DOI:

EANM'25

Annual Congress of the European Association of Nuclear Medicine
October 4–8, 2025 I Barcelona, Spain

Abstracts

EANM Innovation (2025): S1–S1013

**This supplement was not sponsored by outside commercial interests.
It was funded entirely by the association's own resources.**

ELSEVIER

Words of Welcome S3

Programme at a Glance S4

Oral Sessions S7

e-Poster Presentation Sessions S201

e-Posters S405

Authors Index S970

EANM Focus Meeting 7 S1012

ICNC: International Conference On Nuclear Cardiology S1013

Dear Colleagues,

It is with great pleasure that I invite you to the EANM'25—the 38th Annual Congress of the European Association of Nuclear Medicine (EANM). The EANM'25 will be held in the vibrant city of Barcelona from October 4-8, 2025.

This year marks a significant milestone for our association as we celebrate four decades of pioneering advancements and collaborative efforts in the field of nuclear medicine. Our congress will be a unique opportunity to reflect on our journey,celebrate our achievements since 1985, and look ahead to securing the brightest future for our specialty.

The EANM Annual Congress is a truly global event, attracting about 10,000 participants from all over the world. This diverse gathering of professionals provides a rich platform for the exchange of ideas, fostering international collaboration and innovation. We are committed to exploring novel formats and interactions with experts, ensuring that our congress remains at the forefront of scientific discourse and professional development.

One of the highlights of this year's congress will be the continued focus on novel advances in theranostics. This rapidly evolving field continues to revolutionise our approach to diagnosis and treatment, offering unprecedented precision and personalised care for our patients. We have an exciting programme lined up, featuring leading experts who will share their insights and latest research findings.

But our congress is also designed to cater to all fields of research and clinical activity within nuclear medicine. We have specific tracks dedicated to all the various specialities, ensuring that every participant can find sessions relevant to their interests and expertise. Whether you are involved in clinical practice, research, or education, there will be something for you at the EANM'25.

In addition to the scientific sessions, the EANM'25 will provide ample opportunities for networking, collaboration, and professional development. We are particularly proud of our EANM Next-Gen programme, which was launched last year to support our younger collaborators. This initiative offers free registration and accommodation to selected participants to facilitate their attendance and integration into the scientific community, ensuring that the next generation of nuclear medicine professionals is well-represented and engaged. This year again, we will also offer a Young Professionals Lounge for congress participants under 38.

I am also very happy to travel once again to Barcelona, with its rich cultural heritage and dynamic atmosphere, which will serve as the perfect backdrop for our gathering. We look forward to welcoming you to what promises to be an inspiring and memorable event. Your participation and contributions are invaluable to the continued success and growth of our community.

Warm regards,

Valentina Garibotto
EANM Congress Chair 2023–2025

Saturday, October 4, 2025

Location/ Time	Auditorium	Room 212			Location/ Time
08:00–08:30					08:00–08:30
08:30–09:00					08:30–09:00
09:00–09:30					09:00–09:30
09:30–10:00					09:30–10:00
10:00–10:30					10:00–10:30
10:30–11:00					10:30–11:00
11:00–11:30		**Advisory Council Meeting** (11:00–12:30)			11:00–11:30
11:30–12:00					11:30–12:00
12:00–12:30					12:00–12:30
12:30–13:00					12:30–13:00
13:00–13:30					13:00–13:30
13:30–14:00		**Delegates' Assembly** (13:15–14:15)			13:30–14:00
14:00–14:30				**EANM Committee Meetings** (14:00–17:45)	14:00–14:30
14:30–15:00		**Members' Assembly** (14:30–16:30)			14:30–15:00
15:00–15:30					15:00–15:30
15:30–16:00					15:30–16:00
16:00–16:30					16:00–16:30
16:30–17:00					16:30–17:00
17:00–17:30					17:00–17:30
17:30–18:00					17:30–18:00
18:00–18:30	**Opening Ceremony including Awards Ceremony** (18:00–18:35)				18:00–18:30
18:30–19:00					19:30–20:30
20:30–21:00	101 **Plenary 1 Highlights Lecture: Not to Be Missed at All Costs** (18:35–19:35)				20:30–21:00
21:00–21:30	**Welcome Reception** (19:45–21:45)				21:00–21:30
21:30–22:00					21:30–22:00

Sunday, October 5, 2025

Location/ Time	Auditorium	Room 112 (Arena)	Room 113	Room 114	Room 211	Room 117	Room 212	Room 115	Room 133+134	Room 116	Room 111	Location/ Time
	LIVE STREAM									LIVE STREAM		
08:00–08:30	201 CME 1 Inflammation & Infection Committee **The Role of FAPI PET/CT in Inflammation Diseases**	202 Special Track Thyroid Committee **Challenge the Expert: When to Stop Radioiodine?**	203 Learn & Improve Professional Skills (LIPS) Track Translational Molecular Imaging & Therapy Committee **Optical and Multimodal/ Hybrid Tracers: Similarities with Radiotracers, Pitfalls and Regulatoy Issues**	204 M2M Track TROP Session Radiopharmaceutical Sciences + Translational Molecular Imaging & Therapy Committee **New Targets in Oncology**	205 Cutting Edge Science Track TROP Session AI Committe **AI for Segmentation in PET/CT**	206 Clinical Oncology Track TROP Session Oncology & Theranostics Committee **Gynaecological Cancer Staging and Image Guidance**	207 TROP Session Neuroimaging Committee **Movement Disorders**	208 TROP Session Cardiovascular Committee **From Muscle to Calcifications What's New in Cardiac Amyloidosis?**	209 e-Poster Presentations Session 1 Translational Molecular Imaging & Therapy Committee **Preclinical Imaging and Therapy**	210 Technologists' Track Opening CTE 1 Technologists Committee / SNMMI **Technologists' Guide Launch**	211 Theranostics Track TROP Session Oncology & Theranostics Committee **Novel Theranostic Applications**	08:00–08:30
08:30–09:00												08:30–09:00
09:00–09:30												09:00–09:30
09:30–10:00	301 CME 2 Neuroimaging Committee **Paradigm Shift for the Diagnosis of Parkinson Diseases**	302 Special Track Oncology & Theranostics Committee **Debate: A Brave New World: Are All PSMA Radiopharmaceuticals Equal?**	303 Learn & Improve Professional Skills (LIPS) Track Bone & Joint Committee **Bone and Joint Therapies**	304 M2M Track TROP Session Radiopharmaceutical Sciences + Translational Molecular Imaging & Therapy Committee **Tracking/Modulating Pharmacokinetics**	305 Cutting Edge Science Track TROP Session Physics Committee **SPECT Quantification in Therapeutic Applications**	306 Clinical Oncology Track TROP Session Oncology & Theranostics Committee **Breast Cancer Imaging**	307 TROP Session Thyroid Committee **Nuclear Medicine Imaging in Thyroid Disorders: From Thyroid Nodule to Advanced/Refractory Cancer**	308 Joint Symposium 1 Paediatrics Committee / SIOPE **Imaging Biomarkers in Paediatric Oncology 'Whats Next?'**	309 e-Poster Presentations Session 2 Inflammation & Infection Committee **Best e-Posters in Inflammation & Infection**	310 Technologists' Track CTE 2 Technologists Committee **Continuous Education Models for NMTs + Instrumentation and Data Processing**	311 Special Symposium EARL **Clinical Implications of EARL PET/CT Accreditation Standards 2 and a New ^{177}Lu SPECT/CT Accreditation**	09:30–10:00
10:00–10:30												10:00–10:30
10:30–11:00												10:30–11:00
11:00–11:30												11:00–11:30
11:30–12:00	401 Plenary 2 **World's Best Theranostics Comes to EANM'25**											11:30–12:00
12:00–12:30												12:00–12:30
12:30–13:00												12:30–13:00
13:00–13:30	**Lunch Break**			**Satellite Symposium**	**Satellite Symposium**	**Satellite Symposium**	**Satellite Symposium**	**Satellite Symposium**		**Satellite Symposium**	**Satellite Symposium**	13:00–13:30
13:30–14:00												13:30–14:00
14:00–14:30												14:00–14:30
14:30–15:00												14:30–15:00
15:00–15:30	501 CME 3 Physics + Paediatrics Committee **Low Dose Imaging**	502 Special Track Oncology & Theranostics Committee **Debate: Will Alpha Therapy be the Main Radionuclide Therapy Approach in the Future?**	503 Learn & Improve Professional Skills (LIPS) Track Thyroid Committee **Imaging Challenges in Nuclear Endocrinology**	504 M2M Track TROP Session Radiopharmaceutical Sciences + Translational Molecular Imaging & Therapy Committee **Tumour Microenvironment as a Therapeutic Target**	505 Cutting Edge Science Track TROP Session AI Committee **AI Based Segmentation - Cardiac, Lung Ventilation, Bone**	506 Clinical Oncology Track TROP Session Oncology & Theranostics Committee **Lung Cancer Imaging**	507 M2M Track TROP Session Radiopharmaceutical Sciences + Translational Molecular Imaging & Therapy Committee **Prostate Cancer: New Tracers**	508 Joint Symposium 2 Neuroimaging Committee / EAN **Epilepsy: Who is the Right Candidate for Epilepsy Surgery?**	509 e-Poster Presentations Session 3 Radiopharmaceutical Sciences Committee **New Tracers for Radioligand Therapy and Imaging**	510 Technologists' Track Oral Presentations 1 Technologists Committee **PET-CT Studies: Diagnosis and Treatment**	511 Special Symposium 2 EANM Journals - Debate **The Evolving World of Scientific Publishing**	15:00–15:30
15:30–16:00												15:30–16:00
16:00–16:30												16:00–16:30
16:30–17:00	601 CME 4 Cardiovascular Committee **Total Body Imaging: Think Big, Think Forward! (Cardio)**	602 Special Track Oncology & Theranostics Committee + Dosimetry Committee **Debate: Routes to Optimised Theranostics: Is 'Dose' Escalation Enough?**	603 Learn & Improve Professional Skills (LIPS) Track AI Committee **AI for Young Developers in NM**	604 M2M Track TROP Session Radiopharmaceutical Sciences + Translational Molecular Imaging & Therapy Committee **Combining Imaging with Targeted Therapy**	605 Cutting Edge Science Track TROP Session Dosimetry Committee **Radiobiological Mechanisms to Overcome Resistance in TRT**	606 Clinical Oncology Track TROP Session Oncology & Theranostics Committee **Haematology and Lymphoma**	607 TROP Session Neuroimaging Committee **Molecular Imaging of Neurodegeneration: FDG, Amyloid PET and Others**	608 Featured Session Thyroid Committee **Nuclear Medicine Imaging in Medullary and Differentiated Thyroid Cancers**	609 e-Poster Presentations Session 4 Physics Committe **Physics e-Poster Presentations Session**	610 Technologists' Track CTE 3 Technologists Committee **Best Practice in Paediatric Inflammation & Infection Radionuclide Imaging - Heart, Bone and Joint, Kidney and Urinary Tract**	611 Featured Session Paediatrics Committee **Advances in Paediatric Molecular Imaging: Innovations in Oncology, Radiomics and Hybrid Technologies**	16:30–17:00
17:00–17:30												17:00–17:30
17:30–18:00												17:30–18:00
18:00–18:30												18:00–18:30

Monday, October 6, 2025

Location/Time	Auditorium	Room 112 (Arena)	Room 113	Room 114	Room 211	Room 117	Room 212	Room 115	Room 133+134	Room 116	Room 111
	LIVE STREAM									LIVE STREAM	
08:00–08:30	701 CME 5 Thyroid Committee **Parathyroid Carcinoma: Rare but Complex**	702 **Special Track** Inflammation & Infection Committee **Debate: WBC Scintigraphy Scan vs FDG PET/CT in Musculoskelet AI Infections**	703 **Learn & Improve Professional Skills (LIPS) Track** Dosimetry Committee **Statistical Analysis in Clinical Studies and Specifically in Dosimetry**	704 **M2M Track** **TROP Session** Radiopharmaceutical Sciences + Translational Molecular Imaging & Therapy Committee **Preclinical Therapy - Various Targets**	705 **Cutting Edge Science Track** **TROP Session** Physics Committee **PET/CT & PET/MR**	706 **Clinical Oncology Track** **TROP Session** Oncology & Theranostics Committee **Imaging Melanoma and New Targets**	707 **TROP Session** Neuroimaging Committee **Innovations and Methodologies in Nuclear Neuroimaging**	708 **Joint Symposium 3** Oncology & Theranostics Committee / **EORTC** **Oncological Response Criteria for PET: Beyond RECIST, EORTC & PERCIST**	709 **e-Poster Presentations Session 5** Cardiovascular Committee **Cardiovascular e-Poster Presentations Session**	710 **Technologists' Track** **Oral Presentations 2** Technologists Committee **Advanced Practice and Novel Solutions**	711 **Theranostics Track** Oncology & Theranostics Committee **Prostate and Novel Targets**	08:00–08:30
08:30–09:00											08:30–09:00
09:00–09:30											09:00–09:30
09:30–10:00	801 CME 6 Oncology & Theranostics Committee **PET in mCRPC: Toward Multiparametric Multitracer Biomarkers**	802 **Special Track** Cardiovascular Committee **Debate: Myocardial Perfusion Imaging! : Should I Stay with SPECT or Go with PET?**	803 **Learn & Improve Professional Skills (LIPS) Track** Radiation Protection Committee **What Would You Do If…? Radiation Protection Issues in Special Cases of Everyday Practices**	804 **M2M Track** **TROP Session** Radiopharmaceutical Sciences + Translational Molecular Imaging & Therapy Committee **Optimising Radiolabeling and Quality Control: The Key for Clinical Translation**	805 **Cutting Edge Science Track** **TROP Session** AI Committee **Disease Characterisation and Prediction Models**	806 **Clinical Oncology Track** **TROP Session** Oncology & Theranostics Committee **NET Imaging**	807 **Featured Session** Bone & Joint Committee **New Frontiers in Bone and Soft Tissue Imaging**	808 **TROP Session** Thyroid Committee **An Overview on Nuclear Medicine Therapy of DTC Patients: Radioiodine and Beyond**	809 **e-Poster Presentations Session 6** Neuroimaging Committee **Neuroimaging e-Posters**	810 **Technologists' Track** **CTE 4** Technologists Committee **Breathing Knowledge – the New Approaches of PET-CT Lung Scanning**	811 **Special Symposium 3** Dosimetry Committee **Challenges in Dosimetry of Alpha-Emitters**	09:30–10:00
10:00–10:30											10:00–10:30
10:30–11:00											10:30–11:00
11:00–11:30											11:00–11:30
11:30–12:00	901 **Plenary 3** **Referring Patients to Nuclear Medicine: When, How, and Mainly Why?**										11:30–12:00
12:00–12:30											12:00–12:30
12:30–13:00											12:30–13:00
13:00–13:30											13:00–13:30
13:30–14:00	**Lunch Break**			**Satellite Symposium**	**Satellite Symposium**	**Satellite Symposium**	**Satellite Symposium**	**Satellite Symposium**		**Satellite Symposium**	**Satellite Symposium**	13:30–14:00
14:00–14:30											14:00–14:30
14:30–15:00											14:30–15:00
15:00–15:30	1001 CME 7 Oncology & Theranostics Committee **Targeted Radionuclide Therapy Accross Various SST Expressing Tumor Models: a new Framework for Rethinking**	1002 **Special Track** **EANM Sanjiv Sam Gambhir Award – Compete and Win!**	1003 **Learn & Improve Professional Skills (LIPS) Track** Cardiovascular Committee **What to Look at in the Heart and in Vessels on Oncological PET Images**	1004 **M2M Track** **TROP Session** Radiopharmaceutical Sciences + Translational Molecular Imaging & Therapy Committee **Innovations in Translational Oncology**	1005 **Cutting Edge Science Track** **TROP Session** Dosimetry Committee **Personalised Dosimetry and Predictive Modeling**	1006 **Clinical Oncology Track** **TROP Session** Oncology & Theranostics Committee **NET and PRRT**	1007 **TROP Session** Thyroid Committee **Tau PET Imaging**	1008 **Joint Symposium 4** AI Committee / **EFOMP** **Trustful AI in the Clinics**	1009 **e-Poster Presentations Session 7** Radiopharmaceutical Sciences Committee **Radiochemistry and Quality Control**	1010 **Technologists' Track** **Technologists' e-Poster Presentations Session** Technologists Committee **Techs' e-Posters**	1011 **Special Symposium 4** EANM Journals **Scientific Writing in 2025**	15:00–15:30
15:30–16:00												15:30–16:00
16:00–16:30												16:00–16:30
16:30–17:00	1101 CME 8 Radiopharmaceutical Committee **Radiotheranostics 2.0: The Power of Emerging Radioisotopes in Translating Imaging into Personalized Radiotherapy**	1102 **Special Track** Neuroimaging Committee **Round Table: Tau PET Imaging: Ready for Clinical Use**	1103 **Learn & Improve Professional Skills (LIPS) Track** Physics Comittee **Getting Imaging Right with Protocol Optimisation**	1104 **M2M Track** **TROP Session** Radiopharmaceutical Sciences + Translational Molecular Imaging & Therapy Committee **Preclinical Neuroimaging**	1105 **Cutting Edge Science Track** **TROP Session** **ROP Session** AI Committee **AI for Report Generation and Patient Prognostication**	1106 **Clinical Oncology Track** **TROP Session** Oncology & Theranostics Committee **Gastrointestinal Tumour Imaging**	1107 **TROP Session** Thyroid Committee **The Pivotal Role of Nuclear Medicine Imaging to Localise Parathyroid Lesion**	1108 **Joint Symposium 5** Oncology & Theranostics Committee / **EAU** **EANM & EAU Advances in Renal Cancer Research**	1109 **e-Poster Presentations Session 8** Oncology & Theranostics Committee **Cancer Imaging and Therapy**	1110 **Technologists' Track** **CTE 5** Technologists Committee **Dynamic Cardiovascular Hybrid Imaging**	1111 **Featured Session** Cardiovascular Committee **Innovation in Myocardial Perfusion in SPECT**	16:30–17:00
17:00–17:30												17:00–17:30
17:30–18:00												17:30–18:00
18:00–18:30												18:00–18:30

Tuesday, October 7, 2025

Location/Time	Auditorium	Room 112 (Arena)	Room 113	Room 114	Room 211	Room 117	Room 212	Room 115	Room 133+134	Room 116	Room 111
	LIVE STREAM									LIVE STREAM	
08:00–08:30	1201 CME 9 Oncology & Theranostics + Neuroimaging Committee **RLT Applications in Neuro-Oncology**	1202 **Special Track** Physics Comittee **Debate: Quantitative Imaging: What's the Point? (Focus on Kinetic Modeling)**	1203 **Learn & Improve Professional Skills (LIPS) Track** Oncology & Theranostics Committee **Pitfalls in PSMA-Based RLT: Case-Based Review**	1204 **M2M Track** **TROP / Featured Session** Radiopharmaceutical Sciences + Translational Molecular Imaging & Therapy Committee **Combination Therapy - Shaping the Future of TRT**	1205 **Cutting Edge Science Track** **ROP Session** AI Committee **AI Techniques for Patient Classification**	1206 **Clinical Oncology Track** **TROP Session** Oncology & Theranostics Committee **Prostate Cancer Therapy: Dosimetry, SPECT/CT, AI**	1207 **TROP Session** Thyroid Committee **Current and Future Perspective of Nuclear Medicine Imaging in Endocrinological Disorders**	1208 **TROP Session** Cardiovascular Committee **Cardiovascular Infection and Inflammation: Evidence and Novelty**	1209 **e-Poster Presentations Session 9** Dosimetry Committee **Advances in Clinical and Preclinical Dosimetry**	1210 **Technologists' Track** **CTE 6** Technologists Committee **Fibroblast-Activated: the 68Ga-FAPI in Different Types of Cancer**	1211 **EU Policy Symposium 1** Policy & Regulatory Affairs Council **From Policy to Patients: Building Readiness for Nuclear Medicine Innovation in Europe**	08:00–08:30
08:30–09:00												08:30–09:00
09:00–09:30												09:00–09:30
09:30–10:00	1301 CME 10 AI Committee **AI as Accelerator for NM Research**	1302 **Special Track** Oncology & Theranostics Committee **Debate: Residents for Residents**	1303 **Learn & Improve Professional Skills (LIPS) Track** Paediatrics Committee **Update on Pediatric GI Nuclear Studies**	1304 **M2M Track** **TROP / Featured Session** Radiopharmaceutical Sciences + Translational Molecular Imaging & Therapy Committee **Improving Radionuclide Production for Tracer Development**	1305 **Cutting Edge Science Track** **TROP Session** Dosimetry Committee **Quantification and Innovation in Dosimetry**	1306 **Clinical Oncology Track** **TROP Session** Oncology & Theranostics Committee **Prostate Cancer Therapy in HSPC and CRPC**	1307 **TROP Session** Neuroimaging Committee **Neuro-Oncology**	1308 **Joint Symposium 6** Translational Molecular Imaging & Therapy Committee / **ESTRO + RPSC + O&T** **Radiobiological Aspects of PRRT**	1309 **e-Poster Presentations Session 10** Paediatrics Committee **Paediatrics e-Poster Presentations Session**	1310 **Technologists' Track** **Oral Presentations 3** Technologists Committee **Interdisciplinary Nuclear Medicine Workforce Sustainability and Training**	1311 **TROP Session** Case Report Session 1 **Case-based Learning in Theranostics**	09:30–10:00
10:00–10:30												10:00–10:30
10:30–11:00												10:30–11:00
11:00–11:30												11:00–11:30
11:30–12:00	1401 **Plenary 4** **Quo vadis Nuclear Medicine 2040: Who Wins? Team Red or Team Green?**											11:30–12:00
12:00–12:30												12:00–12:30
12:30–13:00												12:30–13:00
13:00–13:30												13:00–13:30
13:30–14:00	**Lunch Break**			**Satellite Symposium**	**Satellite Symposium**	**Satellite Symposium**	**Satellite Symposium**	**Satellite Symposium**		**Satellite Symposium**	**Satellite Symposium**	13:30–14:00
14:00–14:30												14:00–14:30
14:30–15:00												14:30–15:00
15:00–15:30	1501 CME 11 Translational Molecular Imaging & Therapy Committee **A Comprehensive Approach to Preclinical Dosimetry**	1502 **Special Track** Oncology & Theranostics Committee **Challenge the Expert: Lymphoma Evaluation: Do We Need to Go Beyond the Deauville Score?**	1503 **Learn & Improve Professional Skills (LIPS) Track** Neuroimaging Committee **Crazy Enough to Do Molecular Imaging in Psychiatric Disorders?**	1504 **M2M Track** **TROP Session** Radiopharmaceutical Sciences + Translational Molecular Imaging & Therapy Committee **Peptides for All Tastes**	1505 **Cutting Edge Science Track** **TROP Session** Physics Committee **Instrumentation, QC & Standardisation**	1506 **Clinical Oncology Track** **TROP Session** Oncology & Theranostics Committee **Prostate Cancer Therapy: New Tracer**	1507 **TROP Session** Cardiovascular Committee **Myocardial Perfusion on PET: Where Are We Going?**	1508 **Joint Symposium 7** Inflammation & Infection Committee / **EUSEM** **The Role of Nuclear Medicine Imaging in Intensive Care Unit (ICU) Patients**	1509 **e-Poster Presentations Session 11** AI Committee **AI e-Poster Presentations Session**	1510 **Technologists' Track** **CTE 7** Technologists Committee **Hybrid Imaging in Differentiated Thyroid Cancer (DTC) Diagnosis and Treatment**	1511 **EU Policy Symposium 2** Policy & Regulatory Affairs Council **Growing Role of Health Technology Assessment (HTA) in Nuclear Medicine: Implications in Light of the Mew EU HTA Regulation**	15:00–15:30
15:30–16:00												15:30–16:00
16:00–16:30												16:00–16:30
16:30–17:00	1601 CME 12 Oncology & Theranostics Committee **Improving Breast Cancer Care: Highlights from Focus Meeting 6: Staging**	1602 **Special Track** Dosimetry Committee **Round Table: Unlocking the Potential: Can Total Body PET Revolutionise Dosimetry?**	1603 **Learn & Improve Professional Skills (LIPS) Track** Inflammation & Infection Committee **Interpretation of FDG PET/CT in Common Infectious-Inflammatory Diseases**	1604 **M2M Track** **TROP Session** Radiopharmaceutical Sciences + Translational Molecular Imaging & Therapy Committee **Imaging of Non-oncological Targets**	1605 **Cutting Edge Science Track** **TROP Session** Radiation Protection Committee **Radiation Exposure and Protection**	1606 **Clinical Oncology Track** **TROP Session** Oncology & Theranostics Committee **Imaging Prostate Cancer: Prediction and Outcome**	1607 **TROP Session** Neuroimaging Committee **Neurology: Psychiatry, Epilepsy, Inflammation and Others**	1608 **TROP Session** Cardiovascular Committee **Metabolism, Fibrosis and Innervation: The Basis of Cardiomyopathies**	1609 **e-Poster Presentations Session 12** Thyroid Committee **Diagnostic and Therapeutic Approach in Patients with Endocrinological Disorders**		1611 **TROP Session** Case Report Session 2 **Case-based Learning in Nuclear Medicine Beyond Oncology**	16:30–17:00
17:00–17:30												17:00–17:30
17:30–18:00												17:30–18:00
18:00–18:30												18:00–18:30

Wednesday, October 8, 2025

Location/ Time	Auditorium	Room 112 (Arena)	Room 113	Room 114	Rom 211	Room 117	Room 212	Room 115	Room 133+134	Room 116	Room 111	Location/ Time
	LIVE STREAM									LIVE STREAM		
08:00–08:30	1701 CME 13 Dosimetry Committee **Challenges in Red Bone Marrow Dosimetry**	1702 **Special Track** Women Empowerment Initiative + Young Professionals Council **Challenge the Expert: Current Challenges in Career and in Leadership for the Future Generations**	1703 **Learn & Improve Professional Skills (LIPS) Track** Oncology & Theranostics Committee **Structured PET Reporting in Oncology**	1704 **M2M Track TROP Session** Radiopharmaceutical Sciences + Translational Molecular Imaging & Therapy Committee **Antibodies and Co.**	1705 **Cutting Edge Science Track TROP Session** AI Committee **Kinetic Modeling and Parametric Imaging**	1706 **Clinical Oncology Track TROP Session** Oncology & Theranostics Committee **Theranostic and New Therapies**	1707 **TROP Session** Cardiovascular Committee **Atherosclerosis Burden, from Plaque to Perfusion**	1708 **TROP Session** Case Report Session 3 **Case-based Learning PET in Oncology**	1709 **e-Poster Presentations Session 13** Bone & Joint Committe **Bone & Joint e-Poster Presentations Session**	1710 **Technologists' Track Mini Courses** Technologists Committee 1710a **Mini Course 1** (08:00–09:00) 1710b **Mini Course 2** (09:05–10:05) 1710c **Mini Course 3** (10:15–11:15)	1711 **Theranostics Track TROP Session** Oncology & Theranostics Committee **Prostate Cancer Theranostic**	08:00–08:30
08:30–09:00												08:30–09:00
09:00–09:30												09:00–09:30
09:30–10:00	1801 CME 14 Bone & Joint Committee **NM Sports, it's in the Game**	1802 **Special Track** Translational Molecular Imaging & Therapy Committee **Challenge the Expert: How can Lessons from Radiobiology be Applied to the Design of Clinical Trials?**	1803 **Learn & Improve Professional Skills (LIPS) Track** Neuroimaging Committee **PET Response Assessment in Neuro-Oncology**	1804 **M2M Track TROP Session** Radiopharmaceutical Sciences + Translational Molecular Imaging & Therapy Committee **Advances in Preclinical Cardiovascular Imaging**	1805 **TROP Session** Paediatrics Committee **Emerging Roles of Molecular Imaging in Paediatric Oncology, Neurology and Transplant Medicine**	1806 **Clinical Oncology Track TROP Session** Oncology & Theranostics Committee **Prostate Cancer Staging and Restaging**	1807 **TROP Session** Inflammation & Infection Committee **Infection/Inflammation Under the Lens: Innovations in Nuclear Medicine Imaging**	1808 **Joint Symposium 8** Cardiovascular Committee / **EACVI** **Controversies in the Evaluation of Coronary Artery Disease**	1809 **e-Poster Presentations Session 14** Radiation Protection Committee **Radiation Protection e-Poster Presentations Session**		1811 **TROP Session** Oncology & Theranostics Committee **Radioembolisation and Novel Therapies**	09:30–10:00
10:00–10:30												10:00–10:30
10:30–11:00												10:30–11:00
11:00–11:30	1901 **Closing Session** **Farewell Drink**											11:00–11:30
11:30–12:00												11:30–12:00
12:00–12:30												12:00–12:30

- Plenary Sessions
- CME Sessions
- Special Track
- Learn & Improve Professional Skills (LIPS) Track
- Joint Symposia
- M2M Track
- Cutting Edge Science Track
- Clinical Oncology Track
- Special Symposium
- Featured/TROP Session
- e-Poster Presentations
- Technologists' Track Session
- Continuing Medical Education
- Young Professionals

Oral Sessions

OC

Saturday, October 4, 2025, 18:00 - 18:35
Auditorium

Opening Ceremony including Awards Ceremony

OP-001
Opening Ceremony
V. Garibotto; *Geneva University and Geneva University Hospitals, Geneva, SWITZERLAND.*

101

Saturday, October 4, 2025, 18:35 - 19:35
Auditorium

Plenary 1: Highlights: Not to Be Missed at All Costs

OP-002
Highlights Lecture
I. Law; *University of Copenhagen, Faculty of Health and Medical Sciences Consultant, Department of Clinical Physiology and Nuclear Medicine Rigshospitalet, Copenhagen, DENMARK.*

OP-003
Highlights Lecture
S. Massalha; *Rambam Medical Center, Haifa, ISRAEL.*

OP-004
Highlights Lecture
A. Maurer; *FMH Nuklearmedizin, FMH Radiologie Universitätsspital Zürich, Klinik für Nuklearmedizin, Zurich, SWITZERLAND.*

201

Sunday, October 5, 2025, 08:00 - 09:30
Auditorium

CME 1 - Inflammation & Infection Committee: The Role of FAPI PET/CT in Inflammation Diseases

OP-006
Understanding the biology and function of fibroblasts in inflammation
M. Coles; *University of Oxford, Kennedy Institute of Rheumatology, Oxford, Oxford, UNITED KINGDOM.*

OP-007
FAPI PET/CT in cardiac diseases
N. Craig; *University of Edinburgh, BHF Cantre of Cardiovascular Science, Edinburgh, UNITED KINGDOM.*

OP-008
FAPI PET/CT in lung diseases
Anne-L. Deleu; *Institut Jules Bordet, Brussels, BELGIUM.*

OP-009
FAPI PET/CT in rheumatological diseases
M. Sandovici; *University Medical Center Groningen, Department of Rheumatology and Clinical Immunology, Groningen, NETHERLANDS.*

202

Sunday, October 5, 2025, 08:00 - 09:30
Room 112 (Arena)

Special Track 1 - Thyroid Committee: Challenge the Expert: When to Stop Radioiodine?

OP-010
Radioiodine Refractory Thyroid Cancer
D. Deandreis; *Gustav Roussy, Villejuif, FRANCE.*

OP-011
Challengers Cases
B. Pranger; *UMC, Utrecht, NETHERLANDS.*

OP-012a
Challengers Cases
Milou T. Joe Way; *LUMC, Leiden, NETHERLANDS.*

OP-012b
Challengers Cases
D. Maccora; *Nuclear Medicine Unit, IRCCS Regina Elena National Cancer Institute of Rome, Rome, ITALY.*

OP-012c
Challengers Cases
G. Kaya; *Hacettepe Üniversitesi, Ankara, TÜRKIYE.*

OP-012d
Challengers Cases
G. Zwezerijnen; *Amsterdam UMC, Amsterdam, NETHERLANDS.*

203

Sunday, October 5, 2025, 08:00 - 09:30
Room 113

LIPS Session 1 - Translational Molecular Imaging & Therapy Committee: Optical and Multimodal/ Hybrid Tracers: Similarities with Radiotracers, Pitfalls and Regulatoy Issues

OP-013
Can Optical Imaging Replace Radioguided Surgery? – NM Perspective
G. Pisano; *Gemelli University Hospital, Nuclear Medicine, Rome, ITALY.*

OP-014
Surgeon's Perspective – Margins vs. Lymph Nodes
F. Hamdy; *University of Oxford, Nuffield Department of Surgical Sciences, Oxford, UNITED KINGDOM.*

OP-015
PET Tracers for Surgical Guidance, Optical vs Beta Detection
T. Kahl; *University Hospital Essen, Urology, Essen, GERMANY.*

OP-016
Placement of Optical Imaging within Iimage-Guided Interventions
F. van Leeuwen; *Leiden University Medical Center, Interventional Molecular Imaging Laboratory, Leiden, NETHERLANDS.*

204

Sunday, October 5, 2025, 8:00 - 9:30
Room 114

M2M Track - TROP Session - Radiopharmaceutical Sciences + Translational Molecular Imaging & Therapy Committee: New Targets in Oncology

OP-017

In vivo detection of tumor senescence by [^{18}F]FPyGal PET

J. Schwenck, *N. Trautwein, S. Mattern, J. Cotton, F. Reche-Perez, A. Wäschle, B. Gückel, M. Pritzkow, B. Zhou, M. Krüger, W. Ehrlichmann, G. Kienzle, A. Maurer, S. Singer, G. Reischl, L. Zender, B. J. Pichler, C. la Fougere;*
University of Tübingen, Tübingen, GERMANY.

Aim/Introduction: Tumor senescence and the senescence-associated secretory phenotype are crucial factors in the progression and therapeutic resistance of solid tumors. To improve the outcome of cancer patients, the non-invasive in vivo detection of senescence could support therapeutic stratification towards senolytic treatments. Here, we investigated [^{18}F]FPyGal, a first-in-class PET tracer to non-invasively detect the activity of β-galactosidase, a commonly used senescence marker. ***Materials and Methods:*** The radiolabeled β-galactosidase substrate [^{18}F]FPyGal was developed and thoroughly validated in vitro in various tumor cell lines (colon cancer HCT116, lung adenocarcinoma A549, hepatocellular carcinoma Myc^{OE}Akt1) as well as in vivo in experimental tumor models. After a single-dose acute toxicity study in rats, a Phase I clinical study in healthy male volunteers (n=8) using 370±50 MBq [^{18}F]FPyGal and a subsequent Phase II study in patients with lung, esophageal and rectal cancer after neoadjuvant therapy was performed (EudraCT 2019-002846-19). In an interim analysis of the Phase II study (n=14 of 27), the [^{18}F]FPyGal uptake in the tumors was correlated to the ex vivo β-galactosidase activity assessed by X-gal staining in the resected tumor tissue as well as to the immunohistological markers p16, p21, p53 and HMGA2 as at least 3 positive markers are needed to confirm senescence according to current standards. ***Results:*** We observed a reliable detection of tumor senescence in tumor cell lines and in preclinical tumor models. The clinical Phase I study confirmed the safe use of [^{18}F]FPyGal in healthy volunteers with no relevant adverse effects. Dosimetry revealed a low effective whole-body radiation dose (8.1±0.2 µSv/MBq) comparable to other routinely applied PET tracers. The Phase II study in cancer patients after neoadjuvant therapy revealed inhomogeneous [^{18}F]FPyGal uptake patterns in the tumors. After resection, areas with high and low [^{18}F]FPyGal uptake were correlated to the X-gal stained tissue. Tumors with X-gal positive areas greater than the median of all analyzed samples (>0.4%) had a significantly higher [^{18}F]FPyGal tumor uptake (lesion/liver ratio, 46-60 min p.i) than tumors with X-gal positive areas below the median. Furthermore, tumor lesions with senescence confirmed by ≥3 positive markers tended towards a higher [^{18}F]FPyGal uptake compared to lesions evaluated as negative. ***Conclusion:*** We present the first clinical evidence of the successful noninvasive in vivo detection of tumor senescence by [^{18}F]FPyGal PET in cancer patients. Nevertheless, further clinical studies are needed to prove the ability of [^{18}F]FPyGal PET to successfully guide senolytic treatments.

OP-018

Nectin4-Targeted Radiotheranostics Probe: Molecular Imaging-Guided Precision in Cancer Diagnosis and Therapy

M. Hu, *N. Wei, D. Zheng, Y. Song, Y. Feng, B. Yang, W. Hu, X. Wang, Y. Gai, Y. Zhang, X. Lan;*
Wuhan Union Hospital, Wuhan, CHINA.

Aim/Introduction: Nectin cell adhesion molecule 4 (Nectin4) is overexpressed in multiple malignancies, making it a promising molecular target for cancer diagnosis and therapy. This study aimed to develop and evaluate PET imaging and radionuclide therapy probes targeting Nectin4 for noninvasive tumor monitoring and precision radiotheranostics. ***Materials and Methods:*** Two Nectin4-targeting antibody fragments, HA22 and N41 Fab, were radiolabeled with ^{68}Ga and assessed for tumor uptake and imaging contrast in xenograft mice bearing human bladder cancer (SW780) and triple-negative breast cancer (TNBC, MDA-MB-468). The optimal Fab fragment was selected. Along with Minibody and monoclonal antibody (mAb) derivatives, they were then radiolabeled with ^{177}Lu for imaging and therapy. The antitumor effect was evaluated by administering 11.1 MBq of [^{177}Lu]Lu-DOTA-Fab, 11.1 MBq of [^{177}Lu]Lu-DOTA-Minibody, 4.44 or 11.1 MBq of [^{177}Lu]Lu-DOTA-mAb, or phosphate buffered saline (PBS, control) to SW780 (n = 5) and MDA-MB-468 (n = 6) xenograft mice. Blood, major organs, and tumor tissues were collected for biosafety evaluation and efficacy analysis. ***Results:*** Both [^{68}Ga]Ga-NOTA-N41 and [^{68}Ga]Ga-NOTA-HA22 were successfully synthesized with high radiolabeling yields and radiochemical purity. PET imaging revealed significant tumor uptake of [^{68}Ga]Ga-NOTA-HA22 in SW780(4.89±0.44 %ID/g) and MDA-MB-468(4.44±0.69 %ID/g) xenografts at 2 h post-injection. [^{68}Ga]Ga-NOTA-HA22 exhibited a superior tumor-to-muscle ratio compared to [^{68}Ga]Ga-NOTA-N41 (P = 0.014), leading to its selection for therapy. [^{177}Lu]Lu-DOTA-Fab$_{HA22}$, [^{177}Lu]Lu-DOTA-Minibody$_{HA22}$ and [^{177}Lu]Lu-DOTA-mAb$_{HA22}$ were successfully synthesized, exhibiting distinct pharmacokinetics. [^{177}Lu]Lu-DOTA-Fab$_{HA22}$ exhibited peak tumor uptake of 5~6 %ID/g and cleared rapidly with renal excretion. [^{177}Lu]Lu-DOTA-Minibody$_{HA22}$ and [^{177}Lu]Lu-DOTA-mAb$_{HA22}$ demonstrated peak tumor uptake of 10~20 %ID/g and 15~28 %ID/g, and both showed prolonged circulation and hepatobiliary elimination. Substantial tumor growth inhibition without severe toxicity was observed in SW780 and MDA-MB-468 xenograft mice after [^{177}Lu]Lu-DOTA-Fab$_{HA22}$ (11.1 MBq), [^{177}Lu]Lu-DOTA-Minibody$_{HA22}$ (11.1 MBq) or [^{177}Lu]Lu-DOTA-mAb$_{HA22}$ (4.44 MBq) administration. Treatment-related mortality occurred between 14th~16th days in SW780 xenograft mice receiving [^{177}Lu]Lu-DOTA-mAb$_{HA22}$ (11.1 MBq), indicating dose-limiting toxicity. Post-treatment histological analysis revealed significant downregulation of Nectin4 and ki67 in treated tumors, confirming effective tumor suppression. ***Conclusion:*** This study establishes [^{68}Ga]Ga-NOTA-HA22 as a promising PET tracer for Nectin4-expressing tumors and highlights the therapeutic potential of [^{177}Lu]Lu-DOTA-Minibody$_{HA22}$, which presents a novel theranostic approach targeting Nectin4, providing an innovative strategy for the diagnosis and treatment of Nectin4-expressing tumors.

OP-019

Development and preclinical evaluation of PD-L1-targeted small molecule theranostic radionuclide probe

H. Xie[1,2];
[1]West China Hospital of Sichuan University, Chengdu, Sichuan Province, CHINA, [2]Beijing Anzhen Hospital,Capital Medical University, Beijing, CHINA.

Aim/Introduction: Programmed cell death protein ligand 1 (PD-L1) serves as a critical biomarker for predicting immunotherapy outcomes. This study aimed to develop small-molecule theranostic probes for noninvasive PD-L1 quantification and evaluate their potential in targeted radionuclide therapy combined with immune checkpoint blockade. ***Materials and Methods:*** The radiotracers ^{68}Ga-HX-01, ^{68}Ga-HX-02, and ^{68}Ga-HX-03 were synthesized based on the scaffolds of (2-methyl-3-biphenylyl) methanol and [3-(2,3-dihydro-1,4-benzodioxin-6-yl)-2-benzyl] methanol, with modifications to their pharmacokinetic properties achieved through the incorporation of dimeric structures, piperidine acid,

and water-soluble functional groups. The labeling efficiency, stability, and lipophilicity (logP) of the probes were systematically evaluated. Cellular uptake assays and competitive blocking experiments were conducted to assess their target specificity. PET imaging was performed in B16F10 (PD-L1-high) and MCF-7 (PD-L1-low) tumor models to assess targeting efficacy. ^{177}Lu-HX-01-targeted radionuclide therapy (TRT) and its combination therapies with anti-PD-L1 immune checkpoint blockade (ICB) were evaluated using B16F10-bearing mice. The synergistic therapeutic effects of ^{177}Lu-HX-01 TRT and ICB were further validated through histopathological analysis and longitudinal tumor volume monitoring in treated mice. ***Results:*** The compounds HX-01, HX-02, and HX-03 were synthesized via multi-step chemical reactions, and their structures were confirmed by ^{1}H NMR and ^{13}C NMR. In vitro competitive binding assays revealed high PD-L1 affinities, with IC50 values of 28.73 nM (HX-01), 23.42 nM (HX-02), and 15.65 nM (HX-03). Radiolabeling with ^{68}Ga-HX-01, ^{68}Ga-HX-02, and ^{68}Ga-HX-03 through simplified procedures, achieving radiochemical yields >95% with favorable stability (>90% purity at 4 h). PET imaging demonstrated 2-3-fold higher uptake of all tracers in PD-L1-high B16F10 tumors compared to PD-L1-low MCF-7 tumors. At 180 min post-injection (p.i.), ^{68}Ga-HX-02 and ^{68}Ga-HX-03 exhibited tumor-to-muscle ratios of 9-13. The dimeric ^{68}Ga-HX-01 showed prolonged tumor retention with peak uptake of 11.03 ± 1.15 %ID/g (6 h p.i.). In therapeutic studies, ^{177}Lu-HX-01 displayed high PD-L1-specific binding and prolonged intratumoral retention, correlating with significant antitumor efficacy. The combination of ^{177}Lu-HX-01-targeted radionuclide therapy (TRT; 18.5 MBq) and anti-PD-L1 monoclonal antibody (mAb) synergistically suppressed tumor growth (tumor growth inhibition is 87.38%). Mechanistically, ^{177}Lu-HX-01 TRT enhanced immunotherapy by upregulating tumoral PD-L1 expression and promoting $CD8^+$/$CD4^+$ T-cell infiltration, thereby activating T-cell-mediated antitumor immunity. ***Conclusion:*** The developed ^{68}Ga-labeled probes (^{68}Ga-HX-01, ^{68}Ga-HX-02, and ^{68}Ga-HX-03,) enable reliable PD-L1 quantification through molecular imaging. ^{177}Lu-HX-01 demonstrates dual functionality as a targeted radiotherapeutic and immunotherapy enhancer, with its therapeutic synergy arising from localized radiation damage and subsequent T-cell-mediated immune activation. This radiotheranostic strategy provides a promising approach to optimize combination therapies against PD-L1-expressing tumors.

OP-020

Development and Translational Study of Mesothelin-Targeted Molecular Imaging Probes for Early Diagnosis of Ovarian Cancer

Y. Deng, *X. Zhang, X. Lv, Z. Lin, D. Zheng, R. An, Y. Zhang, D. Jiang, X. Lan;*
Union Hospital, Tongji Medical College, Huazhong University of Science and Technology, Wuhan, CHINA.

Aim/Introduction: Early detection of ovarian cancer remains a significant clinical challenge. Mesothelin (MSLN), a tumor-associated antigen, is overexpressed in 80-85% of ovarian cancers, making it an ideal target for molecular imaging. This study aimed to develop and evaluate MSLN-targeted single-chain variable fragment (scFv) and fragment antigen-binding (Fab) probes for PET/CT imaging. ***Materials and Methods:*** Bioinformatics analysis was performed using the GEO and TCGA databases to assess MSLN expression in ovarian cancer and its correlation with prognosis. Differential gene expression, GO, and KEGG pathway analyses were conducted between MSLN-high and MSLN-low groups. For in vitro validation, cellular uptake experiments were performed using MSLN-high/low (OVCAR-3/SKOV3) cell lines and MSLN-blocked controls. Ovarian (OVCAR-3, SKOV3) cancer xenograft models were established for in vivo evaluation of ^{68}Ga-labeled probes via PET/CT imaging, biodistribution, and immunohistochemistry (IHC). For clinical translation, six patients were enrolled following ethical approval. Surgical patients underwent tumor IHC, while non-surgical patients had ascites immunostaining for MSLN validation. ***Results:*** Bioinformatics analysis confirmed MSLN's epithelial-specific expression and identified associated pathways in ovarian cancer, correlating with poor prognosis. In vitro studies demonstrated significantly higher uptake of both probes in MSLN-high cells ($p < 0.01$), which was effectively blocked by MSLN antibodies. In vivo, the ^{68}Ga-scFv probe showed excellent tumor-to-muscle ratios (10.6 ± 1.4 at 2 h) with rapid clearance, while the ^{68}Ga-Fab probe exhibited prolonged tumor retention (6.4 %ID/g ± 0.8 at 4 h) in OVCAR-3 xenograft models. Clinical imaging successfully differentiated MSLN-positive tumors (n=4) from negative cases (n=2), correlating perfectly with pathological findings (tumor/ascites IHC staining). No adverse events were observed during 72-hour safety monitoring. ***Conclusion:*** The ^{68}Ga-labeled scFv and Fab probes demonstrate exceptional specificity and safety for MSLN-targeted imaging. Combined bioinformatics and experimental validation confirms their potential for early ovarian cancer detection, particularly in epithelial subtypes. Ongoing clinical trials are further evaluating their diagnostic performance in larger cohorts.

OP-021

Theranostic potential of kinin B1 receptor targeting in glioblastoma therapy

S. Ghanaatgar[1], *M. Savard*[1], *M. Gagnon*[1], *D. Fortin*[2], *M. Lepage*[3], *B. Guérin*[3], *Y. Dory*[4], *F. Gobeil*[1];
[1]*Department of Pharmacology and Physiology, Faculty of Medicine and Health Sciences, Université de Sherbrooke, sherbrooke, QC, CANADA,* [2]*Department of Surgery, Universite´ de Sherbrooke, Sherbrooke, Quebec, Canada., sherbrooke, QC, CANADA,* [3]*Department of Medical Imaging and Radiation Sciences, Faculty of Medicine and Health Sciences, Université de Sherbrooke, Sherbrooke, Québec, CANADA., sherbrooke, QC, CANADA,* [4]*6Department of Chemistry, Faculté des Sciences, Université de Sherbrooke, Sherbrooke, Québec, Canada, Sherbrooke, QC, CANADA.*

Aim/Introduction: Glioblastoma (GBM), the most common and aggressive primary brain tumor in adults, remains uniformly fatal with no effective therapies available. The inducible kinin B1 receptors (B1R) may be considered attractive targets as biomarkers and for molecular imaging and therapeutic interventions in cancer. This is because they are frequently overexpressed on the surface of cancer cells and play a role in regulating cancer growth. In this study, we examined the theranostic potential of B1R in glioblastoma. ***Materials and Methods:*** Transcriptomic data from the CGGA and TCGA databases, along with IHC and immunoblotting, were used to examine B1R expression in human glioma specimens. The impact of B1R depletion (via shRNA knockdown) on the growth of F98 GBM cells was evaluated both in vitro, using MTT assays, and in vivo, by MRI monitoring of tumor progression in orthotopic rat GBM models using F98-wt and F98-B1R knockdown cells, respectively. Additionally, the theranostic potential of the B1R antagonist 64Cu/NOTA-R954 was tested via PET/CT imaging and targeted radiotherapy in F98wt GBM-bearing rats. ***Results:*** Transcriptomic data identified B1R upregulation in IDH-wildtype gliomas (the most clinically aggressive), correlating negatively with patient survival ($p=0.03$, $\beta=0.538$). Immunohistochemical studies confirmed elevated B1R protein expression in high-grade glioma specimens. MRI demonstrated an approximately 70% reduction in tumor growth in B1R-knockdown F98 models compared to wild-type controls. These in vivo findings were supported by MTT assay results, which showed reduced cell proliferation following B1R knockdown in vitro. PET/CT imaging with 64Cu/NOTA-R954 showed specific localization to GBM tumors, with no detectable uptake in contralateral brain regions. Therapeutic administration of 64Cu/NOTA-R954 —whether as a

single 7.5 mCi dose or fractionated 3.75 mCi doses—significantly prolonged survival compared to untreated controls. ***Conclusion:*** Our results support a role of B1R in GBM development, identifying it as a potential target for brain cancer theranostics. The use of 64Cu/NOTA-R954 yielded promising results in both imaging and therapeutic applications, highlighting the need for further investigation in the context of GBM.

OP-022

In vitro and in vivo preclinical side by side comparison of ^{177} Lu-DOTA-A1K2 and^{161}Tb-DOTA-A1K2 directed against mesothelin.

E. N'Guessan[1], *F. Raes*[1], *M. Ahmadi*[1], *S. Bacot*[1], *L. Dumas*[1], *J. Leenhardt*[2,1], *A. du Moulinet d'Hardemare*[1], *M. Debiossat*[1], *C. André*[1], *J. Durivault*[3], *C. Montemagno*[3], *D. Fagret*[1], *J. Lenormand*[4], *L. Djaileb*[2,1], *U. Köster*[5], *C. Ghezzi*[1], *P. Perret*[1], *C. Lombardi*[1,4], *A. Broisat*[1];
[1]*Univ. Grenoble Alpes, INSERM U1039, LRB, Grenoble, FRANCE,* [2]*CHU Grenoble Alpes, Department of Nuclear Medicine, LRB, Grenoble, FRANCE,* [3]*Departement Biomédical, Centre Scientifique de Monaco, Monaco, MONACO,* [4]*Univ. Grenoble Alpes, CNRS U5525, TIMC-Tree, Grenoble, FRANCE,* [5]*Institut Laue-Langevin, Grenoble, FRANCE.*

Aim/Introduction: Mesothelin (MSLN) is a 40 kDa glycoprotein overexpressed in several malignancies, such as triple-negative breast cancer (TNBC), while its expression in normal tissues is restricted to mesothelium. It has therefore emerged as a promising target for novel therapies, such as immunotoxins, antibody-drug conjugates or CAR-T cells. We hypothesized that, as an alternative strategy, the anti-MSLN single-domain antibody DOTA-A1K2 could be employed as a radio-theranostic agent and that ^{161}Tb might provide additional efficacy over ^{177}Lu, due to abundant Auger electron emission. The aim of this study was therefore to compare in vitro and in vivo the efficacy of ^{177}LuDOTA-A1K2 and ^{161}Tb-DOTA-A1K2. ***Materials and Methods:*** Radiolabeling was performed using n.c.a. ^{177}Lu (ITM radiopharma) and n.c.a. ^{161}Tb (provided by PRISMAP). Then, the efficacy of ^{177}Lu-DOTA-A1K2 and ^{161}Tb-DOTA-A1K2 was investigated using MDA-MB-231 human TNBC cell line, transfected either with MSLN or with LAC-z as negative control. In vitro, clonogenic assay was performed following 24h incubation of either ^{177}Lu-DOTA-A1K2 or 161Tb-DOTA-A1K2. In vivo, their therapeutic efficacy was evaluated up to 9 weeks following a single intravenous injection of 2, 5, 10, or 20 MBq of each radiotracer (n=6-12 per group). ***Results:*** Radiolabeling of DOTA-A1K2 was successfully performed with radiochemical purity >95% for both ^{177}Lu and ^{161}Tb. In vitro, both ^{177}Lu-DOTA-A1K2 and ^{161}Tb-DOTA-A1K2 were found to inhibit colony formation. However, this effect was significantly higher for 161Tb-DOTA-A1K2, with 88% and 78% reduction in colony number at 1 and 0.3 MBq/mL, in comparison to 35% and 24% for ^{177}Lu-DOTA-A1K2 ($P < 0.001$). In vivo, both ^{177}Lu-DOTA-A1K2 and ^{161}Tb-DOTA-A1K2 were found to inhibit tumor growth at 5, 10 or 20 MBq ($p < 0.001$ vs vehicle). However, unlike what was observed in vitro, ^{161}Tb-DOTA-A1K2 was not found to be more potent than ^{177}Lu-DOTA-A1K2 (p=NS). ***Conclusion:*** In vitro, DOTA-A1K2 successfully reduced the viability of MSNL+ cells and, as hypothesized, ^{161}Tb-DOTA-A1K2 was significantly more potent than ^{177}Lu-DOTA-A1K2. In vivo efficacy of DOTA-A1K2 was also demonstrated. However, similar effects were observed using ^{177}Lu and ^{161}Tb. Additional experiments will be conducted to investigate this discrepancy. It might be attributable to mesothelin shedding in vivo, resulting in its release and preventing Auger electrons to reach radiation-sensitive parts of tumor cells, while beta- particles with longer range, might retain this ability. Acknowledgements: This project has received funding from the European Union's Horizon 2020 research and innovation programme under grant agreement No101008571 (PRISMAP), INCA_16111 (PLBIO21-243), Fondation ARC and ANR-11-INBS-0006 (France Life Imaging).

OP-023

Radiosynthesis and Preclinical Evaluation of ^{77}Br-hGTS13 for Non-Small Cell Lung Cancer Treatment

R. Malek, *P. Cheung, A. Moses, S. Abdi, M. Landry, C. Beinat;*
Stanford University, Palo Alto, CA, UNITED STATES OF AMERICA.

Aim/Introduction: System xc- is an amino acid antiporter mediating the exchange of cystine for glutamate. It is overexpressed in multiple cancers such as glioma, pancreatic cancer and Non-Small Cell Lung Cancer (NSCLC) and is associated with cancer cell proliferation, invasion, metastasis, development of chemo-resistance and poor survival. We previously reported [18F]hGTS13 a second-generation radiotracer targeting system xc- showing an improved tumour uptake in NSCLC rat models, and lower pancreas and kidney retention compared to the reference [18F]FSPG. We report here the development and preclinical evaluation of the therapeutic counterpart [77Br]hGTS13 labelled with the Auger electron emitter bromine 77 [77Br]. ***Materials and Methods:*** We synthesized [77Br]hGTS13 by the nucleophilic displacement of the tosyl group by [77Br], followed by a deprotection with HCl. We evaluated the product's stability in human serum by incubation at 37 °C for 30 and 60 min. We then measured its cellular uptake over 0.5, 1, 2 and 4h in the NSCLC cell lines, A549 and H460. We assessed its specificity for system xc- in A549 and H460, by competition with the natural transporter substrate L-glutamic acid, and the system xc--specific inhibitor erastin2 with final well concentrations of 1 mM and 10 µM, respectively. Cells were preincubated for 10 min with the competitor in HBSS, before adding [77Br]hGTS13 (~48 kBq/well) and incubating for 1h. Cells were then lysed and the cell-associated activity counted on a γ-counter and protein content determined using the bicinchoninic acid assay. ***Results:*** [77Br]hGTS13 was obtained with a non-decay corrected radiochemical yield (RCY) at the end of synthesis of 24.2 ± 7.4% (n=7), and in 99% radiochemical purity. Analytical HPLC showed the product remained 96 and 93% intact in human serum after 30 and 60 min incubation, respectively. The cellular uptake of [77Br] hGTS13 peaked at 1 hour in H460 cells with 549 ± 72% uptake per mg protein and then decreased over time. In A549 cells, [77Br]hGTS13 uptake reaches a plateau after 1h then slowly starts decreasing after 2h. The competition assay in A549 cells showed that L-glutamic acid and erastin2 reduced [77Br]hGTS13 uptake by 91 and 98% respectively. In H460 cells, all competitors blocked over 94% of [77Br]hGTS13 uptake. ***Conclusion:*** We successfully radiolabelled 77Br-hGTS13 and showed its stability in human serum. Competition assay proves that our therapeutic counterpart remains a substrate for system xc-. We are now studying its biodistribution in rat models of NSCLC and will then assess its therapeutic efficacy.

OP-024

Radiosynthesis and Evaluation of Novel NTSR1 Targeting Theranostic Probes

F. Zhang, *X. Liu, J. Li, S. Song;*
Department of Nuclear Medicine, Fudan University Shanghai Cancer Center, Shanghai, CHINA.

Aim/Introduction: Neurotensin receptor 1 (NTSR1) has been demonstrated to play a crucial role in the tumorigenesis, proliferation, invasion, and metastasis of various malignancies. It was significantly overexpressed in multiple tumors and emerged as a promising molecular target for clinical diagnosis and therapy. In this study, we designed and synthesized five novel NTSR1-targeted radiopharmaceuticals and evaluated their diagnosis and radiotherapy potential in H1299 xenograft tumor models. ***Materials and Methods:*** Five structurally distinct radiopharmaceuticals were designed, synthesized, and radiolabeled with ^{68}Ga or ^{177}Lu. The radiolabeling efficiency and radiochemical purity (RCP) were determined using Radio-HPLC. The stability, log P values, and in vivo blood clearance half-life were

systematically evaluated. Micro-PET/CT imaging was performed to screen for optimal diagnostic probes. Additionally, micro-SPECT/CT imaging, biodistribution studies, and therapeutic efficacy assessments were conducted to identify suitable radiotherapeutic ^{177}Lu labeled-agents and determine the optimal dosages. ***Results:*** All five radiopharmaceuticals were successfully synthesized with high RCP (>95%). In vitro stability assays confirmed that all probes maintained >95% RCP after 3 h incubation in saline and FBS. Log P measurements indicated favorable hydrophilicity for all probes. Pharmacokinetic analysis revealed significant differences in blood clearance half-lives (Probe 1-5): 3.83 ± 0.76 h, 4.14 ± 0.75 h, 36.0 ± 7.2 min, 29.0 ± 7.0 min, but the data for Probe 5 were not detected yet. Micro-PET/CT imaging demonstrated that the tumor uptake of five probes (Probe 1-5) was 9.50 ± 0.36 %ID/g, 9.17 ± 1.26 %ID/g, 7.77 ± 1.07 %ID/g, 3.97 ± 1.42 %ID/g, and 2.87 ± 0.81 %ID/g. The T/M (Probe 1-5) were 3.17 ± 0.52, 1.63 ± 0.29, 8.66 ± 2.10, 7.46 ± 2.72, and 5.42 ± 2.66. Probe 3 showed significantly high tumor uptake and T/M. Following ^{177}Lu labeling, SPECT imaging of Probes 1 and 2 revealed prolonged tumor retention. Biodistribution studies at 48 h post-injection indicated that the tumor uptake of two probes was 8.12 ± 0.54 %ID/g (Probe 1) and 10.78 ± 1.97 %ID/g (Probe 2), and Probe 1 had superior clearance liver: 0.75 ± 0.12 %ID/g (Probe 1) vs 3.74 ± 0.44 %ID/g (Probe 2). Further long-term biodistribution and therapeutic efficacy studies are ongoing. ***Conclusion:*** We successfully developed five NTSR1-targeted radiopharmaceuticals. ^{68}Ga-labeled Probe 3 emerged as the most promising PET imaging agent, demonstrating high tumor uptake and excellent T/M contrast at 2 h post-injection. Additionally, ^{177}Lu-labeled Probes 1 and 2 exhibited favorable in vivo pharmacokinetics, supporting their potential for targeted radionuclide therapy.

OP-025

Selective Killing of Tumor Associated Macrophages with a [^{177}Lu]Lu-Nanomedicine Unlocks Checkpoint Inhibition

J. Cleland[1], *S. S. Minami*[2], *M. Paborji*[2], *W. Thomas*[2], *X. Li*[2], *H. Roth*[2], *M. Feng*[2], *A. Brus*[3], *R. Stagaard*[3], *S. Al-Haidar*[3], *N. Nielsen*[3], *M. A. Islam*[3];
[1]*Ironfist Therapeutics, Redwood City, CA, UNITED STATES OF AMERICA,* [2]*Programmable Medicine, Redwood City, CA, UNITED STATES OF AMERICA,* [3]*Minerva Imaging ApS, Ølstykke, DENMARK.*

Aim/Introduction: Tumor associated macrophages (TAMs) inhibit T cell engagement and reduce the efficacy of checkpoint inhibitors. Hydroxyl dendrimers (HDs), novel nanomedicines known to selectively target activated macrophages, conjugated with [^{64}Cu]Cu-NOTA without a targeting ligand, demonstrated significant tumor uptake by PET imaging in the 4T1 triple negative breast cancer model. This study next aimed to optimize the chelator for ^{177}Lu and demonstrate the ability of [^{177}Lu]Lu-HDs to unlock checkpoint inhibition and have therapeutic efficacy in the 4T1 tumor model. ***Materials and Methods:*** NOTA, NODAGA, and DOTA conjugates of HDs were synthesized and ^{177}Lu chelation was performed. Stability of the [^{177}Lu]Lu-HDs was evaluated in buffer and plasma. In vivo and ex vivo biodistribution in mice was assessed after a single intravenous administration by SPECT/CT imaging 24 and 96 h after injection in tumor mice and by gamma counting of excised tissues at 24 and 72 h after injection in normal healthy mice. For the efficacy study, mice were implanted subcutaneously with 4T1 cells, known to be unresponsive to anti-PD-1 therapy, and once tumors were ~130 mm^3, mice were treated with either vehicle, 10 mg/kg anti-PD-1 antibody, or [^{177}Lu]Lu-DOTA-HD alone (4.9, 10.1 or 14.9 MBq) or in combination with anti-PD-1 antibody. ***Results:*** ^{177}Lu incorporation was 46.6%, 93.0%, and 98.6% in NOTA, NODAGA, and DOTA-HDs, respectively. In buffer or mouse plasma after 72h at 37°C, [^{177}Lu]Lu-DOTA-HDs radiochemical purity was unchanged (98%), while the other HDs had decreased purity. Ex vivo biodistribution in normal healthy mice indicated the highest uptake of [^{177}Lu]Lu-NOTA-HD in kidney and bone (most likely free ^{177}Lu), whereas [^{177}Lu]Lu-NODAGA-HD and [^{177}Lu]Lu-DOTA-HD had higher uptake in liver and spleen. Treatment with doses of up to 14.9 MBq [^{177}Lu]Lu-DOTA-HD appeared to halt tumor progression and in combination with anti-PD-1 antibody resulted in tumor regression. SPECT/CT scans confirmed tumor uptake and accumulation over time as observed with [^{64}Cu]Cu-NOTA-HD. ***Conclusion:*** These results demonstrated the potential of selective TAM killing as a therapeutic approach in oncology, especially in checkpoint inhibitor resistant tumors. Additional preclinical efficacy studies with [^{177}Lu]Lu-DOTA-HD are planned to include PSMA-negative prostate cancer, which lacks a clear target and remains an unmet medical need.

205

Sunday, October 5, 2025, 8:00 - 9:30
Room 211

Cutting Edge Science Track - TROP Session - AI Committee: AI for Segmentation in PET/CT

OP-026

Application of Automatic Organ Segmentation for Audit and Optimisation in FDG PET/CT

L. Bonney[1,2], *K. M. Bradley*[3], *A. B. Hassan*[2], *D. R. McGowan*[1,4];
[1]*Department of Medical Physics and Clinical Engineering, Oxford University Hospitals NHS Foundation Trust, Oxford, UNITED KINGDOM,* [2]*Sir William Dunn School of Pathology, University of Oxford, Oxford, UNITED KINGDOM,* [3]*Wales Research and Diagnostic Positron Emission Tomography Centre (PETIC), University Hospital of Wales, Cardiff, UNITED KINGDOM,* [4]*Department of Oncology, University of Oxford, Oxford, UNITED KINGDOM.*

Aim/Introduction: Automatic deep-learning based segmentation methods for organs are now well established and known to be highly accurate. This work enables region generation at a much larger scale for lower resource cost than previously possible. This work looked to explore using automatic organ segmentation for image quality control in a large retrospective PET/CT dataset (N=1,000, 3,045 scans). ***Materials and Methods:*** A consecutive single centre patient cohort of 1,000 adult patients who received an FDG PET/CT scan were selected. All PET/CT scans these patients had received in a ten-year period at the centre were included in the analysis (3,045 scans). All scans were acquired on a GE D690 or D710 PET/CT scanner with consistent protocols. Organ segmentation was generated using Total Segmentator [1]. Regions were eroded by 10mm to minimise edge effects and motion artefacts. Methods were designed to have low levels of user input or data cleaning, using a large dataset to mitigate errors. This work validated this approach against published quantitative results in the liver, before exploring more novel areas. ***Results:*** Results in liver reproduced standard results from literature that used more time intensive data annotation methods using spherical volumes of interest amongst other results mean population SUV_{MEAN}=2.09 [2,3]. Automated methods enabled measurement for volumes of interest beyond liver at low resource cost. Notably distributions for organs other than liver including kidneys and lung were relatively narrow and of comparable width to liver [Liver: mean=2.09, std=0.41; Kidney: mean=2.56, std=0.63; Lung: mean=0.51, std=0.18]. Patient groups were compared. An interesting significant difference was observed in standard deviation of SUV in the gluteus maximus between sexes [Male: 0.13, Female: 0.16] with the higher noise observed in women likely explained by sex-based differences in body fat distribution. Application of the measured distributions demonstrated the ability to detect height and weight data entry errors. ***Conclusion:*** Automated organ segmentation methods can enable automated image quality audit in large datasets,

with minimal data cleaning or selection required. This enabled measurement of SUV_{MEAN} distribution for a number of regions little studied before and has potential applications in optimisation, harmonisation and quality control. With the benefit of including data from a representative patient population. The next stage of this work is to extend to more complex image measurements and consider impact in longitudinal data. ***References:*** 1. Wasserthal et al., Radiol Artif Intell., 5:5 (2023)2. Boellard et al., EJNMMI, 42:328-354 (2015)3. Sprinz et al., Sci Rep, 8:2126 (2018)

OP-027

A hybrid deep learning model for tumor and pulmonary nodule segmentation in non-small cell lung cancer using MedSAM.

H. Habchi[1], *B. Daoud*[2], *S. Mensi*[3,4], *K. Chatti*[5];
[1]*Department of Biophysics and Medical Imaging, Higher Institute of Medical Technologies of Tunis, University of Tunis El Manar, Tunis, TUNISIA,* [2]*University of Texas, MD Anderson Cancer Center, Houston, TX, UNITED STATES OF AMERICA,* [3]*Nuclear Medicine department, CHU Sahloul, Sousse, TUNISIA,* [4]*Department of biophysics, School of medicine of Sousse, University of Sousse, Sousse, TUNISIA,* [5]*School of Medicine of Monastir, University of Monastir, Monastir, TUNISIA.*

Aim/Introduction: The segmentation of lung tumor lesions and pulmonary nodules in patients with non-small cell lung cancer (NSCLC) within ^{18}F-FDG PET-CT imaging plays a vital role in choosing the right treatment. However, it is difficult to accurately define the target areas because breathing movements lead to noticeable changes in the shape and size of the tumor between PET and CT scans. Additionally, undetectability of small pulmonary nodules can affect the accuracy of treatment decisions, so complicating the diagnosis of their benign or malignant character. To deal with these challenges, the aim of this study was to develop a specific deep learning model for automatic segmentation of lung tumors and pulmonary nodules structures from PET-CT images. ***Materials and Methods:*** The dataset includes 188 ^{18}F-FDG PET-CT scans of NSCLC patients, with manually segmented tumor lesions (lung tumor and pulmonary nodules) using the PET Tumor Segmentation extension in 3D Slicer and confirmed by our nuclear doctor. The collection includes data from 168 patients who took part in the autoPET MICCAI 2022 challenge and were published in the Cancer Imaging Archive, alongside an additional 20 patients from our institution. We developed a novel hybrid model that integrates PET-CT and CT images for improved medical image segmentation. All the individual input modalities are processed through the Segment Anything in Medical Images (medSAM) model separately to extract features, then merged using an adaptively weighted ensemble approach to produce a more complete segmentation output while using two separate loss functions for joint learning. We then use the same process with nnU-Net and train the individual PET-CT images with medSAM and nnU-Net to evaluate performance. The autoPET data were randomly divided into under 5-fold cross-validation with 100 training, 34 validation, and 34 test PET-CTs, while our institution's data were used as external testing data. The accuracy of the four models was evaluated using the Dice similarity coefficient (DSC) and surface DSC at 2 mm (sDSC2mm). ***Results:*** Hybrid models segmented the tumor lesions more accurately compared with the individual models, and hybrid-medSAM was higher than hybrid-nnUnet. The average DSC values for hybrid-medSAM, hybrid-nnUnet, individual-medSAM, and individual-nnUnet were 0.80±0.016, 0.77±0.047, 0.72±0.018, and 0.71±0.057, respectively. The average sDSC2mm values for hybrid-medSAM, hybrid-nnUnet, individual-medSAM, and individual-nnUnet were 0.83±0.021, 0.81±0.052, 0.76±0.027, and 0.77±0.013, respectively. ***Conclusion:*** Our hybrid-medSAM model is effective for segmenting the tumor lesions in PET-CT images. The proposed model holds promise for its potential application in various cancer types.

OP-028

How accurately can artificial intelligence identify metabolic tumour volume (MTV) in large B-cell lymphoma on ^{18}F-FDG PET/CT? Validation of a Deep Learning tool in a large B-cell lymphoma patient cohort

M. Santoro[1], *S. Proto*[2], *A. Farolfi*[3], *R. Ussia*[3], *S. Fanti*[3,2], *L. Strigari*[1];
[1]*Department of Medical Physics, IRCCS Azienda Ospedaliero-Universitaria di Bologna, Bologna, ITALY,* [2]*Nuclear Medicine, Alma Mater Studiorum University of Bologna, Bologna, ITALY,* [3]*Nuclear Medicine, IRCCS Azienda Ospedaliero-Universitaria di Bologna, Bologna, ITALY.*

Aim/Introduction: Automated segmentation tools for identifying metabolic tumour volume (MTVs) and extracting related features hold significant potential for accelerating standardization and harmonization in multicentric studies. They also enable the broader application of radiomics to predict treatment response and clinical outcomes. A preliminary research version of a commercial deep learning(DL) tool for automatic MTV segmentation on ^{18}F-FDG PET/CT was implemented in our Institution. An independent external validation was conducted using a large monocentric cohort of patients with large B-cell lymphoma, examined across multiple PET/CT scanner vendors. ***Materials and Methods:*** Baseline PET/CT images from different scanners of 94 consecutive patients undergoing CAR-T therapy were analysed. Two experienced nuclear medicine physicians manually delineated MTVs using either freehand contours(MTV_m) or a fixed SUV threshold of 4.0(MTV_{th}). DL-based automatic segmentations(MTV_a) were performed and refined using the liver SUV_{max} as a reference. Inter-method agreement was assessed using relative volume differences, Dice Similarity Coefficient(DSC), and Mean Distance to Agreement(MDA), with results stratified by liver SUV_{max} ranges, i.e., 0≤liver SUV_{max}<4 and liver SUV_{max}≥4. The time required for DL-based segmentation was recorded, and the reproducibility of MTV_a produced by the DL tool was evaluated with the repositioning of the liver volume of interest by two independent operators for the liver SUV_{max} determination. ***Results:*** Based on a total of 188 MTVs, the mean liver SUV_{max} was 3.2±1.03. The median[range] of MTVa and MTV_m or MTV_{th} were 209.1[2.9-8895.3] and 142.4[2.9-7936.3] cm^3, respectively. The mean DSC of MTV_a compared to MTV_m or MTV_{th} was 0.72[0.35-0.93] and 0.68[0.30-0.91], respectively, for 0≤liver SUV_{max}<4. In patients with metastatic liver disease, the mean DSC was lower, i.e., 0.54[0.50-0.58] and 0.70[0.57-0.82] for MTV_a versus MTV_m and MTV_a versus MTV_{th} respectively. When MTV_a underestimated MTV_m or MTV_{th}, the median MDA was 11.5 mm and 5.4 mm, respectively. In other cases, median MDA values resulted in 4.8 mm and 8.58 mm for MTV_a versus MTV_m and MTV_a versus MTV_{th}, respectively. DL-based segmentation was efficient, with a mean[range] processing time of 33[27-40] seconds per patient. Reproducibility of MTV_a between operators was within 10%. ***Conclusion:*** A good agreement between DL-based and expert segmentations was found, with greater divergence at smaller MTVs. The DL-based software speed, reproducibility and level of agreement with expert contours support its potential for future clinical investigations.

OP-029

Evaluation of Single-Channel PET and Dual-Channel PET/CT nnU-Net Deep Learning 3D Segmentations from Diffuse Large B-Cell Lymphoma to Follicular Lymphoma

M. Luo[1,2], *F. Yousefirizi*[2], *C. Gowdy*[3], *J. O*[4], *A. Rahmim*[1,2];
[1]*Faculty of Medicine, The University of British Columbia, Vancouver, BC, CANADA,* [2]*BC Cancer Research Centre, Vancouver, BC, CANADA,* [3]*BC Children's Hospital, Vancouver, BC, CANADA,* [4]*College of Medicine, Seoul St. Mary's Hospital, The Catholic University of Korea, Seoul, KOREA, REPUBLIC OF.*

Aim/Introduction: Accurate segmentation of lymphoma lesions in PET/CT imaging is crucial for the quantification of imaging-based biomarkers, such as total metabolic tumor volume (TMTV). Many studies examining segmentation approaches have focused predominantly on the most common subtypes of lymphoma, including Diffuse Large B-Cell Lymphoma (DLBCL). Although TMTV quantification is well studied, limited research has specifically addressed its application in follicular lymphoma (FL), despite the heterogeneous ^{18}F-FDG uptake patterns commonly encountered in clinical practice and the known limitations of visual assessment in reliably differentiating FL from DLBCL. This study aims to evaluate the performance of single-channel PET and dual-channel PET/CT nnU-Net trained on DLBCL for segmenting lesions in FL. ***Materials and Methods:*** Single- and dual-channel nnU-Net models were trained using a 3D full-resolution architecture with 5-fold cross-validation. Training was performed on a multi-centre dataset of 258 DLBCL cases (n=41 from Center I and n=217 from Center II). For dual-channel input, CT images were resampled using linear interpolation to match the spatial dimensions of PET images. Nuclear medicine physicians provided ground truth reference segmentations. Models were evaluated on 1) 19 FL cases from FOLL12 and RELEVANCE trials benchmarked by Boellaard et al.; and 2) 33 Primary Mediastinal B-Cell Lymphoma (PMBCL) cases from Center I. ***Results:*** In 5-fold cross-validation on DLBCL, the single-channel model achieved a mean Dice score of 0.65±0.05 with a mean intra-fold Dice standard deviation of 0.32 (precision/recall 0.87/0.71). The dual-channel model yielded similar performances with a mean Dice score of 0.65±0.04 with a mean intra-fold Dice standard deviation of 0.33 (precision/recall 0.85/0.72). On FL, mean Dice scores of 0.53±0.25 (precision/recall 0.37/0.81; single-channel) and 0.52±0.29 (precision/recall 0.47/0.60; dual-channel) were achieved. On PMBCL, mean Dice scores of 0.60±0.41 (precision/recall 0.80/0.93; single-channel) and 0.62±0.41 (precision/recall 0.86/0.90; dual-channel) were achieved. Generally, mean relative error (RE) decreased as ground truth lesion volume increased (single-channel: RE 6.34 (0.216mL-21.607mL) to RE 0.27 (501.251mL-5920.354mL); dual-channel: RE 3.75 (0.216mL-21.607mL) to RE 0.22 (501.251mL-5920.354mL)). ***Conclusion:*** Both single- and dual-channel nnU-Net 3D segmentation models demonstrated similar performance with reasonable generalizability to FL. The decrease in performance on FL cases may be due to variability in FDG avidity of FL. These findings suggest that more resource-efficient single-channel models may achieve comparable performance and that segmentation models trained on DLBCL cases may be a good starting point for extension to other lymphoma subtypes.

OP-030

Deep Learning-Driven Automated Segmentation for Mantle Cell Lymphoma in ^{18}F-FDG PET: Towards Prognostic and Clinical Applications

Z. Zhang[1], *W. Xu*[2], *C. Jiang*[1], *H. Huang*[1], *X. Zheng*[2], *Y. Teng*[3], *Y. Liu*[1], *Z. Jiang*[4], *J. Xu*[3], *S. Liu*[2], *R. Tian*[1];
[1]West China Hospital of Sichuan University, Cheng Du, CHINA, [2]School of Computer Science, Nanjing University of Posts and Telecommunications, Nanjing, CHINA, [3]Nanjing Drum Tower Hospital, the Affiliated Hospital of Nanjing University Medical School, Nan jing, CHINA, [4]West China Biomedical Big Data Center, West China Hospital, Sichuan University, Chengdu, Sichuan, China, Cheng Du, CHINA.

Aim/Introduction: This study aims to develop and validate an automated deep learning model for segmenting mantle cell lymphoma (MCL) lesions in 18F-FDG-PET images and to assess its prognostic value. ***Materials and Methods:*** A total of 169 MCL patients from two independent centers (118 patients from West China Hospital and 51 patients from Nanjing Drum Tower Hospital) were included in the study. All patients had histologically confirmed MCL, underwent pretherapy ^{18}F-FDG PET/CT scans, and received R-CHOP-like regimens. A deep learning model based on the nnU-Net architecture was employed to segment MCL lesions, and the derived total metabolic tumor volume (TMTV) was evaluated for prognostic significance. Model performance was evaluated using standard metrics, with the prognostic value of TMTV validated in an external cohort. ***Results:*** Predicted total metabolic tumor volume (pTMTV) demonstrated strong agreement with ground truth TMTV (gtTMTV) in both training and validation cohorts, as shown by Bland-Altman analysis, with biases of −22.9 (−394.1 to 348.3) cm3 in the training cohort and −2.0 (−698.9 to 694.8) cm3 in the validation cohort. Predicted TMTV was identified as an independent predictor of Disease-Free Survival (DFS) in multivariate analysis (HR = 1.001, p = 0.038). The cut-off value for pTMTV to predict DFS was 1068.5 cm^3. Predicted TMTV was significantly associated with DFS, with high pTMTV correlating with poorer DFS (p< 0.05). ***Conclusion:*** The nnU-Net-based automated segmentation model for MCL lesions in FDG-PET images is a reliable and precise tool for TMTV assessment, offering potential to enhance clinical decision-making and prognosis prediction in MCL patients. Funding: This study was supported by the 1·3·5 project for disciplines of excellence, West China Hospital, Sichuan University (grant ZYAI24014).

OP-031

Deep-Learning blind-spots in PET/CT tumour segmentation: validating different deep-learning tumour segmentation models against Nuclear Medicine Physicians/Radiologists and describing their limitations.

D. Lim[1], *N. Leow*[2], *C. Tang*[1], *W. Chua*[1], *W. Tham*[1], *Y. Khor*[1], *D. Ng*[1], *W. Lam*[1];
[1]Singapore General Hospital, Department of Nuclear Medicine and Molecular Imaging, Singapore, SINGAPORE, [2]National University Hospital, Department of Diagnostic Imaging, Singapore, SINGAPORE.

Aim/Introduction: Several imaging biomarkers are shown to correlate well with treatment outcomes and disease prognostication[1]. These biomarkers require tumour segmentation which is tedious to achieve prospectively during reporting. Deep learning models have been developed to improve efficiency of segmentation and generate biomarkers. We validated two deep learning based models on 477 F-18 FDG PET/CTs performed in our institutions on lymphoma patients (n = 216). DICE scores comparing the model performance against Nuclear Medicine Physicians/Radiologists were calculated for 15% of the scans which were randomly selected. The deep learning models validated included a publicly available TMTV segmentation model ("TMTV-net"), and a modified CT-based segmentation model ("Total Segmentator" with SUV thresholding applied. We also present examples of lesions missed by the models and the false positives. ***Materials and Methods:*** DICOM images of 477 F-18 FDG PET/CT studies for 216 patients with lymphoma were extracted. All studies were performed on scanners of the same model and used the same reconstruction methods. A model was developed to segment lesions above the threshold of SUV 4.0 and the output was put through the deep learning model "TotalSegmentator" to exclude sites of physiological FDG-uptake. This model and a publicly available "TMTV-net" were applied on the dataset. For validation, 65 studies (15%) were randomly selected. Manual segmentation of all FDG-avid lesions were performed by Nuclear Medicine Physicians/Radiologists. The DICE score for each model was calculated. Lesions missed or wrongly segmented were tabulated. ***Results:*** The DICE score for TMTV-net was 0.782 on our institution scans. The DICE score for the SUV4.0 thresholding based model was 0.20, likely due to inability to exclude sites of physiological uptake. Examples of false positive lesions segmented by TMTV-net included: IV cannula site and post surgical changes. The model showed incomplete segmentations for large lesions. There was under-segmentation of marrow disease and small volume FDG-avid nodes in patients with extensive nodal disease. The thresholding-based model had more false positives

including: edges of the brain, sites of skin contamination, brown fat and muscle uptake. ***Conclusion:*** Deep learning models can improve efficiency in reporting, however externally developed models run the risk of exhibiting variable performance when applied in a different environment. Thus validation is crucial before incorporation into daily practice. Understanding a model's performance is critical to build upon existing models and to allow for safe use of models in clinical care.

OP-032

Deep-Learning-Based Automated Delineation of Non-Hodgkin Lymphoma in [^{18}F]FDG PET/CT

P. Nikulin[1], *S. Hoberück*[2], *F. Hofheinz*[1], *J. Maus*[1], *C. Hanoun*[3], *A. Hüttmann*[3], *U. Dührsen*[3], *K. Kopka*[1], *J. Kotzerke*[2], *R. A. Bundschuh*[2], *A. Braune*[1];
[1]*Institute of Radiopharmaceutical Cancer Research, Helmholtz-Zentrum Dresden-Rossendorf, Dresden, GERMANY,* [2]*University Hospital Carl Gustav Carus, Department of Nuclear Medicine, Dresden, GERMANY,* [3]*University Hospital Essen, Department of Hematology, Essen, GERMANY.*

Aim/Introduction: Total metabolic tumor volume (TMTV) is a significant prognostic factor in patients with aggressive non-Hodgkin lymphoma. Extraction of image-based biomarkers however requires delineation of all tumor lesions which is non-trivial, time-consuming, and error-prone with the currently available semi-automated methods. The goal of this study was the development and evaluation of a deep-learning-based method for automated delineation of lymphoma in [^{18}F]FDG PET/CT. ***Materials and Methods:*** Automated delineation was performed with a 3D U-Net convolutional neural network (CNN) developed from scratch using nnU-Net framework [1]. 1133 [^{18}F] FDG PET/CT scans of non-Hodgkin lymphoma patients acquired within the PETAL prospective multicenter study [2] were used for network training and testing using a 5-fold cross-validation scheme. The ground truth delineations were developed iteratively by an experienced observer with assistance of intermediate CNN models trained on smaller subsets of the data. All tumor lesions were included regardless of their volume or maximum uptake. ***Results:*** The derived CNN models are capable of accurate delineation, achieving a Dice similarity coefficient of 0.889. The dataset included 6602 tumor lesions which were detected with sensitivity of 0.671 and positive predictive value of 0.809. The average (median) volume of missed lesions was 3.3 (0.5) ml. After exclusion of the outliers (worst 1%), manually and automatically derived TMTVs were highly correlated with R2=0.983 while the mean absolute error of TMTV determination was 13.1 ml with the average TMTV of 133.4 ml. ***Conclusion:*** In this work, we present a CNN able to perform delineation of tumor lesions in lymphoma with only minimal manual corrections possibly required. It thus is able to accelerate study data evaluation in quantitative PET and does also have potential for supervised clinical application. ***References:*** [1] Isensee, F. et al. "nnU-Net: a self-configuring method for deep learning-based biomedical image segmentation." Nat Methods 18, 203-211 (2021)[2] Dührsen, U. et al. "Positron Emission Tomography-Guided Therapy of Aggressive Non-Hodgkin Lymphomas (PETAL): A Multicenter, Randomized Phase III Trial." J Clin Oncol 36, 2024-2034 (2018)

OP-033

Tumour Occurrence Maps: A Fully-Automated Approach for Investigating Generalizability of AI-Based Tumour Segmentation

M. Pires[1], *S. Gutschmayer*[1], *D. Amareller*[2], *E. Bergalla*[3], *S. Chauvie*[3], *A. Frille*[4,5], *S. Hesse*[4], *O. Sabri*[4], *E. M. Abenavoli*[6], *R. Sciagrà*[6], *J. Auriac*[7], *R. Seban*[7,8], *I. Buvat*[7], *T. Beyer*[1], *L. K. S. Sundar*[9];
[1]*QIMP Team, Medical University of Vienna, Wien, AUSTRIA,* [2]*Department of Radiology and Nuclear Medicine, Medical University Vienna, Wien, AUSTRIA,* [3]*Medical Physics Division, Santa Croce e Carle Hospital, Cuneo, ITALY,* [4]*Department of Nuclear Medicine, University Hospital Leipzig, Leipzig, GERMANY,* [5]*Department of Respiratory Medicine, University Hospital Leipzig, Leipzig, GERMANY,* [6]*Division of Nuclear Medicine, Azienda Ospedaliero Universitaria Careggi, Florence, ITALY,* [7]*Institut Curie, Université Paris-Saclay, Inserm LITO U1288, Orsay, FRANCE,* [8]*Institut Curie, Department of Nuclear Medicine, Paris-St-Cloud, FRANCE,* [9]*DIGIT-X Lab, Department of Radiology, LMU, Munich, GERMANY.*

Aim/Introduction: Assisted tumour segmentation in PET/CT is critical for automated biomarker extraction. Despite progress with deep-learning models, dataset construction still relies on blindly accruing large numbers of scans followed by manual segmentation — an inefficient process that burdens clinicians. Deep-learning models only generalize to variations seen during training, making variability critical. By selectively targeting cases that introduce new variations, we can efficiently fill gaps in the training data. Here, we propose Tumour Occurrence Maps (TOMs) — a data-driven framework to characterise tumour spatial distributions and guide efficient training dataset construction. ***Materials and Methods:*** We retrospectively collected 3,857 [18F] FDG-PET images: 170 melanoma cases, 713 lung cancer cases, 2,866 lymphoma cases, and 108 breast cancer cases. Nuclear medicine physicians were instructed to manually segment the entire tumour load on each scan. We trained 4 separate segmentation models — one per cancer type — using nnU-Net with the DA5 trainer. The models' generalizability was evaluated by testing each model on the other tumour types. Performance was quantified using lesion-level sensitivity. TOMs were generated by first obtaining body masks using MOOSE [1]. Tumour segmentations and body masks were registered to a common anatomical template with affine registration, producing three-dimensional voxel-wise probability maps. For each of the 4 TOMs, the proportion of non-zero voxels (%) was computed as a tumour spatial coverage metric. ***Results:*** The lung cancer model achieved the highest cross-cancer sensitivity (72%) with a TOM coverage of 46%, followed by the melanoma model (68% sensitivity, 28% coverage) and the lymphoma model (66% sensitivity, 90% coverage). The breast cancer model showed the lowest performance (45% sensitivity, 17% coverage). However, the non-breast cancer models yielded strong sensitivity on breast cancer cases: melanoma (86%), lung (85%), and lymphoma (83%). This asymmetry suggests that generalisability is driven more by spatial coverage than cancer type. Models trained on anatomically diverse tumours effectively captured breast cancer lesions despite not encountering them during training. In contrast, the breast model's restricted coverage limited its ability to detect lesions beyond its learned distribution. ***Conclusion:*** This study demonstrated the utility of TOMs to quantify anatomical variability of tumours in training datasets. Broader spatial coverage, rather than cancer type, emerged as essential in cross-cancer model generalisability, supporting TOMs as a tool to efficiently curate more variable training datasets for tumour segmentation. ***References:*** [1] Sundar et al. "Fully automated, semantic segmentation of whole-body ^{18}F-FDG PET/CT images based on data-centric artificial intelligence." JNM 63.12 (2022): 1941-1948.

OP-034

Gaze-Guided Clinician-in-the-Loop AI Platform for total tumor volume segmentation in PET/CT and SPECT/CT

R. Hamidpour[1], *A. Toosi*[1,2], *F. Yousefirizi*[1], *Y. Salimi*[3], *H. Zaidi*[3], *C. Uribe*[1,2], *A. Rahmim*[1,2];
[1]*BC Cancer Research Institute, Vancouver, BC, CANADA,* [2]*University of British Columbia, Vancouver, BC, CANADA,* [3]*Geneva University Hospital, Geneva, SWITZERLAND.*

Aim/Introduction: Total-Tumor-Volume(TTV) has emerged as a valuable prognostic biomarker across various cancer types, including PSMA PET/CT, and is needed for dosimetry in SPECT/CT imaging. Routine tumor delineation is an excessive burden on

clinicians and is not routinely performed. Such delineations can also be used to generate additional quantitative features (e.g., radiomics analyses). Meanwhile, interactive foundation models such as MedSAM and nnInteractive can provide strong performance on segmenting tumors. Still, mouse-based interaction models can induce user fatigue in large-scale dataset annotations. In this study, we propose and publicly-share a Gaze-Guided Clinician-in-the-Loop AI platform for TTV segmentations to facilitate feasible, routine quantification guided by clinicians looking at regions-of-interests (ROIs). We compare the results of two foundation models over SPECT/CT and PET/CT imaging, with Gaze-Tracking(GaTr) and Bounding-box(Bbox) prompt-types. ***Materials and Methods:*** We implemented our pipeline for MedSAM and nnInteractive, enabling interactive 2D and 3D segmentations, as an extension to the popular 3D-Slicer platform to simplify the process for public use. The 3D-Slicer extensions were integrated with the GaTr tool by connecting a standard Webcam(60 Frame-Rate-per-Seconds) to the GaTr server and then communicating with the Software Development Kit(SDK). When the physician is looking at a ROI, the GaTr server catches the point over the screen, and our extension retrieves it through the SDK. We utilize this point as a center-of-a-Bbox or a point-prompt to our models. We assessed our study via zero-shot learning to evaluate pipeline performance for 177Lu-DOTATATE-SPECT/CT and 18F-PSMA-PET/CT. ***Results:*** As initial assessment, we compared two prompt-types with nnInteractive over 10 patients from each modality, focusing on the difficult task of segmenting TTV of PSMA-PET and DOTATATE-SPECT. In terms of segmentation-accuracy and interaction-time, nnInteractive for DOTATATE-SPECT/CT with Bbox achieved a Dice-Score(DS) of 0.63+-0.15, while with GaTr, DS over the same dataset was 0.62+-0.17. Meanwhile, the interaction-time median on each prompt-type was 5.65+-2.8s and 0.28+-0.14s, respectively. On the PSMA cohort, nnInteractive achieved DS of 4.56+-1.25s (Bbox) and 0.67+-0.15s(GaTr) while the interaction-time was 4.3+-2.5s(Bbox) and 0.25+-0.02s(GaTr). By contrast, MedSAM with Bbox performed better for SPECT/CT with DS 0.38+-0.38 while DS over PET/CT images was only 0.21+-0.16. MedSAM median-interaction-time was 5.59+-2.04s(SPECT/CT) and 6.72+-1.73s(PET/CT). ***Conclusion:*** Our publicly-shared platform enables significantly-faster segmentations via gaze-tracking coupled with state-of-the-art AI solutions. Researchers and clinicians can take advantage of this system for clinical trials and, ultimately, in routine-care to annotate various types of lesions, cancers, and modalities for quantification, prognosis and dosimetry.

206

Sunday, October 5, 2025, 8:00 - 9:30
Room 117

Clinical Oncology Track - TROP Session - Oncology & Theranostics Committee: Gynaecological Cancer Stagingand Image Guidance

OP-035

Sentinel Lymph Node Biopsy in Breast Cancer: Guideline Updates and Real-World Insights

F. Silva-Ribeiro, *B. Martins, C. V. Pinto, V. C. Sousa;*
Unidade Local de Saúde de Loures / Odivelas, Lisboa, PORTUGAL.

Aim/Introduction: Sentinel lymph node biopsy (SLNB) is the conventional approach for assessing nodal involvement in early-stage breast cancer patients with clinically negative nodes. SOUND and INSEMA trials indicate that omitting SLNB does not compromise invasive disease-free survival. This prompted reevaluation reflected in the April 2025 American Society of Clinical Oncology (ASCO) guideline, supporting omission of SLNB in postmenopausal women ≥50 years, clinically T1, Nottingham grade 1-2, hormone receptor-positive, HER2-negative breast cancer. This study reflects real-world evidence from our institution. ***Materials and Methods:*** Demographic data, tumor profiles, treatment data, incidence of pathological positive lymph nodes and follow-up information (registry of events like breast recurrence, axillary recurrence, distant recurrence and death) of breast cancer patients who underwent lymphoscintigraphy between January 2012 and December 2019, were retrospectively collected and analyzed. This ensured a median (IQR) follow-up of 8 years (6.0-9.8). A subgroup analysis was conducted based on ASCO recommendations for SLNB omission. ***Results:*** Over the eight-year period, 532 breast lymphoscintigraphies were performed, corresponding to 507 patients, with a median age of 62.0 (range: 28-94) of which four were male. Invasive breast cancer was observed in 90.2% (480/532) of cases, of which 265 were cT1, 191 cT2 and 24 >cT2. 86.0% (413/480) were hormone receptor-positive, 86.5% were HER2-negative and, 83.1% (399/480) were low or medium grade tumours (G1: 27.3%, G2: 55.8%, G3 13.3%). Subgroup analysis included 131/507 patients (25.8%) who met SLNB eviction criteria, with median (IQR) age of 65.0 (59.5-73.0). In this subgroup, sentinel lymph node positivity represented 19.8% of cases. The registry of follow-up revealed an event rate of 5.3% (1/131 breast and 1/131 axillary recurrences, 4/131 distant metastases and 1/131 death), occurring at a median (IQR) period of 6 (5-7) years. Of these events, only one was observed in a patient with nodal involvement. ***Conclusion:*** According to current recommendations for SLNB eviction, the incidence of nodal positivity in our subgroup was higher than the INSEMA study (19.8% vs 15.1%). In the subgroup analysis, events were observed in 5.3% (similar to INSEMA rate), with no events reported before 5 years of follow-up. Although longer follow-up periods are needed to clearly evaluate the impact of this recommendation, our data suggests that omitting SLNB in this subgroup may not negatively impact the overall and disease-free survival. ***References:*** Park KU, Somerfield MR, Anne N, et al. Sentinel Lymph Node Biopsy in Early-Stage Breast Cancer: ASCO Guideline Update. J Clin Oncol. Published online April 10, 2025. doi:10.1200/JCO-25-00099

OP-036

Sentinel Node Scintigraphy for Breast Cancer on CZT-Based Whole-Body SPECT/CT: Description of an 18-Month Monocentric Experience and Workflow Efficiency

F. Serani[1], *C. Gagliani*[1], *P. Zucchetta*[2], *R. Simeone*[2], *V. Bodanza*[2], *G. Grassetto*[2], *D. Cecchin*[1];
[1]*Nuclear Medicine Unit, Department of Medicine DIMED, University-Hospital of Padova, Padova, ITALY,* [2]*Nuclear Medicine Unit, University-Hospital of Padova, Padova, ITALY.*

Aim/Introduction: Over the past 18 months, our department has introduced a novel technique for sentinel node scintigraphy in breast cancer patients, utilising a cadmium zinc telluride (CZT)-based whole-body SPECT/CT system. Unlike the traditional method employing liquid crystal collimators and preoperative skin marking, this approach omits skin marking and relies on CT imaging for intraoperative guidance. The aim of this retrospective analysis was to evaluate the feasibility, workflow efficiency, and surgical impact of the new method. ***Materials and Methods:*** We retrospectively reviewed all breast cancer sentinel node scintigraphy procedures performed with the CZT-based system over an 18-month period. A short survey was administered to three breast surgeons to assess their intraoperative experience and

any perceived differences compared to the traditional technique. ***Results:*** A total of 325 breast cancer patients underwent sentinel node scintigraphy. Among these, anomalous lymphatic drainage pathways were identified in 57 cases, clearly visualised through the CT images. The new technique allowed simultaneous acquisition of functional and anatomical information, resulting in reduced procedure times due to the elimination of manual skin marking. Surgeon feedback indicated that none of the respondents noticed the absence of the skin marker during surgery, suggesting no negative impact on surgical localisation or planning. From the nuclear medicine perspective, the improved workflow and enhanced visualisation of "in-transit" lymph nodes and lymphatic vessel tortuosity were identified as major advantages. ***Conclusion:*** The adoption of CZT-based whole-body SPECT/CT for sentinel node scintigraphy in breast cancer patients appears feasible and efficient. It streamlines workflow, enhances anatomical visualisation, and maintains surgical effectiveness. Further studies involving larger cohorts and objective surgical outcome measures are recommended to validate these findings.

OP-037

Systematic evaluation of the performance of hybrid tracers in image-guided sentinel node biopsy

T. Buckle[1], *M. Vreeburg*[2], *F. van Leeuwen*[1], *D. Rietbergen*[1];
[1]*Leiden University Medical Center, Leiden, NETHERLANDS,* [2] *Netherlands Cancer Institute - Antoni van Leeuwenhoek Hospital, Amsterdam, NETHERLANDS.*

Aim/Introduction: In solid tumors patient prognosis is primarily influenced by the presence of nodal metastases, which are found in 10-25% of clinically node-negative patients. Sentinel node biopsy (SNB) has been introduced to address the need to identify micro-metastases. This technology is globally integrated into routine clinical care for e.g. melanoma, oral cavity, penile, breast and gynecological cancer. Since 2011 hybrid SN tracers that contain both a radio- and fluorescent label have been clinically applied. Besides having been applied in 11 tumor types and > 2000 patients, a systematic performance assessment of their use in SNB has not yet been performed. ***Materials and Methods:*** Comprehensive bibliographic screening was performed according to Preferred Reporting Items for Systematic Reviews and Meta-analyses (PRISMA) guidelines for clinical reports (PROSPERO registration number: CRD42023431662, 2011-2024). 61 of the 563 selected articles described clinical use of radioactive and fluorescent hybrid tracers in SNB. Risk of bias assessment was performed using the Newcastle-Ottawa Scale (low risk of bias: ≥7). Tracer preparation, preoperative findings (lymphoscintigraphy, SPECT/CT), intraoperative findings (radioactive and/or fluorescent nodes, sensitivity, specificity, negative predictive value (NPV) and false negative rate), pathological and oncological outcomes (including overall survival/mortality, biochemical and clinical recurrence, disease free survival), and complications were evaluated. ***Results:*** Risk of bias was low in 43% (N= 26) prospective studies performed in head-and-neck-, prostate-, penile-, vulvar-, gastric- and cervical cancer, and melanoma. The remaining studies included insufficient follow-up and/or solely proof-of-principle assessment. Inter-study comparison showed agreement in preoperative SN detection with solely radiolabelled parental SN tracers (e.g., ^{99m}Tc-nanocolloid), and between hybrid tracer variants. An ICG-HSA ratio of 0.5 was deemed most reliable and resulted in all radioactive nodes being fluorescent and vice versa. Intraoperatively, hybrid tracers were shown to outperform optical dyes. Hybrid guidance was proven to be most beneficial in more complex anatomies such as the pelvic- and head-and-neck region (NPV: 93.4-99.7%). Oncological outcome was only reported for penile and prostate cancer showing lower rates of biochemical recurrence (0.79, 95% CI 0.63-0.98) and clinical recurrence (HR 0.76, p=0.035). No tracer-related complications were reported. ***Conclusion:*** Hybrid SN tracers are safe and reliable tracers for SNB, with similar effectiveness as the current golden standard (radioactivity alone). Use of hybrid tracers is most beneficial more complex anatomies (e.g., pelvic and head-and-neck area) and shows favorable effects on oncological outcome. Recommendations for future clinical studies emphasize the need for additional oncological outcome reporting.

OP-038

Diagnostic accuracy and interrater agreement of FDG-PET/CT lymph node staging in high-risk endometrial cancer: The SENTIREC-endo study

J. Holm[1,2], *A. H. Dias*[3], *O. Gerke*[1,2], *A. Loft*[4], *K. Bouchelouche*[3,5], *M. H. Vilstrup*[6], *S. M. Bjørnholt*[7,5], *S. E. Sponholtz*[8], *K. M. Jochumsen*[8], *M. G. Hildebrandt*[1,2], *P. T. Jensen*[7,9];
[1]*Department of Nuclear Medicine, Odense University Hospital, Odense C, DENMARK,* [2]*Department of Clinical research, University of Southern Denmark,, 5230 Odense, DENMARK,* [3]*Department of Nuclear Medicine and PET-centre, Aarhus University Hospital, 8000 Aarhus, DENMARK,* [4]*Department of Clinical Physiology and Nuclear Medicine, Copenhagen University Hospital, Copenhagen, DENMARK,* [5]*Department of Clinical Medicine, Aarhus University, 8000 Aarhus, DENMARK,* [6]*Department of Radiology and Nuclear Medicine, Esbjerg and Grindsted Hospitals, University of Southern Denmark, 6705 Esbjerg, DENMARK,* [7]*Department of Gynecology and Obstetrics, Aarhus University Hospital, Aarhus, DENMARK,* [8]*Department of Gynecology and Obstetrics, Odense University Hospital, 5000 Odense, DENMARK,* [9]*Department of Clinical Medicine, Aarhus University, 8200 Aarhus, DENMARK.*

Aim/Introduction: The SENTIREC-endo study established a safe algorithm combining sentinel lymph node mapping with PET-positive node dissection, achieving results comparable to lymphadenectomy in patients with high-risk endometrial cancer (EC) [1]. This study further evaluates the diagnostic accuracy of [18F]FDG-PET/CT alone for lymph node staging and examines interrater agreement across three Danish centers. ***Materials and Methods:*** This prospective multicenter study included women with high-risk endometrial cancer from the Danish SENTIREC study database (2019-2023). All patients underwent preoperative FDG-PET/CT, with pathology-confirmed results and postoperative clinical information serving as the reference standard. The primary outcome was the diagnostic accuracy FDG-PET/CT, assessed by location, size, and standardized uptake value (SUV). The secondary outcome was interrater agreement between readers at three Danish hospitals. Lymph nodes detected on FDG-PET/CT were classified as 'test-negative' or 'test-positive' for metastasis, with an 'equivocal' category included for interrater agreement evaluations. Readers were blinded to each other and to the reference standard. ***Results:*** Among 227 patients with high-risk endometrial cancer, 52 women (23 %) had lymph node metastasis. FDG-PET/CT diagnosed lymph node metastases with a sensitivity of 56% (CI 95%: 42-68) , specificity of 91% (CI 95%: 86-94) and positive and negative predictive values of 64% (CI 95%: 50-77) and 87% (CI 95%: 82-91), respectively. Sensitivity of paraaortic nodes remained low (56%), while specificity was very high (97%). Lymph node size and SUVmax showed moderate diagnostic value (AUC-ROC ~0.7), limiting their clinical applicability for cutoff determination. Interrater agreement for lymph node classification as 'benign', 'malignant', or 'equivocal' was 95% wich is almost perfect ($\kappa = 0.84$, CI 95%: 0.73-0.94). ***Conclusion:*** FDG-PET/CT demonstrated high specificity but limited sensitivity in staging lymph node metastasis in high-risk endometrial cancer, consistent with previous studies. Due to its excellent specificity and high interrater reliability, FDG-PET/CT is valuable when combined with the highly sensitive sentinel lymph node biopsy for targeted dissection of PET-positive lymph nodes, particularly identifying malignant lymph nodes in the paraaortic region. ***References:*** 1. Bjørnholt, S.M., et al., Identifying safe diagnostic algorithms for sentinel lymph node mapping in high-risk endometrial cancer: The SENTIREC-endo study. Gynecol Oncol, 2024. 182: p. 179-187.

OP-039

Is Visceral Adipose Tissue Metabolism Linked to Aggressiveness in Endometrial Cancer?

J. Sæterstøl[1,2], *J. Lavik*[1], *L. P. Lunde*[1], *C. Krakstad*[3,4], *I. S. Haldorsen*[1,2], *K. E. Fasmer*[1];
[1]*Mohn Medical Imaging and Visualization Centre, Department of Radiology, Haukeland University Hospital, Bergen, NORWAY,* [2]*Department of Clinical Medicine, University of Bergen, Bergen, NORWAY,* [3]*Department of Obstetrics and Gynaecology, Haukeland University Hospital, Bergen, NORWAY,* [4]*Centre for Cancer Biomarkers, Department of Clinical Science, University of Bergen, Bergen, NORWAY.*

Aim/Introduction: Obesity is a well-established risk factor for endometrial cancer. A few studies have also linked visceral obesity to poor disease-specific survival for patients with endometrial cancer. One proposed mechanism is that visceral adipose tissue (VAT) produces cytokines, creating an inflammatory environment that promotes tumorigenesis and poor outcomes. The metabolic activity of VAT can be measured by [^{18}F]fluoro-deoxy-glucose (FDG) positron emission tomography/computed tomography (PET/CT). This study aimed to assess VAT metabolic activity in a large cohort of endometrial cancer patients, and explore whether VAT metabolic activity is related to lymph node metastases (LNM), International Federation of Gynecology and Obstetrics (FIGO) stage, and postoperative histological risk (low risk: endometrioid endometrial cancer (EEC) grade 1-2; high risk: EEC grade 3 and non-EEC). ***Materials and Methods:*** Preoperative [^{18}F]FDG PET/CT scans of 274 patients with endometrial cancer were retrospectively collected and analyzed. The patients were part of a larger prospective population-based study cohort. Metabolic activity of VAT was measured in regions of interest (ROIs) at the level of vertebra L4 on standardized uptake value (SUV) images. The ROIs were individually adjusted to avoid signal interference from adjacent organs/tissues, and confined to VAT by restricting placement to tissue with CT Hounsfield units ranging from -195 to -45. Mean and maximum SUVs in the ROI (VAT_{mean} and VAT_{max}) were recorded for all patients. To account for differences between two PET/CT systems, SUV values were harmonized with ComBat before they were assessed in relation to high-risk features using Kruskal-Wallis equality-of-populations rank test. ***Results:*** Median VAT_{mean} [95% confidence interval (CI)] was 0.26 [0.26,0.28] and the median VAT_{max} [95% CI] was 0.46 [0.44,0.49]. Mean (standard deviation) ROI size was 5.4 (3.8) cm^2. Patients with histologically verified LNM (n=24) had a higher median VAT_{mean} of 0.30 [0.24,0.37] compared to patients verified with no LNM (0.26 [0.25,0.27], p=0.03) (n=123). Similarly, patients with advanced FIGO stage (3-4) (n=47) had a higher median VAT_{mean} of 0.29 [0.25,0.36] compared to patients with low FIGO stage (1-2) (n=227) (VAT_{mean}: 0.26 [0.25,0.27], p=0.03). The VAT_{mean} was not significantly different for high-risk versus low-risk postoperative histology, and VAT_{max} showed no significant associations to LNM, advanced FIGO stage or high-risk histology. ***Conclusion:*** Median VAT_{mean} was higher in patients with LNM and advanced FIGO stage than in patients with no LNM and lower FIGO stage. However, future studies are needed to explore the underlying biological mechanisms linking VAT metabolic activity to aggressive endometrial cancer disease.

OP-040

Prediction of Treatment Response Using PET-CT Radiomics Features in Patients Undergoing Radical Chemoradiotherapy with a Diagnosis of Cervical Cancer

O. Senmevsim[1], *B. Kocabas*[1], *I. F. Ozsarikaya*[2], *S. Butuner*[3], *B. Erol*[4], *Z. Guzeloz*[1];
[1]*Izmir City Hospital, Izmir, TÜRKIYE,* [2]*Ministry of Health Tepecik Training and Research Hospital, Izmir, TÜRKIYE,* [3]*Beykent University, Department of Software Engineering, Istanbul, TÜRKIYE,* [4]*Beykent University, Istanbul, TÜRKIYE.*

Aim/Introduction: There has been an increasing interest in "Radiomics" assessment, which is based on the extraction and analysis of quantitative features from medical images (1-3). Texture features are extracted from statistical matrices based on density spatial distribution relationships and reflect the FDG distribution, and therefore the heterogenity of the tumor (4).In this study, we aimed to develop a classification model that can predict treatment response with FDG/PET-CT radiomics assessment in patients undergoing treatment with a diagnosis of cervical cancer. ***Materials and Methods:*** The study included 62 patients, whose staging and response evaluation FDG/PET-CTs were performed on the same device. These patients underwent brachytherapy after chemoradiotherapy. Complete response was defined as the SUV max value of the tumor or metastatic lymph nodes/node regressing to background activity. Using the staging and response evaluation FDG/PET-CT, the primary tumor and the metastatic lymph node with the highest SUV uptake were manually segmented using LIFEx (Local Image Features Extraction version 7.6.0) software, and ROIs were obtained. Six different machine learning algorithms were developed and their performances were evaluated for the classification problem: decision tree (DT), random forest (RF), k-nearest neighbor (KNN), bagged KNN, support vector machines (SVM), and artificial neural networks (ANN). Performance evaluation was carried out using metrics such as accuracy, precision, recall, F1-score, and area under the curve (AUC). ***Results:*** The median age was 52 (34-78). 41.9% of the patients (n=26) were Stage 1.The most common histology was SCC, at 90.3% (n=58). 56.5% of the patients (n=35) were evaluated as having a complete response, and 43.5% (n=27) as having no complete response. According to the results obtained, the random forest (RF) algorithm showed the highest performance in all metrics (Accuracy: 0.89, Precision: 0.87, Recall: 0.94, F1-Score: 0.89, AUC: 0.96). The RF algorithm was followed by DT and SVM methods. ***Conclusion:*** Our study has revealed the usability of radiomics features in the classification for predicting treatment response in inoperable cervical cancer. ***References:*** 1- Lambin P, Leijenaar RTH, Deist TM, et al. Radiomics: the bridge between medical imaging and personalized medicine. Nat Rev Clin Oncol. 2017;14:749-762. 2- Hatt M, Le Rest CC, Tixier F, Badic B, Schick U, Visvikis D. Radiomics: data are also images. J Nucl Med. 2019;60(suppl 2):38S-44S.3- Mayerhoefer ME, Materka A, Langs G,et al. Introduction to radiomics. J Nucl Med.2020;61:488-495. 4- Zwanenburg A, Vallieres M, Abdalah MA, et al. The image biomarker standardization initiative: standardized quantitative radiomics for high-throughput image based phenotyping. Radiology.2020;295:328-338

OP-041

FDG-PET/CT response assessment is predictive of survival and recurrence in locally advanced cervical cancer

M. Markus[1], *H. Sartor*[2], *M. Bjurberg*[3], *D. Minarik*[4], *E. Trägårdh*[1];
[1]*Clinical Physiology and Nuclear Medicine, Skåne University Hospital, Malmö, SWEDEN,* [2]*Diagnostic Radiology, Department of Translational Medicine, Lund University, Skåne University Hospital, Lund, SWEDEN,* [3]*Department of Hematology, Oncology and radiation Physics, Skåne University Hospital, Lund, SWEDEN,* [4]*Radiation Physics, Department of Hematology, Oncology and Radiation Physics, Skåne University Hospital, Lund, SWEDEN.*

Aim/Introduction: [18F]-fluorodeoxyglucose (FDG) positron emission tomography with computed tomography (PET-CT) is routinely performed in patients with advanced cervical cancer for staging and evaluation of treatment response. The maximum standardised uptake value (SUVmax) is the most used PET parameter in clinical routine but more advanced metabolic parameters (e.g metabolic tumour volume (MTV) and total lesion glycolysis (TLG)) may better predict survival. This study investigates the prognostic significance of SUVmax, MTV, and TLG in assessing treatment response, using overall survival (OS) and

local recurrence as outcome measures. ***Materials and Methods:*** This study included women with locally advanced cervical cancer who were referred for radiochemotherapy between 2011 and 2019 and underwent PET-CT scans at baseline and at a 6-month follow-up post-treatment. Treatment response on PET-CT was evaluated according to the European Organization for Research and Treatment of Cancer (EORTC) criteria, comparing SUVmax, MTV, and TLG. Response outcomes were categorized as complete metabolic response (CMR), progressive metabolic disease (PMD), partial metabolic regression (PMR), or stable disease (SD). These outcomes were correlated with OS and recurrence using regression analysis, and the predictive potential of the different measures was visualized using the C-index. ***Results:*** A total of 133 patients were included in the study. Age- and clinical stage-adjusted analyses revealed a statistically significant association ($p<0.001$) between treatment response and OS for SUVmax (hazard ratio [HR] 16 for PMD, 4.0 for PMR/SD), MTV (HR 16 for PMD, 2.9 for PMR/SD), and TLG (HR 16 for PMD, 2.9 for PMR/SD), with CMR as the reference. Additionally, C-index values from adjusted Cox models were comparable between the PET parameters (SUVmax 0.84, MTV and TLG 0.86). Logistic regression for recurrent disease based on treatment response showed a statistically significant association ($p<0.001$) for all PET parameters, with similar results across the parameters. ***Conclusion:*** Treatment response evaluation using FDG-PET/CT, according to the EORTC criteria, is predictive of OS and local recurrence in patients with advanced cervical cancer. The prognostic value was similar for SUVmax, MTV, and TLG.

OP-042

Avidination for Radionuclide THerapy (ARTHE) in nonpalpable breast cancer. Phase I IRST "Dino Amadori-IRCSS' trial"

M. Sansovini[1], *P. Sanna*[2], *P. Possanzini*[2], *I. Grassi*[1], *P. Caroli*[1], *M. Amadori*[2], *I. Marini*[1], *S. Nicolini*[1], *M. Belli*[1], *L. Fabbri*[1], *E. Scarpi*[1], *A. Curcio*[2], *R. Ciani*[2], *V. Mautone*[1], *V. Di Iorio*[1], *M. Monti*[1], *A. Sarnelli*[1], *A. Miserocchi*[1], *O. Nanni*[1], *M. Costantini*[2], *G. Paganelli*[3], *F. Falcini*[2], *F. Matteucci*[1];
[1]*IRST, Meldola (Fc), ITALY,* [2]*AUSL della Romagna, Forlì, ITALY,* [3]*IOR Istituto Oncologico Romagnolo, Forlì, ITALY.*

Aim/Introduction: Non-palpable breast lesions account for ~30% of breast tumours requiring surgery. Vacuum assisted breast biopsy (VABB) can only completely remove 10-30% of small lesions. Our phase I trial proposes targeted radionuclide therapy after VABB using a biotin-DOTA-90Y compound delivered into the biopsy cavity. The idea is to irradiate and destroy residual microscopic tumour cells in situ. ***Materials and Methods:*** Up to 52 pts were enrolled in Part 1 (18 in dose-escalation phase) and Part 2 (44 in dose expansion). Pts were divided into 6 cohorts in Part 1 to establish biotin-DOTA-^90Y's DLT and MAD. The ARTHE procedure consists of an ultrasound-guided injection of avidin into the breast tissue at the VABB site, followed immediately by an injection of biotin-DOTA-90Y. Avidin dose: 6-10 mg in a volume of 0.3-0.5 mL. Biotin-DOTA-90Y dose: 28-126 MBq (0.2-0.3 mL), with a specific activity of 3.7 GBq/mg. According to worldwide and national norms, pts underwent surgery 4 to7 weeks after ARTHE therapy. ***Results:*** From July 2024 to January 2025, 18 pts underwent VABB for the presence of breast carcinoma with a median size of 10 mm. Histological diagnosis showed ductal carcinoma in situ in 6 pts (33.3%), invasive ductal carcinoma in 1 pts (5.6%), invasive carcinoma of no special type in 5 pts (27.8%) and other hystotypes in 6 pts (33.3%). In Part 1, pts were divided into 3 cohorts of 6 pts each and treated with dose of 90Y-biotin of 28 MBq (dose A), 57MBq (dose B) and 126 MBq (dose C), respectively. Within 1 month after ARTHE, all pts underwent quadrantectomy. Postoperative histological examination showed pCR in 5 pts (27.8%) and persistence of disease in the remaining 13 pts. There were no haematological toxicities or major acute skin toxicities (>G3) at the inoculation site. Grade 1 adverse reactions were reported, consisting of pain (22.2%), erythema (11.1%) and skin toxicity/redness in 1 patient in dose group B (5.5%). ***Conclusion:*** ARTHE may be an interesting nuclear medicine approach as it has proven to be a rapid, minimally invasive procedure with no major side effects. The evaluation of its antitumour activity is in progress and further studies on larger cohorts will be necessary to assess its impact on the management of breast cancer, especially in elderly women with comorbidities that do not recommend a surgical approach ***References:*** Paganelli G, et al. Eur J Nucl.Med mol Imaging.2010; 37: 203-11

OP-043

Combined External Beam Radiation Therapy and Peptide Receptor Radionuclide Therapy in Progressive Meningiomas: A Retrospective Analysis of Feasibility, Safety, and Prognostic Factors

N. Hasenauer[1], *M. Müller*[1], *R. Sweeney*[2], *B. Polat*[3], *H. Hänscheid*[1], *R. A. Werner*[4], *M. Heinrich*[1], *A. K. Buck*[1], *P. E. Hartrampf*[1];
[1]*Department of Nuclear Medicine, University Hospital Wuerzburg, Wuerzburg, GERMANY,* [2]*Department of Radiotherapy and Radiation Oncology, Leopoldina Hospital Schweinfurt, Schweinfurt, GERMANY,* [3]*Department of Radiation Oncology, University Hospital Wuerzburg, Wuerzburg, GERMANY,* [4]*Department of Nuclear Medicine, University Hospital Ludwig-Maximilians-Universitaet Muenchen, Muenchen, GERMANY.*

Aim/Introduction: In patients with irresectable meningiomas, external beam radiation therapy (EBRT) may be limited by the safely deliverable dose, particularly in cases involving multiple lesions or tumors adjacent to critical structures. Combining EBRT with somatostatin receptor (SSTR)-targeted peptide receptor radionuclide therapy (PRRT) may offer a strategy to intensify treatment. The aim of this study was to evaluate the feasibility, safety, and prognostic factors of this combined approach. ***Materials and Methods:*** This monocentric retrospective study analysed 75 patients who received combined standard EBRT and PRRT within a 30-day interval. Baseline clinical, laboratory, and PET-derived parameters (SUVmean, SUVmax, SUVpeak, and SSTR-positive tumor volume) were evaluated for their prognostic value regarding progression-free survival (PFS) using Cox regression models. PFS and OS were estimated using Kaplan-Meier analysis. Toxicity was assessed according to CTCAE v5.0, and clinical follow-up data were reviewed for treatment-related adverse events and subjective outcomes. ***Results:*** After a median follow-up of 57 months, 25/75 patients experienced disease progression, and 17 died. Both, median PFS and median OS had not been reached. Patients with WHO grade I meningioma showed longer PFS (NR) compared with grade II (38 months, HR 5.4, $p<0.01$) and grade III tumors (15.5 months, HR 15.1, $p<0.01$). On univariable analysis, higher WHO grade (HR 4.7, $p<0.01$) as well as elevated baseline levels of C-reactive protein (HR 2.2, $p<0.01$), lactate dehydrogenase (per 100, HR 1.5, $p<0.05$), creatinine (per 0.1, HR 1.3, $p<0.05$), and alkaline phosphatase (per 10, HR 1.5, $p<0.05$) were associated with shorter PFS. In multivariable analysis, WHO tumor grade remained an independent prognostic factor (HR 4.7, $p<0.01$). No associations were found between PET parameters and PFS. Lesion dosimetry after PRRT was available in 37 cases; estimated doses did not differ between patients who received PRRT before versus after EBRT ($P=0.5$). PFS did not significantly differ between patients with solitary versus multifocal meningiomas (HR 0.84, $p=0.7$), nor between patients treated with reduced (<54 Gy) versus standard-dose EBRT (≥54 Gy). 13 patients developed mild (CTCAE I-II) hematologic or renal toxicities. Among 58 patients with available clinical follow-up data, 18 worsened, mainly involving concentration difficulties and fatigue. 44 reported stable or improved well-being. ***Conclusion:*** Combined EBRT and PRRT represents a feasible and well-tolerated treatment option for patients with progressive meningiomas, potentially enabling dose intensification in complex cases. WHO tumor grade is the strongest predictor of PFS, while baseline PET parameters showed no prognostic value.

207

Sunday, October 5, 2025, 8:00 - 9:30
Room 212

TROP Session - Neuroimaging Committee: Movement Disorders

OP-044

Clinical value of ^{18}F-PI-2620 Tau-PET in the diagnostic workup of patients with suspected Progressive Supranuclear Palsy

M. Brendel[1], *C. Palleis*[1], *N. Franzmeier*[1], *J. Gnörich*[1], *A. Jäck*[1], *A. Bernhardt*[1], *S. Katzdobler*[1], *U. Fietzek*[1], *E. Weidinger*[1], *L. Frontzkowski*[1], *S. Roemer-Cassiano*[1], *R. Werner*[1], *A. Zwergal*[1], *H. Barthel*[2], *O. Sabri*[2], *J. Levin*[1], *G. Höglinger*[1];
[1]*LMU Hospital, Munich, GERMANY,* [2]*University of Leipzig, Leipzig, GERMANY.*

Aim/Introduction: Progressive Supranuclear Palsy (PSP) is a rapidly progressing 4-repeat tauopathy, presenting with clinically heterogeneous phenotypes. Currently, diagnoses are based solely on clinical criteria but reliable diagnostic classification remains particularly challenging at early stages. ^{18}F-PI-2620 tau-PET is an evolving neuroimaging biomarker to capture 4-repeat tau (4RT) deposits with clear diagnostic potential in research settings. To determine the added clinical value of ^{18}F-PI-2620 tau-PET in the diagnostic workup of PSP, we evaluated whether ^{18}F-PI-2620-assessed 4RT positivity (i.e. using the basal ganglia as a target readout) predicts subsequent increases of diagnostic certainty for PSP, indicative of 4RT pathology driving clinical progression. ***Materials and Methods:*** We collected monocentric longitudinal data at the LMU Hospital in Munich, from a non-randomized prospective cohort study between October 2018 and December 2024. Data collection included pre-PET visits with routine clinical classification following the Movement Disorders Society PSP criteria. Levels of certainty are graded as suggestive of, possible, probable and definite PSP. In addition, we performed ^{18}F-PI-2620 tau-PET with dichotomous visual read assessments of 4RT pathology by an expert reader and collected clinical follow-up data or autopsy information. ***Results:*** 342 patients with a pre-PET differential diagnosis of PSP were referred to ^{18}F-PI-2620 tau-PET in clinical routine. Of those, 200 patients (61.5% male, mean±sd age 69.2±8.3 years) had a post-PET clinical follow-up between 12-24 months (mean±sd 17.1±4.2 months). 90 patients were rated as suggestive of PSP, 49 as possible PSP and 61 as probable PSP. The two most common differential diagnoses were Parkinson's Disease (39%) and Multiple Systems Atrophy (12%). 68.5% (137/200 patients) were rated 4RT-positive at baseline. The positive predictive value of a positive tau-PET read at baseline for a PSP diagnosis at follow-up visit was 98.5% (135/137 patients). Change to a non-PSP diagnosis at follow-up occurred in 23.5% (47/200 patients), identified by a negative baseline tau-PET in 95.5%. Regarding the diagnosis of suggestive of PSP, 79% of tau-PET-positive patients progressed to a higher diagnostic certainty, 3% had histopathological confirmation of PSP diagnosis, 13% remained suggestive of PSP, and 5% received a non-PSP diagnosis at follow-up. ***Conclusion:*** ^{18}F-PI-2620 tau-PET can successfully identify patients that progress along expected 4RT clinical spectra. This supports ^{18}F-PI-2620 tau-PET as a 4RT biomarker, with the potential to facilitate early biomarker-based diagnosis when clinical criteria may still lack sensitivity and specificity. This development can be transformative for clinical decision making, early identification of PSP and stratifying patients for disease modifying clinical trials.

OP-045

Patterns and their Correlations of PET Imagings with FDG, DAT and Tau in patients with Progressive Supranuclear Palsy

M. Liang[1], *C. Jia*[1], *z. Huang*[1], *T. Zhang*[2], *Q. Li*[1], *T. Yen*[3], *h. Wang*[4], *R. Cui*[1];
[1]*Department of Nuclear Medicine, Peking Union Medical College Hospital Chinese Academy of Medical Sciences and Peking Union Medical College, Beijing, CHINA,* [2]*Beijing Engineering Research Center of Radiographic Techniques and Equipment, Institute of High Energy Physics, Chinese Academy of Sciences, Beijing, CHINA,* [3]*APRINOIA Therapeutics Co, Ltd, Suzhou, CHINA,* [4]*Department of Neurology, Peking Union Medical College Hospital Chinese Academy of Medical Sciences and Peking Union Medical College, Beijing, CHINA.*

Aim/Introduction: The latest diagnostic criteria for Progressive Supranuclear Palsy (PSP) highlight the supportive roles of various PET imaging methods in improving diagnostic accuracy, such as 18F-Fluorodeoxyglucose(18F-FDG), 18F-FP-CIT and Florzolotau(18F) PET. In this study, we simultaneously analyzed the patterns of 18F-FDG, 18F-FP-CIT and Florzolotau(18F) PET imaging and their correlations in a cohort of PSP patients, trying to investigate the interplay between these pathological processes. ***Materials and Methods:*** Twenty-eight patients clinically diagnosed with PSP underwent ^{18}F-FDG, ^{18}F-FP-CIT and Florzolotau(^{18}F) PET examinations, and imaging data were analyzed using voxel-based and region-of-interest (ROI) methods. Standardized uptake value ratios (SUVRs) were compared with age-matched healthy controls, and inter-tracer correlations were assessed. ***Results:*** PSP patients demonstrated elevated Florzolotau(^{18}F) uptake in the thalamus, midbrain, pons, and precentral gyrus. Glucose hypometabolism was prominent in the frontal and parietal lobes, cerebellum, midbrain, medulla, caudate, and thalamus. ^{18}F-FP-CIT PET revealed reduced striatal and midbrain DAT availability. A weak negative correlation was observed between Florzolotau(^{18}F) and ^{18}F-FDG SUVRs in the midbrain (r=-0.39, p=0.04), but no association was found in the frontal cortex (r=0.04, p=0.85). Notably, frontal hypometabolism correlated with hypometabolism in subcortical structures including the thalamus, caudate, pons, and midbrain. Only a moderate negative correlation between ^{18}F-FP-CIT and Florzolotau(^{18}F) SUVRs in the left putamen was observed(r =-0.42, p = 0.03). ***Conclusion:*** The study reveals distinct spatial patterns of tau pathology, metabolism, and dopaminergic degeneration in PSP. The inverse correlation between midbrain tau burden and metabolism suggests region-specific interactions in brainstem regions, while the lack of correlations between tau and metabolism in the frontal cortex, as well as between tau and dopamine transporter (DAT) levels in most regions, points to divergent pathogenic mechanisms across cortical and subcortical areas. These findings highlight the complex, multifactorial nature of PSP pathophysiology, with tau accumulation, metabolic dysfunction, and dopaminergic decline exhibiting region-specific relationships.

OP-046

Association between tau-burden and eye movement disorders in progressive supranuclear palsy

M. Zaganjori[1], *J. Gnörich*[1], *S. Katzdobler*[2], *L. Frontzkowski*[3], *U. Fietzek*[2], *G. Nübling*[2], *J. Levin*[2], *N. Franzmeier*[4], *G. Höglinger*[2], *R. Werner*[1], *M. Brendel*[1], *A. Zwergal*[2];
[1]*Department of Nuclear Medicine, University Hospital, LMU Munich, Munich, GERMANY,* [2]*Department of Neurology, University Hospital, LMU Munich, Munich, GERMANY,* [3]*Institute for Stroke and Dementia Research (ISD), University Hospital, LMU Munich, Munich, Germany, Munich, GERMANY,* [4]*Institute for Stroke and Dementia Research (ISD), University Hospital, LMU Munich, Munich, GERMANY.*

Aim/Introduction: Progressive supranuclear palsy (PSP) is a severe neurodegenerative disorder pertaining to 4R-tau aggregation. PSP can present as different clinical phenotypes including the classical PSP-Richardson Syndrome (RS) type, which is characterized by predominant supranuclear saccadic impairment. Assessing the extent to which tau pathology influences the manifestation of saccadic and other eye movement abnormalities could be crucial to better understanding the pathomechanisms of PSP. In this study, we aimed to explore regional associations between tau burden and differential ocular motor phenotypes in PSP. ***Materials and Methods:*** We included 44 patients with a suspected or probable PSP diagnosis according to current MDS-criteria, of which 28 had PSP-RS. Patients underwent dynamic 60 minute 18-F-PI-2620 tau-PET and a comprehensive video-oculographic ocular motor examination within an interval of 12 months. Distribution volume ratios (DVR) of tau aggregation and perfusion surrogates (R1) were computed for all regions of the brainnetome atlas. Whole brain voxel-wise analysis and region-of-interest-based analysis corrected for age and sex were performed to test for associations between tau burden or perfusion deficits and different eye movement parameters (esp. saccade velocity and latency, smooth pursuit gain, respectively for the vertical and horizontal axis). ***Results: Results:*** Voxel-wise analysis showed that increased tau-PET DVR correlated significantly with decreased saccadic velocity, particularly in the horizontal axis, in the pontomesencephalic brainstem tegmentum (r: -0.4, p< 0.05) and frontal cortex (r: -0.33, p< 0.05), whereas basal ganglia tau-PET DVR did not correlate significantly with saccadic velocity (r: -0.27, p=0.08). Higher mean saccadic latency correlated significantly with increased tau-PET DVR in the temporal (r: 0.38, p<0.05) and occipital cortex (r: 0.31, p<0.05), whereas smooth pursuit did not show any associations. There was no significant association between brain perfusion and saccadic velocity. ***Conclusion:*** Our findings suggest that tau burden in in the pontomesencephalic brainstem tegmentum and frontal cortex has an impact on saccadic phenotypes in PSP.

OP-047

DAT-SPECT profiling for biological definition of two prospective Parkinson's disease cohorts

S. Caminiti[1], *R. Malito*[2], *C. Meneghini*[1], *A. Galli*[3], *P. Mitrotti*[1], *M. Inglese*[4], *C. Zatti*[3], *A. Lupini*[3], *A. Pilotto*[3], *A. Padovani*[3], *M. Avenali*[1], *E. Valente*[1], *C. Tassorelli*[1];
[1]*University of Pavia, Pavia, ITALY,* [2]*IRCCS San Raffaele Hospital, Milan, ITALY,* [3]*University of Brescia, Brescia, ITALY,* [4]*University of Rome Tor Vergata, Rome, ITALY.*

Aim/Introduction: There is a need for simplified classification systems capable of effectively stratifying Parkinson's disease (PD) in routine clinical practice. Objectives: Identification of PD subtypes integrating neuroimaging and clinical features, widely used to support clinical diagnosis. ***Materials and Methods:*** We included, from Parkinson's Progression Markers Initiative (PPMI), n=249 de novo early diagnosed PD patients. Two step clustering analysis was run on 123I-FP-CIT-SPECT striatal uptake [D+/D] and motor impairment [M+/M]. The emerging subgroups were evaluated for demographic, clinical, cerebrospinal fluid biomarkers, brain morphometry and longitudinal clinical progression. Mediation analysis evaluated the effect of biomarkers on the relationship between subgroups and cognitive decline. We validated the proposed classification algorithm through an independent validation cohort (n=84). ***Results:*** Four distinct subtypes emerged: [D+/M+]: poorer memory performance, greater Aβ1-42 and α-synuclein pathology and atrophy in the inferior temporo-occipital cortex. At follow-up D+/M+ showed faster progression of motor disability, motor complications and cognitive decline. [D/M]: higher levels of anxiety and gray matter volume reductions in the precuneus, fusiform gyrus and the precentral gyrus. [D/M+]: marked by pronounced rigidity and apathy, atrophy in motor and sensorimotor areas, and a more rapid progression of rigidity. [D+/M]: severe impulsiveness, lower working memory performance and thalamic atrophy. Aβ1-42 showed significant mediational effect on the relationship between D+/M+ and cognitive decline. The validation cohort supported the clinical findings observed in the PPMI cohort. ***Conclusion:*** PD can be categorized into distinct subgroups using information widely available in clinical and research settings. These data offer valuable insights into the underlying co-pathology, disease progression and severity.

OP-048

Dopamine Loss in Putamen and Caudate Drives Distinct Motor and Cognitive Symptoms in Parkinson's Disease Progression

V. Dzialas[1,2], *K. Giehl*[1,3], *G. N. Bischof*[1,3,4], *A. Ophey*[5], *K. Möllenhoff*[6], *A. Drzezga*[1,3,7], *T. van Eimeren*[1,8];
[1]*Nuclear Medicine, Faculty of Medicine, University Hospital and University of Cologne, Cologne, GERMANY,* [2]*Faculty of Mathematics and Natural Sciences, University of Cologne, Cologne, GERMANY,* [3]*Molecular Organization of the Brain, Institute for Neuroscience and Medicine II, Research Centre Juelich, Juelich, GERMANY,* [4]*Life Molecular Imaging GmbH, Berlin, GERMANY,* [5]*Department of Medical Psychology | Neuropsychology and Gender Studies, Center for Neuropsychological Diagnostics and Intervention (CeNDI), Faculty of Medicine, University Hospital and University of Cologne, Cologne, GERMANY,* [6]*Institute of Medical Statistics and Computational Biology (IMSB), Faculty of Medicine, University of Cologne, Cologne, GERMANY,* [7]*German Centre for Neurodegenerative Diseases, Bonn, GERMANY,* [8]*Department of Neurology, Faculty of Medicine, University Hospital and University of Cologne, Cologne, GERMANY.*

Aim/Introduction: Imaging biomarkers for motor and cognitive progression in Parkinson's disease (PD) remain limited. While the putamen has been associated with motor dysfunction and the caudate nucleus with cognitive impairment, longitudinal studies validating the relationship between dopamine transporter (DaT) decline and symptom progression are scarce. We recently showed that putaminal DaT decline may track motor progression in early PD[1]. However, comparable imaging markers for cognitive decline are lacking. Considering the dual syndrome hypothesis[2], two distinct mechanisms contribute to cognitive impairment in PD: fronto-striatal dopaminergic loss leading to executive dysfunction, and posterior cholinergic degeneration underlying memory and visuospatial deficits. We examined and compared caudate and putamen DaT signal loss as potential longitudinal biomarkers of cognitive decline, particularly in executive functions. ***Materials and Methods:*** We analysed 5-year follow-up data from early-stage PD patients (diagnosis<2 years) enrolled in the Parkinson's Progression Markers Initiative, including scores from nine cognitive tests: Clock Drawing (CDT), Lexical Fluency (FAS), Hopkins Verbal Learning-Revised (HVLT-R), Judgment of Line Orientation (JLO), Letter-Number Sequencing (LNS), Modified Boston Naming (mBNT), Symbol Digit Modalities (SDMT), Semantic Fluency (SE), and Trail Making-A (TMT-A). Based on the dual syndrome hypothesis[2] and PD-MCI criteria[3], we classified LNS, SDMT, SE, TMT-A, and FAS as primarily executive and CDT, JLO, mBNT, and HVLT-R as memory/visuospatial tests. Using linear mixed-effects models, we tested whether cognitive decline was associated with progressive DaT loss in the caudate or putamen, captured by the time×DaT interaction. We hypothesized significant effects only for caudate DaT and executive tests. ***Results:*** 783 participants (~62% male; 62±9 years, MoCA: 27±3) contributed 2148 data points, with 49 patients classified as having mild cognitive impairment at baseline based on expert clinical assessment. Significant interactions (pone-sided<.05) were found between declining caudate DaT signal and worsening performance in LNS, SDMT, SE,

TMT-A, and HVLT-R (Table 1). No such associations were observed for putaminal DaT signals. ***Conclusion:*** audate DaT loss emerged as a promising marker for cognitive decline in PD, particularly in executive functions. Our results mainly aligned with assumptions derived from the dual syndrome hypothesis, while findings for FAS and HVLT-R did not align. This may reflect strong engagement of executive (for HVLT-R) and language/memory functions (for FAS), as also controversially discussed in the literature. Importantly, while cognitive progression was associated exclusively with DaT loss in the caudate, motor symptom progression was linked solely to putamen degeneration—supporting a functional dissociation between striatal subregions in PD. ***References:*** 1)doi:10.1002/ana.27223, 2)doi:10.1159/000341998, 3)doi:10.1002/mds.24893

OP-049

Validation of a 360° CZT-SPECT Normal Database for [123I]-FP-CIT SPECT/CT Imaging

P. Schaefer[1], *M. Doyen*[1], *A. El-Barkaoui*[2], *A. Flaus*[2], *L. Imbert*[1], *A. Verger*[1];
[1]*Nancy University Hospital of Lorraine, Nancy, FRANCE,* [2]*Hospices Civils de Lyon (Lyon University Hospital), Lyon, FRANCE.*

Aim/Introduction: Three-hundred-sixty-degree CZT SPECT cameras provide superior image quality for [123]-FP-CIT SPECT/CT imaging compared to conventional systems, enabling reduced radiotracer doses and acquisition times. However, currently available quantification software still relies on normal databases derived from conventional cameras. This study aimed to validate a locally developed normal database for [123I]-FP-CIT SPECT/CT imaging acquired using a 360° CZT-SPECT system. ***Materials and Methods:*** Patients who underwent [123I]-FP-CIT SPECT/CT imaging using a 360° CZT-SPECT camera (injected dose: 130 MBq; acquisition time: 15 minutes) for suspected Parkinson's disease (PD), and who were clinically classified as either normal or having PD based on follow-up of at least two years post-scan, were included. This CZT-derived normal database was compared with a previously validated database acquired using a conventional SPECT/CT camera (injected dose: 185 MBq; acquisition time: 30 minutes). Specific binding ratios (SBRs) for the striatum and putamen were extracted following CT-based spatial normalization. General linear models (GLMs) were used to assess the effects of age, sex, and age-sex interaction on striatal SBRs in both databases. Additionally, patients with clinically confirmed PD were analyzed for diagnostic performance using semi-quantification with both databases. Sensitivity, specificity, and accuracy were calculated for minimal putaminal SBRs, using cross-validation and optimal thresholds from ROC curve analysis. ***Results:*** The CZT database included 139 patients (mean age 70.1±11.6 years, 77 women), and the conventional database, 233 patients (mean age 62.6±15.8 years, 115 women). Additionally, 107 PD patients (mean age 69.6±9.6 years, 45 women) were included for diagnostic evaluation. GLMs identified a significant effect of age ($p \leq 0.01$) on striatal SBRs in both databases, with no significant effect of sex or age-sex interaction. Age-related decline in SBR was estimated at -7.1% per decade for the CZT database and -4.9% for the conventional one. After age correction, both databases showed low standard deviations and coefficients of variation (CZT: 0.0079 and 0.0021; conventional: 0.0139 and 0.0028). For semi-quantification, the CZT database yielded 76% sensitivity, 84% specificity, and 81% accuracy, compared to 92%, 52%, and 69%, respectively, for the conventional database. ***Conclusion:*** This study presents the first validated normal database for [123I]-FP-CIT SPECT/CT imaging using a 360° CZT-SPECT system. The age-related effects and dispersion were consistent with those observed in a validated conventional database. Importantly, semi-quantification using the CZT-derived database demonstrated superior diagnostic performance in identifying PD, supporting its integration into routine clinical practice for patients imaged with CZT systems.

OP-050

Brain Metabolic Contribution in CANVAS

S. Naranjo Sancho*, C. Vigil Díaz, A. Álvarez Alonso, D. Santirso Rodríguez, G. Morís de la Tassa, J. Álvarez Carriles, M. Álvarez Martínez, A. Álvarez Amigo, J. Guzmán de la Cerda, F. González García;*
Central University Hospital of Asturias, Oviedo, SPAIN.

Aim/Introduction: Cerebellar ataxia, neuropathy and vestibular areflexia syndrome (CANVAS) is a late-onset progressive disorder primarily caused by a recessive expansion in the replication factor C subunit 1 (RFC1) gene. In addition to the classical pathological triad of cerebral atrophy, bilateral vestibular hypofunction and somatosensory impairment, CANVAS frecuently presents with other clinical features, such as autonomic dysfunction or cronic cough. As the condition becomes increasingly recognized, its clinical phenotype continues to expand. Recent studies suggest that cognitive impairment—particularly affecting executive function, language, visuospatial cognition, and emotional-affective regulation—may also be part of the spectrum. ***Materials and Methods:*** We studied 37 patients (24 females, 13 males), aged between 46 and 81 years, with genetically confirmed RFC1 mutation, aiming to evaluate brain metabolic compromise and the potential prevalence of cognitive impairment in this population. All participants underwent a 18F-fluorodeoxyglucose PET/CT (FDG-PET), with both visual and quantitative assessment of the presence, distribution and severity of hypometabolism in the cerebral and cerebellar cortex. Clinical examination findings were compared with the FDG-PET results. ***Results:*** In our series, cerebellar hypometabolism was observed in 67.6% of cases (25/37): severe in 21.6% (8/37), moderate in 16.2% (6/37), and mild in 29.7% (11/37). Vermis involvement was found in 43.2% of patients (16/37), with 37.5% of these (6/16) showing severe hypometabolism and 62.5% (10/16) presenting with mild to moderate changes. Pontine hypometabolism was detected in 43.2% of patients (16/37), most commonly at a moderate level (56.3%, 9/16). Gait disturbances were identified in 31/37 patients and were significantly associated with cerebellar hypometabolism ($p<0.05$). Additionally, cerebral hypometabolism—mainly affecting the medial and/or lateral prefrontal cortex—was observed in 59.5% (22/37), although cognitive decline was identified in only one patient. ***Conclusion:*** FDG PET has proven to be a valuable tool in the evaluation of the cerebellar involvement in CANVAS both visually and quantitatively. Our preliminary findings reveal a consistent pattern of cerebellar hypometabolism associated with the presence of gait disorders in patients with CANVAS. However, significant cognitive decline was not evident in this cohort, despite the prevalence of cerebral hypometabolism. Continued follow-up and the integration of molecular neuroimaging and neuropsychological evaluation are essential to further characterize the clinical phenotype and optimize patient management.

OP-051

In vivo measurement of P-glycoprotein function in the brain and gut of patients with Parkinson's disease: a preliminary [^{18}F]MC225 PET study

G. Salvi de Souza[1,2], *W. Liu*[2], *J. F. Somsen*[2], *P. Mossel*[2,3], *N. A. Verwey*[4], *A. L. Bartels*[5], *S. K. Meles*[6], *C. R. Furini*[1,7], *R. A. Dierckx*[2], *A. A. Lammertsma*[2], *C. Tsoumpas*[2], *G. Luurtsema*[2];
[1]*PUCRS, Porto Alegre, BRAZIL,* [2]*Department of Nuclear Medicine and Molecular Imaging, University of Groningen, University Medical Center Groningen, Groningen, NETHERLANDS,* [3]*Department of Radiology, Leiden University Medical Center,, Leiden, NETHERLANDS,* [4]*Memory clinic, Department of Neurology, Medisch Centrum Leeuwarden, Leeuwarden, NETHERLANDS,* [5]*Department of Neurology, Ommelander Ziekenhuis Groep, Scheemda, NETHERLANDS,* [6]*Department of Neurology, University of Groningen, University Medical Center Groningen, Groningen, NETHERLANDS,* [7]*Laboratory of Cognition and Memory Neurobiology, Brain Institute, PUCRS, Porto Alegre, BRAZIL.*

Aim/Introduction: Parkinson's disease (PD) is a neurodegenerative disorder involving α-synuclein aggregation, neuroinflammation, and blood-brain barrier (BBB) dysfunction. P-glycoprotein (P-gp), an efflux transporter at the BBB, is involved in the clearance of neurotoxins, and reduced P-gp function may contribute to toxin accumulation in the brain[1]. P-gp is also present in the intestines, where it maintains barrier integrity and interacts with the gut microbiota. This study aims to assess P-gp function at the BBB and in the small intestines of PD patients compared to healthy volunteers (HV), using [^{18}F]MC225 positron emission tomography (PET) imaging. ***Materials and Methods:*** Seven HV and four PD subjects underwent 60-min dynamic PET scans using a long axial field of view PET/CT scanner. Five arterial manual blood samples were collected during the scan to estimate plasma-to-whole blood ratios and plasma parent fractions. Brain tissue time-activity curves were extracted using the Hammers maximum-probability atlas. A two-tissue compartment model was used to estimate the brain's volume of distribution (V_T). Parametric Logan V_T images were generated, and V_T values were extracted for the small intestines. ***Results:*** No significant differences were observed between the HV and PD groups in whole blood arterial concentrations or plasma parent fractions. Whole brain V_T values (white and grey matter) showed no significant differences between PD and HV groups. However, regional differences emerged: increases in V_T in the brainstem (14.6%) and pallidum (12.7%) in PD patients suggest potential P-gp alterations in these regions. In contrast, decreases in V_T in the caudate nucleus (-17.9%), ventricles (-29.5%), and corpus callosum (-17.6%) indicate potential reductions in P-gp function. These findings are particularly relevant as the brainstem, pallidum, and caudate nucleus are closely linked with motor control and cognitive functions affected in PD[2]. In the small intestine, mean V_T was 40.7% lower in PD, though not statistically significant. High intersubject variability was observed, and one PD subject with long disease duration showed markedly lower V_T. ***Conclusion:*** Our findings show no significant differences in P-gp function in the BBB and small intestines of PD patients and HV, assessed by [^{18}F]MC225 PET. However, the small sample size limits these results' statistical power and generalizability. Interestingly, changes were observed in brain regions associated with PD pathology, which warrants further investigation in larger PD groups concerning disease stage and symptom severity. ***References:*** 1. Mossel, P. et al. Eur J Nucl Med Mol Imaging 50, (2023)2. Garg A., et al. , Front Neurosci 9, 101 (2015)

OP-052

Study on the Value of Whole-Brain Dopamine Transporter Loss in Parkinson's Disease and Its Subtypes Based on ^{11}C-CFT PET Imaging

X. Guo[1], *J. Li*[1], *J. Guo*[2,3,4], *S. Hu*[1,5,6];
[1]*Department of Nuclear Medicine, Xiangya Hospital, Central South University, Changsha, CHINA,* [2]*Department of Neurology, Xiangya Hospital, Central South University, Changsha, CHINA,* [3]*Key Laboratory of Hunan Province in Neurodegenerative Disorders, Central South University, Changsha, CHINA,* [4]*Hunan International Scientific and Technological Cooperation Base of Neurodegenerative and Neurogenetic Diseases, Changsha, CHINA,* [5]*National Clinical Research Center for Geriatric Disorders, Xiangya Hospital, Central South University, Changsha, CHINA,* [6]*Key Laboratory of Biological Nanotechnology, Changsha, CHINA.*

Aim/Introduction: This study utilized whole-brain ^{11}C-CFT PET imaging to investigate alterations in dopaminergic pathways of Parkinson's disease (PD), explore pathogenic differences between tremor-dominant (TD) and postural instability/gait difficulty (PIGD) subtypes, and develop machine learning models for early PD diagnosis and subtype differentiation. ***Materials and Methods:*** In this retrospective study, we enrolled 197 PD patients (80 TD, 117 PIGD) and 21 age- and gender-matched healthy controls (HCs) underwent ^{11}C-CFT PET scans. Differential analysis was performed across whole-brain regions. Spearman correlation analysis was employed to assess the relationships between regional tracer uptake and clinical scores. Support Vector Machine (SVM), Logistic Regression (LR), and Random Forest (RF) algorithms were used to construct diagnostic and subtype classification models, and the best performing classifier was further applied to subtype classification based on distinct brain regions. ***Results:*** ^{11}C-CFT uptake was reduced not only in nigrostriatal regions but also more extensively in areas associated with other dopaminergic pathways, including the ventral tegmental area, amygdala, nucleus accumbens (NAcc) and insula. Correlation analysis indicated that DAT loss in these limbic regions was correlated with non-motor symptoms, with the NAcc specifically linked to depression and freezing of gait. Compared to the TD group, the PIGD group showed significantly lower ^{11}C-CFT uptake in the putamen, caudate nucleus, pallidum, and NAcc contralateral to the most clinically affected side, and these reductions strongly correlated with PD severity ($|r|>0.4$, $p<0.01$). For early PD diagnosis, SVM, LR, and RF models all achieved perfect discrimination (AUC = 1.00). For subtype differentiation, models based on nigrostriatal regions, extra-nigrostriatal regions, and whole-brain regions yielded AUC values of 0.78 (specificity = 76%, sensitivity = 64%), 0.64 (specificity = 61%, sensitivity = 100%), and 0.84 (specificity = 79%, sensitivity = 94%), respectively. ***Conclusion:*** Our findings demonstrate widespread degeneration across multiple mesolimbic dopamine pathways in PD and highlight the diagnostic value of extra-nigrostriatal regions in early PD detection and subtype differentiation. The progression from TD to PIGD subtype may reflect further deterioration of dopaminergic projections in the striatum, pallidum, and NAcc contralateral to the most clinically affected side. Additionally, we successfully developed effective models for early PD diagnosis and subtype classification.

208

Sunday, October 5, 2025, 8:00 - 9:30
Room 115

TROP Session - Cardiovascular Committee: From Muscle to Calcifications, What's New in Cardiac Amyloidosis?

OP-053

Pittsburgh compound B positron emission tomography detects cardiomyopathy in hereditary transthyretin amyloidosis patients with negative bone scintigraphy

H. Tingen, G. N. Stormezand, J. H. van Snick, ***Y. Hu****, P. A. van der Zwaag, P. van der Meer, B. P. C. Hazenberg, G. Luurtsema, H. L. A. Nienhuis, R. H. J. A. Slart;*
University Medical Center Groningen, Groningen, NETHERLANDS.

Aim/Introduction: Transthyretin (ATTR) amyloidosis is a systemic disease characterized by deposition of misfolded transthyretin protein. Bone scintigraphy can generally diagnose ATTR related cardiomyopathy (ATTR-CM) with high accuracy. However, it has reduced sensitivity in certain transthyretin gene (TTR) variants, which complicates screening and may delay diagnosis of ATTR-CM in individuals carrying these variants. Previous studies suggest that [^{11}C]-Pittsburgh Compound-B ([^{11}C]PiB) positron emission tomography (PET) and can detect cardiac and brain ATTR deposits in patients with TTR variants associated with reduced bone scintigraphy sensitivity. This case series evaluates the effectiveness of PET with [^{11}C]PiB for detecting ATTR-CM and brain involvement in patients with TTR variants associated with reduced bone scintigraphy sensitivity. ***Materials and Methods:*** This prospective case series included four ATTRv amyloidosis patients with TTR variants associated with reduced bone scintigraphy sensitivity,

and two control patients (one ATTRv and one wild-type ATTR (ATTRwt) amyloidosis patient) with cardiac radiotracer uptake bone scintigraphy. All patients underwent diagnostic work-up between April 2024 and March 2025, including [^{11}C]PiB PET/CT. Cardiac and brain [^{11}C]PiB uptake were assessed visually. For cardiac evaluation, target-to-background ratios (TBR) were calculated by comparing myocardial radiotracer uptake to blood pool uptake. TBR ≥1.09 was considered positive for ATTR-CM. For brain analysis, cortical SUV ratios were calculated, comparing radiotracer uptake in the prefrontal cortex, orbitofrontal cortex, temporal cortex and anterior cingulate cortex to uptake in the pons. SUV ratios ≥0.7 were considered positive for brain involvement. ***Results:*** Cardiac [^{11}C]PiB uptake was observed in three of four ATTRv patients despite negative bone scintigraphy. In the one of four patients, there was visually equivocal radiotracer uptake, but elevated TBRs did indicate ATTR-CM. Conversely, both ATTRv and ATTRwt patients with a positive bone scintigraphy had negative or inconclusive [^{11}C]PiB PET results. Brain uptake was observed in two asymptomatic patients, while no uptake was seen in two patients with suspected brain involvement, including one patient with magnetic resonance imaging confirmed leptomeningeal amyloid deposits. ***Conclusion:*** [^{11}C]PiB PET is an effective tool for detecting ATTR-CM in patients with TTR variants associated with reduced bone scintigraphy sensitivity, and could serve as an alternative non-invasive method for cardiac screening in individuals with these variants. However, its utility for detecting brain involvement in symptomatic ATTRv patients remains uncertain and further research is warranted.

OP-054

New Quantitative SPECT-CT Parameters in the Diagnosis of Cardiac Amyloidosis

Ü. Aksu[1], *E. M. Kaya*[1], *D. İnan*[2], *C. Yağmur*[1], *B. E. Akkaş*[1];
[1]*Basaksehir Cam and Sakura City Hospital, Department of Nuclear Medicine, Istanbul, TÜRKIYE,* [2]*Basaksehir Cam and Sakura City Hospital, Department of Cardiology, Istanbul, TÜRKIYE.*

Aim/Introduction: Traditional methods, including visual assessment based on planar imaging and the heart/contralateral lung(H/CL) ratio, are subject to observer variability and may pose diagnostic challenges, particularly in the early stages of the disease or in the presence of blood pool uptake. The aim of this study is to propose a more objective and sensitive method for the diagnosis of ATTR-CA by calculating a quantitative ratio between myocardial wall and blood pool uptake using 99mTc-PYP SPECT/CT. ***Materials and Methods:*** 336 patients who underwent Tc-PYP scintigraphy with suspected cardiac amyloidosis were retrospectively evaluated. Planar and SPECT-CT imaging were performed 1 and 3 hours after injection of 99mTc-PYP. From planar images, the H/CL ratio and Perugini score were determined. On SPECT/CT, spherical volumes of interest (VOI) with a diameter of 1.25 cm were drawn over the septum, left and right ventricular walls, and blood pool, and the S/BP, LV/BP, and RV/BP ratios were calculated. ***Results:*** Nineteen patients with monoclonal gammopathy were excluded from the study. The final cohort consisted of 317 patients (mean age: 62; 56% male). According to planar Perugini scores (PG), patients were grouped as PG 0 (n=84), PG 1 (n=172), and PG 2-3 (n=61). Patients with a C/CL >1.5, Grade 2-3 uptake, no significant blood pool uptake on SPECT and normal hematological tests were considered positive for ATTR-CA. Accordingly, 19 patients were positive (Grade 2-3), 42 patients were suspicious (Grade 2-3), and 256 patients (Grade 0-1) were evaluated as negative. After reevaluation with SPECT/CT, no change was observed in Grade 0-1 patients. Of the 19 patients evaluated as positive in Grade 2-3, 6 were reclassified as negative. Among the 42 suspicious patients, 1 was confirmed as positive, and the remaining 41 were evaluated as negative. This led to reclassification in 14% of the total patient group, while the reclassification rate reached 81% among the suspicious and positive groups. S/BP, LV/BP, and RV/BP ratios were 0.36, 0.40, and 0.38, respectively, in negative patients; 0.47, 0.49, and 0.44 in suspicious patients; and 2.72, 2.37, and 1.32 in positive patients. Using cut-off values of S/BP ≥0.73 and LV/BP ≥0.79, sensitivity was found to be 100% and specificity 92.5%. ***Conclusion:*** Quantitative ratios obtained from SPECT/CT provide higher diagnostic accuracy in the diagnosis of ATTR-CA compared to planar imaging. This method increases diagnostic precision by allowing the reclassification of most suspicious cases as negative and minimizes reader-related errors.

OP-055

A Diagnostic Nomogram for ATTR Cardiac Amyloidosis: Toward Smarter Use of Scintigraphy

A. Agosti[1,2], *G. Garelli*[1,2], *C. Dell'acqua*[1,2], *E. Califaretti*[1], *S. Grimaldi*[1], *M. Finessi*[1], *S. D. Morbelli*[1,2], *A. Lesca*[1], *R. Casoni*[1], *G. Rovera*[1,2];
[1]*Nuclear Medicine Unit, AOU Città della Salute e della Scienza, Turin, ITALY,* [2]*Department of Medical Sciences, University of Turin, Turin, ITALY.*

Aim/Introduction: The advent of disease-modifying therapies for transthyretin (ATTR) cardiac amyloidosis has made early and accurate diagnosis essential, both for timely treatment and genetic screening in at-risk family members. Scintigraphy with bone tracers enables non-invasive diagnosis when Perugini score is ≥2 and no monoclonal component is present. With rising referral rates but many negative results, better pre-test patient selection is needed. This study aimed to develop a clinical nomogram to identify patients at higher likelihood of a positive scintigraphy scan, enhancing diagnostic accuracy while reducing unnecessary imaging. ***Materials and Methods:*** A retrospective analysis was conducted on patients referred at our center for cardiac scintigraphy on suspicion of ATTR cardiac amyloidosis. Collected variables included demographics, imaging, laboratory markers, clinical findings, and comorbidities. Univariate and multivariate logistic regression (R v4.2.1) identified predictors of positive scans (Perugini ≥2), and the multivariate model was used to build a predictive nomogram. Model performance was evaluated via Nagelkerke-R^2, confusion matrix, ROC curve, calibration curve, and internal validation with bootstrapping. ***Results:*** Out of 234 patients referred for cardiac scintigraphy, 127 showed a Perugini score of 0, 12 a score of 1, and 95 a score ≥2. At multivariate logistic regression, male gender (OR 2.70, 95%CI 1.07-7.29, p=0.041), older age (OR 1.11, 95%CI 1.06-1.18, p<0.001), increased interventricular septal thickness (OR 1.40, 95%CI 1.21-1.66, p<0.001), grade II-III diastolic dysfunction (OR 3.23, 95%CI 1.43-7.55, p=0.005) and carpal tunnel syndrome (OR 5.86, 95%CI 2.44-15.16, p<0.001) were independently associated with positive scintigraphy (Perugini ≥2). Other variables - such as ECG low voltages, arrhythmia, and apical sparing - were significant in univariate analysis but not retained in the multivariate model. This could partly be due to the limited availability of apical sparing data in echocardiographic reports, underscoring the need for standardized imaging in suspected cardiac amyloidosis. The model demonstrated good fit (Nagelkerke-R^2 0.55) and diagnostic performance: accuracy 79.1% (95%CI 72.6-84.7), sensitivity 77.6%, specificity 80.2%, PPV 72.8%, NPV 83.9%, and AUC 0.88. Calibration showed good agreement between predicted and observed outcomes. Applying the nomogram at a 5% threshold could have avoided 24.3% of negative scans without missing diagnoses; at 7%, 33.3% of negative scans could be avoided with only 1.3% of true cases missed. ***Conclusion:*** The newly developed nomogram could represent an effective tool for predicting positive cardiac scintigraphy in ATTR amyloidosis, enhancing diagnostic precision while minimizing unnecessary imaging, and is now ready for external validation in an independent cohort.

OP-056

Prevalence and Clinical Outcomes of Incidental Cardiac Uptake in Bone Scintigraphies Unrelated to Cardiac Amyloidosis: The Overlooked ATTR Cohort

R. Sá e Silva, *J. Escaleira, L. Costa, P. Monteiro, L. Lobato, P. Rodrigues;*
Centro Hospitalar Universitário do Porto, Porto, PORTUGAL.

Aim/Introduction: Cardiac amyloidosis (CA), particularly the wild-type transthyretin (ATTRwt-CA), is an underdiagnosed condition with increasing relevance. Bone scintigraphy (BS) using 99mTc-DPD can incidentally reveal cardiac uptake, offering an opportunity for early identification of ATTR-CA. This study aims to evaluate the prevalence of incidental cardiac uptake (ICU) in routine BS performed for non-CA indications, patient's outcomes, and to determine the proportion of patients meeting the 2021-ESC criteria for CA screening. ***Materials and Methods:*** Retrospective, observational study including all BS performed between January/2023-March/2025 for non-CA indications. Two independent readers assessed Perugini's visual score. For patients with ICU, medical records were reviewed to assess referrals to Cardiology consultation (CC); p-value<0.05 was considered statistically significant. ***Results:*** Out of 1561 BS performed for non-CA purposes, ICU was observed in 17 cases (1.1%). After excluding 3repeated exams, 14 cases were analyzed, all conducted in the context of prostate cancer staging or follow-up (71%). Patients, with median age of 85 years, presented with multiple cardiovascular (CV) risk factors. Notably, 50% had pre-existing CV symptoms, dyspnea being the most prevalent (Table I).The Perugini score was positive (score 2/3) in 64% of cases and indeterminate (score 1) in 36%. ICU was detailed in all BS reports, although included in the conclusion only in 43%. Referral to a CC occurred in 29% of patients and more frequent when ICU was mentioned in the BS report conclusion (p=0,015); the patients were diagnosed with ATTRwt-CA after exclusion of monoclonal gammopathies and verifying normal TTR gene sequencing. A diagnostic delay was present, with a median of 18 months between the BS and the ATTR-CA diagnosis.In patients with recent TTE, 71% met screening criteria for CA. "Red flags" included heart failure with preserved ejection fraction (50%), increased septal wall thickness (64%), bilateral carpal tunnel syndrome (14%), AV conduction disorders (29%), and reduced global longitudinal strain (29%). In patients with prior BS, 40% demonstrated positive variation in Perugini score. ***Conclusion:*** Incidental cardiac uptake in BS offers a valuable opportunity for earlier recognition of ATTRwt-CA, particularly in elderly male undergoing BS for prostate cancer staging. Our cohort reinforce the diagnostic complexity by the coexisting CV comorbidities. An attentive incorporation of BS, clinical evaluation and genetic tests lead us to advise a structured direct referral from Nuclear Medicine to Cardiology, adjusting for timely treatment and evading the complexity of a multisystem disease related to heart failure.

OP-057

Implementation of a predictive model for mortality using AI in patients with TTR cardiac amyloidosis confirmed by ^{99m}Tc-DPD scintigraphy.

F. Sebastián Palacid, *N. Álvarez Mena, R. C. Zambrano Infantino, M. García Aragón, B. M. Jaramillo López, Á. R. Suazo Montero, J. Gómez Hidalgo, C. Riola Parada, R. Ruano Pérez;*
Hospital Clínico Universitario Valladolid, Valladolid, SPAIN.

Aim/Introduction: To develop and validate a model to predict mortality risk in patients with TTR cardiac amyloidosis using key clinical parameters to support clinical decision making. ***Materials and Methods:*** A total of 121 patients with a diagnosis confirmed by 99mTc-DPD scintigraphy were included. A 3-year follow-up was performed to determine the number of deaths. The most relevant parameters for the model were identified: age, sex, presence of arrhythmias, arterial hypertension and LVEF calculated by gated SPECT-CT. The prediction model was developed by ChatGPT using Random Forest with class balancing to counteract the imbalance between deceased and non-deceased. Its performance was measured by cross-validation and ROC curve analysis. ***Results:*** The sample consisted of 79 men and 42 women (mean age 78.6 ± 11.7 years). During follow-up, 29 patients (24%) died.LVEF calculated by gSPECT contributed 12% to the overall model power, with the most influential parameters being age (27%) and the presence of arrhythmias (22.5%). The model achieved an overall accuracy of 70.3% and an area under the curve (AUC) of 0.71.In the non-deceased, it achieved an accuracy of 87.5% and a sensitivity of 72.4%; in the deceased, it achieved an accuracy of 38.5% and a sensitivity of 62.5%.In addition, an interface was designed to allow rapid data entry, resulting in efficient risk estimation. ***Conclusion:*** The proposed model represents a practical and effective tool for predicting mortality in patients with TTR cardiac amyloidosis. Its implementation could contribute to better risk stratification, optimise the allocation of clinical resources and promote more personalised care.

OP-058

Myocardium-to-cavity ratio as a novel quantitative index in cardiac amyloidosis: dual-isotope ^{99m}Tc-pyrophosphate/^{201}Tl imaging with D-SPECT

K. Nakajima[1], *S. Yamashita*[2], *T. Kitano*[2], *H. Kato*[2], *H. Yamamoto*[2], *K. Yokoyama*[2];
[1]*Kanazawa University, Kanazawa, JAPAN,* [2]*Public Central Hospital of Matto Ishikawa, Hakusan, JAPAN.*

Aim/Introduction: In cardiac amyloidosis imaging using ^{99m}Tc-pyrophosphate (PYP), the heart-to-contralateral lung (H/CL) ratio from planar images has been widely adopted. However, cardiac-dedicated cadmium-zinc-telluride cameras such as D-SPECT do not employ planar acquisition, and H/CL ratio using an Anger camera has limitations in distinguishing myocardial from blood-pool activity, particularly near the diagnostic threshold of 1.3-1.5. This study aimed to evaluate the feasibility of a myocardium-to-cavity (M/C) ratio, derived from dual-isotope ^{99m}Tc-PYP/^{201}Tl SPECT, as an alternative quantitative index. ***Materials and Methods:*** We studied 121 consecutive patients with suspected cardiac amyloidosis who underwent dual-isotope ^{99m}Tc-PYP/^{201}Tl imaging. The clinical diagnosis of cardiac diagnosis followed Japanese Circulation Society's guidelines. Anterior planar images were acquired with an Anger camera 1 hour post ^{99m}Tc-PYP injection. D-SPECT dual-isotope images were acquired 10 minutes after ^{201}Tl injection at 1 and/or 3 hours after ^{99m}Tc-PYP administration. For M/C ratio calculation, three short-axis slices were summed. The slice with the maximum ^{201}Tl count was used to define myocardial regions with appropriate zooming, and eight circular regions of interest (ROIs) were placed over the myocardium and left ventricular cavity on base, mid, and apical slices (3 added slices ? 3 levels ? 8 ROIs corresponding to 72 volumes of interest). These ROIs were then applied to the ^{99m}Tc-PYP image with a complete match between perfusion and PYP uptake. Diagnostic accuracy of H/CL and M/C ratios was compared. Functional parameters of volume and ejection fraction were obtained from the ^{201}Tl images, and segmental perfusion was compared with ^{99m}Tc-PYP uptake. ***Results:*** Optimal cut-offs were 1.5 for H/CL and 1.0 for M/C ratios. Among 121 patients, 19 (16%) were visually PYP-positive. Both H/CL and M/C ratios were significantly higher in PYP-positive cases. Five patients with H/CL > 1.5 but M/C < 1.0 were visually negative, and correctly classified by M/C ratio. M/C ratio showed 100% sensitivity, specificity, and predictive values. H/CL yielded 100% sensitivity, 95% specificity, 79% positive predictive value, and 100% negative predictive value, reflecting ambiguity near H/CL = 1.5. Among 19 PYP-positive patients, 13 (68%) showed a mismatch pattern—reduced ^{201}Tl uptake corresponding to high ^{99m}Tc-PYP uptake. ***Conclusion:*** In D-SPECT-based imaging, the M/C ratio offers superior diagnostic accuracy over the planar H/CL

ratio, especially in reducing false positives near the conventional threshold. The method is simple, reproducible, and uses a clinically convenient threshold (1.0), making it a promising candidate to replace H/CL when dual-isotope imaging is available.

OP-059

Early-phase 99mTc-HDP planar imaging in suspected cardiac amyloidosis: predictive value of heart-to-contralateral lung ratio for late-phase Perugini scoring

G. Fiorillo[1], *A. Della Morte*[1], *M. Coppola*[1], *M. Scarano*[1], *M. Bellino*[2], *S. Migliarino*[2], *L. Pace*[2];
[1]*Azienda Ospedaliera Universitaria San Giovanni di Dio e Ruggi d'Aragona, Salerno, ITALY,* [2]*Dipartimento di Medicina, Chirurgia e Odontoiatria, Università degli Studi di Salerno (UNISA), Salerno, ITALY.*

Aim/Introduction: Late-phase 99mTc-HDP scintigraphy with Perugini scoring is a widely accepted method to identify transthyretin-related cardiac amyloidosis. However, the diagnostic value of early-phase quantitative indices and tomographic parameters such as SUV from SPECT/CT imaging is still under investigation. This study aims to evaluate whether early heart-to-contralateral lung (H/CL) ratios and quantitative data from SPECT/CT correlate with 3-hour Perugini scores, providing predictive value in the diagnostic workflow. ***Materials and Methods:*** This ongoing retrospective study began in September 2018 and includes 80 patients with suspected cardiac amyloidosis. All patients underwent planar imaging with 99mTc-HDP at both 5-10 minutes (early phase) and 3 hours (late phase), as well as SPECT imaging. Following a technological upgrade in 2023, all patients with a positive Perugini score subsequently underwent SPECT/CT instead of conventional SPECT, allowing extraction of SUVmax and SUVmean values. The myocardial uptake at 3 hours was visually scored using the Perugini scale (0-3). H/CL ratios were calculated for both phases. Pearson and Spearman correlations were used to assess the relationship between early and late-phase indices, SUV values, and Perugini scores. ***Results:*** Out of 80 patients, 18 (22.5%) had positive cardiac uptake (Perugini score ≥1). - H/CL (early phase) showed a strong positive correlation with Perugini score ($r = 0.742$, $p = 0.00099$) - H/CL (late phase) also correlated significantly with Perugini score ($r = 0.744$, $p = 0.00095$) - In the subgroup of patients undergoing SPECT/CT: - The mean SUVmean was 11.06 ± 6.68 (range: 1.579-21.04) - The mean SUVmax was 13.93 ± 6.77 (range: 1.73-22.45) - SUVmean demonstrated a very strong and statistically significant correlation with the Perugini score ($r = 0.851$, $p = 0.00045$) - SUVmax demonstrated a very strong and statistically significant correlation with the Perugini score ($r = 0.851$, $p = 0.00045$) ***Conclusion:*** The H/CL ratio measured in the early phase of 99mTc-HDP planar imaging is strongly predictive of the final Perugini score at 3 hours. These findings support the diagnostic value of early-phase quantification as a non-invasive predictor of cardiac amyloid burden, potentially aiding early diagnosis and improving decision-making in borderline or atypical cases. The transition to SPECT/CT imaging from 2023 has allowed enhanced quantitative assessment, with both SUVmean and SUVmax emerging as reliable markers strongly associated with myocardial amyloid deposition.

OP-060

Aortic valve calcium score from computed tomography for signal localization by cardiac amyloid radionuclide imaging to predict aortic stenosis and assess prognosis in patients with transthyretin cardiomyopathy

G. Bonnans*, R. Engel, E. Cariou, H. Malerbi, S. Cazalbou, Y. Lavie-Badie, E. Cassol, P. Fournier, O. Lairez;*
CHU Rangueil, Toulouse, FRANCE.

Aim/Introduction: Transthyretin cardiomyopathy (ATTR-CM) and aortic stenosis (AS) are two frequently associated pathologies. The diagnosis of ATTR-CM can be made by performing bone scintigraphy with tomographic acquisitions and a computed tomography (CT) scan to localize the signal if positive. Calcifications of the aortic valve can be seen on this CT scan. The aim of this study was to determine whether aortic calcifications on the CT scan performed at the time of bone scintigraphy for the diagnosis of ATTR-CM were predictive of AS and had an impact on prognosis. ***Materials and Methods:*** Consecutive patients referred to nuclear medicine and diagnosed with ATTR-CM on bone scintigraphy after exclusion of monoclonal gammopathy were included. Patients with a history of aortic valve replacement were excluded. CT images performed for signal localization were reviewed for the presence of aortic calcifications. In the presence of calcifications, a calcium score was calculated from axial slices using a threshold of 130 Hounsfield units. Calcium score results were compared with aortic valve hemodynamic parameters assessed by transthoracic echocardiography to classify patients according to the presence and severity of AS. A three-stage visual score was developed to assess the extent of aortic valve calcifications (score 0: absence or spotty calcification; score 1: < 50% of annulus circumference; score 2: ≥ 50%). Receiver operating characteristic (ROC) analysis and Cox proportional hazards models were used for statistical analysis. ***Results:*** Two hundred and sixty-three patients were included. Aortic calcifications based on visual score > 0 were present in 153 (58%) patients. Among them, the median calcium score was 430 [200-1140]. A cut-off calcium score ≥ 380 predicted AS with an area under the ROC curve of 0.93 ($P < 0.0001$), sensitivity 91%, specificity 81%. For severe AS, a threshold ≥ 1690 yielded an AUC of 0.98 ($P < 0.0001$), allowing a sensitivity of 94% and a specificity of 96%. A visual score of 2 predicted severe AS with 94% sensitivity and 90% specificity. Both the aortic valve calcium score and visual score were independent predictors of all-cause mortality during follow-up. ***Conclusion:*** Aortic calcifications on CT scan of bone scintigraphy are found in almost two-thirds of patients with ATTR-CM. Assessed using both a semi-quantitative visual score and a calcium score, they are strong predictors of AS severity and mortality. A calcium score ≥ 1690 and visual score 2 reliably identify severe AS.

OP-061

Coronary Artery Calcification as a Complementary Marker in ATTRV30M Amyloidosis: Insights Across the ^{99m}Tc-DPD Uptake Spectrum

J. Rei da Cruz Escaleira[1,2], *R. Sá e Silva*[3], *J. Bessa*[4], *A. Campos*[4,2,5], *A. Cunha*[4], *J. Silva*[3], *L. Costa*[3], *P. Rodrigues*[6,2], *J. Santos*[4,2,5], *L. Lobato*[4,2,5];
[1]*Department of Nuclear Medicine, Unidade Local de Saúde (ULS) de Santo António, Oporto, PORTUGAL,* [2]*Unit for Multidisciplinary Research in Biomedicine (UMIB), Oporto, PORTUGAL,* [3]*Department of Nuclear Medicine, Unidade Local de Saúde (ULS) de Santo António, Oporto, PORTUGAL,* [4]*Department of Nephrology, Unidade Local de Saúde (ULS) de Santo António, Oporto, PORTUGAL,* [5]*Laboratory for Integrative and Translational Research in Population Health (ITR), Oporto, PORTUGAL,* [6]*Department of Cardiology, Unidade Local de Saúde (ULS) de Santo António, Oporto, PORTUGAL.*

Aim/Introduction: Bone-seeking tracers, such as DPD, are essential for the non-invasive detection of transthyretin(ATTR) amyloid deposits in the heart. Although the mechanism underlying tracer uptake remains unclear, microcalcifications have been proposed as a contributing factor. In addition to interstitial and valvular deposition, ATTR may also involve coronary vessels. This study investigates the extent of coronary artery calcification (CAC) in patients with ATTRV30M amyloidosis. ***Materials and Methods:*** We retrospectively analyzed ATTRV30M patients followed by nephrologists at a single centre from until 2025. Diagnostic criteria for cardiac amyloidosis (CA): interventricular septal thickening≥ 12 mm (without other cause) or a Perugini score≥ 2, besides no plasma cell disease. The cardiorenal assessment was established on the National Amyloidosis Centre (NAC) staging system. CAC was assessed using chest CT scans, either obtained during DPD

SPECT/CT imaging or from unrelated CT studies. CAC severity was graded using a visual ordinal scale as follows: 0,no CAC visualized; 1 (mild), isolated speckles of CAC in any coronary artery; 2 (moderate), greater than mild but less than severe; 3 (severe), at least one coronary segment with contiguous, extensive, or diffuse CAC. ***Results:*** Sixty-nine patients were included, of whom 35 had CA. Among these, 28(85.7%) had a Perugini score of 0 or 1, and only 5(14.3%) had scores of 2 or 3; 12(34.3%) cases with CA experienced heart failure, all with preserved ejection fraction. Ischemic events were infrequent (one myocardial infarction and two strokes). CAC was observed in 17 patients (24.6%), who were predominantly male (70.6%;p=.006) and tended to develop symptoms at a median age of 39 years, five years later than those without CAC(p=.052). No significant relationship was observed between NAC and CAC grades (Table I). A Perugini score of 0 was primarily observed in patients with absent or mild CAC, whereas detectable DPD uptake(score≥1) was more frequently associated with moderate/severe CAC (p<.001;Table II). In multivariate logistic regression adjusted for cardiovascular risk factors, DPD uptake remained an independent predictor of moderate to severe CAC (OR=9.8;p=.022). Conversely, while CAC in this range also predicted DPD uptake (OR=8.1;p=.030), this association may be modulated by sex (OR=4.9; p=.053). The presence of CAC, regardless of severity, was independently associated with CA (OR=5.9; p=.026). ***Conclusion:*** This study is the first to investigate the relationship between CAC/DPD uptake in ATTRV30M amyloidosis. CAC was overall uncommon in non-CA patients; however, it emerged as a potential complementary imaging marker in those with cardiac involvement, highlighting a possible calcium-mediated interplay between amyloid fibrils, the myocardium, and coronary vessels.

209

Sunday, October 5, 2025, 8:00 - 9:30

Room 133+134

e-Poster Presentations Session 1 - TMI&T: Preclinical Imaging and Therapy

EPS-001

3-dimensional Microfluidic "Stacks" Platform for Advanced in vitro Radiobiology Studies

M. Lindsey[1], *E. Recchia*[1,2], *A. Thickens*[1], *M. Bio Idrissou*[1], *O. Kwon*[1], *B. Bednarz*[1], *D. Kosoff*[1,2,3], *R. Hernandez*[1];
[1]*University of Wisconsin-Madison, Madison, WI, UNITED STATES OF AMERICA,* [2]*University of Wisconsin Carbone Cancer Center, Madison, WI, UNITED STATES OF AMERICA,* [3]*William S. Middleton Memorial Veterans' Hospital, Madison, WI, UNITED STATES OF AMERICA.*

Aim/Introduction: Development of robust and predictable methods for drug evaluation is a key priority of the FDA. Microphysiological systems, including spheroid or organ-on-a-chip models, better represent in vivo tissue architectures and biological responses. We have developed a microscale cell culture platform ("Stacks") that permits isotropic dose deposition from radiopharmaceutical therapy (RPT) to 3-dimensional clusters of cells. Our platform captures the increased radioresistance of cells seen in vivo, allowing for robust radiobiological analyses. ***Materials and Methods:*** Absorbed dose from free ^{225}Ac and ^{177}Lu was estimated using the MIRD formalism, with S-values computed in Geant4 with the G4EmLivermorePhysics model for both the Stacks platform and 96-well plate formats. LNCaP metastatic prostate cancer cells were seeded onto either the collagen-fibronectin matrices of the Stacks platform or the 96-well plate at a concentration of 5,000 cells/mL. Radioisotopes were suspended in media and applied at increasing activity concentrations. For ^{225}Ac, treatments were titrated up to 10 µCi/mL (Stacks) or 1 µCi/mL (96-well). For ^{177}Lu, treatments were titrated up to 10 mCi/mL (Stacks) or 200 µCi/mL (96-well). In the Stacks platform, convectively circulating treatment droplets envelope the cell culture, permitting isotropic dose deposition from suspended radioisotopes. Cells were incubated for 96 hours. Cellular vitality in the Stacks platform was determined via bioluminescent imaging with CellTiter-Glo. Cellular vitality in the 96-well plate was determined with PrestoBlue in a live-cell assay. ***Results:*** Computed S-values for the Stacks platform were orders of magnitude larger than those for the 96-well plate, reflecting the significant difference that 3-dimensional geometry plays in dose deposition. The LNCaP cells were more radioresistant in the Stacks platform at the same absorbed dose. For cells treated with 3 Gy ^{225}Ac, vitality was reduced to 29.55±5.15% in the 96-well plate but only 88.52±12.49% in the Stacks platform (p<0.0001). Likewise, for cells treated with 30 Gy ^{177}Lu, vitality was reduced to 32.07±5.76% in the 96-well plate but only 60.01±7.33% in the Stacks platform (p<0001). ***Conclusion:*** We have developed a microfluidic platform that more accurately models in vivo radiation dose response. Despite handling larger absorbed doses, radiobiological studies in the Stacks platform require less activity due to its microscale, making them more economic and limiting exposure. The Stacks platform allows for more clinically relevant in vitro radiobiological modeling without sacrificing throughput.

EPS-002

[^{177}Lu]Lu-PSMA: impacting the full transcriptome of prostate cancer cells.

F. Amoroso[1,2], *B. T. Cornelissen*[1,2];
[1]*Dept. of Nuclear Medicine and Molecular Imaging, University Medical Centre Groningen, Groningen, NETHERLANDS,* [2]*Institute for Radiation Oncology, Department of Oncology, University of Oxford, Oxford, UNITED KINGDOM.*

Aim/Introduction: Radiotherapy is an effective therapeutic option for locally advanced prostate cancer (PCa). However, when PCa progresses, metastatic disease is incurable. Despite the promising results of the clinical trials with ^{177}Lu-labelled PSMA (1), and the ever-mounting interest, treatment with [^{177}Lu]Lu-PSMA is not yet curative. Improving our understanding of the (radio)biology of the damage induced by [^{177}Lu]Lu-PSMA will aid in designing new targeted and more effective treatments for PCa patients. ***Materials and Methods:*** We performed a comprehensive analysis on the full transcriptome of prostate cancer cells (22Rv1, LNCaP and C4-2B), treated with [^{177}Lu]Lu-PSMA for 2 hours, over a period of 6 days, using RNA-Seq. ***Results:*** We recorded a progressive enrichment of genes that are differentially expressed over time as a consequence of [^{177}Lu]Lu-PSMA treatment. Performing pathway analysis, we confirmed the activation of pathways that relate to the induction of genomic reorganization (e.g., of DNA and RNA synthesis-related processes), DNA damage repair (such as Nucleotide Excision Repair) and autophagic processes that are known to correlate with cellular responses to ionizing radiation (2). We also identified new biologies that are impacted by the treatment with this radiolabelled peptide. ***Conclusion:*** With this study we aimed to improve our understanding of the radiobiological effects that beta and gamma emitter [^{177}Lu]Lu-PSMA has on prostate cancer cell lines. Moreover, we shed the light on new pathways that are not strictly related to the induction of the DNA damage and can represent new therapeutic avenues for prostate cancer patients. ***References:*** (1) Novartis. Phase III VISION study. 2021 (2) Chaurasia M, et al., Free Radic Res. 2016;50(3):273-90. doi: 10.3109/10715762.2015.1129534. Epub 2016 Jan 14. PMID: 26764568.

EPS-003

Using ^{18}F-FES PET imaging of ERα re-expression in triple-negative breast cancer in response to anti-platelet derived growth factor C therapy

I. Burvenich[1], *S. Quazi*[1], *N. Huynh*[1], *A. Rigopoulos*[1], *A. McDonald*[1], *U. Ackermann*[2], *A. Scott*[1];
[1]*Olivia Newton-John Cancer Research Institute, Heidelberg, AUSTRALIA,* [2]*Department of Molecular Imaging and Therapy, Austin Health, Heidelberg, AUSTRALIA.*

Aim/Introduction: Monoclonal antibody (mAb) 6B3 can cause re-expression of estrogen receptor alpha (ERα) in triple-negative breast cancer (TNBC) mouse models, via neutralisation of platelet derived growth factor C (PDGF-CC) in the tumour microenvironment (1). Here, we investigated if ^{18}F-FES PET imaging can be used to measure and quantify the re-expression of ERα in TNBC models following mAb 6B3 therapy or genetic ablation of PDGF-C. ***Materials and Methods:*** Ovariectomised BALB/c nude mice were subcutaneously injected with MCF-7 (5x10^6; n=5), 231HMclB2 (3x10^6; n=10) or 231HMclB2$^{pdgfc-/-}$ cells (3x10^6; n=5) in the shoulder. 231HMclB2-tumour-bearing mice were treated with 100 µL of 6B3 (50 mg/kg, twice weekly) or PBS vehicle control (n = 5). To support growth of ERα-expressing tumour cells, all mice received subcutaneous injections of 20µg 17β-estradiol (20µg/20µL; corn oil:ethanol, 9:1) in the nape of their necks starting 2 days prior to cell injection, followed by five injections per week for 5 weeks. Once tumour volumes reached approximately 100mm^3, 17β-estradiol injections were halted 3 days prior to mice receiving ^{18}F-FES (5-11 MBq) to avoid competitive binding to ERα. After 1 hour, a 15-minutes PET acquisition was performed on each mouse. ERα target expression was assessed using immunohistochemistry. ***Results:*** As expected, highly ERα-expressing MCF-7 tumours displayed specific uptake of ^{18}F-FES. In contrast, no uptake of ^{18}F-FES was observed in 231HMclB2$^{pdgfc-/-}$ tumours or 231HMclB2 tumours treated with either 6B3 or PBS. Ex vivo biodistribution study confirmed low uptake of ^{18}F-FES by 231HMclB2$^{pdgfc-/-}$ tumours or 231HMclB2 tumours treated with 6B3. Immunohistochemistry analysis confirmed the deletion of PDGF-C in 231HMclB2$^{pdgfc-/-}$ tumours, however, some ERα expression was observed in 231HMclB2 tumours treated with 6B3. ***Conclusion:*** Although some ERα re-expression was induced in 231HMclB2 tumours treated for 4 weeks with mAb 6B3, the low expression level of ERα could not be detected using ^{18}F-FES PET imaging. ***References:*** 1. Roswall P, et al. Microenvironmental control of breast cancer subtype elicited through paracrine platelet-derived growth factor-CC signaling. Nat Med. 2018 May;24(4):463-473. doi: 10.1038/nm.4494.

EPS-004

3D spheroids for analysis of targeted binding and toxicity of radionuclide-labeled affibodies

I. Zelepukin, *A. Herlina, A. Vorobyeva, V. Tolmachev; Uppsala University, Uppsala, SWEDEN.*

Aim/Introduction: The development of targeted therapeutics requires screening of their binding efficiency and therapeutic effects in cancer cells and tumor models. Tumor spheroids, a 3D cancer in vitro model, serve as a crucial step in the evaluation of therapeutics efficiency. Spheroids partially preserved architecture and features of tumor microenvironment, and can be used for high throughput screening of drugs, which is complicated in animals by ethical reasons. ***Materials and Methods:*** We established a 3D cell culture platform for evaluating the response of spheroids to targeted therapies. The platform features soft agarose microdishes with 81 U-shaped wells. Due to the non-adhesive properties of agarose, cells naturally aggregate into compact spheroids - a phenomenon observed across seven different human and mouse cancer cell lines.We utilized this 3D culture model to investigate the binding specificity and therapeutic efficacy of the $Z_{HER2:48937}$ affibody conjugated with ^{161}Tb. For this aim we prepared spheroids from EMT-HER2 murine cell line with overexpression of human HER2 receptors and parental EMT6/P line without receptors. [^{161}Tb]Tb-$Z_{HER2:48937}$ affibodies had a specific activity of 5 MBq/nmol. For specificity binding testing, spheroids were treated for 24 h with 1 nM solution of [^{161}Tb]Tb-$Z_{HER2:48937}$, while blocking was performed by 1-h preincubation with 100 nM solution of $Z_{HER2:48937}$. For therapy, spheroids were incubated for 8 h or 24 h with 1 nM solution of [^{161}Tb]Tb-$Z_{HER2:48937}$. The toxicity was analyzed by measuring spheroids growth kinetics over 2 weeks and measurement of migration distance of cells after spheroids attachment to adhesive plastic. ***Results:*** The agarose-based microdishes enable consistent formation of multiple spheroids with 6 ± 2% diameter variation. EMT-HER2 spheroids demonstrate specific binding of [^{161}Tb]Tb-$Z_{HER2:48937}$ affibody, which could be prevented by receptor blockade. Specific binding of affibodies was not observed in EMT6/P spheroids. Treatment with [^{161}Tb]Tb-$Z_{HER2:48937}$ has a drastic effect on spheroids growth. Spheroids volume increased ~8 and ~2.2 times in non-treated and 24-h-treated groups, respectively. Incubation of spheroids with [^{161}Tb]Tb-$Z_{HER2:48937}$ for 8 h did not induce decrease of the cells proliferation. Compared to not-treated group, median migration distances were 1.52-fold lower for group treated with [^{161}Tb]Tb-$Z_{HER2:48937}$ for 24 h. ***Conclusion:*** The developed 3D cell culture platform allows to perform screening of various targeted drugs for the development of chemo- and radiopharmaceuticals**.**

EPS-005

Visualizing cerebral plasticity mechanisms using [^{18}F] UCB-H and [^{18}F]FDG in animal models of acute unilateral vestibulopathy

I. Fuxjäger[1], *M. Antons*[2], *R. Oos*[3], *G. Palumbo*[3], *S. Lindner*[3], *S. Ziegler*[3,4], *K. Matiasek*[5], *M. Brendel*[3,6,7], *R. Werner*[3], *A. Zwergal*[1,8];
[1]*German Center for Vertigo and Balance Disorders, LMU University Hospital, LMU Munich, München, GERMANY,* [2]*Department of Radiology, LMU University Hospital, LMU Munich, München, GERMANY,* [3]*Department of Nuclear Medicine, LMU University Hospital, LMU Munich, München, GERMANY,* [4]*Clinic for Nuclear Medicine, Hannover Medical School (MHH), Hannover, GERMANY,* [5]*Section of Clinical & Comparative Neuropathology, Centre for Clinical Veterinary Medicine, LMU Munich, München, GERMANY,* [6]*German Center for Neurodegenerative Diseases (DZNE), München, GERMANY,* [7]*Munich Cluster for Systems Neurology (SyNergy), München, GERMANY,* [8]*Department of Neurology, LMU University Hospital, LMU Munich, München, GERMANY.*

Aim/Introduction: Acute unilateral peripheral vestibular loss in patients can result from lesions in the inner ear or the vestibular nerve. Animal models reflect this by inducing preganglionic (before the Scarpa's ganglion) or postganglionic (after the ganglion) lesions of the VIIIth cranial nerve. Over time, both patients and animals recover through adaptive functional and structural central neural plasticity. However, it is unclear how central compensation mechanisms differ as a function of the peripheral vestibular lesion mechanism. ***Materials and Methods:*** Twenty-four male Sprague Dawley rats (mean age: 9.5 weeks) underwent either unilateral chemical labyrinthectomy (cUL, preganglionic) or unilateral vestibular neurectomy (UVN, postganglionic). All animals received preoperative baseline [^{18}F]FDG and [^{18}F]UCB-H PET scans. Postoperatively, [^{18}F]FDG PETs were conducted weekly for four weeks to depict changes of regional cerebral glucose metabolism (rCGM) as a surrogate for functional plasticity, and [^{18}F]UCB-H PETs at three time points over nine weeks to visualize alterations in synaptic density indicating structural plasticity. Behavioral recovery was assessed weekly using a scoring system and Open Field tests. Regional SUVr values in segmented brain regions (Schiffer rat brain atlas) were compared to baseline and between groups using mixed-effects models and voxelwise SPM analysis. ***Results:*** Both[^{18}F]FDG and [^{18}F]UCB-H PET revealed a similar spatial pattern of affected brain regions in both models. However, while rCGM

changes in the UVN and cUL model appeared to a comparable extent in vestibular network hubs, [^{18}F]UCB-H PET showed more extensive and pronounced alterations in synaptic density in the UVN vs. cUL group. Specifically, synaptic density in the vestibular nuclei was significantly lower after UVN, which was accompanied by compensatory increases in frontal sensorimotor cortical areas. Behavioral data reflected comparable compensation dynamics between groups. ***Conclusion:*** Pre- and postganglionic vestibular lesion models exhibit similar patterns of behavioral recovery and glucose metabolism. However, postganglionic lesions induce more severe and widespread synaptic remodeling. This data suggest that synaptic density imaging may be a more sensitive method to depict subtle differences in mechanisms of lesion-induced adaptive neuroplasticity than traditional techniques such as imaging of glucose metabolism.

EPS-006

ImmunoPET imaging of c-Met using a nanobody-based tracer ^{68}Ga-NOTA-PFCM01 in pancreatic ductal adenocarcinoma

L. Kang, *X. Sun, T. Wang, Q. Yang, L. Song, Y. Lei, W. Huang, Z. Chen, Y. Qiu;*
Dept. of Nuclear Medicine, Peking University First Hospital, Beijing, CHINA.

Aim/Introduction: Pancreatic ductal adenocarcinoma (PDAC) is the most prevalent form of pancreatic cancer, with high malignancy and poor prognosis. The cellular mesenchymal-epithelial transition factor (c-Met) is overexpressed in 84% of PDAC and plays a critical role in tumor progression, which are closely associated with poor patient outcomes. The focus of this study is to develop a new ^{68}Ga-labeled nanobody (^{68}Ga-NOTA-PFCM01) for the visualization of c-Met in PDAC models. ***Materials and Methods:*** By immunizing an alpaca with recombinant human c-Met, the variable domain of the heavy chain of heavy-chain-only antibody (VHH) were screened, and the binding affinity was tested by bio-layer interferometry (BLI). c-Met expression in human PDAC cell lines was evaluated using western blot and flow cytometry. NOTA (1,4,7triazacyclononane-1,4,7-triacetic acid) chelator was labeled the nanobodies with ^{68}Ga. PET imaging and biodistribution studies were performed in tumor xenografts. ***Results:*** PFCM01 was screened with an excellent binding property with the K_D value of 286.2 pM. c-Met expression was the highest in BXPC-3 cells but the lowest in MIA PaCa-2 cells, which were set as the positive and negative models separately. Small animal positron emission tomography/computed tomography (PET/CT) imaging showed that the uptake of ^{68}Ga-NOTA-PFCM01 in BXPC-3 tumors was significantly higher than that in MIA PaCa-2 models. Additionally, no significant tumor uptake was observed in the blocking group, nor in the BXPC-3 tumor model injected with ^{68}Ga-NOTA-NC (a negative control nanobody), demonstrating receptor-specific binding of PFCM01. The biodistribution results showed that the uptake of BXPC-3 tumors (1.14 ± 0.08 %ID/g) is higher than that of MIA PaCa-2 tumors (0.34 ± 0.01 %ID/g, $P < 0.0001$) and tumors in blocking group (0.79 ± 0.11 %ID/g, $P < 0.01$), which was further reinforced the PET imaging results. ***Conclusion:*** ^{68}Ga-NOTA-PFCM01 showed a specific and high tumor uptake in c-Met-positive PDAC models, providing a noninvasive method to assess c-Met expression, suggesting its promise as a prospective PET imaging agent for future clinical applications.

EPS-007

Cancer-associated fibroblasts as a determinant for the tumor cells' response to targeted radionuclide therapy

J. D. Campeiro, *M. J. Klomp, C. D. van der Heide, J. W. K. Zhang, S. U. Dalm;*
Erasmus MC, Rotterdam, NETHERLANDS.

Aim/Introduction: Next to high expression of the targeted biomarker, the radiosensitivity of tumors is key in determining responses to targeted radionuclide therapy (TRT). Research showed that multiple factors can play a role in the tumor cells' radiosensitivity. In line herewith, epithelial-to-mesenchymal transition (EMT), a process which can be induced by cancer-associated fibroblasts (CAFs), results in more aggressive tumors and is associated with resistance to external beam radiotherapy. CAF-induced EMT might also play a role in the observed suboptimal clinical outcomes after TRT. Accordingly, we aimed to determine whether CAF-induced EMT occurs in triple-negative breast cancer (TNBC) cells and how this affects TRT response. ***Materials and Methods:*** CAF-derived conditioned medium (CM) was obtained by culturing 100% confluent human breast CAFs (19TT-F) in fetal calf serum (FCS)-free medium for 3 days. Human TNBC cells (HCC1806, MDA-MB-231 and Hs 578T) were cultured for 4 days in daily refreshed medium containing 4% (v/v) FCS, with (primed) or without (unprimed) 50% (v/v) CM. Subsequently, cells were incubated for 6 days with 0, 1.0, 3.0 or 8.0 MBq/400 µL [^{177}Lu]Lu-DTPA, mimicking the low dose rate of TRT, followed by a viability assay. Moreover, cell morphology and EMT marker mRNA levels, i.e. mesenchymal markers TWIST1, SNAI1, SNAI2, VIM and FN1, and epithelial markers EpCAM and CLDN1, were assessed. ***Results:*** Primed MDA-MB-231 cells demonstrated a slight decrease in cell viability after treatment versus unprimed cells, i.e. 26.8±1.7% versus 33.2±0.7% using 3.0 MBq/400 µL [^{177}Lu]Lu-DTPA. In contrast, treatment with the same activity concentration resulted in 25.9±1.8% viable HCC1806 cells and 26.1±5.9% viable Hs 578T cells in primed condition, versus 7.8±0.6% and 8.4±1.9%, respectively, in unprimed cells. Although a more mesenchymal spindle-like morphology was only observed for primed Hs 578T, all cell lines showed changes in EMT markers; (1) MDA-MB-231 was characterized by decreased EpCAM and CLDN1, and increased SNAI1 and FN1, (2) HCC1806 demonstrated decreased CLDN1, and increased SNAI1 and VIM, and (3) Hs 578T showed a decrease in TWIST1, SNAI1, EpCAM and CLDN1, and an increase in FN1. ***Conclusion:*** Our preliminary results demonstrate that CAF-derived CM induced changes in TNBC cells in terms of EMT profile, suggestive for a more mesenchymal-like state, and radiosensitivity, which seems to be cell line-dependent. Future studies include analysis of relevant protein expression levels and cellular invasion capacity. Moreover, the mechanism underlying cell line-dependent effects and possibilities to reverse EMT to increase radiosensitivity towards TRT will be explored.

EPS-008

Preclinical evaluation of a ^{68}Ga/^{177}Lu theranostic targeting PARP for PARP-expressing cancers

C. Y. Chan[1], *J. Shi*[2], *F. Tsoi*[2], *U. S. Khoo*[2], *E. Parkes*[3], *K. V. Tan*[4];
[1]*The Institute of Cancer Research, London, UNITED KINGDOM,* [2]*University of Hong Kong, Hong Kong, HONG KONG,* [3]*University of Oxford, Oxford, UNITED KINGDOM,* [4]*Perceptive Inc., London, UNITED KINGDOM.*

Aim/Introduction: Radioligand therapy (RLT) represents a promising approach in cancer treatment, leveraging radiopharmaceuticals to deliver highly localised radiation directly to tumour cells. A notable target in this approach is poly(adenosine diphosphate-ribose)-polymerase (PARP), a key enzyme involved in DNA damage repair enzyme. PARP-targeting compounds, when radiolabelled with an appropriate therapeutic radionuclide, can selectively bind to damaged DNA within tumour tissue, where the emission of high-energy ionising radiation induces complex DNA damage ultimately leading to cancer cell death. Coupled with the elevated expression of PARP in many aggressive cancer cells relative to normal tissues (1), enables for more precise delivery of radiopharmaceuticals, hence enhancing the therapeutic index and minimising damage to surrounding tissues. Here, we report the development of KK02, a novel PARP-targeting compound designed for chelation with various radiometals, including ^{68}Ga

and ^{177}Lu, for use in PET imaging and RLT applications. ***Materials and Methods:*** Radiolabelling efficiency, purity and stability of the matched-pair radiopharmaceuticals, [^{68}Ga]Ga-KK02 and [^{177}Lu]Lu-KK02, were assessed using radio-TLC and HPLC. In vitro uptake and specificity of [^{68}Ga]Ga/[^{177}Lu]Lu-KK02 were determined in human triple-negative breast cancer (TNBC) and prostate cancer (PCa) cells. Therapeutic efficacy of [^{177}Lu]Lu-KK02 were evaluated in TNBC cells. In vivo imaging, biodistribution studies and autoradiography were conducted using naïve and TNBC-bearing mouse models. Preliminary assessment of efficacy and safety for [^{177}Lu]Lu-KK02 was performed in a murine PCa models. ***Results:*** [^{68}Ga]Ga-KK02 and [^{177}Lu]Lu-KK02 were obtained in good yields and remained stable in serum. In vitro studies showed selective uptake of [^{68}Ga]Ga/[^{177}Lu]Lu-KK02 across all models, and was dependent on cellular PARP-1 expression levels. A significant reduction in clonogenicity was observed after treatment with only 100 Bq of [^{177}Lu]Lu-KK02 in TNBC cells. In vivo studies demonstrated that both [^{68}Ga]Ga-KK02 and [^{177}Lu]Lu-KK02 exhibited similar hepatobiliary and renal clearance profiles and showed bioequivalence. For [^{177}Lu]Lu-KK02, rapid blood clearance was observed at 1 h (0.14±0.05 %ID/g), with little kidney retention seen at 24 h (0.28±0.05 %ID/g) post-injection. A single, high-dose administration of [^{177}Lu]Lu-KK02 (60 MBq) resulted in a significant delay in MyC-CaP tumour growth compared to the vehicle control, without causing body weight loss and hematopoietic toxicity. ***Conclusion:*** Our study demonstrates the strong potential for KK02 as a theranostic tool for the diagnosis and treatment of PARP-expressing cancers, with improved radiotoxicity profiles. Ongoing investigations are exploring the therapeutic effects of alternative radiometals and the impact of multiple-dose administration. ***References:*** 1. CY Chan, KV Tan, B Cornelissen; Clinical Cancer Research 27 (6), 1585-1594, 2021.

EPS-009

Preclinical Evaluation of a ^{47}Sc-labeled Gastrin Releasing Peptide-based Radioantagonist for the Targeted Management of Breast Cancer

N. Kumar[1], *A. Bilinska*[1], *E. Menéndez*[1], *T. Läppchen*[1], *E. S. Moon*[2], *M. Zoltowska*[3], *D. Pawlak*[3], *I. Cieszykowska*[3], *R. Mikolajczak*[3], *F. Rösch*[2], *A. Rominger*[1], *E. Gourni*[1];
[1]*Department of Nuclear Medicine, Inselspital, Bern University Hospital, University of Bern, Bern, SWITZERLAND,* [2]*Department of Chemistry-TRIGA site, Johannes Gutenberg University of Mainz, Mainz, GERMANY,* [3]*Radioisotope Centre POLATOM, National Centre for Nuclear Research, Otwock, POLAND.*

Aim/Introduction: Radiolabeled gastrin-releasing peptide receptor (GRPR) antagonists appear as promising tools for the management of breast cancer. By targeting GRPR, which is often overexpressed in breast tumors, these radioantagonists enable precise imaging and targeted therapy, offering potential improvements in diagnosis, staging, and treatment monitoring. The goal of the current study was to preclinically evaluate a ^{47}Sc-labeled GRPR-based radioantagonist with the potential to be used for in-vivo imaging and therapy of breast cancer. ***Materials and Methods:*** The statine-based GRPR antagonist (AAZTA^5-Pip-D-Phe-Gln-Trp-Ala-Val-Gly-His-Sta-Leu-NH_2: LF1) was radiolabeled with scandium-47. Detailed in-vitro evaluation, including lipophilicity, protein binding, saturation and internalization studies, was carried out in T47D breast cancer cells. In-vivo studies (biodistribution, metabolic stability, blood and organs clearance kinetics, SPECT/CT imaging) were performed in T47D xenografts. ***Results:*** [^{47}Sc]Sc-LF1 was prepared in high radiochemical purity (> 99 %) with molar activities up to 40 MBq/nmol. [^{47}Sc]Sc-LF1 was stable for 6 days post-labelling and exhibiting a hydrophilic profile with a Log_D value of -2.8. [$^{nat/47}$Sc]Sc-LF1 exhibited affinity for T47D cells, with K_d values of 10.6 ± 3.0 nM and a low internalization rate in the cells, with values below 10% to the total cell bound activity. The metabolite analysis revealed the formation of three hydrophilic metabolites. In-vivo protein binding showed that approximately 3 % of the radioactivity is bound to blood protein after 15 min post-injection of [^{47}Sc]Sc-LF1 in mice. In T47D xenografts, [^{47}Sc]Sc-LF1 exhibited significantly high, retained and specific tumor uptake, with values of 9.5 ± 2.5 and 0.7 ± 0.1 % I.A./g at 1 and 72 h p.i., respectively. Blood retention level of [^{47}Sc]Sc-LF1 was low, decreasing from around 0.6 ± 0.1% IA/g at 1 h p.i to 0.1 ± 0.0 % IA/g at 4 h p.i. The effective half-life in blood was 21.3 min, demonstrating its rapid clearance. The clearance of the radioactivity from non-target organs was significantly faster compared to the tumor uptake with organ-specific half-lives of 2.5, 0.9 and 3.2 h for the kidney, pancreas and tumor, respectively. The favorable pharmacokinetic performance of [^{47}Sc]Sc-LF1 in combination with the excellent imaging properties of scandium-47 led to SPECT/CT images of high contrast. ***Conclusion:*** The high and persistent tumor uptake in the breast tumor model underscores the significant potential of [^{47}Sc]Sc-LF1 as a dual-purpose tool for both SPECT imaging and targeted therapy. ***References:*** This work is a PRISMAP contribution.

EPS-010

Granzyme B-Targeted PET Imaging Enables CarNK Cell Tracking and Prognosis Prediction in Adoptive Immunotherapy

L. Zhang, *X. Lan, Y. Gai, W. Cao;*
Department of Nuclear Medicine, Union Hospital, Tongji Medical College, Huazhong University of Science and Technology, Wuhan, CHINA.

Aim/Introduction: Adoptive cell therapy (ACT) has demonstrated significant potential in cancer immunotherapy, with chimeric antigen receptor-engineered natural killer (CarNK) cells inducing tumor cell DNA damage and apoptosis via perforin-granzyme B delivery. This study aimed to noninvasively quantify CarNK cell infiltration dynamics and predict therapeutic outcomes using [68Ga]Ga-NOTA-GZP positron emission tomography (PET). ***Materials and Methods:*** In vitro, EGFRvIII-Car-NK92(abbreviation: CarNK) cells were co-cultured with A549$^{EGFRvIII+}$ non-small cell lung cancer cells. Cytotoxicity was assessed via LDH release and CCK-8 assays, while CD107a surface expression was analyzed by flow cytometry to evaluate CarNK activation. In vivo, two models were established: 1) Balb/c nude mice subcutaneously injected with CarNK/A549$^{EGFRvIII+}$ mixtures (ratios 1:1, 1:2 to 1:5) underwent [68Ga]Ga-NOTA-GZP PET/CT imaging; 2) SCID NOD mice bearing A549$^{EGFRvIII+}$ subcutaneous tumors received CarNK cell infusion, followed by longitudinal PET imaging at days 1, 3, 7, and 12 post-treatments. Survival analysis correlated imaging metrics with therapeutic efficacy. ***Results:*** In vitro, CarNK cells exhibited peak LDH release at an effector-to-target (E: T) ratio of 5:1, significantly surpassing wild-type NK92 cells ($P < 0.05$), while CCK-8 assays demonstrated minimal residual cell viability in the corresponding groups ($P < 0.05$). Flow cytometry confirmed A549$^{EGFRvIII+}$-specific CarNK activation for 4h (CD107a+ proportion: 21.7% vs. 12.6% in NK92, $P<0.05$). In vivo, Balb/c nude mice with CarNK: A549$^{EGFRvIII+}$=1:5 showed higher tracer uptake ($P<0.05$). In SCID NOD mice, CarNK group achieved maximal the ratios of T/B (The ratios of tumor %ID/g to blood %ID/g was defned as T/B). at day 7, 1.56-fold higher than NK92 controls ($P<0.05$). Kaplan-Meier analysis revealed prolonged median survival in high-uptake cohorts ($P<0.05$). ***Conclusion:*** [68Ga]Ga-NOTA-GZP PET enables noninvasive monitoring of granzyme B activity, indirectly reflecting CarNK infiltration and cytotoxic efficacy. This approach provides a translational imaging biomarker for ACT outcome prediction, with critical implications for personalized immunotherapy.

EPS-011

Dual-Modality NIRF/PET Imaging of Pre-targeted Glycoengineered CAR-NK Cells for Theranostic Monitoring in Glioblastoma

W. Cao, *L. Zhang;*
Department of Nuclear Medicine, Union Hospital, Tongji Medical College, Huazhong University of Science and Technology, 430022, Wuhan, China, Wuhan, CHINA.

Aim/Introduction: Glioblastoma (GBM), the most aggressive primary brain tumor, remains a therapeutic challenge. Despite emerging advances in chimeric antigen receptor (CAR)-engineered immune cell therapy, noninvasive tracking of CAR-NK cells in GBM treatment remains unexplored. This study aimed to develop a bioorthogonal click chemistry-based dual-modality imaging platform for real-time monitoring of adoptively transferred CAR-NK cells. ***Materials and Methods:*** A pre-targeted imaging strategy integrating metabolic glycoengineering and bioorthogonal click chemistry was established. Key procedures included:Cell Models:Lentiviral transduction generated U87-EGFRvIII-overexpressing and control U87-CON cell lines.CAR-NK cells were engineered from NK-92 cells using a second-generation CAR lentiviral vector targeting EGFRvIII. Metabolic Labeling: CAR-NK cells were incubated with N-azidoacetyl-D-mannosamine tetraacetate (Ac4ManNAz) to incorporate azide (N_3) groups onto cell-surface glycans, yielding N_3-CAR-NK cells. Probe Synthesis: NIRF probe: Cy5.5-conjugated dibenzocyclooctyne (DBCO-Cy5.5). PET probe: ^{68}Ga-labeled NETA-DBCO (^{68}Ga-NETA-DBCO). In Vivo Validation: Subcutaneous and orthotopic U87-EGFRvIII glioma models were established. N_3-CAR-NK cells were intravenously administered, followed by NIRF and PET imaging. ***Results:*** In Vitro: Western blot confirmed EGFRvIII overexpression in U87-EGFRvIII cells. Fluorescence microscopy demonstrated stable GFP expression in CAR-NK cells. CCK-8 assays revealed no cytotoxicity of Ac4ManNAz at ≤30 μM ($P>0.05$), while 60 μM reduced viability to 72% ($P<0.05$). LDH assays showed preserved cytolytic activity of 30 μM Ac4ManNAz-treated CAR-NK cells against U87-EGFRvIII ($P>0.05$). In Vivo: In subcutaneous tumors, Cy5.5-CAR-NK cells accumulated specifically by day 3, with signal persistence until day 12. Orthotopic models exhibited higher intracranial NIRF signal vs. controls ($P<0.05$), indicating blood-brain barrier penetration. PET imaging confirmed efficient ^{68}Ga-DOTA-DBCO binding to N_3-CAR-NK cells in vivo. ***Conclusion:*** This study pioneers a pre-targeted dual-modality NIRF/PET strategy for real-time tracking of CAR-NK cells, offering a transformative imaging tool to evaluate adoptive immunotherapy efficacy in GBM, with significant clinical translation potential.

EPS-012

^{225}Ac-NM600 Efficacy in Murine Models of Metastatic and Localized Triple Negative Breast Cancer

Y. Medina Guevara, *H. Comas Rojas, O. Bio Idrissou, L. Lambert, L. Wehner, M. Lindsey, A. Pinchuk, A. Carston, N. Clemons, J. Grudzinski, B. Bednarz, J. Weichert, R. Hernandez;*
University of Wisconsin-Madison, Madison, WI, UNITED STATES OF AMERICA.

Aim/Introduction: Advanced breast cancer remains incurable. The absence of estrogen receptor, progesterone receptor, and HER2 expression in triple-negative breast cancer (TNBC) limits the use of targeted therapies. Chemotherapy offers brief responses with poor prognosis. We have developed several alkyphosphocholine analogs (NM600) as tumor-selective targeted radioligands for radiopharmaceutical therapy (RPT). Herein, we investigate [^{225}Ac]Ac-NM600 therapeutic efficacy and safety in two murine models of TNBC ***Materials and Methods:*** In vitro, cytotoxicity studies were performed in 4T1 (metastatic murine TNBC cells) and 4T07 (non-metastatic murine TNBC cells). Monte Carlo-based ^{225}Ac dosimetry estimates enabled viability and clonogenic survival measurements in cells treated with ^{225}Ac (0.03-1 Gy). In vivo, female Balb/c 10-12 weeks old were subcutaneously implanted with 4T1 or 4T07 cells, and caliper measurement determined tumor volume. NM600 was radiolabeled with ^{225}Ac following previous methods. Longitudinal ex vivo biodistribution studies were performed in mice bearing 4T1 or 4T07 tumor grafts injected with 9.25 kBq [^{225}Ac]Ac-NM600 at 24, 72, 120, and 144 h post-injection (p.i.). Three groups of mice ($n=5$) received IV injections of vehicle, or 9.25 or 18.5 kBq [^{225}Ac]Ac-NM600. Tumor volume and overall survival were monitored thrice weekly. Toxicity was evaluated in groups of Balb/c mice ($n=3$) at days 7, 30, and 120 p.i. through complete blood count (CBC), serum chemistry, and histopathological analysis ***Results:*** In vitro, free ^{225}Ac showed comparable cytotoxicity in 4T1 and 4T07 cells, with an enhanced effect at higher estimated doses. In vivo, ex vivo biodistribution revealed elevated radioactivity in the blood and lungs, followed by a gradual decline over time. Due to the hepatobiliary excretion of [^{225}Ac]Ac-NM600, distribution in normal tissues was most prominent in the liver, with absorbed doses of 57 Gy/μCi and 63 Gy/μCi for mice bearing 4T1 and 4T07 tumors, respectively. Similarly to the liver, uptake in tumor regions progressively increased, resulting in 46 Gy/μCi and 42 Gy/μCi. Mice bearing 4T1 or 4T07 tumors and treated with [^{225}Ac]Ac-NM600 exhibited significant tumor growth inhibition ($p \leq 0.015$). Median survival for mice bearing 4T1 or 4T07 tumors was 18, 30, and 42 days, or 30, 84, and 90 days, for the vehicle, 18.5 kBq, and 9.25 kBq groups, respectively. Mice administered 9.25 or 18.5 kBq of [^{225}Ac]Ac-NM600 exhibited only mild effects, and no treatment-related mortality was observed ***Conclusion:*** These findings underscore the potential of [^{225}Ac]Ac-NM600 as a promising therapeutic agent for TNBC, warranting further assessments of efficacy and potential toxicities in additional TNBC animal models.

EPS-013

Preclinical evaluation of DOTAGA.PEG$_2$.Glu.(FAPI)$_2$, a FAP dimeric inhibitor, for developing theranostic radiotracers in FAP-positive malignancies

N. Kumar[1], *A. Bilinska*[1], *E. Menéndez*[1], *T. Läppchen*[1], *M. Marcel*[2], *F. Rösch*[2], *A. Rominger*[1], *E. Gourni*[1];
[1]*Department of Nuclear Medicine, Inselspital, Bern University Hospital, University of Bern, Bern, SWITZERLAND,* [2]*Department of Chemistry-TRIGA site, Johannes Gutenberg University of Mainz, Mainz, GERMANY.*

Aim/Introduction: Targeting components of the tumor stroma offers a promising theranostic approach for cancer management. Among these components, the fibroblast activation protein (FAP) attracts attention due to its overexpression on cancer activated fibroblasts (CAFs) in various tumor types, while being largely absent in healthy tissues and most non-malignancies. This study aims at preclinical evaluation of DOTAGA.PEG$_2$.Glu.(FAPI)$_2$, a FAP-dimeric-based inhibitor, as a potential precursor for developing theranostic radiopharmaceuticals targeting FAP-positive tumors. ***Materials and Methods:*** DOTAGA.PEG$_2$.Glu.(FAPI)$_2$ was labeled with gallium-68 and lutetium-177. Both radiotracers were evaluated in-vitro (lipophilicity, protein binding, saturation, internalization and externalization) on immortalized CAFs expressing FAP. In-vivo studies (biodistribution, metabolic stability in plasma, blood clearance kinetics, PET/SPECT/CT imaging) were performed in PC3-xenografts. ***Results:*** DOTAGA.PEG$_2$.Glu.(FAPI)$_2$ was radiolabeled with gallium-68 and lutetium-177, in >98% radiochemical purity. The apparent molar activities (Am) ranged from 15-20 GBq/μmol for the ^{68}Ga-labeled and 10-26 GBq/μmol for the ^{177}Lu-labeled tracer. [^{68}Ga]Ga-DOTAGA.PEG$_2$.Glu.(FAPI)$_2$ and [^{177}Lu]Lu-DOTAGA.PEG$_2$.Glu.(FAPI)$_2$ demonstrated Log_D values of -3.0 and -3.3, respectively. Both radiotracers exhibited high FAP affinity (K_d: 0.9-1.2 nM). Internalization was rapid, with up to 95 % of total cell-bound activity internalized within 30 min in CAFs. Externalization studies showed that 35% of the total internalized

activity was released from the cells after 24 h of incubation. Incubation of the radiotracers with human plasma revealed that ~8% and ~4% for [^{68}Ga]Ga-DOTAGA.PEG$_2$.Glu.(FAPI)$_2$ and [^{177}Lu]Lu-DOTAGA.PEG$_2$.Glu.(FAPI)$_2$ was bound to the proteins after 30 and 60 min of incubation. Metabolic studies showed that both tracers are stable in plasma. Biodistribution studies of [^{68}Ga]Ga-DOTAGA.PEG$_2$.Glu.(FAPI)$_2$ at 1, 2, and 3 h p.i. (n=5), revealed high and consistent tumor uptake (19.2±2.7, 18.3±3.3 and 21.4±5.6 %IA/g at 1, 2 and 3 h p.i.) with low blood activity levels at all tested time points (~2.9 %IA/g). For [^{177}Lu]Lu-DOTAGA.PEG$_2$.Glu.(FAPI)$_2$, tumor uptake at 4 h p.i. was 16.1±2.6 %IA/g and decreasing to 3.7±0.2 %IA/g by 48h. Blood retention decreased from ~2.0 %IA/g at 4 h to 0.2 %IA/g at 48 h for [^{177}Lu]Lu- DOTAGA.PEG$_2$.Glu.(FAPI)$_2$. For both tracers, the accumulated activity in the kidneys and liver remained below 3% IA/g and decreased over time, leading to high tumor-to-normal organ ratios at all time points, as confirmed by the high-contrast PET/SPECT/CT images. ***Conclusion:*** The results provide strong evidence for the potential use of DOTAGA.PEG$_2$.Glu.(FAPI)$_2$ as a promising theranostic agent for targeting FAP-positive tumors. The compound demonstrated significant potential to enhance precision oncology by utilizing their ability to both identify and therapeutically address FAP-expressing malignancies.

EPS-014

Development and Evaluation of a BCMA-Targeted Bicyclic Peptide Imaging Probe for Multiple Myeloma Detection

L. Kang[1], *L. Song*[1], *Q. Yang*[1], *Y. Qiu*[1], *Z. Chen*[1], *X. Sun*[1], *W. Huang*[1], *T. Wang*[1], *Z. Wang*[2];
[1]Dept. of Nuclear Medicine, Peking University First Hospital, Beijing, CHINA, [2]Fujian Provincial Key Laboratory of Brain Aging and Neurodegenerative Diseases, School of Basic Medical Sciences, Fujian Medical University, Fuzhou, CHINA.

Aim/Introduction: Multiple myeloma (MM) is a hematologic malignancy marked by abnormal bone marrow plasma cell proliferation and excessive monoclonal immunoglobulin production. Current diagnostic methods, such as bone marrow biopsy and imaging (X-ray, CT, MRI), face limitations in sensitivity, specificity, and non-invasiveness. Although ^{18}F-FDG is widely used for MM diagnosis and monitoring, its lack of specificity remains a challenge. This study aims to develop a BCMA-targeted bicyclic peptide imaging probe to improve stability, specificity, and imaging performance for MM detection. ***Materials and Methods:*** A bicyclic peptide (BCP1) targeting BCMA was synthesized using a 1,3,5-tris(bromomethyl)benzene (TBMB) scaffold, forming a stable structure via cysteine thiol residues. BCP1 was radiolabeled with ^{68}Ga to produce [^{68}Ga]Ga-DOTA-BCP1, with radiochemical purity and stability assessed by HPLC. In vitro uptake experiments in H929 myeloma cells evaluated targeting specificity. PET/CT imaging in H929 (BCMA-positive) and K562 (BCMA-negative) tumor models assessed in vivo targeting efficiency. Pharmacokinetic studies in primates evaluated metabolic pathways and clearance mechanisms. ***Results:*** HPLC analysis confirmed that [^{68}Ga]Ga-DOTA-BCP1 exhibited high radiochemical purity (>95%) and remained stable in physiological saline and FBS for at least 2 hours, with no significant degradation. Cell uptake experiments demonstrated a significantly higher binding rate of [^{68}Ga]Ga-DOTA-BCP1 to H929 myeloma cells (0.497±0.06%) compared to the blocked group (0.225±0.03%, $P < 0.01$) and the BCMA-negative K562 cells (0.255±0.04%, $P < 0.01$), confirming its strong affinity and specificity for BCMA-expressing tumors. PET/CT imaging in tumor-bearing mice revealed rapid and selective accumulation of [^{68}Ga]Ga-DOTA-BCP1 in H929 tumors, with sustained uptake up to 60 minutes post-injection. In contrast, BCMA-negative K562 tumors showed no significant uptake, further validating specificity. Biodistribution analysis quantified tumor uptake, showing significantly higher retention in H929 tumors (1.38±0.08 %ID/g at 30 min, 1.05±0.04 %ID/g at 60 min) compared to K562 tumors ($P < 0.001$). Immunofluorescence staining confirmed high BCMA expression in H929 tumors, correlating with observed imaging results. Pharmacokinetic studies in non-human primates demonstrated that [^{68}Ga]Ga-DOTA-BCP1 exhibited a rapid distribution phase, predominantly renal clearance, minimal hepatic accumulation, and a favorable metabolic profile, supporting its potential for clinical translation. ***Conclusion:*** [^{68}Ga]Ga-DOTA-BCP1 demonstrated strong potential for non-invasive, MM-specific PET imaging, offering a promising alternative to repeated invasive biopsies. Its high specificity, stability, and favorable pharmacokinetics support its clinical application for MM diagnosis and monitoring, making it a viable candidate for future precision imaging of BCMA-positive malignancies.

EPS-015

How does ionizing radiation activate photosensitizers—and how can this improve radiotherapy?

B. Xu[1], *R. Eelkema*[2], *A. G. Denkova*[1];
[1]Department of Radiation Science and Technology, Delft University of Technology, Delft, NETHERLANDS, [2]Depatment of Chemical Engineering, Delft University of Technology, Delft, NETHERLANDS.

Aim/Introduction: Photosensitizers (PSs) have attracted growing attention as potential radiosensitizers due to their ability to generate reactive oxygen species (ROS) when activated by ionizing radiation[1]. Unlike conventional chemotherapeutic agents, which often cause severe systemic side effects, PSs exhibit minimal toxicity in their inactive form, reducing damage to healthy tissue. Even though clinical studies have shown promising results[2-4], the mechanism underlying their activation by ionizing radiation, rather than light, remains unknown. Obtaining an understanding of the activation mechanisms can help to improve their effectiveness when combined with radiotherapy. ***Materials and Methods:*** This study explores the radiation-induced activation of chlorin e6 (Ce6), focusing on how photon energy, dose and dose rate influence the generation of singlet oxygen ($^1O_2$). Experiments were conducted using X-rays (up to 310 kV) and ^{60}Co gamma rays (1.17 and 1.33 MeV) across a range of doses and dose rates. The formation of $^1O_2$ was measured using the singlet oxygen sensor green (SOSG) probe and the imidazole/RNO method. ***Results:*** Our results revealed that both energy and dose rate significantly impact $^1O_2$ production, with unexpectedly high yields observed at very low dose rate. Scavenger experiments further showed that the superoxide anion ($\cdot O_2^-$) is a critical intermediate in the activation pathway. ***Conclusion:*** our results suggest that the typical triplet-state mediated energy transfer involved in light activation does not play a role in ionizing radiation exposure. Instead, our data supports a radical-driven mechanism in which Ce6 radical cations together with $\cdot O_2^-$, play a key role in generating $^1O_2$. The activation at low dose rates (0.005 Gy/min) suggests that photosensitizers are best combined with radionuclide therapy or low dose brachytherapy. ***References:*** 1Owari, T. et al. 5-Aminolevulinic acid overcomes hypoxia-induced radiation resistance by enhancing mitochondrial reactive oxygen species production in prostate cancer cells. British Journal of Cancer 127, 350-363, doi:10.1038/s41416-022-01789-4 (2022).2Schaffer, M. et al. Feasibility of Photofrin II as a Radiosensitizing Agent in Solid Tumors - Preliminary Results. Oncology Research and Treatment 29, 514-519, doi:10.1159/000095979 (2006).3Schwartz, S., Absolon, K. & Vermund, H. Hospital Report Porphyrins, X-Rays and Tumors. Univ. Minnesota Med. Bull. 27, 1-37 (1955).4Pepper, N. B. et al. ALA-RDT in GBM: protocol of the phase I/II dose escalation trial of radiodynamic therapy with 5-Aminolevulinic acid in patients with recurrent glioblastoma. Radiation Oncology 19, doi:10.1186/s13014-024-02408-7 (2024).

EPS-016

Synergistic Antitumor Effects of B-OT and ^{177}Lu-PSMA-617 in PSMA-Positive Prostate Cancer via Transketolase Inhibition

Q. Wu[1,2,3], *T. Zhao*[1,2,3], *X. Yao*[1,2,3], *R. P. Baum*[4], *X. Duan*[1,2,3], *J. Zhang*[1,2,3];
[1]*Departments of Diagnostic Radiology, Yong Loo Lin School of Medicine, National University of Singapore, Singapore, SINGAPORE,* [2]*Theranostics Center of Excellence (TCE), Yong Loo Lin School of Medicine, National University of Singapore, 11 Biopolis Way, Helios, Singapore 138667, Singapore, SINGAPORE,* [3]*Clinical Imaging Research Centre, Centre for Translational Medicine, Yong Loo Lin School of Medicine, National University of Singapore, Singapore 117599, Singapore, SINGAPORE,* [4]*Curanosticum Wiesbaden-Frankfurt, Center for Advanced Radiomolecular Precision Oncology, Wiesbaden, GERMANY.*

Aim/Introduction: Prostate-specific membrane antigen (PSMA)-targeted radioligand therapy (RLT) with ^{177}Lu-PSMA-617 has shown promise in treating PSMA-expressing tumors. However, the efficacy of ^{177}Lu-PSMA-617 RLT remains limited by intrinsic resistance mechanisms in prostate cancer. Benfo-oxythiamine (B-OT), a derivative of oxythiamine, inhibits transketolase in the non-oxidative branch of the pentose phosphate pathway (PPP), thereby reducing ribose-5-phosphate synthesis and impairing DNA repair. We hypothesized that B-OT could act as a radiosensitizer to enhance the efficacy of ^{177}Lu-PSMA-617 therapy in PSMA-positive prostate cancer. Unlike existing combination approaches that focus on DNA repair inhibition or target upregulation, our strategy employs B-OT to induce metabolic crisis through dual mechanisms, depletion of nucleotide precursors essential for radiation damage repair, and reduction of NADPH pools required for oxidative stress defense. ***Materials and Methods:*** PSMA-expressing pip-PC3 xenografts (80-100 mm^3) were randomized to: (1) PBS control, (2) B-OT alone (oral gavage, -2 d pre-RLT then dosing every 3 d), (3) ^{177}Lu-PSMA-617 alone (350 µCi), or (4) combination therapy (n=6/group). Tumor response was assessed by caliper measurements and SPECT/CT imaging (Days 1,2,3,7,14). Terminal IHC analysis evaluated Ki67, TUNEL, DNA damage (γ-H2AX), and metabolic stress markers. Safety was monitored via weight and clinical observation. ***Results:*** The BOT combination group demonstrated superior antitumor activity, achieving complete remission in 33% of mice (2/6 mice) and a 100% objective response rate by Day 14 ($p<0.001$ vs. RLT alone). Quantitatively, the combination yielded a tumor growth inhibition (TGI) of 106.9% and a tumor regression rate of 90.45%, significantly surpassing the effects of RLT monotherapy. Mechanistic studies revealed increased DNA damage, a reduction in tumor nucleotide levels and stable PSMA expression by IHC, verifying target-agnostic action. Importantly, the combination was well-tolerated with no additional toxicity over RLT monotherapy. ***Conclusion:*** B-OT enhances the therapeutic efficacy of ^{177}Lu-PSMA-617 in PSMA-positive prostate cancer by impairing nucleotide synthesis and DNA repair through transketolase inhibition. The oral bioavailability and favorable safety profile of B-OT support clinical translational potential to address RLT resistance in prostate cancer.

EPS-017

Efficacy of FAP-targeted radiopharmaceutical treatment: Comparing [^{177}Lu]Lu-FAP-2286 and [^{161}Tb]Tb-FAP-2286 behavior and efficacy in vitro and in vivo

C. D. van der Heide[1], *C. Ntihabose*[1,2], *H. Ma*[1], *M. Konijnenberg*[1], *Y. Seimbille*[1], *M. Doukas*[3], *D. Stuurman*[1], *C. de Ridder*[4], *E. de Blois*[1], ***S. U. Dalm***[1];
[1]*Department of Radiology & Nuclear Medicine, Erasmus MC, Rotterdam, NETHERLANDS,* [2]*Department of Hospital Pharmacy, Erasmus MC, Rotterdam, NETHERLANDS,* [3]*Department of Pathology, Erasmus MC, Rotterdam, NETHERLANDS,* [4]*Department of Experimental Urology, Erasmus MC, Rotterdam, NETHERLANDS.*

Aim/Introduction: Fibroblast activation protein (FAP), predominantly expressed on cancer-associated fibroblasts (CAFs), is present >90% of solid cancers, making it an ideal target for radionuclide theranostics. Imaging studies using FAP-targeting radiopharmaceuticals are promising, but it remains to be elucidated whether FAP-targeted radionuclide treatment (TRT) is effective. Regarding TRT, the beta-minus, conversion- and auger-electrons emitted by Tb-161 are potentially more cytotoxic than the beta-minus radiation emitted by Lu-177. We aimed to determine FAP-TRT efficacy using radiolabeled FAP-2286, and compared [^{177}Lu]Lu-FAP-2286 and [^{161}Tb]Tb-FAP-2286 treatment. Prior to this, we compared radiopharmaceutical behavior and potential dose-effects. ***Materials and Methods:*** FAP-2286 was labeled with luteium-177 or terbium-161, and radiopharmaceutical stability in mouse serum was determined. FAP affinity and radiopharmaceutical uptake were evaluated in vitro using the FAP-transduced human fibrosarcoma cell line HT1080-FAP. To determine affinity, cells were exposed to 1 nM [^{177}Lu]Lu-FAP-2286/[^{161}Tb]Tb-FAP-2286 (20 MBq/nmol), +/- 10^{-12}-10^{-6} M UAMC-1110. Furthermore, cells were incubated with 1 nM [^{177}Lu]Lu-FAP-2286/[^{161}Tb]Tb-FAP-2286 (20 MBq/nmol), +/- 1 mM UAMC-1110, to determine radiopharmaceutical uptake. Additionally, ex vivo biodistribution studies were performed post injection of 5 MBq/500 pmol in C57BL/6 mice xenografted with FAP-negative mouse pancreatic cancer cells, PDAC229, known to attract CAFs in vivo. Using the biodistribution data, dosimetry calculations were performed to guide subsequent efficacy studies in the same animal model. First, treatment with 4×40 MBq/500 pmol [^{177}Lu]Lu-FAP-2286 or 4×40 MBq/500 pmol [^{161}Tb]Tb-FAP-2286 was compared. Hereafter, treatment with alternating doses of 2×40 MBq/500 pmol of each radiopharmaceutical was evaluated. ***Results:*** FAP-2286 was successfully labeled with lutetium-177 and terbium-161 (RCY>98%, RCP>97%). Radiopharmaceutical stability in mouse serum decreased over time, with <13% intact [^{177}Lu]Lu-FAP-2286/[^{161}Tb]Tb-FAP-2286 present after 24 h. FAP affinity (IC_{50}: 2.9±7.2 nM (Lu-177) and 1.5±3.2 nM (Tb-161)) and in vitro radiopharmaceutical uptake (19.7±6.8% (Lu-177) and 18.5±5.2% (Tb-161) added activity/200,000 cells after 1 h) was comparable. Similarly, ex vivo biodistribution studies showed no relevant differences in radiolabeled FAP2286 uptake in blood, tumor and background organs of PDAC229-xenografted animals, e.g. tumor uptake was 1.85±0.39% and 1.39±0.45% injected dose/g for Lu-177 and Tb-161, respectively, 1 h post injection. Unfortunately, no significant survival benefit was observed in animals treated with 4×[^{177}Lu]Lu-FAP-2286 or 4×[^{161}Tb]Tb-FAP-2286. Remarkably, treatment with 2×[^{161}Tb]Tb-FAP-2286 and 2×[^{177}Lu]Lu-FAP-2286 did show a significant prolonged survival compared to animals receiving vehicle. ***Conclusion:*** We demonstrated that [^{177}Lu]Lu-FAP-2286 and [^{161}Tb]Tb-FAP-2286 have similar behavior. In our in vivo study using a clinically representative mouse model, limited FAP-TRT efficacy was observed, with only tandem treatment with Lu-177 followed by Tb-161 being beneficial.

EPS-018

Biodistribution Study of Intraperitoneally Administered Annexin A1 in Mouse Ovarian Cancer Models

L. Xu[1], *S. K. Singh*[1], *K. R. Smith*[1], *C. Mallett*[1], *D. Agnew*[1], *J. Schnitzer*[2], *K. R. Zinn*[1];
[1]*Michigan State University, East Lansing, MI, UNITED STATES OF AMERICA,* [2]*Proteogenomics Research Institute for Systems Medicine (PRISM), La Jolle, CA, UNITED STATES OF AMERICA.*

Aim/Introduction: A humanized antibody Annexin A1 (hAnnA1) is known to target caveolae on tumor endothelium, leading to hAnnA1 accumulation in the tumor space by a pumping mechanism (1). This study assessed the potential of hAnnA1 for tumor imaging following intraperitoneal (IP) injection of the labeled antibody in immune-competent mouse ovarian cancer

models. ***Materials and Methods:*** FVB (n=8) and C57BL/6 (n=8) female mice were intraperitoneally implanted with luciferase-positive 30200 and HGS2 tumor spheroids, respectively. Bioluminescence imaging (Revvity IVIS) was used to monitor tumor growth in both groups for 3 months prior to IP injection of IRDye680-hAnnA1 mixed with Tc99m-HYNIC-hAnnA1 (HGS2, n=4) or Zr-89-DFO-hAnnA1 (30200, n=4). Strain-matched controls received IRdye680-IgG1 co-injected with Tc99m-HYNIC-IgG1 (HGS2, n=4) or Zr-89-DFO-IgG1 (30200, n=4). Fluorescence imaging (LICORbio Pearl Trilogy) was used to determine antibody localization in mice. PET/MR imaging (7T Bruker BioSpec) was performed following initial injection and 6 hours post-injection for FVB mice. Regions of interest were derived from bioluminescence images (centered on highest intensity pixels) and applied to co-registered PET (MLEM reconstruction with standard corrections) and anatomical MR (3D FISP) images in PMOD to estimate regional radiotracer concentration as %injected dose per mL of tissue (%ID/mL). Biodistribution was conducted for major tissues at 2, 6, and 24 hours to quantify tracer uptake as %injected dose per gram of tissue (%ID/g) using the Gamma Counter (Revvity Wizard2 2480). Statistical analysis (Graphpad) using two-way analysis of variance (ANOVA) with Tukey's test compared antibody uptake levels between tissue groups to assess significance ($p<0.05$). ***Results:*** For both cell lines, labeled hAnnA1 detected by fluorescence and PET were co-localized with the tumor's bioluminescence signal, but not for IgG1 controls. Significantly higher hAnnA1 uptake was observed for 30200 tumors at 2 hours (14.1±2.3 %ID/g for hAnnA1 vs 4.3±1.0 %ID/g for IgG1) and 6 hours (19.9±3.0 %ID/g for hAnnA1 vs 6.5±3.1 %ID/g for IgG1) post-injection ($p<0.05$). hAnnA1 levels (1.9±0.9 %ID/g) were the highest compared to IgG1 (0.02±0.01 %ID/g) at 2 hours post-injection for HGS2 tumors ($p<0.05$). Blood levels of hAnnA1 were highest at 6 hours post-injection (24.5±3.2 %ID/g for 30200 and 22.8±1.4 %ID/g for HGS2). Larger tumors exhibited higher hAnnA1:IgG1 ratios, possibly due to more mature blood vessel formation. hAnnA1/IgG ratios and trends observed in PET data agree with biodistribution results. ***Conclusion:*** hAnnA1 antibody is a promising targeting agent for ovarian cancer, showing high tumor uptake in immune-competent mouse models with minimal off-target binding. ***References:*** 1. Nat Med. 2014 Sep 1; 20(9):1062-8.

EPS-019

Design and Preclinical Evaluation of a Small-Molecule Diagnostic and Therapeutic Radionuclide Probe Targeting Tumor Extracellular Nucleotidase CD73

C. Zhao, *L. Li, X. Wu;*
West China Hospital, Sichuan University, Chengdu, CHINA.

Aim/Introduction: CD73 (Ecto-5'-Nucleotidase, NT5E) inhibits anti-tumor immune responses and promotes tumor immune evasion, metastasis, and drug resistance. Therefore, accurate evaluation of CD73 expression level in tumor tissues is of great significance for tumor targeted therapy and treatment efficacy prediction. This study aims to develop a novel non-nucleotide small-molecule radiotracer targeting CD73 for accurate in vivo PET imaging of CD73 expression. Additionally, radionuclide-labeled therapeutic agents were prepared to achieve integrated diagnosis and therapy targeting CD73. ***Materials and Methods:*** Based on the crystal structure of CD73 protein reported in the literature, we synthesized a series of non-nucleoside small-molecule inhibitors targeting CD73 and screened the test compounds through in vitro enzymatic activity assays. The selected optimal compound was radiolabeled with ^{68}Ga, and its targeting specificity was validated via cellular uptake and competitive binding assays. Then, biodistribution and micro-PET/CT imaging studies were conducted to investigate the in vivo metabolic characteristics and imaging performance of the probe. Subsequently, the compound was radiolabeled with ^{177}Lu to evaluate its antitumor efficacy in LS174T and EMT6 tumor-bearing mice. ***Results:*** Through enzymatic activity assays, the newly synthesized compound HX-6 was selected from seven candidates as having the highest inhibitory activity (IC_{50} = 0.07 μM) and the capability for radioisotope labeling. ^{68}Ga-HX-6 rapidly binds to CD73-positive cells, and this binding can be effectively blocked by the corresponding non-radiolabeled compound, with inhibition rates of 62.5% in LS174T cells and 75.9% in EMT6 cells. Biodistribution studies indicated that ^{68}Ga-HX-6 is primarily metabolized through the liver. Micro-PET/CT imaging demonstrated that ^{68}Ga-HX-6 possesses favorable imaging performance for CD73-positive tumors, with peak tumor uptake reaching 6.98 ± 0.74 %ID/g in LS174T tumors and 6.92 ± 0.65 %ID/g in EMT6 tumors. Moreover, tumor uptake could be effectively blocked by the corresponding non-radiolabeled compound. 177Lu-HX-6 exhibited favorable antitumor efficacy. In LS174T tumor-bearing mice, the best therapeutic outcome was observed with the 37 MBq ^{177}Lu-HX-6 (×4) treatment group, achieving a tumor growth inhibition (TGI) rate of 67.7 ± 5.0%. In EMT6 tumor-bearing mice, the most effective antitumor response was observed with the combination therapy of 37 MBq ^{177}Lu-HX-6 and anti-PD-1, with a TGI of 64.9 ± 4.2%. ***Conclusion:*** ^{68}Ga-HX-6 has a good specific binding power for CD73 and can effectively visualize the content of CD73 in tumor tissues in vivo. ^{177}Lu-HX-6 is a safe and effective radionuclide therapeutic agent, which can significantly delay the growth of CD73-positive tumors.

EPS-020

The absorbed dose-response relationship of the Auger electrons from La-135

M. Crabbe, *K. Spoormans, T. Opsomer, C. Segers, S. Rodriguez Pérez, K. Vermeulen, C. Saldarriaga Vargas, L. Struelens, M. Ooms;*
Belgian Nuclear Research Centre, Mol, BELGIUM.

Aim/Introduction: Auger electron (AE) therapy is expected to be highly efficient for metastatic disease, leading to lower risks of radiotoxicity in healthy tissues. Lanthanum-135 (La-135) has been proposed as a potential candidate for AE therapy, moreover, its production was recently up-scaled to reach a yield and purity suitable for preclinical research (1). In this proof-of-principle study, we assessed the differential dose-response correlation of internalizing (DOTA-TATE) and non-internalizing vectors (DOTA-LM3) labeled with La-135 in in vitro models of neuroendocrine tumors. ***Materials and Methods:*** Quantitative equipment for activity measurements was cross-calibrated based on gamma spectrometry, taking into account relevant geometry and volume effects. Radiochemical conversion (RCC) and purity (RCP) were assessed at molar activities 5-100 MBq/nmol. CA20948 cells (2) were treated with an activity range of 0.31-1.25 MBq/mL of [^{135}La]La-DOTA-TATE and [^{135}La]La-DOTA-LM3 to evaluate the effects on clonogenic potential (CFU) and metabolic activity (MTS). Saturation binding assays were executed for both radioligands at a 0.025-2.5 MBq/mL activity range to verify the subcellular biodistribution parameters. Kinetic uptake data was retrieved from previously published radiolanthanide data (3). To calculate the absorbed dose to the nucleus, the S-values for AE particle emissions were computed via Monte Carlo simulations, while considering a concentric CA20948 sphere model. SPECT imaging of homogeneity and Derenzo phantoms was performed. ***Results:*** Activity calibrations were challenging due to poor reproducibility and extensive non-linearity and measurement geometry effects, which was attributed to substantial low-energy X-ray yield of La-135. The maximum achievable molar activity was 50 MBq/nmol with a RCC and RCP of >99% for [^{135}La]La-DOTA-TATE while this was ~97% and 93%, respectively, for [^{135}La]La-DOTA-LM3. Qualitative SPECT imaging was feasible based on preliminary phantom imaging. The cellular biodistribution pattern of both radioligands corresponded to previous reports with radiolanthanides albeit that K_d and B_{max} of [^{135}La]La-DOTA-LM3 were different in this

study (3). The absorbed dose to the nucleus for both radioligands was very low (<0.15 Gy at 1.25 MBq/mL concentration). No statistically significant biological effects were detected with the CFU or MTS assay. ***Conclusion:*** We conclude that La-135 offers limited therapeutic potential in combination with the respective internalizing and membrane-bound ligands DOTA-TATE and DOTA-LM3 in vitro. Future studies may explore DNA-binding vectors to enable the close-range therapeutic effects of its Auger electrons. ***References:*** 1) Pedersen et al. Applied Radiation and Isotopes. 2023 2) Bernard et al. Nucl Med Commun. 2000 3) Spoormans et al. JNM. 2024

EPS-021

Development of a ^{64}Cu/^{67}Cu theranostic radioligand for imaging and therapy in CXCR4-expressing cancers

I. Astiazaran-Rascon[1], *M. Jaraquemada-Pelaez*[2], *H. Merkens*[1], *N. Colpo*[2], *K. Lin*[2], *F. Benard*[2];
[1]*BC Cancer/UBC, Vancouver, BC, CANADA,* [2]*BC Cancer, Vancouver, BC, CANADA.*

Aim/Introduction: The chemokine receptor 4 (CXCR4) is a G protein-coupled receptor overexpressed in multiple cancers. In recent years, ^{68}Ga and ^{177}Lu-labelled theranostic ligands have been developed for imaging and therapy of CXCR4-expressing cancers. However, their clinical success is limited by biokinetic differences and on-target bone marrow toxicity. The development of copper-based theranostics offers potential advantages due to their identical chemical properties and half-lives optimal for both late timepoint imaging and therapy. A cyclic peptide targeting CXCR4, previously developed in our group, was selected for preclinical evaluation of ^{64}Cu/^{67}Cu-labelled CXCR4 radioligands. ***Materials and Methods:*** A CXCR4-targeting cyclic peptide was chosen for coupling to 1,4,7-triazacyclononane-based chelators (p-SCN-Bn-NOTA and NODAGA). In vitro binding affinity to CXCR4 was evaluated in a competition binding assay. Our lead candidate (NODAGA-BL34) was labelled with [^{64}Cu/^{67}Cu]Cl_2 for in vitro and in vivo characterization. The time-course biodistribution of [^{64}Cu]Cu-NODAGA-BL34 was evaluated by PET imaging and biodistribution studies in two tumour models (Z138 and LTL331R) with different CXCR4 expression levels. Specific binding was confirmed by blocking with unlabeled CXCR4-targeting peptide. [^{67}Cu]Cu-NODAGA-BL34 specific binding was validated through cell uptake and internalization studies. ***Results:*** The BL34 pharmacophore was successfully coupled to three different 1,4,7-triazacyclononane-based chelators. The cold standard, ^{nat}Cu-NODAGA-BL34, showed high in vitro binding affinity to human CXCR4 (IC_{50}= 12.2±3.4 nM). NODAGA-BL34 was radiolabelled with ^{64}Cu and ^{67}Cu with a radiochemical purity of >95%. Moreover, both radioligands resulted in similar partition coefficients. [^{64}Cu]Cu-NODAGA-BL34 showed high tumour uptake at 1h post-injection in Z138 (12.5±1.5 %IA/g) and LTL331R-tumour bearing mice (7.2±2.3 %IA/g). After 24h, tumour uptake values decreased by 48% (6.5±0.3 %IA/g) and 82% (1.3±0.2 %IA/g) in Z138 and LTL331R, respectively. In both models, the tracer was cleared mainly through the renal pathway and the maximum tumour uptake correlates to the CXCR4 protein expression levels observed by western blot. [^{67}Cu]Cu-NODAGA-BL34 resulted in >60% cell uptake after 3 hours in CXCR4-expressing cells. ***Conclusion:*** The results presented show that [^{64}Cu]Cu-NODAGA-BL34 accumulates in the tumour site at high levels in CXCR4-expressing tumour models. Minimal uptake in major organs such as kidneys and liver was observed with time. Currently, in vivo characterization of [^{67}Cu]Cu-NODAGA-BL34 is being performed to design a dose-escalation therapy study.

210

Sunday, October 5, 2025, 08:00 - 09:30
Room 116

CTE 1 - Technologists Committee / SNMMI: Technologists' Guide Launch

OP-062a

Why is it important to talk about Women's Health?
A. Pietrzak*; Greater Poland Cancer Centre/Poznan University of Medical Sciences, Poznan, POLAND.*

OP-062b

Why is it important to talk about Women's Health?
L. Evangelista*; Humanitas University, Department of Bioscience, Pieve Emanuele, Milan, ITALY.*

OP-063

Nuclear Medicine role in Endometriosis
G. Costa*; Unidade Local de Saúde de Coimbra, Serviço de Medicina Nuclear, Coimbra, PORTUGAL.*

OP-064

Promising Radiopharmaceuticals
O. Ramsay*; Dana Farber Cancer Institute, Nuclear Medicine, Boston, Massachusetts, UNITED STATES OF AMERICA.*

OP-065

Radiation Protection Considerations for the Female Worker
V. Rowse*; University Hospitals Sussex NHS Foundation Trust, Nuclear Medicine Physics, Brighton, UNITED KINGDOM.*

211

Sunday, October 5, 2025, 8:00 - 9:30
Room 111

Theranostics Track - TROP Session - Oncology & Theranostics Committee: Novel Theranostic Applications

OP-066

^{68}Ga-NY104 PET/CT for the Detection of Clear Cell Renal Cell Carcinoma in Presurgical Patients With Renal Masses: A Prospective Phase II Study

X. Yan[1], *G. Zheng*[2], *M. Liu*[1], *Y. Zhang*[1], *Y. Xie*[1], *W. Zhu*[1], *L. Huo*[1];
[1]*Department of Nuclear Medicine, Peking Union Medical College Hospital, Chinese Academy of Medical Sciences, Beijing, CHINA,* [2]*Department of Urology, Peking Union Medical College Hospital, Chinese Academy of Medical Sciences, Beijing, CHINA.*

Aim/Introduction: Presurgical detection of clear cell renal cell carcinoma (ccRCC) remains challenging with conventional imaging. Contrast-enhanced CT demonstrates suboptimal specificity due to overlapping enhancement patterns with other renal masses. Carbonic anhydrase IX (CAIX) overexpression in clear cell renal cell carcinoma (ccRCC). We developed ^{68}Ga-NY104, a novel small-molecule PET tracer with high affinity to CAIX, and conducted this prospective study to evaluate its ccRCC detection performance in presurgical patients with renal masses. ***Materials and Methods:*** This prospective single-center phase II trial enrolled 51 patients with renal masses scheduled for surgical resection. All patients underwent intravenous injection of ^{68}Ga-NY104 followed by PET/CT imaging at 45-75 minutes post-injection. Surgical specimens were evaluated for histopathological diagnosis and CAIX expression. Diagnostic metrics including sensitivity, specificity, positive and negative predictive values were calculated against pathological results. ***Results:*** A total of 51 patients with renal masses were evaluated, all of whom underwent surgical resection. Histopathological analysis confirmed 36 ccRCC and

15 non-ccRCC cases. At the patient level, ^{68}Ga-NY104 PET/CT demonstrated 91.7% sensitivity (33/36 ccRCC correctly identified) and 60.0% specificity (9/15 non-ccRCC correctly classified). The positive and negative predictive values were 84.6% (33/39) and 75.0% (9/12), respectively. Six false-positive cases included 3 chromophobe RCCs and 2 oncocytomas and 1 FH-deficient RCC. Two of three false-negative cases were CAIX-negative ccRCC (both with extensive hemorrhage and necrosis) showing limited tracer uptake (SUVmax=4.0 and 0.8). The third case was pathologically confirmed as ccRCC (CAIX-positive by immunohistochemistry), showed moderate uptake (SUVmax=9.0, tumor-blood pool ratio=7.5) but was visually interpreted as negative due to high-uptake of normal renal cortex (SUVmax=28.6,). ***Conclusion:*** ^{68}Ga-NY104 PET/CT demonstrates promising diagnostic performance for ccRCC lesion detection in presurgical patients with renal masses.

OP-067

Relationship between [^{18}F]PSMA-1007 PET parameters and biochemical recurrence-free survival in high-risk prostate cancer patients receiving neoadjuvant hormonal treatment

N. Ahmadi Bidakhvidi[1], *A. Giesen*[2], *G. Devos*[2], *A. Laenen*[3], *M. Baldewijns*[4], *M. Koole*[1], *C. M. Deroose*[1], *W. Everaerts*[5], *S. Joniau*[2], *K. Goffin*[1];
[1]*Nuclear Medicine, University Hospitals Leuven; Nuclear Medicine and Molecular Imaging, Department of Imaging and Pathology, KU Leuven, Leuven, BELGIUM,* [2]*Urology, University Hospitals Leuven; Urogenital, Abdominal and Plastic Surgery, Department of Development and Regeneration, KU Leuven, Leuven, BELGIUM,* [3]*Interuniversity Institute for Biostatistics and Statistical Bioinformatics, Leuven, BELGIUM,* [4]*Pathology, University Hospitals Leuven, Leuven, BELGIUM,* [5]*Urology, University Hospitals Leuven; Laboratory of Ion Channel Research, Department of Cellular and Molecular Medicine, KU Leuven, Leuven, BELGIUM.*

Aim/Introduction: To investigate the relationship between [^{18}F]PSMA-1007 PET parameters and biochemical recurrence-free survival (BCR-FS) in high-risk primary prostate cancer patients receiving neoadjuvant hormonal treatment. ***Materials and Methods:*** This prospective randomized, double-blind, placebo-controlled phase II trial included 89 high-risk primary prostate cancer patients who received a pelvic [^{18}F]PSMA-1007 PET/MRI prior to and following neoadjuvant hormonal treatment. Patients were randomly assigned to neoadjuvant hormonal treatment with degarelix + apalutamide (n=45) or degarelix + matching placebo (n=44) for 3 months followed by radical prostatectomy and extended pelvic lymph node dissection. The following [^{18}F]PSMA-1007 parameters were determined on the pre- and posttreatment [^{18}F]PSMA-1007 PET: (i) semi-quantitative [^{18}F]PSMA-1007 PET parameters such as SUV_{max}, SUV_{mean}, PSMA-expressing volume and total lesion activity, and their absolute and relative differences; (ii) number of pelvic lymph node, distant and extraprostatic metastases determined on [^{18}F]PSMA-1007 PET; (iii) [^{18}F]PSMA-1007 PET-based response criteria (aPERCIST and RECIP 1.0); (iv) molecular imaging TNM-stage as determined by PROMISE version 2. ***Results:*** Thirty-five percent of included patients developed BCR within a median follow-up time of 38 months. Multivariate regression analyses revealed that PSMA-expressing volume posttreatment, the number of distant metastases pretreatment and miN1+miN2 vs. miN0 pretreatment were significant predictors of BCR-FS with hazard ratios of 1.184 (95% CI 1.070-1.309, p=0.0010), 5.820 (95% CI 2.498-13.561, p<0.0001) and 4.024 (95% CI 1.740-9.307, p=0.0011), respectively. ***Conclusion:*** Our results indicate that [^{18}F]PSMA-1007 PET can be a tool to monitor response to neoadjuvant hormonal treatment and that [^{18}F]PSMA-1007 PET can be used to aid in patient stratification for determining which patients would benefit from additional (neo)adjuvant treatment.

OP-068

Integrating PSMA PET with mpMRI Enhances Specificity and Reduces Unnecessary Biopsies in Suspected Prostate Cancer: Interim Results of the BIOPSTAGE Trial

M. Celli[1], *R. Gunelli*[2], *F. Ferroni*[1], *M. Costantini*[2], *A. Prochowski Iamurri*[1], *E. Fragalà*[2], *L. Fantini*[1], *I. Marini*[1], *D. Bezzi*[3], *V. Rossetti*[1], *I. Grassi*[1], *S. Nicolini*[1], *E. Giunta*[1], *S. Bellia*[1], *V. Di Iorio*[1], *F. Foca*[1], *F. Matteucci*[1], *P. Caroli*[1];
[1]*IRCCS Istituto Romagnolo per lo Studio dei Tumori (IRST) "Dino Amadori", Meldola (FC), ITALY,* [2]*Morgagni Pierantoni Hospital, Romagna Local Health Service, 47100 Forlì, Italy, Forlì (FC), Italy, Forlì (FC), ITALY,* [3]*Bufalini Hospital, Romagna Local Health Service, 47100 Cesena, Italy, Cesena (FC), Italy, Cesena (FC), ITALY.*

Aim/Introduction: mpMRI is widely used to guide prostate biopsies but suffers from limited specificity. PSMA PET may complement mpMRI by improving lesion characterization. The BIOPSTAGE trial evaluates whether combining the two modalities enhances diagnostic accuracy and biopsy triage in suspected prostate cancer (PCa). ***Materials and Methods:*** In this single-center prospective study, 96 men with clinical suspicion of PCa underwent [^{68}Ga]Ga-PSMA-11 PET/CT and mpMRI prior to prostate biopsy. Clinically significant PCa (csPCa) was defined as ISUP grade group ≥2. ROC analysis determined optimal semiquantitative PET thresholds (SUVmax ≥9.1; SUVratio ≥3.6). Diagnostic performance and biopsy burden were compared for mpMRI alone, PSMA PET alone, and their integration. ***Results:*** mpMRI alone identified 74 lesions (PI-RADS ≥3), achieving 93.8% sensitivity, 54.6% specificity, PPV of 20.3%, and NPV of 98.6%. PSMA PET identified 25 positive lesions in 21 patients using predefined thresholds, with a sensitivity of 85.7%, specificity of 86.3%, PPV of 48.0%, and NPV of 97.6%. Fourteen lesions were concordant between PET and mpMRI, while 11 were PET-only positive. Implementing an integrated approach that targets only PET-positive lesions would reduce biopsy targets by 66.2% compared to an mpMRI-only strategy. This approach increased specificity from 54.6% (mpMRI alone) to 86.3%. Two small csPCa lesions (5 mm and 8 mm, both ISUP 2) were missed by PET but detected on mpMRI. One PET-only lesion was confirmed as csPCa (ISUP 3). Concordant PSMA PET and mpMRI positive lesions had the highest frequency of csPCa (64.3%), compared to 9.1% in PET-only positive lesions. ***Conclusion:*** The integration of semiquantitative PSMA PET with mpMRI enhances lesion-level specificity and substantially reduces biopsy burden. mpMRI remains important for detecting small or low-uptake tumors, but the combined imaging approach may improve biopsy decision-making in men with suspected PCa.

OP-069

Comparison of PET/CT images with ^{68}Ga-NY104 and ^{18}F-FDG in metastatic clear cell renal cell carcinoma

W. Zhu[1], *X. Li*[2], *G. Zheng*[3], *C. Bai*[2], *Y. Zhang*[3], *L. Huo*[1];
[1]*Department of Nuclear Medicine, Beijing Key Laboratory of Molecular Targeted Diagnosis and Therapy in Nuclear Medicine, Peking Union Medical College Hospital, Chinese Academy of Medical Sciences and Peking Union Medical College, Beijing, CHINA,* [2]*Department of Oncology, Peking Union Medical College Hospital, Chinese Academy of Medical Sciences and Peking Union Medical College, Beijing, CHINA,* [3]*Department of Urology, Peking Union Medical College Hospital, Chinese Academy of Medical Sciences and Peking Union Medical College, Beijing, CHINA.*

Aim/Introduction: To evaluate the role of ^{68}Ga-NY104 PET/CT in metastatic clear cell renal cell carcinoma(ccRCC) in comparison with ^{18}F-FDG PET/CT ***Materials and Methods:*** This prospective single-center study (NCT05879471, IRB I-23YJ610) at Peking Union Medical College Hospital (PUMCH, Beijing, China) evaluated 45 consecutive paired ^{68}Ga-NY104/^{18}F-FDG PET/CT scans via independent interpretations. Inclusion required histologically confirmed ccRCC with radiologically/histologically

proven metastases, no change in ccRCC treatment between two scans, and ≥1-week VEGF-TKI washout if applicable. All patients underwent ^{18}F-FDG PET/CT and ^{68}Ga-NY104 PET/CT within a maximum time interval of 7 days. The primary outcome assessed lesion/region-level sensitivity and specificity of ^{68}Ga-NY104 PET/CT and ^{18}F-FDG PET/CT for ccRCC detection. Secondary outcomes included PPV/NPV, SUV_{max}/TBR (stratified by lesion/region type), imaging-histopathology correlation, identification of previously undetected regions, and the clinical impact (high/medium/low/no) of ^{68}Ga-NY104 PET/CT findings on patient management. ***Results:*** 682 lesions (591 ccRCC, 91 non-ccRCC) and 175 regions were analyzed. The lesion-level sensitivity, specificity, PPV, NPV were 94.4% (95%CI, 92.6%-96.3%), 98.9% (95%CI, 96.7%-100%), 99.8% (95%CI, 99.5%-100%), 73.2% (95%CI, 65.3%-81.0%) for ^{68}Ga-NY104, and 78.2% (95%CI, 74.8%-81.5%), 5.5% (95%CI, 0.8%-10.2%), 84.3% (95%CI, 81.3%-87.3%), 3.7% (95%CI, 0.5%-6.9%) for ^{18}F-FDG. For 591 ccRCC lesions, ^{68}Ga-NY104 showed higher SUV_{max} (12.4±11.8 vs. 7.5±10.7, P<0.001) and TBR (15.3±14.6 vs. 4.7±5.5, P<0.001) than ^{18}F-FDG, whereas non-ccRCC lesions exhibited lower tracer uptake (SUV_{max}: 1.2±0.9 vs. 6.7±3.4; TBR: 1.0±0.6 vs. 3.6±2.9; both P<0.001). The region-level sensitivity, specificity, PPV, NPV were 97.0% (95%CI, 94.2%-99.9%), 97.5% (95%CI, 92.7%-100%), 99.2% (95%CI, 97.8%-100%), 90.7% (95%CI, 82.0%-99.4%) for ^{68}Ga-NY104, and 82.2% (95%CI, 75.8%-88.7%), 10.0% (95%CI, 0.7%-19.3%), 75.5% (95%CI, 68.6%-82.5%), 14.3% (95%CI, 1.3%-27.2%) for ^{18}F-FDG. ^{68}Ga-NY104 demonstrated superior lesion/region-level sensitivity and specificity over ^{18}F-FDG (both P<0.001). Of 99 regions previously identified via other imaging, 90 were detected by either PET. ^{68}Ga-NY104 and ^{18}F-FDG PET identified 47 and 32 additional ccRCC regions, respectively. ^{68}Ga-NY104 PET/CT provided additional radiographic information versus ^{18}F-FDG PET/CT in 37 (37/45, 82%) patients, impacting clinical management in 11 (11/45, 24%: 6 high, 5 medium impact) patients. In the remaining 26 patients, added ^{68}Ga-NY104 data revealed no management changes despite supplementary radiographic information. ***Conclusion:*** ^{68}Ga-NY104 PET/CT demonstrates superior diagnostic accuracy, lesion characterization, and clinical utility compared to ^{18}F-FDG PET/CT in metastatic ccRCC, with significantly higher sensitivity and specificity. Its ability to detect occult lesions and influence clinical management underscores its potential as a transformative tool for staging, therapeutic monitoring, and personalized decision-making in ccRCC, particularly in scenarios where ^{18}F-FDG underperforms.

OP-070

Influence of the injected peptide mass on imaging of prostate cancer: Phase I clinical study with the GRPR-antagonist [^{99m}Tc]Tc-DB8

A. Orlova[1], *V. Chernov*[2], *T. Maina*[3], *B. A. Nock*[3], *P. Kanellopoulos*[1], *M. Larkina*[2], *L. Tashireva*[2], *A. Rybina*[2], *R. Varvashenya*[2], *R. Zelchan*[2], *O. Bragina*[2], *A. Medvedeva*[2], *V. Tolmachev*[1];
[1]*Uppsala University, Uppsala, SWEDEN,* [2]*Cancer Research Institute, Tomsk, RUSSIAN FEDERATION,* [3]*NCSR "Demokritos", Athens, GREECE.*

Aim/Introduction: The gastrin-releasing peptide receptor (GRPR) is highly expressed in many human tumors, including prostate cancer (PCa). Its expression in the early stages of PCa, but not in prostate hyperplasia, allows the discrimination of early neoplastic events from common hyperplasia. [^{99m}Tc]Tc-DB8 is a GRPR-antagonist, demonstrating favorable biodistribution in PCa models in mice1. In the present study, we investigated the diagnostic value of [^{99m}Tc]Tc-DB8 in PCa patients, including tolerability and safety assessments and dosimetry calculations. We also performed a mass escalation study for the first time in PCa patients, aiming to improve diagnostic accuracy. ***Materials and Methods:*** A Phase I clinical study was conducted as a single-center diagnostic open-label exploratory study (ClinicalTrials.gov ID NCT05940298). Single intravenous injections of [^{99m}Tc]Tc-DB8 were performed in a 10 ml solution of 40, 80, or 120 µg of peptide. Patients (n=16 with clinically and radiologically diagnosed and histologically verified naïve hormone-sensitive or castration-resistant PCa) underwent whole-body planar imaging and SPECT-CT acquisition 2, 4, 6, and 24 h post-injection (pi). ***Results:*** The safety and tolerability of single intravenous administration of [^{99m}Tc]Tc-DB8 was confirmed for all tested peptide masses injected. The overall activity distribution was characterized by rapid activity excretion via kidneys. Elevated activity uptake was found in the kidneys and pancreatic tissue in the patients injected with 40 µg of peptide. Activity uptake in other normal tissues was low. Increased injected peptide mass led to faster whole-body activity elimination and blood clearance. The effective doses for individual peptide masses did not differ significantly and were in the range of 0.0038-0.0066 mSv/MBq, which corresponded to 1.6-3.0 mSv/procedure. High contrast images were obtained already 2 h pi of [^{99m}Tc]Tc-DB8 for all tested masses of peptide. Primary PCa lesions were visualized in 14 of 15 patients (93.3%, one patient underwent prostatectomy). The highest activity uptake in primary lesions and the highest tumor-to-background ratios were found for [^{99m}Tc]Tc-DB8 injections with 120 µg. Notably, increase of injected mass resulted in 3-fold lower activity uptake in pancreas and 2.5-fold lower activity uptake in kidneys. ***Conclusion:*** [^{99m}Tc]Tc-DB8 turned out to be a promising tracer in the diagnosis of PCa with SPECT/CT and its diagnostic value improved by increasing injected peptide dose. This concept warrants further clinical validation as a new versatile tool to improve image contrast (and potentially also therapeutic efficacy) of other receptor antagonist radioligands. ***References:*** 1. Nock et al. J Med Chem 2018,61:3138.

OP-071

Deep Learning for Automated Whole-Body Tumor Quantification and Prognostic Stratification of Prostate Cancer on ^{68}Ga-PSMA-11 PET/CT

P. Yang[1], *Q. Pan*[2], *L. Jiang*[1], *Z. Zhao*[1], *L. Li*[1], *Q. Guo*[3], *H. Cai*[1];
[1]*West China Hospital of Sichuan University, ChengDu, CHINA,* [2]*Machine Intelligence Laboratory, College of Computer Science, Sichuan University, ChengDu, CHINA,* [3]*School of Artificial Intelligence,Guangxi Minzu University, Nanning, CHINA.*

Aim/Introduction: To develop a deep learning (DL) approach for fully automated, whole-body tumor quantification on ^{68}Ga-PSMA-11 PET/CT and validate its value in prognostic stratification for prostate cancer (PCa). ***Materials and Methods:*** A total of 782 patients with PCa from two independent medical centers were included in this retrospective study, comprising a training cohort (n = 656), an internal testing cohort (n = 73), and an external testing cohort (n = 53). A whole-body tumor segmentation model of ^{68}Ga-PSMA-11 PET was developed based on a transformer-driven framework MedNeXt. Segmentation performance was evaluated by the Dice similarity coefficient (DSC), intersection over union (IoU), sensitivity, and positive predictive value (PPV). DL-based whole-body quantitative PET metrics, including SUVmax, SUVmean, total tumor volume (TV), and total lesion uptake (TLU) were extracted from the automated segmentations and then utilized to predict overall survival (OS) in another 94 patients with Castration-Resistant Prostate Cancer (CRPC). Furthermore, the prognostic performance of these metrics was further compared with that of the miTNM staging system using Harrell's concordance index (C-index). ***Results:*** For the internal testing cohort, the mean DSC, IoU, Sensitivity, and PPV were 0.75±0.24, 0.64±0.24,0.73±0.26, and 0.81±0.21, respectively. For the external testing cohort, the mean DSC, IoU, Sensitivity, and PPV were 0.81±0.17, 0.71±0.19,0.83±0.18, and 0.82±0.18, respectively. DL-based TV (HR: 4.291, p<0.001) and TLU (HR: 3.215, p<0.001) were significantly associated with poor OS. Among all evaluated features, distant lymph node metastasis (M1a), multiple or diffuse bone metastases [M1b (diss or dmi)], organ metastasis (M1c), and DL-based TV together achieved the highest C-index of

0.800 (95%CI: 0.708-0.892) for OS risk prediction. ***Conclusion:*** The proposed approach demonstrated accurate tumor segmentation on ^{68}Ga-PSMA-11 PET/CT scans. Moreover, DL-based TV and TLU showed potential for improving OS prognostic stratification in patients with CRPC.

OP-072

Comparative diagnostic utility and quantification of PSMA-avid lesions on 99mTc-HYNIC-PSMA-11 SPECT/CT with 68Ga-PSMA PET/CT in metastatic prostate cancer patients.

M. Hooda[1], *B. Singh*[1], *R. Mavuduru*[2], *H. Singh*[3], *A. P. Sharma*[2];
[1]*Department of Nuclear Medicine, Post-graduate institute of medical education and research (PGIMER), Chandigarh, INDIA,* [2]*Department of Urology, Post-graduate institute of medical education and research, (PGIMER), Chandigarh, INDIA,* [3]*Department of Nuclear Medicine, Post-graduate institute of medical education and research, (PGIMER), Chandigarh, INDIA.*

Aim/Introduction: In this study, we assessed the diagnostic-efficacy of ^{99m}Tc-HYNIC-PSMA-11(whole-body and regional-SPECT/CT) and compared it with the 'standard-of-care' ^{68}Ga-PSMA-PET/CT, for the detection of primary and metastatic lesions in prostate cancer (PCa) patients. Additionally, we analysed the correlation between semi-quantitative-parameters i.e. the percentage-quantitative-lesion-uptake (%QLU-SPECT) and (SUVmax-PET) of these techniques. Prior studies have highlighted the potential of ^{99m}Tc-HYNIC-PSMA-11 as a cost-effective alternative to ^{68}Ga-PSMA imaging in clinical management of PCa(1). ***Materials and Methods:*** This prospective study included forty-six male-patients (mean-age 67.2±8.41years) with histologically confirmed PCa and raised PSA-levels. Each patient underwent ^{68}Ga-PSMA-PET/CT followed within-one-week by ^{99m}Tc-HYNIC-PSMA-11 scintigraphy. Patients received an intravenous dose of ^{99m}Tc-HYNIC-PSMA-11 (mean-activity 12.3±1.8mCi). The whole-body anterior& posterior at 2h & 4h and regional SPECT/CT at-3h of the involved/suspected sites were acquired using the dual-headed-gamma-camera (Symbia-T16-Siemens, Erlangen, Germany). The comparative data analysis of the two techniques included the number of metastatic-lesions detected on ^{99m}Tc-HYNIC-PSMA-11 in comparison to ^{68}Ga-PSMA-PET/CT imaging. Further, the correlation between the SPECT and PET-based quantitative-parameters i.e. %quantitative-lesion-uptake (%QLU) and SUV_{max} for the matched PSMA-avid lesions detected on both modalities was also evaluated. The method for SPECT-based quantitative analysis has been described by us elsewhere(2). ***Results:*** The mean PSA-levels among patients was 136.10±447.34ng/mL, with a Median Gleason-score of 4.0+3.0 and an ISUP grade of 4.0. Both imaging modalities detected PSMA-avid lesions in 45/46 patients with no disease evidence in one patient on either scan. The primary lesions (n=45) were detected in all the patients on both the imaging techniques. ^{68}Ga-PSMA-PET/CT detected 252 metastatic lesions (5.6-lesions/patient), while ^{99m}Tc-HYNIC-PSMA-11-SPECT/CT identified 209 lesions (4.6-lesions/patient), including 48/68 pelvic nodes; 45/59 distant nodes; 115/124 skeletal lesions; 1/1 visceral lesion. On 165 matched lesions (45 primary;50 lymph nodes(pelvic & distant) and 69 skeletal lesions) detected on both the modalities, the semi-quantitative analysis provided mean-%QLU of 7.76±9.01 and mean-SUV_{max} of 18.30±12.69 respectively. A highly significant-correlation (r=0.61;p<0.001) was noted with the SUV_{max} values. ***Conclusion:*** With the comparative detection efficiency, ^{99m}Tc-HYNIC-PSMA-11 demonstrates 83% lesion-detection and strong-correlation with SUV_{max}, supporting its use as a cost-effective alternative for evaluating metastatic-PCa when ^{68}Ga-PSMA-PET/CT is unavailable(3). ***References:***
1.Baljinder Singh et,al. Comparison of the diagnostic utility of 99mTc-PSMA scintigraphy versus 68Ga-PSMA-11PET/CT in the detection of metastatic-prostate-cancer and dosimetry-analysis:a gamma-camera-based alternate prostate-specific membrane antigen imaging modality.NuclMedCommun.2021;42(5):482-489.2.Amritjyot Kaur et,al. Quantitative liver-SPECT/CT is a novel tool to assess liver function, prognosis, and response to treatment in cirrhosis. FrontMed(Lausanne).2023Mar22:10:1118531.3.Hooda M, et,al.Can 99mTc-PSMA SPECT/CT Presenting Mirror Image of 68Ga-PSMA-PET/CT Be Used for Response-Assessment to 177Lu-PSMA in Metastatic-Castration-Resistant-Prostate-Cancer?ClinNuclMed.2025.

OP-073

Radionuclide Therapy with FAP-2286 in FAP expressing Relapsed / Refractory Malignancies - Proof of Concept and Up-to-date Single Centre Experience

S. Dash*, V. Malasani, R. Vatsa, A. Raj, V. Hari, D. Pendharkar; Sarvodaya Hospital, Faridabad, INDIA.*

Aim/Introduction: Fibroblast activation proteins (FAP) expressed in specific subtypes of "cancer associated fibroblasts (CAF)" are seen in the tumor microenvironment of several cancer types like pancreatic ductal adenocarcinoma, aggressive subtypes of breast cancers, colorectal& gastric cancers, non-small cell lung cancers, ovarian cancer, sarcomas, hepatocellular, and head & neck squamous cell carcinomas· In addition to increased cell migration, angiogenesis, epithelial-to-mesenchymal transition, immune evasion, FAP expression is also linked to chemotherapy resistance and poor prognosis· Recently FAP targeted radiopharmaceuticals have demonstrated promising potential for diagnosis and therapy· This study shares the experience of FAP-2286 theranostics in a tertiary cancer care center in India, establishing proof of concept, safety for palliation, and survival benefits ***Materials and Methods:*** It is an ongoing interventional study comprising 60 patients with relapsed or refractory disease on established standard treatment with ≥80% positive lesions on FAP-2286 PET- CT scan· Patients who had received two or more doses were included (n¦56) for analysis· Depending upon the tumor subtypes & biological behaviour, genetic studies, and clinical profile, patients received either monotherapy (radiolabeled FAP-2286) or combination therapy (radiolabeled FAP-2286 with targeted/Immunotherapy)· The objective response rate (ORR), progression free survival rate (PFSR) and radiopharmaceutical safety were analyzed· Patients with mixed response and progressive disease were excluded from the study ***Results:*** Of the 56 patients (34M,22F) 14 vs 42 received monotherapy and combination therapy, respectively· 37 patients received 4 radionuclide therapy cycles and are under long-term follow up (Table-1)· 177-Lu-FAP-2286, 225-Ac-FAP-2286, and both (tandem) were administered in n≡46, n≡8, and n≡2 patients, respectively· After 2 cycles, 4/14 and 2/14 of monotherapy arm and 6/42 and 3/42 of combination therapy arm were excluded due to mixed response and disease progression, respectively· The ORR, disease control and mean PFSR for monotherapy vs combination therapy were noted to be 42.9%, 14.2%, and 3.5 months vs 57%, 21.4%, and 8.9 months· Patients with combination therapy also experienced other drug-related adverse effects, notably fatigue, skin reactions, and various GI symptoms ***Conclusion:*** FAPI Theranostics with FAP-2286 seems to be a viable alternative for patients failing on all standard lines of management in FAP expressing malignancies· There is definite evidence of improved quality of life, reduction in disease burden, and survival benefit.

OP-074

A FAP-Directed Theranostic Approach Using [^{203}Pb]/[^{212}Pb]Pb-PSV359: Design of a First-in-Human Phase I/IIa Clinical Trial

S. Mehr[1], *R. Patel*[2], *G. Blitzer*[3], *Y. Lu*[4], *V. Sukrithan*[5], *A. Chauhan*[6], *C. Mari Aparici*[7], *M. Puhlmann*[8], *S. Keefe*[8], *L. Baratto*[8], *E. van Dam*[7], *D. Kurup*[7], *H. Tomash*[8], *W. Yang*[8], *J. Calais*[9];
[1]*Nebraska Cancer Specialists, Omaha, NE, UNITED STATES OF AMERICA,* [2]*UPMC, Pittsburgh, PA, UNITED STATES OF AMERICA,* [3]*U of Wisconsin, Madison, WI, UNITED STATES OF AMERICA,* [4]*MD Anderson, Houston, TX, UNITED STATES OF AMERICA,* [5]*Ohio State University, Columbus, OH, UNITED STATES OF AMERICA,* [6]*Sylvester Comprehensive Cancer Center, University of Miami, Miami, FL, UNITED STATES OF AMERICA,* [7]*Stanford University, Standford, CA, UNITED STATES OF AMERICA,* [8]*Perspective Therapeutics, Seattle, WA, UNITED STATES OF AMERICA,* [9]*UCLA, Los Angeles, CA, UNITED STATES OF AMERICA.*

Aim/Introduction: [^{203}Pb]/[^{212}Pb]Pb-PSV359 is a novel theranostic radiopharmaceutical targeting Fibroblast Activation Protein alpha (FAP-α), which can be overexpressed on tumour or stromal cells in the tumour microenvironment. PSV359 is designed for the delivery

of targeted alpha particle therapy, combining [^{203}Pb]Pb-PSV359 for SPECT imaging and [^{212}Pb]Pb-PSV359 for targeted radiotherapy. Preliminary human imaging data using [^{203}Pb]Pb-PSV359 demonstrated specific and sustained tumour uptake across multiple cancer types, supporting the advancement of this agent into therapeutic studies. We present the design of a first-in-human Phase I/IIa study evaluating safety, dosimetry, and preliminary efficacy in patients with FAP-α-positive tumours. ***Materials and Methods:*** Phase I of the trial follows a modified Toxicity Probability Interval version 2 design. Patients will first undergo [^{203}Pb]Pb-PSV359 imaging to confirm FAP-α expression. [^{212}Pb]Pb-PSV359 will then be administered in dose cohorts ranging from 2.5 mCi to ≤ 10 mCi (92.5 to 370 MBq). A dosimetry sub-cohort will receive scans at multiple time points to characterise biodistribution and radiation exposure. Safety, pharmacokinetics, and efficacy data will be collected at baseline and at regular intervals (every 8 weeks for the first 6 months, then every 12 weeks up to 12 months). Dose-limiting toxicities will be evaluated during cycle 1 as part of the primary objective of the study to determine the recommended Phase 2 dose (RP2D). Imaging assessments to evaluate antitumour efficacy will include FDG PET/CT and MRI or CT scans. Safety will be assessed according to the Common Terminology Criteria for Adverse Events, version 5.0 and efficacy by Response Evaluation Criteria in Solid Tumours v1.1. Expansion cohorts at the RP2D will further characterise the agent's benefit-risk profile across multiple tumour types where FAP-α may play a role in tumourigenesis and/or progression, such as in sarcoma, mesothelioma, colorectal, ovarian, and head and neck cancers. ***Results:*** The study is now actively enrolling. The[PH1] main inclusion criterion of FAP-α expression will be determined by SPECT imaging. Main exclusion criteria include active brain metastasis, the presence of another active secondary malignancy, and known hypersensitivity to the active agent or a history of life-threatening allergic reactions. ***Conclusion:*** [^{203}Pb]/[^{212}Pb]Pb-PSV359 represents a promising approach to targeted alpha therapy in FAP-α-overexpressing solid tumours through selective FAP-α targeting, tumour accumulation, and retention, combined with rapid clearance from normal organs. The ongoing clinical study is designed to rigorously evaluate safety, dosimetry, and initial efficacy outcomes, with the goal of advancing a pan-cancer theranostic agent.

301

Sunday, October 5, 2025, 09:45 - 11:15
Auditorium

CME 2 - Neuroimaging Committee: Paradigm Shift for the Diagnosis of Parkinson's Disease

OP-075
FDG PET: not a physiopathological biomarker but …
C. Boccalini; *Hôpitaux Universitaires de Genève & University of Geneva, Neuroimaging and Innovative Molecular Tracers Lab, Geneva, SWITZERLAND.*

OP-076
Dopaminergic imaging: a good old friend
M. Pardin; *University of Genova, Dipartimento di neuroscienze, riabilitazione, oftalmologia, genetica e scienze materno-infantili - DINOGMI, Genova, ITALY.*

OP-077
MIBG: when, why ?
V. Camacho; *NuclearMedicine Department Hospital de Sant Pau, Universitat Autònoma de Barcelona, Barcelona, SPAIN.*

OP-078
New tracers under development
M. Brendel; *LMU München, Dept. of Nuclear Medicine, Munich, GERMANY.*

302

Sunday, October 5, 2025, 09:45 - 11:15
Room 112 (Arena)

Special Track 2 - Oncology & Theranostics Committee: Debate: A Brave New World: Are All PSMA Radiopharmaceuticals Equal?

OP-079
Point of View: PSMA diagnostics: all equal
D. Oprea-Lager; *Radboud UMC, Department of Medical Imaging, Nijmegen, NETHERLANDS.*

OP-080
Point of View: PSMA diagnostics: there are differences
I. Burger; *Kantonsspital Baden, Nuklearmedizin, Baden, SWITZERLAND.*

OP-081a
Point of View: PSMA therapeutics: all equal
S. Fanti; *University of Bologna, Department of Medical and Surgical Sciences, Bologna, ITALY.*

OP-081b
Point of View: PSMA therapeutics: there are differences
M. Eiber; *Klinikum rechts der Isar der Technischen Universität, Nuklearmedizin, Munich, GERMANY.*

303

Sunday, October 5, 2025, 09:45 - 11:15
Room 113

LIPS Session 2 - Bone & Joint Committee: LIPS Session 2 - Bone & Joint Committee: Bone Palliation Therapies

OP-082
Bone palliation therapies - bone seeking agent radionuclide therapy
K. Liepe; *Klinikum Frankfurt (Oder), Frankfurt, GERMANY.*

OP-083
Radiosynoviorthesis
G. Santo; *Magna Graecia University, Catanzaro, ITALY.*

OP-084
Dosimetry
P. M. Gabiña; *Unidad de Radiofísica y Protección radiológica. Gurutzeta/Cruces University Hospital, Barakaldo, SPAIN.*

304

Sunday, October 5, 2025, 9:45 - 11:15
Room 114

M2M Track - TROP Session - Radiopharmaceutical Sciences + Translational Molecular Imaging & Therapy Committee: Tracking/Modulating

OP-086
Hydrophobic F-base engineering augments aptamer pharmacokinetics for precision oncology: A PET imaging study
S. Yang[1], *Q. Chen*[1], *D. Ding*[2], *X. Lan*[1], *D. Jiang*[1];
[1]*Department of Nuclear Medicine, Union Hospital, Tongji Medical College, Huazhong University of Science and Technology, Wuhan, CHINA,* [2]*Institute of Molecular Medicine (IMM), Renji Hospital, State Key Laboratory of Oncogenes and Related Genes, Shanghai*

Jiao Tong University School of Medicine, and College of Chemistry and Chemical Engineering, Shanghai Jiao Tong University, Shanghai, CHINA.

Aim/Introduction: Aptamers, oligonucleotide sequences with a specific spatial conformation, hold immense potential as cancer-targeting agents but suffer from rapid clearance that compromises tumor accumulation. While hydrophobic F-base engineering have been proposed to enhance aptamer circulation, systematic pharmacokinetic evaluations across tumor models remain lacking. This study addresses this gap by comprehensively assessing the impact of F-base engineering on Sgc8 pharmacokinetics and tumor uptake using positron emission tomography (PET) imaging across multiple tumor models. ***Materials and Methods:*** The Sgc8 aptamer and its F-base derivatives (FSgc8, 2FSgc8) were radiolabeled with Zr-89, with radiochemical purity (>90%) validated by radioactive instant thin layer chromatography (radio-iTLC). Dynamic PET imaging (0-168 h) was conducted in murine MC38 and CT26 colon carcinoma models. Time-activity curves for blood pools and tumors were quantified via the region of interest (ROI) analysis in MC38 models, followed by the area under the curve (AUC) comparisons and tumor-to-blood (T/B) ratio calculations. ***Results:*** F-base modification conferred dose-dependent pharmacokinetic enhancements: 1 h post-injection blood retention increased from 0.05 ± 0.01%ID/g (native Sgc8) to 1.05 ± 0.23%ID/g (FSgc8) and 2.93 ± 0.25%ID/g (2FSgc8), with sustained detection of 2FSgc8 until 168 h. Tumor uptake of 2FSgc8 surpassed FSgc8 until 72 h ($p < 0.05$), achieving 33.2-fold and 1.5-fold increases over Sgc8 and FSgc8, respectively. Despite superior bioavailability (AUC_{blood}: 38.8× Sgc8; 2.4× FSgc8), 2FSgc8 exhibited a declining T/B ratio at 72 h (1.99 vs. 2.58 for FSgc8), suggesting prolonged circulation may reducing tumor-specific enrichment by decreasing intact 2FSgc8 at tumor sites. ***Conclusion:*** Hydrophobic F-base engineering significantly enhances aptamer pharmacokinetics and tumor targeting, positioning it as a transformative strategy for oligonucleotide therapeutics. Ongoing optimization focuses on balancing serum stability and tumor accumulation kinetics to maximize clinical translatability.

OP-087

Linker Modifications in Radiolabeled Rm26-based Antagonists to Gastrin-releasing Peptide Receptor (GRPR) Improved Pharmacokinetics

E. Bezverkhniaia*, A. Abouzayed, P. Kanellopoulos, V. Tolmachev, U. Rosenström, A. Orlova;*
Uppsala university, Uppsala, SWEDEN.

Aim/Introduction: Radionuclide targeting of gastrin-releasing peptide receptor (GRPR) holds significant diagnostic and therapeutic potential. Recently, our group reported the results of the Phase I clinical evaluation of [^{99m}Tc]Tc-maSSS-PEG2-RM26, an antagonist GRPR-targeting SPECT imaging agent [1]. The present study aimed to develop the next generation of RM-26-based GRPR antagonists with enhanced metabolic stability and improved pharmacokinetics. Four new agents containing a sarcosine (Sar) at position 11 to improve the in vivo stability and with more hydrophilic linkers were designed: Pep1 - maSSS-PEG2-[Sar^{11}]RM26, Pep2 - maSSS-PEG6-[Sar^{11}]RM26, Pep3 - maSSS-PEG2-Pip-[Sar^{11}]RM26, Pep4 - maSSS-EEE-[Sar^{11}]RM26. These analogues were compared in vitro and in vivo with [^{99m}Tc]Tc-maSSS-PEG2-RM26. ***Materials and Methods:*** Constructs were radiolabeled with ^{99m}Tc using transchelation from gluconate. In vitro GRPR-binding specificity, cellular processing, and binding kinetics were evaluated using PC-3 cells. Biodistribution and in vivo stability (for the best-performing constructs) were assessed in NMRI mice. Tumor targeting, in vivo specificity, and SPECT/CT imaging were performed in BALB/c nu/nu mice. ***Results:*** All constructs were radiolabeled with radiochemical yields over 95%. The label was stable during 1h in 300-molar excess of L-cysteine and PBS at room temperature. In PC-3 cells, [^{99m}Tc]Tc-Pep1, [^{99m}Tc]Tc-Pep2 and [^{99m}Tc]Tc-Pep3, but not [^{99m}Tc]Tc-Pep4, specifically bound to GRPR and exhibited low nanomolar affinity. When compared in vivo in NMRI mice, new peptides had significantly reduced activity uptake in the liver: [^{99m}Tc]Tc-Pep1 had a 2.3-fold reduction, [^{99m}Tc]Tc-Pep2 - 10-fold reduction, [^{99m}Tc]Tc-Pep3 - 3-fold reduction compared to [^{99m}Tc]Tc-maSSS-PEG2-RM26. This was also reflected in the octanol-water coefficient. Both [^{99m}Tc]Tc-Pep2 and [^{99m}Tc]Tc-Pep3 showed improved metabolic stability (≈ 62% and ≈ 73% of intact radiopeptide respectively) compared with [^{99m}Tc]Tc-maSSS-PEG2-RM26 (≈ 31% of intact radiopeptide), bound specifically to GRPR in vivo, and demonstrated a tendency (not statistically significant) for higher tumor activity uptake compared to the reference. Biodistribution data were confirmed by SPECT/CT imaging. ***Conclusion:*** This study demonstrated the promising impact of linker modification on refining the pharmacokinetic profile of ^{99m}Tc-labeled GRPR-antagonists. Based on the obtained results, the introduction of a hydrophilic PEG2-pip linker or a PEG6 linker, as pharmacokinetic modifiers, has a profound impact on the shift from hepatobiliary excretion towards renal excretion compared to the reference [^{99m}Tc]Tc-maSSS-PEG2-RM26. The use of a PEG6 linker decreased activity uptake in the liver by 10-fold and by 1.3-fold in the gastrointestinal tract. The use of a PEG2-pip linker decreased activity uptake in the liver by 3-fold and by 1.4-fold in the gastrointestinal tract. ***References:*** 1. Chernov et al. Cancers. 2023,15(6):1631.

OP-088

[^{18}F]F-FPy prosthetic group lowers kidney accumulation while retaining tumor uptake in a Glypican-3 targeted nanobody

S. Fayn*[1,2], F. Basuli[1], H. Makala[1], W. Lee[1], M. Ho[1], R. E. Swenson[1], P. L. Choyke[1], O. Jacobson[1], F. E. Escorcia[1];*
[1]National Institutes of Health, Bethesda, MD, UNITED STATES OF AMERICA, [2]University of Oxford, Oxford, UNITED KINGDOM.

Aim/Introduction: Nanobodies (Nbs), or single-domain antibodies (sdAbs), have become a promising tool in helping augment cancer treatment. These sdAbs have good tumor penetration, a half-life amenable to same-day imaging, and renal clearance, making them attractive scaffolds for building radiotheranostics for liver cancer. One limitation of nanobodies for radiopharmaceutical therapy is their high kidney retention, which could result in significant nephrotoxicity. Strategies to reduce kidney uptake of Nbs have been underway, including manipulating prosthetic groups used for labeling. Here, we used a fluorine-18-based labeling strategy with our previously developed Glypican-3 targeted nanobody, ssHN3, with the aim of minimizing kidney retention. ***Materials and Methods:*** We made two new versions of our ssHN3 LPETG-tagged nanobody, including direct lysine-based labeling of [^{18}F]F-FPy, and sortase-based site-specific labeling using triglycine-[^{18}F]F-FPy. Direct labeling was done by combining [^{18}F]F-FPy-TFP with ssHN3 and incubating for 20 min at 37 °C. Site-specific labeled nanobody was prepared by combining H-GGGK-[^{18}F]F-FPy-NH_2, sortase, and ssHN3 and incubating at 4°C for 30 min. Ex vivo biodistribution studies were done in nude athymic mice inoculated with HepG2 GPC3+ and GPC3- tumors. Organs were collected at 1, 2, and 3 h post-injection (p.i.), and activity was measured on a gamma counter to determine conjugate uptake (n = 4-5 per time point). ***Results:*** Radioconjugates were synthesized at high purity (>99%). ssHN3-[^{18}F]F-FPy and ssHN3-GGGK-[^{18}F]F-FPy demonstrated specificity for GPC3+ tumors with 10% and 6% injected activity/gram (IA/g) in HepG2 GPC3+ vs 1.13 and 1.38 %IA/g in HepG2 GPC3- tumors 1 h p.i., respectively (n = 5 for ssHN3-[^{18}F]F-FPy, n = 4 for ssHN3-GGGK-[^{18}F]F-FPy). More importantly, kidney uptake was ~40-fold lower between the two tracers in HepG2 GPC3+ tumors 3 h p.i. (2.37% IA/g for ssHN3-[^{18}F]F-FPy and 3.35% IA/g for ssHN3-GGGK-[^{18}F]F-FPy) compared to our previously developed version ssHN3-Al[^{18}F]F-RESCA (113.36% IA/g 3 h p.i.), and ~62 fold lower compared to our previously developed version ^{89}Zr-ssHN3 (173.77% IA/g 3 h p.i.). ***Conclusion:*** Altogether,

we demonstrated the ability to significantly reduce renal uptake of a nanobody by replacing metal-based chelators with a nonmetal [^{18}F]F-FPy construct. This allows for a higher signal-to-noise in PET/CT imaging of liver tumors, lowers the amount of radioactivity that normal tissue is exposed to, and underscores the approach of using nonmetal-based therapeutic radionuclides (e.g., Iodine-131, Astatine-211). Furthermore, this strategy could be extended to other smaller molecules and antibody fragments with similar challenges and ultimately provide a much-needed library of targeted tools for cancer diagnosis and treatment.

OP-089

Selection of the optimal format of albumin-binding domain-fused CAECAM5-specific affibody for targeted delivery of cytotoxic payload to malignant tumours

V. Tolmachev[1], *E. Papalanis*[1], *R. Li*[2], *M. Oroujeni*[1], *A. J. Herlina*[1], *Y. Liu*[1], *A. Orlova*[3], *E. Bezverkhniaia*[3], *P. Nygren*[2], *T. Gräslund*[2];
[1]*Department of Immunology, Genetics and Pathology (IGP), Uppsala University, Uppsala, SWEDEN,* [2]*KTH-Royal Institute of Technology, Stockholm, SWEDEN,* [3]*Department of Medicinal Chemistry, Uppsala University, Uppsala, SWEDEN.*

Aim/Introduction: A cell surface protein CEACAM5 is overexpressed in colorectal, pancreatic, ovarian and lung carcinomas, but shows low postnatal expression. Thus, CEACAM5 is a potential molecular target for cancer therapy. Affibodies are engineered affinity proteins based on non-immunoglobulin scaffold. They demonstrated capacity of specific delivery of cytotoxic substances to malignant tumours. A dimeric affibody C9-9 binding to CEACAM5 with an apparent affinity of 2 nM has been reported. Fusing affibodies with the albumin-binding domain (ABD) reduces their renal clearance and reabsorption, increases residence in blood and enhances tumour accumulation. This study aimed to characterise fusions of C9-C9 with albumin-binding domain ABD_{035} and select the best variant for development of targeting system. ***Materials and Methods:*** Two variants of the fusion were created, ABD_{035}-C9-C9-EYEC (ABD at the N-terminus) and C9-C9-ABD_{035}-EYEC (ABD at the C-terminus). The chelating sequence -EYEC was incorporated at C-termini of both constructs for labelling with ^{99m}Tc. In vitro binding specificity and internalisation were evaluated using BxPC3, LS174T and HT-29 cells, having high, intermediate and low CEACAM5 expression, respectively. Apparent affinity of interaction with caner cells was measured using LigandTracer. Biodistribution was measured in nude mice bearing human CEACAM5-expressing xenografts 4, 24 and 48 h post- injection (p.i.). ***Results:*** Both constructs showed radiochemical purity >95%, and labels were stable under cysteine challenge. Both [^{99m}Tc]Tc-C9-C9-ABD_{035}-EYEC and [^{99m}Tc]Tc-ABD_{035}-C9-C9-EYEC bound specifically to CEACAM5-expressing cells in vitro, and binding was proportional to the expression level. InteractionMap analysis of the LigandTracer data showed two types of interaction with CEACA5-expressing cells, one with apparent dissociation constant of 550-850 pM and another with 14-19 nM. The strongest interaction was more abundant for [^{99m}Tc]Tc-ABD_{035}-C9-C9-EYEC. After 24-h incubation at 37°C, the internalised fraction was 50-55% for both constructs. The retention of ABD-fused variants in blood 4 h p.i. was >50-fold higher than the retention of non-fused control [^{99m}Tc]Tc-C9-C9-EYEC. Their tumour uptake was six-fold higher and renal uptake was 10-fold lower compared with the uptake of [^{99m}Tc]Tc-C9-C9-EYEC. The blood half-lives were 20.6 and 12.3 h for [^{99m}Tc]Tc-ABD_{035}-C9-C9-EYEC and [^{99m}Tc]Tc-C9-C9-ABD_{035}-EYEC, respectively. The maximum uptake in BxPC3 xenografts (48 h) of [^{99m}Tc]Tc-ABD_{035}-C9-C9-EYEC (59±20 %ID/g) was significantly higher than the uptake of [^{99m}Tc]Tc-C9-C9-ABD_{035}-EYEC (22±7 %ID/g). ***Conclusion:*** Targeting properties of fusions of C9-C9 with ABD depend on the position of domains binding to CEACAM5 and albumin. ABD_{035}-C9-C9-EYEC provides more efficient targeting compared with the counterpart with the C-terminal positioning of ABD_{035}.

OP-090

Oligonucleotide modification minimizes renal uptake of nanobodies

S. Yang[1], *X. Long*[1], *W. Wei*[2], *X. Lan*[1], *D. Jiang*[1];
[1]*Department of Nuclear Medicine, Union Hospital, Tongji Medical College, Huazhong University of Science and Technology, Wuhan, CHINA,* [2]*Department of Nuclear Medicine, Institute of Clinical Nuclear Medicine, Renji Hospital, School of Medicine, Shanghai Jiao Tong University, Shanghai, CHINA.*

Aim/Introduction: Nanobodies, single-domain antibody fragments, are valuable in precision medicine for their superior tumor-targeting ability and rapid clearance from the bloodstream. However, their high renal retention complicates cancer diagnosis, especially in renal metastasis, and radioimmunotherapy. To address this limitation, we developed a novel oligonucleotide-based modification strategy to reduce radioactive retention of nanobodies. ***Materials and Methods:*** A nanobody targeting CD70 (namely B6) was site-specifically conjugated to a 20-base double-stranded nonsense oligonucleotide (dsODN) via a two-step reaction. The B6-dsODN conjugates were purified via size-exclusion chromatography (SEC) and confirmed by polyacrylamide gel electrophoresis (PAGE). The serum stability was assessed by agarose gel electrophoresis after incubation in 90% fetal bovine serum (FBS) at 37°C for 4 hours. The nanobody and ODN components of B6-dsODN were radiolabeled with F-18, respectively (i.e., [^{18}F]B6-dsODN and [^{18}F]dsODN-B6). The renal uptake was compared to [^{18}F]B6 by PET/CT imaging and biodistribution studies in healthy mice. ***Results:*** The PAGE electrophoresis confirmed the conjugation of B6 to dsODN with >95% purity. B6-dsODN showed excellent serum stability, with the majority remaining intact after 4 hours in FBS due to the nuclease resistance of the double-stranded structure. PET/CT imaging in healthy mice showed significantly lower renal uptake of [^{18}F]dsODN-B6 compared to [^{18}F]B6, with a 187-fold reduction. Biodistribution studies at 2 h after injection revealed a >200-fold reduction in renal uptake for [^{18}F]dsODN-B6. However, no difference in renal uptake was observed between [^{18}F]B6-dsODN and [^{18}F]B6. Further analysis confirmed that the F-18 labeled dsODN detached in the kidneys, resulting in reduced renal radioactivity uptake. ***Conclusion:*** This dsODN-based modification strategy effectively reduces renal radioactive uptake of nanobodies, offering a convenient and efficient approach for developing nanobody-derived drugs. Future work will validate the universal applicability of the strategy and evaluate its efficacy in tumor-bearing mice.

OP-091

Assessing the generalizability of a preclinical PBPK model for DOTA-TATE-based radiopharmaceuticals: application to ^{161}Tb, ^{177}Lu, ^{153}Sm and ^{68}Ga

J. Henriot[1], *L. Struelens*[2], *M. Andersson*[3], *S. Rodriguez Pérez*[2], *M. Koole*[4], *C. Saldarriaga Vargas*[2];
[1]*SCK CEN & KU Leuven, Mol, BELGIUM,* [2]*SCK CEN, Mol, BELGIUM,* [3]*SCK CEN & ULB, Mol, BELGIUM,* [4]*KU Leuven, Leuven, BELGIUM.*

Aim/Introduction: [177Lu]Lu-DOTA-TATE combined with [68Ga]Ga-DOTA-TATE is current the theragnostic approach of choice for Peptide Receptor Radionuclide Therapy (PRRT) of Neuro-Endocrine Tumors (NETs). Several research groups are exploring the potential of DOTA-TATE labelled with other radionuclides, such as 161Tb. Considering that pharmacokinetics are predominantly driven by the peptide moiety, we propose a generic preclinical physiologically-based pharmacokinetic (PBPK) model to accurately predict the uptake of various DOTA-TATE-based radiopharmaceuticals in both tumor and organs at risk. ***Materials and Methods:*** A murine whole-body PBPK model for [161Tb]Tb-DOTA-TATE was implemented using MATLAB Simbiology based on a published model (1). The model was initially developed in healthy mice, incorporating novel in vitro binding data (2), plasma protein binding, and competition between labeled and unlabeled DOTA-TATE for receptor targeting. Kinetic parameters and SSTR2

densities were fitted to [161Tb]Tb-DOTA-TATE preclinical biokinetic data. The model was then verified using an independent [161Tb]Tb-DOTA-TATE dataset (3) and further developed and verified using biokinetic data of mice bearing a CA20948 rat pancreatic tumor (4). The generalizability of the model was assessed using preclinical literature biodistribution studies for DOTA-TATE radiolabeled with [68Ga]Ga and various β-emitters. ***Results:*** The developed PBPK model successfully described the pharmacokinetics of [161Tb]Tb-DOTA-TATE both in healthy and tumor-bearing mice. The relative errors for time-integrated activities ranged from -1% to +22% in the kidneys, while a value of -15% was obtained for the tumor. SSTR2 densities emerged as a strain-specific parameter such that fitting was essential to accurately match experimental data. Still, relative SSTR2 levels between organs remained reasonably constant across mice strains with relative simulated expressions of 19 ± 3% for the pancreas, 2 ± 1% for the liver, 1 ± 0% for the spleen, and 10 ± 5% for the lungs (mean ± SD), using kidneys expression levels as reference. Our findings also indicated that our PBPK model can be applied to other DOTA-TATE-based radiopharmaceuticals labeled with [177Lu]Lu, [153Sm]Sm, [68Ga]Ga, showing the potential of a generic model for DOTA-TATE-based PRRT and supporting its clinical translation to predict tumoral and organ uptake of [161Tb]Tb-DOTA-TATE and [177Lu]Lu-DOTA-TATE in NET patients. ***Conclusion:*** These preclinical results constitute a first step towards the broad clinical application of a generalized PBPK model to support dosimetry-based PRRT personalization with radiolabeled DOTA-TATE. ***References:*** (1) Zaid et al. 2021. https://doi.org/10.3390/pharmaceutics13122132. (2) Spoormans et al. 2024 https://doi.org/10.2967/jnumed.124.267873. (3) Busslinger et al. 2024. https://doi.org/10.1007/s00259-024-06827-2. (4) Bernard et al. 2000. https://doi.org/10.1097/00006231-200011000-00015.

OP-092

Association of different forms of non-conjugated astatine-211 to albumin

E. Aneheim[1,2], *S. Lindegren*[1], *H. J. Jensen*[3], *T. Bäck*[1];
[1]*University of Gothenburg, Göteborg, SWEDEN,* [2]*Sahlgrenska University Hospital, Göteborg, SWEDEN,* [3]*Copenhagen University Hospital, Copenhagen, DENMARK.*

Aim/Introduction: Astatine-211 is one of the alpha-particle emitting nuclides investigated for use within Targeted Alpha Therapy (TAT) of disseminated cancer. In previous studies, a difference in blood clearance has been observed when comparing astatinated compounds with their iodinated counterparts. This has been explained by a potentially prolonged retention in the blood by present free astatine. In this work, the spontaneous association of non-conjugated, so called "free" astatine to albumin has been investigated and compared to iodine in vitro under physiological conditions. In addition, the in vivo blood circulation behavior of free astatine was evaluated in comparison to iodine. ***Materials and Methods:*** Astatine solutions were formulated following dry distillation and evaporation to dryness of astatine solvated in $CHCl_3$. In vitro evaluation of astatine and iodine association to albumin was mainly performed using size exclusion chromatography applying both disposable columns (PD10 and NAP10) as well as an FPLC system (ÄKTA) with online UV detection and activity fraction collection. Also methanol precipitation and radio-TLC methods were used for analysis. In vivo evaluation was performed using furry BALB/C mice (3 / group) with both i.v. and i.p. injection of activity, followed by sequential blood sampling from the tail vein and biodistribution. ***Results:*** Oxidized and unmodified forms of free astatine display a significantly higher and more rapid association to albumin in vitro compared to reduced forms, with >97 % compared to <25 % associated after 10 minutes. Both the corresponding oxidized and reduced forms of iodine display a very low and slow association to albumin with < 5% associated after 40 minutes. Oxidized, unmodified and reduced astatine show very similar blood profiles over time as well as a similar uptake in biodistribution after 20-22 h following i.p. injection. Upon i.v. injection a larger difference in blood profiles between the species could be observed, which in turn was different compared to the curve obtained after i.p. injection. In addition an unexpected uptake of Astatine in PBS/1% Asc. in stomach was found. In all cases the blood profile and biodistribution of astatine was significantly different compared to iodine, which displayed a greater and more rapid blood clearance and specific accumulation in thyroid. ***Conclusion:*** Different forms of unbound astatine differ in their association to albumin. However, all investigated forms of free astatine associates to albumin to a much higher degree than iodine. This behavior could explain the prolonged blood circulation of free astatine compared to iodine.

OP-093

Kinetic modelling of [^{89}Zr]Zr-DFO-anti-VEGF PET at different stages of glioblastoma progression

E. Ramos-Docampo[1,2], *M. Muñoz-González*[1], *J. Codesido*[1], *X. García-Otero*[1], *C. Domínguez-Borrero*[1], *S. Groba-de Antas*[1], *N. Gómez-Lado*[1], *P. Aguiar*[1,2], *L. García-Varela*[1,2];
[1]*Molecular Imaging and Pharmacokinetic Modelling Group, Center for Research in Molecular Medicine and Chronic Diseases (CiMUS), University of Santiago de Compostela, Santiago de Compostela, SPAIN,* [2]*Nuclear Medicine and Molecular Imaging Group, Health Research Institute of Santiago de Compostela (IDIS), University Hospital Santiago de Compostela, Santiago de Compostela, SPAIN.*

Aim/Introduction: Kinetic modelling offers a detailed quantification of the radiotracer, enhancing our understanding of tumor antigen dynamics during disease progression and treatment. While standardized uptake values (SUVs) are simple to compute, they are highly variable and influenced by body weight and dose injected estimation errors 1,2. To overcome these limitations, we performed kinetic modelling analysis to characterize the pharmacokinetics of [89Zr]Zr-DFO-anti-VEGF (vascular endothelial growth factor) PET radiotracer during glioblastoma (GBM) development, a highly aggressive brain tumor with poor prognosis 3. This approach may reveal VEGF changes during tumor growth and treatment, which are linked to pharmacoresistance and reduced therapeutic efficacy. ***Materials and Methods:*** GBM models were induced on Sprague-Dawley rats by implanting F98 cells into the frontal cortex and injected with [89Zr]Zr-DFO-anti-VEGF (bevacizumab), following previously described methods 4. Multiple PET/CTs were performed on two groups: rats with 1-week tumor development (n=4) (1W) were scanned at 0, 48, 168, and 240 hours post-injection, and rats with 2-week tumor development (n=2) (2W) were scanned at 0, 5, 9, 14, 23, 26, 30, 48, 72, 144, and 216 hours. Blood and plasma samples were collected before each scan for radioactivity analysis. Tumor volumes of interest were delineated using MRI images acquired one day before PET/CTs. Mean and maximum SUVs, as well as the Patlak influx rate constant (Ki), were calculated for each subject. Differences in SUVs and Ki between groups were assessed using independent t-tests. Correlations between SUV and Ki were also evaluated. ***Results:*** [89Zr]Zr-DFO-anti-VEGF showed >95% purity and a specific activity of 74 MBq/mg. The average tumor volume was 0.0141 cm3 in 1W and 0.092 cm3 in 2W. SUV values showed high variability, especially at early time points and in animals with 1W animals. SUVmean at the final time point was higher in the 2W group ($p = 0.031$), with no significant differences in SUVmax. Ki values were 1.5 times higher in 2W group ($p = 0.036$) and strongly correlated with SUVmean ($R^2 = 0.878$), but not with SUVmax ($R^2 = 0.096$). These changes may reflect increased VEGF expression over tumor progression and/or altered blood-brain barrier (BBB) penetrability at more advanced stages. Further kinetic modeling studies are currently being conducted to better address this issue. ***Conclusion:*** Our findings provided higher Patlak-derived Ki values in the 2W compared to 1W group, supporting significant stage-dependent changes in the pharmacokinetics of the [89Zr]Zr-DFO-anti-VEGF. ***References:*** (1) https://doi.org/10.2967/

jnumed.108.057182. (2) https://doi.org/10.1007/s40336-014-0067-x. (3) https://doi.org/10.1021/acs.jmedchem.1c01946.(4) https://doi.org/10.1016/j.ijpharm.2024.123795.

OP-094

Pharmacokinetics, Tumour and Normal Tissue Uptake, SPECT/CT and Cerenkov Imaging of Radiolabeled Hybrid Gold-Lipid Nanoparticles vs. Gold Nanoparticles in a Human Breast Cancer Xenograft Mouse Model

Z. Cai[1], *A. Momeni*[2], *M. K. Brown*[1], *L. Messier*[2], *M. H. Y. Cheng*[2], *C. A. Brimacombe*[3], *P. R. Cullis*[2], *R. M. Reilly*[1];
[1]University of Toronto, Toronto, ON, CANADA, [2]University of British Columbia, Vancouver, BC, CANADA, [3]Polymorphic BioSciences, Vancouver, BC, CANADA.

Aim/Introduction: Hybrid gold-lipid nanoparticles (AuNP-LNP) enable triggered drug release in tumours by laser irradiation of the encapsulated AuNP. Our aim was to evaluate the pharmacokinetics (PK) and biodistribution (BOD) of AuNP-LNP vs. AuNP in tumour-bearing mice. ***Materials and Methods:*** [^{198}Au]AuNP (^{198}AuNP) or AuNP were synthesized by H[^{198}Au]$AuCl_4$ or $HAuCl_4$ reduction in Na citrate and tannic acid, then conjugated to PEG_{2k}-lipoic acid (LA) or DOTA-PEG_{2k}-OPSS, respectively. DOTA-PEG_{2k}-OPSS-AuNP were complexed to [^{177}Lu]$LuCl_3$. LNP encapsulating ^{198}AuNP or [^{177}Lu]Lu-DOTA-PEG_{2k}-OPSS-AuNP (^{177}LuAuNP) were synthesized at 2.2 x 10^{13} AuNP/µmol lipid. AuNP and AuNP-LNP were characterized by dynamic light scattering (DLS) and transmission electron microscopy (TEM). NRG mice with s.c. 164/8-1B/H2N.Luc+ and MDA-MB-231 human breast cancer tumours were injected intravenously with 3.8-6.3 MBq (2.1-4.8 x 10^{13} AuNP) of ^{177}LuAuNP, ^{177}LuAuNP-LNP, ^{198}AuNP or ^{198}AuNP-LNP. Blood samples were collected up to 120 h post-injection (p.i.). The percent injected dose/g (%ID/g) in the blood vs. time curves were fitted to 2-compartment PK models. SPECT/CT and Cerenkov imaging was performed at 6, 24 and 96 h p.i. BOD was determined ex vivo at 120 h p.i. ***Results:*** The diameter of AuNP by DLS was 7.5±0.7 nm [polydispersity index = 0.13±0.02]. TEM showed a spherical shape with diameter = 5.8±0.9 nm. The diameters of ^{177}LuAuNP, ^{177}LuAuNP-LNP, ^{198}AuNP-LNP were 19±2, 73±1 and 87±25 nm, respectively. Elimination from the blood was slowest for ^{198}AuNP ($t_{1/2}\beta$=36.9 h), then ^{177}LuAuNP (14.9 h), ^{177}LuAuNP-LNP (10.4 h) and ^{198}AuNP-LNP (3.4 h). Uptake in MDA-MB-231 at 120 h p.i. was higher for ^{198}AuNP than ^{198}AuNP-LNP (15± 4 vs 2±1 %ID/g, p=0.046). Uptake (%ID/g) in 164/8-1B/H2N.Luc+ was higher for ^{198}AuNP (6.1±2.7) than ^{198}AuNP-LNP (0.9±0.5), ^{177}LuAuNP (0.40±0.08) and ^{177}LuAuNP-LNP (0.26±0.05). The highest normal tissue uptake (%ID/g) was observed in the spleen and liver for each NP: ^{198}AuNP -LNP (136±6 and 76±5), ^{198}AuNP (19 ± 2 and 15 ± 4), ^{177}LuAuNP-LNP (29±13 and 6.0±0.6) and ^{177}LuAuNP (14±4 and 5.1±0.4), respectively. The kidney uptake of each NP was <2 %ID/g (p=0.769). The tumour uptake of ^{198}AuNP and ^{198}AuNP-LNP were visualized by Cerenkov imaging at 6, 24 and 96 h p.i. and by SPECT/CT at 24 and 96 h p.i. Images by both imaging modalities correlated well. ***Conclusion:*** ^{198}AuNP exhibited the longest blood circulation time and highest tumor uptake. In contrast, ^{198}AuNP-LNP had shortest circulation time, but second highest tumour uptake. ^{198}AuNP would be superior to ^{177}LuAuNP for guiding laser irradiation of AuNP-LNP in tumours by SPECT/CT or Cerenkov imaging.

305

Sunday, October 5, 2025, 9:45 - 11:15
Room 211

Cutting Edge Science Track - TROP Session - Physics Committee: SPECT Quantification in Therapeutic Applications

OP-095

Evaluation of observer accuracy among eight observers in measuring kidney phantom activity concentration of ^{177}Lu using two measurement methods

E. Ilan[1,2], *C. Widström*[1], *T. Sjöholm*[1,2], *A. Moreno Moreno*[1,2], *S. Kvernby*[3], *C. Held*[1], *S. Jacobsson Svärd*[1], *M. Sandström*[1,2];
[1]Medical Physics, Uppsala University, SWEDEN, [2]Nuclear medicine & PET, Uppsala University, SWEDEN, [3]Medical Physics, Lund University, SWEDEN.

Aim/Introduction: Fractionated molecular radiotherapy with 177Lu-DOTATATE is an effective treatment option for patients with generalized neuroendocrine tumors. Absorbed dose (AD) calculations to solid organs have been suggested to optimize the treatment. The uncertainty of the calculated absorbed doses is both dependent on how well the activity concentrations are determined and at what time-point (after therapy) the activity concentration is determined. This study aims to determine the accuracy of measuring activity concentrations in a kidney phantom using two different methods, for eight different observers. ***Materials and Methods:*** A 3D printed kidney phantom described earlier [Jessen et al, 2024] was prepared blindly for the eight observers. The phantom was scanned in two different SPECT/CT systems, GE Discovery 670 with photomultipliers (PMT) and GE 870 CZT (CZT). The activity concentration in the kidneys was determined using two methods, 4 ml VOI (one VOI) and 2.21 ml VOIs (the mean of three 2.21 mL VOIs, non-overlapping). The VOI(s) were placed in area with homogenous uptake. The activity concentrations determined by the observers were compared with the known activity concentration and the accuracy of each activity concentration determination was established. ***Results:*** Across all observers irrespective of method and system, the determined activity concentrations showed an accuracy better than 10%. For the 2.21 ml VOI method, the CZT system yielded a more pronounced underestimation in the left kidney (median, min to max, -6.0%, -8.9 to -1.1) compared to the PMT system (-4.3%, -9.3 to 0.0). In contrast, both systems showed positive deviations in the right kidney, with PMT slightly higher (5.2%, 1.3 to 6.8) than CZT (4.0%, 0.0 to 6.5). For the 4 ml VOI, both systems showed small differences in the left kidney (CZT: -0.9%, -2.9 to 0.4; PMT: -0.4%, -2.0 to 1.5) and identical median values (4.7%) in the right kidney, with overlapping ranges (CZT: 1.0 to 6.0; PMT: 1.9 to 5.4). ***Conclusion:*** The activity concentration was determined with an accuracy better than 10 % for the eight observers. Overall, the 2.21 ml VOI method yielded larger variability and greater differences between kidneys and systems compared to the 4 ml VOI method, which provided more consistent results across both systems and kidneys. ***References:*** Jessen L, Gustafsson J, Ljungberg M, CurkicKapidzic S, Imsirovic M and SjögreenGleisner K. 3D printed non-uniform anthropomorphic phantoms for quantitative SPECT. EJNMMI Phys 11, 8 (2024). https://doi.org/10.1186/s40658-024-00613-7

OP-096

Towards harmonised quantitative SPECT imaging: experiences from the EARL ^{177}Lu SPECT/CT Accreditation pilot study

L. Vávrová[1], *W. Claeys*[2], *A. Denis-Bacelar*[3], *I. Hristova*[4], *M. Lassmann*[1], *M. Koole*[2], *J. Dickson*[5], *J. Tran-Gia*[1];
[1]*Department of Nuclear Medicine, University Hospital Würzburg, Würzburg, GERMANY,* [2]*KU Leuven, Leuven, BELGIUM,* [3]*National Physical Laboratory, Teddington, UNITED KINGDOM,* [4]*EANM Forschungs GmbH, Vienna, AUSTRIA,* [5]*Institute of Nuclear Medicine, University College London Hospitals, London, UNITED KINGDOM.*

Aim/Introduction: Quantitative ^{177}Lu SPECT/CT is increasingly important for dosimetry, treatment verification, and clinical research. However, a lack of harmonised protocols and standardisation limits the comparability of results across centres. The EARL Accreditation Programme aims to provide a framework for harmonisation in ^{177}Lu SPECT/CT. Within this effort, this study evaluates differences in reconstruction approaches and highlights challenges of multi-centre harmonisation. ***Materials and Methods:*** In the ^{177}Lu SPECT/CT Accreditation pilot, data from 29 systems across 25 European sites have been collected to date. Of these, 16 datasets are pending resubmission due to non-compliance with EARL protocol (e.g., phantom mispositioning, inappropriate reconstruction parameters, or data transfer issues). Two Siemens Symbia Pro.specta datasets were excluded due to limitations in exporting scatter projections, required for manufacturer-independent reconstruction. The remaining 11 datasets (5 Siemens, 6 GE) were analysed. Alongside the mandatory manufacturer OSEM reconstructions, data were centrally reconstructed using the vendor-neutral PyTomography platform [1] (20 iterations, 4 subsets, no post-filtering, attenuation correction, triple-energy-window scatter correction, resolution modelling). Images were processed in Python (v3.12.4) to derive image calibration factors (ICFs, Jaszczak phantom) and recovery coefficients (RCs, NEMA phantom with 6 spheres, no background). RCs were calculated using SPECT-based segmentation with a centre-of-mass method and spherical volumes of interest (VOI) defined by the nominal lesion volume. Recovery curves were compared across systems and methods. ***Results:*** ICFs showed strong correlation ($R^2 = 0.999$) between manufacturer and PyTomography reconstructions. Siemens systems yielded higher ICFs (mean ± SD: 19.76 ± 0.43 cps/MBq) than GE (11.80 ± 0.92 cps/MBq), with minimal intra-manufacturer variation. In contrast, RCs showed greater variability, with percentage deviations of 3-14% (Siemens) and 4-54% (GE) for vendor reconstructions, and 4-19% (Siemens) and 4-60% (GE) for Pytomography reconstructions. For manufacturer reconstructions, Siemens generally showed better recovery than GE, while PyTomography showed the opposite trend. Normalising recovery curves to a single manufacturer-specific reference site reduced inter-system variability for both reconstruction methods. Differences may reflect inaccuracies in activity concentration (e.g., lack of traceable activity measurements and/or volume uncertainties in stock solution preparation). Residual discrepancies likely arise from segmentation inconsistencies, particularly for the smallest sphere. ***Conclusion:*** These preliminary findings suggest that harmonisation of quantitative imaging across different SPECT/CT systems and reconstruction methods is achievable but challenging. Scaling recovery curves shows promise for improving consistency, though activity measurement and segmentation issues must still be addressed. Resolving these factors is essential for reliable multicentre dosimetry in ^{177}Lu radiopharmaceutical therapy. ***References:*** [1] Polson et al. arXiv:2309.01977

OP-097

Multicenter Comparison of SPECT/CT Protocols for Quantitative ^{177}Lu Imaging

W. Claeys[1], *K. Baete*[2], *L. Beels*[3], *C. Bernard*[4], *R. Danieli*[5], *Y. D'Asseler*[6], *A. De Crop*[7], *M. Hesse*[8], *V. Nuttens*[9], *B. Vanderlinden*[5], *M. Koole*[1];
[1]*KU Leuven, Leuven, BELGIUM,* [2]*UZ Leuven, Leuven, BELGIUM,* [3]*AZ Groeninge, Kortrijk, BELGIUM,* [4]*C.H.U. Liège, Liège, BELGIUM,* [5]*Institut Jules Bordet, Brussels, BELGIUM,* [6]*UZ Gent, Gent, BELGIUM,* [7]*AZ Delta, Roeselare, BELGIUM,* [8]*Cliniques Universitaires Saint-Luc, Brussels, BELGIUM,* [9]*OLVZ Aalst, Aalst, BELGIUM.*

Aim/Introduction: Following the recent successes of radionuclide therapies for treating neuroendocrine tumors and prostate cancer, the use of ^{177}Lu has grown considerably, with more and more centers performing quantitative ^{177}Lu-SPECT imaging. However, due to a lack of standardization, ^{177}Lu-SPECT image quality can differ significantly across hospitals, making data pooling or reproducible dosimetry estimates challenging. The goal of this study was to assess variability in quantitative ^{177}Lu SPECT-imaging across different systems and hospitals. ***Materials and Methods:*** A uniform cylindrical phantom (6.3l) and a NEMA IEC body phantom containing six hot spheres (13-60mm) and a cold background, were prepared centrally at UZ/KU Leuven. These phantoms were measured during 2 weeks at 8 different sites across Belgium using a representative set of NaI(Tl) and CZT SPECT/CT systems from different manufacturers. Each site scanned the phantoms using their own clinical protocol and a standardized acquisition protocol (TEW, 60 views, 256 matrix) using the 208 keV photopeak. The acquisition duration was adapted to preserve the total number of counts per acquisition. Similarly, reconstructions were performed using each site's clinical protocol as well as a standardized protocol (OSEM, 40 iterations 2 subsets). Most sites used vendor-specific reconstruction software, only two sites reconstructed the images using third-party software. All images were analyzed centrally: based on the uniform cylinder, the calibration factor for each system was determined, which was then used to calculate the recovery coefficients (RCs) from the NEMA IEC body phantom. ***Results:*** The calibration factor was fairly constant across systems from the same manufacturer, (12 or 20 cps/MBq for NaI(Tl) systems, 100 cps/MBq for CZT), regardless of acquisition/reconstruction protocol. The RC curves were little affected by the acquisition protocol but changed significantly with reconstruction settings like number of updates and post filter. Additionally, pre-filtering of the scatter windows turned out to have a major impact on the image quality by improving the scatter estimates. When using standardized acquisition and reconstruction settings, scanners from the same manufacturer had similar RC curves, but differences between manufacturers remained large. In particular, CZT systems had lower RCs than NaI(Tl) systems. ***Conclusion:*** The current diversity in quantitative ^{177}Lu-SPECT protocols leads to significant differences in the SPECT-images generated with different SPECT/CT systems at various hospitals. Standardizing the reconstruction protocol, rather than the acquisition protocol, could more effectively reduce differences between systems from the same vendor, while additional post-filtering would help harmonize systems across different manufacturers.

OP-098

Dual-Peak Image Reconstruction for 177Lu SPECT with CZT Gamma-Camera: Phantom-Based Optimization of Acquisition Time for 177Lu-DOTATATE and 177Lu-PSMA617 Protocols

Y. Cras, *H. Noamen, A. Benhamla, G. Rovera, P. Lacassagne, L. Ferreol, D. Deandreis;*
Gustave Roussy, Villejuif, FRANCE.

Aim/Introduction: Specific Semiconductor CZT-based gamma-camera are able to reconstruct images using both main photopeaks of Lutetium-177 (113 keV and 208 keV). The aim of this

study was to optimize in a NEMA phantom the acquisition time for 177Lu-DOTATATE and 177Lu-PSMA617 protocols by comparing current single-peak reconstructions (113 keV) with dual-peak reconstructions by a CZT gamma-camera. ***Materials and Methods:*** A NEMA IEC image quality phantom was used for this study, with hot background, cold lung insert, and six hot spheres (10-37 mm in diameter). The phantom was filled using a single calibrated syringe (total activity 637 MBq; sphere-to-background ratio: 10.3). It was acquired once using single standardized protocol: 30 minutes for 177Lu DOTATATE and 20 minutes for 177LuPSMA617. A dedicated tool on the CZT system was applied to simulate reduced acquisition times by resampling the raw projection data at 20, 15, and 10 minutes for DOTATATE and 15, 10, and 5 minutes for PSMA617. The standard Single-Peak reconstruction applied 4 iterations, 8 subsets, 2.46 mm voxel size, CT-based attenuation correction, scatter correction, intra-filter convolution and median post-filter for both protocols. Image quality metrics were first assessed on all Time-Points for single-peak reconstructions: background variability, contrast recovery for each sphere, total activity recovery, and sphericity (top 3 spheres). Then, the same variables were compared with dual-peak reconstructions. ***Results:*** For 177Lu-PSMA617, the dual-peak reconstruction (8 iterations, 8 subsets for the 113 keV, 6 iterations, 16 subsets for the 208 keV) at 15 minutes (25% time reduction) preserved image noise, improved contrast for all 6 spheres, provides a total activity recovery of +4%, and maintained sphericity compared to the 20-minute single-peak reference. For 177Lu-DOTATATE, the dual-peak reconstruction (8 iterations, 8 subsets for the 113 keV, 8 iterations, 8 subsets for the 208 keV) at 18 minutes (40% time reduction), found with continuous interpolation of Time-Points by a quadratic trend curve, preserved image noise, improved contrast in 1 sphere, maintained unchanged contrast in 4 out of 6 spheres, provides a total activity recovery of +5%, and preserved sphericity compared to the 30-minute single-peak reference. ***Conclusion:*** Dual-peak image reconstruction using the CZT gamma-camera allowed significant acquisition time reduction for both 177Lu-DOTATATE and 177Lu-PSMA617 protocols without degrading image quality. This phantom-based study supports clinical implementation of shortened protocols. Clinical validation is underway via blinded qualitative and quantitative assessments compared to current routine reconstructions.

OP-099

Evaluation of modified window-based scatter correction in quantitative ^{177}Lu-SPECT for a ring-configured CZT SPECT

I. Ceric Andelius[1,2], *A. Stenvall*[1], *E. Nilsson*[1], *E. Larsson*[1], *J. Gustafsson*[3];
[1]*Radiation Physics, Department of Haematology, Oncology, and Radiation Physics, Skåne University Hospital, Lund, SWEDEN,* [2]*Department of Translational Medicine and Wallenberg Centre of Molecular Medicine, Lund University, Malmö, SWEDEN,* [3]*Medical Radiation Physics, Lund, Lund University, Lund, SWEDEN.*

Aim/Introduction: The aim was to experimentally evaluate ^{177}Lu-activity estimation for a ring-configured CZT gamma camera using a modified window-based scatter correction (MSC) that accounts for the tailing affects seen in CZT gamma cameras. While the original correction addressed tailing in the 208 keV peak only [1], separating primary and scatter photon within the scatter window, the current adaption extents to the 113 keV peak. In the modified version, the primary photons can be added back to the main window (MSC+P). We aim to assess the quantitative effects at 113 keV and 208 keV with respect to bias and precision using TEW, MSC and MSC+P. ***Materials and Methods:*** Phantom experiments with a NEMA-PET body phantom filled with ^{177}Lu were performed on a ring-configured CZT system. The NEMA phantom with six spheres (1.2 mL to 113 mL) had a non-radioactive background. Projections were acquired for 1 h and divided into six 10-minute frames. Reconstruction was performed using OS-EM 2-30 iterations (10 subsets) with compensation for attenuation, scatter (TEW for 113 keV, MSC and MSC+P), distance-dependent spatial resolution, and penetration at 208 keV. Total activity within the entire phantom and volumes-of-interest following the physical size of the spheres were defined and activity-concentration mean relative errors and coefficients-of-variation (CVs) over timeframes were computed for the different number of iterations. ***Results:*** MSC and MSC+P showed similar mean relative errors and CVs for 208 keV. For the smallest and largest NEMA-sphere at 20 iterations, the mean relative errors/CVs were -74 %/17% (MSC) and -78%/20% (MSC+P) and -25%/0.6% (MSC) and -24%/0.7% (MSC+P). At 113 keV, corresponding results for the 113 keV peak were -50%/12% (TEW), -60%/9% (MSC) and -70%/6% (MSC+P) for the smallest sphere (and -10%/0.75% (TEW), -16%/0.6% (MSC) and -22/0.2% (MSC+P) for the largest sphere. Mean relative in total activity at 20 were -4% (MSC) and -2.0% (MSC+P) for the 208 keV peak. Corresponding results for 113 keV were 21% (TEW), -5% (MSC) and 4% (MSC+P). ***Conclusion:*** The MSC and MSC+P resulted in improved signal to noise ratios for the NEMA phantom spheres resulting in reduced coefficient of variation for 113 keV peak and considerably better preservation of total activity. MSC and MSC+P improves the accuracy of quantitative ^{177}Lu-SPECT. ***References:*** Stenvall A, Ceric Andelius I, Nilsson E, Lindvall A, Larsson E, Gustafsson J. Bias and precision of SPECT-based ^{177}Lu activity-concentration estimation using a ring-configured solid-state versus a dual-headed anger system. EJNMMI Phys. 2024 Nov 4;11(1):91

OP-100

Recovery coefficients in Lu-177-SPECT-CT are reduced as a function of activity concentration

V. Reijonen[1], *S. E. A. Kokkonen*[2], *M. Tenhunen*[1];
[1]*Helsinki University Hospital, Helsinki, FINLAND,* [2]*University of Helsinki, Helsinki, FINLAND.*

Aim/Introduction: Quantitative SPECT-CT imaging is used to determine absorbed dose distributions in molecular radiotherapy (MRT). There are initiatives for harmonization of this process, such as EARL Lu-177 Quantitative SPECT accreditation. It is acknowledged that resolution recovery is a key factor to consider, especially due to the importance of tumor dosimetry. Resolution recovery coefficients (RCs) are usually measured using a standardised phantom with fillable inserts, and a constant target activity concentration may be used and established along the harmonization: a level of 2 MBq/ml has been suggested [1]. Subsequently, the acquired RC correction curve is applied to the patient dose calculation. There are several factors contributing to the uncertainty of the RC curve. In this study we evaluated whether activity concentration level affects the RCs. ***Materials and Methods:*** We prepared a solution using left-over no-carried-added Lu-177 from MRT treatments at the activity concentration level of 10 MBq/ml. The six standard sphere inserts (diameters 10, 13, 17, 22, 28 and 37 mm) of a NEMA IEC Body Phantom Set were filled with this solution. A quality assurance sample was taken from each fill syringe to ensure homogeneity of the solution. The background compartment of the phantom was filled with distilled water. The phantom was imaged with our site's clinical Lu-177 SPECT-CT protocol (parameters otherwise as in [1] except for a fixed imaging time, 10 s per projection, and automated quantification reconstruction with i=8, s=4) repeatedly over a period of eight half-lives. Volumes of interest (VOIs) were outlined for the inserts along their external wall on the first-day CT image,

and the RCs were determined based on the first-day imaging, accordingly. The VOIs were transferred to the other time-points with an automated alignment tool (CT-to-CT fusion). ***Results:*** The RCs determined at the initial activity concentration (9.7 MBq/ml) appeared to work within 5% down to 1 MBq/ml scale for the three largest inserts. At 0.5 MBq/ml, the recovered activity concentration in the inserts was 71%, 82%, 84%, 93%, 90% and 99%, respectively. At the lowest activity concentration measured in this series, 0.04 MBq/ml, the recovered activity of the largest insert had declined to 93%. ***Conclusion:*** There appears to be activity concentration dependence in the RC curve behaviour, which starts to manifest at clinically relevant activity concentration levels. This effect should be further studied, especially to improve tumor dosimetry. ***References:*** 1. EANM Forschungs GmbH: Lu-177 EARL Quantitative SPECT prototype, 15 Mar 2022 (update Feb 2025).

OP-101

Assessment of an ultra-fast dual-energy whole-body 360° ^{177}Lu-CZT-SPECT recording developed for the monitoring of ^{177}Lu-PSMA therapy

C. Boursier, *T. Zaragori, A. Zouaoui, A. Verger, P. Marie, L. Imbert; CHRU Nancy, Vandoeuvre-les-Nancy, FRANCE.*

Aim/Introduction: The ^{177}Lu-PSMA therapy monitoring of prostate cancer patients may be performed with high-speed whole-body 360° ^{177}Lu-CZT-SPECT recordings of only 18 min, based on the single 113 keV ^{177}Lu energy peak. However, count sensitivity is two to three times higher for SPECT recorded with dual 113 / 208 keV ^{177}Lu energy peaks. This study assesses the feasibility of an ultra-fast dual-energy whole-body 360° ^{177}Lu-CZT-SPECT recording of only 9 min. Such a short recording time would improve patient comfort and facilitate ^{177}Lu-SPECT scheduling. ***Materials and Methods:*** We selected the list-mode data of high-speed (18 min) whole-body 360° ^{177}Lu-CZT-SPECT recordings acquired the day after injection of 7.4 GBq of ^{177}Lu-PSMA in 20 prostate cancer patients (median age 73 years [interquartile range: 69 - 75 years]) referred to our nuclear medicine department between March and April 2025. SPECT images were reconstructed (i) as previously validated on the single 113 keV ^{177}Lu energy peak on the entire 18-min recording (SINGLE) and (ii) using a new dual 113 / 208 keV ^{177}Lu energy peak-based method applied on only the initial 9-min recording period. We compared SINGLE and DUAL reconstructions, using the parameters for tumor monitoring (SUVmax, SUVmean, and bone tumor volume determined using the standard 3 SUV threshold level), and background activity on a large region-of-interest encompassing the thigh muscles. Reconstruction parameters were previously optimized separately for 113 keV, 208 keV and dual 113 / 208 keV from an IEC body phantom filled in with a 12.7 ratio of ^{177}Lu between hot spheres and background. ***Results:*** Of these patients, 15 were considered to have metastatic bone lesions. SINGLE and DUAL reconstructions provided comparable levels of tumor SUVmax (38.7 [13.0-120.1] vs. 41.2 [10.9-143.0]), tumor SUVmean (7.8 [4.6-11.4] vs. 7.7 [4.3-12.9]), and background SUVmean (0.59 [0.043-0.079] vs. 0.59 [0.038-0.075]). However, tumor volume was lower with DUAL than with SINGLE reconstructions (70.9 [46.4-658.2] ml vs. 115.5 [61.1-550.2] ml, p=0.009), with a median decrease of 21.5 % [15.6-26.6 %] between SINGLE and DUAL reconstructions. ***Conclusion:*** Ultra-fast dual-energy whole-body 360° ^{177}Lu-CZT-SPECT recordings of only 9 min are feasible in cancer patients treated by ^{177}Lu-PSMA, although are associated with smaller tumor volumes than the previous single-energy peak recording method. Therefore, these two methods are not interchangeable when analyzing tumor changes during follow-up.

OP-102

Optimal SPECT Acquisition Settings for Quantitative Ac-225 Dosimetry

L. Polson[1], *S. Kurkowska*[2], *C. Li*[1], *P. Esquinas*[3], *C. Uribe*[1], *A. Rahmim*[1];
[1]*University of British Columbia, Vancouver, BC, CANADA,* [2]*Pomeranian Medical University, Szczecin, POLAND,* [3]*BC Cancer, Vancouver, BC, CANADA.*

Aim/Introduction: Patient specific dosimetry in radiopharmaceutical therapy requires accurate activity maps from SPECT images for personalization of treatment. The isotope Ac-225 is difficult to image with a SPECT system due to (i) a low count rate and (ii) a complex decay chain with contamination from multiple daughter isotopes in each photopeak. This work explores simulation and real phantom experiments to determine the optimal acquisition settings for accurate quantitative imaging of Ac-225. ***Materials and Methods:*** Monte Carlo (MC) simulations from SIMIND and real acquisitions from a Siemens Symbia T2 scanner were considered; the simulation represented the real system. MC simulations: to identify the optimal calibration method, (i) point source scans were acquired and (ii) uniform cylindrical phantoms of varying diameters were imaged and reconstructed. Optimal acquisition and reconstruction parameters were determined using a three-sphere phantom (10:1 source-to-background ratio, 40 min scan time), evaluated across different activity concentrations (0.2, 1, 10 kBq/mL), projection counts (8-128), photopeak/scatter windows (centered on 218 and 440 keV), scatter prefilter widths (0.0, 0.5, 1 cm FWHM), radial distances (15-25 cm), and reconstruction settings (up to 200 iterative updates). Multiple noise realizations were included for each condition, and both calibration methods were compared for converting to activity units. Real acquisitions: optimal settings were then used for a real phantom with spheres containing 10 kBq/mL. All reconstructions used OSEM, considering (i) attenuation and (ii) the collimator detector response, including septal penetration and septal scatter. The triple energy window (TEW) was used for scatter correction. ***Results:*** The optimal calibration was uniform cylinder reconstruction with ≥1 MBq total activity and cylinder diameter <10 cm; the point-source method was suboptimal due to sensitivity variation with source-detector distance. Convergence in a 40 mm sphere required ~100 (218 keV) and ~200 (440 keV) iterations; smaller VOIs required more. RCs in the 72 mm sphere declined with increasing source-detector distance by 18.0% (440 keV) and 10.3% (218 keV) from 15-25 cm. Scatter window width (5% vs. 10%) had little impact, but ≥0.5 cm TEW prefiltering greatly improved accuracy, especially at low activity (e.g., 186.0% vs. 87.3% RC at 200 Bq/mL). Thirty-two projections (in 40 min) balanced angular sampling and TEW precision. In the real phantom, optimal settings achieved RCs of 84.6% (218 keV) and 87.4% (440 keV) in a 60 mm sphere. ***Conclusion:*** Optimal acquisition, calibration, and reconstruction parameters for Ac-225 imaging were established through simulations and validated with a real phantom.

OP-103

Comparative Ac225 performance evaluation for a dual-collimator 3D CZT Camera

R. Zananiri, *A. Devir-Wolfman, L. Tsukerman, J. Bouhnik; GE HeathCare, Haifa, ISRAEL.*

Aim/Introduction: With the growing prominence of theragnostic isotopes in nuclear medicine (NM), Ac225 has emerged as a promising candidate, thanks to its unique combination of alpha and gamma emission properties. The Ac225 decay cascade incorporates gamma emissions from its daughters peaking at 440, 218 and 79 keV. Due to alpha toxicity, the injection doses are generally 10-100 folds less than nominal NM practices. The wide imaging peak ranges and the low activity pose a challenge on imaging Ac225. In this report, we compare the performance of a newly designed CZT-based multi-detector dual collimator 3D camera; deonted as dual-collimator StarGuide (DCS). DCS is equipped with two collimators optimized for high sensitivity (HS) and low penetration (LP) fulfilling the wide energy range needed for NM theragnostic scans. Ac225 performance of this DCS with LP collimators is compared to general purpose NaI based camera (870DR-GEHC) equipped with HEGP. To the best of our knowledge, this study reports the first Ac225 study on a multi-headed, CZT based detector imaging its all three peaks. ***Materials and Methods:*** Camera Design: DCS detectors were mounted on the StarGuide™ gantry. Notably, the detectors accounted for and corrected the Compton scattered photos within the CZT detector throughout the acquisition. Ac225 Phantom Test: A NEMA IEC phantom with spheres filled with 2.7µCi/ml and water background was scanned on both cameras; with LP collimator on DCS and HEGP on 870DR. The net acquisition time for both cases was 60 min. Images for the three peaks were assessed visually and quantitatively: separately and as a summed image of the reconstructions. ***Results:*** DCS possesses an overall equivalent or better image quality for all Ac225 peaks. Specifically, the background around the spheres is better on DCS in comparison to HEGP. The Spheres appear sharper on DCS as opposed to Dual-Head with sizes accurately reflecting the ground truth. The sum of the three Ac225 peaks marks a potential solution to increase the acquisition statistics and/or reduce the scan times for Ac225 patients. ***Conclusion:*** Using LP collimator on DCS provides a great potential to scan Ac225 gaining from the improved camera ring design as well as the ability to acquire all three Ac225 with accuracy. More studies on scan duration and phantoms possessing activity in their background are needed to fully develop an Ac225 patient protocol.

306

Sunday, October 5, 2025, 9:45 - 11:15

Room 117

Clinical Oncology Track - TROP Session - Oncology & Theranostics Committee: Breast Cancer Imaging

OP-104

Pre-treatment [^{18}F]FDG PET/CT and Histopathological Biomarkers in Early Triple-Negative Breast Cancer: Correlation with pCR and Prognostic Value in the SCANDARE Trial

R. Seban[1], *I. Buvat*[2], *L. Cabel*[3], *L. Djerroudi*[4], *L. Champion*[1], *N. Jehanno*[5], *T. Gaillard*[6], *L. Darrigues*[6], *E. Laas*[6], *J. Feron*[6], *V. Fourchotte*[6], *N. Pouget*[7], *C. Bonneau*[7], *C. Le Tourneau*[8], *M. Sablin*[8], *C. Lamy*[8];
[1]*Department of Nuclear Medicine and Endocrine Oncology, Institut Curie, Saint-Cloud, FRANCE,* [2]*Laboratory of Translational Imaging in Oncology, Paris Sciences et Lettres University (PSL) Research, Institut Curie, Orsay, FRANCE,* [3]*Department of Medical Oncology, Institute Curie, Paris, FRANCE,* [4]*Department of Pathology, Institut Curie, Paris-Sciences-Lettres Research University, Paris, FRANCE,* [5]*Department of Nuclear Medicine, Institut Curie, Paris, FRANCE,* [6]*Department of Breast, Gynecological and Reconstructive Surgery, Institut Curie, Paris, FRANCE,* [7]*Department of Breast, Gynecological and Reconstructive Surgery, Institut Curie, Saint-Cloud, FRANCE,* [8]*Department of Drug Development and Innovation (D3i), Paris-Saclay University, Institut Curie, Paris, FRANCE.*

Aim/Introduction: Triple-negative breast cancer (TNBC) is defined by the absence of ER, PR, and HER2 expression. However, androgen receptor (AR) and low HER2 expression have emerged as potential therapeutic targets. Literature suggests that AR-positive TNBC is associated with lower [18F]FDG uptake than AR-negative, while HER2-zero and HER2-low TNBC show similar uptake patterns. We thus aimed to validate the association between pre-treatment [^{18}F]FDG PET/CT parameters and HER2/AR expression, and to identify metabolic and histopathological biomarkers predictive of pathological complete response (pCR), recurrence-free survival (RFS), and breast cancer-specific survival (BCSS) in early-stage TNBC (eTNBC). ***Materials and Methods:*** We analyzed 176 patients with biopsy-proven eTNBC of no special type and other subtypes, prospectively enrolled in the SCANDARE trial (NCT03017573) at Institut Curie between 2017 and 2021. All underwent pre-treatment [^{18}F]FDG PET/CT (~62 min post-injection, median 194 MBq), using three different scanners. Tumours were segmented with a semi-automatic 41% SUVmax threshold, and PET biomarkers were tumor SUVmax and total metabolic tumor volume (TMTV). HER2-low was defined as IHC 1+ or 2+ with negative FISH; AR positivity as >10% nuclear staining. Patients received either neoadjuvant or adjuvant chemotherapy with surgery and radiotherapy. Associations between imaging and histopathological biomarkers with pCR, recurrence-free survival (RFS), and breast cancer-specific survival (BCSS) were assessed . ***Results:*** HER2 status was available for all patients: 76% were HER2-zero and 24% HER2-low. AR status was available for 53% of patients, with 23% AR-positive. No significant differences in clinicopathological features, tumor SUVmax, or TMTV were observed between AR or HER2 subgroups. Neither AR nor HER2 expression was associated with pCR (AR-positive: 22.6% vs. 18.2%, p=0.86; HER2-low: 30.0% vs. 27.8%, p=0.93), RFS (AR: HR=1.0, p=0.95; HER2: HR=0.7, p=0.48), or BCSS (AR: HR=0.7, p=0.66; HER2: HR=1.2, p=0.74). Median follow-up was 5 years; median tumor SUVmax and TMTV were 12.4 and 4.6 cm^3, respectively. High tumor SUVmax (>median) was strongly associated with pCR (p<0.001), while high TMTV predicted poorer RFS (HR=2.5, p=0.02) and BCSS (HR=6.9, p=0.002). ***Conclusion:*** Pre-treatment tumor SUVmax and

TMTV on [18F]FDG PET/CT were predictive of response and survival respectively, while HER2-low and AR-positive phenotypes showed no impact on outcomes. These results align with previous HER2 data. For AR, discrepancies may stem from differing positivity thresholds—1% in prior studies, reflecting the commonly used cutoff in the US, versus 10% in our study, in line with European practice. Further validation in larger cohorts is needed, along with international consensus on AR threshold definition.

OP-105

The impact of [18F]FDG PET/CT in guiding the change of management of triple-negative breast cancer patients: a sub-analysis of the TRINE-PET trial

L. Urso[1], *S. Panareo*[2], *A. Iudicello*[2,3], *D. Albano*[4], *M. L. Calcagni*[5], *A. Mazzoletti*[6], *R. Sciuto*[7], *L. Fantini*[8], *G. Rovera*[9], *L. Sofia*[10], *P. Guglielmo*[11], *S. Sorbello*[12], *M. Bambaci*[13], *S. Ialuna*[14], *A. Miceli*[15], *E. Rizza*[16], *C. Ferrari*[17], *A. Marongiu*[18], *F. Garrou*[19], *D. Bertin*[20], *A. Arnone*[21], *C. Colombo*[22], *A. M. Maffione*[23], *D. Donner*[24], *L. Evangelista*[25];
[1]*University of Ferrara, Ferrara, ITALY,* [2]*University-Hospital of Modena, Modena, ITALY,* [3]*University-Hospital of Ferrara, Ferrara, ITALY,* [4]*University of Brescia, Brescia, ITALY,* [5]*Department of Radiological and Hematological Sciences, Università Cattolica del Sacro Cuore, Rome, ITALY,* [6]*Fondazione Poliambulanza Istituto Ospedaliero, Brescia, ITALY,* [7]*IRCCS Istituto Nazionale Tumori Regina Elena, Rome, ITALY,* [8]*IRCCS IRST "Dino Amadori, Meldola, Meldola, ITALY,* [9]*University of Turin, Turin, ITALY,* [10]*University of Genoa, Genoa, ITALY,* [11]*Humanitas Gavazzeni, Bergamo, ITALY,* [12]*Ospedale GPII, Ragusa, ITALY,* [13]*Humanitas Istituto Clinico Catanese, Catania, ITALY,* [14]*Osp. Riuniti Villa Sofia Cervello, Palermo, ITALY,* [15]*AOU SS. Antonio e Biagio.e c. Arrigo, Alessandria, ITALY,* [16]*Vito Fazzi Hospital, Lecce, ITALY,* [17]*University Aldo Moro, Bari, ITALY,* [18]*University of Sassari, Sassari, ITALY,* [19]*A.O.U. Maggiore della Carità, Novara, ITALY,* [20]*IOV, Padua, ITALY,* [21]*Arcispedale S. Maria Nuova, Reggio Emilia, ITALY,* [22]*Fondazione IRCCS Ca' Granda, Milan, ITALY,* [23]*Santa Maria della Misericordia Hospital, Rovigo, ITALY,* [24]*Santa Chiara Hospital, Trento, ITALY,* [25]*Department of Biomedicine, Humanitas University, Pieve Emanuele, Milan, ITALY.*

Aim/Introduction: triple-negative breast cancer (TNBC) is an aggressive malignancy, and its management remains challenging due to limited therapeutic options. As such, accurate diagnosis is crucial to ensure timely and effective treatment decisions. TNBC is known to be an [18F]-FDG-avid tumor; however, [18F]-FDG PET/CT is still employed in only a limited number of clinical scenarios. TRINE-PET is a large, retrospective, real-world multicenter Italian study designed to investigate the correlation between [18F]-FDG PET/CT findings and survival outcomes in TNBC patients across different clinical stages of the disease. This sub-analysis of the TRINE-PET study aims to assess the clinical impact of [18F]-FDG PET/CT in influencing the changes in patient therapeutic management. ***Materials and Methods:*** data on [18F]-FDG PET/CT in TNBC patients were retrospectively collected from 24 Italian centers. Scans were categorized into four clinical settings: (a) baseline, (b) post-neoadjuvant chemotherapy (NAC), (c) suspected disease recurrence, and (d) patients undergoing systemic therapies. For inclusion, a minimum follow-up of two years was required. Clinical decisions made following [18F]-FDG PET/CT were recorded, and the percentage of changes in patient therapeutic management was calculated for each clinical setting. ***Results:*** a total of 707 [18F]-FDG PET/CT scans from 389 patients (mean age = 54 ± 13 years) were analyzed. The distribution of scans across clinical settings was as follows: baseline = 257, post-NAC = 111, suspected recurrence = 144, and systemic therapy = 195. [18F]-FDG PET/CT led to a change in therapeutic management in 22 (8.6%) baseline cases, 15 (13.5%) post-NAC cases, 42 (29.2%) cases with suspected recurrence, and 68 (35%) cases in patients receiving systemic therapies. ***Conclusion:*** the clinical impact of [18F]-FDG PET/CT in guiding treatment decisions increased with the progression of the stages of disease. A lower influence on patients therapeutic management was observed when PET/CT was performed at baseline or after NAC. In contrast, [18F]-FDG PET/CT significantly influenced therapeutic decisions in patients with suspected recurrence and in those undergoing systemic therapy. ***References:*** DOI: 10.1007/s00259-024-06866-9Acknowledgements: De Rimini M.L., Frega N., Filippi L. and Mattoli M.V.

OP-106

The PET/CT Response Monitoring in Oncology (PREMIO) criteria: A first suggestion to adapt the PERCIST criteria for patient-centric response monitoring of solid tumors in PET/CT scans

S. Hein[1], *N. M. Jakobsen*[2], *M. Naghavi-Behzad*[2], *W. A. Weber*[1], *W. Vach*[3], *M. Grubbe Hildebrandt*[2,4], *M. Vogsen*[5,4];
[1]*Department of Nuclear Medicine, Technical University of Munich, Munich, GERMANY,* [2]*Department of Nuclear Medicine, Odense University Hospital, Odense, DENMARK,* [3]*Basel Academy for Quality and Research in Medicine, Basel, SWITZERLAND,* [4]*Department of Clinical Research, University of Southern Denmark, Odense, DENMARK,* [5]*Department of Oncology, Odense University Hospital, Odense, DENMARK.*

Aim/Introduction: As PERCIST was originally designed for pharmaceutical trials using a study-centric framework, its application in clinical response monitoring may overlook disease progression due to baseline-focused comparisons and may yield false-positive results owing to its generalized definition of new lesions[1]. To address the need for objective response criteria in an international clinical trial, we adapted PERCIST towards a more patient-centric approach for better individual assessment: the PREMIO (PET/CT Response Monitoring In Oncology) criteria. ***Materials and Methods:*** Evolving from the one-lesion PERCIST, we further developed the criteria based on a prospectively acquired dataset of [18F]-FDG-PET/CT response monitoring cases of 87 metastatic breast cancer patients with a median of 6 follow-up scans without therapy change and without influence of the [18F]-FDG-PET on therapy decisions[1]. To determine the suitable SULpeak increase for progression in the PREMIO criteria, the probability for false progression was minimized based on an analysis of SULpeak variation in stable periods. Ideal ground truth time point of progression was determined by consent of two nuclear medicine physicians after validation of progression in the follow-up scans. ***Results:*** The PREMIO criteria are based on three pillars: quantitative assessment, new lesion assessment, and visual assessment. Major changes in PREMIO with respect to PERCIST are: the usage of the nadir scan with the lowest malignant SULpeak as the reference scan for progression in the quantitative assessment; the definition of measurability and assessability on scan level and between current scan and reference scan; a 50% SULpeak increase criterium for progression; definitions for the progression based on visual assessment; the integration of a classification system for new lesions for the examined cancer entity - e.g. the mBI-RADS (metastatic Breast cancer Imaging Reporting and Data System, presented at EANM24); and the introduction of the new category EMD (Equivocal Metabolic Disease), which demands a re-evaluation of a new equivocal lesion (mBI-RADS 3) in the following scan. PREMIO proved better suited for clinical response monitoring than PERCIST, with a positive predictive value of 94% vs. 84% and a negative predictive value of 100% vs. 63%. ***Conclusion:*** The new PREMIO criteria fill the gap for an objective and patient-centric response monitoring system of solid tumors in PET/CT scans, demonstrating promising accuracy results for response monitoring in metastatic breast cancer. The modular approach with possible different molecular imaging RADS also suggests the application in other tumor entities for future perspectives. ***References:*** [1] Vogsen et al. J Nucl Med 2023; 64.3:355-361.

OP-107

HER2-Targeted^{68}Ga-ABS011 positron emitted tomography (PET) in Metastatic Breast Cancer: Intermediate analysis of the HERMIA study.

G. Gebhart[1], *R. Lhommel*[2], *H. Everaert*[3], *O. De Winter*[4], *M. Lonneux*[5], *K. Goffin*[6], *D. Frijns*[7], *E. De Azambuja*[1];
[1]*Hôpital Universitaire de Bruxelles (HUB)-Institut Jules Bordet, Brussels, BELGIUM,* [2]*Cliniques Universitaires Saint-Luc, Brussels, BELGIUM,* [3]*Universitair Ziekenhuis Brussel, Brussels, BELGIUM,* [4]*Onze Lieve Vrouw Ziekenhuis, Aalst, BELGIUM,* [5]*CHIREC AZ Delta, Brussels, BELGIUM,* [6]*Universitair Ziekenhuis Gasthuisberg, Leuven, BELGIUM,* [7]*ABSCINT NV/SA, Liège, BELGIUM.*

Aim/Introduction: The 2016 ZEPHIR study introduced the concept of HER2 tumor heterogeneity, raising concerns about the reliability of HER2 immunohistochemistry (IHC) [1]. The IMPACT-MBC study, presented at ASCO 2024 [2], assessed whole-body HER2 heterogeneity using ^{89}Zr-trastuzumab PET in 200 metastatic breast cancer patients and showed that in a 21% of HER2-negative patients, HER2 PET led to treatment adjustments and improved survival outcomes. However, the clinical use of ^{89}Zr-labeled antibodies is limited due to challenges such as high cost, slow pharmacokinetics, and relatively high radiation doses [3]. Single-domain antibodies (sdAbs) are stable small proteins (12-15 kDa), with high nanomolar affinity, and low immunogenicity [4-7]. When radiolabeled, sdAbs target their antigen rapidly, enabling same-day imaging (i.e. 90 min after administration). Additionally, labeling with gallium-68 significantly reduces the radiation exposure [6-7]. ***Materials and Methods:*** After the successful completion of the Phase I and IIa trials, confirming safety and scan repeatability, the HERMIA Phase IIb study (EU-CT20245114192200) was designed to assess the diagnostic performance of ^{68}Ga-ABS011 PET in determining HER2 expression status and its potential to guide treatment decisions. ^{68}Ga-ABS011 is being compared to current standard diagnostic methods, including IHC/ISH, ^{18}F-FDG PET, and contrast-enhanced CT. Secondary objectives evaluate tumor heterogeneity and correlate the HER2 full body PET/CT images with early metabolic response, and tumor shrinkage after two cycles of T-DXd treatment. ***Results:*** To date, the positive safety profile of the ABS011 tracer was confirmed for 27 trial subjects. Based on intermediate data, temporal and inter-lesion heterogeneity was observed. A preliminary evaluation was performed on 8 out of 27 patients that were eligible for T-DXd treatment, and for which a follow-up ^{18}F-FDG-PET/CT after 2 treatment cycles was available. Positive lesions on HER2 PET/CT with Ga68-ABS011 showed treatment response, assessed via RECIST and PERCIST criteria. ***Conclusion:*** Upon completion of the full HERMIA dataset and confirmation of the diagnostic performance of Ga68-ABS011 PET tracer, a phase III trial evaluating of clinical utility, i.e relationship between HER2 PET/CT and long-term treatment outcomes, is envisioned. ***References:*** 1. Gebhart, G., et al. (2016). Ann Oncol 27(4): 619-624. 2. Eisses, B., et al. (2024). J Nucl Med. 3. Miao, H., et al. (2022). Front Oncol 12: 894767. 4. Ackaert C et al., Front Immunol. 2021;12:632687. 5. Muyldermans S., et al. Protein Eng. 1994;7:1129-1135. 6. Keyaerts M., et al. J Nucl Med. 2016;57:27-33. 7. Gondry, O., et al. (2024). J Nucl Med 65(2): 178-184.

OP-108

Al^{18}F-HER2-BCHImaging as a Non-invasive Approach to Assess Whole-Body HER2 StatusinHER2-Negative, -Low, and -PositiveBreast Cancer

X. Guo[1], *N. Zhou*[1], *J. Liu*[1], *H. Zhu*[2], *Z. Yang*[1];
[1]*Beijing Cancer Hospital, Beijing, CHINA,* [2]*Beijing Cancer Hospital, Beijing, CHINA.*

Aim/Introduction: Understanding which patients with human epidermal growth factor receptor 2 (HER2)-negative or -low metastatic breast cancer benefit from HER2-targeted strategies is urgently needed. We assessed the whole-body heterogeneity of HER2 expression on Al^{18}F-NOTA-HER2-BCH PET and the diagnostic performance in a large series of patients, including HER2-negative and -low breast cancer. ***Materials and Methods:*** In this prospective study conducted from June 2020 to March 2025, participants with newly diagnosed or relapsed breast cancer underwent both Al^{18}F-NOTA-HER2-BCH and ^{18}F-FDG PET/CT. HER2 status was determined by immunohistochemistry and in situ hybridization. Uptake was quantified by maximum standardized uptake value (SUVmax). HER2 immunohistochemistry was related to the quantitative Al^{18}F-NOTA-HER2-BCH uptake of corresponding biopsied lesions and all metastases, uptake heterogeneity, and qualitative scan evaluation. A prediction algorithm for HER2 immunohistochemistry positivity based on uptake was developed. ***Results:*** In 185 participants, HER2 status were positive (3+ or 2+/FISH+), low (1+ or 2+/FISH-), negative (0) in 98, 63, and 24 participants. With increasing HER2 immunohistochemistry status, the uptake of Al^{18}F-NOTA-HER2-BCH was higher (median SUVmax of 12.7, 7.2, and 4.0 for a HER2-positive, -low, -negative, respectively; P< 0.001) in 318 biopsied metastases. High uptake exceeding 10 was observed in 72.6% of HER2-positive participants, and low uptake below 4 predicted 50% of HER2 negative participants. Al^{18}F-NOTA-HER2-BCH uptake in the biopsied metastases with the predefined SUVmax threshold of 2.85 predicted HER2 IHC with a sensitivity of 95.2%, a specificity of 87.1%, of 98.6%, a PPV of 98.6%, and a NPV of 65.9%. The sensitivity, specificity, PPV and NPV of ^{18}F-FDG PET/CT was 84.6%, 83.9%, 97.9%, and 38.2%. Additionally, clear interindividual and intraindividual differences on Al^{18}F-NOTA-HER2-BCH uptake was noted between participants, different metastases in the same participants, even within different organ systems. ***Conclusion:*** Al^{18}F-NOTA-HER2-BCH had good diagnostic performance in breast cancer, showing considerable whole-body HER2 heterogeneity and uptake above background in HER2-negative and -low patients. This provides novel insights into HER2-negative and -low metastatic breast cancer compared with standard HER2 IHC on a single biopsy for identifying patients who may derive clinical benefit from HER2-targeted therapies. ***References:*** 1. Lumish MA, Maron SB, Paroder V, et al. Noninvasive Assessment of Human Epidermal Growth Factor Receptor 2 (HER2) in Esophagogastric Cancer Using (89) Zr-Trastuzumab PET: A Pilot Study. J Nucl Med. 2023;64:724-730.2. Guo X, Zhou N, Liu J, et al. Comparison of an Affibody-based Molecular Probe and (18)F-FDG for Detecting HER2-Positive Breast Cancer at PET/CT. Radiology. 2024;311:e232209.

OP-109

Diagnostic Accuracy of 99mTc-FAPI-46 SPECT/CT in Differentiating Malignant and Benign Breast Masses Classified as BIRADS IV and V: A Prospective Clinical Study

S. Barashki, *K. Aryana, N. Raeisi, R. Sabzi, A. J. Noughabi, H. Soleimani Bami, M. Emadzadeh;*
Mashhad University of Medical Sciences, Mashhad, IRAN, ISLAMIC REPUBLIC OF.

Aim/Introduction: Breast cancer is the most common malignancy among women worldwide, and early, accurate diagnosis is crucial for optimal treatment. The Breast Imaging Reporting and Data System (BIRADS) categorizes lesions based on malignancy risk, with BIRADS IV and V indicating high suspicion. However, many BIRADS IV lesions are benign, leading to unnecessary biopsies. Fibroblast activation protein (FAP), highly expressed in cancer-associated fibroblasts, is a promising target for molecular imaging. 99mTc-FAPI-46 is a novel SPECT radiotracer that may improve diagnostic accuracy while offering wider accessibility compared to PET tracers. We evaluate the diagnostic accuracy of 99mTc-FAPI-46 SPECT/CT in differentiating benign from malignant breast lesions classified as BIRADS IV and V, using histopathology as the reference. ***Materials and Methods:*** Thirty patients (mean age 45 ± 9.1 years, range 30-65) with BIRADS IV or V breast masses

were prospectively enrolled. The cohort included 7 BIRADS 4a, 7 BIRADS 4b, 6 BIRADS 4c, and 10 BIRADS 5 cases. After informed consent, patients received 20 mCi 99mTc-FAPI-46 intravenously. Imaging was performed 1 hour post-injection, including static chest, whole-body, and SPECT/CT scans. Images were interpreted by nuclear medicine specialists blinded to pathology. All patients underwent biopsy, and pathology results served as the gold standard. Tumor-to-contralateral breast and tumor-to-liver uptake ratios were calculated. ROC curve analysis assessed diagnostic performance. ***Results:*** Pathology confirmed 11 benign and 19 malignant lesions. The tumor-to-contralateral breast uptake ratio was significantly higher in malignant lesions (6.2 ± 4.1, range 1.6-17.4) than benign ones (1.1 ± 0.27, range 0.65-1.64; P < 0.001). The tumor-to-liver uptake ratio was also higher in malignant lesions (2.4 ± 1, range 0.9-5.0) compared to benign (0.64 ± 0.32, range 0.23-1.21; P < 0.001). Uptake ratios increased progressively from BIRADS 4a to 5. ROC analysis showed excellent accuracy: tumor-to-contralateral breast ratio had an AUC of 0.995 (95% CI: 0.979-1.000), and tumor-to-liver ratio had an AUC of 0.985 (95% CI: 0.950-1.000), both p < 0.001. A tumor-to-contralateral breast ratio >1.5 yielded 100% sensitivity and 91% specificity; a tumor-to-liver ratio >1.2 showed 94% sensitivity and 100% specificity. ***Conclusion:*** 99mTc-FAPI-46 SPECT/CT offers high sensitivity and specificity in distinguishing malignant from benign BIRADS IV and V breast lesions. Its accessibility and diagnostic performance support its potential as a valuable adjunct in breast cancer evaluation. Further studies are recommended to validate these findings and explore broader clinical applications.

OP-110

The Contribution of Ga-68 FAPI PET/CT in Newly Diagnosed Breast Cancer Patients Receiving Neoadjuvant Chemotherapy

M. Oflas[1], *D. Has Simsek*[1], *R. Yilmaz*[2], *N. Cabioglu*[3], *S. Onder*[4], *E. Isik*[1], *Z. Ozkan*[1], *A. Aydiner*[5], *Y. Sanli*[1], *S. Kuyumcu*[1];
[1]*Istanbul Faculty Of Medicine Department Of Nuclear Medicine, Istanbul, TÜRKIYE,* [2]*istanbul Faculty Of Medicine Department Of Radiology, Istanbul, TÜRKIYE,* [3]*istanbul Faculty Of Medicine Department Of General Surgery, Istanbul, TÜRKIYE,* [4]*Istanbul Faculty Of Medicine Department Of Pathology, Istanbul, TÜRKIYE,* [5]*Istanbul University Institute Of Oncology, Department Of Clinical Oncology, Istanbul, TÜRKIYE.*

Aim/Introduction: This study primarily aims to evaluate the utility of Ga68-FAPI PET/CT in combination with MAMMI PET for assessing pathological response to neoadjuvant chemotherapy (NACT) in breast cancer patients. ***Materials and Methods:*** We retrospectively reviewed breast cancer patients who underwent NACT and had pre/post-therapy imaging with F18-FDG PET/CT, Ga68-FAPI-FAPI PET/CT, and Ga68-FAPI MAMMI PET. Radiological and histopathological findings before and after treatment were documented. Quantitative PET parameters were calculated, and the post-therapy diagnostic performance of PET imagings were assessed using ROC analysis. Threshold values for detecting residual lesions were calculated, and univariate-multivariate analyses were performed for the breast and axilla. ***Results:*** A total of 21 breasts from 20 female patients were included in the study. Residual tumor was detected in 11 breasts (52.4%), while pathological complete response (pCR) was achieved in 10 breasts (47.6%). In visual assessment, the sensitivity, specificity and accuracy for detecting residual tumor in the breast after NACT were 73%, 70% and 71% for of F18-FDG PET/CT; 73%, 80% and 76% for Ga68-FAPI PET/CT; 64%, 70% and 67% for Ga68-FAPI MAMMI PET (including all lesions); 70%, 70% and 70% for Ga68-FAPI MAMMI PET (including the lesions in the field of view); and 100%, 50% and 76% for MRI, respectively. In quantitative analysis, the primary tumor TBR SUVmax value derived from post-therapy Ga68-FAPI MAMMI PET images had the highest diagnostic performance in detecting residual tumor in the breast. A threshold value of 1,35 for the TBR SUVmax value had 91% sensitivity, 80% specificity ,83% PPV, 89% NPV and 86% accuracy. In visual assessment, the sensitivity, specificity and accuracy for detecting residual tumor in the axilla were 33% ,91% and 71% for F18-FDG PET/CT, 50%,100% and 82% for of Ga68-FAPI PET/CT, and 50%,70% and 63% for MRI, respectively. None of the quantitative parameters have been found statistically significant in detecting residual tumor on the axilla. Ga68-FAPI PET/CT downstaged TNM in 15% of patients and upstaged TNM in 5% of the patients. ***Conclusion:*** The diagnostic performance of quantitative parameters derived from Ga68-FAPI PET/ BT combined MAMMI PET was found superior to current diagnostic methods in determination of pathological response of primary tumor, which may prevent unnecessary surgeries by accurate assessment of pCR. The contribution of Ga68-FAPI PET/CT for determination of NACT response in the axilla is limited. Moreover, it is predicted that Ga68-FAPI PET/CT may significantly impact the treatment approach in breast cancer by altering the TNM stage.

OP-111

Prostate-specific membrane antigen expression in patients with metastatic triple negative breast cancer: Final results of the PRISMA study

M. Manley[1], *G. Nader Marta*[2], *A. Arcay Ozturk*[1], *M. Kassas*[1], *L. Taraji*[1], *P. Aftimos*[1], *Z. Wimana*[1], *P. Flamen*[1], *G. Gebhart*[1];
[1]*Institute Jules Bordet, Anderlecht, BELGIUM,* [2]*Dana-Farber Cancer Institute, Boston, MA, UNITED STATES OF AMERICA.*

Aim/Introduction: Radioligand therapy (RLT) targeting prostate-specific membrane antigen (PSMA) prolongs survival in patients with prostate cancer. Immunohistochemistry-based studies suggest that PSMA is highly expressed in the tumor-associated neovasculature of triple-negative breast cancer (TNBC). In this study, we aimed to assess PSMA expression in patients with metastatic TNBC (mTNBC) via [^{68}Ga]Ga-PSMA-11 positron-emission tomography/computed tomography (PSMA PET/CT) to evaluate the feasibility of PSMA-targeted RLT for mTNBC. ***Materials and Methods:*** PRISMA is a prospective, single-center study that enrolled 22 patients with progressive mTNBC. Patients undergoing FDG-PET/CT with PET Response Criteria in Solid Tumors (PERCIST)-evaluable disease underwent PSMA PET/CT. For qualitative analysis, healthy liver uptake was used as a patient-specific reference. Patients were classified as PSMA-positive if PSMA uptake was higher than healthy liver uptake in the majority of lesions. For semi-quantitative analysis, target-lesions (TLs) were segmented and defined as ≥1.5 cm in diameter and PERCIST measurable on FDG PET/CT. TL volumes were propagated to the PSMA PET/CT and anatomically matched to measure maximum standard uptake value corrected for body weight (SUVmax) for each TL. Mann-Whitney U test was used to compare mean SUVmax between subgroups based on age, prior therapy and androgen receptor status. ***Results:*** Twenty patients were evaluable for analysis. On qualitative analysis, 10 (50%) patients were classified as PSMA positive. Semi-quantitatively, the mean SUVmax on PSMA PET/CT of all TLs (total 106) was 6.5 (range 1.4 - 28.0). Overall, 71 (67%) of TLs had PSMA SUVmax greater than their respective healthy liver. In 7 (35%) patients, all TLs showed PSMA uptake higher than healthy liver. In 13 (65%) patients, the majority of TLs demonstrated PSMA SUVmax higher than healthy liver. All TLs exhibited an SUVmax above the patient specific blood pool. Tumor histopathology is available for 16/20 patients, of which 15/16 expressed PSMA in endothelial cells. Mean PSMA SUVmax was higher in patients having received < 3 lines of prior therapy, having undergone immunotherapy and with negative androgen receptor status. ***Conclusion:*** PSMA expression in mTNBC exhibits substantial intra-

and interpatient heterogeneity with frequent mismatching with FDG-avidity. In approximately one third of progressing mTNBC patients all FDG-positive target lesions demonstrated PSMA-expression higher than normal liver on PSMA PET/CT. For this specific subset of patients, who currently have limited therapeutic alternatives, ^{177}Lu-PSMA RLT might become a new therapeutic opportunity.

OP-112

Integrin $\alpha_v\beta_6$-Targeted ^{68}Ga-Trivehexin PET/CT in Breast Cancer: A Prospective Comparison with ^{18}F-FDG

Z. Liu[1], *L. Li*[1], *H. Wu*[1], *Q. Chen*[2], *C. Li*[1], *Y. He*[1];
[1]*Department of Nuclear Medicine, Zhongnan Hospital of Wuhan University, Wuhan, CHINA,* [2]*Department of Pathology, Zhongnan Hospital of Wuhan University, Wuhan, CHINA.*

Aim/Introduction: Breast cancer has become the most commonly diagnosed malignancy worldwide. While ^{18}F-FDG PET/CT is widely used in clinical practice, its limitations—such as reduced sensitivity in low-metabolic tumors and false positives in inflammatory lesions—scan hinder accurate assessment. ^{68}Ga-Trivehexin, an integrin $\alpha_v\beta_6$-targeted tracer, has shown promising results in various tumors but remains unexplored in breast cancer. In this prospective study, we aimed to compare the diagnostic performance of ^{68}Ga-Trivehexin and ^{18}F-FDG PET/CT in breast cancer patients, and to analysis the correlation between tracer uptake and $\alpha_v\beta_6$ expression. ***Materials and Methods:*** Patients with clinically suspected or biopsy-confirmed, treatment-naïve breast cancer were enrolled in this prospective study and underwent both ^{18}F-FDG and ^{68}Ga-Trivehexin PET scans within one week. The primary endpoint was the diagnostic efficacy, using the histological findings from primary tumors and regional lymph nodes, as the gold standard. The secondary endpoint was the comparison of uptake parameters (SUVmax and TBR:tumor-to-background ratios) between the two imaging modalities. Integrin $\alpha_v\beta_6$ expression was evaluated via immunohistochemistry in available surgical specimens. A $p< 0.05$ was considered as statistically significant. ***Results:*** A total of 26 patients (mean age 50.7 ± 9.5 years) were included, comprising 4 triple-negative (TNBC), 4 HER2-positive, 3 Luminal A, and 15 Luminal B cases. Among 46 primary tumors, ^{68}Ga-Trivehexin PET/CT achieved a detection rate of 100% (46/46), compared to 97.83% (45/46) for ^{18}F-FDG ($p=0.317$). Notably, ^{68}Ga-Trivehexin detected a 5-mm ductal carcinoma in situ that was confirmed by postoperative histology but missed by ^{18}F-FDG. Semiquantitative analysis revealed significantly higher TBR with ^{68}Ga-Trivehexin (11.76 vs. 8.61; $p<0.001$). Among 177 regional lymph nodes evaluated, ^{68}Ga-Trivehexin detected 172 metastatic nodes (93.99%) versus 174 (95.08%) with ^{18}F-FDG ($p=0.527$). In 4 TNBC patients (28 nodes), ^{68}Ga-Trivehexin exhibited significantly higher uptake compared to ^{18}F-FDG (SUVmax: 6.72 vs. 4.44; TBR: 10.60 vs. 3.68; all $p<0.001$). Immunohistochemistry confirmed integrin $\alpha_v\beta_6$ expression in 5/6 surgically resected primary tumors. ***Conclusion:*** ^{68}Ga-Trivehexin PET/CT provides superior tumor-specific contrast compared to ^{18}F-FDG, particularly in $\alpha_v\beta_6$-overexpressing subtypes like TNBC. These findings support further clinical validation of ^{68}Ga-Trivehexin for subtype-specific imaging and management of breast cancer.

307

Sunday, October 5, 2025, 9:45 - 11:15
Room 212

TROP Session - Thyroid Committee: Nuclear Medicine Imaging in Thyroid Disorders: From Thyroid Nodule to Advanced/Refractory Cancer

OP-113

A non-invasive approach integrating PET/CT radiomics and ultrasound to improve risk stratification of thyroid incidentalomas detected on FDG PET/CT.

M. Roncali*, G. Ferrulli, R. Durmo, A. Frasoldati, A. Ghidini, S. Piana, M. Bertolini, L. Braglia, A. Filice;*
AUSL-IRCCS di Reggio Emilia, Reggio Emilia, ITALY.

Aim/Introduction: Thyroid incidental uptake (TIU) on FDG PET/CT is a relatively common finding in clinical practice, yet its clinical significance remains controversial. This study aimed to develop an integrated predictive algorithm combining conventional parameters and radiomic features to better assess the risk of malignancy in TIU. ***Materials and Methods:*** We retrospectively analyzed patients who underwent FDG PET/CT between January 2010 and December 2024 for non-thyroid indications, had reported TIU and have fine-needle aspiration cytology available. Patients were classified as positive or negative based on cytological results. Collected covariates included demographics, comorbidities, ultrasound (US) classification, PET/CT semi-quantitative parameters (SUVmax, SUVmean, MTV, TLG) and radiomic features (for a subset of patients) extracted using LifeX software. Statistical analysis was performed by estimating linear and quadratic discriminant analysis classifiers, with previous variable selection according to both a forward (Wilks' lambda based) and bidirectional (prediction accuracy based) stepwise procedure. Accuracies and diagnostic tests performance measures were calculated using a jackknife approach. Statistical analysis was performed using R 4.3.0. ***Results:*** A total of 208 patients (65.4% female; median age 67 years, IQR 58-73) were included. Among them, 68.8% (143/208) had benign nodules, while 31.2% had positive cytology. US categorized nodules as benign in 32.4%, indeterminate in 52.5%, suspect in 14.4%, and malignant in 0.7% of cases rspectively. Median SUVmax was 6.04 (IQR 4.15-8.93), SUVmean 3.56 (IQR 2.32-5.45), MTV 3.09 cm^3 (IQR 1.63-6.94), and TLG 11.34 (IQR 5.80-22.59). In the discriminant analysis on all the sample only US features were consistently selected in all stepwise procedures, with best performance obtained using only suspect/malignancy (with a moderate predictive performance: accuracy 74.4%, positive predictive value 77.3%). Radiomic analyses were available for 96 patients. Among the extracted textures, a geometric feature (NHOpeak) was selected in using the forward procedure, not with the bidirectional (accuracy prediction based) one. The model combining ultrasound and NHOpeak didn't overperformed, in terms of prediction accuracy, if compared with model with US feature only, bothhaving an accuracy of 84.9%, specificity and positive predictive value of 100%, a negative predictive value of 84.2%, and a sensitivity of 21.4%. Further evaluations are in progress. ***Conclusion:*** Ultrasound classification remains the cornerstone for initial TIU risk stratification. However, the integration of radiomic features from FDG PET/CT may enhance diagnostic accuracy, particularly by increasing specificity and PPV, thus minimizing false-positive findings.

OP-114

Diagnostic ^{131}I whole-body scans in the Detection of Differentiated Thyroid Cancer: Comparison with different doses

T. Ming, *f. Kang, w. Ma, j. Wang;*
Department of Nuclear Medicine, Xijing Hospital, Fourth Military Medical University, Xi'an, CHINA.

Aim/Introduction: Compare the diagnostic efficacies of different low-dose diagnostic ^{131}I whole-body scans (Dx-WBS) in differentiated thyroid cancer (DTC). ***Materials and Methods:*** We reviewed data from 1146 consecutive patients with DTC who had total thyroidectomy and were referred for Radioactive iodine (RAI) therapy between April 2022 and April 2025 in Xijing Hospital. They were divided into three groups according to doses of Dx-WBS(353 patients with 5mCi, 609 patients with 3mCi, and 184 patients with 1mCi). The diagnostic efficacy of Dx-WBS was calculated with post-therapy WBS (Rx-WBS) as the reference, and compare diagnostic efficacies of different low-dose Dx-WBS. ***Results:*** In total, 1146 patients [mean age, 40.1±12.0 years; range, 7-77 years; 688 (60%) Female,458 (40%)male] were evaluated. For different doses (5mCi,3mCi and 1mCi) of low-dose diagnostic whole-body scans (Dx-WBS), the detection rates for residual thyroid tissue [99.4% (328/330),91.6% (535/584) and 80.8% (139/172)], lymph node metastasis [61.2% (39/62),58.1% (61/105) and 22.7% (5/22)], and distant metastasis [72.3% (8/11), 71.4% (10/14) and 50.0% (1/2)]. In lymph node metastasis, the diagnostic efficiency of Dx-WBS at a dose of 3mCi is comparable to that of Dx-WBS at a dose of 5mCi. The detection rates are 61.2% and 58.1% respectively, and both have significantly higher detection rates than 1mCi (22.7%). ***Conclusion:*** Dx-WBS with a dose of 3mCi exhibits comparable diagnostic performance to 5mCi for lymph node metastasis. However, both significantly surpasses Dx-WBS with a dose of 1mCi. Therefore, for patients with a high suspicion of lymph node metastases, it is recommended that they undergo a Dx-WBS with a dose of 3mCi.

OP-115

[18F]AlF-NOTA-FAPI-04 PET/CT improves detection of subcentimeter recurrent lesions in differentiated thyroid cancer: acomparative study with [18F]FDG

K. Zheng, *H. Ye;*
Hunan Cancer Hospital, Changsha, CHINA.

Aim/Introduction: Fibroblast activation protein (FAP)-targeted PET/CT has emerged as a promising tool for visualizing tumor stroma. This study aimed to validate the diagnostic efficacy of [^{18}F]AlF-NOTA-FAPI-04 PET/CT in detecting subclinical metastases in recurrent differentiated thyroid cancer (DTC), with direct comparison to [^{18}F]FDG PET/CT. ***Materials and Methods:*** Twenty-three DTC participants with biochemical recurrence (suppressed thyroglobulin [Tg] ≥1 ng/mL or Tg antibodies [Tg-Ab] >115 IU/mL) underwent [^{18}F]AlF-NOTA-FAPI-04 PET/CT, including 16 who underwent paired [18F]FDG scans. Lesion classification followed histopathology or 15.5-month clinical follow-up (median, 8-32 months). ***Results:*** [^{18}F]AlF-NOTA-FAPI-04 PET/CT demonstrated significantly higher lesion-level sensitivity (75% vs 12.5%, P = 0.002) and accuracy (80% vs 26.7%, P < 0.001) than [^{18}F]FDG. Participant-level sensitivity reached 100% (7/7 vs 14.2% [1/7], P =0.003). Notably, 7 cervical lymph node metastases (mean diameter 5.9 ± 1.4 mm) were detected exclusively by FAPI imaging. ***Conclusion:*** [^{18}F]AlF-NOTA-FAPI-04 PET/CT exhibits superior diagnostic performance over [^{18}F]FDG PET/CT in detecting small metastatic lesions in recurrent DTC, potentially enabling earlier intervention and improved patient management.

OP-116

Diagnostic value of [18F]-FDG and [68Ga]-FAPI-04 PET/MRI for lymph node metastasis in papillary thyroid cancer

T. Han[1], *Z. Quan*[1], *H. Wei*[2], *J. Wang*[1], *F. Kang*[1];
[1]*Department of Nuclear Medicine, Xijing Hospital, Fourth Military Medical University, Xi'an, CHINA,* [2]*Department of Thyroid and Breast Surgery, Xijing Hospital, Fourth Military Medical University, Xi'an, CHINA.*

Aim/Introduction: This study aimed to evaluate the diagnostic value of [^{18}F]-FDG PET/MRI for the diagnosis of neck lymph node metastasis (LNM) in patients with initially diagnosed papillary thyroid cancer (PTC) and to compare it with [^{68}Ga]-FAPI-04 PET/MRI. ***Materials and Methods:*** Thirty patients with PTC confirmed by thyroid fine-needle aspiration biopsy were prospectively enrolled and underwent [^{18}F]-FDG PET/MRI; of which, 6 additionally underwent [^{68}Ga]-FAPI-04 PET/MRI within 3 days. According to surgical guidelines, the neck lymph node (LN) was divided into three macroscopic regions: central (VI) and left/right lateral neck (II-V). Images were semi-quantitatively and visually interpreted, and lesions' quantity, location, and uptake values were noted. Diagnostic performance of [^{18}F]-FDG PET/MRI versus US and MRI in N-staging of PTC patients based on regional analysis using postoperative histopathology as the gold standard. Whether the $BRAF_{V600E}$ mutation or not affects metastatic LN radioactivity uptake. Exploring the relevance of dual tracer imaging of metastatic LN radioactivity uptake and its head-to-head comparison for diagnostic efficacy. ***Results:*** A total of 48 macroscopic regions were surgically dissected. The diagnostic efficacy of [^{18}F]-FDG PET/MRI for detecting LNM was higher than that of US and MRI, overall sensitivity, specificity, and accuracy were 71.1% vs. 60.5% vs. 65.8%, 90.0% vs.80.0% vs. 80.0%, and 75.0% vs. 64.6% vs. 68.8%, respectively (all P > 0.05). For the central region (n=30), the sensitivity, specificity, and accuracy of US, MRI, and [^{18}F]-FDG PET/MRI for detecting LNM were 42.9% vs. 47.6% vs. 52.4%, 77.8% vs. 88.9% vs. 88.9%, and 53.3% vs. 60.0% vs. 63.3%, respectively (all P > 0.05). For the lateral region, the sensitivity and accuracy of [^{18}F]-FDG PET/MRI for detecting LNM were significantly superior to those of US (94.1% vs. 82.4%; 94.4% vs. 83.3%; all P < 0.05), while demonstrating comparable specificity. SUV_{max} of metastatic LNs on [^{68}Ga]-FAPI-04 PET/MRI was positively correlated with [^{18}F]-FDG PET/MRI (r=0.8564,95%CI:0.7208-0.9289; P<0.0001). The positive lesion detection rate of dual tracer imaging in 6 patients with PTC is consistent, and the degree of radioactivity uptake of [^{68}Ga]-FAPI-04 was higher than that of [^{18}F]-FDG in both primary lesion and LNM (12.3±5.7 vs. 6.9±5.3;4.5±3.7 vs. 3.4±1.8; all P > 0.05). ***Conclusion:*** [^{18}F]-FDG PET/MRI demonstrated marginally superior diagnostic performance for LNM detection compared to US and MRI, but all three modalities exhibited suboptimal sensitivity, particularly in the central region. Small sample populations revealed no significant differences in [^{68}Ga]-FAPI-04 and [^{18}F]-FDG uptake levels in primary lesion and LNM of PTC.

OP-117

Trop2-Targeted PET/CT with ^{68}Ga-MY6349 for Detecting Metastatic Lesions in Recurrent/Metastatic Thyroid Cancer: Prospective Comparison of Diagnostic Efficacy with ^{18}F-FDG PET/CT

H. Fu[1], *J. Huang*[1], *W. Guo*[1], *H. Wu*[1], *F. Wang*[2], *H. Chen*[1];
[1]*The First Affiliated Hospital of Xiamen University, Xiamen, CHINA,* [2]*Peking University, Beijing, CHINA.*

Aim/Introduction: Trophoblast cell surface antigen 2 (Trop2) targeted molecular imaging with ^{68}Ga-MY6349 has been proposed as a potential modality for visualizing cancerous lesions, but its utility for identifying recurrent/metastatic thyroid cancer (TC) is not well-established in the literature. This study

aims to evaluate the clinical utility of ^{68}Ga-MY6349 PET/CT for detecting metastatic TC and to compare the results with those of ^{18}F-fluorodeoxyglucose (FDG) PET/CT. ***Materials and Methods:*** This was a prospective, single-center, open-label, single-arm comparative imaging trial. Patients with clinically suspected or confirmed recurrent/metastatic TC were prospectively enrolled and underwent paired ^{68}Ga-MY6349 and ^{18}F-FDG PET/CT from November 2023 to March 2024. Histopathology and clinical follow-up (mean 12 months ± 0.7 [standard deviation] (range: 11-13 months) were used as reference standards for the final diagnosis. ^{18}F-FDG and ^{68}Ga-MY6349 uptake were compared by using the Wilcoxon signed-rank test. The McNemar test was used to compare the diagnostic efficacy of the two techniques, and the influence of various clinicopathological characteristics on ^{18}F-FDG and ^{68}Ga-MY6349 uptake was evaluated by Mann-Whitney and Kruskal-Wallis tests. ***Results:*** In total, 113 participants (median age, 51 years [interquartile range, 35-61 years]; 17 men) were evaluated. Among the 113 patients, 89 had papillary thyroid cancer (PTC). The other tumor entities were follicular thyroid cancer (9), Hürthle cell cancer (3), poorly differentiated thyroid cancer (4), differentiated high-grade thyroid cancer (4), medullary thyroid cancer (3), and anaplastic thyroid cancer (1), respectively. In all 113 participants, the ^{68}Ga-MY6349-derived SUV_{max} was higher than the ^{18}F-FDG-derived SUV_{max} in all the lesions (6.43 vs. 2.46, P<0.001), the local recurrence (24.9 vs. 10.7, P = 0.026), metastatic central compartment (12.7 vs. 4.9, P < 0.001), metastatic lateral compartment (11.0 vs. 5.4, P < 0.001), and mediastinal lymph nodes (LNs) (9.5 vs. 4.6, P = 0.012). In PTC lesions, the ^{68}Ga-MY6349-derived SUV_{max} was higher than the ^{18}F-FDG-derived SUV_{max} (8.26 vs. 2.09, P< 0.001). Besides, the ^{68}Ga-MY6349-derived SUV_{max} in PTC lesions was higher than that of non-PTC lesions (8.26 vs. 3.38, P< 0.001). ^{68}Ga-MY6349 PET/CT had a higher sensitivity than ^{18}F-FDG PET/CT for detecting neck lesions (90% vs. 58%; P < 0.001). ***Conclusion:*** ^{68}Ga-MY6349 PET/CT had high screening sensitivity in PTC metastatic lesions, and was superior to ^{18}F-FDG PET/CT for detecting metastatic TC, especially in local recurrence and LNs metastases of PTC.

OP-118

Diagnostic Utility of ^{68}Ga-PSMA PET/CT in Differentiated Thyroid Cancer Patients with Biochemical Recurrence and Negative Conventional Imaging.

C. Sgro[1], *E. Greco*[1], *G. Fuso*[1], *G. Bianciardi*[1], *L. Carrara*[1], *G. Cuzzani*[1], *E. Fortunati*[2], *L. Zanoni*[2], *R. Mei*[2], *L. Vetrone*[2], *A. Golemi*[2], *E. Lodi Rizzini*[3], *L. Calderoni*[2], *E. Tabacchi*[2], *S. Fanti*[1,2];
[1]*Nuclear medicine, Alma Mater Studiorum University of Bologna, Bologna, ITALY,* [2]*Nuclear Medicine, IRCCS, Azienda Ospedaliero-Universitaria di Bologna, Bologna, ITALY,* [3]*Radiation Oncology, IRCCS, Azienda Ospedaliero-Universitaria di Bologna, Bologna, ITALY.*

Aim/Introduction: Differentiated thyroid cancer(DTC) generally exhibits a favourable prognosis following total thyroidectomy and radioactive iodine(I-131)ablation. However, a subset of patients develops biochemical recurrence-elevated thyroglobulin (Tg) or anti-Tg antibodies(AbTg)-with negative or equivocal findings on conventional imaging(ultrasound or CT).In these cases,^{18}F-FDG-PET/CT may be used,although the results may be equivocal. ^{68}Ga-PSMA-PET/CT, although primarily used in prostate cancer, has shown promising results in detecting neoplastic lesions by targeting tumour neovascularisation in other malignancies, including DTC. ***Materials and Methods:*** This study enrolled patients with DTC who underwent thyroidectomy followed by I-131 therapy.All patients had evidence of biochemical progression,defined as increasing Tg or AbTg levels,but negative or indeterminate findings on ultrasound and CT.Each patient underwent an ^{18}F-FDG PET/CT scan,which either failed to localise the disease or was inconclusive.^{68}Ga-PSMA-PET/CT was then performed. PSMA-avid lesions, SUVmax values and uptake distribution were analysed.Histological or radiological follow-up (when available) was used as a reference standard to validate PET results. ***Results:*** 17 patients were included(mean age: 60y.o.):12/17(70%)patients had papillary variant DTC,4/17(26%) had follicular variant and 1/17(6%) had hurtle-cell carcinoma.BRAF, RAS and TERT mutations were tested in 11 patients:8/11(73%) had BRAF mutations, 2/11(18%)had RAS and 4/11(36%)had TERT mutations.Mean basal Tg and Ab-Tg were 32 ng/mL and 42 UI/mL,respectively,at the time of ^{68}Ga-PSMA-PET/CT. 4/17(24%) patients had equivocal CT, 7/17(41%) had equivocal ultrasound, while 6/17(35%) had evidence of biochemical progression with negative imaging. All patients underwent^{18}F-FDG-PET/CT: 12/17(70%) resulted FDG-negative, 4/17(24%) FDG-positive and only 1/17(6%) had equivocal scan.Regarding the ^{68}Ga-PSMA-PET/CT scans:9/17(53%) resulted PSMA-positive while 8/17(47%) PSMA-negative.Two patients had both FDG-PSMA-positive-PET-scan and one resulted FDG-positive but PSMA-negative.SUVmax values of 11 PSMA-positive lesions showed a mean of 2.65, a median of 2.4 and a range of 1.5-3.7. Of the 9 patients with PSMA-positive findings, lymph node metastases were histologically confirmed in 2/9 patients, while 4/9 patients had radiological evidence of metastatic disease(bone, lung, abdominal-lymph nodes); data were not available for the other patient. In patients with negative-scans, the absence of detectable disease supported ongoing surveillance strategies.No clear association was observed between PSMA-expression and histological variants of DTC nor with the presence of BRAF, RAS or TERT mutations. ***Conclusion:*** ^{68}Ga-PSMA-PET/CT appears to be a useful imaging modality in selected DTC patients with biochemical progression and negative or inconclusive conventional imaging.While ^{18}F-FDG-PET/CT remains an important imaging modality for the evaluation of dedifferentiated or radioiodine-refractory thyroid cancer, PSMA-based imaging may serve as a valuable adjunct.Future prospective studies should investigate its diagnostic accuracy, prognostic relevance and potential in theranostic applications.

OP-119

Diagnostic accuracy of ^{18}F-FDG PET/CT compare to 18F-PSMA PET/CT in Radioiodine-Refractory Differentiated Thyroid Carcinoma Patients

A. J. S. Portilho, *M. O. Cerci, S. Kuba, N. T. T. P. Silva, R. N. Tineo, C. A. de Souza, D. E. Zantut-Wittmann, C. D. Ramos;
University of Campinas (UNICAMP), Campinas, BRAZIL.*

Aim/Introduction: While differentiated thyroid carcinoma (DTC) typically has excellent prognosis (10-year survival: 98.4%), 5-15% of cases progress to radioiodine-refractory disease (rRIT), necessitating alternative diagnostic approaches. Emerging evidence suggests prostate-specific membrane antigen (PSMA)-targeted PET/CT may complement ^{18}F-FDG imaging in rRIT-DTC [1], potentially enabling theranostic applications. This study aimed to perform a head-to-head comparison of 18F-PSMA-1007 and ^{18}F-FDG PET/CT for lesion detection and metabolic characterization in rRIT-DTC patients. ***Materials and Methods:*** This cross-sectional study enrolled rRIT-DTC patients with suspected locoregional or metastatic disease. All underwent both ^{18}F-FDG and 18F-PSMA-1007 PET/CT within 7 days. Lesion detection rates and maximum standardized uptake values (SUVmax) were compared across anatomical sites. ***Results:*** Among 23 enrolled patients (16 female, mean age 55.6 ± 18 years), a total of 91 lesions were identified by ^{18}F-FDG PET/CT compared to 87 lesions detected with 18F-PSMA-1007 PET/CT. Both tracers demonstrated similar localization of metastases, with concordant findings in the thyroid bed (6 vs. 5 lesions), cervical lymph nodes (17 vs. 17), thoracic lymph nodes (12 vs. 12), lungs (17 vs. 16), and liver (1 vs. 1). Discrepancies were observed in abdominal lymph nodes (3 detected by ^{18}F-FDG vs. 0 by 18F-PSMA) and bone lesions (4 vs. 6). The median SUVmax across all lesions was higher for ^{18}F-FDG (24.2; range 5.6-80.9) than for 18F-PSMA (17.3; range 4.1-73.3). Notably,

13 patients (56.5%) exhibited at least one lesion with greater 18F-PSMA uptake intensity than 18F-FDG, suggesting interlesional heterogeneity in tracer avidity. ***Conclusion:*** 18F-PSMA-1007 demonstrates comparable lesion detection to ^{18}F-FDG in rRIT-DTC, with heterogeneous uptake patterns suggesting complementary roles. The superior 18F-PSMA uptake in >50% of patients supports further investigation of PSMA-targeted theranostics for selected cases. ***References:*** [1] Rizzo A, et al. Potential Role of PSMA-Targeted PET in Thyroid Malignant Disease: A Systematic Review. Diagnostics (Basel). 2023;13(3):564.

OP-120

Unlocking the Potential of Liquid Biopsy in Advanced Differentiated Thyroid Cancer (DTC): Could [^{18}F]FDG PET/CT Increase the Rate of Informative Liquid Biopsies?

G. Rovera[1], *C. Moneta*[2], *S. Moog*[2], *M. Bani*[3], *J. Hadoux*[2], *A. Ghuzlan*[3], *D. Hartl*[4], *I. Breuskin*[5], *L. Lacroix*[6], *Y. Loriot*[7], *A. Italiano*[8], *B. Besse*[9], *E. Baudin*[2], *L. Lamartina*[2], *D. Deandreis*[1];
[1]*Nuclear Medicine Department, Gustave Roussy, University Paris Saclay, Villejuif, FRANCE,* [2]*Department of Imaging, Endocrine Oncology Unit, Gustave Roussy, University Paris Saclay, Villejuif, FRANCE,* [3]*Department of Pathology, Gustave Roussy, Villejuif, FRANCE,* [4]*Department of Otolaryngology Head and Neck Surgery, Gustave Roussy, University Paris Saclay, Villejuif, FRANCE,* [5]*Department of Head and Neck Oncology, Gustave Roussy, Villejuif, FRANCE,* [6]*Department of Biopathology, Gustave Roussy, Villejuif, FRANCE,* [7]*Early Drug Development Department, Gustave Roussy, Villejuif, FRANCE,* [8]*DITEP, Gustave Roussy, Villejuif, FRANCE,* [9]*Department of Cancer Medicine, Gustave Roussy, Villejuif, FRANCE.*

Aim/Introduction: Liquid biopsy (LB) is a promising technique for less invasive and more comprehensive molecular profiling of cancers. However, data on the use of LB in thyroid cancer, in particular metastatic/locally-advanced DTC are still limited, and LBs are not always concordant with tissue biopsies. LB is thus currently recommended to detect target mutations (BRAF/RET/NTRK fusions) only in absence of a tissue biopsy. The aim of this study was to investigate the association between the [18F]FDG-PET/CT metabolic profile and the diagnostic yield of LB in metastatic/locally-advanced DTC. ***Materials and Methods:*** A retrospective study was conducted on patients with metastatic/locally-advanced DTC who underwent LB at our center (01/2021-01/2024). The concordance between LB results and tissue biopsies was assessed using genetic data from primary-tumor/metastases (NGS/immunohistochemistry). [18F]FDG-PET/CT imaging was reviewed and semiquantitatively analyzed using MIM-v7.3.7 and a 41% SUVmax threshold. Extracted parameters included SUVmax, SUVmean, metabolic tumor volume (MTV) and total lesion glycolysis (TLG) at both lesion and whole-body level. Statistical analysis was performed using SPSS-v29, and differences in PET-derived parameters between concordant/discordant LB cases were assessed using Mann-Whitney test. ***Results:*** 76 patients (median age 61 [range:23-87]) with metastatic/locally-advanced DTC were retrospectively evaluated. At the time of LB, 85.5% of patients were radioiodine-refractory, 90.8% were M1, 40.8% were receiving treatment and 27.6% had already undergone ≥2 lines of treatment. Out of 76 patients, 30 underwent [18F]FDG-PET/CT imaging near the date of liquid biposy. In this sub-cohort, concordance between LB and tissue biopsy was observed in 26.7% (8/30) of patients, while in 73.3% (22/30) LB did not identify the same driver mutation. At [18F]FDG-PET/CT semiquantitative analysis, the median tMTV was found to be significantly higher in patients with concordant LB results (64.0ml [IQR 24.18-128.52] vs 7.6ml [IQR 1.50-18.91], p=0.008). Similarly, the median tTLG was also higher in case of informative LB (358.7 [85.0-851.5] vs 33.9 [10.8-114.3], p=0.031). These findings suggest that [18F]FDG-PET/CT may provide valuable functional information by reflecting the biological aggressiveness of disease and metabolic tumor burden, which could influence the shedding of tumor-derived genetic material into the bloodstream and therefore the rate of LB concordance. On the other hand, no significant differences were found in terms of more conventional metrics such as SUVmax (9.3 vs 11.1) and SUVmean (4.3 vs 3.8). ***Conclusion:*** Higher metabolic tumor burden on [18F]FDG-PET/CT is associated with increased diagnostic yield of liquid biopsy in advanced DTC, suggesting its potential as a complementary tool in patient selection.

OP-121

Intraoperative PET/CT imaging for thyroid cancer, parathyroid adenoma and oncological work-up of cervical lymph nodes with a high resolution mobile PET/CT-camera for surgical specimens

B. Lambert[1], *V. Vergucht*[2], *D. Berwouts*[1], *B. Van Den Bossche*[1], *J. Mertens*[1], *C. Van Haverbeke*[2], *M. Coppens*[2], *C. Gabriel*[3], *M. Rottiers*[2], *A. Decock*[2], *V. Galle*[2], *T. Van Oostveldt*[2], *K. Decaestecker*[2];
[1]*Maria Middelares Hospital - Jan Palfijn Hospital, Gent, Gent, BELGIUM,* [2]*Maria Middelares Hospital, Gent, BELGIUM,* [3]*Maria Middelares Hospital, Gent, BELGIUM.*

Aim/Introduction: This prospective exploratory trial, conducted at Maria Middelares Hospital (Ghent, Belgium), investigates the feasibility of using a mobile specimen PET/CT camera during surgery for thyroid and parathyroid disease, as well as for oncological work-up of suspicious cervical lymph nodes. Patients are injected with a PET tracer prior to surgery, and the resected specimens were scanned intraoperatively. While prior applications of this technology have been reported in breast and prostate cancer, this study explores its potential in new indications. The study is ongoing, with partial results published in a recent paper. ***Materials and Methods:*** Seventeen patients were enrolled for head-and-neck related indications: 8 thyroid cancers, 3 parathyroid explorations and 6 nodal excision biopsies of cervical suspect nodes for oncological work-up. Patients received 1h preoperatively a low activity of [18F]Choline (parathyroid), or [18F]FDG. After surgical excision, specimens were scanned using a mobile specimen PET/CT scanner (AURA10, Xeos Medical, Ghent, Belgium), with imaging completed within 12 minutes post-resection. Imaging results were compared with histopathology to evaluate correlation. ***Results:*** In the thyroid cancer group, 4 patients underwent total thyroidectomy—3 with lymphadenectomy—and 4 resection of recurrent disease. Intraoperative imaging predicted R0 status in all total thyroidectomies and correctly identified a positive margin in a local relapse. In 7/8 cases intraoperative PET/CT confirmed complete removal of all suspicious lymph nodes identified pre-operatively. In all 3 patients suspected of suffering from parathyroid adenoma, intraoperative PET/CT with [18F]Choline showed concordance with pathology.For the oncological work-up of metabolic active cervical lymph nodes of unknown origin, imaging accurately identified malignant involvement in 5/6 patients, including 4 cases of lymphoma, lymph node metastases from breast cancer. One biopsy resection of a neck node in a patient with colorectal cancer was futile: due to adherence the lymph node could not be resected and only non-suspicious tissue was removed. Pathology confirmed all intraoperative PET/CT imaging findings (6/6 concordance with 1 true negative case). ***Conclusion:*** Our initial experiences with intraoperative PET/CT demonstrate the feasibility to assess the surgical margins of tumoral specimens as well as confirmation that the correct nodes/nodules are resected in thyroid cancer, parathyroid exploration and lymph node excision biopsies. ***References:*** Lambert, B. et al. (2025). "Feasibility study on the implementation of a mobile high-resolution PET/CT scanner for surgical specimens: exploring clinical applications and practical considerations". European Journal of Nuclear Medicine and Molecular Imaging. doi: 10.1007/s00259-025-07143-z.

308

Sunday, October 5, 2025, 09:45 - 11:15
Room 115

Joint Symposium 1 - Paediatrics Committee / SIOPE: Imaging Biomarkers in Paediatric Oncology 'Whats Next?'

OP-122
The clinical Role of Imaging Biomarkers in Paediatric Oncology
***H. Deubzer**; Charité – Universitätsmedizin Berlin, Berlin, GERMANY.*

OP-123
Imaging Biomarkers in Paediatric Oncology - Radiology
***A. Littooij**; UMC Utrecht, Utrecht, NETHERLANDS.*

OP-124
Imaging Viomarkers in Paediatric Oncology – Nuclear Medicine
***J. Rogasch**; Charité-Universitätsmedizin Berlin, Berlin, GERMANY.*

309

Sunday, October 5, 2025, 9:45 - 11:15
Room 133+134

e-Poster Presentations Session 2 - Inflammation & Infection Committee: Best e-posters in Inflammation & Infection

EPS-022
Utility of [18F]FDG-PET/CT in the Detection of Infection in Patients with Aortic Prostheses
***B. Hervás-Sanz**[1], L. M. Gràcia-Sánchez[1], F. Escrihuela-Vidal[2,3], I. E. Sánchez-Rodríguez[1], P. C. Notta[1], J. L. Díaz-Moreno[1], C. García-Alcober[4], A. Blasco-Lucas[5], D. Toral-Sepúlveda[5], F. Sbraga[5], M. Potocnik[5], O. Alegre-Canals[6], M. P. Mañas-Jiménez[6], J. Sánchez-Vega[6], I. C. Grau-Garriga[2], D. Berbel-Palau[7], M. Cortés-Romera[1]; [1]Nuclear Medicine-PET (IDI) Department, Bellvitge University Hospital-IDIBELL, L'Hospitalet de Llobregat, SPAIN, [2]Infectious Diseases Department, Bellvitge University Hospital-IDIBELL, L'Hospitalet de Llobregat, SPAIN, [3]Centro de Investigación Biomédica en Red - Enfermedades Infecciosas (CIBERINFEC), Instituto de Salud Carlos III, Madrid, SPAIN, [4]Radiopharmay Department, Bellvitge University Hospital-IDIBELL, L'Hospitalet de Llobregat, SPAIN, [5]Cardiovascular Surgery Department, Bellvitge University Hospital-IDIBELL, L'Hospitalet de Llobregat, SPAIN, [6]Cardiology Department, Bellvitge University Hospital-IDIBELL, L'Hospitalet de Llobregat, SPAIN, [7]Microbiology and parasitology Department, Bellvitge University Hospital-IDIBELL, L'Hospitalet de Llobregat, SPAIN.*

Aim/Introduction: The use of endovascular prostheses for aortic root replacement (Bentall-Bono procedure) and aortic arch/intrathoracic aorta repair (Frozen Elephant Trunk (FET)) is increasingly common in patients with complex acute and chronic aortic disease. Infection of these devices poses significant diagnostic and therapeutic challenges. [18F]FDG-PET/CT may have a clinical impact in detecting infections and guiding their management. The objectives of this study are: to assess the utility of [18F]FDG-PET/CT in detecting aortic prosthetic vascular infections; to identify morphometabolic features that help differentiate between post-surgical inflammatory changes and true infection and to correlate PET/CT findings with clinical data. ***Materials and Methods:*** Retrospective descriptive study of patients with FET and aortic root prostheses who presented clinical suspicion of infection and underwent [18F]FDG-PET/CT between March 2016 and February 2025. Demographic data, vascular device and PET/CT study characteristics were analyzed and compared with the final diagnosis established by a multidisciplinary team. ***Results:*** A total of 18 patients with 22 PET/CT studies were included. Six patients had FET prostheses and 12 had aortic root prostheses. The cohort included 6 women and 12 men, with a mean age of 64 years (30-82). The average time between surgery and PET/CT was 26 months. Of the 22 studies, 10 were classified as positive by PET/CT, 9 of which were true positives and 1 false positive (this case was not clinically considered infected and prolonged antibiotic therapy was not initiated). All 9 studies deemed negative by PET/CT were true negatives. Three studies were considered indeterminate; among these, one was confirmed as positive for infection, the other two were negative. In 7 of the 9 true positive cases, the highest metabolic activity was observed within the prosthetic body, with a mean SUVmax of 6mg/dL. In the remaining 2, the highest uptake was at the suture sites, with a higher mean SUVmax (11mg/dL). In the negative studies, a mean SUVmax of 3mg/dL was observed, attributed to post-surgical inflammatory activity. CT imaging identified suspicious signs of infection (thickening, fat stranding, and para-aortic abscesses) in 8/10 PET/CT-positive cases. Patients with positive PET/CT findings showed higher SUVmax values and greater leukocytosis compared to negative cases. ***Conclusion:*** [18F]FDG-PET/CT is a useful, non-invasive tool for detecting infections associated with aortic endovascular prostheses. It allowed for the safe exclusion of infection in negative cases, avoiding unnecessary surgeries and prolonged antibiotic treatments. PET/CT plays a significant role in the clinical and therapeutic decision-making process for complex patients.

EPS-023
Is ^{18}F-FDG PET/CT useful in suspected Cardiac Implantable Electronic Device infection?
***R. Dobson**, D. Bartholomeusz, S. Jo, M. Bills; Royal Adelaide Hospital, SA Medical Imaging, South Australia, AUSTRALIA.*

Aim/Introduction: Positron Emission Tomography with low dose Computed Tomography (PET/CT) is an established investigation in prosthetic valve endocarditis. The role of PET/CT in the diagnosis of Cardiac Implantable Electronic Device (CIED) related infection is evolving. Diagnosis is difficult but crucial as infection, if confirmed, may result in device removal and associated morbidity. The aim of this study was to evaluate the role of PET/CT in patients with suspected CIED infection. ***Materials and Methods:*** A 12-month (January - December 2024) retrospective review was conducted of PET/CT scans performed at a quaternary public hospital, in patients referred for suspected CIED infection and/or prosthetic valve infective endocarditis (IE). 18F-Flurodeoxyglucose (18F-FDG) PET/CT was performed on Siemens Biograph MCT Flow PET scanners. All patients were instructed to follow a standardised low-carbohydrate diet for 24 hours to supress physiological cardiac uptake and fast for a minimum of 6-hours prior to scanning. Patients were intravenously injected with 285MBq of 18F-FDG. Following a 60-minute uptake period whole-body and dedicated gated cardiac scans were acquired. Scan technique, effectiveness of cardiac diet, clinical context including suspected IE, echocardiography and microbiology results were reviewed with final diagnosis based on clinical consensus. ***Results:*** 53 patients (36 male), median age 76 years (31 - 96 years) underwent PET scans for suspected CIED infection and/or IE. Adherence to the low-carbohydrate diet was noted in 85% of patients, evidenced by sufficient physiologic myocardial suppression. Of the 53 patients, 37 (70%) had CIEDs alone, the remaining 16 (30%) had both CIED and prosthetic valves. Nine cases were positive for CIED infection, and 3 cases were positive for IE. Microbiology was positive in 88%. Of the positive CIED group, 3 suggested pocket infection

and 6 lead infection. The SUVmax mean was 4.19 (range 2.9 - 7.6). Transthoracic echocardiogram (TTE) and transoesophageal echocardiogram (TOE) were performed in 5 of the 9 PET positive lead infections and positive in only 1 case. Patients were discussed at an endocarditis multidisciplinary team meeting. Antibiotic treatment was commenced in patients with results that were consistent with Duke Criteria and clinical consensus for infection. ***Conclusion:*** PET/CT is an important investigation in the diagnosis of CIED infection and has demonstrated value in the context of IE, particularly when echocardiography is inconclusive or negative despite a strong clinical indication. Thus, PET imaging can inform targeted therapeutic decisions, from conservative management to device removal.

EPS-024

Diagnostic value of [^{18}F]FDG PET/CT imaging in LVAD infection

G. Metzger[1], *C. Hosse*[2], *I. Schobert*[2], *I. Just-Lauer*[3], *J. Mulzer*[4], *J. Kolck*[2], *W. Lüdemann*[2], *E. Sodemann*[2], *T. Wallter-Rittel*[2], *E. Potapov*[4], *C. Furth*[1], *G. Böning*[2];
[1]*Charité Universitätsmedizin Berlin - Klinik für Nuklearmedizin, Berlin, GERMANY,* [2]*Charité Universitätsmedizin Berlin - Klinik für Radiologie, Berlin, GERMANY,* [3]*Charité Universitätsmedizin Berlin - Klinik für Herz-, Thorax- und Gefäßchirurgie, Berlin, GERMANY,* [4]*Charité Universitätsmedizin Berlin - Klinik für Herz-, Thorax- und Gefäßchirurige, Berlin, GERMANY.*

Aim/Introduction: Treatment of LVAD infections remains highly challenging. Accurate diagnosis, including precise localization of the affected LVAD component and reliable therapy monitoring, is essential. Current evidence on the diagnostic value of [^{18}F]FDG PET/CT is limited to small case series without clearly defined endpoints. We therefore conducted a clinical analysis with surgical and, where possible, microbiological correlation. ***Materials and Methods:*** This single-center retrospective study included patients with suspected LVAD infection who underwent FDG PET/CT between April 2016 and July 2022 with subsequent cardiac surgical correlation. Microbiological evidence—such as positive driveline swab, blood cultures, or intraoperative confirmation—served as the reference standard. CRP levels and body temperature were recorded to support clinical assessment. Quantitative PET parameters (SUVmax and SUVmean) were measured at key device sites, and concomitant thoracic lymph node involvement was analyzed. ***Results:*** Twenty PET/CT scans were included: 18 with surgical confirmation of LVAD infection and 2 without. FDG PET/CT identified LVAD-specific infections with a sensitivity and specificity of 100%. Affected regions included the cutaneous driveline entry (11%), driveline course (66%), and pump/outflow graft (11%); the inflow cannula was unaffected. The infection site was identified in all cases, with a mean SUVmax of 7.9 and a mean Deauville score of 5. Thoracic lymphadenopathy was present in 65% (n=13) of patients, most frequently with a Deauville score of 5. Notably, there was no significant correlation between C-reactive protein levels or body temperature and confirmed infection (p>0.05). ***Conclusion:*** FDG PET/CT enables accurate, noninvasive diagnosis of suspected LVAD infections, allowing precise localization of affected components and detection of associated inflammatory responses such as thoracic lymphadenopathy. Its diagnostic performance exceeds that of systemic inflammatory markers and supports its clinical use for surgical planning and therapy guidance.

EPS-025

Feasibility of Shortened Total-body ^{18}F-FDG PET/CT Dynamic Acquisition for Parametric Imaging in the Quantitative Evaluation of Takayasu's Arteritis

L. Gao[1], *Y. Ng*[2], *Y. Duan*[1], *Z. Cheng*[1];
[1]*The First Affiliated Hospital of Shandong First Medical University, Jinan, Shandong, CHINA,* [2]*United Imaging Healthcare Group Co., Ltd. Shanghai 201807, China, Shanghai, CHINA.*

Aim/Introduction: Takayasu's arteritis is a systemic inflammatory vasculitis affecting large arteries. ^{18}F-FDG PET/CT is essential for detecting active inflammation, with guidelines recommending 90-120 minute delayed acquisition optimal reliable quantification. Previous study have demonstrated that K_i parametric imaging derived from 60-min dynamic PET (dPET) exhibits superior sensitivity and detectability over 2-hour delayed imaging in visualizing and quantifying TAK-active arteries. However, the clinical implementation of prolonged dynamic acquisition is constrained by patient discomfort and feasibility concerns. This study investigates the potential of further reducing total-body ^{18}F-FDG PET/CT dynamic acquisition time while preserving the diagnostic integrity of parametric imaging in quantitative assessment of Takayasu's arteritis. ***Materials and Methods:*** A retrospective study of eight Takayasu's arteritis patients (3 males, 5 females; mean age: 33.88 ± 6.71 years) was conducted at The First Affiliated Hospital of Shandong First Medical University (March - October 2022). Patients were stratified into active and inactive inflammation groups based on the National Institute of Health (NIH) criteria. All subjects underwent a 1-hour total-body dPET scan followed by a 2-hour delayed static PET acquisition, with a 1-hour static PET image extracted from the 50-60 min dPET data. K_i parametric images were generated using 10, 20, 30, 40 and 60 min dPET data and compared with the 1-hour and 2-hour static PET images. Clinical differences between active and inactive inflammation groups were analyzed using the Chi-square test and Mann-Whitney U test. Image quality metrics, including target-to-background ratio (TBR), contrast-to-noise ratio (CNR), and active lesion detection rates were evaluated across acquisition times using the Friedman test and Fisher's exact probability tests. ***Results:*** There were no statistically significant differences among TBR_{30min}, TBR_{40min}, and TBR_{60min} (P=0.425, 0.772) but were significantly higher than at 1-h and 2-h (P<0.001). While CNR_{30min} and CNR_{40min} was lower than CNR_{60min}, both were significantly higher than at 1-h and 2-h (P<0.001). No significant difference was observed between CNR_{40min} and CNR_{60min} (P=0.460).In both active and inactive inflammation groups, K_{i30min} and K_{i40min} demonstrated significantly higher detection rates for active arteries than 1-h static PET (χ^2=17.711, P=0.001; χ^2=24.348, P<0.001). Although their detection rates also exceeded those of 2-h static PET, the differences were not statistically significant (χ^2=0.031, P=0.861; χ^2=3.396, P=0.093, respectively). ***Conclusion:*** K_i parametric imaging derived from shortened dPET acquisitions is feasible for evaluating arterial inflammation in Takayasu's arteritis, with 30-40 min dPET providing optimal image quality and lesion detectability.

EPS-026

Impact of [^{18}F]FDG PET/CT on therapeutic intent in patients with large vessel vasculitis treated with tocilizumab

N. Canchumanya Huatuco, *A. Caresia Aroztegui, J. Font-Urgelles, V. Vallejos Arroyo, M. Boronat de Ferrater, S. Lafuente Carrasco, M. Salcedo Pujantell, J. Deportós Moreno, M. Solà Suárez, I. Casafont-Solé, A. Riveros Frutos, R. Ugena-García, G. Moragas Freixa;*
Hospital Universitario Hermanos Trias I Pujol, Badalona, SPAIN.

Aim/Introduction: The role of [^{18}F]FDG PET/CT in the diagnosis of large vessel vasculitis (LVV) has been demonstrated. However, there is insufficient scientific evidence on its impact on therapeutic management in case of unclear relapse. Furthermore, it is known that tocilizumab (TCZ) treatment blocks the expression of inflammatory markers, so the use of PET/CT in these patients may be a determining factor for the correct management of LVVs. Therefore, our objective is to determine the impact of PET/CT results on therapeutic intent of patients with LVV in treated with TCZ with clinical suspicion of relapse or disease remission. ***Materials and Methods:*** 26 patients (23 females/3

males; mean age at diagnosis of 69.5 ± 10.4 years) with LVV and ongoing treatment with TCZ were included. All patients underwent contrast enhanced [18F]FDG PET/CT. Images were interpreted using qualitative visual analysis of vascular tracer uptake according to the Total Vascular Score. The change on initial pre-test therapeutic intention was also calculated. ***Results:*** In 19 patients (73%) were studied for suspicion of recurrence. The other 7 (27%) to assess discontinuation of TCZ. The average time between the start of TCZ treatment and the PET/CT scan was 20.1 months (4-63 months).Suspected recurrence group (19 patients): 11 patients (57.9%) tested positive, so treatment was escalated (increase in steroid dose, iv TCZ, or increase in sc TCZ dose). 8 patients (42.1%) had a negative scan, leading to changes in the initial therapeutic intention (mainted treatment and/or decrease in steroid dose).Clinical remission group (7 patients): 6 patients (85.7%) tested negative and clinical remission was confirmed, so the pre-established therapeutic plan of treatment optimization was maintained. Only one patient (14.3%) had a positive PET/CT and treatment was maintained, thus avoiding recurrence due to drug discontinuation.Overall, the actual change in therapeutic management was 9/26 patients, which corresponds to 34.6%. ***Conclusion:*** In our cohort of patients with LVV on active treatment with TCZ, PET/CT scans performed for suspicion of recurrence or for assessing discontinue of TCZ resulted in a 34.6% change in pre-test therapeutic intention.

EPS-027

Diagnostic value of 18F-FDG-PET/CT in detecting vascular graft infection and the role of a complementary labelled leucocyte scan

S. Georga[1], *D. Katsampoukas*[1], *A. Morfesi*[1], *N. Vavlas*[1], *A. Georgiou*[1], *D. Karamanos*[2], *V. Mpalaris*[1], *K. Lazaridis*[1], *E. Moralidis*[1], *G. Arsos*[1];
[1]*Department of Nuclear Medicine, Aristotle University Medical School, Papageorgiou General Hospital, Thessaloniki, GREECE,* [2]*Department of Surgery, Aristotle University Medical School, Papageorgiou General Hospital, Thessaloniki, GREECE.*

Aim/Introduction: Vascular graft infection (VGI) is a severe complication of vascular surgery, associated with high morbidity and mortality. Early diagnosis of VGI is essential for successful treatment and clinical outcome. The study aimed to assess the diagnostic value of 18F-FDG-PET/CT in detecting VGI and, furthermore, to explore the role of the additional performance of Tc-99m-HMPAO-labelled leucocyte-SPECT/CT scan. ***Materials and Methods:*** Fifty two consecutive patients with clinical suspicion of VGI underwent 18F-FDG-PET/CT. Twenty six patients had aortobifemoral grafts, 24 thoracic aorta grafts and 2 axillobifemoral grafts. Median time between graft implantation and imaging was 24 months (range 1-240 months).Vascular prostheses were visually evaluated for the presence, intensity (mild, moderate or intense uptake, using a 3-point scale comparing peri-graft uptake to blood pool activity in the ascending aorta and liver uptake) and pattern (focal/multifocal, heterogenous or homogenous diffuse) of FDG uptake. Maximum standardized uptake value (SUVmax) was also calculated. Focal/multifocal or heterogeneous diffuse, peri-graft intense FDG uptake was suggestive of VGI. A Tc-99m-HMPAO-labelled leucocyte-SPECT/CT scan (LS-SPECT/CT) was additionally performed in 14 patients with equivocal 18F-FDG-PET/CT findings. LS-SPECT/CT was performed and interpreted according to the EANM guidelines. Increased over time leucocyte uptake in the region of vascular graft, in terms of intensity and/or extension, indicated VGI. Final diagnosis was based on surgical/histopathological findings or long-term clinical follow-up. ***Results:*** Twenty nine out of 52 vascular grafts investigated were confirmed as infected. All infected vascular grafts showed intense focal/multifocal or heterogeneous FDG uptake. SUVmax was significantly higher in infected than uninfected vascular grafts (10.3 ± 2.6 vs 3.9 ± 3.7, $p < 0.05$).18F-FDG-PET/CT results were as follows: TP 28, TN 19, FP 6 and FN 0. False positive 18F-FDG-PET/CT results were attributed to inflammation/foreign body reaction, even years after graft implantation, and were reduced by the additional performance of LS-SPECT/CT. Sensitivity, specificity, accuracy, PPV and NPV of 18F-FDG-PET/CT for diagnosing VGI were 100 %, 76%, 90 %, 82% and 100 %, respectively. LS-SPECT/CT showed 100% specificity and PPV and helped to discriminate infection from sterile inflammation/foreign body reaction in patients with equivocal 18F-FDG-PET/CT findings, leading to the correct diagnosis. ***Conclusion:*** FDG-PET is a highly sensitive non-invasive imaging modality for detection of VGI. A negative study excludes VGI. LS-SPECT/CT is a more specific method for diagnosing VGI. Thus, in cases of equivocal FDG-PET findings, the additional performance of LS-SPECT/CT scan helps to discriminate infection from sterile inflammation/foreign body reaction and establish the correct diagnosis.

EPS-028

The post-therapy follow-up of [F[18]]FDG PET in vasculitis

R. Park*, J. McCormick, S. Olson, R. Staff;*
NHS Grampian, Aberdeen, UNITED KINGDOM.

Aim/Introduction: There is little clarity regarding using [18F] FDG PET/CT to monitor the response to treatment for patients with vasculitis[1]. The Scottish guidance states that [18F]FDG PET imaging currently has no role in routine response monitoring. This is likely due to an absence of evidence rather than evidence of its value. This retrospective audit investigated the patient cohort returning for imaging mid/post-treatment. ***Materials and Methods:*** Of the patients (n=93) referred for an [18F]FDG PET/CT scan due to a vasculitis indication between July 2023 and June 2024, 11 patients were imaged as part of mid/post-treatment follow-up. All patients underwent some form of therapy, including steroids and immunosuppressants. To analyse each patient's response to their treatment, the Target to Background Ratio (TBR) was calculated for both imaging sets. This was calculated using the SUV_{max} of the most visually avid area of the aorta and a defined region from the right lobe of the liver. In addition, the extent of the vasculitis was quantified by assessing the uptake in 7 vascular regions, providing a Total Vascular Score (TVS) that was compared before and after treatment. Two blind observers performed scoring, and the inter-rater agreement was found. ***Results:*** Patients had follow-up imaging either once (5), twice (4) or three times (2) after their initial baseline images. The mean interval between baseline and subsequent follow-up was 18 months (range 5-35 months). Nine of those with baseline and follow-up were positive at the first visit. After treatment, the observed TVS for all positive patients had reduced. However, only 4 cases were resolved. Of the positive patient cohort, the calculated TBR reduced (6), stayed the same (2) or increased (1) after treatment. In both instances where a positive repeat scan followed a negative baseline, the TVS and TBRS increased. ***Conclusion:*** For patients with an initial positive diagnosis, the extent of the vasculitis reduced after treatment in all cases, as expected; however, the avidity of the aortic uptake had a mixed response. For patients with a negative to positive disease progression, both the avidity and extent of the uptake increased. The heterogeneity of the follow-up suggests that [18F]FDG PET/CT may have a role in monitoring vasculitis treatment. ***References:*** [1] R.H.J.A. Slart et al. "FDG-PET/CT imaging in large vessel vasculitis and polymyalgia rheumatica: joint procedural recommendation of the EANM, SNMMI, and the PET Interest Group (PIG), and endorsed by the ASNC." European journal of nuclear medicine and molecular imaging, 45(2018):1250-1269.

EPS-029

Tailored Management of Non-Typhoid Salmonella Bacteremia: Insights from 2-[^{18}F]FDG PET/CT Imaging

P. Chuang[1], *C. Huang*[2], *T. Hong*[1], *M. Chiang*[3], *C. Hung*[2], *C. Lu*[1];
[1]*National Taiwan University Cancer Center, Taipei, TAIWAN,* [2]*National Taiwan University Hospital, Taipei, TAIWAN,* [3]*Taipei Medical University Hospital, Taipei, TAIWAN.*

Aim/Introduction: Non-typhoid Salmonella (NTS) bacteremia is associated with significant morbidity and mortality, particularly in high-risk populations such as the elderly and immunocompromised patients. Metastatic infections are not uncommon and may require prolonged antibiotic therapy or surgical intervention to ensure pathogen eradication and prevent recurrence. This study evaluates the utility of 2-[^{18}F]fluorodeoxyglucose (FDG) PET/CT in detecting metastatic foci and guiding individualized treatment strategies. ***Materials and Methods:*** We retrospectively reviewed consecutive patients with NTS bacteremia who underwent 2-[^{18}F]FDG PET/CT between 2018 and 2023. Imaging findings, including visual interpretation and semiquantitative measurements, were analyzed alongside clinical parameters to assess their impact on treatment decisions, such as the duration of antibiotic therapy or surgical management. Recurrence of NTS bacteremia following treatment cessation was recorded and correlated with initial PET/CT findings. ***Results:*** Thirty-three patients (25 men, 8 women; mean age 66.5 ± 13.1 years) were included, with group D Salmonella isolated in 30 cases (90.9%). 2-[^{18}F]FDG PET/CT revealed metastatic infections in 27 patients (81.8%), including mycotic aneurysms (9/27, 33.3%), septic arthritis or spondylodiscitis (9/27, 33.3%), soft tissue abscesses (9/27, 33.3%), and visceral abscesses (7/27, 25.9%). Patients with metastatic infections received significantly longer antibiotics treatment compared to those without (median 10.6 vs. 3.2 weeks, p=0.012), and were more likely to undergo surgery (29.6% vs. 0%, p=0.131). Despite aggressive treatment, 4 of 27 patients (14.8%) with metastatic disease identified on initial PET/CT experienced recurrence within two years after discontinuing antibiotic therapy. The recurrent cases included one mycotic aneurysm, one soft tissue abscess, and two visceral abscesses. The median time to recurrence was 12.1 months. In contrast, no recurrences were documented during follow-up in patients without PET-detected metastatic disease. ***Conclusion:*** 2-[^{18}F]FDG PET/CT effectively detects metastatic foci in NTS bacteremia and plays a pivotal role in tailoring treatment duration and identifying candidates for surgical intervention. Its use may reduce recurrence by supporting evidence-based, personalized management strategies.

EPS-030

Preliminary diagnostic evaluation of CROhn's disease with DYNamic total-body pOsitron emission tomography/computed tomography (CRODYNO) - A single-center prospective study

A. Farolfi[1], *G. Calini*[2,3], *I. Brusa*[1], *D. Dall'Olio*[3], *C. Nanni*[1], *L. Romagnoli*[1], *V. Lucidi*[4], *B. Spencer*[5], *G. Wang*[5], *L. Nardo*[5], *S. Fanti*[1], *A. Di Giorgio*[6];
[1]*Nuclear Medicine, IRCCS Azienda Ospedaliero-Universitaria di Bologna, Bologna, ITALY,* [2]*Surgery of Alimentary Tract, IRCCS Azienda Ospedaliero-Universitaria di Bologna, Bologna, ITALY,* [3]*Department of Medical and Surgical Sciences, Alma Mater Studiorum - University of Bologna, Bologna, ITALY,* [4]*Department of Radiology, IRCCS Azienda Ospedaliero-Universitaria Di Bologna, Bologna, ITALY,* [5]*Department of Radiology, University of California Davis Health, Sacramento, CA, UNITED STATES OF AMERICA,* [6]*Nuclear Medicine, Alma Mater Studiorum - University of Bologna, Bologna, Italy, Bologna, ITALY.*

Aim/Introduction: Crohn's Disease (CD) is a chronic inflammatory disease with rising global prevalence. Magnetic resonance enterography (MRE) excels in surgical indications but is limited in disease staging, particularly regarding activity, mesenteric involvement, and extraintestinal manifestations. Dynamic total-body PET/CT with ^{18}F-fluorodeoxyglucose (FDG-TBPET), with its high sensitivity and ability to quantify kinetic parameters (FDG delivery rate K_1, phosphorylation rate k_3, net influx rate K_i, volume of distribution DV) across the entire body, offers a novel approach for characterizing inflammatory diseases like CD. This study explores its potential in CD assessment and in distinguishing CD from aspecific bowel FDG uptake. ***Materials and Methods:*** Prospective study enrolling CD patients undergoing restaging with MRE and 60-minute dynamic FDG-TBPET (FOV=194cm). Healthy controls (n=10) from UC Davis, California, were stratified based on the presence (n=5) or absence (n=5) of diffuse aspecific FDG bowel uptake. Images were analyzed qualitatively, semiquantitatively (SUV-metrics) and quantitatively using two-tissue compartment models with model selection (2TC, 2TiC; mean absolute scaled error-MASE and the Akaike Information Criterion-AIC for selection). Kinetic parameters were compared between MRE and/or histopathology-positive lesions, healthy intestine/mesentery in CD patients, and intestine/mesentery in healthy controls. VOIs included non-diseased bowel and mesentery in CD patients compared to healthy controls. ***Results:*** Three patients experiencing a CD flare-up underwent MRE and dynamic FDG-TBPET prior to surgery. MRE findings were positive for ileal involvement in two patients and large bowel involvement in one patient. Histological examination of surgical specimens revealed CD in the anal canal and rectum in 1 patient, the ileo-cecal tract in 2 patients, and the ileal mesentery in 1 patient. Across the 3 patients, a total of 8 areas positive for CD were identified via MRE/histology, and corresponding VOIs were generated. While SUV values alone did not discriminate disease from physiological bowel uptake (p=0.147), significant differences in k_3 and K_i values were observed between CD patients and healthy controls (both p<0.001), even in the subgroup of healthy controls with diffuse aspecific bowel uptake (p<0.001), suggesting altered glucose metabolism in CD. Within CD patients, confirmed lesions tended to exhibit a kinetic profile characterized by lower K_1 and higher k_3, particularly in the ileum, but not statistically significant (p>0.05). ***Conclusion:*** These preliminary findings suggest that dynamic FDG-TBPET, by enabling simultaneous assessment of metabolic activity throughout the body, may differentiate pathological inflammation from healthy tissue in CD. Kinetic modeling, particularly k_3 and K_i, may offer a pathophysiological signature of active inflammation beyond SUV-metrics.

EPS-031

Clinical impact of [^{18}F]FDG PET/CT in the assessment of incidental findings related to aesthetic procedures: implications for complication detection and oncological management.

M. Pudis[1], *P. Notta*[1], *C. S. Salomón-Duhalde*[2], *C. Cases-Pellise*[3], *L. Rodríguez-Bel*[1], *L. M. Gracia-Sánchez*[1], *V. A. Carrero-Vasquez*[1], *J. J. Robles-Barba*[1], *A. I. Fritsch-Medina*[1], *P. Perlaza-Jiménez*[1], *A. Tapias-Mesa*[1], *M. Suarez-Piñera*[1], *M. Cortés-Romera*[1];
[1]*Nuclear Medicine - PET (IDI), Bellvitge University Hospital - IDIBELL, L'Hospitalet de Llobregat, SPAIN,* [2]*Nuclear Medicine, Hospital Universitari Son Espases, Palma de Mallorca, SPAIN,* [3]*Nuclear Medicine, Hospital Universitario Virgen del Rocío, Sevilla, SPAIN.*

Aim/Introduction: Aesthetic procedures are increasingly common and often undocumented in medical records. [^{18}F]FDG PET/CT may incidentally detect related findings, which can pose diagnostic challenges in oncological settings. This study aims to assess the role of [^{18}F]FDG PET/CT in identifying such findings and to evaluate their clinical relevance in differential diagnosis, complication detection, and therapeutic decision-making. ***Materials and Methods:*** This retrospective study included 17 aesthetic procedures identified in 15 female patients (mean age: 60 years) who underwent [^{18}F]FDG PET/CT for oncological

evaluation. Incidental findings suggestive of prior aesthetic interventions were identified based on characteristic metabolic activity and morphological alterations observed during image interpretation.As most procedures were not documented in the institutional medical records, confirmation was obtained through structured telephone interviews. Patients were asked to confirm the type of procedure, material used, anatomical location, approximate date, and any associated or persistent symptoms. Only findings with both patient-confirmed history and concordant PET/CT features were included in the analysis. ***Results:*** The most frequent intervention was silicone breast implantation (n=9; eight bilateral). Post-surgical inflammatory changes with low-to-moderate [^{18}F]FDG uptake were observed in seven cases, with five patients reporting persistent postoperative pain. One patient presented an intracapsular rupture requiring explantation, and another showed axillary siliconomas with mild discomfort.Two cases of autologous fat grafting (lipofilling) to the breast revealed areas of fat necrosis, both asymptomatic.Four patients had facial or mandibular fillers: three in the zygomatic region (hyaluronic acid, calcium hydroxyapatite, and biopolymers) and one in the mandible (calcium hydroxyapatite). All demonstrated increased FDG uptake associated with local erythema or warmth. One patient with permanent biopolymers presented with an active infection requiring antibiotic therapy.Two asymptomatic patients with gluteal biopolymer fillers exhibited moderate-to-intense FDG uptake consistent with granulomatous inflammatory reaction. All 17 aesthetic procedures exhibited PET-detectable metabolic alterations, ranging from benign post-procedural inflammation to infectious or granulomatous reactions. In five patients (33%), these findings prompted additional clinical evaluation or therapeutic intervention. ***Conclusion:*** [^{18}F]FDG PET/CT can reveal clinically relevant findings associated with prior aesthetic procedures, even when undocumented in medical records. Recognising these characteristic uptake patterns is essential to avoid misinterpretation—particularly in oncological patients—and to prevent unnecessary biopsies or delays in management. Increased awareness among nuclear medicine specialists is crucial as the prevalence of such interventions continues to rise.

EPS-032

[^{18}F]FAPI Total-Body PET in Metabolic-Dysfunction Associated Steatotic Liver Disease: Preliminary Results

S. Shivani[1], *Y. G. Abdelhafez*[1], *B. A. Spencer*[1], *V. Medici*[1], *V. Lyo*[1], *M. T. Corwin*[1], *K. Chung*[1], *X. Duan*[1], *O. R. Vigil*[1], *I. Tunali*[2], *P. Lacor*[2], *A. T. Hoye*[2], *M. Flitter*[2], *A. McGeehan*[2], *M. Johnson*[2], *E. C. Collins*[2], *G. Wang*[1], *R. Badawi*[1];
[1]*University of California at Davis, Sacramento, CA, UNITED STATES OF AMERICA,* [2]*Eli Lilly, Inc., Indianapolis, IN, UNITED STATES OF AMERICA.*

Aim/Introduction: Fibrosis staging plays a critical role in assessing disease progression and prognosis in metabolic dysfunction-associated-steatotic liver disease (MASLD). Existing non-invasive tests (NITs) including MRI elastography, ultrasound transient elastography, and blood-based scores (Fibrosis-4) have known limitations and invasive liver biopsy remains the gold standard. This highlights the unmet need for reliable NITs to accurately stage liver fibrosis. Fibroblast activation protein (FAP) expression has been shown to correlate with fibrosis severity and staging. This study aims to investigate the potential of quantitative [^{18}F] FAPI PET imaging as an NIT to assess liver fibrosis in MASLD subjects relative to biopsy-confirmed fibrosis stage. ***Materials and Methods:*** This ongoing study has so far recruited eight participants (7 females, 1 male): one healthy volunteer (HV, age: 27), and seven MASLD participants who had undergone liver biopsy within 90 days of PET imaging (fibrosis stages F1/F2 [n=3] and F3/F4 [n=4], age range: 39-69). Fibrosis pathological staging was determined using MASH Clinical-Research-Network criteria. Dynamic total-body PET/CT imaging was performed between 0-60 minutes post-intravenous administration of 215-236 MBq [^{18}F]FAPI-74. Volumes-of-interest (VOIs) were placed on eight liver segments and descending aorta. Liver VOI values were averaged. Liver SUVmean ratio (SUVR) was calculated using descending aorta as reference region. Kinetic modelling was conducted using a dual-input two-tissue compartment model to estimate the net influx rate (K_i). No statistical tests were performed due to the small sample size. ***Results:*** Liver SUVmean, SUVR, and K_i values showed differences between HV and MASLD participants. SUVmean and SUVR measured at 4 mins post-injection (240s to 300s), 20 mins (20 min to 23 min), and 55 mins (55 min to 60 min) were compared. The 4 min data were shown to best separate the groups and are reported here. Participants with stage F3/F4 exhibited a higher median SUVmean of 4.53 [range: 4.12-4.85] and SUVR of 0.64 [0.61-0.68] compared to those with stage F1/F2 (SUVmean: 3.89 [3.79-4.57], SUVR: 0.53[0.48-0.54]) and HV (SUVmean: 3.62, SUVR: 0.48). Similarly, median K_i values reflected differences in tracer retention across groups: HV (0.009), F1/F2 (0.021[0.017-0.023]), and F3/F4 (0.035 [0.027-0.040]). ***Conclusion:*** [^{18}F]FAPI PET demonstrates potential as an imaging NIT For staging liver fibrosis that may be more accurate than existing NITs and avoid the need for liver biopsy. The observed association between liver SUVmean, SUVR, and K_i values and pathology-confirmed fibrosis stages supports its potential for disease stratification in MASLD. These preliminary results warrant validation in larger cohorts.

EPS-033

A Prospective Study on the Diagnosis and Severity Assessment of Interstitial Lung Disease Complicated by Dermatomyositis in Adults Using ^{68}Ga-FAPI PET/CT

J. Hu[1], *X. Sun*[1], *X. Shao*[2], *Q. Qu*[1], *J. Hu*[2], *Q. Zhao*[2], *Y. Jin*[1], *Z. Cheng*[3], *W. Hai*[1], *B. Li*[1], *H. Cao*[2];
[1]*Department of Nuclear Medicine, Ruijin Hospital, Shanghai Jiao Tong University School of Medicine, Shanghai, CHINA,* [2]*Department of Dermatology, Ruijin Hospital, Shanghai Jiao Tong University School of Medicine, Shanghai, CHINA,* [3]*Department of Radiology, Ruijin Hospital, Shanghai Jiao Tong University School of Medicine, Shanghai, CHINA.*

Aim/Introduction: Dermatomyositis is a heterogeneous disease characterized primarily by muscle weakness and multi-organ involvement (e.g., lungs, heart, gastrointestinal tract, kidneys, or associated malignancies). Its common complication and leading cause of death is rapidly progressive interstitial lung disease (RP-ILD). Currently, the early specific screening methods used in clinical practice still have certain limitations. Based on this, this study employs a novel fibroblast activation-targeting tracer—^{68}Ga-FAPI PET/CT—to explore its clinical utility in dermatomyositis patients complicated by interstitial lung disease. ***Materials and Methods:*** Prospective study including 140 dermatomyositis patients who underwent 68Ga-FAPI PET/CT, PFTs and autoimmune blood analysis. Four groups were created: non-ILD subjects and ILD patients with or without infection. For normally distributed continuous data, unpaired t-tests or analysis of variance (ANOVA) were used, while for non-normally distributed continuous data, the Mann-Whitney test or Kruskal-Wallis test was employed to compare variable differences. Pearson or Spearman correlation coefficients were used to analyze associations with clinical indicators. ***Results:*** The sensitivity and specificity of ^{68}Ga-FAPI PET/CT for diagnosing dermatomyositis with non-infectious ILD reached 97.67% and 97.83%, respectively, while for dermatomyositis with infectious ILD, both sensitivity and specificity were 100%. The results showed that in the non-infection group, the maximum value of SUVmax in lung lesions (SUVlung) in patients with anti-synthetase syndrome and MDA5-positive dermatomyositis was significantly higher than in TIF-1γ-positive dermatomyositis patients (P=0.0514). Additionally, SUVlung in MDA5 and Ro-52 double antibody-positive dermatomyositis patients was higher than in MDA5-positive but

Ro-52-negative patients (P=0.0216). In the non-infection state, SUVlung exhibited significant correlations with KL-6 and FVC (r=0.4941, P<0.0001; r=-0.4651, P=0.0001). These correlations strengthened in the infection state (r=0.6529, P<0.0001; r=-0.5020, P=0.0029). ***Conclusion:*** In conclusion, ^{68}Ga-FAPI PET/CT enables accurate diagnosis and severity assessment of interstitial lung disease complicated by dermatomyositis, thereby potentially guiding therapeutic decisions and improving patient prognosis.

EPS-034

[99mTc]DTPA aerosol clearance as an assessment of pulmonary alveolar permeability in long COVID

T. Biggans, *J. Asogan Vaishnavi, P. Guntur Ramkumar; NHS Tayside, Dundee, UNITED KINGDOM.*

Aim/Introduction: Individuals experiencing ongoing symptoms four weeks since onset of Coronavirus disease 2019 (COVID-19) are widely described as suffering from long COVID. Breathlessness is one of the most common of these symptoms. The physiological cause of this breathlessness is unknown with unremarkable findings on CT and lung function tests. The aim of this study was to determine if the clearance rate of 99mTc-diethylenetriaminepentaacetic acid ([99mTc]DTPA) aerosol from the lungs is abnormal in patients suffering from long COVID. This objective marker is representative of alveolar epithelial membrane integrity. Any change in clearance rate would indicate that membrane permeability may have been affected and could be involved in the underlying cause of long COVID symptoms. ***Materials and Methods:*** Participants were recruited from patients who were referred for ventilation/perfusion lung scintigraphy (V/Q scan) at Ninewells Hospital, Dundee, Scotland from July 2022 to June 2023. Participants completed a questionnaire to ascertain smoking habits and any history of lung disease. Dynamic lung scintigraphy was performed following inhalation of [99mTc]DTPA aerosol. Regions of interest (ROIs) were drawn around each lung with corresponding background regions. Background corrected geometric mean time activity curves were generated from these ROIs and the clearance half time was determined from least squares exponential fit of the data. The mean of the clearance half time from both lungs was calculated. Participants were grouped into smokers and non-smokers before being clinically sub-grouped using the questionnaire, relevant clinical history and the final V/Q scan report. The sub-groups were defined as history of interstitial lung or airways disease, history of long COVID and controls. ***Results:*** In total 125 participants were recruited with 21 subsequently excluded for technical reasons. Only 7 of the remaining 104 were smokers which did not allow for subgroup analysis of the smoking group. The mean clearance half time (SD - standard deviation) for non-smokers was 56 min (SD 24), 72 min (SD 23) and 71 min (SD 22) for interstitial lung or airways disease, long COVID and control subgroups respectively. For smokers, the mean clearance half time was 35 min (SD 12). ***Conclusion:*** This study indicates pulmonary alveolar permeability is maintained in long COVID sufferers.

EPS-035

Emotional Stress During the COVID-19 Lockdown: How Negative X/Twitter Posts Correlated with Changes in the Brain's Fear Network

E. Guedj[1], *J. Y. Campion*[2], *T. Horowitz*[1], *F. Barthelemy*[3], *S. Khalfa*[4], *W. El-Hage*[2];
[1]*Aix-Marseille University, Marseille, FRANCE,* [2]*CHRU Tours, Tours, FRANCE,* [3]*APHM, Marseille, FRANCE,* [4]*CNRS, Marseille, FRANCE.*

Aim/Introduction: The COVID-19 pandemic has profoundly affected mental health, with the lockdown period particularly exacerbating negative emotions such as fear, sadness, and uncertainty. This study examines brain metabolic changes associated with the psychological context of the French COVID-19 lockdown. ***Materials and Methods:*** As a proxy measure of this psychological context, we utilized a composite negative-emotion score from an open-source X/Twitter dataset ("The First French COVID-19 Lockdown Twitter Dataset"), previously designed to capture the overall public sentiment during the 55-day lockdown. Using statistical parametric mapping (SPM), this composite negative-emotion score was day-by-day correlated to the whole-brain voxel-based [18F]FDG PET imaging in 95 patients with neurological conditions (p-voxel < 0.001, k > 108). ***Results:*** Results showed a significant negative correlation between daily negative-emotion scores and metabolism in the right ventromedial prefrontal cortex (vmPFC) and anterior cingulate cortex (ACC), key regions within the brain fear circuit. Inter-regional correlation analysis (IRCA) of metabolic connectivity from the right vmPFC/ACC subsequently revealed a right limbic-dominant network encompassing the amygdala, hippocampus, thalamus, and basal ganglia. ***Conclusion:*** These findings highlight the sensitivity of the right vmPFC/ACC to societal emotional stressors, suggesting a potential cerebral substrate for the increase in psychological and psychiatric disorders observed during the pandemic. Future research is required to validate these results in broader populations and explore their longitudinal implications to better understand the neurological and psychiatric impacts of collective stress.

EPS-036

TSPO PET relates to blood markers of vascular regulation, immune cell survival and brain damage in post-COVID syndrome

D. Visser[1], *H. L. D. M. Willemen*[2], *S. S. V. Golla*[1], *R. Boellaard*[1], *H. Knoop*[3], *B. N. M. van Berckel*[1], *J. Bosch*[3], *J. den Dunnen*[4], *N. Eijkelkamp*[2], *N. Tolboom*[5];
[1]*Department of Radiology & Nuclear Medicine, Amsterdam Neuroscience, Amsterdam UMC, Amsterdam, NETHERLANDS,* [2]*Center for Translational Immunology, UMC Utrecht, Utrecht, NETHERLANDS,* [3]*Department of Medical Psychology, Amsterdam UMC, Amsterdam, NETHERLANDS,* [4]*Center for Experimental and Molecular Medicine, Amsterdam UMC, Amsterdam, NETHERLANDS,* [5]*Department of Radiology & Nuclear Medicine, UMC Utrecht, Utrecht, NETHERLANDS.*

Aim/Introduction: The pathophysiology of post-COVID syndrome is still unclear. We previously showed that a subset of post-COVID individuals show neuroinflammatory activity on TSPO PET, indicating pathophysiological heterogeneity of the syndrome(1). Further validation of this neuroinflammatory subtype using blood based biomarkers would greatly aid unravelling the pathophysiology of post-COVID. Therefore, we aimed to identify which blood-based biomarkers associate with neuroinflammatory activity as measured with TSPO PET in post-COVID syndrome patients. ***Materials and Methods:*** We included 31 post-COVID patients (mean age 50±9, 55% female, 26±8 months after initial SARS CoV2 infection) who underwent a 60-minute dynamic [^{18}F] DPA-714 PET with arterial sampling, MRI, and blood-collection on the day of, and prior to, the PET scan. [^{18}F]DPA-714 binding was quantified using binding potential in the global grey matter. Blood samples were analysed using NULISA (Alamar's 120-plex Central Nervous System disease Panel)(2). Regression models and Spearman's correlation were employed to evaluate the the association between neuroinflammatory activity on PET and blood-based markers. Additionally, we compared blood-based markers between patients with high (>mean+1.5SD of a control population) and those with low neuroinflammatory activity on PET using ANOVA and Wilcoxon tests. ***Results:*** Increased [^{18}F] DPA-714 binding on PET associated with higher levels of Vascular endothelial growth factor A (VEGFA; Spearman's rho 0.50, p=0.007), a protein with an important role in angiogenesis and vascular permeability including blood brain barrier permeability, but which also supports neuroprotection and glial growth(3). Post-COVID patients with high binding on PET compared to those with low binding on PET had higher levels of Ficolin-2 (FCN2; p=0.040), a lectin pathway initiator linked to the severity of brain damage(4),

and lower levels of Interleukin-7 (IL7; p=0.049), a cytokine essential for immune cell survival(5). ***Conclusion:*** We identified VEGFA, FCN2, and IL7 to be associated with neuroinflammatory activity as measured with TSPO PET in post-COVID syndrome patients. This might reflect altered vascular regulation, complement activation, and immune dysregulation, which were previously hypothesized as central to the pathophysiology of post-COVID syndrome. These findings reinforce the concept of a distinct neuroinflammatory subtype within post-COVID syndrome. Further validation in larger cohorts is required to confirm and expand upon these results. ***References:*** (1) Visser, D, et al. Varying levels of inflammatory activity in brain and body of patients with persistent fatigue and difficulty concentrating after COVID-19: a TSPO PET study; submitted (2) DOI:10.1038/s41467-023-42834-x (3) DOI:10.4161/org.6.2.11687 (4) DOI:10.1177/0271678X18758881 (5) DOI:10.1016/j.cyto.2022.156049

EPS-037

Synergistic FAPI and PSMA PET/CT Imaging in Primary Sjögren's Syndrome: Comprehensive Evaluation of Inflammatory Burden and Functional Parameters for Clinical Translation

J. Wang, *J. Xiang, R. Wang, X. Peng, Y. Wang, Z. Zhu;*
Peking Union Medical College Hospital, Beijing, CHINA.

Aim/Introduction: Primary Sjögren's syndrome (pSS) is a chronic autoimmune disorder characterized by immune-mediated glandular destruction and sicca symptoms. Pro-inflammatory fibroblasts drive glandular damage, quantifiable via fibroblast activation protein (FAPI) PET/CT, which maps inflammatory activity. Prostate-specific membrane antigen (PSMA) PET/CT, traditionally used in oncology, reveals salivary gland dysfunction in pSS through reduced physiological uptake. Combining these modalities offers a dual-perspective approach to evaluate inflammation and functional decline in pSS. ***Materials and Methods:*** Thirty-five pSS patients underwent paired [^{68}Ga]Ga-FAPI-04 and [^{68}Ga]Ga-PSMA PET/CT imaging (February 2024-March 2025). Salivary gland uptake was compared to 35 age-/sex-matched breast cancer controls. Standardized uptake values (SUVmax/mean), salivary gland ultrasonography (SGUS) scores, and clinical indices (ESSDAI, ESSPRI, IgG, RF, ESR) were analyzed. Histopathological validation was performed using FAPI/PSMA immunohistochemistry on labial gland biopsies. ***Results:*** pSS patients exhibited higher FAPI uptake (SUVmax: 3.42 ± 1.25 vs. 2.08 ± 0.42, $p < 0.001$) and reduced PSMA uptake (SUVmean: 5.39 ± 2.77 vs. 10.60 ± 2.02, $p < 0.0001$) compared to controls. The functional-to-inflammatory ratio (FPR = FAPI SUVmax/PSMA SUVmean) correlated with SGUS scores (parotid: $r = 0.58$, $p < 0.05$; submandibular: $r = 0.63$, $p < 0.01$), disease activity (ESSDAI: $r = 0.3$; ESSPRI: $r = 0.4$), and serologic markers (IgG/RF/ESR, $p < 0.05$). FAPI PET strongly correlated with fibroblast activation on immunohistochemistry ($r = 0.72$, $p < 0.001$), while PSMA PET moderately aligned with glandular function ($r = 0.51$, $p < 0.05$). ***Conclusion:*** The functional-to-inflammatory ratio (FPR) integrates FAPI PET/CT (inflammation) and PSMA PET/CT (glandular function) into a novel biomarker for stratifying pSS severity and guiding therapy. Histopathological validation reinforces its biological relevance, supporting future applications in precision management.

EPS-038

Imaging Phenotypes of Idiopathic Inflammatory Myositis using ^{18}F-FDG PET/MR

Y. Zhang, *B. Zhang, B. Li, X. Zhang;*
The First Affiliated Hospital, Sun Yat-Sen University, Guangzhou, CHINA.

Aim/Introduction: Idiopathic inflammatory myositis (IIM) comprises a heterogeneous group of autoimmune disorders involving muscle inflammation and increased malignancy risk. ^{18}F-FDG PET/MR imaging shows promise for evaluating muscle involvement. This study aimed to derive novel imaging phenotypic clusters of muscle involvement using ^{18}F-FDG PET/MRI. ***Materials and Methods:*** This retrospective study included patients fulfilling classification criteria for IIM who underwent ^{18}F-FDG PET/CT with whole-body MRI or ^{18}F-FDG PET/MRI. Muscle enzyme levels were collected. Muscle oedema (scores 0-2), fatty infiltration (0-1), and atrophy (0-1) were evaluated across 42 muscle groups. Fasciitis (0-1) and subcutaneous oedema (0-1) were assessed in 8 regions. Muscle ^{18}F-FDG uptake was measured via target-to-background ratio (TBR: muscle SUVmax / liver SUVmean). Mean scores for each parameter were calculated per patient. Hierarchical clustering analysis using z-transformed mean TBR, oedema, fatty infiltration, atrophy, fasciitis, and subcutaneous oedema scores identified patient subgroups. ***Results:*** Seventy-two IIM patients (n=48 female [66.7%]; median age 51.0 [IQR 34.5, 59.5] years) were included. Subtypes were antisynthetase syndrome (11/72, 15.3%), dermatomyositis (DM, 47/72, 65.3%), immune-mediated necrotizing myopathy (IMNM, 8/72, 11.1%), and polymyositis (PM, 6/72, 8.3%). Four clusters emerged. Cluster 1 (n=32) showed moderate ^{18}F-FDG uptake, severe muscle oedema, mild fatty infiltration/atrophy, and moderate fasciitis/subcutaneous oedema; DM was most frequent (22/32, 68.8%), CK levels were moderately elevated (255.5 [IQR 66.0, 910.0] U/L), and 3/32 (9.4%) had malignancy. Cluster 2 (n=26) exhibited mild muscle involvement on PET/MRI with mild fasciitis/subcutaneous oedema; DM (15/26, 57.7%) and antisynthetase syndrome (6/26, 23.1%) were common, CK levels were not evidently elevated (82.0 [IQR 57.0, 188.0] U/L), and 3/26 (11.5%) had malignancy. Cluster 3 (n=9) displayed high ^{18}F-FDG uptake, severe muscle oedema, severe fatty infiltration/atrophy, and moderate fasciitis/subcutaneous oedema; IMNM (4/9, 44.4%) and PM (3/9, 33.3%) were frequent, CK levels were significantly elevated (2,094.0 [IQR 318.0, 2,899.0] U/L), with no malignancies detected. Cluster 4 (n=5) had high ^{18}F-FDG uptake, severe muscle oedema, mild fatty infiltration/atrophy, and severe fasciitis/subcutaneous oedema; all patients had DM, CK levels were elevated (398.0 [IQR 229.0, 860.0] U/L), and 2/5 (40.0%) had malignancy. ***Conclusion:*** Distinct imaging phenotypes within IIM can be identified using ^{18}F-FDG PET/MR biomarkers and clustering analysis. These clusters exhibit different patterns of muscle inflammation, damage, and extramuscular involvement, potentially reflecting different underlying pathologies or disease stages and showing varied associations with specific IIM subtypes and malignancy risk. ^{18}F-FDG PET/MR shows promise in characterizing the heterogeneity of IIM.

EPS-039

Role of ^{68}Ga-FAPI PET/CT in assessing liver fibrosis in chronic liver disease

S. Singh, *M. Ora, S. Gambhir;*
SGPGIMS, Lucknow, INDIA.

Aim/Introduction: Chronic liver disease (CLD) is a global health burden and it requires accurate fibrosis staging, but liver biopsy's invasiveness and non-invasive methods limited resolution create diagnostic gaps. Fibroblast activation protein (FAP), expressed in hepatic stellate cells during fibrogenesis, offers a novel target. ^{68}Ga-FAPI PET/CT enables whole-liver quantification of fibrotic activity via SUV measurements, potentially detecting early fibrosis before structural changes occur. This study evaluates its role versus traditional methods. ***Materials and Methods:*** This prospective study was conducted in the Department of Nuclear Medicine at SGPGIMS, enrolling 30 chronic liver disease (CLD) patients (stratified into Child-Pugh classes A, B, and C; n=10 each) and 10 healthy controls. Inclusion criteria comprised adults (≥18 years) with confirmed CLD who provided informed consent, while exclusion criteria eliminated patients with liver masses/malignancy, pregnancy/lactation, or inability to cooperate. All participants underwent baseline evaluation including medical

history, CBC, liver function tests, viral markers, APRI, and FIB-4 scoring. Each patient received ^{68}Ga-FAPI PET/CT imaging following standardized protocols (150 MBq IV, 60-minute uptake period), with qualitative (visual assessment) and quantitative (SUVmax) analysis performed by an experienced nuclear medicine physician blinded to clinical data. Statistical analysis included correlation of FAPI uptake with Child-Pugh class and non-invasive biomarkers, along with group comparisons. ***Results:*** The study included 30 CLD patients (Child-Pugh A/B/C: 10 each) and 10 controls. ^{68}Ga-FAPI PET/CT demonstrated significantly higher hepatic uptake in CLD patients versus controls (mean SUVmax 4.8 (2.7-5.7) vs 1.0 (0.8-1.2), p<0.001). FAPI avidity correlated strongly with disease severity, showing progressive SUVmax increases across Child-Pugh classes (A: 3.0 (2.0-3.8), B: 5.5 (3.9-6.8), C: 5.3 (4.6-6.1); p<0.001). ***Conclusion:*** ^{68}Ga-FAPI PET/CT emerges as a transformative, non-invasive tool for liver fibrosis assessment, demonstrating strong correlation with disease severity and superior diagnostic accuracy to conventional biomarkers. Its ability to quantify fibrotic activity through SUVmax measurements and detect regional heterogeneity offers distinct advantages over current standards, potentially reducing reliance on invasive biopsies. These findings position FAPI-PET as a promising technique for personalized management of chronic liver disease, particularly for monitoring progression and therapeutic response.

EPS-040

[18F]FDG-PET/CT value in the assessment of treatment response in patients with extrapulmonary tuberculosis

M. Tormo Ratera[1], *M. Cortés-Romera*[1], *M. Santin*[2], *A. Fritsch-Medina*[1], *S. Pérez-Recio*[2], *M. Grijota-Camino*[2], *P. Perlaza-Jiménez*[1], *J. Diaz-Moreno*[1], *A. Bagán-Trejo*[1], *J. Robles-Barba*[1];
[1]*Nuclear Medicine-PET (IDI) Department, Hospital Universitari de Bellvitge-IDIBELL, L'Hospitalet de Llobregat, SPAIN,* [2]*Infectious Diseases Department, Hospital Universitari de Bellvitge-IDIBELL, L'Hospitalet de Llobregat, SPAIN.*

Aim/Introduction: The aim of this study is to evaluate the utility of [18F]FDG-PET/CT in assessing the response to antituberculosis treatment in patients with extrapulmonary tuberculosis (TB-E). ***Materials and Methods:*** Retrospective cohort study, including 20 patients diagnosed with TB-E, all of whom underwent a baseline [18F]FDG-PET/CT prior to treatment and another for assessment of the response to antituberculosis treatment.Demographic and diagnostic data (IGRA, PPD, cultures, and biopsies) were collected. [18F]FDG-PET/CT semi-quantitative (SUVmax, ΔSUVmax) and visual parameters were analysed. Lesions with activity greater than the hepatic reference were considered pathological, and a complete metabolic response (CMR) was defined as a reduction in uptake (≤hepatic). ***Results:*** The median age at diagnosis was 49 years (7 women). At diagnosis, 90% (18/20) of the patients had a positive IGRA, 10% (2/20) a positive PPD, 20% (4/20) positive cultures, and 35% (7/20) compatible biopsies.Baseline [18F]FDG-PET/CT images showed pathological findings in 100% of the patients: 75% (15/20) showed only lymph node involvement, 20% (4/20) both lymph node and extranodal involvement, and 5% (1/20) only extranodal involvement. The mean baseline SUVmax was 9.03 ± 4.8. The median duration of antituberculosis treatment was 6 months (range 3-9 months), and the interval between the start of treatment and the post-treatment [18F]FDG-PET/CT was 6 months (range 2-18). The mean post-treatment SUVmax was 3.37 ± 3.12. CMR was observed in 50% of the patients. Moreover, 95% of the patients showed a reduction in SUVmax, with a mean ΔSUVmax of 61.3% (range 6%-86%). One patient exhibited an increase in both SUVmax and the number of lesions, which led to a concomitant diagnosis of urothelial carcinoma. ***Conclusion:*** [18F]FDG-PET/CT has proven to be useful in assessing the response to antituberculosis treatment in patients with TB-E, showing a good correlation between semi-quantitative and visual parameters and clinical response.

EPS-041

FDG-PET/CT Patlak Parametric Imaging in Patients with Alveolar Echinococcosis

B. Sah[1], *L. Husmann*[1], *F. Kotasidis*[2], *A. Maurer*[1], *C. Meyer zu Schwabedissen*[1], *A. Deibel*[1], *M. Huellner*[1];
[1]*University Zurich/University Hospital Zurich, Zurich, SWITZERLAND,* [2]*University Zurich/GE Healthcare, Zurich/Waukesha,USA, SWITZERLAND.*

Aim/Introduction: To determine the role of whole-body dynamic (WBD) / Patlak parametric ^{18}F-fluorodeoxyglucose (FDG) positron emission tomography/computed tomography (PET/CT) in patients with alveolar echinococcosis (AE). This technique allows separating metabolized from unmetabolized FDG in the blood pool and tissue, potentially providing complementary qualitative information and superior quantification to standard static PET/CT images. ***Materials and Methods:*** We prospectively analysed 20 PET/CT datasets performed for staging or therapy monitoring in patients with confirmed AE. Dynamic and standard static PET/CT datasets were acquired in all patients, and quantitative imaging parameters were measured in the lesion with the highest uptake (i.e., maximum standardized uptake value (SUVmax) and Patlak parameters) and compared to normal liver tissue (SUVratio and Patlak ratio). ***Results:*** Mean SUVmax in AE manifestations was 5.7±3.1 (3.2-13.9), compared to 3.2±0.4 (2.5-4.2) in non-infected liver tissue, respective values for Patlak were 13.0±8.6 (2.7-35.5) and 4.9±2.8 (0.6-12.1). SUVratio (1.8±1.1; 1.0-5.2) was significantly lower (P<0.001) than Patlak ratio (3.2±3.2; 1.1-15.6). Both ratios correlated significantly with E. granulosus hydatid fluid (EgHF) antibodies (SUVratio r=0.73, P<0.001; Patlak ratio r=0.85, P<0.001). ***Conclusion:*** WBD PET/CT yields higher lesion-to-background contrast and may therefore have the potential to increase sensitivity in the assessment of hepatic AE.

EPS-042

Neuroimmune activation in temporal lobe epilepsy patients with worsening seizure following the COVID-19 pandemic: A [^{18}F]DPA-714 PET/MR study

L. Xiao[1], *L. Feng*[1], *Y. Tang*[1], *S. Hu*[1], *K. Shi*[2];
[1]*Xiangya Hospital Central South University, Changsha, CHINA,* [2]*University Hospital Bern, Bern, SWITZERLAND.*

Aim/Introduction: Temporal lobe epilepsy (TLE) patients frequently experience worsening epilepsy following COVID-19, referred to as post-COVID-19 active TLE. While neuroinflammatory changes are suspected in these patients, measurements of both central and systemic inflammation in the brain remain unexplored. To investigate whether the translocator protein standardized uptake value ratio (TSPO SUVr), a quantifiable marker of neuroinflammation using positron emission tomography (PET), is elevated in the brains of patients with post-COVID-19 active TLE. Additionally, we examine correlations between TSPO SUVr and inflammatory factors to identify potential peripheral blood inflammatory predictors of post-COVID-19 active epilepsy. ***Materials and Methods:*** This prospective single-center study was conducted at Xiangya Hospital of Central South University from June 2023 to May 2024. It included 24 TLE patients (12 with post-COVID-19 active TLE, 12 with post-COVID-19 non-active TLE) and 9 healthy controls (HCs), comparing serum inflammatory factors and TSPO SUVr across participants. TSPO SUVr was measured using the TSPO radioligand fluorine [^{18}F]DPA-714 PET, and the serum inflammatory factors levels were quantified using enzyme-linked immunosorbent assay (ELISA) kits. ***Results:*** The study involved 33 participants. In comparison to non-active TLE patients and HCs, the active TLE group exhibited significantly higher levels of IL-1β, IFN-γ, TNF-α, IL-5, and IL-10 ($P < 0.05$). Notable increases in TSPO SUVr were observed in specific regions, including the left temporal gyrus, right inferior frontal gyrus, and right cingulum ($P < 0.001$ uncorrected, clusters of ≥ 200 voxels). IL-1β, IL-10, and IFN-γ demonstrated the strongest associations with TSPO SUVr in the left temporal gyrus. ***Conclusion:*** Our study highlights

the presence of widespread neuroinflammation in the brain and increased levels of inflammatory cytokines in the plasma of individuals with post-COVID-19 active TLE. Furthermore, strong correlations between plasma levels of IL-1β, IL-10, and IFN-γ and neuroimmune activation suggest the potential for integrating plasma inflammatory factors with TSPO PET as a dependable approach for clinical diagnosis, dynamic monitoring, and assessment of immune-based therapeutic efficacy in TLE-associated neuroinflammation. ***References:*** 1.Depressive and Cognitive Symptoms. JAMA Psychiatry. Aug 1 2023;80(8):787-795. doi:10.1001/jamapsychiatry.2023.1321 IF: 22.5 Q1 B1 IF: 22.5 Q1 B1 2.Huang S, Gao Z, Wang S. China's COVID-19 reopening measures-warriors and weapons. Feb 25 2023;401(10377):643-644. doi:10.1016/S0140-6736(23)00213-1 IF: 98.4 Q1 B1 IF: 98.4 Q1 B1 3.Cagnazzo F, Arquizan C, Derraz I, et al. Neurological manifestations of patients infected with the SARS-CoV-2: a systematic review of the literature. . Aug 2021;268(8):2656-2665. doi:10.1007/s00415-020-10285-9 IF: 4.8 Q1 B2 IF: 4.8 Q1 B2

310

Sunday, October 5, 2025, 09:45 - 11:15
Room 116

CTE 2 - Technologists Committee: Continuous Education Models for NMTs + Instrumentation and Data Processing

OP-126
Entry Level Education in Nuclear Medicine: Establishing the Foundations for Lifelong Learning
R. McDade; *Dept of Clinical Physics & Bio-Engineering, Glasgow Royal Infirmary, Nuclear Cardiology, Glasgow, UNITED KINGDOM.*

OP-127
Continuous Professional Development: A World of Opportunities
A. Geão; *Hospital Cuf Descobertas, Medicina Nuclear, Lisboa, PORTUGAL.*

OP-128
Instrumentation, Data Processing and Dosimetry– a Learning Gap?
T. Yamamoto; *Kyorin University, Department of Medical Radiological Technology, Mitaka, Tokyo, JAPAN.*

311

Sunday, October 5, 2025, 09:45 - 11:15
Room 111

Special Symposium 1 - EARL: Clinical Implications of EARL PET/CT Accreditation Standards 2 and a New 177Lu SPECT/CT Accreditation: Results, Specifications and Future Directions

OP-130
Clinical Implications of EARL PET/CT Accreditation Standards 2: Enhancing Diagnostic Quality and Patient Outcomes
R. Boellaard; *VU University Medical Center, Amsterdam, NETHERLANDS.*

OP-131
177Lu SPECT/CT Accreditation: Results, Specifications, and Future Directions
A. Denis-Bacelar; *National Physical Laboratory, Teddington, UNITED KINGDOM.*

401

Sunday, October 5, 2025, 11:30 - 13:00
Auditorium

Plenary 2: World's Best Theranostics Comes to EANM'25

OP-132
Maximising the Potential of PSMA-Targeted Therapies: New Horizons in Oncology
G. Kong; *Peter MacCallum Cancer Centre, Molecular Imaging and Therapeutic Nuclear Medicine, University of Melbourne, Melbourne , AUSTRALIA.*

OP-133
The Power of Targeted Alpha Therapy: From Physics to Patient Outcomes
M. Sathekge; *Steve Biko Academic Hospital, Department of Nuclear Medicine, Pretoria, SOUTH AFRICA.*

OP-134
Transforming Cancer Care: Advances in Precision Oncology and Theranostic Approaches
H. Jacene; *Dana-Farber Cancer Institute, Department of Imaging, Boston, UNITED STATES OF AMERICA.*

OP-135
Radium-223 Through the Ages: From Discovery to Modern Applications
E. Etchebehere; *University of Campinas (UNICAMP), Division of Nuclear Medicine, Campinas, BRAZIL.*

OP-136
Expanding Horizons: Modernising Nuclear Medicine Infrastructure for Tomorrow's Challenges
R. Kumar; *All India Institute of Medical Sciences, Department of Nuclear Medicine, New Delhi, INDIA.*

OP-137
Astatine-211 - a Targeted Alpha Therapy for Thyroid Cancer: Advances and Challenges
T. Watabe; *Graduate School of Medicine, The University of Osaka, Osaka, JAPAN.*

501

Sunday, October 5, 2025, 15:00 - 16:30
Auditorium

CME 3 - Physics + Paediatrics Committee: Low Dose Imaging

OP-138
Where Are We Now, and How Low Can We Go?
J. Dickson; *University College London Hospitals, Institute of Nuclear Medicine, London, UNITED KINGDOM.*

OP-139
Role of AI in Low Dose Imaging
L. Imbert; *University Hospital of Nancy, Department of Nuclear Medicine, Nancy, FRANCE.*

OP-140
Nuclear Medicine Imaging of Vulnerable Patients
P. Zucchetta; *Padua University Hospital, Department of Nuclear Medicine, Padua, ITALY.*

OP-141
Role of Total Body PET in Low Dose Imaging
S. Ivashchenko; *University Medical Center Groningen, Department of Nuclear Medicine and Molecular Imaging, Groningen, NETHERLANDS.*

502

Sunday, October 5, 2025, 15:00 - 16:30
Room 112 (Arena)

Special Track 3 - Oncology & Theranostics Committee: Challenge the Expert: Will Alpha Therapy be the Main Radionuclide Therapy Approach in the Future?

OP-142
Pro: A Breakthrough that Should Improve Response and Long Term Outcome
***D. Deandreis**; Institut Gustave Roussy, University of Turin, Villejuif/Turin, FRANCE / ITALY.*

OP-143
Contra: Complex Techniques Difficult to Validate at the Era of Effective 177Lu-Theranostic Approaches
***C. Bailly**; Nantes University Hospital, Nuclear Medicine, Nantes, FRANCE.*

503

Sunday, October 5, 2025, 15:00 - 16:30
Room 113

LIPS Session 3 - Thyroid Committee: Imaging Challenges in Nuclear Endocrinology

OP-145
Challenges in Scintigraphic Imaging of Hyperparathyroidism
***P. Petranovic Ovčariček**; Department of Oncology and Nuclear Medicine, University Hospital Center Sestre Milosrdnice, Zagreb, CROATIA.*

OP-146
Challenges in Staging and Restaging of Sporadic and MEN-related MTC
***D. Taieb**; APHM-AMU, Marseille, FRANCE.*

OP-147
Challenges in Nuclear Endocrinology Resolved by Ultrasonography
***S. Ilgan**; GATA Medical Faculty, Ankara, TÜRKIYE.*

504

Sunday, October 5, 2025, 15:00 - 16:30
Room 114

M2M Track - TROP Session - Radiopharmaceutical Sciences + Translational Molecular Imaging & Therapy Committee: Tumor Microenvironment as a Therapeutic Target

OP-149
Tumour Heterogeneity in FAP Expression Exposes a Dual Role for FAP-Expressing CAFs in FAP-Targeted Radionuclide Therapy
***C. Wu**, A. Kurniawan, Z. Ming, G. Li, W. Noordzij, A. W. J. M. Glaudemans, I. F. Antunes, B. Cornelissen;*
University Medical Center Groningen, Groningen, NETHERLANDS.

Aim/Introduction: Despite promising therapeutic efficacy in preclinical studies, fibroblast activation protein-targeted radionuclide therapy (FAP-TRT) has shown limited clinical benefit. This study aims to clarify the dual role of FAP-expressing cancer-associated fibroblasts (CAFs) as therapeutic targets and potential tumour-promoting components during FAP-TRT with [^{161}Tb]Tb-FAPI-46, using 2D and 3D co-culture models of pancreatic ductal adenocarcinoma (PDAC). ***Materials and Methods:*** Immunofluorescence staining of alpha-smooth muscle actin (α-SMA) and FAP was performed on tumour sections from 10 PDAC patients, and the proportions of FAP-positive CAFs and tumour cells were enumerated. FAP expression in PSN-1 cells (human PDAC) and CAFs was measured by immunofluorescence. Uptake, internalisation, efflux, and specific binding of [^{161}Tb]Tb-FAPI-46 (40 MBq/nmol) were assessed in PSN-1 and CAFs at low (10 kBq) and high (4000 kBq) activities. Therapeutic effects of [^{161}Tb]Tb-FAPI-46 at various activities (0-4000 kBq) were evaluated in 2D clonogenic assays and 3D spheroid models, both in monoculture and co-culture conditions with different tumour-to-CAFs ratios (1:2 and 1:5). Spheroid growth was monitored for up to 13 days. ***Results:*** FAP expression varied widely among PDAC samples, with FAP-positive stromal and tumour cells ranging from 38-88% and 6.8-30%, respectively. PSN-1 cells showed lower uptake of [^{161}Tb]Tb-FAPI-46 than CAFs. High and low-added activities displayed distinct uptake/internalisation patterns in both PSN-1 and CAFs. In 2D clonogenic assays, no significant cytotoxicity to PSN-1 cells was observed in either mono- or co-culture models. In 3D spheroids, a paradoxical tumour-growth-promoting effect was seen at intermediate added activities (2000 kBq), especially in the 1:2 PSN-1: CAFs spheroid, where tumour growth temporarily accelerated markedly (P=0.002) (Table 1). This suggests that sublethal irradiation of CAFs may (transiently) stimulate tumour proliferation. By day 13, representing the long-term treatment response, all models exhibited activity-dependent growth inhibition, with 4000 kBq achieving the strongest effect ($P < 0.001$). However, the extent of inhibition decreased with increasing CAFs proportion, indicating that CAFs abundance may attenuate the long-term efficacy of FAP-TRT on tumour cell growth, even at high doses. The discrepancy between 2D and 3D model responses emphasises the importance of spatial architecture and tumour-CAFs interactions in mediating FAP-TRT efficacy. ***Conclusion:*** FAP expression and CAFs proportions critically influence FAP-TRT efficacy. While they enhance tracer uptake in cancerous tissue as a whole, excessive CAFs may promote tumour growth when exposed to subtherapeutic amounts of FAP-TRT. These findings highlight the importance of patient selection, dose optimisation, and CAFs composition and spatial arrangement for effective FAP-TRT.

OP-150
Investigating Fibroblast Activation Protein Binding of the dimeric DOTAGA.Glu.$(FAPI)_2$ labelled with Terbium-161 in Ovarian Cancer Models Incorporating the Tumor Microenvironment
***S. Van Mechelen**[1,2], K. Vermeulen[1], T. Opsomer[1], Z. Janssen[1], J. Buset[1], M. Ooms[1], F. Rösch[3], A. Coosemans[2], K. Tabury[1], I. Primac[1];*
[1]SCK CEN, Mol, BELGIUM, [2]KU Leuven, Leuven, BELGIUM, [3]Johannes Gutenberg University, Mainz, GERMANY.

Aim/Introduction: Radiotheranostics targeting the tumour stroma, particularly cancer-associated fibroblasts (CAFs) expressing fibroblast activation protein (FAP), offer a promising pan-cancer approach for the treatment of various malignancies, including ovarian cancer (OC). High-affinity, long-retention FAP-targeting radioligands are essential to maximise tumour uptake and therapeutic impact. This study preclinically evaluates the potential of a dimeric FAP inhibitor, DOTAGA.Glu.$(FAPi)_2$, labelled with the β- and Auger/conversion electron-emitting radionuclide Terbium-161 (^{161}Tb) in FAP-expressing OC models. ***Materials and Methods:*** A panel of OC cell lines and CAFs was characterized for FAP expression using Western blotting and immunofluorescence imaging. DOTAGA.Glu.$(FAPi)_2$ was radiolabelled with ^{161}Tb (100

MBq/nmol), achieving radiochemical purities exceeding 98%. Radioligand uptake was measured in CAF and OC monocultures at different timepoints (0.5-4 hours), while binding affinities were determined at one hour in co-culture models of FAP-positive CAFs and OC cells. A comparison with the clinically established monomeric analogue FAPI-46 was also included. Ex vivo tissue binding was analyzed by autoradiography on OC-CAF xenograft sections, and data were correlated to FAP histology. ***Results:*** Significantly elevated FAP expression was detected in CAFs compared to OC cell lines, as confirmed by both Western blotting and immunofluorescence. Correspondingly, radioligand uptake in CAFs peaked at 1 hour (38.9% ± 0.6% added activity (AA)/10^5 cells), while uptake in OC cells remained minimal (0.92% ± 0.01% AA/10^5 and 2.4% ± 0.1% AA/10^5 for OC cells). [161Tb]Tb-DOTAGA.Glu.$(FAPi)_2$ demonstrated a 3.1-fold increase in cellular uptake relative to [^{161}Tb]Tb-FAPI-46 and exhibited high FAP-binding affinity, with nanomolar dissociation constants in OC-CAF co-culture models. Autoradiographic analysis of OC-CAF xenograft tissues revealed a significantly greater tumour-associated specific binding for the dimeric radioligand (18.1 ± 1.7 DLU/mm^2) compared to the monomeric counterpart (6.0 ± 0.8 DLU/mm^2, $p < 0.0001$), alongside minimal non-specific uptake in healthy organs. These findings were consistent with FAP expression patterns observed in tumour histology. ***Conclusion:*** [^{161}Tb]Tb-DOTAGA.Glu.$(FAPi)_2$ exhibits markedly improved tumour targeting and binding in biologically relevant FAP-expressing ovarian cancer models. These findings support its further development as a potent radioligand for the targeted treatment of FAP-positive tumours, including ovarian cancer.

OP-151

Safety, Biodistribution, and Dosimetry of Fibroblast Activation Protein and Integrin $\alpha_v\beta_3$ dual Targeting radioligand ^{177}Lu-DOTA-FAPI-RGD: Preclinical and First-in-Human Results

J. Xiang[1,2], *X. Wen*[3], *R. Wang*[1,2], *J. Wang*[1,2], *X. Peng*[1], *Y. Wang*[1,2], *Z. Zhu*[1], *J. Zhang*[4];
[1]*Peking Union Medical College Hospital, Beijing, CHINA,* [2]*Peking Union Medical College, Beijing, CHINA,* [3]*Theranostics Center of Excellence (TCE), Yong Loo Lin School of Medicine, National University of Singapore, Singapore, SINGAPORE,* [4]*Department of Diagnostic Radiology, Yong Loo Lin School of Medicine, National University of Singapore, Singapore, SINGAPORE.*

Aim/Introduction: Fibroblast activation protein (FAP) and integrin αvβ3 are promising targets for cancer theranostics. We developed a novel dual-targeting radiotheranostic agent, ^{177}Lu-DOTA-FAPI-RGD, and conducted a first-in-human study to evaluate its safety, biodistribution, dosimetry, and preliminary therapeutic efficacy in patients with advanced adenocarcinomas. ***Materials and Methods:*** DOTA-FAPI-RGD was synthesized by conjugating a FAPI inhibitor, an RGDfK peptide and a DOTA chelator. The biodistribution and preclinical pharmacokinetics of ^{177}Lu-DOTA-FAPI-RGD were determined in HT1080-FAP and U87MG xenograft models. Nine patients with advanced adenocarcinomas and positive ^{68}Ga-FAPI-RGD PET/CT underwent treatment with 2.0±0.3 GBq (range, 1.6-2.4 GBq) of ^{177}Lu-DOTA-FAPI-RGD. ***Results:*** ^{177}Lu-DOTA-FAPI-RGD showed high radiochemical purity and stability (≥96 h). It demonstrated strong dual-target binding in vitro and sustained tumor uptake with favorable tumor-to-background ratios in vivo. ^{177}Lu-DOTA-FAPI-RGD was well-tolerated in humans. The whole-body effective dose was 0.08±0.02 Sv/GBq. Mean absorbed doses were: red marrow, 0.04±0.01 Gy/GBq; liver, 0.50±0.31 Gy/GBq; and kidneys, 0.31±0.11 Gy/GBq. Tumor-absorbed doses reached 6.10±1.42 Gy/GBq (lung metastases) and 4.20±0.84 Gy/GBq (lymph nodes). No grade 4 adverse events occurred. Grade 3 adverse events included thrombocytopenia (n=3), leukopenia (n=2), and anemia (n=1). Preliminary therapeutic outcomes showed a partial response in 2 patients (22.2%), stable disease in 6 (66.7%), and progression in 1 (11.1%), resulting in an objective response rate of 22.2% and disease control rate of 88.9%. ***Conclusion:*** ^{177}Lu-DOTA-FAPI-RGD showed adequate radiochemical purity and stability, persistent tumor uptake and high tumor-to-background ratios during the preclinical evaluation. ^{177}Lu-DOTA-FAPI-RGD also demonstrated acceptable safety, significant tumor uptake, and promising efficacy in patients, supporting further investigation in dose-escalation and multi-cycle trials.

OP-152

Head-to-head comparison of FAP-targeting single domain antibody 4AH29 vs peptide FAP-2286

N. Dumauthioz*, L. Navarro, M. Berdal, S. Nagachinta, S. Massa, A. R. Pombo Antunes, J. Dewulf, D. Mantzilas, M. D'Huyvetter;*
Precirix, Brussels, BELGIUM.

Aim/Introduction: The FAP-targeting sdAb 4AH29 was developed previously, with exceptional binding kinetics and sustained tumour retention, which translates in proper therapeutic efficacy as a single agent[1]. ^{177}Lu-labelled FAP-2286 is generally considered as most clinically advanced[2], however its perceived limited tumour retention might impact its effectiveness. This study head-to-head compares sdAb 4AH29 and peptide FAP-2286 for their in vitro and in vivo tumour retention, resulting dosimetry, and eventual therapeutic efficacy in U87 (FAP expression on tumour cells) and HT29 (FAP expression in stroma) tumour bearing mice. ***Materials and Methods:*** In vitro cell retention of [^{177}Lu]Lu-DOTA-4AH29 or [^{177}Lu]Lu-DOTA-FAP-2286 was assessed until 24h on U87 cells. Their biodistribution was evaluated in U87 and HT29 tumour xenografted mice, by i.v. injecting both ^{177}Lu-labelled compounds (3.9±0.1MBq, 1nmol) and assessing radioactive uptake in relevant organs and tissues until 168h p.i. The obtained data was used for dosimetry calculations. Finally mice with established U87 tumours were treated with a single administration of ~60 MBq (1 nmol) of [^{177}Lu]Lu-DOTA-4AH29 or [^{177}Lu]Lu-DOTA-FAP-2286, after which animals are monitored for general wellbeing and tumours volume until end of study. Statistics are done via one-way ANOVA (Tukey correction). ***Results:*** In vitro, [^{177}Lu]Lu-DOTA-4AH29 showed sustained cell-associated activity until 24h, whereas it dropped to baseline within the first hours for [^{177}Lu]Lu-DOTA-FAP-2286, indicating a rapid dissociation from U87 cells for the latter. In vivo, U87 tumour uptake was 2.8±1.0%IA/g for [^{177}Lu]Lu-DOTA-4AH29 and 9.8±2.3%IA/g for [^{177}Lu]Lu-DOTA-FAP-2286 at 1h. In the case of [^{177}Lu]Lu-DOTA-4AH29 this was retained up to 72h (2.3±0.8%IA/g), whereas for [^{177}Lu]Lu-DOTA-FAP-2286, uptake dropped to 0.96±0.4%IA/g by 24h and 0.44±0.14%IA/g at 72h. The prolonged retention resulted in a threefold higher absorbed dose to the tumour [^{177}Lu]Lu-DOTA-4AH29. Similar retention trends were obtained in HT29 tumours, however at lower absolute uptake given the lower FAP-expression in this model. HT29 tumour uptake measured rather similar for both [^{177}Lu]Lu-DOTA-4AH29 and [^{177}Lu]Lu-DOTA-FAP-2286 (1.14±0.35 vs 1.10±0.4%IA/g) early after administration in line with the results obtained in U87 tumours, improved tumour retention was observed for [^{177}Lu]Lu-DOTA-4AH29 over time, resulting in a twofold higher absorbed dose to tumour. Treatment with [^{177}Lu]Lu-DOTA-4AH29 significantly delayed tumour development vs vehicle (p=0.0124), and showed superior anti-tumour effects over treatment with [^{177}Lu]Lu-DOTA-FAP-2286 (p=0.0362) at 43 days after U87 tumor cell inoculation. ***Conclusion:*** These preclinical results underline the potential benefit of radiolabelled 4AH29 over radiolabelled FAP-2286 because of its improved tumour retention and more pronounced anti-tumour effect, and warrants its translation into the clinic. ***References:*** 1. Dekempeneer,JNM,64,1941-1948,(2023). 2. NCT04939610,ClinicalTrials.gov.

OP-153

eFAP-51: a promising dimeric FAP inhibitor with prolonged tumor retention for cancer radionuclide therapy

H. Ma, *L. Li, A. Piet, C. de Ridder, D. Stuurman, P. Paraiso, Y. Seimbille;*
Erasmus MC, Rotterdam, NETHERLANDS.

Aim/Introduction: Fibroblast activation protein (FAP) is a membrane-bound serine protease highly expressed in cancer-associated fibroblasts but minimally present in normal tissues, making it a promising bio-target for cancer. Although small-molecule FAP inhibitors have shown utility in tumor imaging, their short residence time limits therapeutic use. To address this limitation, we tested two quinoline-based monomeric FAP inhibitors—eFAP-9 and eFAP-12—from our in-house library. eFAP-9 exhibited tumor uptake comparable to the clinical reference FAPI-46, while eFAP-12 demonstrated a 1.7-fold longer tumor half-life. Building on these results, we designed dimeric analogs—eFAP-51 and eFAP-52—to enhance tumor retention through multivalency. ***Materials and Methods:*** eFAP-9 and eFAP-12 were synthesized using an 8-quinolinecyanopyrrolidine (8-QCP) scaffold. Dimers eFAP-51 and eFAP-52 were constructed by linking the respective monomers via a triazine-based platform. All compounds were radiolabeled with indium-111 and/or lutetium-177 and we evaluated their stability in PBS/mouse serum. Enzymatic inhibition was assessed against human/murine FAP, prolyl endopeptidase (PREP), and dipeptidyl peptidase-4 (DPP4). Cellular uptake was determined in HT-1080.hFAP cells. SPECT/CT imaging and biodistribution were performed in HT-1080.hFAP tumor-bearing NMRI-Foxn1^nu/nu mice. ***Results:*** All compounds were synthesized and radiolabelled with high RCY (>95%) and RCP (>96%). Both monomers and dimers exhibited potent FAP inhibition (IC_{50} < 3 nM), strong selectivity over PREP (SI >10), or DPP4 (IC_{50} > 1 mM). eFAP-9 (26.6 ± 2.3% AD) and eFAP-12 (12.0 ± 4.1% AD) showed comparable uptake in HT-1080.hFAP cells to FAPI-46 (17.2 ± 4.3% AD). eFAP-51 achieved the highest uptake (33.7 ± 4.0% AD), resulting in a 1.3-fold increase over eFAP-9, while eFAP-52 (12.5 ± 0.5% AD) performed similarly to eFAP-12. In vivo, eFAP-9 and eFAP-12 displayed tumor uptake similar to FAPI-46 at 1 h p.i., but retention declined over 24 h. In contrast, high tumor uptake (3.2% ID/g) of eFAP-51 remained over 48 h, 9-fold higher than eFAP-9 (0.35% ID/g). eFAP-52 also outperformed its monomer eFAP-12 (1.8 vs. 0.4% ID/g). Both dimers exhibited 2-4-fold higher retention than FAPI-46 (0.71% ID/g) at 48 h and showed minimal off-target accumulation with renal clearance profiles similar to monomers. ***Conclusion:*** Dimeric eFAPs demonstrated high FAP affinity, in vitro stability, and specificity, comparable to their monomeric analogs. While monomers showed modest pharmacokinetic improvement over FAPI-46, dimerization significantly enhanced tumor uptake and retention. eFAP-51, in particular, stands out as a strong candidate for FAP-targeted radioligand therapy. These findings pave the way for multivalent FAP inhibitors in next-generation cancer theranostics. ***References:*** Fibroblast activation protein, dimeric small-molecule analog, radionuclide theranostic application.

OP-154

^{67}Cu-, ^{161}Tb- and ^{177}Lu-radiolabeled antibody derivatives addressing fibroblast activation protein for radionuclide therapy

C. Neuber, *M. Kubeil, L. Loureiro, S. Brühlmann, N. Berndt, C. Arndt, A. Feldmann, K. Kopka, M. Bachmann, J. Pietzsch;*
Helmholtz-Zentrum Dresden-Rossendorf, Dresden, GERMANY.

Aim/Introduction: Fibroblast activation protein alpha (FAP) is expressed on the surface of cancer-associated fibroblasts (CAFs) but, in contrast, is mostly absent in healthy adult tissue. Therefore, imaging of this promising tumor marker provides an excellent tumor-to-background contrast. Various attempts have been made to exploit this property also for development of (radionuclide) therapeutics. In our previous preclinical study, a human IgG4-based, FAP-specific target module (anti-FAP-IgG4) was shown to be not only effective in universal chimeric antigen receptor (UniCAR) T-cell immunotherapy but also, when radiolabeled with ^{64}Cu, to be a highly specific diagnostic PET tracer for the detection of human FAP in vivo [1]. Subsequently, we aim at the use of radiolabeled anti-FAP-IgG4 for targeted radionuclide therapy (TRT). ***Materials and Methods:*** To be labeled with the beta particle emitting radionuclides ^{67}Cu, ^{161}Tb, and ^{177}Lu, anti-FAP-IgG4 was modified with the complexing agent NODA-GA (for ^{67}Cu) or DTPA-CHX-A" (for ^{161}Tb or ^{177}Lu). Pharmacokinetics of the radiolabeled compounds were determined by SPECT/CT imaging and ex vivo biodistribution experiments, which also allow for dosimetry. Therapeutic effects of different activity amounts of [^{67}Cu]Cu-, [^{161}Tb]Tb-, and [^{177}Lu]Lu-anti-FAP-IgG4 (3.2-18 MBq per mouse) on tumor growth and potential adverse side effects, e.g. on the hematopoietic system, were assessed by regular tumor size and weight monitoring for 120 days as well as by blood and urine analysis, respectively. ***Results:*** Radiolabeling with ^{67}Cu, ^{161}Tb, and ^{177}Lu showed high radiochemical yields and purities as well as good molar activities ≥40 GBq/µmol. SPECT/CT imaging revealed an excellent FAP-specific tumor uptake 24 hours post i.v. injection in mice bearing genetically modified HT1080 tumor xenografts overexpressing human FAP (HT1080-hFAP). In line with this, all radioligands caused a significant tumor growth inhibition within 72 hours retaining for up to 120 days. Nevertheless, clear differences between [^{67}Cu]Cu-, [^{161}Tb]Tb-, and [^{177}Lu]Lu-anti-FAP-IgG4 could be observed with regard to long-term tumor control and adverse side effects, requiring the need for individual activity amount adjustments. ***Conclusion:*** In conclusion, we demonstrated in the HT1080-hFAP model the suitability of anti-FAP-IgG4 not only for immunotherapeutic approaches using UniCAR T-cells but, after radiolabeling with appropriate radionuclides, also for diagnostic PET and SPECT imaging as well as TRT. ***References:*** [1] Loureiro LR, Hoffmann L, Neuber C, Rupp L, Arndt C, Kegler A, Kubeil M, Hagemeyer CE, Stephan H, Schmitz M, Feldmann A, Bachmann M. Journal of Experimental & Clinical Cancer Research 2023, 42, 341.

OP-155

A Phase I Clinical Study of Evaluating the Safety and Preliminary Efficacy of ^{177}Lu-FAPI-XT in Advanced Solid Tumors with Fibroblast Activation Protein Expression

H. Liu[1], *R. Guo*[2], *X. Zhang*[1], *H. Ji*[1], *S. Sun*[1], *S. Sun*[3], *J. Liu*[4], *Z. Yang*[2], *R. Wang*[1];
[1]*Department of Nuclear Medicine, the First Medical Center of Chinese PLA General Hospital, Beijing, CHINA,* [2]*Department of Nuclear Medicine, Peking University Cancer Hospital & Institute, Beijing, CHINA,* [3]*Sinotau Pharmaceutical Group, Beijing, CHINA,* [4]*Department of Bone and Soft Tissue Tumor, Peking University Cancer Hospital & Institute, Beijing, CHINA.*

Aim/Introduction: To investigate the safety profile, radiation dosimetry characteristics, and preliminary therapeutic potential of ^{177}Lu-FAPI-XT in patients of advanced solid tumors with fibroblast activation protein (FAP)-positive. ***Materials and Methods:*** Fourteen patients with histologically confirmed FAP-positive advanced malignancies who had progressed on standard therapies received intravenous administration of ^{177}Lu-FAPI-XT. Quantitative dosimetric analysis was performed to determine the percentage of injected activity (%ID), residence time, absorbed dose of per organ, and total effective dose using hybrid SPECT/CT imaging. Tumor response was assessed according to RECIST 1.1 criteria. ***Results:*** Peak organ uptake (%ID) occurred at 1-hour post-injection, with pulmonary parenchyma (3.878±1.331%) and red marrow (2.014±1.843%) demonstrating the highest accumulation. Prolonged tracer retention was observed in lungs (0.853±0.339 h) and hematopoietic system (0.659±0.373 h). Mean absorbed doses of per unit activity were kidney 0.13±0.047 Gy/GBq, lung 0.103±0.077 Gy/GBq, and red marrow 0.05±0.015 Gy/GBq. Tumor-absorbed doses ranged from 0.063 to 3.089 Gy/GBq. The treatment demonstrated favorable safety profiles with no

grade ≥3 adverse events. Six-month disease control rate (DCR) was 21.4% (3/14 partial responses), with fibroblastic sarcoma subgroup showing 37.5% DCR (3/8). Notably, one malignant solitary fibrous tumor case maintained stable disease for 9.4 months, while two myo-fibroblastic sarcoma cases exhibited significant reduction in FAPI PET/CT uptake activity. ***Conclusion:*** ^{177}Lu-FAPI-XT exhibits manageable toxicity and promising disease control efficacy in treatment-refractory and FAP-expressing malignancies. The favorable dosimetric profile supports further clinical investigation, particularly dose-escalation studies in mesenchymal neoplasms.

OP-156

Increasing the Residence Time of FAP Radioligands Using a Ketoamide FAPI

A. de Groot[1], *P. Brzeminski*[2], *D. Wilocx*[3], *E. Verhulst*[1], *S. Peeters*[2], *A. Fabisiak*[2], *I. De Meester*[1], *P. Van Der Veken*[2], *F. Elvas*[3];
[1]*Laboratory of Medical Biochemistry (LMB), University of Antwerp, Antwerp, BELGIUM,* [2]*Laboratory of Medicinal Chemistry (UAMC), University of Antwerp, Antwerp, BELGIUM,* [3]*Molecular Imaging and Radiology (MIRA), University of Antwerp, Antwerp, BELGIUM.*

Aim/Introduction: Fibroblast activation protein alpha (FAP) is a promising pan-tumor target, with diagnostic radiotracers demonstrating significant success across various cancer types. However, therapeutic translation remains a major challenge, primarily due to suboptimal radiation doses. Limited radioligand retention in the tumor has been identified as one of the potential causes[1]. We hypothesized that increasing FAP residence time could improve tumor retention and efficacy. In this study, we present a novel FAP-targeting radioligand, [^{177}Lu]Lu-DOTA-UAMC5947, featuring an alpha-ketoamide warhead and a quaternary ammonium linker to optimize both pharmacokinetics and pharmacodynamics. The goal is to enhance tumor retention to improve the efficacy of FAP-targeted radiotherapeutics. ***Materials and Methods:*** A novel ketoamide-FAP ligand derivatized with DOTA (UAMC5946) was radiolabelled with Lu-177 to generate [^{177}Lu]Lu-DOTA-UAMC5947. Inhibition and kinetic enzyme assays determined binding specificity, affinity and kinetic parameters. The lipophilicity and stability were evaluated. Cellular uptake, binding specificity and distribution were determined in CT-5.3-hTERT cancer-associated fibroblasts (CAFs) up to 48h. SPECT/CT imaging and ex vivo biodistribution were performed from 4h up to 96h p.i. in U-87 MG xenografts. ***Results:*** ^{Nat}Lu-complex (UAMC5947) exhibited potent FAP inhibition, with an IC_{50} of 1.6 nM and an exceptionally slow dissociation rate (k_{off} = 0.00006 s^{-1}), corresponding to an in vitro FAP-residence time of 286 minutes. Moreover, it exhibited high selectivity (SI > 625) over DPP2, DPP4, DPP8 and DPP9 and an SI over prolyl oligopeptidase of 2. The Lu-177 labeled ligand was obtained with a radiochemical purity >95%, and exhibited very good stability in PBS, and mouse plasma (>69% intact after 96h). In cell-based assays using CAFs, [^{177}Lu]Lu-DOTA-UAMC5947 showed specific binding, sustained cellular retention over 48h, and minimal efflux. SPECT/CT imaging revealed fast clearance via the kidney resulting in low background and good tumor visualisation from 4h until 96h p.i.. Accordingly with the hydrophilicity profile (logD = -2.5), the radioligand showed fast blood clearance (1.99±0.08%IA/g at 4h p.i.) with excretion through the kidneys (4.39±2.99%IA/g at 4h p.i.). [^{177}Lu]Lu-DOTA-UAMC5947 showed high and persistent tumor uptake from 4h p.i. (18.92±1.99%IA/g) with negligible tumor washout 96h p.i. (22.31±3.82%IA/g at 4h p.i.). ***Conclusion:*** [^{177}Lu]Lu-DOTA-UAMC5947 demonstrated strong FAP binding, excellent stability, and prolonged tumor retention with low background uptake, making it a promising candidate for FAP-targeted radiotherapy. Its ability to enhance intratumoral residence time may help overcome current limitations in radioligand therapy. In vivo efficacy studies in murine tumor models are currently underway to further assess its therapeutic potential. ***References:*** [1]Mori et al, npj imaging, 2024.

OP-157

An MAE_3-DOTA-Conjugated FAP Inhibitor for TargetedRhenium-188 Radionuclide Therapy

M. Xu*, Z. Liu;*
Changping Laboratory, Beijing, CHINA.

Aim/Introduction: Rhenium-188 (^{188}Re) is a promising radionuclide for targeted radionuclide therapy due to its cost-effectiveness, high-energy β^- emissions for therapeutic efficacy, and γ emissions enabling SPECT imaging. However, the complex coordination chemistry of rhenium poses significant challenges in developing stable bifunctional chelators. Here, we designed four fibroblast activation protein (FAP)-targeted radiotracers: ^{188}Re-labeled MAS_3-FAPI, MAS_3-DOTA-FAPI, MAE_3-FAPI, and MAE_3-DOTA-FAPI, aiming to offer synergize therapeutic precision with diagnostic capabilities. ***Materials and Methods:*** Radiolabeling was achieved using triamidomonothiol (N_3S) chelator framework, mercaptoacetyl-Ser-Ser-Ser (MAS_3) and mercaptoacetyl-Glu-Glu-Glu (MAE_3). The 1,4,7,10-Tetraazacyclododecane-1,4,7,10-tetraacetic acid (DOTA) was used to modulate the pharmacokinetic properties. Radiolabeling efficiency, in vitro stability, and hydrophilicity were systematically compared. The tracers were further evaluated through FAP protein/cell binding assays, SPECT/CT imaging, biodistribution studies, and therapeutic efficacy assessments in HT1080-FAP xenograft model. ***Results:*** All the radiotracers exhibited efficient radiolabeling with yields exceeding 80%. MAE_3-based chelators demonstrated good stability (radiochemical purity >96% at 6 h). In vitro studies confirmed FAP-specific binding, while in vivo SPECT imaging revealed distinct pharmacokinetic profiles: DOTA-modified tracers (MAS_3-DOTA-FAPI and MAE_3-DOTA-FAPI) showed enhanced tumor uptake and prolonged retention, with significantly reduced hepatic/intestinal accumulation. Notably, [^{188}Re]Re-MAE3-DOTA-FAPI achieved potent tumor growth inhibition (100% reduction vs. controls) with negligible off-target toxicity. ***Conclusion:*** In this study, the potential of ^{188}Re-targeted radionuclide therapy was evaluated through the development and in vitro and in vivo assessment of ^{188}Re-labeled radiopharmaceuticals. This study establishes [^{188}Re]Re-MAE_3-DOTA-FAPI as an optimized therapeutic agent, combining MAE_3's robust chelation stability with DOTA-driven pharmacokinetic refinement. Its high tumor specificity, sustained intralesional retention, and potent therapeutic efficacy underscore strong potential for clinical translation.

505

Sunday, October 5, 2025, 15:00 - 16:30
Room 211

Cutting Edge Science Track - TROP Session - AI Committee: AI Based Segmentation - Cardiac, Lung Ventilation, Bone

OP-158

Towards reliable automation of anatomical segmentation in whole-body bone scintigraphy using deep learning

I. Correia[1,2], *F. Oliveira*[1], *C. S. Constantino*[1], *L. C. Silva*[1], *J. Castanheira*[1], *Â. Ferreira*[1], *R. Teixeira*[1], *D. C. Costa*[1];
[1]*Champalimaud Clinical Centre, Champalimaud Foundation, Lisbon, PORTUGAL,* [2]*Faculdade de Ciências, Universidade de Lisboa, Lisbon, PORTUGAL.*

Aim/Introduction: This project aims to assess the performance of deep-learning-based (DL) automatic anatomical segmentation of bone scintigraphy (BS) images. In combination with lesion segmentation and classification models, it can be used to generate lesion location reports to support clinical interpretation. Therefore, interpretation time and inter-reader variability are reduced to

improve clinical workflows. ***Materials and Methods:*** 255 total-body BS (anterior and posterior projections) from 189 patients were retrospectively collected for training and testing. Patients were injected with 99mTc-HDP (677±51.55 MBq) and scanned 2-4 hours post-injection using a Philips BrightView® dual-head gamma camera with LEHR collimators. Scans were acquired continuously at 14 cm/min, resulting in 512×1024 resolution images (2×2 mm^2 pixels). Patients (107 female, 82 male, mean age 70±13 years) were diagnosed with breast (N=99), prostate (N=66), or other cancers (N=24). Scans were acquired for staging or reassessment of bone metastases. From the full dataset, 50 patients were randomly selected for testing, ensuring no patient testing-training overlap and balanced sex distribution. The remaining scans (N=205) were used for network training. Both anterior and posterior projections were manually segmented under the supervision of an experienced nuclear medicine physician, covering the entire skeleton. The resulting masks contained 31 bones/bone structures for the anterior and 28 for the posterior projections. The training and inference were done using the nnU-Net framework [1], with one input channel per projection segmentation. Model performance was evaluated using manual segmentation as the ground truth. The Dice similarity coefficient (DSC) was computed per patient, weighted by label size. Bones/bone-structures-wise DSC across patients were also calculated. ***Results:*** The average DSC was 0.970 (range: 0.928-0.983) for anterior and 0.969 (range: 0.851-0.987) for posterior projections. Regarding bones/bone-structures-wise DSC, the skull achieved the highest mean score (0.993) in both projections. The lowest mean values were observed for the left radius (0.788 for anterior, and 0.781 for posterior projections), likely due to high variability in arm positioning and frequent partial cropping, rather than low uptake. The lowest score per patient resulted from the model mislabelling of symmetrical structures (left/right swap) despite the segmentation itself being anatomically correct, requiring potential architectural or input refinements. ***Conclusion:*** The proposed DL approach effectively identifies the skeletal structures in BS images, achieving high segmentation accuracy. While further validation is still needed across broader clinical scenarios to validate this tool and promote its integration in lesion detection models, it potentially paves the way for clinically meaningful automation. ***References:*** [1] Isensee, et al., (2021). doi:10.1038/s41592-020-01008-z

OP-159

Deep Learning Segmentation for Myocardial Perfusion Imaging SPECT

T. Huxohl[1], *M. Günter*[2];
[1]*Heart and Diabetes Center NRW, Bad Oeynhausen, GERMANY,* [2]*Bielefeld University, Bielefeld, GERMANY.*

Aim/Introduction: Segmentation of the myocardium in myocardial perfusion SPECT images is an important preprocessing step. It facilitates downstream tasks such as reorientation and polar map generation required for clinical interpretation. In this work, a deep learning approach is implemented, and evaluated on three different SPECT scanners. ***Materials and Methods:*** Using a dataset of 437 SPECT/CT scans acquired with a Siemens Symbia Intevo scanner, initial segmentation masks were generated from attenuation maps using TotalSegmentator [1]. To deal with registration errors, the masks were shifted to maximize the activity under the mask. Furthermore, all masks were dilated, smoothed, manually refined and checked. With about 20% of the scans retained for testing, this dataset is used to train an nnU-Net [2] to segment the myocardium in MPI SPECT scans. The resulting model is evaluated qualitatively and using the Dice coefficient. In addition, the model is evaluated qualitatively on data from two other scanners: 64 scans acquired with a GE Discovery 530c and 47 scans acquired with a Philips Cardio-MD scanner. ***Results:*** The trained model achieves a Dice coefficient of 0.83±0.04 on the Siemens Symbia Intevo test data. In a qualitative evaluation, the segmentation masks for the other two scanners show a very good fit. ***Conclusion:*** An nnU-Net performs well for the segmentation of the myocardium in myocardial perfusion SPECT images across multiple scanners. In future work, we want to evaluate the segmentation masks with respect to two downstream tasks: (1) reorientation, and (2) image registration by comparing SPECT segmentation masks with CT segmentation masks generated with TotalSegmentator. ***References:*** [1] J. Wasserthal et al., "TotalSegmentator: Robust Segmentation of 104 Anatomic Structures in CT Images," Radiology: Artificial Intelligence, vol. 5, no. 5, p. e230024, Sep. 2023, doi: 10.1148/ryai.230024. [2] F. Isensee, P. F. Jaeger, S. A. A. Kohl, J. Petersen, and K. H. Maier-Hein, "nnU-Net: a self-configuring method for deep learning-based biomedical image segmentation," Nat Methods, vol. 18, no. 2, Art. no. 2, 2021, doi: 10.1038/s41592-020-01008-z.

OP-160

Left Ventricle Segmentation in Dynamic ^{82}Rb PET/CT Using Deep Convolutional Neural Networks

M. Amirian[1,2], *A. Chevalley*[1,2], *V. Andrearczyk*[1,2], *R. Klein*[3], *R. DeKemp*[4], *E. Moulton*[5], *C. Kamani*[2], *J. Prior*[2], *M. Jreige*[2], *A. Depeursinge*[1,2];
[1]*University of Applied Sciences and Arts of Western Switzerland (HES-SO), Sierre, SWITZERLAND,* [2]*Department of Nuclear Medicine and Molecular Imaging, Centre Hospitalier Universitaire Vaudois (CHUV), Lausanne, SWITZERLAND,* [3]*Division of Nuclear Medicine and Molecular Imaging, University of Ottawa, Ottawa, ON, CANADA,* [4]*Division of Cardiology, University of Ottawa Heart Institute, Ottawa, ON, CANADA,* [5]*Jubilant DraxImage Inc, Kirkland, QC, CANADA.*

Aim/Introduction: Precise delineation of the left ventricle (LV) enables advanced analyses of endo-to-epicardium blood perfusion patterns and their gradients in PET, which can support various clinical applications, including coronary microvascular dysfunction. Approaches like simple thresholding or semi-automatic curve fitting often fall short in accurately capturing the LV boundaries in dynamic ^{82}Rb PET/CT. They also require expert manual input. This study presents a reliable manual, multi-modal LV delineation strategy, and a fully automatic segmentation algorithm using deep convolutional neural networks (CNNs). ***Materials and Methods:*** We manually segmented 40 non-gated dynamic PET/CT volumes from 20 patients, acquired under both rest and stress examinations. The cohort consists of patients who underwent ^{82}Rb PET/CT examinations for revascularization and includes several cases with evident apex thinning and hypoperfused septal and lateral walls. To support accurate delineation, multiple time frames—including early and late uptake phases—were used to segment the LV while excluding the blood pool. Additionally, computed tomography (CT) scans were used as a sanity check to ensure that the contours remained within the LV muscle tissue. This dataset was then used to train and evaluate an nnU-Net architecture [1] using a 5-fold cross-validation. The results are compared to a simple semi-automatic baseline thresholding method. ***Results:*** Best segmentation performance using semi-automatic baseline thresholding was achieved with a threshold equal to 35% of the highest photon count inside the LV, which achieved a mean Dice of 0.7452 and a balanced accuracy of 0.9101. The fully automatic nnU-Net outperformed this baseline by a large margin, achieving a Dice of 0.8701 and a balanced accuracy of 0.9392. Thresholding especially fails to contour the LV in ischaemic patients in the presence of hypoperfused septal and lateral walls or apex thinning. In such cases, the performance gap between the best nnU-Net and thresholding is even more pronounced, with nnU-Net achieving a Dice of 0.8525 compared to 0.7026 for thresholding. This performance gap is also more evident in stress examinations compared to rest, where nnU-Net boosts the Dice from 0.7387 (using thresholding) to 0.8696 for stress. ***Conclusion:***

Deep CNNs enable fully automated segmentation of ^{82}Rb dynamic PET sequences. It eliminates the need for human expert intervention in segmentation and achieves a relative improvement of 21% for patients with hypo-perfused tissues compared with the baseline thresholding algorithm. ***References:*** [1] Isensee F, Jaeger PF, Kohl SA, Petersen J, Maier-Hein KH. nnU-Net: a self-configuring method for deep learning-based biomedical image segmentation. Nature methods. 2021 Feb;18(2):203-11.

OP-162

Segmenting Pulmonary Embolism in Ventilation/ Perfusion (V/Q) Scans: Benchmarking nnUnet, SwinUnet, and BTUnet

A. Jabbarpour[1,2], *S. Kaviani*[3,4,5], *E. Moulton*[4], *W. Zeng*[6], *S. Ghassel*[7], *R. Akbarian*[6], *A. Couture*[8], *A. Roy*[9], *R. Liu*[9], *Y. A. Lucinian*[8], *N. Hejji*[10], *S. AlSulaiman*[6], *F. Shirazi*[6], *E. Leung*[11,12], *R. Klein*[12,13,5];
[1]*Department of Medical Physics, Carleton University, Ottawa, Ontario, Canada, Ottawa, ON, CANADA,* [2]*Ottawa Hospital Research Institute, Ottawa, ON, CANADA,* [3]*Division of Nuclear Medicine and Molecular Imaging, Faculty of Medicine, University of Ottawa, Ottawa, ON, CANADA,* [4]*Jubilant DraxImage, Montreal, QC, CANADA,* [5]*Electrical Engineering and Computer Science, University of Ottawa, Ottawa, Ontario, Canada., Ottawa, ON, CANADA,* [6]*Department of Nuclear Medicine and Molecular Imaging, The Ottawa Hospital, Ottawa, Ontario, Canada, Ottawa, ON, Canada, Ottawa, ON, CANADA,* [7]*Electrical Engineering and Computer Science, University of Ottawa, Ottawa, ON, Canada, Ottawa, ON, CANADA,* [8]*Hôpital Maisonneuve-Rosemont, Montreal, QC, CANADA,* [9]*McGill University Faculty of Medicine, Montreal, QC, CANADA,* [10]*Department of Nuclear Medicine and Molecular Imaging, The Ottawa Hospital, Ottawa, Ontario, Canada, Ottawa, ON, Canada, Montreal, QC, CANADA,* [11]*Division of Nuclear Medicine and Molecular Imaging, Faculty of Medicine, University of Ottawa, Ottawa, Ontario, Canada., Ottawa, ON, CANADA,* [12]*Department of Nuclear Medicine and Molecular Imaging, The Ottawa Hospital, Ottawa, Ontario, Canada, Ottawa, ON, CANADA,* [13]*Department of Medical Physics, Carleton University, Ottawa, Ontario, Canada, Ottawa, ON, CANADA, Ottawa, ON, CANADA.*

Aim/Introduction: Clinical guidelines (PIOPED/EANM) for pulmonary embolism (PE) diagnosis rely on qualitative assessment of segmental/subsegmental perfusion defects in ventilation-perfusion (V/Q) scintigraphy. Annotation of segmental defects is limited by interobserver variability and is labor-intensive, so is seldom performed clinically, undermining communication of findings. To address this, we trained and validated three AI 2.5D models—nnUnet, SwinUnet, and Bottle neck transformer Unet (BTUnet)—for automated, reproducible defect segmentation in planar V/Q scans. ***Materials and Methods:*** Planar lung V/Q image data were sources from The Ottawa Hospital (TOH) and University Health Toronto (UHT). Both using a 256x256 grid with a ^{99m}Tc energy peak of 140±7.5% [129-150] keV, across six standard projections: anterior, posterior, and left/right anterior/posterior obliques. Ventilation at TOH was performed using Technegas, while UHT used various aerosolized agents. Both centers used ^{99m}Tc-MAA for perfusion. Models were trained on data from 1,313 patients (7,878 projections) and validated on 329 patients (1,974 projections) group-wise split by patient IDs and equally stratified by PIOPED categories. The BTUnet model was in-house developed and incorporated a lightweight transformer block within the bottleneck of the Unet architecture. Each model was trained on 6 consecutive paired V/Q images stacked channel-wise and corresponding annotated masks using a combined cross-entropy and Dice loss. Model performance was assessed on a hold-out test set of 46 images (276 projections), using FROC analysis and calculating sensitivity at 1 and 0.5 false positive rate (FPR) and Dice scores. Predicted defects were considered true positives if their centroids were within 1.95 cm (10 pixels) of the ground truth. Model results were compared to annotations by seven nuclear medicine physicians of the same images. ***Results:*** BTUnet, SwinUnet, and nnUnet mean ± std Dice scores were 0.51±0.37, 0.48±0.36, 0.48±0.40, respectively. BTUnet, SwinUnet, nnUnet, and for physicians mean ± std sensitivity at 1 FPR were 0.495±0.028, 0.462±0.030, 0.386±0.028, 0.572±0.058 and at 0.5 FPR were 0.400±0.041, 0.374±0.045, 0.374±0.044, and 0.459±0.057, respectively. Thus, BTUnet was the only model whose performance approached that of human readers, but did not reach the same level ($p<0.001$). ***Conclusion:*** Our top-performing AI model, BTUnet, robustly segmented vascular perfusion defects on V/Q scintigraphy, approaching the performance of expert physician assessments, but not matching it. Its ability to provide rapid and consistent segmentation marks its potential to enhance diagnostic efficiency and support the integration of AI-driven tools into standard clinical workflows for PE evaluation. Future work may aim to improve model performance by using all projections concurrently.

OP-163

Improved Differential Diagnosis of Parkinsonian Syndromes Using Quantitative Dual-Phase [^{18}F]FP-CIT PET

H. Yoon[1], *D. Kim*[2], *S. Lee*[2], *S. Lee*[1], *M. Park*[3], *M. Yun*[1];
[1]*Yonsei University College of Medicine, Seoul, KOREA, REPUBLIC OF,* [2]*Yonsei University, Seoul, KOREA, REPUBLIC OF,* [3]*UT Southwestern Medical Center, Dallas, TX, UNITED STATES OF AMERICA.*

Aim/Introduction: Dual-phase [^{18}F]FP-CIT PET/CT has proven valuable for the differential diagnosis of parkinsonian syndromes. Early-phase images resemble [^{18}F]FDG PET scans, reflecting cerebral perfusion and neuronal activity, while delayed-phase images depict striatal dopamine transporter binding. With increasing interest in artificial intelligence (AI)-based diagnostic tools, we hypothesized that combining early- and delayed- phase imaging would allow diagnosis and differential diagnosis of Parkinsonism. This study aimed to quantitatively analyze and classify dual-phase [^{18}F]FP-CIT PET/CT images using a machine learning algorithm, and to evaluate whether the inclusion of early-phase features improves the accuracy of differential diagnosis. ***Materials and Methods:*** We retrospectively collected dual-phase [^{18}F]FP-CIT PET/CT images from 435 subjects (normal = 188, idiopathic Parkinson's disease (IPD) = 111, atypical Parkinson's disease (APD) =136) at a single center. To measure regional uptake, segmentation masks of the ventral striatum, putamen and caudate were obtained from CT images using a deep learning model. Based on anterior commissure (AC)-posterior commissure (PC) landmarks, the mask was divided into 12 regions of interest (ROIs): anterior putamen, anterior caudate, posterior putamen, posterior caudate, ventral putamen, and ventral striatum (left and right). Binding potential (BPnd) and standardized uptake value ratios (SUVRs) were extracted from delayed and early-phase images, respectively, using the occipital cortex (delayed) and cortical white matter (early) as reference regions. In addition to BPnd and SUVRs for each ROI, 18 inter-regional ratios were derived and included as features. For early-phase features, SUVRs from 26 regions outside the basal ganglia were also incorporated. Two XGBoost classifiers were trained to categorize patients into normal, IPD, or APD groups using 10-fold stratified cross-validation. One model was trained using delayed-phase features only, while the other utilized both delayed- and early-phase features. Model performance was evaluated based on accuracy and F1 score. ***Results:*** The model trained solely on delayed-phase features achieved an accuracy of 0.834 ± 0.057 and an F1 score of 0.823 ± 0.063 (mean ± standard deviation). The model incorporating both delayed- and early-phase features demonstrated higher performance, with an accuracy of 0.917 ± 0.039 and an F1 score of 0.915 ± 0.041 (mean

± standard deviation). ***Conclusion:*** Incorporating early-phase features alongside delayed-phase features significantly improves machine learning-based differential diagnosis of parkinsonian syndromes. The enhanced accuracy and F1 scores highlight the added value of dual-phase [^{18}F]FP-CIT PET/CT as a more informative and comprehensive imaging modality for AI-assisted diagnosis.

OP-164

Seg V/Q: Building a Large-Scale Database of Lung Ventilation-Perfusion Scintigraphy Annotated for Pulmonary Embolism Mismatch Defects (VQ4PEDB) With the Help of AI

A. Jabbarpour[1], *S. Kaviani*[2,3], *E. Moulton*[3,4], *S. Ghassel*[5], *W. Zeng*[6], *R. Akbarian*[7], *A. Couture*[8], *A. Roy*[9], *R. Liu*[9], *Y. A. Lucinian*[8], *N. Hejji*[6], *S. AlSulaiman*[6], *F. Shirazi*[6], *E. Leung*[6], *R. Klein*[6];
[1]*Carleton University, Ottawa, ON, CANADA,* [2]*Division of Nuclear Medicine and Molecular Imaging, Faculty of Medicine, University of Ottawa, Ottawa, Ontario, Canada., Ottawa, ON, CANADA, Ottawa, ON, CANADA,* [3]*Jubilant DraxImage, Montreal, QC, CANADA, Montreal, QC, CANADA,* [4]*Electrical Engineering and Computer Science, University of Ottawa, Ottawa, Ontario, Canada., Ottawa, ON, CANADA,, Ottawa, ON, CANADA,* [5]*Electrical Engineering and Computer Science, University of Ottawa, Ottawa, Ontario, Canada, Ottawa, ON, CANADA,* [6]*Department of Nuclear Medicine and Molecular Imaging, The Ottawa Hospital, Ottawa, Ontario, Canada, Ottawa, ON, CANADA,* [7]*Electrical Engineering and Computer Science, University of Ottawa, Ottawa, Ontario, Canada, Ottawa, ON, CANADA,* [8]*Hôpital Maisonneuve-Rosemont, Montreal, QC, CANADA, Montreal, QC, CANADA,* [9]*McGill University Faculty of Medicine, Montreal, QC, CANADA,, Montreal, QC, CANADA.*

Aim/Introduction: Pulmonary embolism (PE) can be reliably diagnosed using ventilation-perfusion (V/Q) scintigraphy, yet subjective interpretation and labor-intensive annotation impede both clinical consistency and the development of AI-driven image processing tools. To overcome these limitations, we have been constructing VQ4PEDB, the first large-scale annotated database of V/Q studies, leveraging Seg V/Q, a hybrid AI-human workflow to enhance the scalability of high-quality PE defect annotation. ***Materials and Methods:*** We analyzed 2,137 planar V/Q studies from The Ottawa Hospital, classified by modified PIOPED criteria. In phase one, 1,485 studies were manually annotated by 10 nuclear medicine physicians using the V7 Darwin platform, segmenting perfusion defects across six standard projections: anterior, left anterior oblique, left posterior oblique, posterior, right posterior oblique, and right anterior oblique. In phase 2, the remaining 652 studies were annotated using Seg V/Q software, an in-house developed GUI incorporating a Bottle Neck Transformer Unet (BTUnet) segmentation model. The model, pre-trained on phase 1 data, generated preliminary defect masks that annotators refined to finalize the segmentations. Annotation times were compared between phases. Furthermore, the proportion of BTUnet annotations requiring human corrections were also evaluated. ***Results:*** The phase 1 cohort included 669 normal studies and 816 with perfusion defects (138 high, 168 intermediate, 266 low, 244 very low probability). The distribution of PIOPED scores were similar between phases. AI integration reduced mean annotation time by 65% (1.24 ± 1.67 vs. 3.50 ± 4.20 minutes; $p < 0.0001$). Critically, 25% of cases required extensive corrections to BTUnet generated defect annotations, 20% of cases required moderate boundary corrections, 35% required only minor boundary edits, with no significant accuracy loss (<2 cm border deviations), and 20% did not require adjustment. ***Conclusion:*** Seg V/Q using AI-generated initial annotations significantly shortened the time required to annotate lung V/Q mismatch defects in planar scintigraphy, while preserving label fidelity. The resulting VQ4PEDB enables the development and validation of diagnostic clinical tools for the accurate detection of PE.

OP-165

Long-term surveillance of an AI segmentation tool in clinical practice

J. Taylor*, P. Metherall;*
Sheffield Teaching Hospitals, Sheffield, UNITED KINGDOM.

Aim/Introduction: Ongoing surveillance of AI tools is a requirement of EU legislation. Such procedures ensure that software performance remains consistent and that user behaviour does not shift significantly over time (e.g. due to automation bias). The aim of this study was to evaluate the long-term performance of a clinically implemented AI tool for automated segmentation of Multi-Gated Acquisition (MUGA) scans. We assessed: • Time required for users to check/edit auto-generated regions • Extent of user editing • Evidence of performance drift or automation bias over time ***Materials and Methods:*** All stages of MUGA scan processing were automatically recorded in a bespoke local database, with associated timestamps. Records between November 2022 to April 2025 were analysed. Tool performance and user editing were evaluated by comparing the ejection fraction (EF) result generated from fully automated regions to the final EF result after human quality checking. To further assess human intervention, 20 cases from two time points (Feb 2023 and Feb 2025) were selected. Left ventricular segmentation areas were measured across all 24 frames of each acquisition, comparing automated vs. manually adjusted results. ***Results:*** Full dataset: Across 625 samples, the mean absolute EF difference between automated and final results was 2.2% (SD 2.6%), suggesting small underestimation by the AI. The mean time for quality checking/editing was 13.5 minutes (SD 22.3 mins), with the high variability likely reflecting workflow interruptions. Frame-by-frame analysis showed systematic overestimation of left ventricular area by the AI, most notably at end-systole (mean difference 0.5 cm^2 across all frames; 1.2 cm^2 at end-systole). Timeline analysis: EF data split into 6-month periods showed no significant trend in absolute EF difference, suggesting stable performance and no increase in automation bias. Similarly, comparing 2023 and 2025 cohorts for per-frame segmentation areas revealed no significant change over time. ***Conclusion:*** This clinically implemented AI tool showed consistent long-term performance in MUGA scan segmentation. A small underestimation of EF was observed, likely due to systematic overestimation of end-systolic size. However, no evidence of performance drift or automation bias was found since implementation.

OP-166

Deep Learning-Based Segmentation of Carotid Arteries for Reliable PET Metric Extraction on a Clinical Dataset of 192 [^{64}Cu]Cu-DOTATATE PET/CT Scans

A. Kristensen Vølund*, V. M. B. Frederiksen, J. S. Madsen, M. E. K. Jensen, A. Clemmensen, R. S. Ripa, A. Kjaer;*
Cluster for Molecular Imaging, Copenhagen University Hospital - Rigshospitalet, Department of Biomedical Sciences, University of Copenhagen, Copenhagen, DENMARK.

Aim/Introduction: The carotid artery bifurcation is a common and critical location for atherosclerotic plaques to develop. If such a plaque becomes unstable, it may lead to stroke. Positron emission tomography (PET) has shown potential in imaging atherosclerotic cardiovascular disease [1], however assessing the radiotracer uptake requires manual annotation of the arteries, which is a time-consuming task. The aim of this study was to train a deep learning model to perform segmentation of the carotid arteries for reliable PET metric extraction ***Materials and Methods:*** In total, 192 clinical [^{64}Cu]Cu-DOTATATE PET/CT scans were included. First, all carotid arteries were manually annotated by trained raters. Second, a 3D nnU-Net model [2] was trained on 154 of the CT scans and the corresponding human annotations of both left and right carotid artery. The performance of the model was evaluated on a test

set consisting of 38 PET/CT scans not used for training. Four PET metrics were extracted: SUV_{max}, $mSUV_{max}$, TBR_{max} and $mTBR_{max}$. In addition, intra- and inter-rater reliability of the manual annotation method was assessed. ***Results:*** The model obtained a Dice score of 0.86±0.11 and 0.88±0.04 for, respectively, the left and right carotid artery on the test set compared to the human annotations. For all four PET metrics, the intraclass correlation coefficient (ICC) was ≥0.96. Bland-Altman analysis showed that the bias ± limits of agreement (LoA) between the model and the human annotations were 0.07±0.64, 0.05±0.15, 0.07±0.89 and 0.07±0.24 for SUV_{max}, $mSUV_{max}$, TBR_{max} and $mTBR_{max}$, respectively. For the intra-rater reliability, the bias ± LoA were 0.10±0.57, 0.00±0.08, -0.06±0.94 and -0.10±0.32, and for the inter-rater reliability bias ± LoA were 0.00±0.94, 0.04±0.09, -0.01±1.52 and 0.03±0.27. The model segments the carotid arteries in just 63 seconds per scan, while the manual annotation takes 14.5 minutes on average per scan. ***Conclusion:*** The width of the LoA for the model was comparable to that of the human intra- and inter-rater variability for all four PET metrics. This, in addition to high ICCs, indicates that the model's ability to create reliable segmentations for PET metric extraction is excellent. A 93% reduction in segmentation time compared to the manual annotation underscores the potential in applying automated segmentation in cardiovascular nuclear imaging. ***References:*** [1] Maier, A. et al. (2024). Uncovering atherosclerotic cardiovascular disease by PET imaging. Nature reviews cardiology, 21, 632-651. [2] Isensee, F. et al. (2021). nnU-Net: a self-configuring method for deep learning-based biomedical image segmentation. Nature methods, 18(2), 203-211.

506

Sunday, October 5, 2025, 15:00 - 16:30
Room 117

Clinical Oncology Track - TROP Session - Oncology & Theranostics Committee: Lung Cancer Imaging

OP-167

Integrin $\alpha_v\beta_6$ Targeting ^{68}Ga-Trivehexin PET/CT for Imaging Non-Small Cell Lung Cancer: A Prospective Study

W. Hq[1], *C. Li*[1], *L. Li*[1], *Q. Chen*[2], *Y. He*[1];
[1]*Department of Nuclear Medicine, Zhongnan Hospital of Wuhan University, Wuhan, CHINA,* [2]*Department of Pathology, Zhongnan Hospital of Wuhan University, Wuhan, CHINA.*

Aim/Introduction: This study aimed to investigate and compare the diagnostic performance of ^{68}Ga-Trivehexin and ^{18}F-FDG PET/CT for detecting mediastinal and hilar lymph node metastasis in non-small cell lung cancer (NSCLC), and further explore their impacts on patients' therapeutic management. ***Materials and Methods:*** Forty patients with histologically confirmed NSCLC were prospectively enrolled and underwent paired ^{68}Ga-Trivehexin and ^{18}F-FDG PET/CT within one week (NCT05835570). The maximum standardized uptake value (SUVmax), target-to-background ratio (TBR) and target-to-liver ratio (TLR) were accessed for paired positive lesions. The diagnostic performance of ^{68}Ga-Trivehexin and ^{18}F-FDG was compared for the detection of primary tumors, lymph nodes and distant metastases. The reference standard was based on histopathological findings, typical radiological manifestations, clinical imaging follow-up of no less than 3 months. Wilcoxon signed-rank test or Mann-Whitney U test was used to compare these indicators between the two groups. ***Results:*** For regional lymph nodes, ^{68}Ga-Trivehexin exhibited higher diagnostic sensitivity (61.5% vs. 53.8%), specificity (98.4% vs. 81.5%), and accuracy (94.9% vs. 78.8%) compared to ^{18}F-FDG (all $p < 0.05$). For primary tumors, the detection efficiency of ^{18}F-FDG and ^{68}Ga-Trivehexin PET/CT is equal (100%). For distant metastases, ^{68}Ga-Trivehexin detected more lesions than ^{18}F-FDG (27 vs. 21), and with higher TLR for liver (22.57 vs 10.07, $p = 0.016$) and bone metastases (13.64 vs 6.65, $p < 0.001$). In particular, for brain metastases, the TBR of ^{68}Ga-Trivehexin was 89.1 times that of ^{18}F- FDG (96.23 vs 1.08, $p = 0.004$). For N-staging, ^{68}Ga-Trivehexin PET/CT showed that 84.2% (16/19) of the patients were consistent with pathological N-staging. A total of 16 patients changed their therapeutic regimens according to ^{68}Ga-Trivehexin PET/CT compared with ^{18}F-FDG PET/CT. ***Conclusion:*** Our study demonstrated that ^{68}Ga-Trivehexin PET/CT is significantly superior to ^{18}F-FDG PET/CT in identifying lymph node metastasis in NSCLC. ^{68}Ga-Trivehexin PET/CT showed a comparable diagnostic performance with ^{18}F-FDG for detecting primary tumors and distant metastases except for brain metastasis.

OP-168

[68Ga]Ga-FAPI-46 PET/CT for Staging Suspected/Confirmed Lung Cancer: Results on the Non-Surgical Cohort within a Monocentric Prospective Trial

E. Fortunati[1], *L. Zanoni*[2], *G. Cuzzani*[3], *C. Nanni*[1], *C. Malizia*[1], *F. Lodi*[1], *V. Cabitza*[1], *I. Brusa*[1], *S. Emiliani*[1], *M. Assenza*[4], *L. Vetrone*[1], *F. Antonacci*[5], *F. Giunchi*[6], *A. Degiovanni*[6], *M. Ferrari*[7], *F. Natali*[7], *T. Galasso*[7], *G. Bandelli*[7], *P. Candoli*[7], *A. D'Errico*[6], *P. Solli*[5], *S. Fanti*[1,3];
[1]*Nuclear Medicine, IRCCS, Azienda Ospedaliero-Universitaria di Bologna, Bologna, ITALY,* [2]*Nuclear Medicine, AST Pesaro-Urbino, Pesaro, ITALY,* [3]*Nuclear Medicine, Alma Mater Studiorum University of Bologna, Bologna, ITALY,* [4]*Professional Development and Implementation of Research in Health Professional Unit, IRCCS Azienda Ospedaliero-Universitaria di Bologna, Bologna, ITALY,* [5]*Division of Thoracic Surgery, IRCCS, Azienda Ospedaliero-Universitaria di Bologna, Bologna, ITALY,* [6]*Pathology, IRCCS, Azienda Ospedaliero-Universitaria di Bologna, Bologna, ITALY,* [7]*Interventional Pulmonology Unit, IRCCS, Azienda Ospedaliero-Universitaria di Bologna, Bologna, ITALY.*

Aim/Introduction: To evaluateT&N-staging diagnostic performances of [68Ga]Ga-FAPI-46 (FAPI) and [18F]F-FDG-PET/CT (FDG) in a suspected/confirmed lung cancer (LC) non-surgical cohort. ***Materials and Methods:*** Among patients with suspected/confirmed LC enrolled in a prospective-monocentric-trial (EudraCT:2021-006570-23;concluded)to perform additional FAPI over conventional-staging-flow-chart(including FDG), only non-surgical patients were included. Results on surgical cohort(n=50) were already published. Visual-positivity-criteria was defined forT&N as uptake higher than mediastinal-blood-pool(MBP). Agreement(%) between FAPI/FDG and histopathology was assessed byTNM-StagingAJCC8thEdition. PET-semiquantitative-parameters were measured forT&N: SUVmax,target-to-background-ratios(TBRs:SUVmaxLesion/SUVmeanBackground) using MBP, liver(L) and pulmonary-parenchyma(P), as backgrounds. FAPI-PET/CT visual&semiquantitative-performances(ROC-AUC forSUVmax and TBRs) were analysed per-patient and per-T&N-regions, compared to FDG. Transthoracic-needle-biopsy(TTNB) and endobronchial-ultrasound-guided-transbronchial-needle-aspiration(EBUS-TBNA)results were considered as standard-of-reference; without TTNB/EBUS-TBNA, radiological/clinical follow-up(FU;1year) were considered to validate PET results. ***Results:*** 63FAPI were performed out of 64patients enrolled(26May22-30Nov23). 3/63patients(mean-age:67y[52-83];M:F=8:5) did not undergo surgery and were included in this subgroup-analysis: 46%(6/13)T0N0-benign, 15%(2/13)T2N2, 15%(2/13)T3N2, 8%(1/13) T3N1(drop out from surgery), 8%(1/13)T1N3, 8%(1/13)T1N0(RT-treated). 92%of patients(12/13)underwentTTNB/EBUS-TBNA: biopsies results were present forT in 77%of patients(10/13) and for N in69%(9/13). Subsequent clinical-imaging-FU was used to validate PET results in the remaining 3/13-T patients and 4/13-N patients. Agreement(%) with histopathological-T&N-results(FAPIvsFDG) was: T-60%vs60%, N-95%vs75%; Cohen's k were also measured

0.29vs0.23 and 0.90vs0.51 respectively.Among the13 patients of the non-surgical cohort, 77%(10/13) presented 10lesions(T) which were examined(1Tfor each patient). 60%resulted benign(6/10): 83%(5/6)inflammatory nodules (3/5concordantFDG&FAPI-FP, 1/5discordantFDG-VN/FAPI-FP, 1/5concordantFDG&FAPI-VN) and 17%(1/6)mycotic infection-concordantFDG&FAPI-TN.40%(4/10) resulted malignant: 75%(3/4)adenocarcinoma(2/3concordantFDG&FAPI-TP, 1/3dicordantFDG-FN/FAPI-TP) and 25%(1/4) adeno-squamous-carcinoma(concordantFDG&FAPI-TP). The remaining 23%of patients(3/13) were judged concordant for T with the N-biopsy results(2/3adenocarcinoma,concordantFDG&FAPI-TP) or with radiological/clinical-FU(1/3absence of tumour,concordantFDG&FAPI-TN).Among the 69%of patients(9/13) with N-biopsies results, 56%of patients(5/9) showed lymph node metastases of adenocarcinoma(2/5N2 concordantFDG&FAPI-TP, 1/5discordantN2FDG-TP/N1FAPI-FN, 1/5N1concordantFDG&FAPI-TP, 1/5discordantN0FDG-FN/N3FAPI-TP)and 11%(1/9)metastases of adeno-squamous carcinoma(concordantFDG&FAPI-TP). 33%of patients(3/9) resulted negative for N-metastases:2/3concordantFDG&FAPI-TN, 1/3discordantFDG-FP/FAPI-TN. 31% of patients(4/13)did not undergo N-biopsies and were judged negative for metastases with radiological/clinical-FU(all concordantFDG&FAPI-TN).20 lymph-nodal stations were analysed(EBUS-TBNA): 55%(11/20) resulted positive for metastases. 82%(9/11)were adenocarcinoma metastases: 4/9concordantFDG&FAPI-TP, 1/9discordantFDG-TP/FAPI-FN, 4/9discordantFDG-FN/FAPI-TP. 18%(2/11)were adeno-squamous carcinoma metastases:2/2concordantFDG&FAPI-TP. 45%of lymph nodal station(9/20)resulted negative for metastases:8/9concordantFDG&FAPI-TN and 1/9discordantFDG-FP/FAPI-TN.AnalysesT-per-patient(n=13) and per-region(n=13),Visual(FAPIvsFDG): TN3vs4, FN0vs1, TP7vs5, FP3vs3; sensitivity100%vs83%, specificity50%vs57%, PPV70%vs63%, NPV100%vs80%, accuracy77%vs69%.AnalysesN-per-patient(n=13);Visual(FAPIvsFDG): TN7vs6, FN1vs1, TP5vs5, FP0vs1; sensitivity83%vs45%, specificity100%vs86%, PPV100%vs83%, NPV88%vs86%, accuracy92%vs85%.AnalysesN-per-region(n=20);Visual(FAPIvsFDG): TN9vs8, FN1vs4, TP10vs7, FP0vs1; sensitivity91%vs54%, specificity100%vs89%, PPV100%vs88%, NPV90%vs67%, accuracy95%vs75%.SUVmax, TBRs parameters performed similarly, better for N(AUCs p< 0.001 in all cases) than forT, not significantly different between the two tracers although slightly in favour of FAPI for N (N-AUCs FAPI>0.90 vs FDG>0.78); T-AUCs ranging from0.83 of FAPI-TBR-L to0.90 of FAPI-SUVmax). ***Conclusion:*** In a suspected/confirmed LC-non-surgical cohort, diagnostic performances forT&Nstaging were slightly in favour of FAPI in all cases (except for T-specificity).

OP-169

FAPI PET/CT response assessment in non-small cell lung cancer (NSCLC) patients: interim results of a prospective exploratory imaging study

A. Deleu, *T. Berghmans, M. Brandão, A. Goudsmit, K. Stathopoulos, A. Arçay Öztürk, C. Marin, L. Taraji, S. Nisar, Z. Wimana, S. Vercauteren, B. Vanderlinden, P. Flamen;*
Jules Bordet Institute - H.U.B., Brussels, BELGIUM.

Aim/Introduction: Fibroblast activation protein inhibitor (FAPI) PET/CT is emerging as promising pan-cancer molecular imaging technique.(1) In non-small cell lung cancer (NSCLC), FAPI outperforms [^{18}F]FDG PET/CT in mediastinal lymph node staging and the detection of brain, pleural, and bone metastases. (2) However, current evidence remains insufficient for clinical implementation of FAPI PET/CT, particularly regarding its potential for evaluating treatment response.Therefore, the aim of this interim analysis is to evaluate tumor response assessment with FAPI PET/CT, as secondary objective of a prospective study (ClinicalTrials.gov; NCT06107608). Moreover, we aimed to validate the immune PET response criteria in solid tumors (iPERCIST) using [^{18}F]FDG PET/CT in NSCLC. ***Materials and Methods:*** Stage III/IV NSCLC patients underwent both [^{68}Ga]Ga-FAPI-46 and [^{18}F]FDG PET/CT at baseline and after 2 cycles of (chemo)immunotherapy. Response was evaluated according to iRECIST. PET parameters were assessed quantitatively on both [^{18}F]FDG and FAPI PET/CT. A correlation analysis of the relative change in [^{18}F]FDG and FAPI PET parameters in the primary tumor after 2 treatment cycles was performed. The difference in the kinetics of FAPI PET imaging biomarkers between the iRECIST response categories was analyzed using an unpaired T-test. ***Results:*** In the 25 patients included so far, a high FAPI uptake was observed with a mean SUVmax of 14.8 in the primary lung tumor on the baseline FAPI PET/CT (range 5.9 - 23.4). After two treatment cycles, both iRECIST and iPERCIST evaluations were available for 17 patients, revealing a near-complete concordance in response categories (Table 1). Regarding the SUVmax changes of the primary tumor after 2 treatment cycles, a significant strong correlation was found between [^{18}F]FDG and FAPI PET/CT ($n = 15$; $r = 0.76$; $p=0.001$). There was a significant difference in relative FAPI ΔSUVmax between the iRECIST partial response (iPR; mean ΔSUVmax -49%) and stable disease (iSD; mean ΔSUVmax -3%) response categories ($p=0.001$). ***Conclusion:*** FAPI PET/CT demonstrates significant potential as a sensitive and reliable imaging modality for assessing treatment response in patients with NSCLC, as evidenced by this interim analysis showing a strong correlation with established response evaluation criteria. Additionally, the analysis highlights the validation of the iPERCIST response criteria in this small cohort of NSCLC patients. Further inclusion is needed to confirm these findings in a larger cohort of patients. ***References:*** 1.Kratochwil C et al. (68)Ga-FAPI PET/CT:Tracer Uptake in 28 Different Kinds of Cancer. J Nucl Med.2019;60(6):801-5. 2.Deleu AL et al. FAPI PET in the Management of Lung Tumors. Semin Nucl Med.2025;55(2):202-11.

OP-170

Imaging tumor-infiltrating CD8+ T-cells upon neo-adjuvant treatment with aPD-L1 in non-small cell lung cancer patients

E. Van Genugten[1], *B. Piet*[1], *I. A. E. van der Hoorn*[1], *K. Schmiedehausen*[2], *F. Ciompi*[1], *C. Jacobs*[1], *M. M. van den Heuvel*[1], *J. J. M. de Vries*[1], *E. H. J. G. Aarntzen*[1];
[1]*Radboud UMC, Nijmegen, NETHERLANDS,* [2]*ImaginAb, Calabasas, CA, UNITED STATES OF AMERICA.*

Aim/Introduction: Presence, localisation and function of CD8 T-cells has prognostic and predictive impact in numerous cancer types[1]. [89Zr]Zr-crefmirlimab berdoxam[2] targeting human CD8a has been introduced to non-invasively detect and monitor CD8 T-cell tumor infiltration[3]. Taking advantage of the neoadjuvant setting, we characterized [89Zr]Zr-crefmirlimab berdoxam as imaging biomarker in early-stage non-small lung cancer patients(NSCLC) upon anti-PD-L1 immune therapy. ***Materials and Methods:*** Eight early-stage NSCLC patients enrolled in a prospective study(NCT03853187) underwent PET/CT imaging 24h p.i. of [89Zr]Zr-crefmirlimab berdoxam(1.5mg protein dose, 37±10%MBq radioactivity dose) and CT-perfusion imaging 4 weeks after start of anti-PD-L1 immune therapy and within 3 days prior to curative resection. Standardized uptake values(SUV) were determined on tumor, tumor-draining lymph nodes(TDLN), distant lymph nodes(LN), spleen and bone marrow. CT images were coregistered and analyzed with the help of a perfusion model to extract hemodynamic parameters of the tumor. Whole-tumor sections were used for autoradiography while consecutive tissue slides were stained immune histochemical(IHC) for CD8 and quantified using Hover-Net algorithm[4] and density maps. A multiplex IHC panel to simultaneously detect multiple lymphocyte populations developed in-house[5] and CODEX[6] stained tissue microarrays were used to characterize tumor-infiltrating CD8 cell

populations. ***Results:*** Tracer uptake in T1b-2bN0-1M0 resectable NSCLC tumors ranged from SUVmean 0.7-2.7 while uptake in lymphoid structures such as TDLN SUVmean exceeded that of the tumor, ranging 1.5-12.3. IHC revealed prominence of different subsets of CD8 cells in the tumor and TDLN, suggesting different subsets contributing to the PET signal. CT-perfusion of the tumor revealed no limitations in [89Zr]Zr-crefmirlimab uptake due to perfusion or permeability, and autoradiography demonstrated good spatial correlation between signal and localization of CD8 lymphocytes. Except for one subject(DON430) with exceptional high CD8 density(2604 cells/mm2) and small tumor(0.5mL), tracer uptake correlates with IHC CD8 cell densities. Tumor SUV was associated with proportion of CD103-negative CD8 cells, concluding that non-tissue resident CD8 cells contribute most to tumor-related PET-signal. ***Conclusion:*** [89Zr]Zr-crefmirlimab berdoxam tumor uptake colocalizes and correlates with CD8 cell density and is independent of perfusion, but high cell density and partial volume effect may have impact on quantification. Tracer uptake in the tumor is determined by non-tissue resident CD8 cells, suggesting that distant labeling and subsequent infiltration is a dominant mechanism of tracer accumulation. Further analysis of CD8 distribution patterns beyond the tumor will help increase our understanding of the complex anti-tumor immune response. ***References:*** [1]Bruni, NatRevCancer,2020[2] Farwell, JNuclMed2022[3]Krekorian, Theranostics2019[4] Graham, MedImageAnal2019[5]Gorris, JVisExp2023[6]Black, NatureProtocols2021

OP-171

Integrating PET/CT Radiomics from Primary Tumors and Metastatic Lymph Nodes for Enhanced Survival Prediction in NSCLC Patients Undergoing Radical Radiotherapy

K. Albattat;
Cardiff University, Cardiff, UNITED KINGDOM.

Aim/Introduction: Lymph node (LN) metastasis is a critical prognostic factor in non-small cell lung cancer (NSCLC), yet survival prediction models often rely solely on primary tumor characteristics [1]. This study aims to determine whether integrating radiomic features from metastatic lymph nodes with those from the primary tumor can significantly improve survival prediction in NSCLC patients undergoing radical radiotherapy. We further evaluated whether incorporating lymph node burden (LN station count) and spatial spread (average nodal distance from the tumor) could enhance prognostic performance. We hypothesized that a combined radiomic model would outperform models based on primary tumor or lymph node features alone. ***Materials and Methods:*** This retrospective study included 147 NSCLC patients with mediastinal or hilar LN metastases. Three cohorts were analysed: (1) Primary Tumour Cohort (n=147), (2) LN Cohort (224 metastatic LNs), and (3) Combined Cohort (n=294 lesions). Patients were stratified into training (70%) and test (30%) sets while maintaining event/non-event balance to reduce validation bias. Radiomic features were extracted from PET/CT images using standardised lesion segmentation protocols. LASSO regression with 10-fold cross-validation was applied separately to each cohort's training set to select predictive features for four survival endpoints: overall survival (OS), progression-free survival (PFS), 2-year OS, and 2-year PFS. Features selected in at least 3 of the 4 LASSO runs were retained. Cox regression was used for OS and PFS, and logistic regression for 2-year outcomes. ***Results:*** Calibration curves indicated the primary tumor cohort had the best alignment with the reference line, suggesting reliable probability estimates. The LN cohort showed the greatest deviation, while the combined cohort had reasonable calibration with greater fluctuation at higher probabilities. Cox regression analysis showed the combined model yielded the best overall fit ($\chi^2 = 30.981$, $p = 0.002$), significantly improving survival prediction. The primary-only model was marginally significant ($p = 0.018$), and the LN-only model was not significant ($p = 0.077$). ***Conclusion:*** Combining radiomic features from primary tumors and metastatic lymph nodes enhances the predictive accuracy of survival models in NSCLC. Despite slightly better calibration in the primary-only model, the combined approach provides a more comprehensive, statistically robust, and clinically valuable prediction of patient outcomes, supporting its potential integration into personalized treatment planning ***References:*** [1] Hellwig D, et al. "Lymph node staging in non-small cell lung cancer using FDG-PET: evidence for improved diagnostic accuracy and impact on patient management." J Thorac Dis. 2014;6(6):453-461.

OP-172

All you need is Δ SUVmax! Response prediction of preoperative immune checkpoint inhibition by dual time point FDG PET/CT in patients with resectable NSCLC in a prospective setting.

H. Hautzel[1], *M. Wiesweg*[2], *T. Plönes*[3,4], *D. Theegarten*[5], *D. Kersting*[1], *C. Aigner*[3,6], *K. Herrmann*[1], *M. Schuler*[2];
[1]*Department of Nuclear Medicine, University Hospital Essen, University Duisburg - Essen, Essen, GERMANY,* [2]*Department of Medical Oncology, University Hospital Essen, University Duisburg - Essen, Essen, GERMANY,* [3]*Department of Thoracic Surgery, University Hospital Essen, University Duisburg - Essen, Essen, GERMANY,* [4]*Department of Surgery, Division of Thoracic Surgery, University Hospital Carl Gustav Carus, Technical University Dresden, Dresden, GERMANY,* [5]*Institute for Pathology, University Hospital Essen, University Duisburg - Essen, Essen, GERMANY,* [6]*General Hospital Vienna, Department of Thoracic Surgery, Medical University Vienna, Vienna, AUSTRIA.*

Aim/Introduction: Immune checkpoint inhibition (ICI) is increasingly used as neoadjuvance prior to surgery in resectable non-small-cell-lung-cancer (NSCLC). A prospective, randomized, multicenter study, NEOpredict-Lung, explores the potential of short-term preoperative ICI with nivolumab (anti PD-1 antibody) with/without relatlimab (anti-LAG-3 antibody) in patients with NSCLC stages I B, II or III A (1). Aim of the present analysis was to explore various parameters derived from two subsequent ^{18}FDG PET/CT scans for the non-invasive prediction of an ICI induced major pathological response. ***Materials and Methods:*** NEOpredict-Lung (NCT04205552) required imaging-based staging at initial NSCLC diagnosis and immediately prior to surgery. ^{18}FDG PET/CT at baseline (PET1) and pre-surgically (PET2) after two cycles of ICI was prospectively included at our center. The pathological response rates (IASLC criteria) in the resected tumors served as reference standard. A major pathological response (MPR) with viable tumour cells ≤10% was regarded as clinically relevant response to ICI (1). In that trial, PERCIST1.0 and RECIST1.1 were used to separate ICI responders from non-responders. Here, the predictive value of additional PET-derived parameters were tested by ROC analyses: single PET/CT scan variables (PET1-SUVmax, PET1-MTV, PET1-TLG, PET2-SUVmax, PET2-MTV, PET2-TLG) and comparative parameters (ΔSUVmax in %, ΔMTV in %, ΔTLG in %). The area-under-the-curves (AUC) were compared to those of PERCIST1.0 and RECIST1.1. ***Results:*** 31 patients with baseline ^{18}FDG PET/CT (median 22 days before ICI inititation) were included. The second ^{18}FDG PET/CT was performed at a median of 4 days before surgery. MPR was achieved in 8/31 patients. ROC of PERCIST1.0 revealed a high AUC of 0.913 while the ROC of RECIST1.1 demonstrated an AUC of 0.541. Taking that PERCIST1.0 AUC as cutting point which indicates a comparable or better prediction capability all single PET/CT parameters (from PET1-SUVmax: AUC 0.408 to PET2-SUVmax: AUC 0.877) and the dual time point PET parameter ΔMTV (AUC 0.85) failed. However, the dual time point PET parameters ΔTLG (AUC 0.931) performed non-inferior and ΔSUVmax (AUC 0.983) better than PERCIST1.0. ***Conclusion:*** ^{18}FDG

PET/CT PERCIST1.0 is recommended in scientific trials as a robust strategy for non-invasive response prediction. This holds true in neoadjuvant ICI before NSCLC resection as well. However, from our prospective data one might infer that the less elaborate and faster to achieve parameter ΔSUVmax is at least comparable in this specific setting and therefore qualifies as straightforward analytical approach in the clinical routine setting of neoadjuvant ICI and NSCLC. ***References:*** Schuler M et al.: Nat Med. 2024. doi: 10.1038/s41591-024-02965-0

OP-173

A Three-Factor Model for Clinical Decision-making in NSCLC Patients treated with Tyrosine Kinase Inhibitors

F. Orlhac[1], *N. Hovhannisyan-Baghdasarian*[1], *H. Fokem-Fosso*[1], *M. Luporsi*[1], *C. Nioche*[1], *H. Tissot*[1,2], *G. Lemoudda*[1], *F. Beltgens*[3], *D. Bruyat*[4], *E. Dansin*[5], *P. Demontrond*[6], *P. Dubray-Longeras*[7], *R. Gervais*[6], *A. Lagrange*[8], *A. Madroszyk*[4], *M. Pérol*[9], *X. Quantin*[10], *C. Quere*[4], *P. Saintigny*[9], *R. Seban*[1,2], *J. Simonnet*[11], *Q. Thomas*[10], *A. Livartowski*[12], *P. Salamoun-Feghali*[12], *N. Hegarat*[12], *N. Girard*[12], *I. Buvat*[1];
[1]*Institut Curie, Université PSL, Inserm, U1288, LITO, Orsay, FRANCE,* [2]*Institut Curie, Department of Nuclear Medicine, Paris-St Cloud, FRANCE,* [3]*Centre Georges-François Leclerc, Department of Anatomopathology, Dijon, FRANCE,* [4]*Institut Paoli-Calmettes, Department of Oncology, Marseille, FRANCE,* [5]*Centre Oscar Lambret, Department of Oncology, Lille, FRANCE,* [6]*Centre François Baclesse, Department of Oncology, Caen, FRANCE,* [7]*Centre Jean Perrin, Department of Oncology, Clermont-Ferrand, FRANCE,* [8]*Centre Georges-François Leclerc, Department of Oncology, Dijon, FRANCE,* [9]*Centre Léon Bérard, Department of Oncology, Lyon, FRANCE,* [10]*Institut du Cancer, Department of Oncology, Montpellier, FRANCE,* [11]*Centre Bergonié, Department of Oncology, Bordeaux, FRANCE,* [12]*Institut Curie, Institut du Thorax Curie-Montsouris, Paris, FRANCE.*

Aim/Introduction: To develop a clinico-radiomic signature to predict treatment duration under tyrosine kinase inhibitors (TKIs) in non-small cell lung cancer (NSCLC) patients. ***Materials and Methods:*** Pre-treatment [18F]FDG-PET/CT scans from 184 advanced NSCLC patients treated with TKIs before 2021 were retrospectively collected in 9 centers (training cohort), along with 57 patients treated from 2021 onward (testing cohort). All lesions were segmented by an expert using a 4 SUV threshold. The brain was segmented using TotalSegmentator on the CT, and copied onto the PET. Using LIFEx (www.lifexsoft.org, v7.8.0) [1], four PET features were extracted: Total Metabolic Tumor Volume (TMTV), the largest distance between two lesions (Dmax), the maximum uptake across all lesions (maxSUVmax), and the whole-brain average FDG uptake ($SUVmean_{Brain}$). For the training cohort, a conditional inference tree [2] was constructed to predict treatment duration under TKIs using the PET-derived features, patient age, gender, BMI, and the presence of an EGFR exon 19 mutation. Model performance was evaluated using Kaplan-Meier analysis and log-rank tests based on TKI treatment duration. ***Results:*** In the training cohort, the decision tree identified three key variables: $SUVmean_{Brain}$, EGFR exon 19 mutation status, and maxSUVmax. Patients were stratified into two groups (log-rank test: p<0.0001): low-risk group (n=42) - characterized by high $SUVmean_{Brain}$ (>5.9 SUV), the presence of an EGFR exon 19 mutation, and a maxSUVmax less than 18.3 SUV units, versus high-risk group (n=142), corresponding to all other patients. At 1 year, 93% of low-risk patients remained on TKI treatment compared to 64% of high-risk patients; at 3 years, these rates were 58% and 18%, respectively. In the testing cohort, the model identified 12 low-risk patients and 45 high-risk patients, with a significant difference in treatment duration curves between the two groups (log-rank test: p=0.019): 92% remained on TKI therapy at 1 year in the low-risk group, compared to 66% in the high-risk group. No significant association was found between $SUVmean_{Brain}$ values and the presence of brain metastases (Wilcoxon test: p=0.631 and 0.546, respectively). ***Conclusion:*** The three-factor decision tree developed and subsequently validated on a testing cohort enables identification of patients likely to benefit from TKI. This signature requires further validation on a larger scale and deeper understanding of the predictive value of $SUVmean_{Brain}$. It could help to guide treatment intensification strategies for patients classified as high-risk. ***References:*** [1] Nioche et al. Cancer Res 2018. [2] Hothorn & Zeileis J Mach Learn Res 2015.

OP-174

PET/CT Metabolic Parameters Correlation of Invasive Lung Adenocarcinoma Histological Grading to Optimize Surgical Decisions

X. Shen*, T. Chen, J. Wen, J. Deng, Y. She, D. Xie, C. Chen; Shanghai Pulmonary Hospital, Shanghai, CHINA.*

Aim/Introduction: The International Association for the Study of Lung Cancer (IASLC) has proposed a grading system for invasive lung adenocarcinoma which has been validated as being a reliable prognostic biomarker. However, given the reliance of this grading system on comprehensive histological evaluation, preoperative grading remains indeterminate. In the present study, we examined the substantial relationship between positron emission tomography/computed tomography (PET/CT) metabolic parameters and the IASLC proposed grading system, while also investigating its potential clinical utility. ***Materials and Methods:*** This study included a total of 1,837 patients who underwent preoperative PET/CT scan and complete resection for clinical stage IA lung adenocarcinoma. A logistic regression model was implemented to estimate the odds ratios (ORs) and 95% confidence intervals (CIs) for clinical and pathological variables. Furthermore, we employed receiver operating characteristic curve analysis to ascertain optimal cutoff values for PET/CT metabolic parameters. Survival analysis was conducted using the Kaplan-Meier method. ***Results:*** The multivariate logistic regression analysis of Grade 3 tumors revealed that male gender, pure solid radiological types, and maximum standardized uptake value (SUVmax) were significant predictive factors (p<.001 for all). The interaction between radiological type and SUVmax was significant (OR 1.31, 95% CI 1.27-1.34, p<.001), indicating that the optimal cutoff value of SUVmax for predicting grade 3 tumors may vary among subsolid and solid nodules. The optimal cutoff value for grade 3 tumor prediction was determined to be 3.35 for the entire cohort, 4.25 for pure solid nodules, and 2.30 for subsolid nodules, with area under the curve values of 0.852, 0.791, and 0.795, respectively. The violin plots demonstrated that the proportion of high-grade patterns in Grade3 lung adenocarcinoma was notably higher in pure solid nodules than in subsolid nodules, which partly explains the potential reason for the different prediction cutoff values. Survival analysis revealed that sublobar resection was associated with a markedly worse prognosis than lobectomy for patients with pure solid nodules and an SUVmax greater than 4.25 (p<.01 for both recurrence-free survival and overall survival). Conversely, the survival rate of sublobar resection and lobectomy was comparable in the entire cohort and subsolid nodules (p>.05 for all). ***Conclusion:*** The SUVmax harbors the potential to predict the histological grade, and the predicted cutoff value varies by radiological nodule type. Preoperative prediction of histologic type facilitates individualized surgical decision-making for clinical stage IA invasive lung adenocarcinoma. The clinical versatility of PET/CT metabolic parameter prediction contributes to further validation for replication.

OP-175

Added Value of Zero-Time Echo (ZTE) Sequence in Evaluating ^{18}F-FDG Positive Pulmonary Nodules on ^{18}F-FDG PET/MRI in Oncologic Patients: Preliminary Findings

S. Gulbahar Ates, *U. Aydos, S. B. Kucukali, S. Demir, U. O. Akdemir, L. O. Atay;*
Gazi University Faculty of Medicine, Ankara, TÜRKIYE.

Aim/Introduction: This study aimed to evaluate the effectiveness of zero-time echo (ZTE), T1-weighted water (T1_W), in-phase (T1_IP), and out-of-phase (T1_OP) MR sequences in identifying anatomical correlates of FDG-avid pulmonary nodules, and to optimize PET/MRI protocol for lung nodules. ***Materials and Methods:*** Patients who underwent FDG PET/MRI for oncologic indications, had either simultaneous thoracic PET/CT or a diagnostic CT within one month, and had at least one FDG-avid pulmonary nodule were included. The number of FDG-avid nodules, the localization, SUVmax, detectability of nodules, and sizes of the two largest and the smallest nodules on each sequence and CT were recorded. The presence and size of nodules on CT were accepted as the reference. The detection rates of nodules across sequences were compared using Cochran's Q and McNemar tests, while nodule sizes were compared using Friedman and Wilcoxon tests. The relationship between nodule detectability on MR sequences and their location or SUVmax was evaluated using Mann-Whitney U test. ***Results:*** 112 nodules from 65 patients (42 males (64.6%), 23 females (35.4%); median age 63 (53.5-68.5)) were included. The mean number of FDG-avid nodules per patient was 2.9±3.2. The median size of nodules on CT was 8 mm (3-27). Nodule detection rates for MR sequences were calculated as 33.9% for T1_W, 64.3% for T1_IP, 73.2% for T1_OP, and 97.3% for ZTE ($p<0.001$). ZTE demonstrated a significantly higher detection rate than other T1-weighted MR sequences ($p<0.001$). Among the three nodules not visualized on ZTE, two were ≤4 mm, and one, despite being 13 mm, was perihilar and indistinguishable from bronchovascular structures. When the T1-weighted sequences were compared with each other, the detection rate of T1_OP was significantly higher than the others, and T1_IP was significantly superior to T1_W ($p<0.05$). For nodules ≤ 4 mm in size, the detection rates were 5.9% for T1_W, 23.5% for T1_IP, 41.2% for T1_OP, and 88% for ZTE. When nodule sizes measured on MR sequences were compared to CT, no significant difference was observed between ZTE and CT ($p=0.083$), while T1 sequences underestimated nodule sizes ($p<0.001$). SUVmax of nodules detectable on T1 sequences were significantly higher than those of undetectable ones($p<0.001$). No significant association was found between nodule localization and detectability ($p>0.05$). ***Conclusion:*** The ZTE sequence outperforms other T1-weighted MR sequences in detecting FDG-avid pulmonary nodules on PET/MRI, with detection rates similar to CT, thereby reducing the need for additional thoracic CT scans.

507

Sunday, October 5, 2025, 15:00 - 16:30
Room 212

M2M Track - TROP Session - Radiopharmaceutical Sciences + Translational Molecular Imaging & Therapy Committee: Prostate Cancer: New Tracers

OP-176

Preclinical development of novel AR-targeted PET radioactive probe in prostate cancer

S. Lin, *B. Gu, X. Wang, S. Song;*
Fudan University Shanghai Cancer Center, Shanghai, CHINA.

Aim/Introduction: Prostate cancer is an androgen-dependent malignancy. Therefore, patients with prostate cancer receive endocrine therapy as a routine treatment. However, the heterogeneous expression of androgen receptor (AR) in prostate cancer patients presents significant challenges for the selection of appropriate anti-androgen therapies. Thus, in this study, we aimed to develop AR-targeted ^{68}Ga-IsosilybinB-FZAR PET radiotracer for detecting AR expression in prostate cancer. ***Materials and Methods:*** An AR-targeted radioactive probe ^{68}Ga-IsosilybinB-FZAR was synthesized, and the radiochemical purity and stability were evaluated by radio-HPLC. The positive or negative expressing-AR cell lines were screened by western blot assay. The targeting performance of ^{68}Ga-IsosilybinB-FZAR was characterized in vitro and in vivo. PET/CT imaging of tumor-bearing mouse models was used to assess the distribution and metabolism of ^{68}Ga-IsosilybinB-FZAR in vivo. Tumor autoradiography and immunohistochemistry were employed to validate the expression of AR in tumor tissues. ***Results:*** The radiochemical purity of ^{68}Ga-IsosilybinB-FZAR was more than 95%, and exhibited high stability in saline and fetal bovine serum for 2 h. IsosilybinB-FZAR showed a high binding affinity to AR with an excellent K_d value of 23.34 nM. PET/CT imaging of the tumor-bearing mice showed that ^{68}Ga-IsosilybinB-FZAR could specifically aggregate in AR-positive LNCaP tumors (0.5 h: 8.10 ± 0.44 %ID/g; 1 h: 6.83 ± 0.55 %ID/g; 2 h: 5.80 ± 0.46%ID/g) and 22RV1 tumors (0.5 h: 5.33 ± 0.91 %ID/g; 1 h: 3.23 ± 0.95 %ID/g; 2 h: 2.13 ±0.47 %ID/g), whereas the AR-negative PC-3 tumors revealed significantly lower uptake of ^{68}Ga-IsosilybinB-FZAR (0.5 h: 1.50 ± 0.20 %ID/g; 1 h: 0.20 ± 0.17 %ID/g; 2 h: 0.50 ± 0.36 %ID/g, P all < 0.05). Furthermore, ^{68}Ga-IsosilybinB-FZAR was mainly metabolized through liver and urinary system in vivo. Moreover, immunochemistry demonstrated the high expression of AR for LNCaP tumor, intermediate expression for 22RV1 tumor, and negative expression for PC-3 tumor, which in consistent with the results of the tumor autoradiography. The results of H&E staining confirmed the biocompatibility of ^{68}Ga-IsosilybinB-FZAR in vivo. ***Conclusion:*** As the first ^{68}Ga-labelled AR inhibitor, ^{68}Ga-IsosilybinB-FZAR exhibited high affinity and strong specificity to AR-positive cells, suggesting it's a promising PET imaging agent for the management of patients with prostate cancer.

OP-177

Uncovering the Mechanisms of Action of 212Pb-based PSMA-targeting Radioligand Therapies

F. Liu, *A. Prior, M. E. Monterosso, D. Boucher, S. Shakti, K. Li, A. Sydes, A. Jones, J. Hesse, C. Kim, A. Horsfall, K. Kuan, W. Tieu, S. Rose, A. Karmann, S. Puttick, G. Li, T. Kryza;*
AdvanCell Pty Ltd, Brisbane, AUSTRALIA.

Aim/Introduction: Prostate-specific membrane antigen (PSMA)-targeted radioligand therapy (RLT) with lutetium-177 (^{177}Lu), a beta-emitter, has been clinically proven to be efficacious for the treatment of prostate cancer (PC). Although emerging clinical data indicate better efficacy with alpha-emitters, the toxicities associated with actinium-225 (^{225}Ac) may limit its broad application, and application in earlier lines of treatment. Lead-212 (^{212}Pb), is a promising isotope for targeted alpha therapy with high linear energy transfer, a half-life of 10.6 hours, and a simple decay scheme. These properties promote efficient killing of PSMA$^+$ PC cells while limiting off-target toxicities. Here we present combined in vitro and in vivo models, omics approaches, and functional assays elucidating the intrinsic cellular mechanisms of response to ^{212}Pb-PSMA RLT. ***Materials and Methods:*** ^{212}Pb-ADVC001, a novel ^{212}Pb-based PSMA-targeting RLT currently in Phase I/II clinical development (NCT05720130) for the treatment of metastatic castration-resistant prostate cancer (mCRPC), was used as ^{212}Pb RLT. The cytotoxic activity in PC cell lines was measured by cell viability assays and in vivo studies. The kinetic mechanisms associated with ^{212}Pb-ADVC001 mediated cell-death were assessed in vitro and ex

vivo using transcriptomics and proteomics approaches, and their impact on the PC cell cycle by flow cytometry. ***Results:*** ^{212}Pb-ADVC001 displayed potent cytotoxic activity with an average EC50 of 2.7, 7.2 and 3.3 kBq/mL in PC cell lines PC-3-PIP (PSMA^{high}), C4-2 (PSMA^{int}) and LNCaP (PSMA^{int}), respectively. Transcriptomic analysis of in vitro treated PC cells and proteomic analysis of tumors harvested longitudinally revealed multiple mechanisms of action involving DNA damage, cell cycle arrest and cell death, and immune response modulation. In vitro cell cycle experiment further confirmed that ^{212}Pb-ADVC001 caused significant DNA damage, and reduced DNA content in the S-phase of the cell cycle with a concomitant increase in the G1 and G2/M-phase arrest compared to ^{177}Lu-PSMA-I&T ($p<0.05$). ***Conclusion:*** Transcriptomic and proteomic analyses indicate multiple ^{212}Pb-PSMA treatment mechanisms of action collectively resulting in effective cancer cell kill. Mechanistic studies furthered the understanding of PC radiobiology and cellular responses to beta- and alpha-based RLT with the identification of a cell cycle arrest in PC specifically induced by ^{212}Pb-PSMA.

OP-178

First-in-human study of novel PSMA-targeted agents, [^{68}Ga]Ga-AAZTA-PSMA-093 and [^{68}Ga]Ga-AAZTA-NI-PSMA-093: dosimetry and initial evaluation in prostate cancer patients

G. Wang[1], *Y. Lai*[1], *W. Jin*[2], *Y. Luo*[2], *H. F. Kung*[3], *L. Zhu*[2], *W. Miao*[1];
[1]*the First Affiliated Hospital, Fujian Medical University, Fuzhou, CHINA,* [2]*Beijing Normal University, Beijing, CHINA,* [3]*University of Pennsylvania, Philadelphia, PA, UNITED STATES OF AMERICA.*

Aim/Introduction: Our team previously designed two novel PSMA-targeted compounds, AAZTA-PSMA-093 and AAZTA-NI-PSMA-093 (incorporating a hypoxia-sensitive nitroimidazole[NI]-moiety). Preclinical studies had confirmed their favorable tumor uptake and retention characteristics. This prospective trial aimed to further evaluate the clinical application value of both agents in prostate cancer (PCa) patients. ***Materials and Methods:*** A total of 60 patients were enrolled in the study, 30 patients underwent a head-to-head comparison between [^{68}Ga]Ga-AAZTA-PSMA-093 and [^{68}Ga]Ga-PSMA-11/[^{68}Ga]Ga-PSMA-617 PET/CT, while another 30 patients were compared between [^{68}Ga]Ga-AAZTA-NI-PSMA-093 and [^{68}Ga]Ga-AAZTA-PSMA-093 PET/CT. The number of tumors and the maximum standardized uptake value (SUV_{max}) for tumors were measured and recorded. Besides, we calculated the SUV_{max} differences of (ΔSUV_{max}) between [^{68}Ga]Ga-AAZTA-NI-PSMA-093 minus [^{68}Ga]Ga-AAZTA-PSMA-093 PET/CT for further analysis. ***Results:*** The patients tolerated [^{68}Ga]Ga-PSMA PET/CT scans well. Both [^{68}Ga]Ga-AAZTA-PSMA-093 and [^{68}Ga]Ga-AAZTA-NI-PSMA-093 showed human biodistribution similar to other PSMA-targeting radiopharmaceuticals. [^{68}Ga]Ga-AAZTA-PSMA-093 PET/CT exhibited higher tumor uptake compared to [^{68}Ga]Ga-PSMA-11 (SUV_{max}: 22.2 ± 10.8 vs. 20.4 ± 14.8, P = 0.025) and [^{68}Ga]Ga-PSMA-617 PET/CT (SUV_{max}: 20.1 ± 12.7 vs. 10.8 ± 8.7, P < 0.001), with a comparable detected number of tumors. [^{68}Ga]Ga-AAZTA-NI-PSMA-093 showed further improved tumor uptake relative to [^{68}Ga]Ga-AAZTA-PSMA-093 PET/CT (SUV_{max}: 17.8 ± 14.0 vs. 16.3 ± 11.5, P = 0.009), particularly in large-volume intraprostatic lesions (ΔSUV_{max} for tumor with diameter of ≥ 2.5 cm and < 2.5 cm, median 0.7 [IQR -2.2 - 8.0] vs. median -2.7 [IQR -5.4 - -0.4], P = 0.039) and primary PCa with high Gleason Score (Gleason Score ≥ 8 and < 8, median 1.1 [IQR -2.5 - 7.3] vs. median -2.4 [IQR -5.9 - -0.1], P = 0.041). However, within the limited sample size, there was no statistically significant difference in prostate cancer lesion detection rates between the two agents. ***Conclusion:*** Both AAZTA-PSMA-093 and AAZTA-NI-PSMA-093 represent promising PSMA-targeted radiopharmaceuticals with high clinical potential. The uptake of [^{68}Ga]Ga-AAZTA-NI-PSMA-093 in high tumor burden prostate cancer and metastatic lesions than that of [^{68}Ga]Ga-AAZTA-PSMA-093 may be attributed to its hypoxia-responsive moiety, which may provide new direction for precision imaging and therapy of PCa in the future. Further research is required to validate these findings.

OP-179

Preclinical Assessment of Novel [^{99m}Tc][Tc(N)(PNP3OH)]$^{2+}$-labelled PSMA inhibitor with Improved Pharmacokinetics for Enhanced Prostate Cancer Detection

C. Bolzati[1], *J. Kleynhans*[2], *C. Gobbi*[1], *I. Hawala*[3], *S. Ghiani*[4], *A. Maiocchi*[5], *F. Cleeren*[2], *N. Salvarese*[1];
[1]*Institute of Condensed Matter Chemistry and Energy Technologies ICMATE-CNR, PADOVA, ITALY,* [2]*Laboratory for Radiopharmaceutical Research, Department of Pharmaceutical and Pharmacological Sciences, KU Leuven, Leuven, BELGIUM,* [3]*Dipartimento di Biotecnologie Molecolari e Scienze per la salute, Centro di Imaging Molecolare, Università degli Studi di Torino, Torino, ITALY,* [4]*Bracco Research Centre, Bracco Imaging SpA, Torino, ITALY,* [5]*Bracco SpA, Milano, ITALY.*

Aim/Introduction: Prostate-specific membrane antigen (PSMA) is an optimal biotarget for prostate cancer (PCa) diagnosis and therapy due to its overexpression in PCa lesions. PSMA also appears to play an important role in triple negative breast cancer and renal cancer, opening the possibility of broadening the application to non-prostatic tumors. Although ^{68}Ga-labelled small molecular weight PSMA inhibitors (PSMAi) have proved high specificity in PCa detection by PET, limited availability and high cost of PET equipment hinder their use in routine clinical practice, especially in remote areas. Recently, several ^{99m}Tc-labelled PSMAi derivatives have been evaluated as more cost-effective analogues of ^{68}Ga- or ^{111}In-tracers for PCa diagnosis. Although these offer advantages over ^{111}In-PSMAi, none outperform the corresponding PET agents. Drawbacks are due to their kidney accumulation and unfavourable clearance from hepatobiliary and intestinal tracts. However, the low-cost and easily available SPECT technique, which predominantly utilizes technetium-99m, could provide a viable alternative for large-scale clinical implementation. Exploiting the advantages of the [TcN(PNP)]-system (PNP=bisphosphino-amine), our aim is to develop a novel ^{99m}Tc-labelled PSMAi with enhanced pharmacological/pharmacokinetic properties to improve lesion detection in primary tumours and metastases during SPECT imaging and surgical procedures. ***Materials and Methods:*** [^{99m}Tc][Tc(N)(PNP3OH)]$^{2+}$-labelled PSMAi (PNP3OH=N,Nbis[(di-hydroxymethylphosphinoethyl)]methoxyethylamine), ^{99m}Tc1 (WO2018109164A1), was prepared, preclinically evaluated, and compared with the clinically tested [^{99m}Tc][Tc-HYNIC]-iPSMA. Log $D_{7.4}$, stability, and target affinity in PSMA(+) (PC3-PIP, LNCaP) and PSMA(-) PC3 cell lines were assessed. Biodistribution and imaging studies of ^{99m}Tc1 were accomplished in PC3-PIP/PC3 tumour-bearing mice. ***Results:*** ^{99m}Tc1 was efficiently prepared with RCP>95% (molar activity 30 GBq/μmol). The compound showed low lipophilicity (^{99m}Tc1 $LogD_{7.4}$ = -2.38), minimal plasma proteins binding, and high in vivo stability. Internalization in PSMA(+) cells was high (13.70±1.0 - 12.49±0.5 %/10^6 cells). Uptake was reduced by lowering the temperature and also effectively blocked with H3NSCys-PSMAi excess. Biodistribution studies display a high and specific tumor uptake of ^{99m}Tc1, the positive-to-negative ratio was 4.37 vs 2.87 of [^{99m}Tc][Tc-HYNIC]-iPSMA. The clearance from the non-target organ was faster for ^{99m}Tc1 than [^{99m}Tc][Tc-HYNIC]-iPSMA, and accordingly a higher target-to-background ratio was reached. No uptake was evident in spleen, and, more importantly, at 1 h after injection a negligible kidneys accumulation was found, which became undetectable at 4 h. ***Conclusion:*** The high tumour uptake and unprecedent clearance of ^{99m}Tc1 from blood and non-target tissues make it a promising new radioligand for PSMA SPECT imaging and RGS. Acknowledgments to Bracco-SpA, AIRC (IG-2020, ID-24528) and Fonds Wetenschappelijk Onderzoek - Vlaanderen (Post-doc grant 1226524 N-7029).

OP-180

Mouse digital twin for [^{177}Lu]Lu-PSMA10.1 to enable individualised therapy.

G. Costa[1,2], *E. Yousefzadeh-Nowshahr*[1], *V. Vasic*[1], *B. Sun*[3], *L. Nagel*[3], *A. Wurzer*[3], *F. Schilling*[3], *A. Beer*[2], *W. Weber*[3], *S. Kossatz*[3], *G. Glatting*[1,2];
[1]*Uni Ulm, Ulm, GERMANY,* [2]*Uniklinik Ulm, Ulm, GERMANY,* [3]*Technische Universität München, Munich, GERMANY.*

Aim/Introduction: Although prostate-specific membrane antigen (PSMA) labelled with Lutetium-177 (^{177}Lu) is a well-established therapy for prostate cancer, the variability in the effectiveness of treatments is not fully understood. Exploring the pharmacokinetics through a physiologically based pharmacokinetic (PBPK) model may assist in understanding this variation which could, help individualising the therapy. Among different PSMA ligands, the radiohybrid rhPSMA-10.1 has the advantage of identical pharmacokinetics when used for PET imaging as [^{18}F]-^{nat}Lu-rhPSMA-10.1 and for therapy as ^{nat}F-[^{177}Lu]rhPSMA-10.1. The ligand also shows low kidney uptake and fast blood pool excretion while maintaining high tumour accumulation. This work aims to develop a digital twin with PBPK models and define an optimal SPECT imaging schedule for imaging-based dosimetry for mice after rhPSMA-10.1 infusion. ***Materials and Methods:*** The digital twins were developed by adapting an available human PBPK model [1] and fitting its parameters (e.g. receptor densities, blood flows, glomerular filtration rate, etc.) to biodistribution studies from 5 mice that received [^{177}Lu]Lu-PSMA10.1. The time-activity curves were generated for typical clinical schedules (4 h to 7 d), and assuming a human-to-mouse time scaling factor of about 7 and restrictions under animal welfare and working hours. Schedules with 2, 3, 4, and 5 time points were evaluated with combinations of 30 min, 3 h, 6 h, 24 h, and 48 h after injection, where the kidneys, tumour, and liver activities were simulated using the digital twin with an added 20% Gaussian noise to mimic measurement errors. The parameters of the PBPK model were fitted to these measurements. This process was replicated 1000 times, and the time-integrated activity (TIA) was calculated and compared with the digital twin. The relative root mean squared error (rRMSE) with the lowest value was ranked as the best schedule. ***Results:*** 20,000 replications were computed, and the rRMSE was the lowest for the schedule (3h, 6h, 24 h) when compared to all two- or three-timepoint schedules, with rRMSE being 11.0%, 11.4%, and 6.8% for the kidneys, tumour, and liver, respectively. The 5-timepoint schedule (not allowed for this project) yielded the lowest rRMSE for the organs mentioned above, with 8.6%, 9.4%, and 4.0%, respectively. ***Conclusion:*** A therapy measurement protocol at 3h, 6h, and 24 h after injection yielded optimal imaging-based dosimetry. By adding a 30-minute time point, a similar or worse rRMSE was found, suggesting that an (difficult to obtain) early time point is not necessary. ***References:*** [1] Kletting et al., J Nucl Med 2019

OP-181

A Preclinical Evaluation on the Radiohybrid Tandem [^{18}F]La- and [^{225}Ac]Ac-rhPSMA-10.1 for Targeted Alpha Therapy of Prostate Cancer

B. Sun[1,2], *A. Morgenstern*[3], *F. Bruchertseifer*[3], *S. Kossatz*[1,2], *M. Eiber*[1], *W. Weber*[1], *C. D'Alessandria*[1], *A. Wurzer*[1];
[1]*Department of Nuclear Medicine, TUM University Hospital, School of Medicine and Health, Technical University of Munich, Munich, GERMANY,* [2]*Central Institute for Translational Cancer Research (TranslaTUM), Technical University of Munich, Munich, GERMANY,* [3]*European Commission, Joint Research Centre, Directorate for Nuclear Safety and Security, Karlsruhe, GERMANY.*

Aim/Introduction: Prostate-specific membrane antigen (PSMA)-targeted alpha therapy emerged as a promising treatment option for advanced metastatic castration-resistant prostate cancer. Imaging and dosimetry of ^{225}Ac-PSMA ligands remain challenging because of suboptimal decay properties for SPECT. Radiohybrid (rh) ligands can be labelled with a radiometal for therapy or ^{18}F for imaging. The ^{18}F-labelled ligand, complexed with the natural metal, displays the identical chemical structure and pharmacokinetics compared to the therapeutic agent. In the present study, we therefore evaluated a rh ^{225}Ac-labelled PSMA-targeted ligand ([^{225}Ac]Ac-rhPSMA-10.1). [^{18}F]La-rhPSMA-10.1, complexed with natural lanthanum, mimicking the complex structure of ^{225}Ac, was investigated as a corresponding PET imaging agent. ***Materials and Methods:*** Cell studies (affinity, internalization, externalization) of [^{225}Ac]Ac-rhPSMA-10.1 and [^{18}F]La-rhPSMA-10.1 were performed on LNCaP and PC3Pip cells in comparison to the references [^{225}Ac]Ac-PSMA-I&T and [^{225}Ac]Ac-PSMA-617. For evaluation of the efficacy, LNCaP tumour-bearing mice (groups n=6) received a single injection of different doses of [^{225}Ac]Ac-rhPSMA-10.1 (20, 30 and 40 kBq; 0.2-0.4 nmol), [^{225}Ac]Ac-PSMA-I&T (20 kBq; 0.2 nmol), versus non-radioactive rhPSMA-10.1 (control; 1 nmol) and were followed for 60 days. The pharmacokinetics of [^{18}F]La-rhPSMA-10.1 were determined via PET-imaging and ex-vivo biodistribution analysis (10 min-4 h p.i.). ***Results:*** [^{225}Ac]Ac-rhPSMA-10.1 (4-7 MBq, 0.1-0.2 MBq/nmol) and [^{18}F]La-rhPSMA-10.1 (1-4 GBq, 50±4% radiochemical yield, 10-30 MBq/nmol) were prepared with ≥95% radiochemical purity. [^{225}Ac]Ac-rhPSMA-10.1 and [^{18}F]La-rhPSMA-10.1 displayed nearly identical cellular uptake and retention, falling in a similar range as the references. For all injected activities, tumour volumes declined in a similar way from day 7 p.i. onwards. At day 28, mean tumour volume relative to baseline had decreased by 39±17% for [^{225}Ac]Ac-PSMA-I&T; and 44±25%, 54±21%, 54±12% for 20, 30 and 40 kBq [^{225}Ac]Ac-rhPSMA-10.1, respectively. Median survival was 12 d in the control group and was not reached for the 20 and 30 kBq [^{225}Ac]Ac-rhPSMA-10.1 groups. In the 20 kBq [^{225}Ac]Ac-PSMA-I&T and 40 kBq [^{225}Ac]Ac-PSMA-rhPSMA-10.1 groups, two and three mice, respectively, had to be sacrificed due to low body condition scores, resulting in median survival of 59 and 60 days. [^{18}F]La-rhPSMA-10.1 demonstrated fast clearance from background tissues via renal excretion and tumour uptake of 12.8±4.2 %ID/g at 10 min, which was maintained over 4 h (12.7±3.1 %ID/g). ***Conclusion:*** [^{225}Ac]Ac-rhPSMA-10.1 revealed high anti-tumour efficacy with low side effects at 20 and 30 kBq, highlighting its potential for targeted alpha therapy of prostate cancer. [^{18}F]La-rhPSMA-10.1 showed favourable pharmacokinetics for PET-imaging and further studies on its suitability as a PET-surrogate for [^{225}Ac]Ac-rhPSMA-10.1 have been initiated.

OP-182

From DNA-encoded chemistry to ACP3-targeted radioligand therapeutics against prostate cancer

S. Cazzamalli[1], *S. Oehler*[1], *T. Georgiev*[1], *F. Migliorini*[1], *A. Ciamarone*[1], *P. Faviana*[2], *F. Bartoli*[2], *J. Mock*[1], *E. Puca*[1], *D. Neri*[1];
[1]*Philochem AG, Otelfingen, SWITZERLAND,* [2]*University of Pisa, Pisa, ITALY.*

Aim/Introduction: Efficient targeting of disseminated solid tumors remains a critical challenge in oncology. While selective monoclonal antibodies can be easily raised against tumor targets, their size hinders rapid and homogeneous tumor penetration [1]. Small organic ligands with ultra-high affinity for tumor-specific markers offer superior pharmacokinetics and tumor penetration [1,2]. Here, we report the discovery of OncoACP3 (ProX1), the first-in-class high-affinity small molecule ligand for prostatic acid phosphatase (ACP3), a promising, underexplored prostate cancer target for radioligand theranostic applications with minimal expression in healthy organs [3]. ***Materials and Methods:*** OncoACP3 was identified through high-throughput screening of DNA-encoded chemical libraries (DELs) [4]. Binding affinity to ACP3 was assessed via surface plasmon resonance. OncoACP3 was conjugated to Lutetium-177 (^{177}Lu) for in vivo evaluation. Tumor targeting, pharmacokinetics, biodistribution, and therapeutic efficacy were investigated in mouse models bearing ACP3-

positive tumors. ***Results:*** OncoACP3 demonstrated picomolar affinity for ACP3 and negligible off-target binding. Radiolabeled ^{177}Lu-OncoACP3 selectively accumulated in ACP3-positive tumors with exceptionally high tumor-to-blood ratios (>148 at 2 h) and prolonged tumor residence time ($t_1/_2$ > 72 h). In in vivo therapy experiments, low-dose administration (5-20 MBq/injection) of ^{177}Lu-OncoACP3 led to complete tumor regression in mice, without observable toxicity. Notably, no significant uptake was detected in kidneys or salivary glands, suggesting a more favorable safety profile than PSMA-targeting agents [5]. ***Conclusion:*** OncoACP3 represents a potent and selective tumor-targeting ligand for prostate cancer, offering advantages over existing PSMA-targeted therapies. These findings highlight the potential of DEL-derived ligands for targeting tumor-specific antigens with high precision and minimal off-target effects. OncoACP3 may pave the way for new targeted radiopharmaceuticals against local and metastatic prostate cancer. ***References:*** (1) Thurber, G. M., Schmidt, M. M. & Wittrup, K. D. Antibody tumor penetration: Transport opposed by systemic and antigen-mediated clearance. Advanced Drug Delivery Reviews 60, 1421-1434 (2008).(2) Cazzamalli, S., Dal Corso, A., Widmayer, F. & Neri, D. Chemically defined antibody- and small molecule-drug conjugates for in vivo tumor targeting applications: A comparative analysis. J Am Chem Soc 140, 1617-1621 (2018).(3) The human protein atlas. Available from: https://www.proteinatlas.org/ENSG00000014257-ACP3. Accessed 25 Jan 2024.(4) Neri, D. & Lerner, R. A. DNA-Encoded Chemical Libraries: A Selection System Based on Endowing Organic Compounds with Amplifiable Information. Annu Rev Biochem 8, (2018).(5) Kratochwil, C. et al. PSMA-targeted radionuclide therapy of metastatic castration-resistant prostate cancer with 177Lu-Labeled PSMA-617. Journal of Nuclear Medicine 57, 1170-1176 (2016).

OP-183

Radiolabeling of PSMA-functionalized Gold Nanoparticles with Terbium-161 for prostate cancer theranostics

A. Apostolopoulou*[1], D. Bajwa[1], E. Salvanou[1], S. Koelewijn[2], P. van Overeem[2], C. Liolios[1], S. Xanthopoulos[1], P. Koźmiński[3], P. Bouziotis[1]; [1]National Center for Scientific Research "Demokritos", Athens, GREECE, [2]Terthera b.v., Breda, NETHERLANDS, [3]Centre of Radiochemistry and Nuclear Chemistry, Institute of Nuclear Chemistry and Technology, Warsaw, POLAND.*

Aim/Introduction: Gold nanoparticles (AuNPs) have been widely used in cancer diagnosis and therapy since their nanoscale size offers several advantages such as low toxicity, satisfactory biocompatibility and enhanced permeability due to the EPR effect. By introducing targeting moieties, AuNPs can go directly to tumor sites and remain there, thus minimizing side effects. Terbium-161 (^{161}Tb) is a radiolanthanide with a half-life of 6.9 days that decays to stable Dysprosium-161 (^{161}Dy) through beta– (β^-) emission. This isotope emits a considerable number of conversion and Auger electrons along with beta particles, which deliver localized radiation within cancer cells, enhancing the damaging of the DNA of tumors. The aim of our study was to radiolabel AuNPs with and without a PSMA-targeting molecule with ^{161}Tb. Radiolabeling was achieved via the macrocyclic TADOTAGA chelator, which is extensively used for binding trivalent metals such as ^{161}Tb. The AuNPs were functionalized with TADOTAGA through the available thiol group which forms very strong Au-S bonds. ***Materials and Methods:*** AuNPs with the TADOTAGA chelator (AuNPs@TADOTAGA) and the PSMA-targeting molecule (AuNPs@TADOTAGA@PSMA) were radiolabeled with $^{161}TbCl_3$. Radiolabeling yield was determined by instant thin-layer chromatography (ITLC). In vitro stability studies were also carried out for both radiolabeled AuNPs in the presence of PBS (pH 7.4) at RT, as well as in Human Serum and DTPA as the competing chelating agent at 37°C, for up to 15 days. In vitro cytotoxicity studies were also carried out against LNCaP and PC3 cell lines up to 72 h using the MTT colorimetric assay. ***Results:*** The nanoparticles were radiolabeled after incubation at 70°C achieving a radiolabeling yield of more than 95% for both nanoconstructs. They also demonstrated unique in vitro stability in all solutions, as evaluated by ITLC analysis which makes them both very promising candidates for in vivo applications. The cytotoxicity studies revealed [^{161}Tb]Tb-AuNPs@TADOTAGA cause a greater reduction in cell viability in LNCaP cells, while PC3 cells display higher resistance to the ^{161}Tb-labeled AuNPs. Functionalization with PSMA ([^{161}Tb]Tb-AuNPs@TADOTAGA@PSMA) further enhances cytotoxicity in LNCaP cells, thus confirming the role of PSMA targeting. In contrast, PC3 cells (which are PSMA negative), show minimal changes in viability. ***Conclusion:*** Based on these preliminary results, we conclude that both ^{161}Tb-labeled nanocomplexes should be further investigated in athymic mice bearing LNCaP tumor xenografts, to assess their potential tumor accumulation with and without targeting. ***References:*** [1] Salvanou, E.-A. et al., Materials 2025, 18, 248. [2] Salvanou, E.-A. et al., Pharmaceutics 2020, 12, 188.

OP-184

From Beta to Alpha: A Preclinical Comparison of ^{177}Lu-, ^{225}Ac- and ^{212}Pb-labeled PSMA-N139

L. Joosten*[1], G. Franssen[1], D. Löwik[2], P. Laverman[1], J. Nagarajah[1], Y. Buchatskaya[3], M. Konijnenberg[4], S. Heskamp[1], Y. Derks[1]; [1]Radboud University Medical Center, Nijmegen, NETHERLANDS, [2]Radboud University, Nijmegen, NETHERLANDS, [3]Nuclear Research & Consultancy Group, Petten, NETHERLANDS, [4]Erasmus University Medical Center, Rotterdam, NETHERLANDS.*

Aim/Introduction: Prostate-specific membrane antigen (PSMA)-targeted radioligand therapy (RLT) represents a promising approach for the treatment of metastatic prostate cancer (mPCa). While β-emitting radionuclides such as ^{177}Lu have been widely studied, increasing interest has turned towards more potent α-emitters, including ^{225}Ac and ^{212}Pb. Here, we compared the biodistribution and dosimetry of a novel DOTA-conjugated PSMA ligand (PSMA-N139), labeled with ^{177}Lu, ^{225}Ac and ^{212}Pb. ***Materials and Methods:*** PSMA-N139 was radiolabeled with ^{177}Lu, ^{225}Ac or ^{212}Pb. Stability in human serum was assessed up to 4h at 37 °C. PSMA-specific binding and internalization were evaluated using LS174T-PSMA cells. Tumor and normal tissue uptake were determined in BALB/c nude mice bearing subcutaneous LS174T-PSMA and LS174T-WT tumors, at multiple timepoints post injection (up to 168h p.i.). Mice received 0.3 nmol radiolabeled PSMA-N139 (^{177}Lu: 2.2 MBq, ^{225}Ac: 14 kBq, ^{212}Pb: 48 kBq). Tumor and organ absorbed doses will be calculated based on the time-activity curves extrapolated from the biodistribution data (ongoing). ***Results:*** PSMA-N139 was labeled with ^{177}Lu (molar activity (MA): 7.35 MBq/nmol, radiochemical purity (RCP): 100%), ^{225}Ac (MA: 45.8 kBq/nmol, RCP: 89.1%) and ^{212}Pb (MA: 160.1 kBq/nmol, RCP: 95.2%), which remained stable up to 4h. PSMA-specific binding and internalization was observed for all three radiopharmaceuticals. In vivo, all radiolabeled PSMA-N139 showed rapid blood clearance and low accumulation in non-target organs. High uptake in the PSMA-positive tumor was observed for PSMA-N139 labeled with ^{177}Lu, ^{225}Ac or ^{212}Pb, with prolonged retention. For example, tumor uptake of ^{177}Lu-, ^{225}Ac-, and ^{212}Pb-PSMA-N139 was 15.9 ± 4.3, 17.2 ± 5.3, and 18.0 ± 5.2 %ID/g, respectively (4h p.i.), and 13.8 ± 3.1, 15.9 ± 5.2, and 14.9 ± 2.4 %ID/g, respectively (24h p.i.). Tumor uptake was still high 7 d p.i. for ^{225}Ac (9.0 ± 2.6 %ID/g) and appreciable for ^{177}Lu (3.3 ± 0.9 %ID/g). As expected, accumulation in the kidney was observed, which decreased rapidly over time. However, kidney accumulation differed significantly between radionuclides: 25.9 ± 8.6, 32.0 ± 5.1, and 67.6 ± 9.4 %ID/g for ^{177}Lu-,^{225}Ac-, and ^{212}Pb-PSMA-N139, respectively (1h p.i.), and 1.8 ± 0.3, 2.6 ± 0.4, and 8.8 ± 3.1 %ID/g, respectively (24h p.i.). ***Conclusion:*** This study presents a direct preclinical comparison of ^{177}Lu-,^{225}Ac-, and ^{212}Pb-

labeled PSMA-N139 and is the first head-to-head comparison of these three isotopes. All three radiopharmaceuticals showed PSMA-specific tumor uptake with good retention. These results show that PSMA-N139 can be used as a versatile platform for PSMA-targeted RLT using β- or α-emitters.

508

Sunday, October 5, 2025, 15:00 - 16:30
Room 115

Joint Symposium 2 - Neuroimaging Committee / EAN: Epilepsy: Who is the Right Candidate for Epilepsy Surgery?

509

Sunday, October 5, 2025, 15:00 - 16:30
Room 133+134

e-Poster Presentations Session 3 - Radiopharmaceutical Sciences Committee: New Tracers for Radioligand Therapy and Imaging

EPS-043

Preclinical Evaluation of a Novel NK-1R-Targeting Radiotracers for Theranostic Applications in Cancers

S. Chopra[1], *H. Yushchyshyna*[1], *T. Xu*[1], *O. Vorontsova*[1], *P. Jha*[1], *H. Westin*[2], *U. Rosenström*[3], *U. Yngve*[4,3], *M. Nestor*[1];
[1]*Department of Immunology, Genetics and Pathology, Science for Life Laboratory (SciLifeLab), Uppsala University, Uppsala, SWEDEN,* [2]*Ridgeview Instruments AB, Uppsala, SWEDEN,* [3]*Department of Medicinal Chemistry, Uppsala University, Uppsala, SWEDEN,* [4]*Science for Life Laboratory (SciLifeLab), Drug Discovery and Development platform, Uppsala, SWEDEN.*

Aim/Introduction: The Neurokinin-1 receptor (NK1R), a member of the G-protein-coupled receptor family, is activated by Substance P. It exists in two isoforms: a full-length (407 amino acids) and a truncated form (lacking 96 residues). NK1R is often overexpressed in cancers, with isoform patterns varying by tumor type—for example, neuroblastoma and breast cancer mainly express the truncated form, while NSCLC may express both. NK1R promotes tumor growth, angiogenesis, metastasis, and inhibits apoptosis, making it a promising theranostic target. ***Materials and Methods:*** Over sixty novel, stable, iodine-containing small molecules were synthesized as potential NK1R-targeting agents. LigandTracer technology was used to screen compounds and assess their binding affinity through competition studies, where FAM-labeled Substance P (FAM-SP) was displaced by an equimolar concentration of molecules. The binding kinetics of FAM-SP to NK1R-transfected cells served as reference molecule. Pharmacokinetic properties were evaluated through in-vitro ADME profiling. Based on these results, top candidates were selected, radioiodinated with [125I], and were isolated using HPLC. Binding of the lead compound was validated on cells transfected with both the full-length and truncated forms of NK1R. Biodistribution studies were carried out in mice bearing NK1R-positive tumors to assess distribution profile of lead molecule. Additionally, in-vivo specificity was evaluated using mice bearing both NK1R-positive and NK1R-negative tumor-xenografts to confirm selective targeting. ***Results:*** Compounds were ranked based on their ADME profiles and ability to displace FAM-SP in competitive binding assays. FAM-SP binding studies to NK1R demonstrated two binding affinities of 171nM and 17nM. Radioiodination of the top candidate was successfully achieved, and post-purification, the compound demonstrated a purity ≥98%. Successful binding of the lead compound was confirmed in cells transfected with either the full-length or truncated form of NK1R. The top candidate exhibited a binding affinity in the picomolar range[UY1] [MN2] , that could be blocked by an excess of the known NK1R inhibitor Aprepitant. In-vivo biodistribution studies revealed a tumor-to-blood ratio exceeding 70 at 24 hours p.i.. Furthermore, selective accumulation was observed in NK1R-positive tumors compared to NK1R-negative tumors. ***Conclusion:*** The lead radioiodinated small molecule demonstrated excellent in vitro binding properties, high specificity for NK1R, and favorable pharmacokinetics. It successfully bound to both full-length and truncated isoforms of NK1R in-vitro, with significantly higher tumor accumulation observed in vivo in NK1R-positive tumors compared to NK1R-negative controls. These findings highlight its strong potential as a promising theranostic agent for imaging and targeted therapy of NK1R-expressing cancers.

EPS-044

Preclinical and first-in-human study of dosimetry and safety for a novel radiopharmaceutical targeting the EGFR mutation in patients with non-small cell lung cancer (NSCLC)

S. Jedidi[1,2], *A. Courteau*[1,2], *B. Presles*[2], *P. S. Bellaye*[1], *B. Collin*[1,2], *N. Isambert*[3], *M. Chafai El Alaoui*[1], *A. Daoust*[4], *C. Berthet*[4], *A. Cochet*[1,2], *J. M. Vrigneaud*[1,2];
[1]*Centre Georges-François Leclerc, Dijon, FRANCE,* [2]*Institut de Chimie Moléculaire de l'Université de Bourgogne (ICMUB), UMR CNRS6302, Université Bourgogne Europe, Dijon, FRANCE,* [3]*CHU Poitiers, Poitiers, FRANCE,* [4]*Oncodesign Precision Medicine, Dijon, FRANCE.*

Aim/Introduction: [18F]-Florepizol is a novel fluorinated PET radiopharmaceutical for imaging of mutated EGFR in non-small cell lung cancer (NSCLC). Biodistribution and absorbed doses of normal organs were quantified in rats and subsequently evaluated in a Phase 0/1 firstinhuman dosimetry study, to determine its safety for clinical use. ***Materials and Methods:*** In the preclinical study, 42 Sprague-Dawley rats (21 males, 21 females) received [18F]-Florepizol intravenously (4.0±0.4 MBq). Animals were sacrificed at 5, 15, 30, 60, 120, 240, and 360 min post-injection. Organs were harvested, weighed, and radioactivity was quantified using a gamma counter. In the clinical study, eight NSCLC patients (4 males, 4 females; 70 ±9 years; 64 ±10 kg) received 300.8 ±36.3 MBq of [18F]-Florepizol as a single intravenous bolus. Eight serial whole-body PET/CT scans were acquired over 4 h, with urine and blood samples collected between or after each scan. Source organs were segmented on CT images using the AI-based tool TotalSegmentator. For both datasets, time-activity curves were fitted and optimised based on the Akaike Information Criterion. Time-integrated activity coefficients of human and animal (with allometric scaling) were then computed and processed in OLINDA/EXM 2.0 for confrontation. ***Results:*** For the preclinical study, the highest fractions of injected activity were found in the colon (20.1% in males, 17.4% in females), bladder (21.3% in males, 15.9% in females), and liver (10.6% in males, 10.4% in females). The corresponding absorbed doses per injected activity were highest in the bladder (0.16 mGy/MBq in females, 0.13 mGy/MBq in males), followed by the colon (0.08 mGy/MBq in females, 0.09 mGy/MBq in males) and liver (0.01 mGy/MBq in both sexes). In patients, the liver retained the highest fraction of injected activity (64.9% in males, 50.6% in females), followed by the small intestine (18.3% in males, 31.9% in females) and gallbladder (12.9% in males, 12.1% in females). The absorbed doses per injected activity reached 0.19±0.02 mGy/MBq in males and 0.20±0.01 mGy/MBq in females for the liver, 0.16±0.05 and 0.16±0.10 mGy/MBq for the gallbladder, and 0.03±0.01 and 0.09±0.04 mGy/MBq for the small intestine. No serious adverse events were recorded across the patient study. ***Conclusion:*** Substantial differences were observed between absorbed doses in human and animal studies. For patients, the

liver and gallbladder were the two dose-critical organs. The mean effective dose was 0.024±0.001 mGy/MBq, supporting its clinical use as a safe molecular imaging tool for EGFR-driven NSCLC.

EPS-045

Design, Synthesis and Preclinical Evaluation of Small Molecular Radiotracers Targeting AVPR2 for PET Imaging in Renal Cell Cancer Xenograft Mice

S. Huang, *T. Tian, R. Huang;*
West China Hospital of Sichuan University, Chengdu, Sichuan, CHINA.

Aim/Introduction: Arginine vasopressin receptor 2 (AVPR2) is a G-protein-coupled receptor expressed in the renal collecting ducts, distal tubules, and nephrons. Its primary function is to regulate water and electrolyte homeostasis through interaction with arginine vasopressin. However, recent studies have shown that AVPR2 activation promotes the proliferation of renal cell carcinoma, and AVPR2 is highly expressed in renal cancer cells. Importantly, AVPR2 antagonists have demonstrated potential in suppressing tumor growth. Therefore, the aim of this study is to develop radiotracers targeting AVPR2 for PET imaging of renal cancer. ***Materials and Methods:*** Radiotracers of ^{68}Ga-HX01, ^{68}Ga-HX02, ^{68}Ga-HX03 were synthesized based on benzodiazepine derivative and tolvaptan. The stability of ^{68}Ga-HX01, ^{68}Ga-HX02 and ^{68}Ga-HX03 after incubation in 0.9% saline and fetal bovine serum (FBS) at 37 °C for 0 h, 1 h, 2 h and 4 h were measured by radioactive thin layer chromatography. ^{68}Ga-HX01, ^{68}Ga-HX02 and ^{68}Ga-HX03 were partitioned between 500 µl n-octanol and 500 µl deionized water to evaluate the lipophilicity of them. Cellular uptakes and blocking in Caki-1cell were performed to confirm their specificity for AVPR2. ^{68}Ga-HX01, ^{68}Ga-HX02 and ^{68}Ga-HX03 were used for PET imaging in Caki-1cell xenograft mice to evaluate the expression of AVPR2. ***Results:*** The radiochemical yields of ^{68}Ga-HX01, ^{68}Ga-HX02 and ^{68}Ga-HX03 were all > 99.0%. The Log P of ^{68}Ga-HX01, ^{68}Ga-HX02 and ^{68}Ga-HX03 were respectively -1.77 ± 0.01, -1.90 ± 0.04 and -2.77 ± 0.05, which indicated ^{68}Ga-HX01, ^{68}Ga-HX02 and ^{68}Ga-HX03 were hydrophilic. As for the stability of ^{68}Ga-HX01, ^{68}Ga-HX02 and ^{68}Ga-HX03 in FBS and 0.9% saline, the radiochemical purities of ^{68}Ga-HX01, ^{68}Ga-HX02 and ^{68}Ga-HX03 were still over 95.0% after 4h. In vitro, the uptake rates of ^{68}Ga-HX01, ^{68}Ga-HX02 and ^{68}Ga-HX03 in Caki-1 cells continuously increased at 15min, 30min, 60min and 120min. Blocking studies found the uptake rates of ^{68}Ga-HX01, ^{68}Ga-HX02 and ^{68}Ga-HX03 in 60min declined from 1.24 ± 0.07 %, 0.69 ± 0.02 %, 0.36 ± 0.02 % to 0.44 ± 0.03 %, 0.28 ± 0.04 %, 0.21 ± 0.04 % with statistically significant. In vivo, preclinical PET/CT found ^{68}Ga-HX02 and ^{68}Ga-HX03 showed fast excretion from tumor and ^{68}Ga-HX01 had excellent retention capacity in tumor. The ^{68}Ga-HX01 uptake of tumor at 30 min, 60 min and 120 min were 5.36 ± 2.03 %ID/g, 4.51 ± 1.23 %ID/g and 4.20 ± 1.48 %ID/g, respectively. ***Conclusion:*** PET imaging with ^{68}Ga-HX01 is an effective tool to evaluate the expression of AVPR2.

EPS-046

Replacing Ahx with Pip-Lys and the C-terminal Pro with Tic for [^{68}Ga]Ga-Z01115 to improve its bradykinin B1 receptor-targeting capability for positron emission tomography

F. Radnia, *S. Jozi, C. Chen, L. Wang, H. Merkens, P. Ng, F. Bénard, K. Lin;*
BC Cancer Research Institute, Vancouver, BC, CANADA.

Aim/Introduction: Bradykinin B1 receptor (B1R), a G protein-coupled receptor, has minimal expression in healthy tissues but is overexpressed in many cancers, making it a promising diagnostic target. Our previous studies showed that the B1R-targeted agonist PET tracer [^{68}Ga]Ga-Z01115 (^{68}Ga-DOTA-Ahx-Lys-Arg-Pro-Hyp-Gly-Cha-Ser-Pro-D-Phe) had good binding affinity (K_i = 25.4 nM) and tumor uptake in B1R-expressing HEK293T::hB1R xenografts (5.65 %ID/g at 1 h post-injection). This study explored the impact of (1) replacing the Ahx linker with a cationic Pip-Lys, and (2) substituting the C-terminal Pro with the unnatural amino acid Tic on its B1R-targeting capability. ***Materials and Methods:*** Two B1R-targeted peptides, AR-B1R-D (DOTA-Pip-Lys-Lys-Arg-Pro-Hyp-Gly-Cha-Ser-Pro-D-Phe) and AR-B1R-E (DOTA-Pip-Lys-Lys-Arg-Pro-Hyp-Gly-Cha-Ser-Tic-D-Phe), were synthesized via solid-phase synthesis. ^{nat}Ga and ^{68}Ga complexations were performed in sodium acetate buffer (0.1 M, pH 4.5) and HEPES buffer (2 M, pH 5.0), respectively. B1R binding affinities were measured via in vitro competition assays using B1R-expressing CHO-K1 cell membranes and [^{3}H]-[Leu^{9},des-Arg^{10}]Kallidin as the radioligand. Intracellular calcium release was measured in HEK293T::hB1R cells using the FLIPR Calcium 6 Assay Kit. The agonist and antagonist controls were Lys-[des-Arg^{9}] Bradykinin and Lys-[Leu^{8},des-Arg^{9}]Bradykinin, respectively. PET/CT imaging and biodistribution studies were conducted at 1 h post-injection in NRG mice bearing both B1R-positive HEK293T::hB1R and B1R-negative HEK293T tumor xenografts. ***Results:*** AR-B1R-D and AR-B1R-E were synthesized in 6% and 11% yields, respectively. ^{nat}Ga-AR-B1R-D and ^{nat}Ga-AR-B1R-E were obtained in 50% and 80% yields, respectively. ^{68}Ga-labeled tracers were obtained in 37-50% decay-corrected radiochemical yields with >98% radiochemical purity. Binding assays showed that Ga-AR-B1R-D and Ga-AR-B1R-E effectively inhibited binding of [^{3}H]-[Leu^{9},des-Arg^{10}]Kallidin to B1R-expressing CHO-K1 cell membranes with K_i values of 2.30 and 1.67 nM, respectively. Ga-AR-B1R-D induced strong calcium release similar to the agonist control, while Ga-AR-B1R-E showed a moderate response, resembling the antagonist control. Both [^{68}Ga] Ga-AR-B1R-D and [^{68}Ga]Ga-AR-B1R-E enabled clear visualization of HEK293T::hB1R tumors, but not the B1R-negative HEK293T tumors in PET images, and their excretion was mainly via the renal pathway. The tumor uptake values of [^{68}Ga] Ga-AR-B1R-D and [^{68}Ga] Ga-AR-B1R-E were 8.02 ± 2.09 and 11.2 ± 4.83 %ID/g, respectively. The uptake values of collected normal organs/tissues except kidneys were minimal (<1 %ID/g) for both tracers. ***Conclusion:*** Our data demonstrate that replacing Ahx in [^{68}Ga]Ga-Z01115 with a cationic linker Pip-Lys improves B1R binding affinity and tumor uptake. Further improvement in B1R binding affinity and tumor uptake could also be achieved by replacing the C-terminal Pro with Tic. However, this additional replacement converts an agonist to an antagonist.

EPS-047

Radiosynthesis and evaluation of a novel ^{68}Ga labeled B7-H3 targeted peptide

F. Zhang, *J. Li, S. Song;*
Department of Nuclear Medicine, Fudan University Shanghai Cancer Center, shanghai, CHINA.

Aim/Introduction: B7 homolog 3 protein (B7-H3, also known as CD276), a recently identified immunoregulatory protein member of the B7 family, is overexpressed in various tumors and within the tumor mircroenvironment (TME). Several therapeutic agents targeting B7-H3 have advanced to clinical trials, demonstrating promising efficacy. To enable precise and non-invasive monitoring of B7-H3 expression in vivo, we developed a novel ^{68}Ga-labeled peptide-based radiotracer. This tracer facilitates highly specific and selective molecular imaging of B7-H3 via positron emission tomography (PET). ***Materials and Methods:*** ^{68}Ga-DOTA-B7H3 was successfully synthesized, and its radiochemical purity (RCP) was assessed by Radio-TLC and Radio-HPLC. Additional evaluations included stability testing, determination of the octanol/water partition coefficient (log P), and measurement of its biological half-life. The binding affinity of ^{68}Ga-DOTA-B7H3 to B7-H3 protein was quantified using surface plasmon resonance (SPR). Furthermore, cellular uptake assays and PET imaging studies were conducted across six tumor cell lines (5-8F, C666-1, HT29, SKOV3, PC3, H1299) with varying B7-H3 expression levels. ***Results:*** ^{68}Ga-DOTA-B7H3

exhibited high radiolabeling efficiency, with stability in saline and serum remaining above 95% over 2 hours. The log P value was determined to be -2.1 ± 0.12 (n = 5), indicating pronounced hydrophilicity. The blood half-life of the probe was 17.2 ± 1.4 min (n = 5). SPR analysis revealed a dissociation constant (K_D) of 83.22 nM, while the half-maximal inhibitory concentration (IC_{50}) in 5-8F cells was 73.5 nM. Cellular uptake was significantly higher in non-blocked groups compared to blocked controls and exhibited a positive correlation with B7-H3 expression across different cell lines. PET imaging demonstrated differential tumor uptake at 30 minutes post-injection, with the highest accumulation observed in the 5-8F model (2.53 ± 0.06 %ID/g_{max}), followed by HT-29 (2.07 ± 0.06 %ID/g_{max}), SKOV3 (1.93 ± 0.23 %ID/g_{max}), C666-1 (1.67 ± 0.38 %ID/g_{max}), PC-3 (1.57 ± 0.25 %ID/g_{max}), and H1299 (0.99 ± 0.01 %ID/g_{max}) (n = 3). These findings were consistent with Western blot (WB) analysis of B7-H3 expression levels. ***Conclusion:*** The successful synthesis of ^{68}Ga-DOTA-B7H3 was achieved with high radiochemical purity. The probe demonstrated strong binding affinity for B7-H3, and tumor uptake correlated with B7-H3 expression, confirming its specificity. These results suggest that ^{68}Ga-DOTA-B7H3 represents a promising diagnostic tool for the non-invasive detection of B7-H3-expressing malignancies in clinical settings.

EPS-048

Preclinical evaluation of a novel click-cleavable radioimmunoconjugate for improved therapy of HER2 expressing tumours

M. H. M. E. van Stevendaal[1], *K. E. de Roode*[1], *L. H. M. Zijlmans*[1], *B. Matthee*[1], *M. W. Konijnenberg*[2], *M. S. Robillard*[1], *R. Rossin*[1];
[1]Tagworks Pharmaceuticals, Nijmegen, NETHERLANDS, [2]Erasmus Medical Center, Rotterdam, NETHERLANDS.

Aim/Introduction: Radioimmunotherapy (RIT) is hampered by the long circulation of mAbs, resulting in dose-limiting toxicity. Tagworks' TGW211 program aims at solving this issue for HER2+ tumours. A trastuzumab conjugate, TGW211-DC, functionalized with DOTA via a cleavable trans-cyclooctene (TCO) linker, releases the radiolabel in circulation upon a bioorthogonal click-to-release reaction with a cell-impermeable tetrazine trigger (TRG001), boosting target-to-nontarget ratios. ***Materials and Methods:*** Release of [^{111}In]In-DOTA from [^{111}In]In-TGW211-DC upon addition of a trigger was measured in PBS and serum. [^{111}In]In-TGW211-DC binding and internalization were characterized using HER2-expressing BT-474 cells. In vivo pharmacokinetics and biodistribution were determined in nude mice +/- BT-474 xenografts, alone or in combination with a trigger. The toxicity of a single i.v. TGW211-DC dose, with or without TRG001, was evaluated in mice with a 1- and 14-day observation period. Safety of TRG001 alone was evaluated in rat and cynomolgus monkey in a repeat-dose 5-week toxicology study. Clinical data for [^{89}Zr]Zr-trastuzumab were used to estimate dosimetry of TGW211-DC +/- TRG001 for different long-lived nuclides (^{177}Lu and ^{225}Ac) using IDAC-Dose 2.1 and OLINDA. ***Results:*** [^{111}In]In-TGW211-DC showed strong in vitro binding (KD = 8.4 nM), and internalization. The trigger rapidly released the [^{111}In]In-DOTA-fragment in plasma (91.8% in 5 min). In healthy mice, [^{111}In]In-TGW211-DC was highly stable (>20d isomerization half-life for the TCO linker) while it gave fast and efficient release of the short-circulating radioactive fragment (64.5 min mean residence time) upon reaction with trigger in blood. In mice bearing BT-474 xenografts, maximal tumour internalization was reached at 72 hrs p.i. TGW211-DC +/- TRG001 and TRG001 alone were well tolerated: the no-observed-adverse-effect-level (NOAEL) of i.v. dosed TGW211-DC +/- TRG001 (62.78 mg/kg) in mouse was 55 mg/kg (TGW211-DC), and the NOAEL of TRG001 alone was 700 mg/kg/dose and 300 mg/kg/dose in rat and cynomolgus monkey, respectively. Dosimetry modelling projected that future clinical cleavable HER2-RIT could afford a maximal decrease in effective dose in bone marrow, kidney and liver when TRG001 is administered 24 hrs after dosing radiolabelled TGW211-DC (up to 92% for ^{225}Ac and 88% for ^{177}Lu). TRG001 administration after 72 hrs was projected to result in effective dose reductions of up to 80% and 72% for ^{225}Ac and ^{177}Lu respectively. ***Conclusion:*** Click-cleavable [^{111}In]In-TGW211-DC improved tumour-to-blood ratios in mice. Extensive toxicological evaluation of TGW211-DC and TRG001, alone or in combination, revealed no significant adverse effects, demonstrating safety. Dosimetry simulations illustrated the potential benefit of click-cleavable radioimmunotherapy for patients with HER2+ cancers.

EPS-049

PET imaging of PARP-1 expression using a novel ^{18}F-labeled probe based on Quinazoline-2,4(1 H,3 H)-dione Scaffold

Y. Zou, *H. Wang, M. Hu, W. Chen, R. Tian;*
Sichuan University, west china hospital, Chengdu, Sichuan, CHINA.

Aim/Introduction: Poly (ADP-ribose) polymerase-1 (PARP-1) inhibitors (PARPi) have been approved for treating cancers with homologous recombination deficiency (HRD). Although recent studies demonstrate their promising efficacy, predicting patient response is complicated by intra-tumor heterogeneity and the limited predictive power of histology-based HRD assessments. To better predict responses to PARPi treatment and stratify patients, several PARP-targeting probes, including ^{18}F-FTT and ^{18}F-PARPi, which enable noninvasive and systemic monitoring, have been reported and entered clinical trials[1]. However, limited by labeling methods, the synthesis of reported probes was cumbersome with low yields. Based on the core binding structure of Senaparib, we aimed to synthesize a novel probe targeting PARP-1 for PET with high feasibility, high binding selectivity, and a favorable tumor-to-background ratio. ***Materials and Methods:*** Based on the quinazoline-2,4(1H,3H)-dione scaffold (Senaparib), we synthesized a PARP-targeting precursor suitable for ^{18}F labeling. ^{18}F-PARP-HX-2 was synthesized using a modified photoredox-mediated ^{18}F-deoxyfluorination and radio-HPLC preparation[3]. In vitro experiments, the lipid-water partition coefficient and cellular uptake of ^{18}F-PARP-HX-2 were measured. Initial PET/CT imaging of ^{18}F-PARP-HX-2 was evaluated in U87MG xenograft models. ***Results:*** ^{18}F-PARP-HX-2 was obtained with high radiochemical purity (≥95%). The Log $D_{7.4}$ of ^{18}F-PARP-HX-2 was 1.36 ± 0.06, indicating its lipophilic nature. There was a significant reduction in cellular uptake of ^{18}F-PARP-HX-2 in the blocked group compared to the control group (7.47 ± 0.20% reduce to 3.19 ± 0.06%, $P < 0.01$). Preliminary PET/CT imaging showed a high tumor-to-muscle ratio (tumor: SUV_{max} = 0.59 ± 0.03, muscle: SUV_{max} = 0.11 ± 0.01 at 1h pi) and fast hepatobiliary excretion in U87MG xenograft models. The blocking experiment demonstrated a significant reduction of ^{18}F-PARP-HX-2 in tumor accumulation (SUV_{max} = 0.59 ± 0.03 reduce to SUV_{max} = 0.11 ± 0.03 at 1h pi, $P < 0.01$). ***Conclusion:*** Photocatalytic radiofluorination enables the facile synthesis of a PARP-1-targeted probe with high specificity and favorable contrast. Further studies on treatment response prediction will be performed in preclinical models. ***References:*** 1. Pantel AR, Gitto SB, Makvandi M, et al. [18F]FluorThanatrace ([18F]FTT) PET Imaging of PARP-Inhibitor Drug-Target Engagement as a Biomarker of Response in Ovarian Cancer, a Pilot Study. Clin Cancer Res. 2023.29(8):1515-1527. 2. Wei Chen, Yueqi Wang, Lili Pan et al. Simplified radiolabeling process toward rapid photoredox-catalyzed aryl 18F-fluorination and PET tracer development, 2025, PREPRINT available at Research Square [https://doi.org/10.21203/rs.3.rs-4325597/v1]

EPS-050

^{177}Lu-labelled CEACAM5-binding affibody for radionuclide therapy

E. Papalanis[1], *R. Li*[2], *M. Oroujeni*[1], *A. Orlova*[1], *E. Bezverkhniaia*[1], *P. Nygren*[2], *T. Gräslund*[2], *V. Tolmachev*[1];
[1]*Uppsala University, Uppsala, SWEDEN,* [2]*KTH, Stockholm, SWEDEN.*

Aim/Introduction: The carcinoembryonic antigen adhesion molecule 5 (CEACAM5) is expressed in many types of cancer including colorectal, lung, breast, ovarian, gastric and pancreatic cancer. Affibody molecules are engineered scaffold proteins that can be selected to bind specifically to desired proteins. We developed a dimeric C9-C9 affibody construct binding to CEACAM5 for delivery of cytotoxic payloads to malignant tumours. To improve targeting and reduce renal uptake, a fusion of C9-C9 with the albumin-binding domain ABD_{035} was created. We found that the N-terminal positioning of ABD_{035} (construct designated as ABD_{035}-C9-C9) provided better targeting compared with C-terminal positioning. This study aimed to evaluate the targeting properties of the ^{177}Lu-labeled ABD_{035}-C9-C9 in vitro and in vivo. ***Materials and Methods:*** Maleimido derivatives of DOTA and DOTAGA chelators were conjugated to C-terminal cysteine of ABD_{035}-C9-C9. The conjugates were labelled with ^{177}Lu and purified using size-exclusion chromatography. CEACAM5-expressing cell lines with high, intermediate and low expression levels were used (BxPC3>LS174T>>HT-29) to evaluate the constructs. The kinetics of binding to living cells was evaluated using LigandTracer. The biodistribution properties of [^{177}Lu]Lu-ABD_{035}-C9-C9-DOTA and [^{177}Lu]Lu-ABD_{035}-C9-C9-DOTAGA were compared in nude mice with BxPC3 tumours. The best variant was selected and a biodistribution analysis was performed 4, 24, 72, 168 and 336h pi. The Area Under Curve (AUC) for decay uncorrected biodistribution data was calculated to compare absorbed doses delivered to tumours and normal organs. ***Results:*** Radiolabelling of both constructs was successful with radiochemical purities exceeding 95%. Both [^{177}Lu]Lu-ABD_{035}-C9-C9-DOTA and [^{177}Lu]Lu-ABD_{035}-C9-C9-DOTAGA demonstrated saturable binding in vitro, which was proportional to CEACAM5 expression levels in cell lines. The internalised fraction for both variants was around 40% after 24 h. InteractionMap analysis by Ligand Tracer revealed two interactions, with higher affinity (880-1000 pM) and with lower affinity (27-41 nM). The higher affinity was more abundant for [^{177}Lu]Lu-ABD_{035}-C9-C9-DOTA. The in vivo experiments demonstrated significantly ($p<0.05$) lower kidney uptake at 48 h post-injection of [^{177}Lu]Lu-ABD_{035}-C9-C9-DOTA compared with [^{177}Lu]Lu-ABD_{035}-C9-C9-DOTGA (19±1 and 29±2%ID/g, respectively). The DOTA-conjugated variant was selected for further studies. The uptake of [^{177}Lu]Lu-ABD_{035}-C9-C9-DOTA in BxPC3 xenografts (29±2%ID/g) was significantly higher than in HT-29 xenografts, showing CEACAM5-dependent uptake in vivo. Fusion with ABD_{035} increased tumour uptake 3.6-fold and decreased renal uptake 14-fold. AUC for the BxPC3 tumours were 4.1-, 3.4- and 23-fold bigger than AUCs for the liver, kidneys and bones, respectively. ***Conclusion:*** Conjugation of ABD_{035}-C9-C9 with DOTA leads to better targeting properties. [^{177}Lu]Lu-ABD_{035}-C9-C9-DOTA is a promising construct for therapy of CEACAM5 expressing tumours.

EPS-051

Preparation and application of novel EBNA1-targeted PET radioactive probe

B. Gu*, F. Zhang, J. Li, S. Song;*
Fudan University Shanghai Cancer Center, Shanghai, CHINA.

Aim/Introduction: Epstein-Barr nuclear antigen 1 (EBNA1), a viral nucleoprotein encoded by EBV, plays an important role in inducing nasopharyngeal carcinoma (NPC). This study aims to develop an EBNA1-targeted PET radiotracer for detecting EBV in EBV-associated NPC tumor-bearing mouse models. ***Methods:*** An EBNA1-targeted radioactive probe ^{68}Ga-NOTA-FZEB was synthesized, and the radiochemical purity and stability were evaluated by radio-HPLC. The positive or negative expressing-EBNA1 NPC cell lines were screened by western blot assay. The targeting performance of ^{68}Ga-NOTA-FZEB was characterized in vitro and in vivo. PET/CT imaging of tumor-bearing mouse model was used to assess the distribution and metabolism of ^{68}Ga-NOTA-FZEB in vivo. ***Results:*** The radiochemical purity of ^{68}Ga-NOTA-FZEB was more than 95%, and exhibited high stability in saline and fetal bovine serum for 3 h. In vitro cell uptake studies showed that EBNA1-positive C666-1 cells revealed significantly higher uptake of ^{68}Ga-NOTA-FZEB than EBNA1-negative 5-8F cells ($P < 0.001$). PET/CT imaging of the tumor-bearing mice showed that ^{68}Ga-NOTA-FZEB could specifically aggregate in EBNA1-positive C666-1tumors, whereas the EBNA1-negative 5-8F tumors revealed significantly lower uptake of ^{68}Ga-NOTA-FZEB (%ID/g: 2.87 ± 1.10 vs. 0.97 ± 0.12, $P < 0.001$). Moreover, ^{68}Ga-NOTA-FZEB was mainly metabolized through liver and urinary system in vivo. The results of H&E staining confirmed the biocompatibility of ^{68}Ga-NOTA-FZEB in vivo. ***Conclusion:*** As the first ^{68}Ga-labelled EBNA1-tageted polypeptide, ^{68}Ga-NOTA-FZEB exhibited high affinity and strong specificity to EBNA1-positive cells, suggesting it's a promising PET imaging agent for the management of EBV-associated NPC patients.

EPS-052

PET imaging of TIM-3 enables sensitive monitoring of immunotherapy

H. Yang*, L. Feng, D. Jiang;*
Department of Nuclear Medicine, Union Hospital, Tongji Medical College, Huazhong University of Science and Technology, Wuhan, CHINA.

Aim/Introduction: T-cell immunoglobulin and mucin domain-3 (TIM-3) is primarily expressed on CD4+ and CD8+ T cells, serving as a critical immune checkpoint. Elevated TIM-3 expression has been shown to correlate with impaired function and exhaustion of CD8+ T cells and natural killer cells, making it a highly promising target for immunotherapy. Although immunotherapy has revolutionized cancer treatment, it demonstrates significant efficacy in only a subset of patients. Early identification of responders could potentially improve patient management and treatment outcomes during immunotherapy. This study aims to develop a positron emission tomography (PET) probe for the non-invasive characterization of TIM-3 expression, thereby providing a novel approach to monitor cancer immunotherapy efficacy. ***Materials and Methods:*** We synthesized the TIM-3-targeted peptide imaging probe 68Ga-NOTA-P2 and conducted a series of in vitro and in vivo experiments to assess its biodistribution, specificity, and pharmacokinetic properties, with the aim of evaluating its potential for non-invasive imaging of TIM-3 expression in tumors. The performance of 68Ga-NOTA-P2 in targeting TIM-3 expressing tumors was validated using PET/CT imaging in mouse models of colorectal cancer, melanoma, and lung cancer, both in baseline conditions and following immune activation. Additionally, the expression levels of TIM-3 in CT26, MC38, B16F10, and LLC tumors were assessed before and after immune activation using Western blot and flow cytometry analyses to confirm the probe's targeting efficacy. ***Results:*** 68Ga-NOTA-P2 PET imaging enables the non-invasive detection of TIM-3 expression levels across various tumor models, providing insights into the distribution of TIM-3-positive cells within these tumors. Additionally, in tumor models treated with a stimulator of interferon genes (STING) agonist, this imaging modality reveals a phenotypic shift from immunologically "cold" to "hot" tumors, as evidenced by an increase in tracer uptake from 1.70 (±0.18) to 2.93 (±0.21) %ID/g in CT26 tumor models. These imaging findings are corroborated by Western blot and flow cytometry analyses, which further validate the observed changes in TIM-3

expression. ***Conclusion:*** 68Ga-NOTA-P2 PET imaging enables the non-invasive assessment of early responses to immunotherapy by targeting TIM-3 expression in colorectal cancer, melanoma, and lung cancer models. These results highlight the feasibility of employing 68Ga-NOTA-P2 PET for TIM-3 tracking and suggest new avenues for optimizing TIM-3-targeted immunotherapy through this novel imaging strategy.

EPS-053

Tissue Factor-targeted PET imaging for Early Diagnosis of Pancreatic Cancer

W. Li, *S. Cheng, R. An, Y. Zhang, X. Lan, D. Jiang;*
Department of Nuclear Medicine, Union Hospital, Tongji Medical College, Huazhong University of Science and Technology, Wuhan, CHINA.

Aim/Introduction: Pancreatic cancer (PC) is an extremely malignant tumor with a dismal five-year survival rate of 13% worldwide. Moreover, PC often remains silent until reaching late stages, making it difficult to detect, therefore resulting in delayed intervention and increased morality. Tissue factor (TF), a protein involved in coagulation, is overexpressed by many tumor cells, especially PC cells, due to its involvement in multiple signaling pathways. Herein, we developed a Fab fragment-based PET tracers targeting TF and evaluated its diagnostic performance in murine models of PC. ***Materials and Methods:*** We radiolabeled anti-TF Fab fragment (TF903) with zirconium-89 (^{89}Zr, $t_{1/2}$= 78.4 h) and gallium-68 (^{68}Ga, $t_{1/2}$=68 min) to obtain TF-targeting PET tracers [^{89}Zr]Zr-DFO-TF903 and [^{68}Ga]Ga-NOTA-TF903. We evaluated the radiolabeling yield, radiochemical purity, and in vitro stability, and tested the in vitro binding affinity of the tracer by cell uptake studies. After that, we performed PET imaging and ex vivo biodistribution studies in pancreatic tumor-bearing mice (Panc02 and ASPC-1) to evaluate imaging performance and biodistribution of radiolabeled TF903. Tumor and major tissues were collected for further immunohistochemical and immunofluorescence staining. ***Results:*** [^{89}Zr]Zr-DFO-TF903 and [^{68}Ga]Ga-NOTA-TF903 were synthesized with satisfactory radiocharacteristics: high radiolabeling yields, radiochemical purity, and stability. Both murine PC cell line Panc02 and human PC cell line AsPC-1 were found to be TF-positive and our in vitro and in vivo experiments demonstrated that TF903-based PET tracers had strong binding affinity for this target. [^{68}Ga]Ga-NOTA-TF903 PET imaging and ex vivo biodistribution studies at 2 h post-injection revealed stable circulation of the tracer in the blood pool, and the probe showed a significantly higher tumor uptake (3.54-5.38% ID/g; 2 h p.i), three times higher than the muscle (1.02-1.64% ID/g; 2 h p.i). [^{89}Zr]Zr-DFO-TF903 PET imaging at longer time points showed an upward trend of tumor accumulation over time, substantiating the specific and strong binding of the probe in vivo. Immunohistochemical analysis also proved the specific binding of TF903. ***Conclusion:*** We successfully developed a TF-targeting Fab fragment probe, which demonstrated satisfactory PET imaging results in terms of tumor uptake and specific binding affinity to PC. The demonstrated properties highlight its potential as next-generation radiopharmaceuticals, which could significantly enhance diagnostic capabilities in nuclear oncology through timely identification of pancreatic malignancies.

EPS-054

First in Man Microdose Trial of [^{68}Ga]Ga-R54, CXCR4 Targeted PET tracer. Comparison with [^{18}F]-FDG and proof of concept in lung cancer models

A. Trotta[1], *L. Portella*[1], *M. Aurilio*[1], *C. D'alterio*[1], *L. D'Ambrosio*[1], *C. Maisto*[1], *A. Morisco*[1], *F. Manna*[1], *A. Luciano*[1], *G. Palma*[1], *G. Di Maiolo*[1], *F. Bruzzese*[1], *R. De Marino*[1], *A. Esposito*[1], *A. Rossi*[1], *F. Ricci*[1], *M. Cerrone*[1], *G. De Feo*[1], *S. Di Maro*[2], *S. Lastoria*[1], *S. Scala*[1];
[1]*Istituto Nazionale Tumori, Fondazione "G. Pascale" -IRCCS, Napoli, ITALY,* [2]*Università della Campania L. Vanvitelli, Caserta, ITALY.*

Aim/Introduction: CXCR4 is overexpressed on the majority of haematological and solid cancers and correlates with metastatic features. CXCR4 is a potential imaging target for the accuracy of diagnosis, staging and predictive treatment efficacy. [^{68}Ga]Ga-Pentixafor is the most advanced CXCR4 targeting PET tracer, nevertheless the sensitivity and specificity toward solid tumors is modest. A new CXCR4-targeting PET tracer, [^{68}Ga]Ga-R54 (PCT/EP2020/087792), specifically accumulated in CXCR4+ tumours in human xenograft models. Aims of the work are to extend the in vivo specificity and imaging efficacy of [^{68}Ga]Ga-R54 in lung cancer xenograft models and to proceed with a First in Man, Microdose trial to identify [^{68}Ga]Ga-R54 Pharmacokinetics/ Pharmacodynamic in metastatic/ advanced solid tumors. Toxicity and toxicokinetic study in rats demonstrated non-evident 2 and 14 days post-injection (p.i.) toxicity. A monocentric, nonrandomized, open label clinical trial with [^{68}Ga]Ga-R54 (R4-FOUR-PET EUCT:2024-513303-14-00) was recently approved. ***Materials and Methods:*** PET/CT imaging and biodistribution was conducted on athymic mice bearing subcutaneous H69 (SCLC, high CXCR4) and H460 (NSCLC, moderate CXCR4) tumors. R4-FOUR-PET will enrol 5-10 patients CXCR4+ advanced cancers (breast, colon, lung, pancreas and ovarian). Primary objective is to evaluate pharmacokinetics and pharmacodynamics of a single microdose (<100 µg) of [^{68}Ga]Ga-R54. Comparison with [18F]-FDG and correlation between SUVmax and CXCR4 IHC expression will be conducted. ***Results:*** Biodistribution studies in H69 and H460 xenograft models revealed high and specific tumour uptake in both tumors after 1 hour post injection (H69-tumor uptake: 12.2±1%ID/g; H460-tumor uptake: 2±0.4%ID/g) and rapid renal excretion. Competition with cold R54 reduced [^{68}Ga]Ga-R54 uptake by approximately 90% and 60% respectively showing CXCR4 specificity. Compared to [^{18}F]-FDG, [^{68}Ga]Ga-R54 showed significantly higher uptake in H69 tumors (12.2±1%ID/g vs 3.75±0.6%ID/g, p<0.001). Consistently, PET/CT scans clearly visualized tumors at 1 hour post tracer administration with significant reduction in accumulation due to cold R54. To date, 4 ovarian, 1 colon, 2 lung and 2 breast cancer patients were enrolled in the R4-FOUR-PET trial and the first patient (ovarian cancer CXCR4+) was injected with [^{68}Ga]Ga-R54. [^{68}Ga]Ga-R54 visualized metastatic lesion CXCR4+ with good image contrast at 1h p.i. and is not associated with any toxicity. ***Conclusion:*** [^{68}Ga]Ga-R54 can be used to image CXCR4 expressing SCLC/NSCLC xenografts. [^{68}Ga]Ga-R54 can be used to visualize CXCR4+ tumors in metastatic ovarian cancer patients.

EPS-056

Drug Kinetics and Therapeutic Efficacy of Non-targeted Astatine-labeled Gold Nanoparticles Administered Locally to Tongue Cancer

H. Kato[1], *H. Shimamoto*[2], *Y. Kadonaga*[1], *K. Ooe*[1], *S. Yamamoto*[3], *X. Huang*[4], *E. Hilmayanti*[5], *A. Shimoyama*[5], *K. Kabayama*[1], *A. Toyoshima*[6], *S. Murakami*[2], *K. Fukase*[6];
[1]*Institute for Radiation Sciences, The University of Osaka, Suita, Osaka, JAPAN,* [2]*School & Graduate School of Dentistry The University of Osaka, Suita, Osaka, JAPAN,* [3]*Waseda Research Institute for Science and Engineering, Tokyo, JAPAN,* [4]*Immunology Frontier Research Center (IFReC), Osaka University, Suita, Osaka, JAPAN,* [5]*Department of Chemistry, Osaka University Graduate School of Science, Toyonaka, Osaka, JAPAN,* [6]*Institute for Radiation Sciences, The University of Osaka, Toyonaka, Osaka, JAPAN.*

Aim/Introduction: Although surgery is the treatment of choice for early-stage tongue cancer, less invasive treatment is awaited because of the impact on quality of life, such as taste disorder and deterioration of speaking. We focused on locoregional administration of non-targeted RI labeled nanoparticles because of their versatility and fast drug excretion rate. In this study, we evaluated the efficacy and pharmacokinetics of [^{211}At]AuNP-S-mPEG (AuNP@PEG), a drug consisting of polyethylene glycol-modified gold nanoparticles labeled with the alpha-ray nuclide

astatine-211, administered locoregionally to tongue cancer patients. The AuNP@PEG was optimized with respect to particle size, particle morphology, PEG size, dosage, and administration method. ***Materials and Methods:*** We varied the administered AuNP size from 2 nm to 30 nm and the PEG chain length from 1kDa to 20 kDa. In addition, the drug AuNR@PEG was prepared by replacing AuNPs with gold nanorods (AuNR). The human pancreatic cancer cell line SAS was transplanted into the lateral abdomen of nude mice. One week after transplantation, the drug was administered slowly into the tumor and changes in tumor size and body weight were observed. In addition, we examined systemic and intratumor drug distribution after administration, respectively. ***Results:*** The locally administered drug effectively inhibited tumor growth of tongue cancer without serious side effects. No significant differences in efficacy were observed for AuNP and PEG sizes, but AuNR@PEG was less effective. The effect was enhanced in a dose-radioactivity-dependent manner, and divided dosing was more effective than single dosing. AuNP@PEG diffused slowly and uniformly into the tumor, while the distribution of AuNR@PEG within the tumor was heterogeneous. Smaller AuNPs showed faster systemic elimination. Intratumor administration of [^{198}Au]AuNP@PEG with a particle size of 5 nm and tracking of drug distribution up to 5 days after administration revealed that AuNPs persist in the liver, and spleen and in the tumor. ***Conclusion:*** Intratumoral administration of non-targeted astatine-labeled gold nanoparticles strongly inhibited tongue cancer growth in a radioactivity-dependent manner without apparent side effects. It was found that fractional dosing is more effective and that smaller gold nanoparticles are optimal for excretion.

EPS-057

Development of fluorinated D-peptide radiopharmaceutical with significantly high tumor uptake for potential combination immunotherapy

C. Liu[1], *S. Zhang*[1], *W. Liu*[1], *Q. Lu*[1], *F. Wang*[2], *R. Wang*[1], *K. Hu*[1]; [1]*Institute of Materia Medica, Chinese Academy of Medical Sciences and Peking Union Medical College, Beijing, CHINA,* [2]*Department of Nuclear Medicine, Nanjing First Hospital, Nanjing Medical University, Nanjing, CHINA.*

Aim/Introduction: [^{68}Ga]DPA exhibits diagnostic potential for non-invasive PD-L1 detection but suffers from suboptimal tumor uptake and transient retention time. The fluorine modification enhances both pharmacokinetic properties and tumor-targeting capacity. In this study, we developed DPA analogs via amino acid substitution with fluorinated optimization to improve tumor uptake and retention time. Furthermore, the optimized ^{177}Lu-labeled fluorinated DPA analog was evaluated for radionuclide therapeutic potential alone or in combination with immunotherapy in triple-negative breast cancer. ***Materials and Methods:*** Peptides were radiolabeled with ^{68}Ga for PET imaging in A375-PD-L1 tumor-bearing mice, with 3.7 MBq administered intravenously per mouse and PET/CT scans acquired at 0.5h/1h post-injection. For therapy, D3 and DPA-5F analogs were labeled with ^{177}Lu. BALB/c mice with bilateral 4T1 tumors were randomized into six groups. Primary tumors received 18.5 MBq ^{177}Lu-ligands intratumorally (monotherapy) or combined with 200 μg intraperitoneal anti-PD-1 every 3 days. Post-treatment, tumors were analyzed for DCs (anti-CD11c-APC/CD80-FITC/CD86-PE) and T cell subsets (anti-CD3-FITC/CD8-PE-Cy7/CD4-PE-Texas Red) via flow cytometry. ***Results:*** A two-stage screening strategy was conducted. In the first alanine scanning round, DPA analogs were assessed for binding affinity to human PD-L1 protein using BLI assay and evaluated for in vivo imaging performance using PET/CT scanning. The D3 analog demonstrated superior tumor uptake (5 %ID/g) compared to the parental DPA peptide (3.5 %ID/g). For subsequent optimization, we designed a series of fluorinated peptides based on D3. Second-stage PET evaluation identified DPA-5F as the lead compound, demonstrating peak tumor uptake (15.3 %ID/g) at 30 minutes, and prolonged retention time evidenced by the sustained tumor uptake through 4 h. To further investigate radionuclide therapeutic potential of [^{177}Lu]5F and combination therapy with anti-PD-1, 4T1 tumor-bearing mice were randomized into six groups: 1) control, 2) anti-PD-1, 3) [^{177}Lu]D3, 4) [^{177}Lu]5F, 5) [^{177}Lu]D3 + anti-PD-1, and 6) [^{177}Lu]5F + anti-PD-1. After 13-day treatment, group 6 exhibited significant antitumor efficacy. To understand this phenomenon, DC infiltration was first analyzed, revealing maximal DC accumulation in group 4. Flow cytometry analysis demonstrated increased percentages of CTLs and Th cells in group 4 (primary tumors) and group 6 (distant tumors). ***Conclusion:*** This investigation demonstrates that the fluorinated compound [^{68}Ga]DPA-5F achieves both increased tumor uptake and prolonged tumor retention. The combination therapy ([^{177}Lu]DPA-5F + anti-PD-1) effectively exerts potent antitumor effects, demonstrating the synergistic potential of radionuclide therapy and immunotherapy.

EPS-058

Preclinical Evaluation of a PSMA-targeting Theranostic Candidate with Reduced Gland Uptake

G. Chen, *X. Hu, Y. Cao, M. Hong, S. Xu, J. Wen; RadAlliance Therapeutics Inc, San Diego, CA, UNITED STATES OF AMERICA.*

Aim/Introduction: Although PSMA-617 has demonstrated superior commercial value, xerostomia caused by its undesired salivary gland uptake is still the issue to be solved. A novel PSMA agent REX003 has been investigated to address PSMA-617's unsolved challenges, particularly the undesired salivary gland uptake. ***Materials and Methods:*** Ga68, Cu64, Lu177, and Ac225 labeled REX003 were evaluated under in vitro, ex vivo and in vivo conditions, head to head to compare with PSMA-617. PSMA binding specificity and affinity were demonstrated. Biodistributions of Lu177-REX003 in xenograft mice with different PSMA expression level were used to assess its tumor-targeting specificity. A separated hot blood PK measurement was performed to evaluate blood exposure difference. PET imaging of Cu64-REX003 on the same NHP (n=2) was used to compare gland uptake. Both Lu177-REX003 and Ac225-REX003 were used to compare efficacy in xenograft model vs benchmark compound. ***Results:*** Preclinical evaluation of Lu-177-labeled REX003 has demonstrated its bigger therapeutic windows to PSMA-617 on salivary gland uptake of 8-fold+, on blood toxicity of 2-fold+ and on kidney 20-90%. Ac225-labeled REX003 could have more potential over PSMA-617 due to its PK profile and gland uptake selectivity. ***Conclusion:*** REX003, a PSMA-targeting agent with versatile radionuclides shows great potential in treatment and diagnosis of PSMA-positive prostate cancer.

EPS-059

Development and Preclinical Evaluation of Novel PSMA-Targeted Nanobody Radiopharmaceuticals for Prostate Cancer Treatment

B. Yang, *Y. Gai, Y. Liu, J. Hu, X. Zhang, M. Li, Y. Zhang, R. An, X. Lan; Department of Nuclear Medicine, Union Hospital, Tongji Medical College, Huazhong University of Science and Technology, Wuhan, CHINA.*

Aim/Introduction: Prostate-specific membrane antigen (PSMA) exhibits specific high expression in prostate cancer (PCa) and low expression in normal tissues. Its expression level is highly correlated with tumor aggressiveness, making it a classical target for PCa. Currently, most proteins identified with sufficiently high affinity (in the nmol range) for the extracellular region of PSMA are monoclonal antibodies or antibody fragments. Nanobodies represent the smallest antibody units capable of stably binding

to antigens identified so far. Compared to traditional monoclonal antibody molecules, nanobodies, due to their smaller molecular weight, can directly penetrate dense tumor tissues. Structurally, they have a longer antigen-binding domain compared to traditional VH domains, resulting in stronger affinity for antigens. ***Materials and Methods:*** Three novel PSMA-specific antibodies, AP01, AP02 and AP03, were produced and labeled with ^{177}Lu to develop radiopharmaceuticals. The stability study and partition coefficient were determined. A series of cell assays was performed to identify the binding affinity and PSMA specificity in vitro. We performed SPECT/CT imaging and biodistribution studies with [^{177}Lu]Lu-AP01, [^{177}Lu]Lu-AP02 and [^{177}Lu]Lu-AP03 in subcutaneous LNCaP patient-derived xenograft models. ***Results:*** All radiopharmaceuticals were successfully prepared with high purity and stability. [^{177}Lu]Lu-AP01 was stable in saline for at least 120 h. They exhibit excellent stability in vitro with good water solubility. The [^{177}Lu]Lu-AP01, [^{177}Lu]Lu-AP02 and [^{177}Lu]Lu-AP03 exhibited high PSMA-binding affinity and specificity both in vitro and in vivo. Compared with the [^{177}Lu]Lu-AP02 and [^{177}Lu]Lu-AP03, [^{177}Lu]Lu-AP01 demonstrated remarkably enhanced tumor accumulation and tumor-to-nontumor ratios (28.58 ± 4.25 %ID/g for [^{177}Lu]Lu-AP01 vs. 16.10 ± 1.54 %ID/g for [^{177}Lu]Lu-AP02 and 15.45 ± 0.65 %ID/g for [^{177}Lu]Lu-AP02 at 48h post-injection). ***Conclusion:*** A series of novel PSMA-targeted nanobody radiopharmaceuticals have been developed and evaluated in vitro and in vivo. Significantly improved tumor uptake and retention were observed for [^{177}Lu]Lu-AP01. The favorable in vivo pharmacokinetics and excellent tumor accumulation, make it a promising radiopharmaceutical for prostate cancer treatment.

EPS-060

Development of [^{68}Ga]Ga-B6FA-01 as a Novel Radiotracer for Dual $\alpha_v\beta_6$and FAP-targeted Tumor PET Imaging

K. Xu[1], *Y. Wang*[1], *Y. Gai*[2], *P. Lei*[3], *Z. Xiao*[1], *Y. He*[1];
[1]*Department of Nuclear Medicine, Zhongnan Hospital of Wuhan University, Wuhan, Wu Han, CHINA,* [2]*Department of Nuclear Medicine, Union Hospital, Tongji Medical College, Huazhong University of Science and Technology, Wu Han, CHINA,* [3]*Department of Immunology, School of Basic Medicine, Tongji Medical College, Huazhong University of Science and Technology, Wu Han, CHINA.*

Aim/Introduction: To overcome the limitation and imperfection on account of the tumor heterogeneity in single-targeting imaging, we developed a bi-specific tracer [^{68}Ga]Ga-B6FA-01, targeting two different chosen cell surface biomarkers, fibroblast activating protein (FAP) and integrin $\alpha_v\beta_6$. ***Materials and Methods:*** [^{68}Ga]Ga-B6FA-01 was designed and synthesized on the basis of quinoline-based FAP inhibitors (FAPI-04) and cyclic RGD peptide monomers1. In vitro formulation stability and metabolic stability were evaluated in PBS and serums (including mice, rats, NHPs, and human), respectively. Further preclinical evaluations of cell uptake and micro-PET/CT imaging were conducted with FAP-$\alpha_v\beta_6$ dual over-expressed HT1080 cells, and corresponding tumor xenograft models. ***Results:*** [^{68}Ga]Ga-B6FA-01 exhibited excellent formulation stability (>99% remained at 3h in PBS), and first-class metabolic stability in serums (>99% remained at 2h in mice, rats, NHPs, and human, respectively). Dual-target binding affinity was revealed significantly in the blocking cell uptake experiments with FAPI-04 ($P < 0.001$) and Trivehexin ($P < 0.001$) as the competitors. In PET/CT imaging, prolonged uptake values were observed (9.42±0.37, 2.62±1.15, and 4.02±1.04 %ID/g at 4h p.i. of [^{68}Ga]Ga-B6FA-01, [^{68}Ga]FAPI-04, and [^{68}Ga]Trivehexin, respectively), and optimized tumor/kidney ratio was revealed (4.68±0.82, and 0.18±0.02 of [^{68}Ga]Ga-B6FA-01, and [^{68}Ga]Trivehexin at 4h p.i.). Co-administration of unlabeled FAPI-04, Trivehexin, and both FAPI-04 and Trivehexin significantly lowered the tumor uptake (0.80±0.12, 1.57±0.16, and 0.60±0.09 compared with 1.37±1.38 %ID/g in baseline group at 1h p.i., respectively). ***Conclusion:*** This work demonstrated a FAP-$\alpha_v\beta_6$ dual-targeting tracer [^{68}Ga]Ga-B6FA-01, resulting in superior tumor uptake and retention time compared with mono-targeting tracers [^{68}Ga]Ga-FAPI-04 and [^{68}Ga]Ga-Trivehexin, and improved renal clearance over the trimer tracer [^{68}Ga]Ga-Trivehexin. Our findings strengthened the potential feasibility of heterodimeric tracers in clinical tumor PET imaging. ***References:*** 1.Neil Gerard Quigley et al, RSC Med. Chem. 2023, 14, 1564.

EPS-061

Preclinical Evaluation of [^{64}Cu]CuNODAGAPSMAI&T for Prostate Cancer Theranostics

D. Rodrigues[1], *A. I. Fonseca*[2], *J. Sereno*[1], *S. do Carmo*[1,2], *V. Marques*[2], *I. Hrynchak*[2], *J. N. Moreira*[3,4,5], *C. Gomes*[5,6,7], *A. Abrunhosa*[1];
[1]*ICNAS/CIBIT, Coimbra, PORTUGAL,* [2]*ICNAS Pharma, Coimbra, PORTUGAL,* [3]*CNC, Coimbra, PORTUGAL,* [4]*Faculty of Pharmacy, Coimbra, PORTUGAL,* [5]*CIBB, Coimbra, PORTUGAL,* [6]*Faculty of Medicine, iCBR, Coimbra, PORTUGAL,* [7]*CACC, Coimbra, PORTUGAL.*

Aim/Introduction: Prostate cancer (PCa) remains one of the most commonly diagnosed malignancies and a leading cause of cancerrelated mortality among men worldwide. Prostatespecific membrane antigen (PSMA) is a wellestablished biomarker overexpressed in PCa, making it an attractive target for both diagnostic imaging and targeted radionuclide therapy. Owing to its unique physical decay properties, copper64 has steadily gained traction in nuclear medicine. In this study, we evaluated the theranostic potential of [^{64}Cu]CuNODAGAPSMAI&T, a novel PSMAtargeting radioconjugate, in a preclinical model of PCa. We aimed to assess its in vivo imaging characteristics, ex vivo biodistribution, dosimetry, and therapeutic efficacy in tumourbearing mice. ***Materials and Methods:*** Copper64 was obtained inhouse by proton irradiation of enriched nickel64 liquid targets in a biomedical cyclotron, followed by postprocessing and NODAGAPSMAI&T radiolabelling. The radiochemical purity and stability of the radiolabelled compound was assessed by radioHPLC and iTLC. For in vivo PET/MR imaging and ex vivo biodistribution studies, Swiss nude mice were subcutaneously inoculated with PC3PIP (PSMApositive) or PC3Flu (PSMAnegative) cells. Dosimetric calculations were performed with OLINDA/EXM® software. The therapeutic efficacy of [^{64}Cu]CuNODAGAPSMAI&T was evaluated in PC3PIP tumourbearing mice. ***Results:*** [^{64}Cu]CuNODAGAPSMAI&T was consistently produced with high radiochemical yields (>85%) and suitable molar activities (20-30 GBq/µmol) for preclinical use. The radiochemical purity of the final product remained above 95% for at least 24 h after the end of synthesis. PET/MR imaging showed strong and selective uptake in PSMApositive tumours, but no uptake in PSMAnegative counterparts (~6% vs ~0.3% ID/g, respectively), confirming target specificity. There was no radiopharmaceutical accumulation in nontargeted organs or tissues besides the kidneys and the urinary bladder, indicative of its renal excretion. These findings were corroborated by the ex vivo biodistribution analysis. In PSMApositive tumourbearing mice, treatment with [^{64}Cu]CuNODAGAPSMAI&T significantly delayed tumour growth and extended survival compared to untreated controls. Dosimetric calculations expectedly identified the kidneys as the doselimiting organs, receiving an absorbed dose of 1.03e-01 mGy/MBq. The effective dose was estimated at 6.60e-03 mSv/MBq. ***Conclusion:*** [^{64}Cu]CuNODAGAPSMAI&T demonstrated excellent in vivo stability, high tumour uptake and specificity, and a favourable biodistribution profile, ultimately resulting in effective tumour growth control and improved survival in a preclinical PCa model. The dual capability of the radiopharmaceutical for both highcontrast PET imaging and targeted radionuclide therapy underscores its strong potential as a versatile theranostic agent. Altogether, these findings encourage further investigation

and support the progression of [^{64}Cu]CuNODAGAPSMAI&T toward clinical translation for the personalized management of PSMAexpressing PCa.

EPS-062

Discovery and preclinical characterization of ETN029, a novel radiotherapeutic agent for the treatment of DLL3-expressing cancers

A. Savinainen, *L. Wu, T. Bruton, A. Chonkar, J. Cupido, J. Dearling, C. Huang, K. Lee, Z. Ma, H. Mok, K. Nabi, A. Salih, A. Sutton, L. Tavera, M. Wan, Z. Weng, X. Xu, J. Xu, A. Zidell, A. Ricardo; Mariana Oncology a Novartis Company, Watertown, MA, UNITED STATES OF AMERICA.*

Aim/Introduction: Neuroendocrine neoplasms (NENs), including small cell lung cancer (SCLC) and neuroendocrine prostate cancer (NEPC), commonly exhibit upregulated surface expression of the atypical notch Delta-like ligand 3 (DLL3). ETN029 is a novel macrocyclic peptide binder to DLL3 designed to achieve high, rapid uptake and retention in tumor tissue and fast clearance of the unbound compound via the renal route. We have demonstrated that ETN029 has excellent binding kinetics and a favorable tumor:kidney (T/K) ratio and that a single dose of ^{225}Ac-ETN029 results in robust and sustained tumor regression and prolonged survival in a dose-dependent manner in subcutaneous cell-derived xenograft (CDX) SCLC models. Further, we have characterized the in vivo anti-tumor activity of ^{225}Ac-ETN029 in combination with different elements of standard-of-care for SCLC, including chemotherapy (cisplatin/etoposide) in CDX models and anti-programmed cell death ligand 1 (anti-PD-L1) checkpoint inhibitor therapy in a syngeneic model. ***Materials and Methods:*** Binding affinity and selectivity were characterized using surface plasmon resonance (SPR). Cell binding and internalization were determined in a cell-based assay in cell lines expressing DLL3. In vivo biodistribution and anti-tumor activity was assessed in mouse models expressing DLL3. ***Results:*** ETN029 binds rapidly and selectively to human DLL3 with picomolar affinity. ^{177}Lu-ETN029 exhibited high cell binding and internalization in DLL3 expressing cells. Biodistribution studies of ^{177}Lu-ETN029 in a mouse CDX model demonstrated rapid radionuclide tumor uptake, persistent tumor retention throughout the study, and a favorable T/K ratio. In vivo efficacy studies in CDX and syngeneic mouse models with tumors expressing human DLL3 demonstrated robust and sustained dose-dependent tumor regression and prolonged survival after a single dose of ^{225}Ac-ETN029 (0.25-1 µCi). While the highest dose of ^{225}Ac-ETN029 (1 µCi) resulted in complete tumor regression, therapy with either cisplatin/etoposide or anti-PDL-1 alone resulted in moderate tumor growth inhibition. When a low dose of ^{225}Ac-ETN029 (0.25 µCi) was combined either with chemotherapy in a CDX model or with anti-PD-L1 in a syngeneic model, the efficacy was improved over either treatment alone. ***Conclusion:*** Taken together, these studies support the use of ^{225}Ac-ETN029 either as single agent treatment or in combination with standard-of-care chemo- and/or immunotherapy in patients with SCLC and potentially other DLL3-expressing solid tumors.

EPS-063

High and Flow-Independent Extraction Fraction of ^{99m}Tc-4BOH in Langendorff Rat Hearts vs. Clinical SPECT Tracers

D. Ding[1], *Y. Gu*[1], *Y. Zhang*[2], *Z. Lv*[2], *L. Sun*[2], *J. Wang*[2], *F. Guo*[3], *W. Fang*[1], *T. Ma*[2], *L. Wang*[1];
[1]*Fuwai Hospital, National Center for Cardiovascular Diseases, Chinese Academy of Medical Sciences, Beijing, CHINA,* [2]*Tsinghua University, Beijing, CHINA,* [3]*Greater bay area national center of technology innovation, Guangdong, CHINA.*

Aim/Introduction: The novel SPECT myocardial perfusion tracer ^{99m}Tc-4BOH has shown preclinical advantages, including prolonged myocardial retention and high heart-liver contrast. This study evaluated the first-pass extraction fraction (EF) of ^{99m}Tc-4BOH in isolated rat hearts using the Langendorff perfusion method against ^{99m}Tc-Teboroxime and ^{99m}Tc-Sestamibi. ***Materials and Methods:*** Hearts from anesthetized male SD rats (275-325g, n=29) were aortic-cannulated and perfused non-recirculatingly with Krebs-Henseleit buffer at three controlled flow rates (5.0, 8.4, and 16.0 mL/min). ^{99m}Tc-Teboroxime, ^{99m}Tc-4BOH, and ^{99m}Tc-Sestamibi were separately tested by delivering a single bolus injection (1 mCi in 0.1 mL) to 3 to 4 isolated hearts at each specified flow rate. The time-activity curve in the heart was recorded over 10 min with Handheld Self-Collimation Gamma Camera. EF was quantified using the Raichle B/A ratio method. ***Results:*** ^{99m}Tc-4BOH exhibited a high overall EF of 93.98 ± 4.54% (n=10), which was comparable to that of ^{99m}Tc-Teboroxime (96.90 ± 1.95%, n=9; $p>0.05$), and significantly higher than ^{99m}Tc-Sestamibi (30.70 ± 7.31%, n=10; $p<0.01$). The EF measured at flow rates of 5.0, 8.4, and 16.0 mL/min were well-maintained for ^{99m}Tc-4BOH, with values of 93.37 ± 4.43%, 92.23 ± 6.92%, and 96.53 ± 0.67%, respectively ($p>0.05$). Similarly,^{99m}Tc-Teboroxime demonstrated stable EF values of 97.40 ± 0.57%, 98.10 ± 2.44%, and 95.18 ± 1.41% ($p>0.05$). In contrast, ^{99m}Tc-Sestamibi showed a significant decline in EF from 39.19 ± 4.93% to 30.88 ± 2.68% and 24.20 ± 3.25% ($p < 0.01$) at these flow rates. ***Conclusion:*** The high EF and the flow-independent characteristic of ^{99m}Tc-4BOH indicates its potential as a promising myocardial perfusion imaging agent, which may offer enhanced accuracy in blood flow quantification compared to conventional SPECT tracers.

510

Sunday, October 5, 2025, 15:00 - 16:30
Room 116

Technologists' Track Oral Presentations 1 - Technologists Committee: PET-CT Studies: Diagnosis and Treatment

OP-883

Evaluation of Automatic Selective Body Part Reconstruction on a Long Axial Field of View PET/CT System

M. Olhaye, *H. Danielsen;*
Aarhus University Hospital, Aarhus, DENMARK.

Aim/Introduction: An inherent challenge on Long Axial Field of View (LAFOV) PET/CT scanner is handling very large data amounts due to their high sensitivity. Reconstruction times for full data set can be quite long, and, in some cases, only selective organ areas are of interest for the clinical reading. To mitigate this issue Siemens Healthineers introduced SMART Image Framer which selectively reconstructing up to four predefined areas - liver, brain, heart, and head/neck - in PET scans based on anatomical information acquired from the CT localizer radiograph. This study aims to evaluate the effectiveness and limitations of this application over a period of two months. ***Materials and Methods:*** One hundred patients, including five children aged 2-13 years, were scanned. Each patient's data was reconstructed using the SMART Image Framer for all four anatomic areas. The cohort included various scan protocols, bed positions, tracers, and patients of different ages and sizes. Data was assessed according to correct anatomy placement, misplaced anatomy, or failed reconstruction. Only single-bed examinations were included. ***Results:*** Of the 386 reconstructions, 40 were unusable, with 37 failed and three misplaced, yielding a success rate of 89.6%. The application bases reconstructions on the last acquired localizer in the protocol, leading to 7% of failures. In protocols where posterior-anterior localizer was scanned before lateral localizer, only the brain area

was reconstructed. Combined protocols with two localizers covering the torso and legs separately failed to reconstruct any anatomy of interest unless reconstructions were initiated before the second appended localizer was performed. 1.8% of failures were due to small or abnormal anatomy with lower success rates in children and for one patient with an enlarged liver. 1.3% failed for unknown reasons, including one case where only half the brain area was reconstructed. ***Conclusion:*** Overall, the study shows a promising tool with a high success rate. As long as the different limitations are known, the SMART image framer is easily applied and works well across a variety of protocols and patient groups. It significantly reduces data volume by selecting only relevant organ areas, enhancing daily clinical efficiency.

OP-884

Personnel dose in the [^{18}F]FDG workflow: LAFOV PET/CT versus SAFOV PET/CT

J. Effing, *T. Young-Mylvaganan, E. C. Streefkerk, J. Maarsen, E. A. Aalbersberg;*
The Netherlands Cancer Institute, Amsterdam, NETHERLANDS.

Aim/Introduction: The new highly sensitive LAFOV PET/CT (Siemens Biograph Vision Quadra) allows further reduction in administered activity and scan duration, which can lead to a significant reduction in dose exposure of PET/CT-related nuclear medicine personnel. The aim of this study is to determine the impact on the external radiation exposure of personnel on LAFOV PET/CT compared to SAFOV PET/CT. ***Materials and Methods:*** For dose analysis, data from all personnel (laboratory technologists, medical assistants and PET technologists) who worked on SAFOV PET/CT with full-dose (3.5 MBq/kg) were collected from July 2023 to December 2023, which was compared to data from July 2024 to December 2024 with low-dose (1.5 MBq/kg) on LAFOV PET/CT. During these periods, all personnel wore Thermo Luminescent Dosimeters (TLD) badges in the upper pocket of their uniform, for the preparation and administration of the radiopharmaceuticals, and patient positioning for the scan. During preparation, laboratory technologists wore extremity dosimeters on both hands, on the palmar side. ***Results:*** The average prepared dose of [^{18}F]FDG was 481 MBq (2278 injections) for SAFOV PET/CT and 271 MBq (2342 injections) for LAFOV PET/CT, resulting in a [18F]FDG dose reduction of 43.6%. With the introduction of LAFOV PET/CT, an average reduction of 52.4% was achieved for the external dose of laboratory technologists; from 17.11 µSv to 8.15 µSv. The extremity doses remained the same, 24.9 µSv compared to 23.6 µSv.The total amount of injected [^{18}F]FDG by the medical assistants was reduced from 562 GBq to 277 GBq, with a mean activity of 272 MBq reduced to 123 MBq per patient. This results in an average exposure dose from 17.29 µSv to 6.68 µSv per day, which is a 61.4% reduction. During the positioning of patients on the scanner, the personnel dose was also lowered from 2.71 µSv to 1.32 µSv per patient: a 51.3% reduction. ***Conclusion:*** By reducing the administered dose from 3.5 MBq/kilogram to 1.5 MBq/kilogram, the dose received by personnel has been drastically reduced. During all activities with [^{18}F]FDG, a clear decrease is seen.

OP-885

Optimising Zr-89-Trastuzumab PET/CT Imaging: Protocol Design for Short and Long Axial Field-of-View Systems

M. van der Vegt, *A. I. van Erp - Zeilstra, A. W. J. M. Glaudemans, W. Noordzij, R. H. J. A. Slart, E. H. J. G. Aarntzen, A. H. Brouwers, O. V. Ivashchenko;*
University Medical Centre Groningen, Groningen, NETHERLANDS.

Aim/Introduction: Imaging with radiolabelled therapeutic monoclonal antibodies plays a growing role in tumour characterisation prior to treatment initiation, as well as in drug development to assess biodistribution and pharmacokinetics. However, the inherently low activity of Zr-89 necessitates lengthy PET/CT acquisition times. Long Axial Field-of-View (LAFOV) PET/CT systems offer increased sensitivity and improved image quality, making them well-suited for Zr-89 imaging. Yet, optimised protocols across different PET/CT platforms remain undefined, and the minimum image quality needed for reliable interpretation is unclear. This study aimed to determine the minimal image quality requirements for Zr-89-trastuzumab imaging on either digital Short Axial Field-of-View (SAFOV) and LAFOV PET/CT systems. ***Materials and Methods:*** Twenty breast cancer patients were analysed, scanned between April 2021 and September 2024, imaged with SAFOV or LAFOV PET/CT systems (10/system). The mean administered activity was 37.5±10% MBq and all scans were conducted on day 4 postinjection. Reconstructions were performed to simulate varying scan durations: 100%, 50%, and 33% of mean LAFOV count statistics, plus matched and 50% SAFOV count levels. SAFOV scans were reconstructed at 100%, 75%, 50%, and 25% of their typical duration. LAFOV data were reconstructed using high sensitivity (HS) and ultra-high sensitivity (UHS) mode. All images were reconstructed using clinical and Zr-89 EARL settings. Five nuclear medicine physicians rated image quality using a 5-point Likert-scale. Quantitative evaluation was based on signal-to-noise ratio (SNR) and tumour-to-background ratio (TBR) in lesions, spleen and blood pool. Liver was excluded as normal organ due to metastatic involvement in some patients. ***Results:*** Physicians required different SNR thresholds in the spleen for acceptable quality: SAFOV = 5.39, LAFOV-HS = 11.06, LAFOV-UHS = 10.83. At equal count statistics, LAFOV-HS and SAFOV scans showed no significant SNR difference (SNR-LAFOV-HS = 8,30, SNR-SAFOV = 7,39, p = 0.135). However, LAFOV-UHS scans showed significantly higher SNR (SNR-LAFOV-UHS = 10,34, SNR-SAFOV = 7,39, p = 0.005). Tumour SNR and TBR remained stable across scan times and systems. Scan time could be reduced by up to 67% with LAFOV and 50% with SAFOV without compromising diagnostic quality. SNR loss became significant only below 50% of standard SAFOV scan duration. ***Conclusion:*** Spleen SNR declines with shorter scans, but lesion visibility and TBR remain unaffected. LAFOV PET/CT enables shorter, high-quality Zr-89 scans. For 37 MBq injections with a skull-to-proximal femur scan on day 4 postinjection, we recommend 9.7-minute LAFOV-UHS and 1.1 mm/sec SAFOV acquisitions for optimal efficiency and image quality.

OP-886

Optimising Post-Yttrium-90 Radioembolization PET/CT Scan Times: A Comparative Evaluation of Standard and Long Axial Field-of-ViewDigital PET/CT in Clinical Practice

T. Stark, *N. Reitsma, W. Noordzij, O. V. Ivashchenko;*
UMCG, Groningen, NETHERLANDS.

Aim/Introduction: Post-treatment PET/CT imaging is essential for assessing the therapeutic efficacy of yttrium-90 (Y-90) radioembolisation. However, Y-90's extremely low positron emission yield (0.003%, compared to 98% for F-18) necessitates extended acquisition times, even with high administered activities (3-5 GBq). Building on prior phantom-based optimisation work, this study retrospectively evaluates and refines scan durations for both standard axial field-of-view (SAFOV) and long axial field-of-view (LAFOV) digital PET/CT systems in clinical practice. The aim is to minimise scan time without compromising quantitative accuracy or diagnostic image quality. ***Materials and Methods:*** Twenty patients who underwent post-radioembolization Y-90 PET/CT scans were included (10 SAFOV, 10 LAFOV). The mean administered activity was 2.5 GBq (range: 0.5-7.5 GBq), with an average imaging delay of 20.6 hours. To standardise image quality, the average total scan count from the SAFOV group (18,300,815 counts/scan) was used as a reference, reflecting administered activity, acquisition time, and scanner sensitivity. Simulated reconstructions were generated at 200%, 150%, 100%, 75%, and 50% of baseline counts.

All scans were reconstructed using consistent parameters (3D OSEM, 4 iterations, 5 subsets, 7 mm Gaussian filter, PSF modelling), with both full and partial sensitivity modes assessed for LAFOV systems. Although partial mode introduces a non-uniform image profile, it doubles the sensitivity at the centre of the field of view. Quantitative analysis included total activity (MBq), average activity concentration (Bq/ml), signal-to-noise ratio (SNR), tumour-to-background ratio (TBR), and contrast-to-noise ratio (CNR) in hepatic and tumour regions. ***Results:*** Tumour activity remained stable across all reconstructions (≤7% deviation). CNR and SNR improved with increasing scan duration. SNR rose from 2.54 ± 0.52 (50%) to 3.57 ± 1.06 (200%). CNR gains plateaued beyond 100%. For accurate quantification, 100% scan statistics were sufficient — equivalent to 8 minutes on SAFOV and 0.7-1.4 minutes on LAFOV for 2.5 GBq. For optimal SNR, 150% statistics were ideal (11 minutes SAFOV; 1-2 minutes LAFOV). Below 1 GBq, SAFOV required ≥30 minutes per bed for acceptable SNR, making LAFOV preferable. ***Conclusion:*** Quantification accuracy is maintained across a range of acquisition durations for both scanner types. However, tumour detectability, vital for post-therapy dosimetry, requires at least 11 minutes (SAFOV) or 1-2 minutes (LAFOV) for 2.5 GBq. For lower activities, LAFOV is recommended due to its higher sensitivity. To ensure consistent dosimetric accuracy, scan duration must be tailored to administered activity and system sensitivity. ***References:*** Croes, G., et al. (2023). EANM'23 Abstract Book Congress Sep 9-13, EPS-233.

OP-887

Optimization and harmonizaton of image reconstructions in [^{18}]F-FDG brain PET/CT for dementia

R. Klausen[1], *P. Braad*[2];
[1]*Department of Radiology, Hospital of Southern Denmark, Aabenraa, DENMARK,* [2]*Department of Clinical Imaging, Odense, DENMARK.*

Aim/Introduction: Time-of-flight (TOF) and block-sequential regularized expectation maximization (BSREM) reconstruction techniques, available on modern digital PET/CT systems, enhance quantitative accuracy and are recommended by the EANM procedure guidelines for [^{18}F]-FDG PET brain imaging. However, diagnostic tools such as 3D-SSP (Cortex-ID), which support dementia evaluation by comparing patient scans to a normal database, require that image reconstructions closely match those used to build the database. This study aimed to evaluate how BSREM reconstructions with and without TOF can be harmonized to comply with Cortex-ID. ***Materials and Methods:*** The Hoffmann 3D Brain Phantom (Data Spectrum) was filled with an aqueous homogeneous solution of [^{18}F]-FDG with a concentration of 36 kBq/ml and subsequently scanned on a Discovery MI 6R gen2 PET/CT system (GE Healthcare) using a standard 12.5 min static brain PET protocol. Phantom images were reconstructed in a field-of-view of 25 cm with a matrix size of 256 using the default ordered subset expectation maximization (OSEM) method (3 iterations/16 subsets) and compared to BSREM reconstructed images (w/wo TOF) with β parameters ranging from 100 to 2000. Images were segmented into grey and white matter regions and quantitation of each tissue type was calculated in 83 brain regions by registering the phantom to the Hammersmith brain atlas (n30r83). 5 patient scans were reconstructed using similar settings and the impact on Z-scores calculated by Cortex-ID was assessed. ***Results:*** TOF-BSREM underperformed compared to BSREM. Images reconstructed using BSREM with a β value of 1000 most closely matched the reference method in both visual quality and quantitative accuracy. On average, the deviations from the reference method were 1.8% in grey matter and -0.6% in white matter. Variations in individual brain regions ranged from -5% to 6% in grey matter and and -1% to 9% in white matter. In high-contrast areas, differences exceeding 10% were observed. Among patients, Z-scores derived from BSREM images were more consistent with the reference scores than those from TOF-BSREM. The mean absolute Z-score difference was 0.1 while differences up to 0.4 were measured in individual brain regions. ***Conclusion:*** Modern BSREM and TOF-based reconstruction techniques enhance image quality and uptake quantification. However, aligning these reconstructions with the normal database in 3D-SSP methods remains challenging, and care should be exercised when using BSREM for Z-score analysis in the evaluation of brain disorders.

OP-888

PET/CT imaging of Blood-Brain Barrier Integrity and inflammatory tracers during Alzheimer's Disease

B. Alenezi[1], *S. Paisey*[2], *T. Hughes*[3], *T. Webberley*[4], *D. Michael*[5], *S. Plummer*[6], *S. Plummer;*
[1]*Cardiff University, CF10 5NG, UNITED KINGDOM,* [2]*Wales Research and Diagnostic PET Imaging Centre, school of Medicine, Cardiff University Heath Park., Cardiff. CF14 4XN, UNITED KINGDOM,* [3]*Division of Infection and Immunity, Henry Wellcome Building, School of Medicine, Cardiff University Heath Park., Cardiff. CF14 4XN, UNITED KINGDOM,* [4]*Cultech Limited, Unit 2 Christchurch Road, Baglan Industrial Park, Port Talbot SA12 7BZ, UK., UNITED KINGDOM,* [5]*Cultech Limited, Unit 2 Christchurch Road, Baglan Industrial Park, Port Talbot SA12 7BZ, UK., UNITED KINGDOM,* [6]*Cultech Limited, Unit 2 Christchurch Road,, Baglan Industrial Park, Port Talbot SA12 7BZ, UK., UNITED KINGDOM.*

Aim/Introduction: Alzheimer's Disease (AD), the most common cause of dementia, is increasingly associated with immune system dysfunction, especially complement activation. Immuno-PET, which merges PET imaging's sensitivity with monoclonal antibody specificity, allows precise detection of disease-related targets. BB5.1, an antibody against murine complement protein C5, holds promise for imaging neuroinflammation. High-fat diets exacerbate inflammation, cognitive decline, and synaptic loss in 3xTg-AD mice—effects reduced by probiotic supplementation. We hypothesize that neurodegeneration and blood-brain barrier disruption in AD will allow radiolabeled BB5.1 to cross into the brain and visualize complement activity via immuno-PET. ***Materials and Methods:*** To investigate our hypothesis, in-vivo imaging was conducted on 3xTg-AD mice using ^{89}Zr-labeled BB5.1 to assess antibody biodistribution and brain penetration, and ^{18}F-FDG to evaluate brain metabolism. Imaging was performed at baseline (6 months) and endpoint (9 months), including PET/CT scans at 24h, 72h, and 144h post-injection of 2 MBq ^{89}Zr-BB5.1 or control antibody (^{89}Zr-D1.3), and 192h with 10 MBq ^{18}F-FDG. Mice were then assigned to one of four dietary groups (HFD±probiotics, chow±probiotics) for three months. Cognitive function was assessed by novel object recognition, inflammatory disease markers, and BBB integrity were evaluated by immunohistochemistry and qPCR. ***Results:*** In vitro hemolysis assays confirmed that ^{89}Zr-BB5.1 retained its ability to inhibit complement protein C5, indicating preserved biological activity. SDS-PAGE and RadioTLC analyses confirmed structural stability and successful radiolabeling with minimal impurities. PET/CT imaging showed reduced brain uptake of ^{89}Zr-BB5.1 in the high-fat diet control (HFDC) group compared to the chow control (ChowC) and high-fat diet probiotic (HFDP) groups. Behavioral analysis showed that HFDP group exhibited a slightly higher mean discrimination ratio compared to the HFDC group, indicating a trend toward improved performance potentially associated with probiotic supplementation. Immunohistochemistry analysis showed a significant increase in microglial expression and activation, evidenced by elevated levels of the proinflammatory marker CD11b, in the hippocampus and cortex of HFDC mice. ***Conclusion:*** The mAb ^{89}Zr-BB5.1 targeted against C5 complement protein was assessed as a BBB patency and complement activation PET tracer in mouse models of AD. Counter to expectation the percentage of injected dose found in the brain inversely correlated with AD progression, measured by microglial activation, suggesting a confounding influence of HFD on BBB penetration potential of

^{89}Zr-BB5.1. qPCR is underway to assess the C5 expression in the livers and brains of mice from the study. Increased peripheral C5 expression in the HFD groups would explain the unexpected PET results.

OP-889

Dynamic Dual-PET imaging for simultaneous metabolic and perfusion information for cardiac imaging

Â. Cardoso[1], *A. Lopez-Montes*[1], *H. Sari*[1,2], *K. Zeimpekis*[1], *N. Rathod*[1], *N. Encina*[3], *J. L. Herraiz*[3], *A. Rominger*[1], *K. Shi*[1], *F. Caobelli*[1];
[1]*Inselspital, University Hospital Bern, Department of Nuclear Medicine, Bern, SWITZERLAND,* [2]*Advanced Clinical Imaging Technology, Siemens Healthcare AG, Lausanne, SWITZERLAND,* [3]*Universidad Complutense de Madrid, Madrid, SPAIN.*

Aim/Introduction: Assessment of both perfusion (e.g. using 82Rb-Cl) and metabolism (18F-FDG) is crucial in some applications of cardiac PET. Traditionally, separate scans are required due to indistinguishable annihilation photons from different tracers. Recently proposed multiplexed PET (mPET) based on triple coincidences from isotopes like 82Rb, enables separation of two PET signals from the same acquisition. However, low probability (~13%) of triple emission in 82Rb challenges mPET. This study explores an alternative: leveraging tracer half-life differences and biodistribution patterns to enable dual-tracer separation in standard dynamic PET. ***Materials and Methods:*** Differences in half-lives of 82Rb (76s) and 18F (109min) and in their dynamic distribution can be leveraged to achieve dynamic separation of both isotopes. We developed a method for separation of 18F and 82Rb signals in a long axial field-of-view scanner assuming 18F distribution to be constant in a single frame (20s frame). The baseline 18F component was initialized from late frames after 82Rb has decayed and iteratively refined for every time frame. The method was tested using a NEMA IQ phantom with a background activity of 3.3 kBq/ml of 18F and different concentrations of 18F and 82Rb in the spheres ranging from 0 to 4 times the activity concentration in the background. Moreover, we tested our method on a healthy volunteer injected with ^{18}F-FDG (60MBq) followed by 82Rb (185MBq). ***Results:*** In the phantom study, 18F activity after separation showed deviations of less than 6% from pre-82Rb values, even in regions with overlapping tracer distribution, where accuracy remained within 5%. In the clinical case, 82Rb images generated by our method closely matched those from a separate 82Rb-only scan. Compared to mPET, our method produced lower image noise and better tracer separation, especially near the injection site, where 82Rb activity was dominant and mPET failed to isolate 18F. Importantly, myocardial dynamics post-separation aligned well with prior 82Rb images. This approach enables accurate dual-tracer imaging for simultaneous perfusion and metabolism assessment in a single scan. ***Conclusion:*** This study demonstrates the feasibility of separating 18F and 82Rb signals by exploiting their distinct dynamic distributions. The method proved effective in both phantom experiments and a clinical case, paving the way for simultaneous assessment of perfusion and metabolism in a single PET scan. This approach could streamline cardiac imaging by enabling double-isotope studies without additional dose or scan time. Future work will explore combining this strategy with mPET to further enhance isotope separation.

OP-890

Defining the Optimal Timeframe For Left Ventricular Volume Measurements in Gated Reconstructions of ^{13}N[NH_3] PET/CT in Adenosine-stressed Patients

L. Does[1], *R. J. J. Knol*[1], *S. T. Martínez-Lucio*[2], *F. M. van der Zant*[1], *S. V. Lazarenko*[1];
[1]*Noordwest Ziekenhuis, Alkmaar, NETHERLANDS,* [2]*UMCG, Groningen, NETHERLANDS.*

Aim/Introduction: In proven ischemia, the left ventricle (LV) is known to temporarily dilate upon stress. The objective of the present study was to define the optimal timeframe to measure LV dilation in gated reconstructions of [^{13}N]NH_3 PET/CT scans while using adenosine as the stressor. ***Materials and Methods:*** [^{13}N]NH_3 PET/CT datasets of 10 patients referred to the Department of Nuclear Medicine between December 2020 and June 2023 were retrospectively included in this study. All patients had proven myocardial ischemia. In these patients, the end-diastolic LV volume was compared between rest (at 12-15 min after starting acquisition) and stress (at 1-3, 5-7, and 9-11 min after starting adenosine administration). Measurements were performed with two software packages, i.e. Cedars QGS and Corridor 4DM. Means ± SD were calculated. Data were checked for normal distribution, and differences were evaluated with paired T-tests. A two-tailed $p<0.05$ was considered significant. ***Results:*** Cedars: The mean LV end-diastolic volume at rest proved to be 125.4±28.9 ml. During adenosine stress, the LV volume was 130.1±34 ml when measured between 1-3 minutes after starting adenosine stress (not significantly different from rest, p=0.210). At 5-7 min, this was 141.6±37.4 ml (significantly different from rest, p=0.005), whereas at 9-11 min a LV volume of 136.7±33.9 ml was measured (significantly different from rest, p=0.006). 4DM: Rest LV end-diastolic volume was 136.4±35.5 ml. Between 1-3 min in stress, this was 140.3±40.9 ml (not significantly different, p=0.483). Between 5-7 min stress, the LV volume was measured as 158.2±42.3 ml (significant, p=0.004), and between 9-11 min, the LV volume was measured as 152.8±36.6 ml (significant, p=0.004). Also, the data suggest that the pattern of LV dilation is variable among patients. While dilation of the LV remains stable during stress in some patients, others show dilation initially, followed by normalization over time. ***Conclusion:*** The optimal timeframe for LV volume measurements in gated reconstructions is between 5-7 minutes after starting adenosine administration, independent of the software package used. Absolute LV volume measurements show variation between software packages.

OP-891

Data-driven energy efficiency in a high-throughput PET/CT department: a model for sustainable nuclear medicine

M. De Summa[1], *S. Spinosa*[1], *S. Fusaro*[1], *S. Annunziata*[2], *M. Calcagni*[2];
[1]*MEDIPASS Ergèa Group, Rome, ITALY,* [2]*Nuclear Medicine Unit, Department of Diagnostic Imaging, Oncological Radiotherapy and Hematology, Fondazione Policlinico Universitario Agostino Gemelli, Rome, ITALY.*

Aim/Introduction: The healthcare sector is increasingly called to contribute to global sustainability goals. Nuclear medicine departments, due to their high technological intensity, are significant energy consumers. This project investigates a data-driven model to optimize energy use in a high-throughput PET/CT department, aiming to reduce environmental impact, operational costs, and energy waste without compromising diagnostic efficiency. The initiative aligns with broader green healthcare strategies and highlights the role of digital monitoring and clinical engineering in sustainable process governance. ***Materials and Methods:*** An advanced energy monitoring platform was integrated into a high-volume PET/CT department (approx. 50 exams/day). Real-time energy consumption data from imaging systems and facility environments were collected and visualized through a dedicated dashboard. Key inefficiencies were identified, including prolonged standby modes, suboptimal temperature/humidity settings, and peak-time overuse. Based on these insights, automated strategies were developed for: 1 smart shutdown of imaging systems during idle periods, 2 dynamic control of climate conditions based on room occupancy, and 3 rescheduling of energy-intensive tasks to off-peak hours. The model was simulated under various operational scenarios to estimate efficiency gains. ***Results:*** Preliminary simulation results indicate that implementing the proposed energy optimization strategies could lead to a 22%

reduction in overall energy consumption. Environmental efficiency, measured as energy usage per exam, improved by approximately 18%. Furthermore, the estimated economic savings reached 15% of the annual energy-related operational costs. Importantly, these outcomes were achieved without any measurable impact on patient throughput or diagnostic workflow, suggesting that sustainability can be enhanced without compromising service quality. ***Conclusion:*** This study demonstrates the potential of a data-driven approach to improve energy efficiency in Nuclear Medicine departments, particularly in high-throughput PET/CT settings. By leveraging real-time monitoring and automated adjustments, it is possible to reduce environmental impact and operational costs while maintaining clinical performance. The model presents a scalable, replicable framework that supports digital sustainability in healthcare and reinforces the strategic role of clinical engineering in process optimization. Future steps include real-world implementation and long-term impact assessment.

511

Sunday, October 5, 2025, 15:00 - 16:30
Room 111

Special Symposium 2 - EANM Journals - Debate: The Evolving World of Scientific Publishing

OP-189
Ethics and Metrics in 2030
E. Bertran, *Elsevier B.V., Amsterdam, NETHERLANDS.*

OP-190
Publications, Journals and Clinical Excellence
A. Scott; *ONJCRI and Austin Health, Melbourne, AUSTRALIA.*

OP-191
Portrait of a Perfect journal
A. Lazar; *Vita-Salute San Raffaele University, Dep. Nuclear Medicine, San Raffaele Hospital; Milan, ITALY.*

601

Sunday, October 5, 2025, 16:45 - 18:15
Auditorium

CME 4 - Cardiovascular Committee: Total Body Imaging: Think Big, Think Forward! (Cardio)

OP-193
Long axial field of view CZT cameras: physical principles CZT cameras
L. Imbert; *Department of Nuclear Medicine and Nancyclotep Imaging Platform, IADI, INSERM U1254, Université de Lorraine, CHRU Nancy, Nancy, FRANCE.*

OP-194
Advances in cardiovascular imaging with CZT cameras
J. Diekmann; *Department of Nuclear Medicine, Hannover Medical School, Hannover, GERMANY.*

OP-195
New PET systems: more than a longer field of view
S. Vanderberghe; *Department of Electronics and Information Systems, Medical Image and Signal Processing, Ghent University, C. Heymanslaan 10, Ghent, BELGIUM.*

OP-196
LAFOV PET in cardiovascular imaging
F. Caobelli; *Department of Nuclear Medicine, University of Bern, Bern, SWITZERLAND.*

602

Sunday, October 5, 2025, 16:45 - 18:15
Room 112 (Arena)

Special Track 4 - Oncology & Theranostics Committee + Dosimetry Committee: Debate: Routes to Optimised Theranostics: Is 'Dose' Escalation Enough?

OP-197
'Targeted radionuclide therapy trials should follow models from drug-based oncology – with activity escalation similar to chemotherapy paradigms'
F. Kraeber Bodéré; *Nuclear Medicine Center, CHU Nantes, Nantes, FRANCE.*

OP-198
'Targeted radionuclide therapy trials should follow radiotherapy logic – guided by absorbed dose, not just injected activity'
J. Wadsley; *Sheffield Teaching Hospitals NHS Foundation Trust, Sheffield, UNITED KINGDOM.*

603

Sunday, October 5, 2025, 16:45 - 18:15
Room 113

LIPS Session 4 - AI Committee: AI for Young Developers in Nuclear Medicine

OP-200
Data Preparation for AI
D. Kersting; *University of Essen, Department of Nuclear medicine, Essen, GERMANY.*

OP-201
Basics of Coding for AI
C. Constantino; *Champalimaud Foundation, Nuclear Medicine-Radiopharmacology, Lisbon, PORTUGAL.*

OP-202
Best Practices for Model Development
L. Cavinato; *Politecnico di Milano, Department of Mathematics, Milan, ITALY.*

OP-203
Large Language Models for Coding and Scientific Writing
G. Prenosil; *University of Bern, Department of Nuclear Medicine, Bern, SWITZERLAND.*

604

Sunday, October 5, 2025, 16:45 - 18:15
Room 114

M2M Track - TROP Session - Radiopharmaceutical Sciences + Translational Molecular Imaging & Therapy Committee: Combining Imaging with Targeted Therapy

OP-204
IL-13Rα2-Targeted Radiotheranostics for Sarcoma: Advancing Precision Antibody-Based Therapy
P. Jeanjean[1], *M. Kumpf*[1], *S. Lee*[1], *L. Carter*[1], *S. Lovibond*[1], *L. Gajecki*[1], *S. Krebs*[2], *D. Veach*[1];
[1]*Memorial Sloan Kettering Cancer Center, New York, NY, UNITED STATES OF AMERICA,* [2]*MD Anderson Cancer Center, Huston, TX, UNITED STATES OF AMERICA.*

Aim/Introduction: Despite initial responses with standard-of-care treatment, soft-tissue sarcomas recur at a high rate (50-70%) and patients with an advanced-stage disease have few effective therapeutic options. Novel therapeutic strategies are urgently needed.(1) Interleukin-13 receptor alpha-2 (IL-13Rα2) is a high-affinity cell surface receptor for interleukin-13. IL-13Rα2 is classified as cancer/testis-like antigen due to its overexpression in several malignancies, including sarcomas, while being largely absent in normal tissues. Its overexpression also correlates with poor prognostic.(2) We developed KLG-3, an Fc-optimized IgG4 human monoclonal IL-13Rα2-targeted antibody to detect and treat IL-13Rα2 positive malignancies, like sarcomas.(3) This project evaluates KLG-3 as a theranostic radioimmunopharmaceutical in two models of leiomyosarcoma (LMS), the most common soft-tissue sarcoma. ***Materials and Methods:*** IL-13Rα2 expression in human LMS-derived cell lines, SK-UT-1 and RKN, was assessed by flow cytometry. Immuno-PET/CT imaging with 5µg of ^{89}Zr-labeled KLG-3 (0.9MBq) or control IgG was performed in mice bearing subcutaneous LMS tumors (N=4/group) to assess tumor uptake and biodistribution. For therapy, SK-UT-1 tumor-bearing mice received a single intravenous dose of ^{225}Ac-KLG-3 or ^{225}Ac-IgG (N=4/group). Therapeutic efficacy and systemic toxicity of 18.5, 9.25 or 3.7kBq per 5µg dose were evaluated by monitoring tumor growth, body weight, hematology and blood chemistry. ***Results:*** Immuno-PET imaging revealed high tumor uptake of ^{89}Zr-KLG-3 at 3d post-injection, with 43.1+10.8%ID/g (SK-UT-1) and 37.0+7.4%ID/g (RKN), followed by a plateau and gradual clearance over 14d. High tumor-to-background ratios (heart, kidney, muscle) were observed. Tumor uptake in ^{89}Zr-IgG group was similar to blood pool. Prospective PET imaging-derived dosimetry estimated maximum tolerated dose (MTD) on bone marrow of 18.5-37kBq for ^{225}Ac-KLG-3 and 18.5MBq for ^{177}Lu-KLG-3. The ongoing ^{225}Ac-KLG-3 pilot therapy study in a large tumor-burden model demonstrates tumor growth delay and increases in overall survival in the 18.5 kBq of ^{225}Ac-KLG-3 group only (32.5d; 2/4 deaths) compared to control (24.5d; 4/4 deaths). No evidence of acute toxicity has been observed in surviving animals at day 25; non-responders were euthanized at endpoint due to disease progression. ***Conclusion:*** These findings suggest that KLG-3 is a promising radioimmunotherapeutic agent for IL-13Rα2-positive sarcomas. ^{89}Zr-KLG-3 immuno-PET clearly delineated tumors in LMS xenografts and cleared well from off-target tissues. At 18.5kBq, ^{225}Ac-KLG-3 was well tolerated, resulted in significant therapeutic effect without evidence for acute toxicity. Ongoing dose-escalation studies will confirm the ^{225}Ac- and ^{177}Lu-KLG-3 MTD and compare therapeutic efficacy of α- versus β-emitting isotopes for KLG-3-based radioimmunotherapy. ***References:*** 1. Bourcier K (2019). 2. Jaén M (2022). 3. Gajecki L (2025)

OP-205

High Activity, Pain Relief, and Low Toxicity of ^{177}Lu-Labeled DOTA-IBA in the theranostics of Bone Metastases from Multiple Tumors: A Preliminary Clinical Trial

C. Qi[1,2], *C. Tian*[1,2], *F. Wu*[1,2], *J. Yang*[1,2], *W. Wang*[1,2], *X. Li*[3], *Y. Chen*[1,2];
[1]*Affiliated Hospital of Southwest Medical University, Luzhou, CHINA,* [2]*Nuclear Medicine and Molecular Imaging Key Laboratory of Sichuan Province*, *Southwest Medical University, Luzhou, CHINA,* [3]*Vienna General Hospital, Vienna, AUSTRIA.*

Aim/Introduction: ^{177}Lu-DOTA-IBA has been proven to be an excellent therapeutic radiopharmaceutical for bone metastases. This study aimed to explore its application value in bone metastases from various tumors. ***Materials and Methods:*** Advanced tumor patients with bone metastases and poor clinical outcomes were recruited for a study on ^{68}Ga/^{177}Lu-DOTA-IBA. Biochemical and hematological tests were performed before PET/CT examinations. Patients received ^{68}Ga-DOTA-IBA (0.05 mCi/kg) and ^{18}F-FDG (0.15 mCi/kg) intravenously on consecutive days, and PET/CT imaging was carried out 1.5-2 hours and 1 hour after administration, respectively. Nuclear medicine physicians evaluated patients' eligibility for ^{177}Lu-DOTA-IBA treatment based on their conditions and lesion imaging features. Eligible patients received 2 to 6 treatment cycles. After slowly intravenous infusion of 30 mCi of ^{177}Lu-DOTA-IBA, whole-body planar imaging (including anterior and posterior views) and single-photon emission computed tomography (SPECT)/CT imaging of the target area were performed at 4 hours, 24 hours, 48 hours, 72 hours, and 168 hours to assess biodistribution and dosimetry. The treatment efficacy and adverse events were evaluated by analyzing the changes in clinical symptoms, imaging comparisons, and biochemical indicators. ***Results:*** The research team has performed ^{68}Ga-DOTA-IBA imaging on more than 1,000 patients and administered ^{177}Lu-DOTA-IBA treatment to more than 300 patients. Groups A-F in the figure respectively display the maximum intensity projection (MIP) images of ^{68}Ga-DOTA-IBA PET/CT of patients with bone metastases from prostate cancer, lung cancer, breast cancer, pancreatic cancer, pheochromocytoma, and liver cancer before and after treatment. The ^{68}Ga/^{177}Lu-DOTA-IBA drug showed good tolerability, and no severe drug-related adverse events were observed in the studied cases. In a few cases, mild to moderate leukopenia occurred in treated patients. ^{68}Ga-DOTA-IBA is mainly excreted through the renal pathway and has minimal distribution in normal bone tissues. Similarly, ^{177}Lu-DOTA-IBA is also mainly excreted through the renal pathway and shows uptake and long-term retention in the areas detected as positive by ^{68}Ga-DOTA-IBA PET/CT. Bone pain relief was observed in 82.7% of the cases. From imaging results such as osteogenic reactions, it can be seen that this treatment showed significant therapeutic effects in some metastatic lesions. ***Conclusion:*** The current treatment cases illustrate the efficacy and safety of ^{68}Ga-DOTA-IBA PET/CT for disease imaging and ^{177}Lu-DOTA-IBA for treating bone metastases from various tumors. The integrated diagnostic and therapeutic approach of ^{68}Ga/^{177}Lu-DOTA-IBA is expected to make substantial contributions to the management of bone pain and bone metastases in cancer patients.

OP-206

Preclinical Evaluation of NYM096: A Novel ^{68}Ga/^{177}Lu-Labeled CAIX-Targeting Theranostic Pair for Clear Cell Renal Cell Carcinoma

W. Zhu[1], *S. Yang*[2], *W. Lv*[2], *W. Eng*[2], *P. Fang*[2], *L. Huo*[1];
[1]*Peking Union Medical College Hospital, Beijing, CHINA,* [2]*Norroy Bioscience Co., Ltd., Wuxi, CHINA.*

Aim/Introduction: Carbonic anhydrase IX(CAIX), markedly overexpressed in clear cell renal cell carcinoma (ccRCC) with restricted expression in healthy tissues, represents an ideal target for tumor-selective theranostics. This study investigated the diagnostic and therapeutic potential of NYM096, a novel ^{68}Ga/^{177}Lu-labeled small-molecule conjugate targeting CAIX, in ccRCC xenograft models. ***Materials and Methods:*** OS-RC-2 human ccRCC cancer cells were subcutaneously transplanted in BALB/c(nu/nu) mice (6 week-old). For PET imaging, ^{68}Ga-NYM096 (80±10uCi, n=4) was intravenously administered to tumor-bearing mice followed by scans at 0.5, 1, and 2 hours post-injection (p.i.). For biodistribution evaluation, ^{177}Lu-NYM096 (300± 20 uCi) was injected (n= 3 per time point), and mice were sacrificed for organ harvesting at 4 and 48 hours. Therapeutic experiments included three dose groups (0.22, 0.67, 2 mCi; n=6 /group) and a saline control (n=6), with blinded assessment of tumor volume and body weight monitored for 35 days. ***Results:*** PET imaging demonstrated rapid and specific delineation of OS-RC-2 xenografts using ^{68}Ga-NYM096, with progressive tracer accumulation peaking at 16.8 ± 3.2% ID/g by 2 hours p.i. and a tumor-to-muscle ratio of 12.8. The tracer was predominantly cleared via the renal pathway. Biodistribution studies revealed tumor-specific accumulation of

^{177}Lu-NYM096, achieving 16.0 ± 4.1% ID/g at 4 h and sustained retention of 6.3 ±2.6% ID/g at 48 h, significantly exceeding muscle tissue levels ($P < 0.05$). Therapeutic evaluation confirmed dose-dependent tumor growth inhibition ($P < 0.05$ for all doses vs control). In the high-dose (2 mCi) treatment group, tumors shrunk without regrowing up to 35 days after a single dose and the tumor growth inhibition rate was over 85%. Furthermore, histopathological analysis of major organs (heart, liver, kidneys, etc.) showed no significant differences in H&E staining scores between treatment and control groups. ***Conclusion:*** The CAIX-targeted theranostic pair ^{68}Ga/^{177}Lu-NYM096 demonstrates precise tumor visualization and potent therapeutic efficacy in ccRCC models, with preserved organ safety supporting clinical translation.

OP-207

Preclinical Evaluation of NYM097: A Novel ^{68}Ga/^{177}Lu-Labeled FAP-Targeting Theragnostic Pair for Pan-Cancer

F. Cui[1], *S. Yang*[2], *W. Lv*[2], *M. Ren*[2], *W. Eng*[2], *P. Fang*[2];
[1]*Department of Oncology, The People's Hospital of Ma Anshan, Ma Anshan, CHINA,* [2]*Norroy Bioscience Co., Ltd., Wuxi, CHINA.*

Aim/Introduction: Fibroblast activation protein alpha (FAP), markedly overexpressed in various solid tumor tissues with restricted expression in healthy tissues, represents an ideal target for tumor-selective theragnostic. This study investigated the diagnostic and therapeutic potential of NYM097, a novel ^{68}Ga/^{177}Lu-labeled small-molecule conjugate targeting FAP, in FAP humanized MC38 syngeneic mouse model. ***Materials and Methods:*** FAP humanized MC38 cells (B-hFAP MC38) were subcutaneously transplanted in C57BL/6 mice (6-8 weeks-old). For PET imaging, ^{68}Ga-NYM097 (80±16 μCi, n=5) was intravenously administered to the tumor-bearing mice followed by scans at 1, 2, and 4 hours post-injection (p.i.). For biodistribution evaluation, ^{177}Lu-NYM097 (300± 60 μCi) was injected (n=3 per time point), and mice were sacrificed for organ harvesting at 4 and 48 hours. Therapeutic experiments included a dose group (2 mCi; n=6) and a saline control (n=6), with blind assessment of tumor volume and body weight monitored for 19 days. ***Results:*** PET imaging demonstrated rapid and specific delineation of B-hFAP MC38 syngeneic models using ^{68}Ga-NYM097, with progressive tracer accumulation peaking at 3.6±2.0% ID/g by 1 hours p.i. and a tumor-to-muscle ratio of 13.1. The tracer was predominantly cleared via the renal pathway. Biodistribution studies revealed tumor-specific accumulation of ^{177}Lu-NYM097, achieving 9.6±0.2% ID/g at 4 h and sustained retention of 3.7±0.5% ID/g at 48 h, significantly exceeding muscle tissue levels. Therapeutic evaluation confirmed 2 mCi ^{177}Lu-NYM097 could significantly inhibit tumor growth (Tumor growth inhibition rate was 62.3%; $P<0.05$ for vs control), and animals have good tolerance to treatment during the experiment. ***Conclusion:*** The FAP-targeted theragnostic pair ^{68}Ga/^{177}Lu-NYM097 demonstrates precise tumor visualization and potent therapeutic efficacy in tumor models, with well safety supporting clinical translation.

OP-208

Identification and characterization of ^{64}Cu- and ^{225}Ac-PD-32766, a Carbonic Anhydrase IX targeting macrocyclic peptide radiotheranostic pair for clear cell renal cell carcinoma (ccRCC)

S. Tsuchida[1], *Y. Mizukoshi*[1], *S. Kato*[1], *H. Inaba*[1], *T. Kotake*[1], *T. Aoki*[1], *H. Shimizu*[1], *Y. Funase*[2], *N. Kanazawa*[2], *H. Yanagida*[1], *H. Kitamura*[1], *K. Matsuhara*[2], *K. Suzuki*[2], *S. Matsushima*[2], *M. Murakami*[1,2];
[1]*PeptiDream Inc., Kanagawa, JAPAN,* [2]*PDRadiopharma Inc., Chiba, JAPAN.*

Aim/Introduction: Carbonic Anhydrase IX (CA9) is a zinc metalloenzyme that contributes to the pH regulation of cells and tissues by catalyzing the conversion of carbon dioxide and water into bicarbonate and protons. CA9 expression is regulated by HIF1a and has been shown to be upregulated in hypoxic tumor microenvironments, including clear cell renal cell carcinoma (ccRCC), identifying CA9 as an attractive therapeutic target. Utilizing our proprietary Peptide Discovery Platform System (PDPS), PeptiDream has identified PD-32766, a novel macrocyclic peptide specifically targeting CA9 that can be labeled with radionuclides such as ^{64}Cu and ^{225}Ac enabling both PET imaging and targeted alpha therapy. Here we report the radiotherapeutic potential of PD-32766 for ccRCC. ***Materials and Methods:*** PD-32766 was identified from PDPS libraries containing trillions of macrocyclic peptides with non-canonical amino acids that were selected against CA9 using mRNA display and directed evolution. The binding affinity of PD-32766 was measured by SPR and the in vitro cellular internalization of PD-32766 was confirmed by confocal microscopy with fluorescent labelled PD-32766. ^{64}Cu- or ^{225}Ac-PD-32766 was dosed to VMRC-RCW (ccRCC cell line) xenograft mice and the percentage of injected dose (%ID/g) in tumors and major organs was quantified by cut and count method. For the PET imaging study, ^{64}Cu-PD-32766 was dosed to VMRC-RCW xenograft mice and scanning was performed at 1, 4, 24, 48 hrs. To measure efficacy, single dosing of ^{225}Ac-PD-32766 (30, 60, 120 kBq/mouse) was conducted in VMRC-RCW xenograft mice and the tumor volume was measured for up to 50 days after dosing. To estimate the dosimetry in adult human subjects, SD rats were injected with ^{225}Ac-PD-32766 and sacrificed at 0.083, 1, 4, 24, 48, 120, and 168 hours post injection to evaluate blood and tissue radioactivity concentration. ***Results:*** PD-32766 exhibited strong and specific binding to CA9 and fluorescence labeled PD-32766 was internalized in VMRC-RCW (CA9-expressing cell line), but not 786-O (CA9-negative cell line). Biodistribution studies with ^{64}Cu- and ^{225}Ac-PD-32766 showed significant and specific tumor accumulation in VMRC-RCW xenograft models, with enrichment of tumor accumulation over off target. PET imaging with ^{64}Cu-PD-32766 clearly detected tumors, consistent with the biodistribution data. In the efficacy study, ^{225}Ac-PD-32766 showed remarkable and dose dependent tumor volume reduction and prolonged overall survival, strongly suggesting robust anti-tumor effects with dosimetry experiments confirming fast renal clearance from blood. ***Conclusion:*** CA9 targeting PD-32766 is a promising radiotheranostic peptide for ccRCC.

OP-209

A Novel [^{11}C]/[^{211}At]-Labeled Radiopharmaceutical Pair Targeting mGluR1 for Melanoma Imaging and Therapy

L. Xie[1], *M. Hanyu*[1], *M. Fujinaga*[1], *Y. Zhang*[1], *T. Kokufuta*[1], *W. Mori*[1], *K. Minegishi*[1], *L. Zhang*[1,2], *R. Luo*[1,2], *H. Wakizaka*[1], *M. Zhang*[1];
[1]*National Institutes for Quantum Science and Technology, Chiba, JAPAN,* [2]*Department of Nuclear Medicine, Nanjing First Hospital, Nanjing Medical University, Nanjing, CHINA.*

Aim/Introduction: Metabotropic glutamate receptor 1 (mGluR1), an oncoprotein involved in glutamine metabolism and frequently overexpressed in a wide range of cancers, including melanoma, represents a promising target for pan-cancer management (1-2). Here, we developed a novel pair of mGluR1-targeted radiopharmaceuticals that combines positron emission tomography (PET) imaging and targeted alpha(α) therapy (TAT) for cancer diagnosis and therapy. ***Materials and Methods:*** Two small-molecule radiopharmaceuticals were synthesized by labeling the same small-molecule compound with either a diagnostic isotope ^{11}C or an α-emitting therapeutic isotope ^{211}At: 3-iodo-N-[4-[6-(methylamino)pyrimidin-4-yl]-1,3-thiazol-2-yl]-N-[^{11}C]methylbenzamide([^{11}C]IMTM) for PET imaging, and 3-[^{211}At]-astato-N-[4-[6-(methylamino)pyrimidin-4-yl]-1,3-thiazol-2-yl]-N-methylbenzamide ([^{211}At]AMTM) for TAT. Their diagnostic and therapeutic effects were assessed in vitro and in vivo using mGluR1-expressing B16F10 melanoma cells and corresponding tumor-bearing mouse models. ***Results:*** Both [^{11}C]IMTM and [^{211}At]

AMTM showed high binding affinity and specificity for mGluR1 in B16F10 cells in vitro. PET imaging with [^{11}C]IMTM clearly visualized subcutaneous and metastatic tumors in B16F10 melanoma models. [^{211}At]AMTM anchored to mGluR1, downregulated this oncoprotein expression, and was subsequently internalized to trigger cancer cell senescence via the p21/caveolin-1 pathway. In vivo, a single dose (2.96 MBq) of [^{211}At]AMTM significantly inhibited tumor growth and doubled survival in both subcutaneous and metastatic melanoma models. No significant body weight loss or adverse effects on liver or kidney function were observed in treated mice during the study period. ***Conclusion:*** The radiopharmaceutical pair [^{11}C]IMTM and [^{211}At]AMTM shows strong precise as mGluR1-targeted radiopharmaceuticals for radiotheranostics. They offer a precise and effective option for diagnosing and treating mGluR1-expressing cancers, such as melanoma, and hold considerable potential for clinical translation.
References: 1. Pollock PM, et al. Nat Genet. 2003; 34:108-112. 2. Xie L, et al. Cell Rep Med. 2023;4:100960.

OP-210

Theranostic role of^{89}Zr and^{177}Lu labeled B7H3 probe in prostate cancer

L. Kang, *Y. Qiu, T. Wang, Q. Yang, L. Song, Y. Lei, X. Sun;*
Dept. of Nuclear Medicine, Peking University First Hospital, Beijing, CHINA.

Aim/Introduction: B7-H3 is a cell surface immunomodulatory glycoprotein overexpressed in prostate cancers (PCs). Understanding its expression in PC lesions and exploring the integration of diagnosis and treatment are essential for the development of B7-H3 targeted therapy and patient selection. BH201 is an antibody-drug conjugate targeting B7H3 that has been shown to be effective against small cell lung cancer and nasopharyngeal carcinoma. Therefore, ^{89}Zr/^{177}Lu-labeled BH201 was investigated for its theranostic role in PCs. ***Materials and Methods:*** BH201 was radiolabeled with ^{89}Zr and ^{177}Lu. Flow cytometry was conducted to assess the binding affinity of BH201. Sequential positron emission tomography (PET) imaging was performed in PC tumor bearing mice following the administration of ^{89}Zr-labeled BH201. A treatment study was subsequently performed after the administration of ^{177}Lu-labeled BH201. Tumor volume was monitored, and single-photon emission computed tomography (SPECT) imaging along with biodistribution studies were executed. Safety evaluation was performed including body weight, blood cell measurement, and hematoxylin-eosin (H&E) staining of major organs. ***Results:*** FITC-labeled BH201 showed a strong binding affinity to B7H3 in PC 22RV1 cells by flow cytometry. Tumor uptake of ^{89}Zr-labeled BH201 peaked at 144 h (19.43 ± 3.24 %ID/g), which was significantly higher than that of blocking group (7.10 ± 0.96 %ID/g). After treatment with 7.4 MBq ^{177}Lu-labeled BH201, the tumor volume was significantly reduced, and the standardized tumor volume at day 20 was significantly less than that in the ^{177}Lu-labeled IgG group (71.11 ± 20.65% vs 272.50 ± 154.37%). Moreover, SPECT images confirmed high contrast between tumors and normal organs, indicating selective tumor uptake of ^{177}Lu-labeled BH201. No discernible abnormalities in blood cells, and no evident histopathological abnormality observed in liver, spleen, and kidney. ***Conclusion:*** The ^{89}Zr/^{177}Lu-labeled BH201 compound has the potential to serve as a specific marker for prostate cancers, offering diagnostic value and enhancing understanding of targeted therapeutic approaches for PCs treatment. Further clinical evaluation and translation of this compound could be highly significant for advancing PCs management.

OP-211

Theranostic Anti-CD38 Antibody for Combined Positron Emission Tomography and Lutetium-177 Radionuclide Therapy in Lymphoma

C. Petitot[1,2,3], *A. Kownacka*[1,3], *A. M. M. Dias*[2,3], *D. Vivier*[2], *M. Moreau*[2,3], *M. Claron*[2], *M. Guillemin*[3], *J. Simonet*[3], *J. Frenay*[3,4], *A. Helbling*[2,3], *A. Courteau*[2,3], *A. Cochet*[2,3], *F. Denat*[2], *P. Bellaye*[1,3], *C. Rossi*[1,5], *F. Girodon*[1,5], *B. Collin*[2,3];
[1]CTM - UMR INSERM 1231, Dijon, FRANCE, [2]ICMUB - UMR CNRS 6302, Dijon, FRANCE, [3]IMATHERA, BioSanD - UMS INSERM 58, Centre Georges-François Leclerc, Dijon, FRANCE, [4]ICB - UMR CNRS 6303, Dijon, FRANCE, [5]CHU François Mitterrand, Dijon, FRANCE.

Aim/Introduction: CD38 is a transmembrane glycoprotein overexpressed in haematologic malignancies, promoting tumour growth and immune evasion. Its overexpression in lymphoid malignancies renders CD38 an attractive theranostic target with antibodies such as isatuximab (ISA). The aim of our study was to design and develop an ISA-based radiotheranostic platform for both positron emission tomography (PET) imaging and targeted radionuclide therapy (TRT) in a CD38-positive lymphoma model. ***Materials and Methods:*** ISA was site-specifically conjugated to a bischelate scaffold (DFO-DOTAGA) and radiolabelled with either zirconium-89 ([^{89}Zr]Zr-DFO-DOTAGA-ISA) or lutetium-177 ([^{177}Lu]Lu-DFO-DOTAGA-ISA). In vitro binding assays were perfomed to confirm that conjugation and radiolabeling preserved CD38 affinity. Ramos Burkitt's lymphoma cells were implanted subcutaneously in Swiss nude mice (n = 12). Six mice received 50 µg of [^{89}Zr]Zr-DFO-DOTAGA-ISA (5 MBq) intravenously; PET scans were acquired at 6, 24, 48, 72 and 96h post-injection (p.i.), followed by ex vivo γ-counting at 96h. Specificity was confirmed by co-injection of a 100-fold excess of unlabelled ISA (blocking group, n = 3). For TRT, mice (n = 10 per group) received 25 µg of [^{177}Lu]Lu-DFO-DOTAGA-ISA at low (3 MBq), medium (7 MBq) or high (11 MBq) doses whereas control groups (n = 6) received either PBS or [^{177}Lu]Lu-DFO-DOTAGA-isotype (IgG1) at 3, 7 or 11 MBq. Single-photon emission computed tomography (SPECT) was performed at 48 h p.i., and mice were monitored for body weight loss, tumour volume, and complete blood count. ***Results:*** After radiolabeling and purification, the radiochemical purity of ISA exceeded 95% with a specific activity of 300 MBq/mg. In vitro experiments demonstrated good binding properties (Kd = 0.48 nM) close to the native antibody. PET imaging revealed progressive tumour uptake, peaking at 26.4 ± 1.5 %ID/g at 96h, while blocking reduced uptake by 3.5-fold (7.9 ± 1.5 %ID/g), as confirmed by ex vivo biodistribution. SPECT confirmed tumoral uptake in TRT groups. High-dose TRT induced significant tumour regression sustained for 10 days and improved survival compared with controls with no significant weight loss or haematological toxicity. ***Conclusion:*** Our study demonstrates that radiolabelled ISA may represent a promising radiotheranostic agent for CD38-positive lymphomas. The versatility of the DFO-DOTAGA bischelate enables TRT with 177Lu, supported by PET-derived dosimetry data. This strategy represents an initial step towards personalised treatment approaches, with the potential to enhance therapeutic efficacy while minimising adverse effects in various CD38 positive lymphoid malignancies.

OP-212

A Novel CEA-Targeted Nanobody Conjugated with Radionuclides for the Theranostics of Colorectal Cancer

W. Wang, *C. Lu, M. Zhou, S. Hu;*
Xiangya Hospital of Central South University, Changsha City, CHINA.

Aim/Introduction: Colorectal cancer (CRC) is a highly lethal malignancy worldwide, with a 5-year survival rate of less than 20% in metastatic patients. There is an urgent need for novel targeted diagnostic and therapeutic strategies. Carcinoembryonic antigen

(CEA) is overexpressed in most CRCs and serves as a potential target for diagnosis and therapy. This study developed a novel CEA-targeted theranostic nanoprobe, [^{68}Ga/^{177}Lu]Ga-Nb-CEA-21, and evaluated its potential utility for non-invasive PET/CT imaging and radionuclide-targeted therapy (TRT) in colorectal cancer (CRC). ***Materials and Methods:*** CEA-specific nanobodies were selected using camel immunization and phage display technology. The affinity and stability of these nanobodies were confirmed by ELISA. High-affinity, stable nanobodies (e.g., CE-21, CE-88) were used to construct monovalent (CE-21), bivalent (CE-21-21), and trivalent (CE-21-21-21) structures, followed by molecular docking for target verification. Radiolabeling was performed with ^{68}Ga/^{177}Lu, and the radiochemical purity (>95%) and in vitro stability of the probes were measured using Radio-HPLC. Their targeting ability and biocompatibility were evaluated at the cellular level. PET/CT imaging of LS174T xenograft tumor models was performed using the [^{68}Ga] probe, and the [^{177}Lu] probe was tested in dose-dependent therapy experiments (7.4/18.5 MBq). Efficacy and safety were evaluated using HE staining, γH2A.X immunohistochemistry, and biochemical assays for liver and kidney function. ***Results:*** ELISA screening identified CE-21, CE-85, and CE-88 as high-affinity binders to CEA, with CE-21 and CE-88 demonstrating superior stability. The synthesized [^{68}Ga]Ga-Nb-CEA-21 probe remained stable in saline/serum for 4 hours, and PET/CT imaging showed tumor uptake of 3.67±0.05 %ID/g, with a T/M ratio of 15.98±3.18 at 1 hour post-injection, outperforming other variants. In therapy experiments, even the 7.4 MBq low-dose group significantly inhibited tumor growth (t-test, p=0.003). The 18.5 MBq group extended survival to twice that of the saline control group (Log-rank test, p<0.0001), with no significant liver or kidney toxicity. ***Conclusion:*** The [^{68}Ga]Ga-Nb-CEA-21 probe enabled precise PET/CT imaging of CEA-positive CRC, while the [^{177}Lu]Lu-Nb-CEA-21 probe demonstrated significant anti-tumor effects at low doses. This dual-modality probe provides an effective tool for integrated CRC diagnosis and treatment, showing significant clinical translation potential.

605

Sunday, October 5, 2025, 16:45 - 18:15
Room 211

Cutting Edge Science Track - TROP Session - Dosimetry Committee: Radiobiological Mechanisms to Overcome Resistance in TRT

OP-213

Can antigenicity counterbalance tumor low absorbed dose in targeted alpha therapy?

J. Pouget[1], *A. Parach*[1], *T. David*[1], *J. Karam*[1], *F. Bruchertseifer*[2], *A. Morgenstern*[2], *M. Jarlier*[3], *M. Bardiès*[1], *E. Deshayes*[1], *A. Gudin-De-Vallerin*[3], *F. Boissière-Michot*[3], *E. Crapez*[3], *J. Constanzo*[1]; [1]*INSERM, Montpellier, FRANCE,* [2]*European Commission, Joint Research Centre, Karlsruhe, GERMANY,* [3]*Institut régional du Cancer, Montpellier, FRANCE.*

Aim/Introduction: Preclinical and clinical studies increasingly show that the immune response plays a major role in radiotherapy. Here, we investigated the role of major histocompatibility complex class I (MHC-I) molecules recognized by cytotoxic CD8$^+$ T cells in the response to targeted alpha therapy (TAT). ***Materials and Methods:*** Two murine melanoma cell lines that express low or high MHC-I levels (B16F10 MHC-I^{low} and B16K1 MHC-I^{high}) were grafted in syngeneic or athymic/nude mice and the response to a single injection of [^{225}Ac]Ac-DOTA-TA99 monoclonal antibodies (9.25 or 18.5 kBq) was assessed and related to dosimetry. For clinical relevance, MHC-I expression was determined in samples from patients with well-differentiated, iodine-avid metastatic thyroid cancer and well-differentiated grade 2 midgut neuroendocrine tumors. ***Results:*** TAT efficacy was enhanced by T-cell presence and MHC-I expression. In mice harboring B16F10 and B16K1 melanoma tumors, TAT showed a stronger anti-tumor effect in C57BL/6J (immunocompetent) than in athymic/nude (immunodeficient) animals, suggesting a crucial role of T cell-mediated immune responses. Moreover, the response to irradiation was the same in B16K1 MHC-I^{high} tumors with low absorbed dose of TAT and in B16F10 MHC-I^{low} tumors with four times higher absorbed dose. These results indicate that CD8$^+$ T cells can counterbalance low tumor irradiation. Conversely, delivering high absorbed doses leads to side effects, and seems to prevent the immune system activation, thereby not taking advantage of these mechanisms. Our results also indicate that MHC-I can be used as a predictive biomarker of TAT response in lesions receiving low absorbed doses, and that TAT treatment regimens should be re-considered in function of the MHC-I expression level. ***Conclusion:*** This study shows that MHC-I expression can predict TAT immunostimulatory effects. This is relevant in metastatic disease where lesions in the same patient can receive very low or very high absorbed doses.

OP-214

Targeted Radionuclide Therapy as Immune Adjuvant for Cancer Treatment: Comparing Beta and Alpha Emitter Absorbed Doses to Stimulate Anti-Tumor Responses.

J. Pouget[1], *T. David*[1], *S. Atis*[1], *A. Pichard*[2,3], *S. Frost*[3,4], *J. Constanzo*[1]; [1]*INSERM, Montpellier, FRANCE,* [2]*Institut Roche, Boulogne-Billancourt, FRANCE,* [3]*Roche Pharma Research and Early Development, Roche Innovation Center Basel, Basel, SWITZERLAND,* [4]*Roche Pharma Research and Early Development, Roche Innovation Center Welwyn, Welwyn Garden City, UNITED KINGDOM.*

Aim/Introduction: Targeted radionuclide therapy (TRT) has significantly advanced the treatment for neuroendocrine tumors and prostate cancer, but its curative potential remains limited. While external beam radiotherapy can induce immunogenic cell death and transform "cold" (immune-desert) tumors into "hot" (immune-inflamed) at specific doses, these parameters remain undefined for TRT. A recent study from our group demonstrates that alpha-TRT efficacy is enhanced by MHC-I expression and CD8+ T cell infiltration, even at low absorbed dose[1]. Here, we investigate in BALB/c mice orthotopically engrafted with the mouse mammary tumor cell line TUBO, the role of absorbed dose of radiopharmaceuticals modulating anti-tumor immune response, comparing a beta emitter (^{177}Lu) and an alpha emitter (^{212}Pb). ***Materials and Methods:*** In vivo biodistribution of ^{177}Lu- and ^{212}Pb-labeled anti-HER2 antibodies (^{177}Lu-TRT and ^{212}Pb-TRT) was determined to calculate tumor absorbed doses (Gy) using MIRD formalism. Next, the therapeutic efficacy (tumor growth and survival) of increasing ^{177}Lu-TRT activities (1-5-10 MBq, absorbed doses of 2-11-22 Gy) was assessed. Immunogenicity markers on tumor cells and immune cell populations in tumors post-treatment were analyzed by multi-color flow cytometry. ***Results:*** ^{177}Lu-TRT significantly improved tumor control and survival at absorbed doses above 2 Gy, with median survival increasing from 23 days (control) to 33 days (2 Gy), 78 days (11 Gy), and >110 days (22 Gy). Complete responses were observed in 30% (11 Gy) and 67% (22 Gy) of mice at day 74. Subsequent rechallenge of tumor-free mice with five-fold TUBO cells revealed enhanced protection in the 11 Gy group compared to the 22 Gy group, suggesting a potential in situ vaccine-like effect, inversely correlated with the tumor absorbed dose. Immunophenotyping revealed decreased immunosuppressive M2-like macrophages at both 11 Gy and 22 Gy, but significant CD8+ T cell infiltration occurred only at 11 Gy. In vitro studies demonstrated that ^{212}Pb-TRT induced higher expression of immunogenicity markers on tumor cells

compared to ^{177}Lu-TRT, potentially leading to better recognition by anti-tumor immune cells. ***Conclusion:*** Despite superior TUBO tumor control at higher absorbed doses, the intermediate ^{177}Lu-TRT dose resulted in enhanced long-term protective vaccine-like effects. In vitro, the stronger immunomodulatory profile of ^{212}Pb-TRT suggests that the alpha emitter may be more effective at activating immune responses. These findings indicate that an intermediate absorbed dose combined with immune checkpoint inhibitors may produce optimal therapeutic responses through enhanced immune system activation. ***References:*** MHC-I-Driven Antitumor Immunity Counterbalances Low Absorbed Doses of Radiopharmaceutical Therapy. Constanzo et al., 2025 - J Nucl Med

OP-215

Targeted Radionuclide Therapy Against Cancer-Associated Fibroblasts: A Promising Alternative or Complement to External Beam Radiotherapy

J. Pouget[1], *L. Ordas*[1], *S. Atis*[2], *S. Poty*[1], *A. Parach*[1], *T. Lahoutte*[2], *L. Navarro*[2], *M. D'Huyvetter*[2];
[1]*INSERM, Montpellier, FRANCE,* [2]*PRECIRIX, Brussels, BELGIUM.*

Aim/Introduction: The tumor microenvironment plays a crucial role in driving cancer progression. It is composed of the extracellular matrix and various non-cancerous cells, notably cancer-associated fibroblasts (CAFs). Conventional therapies, including chemotherapy and external beam X-ray radiotherapy (EBRT), often show limited success in improving patient survival. This limitation is largely attributed to pronounced desmoplasia, with CAFs identified as key contributors and potential therapeutic targets. Studies have shown that EBRT induces a senescence-associated secretory phenotype (SASP) in CAFs, which can enhance tumor cell invasion and growth. In this study, we investigate and compare the in vitro biological response of CAFs to EBRT and targeted radionuclide therapy (TRT). ***Materials and Methods:*** In vitro, immortalized human CAFs were exposed to TRT using single-domain antibodies radiolabeled with ^{177}Lu (^{177}Lu-sdAb; 0-8 MBq/mL), or to X-ray irradiation (0, 2, 4, 8 Gy). Clonogenic survival, proliferation, cell cycle progression, and senescence induction (assessed via β-galactosidase activity, persistent DNA damage, and lamin B1 expression) were evaluated. The CAF secretome following both treatments was analyzed using a multiplex cytokine array . In vivo, immunodeficient mice bearing subcutaneous patient-derived xenograft (PDX) ovarian tumors were treated with either various activities of ^{177}Lu-sdAb, different X-ray fractionation schemes, or a combination of TRT and EBRT. Tumor growth was monitored, and treatment-related toxicity was assessed. Dosimetry was performed at both the cellular and whole-body levels, and the biologically effective dose (BED) was used to compare the different radiotherapy modalities. ***Results:*** Clonogenic survival of CAFs decreased with increasing activity/dose following both EBRT and TRT. Specifically, CAF survival at 2 Gy or 2 MBq/mL (0.8 Gy) was approximately 50% and 55%, respectively. However, while clonogenic death was associated with cell proliferation arrest and senescence induction accompanied by SASP after EBRT, this was not observed following TRT. Interestingly, only the secretome of TRT-treated CAFs induced a cytotoxic bystander effect, reducing tumor cell clonogenic survival to 70%. In vivo, tumor growth was delayed after both TRT and X-ray irradiation, and BED was indicative of a long-term response. However, relapse was observed 140 days post-therapy with EBRT, while stable disease was maintained with TRT. ***Conclusion:*** Our findings suggest that CAF-targeted radionuclide therapy represents a promising strategy in cancer treatment. For an equivalent BED, continuous low dose rate irradiation of CAFs appears to be more advantageous than conventional EBRT. These results support the potential of TRT alone or in combination with EBRT as an effective therapeutic approach.

OP-216

Mechanistic insights into HSP90 inhibition as a sensitization strategy for PRRT

M. Sabatella*, P. Engbers, T. Reuvers, T. Heredia Genestar, J. Chang, N. Verkaik, J. Nonnekens;*
Erasmus Mc, Rotterdam, NETHERLANDS.

Aim/Introduction: Peptide receptor radionuclide therapy (PRRT) employing [^{177}Lu]Lu-[DOTA-Tyr^3]octreotate (^{177}Lu-DOTA-TATE) has been established as treatment for patients with metastatic neuroendocrine tumors (NETs) overexpressing the somatostatin receptor (SSTR). While PRRT improves survival and quality of life, curative responses remain rare [1]. One way to enhance PRRT therapeutic efficacy is combining it with radiosensitizing agents such as heat shock protein 90 (HSP90) inhibitors. HSP90 is a highly conserved molecular chaperone essential for the maturation and stabilization of over 200 proteins, including proteins involved in the DNA damage response and oncogenic signaling [2]. HSP90-inhibition has been shown to potentiate PRRT [3], however the mechanism behind this radiosensitizing effect remains unknown. This study aimed to elucidate mechanisms involved in the radiosensitizing effect of HSP90 inhibition. ***Materials and Methods:*** We investigated the radiosensitizing potential of HSP90 inhibitor ganetespib in two NET cell lines: GOT1 and BON1-SSTR2. Cells were treated with X-ray as external beam radiotherapy (EBRT, 2 Gy) or PRRT (1 MBq/mL) alone or in combination with ganetespib and assessed cell viability (CellTiter-Glo assay) and cell death (flow cytometry). To investigate the influence of HSP90-inhibition on various DNA repair pathways, an end-joining assay was performed, as well as RAD51 (homologous recombination specific) and 53BP1 (double strand breaks in general) foci quantification. To investigate whether non-DNA damage response related mechanisms were involved in the radiosensitization potential of HSP90-inhibition, RNA sequencing was performed post-treatment, followed by differential expression and pathway enrichment analyses. ***Results:*** Ganetespib enhanced the cell killing efficacy of both PRRT and EBRT in GOT1 and BON1-SSTR2 cells. Although HSP90 inhibition reduced RAD51 foci numbers, its effect on non-homologous end joining and DNA damage persistence was limited. Transcriptomic analysis revealed enrichment of proteotoxic stress-related pathways - such as protein folding and stabilization - following combination treatment, which was consistent with effects observed in HSP90 inhibitor monotherapy. ***Conclusion:*** Since we do not find significant effects of HSP90-inhibition on direct DNA repair or transcriptomic responses, our findings suggest that HSP90 inhibition radiosensitizes NET cells by inducing a pleiotropic effect on multiple stress-related pathways rather than solely through disruption of DNA damage response mechanisms. This effect is likely driven by impaired proteostasis and induction of proteotoxic stress. ***References:*** [1] Strosberg, J.R., et al. (2021), Lancet Oncol. 22(12): p. 1752-1763. [2] Pennisi, R., P. Ascenzi, and A. di Masi (2015), Biomolecules, 2015. 5(4): p. 2589-618. [3] Lundsten, S., et al. (2020), Eur J Nucl Med Mol Imaging, 2020. 47(4): p. 980-990.

OP-217

Synthetically Lethal DNA Damage Response Inhibition Enhances [^{177}Lu]Lu-PSMA-617 Cure Rates in Advanced Prostate Cancer

M. Bio Idrissou*, E. Santos, H. Comas Rojas, A. Carston, O. Kwon, L. Wehner, N. Clemons, J. Munson, L. Batley, Y. Medina Guevara, I. Lambert, A. Pinchuk, B. Bednarz, G. Iyer, R. Hernandez;*
University of Wisconsin-Madison (UW-Madison), Madison, WI, UNITED STATES OF AMERICA.

Aim/Introduction: [^{177}Lu]Lu-PSMA-617 has shown unprecedented therapeutic activity in metastatic castration-resistant prostate cancer (mCRPC). However, nearly half of the treated patients do not respond, and curative responses remain rare. We aim to expand [^{177}Lu]Lu-PSMA-617's efficacy by blunting the DNA

damage repair (DDR) response of mCRPC through a combination of poly(ADP-ribose) polymerase 1 (PARP1) and bromodomain and extra-terminal (BET) protein inhibition. ***Materials and Methods:*** A panel of prostate cancer (PCa) cells, including PC3-PIP, LNCaP, and 22Rv1, were treated with ^{177}Lu_(0.3-3 Gy), alone or combined with Talazoparib (PARP Inhibitor: TAZ), ABBV-075 (BET inhibitor), or both. Cell cycle profiling, RNA-sequencing, viability, clonogenic assays, and γ-H2AX staining were conducted. In vivo, PC3-PIP xenograft mice (N=5-10) received [^{177}Lu]Lu-PSMA-617_(37 MBq) with or without daily TAZ_(0.5 mg/kg), ABBV-075_(1 mg/kg), or both for 14 days. Controls received saline or monotherapy. Tumor progression, survival, and toxicity were monitored, with safety evaluated in naïve mice through hematology, biochemistry, and histopathology. ***Results:*** ABBV-075 treatment led to an increase in G1 arrest from 56.7 ±4.1 to 81.7 ±0.3% ($p < 0.04$) while TAZ and ^{177}Lu led to G2 arrest, from 17.9 ±4.1 to 85.1 ±0.2 and 81.3 ±0.1, respectively ($p < 0.02$) in AR-negative PC3-PIP cells. Importantly, ^{177}Lu+TAZ+ABBV-075 resulted in dual-phase (G1/G2) arrest, and the highest reduction in S-phase 9.6 ±1.2% versus 25.3 ±3.1% (control), 15.5 ±0.9% (^{177}Lu), 24.5 ±0.4% (^{177}Lu+TAZ), and 17.9 ±2.1% (^{177}Lu+ABBV-075). On the other hand, AR-positive LNCaP and 22Rv1 cells exhibited G1 arrest. RNA-sequencing data showed significant downregulation of key DDR-associated genes, including BRCA1/2, XRCC2, and RAD51 (Log_2FC: - 2 to - 4, $p < 0.001$) following ABBV-075 or ^{177}Lu+ABBV-075 treatments, across PCa cells. Viability and clonogenic assays corroborated enhanced cytotoxicity in all combination treatments, with the triple combination treatment (^{177}Lu+TAZ+ABBV-075, $p < 0.02$) consistently achieving the highest potency. Consequently, ^{177}Lu+TAZ+ABBV-075 displayed the highest number and persistent DNA breaks (γH2AX foci) compared with other treatments in PC3-PIP. In vivo, [^{177}Lu]Lu-PSMA-617+TAZ+ABBV-075 showed the highest efficacy (N= 8/8 complete response, $p < 0.05$) in the PC3-PIP xenograft model. No increase in toxicity was observed in combination treatments compared to [^{177}Lu]Lu-PSMA-617. ***Conclusion:*** Our result proved that pharmacologically induced G1/G2-phase arrest, S-phase suppression, and DDR downregulation are an effective radiosensitization strategy in mCRPC. This premise was demonstrated in vivo by the enhanced efficacy and curative rates achieved by the triple combination of TAZ+ABBV-075+[^{177}Lu]Lu-PSMA-617. Importantly, this enhanced treatment potency did not come with a safety tradeoff, thus suggesting an improvement in the overall therapeutic window.

OP-218

Transcriptional Silencing of DNA Repair Improves Targeted Alpha Therapy in Advanced Prostate Cancer

M. Bio Idrissou, *E. Santos, H. Comas Rojas, A. Carston, O. Kwon, L. Wehner, N. Clemons, J. Munson, L. Batley, Y. Medina Guevara, L. Lambert, A. Pinchuk, B. Bednarz, G. Iyer, R. Hernandez;*
University of Wisconsin-Madison (UW-Madison), Madison, WI, UNITED STATES OF AMERICA.

Aim/Introduction: Approximately 40% of metastatic castration-resistant prostate cancer (mCRPC) patients treated with [^{225}Ac]Ac-PSMA fail to respond, and cure rates remain at single-digit percentages. Unfortunately, xerostomia prohibits further dose escalation. Our approach to improve treatment responses in mCRPC involves Bromodomain and Extraterminal protein (BET) inhibition to suppress double-strand DNA repair genes and enhance the radiobiological efficacy of [^{225}Ac]Ac-PSMA. ***Materials and Methods:*** In vitro, PC3-PIP, LNCaP, and 22Rv1 cells were treated with ^{225}Ac (0.03-1 Gy) ± ABBV-075 (500 nM), a BET inhibitor (BETi). Assays included cell cycle analysis, RNA-sequencing, viability, clonogenic survival, and γH2AX (DNA breaks) staining. In vivo, nude mice bearing PC3-PIP xenografts (N=4-8) received ABBV-075 (1 mg/kg, 14 days) starting 3-days before, 3-days after, or with [^{225}Ac]Ac-PSMA (37 kBq, IV). Tumor growth and survival were monitored thrice weekly. Safety was assessed in naïve mice through biochemistry, complete blood count, and histopathology at days 7, 28, or 120. ***Results:*** In AR-negative PC3-PIP cells, ABBV-075 treatment significantly increased the G1 cell population from 56.7 ±4.1 to 81.7 ±0.3% ($p < 0.04$). On the other hand, ^{225}Ac primarily induced G2 arrest, from 17.9 ± 0.2 (control) to 78.9 ±0.2% ($p = 0.0037$). Combination of ABBV-075 with ^{225}Ac led to dual-phase (G1/G2) arrest and significantly reduced the S-phase population from 25.3 ±3.1% (control) to 10.53 ±3.2% ($p < 0.05$). AR-positive LNCaP and 22Rv1 cells mostly exhibit a G1-phase arrest. As expected, RNA-sequencing data revealed that ABBV-075 treatment was associated with downregulation of key DNA damage repair (DDR) genes, including BRCA1/2, XRCC2, and RAD51 (Log_2FC -2 to -6, $p < 0.001$), thereby sensitizing PCa cells to ^{225}Ac radiation. Viability and clonogenic assays revealed significantly enhanced cytotoxicity with ABBV-075 + ^{225}Ac ($p < 0.02$) across cell lines, resulting in a consistent 6 to 10-fold increase in relative biological effectiveness (RBE) compared to ^{225}Ac alone. Furthermore, ABBV-075 + ^{225}Ac induced sustained γH2AX foci, reflecting the diminished repair capacity in ABBV-075-treated cells. In vivo, all three tested combination treatments significantly enhanced tumor growth delay and extended overall survival compared to [^{225}Ac]Ac-PSMA alone ($p < 0.02$), with no noticeable toxicity. ***Conclusion:*** Our data provides a robust mechanistic and efficacy foundation warranting further exploration of BETi in combination with [^{225}Ac]Ac-PSMA in mCRPC. The observed dual-phase cell cycle arrest, downregulation of key DNA repair genes, and sustained DNA breaks in PCa cells demonstrate strong radiosensitization by ABBV-075, enhancing efficacy. Future efforts will focus on clinical translation and potential expansion to other RPT indications.

OP-219

Dissecting the Transcriptional and Cell Cycle effects of Alpha and Beta emitting Radionuclides on Prostate Cancer Cells

M. Bio Idrissou, *E. Santos, O. Kwon, B. Bednarz, G. Iyer, R. Hernandez;*
University of Wisconsin-Madison (UW-Madison), Madison, WI, UNITED STATES OF AMERICA.

Aim/Introduction: Radiopharmaceutical therapies (RPT) such as [^{177}Lu]Lu-PSMA-617 and [^{225}Ac]Ac-PSMA-617 have shown clinical benefit in patients with advanced prostate cancer (PCa), but only in half of the patients treated. To understand the mechanisms behind treatment failures, we performed comprehensive transcriptional and phenotypic profiling across a panel of PCa cell lines treated with ^{177}Lu or ^{225}Ac. ***Materials and Methods:*** PC3-PIP, LNCaP, and 22Rv1 were treated (24h) in vitro with ^{177}Lu (0.3-3 Gy) or ^{225}Ac (0.03-1 Gy). A comprehensive battery of in vitro assays, including flow cytometry, RNA-sequencing, γH2AX immunofluorescence, and clonogenic, was performed to assess treatment effects on cell cycle, gene expression, DNA repair dynamics, and radiosensitivity. ***Results:*** ^{177}Lu and ^{225}Ac treatments resulted in dose-dependent G2-phase arrest, increasing from 17.9 ±0.2 (control) to 83.8 ±0.9% and 78.9 ±0.2% ($p = 0.0037$) at 1 Gy in PC3-PIP_(PSMA+/AR-) cells. AR-positive LNCaP and 22Rv1 cells showed a trend towards G1-phase increases ($p > 0.05$). RNA-sequencing revealed broader changes in gene regulation for ^{177}Lu (3,257 DEGs: Differentially Expressed Genes) than for ^{225}Ac (1,451 DEGs) in PC3-PIP. Both treatments upregulated CCNG2 and BBC3 genes, involved in cell-cycle arrest and apoptosis, while ^{225}Ac uniquely downregulated DNA repair genes such as LIG1, and RAD54L (Log_2FC: -1.5 to -1.66; padj <0.005). In LNCaP cells, ^{225}Ac elicited stronger p53 pathway activation, with upregulation of TP53I3, and CDKN1A (Log_2FC: 3.27-6.41; padj <1E-3), and downregulated multiple homologous recombination (HR) genes, including BRCA1/2 (Log_2FC: -1.18 to -6.09; padj <1E-10), while ^{177}Lu induced less pronounced pro-apoptotic responses.

In 22Rv1, ^{225}Ac induced fewer DEGs (538 vs. 2,588 with ^{177}Lu) but robustly upregulated CDKN1A and BBC3 (Log_2FC: 2.35 to 2.99; padj <1E-40) and suppressed DNA repair genes. Several senescence markers (≥80) were significantly upregulated (Log_2FC >3; padj <0.0001) alongside cell cycle arrest across PCa cell lines. Notably, DNA repair genes were not upregulated, suggesting early responses prioritize arrest over repair. Immunofluorescence showed more persistent clustered DNA breaks with ^{225}Ac than ^{177}Lu. Clonogenic survival assay confirmed higher cytotoxicity of ^{225}Ac, with relative biological effectiveness (RBE) ranging from 6.2 to 10.1 across cell lines. ***Conclusion:*** Our data identified cell cycle arrest and senescence rather than enhanced DNA repair as key early responses and potential contributors to radioresistance in PCa cells. ^{225}Ac demonstrates superior cytotoxicity compared to ^{177}Lu, despite eliciting a more limited transcriptional response. We will continue mining our RNA-sequencing data and identifying potential PCa vulnerabilities that can be tackled pharmacologically to augment the depth and durability of RPT therapeutic responses.

OP-220

Phosphoproteomics Analysis of Signaling Networks in Response to Terbium-161 and Lutetium-177 Radioimmunotherapy in Ovarian Cancer and Lymphoma Models

M. Grzmil[1], *E. Rioja-Blanco*[1,2], *T. Todorov*[1,2], *P. Grundler*[1], *A. Moiseeva*[1], *N. van der Meulen*[1,3], *Y. Banz*[4], *C. Schlapbach*[5], *U. Novak*[6], *J. Grünberg*[1], *R. Schibli*[1,2], *M. Behe*[1];
[1]*Center for Radiopharmaceutical Sciences, PSI Center for Life Sciences, Villigen PSI, SWITZERLAND,* [2]*Department of Chemistry and Applied Biosciences, ETH Zurich, Zurich, SWITZERLAND,* [3]*Laboratory of Radiochemistry, PSI Center for Nuclear Engineering and Sciences, Villigen PSI, SWITZERLAND,* [4]*Institute of Tissue Medicine and Pathology, University of Bern, Bern, SWITZERLAND,* [5]*Department of Dermatology, Inselspital, Bern University Hospital, University of Bern, Bern, SWITZERLAND,* [6]*Department of Medical Oncology, Inselspital, Bern University Hospital, University of Bern, Bern, SWITZERLAND.*

Aim/Introduction: Radioimmunotherapy (RIT) combines the specificity of monoclonal antibodies with the cytotoxic radionuclides. Terbium-161 (Tb-161) offers an advantage over the clinically established lutetium-177 (Lu-177) by emitting both β^- particles and ultra-short-range conversion and Auger electrons (CE/AE), enhancing its potential to eradicate single cancer cells and metastases. This study investigates and compares molecular responses to Tb-161- and Lu-177-based RIT in two distinct cancer models: L1 cell adhesion molecule (L1CAM) overexpressing high-grade serous ovarian cancer (HGSOC) and CD30-positive T-cell lymphoma. ***Materials and Methods:*** Anti-L1CAM monoclonal chCE7 antibodies were radiolabeled to produce [^{161}Tb]Tb-DOTA-chCE7 and [^{177}Lu]Lu-DOTA-chCE7 radioimmunoconjugates (RICs) for the treatment of ovarian cancer OVCAR8 cells, whereas in the lymphoma model, CD30-targeted RICs ([^{161}Tb]Tb-cAC10 and [^{177}Lu]Lu-cAC10) were assessed for RIT of Karpas 299-tumor bearing nude mice. Tandem mass tagging (TMT)-based integrated phosphoproteomics and proteomics was employed for MS-based peptide identification and quantification. Comparative bioinformatics analyzed signaling network alterations in response to RIT with Tb-161 and Lu-177. ***Results:*** In ovarian cancer cells, phosphoproteomics combined with matching proteomics quantified 22101 phosphopeptides and 7484 proteins, whereas in the lymphoma model, 12548 phosphopeptides and 7763 proteins were quantified. Both [^{177}Lu]Lu-DOTA-chCE7 and [^{161}Tb]Tb-DOTA-chCE7 treatments induced pathways involved in DNA damage response (DDR) and repair, signal transduction (including EGFR, VEGFR, and mTOR signaling), mRNA processing, cell cycle and cytoskeleton regulation, translation, apoptosis, and glycogen metabolism. Similarly, in lymphoma in vivo model both [^{177}Lu]Lu-cAC10 and [^{161}Tb]Tb-cAC10 induced alterations in DDR and replication stress response (RSR), cell cycle arrest, and protein metabolism regulation. To further investigate the potential differences between both radionuclides, we directly compared the phosphopeptide abundance after Tb-161 and Lu-177 RITs. While most alterations were common to both treatments, the phosphorylation of a few proteins associated with chromatin methylation, GTPase activation, and chromosome structure was either uniquely induced or significantly more pronounced with Tb-161 as compared to Lu-177 RIT. We are currently conducting further bioinformatics analyses and validation study. ***Conclusion:*** This dual-model study underscores the potential of Tb-161 and Lu-177 to activate signaling networks in both solid and hematologic malignancies. Through in-depth proteomic and phosphoproteomics profiling, the study provides comprehensive insights into the molecular responses triggered by β^- and CE/AE radiation. ***References:*** E. Rioja-Blanco, Y. Banz, C. Schlapbach, U. Novak, T. Chiorazzo, N. L. Bertschi, P. Bernhardt, P. V. Grundler, N. P. van der Meulen, M. Grzmil, R. Schibli, M. Behe. Terbium-161 radioimmunotherapy as a novel treatment for CD30+ lymphomas. J Nucl Med. 2025. In press

OP-221

Live-cell imaging of [^{177}Lu]Lu-DOTA-TATE: towards linking intracellular distribution and DNA damage kinetics for improved dosimetry

J. Nonnekens*, P. Engbers, T. de Wolf, G. Tamborino, J. Zink, D. Chapeau, Y. Seimbille, M. Sabatella;*
Erasmus MC, Rotterdam, NETHERLANDS.

Aim/Introduction: Peptide receptor radionuclide therapy (PRRT) using [^{177}Lu]Lu-[DOTA-Tyr^3]octreotate ([^{177}Lu]Lu-DOTA-TATE) is effective in treating metastatic neuroendocrine tumors, yet curative responses remain rare due to therapeutic limitations and toxicity. Compared to external beam radiotherapy (EBRT), little is known about the radiobiological effects of PRRT. Given their distinct irradiation kinetics, PRRT likely has a different dose-effect relationship than EBRT. Determining these relationships requires precise knowledge on the absorbed cellular doses, which are influenced by intracellular radiopharmaceutical localization. Due to its limited spatial resolution, nuclear imaging cannot resolve subcellular radiopharmaceutical distribution. Therefore, we employed confocal microscopy, which offers sub-micrometer resolution, to accurately map intracellular localization. This study aimed to correlate the subcellular distribution of [^{177}Lu]Lu-DOTA-TATE with DNA damage kinetics using live-cell microscopy, as a basis for improving microdosimetric modeling. ***Materials and Methods:*** To evaluate DNA damage kinetics induced by [^{177}Lu]Lu-DOTA-TATE and compare it to EBRT, we used CRISPR/Cas9 genome editing to create a functional 53BP1-mClover knock-in (53BP1 is a marker for DNA double strand breaks (DSBs)) in the human osteosarcoma cell line U2OS which overexpress the somatostatin receptor 2 (SSTR2). Cells were treated with equitoxic doses of EBRT (2 Gy) or [^{177}Lu]Lu-DOTA-TATE (1 MBq/mL) and 53BP1 foci formation and resolution were tracked for 24h by live cell imaging. DNA damage kinetics were quantified using an artificial intelligence-driven pipeline which includes fully automatic cell nucleus detection, reduction of noise, and detection and tracking of DNA repair foci. To visualize radiopharmaceutical distribution, we created a fluorescently labelled [^{177}Lu]Lu-DOTA-TATE (Cy5-[^{177}Lu]Lu-DOTA-TATE). U2OS-SSTR2 53BP1 mClover cells were incubated with Cy5-[^{177}Lu]Lu-DOTA-TATE for 2 hours, and radiopharmaceutical internalization and 53BP1 foci dynamics were co-imaged during and after the incubation period. ***Results:*** Competition binding assays showed limited influence of Cy5 on the binding affinity of [^{177}Lu]Lu-DOTA-TATE . Live-cell imaging revealed dynamic internalization of Cy5-[^{177}Lu]Lu-DOTA-TATE and localization close to the nucleus, consistent with localization to the Golgi apparatus. Quantification of 53BP1 foci numbers revealed

differential kinetics upon EBRT and PRRT, while 53BP1 foci track durations showed the same distributions. ***Conclusion:*** Differences in 53BP1 foci formation illustrate the distinct therapeutic window between EBRT and PRRT, while the similar foci track duration, reflecting DSB persistence, suggests comparable DSB complexity. Ongoing analyses aim to directly link Cy5-[^{177}Lu]Lu-DOTA-TATE localization with DNA damage induction. These insights will support more accurate dosimetric modeling and help refine the dose-effect relationship of PRRT relative to EBRT, ultimately improving its therapeutic efficacy.

606

Sunday, October 5, 2025, 16:45 - 18:15
Room 117

Clinical Oncology Track - TROP Session - Oncology & Theranostics Committee: Haematology and Lymphoma

OP-222

Dual time point lymphoma [^{18}F]FDG Total-Body PET/CT - a prospective single center AI-aided study to assess therapy response prediction

*C. Mingels[1], **F. Sen**[2], H. Nalbant[2], K. Chung[2], N. S. Esteghamat[3], M. Rokni[2], J. M. Tuscano[3], A. Rominger[1], Y. Abdelhafez[2], R. D. Badawi[2], B. Spencer[2], L. Nardo[2];*
[1]Department of Nuclear Medicine, Inselspital, Bern University Hospital, University of Bern, Bern, SWITZERLAND, [2]Department of Radiology, University of California Davis, Sacramento, CA, UNITED STATES OF AMERICA, [3]Department of Bone Marrow Transplant, University of California Davis, Sacramento, CA, UNITED STATES OF AMERICA.

Aim/Introduction: To evaluate dual time point (DTP) [^{18}F]FDG total-body (TB) PET/CT with regard to therapy response evaluation. We hypothesized that DTP TB imaging might be able to provide new biomarkers for therapy response assessment in lymphoma patients. ***Materials and Methods:*** A total of 75 lymphoma patients received DTP [^{18}F]FDG TB PET/CT imaging 60- and 120-minutes post injection for staging and restaging. PET images were segmented using an artificial intelligence (AI)-driven algorism. Segmentation was scrutinized and edited by a nuclear medicine physician. Lesion uptake was characterized by standardized uptake values (SUV), metabolic tumor volume (MTV) and total lesion glycolysis (TLG) on a lesion--basis and by total metabolic tumor volume (TMTV) and TLG on a per-patient basis. $SUV_{mean/max/peak}$ was used to calculate the tumor-to-background ratio (TBR) and contrast-to-noise ratio (CNR). Follow up data (12±2 month) were used to assess overall (OS) and progression free survival (PFS). ***Results:*** A total of 977 lesions were identified and analyzed. DTP imaging showed no significant difference regarding the tumor uptake between the two analyzed time points (SUV_{max} 60min: 3.89±3.43 vs. 120min: 3.65±3.37, p=0.09). MTV and TLG were also not significantly different between the two timepoints (MTV p=0.72; TLG p=0.56). However, TBR and CNR were significantly higher in late TB PET images (TBR 60min: 3.32±4.54 and 120min 6.40±6.28, p<0.01; CNR 60min: 13.56±23.07 vs. 120 min: 30.44±41.19, p<0.01). Patients with high lesion uptake (SUV_{max}>11.0) showed significantly shorter OS than patients with low [^{18}F]FDG uptake in both time points (p<0.05). PFS was not different in patients with high and low lesion uptake. TMTV over 20ml was prognostic for shorter PFS (median 18 month) in both time points. However, OS was not different in patients with high and low TMTV. ***Conclusion:*** DTP [^{18}F]FDG TB PET/CT is a useful tool to assess new biomarkers in lymphoma patients to evaluate patients' outcome prediction. With its long--axial field-of-view (> 100cm) it enables to scan the entire patient in a single bed position. SUV_{max} was prognostic for OS and TMTV for PFS in our small study cohort. Larger studies are necessary to confirm our results and apply TB PET's new prognostic biomarker on different lymphoma subtypes.

OP-223

Quantitative Dual-Tracer PET Biomarkers for Optimizing Patient Selection in CXCR4-Targeted Radioligand Therapy for Multiple Myeloma

***N. Dreher**[1], S. Xue[2], S. Kraus[3], J. S. Enke[1], K. Michalski[4], M. Hacker[2], H. Einsele[3], A. K. Buck[4], X. Li[2], C. Lapa[1];*
[1]Nuclear Medicine, Faculty of Medicine, University of Augsburg, Augsburg, GERMANY, [2]Division of Nuclear Medicine, Department of Biomedical Imaging and Image-guided Therapy, Vienna General Hospital, Medical University of Vienna, Vienna, AUSTRIA, [3]Department of Internal Medicine II, University Hospital Würzburg, Würzburg, GERMANY, [4]Department of Nuclear Medicine, University Hospital Würzburg, Würzburg, GERMANY.

Aim/Introduction: CXCR4-directed radioligand therapy (CXCR4-RLT) is an emerging treatment modality for patients with relapsed or refractory (r/r) multiple myeloma (MM). However, heterogeneous treatment responses underscore the limitations of current patient selection approaches, which to a certain extent rely on qualitative assessments of CXCR4/FDG-PET concordance. This study evaluates whether quantitative imaging biomarkers derived from dual-tracer PET/CT can enhance patient stratification and predict therapeutic response and survival outcomes. ***Materials and Methods:*** We retrospectively analyzed 28 patients with r/r MM who underwent CXCR4-directed [^{68}Ga]Ga-PentixaFor and [^{18}F]FDG PET/CT imaging prior to CXCR4-RLT. Lesions and organs were segmented using a deep learning-based pipeline, followed by dual-tracer image fusion. Quantitative imaging features—including SUVmean, SUVmax, molecular tumor volume (MTV), total lesion glycolysis (TLG), and total lesion CXCR4 uptake (TLC)—were extracted from both concordant and discordant lesions. Treatment response was assessed based on International Myeloma Working Group (IMWG) criteria. Decision tree analysis was used to identify imaging biomarkers associated with treatment response and 6-month survival. Furthermore, a survival tree was constructed to identify imaging-based risk stratification rules using time-to-event data. Imaging features selected by the survival tree were further evaluated using Kaplan-Meier survival analysis, with statistical significance assessed by log-rank tests. ***Results:*** Decision tree analyses identified complementary imaging biomarkers predictive of treatment response and 6-month survival following CXCR4-RLT in MM. For treatment response, CXCR4-MTV ≤ 450 cm^3 was the primary stratification feature, with all such patients responding to therapy. In patients with higher tumor burden, non-response was linked to CXCR4-SUVmax > 23.7 and FDG-SUVmax > 9.0, while lower CXCR4-SUVmean within $CXCR4^+$/FDG^+ overlap regions (≤ 3.12) was associated with improved response. For 6-month survival, FDG-SUVmean with a threshold of ≤ 6.61 within $CXCR4^+$/FDG^+ overlap regions was associated with significantly improved survival. Survival tree analysis further identified FDG-TLG as the strongest survival predictor, with values > 2276 significantly associated with reduced survival (p < 0.01, HR = 4.1). ***Conclusion:*** Quantitative imaging features from dual-tracer PET/CT are strong indicators of both treatment response and short-term survival following CXCR4-RLT in MM. Both CXCR4 tumor burden and metabolic activity in $CXCR4^+$/FDG^+ concordant lesions are key predictors of response and short-term survival following CXCR4-RLT. FDG-TLG was identified as the strongest predictor of overall survival, with high values linked to significantly reduced survival. These findings underscore the prognostic value of integrating lesion-level dual-tracer imaging biomarkers to guide patient selection and risk assessment.

OP-224

SAFOV vs LAFOV PET/CT in Lymphoma: Impact on Staging and Metabolic Response Assessment

S. Proto[1], *A. Di Giorgio*[1], *C. Malizia*[2], *M. Assenza*[3], *M. Stasolla*[1], *E. Fortunati*[2], *A. Farolfi*[2], *C. Pellegrini*[4], *B. Casadei*[4], *P. L. Zinzani*[4,5], *S. Fanti*[1,2], *C. Nanni*[2];
[1]*Nuclear Medicine, Alma Mater Studiorum Bologna, Bologna, ITALY,* [2]*Nuclear Medicine, IRCCS Azienda Ospedaliero-Universitaria di Bologna, Bologna, ITALY,* [3]*Professional Development and Implementation of Research in Health Professional Unit, IRCCS Azienda Ospedaliero-Universitaria di Bologna, Bologna, ITALY,* [4]*Istituto di Ematologia e Oncologia Medica "L. & A. Seragnoli" IRCSS Azienda Ospedaliero-Universitaria Policlinico-S.Orsola Malpighi, Bologna, ITALY,* [5]*Dipartimento di Scienze Mediche e Chirurgiche, Università di Bologna, Bologna, ITALY.*

Aim/Introduction: Long-axial-field-of-view PET (LAFOV-PET) provides superior sensitivity and spatial resolution compared to conventional short-axial-field-of-view PET (SAFOV-PET). As the Deauville Score (DS) was established using SAFOV-PET, it is essential to evaluate the concordance between these two modalities in lymphoma assessment. This study aims to compare LAFOV-PET and SAFOV-PET in lymphoma staging and treatment response evaluation. ***Materials and Methods:*** Patients with a confirmed diagnosis of lymphoma underwent [18F]FDG-PET/CT imaging 60 minutes post-injection, first using SAFOV-PET, immediately followed by LAFOV-PET (Protocol number: 598/2024/Oss/AOUBo). Depending on the clinical indication, some patients underwent multiple paired scans. The two acquisitions were compared based on positivity/negativity concordance, number of detected lesions, SUVmax-SUVmean in the reference lesion and reference regions (liver-lv, bloodpool-bp, bone marrow-bm), metabolic-tumour-volume (MTV), total-lesion-glycolysis (TLG) and DS classification. ***Results:*** Seventeen patients underwent paired PET/CT imaging, contributing a total of 34 scan pairs for analysis. Overall agreement for lesion positivity/negativity between SAFOV-PET and LAFOV-PET was 94.1% (32/34 scans; Cohen's kappa-κ = 0.88), with lesion count agreement at 76.5% (26/34; weighted κ = 0.80). LAFOV-PET showed higher median SUVmax in reference lesions: 7.1 (IQR 2.6-14.4) vs 5.7 (IQR 2.4-12.3) in SAFOV-PET. Conversely, reference tissues showed lower median SUVmax on LAFOV-PET vs SAFOV-PET: lv 2.4 vs 3.6, bp 1.7 vs 2.6, bm 2.4 vs 3.0 respectively, reflecting enhanced image contrast. MTV (mean 242.3 cm^3 vs 228.6 cm^3) and TLG (mean 1012.4 vs 927.5) were also higher on LAFOV-PET vs SAFOV-PET. DS classification agreement was 91.2% (31/34 scans; weighted κ = 0.93), with phase-specific agreement of 85.7% pre-therapy (12/14 scans; κ = 0.76), 100% interim (8/8 scans; κ = 1.0) and 91.7% post-therapy (11/12 scans; κ = 0.93). ***Conclusion:*** The higher sensitivity of LAFOV-PET allows the detection of additional lesions, particularly at baseline, and yields higher SUVmax values at target lesions along with slightly lower background uptake in reference tissues. This results in improved lesion-to-background contrast compared to SAFOV-PET, likely reflecting superior image quality and signal-to-noise characteristics. Despite these technical differences, the high concordance in DS classification, especially during interim and post-therapy phases, confirms that response assessment remains consistent. These findings support the continued applicability of established DS-based criteria to LAFOV-PET in clinical lymphoma evaluation.

OP-225

Prognostic Value of Baseline ^{18}F-FDG PET/CT-Derived Total Metabolic Tumor Volume of Bone Marrow in Multiple Myeloma Patients (CASSIOPET Cohort)

S. Ahrari[1], *B. Jamet*[1], *S. Zweegman*[2], *A. Perrot*[3], *C. Hulin*[4], *D. Caillot*[5], *T. Facon*[6], *X. Leleu*[7], *K. Belhadj*[8], *E. Itti*[9], *L. Karlin*[10], *C. Bailly*[1,11], *M. Levin*[12], *M. C. Minnema*[13], *C. Bodet-Milin*[1,11], *B. De Keizer*[14], *J. Corre*[15], *P. Sonneveld*[16], *C. Touzeau*[17,11], *P. Moreau*[17,11], *F. Kraeber-Bodéré*[1,11], *T. Carlier*[1,11];
[1]*Service de Médecine Nucléaire, University Hospital Hôtel-Dieu, Nantes, FRANCE,* [2]*Amsterdam UMC, Vrije Universiteit Amsterdam, Cancer Center Amsterdam, Department of Hematology, Amsterdam, NETHERLANDS,* [3]*CHU de Toulouse, IUCT-O, Université de Toulouse, UPS, Service d'Hématologie, Toulouse, FRANCE,* [4]*Department of Hematology, Hôpital Haut Lévêque, University Hospital Bordeaux, Pessac, FRANCE,* [5]*CHU Dijon, Hôpital Du Bocage, Dijon, FRANCE,* [6]*University of Lille, CHU Lille, Service des Maladies du Sang, Lille, FRANCE,* [7]*CHU Poitiers, Hôpital la Milétrie, Poitiers, FRANCE,* [8]*Hôpital Henri Mondor, Lymphoid Malignancies Unit, Créteil, FRANCE,* [9]*Department of Nuclear Medicine, Hôpital Henri Mondor, Créteil, FRANCE,* [10]*Centre Hospitalier Lyon-Sud Hématologie (HCL), Pierre–Bénite, FRANCE,* [11]*CRCI2NA, INSERM, CNRS, Université d'Angers, Université de Nantes, Nantes, FRANCE,* [12]*Albert Schweitzer Ziekenhuis, Dordrecht, NETHERLANDS,* [13]*Department of Hematology, University Medical Center Utrecht, Utrecht, NETHERLANDS,* [14]*Department of Nuclear Medicine and Radiology, University Medical Center Utrecht, Utrecht, NETHERLANDS,* [15]*Unité de Genomique du Myélome, IUC-T Oncopole, Toulouse, FRANCE,* [16]*Erasmus MC Cancer Institute, Rotterdam, NETHERLANDS,* [17]*Hematology, University Hospital Hôtel-Dieu, Nantes, FRANCE.*

Aim/Introduction: Multiple myeloma (MM) is a heterogeneous hematologic malignancy whose outcome in some patients is difficult to predict using conventional factors. This study evaluates the interest of total metabolic tumor volume of the bone marrow (TMTV-BM), derived from 2-[^{18}F]fluoro-2-deoxy-D-glucose (^{18}F-FDG) positron emission tomography/computed tomography (PET/CT) at baseline, in predicting survival outcomes in a multicenter cohort of newly diagnosed MM patients. ***Materials and Methods:*** Patients were enrolled in the CASSIOPET protocol, an ancillary study of the CASSIOPEIA protocol sponsored by the IFM group. The total population underwent whole-body ^{18}F-FDG PET/CT imaging before treatment. The population treated with Daratumumab after the first and/or second randomization was termed the DARA population. Skeleton, liver, and skull were automatically segmented from the CT images using the pre-trained MOOSE algorithm, with manual corrections applied as needed. CT-based skeletal and liver segmentations were then resampled and applied to standardized uptake value PET images. To reduce the influence of intense brain ^{18}F-FDG uptake, the skull was excluded from analysis. TMTV-BM was defined as the number of voxels with uptake greater than the median liver uptake. The potential of TMTV-BM, in combination with clinical and conventional PET-derived features, for progression-free survival (PFS) and overall survival (OS) was evaluated. In the total population, three additional treatment arm features were also considered according to the CASSIOPEIA study design. Four machine learning algorithms were trained using uncorrelated features from consensus-based hierarchical clustering and feature selection, with hyperparameter optimization performed using three outer/inner fold nested cross-validation. Final predicted risk scores for the outer test samples were calculated by averaging the predictions of the four optimized models in each outer fold. Feature importance was assessed using Shapley additive explanation values. ***Results:*** The total population comprised 239 patients, of which 172 were classified as the DARA population. In the total population, the final model achieved a concordance index (C-index) of 0.642±0.007 for PFS and 0.577±0.020 for OS. In the DARA population, C-indices of 0.619±0.032 and 0.642±0.069 were observed for PFS and OS, respectively. TMTV-BM was the most informative feature for predicting OS in the total population and PFS in the DARA population. It ranked third for PFS in the total population, following two treatment arm combinations, and third for OS in DARA, after R-ISS and IMPeTUs criteria. ***Conclusion:*** Our results highlight the considerable potential of TMTV-BM, which may play a critical role in identifying high-risk MM patients at baseline in future clinical practice.

OP-226

Baseline [^{18}F]FDG PET Biomarkers of Host and Tumor Predict Efficacy and CRS in Multiple Myeloma Patients Treated with CAR T Cells

S. Xue[1], *Y. Jia*[1], *J. Chen*[2], *G. Hu*[3], *M. Hacker*[1], *X. Li*[1], *Z. Cai*[2];
[1]*Division of Nuclear Medicine, Department of Biomedical Imaging and Image-guided Therapy, Vienna General Hospital, Medical University of Vienna, Vienna, AUSTRIA,* [2]*Marrow Transplantation Center, Department of Hematology, The First Affiliated Hospital, School of Medicine, Zhejiang University, Hangzhou, CHINA,* [3]*Department of Nuclear Medicine, The First Affiliated Hospital, Zhejiang University School of Medicine, Hangzhou, CHINA.*

Aim/Introduction: Chimeric antigen receptor T-cell (CAR-T) therapy has transformed the management of relapsed/refractory multiple myeloma (r/r MM), yet therapeutic response and toxicity—particularly cytokine release syndrome (CRS)—remain highly variable. Although tumor burden is often quantified on [^{18}F]FDG PET/CT, the metabolic activity of immune-related organs may reflect host immune status and influence CAR-T outcomes. ***Materials and Methods:*** We retrospectively evaluated baseline [^{18}F]FDG PET/CT scans from 120 patients with r/r MM treated with BCMA-directed CAR-T therapy. Quantitative metrics were extracted from both tumor lesions and immune-related organs, including the spleen, liver, and bone marrow. Treatment response was defined by IMWG criteria, and CRS was graded per ASTCT guidelines. A transformer-based machine learning model was trained to integrate PET-derived and clinical features for predicting both therapeutic response and CRS severity. ***Results:*** Patients with lower spleen SUVmean at baseline were significantly more likely to achieve a deep treatment response (≥VGPR) (OR 3.8, 95% CI: 1.7-8.3; P < 0.001). Conversely, elevated metabolic activity in extramedullary lesions—especially high SUVmax and metabolic tumor volume (MTV)—was associated with poor response (OR 0.4, 95% CI: 0.2-0.8; P = 0.007). For toxicity, increased liver and spleen total lesion glycolysis (TLG) independently predicted grade ≥2 CRS (OR 3.2, 95% CI: 1.5-6.9; P < 0.001). The integrated model combining imaging and clinical data achieved an AUC of 0.83 for predicting treatment response and 0.79 for CRS severity. ***Conclusion:*** Baseline [^{18}F]FDG PET/CT features—particularly spleen SUVmean and liver/spleen TLG—are associated with both therapeutic efficacy and immune-mediated toxicity in CAR-T-treated multiple myeloma. These imaging biomarkers may reflect host immune readiness and systemic inflammation, offering a noninvasive tool for pre-infusion risk stratification. Prospective studies are warranted to validate these findings, including correlation with peripheral and tumor-associated immune profiles assessed via flow cytometry and tissue sampling.

OP-227

FAST Score : A Machine Learning-Based Model Predicting Early Relapse after CAR T-cells in Follicular Lymphoma:Results from the French DESCAR-T Registry

Y. Al Tabaa[1], *X. Palard-Novello*[2], *G. Cartron*[3], *C. Thieblemont*[4], *D. Blaise*[5], *C. Rossi*[6], *R. Houot*[7], *F. Bodere*[8], *B. Tessoulin*[9], *F. Lebras*[10], *O. Hermine*[11], *F. Morshhauser*[12], *E. Van Zele*[13], *V. Dupont*[14], *R. Ricci*[13], *E. Bachy*[15], *L. Ysaebert*[16];
[1]*Scintidoc Nuclear Medicine Center, Montpellier, FRANCE,* [2]*Nuclear Medicine Center, Rennes, FRANCE,* [3]*Hematology Department, CHU Montpellier, Montpellier, FRANCE,* [4]*Hematology Department, Saint-Louis Hospital, Paris, FRANCE,* [5]*Hematology Department, Insitiut Paoli Clamettes, Marseille, FRANCE,* [6]*Hematology Department, CHU Dijon, Dijon, FRANCE,* [7]*Hematology Department, CHU Rennes, Rennes, FRANCE,* [8]*Nuclear Medicine Center, CHU Nantes, Nantes, FRANCE,* [9]*Hematology Department, CHU Nantes, Nantes, FRANCE,* [10]*Hematology Department, CHU Henri Mondor, Créteil, FRANCE,* [11]*Hematology Department, CHU Necker, Paris, FRANCE,* [12]*Hematology Department, CHU Lille, Lille, FRANCE,* [13]*LYSA-IM, Créteil, FRANCE,* [14]*LYSARC, Pierre Bénite, FRANCE,* [15]*Hematology Department, CHU Lyon Sud, Lyon, FRANCE,* [16]*Hematology Department, Oncopole Toulouse, Toulouse, FRANCE.*

Aim/Introduction: Patients with relapsed or refractory Follicular Lymphoma (R/R-FL) often experience brief progression-free survival (PFS) after two or more therapies. CAR-T-cell-therapy was recently approved for these patients, demonstrating high complete response rates and extended PFS in phase II studies. Predicting outcomes after CAR-T-cell-therapy could guide further treatment in FL patients at high risk of relapse. We aim to evaluate early relapse predictors using machine learning (ML) models after CAR-T-therapy in R/R-FL patients. ***Materials and Methods:*** Patients with R/R-FL from the DESCAR-T-registry (NCT04328298), treated with tisagenlecleucel (tisa-cel) or axicabtagene-ciloleucel (axi-cel), and with FDG-PET/CT before lymphodepletion (Pre-LD) and 1,3,6, and 12 months (M) after infusion, available for central review, were included. Total Metabolic Tumor Volume (TMTV) and SUVmax were measured and Deauville score (DS) was registered. PFS is the time between CAR-T-cell infusion and progression or death during follow-up. Four models (random forest,logistic regression,decision tree,XGBoost) were trained (80% dataset) and tested (20%) to predict progression at M3. Model performance was assessed using AUC, sensitivity, specificity, and predictive values, including clinical (age,sex,Ann-Arbor stage,ECOG,prior treatment), biological (LDH,ferritin,CRP at infusion), and imaging parameters (pre-LD SUVmax and TMTV). The best predictive factors from the best ML model were then computed in a multivariate Cox model to establish a score based on Hazard Ratios values. Cutoff values for quantitative variables prior to the Cox model were estimated to maximize the log-rank statistics. ***Results:*** FDG-PET/CT were available for 94 R/R-FL patients (77 treated with tisa-cel,17 with axi-cel), predominantly male (71.3%),mean age of 62 years, mostly in advanced-stage disease (69.9% Ann-Arbor stage III-IV). Median follow-up since infusion was 7.1 months with 21 patients experiencing progression/relapse before M3. Death rate was 5.3% (5patients), preventing OS analysis. At M1, 75 patients (79.8%) had a complete response (CR,DS1-3) and 56 (77.7%) maintained CR at M3. One patient with DS4 at M1 showed a CR at M3.Random Forest was the best-performing model (AUC:1.0) outperforming other models (Logistic Regression:0.89;XGBoost:0.75;Decision Tree:0.73). A prognostic score (FAST) ranging 0-8 points (pts) was developed including retained predictors from Random Forest (elevated ferritin:1pt, Age<71years:3pts, pre-LD SUVmax>8.4:3pts, pre-LD TMTV>448 ml:1 pt) and distinguished 3 risk groups: 1)0-3:low risk (n=23,100% PFS at 12 months), 2)4-6:intermediate risk (n=39,69%) and 3)7-8pts:high risk (n=32,51%). ***Conclusion:*** We introduce a novel prognostic score FAST (elevated ferritin and age at infusion, SUVmax and TMTV pre-LD) allowing improved accuracy of early risk stratification that could drive post-CAR-T monitoring and therapeutic strategies.

OP-228

Prognostic significance of image-based biomarkers in baseline FDG PET/CTs of patients with DLBCL from the CALGB50303 study - Comparison of manual and AI-based segmentation

D. Hellwig[1,2], *J. Mikolajczak*[2], *V. Langguth*[2], *A. Hellwig*[2], *D. Schmidt*[2];
[1]*University Regensburg, Regensburg, GERMANY,* [2]*Department of Nuclear Medicine, University Hospital Regensburg, Regensburg, GERMANY.*

Aim/Introduction: Image-based biomarkers (IBBs) gain importance as their prognostic relevance is recognized for several tumor entities, e.g. aggressive non-Hodgkin's lymphoma (aNHL). For clinical stratification of patients, cut-off values for parameters like metabolic tumor volume (MTV) or total lesion glycolysis (TLG) must be established by rigorous methodology and prospectively confirmed in trials. Here we intend to derive thresholds for MTV and TLG from FDG PET/CT images from a prospective trial to be used as risk stratificator in the analysis of further prospective

trials in aNHL. ***Materials and Methods:*** PET/CT image data of the randomized CALGB50303 trial (testing standard versus experimental chemoimmunotherapy in aNHL) [1] acquired in the imaging substudy CALGB580603 [2] were obtained from The Cancer Imaging Archive (TCIA) [3]. Baseline FDG PET/CTs were used to measure total MTV and TLG by delineating lymphoma manifestations using 41% of the lesional SUV maximum (SUVmax), restricted to lesions volume above 1 mL, using a CE-certified analysis tool (MTV_syngo, TLG_syngo) or a self-trained convolutional neural network (MTV_unet, TLG_unet) based on the nnU-Net framework [4] trained with a subset of lymphoma patients (n=131) from the AutoPET data set [5] without further supervision. Results were analysed for prognostic relevance compared to clinical parameters by log-rank tests and Cox-regression using follow-up data from TCIA. ***Results:*** Baseline PET/CT was available for 150 of 155 patients in the imaging substudy. MTV_syngo and MTV_unet as well as TLG_syngo and TLG_unet were highly correlated (r>0.95, p<0.001). Larger deviations between manual and AI-based segmentation were classified as related to false-positive and false-negative results of AI. Optimal cut-offs were 150 mL for both MTV_syngo and MTV_unet for progression-free survival and 650 mL for overall survival (OS). p-values for IBBs from manual segmentation were lower (and thus Hazard ratios higher) than from AI-based IBBs. No differences in demographics, IBBs, response rate, or survival were observed between treatment arms or age groups ≤60 and >60 years (p>0.10). ***Conclusion:*** TCIA is a valuable source to establish IBBs from reused imaging data of prospective trials. As neither treatment arms nor age affected outcome, IBBs derived here can be used in further prospective trials as already planned for the currently finished OPTIMAL>60 trial (NCT01478542). ***References:*** 1. Bartlett et al. J Clin Oncol 2019, https://doi.org/10.1200/JCO.18.01994 2. Schöder H et al. Blood 2020, https://doi.org/10.1182/blood.2019003277 3. Clark et al. J Dig Imag 2013, https://doi.org/10.1007/s10278-013-9622-7 4. Isensee et al. Nature Methods 2021, https://doi.org/10.1038/s41592-020-01008-z 5. Gatidis et al. Nature Machine Intelligence 2024, https://doi.org/10.1038/s42256-024-00912-9

OP-229

Irregular, Highly Metabolically Active Lesions Predict Early Progression in B-cell Lymphoma Patients Treated with CAR T-cells.

S. Sabir[1,2], *Y. Chen*[2], *A. Mártínez-Rubio*[3], *L. Martín-Martín*[4], *L. Lopez-Corral*[5], *J. C. Canadas Salazar*[5], *C. Montes-Fuentes*[5], *M. Tamayo Alonso*[5], *A. Cedillo*[6], *P. Balsalobre*[6], *P. Barba*[7], *A. Perez-Martinez*[8], *V. M. Pérez García*[2];
[1]*University Carlos III, Madrid, SPAIN,* [2]*Mathematical Oncology Laboratory (MOLAB), Instituto de Matemática Aplicada a la Ciencia y la Ingeniería, University of Castilla-La Mancha, Ciudad Real, SPAIN,* [3]*Universidad de Cádiz, Cadiz, SPAIN,* [4]*University of Salamanca, Salamanca, SPAIN,* [5]*Hospital Universitario de Salamanca, Instituto de Investigación Biomédica de Salamanca (IBSAL), Salamanca, SPAIN,* [6]*Grupo Español de Trasplante Hematopoyético y Terapia Celular, Madrid, SPAIN,* [7]*Hospital Universitari Vall d'Hebron, Barcelona, SPAIN,* [8]*University Hospital La Paz, Madrid, SPAIN.*

Aim/Introduction: CAR T-cell therapy has become a standard treatment for relapsed/refractory aggressive B-cell lymphoma (r/r ABCL) [1,2]. However, predicting the long-term outcome remains challenging. The primary aim of this study was to identify reliable morphological molecular imaging biomarkers predicting the long-term therapeutic outcomes of CAR T-cell therapy in relapsed/refractory aggressive B-cell lymphoma (r/r ABCL). ***Materials and Methods:*** Multicenter study of 63 r/r ABCL patients from four institutions treated with CAR T-cells. Data included detailed clinical records, longitudinal CAR T-cell expansion (via PCR or flow cytometry), and baseline PET scans. Median SUVmax was 18.63; median lesions per patient:4; MTV: 127.1 cm^3; TLG: 804.9 g. Known prognostic factors (e.g., ECOG performance status, pre-apheresis LDH) were analyzed [3]. PET scans were segmented with MIM Encore and processed for morphological, metabolic, and radiomic features using MATLAB's radiomic functions (R2024a). Survival analyses (Cox regression, Kaplan-Meier estimates, log-rank tests) assessed links between imaging, CAR T-cell dynamics, and progression free survival (PFS). A compartmental mechanistic model explored tumor growth, immune suppression, and treatment effects on PFS. ***Results:*** Median patient age was 61 years (range 32-79), with a median of 2 prior therapy lines. A multivariate Cox model identified SUVmax of the most irregular lesion (SUVmaxMinSpher) as the only significant predictor of shorter PFS (p = 0.029) [4,5]. Univariate analysis confirmed this (p = 0.001), with Kaplan-Meier survival differences above/below the median (log-rank p = 0.0044). The effect remained significant across the two CAR T-cell products tested (likelihood ratio p = 0.09). Simulations suggest larger contact surfaces in irregular lesions promote immune suppression, reducing CAR T-cell efficacy [6,7]. High SUVmaxMinSpher patients had slower expansion (peak at 21 vs. 7 days) but stronger response (p = 0.05) [8]. ***Conclusion:*** Prognosis was worse for r/r ABCL patients post-CAR T-cell therapy with highly metabolically active, irregular lesions. Thus this biomarker may help to identify patients at elevated risk of disease progression following CAR T-cell treatment for B-cell lymphoma. ***References:*** 1. Roschewski et al, New England Journal of Medicine 2022; 386: 692-696. 2. Neelapu et al, Blood 2023; 141:2307-15. 3. Jain, M. D. et al, In Journal of Clinical Oncology 2024; 42: 3581-3592. 4. Ferrer-Lores et al, American Journal of Cancer Research 2023; 13:509-525. 5. Davey et al, Radiotherapy and Oncology 2020; 143:73-80. 6. Sabir et al., Bull Math Biol 2025,40. 7.Sheng et al, Biomarker Research 2024; 12:104. 8.Mussetti et al, American Society of Hematology 2023; 1:357-363.

OP-230

Risk Prediction of ^{68}Ga-FAPI-46 PET/CT-Derived Parameters in Lymphoma Patients

X. Chen[1], *T. Yuan*[2], *X. Wang*[3];
[1]*Beijing Tsinghua Changgung Hospital, School of Clinical Medicine , Tsinghua University, Beijing, CHINA,* [2]*Peking University First Hospital, Beijing, CHINA,* [3]*National Cancer Center/National Clinical Research Center for Cancer/Cancer Hospital, Chinese Academy of Medical Sciences and Peking Union Medical College, Beijing, CHINA.*

Aim/Introduction: we aimed to evaluate and compare in vivo tumor metabolism and cancer-associated fibroblast activation using ^{68}Ga-FAPI PET/CT for prediction of survival in lymphoma patients. ***Materials and Methods:*** Participants with different lymphoma subtypes, who were prospectively recruited from May 2020 to December 2021, underwent ^{68}Ga-FAPI and ^{18}F-FDG PET/CT. The tracer uptake was determined as maximum tumor standardized uptake value (SUV_{max}), FAPI-avid tumor volume (FTV), total lesion FAP expression (TLF) and target-to-liver ratios (TLR). Paired parameters were compared using the paired t test or the Wilcoxon matched-pairs signed-rank test. Kaplan-Meier curves were generated to calculate progression-free survival (PFS) and overall survival (OS) rates, and Cox regression analysis was performed to determine which PET/CT parameters were prognostic factors for PFS and/or OS. ***Results:*** In total, 201 participants (median age: 52 years [interquartile range: 18-79 years]; 99 women) were included. The median follow-up of 30.0 months (range, 3.6—101.1). Receiver-operating-characteristic curve analysis identified SUV_{max}, FTV, TLF, and TLR were not significant predictors for 2-year PFS and OS of total lymphomas and Aggressive B-cell lymphomas, that all the p values were greater than 0.05. TLR was significantly associated with OS of Aggressive T-cell lymphomas in the univariate analysis. Furthermore, in patients with Diffuse large B-cell lymphoma (DLBCL), SUV_{max} and

TLR were significantly associated with PFS and OS in the univariate analysis, and TLR was an independent risk factor for both PFS (HR, 0.155; 95% CI, 0.047-0.511; P = 0.002) and OS (HR, 0.154; 95% CI, 0.036-0.657; P = 0.011) in the multivariate analysis. ***Conclusion:*** This pilot study revealed that it appears unlikely that ^{68}Ga-FAPI-46 PET/CT-derived markers will generally replace ^{18}F-FDG PET/CT for prognostic stratification, yet it may have prognostic value for patients with DLBCL treated with standard chemotherapy, with TLR particularly promising.

607

Sunday, October 5, 2025, 16:45 - 18:15
Room 212

TROP Session - Neuroimaging Committee: Molecular Imaging of Neurodegeneration: FDG, Amyloid PET and Others

OP-231

Wavelet Diffusion Modeling Enables Individualized FDG-PET Synthesis for Early Diagnosis of Neurodegenerative Diseases

S. Xue[1], *J. Ding*[2], *M. Hacker*[1], *J. Zhao*[2], *X. Li*[1];
[1]*Division of Nuclear Medicine, Department of Biomedical Imaging and Image-guided Therapy, Vienna General Hospital, Medical University of Vienna, Vienna, AUSTRIA,* [2]*Department of Nuclear Medicine, Shanghai East Hospital, Tongji University School of Medicine, Shanghai, CHINA.*

Aim/Introduction: Neurodegenerative diseases such as Alzheimer's disease (AD) and Parkinson's disease (PD) are irreversible, but early intervention during the presymptomatic stage can slow disease progression. FDG-PET enables the detection of glucose metabolism changes in the brain, offering potential for early diagnosis. However, individual variability in FDG metabolism poses challenges for quantitative assessment. This study aims to develop a deep learning model capable of generating individualized healthy FDG-PET templates to facilitate voxel-wise comparison and precise identification of metabolic changes. ***Materials and Methods:*** A Wavelet Diffusion Model (WaveDM) was employed to synthesize FDG-PET images from T2-weighted MRI. This generative framework combines wavelet decomposition and diffusion modeling for high-resolution 3D image-to-image translation. A dataset of 1,060 paired PET/MRI scans was used for training and validation (9:1 split), with an additional 158 AD cohort scans (Normal Control (NC), Mild Cognitive Impairment (MCI), and AD) for testing. Model performance was compared to a 3D U-Net baseline using normalized root mean square error (NRMSE), peak signal-to-noise ratio (PSNR), and structural similarity index measure (SSIM). Qualitative assessments are ongoing, with physicians reviewing the synthesized PET images and evaluating diagnostic accuracy in differentiating AD, MCI, and NC using voxel-wise difference maps from the individualized healthy templates. ***Results:*** The WaveDM model demonstrated superior performance compared to the baseline U-Net model on the validation dataset, achieving a 12.3% increase in PSNR, a 6.6% improvement in SSIM, and a 20.5% reduction in NRMSE. Testing on the AD cohort demonstrated the model's ability to differentiate between NC, MCI, and AD through voxel-wise difference map analysis. ***Conclusion:*** The WaveDM framework provides a robust and versatile approach for generating individualized FDG-PET templates from MRI data. By enabling precise voxel-wise metabolic assessment, it shows great promise in enhancing the early diagnosis and management of neurodegenerative diseases. Moreover, this technique is adaptable to various neurological conditions, including the early detection of brain tumors or other disorders with detectable metabolic changes on neuro-PET imaging, broadening its potential clinical applications.

OP-232

Fronto-striatal disconnection contributes to striatal degeneration in behavioural variant frontotemporal dementia: preliminary results

S. Xie[1,2], *Y. Mayr*[1,2], *T. Grimmer*[3], *I. Yakushev*[1,2];
[1]*Department of Nuclear Medicine, School of Medicine, Klinikum Rechts der Isar, Technical University of Munich, Munich, GERMANY,* [2]*Graduate School of Systemic Neurosciences, Ludwig Maximilian University of Munich, Munich, GERMANY,* [3]*Department of Psychiatry and Psychotherapy, School of Medicine, Klinikum Rechts der Isar, Technical University of Munich, Munich, GERMANY.*

Aim/Introduction: Behavioral variant frontotemporal dementia (bvFTD) is traditionally characterized by frontal and temporal cortical degeneration, yet mounting evidence identifies striatal degeneration as a critical component of disease pathophysiology with significant implications for patient prognosis. While pathological aggregation of tau and TDP-43 proteins is considered a primary driver of striatal degeneration, fronto-striatal disconnection may represent an important secondary mechanism. This study investigated the relationship between striatal degeneration and fronto-striatal disconnectivity in bvFTD. ***Materials and Methods:*** A group of 19 individuals with mild bvFTD and 19 matched healthy controls (HC) underwent FDG-PET and diffusion weighted imaging (DWI). Standardized uptake value ratios (SUVr) in the frontal and striatal regions were quantified with reference to the cerebellar grey matter after correction for partial volume effects. White matter tracts of the frontal and striatal regions were reconstructed using probabilistic tractography. We specifically isolated white matter tracts a) within the frontal lobe and b) those between the frontal lobe and striatum. Node strength was used as index of anatomical connectivity (AC). ***Results:*** Frontal and striatal SUVr was lower in bvFTD patients relative to HC by 25% and 23% (both $p<0.001$), respectively. Frontal and fronto-striatal AC was lower in bvFTD patients relative to HC by 21% and 15% (both $p<0.001$), respectively. Notably, a robust correlation ($r=0.99$, $p<0.001$) was observed between fronto-striatal AC and SUVr across four key striatal regions (bilateral putamen and caudate nuclei). ***Conclusion:*** While further analyses are ongoing, we found a pronounced striatal hypometabolism and fronto-striatal disconnection in patients with bvFTD. These patterns were strongly related at the level of key striatal regions. Even though preliminary, this study provides the first direct evidence that deafferentation from frontal cortex contributes to striatal degeneration in bvFTD. Beyond improving understanding of disease pathophysiology, these results may guide future therapeutic approaches targeting secondary neurodegeneration to slow disease progression in bvFTD.

OP-233

Multimodal Characterisation of Cerebral Amyloid Angiopathy in Mild Cognitive Impairment Using Amyloid PET/MRI and FDG-PET

M. Pudis, *L. Rodríguez-Bel, M. Suarez-Piñera, B. Hervás-Sanz, J. Diaz-Moreno, M. Zamorano-Rivas, A. Bagan-Trejo, A. Dacosta-Escobar, C. Martínez-Ramos, M. Cortés-Romera;*
Nuclear Medicine - PET (IDI), Bellvitge University Hospital - IDIBELL, L'Hospitalet de Llobregat, SPAIN.

Aim/Introduction: This study aimed to describe amyloid PET findings in patients with mild cognitive impairment (MCI) who met the Boston Criteria 2.0 for cerebral amyloid angiopathy (CAA). We hypothesised that a multimodal imaging approach combining PET and MRI could reveal distinctive patterns of amyloid deposition and metabolic alterations, indicative of underlying mixed pathology. ***Materials and Methods:*** We retrospectively

included consecutive patients referred for [^{18}F]flutemetamol PET/MR in our centre between 2023 and April 2025. From a cohort of 412 subjects with cognitive complaints, we selected those meeting Boston 2.0 criteria for possible or probable CAA based on MRI findings, including lobar haemorrhages, cortical superficial siderosis, and cerebral microbleeds. Sixteen patients fulfilled inclusion criteria (12 men, 4 women; mean age 75 years [68-80]). Amyloid PET was analysed visually and semi-quantitatively, with SUVr and Centiloid conversion (whole cerebellum as reference). Occipital-to-frontal and occipital-to-global SUVr ratios were also calculated. FDG PET (n = 7) was assessed visually and using voxel-wise comparison to a normative database. Blood biomarkers (pTau and beta-amyloid 42/40) were available in five patients. Neuropsychological assessments complemented imaging data. ***Results:*** Amyloid PET was visually positive in 14/16 patients (88%). Mean SUVr was 0.75 (range 0.47-0.97); mean Centiloid value was 89.4 (range 38.6-205). One patient had discordant findings, with a small focus in the left frontal and insular cortices (SUVr 0.47; Centiloid 38.6). Of the 10 patients classified as probable CAA, 9 were PET positive; of the 6 possible CAA cases, 5 were PET positive. Occipital-to-frontal SUVr ratio >1 in 7 patients; occipital-to-global >1 in 6. No clear pattern differences were seen among PET-positive cases (5 posterior-predominant, 9 anterior-predominant). MRI revealed >10 lobar microbleeds in 9 patients, mainly frontoparietal and occipital; cortical superficial siderosis in 8; lobar haemorrhage in 6. FDG PET showed AD-like hypometabolism in 5 cases (matching blood biomarkers) and frontotemporal pattern in 2, including the only amyloid-negative case. ***Conclusion:*** Only 16 out of 412 patients (~4%) met imaging-based Boston Criteria 2.0 for CAA in our memory clinic cohort. Most patients demonstrated a high amyloid burden, although PET-negative cases and atypical regional patterns were observed. The integration of amyloid PET/MRI and FDG PET enhances the diagnostic characterisation of CAA and reveals overlap with Alzheimer's and other pathologies. These findings support the clinical relevance of multimodal imaging approach in evaluating complex dementia cases.

OP-234

Robustness of the Centiloid Scale to Data Decimation using Florbetaben PET

J. Perucho, *B. Spottiswoode, R. Fahmi;*
Siemens Medical Solutions USA, Inc., Knoxville, TN, UNITED STATES OF AMERICA.

Aim/Introduction: Amyloid-β (Aβ) positron emission tomography (PET) imaging is an essential diagnostic tool for Alzheimer's Disease (AD). Florbetaben (FBB), one of three clinically approved amyloid-PET radiotracers, typically requires 20-minute-long acquisitions. Quantification of these radiotracers can be standardized with the Centiloid (CL) method. Previous studies demonstrated the feasibility of reducing scan time without compromising AD diagnosis. This study aims to assess the robustness of CL values to the shortening of PET scans on a digital ultrafast time-of-flight (TOF) system. ***Materials and Methods:*** Co-registered dynamic (four 5-min frames) FBB-PET images from 50 subjects acquired on SiPM PET-CT scanner with 214ps TOF resolution were obtained from the ADNI database. For each scan, 5-, 10-, 15-, and 20-min summed frames were generated. Each frame was used to calculate CL values with a commercial package using a PET-only processing pipeline with tracer-specific target regions, and either the whole-cerebellum (WCB) or the cerebellar-gray-matter (CGM) as the reference region (RR). CL values corresponding to shorter scans were compared to those calculated using the 20-min summed image. Subjects were then dichotomized into positive and negative Aβ status using a threshold of 30 CL[1] to investigate bias in CL levels. ***Results:*** Using ANOVA tests, no group differences were found between CL values across all summed frames using WCB as the RR (p=0.259), whereas a significant difference was found when CGM was used as the RR (p=0.019). There was no significant difference between 5-min and 20-min CL values when using the WCB as the RR (p=0.376), but there was a significant difference when using the CGM as the RR (p=0.019) as determined by paired t-tests. Bland-Altman analysis resulted in a bias of -0.91 (Limits of Agreement (LoA): -15, 13) CL and -4.04 (LoA: -27, 19) CL for WCB and CGM as RR, respectively. This pattern was consistent when considering Aβ+ and Aβ- groups separately with p=0.451 and p=0.658 when comparing 5-min vs. 20-min CL, respectively, using WCB as the RR versus p=0.030 and p=0.396, respectively when using CGM as the RR. ***Conclusion:*** Decimated (5-min) FBB scans from an ultrafast-TOF PET scanner produced CL measurements that are not significantly different from CL measures from standard 20-min scans when the WCB was used as the RR. The error introduced by data-decimation falls within CL test-retest variability. Decimations to lower frame lengths and with other tracers will be investigated. ***References:*** 1. L. E. Collijet al., Alz. & Dement. 20(12), 9037-9048 (2024). DOI: 10.1002/alz.14336.

OP-235

Impact of Deep Learning-Based Noise Reduction on Centiloid Quantification in Reduced-Dose Amyloid PET Imaging

A. Tahmazov[1], *M. Doyen*[2,1], *S. Heyer*[1], *L. Imbert*[1,2], *A. Verger*[1,2];
[1]*Department of Nuclear Medicine and Nancyclotep Imaging Platform, University of Lorraine, Nancy Regional Hospital Centre, Nancy, FRANCE,* [2]*University of Lorraine, IADI, INSERM U1254, Nancy, FRANCE.*

Aim/Introduction: Quantitative analysis of amyloid PET imaging plays a critical role in selecting and monitoring patients undergoing anti-amyloid therapy. This study evaluates the impact of a deep learning-based noise reduction algorithm on centiloid (CL) quantification when simulating reduced injected doses of [^{18}F]flutemetamol. ***Materials and Methods:*** Patients with objective cognitive impairment who underwent list-mode [^{18}F]flutemetamol PET scans (185 MBq, acquired 90-110 minutes post-injection) were included. Standard images were visually assessed as amyloid-positive or -negative by expert nuclear medicine physicians. Simulated reduced-dose images (50%, 25%, 12.5%, and 5% of the original dose) were generated, and a deep learning noise reduction algorithm (DLNRA) was applied, resulting in ten reconstructions per patient. CL values were calculated using a validated in-house MATLAB pipeline, using the whole cerebellum as the reference region and converted to [^{18}F]flutemetamol-equivalent centiloid values. Differences in CL values between the full-dose reference and the reduced-dose images (with and without DLNRA) were analyzed. ***Results:*** A total of 310 PET reconstructions from 31 patients (mean age 71.6 years; 12 women; 17 visually positive scans; median CL: 8.1 [range -2.7 to 49.1]) were analyzed. Among the 17 visually positive cases, 4 were classified as CL-negative (CL < 24). CL values increased both at the 50% dose level and with DLNRA application (respectively +3% and +7% in medians, $p < 0.01$). Across the cohort, the full-dose DLNRA images showed a median CL deviation of less than 10% from the reference (6%), with only two amyloid-negative patients exceeding a 10% difference. In patients eligible for anti-amyloid therapy follow-up (CL > 24), all reconstructions, especially full-dose DLNRA and 50% dose images (with or without DLNRA) with no individual case exceeding a CL 10% deviation, showed a median CL deviation of less than 10% from the reference. ***Conclusion:*** While reduced-dose imaging can impact CL quantification, applying DLNRA to full-dose images maintains robust quantitative accuracy. In longitudinal anti-amyloid treatment monitoring, reducing the dose by up to 50%—with or without DLNRA—is feasible, although the impact on visual interpretation warrants further investigation. ***References:***

1. Klunk WE, Koeppe RA, Price JC, Benzinger TL, Devous MD, Jagust WJ, et al. The Centiloid Project: Standardizing quantitative amyloid plaque estimation by PET. Alzheimers Dement. janv 2015;11(1):1.

OP-236

Synthetic [18F]AV45 PET Image Generation from [18F] FDG PET and MRI Using Multimodal Deep Learning: A High-Accuracy Alternative for Amyloid-β Assessment

Y. Zhang[1], *X. Fu*[2], *H. Shao*[1], *Y. Jin*[2], *N. Zhang*[2], *Z. Hu*[2], *Y. Wang*[1], *G. Huang*[1], *J. Liu*[1];
[1]*Department of Nuclear Medicine, Institute of Clinical Nuclear Medicine, Ren Ji Hospital, Shanghai Jiao Tong University School of Medicine, Shanghai, CHINA,* [2]*Research Center for Medical AI, Shenzhen Institute of Advanced Technology, Chinese Academy of Sciences Key Laboratory of Biomedical Imaging Science and System, Chinese Academy of Sciences, State Key Laboratory of Biomedical Imaging Science and System, Shenzhen, CHINA.*

Aim/Introduction: Alzheimer's disease (AD) is characterized by amyloid-β (Aβ) pathology, the accurate detection of which is critical for early diagnosis and intervention. While [^{18}F]Florbetapir (AV45) PET imaging serves as a gold standard for quantifying Aβ deposition, its clinical utility is limited by high costs and limited accessibility. To address this challenge, we developed a novel deep learning approach to synthesize AV45 PET images from more widely available [^{18}F]FDG PET and T1-weighted MRI (T1WI) data acquired on an integrated PET/MR scanner. ***Materials and Methods:*** This study utilized a dataset of 249 patients with paired [^{18}F]FDG PET, T1WI, and [^{18}F]AV45 PET scans. We developed a multimodal deep learning framework based on ControlNet and Stable Diffusion to synthesize AV45 PET images from [^{18}F] FDG PET and T1WI inputs, training the model to capture Aβ deposition patterns through cross-modal feature fusion. To evaluate synthetic image accuracy, we quantified Aβ load using Centiloid (CL) values for both synthetic and real [^{18}F]AV45 PET scans, then classified the images into three clinical categories based on CL thresholds: negative (CL ≤ 12), weakly positive (12 < CL < 30), and positive (CL ≥ 30). Statistical agreement was assessed through Pearson correlation (for CL values) and Cohen's Kappa (for classification consistency). ***Results:*** The synthetic [^{18}F]AV45 PET images demonstrated high fidelity to real scans, with an MAE of 6.55, an MSE of 76.58, an excellent Pearson correlation of 0.97 ($P < 0.001$) , and a regression slope of 1.02 (intercept = 0.06, $R^2 = 0.95$) in Aβ quantification. Classification analysis revealed 95.8% overall consistency between synthetic and real images, achieving perfect agreement for negative and positive categories, while 3 of 10 weakly positive cases were misclassified as negative. For classification consistency, a strong Cohen's kappa coefficient of 0.93 was reflected. These results indicate the model's high accuracy in replicating definitive amyloid status while suggesting the need for improved sensitivity in borderline cases. ***Conclusion:*** This study demonstrates that synthetic [^{18}F]AV45 PET images generated from [^{18}F]FDG PET and MRI T1WI using a multimodal deep learning model achieve high accuracy in amyloid-β assessment, offering a cost-effective alternative where amyloid imaging is unavailable. Further optimization is needed for weakly positive cases.

OP-237

Assessment of reactive astrogliosis by [^{18}F]F-DED PET imaging across all stages of the Alzheimer's continuum

M. Zeinaki[1], *B. S. Rauchmann*[2,3,4], *J. S. Dorneich*[1], *L. Tagnin*[1], *L. Vogler*[1], *J. Gnörich*[1], *G. Höglinger*[4,5,6], *R. A. Werner*[1], *L. Frontzkowski*[1,7], *F. Hirsch*[7], *D. Janowitz*[7], *K. Bürger*[4,7], *J. Vöglein*[4,5,6], *S. Lindner*[1], *J. Levin*[4,5,6], *G. N. Bischof*[8,9], *N. Franzmeier*[5,7], *R. Perneczky*[3,4], *M. Brendel*[1,4,5];
[1]*Department of Nuclear Medicine, University Hospital LMU, Munich, GERMANY,* [2]*Institute of Neuroradiology, University Hospital LMU, Munich, GERMANY,* [3]*Department of Psychiatry and Psychotherapy, University Hospital LMU, Munich, GERMANY,* [4]*German Center for Neurodegenerative Diseases, DZNE, Munich, GERMANY,* [5]*Munich Cluster for Systems Neurology, SyNergy, Munich, GERMANY,* [6]*Department of Neurology, University Hospital LMU, Munich, GERMANY,* [7]*Institute for Stroke and Dementia Research (ISD), University Hospital LMU, Munich, GERMANY,* [8]*Department of Nuclear Medicine, University Hospital of Cologne, Cologne, GERMANY,* [9]*Life Molecular Imaging (LMI), Berlin, GERMANY.*

Aim/Introduction: A growing body of research highlights neuroinflammation as a key factor in neurodegenerative diseases like Alzheimer's (AD), characterized by cognitive decline, functional impairment and currently limited treatment options. This study investigates the spatiotemporal dynamics of reactive astrogliosis, captured by the MAO-B specific radiotracer [^{18}F] Fluorodeprenyl-D2 ([^{18}F]F-DED), across all clinical AD stages, and in relation to beta-amyloid and tau pathology. ***Materials and Methods:*** Our multimodal study included 25 AD patients and 11 age-matched controls who underwent dynamic (0-60 min p.i.) [^{18}F]F-DED PET, along with native T1-weighted cMRI for spatial normalization. The data were processed using the PMOD software and volumes of distribution (VT) were calculated using a One-Tissue-Compartment model (1TC2k) with carotid image-derived input function. AD patients were classified into three subgroups: subjective memory complaints (SMC), mild cognitive impairment (MCI), and dementia (mild, moderate, severe DEM). MMSE scores, CSF Amyloid-beta 42/40 ratios and phosphorylated Tau-181 were recorded together with amyloid and tau load measurement via [^{18}F]Flutemetamol and [^{18}F]PI-2620 PET imaging. Using statistical parametric mapping (SPM), VT images of AD patients were compared voxel-wise to controls and also correlated with centiloid scores and metatemporal tau levels. In addition, intergroup comparisons and tracer correlations were subsequently cross-validated with VOI-based astrocyte PET quantification. ***Results:*** AD patients exhibited significantly higher [^{18}F]F-DED binding than controls, with highest differences in the white matter of the temporal and frontal lobe ($p(FWE) < 0.05$). VT increases were already strong at SMC stage and did not differ significantly from MCI and DEM stages across all brain regions. The explorative SPM analysis of all AD patients revealed a positive correlation between [^{18}F]F-DED VT and centiloid-amyloid, primarily in the ACC, parietal and temporal regions, as well as a negative correlation with metatemporal-tau, especially in the temporal, frontal and occipital white matter ($p < 0.05$, uncorrected). ***Conclusion:*** Our results suggest that [^{18}F]F-DED tracer binding is noticeably elevated in patients across the AD continuum and closely associated with underlying AD pathophysiology, potentially establishing it a promising biomarker for assessing reactive astrogliosis in early-stage AD.

OP-238

Metabotropic Glutamate Receptor 5 is associated with Plasma GFAP Dependent on Age

T. Hu[1], *Y. Wang*[1], *J. Wang*[1], *X. Mao*[1,2], *S. Ren*[1], *K. He*[1], *Z. Lin*[3], *Y. Wei*[3], *Y. Yang*[4], *Y. Guan*[1], *Q. Huang*[1], *B. Li*[5], *F. Xie*[1];
[1]*Department of Nuclear Medicine & PET Center, Huashan Hospital, Fudan University, Shanghai, CHINA,* [2]*Center for Molecular Imaging and Translational Medicine, State Key Laboratory of Molecular Vaccinology and Molecular Diagnostics, School of Public Health, Xiamen University, Xiamen, CHINA,* [3]*United Imaging Healthcare Co., Ltd., Shanghai, 201807, China, Shanghai, CHINA,* [4]*Beijing United Imaging Healthcare Co., Ltd., Beijing, 100094, China, Beijing, CHINA,* [5]*Department of Neurology and Institute of Neurology, Ruijin Hospital, Shanghai Jiao Tong University School of Medicine, Shanghai, CHINA.*

Aim/Introduction: Metabotropic glutamate receptor subtype 5 (mGluR5) has been implicated in the pathogenesis of Alzheimer's disease (AD), and various plasma biomarkers have been shown to play a role in AD. However, the relationship between mGluR5 availability, measured with ^{18}F-PSS232 PET, and these plasma

biomarkers has not been thoroughly investigated. This study aims to assess the relationship between mGluR5 availability and plasma biomarkers. ***Materials and Methods:*** This cross-sectional study included 71 participants, consisting of 17 cognitively unimpaired (CU) individuals, 10 with early-onset cognitive impairment (EOCI), and 44 with late-onset cognitive impairment (LOCI). The Aβ pathology was quantified using the ^{18}F-Florbetapir PET, whereas mGluR5 availability was assessed using ^{18}F-PSS232 PET. Partial correlation analyses were applied to explore the correlation between mGluR5 availability and various plasma biomarkers, including plasma glial fibrillar acidic protein (GFAP), neurofilament light chain (NfL), and tau phosphorylated at T181 (p-tau181). Mediation analysis was performed to determine whether plasma GFAP mediated the association between age and entorhinal mGluR5 availability. A series of interaction analyses was conducted to explore the potential confounding effects of extraneous variables on the correlation between mGluR5 and GFAP. ***Results:*** The mGluR5 availability was associated with increased plasma GFAP levels, but not plasma NfL and ptau-181 in individuals over 65 years old and within the LOCI group. Plasma GFAP partially mediated the correlation of age and entorhinal mGluR5 availability (indirect effects = 0.007, SE = 0.014, 95% CI [0.001, 0.014]; direct effects = 0.019, SE = 0.034, 95% CI [0.003, 0.034]). The positive relationship of mGluR5 with plasma GFAP in the LOCI group only survived in the Aβ positive subgroup (r = 0.475, p = 0.011), as well as in groups with lower plasma Aβ42/Aβ40 ratios (r = 0.513, p = 0.025) and higher plasma NfL levels (r = 0.593, p = 0.007). ***Conclusion:*** This study indicated that age played a key role in the investigations of mGluR5 and plasma GFAP in AD. Increased mGluR5 availability is significantly associated with elevated plasma GFAP levels dependent on age.

OP-239

Cardiac Amyloid Deposits as a Cause of Cardiac Dysfunction in Alzheimer's Disease (CACAO-PET): A Prospective Study

D. Kersting[1], *T. Goerttler*[2], *I. Trender-Gerhard*[2], *M. Chodyla*[3], *A. Küper*[1], *A. Gerhard*[4], *L. Kessler*[3], *T. Schlosser*[3], *G. Davidzon*[5], *M. Papathanasiou*[6], *C. Rischpler*[7], *W. Fendler*[1], *C. Deuschl*[3], *T. Rassaf*[8], *K. Herrmann*[1], *R. Dodel*[9], *S. Settelmeier*[8];
[1]*Department of Nuclear Medicine, University Hospital Essen, University of Duisburg-Essen, Essen, GERMANY,* [2]*Department of Neurology and Center for Translational Neuro- and Behavioral Sciences (C-TNBS), University Hospital Essen, University of Duisburg-Essen, Essen, GERMANY,* [3]*Institute for Diagnostic and Interventional Radiology and Neuroradiology, University Hospital Essen, University of Duisburg-Essen, Essen, GERMANY,* [4]*Department of Geriatric Medicine, Klinikum Hochsauerland GmbH, Arnsberg, GERMANY,* [5]*Department of Radiology, Stanford University School of Medicine, Stanford, CA, UNITED STATES OF AMERICA,* [6]*Department of Cardiology and Angiology, University Hospital Frankfurt, Frankfurt am Main, GERMANY,* [7]*Department of Nuclear Medicine, Klinikum Stuttgart, Stuttgart, GERMANY,* [8]*Department of Cardiology and Vascular Medicine, West German Heart and Vascular Center, University Hospital Essen, University of Duisburg-Essen, Essen, GERMANY,* [9]*Department of Geriatric Medicine, University of Duisburg-Essen, Essen, GERMANY.*

Aim/Introduction: Alzheimer's disease (AD) and Cardiac amyloidosis (CA) are both associated with amyloid deposits but of different chemical composition. We used combined cerebral and cardiac amyloid PET/MRI in a "one-stop-shop" approach to investigate co-occurrence and potential correlation between cerebral amyloid deposits (indicating AD) and cardiac amyloid deposits (indicating CA). ***Materials and Methods:*** We included persons with clinically diagnosed mild cognitive impairment (MCI) or mild dementia suspected of AD who were referred for cerebral amyloid PET in this prospective study. Exclusion criteria included pre-existing cardiac conditions and contraindication for MRI. Dynamic cardiac PET/MRI data were acquired for 60 min directly after injection of 298 MBq ± 30 MBq [^{18}F]F-Florbetaben (mean ± SD). Approximately 65 minutes after tracer injection, a static brain PET/MRI was performed for 15 minutes. All patients underwent CA-specific laboratory tests and echocardiography. Primary study endpoint was the frequency of cardiac amyloid deposits in patients with cerebral amyloid deposition. For detection of cardiac amyloid, visual evaluation of static PET images (reconstructed from minutes 40-60 p.i.) and analysis of the established myocardial tracer retention (MTR) from left ventricular uptake curves were performed. The Centiloid scale was used to evaluate the extent of cerebral amyloid deposition. ***Results:*** We screened N=64 patients with MCI and mild dementia who were referred for amyloid PET imaging. Of these, N=15 patients (10 female, 5 male, mean ± SD age 69 ± 7 years) were included (main exclusion criteria: inability for MRI due to neuropsychologic reasons). Amyloid-related brain alterations consistent with AD were detected in N=12/15 patients (80%), one patient presented with cerebral amyloid angiopathy. Median ± IQR Centiloid score was 102.7 ± 43. No signs of cardiac amyloid deposits were detected by visual evaluation or evaluation of the MTR (median ± IQR MTR: 29.8 ± 2.6). Cardiac MRI did not reveal any patients with suspected CA (median ± IQR T1 relaxation time: 1254 ms ± IQR 47.5 ms, no detection of transmural late gadolinium enhancement, only one patient with left ventricular hypertrophy that was asymmetric and probably post-ischemic). ***Conclusion:*** No co-occurrence of cerebral and cardiac amyloid deposits was found in our primary analysis of PET and MRI data. Analysis of secondary endpoints (including laboratory values and echocardiographic findings) is ongoing. Currently, the study data does not support routine combined amyloid imaging in order to simultaneously detect cardiac amyloid deposition in patients with MCI or suspected AD.

608

Sunday, October 5, 2025, 16:45 - 18:15
Room 115

Featured Session - Thyroid Committee: Nuclear Medicine Imaging in Medullary and Differentiated Thyroid Cancers

OP-240

Invited Speaker

M. Tuncel;
Nuclear Medicine, Ankara, TÜRKIYE.

OP-241

Evaluation of F-18 FDG PET/CT and Ga-68 DOTATOC PET/CT scans in Assessing Patients with Differentiated Thyroid Carcinoma Exhibiting Elevated Serum Thyroglobulin Levels and Negative Whole-Body Scans with I-131 (TENIS Syndrome)

A. Aghaee*, M. Esmatinia, K. Aryana;*
Nuclear Medicine Research Center,Mashhad University Of Medical Sciences, Mashhad, IRAN, ISLAMIC REPUBLIC OF.

Aim/Introduction: This study aims to critically assess the effectiveness of ^{18}F-FDG PET/CT and 68Ga-DOTATOC PET/CT in detecting recurrent or metastatic differentiated thyroid cancer (DTC) in patients with elevated serum thyroglobulin(Tg) levels and negative I-131 whole-body scans. The study investigates the potential of these diagnostic tools to enhance the identification of residual or recurrent disease, thereby refining treatment strategies for DTC patients. ***Materials and Methods:*** This retrospective study examined 20 patients with DTC at the thyroid clinic of the Ghaem Hospital's nuclear medicine ward in Mashhad. The study

focused on patients who exhibited recent negative whole-body I-131 scans and serum Tg levels exceeding 10 ng/mL following thyroid-stimulating hormone (TSH) stimulation via levothyroxine withdrawal, Each patient underwent an initial ^{18}F-FDG PET/CT scan, followed by a Ga-68 DOTATOC PET/CT scan within one week. ***Results:*** A total of 20 patients with TENIS syndrome were evaluated;19 had papillary thyroid cancer (PTC), and 1 had follicular thyroid cancer (FTC). Both imaging modalities identified 23 out of 27 lesions. The 68Ga-DOTATOC and ^{18}F-FDG scans were positive in 65% and 70% of patients, respectively. Most patients were classified as stage IV according to the seventh edition of the AJCC staging system, while 10 patients were classified as stage I according to the eighth edition. Among the patients with positive 68Ga-DOTATOC results, 13 were candidates for therapy: six received Lu-177-DOTATATE, five underwent surgery, one had surgery combined with radiotherapy, and one received both Lu-177-DOTATATE and radiation therapy. Of the 14 patients with positive ^{18}F-FDG scans, six underwent surgery, and one received a combination of [KA(3] radiation and surgery. No statistically significant relationship was observed between the positive and negative results of both PET tracers (P=1), [KA(5] nor between the 68Ga-DOTATOC and ^{18}F-FDG scan results and patient Tg levels (P=0.67). However, a significant association was noted between Tg levels and ^{18}F-FDG scan results, particularly under non-TSH stimulation conditions (P=0.015), but not in the TSH stimulation state (P=0.262). No[KA(6] association was found between Tg levels and tumor subtypes (P=0.602). ***Conclusion:*** : 68Ga[KA(1] -DOTATOC PET/CT demonstrates somatostatin receptor expression in patients with negative whole-body iodine scans and elevated Tg levels, indicating its potential as a viable alternative diagnostic modality for restaging and metastatic evaluation. The positive results from both imaging techniques showed no significant differences. The study suggests that 68Ga-DOTATOC PET/CT may assist in guiding therapy with Lu-177-DOTATATE for patients exhibiting positive FDG PET/CT results who require systemic treatment.

OP-242

Evaluating the Detection Rate of DTC Metastatic Lesions Using Technetium-99m FAPI Scan in Patients with Elevated Thyroglobulin and Negative Iodine Scan

A. Aghaee[1], *S. Soltani*[2], *K. Aryana*[1], *A. Vasei*[1], *S. Zakavi*[1], *F. Karamian*[1];
[1]*Nuclear Medicine Research Center, Mashhad University of Medical Sciences, Mashhad, IRAN, ISLAMIC REPUBLIC OF,* [2]*Kidney Transplantation Research Center, Research Center, Mashhad University of Medical Sciences, Mashhad, IRAN, ISLAMIC REPUBLIC OF.*

Aim/Introduction: Conventional imaging methods like WBIS often fail to detect these metastases in TENIS (thyroglobulin elevated and negative iodine scan) patients due to the inability of certain cancer cells to capture iodine. Fibroblast Activation Protein (FAP), has emerged as a significant biomarker in oncology. FAP-targeted imaging techniques, such as Fibroblast Activation Protein Inhibitor (FAPI) SPECT imaging, offer enhanced tumor visualization with high sensitivity and specificity. This Study aims to evaluate the detection rate of metastatic lesions using technetium-99m FAPI scans in TENIS patients. ***Materials and Methods:*** This prospective study included eight eligible patients referred to Ghaem Hospital's clinic in 2024. Eligible patients had a confirmed diagnosis of DTC, elevated serum thyroglobulin levels (> 10 ng/mL, excluding those with a doubling time of more than five years), and negative iodine scan results within the past six months. All patients had recently undergone neck ultrasonography and thoracic HRCT or FDG PET/CT, which identified the locations of metastases. Our aim was to assess the FAPI avidity of these metastatic lesions. ***Results:*** A total of eight patients with PTC (median age 49 years; range 25-64 years; 3 [37.5%] men and 5 [62.5%] women) underwent [99mTc] FAPI SPECT/CT. The tumor subtypes included: classic (n=3), follicular variant (n=2), classic with follicular areas (n=1), and not reported (n=1). Seven patients had positive FAPI scans, while one patient had a negative scan. In recent lung and mediastinal HRCT and/or FDG PET/CT scans of the seven positive patients, a total of 20 metastatic lesions were detected. All metastatic lesions in four patients showed FAPI avidity, 90% in one patient showed FAPI avidity, and 50% in two patients showed FAPI avidity. Our study found an overall FAPI avidity of approximately 73%. No drug-related side effects occurred during or after [99mTc] FAPI injection, and SPECT/CT imaging was well tolerated by all patients. No new symptoms were reported during the observation period. ***Conclusion:*** In conclusion, the study's findings suggest that technetium-99m FAPI scans are promising in enhancing the detection of metastatic lesions in TENIS patients. These results have significant implications for clinical practice, supporting further exploration and eventual integration of this imaging technique into standard care protocols for TENIS patients. We believe this new imaging modality has the potential to transform the evaluation and management of TENIS patients.

OP-243

Identification of Rare and Unusual Sites of Metastatic Localizations in Differentiated Thyroid Carcinoma by Means of I-124 PET-CT. A National Cancer Institute of Malaysia Review.

M. Abdul Onny[1,2], *N. Mokhtar*[1], *N. Sulaiman*[1], *A. Kindu*[1], *N. Ali*[1];
[1]*National Cancer Institute Malaysia, Putrajaya, MALAYSIA,*
[2]*University Medical Center Groningen, Groningen, NETHERLANDS.*

Aim/Introduction: Differentiated thyroid carcinoma (DTC) is the 7th most common cancer in Malaysia, predominantly in female with age incident rate of 3.2. A local or regional disease has an excellent 5-year survival of >98% but drop drastically with distant metastasis (50%). The common sites of metastases are lung and bone. However, presence of rare metastatic sites such as brain, kidney, adrenal and pituitary carry poorer prognosis hence, identification of these unusual sites is paramount in allowing prompt initiation of therapies. Thyroidectomy followed by radioiodine therapy (RAI) are the standard-of-care but other form of therapies such as targeted radiotherapy or systemic therapy are useful in advance cases. The advancement of radiopharmaceutical and imaging technique has led to the utilization of I-124 PET-CT which has revolutionized the management of DTC particularly in detecting previously unseen lesions and utilized for personalized RAI treatment through dosimetry. ***Materials and Methods:*** We conduct a retrospective review of the DTC cases which had undergone I-124 PET-CT scans for dosimetry from year 2015-2023. A total of 83 patients had undergone a total of 117 imaging procedures. Each case was reviewed and sites of metastases were identified. Cases with uncommon metastasis were specifically identified. ***Results:*** 15 cases (11-female and 4-male) with mean age of 47.2-year-old, (range 22-78) were identified. Patients had total thyroidectomy followed by varying courses of RAI (range 1-6 courses) via empirical or dosimetry-guided dosing with mean total cumulative dose of (847.3mCi, range 300-2000). The metastatic sites were renal(3), skeletal muscles(4), brain(2), adrenal(1), breast(1), pituitary(1), heart(2), and sphenoid sinus(1) in addition to the usual lung and bone metastases. ***Conclusion:*** The significantly higher resolution of I-124 PET-CT which translate to better sensitivity has resulted in detection of more sites of metastasis. In addition, it led to escalation of treatment including metastatic targeted or systemic therapies. Furthermore, it is invaluable for personalised RAI through its dosimetry capabilities. ***References:*** 1. Azizah,A.M., et al,(2019) 'Malaysia National Cancer Registry Report 2012-2016'. 2. Avram,A.M. et al.(2022) 'SNMMI Procedure Standard/EANM Practice Guideline for Nuclear Medicine Evaluation and Therapy of Differentiated Thyroid Cancer: Abbreviated Version', Journal of

Nuclear Medicine, 63(6), pp.15N-35N. 3. Song,S.J. et al.(2011) 'Rare metastases of differentiated thyroid carcinoma: Pictorial Review', Endocrine-Related Cancer, 18(5), pp.R165-R174. 4. Bashank,N. et al. (2022) 'Rare sites of metastases in patients with differentiated thyroid carcinoma and added value of SPECT/CT over planar whole body radioactive iodine scan', European Journal of Hybrid Imaging, 6(1). doi:10.1186/s41824-022-00155-0.

OP-244

Diagnostic performance of [^{68}Ga]OncoFAP-PET compared with [^{18}F]DOPA-PET in patients with recurrent medullary thyroid carcinoma

W. Roll, *D. Ventura, M. Schäfers, B. Noto, P. Backhaus, K. Rahbar, B. Riemann, P. Schindler;*
University Hospital Münster, Münster, GERMANY.

Aim/Introduction: Molecular imaging of advanced or recurrent medullary thyroid cancer (MTC) remains a clinical challenge. Currently, [^{18}F]DOPA-positron emission tomography (PET) has demonstrated the highest sensitivity, though this has only been shown to reach 70%. Fibroblast activation protein (FAP) inhibitor (FAPI) PET-based imaging has emerged as a valuable imaging modality in the context of several malignancies, exhibiting favorable uptake and sensitivity. The aim of this study is to evaluate the detection rate of FAPI-PET with [^{68}Ga]OncoFAP in comparison with [^{18}F]DOPA-PET, given the high level of fibroblast activation of MTCs. ***Materials and Methods:*** Eight patients were analyzed who had histologically proven MTC and suspicion of recurrence with elevated tumor marker level calcitonin. The patients underwent both [^{18}F]DOPA and [^{68}Ga]OncoFAP-PET. The comparative analysis included both a patient-based and a lesion-based approach. Our quantitative analysis compared maximum and mean standardized uptake values (SUV_{max}/SUV_{mean}), metabolic tumor volume (MTV), and maximum tumor-to-background ratios (TBR_{max}). ***Results:*** The median time between the two PET acquisitions was 30.4 d (range: 7-56 d). A total of 35 tracer-avid lesions were detected in both imaging modalities. [^{68}Ga]OncoFAP-PET detected significantly more lesions than [^{18}F]DOPA-PET (34 [97%] vs. 16 [46%], $P < 0.001$). A total of 15 (43%) lesions presented with elevated uptake in [^{68}Ga]OncoFAP and [^{18}F]DOPA-PET, while 19 (54%) were only [^{68}Ga]OncoFAP-positive and 1 (2.9%) was only [^{18}F]DOPA-positive. Quantitative analysis with TBR_{max} revealed significantly higher tracer affinity for [^{68}Ga]OncoFAP, e. g., blood pool TBR_{max} with 6.3 vs. 3.5 ($P < 0.001$). ***Conclusion:*** In this limited patient cohort, the lesional detection rate of [^{68}Ga]OncoFAP-PET was superior to that of [^{18}F]DOPA-PET. Further prospective multicentric investigations with larger patient numbers are warranted.

OP-245

Comparison of ^{68}Ga-FAPI and ^{18}F-DOPA PET/CT in patients with medullary thyroid cancer

D. Hescheler[1], *D. Atiyat*[1], *A. Heinzel*[2], *K. Lorenz*[3], *P. Reschke*[4], *E. Epphard*[1], *J. Wuestemann*[1], *M. C. Kreissl*[1];
[1]*Division of Nuclear Medicine, Department of Radiology and Nuclear Medicine, University Hospital Magdeburg, Magdeburg, Germany, Magdeburg, GERMANY,* [2]*Department of Nuclear Medicine, University Medicine Halle, Halle, Germany,, Halle, GERMANY,* [3]*Department of Visceral, Vascular and Endocrine Surgery, University Medicine Halle, Halle, Germany, Halle, GERMANY,* [4]*University Hospital Frankfurt, Frankfurt, GERMANY.*

Aim/Introduction: Accurate staging is critical for the management of medullary thyroid cancer (MTC). The abundant stroma in most thyroid cancers, including MTC, opens new opportunities to target cancer-associated fibroblasts (CAFs) for novel molecular imaging and therapeutic targets. Fibroblast activation protein inhibitor (FAPi) molecules labeled with [^{68}Ga] Ga have enabled alternative molecular diagnostics of thyroid cancer. The aim of this study was to compare PET/CT using ^{68}Ga-RTX-1363R (^{68}Ga-FAPI) and PET/CT using ^{18}F-DOPA PET/CT for the staging of MTC. ***Materials and Methods:*** In this retrospective study, ^{18}F-DOPA- and ^{68}Ga-FAPI-PET/CT imaging was compared using per-patient analysis and per-lesion analysis in patients with MTC. The results of the two scans were correlated with morphological findings (CT/MRI/sonography) or histology. Quantitative assessment included a comparison of standardized uptake values and tumor background ratio (TBR). ***Results:*** 9 patients with a mean age of 55 years (34 - 80 years) and 62 lesions were included in the study. In the group of patients with lymph node metastases (n=4), more patients were detected with ^{68}Ga-FAPI than with ^{18}F-DOPA (100% (4/4) patients vs. 50% (2/4) patients). Accordingly, the analysis per lesion showed a higher detection rate with higher TBR values for lymph node metastases with ^{68}Ga-FAPI than with ^{18}F-DOPA (true-positive [TP] 100% [8 of 8] vs. 50% [4/8]), mean TBR 10.9 vs. 6.9). In the group of patients with liver metastases (n=3), all patients were detected with both ^{68}Ga-FAPI and ^{18}F-DOPA. The analysis per lesion also showed a higher detection rate with higher TBR values for liver metastases (TP 100 % [22/22] vs. 22.7 % [5/22], mean TBR 24.1 vs. 2.7). In the group of patients with lung metastases (n=3), more patients were detected with ^{68}Ga-FAPI than with ^{18}F-DOPA (100 % (3/3) patients vs. 67 % (2/3) patients). Per lesion analysis showed a higher detection rate with higher TBR values for lung metastases (TP 86% [12/14] vs. 43% [6/14], TBR 6.1 vs. 3.6). ***Conclusion:*** ^{68}Ga-FAPI PET shows a higher detection rate with higher TBR values in metastases of MTC. ^{68}Ga-FAPI PET/CT could improve the diagnosis of MTC.

OP-246

Early or delayed 18F-DOPA PET/CT for MTC primary tumour detection

G. Bianciardi[1], *E. Fortunati*[2], *E. Tabacchi*[2], *I. Brusa*[2], *D. Dall'Olio*[3], *M. Assenza*[4], *E. Greco*[1], *C. M. P. Sgro*[1], *G. A. Fuso*[1], *L. Carrara*[1], *G. Cuzzani*[1], *L. Zanoni*[5], *L. Calderoni*[2], *S. Fanti*[1,2], *V. Ambrosini*[1,2];
[1]*Nuclear Medicine, Alma Mater Studiorum, University of Bologna, Bologna, ITALY,* [2]*Nuclear Medicine, IRCCS Azienda Ospedaliero-Universitaria di Bologna, Bologna, ITALY,* [3]*Department of Medical and Surgical Sciences, University of Bologna, Bologna, ITALY,* [4]*Professional Development and Implementation of Research in Health Professional Unit, IRCCS Azienda Ospedaliero-Universitaria di Bologna, Bologna, ITALY,* [5]*Nuclear Medicine, AST Pesaro-Urbino, Pesaro, ITALY.*

Aim/Introduction: Medullary thyroid carcinoma (MTC) is a rare neuroendocrine tumour accounting for 1-2% of all thyroid cancers. 18F-DOPA PET/CT is an established imaging tool for MTC staging, although the optimal acquisition timing remains controversial. Aim of the study was to retrospectively compare both visually and semiquantitatively early and delayed images in patients with histologically confirmed MTC. ***Materials and Methods:*** Among 18F-DOPA PET/CT scans performed between 2022 and 2025 in confirmed MTC pts, only those studied for staging were included. According to EANM guidelines, 60minutes standard acquisition was preceeded by an early acquisition centered on the thyroid [1]. Primary tumours' SUVmax and contrast-to-noise ratio (CNR) were measured on early and delayed images [2]. ***Results:*** Overall, 16 patients (33% male; mean age 52 years) were included. 18F-DOPA PET/CT was positive in all primary lesions at the early acquisition while in 6 cases visual lesion detection was not possible in the delayed scans. SUVmax values were higher on early acquisitions in all patients. CNR values decreased between early and delayed scans in the entire study population, with a mean reduction of 62% (range 15-100%). In 6/16 patients, while the delayed- CNR fell below 5 (a critical threshold for reliable lesion detection) [2], the early -CNR always remained above 6. In 3/6 with delayed-CNR below 1, visual lesion detection was not possible. In 10/16 cases, a detailed pathologic report including differentiation grade was available: low-grade MTC was observed in 4/10 (all presenting delayed- CNR <5) while high-grade MTC was detected

in the remaining 6/10 (with delayed-CNR>6). ***Conclusion:*** Our preliminary data show that 18F-DOPA PET/CT early acquisition detected the primary tumour in all cases. Although limited by the small cohort of retrospective patients included in the study, performing delayed imaging alone would have resulted in a higher rate of false-negative findings. ***References:*** [1] Giovanella L, Treglia G, Iakovou I, Mihailovic J, Verburg FA, Luster M. EANM practice guideline for PET/CT imaging in medullary thyroid carcinoma. Eur J Nucl Med Mol Imaging. 2020 Jan;47(1):61-77. doi: 10.1007/s00259-019-04458-6. Epub 2019 Sep 4. PMID: 31482429. [2] Bao Q, Chatziioannou AF. Estimation of the minimum detectable activity of preclinical PET imaging systems with an analytical method. Med Phys. 2010 Nov;37(11):6070-83. doi: 10.1118/1.3495817. PMID: 21158319; PMCID: PMC2994933.

OP-247

Feasibility of ^{68}Ga-SSO-120 PET/CT Imaging in Medullary Thyroid Carcinoma: A Retrospective Analysis

I. Ciuciulkaite, *T. Brandenburg, W. Jentzen, W. Fendler, P. Fragoso Costa, M. Nader, S. Himmen, H. Lahner, L. Umutlu, D. Führer-Sakel, K. Herrmann, H. Hautzel, D. Kersting;*
Essen University Hospital, Essen, GERMANY.

Aim/Introduction: Most patients with medullary thyroid carcinoma (MTC) present with advanced, metastatic disease. Somatostatin receptor (SSTR) expression in MTC offers diagnostic and therapeutic potential. However, SSTR agonist-based PET/CT imaging has shown suboptimal detection rates in MTC. Newer SSTR antagonists provide improved sensitivity, lesion detection, and image contrast in imaging, as well as higher tumour uptake, longer tumour residence time, and better tumour-to-kidney dose ratios in therapeutic settings. This study aimed to investigate the feasibility of PET/CT with ^{68}Ga-SSO-120, an SSTR antagonist, in patients with MTC. ***Materials and Methods:*** Patients with newly diagnosed MTC or elevated calcitonin levels who underwent whole-body ^{68}Ga-SSO-120-PET/CT were retrospectively included. The mean administered activity was 134.7 MBq, with a mean uptake time of 63 minutes. Lesions with uptake above background were evaluated across five anatomical regions (thyroid bed, regional lymph nodes, liver, bone, and other metastases), according to the 8th edition TNM classification. SUVmax, SUVmean, SUVpeak, and peak tumour-to-liver ratio (TLRpeak) were measured for each lesion, with TLRpeak calculated by dividing lesion SUVpeak by liver SUVmean. For theranostic evaluation, whole-body (WB) SUVmean and TLRmean were assessed per patient. WB SUVmean was the mean SUV in all PET-positive lesions per patient, and WB TLRmean was calculated by dividing WB SUVmean by liver SUVmean. Continuous variables were reported as medians and ranges; categorical variables as counts and percentages. ***Results:*** Thirty-five patients were included. 68Ga-SSO-120-positive tumours were detected in 24 patients (68.6%) and in 41 of 175 evaluated regions (23.4%). Patient-based median SUVmax, SUVpeak, and TLRpeak values were 5.7 (1.6-20.9), 4.0 (1.4-14.9), and 1.0 (0.4-4.8), respectively. Region-based median SUVmax values were 3.9 (2.2-12.3) for the thyroid bed, 5.1 (1.6-20.9) for lymph node, 7.6 (4.2-12.0) for liver, 4.6 (2.0-10.0) for bone, and 3.7 (2.0-8.9) for other metastases. Lesion-based analysis identified 10 lesions in the thyroid bed, 43 lymph node, and 58 distant metastases, with median SUVmax values of 3.6 (2.1-12.5), 4.8 (1.0-21.5), and 4.6 (1.4-19.6), respectively. Median WB SUVmean and TLRmean were 2.8 (range 0.9-11.5) and 0.9 (range 0.1-3.8), respectively. WB TLRmean was <1 in 62.5% of patients, between 1-3 in 33.3%, and >3 in 4.2%. ***Conclusion:*** ^{68}Ga-SSO-120-PET/CT demonstrated potential for imaging in patients with MTC. Further investigation is warranted to identify predictive parameters for high tumour uptake and select patients who might benefit from SSTR antagonist PRRT.

OP-248

Temporal Kinetics of 18F-DOPA in Medullary Thyroid Carcinoma: The Added Value of Dynamic PET

G. Bianciardi[1], *E. Fortunati*[2], *E. Tabacchi*[2], *I. Brusa*[2], *D. Dall'Olio*[3], *M. Assenza*[4], *E. Greco*[1], *C. M. P. Sgro*[1], *G. A. Fuso*[1], *L. Carrara*[1], *G. Cuzzani*[1], *L. Zanoni*[5], *L. Calderoni*[2], *S. Fanti*[1,2], *V. Ambrosini*[1,2];
[1]*Nuclear Medicine, Alma Mater Studiorum University of Bologna, Bologna, ITALY,* [2]*Nuclear Medicine, IRCCS Azienda Ospedaliero-Universitaria di Bologna, Bologna, Italy, Bologna, ITALY,* [3]*Department of Medical and Surgical Sciences, University of Bologna, Bologna, Italy, Bologna, ITALY,* [4]*Professional Development and Implementation of Research in Health Professional Unit, IRCCS Azienda Ospedaliero-Universitaria di Bologna, Bologna, ITALY,* [5]*Nuclear Medicine, AST Pesaro-Urbino, Pesaro, ITALY.*

Aim/Introduction: 6-[^{18}F]fluoro-L-DOPA(18F-DOPA)-PET/CT is the gold standard imaging for staging/restaging medullary thyroid carcinoma (MTC), a rare neuroendocrine tumour. Dynamic PET/CT acquisitions allow analysis of tracer kinetics, potentially improving the detection and characterization of T (primary tumour), lymphnode involvement (N) and distant metastases (M). Aim: to evaluate 18F-DOPA pharmacokinetics in dynamic-uExplorer LAFOV-PET in MTC patients. ***Materials and Methods:*** Among patients who underwent 18F-DOPA-PET/CT for suspected/known MTC, only those with pathological confirmation were retrospectively included. Dynamic-LAFOV- 18F-DOPA-PET/CT images were acquired over 25minutes (intravenous injected activity:3MBq/kg) completed by standard static 60-minutes acquisition (STD). Volumes of interest were manually drawn over lesions sites and reference healthy tissue(contralateral thyroid lobe) by experienced nuclear medicine physicians. 18F-DOPA uptake and pharmacokinetics were evaluated using standardized uptake value (SUV), graphical analysis (Patlak and RE-plots) and two-tissue compartment models, including both the reversible (2TC) and irreversible (2TiC) approaches. Mean absolute scaled error (MASE) and Akaike Information Criterion (AIC) were used to assess the best fitting model for each VOI. ***Results:*** Ten MTC-confirmed patients (males:females=2:8;mean age:66.2years) were included. PET/CT was positive in 8/10 patients (at≥1 site: T in 4/8; N in 4/8; M in 3/8, all positive at bone level, 1 also at liver level) and true negative in 2/10. 18F-DOPA demonstrated rapid blood clearance and early accumulation in both pathological lesions and background tissues, typically within 1-2minutes post-injection. All VOIs were better fitted by reversible kinetic models (RE-plots and 2-tissue compartment reversible model-2TC), which provided significantly higher mean distribution volume (DV) values in all lesions (DV_T=3.8±2.1,DV_N=2.0±1.3,DV_M=3.9±2.8) compared to reference healthy thyroid tissue (DV_thyroid=0.7). The rate constant k4 was markedly decreased in pathological VOIs (k4_T= 0.1±0.02,k4_N=0.1±0.08,k4_M=0.1±0.1) compared to normal thyroid tissue (k4_thyroid=0.5±0.06), reflecting increased tumour tracer retention. Time-activity-curves showed a trend towards uptake reduction over the dynamic-acquisition time-frame, especially at primary and nodal level. STD confirmed reduction of the uptake, except for some bone lesions that either became apparent only in STD or increased uptake. ***Conclusion:*** MTC lesions demonstrate intense 18F-DOPA uptake and retention, as reflected by elevated DV and reduced k4 value compared to background healthy tissues. A relatively rapid wash-out was observed in several lesions, particularly at primary and nodal level, suggesting heterogeneity in tracer handling and lesions' metabolic activity supporting the potential added value of early dynamic acquisitions to define the best time-frame-window for image acquisition.Further studies are needed to elucidate the metabolic behaviour mechanisms at the basis of lesions' differential tracer retention/clearance.

609

Sunday, October 5, 2025, 16:45 - 18:15
Room 133+134

e-Poster Presentations Session 4 - Physics
Committee: Physics e-Poster Presentations Session

EPS-073

Dynamic ^{18}F-FDG PET/CT Imaging Combined with Machine Learning Models for Improved Classification of Solitary Pulmonary Lesions: A Series of Studies

Y. Luo, *L. Huang, W. Ma, J. Liu;*
The Second Hospital of Lanzhou University (Second Clinical Medical College), lanzhou, CHINA.

Aim/Introduction: Accurate differentiation of solitary pulmonary lesions (SPLs) has long been a clinical challenge. This study aimed to integrate dynamic ^{18}F-fluorodeoxyglucose (FDG) PET/CT imaging with machine learning (ML) to improve the diagnostic accuracy of SPL classification in terms of benign/malignant nature and histopathological subtypes. ***Materials and Methods:*** Retrospective analysis of dynamic PET/CT imaging data from 150 SPL patients enrolled between 2017 and 2025 (scanned at 1, 2, 3, and 4h after ^{18}F-FDG injection) was conducted. Metabolic parameters (SUVmax, SUVmean, standardized SUV [stdSUV], metabolic homogeneity) were extracted and to assess their diagnostic efficacy, and dynamic metabolic curves(DMCs) were fitted for observation. Six ML models were constructed, and their performance was evaluated through ROC-AUC analysis, 10-fold cross-validation, and external validation. ***Results:*** In the discrimination of benign and malignant SPLs, thresholds based on 4-h average stdSUV (stdSUVavg4h: 2.7 for benign vs. malignant, 4.76 for squamous cell carcinoma vs. tuberculosis, 4.12 for squamous cell carcinoma vs. inflammatory lesions, 2.36 for adenocarcinoma vs. inflammatory lesions) and stdSUVmax4h(7.43 for squamous cell carcinoma vs. adenocarcinoma, 6.20 for tuberculosis vs. inflammatory lesions) demonstrated good classification accuracy (AUC: 0.82-0.97); the ability to discriminate adenocarcinoma from tuberculosis was limited. DMCs showed that the DMCs of malignant SPLs were generally higher than those of benign lesions (squamous cell carcinoma > adenocarcinoma > tuberculosis > inflammatory lesions); over time, the DMCs of lung cancer and tuberculosis continued to rise (with tuberculosis showing a smaller increase than lung cancer), while the DMCs of inflammatory lesions decreased to varying degrees. DMCs also showed good efficacy in differentiating adenocarcinoma from tuberculosis. ML models further enhanced the classification capability of PET/CT for SPLs, with the random forest (RF) model achieving the best performance (AUC: 0.97, sensitivity: 93%, specificity: 89%); additionally, ML models using dual-time-point (1,4h) and four-time-point (1, 2, 3, and 4 hours) imaging exhibited comparable efficiency, reducing radiation exposure by 40%. ***Conclusion:*** Multi-phase ^{18}F-FDG PET/CT imaging combined with DMC analysis and ML models can effectively distinguish the benign/malignant nature and subtypes of SPLs. Dual-time-point (1, 4h) imaging reduces the number of scans while maintaining diagnostic accuracy, supporting its clinical adoption. ***References:*** Luo Y. Differential diagnosis of lung cancer and tuberculosis based on 18F-fluorodeoxyglucose PET/CT multi-time points imaging. Nucl Med Commun. 2023; 44(8): 732-740.

EPS-074

Effect of data-driven motion correction for respiratory movement on lesion detectability in PET-CT: a phantom study

M. de Winter[1], *R. Gevers*[1], *J. Lavalaye*[1], *J. Habraken*[1], *M. Maspero*[2]; *[1]Sint Antonius Hospital, Nieuwegein, NETHERLANDS, [2]University Medical Center Utrecht, Utrecht, NETHERLANDS.*

Aim/Introduction: While DDMC techniques have proven to enhance the visibility of lesions affected by motion, their impact on overall detectability remains unclear. This study investigates whether data-driven motion correction (DDMC) improves lesion detectability in PET-CT. ***Materials and Methods:*** A moving platform simulated respiratory motion in a NEMA-IEC body phantom with varying amplitudes (0, 7, 20, 30 mm) and target-to-background ratios (2, 5, 10.5). Scans were reconstructed with and without DDMC, and the spherical targets' maximal and mean recovery coefficient (RC) and contrast-to-noise ratio (CNR) were measured. ***Results:*** DDMC results in higher RC values in the target spheres. CNR values increase for small, high-motion affected targets but decrease for larger spheres with smaller amplitudes. A sub-analysis shows that DDMC increases the contrast of the sphere and the background noise by 17%. ***Conclusion:*** While DDMC significantly enhances contrast (RC), its impact on detectability (CNR) is less profound due to increased background noise. CNR improves for small targets with high motion amplitude, potentially enhancing the detectability of low-uptake lesions. Given that the increased background noise may reduce detectability for targets unaffected by motion, we suggest that DDMC reconstructions are used best in addition to non-DDMC reconstructions.

EPS-075

Linearity and Dynamic Range of Digital PET Systems for Myocardial Blood Flow Quantification

R. DeKemp[1], *J. Huettges*[2], *J. Abele*[3], *R. Hung*[3], *M. Iwanochko*[4], *M. Alwan*[5], *M. Al Mallah*[5], *S. Chih*[1]; *[1]University of Ottawa Heart Institute, Ottawa, ON, CANADA, [2]Cardiac Imaging Inc, Houston, TX, UNITED STATES OF AMERICA, [3]University of Alberta Hospital, Edmonton, AB, CANADA, [4]University Health Network, Toronto, ON, CANADA, [5]Houston Methodist Hospital, Houston, TX, UNITED STATES OF AMERICA.*

Aim/Introduction: Digital PET-CT scanners have generally improved performance over PMT-based systems, however their accuracy for quantification of myocardial blood flow (MBF) has not been evaluated systematically. Rb-82 is the most commonly used tracer for MBF imaging but may exceed the count-rate limits for linearity and accuracy at the guideline-recommended dose of 10 MBq/kg. This study aimed to characterize the dynamic range of four current digital PET-CT scanners based on established methodologies (Renaud et al. JNM 2017). ***Materials and Methods:*** Rubidium-82 (2000-3000 MBq) was injected directly into the heart wall of a cardiac insert within large and small torso phantoms (Spectrum Dynamics) to simulate different patient sizes. List-mode scans (6 min) were started at the end-of-injection when the heart wall activity was well-mixed and homogeneous. Dynamic images were reconstructed with all corrections enabled, and volumes of interest were drawn around the entire cardiac insert to measure the total (decay-corrected) activity vs time. Three different metrics were used to evaluate scanner dynamic range defined at the measured heart wall activity with <10% bias relative to the end-of-scan value used as the accuracy standard: 1. True activity in the LV heart wall, 2. Prompt coincidence count-rate, 3. Coincidence dead-time correction factor. ***Results:*** For all systems, the prompt count-rates and dead-time factors increased monotonically with total activity in the LV heart wall. At the 10% bias limit, true heart wall activity was systematically higher in the large vs small phantom due to higher attenuation losses. Conversely, the

prompt count-rates were systematically lower in the large vs small phantoms at the 10% bias limit, due to changes in patient scatter and dead-time corrections. Dead-time factors were higher in the large vs small phantom due to increased incidence of scattered events. ***Conclusion:*** The dynamic range available for accurate measurement of cardiac activity varies greatly among current digital PET-CT scanners. The prompt count-rate and total activity limits (at 10% bias) will vary between patients based on the discrepant results in the small and large torso phantoms. Cardiac-specific performance standards may be required to characterize the high-count-rate accuracy for quantification of myocardial blood flow using rubidium-82 PET imaging. ***References:*** 1. Renaud⋯ deKemp. Characterization of 3-Dimensional PET Systems for Accurate Quantification of Myocardial Blood Flow. J Nucl Med. 2017 Jan;58(1):103-109. 2. Gao⋯ deKemp. Rubidium-82 dose effects on myocardial blood flow measurements using a digital positron emission tomography - computed tomography scanner. J Nucl Cardiol. 2025 Jan;43:102073.

EPS-076

^{82}Rb Myocardial perfusion imaging - how high can you go?

C. López Martínez[1], *H. McMeekin*[1,2], *M. Burniston*[1], *B. Sanghera*[1]; [1]*Barts Health NHS Trust, London, UNITED KINGDOM,* [2]*Hermes Medical Solutions, London, UNITED KINGDOM.*

Aim/Introduction: Cardiac positron emission tomography/computed tomography (PET/CT) with rubidium-82 (^{82}Rb) is a powerful tool in the diagnosis of coronary arterial disease and microvascular disease. Myocardial blood flow rates (MBFs) are determined from the first-phase dynamic data. Due to the short half-life of ^{82}Rb (75 seconds), the first-pass phase can have extremely high count-rates which may saturate the detectors, making deadtime correction factors (DTCFs) insufficient and resulting in reduced MBF quantitative accuracy. This work characterises the count-rate performance of the scanner, aiming to find an upper limit to the weight-based dosing for accurate activity quantitation in the dynamic image. ***Materials and Methods:*** The method by (Renaud, et al.) was reproduced: 2220 MBq of ^{82}Rb were injected into the myocardium insert of a cardiac anthropomorphic phantom and dynamic images were acquired. The activity in the myocardium was measured and DTCF information was collected at each time frame. 10% difference between the measured and known myocardial activity was chosen as the maximum allowable error; the DTCFs at these count rates were recorded to establish the dynamic range. Similar acquisitions and analyses were repeated with two larger phantom sizes and with an ^{18}F-FDG source outside the FOV. The known activities corresponding to the dynamic range limits were converted into activity-per- weight to establish limits for quantitatively accurate scanning. ***Results:*** The scanner underestimates activity in the myocardium at high count-rates. Dynamic range limits were measured as DTCFs of 1.45, 1.80, 1.83 and 1.68 for the acquisitions with the standard phantom size, two larger phantom sizes, and activity outside the FOV, respectively. The maximum activity per weight for quantitative accuracy was calculated as 14.50 MBq/kg. ***Conclusion:*** The count-rate limitations of a PET/CT scanner depend on patient size; the scanner can process higher DTCFs for larger patients due to the increased attenuation. Having a source of activity outside the FOV increases the DTCF limit, as expected, as the total counts received by the detectors are greater. If a large proportion of these counts originate from outside the FOV then the maximum myocardial activity for quantitative accuracy will be reduced. The activity-per-weight currently administered to patients of 10 MBq/kg is below the limit for quantitative accuracy found in this work, inferring the weight-based dosing is optimised for MBF accuracy. ***References:*** Renaud, J. M., et al., Characterization of 3-Dimensional PET Systems for Accurate Quantification of Myocardial Blood Flow, J Nucl Med, 58, 103-109 (2017)

EPS-077

Potential of Lean Body Mass-Adjusted FDG PET/CT Parameters to Predict Pathologic Findings in Overweight Endometrium Cancer Cases

F. Avci[1], *A. Tunc*[1], *B. K. Erkek*[2], *A. A. Ozsaran*[3], *G. Serin*[4], *O. Zekioglu*[4], *Z. Burak*[1]; [1]*Ege University, Nuclear Medicine, Izmir, TÜRKIYE,* [2]*Agri Training and Research Hospital, Nuclear Medicine, Izmir, TÜRKIYE,* [3]*Ege University, Obstetrics and Gynecology, Izmir, TÜRKIYE,* [4]*Ege University, Pathology, Izmir, TÜRKIYE.*

Aim/Introduction: This study aims to evaluate the potential of metabolic and volumetric F-18 FDG PET/CT parameters, adjusted for lean body mass (LBM), in predicting pathological findings in overweight patients diagnosed with endometrial cancer who underwent preoperative PET/CT imaging. ***Materials and Methods:*** Between 2021 and 2024, a total of 80 endometrial cancer patients with a body mass index (BMI) ≥25 kg/m^2, who had not received neoadjuvant therapy prior to undergoing total abdominal hysterectomy and bilateral salpingo-oophorectomy (TAH-BSO), were included. Demographic and postoperative pathological data were obtained from the hospital's electronic records. PET/CT images were evaluated both visually and semi-quantitatively to calculate tumor-associated parameters, including SULmax, SULmean, SULpeak, metabolic tumor volume (MTV), and total lesion glycolysis adjusted for lean body mass (TLG-LBM). Histopathological and immunohistochemical features of tumors were analyzed. Results were retrospectively analysed using SPSS v25. ***Results:*** The mean age at diagnosis was 60.34 years (44-84), and the mean BMI was 34.48 kg/m^2 (25.01-55.10). PET parameters are presented in Table 1. Among the cases, 69 were endometrioid, 5 mucinous, 3 serous, and 3 carcinosarcoma. The average tumor size was 3.96 cm (1-9 cm), and staging revealed 10 cases at Stage I, 56 at Stage II, and 14 at Stage III. Lymphovascular invasion was detected in 22 cases, and cervical involvement in 9 cases. Lymph node dissection was performed in 60 patients, 6 of whom had micrometastases. SULmean showed weak but statistically significant correlations with age (r=0.25), tumor size (r=0.34), Ki-67 index (r=0.25), and estrogen receptor percentage (r=-0.25) ($p<0.05$). SULmax also showed a weak but significant correlation with the Ki-67 index (r=0.26). Estrogen receptor expression, a known favorable prognostic factor, was inversely correlated with PET parameters, excluding MTV. No significant relationships were found between PET parameters and progesterone receptor levels or p53 expression. Histologic grade correlated significantly with SULmax ($p=0.008$), SULmean, and SULpeak. Interestingly, SULmean values were significantly higher in patients with lymphovascular invasion ($p=0.008$) and lymph node metastasis ($p=0.011$). However, no significant associations were found between PET parameters and histologic subtype, myometrial invasion, or cervical involvement. ***Conclusion:*** Our findings suggest that in overweight patients with endometrial cancer, SUL parameters play a more effective role than SUV parameters in assessing clinical and pathological characteristics. Specifically, SULmean demonstrated significant correlations with prognostically critical variables. These results indicate that SULmean may serve as a potential tool in the diagnostic stratification and treatment planning of endometrial cancer.

EPS-078

Optimization of Whole-Body Dynamic ^{68}Ga PET Acquisition Protocols Using a 32 cm Axial Field of View: A Phantom Study

Q. Maronnier, *S. Brillouet, C. Lamesa, F. Courbon, O. Caselles;*
Oncopole Claudius Regaud, Toulouse, FRANCE.

Aim/Introduction: Dynamic PET imaging provides additional clinical insights over static imaging, potentially enhancing patient selection for targeted therapies. However, traditional PET systems are limited by narrow axial fields of view (FOV), restricting whole-body (WB) radiotracer kinetic assessment. WB dynamic imaging can be performed using image-derived input function (IDIF) from a blood pool and sequential WB passes [1]. This study aims to produce optimized protocols for WB dynamic acquisitions with ^{68}Ga-labeled radiotracers, ensuring reliable semi-quantitative metrics while increasing the number of WB passes for improved kinetic analysis. ***Materials and Methods:*** Phantom experiments were conducted on a 32cm axial FOV PET/CT system using ^{68}Ga, with two components: simulating the IDIF and multiple WB passes. These included evaluating bolus measurement accuracy and assessing image quality and quantification. A Jaszczak phantom, with a 10cc syringe (25mm cross-section) containing ^{68}Ga, was used for bolus measurement accuracy. 6 minutes scan time was rebinned into 12×5s, 6×10s, and 8×30s frames. Derived from the EARL image quality procedure, a body phantom containing spheres of 10 to 37mm in diameter with a contrast ratio of 10.15 was scanned over one hour. The data were then rebinned with various framing (1, 1.5, 2, and 2.5 min/FOV) and reconstruction parameters (β of 750, 1000, and 1250). Mean and maximum recovery coefficients (RC) were calculated and compared to the reference clinical protocol used for static imaging (2.5 min/FOV, β = 750). ***Results:*** Two dynamic acquisition protocols were designed, one with 4 bed positions (vertex-thighs) and the other with 8 bed positions (total-body), both incorporating IDIF and WB passes. In the IDIF experiment, less than 5% variation in RCmean and RCmax was observed. In the WB experiment, the coefficient of variation over frames from the phantom background was 10.1% for the optimized series and 10.2% for the reference series. The standard deviation of RCmean and RCmax in spheres over frames was generally lower and more consistent for the optimized series. A slight decrease in RC metrics was noted, with the largest difference observed in the smallest target (12% for RCmax and 9% for RCmean). ***Conclusion:*** We produced dynamic ^{68}Ga PET acquisition protocols that provide reliable semi-quantitative metrics with minimal variation across frames while allowing for an increased number of WB passes within the same acquisition time. ***References:*** 1. Dias AH, Jochumsen MR, Zacho HD, Munk OL, Gormsen LC. Multiparametric dynamic whole-body PSMA PET/CT using [68Ga]Ga-PSMA-11 and [18F]PSMA-1007. EJNMMI Res. 2023 Apr 15;13(1):31.

EPS-079

Optimisation of [^{18}F]FDG dosage for quantitative whole-body PET: ensuring image quality anthropometric independency and EARL harmonisation

I. Baltabaev, *A. Khalimon, A. Nikiforuk, B. Shvets, M. Khodzhibekova, G. Khamadeeva, D. Khodakova, T. Lazutina, I. Pylova, A. Leontev;*
P. Hertsen Moscow Oncology Research Institute - branch of the National Medical Research Radiological Centre of the Ministry of Health of the Russian Federation, Moscow, RUSSIAN FEDERATION.

Aim/Introduction: Consistent image quality independent of patient-specific anthropometric variability in whole-body PET imaging remains a challenge when using standardised [^{18}F]FDG dosing protocols. This study aimed to develop and validate an optimised anthropometry-based dosing regimen for [^{18}F]FDG administration, with a focus on EARL2-harmonisation and reduction of signal-to-noise ratio (SNR) dependency on anthropometric parameters. ***Materials and Methods:*** A total of 250 patients were included in a prospective study: 90 to determine a new dosage protocol and 160 for its validation. The local [^{18}F]FDG dosing regimen, clinical PET/CT acquisition protocol (3min/bed) and two EARL2-harmonised reconstructions (BSREM with β=400 and 3D-OSEM+PSF with 11 iterations, 6 subsets, 5 mm Gaussian filter) were utilised. Liver SNR was measured and normalised to administered activity for both reconstructions. Acceptable SNR (SNR_{acc}) was determined by physicians based on visual assessment. The dependence of normalised SNR on various patient-specific parameters was analysed using multiple regression models. The anthropometric parameter and regression model with the highest R^2, along with the predefined SNR_{acc}, were used to determine the new dosing regimen, which was prospectively validated using only BSREM reconstruction method. Additionally, minimum acceptable EARL2-compliant activity was derived from NEMA IEC Body Phantom NU2-2018 acquisition conducted in accordance with the EARL ^{18}F-standards accreditation manual. ***Results:*** The best regression model between patient-specific anthropometric parameters and normalized SNR was observed for body surface area (Haycock formula) and body weight. SNR_{acc} was defined as 17 for BSREM and 10.5 for 3D-OSEM+PSF. Due to its practical simplicity, body weight was selected as the patient-specific parameter for the new dosing regimen. The power-law model demonstrated the best fit, yielding R^2=0.67 for BSREM and R^2=0.59 for 3D-OSEM+PSF ($p<0.001$). Consequently, administered activity was defined as $A=4.31\times m^{1.04}$ for BSREM and $A=1.2\times m^{1.34}$ for 3D-OSEM+PSF. After the validation with BSREM reconstruction, the new regimen demonstrated no correlation between SNR and body weight (r=-0.05 and p=0.53) and reduction in SNR's coefficient of variation to 8.8% compared to 14.3% observed with the local dosing regimen, with a mean value of SNR 16.9. The minimum acquisition time per bed ensuring EARL2-harmonisation was derived from the phantom study and accounted for 75 seconds for BSREM. Using reference activity and weight values of the phantom (300MBq and 75kg), minimum acceptable activity was set as $A_{min}=1.4\times m^{1.04}$ for clinical 3min/bed acquisition protocol with BSREM algorithm. ***Conclusion:*** The proposed patient-specific anthropometry-based optimisation of [^{18}F]FDG dosing regimen improves image quality stability and satisfies EARL2-harmonisation standards in quantitative whole-body PET imaging.

EPS-080

A Systematic Exploratory Study on SUV Harmonization for Long Axial PET/CT

Y. Li, *X. Lu, H. Pang;*
Department of Nuclear Medicine, The First Affiliated Hospital of Chongqing Medical University, Chongqing, CHINA.

Aim/Introduction: European Association of Nuclear Medicine (EANM) have launched EANM Forschungs GmbH (EARL) to achieve harmonization of standard uptake value (SUV), which aimed to align SUV obtained from different scanners and algorithms. EARL developed the standard protocol of SUV harmonization for short-axis PET (SaPET). However, Long-axis PET (LaPET) demonstrated completely different scan mode and SUV harmonization logic when compared to SaPET, and there were no relative studies specifically focused on the SUV harmonization of LaPET. Our purposes were to perform systematical researches on SUV harmonization of LaPET, establish the standardized protocol and conduct clinical validation to verify its efficacy. ***Materials and Methods:*** Firstly, we compared the SUVs of NEMA IEC phantoms obtained from different scanners (SaPET and LaPET) and algorithms. Secondly, to explore the SUV harmonization protocol for LaPET, a specific scan mode was proposed. The long-axial detector was divided into five parts according to the patient position, within which most patient's head and neck, chest,

abdomen, pelvis and leg could be correspondingly placed. After 5 times of scanning (one-bed, phantom placed at the middle of each part), SUV harmonization for each scan was performed. Post-filters (F-brain, F-chest, F-abdomen, F-pelvis and F-leg, namely filter of corresponding position) were then determined, and recovery coefficients (RC) were calculated. The the root mean square error (RMSE) of adjusted RC to RCexpected was then calculated to describe the success of harmonization. Finally, we applied the SUV harmonization to the DICOMs of the same patient obtained from LaPET and SaPET. ***Results:*** The phantom SUVs varied between SaPET and LaPET, as well as among different algorithms, confirming the necessity of SUV harmonization. The RMSE of adjusted RC to RCexpected were 0.048, 0.045, 0.053, 0.061 and 0.045 for head and neck, chest, abdomen, pelvis and leg positions under our clinically reconstruction algorithms (3i20s, Gaussian post-filtering 2mm), respectively. Meanwhile, SUVs from the same patient significantly differed from LaPET to SaPET, and SUV harmonization explained a lot for the abnormal SUV observed in clinic. ***Conclusion:*** SUV harmonization showed great significance between SaPET and LaPET, and special harmonization protocol showed be established for LaPET, by which each body part showed be harmonized separately according to its position in detector.

EPS-081

Validation of image-derived SUV estimates for ultra-low ^{18}F-FDG PET imaging using a large axial field-of-view PET/CT system

C. Smith, *G. J. C. Zwezerijnen, J. Heijmen, M. E. den Hollander, J. M. Zijlstra, C. Menke-van der Houven van Oordt, I. Bahce, M. Yaqub, R. Boellaard;*
Amsterdam UMC, Amsterdam, NETHERLANDS.

Aim/Introduction: Large-axial field of view (LAFOV) PET/CT systems enable image-derived quality control of standardised uptake values (SUV) by extracting ^{18}F-FDG activity and body weight from the total and half-body scans [1]. Additionally, these systems offer ultrahigh sensitivity and signal-to-noise ratios, allowing lower tracer doses and shorter acquisition times. This study examined whether previously published QC methods remain valid when using significantly lower ^{18}F-FDG activities with LAFOV PET/CT. ***Materials and Methods:*** Ten patients with cancerous tumours underwent two ^{18}F-FDG PET/CT scans: one with standard activity (3.0 MBq/kg) and, within 7 days, one with ultra-low activity (0.3 MBq/kg). List-mode data of both scans were resampled to simulate activities of 0.3 and 0.03 MBq/kg. We applied linear regressions from Smith et al. [1] to the test, retest, and simulated activities to assess their applicability at lower activities. ***Results:*** Image-derived body weight significantly predicted reported body weight across test, retest, and simulated 0.3 and 0.03 MBq/kg scans for both total (r= 0.964; r= 0.982; r= 0.964; r= 0.918) and half body (r= 0.988; r= 0.988; r= 0.988; r= 0.976) data, respectively. A small underestimation at simulated 0.03 MBq/kg was found but could be corrected with additional Gaussian filtering. Image based estimated ^{18}F-FDG activity showed biases of more than 15% in case of half body retest scans (when using low injected activities) which improved to within 5% after adding an interaction term between image based activity and patient length in the original independent training fits. Image based estimated ^{18}F-FDG activity accurately (within 5%) predicted reported injected activity across test, retest, and simulated 0.3 and 0.03 MBq/kg scans for both total (r= 0.964; r= 0.964; r= 0.973; r= 0.964) and half body (r= 0.964 r= 0.976; r= 0.973; r= 0.988) data, respectively. ***Conclusion:*** Body weight and injected activity can be accurately derived from total and half-body scans, even at significantly reduced doses (0.3 MBq/kg). This supports continuing to use image-derived QC for SUV calculation for high and low-activity protocols. Standardisation of low-dose protocols for LAFOV PET/CT systems aligns with ALARA/ALAPA principles, which is particularly relevant for radiation-sensitive patients such as children and pregnant women. ***References:*** Smith, C. L., Zwezerijnen, G. J., den Hollander, M. E., Weijland, J., Yaqub, M., & Boellaard, R. (2024). Mitigating SUV uncertainties using total body PET imaging. European Journal of Nuclear Medicine and Molecular Imaging, 51(4), 1070-1078.

EPS-082

Redefining Ultra-low Dose: Full-sensitivity LAFOV PET/CT for Paediatric Imaging

G. C. van den Oever, *J. H. van Snick, K. P. Koopmans, E. H. J. G. Aarntzen, R. H. J. A. Slart, W. Noordzij, A. H. Brouwers, G. N. Stormezand, T. Velleman, A. W. J. M. Glaudemans, O. V. Ivashchenko;*
University Medical Center Groningen, Groningen, NETHERLANDS.

Aim/Introduction: Long axial field-of-view (LAFOV) PET/CT systems, with scans over 1 metre, offer superior sensitivity. This enables faster scanning and reduced radiopharmaceutical doses, benefitting paediatric imaging due to children's higher radiosensitivity. However, no international guidelines for paediatric LAFOV PET/CT dosing exist. While early studies suggest substantial dose reduction potential, recent advances including full-acceptance angle acquisition have doubled sensitivity. This mode can cause non-uniform image quality unless scanning is performed in multiple bed positions, which is often unnecessary in children, as most major organs fall within 1 metre. Bed movement may also increase stress or necessitate sedation. This study investigates optimal use of full-sensitivity LAFOV PET/CT in paediatrics, balancing dose reduction and diagnostic quality. ***Materials and Methods:*** This retrospective study included 56 [^{18}F]FDG-PET/CT scans from patients aged 0.2-17.5 years (mean 9.9 ± 5.2), performed for oncological (n=25) or infectious/inflammatory (n=31) indications. Reference image quality (RIQ) was defined from average count statistics per bodyweight from scans conducted at our centre between October 2021 and December 2024. Full-sensitivity reconstructions were created at 0.39%, 1.56%, 6.25%, 12.5%, and 25% of RIQ, following evidence of a 50% dose reduction with partial system sensitivity. Three nuclear medicine specialists rated image quality on a 5-point Likert scale, with 3 considered clinically acceptable, and re-evaluated images after reviewing clinical indications. Signal-to-noise ratio (SNR) in the liver, tumour-to-background ratio (TBR), and lesion SUVs were analysed. SNR liver was normalised for administered activity and scan duration. Optimal dose-modelling parameters (weight, height, BMI, bodyweight-per-height (BWH), and body surface area) were determined using goodness-of-fit metrics and F-tests. ***Results:*** An SNR of 12.3 correlated with clinically acceptable quality. Primary oncological scans with previously unacceptable Likert scores were upon re-evaluation more frequently rated as clinically acceptable than follow-up scans ($p = 0.03$). TBR showed no significant change across reconstruction percentages. Weight and BWH showed the best fit ($R^2 = 0.88$ and 0.89), with no significant difference between models ($F = 2.13$, $p = 0.15$). Weight was selected due to ease of clinical use. The resulting model indicated a 97% (96-98) dose reduction compared to current EANM guidelines. ***Conclusion:*** Full-sensitivity LAFOV PET/CT achieves a 97% dose reduction in paediatric imaging while maintaining clinically acceptable quality. Weight and BWH are optimal for dose modelling, highlighting LAFOV PET/CT's potential in paediatrics and the need for further protocol optimisation. ***References:*** 1) van der Kaap, et al. DOI:10.1007/s00259-024-06838-z. 2) EANM Dosage Card 2016. 3) de Groot, et al. DOI:10.1186/2191-219X-3-63

EPS-083

The effect of Dead Time Correction on the accuracy of brain PET imaging quantification

A. Issa[1], *J. Scheins*[1], *L. Tellmann*[1], *C. Brambilla*[1], *P. Lohmann*[1], *H. Herzog*[1], *N. Shah*[1,2,3], *C. Lerche*[1];
[1]*Institute of Neuroscience and Medicine 4, INM-4, Forschungszentrum Jülich GmbH, Jülich, GERMANY,*
[2]*Institute of Neuroscience and Medicine 11, INM-11, JARA, Forschungszentrum Jülich, Germany, Jülich, GERMANY,*
[3]*Department of Neurology, RWTH Aachen University, Aachen, Germany, Aachen, GERMANY.*

Aim/Introduction: One of the most important corrections to allow accurate image quantification is the dead time correction (DTC). In our institute, we run a dedicated Siemens 3T MR BrainPET insert which utilizes a global DTC. This method is based on an average DTC factor estimated for all detector blocks. However, it fails to account for count rate variations of the individual blocks, which can depend on their positions. Additionally, MR compatibility limits the placement of radiation shields, making it difficult to reduce these variations. To address this, we have implemented a block-pairwise method for DTC at the level of individual scintillation block detector pairs. ***Materials and Methods:*** The new DTC method utilizes delayed random coincidence count rates to estimate the dead time function (D*f*) for individual block pairs. This method was evaluated through decay experiments using phantom measurements with both homogeneous and inhomogeneous activity distributions. We compared the two DTC methods and evaluated the differences in the quantification of images using three tracers. We analyzed the impact on the time-activity curves (TACs) of [^{11}C]ABP688, as well as derived quantities such as the non-displaceable binding potential (BP_{ND}) and the total distribution volume (V_T). Additionally, we assessed [^{18}F]-FET TACs, including the tumor-to-background ratios (TBR_{max} and TBR_{mean}). Finally, applying kinetic modeling, we evaluated the effects on [^{15}O]H_2O TACs, obtained the regional cerebral blood flow (rCBF), the rate constant k_2, and the V_T. ***Results:*** The validation of the phantom measurements indicated that the global DTC introduced significant biases, particularly in areas with high activity concentrations. In contrast, the block-pairwise method resulted in less bias in these regions, even though the noise levels were comparable for both methods. The evaluation of patient and volunteer measurements revealed a notable difference between the two DTC methods. For the [^{11}C]ABP688 measurements, the global method exhibited a significant bias in V_T across all relevant brain regions. For [^{18}F]-FET, we found a difference of up to 10% in the TBR_{max} between the two methods. The evaluation of [^{15}O]H_2O measurements revealed that the global method showed a significant bias in rCBF, k_2, and V_T in both gray matter and white matter regions. ***Conclusion:*** The developed block-pairwise method corrected DT losses more accurately when applied to acquisitions with the 3T MR-BrainPET insert, consistently increasing the quantitation accuracy for different tracers and quantities.

EPS-084

Optimization of the imaging protocols for a SAFOV digital PET/CT

C. Steenhout, *C. Bernard, D. Palmeri, L. Seidel, C. Lachapelle, S. Marchiori, A. Jadoul, C. Derwael, P. Lovinfosse, N. Withofs, R. Hustinx;*
CHU Liège, Liège, BELGIUM.

Aim/Introduction: Digital Positron Emission Tomography/Computed Tomography (PET/CT) has improved image quality and lesion detection compared to analog PET. This study aims at optimizing the counting statistics, i.e. scanning time/injected activity in clinical protocols with the digital PET/CT Siemens Biograph Vision 600 system. ***Materials and Methods:*** One-hundred-and-fifty patients who underwent [^{18}F]FDG (n=100, 2.5 MBq/kg), [^{68}Ga]Ga-PSMA-11 (n=30, 1 MBq/kg) and [^{68}Ga]Ga-DOTANOC (n=20, 1 MBq/kg) PET/CT scans were retrospectively evaluated. According to our clinical protocol, a typical 170-cm subject underwent a whole-body (WB) study in 400 seconds and a total-body (TB) study in 596 seconds. The list-mode PET data were reconstructed using the clinical reconstruction protocol (hereafter referred to as "100%"), and using 80, 60, 40 and 20% of the acquired counts. Each dataset was evaluated by at least 2 nuclear medicine physicians regarding the image quality, using a 5-point Likert-scale. Three categories were considered for statistical purposes: Likert 1-2 as "clinically insufficient", Likert 3 as "fair" and Likert 4-5 as "clinically good". Lesion detection capability was assessed by reporting visible lesions (from "no" to "more than 10" lesions). Agreement between the observers was assessed by Cohen's Kappa coefficient (κ) and by Intraclass Correlation Coefficient (ICC). Youden indexes were calculated establishing the maximal weight keeping a good image quality while reducing the acquired counts. In addition, reconstructed images were quantitatively assessed for comparison of standardized uptake values (SUVs) and noise. ***Results:*** There is a significant agreement between observers regarding both the overall image quality (considering Likert 1-2-3 versus 4-5: $0.36 \leq \kappa \leq 0.82$) and the number of detected lesions ($0.82 \leq ICC \leq 0.99$).The 60% counts datasets were considered as "clinically good" in 62% of the [^{18}F]FDG, 53.3% of the [^{68}Ga]Ga-PSMA-11 and 80% of the [^{68}Ga]Ga-DOTANOC scans, respectively. Regarding "clinically good" image quality, Youden indexes are 76kg, 78kg and 70kg for [^{18}F]FDG and [^{68}Ga]Ga-PSMA-11 and [^{68}Ga]Ga-DOTANOC, respectively. Below these thresholds, the proportion increases to 72.4%; 78.6% and 100%, respectively. For each radiotracer, no significant difference ($p > 0.05$) was found between lesion SUVs comparing 100% and other reconstructions, but an increase in noise was observed. ***Conclusion:*** Compared to the default protocol (i.e. 2,5 MBq/kg [^{18}F]FDG and 400 seconds for a 170-cm individual), the scanning time and/or injected activity could be reduced by 40% for patients weighting less that 76 kg and 20% for those weighting more, without significant loss of quality. Results are comparable with [^{68}Ga] labeled compounds.

EPS-085

Evaluation of deep learning-based reconstruction models on non-TOF BGO PET/CT: Impact of acquisition times and BSREM penalization factors

S. Kvernby[1,2], *A. Stenvall*[1], *E. Trägårdh*[2,3], *D. Minarik*[1,2];
[1]*Radiation Physics, Department of Hematology, Oncology and Radiation Physics, Skåne University Hospital, Sweden, Lund, SWEDEN,* [2]*Department of Translational Medicine and Wallenberg Centre of Molecular Medicine, Lund University, Malmö, SWEDEN,*
[3]*Department of Clinical Physiology and Nuclear Medicine, Skåne University Hospital, Malmö, SWEDEN.*

Aim/Introduction: A new generation PET scanners based on BGO detectors, without time of flight (TOF) capability, are now available. They incorporate deep learning-based (DLb) models to compensate for the lack of TOF. These DLb-TOF models have not been evaluated with block-sequential regularized expectation maximization (BSREM) reconstruction methods for different acquisition times. This study aims to evaluate the impact of different acquisition times combined with different BSREM penalization factors (β) on image quality and lesion detectability for FDG whole-body images using DLb-TOF models. ***Materials and Methods:*** Fourteen patients referred for a clinical FDG PET scan were included. Each patient was injected with 3.5 MBq/kg of [^{18}F]-FDG and underwent a whole-body PET acquisition (120 s/bed) on a digital BGO PET/CT (32 cm FOV) 60 minutes post-injection. Data were reconstructed into images (384x384 matrix) representing different acquisition times (120s, 90s, 60s, 45s, 30s and 15s) using BSREM with various penalization factors (β50, β100, β300, β500, β700, β900 and β1100) and with three DLb-TOF

models (Low, Medium and High). Volumes of interest were placed in the liver and in two avid lesions for each patient. SNR were calculated as $SUVmean_{liver}/SD_{liver}$ and detectability were calculated as $SUVpeak_{tumor}/SUVpeak_{liver}$. ***Results:*** SNR increased with longer acquisition times and higher β-factors (range: 0.7 (β50/15s) - 24.3 (β1100/120s)). Applying DLb-TOF models increased SNR for all acquisition times and β-factors, with the Low DLb-TOF model producing the largest increase (66%). Lesion detectability depended on the acquisition time and β-value. For the longest acquisition times (120s and 90s), the highest detectability were observed at β100, while shorter acquisition times (60s-15s), required a higher β-value (β300) for optimal detectability. For the DLb-TOF models, the High DLb-TOF model provided the highest detectability, but varying with acquisition time and β-value. The Low DLb-TOF model achieved the highest detectability at lower β-values compared to the High DLb-TOF model. ***Conclusion:*** SNR increased with higher β-values, longer acquisition times, and the application of DLb-TOF models. Lesion detectability depended on the β-value, acquisition time, and the DLb-TOF model used. The Low DLb-TOF model had the best SNR but at the expense of detectability. The optimal parameters for the evaluated BGO PET/CT system, balancing SNR and lesion detectability within a clinical reasonable acquisition time, were 60-90 s with β-values of 500-300, in combination with the Medium DLb-TOF model.

EPS-086

Performance Evaluation of Advanced PET Reconstruction Algorithms Using Phantom and Patient Datasets

P. Goorhoo*, M. Qebetu, K. Banda, K. Legodi, C. Davis, L. Smith, S. Sibiya, A. Mdlophane, S. Mdanda, K. Mokoala, M. Sathekge, K. Ramonaheng;*
Nuclear Medicine Research Infrastructure (NuMeRI), Pretoria, SOUTH AFRICA.

Aim/Introduction: Quantitative accuracy and spatial resolution in PET imaging are limited by partial volume effects (PVEs). Advances in digital PET/CT systems, such as LYSO crystals, SiPMs, and deep learning-based reconstruction algorithms, have improved image quality and reduced PVEs. This study assesses the quantitative and qualitative performance of the 3D-Ordered Subset Expectation-Maximization (OSEM), Hyper Iterative, and Hyper DPR (Deep Progressive Reconstruction) algorithms by evaluating recovery coefficients (RCs), overall system performance using the Jaszczak phantom, and SUVmean analysis from three patient datasets. ***Materials and Methods:*** PET/CT imaging was performed using the uMI 550 digital system (United Imaging Healthcare). The NEMA IEC Body Phantom and Jaszczak phantom, both filled with Fluorine-18, were used to simulate clinical imaging scenarios. Clinical data from three patients were also acquired using standard acquisition parameters. PET data was acquired in list mode with a single 15-minute bed position. Reconstruction was performed using 3D-OSEM (2-10 iterations, 20 subsets), Hyper Iterative (strengths 0.2-1.0), and Hyper DPR (strengths 1-5), across acquisition durations ranging from 10 to 90 seconds. Image analysis was carried out using AMIDE and ImageJ to evaluate RCs, image contrast, spatial resolution, uniformity, and SUVmean from the clinical datasets. Optimized reconstruction settings were identified based on the phantom analysis and subsequently applied to the patient data; semi-quantitative analysis for the patient data was performed. ***Results:*** Hyper DPR showed RCs, with values increasing from 0.613 ± 0.041 (10 mm) to 0.824± 0.005 (37 mm) at strength 5 with 90 seconds. Optimal hot (0.849 ± 0.003) and cold contrast (0.723 ± 0.003) were observed. Spatial resolution allowed visualization of all rods ≥6.4 mm. Hyper Iterative achieved stable RCs across strengths and durations, peaking at 0.820 ± 0.002 (37 mm), with consistent contrast and uniformity values (1.277% differential; 1.825% integral). 3D-OSEM exhibited minimal variation across iterations, reaching an RC of 0.830 ± 0.002 (37 mm). OSEM with PSF-on and TOF-off yielded the highest hot/cold contrast and spatial resolution, with 27 of 32 rods (6.4 mm) resolved. Clinical Data: Analysis of three patient datasets confirmed consistent SUVmean values for OSEM and Hyper Iterative reconstructions. Hyper DPR yielded the highest SUVmean at strength 5. ***Conclusion:*** Overall, the selection of reconstruction algorithm and optimization of parameters play a critical role in enhancing PET image quality and semi-quantitative analysis, with Hyper DPR demonstrating the potential for minimizing PVEs and improving quantification accuracy in digital PET/CT imaging.

EPS-087

Clinical Protocol Simulations and Phantom Validations for a dual-collimator 3D CZT Camera

R. Zananiri*, Y. Odes, O. Ziv, A. Shtangel, N. Didi, B. Yuzefovich, J. Sachs, A. Efrati, H. Kosovezer, G. Rabin, A. Devir-Wolfman, J. Bouhnik;*
GE HeathCare, Haifa, ISRAEL.

Aim/Introduction: With the emergence of 3D-CZT SPECT cameras over the last years, many clinical protocols have been developed, showing their potential in clinical practice. In this report, we introduce a GE Healthcare StarGuide™-based system design equipped with smaller pixels and two collimators, noted the dual-collimator StarGuide (DCS). The high sensitivity (HS) collimator is designed to enable swift acquisition durations with increased sensitivity (~1.9x) without compromising the physical resolution of StarGuide™. Beyond the physical detector design, DCS is equipped with deep learning (DL) reconstructions for image enhancement and/or scan time reduction. Here, we report the simulation and phantom validations for whole body bone (WBB), cardiac, DaTScan, and Lu177 protocols in comparison to StarGuide™ and dual-head NaI-based camera. ***Materials and Methods:*** WBB: Simset-XCat male95 and female50 with 8:1 features to background (F:B) ratio were scanned and DL-reconstructed, in StarGuide™ and DCS-HS. DCS-HS WBB scans were optimized for (1.5′, 3′ and 1.5′ for head, torso and legs, respectively) as opposed to 4′, 8′ and 4′ for the same body parts in StarGuide™. Additionally, a 5.4mCi, 8:1 IEC NEMA body phantom was acquired for physical validation. Phantoms were assessed for image quality (IQ) using Contrast, CNR and Background Variability, following NEMA. Cardiac: Simset-XCat gated cardiac phantom was scanned and DL-reconstructed, in StarGuide™ and DCS-HS. Additionally, a static anthropomorphic torso phantom was acquired on DCS and StarGuide. Data was assessed visually and quantitatively for Image quality using Xeleris-Myovation app. DaTScan: Simset-XCat Striatal patient was scanned and reconstructed in StarGuide™ and DCS-HS. Additionally, a striatal phantom was filled with a left 8:1 and right 10:1 F:B ratio and scanned on DCS-HS, StarGuide and 870DR-LEHRS for comparison. Xeleris DaT-Quant app was used to assess the result quantitatively. Lu177: 54 mCi IEC Phantom acquisitions with F:B 8:1 was scanned on StarGuide™, DCS-HS, DCS-LP. Data was assessed for IQ using Contrast, CNR and Background Variability, following NEMA NU-1-2023. ***Results:*** WBB: Comparable IQ at 15′ WBB scan versus StarGuide in 40′. Cardiac: Improved gated IQ for 4′/6′stress/rest versus StarGuide at same acquisition durations DatScan: Comparable IQ at 7.5′ versus StarGuide 15′. Lu177***:*** Comparable IQ for DCS-HS at 9′ eye-to-thigh on IQ (4 FOVs) scan versus 12′ for StarGuide™. ***Conclusion:*** Here, we show the potential of the double sensitivity of DCS (versus StarGuide™) enabling faster clinical scans. Patient scans are needed to verify the protocols developed and further optimizations are needed to show the potential of this system design.

EPS-088

Characterisation of Tungsten-Collimator Penetration in Cadmium Zinc Telluride-based Detectors for ^{123}I: A Monte Carlo Simulation Study

I. Ceric Andelius[1,2], *P. Kalaitzidis*[1], *J. Oddstig*[1,2], *D. Roth*[3], *M. Ljungberg*[3];
[1]*Radiation Physics, Department of Haematology, Oncology, and Radiation Physics, Skåne University Hospital, Lund, SWEDEN,* [2]*Department of Translational Medicine and Wallenberg Centre of Molecular Medicine, Lund University, Malmö, SWEDEN,* [3]*Medical Radiation Physics Lund, Lund University, Lund, Sweden, Lund, SWEDEN.*

Aim/Introduction: Although ^{123}I primarily emits photons at 159 keV, additional emissions of higher energy photons (248-784 keV) contribute to image degradation due to scatter and collimator penetration, potentially affecting quantitative imaging. Previous research has demonstrated that tungsten collimators enhance image quality for NaI(Tl)-based SPECT cameras [1]. The integration of tungsten collimators with Cadmium Zinc Telluride (CZT) detectors may further improve image quality and quantitative accuracy, leveraging the inherent properties of CZT detectors. This simulated study compares the ^{123}I spectra for a dual-headed CZT-SPECT system equipped with either tungsten or lead collimators. ***Materials and Methods:*** The energy spectrum for the ^{123}I NEMA body phantom was simulated for a full-sized system with a parallel hole collimator using the SIMIND Monte Carlo code, which includes a model for CZT charge induction [2]. Spectra and planar images were generated for a point source in air and inside an 11 cm water phantom, and line-spread functions (LSFs) were calculated. Additionally, SPECT images of a NEMA phantom with spheres of various activity concentrations and radii were simulated for both hot and cold cases. The phantom was placed 15 cm from the detector. In both studies, the fractions of detections originating from geometrically collimated (gc), septal penetrated (pc), and collimator scattered (sc) photons within the main energy window (143-167 keV) were calculated. ***Results:*** The point source simulations indicate that tungsten collimators exhibit lower penetration compared to lead collimators. Specifically, the percentage gc/pc/sc fractions of tungsten [69.1/15.4/15.5] were more favourable when compared to lead [58.3/26.2/15.5]. Therefore, the tails of the LSFs are significantly reduced, resulting in enhanced spatial resolution and improved contrast in reconstructed images. The sensitivities for the point source simulation were 28.83 and 34.4 cps/MBq for tungsten and lead, respectively. No significant difference in phantom scatter-to-total fractions between tungsten and lead was observed. ***Conclusion:*** The use of tungsten collimators will reduce collimator penetration significantly and result in improved spatial resolution and contrast in reconstructed images. ***References:*** 1. Pirayesh Islamian J, Ljungberg M. Evaluation of Improved Imaging Properties with Tungsten-Based Parallel-Hole Collimators: A Monte Carlo Study. World J Nucl Med. 2024. 2. Roth D, Larsson E, Ljungberg M, Sjogreen Gleisner K. Monte Carlo modelling of a compact CZT-based gamma camera with application to (177)Lu imaging. EJNMMI Phys. 2022;9(1):35.

EPS-089

The effect of SPECT pulmonary ventilation/perfusion scintigraphy on the efficacy of pulmonary endarterectomy in treating chronic thromboembolic pulmonary hypertension

P. Han, *R. Ma, W. Xie, H. Li, Q. Huang, Z. Zhai, L. Fu;*
China Japan Friendship Hospital, Beijing, CHINA.

Aim/Introduction: Surgery is the definitive treatment for chronic thromboembolic pulmonary hypertension (CTEPH). Pulmonary endarterectomy (PEA) can effectively restore pulmonary blood perfusion, reduce pulmonary arterial pressure, and yield excellent outcomes. Evaluating PEA's effectiveness is crucial for enhancing patient management, boosting treatment success rates, and improving prognosis. This study explored the utility of quantitative analysis of pulmonary Ventilation/Perfusion (V/Q) scintigraphy in assessing PEA efficacy in CTEPH patients. ***Materials and Methods:*** This retrospective study included patients with CTEPH who underwent PEA at our hospital between April 2018 and December 2024. Enrolled patients underwent SPECT pulmonary V/Q scintigraphy within 2 weeks preoperatively and follow-up right heart catheterization (RHC) and V/Q scans 3-6 months postoperatively. We analyzed pre- and postoperative clinical data and parameters from RHC and SPECT V/Q scans. ***Results:*** Sixty patients were enrolled, including 43 (71.7%) male, with an average age of 49 ± 14 years. Post-PEA, significant improvements were observed in SPECT V/Q scan parameters, including total segmental perfusion defects (TSPDs), Begic's score, volume percentage of mismatched defects (VPMD) calculated by software, NYHA classification, six-minute walk distance (6MWD), NT-proBNP levels, and RHC-associated parameters [systolic pulmonary arterial pressure (sPAP), mean pulmonary arterial pressure (mPAP) and pulmonary vascular resistance(PVR)] (Table 1, P all < 0.001). The parameters of V/Q scans and clinical information presented a positive correlation with mPAP, sPAP, and PVR, with correlation coefficients (r) ranging from 0.44 to 0.51 and P all < 0.05. In 23 patients who underwent V/Q imaging 1-2 years postoperatively, TSPDs, Begic's score, and VPMD showed no significant changes compared to earlier postoperative assessments (P value: 0.33, 0.19, 0.14, respectively). ***Conclusion:*** PEA surgery leads to significant improvements in pulmonary perfusion, which presented positive correlations with hemodynamic parameters. Pulmonary blood flow perfusion tends to stabilize around six months post-surgery. Our findings underscore the value of quantitative V/Q scintigraphy analysis in evaluating postoperative outcomes in CTEPH patients.

EPS-090

Comparison of Three Diagnostic Strategies for Suspicion of Pulmonary Embolism: Planar Ventilation-Perfusion Scan (V/Q), Computed Tomography Pulmonary Angiography (CTPA), and Single Photon Emission Computed Tomography Ventilation-Perfusion Scan (SPECT V/Q): a multicenter, non-inferiority randomized controlled trial

R. Le Pennec[1], *P. Le Roux*[1], *P. Robin*[1], *F. Couturaud*[1], *M. Righini*[2], *A. Trinh-Duc*[3], *P. Roy*[4], *E. Leung*[5], *A. Helias*[6], *L. Bertoletti*[7], *C. Revel*[8], *O. Sanchez*[9], *J. Schmidt*[10], *C. Moreau-Triby*[11], *D. Goetghebeur*[1], *H. Robert-Ebadi*[12], *M. Blondon*[12], *D. Momboisse*[3], *P. Guillo*[1], *G. Le Gal*[5], *P. Salaün*[1];
[1]*Brest University Hospital, Brest, FRANCE,* [2]*HUG, Génève, SWITZERLAND,* [3]*Agen Hospital, Agen, FRANCE,* [4]*Angers University Hospital, Angers, FRANCE,* [5]*Ottawa Hospital, Ottawa, ON, CANADA,* [6]*Toulon Hospital, Toulon, FRANCE,* [7]*Saint Etienne University Hospital, Saint Etienne, FRANCE,* [8]*Saint Denis La Reunion Hospital, Saint Denis La Reunion, FRANCE,* [9]*APHP, Paris, FRANCE,* [10]*Clermont Ferrand University Hospital, Clermont Ferrand, FRANCE,* [11]*Lyon University Hospital, Lyon, FRANCE,* [12]*HUG, Genève, SWITZERLAND.*

Aim/Introduction: Nuclear medicine physician community has widely adopted single-photon emission computed tomography (SPECT) V/Q instead of planar ventilation/perfusion (V/Q) scan for pulmonary embolism (PE) diagnosis. However, to date, no management outcome study or randomized trial has evaluated an algorithm based on SPECT V/Q for PE diagnosis. Due to this lack of supporting evidence, ESC/ERS recommendations state: "SPECT may be considered for PE diagnosis with class of recommendation IIb (efficacy is less well established by evidence)". To fill this knowledge gap, and address the discrepancy between clinical and nuclear medicine physician' point of view, we conducted a randomized controlled trial comparing SPECT V/Q, CTPA, and

planar V/Q scan-based strategies in patients with suspected PE. NCT 02983760 ***Materials and Methods:*** In a multicenter, non-inferiority trial, we randomized patients with clinical suspected PE and either non-high pre-test probability but positive d-dimer, or high pre-test probability , into three arms using a diagnostic algorithm based on either SPECT V/Q, CTPA, or planar V/Q scan, with an unbalanced allocation (2:1:1). The primary outcome was the 3-month risk of venous thromboembolism (VTE) in patients left untreated after a negative diagnostic work-up, comparing SPECT V/Q patients to the combined group of CTPA and planar V/Q patients with a non-inferiority margin of 1%. Secondary outcomes included PE diagnosis rates. The trial was prematurely discontinued in October 2024 due to slow patient recruitment and funding expiry. ***Results:*** Between July 2017 and October 2024, we randomized 603 patients with either a positive d-dimer or high pre-test probability. PE was diagnosed in 61/303 (20.3%), 31/150 (20.7%) and 24/150 (16.1%) in the SPECT V/Q, CTPA and planar V/Q scan arms, respectively. The 3-month VTE risk among negative, untreated patients was 1/221 (0.5% ; 95%CI 0.0% to 2.5%), 0/107 (0.0% ; 95%CI 0.0% to 3.4%) and 1/118 (0.8% ; 95%CI 0.0% to 4.6%), respectively. The difference in the 3-month outcome rate between the SPECT V/Q and the combined CTPA and planar V/Q arm was 0% (95%CI -1.2% to 1.3%), p for non-inferiority 0.75. ***Conclusion:*** Although we could not demonstrate the non-inferiority of SPECT V/Q as compared with CTPA and planar V/Q based strategies, the 3-month risk of VTE in patients left untreated after a negative SPECT V/Q was in range with accepted standards, supporting the safety of ruling out PE based on a negative SPECT-based algorithm. PE diagnosis rate was in line with that observed when using previously validated imaging modalities.

EPS-091

Optimizing Quantitative ^{177}Lu SPECT-CT: Effects of OSEM Parameters and Deadtime

R. Albergueiro[1,2], *A. Carvalho*[1], *J. Santos*[2];
[1]*Unidade Local de Saúde do São João, Porto, PORTUGAL,* [2]*IPO Porto Research Center, Porto, PORTUGAL.*

Aim/Introduction: Quantitative SPECT-CT imaging plays a crucial role in dosimetry after ^{177}Lu radiopharmaceutical therapy. This study aims to optimize quantification by: (1) evaluating the influence of OSEM reconstruction parameters; (2) assessing gamma camera performance via deadtime (DT) analysis in post-therapy acquisitions to define optimal imaging timing; and (3) investigating the stability of the calibration factor (CF) using consistent acquisition and reconstruction conditions. ***Materials and Methods:*** A NEMA IEC phantom containing six spherical inserts was filled with 7.9GBq of ^{177}Lu, using a sphere-to-background ratio of approximately 10:1. Ten SPECT-CT time point acquisitions were performed on a Symbia Intevo 6 system at decreasing activity levels, using a 208keV±10% energy window. Images were reconstructed using OSEM with Hybrid Recon™, varying the number of iterations from 8 to 32 while fixing the number of subsets at 4. Quantitative and qualitative metrics were assessed, including contrast recovery coefficients (CRCs), coefficients of variation (CV), contrast-to-noise ratio (CNR), CF, and activity recovery coefficients (ARCs). Following reconstruction parameter optimization, the system's count rate performance was analyzed by plotting measured count rate versus true activity and fitting the data to a paralyzable detector model to estimate DT. CF was evaluated across all time points to confirm consistency over a broad activity range. ***Results:*** The optimal balance between contrast, noise, and activity quantification was achieved with OSEM reconstruction using 24 iterations and 4 subsets. This configuration yielded the highest CRCs and ARCs across all spheres, while maintaining a CV around 5%. All spheres were detectable according to the Rose criterion, indicating adequate CNR. The CF remained stable at (18.3 ± 0.3)cps/MBq, regardless of the iteration number. Count rate analysis showed a linear relationship with activity, with a slope of (17.97 ± 0.02)cps/MBq and an R^2 of 0.9988. Fitting to a paralyzable model was not applicable due to the absence of detector saturation, indicating that SPECT/CT acquisitions can be performed on the day of therapy without significant DT effects. CF values were consistent across all time points, averaging (18.0 ± 0.5)cps/MBq and ranging from 17.3 to 18.7cps/MBq, further supporting the minimal impact of DT. ***Conclusion:*** OSEM reconstruction with 24 iterations and 4 subsets provided optimal image quality and quantification. The linear detector response and consistent calibration factors confirm negligible DT effects, even at activities up to 8 GBq, due to the low γ yield and minimal bremsstrahlung of ^{177}Lu. These findings support reliable quantitative SPECT-CT for post-therapy dosimetry, protocol standardization, and inter-patient dose comparison.

EPS-092

Acquisition and Reconstruction Parameters for ^{32}P Imaging in a CZT Gamma Camera

P. Guardiola-Zaragoza[1], *D. Sánchez-Artuñedo*[1], *I. Navales-Mateu*[2], *M. López-Arribas*[2], *D. Borrás-Sánchez*[2], *C. Gamez-Cenzano*[2], *M. Beltran-Vilagrasa*[1];
[1]*Servei de Física i Protecció Radiològica. Hospital Universitari Vall d'Hebron, Barcelona, SPAIN,* [2]*Servei de Medicina Nuclear. Hospital Universitari Vall d'Hebron, Barcelona, SPAIN.*

Aim/Introduction: Phosphorus-32 (^{32}P), a pure beta emitter, is implanted intratumoral for the treatment of locally advanced pancreatic cancer. After treatment, a bremsstrahlung SPECT/CT image is acquired to verify the correct administration. Post-treatment imaging is challenging due to the low administered activities and the bremsstrahlung spectra. New CZT gamma cameras as StarGuide (GE Healthcare) have higher sensitivity, therefore could enhance ^{32}P SPECT imaging. This works aims to assess the minimum ^{32}P activity visually detectable in a StarGuide, and the acquisition and reconstruction parameters that improve image quality. ***Materials and Methods:*** Syringes with different punctual activities of ^{32}P: 0.4, 0.8, 2.9, 4.5, 10.3 and 14.7 MBq were prepared. Each syringe was placed in a water-filled Jaszczack phantom. SPECT/CT images were acquired with acquisition parameters: •Time: 30 min. •Emission Window: 75 keV (±25%). Reconstruction parameters were: •Algorithm: Q.Clear (20 iterations, 10 subsets). •Regularisation method: RDP, γ=1, β=0.2. • Attenuation correction and resolution recovery correction. The camera sensitivity was calculated for each image. To assess the visual detectability of the syringes, reconstructions were created varying the acquisition time: 10 and 20 min. We determined the minimum activity visually detectable and its corresponding contrast-to-noise ratio (CNR) threshold value. We fitted a power curve of the CNR versus the product activity×time. Setting the CNR value to $CNR_{threshold}$, we established the formula relating the minimum acquisition time (t_{min}) and the administered activity. To assess the impact of the reconstruction parameters in the image quality, additional reconstructions were created varying iterations and subsets, regularisation method (MRP), and the γ and β values. For each SPECT we calculated the contrast, the CNR and the tomographic spatial resolution with the FWHM, the MTF50% and the MTF10%. ***Results:*** The mean camera sensitivity value was 15.7 cps/MBq. The minimum activity visually detectable was 0.8 MBq with a $CNR_{threshold}$ of 13.2. The fitted relation was $CNR = 0.8\times(activity\times time)^{0.5}-10.6$ (R^2=0.96). The t_{min} value regarding the administered activity can be calculated from: $activity \times t_{min} = 922.2$ MBq s. Using the MRP regularisation method, the mean FWHM in all directions was reduced by 0.9 mm, and the MTF50% and MTF10% increased by 0.002 mm^{-1}. Default reconstruction parameters optimized the CNR values. ***Conclusion:*** The minimum ^{32}P activity detectable in a StarGuide with a 30 min acquisition time is 0.8 MBq. Based on the administered activity, acquisition time can be tailored with the obtained formula. The MRP regularisation method improves tomographic spatial resolution.

EPS-093

Phantom-based characterisation of an ultra-fast and ultra-low-dose tomographic molecular breast imaging system

A. Cherlin[1], *K. Erlandsson*[2], *N. Atkins*[1], *M. Exley*[1], *I. Baistow*[1], *K. Thielemans*[2], *B. Hutton*[2];
[1]*Kromek Ltd, Sedgefield, UNITED KINGDOM,* [2]*Institute of Nuclear Medicine, University College London, London, UNITED KINGDOM.*

Aim/Introduction: Molecular Breast Imaging (MBI) demonstrates high sensitivity for the detection of breast cancer, particularly in dense breast tissue. Despite its diagnostic advantages, the clinical adoption of MBI has been limited by ~40 minutes acquisition time and higher radiation dose (~2.4 mSv) compared to mammography (~0.5 mSv). In alignment with the 2018 ACR recommendations, implementation of MBI for screening requires a reduction in radiation dose to ≤1 mSv. Also, a substantial decrease in scan time is required to improve patient throughput. In response to these requirements, a novel MBI prototype has been developed and evaluated. ***Materials and Methods:*** The prototype is comprised of two heads, each having a 4x6 array of 3D position-sensitive 5 mm thick CZT detectors covering the FOV of 132 mm x 88 mm, and a densely packed multi-pinhole 3D-printed tungsten collimator with 294 pinholes. The detectors have an 11x11 array of 2 mm pixels. The acquired images include significant multiplexing due to overlap of pinhole data, resulting in adverse artefacts which are mitigated by de-multiplexing algorithms that benefit from 3D position of interaction information. The detector data is analysed using a machine-learning model providing significant improvement in sub-pixel position resolution. The performance is characterised using Tc99m-filled phantoms comprised of 5 to 10 mm spherical lesions with uniform background. Non-Local Means noise filtering is applied to the reconstructed images. ***Results:*** Initial prototype evaluation using 2D projection images demonstrated a significant advancement in detector resolution, achieving 5×5 sub-pixelisation, or the position resolution of 450 µm and average depth resolution of ~700 µm. This improvement in the image resolution surpasses the performance of existing SPECT and MBI systems utilizing CZT detectors. The results have been validated through simulated and experimental image reconstructions, showing enhancement in image quality and improved de-multiplexing algorithm performance. Dose/time reduction factors were estimated based on published count density data for a standard administered 300 MBq clinical activity. Preliminary results show the reduction factor of 8 for ≥6 mm lesions. ***Conclusion:*** The novel detector, collimator and image reconstruction technology implemented in the prototype enhance the performance of tomographic image reconstruction and allow significant reduction of scan time while maintaining the radiation dose below 1 mSv. Current results show the potential to shorten the scan time from 40 to 10 min for ≥6 mm lesions. Further work on improving the results and comparison with an existing commercial MBI scanner is ongoing and will be reported.

610

Sunday, October 5, 2025, 16:45 - 18:15

Room 116

CTE 3 - Technologists Committee: Best Practice in Paediatric Inflammation & Infection Radionuclide Imaging - Heart, Bone and Joint, Kidney and Urinary Tract

OP-249

The [18F]FDG PET-CT in Inflammation of Unknown Origin Among Children

D. Albano*; ASST Spedali Civili of Brescia, Università degli di studi of Brescia, Brescia, ITALY.*

OP-250

Musculoskeletal Diseases – State-of-the-Art in Hybrid Imaging

B. Rodriguez-Alfonso*; Nuclear Medicine Department, Hospital Universitario Puerta de Hierro, Majadahonda, Madrid, SPAIN.*

OP-251

When the Kidneys Fail: The Urinary Tract Inflammation & Infection Molecular Diagnosis

R. Madru*; Medical Physicist at Skane University Hospital, Department of Medical Radiation Physics, Lund, SWEDEN.*

611

Sunday, October 5, 2025, 16:45 - 18:15

Room 111

Featured Session - Paediatrics Committee: Advances in Paediatric Molecular Imaging: Innovations in Oncology, Radiomics and Hybrid Technologies

OP-253

Invited Speaker

C. Olianti; ITALY.

OP-254

Impact of Interim ^{18}F-FDG PET/CT Metabolic Parameters and Deauville Score on Outcomes of Pediatric Hodgkin Lymphoma

O. Kodaz[1], *A. Pala*[1], *G. Kaya*[2], *B. Volkan Salanci*[1], *P. Ozgen Kiratli*[1];
[1]*Hacettepe University Department of Nuclear Medicine, Ankara, TÜRKIYE,* [2]*Yozgat City Hospital Department of Nuclear Medicine, Yozgat, TÜRKIYE.*

Aim/Introduction: Assessing interim 18F-FDG-PET/CT (iPET) scans in pediatric Hodgkin lymphoma (HL) patients present significant challenges. In addition to the established Deauville-Score (DS), metabolic parameters derived from PET/CT imaging, such as total lesion glycolysis (TLG), metabolic tumor volume (MTV), and quantitative PET (qPET), are also critical. This study aims to investigate the prognostic value of iPET in pediatric-HL patients by comparing visual analysis with semiquantitative analysis. ***Materials and Methods:*** iPET images of pediatric FDG-avid HL patients were evaluated retrospectively. Tumor-segmentation was defined using the threshold SUVmax of 2.5, and the MTV&TLG values were obtained. DS were also recorded for each patient. qPET was calculated by dividing the SUVpeak of residual tumors by the average liver uptake, which is measured using standardized volumes of interest. MTV&TLG values greater than 0 and DS values of 4 or higher were considered residual disease. Survival analysis and diagnostic parameters of each patient were examined. Death and disease progression were accepted as an event. Kaplan-

Meier curves and the log-rank test were used to compare survival experiences between metabolic PET parameters at cut-off values (ROC-curve and Youden Index). ***Results:*** A total of 50 pediatric-HL patients (F/M: 18/32; mean age: 12.4 year, SD: 3.92) who were diagnosed between 2014 and 2024 were included. Nodular sclerosing (54%) and mixed cellularity (20%) were the most common subtypes. On iPET scans, median MTV was 0 cm3 (range: 0-30.7), TLG was 0 (range: 0-109.81), DS was 2 (range: 1-5), and qPET was 0.465 (range: 0-3.43). On MTV&TLG analysis, 10 patients were positive for the minimal residual disease, while 17 were positive in the DS group. None of the patients was classified negative on DS but positive on MTV&TLG. Patients accepted positive with MTV&TLG and DS differed significantly from each other (p<0.001). Mean time to event was shorter in patients who were positive for both MTV&TLG and DS compared to those positive for only DS (52.4 vs 101.7; p=0.29). Cox analysis showed that the proportional hazard ratio was 5.3 for MTV&TLG positivity (lower 0.6 and upper 47.9, CI 95%; p=0.134). Positive-predictive value of MTV&TLG positivity was %70. The optimal cut-off value for qPET was found to be 1.53; qPET positivity was significantly associated with EFS (42.3 vs 106.7; p<0.001). ***Conclusion:*** MTV&TLG and DS assessments, although it didn't reach statistical significance, differ in pediatric HL patients. MTV&TLG appear superior to DS in these patients. Additionally, qPET values are predictive for EFS.

OP-255

The value of PET/MR in prognostic evaluation of nephroblastoma in children

Y. Xu*;*
Hangzhou Universal Medical Imaging Diagnostic Center, Hangzhou, CHINA.

Aim/Introduction: To assess the prognostic value of ^{18}F-FDG PET/MR-derived metabolic parameters and clinicopathological features in pretreatment nephroblastom. ***Materials and Methods:*** A retrospective cohort of 92 children with newly diagnosed nephroblastom undergoing ^{18}F-FDG PET/MR was analyzed. Clinicopathological variables (e.g., histology subtype, lymph node involvement, serum lactate dehydrogenase [LDH]) and metabolic indices, including maximum standardized uptake value (SUVmax), metabolic tumor volume (MTV), and total lesion glycolysis (TLG), were evaluated using univariate and multivariate Cox regression models to predict event-free survival (EFS) and overall survival (OS). ***Results:*** During a median follow-up of 42 months, disease progression or relapse occurred in 32 patients (34.78%). Univariate analysis revealed that, unfavorable histology (P=0.007), lymph node metastasis (P=0.004), elevated LDH (P=0.018), MTV (P=0.005), and TLG (P=0.008) were significantly associated with reduced EFS and OS. Multivariate analysis identified TLG (EFS: P=0.013; OS: P=0.017) and lymph node metastasis (EFS: P=0.025; OS: P=0.031) as independent prognostic factors for both endpoints. Additionally, MTV remained predictive of OS (P=0.029). ***Conclusion:*** Pretreatment ^{18}F-FDG PET/MR offers critical prognostic insights in pediatric nephroblastom. Higher TLG, lymph node metastasis, and increased MTV correlate with adverse outcomes, underscoring their potential for refining risk-adapted treatment strategies and improving clinical decision-making.

OP-256

Early TreatmentResponse Assessment with 68GaDOTANOC PET/CT: Superior Concordance with Clinical Outcome

N. Kundu*, D. Khan, S. Sagar, A. Mahalik, A. Roy, A. K. Pandey, R. Kumar;*
AIIMS New Delhi, Delhi, INDIA.

Aim/Introduction: Recent advancements in histopathological assessment and functional imaging modalities have significantly enhanced the diagnostic accuracy and restaging processes in pediatric neuroblastoma. These developments have facilitated more accurate quantification of tumor burden and improved evaluation of therapeutic response, thereby supporting more individualized and effective treatment stratification strategies.Although the International Neuroblastoma Response Criteria endorse the use of metaiodobenzylguanidine (mIBG) scintigraphy or [F-18]2-fluoro-2-deoxyglucose (FDG) PET/CT for disease evaluation, the present study aims to assess and compare the efficacy of 68Ga-DOTANOC PET/CT and mIBG scintigraphy in classifying early treatment response following induction chemotherapy in patients with high-risk neuroblastoma. ***Materials and Methods:*** 19 pediatric patients with known neuroblastoma underwent baseline and posttherapy 68GaDOTANOC PET/CT and 131ImIBG planar +/-SPECT/CT imaging after initial chemotherapy. Both the pre and post chemotherapy 68Ga-DOTANOC PET MIP and 131I-mIBG planar were compared to look for response assessment. Responses were defined by reduction/disappearance of DOTANOC or mIBG avid lesions and SIOPEN score decrease ≥50 % (partial) or 100 % (complete). Imaging findings were crosschecked with clinical/marrow status at 6 months. ***Results:*** Median follow-up period was 4 months, ranging from 2 to 11 months. Of these 19 patients, 12 underwent both 68Ga-DOTANOC and 131I-mIBG at baseline and follow-up. 18 out of 19 patients received chemotherapy, while one patient received mIBG therapy. Patients received an average of 5 chemotherapy cycles, with minimum of 3 cycles, and maximum of 8 cycles. Due to technical issues and unavailability of radiotracer, 7 patients underwent only 131I-mIBG on follow-up. DOTANOC and mIBG were concordant in 10/12 paired followups. All six complete/partial responses confirmed clinically were DOTANOCpositive; mIBG missed two partial responses owing to baseline underrepresentation of marrow disease. Two discordant cases (DOTANOCPR vs mIBGSD) involved extensive baseline DOTANOC+/mIBG- marrow spread that regressed on PET but remained occult on planar scans. Among 14 patients with available marrow histology, positivity at diagnosis predicted nonresponse (P = 0.03). Male sex also associated with poorer imaging outcome (P = 0.02). ***Conclusion:*** DOTANOC PET/CT demonstrates superior sensitivity to early therapeutic change, especially in initially mIBGoccult marrow metastases, and aligns more faithfully with shortterm clinical remission. Baseline marrow infiltration and male sex emerged as adverse predictors, suggesting intensified or alternative approaches for these subsets. Thus, DOTANOCbased response criteria may merit incorporation into future responseadapted protocols.

OP-257

Comparative Analysis of Diagnostic Efficacy:[^{68}Ga] DOTATATE PET/CT Versus[^{123}I]MIBG Scintigraphy in Paediatric Neuroblastoma Detection

N. Gülaldi*, A. Karacan;*
University of Health Sciences, Ankara Bilkent City Hospital, Department of Nuclear Medicine, Ankara, TÜRKIYE.

Aim/Introduction: [^{123}I]MIBG scintigraphy is used routinely for staging and treatment response evaluation of pediatric neuroblastoma patients. [^{68}Ga]DOTATATE PET/CT imaging has also gained popularity in recent years. We aimed to reveal the diagnostic performance of the Somatostatin PET/CT results to find if it is logical to add this modality for the clinical evaluation of the patients. ***Materials and Methods:*** Fourteen children diagnosed with neuroblastoma between March 2019 and July 2024 were included in the study (age-10 months-7 years). [^{68}Ga]DOTATATE PET/CT study was performed within 1 month in addition to the [^{123}I]MIBG scan with SPECT/CT study for the lesion area when the treatment administration was not started or was equal. Soft tissue and bone involvement groups were noted and because of their non-homogeneous distribution pattern, they were evaluated by the Wilcoxon-signed rank test. ***Results:*** 6 of 14 patients had

only soft tissue lesions detected by both imaging modalities. In 1 patient, soft tissue lesions were visualized with [^{68}Ga]DOTATATE in a larger area. In 3 patients, bone lesions were present and although detected by both imaging modalities, more bone lesions were recorded by [^{68}Ga]DOTATATE in 2 patients. In 1 patient, both imaging modalities were negative despite the presence of anatomical lesions. In 2 patients, bone marrow metastases were detected only with [^{68}Ga]DOTATATE PET/CT. 2 patients showed soft tissue uptake on [^{123}I]MIBG only. No statistically significant superiority was found between the two imaging modalities (p>0,05). Only borderline values were obtained with a hypothesis that [^{68}Ga]DOTATATE PET/CT was superior to [^{123}I]MIBG scan (p=0,07). ***Conclusion:*** According to our study, [^{68}Ga]DOTATATE PET/CT scan can be used as a complementary imaging modality in pediatric neuroblastoma patients. We believe that because of the superior image quality of PET/CT compared to SPECT/CT images, somatostatin imaging can detect a higher number of lesions, especially in bone and bone marrow if done in larger series. [^{123}I]MIBG scan looks like better delineates soft tissue involvement. We also believe that scoring should be performed by evaluating both modalities together especially if the treatment algorithm will change according to the presence of active metastatic bone lesions or soft tissue lesions.

OP-258

The value of ^{18}F-FDG PET/MR radiomic features in predicting WT1 and CTNNB1 mutations in nephroblastoma in children

Y. Xu;
Hangzhou Universal Medical Imaging Diagnostic Center, Hangzhou, CHINA.

Aim/Introduction: This study aims to evaluate the predictive capability of ^{18}F-FDG PET/MR radiomics features for identifying WT1 and CTNNB1 mutations in nephroblastoma in children, critical molecular alterations associated with tumor progression and therapeutic resistance. ***Materials and Methods:*** A retrospective analysis was performed on 115 nephroblastoma patients (median age 3.2 years, range 0.6-14.1 years). Clinical parameters, including tumor stage, histological subtype, and serum lactate dehydrogenase (LDH) levels, were incorporated into a clinical model (C_model). Radiomic features were extracted from pre-treatment PET/MR images using the PyRadiomics platform. The Least Absolute Shrinkage and Selection Operator (LASSO) regression was applied to select significant radiomic features and construct a radiomics model (R_model). Predictive performance of C_model, R_model, and a combined model (CR_model) was assessed via receiver operating characteristic (ROC) analysis. A nomogram integrating radiomics scores (rad-score) and clinical variables was developed. ***Results:*** Patients were stratified into a training cohort (n=80) and a validation cohort (n=35). LASSO identified 7 radiomic features for WT1 mutations and 6 features for CTNNB1 mutations. The R_model achieved AUCs of 0.91 (training) and 0.88 (validation) for WT1, and 0.89 (training) and 0.86 (validation) for CTNNB1. The C_model showed lower performance (AUCs: 0.74-0.78). The CR_model demonstrated superior predictive ability, with AUCs of 0.96 (WT1) and 0.94 (CTNNB1) in training, and 0.92 (WT1) and 0.90 (CTNNB1) in validation ($P < 0.05$). ***Conclusion:*** Pre-therapeutic ^{18}F-FDG PET/MR radiomics features effectively predict WT1 and CTNNB1 mutations in nephroblastoma, providing a non-invasive method to enhance molecular subtyping, risk stratification, and personalized treatment planning. This approach may reduce reliance on invasive biopsies and optimize clinical management.

OP-259

Incidental Detection of Non-Ossifying Fibroma in Pediatric Oncology: FDG PET/CT Features and Diagnostic Pitfalls

B. Arca[1], *E. G. Isik*[1], *Z. Bayramoglu*[2], *K. Aslaner*[1], *Z. G. Ozkan*[1], *S. Kuyumcu*[1];
[1]*Istanbul University, Istanbul Faculty of Medicine, Nuclear Medicine Department, Istanbul, TÜRKIYE,* [2]*Istanbul University, Istanbul Faculty of Medicine, Radiology Department, Istanbul, TÜRKIYE.*

Aim/Introduction: Non-ossifying fibromas (NOFs) are common benign bone lesions frequently encountered in radiological practice. Typically arising during childhood, they are often (~75%) detected incidentally in the second decade of life. NOFs are usually located in the metaphyseal-diaphyseal regions of the femur or tibia and may show increased FDG uptake on PET/CT, mimicking bone metastases. This study aims to evaluate the visual and quantitative features of incidentally detected NOFs in pediatric patients undergoing F-18 FDG PET/CT. ***Materials and Methods:*** F-18 FDG PET/CT scans performed in pediatric patients (≤18 years old) at our clinic between 2015 and 2024 were retrospectively analyzed. Patients were categorized based on clinical indications. Lesion localization and size were recorded. Mean and maximum standardized uptake values (SUVmax and SUVmean) were calculated and compared with the mediastinal blood pool, the liver (right lobe), and, if present, the primary tumor. ***Results:*** Among 1,500 pediatric FDG PET/CT scans, 40 lesions from 32 patients (mean age: 15 years (6-18); 62% male) were retrospectively evaluated. Clinical details are summarized in Table 1. Regarding the localization of the NOF lesions: 24 were located in the distal femur, 2 in the femoral head region, 11 in the proximal tibia, 1 in the distal tibia, and single cases in the humerus and iliac bone. The mean craniocaudal length of the lesions was 14.2 mm (8-70 mm). The average SUVmax and SUVmean were 2.9 (0.5-19.9) and 1.1 (0.2-4.0) respectively. Reference average SUVmax values were 2.1 (0.6-3.4) for the liver and 1.5 (0.4-3.4) for the mediastinal blood pool. Among 24 patients with malignancy, 6 had undergone surgery. In the remaining 18, the average SUVmax of the primary malignant lesions was 11,9 (3,3-24,5). SUVmax exceeded liver and mediastinal reference values in 48% (n:19) and 60% (n:24) of NOF lesions, respectively. In two patients, the NOF lesions demonstrated higher SUVmax values than the primary tumor (4.7 vs. 3.3 and 19.9 vs. 6.7). In this subgroup, the average NOF SUVmax was calculated as 4.4. ***Conclusion:*** Non-ossifying fibromas (NOFs) are common benign bone lesions typically asymptomatic in nature. However, their variable metabolic activity on FDG PET/CT can lead to misinterpretation as a malignant lesion, potentially impacting disease staging and clinical management. Therefore, the morphological clues from the CT component of PET/CT and, lesion localization are essential for accurate diagnosis and to avoid diagnostic pitfalls due to FDG uptake.

OP-260

Gallium-68 labelled satoreotide trizoxetan in pediatric patient with neuroblastoma: biodistribution and radiation dosimetry results

L. Teles[1], *R. van Rooij*[1,2], *M. van Noesel*[1,3], *A. Poot*[1,2], *N. Tolboom*[1,2], *A. Braat*[1,2,4];
[1]*Princess Máxima Center for Pediatric Oncology, Utrecht, NETHERLANDS,* [2]*University Medical Center Utrecht / Wilhelmina Children's Hospital, Utrecht, NETHERLANDS,* [3]*Division Imaging and Cancer, University Medical Center Utrecht, Utrecht, NETHERLANDS,* [4]*Netherlands Cancer Institute, Utrecht, NETHERLANDS.*

Aim/Introduction: The current clinical standard for neuroblastoma (NBL) imaging is based on metaiodobenzylguanidine (mIBG), which has multiple known limitations. These limitations can be overcome by somatostatin receptor (SSTR) targeted positron

emission tomography (PET/CT) imaging. Experience with SSTR2 agonists already exists, but a subsequent improvement will be SSTR2 antagonist imaging with [^{68}Ga]Ga-satoreotide trizoxetan ([^{68}Ga]Ga-SSO120 or [^{68}Ga]Ga-SATO).[1,2] This antagonist targets both active and inactive receptors, instead of active ones alone, potentially improving lesion detection. Here we present the biodistribution and radiation exposure results of [^{68}Ga]Ga-SATO PET/CT imaging in paediatric patients with NBL. ***Materials and Methods:*** After administering 2 MBq/kg of [^{68}Ga]Ga-SATO, a 60-min dynamic and a static PET/CT (2h post-injection) were acquired. Standardized uptake values (SUV_{max}, SUV_{mean}, SUV_{peak}) were measured in suspected tumour lesions and various tissue compartments. Tumour-to-liver ratios (TLR) were calculated. Organs were automatically segmented with TotalSegmentator, followed by manual adjustment in MIM Software. Radiation dose to various organs and the total-body effective dose were computed via OLINDA/EXM software V1.0 (based on a 5-year-old phantom model). ***Results:*** Five patients underwent dynamic [^{68}Ga]Ga-SATO PET/CT scanning with, in total, 17 suspected NBL lesions. Median administered activity was 2.5 MBq/kg (range 2.1-2.8 MBq/kg). At 60 min post-injection, mean tumour SUV_{max} and SUV_{peak} were 5.41 (1.89 - 18.27) and 3.72 (1.23 - 14.93), and TLR was 2.43. The highest exposure was in the bladder (22.3 ± 4.3 µSv/MBq) due to renal excretion of [^{68}Ga]Ga-SATO, like most radiopharmaceuticals. The effective dose was 0.0875 ± 0.0135 mSv/MBq. Quantitative analysis of imaging showed clear improvement over mIBG imaging. ***Conclusion:*** These results show that [^{68}Ga]Ga-SATO PET/CT is safe and feasible in NBL patients with a low effective radiation dose in individual organs, and that it is capable of detecting NBL lesions with a good target-to-noise ratio. Future work will directly compare the lesion detection ability of [^{68}Ga]Ga-SATO PET/CT against standard mIBG imaging. ***References:*** 1. Virgolini I, Bahri S, Kjaer A, et al. A Randomized, Factorial Phase II Study to Determine the Optimal Regimen for 68Ga-Satoreotide Trizoxetan as an Imaging Agent in Patients with Gastroenteropancreatic Neuroendocrine Tumors. J Nucl Med. 2022;63(3):376-383. doi;10.2967/jnumed.121.261936

OP-261

Stable clinical metrics of metabolic activity in synthetic CT based pediatric PET during and following treatment from a LAFOV scanner

S. Honoré d'Este[1], *M. E. Montgomery*[1], *F. L. Andersen*[1,2], *C. Schulze*[1], *E. S. Saxtoft*[1], *C. N. Ladefoged*[1], *K. F. Andersen*[1];
[1]*Department of Clinical Physiology and Nuclear Medicine, Copenhagen University Hospital, Copenhagen, DENMARK,*
[2]*Department of Clinical Medicine, University of Copenhagen, Copenhagen, DENMARK.*

Aim/Introduction: In a previous study, we demonstrated the potential of an Artificial Intelligence (AI) based synthetic Computed Tomography (sCT) generated from non-attenuation correction (NAC) Positron Emission Tomography (PET) data for use in attenuation correction in a pediatric population. The model allows for elimination of the additional and conventionally utilized AC-CT, reducing overall radiation exposure while limiting motion artefacts and inconsistencies due to hyperdense CT structures. The improved image quality ensures more definitive tumor margins and ultimately leads to superior tumor delineation. This study aims to quantify clinical metrics to evaluate diagnostic performance of the AI based sCT for PET attenuation correction both during initial staging and treatment response assessment in the same pediatric cohort. ***Materials and Methods:*** 14 oncologic pediatric patients (1y-17y) with [18F]FDG avid lesions were included. Four patients had multiple scans performed during the inclusion period, leading to an included total of 20 scans from the initial test cohort[1]. Imaging was performed on 106cm Long-Axial-Field-Of-View (LAFOV) PET/CT. An ultra-low-dose CT (ULDCT) was acquired for conventional attenuation correction. A standard protocol of 1.5MBq/kg [18F]FDG administered 60min prior to 5min scanning was applied. The sCT was generated from the NAC-PET data, through a 3D parameter transferred conditional generative adversarial network (cGAN), previously described in detail[2]. Attenuation correction was performed two ways: from the sCT (sPET) and from the conventional ULDCT (cPET). Blinded lesion delineation and corresponding background liver volume-of-interests (VOI), diameter of 3cm (1cm in two cases), were drawn for comparative and quantitative analysis. ***Results:*** A total of 55 lesions (n_{lung}=3, n_{bone}=7, $n_{soft\ tissue}$=45) were identified and analyzed. We measured no significant difference in image noise depicted as mean Coefficient Of Variance (COV) ± standard deviation (SD) (COV_{sPET}=0.07 ±0.03, COV_{cPET}=0.07 ±0.02, p=0.55), in maximal Standardized Uptake Value (SUV_{max}) (p=0.06-0.83) or in SUV_{peak} (p=0.09-1.00) in either tissue subgroup. In soft tissue lesions the sPET reached higher clinical metrics than cPET when comparing Metabolic Tumor Volume with threshold of 40%SUV_{max} (MTV) and Tumor Lesion Glycolysis (TLG) with a borderline significant difference observed (P_{MTV}=0.04, P_{TLG}=0.04). We found that these results remained constant during and following scheduled treatment in the four repeat patients. ***Conclusion:*** The sPET images demonstrate image noise equal to that of cPET. Further clinical metrics of metabolic activity in lung, bone and soft tissue lesions remained stable both during initial staging and following treatment indicating useability in response assessment criteria such as Deauville and PERCIST. ***References:*** [1] doi:10.3390/diagnostics14242788 [2] doi:10.3390/diagnostics13243661

OP-262

Potential for Shortening Acquisition Time or Administered Activity in Paediatric Bone Scans with a 360-Degree Digital SPECT/CT Camera

Z. Bar-Sever[1], *S. Caduri*[1], *A. P. Steinmetz*[2];
[1]*Schneider Children's Medical Center of Israel, Petach Tikva, ISRAEL,* [2]*Rabin Medical Center, Petach Tikva, ISRAEL.*

Aim/Introduction: To determine if the superior sensitivity and spatial resolution of 360-degree CZT Digital SPECT/CT cameras over conventional SPECT/CT allows shortening of acquisition time or dose reduction in pediatric bone scans ***Materials and Methods:*** 22 successive bone scans of children (ages 3-17, mean 10.2 years) were retrospectively analyzed. Injected activity was based on the EANM dosage calculator. Vendor-recommended acquisition included a blood pool (BP) SPECT covering the trunk, pelvis, and lower extremities (50 seconds per bed position), and whole-body skeletal SPECT (trunk and pelvis, 5 minutes per bed, head and feet, 3 minutes). Original study counts (100%) were truncated by 30% and 50% to simulate acquisition time or dose reduction. The 100%, and the resulting 70%, and the 50% count groups were reconstructed using similar OSEM parameters without CT-based attenuation correction or image enhancement. All reconstructions were presented in random order to an experienced reader blinded to the clinical and truncation data. Each reconstruction was evaluated for the following parameters: Overall blood pool and skeletal image quality (Likert scale 1-5). Uptake in 4 skeletal landmarks (1st metatarsal growth center, metacarpophalangeal joints, occipital protuberance, and anterior ribs) was graded 0-2 and summed. Abnormal tracer uptake was recorded. Differences between count groups were analyzed with the Mann-Whitney U test. ***Results:*** Mean Likert scores for the 100%, 70%, and 50% groups were 4.45, 4.09, and 3.81 for the whole-body skeletal SPECT, and 4.09, 3.53, and 3.27 for the BP SPECT, respectively. No significant differences were noted between the 100% and 70% skeletal SPECT groups. Differences were significant between the 100% and 50% skeletal SPECT and between the 100%, 70%, and 50% BP SPECT groups. The visibility of kidneys, ureters, and arteries was not significantly different between the groups. The mean cumulative skeletal landmark score was 6.5, 6.27, and 5.95 for the 100%, 70%, and 50% count groups, with no statistically significant differences.

Abnormal uptake was present in 7 studies and interpreted as spondylolysis, osteomyelitis (2 cases), fibrous dysplasia, condylar hyperplasia, and osteoid osteoma (2 cases). These findings were all seen on the BP and skeletal phase SPECT following 30 and 50% count truncations (except for condylar hyperplasia on the 50% truncation). ***Conclusion:*** Reducing vendor-recommended acquisition time or the EANM-recommended injected activity by 30% does not compromise the diagnostic quality of pediatric bone scans when performed with a 360-degree digital CZT SPECT/CT camera. These preliminary observations should be substantiated in larger cohorts.

701

Monday, October 6, 2025, 08:00 - 09:30
Auditorium

CME 5 - Thyroid Committee: Parathyroid Carcinoma: Rare but Complex

OP-263
Beyond the Surface: Advanced Ultrasonographic Detection and Characterization of Parathyroid Carcinoma
M. Tuncel; *Hacettepe University, Department of Nuclear Medicine, Ankara, TÜRKIYE.*

OP-264
From Detection to Decision: [99mTc]MIBI Scintigraphy in Parathyroid Cancer Mapping
A. Campennì; *University of Messina, Department of Biomedical and Dental Sciences and Morpho-Functional Imaging, Messina, ITALY.*

OP-265
[18F]fluorocholine PET/CT(MR): A Molecular Beacon in Parathyroid Cancer Imaging
M. W. Huellner; *University Hospital Zurich, Department of Nuclear Medicine, Zurich, SWITZERLAND.*

OP-266
Decoding Parathyroid Malignancy: [18F]FDG and beyond
D. Deandreis; *Gustave Roussy and Paris Saclay University, Nuclear Medicine and Endocrine Oncology, Paris, FRANCE.*

702

Monday, October 6, 2025, 08:00 - 09:30
Room 112 (Arena)

Special Track 5 - Inflammation & Infection: Debate: WBC Scintigraphy Scan vs FDG PET/CT in Musculoskeletal Infections

OP-267
WBC Scintigraphy in Musculoskeletal Infections
C. Lauri; *Sant'Andrea Hospital, "Sapienza" University of Rome, Department of Medical-Surgical Sciences and of Translational Medicine, Rome, ITALY.*

OP-268
FDG-PET/CT in Musculoskeletal Infections
E. Arnon-Sheleg; *Galilee Medical Center, Departments of Nuclear Medicine and Diagnostic Radiology, Nahariya, ISRAEL.*

703

Monday, October 6, 2025, 08:00 - 09:30
Room 113

LIPS Session 5 - Dosimetry Committee: Statistical Analysis in Clinical Studies and Specifically in Dosimetry

OP-270
Statistics for Clinical Trials and Dosimetry Studies (Basics and Practice)
L. Strigari; *IRCCS Azienda Ospedaliero-Universitaria di Bologna, Department of Medical Physics, Bologna, ITALY.*

OP-271
Routine or Puzzling Concepts? Uncertainty, Bias, Accuracy and Others (Basics and Practice)
M. Brambilla; *AOU Maggiore della Carità, Novara, Department of Medical Physics, Novara, ITALY.*

OP-272
Correlations and Models (Basics and Practice)
O. Ivashchenko; *University Medical Centre Groningen, Groningen, NETHERLANDS.*

OP-273
How Statistical Methods Can Improve Dosimetry?
G. Glatting; *Universitätsklinikum Ulm, Nuklearmedizin, Ulm, GERMANY.*

704

Monday, October 6, 2025, 8:00 - 9:30
Room 114

M2M Track - TROP Session - Radiopharmaceutical Sciences + Translational Molecular Imaging & Therapy Committee: Preclinical Therapy - Various Targets

OP-274
Engineered Helper Lipid Extracellular Vesicles for Pulmonary siRNA Delivery: PET Imaging-Guided Therapy of Lung Metastasis
R. Guo, *X. Lan, R. An, D. Jiang;*
Department of Nuclear Medicine, Union Hospital, Tongji Medical College,Huazhong University of Science and Technology, Wuhan, CHINA.

Aim/Introduction: Pulmonary diseases, including malignancies and chronic airway diseases, pose substantial global health challenges requiring advanced therapies. While extracellular vesicles (EVs) show promises as natural delivery vectors, their clinical application is limited by hepatic tropism. To date, no rational design for selectively lung-targeted EVs has been developed. We modulated tumor-derived microvesicles (TMVs) with cationic DOTAP lipids to alter their internal charge and tissue tropism. We accurately tracked the biodistribution of TMVs-DOTAP in vivo via high-sensitivity positron emission tomography (PET) imaging, indicating their enhanced lung-targeting specificity. Furthermore, we developed an innovative siRNA delivery system, TMVs-DOTAP/siPD-L1, which specifically and effectively targets PD-L1 and enhances tumor immune responses. Mechanistic studies revealed the role of the protein corona in determining tissue tropism. ***Materials and Methods:*** To prepare TMVs-DOTAP, the DOTAP solution dissolved in anhydrous ethanol (50 mg/mL) was mixed with TMVs in a 1:10 volume ratio. PET/CT imaging was conducted to observe the distribution of ^{68}Ga-TMVs and ^{68}Ga-

TMVs-DOTAP in healthy mice, using a micro-PET/CT scanner. To assess the knockdown efficiency of PD-L1 protein, TMVs-DOTAP/siNC and TMVs-DOTAP/siPD-L1 were incubated with B16F10 cells for 48 h. Subsequently, intrapulmonary delivery and in vivo anti-tumor efficacy of TMVs-DOTAP/siPD-L1 were validated. Moreover, we systematically evaluated the compositional and quantitative alterations in the protein corona on TMVs-DOTAP/siNC. ***Results:*** The TMVs and TMVs-DOTAP were dispersed in PBS, with hydrodynamic diameters of 211.03 ± 17.94 and 241.81 ± 39.36 nm respectively. PET/CT imaging revealed that TMVs-DOTAP selectively accumulated in the lung (10.45 ± 0.32%ID/g at 0.5 h p.i.), while the signal in the liver significantly reduced to 2.15 ± 1.58%ID/g at 0.5 h p.i.. The results suggest that DOTAP modification enables tissue-specific retargeting of TMVs from the liver to the lung. Encouraged by the strong lung-targeting ability of engineered nanovesicles TMVs-DOTAP in vivo, we designed TMVs-DOTAP/siPD-L1 as a potential therapeutic strategy for lung metastasis. The TMVs-DOTAP/siNC group exhibited elevated levels of key pulmonary delivery-associated proteins, including fibrinogen, vitronectin, apolipoprotein A-I, and prothrombin, compared to the TMVs group. Our findings highlight the complex relationship between protein corona composition and organ-targeting outcomes of EVs. ***Conclusion:*** We developed a lung-targeted EVs platform, TMVs-DOTAP, and tested its feasibility using TMVs-DOTAP/siPD-L1 for the treatment of lung metastasis. This platform circumvents liver-specific delivery mechanisms, enabling effective access to lung tissue and enhancing therapeutic efficacy in the lung metastasis model. ***References:*** Selective organ targeting (SORT) nanoparticles for tissue-specific mRNA delivery and CRISPR-Cas gene editing. Nat Nanotechnol 15, 313-320 (2020).

OP-275

Preclinical Comparison of [^{161}Tb]Tb-NM600 and [^{177}Lu]Lu-NM600 in a Murine Triple Negative Breast Cancer Model

Y. Medina Guevara, *H. Comas Rojas, O. Bio Idrissou, L. Lambert, A. Pinchuk, L. E. Wehner, A. Carston, N. Clemons, J. Weichert, R. Hernandez;*
University of Wisconsin-Madison, Madison, WI, UNITED STATES OF AMERICA.

Aim/Introduction: Triple-negative breast cancer (TNBC) is characterized by aggressive behavior, a high propensity for metastatic spread, and poor survival. These outcomes are largely attributable to the frequent presence of micrometastatic disease at diagnosis and the lack of effective molecularly targeted therapies. To improve the clinical efficacy of radiopharmaceutical therapy (RPT) in TNBC, we evaluated NM600, an alkylphosphocholine analog that demonstrates enhanced tumor uptake and retention. NM600 was used to deliver Terbium-161, whose Auger/Conversion electron emissions are optimally suited for treating disseminated and occult disease. ***Materials and Methods:*** We radiolabeled NM600 with ^{161}Tb and ^{177}Lu under similar reaction conditions and molar activity. The radiochemical stability of the compounds was assessed in saline and human serum using iTLC. For in vitro cytotoxicity studies, 4T1 cells (metastatic murine TNBC) were incubated with increasing activities of free ^{177}Lu or ^{161}Tb (0-2 MBq/mL), or with their respective NM600-labeled forms, and cell viability was measured. In vivo, therapy studies were conducted in 8-week-old female Balb/c mice (***n*** = 5 per group) bearing 4T1 tumors. Mice were intravenously injected with [^{161}Tb]Tb-NM600 (250 or 500 µCi), [^{177}Lu]Lu-NM600 (250 µCi), or vehicle. Tumor growth, animal survival, and overall well-being were monitored thrice weekly. Treated mice also underwent serial SPECT/CT scans from 2 to 168 hours post-injection (p.i.) to evaluate radioligand biodistribution and estimate radiation dosimetry. Toxicological studies conducted in 8-week-old female Balb/c mice are currently underway to assess the safety profile of [^{161}Tb]Tb-NM600. ***Results:*** [^{161}Tb]Tb-NM600 achieved >95% radiolabeling yield and radiochemical purity, remaining stable in human serum for up to 168 hours (~98 %). Treatment with free ^{161}Tb and ^{177}Lu showed non-statistically differences, but [^{161}Tb]Tb-NM600 resulted in statistically significant increased cytotoxicity at 2 MBq/mL (p=0.03), compared to [^{177}Lu]Lu-NM600, highlighting the dosimetric advantage of ^{161}Tb's low-energy Auger electrons. SPECT/CT imaging revealed higher tumor uptake of [^{161}Tb]Tb-NM600 compared to [^{177}Lu]Lu-NM600, with mean committed tumor doses of 50 Gy and 30 Gy, respectively. In therapeutic studies, mice treated with [^{161}Tb]Tb-NM600 exhibited tumor regression and prolonged survival compared to control or those receiving the [^{177}Lu]Lu-NM600. Overall survivals of 11, 21, and 29 days were recorded for vehicles, [^{177}Lu]Lu-NM600 and [^{161}Tb]Tb-NM600, respectively. No overt radiotoxicity was observed with either treatment. ***Conclusion:*** Our findings demonstrate the enhanced pharmacologic profile of [^{161}Tb]Tb-NM600, resulting in superior dose deposition and therapeutic efficacy compared to [^{177}Lu]Lu-NM600. These results reinforce the promise [^{161}Tb]Tb-NM600 as a compelling RPT agent, particularly for the treatment of residual or micrometastatic disease.

OP-276

Radium-223-Loaded Radioactive Metal-Organic Framework Induces Alpha-Particle-Driven PANoptosis to Halt Cancer Progression

F. Yu[1], *J. Zhang*[1], *K. Kabayama*[2], *K. Fukase*[2], *T. Watabe*[2], *Y. Feng*[3], *K. Shi*[4];
[1]*Department of Nuclear Medicine, Shanghai Tenth People's Hospital and Institute of Nuclear Medicine, School of Medicine, Tongji University, Shanghai, CHINA,* [2]*Institute for Radiation Sciences, Osaka University, Osaka, JAPAN,* [3]*Department of Radiology, Duke University Medical Center, Durham, NC, UNITED STATES OF AMERICA,* [4]*Department of Nuclear Medicine, Inselspital, University of Bern, Bern, SWITZERLAND.*

Aim/Introduction: Radium-223 (^{223}Ra) is a potent alpha-particle-emitting radionuclide that effectively induces double-strand DNA breaks in tumor cells, which makes it a promising candidate for cancer therapy. However, the precise mechanisms of action of ^{223}Ra, beyond its DNA damage capabilities, remain poorly understood. This study aims to explore the effects of ^{223}Ra on gene expression related to PANoptosis, a cell death mechanism that integrates pyroptosis, apoptosis, and necroptosis, in Lewis lung carcinoma (LLC) cells. The study also investigates the potential of ^{223}Ra-MOF-74(Fe) nanoplatforms in enhancing therapeutic efficacy and overcoming apoptosis resistance in cancer therapy. ***Materials and Methods:*** In this study, a ^{223}Ra-MOF-74(Fe) nanoplatform was developed to deliver radium-223 to the target cells. RNA sequencing was employed to analyze gene expression changes in LLC cells treated with the nanoplatform, with a focus on pathways related to PANoptosis. In vitro experiments were conducted to measure the production of reactive oxygen species (ROS) and assess mitochondrial dysfunction. Tumor growth inhibition was evaluated in vivo, and off-target toxicity was assessed to determine the safety profile of the treatment. ***Results:*** The RNA sequencing analysis revealed that treatment with ^{223}Ra-MOF-74(Fe) significantly alters gene expression patterns associated with PANoptosis, resulting in the activation of pyroptosis, apoptosis, and necroptosis pathways. In vitro experiments showed that ^{223}Ra-MOF-74(Fe) markedly increased ROS production and caused mitochondrial dysfunction in LLC cells. These cellular effects were associated with the activation of PANoptosis pathways. In vivo, ^{223}Ra-MOF-74(Fe) demonstrated strong tumor growth inhibition in LLC tumor-bearing mice, with minimal off-target toxicity, suggesting its potential as an effective cancer treatment with a favorable safety profile. ***Conclusion:*** This study provides new insights into the novel mechanism by which ^{223}Ra-MOF-74(Fe) induces PANoptosis in tumor cells. By enhancing ROS production and mitochondrial dysfunction, ^{223}Ra-MOF-74(Fe) activates the PANoptosis pathways, offering a promising strategy to overcome apoptosis resistance in cancer therapy. The results demonstrate the therapeutic potential of this nanoplatform in inhibiting tumor growth while minimizing toxicity, providing a new avenue for effective cancer treatment.

OP-277

Conjugation and Radiolabelling of anti-EphA3 Antibody [^{225}Ac]Ac-macropa-tzPEG$_3$Sq-chIIIA4 and Preclinical Evaluation in a Murine Glioblastoma Model

C. Wichmann[1], *K. Morgan*[2], *L. Osellame*[1], *Z. Cao*[1], *N. Guo*[1], *H. Gan*[1], *I. Burvenich*[1], *P. Donnelly*[2], *A. Scott*[1];
[1]*Olivia Newton-John Cancer Research Institute, Heidelberg, AUSTRALIA,* [2]*University of Melbourne, Parkville, AUSTRALIA.*

Aim/Introduction: Alpha-particle based radioimmunotherapy has shown success in clinical malignancies. ^{225}Ac-Labelled antibodies or peptides demonstrated effective treatment in patients with myeloid leukemia or mCRPC. Macropa is a promising chelator capable of forming stable complexes with Ac-225. Here we explore radioimmunotherapy with ^{225}Ac-labelled H$_2$macropa-chIIIA4 which binds EphA3 receptor on tumour cells as well as in the tumour microenvironment. ***Materials and Methods:*** Conjugation of chIIIA4 to H$_2$macropa-tzPEG$_3$SqOEt and radiolabelling with Ac-225 was optimized. Affinity of immunoconjugates was confirmed using FACS. Radioimmunoconjugates were characterised by TLC, HPLC, and immunoreactive fraction, and stability evaluated in human serum. In-vitro efficacy of [^{225}Ac]Ac-macropa-tzPEG$_3$-chIIIA4 (^{225}Ac-chIIIA4) in U251 glioma cells was evaluated against ^{225}Ac-IgG1, ^{225}Ac-only, and chIIIA4 controls using MTS cytotoxicity assays. Biodistribution of ^{225}Ac-chIIIA4 and ^{225}Ac-IgG1 control was determined in a murine U251 xenograft model. In-vivo therapy studies with ^{225}Ac-chIIIA4 were performed in the same model and evaluated against ^{225}Ac-labelled and unlabelled controls. ***Results:*** Labelling of H$_2$macropa-tzPEG$_3$Sq-chIIIA4 with Ac-225 showed quantitative conversion after 15 and 5 minutes for 10^{-7} M and higher concentrations of chelator, respectively. At EOS, typical apparent specific activity was 37 MBq/mg and radiochemical purity was always >99%. SE-HPLC of unlabelled and ^{225}Ac-labelled immunoconjugates showed negligible levels of protein aggregation and immunoreactivity in U251 cells was >98%. Stability in human serum was excellent with radiochemical purity and immunoreactivity >95% and 60% after 7 days, respectively. In-vitro efficacy of ^{225}Ac-chIIIA4 in U251 cells was evident in cytotoxicity assays, although low grade bystander effects were observed with ^{225}Ac-containing controls. Biodistribution of ^{225}Ac-chIIIA4 in U251 murine xenograft models showed maximum tumour uptake of 20 %ID/g on day 2 post-injection. General organ uptake was low (<9 %ID/g) apart from high uptake in spleen and liver which naturally express EphA3 receptor. Single-dose treatment with ^{225}Ac-chIIIA4 (18.5 kBq) was well tolerated and demonstrated significant, sustained tumour growth inhibition, with all mice achieving at least partial response at study termination (day 53 post-treatment). Mice in the chIIIA4 treated cohort reached ethical endpoint on day 13 due to progressive disease. Mean tumour volume in the ^{225}Ac-chIIIA4 cohort was significantly lower compared to the ^{225}Ac-IgG1 treated cohort (7.4±4.5 mm3 vs 226±70 mm3, p=0.0022) with all mice in the latter cohort showing progressive disease. ***Conclusion:*** Radiosynthesis of ^{225}Ac-chIIIA4 was achieved in quantitative radiochemical yield and passing quality control criteria typical for clinically applied radiopharmaceuticals. In-vivo therapy studies showed prolonged survival and eradication of tumours in the ^{225}Ac-chIIIA4 treated cohort compared to controls.

OP-278

Preclinical Assessment of ^{177}Lu- and ^{161}Tb-Labeled DZ-HX3 Cyanine Probes for Theranostic Targeting of Solid Tumors

W. Wang[1], *M. Huang*[1], *Y. Wang*[2], *R. Wang*[1], *Y. Zhang*[3], *R. Tian*[1];
[1]*Department of Nuclear Medicine, West China Hospital, Sichuan University, Chengdu, CHINA,* [2]*Department of Nuclear Medicine and Clinical Nuclear Medicine Research Lab, West China Hospital, Sichuan University, Chengdu, CHINA,* [3]*Department of Biomedical Sciences, Cedars-Sinai Medical Center, Los Angeles, CA, UNITED STATES OF AMERICA.*

Aim/Introduction: Radionuclide-based agents with broad-spectrum antitumor activity and theranostic potential represent a promising approach to address tumor heterogeneity and therapeutic resistance. DZ-1, a heptamethine carbocyanine dye, demonstrates broad tumor selectivity through preferential uptake and mitochondrial/lysosomal localization in diverse cancer types. Previous studies showed that conjugating DZ-1 with chemotherapeutics facilitates efficient intracellular delivery and tumor suppression. This study developed and systematically evaluated the preclinical targeting, efficacy, and safety of ^{177}Lu- and ^{161}Tb-labeled DZ-HX derivatives. ***Materials and Methods:*** A modified DZ-HX3 platform was synthesized with enhanced molecular stability and metabolic properties. Cellular uptake was assessed in H1975, HeLa, and MIA PaCa-2 cell lines. In vitro validation included cell binding assays and dose-dependent cytotoxicity evaluations (0-3.7 MBq). Pharmacokinetic profiles were assessed via serum clearance studies and Micro-SPECT imaging. Biodistribution was analyzed across time points (4-168 h), comparing tumor and normal organ uptake. Therapeutic efficacy was evaluated in subcutaneous and orthotopic tumor models using single and multiple-dose regimens (18.5, 7.4, 3.7 MBq), combined with serial SPECT/CT imaging and tumor volume measurements. All studies included blood work and histopathology of major organs for safety assessment. ***Results:*** High uptake was observed in tumor cells, peaking at 5.45 ± 0.57% (HeLa) and 7.38 ± 0.21% (H1975). Cytotoxicity assays revealed dose-dependent reductions in viability, with 3.7 MBq exposure lowering cell viability to < 35% ($P < 0.0001$ vs. free radionuclides). Micro-SPECT/CT imaging showed rapid tumor localization within 24 h, peaking at 48 h (^{177}Lu-DZ-HX3: 13.85 ± 1.31 %ID/g; ^{161}Tb-DZ-HX3: 19.56 ± 0.99 %ID/g in HeLa). This differential uptake persisted in MIA PaCa-2 models (^{177}Lu-DZ-HX3: 11.39 ± 2.90 %ID/g; ^{161}Tb-DZ-HX3: 21.24 ± 6.84 %ID/g at peak), with both probes maintaining >7 %ID/g tumor retention at 96 h. The tumor-to-muscle ratio reached 24.62 ± 8.96, highlighting strong tumor specificity.Therapeutic outcomes reflected these pharmacokinetic advantages. High-dose ^{177}Lu-DZ-HX3 treatment achieved tumor inhibition rates of 87.20% (H1975), 93.90% (HeLa), and 90.61% (MIA PaCa-2), while ^{161}Tb-DZ-HX3 at 18.5 MBq showed 97.14% (HeLa) and 97.96% (MIA PaCa-2) inhibition. Fractionated low-dose ^{177}Lu-DZ-HX3 (11.1 MBq) induced complete remission in 43% of orthotopic lung cancer models, with no recurrence observed during 60-day monitoring. Treatment was generally well tolerated, with no significant histopathological findings or weight loss. ***Conclusion:*** ^{177}Lu- and ^{161}Tb-labeled DZ-HX3 demonstrated strong tumor targeting and therapeutic efficacy. While ^{161}Tb-DZ-HX3 showed slightly greater tumor uptake and inhibition, both agents effectively suppressed tumor growth, with ^{177}Lu-DZ-HX3 inducing complete remission in orthotopic models. These results support further development for targeted radionuclide therapy.

OP-279

Simultaneous Alpha- and Beta-Particle Digital Autoradiography for Evaluating Co-Therapy and Theranostic Differential Activity Uptake Distributions: Initial Results in Pre-Clinical Studies of Co-Injected Ac-225 with Lu-177 and with Diagnostic PET Tracers

B. W. Miller[1,2], *S. S. Rinne*[3], *N. Aguirre*[4], *B. Vaughn*[5], *A. Wacker*[6], *A. Le Roux*[4], *J. Kelly*[6], *S. M. Cheal*[6];
[1]*The University of Arizona, Tucson, AZ, UNITED STATES OF AMERICA,* [2]*QScint Imaging Solutions, LLC, Tucson, AZ, UNITED STATES OF AMERICA,* [3]*Uppsala University, Uppsala, SWEDEN,* [4]*Memorial Sloan Cancer Center, New York, NY, UNITED STATES OF AMERICA,* [5]*Convergent Therapeutics, Cambridge, MA, UNITED STATES OF AMERICA,* [6]*Weill Cornell Medicine, New York, NY, UNITED STATES OF AMERICA.*

Aim/Introduction: The development of a quantitative digital autoradiography system, called iQID (ionizing-radiation Quantum

Imaging Detector), represents a significant advancement in the field of molecular imaging. This system is capable of simultaneously imaging alpha- and beta-particle emissions (co-therapy electrons or positrons), providing enhanced resolution, quantification capabilities, and specificity in pre-clinical digital autoradiography studies. ***Materials and Methods:*** The iQID system leverages a novel particle discrimination method where alpha and beta particles are distinguished from one another based on event area and summed signal within the event cluster. We utilized the iQID device to simultaneously image alpha-emitting Ac-225 and beta-emitting tracers (labeled with Lu-177, Zr-89, or Ce-134) in pre-clinical organ samples. Organs samples were prepared by co-injection of 225Ac-labeled radioligands with their either Lu-177 (therapeutic electron), Zr-89 (diagnostic positron) or Ce-134 (diagnostic positron) labeled analogues. Monoisotope injections were included as control. Tissue was collected 24h after administration of the radioligand, flash frozen in OCT, and sectioned (7µm) on to Gadox (Gd2O2S) scintillation paper, which is sensitive to both alphas and beta emitters. Tumors and normal organs were imaged. Listmode data for each detected particle and energy cuts to discriminate between particles were used to construct digital autoradiographs (pixel values in units of counts detected) of total-counts images, alpha-only images, and beta-only images. ***Results:*** Distinct uptake patterns were observed between the alpha and beta emitters, exhibiting different uptakes at both cellular and sub-organ levels. The differences in signal acquisition between the particles suggest variability in tracer localization and retention, underscoring the importance of evaluating diagnostic and therapeutic strategies at resolutions higher than those achievable with PET or SPECT imaging. ***Conclusion:*** Our findings highlight the need in radiopharmaceutical development for precise analysis of radionuclide distributions at near-cellular levels. This study demonstrates the potential of the iQID system to facilitate the concurrent imaging of multiple particle types, offering a novel approach for evaluating complex radiopharmaceuticals and their therapeutic potential, particularly for co-therapies (e.g., Ac-225 and Lu-177) and positron radionuclide imaging pairs. ***References:*** Miller, Brian W., et al. "Quantitative single-particle digital autoradiography with α-particle emitters for targeted radionuclide therapy using the iQID camera." Medical physics 42.7 (2015): 4094-4105.

OP-280

Targeted Alpha Therapy (TAT) in AML: CD38 as a Promising Alternative to CD33

M. Sorin[1], *S. Gouard*[1], *S. Marionneau-Lambot*[1,2], *C. Maingueneau*[1], *A. Morgenstern*[3], *F. Bruchertseifer*[3], *M. Chérel*[1,4], *F. Haddad*[5,6], *M. Allard*[1], *J. Gaschet*[1];
[1]Nantes Université, Inserm, CNRS, Université d'Angers, CRCI2NA, Nantes, FRANCE, [2]Nantes University Hospital, Nantes, FRANCE, [3]European Commission, Joint Research Centre, Directorate for Nuclear Safety and Security, Karlsruhe, GERMANY, [4]ICO-René Gauducheau Cancer Center, Saint-Herblain, FRANCE, [5]GIP ARRONAX, Saint-Herblain, FRANCE, [6]Nantes Université, IMT Atlantique, CNRS-IN2P3, SUBATECH, Nantes, FRANCE.

Aim/Introduction: Acute Myeloid Leukemia (AML) is the most common leukemia in adults, characterized by a poor prognosis and a 5-year survival rate below 30%, largely due to chemoresistance. Targeted alpha-therapy (TAT) has emerged as a promising approach for treating disseminated tumors such as AML. Clinical trials using a [^{225}Ac]Ac-anti-CD33 monoclonal antibody (mAb) have demonstrated encouraging responses, as CD33 is expressed in 85-90% of AML cases. However, this approach is frequently associated with prolonged myelosuppression, primarily due to CD33 expression on normal hematopoietic cells. To broaden therapeutic options while minimizing off-target toxicity, we explored CD38 as an alternative and innovative target. CD38 is a well-established therapeutic antigen in multiple myeloma, where daratumumab, an anti-CD38 mAb, has shown remarkable efficacy. Although CD38 expression in AML is heterogeneous, daratumumab has demonstrated only modest anti-tumor activity in this context. We hypothesize that using [^{225}Ac]Ac-anti-CD38 mAb for TAT could overcome these limitations and provide a novel therapeutic strategy for AML, particularly in patients with higher CD38 expression than CD33. ***Materials and Methods:*** The human AML cell lines, MOLM-14 and THP-1 were characterized for their expression of CD33 and CD38 and use to establish disseminated preclinical AML models in NSG mice. Anti-CD33 and anti-CD38 mAbs underwent comprehensive characterization and their radiolabelling with [^{225}Ac] was optimized. The maximum tolerated activity (MTA) was determined in naïve animals. Efficacy studies were performed 6 days post-engraftment, assessing the impact of TAT on median survival (MS) of mice bearing either MOLM-14 or THP-1 disseminated AML models. ***Results:*** Both MOLM-14 and THP-1 cell lines expressed CD33 and CD38. MOLM-14 cells had a higher density of CD33 binding, while THP-1 cells showed greater CD38 expression. The MTA for [^{225}Ac]Ac-anti-CD33 mAb in naïve NSG mice was established at 0.5 kBq/g. Treatment with either [^{225}Ac]Ac-anti-CD33 or [^{225}Ac]Ac-anti-CD38 mAb at 0.5 kBq/g significantly prolonged MS in both disseminated MOLM-14 and THP-1 AML models compared to non-radiolabeled counterparts or a [^{225}Ac]Ac-isotype control mAb. Consistent with antigen expression, [^{225}Ac]Ac-anti-CD33 mAb was more effective in the MOLM-14 AML model compared to [^{225}Ac]Ac-anti-CD38 mAb. Conversely, in the THP-1 AML model, [^{225}Ac]Ac-anti-CD38 mAb demonstrated superior efficacy over [^{225}Ac]Ac-anti-CD33 mAb. Toxicity analyses are ongoing. ***Conclusion:*** This study demonstrates that CD38-targeted TAT could offer a promising alternative to CD33 in AML, potentially reducing off-target toxicity. In particular, for AML cases with higher CD38 expression than CD33, CD38-directed TAT could provide enhanced therapeutic efficacy, offering a novel therapeutic avenue for treating AML.

OP-281

The dose-response effects of ^{225}Ac-Labeled MOF regulates endoplasmic reticulum stress to induce antitumor immunity

F. Yu[1], *X. Luan*[1], *T. Watabe*[2], *Y. Feng*[3], *K. Shi*[4], *K. Kabayama*[2], *K. Fukase*[2];
[1]Department of Nuclear Medicine, Shanghai Tenth People's Hospital and Institute of Nuclear Medicine, School of Medicine, Tongji University, Shanghai, CHINA, [2]Institute for Radiation Sciences, Osaka University, Osaka, JAPAN, [3]Department of Radiology, Duke University Medical Center, Durham, NC, UNITED STATES OF AMERICA, [4]Department of Nuclear Medicine, Inselspital, University of Bern, Bern, SWITZERLAND.

Aim/Introduction: Radionuclide therapy has emerged as a critical modality for cancer treatment, with growing interest in its potential to activate immune responses. Alpha radionuclides are particularly notable for their unique characteristics of high energy and short range, allowing them to induce cell death with exceptional efficiency. Among alpha radionuclides, ^{225}Ac has gained significant attention for its clinical applications. This study investigates the mechanisms by which low-dose ^{225}Ac-labeled metal-organic frameworks (^{225}Ac/MOF) induce endoplasmic reticulum stress (ERS) and immune activation. ***Materials and Methods:*** ^{225}Ac/MOF was developed to deliver Actinium-225 to the target cells, the materials are characterized first to clarify their basic properties. Subsequently, cell experiments with different nuclide concentrations were conducted, including cytotoxicity tests, ROS generation determination, cell cycle experiments, apoptosis experiments. At the same time, the safety of ^{225}Ac/MOF material was also verified. The experiment conducted RNA sequencing for both high and low dose groups to verify the effects of different nuclide doses on cells. The relationship between endoplasmic reticulum stress and the activation of anti-tumor immunity at different doses was verified at the animal experiment level. ***Results:*** The results demonstrated that, compared to high-

dose treatment (11.10 kBq), low-dose radionuclide therapy (3.70 kBq) more effectively induces endoplasmic reticulum stress, significantly upregulating CHOP expression ($p < 0.01$). The increased CHOP level further promotes the translocation of HMGB1 from the intracellular to the extracellular space, ultimately eliciting a more pronounced antitumor immune response. Animal experiments also proved this point. Mice in the low-dose group (3.70 kBq) were superior to those in the high-dose group (11.10 kBq) in terms of tumor size and survival time. As for ERS and tumor immune activation markers, the low-dose group is also better than the high-dose treatment. ***Conclusion:*** In conclusion, our study reveals the mechanisms by which ^{225}Ac/MOF regulate ER stress to enhance antitumor immunity. The activation of the CHOP and HMGB1 pathways represents a key axis in this process. These findings provide new insights into optimizing radionuclide therapy strategies and provide a theoretical basis for incorporating ER stress-induced immune regulation into comprehensive cancer treatment regimens. Moreover, ^{225}Ac/MOF treatment exhibited a distinct dose-dependent effect, highlighting the importance of optimizing the dose to achieve a balance between therapeutic efficacy and minimizing adverse effects.

OP-282

^{191}Pt-labeled agents targeting tumor DNA in vivo: compound design and biological evaluation for targeted Auger electron therapy

H. Obata[1], *A. B. Tsuji*[1], *Y. Feng*[2], *M. R. Zalutsky*[2], *M. R. Zhang*[1]; *[1]National Institutes for Quantum and Radiological Science and Technology, Chiba, JAPAN, [2]Duke University Medical Center, Durham, NC, UNITED STATES OF AMERICA.*

Aim/Introduction: Pt-191-labeled agents are promising candidates for DNA-targeted Auger electron cancer therapy, but there has yet to be an established drug design that enables targeting tumor DNA efficiently in vivo. Herein, we explored linker structures for ^{191}Pt-labeled complexes targeting both tumor antigen and genomic DNA, and demonstrated DNA binding of novel ^{191}Pt-labeled complexes in targeted tumors in vivo. ***Materials and Methods:*** We synthesized six different conjugates composed of a trithiol ligand for ^{191}Pt labeling, Hoechst for DNA binding, and a glutamic acid-urea-lysine moiety for targeting prostate-specific membrane antigen (PSMA) (Trithiol-Hoechst-PSMA: THP1, 2-4, 2-8, 3-4, 3-8, 4). They contain different structures and lengths of linkers between either side of the trithiol ligand and Hoechst/the PSMA-targeted moiety. After ^{191}Pt labeling, the DNA binding ability and PSMA targeting specificity of the [^{191}Pt]Pt-THP complexes were evaluated in cell experiments, and their biodistribution was investigated in mice bearing tumors with/without PSMA expression. Finally, tumor DNA binding of [^{191}Pt]Pt-THP3-4 and 3-8 was evaluated in vivo. ***Results:*** All six [^{191}Pt]Pt-THP complexes were obtained with radiochemical yields of 60-80%, and ^{191}Pt-labeled products were successfully separated from their precursors. [^{191}Pt]Pt-THP3-4 and 3-8, in which Hoechst is on one side of the trithiol ligand across a linear PEG linker and the PSMA-targeted moiety on another side across a C4 linker, maintained PSMA targeting specificity and DNA binding ability in cultured cells than the other complexes. In vivo experiments for [^{191}Pt]Pt-THP3-4 and 3-8 showed rapid drug clearance from normal organs and long retention in the kidneys and tumors expressing PSMA. Notably, the two complexes exhibited almost the same DNA binding ratio in PSMA-positive tumors in vivo as in the cultured cells. ***Conclusion:*** This study demonstrated that two novel ^{191}Pt-labeled agents efficiently bind the genomic DNA of PSMA-positive tumors in vivo. Comparison of six different [^{191}Pt]Pt-THP complexes suggests that two linkers (1) a PEG linker between the trithiol ligand and the Hoechst compound and (2) a C4 linker between the trithiol ligand and the PSMA ligand were crucial for delivering ^{191}Pt-labeled complexes to tumor DNA. These findings would facilitate drug development using Pt radionuclide for radiopharmaceutical therapy, especially DNA-targeted Auger electron cancer therapy.

705

Monday, October 6, 2025, 8:00 - 9:30

Room 211

Cutting Edge Science Track - TROP Session - Physics Committee: PET/CT & PET/MR

OP-283

Evaluation of MRgTOF-BSREM PET Reconstruction for Accurate T Classification in Oral Cancer

M. Nogami[1,2], *J. Inoue Inukai*[3], *F. Zeng*[3], *N. Sugiyama*[3], *M. G. Spangler-Bickell*[4], *T. Kurimoto*[5], *K. Kubo*[1], *Y. Kiyono*[2], *T. Murakami*[3,1]; *[1]Department of Radiology, Kobe University Hospital, Kobe, JAPAN, [2]Biomedical Imaging Research Center, University of Fukui, Fukui, JAPAN, [3]Department of Radiology, Kobe University Graduate School of Medicine, Kobe, JAPAN, [4]GE HealthCare, Waukesha, WI, UNITED STATES OF AMERICA, [5]GE HealthCare, Hino, JAPAN.*

Aim/Introduction: For pretreatment staging of oral cancer, PET/MRI is known to outperform PET/CT in assessing local tumor extension due to its superior soft tissue contrast and simultaneous acquisition capabilities. However, PET inherently suffers from partial volume effects, leading to underestimation of tracer uptake. The newly proposed PET image reconstruction method—MR-guided Time-of-Flight Block Sequential Regularized Expectation Maximization (MRgTOF-BSREM)—leverages anatomical information from simultaneously acquired MRI to guide noise control in BSREM reconstruction, thereby allowing PET reconstruction with enhanced spatial resolution. The aim of this study was to evaluate the diagnostic performance of MRgTOF-BSREM for assessing local tumor invasion in oral cancer patients and to compare its semiquantitative metrics (SUV) with those of conventional reconstruction, in order to assess its clinical utility. ***Materials and Methods:*** A retrospective analysis was performed on 54 consecutive patients who underwent FDG PET/MRI for pretreatment staging of oral cancer. Head and neck PET list-mode data were reconstructed using MRgTOF-BSREM and the conventional TOF-Ordered Subset Expectation Maximization (TOF-OSEM) method. MRgTOF-BSREM reconstruction incorporated simultaneously acquired 3D T2-weighted sagittal MRI as a prior in BSREM, with both PET and MRI data corrected for motion using PET list-mode live reconstruction. Two readers independently interpreted fused PET/MRI images of the head and neck. Pathological findings after surgery were used as the reference standard. Agreement in T classification (TNM system) was assessed using the kappa statistic, and diagnostic confidence (rated on a 5-point scale) was compared using the Wilcoxon test. SUVmax of the primary tumor was measured and compared between methods using intraclass correlation coefficient (ICC) and Bland-Altman analysis. ***Results:*** Agreement with pathological T classification was higher with MRgTOF-BSREM (reader 1: $\kappa = 0.787$; reader 2: $\kappa = 0.749$) than with TOF-OSEM (reader 1: $\kappa = 0.738$; reader 2: $\kappa = 0.721$). Diagnostic confidence was significantly higher with MRgTOF-BSREM than with TOF-OSEM for both readers ($p = 0.038$ and 0.034, respectively). SUVmax of the primary tumor showed excellent correlation between MRgTOF-BSREM and TOF-OSEM (ICC = 0.975), with a minimal mean difference of 0.004 (upper and lower limits of agreements: 4.334 and -4.342, respectively). ***Conclusion:*** MRgTOF-BSREM PET reconstruction in PET/MRI improves diagnostic performance in assessing local tumor extension in oral cancer patients, while maintaining excellent quantitative agreement with conventional methods.

References: 1.Khalighi MM, et al. J Nucl Med.2020;61:1477-1477. 2. Spangler-Bickell MG, et al. J Nucl Med.2021 Feb;62(2):287-292. 3.Spangler-Bickell MG, et al. J Nucl Med.2022 Oct;63(10):1604-1610.

OP-284

BrainPET-7T: an Ultra-high filed MRI compatible PET insert for neuroscience

C. Lerche[1], *D. Niekaemper*[1], *J. Scheins*[1], *L. Tellmann*[1], *C. Régio Brambilla*[2], *C. Choi*[1], *E. Farrher*[1], *J. Felder*[1,3], *D. Arutinov*[4], *R. Heil*[4], *W. Silex*[4], *S. van Waasen*[4], *D. Grunwald*[5], *M. Lennartz*[5], *T. Meurer*[5], *G. Natour*[5,6], *B. Weissler*[7,8], *F. Mueller*[7], *D. Schug*[7,8], *E. Gegenmantel*[8], *H. Radermacher*[7], *O. Mülhens*[8], *M. Lang*[9], *P. Gebhardt*[10], *J. Lefaucheur*[11], *Z. Chen*[12], *G. Egan*[12], *V. Schulz*[7,8], *J. Shah*[1,13,14]; [1]*Institute of Neuroscience and Medicine 4, Forschungszentrum Jülich GmbH, Juelich, GERMANY,* [2]*Forschungszentrum Jülich GmbH, Institute of Neuroscience and Medicine 4, Jülich, GERMANY,* [3]*Affinity Imaging GmbH, Jülich, GERMANY,* [4]*Integrated Computing Architectures - Peter Grünberg Institute 4, Forschungszentrum Jülich GmbH, Juelich, GERMANY,* [5]*Institute of Technology and Engineering, Forschungszentrum Jülich GmbH, Juelich, GERMANY,* [6]*Mechanical Engineering, Rheinisch-Westfälische Technische Hochschule, Aachen, GERMANY,* [7]*Institute of Imaging & Computer Vision, Rheinisch-Westfälische Technische Hochschule, Aachen, GERMANY,* [8]*Hyperion Hybrid Imaging Systems GmbH, Aachen, GERMANY,* [9]*Institute of Neuroscience and Medicine 5, Forschungszentrum Jülich GmbH, Juelich, GERMANY,* [10]*Institute of Experimental Molecular Imaging, Rheinisch-Westfälische Technische Hochschule, Aachen, GERMANY,* [11]*Inviscan Imaging Systems SA, Strasbourg, FRANCE,* [12]*Monash Biomedical Imaging, Monash University, Clayton, AUSTRALIA,* [13]*Department of Neurology, Rheinisch-Westfälische Technische Hochschule, Aachen, GERMANY,* [14]*Affinity Imaging GmbH, Juelich, GERMANY.*

Aim/Introduction: Simultaneous MR/PET imaging offers a huge potential for neuroscience, especially for correlating processes of neuronal activity during cognitive or pharmacological challenges with the binding characteristics of neurotransmitters. We recently developed and built an ultra-high field MRI-compatible PET insert for neuroscientific imaging in humans with high sensitivity and high homogeneous spatial resolution. The design and the imaging performance of this system will be presented. ***Materials and Methods:*** The PET insert was built for a human 7T MRI scanner and comprises a total of 8 ultra-high field compatible PET modules in a carbon fibre housing. Each module has 3 × 5 pixelated scintillation detector blocks with three staggered layers of LSO scintillator coupled to arrays of digital SiPMs. The three staggered layers are used for depth of interaction detection. The BrainPET-7T insert is equipped with liquid cooling for optimal temperature stabilization, a low noise power supply unit, and a mostly (approx. 92% transmission) gamma-ray transparent 8-channel prototype transceiver array. In a baseline performance evaluation without MR system, we determined system sensitivity, noise-equivalent count rates (NECR), and spatial resolution (determined with mini-Derenzo phantom). In a second evaluation, we determined the PET inserts´ RF noise detectable with the MR system. We also measured prompt and true coincidence count rates with MP2RAGE, TSE, FLAIR, and EPI MR imaging sequences at different typical activities between 20 and 160 MBq and acquired simultaneous MR/PET images of different phantoms including fruits and an anthropomorphic head phantom. ***Results:*** The transversal spatial resolution was determined to be ≈ 1.6 mm at the isocentre and at 10 cm off-centre. No difference in spatial resolution was observed when comparing the spatial resolution from the baseline performance evaluation and from the performance evaluation with running MR. The peak NECR was measured to be 414 kcps at 12 kBq/ml and the system sensitivity with a shielded RF coil array was 57.2 kcps/MBq (energy window: 420-650 keV, coincidence window: 2.5 ns). During repetition of the NECR measurement with running MR sequences, no influence on coincidence resolving time, energy resolution, and count rates by MR sequences was observed for the tested sequences. No visible image artefacts were observed in MR or PET images when simultaneously acquiring data. ***Conclusion:*** The new BrainPET-7T system provides simultaneous high-quality PET and MR images. No mutual interference or incompatibility have been observed in the reconstructed images when acquiring MR and PET data simultaneously.

OP-285

Impact of MR-Guided TOF-BSREM Reconstruction on Visual Interpretation in [^{18}F]Flutemetamol PET/MR

J. Inoue Inukai[1], *M. Nogami*[2,3], *F. Zeng*[2], *K. Kubo*[2], *T. Kurimoto*[4], *F. Kotasidis*[5,6], *M. Spangler-Bickell*[6], *M. W. Huellner*[5], *T. Murakami*[1,2]; [1]*Department of Radiology, Kobe University Graduate School of Medicine, Kobe, JAPAN,* [2]*Department of Radiology, Kobe University Hospital, Kobe, JAPAN,* [3]*Division of Medical Imaging, Biomedical Imaging Research Center, University of Fukui, Fukui, JAPAN,* [4]*GE Healthcare, Hino, JAPAN,* [5]*Department of Nuclear Medicine, University Hospital Zurich and University of Zurich, Zurich, SWITZERLAND,* [6]*GE Healthcare, Waukesha, WI, UNITED STATES OF AMERICA.*

Aim/Introduction: [^{18}F]Flutemetamol PET is a type of amyloid PET that enables visualization of fibrillar β-amyloid plaques, aiding in the diagnosis of mild cognitive impairment due to Alzheimer's disease. Visual interpretation as positive or negative is required. However, in some cases, uptake in the cortical margins remains ambiguous owing to partial-volume effects. Time-of-flight (TOF) block-sequential regularized expectation maximization (BSREM) allows for highly converged PET image reconstruction while maintaining quantifiability and image quality. Furthermore, MR-guided BSREM, which incorporates voxel-level MR anatomical priors into the PET regularization process, is expected to improve the noise control and spatial accuracy. This study aimed to evaluate whether MR-guided TOF-BSREM improves reader confidence in the binary classification of amyloid PET findings compared with conventional TOF-ordered subset expectation maximization (OSEM) reconstruction. ***Materials and Methods:*** This study analyzed a total of 41 cases who underwent Flutemetamol PET/MR imaging—using the same PET/MRI scanner, 11 cases were conducted at Institution 1 and 30 cases at Institution 2. For each subject, PET images were reconstructed using both conventional TOF-OSEM and MR-guided TOF-BSREM methods. Centiloid scales were calculated using both reconstruction methods and assessed for correlations. Visual interpretation was conducted according to the standardized Flutemetamol PET reading methodology, in which each brain region was assessed individually. Two experienced readers independently evaluated both conventional and MR-guided TOF-BSREM reconstructed images, assigning a 5-point score for each region as well as for the overall classification of amyloid positivity or negativity. The diagnostic performance was compared using receiver operating characteristic analysis and the DeLong test. Confidence score distributions were assessed using the Wilcoxon signed-rank test and visualized using histograms. The reference standard for amyloid positivity or negativity was determined by consensus among the two readers and a third independent expert. ***Results:*** The centiloid scales between the two reconstruction methods showed a strong positive correlation ($r = 0.997$). In visual interpretation, both readers showed higher area under the curves for MR-guided TOF-BSREM than for conventional TOF-OSEM (Reader 1: 0.997 > 0.974; Reader 2: 0.993 > 0.971). Although the difference in confidence score distribution was not statistically significant ($p = 0.068$), the histograms suggested a greater proportion of extreme confidence scores with MR-guided TOF-BSREM, indicating more definitive interpretations. ***Conclusion:*** MR-guided TOF-BSREM reconstruction for Flutemetamol PET/MR may enhance reader confidence in binary visual interpretation, potentially leading

to more reliable assessments of amyloid positivity or negativity compared to conventional reconstruction. ***References:*** 1) JAMA Neurol. 2015;72:287-294. 2) J Nucl Med. 2007;48:932-945.

OP-286

New Discoveries in Systemic Amyloidosis: A Network of Brain and Organ Relationships Based on ^{11}C-PiB PET/MRI

S. Wei, *W. Ruan, Z. Zhou, D. Zheng, Y. Lv, Z. Dai, Y. Gai, X. Lan, C. Qin;*
Department of Nuclear Medicine, Union Hospital, Tongji Medical College, Huazhong University of Science and Technology, Wuhan, China, CHINA.

Aim/Introduction: Primary systemic amyloidosis is a disorder characterized by abnormal extracellular amyloid protein deposition, resulting in multi-organ dysfunction. ^{11}C-PiB PET is widely used to diagnose Alzheimer's disease and has shown potential in assessing systemic amyloidosis. However, the correlation between brain ^{11}C-PiB uptake and other organs, as well as between different organ uptake, remains unclear. This study explores the correlation between amyloid protein deposition in the brain and various organs. ***Materials and Methods:*** A retrospective analysis was conducted on patients who underwent whole-body ^{11}C-PiB PET/MRI for suspected or confirmed systemic amyloidosis. Brain PET images were segmented into 70 regions in MATLAB with SPM12, and SUV values were extracted for each region. ROIs were delineated in multiple organs to acquire UVmax. Pearson correlation coefficients (r) and p-values were calculated between various brain regions and multiple organs, as well as across different organs, using Python programming to assess the correlation of amyloid deposition among different organs. ***Results:*** Fifty patients with systemic amyloidosis (case group), 9 with other plasma cell diseases, and 4 controls were included. In the control group, 57, 22, and 24 brain regions exhibited extremely strong correlations with spleen, renal parenchyma, and bone marrow, respectively (with the strongest correlation being r = 0.981-0.997, all P < 0.05). In the other plasma cell disease group, 60, 23, 6, and 31 brain regions had strong correlations with myocardium, spleen, renal parenchyma, and bone marrow, respectively (r = 0.742-0.814, all P<0.05). All brain regions showed a poor or no correlation with lung, liver, gastric wall, and pancreas in the aforementioned two groups. Conversely, in the case group, merely 22 and 4 brain regions weakly correlated with pancreas and bone marrow (r = 0.345, 0.340, all P<0.05), while all showed poor or no correlation with lung, myocardium, liver, spleen, gastric wall, and renal parenchyma. Meanwhile, clear organ correlations were exhibited in the non-amyloidosis groups (the control group and other plasma cell disease groups), including myocardium-bone marrow, myocardium-spleen, myocardium-gastric wall, lung-liver, spleen-gastric wall, spleen-bone marrow, and gastric wall-bone marrow (r = 0.678-0.857; all P <0.05). However, these organ correlations significantly decreased or even vanished in the case group. ***Conclusion:*** We preliminarily constructed a network of relationships between PiB uptake in the brain and multiple organs, as well as between organs. Primary systemic amyloidosis significantly disrupts the correlation of PiB uptake between the brain and various organs, as well as between organs.

OP-287

Posterior Putamen Vulnerability in Parkinson's Disease: Multimodal ^{18}F-FPCIT PET/MRI Reveals Iron-Mediated Nigrostriatal Degeneration and Microstructural Decoupling

H. Lin[1], *Y. Wei*[2], *Y. Zhu*[1], *Z. Lin*[2], *Y. Yang*[3], *C. Zuo*[1];
[1]Deparment of Nuclear Medicine / PET Center, Huashan Hospital, Fudan University, Shanghai, CHINA, [2]United Imaging Healthcare Co., Ltd., Shanghai, CHINA, [3]Beijing United Imaging Healthcare Co., Ltd., Beijing, CHINA.

Aim/Introduction: Parkinson's disease (PD) is characterized by posterior-to-anterior striatal dopaminergic denervation, most pronounced in the posterior putamen (pPut). However, the microstructural mechanisms driving this spatial gradient remain unclear. This study investigates nigrostriatal pathway alterations by correlating substantia nigra pars compacta (SNc) iron deposition/diffusion metrics with striatal dopamine transporter availability (DaT-SBR) to elucidate why pPut is preferentially affected. ***Materials and Methods:*** We performed ^{18}F-FPCIT PET/MRI in 53 PD patients and 10 controls. Striatal DaT-SBR (caudate, anterior/middle/posterior putamen [aPut/mPut/pPut]) and SNc microstructural metrics (iron deposition via quantitative susceptibility mapping; diffusion tensor imaging [DTI: axial/mean/radial diffusivity (AD/MD/RD), fractional anisotropy [FA]) were analyzed. Group differences and SNc-striatal correlations were assessed using general linear models adjusted for age, disease duration. ***Results:*** PD patients exhibited marked DaT-SBR reductions in bilateral caudate and putamen (p<0.0001 vs. controls), with maximal loss in the right pPut. A posterior-to-anterior DaT-SBR gradient was confirmed (aPut>mPut>pPut, all p<0.0001). SNc iron deposition inversely correlated with DaT-SBR in the clinically affected hemisphere's right caudate (R=−0.548, P=0.001) and pPut (R=−0.422, P=0.016), and contralaterally in the left caudate (R=−0.486, P=0.005). No associations were observed in aPut/mPut or left putamen (P>0.05). Adjusted for covariates, SNc DTI metrics demonstrated distinct spatial patterns: SNc AD/MD/RD positively correlated with putaminal diffusivity (MD/AD/RD: R=0.421-0.518, P≤0.009), strongest in aPut and weakening in pPut. Conversely, SNc FA negatively correlated with caudate diffusivity (R=−0.418-−0.430, P≤0.003). Notably, SNc AD/MD showed inverse correlations with pPut FA (R=−0.295-−0.306, P≤0.044), suggesting microstructural decoupling in posterior regions. ***Conclusion:*** This multimodal study reveals two key mechanisms underlying pPut vulnerability in PD: (1) Stronger nigrostriatal associations in anterior regions (SNc diffusivity-aPut diffusivity) may reflect compensatory axonal plasticity, while weaker posterior correlations (SNc-pPut) indicate disrupted connectivity. (2) Inverse SNc iron-DaT-SBR links in pPut and caudate suggest iron-mediated dopaminergic toxicity, particularly in the clinically affected hemisphere. The posterior-anterior DaT-SBR gradient mirrors diminishing SNc-striatal microstructural coherence, supporting a model where posterior striatal regions are more susceptible due to both reduced compensatory capacity and iron-related neurodegeneration. These findings provide novel insights into the microstructural basis of PD's spatial progression, emphasizing SNc iron homeostasis and axonal integrity as potential therapeutic targets.

OP-288

Impact of Continuous Bed Motion on Image Quality and Quantification with a LAFOV PET/CT: A Comparative Study

F. Schmidt[1,2], *W. Lan*[1], *P. M. Linder*[1], *E. Calderón*[1], *C. la Fougère*[1,3];
[1]Nuclear Medicine and Clinical Molecular Imaging, University Hospital Tuebingen, Tuebingen, GERMANY, [2]Werner Siemens Imaging Center, Dep Preclinical Imaging and Radiopharmacy, University of Tuebingen, Tuebingen, GERMANY, [3]Cluster of Excellence iFIT (EXC 2180) "Image Guided and Functionally Instructed Tumor Therapies", University of Tuebingen, Tuebingen, GERMANY.

Aim/Introduction: To extend the axial coverage of 106 cm of a long axial field of view (LAFOV) PET/CT scanner, continuous bed motion (CBM) has been introduced. In this study, we evaluated the impact of CBM compared to standard step-and-shoot (SS) acquisition on image uniformity, noise characteristics, and potential discrepancies in quantification. ***Materials and Methods:*** Ten oncological patients underwent sequential [18F]-FDG or [18F]-PSMA PET/CT scans (2 MBq/kg, 60 min p.i.) scans using a standard protocol at your institute (SS, 300 s, 4 iterations/5

subsets OP-OSEM with PSF+TOF, ultra-high-sensitivity (UHS) mode) and additional CBM (bed speed 2.8 mm/s, 106 cm, 380 s, UHS). SUVmean, SUVmax and coefficient of variation (CV) were determined for lesions and liver to assess quantification and noise. A uniform cylindrical phantom (diameter: 5.5 cm, length: 140 cm) filled with 2 kBq/ml F-18 was scanned with CBM at various speeds (2.8 mm/s to 50 mm/s) and compared to SS protocols (300 s and 380 s). Image uniformity (percentage standard deviation of mean activity concentration) and noise (CV) were evaluated over the central 80 cm axial FOV. Additionally, a NEMA NU-2 2018 IEC phantom (sphere-to-background ratio 4:1, 2 kBq/ml F-18) was used to compare contrast recovery coefficients (CRC) for different sphere sizes at axial positions of 0, 45, and 50.5 cm for CBM vs. SS. ***Results:*** For patient data, strong correlations were observed between SS and CBM across all quantitative parameters ($R^2 > 0.98$). Mean lesion SUVmean was 9.1 ± 8.1 (SS) vs. 8.3 ± 7.3 (CBM), SUVmax 14.7 ± 14.2 (SS) vs. 13.7 ± 13.0 (CBM), and lesion CV 20.5 ± 3.9% (SS) vs. 20.3 ± 4.2% (CBM). Liver SUVmean remained stable 8.9 ± 4.3 (SS) vs. 9.0 ± 4.4 (CBM), with comparable noise levels of 7.1 ± 1.1% (SS) vs. 6.6 ± 1.2% (CBM). Phantom studies confirmed a high uniformity of 0.9% (CBM, 2.8mm/s) comparable to 0.7% (SS, 380 s), with degradation at higher speeds to 3.6% (50 mm/s). CV was slightly increased with CBM (5.9 ± 1.0%) compared to 4.7±0.7% (SS, same 380 s), but comparable to 300 s SS with 5.4±0.8%. CRC values were preserved with CBM, e.g., with 0.46 (10 mm sphere) and 0.75 (28 mm) at center FOV, comparable to SS (0.46 / 0.76). Even at off-center positions, CBM maintained quantification for slow speeds, but showed degradation at high speeds, e.g., 50.5 cm, 8.4 mm/s CRC 0.38 (10 mm) / 0.69 (28 mm). ***Conclusion:*** CBM acquisition on LAFOV PET/CT systems enables extended axial imaging without introducing inhomogeneities or great deviations in quantification compared to conventional SS protocols. Slight increases in image noise under CBM can be compensated by modest extensions of scan duration.

OP-289

Less Is More: Tailored Low-Dose [^{18}F]FDG PET/CT Imaging in Pregnant Patients Using LAFOV Technology

I. S. Deurloo[1,2], *M. M. Steemers-de Boer*[3], *J. H. van Snick*[2], *K. P. Koopmans*[2], *R. H. J. A. Slart*[2], *W. Noordzij*[2], *A. H. Brouwers*[2], *G. N. Stormezand*[2], *T. Velleman*[2], *E. H. J. G. Aarntzen*[2], *B. J. de Wit - van der Veen*[3], *W. V. Vogel*[3], *S. M. Jansen*[3], *A. J. A. T. Braat*[3,4], *A. W. J. M. Glaudemans*[2], *O. V. Ivashchenko*[2];
[1]*Isala, Zwolle, NETHERLANDS,* [2]*University of Groningen, University Medical Centre Groningen, Groningen, NETHERLANDS,* [3]*Netherlands Cancer Institute, Amsterdam, NETHERLANDS,* [4]*University Medical Centre Utrecht, Utrecht, NETHERLANDS.*

Aim/Introduction: PET/CT is essential for diagnosing and monitoring cancer in pregnant patients. The recent introduction of long axial field-of-view (LAFOV) PET/CT scanners—offering up to 10× higher sensitivity than conventional PET—presents a unique opportunity to reduce radiopharmaceutical dose, especially important due to foetal radiosensitivity and the need for repeated imaging of pregnant oncological patients. However, standard adult imaging protocols are still commonly used during pregnancy. In clinical practice, PET dose and scan time are guided by desired image quality, often including a buffer to account for variability in preferences of physicians. For pregnant patients, minimizing this buffer to reduce foetal exposure is essential. Additionally, altered maternal body composition may render conventional adult dose models suboptimal. This study evaluates the image quality-dose trade-off in pregnant patients scanned with LAFOV PET/CT and identifies the most predictive body composition metric for image quality to support development of a tailored dose model. ***Materials and Methods:*** PET/CT scans from 11 pregnant patients, acquired using a LAFOV PET/CT system and ultra-low-dose CT (tin filter), were retrospectively analysed. [^{18}F]FDG was administered using either a quadratic (0.26 MBq/kg^2) or linear (0.3 MBq/kg) regimen, with 15-20 minute acquisitions—approximately 7-fold lower than standard adult dosing. A reference image quality (RIQ), based on average counts per kg, was defined. Images were reconstructed at 100-12.5% RIQ with clinical and EARL2 settings, and assessed by 11 physicians using a 1-5 Likert scale (≥3 = acceptable). Liver signal-to-noise ratio (SNR) served as an objective image quality metric. The minimum required scan statistics was modelled based on the SNR threshold for acceptable image quality and patient body composition. Foetal dose was estimated using uterine segmentation, PET conversion factors[1], and SSDE-adjusted CTDIvol. ***Results:*** SNR correlated well with Likert scores (R^2 = 0.80), with an SNR of 10.72 corresponding to acceptable image quality. Body surface area (BSA) was the best predictor for required image quality (R^2 = 0.85), outperforming weight, weight/height, and body-mass-index. The proposed model (A[MBq] × t[min] = 25.21 × BSA^1.8) yields a PET dose of 5.2 MBq for a 75 kg/170 cm patient, reducing dose by 74-97% compared to current protocols. Estimated foetal doses are expected to be 0.0049 mGy (PET) and 0.31 mGy (CT) after introduction of the proposed protocol. ***Conclusion:*** LAFOV PET/CT enables substantial [^{18}F]FDG dose reduction in pregnant patients. A BSA-based dose model provides optimal prediction of image quality while ensuring minimal foetal exposure. ***References:*** [1]Zanotti-Fregonara et al., J Nucl Med. 2016;57(11):1760-1763.

OP-290

^{212}Pb PSMA imaging by pair production PET confirms localisation of alpha emissions within tumour lesions

M. Griffiths[1], *L. Campbell*[1], *M. Latter*[1], *D. Wyld*[1], *E. OMahoney*[2], *I. Holmes*[2], *L. Katchel*[2], *S. Baker*[2], *A. Hansen*[2], *M. Baronet*[3], *S. Rose*[3], *A. Karmann*[3], *D. Pattison*[1];
[1]*Royal Brisbane and Women's Hospital, Brisbane, AUSTRALIA,* [2]*Princess Alexandra Hospital, Brisbane, AUSTRALIA,* [3]*AdvanCell, Sydney, AUSTRALIA.*

Aim/Introduction: ^{212}Pb PSMA SPECT/CT imaging has been shown to confirm the localisation of the in vivo alpha generator ^{212}Pb in PSMA-avid tumour lesions. ^{212}Pb decays into ^{212}Bi (60 min half-life) which either emits an alpha particle or decays into ^{212}Po (3 µs half-life) which emits an alpha particle; neither ^{212}Bi nor ^{212}Po produce imageable emissions. The alpha emitting ^{212}Bi atoms decay into ^{208}Tl (3 min half-life) which emit a 2.6MeV gamma. 2.6 MeV gamma interactions with atomic nuclei can cause pair production allowing imaging with a PET camera. The number of positrons per voxel is dependent on the number of gamma rays in the voxel and the density of the material. As photon density decreases with 1/distance^2 the highest photon density is associated with the highest concentration of ^{209}Tl / ^{212}Bi. We have investigated PET imaging of the ^{212}Pb decay chain in phantoms and in patients receiving ^{212}Pb-ADVC001 in the TheraPb trial (NCT05720130). ***Materials and Methods:*** ^{212}Pb point sources in glass capillary tubes in water filled phantoms were imaged to determine the FHWM. An IEC phantom was imaged with activities matching patient concentrations of 160 MBq administration of ^{212}Pb-ADCV001. Patient imaging following administration of 160 and 200 MBq of ^{212}Pb-ADVC001 were performed at two clinical sites using Siemens Vision PET cameras. ***Results:*** The FWHM of ^{212}Pb on the Vison was 4.9 mm. An IEC phantom with a concentration simulating a 160 MBq administration of ^{212}Pb-ADVC001, with zero background, allowed visualisation of the 13 mm sphere. There was increased background between the two largest spheres indicating pair production around the ^{212}Pb sources. The recorded counts were linear with radioactivity. Clinical imaging of ^{212}Pb PET pair production is feasible. Conventional scatter correction is not suitable due to the high proportion of down scattered gamma rays in the PET energy window compared to the number of pair production positrons. Blood pool activity in early time point images and out of field activity contribute to image background. Transaxial slices show diffuse localisation however MIP images provide a clearer indication of localisation of positrons hence ^{208}Tl and ^{212}Bi in lesions concordant with diagnostic PSMA PET imaging. ***Conclusion:*** Clinical ^{212}Pb PSMA PET imaging of ^{208}Tl gamma pair production confirms the localisation of ^{208}Tl, ^{212}Bi and hence alpha emissions from ^{212}Pb-ADVC001within PSMA-avid tumour lesions. Investigation of post processing of pair production PET images is needed to enhance image quality.

OP-291

A PET/CT Phantom Study on the Potential Overcorrection of Lesion Activity in Cortical Bone like Structures and a Potential Solution

J. Ni, *A. Haslauer, S. Nekolla;*
Department of Nuclear Medicine, TUM Klinikum Rechts der Isar, Technical University Munich, School of Medicine & Health, Munich, GERMANY.

Aim/Introduction: In PET/CT systems, an attenuation map (μ-map) is generated by extrapolating the CT Hounsfield units to 511 keV PET linear attenuation coefficients (LAC). However, due to the higher photoelectric effect at lower CT energies, high-density tissues like cortical bone may cause overcorrection of lesion activity. ***Materials and Methods:*** A 3D printed phantom (500 HU) using stone-like PLA based filament was used to simulate cortical bone. Different sized holes in the phantom wall allowed the lesions to simulate cortex intrusion. PCR tubes of different diameters (7mm, 10mm, 15mm) containing solidified mixture of ^{18}F-FDG and dental gypsum were fixed in dedicated cavities to simulate bone lesions, and the phantom was placed in a water bucket simulating a body. Identical tubes filled only with ^{18}F-FDG solution were fixed in the water bucket to simulate soft tissue lesions as reference. Additionally, two 28mm-diameter tubes containing ^{18}F-FDG solids and solution, respectively, were fixed in the cavity of the phantom to minimize partial volume effects. Scans were performed in a clinical digital PET/CT. To evaluate potential overcorrection, we used a cardiac-metal-artifact-reduction (cMAR) option, which is originally developed to reduce metal induced attenuation artifacts. This technique clips the LAC greater than 0.1 cm^{-1} in the μ-map to 0.1 cm^{-1}, and was used to evaluate the effect of the absence of cortical bone tissue in the attenuation correction. PET data were reconstructed using six different methods (FBP-TOF, OP-TOF, OP-TO PSF-TOF, and their corresponding cMAR versions) ***Results:*** For lesions with diameters of 7mm, 10mm, and 15mm, in reconstructions without cMAR, the mean and maximum tracer uptake concentrations in simulated bone lesions were significantly higher than those in soft tissue lesions, with the difference increasing with lesion size. FBP-TOF as most analytical reconstruction approach showed the most significant overestimation in the maximum value (up to 17.5% at 15 mm). cMAR significantly reduces the overestimation across all reconstruction methods, especially in PSF-TOF cMAR, where the differences dropped below 4% for all sized lesions. For the 28mm-diameter lesions, cMAR reduced the overestimation of the maximum tracer uptake concentration from more than 10% to approximately 0% in all reconstruction methods. ***Conclusion:*** In PET/CT scans, the tracer uptake concentration is potentially overestimated in bone cortical invasion lesions. This can be attributed to an overcorrection in high-density tissue due to technical limits of the CT to 511keV extrapolation. Clipping cortical bone LAC in attenuation correction could be a potential solution.

706

Monday, October 6, 2025, 8:00 - 9:30
Room 117

Clinical Oncology Track - TROP Session - Oncology & Theranostics Committee: Imaging Melanoma and New Targets

OP-292

The MELATEP study: Diagnostic performance of [18F]FDG-PET/CT follow-up for patients on adjuvant immunotherapy for melanoma in real-life setting

A. Bauduer, *V. Sibaud, C. Pages, F. Courbon, M. Terroir;*
Oncopole, Toulouse, FRANCE.

Aim/Introduction: There is no international consensus on the optimal follow-up for patients treated with adjuvant immunotherapy after melanoma resection. Although [18F]FDG-PET/CT is frequently used, its relevance remain debated. The objective was to evaluate the diagnostic accuracy of FDG-PET/CT in real-life setting. ***Materials and Methods:*** This was a single-center retrospective study enrolling 278 patients with resected stage IIB to IV melanoma treated with adjuvant immunotherapy : 151 patients were monitored by CT and 127 patients by FDG-PET/CT. Recurrence was confirmed by biopsy, other imaging or clinical follow-up. Incidence of recurrence, sensitivity, specificity, median time to detect recurrence and mean lesion size were outcome measures. ***Results:*** Median follow-up was 31 months. 42% recurrences were observed : 39% by CT (59/151) and 45% by FDG-PET/CT (57/127). Sensitivity and specificity were respectively 89% and 91% for FDG-PET/CT and 73% and 99% for CT. The median time to detect recurrence was 9 months for FDG-PET/CT and 12 months for CT. The main site of recurrence was lymph nodes in both groups. The mean lesion size detected was 21 mm by CT and 16 mm by FDG-PET/CT. 18% of total recurrences were missed by cross-sectional imaging. The false negative rates were 25% in the CT group (15/59) and 11% in the FDG-PET/CT group (6/57). The skin represented by far the main site of recurrence (81%), of which 76% occurring on limbs. These lesions were discovered by clinical follow-up or ultrasound. 69% of patients received adjuvant immunotherapy for a minimal 12 month-duration. The main cause of premature discontinuation was toxicity occurring in 18% of patients. Gastrointestinal and hepatic toxicities were the most frequent (47% of all toxicities). ***Conclusion:*** [18F]FDG-PET/CT is an effective tool for monitoring patients treated with adjuvant immunotherapy for melanoma. In comparison with CT, it detects smaller recurrences at an earlier stage. It seems particularly relevant for cutaneous recurrence especially on limbs. Its lower specificity should encourage early reassessment in case of doubtful imaging. ***References:*** Andersen, J.A.S., Spatzek, A.D., Vilstrup, M.H. et al. The diagnostic accuracy and clinical impact of FDG-PET/CT follow-up for patients on adjuvant immunotherapy for high-risk malignant melanoma. Eur J Nucl Med Mol Imaging 49, 2342-2351 (2022)

OP-293

DYNAMO: Dynamic Total Body FDG PET/CT and Kinetic Modeling for Early Lesion-Level Response Assessment in Metastatic Melanoma Undergoing Immunotherapy - Preliminary Results from a Prospective Study

A. Di Giorgio[1], *D. Dall'Olio*[2], *I. Brusa*[3], *P. Marchese*[4], *G. Siepe*[5], *M. Assenza*[6], *A. Zappacosta*[3], *C. Nanni*[3], *B. Melotti*[4], *G. Castellani*[2,7], *S. Fanti*[1,3], *A. Farolfi*[3];*
[1]Nuclear medicine, Alma Mater Studiorum University of Bologna, Bologna, ITALY, [2]Department of Medical and Surgical Sciences, University of Bologna, Bologna, ITALY, [3]Nuclear Medicine, IRCCS Azienda Ospedaliero-Universitaria di Bologna, Bologna, ITALY, [4]Medical Oncology, IRCCS Azienda Ospedaliero-Universitaria di Bologna, Bologna, ITALY, [5]Radiation Oncology, IRCCS Azienda Ospedaliero-Universitaria di Bologna, Bologna, ITALY, [6]Professional Development and Implementation of Research in Health Professions Unit, IRCCS Azienda Ospedaliero-Universitaria di Bologna, Bologna, ITALY, [7]IRCCS Azienda Ospedaliero-Universitaria di Bologna, Bologna, ITALY.

Aim/Introduction: Malignant melanoma, characterized by its aggressive nature with rising incidence and frequent metastasis, remains a challenge for timely treatment response assessment despite advancements like immunotherapy and stereotactic radiotherapy. Long-axial field-of-view(LAFOV)-PET/CT, a recent technology enabling sensitive, single-bed dynamic whole-body imaging, may improve early detection of therapeutic response and disease progression. Preliminary data suggest LAFOV-PET/CT offers superior lesion detection and earlier identification of therapy-induced metabolic changes over conventional PET/CT. This prospective study(DYNAMO) investigates whether dynamic LAFOV FDG PET/CT with kinetic modeling can identify early metabolic changes in melanoma lesions predictive of treatment response ***Materials and Methods:*** Prospective single-center study consecutively enrolling treatment-naïve metastatic melanoma

patients initiating first-line systemic immunotherapy(CE AVEC:447/2024/Oss/AOUBo). Patients underwent a 60-minutes total-body dynamic [18F]-FDG PET/CT scan using the uExplorer system. Images were evaluated qualitatively and quantitatively for metabolic and dynamic parameters. [18F]-FDG uptake and pharmacokinetics were assessed by SUV by two–tissue compartment models(reversible 2TC, irreversible 2TiC). Model selection used mean absolute scaled error(MASE) and the Akaike Information Criterion(AIC). A post-treatment [18F]-FDG-PET/CT was performed on a digital tomograph for response assessment. Lesions were defined as responding if they demonstrated complete metabolic resolution or a reduction in SUVmax on follow-up imaging. Kinetic parameters(K_1, k_2, k_3, K_i, DV) were compared between responding and non-responding lesions and with healthy reference tissues. Lesions treated with concurrent stereotactic body radiation therapy(SBRT) were excluded. ***Results:*** Fourteen patients(median age 65 years, IQR 63-71; 50% female) underwent dynamic PET/CT. Four patients completed follow-up with post-treatment scans. Overall, 12(85%) patients had positive baseline scanfor metastatic disease (median lesion SUVmax 6.1, IQR 4.0-8.8, SUVmean 4.0, IQR 3.2-5.7), while 2(15%) were negative. Among the 14 patients, a total of 34 FDG-positive lesions were identified: 14(41%) pulmonary and 20(58%) lymphatic/subcutaneous metastases. Kinetic parameters K_1, k_2, k_3, K_i, and DV) significantly differed between lesions and healthy reference tissues such as liver(p=0.0019), lung parenchyma(p=0.0006), and muscle(p=0.006). In a region-based analysis, among 12 lesions with paired pre- /post-scans, responding lesions demonstrated statistically significant differences in K_1(p=0.0136), k_3(p=0.0087) , and K_i(p=0.0055) compared to non-responding lesions. Baseline SUVmax and SUVmean did not significantly differ between responding and non-responding lesions(p=0.1047 and p=0.0896, respectively). ***Conclusion:*** Dynamic LAFOV-FDG PET enables extraction of Kinetic parameters that may outperform conventional SUV in early discrimination of treatment response in metastatic melanoma. K_1, k_3, and K_i appear particularly promising for lesion-level response assessment. These preliminary data support the potential role of dynamic LAFOV-[18F] FDG-PET/CT as a biomarker for guiding immunotherapy in melanoma.

OP-294

Artificial intelligence-assisted assessment of metabolic response to tebentafusp in metastatic uveal melanoma: a long axial field-of-view [^{18}F]FDG PET/CT study

C. Sachpekidis[1], *D. Machiraju*[2], *C. Ziener*[1], *L. Edenbrandt*[3], *J. C. Hassel*[4], *A. Dimitrakopoulou-Strauss*[1];
[1]*German Cancer Research Center (DKFZ), Heidelberg, GERMANY,* [2]*National Center for Tumor Diseases (NCT), Heidelberg, GERMANY,* [3]*Sahlgrenska University Hospital, Gothenburg, Gothenburg, SWEDEN,* [4]*National Center for Tumor Diseases (NCT), University Hospital Heidelberg, Heidelberg, GERMANY.*

Aim/Introduction: Tebentafusp, a T-cell receptor-bispecific molecule targeting glycoprotein 100 and CD3, is the first systemic therapy to significantly improve survival in treatment-naïve HLA-A*02:01+ adult patients with unresectable or metastatic uveal melanoma (mUM). To identify potential surrogate markers of response, we investigate the prognostic value of [^{18}F]FDG PET/CT in monitoring treatment response in mUM patients receiving tebentafusp. ***Materials and Methods:*** Fifteen patients with mUM undergoing tebentafusp therapy were evaluated with [^{18}F]FDG PET/CT at baseline and at 3 months, using a long axial field of view (LAFOV) PET/CT system (Biograph Vision Quadra, Siemens Healthcare). Tumor response was assessed according to PET-based metabolic criteria: EORTC, PERCIST, and immunotherapy-modified PERCIMT. Metabolic responses were classified into complete metabolic response (CMR), partial metabolic response (PMR), stable metabolic disease (SMD), or progressive metabolic disease (PMD), and dichotomized into disease control (DC = CMR + PMR + SMD) vs. PMD. Whole-body metabolic tumor volume (MTV) and total lesion glycolysis (TLG) were quantified using a 3D AI-based tool (RECOMIA), with occasional manual refinements for optimal delineation. Liver tissue MTV and TLG were also calculated. Overall survival (OS) was assessed for all patients. ***Results:*** Median follow up [95% CI] was 14.1 months [12.9 months - NA]. PET-based response assessments yielded the following disease control rates and corresponding median OS:• EORTC: 4 DC (OS: 24.5 months, 95% CI: NA-NA); 11 PMD (OS: 14.6 months, 95% CI: 14.3-NA)• PERCIST: 6 DC (OS: 24.5 months, 95% CI: NA-NA); 9 PMD (OS: 14.6 months, 95% CI: 14.3-NA)• PERCIMT: 9 DC (OS: 24.5 months, 95% CI: 14.6-NA); 6 PMD (OS: 14.3 months, 95% CI: 3.3-NA)Across all criteria, patients achieving DC showed a trend toward improved OS, most notably with PERCIST (p=0.08). AI-derived metrics revealed that high whole-body baseline MTV and TLG (above median) of tumor lesions were associated with significantly shorter OS (MTV: 16.9 vs. 27.2 months; TLG: 16.9 vs. 27.2 months; p<0.05). Similarly, elevated MTV and TLG at 3 months were predictive of poorer survival (MTV: 14.3 vs. 24.5 months; TLG: 14.3 vs. 24.5 months; p<0.05). Additionally, increased liver MTV and TLG at 3 months were associated with shorter survival (p < 0.05). ***Conclusion:*** Automated volumetric assessment of [^{18}F]FDG PET/CT using whole-body and liver MTV and TLG provides robust prognostic insights in tebentafusp-treated mUM patients. These AI-derived metrics outperform conventional PET response criteria and offer a promising tool for response monitoring and risk stratification.

OP-295

Pseudoprogression Rates in the Dutch Melanoma Population suggest Opportunities for Cost-Effective Use of [^{18}F]FDG PET/CT during Therapy with Immune Checkpoint Inhibitors

S. van Mossel[1,2], *D. Vriens*[3], *D. Kersbergen*[1], *M. Bloem*[4], *E. Kapiteijn*[1], *H. Koffijberg*[2], *S. Saing*[2], *L. De Geus-Oei*[1,2,5];
[1]*Leiden University Medical Center, Leiden, NETHERLANDS,* [2]*University of Twente, Enschede, NETHERLANDS,* [3]*Radboud University Medical Center, Nijmegen, NETHERLANDS,* [4]*Dutch Institute for Clinical Auditing, Leiden, NETHERLANDS,* [5]*Delft University of Technology, Delft, NETHERLANDS.*

Aim/Introduction: Unconventional modes of responses, beyond RECIST criteria (v1.1), are frequently observed in patients treated with immune checkpoint inhibitors, showing delayed apparent therapy efficacy. Therefore, healthcare professionals in melanoma care should reconsider the conventional ways of interpreting radiological tumour responses. The joint EANM/SNMMI/ANZSNM practice guidelines on recommended use of [^{18}F]FDG PET/CT during immunomodulatory treatments in patients with solid tumours provide procedure standards for a more accurate interpretation of tumour responses in the rapidly evolving immunotherapeutic landscape. [^{18}F]FDG PET/CT is especially recommended early after therapy initiation, commonly after 8-12 weeks (3-4 cycles), to complement contrast-enhanced CT and resolve discordant findings related to pseudoprogression and mixed or dissociated responses. This study builds on the joint EANM/SNMMI/ANZSNM practice guidelines. It indicates pseudoprogression rates in the Dutch Melanoma Treatment Registry (DMTR) and relates decreasing pseudoprogression rates, when using [^{18}F]FDG PET/CT, to potential cost savings and clinical benefits for melanoma patients. ***Materials and Methods:*** This study consisted of a care pathway analysis to map the specific clinical decisions for melanoma patients in the Netherlands and a review of a Dutch response-based survival model [1]. In 514 patients from the Dutch response-based survival model with known response status at 3 and 6 months after therapy initiation, changes in response status were analysed. Pseudoprogression and mixed responses were related to the costs of ineffective therapy in the event of true

tumour progression, and missing an early opportunity to shift to alternative treatment options. ***Results:*** Pseudoprogression was suggestive for at least 23 patients. Ineffective therapy in the event of true tumour progression was suggestive for 262 patients, resulting in premature death within 6 months after therapy initiation in 147 patients. A subgroup of at least 39 patients was suggestive of missing an early opportunity to start an alternative (likely effective) treatment. Immunotherapy-related costs were estimated at €10,000 per month per patient, where medication costs contribute to at least 80% of these costs. High therapy costs contrast sharply with the cost of [^{18}F]FDG PET/CT estimated at €1,000 per scanning procedure, suggesting an opportunity for cost-effective use of [^{18}F]FDG PET/CT compared to usual care. ***Conclusion:*** We suggest a clear opportunity for potential cost-effective use of [^{18}F]FDG PET/CT during immunomodulatory treatments. However, full health economic evaluations are lacking (but needed). ***References:*** [1] van Breeschoten J et al. Population mortality in advanced melanoma patients with and without response and progression; data from the Dutch Melanoma Treatment Registry. Eur J Cancer. 2023 Mar;182:132-143

OP-296

Comparison of melanin-targeted [^{18}F]DMPY2 and [^{18}F] FDG PET/CT in Advanced Melanoma Patients

Y. Yang, *M. Zhou, J. Su, X. Chen, S. Hu;*
Xiangya Hospital, Central South University, Changsha, CHINA.

Aim/Introduction: Our previous research demonstrated that a melanin-targeted PET probe [^{18}F]DMPY2 outperformed [^{18}F]FDG in detecting primary lesions and sentinel lymph nodes in operable melanoma patients [1]. This study aims to compare the diagnostic efficacy of [^{18}F]DMPY2 PET/CT and [^{18}F]FDG PET/CT in advanced melanoma patients, with a focus on detecting small-sized (<1 cm) metastases in the brain and liver, where [^{18}F]FDG typically shows limited sensitivity. ***Materials and Methods:*** Twenty-six patients (14 men, 12 women; mean age: 54 ± 18 years; mean weight: 60.54 ± 2.14 kg) with histologically confirmed melanoma underwent both [^{18}F]DMPY2 PET/CT and [^{18}F]FDG scans within one week. The mean injected activities were 6.56 ± 0.22 mCi for [^{18}F]DMPY2 and 6.64 ± 0.26 mCi for [^{18}F]FDG. Lesion positivity rates and standardized SUVmax (calculated as SUVmax divided by the aortic arch SUVmean) were compared between the two tracers in both patient- and lesion-based analyses. ***Results:*** The cohort comprised eleven melanoma patients undergoing initial staging and fifteen under restaging, including nine with stage III and seventeen with stage IV disease. Both [^{18}F]DMPY2 and [^{18}F]FDG detected all eleven primary lesions, with comparable SUVmax values (14.24 vs. 6.04, $p = 0.016$). Moreover, [^{18}F]DMPY2 PET/CT demonstrated significantly higher SUVmax values in brain (14.28 vs. 0.68, $p < 0.0001$), liver (10.65 vs. 4.76, $p = 0.0005$), lung (8.80 vs. 4.84, $p = 0.028$), bone (14.71 vs. 5.71, $p = 0.009$), lymph node (11.82 vs. 7.28, $p < 0.0001$), and other metastatic lesions (20.02 vs. 6.71, $p = 0.0002$) compared to [^{18}F]FDG. In terms of sensitivity, [^{18}F]DMPY2 PET/CT was superior to [^{18}F]FDG PET/CT across brain metastases (100% [4/4] vs. 25% [1/4]) and liver (100% [6/6] vs. 83% [5/6]). It was comparable to [^{18}F]FDG PET/CT in primary tumors, lung, bone, lymph nodes, and other metastases. Lesion-based analysis showed that [^{18}F]DMPY2 identified 45 more metastatic foci than [^{18}F]FDG in brain (13 vs. 1), liver (41 vs. 35), lungs (144 vs. 133), bone (209 vs. 202), lymph nodes (299 vs. 290), and other metastases (90 vs. 89). ***Conclusion:*** [^{18}F] DMPY2 PET/CT demonstrates superior diagnostic performance compared to [^{18}F]FDG PET/CT in advanced melanoma, particularly in detecting small-sized metastases in the brain and liver. [^{18}F] DMPY2 may serve as a promising imaging agent for accurate staging and comprehensive assessment of metastatic burden in melanoma patients. ***References:*** [1] Yang, Y., Ming Z., Shuang, Z., et al. (2025). First-in-human PET imaging and evaluation of melanin-targeted [^{18}F]DMPY2 in malignant melanoma patients. Theranostics. Doi:10.7150/thno.109243

OP-297

[^{68}Ga]Ga-DPI-4452 PET/CT for Staging of Patients with Clear Cell Renal Cell Carcinoma (ccRCC)

A. Küper[1], *D. Kersting*[1], *K. Pabst*[1], *M. Nader*[1], *C. Darr*[2], *L. Umutlu*[3], *U. Krafft*[2], *V. Grünwald*[2], *B. Hadaschik*[2], *K. Herrmann*[1], *W. Fendler*[1];
[1]*Department of Nuclear Medicine, University Hospital Essen, GERMANY,* [2]*Department of Urology, University Hospital Essen, GERMANY,* [3]*Department of Radiology, University Hospital Essen, GERMANY.*

Aim/Introduction: The aim of this study was to evaluate the diagnostic accuracy of [^{68}Ga]Ga-DPI-4452 PET/CT in comparison to conventional imaging (+/- [^{18}F]FDG PET/CT), as well as its safety and theranostic potential in ccRCC. ***Materials and Methods:*** From July 2024 to March 2025, 20 patients (62y, IQR 14y) with histologically confirmed ccRCC (T1, n=5; T2, n=3; T3, n=6; T4, n=0; unknown, n=6) were examined. 15 patients also underwent [^{18}F] FDG PET/CT (≤ 2 weeks). Each scan was assessed for the presence of primary tumor or recurrence, as well as for the detection of metastases in local and distant lymph nodes, liver, bones, and other regions. The analysis included SUVmax/SUVmean tumor-to-liver ratios (TLR), and tumor volume (presented as mean ± SD). ***Results:*** The average injected activity was 84 MBq for [^{68}Ga]Ga-DPI-4452 and 260 MBq for [^{18}F]FDG, with an average uptake time of 46 to 76 minutes. No acute or long-term side effects were observed. Two out of 20 patients (10 %) showed no viable tumor in the current examinations; both were receiving targeted therapy. One of them had residual pulmonary metastases and presumably reactive hilar lymph nodes on CT, without DPI or FDG uptake uptake. A total of 36 [^{68}Ga]Ga-DPI-4452-positive regions were detected in 18 (90 %) patients. In patients who received dual PET/CT imaging, 25 [^{68}Ga] Ga-DPI-4452-positive regions were identified, 9 of them were also detected by [^{18}F]FDG PET/CT (36 %) and one confirmed by biopsy (4 %). No [^{18}F]FDG-positive [^{68}Ga]Ga-DPI-4452-negative regions were detected. The average SUVmax of all [^{68}Ga]Ga-DPI-4452-positive regions was 54.5 ± 65.1. The highest regional uptake was measured in bone metastases (average SUVmax 139.2 ± 146.6), and the highest physiological uptake in the stomach (average SUVmax: 77.0 ± 53.9). Tumor segmentation revealed 131 [^{68}Ga]Ga-DPI-4452-positive lesions (total volume 380.6 cm^3). The average SUVmean for all [^{68}Ga]Ga-DPI-4452-positive lesions was 27.4 ± 31.4. [^{68}Ga]Ga-DPI-4452 showed a high TLR with a global average TLR (SUVmean / liver SUVmean) of 10.3 ± 8.0 ***Conclusion:*** [^{68}Ga] Ga-DPI-4452 PET/CT is a promising imaging tool for ccRCC with superior detection when compared to [^{18}F]FDG PET/CT. High SUV values indicate potential for a theranostic application.

OP-298

First-in-Human Phase I Study of [^{68}Ga]Ga-OncoCAIX: Preliminary Results on Safety, Dosimetry, Pharmacokinetics, and Diagnostic Performance

F. Gelardi[1], *M. Sollini*[2,1], *C. Pini*[2,1], *L. Antunovic*[1], *A. Maielli*[1], *R. Petrelli*[1], *G. Bonfitto*[1], *A. Tudda*[1], *M. Minotti*[1], *J. Mock*[3], *S. Cazzamalli*[3], *S. Oehler*[3], *M. Müller*[3], *D. Neri*[3], *A. Alessi*[4], *P. Erba*[5,6], *A. Chiti*[2,1];
[1]*IRCCS Ospedale San Raffaele, Milan, ITALY,* [2]*Università Vita-Salute San Raffaele, Milan, ITALY,* [3]*Philochem AG, Otelfingen, SWITZERLAND,* [4]*Fondazione IRCCS Istituto Nazionale dei Tumori di Milano, Milan, ITALY,* [5]*Università degli Studi di Milano-Bicocca, Milan, ITALY,* [6]*ASST Azienda Ospedaliera Papa Giovanni XXIII, Bergamo, ITALY.*

Aim/Introduction: Conventional imaging techniques remain limited in accurately characterising and staging clear cell renal cell carcinoma (ccRCC). Carbonic anhydrase IX (CAIX), a transmembrane protein overexpressed in ccRCC, has emerged as a promising molecular target for imaging. [^{68}Ga]Ga-OncoCAIX is a novel radiopharmaceutical with high in vitro selectivity for CAIX and a favourable biodistribution in preclinical models, showing high tumour-specific uptake and minimal background in healthy tissues, including the kidney. We report the preliminary first-in-

human data from an ongoing multicentre, prospective, phase I clinical trial evaluating the safety, dosimetry, pharmacokinetics, and diagnostic performance of [^{68}Ga]Ga-OncoCAIX in patients with suspected ccRCC. ***Materials and Methods:*** The present study is planned to include up to 20 patients with renal masses suspected of ccRCC. Enrolled patients are divided into two cohorts: cohort A includes six patients with suspected primary tumour only, while cohort B can also include patients with metastatic disease. All patients receive a single intravenous administration of 250 MBq of [^{68}Ga]Ga-OncoCAIX, followed by serial PET/CT imaging at 0 - 30 min, 60 min, and 120 min post-injection. Blood and urine samples are collected at predefined time points to assess pharmacokinetics and excretion. Adverse events (AEs) are reported and graded according to Common Terminology Criteria for Adverse Events (CTCAE) v.5.0. Where available, [^{68}Ga]Ga-OncoCAIX PET imaging results are correlated with histopathological findings from biopsy or surgical specimens. ***Results:*** As of 2 May, three patients have been enrolled and undergone [^{68}Ga]Ga-OncoCAIX PET imaging. All patients presented with an incidental renal mass on contrast enhanced CT suspicious for ccRCC and were scheduled for surgical resection. No adverse events were reported during the study. [^{68}Ga]Ga-OncoCAIX showed favourable biodistribution with renal excretion, low activity in healthy kidney parenchyma and physiological uptake in the gastrointestinal tract, particularly in the stomach. In two patients, moderate radiopharmaceutical uptake was observed in the suspected renal mass early at the post-injection acquisition, with increasing intensity at 60- and 120-minutes scans (SUVmax 25.5 and 60.8 at 60 minutes, respectively). One patient showed no significant uptake in the suspected renal lesion. ***Conclusion:*** Preliminary first-in-human data showed that [^{68}Ga]Ga-OncoCAIX is safe and well tolerated, with favourable biodistribution and low background activity in healthy kidney tissue. Early imaging results suggested promising tumour-to-background contrast in suspected ccRCC lesions. Histopathological confirmation will determine the diagnostic accuracy for ccRCC discrimination and potential clinical utility.

OP-299

The impact of ^{68}Ga-Pentixafor PET/CT imaging with solid tumours, a comparison with ^{18}F-FDG: a prospective cross-sectional study

B. Hadebe-Chonco[1], *L. Harry*[1], *N. Ndlovu*[1], *M. Patel*[1], *L. Gabela*[1], *S. Masikane*[1], *V. Pillay*[1], *T. Nxasana*[1], *T. Mkhize*[1], *M. Msimang*[2], *M. Sathekge*[3], *M. Vorster*[1];
[1]*University of KwaZulu Natal, Nuclear Medicine Department, Durban, SOUTH AFRICA,* [2]*University of KwaZulu Natal, Anatomical Pathology Department, Durban, SOUTH AFRICA,* [3]*Department of Nuclear Medicine, University of Pretoria, Pretoria, SOUTH AFRICA.*

Aim/Introduction: ^{68}Ga-Pentixafor, offers a novel, non-invasive imaging tool for CXCR4 expression. Although it has shown promising utility in hematological malignancies, evidence in solid tumours remains limited. This study aimed to evaluate the impact of ^{68}Ga-Pentixafor PET/CT in patients with solid tumours, comparing uptake patterns with ^{18}F-FDG PET/CT and CXCR4 immunohistochemistry (IHC) to determine whether CXCR-4 targeted imaging may be a surrogate for IHC staining. ***Materials and Methods:*** One hundred and nineteen patients with histologically proven cancers of the breast (n=53), head and neck (n=23), gynecological (34), male genitourinary tract (n=2), gastrointestinal tract (n=6), lung (n=1) and pancreas (n=1) underwent ^{68}Ga-Pentixafor PET/CT imaging. ^{18}F-FDG PET/CT images were available in 92/119 cases (77%). Semi-quantitative parameters including maximum standardized uptake values (SUVmax), total lesion uptake (TLU), metabolic tumour volume (MTV) and tumour-to-background ratios (TBR) of primay lesions were measured and correlated with HIV status, tumour grade and CXCR4 immunohistochemistry staining (n=69) using the t-test or Wilcoxon test as appropriate. Pearson correlation coefficients were used to assess the correlation between ^{68}Ga-Pentixafor uptake and overall survival. ***Results:*** Seventy-nine percent (94/119) were female, the median age (Q1-Q3) was 53.0(47.0-68.0). Forty five percent (55/119) of patients (46%) were HIV positive. ^{68}Ga-Pentixafor uptake was visually detectable in 105/119 (88%) of the primary tumours and was generally lower and more heterogeneous than ^{18}F-FDG. However, high uptake was observed in aggressive tumour subtypes, including triple-negative breast cancer (TNBC), high-grade tumours and HIV-positive patients. HIV-positive patients were significantly younger median age (IQR) 48.0(42.5-58.0) compared to HIV-negative 53.0(47.0-68.0) p=0.012. Triple-negative breast cancer, vulva, ovarian and nasopharyngeal carcinomas demonstrated higher ^{68}Ga-Pentixafor avidity than the other solid tumours. A significant positive correlation was found between ^{68}Ga-Pentixafor uptake and CXCR4 IHC expression in head and neck cancer r= 0,5 p=0,02. Notably, ^{68}Ga-Pentixafor detected additional metastatic lesions in the brain and skull, while ^{18}F-FDG remained superior in identifying skeletal metastases. A weak negative correlation was also noted between ^{18}F-FDG SUVmean and overall survival r=-0,1983 (p=0.057). ***Conclusion:*** ^{68}Ga-Pentixafor uptake was high in triple-negative breast cancer, vulva, ovarian and nasopharyngeal carcinomas. ^{68}Ga-Pentixafor PET/CT may complement ^{18}F-FDG, adding value particularly in the detection of brain lesions and in HIV-infected individuals with breast cancer. Future studies should explore its value in prognostication and guiding CXCR4-targeted therapies. The high uptake of ^{68}Ga-Pentixafor in HIV-infected patients with solid malignancies emphasizes the importance of exploring the potential synergistic effect of CXCR4 targeted therapies in these patients.

OP-300

Prospective Head-to-Head Comparison of ^{18}F-FDG PET/CT and ^{18}F-FAPI-42 PET/CT for Assessing Inguinal Lymph Node Metastases in Penile Squamous Cell Carcinoma

X. Tong[1], *W. Ouyang*[1], *W. Hou*[1], *C. Zhou*[1], *H. Fu*[1], *J. Liu*[1], *Q. Wang*[1], *Z. Liu*[2], *K. Cao*[1], *K. Yao*[1], *X. Li*[3], *L. Wang*[1], *M. Zhao*[1];
[1]*Third Xiangya Hospital of Central South University, Changsha, Hunan, CHINA,* [2]*The Affiliated Cancer Hospital of Xiangya School of Medical, Changsha, Hunan, CHINA,* [3]*Medical University of Vienna, Vienna, Austria, AUSTRIA.*

Aim/Introduction: This study aimed to compare the diagnostic performance of ^{18}F-FAPI-42 PET/CT and ^{18}F-FDG PET/CT in detecting inguinal lymph node (ILN) metastases in penile squamous cell carcinoma (PSCC) and to explore the correlation between tracer uptake and fibroblast activation protein (FAP) and glucose transporter 1 (GLUT1) expression. ***Materials and Methods:*** This prospective study included 21 patients with clinically node-positive (cN+) PSCC, who underwent both ^{18}F-FDG PET/CT and ^{18}F-FAPI-42 PET/CT within one week prior to surgical resection. Visual PET/CT interpretations were compared with histopathological findings, and quantitative PET parameters (SUVmax, SUVmean, TBR) were analyzed. McNemar's test was used to compare diagnostic performance metrics, and Spearman's correlation assessed the relationship between tracer uptake and immunohistochemical FAP/GLUT1 expression ***Results:*** A total of 359 lymph nodes were dissected. ^{18}F-FAPI-42 PET/CT exhibited superior diagnostic performance compared to ^{18}F-FDG PET/CT, with higher staging accuracy (99.72% vs. 91.92%), sensitivity (95.65% vs. 86.96%), and specificity (100% vs. 92.26%). ^{18}F-FAPI-42 identified 22 of 23 metastatic LNs, whereas ^{18}F-FDG PET/CT identified 19. Additionally, ^{18}F-FDG PET/CT produced 26 false positives, while ^{18}F-FAPI-42 PET/CT had none, highlighting its superior specificity in differentiating metastatic from inflammatory lymphadenopathy. In patient-based analyses, ^{18}F-FDG PET/CT demonstrated diagnostic performance with 9 true-positive, 1 false-negative, 8 true-negative, and 3 false-positive cases, yielding an overall accuracy of 80.95%. In comparison, ^{18}F-FAPI PET/CT exhibited superior diagnostic capability, achieving 100% accuracy in detecting LNs metastases among PSCC, with no false-positive or false-negative results observed. Immunohistochemical analysis revealed a strong correlation between FAP expression and ^{18}F-FAPI-42 SUVmax ($r = 0.78$, $P < 0.001$), while GLUT1 expression correlated with ^{18}F-FDG SUVmax ($r = 0.81$, $P < 0.001$) ***Conclusion:*** ^{18}F-FAPI-42 PET/CT outperformed ^{18}F-FDG PET/CT in ILN staging, demonstrating higher accuracy and specificity with fewer false positives. These findings suggest that ^{18}F-FAPI-42 PET/CT could

refine nodal staging, reduce unnecessary inguinal lymph node dissection (ILND), and enhance clinical decision-making in PSCC management.

707

Monday, October 6, 2025, 8:00 - 9:30
Room 212

TROP Session - Neuroimaging Committee: Innovations and Methodologies in Nuclear Neuroimaging

OP-301

First-in-human study of a ^{18}F-labeled PET tracer for glutamate AMPA receptors, [^{18}F]K-40

S. Ichijo[1], *Y. Kimura*[2], *T. Arisawa*[1], *M. Hatano*[1], *W. Nakajima*[1], *T. Miyazaki*[1], *T. Eiro*[1], *Y. Takada*[1], *R. Iai*[1], *A. Sano*[1], *M. Sonoda*[1], *Y. Takayama*[1], *T. Takahashi*[1];
[1]*Yokohama City University, Yokohama, JAPAN,* [2]*Kindai University, Osaka, JAPAN.*

Aim/Introduction: Although alteration of glutamate α-amino-3-hydroxy-5-methyl-4-isoxazole propionic acid receptor (AMPAR) distribution has been believed to underlie physiological and pathological neuronal function, there has been no modality to evaluate AMPA receptors in the living human. [11C]K-2, the PET tracer we previously developed, is the first and only technology to visualize AMPAR densities in the living human brain. Despite its favorable kinetics as a PET tracer, the short half-life of the 11C limits availability of [11C]K-2. We recently developed an 18F-labeled PET tracer, [18F]K-40, which demonstrated AMPAR-specific binding properties and brain distribution similar to that of [11C]K-2 in preclinical studies. The purpose of this first-in-human study is to evaluate the properties of [18F]K-40 in the human and to compare the kinetics and PET images of [18F]K-40 with those of [11C]K-2. ***Materials and Methods:*** Five healthy volunteers were enrolled and underwent dynamic PET scanning using [18F]K-40 and [11C]K-2. Non-displaceable binding potential (BPND) with white matter as reference was calculated by Logan graphical analysis using tissue time-activity curves (tTACs), and VT of [18F]K-40 was calculated using plasma time-activity curves (pTACs). The intraindividual correlation between the BPND values obtained for [18F]K-40 and [11C]K-2 was examined. To optimize the time window for PET scanning, BPND and standardized uptake value ratio (SUVR) were evaluated. ***Results:*** The tTACs of [18F]K-40 showed similar curves to those of [11C]K-2. Logan graphical analysis using pTACs revealed reversible binding of [18F]K-40. BPND obtained with [18F]K-40 and [11C]K-2 significantly correlated in each corresponding region and showed very good correlation, which indicated that K-40, as observed with K-2, can provide PET images that reflect the amount of AMPA receptors. A good linear relationship was observed between BPND and the summation image of SUVR between 40 and 50 minutes after radiotracer injection. ***Conclusion:*** [18F]K-40, as [11C]K-2, has favorable binding properties as an AMPA-PET tracer. Thus, [18F]K-40 could characterize AMPAR distribution in pathophysiological conditions of the brain and facilitate the development of novel diagnostics of neuropsychiatric disorders.

OP-302

Quantitative Detection of Limbic-predominant Age-related TDP-43 Encephalopathy (LATE) Using Brain FDG PET: An IAEA Multinational Neuroimaging Consortium

T. Thientunyakit[1], *J. Arbizu*[2], *M. Garcia-Granero*[3], *D. Cross*[4], *A. Damián*[5], *J. Warwick*[6], *J. Jamsek*[7], *J. Reimand*[8], *M. Tripathi*[9], *M. Trošt*[7], *N. Sultana*[10], *O. Pellet*[11], *D. Paez*[11], *S. Minoshima*[4];
[1]*Faculty of Medicine Siriraj Hospital, Mahidol University, Bangkok, THAILAND,* [2]*Clinica Universidad de Navarra, Pamplona, SPAIN,* [3]*Consultoria Estadistica Marta Garcia-Granero, Pamplona, SPAIN,* [4]*The University of Utah, Salt Lake City, UT, UNITED STATES OF AMERICA,* [5]*Centro Uruguayo de Imagenología Molecular (CUDIM), Montevideo, URUGUAY,* [6]*Stellenbosch University, Stellenbosch, SOUTH AFRICA,* [7]*University Medical Centre Ljubljana, Ljubljana, SLOVENIA,* [8]*North Estonia Medical Centre, Tallinn, ESTONIA,* [9]*All India Institute of Medical Sciences, New Delhi, INDIA,* [10]*NINMAS, Bangladesh Atomic Energy Commission (BAEC), Dhaka, BANGLADESH,* [11]*The International Atomic Energy Agency, Vienna, AUSTRIA.*

Aim/Introduction: Limbic-predominant age-related TDP-43 encephalopathy (LATE) is increasingly recognized among dementia patients. Brain FDG PET has revealed unique metabolic signatures associated with LATE. This study investigated a quantitative method for detecting LATE-related changes in brain FDG PET based on autopsy-confirmed LATE and Alzheimer's disease (AD) cases. The method was applied to mild cognitive impairment or mild AD patients with possible comorbidities recruited through the International Atomic Energy Agency (IAEA) Multinational Neuroimaging Consortium. ***Materials and Methods:*** Brain FDG PET scans from 4 groups were analyzed with NEUROSTAT/3D-SSP: 133 IAEA cohort cases from 6 countries (mean age 67.8±9.1 years, MMSE 24.7±3.5, CDR 0.6±0.4); 6 autopsy-confirmed LATE cases (ADNI); 32 autopsy-confirmed AD cases (University of Utah); and 20 healthy controls with negative amyloid PET. Group Z-score maps for autopsy-confirmed LATE and AD were generated using the healthy controls for reference. Individual Z-score maps of the IAEA cohort cases were generated using the same controls. To quantify individual's disease patterns, Z-score products were calculated by multiplying each individual's Z-score map with the disease template (LATE or AD) on a pixel-by-pixel basis, averaging across the brain. Z-score product thresholds of 16 (Z=4x4) and 9 (Z=3x3) were used to identify probable LATE and AD, respectively. ***Results:*** The autopsy-proven LATE template demonstrated unique hypometabolism in the medial temporal lobe, anterior temporal lobe, and inferior frontal lobe, contrasting with the relatively mild medial temporal hypometabolism in AD. Among the IAEA cohort, 8 patients (6%) were identified as probable LATE (mean age 67.3±8.1, MMSE 23.9±3.1, CDR 0.79±0.3) and 15 (11%) showed features of both LATE and AD (mean age 71.1±8.8, MMSE 21.1±2.2, CDR 0.80±0.3), indicating a total 17% prevalence of LATE pathology. Visual inspection confirmed typical LATE patterns in these patients, and 17 additional cases (13%) showed subthreshold LATE features. Among probable LATE cases, 77% had positive amyloid biomarkers (amyloid PET or CSF analysis). ***Conclusion:*** Brain FDG PET combined with Z-score product analysis based on autopsy-confirmed LATE and AD cases reveled probable LATE pathology in patients with MCI or mild AD. While LATE findings can exist independently, a larger proportion of cases demonstrated co-existing LATE and AD pathologies, further supported by positive amyloid biomarkers. The notable presence of LATE pathology in this population underscores the need for further investigation into the epidemiology of LATE and its potential synergistic relationship with AD.

OP-303

Variations in Glucose Metabolism Covariance Pattern Linked to Aβ Status in Subjective Cognitive Decline

R. Devi[1], *M. Daamen*[1,2], *E. Duezel*[3,4,5], *M. Essler*[6], *F. C. Gaertner*[6], *J. Hellmann*[7,8,9], *F. Jessen*[1,10,11], *C. Laske*[12,13,14], *O. Peters*[7,8,9], *J. Priller*[7,15,16], *A. Spottke*[1,17], *S. Teipel*[18,19], *N. Upadhyay*[1,2], *M. Wagner*[1,20], *H. Boecker*[1,2];
[1]*German Center for Neurodegenerative Diseases (DZNE), Bonn, GERMANY,* [2]*Clinical Functional Imaging Lab, Department of Nuclear Medicine, University Hospital Bonn, Bonn, GERMANY,* [3]*German Center for Neurodegenerative Diseases (DZNE), Magdeburg, GERMANY,* [4]*Insitute of Cognitive Neurology and Dementia Research (IKND), Magdeburg, GERMANY,* [5]*Department for Psychiatry and Psychotherapy, University Hospital Magdeburg, Magdeburg, GERMANY,* [6]*Department of Nuclear Medicine, University Hospital Bonn, Bonn, GERMANY,*

[7]German Center for Neurodegenerative Diseases (DZNE), Berlin, GERMANY, [8]Department of Psychiatry and Neurosciences, Charité Universitätsmedizin Berlin, Berlin, GERMANY, [9]Experimental and Clinical Research Center, Charité Universitätsmedizin Berlin, Berlin, GERMANY, [10]Department of Psychiatry, University of Cologne, Cologne, GERMANY, [11]Excellence Cluster on Cellular Stress Responses in Aging-Associated Diseases (CECAD), University of Cologne, Cologne, GERMANY, [12]German Center for Neurodegenerative Diseases (DZNE), Tübingen, GERMANY, [13]Section for Dementia Research, Hertie Institute for Clinical Brain Research, Tübingen, GERMANY, [14]Department of Psychiatry and Psychotherapy, University of Tübingen, Tübingen, GERMANY, [15]Department of Psychiatry and Psychotherapy, Charité Universitätsmedizin Berlin, Berlin, GERMANY, [16]University of Edinburgh and UK DRI, Edinburg, UNITED KINGDOM, [17]Department of Neurology, University Hospital Bonn, Bonn, GERMANY, [18]German Center for Neurodegenerative Diseases (DZNE), Rostock, GERMANY, [19]Department of Psychosomatic Medicine, Rostock University Medical Center, Rostock, GERMANY, [20]Department of Old Age Psychiatry and Cognitive Disorders, University Hospital Bonn, Bonn, GERMANY.

Aim/Introduction: Subjective Cognitive Decline (SCD) lies between cognitively normal individuals and those with Mild Cognitive Impairment (MCI) on the Alzheimer's Disease (AD) clinical continuum. While not all SCD individuals progress into MCI or AD dementia, concomitant Amyloid-beta (Aβ) positivity significantly increases the risk[1]. Investigating differences in glucose metabolism between Aβ-positive and Aβ-negative SCD patients offers a unique opportunity to help illuminate early metabolic changes associated with amyloid pathology, providing insights into the mechanisms driving clinical progression. ***Materials and Methods:*** FDG-PET and MPRAGE data of SCD participants were obtained from the DELCODE[2] study. Using established analysis pipelines for FBB-PET (PMID: 37070734), Aβ status was determined using centiloid (CL) scores from corresponding FBB-PET data, classifying Aβ-negative (CL≤12), Aβ-positive (CL>30), and Intermediate (12<CL≤30). Glucose metabolism of 24 Aβ-positive participants (73.4±5.2 years; 13 male) were compared with 24 demographically matched Aβ-negative participants (71.5±5.1 years; 13 male) using Scaled Sub-Profile Modeling (SSM) PCA[3]. Preprocessed (motion-corrected, co-registered, smoothened, spatially normalized, and intensity-normalized[4]) FDG-PET data were analyzed in ScanVP[5]. The glucose metabolism covariance pattern that best separated the two groups was identified based on combinations of Group-Invariant Subprofiles (GIS) whose resulting scores separated the two groups with the minimum Akaike Information Criterion value. The pattern was verified using Leave-One-Out-Cross-Validation (LOOCV), and further validated against similarly preprocessed FDG-PET data from 19 Intermediates. ***Results:*** A glucose metabolism covariance pattern was identified that significantly separated Aβ-positive from Aβ-negative participants: p=0.00011 (two-tailed Student's t-test, unequal variance), AUC=0.80, Sensitivity=0.71, Specificity=0.79 and Accuracy=0.75. Key regions showing hypermetabolism included cingulate/paracingulate gyri, thalamus, insula, putamen and left cerebellum, while hypometabolism predominated in the occipital/temporal/parietal/frontal lobes, caudate, and hippocampal regions. Subject scores of LOOCV-generated patterns correlated highly with the original pattern (r=0.96±0.03). Additionally, the scores of the Intermediate participants (z=0.66±0.94) lay between those of the Aβ-negative (z=0.00±0.82) and Aβ-positive groups (z=1.05±0.89) and were significantly different from Aβ-negative scores (p=0.019). ***Conclusion:*** This study successfully identified a glucose metabolism covariance pattern that distinguishes Aβ-positive from Aβ-negative SCD participants, highlighting early metabolic changes associated with amyloid pathology. The Intermediate group's scores suggest a continuum of metabolic alterations across the SCD spectrum, underscoring the value of FDG-PET in identifying early biomarkers for AD progression. ***References:*** [1] Elman et al., Biol. Psych., 2021; [2] Jessen et al., Alzheimer's Research & Therapy, 2018; [3] Moeller et al., JCBFM, 1987; [4] López-González et al., NeuroImage, 2020; [5] Spetsieris et al., JoVE., 2013.

OP-304

The interaction among Amyloid, tau and FDG metabolism in Alzheimer's disease using PET-based Braak staging

G. Huang[1], *Y. Zhou*[1], *H. Shao*[1], *J. Hao*[2], *L. Qi*[2], *J. Liu*[1], *C. Zhang*[1]; *[1]Renji Hospital, Shanghai Jiao Tong University School of Medicine, Shanghai, CHINA, [2]United Imaging Healthcare, Shanghai, CHINA.*

Aim/Introduction: Alzheimer's disease (AD) is characterized by the accumulation of amyloid-β (Aβ) plaques and tau neurofibrillary tangles, followed by neurodegeneration and progressive cognitive decline. The ATN framework, a biomarker-based diagnostic system for AD, categorizes amyloid-β (A), tau (T), and neurodegeneration (N) biomarkers as core diagnostic components. This study applies the Braak neurofibrillary tangle staging system to PET imaging data in AD patients. Within the ATN framework, we investigate the dynamic interplay between FDG metabolism, Aβ, and tau across different AD stages, as well as their associations with cognitive performance. ***Materials and Methods:*** All participants (n = 84; mean age 68.58 ± 7.51 years; age range 56-81; 64.3% female; MMSE score 15.73 ± 7.08; MoCA score 11.30 ± 6.29) underwent standardized clinical evaluations, including comprehensive history collection, neurological examinations, caregiver interviews, and multimodal neuroimaging: brain [^{18}F]FDG PET/MR, [^{18}F]Florbetapir PET/CT (Aβ-PET), and [^{18}F]PI2620 PET/CT (tau-PET). Cognitive assessments included the Mini-Mental State Examination (MMSE) and Montreal Cognitive Assessment (MoCA). Consensus diagnoses were provided by a multidisciplinary team. Image preprocessing involved partial volume effect correction and segmentation using the AAL brain atlas via uWS-MI/MR software. Reference regions were defined as cerebellar grey matter for Aβ-PET and tau-PET, and the entire cerebellum for FDG-PET. Braak stage-specific regions of interest (ROIs) were analyzed to calculate standardized uptake value ratios (SUVRs). Mediation analysis evaluated causal pathways among biomarkers, while Pearson correlations assessed associations between biomarker SUVRs and cognitive scores. ***Results:*** AD exhibited Braak stage-dependent biomarker dynamics: Aβ directly drove early FDG hypometabolism (Braak I/II: $\beta = 0.32$, $p = 0.003$; Braak III: $\beta = 0.29$, $p = 0.006$), whereas tau mediated late-stage metabolic decline (Braak V: $\beta = -0.51$, $p < 0.001$). Braak IV demonstrated synergistic Aβ-tau effects (combined $\beta = -0.62$, $p < 0.001$). FDG-PET SUVRs strongly correlated with MMSE/MoCA scores across Braak stages (Braak I-V: $R > 0.3$, $p < 0.05$), while tau-PET SUVRs showed inverse correlations (Braak I-V: $R < -0.3$, $p < 0.05$). Aβ-PET exhibited no significant cross-biomarker associations. ***Conclusion:*** Multimodal PET biomarker analysis enhances diagnostic accuracy by capturing complementary pathological and metabolic signatures in AD. Braak staging elucidates stage-specific contributions of Aβ and tau to neurodegeneration, with PET-Braak stages correlating with biomarker progression and cognitive decline. These findings underscore the potential of in vivo PET staging to refine AD diagnosis and monitor disease trajectory.

OP-305

Glymphatic system dysfunction is strongly linked to neurodegeneration and serves as a bridge between ATN biomarkers and cognitive decline in sex-dependent in Alzheimer's disease

J. Wang;
Department of Nuclear Medicine & PET Center, Huashan Hospital, Fudan University, Shanghai, China, Shanghai, CHINA.

Aim/Introduction: To elucidate how glymphatic function disruption affects AD pathology and explore its relationships with ATN biomarkers, with a focus on the effects of sex and amyloid

status on these relationships. ***Materials and Methods:*** We recruited 1,135 individuals from the Chinese Preclinical Alzheimer's Disease Study (CPAS), including 247 AD patients, 283 individuals with mild cognitive impairment (MCI), and 605 cognitively unimpaired (CU) participants. All participants underwent Aβ-PET, diffusion magnetic resonance imaging (MRI), and neuropsychological assessments; additionally, 695 participants underwent FDG-PET, 394 underwent tau-PET, and 615 provided blood samples to measure plasma ATN biomarkers. Glymphatic function was evaluated using the diffusion tensor imaging analysis along the perivascular space (DTI-ALPS) index. A one-way analysis of variance was conducted to examine the differences among DTI-ALPS, imaging, and blood ATN biomarkers. Partial correlation and mediation models were employed to investigate the associations among glymphatic function, ATN biomarkers, and cognition. ***Results:*** The AD group has a lower ALPS index than the MCI group and CU, and MCIs are also lower than CUs. The Aβ-positive group had a lower ALPS index than the Aβ-negative group, and the male group had a lower ALPS index than the female group. The ALPS index was negatively associated with amyloid deposition, tau burden and plasma p-tau 181 and neurofilament light (NfL), and positively associated with glucose metabolism and hippocampal volume only in females. ALPS-index showed significant mediation effects between global amyloid deposition and meta-temporal lobe tau burden, between global amyloid deposition and plasma p-tau 181. The ALPS index mediates the associations of Aβ pathology with neurodegeneration and tau pathology with neurodegeneration in the female or Aβ-positive groups. The ALPS index was positively associated with global cognition, memory, language and executive function. The ALPS index mediates the associations of Aβ pathology with global cognition, and tau pathology with global cognition in the female or Aβ-positive groups, and neurodegeneration with global cognition only in the female group. ***Conclusion:*** Compared to CU, a significant reduction in ALPS-indexes in MCI and AD patients, and males exhibit lower ALPS-indexes than females. The ALPS-index was correlated with ATN biomarkers and mediated key relationships among Aβ, tau pathology, neurodegeneration, and cognition in a sex manner. The impaired glymphatic function bridges the link between Aβ pathology, tau pathology, neurodegeneration and cognitive decline in a sex-dependent manner. These findings suggest that glymphatic dysfunction plays a critical role in the pathogenesis of AD in a sex-dependent manner.

OP-306

Amyloid PET/CT could not replace tau PET/CT for Alzheimer's disease in terms of disease staging and predicting outcome: a large cohort single-institutional study

S. Chen, *Y. Leung, K. Wu, Y. Wong, S. Cheung, Y. Yip, K. Cheng, C. Ho;*
Hong Kong Sanatorium & Hospital, Hong Kong, HONG KONG.

Aim/Introduction: The AT[N] criteria of the 2018 NIA-AA Research Framework specifies that the Alzheimer's disease (AD) pathway is defined by in vivo biomarkers of β-amyloid (A) and tau (T). Amyloid is generally regarded as a Core 1 initiator for early detection of pathological change, while tau is a Core 2 driver as a continuous variable related to symptom severity and prognosis prediction. Existing data on AD PET/CT studies are mostly collected from small multicenter trials, which are inevitably heterogeneous, and largely on amyloid-burden. We therefore performed a large cohort, single-institutional PET/CT study with dual-tracers, ^{11}C-PIB (amyloid) and ^{18}F-T807 (tau), on patients clinically suspected of AD, aiming at comparing head-to-head the diagnostic power and severity correlation/prediction of AD between these 2 tracers. ***Materials and Methods:*** During the last 4 years, 863 patients (M:371, F:492; age range:48-92 years, mean=70.4±8.0 years) with decreased short-term memory, but with no history of other neurodegenerative disease, were consecutively recruited. They all underwent ^{11}C-PIB and ^{18}F-T807 PET/CT in 2 separate days. ^{11}C-PIB PET was scanned at 5 & 35 minutes and ^{18}F-T807 PET began at 85 minutes post injection, each for 10-min static imaging. Global cortical-to-cerebellum SUV ratio (SUVR) was calculated for both ^{11}C-PIB and ^{18}F-T807 PET. ^{11}C-PIB "global-retention">=1.42 was taken as threshold for positive amyloid-burden (by prior studies). In amyloid-positive patients, correlation analysis was performed between global SUVR of ^{11}C-PIB ($SUVR_{amyloid}$) and ^{18}F-T807 ($SUVR_{tau}$). ***Results:*** 530/863 (61.4%) patients had negative ^{11}C-PIB PET (mean $SUVR_{amyloid}$=1.10±0.07, median $SUVR_{amyloid}$=1.10). For these [A-] PET patients, ^{18}F-T807 PET also showed minimal-to-no uptake (mean $SUVR_{tau}$=1.06±0.05, median $SUVR_{tau}$ =1.03), categorized as [T-] PET. The remaining 333/863 (38.6%) patients had positive ^{11}C-PIB [A+] PET with $SUVR_{amyloid}$ ranging from 1.17 to 2.24 ($SUVR_{amyloid}$=1.55±0.21). The head-to-head ^{18}F-T807 PET varied significantly among [A+] patients, ranging from zero to intense ^{18}F-T807 uptake ($SUVR_{tau}$ range:0.9-2.34, mean:1.25±0.24). In these [A+] patients, amyloid-burden showed no significant difference between [T+] (N=177/333) and [T-] patients (N=156/333): $SUVR_{amyloid}$=1.58±0.20 vs. 1.49±0.20, P>0.05; while corresponding $SUVR_{tau}$=1.39±0.23 vs. $SUVR_{tau}$=1.05±0.05, respectively, P<0.05. Correlation analysis also indicated that amyloid-burden did not correlate with tau-burden in AD patients (r=0.260, P>0.05), suggesting that amyloid-PET is less optimal for predicting AD disease severity quantified by tau-PET. ***Conclusion:*** ^{11}C-PIB PET/CT is valuable for diagnosing AD at an earlier phase. In [A-] patients, tau-PET may not be necessary. However, when ^{11}C-PIB PET is positive, integration of tau-PET is highly suggested to refine AD staging, potentially for severity grading and predicting treatment response.

OP-307

The role of metabolism first or amyloid first approach in the assessment of patients with early cognitive impairment due to Alzheimer's disease

A. Damian[1], *M. Trošt*[2], *J. Jamsek*[3], *T. Thientunyakit*[4], *M. Garcia Granero*[5], *J. Warwick*[6], *J. Reimand*[7], *M. Perovnik*[2], *N. Sultana*[8], *O. Pellet*[9], *F. Mariani*[10], *D. Cross*[11], *M. Tripathi*[12], *D. Paez*[9], *J. Arbizu*[13], *S. Minoshima*[11];
[1]*Uruguayan Centre of Molecular Imaging (CUDIM), Montevideo, URUGUAY,* [2]*University Medical Centre, Ljubljana, SLOVENIA,* [3]*UMC Ljubljana, Ljubljana, SLOVENIA,* [4]*Faculty of Medicine Siriraj Hospital, Mahidol University, Bangkok, THAILAND,* [5]*Consultoria Estadistica Marta Garcia-Granero,, Pamplona, SPAIN,* [6]*Stellenbosch University, Stellenbosch, SOUTH AFRICA,* [7]*North Estonia Medical Centre, Tallinn, ESTONIA,* [8]*NINMAS, Bangladesh Atomic Energy Commission (BAEC), Dhaka, BANGLADESH,* [9]*International Atomic Energy Agency, Vienna, AUSTRIA,* [10]*Departamento de Neuropsicología, Hospital de Clínicas, Universidad de la República (UdelaR), Montevideo, URUGUAY,* [11]*The University of Utah, Salt Lake City, UT, UNITED STATES OF AMERICA,* [12]*All India Institute of Medical Sciences, New Delhi, INDIA,* [13]*Clinica Universidad de Navarra, Pamplona, SPAIN.*

Aim/Introduction: Recently, algorithms have been developed to utilize molecular imaging techniques for evaluating patients presenting with clinical symptoms of Alzheimer's disease (AD). However, there is still no clinical validation of the use of these algorithms in patient series. The aim of this study was to compare the metabolism first versus the amyloid first approach to elucidate the cause of early cognitive decline in patients with suspected early AD. ***Materials and Methods:*** In this prospective multicentre study that recruited patients with possible or probable early AD and MCI due to AD, all patients underwent full neuropsychological examination, MRI, ^{18}F-FDG PET/CT, and determination of amyloid status (PET/CT and/or CSF analysis). The diagnosis made after ^{18}F-FDG or amyloid determination was compared with the

consensus diagnosis which was determined based on metabolic brain pattern and amyloid status. ***Results:*** Out of 133 patients recruited, 96 underwent both ^{18}F-FDG and amyloid determination and were analysed. Thirteen patients were excluded from the further analyses due to discrepant result of amyloid and metabolic brain evaluation. The amyloid status was positive (amy+) in 55/83 patients, while metabolic brain changes were characteristic for AD in 45/83 (all amy+), DLB in 5/83 (all amy +), FTD in 5/83 (all amy-), and with LATE (all amy-) in 2/83. 2/83 had normal brain metabolism (1 amy+), 23/83 had metabolic changes consistent with age related atrophy (10 amy+) and in 1/83 the finding was indeterminate (amy+). ^{18}F-FDG imaging was consistent with the consensus diagnosis in 73/83 patients, while amyloid was consistent in all cases. ***Conclusion:*** While determination of amyloid status could confirm or exclude the diagnosis of AD, ^{18}F-FDG PET provides broader diagnostic insight, differentiating among various neurodegenerative disorders, including AD and DLB. While the combination of both modalities likely provides the most accurate diagnosis, a metabolism-first approach may be especially valuable in resource-constrained countries where amyloid determination is limited.

OP-308

Multiorgan Metabolic Dysregulation in Alzheimer's Disease: Total-body PET/CT Reveals Systemic Network Interactions with Amyloid Burden

R. Xu[1], *Y. Duan*[2], *L. Gao*[2], *Y. Chen*[1], *H. Han*[1], *Z. Cheng*[2], *Z. Xie*[1,3];
[1]*Institute of Medical Technology, Peking University Health Science Center, Peking University, Beijing, CHINA,* [2]*Department of Nuclear Medicine, The First Affiliated Hospital of Shandong First Medical University Shandong Provincial Qianfoshan Hospital, Jinan, CHINA,* [3]*National Biomedical Imaging Center, Peking University, Beijing, CHINA.*

Aim/Introduction: Alzheimer's disease (AD) is increasingly recognized as a systemic disorder, with pathological changes extending beyond the brain to peripheral organs. A common feature of these systemic processes is disrupted energy metabolism[1]. However, traditional PET imaging has been limited in assessing such information due to its restricted axial field of view. Total-body PET overcomes these limitations, enabling simultaneous imaging of multiple organs. In this study, we utilized two tracers to elucidate the interplay between cerebral amyloid-beta deposition and systemic glucose metabolism, aiming investigate the systemic manifestations of AD. ***Materials and Methods:*** Sixty-four AD patients were enrolled, and data were acquired using uEXPLORER with both [^{18}F]-Flobetapir and [^{18}F]-FDG tracers. A total of 131 whole-body and 83 brain regions were segmented via the MPUM model using CT images, from which SURr values were extracted. To further quantify the amyloid load, the Centiloid (CL) scores were calculated from six representative VOIs (medial orbitofrontal, lateral temporal, parietal, anterior cingulate gyrus, posterior cingulate gyrus, and precuneus), following the AHEAD 3-45 classification (CL ≤20, 20< CL<40, CL≥40)[2,3]. A metabolic connectivity matrix with a size of 214×214 was constructed using FDG tracers, employing Pearson correlation coefficients. This matrix was then analyzed to assess the topological properties of the network across different CL groupings. Additionally, we computed edge correlations between the population-based residual matrix and CL scores, selecting significant edges ($p<0.01$) as positive (Σ^+) or negative (Σ^-) features. An ensemble model for CL prediction was trained using the edge features and validated on test data. ***Results:*** Our study identified CL-dependent brain-body connectivity alterations in amyloid pathology. The CL<20 subgroup exhibited compensatory hyperconnectivity between the inferior parietal lobule and posterior orbital gyrus ($\Delta=0.97$), alongside elevated cardiocentric connectivity ($\Delta=0.98$) , whereas CL>40 subgroup demonstrated uterine-brain hyperconnectivity ($\Delta=1.28$), suggesting potential neuroendocrine dysregulation. Network analysis revealed 18 positive and 37 negative edges. Our predictive model demonstrated strong validity ($R^2=0.912$), robustly linking CL thresholds to these distinct connectivity patterns. ***Conclusion:*** By revealing the relationship between systemic metabolic networks and amyloid burden, our proposed approach characterize AD's systemic pathology, potentially facilitating more precise disease subtyping. ***References:*** ULLAH R, et al. Ageing Res Rev, 2021, KLUNK W E, et al, Alzheimers Dement, 2015. RAFII M S, et al. Alzheimers Dement, 2023.

OP-309

PET imaging of βAmyloid Load Across the Spectrum of Dementia with Lewy Bodies

M. Yoshita[1], *S. Tsuji*[2], *K. Yokoyama*[2];
[1]*NHO Hokuriku National Hospital, Nanto, JAPAN,* [2]*Public Central Hospital of Matto Ishikawa, Hakusan, JAPAN.*

Aim/Introduction: Dementia with Lewy bodies (DLB) is characterized by predominant deficits in executive and visuospatial functions, accompanied by clinical features including parkinsonism, fluctuating cognition, visual hallucinations, and REM sleep behavior disorder. The role of β-amyloid (Aβ) plaques in DLB, especially during prodromal stages, remains unclear. This study investigates Aβ load throughout the DLB spectrum, from isolated REM sleep behavior disorder (iRBD) to mild cognitive impairment with Lewy bodies (MCI-LB) and fully developed DLB. ***Materials and Methods:*** A consecutive cross-sectional study was conducted on patients diagnosed iRBD, MCI-LB, or DLB at the Public Central Hospital of Matto Ishikawa Dementia Research Center. Aβ levels were measured using Pittsburgh compound B (PiB) PET, and Centiloid (CL) scale was calculated. Comparisons were made amongst clinical groups. Multiple linear regression tested interactions between sex and APOE ε4 status on PiB CL along the DLB spectrum. ***Results:*** The study included 84 patients: 4 with iRBD, 36 with MCI-LB, and 44 with DLB. Global cortical PiB CL was significantly higher in DLB than MCI-LB and iRBD. The DLB group had the highest proportion of Aβ positive patients (72%), followed by MCI-LB (42%), and iRBD (0%). Woman displayed higher PiB CL with advancing age compared to men. APOE ε4 carriers exhibited higher PiB CL in MCI-LB ($p < 0.03$) and DLB ($p< 0.03$). ***Conclusion:*** Aβ load increases further along the DLB spectrum, with significant elevation in the predementia stage of MCI-LB and DLB compared to iRBD. APOE ε4 carriers and older women tend to have higher Aβ levels. Reducing Aβ levels in DLB clinical trials may benefit early-stage patients or those with certain genetic profiles, aiding in developing disease-modifying treatments.

708

Monday, October 6, 2025, 08:00 - 09:30
Room 115

Joint Symposium 3 - Oncology & Theranostics Committee / EORTC: Oncological Response Criteria for PET: Beyond RECIST, EORTC & PERCIST

OP-310

The Importance of Molecular Imaging Response Criteria: Rationale and Overview of the Landscape

E. Lopci*; IRCCS–Humanitas Research Hospital, Nuclear Medicine, Milan, ITALY.*

OP-311

Overview of PET Response Criteria in Haematological Malignancies (Lymphoma & Multiple Myeloma)

C. Nanni*; IRCCS Azienda Ospedaliero-Universitaria di Bologna, Bologna, ITALY.*

OP-312

Risk and Response Assessment in Prostate Cancer Using PSMA-PET

***W. Fendler**; Universitätsklinikum Essen, Klinik für Nuklearmedizin, Essen, GERMANY.*

OP-313

How to Define Response for Somatostatin Receptor PET?

***C. Deroose**; UZ Leuven, Nuclear Medicine, Leuven, BELGIUM.*

709

Monday, October 6, 2025, 8:00 - 9:30

Room 133+134

e-Poster Presentations Session 5 - Cardiovascular Committee: Cardiovascular e-Poster Presentations Session

EPS-094

Prediction value of cingulate gyrus activity by brain FDG PET for sudden cardiac death in patients with HFrEF

***Y. Zhao**[1], M. Yun[1], Z. Shi[1], Y. Bai[2], X. Zhang[1];*
[1]Laboratory for Molecular Imaging, Department of Nuclear Medicine, Beijing Anzhen Hospital, Capital Medical University, Beijing, CHINA, [2]Department of Nuclear Medicine, the First Affiliated Hospital of Zhengzhou University, Zhengzhou, CHINA.

Aim/Introduction: The brain regulates the heart through the autonomic nervous system (ANS). Disruptions in cardio-neural interactions can affect disease prognosis in patients with heart failure. This study investigated the relationship between ANS-linked neuro-metabolism and left ventricular (LV) diastolic dysfunction in patients with heart failure and reduced ejection fraction (HFrEF), as well as its correlation with sudden cardiac death (SCD)-related events. ***Materials and Methods:*** This retrospective study included 196 (age 58.0 years [IQR: 49-65 years], 88.8% men) patients with HFrEF, who underwent gated single photon emission computed tomography (SPECT) myocardial perfusion imaging (G-MPI) and brain ^{18}F-fluorodeoxyglucose positron emission tomography. The parameters of LV systolic and diastolic function, including left ventricular ejection fraction (LVEF), end-diastolic volume (EDV), end-systolic volume (ESV), peak ejection rate (PER), and peak filling rate (PFR), were evaluated by quantitative GMPI. Cingulate gyrus glucose metabolism activity was analyzed by SPM12 software. Relationships between the brain metabolism and SCD-related events were assessed using Cox models and mediation analyses. ***Results:*** Overall, 22 patients (11.2%, median follow-up: 3.8 years) experienced SCD-related events. Compared to those without SCD-related events, patients with SCD-related events had a lower LVEF (15.0 [13.8-19.3] vs. 21.0 [17.0-25.0], $P < 0.001$), PER (0.58 [0.51-0.79] vs. 0.82 [0.66-1.07], $P < 0.001$), PFR (0.59 [0.48-0.76] vs. 0.80 [0.64-1.04], $P < 0.001$), cingulate gyrus activity (1.01 [0.93-1.05] vs. 1.04 [0.97-1.12], $P = 0.019$), and a higher EDV (250.5 [192.5-345.3 vs. 200.5 [156.75-262.5], $P = 0.014$) and ESV (214.5 [148.8-296.0] vs. 156.0 [116.8-215.3], $P = 0.006$). Patients with reduced metabolism in the cingulate gyrus were more likely to exhibit severe LV diastolic dysfunction (PER: 0.76 [0.60-1.01] vs. 0.89 [0.70-1.09]; PFR: 0.75 [0.60-0.96] vs. 0.88 [0.70-1.08], all $P < 0.05$) and had a higher incidence of SCD-related events (52.9% vs. 36.2%, $P = 0.033$). Furthermore, cingulate gyrus metabolism activity showed significant correlations with LV diastolic function (all $P < 0.05$). Cingulate gyrus metabolism activity (HR: 9.286, 95% CI 1.247-69.169, $P = 0.03$) was strongly associated with SCD-related events after adjustment for clinical information and LV functional parameters. Additionally, cingulate gyrus activity was linked to SCD-related events through its relationship with LV diastolic function. ***Conclusion:*** Cingulate gyrus activity displayed significant independent prognostic value for risk stratification of SCD-related events in patients with HFrEF. Impairment in cingulate gyrus metabolism may contribute to the occurrence of SCD-related events, potentially mediated by LV diastolic function.

EPS-095

Serial FDG PET analysis for detection of cardiotoxicity of breast cancer chemotherapy

***Y. Izoe**[1], M. Nagao[2], H. Tsukada[2], S. Watanabe[2], Y. Maekawa[2], A. Yamamoto[2], Y. Satoh[3], H. Saya[1], S. Akashi-Tanaka[2], S. Sakai[2];*
[1]Fujita Health University, Toyoake, JAPAN, [2]Tokyo Women's Medical University, Shinjuku-ku, JAPAN, [3]Fujita Medical Innovation Center Tokyo, Ota-ku, JAPAN.

Aim/Introduction: In breast cancer patients undergoing repeated chemotherapy, cancer therapy-related cardiac dysfunction is an important prognostic factor. However, there are no useful tools for its prediction. Myocardial accumulation on FDG PET is influenced by blood glucose level and insulin activity and fluctuates between individuals with poor reproducibility. Therefore, it is difficult to distinguish physiologic from pathologic accumulation, and myocardial accumulation on FDG PET during oncology has not been used for complication assessment. We quantitatively evaluated myocardial accumulation using FDG PET performed consecutively during breast cancer chemotherapy to assess the potential for cardiotoxicity by chemotherapy regimen. ***Materials and Methods:*** We analyzed 535 FDG PET examinations performed before and after chemotherapy in 108 patients with breast cancer between January 2014 and February 2025. On pre- and post-treatment FDG PET, the mean values within the volume of interest (size 1.5cm3) of myocardium with the highest accumulation and descending aorta on the same cross-section were measured, and the ratio of the two was defined as the myocardial standard uptake ratio (M-SUR). Chemotherapy was classified into four regimens: anthracyclines, human epidermal growth factor receptor 2 (HER2) inhibitors, immune check inhibitors (ICI), and others (eribulin, paclitaxel, and docetaxel, etc.). When single or multiple chemotherapy regimens were administered in the same patient, pre- and post- data sets for each chemotherapy regimen were compared using Wilcoxon matched-pairs signed rank test. Patients with other cancers, cardiac metastases or diabetes were excluded. ***Results:*** The average observation period and number of PET scans per patient is 39 months and 5.0 scans. A total of 309 pre- and post-chemotherapy data sets were obtained, of which 34 were for anthracyclines (n=17), 146 were for HER2 inhibitors (n=40), 20 were for ICI (n=9), and 109 were for others (n=54). M-SUR after chemotherapy was significantly higher than before chemotherapy in the anthracyclines (4.66±3.94 vs. 3.19±2.10, $p<0.0001$) and ICI (4.98±4.27 vs. 3.02±2.21, $p=0.0328$) groups. On the other hand, in the HER2 inhibitor and the other groups, M-SUR tended to be lower after chemotherapy than before, but the difference was not significant (HER2 inhibitor: 4.91±4.44 vs. 4.31±3.22; the other: 4.22±3.16 vs. 3.76±3.01). ***Conclusion:*** Serial analysis of pre- and post-chemotherapy FDG PET revealed different responses to myocardial accumulation depending on the chemotherapy regimen. With anthracycline and ICI, there is a significant increase in myocardial uptake after chemotherapy. Analysis of myocardial accumulation on FDG PET, which has been underutilized, has the potential to detect cardiotoxicity of chemotherapy.

EPS-096

Left ventricular volumes and ejection fraction by [^{13}N]-NH^3 positron emission tomography are dependent on the reconstruction method: A head-to-head comparison with cardiovascular magnetic resonance

***S. Kvernby**[1,2], J. Oddstig[1,2], F. Hedeer[3], S. Akil Engblom[3];*
[1]Radiation Physics, Department of Hematology, Oncology and Radiation Physics, Skåne University Hospital, Sweden, Lund, SWEDEN, [2]Department of Translational Medicine and Wallenberg Centre of Molecular Medicine, Lund University, Malmö, SWEDEN, [3]Clinical Physiology, Department of Clinical Sciences Lund, Lund University, Skåne University Hospital, Lund, SWEDEN.

Aim/Introduction: Myocardial perfusion imaging using positron emission tomography (PET) enables assessment of left ventricular ejection fraction (EF) by determining left ventricular end diastolic volume (EDV), end systolic volume (ESV) and stroke volume (SV). Choice of PET image reconstruction method (OSEM or BSREM) and reconstruction parameters (number of iterations and subsets or penalization factor β) impacts the image quality. The aim of this study was to investigate to what extent the choice of reconstruction method and reconstruction parameters affects the assessment of left ventricular volumes and EF determined by [^{13}N]-NH^3 PET in a head-to-head comparison with cardiovascular magnetic resonance (CMR). ***Materials and Methods:*** Twenty-three patients with suspected or established chronic coronary syndrome were examined with CMR and [^{13}N]-NH^3 PET during rest on the same day. The PET-data were reconstructed into gated images with 8 bins, using six different PET image reconstructions (TOF-OSEM-2 iterations/16 subsets (2/16) - 3 mm post filter, TOF-OSEM-5 iterations/16 subsets (5/16) - 3 mm post filter, TOF-OSEM-6 iterations/24 subsets (6/24) - 3 mm post filter, BSREM-β50, BSREM-β100 and BSREM-β300). EDV, ESV, SV and EF were assessed and compared between all PET reconstruction methods and with CMR findings. Statistical differences were evaluated using paired sample t-Test. ***Results:*** Regardless of reconstruction method, left ventricular volumes by [^{13}N]-NH^3 PET were significantly smaller ($p<0.001$) than the volumes from CMR, where the smallest difference between the two modalities was found when using TOF-OSEM-6/24 or BSREM-β50 (average agreement with CMR; EDV: -54.5 ml, ESV: -19.8 ml, SV: -33.8 ml), while the largest difference was found when using TOF-OSEM-2/16 (average agreement with CMR; EDV: -63.1 ml, ESV: -27.9 ml, SV: -35.0 ml). Compared with CMR, EF by PET was significantly higher ($p<0.001$) using TOF-OSEM-2/16 or BSREM-β300 reconstructions (4.1% increase), while no difference was found for the other reconstructions. A significant smaller ($p<0.01$) EDV and ESV together with a larger EF could be seen for two of the PET reconstruction methods (TOF-OSEM-2/16 and BSREM-β300), when comparing them with the PET reconstruction producing the largest volumes and smallest EF (TOF-OSEM-6/24). No significant difference ($p>0.05$) in SV could be seen between the different PET reconstruction methods. ***Conclusion:*** The choice of reconstruction method affects the assessment of cardiac left ventricular volumes and EF from [^{13}N]-NH^3 ammonia PET. The largest volumes and best agreement with CMR were found with OSEM reconstruction using a high number of iterations and subsets, or with BSREM reconstruction using a low penalization factor.

EPS-097

Clinical Validation of Automated Convolutional Neural Network Screening of Incidental Cardiac Uptake on Bone Scintigraphy

V. Uusitalo, *H. Halme, T. Ahokas, E. Hippeläinen;*
Helsinki University Hospital, Helsinki, FINLAND.

Aim/Introduction: We validate a convolutional neural network tool designed for the automatic detection of incidental cardiac uptake suggestive of transthyretin amyloidosis (ATTR) on bone scintigraphy. In the case of incidental cardiac uptake, our algorithm can alert the nuclear medicine technician to obtain additional cross-sectional imaging and notify the clinical reader of the possibility of ATTR cardiomyopathy. ***Materials and Methods:*** We utilized a previously designed neural network to retrospectively analyze cardiac uptake on 1325 [^{99m}Tc]Tc-HMDP scintigraphs, which were imaged due to non-cardiac indications at Helsinki University Hospital, Finland. Images were read by an experienced nuclear medicine physician and were labeled as negative (Perugini grade 0 or 1) or positive (Perugini grade 2 or 3) for cardiac uptake. ***Results:*** The mean age was 75 ± 12 years, and 37% were female. There were 30 positive cases of cardiac uptake detected by a nuclear medicine physician (2.3%). Four images (0.3%) were excluded for being non-diagnostic for cardiac analysis. The area under the curve (AUC) for automated detection of cardiac uptake compared to the human reference was 0.87. In the automated screening, there were no false negative cases, 997 true negatives, 342 false positives, and 30 true positives, respectively. Thus, the human reader did not reclassify any negative cases by the neural network but downgraded 92% of positive cases to non-significant cardiac uptake. ***Conclusion:*** An automated novel neural network can safely exclude significant incidental cardiac uptake suggestive of ATTR cardiomyopathy on bone scintigraphy. Cardiac imaging specialists should review any positive results from automated screening. Our algorithm can be utilized for online image surveillance to identify incidental cardiac uptake during bone scintigraphy, alerting technicians and reading physicians to the possibility of ATTR cardiomyopathy.

EPS-098

Graph Theory Analysis of Brain Functional and Metabolic Network Alterations in Heart Failure Patients: a simultaneous PET/MR study

C. Zheng[1], *R. Qin*[1], *N. Li*[2], *J. Lu*[1];
[1]*Xuanwu Hospital, Capital Medical University, Beijing, CHINA,*
[2]*Beijing United Imaging Research Institute of Intelligent Imaging, Beijing, CHINA.*

Aim/Introduction: Graph theory analysis elucidates complex brain network topology, aiding understanding of neurological impacts. Heart failure (HF) is known to impact both brain function and metabolism. This study investigated alterations in brain functional (fMRI-derived) and metabolic (FDG-PET-derived) networks in patients with distinct HF phenotypes (preserved vs. reduced ejection fraction: HFpEF vs. HFrEF) using simultaneous PET/MR and graph theory. ***Materials and Methods:*** The study included 68 subjects, including 27 patients with HFpEF, 27 patients with HFrEF, and 14 healthy controls (HC). All participants underwent integrated 18F-fluorodeoxyglucose ([^{18}F-FDG) PET/MR scans, which included 3D TIWI and resting-state functional MRI sequences. The DPARSFA software and in-house MATLAB scripts were utilized to preprocess fMRI and PET imaging. Brain parcellation was based on the Anatomical Automatic Labeling (AAL) atlas. The individual functional network was constructed by calculating Pearson's correlation of temporal signals between all brain region pairs, and the average is used as the group-level correlation matrix. Additionally, the Pearson's correlation of standardized uptake values ratio (SUVr) across brain regions within the cohort was utilized to generate a group-level metabolic network. To calculate the global characteristic parameters related to graph theory, area-under-the-curve (AUC) was integrated across a range of network sparsity to summarize network properties. The difference of each network property between the three groups was evaluated by using a nonparametric permutation approach with 10000 permutations. ***Results:*** The global connectivity characteristics of brain functional networks and metabolic networks differ significantly in HF. While no significant differences are observed in the global properties of functional networks among the HFpEF, HFrEF, and healthy control groups, the metabolic networks exhibit marked disruption in HF. Compared to HFrEF, HFpEF demonstrates significant alterations in global network metrics, including decreased normalized clustering coefficient (nCp) and small-worldness (sigma), along with increased characteristic path length (Lp), as revealed by permutation testing ($P < 0.05$ for all). Especially when sparsity thresholds exceed 0.3, the small-world index falls below 1, suggesting a shift toward global network segregation and a significant decline in network stability. ***Conclusion:*** HF patients exhibit differential alterations in brain functional and metabolic networks. Metabolic network topology appears more sensitive to HF-related pathological changes, particularly distinguishing between HFpEF and HFrEF phenotypes. These findings suggest

that graph analysis of brain metabolic networks could offer valuable pathophysiological insights, and its topological features hold potential as biomarkers for assessing HF-related brain injury.

EPS-099

Impact of CT-free Attenuation Correction on Left Ventricular Ejection Fraction and Volumes obtained from a dedicated Cardiac CZT SPECT Camera

V. Roelants[1], *M. Hesse*[2], *F. Dupont*[2], *N. Laajimi*[2], *A. Oulad Bouchetta*[2], *R. Lhommel*[2];
[1]*Cliniques Universitaires Saint-Luc, Brussels, BELGIUM,* [2]*Cliniques Universitaires Saint-Luc - Université Catholique de Louvain, Brussels, BELGIUM.*

Aim/Introduction: Attenuation-correction (AC) improves the diagnostic accuracy of myocardial perfusion scintigraphy (MPS). In the CASCTEC study we developed an approach generating CT-free attenuation maps for pinhole CZT cameras (pinhole CZT), based on emission scans only. In this work, we evaluated the effect of CT-free AC on the determination of left ventricular ejection fraction (LVEF), end-systolic (ESV) and end-diastolic (EDV) volumes using a pinhole CZT. ***Materials and Methods:*** Twenty-seven patients (19 male; age: 67 ± 15 years, BMI: 28 ± 6 kg/m2) with suspected or known coronary artery disease referred for a two-day stress/rest MPS have been included at this stage. 5-minute ECG-gated (16 bins) acquisitions were performed on a pinhole CZT 30-60 minutes after injection of 359 ± 18 MBq of a 99mTc-labeled tracer. This acquisition was immediately followed by an additional 5-minute acquisition after retracting the detectors without moving the patient. It allowed to delineate the patient body contour, and together with the first acquisition, enabled the segmentation of soft and lung tissues to produce an attenuation map. Each frame of the ECG-gated acquisition was reconstructed using the manufacturer algorithm without and with AC, then smoothed using a 1-2-1 temporal filter. LVEF, ESV and EDV were calculated from each reconstruction using Quantitative Gated SPECT software (QGS). Results were analyzed using linear regression and Wilcoxon Signed-Rank test, while Bland-Altman plots served to evaluate the level of agreement. ***Results:*** LVEF, ESV and EDV values were automatically obtained for 23 patients. Manual adjustment of the LV contour was required in the remaining 4 patients. The comparison between NC and AC images gave the following results: 60.6 ± 8.9 % vs 54.8 ± 8.4 % (p<0.001) for LVEF; 100.5 ± 30.2 ml vs 104.3 ± 31.4 ml (p<0.001) for EDV and 41.5±19.2ml vs 49.0±20.8ml (p<0.001) for ESV. Linear correlation was excellent for LVEF (R=0.94, p< 0.001) and for both EDV (R=0.98, p<0.001) and ESV (R=0.96, p<0.001). However, Bland-Altman analysis revealed a significant bias of -5.74% for LVEF (95% limit of agreement: -12.0 to 0.54%), of 3.8ml for EDV (95% limit of agreement: -7.4 to 14.9ml) and of 7.6 ml for ESV (95% limit of agreement: -3.4 to 18.5ml). ***Conclusion:*** LVEF and volumes determined by QGS from CT-free AC pinhole CZT MPS strongly correlated with NC values. However, CT-free AC introduced significant bias (underestimation of LVEF and overestimation of LV volumes) making the two methods non-interchangeable.

EPS-100

FAPI SPECT/CT to Evaluate Fibrosis Burden of Right Ventricular in CTEPH: Correlation with Echocardiographic Strain Parameters and Response to BPA

K. Wang*, X. Li, S. Song, W. Fang, L. Wang, C. Yan;*
Chinese Academy of Medical Sciences & Peking Union Medical College, Fuwai Hospital, Beijing, CHINA.

Aim/Introduction: Prognosis in chronic thromboembolic pulmonary hypertension (CTEPH) is strongly determined by right ventricular (RV) function, which deteriorates partly due to myocardial fibrosis. Radiolabeled fibroblast activation protein inhibitors (FAPI) offer a novel way to visualize the fibrosis progression in vivo. This study aims to assess FAPI SPECT/CT as a potential imaging biomarker to evaluate the fibrosis burden and to investigate the association between RV FAPI uptake parameters with RV strain parameters derived from speckle tracking echocardiography, both at baseline and after balloon pulmonary angioplasty (BPA). ***Materials and Methods:*** We enrolled 37 CTEPH patients who completed baseline ^{99m}Tc-FAPI SPECT/CT, strain echocardiography, and right heart catheterization (RHC) before the initial BPA. Baseline FAPI parameters (Fibroblast Activation Volume [FAV], SUV_{peak}, TBR_{peak}) and RV strain parameters (free wall strain [FWS] and global strain [GS]) were collected. RV-pulmonary artery coupling was calculated as RVFWS/sPAP (estimated systolic pulmonary artery pressure). Ten patients underwent complete re-examination (including FAPI SPECT/CT) after the first BPA. ***Results:*** Baseline RV FAPI uptake varied with mean ± SD values of 2.27 ± 0.97 for SUV_{peak} (range: 1.04-4.19), 2.92 ± 0.96 for TBR_{peak} (range: 1.44-4.76), and 128 ± 118 mL for FAV (range: 0-525 mL). Echocardiographic strain analysis yielded a mean FWS of -14.7 ± 6.28 % and a median RVFWS/sPAP of -0.23 ± -0.18. Baseline TBR_{peak} of free wall (FW) correlated with longitudinal diameter of RV (r = 0.541, p = 0.001), FWS (r = 0.386, p = 0.018) and RVFWS/SPAP (r = 0.347, p = 0.026). Response to the first BPA varied among patients; not all showed improvement in hemodynamics or RV strain. Nonetheless, changes (Δ) in FW TBR_{peak} significantly correlated with changes (Δ) in FWS (r = -0.721, p = 0.019) and ΔRVFWS/SPAP (r = -0.636, p = 0.048). This finding reflects a concordance between changes in FAPI uptake and changes in strain parameters: greater reductions in FAPI uptake paralleled greater improvements in strain, while increased uptake was associated with strain deterioration. ***Conclusion:*** FAPI SPECT/CT emerges as a promising imaging biomarker for assessing RV involvement in CTEPH. The significant correlation between RV FAPI uptake with baseline myocardial strain parameters, as well as the association between changes in FAPI uptake and changes in RV strain following BPA suggests its potential utility in assessing response to treatment.

EPS-101

Detection of myocardial metabolic abnormalities by ^{18}F-FDG and preliminary mechanism analysis in mice with Anthracycline cardiotoxicity: A corresponding ^{18}F-FDG PET/MRI observation

T. Yuan[1], *X. Chen*[1], *M. Wei*[1], *X. Lin*[1], *H. Zhu*[1], *Z. Yang*[1], *X. Wang*[2];
[1]*Peking University Cancer Hospital & Institute, Beijing, CHINA,* [2]*Key Laboratory of Carcinogenesis and Translational Research (Ministry of Education/Beijing), NMPA Key Laboratory for Research and Evaluation of Radiopharmaceuticals (National Medical Products Administration), Beijing, CHINA.*

Aim/Introduction: The present translational study aimed to verify whether serial ^{18}F-FDG PET predicts doxorubicin cardiotoxicity and preliminary mechanistic insights. ***Materials and Methods:*** Twenty mice were allocated into four groups: five received 5-6 weekly intraperitoneal doxorubicin (5 mg/kg) and were sacrificed at week 7; five each underwent 4- or 3-week regimens (terminated at weeks 5/4); and five controls received six weekly intraperitoneal saline injections before sacrifice at week 7. Histopathological changes were identified by light and electron microscopy. Prospective cohort study (NCT04555642) with ethics approval, enrolling lymphoma survivors post ≥3 cycles of anthracycline regimens underwent ^{18}F-FDG PET/CT and PET/MRI. ^{18}F-FDG PET/MRI parameters (including PET and CMR parameters) for toxicity prediction were established via ROC curve analysis. Early cardiotoxicity was observed by ECG within two weeks near-PET/MRI. ***Results:*** In mice, ^{18}F-FDG radiotracer distribution analysis revealed significantly elevated myocardial uptake in the 4 and 5-6 weekly doxorubicin doses compared to control group (P<0.05). Progressive pathological changes were observed with increasing chemotherapy cycles: mice exhibited graded myocardial

injuries ranging from mild subendocardial edema to myocardial disintegration, accompanied by mitochondrial vacuolization and nuclear swelling/vacuolization. Mild subendocardial fibrosis became detectable starting at 4 cycles, persisting through 5-6 cycles. Ultrastructural analysis demonstrated distinct mitochondrial alterations: those receiving 5-6 weekly doxorubicin doses exhibited pronounced mitochondrial swelling, disrupted cristae, and vacuolated structures. The specificity, positive predictive value and accuracy of $SUV_{max\text{-}heart}$ (cutoff 8.8) were 87.1%, 71.4% and 84.1% for the $SUV_{max\text{-}heart}$ were better than $SUV_{max\text{-}heart}/SUV_{max\text{-}mediastinum}$, $SUV_{max\text{-}heart}/SUV_{max\text{-}liver}$, and $SUV_{max\text{-}heart}/SUV_{max\text{-}muscle}$ ratios. There was no available parameters of MRI using ROC curve analysis with P values >0.05. Moreover, myocardial uptake values exhibited an increasing trend with successive chemotherapy cycles. Notably, while no significant differences in these parameters were observed between ECG-positive and negative groups at 3-4 treatment cycles (P>0.05), the ECG-positive subgroup receiving 7-8 chemotherapy cycles showed significantly elevated values across all four PET parameters compared to their ECG-negative counterparts All P<0.05). Cardiac structural analysis revealed that ECG-positive patients post-chemotherapy had significantly lower indexed EDV/BSA. Furthermore, patients completing 7-8 chemotherapy cycles demonstrated reduced LVEF, decreased indexed EDV, and lower septal wall T1 values compared to ECG-negative controls (all P<0.05). ***Conclusion:*** Cumulative chemotherapy induces dose-dependent cardiotoxicity, evidenced by elevated PET metabolic parameters ($SUV_{max\text{-}heart}$ AUC=0.844) and impaired cardiac function in ECG-positive patients, particularly after 7-8 cycles. Animal studies corroborate progressive myocardial damage, from mitochondrial vacuolization to fibrosis, aligning with clinical PET findings. PET/CT demonstrates superior sensitivity over MRI for early detection.

EPS-102

First total-body dynamic imaging and kinetic modeling of ^{18}F-flurpiridaz quantifying perfusion and mitochondrial complex I distribution in healthy volunteers

H. Song[1,2,3], *J. Zhao*[1,2,3], *Z. Xiang*[1,2,3], *Z. Qin*[1,2,3], *Y. Wang*[4], *P. Wu*[1,2,3], *S. Li*[1,2,3];
[1]*Department of Nuclear Medicine, First Hospital of Shanxi Medical University, Taiyuan, CHINA,* [2]*Shanxi Key Laboratory of Molecular Imaging, Shanxi Medical University, Taiyuan, CHINA,* [3]*Collaborative Innovation Center for Molecular Imaging of Precision Medicine, Taiyuan, CHINA,* [4]*United Imaging Healthcare, Shanghai, CHINA.*

Aim/Introduction: High-resolution mitochondrial complex I-(MC-I) targeting probe ^{18}F-flurpiridaz combined with total-body PET/CT can unleash its potential in future pathological studies beyond myocardial perfusion imaging. Yet the most appropriate kinetic model for total-body ^{18}F-flurpiridaz quantification has not yet been proposed. We aim to obtain preliminary data on total-body pharmacokinetics of ^{18}F-flurpiridaz in healthy volunteers as a potential quantitative biomarker for both perfusion and MC-I activity. ***Materials and Methods:*** Nine healthy volunteers underwent 60-minute dynamic total-body ^{18}F-flurpiridaz PET/CT scans. Multiple normal organ VOIs were generated with an automated CT-based total-body segmentation method on motion-corrected total-body dynamic imaging to obtain time-activity curves (TACs). Descending aorta was chosen as the input function for most of the organs except for lung, where the pulmonary artery was used. Both irreversible (2T3K) and reversible (2T4K) two-tissue compartment model with blood volume and time delay correction were applied to compare their fitting quality using the Akaike Information Criterion (AIC). Logan and Patlak graphical analyses were also used to verify the reversibility of ^{18}F-flurpiridaz kinetics in different organs, as well as providing simplified quantification surrogates for MC-I distribution. ***Results:*** The 2T4K model demonstrated superior fit for most organs compared to 2T3K, excluding liver and lung where irreversibility predominated. The rate constants demonstrated organ-specific pattern. The perfusion rate K_1 ranged from 0.05 ml/cm^3/min in spinal cord to 2.62 ml/cm^3/min in right renal cortex. The backward flux k_2 varied from 0.04 min^{-1} in liver to 1.64 min^{-1} in left lung's upper lobe. The k_3 representing specific binding to MC-I peaked in thyroid as 0.64 min^{-1} vs. 0.00 min^{-1} in liver, and the reversible binding parameter k_4 varied from 0.07 min^{-1} in myocardium to 0.90 min^{-1} in thyroid. The renal cortex has the highest distribution volume (V_T) of 17.71 ml/g, while the middle right lung lobe had the lowest V_T (0.74 ml/g). Logan analysis with t*=10 min demonstrated higher R^2 in most organs compared to Patlak analysis, verifying the reversible kinetics of ^{18}F-flurpiridaz. Strong correlations were observed between Logan-V_T and 2T4K-V_T(r=0.97, P<0.0001), suggesting that they can be used as promising surrogates for MC-I distribution. ***Conclusion:*** This study delivers the first evidence of ^{18}F-flurpiridaz's reversible binding kinetics across multiple organs in human. Total-body ^{18}F-flurpiridaz dynamic imaging exhibits distinct kinetic rates across various organs. Mapping the multi-organ pharmacokinetic parameters of ^{18}F-flurpiridaz has the potential to enable pathological correlation in future perfusion/MC-I studies.

EPS-103

Prognostic Value of Stress Myocardial Perfusion Entropy (MPE) in Patients with Normal Single-Photon Emission-Computed Tomography (SPECT) Myocardial Perfusion Imaging

L. Djaileb[1], *N. De Leiris*[1], *M. Desvignes*[2], *D. Fagret*[1], *C. Ghezzi*[3], *G. Barone-Rochette*[1], *L. Riou*[3];
[1]*University Grenoble Alpes, Grenoble, FRANCE,* [2]*Gipsa-Lab, University Grenoble Alpes, Grenoble, FRANCE,* [3]*Univ. Grenoble Alpes, INSERM, LRB, Grenoble, FRANCE.*

Aim/Introduction: Stress myocardial perfusion entropy (MPE) as computed from routinely acquired SPECT myocardial perfusion images showed an added prognostic value over clinical risk factors, stress test EKG and summed stress score (SSS) in high-risk type 2 diabetic patients (1). The relationship between increased MPE and coronary microvascular dysfunction (CMVD) have been suggested in a preclinical model (2). Our aim was to assess the prognostic value of MPE in low-risk patients with normal SPECT myocardial perfusion imaging. ***Materials and Methods:*** Consecutive patients with normal myocardial perfusion (SSS <4) and a normal left ventricular ejection fraction (> 45%) were retrospectively enrolled in the study. Myocardial perfusion imaging using ^{201}Tl was performed on a CZT cardiac dedicated camera following exercise testing or pharmacological testing. MPE was determined from SPECT myocardial perfusion images as previously described (1). The primary endpoint was the occurrence of a cardiovascular event (cardiovascular death, non-fatal myocardial infarction, coronary angiography with or without revascularization, and stroke). Univariate and multivariable Cox models were performed to assess the prognostic value of MPE for cardiovascular events. ***Results:*** From May 2011 to September 2012, 472 patients were identified. 29/472 (6%) were lost to follow-up. 443 patients were included in this analysis. The primary endpoint occurred in 73 patients during follow-up (3.3 ± 0.4 years). In a multivariate analysis, age (HR 1.04 [1.01; 1.06] p <0.0001) and stress entropy (HR: 1.6 [1.004; 2.56], p=0.04) were independent predictors of cardiovascular events. In survival analysis, patients with elevated MPE (> 4.06) underwent more events than those with a lower MPE (<4.06) (log rank = 0.04). ***Conclusion:*** MPE determined from thallium-201 stress CZT SPECT perfusion imaging improved prognostic risk assessment of cardiovascular event in patients with normal myocardial perfusion scintigraphy. ***References:*** (1) Djaileb, L. et al. Prognostic value of SPECT myocardial perfusion entropy in high-risk type 2 diabetic patients. Eur J Nucl Med Mol

Imaging 48, 1813-1821 (2021). (2) Carabelli, A. et al. Noninvasive assessment of coronary microvascular dysfunction using SPECT myocardial perfusion imaging and myocardial perfusion entropy quantification in a rodent model of type 2 diabetes. Eur J Nucl Med Mol Imaging 49, 809-820 (2022).

EPS-104

Incidence of Cardiotoxicity Assessed with CZT-ERNA in Patients Undergoing Medical Cancer Therapy: A 12-year real-word experience

J. E. Larsson, *M. Ø. Nielsen, B. Zerahn;*
Department of Nuclear Medicine, Copenhagen University Hospital – Herlev, Copenhagen, DENMARK.

Aim/Introduction: Medical cancer therapies (MCT) have undergone a remarkable transformation during the recent decades with the addition of new therapeutic modalities. Nonetheless, adverse effects remain significant. In this context, incidences of cardiotoxicity, as assessed with cadmium-zinc-telluride (CZT) equilibrium radionuclide angiography (ERNA) imaging, are limited. Therefore, the aim of this study was to determine the incidence and risk factors for cardiotoxicity in patients undergoing contemporary MCT under surveillance with CZT-ERNA. ***Materials and Methods:*** We included all adult patients who underwent first-time and follow-up assessment of cardiac function with CZT-ERNA within 6 months in relation to MCT at a European university hospital between 2012 and 2024. The primary outcome was cardiotoxicity, defined as a reduction in left ventricular ejection fraction (LVEF) ≥ 10% from baseline to < 50% during the first year, and was estimated using cumulative incidence functions. Secondary outcomes included the estimated proportion of patients with recovery of LVEF to ≥ 50%, and risk factors for cardiotoxicity. Risk factors were estimated with multiple logistic regression adjusted for age, sex, body mass index, and type of cancer in landmark analyses of survivors > 9 months. ***Results:*** Of 5,937 patients with a first-time CZT-ERNA, 953 patients (54% females, mean age 63 years, SD 14.4) had a follow-up assessment within 6 months and a total of 3,236 examinations during the first year. Most patients had sarcoma (30%), melanoma (23%), and breast cancer (20%). The overall incidence of cardiotoxicity was 115/953 ~ 12.1% (95% CI 10.0-14.1) with best/worst case sensitivity analysis: 1.9-18.0%. Median time to cardiotoxicity was 125 days [Q1-Q3 82-184 days] and reversibility was observed in 61 patients (61/115 ~ 53%). Baseline LVEF (adjusted OR / 10% increase 0.50; 95% CI 0.40-0.62; p <0.001), end-systolic volume (adjusted OR / 10 ml increase 1.47; 95% CI 1.28-1.69; p < 0.001) and end-diastolic volume (adjusted OR / 10 ml increase 1.13; 95% CI 1.03-1.24; p=0.01) were associated with cardiotoxicity. ***Conclusion:*** Cardiotoxicity occurred in approximately 12% of all cancer patients referred for CZT-ERNA surveillance during MCT. Risk factors were larger left ventricular volumes and lower LVEF at baseline.

EPS-105

Clinical Outcomes and Management Following Abnormal SPECT Myocardial Perfusion Imaging

B. Miles, *K. Atieh, K. Mason, U. Oza;*
Baylor University Medical Center, Dallas, TX, UNITED STATES OF AMERICA.

Aim/Introduction: Stress myocardial perfusion imaging with single photon emission computed tomography (SPECT) is a widely implemented imaging choice to assess for inducible reductions in coronary arterial flow during times of increased myocardial demand. While coronary angiography is the gold standard to evaluate flow-limiting coronary blood flow, this invasive imaging modality is associated with risks of traumatic vascular complications and contrast induced complications. Compared to coronary angiography, nuclear stress testing has fewer risks. These complications include short-lived arrhythmias and chest pain which typically subside upon return to resting heart rate. Many patients who present with angina can undergo nuclear stress testing to assess for underlying inducible reduced coronary flow. The purpose of this study was to assess the rate of interventions in patients who underwent nuclear cardiac stress testing and were found to have abnormal findings. ***Materials and Methods:*** This global population-based retrospective cohort study was designed utilizing the STROBE (Strengthening the Reporting of Observational Studies in Epidemiology) guidelines. We accessed the anonymized medical record information of more than 165 million patients in 144 large healthcare organizations internationally. The patient cohort was created by using International Classification of Disease 10 (ICD-10) codes, Current Procedural Terminology (CPT) codes, and medication codes. Patients in this study had to have no personal history of TIA or stroke (Z86.73), and no history of peripheral vascular disease (I73). They were required to have undergone myocardial perfusion imaging (CPT 78452) with an abnormal outcome (R94.39). This resulted in 88,522 patients. They were then evaluated for the outcomes of angioplasty with or without stents, coronary artery bypass grafting, or medical management (aspirin with either clopidogrel, prasugrel, or ticagrelor) within the subsequent 3 months. ***Results:*** 41.8% of patients with abnormal nuclear medicine stress testing were managed with intervention of any type. The most common intervention was medical management (41.6%), followed by angioplasty with or without stents (5.3%) and coronary artery bypass grafting (2.9%). ***Conclusion:*** Stress myocardial perfusion imaging with single photon emission computed tomography (SPECT) is used to assess for inducible reductions in coronary arterial flow during times of increased myocardial demand and has less risks than coronary angiography. Our study has shown that abnormal nuclear stress myocardial perfusion images often lead to interventions within 3 months of testing in patients, with the most common intervention being medical management. These findings highlight the utility of nuclear stress imaging in the management of patients with chest pain.

EPS-106

Potential link between left ventricular mechanical dyssynchrony (LVMD) and coronary microvascular dysfunction (CMD) in suspected coronary arteries disease (CAD) patients: a preliminary study based on CZT-SPECT

H. Zhang[1], *F. Caobelli*[2], *K. Shi*[2], *F. Yu*[1];
[1]*Tongji University School of Medicine,shanghai Tenth people's hospital, Shanghai, CHINA,* [2]*Department of Nuclear Medicine, Inselspital, Bern University Hospital, University of Bern, Bern, SWITZERLAND.*

Aim/Introduction: It is still unclear whether left ventricular mechanical dyssynchrony (LVMD) is implicitly tied to the pathogenesis of coronary microvascular dysfunction (CMD). This preliminary study aimed to demonstrate the correlation between LVMD and CMD by CZT-SPECT myocardial perfusion imaging (MPI). ***Materials and Methods:*** A cohort of 142 suspected CAD patients who were referred to D-SPECT MPI were retrospectively analyzed and divided into two groups: the CMD group and the non-CMD group. CMD was defined as CFR <2.5 and LVMD was diagnosed through phase bandwidth (PBW) and phase standard deviation (PSD) value exceeded mean+2SD for control patients. ***Results:*** A total of 142 patients were recruited for this study and divided into two groups: CMD group (n =62, 32 males, 30 females; mean age 68.69±9.08 years) and non-CMD group as controls (n = 80, 47 males, 33females; mean age 63.55±11.35 years).Among the 62 CMD patients, 26 (41.9%) had LVMD, including stress LVMD 19 cases, rest LVMD 16 cases, and both stress/rest LVMD 9 cases. The phase analysis parameters of two groups showed statistically significant differences, PBW (P<0.001; P<0.001), PSD (P<0.001; P<0.001) and Entropy (P<0.001; P=0.011) were significantly elevated in the CMD group. Compared with the non-LVMD group, the parameters of stress/rest left ventricular function were worse

in the LVMD group, with left ventricular ejection fraction (LVEF) (P=0.002; P=0.001), perk ejection ratio (PER) (P=0.003; P=0.001), peak fraction ratio (PFR) (P=0.034; P=0.010) were lower, and ESV (P=0.014; P=0.026) was higher. There was a moderate negative correlation between CFR and Stress PBW (r=-0.22, P=0.014), Stress PSD (r=-0.25, P=0.011), Rest PBW (r= -0.19, P=0.037). Meanwhile, multivariate regression analysis suggested that stress LVMD was an independent risk factor for CMD (OR: 22.52, 95% CI: 2.45-206.80, P=0.006). ***Conclusion:*** There is a clear correlation between LVMD and CMD, which provides incremental value for the early diagnosis of CMD in suspected CAD patients.

EPS-107

Functional Evaluation of Cardiac Cell Membrane Transporter P-Glycoprotein in healthy volunteers with [^{18}F]MC225-PET imaging- a feasibility study

W. Liu[1], *J. Somsen*[1], *G. S. d. Souza*[1], *P. Mossel*[2], *A. Bartels*[3], *R. Slart*[1], *G. Luurtsema*[1];
[1]*University Medical Center Groningen, Groningen, NETHERLANDS,*
[2]*Leiden University Medical Center, Leiden, NETHERLANDS,*
[3]*Ommelander Ziekenhuis Groep, Scheemda, NETHERLANDS.*

Aim/Introduction: P-glycoprotein (P-gp) is an efflux transporter that regulates the distribution of various compounds across multiple organs, including the heart and brain. Cardiac P-gp plays a crucial role in protecting against cardiotoxicity and also in modulating the efficacy of P-gp-related cardiovascular drugs, such as beta-blockers and digoxin. [^{18}F]MC225-PET imaging has been identified as a promising tool for assessing P-gp function at the blood-brain barrier (BBB) in the past. This feasibility study aims to assess cardiac P-gp function with [^{18}F]MC225-PET imaging, in healthy volunteers. ***Materials and Methods:*** Six healthy volunteers (3 females, 60.67 ± 3.21 years; 3 males, 66.25 ± 3.59 years, all free of medications affecting P-gp function, underwent 60-minute dynamic [^{18}F]MC225 LAFOV PET scans (injected activity: 214.9 ± 92.36 MBq). Whole-blood time activity curves was derived from the internal aortic arch. The image derived input function (IDIF) was calibrated using the arterial manual samples, and adjusted for the plasma-to-whole blood ratio and corrected for plasma parent fraction. Kinetic parameters were calculated using different compartment models, including the reversible one-tissue compartment model and both reversible and irreversible two-tissue compartment models. ***Results:*** Sixty minutes post-injection, the plasma parent fraction was 64.61 ± 10.17%, with males showing 63.55 ± 16.26% and females 65.66 ± 6.41%. [^{18}F] MC225 PET imaging showed increased uptake in the heart wall. The reversible two-tissue compartment model provides the best fit for characterizing P-gp function in the human heart. Kinetic parameters were used to assess cardiac P-gp function and are presented in Table 1. The volume of distribution (VT) in healthy volunteers was 22.26 ± 2.23 mL·cm-3 for females and 27.12 ± 8.43 mL·cm-3 for males. ***Conclusion:*** This is the first evaluation of cardiac P-gp function in healthy volunteers using [^{18}F]MC225 PET. Although the small sample size limits statistical power, the findings still demonstrate the potential for future applications of [^{18}F]MC225 PET in assessing or predicting cardiotoxicity and the treatment effects of P-gp substrate medications.

EPS-108

Diagnostic Performance of NaI(Tl) SPECT Myocardial Blood Flow Quantification versus Relative MPI in Detecting Hemodynamically Significant Stenosis: A Prospective Study Using ICA with Wire-Based FFR as Reference

R. Sun, *Z. Zhang, K. Han, X. Wang, L. Wang, W. Fang;*
Chinese Academy of Medical Sciences Fuwai Hospital, Beijing, CHINA.

Aim/Introduction: This prospective study compared the diagnostic performance of myocardial blood flow (MBF) quantification derived by NaI (Tl) SPECT with relative myocardial perfusion imaging (MPI) in detecting hemodynamically significant stenosis in patients with coronary intermediate stenosis, using invasive coronary angiography (ICA) with wire-based fractional flow reserve (FFR) as reference. ***Materials and Methods:*** We enrolled 102 patients (age 58 ± 9 years, 64.7% male) with ≥ 1 coronary intermediate stenosis (50% ~ 90% diameter stenosis [DS]) by coronary CTA scheduled for clinically indicated SPECT MPI were prospectively enrolled in this study. All participants underwent both SPECT MPI and SPECT MBF quantification, followed by ICA with FFR measurements for intermediate stenosis. Vessel-level rest MBF, stress MBF and myocardial flow reserve (MFR) were obtained by NaI (Tl) SPECT. A SSS of ≥ 4 was considered abnormal on relative MPI. Hemodynamically significant stenosis was defined as > 90% DS on ICA or wire-based FFR ≤ 0.80. The optimal cut-off values of MBF and MFR were determined by ROC curve analysis and the Youden index. Areas under the curve were compared using DeLong method. The diagnostic indicators were compared using generalized estimating equations (GEE) to adjust for correlation between multiple vessels within the same patient. ***Results:*** Among 301 vessels included in the final analysis, hemodynamically significant stenosis was identified in 71 vessels (23.5%), including: 19 vessels with > 90% DS, 52 vessels with FFR ≤ 0.80 (from 124 vessels with FFR measurements,excluding 5 with missing data) and 158 vessels with < 50% DS. The optimal cut-off value on vessel level was 1.62 mL/min/g for stress MBF (AUC: 0.719; sensitivity: 66.2%, specificity: 79.6%, PPV: 50.0%, NPV: 88.4%, accuracy: 76.4%) and 1.99 for MFR (AUC: 0.691; sensitivity: 62.0%, specificity: 83.5%, PPV: 53.7%, NPV: 87.7%, accuracy: 78.4%). The AUC, sensitivity, specificity, PPV, NPV and accuracy for relative MPI was 0.561, 22.5%, 89.6%, 40.0%, 78.9% and 73.8%, respectively. The diagnostic AUC and sensitivity of stress MBF and MFR were significantly higher than relative MPI (all P < 0.0001). ***Conclusion:*** Quantitative MBF assessment by NaI (Tl) SPECT demonstrated superior diagnostic performance, particularly sensitivity, compared to relative MPI in detecting hemodynamically significant stenosis determined by ICA with wire-based FFR. This study supports its potential as a non-invasive tool for functional evaluation of hemodynamically significant stenosis.

EPS-109

Pre-administration of caffeine anhydrous has the potency to suppress myocardial [^{18}F]-FDG uptake: a feasibility study

C. P. W. Cox, *Q. G. de Lussanet de la Sablonière, T. Mulders, L. H. Graven, F. A. Verburg, T. Brabander;*
Erasmus MC, Rotterdam, NETHERLANDS.

Aim/Introduction: Positron emission tomography/Computed tomography (PET/CT) with [^{18}F]-2-fluoro-2-deoxyglucose ([^{18}F]-FDG) has an increasingly relevant role in diagnosis and treatment management of cardiac inflammation and infection. A major problem of cardiac [^{18}F]-FDG PET/CT is physiological myocardial [^{18}F]-FDG uptake, which could complicate the differentiation between physiological uptake in the normal myocardium and inflammation. Despite dietary manipulation, extended fasting and possibly additional intravenous heparin to suppress the physiological myocardial uptake, 5-20% of the patients still present inadequate myocardial uptake suppression and further improvement of the protocol is needed. These patients may benefit from additional caffeine anhydrous pre-administration, as it reduces insulin-dependent GLUT4 myocardial glucose uptake and increases free fatty acid levels, which stimulate myocytic free fatty acid oxidation. The aim of this study is to investigate the feasibility of additional caffeine anhydrous pre-administration on myocardial [^{18}F]-FDG uptake suppression. ***Materials and Methods:*** Eight adult patients who showed inadequate myocardial [^{18}F]-FDG suppression with the standard high-fat no-carbohydrate diet and 12 hours fasting on a routine [^{18}F]-FDG PET/CT with indication of inflammation or infection were included. An additional study PET/CT was performed with the standard diet and an additional caffeine anhydrous food supplement

tablet (200 mg) one hour prior to [^{18}F]-FDG injection. Both PET/CT scans were independently scored with a blind assessment of left ventricular myocardial [^{18}F]-FDG uptake for each of the 17 segments, as well as for overall image quality. Additionally, SUV measurements were taken for extra-cardiac image quality. Patients were monitored by measuring blood pressure and heart rate, and blood samples were analyzed for blood glucose and free fatty acid levels. ***Results:*** Additional caffeine supplementation prior to [^{18}F]-FDG administration resulted in a significantly lower total number of segments with inadequate suppression ($p<0.001$). Only three patients still showed inadequate suppression. Among them, two showed a significant decrease in the number of inadequate segments, all of which were in the basal and mid postero-anterolateral segments. No significant differences ($p>0.05$) were found on visual and semi-quantitative extra-cardiac image quality and sarcoid lesions. All patient monitoring parameters remained stable compared to before caffeine intake, except a significant ($p<0.001$) decrease (-8 beats/minutes) in mean heart rate before [^{18}F]-FDG injection and a significant ($p<0.05$) increase (+8 mmHg) of mean systolic blood pressure after PET/CT. Patients did not report any symptoms associated with caffeine. ***Conclusion:*** Additional caffeine anhydrous pre-administration one hour before [^{18}F]-FDG injection has potency to improve myocardial [^{18}F]-FDG uptake suppression, while maintaining extra-cardiac visual and semi-quantitative image quality.

EPS-110

Agreement of ^{68}Ga-DOTANOC PET/CT with ^{18}F-FDG PET/CT and Cardiac MR in sarcoid patients with suspected cardiac involvement

R. Solanki*, A. Sood, B. Mittal;*
Post Graduate Institute of Medical Education and Research, Chandigarh, INDIA.

Aim/Introduction: Cardiac magnetic resonance imaging (CMR) and positron emission tomography (PET) are helpful in the early diagnosis and follow-up of cardiac sarcoidosis (CS). ^{18}F-FDG PET/CT in CS is one of the major criteria in diagnosing disease activity of CS, and helps in therapy monitoring however, requires stringent patient preparation/ dietary modifications for suppressing myocardial FDG uptake. ^{68}Ga-DOTANOC imaging for somatostatin receptors (SSTR) expressed in sarcoid granulomas, maybe an alternative, as it shows minimal physiological myocardial uptake & does not require dietary modifications to suppress myocardial radiotracer activity. ***Materials and Methods:*** This prospective study enrolled twenty-three patients, either biopsy-proven pulmonary sarcoidosis patients with suspected cardiac involvement or patients presenting with a primary cardiac abnormality with clinical features & histopathological diagnosis from a systemic site. Patients underwent CMR, ^{13}N-NH_3, ^{18}F-FDG (after low carbohydrate high fat protein diet preparation), and ^{68}Ga-DOTANOC PET/CT studies. Patient wise and cardiac segment wise analysis was done using Cohen's kappa to assess inter-modality agreement among three modalities. Mean SUVmax and target to background blood pool ratio (TBR) for positive lesions on DOTANOC and FDG PET were also calculated. ***Results:*** All patients underwent ^{68}Ga-DOTANOC & ^{18}F-FDG PET/CT, whereas only 19 patients could undergo CMR. ^{68}Ga-DOTANOC & CMR showed almost perfect intermodality agreement on segment-wise analysis [Cohen's kappa 0.88 (p-value 0.004)] and good intermodality agreement on patient-wise analysis [Cohen's kappa 0.51 (p-value 0.003)]. ^{18}F-FDG PET/CT showed almost perfect intermodality agreement with CMR on segment-wise analysis [Cohen's kappa 0.80 (p-value 0.004)] and good intermodality agreement on patient-wise analysis [Cohen's kappa 0.77 (p-value 0.001)]. Mean lesion SUVmax and TBR were not significantly different for ^{68}Ga-DOTANOC (6.6 ± 2.8 & 3.4 ± 1.4 respectively) and ^{18}F-FDG (9.0 ± 5.4 & 3.6 ±1.2 respectively). ***Conclusion:*** In conclusion, ^{68}Ga-DOTANOC PET/CT emerges as a highly effective and convenient imaging modality for diagnosing and managing cardiac sarcoidosis, demonstrating diagnostic performance comparable to ^{18}F-FDG PET/CT and cardiac magnetic resonance (CMR). Its favorable imaging characteristics, including high target-to-background ratios and reduced physiological myocardial uptake, enhance its utility in accurately detecting active cardiac sarcoid lesions. Furthermore, the streamlined preparation process and lack of dietary restrictions offer significant advantages in clinical practice, improving patient compliance and potentially less indeterminate results for reporting physician. The results of this study support the integration of ^{68}Ga-DOTANOC PET/CT into the diagnostic algorithm for cardiac sarcoidosis, warranting further prospective studies to validate its role and optimize its application in routine clinical settings.

EPS-112

The relationship between myocardial blood flow assessed by dynamic CZT-SPECT and the radiomics features of coronary artery calcification in NOCAD patients

K. Zavadovsky*, A. Maltseva, I. Taskaev, A. Dasheeva, A. Mochula;*
Cardiology Research Institute, Tomsk National Research Medical Center, Russian Academy of Sciences, Tomsk, RUSSIAN FEDERATION.

Aim/Introduction: Coronary artery calcification (CAC) is a marker of cardiovascular disease risk. Although myocardial blood flow (MBF) impairment and CAC have a weak inverse correlation, radiomics analysis of CAC may offer a more informative approach for evaluating MBF compared to the Agatston Calcium Score. Therefore, this study aimed to assess the relationship between MBF and radiomics features of CAC in patients with non-obstructive coronary artery disease (NOCAD). ***Materials and Methods:*** Based on CCTA results, 34 NOCAD patients (stenosis <50%; 23 men; mean age 59.0±9.6 years) were included in the study. We assessed CAC using the Agatston Calcium Score and the Calcium Volume Score. All patients underwent dynamic CZT-SPECT to assess stress and rest myocardial blood flow (SMBF or RMBF) and myocardial flow reserve (MFR) [1,2]. Radiomics features of CAC were additionally estimated using the Pyradiomics module in 3D Slicer 5.7.0. ***Results:*** Based on SMBF values, patients were divided into two groups: reduced SMBF (<1.5; n=19) and normal SMBF (≥1.5; n=15). The Agatston Calcium Score showed no significant difference between groups: 62.0 (44.0; 246.0) vs. 39.0 (17.0; 102.0), whereas patients with reduced SMBF had significantly higher the Calcium Volume Scores: 30.0 (17.0; 90.0) vs. 12.0 (4.0; 28.0) mm3. SMBF demonstrated significant inverse correlations with radiomics features: Glszm-SizeZoneNonUniformity (ρ=-0.37), Firstorder-Energy (ρ=-0.37), Glrlm-RunLengthNonUniformity (ρ=-0.37), Voxel count (ρ=-0.37), Gldm-DependenceEntropy (ρ=0,38), Firstorder-TotalEnergy (ρ=-0.39), Shape-VoxelVolume (ρ = -0.39), Glszm-ZoneEntropy (ρ=-0.40), Shape-MeshVolume (ρ=-0.42), Glcm-Idn (ρ=-0.43), Glcm-Idmn (ρ=-0.44), with a stronger correlation than the Agatston Score (ρ=-0.37). MFR showed significant inverse correlations with Firstorder-Minimum (ρ=-0.40), Shape-Sphericity (ρ=-0.40), Shape-MeshVolume (ρ=-0.39), Glrlm-RunLengthNonUniformity (ρ=-0.39), Glcm-Idmn (ρ=-0.39), Glszm-ZoneEntropy (ρ=-0.39), Shape-MajorAxisLength (ρ=-0.39), Shape-MinorAxisLength (ρ=-0.41), Glszm-GrayLevelNonUniformity (ρ=-0.42), Shape-Maximum3DDiameter (ρ=-0.42), Gldm-GrayLevelNonUniformity (ρ=-0.43), Glrlm-GrayLevelNonUniformity (ρ=-0.44), with a stronger correlation than the Agatston Score (ρ=-0.37) and Calcium Volume Score (ρ=-0.39). ***Conclusion:*** SMBF and MFR had significant inverse relationship with radiomics features of CAC. This approach offers a novel and potentially more effective method for assessing the impact of CAC on myocardial perfusion in NOCAD patients compared to the conventional the Agatston Calcium Score. ***References:*** 1.Mochula A, et al. The Influence of Kinetic Models and Attenuation Correction on Cadmium-Zinc-Telluride Single-Photon Emission Computed Tomography (CZT SPECT)-Derived Myocardial Blood Flow and Reserve: Correlation with Invasive Angiography Data. J Clin Med. 2024;13(5):1271. DOI: 10.3390/jcm13051271. 2.Zavadovsky KV, et al. Myocardial Blood Flow and Flow Reserve in Patients With Acute Myocardial Infarction and Obstructive and Non-Obstructive Coronary Arteries: CZT SPECT Study. Front Nucl Med. 2022;2:935539. DOI: 10.3389/fnume.2022.935539.

EPS-113

Early Detection of Anthracycline Combined with Immune Checkpoint Inhibitor Therapy-Related Cardiotoxicity Using [18F]FDG PET MRI

Y. Cai[1], *T. Yuan*[2], *X. Xu*[3], *Y. Sun*[4], *X. Chen*[5], *h. zhu*[3], *T. Wu*[1], *Z. Yang*[3], *X. Wang*[1];
[1]Department of Nuclear Medicine, National Cancer Center/ National Clinical Research Center for Cancer/Cancer Hospital, Chinese Academy of Medical Sciences and Peking Union Medical College,, Beijing, CHINA, [2]Department of Nuclear Medicine, Peking University First Hospital,, Beijing, CHINA, [3]Key Laboratory of Carcinogenesis and Translational Research (Ministry of Education/Beijing), Department of Nuclear Medicine, Peking University Cancer Hospital & Institute, Peking University, Beijing, CHINA, [4]Department of Pathology, Fuwai Hospital, National Cardiovascular Center, Chinese Academy of Medical Sciences and Peking Union Medical College, Beijing, CHINA, [5]Key Laboratory of Carcinogenesis and Translational Research (Ministry of Education/Beijing), Department of Nuclear Medicine, Peking University Cancer Hospital, Beijing, CHINA.

Aim/Introduction: To verify whether [18F] F -FDG PET/MRI can predict Anthracycline Combined with immune check point inhibitor Therapy-Related Cardiotoxicity ***Materials and Methods:*** Experimental procedures were carried out on female BALB/c mice, ranging from 6 to 8 weeks in age and weighing 18-20 g. The mice were divided into PD-1group, P-A group (anti-PD-1 + doxorubicin), and control group. Cardiac uptake of radiopharmaceuticals was evaluated via γ-counting and PET/MRI imaging. Combined with light microscopy (H&E, Masson's trichrome, CD68 immunostaining) to observe myocardial pathological changes. Human trials included 29 lymphoma patients undergoing anthracycline and PD-1 therapy. Cardiotoxicity was defined per 2022 ESC criteria, with patients stratified into ECG[+] (n=18) and ECG[-] (n=11) groups. Cardiac toxicity was assessed using [18F] F -FDG PET/MRI. Diagnostic accuracy was determined via ROC curve analysis. Data were analyzed with SPSS and GraphPad Prism ($p<0.05$) ***Results:*** In animal experiments, there was no basic uptake in myocardium in control group, the myocardium showed increased uptake of [18F] F -FDG in 4-week PD-1 group,6-week PD-1 group and P-A groups, The myocardial cell swelling and degeneration and focal macrophage infiltration of the epicardium were observed in 4-week PD-1 group , 6-week PD-1 group and P-A groups by optical microscope. In clinical studies, the [18F] F -FDG SUVmax_heart in ECG(+) group was higher than that in ECG(-) group, and GLS, GRS, GCS in ECG(+) group were lower than that the in ECG(-) group (all P values <0.05). Following 3-4 cycles of PD-1 inhibitor therapy, SUVmax_heart were elevated in the ECG(+) group compared to ECG(-) group. SUVmax_heart exhibited optimal diagnostic performance for cardiotoxicity injury (cut-off: 3.0; AUC=0.768; sensitivity=77.8%; specificity=81.8%; PPV=77.8%; NPV=81.8%; accuracy=79.3%). ***Conclusion:*** [18F] F -FDG PET/MR imaging can identify anthracycline/PD-1-induced cardiotoxicity in lymphoma patients at an early stage. anthracycline Combined with Immune checkpoint inhibitor therapy may induce myocardial damage, manifesting as reduced left ventricular full-thickness wall motion, with SUVmax_heart serving as a sensitive diagnostic parameter for cardiotoxicity.

EPS-114

Low myocardial flow reserve would predict all-cause mortality, cardiovascular mortality, and non-cardiovascular mortality in end stage kidney disease patients

S. Ohshima;
Kaikoukai Nagoya Kyoritsu Hospital, Nagoya, JAPAN.

Aim/Introduction: We have reported that low myocardial flow reserve (MFR) would predict all cause mortality and major cardiovascular event in end stage kidney disease (ESKD) patients. However it is unclear about the prognostic value of low MFR in cardiovascular(CV) or non CV mortality in these patients. In this study, we investigated the prognostic value of low MFR in all-cause mortality, cardiovascular (CV) mortality and non- CV mortality in ESKD patients. ***Materials and Methods:*** 1020 HD patients who underwent N^{13}-NH_3-PET myocardial perfusion imaging (MPI) suspected for ischemic heart disease were included. They are divided into two groups according to median value of MFR (2.0). We collected all-cause mortality, CV mortality and non-CV mortality. We have followed them for 1282 days. ***Results:*** We found any cause of death were 285 cases (the high MFR group vs the low MFR group; 165 (35.5%) vs 118 (21.3%), $p<0.001$), CV death were 121 cases (52 (9.4%) vs 68 (14.6%), $p=0.010$) and non-CV death were 164 cases (66(11.9%) vs 97 (20.9%, $p<0.001$)). Kaplan-Meier curve analysis and Cox regression model showed the low MFR groups had poor prognosis for all-cause mortality (log rank; $p<0.001$, hazard ratio (HR); 1.9964, 95% confidential interval (CI); 1.576-2.529), CV mortality (log rank; $p=0.0009$, HR; 1.834, 95%CI; 1.278-2.633) and non-CV mortality (log rank; $p<0.0001$, HR; 2.213, 95%CI; 1.555-2.907). Furthermore, multivariate cox regression model analysis showed the continuous value of MFR was an independent predictor for both all-cause mortality (HR0.180, 95%CI 0.074-0.435, $p=0.0001$) and non-CV mortality (HR0.553, 95% CI0.397-0.769, $p=0.0004$). ***Conclusion:*** In ESKD patients, low MFR would be an important predictor for all-cause mortality, CV mortality and non-CV mortality.

710

Monday, October 6, 2025, 8:00 - 9:30
Room 116

Technologists' Track Oral Presentations 2 - Technologists Committee: Advanced Practice and Novel Solutions

OP-314

Filling A Void: An altered teaching method for Nuclear Medicine Technology in Australia

M. Scalzo[1], *K. Metzger*[1], *T. Pearson*[2], *J. Barlow*[3];
[1]RMIT University, Melbourne, AUSTRALIA, [2]Royal Brisbane and Women's Hospital, Brisbane, AUSTRALIA, [3]Queensland X-ray, Brisbane, AUSTRALIA.

Aim/Introduction: In response to insights from multiple workforce summits, RMIT University has developed the Embedded Student Model (ESM), a groundbreaking initiative designed to integrate academic theory with Work Integrated Learning (WIL). This transformative framework, created in collaboration with industry partners, equips students with clinical expertise, critical thinking, and professional skills essential for success in Nuclear Medicine imaging. The ESM addresses workforce shortages, combats student "placement poverty," enhances employability, and aspires to establish a replicable model for innovation in higher education. ***Materials and Methods:*** The ESM will balance academic instruction with industry engagement, addressing RMIT's limited presence outside Victoria through collaboration with public and private partners. This innovative apprenticeship-style approach integrates three days of remote learning with two days of practical experience each week, preparing students for professional success. RMIT University ensures quality teaching, learning outcomes, and a supportive student experience for remotely delivered content. Combining theoretical knowledge with hands-on training, the ESM uses capability-based assessments and a real-world capstone project to equip graduates with the academic credentials and practical expertise needed for workforce readiness. ***Results:*** The ESM will deliver immediate impact beyond graduate numbers and job placements by addressing "placement poverty," as highlighted in the 2024 Australian Universities Accord. Through sustained industry partnerships, RMIT University provides students with real-world exposure, mentorship, and networking opportunities,

ensuring they graduate with in-demand skills aligned with workforce needs. This innovative approach not only tackles student hardships but also serves as a scalable and adaptable model for other educational programs. By expanding the ESM to States and Territories lacking undergraduate Nuclear Medicine training, RMIT can benefit the Nuclear Medicine profession Australia-wide. The program's inception, demonstrates how public and private industry collaborations can address shared challenges, enhancing both education and workforce readiness. ***Conclusion:*** The ESM bridges academia and industry, addressing skills gaps and combating placement poverty. By integrating theoretical learning with practical experience, it prepares graduates for meaningful careers. This innovative model has the potential to transform education, foster workforce readiness, and serve as a blueprint for both national and global adoption.

OP-315

Revisiting SeHCAT: A Familiar Tool with Renewed Clinical Significance in Nuclear Medicine

M. Ryser, *S. Figueiredo, J. O. Prior, P. Ferreira, M. Nicod-Lalonde;*
CHUV, Lausanne, SWITZERLAND.

Aim/Introduction: Bile acid malabsorption (BAM) is a prevalent etiology of chronic diarrhea. A sensitive and specific diagnostic method for this pathology is the SeHCAT (selenium-75 homochlic acid taurine) procedure. This test is experiencing a resurgence in the field of Nuclear Medicine, particularly with the introduction of new treatments options. The aim of this work is to describe how we implemented this procedure in our Nuclear Medicine Department and to share our experience. ***Materials and Methods:*** For the successful implementation of the SeHCAT investigation procedure in our Nuclear Medicine Department, we did a comprehensive review of existing literature and a collaborative discussion with a multidisciplinary team, including Nuclear Medicine Physicians, Gastroenterologists, Nuclear Medicine Technologists and the nursing staff. Several criteria had to be considered to establish an optimal protocol: patient preparation, radiopharmaceutical availability, acquisition parameters (timing post-radiopharmaceutical administration, imaging modalities, energy window specifications, collimation technique), interpretation criteria and waste management. ***Results:*** The implementation process in our department for this procedure took us 3 months. After considering all the above-mentioned criteria, a standardized protocol was developed and implemented. Our first patient was assessed in August 2024, and, by March 2025, we had conducted examinations on three patients. Our results revealed that two patients exhibited severe BAM, while one presented with mild BAM. The results of SeHCAT investigation guided subsequent therapeutic management. Specifically, the introduction of Colestyramine, a bile acid sequestrant, in the two patients with severe BAM led to a good response in controlling diarrhea, which was not the case in the patient presenting with mild BAM. ***Conclusion:*** Through the dedicated efforts of our multidisciplinary team, The SeHCAT investigation procedure was safely and efficiently implemented in our department. SeHCAT investigation enables us to effectively address the diagnostic needs of gastroenterologists, thereby enhancing patient care in the context of BAM.

OP-316

Correlating Subjective Evaluations in Equine Nuclear Scintigraphy with Radiomic Profiles, Serum Osteocalcin and C-Terminal Telopeptides of Type I Collagen

P. Tually[1], *J. Meadows*[1], *S. Tagore*[1], *G. Currie*[2];
[1]*TeleMedVET, Perth, Western Australia, AUSTRALIA,* [2]*Charles Sturt University, Wagga Wagga, AUSTRALIA.*

Aim/Introduction: The racehorse industry is facing increasing scrutiny under its social licence to operate, particularly concerning preventable injuries such as stress fractures. Advanced imaging tools like PET and SPECT and the emergence of blood biomarkers offer new opportunities to identify bone fatigue earlier and mitigate musculoskeletal injury (MSI) risk.This study aimed to explore the relationship between serum bone turnover markers and regional radiomic features from planar and SPECT imaging in Thoroughbred racehorses, to assess the potential of combined modalities in improving early detection of subclinical bone stress. ***Materials and Methods:*** A prospective study was conducted across two jurisdictions—Western Australia and Hong Kong—using clinically lame Thoroughbred racehorses undergoing nuclear scintigraphy. Blood samples were collected pre-radiotracer injection and analysed for osteocalcin (OC) and C-terminal telopeptides of type I collagen (CTX) using equine-specific ELISA kits. Samples were processed and analysed at a single laboratory to ensure consistency. In Australia, horses received standardised scintigraphic imaging with a SPECT-capable gamma camera (Millennium MPR, GE Healthcare). Radiomic features were extracted from predefined regions of interest using decay-corrected geometric mean values. Relative radiomic asymmetry (left vs right) and serum marker levels were assessed for association. ***Results:*** Horses with both elevated OC levels and asymmetry in radiomic values above a defined threshold were more likely to demonstrate regions of increased radiopharmaceutical uptake suggestive of developing bone pathology. While CTX alone was not associated with increased radiotracer uptake, the OC:CTX ratio appeared informative. Combined biomarker-radiomic screening identified a subset of high-risk cases not readily apparent from imaging or blood data alone. ***Conclusion:*** This study supports the feasibility of integrating radiomic and serum biomarker data to enhance early MSI risk detection in racehorses. Given the industry's need to address welfare concerns, particularly around preventable injuries, tools like SPECT imaging and OC:CTX analysis could contribute to improved monitoring protocols. Multimodal screening may play a future role in protecting horse welfare and supporting the industry's ongoing social legitimacy.

OP-317

Relationship of point-of-care β-hydroxybutyrate measurements with myocardial glucose uptake: an observational study.

S. Bourouis, *C. Derneden, Q. Shagera, F. Jamar, O. Gheysens, V. Depoortere;*
Cliniques universitaires Saint-Luc, Bruxelles, BELGIUM.

Aim/Introduction: 18F-FDG-PET/CT is widely used to diagnose inflammatory/infectious cardiac diseases. A limitation of 18F-FDG-PET is the physiological myocardial glucose uptake, which may interfere with image interpretation. Adequate suppression of physiological myocardial glucose uptake is crucial. To achieve adequate myocardial glucose suppression (MGS), patients follow a high-fat, low-carbohydrate diet for 24-48 hours combined with prolonged fasting (>12 hours) before FDG injection. Despite this, up to 20% scans remain non-diagnostic due to inadequate suppression. While dietary logs are often reviewed, no consistent link between nutrient intake and MGS was confirmed. Recent studies showed an inverse correlation between β-hydroxybutyrate (BHB) levels - a ketone body produced during fasting - and myocardial glucose uptake. BHB can be measured easily with point-of-care devices, making it a potentially useful tool. This observational study aimed to assess the relationship between BHB levels and MGS 18F-FDG-PET/CT. ***Materials and Methods:*** We studied 102 patients undergoing 18F-FDG-PET/CT for oncologic or cardiac inflammatory/infectious evaluation. All patients had capillary BHB levels checked prior to FDG injection using a point-of-care device. 72 patients with suspected cardiac conditions followed a dietary regimen with prolonged fasting. PET scans were performed 60-90 minutes post-injection and MGS was assessed

visually by experienced nuclear medicine physicians using a 4-point scale : diffuse myocardial uptake (score 0), uptake at the basolateral wall or basal ring sign (score 1), myocardial uptake equal to left ventricular bloodpool (score 2) and myocardial uptake less than left ventricular bloodpool (score 3). Scores 2 and 3 were considered as optimal suppression. ***Results:*** Cardiac 18F-FDG-PET scores were: 0 (19), 1 (12), 2 (35) and 3 (36). Median (IQ range) BHB values were significantly lower for scores 0 and 1 compared to 2 and 3, i.e. 0.1 (0.1-0.7), 0.2 (0.1-0.4), 0.8 (0.4-1.2) and 0.8 (0.4-1.2) mmol/L, respectively. When combining scores 0/1 and 2/3, median (IQ range) BHB values were significantly lower for scores 0/1, 0.2 (0.1-0.4) vs 0.8 (0.4-1.2), respectively; P<0.01. Patients with adequate preparation had higher BHB levels than those without (0.7 vs 0.2 mmol/L; P<0.05). ROC curve analysis yielded an AUC of 0.8, with a BHB cutoff of ~0.45 mmol/L predicting good MGS (sensitivity 73%, specificity 77%). Correlation between BHB and glucose was weak (R = -0.24). ***Conclusion:*** Point-of-care BHB measurement is feasible and levels correlate inversely with myocardial glucose uptake. Dietary preparation increases BHB levels, and BHB monitoring may help optimize the management of patients referred for cardiac inflammatory/infectious evaluation.

OP-318

Design and Fabrication of Spherical Inserts using Stereolithography for 10 L Imaging Validation Phantom

N. Salkica[1], *M. Jusufbegović*[2], *A. Beganović*[3], *A. Skopljak-Beganović*[3], *S. Hadžimusić*[1], *E. Tinjak*[4];
[1]*Clinic of Nuclear Medicine, Sarajevo, BOSNIA AND HERZEGOVINA,* [2]*Clinic of Radiology, Sarajevo, BOSNIA AND HERZEGOVINA,* [3]*Department for Medical Physics and Radiation Protection, Sarajevo, BOSNIA AND HERZEGOVINA,* [4]*Clinic of Oncology, Sarajevo, BOSNIA AND HERZEGOVINA.*

Aim/Introduction: Imaging validation phantoms are commonly used for calibration, resolution testing, and contrast evaluation in imaging modalities such as positron emission tomography (PET), single-photon emission computed tomography (SPECT), and computed tomography (CT). The focus is on achieving dimensional and volumetric accuracy, optical clarity, and mechanical robustness to ensure valid and reproducible experimental outcomes. The aim of this study is to design and construct six spherical inserts for 10 L acrylic phantom with (inner diameters: 10, 13, 17, 22, 28, and 37 mm) using stereolithography (SLA) and clear photopolymer resin. ***Materials and Methods:*** The phantom was designed using parametric computer-aided design (CAD) software, ensuring precise manipulation of geometry and dimensional tolerances. The nominal dimensions of 24.1 × 30.5 × 24.1 cm were chosen to provide a total volume of 10 L. Wall thicknesses between 3-5 mm were selected to optimize the balance between mechanical rigidity and attenuation effects. To reduce resin consumption, the external container was partitioned into multiple panels for bonding. Six spherical inserts, with internal diameters of 10, 13, 17, 22, 28, and 37 mm, were designed with shell thicknesses of 1-2 mm. These inserts were equipped with integrated fill ports or vent channels to facilitate fluid introduction and removal. Mounts or rods inside the main phantom volume ensured stable positioning of the spheres. For the SLA printing process, a clear resin was selected based on compatibility with the SLA machine and its mechanical and optical properties. Post-processing included UV-curing to stabilize the prints, followed by wet-sanding and polishing to enhance optical clarity. Final assembly used UV-curing adhesives or epoxy formulations, with leakage testing conducted under internal pressure. ***Results:*** The assembled 10 L acrylic phantom was dimensionally accurate, with all six spherical inserts positioned securely within the main phantom volume. Attenuation characteristics of materials used for phantom production was assessed and found to be suitable for imaging validation. Leakage testing confirmed the integrity of the seals at all interfaces, and no significant seepage was observed. ***Conclusion:*** The construction of a 10 L acrylic phantom with six spherical inserts using SLA and clear resin is a feasible and effective approach for producing a dimensionally precise and transparent phantom for advanced imaging validation and calibration studies. Attention to design details, material properties, print orientation, support strategies, and post-processing techniques is essential to ensure the phantom's accuracy and reliability. The fabricated phantom is suitable for use in PET, SPECT, and CT imaging applications, offering a robust tool for calibration and testing.

OP-319

Evaluating the Effectiveness of Virtual Reality as a distraction tool in Pediatric Scanning Procedures - To Enhance Image Quality and Reducing Anesthesia use

N. Svendsen*, V. Setterberg;*
Rigshospitalet, Copenhagen, DENMARK.

Aim/Introduction: Distraction during such procedures is essential in pediatric care. Effective techniques reduce anxiety, promote trust, and prevent delays in language and speech development. VR glasses, with healthcare-specific games, offer a promising distraction tool. The glasses feature calming, engaging games to help the child remain still and reduce distress. We have modified the user interface from vertical to horizontal gameplay, so it can now be used during scanning procedures. Including a 180-degree field of view so the child can keep the head in one position. ***Materials and Methods:*** The Pediatric Technologist Team is often consulted within the department when children struggle to cooperate during scanning procedures, due to fear, anxiety, or restlessness. We introduced the VR-glasses for scanning procedures in 30 children aged 5-13 y. as a distraction tool in these cases where standard distraction (movies in the ceiling etc.) was not sufficient. The remote control is functioning with only small movements of the hand, that do not interfere with the scanning procedure. ***Results:*** A total of 30 children used the VR glasses during scanning procedures. During the test period the intervention was ineffective in 4 of the 30 children; with 3 children not being able to distract the children and 1 child declining to use the glasses. And in the remaining 26 children the procedure was performed successfully with satisfied child and parents and a high-quality study. Most of the children had renographies, hepatobiliary scintigraphies or SPECT/CT of the abdomen or the extremities performed. The VR intervention allowed the children to remain still and calm, reducing the need for anesthesiologic support. ***Conclusion:*** In the majority of children that needed extra distraction, VR glasses were more effective than standard distraction methods. Unlike passive techniques, as movie in the ceiling etc., VR allows children to actively engage in an immersive environment, fostering deeper focus, distracted the child, and improved cooperation. This active participation proved more effective in reducing stress compared to standard methods, which is not engaging the child in the same manner. The use of VR glasses furthermore reduced the need for anesthesiologic intervention and rescheduling of the scan. The experience helped children become fully engaged, often losing awareness of time and surroundings. These results suggest that VR is a promising tool in pediatric imaging as an extra tool for distraction.

OP-320

Preclinical PET Imaging of B7-H3 Expression Using Affibody Molecules Labelled with Positron-Emitting Gallium-68

M. Oroujeni[1], *V. Tolmachev*[1], *E. A. Bezverkhniaia*[1], *E. Papalanis*[1], *A. Mujahid Bin Muhammad*[1], *A. Verabyova*[1], *E. Gunneriusson*[2], *S. Klint*[2], *E. Ryer*[2], *M. Carlqvist*[2], *W. Kazmierczak*[2], *A. Orlova*[1], *F. Y. Frejd*[2];
[1]*Uppsala University, Uppsala, SWEDEN,* [2]*Affibody AB, Stockholm, SWEDEN.*

Aim/Introduction: Affibody molecules, non-immunoglobulin scaffold proteins, have a high potential as probes for molecular imaging of different molecular targets. One of the molecular targets for radionuclide diagnosis and therapy is B7-H3 (known as CD276), which is overexpressed in various cancers, whereas its expression is low in most normal organs and tissues. The visualization of expression levels of B7-H3 has been performed using Affibody molecules labelled with Tc-99m. However, radionuclide molecular imaging using PET offers several advantages such as superior sensitivity, quantitation accuracy, and better spatial resolution compared to SPECT. In this study, we aimed to introduce a radiotracer for PET imaging of B7-H3 using Affibody molecules labelled with Ga-68. ***Materials and Methods:*** To design imaging agents for labeling with the generator-produced positron-emitting radionuclide ^{68}Ga, the macrocyclic triaza chelator (2-[4,7-bis(carboxymethyl)-1,4,7-triazonan-1-yl]acetic acid) (NOTA) chelator was site-specifically coupled to the C-termini of the anti-B7-H3 Affibody molecules. Four different variants of Affibody molecules, ZB7-H3_2, ZB7-H3_3, ZB7-H3_4, and ZAC12 (as control) were produced, characterized, and labelled with ^{68}Ga. In vitro characterization was performed on B7-H3-expressing cell lines. A head-to-head biodistribution of Affibody molecules labelled with ^{68}Ga was studied in mice bearing B7-H3-expressing SKOV-3 xenografts. PET/CT imaging was performed to confirm the biodistribution results. ***Results:*** All variants were successfully labelled with ^{68}Ga with high radiochemical yield and purity and demonstrated specific binding to B7-H3-expressing cells in vitro and in vivo. ^{68}Ga-labelled conjugates bound specifically to B7-H3-expressing cells in vitro and in vivo. Biodistribution demonstrated that the blood concentration of [^{68}Ga]Ga $Z_{B7\text{-}H3\text{—}2}$ (0.24±0.03 %ID/g) and [^{68}Ga]Ga $Z_{B7\text{-}H3\text{—}3}$ (0.27±0.02 %ID/g) was significantly ($p < 0.05$) higher than for the control variant, [^{68}Ga]Ga-Z_{AC12} (0.11±0.01 %ID/g) 2 h after injection. [^{68}Ga]Ga-ZB7-H3_2 had the highest tumor accumulation only 2 h after administration, which was 2.8-fold higher than for the control ZAC12. Tumor-to-liver ratio was significantly ($p < 0.05$) higher for [^{68}Ga]Ga-$Z_{B7\text{-}H3\text{—}2}$ (7.5±0.7) than for [^{68}Ga]Ga-$Z_{B7\text{-}H3\text{—}3}$ (3.9±0.2) and [^{68}Ga]Ga-$Z_{B7\text{-}H3\text{—}4}$ (4.4±0.8). There was a tendency for higher tumor-to-organ ratios compared to the other variants, resulting in higher imaging contrast using [^{68}Ga]Ga-ZB7-H3_2 for preclinical PET imaging of B7-H3-expressing tumors. ***Conclusion:*** The use of an Affibody-based tracer containing a NOTA chelator at the C-terminus provides labeling of the anti-B7-H3 Affibody molecule with ^{68}Ga. The newly introduced Affibody-based tracers are suitable for preclinical imaging of B7-H3 expressing tumors already 2 h after injection. [^{68}Ga]Ga-ZB7-H3_2 could be a promising candidate for further development aiming at clinical imaging in the future.

OP-321

Using AI to assess PRRT response in ^{177}Lu-DOTATATE post-treatment scans: creation of a Python-based tool to automate inter-cycle comparison

F. Montanini[1], *E. M. Abenavoli*[2], *V. Briganti*[2], *M. Nerattini*[3], *A. Lastrucci*[4], *C. Galeotti*[1], *R. Ricci*[4], *R. Sciagrà*[2,3], *V. Berti*[2,3];
[1]*Nuclear Medicine Unit, Department of Health and Rehabilitation Technical Professions, Careggi University Hospital, Florence, ITALY,* [2]*Nuclear Medicine Unit, Department of Diagnostic Services, Careggi University Hospital, Florence, ITALY,* [3]*Department of Experimental and Clinical Biomedical Sciences 'Mario Serio', University of Florence, Florence, ITALY,* [4]*Department of Health and Rehabilitation Technical Professions, Careggi University Hospital, Florence, ITALY.*

Aim/Introduction: Accurate assessment of treatment response in patients with metastatic neuroendocrine tumors (NETs) undergoing ^{177}Lu-DOTATATE therapy is essential for effective clinical management. Visual comparison of post-treatment whole-body (WB) acquisitions between consecutive cycles is often a challenging procedure, especially when evaluating the liver, due to the complex and variable distribution of lesions. This work aimed to develop an automated Python based software solution to quantitatively compare liver uptake across treatment cycles, overcoming the limitations of subjective visual analysis by providing a standardized and reproducible method to evaluate disease progression or regression. ***Materials and Methods:*** A custom software tool was developed using Python 3.13, leveraging artificial intelligence models to streamline coding. The software imports DICOM files of anterior and posterior WB acquisitions from two ^{177}Lu-DOTATATE treatment cycles. Images are then normalized by dividing pixel values by the mean counts value of a reference region, selectable as either the third lumbar vertebra or spleen. Automatic liver segmentation is performed on both anterior and posterior views of each cycle, with an option for manual adjustment of region-of-interest (ROI) contours to ensure accuracy. The segmented liver ROIs are registered and transformed to align perfectly between cycles, enabling direct comparison. Differences in uptake are calculated, with increased counts indicating lesion progression and decreased counts suggesting lesion response. The software finally generates a numerical and visual report summarizing changes. Extensive testing and debugging ensured robust functionality across various datasets. ***Results:*** The software successfully processed WB acquisitions, accurately segmenting the liver and aligning ROIs between cycles. Normalization using reference regions standardized counts values, ensuring reliable comparisons. The automated analysis highlighted uptake differences, with visual reports clearly depicting areas of increased or decreased counts. Testing confirmed the tool's ability to quantify disease changes rapidly, offering a significant improvement over visual assessment by providing objective data at a glance. ***Conclusion:*** This automated tool enhances the evaluation of ^{177}Lu-DOTATATE treatment response by quantifying liver uptake changes with precision and consistency in patients with metastatic NETs. By overcoming the limitations of subjective visual assessment, the tool offers a robust complement to qualitative evaluation, enabling clinicians to detect subtle variations in disease progression or regression with greater confidence. Future developments aim to expand the software's functionalities to include SPECT/CT acquisitions and whole-body lesion analysis, further broadening its applicability. ***References:*** •Weber et al. (2020). Quantitative imaging biomarkers for nuclear medicine: from SUV to AI. European Journal of Nuclear Medicine and Molecular Imaging, 47(6), 1400-1412.

OP-322

Development of a Dynamic Flow Phantom for Routine Calibration and Quality Control in [^{82}Rb]RbCl PET imaging.

S. Mallem[1], *M. Bernardini*[2];
[1]*INSERM - U970 PARCC, Paris, FRANCE,* [2]*Hôpital Européen Georges Pompidou AP-HP, Paris, FRANCE.*

Aim/Introduction: [^{82}Rb]RbCl PET is increasingly used for myocardial perfusion imaging due to its ability to provide fast, quantitative assessment of myocardial blood flow. However, its short half-life (76 s) and automated injection systems complicate calibration and PET system quality control. Unlike [^{18}F]FDG, no standard phantom can be manually filled to verify the accuracy of injected activity and image quantification in clinical settings. We developed and validated a simple dynamic flow phantom to enable calibration and routine quality control for [^{82}Rb]RbCl PET. ***Materials and Methods:*** The system included a cylindrical phantom (as used for [^{18}F]FDG), connected to silicone tubing, a peristaltic pump, and a 3D-printed open injection chamber allowing automated injection without air bubble introduction. The circuit provided continuous flow, simulating clinical injection

conditions : early input function and later homogeneous distribution can be visualized. To calculate the total system volume, a known activity of [^{18}F]FDG was injected, and volumic activity was determined via gamma counter measurements after homogenization. PET acquisition started at injection time, and dynamic reconstruction showed tracer homogeneity suitable for quantification at 2 minutes. Quantitative analysis was performed over the 2-5 minute interval, in line with clinical protocols. The same procedure was applied with [^{82}Rb]RbCl at different activity levels. Image-based activity was compared with expected values to assess PET quantification accuracy and the reliability of the injected activity reported by the injector. ***Results:*** With [^{18}F]FDG, mean SUV was 0.97, corresponding to -3% deviation from expected activity. This confirmed both the accuracy of PET quantification for [^{18}F]FDG and the ability of the phantom to achieve homogeneous distribution within 2 minutes. With [^{82}Rb]RbCl, quantification was systematically lower than expected. A correction factor was derived for [^{82}Rb]RbCl acquisitions : the average deviation was −9% at high activity (1,480 MBq) and −5% at low activity (740 MBq), remaining within the commonly accepted ±10% tolerance for PET quantification. ***Conclusion:*** The dynamic flow phantom developed provides a practical and reproducible tool for [^{82}Rb]RbCl PET calibration and quality control. It allows realistic simulation of clinical injection, accurate verification of PET quantification, and consistent comparison between measured and injector-reported activity. The setup is easy to implement and suitable for integration into routine quality control procedures. ***References:*** Jensen, EJNMMI Phys, 2022 Bui, J Nucl Cardiol, 2020 Koenders, J Nucl Cardiol, 2022 Armstrong, J Nucl Cardiol, 2022 van Dijk, EJNMMI Phys, 2022 Gould, J Nucl Cardiol, 2011 Prior, Eur J Nucl Med Mol Imaging, 2012

711

Monday, October 6, 2025, 8:00 - 9:30
Room 111

Theranostics Track - Oncology & Theranostics Committee: Prostate and Novel Targets

OP-323

[^{177}Lu]Lu-PSMA-617 SPECT/CT as an Early Response Biomarker for Prediction of Progression Free and Overall Survival in Patients with Metastatic Castration Resistant Prostate Cancer Treated with Enzalutamide and [^{177}Lu]Lu-PSMA-617 within the ENZA-p Trial (ANZUP 1901)

N. Ayati[1,2], *N. Papa*[3], *S. Subramaniam*[4,5], *M. Crumbaker*[1,3,6], *E. Askari*[7], *R. Alipour*[8,9], *A. Iravani*[10], *S. Khan*[1], *S. Yadav*[11], *M. Eiber*[12], *R. Francis*[13,14], *A. Nguyen*[1], *M. Hofman*[8,9], *S. Sandhu*[8,9], *T. Hioki*[1], *J. Oorschodt*[15], *K. Devitt*[1], *K. Willowson*[16,17], *S. Sharma*[1], *A. Stancu*[18], *S. Chauvie*[19], *P. Wilson*[20], *M. Stockler*[4], *I. Davis*[21,22], *L. Emmett*[1,2,3]; [1]*St Vincent's Hospital, Sydney, AUSTRALIA,* [2]*St Vincent's Clinical School, University of New South Wales, Sydney, AUSTRALIA,* [3]*Garvan Institute of Medical Research, Sydney, AUSTRALIA,* [4]*NHMRC Clinical Trials Centre, University of Sydney, Sydney, AUSTRALIA,* [5]*Department of Medical Oncology, Bankstown-Lidcombe Hospital, Sydney, AUSTRALIA,* [6]*Department of Medical Oncology, Kinghorn Cancer Centre, St Vincent's Hospital, Sydney, AUSTRALIA,* [7]*Nuclear Medicine Research Centre, Mashhad University of Medical Sciences, Mashhad, IRAN, ISLAMIC REPUBLIC OF,* [8]*Prostate Cancer Theranostics and Imaging Centre of Excellence (ProsTIC); Molecular Imaging and Therapeutic Nuclear Medicine, Cancer Imaging, Peter MacCallum Cancer Centre, Melbourne, AUSTRALIA,* [9]*Sir Peter MacCallum Department of Oncology, The University of Melbourne, Melbourne, AUSTRALIA,* [10]*Department of Radiology, University of Washington, Seattle, WA, UNITED STATES OF AMERICA,* [11]*Department of Radiology and Biomedical Imaging, University of California San Francisco, San Francisco, CA, UNITED STATES OF AMERICA,* [12]*Department of Nuclear Medicine, Rechts der Isar Medical Center, Technical University of Munich, Munich, GERMANY,* [13]*Department of Nuclear Medicine, Sir Charles Gairdner Hospital, Perth, AUSTRALIA,* [14]*Medical School, University of Western Australia, Perth, AUSTRALIA,* [15]*Eindhoven University of Technology, Eindhoven, NETHERLANDS,* [16]*Royal North Shore Hospital, St. Leonards, Sydney, AUSTRALIA,* [17]*Institute of Medical Physics, School of Physics, University of Sydney, Camperdown, Sydney, AUSTRALIA,* [18]*Dixit Srl, Torino, ITALY,* [19]*Division of Medical Physics, 'Santa Croce e Carle' Hospital, Cuneo, ITALY,* [20]*MIM Software, A GE HealthCare Company, Cleveland, OH, UNITED STATES OF AMERICA,* [21]*Monash University Eastern Health Clinical School, Melbourne, AUSTRALIA,* [22]*Eastern Health, Melbourne, AUSTRALIA.*

Aim/Introduction: [^{177}Lu]Lu-PSMA single photon emission computed tomography (SPECT)/CT is a promising early response biomarker for [^{177}Lu]Lu-PSMA therapy in retrospective studies and an affordable alternative to PSMA-PET. ENZA-p is a prospective randomised phase II trial in metastatic castrate resistant prostate cancer (mCRPC). This ENZA-p sub-analysis aims to determine if a week 6 [^{177}Lu]Lu-PSMA-617 SPECT/CT is prognostic for clinical outcomes. ***Materials and Methods:*** Eligible participants (pts) were randomised (1:1) to either enzalutamide 160 mg daily or enzalutamide 160 mg daily +[^{177}Lu]Lu-PSMA-617 7.5 GBq (2 or 4 doses). All patients in the combination arm underwent a 25-minute SPECT/CT 24 hours after each [^{177}Lu]Lu-PSMA-617 therapy, with SPECT/CT imaging acquisition protocols, cameras and image reconstruction parameters standardised across the 15 trial sites. SPECT/CT images were centrally quantified with semi-automated software to derive total tumour volume (TTV) and standardised uptake value (SUV)mean. Reduction of >90% in SPECT-TTV and SUVmean at 6 weeks were considered significant. Change in SPECT/CT quantitative parameters (TTV and SUVmean) between dose 1 and dose 2 were correlated with clinical outcomes. ***Results:*** ENZA-p randomised 162 pts of whom

81 received enzalutamide plus (2 or 4 doses) 7.5Gbq ^{177}Lu]Lu-PSMA-617. 74/81 (91%) had analysable SPECT/CT. Median PSA-PFS was 12 months (95%CI: 10-16) with median overall survival 33 months (95%CI: 27-35). The median change in SPECT-TTV was -57% (IQR: -89% to -38%), with 24% of pts demonstrating a 90% reduction in SPECT-TTV at 6 weeks, 61% a 50% reduction, and 4.1% any rise in SPECT-TTV. Median PSA-PFS for pts with ≥90% volume response was 17 months (95%CI: 9.6-NE) vs 11 months (95%CI: 9.6-15) for <90% volume response, HR=0.56 (95%CI: 0.29-1.09). Median OS for pts with ≥90% volume response was 36 months (95%CI: 33-NE) vs 32 months (95%CI: 27-34) for <90% volume response, HR=0.49 (95%CI: 0.21-1.10). The median change in SUVmean was -30% (IQR: -56% to -13%), with 15% of pts demonstrating a 90% reduction in SUVmean at 6 weeks, 30% a 50% reduction, and 15% any rise in SUVmean. Median PSA-PFS for pts with ≥90% decrease in SUVmean at 6 weeks was 22 months (95%CI: 6.8-NE) vs 11 months (95%CI: 10-15) for <90% decrease, HR=0.45 (95%CI: 0.19-1.06). Median OS for pts with ≥90% decrease in SUVmean was not reached (95%CI: 21-NE) vs 32 months (95%CI: 27-34) for <90% decrease, HR=0.28 (95%CI: 0.08-0.90). ***Conclusion:*** [^{177}Lu]Lu-PSMA SPECT/CT quantitative parameters at 6-weeks is a candidate early prognostic biomarker for PSA-PFS and OS with enzalutamide plus ^{177}Lu]Lu-PSMA-617 therapy.

OP-324

Impact of PET-Guided Versus Conventional Imaging-Guided Metastasis-Directed Therapy on Clinical Outcomes in Oligometastatic Castration Resistant Prostate Cancer (omCRPC): A Secondary Analysis of the PRECISE-MDT Study

F. Lanfranchi[1], *D. Albano*[2], *F. Linguanti*[3], *L. Urso*[4], *A. Rizzo*[5], *D. Dubois*[1], *F. Dondi*[2], *E. M. Abenavoli*[6], *L. Vaggelli*[6], *N. Ortolan*[4], *F. Garrou*[7], *S. Grimaldi*[7], *P. Ghedini*[8], *A. Iudicello*[8], *G. Rovera*[7], *D. Vita*[1], *M. Salgarello*[9], *M. Racca*[5], *M. Bartolomei*[4], *S. Panareo*[8], *F. Bertagna*[2], *S. Morbelli*[7], *G. Sambuceti*[1], *L. Belgioia*[1], *M. Bauckneht*[1];
[1]*IRCCS Ospedale Policlinico San Martino, Genova, ITALY,* [2]*Nuclear Medicine, ASST Spedali Civili di Brescia, Brescia, ITALY,* [3]*Nuclear Medicine, Ospedale San Donato, Arezzo, ITALY,* [4]*Nuclear Medicine, University Hospital of Ferrara, Ferrara, ITALY,* [5]*Nuclear Medicine, Candiolo Cancer Institute, FPO-IRCCS, Torino, ITALY,* [6]*Nuclear Medicine, Careggi University Hospital, Firenze, ITALY,* [7]*Nuclear Medicine, AOU Città della Salute e della Scienza di Torino, Torino, ITALY,* [8]*Nuclear Medicine, University Hospital of Modena, Modena, ITALY,* [9]*Nuclear Medicine, IRCCS Ospedale Sacro Cuore Don Calabria, Negrar, ITALY.*

Aim/Introduction: The ideal imaging modality to guide metastasis-directed therapy (MDT) in oligometastatic castration-resistant prostate cancer (omCRPC) has yet to be fully established. The ARTO trial demonstrated that adding MDT to systemic treatment improves oncological outcomes in omCRPC. However, preliminary data from the MEDCARE trial suggest that the diagnostic accuracy of imaging tools may influence MDT efficacy in this clinical setting. Therefore, we aimed to evaluate the impact of PET-guided versus conventional imaging-guided MDT on clinical outcomes in omCRPC patients. ***Materials and Methods:*** We performed a secondary analysis using data from the PRECISE-MDT study, focusing on omCRPC patients treated with stereotactic body radiotherapy (SBRT) guided by either PET (PSMA or choline) or conventional imaging (CI). All patients received systemic treatment in addition to MDT. Inverse probability of treatment weighting (IPTW) was applied to adjust for AJCC stage, ISUP Grade Group, PSA value at the time of MDT, metastatic site, and number of metastases. Outcomes included progression-free survival (PFS), time to systemic treatment change (PFS2), and overall survival (OS). PSA response rates (PSA50 and PSA90) were also assessed. All survival analyses were censored at 48 months. ***Results:*** The IPTW-adjusted analysis showed significantly improved PFS in the PET-guided group compared to the CI-guided group (median 14.23 vs. 8.30 months; p=0.0422; HR=0.53; 95% CI [0.28, 0.99]) and a trend toward improved PFS2 favoring PET guidance (median 27.10 vs. 12.90 months; p=0.0840; HR=0.49; 95% CI [0.22, 1.12]). No significant difference was observed in OS (median not reached in either group; p=0.4042; HR=0.55). PSA50 response rates were comparable between groups (49.2% PET vs. 47.1% CI), as were PSA90 rates (24.6% PET vs. 23.5% CI). ***Conclusion:*** PET-guided MDT significantly prolongs the time to progression and shows a trend toward delaying systemic treatment change compared to conventional imaging-guided MDT in omCRPC patients, although PSA response profiles were substantially overlapping between groups. These findings support the use of next-generation imaging to optimize patient selection and treatment outcomes in the omCRPC setting, when MDT is chosen to intensify systemic treatment.

OP-325

Assessment of PARPi-uptake in metastatic castration resistant prostate cancer patients using [^{18}F]PARPi- and [^{68}Ga]PSMA PET/CT

H. Einspieler*, H. Ofner, M. Ozenil, C. P. Spielvogel, I. K. Langrate, M. R. Hassler, L. Nics, K. Bamminger, P. A. T. Baltzer, S. F. Shariat, M. Hacker, G. Kramer, S. Rasul;*
Medical University of Vienna, Vienna, AUSTRIA.

Aim/Introduction: [^{18}F] Poly-ADP-ribose polymerase inhibitors (PARPi) are a novel class of radiotracers that allow non-invasive PET imaging of PARP1 expression. In this study, we aimed to quantify PARPi uptake in tumor lesions of patients with metastatic castration-resistant prostate cancer (mCRPC) and to compare these findings with prostate-specific membrane antigen (PSMA) expression using PET/CT imaging. ***Materials and Methods:*** [^{18}F] PARPi and [^{68}Ga]Ga-PSMA-11 PET/CT scans from 22 male patients with mCRPC were retrospectively analysed. Lesions with relevant PARPi uptake (higher than background) were delineated and correlated with their PSMA-expression using standardized uptake values (SUV). Additionally, a comparison was performed to investigate the effects of homologous recombination deficiency (HRD) alterations on PARPi tumor uptake. ***Results:*** Most metastatic PCa lesions that exhibited PARPi uptake were located in the bones (n=57), with mean SUVmax values of 4.9 ± 1.5 for PARPi and 30.9 ± 28.3 for PSMA. Additionally, 3 local prostate lesions, 14 lymph nodes and 4 further metastatic lesions were detected. Significant correlations were identified between PARPi- and PSMA uptake, as measured by SUVmean (r=0.48, p<0.001), SUVpeak (r=0.48, p<0.001) and SUVmax (r=0.43, p<0.001) of the osseous metastatic lesions and SUVpeak (r=0.49, p=0.04) of extraosseous lesions. No significant differences were found between PARPi uptake of metastatic lesions in patients with or without HRD alterations (all p>0.05). ***Conclusion:*** Considerable uptake of [18F]PARPi was observed in multiple lesions in mCRPC patients, suggesting the potential of using [18F]PARPi as a diagnostic imaging tool in mCRPC patients. Further studies are needed to evaluate the clinical benefit of this innovative radiotracer. In the future, the use of PARPi PET imaging may support personalised treatment strategies and be a helpful tool in clinical decision making.

OP-326

Diagnostic Performance, Safety, and Pharmacokinetics of [^{68}Ga]Ga-OncoACP3 in Prostate Cancer - Preliminary Results from a Prospective Phase I Clinical Trial

C. Pini[1], *F. Gelardi*[1], *M. Sollini*[1,2], *L. Antunovic*[2], *R. Di Donato*[2], *G. R. Bonfitto*[2], *A. Piai*[3], *R. Petrelli*[2], *M. Minotti*[2], *J. Mock*[4], *S. Cazzamalli*[4], *S. Oehler*[4], *A. Ciamarone*[4], *F. Migliorini*[4], *D. Neri*[4], *M. Kirienko*[5], *P. A. Erba*[6,7], *A. Chiti*[1,2];
[1]*Vita-Salute San Raffaele University, Milan, ITALY,* [2]*Department of Nuclear Medicine, IRCCS Ospedale San Raffaele, Milan, ITALY,* [3]*Medical Physics Department, IRCCS Ospedale San Raffaele, Milan, ITALY,* [4]*Philochem AG, Otelfingen, SWITZERLAND,* [5]*Nuclear Medicine, Fondazione IRCCS Istituto Nazionale dei Tumori di Milano, Milan, ITALY,* [6]*School of Medicine and Surgery, University of Milano-Bicocca, Milan, ITALY,* [7]*Nuclear Medicine Unit, ASST Papa Giovanni XXIII Hospital, Bergamo, ITALY.*

Aim/Introduction: Acid Phosphatase 3 (ACP3) is an emerging promising theranostic target for prostate cancer (PCa). It is expressed on the surface of PCa cells in most primary and metastatic lesions. ACP3 shows higher and more homogeneous expression

than PSMA in both low- and high-ISUP grade tumours as well as in metastases, while not being expressed in healthy organs such as salivary glands, kidneys, and gastrointestinal tract. We present preliminary data from an ongoing prospective, multicentre, phase I clinical trial investigating safety, dosimetry, pharmacokinetics, and diagnostic performance of [^{68}Ga]Ga-OncoACP3, a novel high-affinity ligand of ACP3 discovered from DNA-Encoded Chemical Libraries, in PCa patients. ***Materials and Methods:*** 20 patients with a confirmed diagnosis of PCa are planned for enrolment starting from April 2025 in two cohorts: Cohort A, 5 patients with primary tumour only; Cohort B, 15 patients with or without metastatic disease. Each patient receives an intravenous administration of 250 MBq [^{68}Ga]Ga-OncoACP3, followed by PET/CT imaging at 0-20, 60-, and 120-min post-injection. Blood and urine samples are collected at predefined timepoints to assess pharmacokinetics. Adverse events are reported according to CTCAE v.5.0. When available, [^{68}Ga]Ga-OncoACP3 PET imaging results are compared to PSMA PET and correlated with pathological findings from biopsy or surgery. ***Results:*** As of April 25th, two patients have been enrolled and completed [^{68}Ga]Ga-OncoACP3 PET imaging. No adverse events have occurred. [^{68}Ga]Ga-OncoACP3 demonstrated a mixed hepatobiliary and renal excretion, with no uptake in salivary glands. Suspect PCa lesions were visible on both 60- and 120-min post-injection acquisitions. Patient 1 previously underwent prostatectomy for ISUP 3 PCa and presented with biochemical relapse (PSA=0.26 ng/mL). PSMA PET showed an area of faint uptake (SUVmax=3.5) below the prostatic bed and an unspecific uptake in one rib (SUVmax=5.3). [^{68}Ga]Ga-OncoACP3 PET revealed intense uptake (SUVmax=16) in the same region of the prostate bed, with no bone uptake. Patient 2 presented with a history of multiple biochemical relapses of ISUP 5 PCa, with no evidence of disease at PSMA PET, subsequently treated with cycles of enantone (last administered on August 2024). [^{68}Ga]Ga-OncoACP3 PET, performed with PSA=5.3 ng/mL, detected intense uptake in a precaval adenopathy (SUVmax=26.4) and a moderate uptake in D9 (SUVmax=10.8). ***Conclusion:*** [^{68}Ga]Ga-OncoACP3 resulted safe and showed favourable biodistribution and targeting characteristics for PET imaging of PCa. [^{68}Ga]Ga-OncoACP3 could represent a valuable advancement over current PSMA-targeting modalities across the whole natural history of the disease, and particularly in theranostic applications.

OP-327

Theranostic targeting of the prostatic acid phosphatase (ACP3) with [^{68}Ga]Ga-OncoACP3-DOTA and [^{177}Lu]Lu-OncoACP3-DOTA in prostate cancer patients

P. Backhaus[1,2], *K. E. Seifert*[2,3], *S. Cazzamalli*[4], *S. Oehler*[4], *F. Migliorini*[4], *A. Ciamarone*[4], *T. Georgiev*[4], *J. Mock*[4], *M. Bögemann*[3], *H. Breyholz*[1], *D. Ventura*[1,2], *F. Landau*[1,2], *F. Büther*[1,2], *E. Puca*[4], *D. Neri*[4], *K. Rahbar*[1], *A. J. Schrader*[3], *M. Schäfers*[1,2];
[1]*Department of Nuclear Medicine, West German Cancer Center, University Hospital Münster, Münster, GERMANY,* [2]*European Institute for Molecular Imaging, University of Münster, Münster, GERMANY,* [3]*Department of Urology, Werst German Cancer Center, University Hospital Münster, Münster, GERMANY,* [4]*Philochem AG, R&D department, Otelfingen, SWITZERLAND.*

Aim/Introduction: Prostatic acid phosphatase 3 (ACP3) shows high expression in prostate cancer (PC) and barely any expression in healthy organs. Recently, a first-in-class high-affinity ACP3 ligand was isolated from a DNA-encoded chemical library [1]. In this retrospective analysis, the first 25 PET with [^{68}Ga]Ga-OncoACP3-DOTA (OncoACP3) and the first patient treated with [^{177}Lu]Lu-OncoACP3-DOTA were analyzed. ***Materials and Methods:*** Chemically pure OncoACP3-DOTA precursor was provided by Cazzamalli et al. [1] The radiotracer was produced and used according to Section 13(2b) of the German Medicinal Products Act. SUV_{mean} of normal organs and PC lesions' SUV_{max} for [^{68}Ga]Ga-OncoACP3 were compared against a PSMA-targeting radioligand (i.e., [^{18}F]F-PSMA-1007 or [^{68}Ga]Ga-PSMA-11) by Wilcoxon rank sum test. Superior diagnostic performance of either tracer was awarded if 50 % higher uptake or 10 % more PC lesions were detected. ***Results:*** 25 male PC patients received PET scans 62 min (mean) after injection of 145 MBq (median) OncoACP3. No side effects were observed. All patients had received PSMA-PET scans (23/25 [^{18}F]PSMA-1007, 2/25 [^{68}Ga]Ga-PSMA-11-PET) 17 days (mean) before the OncoACP3-PET. In comparison to [^{18}F]PSMA-1007, OncoACP3 uptake was significantly lower in the liver, kidney, parotid gland and small intestine (all $p < 0.002$). Blood retention was significantly higher for OncoACP3 ($p < 0.001$). OncoACP3-PET demonstrated PC manifestations in all 25 patients. In 11 patients with locoregional PC, performance was better for OncoACP3 in 6 and for PSMA in 3 patients (mean SUV_{max} OncoACP3 vs. PSMA: 24.1 vs. 11.2, n.s.). In 11 patients with lymph node metastases, performance was better for OncoACP3 in 4 and for PSMA in 2 patients (mean SUV_{max} OncoACP3 vs. PSMA: 20.2 vs. 14.9, p 0.018). In 17 patients with osseous metastases, diagnostic performance was better for OncoACP3 in 5 and for PSMA in 7 patients (mean SUV_{max} OncoACP3 vs. PSMA: 17.7 vs. 18.5, n.s.). OncoACP3 PET impacted further diagnostic work-up in 7 and therapy decisions in 8 patients. One patient was treated with two cycles of [^{177}Lu]Lu-OncoACP3 in compassionate use with 2.4 and 5.0 GBq. Treatment was well tolerated, PSA with a prior doubling time of < 1 month demonstrated response (1st cycle 46.5 ng/ml, 2nd cycle 48.3 ng/ml, 5 weeks after 2nd cycle 23.1 ng/ml). ***Conclusion:*** First theranostic ACP3-targeting demonstrates great potential of the ligand OncoACP3-DOTA in prostate cancer patients. ***References:*** [1] (Cazzamalli et al. J Nucl Med. 2024; 65:241120.)

OP-328

FAPStera: Comparison of [^{18}F]DCFPyL and [^{18}F]FAPI-74 PET/CT imaging in metastatic prostate cancer

H. Minn[1], *A. Hyväkkä*[1], *M. Sundvall*[1], *V. Sivonen*[1], *K. Mattila*[1], *M. Anttinen*[2], *O. Ettala*[2], *M. Högerman*[2], *A. Kirjavainen*[3], *O. Eskola*[3], *S. Forsback*[3], *V. Saunavaara*[4], *M. Seppänen*[5], *S. Malaspina*[5];
[1]*Department of Oncology and FICAN West Cancer Centre, University of Turku and Turku University Hospital, Turku, FINLAND,* [2]*Department of Urology, University of Turku and Turku University Hospital, Turku, FINLAND,* [3]*Radiopharmaceutical Chemistry, Turku PET Centre, University of Turku, Turku, FINLAND,* [4]*Department of Medical Physics and Turku PET Centre, Turku University Hospital, Turku, FINLAND,* [5]*Department of Nuclear Medicine and Turku PET Centre, University of Turku and Turku University Hospital, Turku, FINLAND.*

Aim/Introduction: To compare PET/CT imaging targeting prostate-specific membrane antigen (PSMA) and fibroblast activation-protein (FAP) in metastatic hormone sensitive (mHS) and castration resistant (mCR) prostate cancer (PC). PSMA imaging is regarded as a game changer in evaluation of metastatic PC owing to its high sensitivity and value in radiotheranostics. However, other molecular targets such as FAP may be useful in patients with metastases showing low affinity for PSMA. ***Materials and Methods:*** FAPStera (EudraCT:2022-003788-13) is an ongoing prospective study, having enrolled 14/15 men with mHSPC and 20/25 men with mCRPC. Patients were required to present with at least one metastasis on conventional imaging (CT/MRI or bone SPECT). The median age was 73 (range, 61-83), 55 % had Gleason 4+5 PC and median pre-scan PSA was 55 ng/mL (range, 2-2000). The patients underwent long-axial field-of-view whole-body PET/CT twice within 2 weeks in random order with fluorine-18 labeled DCFPyL (PSMA) or FAP inhibitor FAPI-74. Each scan was reviewed by two experienced nuclear medicine physicians and the observed metastases were divided in groups as follows: pelvic lymph nodes, extra-pelvic lymph nodes, skeletal and visceral. SUVmax of the metastatic lesions was measured. Positivity on both PET scans was assessed according to predefined criteria. Clinical and tracer uptake data was analyzed using standard non-parametric statistical tests. ***Results:*** A total of 1097 lesions were identified in

34 patients with mPC. There were 9% (n=94) pelvic nodal, 12% (n=127) extra-pelvic nodal, 76% (n=833) skeletal, and 4% (n=43) visceral metastases, respectively. In skeletal, [^{18}F]DCFPyL imaging detected 99% (n=826/833) and [^{18}F]FAPI-74 58% (n=484/833) of the lesions, while that in pelvic nodal was 100% (n=94/94) with [^{18}F]DCFPyL and 52% (n=49/94) with [^{18}F]FAPI-74. In extra-pelvic nodes PSMA detected 86% (n=109/127) and [F]FAPI-74 55% (n=70/127) of lesions, while in visceral metastases [^{18}F]DCFPyL found 93% (n=40/43) and [^{18}F]FAPI-74 72% (n=31/43) lesions. Overall, 3% (n=28/1097) of metastases were negative for PSMA, 14% (n=18/127) of extra-pelvic nodal and 7% (n=3/43) of visceral metastases. Of these PSMA-negative lesions 61% (n=17/28) were positive for [^{18}F]FAPI-74. Generally metastatic lesions had higher SUVmax for [^{18}F]DCFPyL (median 25; range, 0-203) than [^{18}F]FAPI-74 (median 3.1; range, 0.1-23.2), although few cases in visceral lesions showed the opposite pattern of uptake. ***Conclusion:*** PSMA PET/CT remains the preferred molecular imaging method for evaluating metastatic PC. However, [^{18}F]FAPI-74 PET/CT may assist in selection of patients for theranostic approaches using alpha- or beta emitters especially in cases with multiple PSMA-negative lesions showing uptake of [^{18}F]FAPI-74.

OP-329

Impact of Radiotherapy on Overall Survival in Prostate Cancer Patients with Biochemical Recurrence Staged by PROMISE Criteria Using PSMA-PET

C. Civan[1], *M. J. Karpinski*[1,2], *S. Hoberück*[3], *K. Herrmann*[1], *K. Rahbar*[2], *M. Bögemann*[4], *L. Nikoukar*[2], *M. Schäfers*[2], *M. Miederer*[5], *T. Hölscher*[3], *S. Rasul*[6], *C. H. Pfob*[7], *K. Goffin*[8], *A. Gafita*[9], *J. Hüsing*[10], *J. Calais*[11], *M. S. Hofman*[12], *T. A. Hope*[13], *T. Soeterik*[14], *A. D. Giorgio*[15], *L. M. Unterrainer*[16], *A. Holzgreve*[16], *G. T. Sheikh*[16], *I. Rauscher*[17], *M. Eiber*[17], *B. A. Hadaschik*[18], *M. Stuschke*[19], *W. P. Fendler*[1], *N. Guberina*[19], *PROMISE Registry Group;*
[1]*Department of Nuclear Medicine, DKTK and NCT University Hospital Essen, Essen, GERMANY,* [2]*Department of Nuclear Medicine, University Hospital Münster, Münster, GERMANY,* [3]*Department of Nuclear Medicine, University Hospital Carl Gustav Carus, Technical University Dresden, Dresden, GERMANY,* [4]*Department of Urology, University Hospital Münster, Münster, GERMANY,* [5]*Department of Translational Imaging in Oncology, National Center for Tumour Diseases (NCT/UCC) Dresden: Faculty of Medicine and University Hospital Carl Gustav Carus, University of Technology Dresden, Dresden, GERMANY,* [6]*Department of Biomedical Imaging and Image-guided Therapy, Division of Nuclear Medicine, Medical University Vienna, Vienna, AUSTRIA,* [7]*Department of Nuclear Medicine, University of Augsburg, Augsburg, GERMANY,* [8]*Department of Nuclear medicine, University Hospitals Leuven, KU Leuven, Leuven, BELGIUM,* [9]*Johns Hopkins University School of Medicine, The Russell H. Morgan Department of Radiology, Baltimore, MD, UNITED STATES OF AMERICA,* [10]*Cancer Registry North-Rhine Westphalia, Bochum, GERMANY,* [11]*Ahmanson Translational Theranostics Division, David Geffen School of Medicine at UCLA,, Los Angeles, CA, UNITED STATES OF AMERICA,* [12]*Sir Peter MacCallum Department of Oncology and Department of Medicine, University of Melbourne, Melbourne, AUSTRALIA,* [13]*Department of Radiology and Biomedical Imaging, University of California San Francisco, San Francisco, CA, UNITED STATES OF AMERICA,* [14]*Department of Urology, St Antonius Ziekenhuis Nieuwegein/Utrecht,, Utrecht, NETHERLANDS,* [15]*Department of Nuclear Medicine, Alma Mater Studiorum, University of Bologna, Bologna, ITALY,* [16]*Department of Nuclear Medicine, LMU University Hospital, LMU Munich, Munich, Germany, Munich, GERMANY,* [17]*Department of Nuclear Medicine, School of Medicine and Health, Klinikum Rechts der Isar, Technical University Munich, Munich, Germany, Munich, GERMANY,* [18]*Department of Urology, University Hospital Essen, Essen, Germany, Essen, GERMANY,* [19]*Department of Radiotherapy, West German Cancer Center, University Hospital Essen, University of Duisburg-Essen, Essen, GERMANY.*

Aim/Introduction: Prostate Cancer Molecular Imaging Standardized Evaluation (PROMISE) criteria have been established for standardized assessment of PSMA-PET. We aimed to investigate the impact of radiotherapy (RT) on overall survival (OS) across different stages determined by PROMISE using PSMA-PET in prostate cancer patients with biochemical recurrence (BCR). ***Materials and Methods:*** We included prostate cancer patients with biochemical recurrence following definitive therapy, who were recruited from a large international multi-center registry study. All patients underwent PSMA-PET at 20 centers worldwide, with known PSA level at the time of imaging and management plan determined after PSMA-PET. Molecular imaging TNM (miTNM) stages of all patients were determined according to PROMISE. Patients were divided into risk groups based on PSA levels (any PSA level; PSA level between 0-0.5 ng/ml; PSA level >0.5ng/ml). ***Results:*** Our cohort included 2738 patients, who underwent PSMA-PET between May 2013 and October 2024. The median follow-up duration was 5.1 years (3.6-6.8 years). As of data-cutoff, 390 patients (14.2%) had died. miTNM stages were: T0N0M0 in 791 patients (29%), TxNxM0 in 960 patients (35%), TxNxM1 in 987 patients (36%). The median time interval from PSMA-PET to RT was 1.9 months (1.0-3.6 months). Patients with salvage RT eligibility (T0N0M0 or TxNxM0) treated with RT had significantly longer OS compared to patients who were not treated (7 years survival rates: 90% vs 84%, p=0.0395). In the subgroup of T0N0M0, OS was significantly longer in RT group (7 years survival rates: 92% vs 87%, p=0.0179, In TxNxM1 group, RT was associated with significantly better OS at any PSA level as well as in patients who had PSA level>0.5 ng/ml (7 years survival rates: 77% vs 66%, p<0.001). ***Conclusion:*** This study highlights that prostate cancer patients in biochemical recurrent stage, who were treated with RT, had significantly longer OS across different PSMA-PET PROMISE stages. Longer OS was also observed in patients undergoing salvage RT for BCR with negative PSMA findings (T0N0M0) and in patients with PET metastatic disease undergoing palliative RT.

OP-330

Kinetic Profiling of [^{68}Ga]Ga-PSMA-11 Using Total-Body PET in Suspected Prostate Cancer: Preliminary Results from the Prospective FUPERMAN Study

A. Farolfi[1], *I. Brusa*[1], *D. Dall'Olio*[2], *C. M. P. Sgro*[3], *L. Bianchi*[4], *R. Mei*[1], *C. Nanni*[1], *P. Castellucci*[1], *S. Fanti*[1];
[1]*Nuclear Medicine, IRCCS Azienda Ospedaliero-Universitaria di Bologna, Bologna, ITALY,* [2]*Department of Medical and Surgical Sciences, Alma Mater Studiorum - University of Bologna, Bologna, ITALY,* [3]*Nuclear Medicine, Alma Mater Studiorum - University of Bologna, Bologna, ITALY,* [4]*Division of Urology, IRCCS Azienda Ospedaliero-Universitaria di Bologna, Bologna, ITALY.*

Aim/Introduction: Multiparametric MRI (mpMRI) is the cornerstone for prostate cancer (PCa) diagnosis but shows limited sensitivity in PI-RADS 1-3 lesions, risking underdetection of clinically significant prostate cancer (csPCa). The FUPERMAN study investigates the added diagnostic value of PSMA-PET in patients with negative/equivocal mpMRI findings, using real-time PSMA-PET/fusion-target biopsy. In this sub-analysis, we leveraged dynamic total-body PET to explore [^{68}Ga]Ga-PSMA-11 pharmacokinetics, aiming to identify kinetic parameters that distinguish malignant from benign prostate lesions. ***Materials and Methods:*** FUPERMAN is a prospective, single-center study enrolling men with suspected PCa (PSA≥4ng/mL, PSA density≥0.1ng/mL^2, family PCa history) and negative/equivocal mpMRI (PI-RADS 1-3). This sub-analysis included patients who underwent 60-min dynamic [^{68}Ga]Ga-PSMA-11 PET on a total-body system (FOV=194 cm) within 6 months of mpMRI. Volumes of interest (VOIs) were manually delineated on intraprostatic areas with increased uptake and on reference prostate tissue without significant uptake. Lesions were scored using the PRIMARY Score (PS), with PS ≥3 considered positive and targeted with transperineal PSMA-PET/fusion-target biopsy; all patients also underwent systematic biopsy. csPCa was defined as ISUP grade group ≥2. Kinetic analysis included time-activity curves, graphical models (Patlak, RE), and compartment models (1TC, 2TC, 2TiC). Model fit was assessed using mean absolute scaled error and Akaike Information Criterion. ***Results:***

Ten men were enrolled (median age: 62, PSA: 16.09 ng/mL, dPSA: 0.45 ng/mL^2). Among 16 lesions, 2 had PS 2 (0% csPCa), 5 had PS 3 (40% csPCa), 4 had PS 4 (25% csPCa) and 5 had PS 5 (100% csPCa). Eight lesions were negative for csPCa on histology (PET+/csPCa-). Patlak modeling fit 4/5 PS 5 lesions best, suggesting irreversible uptake; all others fit better with reversible models (RE), similar to 8/8 lesions PET+/csPCa- and normal prostate. Compartment analysis revealed that all PS 3-4-5 lesions, PET+/csPCa- lesions and reference prostate were best described by irreversible uptake (2TiC). K1, k3, and Ki were significantly higher in PS 3-4-5 lesions vs reference tissue ($p<0.05$). Ki strongly correlated with SUVmax/SUVmean (Rho>0.8, $p<0.001$), while k_2 inversely (Rho=-0.83, $p=0.0053$). Ki outperformed SUV in sensitivity (89% vs 78%, both at 94% specificity). Among PS 3 lesions, k3 best distinguished csPCa from false-positive PET findings ($p=0.037$). ***Conclusion:*** Dynamic [^{68}Ga]Ga-PSMA-11 total-body PET reveals promising kinetic biomarkers, particularly Ki and k3, for identifying csPCa in patients with inconclusive mpMRI. Kinetic modeling (i.e. k3) enhances specificity in PRIMARY score 3 lesions where visual and SUV-based evaluation often fail. Further validation is ongoing.

OP-331

^{177}Lu-PSMA-1 applied to ccRCC

***A. Giraudet**, A. Vinceneux, A. Sanchez-Lajusticia, G. Garin, J. Badel, D. Perol, A. Bidaux, C. Cropet, C. Trolliet, D. Kryza; Centre Léon Bérard, Lyon, FRANCE.*

Aim/Introduction: PSMA is over expressed in 86-100% of clear cell RCC (ccRCC)(1). PSMA-PET in ccRCC have demonstrated a greater sensitivity compared to conventional imaging(2). ^{177}Lu-PSMA is safe, increases OS for prostate cancer patients. PRADR is an ongoing prospective phase I/II study evaluating its tolerability and efficacy for metastatic ccRCC (mccRCC) patients pre-treated with immunotherapy and TKI. We report preliminary results of the safety run cohort concerning PSMA-PET and ^{177}Lu-PSMA SPECT-CT findings. ***Materials and Methods:*** This prospective multicentrique phase I/II study planned to include up to 42 patients, including 6 patients in a safety run conducted in Léon Bérard Cancer Center, treated with maximum 4 cycles of 7.4 GBq of ^{177}Lu-PSMA-1 radiolabeled on site. A positive lesion on PSMA PET had to demonstrate a lesion SUV max/liver SUVmean ≥ 1.5. Patient eligibility required at least 50% of positive supracentimetric extrahepatic lesions, and ≥ 80 % of positive supracentimetric liver metastatic in case of liver mets. Whole body SPECT-CT on 360° CZT-CT was repeated at 4h, 24, and D7 after injection at cycle 1 for dosimetry purpose. Lesions uptake was visually compared to background and normal liver uptake. Treatment tolerance and efficacy is still evaluated. ***Results:*** Eleven patients included in the safety run were screened. Six of them fulfilled PSMA-PET positivity criteria and up to day had received at least one cycle of ^{177}Lu-PSMA-1. Treated patients presented with bone (N=5 patients), pleural (N=2), lung (N=4), liver (N=1), peritoneal (N=3), nodal (N=3), soft tissues (N=4), adrenal (N=2), pancreatic (N=2) metastases. In all patients, lesions uptake highly decreased over time on repeated ^{177}Lu-PSMA SPECT-CT and demonstrated a complete clearance of all lesions in 4/6 patients, and almost in the remaining. Despite intense lesions uptake on H4 SPECT-CT, 5/6 patients demonstrated at least 1 supra-centimetric lesion showing no uptake. ***Conclusion:*** In highly selected mccRCC patients on lesions uptake intensity on PSMA-PET, ^{177}Lu-PSMA lesions uptake is highly heterogenous in the same patient, and tends to demonstrate an almost complete wash-out on D7 SPECT-CT in all patients. ***References:*** (1). Chang SS, et al. Metastatic renal cell carcinoma neovasculature expresses prostate-specific membrane antigen. Urology. 2001 Apr;57(4):801-5. doi: 10.1016/s0090-4295(00)01094-3. PMID: 11306418.(2). Singhal T, et al. Role of PSMA-targeted PET-CT in renal cell carcinoma: a systematic review and meta-analysis. Ann Nucl Med. 2024 Mar;38(3):176-187. doi: 10.1007/s12149-024-01904-w. Epub 2024 Feb 10. PMID: 38340144.

801

Monday, October 6, 2025, 09:45 - 11:15

Auditorium

CME 6 - Oncology & Theranostics Committee: PET in mCRPC: Toward Multiparametric Multitracer Biomarkers

OP-332

Evaluating mCRPC with PSMA PET: Strengths and Pitfalls

***I. Burger**; Kantonsspital Baden, Nuclear Medicine, Baden, SWITZERLAND.*

OP-333

Multi-Tracer PET/CT for the Characterisation and Prognostication of mCRPC: the 3TMPO Study

***Jean-M. Beauregard**; CHU de Quebec, Université Laval, Quebec City, Quebec, CANADA.*

OP-334

Standardised Assessment: Promise V2 and Beyond

***W. Fendler**; Universitätsklinikum Essen, Klinik für Nuklearmedizin, Essen, GERMANY.*

OP-335

Multimodal Imaging in mCRPC: A Game Changer

***N. Tunariu**; The Institute of Cancer Research, Division of Radiotherapy and Imaging, Sutton, UNITED KINGDOM.*

802

Monday, October 6, 2025, 09:45 - 11:15

Room 112 (Arena)

Special Track 6 - Cardiovascular Committee: Challenge the Expert: Myocardial Perfusion Imaging : Should I Stay with SPECT or Go with PET?

OP-336

I Should Definitely Stay with SPECT for Myocardial Perfusion Imaging

***M. Bailly**; CHU Orléans, Department of Nuclear Medicine, Orléans, FRANCE.*

OP-337

I Should Definitely Move to PET for Myocardial Perfusion Imaging

***P. Arumugam**; Manchester University, Department of Nuclear Medicine, Manchester, UNITED KINGDOM.*

803

Monday, October 6, 2025, 09:45 - 11:15

Room 113

LIPS Session 6 - Radiation Protection Committee: What Would You Do If…? Radiation Protection Issues in Special Cases of Everyday Practices

OP-338

After an Imaging Procedure, It Is Realised that the Patient Is Pregnant. What Would You Do?

***I. Schatka**; Department of Nuclear Medicine, Charité-Universitätsmedizin , Berlin, GERMANY.*

OP-339

A Breast-feeding Patient Needs a NM Scan or NM Treatment. What Would You Do?

***S. Leide Svegborn**; Department of Medical Radiation Physics, Skåne University Hospital, Lund University, Lund, SWEDEN.*

OP-340

A Patient Treated with Lu-177, I-131 or Ra-223 Needs to Be Transferred to an Intensive Care Unit or Any Other Department of the Hospital. What Would You Do?

J. Kurth; *University Medical Center Rostock, Department of Nuclear Medicine, Rostock, GERMANY.*

OP-341

How Do You Report SUV in PET in Case of an Extravasation?

J. van der Pol; *Department of Radiology and Nuclear Medicine, Maastricht University Medical Center, Maastricht, NETHERLANDS.*

OP-342

A patient Who Has Recently Undergone a Nuclear Medicine Procedure Sets Off an Alarm at an Airport Security Scanner. What Would You Do?

A. Stenvall; *Radiation Physics, Skåne University Hospital, Lund, SWEDEN.*

804

Monday, October 6, 2025, 9:45 - 11:15

Room 114

M2M Track - TROP Session - Radiopharmaceutical Sciences + Translational Molecular Imaging & Therapy Committee: Optimising Radiolabeling and Quality Control: The Key for Clinical Translation

OP-343

Optimization and Scale-Up of ^{177}Lu Radiolabeling of PSMA-ALB-56 for Automated Patient Dose Preparation

C. Fersing[1,2], *J. Torchio*[1], *S. Renaud*[1], *L. Rubira*[1], *J. Vanney*[1]; [1]*Montpellier Cancer Institute, Nuclear Medicine Unit, Montpellier, FRANCE,* [2]*IBMM, Univ Montpellier, CNRS, ENSCM, Montpellier, FRANCE.*

Aim/Introduction: Targeted radionuclide therapy using ^{177}Lu-labeled ligands of the prostate-specific membrane antigen (PSMA) is now established as an effective treatment for metastatic castration-resistant prostate cancer. Recently, chemical modification of PSMA radioligands with albumin-binding motifs has shown promise in improving biodistribution and tumor uptake. Among these, PSMA-ALB-56 has demonstrated excellent preclinical results and is now entering clinical evaluation. However, current literature describes its ^{177}Lu radiolabeling using conventional conditions, with limited investigation into process optimization [1]. Thus, a study was conducted to explore key synthesis parameters for [^{177}Lu]Lu-PSMA-ALB-56. Optimized conditions were subsequently scaled up using an automated radiolabeling protocol suitable for clinical dose preparation. ***Materials and Methods:*** Radiolabeling conditions for [^{177}Lu]Lu-PSMA-ALB-56 were evaluated using manual, non-purified syntheses. No-carrier-added $^{177}LuCl_3$ (3.27 GBq/mg) was used. The effect of five different buffer systems on the radiochemical purity (RCP) of the complex was assessed. RCP was determined by high-performance liquid chromatography (HPLC). The influence of four antioxidants on complex stability over 48 h was also evaluated by HPLC. Each condition was tested in triplicate. Optimized parameters were then transferred to an automated procedure using a ^{68}Ga workflow. Three batches were produced and analyzed for RCP, radiochemical yield (RCY), 120 h stability, radionuclidic purity and radionuclide identity. ***Results:*** Twenty-seven radiolabeling reactions were performed manually using 25 µg of PSMA-ALB-56 and 80 MBq of ^{177}Lu, heated at 98 °C for 30 min. Three buffers (1 M ammonium acetate, 1.8 M ascorbic acid, 1.25 M HEPES) yielded excellent RCPs (>98%). Lower molarity buffers (0.1 M ammonium or sodium acetate) gave similar results. Maintaining pH ~4.5 was critical. Methionine and ascorbic acid preserved RCP >97% over 48 h, while 3.5 mM gentisic acid improved peak resolution on HPLC. Cysteine inhibited complexation. Automated syntheses yielded [^{177}Lu]Lu-PSMA-ALB-56 in 30 min with RCP of 98.9 ± 0.1% post-purification on C_{18} cartridge. Methionine 18.75 mg/mL in the reaction medium and ascorbate 3.6 mg/mL in the final formulation maintained RCP >95% over 120 h. Mean radiochemical yield was 86.5 ± 0.5%, with final vial recovery of 87.4 ± 0.5% and apparent molar activity of 40.1 ± 2.3 GBq/µmol. Radionuclidic purity and identity matched ^{177}Lu specifications. ***Conclusion:*** The use of 0.11 M sodium acetate (0.25 mL) and 25.7 mg/mL methionine (1.5 mL) at pH 4.5 (0.65 mL of HCl 0.1 M) enabled efficient automated production of [^{177}Lu]Lu-PSMA-ALB-56. Three test batches (>2 GBq) demonstrated excellent stability over 5 days, and doubling the starting activities would allow GMP-compliant production of patient doses. ***References:*** [1] C. A. Umbricht, et al. Mol Pharm. 2018, 15, 2297−2306.

OP-344

Fully compliant automated cassette-based sterility testing of radiopharmaceuticals on miniAllinOne

T. Vergote[1], *C. Vriamont*[1], *P. Novelli*[1], *F. De Meeus d'Argenteuil*[1], *K. Van Butsele*[1], *G. Zeiske*[2], *M. Nousch*[2]; [1]*Trasis, Ans, BELGIUM,* [2]*CUP Contract Labs, Radeberg, GERMANY.*

Aim/Introduction: Sterility testing is mandatory for all parenteral (radio)pharmaceuticals intended for human use, as required by European and US Pharmacopeias [1,2]. In the US, the test must be conducted within 30 hours post-manufacturing. However, radioactivity introduces unique challenges. Few facilities, like Cup Lab (DE), are authorized to conduct such tests. Radioactivity can also cause false negatives due to bacteriostatic or bactericidal effects, potentially allowing bacteria to proliferate post-administration. A solution is needed that complies with regulations, is simple, robust, economical, and eliminates radioactivity interference to ensure accurate results. ***Materials and Methods:*** A sterile, single-use cassette system was developed, integrating components for immediate, automated sterility testing, including filtration membrane and culture media. The sterility of the setup was evaluated, along with its ability to support aerobic and anaerobic microbial growth. Reference strains recommended by pharmacopeias were introduced into the filtration units, followed by growth media, and microbial growth was monitored. Aerobic (TSB at 25°C) and anaerobic (FTM at 32°C) growth were tested. Initial sterility tests on freshly produced radiopharmaceuticals show promising results. ***Results:*** Unlike manual methods, this approach enables immediate post-production testing in a simple, fully automated way, ensuring operator safety from radiation. The single-use cassette includes four filter units serving as test chambers for sterility and controls, designed to detect biological contaminants. Within a laminar flow hood, the cassette is placed on the miniAllinOne synthesizer and connected to buffers, media, and sample. The automated process then runs independently. Initial sterile runs confirmed absence of growth. When reference microorganisms (≤100 CFU) were added, robust growth occurred for Bacillus spizizenii, Clostridium sporogenes, Pseudomonas paraeruginosa, and Staphylococcus aureus within three days, and for Candida albicans and Aspergillus brasiliensis within five days. Preliminary automated tests on batches of radiopharmaceuticals meet sterility requirements, with approximately 30 minutes needed to prepare both test and control samples for incubation. ***Conclusion:*** This closed, sterile system reduces contamination risks and integrates into automated workflows, minimizing human intervention. It complies with both European and American Pharmacopeia sterility testing standards and supports growth of critical reference microorganisms. This proof-of-concept shows strong potential to standardize sterility testing in radiopharmaceutical quality control, enabling routine implementation across the industry. ***References:*** [1] Ph. Eur., Chapter 2.6.1. Sterility [2] USP, Chapter <71> Sterility Tests

OP-345

^{225}Ac-radiopharmaceuticals and Their Daughters - HPLC-Based Liquid Scintillation Detection for Routine Characterization

***G. Claude**, M. Balzer, W. Brenner, S. Spreckelmeyer;*
Charité – Universitätsmedizin Berlin, Klinik für Nuklearmedizin, Berlin, GERMANY.

Aim/Introduction: Targeted alpha therapies using actinium-225 (^{225}Ac) are gaining momentum. While significant progress has been made in the production and quality control of ^{225}Ac-radiopharmaceuticals, analytical methods for reliable identity assessment as required for the determination of radiochemical purity and stability remain limited.[1] High-performance liquid chromatography (HPLC) with fraction collection has been previously suggested but lacks speed and resolution, making it cumbersome for routine application. We present a streamlined method using HPLC coupled with inline liquid scintillation counting (LSC) to analyze [^{225}Ac]Ac-PSMA-I&T and [^{225}Ac]Ac-DOTATOC (collectively referred to as ^{225}Ac-RPs), enabling the differentiation between ^{225}Ac and its daughter nuclides in a single chromatographic run. ***Materials and Methods:*** ^{225}Ac-RPs were analyzed using a Ramona Star radio-HPLC system equipped with inline LSC detection. Various scintillation cocktail ratios were tested to ensure sufficient signal intensity while minimizing radioactive waste. Chromatograms were analyzed for reproducibility and signal patterns. Different formulations (e.g., reaction formulation, stabilized formulation with DTPA) were tested to probe the stability of the complexes and the behavior of free or recoiled daughter nuclides. ***Results:*** Our method provided reproducible retention times for ^{225}Ac-RPs, allowing clear differentiation between [^{225}Ac]Ac-PSMA-I&T and [^{225}Ac]Ac-DOTATOC. Three distinct peaks were consistently observed in all preparations, corresponding to complexes of ^{213}Bi-RP, ^{209}Pb-RP, and ^{225}Ac-RP. This observation aligns with known coordination chemistry of ^{213}Bi and ^{212}Pb at room temperature.[2,3] Fraction collection followed by gamma spectrometry enabled unambiguous identification of the ^{213}Bi-RP and ^{225}Ac-RP. Upon addition of DTPA, the peaks corresponding to ^{213}Bi-RP and ^{209}Pb-RP eventually disappeared, suggesting either decomplexation or failure of newly formed daughter nuclides to form DOTA or DOTAGA complexes in presence of DTPA. Reducing the volume of the scintillation cocktail successfully limited waste without compromising signal intensity. ***Conclusion:*** We successfully demonstrated the next step towards radiochemical purity determination of ^{225}Ac-radiopharmaceuticals, including their daughter nuclides ^{213}Bi and ^{209}Pb. ***References:*** (1) Hooijman, E. L. et al. Ac-225 radiochemistry through the lens of [225Ac]Ac-DOTA-TATE. EJNMMI Radiopharm. Chem. 2025, 10, 9. (2) Šimeček, J.; et al. Efficient formation of inert Bi-213 chelates by tetraphosphorus acid analogues of DOTA: towards improved alpha-therapeutics. EJNMMI Res. 2018, 8, 78. (3) Horak, E. et al. Radioimmunotherapy targeting of HER2/neu oncoprotein on ovarian tumor using lead-212-DOTA-AEI. J. Nucl. Med. 1997, 38, 1944-1950.

OP-346

Nitrosoarenes for ^{18}F-labeling - insights into substrate scope

***M. Laube**[1], S. Roscales[2], J. Pietzsch[1,3], A. G. Csákÿ[2];*
[1]Helmholtz-Zentrum Dresden-Rossendorf, Dresden, GERMANY, [2]Instituto Pluridisciplinar, Universidad Complutense de Madrid, Madrid, SPAIN, [3]Faculty of Chemistry and Food Chemistry, School of Science, Technische Universität Dresden, Dresden, GERMANY.

Aim/Introduction: Nitrosoarenes are versatile organic building blocks that are considered both good nucleophiles and electrophiles and therefore offer diverse applications for the formation of new C-N bonds and heterocycles.[1] Herein, we report initial findings on the [^{18}F]fluoro-for-nitroso exchange and systematically investigate the scope and limitations of this completely novel radiofluorination approach. ***Materials and Methods:*** Nitroso compounds were obtained by oxidation of the corresponding anilines with Oxone[2]. Radiofluorination reactions were screened using our recently described microliter scale radiofluorination approach in HPLC vials [3] comprising concentration of K_2CO_3 for QMA elution (29.4 mM (normal) vs. 7.3 mM (¼ base)), reaction temperature (90°C, 110°C, 130°C), and solvent (MeCN, DMF, DMSO) as parameters. The radiochemical conversion (RCC) was determined by radio-TLC and radio-HPLC. Isolated RCY were determined after semi-preparative HPLC. Product identification was performed by standard addition using the authentic non-radioactive reference substances. ***Results:*** A set of 18 nitroso-substituted compounds was synthesized in yields of 56-89% starting from commercially available amines utilizing a simple, high-yielding synthetic strategy towards nitrosoarenes bearing different functional groups. Substrate scope covered the nitroso derivatives of unsubstituted benzene and pyridine, as well as arenes bearing substituents like CN, CHO, CF_3, NO_2, CO_2Et, Cl, OMe, Me, Br, COPh alone or in combination at specified positions to get insights into the effects of electron withdrawing or donating groups. The formation of the ^{18}F-labeled product resulting from [^{18}F]fluoro-for-nitroso exchange could be observed and verified by standard addition and analysis by radio-HPLC. RCC as a measure for radiolabeling efficacy was found to vary in this subset between 2-78% while isolated RCY varied between 2-54% for 13 selected precursors. Application of normal K_2CO_3 concentration and higher temperatures of 110°C or 130°C in DMSO or DMF was found to be advantageous for the reaction. ***Conclusion:*** To the best of our knowledge, this work represents the first example for a [^{18}F] fluoro-for-nitroso exchange which might prove to be a useful tool for ^{18}F-chemistry based on accessibility of nitrosoarenes starting from anilines. The radiofluorination approach tolerates a variety of electron donating or withdrawing groups and can be applied to the radiofluorination of heterocycles like pyridine, too. ***References:*** [1] Roscales, S.; Csákÿ, A. G. Chem. Soc. Rev. 2020, 49, 5159. [2] Priewisch, B.; Rück-Braun, K. J. Org. Chem. 2005, 70, 2350. 3) Laube et al. Nucl. Med. Biol. 2021, 96-97:S61.

OP-347

PYTA is the new DOTA - A versatile chelator for targeted radionuclide therapy

***M. Cheveau**[1,2], M. Moreau[2], A. Grohmann[1], S. Robert[1], M. Mendes-Arnaud[1], D. Vivier[2], A. Cochet[2,3], B. Collin[2,3], F. Boschetti[1], S. Poty[2], F. Denat[2];*
[1]Chematech-MDT, Dijon, FRANCE, [2]ICMUB, UMR 6302, CNRS, Université Bourgogne Europe, Dijon, FRANCE, [3]Centre Régional De Lutte Contre Le Cancer Georges François Leclerc, Dijon, FRANCE.

Aim/Introduction: Targeted radionuclide therapy (TRT) is experiencing an exponential growth with rising interests in several radionuclides including: ^{225}Ac (α), ^{177}Lu (β^-) and ^{161}Tb (β^-, AE, IC). Yet, those radionuclides present distinct coordination properties. DOTA remains the gold-standard for those three radionuclides, despite suboptimal coordination properties toward ^{225}Ac and ^{161}Tb. This prompted the quest for a "magic chelate", which would surpass DOTA's versatility: Macropa demonstrated impressive performances with ^{225}Ac but poor affinity for ^{177}Lu, Crown presented valuable chelation properties for ^{161}Tb but showed progressive in vivo release of ^{225}Ac. We recently reported the synthesis and evaluation of PYTA-based bifunctional chelators (BFCs) in a study that highlighted outstanding chelation properties with ^{225}Ac compared to gold-standards. Herein, we exemplify the high versatility of PYTA BFCs with radiochemical and in vivo evaluations with ^{177}Lu, ^{161}Tb, and ^{111}In. ***Materials and Methods:*** PYTA BFCs were conjugated to a PSMA ligand and panitumumab (anti-EGFR IgG_2). Radiochemical performances were compared to gold-standards (DOTA, Macropa, Crown) and stabilities were tested in reference media (PBS, EDTA, serum).

^{177}Lu/^{161}Tb/^{111}In-panitumumab conjugates biodistribution were evaluated in mice bearing EGFR^{+} (BxPC3) subcutaneous tumors up to 15 days post-intravenous injection, along with SPECT/CT imaging. Dosimetry is reported based on biodistribution data. ***Results:*** PYTA-conjugates demonstrated excellent radiochemical yields (>97%) under mild conditions with all radionuclides, with high specific activities (600MBq/mg for ^{111}In, 1.2GBq/mg with ^{177}Lu and ^{161}Tb) and prolonged stabilities (~95% after 7 days in serum). In comparison, Macropa displayed a low affinity for these radionuclides and Crown demonstrated detrimental instability with ^{177}Lu, in line with our previous ^{225}Ac results, and a low affinity for ^{111}In. Finally, DOTA was outperformed in every radiolabeling assays and did not demonstrate enhanced stability compared to PYTA. Biodistribution studies and SPECT/CT images of PYTA-panitumumab radioconjugates revealed a high and specific accumulation in the tumor (40-80%IA/g 6 to 9 days post-injection) and low non-specific accumulation in healthy organs known to accumulate free radiometals, especially liver and bones (<5%IA/g), highlighting the in vivo stability of PYTA radiocomplexes. Dosimetry based on biodistribution data report therapeutic indexes >10 in all organs. ***Conclusion:*** PYTA BFCs display unprecedented radiochemical performances toward ^{225}Ac, ^{177}Lu, ^{161}Tb and ^{111}In, outperforming gold-standards. In vivo assessment revealed the enhanced stability of PYTA radioconjugates, in line with our previous ^{225}Ac study. This study showcases the unmatched versatility of PYTA BFCs, propelling them to the forefront as a transformative breakthrough for the development of TRT. ***References:*** Cheveau, M et al. ChemRxiv. 2025. https://doi.org/10.26434/chemrxiv-2025-q2t1b.

OP-348

Chelating [^{227}Th]Th^{4+} For Peptide Receptor Radionuclide Therapy Of Neuroendocrine Tumours

L. Wharton[1], *S. W. McNeil*[1,2], *H. Meeres*[1,2], *D. Zhang*[1,2], *A. Ingham*[3], *H. Merkens*[4], *M. Osooly*[5], *C. Rodríguez-Rodríguez*[6,7,8], *F. Bénard*[4,9], *H. Yang*[1,2,10];
[1]*TRIUMF, Vancouver, BC, CANADA,* [2]*Department of Chemistry, University of British Columbia, Vancouver, BC, CANADA,* [3]*Memorial Sloan Kettering Cancer Center, New York City, NY, UNITED STATES OF AMERICA,* [4]*British Columbia Cancer Research Centre, Vancouver, BC, CANADA,* [5]*Alpha 9 Oncology, Vancouver, BC, CANADA,* [6]*Centre for Comparative Medicine, Vancouver, BC, CANADA,* [7]*Faculty of Pharmaceutical Sciences, University of British Columbia, Vancouver, BC, CANADA,* [8]*Department of Physics and Astronomy, University of British Columbia, Vancouver, BC, CANADA,* [9]*Department of Radiology, University of British Columbia, Vancouver, BC, CANADA,* [10]*Department of Chemistry, Simon Fraser University, Vancouver, BC, CANADA.*

Aim/Introduction: Thorium-227 represents an interesting candidate for targeted alpha therapy (TAT) given its relatively long half-life, 18.7 days, and the cascade of short-lived, high-potency, alpha-emitting daughter progeny in its decay scheme. However, to date few chelators exist which can effectively and stably bind [^{227}Th]Th^{4+} at molar activities high enough for TAT. Furthermore, clinical studies with Th-227 have exclusively focused on antibody-based targeting strategies. We hypothesized that Th-227 could be effectively paired with fast-circulating peptide-based targeting vectors, if a suitable chelator could be identified. We aimed to evaluate the radiolabelling properties of a pool of potential chelators, and investigate for the first time, the feasibility of peptide-based targeting with Th-227 in a preclinical mouse model. ***Materials and Methods:*** An array of potential [^{227}Th]Th^{4+} chelators were screened using freshly purified Th-227 obtained from an ^{227}Ac/^{227}Th generator. Radiochemical yields were determined by radio-TLC and gamma spectroscopy, and the most favourable candidates taken forward for further investigation using concentration-dependent radiolabelling and human serum stability studies. A ^{227}Th-labelled peptide-based bioconjugate, [^{227}Th]Th-noneunpaX-Ahx-TATE, was prepared and characterized using radio-TLC, radio-HPLC, log$D_{7.4}$ measurements, and serum stability studies. Preclinical evaluation of [^{227}Th]Th-noneunpaX-Ahx-TATE was undertaken in male NRG mice bearing AR42J tumours and biodistribution studies performed at 3 h post-injection. Optimised methods for evaluation of Th-227 biodistribution and dissemination between parent and daughter progeny uptake were developed, allowing for routine detection. ***Results:*** An initial screening of potential chelators for [^{227}Th]Th^{4+} identified H_4noneunpaX as an efficient ligand, demonstrating radiolabelling with [^{227}Th]Th^{4+} at concentrations of 10^{-6} M (A_m = 272 kBq/nmol) under mild conditions (ambient temperature, 15 min). The coordination characteristics of [Th(noneunpaX)] were thoroughly investigated through ^{1}H NMR spectroscopy, mass spectrometry, and DFT calculations, indicating the formation of a single monomeric complex. [^{227}Th]Th-noneunpaX-Ahx-TATE was prepared with high molar activities (A_m = 500 kBq/nmol), and fully characterised by radio-TLC, gamma spectroscopy, and radio-HPLC, showing a single peak, with RCP >99.7%. Preclinical evaluation of [^{227}Th]Th-noneunpaX-Ahx-TATE in AR42J tumour bearing mice, showed good tumour uptake (25.8±6.2 %IA/g) at 3 h post injection and fast clearance via the renal pathway. Low retention in non-target organs was seen, with notably low uptake in bone, implying good radiotracer stability in vivo. ***Conclusion:*** H_4noneunpaX was identified as a versatile chelator which can be labelled with [^{227}Th]Th^{4+} under mild conditions and demonstrates high in vivo stability and tumour uptake when coupled to a peptide-targeting vector.

OP-349

Impact of formulation buffers on the radiolysis and stability of RHN001-Tx (^{188}Re-PSMA)

A. Mdlophane[1,2], *S. Mdanda*[1,2], *S. M. Sibiya*[1,2], *M. Qebetu*[1,2], *K. Ramonaheng*[1,2], *M. M. Sathekge*[1,2,3], *F. L. Giesel*[4], *J. Cardinale*[4];
[1]*Nuclear Medicine Research Infrastructure, Pretoria, SOUTH AFRICA,* [2]*University of Pretoria, Pretoria, SOUTH AFRICA,* [3]*Steve Biko Academic Hospital, Pretoria, SOUTH AFRICA,* [4]*Medical Faculty and University Hospital Duesseldorf, Duesseldorf, GERMANY.*

Aim/Introduction: RHN001 is a novel PSMA-targeting theragnostic ligand which can be labelled with Technetium-99m and Rhenium-188. A first in man study with ^{188}Re-labelled RHN001-Tx (formerly GCK01) in the treatment of prostate cancer has been reported(1). The ligand is subject of the recently started RHINO trial - a prospective phase-I/II clinical trial. The objective of the current project was to optimise the formulation by incorporation of suitable stabilizers and reduction of the radiolytic effect of β-emissions. ***Materials and Methods:*** Preparation of RHN001-Tx was conducted as previously reported (1). After cartridge extraction, RHN001-Tx was reformulated in 4 different buffers: Formulation 1 was simple phosphate buffered saline with sodium ascorbate as anti-oxidant; Formulation 2 was a typical ^{225}Ac-formulation buffer based on sodium acetate/ascorbate in saline with additional diethylenetriamine pentaacetic acid (DTPA); Formulation 3 and 4 were composed from sodium acetate and -ascorbate in saline with or without gentisic acid. The impact on radiolytic stability was determined by radioHPLC at the end of synthesis (EoS), 3 h and 6 h post-synthesis. ***Results:*** Formulation 1 resulted in poor and quickly dropping radiochemical purity (RCP, not quantifiable). In formulation 2 the DTPA caused transchelation of the ligand to DTPA increasing over time. Formulation 3 showed improved stability of the labelled product (RT 6.15 min) with 99 % RCP at EoS, dropping to 95.4 % and 92.7 % at 3- and 6 h, respectively. Finally, the addition of gentisic acid in formulation 4 resulted in the best radiolytic stability with 98.9 %, 97.6 % and 96.4 % RCP at EoS, 3- and 6 h, respectively. ***Conclusion:*** Surprisingly, our standard formulations did not work for stabilizing RHN001-Tx. However, we were able to identify a suitable formulation buffer based on an adapted version of a previously used buffer for ^{225}Ac-

Radiopharmaceutical formulations. In the new formulation we were able to validate an excellent shelf-life of up to 6 h for RHN001-Tx. Validation for the more recent preparation procedure and even longer shelf-lives are currently under investigation. ***References:*** (1)Cardinale J, Giesel FL, Wensky C, Rathke HG, Haberkorn U, Kratochwil C. PSMA-GCK01: A Generator-Based 99mTc/188Re Theranostic Ligand for the Prostate-Specific Membrane Antigen. Journal of Nuclear Medicine. 2023;64(7):1069-75.

OP-350

3p-C-DEPA$_{-TFP}$-PEG$_4$ as an effective bifunctional chelator for radiolabelling ^{161}Tb and ^{225}Ac for theranostic applications

J. Pougoue Ketchemen[1], *S. Ahenkorah*[2], *E. Nwangele*[1], *F. Njotu*[1], *D. Fon*[1], *M. Khosravifarsani*[1], *K. Bato*[1], *M. Ooms*[3], *C. Van Laere*[3], *S. Leekens*[4], *F. Cleeren*[4], *H. Fonge*[1];
[1]*Université Laval, Quebec, QC, CANADA,* [2]*University of Iowa Health Care, Iowa, IA, UNITED STATES OF AMERICA,* [3]*Belgian Nuclear Research Center (SCK CEN), Mol, BELGIUM,* [4]*University of Leuven, Leuven, BELGIUM.*

Aim/Introduction: Terbium-161 (^{161}Tb) with simultaneous γ-emissions of 48.9 keV and 74.6 keV is suitable for micro SPECT imaging while its β-emission (154 keV) and Auger-electrons (≤40 keV) are also ideal for therapy. Actinium-225's (^{225}Ac) alpha-emissions of 5.8 MeV make it ideal for therapy against cancers. 3p-C-DEPA is a potential good chelator for both ^{225}Ac and ^{161}Tb. Simultaneous/concomitant use of ^{225}Ac and ^{161}Tb-labelled radiopharmaceuticals are potentially effective for radiotherapy of malignancies because it would take advantage of three potent radionuclide classes (beta, alpha and Auger/conversions electrons). ***Materials and Methods:*** The BFC 3p-C-DEPA$_{-TFP}$-PEG$_4$ was conjugated to the model antibody trastuzumab followed by radiolabeling with [^{161}Tb]TbCl$_3$ or [^{225}Ac]AcCl$_3$ using standard conditions (2 h at 40 °C (^{161}Tb) and ^{225}Ac (37°C)). Benchmarks BFCs, DOTA$_{-SCN}$, 3p-C-DEPA$_{-SCN}$ and Macropa$_{-SCN}$ were used for trastuzumab conjugation and radiolabeling. The in vitro stability of the corresponding radioconjugates was determined in PBS and human serum for a period of 4 (^{161}Tb) to 10 (^{225}Ac) days. The radioimmunoconjugates (RICs) were evaluated in vivo using biodistribution in non-tumor bearing Balb/C mice and will be done in JIMT-1 athymic Balb/C nude mice. Concomitant radiotherapy of [^{161}Tb]Tb-3p-C-DEPA$_{-TFP}$-PEG$_4$-trastuzumab and [^{225}Ac]Ac-3p-C-DEPA$_{-TFP}$-PEG$_4$-trastuzumab will be done in HCC1954/JIMT-1 xenografts, 4T1-HER2 syngeneic models and patient-derived xenografts. ***Results:*** The HPLC and bioanalyzer analysis of the immunoconjugates 3p-C-DEPA$_{-TFP}$-PEG$_4$-trastuzumab, DOTA$_{-NCS}$-trastuzumab, 3p-C-DEPA$_{-NCS}$-trastuzumab and Macropa$_{-NCS}$-trastuzumab showed 98% purity with less than 2% impurities. A RCC of 93.5% was obtained for [^{225}Ac]Ac-3p-C-DEPA$_{-TFP}$-PEG$_4$-trastuzumab, 90.4% for [^{225}Ac]Ac-DOTA$_{-NCS}$-trastuzumab, 97.3% for [^{225}Ac]Ac-3p-C-DEPA$_{-NCS}$-trastuzumab and 95.9% for [^{225}Ac]Ac-Macropa$_{-NCS}$-trastuzumab after 2 h incubation at 37°C. Furthermore, a RCC of 90.8% was obtained for [^{161}Tb]Tb-3p-C-DEPA$_{-TFP}$-PEG$_4$-trastuzumab, 83.2% for [^{161}Tb]Tb-DOTA$_{-NCS}$-trastuzumab after 2 h incubation at 40°C. Excitingly, in PBS, 91.3 ± 4.3%, 60.1 ± 0.6%, 48.3 ± 1.2%, and 81.9 ± 5.6% intact radiocomplexes were observed after 10 d for [^{225}Ac]Ac-3p-C-DEPA$_{-TFP}$-PEG$_4$-trastuzumab, [^{225}Ac]Ac-DOTA$_{-NCS}$-trastuzumab, [^{225}Ac]Ac-3p-C-DEPA$_{-NCS}$-trastuzumab and [^{225}Ac]Ac-Macropa$_{-NCS}$-trastuzumab, respectively. In contrast, [^{161}Tb]Tb-3p-C-DEPA$_{-TFP}$-PEG$_4$-trastuzumab was found to be less stable with only 36.7 ± 7.9% and 71.1 ± 3.2% of intact radiocomplex remaining after 4 days in PBS and human serum, respectively. There were no major significant differences between the biodistribution profile of [^{225}Ac]Ac-3p-C-DEPA-$_{NCS}$-trastuzumab, [^{225}Ac]Ac-DOTA$_{-NCS}$-trastuzumab and [^{225}Ac]Ac-Macropa$_{-NCS}$-trastuzumab in all organs of interest ($p > 0.05$ for all organs). However, the liver uptake of [^{225}Ac]Ac-DOTA$_{-NCS}$-trastuzumab (14.1 ± 2.9% IA/g) was higher than [^{225}Ac]Ac-3p-C-DEPA$_{-NCS}$-trastuzumab (9.0 ± 3.3% IA/g) ($p=0.04$). Additional in vitro and in vivo experiments are ongoing. ***Conclusion:*** 3p-C-DEPA$_{-TFP}$-PEG$_4$ is a promising chelator especially for ^{225}Ac with a good RCC under mild conditions, and stability in vitro.

OP-351

Bischelate Strategy for a "Pseudo-Theranostic Pair" (PET and RIT): Synthesis and in vivo Evaluation of the First Site-Specific DFO/DOTAGA Immunoconjugate

D. Vivier[1], *M. Grah Kple*[1], *J. Ariztia*[1], *M. Moreau*[1], *M. Claron*[1], *A. Laouafa*[1], *A. Kownacka*[2], *C. Petitot*[2], *J. Simonet*[2], *R. Ruffin*[2], *A. Oudot*[2], *B. Collin*[2], *F. Denat*[1];
[1]*Université Bourgogne Europe, CNRS, ICMUB UMR 6302, Dijon, FRANCE,* [2]*Centre Georges François Leclerc, IMATHERA, BioSanD – UMS INSERM 58, Dijon, FRANCE.*

Aim/Introduction: Targeted radiotherapy (TRT), recently propelled by the approval of Lutathera® and Pluvicto®, offers a promising approach for treating metastatic cancers by delivering therapeutic radionuclides directly to tumor cells, reducing systemic toxicity compared to conventional treatments. To optimize patient selection and monitor efficacy, TRT is often combined with PET imaging under the radiotheranostic paradigm. However, when different radionuclides are used for therapy and diagnosis, the choice of chelator becomes a key limitation, as most are optimized for a single radiometal. To address this, we developed a DOTAGA/DFO dual-chelator platform based on L-lysine, tailored for the pseudo-theranostic pair ^{177}Lu/^{89}Zr. This strategy allows site-specific assembly of bischelate immunoconjugates via microbial transglutaminase (MTGase)-mediated conjugation, offering an efficient solution for accommodating therapeutic and diagnostic radionuclides in one construct. ***Materials and Methods:*** Starting from Boc-L-Lys(Fmoc)-OH, we synthesized a DFO-Lys-DBCO probe combining a deferoxamine (DFO) chelator for PET and a DBCO handle for strain-promoted azide-alkyne cycloaddition (SPAAC). Enzymatic conjugation to trastuzumab (Tzb) via MTGase, followed by SPAAC with an azide-functionalized DOTAGA chelator, yielded the bischelate immunoconjugate ss-Tzb-DFO-DOTAGA. Each step was monitored by mass spectrometry. The resulting immunoconjugate was radiolabeled with either ^{89}Zr or ^{177}Lu, and its stability was evaluated in PBS and plasma over 7 days. In vivo studies were conducted in mice bearing HCC1954 xenografts (HER2-overexpressing cell line, resistant to Tzb). PET or SPECT imaging with [^{89}Zr]Zr-ss-Tzb-DFO-DOTAGA or [^{177}Lu]Lu-ss-Tzb-DFO-DOTAGA were performed at 24, 72, and 168 hours post-injection to monitor biodistribution. An additional group received [^{89}Zr]ss-Tzb-DFO-DOTAGA(Lu) — where DOTAGA was pre-loaded with cold lutetium — to assess the influence of the second chelator occupancy. ***Results:*** The DFO-Lys-DBCO probe was synthesized in four steps (39% overall yield). Enzymatic conjugation yielded ss-Tzb-DFO-DBCO with a grafting ratio of 2; the subsequent SPAAC introduced an average of 1.8 DOTAGA per antibody. Radiolabeling confirmed excellent selectivity of DFO for ^{89}Zr and DOTAGA for ^{177}Lu, with radiochemical purities above 94% before purification. The bischelate conjugate exhibited stability comparable to monochelate controls (≥95% after 7 days). Analysis of biodistribution and imaging data is currently underway. ***Conclusion:*** This work reports the first site-specific, dual-chelator immunoconjugate for theranostic applications. Its modular two-step assembly enables easy adaptation to a range of therapeutic radiometals, including β- and α-emitters. Preliminary findings suggest that the choice of radiometal has minimal impact on the in vivo behavior of the bischelate immunoconjugate, supporting its potential as a versatile radiotheranostic platform pending full data analysis.

805

Monday, October 6, 2025, 9:45 - 11:15
Room 211

Cutting Edge Science Track - TROP Session - AI Committee: Disease Characterisation and Prediction Models

OP-352

Reactive Evaluation - A Novel Alternative to Transfer Learning to Handle Multi-Centric Variations in Prostate Cancer Cohorts

L. Papp[1], *S. Wail*[2], *D. Haberl*[1], *L. Dolezel*[2], *M. Hacker*[1], *R. A. Bundschuh*[3], *C. Lapa*[4], *R. Laudicella*[5], *I. Burger*[6], *W. Drexler*[1];
[1]*Medical University of Vienna, Vienna, AUSTRIA,* [2]*Telix Pharmaceuticals, Melbourne, AUSTRALIA,* [3]*Universitätsklinikum Carl Gustav Carus Dresden, Dresden, GERMANY,* [4]*Universitaetsklinikum Augsburg, Augsburg, GERMANY,* [5]*Università di Messina, Messina, SWITZERLAND,* [6]*Kantonspital Baden, Baden, SWITZERLAND.*

Aim/Introduction: Metabolic, imaging apparatus and clinical workflow variations across different medical imaging centres are challenging efforts to build highly-generalisable, multi-centric AI models. Next to techniques e.g. ComBat or cycleGAN harmonisation, transfer learning (TL) can be used to fine-tune a trained model to another data source's characteristics. This, however, complicates clinical adoption and does not result in a singular model. Here, we present a novel technique, called Reactive Evaluation (RE), which dynamically weights model predictions during inference-time, based on a target data source's distribution, without the need to perform any model tuning or TL. ***Materials and Methods:*** Three prostate cancer ^{68}Ga-PSMA-11 image datasets, including a PET/MRI (11 ISUP<2 vs 17 ISUP≥2) from Austria, a PET/MRI (49 ISUP<2 vs. 75 ISUP≥2) from Switzerland and a PET/CT (25 ISUP<2 vs 25 ISUP≥2) from Germany were collected. All cohorts underwent a 2x2x2mm PET resolution normalisation. This was followed by automated prostate and lesion detection and IBSI 1.0 radiomic feature extraction of lesions in the prostate. Automated machine learning was employed to build mixed-stacked ensemble learners to predict low or high risk prostate cancer per-patient. The following scenarios were employed for training: Scenario1 - Switzerland (train)-Austria (validate+test); Scenario 2 - Germany (train)-Switzerland (validate+test); Scenario 3 - Switzerland (train)-Germany (validate+test). In all scenarios, the non-training set was split to 50-50% for validation and test sets, while maintaining a balanced test split ratio of ISUP<2 vs. ISUP≥2 cases. The 50% validate set was the reference dataset for RTE weighting, and the other 50% test set was evaluated by the model, while employing RE at inference-time. The same evaluation was repeated without RE on the test datasets for comparison. ***Results:*** The balanced accuracy (BACC) with RE was 0.84 in Scenario 1, while it was 0.78 without RE. In Scenario 2, BACC was 0.67 with RE and 0.63 without RE. In Scenario 3, BACC was 0.67 with RE and 0.60 without RE. ***Conclusion:*** We demonstrate that RE can yield 3.3 - 7.1% BACC increase in multi-centric prostate cancer cohorts without the need for TL and even when PET/CT and PET/MRI data are mixed. Since RE does not retrain base models, it has the potential to dynamically become increasingly more accurate as additional representative validation samples are provided to it over time. This simplifies efforts to minimise the impact of imaging variability in AI models and allows the generalisability of such models across multiple imaging sites.

OP-353

PSMA PET radiomics in risk stratification of prostate cancer; A machine learning approach

K. Mathiazhagan*, K. B. Chandra, R. Kumar, C. D. Patel, A. Seth, S. Kaushal, G. Priyanka;*
All India Institute of Medical Sciences, Delhi, INDIA.

Aim/Introduction: Aim of the study was to assess the role of PSMA PET radiomics in risk stratification of prostate cancer. The primary and secondary objective was to assess the feasibility of PSMA PET radiomics in predicting NCCN risk groups and ISUP grades in prostate cancer. ***Materials and Methods:*** Data from pathologically confirmed treatment-naïve prostate cancer patients who underwent 68Ga-PSMA-11 PET/CT between January,2018 - August,2024 were analyzed. Primary target outcome was high-very high NCCN risk. Secondary outcome was identification of high-risk ISUP grade group (≥4), based on pathology. Radiomics features were extracted from primary lesion segmentations using whole prostate Region of interest. A total of 110 and 112 clinico-imaging and radiomics features were analyzed for NCCN risk and ISUP grade group prediction analyses respectively. Sampling with Bootstrapping allocated 189 patients (January,2018 - December,2023) to training set, with 75 patients reserved for validation. An independent cohort of 66 patients (January,2023 - August,2024) was used for testing. Feature selection was performed using Gini Index and 10 ML algorithms were trained via stratified 10-fold cross-validation. After validation, model evaluation for generalizability was tested on unseen testing set. ***Results:*** The study included 255 male patients. High-very high NCCN risk was observed in 142/189 (75.1%) of patients in the training/validation sets and 40/66 (60.6%) in the testing set (P = 0.028). High-risk ISUP grade groups were present in 65.1% (123/189) of the training/validation set and 62.1% (41/66) of the testing set (P = 0.766). For primary objective, eight ML algorithms achieved >0.800 in all performance metrics during cross-validation, with k-Nearest Neighbors (kNN) performing the best (AUC 0.964). On validation, kNN still achieved the highest AUC of 0.785. Testing on the independent dataset showed seven ML models maintained strong performance (AUC >0.700). Gradient Boosting (xgboost) had the highest AUC-0.782, CA-0.712, F1 score-0.782, Precision-0.723, and Recall-0.850. For secondary objective, eight ML algorithms achieved >0.800 performance metrics during cross-validation, with Gradient Boosting (catboost) showing the best results (AUC 0.953). During validation, seven ML algorithms maintained >0.700 in all metrics, with Random Forest achieving the best AUC of 0.795. Seven models in independent test set maintained strong performance (>0.700 in all metrics with Gradient Boosting (xgboost) achieving the highest performance metrics (AUC-0.812, CA-0.803, F1 score-0.840, Precision-0.850, and Recall-0.829). ***Conclusion:*** Machine learning using PSMA PET radiomics can predict high-very high NCCN risk and ISUP grade groups in treatment-naïve prostate cancer patients with robust performance and generalizability.

OP-354

Training Classical Neural Networks with Quantum Learning to Improve Cancer Prediction Models

L. Papp[1], *S. Moradi*[1], *D. Haberl*[1], *C. Spielvogel*[1], *Z. Ritter*[2], *A. Boukhari*[3], *M. Hatt*[3], *W. Drexler*[1];
[1]*Medical University of Vienna, Vienna, AUSTRIA,* [2]*Medical University of Pécs, Pécs, HUNGARY,* [3]*University of Brest, LaTIM, INSERN, Brest, FRANCE.*

Aim/Introduction: Deep Learning (DL) is at the forefront of modern nuclear medicine (NM) data research. However, most cohorts are small, which hinders the training and generalizability of highly complex DL models. As such, most NM-specific DL prediction models are either systematically over- or under-fitted to small training data, preventing them to unlock their true potential (1). In this study, we demonstrate that classical DL models can be trained with quantum learning (QL), requiring significantly less trainable parameters than conventional learners (CL). This technique is called variational quantum-classical computing. Furthermore, we show that QL trains models with better predictive DL performance than relying on conventional DL learners, due to the reduced

number of trainable parameters. ***Materials and Methods:*** Two open-access PET/CT and clinical multi-centric datasets, including diffuse large b-cell lymphoma (DLBCL) to predict two-years survival and the head and neck dataset (HECKTOR) to predict HPV status were utilized. DLBCL had 40-44, and HECKTOR had 158-74 train-test splits from different centers. A one hidden layer classical neural network was trained with 16 neurons, and 305 weights for DLBCL. In case of HECKTOR, 25 neurons and 951 weights were trained. These trainings with CL were done with Adam optimizer through 100 epochs. The same classical model schemes were also independently trained with QL through 10-epochs where a 9 and a 10-qubit circuit were optimized for DLBCL and HECKTOR, respectively. In these circuits, the number of parameters to train was 36 and 40 for DLBCL and HECKTOR, respectively. In the trained models, confusion matrix analytics were utilized, from which sensitivity (SNS), specificity (SPC) and balanced accuracy (BAcc) were calculated over test cases. ***Results:*** In DLBCL, QL yielded 63% SNS, 86% SPC, and 74% BAcc, while CL yielded 59% SNS, 85% SPC and 72% BACC. In HECKTOR, QL yielded 93% SNS, 53% SPC, and 73% BAcc, while CL yielded 91% SNS, 52% SPC and 71% BAcc. ***Conclusion:*** Quantum learning was capable to train classical DL models with significantly less parameters compared to classical learning algorithms, while also yielding a higher predictive performance. This parameter advantage is larger as the model complexity increases, making our findings scalable to larger DL models. With these findings, we demonstrated not only the technical feasibility but also the disruptive potential of QL in future NM-DL applications. ***References:*** 1. Piffer S, et al., Tackling the small data problem in medical image classification with artificial intelligence: a systematic review. DOI:10.1088/2516-1091/ad525b

OP-355

Time-activity Curves Learning for Differentiating Benign and Malignant Lung Lesions with Dynamic [18F]FDG-PET

T. Sun[1], *Z. Yao*[1], *Y. Wang*[2], *Y. Wu*[3], *Y. Liang*[2], *M. Wang*[3];
[1]*Chinese Acedemy of Sciences, Shenzhen, CHINA,* [2]*Shenzhen Cancer Hospital, Shenzhen, CHINA,* [3]*Henan Provicial People's Hospital, Zhengzhou, CHINA.*

Aim/Introduction: Dynamic [18F]FDG-PET is an emerging imaging modality that captures the temporal metabolic behavior of lesions. This study aimed to evaluate whether the intrinsic information embedded in time activity curves (TACs), when analyzed with artificial intelligence, can improve the differentiation between benign and malignant pulmonary lesions. ***Materials and Methods:*** A total of 229 patients with clinically suspected lung cancer were enrolled, comprising both representative subtypes of lung cancer and benign pulmonary lesions. Among them, 187 patients from the same institution were randomly assigned to training (n = 149) and internal validation (n = 38) cohorts using an 8:2 split. An independent external testing set of 42 patients was collected from a different institution. TACs were extracted from manually segmented lung regions of interest (ROIs). An unsupervised clustering algorithm was first used to divide the TACs within each ROI into high- and low-metabolism groups. A deep learning model combining Long Short-Term Memory (LSTM) and Convolutional Neural Networks (CNN) was subsequently trained to generate a risk score per patient based on the clustered TACs. Receiver Operating Characteristic (ROC) analysis was performed to evaluate classification performance. ***Results:*** The proposed TAC-based model significantly distinguished between benign and malignant lesions across both datasets ($p < 0.05$). It outperformed conventional static metrics such as SUVmax and Ki. In the internal validation set, the model achieved an AUC of 0.909, with a sensitivity of 0.818, specificity of 1.000, and F1-score of 0.914. In comparison, SUVmax showed lower diagnostic accuracy (AUC = 0.727), as did Ki (AUC = 0.703). For the external test set, the TAC model maintained high performance (AUC = 0.892), outperforming SUVmax (AUC = 0.716) and Ki (AUC = 0.714). ***Conclusion:*** We proposed a novel diagnostic model that integrates time-series learning models. This approach demonstrated superior performance over conventional quantitative PET parameters in differentiating benign from malignant lung lesions, and holds promise for enhancing clinical diagnostic decision-making in pulmonary oncology.

OP-356

Machine Learning-Based Prediction of Radiochemotherapy Response in NSCLC Using ^{18}F-FDG PET/CT

R. Da-ano[1], *O. Tankyevych*[2], *Y. Mtazaoui*[2], *C. Cheze Le Rest*[2], *D. Visvikis*[1];
[1]*INSERM - DR GRAND OUEST/ LaTIM U1101, Brest, FRANCE,* [2]*Nuclear Medicine, University of Poitiers, Poitiers, FRANCE.*

Aim/Introduction: Predicting the response to concurrent chemoradiotherapy in stage III non-small cell lung cancer (NSCLC) is essential for personalized treatment planning. This study aimed to explore the use of ^{18}F-FDG PET/CT imaging alongside machine learning techniques, to predict radiochemotherapy response in NSCLC patients. The hypothesis was that combining clinical parameters with PET/CT data, could effectively predict pathological response with high accuracy. ***Materials and Methods:*** The clinical data of 158 patients with stage III NSCLC from 2 institutions (105 from Poitiers and 53 from Tours) were collected. The primary endpoint was the response to concurrent chemoradiotherapy assessed using RECIST criteria (complete response, partial response, stable disease vs progression). Random Forest (RF) was employed as the machine learning algorithm to predict the response based on radiomics derived from PET/CT combined with clinical parameters (age, gender, histology, stage). The model's performance was evaluated using accuracy and Area Under the Curve (AUC) metrics for both untransformed and combat-version PET/CT data. ***Results:*** The RF model showed a significant difference in performance between the untransformed and combat-version PET/CT data on the test set. The combat-version showed an increased performance with an AUC of 0.78 and accuracy of 92% compared to its untransformed counterpart with an AUC of 0.75 and an accuracy of 91%. These results demonstrate that applying the combat harmonization to the PET/CT data issued from different institution resulted in a slight but consistent improvement in the model's ability to predict radiochemotherapy response, suggesting that data preprocessing plays a role in enhancing the predictive accuracy. ***Conclusion:*** Using ^{18}F-FDG PET/CT data, this study shows that machine learning models can accurately forecast how NSCLC patients would respond to radiochemotherapy. The advantage of data preprocessing approaches was demonstrated by the combat-version PET/CT data's better predictive accuracy when compared to untransformed data. These results provide credence to the generalizability of PET/CT imaging in conjunction with machine learning as a non-invasive way of enhancing individualized treatment plans for non-small cell lung cancer. ***References:*** [1] Yoo J, Lee J, Cheon M, Woo SK, Ahn MJ, Pyo HR, Choi YS, Han JH, Choi JY. Predictive Value of ^{18}F-FDG PET/CT Using Machine Learning for Pathological Response to Neoadjuvant Concurrent Chemoradiotherapy in Patients with Stage III Non-Small Cell Lung Cancer. Cancers (Basel). 2022 Apr 14;14(8):1987. doi: 10.3390/cancers14081987. PMID: 35454899; PMCID: PMC9031866.

OP-357

Dual-Attention Deep Learning Framework for Non-Invasive Histological Subtyping of Lung Cancer Using ^{18}F-FDG PET/CT Imaging

Y. Jia[1], *X. Zhu*[2], *M. Hacker*[1], *X. Li*[1], *Y. Wu*[2], *S. Xue*[1];
[1]Division of Nuclear Medicine, Department of Biomedical Imaging and Image-guided Therapy, Vienna General Hospital, Medical University of Vienna, Vienna, AUSTRIA, [2]Department of Nuclear Medicine, Peking University Cancer Hospital Inner Mongolia Hospital/Cancer Hospital Affiliated to Inner Mongolia Medical University, Hohhot, CHINA.

Aim/Introduction: Accurate histological subtyping of lung cancer is essential for selecting appropriate, subtype-specific therapies. Yet current diagnostic practice relies on invasive biopsies, which carry procedural risks and may fail to capture tumor heterogeneity. To address these limitations, we developed a dual-attention deep learning framework that non-invasively classifies lung cancer subtypes using baseline ^{18}F-FDG PET/CT imaging. This diagnostic model also serves as the first component of our multi-modal foundation model for lung cancer, with future applications in predicting therapeutic response and survival to support personalized treatment planning. ***Materials and Methods:*** We retrospective included 1,042 patients with pathologically confirmed lung cancer from two independent clinical centers. All patients underwent baseline ^{18}F-FDG PET/CT imaging prior to any therapeutic intervention, and only untreated primary tumors were analyzed. We developed a dual-stream convolutional neural network comprising: (1) modality-specific branches for extracting metabolic (PET) and anatomical (CT) features, (2) lesion-guided spatial attention using annotated tumor masks to enhance focus on diagnostically relevant regions, and (3) bidirectional cross-modality attention for effective PET/CT feature fusion. Performance was evaluated using accuracy, F1-score, and area under the receiver operating characteristic curve (AUROC). ***Results:*** Our model achieved robust performance in lung cancer subtyping, with an overall accuracy of 82.3% (95% CI: 79.3-88.2%), an F1-score of 0.81, and an AUROC of 0.89 across all classes. Subtype-specific performance was consistent: ADC reached 85.4% accuracy (F1-score: 0.85; AUROC: 0.91), SCC 86.1% accuracy (F1-score: 0.85; AUROC: 0.91), and SCLC 75.6% accuracy (F1-score: 0.74; AUROC: 0.83). ***Conclusion:*** The proposed dual-attention deep learning framework enables accurate, non-invasive subtyping of untreated primary lung tumors using preoperative PET/CT imaging. By combining interpretability and generalizability, this work serves as a critical diagnostic component in the development of a larger lung cancer foundation model designed to support personalized prognostication and therapy planning.

OP-358

Evaluating tumour heterogeneity and therapy response with AI-assisted longitudinal analysis of FDG- and PSMA-PET/CT

L. Förner[1,2], *K. Tehlan*[1,2], *E. Gastreich de Llanes*[1], *J. Enke*[1], *Z. Reinke*[1], *K. Hildebrand*[1], *P. Hoffmann*[1], *M. Trepel*[1], *R. Claus*[1], *C. Lapa*[1], *T. Wendler*[1,2], *LF and KT are first authors with equal contribution;*
[1]University Hospital Augsburg, Augsburg, GERMANY, [2]Technical University of Munich, Munich, GERMANY.

Aim/Introduction: The introduction of AI-assisted image analysis tools and liquid biopsies where genetic traces such as circulating tumour DNA (ctDNA) are analysed opens new possibilities to track heterogeneity and treatment response in metastatic cancer patients. In the frame of the Augsburg Longitudinal Plasma Study (ALPS) [1], we set up an automatic imaging pipeline to evaluate FDG- and PSMA-PET/CT (FPC and PPC) over time and evaluate it in a first cohort. ***Materials and Methods:*** 29 metastasized castration-resistant prostate cancer patients enrolled in ALPS underwent multiple FPC and PPC, as well as Lu-177-PSMA radioligand therapy (RLT), external beam radiation therapy of the metastases (EBRT), ARPI or chemotherapy (CTx). We used the AutoPET III automatic tumour segmentation [2], implemented multiple PET/CT metrics, and applied them on all available FPC and PPC at patient and organ level. We then analysed the trends in the view of the dates RLT were applied. ***Results:*** Patients got 2-5 FPC, 2-11 PPC, 3.8±2.5 (0-8) RLT cycles or 0.4±0.9 (0-4) EBRT over 51±39 (2-148) weeks, with 7 of them deceasing and 13 dropping-out. 8 patients got ARPI and 5 CTx. During the RLT, SUVmean, SUV standard deviation (SUVstd), and Dmax dropped significantly in PPC (-24.8%, -48.7% and -2.2% respectively). For FPC, while RLT reduced most tumour metrics (-9.8%, -13.2% and +2.2% respectively) no reduction was significant. Matched comparison of FPC and PPC during RLT showed significant differences in SUVstd (p=5.4E-5), Dmax (p=6.6E-4) and total tumour surface area (p=6.4E-8). ***Conclusion:*** Significant drops in tumour metrics for PPC confirm therapy effectiveness and reduced heterogeneity in PSMA-avid disease after RLT, while FDG-avid heterogeneity does not follow the same decreasing pattern. Matched analysis shows significant differences between the two tracers' heterogeneity profiles, growth patterns, and lesion size distribution during RLT. This highlights the potential emergence or selection of aggressive tumour subpopulations inherently resistant to PSMA-targeted therapies or potentially driven by therapeutic selection pressure. While we did not annotate tumours manually, the segmentations were qualitatively evaluated and the longitudinal curves derived from the pipeline agree with the development of the patients. Including radiology reports as validation for the segmentation, correlating the results with dosimetry, PSA and ctDNA values, and repeating the analysis for other therapies are next steps towards better understanding heterogeneity and correlation between image findings and genetic biomarkers in metastatic prostate cancer. ***References:*** [1] Sommer S et al. J Lab Med. 2024 Jun 1;48(3):107-19.[2] Rokuss M et al. arXiv preprint arXiv:2409.09478, 2024.

OP-359

AI-Assisted Detection of Prostate Cancer Lesions on 18F-Flotufolastat PET/CT: Agreement with Expert Readers.

P. Blanc-Durand[1], *C. Besnier*[1], *A. Dujardin*[2], *R. Penny*[3], *E. Itti*[1];
[1]CHU Henri Mondor, Créteil, FRANCE, [2]PAIRE, Paris, FRANCE, [3]Blue Earth Diagnostics, Oxford, UNITED KINGDOM.

Aim/Introduction: Assistance in diagnosis and lesion detection using artificial intelligence is rapidly expanding, particularly in PET/CT diagnostic imaging. The aim of this study is to evaluate the detection performance of an algorithm for identifying high uptake foci on 18F-flotufolastat PET/CT. ***Materials and Methods:*** Patients were included from the LIGHTHOUSE study (NCT04186819)[1], which enrolled those with newly diagnosed unfavourable intermediate-, high-, or very high-risk prostate cancer. Three expert nuclear medicine physicians independently annotated lesions consistent with prostate cancer, forming a consensus ground truth (any lesion identified by at least one reader). The evaluated algorithm, Pionus v1.5.0 (PAIRE, Paris, France), is a convolutional neural network trained on 4,872 FDG PET/CT scans and fine-tuned on 525 PSMA PET/CT scans from the AUTOPET challenge.Predicted lesions were compared to the consensus read and classified as true positives, false positives (detected by the algorithm but not by any physician), or false negatives (missed by the algorithm but detected by at least one physician). Performance was assessed at lesion and patient levels using agreement, positive predictive value (PPV), and false positive rate (FPR). No pathology-based gold standard was used for comparison. ***Results:*** Imaging data from 352 patients enrolled in the LIGHTHOUSE study were analyzed. The algorithm achieved an overall lesion-level agreement of 90% versus the ground truth, of the human reviewers. Agreement for prostate lesions was 90%, for nodal lesions 73%, and for metastatic lesions 80%. The positive predictive value was 47%,

corresponding to a median of 2 false positives per scan and an estimated false positive rate of 53%. At the patient level, the algorithm demonstrated excellent performance, with an overall agreement versus the physician reads of 98%. Agreement for detecting prostate involvement was 98%, for nodal involvement 92%, and for metastatic disease 98%. ***Conclusion:*** These results indicate that the algorithm performs reliably in identifying both primary and secondary prostate cancer lesions and shows lesion-level agreement comparable to expert human readers, particularly in the detection of metastatic disease. ***References:*** 1) Surasi DS, Eiber M, Maurer T, Preston MA, Helfand BT, Josephson D, Tewari AK, Somford DM, Rais-Bahrami S, Koontz BF, Bostrom PJ, Chau A, Davis P, Schuster DM, Chapin BF; LIGHTHOUSE Study Group. Diagnostic Performance and Safety of Positron Emission Tomography with ^{18}F-rhPSMA-7.3 in Patients with Newly Diagnosed Unfavourable Intermediate- to Very-high-risk Prostate Cancer: Results from a Phase 3, Prospective, Multicentre Study (LIGHTHOUSE). Eur Urol. 2023 Oct;84(4):361-370. doi: 10.1016/j.eururo.2023.06.018. Epub 2023 Jul 5. PMID: 37414702

806

Monday, October 6, 2025, 9:45 - 11:15
Room 117

Clinical Oncology Track - TROP Session - Oncology & Theranostics Committee: NET Imaging

OP-361

A phase I/II study of [^{61}Cu]Cu-NODAGA-LM3 for the detection of neuroendocrine tumours: Preliminary results of the COPPER PET in NET Trial

G. Nicolas[1], *A. Chirindel*[1], *F. Kaul*[1], *L. McDougall*[1], *A. Johayem*[2], *A. Llamazares*[2], *M. Baier*[3], *N. Schubert*[3], *F. De Rose*[3], *B. Pais*[3], *L. Jaafar-Thiel*[3], *M. Alejandre Lafont*[1], *A. Bauman*[1], *M. Fani*[1], *D. Wild*[1]; [1]*Department Theragnostics, University Hospital Basel, Basel, SWITZERLAND,* [2]*Department of nuclear Medicine, University Hospital Zurich, Zürich, SWITZERLAND,* [3]*Nuclidium AG, Basel, SWITZERLAND.*

Aim/Introduction: (Pre)clinical data suggest that somatostatin receptor (sstr) antagonists, when radiolabelled with gallium-68, offer superior imaging performance over agonists in patients with neuroendocrine tumours (NETs). [^{61}Cu]Cu-NODAGA-LM3 is a novel PET tracer targeting sstr subtype 2 that may overcome the production, resolution, and logistics limitations of [^{68}Ga]-based tracers. Copper-61 is cyclotron produced and has a longer half-life compared to Ga-68 or F-18, which are currently used for sstr2-targeting PET tracers, enabling delayed imaging and easier logistics. Additionally, Cu-61 has a high positron fraction enhancing image quality per administered activity. We report first-in-human data on safety, biodistribution, dosimetry, blood pharmacokinetics, image quality, and lesion detection with [^{61}Cu]Cu-NODAGA-LM3. ***Materials and Methods:*** This ongoing, randomized, controlled, reader-blind, phase I/II PET/CT study (NCT06455358) includes 22 patients with sstr2-positive well-differentiated gastroenteropancreatic or bronchopulmonary NETs. Each patient undergoes both [^{61}Cu]Cu-NODAGA-LM3 (1h and 3h post-injection) and [^{68}Ga]Ga-DOTA-TOC (1h p.i.) PET/CT imaging on the same scanner within 28 days and, if applicable, 14±2 days after somatostatin analogue injection. Co-primary endpoints are safety and sensitivity of [^{61}Cu]Cu-NODAGA-LM3. Sensitivity will be tested for noninferiority against [^{68}Ga]Ga-DOTA-TOC using a mixed-effects logistic regression model. Biopsy and/or composite imaging during 2-7 months of follow-up serve as gold standard. Adverse events will be monitored up to one day after administration using the Common Terminology Criteria for Adverse Events version 5.0. Main secondary outcomes are biodistribution, pharmacokinetics, dosimetry, and lesion detection. Six patients undergo additional PET/CT 18h p.i for dosimetry. The PET/CT results at 1h and 3h p.i. are compared to determine optimal imaging time. ***Results:*** To date, 9 patients have completed imaging and 4 completed full dosimetry without any adverse events. [^{61}Cu]Cu-NODAGA-LM3 demonstrated rapid blood clearance (median half-life: 15.3 minutes [13.4-25.3] and a residence time of 77.1 minutes [67.9-101.3]). Biodistribution was favourable, with 53% lower median liver SUVmax 2.7 [2.5-3.2]) and 63% lower median spleen SUVmax (9.0 [6.4-10.3]) compared to [^{68}Ga]Ga-DOTA-TOC (liver: 5.8 [4.2-6.7], spleen: 24.0 [18.9-25.8]). Median of the mean SUVmax for the three hottest matched lesions, tumour uptake was 21% higher with [^{61}Cu]Cu-NODAGA-LM3 (19.6 [8.9-22.5] vs. 16.2 [11.7-19.3]), improving lesion detectability and tumour-to-background contrast. The median effective dose was 5.0 mSv [4.2-5.7]. Image quality was rated superior in 8/9 cases in blinded review. ***Conclusion:*** [^{61}Cu]Cu-NODAGA-LM3 demonstrated excellent safety, favourable pharmacokinetics, biodistribution, dosimetry, and superior lesion detectability in patients with NETs. These preliminary findings support the clinical potential of sstr2 antagonists and suggest potential for broader clinical use.

OP-362

Head-to-head comparison of [^{18}F]AlF-NOTA-TATE and [^{68}Ga]Ga-DOTA-TATE PET/CT in Patients with Neuroendocrine Tumors: a prospective study

H. Liu*, G. Ma, H. Wen, X. Zhang, R. Wang, J. Zhang; Department of Nuclear Medicine, The First Medical Centre, Chinese PLA General Hospital, Beijing, CHINA.*

Aim/Introduction: A prospective comparison was made between [^{18}F]AlF-NOTA-TATE and the routinely used clinical imaging agent [^{68}Ga]Ga-DOTA-TATE in patients with neuroendocrine tumors (NETs) regarding diagnostic performance, pharmacokinetic features, and safety, and the clinical application potential of the former as an alternative was explored. ***Materials and Methods:*** The [^{18}F]AlF-NOTA-TATE was synthesized automatically by employing the self-developed direct purification technology of column chromatography, and the quality control standards were stringently adhered to. A clinical comparative study enrolled 20 patients with suspected or confirmed NETs (median age 52 years). All patients accomplished PET/CT imaging of [^{18}F]AlF-NOTA-TATE (dose 7.8 ± 1.8 mCi) and [^{68}Ga]Ga-DOTA-TATE (dose 3.9 ± 0.6 mCi) within 3 days. Image analysis encompassed parameters such as the detection rate of lesions, the maximum standardized uptake value (SUVmax), the tumor/background ratio (TBR), etc., while the radiation dosimetry and the characteristics of biodistribution were simultaneously evaluated. ***Results:*** Among the 20 patients, 13 were diagnosed as NETs and 7 showed negative imaging results or were diagnosed with non-NET lesions. The total detection rate of lesions by [^{18}F]AlF-NOTA-TATE was consistent with that of [^{68}Ga]Ga-DOTA-TATE, but the former showed higher uptake in the liver (SUVmax: 63.9 ± 24.9 vs. 37.2 ± 6.2, P = 0.009), lymph nodes (SUVmax median: 33.8 vs. 22.4, P = 0.021), and bone metastases (SUVmax: 112.9 ± 20.7 vs. 66.1 ± 6.7, P < 0.001). In terms of TBR, [^{18}F]AlF-NOTA-TATE was superior to the control group in liver lesions (77.8 ± 32.4 vs. 57.3 ± 17.6, P = 0.040) and bone metastasis lesions (135.2 ± 28.6 vs. 89.3 ± 18.9, P = 0.001). The biodistribution showed that the physiological uptake of [^{18}F]AlF-NOTA-TATE was higher in normal organs such as the pituitary gland and spleen, but lower in the brain and cardiac ventricles. Dosimetry assessment indicated that the effective dose was 0.021 ± 0.007 mSv/MBq, with the highest absorbed dose in the spleen (0.109 ± 0.059 mGy/MBq), and the safety was good. ***Conclusion:*** [^{18}F]AlF-NOTA-TATE exhibits comparable lesion detection rate to [^{68}Ga]Ga-DOTA-TATE in NETs diagnosis, and has higher tumor uptake and better TBR, especially in the detection of micrometastases. Its automated

synthesis process is simple, with a long half-life, and can overcome the supply limitation of gallium-68 imaging agents. It is expected to become a new alternative solution for the diagnosis and treatment of NETs.

OP-363

Intra-individual Comparison of 68Ga-DOTA-TOC PET/CT and 18F-SiTATE PET/CT: Frequency of Pitfalls in patients with neuroendocrine tumors (G1-G2)

K. Hansen, *J. Q. Petzold, M. C. M. Gammel, A. Richter, W. A. Weber, M. Eiber, I. Rauscher, S. Notohamiprodjo;*
TUM Klinikum Rechts der Isar, Munich, GERMANY.

Aim/Introduction: 18F-SiTATE is a promising new SSTR-PET tracer for imaging neuroendocrine tumors (NET). We retrospectively evaluated the frequency and characteristics of non-tumor-related uptake in comparison to 68Ga-DOTA-Toc. ***Materials and Methods:*** 40 NET patients (G1-G2) were included, who underwent 68Ga PET/CT and, as a follow-up 12.5 ± 6.4 months later 18F-SiTATE PET/CT. All PET/CT scans (n=80) were reviewed by 2 nuclear medicine physicians. PET positive focal findings attributed to a benign origin based on known pitfalls and information from CT were analyzed. The maximum and mean uptake intensity (SUVmax/mean) of these benign findings was measured using a 50% isocontour volume of interest and compared between tracers. For intra-individual comparison, the same benign lesion was analyzed on both scans. Paired differences were approximately normally distributed (Shapiro-Wilk), allowing statistical evaluation using a two-tailed paired t-test. ***Results:*** Overall, a total of 365 benign focal findings were identified: 164 on 68Ga-DOTA-TOC PET/CT and 201 on 18F-SiTATE PET/CT. In 56% this was due to focal uptake by normal organs with somatostatin receptor expression in 20% due to benign osseous lesions, and in 24% due to inflammatory lesions. 68Ga-DOTA-TOC SUVmax values for findings in these three categories were 7.48 ± 6.29, 3.10 ± 1.50, and 7.45 ± 4.81, respectively, while the corresponding values for 18F-SiTATE were 7.95± 6.66, 4.30 ± 1.75, and 6.22 ± 2.98, respectively. Regionally, SUVmean and SUVmax values across specific anatomical sites—including the processus uncinatus, and cervical and presacral ganglia—were largely similar between 18F-SiTATE and 68Ga, with minimal variation. However, 18F-SiTATE demonstrated prominent gallbladder uptake in 22 out of 28 patients (SUVmax 13.57 ± 5.40), whereas no such uptake was observed with 68Ga. In a paired comparison of the highest-uptake benign osseous lesion per patient, 18F-SiTATE showed significantly higher SUVmax values than 68Ga-DOTA-TOC (mean difference: 1.37; 95% CI: 1.88 to 0.86; $p < 0.0001$). ***Conclusion:*** In this preliminary analysis physiological findings were largely similar between 18F-SiTATE and 68Ga-DOTA-TOC. Yet 18F-SiTATE showed significantly higher uptake in the gallbladder and benign osseous findings compared to 68Ga-DOTA-TOC. These differences should be considered when evaluating 18F-SiTATE PET/CT studies.

OP-364

High versus Low Specific Activity in the Biodistribution of [18F]SiTATE: A Matched-pair Analysis of clinical PET Data

J. Petzold[1], *S. Notohamiprodjo*[1], *A. Richter*[1], *A. Wurzer*[1], *P. Bösl*[1], *S. Fischer*[1], *S. Lindner*[2], *J. Allmann*[1], *W. Weber*[1], *M. Eiber*[1], *I. Rauscher*[1];
[1]*TUM University Hospital, Munich, GERMANY,* [2]*LMU University Hospital, Munich, GERMANY.*

Aim/Introduction: [18F]SiTATE is a novel somatostatin receptor-targeting PET-agent with potential clinical advantages based on its F18-label consisting in longer half-life and large batch production. This potentially opens up the possibility of centralised production with distribution to peripheral PET centres without their own cyclotron. However, longer transport routes and thus longer time periods between batch production and injection lead to lower specific activities. We have therefore investigated, whether the specific activity influences its normal organ uptake. ***Materials and Methods:*** A total of 40 patients with gastroenteropathic and pulmonal neuroendocrine tumors (G1-G3) were retrospectively selected based on the specific activity of injected [18F]SiTATE and sub-grouped in patients receiving high (mean value, 114,09 MBq/µg, n=20) versus low specific activity (mean value, 29,02 MBq/µg, n=20). SUVmean was determined within standardized isocontour volumes of interest with 50% of the SUVmax and a diameter of 3 cm in the submandibular gland, thyroid gland, blood pool, lung, spleen, liver, adrenal gland, kidney, pancreas, urinary bladder, prostate, bone and muscle. Differences in mean SUVmean values were compared using a student t-test. ***Results:*** In the sub-group of patients with high specific activity the median SUVmean in the submandibular gland, thyroid gland, blood pool, lung, spleen, liver, adrenal gland, kidney, pancreas, urinary bladder, prostate, bone and muscle were 2.29, 3.87, 1.38, 0.35, 40.46, 7.37, 21.50, 17.87, 8.59, 18.13, 5.43, 1.32, 0.88, respectively. In the sub-group of patients with low specific activity the median SUVmean in the submandibular gland, thyroid gland, blood pool, lung, spleen, liver, adrenal gland, kidney, pancreas, urinary bladder, prostate, bone and muscle were 1.94, 3.39, 1.22, 0.32, 39.10, 6.52, 21.79, 20.21, 8.12, 15.50, 5.36, 1.16, 0.76. Of all regions tracer uptake in the submandibular gland, musculature and blood pool were slightly but statistically significantly higher in the high-specific-activity group (median SUVmean: 2.29 vs. 1.94, $p = 0.047$; 0.88 vs. 0.76, $p = 0.038$; 1.38 vs. 1.22, $p = 0.024$ respectively). No other statistically significant differences were found for normal organs. ***Conclusion:*** A 4-fold decrease in specific activity has only minor effects on the biodistribution of [18F]SiTATE, which are most likely not clinically relevant. These findings suggest that [18F]SiTATE can be centrally produced and transported to PET clinics in a similar way to [18F]FDG.

OP-365

First histological ex vivo validation of the novel [18F]SiTATE SSTR PET tracer

N. Trautwein[1], *S. Mattern*[2], *M. Hinterleitner*[3], *G. Reischl*[4], *R. Schirrmacher*[5], *V. Steger*[6], *S. Nadalin*[7], *K. Nikolaou*[8], *J. Schwenck*[1], *S. Singer*[9], *C. la Fougère*[1];
[1]*Nuclearmedicin Tuebingen, Tübingen, GERMANY,* [2]*Pathology Tuebingen, Tübingen, GERMANY,* [3]*Internal Medicine VIII Tuebingen, Tübingen, GERMANY,* [4]*Preclinical imaging and radiopharmacy Tuebingen, Tübingen, GERMANY,* [5]*Medical Isotope and Cyclotron Facility, Alberta, AB, CANADA,* [6]*Department of Thoracic and Cardiovascular Surgery Tuebingen, Tübingen, GERMANY,* [7]*Department of General, Visceral and Transplant Surgery Tuebingen, Tübingen, GERMANY,* [8]*Department of Diagnostic and Interventional Radiology Tuebingen, Tübingen, GERMANY,* [9]*Patology Tuebingen, Tübingen, GERMANY.*

Aim/Introduction: The utilization of radiolabeled somatostatin analogs (SSAs), exemplified by [68Ga]Ga-DOTA-SSAs, has profoundly impacted imaging and therapeutic methodologies. However, their utilization is limited by the high cost of generators and the brief half-life of 68Ga. Conversely, [18F]SiTATE emerges as a compelling alternative, boasting the advantages of the prolonged half-life of 18F and the high output of cyclotron-based production. This study aims to provide the first histological ex vivo validation of [18F]SiTATE. ***Materials and Methods:*** 47 patients (57% male, mean age 66.9 ± 14.9 years) with histologically confirmed well-differentiated neuroendocrine neoplasms (NENs) who underwent [18F]SiTATE PET scan followed by surgery within four months were retrospectively included in this study. The quantification of lesion uptake was performed using SUVmean, SUVpeak, SUVmax, and the tumor-to-liver ratio (TLR). The histological SSTR2 expression levels were determined using H-scores, with thresholds delineating SSTR scores 1-3. The accuracy of PET imaging for preoperative metastatic detection was evaluated against surgical histology. ***Results:*** The findings revealed a significant correlation between [18F]SiTATE uptake (SUVmean and TLR) and SSTR2 H-scores ($r = 0.618$, $r = 0.622$; $P < 0.0001$). Furthermore, a SSTR score of 3 was

found to be associated with elevated SUVmean and TLR levels (P < 0.0001). Among the 35 patients who underwent primary resection and lymphadenectomy, PET imaging exhibited a sensitivity of 73.9% and a specificity of 100%. ***Conclusion:*** [^{18}F]SiTATE PET imaging demonstrated a strong correlation with histological SSTR expression, underscoring its potential application in staging and guiding therapeutic decisions in NENs. This novel ^{18}F-labeled tracer demonstrates comparable specificity to historical [^{68}Ga]Ga-DOTA-SSA data, while also exhibiting the potential to enhance sensitivity in detecting locoregional metastases. Further head-to-head comparisons of [^{18}F]SiTATE with [^{68}Ga]Ga-DOTA-SSA and histological validation are warranted to optimize its diagnostic accuracy and clinical impact. ***References:*** Leupe H, Ahenkorah S, Dekervel J, et al. (18)F-Labeled Somatostatin Analogs as PET Tracers for the Somatostatin Receptor: Ready for Clinical Use. J Nucl Med. 2023;64(6):835-41. Calderón E, Kiefer LS, Schmidt FP, et al. One-day dual-tracer examination in neuroendocrine neoplasms: a real advantage of low activity LAFOV PET imaging. Eur J Nucl Med Mol Imaging. 2025.

OP-366

Retrospective Evaluation of [^{18}F]AlF-NOTA-Octreotide PET/CT in 288 Patients Referred for SSTR PET/CT

H. Leupe[1], *S. De Buyst*[1], *J. Dekervel*[1], *F. Cleeren*[2], *C. Dooms*[1], *K. Goffin*[1], *S. Jentjens*[1], *L. Boeckxstaens*[1], *F. Van Herpe*[1], *E. Van Cutsem*[1], *P. Clement*[1], *G. Rasschaert*[1], *G. Bormans*[2], *C. Verslype*[1], *C. Deroose*[1];
[1]*UZ Leuven, Leuven, BELGIUM,* [2]*KU Leuven, Leuven, BELGIUM.*

Aim/Introduction: [^{18}F]AlF-NOTA-octreotide has emerged as a reliable tracer for somatostatin receptor (SSTR) PET/CT in patients with neuroendocrine neoplasms (NENs). Although effective and logistically advantageous, there remains limited data on its routine clinical application, particularly for specific NEN subtypes less represented in the prospective trials that evaluated its diagnostic accuracy (e.g. NET G3) (1-3). This study aims to assess the real-world clinical use of [^{18}F]AlF-NOTA-octreotide PET/CT, with an emphasis on uptake characteristics and referral patterns at our institution. ***Materials and Methods:*** A retrospective analysis was conducted on all patients referred for SSTR PET/CT at University Hospitals Leuven between March 1, 2023, and January 18, 2024. Relevant clinical and demographic data, along with procedural details, were collected. PET/CT imaging data was analyzed to quantify uptake parameters. Image analysis was performed using MIM version 7.3.4 (MIM Software Inc., Cleveland, Ohio). SSTR-positive lesions were delineated semi-automatically using a relative threshold based on SUV_{mean} of the liver (1.5 x SUV_{mean} + 2 SD). ***Results:*** A total of 322 [^{18}F]AlF-NOTA-octreotide PET/CT scans from 288 patients were evaluated, with besides 175 patients with gastroenteropancreatic (GEP) NET, 15 patients presenting with G3 NET, 15 with paraganglioma/pheochromocytoma (PPGL), 5 with neuroendocrine carcinoma (NEC) and 40 with lung NET (table 1). In total, 4677 lesions were analyzed. Average injected activity was 208.5 ± 73.6 MBq (2.8±0.88 MBq/kg), and the mean uptake time before imaging was 121 ± 14 minutes. Analysis of the referral patterns by SNMMI appropriate use criteria (AUC) showed that the majority of patients were referred for 'Monitoring of NETs seen predominantly on SSTR PET', followed by 'Initial staging after histologic diagnosis'. Mean SUV_{max} ± SD per WHO tumor grade show comparable uptake in G1 (12.1±9.8), G2 (16.0±17.9), G3 (13.0±12.3) NET and NEC (13.4±5.5). Mean SUV_{max} per NET lesion organ site was highest for pancreas (23.0±28.9), followed by liver (16.0±15.5), small intestine (15.9±15.6) and lymph node (15.6±14.3). Mean SUV_{max} per primary tumor was highest for appendixNET (29.9±29.4), followed by gastricNET (20.4±18.2), rectumNET (17.5±13.6), pancreasNET (14.7±16.7) sigmoidNET (14.5±13.0), smallintestineNET (13.5±13.6) and lungNET (8.7±9.0). ***Conclusion:*** This study provides essential real-world data supporting the routine clinical use of [^{18}F]AlF-NOTA-octreotide PET/CT in NET patient management. Quantitative analysis shows sufficient tracer uptake in NET lesions irrespective of tumor grade, lesion organ and primary tumor origin. ***References:*** 1. Pauwels E,JNuclMed.2023Apr;64(4):632-638.PMID:36265911. 2. Pauwels E,EJNMMI.2020Dec;47(13):3033-3046.PMID: 32617641. 3. Boeckxstaens L,EJNMMIRes.2023Jun;13(1):53.PMID: 37261615.

OP-367

[^{68}Ga]Ga-FAPI PET/MR Imaging for Predicting Invasive Potential in Pituitary Neuroendocrine Tumors

Y. Xi[1], *J. Li*[2], *X. Wang*[2], *Y. Lu*[2], *W. Sun*[1], *X. Zhang*[1], *W. Hai*[1], *B. Li*[1], *S. Lin*[2];
[1]*Department of Nuclear Medicine, Ruijin Hospital, Shanghai Jiaotong University, School of Medicine, Shanghai, CHINA,* [2]*Department of Neurosurgery, Ruijin Hospital, Shanghai Jiaotong University, School of Medicine, Shanghai, CHINA.*

Aim/Introduction: Pituitary neuroendocrine tumor (PitNET) is a common benign tumor in the brain, which exhibits benign behavior. But about 35% of them show invasive growth. This study aimed to use [^{68}Ga]Ga-FAPI PET/MR for early detection of tumor invasion, which beneficial for guiding the development of treatment strategies for reducing recurrence rates. ***Materials and Methods:*** Twenty Patients who found a pituitary mass with KNOSP Level II-IV or suspicion bone invasion were collected from December 2023 to November 2024. All patients underwent [^{68}Ga]Ga-FAPI PET/MR, and then performed transnasal hypophysectomy within one week. Region of interests (ROIs) were drawn to obtain the maximum standardized uptake value (SUV_{max}) in five areas for each tumor: Left cavernous sinus; Right cavernous sinus; Bottom of the tumor; Top of the tumor; The sphenoid sinus mass if the tumor invaded. The invasion into surrounding tissues in each area was evaluated during hypophysectomy. Then, Drew ROC curve and calculated Youden Index to obtain the best cut-off value of SUV_{max} for prediction the invasiveness and the diagnostic accuracy. Pathological diagnosis was obtained to differentiate tumor type. ***Results:*** 85 areas were evaluated in 20 patients. The tumor size was correlated with SUV_{max} in the bilateral cavernous sinus (p=0.002 and p=0.046). The KNOSP level of the bilateral cavernous sinuses was significant correlated with SUV_{max} (p<0.001). The SUV_{max} of area with KNOSP ≥ 2 was significantly higher than that with KNOSP < 2 (p=0.006). The pathological types of high invasive potential PitNETs (PIT-1 / T-PIT / null cell) had a greater impact on [^{68}Ga]Ga-FAPI radioactive uptake with a higher SUV_{max} (p<0.001). Then, this study found a correlation between SUV_{max} and the percentage of Ki67 expression (p=0.021). The SUV_{max} with Ki67 > 1% was significantly higher than that with Ki67 ≤ 1% (p=0.009). Importantly, SUV_{max} of invasive tumors was significantly higher than that of non-invasive ones (p<0.001). To predict the invasiveness of pituitary tumors through SUV_{max}, drew ROC curve and obtained AUC as 0.88 (p<0.001). Calculated Youden Index as the maximum value 0.68 while cut-off value of SUV_{max} was 1.7. In this cut-off value, the diagnostic accuracy was 92.31%, and sensitivity, specificity was 90.70%, 94.29%, respectively. ***Conclusion:*** [^{68}Ga]Ga-FAPI PET/MR accurately evaluated the invasiveness and site of invasion of pituitary tumors. [^{68}Ga]Ga-FAPI radioactive uptake was affected by tumor size, The relationship between tumors and cavernous sinus, and tumor type.

OP-368

Validation of PET Response Evaluation Criteria in Neuroendocrine Tumors (PERCIN) in an Independent Cohort.

A. Chaban[1], *L. Unterrainer*[2], *R. Werner*[2], *A. Holzgreve*[2], *L. Bodei*[3], *W. Weber*[1], *G. Sheikh*[2];
[1]*Klinik und Poliklinik für Nuklearmedizin, Klinikum Rechts der Isar, Technische Universität München, München, GERMANY,* [2]*Klinik und Poliklinik für Nuklearmedizin, LMU Klinikum München, München, GERMANY,* [3]*Department of Radiology, Memorial Sloan Kettering Cancer Center, New York, USA, New York, NY, UNITED STATES OF AMERICA.*

Aim/Introduction: We have recently proposed criteria for assessment of tumor response to therapy by measuring changes of the somatostatin receptor-positive tumor volume (SRV) with PET (PERCIN). In the development cohort, tumor response according to PERCIN had a higher prognostic value than tumor response according to morphologic imaging (RECIST). The goal of the present study was to externally validate the prognostic value of PERCIN in an independent patient population imaged and treated at another medical center. ***Materials and Methods:*** This retrospective, single-center validation study included 100 patients with gastroenteropancreatic neuroendocrine tumors (GEP-NETs, G1: 35, G2: 62, G3: 3), who underwent somatostatin receptor PET/CT (SSR-PET/CT) before and after four cycles of SSR-targeted radiopharmaceutical therapy. SRV was delineated by using background tissue-dependent threshold values (for liver metastases, voxels with a SUVbw more than 2.2 g/ml higher than the maximum liver SUVbw were included in the total tumor volume; for lung and bone metastases, voxels with a SUVbw of more than 3.0 g/ml; and for all other metastases, voxels with a SUVbw higher than the maximum liver SUVbw). Based on these volumes, treatment response was evaluated according to PERCIN as follows: complete response (CR) - absence of any uptake on follow-up PET; partial response (PR) - no new lesions and ≥40% decrease in SRV; progressive disease (PD) - new lesion on follow-up PET and/or ≥20% increase in SRV; stable disease (SD) - no new lesions with <40% decrease or <20% increase in SRV. Patient groups defined by PERCIN were correlated with progression-free survival (PFS). For comparison, response was also evaluated using RECIST (CT-based) and PERCIST (PET-based). ***Results:*** After a follow-up time of 4.2-137.8 months (median = 27.8 months), the median PFS was 35.6 months. PERCIN demonstrated the highest concordance with PFS (p<0.001, c-index=0.75). Median PFS for PERCIN PR, SD, and PD was 48,5 months (45 patients), 34 months (34 patients), and 12.5 months (20 patients). Tumor response according to PERCIST also had significant prognostic value but showed a lower concordance level than PERCIN (p<0.001, c-index=0.69), whereas tumor response according to RECIST failed to achieve statistical significance (p=0.84, c-index=0.52). ***Conclusion:*** External validation of the PERCIN criteria confirmed its strong prognostic value in patients with GEP-NETs undergoing somatostatin receptor-targeted radiopharmaceutical therapy. The prognostic value of tumor response according to PERCIN was superior to existing PET and CT-based criteria.

OP-369

Impact of peptide dose on tumor and normal organ somatostatin receptor expression at PRRT; Measurements on ^{68}Ga-DOTATOC-PET in a simulated therapy setting

E. Ilan[1,2], *U. Jahn*[3], *A. Sundin*[3];
[1]*Medical Physics, Uppsala University, SWEDEN,* [2]*Nuclear medicine & PET, Department of Surgical Sciences, Uppsala University, SWEDEN,* [3]*Radiology & Molecular Imaging, Department of Surgical Sciences, Uppsala University, SWEDEN.*

Aim/Introduction: Disseminated small intestinal neuroendocrine tumors (SI-NET) are primarily treated with long-acting somatostatin analogs (SSA) and peptide-receptor- radionuclide-therapy (PRRT). Debate remains about whether SSA block the uptake of ^{177}Lu-DOTATATE at PRRT and their influence on the tumor versus normal organ receptors. This study aimed to assess whether previously observed uptake differences between large (>4cm) and small (>1cm to<4cm)SI-NET metastases versus normal organs persist in a simulated PRRT setting, when injecting intravenous SSA at amounts comparable to PRRT, before and after a preload of 400µg intravenous octreotide(Sandostatin), and measured on ^{68}Ga-DOTATOC-PET. ***Materials and Methods:*** Ten patients with SI-NET, underwent three ^{68}Ga-DOTATOC-PET/CT examinations (dynamic and static whole-body (WB) PET). Each PET/CT session started by infusion of 167±21MBq(mean±SD) of ^{68}Ga-DOTATOC. Before the last two PET/CT scans an extra intravenous infusion of 150µg octreotide, was administered to mimic the PRRT, and five hours prior to the last PET/CT, a single intravenous infusion of 400µg octreotide. In each patient, the median tumor SUV and tumor net-influx-rate(K_i) of all tumors, large tumors and small tumors, respectively, were determined using 50% iso-contour VOIs. For normal organs (liver,right and left kidney, spleen, pancreas and bone marrow) SUV was determined placing a spherical VOI (1.5cm in diameter) in a representative healthy part of the respective organs. ***Results:*** In the large tumor group, SUV and K_i remained stable across all peptide concentrations (p>0.05), while the remaining tumor groups demonstrated progressive SUV reductions. K_i values declined consistently in all median tumors, while small tumors showed a reduction between the first and second dynamic scans but stabilized following additional peptide at the third time-point. Across all peptide concentrations, SUV and K_i was consistently lower in small tumors than in large tumors. For healthy organs, a significant SUV decline was observed after the first octreotide injection (150µg), in the second WB scan, with the spleen showing further reduction after peptide pre-loading prior to the third WB. The spleen showed the largest SUV decrease(50%), followed by the liver(45%), pancreas(30%), kidneys(20%) and bone marrow(25%).Tumor-to-kidney ratios were stable in large tumors but decreased in small tumors after preloading. Tumor-to-spleen ratios increased initially, then decreased only in small tumors. Ratios to liver, pancreas, and bone marrow were high due to their low baseline uptake. ***Conclusion:*** Large SI-NETs are not influenced by high amounts of injected peptide,while small NETs appear to reduce their uptake in the presence of higher peptide amounts, equivalent to receptor down regulation.

807

Monday, October 6, 2025, 9:45 - 11:15
Room 212

Featured Session - Bone & Joint Committee: New Frontiers in Bone and Soft Tissue Imaging

OP-370

Invited Speaker

R. Graham;
Radiology Department, Royal United Hospitals Bath NHS FT, Bath, UNITED KINGDOM.

OP-371

Correlation analysis of ^{68}Gallium-FAPI- and ^{18}Fluor-FDG-uptake of joints and periarticular tissue with structured pain anamnesis in 171 patients

M. Röhrich[1], *L. Brückner*[2], *A. Spektor*[1], *P. Kvacskay*[3], *M. Schreckenberger*[1], *H. Lorenz*[3], *U. Haberkorn*[2], *W. Merkt*[4];
[1]*University Hospital Mainz, Mainz, GERMANY,* [2]*University Hospital Heidelberg, Heidelberg, GERMANY,* [3]*University Hospital Heidelberg, Mainz, GERMANY,* [4]*University Hospital Düsseldorf, Düsseldorf, GERMANY.*

Aim/Introduction: In both ^{68}Gallium-FAPI-PET and ^{18}Fluor-FDG-PET, joint-associated tracer uptake is a common finding. While ^{18}Fluor-FDG reflects glucose metabolism of inflammatory cells, ^{68}Gallium-FAPI-PET reflects activation of fibroblasts involved in chronic, fibrotic processes. To date, it is not clear, which of these tracers is superior with respect to the depiction of articular pain, the major symptom of joint diseases like osteoarthritis or rheumatoid arthritis. In this retrospective analysis, we correlate ^{68}Gallium-FAPI- and ^{18}Fluor-FDG-PET-imaging findings with a structured joint-related pain anamnesis in 171 patients. ***Materials and Methods:*** Patients, who underwent either 68Gallium FAPI-PET/CT (85 patients) or 18Fluor-FDG-PET/CT (86 patients), filled in a structured anamnesis form, which covered history of joint diseases, pain medication, the presence, localization and intensity of joint-related pain as well as clinically established quality of life-centered scoring systems: 1. Shoulder Pain and Disability Index (SPADI), 2. Western Ontario and McMaster Universities Arthritis

Index (WOMAC), which depicts hip- and knee related pain and 3. Knee Injury and Osteoarthritis Outcome Score (KOOS). PET-signals of shoulders, hips and knees as well as corresponding periarticular tissues were delineated by isocontouring and SUVmax and SUVmean were extracted. Imaging and anamnesis results were analyzed descriptively and the results of the scoring systems were correlated with PET-imaging parameters. ***Results:*** Joint-related pain was present in 41/85 (68Gallium FAPI-PET/CT) and 49/86 (18Fluor-FDG-PET/CT) patients. Differences in PET-signal intensities between pain-affected and pain-free joints and periartcular tissue (shoulder, hip and knee) were markedly more pronounced in 68Gallium FAPI-PET/CT than in 18Fluor-FDG-PET/CT. For instance, 68Gallium FAPI-uptake in pain-positive shoulder-joints was significantly: higher than in pain-negative ones (average SUVmax / mean 2.56+/-0.99 and 0.90+/-0.56 (pain-positive) versus 1.87+/-0.94 and 0.66+/-0.27 (pain-negative). However, 18Fluor-FDG-uptake of shoulder joints was mostly independent from pain (average SUVmax / mean 2.27+/-0.83 and 1.20+/-0.31 (pain-positive) versus 2.46+/-1.06 and 1.11+/-0.36 (pain-negative). Hips and knees showed similar results. Correlations between 68Gallium FAPI-PET/CT / 18Fluor-FDG-PET/CT signalling parameters and results of corresponding established scoring systems (SPADI, WOMAC, KOOS) were positive and significant for almost all parameters in both tracers. However, 68Gallium FAPI-PET/CT showed markedly higher positive correlations for periarticular tissue than 18Fluor-FDG-PET/CT. ***Conclusion:*** Overall, 68Gallium-FAPI-PET showed a more pronounced positive correlation with joint-related pain than 18Fluor-FDG-PET/CT. Thus, it appears promising to include 68Gallium-FAPI-PET into the assessment and therapy response evaluation of diseases with joint-related pain, such as osteoarthritis and rheumatoid diseases.

OP-372

Diagnosis of Prosthetic Loosening Following Total Knee Arthroplasty: A Quantitative SPECT/CT Approach

J. Rei da Cruz Escaleira[1,2], *R. Sá e Silva*[1], *M. Oliveira*[1], *L. Costa*[1], *A. Vilaça*[3];
[1]*Department of Nuclear Medicine, Unidade Local de Saúde (ULS) de Santo António, Oporto, PORTUGAL,* [2]*Unit for Multidisciplinary Research in Biomedicine (UMIB), Oporto, PORTUGAL,*
[3]*Department of Orthopedics, Unidade Local de Saúde (ULS) de Santo António, Oporto, PORTUGAL.*

Aim/Introduction: Single-photon emission computed tomography/computed tomography (SPECT/CT) has emerged as a promising modality for assessing prosthetic loosening after total knee arthroplasty (TKA). However, persistent postoperative physiological uptake can obscure interpretation, making early diagnosis particularly challenging. This study aimed to evaluate the role of quantitative SPECT/CT in enhancing diagnostic accuracy and supporting clinical decision-making. ***Materials and Methods:*** We retrospectively analyzed patients with cemented total knee prostheses (TKPs) under follow-up by orthopedic specialists at a single center who underwent ^{99m}Tc-labeled bisphosphonate SPECT/CT within the past two years. Knees were stratified by time since surgery into early(<5 years) and late(≥5 years) groups. Suspected loosening was defined by the presence of periprosthetic radiolucent lines (RL)≥2 mm on knee radiographs in the early group, and by visual assessment of increased periprosthetic tracer uptake on SPECT/CT without an alternative cause in the late group. Peak standardized uptake value (SUV_{peak}) was calculated using dedicated software, with spherical volumes of interest (VOIs) placed in five component regions: the tibial stem (TS) tip, medial and lateral tibial plateaus (TP), and medial and lateral femoral condyles (FC). ***Results:*** Forty-seven patients were included (85.9% women, 54.7% obese), with a median age of 74 years[IQR: 67-76]. Sixty-four TKPs were evaluated; 36 (56.3%) were imaged <5 years post-surgery, and 28 at ≥5 years. In the early group, SUV_{peak} values were significantly higher in TKPs with suspected loosening than in radiographically normal implants across all assessed regions, with the most pronounced differences at both TP(p<.001). In the late group, SUV_{peak} was significantly elevated in scans with loosening suspicion at the TS tip(p=.002) and lateral TP(p=.033), with close but non-significant trends in other regions, except the lateral FC(table I). Receiver operating characteristic (ROC) analysis identified optimal SUV_{peak} thresholds for detecting TKPs loosening (table II). In the early group, the medial TP showed the highest diagnostic performance, with a cut-off of 4.8 yielding 70.0% sensitivity and 96.2% specificity(AUC=0.900). In the late group, the TS tip provided the best accuracy, with a cut-off of 2.3 achieving 61.5% sensitivity and 100% specificity (AUC=0.831). Varus-aligned knees(n=42) demonstrated a significantly higher medial-to-lateral SUVpeak ratio compared to neutrally aligned knees (1.17 vs. 1.03, p=.028). ***Conclusion:*** This study supports the use of quantitative SPECT/CT as a practical tool for evaluating suspected prosthetic loosening following TKA. Time-based SUV_{peak} cut-offs may enhance interpretation across postoperative phases—particularly in the early period—by increasing diagnostic accuracy and potentially optimizing patient management while avoiding unnecessary interventions.

OP-373

Usefulness of Quantitative 99mTc-WBC SPECT/CT for Infection Detection

A. Skriabina*, M. Jreige, J. O. Prior, N. Schaefer, M. Nicod-Lalonde; CHUV, Lausanne, SWITZERLAND.*

Aim/Introduction: WBC scintigraphy is a well-known imaging modality for detecting infection. The diagnosis of infection is made by visual and semi-quantitative assessment on planar and/or SPECT/CT images. We aimed to investigate the added value of SPECT/CT quantification for the detection of infection. ***Materials and Methods:*** We retrospectively evaluated all patients with suspicion of infection undergoing ^{99m}Tc-Scintimun or in vitro ^{99m}Tc-labelled WBC scintigraphy with quantitative SPECT/CT (4h and/or 24h post-injection). Patients who refused the hospital's general consent and who did not have available follow-up were excluded from the analysis. Microbiological results and radiological follow-up were retrieved from the patient's electronic file. For planar semi-quantitative analysis, regions of interest (ROI) were drawn on the suspected site of infection and on the contralateral limb at 4 and 24 hours, and static ratio (ROI lesion/ROI contralateral at 24h)/(ROI lesion/ROI contralateral at 4h) was calculated. Lesion SUV_{max} and SUV_{peak} were measured from 4h and 24h SPECT/CTs. ROC analysis was performed to compare diagnostic accuracy of the different parameters. ***Results:*** In total, 55 WBC scans in 52 patients (39M/13F, aged 23 to 87 years) were included. Follow-up showed infection in 16/55 (29%) (15 on biological samples and 1 on radiological follow-up). The AUCs of the static ratio, SUV_{max}@4h and SUV_{max}@24h were not statistically different: 0.79 [95%CI 0.62-0.96], 0.71[0.57-0.86] and 0.71 [0.57-0.85], respectively. Similar results were found for SUV_{peak}. In a subgroup of 45 patients with no bone marrow surrounding the lesion suspected of infection, the AUCs of the static ratio, SUV_{max}@4h and SUV_{max}@24h were 0.76 [0.56-0.95], 0.79 [0.65-0.94] and 0.82 [0.69-0.96], respectively. In this subgroup, quantitative SPECT/CT parameters at a single timepoint @24h had a higher diagnostic accuracy than planar analysis using two timepoints @4 and @24h, although the difference was not statistically significant. ***Conclusion:*** Our preliminary data show similar specificity and sensitivity of quantitative SPECT/CT parameters at a single timepoint either 4h or 24h for the diagnosis of infection compared to standard dual-time planar imaging. Quantitative SPECT parameters may replace the time-consuming dual-acquisition protocol on 2 separate days, particularly in patients with no bone marrow surrounding the suspected infected lesion. These promising results remain to be confirmed in a larger population sample.

OP-375

A prospective observational study on long-term results of ^{90}Yttrium and 166-Holmium radiosynoviorthesis of chronic knee synovitis in rheumatoid arthritis.

M. Szentesi, *E. Takács, A. Radácsi;*
Hospital of the Hospitaller Brothers of St. John of Budapest, Budapest, HUNGARY.

Aim/Introduction: Examination of anti-inflammatory effect of 90-Yttrium and 166-Holmium injections in Rheumatoid Arthritis (RA) patients. ***Materials and Methods:*** After the treatment, we performed a long-term, prospective follow-up. In our present work We report the 10-year results of 345 RA patients. All patients provided written informed consent. In all patients inflammatory knee joint disease was diagnosed on the basis of the American College of Rheumatology. 312 of 345 patients with RA were seropositive, 33 seronegative. Mean age of 108 male and 237 female patients was 61.6 years (range 40-84) years. In 180 patients the right knee, in 165 the left knee was treated by RSO. Steinbrocker functional stadium II was observed in 165, stadium III in 165 and stadium IV in 15 of them. By radiography grades I (n= 9), II (n=201), III (n= 135) were observed. Grading was done according to Steinbrocker anatomic score. Mean duration of disease was 7.3 years (0.5-25), of synovitis (6.4 years (0.5-24) Mean number of punctions of the treated joint prior to radiosynovectomy was 12.3 per patient and of steroid administrations prior to radiosynovectomy 10.2. In 25 patients a systemic steroid therapy has been performed. Evaulation was based on the criteria as described by Müller, Rau and Scütte the score system was developed by the authors. ***Results:*** Excellent and good results in RA patients were achieved in 78.5% in the first 5 years and 65.8% in 10 years after RSO. Excellent and good results were achived in 89,6%/5 years and 79,2%/ 10 years in local stadium II, in the first 5 years, while excellent and good results were found in 62,3% in local stadium III. Ten years after RSO 70,43% of patients did not need another punction. These results prove that RSO must be done in the early X-ray phase I-II. The effectiveness is worsened significantly by the stadium of the disorder and the local x ray phase and diagnosis. P 0.00001. ***Conclusion:*** RSO is as effectiv method of treating chronic synovitis as surgical synovectomy. Even after a ten-years period 78,5% the findings were rated as excellent or good. 70,43% of the patients do not need another punction even after a ten years period. The treatment must be done in RA Steinbrocker stadium I-II, local stadium I-II.

OP-376

Somatostatin Receptor-directed PET/CT: A key factor in diagnosis and treatment of tumour-induced Osteomalacia

M. Heinrich[1], *A. Kosmala*[1], *A. Dierks*[2], *F. Genest*[3], *S. Achtziger*[3], *P. Raab*[3], *A. K. Buck*[1], *C. Lapa*[2], *L. Seefried*[3], *K. Michalski*[1];
[1]*Universitätsklinikum Würzburg, Würzburg, GERMANY,* [2]*Universitätsklinikum Augsburg, Augsburg, GERMANY,* [3]*Universität Würzburg, Würzburg, GERMANY.*

Aim/Introduction: To evaluate the efficacy of somatostatin receptor (SSTR)-directed positron emission tomography/computed tomography (PET/CT) in localizing phosphaturic mesenchymal tumours (PMT) in patients with tumour-induced osteomalacia (TIO) and to explore relationships between imaging parameters and biochemical markers. ***Materials and Methods:*** This retrospective analysis included 20 patients with suspected TIO who underwent SSTR-directed PET/CT. PET/CT parameters and findings were analysed in combination with biochemical markers and clinical outcome. Patients with a delineable SSTR-positive tumour on PET underwent surgical resection, while those without a discernible tumour but persistent renal phosphate wasting were continued or initiated on medical treatment. Follow-up assessments included laboratory values and clinical examinations. ***Results:*** PMT were detected in 12 out of 20 patients (60 %) on PET and were subsequently resected. Phosphorus levels (0.56 mmol/l vs 0.84 mmol/l; U = 20.5; r = 0.26; p = 0.03), tubular reabsorption of phosphate (TRP; 62 % vs 87 %; U = 4; r = 0.77; p < 0.01) and tubular maximum of phosphate reabsorption over GFR (TmP/GFR; 0.58 mmol/l vs 0.87 mmol/l; U = 16.5; r = 0.44; p = 0.07) were lower in patients with detected PMT compared to those without. Fibroblast growth factor 23 (FGF23) elevation was not higher in PMT positive patients with 253 % vs 134 % above the upper limit of normal (ULN; U = 47; p = 0.97). Total lesion uptake (TLU) of the tumours showed a significant negative correlation with TmP/GFR (r = - 0.71; r = 0.02; p = 0.03). A maximum standardized uptake value (SUVmax) threshold of 7.6 differentiated PMT from bone fractures with 83 % sensitivity and 100 % specificity. All resected tumors showed histological expression of SSTR2. Post-resection follow-up confirmed clinical cure in all cases with improvements in phosphate levels, TmP/GFR and TRP, while FGF23 levels varied. ***Conclusion:*** Patients with a lower TmP/GFR show a higher TLU in SSTR-directed PET/CT for PMT. In SSTR-directed PET/CT, a clear distinction between PMT and bone fracture is possible with a SUVmax threshold of 7.6. The integration of PET derived TLU, along with TmP/GFR could improve diagnosis and treatment planning for TIO.

OP-377

'New Normal': Reporting Bone SPECT/CT scans reconstructed with a Bayesian Algorithm using Anatomical Information

H. McMeekin, *H. Mohan, A. Syed;*
Barts Health NHS Trust, London, UNITED KINGDOM.

Aim/Introduction: Anatomical information from a CT can be used in Bayesian SPECT reconstruction algorithms to reduce noise and increase resolution. The superior quantitative performance of these algorithms has been demonstrated (1); we investigated the impact of a Bayesian algorithm with an anatomically guided relative difference prior (AMAP-R) based on visual assessment for routine clinical reporting. ***Materials and Methods:*** 20 patient Tc-99m HDP bone SPECT/CT scans were independently reviewed by two experienced nuclear medicine consultants. A Bayesian SPECT reconstruction algorithm (AMAP-R) using anatomical prior information based on the patient's CT scan was optimised and implemented retrospectively using vendor neutral reconstruction software. CT attenuation correction, Monte-Carlo scatter correction, and resolution recovery were applied during the iterative reconstruction loop of 6 iterations and 15 subsets. After an initial optimisation study for visual assessment, the following parameters were used for the AMAP-R algorithm: Bayesian weight 0.1; RDP gamma 1; similar neighbours 8. The images were scored for image quality and diagnostic confidence compared to the current clinical reconstruction: the camera manufacturer OSEM algorithm with CT attenuation correction using 4 iterations, 8 subsets, and a 9mm Gaussian FWHM post-filter. Any change in clinical interpretation was noted and described. ***Results:*** Averaged results from both reviewers were: 75% had better image quality; 23% had higher diagnostic confidence; 18% clinical interpretation may change. Facet joint uptake was more clearly localised in some cases, and there was increased visibility of degenerative change. No scans were found to have worse image quality or lower diagnostic confidence. ***Conclusion:*** Bayesian SPECT reconstruction for bone SPECT/CT scans offers increased image quality and diagnostic confidence in some cases, as well as impacting clinical interpretation. The 'new normal' must be established for these images, which could offer increased sensitivity for identifying facet joints and other degenerative disease sites as possible pain generators. ***References:*** 1. Kangasmaa, T.S., Constable, C. & Sohlberg, A.O. Quantitative bone SPECT/CT reconstruction utilizing anatomical information. EJNMMI Phys 8, 2 (2021). https://doi.org/10.1186/s40658-020-00348-1

OP-378

Diagnostic Performance of 360° CZT-SPECT/CT Using [^{99m}Tc]Tc-HDP for Detecting Active Lumbar Inflammation in Degenerative Disc Disease: Correlation with MRI Findings

S. Peralta[1], *F. Mínguez*[1], *M. Romera*[1], *A. Basanta*[1], *M. Rodríguez-Fraile*[1], *V. Betech-Antar*[1], *F. Pareja*[1], *A. F. Hendy*[1], *G. Quincoces*[1], *R. Cuevas*[1], *A. Martínez*[1], *V. Rodrigo*[1], *N. Varela*[1], *E. F. Guillén*[2], *J. J. Rosales*[1], *J. Arbizu*[1];
[1]*Clinica Universidad de Navarra, Pamplona, SPAIN,* [2]*Clinica Universidad de Navarra, Madrid, SPAIN.*

Aim/Introduction: To evaluate the correlation between semiquantitative parameters of [99mTc]Tc-HDP 360° CZT-SPECT/CT (SPECT/CT) and active inflammatory changes on Magnetic Resonance Imaging (MRI) in patients with lumbar pain and degenerative disc disease. ***Materials and Methods:*** We included patients with lumbar pain who underwent SPECT/CT using a VERITON-CT version 300 (Spectrum Dynamics Medical) and MRI. SUVmax was measured by placing a rectangular Volume of Interest (VOI) that included the superior and inferior vertebral endplates from T12 to S1. Active inflammation was classified as present or absent based on MRI findings. Groups were compared using the Mann-Whitney U test. Optimal SUVmax cut-off values for detecting active inflammation were determined by ROC curve analysis. ***Results:*** A total of 61 patients (mean age: 60.9 ± 15.8 years; 55.7% female, 44.3% male) and 366 lumbar vertebral segments were analyzed. Active inflammation was identified on MRI in 41 segments from 26 patients (42.6%), while 325 segments from 35 patients showed no inflammatory changes. The most frequently affected spinal level was L5-S1, accounting for 13 out of 41 segments with inflammation (31.7%). Segments with active inflammation exhibited significantly higher SUVmax values, with a median of 9.0 (IQR: 7.4-11.2), compared to 6.4 (IQR: 5.0-7.4) in non-inflammatory segments ($p < 0.001$). An optimal SUVmax cut-off of 7.9 provided a sensitivity of 68.2%, specificity of 83.7%, positive predictive value (PPV) of 34.5%, negative predictive value (NPV) of 95.4%, and overall accuracy of 81.2% (AUC: 0.830; 95% CI: 0.758-0.902). ***Conclusion:*** Semiquantitative analysis of [99mTc]Tc-HDP using 360° CZT-SPECT/CT demonstrates good diagnostic performance in identifying active inflammatory changes in the lumbar spine of patients with degenerative disc disease. The high negative predictive value (95.4%) supports its use as a complementary imaging modality to rule out active inflammation when MRI is unavailable or contraindicated.

808

Monday, October 6, 2025, 9:45 - 11:15
Room 115

TROP Session - Thyroid Committee: An Overview on Nuclear Medicine Therapy of DTC Patients: Radioiodine and Beyond

OP-379

rTSH vs Endogenous Stimulation: Different Roads, Same Destination in Thyroid Cancer Treatment

S. Paiva*, S. Barata, I. Casimiro, D. Carvalho, J. Rebelo, G. Costa; ULS Coimbra, Coimbra, PORTUGAL.*

Aim/Introduction: Differentiated thyroid carcinoma (DTC) is the most common endocrine malignancy, with an excellent prognosis and 5-year survival rate. However, recurrence risk persists, particularly among intermediate and high-risk groups. Current guidelines recommend individualized strategies for postoperative radioiodine (RAI) therapy, with TSH stimulation achieved either by thyroid hormone withdrawal or recombinant human TSH (rTSH). The optimal stimulation method regarding disease control remains under investigation. This study aimed to compare disease recurrence rates (that required adicional RAI treatments) and progression-free survival (PFS) between stimulation methods in patients with no RAI uptake outside the thyroid bed in the whole-body post-RAI treatment scan. ***Materials and Methods:*** This retrospective cohort study included 315 patients with DTC who underwent total thyroidectomy followed by RAI therapy. Patients were stratified according to TSH stimulation: endogenous (n=163) or rTSH (n=152). Collected data included age, gender, histological type, AJCC/TNM staging and RAI activity. PFS was defined as time from RAI therapy to recurrence or last follow-up, with patients without recurrence censored at last contact. Statistical comparisons used the Chi-square test and Kaplan-Meier survival analysis with the log-rank test. Statistical analysis was performed using SPSS-Statistics v.30.0. $P<0.05$ were considered statistically significant. ***Results:*** There were no significant differences between the endogenous and rTSH groups regarding gender distribution (female 71.8% vs 76.3%, p=0.74), mean age at first RAI treatment (50.9 vs 53.6 years, p=0.07), histological type (papillary carcinoma 85.3% vs 85.5%, p=0.45), or AJCC staging (Stages I-II in 98.8% vs 97.4%, p=0.58). Recurrence that required additional RAI treatments, occurred in 11.7% of patients in the endogenous group and 11.8% in the rTSH group (p=0.934). Mean time to recurrence was 21.8 months (range: 4.4-98.1) for endogenous stimulation and 27.5 months (range: 2.6-79.2) for rTSH. Kaplan-Meier analysis showed no significant difference in PFS between groups (log-rank p=0.925). ***Conclusion:*** In this cohort, the method of TSH stimulation did not significantly influence recurrence rates or progression-free survival. These results support rTSH as an effective and safe alternative, particularly for patients with comorbidities, aligning with current recommendations for individualized management of DTC. ***References:*** Avram AM, Giovanella L, Greenspan B, et al. SNMMI Procedure Standard/EANM Practice Guideline for Nuclear Medicine Evaluation and Therapy of Differentiated Thyroid Cancer: Abbreviated Version. J Nucl Med. 2022;63(6):15N-35N.

OP-380

The total diameter impacts on the response to treatment of multifocal differentiated thyroid cancers

A. Campenni[1], *M. Martini*[2], *P. Petranovic Ovcaricek*[3], *R. M. Ruggeri*[4], *A. Nicocia*[5], *A. Alibrandi*[6], *F. Capoccetti*[7], *V. Zuccalà*[2], *F. Minutoli*[1], *G. Fadda*[2], *L. Giovanella*[8];
[1]*Department of Biomedical and Dental Sciences and Morpho-Functional Imaging, University of Messina, Messina, Italy; Unit of Nuclear Medicine, University Hospital "Gaetano Martino", Messina, Italy, Messina, ITALY,* [2]*Department of Human Pathology in Adult and Developmental Age "Gaetano Barresi", University of Messina, 98125 Messina, Italy, Messina, ITALY,* [3]*Department of Oncology and Nuclear Medicine, University Hospital Center Sestre Milosrdnice, Zagreb, CROATIA; School of Medicine, University of Zagreb, Zagreb, Croatia, Zagreb, CROATIA,* [4]*Endocrine Unit, Department of Human Pathology of Adulthood and Childhood DETEV, University Hospital "Gaetano Martino", Messina, Messina, ITALY,* [5]*Unit of Nuclear Medicine, University Hospital "Gaetano Martino", Messina, Italy, Messina, ITALY,* [6]*Unit of Statistical and Mathematical Sciences, Department of Economics, University of Messina, Messina, ITALY,* [7]*Nuclear Medicine Unit, Service Department Macerata Hospital, ASUR Marche AV3, 62100 Macerata, Macerata, ITALY,* [8]*Department of Nuclear Medicine, Gruppo Ospedaliero Moncucco SA, Clinica Moncucco, Via Soldino 10, Lugano, SWITZERLAND; Clinic for Nuclear Medicine, University Hospital of Zürich, Zürich, Switzerland, Lugano, SWITZERLAND.*

Aim/Introduction: In low-to-intermedite risk papillary thyroid cancer (PTC), multifocality is no longer considered "per sè" as an additional risk factor suggesting post-operative adjuvant iodine-131 administration. However, many studies showed a significantly different prognosis in patients with larger total diameters (i.e. obtained by summing the diameter of any single

foci). This study was prompted to evaluate if total diameter (sumD) should be taken into account to administrate radioiodine in PTC patients. ***Materials and Methods:*** The records of 115 multifocal PTC patients (mPTC) [F=83, M=32] affected by low-to-intermediate risk PTC were reviewed. All patients underwent (near)-total thyroidectomy followed by risk-adapted iodine-131 therapy (RIT). A post-therapy whole-body scan (pT-WBS) integrated with single photon emission tomography-computed tomography (SPECT/CT), was obtained in all cases 2-5 days after RIT. In all patients, the response to initial treatments was assessed 8 to 12 months after RIT according to 2015 American Thyroid Association (ATA) guidelines. Patients were monitored in a mean follow-up of 20.6 months. ***Results:*** In our cohort, the mean sumD size was 22.67±15.25 mm. In 24 out of all (20.9%) mPTC patients, loco-regional lymph node metastasis were ascertained by histopathological analysis (i.e., pN1). Interestingly, the mean sumD was larger in these patients compared with pN0 ones (23.9±4.4 mm vs 21.9±4.1mm, p= 0.043). Overall, 87 (75.6%) and 28 (24.4%) out of 115 patients presented an ER or a less than ER, respectively. Noteworthy, the sumD was larger in patients having a less than ER compared to patients with ER [27.1 mm±14.2 vs 21.3 mm±12.3, respectively (p=0.039)]. At receiver operating characteristic (ROC) analysis, the optimal sumD cutoff to predict a less than ER to initial treatments was set at 21.5 mm (AUC= 0.783). Accordingly, the overall sensitivity, specificity, accuracy, positive predictive value (PPV), and negative predictive value (NPV) were 96.43, 59.77, 68.70, 43.55, 98.11 respectively .The risk of having a less than ER is about 96.4% (27/28) higher in mPTC patients with a total mean size ≥21.5 mm than in other patients 40.2% (35/87) (OR=40.11; 95%C.I. 5.21-308.93). Interestingly, sumD overperformed gender, age, histological variant, pT-staging, lesions topography, and BRAF mutation in predicting less than ER. ***Conclusion:*** In low-to-intermediaterisk mPTC patients, the sumD significantly predicts the response to adjuvant treatment and we suggest to take it into account in postoperative decision making. In particular, a sumD≥21.5 mm identifies patients having a higher prevalence of residual lymph node metastasis after surgery with attached worse response to adjuvant therapy.

OP-381

Comparison of long-term survival with and without radioiodine therapy in low-risk differentiated thyroid cancer (ESTIMABL2-like): A SEER based analysis.

H. Weis[1], *K. Schmidt*[1], *M. Hellmich*[2], *J. Heilinger*[1], *A. Drzezga*[1], *M. Schmidt*[1];
[1]*Department of Nuclear Medicine, Faculty of Medicine and University Hospital of Cologne, Cologne, GERMANY,* [2]*Institute of Medical Statistics and Computational Biology, Faculty of Medicine and University Hospital of Cologne, Cologne, GERMANY.*

Aim/Introduction: In patients with low-risk differentiated thyroid cancer (DTC, i.e. papillary- and follicular thyroid cancer (PTC, FTC)) postsurgical radioiodine therapy (RAI) is matter of controversial debate. Long-term survival data are scarce and partially conflicting. A single prospective study showed that a treatment avoiding RAI was non-inferior compared to RAI for a composite of low-risk DTC patients, yet follow-up time was relatively short (<5 years) and FTC were underrepresented (only 3.1 % of patients (n=24)) [ESTIMABL2, (1,2)]. We analysed long-term relative survival (> 10 years) of low risk DTC patients based on the large Surveillance, Epidemiology, and End Results Program database (SEER). ***Materials and Methods:*** We retrospectively analysed survival relative to the proportion of expected survivors in a comparable set of cancer free individuals (relative survival, RS) as a robust measure of net survival. We compared survival with and without RAI in cohort of low risk DTC patients (pT1am, pT1b, N0, NX). 199,789 patients with thyroid cancer were identified from the year 2000 until 2021. Patients were subdivided based on histology (PTC and FTC) and TNM. Lymph node involvement (N1) was additionally analysed. Relative survival was compared for each subgroup with and without RAI by a specific z-test. Additionally, overall survival was analysed. ***Results:*** Relative survival was higher even in certain low-risk subgroups after RAI in case of a long enough follow-up time: For PTC without lymph node involvement no relevant difference between subgroups could be detected. In contrast, if lymph node involvement prevails, relative survival was higher in the RAI-group after a long follow-up time of ten years (2.6 % difference, p=0.023). For FTC, in an ESTIMABL2-like cohort, relative survival was significantly higher by 0.5 % with RAI after 5 years (p=0.029), which could not be detected after only three years (0.38 % difference, p=0.15). The relative survival benefit increased up to 4.4% after eleven years. In addition, overall survival was higher by 3.6% after five years, increasing up to 7.3% after 11 years. ***Conclusion:*** Subgroups of patients with low-risk differentiated thyroid cancer in an ESTIMABL2-like cohort have, depending on histology, a higher survival after RAI compared to patients not undergoing RAI during long term follow-up. ***References:*** [1] Leboulleux S et al., N Engl J Med. 2022;386:923. [2] Leboulleux S et al., Lancet Diabetes Endocrinol. 2025;13:38

OP-382

Development and Validation of a Dynamic Risk-Adaptive Algorithm for Radioactive Iodine (RAI) Dosimetry in Thyroid Cancer: Integrating Clinical Guidelines and Machine Learning

W. Song, *X. Zhang, M. Li, X. Lan;*
Union Hospital, Huazhong University of Science and Technology, Wuhan, CHINA.

Aim/Introduction: Radioactive iodine (RAI) therapy is critical for differentiated thyroid cancer (DTC) management, yet optimal dosing remains challenging, particularly for patients requiring multiple treatments. Current approaches often rely on static empirical protocols, neglecting dynamic risk stratification, individualized biomarker trends (e.g., Tg kinetics), and evolving guidelines (e.g., 2021 Chinese RAI Guidelines).To develop and validate a computational algorithm integrating real-time treatment response assessment, quantitative imaging biomarkers, and guideline-based clinical rules to optimize RAI dosing for both initial and repeat therapies. ***Materials and Methods:*** A hybrid model was constructed using retrospective data from 600 DTC patients, incorporating: XGBoost-based prediction of baseline dose using features including Tg slope, nodal metastasis ratio, and SPECT/CT-derived iodine avidity. Dose adjustments based on Guidelines (e.g., renal function limits, pediatric BSA scaling, lung metastasis fractionation). Bone marrow dose estimation (threshold ≤2 Gy) and dynamic TSH suppression targets. Validation was performed prospectively in 200 patients, comparing algorithm recommendations to expert panel decisions. ***Results:*** The algorithm demonstrated high concordance (92%) with guideline-recommended dosing ranges, evidenced by strong inter-rater reliability (κ=0.85). For patients requiring repeat therapies, the model reduced over-dosing instances (>200 mCi) by 40% compared to traditional protocols, while preserving equivalent biochemical response rates (Tg reduction ≥25% in 78% vs. 75%, p=0.32). Critically, safety outcomes improved significantly: real-time dose fractionation alerts reduced post-treatment bone marrow suppression from 18% to 6% (p<0.01), underscoring its capacity to balance efficacy with reduced hematologic toxicity. These results validate the algorithm's dual role in standardizing dose selection and enhancing patient safety in complex multi-therapy scenarios. ***Conclusion:*** This dynamic risk-adaptive algorithm enables precision RAI dosing by harmonizing guideline mandates, quantitative biomarkers, and patient-specific safety thresholds. It addresses critical gaps in managing multi-therapy patients and provides a scalable framework for integrating evolving evidence into clinical workflows. ***References:*** 1. Patterns of Use,

Efficacy, and Safety of Treatment Options for Patients with Graves' Disease: A Nationwide Population-Based Study[J].Thyroid: official journal of the American Thyroid Association.2020,30(3).357-364. DOI:10.1089/thy.2019.0132 .2. Stachura Albert,Gryn Tomasz,Kałuża Bernadetta, et al. Predictors of euthyreosis in hyperthyroid patients treated with radioiodine 131I–: a retrospective study[J].BMC Endocrine Disorders.2020,20(1).DOI:10.1186/s12902-020-00551-2 .

OP-383

Single-time-point Iodine-124 PET/CT imaging for patients with differentiated thyroid carcinoma to predict therapeutic efficacy

***M. Sadeghi Panah**, W. Jentzen, H. Hautzel, R. Görges, W. P. Fendler, K. Herrmann, I. Čiučiulkaitė, P. Fragoso Costa, D. Kersting; University Hospital, Essen, GERMANY.*

Aim/Introduction: A two-time-point ^{124}I-PET/CT lesion dosimetry protocol has been performed for years at our institution in selected DTC patients prior to planned radioiodine therapy (RIT). These scans were conducted approximately 24-h and 96-120-h after ^{124}I administration. The aim of this work was to utilise only the 24-h-time-point ^{124}I PET/CT data set to statistically predict therapeutic efficacy using standard activities. This simplified approach has advantages for patient comfort and logistics. ***Materials and Methods:*** Dosimetry data from 397 patients with 796 lesions were analysed retrospectively (2009 to 2023). The following lesion characteristics were recorded: (a) histology (papillary and follicular), (b) lesion type (residual thyroid tissue, lymph node metastases, lung metastases, bone metastases), (c) RIT for initial ablation or after completed first RIT, (d) predicted ^{131}I lesion absorbed doses (in Gy/GBq) derived from two-time-point ^{124}I dosimetry and (e) ^{124}I SUVmax. The lesions were then categorised into subgroups based on their histology, lesion type and therapeutic RIT state. Their ^{124}I 24-h SUVmax was correlated with the ^{131}I lesion absorbed dose estimated by the two-time-point ^{124}I dosimetry. Reaching established target absorbed doses (100 Gy for lymph node metastases, 85 Gy for lung metastases, 300 Gy for residual thyroid tissue and 350 for bone metastases) by using standard ^{131}I activities of 3.7 GBq, 7.4 GBq and 11.1 GBq was considered to be therapeutically effective. Spearman correlation coefficients (CC) and their confident intervals (CI) were determined for each subgroup. Histology was not considered for residual thyroid tissue. ***Results:*** A significant correlation of SUVmax with lesional absorbed dose was found for 4 subgroups: residual thyroid tissue (CC=0.93, n=214) and lymph node metastases in papillary DTC (CC= 0.93, n=182) before first RIT as well as residual thyroid tissue (CC=0.90, n= 36) and lymph node metastases in papillary DTC (CC=0.82, n= 67) after at least one RIT. For example, a 24h SUVmax >120 for thyroid remnant or >60 for lymph node metastases (papillary) and a planned activity of 3.7 GBq will achieve the target dose in 90% of the lesions. ***Conclusion:*** Single-time-point ^{124}I PET allows the prediction of therapeutic efficacy for selected subgroups. For lesions with low SUVmax the pretherapeutic dosimetry can be completed by performing the second PET imaging after 96-120-h.

OP-384

Optimized ^{131}I therapy of metastatic differentiated thyroid cancer with ^{124}I PET dosimetry: update of an ongoing phase II trial

***C. Chiesa**[1], G. Gorgoni[2], F. Rubino[1], L. Olivari[2], S. Mazzaglia[1], F. Severi[2], M. Kirienko[1], V. Fuoco[1], C. Ingraito[3], A. Alessi[1], A. Lorenzoni[1], L. De Cecco[1], K. Massri[4], L. Dellavedova[4], A. Muni[5], E. Pomposelli[5], M. Rodari[6], M. Rubino[7], F. Zerbini[8], R. Maggiore[9], A. Chiti[10,9], L. Grappeja[11], B. Parducci[12], E. Mesiani[12], E. Seregni[1], M. Salgarello[2], M. Maccauro[1];*
[1]Foundation IRCCS Istituto Nazionale Tumori, Milano, ITALY, [2]IRCCS Sacro Cuore Don Calabria, Negrar, ITALY, [3]Specialization School for Medical Physics, University of Milan, Milano, ITALY, [4]Hospital of Legnano, Legnano, ITALY, [5]Azienda Ospedaliera Nazionale SS. Antonio e Biagio e Cesare Arrigo, Alessandria, ITALY, [6]Humanitas Clinical Institute, Rozzano, ITALY, [7]European Institute for Oncology, Milano, ITALY, [8]Policlinico di Monza, Monza, ITALY, [9]IRCCS Ospedale San Raffaele, Milano, ITALY, [10]Faculty of Medicine and Surgery, Vita-Salute San Raffaele University, Milano, ITALY, [11]Specialization school in Nuclear Medicine, University of Milan, Milano, ITALY, [12]Specialization School in Nuclear Medicine, University of Milan, Milano, ITALY.

Aim/Introduction: This prospective study aims at demonstrating that the first treatment with ^{131}I of metastatic differentiated thyroid cancer (MDTC), optimized with dosimetric treatment planning with ^{124}I, provides an objective response rate on soft tissue metastases at 6 months higher than the fixed activity administration schema. ***Materials and Methods:*** Patients are enrolled if they have known DTC metastases to soft tissues, if they were not treated in the previous 5 years, except with surgery or radiotherapy. They are prepared with hormone withdrawal both for treatment planning and therapy. Oral administration of liquid ^{124}I (100 MBq) is followed by blood sampling and whole body counting at 2, 6, 24, 96 h. PET scans are taken at 24 and 96 h. Lesion post-therapy dosimetry is performed on dead time corrected SPECT/CT taken at 24 and 96 h. A composite response is assessed with ^{18}F-FDG-PET, contrast-enhanced CT/MRI, ^{124}I PET and thyroglobulin level, 6 months after one or two optimized treatments. ***Results:*** We studied 28 patients with ^{124}I. Eleven (39%) were dropped out for absence of ^{124}I uptake by metastases. Seventeen patients received 26 optimised treatments with median 11 GBq, IQR 8-13.5 GBq, range 4-20 GBq. In 10/26 (38%) administrations, the limit of 2 Gy to blood prevented us to administer more than our standard activity for MDTC (8 GBq). In 14/26 (54%) treatments, we administered almost the maximum tolerable activity. Treatment planning modified our standard activity in 22/26 treatments (85%). Three females over 70 exhibited G2/G3 haematological toxicity. Moderate sialadenitis was reported by 5 patients. Among 8 patients who reached the end of the study, we had 3 CR (one with a massive skull metastases), 4 PR and 1 PD. ***Conclusion:*** ^{124}I PET showed extraordinary diagnostic sensitivity, higher than post-therapy ^{131}I SPECT/CT. This was essential for a perfect staging before the first treatment. Known the high threshold necessary to reach CR with bone metastases (350-650 Gy [1]), a correct staging allowed to plan the maximal tolerable activity in presence of bone lesions. Lesion dosimetry was less impacting than blood dosimetry, since intra-patient heterogeneity, their number and their undetectability on CT made global prediction of absorbed dose unfeasible in many cases. This fact remarks the clinical usefulness with bone lesions in MDTC of maximization based on pre-treatment blood dosimetry with ^{131}I, feasible even in absence of ^{124}I. The study is funded by the AIRC Foundation. ***References:*** [1] Jentzen et al J Nucl Med. 2016 Oct;57(10):1499-1504

OP-385

Redifferentiation of Radioiodine-Refractory Thyroid Cancer following Genotype-Guided MAPK/BRAF Inhibition

***C. Laschinsky**[1], M. M. Weber[2], B. Riemann[3], T. Brandenburg[1], D. Führer-Sakel[1], D. Gröner[4], M. C. Kreissl[5], F. Weber[1], K. Herrmann[1], W. Jentzen[1], H. Grafe[1], C. Rischpler[6], S. Theurer[1], A. Bockisch[1], J. Nagarajah[7], W. P. Fendler[1], D. Kersting[1];*
[1]Universitätsklinikum Essen, Essen, GERMANY, [2]Medizin Center Bonn, Bonn, GERMANY, [3]Universitätsklinikum Münster, Münster, GERMANY, [4]Universitätsklinikum Frankfurt, Frankfurt, GERMANY, [5]Universitätsklinikum Magdeburg, Magdeburg, GERMANY, [6]Universitätsklinikum Stuttgart, Stuttgart, GERMANY, [7]Röntgeninstitut, Düsseldorf, GERMANY.

Aim/Introduction: In patients with BRAF-wild type (BRAF-WT) radioiodine-refractory thyroid cancer, inhibition of the mitogen-activated protein kinase (MAPK) pathway using a mitogen-

activated protein kinase (MEK) inhibitor can restore iodine uptake. In contrast, patients with BRAFV600E mutations typically require specific BRAF inhibition to achieve similar effects. This report presents the final analysis of the ERRITI trial's primary endpoint—redifferentiation rate—for a genotype-guided MAPK modulation strategy: trametinib (a MEK inhibitor) for BRAF-WT patients and a combination of trametinib with dabrafenib (a BRAF inhibitor) for BRAFV600E patients. Additional outcomes related to clinical redifferentiation outside the study and survival are also described. ***Materials and Methods:*** ERRITI was a prospective, interventional, single-center, two-arm phase II trial (NCT04619316) including 29 patients with radioiodine-refractory thyroid cancer. Patients received redifferentiation therapy for at least 21 ± 3 days. Additionally, outcomes from seven patients treated with comparable clinical protocols outside the trial were included. The primary endpoint was the redifferentiation rate, evaluated via ^{123}I scintigraphy and ^{124}I PET imaging. Redifferentiation rates between BRAF-WT and BRAFV600E groups were compared using the X2 test. Patients demonstrating restored radioiodine uptake underwent dosimetry-guided high-activity ^{131}I therapy. Time to treatment failure (TTF) was defined from the start of redifferentiation therapy to disease progression, initiation of new therapy, or death. Cox regression analysis was used to assess the associations of redifferentiation success and BRAF status with TTF and overall survival (OS), reporting hazard ratios (HR) with 95% confidence intervals (CI). Adverse events (AEs) were reported from trial participants who underwent active AE monitoring. ***Results:*** Redifferentiation was successful in 16/36 patients (44.4%), with similar rates for BRAF-WT (42.9%) vs. BRAFV600E (46.7%) groups (p=1.0). Among ERRITI trial participants, 11/29 (37.9%) achieved redifferentiation. Radioiodine therapy was administered at a mean activity of 10.1 GBq. AEs occurred in 22/29 patients (75.9%), only 3 grade 3/4, all resolved completely. Patients with successful redifferentiation had significantly longer TTF (median: 19.4 months vs. 12.8 months, HR: 0.42, 95%-CI: 0.179-0.997, p=0.049), while OS did not differ significantly (median: 57.9 months vs. not reached, HR: 2.39, 95%-CI: 0.672-8.499, p=0.178). Similarly, no significant differences in TTF or OS were observed between BRAF-WT and BRAFV600E patients. ***Conclusion:*** Genotype-guided MAPK modulation achieved redifferentiation in nearly half of patients, with comparable efficacy in BRAF-WT and BRAFV600E subgroups. Redifferentiation in combination with radioiodine therapy was associated with prolonged TTF, supporting its potential in managing radioiodine-refractory thyroid cancer. ***References:*** doi: 10.1158/1078-0432.CCR-22-0437

OP-386

From Resistance to Response: BRAF/MEK Inhibition Revives RAI Uptake in RAIR-DTC

M. Demirkol[1], *G. Kaya*[2], *H. Seymen*[3], *F. Alagöl*[3], *F. Selçukbiricik*[3];
[1]*Amerikan Hospital, Istanbul, TÜRKIYE,* [2]*Republic of Turkiye, Ministry of Health, Yozgat State Hospital, Nuclear Medicine Dept., Yozgat, TÜRKIYE,* [3]*Koc University Hospital, Istanbul, TÜRKIYE.*

Aim/Introduction: Differentiated thyroid cancer (DTC) is commonly diagnosed early, but some patients develop metastatic disease. Locoregional metastases are surgically treated, while distant ones, especially to lung and bone, often require radioactive iodine (RAI) therapy. A subset develops RAI-refractory (RAIR) disease, where lesions fail to uptake iodine. Interestingly, redifferentiation with targeted agents like BRAF and MEK inhibitors may restore RAI avidity, but optimal management remains unclear. ***Materials and Methods:*** We retrospectively analyzed patients with metastatic papillary or follicular thyroid carcinoma treated at Koç University (2018-2025). Inclusion required prior RAI post-thyroidectomy and RAIR disease, defined by lack or loss of RAI uptake, progressive lesions, rising thyroglobulin (Tg), or FDG uptake. Imaging included whole-body scintigraphy, [^{18}F]FDG PET/CT, and CT/MRI. Patients received trametinib alone or with dabrafenib/vemurafenib for 4-6 weeks. RAI therapy followed redifferentiation. Uptake and dosimetry were evaluated with standard software. Tg trends, imaging, and response (RECIST 1.1) were assessed. Toxicity was graded by CTCAE v5. ***Results:*** Nine patients (2 male, 7 female; median age >55 in 66%) were analyzed. Most (66%) had classical papillary DTC; 77% had BRAF mutations. Combination redifferentiation was used in all BRAF-mutant cases. After a median 6-week therapy, 88% showed restored RAI uptake and received RAI (5.5-9.1 GBq). Median follow-up was 27 months. Post-RAI, 75% achieved partial response, 12.5% had stable disease, and 12.5% progressed. No grade ≥3 toxicity occurred. ***Conclusion:*** Redifferentiation, particularly in BRAF-mutant RAIR-DTC, can re-enable effective RAI therapy, with most patients showing clinical benefit. Restoration of iodine uptake is necessary but not always predictive of response. Even without major tumor shrinkage, redifferentiation revealed occult disease, aiding treatment planning. Anti-Tg interference was clarified in 3 patients. Therapy was well tolerated, even in older patients. Future directions include optimizing redifferentiation duration, integrating genomic profiling, and leveraging personalized dosimetry to enhance outcomes. Redifferentiation using BRAF/MEK inhibitors is safe and effective in selected RAIR-DTC patients, enabling RAI therapy and meaningful responses. Personalized approaches based on tumor biology are essential to advance care.

OP-387

First-in-Human SPECT/CT Imaging and Dosimetry of [^{211}At]NaAt in Refractory Thyroid Cancer in Alpha-T1 Trial

T. Watabe[1], *H. Sasaki*[2], *T. Kamiya*[2], *K. Mukai*[1], *S. Naka*[2], *A. Fukuhara*[1], *Y. Shirakami*[1], *K. Ooe*[1], *H. Haba*[3], *A. Toyoshima*[1], *K. Isohashi*[1], *I. Shimomura*[1], *N. Tomiyama*[1];
[1]*The University of Osaka, Suita, JAPAN,* [2]*The University of Osaka Hospital, Suita, JAPAN,* [3]*RIKEN, Wako, JAPAN.*

Aim/Introduction: Radioactive iodine (RAI) therapy with ^{131}I has long been used to treat patients with differentiated thyroid cancer. However, some patients develop resistance to repeated RAI therapy, even in regions with adequate iodine uptake. Astatine (^{211}At), a cyclotron-produced alpha emitter, has garnered attention as a novel NIS-targeted alpha therapeutic agent. In this first-in-human clinical trial (Alpha-T1 trial), we aimed to evaluate dosimetry of [^{211}At]NaAt using SPECT/CT imaging in patients with RAI-refractory thyroid cancer. ***Materials and Methods:*** Patients with metastatic differentiated thyroid cancer who had received at least three prior RAI treatments were enrolled (n = 11). A single intravenous administration of [^{211}At]NaAt was performed under recombinant human TSH (rhTSH) stimulation. Dose escalation followed a modified 3+3 design, with dose levels of 1.25 MBq/kg (n=2), 2.5 MBq/kg (n=3), and 3.5 MBq/kg (n=6). SPECT/CT imaging was conducted at 1, 3, and 24 hours post-administration using the VERITON-CT system (Spectrum Dynamics Medical) equipped with a full-ring cadmium zinc telluride detector, targeting the 79 keV X-rays emitted by the daughter nuclide ^{211}Po. Regions of interest were manually delineated in major organs using PMOD software, and residence times were derived from time-activity curves using the trapezoidal integration method. Absorbed doses were estimated using IDAC-Dose 2.1. Adverse events were evaluated according to CTCAE v5.0 criteria. ***Results:*** At 3 hours post-administration, physiological uptake was observed in the stomach (SUVmean = 3.47 ± 1.35) and bladder (3.62 ± 0.68), followed by the spleen (2.70 ± 0.51) and salivary glands (2.21 ± 0.66). Relatively high absorbed doses were recorded in the stomach (2.75 ± 1.46 mGy/MBq) and salivary glands (1.96 ± 0.80 mGy/MBq), while the red bone marrow received 0.57 ± 0.15 mGy/MBq. Dose-limiting toxicity (grade 3 lymphopenia or leukopenia persisting for more than one week) was observed at the 3.5 MBq/kg dose level (50%). The common adverse events were anemia (Grade 1: 55%), leukopenia

(Grade 2: 27%, Grade 3: 36%), thrombocytopenia (Grade 1: 18%), salivary gland swelling (grade 1: 9%, grade 2: 64%), xerostomia (grade 1: 36%, grade 2: 18%), and gastrointestinal symptoms such as nausea (grade 1: 9%, grade 2: 82%), anorexia (grade 2: 27%), and vomiting (grade 2: 36%). ***Conclusion:*** This study demonstrates the feasibility of performing dosimetry for targeted alpha therapy with [^{211}At]NaAt in patients with RAI-refractory thyroid cancer. Similar to ^{131}I and ^{177}Lu, ^{211}At enables SPECT imaging, making it a promising for predicting treatment-related toxicities during dose escalation and assessing therapeutic efficacy. ***References:*** NCT05275946

809

Monday, October 6, 2025, 9:45 - 11:15
Room 133+134

e-Poster Presentations Session 6 - Neuroimaging Committee: Neuroimaging e-Posters

EPS-115
Alzheimer's Disease Detection Using FDG-PET and Clinical Data with a 3D CNN and Grad-CAM Visualization

Z. Tekgul[1], *E. Balci*[2], *O. Akdemir*[2], *S. Sagiroglu*[1], *L. Atay*[2];
[1]*Gazi University Faculty of Engineering, Department Of Computer Engineering, Ankara, TÜRKIYE,* [2]*Gazi University Medical Faculty, Department of Nuclear Medicine, Ankara, TÜRKIYE.*

Aim/Introduction: Early and accurate detection of Alzheimer's disease (AD) is critical for timely intervention and patient care. We propose a 3D convolutional neural network (3D CNN) that integrates full volumetric FDG-PET scans with demographic and clinical variables to classify amyloid PET positivity. Our dataset comprises 212 subjects from ADNI, including age, sex, APOE genotype, and MMSE scores, which are concatenated with imaging features to improve both accuracy and explainability. ***Materials and Methods:*** Data from patients with mild cognitive impairment obtained from the ADNI dataset confirmed by 2 experienced nuclear medicine experts were used and 10 Fold Cross Correlations were applied in training. The created 3D CNN models have 3x3D-Conv layers, each followed by Max Pooling and Batch Normalization. After them, 1xAverage Pooling layer exists. Demographic information is given into a Dense layer. The output of the convolution layers and demographic data were combined and passed through 3xDense and 2xDropout layers. Adam Optimizer and Cross Entropy were used as error function in model optimization. 3D Grad-CAM was used as XAI method to make the decision-making process of the models interpretable. ***Results:*** Two models were trained with 212 and 159 patient data because of imbalance data among classes. Two models showed promising results in predicting amyloid PET positivity by achieving 80.66% and 96.86% Accuracy and 85.20% and 97.58% F1 Scores, respectively. The model having more balanced data achieves the task with high accuracy. Additionally, the trained models, unlike traditional 2D slice-based models, process full volumetric data, thus preserving spatial continuity and eliminating possible information loss in the third dimension. As a result of the visualization obtained with Grad-CAM in both 2D slice and full 3D volumetric format, the brain features that provide the most important contribution to the model estimation were successfully determined and insights were provided regarding the neurobiological patterns associated with amyloid positivity. ***Conclusion:*** Combining full-volume PET with clinical data in a 3D CNN substantially enhances classification performance and provides transparent, regional insights via explainable AI. This framework may support earlier, more reliable detection of amyloid pathology and deepen understanding of underlying neurobiological patterns.

EPS-117
Robustness of the Centiloid Scale Against Different Reconstructions and Reference Regions

K. Hirschmüller[1], *E. Prieto*[1], *F. Mínguez*[1], *R. Fahmi*[2], *E. F. Guillen*[3], *R. Cuevas*[1], *A. Martínez*[1], *B. Echeveste*[1], *M. Riverol*[1], *J. Arbizu*[1];
[1]*Clínica Universidad de Navarra, Pamplona, SPAIN,* [2]*Siemens Healthineers, Knoxville, TN, UNITED STATES OF AMERICA,* [3]*Clínica Universidad de Navarra, Madrid, SPAIN.*

Aim/Introduction: Centiloid (CL) scale is a standardised metric for quantifying amyloid-PET acquired with different tracers. The aim of this study was to test the impact of different technical factors on the calculated CL values. ***Materials and Methods:*** Sixty-eight (N=68) amyloid PET images acquired at our institution were retrospectively reviewed. Two different tracers were included: 16 ^{18}F-florbetaben (FBB) and 52 ^{18}F-flutemetamol (FMM) datasets. Images were processed using a commercially available solution to calculate Centiloid. Four different options were considered for each tracer, including two different reconstructions (Rec1: OSEM3D, 3i21s, with TOF and 5 mm Gaussian filter, and Rec2: OSEM3D, 3i21s, with PSF+TOF and 2mm Gaussian filter) and two different reference regions (RR) (pons and whole cerebellum (WCb) for FMM, and the cerebellar grey matter (GMCb) and WCb for FBB). Statistical analyses were performed to evaluate the impact of the reconstruction and the choice of RR on the calculated CL values. Bland-Altman plots, Lin's concordance correlation coefficient (CCC) and Wilcoxon tests were used. ***Results:*** When WCb was used as RR, concordance between CL values corresponding to the two considered reconstructions was almost perfect, with CCC > 0.99 and with 95% limits of agreement (LoA) within ±10 CL. However, this was not the case when the pons (for FMM) and the GMCb (for FMM) were used as RRs with 0.95 < CCC < 0.99 and with 95% LoA reaching ± 20 CL. Concordance between pons- and WCb-derived CLs was poor for FMM, with mean differences of 16.2 CL for Rec1 and 24.4 CL for Rec2. However, the concordance between FBB CL values obtained with GMCb and those obtained with WCb was much higher and with much lower mean differences (i.e., -7.6 CL for Rec1 and -2.1 CL for Rec2). ***Conclusion:*** The CL metric is more robust against differences in reconstruction when the WCb is used as RR. CL derived from FMM images using the pons as RR show the highest sensitivity to image resolution. Significant differences were obtained between CL values calculated with pons and WCb for our FMM cohort, and more so with PSF reconstruction.

EPS-118
Glymphatic system dysfunction and retinal vascular changes in Alzheimer's disease

Z. Chen[1], *S. Yan*[1], *S. Bi*[1], *Z. Qi*[1], *B. Cui*[1], *N. Li*[2], *Y. Hu*[3], *J. Lu*[1];
[1]*Department of Radiology & Nuclear Medicine, Xuanwu Hospital, Capital Medical University, Beijing, CHINA,* [2]*Beijing United Imaging Intelligence Imaging Technology Research Institute, Beijing, CHINA,* [3]*United Imaging Healthcare, Shanghai, CHINA.*

Aim/Introduction: This study investigated the mediating role of glymphatic system dysfunction in the relationship between retinal vascular alterations and cognitive impairment in Alzheimer's disease (AD). By integrating multimodal neuroimaging and retinal assessments, we explored the eye-brain axis as a non-invasive biomarker for early AD detection. ***Materials and Methods:*** Thirty-one AD patients and 24 healthy controls (HC) underwent 3D T1-weighted imaging (3D T1WI), diffusion tensor imaging (DTI), and retinal fundus photography. Glymphatic metrics included hippocampus_perivascular space (Hip_PVS), basal ganglia_PVS, white matter_PVS, free water and diffusion tensor image analysis along the perivascular space (DTI-ALPS) index, and. Retinal vascular parameters (RVPs) comprised fractal dimension (FD) and vascular density (VD), mean arterial caliber, and mean venous caliber. Using the minimum bounding circle of the optic disc as the diameter (papilla-diameter, PD), VD (total, 0.5-1.0 PD, 1.0-1.5 PD, 1.5-2.0 PD,

2.0-2.5 PD) was calculated, as well as for mean arterial caliber and mean venous caliber. Statistical analyses included group comparisons, spearman correlations, mediation analysis. Bagged Trees models were trained to distinguish AD patients from HC, and area under the curve (AUC) of receiver operating characteristic (ROC) was performed to evaluate classification performance. Covariates included age, gender, education, hypertension, diabetes, hyperlipidemia. Multiple comparisons correction was performed using the false discovery rate (FDR). ***Results:*** AD patients exhibited elevated Hip_PVS ($P_{FDR} < 0.001$), reduced DTI-ALPS index ($P_{FDR} = 0.008$), and higher free water ($P_{FDR} < 0.001$) compared to HC. FD, VD (total), VD (0.5-1.0 PD), and VD (1.0-1.5 PD) were significantly lower in AD (all $P_{FDR} < 0.05$) and correlated with Hip_PVS (r = -0.353 to -0.434, $P_{FDR} < 0.05$). Mini-Mental State Examination (MMSE) score showed negative correlation with Hip_PVS (r = -0.647, $P_{FDR} < 0.001$), while positively correlating with FD, VD (total), VD (0.5-1.0 PD), and VD (1.0-1.5 PD) (r = 0.306 to 0.410, $P_{FDR} < 0.05$). Mediation analysis revealed that Hip_PVS mediated the effects of FD, VD (total), VD (0.5-1.0 PD), and VD (1.0-1.5 PD) on MMSE score with indirect effect ranging from 27.580 to 123.584. The retinal combination model, incorporating FD, VD (total), VD (0.5-1.0 PD), and VD (1.0-1.5 PD), achieved AUC of 0.768 for distinguishing AD from HC, and the retinal combination + Hip_PVS model yielded higher AUC of 0.877. ***Conclusion:*** Hip_PVS-mediated glymphatic dysfunction bridges retinal vascular changes and cognitive decline in AD. Integrating retinal and glymphatic biomarkers enhances diagnostic performance, underscoring the retina as a non-invasive window for early AD detection.

EPS-119

Multi-site, prospective trial of FET-PET In Glioblastoma (FIG) Study (TROG 18.06):Results of central review of FET-PET biologic target volume delineation for radiation planning.

A. Scott[1], *R. Francis*[2], *S. Lee*[1], *E. Lau*[3], *E. Thomas*[2], *A. Moore*[4], *D. Pattison*[5], *T. Akhurst*[6], *E. Hsiao*[7], *G. Schembri*[7], *P. Lin*[8], *I. Kirkwood*[9], *D. Krishna*[10], *S. Ngai*[11], *S. Beuzeville*[12], *D. Wong*[13], *N. Barry*[14], *M. Ebert*[2], *H. Gan*[1], *S. Ng*[1], *M. Pinkham*[11], *D. Bailey*[7], *E. Koh*[15];
[1]*ONJCRI and Austin Health, Heidelberg, AUSTRALIA,* [2]*Sir Charles Gairdiner Hospital, Perth, AUSTRALIA,* [3]*Austin Health, Heidelberg, AUSTRALIA,* [4]*TROG, Newcastle, AUSTRALIA,* [5]*Royal Brisbane and Womens Hospital, Brisbane, AUSTRALIA,* [6]*Peter MacCallum Cancer Centre, Melbourne, AUSTRALIA,* [7]*Royal North Shore Hospital, St Leonards, AUSTRALIA,* [8]*Liverpool Hospital, Sydney, AUSTRALIA,* [9]*Royal Adelaide Hospital, Adelaide, AUSTRALIA,* [10]*Canberra Hospital, Canberra, AUSTRALIA,* [11]*Princess Alexandra Hospital, Brisbane, AUSTRALIA,* [12]*St George Hospital, Sydney, AUSTRALIA,* [13]*Wesley Hospital, Brisbane, AUSTRALIA,* [14]*University of Western Australia, Perth, AUSTRALIA,* [15]*Liverpool Hospital, Liverpool, AUSTRALIA.*

Aim/Introduction: To update regarding the prospective multi-site trial evaluating O-(2-[^{18}F]-fluoroethyl)-L-tyrosine Positron Emission Tomography (FET-PET) in Glioblastoma (FIG) study, and to report the impact of central Nuclear Medicine physician (NMP) review of prospective FET-PET1 delineation of the biological target volume (BTV) for radiotherapy (RT) planning. ***Materials and Methods:*** Adult GBM participants across 11 Australian sites undergo FET-PET post-surgery/pre-chemo-RT [CRT] (FET-PET1), one month post CRT (FET-PET2) and at suspected progression vs pseudoprogression evaluation timepoint (FET-PET3). Group 1 participants enter at timepoint 1 (FET-PET1 with MRI1), with Group 2 at timepoint 2. Adjuvant RT target volumes are derived per standard contrast MRI, with hybrid post-hoc RT volumes then incorporating the FET-PET1 NM-derived BTV utilising MiM version 7.0 to evaluate the impact of FET PET on potential treatment planning. All trial sites and NMP have passed credentialling which included three benchmarking cases involving FET1-BTV delineation. ***Results:*** Recruitment commenced in January 2021, with 247 (n=156 Group 1 and n=91 Group 2) participants enrolled to date with n=143 evaluable Group 1 data. Trial credentialling demonstrated variations in FET-PET1-derived BTV in 25/72 (34.7%)-13 minor and 12 major. Currently, 121/143 participant FET-PET1 with BTV delineation cases across 11 sites have undergone central NMP review, with 18/121 (14.9%) requiring resubmission. Reasons for resubmission/protocol deviation included incorrect imaging sequence selection within MiM workflow (n=3), static GTV overcontouring (n=12), dynamic volume of interest change in size/position during workflow (n=1) and static FET interpretation issues (n=2). ***Conclusion:*** This trial has demonstrated the importance of credentialling and central review of prospective FET-PET-derived BTV delineation in ensuring protocol adherence. The FIG study is the largest prospective multi-site study of its kind addressing FET-PET's impact on radiation planning and in management of pseudoprogression and prognostication. Analysis of trial FET-PET BTV data is continuing, as is recruitment for evaluable patients to address progression vs pseudoprogression post CRT.

EPS-120

Metabolic activity of proton radiation therapy related effects in gliomas measured with [18F]FET PET imaging

K. Madsen[1], *A. Muhic*[2,3], *J. Skjøth-Rasmussen*[4], *J. Carlsen*[5], *D. Scheie*[6], *I. Law*[1], *O. Henriksen*[1];
[1]*Department of Clinical Physiology, Nuclear Medicine and PET, Copenhagen University Hospital Rigshospitalet, Copenhagen, DENMARK,* [2]*Department of Oncology, Copenhagen University Hospital Rigshospitalet, Copenhagen, DENMARK,* [3]*Danish Centre for Particle Therapy, Aarhus University Hospital, Aarhus, DENMARK,* [4]*Department of Neurosurgery, Copenhagen University Hospital Rigshospitalet, Copenhagen, DENMARK,* [5]*Department of Radiology, Copenhagen University Hospital Rigshospitalet, Copenhagen, DENMARK,* [6]*Department of Pathology, Copenhagen University Hospital Rigshospitalet, Copenhagen, DENMARK.*

Aim/Introduction: Proton radiation therapy (PRT) has since 2019 become a treatment option alongside photon therapy in Denmark. PRT reduces doses to normal brain structures and for gliomas PRT has been considered in oligodendroglioma WHO grade 2-3 (O2-3) and astrocytoma IDH mutated WHO grade 2-4 (A2-4). Concerns have been raised regarding the frequency of proton treatment-related effects (PTRE). We previously found the metabolic activity measured by [18F]FET PET imaging separates tumor relapse from PTRE at an early stage with an optimal TBRmax cut-off at 2.2. The aim of this study is to characterize the time course of metabolic activity within PRTE lesions verified by histopathology. ***Materials and Methods:*** Forty-nine patients (mean age 41 years range 23-65) from Rigshospitalet, Copenhagen, Denmark suffering from glioma were treated with PRT at the Danish Centre for Particle Therapy until October 2022 and followed for minimum 2.5 years until March 2025. At regular follow-up MRI new contrast enhancing lesions were found in 29 patients of which eight patients fulfilled the inclusion criteria for the study, i.e. [18F]FET PET imaging and biopsy showing only PTRE (initial pathology O3 n=5, A3 n=2 A4 n=1). Patients were subsequently followed with regular MRI and median four [18F]FET PET scans (range 1-8). ***Results:*** Regarding the eight included patients PTRE emerged at MRI median 10 months after PRT (range 7-24), and all but one subsequently developed multiple lesions during the follow-up period. The TBRmax peaked at a median of 11 months (range 0-22) after PTRE emerged at MRI. Regarding the majority of lesions TBRmax remained below the cut-off at 2.2, however, three patients each developed one lesion with higher intensity, with a peak TBRmax at 2.5-3.5. ***Conclusion:*** Our study indicates that PTRE may emerge relatively late after PRT and might also have a prolonged course. The metabolic activity of PTRE lesions usually stays below 2,2 but lesions may develop higher metabolic intensity. However, our study only included patients where biopsy was required, which might select the most severe cases.

EPS-121

[18F]FDOPA PET/MRI in Brain Metastases: Effect of Immunotherapy in Detecting Tumor Relapse

M. Suárez-Piñera[1], *C. Cases Pellise*[2], *C. Salomón*[3], *N. Vilariño Quintela*[4], *R. Velasco Fargas*[5], *M. Pudis*[1], *L. Rodriguez-Bel*[1], *B. Hervás Sanz*[1], *M. Cortés-Romera*[1];
[1]*Hospital Universitario de Bellvitge. (Nuclear-Medicine Department), Barcelona, SPAIN,* [2]*Department of Nuclear Medicine. Hospital Universitario Virgen del Rocio, Sevilla, SPAIN,* [3]*Department of Nuclear Medicine. Hospital Universitario Son Espases, Palma. Islas Baleares, SPAIN,* [4]*Medical Oncology Department, Catalan Insitute of Oncology, L' Hospitalet, Barcelona, SPAIN,* [5]*Department of Neurology, Institut Català d'Oncologia (ICO)-Hospital Universitari de Bellvitge, Barcelona, SPAIN.*

Aim/Introduction: To assess the possible effect of concurrent immunotherapy with immune check point inhibitors (ICIs) on 18F-FDOPA PET/MRI imaging, in patients with brain metastases (BM) treated and suspected of tumor relapse (TR) versus treatment related changes (TRC). ***Materials and Methods:*** A retrospective analysis was performed on 37 ^{18}F-FDOPA PET/MRI (FDOPA-PET) scans from 37 patients (including 53 BM), from different primary tumors. Patients had received surgery combined with hypofractionated stereotactic radiation therapy or radiosurgery alone. A subset of patients had received, immunotherapy using ICI. Images were analyzed visually and quantitatively. Semiquantitative evaluation included measurement of SUVmax and lesion-to-striatum (L/S) and lesion-to-cortex (L/C) SUVmax ratios. Patients were categorized based on whether they were undergoing ICI at the time of imaging. Lesion etiology for TR vs TRC interpretation was determined through clinical-radiological follow-up (at least 6 months) and/or histopathology. Statistical analysis was performed using non-parametric tests (Mann Whitney test) to compare differences between groups (immunotherapy vs. no immunotherapy). ***Results:*** The most common primary malignancy was lung adenocarcinoma (23/37, 62.%), followed by breast cancer (6/37), renal cancer (3/37), melanoma (2/37), small cell lung cancer (1/37), pulmonary neuroendocrine tumor (1/37) and colon neuroendocrine tumor (1/37). At the time of the PET/MRI 17/37 (46%) of patients (23 lesions) were receiving ICIs. Among the 53 analyzed lesions, 22 were finally considered as TR. A mean L/S of 1.12vs0.92 and L/C of 2.00vs1.67 differentiated TR from TRC in no ICI patients. A mean L/S of 1.24vs0.90 and L/C of 2.02vs1.41 differentiated TR from TRC in patients on ICI. No statistically significant differences ($p > 0.05$) between the two groups were observed regardless of lesion classification. However, both visual and semiquantitative analysis showed an overall trend towards higher uptake in patients undergoing ICI with higher SUVmax values and L/S ratios, this difference was even more pronounced in PET/MRI-positive cases both in SUVmax (U=53.0, p=0.118) and L/E ratio (U=64.0, p=0.316). The results of lower L/C ratio in patients receiving immunotherapy in PET/MRI-negative lesions this could be related to the increased cortical uptake under the influence of ICIs. ***Conclusion:*** Despite slightly higher FDOPA-PET activity in BM undergoing ICIs was observed, the preliminary analysis do not show significant differences. Nevertheless, studies with larger samples should be performed to confirm these negative results. Our findings support the utility of FDOPA-PET imaging for BMs assessment, regardless of the patient's immunotherapy status.

EPS-122

Analytic processing of dynamic ^{18}F-FET PET Time Activity Curves in patients affected by different grades of gliomas.

C. Pettinato[1], *L. Savio*[2], *A. Castello*[3], *L. Florimonte*[3], *G. Zuccotti*[4], *F. Buffoni*[3], *C. Canzi*[1], *A. Barantani*[1], *M. Schiavini*[3], *E. Galli*[3], *M. Arnaboldi*[3], *M. Campoleoni*[1], *M. Castellani*[3];
[1]*Health Physics - Fondazione IRCCS Ca' Granda - Ospedale Maggiore Policlinico, Milan, ITALY,* [2]*Department of Physics - University od Milan, Milan, ITALY,* [3]*Nuclear Medicine - Fondazione IRCCS Ca' Granda - Ospedale Maggiore Policlinico, Milan, ITALY,* [4]*Nuclear Medicine - Regional Hospital U. Parini, Aosta, ITALY.*

Aim/Introduction: The analysis of 18F-FET Time Activity Curves (TAC) based on SUVmax uptake patterns is useful to differentiate between high-grade and low-grade gliomas. Typically, high-grade gliomas exhibit an early peak followed by a decrease, while low-grade gliomas tend to show a gradual increase over time. Some lesions may plateau after an initial rise. However, visual interpretation of these curves can be challenging due to image noise affecting SUVmax measurements and ambiguous curve trends in some cases. Our study aimed to develop an objective method for characterizing 18F-FET TAC uptake patterns through analytical curve processing. ***Materials and Methods:*** 51 patients affected by different grade gliomas (2021 WHO classification) underwent a 40-minute dynamic 18F-FET PET/CT scan. Of these, 19 patients were evaluated at initial diagnosis, and 32 at disease relapse. Overall, 59 lesions were analyzed: 35 were high-grade (12 glioblastomas and 1 astrocytoma at diagnosis; 19 glioblastomas and 3 astrocytomas at relapse), and 24 were low-grade (2 astrocytomas, 2 oligodendrogliomas, and 2 gangliogliomas at diagnosis; 11 astrocytomas, 6 oligodendrogliomas, and 1 ganglioglioma at relapse). SUVmax TACs were extracted from dynamic imaging data using a 40% threshold VOI on the lesions. The final 20 minutes of each TAC were fitted with a linear regression model to calculate the angular slope. In particular, we defined a plateau as any slope within the range of ±5°; while slopes >5° were considered increasing, and those <−5° decreasing. ***Results:*** None of 13 high-grade lesions at diagnosis showed an increasing uptake pattern: 10/13 showed decreasing curves (mean slope: −13.4°), and 3/13 plateau patterns (mean slope: −0.02°). In the relapse group, 13/22 high-grade lesions exhibited plateau curves (mean slope: −0.9°), 3/22 increasing curves (mean slope: 7.6°), and 6/22 were decreasing (mean slope: −8.9°). 5/6 low-grade lesions at diagnosis showed plateau curves (mean slope: −0.3°), and 1/6 was decreasing (slope: −11.5°). In contrast, 5/18 low-grade lesions at relapse exhibited increasing curves (mean slope: 9.8°), 10/18 plateau curves (mean slope: 0.7°), and 3/18 decreasing curves (mean slope: −8.5°). ***Conclusion:*** Evaluating TAC slopes allows for a more objective classification of uptake patterns. Our findings revealed distinct TAC behaviour between diagnosis and relapse, particularly among high-grade gliomas. Notably, relapsed high-grade lesions exhibited all curve types, including increasing patterns traditionally associated with low-grade gliomas. Our results showed a kinetic shift at relapse in the TAC patterns, which could help clinicians for identifying glioma patients who are likely to benefit from treatments.

EPS-123

Noninvasive Assessment of IDH Mutation Status and WHO Grade in Untreated Prospective Glioma Patient Cohort using Integrated ^{18}F-FET PET/MR

B. Yu[1], *W. Zhou*[1], *M. Li*[1], *Z. Lin*[2], *Y. Wei*[2], *X. Chen*[2], *Y. Yang*[3], *T. Hua*[1];
[1]*Department of Nuclear Medicine & PET Center, Huashan Hospital, Fudan University, Shanghai, CHINA,* [2]*United Imaging Healthcare Co., Ltd., Shanghai, Shanghai, CHINA,* [3]*Beijing United Imaging Healthcare Co., Ltd., Beijing, Beijing, CHINA.*

Aim/Introduction: Isocitrate dehydrogenase (IDH) mutation status and WHO grade are essential markers for glioma stratification and therapeutic decision-making. This study aimed to evaluate the diagnostic performance of multiparametric PET/MR, combining O-(2-^{18}F-fluoroethyl)-L-tyrosine positron emission tomography (^{18}F-FET PET) and intravoxel incoherent motion (IVIM) imaging, for the noninvasive assessment of IDH mutation status and WHO grade. ***Materials and Methods:*** 86 untreated prospective glioma patients (IDH-mutant type: 46; IDH-wild type: 40) underwent simultaneous ^{18}F-FET PET and IVIM imaging using an integrated PET/MR (uPMR790, United Imaging Healthcare, Shanghai, China). The max, peak, and mean tumor-to-brain ratio (TBR_{max}, TBR_{peak}, TBR_{mean}), metabolic tumor volume (MTV), and total lesion glycolysis (TLG) were derived from whole-tumor segmentations based on PET images. IVIM metrics of the tumor, including the standard

apparent diffusion coefficient (sADC), true diffusion coefficient (D), pseudo diffusion coefficient (D*), perfusion fraction (f), relative blood flow (rBF), distributed diffusion coefficient (DDC) and water molecular diffusion heterogeneity index (α) were measured. Logistic regression and receiver operating characteristic (ROC) analysis were performed to evaluate the predictive value of PET indicators, IVIM indicators and their combined use for IDH mutation and WHO grade. ***Results:*** Univariate logistic regression showed that TBR_{max} (p = 0.015), TBR_{peak} (p = 0.016), and TBR_{mean} (p = 0.007) were significantly negatively associated with IDH mutation status, indicating lower uptake in IDH-mutant gliomas. Among IVIM parameters, IDH-mutant gliomas exhibited lower f (p = 0.003), rBF (p = 0.003), but higher α (p = 0.001). Age was a significant predictor of IDH mutation (p = 0.027), with mutations more common in younger patients. A multivariate model combining TBR_{mean}, f, rBF, α, and age achieved the highest predictive performance for IDH mutation status, with an AUC of 0.8147. TBR_{max} (p = 0.001), TBR_{peak} (p = 0.003), TBR_{mean} (p =0.006), and age (p = 0.003) were positively associated with WHO grade, while D (p = 0.038) and sADC (p = 0.048) were negatively associated. A combined model incorporating TBR_{max}, D, and age yielded the best diagnostic performance, with an AUC of 0.8322. ***Conclusion:*** Multiparametric ^{18}F-FET PET/MR imaging demonstrates significant promise for the noninvasive evaluation of IDH mutation status and WHO grade in glioma patients. The combination of metabolic and diffusion-perfusion parameters enhances evaluation performance, supporting its clinical utility in glioma management.

EPS-124

MRI radiomic analyses to predict the clinical utility of additional [^{18}F]FET PET imaging in glioblastoma patients

L. Kaiser[1], *A. J. Zounek*[1], *E. Istrefi*[1], *J. Isakaj*[1], *E. Barci*[1], *J. Reis*[2], *R. Forbrig*[2], *B. Wiestler*[3], *K. J. Müller*[1], *L. von Baumgarten*[4], *M. J. Mair*[1,5], *S. Ziegler*[6,1], *N. L. Albert*[1];
[1]*Department of Nuclear Medicine, LMU University Hospital, LMU Munich, Munich, GERMANY,* [2]*Institute of Neuroradiology, LMU University Hospital, LMU Munich, Munich, GERMANY,* [3]*Department of Neuroradiology, Klinikum Rechts der Isar, Technical University of Munich, Munich, GERMANY,* [4]*Department of Neurosurgery, LMU University Hospital, LMU Munich, Munich, GERMANY,* [5]*Division of Oncology, Department of Medicine I, Medical University of Vienna, Vienna, AUSTRIA,* [6]*Department of Nuclear Medicine, Hannover Medical School (MHH), Hannover, GERMANY.*

Aim/Introduction: MRI remains the primary imaging modality for managing glioblastoma, and contrast-enhancement on MRI usually represents the target volume for local therapies such as surgical resection or irradiation. However, MRI may fail to capture the full extent of the tumor, while [^{18}F]FET PET imaging can help to reveal metabolically active tumor parts beyond those visible on contrast-enhanced MRI in a significant number of cases. This study explores whether radiomic features extracted from MRI can predict the presence of tumor parts outside the contrast-enhancing volumes, thus identifying patients who may benefit from additional [^{18}F]FET PET imaging for local therapy planning. ***Materials and Methods:*** The study cohort consisted of 239 patients newly diagnosed with glioblastoma. All patients underwent preoperative [^{18}F]FET PET scans. PET tumor boundaries were determined using a 1.6-fold background intensity threshold. MRI tumor volumes, including regions of contrast enhancement and T2 signal hyperintensity, were delineated using the BraTS toolkit. The spatial overlap and maximum Hausdorff distance between PET and MRI-defined tumor volumes were assessed. Radiomic features were derived from T1-weighted contrast-enhanced and T2-weighted MRI images. A logistic regression model with nested cross-validation (5 folds, 50 repeats) was employed to classify cases where [^{18}F]FET PET revealed more than 1 ml of tumor tissue beyond the MRI-defined region and with a Hausdorff distance exceeding 1 cm. ***Results:*** 145/239 patients (61%) exhibited PET-detected tumor exceeding the MRI-defined areas, while the remaining 94 patients (39%) showed PET activity confined within or marginally exceeding contrast-enhancing MRI volumes. The overall Dice similarity coefficient between MRI and PET volumes was 0.37. The radiomics-based model achieved an area under the curve (AUC) of 0.78 in identifying patients with PET volumes significantly exceeding MRI (positive predictive value of 0.80 and negative predictive value of 0.60). ***Conclusion:*** MRI radiomics demonstrated moderate performance in predicting glioblastoma patients in whom additional [^{18}F]FET PET visualizes tumor tissue beyond contrast enhancement on MRI. Future studies are warranted to assess whether this strategy can enhance local therapy planning by enabling more selective application of [^{18}F]FET PET in clinical practice.

EPS-125

Can radiomics from conventional MRI forecast [^{18}F]FET PET positivity in patients with suspected low-grade gliomas?

L. Kaiser[1], *A. J. Zounek*[1], *E. Istrefi*[1], *J. Isakaj*[1], *E. Barci*[1], *J. Reis*[2], *R. Forbrig*[2], *B. Wiestler*[3], *K. J. Müller*[4], *L. von Baumgarten*[5], *M. J. Mair*[1,6], *S. Ziegler*[7,1], *N. L. Albert*[1];
[1]*Department of Nuclear Medicine, LMU University Hospital, LMU Munich, Munich, GERMANY,* [2]*Institute of Neuroradiology, LMU University Hospital, LMU Munich, Munich, GERMANY,* [3]*Department of Neuroradiology, Klinikum Rechts der Isar, Technical University of Munich, Munich, GERMANY,* [4]*Department of Neurology, LMU University Hospital, LMU Munich, Munich, GERMANY,* [5]*Department of Neurosurgery, LMU University Hospital, LMU Munich, Munich, GERMANY,* [6]*Division of Oncology, Department of Medicine I, Medical University of Vienna, Vienna, AUSTRIA,* [7]*Department of Nuclear Medicine, Hannover Medical School (MHH), Hannover, GERMANY.*

Aim/Introduction: In patients with suspected low-grade glioma on MRI, [^{18}F]FET PET is regularly performed to localize regions for targeted biopsy. Nevertheless, approximately one-third of these non-enhancing gliomas do not exhibit elevated tracer uptake on [^{18}F]FET PET. Given the growing demand for PET scans, the prediction of PET negativity could avoid performing scans with negative outcome. This study, therefore, sought to determine whether radiomics derived from standard MRI sequences could forecast [^{18}F]FET positivity in patients with suspected low-grade gliomas. ***Materials and Methods:*** The study included 282 individuals with newly diagnosed gliomas who underwent preoperative [^{18}F]FET PET and exhibited no contrast enhancement on MRI. Tumor regions were segmented using the BraTS toolkit, and radiomic features were extracted from both contrast-enhanced T1 and T2-weighted MRI images. A logistic regression model with nested cross-validation (5 folds, 50 repeats) was employed to predict [^{18}F]FET positivity, defined as tumor regions exhibiting significant uptake (> 1.6 times the background activity). ***Results:*** 192/282 cases (68%) demonstrated positive [^{18}F]FET uptake, while 90 cases (32%) did not meet the threshold for significant uptake and were classified as [^{18}F]FET-negative. The radiomics-based classification model achieved an area under the curve (AUC) of 0.64, with a positive predictive value of 0.78 and a negative predictive value of 0.45. ***Conclusion:*** Radiomics derived from MRI provided only a limited predictive power in identifying [^{18}F]FET positivity among non-enhancing gliomas, suggesting that PET should be performed in all patients. Further research is needed to determine whether deep learning approaches can enhance predictive accuracy, or whether these findings instead indicate that morphologic texture features from MRI are insufficient to predict if [^{18}F]FET PET can provide additional information to guide biopsy in patients with suspected low-grade glioma.

EPS-126

SSTR-PET Characteristics of Meningiomas: a Retrospective Comparison of Gallium-68- and Fluorine-18-labelled Tracers

L. Degryse[1], *L. Teles*[2], *S. De Vleeschouwer*[1], *L. Boeckxstaens*[1], *S. Jentjens*[3], *W. Deckers*[1], *G. Schramm*[1], *M. Lambrecht*[1], *J. Daisne*[4], *K. Van Laere*[1], *P. Clement*[1], *K. Goffin*[1], *C. M. Deroose*[1];
[1]*University Hospitals Leuven, Leuven, BELGIUM,* [2]*Princess Máxima Center for Pediatric Oncology, Utrecht, NETHERLANDS,* [3]*Maastricht University Medical Center, Maastricht, NETHERLANDS,* [4]*ZAS, Antwerp, BELGIUM.*

Aim/Introduction: Meningiomas frequently overexpress somatostatin receptor (SSTR) subtype 2, which is targeted on SSTR-PET imaging [1]. While [^{68}Ga]Ga-DOTATATE/TOC are well-established radiotracers for this purpose, emerging fluorine-18-labelled agents such as [^{18}F]AlF-NOTA-Octreotide (^{18}F-AlF-OC) offer practical advantages, including a longer physical half-life and centralized production [2-4]. We retrospectively studied quantitative uptake metrics across different delineation strategies using both gallium-68 and fluorine-18-labelled tracers. ***Materials and Methods:*** Patients with SSTR-PET imaging at our institution between 1/01/2007 and 1/03/2024, either demonstrating a meningioma or referred for its evaluation, were included. For individuals with multiple scans, only the first scan was analysed. Three radiotracers were used over the study period: [^{68}Ga]Ga-DOTATATE/TOC (N=137, 2.2 MBq/kg, scan 30-60 minutes post-injection), and ^{18}F-AlF-OC (N=15, 2-4 MBq/kg depending on yield, scan 120 minutes). SSTR uptake in meningiomas measuring ≥ 1 cm^3 was quantified using 3 lesion delineation strategies [5]: (1) a fixed SUV threshold of 2.3; (2) a relative threshold of 1.73×SUV_{peak} of a reference meningeal region; (3) a relative threshold of 11% of the SUV_{max}. Physiological uptake was quantified using spherical VOIs in non-pathological spleen, liver, left ventricle, vertebrae and meningeal tissue. ***Results:*** Overall, 171 distinct SSTR-expressing meningiomas (97.7%) and 4 non-SSTR-expressing meningiomas (2.3%) were documented in 152 patients. Most SSTR-expressing meningiomas were localised at the convexity (43.3%), skull base (32.7%) or falx (18.7%). Two patients had an optic nerve sheath meningioma (1.2%) and one had a spinal meningioma (0.6%). Quantitative analysis of lesions ≥1cm^3 revealed robust uptake for both ^{18}F-AlF-OC (N=7) and [^{68}Ga]-DOTATATE/TOC (N=79), with mean SUV_{max} values of 12.8, 12.8, and 13.5 for the former and 13.4, 13.4, and 15.5 for the latter across the three delineation strategies, respectively. Corresponding SUV_{mean} values were 5.2, 3.2, and 4.6 for ^{18}F-AlF-OC and 5.0, 3.0, and 4.8 for [^{68}Ga]-DOTATATE/TOC, respectively. Physiological uptake in all organs was comparable between both tracers. Across all delineation strategies, both tracers achieved high tumourtomeningeal ratios, yielding excellent lesiontobackground contrast. Tumourtoliver ratios exceeded 1 in every 18F-AlF-OC scan and in > 50 % of [^{68}Ga] GaDOTATATE/TOC scans, corresponding to a Krenning score ≥ 3. ***Conclusion:*** SSTR-PET imaging reveals high and consistent uptake in meningiomas across both [^{68}Ga]-DOTATATE/TOC and ^{18}F-AlF-OC. Quantitative parameters were robust across delineation strategies, and no relevant differences in uptake were observed between both tracers. These findings support the clinical interchangeability of ^{18}F-AlF-OC and [^{68}Ga]-labelled tracers for meningioma imaging.
References: 1.Albert NL, EJNMMI.2024;51(12):3662-3679 2.Pauwels E, EJNMMI.2023;47(13):3033-3046 3.Pauwels E, JNM.2023;64(4):632-638 4.Pauwels E, AJNMMI. 2018;8(5):311-331 5.Boursier C, EurRadiol.2023;33(10):7089-7098

EPS-127

Calibration of 3D ring-design SPECT/CT system to ENC-DAT database

T. Noponen*, H. Suoraniemi, A. Rissanen, M. Seppänen;*
Turku University Hospital, Turku, FINLAND.

Aim/Introduction: 3D ring-design SPECT/CT (3D-SPECT) is a desirable system for imaging small objects such as striatum in [^{123}I]-FP-CIT dopamine transporter (DAT) imaging. The reporting of DAT images relies nowadays on a reliable reference database to quantify precisely whether the striatal uptake level is normal. Widely accepted European Normal Control database of DaTscan (ENC-DAT) has been acquired using dual-head SPECT systems (2D-SPECTs) and requires a striatal phantom based calibration to adjust the specific SPECT system to that database. In this study, 3D-SPECT with the optimized reconstruction protocol is calibrated to the ENC-DAT database and compared with the calibration results of 2D-SPECTs. ***Materials and Methods:*** A brain phantom with realistic head and striatal structures was filled with ^{123}I solution so that the right striatum has 28% higher activity concentration than the left striatum. Three different background activity levels were used and on each level the phantom was imaged using three different imaging systems, 3D-SPECT, analog and digital 2D-SPECT. The six striatum-to-background activity concentration ratios (SBR) (ranging from 2.7 to 11.6) were verified using a well counter. The images were reconstructed and the SBRs quantified from the SPECT images as well. The optimal image reconstruction parameters were defined for the 3D-SPECT by maximizing the SBR in SPECT images. The linear equation was fitted between the well counter and image based SBRs and the slope and r^2 values of the equation were calculated for each SPECT measurement. The slope values will be used to adjust the measurements of each SPECT system to the ENC-DAT database. ***Results:*** Optimal reconstruction (Bayesian penalized-likelihood algorithm with a novel scatter correction, beta = 0.01 and gamma = 3.0) increased the contrast in 3D-SPECT images 26% compared to a standard manufacturer reconstruction. The 3D-SPECT images had the highest slope (s) values and SBRs (s=0.510, SBRs = 1.8-6.3) compared to the values of analog (s=0.413, SBRs = 2.1-5.6) and digital 2D-SPECT (s=0.408, SBR = 1.7-5.3) meaning that 3D-SPECT images have the highest striatal contrast. The r^2 values of the slope fits were very high for each system (3D-SPECT: 0.993, analog 2D-SPECT: 0.995, and digital 2D-SPECT: 0.998) proving that the calibration procedure succeeded reliably. ***Conclusion:*** Our results show that 3D-SPECT can be reliably calibrated to the ENC-DAT database. This makes possible the utilization of well-established database for clinical reporting of 3D-SPECT DAT images. An optimized 3D-SPECT provides the higher SBRs than 2D-SPECTs showing the advantage of 3D-SPECT for DAT imaging.

EPS-128

Clinical Impact of Dual-Biomarker PE2I-PET in the Differential Diagnosis of Parkinsonian Syndrome: A Retrospective Study

T. Crnic Bojkovic[1], *L. Falk*[1], *L. Appel*[1], *C. Widström*[1], *D. Nyholm*[2], *J. Sörensen*[1], *T. Danfors*[1], *M. Lubberink*[1], *M. Jonasson*[1];
[1]*Department of Surgical Sciences, Molecular Imaging and Medical Physics, Uppsala University, Uppsala, SWEDEN,* [2]*Department of Medical Sciences, Neurology, Uppsala University, Uppsala, SWEDEN.*

Aim/Introduction: Dynamic PE2I-PET assesses both dopamine transporter (DAT) availability and cerebral blood flow ratio (CBFR), the latter as an alternative to FDG as a marker of brain function. It may support differential diagnosis of early-stage parkinsonian disorders, where clinical assessment is challenging. This study aims to explore the impact of [^{11}C]PE2I-PET on clinical diagnosis in patients evaluated for parkinsonism or related neurodegenerative disorders. ***Materials and Methods:*** We retrospectively reviewed 432 patients (mean age 72; 35% females) who underwent 40-min dynamic [^{11}C]PE2I-PET at Uppsala University Hospital (2015-2023). Patients were included for whom diagnoses by a referring clinician were available from the Uppsala County diagnosis register both prior to and after the PET scan. Parametric images of specific binding ratio (30-40 min; DAT) and CBFR were calculated using a basis function implementation of the simplified reference tissue model with cerebellum as reference region. These images were read by experienced nuclear medicine physicians to obtain the most probable image-based differential diagnosis[1]. Pre- and post-

PET diagnoses were based on the last relevant clinical diagnosis before and after PET. Patients were classified into six diagnostic categories: Parkinson's disease (PD), Lewy body dementia (LBD), progressive supranuclear palsy (PSP), multiple system atrophy (MSA), other dementias, and other non-parkinsonian/unspecified disorders. For comparison with clinical diagnosis, a 'normal scan' PET reading was grouped with the latter for diagnostic comparison. Diagnostic agreement and change were assessed by comparing clinical diagnoses and PET reading overall and within diagnostic groups. Diagnostic changes were interpreted as shifts in clinical confidence. ***Results:*** Pre-PET, PET reading and post-PET diagnoses were distributed as PD: 20%, 30%, and 27%; LBD: 1%, 15% and 11%; PSP: 1%, 5% and 3%; MSA: 1%, 4% and 5%; other dementias: 4%, 5% and 8%; other non-parkinsonian/unspecified disorders: 74%, 42% and 47%. The post-PET diagnosis differed from the pre-PET diagnosis in 42% of cases. Of these, the post-PET diagnosis agreed with the PET reading in 62% of cases ($\kappa = 0.53$, $p < 0.001$). Overall, the post-PET diagnoses agreed in 67% of cases with the PET reading ($\kappa = 0.53$, $p < 0.001$). Non-parkinsonian/unspecified cases decreased markedly after PET from 318 to 202, a 37% reduction. ***Conclusion:*** In this retrospective study, [^{11}C]PE2I PET was associated with changes in clinical diagnoses in more than 40% of patients, and increased agreement with post-PET diagnoses, suggesting a role in refining and supporting clinical decision-making. ***References:*** [1]Crnic Bojkovic et al, EANM Technologist Guide 2024, Chapter 5

EPS-130

A Head-to-head Comparison of ^{18}F-DPA714 PET and ^{18}F-FDG PET in the diagnosis of Autoimmune Encephalitis

M. Zhang[1], *H. Meng*[2], *S. Chen*[2], *H. Wang*[1], *B. Li*[1];
[1]*Department of Nuclear Medicine, Ruijin Hospital, Shanghai Jiao Tong University School of Medicine, Shanghai, CHINA,*
[2]*Department of Neurology, Ruijin Hospital, Shanghai Jiao Tong University School of Medicine, Shanghai, CHINA.*

Aim/Introduction: The positive detection rate of MRI in autoimmune encephalitis (AIE) patients is relatively low, often failing to make a rapid and accurate localization diagnosis. Both ^{18}F-DPA714 [1] and ^{18}F-FDG [2] PET demonstrated their advantages in the diagnosis of AIE by characterizing microglial TSPO expression and glucose metabolism levels, respectively. Therefore, the aim of this study was to conduct a head-to-head comparison of the diagnostic value between ^{18}F-DPA714 and ^{18}F-FDG PET in patients with AIE. ***Materials and Methods:*** This cross-sectional study included 23 antibody-positive and 2 possible antibody-negative AIE patients, along with 10 healthy controls (HCs). All patients underwent sequential ^{18}F-DPA714 PET/MRI and ^{18}F-FDG PET/CT examinations within one week. A follow-up of 6 to 12 months after the baseline examinations was performed to assess the change of patients' clinical symptoms. Positive findings for ^{18}F-DPA714 PET were defined as Z-score above 2.0 in the corresponding brain regions of HCs. Positive results for ^{18}F-FDG PET were indicated by the Z-score above 2.0 or below -2.0 obtained after comparison with the normal population database. ***Results:*** Both ^{18}F-FDG PET and ^{18}F-DPA714 PET showed higher positivity rates than MRI (81% vs 44%, $P = 0.006$ and 76% vs 44%, $P = 0.008$, respectively). A statistically significant association was found between the ^{18}F-DPA714 but not ^{18}F-FDG uptake and the mRS scores ($P = 0.032$) or CASE scores ($P = 0.006$). Patients with epilepsy showed a significantly higher uptake in the whole-cortex of both ^{18}F-DPA714 ($P = 0.001$) and ^{18}F-FDG ($P = 0.005$) as well as in the temporal lobe of ^{18}F-FDG ($P = 0.022$) compared to those patients without. Higher ^{18}F-DPA714 standardized uptake value ratio (SUVR, $P<0.001$) and lower ^{18}F-FDG SUVR ($P<0.001$) in the whole-cortex of patients with long-term cognitive impairment than those patients without were observed. ***Conclusion:*** ^{18}F-DPA714 PET showed its better correlation with disease severity of AIE than ^{18}F-FDG PET, serving as a supplementary tool to ^{18}F-FDG PET and MRI. ***References:*** 1. Zhang M, Meng H, Zhou Q, et al. Microglial Activation Imaging Using (18)F-DPA-714 PET/MRI for Detecting Autoimmune Encephalitis. Radiology. 2024;310:e230397.2. Solnes LB, Jones KM, Rowe SP, et al. Diagnostic Value of (18)F-FDG PET/CT Versus MRI in the Setting of Antibody-Specific Autoimmune Encephalitis. J Nucl Med. 2017;58:1307-1313.

EPS-131

In search of the optimal pseudo-reference region for the quantification of synaptic density using Positron Emission Tomography imaging with [^{11}C]UCB-J in Alzheimer's Disease

I. Arino[1], *A. Dubois*[1], *P. Testard*[2], *M. Tonietto*[3], *G. Klein*[3], *C. Clerget*[1], *P. Gervais*[1], *A. Pinon*[1], *B. Zinnhardt*[3], *I. Gerlach*[1], *M. Ly-Le Moal*[3], *A. Petiet*[4], *T. Lebouvier*[5], *D. Wallon*[6], *G. Dorothée*[7], *M. Potier*[8], *A. Kas*[9], *M. Sarazin*[2,1], *M. Bottlaender*[1], *J. Lagarde*[1,2];
[1]*Université Paris-Saclay, BioMaps, CEA, Inserm Service Hospitalier Frédéric Joliot, Orsay, FRANCE,* [2]*Service de Neurologie de la Mémoire et de Langage, GHU Paris Psychiatrie et Neurosciences, 75014 Paris, FRANCE,* [3]*Roche Pharma Research and Early Development, Neuroscience and Rare Diseases, Roche Innovation Center, Basel, SWITZERLAND,* [4]*Institut Roche, 92100 Boulogne-Billancourt, FRANCE,* [5]*Univ Lille, Inserm U1172, Lille, France ; CHU de Lille, DISTALZ, F-59000 Lille, FRANCE,* [6]*Normandie Univ, UNIROUEN, Inserm U1245; CHU Rouen, Department of Neurology and CNR-MAJ, F 76000 Rouen, FRANCE,* [7]*Sorbonne Université, Inserm ; Centre de Recherche Saint-Antoine, CRSA, Immune System and Neuroinflammation Laboratory, Hôpital Saint-Antoine, Paris, FRANCE,* [8]*Paris Brain Institute (ICM), Centre National de la Recherche Scientifique (CNRS) UMR 7225, INSERM U1127, Hôpital de la Pitié-Salpêtrière, Sorbonne Université, Paris, FRANCE,* [9]*Service de médecine nucléaire, Hôpital Pitié-Salpêtrière, 75013 Paris, FRANCE.*

Aim/Introduction: Gold standard PET quantification implies arterial blood sampling. This procedure is invasive and involves a number of constraints and contraindications. There are alternative methods that avoid arterial samples, one of which uses reference or pseudo-reference regions. The choice of this reference region is critical to the validity and accuracy of the analysis. The synaptic vesicle glycoprotein 2A (SV2A) radiotracer [^{11}C]UCB-J has ideal imaging characteristics to quantify synaptic loss in Alzheimer's disease (AD). The pseudo-reference region conventionally used for this radiotracer is the centrum semiovale (CS). However, recent studies suggest that using the whole cerebellum as an alternative reference region would provide a more robust signal than the small centrum semiovale region.[1] ***Materials and Methods:*** Fifty-two subjects (33 AD patients and 19 healthy controls) underwent a 70 min PET/MR after i.v. injection of [^{11}C]UCB-J (314±30 MBq). Anatomical MRIs were segmented using FastSurfer and 6 potential pseudo-reference regions were drawn (after erosion to avoid partial volume effect): whole cerebellum, cerebellar gray matter, pons and CS defined in 3 different ways: i) from MNI template applied to subject after normalization with ANTs library (mean vol ± SD: 1.6±0.2 mL), ii) from individual MRI eroded total white matter (15.7±8.5 mL), iii) and after exclusion of the white matter lesions (10.7±7.4 mL). SUV values (50-70 min) of each reference region were analyzed for all subjects. DVR using SRMT2 model and SUVr (50-70 min) were calculated with each reference region and investigated for 13 cortical regions of interest. ***Results:*** Mean SUV values between AD patients and controls did not differ in any of the pseudo-reference regions. Coefficient of variation of SUV were comparable across pseudo-reference regions except for the Pons where it was more variable. DVR values were significantly decreased in temporo-parietal regions in AD patients compared to controls with both whole cerebellum and individually defined CS (Cohen's $d>1$). Results were less pronounced (NS in the left temporal mesial ROI) with the CS from the template (Cohen's $d=0.9$), and non-significant in most regions with the pons. The SUVr

(50-70min) showed similar results to DVR. ***Conclusion:*** SUVs in CS and whole cerebellum showed good stability between controls and patients. Careful CS definition by delineation on individual MRI instead of applying a template improved robustness for its use as a reference region. Under these conditions, the CS and whole cerebellum reference regions lead to similar results using DVR and SUVR quantification. ***References:*** 1.Mecca AP et al. 2020.

EPS-132

^{18}F-SynVesT-1 PET Imaging Reveals Synaptic Density Abnormalities and Brain Network Alterations in Tinnitus Patients: A Pilot Study

J. Zhong, *S. Hu;*
Xiangya Hospital,Central South University, Changsha, CHINA.

Aim/Introduction: The prevalence of tinnitus is as high as 10% to 30% of the population, and it has become a major global health problem.At present, the pathogenesis of tinnitus is not completely clear, and its neurophysiological basis needs to be further studied.The hypothesis of increased neuronal activity is confirm by ^{18}F-fluorodeoxyglucose (^{18}F-FDG) in primary and chronic tinnitus patients, but the abnormalities of synaptic density has not been tested directly by synaptic vesicle protein 2A (SV2A). In this positron emission tomography (PET) study with the new tracer ^{18}F-SynVesT-1, we evaluated SV2A abnormalities in patients with primary and chronic tinnitus and compared the pattern to ^{18}F-fluorodeoxyglucose (^{18}F-FDG). ***Materials and Methods:*** 28 patients with acute and chronic tinnitus and 24 healthy controls were recruited. Acute and chronic tinnitus patients underwent magnetic resonance imaging (MRI) and static PET imaging with both ^{18}F-SynVesT-1 and ^{18}F-FDG, while the controls only PET with ^{18}F-SynVesT-1 and MRI. Brain network assessment of PET with ^{18}F-SynVesT-1 was undertaken. Standardized uptake value (SUV) of ^{18}F-SynVesT-1 and ratio (SUVr) were computed between regions of interest. Electroencephalographs (EEGs)was applied in tinnitus patients and healthy controls. Correlations between synaptic density and clinical features in tinnitus were also analyzed. ***Results:*** Chronic tinnitus patients showed increased ^{18}F-SynVesT-1 uptake in 14 brain areas, including the limbic lobe, temporal lobe, and parahippocampal gyrus, corresponding to high metabolism detected by ^{18}F-FDG. Acute tinnitus patients had decreased synaptic density in five brain areas, including the bilateral frontal lobe and left occipital lobe. ^{18}F-SynVesT-1 uptake had a broader pattern than ^{18}F-FDG ($P<0.05$). SUVR of the two tracers was positively correlated in the insula lobe but not in the parahippocampal gyrus, temporal lobe, paracentral lobule, or occipital lobe. Brain network connectivity was enhanced in tinnitus patients, with better connectivity in acute vs. chronic patients. EEG microstate analysis showed alternating patterns in both groups.THI scores were negatively correlated with bilateral hippocampus, amygdala, left putamen, and medial cingulate gyrus. ***Conclusion:*** SV2A PET with ^{18}F-SynVesT-1 represents a promising tool for elucidating the synaptic basis of tinnitus and its associated brain network changes. SV2A PET with 18F-SynVesT-1 is the first in vivo evidence confirming to the hypothesis of changed neuronal activity in tinnitus. Our findings provide further incentive to evaluate interventions that restore synaptic connections to treat tinnitus.

EPS-133

Evidence for brain glial activity in chronic migraine patients: A [^{11}C] PBR28 PET/MR study

Y. Chang, *R. Wang;*
Chinese PLA General Hospital, Beijing, CHINA.

Aim/Introduction: Although neuroinflammation may play a key role in the pathology of migraine and the process of chronification, with implications for disease treatment, the role of microglia in chronic migraine (CM) remains unknown. We investigated whether neuroinflammation is involved in the pathophysiology of CM and whether pro-inflammatory signals are associated with clinical features. ***Materials and Methods:*** This study is divided into two parts. The first part comprises an animal experiment using a chronic migraine (CM) mouse model induced by repeated nitroglycerin (NTG) injections. The distribution pattern of activated microglia in the brains of these mice was evaluated using [^{11}C]PBR28 micro-positron emission tomography (Micro-PET). To further verify the spatial specificity of TSPO (translocator protein) signals, [^{11}C]PBR28 autoradiography was performed. The second part of the study involves a clinical research trial. Nineteen individuals with CM and 10 healthy controls (HCs) underwent integrated brain positron emission tomography (PET)/magnetic resonance (MR) via the translocator protein (TSPO) radioligand [^{11}C] PBR28, a marker of glial activation, together with the quantification of blood plasma inflammatory cytokine/chemokine. The volume in regions of interest (ROI) was calculated using MRI data. The standardized uptake value ratio (SUVR) was extracted for ROI in [^{11}C] PBR28 uptake. The Spearman's rank correlation coefficient between [^{11}C] PBR28 SUVR and changes in plasma factors was calculated. ***Results:*** Micro-PET imaging demonstrated that during the chronicization process of CM induced by repeated NTG injections, there was an increased uptake of radioactivity in the pons, hypothalamus, and amygdala. Complementary in vivo autoradiography revealed a concentrated accumulation of radioactive signals in the medulla oblongata, cerebellum, hypothalamus, midbrain, and basal ganglia, indicating elevated TSPO expression in brain microglia. CM patients had a significantly higher Hamilton Depression Rating Scale (HAMD) and Hamilton Anxiety Rating Scale (HAMA) scores than that in HCs ($p<0.05$). Participants with CM exhibited reduced volume in the thalamus ($p=0.012$), compared with HCs. [^{11}C] PBR28 binding was significantly increased in the midbrain, occipital lobe and vermis, along with increased interictal plasma interleukin-8 (IL-8) and CX3CL1 levels, in individuals with CM compared with HCs. The midbrain levels of TSPO were negatively correlated with the headache frequency ($r=-0.462$, $p=0.046$). ***Conclusion:*** The present findings demonstrated increased central inflammation in CM participants compared to HCs, providing imaging evidence implicating inflammation in the pathophysiology of CM. The reduction in volume within the thalamus may contribute to migraine chronification.

EPS-134

Simplified Quantification of Brain Estrogen Receptors with Fluoroestradiol PET: Evidence Supporting a 30-60 Minute Window for SUVR Calculation

M. Nerattini[1], *V. Berti*[1], *D. C. Matthews*[2], *S. Williams*[3], *C. Andy*[3], *F. Fauci*[3], *C. Boneu*[3], *T. Ajila*[3], *S. Pahlajani*[3], *M. Battista*[3], *R. Andrews*[2], *A. Pupi*[1], *R. Diaz Brinton*[4], *J. P. Dyke*[3], *L. Mosconi*[3];
[1]*University of Florence, Florence, ITALY,* [2]*ADM Diagnostics, Northbrook, IL, UNITED STATES OF AMERICA,* [3]*Weill Cornell Medicine, New York, NY, UNITED STATES OF AMERICA,* [4]*University of Arizona, Tucson, AZ, UNITED STATES OF AMERICA.*

Aim/Introduction: 17β-estradiol (E2), the most potent endogenous estrogen, modulates neurophysiology and neuropathology via estrogen receptors (ERs) in the brain. The menopause-related decline in E2 has been linked to neurological symptoms and conditions, including Alzheimer's disease. Positron Emission Tomography (PET) with 16α-[18F]fluoro-17β-estradiol (18F-FES) is the only in vivo technique available to assess ER expression in the human brain. However, brain 18F-FES PET studies in women remain limited and typically rely on complex kinetic modeling. Here, we aim to evaluate simplified standardized uptake value ratio (SUVR)-based methods and to identify an optimal static imaging window to enhance clinical feasibility. ***Materials and Methods:*** Fifty-five healthy women (ages 40-65)—18 premenopausal, 18 perimenopausal, and 19 postmenopausal—underwent 90-minute dynamic 18F-FES PET imaging. Parametric binding potential (BPnd) maps were generated using voxel-wise Logan plots with cerebellar gray matter as the reference region. Static images were extracted

for five 20-minute intervals (30-50, 40-60, 50-70, 60-80, and 70-90 minutes post-injection). The pituitary was selected as the primary region of interest (ROI) based on consistent evidence of specific ER binding. Exploratory ROIs included ER-rich hypothalamus, hippocampus, amygdala, caudate, frontal, and cingulate cortex. SUVRs were computed using the same cerebellar reference and compared to distribution volume ratios (DVR = BPnd + 1) via Pearson correlations, intraclass correlation coefficients (ICC), and model selection procedures (stepwise regression and LASSO with AIC). The reference ROI was restricted to cerebellar crus II gray matter, refined with supervised clustering to ensure low, exposure-invariant uptake, thus satisfying normalization criteria. Group differences in SUVRs between pre- and postmenopausal women were also tested. ***Results:*** Pituitary SUVRs showed strong agreement with DVRs, performing best in earlier time intervals. All correlations were significant ($p < 0.001$), peaking at 30-50 minutes ($r = 0.96$, ICC = 0.973). Data-driven analyses identified 30-50 minutes as optimal, closely followed by 40-60 minutes. Findings align with 18F-FES pharmacokinetics—rapid uptake in ER-rich tissue within 20-30 minutes and return to sub-physiological levels by ~1 hour. The selected intervals revealed significantly higher pituitary SUVRs post-menopause ($d = 0.927$, $p = 0.021$ for 30-50 minutes; $d = 0.911$, $p = 0.023$ for 40-60 minutes), consistent with prior evidence of ER upregulation post-menopause. Similar results were observed in exploratory ROIs. ***Conclusion:*** The 30-60 minute SUVR window provides a reliable and practical alternative to kinetic modeling for quantifying pituitary 18F-FES uptake, supporting broader clinical and research application.

EPS-135

Precision Diagnostics in Neurodegeneration via AI-Augmented PET/MRI Fusion of ASL, DTI, and PET

J. Strobel[1], *J. Kassubek*[2], *G. Grön*[3], *A. J. Beer*[4], *M. Beer*[5], *H. Müller*[1], *N. Sollmann*[1];
[1]*Department of Nuclear Medicine and Department of Diagnostic and Interventional Radiology, University Hospital Ulm, Ulm, GERMANY,* [2]*Department of Neurology, University Hospital Ulm, Ulm, GERMANY,* [3]*Department of Psychiatry and Psychotherapy III, University Hospital Ulm, Ulm, GERMANY,* [4]*Department of Nuclear Medicine, University Hospital Ulm, Ulm, GERMANY,* [5]*Department of Diagnostic and Interventional Radiology, University Hospital Ulm, Ulm, GERMANY.*

Aim/Introduction: This study explores a novel approach to neuroimaging for neurodegenerative diseases (NDD) using a hybrid PET/MRI platform that combines Arterial Spin Labeling (ASL), Diffusion Tensor Imaging (DTI), and Positron Emission Tomography (PET). The goal was to integrate these modalities for a comprehensive analysis of NDDs in patients with conditions like Alzheimer's disease, frontotemporal dementia, and primary progressive aphasia. By leveraging the strengths of each imaging technique—ASL for measuring cerebral blood flow, DTI for assessing white matter integrity, and PET for evaluating metabolic and molecular activity—the study aims to enhance diagnostic accuracy, facilitate early detection, and improve understanding of disease-specific patterns. This multimodal strategy may offer valuable insights into the complex pathophysiology of NDDs and support the development of targeted therapeutic interventions. ***Materials and Methods:*** In this study, 76 patients with NDD were examined using the Siemens Biograph PET/MRI system. The standardized acquisition and analysis protocols allowed comparisons between patients and a control group. Specific brain structures of interest were identified based on prior research, and region-of-interest (ROI) analysis was conducted. An artificial intelligence (AI)-based support vector machine (SVM) was employed to categorize different neurodegenerative pathologies. ***Results:*** PET imaging achieved 92.0% accuracy in distinguishing NDD patients from controls and 78.1% for differentiating among NDD types. Combined ASL/DTI matched or exceeded PET accuracy for nfvPPA (81.0%) and lgPPA (94.7%), but was lower for AD (76.3%) and svPPA (88.9%). Voxel-wise analysis revealed overlap between PET and ASL clusters, especially in left-lateralized regions for svPPA and lgPPA. ***Conclusion:*** The study reveals significant differences in PET, ASL, and DTI measurements between neurodegenerative disease (NDD) patients and healthy controls. PET imaging demonstrated a high overall classification accuracy of 92% in distinguishing NDD cases, while ASL and DTI offered comparable or even superior performance in identifying specific subtypes, particularly non-fluent variant primary progressive aphasia (nfvPPA) and logopenic variant PPA (lgPPA). Voxel-wise analysis highlighted notable spatial overlap between PET and ASL signal clusters, especially in left-lateralized brain regions associated with semantic variant PPA (svPPA) and lgPPA. Furthermore, DTI detected complementary white matter alterations in these areas, emphasizing the structural underpinnings of disease progression. This integrated, multimodal imaging strategy underscores the potential of combining MRI and PET to provide a more comprehensive diagnostic picture—targeting both structural and molecular biomarkers in a single session. Such a "one-stop-shop" approach enhances diagnostic precision while streamlining the evaluation process for NDDs.

810

Monday, October 6, 2025, 09:45 - 11:15
Room 116

CTE 4 - Technologists Committee: Breathing Knowledge – the New Approaches of PET-CT Lung Scanning

OP-388

The Impact of PET/CT in Patients with Lung Cancer

R. Mei*; Nuclear Medicine, IRCCS Policlinico S.Orsola Malpighi, Bologna, ITALY.*

OP-389

The Role of the Technologists in PET/CT Lung Imaging: Techniques and Patient Care

S. Valente*; Hospital Lusíadas Lisboa, Nuclear Medicine, Lisbon, PORTUGAL.*

OP-390

A Step into the Future: Perspectives for Lung Cancer in Nuclear Medicine

H. Hautzel*; University Hospital Essen, Nuclear Medicine, Essen, GERMANY.*

811

Monday, October 6, 2025, 09:45 - 11:15
Room 111

Special Symposium 3 - Dosimetry Committee: Challenges in Dosimetry of Alpha-Emitters

OP-392

Need of Validated Primary and Secondary Standards to Calibrate Alpha Emitters in Radionuclide Calibrators

A. Denis-Bacelar*; National Physical Laboratory (NPL), London, UNITED KINGDOM.*

OP-393

Feasibility of SPECT–Based Dosimetry of Alpha Emitters

J. Gustafsson*; Lund University, Medical Radiation Physics, Lund, SWEDEN.*

OP-394
How to Address Daughters' Redistribution in Dosimetry of Alpha Emitters
***A. Delker**; Ludwig-Maximilians-Universität, Munich, GERMANY.*

OP-395
Small Scale Dosimetry and Microdosimetry to Better Understand Treatment Outcomes
***P. Mínguez Gabiña**; Gurutzeta/Cruces University Hospital, Department of Medical Physics, Barakaldo, SPAIN.*

901

Monday, October 6, 2025, 11:30 - 13:00
Auditorium

Plenary 3: Referring Patients to Nuclear Medicine: When, How and Mainly Why?

OP-396
Never without Nuclear Medicine in Prostate Cancer, is Kidney Cancer Next in Line?
***S. Muselaers;** Radboudumc, Nijmegen, NETHERLANDS*

OP-397
New Targets in Kidney Cancer
***L. Lindenberg**; National Cancer Institute, Center for Cancer Research, National Institutes of Health, Bethesda, UNITED STATES OF AMERICA.*

OP-398
Nuclear Medicine Is Routine in Lung Cancer and Optional in the Majority of Breast Cancers
***A. Gennari**; University of Piemonte Orientale, Department of Oncology, Maggiore University Hospital, Novara, ITALY.*

OP-399a
New Frontiers in Breast Cancer Molecular Imaging
***G. Ulaner**; Hoag Family Cancer Institute, Irvine, UNITED STATES OF AMERICA.*

OP-399b
Nuclear Medicine has Revolutionised the Alzheimer's Disease Landscape, is Parkinson's Disease the Next?
***D. Ferreira Padilla**; Karolinska Institute, Solna, SWEDEN.*

OP-399c
Parkinson's Disease Can Only Be Understood with Molecular Imaging
***G. Hoeglinger**; LMU Klinikum, Munich, GERMANY.*

1001

Monday, October 6, 2025, 15:00 - 16:30
Auditorium

CME 7 - Oncology & Theranostics Committee: Targeted Radionuclide Therapy Accross Various SST Expressing Tumor Models: a new Framework for Rethinking

OP-400
The "mild" tumour model (midgut/PPGL/ G1-G2 meningioma/typical lung carcinoids)
***V. Ambrosini**; Alma Mater Studiorum, University of Bologna, Bologna, Italy; Nuclear Medicine, IRCCS, Azienda Ospedaliero-Universitaria di Bologna, Bologna, ITALY.*

OP-401
The "aggressive" tumour model (heavily treated GEP-NET/ atypical lung carcinoids)
***D. Taïeb**; Marseille University Hospitals, APHM/AMU, Departement of Nuclear Medicine, Marseille, FRANCE.*

OP-402
The "highly aggressive" tumour model (SCLC-LCLC/G3 GEP-NET/G3 meningioma/Merckel)
***M. Mileva**; Institut Jules Bordet, Brussels, BELGIUM.*

OP-403
When passing the baton to alpha?
***E. Deshayes**; Institut du Cancer de Montpellier, Université de Montpellier, Montpellier, FRANCE.*

1002

Monday, October 6, 2025, 15:00 - 16:30
Room 112 (Arena)

Special Track 7: Award Session: EANM Sanjiv Sam Gambhir Award - Compete and Win!

1003

Monday, October 6, 2025, 15:00 - 16:30
Room 113

LIPS Session 7 - Cardiovascular Committee: What to look at in the Heart and in Vessels on Oncological PET Images

OP-407
What to Look for On Low-Dose CT
***M. Badarna**; Rambam Healthcare campus, Nuclear medicine, Haifa, ISRAEL.*

OP-408
What to Look for in the Heart on FDG-PET
***N. Mikail**; APHP Paris Centre, Nuclear Medicine, Paris, FRANCE.*

OP-409
What to Look for in the Vessels on FDG-PET
***J. Bucerius**; Graz University Hospital, Nuclear Medicine Department, Graz, AUSTRIA.*

OP-410
What to Look for with Tracers Other than FDG
***A. Kjær**; University of Copenhagen, Copenhagen, DENMARK.*

1004

Monday, October 6, 2025, 15:00 - 16:30
Room 114

M2M Track - TROP Session - Radiopharmaceutical Sciences + Translational Molecular Imaging & Therapy Committee: Innovations in Translational Oncology

OP-411
Preclinical Evaluation of 3B031: A Novel FAP-Targeting Peptide Radioligand with High Tumor Retention and Promising Tumor-to-Kidney Ratio
***W. XU**, J. Zhang;*
PepLib, Metuchen, NJ, UNITED STATES OF AMERICA.

Aim/Introduction: Fibroblast activation protein (FAP) is a membrane-bound serine protease highly expressed in cancer-associated fibroblasts across various solid tumors, making it a compelling target for peptide-based radioligand therapy. However, existing agents such as FAP2286 show notable off-target uptake, particularly in the kidneys, which may limit their clinical utility. We have developed an integrated peptide discovery

platform that combines disulfide-rich peptide phage display with AI-driven in silico peptide design platform to accelerate the development of highly specific and stable peptide radioligands. Using this platform, we developed 3B031, a novel FAP-targeting peptide radioligand with enhanced tumor selectivity and low kidney uptake. ***Materials and Methods:*** 3B031 was discovered through in house peptide library screening and computational design, followed by conjugation with DOTA and radiolabeling with Gallium-68. Surface plasmon resonance was used to determine binding affinity to recombinant human FAP. Plasma stability was evaluated in mouse serum. For in vivo evaluation, BALB/c nude mice bearing subcutaneous HT1080-FAP xenografts were injected intravenously with ^{68}Ga-3B031. PET/CT imaging and ex vivo biodistribution were conducted at 4 hours post-injection. A head-to-head comparison with Novartis's FAP2286 was performed under matched conditions. ***Results:*** 3B031 demonstrated high binding affinity to human FAP with a K_D of 3.7 nM and excellent serum stability. In vivo PET imaging revealed strong tumor localization and minimal non-target organ accumulation. Biodistribution analysis showed high tumor uptake and significantly reduced renal accumulation, resulting in a tumor-to-kidney ratio of approximately 5 at 4 hours post-injection. In comparison, FAP2286 showed a tumor-to-kidney ratio of approximately 2. Under identical conditions, 3B031 outperformed FAP2286 in terms of higher binding affinity, greater tumor retention, lower kidney uptake, and superior tumor-to-kidney ratio. ***Conclusion:*** 3B031 represents a promising next-generation FAP-targeting peptide radioligand with significantly improved pharmacokinetics and tumor selectivity compared to FAP2286. These preclinical results support its advancement into IND-enabling studies and clinical evaluation for diagnostic imaging and potential radiotherapeutic applications in FAP-expressing tumors. ***References:*** 1. Loktev A, Lindner T, Burger EM, et al. Development of Fibroblast Activation Protein-Targeted Radiotracers with Improved Tumor Retention. J Nucl Med. 2019;60(10):1421-1429.

OP-412

mRNA Display-enabled De Novo Discovery of Covalent Macrocyclic Peptide Radiotracers Targeting Fibroblast Activation Protein

X. Cui[1], *P. Liu*[1], *Y. Yang*[2], *Y. Yin*[2], *Z. Liu*[1,3];
[1]*Changping Lab, Beijing, CHINA,* [2]*Shandong University, Qingdao, CHINA,* [3]*Peking University, Beijing, CHINA.*

Aim/Introduction: Current targeted radionuclide therapies (TRT) face challenges with radioligands such as rapid clearance and off-target uptake. This study aimed to exploit mRNA display technology to engineer macrocyclic peptide-based covalent targeted radioligands (CTRs)[1] targeting fibroblast activation protein (FAP), a tumor stromal marker, to achieve prolonged intratumoral retention and enhanced therapeutic precision. ***Materials and Methods:*** A library of >10^{12} macrocyclic peptides incorporating 4-fluorosulfonyloxy-L-phenylalanine (FSY) was ribosomally synthesized using the Flexible In vitro Translation (FIT) system. The Random non-standard Peptide Integrated Discovery (RaPID)[2] platform enabled de novo screening against human FAP. High-affinity hits were conjugated with DOTA for radiolabeling (^{68}Ga/^{177}Lu). Covalent binding kinetics were assessed via SDS-PAGE/autoradiography and surface plasmon resonance (SPR). Pharmacokinetics, stability, and tumor targeting were evaluated in HT-1080-FAP xenograft models using PET/CT imaging, with lipophilicity (Log P) and in vitro stability under radiolabeling conditions (pH 4.0, 90°C) further characterized. ***Results:*** Three CTRs—DOTA-4D-2, -4D-5, and -4D-12—exhibited subnanomolar affinity (K_D = 0.12-0.22 nM) and rapid covalent engagement with FAP (>50% yield within 30 min in vitro). [^{68}Ga]Ga-DOTA-4D-5 demonstrated superior tumor retention, with uptake increasing from 1.77-fold (30 min) to 4.24-fold (5 h) compared to its non-covalent analog, alongside optimal tumor-to-muscle ratios (50.3 ± 21.1). Log P values (−1.92 to −2.15) correlated with reduced non-specific organ uptake, while tandem MS confirmed irreversible binding to tyrosine Y541 in FAP. Stability assays revealed <5% hydrolysis for DOTA-4D-5 under radiolabeling conditions, underscoring robustness. In contrast, non-covalent controls showed rapid washout (tumor uptake decline >60% at 5 h), highlighting the critical role of FSY-mediated covalent bonding. ***Conclusion:*** This study establishes mRNA display as a powerful tool for developing FAP-targeted covalent macrocyclic peptide radiotracers. The integration of FSY enables durable tumor retention through tyrosine-selective sulfur(VI) fluoride exchange (SuFEx), overcoming limitations of conventional non-covalent agents. The optimized CTRs, particularly DOTA-4D-5, exhibit exceptional pharmacokinetic profiles and imaging contrast, positioning them as promising candidates for clinical TRT. This platform broadens the scope of covalent drug design to non-cysteine residues, offering a transformative strategy for precision oncology. ***References:*** (1) Cui, X.-Y. et al. Covalent Targeted Radioligands Potentiate Radionuclide Therapy. Nature 2024, 630, 206-213. (2) Goto, Y.; Suga, H. The RaPID platform for the discovery of pseudo-natural macrocyclic peptides. Acc. Chem. Res. 2021, 54, 3604-3617.

OP-413

Development of ^{161}Tb Radioimmunotherapy for the Treatment of T-cell Lymphomas

E. Rioja Blanco[1,2], *Y. Banz*[3], *C. Schlapbach*[4], *U. Novak*[5], *T. Chiorazzo*[1], *N. Bertschi*[4], *P. Bernhardt*[6,7], *P. Grundler*[1], *N. van der Meulen*[1,8], *M. Grzmil*[1], *R. Schibli*[1,2], *M. Behe*[1];
[1]*Center for Radiopharmaceutical Sciences, PSI Center for Life Sciences, Villigen PSI, SWITZERLAND,* [2]*Department of Chemistry and Applied Biosciences, Institute of Pharmaceutical Sciences, ETH Zurich, Zurich, SWITZERLAND,* [3]*Institute of Tissue Medicine and Pathology, University of Bern, Bern, SWITZERLAND,* [4]*Department of Dermatology, Inselspital, Bern University Hospital, University of Bern, Bern, SWITZERLAND,* [5]*Department of Medical Oncology, Inselspital, Bern University Hospital, University of Bern, Bern, SWITZERLAND,* [6]*Department of Medical Radiation Sciences, Institute of Clinical Sciences, Sahlgrenska Academy at University of Gothenburg, Gothenburg, SWEDEN,* [7]*Department of Medical Physics and Biomedical Engineering, Sahlgrenska University Hospital, Gothenburg, SWEDEN,* [8]*Laboratory of Radiochemistry, PSI Center for Nuclear Engineering and Sciences, Villigen PSI, SWITZERLAND.*

Aim/Introduction: Lymphoma remains a major global health concern. Despite therapeutic advances, managing advanced and relapsed cases, particularly aggressive T-cell lymphoma subtypes, remains an unmet clinical need. Radioimmunotherapy (RIT) with terbium-161 offers a promising strategy, especially for patients at advanced stages of disease. Terbium-161 emits both β^--particles and conversion and Auger electrons, enabling the targeted elimination of large tumor masses as well as small lesions and single cancer cells. In this study, we preclinically evaluate a novel terbium-161-labeled anti-CD30 RIT in comparison to the clinical benchmark lutetium-177 in various T-cell lymphoma models, including a newly developed, clinically relevant disseminated mouse model. ***Materials and Methods:*** The DOTA-conjugated anti-CD30 antibody cAC10 was radiolabeled with terbium-161 or lutetium-177, achieving high specific activities. In vitro cytotoxicity and clonogenic survival were assessed in CD30+ T-cell lymphoma cell lines. In vivo biodistribution and dosimetry were evaluated in a lymphoma xenograft mouse model. Therapeutic efficacy was studied in both localized and disseminated lymphoma models. For the latter, EL4 murine T-cell lymphoma cells were stably transduced with human CD30 (EL4-hCD30+) and inoculated intravenously into immunocompetent mice. Engraftment and disease distribution were assessed via SPECT/CT imaging,

autoradiography, and immunofluorescence staining. ***Results:*** [^{161}Tb]Tb-cAC10 demonstrated superior CD30-specific cytotoxicity across all tested lymphoma cell lines, with IC_{50} values up to 43-fold lower than [^{177}Lu]Lu-cAC10. Clonogenic assays confirmed a markedly stronger reduction in survival with terbium-161. In vivo, both radioimmunoconjugates displayed comparable biodistribution with high tumor uptake (31.0 ± 7.4 %IA/g at 48 h) and low background accumulation. Terbium-161 delivered a 1.5-fold higher tumor-absorbed dose compared to lutetium-177 counterpart. In a localized lymphoma model, a single dose of [^{161}Tb]Tb-cAC10 significantly prolonged median survival (41 days) compared to lutetium-177 (21 days) and controls (12-15 days). The disseminated model showed successful engraftment in clinically relevant sites, including bone marrow. Therapeutic studies in this model are ongoing, and we anticipate an even greater therapeutic benefit for terbium-161 due to its capacity to effectively irradiate single cells and smaller tumor lesions. ***Conclusion:*** To our knowledge, this study presents the first evaluation of terbium-161 RIT for the treatment of hematological malignancies, introducing a novel disseminated mouse model that better reflects the clinical landscape of advanced-stage lymphomas. Terbium-161 RIT demonstrates superior therapeutic potential offering a promising therapeutic option for T-cell lymphomas.

OP-414

Tb, or Not Tb - Exploring Terbium-161 for CD44v6-Targeted Radionuclide Therapy

A. Gustafsson[1], *S. S. Rinne*[1], *T. Xu*[1], *K. Bratteby*[2,3], *A. Lundgren Mortensen*[1,2], *P. Bernhardt*[4,5], *M. Nestor*[1];
[1]*Uppsala University, Uppsala, SWEDEN,* [2]*Karolinska Institutet, Stockholm, SWEDEN,* [3]*Karolinska University Hospital, Stockholm, SWEDEN,* [4]*University of Gothenburg, Gothenburg, SWEDEN,* [5]*Sahlgrenska University Hospital, Gothenburg, SWEDEN.*

Aim/Introduction: Pancreatic cancer remains among the deadliest malignancies, with limited treatment options and poor prognosis. [^{177}Lu]Lu-DOTA-AKIR001, a lutetium-177-labeled full-length human IgG1 antibody targeting CD44v6, has demonstrated therapeutic potential for targeted radionuclide therapy of several malignancies, including pancreatic cancer. Terbium-161, a promising alternative to lutetium-177, emits not only medium-energy beta particles but also conversion and Auger electrons, potentially offering complementary therapeutic benefits. This study evaluated [^{161}Tb]Tb-DOTA-AKIR001 as an alternative CD44v6-targeted therapeutic agent. ***Materials and Methods:*** AKIR001 was labelled with terbium-161 from PRISMAP. Radiochemical stability of [^{161}Tb]Tb-DOTA-AKIR001, with and without 50 mg/ml ascorbate, was assessed in PBS, mouse serum, and EDTA using ITLC or HPLC. CD44v6 expression and binding specificity were validated in vitro. Biodistribution was assessed in immunodeficient BALB/c nu/nu mice bearing subcutaneous human pancreatic ductal adenocarcinoma xenografts. Dosimetry calculations were based on TIACs from bi-/tri-exponential fits and absorbed energy per decay from MOBY phantom or Monte Carlo models; marrow activity concentration was estimated at 36% of blood activity concentration. Therapeutic efficacy was assessed in xenograft-bearing animals receiving either 4 MBq, 2 × 4 MBq(fractionated one week apart), or 8 MBq of [^{161}Tb]Tb-DOTA-AKIR001 and compared to 4 MBq and 12 MBq [^{177}Lu]Lu-DOTA-AKIR001. Tumour uptake was verified via small-animal SPECT imaging, and haematologic toxicity was monitored through serial blood sampling. ***Results:*** [^{161}Tb]Tb-DOTA-AKIR001 showed high radiochemical yields (>95%) and stability (>95% at 24 h) in presence of 50 mg/ml ascorbate. In vitro assays confirmed specific, picomolar-affinity binding to CD44v6-positive cells. [^{161}Tb]Tb-DOTA-AKIR001 tumor uptake exceeded 150% IA/g at 96 h p.i., with favourable tumour-to-organ ratios. The mean absorbed tumour dose was calculated to be 32 Gy/MBq, with a tumour-to-bone marrow absorbed dose ratio of 28. An activity-dose-dependent anti-tumour effect was observed, with greatest tumour regression in the 8 MBq single-dose group. At equivalent activity (4 MBq), [^{161}Tb]Tb-DOTA-AKIR001 outperformed [^{177}Lu]Lu-DOTA-AKIR001. Comparable efficacy was observed between 8 MBq [^{161}Tb]Tb-DOTA-AKIR001 and 12 MBq [^{177}Lu]Lu-DOTA-AKIR001. Mild to moderate haematological effects, including lymphopenia and anaemia, were observed in an activity-dose-dependent manner. Animal weights remained stable. ***Conclusion:*** [^{161}Tb]Tb-DOTA-AKIR001 demonstrated excellent radiochemical stability, favorable biodistribution and dosimetry, and promising therapeutic efficacy. Hematologic changes were more pronounced compared to previous observations with [^{177}Lu]Lu-DOTA-AKIR001; however, the observed anti-tumor effects and potential therapeutic benefits of terbium-161 support its continued exploration alongside of [^{177}Lu]Lu-DOTA-AKIR001. The emission profile of terbium-161 may offer added advantages in certain therapeutic contexts, highlighting [^{161}Tb]Tb-DOTA-AKIR001 as a highly promising candidate for further preclinical development in targeted radionuclide therapy.

OP-415

A feasibility study of SmartCC platform for a two-step pretargeted radioimmunotherapy (PRIT): taking GD2-expressing neuroblastoma as an example

Z. Qiao*, H. Qi, Y. Yang, C. Wei, T. Xu;*
SmartNuclide Biotech, Suzhou, CHINA.

Aim/Introduction: To improve the therapeutic index (TI) of the pretargeted radioimmunotherapy (PRIT), we developed a bispecific fusion protein for two-step PRIT, comprising (i) a tumor-targeting domain, (ii) a lanthanide metal (Ln)-DOTA binding domain, and (iii) a novel tetramerization domain derived from human. There, home-made tetramerization domain library, referred to as SmartCC, mediate the self-assembly and disassembly of the bispecific fusion protein. The tetramer demonstrated high avidity for tumor binding while exhibiting rapid blood clearance upon disassembly into small monomers (<70 kDa). Furthermore, the SmartCC can modulate the pharmacokinetics of proteins, consequently, enhancing the biologic effect of radiation dose to tumor and widening therapeutic window. In this present study, we tested the feasibility of SmartCC platform for PRIT using GD2-expressing neuroblastoma as a model. ***Materials and Methods:*** A library of SmartCCs capable of modulating the pharmacokinetic properties of tumor-targeting antibodies was established and used for in vivo screening to identify GD2-SmartCCs exhibiting the favorable TI. In a typical PRIT, protein was intravenously administrated to IMR32 tumor-bearing mice, followed by the injection of a ^{177}Lu-DOTA-Bn. The PRIT parameters were optimized, including protein dose, ^{177}Lu-DOTA-bn dose, and the time interval between protein and ^{177}Lu-DOTA-Bn administration. Ex vivo biodistribution, dosimetry, tumor inhibition, and toxicity studies were evaluated to assess the effects of PRIT. ***Results:*** The selected bispecific fusion protein (SNA025) was identified through in vivo screen studies. The optimized PRIT parameters of SNA025-PRIT were: 1) 1.0 nmol of protein dose, 2) 48-hour injection intervals, 3) 18.5 MBq of ^{177}Lu- DOTA-Bn. The ex vivo biodistribution studies showed the tumor and kidney uptake were 16.60 ± 2.51 and 1.33 ± 0.18 %ID/g at 24 h postinjection, respectively, with significant tumor retention of 32.58 ± 3.68 %ID/g at 120 hours post-injection. The adsorbed dose of tumor, blood and kidney was 399 cGy/MBq, 0.7 cGy/MBq (TI=589) and 13.1 cGy/MBq (TI=30.5), respectively. Complete IMR32tumor growth inhibition was observed using two doses of SNA025-PRIT (18.5 MBq). Notably, no obvious toxicity or body weight decrease was observed during the PRIT ***Conclusion:*** In summary, we established a SmartCC library with ability to modulate antibody pharmacokinetics and tumor uptake. Taking GD2 as an example, we identified SNA025-PRIT with high tumor

uptake, prolonged retention, low normal tissue uptake, and a favorable safety profile. These preclinical findings highlight the potential of our SmartCC platform for PRIT in diverse tumor targets.

OP-416

Novel SSTR2 RPT agent RYZ401 demonstrates significant improvement in Biodistribution and Efficacy compared to DOTATATE

T. Lo, *T. Chung, L. Nyiranshuti, N. Bakes, S. Richardson, S. Richardson, A. Noncovich, A. Hudson, P. Napier, N. Smith, A. Bhat; RayzeBio, a subsidiary of Bristol-Myers Squibb, San Diego, CA, UNITED STATES OF AMERICA.*

Aim/Introduction: Somatostatin receptor type 2 (SSTR2) is found in various cancers, including gastroenteropancreatic neuroendocrine tumors (GEP-NETs), lung, and breast cancers. [^{177}Lu]Lu-DOTATATE is a radiopharmaceutical therapy (RPT) for SSTR2-positive GEP-NETs but has limitations due to prolonged kidney retention, raising the risk of radiation-induced nephropathy. To mitigate such risk, a long Lys-Arg infusion was required during the treatment of [^{177}Lu]Lu-DOTATATE. In addition, high kidney retention restricts the dose that can be safely administered to GEP-NET patients which further impacts the therapeutic efficacy. RYZ401 is a highly selective SSTR2 agonist conjugated with DOTA-chelator allowing labeling with various radioisotopes including ^{177}Lu and ^{225}Ac. RYZ401 was designed to improve tumor retention and accelerate renal clearance compared to DOTATATE. The aim of this study was to use multilayer imaging approaches to evaluate the biodistribution and treatment efficacy of RYZ401 in SSTR2-positive tumor xenograft model compared to DOTATATE based RPT agents. ***Materials and Methods:*** An SSTR2 expressing, non-small cell lung cancer (NSCLC) xenograft mouse model was used in the following in vivo studies. To evaluate the in vivo biodistribution between [^{177}Lu]Lu-RYZ401 and [^{177}Lu]Lu-DOTATATE, a comparative longitudinal Single Photon Emission Computed Tomography (SPECT) imaging combined with Area Under the Curve ($AUC_{2\text{-}168h}$) of Time Activity Curves (TAC) between 2h to 168h post-injection was performed. To validate the treatment efficacy, a head-to-head ^{225}Ac efficacy study between [^{225}Ac]Ac-RYZ401 and [^{225}Ac]Ac-DOTATATE in mice bearing large tumors (410-1300mm^3) was conducted and ^{225}Ac treatment outcome was monitored by SSTR2-targeting Positron Emission Tomography (PET) imaging using [^{68}Ga]Ga-DOTATATE. ***Results:*** Longitudinal SPECT imaging with [^{177}Lu]Lu-RYZ401 displayed a 62% lower kidney uptake (Kidney AUC_{RYZ401}=103; Kidney $AUC_{DOTATATE}$=166) and 303% longer tumor retention (Tumor AUC_{RYZ401}=1619; Tumor $AUC_{DOTATATE}$=534) compared to [^{177}Lu]Lu-DOTATATE. An ^{225}Ac efficacy study was conducted by injection of 111 kBq of [^{225}Ac]Ac-RYZ401 and [^{225}Ac]Ac-DOTATATE in an SSTR2 expressing NSCLC xenograft mouse model. Both [^{225}Ac]Ac-RYZ401 and [^{225}Ac]Ac-DOTATATE showed tumor volume suppression by 4 weeks post-treatment. However, the recurrence of [^{68}Ga]Ga-DOTATATE-positive tumors were detected only in the [^{225}Ac]Ac-DOTATATE-treatment group by week 7. On the other hand, no detectable [^{68}Ga]Ga-DOTATATE-positive PET signal was observed in the [^{225}Ac]Ac-RYZ401 treatment group while maintaining tumor volume suppression. ***Conclusion:*** Preclinical in vivo imaging reveals that RYZ401 has an improved biodistribution profile compared to DOTATATE. [^{225}Ac]Ac-RYZ401 further demonstrates an effective treatment outcome compared to [^{225}Ac]Ac-DOTATATE. Therefore, [^{225}Ac]Ac-RYZ401 as a therapeutic agent has the potential to deliver more effective ^{225}Ac treatment to tumors while reducing kidney radiation dose.

OP-417

Tumor-stroma dynamics define FAP optimum imaging and therapeutic windows in the management of glioblastoma

A. Bilinska[1], *N. Kumar*[1], *E. Menéndez*[1], *T. Läppchen*[1], *F. Rösch*[2], *A. Rominger*[1], *E. Gourni*[1];
[1]*Department of Nuclear Medicine, Inselspital, Bern University Hospital, University of Bern, Bern, SWITZERLAND,* [2]*Department of Chemistry—TRIGA site, Johannes Gutenberg University of Mainz, Mainz, GERMANY.*

Aim/Introduction: Glioblastoma is one of the most aggressive cancers, with a poor survival rate. The transforming growth factor-beta (TGF-β) signaling pathway plays a significant role in regulating glioblastoma and is known to induce fibroblasts activation, leading to the expression of Fibroblast Activation Protein (FAP). This study investigates the natural tumor-stroma interactions in glioblastoma, identifying an optimal window for FAP-targeted radiopharmaceutical imaging and therapy. ***Materials and Methods:*** PET/CT scans were performed on U87MG xenografts using [^{68}Ga]Ga-DATA.SA.FAPI and [^{68}Ga]Ga-DOTAGA.Glu.$(FAPI)_2$ on days 7, 11 and 15 following tumor cell implantation. PET/CT images were obtained 1hour p.i.. On day 11, an additional cohort of U87MG xenografts was injected with [^{18}F]F-FDG and PET/CT was performed under identical conditions. To monitor tumor-stroma interactions, immunohistochemical staining and qPCR were performed. ELISA was conducted on murine blood samples, collected on the same days. A 48-hour co-culture experiment was conducted using U87MG cells with either cancer-associated fibroblasts (CAFs) or normal fibroblasts (NAFs). Following the co-culture, gene expression analysis was performed, focusing on key genes involved in glioblastoma progression, including FAP and TGF-β. ***Results:*** Tumor uptake significantly increased from day 7(3.7±0.4 %IA/g) to day 11 (7.7±1.3 %IA/g) to day 15 (13.8±1.4 %IA/g), and both radiotracers displayed the same pattern. In contrast, the FDG scan did not show any increase in tumor uptake at day 11 (4.14±1.5%IA/g). The tumor sizes did not significantly change throughout the entire experiment. The levels of murine and human circulating FAP were at the same level at the three tested days, being 130 and 10 µg/ml, respectively. Both human and FAP protein levels increase over days was detected by immunohistochemistry. These was consistent with the significantly increased relative mRNA levels of FAP detected by qPCR. The relative levels of human TGF-β were stable in all the tumors while murine significantly increased, pointing the stroma activation. Co-culture of U87MG cells with CAFs caused the upregulation of FAP expression in cancer cells. Meanwhile, co-culture of U87MG with NAFs led to the upregulation of FAP, CD44 and TGF-β expression in NAFs, indicating their activation. Addition of TGF-β inhibitor to the co-culture of U87MG and NAFs, decreased the mRNA levels of FAP however remained higher than those in NAFs alone. ***Conclusion:*** Our results highlight the role of tumor-stroma dynamics in shaping FAP expression, offering a strategic imaging and therapeutic windows for FAP-based theranostics. These insights provide a biological basis for enhancing clinical translation of FAP-based approaches in glioblastoma.

OP-418

Novel CAIX-Targeted Radiotracer for Precision PEC/CT Imaging of Renal Cell Carcinoma

S. Cheng[1], *X. Niu*[2], *Y. Zhang*[1], *X. Lan*[1], *P. Teng*[2], *D. Jiang*[1];
[1]*Department of Nuclear Medicine, Union Hospital, Tongji Medical College, Huazhong University of Science and Technology, Wuhan, CHINA,* [2]*College of Pharmaceutical Sciences, National Key Laboratory of Advanced Drug Delivery and Release Systems, Zhejiang University, Hangzhou, CHINA.*

Aim/Introduction: Carbonic anhydrase IX (CAIX) is a well-established marker of hypoxia that has been famed as a promising target for solid malignancies. In renal cell carcinoma (RCC), CAIX expression is unique as it is driven by the loss-function mutations in the VHL gene and subsequent accumulation of downstream HIF-1α in the nucleus, even in the absence of hypoxia. Limited theragnostic options are available for advanced or metastatic RCC, spurring the development of CAIX-targeted radiopharmaceuticals. However, substantial physiological uptake in the gastrointestinal and biliary system remains a persistent concern. This study aims to develop novel CAIX-targeted PET/CT imaging tracers and explore their potential for RCC detection

and metastasis visualization in preclinical models. ***Materials and Methods:*** CAIX expression was analyzed across several tumor cell lines using western blot. Fourteen novel CAIX-specific cyclic peptides were synthesized, functionalized with DOTA chelators, and radiolabeled with gallium-68 (^{68}Ga, $T_{1/2}$ ~ 68 min). Their in vivo distribution was initially evaluated by PET/CT imaging. Mice bearing subcutaneous OS-RC-2 clear cell RCC xenograft were intravenously injected with 4.63 ± 0.93 MBq of radiotracer and images acquired at 15, 30, 60, and 120 min post-injection. Region of interest (ROI) analyse of the images and ex vivo biodistribution, following the last imaging time point, quantified the tumor and major tissue uptake as percent of injected dose per gram of tissue (%ID/g; mean ± SD). Tumor tissues were subsequently collected for immunohistochemistry. ***Results:*** All the radiotracers were synthesized with high radiolabeling yields and radiochemical purity exceeding 95%. Longitudinal in vivo PET/CT screening of OS-RC-2 human xenograft mouse models identified [^{68}Ga]Ga-RCC78 as the most promising candidate, displaying high and sustained tumor uptake alongside rapid background clearance. Biodistribution studies revealed tumor uptake as 4.65 ± 1.00 %ID/g, yielding a tumor-to-background ratio of 41.30 ± 7.01 at 2 h post-injection. Notably, normal tissue uptake was minimal, with gastrointestinal background uptake recorded at only 0.17 ± 0.04 %ID/g at 2 h post-injection. The renal accumulation related to drug excretion remained with acceptable limits (4.40 ± 1.36 %ID/g at 2 h post-injection). Western-blot and immunohistochemical results confirmed CAIX expression in tumor tissues. ***Conclusion:*** We have successfully developed several CAIX-specific radiotracers with outstanding imaging profiles. Among them, [^{68}Ga]Ga-RCC78 stand out for its high tumor contrast and negligible gastrointestinal background. These results lay the groundwork for further optimization of [^{68}Ga]Ga-RCC78 and its progression toward clinical translation in CAIX-targeted RCC imaging.

OP-419

Nectin-4 targeted PET imaging of advanced urothelial carcinoma: tracer development and preclinical evaluation

X. Long*, X. Nian, Y. Zhang, R. An, D. Jiang;*
Department of Nuclear Medicine, Union Hospital, Tongji Medical College, Huazhong University of Science and Technology, Wuhan, CHINA.

Aim/Introduction: Nectin cell adhesion molecule 4 (Nectin-4), a type I transmembrane cell adhesion protein, has been demonstrated to be overexpressed in a variety of tumors, making it an attractive marker for targeted therapies such as antibody-drug conjugates (ADCs). Of great note, the FDA-approval of the first Nectin-4 targeted ADC drug, enfortumab vedotin (EV) offers a promising future for patients with advanced urothelial cancer (UC). However, successful patient selection with PET imaging to noninvasively quantify nectin-4 expression would help to predict treatment response and improve overall therapeutic efficacy. Here, we aim to develop two novel Nectin-4 targeting single-domain antibody (sdAb) tracers and evaluate their diagnostic performance in preclinical UC xenograft models. ***Materials and Methods:*** Two sdAbs, namely the sdAb monomer BS8 and homodimer BS11 were successfully obtained, and their purities and binding kinetics were determined by SDS-PAGE and HPLC. By labeling the two sdAbs with ^{68}Ga ($t_{1/2}$ = 1.1 h), we developed two Nectin-4-targeted PET imaging probes [^{68}Ga]Ga-NOTA-BS8 and [^{68}Ga]Ga-NOTA-BS11. Subcutaneous and orthotopic xenograft models were prepared using Nectin-4 positive sw780 and HT1376 cell lines, respectively. ImmunoPET imaging and ex vivo biodistribution studies were performed in tumor-bearing mice to evaluate imaging performance and systemic distribution of two radiotracers. IHC staining was used to screen the expression of Nectin-4 in UC tissues. ***Results:*** The molecular weight of BS8 and BS11 were approximately 15 kDa and 30 kDa, respectively. [^{68}Ga]Ga-NOTA-BS8 and [^{68}Ga]Ga-NOTA-BS11 showed high radiochemical purities. PET/CT imaging with [^{68}Ga]Ga-NOTA-BS8 and [^{68}Ga]Ga-NOTA-BS11 demonstrated a high tumor-to-background ratio in sw780 subcutaneous models at 2 h post-injection, with the latter showing better diagnostic potential supported by higher tumor uptake (2.10 ± 0.32 %ID/g vs. 3.09 ± 0.44 %ID/g, n=3). Apart from high uptake in the kidney, minimal radioactivity was detected in other healthy tissues and organs. In the orthotopic xenograft models, ex vivo PET imaging and biodistribution studies clearly delineated tumors in the bladder wall, suggesting great potential of transforming BS11 from diagnostic PET imaging to targeted radiotherapy of primary UC lesions, by either bladder irrigation or systemic administration. ***Conclusion:*** In this study, we successfully developed two sdAb-based PET tracers for Nectin-4 imaging in vivo. ImmunoPET of UC xenograft models demonstrated high tumor uptakes, supporting the application of [^{68}Ga]Ga-NOTA-BS11 as a companion diagnostic tool for optimizing treatments targeting Nectin-4, which may further support Nectin-4 targeted radiotherapy and personalized UC cancer management.

1005

Monday, October 6, 2025, 15:00 - 16:30
Room 211

Cutting Edge Science Track - TROP Session - Dosimetry Committee: Personalised Dosimetry and Predictive Modeling

OP-420

Predictive Dosimetry in PSMA-targeted Radiopharmaceutical Therapies Guided by Physiologically-Based Pharmacokinetic (PBPK) Modeling and Artificial Intelligence

H. Abdollahi*, A. Rahmim, J. Fowler, C. Uribe;*
BC Cancer Agency, Vancouver, BC, CANADA.

Aim/Introduction: Predictive dosimetry from pre-therapy PET/CT remains a key challenge for optimizing radiopharmaceutical therapy (RPT). We developed a computational framework combining PBPK modeling and AI to predict absorbed dose and biologically effective dose (BED) in tumors and organs-at-risk for PSMA-targeted RPT. By analyzing time activity curves (TACs) from various radiopharmaceuticals, the framework enables systematic in silico evaluation of predictive dosimetry. ***Materials and Methods:*** We used a PBPK modeling approach, representing each organ with vascular, interstitial, binding, and intracellular compartments, with exchanges governed by ODEs. These models simulated PSMA PET and SPECT TACs for 640 virtual patients, focusing on tumors, kidneys, and salivary glands. For each patient, F-18, Ga-68, and Cu-64 TACs were matched to Lu-177 TACs by varying parameters such as association, dissociation, release, and receptor binding rates. Radiomics and kinetic features were extracted, and a nested ML pipeline using Random Forest, Extra Trees, Ridge, and SVR with RFE, LASSO, and RF importance was applied to predict absorbed dose and BED. Performance was evaluated via 5-fold nested cross-validation using MAPE. ***Results:*** Cu-64 consistently yielded the best mean MAPE values for both dose (7.1%, 8.2%, 6.7%) and BED (7.3%, 9.0%, 5.9%) across all tumor volumes (TV = 1, 0.01, 0.001 Liters), outperforming F-18 and Ga-68. Across all evaluated organs and volumes, Cu-64 demonstrated least prediction errors compared to the other radiopharmaceuticals. For dose, MAPE in the kidney decreased from 8.5% at TV = 1 to 3.5% at TV = 0.001, and in the salivary gland from 9.9% to 3.8%. For BED, MAPE in the kidney ranged from 9.3% to 3.7%, and in the salivary gland from 9.2% to 4.4%. Tumor predictions also showed favorable trends,

with Cu-64 achieving the lowest MAPE values of 7.1%, 8.2%, and 6.7% for dose, and 7.3%, 9.0%, and 5.9% for BED at TV = 1, 0.01, and 0.001, respectively. Cu-64 consistently showed the lowest error rates across all tumor volumes and organs. ***Conclusion:*** Cu-64 showed the highest overall accuracy in modeling both dose and BED across all tumor and organs. While Ga-68 performed similarly for tumor BED at intermediate volume, Cu-64 consistently had the lowest prediction errors, likely due to its longer half-life and enhanced delayed imaging capabilities, supporting its selection as the most reliable radiotracer. Clinical validation is ongoing. This integration of modeling and AI enables systematic in silico assessment of radiopharmaceutical behavior and offers a robust platform for predictive dosimetry and optimized RPT.

OP-421

Optimization of ^{177}Lu-PSMA Dosimetry Imaging Schedules using Physiologically-Based Pharmacokinetic (PBPK) Modeling

J. Fowler[1,2], *M. Sabouri*[1,2], *A. Rahmim*[1,2], *C. Uribe*[1,2];
[1]*BC Cancer Research Institute, Vancouver, BC, CANADA,* [2]*University of British Columbia, Vancouver, BC, CANADA.*

Aim/Introduction: Absorbed dose calculations in radiopharmaceutical therapies (RPTs) rely on fitting single photon emission computed tomography (SPECT) data. The timing and frequency of SPECT acquisitions strongly influence the fitting process, and therefore the estimated doses. This study optimized 2-, 3-, and 4-time-point sampling schedules for ^{177}Lu prostate-specific membrane antigen (PSMA) RPTs using a diverse dataset generated via advanced computational modeling. ***Materials and Methods:*** Using our validated physiologically-based pharmacokinetic (PBPK) model, we simulated the biodistribution of ^{177}Lu-PSMA (7.4 GBq) in 100 virtual patients with varied pharmacokinetics. This model, originally developed in MATLAB SimBiology, was adapted and implemented in Python (publicly available) to enable flexible, large-scale studies. Time-activity curves (TACs) were generated for the kidneys, salivary glands, and a primary tumor in each patient. To correctly simulate noise propagation in expectation maximization reconstructions, log-normal noise was added with a standard deviation proportional to the square root of the activity, scaled by a factor α derived from phantom studies and simulations. Three noise realizations per patient yielded 300 virtual studies. Activity sampling occurred hourly for 6 hours, every 2 hours to 48 hours, and every 24 hours to 144 hours. All possible 2-, 3-, and 4-time-point combinations resulted in 465, 4495, and 31465 unique schedule combinations, and were evaluated using the Levenberg-Marquardt least-squares method. A mono-exponential model was applied to all 2-, 3-, & 4-point schedules, while a 3-term bi-exponential model was applied to 3- & 4-point schedules. The optimal schedule in each category minimized the relative error in the estimated time-integrated activity (TIAC) (proportional to the estimated dose when neglecting cross-radiation). ***Results:*** Mean absolute percent error (MAPE) varied across sampling schedules. The optimal 2-point schedule was [12, 72] hours (MAPE: 4.42%). The optimal 3-point schedule was [12, 72, 144] hours, with MAPEs of 3.40% (mono-exponential) and 3.06% (bi-exponential). The best 4-point schedule was [10, 12, 72, 144] hours, yielding MAPEs of 3.39% and 3.06%, respectively. ***Conclusion:*** Validated computational modeling (specifically, PBPK modeling) holds significant potential in guiding optimized RPTs. This work demonstrates that the timing and frequency of SPECT scans have a significant impact on the accuracy of absorbed dose calculations in radiopharmaceutical therapy. Optimizing imaging schedules should be a key consideration in the design of clinical trials and treatment protocols. Thoughtful selection of time points can increase dosimetry accuracy, ultimately supporting more informed clinical decision-making and potentially improving patient outcomes.

OP-422

Progress Update on Personalized Single-Timepoint Kidney Dosimetry in 177Lu-DOTATATE PRRT Using Deep Learning-Based Segmentation: A Multi-Center Study

M. Reymann[1], *L. Bönsel*[1], *S. M. Montenegro*[1], *D. L. Bailey*[2], *A. H. Vija*[3];
[1]*Siemens Healthineers AG, Forchheim, GERMANY,* [2]*Royal North Shore Hospital, Sydney, AUSTRALIA,* [3]*Siemens Medical Solutions USA, Inc., Hoffman Estates, IL, UNITED STATES OF AMERICA.*

Aim/Introduction: Due to inter-patient variability, especially in kidney radiosensitivity, personalized dosimetry is recommended for [^{177}Lu]Lu-DOTATATE PRRT. Single-timepoint dosimetry (1TP) offers a practical alternative to full time-activity sampling (FTP) by reducing burden on patients and clinics [1, 2]. As part of a multi-center study, we are evaluating the feasibility of a population-based 1TP approach [3]. This update summarizes project status and challenges in aligning heterogeneous data. ***Materials and Methods:*** Over five years, patient data were collected from three clinical sites using Symbia Intevo Bold SPECT/CT systems with medium-energy collimators. Imaging protocols varied: two sites acquired at 0.5, 24, 48, and 72 h post-injection, while the third used 0.5, 4, 24, and either 96 or 120 h. Patient preparation varied: amino acid infusions ranged from 25-30 g lysine/arginine over 3-4 hours; premedication included IV or oral ondansetron, with or without dexamethasone. Some patients also received capecitabine-based radiosensitizers per local protocols. SPECT images were reconstructed at a core laboratory using CG reconstruction with attenuation-correction, scatter-correction, and varying PSF, then smoothed with a 16 mm FWHM Gaussian. Kidney segmentation used a deep learning-based model [4]. Ongoing efforts aim to standardize imaging and patient management across centers for comparability and model-based analysis. The impact of protocol differences on 1TP feasibility will inform optimal protocol design. ***Results:*** A total of 65 patients were included across three clinical centers. Of 177 available treatment cycles, 134 included four measurement timepoints and were eligible for single- vs. four-timepoint dosimetry comparison. Mean injected activities were 6.46±0.44 GBq (D1), 7.41±0.04 GBq (D2), and 7.90±0.12 GBq (AUS), reflecting protocol and delivery differences. Imaging timepoints clustered consistently within centers, with protocol variations evident in relative acquisition times. Projection durations also varied across sites. Registration quality was impacted by CT availability: at a site with only baseline CT, 91% of registrations required adjustment, versus 45-71% at sites with CT at each timepoint - highlighting the influence of protocol design on alignment and motion correction. ***Conclusion:*** The curated dataset is ready for evaluating biodistribution and dosimetry across platforms and timepoints. Preliminary analysis shows that imaging schedules, injected activity, and patient preparation affect data consistency. Addressing these variations is essential before robust evaluation of single-timepoint dosimetry. Future work will focus on harmonizing data across sites for reliable analysis under real-world conditions. ***References:*** [1]: Willowson et al., EJNMMI Phys, 2018. [2]: Wang etal., J Nucl Med, 2023. [3]: Madsen etal., Medical Physics, 2018. [4]: Wasserthal et al., Radiology: Artificial Intelligence, 2023.

OP-423

Towards Personalised Dosimetry: Predicting Radiological Response in Neuroendocrine Tumours Treated with [^{177}Lu]Lu-DOTATATE Using Cyclic Changes and Absorbed Dose

M. Macsuka[1], *B. Driscoll*[2], *I. W. T. Yeung*[3], *J. Publicover*[4], *U. Metser*[5], *R. Juergens*[6], *S. D. Myrehaug*[7], *D. Laidley*[8], *R. K. Wong*[2], *D. R. McGowan*[1], *K. A. Vallis*[1];
[1]*Department of Oncology, University of Oxford, Oxford, UNITED KINGDOM,* [2]*Radiation Medicine Program, Princess Margaret Cancer Centre, University Health Network, Toronto, ON, CANADA,*

[3]Southlake Regional Health Centre, Newmarket, ON, CANADA, [4]University Health Network, Toronto, ON, CANADA, [5]Joint Department of Medical Imaging, University Health Network, Toronto, ON, CANADA, [6]Division of Medical Oncology, Juravinski Cancer Centre, Hamilton, ON, CANADA, [7]Department of Radiation Oncology, Odette Cancer Centre, Sunnybrook Health Sciences Centre, University of Toronto, Toronto, ON, CANADA, [8]University of Western Ontario, London, ON, CANADA.

Aim/Introduction: Current [^{177}Lu]Lu-DOTATATE treatment protocols for neuroendocrine tumours (NETs) apply fixed administered activities without individual optimisation. Given the late-responding nature of NETs, identifying biomarkers that predict treatment efficacy could enable adaptive therapeutic strategies. ***Materials and Methods:*** Patients with positive [^{68}Ga]Ga-DOTATATE scans and confirmed NETs were enrolled in the OZMOSIS OZM-067 trial (NCT02743741) and were treated with 4 cycles of [^{177}Lu]Lu-DOTATATE and imaged at 4, 24, and 72 hr post-injection after each cycle. The injected activity varied depending on the kidney dose. Out of the 90 patients in the full dataset, 73 patients and 140 tumours were included in this analysis, after excluding tumours less than 10 ml in volume. Eligible tumours were segmented using a semi-automatic adaptive thresholding method. Partial volume correction was based on recovery coefficients from phantom data. Dose rate curves were fitted using a monoexponential clearance model. Absorbed dose to tumours (Gy) and administered activity (GBq) were recorded for all treatment cycles. Patients were considered responders if they exhibited a partial response (PR) at any time point, as defined by RECIST 1.1. The average total tumour dose and the average change in Gy/GBq across all eligible tumours per patient were also recorded. ***Results:*** A systematic and statistically significant ($p<0.0001$) serial decline in Gy/GBq was observed across treatment cycles, with reductions of approximately 9%, 21%, and 31% in cycles 2, 3, and 4, respectively, relative to cycle 1. A greater reduction in Gy/GBq correlated with an increased likelihood of PR. Specifically, 65% of patients with an average Gy/GBq decrease of at least 50% had PR. A dose-response relationship was also established, starting from 4% probability of PR at low doses, increasing to 28% at 100 Gy before finally plateauing at 45% at the highest doses. Total absorbed dose and Gy/GBq decrease were observed to be uncorrelated. Interestingly, we found that 10 out of 11 patients with an average absorbed dose of at least 100 Gy to their tumours and a decrease in Gy/GBq of at least 50% presented with PR. Ongoing analysis is focused on modelling optimal injected activities based on imaging data, considering organ dose limits and radiobiology. ***Conclusion:*** Cyclic changes in absorbed dose combined with total absorbed dose could serve as a simple and meaningful predictive imaging biomarker that is easily translatable to existing clinical practice. Monitoring these changes could inform personalised treatment adaptations, enhancing therapeutic efficacy and guiding early treatment decisions.

OP-424

Systematic Comparison of Reported PRRT Tumour Dose-Response Relationships in an Independent Cohort; Pilot Results for Tumour Absorbed Dose

M. Kvassheim[1,2], *H. Ramsvik*[1], *T. Husevåg*[1], *J. Blakkisrud*[1], *C. Stokke*[1,3];
[1]*Department of Physics and Computational Radiology, Division of Radiology and Nuclear Medicine, Oslo University Hospital, Oslo, NORWAY,* [2]*Institute of Clinical Medicine, University of Oslo, Oslo, NORWAY,* [3]*Department of Physics, University of Oslo, Oslo, NORWAY.*

Aim/Introduction: A systematic review revealed thirteen publications (1-13) investigating PRRT tumour dose-response relationships. We aim to investigate if the correlations can be reproduced with our patient data. This work presents results for a pilot cohort. ***Materials and Methods:*** The methods for dosimetry and response evaluation were implemented as described in each publication in Slicer (v5.6.0), adapted as closely as feasible with our data (SPECT/CTs day 0, 1, 4, and 7 (cycle 1), day 1 (cycle 2-4), day 0 or 7 (cycle 4)). We implemented eight dosimetry methods (1-9) for a pilot cohort of 4 patients and 10 lesions. For publications reporting Pearson correlations we estimated the required sample size to achieve statistical power of 0.80 and 0.90 (alpha = 0.05) using G*Power (v3.1). ***Results:*** The percentage difference between the smallest and largest C1 tumour dose across methodologies varied between 65% and 129% (mean difference 91%). Differences in segmentation, integration methods, and imaging timepoints were contributors to variations in absorbed dose. For activity quantification by spherical VOIs of diameters 1.2 cm and 2 cm as used in (1) and (2), single-timepoint dosimetry (1) on average gave a 26% higher cycle 1 lesion dose compared to the 3-timepoint dosimetry in (2). (4-6) fit a monoexponential to threshold-based activity concentrations from day 1, 4, and 7, while (7) used CT-based segmentations and trapezoidal integration combined with a monoexponential to day 1 and 7, and the average absolute percentage difference in C1 tumour dose was 19%. Sample size calculations for Pearson correlation coefficients with p-values < 0.2 indicated that 236 or 177 lesions and 94 or 71 patients are required for power of 0.9 or 0.8, respectively. When restricting to coefficients with p-values < 0.05, the required sample sizes decreased to 113 or 85 lesions and 36 or 27 patients, for power of 0.9 or 0.8, respectively. ***Conclusion:*** Preliminary investigations in the pilot cohort indicate marked variability in tumour doses calculated across methods, which may explain reported differences in dose-response relationships. Ongoing analysis will assess the reproducibility of the dose-response relationships using an expanded cohort and response data. ***References:*** (1) Ha, EJNMMIPhys. 2024;11(1):14. (2) Del Prete, EurJNuclMedMolImaging. 2017;44(9):1490-1500. (3) Hebert, JNuclMed. 2024;65(6):923-930. (4) Ilan, JNuclMed. 2015;56(2):177-82. (5) Jahn, Cancers. 2021;13(5):962. (6) Jahn, Neuroendocrinology. 2020;110(7-8):662-670. (7) Maccauro, EurJNuclMedMolImaging. 2024;52(1):291-304. (8) Del Prete, EurJNuclMedMolImaging. 2019;46(3):728-742. (9) Mileva, JNuclMed. 2024;65(2):236-244. (10) Warfvinge, JNuclMed. 2024;65(7):1070-1075. (11) Alipour, EurJNuclMedMolImaging. 2023;50(10):2997-3010. (12) Gålne, EJNMMIRep. 2024;8(1):24. (13) Bodei, JNuclMed. 2025;66(3):449-456.

OP-425

RADIO-MARKER Study: Biomarker identification of radionuclide therapy-induced radiation responses

J. Nonnekens[1], *N. Becx*[1], *P. Morvay*[2], *T. de Wolf*[1], *P. Davies*[2], *G. Tamborino*[1], *R. Brandt*[1], *G. O'Brain*[2], *T. Heredia Genestar*[1], *M. Konijnenberg*[1], *H. Hofland*[1], *C. Badie*[2], *L. Cruz Garcia*[2];
[1]*Erasmus MC, Rotterdam, NETHERLANDS,* [2]*UK Health Security Agency, Chilton, UNITED KINGDOM.*

Aim/Introduction: Peptide receptor radionuclide therapy (PRRT) with ^{177}Lu-DOTATATE is an internal radiation treatment for patients with a neuroendocrine tumor (NET). Exposure to ^{177}Lu-DOTATATE induces cellular responses, including DNA damage response activation and gene expression changes. Understanding these radiobiological effects may facilitate biomarker identification for predicting PRRT toxicity and efficacy. Prior studies have shown correlation between radiation dose to the blood and DNA double strand break induction in peripheral blood mononuclear cells (PBMCs) or DNA damage response activation in the blood for PRRT-like treatments. This pilot study investigated the feasibility of liquid biopsies to assess radiation-induced DNA damage and transcriptional changes following PRRT. These irradiation responses could serve as potential biomarker for predicting PRRT outcomes. ***Materials and Methods:*** Patients with gastroenteropancreatic NET receiving their first cycle of 7.4 GBq ^{177}Lu-DOTATATE were included. Blood samples were collected at baseline, 4 hours, 24

hours and 8 weeks post-PRRT. PBMCs were isolated to assess DNA damage using 53BP1 immunofluorescence staining as marker for DNA double strand breaks in 10 patients. The absorbed dose to the blood was calculated by converting radioactive levels measured in a gamma counter using the MIRD formalism. Transcriptomic effects of selected genes were analyzed in whole blood by qPCR, and full transcriptome analysis was performed in 3 patients using cDNA nanopore sequencing (PromethION 2 Solo, Oxford Nanopore Technologies). ***Results:*** Following PRRT, the average number of 53BP1 foci per nucleus increased by 0.57±0.07 (mean±SEM) ($p<0.001$) and 0.34±0.13 (mean±SEM) ($p=0.02$) at 4 and 24 hours, respectively, compared to baseline. The absorbed dose to blood was on average 34.61±13.49 mGy (mean±SD) at 4 hours and 93.98±33.60 mGy (mean±SD) at 24 hours. A significant correlation was found between the number of radiation-induced foci and absorbed dose to the blood. Despite the low dose to circulating PBMCs, qPCR analysis showed significant upregulation of DNA damage response genes FDXR, MDM2, GADD45 and DDB2 after 24 hours. For the first time, full transcriptome sequencing showed significant upregulation of DNA damage response genes at 4 and 24 hours post-PRRT, alongside a striking downregulation of immune response genes at 8 weeks. ***Conclusion:*** Our results here show for the first time direct evidence that PRRT with ^{177}Lu-DOTATATE induces measurable transcriptional changes in PBMCs, linking radiation dose to molecular response. These findings introduce novel biomarkers candidates for predicting clinical outcomes of PRRT and highlight the potential of sequencing-based liquid biopsies for radiation response monitoring.

OP-426

Comparison of radiation-induced DNA damage in PBMCs and absorbed dose to the blood between two therapy cycles with [^{177}Lu]Lu-PSMA-617

N. Zindler[1], *H. Scherthan*[2], *S. Schumann*[1], *P. E. Hartrampf*[1], *I. Strobel*[1], *M. Lassmann*[1], *U. Eberlein*[1];
[1]*University Hospital Würzburg, Würzburg, GERMANY,*
[2]*Bundeswehr Institute of Radiobiology affiliated to the University of Ulm, Munich, GERMANY.*

Aim/Introduction: The aim was to compare radiation-induced DNA double strand break (DSB) damage and repair in peripheral blood mononuclear cells (PBMCs) in-vivo and ex-vivo, as well as the absorbed doses to the blood between the first and third cycles of [^{177}Lu]Lu-PSMA-617 therapy in patients with prostate cancer. ***Materials and Methods:*** Blood samples were collected from eight patients before therapy for ex-vivo analysis and to obtain background values. Ex-vivo irradiation with [^{177}Lu]$LuCl_3$ solution was performed to result in 50mGy absorbed dose to the blood. PBMCs were isolated and fixed with ethanol before and immediately after irradiation or after 3h, 6h or 24h. After administration of 7.4GBq [^{177}Lu]Lu-PSMA-617 blood samples were collected at 1h and 24h for in-vivo analysis. All samples were analyzed for DSB foci by manually enumerating γH2AX+53BP1 colocalizing foci in 100 cells per sample. The number of radiation-induced foci (RIF) was determined by subtracting the average number of foci per cell of each non-irradiated sample from the corresponding irradiated samples. The absorbed dose to the blood was calculated for each patient at 1h, 24h and the total absorbed dose using blood sample measurements with a calibrated germanium detector, patient-specific dose rate measurements, and whole-body imaging. To account for inter-patient variability, RIF numbers at 1h post-therapy were normalized to the absorbed dose to the blood. Paired t-tests were used to test for differences in all parameters between the first and third treatment cycles. ***Results:*** RIF numbers were quantified in both ex-vivo and in-vivo samples across the first and third therapy cycles. In the ex-vivo analysis, RIF values decreased with repair time for both cycles: 0h(n=8): 0.75±0.25(first cycle), 0.60±0.18(third cycle); 3h(n=8): 0.41±0.16, 0.31±0.21; 6h(n=7): 0.21±0.21, 0.21±0.14; 24h(n=7): 0.15±0.25, -0.02±0.16. In-vivo RIF numbers at 1h and 24h post-injection were similar for both cycles: 1h(n=7): 0.46±0.21, 0.49±0.10; 24h(n=7): 0.51±0.33, 0.45±0.20. The absorbed dose to the blood was similar for both cycles:1h: (28±6)mGy, (29 ±7)mGy;24h: (225±65)mGy, (245±65) mGy; total: (293±70)mGy, (298±62)mGy. Normalized RIF/mGy values were similar: 1h: (0.016±0.006)mGy^{-1}, (0.017±0.003)mGy^{-1}. No statistically significant differences were observed between the two cycles ($p>0.05$) for all parameters, indicating consistent levels of radiation-induced DNA damage and absorbed dose to the blood across repeated treatment cycles. ***Conclusion:*** Further patient recruitment is needed to increase the statistical power of the study. In addition, clinical parameters, tumor doses and organ doses will be analyzed across treatment cycles to identify potential correlations between these variables and the observed DNA damage and repair.

OP-427

Potential for home-based blood sampling for estimating maximum tolerated activity for [131I]-NaI dosimetry-patients

S. Synnes Lindseth[1], *L. T. G. Mikalsen*[1], *A. Tulipan*[2,3], *E. Hernes*[2], *C. Stokke*[1,4];
[1]*Department of Physics and Computational Radiology, Division of Radiology and Nuclear Medicine, Oslo University Hospital, Oslo, NORWAY,* [2]*Department of Nuclear Medicine, Division of Radiology and Nuclear Medicine, Oslo University Hospital, Oslo, NORWAY,* [3]*Department of Radiology, Nuclear medicine/PET-centre, Haukeland University Hospital, Bergen, NORWAY,* [4]*Department of Physics, University of Oslo, Oslo, NORWAY.*

Aim/Introduction: Patients at Oslo University Hospital (OUS) undergoing pre-therapeutic [131I]-NaI dosimetry for differentiated thyroid cancer currently visit the hospital four times over the course of one week for venous blood sampling and whole-body probe measurements. These measurements are used to estimate blood and whole-body retention times (τ_b and τ_{wb}, respectively) to calculate the maximum tolerated activity (MTA), in accordance with EANM guidelines. We present a simulation study investigating a novel approach in which patients collect capillary blood samples at home. The aim is to assess whether this procedure can produce MTA-estimates comparable to the current clinical protocol, thereby demonstrating the feasibility for future clinical studies. ***Materials and Methods:*** In a retrospective data analysis of 56 patients who underwent MTA estimation at OUS between 2020 and 2025, we divided the patients into a training set (n = 40) and a validation set (n = 16). A linear regression model to predict the dose factor (D/A) from τ_b was developed using the training set and validated via five-fold cross-validation. For each patient in the validation set, 1500 bootstrap samples of τ_b were generated to simulate 20 µL capillary microsampling based on the measured activity concentration in the collected venous blood samples. Uncertainty in each simulated τ_b was modelled by incorporating a 5% relative standard error in sample volume, expected count rate, and acquisition time. Simulated MTA-values (MTA_{home}) were computed by dividing the 2 Gy absorbed dose limit by the simulated D/A-values and compared to the reference MTA-values. ***Results:*** Reference MTA-values for the 56 patients ranged from 5 to 30 GBq (6 to 26 GBq for the validation patients). The regression model showed strong predictive performance, with an $R^2 = 0.96 \pm 0.02$ across the five cross-validation folds. Predicted MTA_{home}-values had a mean relative error of 10 ± 8 % across all iterations with a root mean squared error of 1.57 GBq compared to the reference values. ***Conclusion:*** Our analysis suggests that home-based capillary blood sampling for MTA estimation may provide estimates comparable to those obtained through the current

hospital-based protocol. This new approach could significantly reduce the need for hospital visits, and further evaluation in a prospective clinical study is planned.

OP-428

Long-Term Renal Safety of Personalized [^{177}Lu]Lu-DOTA-TATE PRRT: Evidence from the NCT02754297 trial Supporting Absorbed Doses Beyond Conventional Limits

S. Kurkowska[1], *P. L. Esquinas*[2], *A. Rahmim*[1], *X. Hou*[2], *F. A. Buteau*[3], *A. Beaulieu*[3], *G. April*[3], *F. Arsenault*[3], *J. M. Beauregard*[3], *C. Uribe*[2];
[1]*BC Cancer Research Institute, Vancouver, BC, CANADA,* [2]*BC Cancer, Vancouver, BC, CANADA,* [3]*CHU de Québec – Université Laval, Quebec City, QC, CANADA.*

Aim/Introduction: Peptide receptor radionuclide therapy (PRRT) with [177Lu]Lu-DOTA-TATE is a well-established therapy for neuroendocrine neoplasms. Fixed-activity injections lead to substantial absorbed dose variability in tumors and organs and can leave many patients undertreated. To address this limitation, the Phase II P-PRRT clinical trial (NCT02754297) evaluated a personalized approach designed to maximize tumor irradiation while preserving renal function, using individualized dosimetry to achieve a targeted renal dose of 26.5Gy (updated from 23Gy after SPECT recalibration). We present the long-term kidney safety outcomes of this personalized approach. ***Materials and Methods:*** We analysed 189 treatment-naïve patients who underwent four cycles of PRRT. Administered activity was individually tailored: initial cycles were personalized based on glomerular filtration rate (GFR) and body surface area, subsequent cycles were based on SPECT/CT kidney dosimetry. Dose reductions (25-50%) were applied to patients with renal/hematologic risk factors. Kidney dosimetry used simplified small-sphere VOI segmentation, monoexponential modelling and OLINDA-derived S-values. Renal safety was monitored via serial eGFR measurements and CTCAE grading. Longitudinal kidney function changes were evaluated using mixed-effects modelling with random intercepts and slopes, adjusting for baseline function, follow-up time, and cumulative renal dose. ***Results:*** Patients received a median cumulative injected activity of 34.97 GBq (range: 5.89-102.67 GBq), resulting in a median cumulative renal absorbed dose of 26.16 Gy (range: 9.54-36.96 Gy). Over a median follow-up duration of 20 months (range: 6-81 months), clinically significant renal toxicity occurred in only four patients: one progressed from baseline Grade 3 to Grade 4 (5.89 GBq; 20.4 Gy, cumulative) and three progressed from baseline Grade 2 to Grade 3 (6.3-13.7 GBq; 18.7-21.8 Gy, cumulative). The cohort showed a 4.68% annual decline in eGFR ($p<0.001$), with substantial interpatient variability. Mixed-effects modelling identified baseline eGFR as the strongest predictor of renal outcome ($\beta=-0.161$, $p<0.001$). Cumulative renal absorbed dose showed no significant association with kidney function changes ($p = 0.178$), likely reflecting the intentional prescription of injected activities to achieve doses below the toxicity threshold. Notably, over half of the patients safely received a cumulative activity exceeding the standard 29.6 GBq (4×7.4 GBq). ***Conclusion:*** Personalized PRRT approach demonstrates long-term renal safety, challenges the conventional 23Gy renal absorbed dose limit, and underscores radiobiological differences from external beam radiotherapy, suggesting current limits may unnecessarily restrict therapeutic potential. The strong association between baseline kidney function and renal outcomes emphasizes the need for careful patient stratification, while supporting dose escalation beyond traditional thresholds for patients with preserved renal function.

1006

Monday, October 6, 2025, 15:00 - 16:30
Room 117

Clinical Oncology Track - TROP Session - Oncology & Theranostics Committee: NET and PRRT

OP-429

Dosimetry of [^{177}Lu]Lu-edotreotide in patients with grade 1 or grade 2 gastroenteropancreatic neuroendocrine tumours: Results from the COMPETE Phase 3 trial

E. Deshayes[1], *A. M. García-Burrilo*[2], *H. Amthauer*[3], *C. Ansquer*[4], *R. Garcia-Carbonero*[5], *A. Teulé Vega*[6], *H. J. Verberne*[7], *J. B. Cwikla*[8], *R. Srirajaskanthan*[9], *A. Buck*[10], *C. M. Grana*[11], *R. P. Baum*[12], *L. O. Dierickx*[13], *M. Michael*[14], *J. Strosberg*[15], *L. De Mestier*[16], *M. Pavel*[17], *P. Jimenez-Fonseca*[18], *A. Kollàr*[19], *B. Viglianti*[20], *A. Kluge*[21], *P. Ritt*[22], *C. Lachachi*[23];
[1]*SFMN, Montpellier Cedex 5, FRANCE,* [2]*Vall d'Hebron University Hospital, Barcelona, SPAIN,* [3]*Charité – Universitätsmedizin Berlin, Corporate Member of Freie Universität Berlin and Humboldt-Universität zu Berlin, Berlin, GERMANY,* [4]*Centre Hospitalier Universitaire de Nantes, Nantes, FRANCE,* [5]*Hospital Universitario 12 de Octubre, Imas12, UCM, Madrid, SPAIN,* [6]*Institut Català d'Oncologia, Barcelona, SPAIN,* [7]*Amsterdam UMC, Amsterdam, NETHERLANDS,* [8]*Diagnostic and Therapeutic Center – Gammed, Warsaw, POLAND,* [9]*King's College Hospital, London, UNITED KINGDOM,* [10]*Universitätsklinikum Würzburg, Würzburg, GERMANY,* [11]*IRCCS European Institute of Oncology Milano, Milano, ITALY,* [12]*Curanosticum Wiesbaden-Frankfurt, Wiesbaden, GERMANY,* [13]*Institut Universitaire du Cancer Toulouse Oncopole, Toulouse, FRANCE,* [14]*Peter MacCallum Cancer Centre, University of Melbourne, Melbourne, AUSTRALIA,* [15]*Moffitt Cancer Center, Tampa, FL, UNITED STATES OF AMERICA,* [16]*Beaujon Hospital, Clichy, FRANCE,* [17]*Universitätsklinikum Erlangen, Erlangen, GERMANY,* [18]*Hospital Universitario Central de Asturias, Oviedo, SPAIN,* [19]*Universitätsspital Bern, Bern, SWITZERLAND,* [20]*University of Michigan Medical Center, Ann Arbor, MI, UNITED STATES OF AMERICA,* [21]*ABX-CRO advanced pharmaceutical services Forschungsgesellschaft mbH, Dresden, GERMANY,* [22]*ITM Oncologics GmbH, Garching, GERMANY,* [23]*Edouard Herriot Hospital, Lyon, FRANCE.*

Aim/Introduction: COMPETE is a Phase 3, multicentric, randomised, controlled and open-label trial, comparing efficacy and safety of [^{177}Lu]Lu-edotreotide with everolimus in patients with grade 1 or grade 2 gastroenteropancreatic neuroendocrine tumours (GEP-NETs). This is the first Phase 3 trial reporting dosimetry assessments in all patients treated with a radiopharmaceutical therapy ([^{177}Lu]Lu-edotreotide). Here, we report the dosimetry assessments with regard to efficacy and safety of [^{177}Lu]Lu-edotreotide. ***Materials and Methods:*** Patients (aged ≥18 years) with grade 1 or grade 2 inoperable, progressive, somatostatin receptor-positive GEP-NETs (Ki-67 ≤20%) were randomised (2:1) to receive [^{177}Lu]Lu-edotreotide (max. 4 cycles of 7.5 GBq/cycle every 3 months, or until disease progression) versus everolimus (10 mg daily up to 30 months, or until disease progression). The primary endpoint was progression free survival (PFS) per RECIST v1.1. Absorbed dose (AD) for target tumours and all organs besides red marrow were determined imaging based (planar and SPECT) at cycle 1. Red marrow dosimetry was performed in a subset of patients (n=20) with additional blood samples at prespecified timepoints to determine the time-activity curves of blood. ***Results:*** A total of 309 patients were randomised to [^{177}Lu]Lu-edotreotide (n=207) versus everolimus (n=102). The median PFS for [^{177}Lu]Lu-edotreotide was significantly prolonged compared to everolimus (23.9 versus 14.1 months, p=0.022; HR: 0.67, 95% CI: 0.48-0.95). Dosimetry evaluations were performed

in all the patients treated with [^{177}Lu]Lu-edotreotide. Mean AD and AD coefficient in evaluable tumour lesions (n=157) were 27.5 Gy/7.5 GBq and 3.67 Gy/GBq, respectively. The mean AD coefficients in kidneys, whole body, liver, spleen, urinary bladder wall and red marrow were 0.42, 0.03, 0.03, 0.31, 0.63, 0.02 Gy/GBq, respectively. Corresponding ADs were 3.1, 0.2, 0.2, 2.4, 4.7 and 0.1 Gy/7.5 GBq, respectively. Additionally, the moderate AD levels in normal organs support the favourable safety profile of [^{177}Lu]Lu-edotreotide. A lower frequency of renal treatment-emergent adverse events was observed with [^{177}Lu]Lu-edotreotide versus everolimus (14.7% versus 21.2%); haematuria and proteinuria being the most common. Similarly, haematological treatment-emergent adverse events were comparable with [^{177}Lu]Lu-edotreotide versus everolimus (40.1% versus 41.4%), with the most common events being anaemia, lymphopenia and thrombocytopenia. ***Conclusion:*** The results showed that ADs to normal organs were lower than the established thresholds[1]. Substantially higher AD in tumour lesions compared to normal organs suggests a favourable therapeutic index. The dosimetry assessments are in agreement with the efficacy and safety outcomes of the trial. ***References:*** 1. Wahl RL et al, 2021. J.Nuc.Med 62:23-35S.

OP-430

A decade of Peptide Receptor Radionuclide Therapy with 177Lu-DOTATATE: Results from the Spanish SEPTRALU Registry

M. Mitjavila Casanovas[1], *V. Pubul*[2], *P. Bello*[3], *A. García Burillo*[4], *M. Castellón*[5], *L. García Cañamaque*[6], *A. Piñeiro*[7], *M. Velasco*[8], *M. Nevares*[9], *R. Valverde*[10], *A. Padilla*[11], *B. Llana*[12], *Z. Nogareda*[2], *A. Custodio*[13], *J. Hernando*[4], *D. Balaguer*[14], *J. Arbizu*[15], *M. Tabuenca*[16], *D. Gomez Sanchez*[17], *M. Orduña*[18], *J. Ardila*[19], *P. Jimenez-Fonseca*[12], *A. Carmona-Bayonas*[20];
[1]*Hospital Universitario Puerta de Hierro Majadahonda, Madrid, SPAIN,* [2]*Complejo Hospitalario Universitario de Santiago, Santiago de Compostela, SPAIN,* [3]*Hospital Universitario La Fe, Valencia, SPAIN,* [4]*Hospital Universitario Vall d'Hebron, Barcelona, SPAIN,* [5]*Hospital Universitario Virgen de la Arrixaca, Murcia, SPAIN,* [6]*Hospitales H.M. Sanchinarro, Madrid, SPAIN,* [7]*Hospital Universitario Virgen de las Nieves, Granada, SPAIN,* [8]*Hospital Universitario de la Santa Creu i Sant Pau, Barcelona, SPAIN,* [9]*Hospital Universitario de Burgos, Burgos, SPAIN,* [10]*Hospital Universitario de Cruces Cruces, Bilbao, SPAIN,* [11]*Hospital General Universitario de Ciudad Real, Ciudad Real, SPAIN,* [12]*Hospital Universitario Central de Asturias, Oviedo, SPAIN,* [13]*Hospital Universitario La Paz, Madrid, SPAIN,* [14]*Hospital Universitario Doctor Pesset, Valencia, SPAIN,* [15]*Clínica Universidad de Navarra, Pamplona, SPAIN,* [16]*Hospital Universitario 12 de Octubre, Madrid, SPAIN,* [17]*Hospital Universitario de Navarra, Pamplona, SPAIN,* [18]*Hospital Universitario Ramón y Cajal, Madrid, SPAIN,* [19]*Hospital Universitario Gregorio Marañón, Madrid, SPAIN,* [20]*Hospital General Universitario Morales Meseguer, Murcia, SPAIN.*

Aim/Introduction: 177Lu-DOTATATE (PRRT) has become a cornerstone in the treatment of advanced and unresectable gastroenteropancreatic neuroendocrine tumors (GEP-NETs). Objective: To describe the accumulated clinical experience with PRRT in a real-life context. ***Materials and Methods:*** Data were obtained from the SEPTRALU registry which includes consecutively recorded patients with NETs treated with 177Lu-DOTATATE across 26 Spanish hospitals. Survival was evaluated using Kaplan-Meier estimates, and toxicity was graded according to CTCAEv3.0. ***Results:*** A total of 919 patients were recorded (December 2017/April 2025) with a mean age of 66 years (range, 12-91) and 58% were male. Functioning NETs were present in 28%, including 5% carcinoid syndrome. Most tumors were well-differentiated (90%), with a median Ki67 of 6% (range: 1-80%). Primary tumor sites included the pancreas (35%), small intestine (31%), lung (9%), pheochromocytoma/paraganglioma (PPGL) (5.5%), other digestive tract locations (5.5%), and unknown origin (7%). Metastases were most frequently located in the liver (88.8%), lymph nodes (65%), bone (28%), peritoneum (18%), and lung (9%). Prior treatments included primary tumor resection (53%), metastasectomy (24%), and locoregional liver therapies (12%). Radiologic response was: partial response (23%), disease control (76%), progression (9%), and unavailable or non-measurable lesions (15%). Pancreatic NETs had higher response rates (30.4%) compared to intestinal NETs (16%). Progression-free survival was 33.3 months, with site-specific variation: intestine (42.5), PPGL (33.6), pancreas (28), and lung (19.6 months). Overall survival was 52.7 months, similar between pancreatic NETs (61.23, 95% CI, 53.5-69.0 months) and ileal NETs (57.9, 95% CI, 49.1-66.7 months; p=0.17). Grade 3-4 toxicity was low (2.3%). The most common adverse effects were nausea (20%), hematologic (18%), emesis (14%), asthenia (13%), urticaria (9%), and alopecia (6%). ***Conclusion:*** This large real-world series confirms the efficacy and safety profile of 177Lu-DOTATATE in the treatment of advanced and unresectable NETs of various origins.

OP-431

Safety and Efficacy of ^{177}Lu-LNC1010 in Advanced SSTR-Positive Neuroendocrine Tumors: A Single-Center, Single-Arm, Phase II Study

W. Guo[1], *Y. Chen*[1], *H. Fu*[1], *L. Zhao*[1], *J. Zhang*[2], *X. Chen*[2], *H. Chen*[1];
[1]*The first affiliated hospital of Xiamen University, Xiamen City, CHINA,* [2]*Yong Loo Lin School of Medicine, National University of Singapore, Singapore, SINGAPORE.*

Aim/Introduction: This open-label, single-arm, single-center phase II clinical trial evaluated the safety and efficacy of ^{177}Lu-LNC1010, an optimized long-acting somatostatin analog (SSA), in patients with metastatic neuroendocrine tumors (NETs). ***Materials and Methods:*** A total of 20 patients with histologically confirmed, unresectable metastatic NETs and progressive disease after prior treatment with SSA and/or tyrosine kinase inhibitors were enrolled. Participants received up to four cycles of peptide receptor radionuclide therapy (PRRT) with a fixed dose of ^{177}Lu-LNC1010 (3.33 GBq per cycle) administered at 8-week intervals, as recommended by a prior phase I clinical trial. Adverse events (AEs) and treatment-related adverse events (TRAEs) were graded according to the National Cancer Institute Common Terminology Criteria for Adverse Events (CTCAE), version 5.0. Treatment response was assessed using RECIST version 1.1. Kaplan-Meier analysis was performed to estimate progression-free survival (PFS) and overall survival (OS). ***Results:*** A total of 20 patients (9 males, 11 females; median age 53 years) received 62 cycles of ^{177}Lu-LNC1010 PRRT. Grade 3 or 4 treatment-related hematotoxicities occurred in six patients (30%), with thrombocytopenia, leukopenia, and neutropenia being the most common. One patient (5%) developed grade 3 TRAE-related hepatotoxicity after three cycles of PRRT. No grade ≥3 nephrotoxicity was observed. According to RECIST 1.1, disease control was achieved in 19 of 20 patients (95%). Among the 16 patients evaluable by imaging, 15 (93.8%) achieved disease control, including six with partial response (PR) and nine with stable disease (SD). After a median follow-up of 19.5 months (range 0-29), 8 patients (40%) had died, while 12 patients (60%) survived. The median PFS was 12 months (95% confidence interval [CI]: 9.82-14.18), and the median OS was 22 months (95% CI: 17.16-26.84). Disease control was significantly associated with prolonged PFS and OS ($P < 0.001$). ***Conclusion:*** PRRT with 3.33 GBq of ^{177}Lu-LNC1010 was well tolerated and demonstrated an acceptable safety profile. A high disease control rate (93.8%) was achieved, which was positively correlated with improved PFS and OS.

OP-432

Radiolabeled Somatostatin Receptor (SSTR) Antagonist versus Agonist for Peptide Receptor Radionuclide Therapy in Patients with SSTR positive Neuroendocrine Tumors - a retrospective Basket study

A. Mushaweh[1], *C. Eigler*[1], *L. McDougall*[1], *A. Bauman*[1], *E. Christ*[2], *P. Bernhardt*[3], *G. Nicolas*[1], *M. Fani*[1], *D. Wild*[1];
[1]*Department Theragnostics, University Hospital of Basel, Basel, SWITZERLAND,* [2]*Department of Endocrinology, Diabetology and Metabolism, University Hospital of Basel, Basel, SWITZERLAND,* [3]*Department of Medical Radiation Sciences, Institute of Clinical Sciences, Sahlgrenska Academy at University of Gothenburg, Gothenburg, SWEDEN.*

Aim/Introduction: Peptide Receptor Radionuclide Therapy (PRRT) with lutetium-177 labeled somatostatin receptor (SSTR) ([^{177}Lu]Lu-DOTATOC or -DOTATATE) has limited response rate and durability. The SSTR antagonist [^{177}Lu]Lu-DOTA-JR11 offers potentially increased tumor doses with better efficacy. Our aim was to conduct an intrapatient comparison of tumor and organ absorbed doses, safety, and median progression free survival (PFS) after therapy with [^{177}Lu]Lu-DOTATOC and [^{177}Lu]Lu-DOTA-JR11 in patients with early relapsing metastatic neuroendocrine tumors (NETs) after standard PRRT. ***Materials and Methods:*** In this preplanned retrospective, single-center, open label study, 15 consecutive patients with metastatic NETs and progression ≤ 12 months after last PRRT with [^{177}Lu]Lu-DOTATOC (2-4 cycles, 5.6- 7.5 GBq/cycle, total 39 cycles) were included. The patients received a rechallenge PRRT with 1-2 cycles [^{177}Lu]Lu-DOTATOC (standard injected activity: 5.1- 7.4 GBq/cycle, total 18 cycles) followed by 1-2 cycles [^{177}Lu]Lu-DOTA-JR11 (2 GBq/m2 × body surface area: 2.7-4.8 GBq/cycle, total 18 cycles) in an interval of 10±1 weeks. Endpoints: Progression free survival (follow-up with imaging every 3-6 months), safety (CTCAE V 5.0), and imaging-based tumor and organ absorbed doses (3D dosimetry using Olinda). ***Results:*** The median (range) of the mean tumor, kidney and bone marrow absorbed doses of one treatment cycle were 18.5 (1.0-354), 2.2 (1.1-6.7) Gy/cycle and 0.54 (0.32-0.66) for [^{177}Lu]Lu-DOTA-JR11 and 12.9 (0.8-223), 2.0 (0.9-4.1) and 0.21 (0.11-0.41) Gy/cycle for [^{177}Lu]Lu-DOTATOC, respectively. Tumor-to-bone marrow dose ratios of both compounds were in the same range. There were two reversible grade 3 adverse events (lymphopenia, hypoalbumenia) after [^{177}Lu]Lu-DOTATOC therapy, and six reversible grade 3 adverse events (anemia, lymphopenia) after [^{177}Lu]Lu-DOTA-JR11 therapy. No grade ≥4 events occurred. Median PFS was 11 months (95% CI: 9-13) after standard therapy with 2-4 cycles [^{177}Lu]Lu-DOTATOC and 14 months (95% CI: 10-18) after 1-2 cycles [^{177}Lu]Lu-DOTATOC plus 1-2 cycles [^{177}Lu]Lu-DOTA-JR11 (Hazard ratio 0.34, p=0.007) in the same NET patients. ***Conclusion:*** The median (range) tumor absorbed dose per cycle is 2.1 (0.9-6.4) times higher with [^{177}Lu]Lu-DOTA-JR11 compared to [^{177}Lu]Lu-DOTATOC in the same patients resulting in a median PFS benefit of 3 months (95% CI: 1.4-10.8) for early relapsing NET patients following standard PRRT. No relevant or persistent adverse events were detected which justifies further prospective evaluation of [^{177}Lu]Lu-DOTA-JR11 in early relapsing NET patients.

OP-433

Safety Profile of [^{177}Lu]Lu-DOTATATE: A Disproportionality Analysis of Adverse Events from the WHO Global Pharmacovigilance Database

J. Vigne*, T. Ladrière, B. Chrétien, A. Bignon-Bretagne, K. Bouhier-Leporrier, C. Dolladille;*
University Hospital of Caen, Caen, FRANCE.

Aim/Introduction: Peptide receptor radionuclide therapy (PRRT) with [177Lu]Lu-DOTATATE has become an effective treatment for patients with metastatic or inoperable neuroendocrine tumors (NETs), owing to its targeted action on somatostatin receptors. While clinical trials, such as NETTER-1[1], have demonstrated its efficacy and overall safety in a limited population of selected patients, real-world safety data remain scarce. ***Materials and Methods:*** This study utilized VigiBase®, the World Health Organization›s global database of individual case safety reports (ICSRs), to evaluate the safety profile of [177Lu]Lu-DOTATATE under real-world conditions. A retrospective disproportionality analysis was performed on all reports submitted up to March 1st, 2024, after deduplication. Safety signals were identified using the Information Component (IC) metric, which estimates the strength of association between a drug and a specific adverse event. A positive lower limit of the 95% confidence interval (IC025 > 0) was considered indicative of a statistically robust association. ***Results:*** Among 3,984 reports analyzed, 86% were submitted between 2021 and 2024, predominantly from the Americas (65%), and primarily by physicians (45%). Adverse events were categorized into 13 main classes and 37 subclasses. The most significant associations were observed with hematologic disorders (IC025 = 2.15), hepatic disorders (IC025 = 1.43), renal failure (IC025 = 1.16), infections (IC025 = 0.91), and malignant hematologic neoplasms (n = 43, IC025 = 2.48). Temporal relationships between treatment and event resolution were supported by dechallenge data in multiple cases. The most frequently co-reported adverse events included hematologic and gastrointestinal disorders within the top 25 co-occurrence patterns. Median time-to-onset ranged from 16 days (metabolic disorders) to 815.5 days (hematologic malignancies). ***Conclusion:*** This global pharmacovigilance study provides valuable insights into the real-world safety profile of [177Lu]Lu-DOTATATE and may contribute to optimizing its clinical use in NET management. ***References:*** 1.Strosberg Jonathan, El-Haddad Ghassan, Wolin Edward, Hendifar Andrew, Yao James, Chasen Beth, et al. Phase 3 Trial of 177Lu-Dotatate for Midgut Neuroendocrine Tumors. New England Journal of Medicine. 2017;376:125-35.

OP-434

Impact of ^{18}F-FDG PET in Patients with Advanced Metastatic Neuroendocrine Tumors Undergoing Rechallenge PRRT: Final Results from a Multicenter WARMTH Study

G. Santo[1], *M. Rodrigues*[1], *D. Paez*[2], *L. Kabasakal*[3], *K. Kairemo*[4], *C. Grana*[5], *R. Baum*[6], *G. di Santo*[1], *I. J. Virgolini*[1];
[1]*Department of Nuclear Medicine, Innsbruck Medical University, Innsbruck, AUSTRIA,* [2]*Nuclear Medicine and Diagnostic Imaging Section, Division of Human Health, International Atomic Energy Agency, Vienna, AUSTRIA,* [3]*Department of Nuclear Medicine, Faculty of Medicine, Yeditepe University School of Medicine, İstanbul, TÜRKIYE,* [4]*Nuclear Medicine & Theragnostics, Docrates Cancer Center, Helsinki, FINLAND,* [5]*Radiometabolic Therapy Unit, IRCCS IEO European Institute of Oncology, Milan, ITALY,* [6]*Theranostics Centre for Molecular Radiotherapy and Precision Oncology, Zentralklinik,, Bad Berka, GERMANY.*

Aim/Introduction: The aim of this multicenter study was to evaluate the impact of metabolic status and its changes measured by ^{18}F-FDG PET on treatment response and survival in advanced/metastatic NET patients undergoing rechallenge PRRT. ***Materials and Methods:*** A total of 100 patients were retrospectively included. All patients received two PRRT courses and underwent both ^{68}Ga-DOTA-TOC/TATE and ^{18}F-FDG PET/CT (before PRRT, 3-months after PRRT, and every 6-9 months thereafter). Baseline patient characteristics were correlated with FDG-positivity at baseline and during treatment. Metabolic status and its changes (no change vs. FDG+/FDG– vs. FDG–/FDG+) at baseline, after the first and the second treatment course were correlated with response, time-to-progression(TTP), and overall survival(OS). ***Results:*** In 43/100 patients(G1:17%, G2:67%, G3:19%), primary tumor site was pancreas, liver was involved in 90% of cases. 50% of patients were FDG-positive prior to treatment. There was a trend toward significance for a higher prevalence of FDG-positivity in patients with pancreatic-NETs compared to other primary sites (60% vs.

42%,p=0.053). After the first PRRT course, 37% were FDG-positive:20 patients became metabolically negative, while 7 became FDG-positive. Post-treatment metabolic status correlated significantly with NET grade (FDG+ G1:19%, G2:33%, G3:66%;p=0.009). There was a trend toward significance in G1/G2 patients converting from FDG+ to FDG− compared to G3 patients (p=0.054). After the rechallenge, 41% were FDG-positive: 27 patients converted to FDG−, 16 became FDG+. The correlation between NET grade and metabolic status persisted after rechallenge (FDG+ G1:25%, G2:31%, G3:89%;p<0.0001), indicating that FDG+ status increased progressively in G3 patients (p=0.023). Conversely, in G2-NET there was an increase in those who became FDG− after rechallenge compared to the first course (+7patients). At a median follow-up of 24 months after the initial treatment, 39% of patients had progressed. FDG-status after the first treatment was significantly correlated with TTP (FDG+12 months [95%CI:8.7-15.3] vs. FDG− not reached,p<0.0001). Also changes in glucose metabolism were associated with TTP (p<0.001). After a median follow-up time of 117.6 months(range:38.4-180), FDG-status after the first treatment was significantly correlated with OS (mOS:FDG+94.8 months[95%CI:85.1-104.5] vs. FDG−144 months[95%CI:142.2-145.7],p<0.0001). Patients who became metabolically negative after the initial treatment had the best mOS(p=0.034). Overall response after rechallenge correlated significantly with survival (p=0.002). ***Conclusion:*** Assessment of metabolic status before PRRT and during follow-up allows prediction of TTP and OS, even in patients considered for rechallenge. NET grade influences changes in metabolic status. Standardization of the use of dual-tracer imaging in patients receiving PRRT could guide clinical management.

OP-435

[^{177}Lu]Lu-DOTA-LM3 for PRRT in Metastatic NET: Dosimetry, Response and Safety

T. Speicher, *A. Schaefer-Schuler, M. Mavrommatis, M. B. Bastian, A. Blickle, S. Maus, M. Bartholomä, C. Burgard, F. Rosar, S. Ezziddin; Nuclear Medicine, Saarland University Hospital, Homburg, GERMANY.*

Aim/Introduction: Recently, somatostatin receptor (SSTR) antagonists have gained attention for peptide receptor radionuclide therapy (PRRT) due to their higher receptor binding capacity and promising preclinical results. This study aimed to evaluate the dosimetry, response and safety of the ^{177}Lu-labeled SSTR antagonist [^{177}Lu]Lu-DOTA-LM3 in patients with metastatic NET. ***Materials and Methods:*** This retrospective study included 12 patients with advanced NET undergoing [^{177}Lu]Lu-DOTA-LM3 PRRT; hybrid dosimetry using serial planar whole-body and SPECT/CT imaging at 24 h, 48 h, and beyond 72 h post-injection; absorbed dose estimation for kidneys and spleen through IDAC 2.1 in combination with the IDAC reference man model. Tumor absorbed doses based on sphere model with ^{177}Lu dose factors interpolated according to mass of each lesion (determined by CT imaging). Adverse events according to CTCAE v5.0, response by EORTC and RECIST 1.1 criteria. ***Results:*** A total of 21 treatment cycles were administered (mean activity: 5.02±0.66 GBq per cycle). The primary tumor site was pancreatic (33%), intestinal (42%), or other (25%). Tumor grading was G1 (18%), G2 (45%), and G3 (36%). According to RECIST 1.1, partial response was observed in 28%, stable disease in 57%, and progression in 14%. EORTC criteria showed response in 33%, stable disease in 44%, and progression in 22%. Metastatic lesions were predominantly hepatic (34 lesions in 10/12 patients), with lymph node and bone involvement in 5/12 patients each**.** Tumor lesion dosimetry revealed considerable intra- and inter-patient variability, with a mean absorbed dose of 3.12±1.9 Gy/GBq (range: 0.36-7.59 Gy/GBq). The mean absorbed doses to the kidneys and the spleen were 1.08±0.53 Gy/GBq and 1.08± 0.75 Gy/GBq, respectively. Three patients showed renal doses ≥2.0 Gy/GBq. Tumor-to-organ dose ratios averaged 3.15±1.99 (kidneys) and 3.72±3.28 (spleen). Alongside several low-grade adverse events, one patient developed hepatotoxicity (CTC-3). No grade 4 or 5 toxicities occurred, despite elevated renal doses in some patients. ***Conclusion:*** [^{177}Lu]Lu-DOTA-LM3 therapy delivers high absorbed doses to tumor lesions with a favorable tumor-to-kidney dose ratio and benign toxicity profile. These findings support exploration of this promising therapeutic option in patients with advanced NET.

OP-436

Novel FAP-Targeted Radiopharmaceutical Therapy with ^{177}Lu/^{90}Y/^{225}Ac-3BP-3940 in Patients with Pancreatic Ductal Adenocarcinoma (PDAC)

J. Zhang[1], *J. Li*[1], *A. Eismant*[2], *L. Greifenstein*[2], *A. Klega*[2], *C. Landvogt*[2], *C. Mueller*[2], *T. Zhao*[1], *O. Klein*[3], *B. Jaeschke*[3], *R. P. Baum*[2]; [1]*National University of Singapore, Singapore, SINGAPORE,* [2]*Center for Advanced Radiomolecular Precision Oncology, Wiesbaden, GERMANY,* [3]*Helios DKD Klinik, Wiesbaden, GERMANY.*

Aim/Introduction: Pancreatic ductal adenocarcinoma (PDAC) is characterized by poor prognosis and limited treatment options in advanced stages. Fibroblast activation protein (FAP) is a promising theranostic target due to its high stromal expression in PDAC. This study reports first-in-human results of FAP-targeted radiopharmaceutical therapy (FRT) using ^{177}Lu-, ^{90}Y-, and ^{225}Ac-labelled 3BP-3940 in 26 patients with metastatic, treatment-refractory PDAC. ***Materials and Methods:*** Between March 2021 and March 2025, 26 patients with metastatic, treatment-refractory PDAC were treated with 3BP-3940-based FRT. Patient selection was based on FAP expression assessed by pre-treatment ^{68}Ga-3BP-3940 PET/CT imaging. Treatments involved either monotherapy or tandem administration of ^{177}Lu-, ^{90}Y-, or ^{225}Ac-labelled 3BP-3940. Adverse events were evaluated using CTCAE version 5.0. Tumor response was assessed by molecular imaging, and overall survival was measured from the initiation of FRT. ***Results:*** FRT with ^{177}Lu-/^{90}Y-/^{225}Ac-3BP-3940 was well tolerated in all patients. The mean cumulative radioactivity/patient were 18±13 GBq for ^{177}Lu, 10±5 GBq for ^{90}Y and 18±10 MBq for ^{225}Ac. Reported side effects included pain in 6/26 patients, 6/26 nausea, 2/26 vomiting, 1/26 diarrhoea, 3/26 partial alopecia, and 1/26 intensified fatigue. One patient experienced Grade 3 toxicity (CTCAE) after the second treatment cycle. No other clinically relevant adverse effects or pharmacologic abnormalities were observed. Post-therapy whole-body imaging and SPECT/CT scans showed intense tumor uptake and prolonged retention, with consistently high tumor-to-background ratios across all patients. Among the 12 patients evaluated after one FRT cycles, molecular imaging responses included partial remission in 58%, mixed response in 8%, stable disease in 25%, and progressive disease in 8%; responses in 13 patients after two cycles included partial remission in 38%, mixed response in 15%, stable disease in 15%, and progressive disease in 31%. Until the study cutoff date in early April 2025, 22 of 26 patients (85%) with PDAC died. The median follow-up time was 17 months, and the median overall survival from the start of FRT was 7 months. ***Conclusion:*** FAP-targeted PTRT using 3BP-3940 labeled with ^{177}Lu, ^{90}Y, or ^{225}Ac is feasible and well tolerated in patients with advanced pancreatic ductal adenocarcinoma. The therapy demonstrated favorable safety, low off-target uptake, and high tumor retention with excellent tumor-to-background contrast. Molecular imaging confirmed objective responses in a subset of patients, and the observed median survival of 7 months from the start of FRT in this heavily pre-treated population is highly encouraging. These first-in-human findings support further clinical evaluation of 3BP-3940 FRT in larger, randomised controlled trials.

OP-437

Changes in Brain Glucose Metabolism Induced by Long-Acting Somatostatin Analogues Therapy in Patients with Neuroendocrine Tumors: a ^{18}F-FDG PET Study

A. Martini[1], *F. De Lauro*[2], *G. Bianciardi*[3], *S. Fanti*[4], *S. Lastoria*[2], *S. Sestini*[1];
[1]*Unit of Nuclear Medicine, Department of Diagnostic Imaging, N.O.P. - S. Stefano, U.S.L. Toscana Centro, Prato, ITALY,* [2]*Nuclear Medicine Unit, Istituto Nazionale Tumori di Napoli, IRCCS "G. Pascale", Naples, ITALY,* [3]*Nuclear Medicine, Alma Mater Studiorum University of Bologna, Bologna, ITALY,* [4]*Nuclear Medicine, Alma Mater Studiorum University of Bologna,IRCCS Azienda Ospedaliero-Universitaria di Bologna, Bologna, ITALY.*

Aim/Introduction: although analogues of the peptide somatostatin (SSA) present a high binding to brain SSR2-5, the low entry-rate of SSA into the brain has favored the idea that they cross the blood-brain-barrier (BBB) not in amount sufficient to affect brain functions. In contrast, no work has been done to confirm this hypothesis. Aim of this study was to investigate the potential off-target clinical and regional brain metabolism effects produced by the long-lasting stimulation of low entry-rate of SSA on brain somatostatin receptors in patients with NETs who were candidates for radioligand therapy. ***Materials and Methods:*** we included 25 patients (mean age 59 ± 12 y) with NETs treated with SSA from 6 up to 84 months. All patients underwent a baseline [^{18}F]-FDG PET together with neurological cognitive assessment. Brain hypo- and hypermetabolism were analysed using an optimised and validated voxel-based SPM method at the single-subject and group levels, based on comparisons with a large and well-selected dataset of healthy controls. A Pearson correlation analyses was performed to investigate the relationship between treatment duration and both the cluster extent and severity (mean T-score) of affected brain regions. ***Results:*** singlesubject and grouplevel analyses showed hypometabolism in cortical and sub-cortical regions including the bilateral OFC (BA11), DLPFC (BA9,10,46), VLPFC (45,47), the bilateral middle temporal pole (BA38) and hyppocampus (BA36), the left superior middle inferior temporal gyrus (BA22, 21, 20) and amygdala (BA28), and the bilateral caudate nuclei. The hypometabolism commonality analysis showed the left fronto-temporal cortices and caudate nuclei as the hypometabolic hallmark for the "whole group", with more limited involvement of the right middle temporal cortex and OFC. Correlation analysis demonstrated that patients with longer treatment with SSA present a higher extension and severity of hypometabolism. Besides, patients with longer SSA exposure reported new-onset mood instability, irritability and slight motor disturbances. ***Conclusion:*** this study provides the first evidence that exposure of low but long-lasting entry-rate of SSA in patients with NETs yields a dysfunction of brain regions expressing SSR2-5. The severity of neural dysfunction appears to correlate with treatment duration and could result in the emergence of positive neuropsychiatric symptoms. According with current knowledge of somatostatinergic networks in the brain, this effect could reflect an excessive inhibition of glutamatergic fronto-temporal pathways, e.g. low concentrion of SSA may cross the BBB and could enhance the inhibitory effect of endogenous SST-14 released by SST-INs interneurons and long-range SST-neurons.

1007

Monday, October 6, 2025, 15:00 - 16:30
Room 212

TROP Session - Neuroimaging Committee: Tau PET Imaging

OP-438

Spatial match and mismatch of tau pathology and hypometabolism at individual level

C. Boccalini[1], *D. E. Peretti*[1], *A. Mendes*[1], *M. Scheffler*[2], *N. Ashton*[3], *H. Zetterberg*[3], *K. Blennow*[3], *G. B. Frisoni*[1], *V. Garibotto*[1];
[1]*University of Geneva, Geneva, SWITZERLAND,* [2]*Geneva University Hospitals, Geneva, SWITZERLAND,* [3]*University of Gothenburg, Gothenburg, SWEDEN.*

Aim/Introduction: Neurodegeneration seems to be mostly driven by tau pathology in Alzheimer's disease (AD). However, despite the similar topographies, there is still variability in the tau accumulation and neurodegeneration patterns across the brain with some regions being more vulnerable to one or another pathology. This study aimed to investigate the spatial mismatch between regional tau pathology and brain metabolism as a measure of neurodegeneration at the individual level and evaluate its impact on patients' clinical and biomarker profiles. ***Materials and Methods:*** We included 137 amyloid-positive and clinically impaired patients from Geneva Memory Clinic (N=57) and ADNI (N=80), who underwent both 18F-Fluorodeoxyglucose (FDG)-PET to assess brain metabolism and 18F-Flortaucipir Tau-PET for tau burden within 1 year. The single-subject procedure (involving a voxel-wise comparison versus a group of amyloid-negative cognitively unimpaired subjects) was applied to calculate hypometabolism and tau maps and their spatial overlap by the Dice coefficient. Hypometabolic and tau maps' extents and delta (Δ) scores were used to classify the prevalent pathology. Differences in demographic and clinical features, neuroimaging-derived features, fluid biomarkers and cognitive trajectories were tested between match and mismatch groups. ***Results:*** We identified 22 patients with spatial match and 115 with mismatch, of which 23 showed hypometabolism-predominant mismatch and 92 tau-predominant mismatch. Patients with hypometabolism/tau match were younger and more cognitively impaired, with higher amyloid, neocortical tau, cortical atrophy, and level of glial fibrillary acidic protein (GFAP) in plasma than both mismatch groups ($p<0.005$). When we focus on differences between hypometabolism- and tau-predominant cases, we found the former showing less amyloid and tau burden ($p<0.005$), but a trend for higher inflammation as measure by GFAP than tau-predominant cases. However, we did not find differences in copathologies as measured by white matter lesion volumes and alpha-synuclein in cerebrospinal fluid ($p>0.05$). Match cases showed a significantly steeper cognitive decline than both mismatch cases, controlling for other imaging biomarkers ($p<0.001$). ***Conclusion:*** Spatial overlap between hypometabolism and tau deposition was associated with a severe clinical and biomarker phenotype with the worst prognosis, whereas spatial decoupling between tau and hypometabolism showed a slower cognitive decline. Patients with greater hypometabolism than tau deposition had lower amyloid and neocortical tau burden than tau-prevalent patients suggesting other contributors to neurodegeneration in addition to AD pathologies. Spatial match between tau and hypometabolism can provide additional information in AD identifying different phenotypes.

OP-439

Mapping Clinical and Tau Trajectories in Alzheimer's Disease: Prognostic and Monitoring Utility of 18F-Florzolotau Tau-PET in a Real-Word Memory Clinic Cohort

J. Lu[1], *J. Wang*[2], *H. Zhang*[1], *J. Wu*[2], *Y. Yang*[1], *M. Wang*[3], *X. Ma*[2], *W. Bao*[1], *Z. Xiao*[2], *H. Lin*[1], *X. Zhou*[2], *Z. Ju*[1], *S. Yan*[2], *F. Jiao*[1], *X. Liang*[2], *Y. Liu*[1], *L. Zheng*[2], *M. Li*[1], *J. Ge*[1], *D. Ding*[2,4,5], *T. Yen*[6], *Y. Guan*[1,4,5], *C. Zuo*[1,4,5], *Q. Zhao*[2,4,5], *the Shanghai Memory Study (SMS);*
[1]*Department of Nuclear Medicine &PET Center, Huashan Hospital, Fudan University, Shanghai, CHINA,* [2]*Department and Institute of Neurology, Huashan Hospital, Fudan University, Shanghai, CHINA,* [3]*Institute of Biomedical Engineering, School of Life Sciences, Shanghai University, Shanghai, CHINA,* [4]*National Clinical Research Center for Aging and Medicine, Huashan Hospital, Fudan University, Shanghai, CHINA,* [5]*National Center for Neurological Disorders, Huashan Hospital, Fudan University, Shanghai, CHINA,* [6]*APRINOIA Therapeutics Co. Ltd, Suzhou, CHINA.*

Aim/Introduction: Despite growing recognition of clinical-biological construct of Alzheimer's disease (AD), evidence supporting the prognostic and monitoring utility of Tau-PET in real-world settings remains limited. This study aimed to bridge the translational gap between Tau-PET research and clinical practice and offer insights into optimizing AD management with ^{18}F-Florzolotau Tau-PET in memory clinic populations. ***Materials and Methods:*** Memory clinic outpatients and cognitively unimpaired volunteers who accepted assessment of AD core biomarkers, Amyloid-PET or plasma p-tau 217 (core 1) and ^{18}F-Florzolotau Tau-PET (core 2), and longitudinal follow-up were included. The prognostic utility was explored in 242 participants with clinical follow-ups (median [range] interval: 1.42 [0.60 ~ 5.93] years) using binary clinical outcomes (progressive versus stable) and the annualized cognitive declines as endpoints. The disease monitoring potential was explored in the subset with Tau-PET follow-ups (n = 81, median [range] interval: 1.94 [0.87 ~ 5.35] years) by comparing the tau trajectories between clinically progressive and stable groups, and the correlation between annualized cognitive declines and annualized tau increases. ***Results:*** Baseline Tau-PET predicted the binary clinical outcomes and the annualized cognitive declines, with continuous measurement, neocortical standardized uptake value ratio (SUVR), showing the best incremental prognostic value to demographic characteristics in the entire cohort (AUC [95% CI] = 0.83[0.77 ~ 0.88] versus 0.67 [0.60 ~ 0.74], p-value < 0.001). Longitudinal Tau-PET analysis depicted a diffuse spatiotemporal pattern of tau accumulation, with tau trajectories closely paralleling clinical cognitive trajectories. Within the AD spectrum sub-cohort, clinically progressive individuals exhibited accelerated tau accumulation than stable cases, most notably in later-involved regions, namely, the precentral gyrus (β [95% CI] = 0.07 [0.02 ~ 0.11] SUVR/year, p-value = 0.007) and supplementary motor area (β [95% CI] = 0.08 [0.02 ~ 0.14] SUVR/year, p-value = 0.017). The annualized rates of tau accumulation correlated with annualized rates of cognitive declines in both traditional (medial temporal lobe and neocortical area) and later-involved regions. ***Conclusion:*** The memory clinic-based longitudinal study confirmed the prognosis and disease monitoring potential of ^{18}F-Florzolotau Tau-PET in AD. Later-involved cortical regions demonstrated greater sensitivity to progression than canonical tau-vulnerable areas, highlighting their potential clinical utility in tracking trajectories and reinforcing the critical need for stage-specific biomarker frameworks tailored to the real-world settings.

OP-440

Tau-PET imaging of advanced primary age-related tauopathy mimicking early-stage AD

M. Grothe[1], *A. Moscoso*[2], *M. A. Labrador-Espinosa*[2], *J. Silva-Rodríguez*[1], *F. Heeman*[2], *A. Costoya-Sánchez*[3], *V. Camacho*[4], *M. van Essen*[5], *I. Mainta*[6], *A. Perissinotti*[7], *O. Rodríguez-Fonseca*[8], *F. Ribaldi*[6], *M. D. Devous*[9], *M. J. Pontecorvo*[9], *G. B. Frisoni*[6], *V. Garibotto*[6], *M. Schöll*[2];
[1]*CIEN Foundation, Madrid, SPAIN,* [2]*University of Gothenburg, Gothenburg, SWEDEN,* [3]*University of Santiago de Compostela, Santiago de Compostela, SPAIN,* [4]*Universitat Autònoma de Barcelona, Barcelona, SPAIN,* [5]*Sahlgrenska University Hospital, Gothenburg, SWEDEN,* [6]*Geneva University Hospitals, Geneva, SWITZERLAND,* [7]*Hospital Clínic Barcelona, Barcelona, SPAIN,* [8]*Lucus Augusti University Hospital, Lugo, SPAIN,* [9]*Avid Radiopharmaceuticals, Philadelphia, PA, UNITED STATES OF AMERICA.*

Aim/Introduction: Primary age-related tauopathy (PART) is typically limited to the medial temporal lobe, but in rare cases it can also show a more extensive distribution that associates with cognitive deficits mimicking Alzheimer's disease (AD), a condition that has been termed tangle-predominant dementia. It remains unknown whether this condition can be detected in-vivo using PET imaging. ***Materials and Methods:*** We first studied the ante-mortem tau- and Aβ-PET imaging (Flortaucipir, Florbetapir), CSF biomarker, and cognitive characteristics of an autopsy case with neuropathologically-confirmed tangle-dominant disease (Braak V, Thal 0, CERAD 0). We then used a large in-vivo cohort of 2402 older individuals to screen Aβ-PET-negative ('A-'; <24.4 Centiloids) individuals for those with elevated neocortical tau-PET (Flortaucipir) signal ('T+', positive visual read), and studied their cognitive, genetic, and CSF biomarker characteristics. ***Results:*** In PET scans acquired 1.8 years before death, the tangle-dominant autopsy case had a negative Aβ-PET (-7 Centiloids) but showed clearly elevated tau-PET signal in temporo-parietal regions, leading to a positive visual read (Fig-1). Repeated CSF measurements (N=8, 2-13 years before death) were constantly negative for $A\beta_{42}$ (>2000 pg/ml) but positive for p-tau_{181} (>30 pg/ml). Last clinical diagnosis before death was aMCI. In the in-vivo cohort, only 3.6% (45/1264) of A- individuals were T+, but this proportion was significantly higher (9.9%) in cognitively impaired individuals (aMCI/AD dementia). A-T+ showed a temporo-parietal tau-PET signal that was spatially similar but less pronounced compared to A+T+. CSF p-tau_{181} levels were significantly elevated in A-T+ compared to A-T- (p=0.01), but $A\beta_{42}$ levels did not differ (p=0.60). APOE-ε4 frequency in A-T+ (37%) was markedly lower than for A+T+ (69%, p<0.001). ***Conclusion:*** We provide converging neuropathologic and fluid biomarker evidence that tau-PET can detect advanced forms of PART (i.e., tangle-dominant disease), a condition that is phenotypically similar to early-stage AD but has a different genetic background.

OP-441

Inhibitory and Promotive Effects of Amyloid-β on Tau Growth: A Stage-dependent Analysis in Alzheimer's Disease

T. Zhang, *B. Nie, B. Shan;*
Institute of High Energy Physics, CAS, Beijing, CHINA.

Aim/Introduction: Alzheimer's disease (AD) is characterized by β-amyloid (Aβ) plaque and tau neurofibrillary tangles. However, the interaction between these two pathologies remains unclear. This study investigates how tau growth rates are influenced by local Aβ standardized uptake value ratio (SUVR), Aβ accumulation rates, and pre-existing tau deposition. ***Materials and Methods:*** Data were sourced from the Alzheimer's Disease Neuroimaging Initiative. Participants (n = 847) who underwent Aβ and tau PET scans within six months were included to compute individual spatial Pearson correlations between the Aβ and tau SUVR. These spatial correlations were examined against Aβ plaques burden (Centiloid). Participants with multiple Aβ (n = 973) or tau (n = 428) PET scans were used to estimate SUVR values and annual growth rates using linear regression at each subject's midpoint age (baseline age plus half follow-up duration). Subjects were classified as healthy controls (HC), cognitively normal (CN), mild cognitive impairment (MCI), or dementia (AD) based on clinical diagnosis. Path analyses using standardized regression coefficients (β) assessed the influence of Aβ SUVR, Aβ accumulation rates, and tau deposition on tau growth rates at both group and individual levels. ***Results:*** A significant negative correlation was observed between Aβ-tau spatial correlation and Aβ burden (r = -0.719, P < 0.001). Group-level analysis revealed Aβ SUVR negatively

influenced tau growth in HC, CN, and MCI (β = -0.581, -0.487, -0.303 respectively, all P < 0.001), but not AD (β = -0.048, P = 0.560). Tau deposition positively affected tau growth across all groups (HC: β = 0.795; CN: β = 0.640; MCI: β = 0.543; AD: β = 0.265; all P < 0.001). Aβ accumulation rates were also positively associated with tau growth (HC: β = 0.430; CN: β = 0.620; MCI: β = 0.650; AD: β = 0.693; all P < 0.001). At the individual level, the path coefficients from Aβ SUVR to tau growth rates were significantly associated with cognitive measures (β vs CDRSB: r = 0.385; β vs MMSE: r = -0.332; both P < 0.001) and Aβ burden (r = 0.317, P < 0.001). ***Conclusion:*** Tau growth is driven by both self-replication and Aβ accumulation rates, the latter of which may reflect underlying levels of Aβ oligomers. Conversely, Aβ SUVR—potentially capturing both plaques and nonspecific binding—was associated with suppressed local tau growth, though this inhibitory effect weakened with advancing disease. These findings highlight stage-dependent nature of Aβ-tau interactions in AD.

OP-442

Correlation between Tau PET imaging and fluid biomarkers in individuals with Down syndrome

P. Stefaneli Mormandi[1], *V. Camacho*[1], *L. Vaqué-Alcázar*[2,3], *M. Calls-Calahorro*[1], *Y. Delisau*[1], *B. Serrallonga*[1], *I. Barroeta*[2,4], *D. Alcolea*[2,5], *M. Carmona-Iragui*[4,2,5], *J. Fortea*[2,4,5], *A. Fernández-León*[1], *S. Asadurova*[1], *M. Velasco-Nuño*[1], *A. Flotats-Giralt*[1];
[1]Nuclear Medicine Department, Hospital de la Santa Creu i Sant Pau, Barcelona, SPAIN, [2]Sant Pau Memory Unit, Department of Neurology, Hospital de la Santa Creu i Sant Pau, Barcelona, SPAIN, [3]Department of Medicine, Faculty of Medicine and Health Sciences, Institute of Neurosciences, University of Barcelona, Institut d'Investigacions Biomèdiques August Pi i Sunyer (IDIBAPS), Barcelona, SPAIN, [4]Barcelona Down Medical Center, Fundació Catalana de Síndrome de Down, Barcelona, SPAIN, [5]Center of Biomedical Investigation Network for Neurodegenerative Diseases (CIBERNED), Madrid, SPAIN.

Aim/Introduction: Down syndrome (DS) arises from chromosome 21 trisomy, leading to extra APP gene copy and triggering early-onset Alzheimer's disease (AD) pathology. Almost all individuals over 40 years of age with DS display the neuropathological features of AD. Understanding AD biomarker trajectories is necessary for DS-specific clinical interventions and interpretation of eventual drug-related changes. The aim of this study is to correlate Tau ([18F]PI2620) PET findings with biomarkers in cerebrospinal fluid (CSF) and plasma in adults with DS. ***Materials and Methods:*** Fifty-eight subjects with DS who underwent brain [^{18}F]PI2620 PET/CT were included (38% women; mean age 46.6 years [30-63.8]). Brain Tau quantification was based on analysis of the standardized uptake value ratio (SUVr) for each Braak stage. Biomarkers were determined using ultrasensitive immunoassay techniques: glial fibrillary acidic protein (GFAP) in plasma (n=27); p-Tau181 in CSF (n=18) and plasma (n=27); p-Tau217 in plasma (n=44); amyloidβ42/40 ratio in CSF (n=18); neurofilament light (NfL) in CSF (n=9) and plasma (n=21). Spearman's correlation coefficient was used to evaluate the relationship between [^{18}F] PI2620 uptake in Braak stages and biomarkers. ***Results:*** A positive correlation was observed between [^{18}F]PI2620 uptake for all Braak stages and values of GFAP in plasma, p-Tau181 in CSF, p-Tau181 in plasma and p-Tau217 in plasma (all p-values <0.01). A negative correlation between [^{18}F]PI2620 uptake and Aβ42/40 ratio values in CSF was noted for all Braak stages (all p-values <0.01). No significant correlation was found between [^{18}F]PI2620 uptake and NfL values in CSF or in plasma. ***Conclusion:*** The results reinforce the interconnectedness of tau deposition, neuronal injury, and inflammatory responses throughout AD progression. Interestingly, the absence of correlation with NfL levels suggests a differential sensitivity or temporal relationship of this marker. Taken together, our findings support the combined use of [^{18}F]PI2620 PET and fluid biomarkers for understanding AD in DS and aiding diagnosis, monitoring, and treatment evaluation.

OP-443

Comparability of [^{18}F]-FDG and Early-Phase amyloid and tau PET in detecting LATE Pattern in in amnestic mild cognitive impairment

G. Mathoux[1], *C. Boccalini*[2], *D. E. Peretti*[2], *M. Scheffler*[1], *G. B. Frisoni*[1], *V. Garibotto*[1];
[1]Hôpitaux Universitaires de Genève, Genève, SWITZERLAND, [2]Geneva University, Genève, SWITZERLAND.

Aim/Introduction: In the lack of specific biomarkers for limbic-predominant age-related TDP-43 encephalopathy (LATE), [18F]-FDG-PET can provide supportive information revealing characteristic hypometabolic patterns involving medial temporal and limbic regions and a relative sparing of the inferolateral temporal cortex.Early-phase PET (ePET), derived from dual-phase amyloid or tau PET protocols, can replace 18F-FDG-PET imaging in most neurodegenerative cases, showing typical disease patterns. This study aimed to investigate the ability of ePET in detecting the characteristic LATE-like pattern using [18F]-FDG-PET as gold standard in amnestic mild cognitive impairment (aMCI). ***Materials and Methods:*** We included 61 aMCI patients who underwent both FDG-, amyloid-, and tau-PET, with a dual-phase protocol (either from [18F]-Florbetapir, or [18F]-Flutametamol or [18F]-Flortaucipir). Two trained raters independently and blindly visually assessed FDG and ePET images with single-subject maps, classifying each scan into: Normal, Alzheimer's disease (AD)-like, LATE-like, or Other; discrepancies were resolved by consensus. Concordance between FDG and ePET classifications was evaluated using Cohen's κ. Standardized uptake value ratios (SUVR) were extracted, and the inferior-to-medial temporal (IMT) ratio was calculated by dividing the SUVR of the inferior temporal lobe by the combined SUVR values of the amygdala and hippocampus to evaluate the correlation of ePET and their respective ^{18}F-FDG PET scans. ***Results:*** FDG-based classification identified 23 Normal, 23 AD-like, 8 LATE-like, and 7 "other" patterns and ePET 24 Normal, 12 AD-like, 14 LATE-like, and 11 "other".Overall concordance between ePET and [^{18}F]-FDG PET was fair (κ=0.35), improving to κ=0.42 when "Other" patterns were excluded. Discordant cases mainly involved (n=14) scans classified as AD-like on FDG but reclassified by ePET; notably, 11 of these 14 were amyloid and tau positive, consistent with AD etiology.We found significantly lower IMT ratio in AD-like than in LATE-like patients with both FDG and ePET (p<0.05). Strong correlations were found between IMT measured by perfusion and by FDG (r=0.67, p<0.05). ***Conclusion:*** The fair agreement between ePET and [^{18}F]-FDG-PET classifications and the significant correlation in IMT ratio might support the use of ePET to identify LATE-like patterns. Without TDP-43-specific biomarkers, dual-phase amyloid or tau PET offers a broadly accessible, cost-effective strategy to raise clinical suspicion for LATE. However, these findings represent preliminary data from aMCI subsample, which we plan to extend to a larger cohort. Moreover, methodological differences and the relatively small size of ePET control database could have contributed to discordant cases and highlight the need of larger and harmonized datasets to refine and validate this approach.

OP-444

Neuropathological Tau Deposition Mediates the Relationship Between Glymphatic dysfunction and Hippocampal Neurodegeneration in Patients with Mild Cognitive Impairment

X. Xu[1], *B. Zhang*[2], *W. Zhang*[2], *J. Chen*[2];
[1]Nanjing Drum Tower Hospital Clinical College of Nanjing Medical University, Nanjing, CHINA, [2]Department of Radiology, Nanjing Drum Tower Hospital, Affiliated Hospital of Medical School, Nanjing University, Nanjing, 210008, China, Nanjing, CHINA.

Aim/Introduction: The glymphatic system, an astrocytic aquaporin 4 (AQP4)-dependent clean system, is a network of functional conduits in the brain for removing metabolic waste and protein deposition. While extensive studies have found Aβ

is closely associated to the glymphatic system, the role of tau pathology in glymphatic dysfunction and its association with neurodegeneration in the Alzheimer Disease (AD) spectrum remain unclear. The aim of this study was to assess how regional tau deposition affect the relationship between glymphatic dysfunction and neurodegeneration in early AD. ***Materials and Methods:*** Cognitively normal (CN, n = 52) controls, mild cognitive impairment (MCI, n = 38) patients, and those with significant memory concern (SMC, n = 46) were included from the Alzheimer's Disease Neuroimaging Initiative database. Regional tau deposition was assessed using positron emission tomography. The glymphatic activity was evaluated using diffusion tensor image analysis along the perivascular space (DTI-ALPS), and neurodegeneration determined by hippocampal volume measured in MRI. Correlation analysis and mediation analysis were used to evaluate the relationship between regional tau SUVR and DTI-ALPS cognitive function scores. Additionally, this study explored how Aβ and APOEε4 status infuence the associations between altered glymphatic activity and tau uptake using hierarchical moderated multiple regression. ***Results:*** Our results showed a significant correlation between tau PET in the right fusiform gyrus and parahippocampal gyrus, and diffusion tensor image analysis along the perivascular space (ALPS) index, which was independent of Aβ and APOE genes statue. Pathological tau deposition could mediate the relationship between glymphatic function and neurodegeneration (indirect effect: 0.012, 95%CI: 0.001, 0.029) rather than ALPS mediates the relationship of tau and neurodegeneration. The relationship between glymphatic function and cognitive decline was fully mediated by tau deposition in specific brain region and neurodegeneration (indirect effect: -1,935, 95%CI: -3.416 — -0.687). ***Conclusion:*** In patients with mild cognitive impairment, the combination of tau PET and MRI provides a powerful approach to identify vulnerable brain regions to tau pathology and its association with glymphatic dysfunction, which appears to be independent of Aβ and APOE ε4 status. Although neural atrophy is irreversible, enhancing glymphatic drainage to mitigate tau-associated neurodegeneration could be a promising therapeutic approach. Our results suggest that targeting tau pathology in the right fusiform gyrus and inferior temporal lobe, along with improving the glymphatic drainage, could offer a potential therapeutic strategy in the early stage of AD.

OP-445

Amyloid and tau changes in preclinical autosomal dominant Alzheimer's disease mutation carriers: a dual-tracer PET/MRI qualitative and quantitative analysis

L. Fu[1], *Z. Zhou*[2], *J. Gao*[1], *Q. Wang*[3], *Q. Wang*[3];
[1]Department of Nuclear Medicine,China-Japan Friendship Hospital, Beijing, CHINA, [2]Department of Neurology,China-Japan Friendship Hospital, Beijing, CHINA, [3]Innovation Center for Neurological Disorders and Department of Neurology, Xuanwu Hospital, Capital Medical University, Beijing, CHINA.

Aim/Introduction: Autosomal dominant Alzheimer's disease (ADAD) offers a distinct framework to study the preclinical phase of Alzheimer's disease (AD), given its predictable symptom onset and high penetrance of causative mutations. The study aims to investigate the spatial distribution and temporal progression of amyloid-beta (Aβ) and tau pathologies, and to assess the application of the centiloid scale (CLs) of PIB-PET in evaluating asymptomatic ADAD patients. ***Materials and Methods:*** Participants were recruited from the Chinese Familial Alzheimer's Disease Network, comprising 19 asymptomatic ADAD mutation carriers and 21 cognitively normal healthy controls (CN). We conducted 20-minute PIB-PET scans (40-60 min uptake) and 20-minute MK6240-PET scans (70-90 min uptake). The cortical-to-cerebellum standardized uptake value ratio (SUVR) was calculated, and CLs of PIB-PET were calibrated using GAAIN datasets. Qualitative analysis categorized ADAD carriers with significant ^{18}F-MK6240 uptake in intracranial regions as Group 2 (both PIB-PET and MK6240-PET positive); others were Group 1(PIB-PET positive or negative; MK6240-PET negative). ***Results:*** Compared to CNs and Group 1, Group 2 participants exhibited significantly higher ^{11}C-PIB uptake in the neocortex but predominant in the striatum (F=20.727, P<0.05) and increased ^{18}F-MK6240-PET uptake in the medial temporal (MTL, P<0.001) and other cortical regions (P<0.05). No statistic difference in the radioactive accumulation of both tracers were observed between CNs and Group 1. In mutation carriers, higher Tau PET binding in MTL and other cortical regions were correlated with shorter estimated years to onset (P=0.02). A 45-year-old female subject with a PSEN2 gene mutation and an MMSE score of 24 had a CL value of 9.25 and an SUVR of 1.10, with visibly increased ^{11}C-PIB uptake in the striatum and MK6240 retention in the MTL. ***Conclusion:*** This study elucidates the spatiotemporal progression of Aβ and tau pathologies in preclinical ADAD, supporting the hypothesis that Aβ accumulation precedes tau pathology. The prominent Aβ deposition in the striatum but less in the cortex in preclinical ADAD may lead to false-negative results in quantitative analysis. Caution should be exercised in early diagnosis and patients' management for ADAD using Centiloid quantification.

OP-446

Could [^{18}F]PI-2620 be used as a biomarker for progressive supranuclear palsy?

A. Bronte[1,2], *E. Prieto*[1], *G. Martí-Andrés*[3], *D. Pigg*[4], *F. Mínguez*[1], *F. Pareja*[1], *G. Quincoces*[1], *M. Erro*[3], *J. Arbizu*[1];
[1]Clínica Universidad de Navarra, Pamplona, SPAIN, [2]Hospital Universitari de Son Espases, Palma, SPAIN, [3]Hospital Universitario de Navarra, Pamplona, SPAIN, [4]Siemens Medical Solutions USA, Knoxville, TN, UNITED STATES OF AMERICA.

Aim/Introduction: Progressive supranuclear palsy (PSP) is a primary 4-repeat (4R) tauopathy. [^{18}F]PI-2620 is a second-generation tau-PET tracer with high affinity to 4R deposits, that has been described to aid in the diagnosis and differentiation of patients with suspected PSP. The aim of our study was to investigate the 4R-tau deposition in patients with clinically diagnosed PSP. ***Materials and Methods:*** We conducted a prospective study in probable or possible PSP patients (diagnosed according to Movement Disorder Society PSP criteria) and controls (healthy and Parkinson disease (PD) controls). All individuals underwent a dynamic [^{18}F]PI-2620 PET scan from 0 to 60 minutes post-injection. Carotid artery image-derived input functions were generated over the 60-minute dynamic [^{18}F] PI-2620 PET. Volume of distribution was calculated using Logan plot, and referred to inferior cerebellum grey matter distribution volume ratios (DVR) were achieved in putamen (P), globus pallidus (GP), globus pallidus externus (GPe), globus pallidus internus (GPi), substantia nigra (SN), subthalamic nucleus (StN), dentate nucleus (DN), dorsomedial (MPF) and dorsolateral prefrontal cortex (LPF). Differences in DVRs among patients with Richardson's syndrome variant of PSP (PSP-RS), non-Richardson variants of PSP (PSP-Non-RS) and control patients were explored using SPSS version 20. ***Results:*** 31 patients were included (18 men; Age 72.3 ± 5.9): 28 PSP (PSP Rating Scale score 38.1 ± 15.5) and 3 Controls (2 Healthy and 1 PD controls). PSP patients were subclassified as 18 PSP-RS and 10 PSP-Non-RS (2 Parkinsonian, 1 Speech&language, 5 Frontal, 1 Oculomotor, 1 Postural instability). PSP-RS DVRs (mean±SD): P (1.23±0.10), GP (1.30±0.12), Gpe (1.32±0.11), Gpi (1.28±0.17), SN (1.22±0.12), StN (1.24±0.16), DN (1.21±0.08), MPF (0.93±0.10), LPF (1.00±0.06). PSP-Non-RS DVRs: P (1.30±0.08), GP (1.36±0.12), Gpe (1.39±0.13), Gpi (1.33±0.16), SN (1.20±0.10), StN (1.25±0.12), DN (1.20±0.05), MPF (0.97±0.05), LPF (1.03±0.05). And Controls DVRs: P (1.14±0.13), GP (1.21±0.11), Gpe (1.23±0.12), Gpi (1.17±0.11), SN (1.23±0.10), StN (1.21±0.05), DN (1.19±0.07), MPF (0.97±0.01), LPF (0.97±0.02). The statistical analysis identified a significant overall

group difference for the Putamen DVR (p = 0.039), with post-hoc testing indicating significant higher DVR values in the PSP-Non-RS group compared to the Control group (p = 0.043). No other differences in DVR values were found among groups. ***Conclusion:*** [^{18}F]PI-2620 PET imaging may aid the diagnosis of patients with PSP by providing greater specificity for 4R tau deposition. In our study, we observed that PSP patients, particularly those with PSP-Non-RS, exhibit differential increases in specific subcortical structures related to PSP-associated tau 4R deposition.

1008

Monday, October 6, 2025, 15:00 - 16:30
Room 115

Joint Symposium 4 - AI Committee / EFOMP: Trustful AI in the Clinic

OP-447
Ethical AI and the EU AI Act
S. Zipponi; *, Milan, ITALY.*

OP-448
Explainable AI for NM
M. Hatt; *INSERM, LaTIM, UMR 1101, Brest, FRANCE.*

OP-449
Trustworthy image processing with AI
O. Diaz; *Dept of Mathematics and Computer Science, University of Barcelona, Barcelona, SPAIN.*

1009

Monday, October 6, 2025, 15:00 - 16:30
Room 133+134

e-Poster Presentations Session 7 - Radiopharmaceutical Sciences Committee: Radiopharmacy e-Poster Presentations Session Radiochemistry and Quality Control

EPS-136
A Novel Substance P Derivative Labeled With Ga68 and Lu177 as Candidates for diagnosis and Therapy of Glioblastoma Tumor
J. Abedi[1]*, s. Mozaffari*[1]*, H. Khoshhosn*[1]*, R. Nami*[1]*, N. Soltani*[1]*, M. Mehrazi*[2]*, M. Mokhtari*[1]*;*
[1]Pars Isotope Company, Tehran, IRAN, ISLAMIC REPUBLIC OF, [2]Trauma and Injury Research Center, Iran University of Medical Science, Tehran, IRAN, ISLAMIC REPUBLIC OF.

Aim/Introduction: Glioblastoma (GBM) is a highly aggressive brain tumor with limited effective treatment options. Substance P (SP) and its receptor, neurokinin-1 (NK1R), are known to be overexpressed in GBM, making them promising targets for novel therapies. In this study, we designed and synthesized a new SP-derived compound containing DOTA chelator. Then, we aimed to validate the methods for the labeling and quality control of it with gallium (^{68}Ga) and Lutetium (^{177}Lu) to enhance its diagnostic and potential therapeutic applications. In-vivo bio distribution studies on normal mice were done ***Materials and Methods:*** A new SP-based analog was designed and evaluated by docking software, then synthesized and radiolabeled with Ga68 and Lu177. The labeling process and quality control of this new compound were validated through a series of experiments. The stability, protein binding and partition coefficient were examined. Furthermore, biodistribution studies in normal mice and dosimetry investigations were performed. ***Results:*** The novel SP derivative was significantly interacted with crystal structure of NK_1R from PDB and displayed binding energies around -8 kcal/mol. The radiolabeling method showed an average radiochemical yield of 65% and the radiochemical purity more than 98% after work up preparation for ^{68}Ga. Also, the average radiochemical yield and purity (without any work up) was more than 98% for ^{177}Lu. Protein binding to human serum was 51% and 63% for ^{68}Ga and ^{177}Lu respectively. It was stable up to 4 h after labeling with ^{68}Ga and was stable up to 5 days with ^{177}Lu in saline and human serum. A value of -1.26 log P was calculated for radiolabeled peptide with ^{68}Ga and -0.82 log P was calculated with ^{177}Lu. The most accumulation of ^{68}Ga activity in normal organs were done in kidneys, intestines and salivary glands regions 1 h and 2 h post-injection of radiopeptide. ***Conclusion:*** Our newly synthesized SP derivative demonstrates good radiolabeling capability and stability make it a promising candidate for future GBM diagnostics and targeted radionuclide therapy of GBM metastatic cancers. Also, our studies on GBM cell lines and preclinical investigations using xenograft mice models to assess tumor uptake are on going for further analysis and conclusions. ***References:*** Glioblastoma Multiforme: A Review of its Epidemiology and Pathogenesis through Clinical Presentation and TreatmentSynthesis and evaluation of a novel 64Cu/67Ga-labeled neurokinin 1 receptor antagonist for in vivo targeting of NK1R-positive tumor xenografts

EPS-137
Streamlining [^{18}F]F-JK-PSMA-7 production: A GMP-compliant alternative to HPLC purification using solid-phase extraction
E. Cazzola, *C. Favaretto, L. Pennacchio, J. Amico, D. Peruzzi, N. Bergamaschi, P. Bovone, M. Malachini, G. Gorgoni;*
Ospedale Sacro Cuore, Negrar, ITALY.

Aim/Introduction: [^{18}F]F-JK-PSMA-7 is a fluorinate-18 PSMA alternative tracer used for PET imaging of prostate cancer. Thanks to its high specificity and affinity for PSMA, it enables effective detection, staging, and monitoring of disease progression as well as treatment response [1]. Currently, its production involves nucleophilic aromatic substitution followed by acid deprotection and High-Performance Liquid Chromatography (HPLC) purification in a Trasis AllinOne (AIO) module. However, HPLC purification is a bottleneck due to limited module availability and potential technical failures. This study explores an alternative purification pathway to streamline the production by reducing synthesis steps and time. ***Materials and Methods:*** [^{18}F]F-JK-PSMA-7 was synthesized using a Trasis AIO module, following the standard AIO protocol up to the crude reactor step. At this stage, the reaction was quenched and transferred outside the module for further processing. Various solid-phase extraction (SPE) systems, including C-18, HLB, and CM cartridges, were tested for purification. The obtained purified solutions were analyzed via HPLC and Thin Layer Chromatography (TLC) to compare yields, radiochemical purity (RCP), and chemical purity against the non-purified crude product. ***Results:*** After the synthesis, HPLC analysis of the crude reaction mixture identified impurities, including unbound fluorine-18, partially deprotected intermediates and unknown species. Among all the processes tested, purification of [^{18}F]F-JK-PSMA-7 using C-18 cartridges effectively trapped the product, with water washes efficiently removing inorganic impurities while retaining the desired compound on the cartridge. Additional washing steps with water and 20% ethanol further eliminated residual impurities. The final elution with 2 mL of 50% ethanol achieved a recovery yield of approximately 70%, a radiochemical purity (RCP) exceeding 99%, and chemical impurity levels compliant with the limits specified in the draft monograph reported in Pharmeuropa [2] . The same process using HLB cartridges resulted in high purity product, though recovery was initially low (55%). Recovery efficiency was significantly improved by replacing

water with saline in all solutions. ***Conclusion:*** Cartridge-based SPE purification presents a robust and GMP-compliant alternative to HPLC for the production of [^{18}F]F-JK-PSMA-7. This method streamlines operations, reduces the risk of cross-contamination and operator errors, and improves the overall reliability of synthesis. Furthermore, it significantly shortens production time and enhances yield while maintaining full compliance with the draft European Pharmacopoeia monograph for [^{18}F]F-JK-PSMA-7. ***References:*** [1] B. D. Zlatopolskiy et al., J Nucl Med, 2019, 60:6. [2] Pharmeuropa vol 36.1., 2024.

EPS-138

Quality control of Actinium-225: Francium-221 to be or not to be?

D. Abou[1,2], *M. Toro-Gonzalez*[1], *L. Wheeless*[1], *L. Van Epern*[1], *M. Hommen*[1], *V. Tangadanchu*[1], *C. Hawkins*[1], *T. Drum*[1], *D. Devries*[1]; *[1]Northstar Medical Radioisotopes LLC., Beloit, WI, UNITED STATES OF AMERICA, [2]Washington University School of Medicine, Mallinckrodt Institute of Radiology, St. Louis, MO, UNITED STATES OF AMERICA.*

Aim/Introduction: Actnium-225 radiopharmaceuticals have drawn great interest in cancer therapy due to their tumor-specific delivery of cytotoxic alpha-particles. Detection and quality control (QC) is a critical issue for these potent agents. Direct ^{225}Ac (9.92 days) detection is challenging, however gamma-emitting progeny include ^{221}Fr (4.8 min, 218 keV) and ^{213}Bi (45 min, 440 keV). There is no consensus for best practice of ^{225}Ac QC. We compared multiple analytical methods for accurate quantification of ^{225}Ac and Drug Product (DP) radiochemical purity (RCP%) across several techniques. ***Materials and Methods:*** Accurate ^{225}Ac quantification was first evaluated using both ^{221}Fr and ^{213}Bi in gamma-ray spectroscopy over 30 d. In a DP context, the RCP% of an ^{225}Ac-labeled DOTA-peptide was defined by Thin Layer Chromatography (TLC) at secular equilibrium for ^{221}Fr and ^{213}Bi. We compared two TLC plate readers: a gas proportional counter, under mixed emission and alpha specific parameters; and a plastic silicon photomultiplier detector. TLC sections were also evaluated using High Purity Germanium (HPGe), liquid scintillation (LS) and NaI gamma-well counting. We correlated these methods to gamma counting of HPLC fractions measured at both equilibriums utilizing multiple energy windows. All instruments were checked for suitability of ^{225}Ac detection with determination of linearity (R^2>0.99) and limit of quantification (LOQ). ***Results:*** ^{225}Ac decay measured using HPGe demonstrated alignment to the reported half-lives for both ^{213}Bi and ^{221}Fr. Each instrument reported different LOQs with 0.5 nCi for NaI, 20 pCi for LS, and 400 pCi (^{213}Bi)/980 pCi (^{221}Fr) for HPGe. These values placed LS and HPGe as the most sensitive tools to quantify ^{225}Ac on TLC. TLC plate-reader using the plastic silicon detector resulted in significant RCP% differences between 30 min and >5h readings, whereas the gas proportional counter showed no-significant differences between alpha-specific (30 min) and the mixed-isotope setting (>5h). HPGe-TLC demonstrated equivalent RCP% for both ^{221}Fr and ^{213}Bi at equilibrium. NaI and LS significantly underestimated RCP% at 30 min. Finally, gamma counting of HPLC fractions resulted in 3-5 % underestimation at ^{221}Fr equilibrium. ***Conclusion:*** ^{225}Ac half-life determination was equivalent using ^{221}Fr or ^{213}Bi gamma-rays. Early measurements at 30 min accurately reported RCP% using HPGe and the gas proportional TLC reader. However, all other techniques required ^{213}Bi equilibrium for accurate determination. With the low radioactive concentration of ^{225}Ac radiopharmaceutical, the ultra-low sensitivity of HPGe or LS meet the requirement of detection at 0.5% ^{225}Ac impurities, where other instruments fail.

EPS-139

Direct Alpha Spectroscopy for Detection of ^{225}Ac Radiopharmaceuticals in Cancer Cells

M. Farasat[1], *B. Saeedi Saghez*[1], *L. Wharton*[1], *S. Shapiro*[2], *C. Vinnick*[3], *M. Daignault*[3], *M. Kostashuk*[4], *N. Pranjatno*[3], *M. Weiman*[1], *C. Andreoiu*[3], *H. Yang*[1], *P. Kunz*[1]; *[1]TRIUMF, Vancouver, BC, CANADA, [2]University of British Columbia, Vancouver, BC, CANADA, [3]Simon Fraser University, Burnaby, BC, CANADA, [4]McMaster University, Hamilton, ON, CANADA.*

Aim/Introduction: Targeted alpha therapy (TAT) employs alpha-emitting radionuclides conjugated to tumour-specific ligands to deliver highly localized cytotoxic radiation, offering significant potential for treating metastatic cancers. Among these radionuclides, Actinium-225 (^{225}Ac, $t_1/_2$ = 9.9 days) stands out due to its emission of four high-energy alpha particles through its decay chain, resulting in potent, localized tumour cell damage. However, complete retention of ^{225}Ac and its radioactive daughters at the target site is uncertain due to nuclear recoil, leading to redistribution and potential off-target toxicity. Thus, there is a critical need for methods that allow direct, real-time observation of alpha-emitting radiopharmaceuticals in live cells to better understand uptake, retention, and redistribution dynamics. This study aims to address these challenges by developing a direct alpha spectroscopy method for in vitro investigation of ^{225}Ac radiopharmaceuticals. ***Materials and Methods:*** AR42J rat pancreatic tumour cells expressing somatostatin receptor 2 (SSTR2), were incubated with three radiopharmaceutical formulations: [^{225}Ac]Ac-crown-TATE, [^{225}Ac]Ac-DOTA-TATE, and [^{225}Ac]Ac^{3+}. Post-incubation, cells were separated from the supernatant and transferred to polypropylene sample cups with thin Mylar foil bottoms. Reference samples were prepared using the same procedure but without cells. The sample cups were positioned approximately 100 µm from the custom designed Bio-sample Alpha Detector (BAD) system, a silicon-based detector for direct alpha spectroscopy operating under ambient conditions. Decay spectra were recorded for incubated cells resuspended in media, corresponding supernatants, and reference samples. Comparative analysis of the spectral profiles was conducted to evaluate uptake and validate the method. ***Results:*** Distinct alpha spectral signatures were observed between cell samples, supernatants, and reference controls, confirming cellular uptake of the radiopharmaceuticals. Detection of ^{213}Po, a decay daughter of ^{225}Ac, in the supernatant indicates partial retention and release of decay products from the cells, offering insights into intracellular retention and radionuclide redistribution. Preliminary data support the feasibility of using the BAD system for the quantitative assessment of alpha-emitting radiopharmaceuticals in biological samples. Geant4 simulations confirmed the alignment of experimental data with theoretical models, validating the method's accuracy. ***Conclusion:*** The BAD system offers a novel, vacuum-free method for the direct detection of alpha emissions in biological samples. This approach enables quantification of cellular uptake and analysis of ^{225}Ac retention and redistribution. It offers a valuable tool for studying radionuclide behavior and microdosimetry in radiopharmaceutical research.

EPS-140

Development and Optimization of [68Ga]68Ga-DOTA-EMP-100 for Non-invasive PET Imaging and Targeted Radioligand Therapy of c-MET Overactivation in Cancer

S. Migliari[1], *C. Portal*[2], *A. Gibson*[2], *A. Gagliardi*[1], *A. Guercio*[1], *M. Scarlattei*[1], *G. Baldari*[1], *L. Ruffini*[1]; *[1]Nuclear Medicine Division, Azienda Ospedaliero-Universitaria of Parma, Parma, ITALY, [2]Edinburgh Molecular Imaging Ltd., Edinburgh, UNITED KINGDOM.*

Aim/Introduction: c-MET is a transmembrane receptor involved in various biological processes, including cell proliferation and migration, particularly during cancer invasion. Overactivation

of the HGF/c-MET signaling pathway is associated with many cancers, making its inhibition a promising therapeutic strategy. Although c-MET expression is typically assessed through immunohistochemistry on tissue samples, this technique has certain limitations. PET-CT offers the potential for in vivo mapping of c-MET-expressing lesions, enabling whole-body detection. The development of a specific c-MET radioligand for PET imaging and radioligand therapy offers a potential alternative, allowing non-invasive, real-time monitoring of target expression while simultaneously enabling a targeted treatment approach. Several radiopharmaceuticals are being developed for this purpose but are not yet used routinely in clinical practice. EMP100 is a cyclic oligopeptide linked to a DOTA chelator, exhibiting nanomolar affinity for c-MET (3.0 ± 0.5 nM) [1-2]. The aim of this project was to establish an automated radiolabelling method for the radiopharmaceutical [^{68}Ga]Ga-DOTA-EMP100. ***Materials and Methods:*** Radiosynthesis of [^{68}Ga]Ga-DOTA-EMP100 was performed using a GMP-certified ^{68}Ge/^{68}Ga generator connected to an automated synthesis module. The radiopharmaceutical production was optimized, scaling down the amount of DOTA-EMP-100 from 50 to 20 µg (50-40-30-20 µg). Synthesis efficiency and release criteria were assessed according to Ph. Eur. for all the final products evaluating radiochemical yield (RY%), radiochemical purity (RCP% = 100%-colloids-ions), presence of free gallium (by Radio-UV-HPLC) and gallium colloids (by Radio-TLC), molar activity (Am), chemical purity, pH and LAL test. Once the method was optimized, the process and the final product were validated with three consecutive syntheses whose stability was assessed over time. ***Results:*** Best results were yielded with 40 µg DOTA-EMP-100 with optimal RY% (64.93%), RCP% (100%) and molar activity (53.08 GBq/µmol). The process validation (three batches produced on three different days) confirmed optimal RY% (mean value 64.50 %) and molar activity (mean value 53.41 GBq/µmol). Finally, the stability of [^{68}Ga]Ga-DOTA-EMP100 was evaluated at room temperature over a 4-hour period, with satisfactory results regarding its appearance, pH, radiochemical purity, and sterility. ***Conclusion:*** [^{68}Ga]Ga-DOTA-EMP100 was successfully synthesised according to Ph. Eur. criteria and is now available for clinical development in PET-CT imaging. ***References:*** [1] Mittlmeier LM, et al. Eur J Nucl Med Mol Imaging. 2022 Apr;49(5):1711-1720. [2] Rusu T, et al. EJNMMI Radiopharm Chem. 2023 Oct;8(1):30.

EPS-141

Development of CYP11B2 selective pyridinylbenzimidazole derivatives for pathological analysis of primary aldosteronism

Y. Yagi[1], *H. Kimura*[2], *R. Fuseda*[3], *T. Murakami*[4], *M. Omokawa*[5], *S. Kise*[6], *M. Sone*[7], *H. Yasui*[3], *N. Inagaki*[4], *H. Saji*[8];
[1]*Kyoto University of Medical Science, Nantan, JAPAN,* [2]*Agency for Health, Safety and Environment, Kyoto University, Kyoto, JAPAN,* [3]*Kyoto Pharmaceutical University, Kyoto, JAPAN,* [4]*Kyoto University Hospital, Kyoto, JAPAN,* [5]*Okayama University, Okayama, JAPAN,* [6]*Kanazawa University, Kanazawa, JAPAN,* [7]*St. Marianna University School of Medicine, Kawasaki, JAPAN,* [8]*Graduate School of Pharmaceutical Sciences, Kyoto University, Kyoto, JAPAN.*

Aim/Introduction: Primary aldosteronism (PA) is a type of secondary hypertension caused by excessive production of aldosterone in the adrenal glands, accounting for 5-10% of hypertension cases. This condition is heterogeneous, with treatment options varying based on whether it is unilateral or bilateral. Unilateral PA can be effectively treated through surgery, highlighting the importance of accurate diagnosis. However, invasive procedures like adrenal vein sampling are often necessary, as non-invasive imaging techniques such as CT and MRI may not provide sufficient diagnostic information. We propose that a non-invasive nuclear medicine diagnostic approach could enhance the diagnosis of PA. To this end, we have developed a molecular probe specific to CYP11B2, which is overexpressed in patients with PA. We focused on a pyridinylbenzimidazole structure known for its selective inhibitory activity against CYP11B2 and proceeded to synthesize and evaluate its derivatives. ***Materials and Methods:*** We developed and synthesized four derivatives of pyridinylbenzimidazole (designated as PBI-1 to PBI-4). Their inhibitory effects on CYP11B2 and selectivity against CYP11B1 were assessed using V79 cells transfected with these enzymes. The synthesized derivatives were subsequently radiolabeled with either I-125 or F-18, and a biodistribution study of the radiotracers was conducted in healthy mice. Lastly, we performed in vitro autoradiography (ARG) using adrenal tissue slices from patients with PA to assess the selectivity for CYP11B2 compared to CYP11B1. ***Results:*** We obtained iodine-containing PBI-1 and PBI-2 for SPECT and fluorine-containing PBI-3 and PBI-4 for PET with relatively good yields. Inhibition assays revealed that PBI-2 and PBI-4, which are fluorochlorobenzene-containing compounds, exhibited high inhibitory activity and selectivity (IC_{50}: PBI-2 = 0.47±0.19 nM, PBI-4 = 0.25±0.05 nM; Ratio: PBI-2 = 245, PBI-4 = 625). We obtained [^{125}I]PBI-2 and [^{18}F]PBI-4. The biodistribution experiment of [^{18}F]PBI-4 showed accumulation in the adrenal glands (5.76±2.00 %ID/g at 5 min). In vitro ARG analysis using human adrenal slices demonstrated higher accumulation of radioactivity in the CYP11B2 region compared to the CYP11B1 region. This result is consistent with the findings from the cell experiments. Therefore, these results suggest that [^{18}F]PBI-4 has high selectivity for CYP11B2. ***Conclusion:*** The newly designed radioiodinated [^{18}F]PBI-4 may serve as a promising PET probe for imaging primary aldosteronism. ***References:*** ACS Medicinal Chemistry Letters 6 (5), pp 573-578, (2015)

EPS-142

La-[$^{18/19}$F]fluoride Complexes: a novel addition to the radiofluorination family.

R. Faizova[1], *S. Gruber*[2], *L. Mu*[3], *M. Schottelius*[1], *M. Behe*[4];
[1]*Lausanne University Hospital, Lausanne, SWITZERLAND,* [2]*ETH Zurich, Zurich, SWITZERLAND,* [3]*ETH Zurich, Zürich, SWITZERLAND,* [4]*Paul Scherrer Institute, Villigen, SWITZERLAND.*

Aim/Introduction: Theranostics, an approach combining diagnostic imaging and targeted therapy, has seen an explosion of research and clinical applications in recent years. With fluorine-18 being the most widely clinically used PET isotope, many groups are developing various strategies for incorporating fluorine-18 into theranostic companion tracers. Among modern ^{18}F-labeling strategies, the one-step synthesis of metal-[^{18}F]fluoride coordination species has emerged as a particularly straightforward radiofluorination method, with examples including AlF^{2+}, ScF^{2+}, GaF^{2+}, and FeF^{2+} coordination complexes. Here, we introduce a new member of the family: a series of novel La-[$^{18/19}$F]fluoride complexes, alongside studies of their stability and reactivity. ***Materials and Methods:*** A series of La-[^{19}F]fluoride coordination complexes with various macrocyclic chelators (DOTA, DOTAM, macropa, and DOTpy) was prepared, both in organic and aqueous media. The ^{19}F-fluorination of the resulting La complexes was investigated in organic and aqueous media. The reactions were monitored by ^{19}F and ^{1}H NMR spectroscopy, LC-MS, and X-ray spectroscopy. Upon verification of [^{19}F]LaF complex formation, selected complexes were further evaluated for ^{18}F-fluorination, and their stability and reactivity were assessed in vitro. Additionally, a DFT study was conducted to further elucidate the factors governing the stability and reactivity of the different La-fluoride complexes. ***Results:*** Generally, the stability in and reactivity with water of the La-chelates was found to strongly depend on the chelator used, with chelators providing more electronegative donor atoms resulting in lower stability of the corresponding La-complexes towards defluorination. The [^{19}F]LaF complexes with macropa and DOTpy were found to be particularly stable in organic solution and were isolated and fully characterized. Furthermore, for the DOTpy-complex, ^{18}F-fluorination (MeOH, 60°C, 20 min) yielded the desired [^{18}F][LaF(DOTpy)]OTf_2 in 90% radiochemical

yield (based on starting ^{18}F-fluoride). The results of the DFT study will be reported. ***Conclusion:*** In this study, we have demonstrated the synthesis of first-in-class La[$^{19/18}$F]fluoride coordination complexes with several (macrocyclic) chelators. The stability of the resulting [$^{18/19}$F]LaF complexes was found to be inversely correlated with the ligand's electron-donating properties, with less electronegative ligands resulting in more stable complexes. This work serves as a proof-of-concept and offers new possibilities for theranostic approaches beyond [La-F] chemistry. Specifically, the further development and application of this approach to ^{225}Ac-radiopharmaceuticals is currently being investigated, which may enable personalized dosimetry and therapy control of ^{225}Ac-based targeted alpha therapy on quantitative PET imaging.

EPS-143

Radiochemistry and Evaluation of Novel Selective α-Synuclein Fibrils tracers for Parkinson's Disease

N. Mortazavi Golsefidi[1], *B. Uzuegbunam*[2], *M. Luster*[1], *D. Librizzi*[1,3], *B. Hooshyar Yousefi*[1,4];
[1]*Department of Nuclear Medicine, School of Medicine, Philipps University Marburg, Marburg, GERMANY,* [2]*Department of Nuclear Medicine, Technical University of Munich, and Isotope Technologies Munich (ITM), Munich, GERMANY,* [3]*Department of Nuclear Medicine, University Hospital OWL, Evangelisches Klinikum Bethel, Bielefeld, GERMANY,* [4]*Preclinical Imaging Core Facility, Center for Tumor Biology and Immunology (ZTI), Philipps University Marburg, Marburg, GERMANY.*

Aim/Introduction: A selective ^{18}F-labelled tracer for the detection of α-synuclein fibrils (α-syn) is crucial for early diagnosis and better understanding of Parkinson's disease (PD) and other α-synucleinopathies. Existing imaging techniques lack the specificity and sensitivity required for in vivo detection of α-syn fibrils, presenting a significant challenge worldwide. Developing selective ^{18}F-labeled positron emission tomography (PET) tracers is therefore an urgent unmet need, with the potential to revolutionize clinical diagnosis, enable precise patient stratification, and monitor therapeutic interventions. 4,4´-Disarylbisthiazoles (DABTA) have shown exceptional binding affinity to α-syn and high selectivity over β-amyloid plaques (Aβ) and tau fibrils, making them promising PET tracer candidates. These ligands were designed to be easily labeled with fluorine-18 ([^{18}F]), a radionuclide with an optimal half-life and energy profile for PET imaging. ***Materials and Methods:*** In this study, over 80 DABTAs with tailored functional groups were evaluated, and 10 lead compounds were identified for radiolabeling via ^{18}F-nucleophilic substitution using various leaving groups. The radiotracers were purified using high-performance liquid chromatography (HPLC) and comprehensively characterized through in vitro and in vivo studies. Typical preclinical evaluation and autoradiography on post-mortem human brain tissues from subjects of Multiple System Atrophy (MSA) with Glial Cytoplasmic Inclusions (GCIs), Dementia with Lewy Bodies/Parkinson's Disease (DLB/PD), Aβ- and tau-pathology, and healthy control were carried out. ***Results:*** Radiolabeling was accomplished through a one-step procedure, achieving radiochemical yields (RCYs) of 4-32% (n = 43), with a radiochemical purity of over 99% confirmed by HPLC and radio-TLC. Non-radioactive reference compounds validated the tracer identities. Notably, FS4, FS5, FS8, and FS9 exhibited significantly higher RCYs (14-32%). Post-mortem autoradiography at 0.2 MBq/mL demonstrated high-contrast binding for most of DABTAs, particularly [^{18}F]FS4, [^{18}F]FS5 and [^{18}F]FS9, in α-synuclein-rich brain regions. ***Conclusion:*** All lead DABTAs were successfully radiolabeled, with FS4, FS5, and FS9 displaying superior radiochemical yields and imaging performance. Their strong binding specificity and enhanced imaging capabilities in small animal imaging highlight their potential for translational research, including longitudinal PET/CT studies in PD animal models (will be presented in another abstract). These findings contribute to our effort in developing effective diagnostic tools for neurodegenerative diseases.

EPS-144

CADD-Guided Optimization and Synthesis of Novel CD13-Targeting PET Probes for Precision Management of Prostate Cancer

T. Liying, *Z. Ming, H. Shou;*
Xiangya Hospital, Central South University, Hunan Province, CHINA.

Aim/Introduction: Prostate cancer (PCa) ranks as the second most prevalent malignancy among men worldwide, with both incidence and mortality rates continuing to rise annually. Early and precise diagnosis and treatment are critical for improving patient prognosis. Previous research identified CD13 as a novel molecular target highly expressed in PCa, leading to the development of the targeted probe [^{18}F]AlF-CD13-L1. However, this probe exhibited limited binding affinity for CD13. Given the demonstrated efficacy of computer-aided drug design (CADD) in optimizing molecular structures for enhanced pharmacological properties, this study aims to employ CADD-based rational optimization of the precursor CD13-L1 to develop a next-generation probe with superior CD13 affinity. ***Materials and Methods:*** The CADD-optimized precursors were radiolabeled with ^{68}Ga, yielding probes [^{68}Ga]Ga-CD13-L2 and [^{68}Ga]Ga-CD13-L3. Cellular uptake studies and small-animal PET/CT imaging were performed using CD13-expressing prostate cancer cells line PC3 and corresponding xenografts. Tumor tissues were analyzed via IHC and HE staining. For therapy evaluation, CD13-L3 was labeled with ^{177}Lu, and the efficacy of [^{177}Lu]Lu-CD13-L3 was assessed in PC3 xenografts, with [^{177}Lu]Lu-CD13-L1 as a control. ***Results:*** We successfully optimized and synthesized two novel CD13-targeting precursor through CADD. The cellular uptake of [^{68}Ga]Ga-CD13-L3 in PC3 cells reached 1.99 ± 0.06%, demonstrating significantly higher accumulation compared to [^{68}Ga]Ga-CD13-L1 and [^{68}Ga]Ga-CD13-L2 (0.7 ± 0.08% and 1.19 ± 0.01%, respectively). This uptake was specifically inhibited by excess unlabeled peptide for all three probes. In PC3 xenograft models, PET imaging at 30, 60, and 90 minutes post-injection revealed superior tumor uptake of [^{68}Ga]Ga-CD13-L3 (2.04 ± 0.11 %ID/g at 90 min) versus [^{68}Ga]Ga-CD13-L1 and [^{68}Ga]Ga-CD13-L2 (0.4 ± 0.04 and 0.72 ± 0.10 %ID/g, respectively). Histopathological analysis confirmed successful tumor engraftment (HE staining) and high CD13 expression in tumor tissue (IHC). Therapeutic evaluation demonstrated that [^{177}Lu]Lu-CD13-L3 significantly inhibited tumor growth ($P < 0.005$) and extended survival compared to both saline controls and [^{177}Lu]Lu-CD13-L1 treatment groups. ***Conclusion:*** We have successfully optimized CD13-targeting precursors and synthesized novel PET probes with enhanced binding affinity. These advancements are anticipated to fully unlock the clinical potential of CD13 in prostate cancer (PCa) applications, ultimately advancing precision diagnosis and targeted therapy for PCa.

EPS-145

Developing covalent radiotracers for detection of neurodegenerative proteinpathies

P. Liu[1], *Z. Liu*[1,2];
[1]*Changping Labrotary, Beijing, CHINA,* [2]*Peking University, Beijing, CHINA.*

Aim/Introduction: To address the critical unmet challenge of developing PET radiotracers for low-abundance pathological aggregates in neurodegenerative diseases, we aimed to harness covalent radiotracers, a novel theranostic strategy, to overcome limitations in target engagement and signal-to-noise ratios.[1] These aggregates include Non-Alzheimer's tauopathies (e.g., progressive supranuclear palsy (PSP), corticobasal degeneration (CBD)), α-Synuclein in Parkinson's disease (PD), TDP-43 inclusions

in frontotemporal dementia (FTD) and amyotrophic lateral sclerosis (ALS). ***Materials and Methods:*** Building on the covalent radiotracer paradigm pioneered by Liu et al.[1], we employed computer-aided drug design (CADD) to develop irreversible covalent probes targeting tau protein. A covalent screening assay was developed to evaluate synthesized compounds for pathological tau aggregates using autoradiography with human postmortem brain tissue slices. Lead covalent molecules were further characterized for binding affinity (K_d) and kinetics across tauopathy subtypes, as well as selectivity against off-target tissues (e.g., amyloid-laden AD cortex and α-synuclein-rich PD midbrain). Pharmacokinetic profiles of the top candidate were assessed in healthy rats via dynamic PET imaging and ex vivo biodistribution studies to quantify brain uptake, clearance rates, and off-target retention. ***Results:*** The covalent tau probes demonstrated high specificity for pathological aggregates in human postmortem brain tissues, with autoradiography revealing preferential binding to tau lesions in AD, PSP, and CBD cases. The lead compound, Tau-3, exhibited nanomolar binding affinity for non-AD-derived tau fibrils and slower dissociation kinetics compared to non-covalent reference tracers (>3-fold improvement). Selectivity profiling confirmed negligible off-target binding to amyloid-β plaques in AD cortex or α-synuclein aggregates in Parkinson's disease (PD) midbrain. In healthy rats, dynamic PET imaging demonstrated rapid blood-brain barrier penetration and efficient systemic clearance, with ex vivo biodistribution studies revealing minimal residual brain activity (<1% ID/g at 90 min). ***Conclusion:*** These results validate the potential of covalent probes for detecting sparse pathological aggregates. Clinical translation is now underway through investigator-initiated trials (IITs) to evaluate efficacy in humans. This work establishes a foundational platform for developing next-generation neurological covalent probes tailored to low-abundance aggregates, bridging the gap between preclinical validation and clinical application. The platform holds transformative potential for addressing the unmet diagnostic needs across diverse proteinopathies. ***References:*** Cui et al., Nature 2024, 630, 206

EPS-146

Tetrazine Ligation Meets αvß6 Integrin-Targeted PET Imaging: Radiosynthesis and Preclinical Evaluation of ^{18}F-Flutrahexin

M. Martin[1], *V. Morath*[2], *F. Reissig*[3], *U. M. Battisti*[1,4], *N. Holzleitner*[2,5], *S. Stangl*[2,5], *V. Shalgunov*[1,6], *A. T. I. Jensen*[1], *J. Notni*[3], *S. Kossatz*[2,5], *M. M. Herth*[1,4,6];
[1]*TetraKit Technologies ApS, Copenhagen, DENMARK,* [2]*Department of Nuclear Medicine, TUM University Hospital, School of Medicine and Health, Technical University Munich, Munich, GERMANY,* [3]*TRIMT GmbH, Radeberg, GERMANY,* [4]*University of Copenhagen, Department of Drug Design and Pharmacology Faculty of Health and Medical Sciences, Copenhagen, DENMARK,* [5]*Central Institute for Translational Cancer Research (TranslaTUM), School of Medicine and Health, Technical University, Munich, GERMANY,* [6]*Rigshospitalet, Department of Clinical Physiology, Nuclear Medicine & PET, Copenhagen, DENMARK.*

Aim/Introduction: The integrin αvβ6 is a transmembrane receptor that is overexpressed in various epithelial cancers. The αvβ6-targeting radioligand ^{68}Ga-Trivehexin consists of three cyclic nonapeptides attached to a central TRAP-chelator and showed highly promising tumor imaging capabilities (pre) clinically in various cancers. These include pancreatic (PDAC), lung (NSCLC), head and neck (HNSCC), papillary thyroidal Ca, parathyroid adenoma including brain metastases as well as (lung) fibrosis. Here we report the synthesis and preclinical evaluation of ^{18}F-Flutrahexin, an ^{18}F-labelled analog of ^{68}Ga-Trivehexin, comprising three nonapeptide targeting vectors, a DOTPI chelator and the trans-cyclooctene T4CO to be labelled via tetrazine ligation. ***Materials and Methods:*** The tetrazine ^{18}F-FlutraTag was synthesized from the corresponding nosyl precursor (dried ^{18}F-tetrabutylammonium fluoride, MeCN, 100 °C, 3 min). The purified ^{18}F-FlutraTag was then clicked to the T4CO-modified click precursor in the presence of gentisic acid. After acid-mediated oxidation (r.t., 30 min), ^{18}F-Flutrahexin was purified by C18-SPE, eluted with EtOH, concentrated, and diluted with PBS. The pharmacokinetic profile of ^{18}F-Flutrahexin was investigated via dynamic and static PET imaging in healthy female Sprague-Dawley rats and mice bearing αvβ6-expressing human lung adenocarcinoma xenografts (H2009), followed by organ biodistribution via gamma-counting. In vivo specificity was assessed via blocking with ^{nat}Ga-Trivehexin. Gelofusine co-injection was investigated for kidney protection. ***Results:*** ^{18}F-FlutraTag was obtained in RCY = 10-30% and RCP > 98%. After quantitative click and oxidation ^{18}F-Flutrahexin was obtained from ^{18}F-FlutraTag in RCY = 60-80%, RCP > 95% and molar activity A_m = 9-20 GBq/µmol. In healthy rats, the radiotracer showed fast clearance from blood, renal excretion and high uptake only in the kidneys, which was reduced by a factor of 3 with gelofusine (90 min p.i.: 30 vs. 9 %ID/g). In xenograft-bearing mice, PET imaging visualized H2009 xenografts with high tumor-to-background contrast. Tumor uptake reached 7% ID/g 90 min p.i., while uptake in other organs was overall low, except for the kidneys, resulting in a tumor-to-blood ratio of 3 and tumor-to-muscle ratio of 14 (90 min p.i). Specificity was demonstrated by blocking with excess ^{nat}Ga-Trivehexin, which reduced tumor uptake from 7 to 1 %ID/g. ***Conclusion:*** Overall, ^{18}F-Flutrahexin performed similar to ^{68}Ga-Trivehexin and offers a promising alternative to for high-resolution PET imaging of αvβ6-positive tumors. Furthermore, it seems feasible to expand to a theranostic approach by using tetrazines labelled with radiohalogens like iodine-131 or astatine-211 in combination with gelofusine kidney protection.

EPS-147

Synthesis and Evaluation of a High Affinity and Long-time Retention CXCR4-Targeted Probe

X. Yu, *M. Zhang, G. Li, W. Yang, J. Wang, F. Kang;*
Xijing Hospital, Fourth Military Medical University, Xi'an, Shaanxi, CHINA.

Aim/Introduction: C-X-C chemokine receptor type 4 (CXCR4) is indispensable to the development of many inflammatory disorders and malignant tumors, such as multiple myeloma and non-Hodgkin lymphomas. ^{68}Ga-PentixaFor, a radioligand targeting CXCR4, exhibits a strong affinity for CXCR4 both in vivo and in vitro. However, ^{68}Ga-PentixaFor PET still has some limits. This study aimed to develop a higher affinity and long-time retention radiotracer for CXCR4-targeted imaging to improve the detection efficiency. ***Materials and Methods:*** The new precursor Pentikra was synthesized with a positively charged tripeptide linker, D-Lys-D-Arg-D-Ala, between the chelator and the targeting peptide of iodoCPCR4. The in vitro stability of ^{68}Ga-Pentikra was evaluated in both PBS and mouse serum. The partition coefficient of ^{68}Ga-Pentikra was evaluated. The cell binding and internalization studies of ^{68}Ga-Pentikra, ^{68}Ga-PentixaFor and ^{68}Ga-PentixaTher were performed in CXCR4 positive cells (CHO-hCXCR4). The affinity assay of these three tracers was performed with CHO-hCXCR4cell line. Static PET imaging studies (1h, 2h, 3h and 4h p.i.) were performed in CHO-hCXCR4 and CHO-control tumor xenograft bearing NOD-SCID mice respectively, and the 90-min dynamic imaging PET studies of the three tracers were performed with CHO-hCXCR4 tumor xenograft bearing NOD-SCID mice only. ***Results:*** ^{68}Ga-Pentikra was stable in both PBS and mouse serum for 2 h. The lipophilicity of ^{68}Ga-Pentikra were -2.88 ± 0.14, which was comparable to those of ^{68}Ga-PentixaFor and ^{68}Ga-PentixaTher. The IC_{50} of Pentikra was 21.95 ± 6.66 nM, which was significantly lower than those of PentixaFor and PentixaTher (477.8 ± 14.86

and 277.5 ± 8.75 nM). In cell studies, the total binding rate and the internalization rate of ^{68}Ga-Pentikra at 120 min was 49.3 ± 4.4% and 20.9 ± 0.92%, which was significantly higher than those of ^{68}Ga-PentixaFor and ^{68}Ga-PentixaTher. PET studies, though the hepatic of ^{68}Ga-Pentikra is high, the SUVmean of ^{68}Ga-Pentikra in CHO-hCXCR4 tumor was 4.25 ± 1.02, which was higher than those of ^{68}Ga-PentixaFor and ^{68}Ga-PentixaTher (3.95 ± 0.60 and 2.25 ± 0.73). In the dynamic PET imaging, the tumor accumulation of ^{68}Ga-Pentikra kept increasing within 90 minutes, which was similar to those of ^{68}Ga-PentixaFor and ^{68}Ga-PentixaTher. ***Conclusion:*** In this study, a novel CXCR4-targeted probe was successfully synthesized and labeled with ^{68}Ga. Due to the high affinity of ^{68}Ga-Pentikra to hCXCR4 and the enhanced cellular retention in CXCR4 overexpressed tumors, ^{68}Ga-Pentikra may have great potential in the application of CXCR4 targeted diagnosis and treatment.

EPS-148

Chelator-free gallium-68 labeling of Nanoclays for in vivo tracking

N. Liu;
The First Affilated Hospital, Zhejiang University School of Medicine, Hangzhou, CHINA.

Aim/Introduction: Nanoclays are an important class of mineral-based herbal medicines that have been widely studied as nanocarriers for drug delivery owing to their large specific surface area, abundant porosity, good adsorption properties, and biocompatibility. However, the lack of comprehensive understanding of their in vivo biological fate has restricted their further clinical development and utilization. Radiolabeling of probes for positron emission tomography (PET) imaging can track the probes with high sensitivity and quantitativity. Herein, we envisioned to use chelator-free gallium-68-labeling to evaluate the radiopharmacokinetics of nanoclays. ***Materials and Methods:*** ^{68}Ga-labeled nanoclays were prepared by simple mixture. Size distribution and zeta potentials of nanoclays were analyzed on a Malvern Zetasizer. The radiolabeling yield of 68Ga was tested by Mini-Scan radio-TLC Strip Scanner. The labeling mechanisms was explored by density functional theory (DFT) calculations. The in vivo stability and biodistribution evaluations of nanoclays were verified by PET imaging after intravenous or gavage administration. ***Results:*** $^{68}Ga^{3+}$ can be radiolabeled on all these three nanoclays with relative high labeling yields upon a short reaction time of 10 min at 37 °C. And this labeling method exhibits good radiochemical purity and serum stability. DFT calculations revealed that the strong Coulomb adsorption between gallium ions and nanoclays contributed to this reliable radiolabeling. Importantly, the PET imaging after intravenous or gavage administration shows good in vivo radiostability during the observation time, confirming the tracing feasibility of nanoclays. ***Conclusion:*** This work provides a simple and stable radiolabeling method to visualize the biological fate of nanoclays in vivo, contributing to understanding of the metabolic pathway and possible biomedical applications of nanoclays. ***References:*** [1] J. Mater. Chem. B 2020, 8, 7335-7351. [2] Natl. Sci. Rev. 2022, 9, nwac119. [3] ACS Nano 2022, 16, 5036-5061.

EPS-149

Production of 64Cu with hybrid target

D. Szikra[1], *V. Forgács*[1], *M. Fodor*[2], *Z. Szücs*[2];
[1]*University of Debrecen, Division of Nuclear Medicine, Medical Imaging Department, Debrecen, HUNGARY,* [2]*Radiochemical Laboratory, HUN-REN Institute for Nuclear Research, Debrecen, HUNGARY.*

Aim/Introduction: 64Cu production on medium energy cyclotrons, equipped with solid target systems, is a well established procedure. The most widely used method is the 64Ni(p,n)64Cu reaction, starting from enriched 64Ni, electroplated onto an appropriate backing material. After irradiation, the target is transferred to a hot cell for dissolution and purification. The implementation of this production method requires the installation of a solid target system with shuttle transport and a dissolution unit in a dedicated hot cell. This requires high investment, which inhibits the broader application of 64Cu labelled tracers. Liquid targets are easier to install and use, but the achievable yields are significantly lower. Dissolution of the irradiated target material inside the target simplifies activity transfer between the cyclotron- and the hot cell and saves precious hot cell space in the cleanroom. ***Materials and Methods:*** Natural- or enriched 64Ni was electroplated onto platinum backings (22x0.5 mm) and mounted on the target holder of a hybrid target system. The targets were irradiated with 50-70 uA 12 MeV proton beam for 1-3 h. The irradiated nickel was dissolved from the backing with 2 ml 6 M HCl at room temperature by applying 3V constant voltage beween the backing and a platinum wire electrode, fixed into the dissolution chamber of the target. The dissolution could be monitored in real time with the observation of the cell current. After the drop of cell current, the target solution was transferred from the target to a collection vial via a PEEK capillary line and loaded onto an AG1X8 column on a Trasis miniAiO module. The purified 64Cu was eluted from the column with 8 ml 0.01 M HCl. ***Results:*** Up to 56,78 GBq 64Cu was produced from 200 mg 64Ni with 70 uA beam current during 3 hour irradiation. The dissolution of the target material was complete in 20 minutes. No nickel residues were remained on the backing. Recycling of the enriched target material was performed with approx. 2% loss. ***Conclusion:*** A new method was developed for the room temperature dissolution of irradiated nickel target material. Efficient 64Cu production was realized using the combination of a hybrid target and a Trasis miniAiO module.

EPS-150

Method for producing medical ^{90}Y via radionuclide generator: improving quality and efficiency

A. Baimukhanova[1,2], *G. Magomedov*[2,3], *V. Pokalchuk*[3], *E. Magomedbekov*[3], *D. Karaivanov*[2], *D. Filosofov*[2];
[1]*Institute of Nuclear Physics of the Republic of Kazakhstan, Almaty, KAZAKHSTAN,* [2]*Joint Institute for Nuclear Research, Dubna, RUSSIAN FEDERATION,* [3]*D. I. Mendeleev Russian University of Chemical Technology, Moscow, RUSSIAN FEDERATION.*

Aim/Introduction: A radionuclide generator provides a convenient way of producing radioisotopes. Generators based on long-lived parent radionuclides are commonly used to obtain medically relevant isotopes—for example, ^{68}Ge ($T_{1/2}$ = 270.93 d) → ^{68}Ga ($T_{1/2}$ = 67.71 min), ^{229}Th ($T_{1/2}$ = 7880 y) → ^{225}Ac ($T_{1/2}$ = 9.92 d), etc. However, over time, the quality of the radiopreparation tends to degrade due to increasing breakthrough of the parent radionuclide and decreasing yields of the daughter product. This issue necessitates the development of new chemical systems and generator configurations. One promising approach is the reverse scheme, which confines the parent radionuclide within a narrow zone on the column. This enhances the stability of the generator's performance over time and improves the quality of the radiopharmaceuticals produced[1]. In this work, we consider the potential for producing ^{90}Y using a ^{90}Sr ($T_1/_2$ = 28.91 y) → ^{90}Y ($T_1/_2$ = 64.05 h) radionuclide generator based on a reverse-tandem scheme. ***Materials and Methods:*** For developing the generator scheme, the distribution coefficients (K_d) of Sr(II) and Y(III) in a system containing ion-exchange resin and a mixed citric acid and ammonia acetate medium were determined in a previous study[2]. Based on these K_d values, efficient separation was achieved using Dowex 50×8 with a 0.1 M CH_3COOH / 0.5 M CH_3COONH_4 solution, where a separation factor is 13. The tandem part of the generator based on the solid extraction chomatography in hydrochloric acid media. ***Results:*** This radionuclide generator achives a ^{90}Y yield of more than 70%, which is a key indicator of its high efficiency in isolating and producing the desired isotope.

The low breakthrough of ^{90}Sr, less than $4{\cdot}10^{-3}$, further highlights the generator's effectiveness in minimizing the contamination of the final radiopharmaceutical product with the parent radionuclide. ***Conclusion:*** The alternative method for producing of ^{90}Y has been developed based on reverse-tandem scheme of the radionuclide generator. The resulting generator parameters ensure the production of high-purity 90Y, which is crucial for medical applications where precise dosimetry and minimal side effects are essential. The combination of a high yield and minimal breakthrough makes this generator particularly reliable and suitable for clinical use, offering stable and reproducible results over time. ***References:*** 1. D. V. Filosofov, N. S. Loktionova and F. Rösch, Radiochim Acta, 2010, 98, 149-156 2. J. Dadakhanov, A. Marinova, A. Baimukhanova, D. Karaivanov, N. Temerbulatova, J. Kozempel, F. Roesch and D. Filosofov, J Radioanal Nucl Chem, 2021, 327, 1191-1199.

EPS-151

Development of novel nanobody-based ^{68}Ga and ^{131}I radiotracers for detecting MUC16 expression in vivo

J. Han, *Y. He;*
Fudan University, Shanghai, CHINA.

Aim/Introduction: MUC16, a high-molecular-weight glycoprotein, is highly expressed in various tumors and is limited to epithelial cells of several tissues. It has already been proven to be a sensitive biomarker and a promising therapeutic target for cancer. However, it still lacks small molecule tools to map the target in vivo. Here, we describe the generation of nanobody-based Immuno-PET/-SPECT tracers that could precisely and rapidly monitor MUC16 expression in vivo. ***Materials and Methods:*** Nanobody was obtained via immunization of llama using a fragment close to N sites. The initial screening of nanobodies was evaluated through an enzyme-linked immunosorbent assay to get lead molecule VHH HF-07. Further, VHH was conjugated with p-SCN-Bn-NOTA to get NOTA HF-07, and the conjugate was continuously radiolabeled with ^{68}Ga to get the radiotracer [^{68}Ga]Ga-NOTA-HF-07. In radioiodination, HF-07 was radiolabeled, followed by two-step procedures with iso-[^{131}I]SGMIB to get iso-[^{131}I]I-SGMIB-HF-07. The radiochemical purity and in vitro stability were tested by radio-thin-layer chromatography and size exclusion chromatography, respectively. The binding of the tracers was validated by saturation binding assay. The capacity of the radiotracer to quantify the MUC16 expression was investigated in vivo in NCG mice bearing OVCAR-3 tumor models through small animal PET-CT and SPECT-CT scanners for ^{68}Ga and ^{131}I tracers, respectively. Finally, the tracers were evaluated by ex vivo biodistribution at 60 min post-injection. ***Results:*** HF-07 shows a high binding affinity toward MUC16 with an EC_{50} value of 1.3 nM. And it was still kept in the nanomolar range after conjugation and radiolabeling. ^{68}Ga and ^{131}I tracers were obtained at high radiochemical purity (>99%) with moderate radiochemical yields, 32 ± 11% for g [^{68}Ga]Ga-NOTA-HF-07 (n = 9, decay-corrected) and 22 ± 6% for iso-[^{131}I]I-SGMIB-HF-07 (n = 6, decay-corrected). Both ^{68}Ga and ^{131}I radiotracers were stable after 240 min incubation at room temperature. Micro PET/CT imaging of [^{68}Ga]Ga-NOTA-HF-07 demonstrated clear and efficient tumor visualization using NCG mice bearing OVCAR-3 xenografts with a high level of MUC16 expression. In micro SPECT/CT scan, iso-[^{131}I]I-SGMIB-HF-07 showed a longer half-life and still had uptake after 24hrs. In biodistribution studies, [^{68}Ga]Ga-NOTA-HF-07 displayed radioactivity accumulation of 1.95 ± 0.89 %ID/g and iso-[^{131}I]I-SGMIB-HF-07 showed 6.06 ± 0.48 %ID/g in OVCAR-3 xenografts at 60 min post-injection. ***Conclusion:*** Two novel nanobody-based probes targeting MUC16, [^{68}Ga]Ga-NOTA-HF-07 and iso-[^{131}I]I-NOTA-HF-07, have been developed. These tracers allow for the early acquisition of the target with clear image quality. The results revealed the radiotracer's great potential for further theranostic research.

EPS-152

Discovery of a novel [^{18}F]-labeled phenylalanine derivative PET tracer for preclinical tumor imaging

Y. Xie, *Y. Wang, H. Zhou, M. Hu, W. Chen;*
West China Hospital, Sichuan University, Chengdu, CHINA.

Aim/Introduction: Accurate diagnosis of glioma is challenging due to its invasive nature and blockade of the blood-brain barrier. Amino acid PET probes targeting large neutral amino acid transporter type-1 (LAT-1) can assist in the noninvasive grading and treatment monitoring. This study aims to develop a novel PET tracer [^{18}F]fluoro-methylated-phenylalanine ([^{18}F]FMP) through direct photocatalyzed ^{18}F-deoxyfluorination that could improve the ability to differentiate non-neoplastic lesions and identify tumor extent. ***Materials and Methods:*** [^{18}F]FMP was prepared through photocatalyzed azeotropic drying-free ^{18}F-deoxfluorination[1]. Cellular uptake experiment was performed in MCF7 and U87MG cells (n=3). Biodistribution studies and imaging efficacy were evaluated in rodent models (n=5). ***Results:*** [^{18}F]FMP demonstrated high radiochemical purity (>99%) and yield (28.3 ± 1.1%, n=3, non-decay corrected). As a pan-cancer probe, the micro-PET in MCF7 and U87MG tumor-bearing mice showed superior tumor uptake for [^{18}F]FMP (SUV_{max} = 6.03 ± 0.34, 2.89 ± 0.43) compared to [^{18}F]FET (SUV_{max} = 3.30 ± 0.36, 1.42 ± 0.15) with high stability. Biodistribution of U87MG tumor in mice at 15, 30, 60, and 120 minutes after intravenous administration was 10.76 ± 1.24%ID/g, 9.58 ± 1.95%ID/g, 8.44 ± 0.96%ID/g, and 9.26 ± 1.80%ID/g. Competition inhibition assays of in vitro cancer cells and in vivo micro-PET imaging suggested [^{18}F]FMP is LAT-1 specific. ***Conclusion:*** We successfully developed a novel radiotracer [^{18}F]FMP via an efficient azeotropic drying-free photolabeling method. [^{18}F]FMP retained the advantageous properties of common amino acid PET tracers while enhancing tumor uptake and tumor-to-background ratio. Preliminary studies indicated the potential of [^{18}F]FMP in clinical applications of brain tumors. ***References:*** [1] Wei Chen, Yueqi Wang, Lili Pan et al. Simplified radiolabeling process toward rapid photoredox-catalyzed aryl ^{18}F-fluorination and PET tracer development, 09 February 2025, PREPRINT (Version 1) available at Research Square [https://doi.org/10.21203/rs.3.rs-4325597/v1]

EPS-153

Radiolabeling of Gold Nanoconstructs with Particle-Emitting Radioisotopes

A. Apostolopoulou[1], *E. A. Salvanou*[1], *D. E. Bajwa*[1], *C. Liolios*[1], *S. Xanthopoulos*[1], *F. Denat*[2], *G. Laurent*[3], *R. Bazzi*[3], *S. Roux*[3], *P. Bouziotis*[1];
[1]*National Center for Scientific Research "Demokritos", Athens, GREECE,* [2]*Institut de Chimie Moléculaire de l'Université de Bourgogne, Dijon, FRANCE,* [3]*Université Marie et Louis Pasteur, CNRS, Chrono-environnement, Besançon, FRANCE.*

Aim/Introduction: Actinium-225 (^{225}Ac, alpha-emitter, $t_{1/2}$ = 9.9 days) and Lutetium-177 (^{177}Lu, beta-emitter, $t_{1/2}$ = 6.71 days) are two promising radioisotopes with substantial potential for a wide range of applications in radiotherapy of cancer. Gold Nanoparticles (AuNPs) functionalized with the chelator TADOTAGA are useful multifunctional carriers for these isotopes. The aim of the current study was the development and evaluation of gold nanoparticles (AuNPs) and gold nanoflowers (AuNFs) radiolabeled with ^{225}Ac and ^{177}Lu via TADOTAGA as an injectable radiopharmaceutical form of therapy for the treatment of cancer. ***Materials and Methods:*** AuNPs/AuNFs were radiolabeled with $^{225}AcCl_3$ (~80 KBq) and $^{177}LuCl_3$ (~10 MBq) using trace-free sodium acetate buffer 0.2 M (pH 5.6) followed by incubation at 75°C. Radiolabeling yield and in vitro stability were evaluated by instant thin-layer chromatography (ITLC). Stability studies were carried out in PBS and sodium acetate over 12-14 days. Cytotoxicity of both bare and radiolabeled nanostructures was assessed using

the MTT assay in U87MG and 4T1 cells over 24, 48, and 72 hours. Therapeutic efficacy of ^{225}Ac-AuNPs and ^{225}Ac-AuNFs was further investigated in a 4T1 tumor-bearing mouse model for 15 days post-administration. ***Results:*** Radiolabeling with ^{225}Ac led to >90% radiolabeling yield for both AuNPs/AuNFs maintaining ~80% stability in PBS and ~85% in sodium acetate up to 14 days post-incubation, as evaluated by TLC analysis. Additionally, radiolabeling with ^{177}Lu resulted in excellent radiolabeling yield for the AuNPs (>97%) while [^{177}Lu]Lu-AuNFs exhibited poor labeling efficiency. Bare AuNPs exhibited minimal cytotoxicity at all concentrations and timepoints examined, while bare AuNFs demonstrated significant toxicity, particularly in U87MG cells. Radiolabeled [^{225}Ac]Ac-AuNFs presented reduced cell viability in both lines (as low as 18.13% in 4T1 at 72 h), while [^{225}Ac]Ac-AuNPs appeared less toxic (minimum 74.94% viability). In addition, cells incubated with [^{177}Lu]Lu-AuNPs maintained high viability (>85%), reinforcing their safety profile. Regarding the therapeutic efficacy study, both [^{225}Ac]Ac-AuNPs/AuNFs reduced tumor growth in 4T1 models. ***Conclusion:*** AuNPs and AuNFs can be effectively radiolabeled with ^{225}Ac, leading to stable nanoconstructs, while [^{225}Ac]Ac-AuNFs demonstrated enhanced cytotoxicity in both cell lines. Both [^{225}Ac]Ac-AuNFs/AuNPs demonstrated a similar therapeutic effect after intratumoral administration in 4T1 tumor xenografts. These results warrant further in vivo investigation for targeted radionuclide therapy in tumor xenografts. ***References:*** [1] Salvanou, E.-A. et al., A Proof-of-Concept Study on the Therapeutic Potential of Au Nanoparticles Radiolabeled with the Alpha-Emitter Actinium-225, Pharmaceutics 2020, 12, 188.

EPS-154

Development of a cGMP-compliant automated synthesis of the radiotherapeutic [^{177}Lu]Lu-ABY-271: Enabling reliable radiolabelling for a first-in-human phase I study

S. Omer[1], *M. Ferrat*[1], *E. Jussing*[1], *N. Molina*[2], *T. Tegnebratt*[2], *J. Garousi*[2], *H. Alfredéen*[1], *J. Ödling*[3], *L. Bremer*[3], *H. Bönisch*[3], *S. Wood*[3], *F. Y. Frejd*[3], *M. M. Moein*[2], *T. A. Tran*[1];
[1]*Karolinska Institutet, Solna, SWEDEN,* [2]*Karolinska University Hospital, Solna, SWEDEN,* [3]*Affibody AB, Solna, SWEDEN.*

Aim/Introduction: Human Epidermal Growth Factor Receptor 2 (HER2) is overexpressed in several malignancies, including breast, ovarian, gastric and oesophageal cancers. Approximately 15-20% of breast cancer tumors express HER2, and the development of HER2-targeted theranostic radiopharmaceuticals enables a personalised "see and treat" approach, facilitating non-invasive tumor characterisation followed by targeted therapy. In this context, the Affibody® molecule [^{68}Ga]Ga-ABY-025 has been clinically evaluated as a HER2 PET imaging tracer in metastatic breast cancer [1], and ongoing for oesophageal cancers (NCT05619016) and as an image-guided selection tool for antibody drug conjugates (ADC) treatment (NCT06830382). Molecular radiotherapy with the ABY-025 derived HER2 targeted Affibody molecule [^{177}Lu]Lu-ABY-271 might provide an alternative treatment for those patients who do not respond to current ADC treatment. For clinical translation, we developed a robust manual radiolabelling protocol that was transferred to a cGMP automatic synthesis, enabling reliable and reproducible manufacturing of [^{177}Lu]Lu-ABY-271 for a first-in-human phase I study in HER2-positive breast cancer patients. ***Materials and Methods:*** Manual radiolabeling of [^{177}Lu]Lu-ABY-271 was scaled up and optimized from earlier preclinical conditions [2]. DOTA-conjugated ABY-271 (2 mg) and $^{177}LuCl_3$ (0.5 - 5 GBq) were used for radiolabelling. Reaction was performed in a sodium acetate/sodium ascorbate buffer at 65 °C for 30 minutes, in a volume of 4 mL, during gentle mixing. The crude product was purified using solid phase extraction (SPE), eluted in a final formulation buffer with ethanol. Following establishment of an optimized protocol, the labelling was transferred to a cGMP-compliant automated synthesis on Modular-Lab PharmTracer (Eckert & Ziegler). ***Results:*** During manual labelling, key parameters influencing yield and stability, including maintaining optimal pH to avoid denaturation, and incorporating sodium ascorbate to limit possible radiolysis, were established. Those conditions were then transferred to a disposable cassette-based, programmed labelling sequence. The fully automated process resulted in a ready-to-use [^{177}Lu]Lu-ABY-271 product containing an activity range of choice 0.5 - 3.3 GBq, 2-12 mg peptide in a volume of 18-22 mL; stable up to 4 days EOS (End of Synthesis), fulfilling the specified GMP standards of a sterile product with RCP > 95%. ***Conclusion:*** This study presents an optimized manual radiolabeling protocol for [^{177}Lu]Lu-ABY-271. Critical parameters impacting the yield and product stability were established and supported the translation of this protocol to GMP-compliant radiosynthesis for clinical use. ***References: References:*** 1. Altena et al JNM, 2024 ; 2. Liu Y et al. Eur J Nucl Med Mol Imaging (2024) 51 (Suppl 1)

EPS-155

Photocatalyzed nucleophilic ^{18}F-deoxyfluorination of highly electron-rich catechol derivatives for [^{18}F]FDOPA synthesis

W. Chen, *M. Hu, Y. Wang, C. Zheng;*
West China Hospital, Sichuan University, Chengdu, CHINA.

Aim/Introduction: Despite much progress having been made in synthesizing the multifunctional clinical PET tracer [^{18}F]FDOPA in the past decades, the established strategies, particularly the preferred direct nucleophilic ^{18}F-fluorination, generally involve complex precursor synthesis and provide unsatisfactory RCYs for scale-up automatic production. Thus, a simple and automatable direct labeling approach using a stable precursor under mild conditions is still attractive for the daily production of the [^{18}F]FDOPA when the current established methods are inaccessible or not well-performed in certain centers or labs. ***Materials and Methods:*** The precursors were prepared from a simple three-step synthesis. The challenging nucleophilic ^{18}F-fluorination of the highly electron-rich catechol moiety was performed under azeotropic drying-free photolabeling conditions[1]. The automatic synthesis was tested on the Allinone radiosynthesis module. ***Results:*** More than 20 novel precursors were rapidly obtained, and the precursors were stable at room temperature for more than 2 years. The labeling RCCs (radiochemical conversions) of the key ^{18}F-labeled intermediates for the subsequent deprotection was up to 70%. The [^{18}F]FDOPA was successfully produced in more than 20% non-decay corrected RCY in 98 minutes with >99% ee and purity on a commercial automatic radiosynthesis module. ***Conclusion:*** We successfully established a novel synthetic routine for the [^{18}F]FDOPA enabled by the photocatalyzed azeotropic drying-free ^{18}F-deoxyfluorination. The readily available and stable precursor makes this transition-metal-free approach an attractive routine for daily production of [^{18}F]FDOPA with high molar activity, and it also paved the way for the nucleophilic ^{18}F-fluorination of other catechol derivatives for PET tracer development and production. ***References:*** [1] Wei Chen, Yueqi Wang, Lili Pan et al. Simplified radiolabeling process toward rapid photoredox-catalyzed aryl ^{18}F-fluorination and PET tracer development, 09 February 2025, PREPRINT (Version 1) available at Research Square [https://doi.org/10.21203/rs.3.rs-4325597/v1]

EPS-156

Routine Radiolabeling of FAP Peptide 3BP-3940 with Y-90, Lu-177, and Ac-225 for FAP-Targeted Radiopharmaceutical Therapy (FTRT): Production and Performance Data from 5 Years and 90+ Clinical Batches

L. Greifenstein, *S. Stephan, C. Mueller, C. Landvogt, R. P. Baum;*
Curanosticum MVZ GmbH, Wiesbaden, GERMANY.

Aim/Introduction: Fibroblast activation protein (FAP) is highly expressed in cancer-associated fibroblasts and represents a promising target for radiopharmaceutical therapy (FTRT). The FAP-targeting ligand 3BP-3940 was developed for theranostic applications and allows labelling with various therapeutic radionuclides. This work presents a five-year clinical routine

experience with radiolabelling 3BP-3940 using Yttrium-90 (Y-90), Lutetium-177 (Lu-177), and Actinium-225 (Ac-225), focusing on production reliability, radiochemical purity, and regulatory compliance. ***Materials and Methods:*** Radiolabelling was performed under GMP-like conditions using standard protocols optimized for each radionuclide. Over a five-year period, a total of 103 syntheses were conducted: 20 with Y-90, 56 with Lu-177, and 27 with Ac-225 for a total of more than 300 patient doses. Radiochemical purity was assessed via radio-HPLC and radio-TLC. Each production batch was evaluated for compliance with internal quality standards. Data on labelling yields, quality control results, and batch failures were systematically recorded and analysed. ***Results:*** Of the 103 productions, 101 resulted in radiopharmaceuticals meeting the predefined quality criteria for patient administration, including 15 syntheses with out-of-expectation or out-of-specification observations. Mean radiochemical purity exceeded 95% for all three radionuclides. The average synthesis time was under 60 minutes for Y-90 and Lu-177, and approximately 90 minutes for Ac-225. No production-related technical failures or contaminations occurred during the study period. Deviations in yields occurred, but mean RCY were higher than 90% for Lu-177 and Ac-225 and above 85 % for Y-90. Issues of peptide stability that were already reported for the Y-90 labelling occurred as well for the Lu-177 protocol and were solved by the addition of L-Methionine to the reaction buffer [1]. Therefore, mean RCPs of 96,7 % were increased to 98,7 % determined by radio-HPLC ***Conclusion:*** The FAP ligand 3BP-3940 can be reliably labelled with Y-90, Lu-177, and Ac-225 under routine clinical conditions, enabling flexible and effective FAP-targeted radiopharmaceutical therapy. The high success rate over five years and more than 100 total productions support the feasibility and safety of implementing FTRT with 3BP-3940 in broader clinical practice. ***References:*** [1] Greifenstein et al., iScience 26, 108541, 2023

e-Poster Presentation Sessions

1010

Monday, October 6, 2025, 15:00 - 16:30
Room 116

Technologists' e-Poster Presentations Session - Technologists Committee: Techs' e-Posters

TEPS-001

Extravasations in Nuclear Medicine: Mechanisms, Consequences and Dosimetry

C. Sobral*, A. Rodrigues Teixeira, M. Nicod Lalonde, J. Prior, S. Medici;*
Centre Hospitalier Universitaire Vaudois (CHUV), Lausanne, SWITZERLAND.

Aim/Introduction: Radiopharmaceutical extravasation refers to the unintended leakage or administration of a radiopharmaceutical outside the injection vein, which can lead to localized accumulation in surrounding tissues rather than systemic circulation. We aimed to retrospectively analyze cases of extravasation that occurred in the department since 2019 to estimate incidence and frequency of paravenous events, as well as to evaluate side effects, specific measures implemented and dosimetry with the goal of establishing a decision-making flowchart. ***Materials and Methods:*** All reported extravasations to our critical incident reporting system from 2019 to 2024 were analyzed, focusing on variables such as the isotope used, dosimetry, need to repeat examinations or injections, manual versus automatic injection, immediate and delayed symptoms, presence of pre-existing catheters and actions taken. ***Results:*** A total of 17 extravasations were documented between 2019 and 2024, involving isotopes Ga-68 (6%), Rb-82 (12%), F-18 (53%), and Tc-99m (29%). Manual injections accounted for 35% of cases. Observed consequences included 59% experiencing partial reinjection of the radiopharmaceutical, 24% requiring repeat CT scans, 24% reporting immediate pain at the injection site and 12% exhibiting redness or swelling. No patients experienced delayed side effects and 35% had pre-existing catheters. Skin dosimetry values ranged from 0.021 Gy to 3.1 Gy.The adverse effects of extravasation depend on the radiopharmaceutical used, the volume and the activity administered. No long-term side effects were observed and no extravasation involving therapeutic radiopharmaceuticals was identified. Immediate post-extravasation interventions, such as massage, limb elevation, and application of cold compresses are recommended to prevent repeat examinations or reinjections. ***Conclusion:*** The consequences of extravasation can be minimized through prompt and proper management and established action protocols, thereby reducing associated side effects. Dosimetric evaluation may be necessary to exclude deterministic effects and facilitate proactive measures. Adecision-making flowchart has been consequently established to determine when dosimetric evaluation or additional local CT is recommended. ***References:*** Barré , E., Nguyen, M.-L., Bruel, D., Fournel, C., Hosten, B., Lao, S.,⋯ Rizzo-Padoin, N. (2013). Extravasation des médicaments radiopharmaceutiques : mesures préventives et prise en chargerecommandées par la SoFRa (Société française de radiopharmacie). Annales Pharmaceutiques Françaises, 71(4), 216224. https://doi.org/10.1016/j.pharma.2013.05.001

TEPS-002

A Novel ^{67}Ga-Labeled CXCR4-Targeted Tracer: Radiolabeling Performance, Stability, and In Vivo Evaluation in Atherosclerotic Models

S. Chen*, M. Chen, C. Chen, C. Hsia, M. Weng, Y. Chang, W. Chen;*
National Atomic Research Institute, Taoyuan, TAIWAN.

Aim/Introduction: Current imaging tools for atherosclerosis often detect disease only after structural plaque formation or vascular occlusion. CXCR4 (C-X-C motif chemokine receptor 4) has emerged as a key inflammatory biomarker during the early stages of atherosclerosis. It is highly expressed by macrophages, T cells, and endothelial cells in the atherosclerotic plaque microenvironment. This study aims to develop and evaluate a novel ^{67}Ga-labeled CXCR4-targeted tracer (APD) for SPECT/CT imaging, with the potential to noninvasively detect early vascular inflammation and facilitate preclinical translation. ***Materials and Methods:*** APD, a cyclen-based bifunctional chelator incorporating pyridylmethylamine moieties, was synthesized for stable radiometal chelation and specific CXCR4 binding. Radiolabeling was achieved by reacting APD with [^{67}Ga]$GaCl_3$ in sodium acetate buffer (80-95 °C, 10-30 min). Radiochemical purity was assessed by radio-TLC and radio-HPLC. The stability of ^{67}Ga-APD was evaluated by storing the tracer at room temperature for 2 hours and reanalyzing by HPLC. For in vivo studies, ApoE^{-}/$^{-}$ mice fed a high-fat diet for 8 weeks received tail vein injection of ^{67}Ga-APD. SPECT/CT imaging was conducted from 0 to 2 hours post-injection, followed by quantitative image analysis. ***Results:*** Radiolabeling yield and radiochemical purity of ^{67}Ga-APD exceeded 90%, as confirmed by both ITLC and HPLC. The tracer demonstrated high stability, maintaining >90% purity at room temperature for up to 2 hours. In vivo imaging revealed increased tracer uptake in the aortic arch and abdominal vasculature of ApoE^{-}/$^{-}$ mice—regions typically associated with early vascular inflammation. ***Conclusion:*** ^{67}Ga-APD is a promising CXCR4-targeted SPECT/CT imaging agent, demonstrating excellent labeling efficiency, radiochemical stability, and preliminary in vivo uptake in vascular regions associated with inflammation, including the coronary arteries. These features support its potential for early detection of atherosclerosis and compatibility with clinical imaging workflows.

Note: APD is a proprietary compound under IP protection. ***References:*** 1.Pharm Anal Acta. 2024 Jan 5;15(1). 2. Labelled Comp Radiopharmac. 2018 May 15;61(5):438-46.

TEPS-003

Injection Method Alters Diagnostic Confidence and Quantitative Metrics in [^{18}F]Fluorocholine PET/CT for Parathyroid Adenomas

M. Rode, *H. Reilev Møller, P. Abadi, H. Juel Nissen;*
University Hospital of Southern Denmark, Vejle, DENMARK.

Aim/Introduction: Studies evaluating [^{18}F]fluorocholine PET/CT for parathyroid adenoma localisation fail to report the injection method utilized, whether it was a manual injection method (MIM) or with an automated injection system (AIS). At our department, MIM was initially used, before switching to an AIS. However, after using the AIS, the physicians began noticing retention of the radiotracer within the veins leading from the injection site, which had not been as present when previously. The aim of this study was to evaluate whether this retention had a clinical impact or was just a visual distraction. ***Materials and Methods:*** A retrospective study compared the two injection methods from two identical patient groups consisting of 60 patient each. Two physicians, blinded to injection method, would determine if retention was present in the images and whether this affected their interpretation. A diagnostic confidence score per lesion from 1(low)-3(high), was noted for the 120 patients in the original description. These scores were compared to determine, if a significant difference between the two patient groups was present. Quantitative measures were determined based on the SUVmean of the reported parathyroid adenomas along with the thyroid and salivary glands as a reference point, to calculate parathyroid/thyroid and parathyroid/salivary gland ratios. ***Results:*** There was a significant difference in presence of retention, with 36 patients in the MIM-group and 53 patients in the AIS-group, p=.0004. However, the accumulation was not determined to influence the interpretation of the images for any patient. Two patients in the MIM-group had a negative scan, compared to nine patients in the AIS-group. A significant difference of the reported diagnostic confidence scores was observed, as more lesions with a high score in the MIM-group was reported, p>.0001. Quantitative measurement revealed a significant difference in SUVmean from the reported adenomas, with 7.52 in the MIM-group and 6.17 in the AIS-group, p=.002). A significant difference was also determined when comparing the parathyroid/thyroid ratio, with 1.75 compared to 1.50 in the MIM and AIS groups, respectively, p=.013. This difference was also present when comparing the parathyroid/salivary gland ratios, with 0.75 in the MIM-group and 0.65 in the AIS-group, p=.014. ***Conclusion:*** While the retention of radiotracer did not appear to influence the evaluation of imaging visually, the difference in diagnostic confidence scores, SUVmean and both ratios could indicate an aspect of potential clinical impact. Thus, manual injection method might be the method of choice, to ensure optimal image quality.

TEPS-004

Optimizing the Use of a Single Radiopharmaceutical Production for Increased Throughput of Patients with Primary Hyperparathyroidism in[^{18}F]Fluorocholine-PET Without Compromising Image Quality

M. Matkovic[1], *F. Hedeer*[1], *A. Stenvall*[2], *J. Oddstig*[2], *U. Bitzén*[1];
[1]*Department of Clinical Physiology and Nuclear Medicine, Lund, SWEDEN,* [2]*Radiation Physics, Department of Haematology, Oncology and Radiation Physics, Skåne, SWEDEN.*

Aim/Introduction: [^{18}F]Fluorocholine-PET in primary hyperparathyroidism was introduced at our department three years ago and replaced ultrasound and parathyroid scintigraphy as conventional first line preoperative imaging modality shortly thereafter. The aim of this study was to increase the throughput of patients with hyperparathyroidism in [^{18}F]Fluorocholine-PET by efficient use of a single production of [^{18}F]Fluorocholine while preserving high image quality. ***Materials and Methods:*** The local cyclotron unit can ensure a production of 27 GBq [^{18}F]Fluorocholine per production. When [^{18}F]Fluorocholine-PET was introduced at our department patients were scanned on digital PET/CT scanners 60 minutes after an intravenous injection of 4 MBq/kg. With a 20 cm axial field of view (aFOV) and 25% overlap two bed positions were required to cover a scanning volume from the base of the scull to the diaphragm. Acquisition time was 4 minutes/bed position and for image reconstruction a block-sequential regularized expectation maximization (BSREM) algorithm with beta value 400 was applied. Using two scanners in parallel during six hours, nine patients per scanner, i.e. 18 patients in total were examined per occasion. To maximize the number of patient doses per production of [^{18}F]Fluorocholine, the amount of administered activity was adjusted. A 25% reduction in injected activity from 4 to 3 MBq/kg was compensated by a 25% increase in acquisition time from 4 to 5 minutes/bed position. Adding a newly installed digital PET/CT scanner to work in parallel, scanner capacity was increased from two to three scanners. With a 32 cm aFOV, one bed position was sufficient to cover the volume of interest. For this scanner acquisition time was 6 minutes for the single bed position and for image reconstruction a BSREM algorithm with beta value 300 was applied. These adjustments required allocated injection rooms to be increased from six to ten and technicians from eight to twelve. ***Results:*** The number of scanned patients per occasion was increased from 18 to 27, i.e. a 50 % increase per production of [^{18}F]Fluorocholine. Additional positive consequences were fewer production occasions needed to match referral inflow, increased cost effectiveness and decreased radiation exposure to patients and technicians. ***Conclusion:*** Increasing demands for a high patient throughput and availability, resource utilization and cost effectiveness in [^{18}F]Fluorocholine-PET could be met by awareness and conscious planning without compromising image quality.

TEPS-005

Clinical Utility of Lacrimal Scintigraphy in the Management of Epiphora

L. Crook, *R. Sajjan, B. Sathyamurthi, S. Muthu;*
Department of Nuclear Medicine, Manchester Foundation Trust, Manchester, UNITED KINGDOM.

Aim/Introduction: Lacrimal dacroscintigraphy is a functional imaging study performed to investigate epiphora by assessing the drainage of the nasolacrimal system, when anatomical patency is maintained. Our aim was to evaluate the effectiveness of the study and to demonstrate the level of impairment in the nasolacrimal system which could aid in the management of patients. ***Materials and Methods:*** We retrospectively identified 37 patients over a 3-year period who had undergone lacrimal scintigraphy from Sept 2022 to Jan 2025. Scans were acquired using 1 drop Tc-99m Sodium Pertechnetate into each eye (maximum of 4 MBq). Initial dynamic images, post saline wash dynamic images and postnasal blow static images were acquired using the Siemens Symbia S camera with a pin hole collimator. ***Results:*** In our study, the scan was abnormal in 35 patients (95%) and normal in 2 patients (5%). Out of 35 abnormal scans, impairment in drainage was seen bilaterally in 65% of patients and unilaterally in 35% of patients. When the level of impairment was assessed, we noticed the abnormality was predominantly at the ductal level, followed by pre-sac and preductal levels. The scan was concordant with clinical symptoms in 62% of patients and discordant in 38%. 86% of discordance was with respect to the laterality of the symptoms (either unilateral or bilateral), except in 2 symptomatic patients (14%) where the scan was normal thus excluding functional impedance. Three patients (8%) have undergone surgery, and 8 patients (21%) are

awaiting surgery. The rest of the patients were managed medically such as warm compression, trial of lid taping, lubrication, botox, punctal plugs and treatment with olopatadine drops. There were also plans for routine follow-up, including patients with discordant findings. Few patients refused surgery after treatment discussion. ***Conclusion:*** Lacrimal scintigraphy identified abnormal drainage in most patients and was also helpful in excluding functional impedance in few symptomatic patients. Furthermore, the demonstration of level of abnormality in the scan played an important role in deciding patient management. In addition, the identification of abnormality in the asymptomatic eye may help in early intervention and prevention of epiphora.

TEPS-006

How to Ensure Sustainability and Research Governance in Nuclear Medicine? A UK Single-Site Experience.

D. Ribeiro, *M. Ratola, Z. Kingsmell;*
King's College Hospital NHS Foundation Trust, London, UNITED KINGDOM.

Aim/Introduction: A quality management system (denominated Q-Pulse) was implemented for use of the Radiology Care Group, at King's College Hospital National Health Service (NHS) Foundation Trust, in 2022. In 2023, it started being actively used for the management and governance of research studies. This report aims to describe our department's experience in using a quality management system to ensure regulatory compliance and foster sustainable approaches in Nuclear Medicine. ***Materials and Methods:*** The "Documents" module on Q-Pulse allows for studies to be created and the relevant documents to be saved under a study placeholder. Moreover, when a clinical trial undergoes an amendment, the study placeholder can be revised and the research documentation up versioned. An audit was conducted to understand the sustainability impact of using this system, within the Nuclear Medicine department. The total number of pages for all research documentation was compared against the number of pages that are currently being printed. This metric will act as a surrogate for understanding the effect of using Q-Pulse on the environmental and economic pillars of sustainability. ***Results:*** Out of the 78 studies uploaded onto the Radiology quality management system, 33 of them required Nuclear Medicine support, with bone densitometry (DEXA) and Positron Emission Tomography (PET)-Computed Tomography (CT) being the most common modalities. Twenty out of the 33 studies had dedicated imaging manuals which were printed and kept as hard copies, in case of an informatics outage. All other study documents were kept on Q-Pulse. The total number of pages for all the research documentation (including the dedicated imaging manuals) amounted to 6266 pages, whereas the total number of pages for the imaging manuals alone corresponded to 948 pages. As physical copies are only kept for the latter, this corresponds to only 15.13% of research documents being printed. This approach leads to a decrease in solid waste (as fewer documents are printed and, when revisions are required, less paper will go to the recycling bin) and a decrease on the money spent on consumables (both paper and ink cartridges). ***Conclusion:*** Whilst imaging documentation can be stored within normal computer drives, this does not represent a safe approach to managing research documentation (amendments cannot be tracked and documents can be inadvertently deleted). Moreover, printing all documents associated with a research study represents a significant environmental and economic burden. Quality management systems represent a suitable approach for balancing research governance and sustainability.

TEPS-007

Biodistribution of BMMSC-Derived Exosomes for Alzheimer's Disease

M. Wang, *C. Ho, C. Chan, K. Cheng, H. Yu, C. Kuo, C. Yang, S. Liu;*
National Atomic Research Institute, Taoyuan, TAIWAN.

Aim/Introduction: Alzheimer's disease (AD), the leading cause of dementia, is characterized by severe memory and cognitive decline. Interestingly, AD frequently co-occurs with osteoporosis, hinting at shared underlying pathological pathways. This study aimed to compare bone quality and the biodistribution of bone marrow mesenchymal stem cell-derived exosomes (BMMSC-Exos) in the 5xFAD mouse model of Alzheimer's disease and normal B6 mice. ***Materials and Methods:*** Bone marrow mesenchymal stem cell (BMMSC)-derived exosomes were isolated using tangential flow filtration followed by fast protein liquid chromatography. For biodistribution analysis, exosomes were conjugated with p-SCN-Bn-DOTA and radiolabeled with Gallium-67 before being administered to both aged (66 weeks) 5xFAD mice and age-matched normal B6 mice. ***Results:*** Our findings demonstrated a significantly higher accumulation of Ga-67 labeled exosomes in the hip bone, sacrum, and ilium of aged (66 weeks) Alzheimer's disease mice compared to their normal counterparts. Furthermore, we observed lower bone density in these same skeletal sites of the aged Alzheimer's disease mice. ***Conclusion:*** Given the association of Alzheimer's disease with aging, we propose that elderly individuals with AD may also be susceptible to osteoporosis. The observed preferential accumulation of BMMSC-Exos in the sacrum, hip bone, and ilium of aged AD mice suggests a potential therapeutic role for BMMSC-derived exosomes in addressing bone loss often associated with advanced age and potentially exacerbated by AD.

TEPS-008

Development and validation of a 3D-printed phantom for PET texture analysis

K. Honda[1], *K. Okuda*[1], *H. Yamamoto*[2], *R. Mori*[1], *S. Hosokawa*[1], *Y. Takahashi*[1];
[1]*Guraduate School of Health Sciences, Hirosaki University, Aomori, JAPAN,* [2]*Hirosaki University Hospital, Aomori, JAPAN.*

Aim/Introduction: Texture analysis can quantify surface conditions such as roughness and smoothness and spatial variations in voxel intensity within a volume of interest (VOI) in medical images. However, a dedicated PET phantom for texture analysis has not yet been developed. Here, we created spherical components containing acrylic beads for a National Electrical Manufacturers Association (NEMA) body phantom using a 3D printer. The aim was to validate the bead-filled spherical phantom for evaluating heterogeneous ^{18}F-fluorodeoxyglucose (FDG) distribution. ***Materials and Methods:*** To simulate the heterogeneous distribution of ^{18}F-FDG, we created spherical phantoms containing acrylic beads using a fused deposition modeling 3D printer. Three sets of spherical phantoms were produced: 10-, 13-, 17-, 22-, 28-, and 37-mm spherical phantoms without beads (SP0) and with 5-mm beads (SP1); and 37-mm phantoms in which the proportion of 5- and 10-mm beads was varied (SP2). PET images were acquired using a Discovery MI PET/CT scanner (GE Healthcare, USA) after the sphere and background radioactivity concentrations were adjusted to 10.2 and 2.55 kBq/mL, respectively. We reconstructed PET data using the Q.Clear algorithm and β-values ranged from 100-600. Standardized uptake values (SUV) and texture features were calculated using LIFEx software v. 7.60 (https://www.lifexsoft.org). A VOI was drawn on the central transaxial slice of a spherical phantom image. We evaluated ^{18}F-FDG images by analyzing 22 texture features that we previously identified. ***Results:*** The mean SUV (SUV_{mean}) values of 37-mm spheres were 3.76 for SP0, 1.54 for SP1, and 1.33 - 1.69 for SP2 in the β-value of 300. The maximum SUV (SUV_{max})values were also 4.42 for SP0, 1.93 for SP1, and 1.95 -

4.08 for SP2. The highest values of SUV_{max} and SUV_{mean} were shown in SP2 filled with only 10 mm beads, while the lowest values were shown in SP2 with 20 % of 10 mm beads for SUV_{mean} and that with 60 % of them for SUV_{max}. Heterogeneous FDG distributions were detectable using 22 texture features under various levels of statistical noise by adjusting β-values. We could classify 22 texture features into two groups: 12 texture features show higher values with increasing heterogeneity, while 10 texture features show lower values. ***Conclusion:*** The developed acrylic beads phantoms could represent heterogeneous ^{18}F-FDG distributions. We selected 22 texture features that could gradually capture image heterogeneity. Spherical components containing acrylic beads might serve as a standard phantom for PET texture analysis.

TEPS-009

Implementing a safe workflow for intra-operative PET/CT imaging of surgical specimen

F. Verschure, *B. Lambert, V. Vergucht, N. Dhont, B. De Paepe, V. Piens, M. Colle, B. Gevaert, L. Meiresonne;*
Maria Middelares, Gent, BELGIUM.

Aim/Introduction: We installed a mobile PET/CT-scanner, designed to acquire high-resolution images of surgical specimens. This camera aims to assess the metabolic activity of tissue and especially its margins in the operating room. In this presentation document, we addressed various safety issues when implementing intra-operative PET/CT imaging. We developed a workflow to achieve high quality intra-operative PET/CT images while maintaining ALARA principles. ***Materials and Methods:*** Intravenous PET-tracer injection (F18-PSMA for prostate cancer patients; FDG for remaining patients; 0.8-4MBq/kg) was done 60-90min before tumour resection. After resection, the specimen was scanned in the operating room for 12min with the AURA10 PET/CT-camera (XEOS) and the specimen was sent for pathology. We developed a work flow to minimize exposure to ionizing radiation. In the first 20 procedures our workflow was tested: We conducted dose rate measurements from injection till transfer to the recovery ward. For patients with a bladder catheter, measurements close to the urinary bag with and without lead shielding were carried out. Surgeons, nurses, and anaesthesiologists were additionally monitored by an electronic dosimeter during the entire procedure. The patient had to remain in bed post-injection to limit close contact with other patients or personnel. In case of a short-lasting surgical procedure the patient was injected with the PET-tracer at the nuclear medicine department. The patient awaited surgery at the nuclear medicine department, in a controlled area. Potential contaminations of the surgical room, instruments and waste were monitored by a survey meter. The specimens were fixed in formaldehyde for 24h before processing. No additional radioprotective measures were taken concerning the specimen. Image quality allowed us to lower the administered activity from 4MBq/kg to 0.8-1MBq/kg. ***Results:*** Dose rates around the patient dropped by a factor >5 when measured at the side of the feet instead of trunk. Normalized to an injected activity of 1MBq/kg, the estimated median absorbed doses per procedure were 15.6µSv(range 0,7-140,8) and 14,1µSv(0,5-46,2) for the surgeons and instrumenting nurses. The diuresis was kept low during urological surgery, with dose rates of 14 µSv/h near the urine bag. We positioned the bag at the far side of the surgeon, with lead shielding. At the surface of the suction unit the dose rate was 3 µSv/h. Measurements with a survey meter didn't reveal contaminations of the room. There was no need to shield the surgical specimen itself. ***Conclusion:*** We developed a safe workflow to implement intra-operative PET/CT in a general hospital.

TEPS-010

Evaluation of a reduced dose 123I-Ioflupane in patients examined with SPECT for clinically uncertain parkinsonism

G. Abell[1], *S. Skauge*[1], *T. Keil*[1], *S. Øen*[1], *A. Karlberg*[1,2];
[1]*Department of Radiology and Nuclear Medicine, St. Olavs hospital, Trondheim University Hospital, Trondheim, NORWAY,* [2]*Department of Circulation and Medical Imaging, Norwegian University of Science and Technology, Trondheim, NORWAY.*

Aim/Introduction: Dopamine transporter imaging with 123I-Ioflupane is regularly used in patients with clinically uncertain Parkinsonian Syndromes. EANM/SNMMI guideline recommends administering 110-250 MBq and acquiring > 1.5 Mcts in the SPECT images for this examination. The aim of this retrospective study was to evaluate if halving the dose of 123I-Ioflupane (from 185 MBq to 92.5 MBq) affects the reported diagnoses in these patients. ***Materials and Methods:*** Patients examined with DaTSCAN for clinically uncertain Parkinsonian Syndromes (n=631) were included in this study. SPECT-acquisitions (180 min post injection) were performed on a dual head digital SPECT/CT-system with wide energy high resolution parallel-hole collimators, 159 keV±10% energy window, 30 sec/frame, 11-15 cm rotational radius, 360° rotation and 3° angular step. The «standard-dose group» (n=340) and the «half-dose group» (n=291) were compared for discrepancies. The nuclear medicine physicians' reported diagnoses were categorized into «normal», «pathological» or «uncertain». Striatal binding ratios (SBR) for striatum (L/R), putamen (L/R) and caudatus (L/R) were assessed for quantitative analysis. A Z-test was used to compare differences in proportions between reported diagnoses in the standard-dose group and half-dose group, and the Mann-Whitney U test were applied to compare differences in SBR between patients reported as normal and pathological. An alpha level of 0.05 were used for all statistical tests. ***Results:*** The mean total detected events were 4.6±0.7 Mcts and 2.5±0.4 Mcts in the standard-dose group and the half-dose group respectively. The proportion of patients reported as normal increased significantly with half-dose compared to standard-dose (+0.10, 95%CI [0.02, 0.18], p=0.012), while the proportion of patients reported as pathological and uncertain decreased (-0.08, 95%CI [-0.16, 0.001], p=0.053 and -0.02, 95%CI [-0.07, 0,02], p=0.322, respectively). However, dose differences did not significantly impact the median SBR-values for the cerebral regions in patients reported as normal, pathological and uncertain. ***Conclusion:*** A significant larger proportion of patients was reported as normal in the half-dose group compared to the standard-dose group. However, half-dose of 123I-Ioflupane fulfills the guidelines' criteria of > 1.5 Mcts in the SPECT-images, and the SBR- values were similar between the the two dose groups, supporting halving the dose in patients examined with SPECT for clinically uncertain parkinsonism.

TEPS-011

Pharmacokinetics and Dosimetry of ^{177}Lu-DOTATATE in Patients with Advanced well-differentiated, gastroenteropancreatic neuroendocrine tumours: results from a Sub-study of the phase 3 XT-XTR008-3-01 trial

H. Zhou[1], *A. Yin*[2], *R. Wang*[1];
[1]*Chinese PLA general hospital, Beijing, CHINA,* [2]*Beijing Sinotau Intl. Pharmaceutical Technology Co., Ltd., Beijing, CHINA.*

Aim/Introduction: While receptor radionuclide therapy (PRRT) with 177Lu-DOTATATE is well established for treatment of GEP-NETs with somatostatin receptor expression, no data in Chinese populations has been reported yet. Herein, we present the results of a sub-study focusing on the exploratory PK and Dosimetry profile of a phase 3 clinical trial on XTR008 (XT-XTR008-3-01, NCT05459844), the first generic version of 177Lu-DOTATATE developed in China. ***Materials and Methods:*** From October 25, 2022 to May 11,

2023, 10 patients with well-differentiated, locally advanced or metastatic GEP-NETs were enrolled. Patients were administered with 4 cycles of ^{177}Lu-DOTATATE (7·4 GBq /cycle, cumulative 29.6 GBq. After the first dose, whole-body planar scintigraphy (6 time points up to 7 days) and abdominal SPECT/CT (24 and 48 h) were performed. Blood and urine samples were collected to determine PK parameters. Safety and efficacy were evaluated according to NCI-CTCAE version 5.0 and RECIST 1.1. ***Results:*** 177Lu-DOTATATE reached highest in blood at 15 min after starting infusion, then decreased with the T1/2 of 37.36±16.44 hours. Cumulative urine activity was 60.38% within 16 hours. The estimated absorbed dosed for four treatment cycles to kidneys and red marrow were 18.914 ± 6.242 Gy (excluding one patient with multifocal nephrolithiasis and absorbed dose to kidneys of 77.1Gy, who had grade 2 creatinine elevation and renal impairment) and 1.199 ± 0.337 Gy, respectively. Two other patients had absorbed doses to kidneys higher than 23 Gy (25.9 Gy, 23.1 Gy), neither developed renal toxicity. The most common TRAEs were haematological toxicities, most of which were grade 1 or 2 (81/98). No significant differences in absorbed doses between patients with and without treatment-related organ-specific toxicities was observed, while the dose to spleen between patients with and without haematological TRAEs (1.058875±0.6156 and 0.77025±0.9896) and ≥grade 3 haematological TRAEs (0.5935±0.3147 and 1.1031±0.6815) showed a numerical difference, though not statistically significant. The tumour absorbed dose ranged from 0.312 to 9.78 Gy/GBq, indicating inter- and intra-patient variabilities. Three patients achieved partial response (ORR 30%), with no significant difference in tumour absorbed doses compared with no-responders (2.68±2.53 Gy/GBq vs. 2.93±1.81 Gy/GBq, p=0.44). Pearson Correlation Analysis indicated a moderate but not statistically significant correlation coefficient (r=0.016, p>0.05) between tumour absorbed dose and tumour size change. ***Conclusion:*** PRRT with ^{177}Lu-DOTATATE showed showed favourable tolerability, PK and dosimetry outcomes in Chinese patients, supporting the potential application of XTR008 in Chinese patients with well-differentiated GEP-NETs.

TEPS-012

Split renal function in living kidney donors derived from ^{99m}Tc-DTPA vs ^{99m}Tc-DMSA: a preliminary evaluation

N. Laajimi, *A. Bouzidi, S. Bourouis, F. Dupont, N. Kanaan, R. Lhommel, F. Jamar, O. Gheysens, V. Depoortere;*
Cliniques Universitaires Saint-Luc, Bruxelles, BELGIUM.

Aim/Introduction: The global shortage of deceased kidney donors has led to an increased reliance on living kidney donors. Accurate pre-transplant assessment of donor renal function of essential for determining which kidney to donate and ensuring adequate long-term function in the remaining kidney. Radioisotopic methods are commonly used for this purpose, with 51Cr-EDTA and 99mTc-DMSA being gold standards for measuring absolute glomerular filtration rate (GFR) and split renal function, respectively. At our center, both tests were routinely performed, with a great advantage that both examinations could be performed on the same day. However, 51Cr-EDTA is no longer commercially available. 99mTc-DTPA is a potential alternative, capable of measuring absolute GFR via a single-injection two-sample method, and also offering split renal function data through a short dynamic acquisition. This dual capability could eliminate the need for an additional 99mTc-DMSA scan. This preliminary study aimed to evaluate whether 99mTc-DTPA can accurately measure split renal function compared to the 99mTc-DMSA standard. ***Materials and Methods:*** Eight patients undergoing evaluation for living kidney donation were included. Split renal function was measured using three methods: conventional geometric mean 99mTc-DMSA (DMSA, reference), posterior 99mTc-DTPA (DTPA PA), and both antero-posterior and postero-anterior 99mTc-DTPA with geometric mean (DTPA GM) using a 120-180 second post-injection window. Manual regions of interest were drawn around each kidney with background correction. Three experienced technologists independently analyzed all images. Results were expressed as the absolute deviation from equal split function (50/50), using Spearman correlation and Bland-Altman plots (mean ± 1.96SD). ***Results:*** Correlation coefficients for DMSA-DTPA PA, DMSA-DTPA GM, and DTPA PA-DTPA GM were 0.37, 0.53, and 0.91, respectively. Mean differences from DMSA were -3.52 ± 9.62% for DTPA PA and -2.49 ± 6.92% for DTPA GM. DMSA had significantly lower inter-observer variability compared to DTPA. Based on DMSA, 7 of 8 patients met the 45-55% eligibility window for donation. However, only 4-5 were eligible based on DTPA GM and 2-3 based on DTPA PA. ***Conclusion:*** This preliminary study suggests that 99mTc-DTPA cannot reliably replace 99mTc-DMSA for assessing split renal function in living kidney donor evaluation. While 99mTc-DTPA is suitable for measuring absolute GFR, accurate assessment of split function is obtained with 99mTc-DMSA. Therefore, a combined approach using 99mTc-DTPA/99mTc-DMSA on different days remains necessary for accurate donor evaluation.

TEPS-013

The Impact of PET/MRI Imaging and Tumor Markers on the Diagnosis of Prostate Cancer

M. Nürnberger[1], *S. Djouraev*[2], *M. Hacker*[1], *R. Agha Mohammadi Sareshgi*[2], *S. Rasul*[1];
[1]*Universitätsklinikum AKH Wien, Wien, AUSTRIA,* [2]*FH Campus Wien, Wien, AUSTRIA.*

Aim/Introduction: Investigation of the Diagnostic Value of PSA Density and Standardized Uptake Values (SUV) in PSMA-PET Scans in Patients with Therapy-Naïve Primary Prostate Cancer and their Influence on the Recurrence Rate and Histology. ***Materials and Methods:*** For the quantitative analysis, pre-existing PET/MRI scans of 19 patients with primary prostate cancer were used and further processed. Based on the imaging datasets, prostate volume was determined, and SUVmean, SUVmax, and SUVpeak were assessed using manually delineated volumes of interest. Additionally, clinical data such as PSA levels, the presence of biochemical recurrence (BCR), and histological findings were documented. With the collected data, statistical procedures could be applied, and the results were interpreted. Using Spearman correlation tests, the correlation between PSA density and SUVs, as well as between the histopathological ISUP score, PSA density, and SUVs, was determined. The influence of prostate cancer histology on PSA density and PSMA SUV was analysed by examining the relationship between the ISUP score and clinical parameters. To identify differences in these parameters between patients with and without biochemical recurrence (BCR), the T-Test and the Mann-Whitney U-test were performed. ***Results:*** A moderate correlation between the ISUP score and PSMA SUVs of the lesion was seen, with correlation coefficients ranging from 0.521 to 0.579 and p-values below 0.05. The investigation into whether there is a correlation between PSA density and various PSMA SUVs in prostate cancer patients revealed an overall weak to very weak correlation between the parameters, with correlation coefficients ranging from 0.190 to 0.437. However, this correlation was not statistically significant (p-values > 0.05). With p-values ranging from 0.234 to 0.731 the evaluation of the impact of recurrence rates on PSA density and PSMA SUVs demonstrated no statistically significant differences between patients with and without BCR. ***Conclusion:*** The moderate correlation between the ISUP score and PSMA SUV supports the reliability of SUV, as it indicates both the presence of prostate cancer and the aggressiveness of the disease. Furthermore, the findings suggest that neither PSA density nor PSMA SUV provide insights into the risk of biochemical recurrence.

TEPS-014

Cardiac Stress Testing: Is it time for NMTs to take the lead? - St. Barts Centre

A. Tsvetanova;
Barts Health NHS Trust, London, UNITED KINGDOM.

Aim/Introduction: Myocardial Perfusion Scan (MPS) stress testing for Nuclear Medicine Technologists was implemented in the PET-CT service, St. Barts Hospital in January 2025. The primary aims were to support the Rb-82 service demand and optimise patient workflow and ensure staff were appropriately trained to perform a safe and efficient MPS procedure.As to provide a common standard for patients and professionals, the British Society of Nuclear Medicine (BNMS) issued training guidelines and assesment on how to achieve clinical competencies in MPS stress testing which were incorporated in our inhouse training. ***Materials and Methods:*** Staff underwent an external intensive two-day training course workshop that delivered the core and knowledge for stress testing. The inhouse training comprised a combination of both basic clinical skills and specific cardiac skillset culminating into a series of assesments of all relevant modules related to cardiac stress testing.To be deemed competent to practice, staff were required to complete a minimum of 50 vasodilator stress tests showcasing their ability to use stress technique safely and effectively and conduct them without adverse events that would require sepervision intervention, retest or unnecessary radiation exposure. A retrospective audit was them conducted to a minimum of 20 clinical cases performed by staff undergoing the training to assess patient care outcomes and experience. ***Results:*** Since implementing Cardiac Stress Testing lead by technologists, we have been able to run a continous service and accomodate 1-2 additional Rb-82 patients a day. Rb-82 MPS appointment's cancelation rate due to list delays decreased from 10.6% in 2024 to 6.8% (Jan-March 2025).Currently, we are still collecting data on staff feedback and patient's experience. However, so far, the overall feedback has been positive. Furthermore, we haven't had any reportable clinical incidents related to Rb-82 MPS Cardiac Stressing. ***Conclusion:*** Effective communication alongside with experience and skills play a vital role in cardiac stress training. It is therefore essential for technologists to adhere to strighten safety protocols to protect themselves and others from potential hazards.

TEPS-015

Analysis of Image Artifacts in TOF-PET/CT - Impact of Defective Block Detectors on Image Quality

J. Teng[1,2], *S. Djouraev*[1], *R. A. M. Sareshgi*[1], *I. Rausch*[2];
[1]*FH Campus Wien, Vienna, AUSTRIA,* [2]*Center for Medical Physics and Biomedical Engineering, Medical University of Vienna, Vienna, AUSTRIA.*

Aim/Introduction: This study investigates the impact of defective block detectors on image quality and quantification in time-of-flight PET systems, with a focus on artifact severity and the clinical relevance of detector failures. ***Materials and Methods:*** Phantom data were acquired using a Siemens Biograph TruePoint system without time-of-flight and a Siemens Biograph mCT system with time-of-flight. Various detector failure scenarios were simulated by virtually disabling individual block detectors during image reconstruction. Image reconstruction was performed using filtered back projection and ordered subset expectation maximization, with and without time-of-flight information. To highlight the robustness of filtered back projection against artifact formation, additional simulations were conducted involving both localized bucket failures and block detector defects distributed across all detector rings. Image quality was evaluated through visual inspection and quantitative analysis of background variability and recovery coefficients. ***Results:*** The number and spatial distribution of defective detectors influenced the severity of image artifacts. [1] Reconstructions with time-of-flight showed more spatially confined artifacts, while those without time-of-flight revealed larger regions of signal loss. [2,3] Time-of-flight notably improved image quality in iterative reconstructions, while filtered back projection particularly benefited the image quality in peripheral phantom regions. Even under extended failure scenarios, filtered back projection resulted only in minor contrast reductions without the appearance of significant artifacts. The largest improvements in background variability were observed with the use of time-of-flight, decreasing from 11 percent to 5.9 percent in filtered back projection for a 90-degree defect configuration, and from 33.7 percent to 17.3 percent in iterative reconstruction for a 180-degree configuration. ***Conclusion:*** Time-of-flight PET systems demonstrate higher tolerance to detector failures compared to non-time-of-flight systems. Filtered back projection in particular shows strong robustness, even in the presence of extensive or distributed detector defects. Preliminary results from phantom studies suggest that PET systems may remain conditionally usable in clinical settings despite multiple block detector failures. Further validation using patient data is ongoing. ***References:*** [1] Elhami E, Samiee M, Demeter S, Leslie WD, Goertzen AL. On the significance of defective block detectors in clinical (18)F-FDG PET/CT imaging. Mol Imaging Biol. 2011;13(2):265-74. doi:10.1007/s11307-010-0362-5 Cited in: PubMed; PMID 20544294.[2] Schaart DR. Physics and technology of time-of-flight PET detectors. Phys Med Biol. 2021;66(9). doi:10.1088/1361-6560/abee56 Cited in: PubMed; PMID 33711831.[3] Zatcepin A, Ziegler SI. Detectors in positron emission tomography. Z Med Phys. 2023;33(1):4-12. doi:10.1016/j.zemedi.2022.08.004 Cited in: PubMed; PMID 36208967.

TEPS-016

Using the Monte Carlo Code RayXpert to Solve Radiation Protection Issues in Six Brachytherapy Rooms

J. Hemptinne, *I. Duarte, C. Dossat, N. Chatry;*
TRAD Tests & Radiations, Labège, FRANCE.

Aim/Introduction: The project consisted in performing a radiation protection study on six brachytherapy rooms at Institut Gustave Roussy, France. The aim was to respect the French Nuclear Safety Association (ASN) requirements regarding the dose inside and outside the rooms. In this context, two main families of calculation codes can be used for this purpose: Monte Carlo codes and deterministic (point-kernel) codes. ***Materials and Methods:*** In order to achieve a radiological zoning, the Monte Carlo software RayXpert® has been used. Its 3D interface allowed to efficiently and precisely model the infrastructure considered, including the six brachytherapy rooms, and import CAD files at the STEP format in the case of complex geometries. After this step, the sources definition and mapping setup allowed to derive results on the whole structure, including dose maps and regulatory zonings. Moreover, from the results of a preliminary study of the facility design, it has been possible to determine and/or optimize the radiological design. ***Results:*** The presentation will focus, as in the context of brachytherapy, on radiation protection issues due to the effects of injected radioactive sources in patients, such as ^{18}F or ^{192}Ir. A first investigation with a deterministic approach allowed to estimate a preliminary radiological design of the facility by using the point-kernel method. This first investigation had to be extended and completed with a Monte Carlo calculation code, here RayXpert®, which enables to consider scattered radiation. Combined with dose mapping, the software allowed to identify the origin of the dose contribution in certain areas. This feature enables to recreate particle paths, and consequently orientate efficiently the radiological design of the infrastructure considered. As a result, by employing both types of calculation codes, radiological design can be optimized, unlike using only a code based on the point-kernel method, which can be too simplistic and limiting. ***Conclusion:*** Calculation codes are widely used for radiological studies, and are in continuous development. Moreover,

Monte Carlo calculation codes bring extra precision to results and, combined with an ergonomic 3D interface like in RayXpert®, can contribute to efficiently realize radiological studies. In the context of the radiation protection study of six brachytherapy rooms at the Institut Gustave Roussy, RayXpert® has been necessary to optimize the shielding. Such tool can also be used for other projects within the nuclear medicine field, such as radiation protection on isotope production facilities, equipment shielding, waste and storage management, among many others.

TEPS-017

The updated capabilities for Registered Nuclear Medicine Technologist practice in Australia

***T. Pearson**, C. Miller, A. Reinhard;*
Medical Radiation Practice Board of Australia, Melbourne, AUSTRALIA.

Aim/Introduction: The Medical Radiation Practice Board of Australia (MRPBA) professional capabilities ("Capabilities") for Nuclear Medicine Technologist (NMT) set the standard for Registration in Australia. The Capabilities need to evolve to ensure that they remain current and are updated every 3-5 years. The Capabilities are primarily used to determine: 1. Entry level requirements for Practitioners entering or re-entering the Profession. 2. Requirements for Australian programs of study to be accredited as a pathway leading to Registration with the MRPBA. The Capabilities are also used to guiding continuous professional development (CPD) activities of already Registered NMT's in Australia. In 2025 the capabilities were updated with the aim of ensuring they align to contemporary and emerging practise. ***Materials and Methods:*** In 2024 the MRPBA undertook a scan of current and emerging NMT practices in Australia and drafted an update to the existing approved Capabilities (approved in 2020). This draft was distributed for initial targeted consultation with relevant key stakeholders, including NMT Professional Bodies, radiation licencing bodies, public and private employer groups and Education providers. This feedback was considered before an open broader public consultation for all other stakeholders. A new updated Professional Capabilities for Medical Radiation Practice was then drafted and presented to the MRPBA for approval. ***Results:*** The MRPBA approved and published the new NMS professional capabilities in mid-2025. Key updates for NMT professional practice include:1. Cultural capability2. Artificial intelligence3. Theranostics4. Radiopharmacy practice5. Leadership and Stewardship in practise. ***Conclusion:*** The MRPBA Professional capabilities for NMT practice have now been implemented in Australia. The process, feedback received, changes made and final MRPBA NMT Professional capabilities for practise in Australia will be the focus of this presentation.

TEPS-018

Comparison of Two Synthesis Methods for ^{68}Ga PSMA-11

***G. Walker**, K. Allen;*
IDX Group Lake Imaging, Ballarat, AUSTRALIA.

Aim/Introduction: The introduction of a simplified, "cold kit" solution for PSMA synthesis may hold promise for faster production times, cost reduction, and ultimately improved access to PET prostate imaging services. We performed a detailed comparison of time, workflow, costs, and radiation dose for a cassette-based method against cold kit synthesis in order to accurately identify and quantify any available efficiencies. ***Materials and Methods:*** Two operators undertook multiple production runs (n=5) for each PSMA synthesis method: lyophilized "cold kit" and cassette-based. Standard manufacturers' protocol was followed, with timing of each step recorded to the nearest 5s, and radiation exposure recorded at chest level for the entire procedure. Radiation dose was averaged for each method, then extrapolated to several time points over generator lifespan to estimate an annual dose to a typical operator. Quality control procedures including TLC and HPLC were performed as required, and also timed and included in the analysis. Any effects of time delays on ultimate injectable product yield were also calculated. Details of consumable items, labour and generator costs were tabulated and compared. ***Results:*** Cold kit synthesis achieved reductions of up to 40% in production time, 65% for radiation dose, and measurable cost savings, compared to a cassette-based method. ***Conclusion:*** In this analysis, significant savings in all areas, including time, cost, and radiation exposure were demonstrated in favour of cold kit synthesis. Implications for improving global access to PSMA PET diagnostic imaging are significant.

TEPS-019

Preclinical Biodistribution Study of [^{68}Ga]Ga-FAPI-46 in a Breast Cancer Mouse Model

***H. Hassan**[1], M. F. Othman[2], W. H. B. Wan Kamal[3], N. N. Jafperi[2], S. Mohamad[3], A. S. Sued[3], S. A. Muhamad[3], H. R. Abdul Razak[4], M. H. Zakaria[5];*
[1]Centre for Diagnostic Nuclear Imaging, Serdang, Selangor, MALAYSIA, [2]Universiti Teknologi MARA, Bandar Puncak Alam, MALAYSIA, [3]Malaysian Nuclear Agency, Kajang, MALAYSIA, [4]University of Exeter, Exeter, UNITED KINGDOM, [5]Universiti Putra Malaysia, Serdang, MALAYSIA.

Aim/Introduction: Fibroblast Activation Protein (FAP) and Cancer-Associated Fibroblasts (CAFs) are critical in cancer growth and metastasis, making them valuable targets for imaging and treatment monitoring. Fibroblast Activation Protein Inhibitor (FAPI) selectively binds to FAP on cancer cells and CAFs, demonstrating high sensitivity and specificity for early cancer detection. This study investigates [^{68}Ga]Ga-FAPI-46 biodistribution in a breast cancer mouse model, addressing limited supporting evidence. ***Materials and Methods:*** MCF7 breast cancer cells were subcutaneously injected into the mammary gland of female BALB/c nude mice (18 weeks old). Tumour growth was monitored biweekly, and mice were randomized into experimental and control groups (~2-weeks post-inoculation, n=3). The experimental group received [^{68}Ga]Ga-FAPI-46 while the control group received free ^{68}Ga via tail vein injection (3.7-7.4 MBq). After 1-hour, relevant organs and tumours were dissected, weighed and analysed for radioactivity using a gamma counter to assess biodistribution. ***Results:*** In the experimental group, [^{68}Ga]Ga-FAPI-46 exhibited remarkable uptake in the intestine (9.55% ID/g), heart (5.82% ID/g) and kidneys (4.15% ID/g), indicating its affinity for high metabolism tissues. Tumours uptake averaged 0.92% ID/g, highlighting its potential for targeted imaging of FAP-expressing tumours. Uptake was lower in muscle, bone and stomach. No tumour uptake was observed in the control group, with biodistribution predominantly in the blood (29.1% ID/g), lungs (18.5% ID/g) and bones (13.4% ID/g). ***Conclusion:*** [^{68}Ga]Ga-FAPI-46 showed significant uptake in the tumours, intestine, heart and kidneys, with biodistribution patterns similar to other studies. These findings support its potential as a targeted imaging agent for FAP-expressing tumours, enhancing FAPI-PET imaging in clinical.

TEPS-020

Utility of Tc-99m HMDP SPECT with synthetic planar images and SUV ratio for the diagnosis of cardiac amyloidosis

***Y. Miyazaki**[1], M. Nogami[1,2], Y. Izawa[3], H. Hashimura[4], K. Kubo[1], A. Kusaka[1], T. Murakami[1,4];*
[1]Department of Radiology, Kobe University Hospital, Kobe, JAPAN, [2]Biomedical Imaging Research Center, University of Fukui, Fukui, JAPAN, [3]Division of Cardiovascular Medicine, Department of Internal Medicine, Kobe University Graduate School of Medicine, Kobe, JAPAN, [4]Department of Radiology, Kobe University Graduate School of Medicine, Kobe, JAPAN.

Aim/Introduction: In Technetium-99m hydroxymethylene diphosphonate (Tc-99m HMDP) imaging for cardiac amyloidosis, few studies have demonstrated the usefulness of the heart-to-contralateral (H/CL) ratio and standardised uptake value (SUV) ratio. In addition, the usefulness of synthetic planar images generated from single photon emission computed tomography (SPECT) is unclear. This study aimed to investigate whether synthetic planar images and SUV ratios correlate with conventional methods. ***Materials and Methods:*** Eleven consecutive patients who underwent Tc-99m HMDP imaging for suspected cardiac amyloidosis at our institution were enrolled. Synthetic planar images were generated from SPECT images using a commercially available scanner (Symbia Pro.specta, Siemens Healthineers). The spherical volume of interest was set in the cardiac and contralateral regions on the SPECT images, and the SUV_{mean} ratio was calculated. The visual scores (Perugini score) were assessed by two nuclear medicine physicians. The correlation and inter-observer agreement of the visual scores between the synthetic and conventional planar images were evaluated using Spearman's rank correlation efficient and Kappa coefficient. The correlation and reproducibility between the synthetic and conventional planar H/CL ratios were evaluated using Pearson's correlation coefficient ant the Bland-Altman plot. The correlation and reproducibility between the SUV_{mean} ratio and the conventional planar H/CL ratio were evaluated using Pearson's correlation coefficient and the Bland-Altman plot. Receiver operating characteristic (ROC) analysis was performed to assess the diagnostic performance of the SUV_{mean} ratio using the visual score as the reference standard. ***Results:*** The visual scores for synthetic and conventional planar images showed substantial agreement ($k = 0.80$, $p < 0.05$) and a significant correlation ($r = 0.94$, $p < 0.05$). A significant correlation was observed between the H/CL ratios of the two types of planar images ($r = 0.99$, $p < 0.05$). Additionally, good reproducibility was observed between the H/CL ratios of both images (mean difference, -0.00055, 95% CI, -0.041 to 0.040). The SUV_{mean} ratio was highly correlated with the H/CL ratio of the conventional planar images ($r = 0.98$, $p < 0.05$). The Bland-Altman analysis showed that the SUV_{mean} ratio overestimated the H/CL ratio in the high SUV region. In the ROC analysis, the SUV_{mean} ratio demonstrated diagnostic ability with 100% sensitivity and 100% specificity, with a cutoff value of 2.31. ***Conclusion:*** Tc-99m HMDP SPECT with synthetic planar imaging and SUV_{mean} ratio demonstrated equivalent performance to the conventional method, suggesting its potential as a robust method for the diagnosis of cardiac amyloidosis.

TEPS-021

First clinical results for the unique TB-PET IMAS with TOF and DOI capabilities

A. González[1], *D. Sanchez*[2], *S. Jimenez-Serrano*[1], *A. Anreus*[1], *E. Y. Ulin-Briseño*[1], *A. Gonzalez-Montoro*[1], *M. Freire*[1], *J. Alamo*[3], *J. Barbera*[3], *A. Rios*[4], *J. M. Benlloch*[1], *B. Martinez Sanchís*[5], *A. S. Canoves Llombart*[5], *I. Torres Espallardo*[5];
[1]*Consejo Superior de Investigaciónes Cientificas, CSIC-i3M, Valencia, SPAIN,* [2]*Oncovision, SA, Valencia, SPAIN,* [3]*Oncovision SA, Valencia, SPAIN,* [4]*Full Body Insight, Valencia, SPAIN,* [5]*Hospital Universitario y Politécnico La Fe, Valencia, SPAIN.*

Aim/Introduction: Total Body - Positron Emission Tomography (TB-PET) systems are very attractive given their unique feature of a long axial field view (FOV). This allows for a significantly increased in system sensitivity and, thus, to reduce the patient dose, scanning time, or a compromise between both. In this work we present the first clinical results of a unique TB-PET, named IMAS, simultaneously enabling time of flight (TOF) and impact depth of interaction (DOI) capabilities. IMAS is installed at the largest hospital in our region: La Fe hospital. ***Materials and Methods:*** IMAS is based on the novel semi-monolithic scintillator geometry. The system has 82 cm in diameter and 71 cm axial coverage, and is made of 5 rings, each measuring 10 cm in axial direction. Novel electronics permit to decrease by a factor of 4 the total number of readout channels, without almost impacting the performance. IMAS is installed together with a standard CT. IMAS has been characterized following the NEMA 2018 protocol. A clinical validation is currently undergoing with patients that are programmed for a conventional PET/CT (Philips Gemini TF), for comparison purposes. Few patients have been already scanned, first in the PET/CT and later in IMAS. Currently, attenuation correction on the IMAS was carried out co-registering the CT of the PET/CT using deformable models. ***Results:*** Pilot results of the IMAS performance have shown an unprecedented homogeneous spatial resolution across the entire FOV below 4 mm. This is obtained because of the use of accurate DOI information during the reconstruction process. The system sensitivity is around 7% for a source located at the center FOV. The system TOF has been determined to be 480 ps, but an improvement close to 350 ps is reachable after a more accurate time skew calibration.The preliminary clinical image quality seems to be superior to the conventional PET/CT. In one of the patients, in which a multi-centric lesion was observed in the axilla, this was clearly resolved with IMAS, but blurred with the PET/CT. ***Conclusion:*** TB-PET imaging shows clear sensitivity advantages over conventional PET. IMAS is a system that saves part of the cost by using an architecture including gaps. The unique feature in clinical PET scanners enabling DOI, results in a homogeneous spatial resolution better than 4 mm.Clinically, the increased sensitivity and accurate impact determination, significantly improve the diagnostic prediction when compared to conventional PET.

1011

Monday, October 6, 2025, 15:00 - 16:30
Room 111

EANM Journals - Scientific Writing in 2025

OP-450a

LLM: Do and Do Not

L. Papp; *Medical University of Vienna, Vienna, AUSTRIA.*

OP-450b

How to Prepare and Share Your Data

R. Ni; *University Zurich, Zurich, SWITZERLAND.*

OP-450c

How to Write a Great Paper without LLMs

M. Andrade; *Grand Hôpital de Charleroi, Charleroi, BELGIUM.*

1101

Monday, October 6, 2025, 16:45 - 18:15
Auditorium

CME 8 - Radiopharmaceutical Committee - Radiotheranostics 2.0: The Power of Emerging Radioisotopes in Translating Imaging into Personalised Radiotherapy

OP-450d

Most Promising Radionuclides for Immediate Clinical Impact

K. Herrmann*; Herrmann, University Hospital Essen, Essen, GERMANY.*

OP-450e

Radiometals for Imaging and Radioligand Therapy

M. Ma*; King's College London, Department of Imaging Chemistry, London, UNITED KINGDOM.*

OP-450f
Terbium-based Theranostic Pairs
C. Favaretto; *IRCCS Ospedale Sacro Cuore Don Calabria, Department of Radiopharmacy, Verona, ITALY.*

OP-450g
Bringing Theranostics to the Clinic: Main Clinical Issues
A. Iagaru; *Stanford University Medical Center, Department of Nuclear Medicine, Stanford, UNITED STATES OF AMERICA.*

1102

Monday, October 6, 2025, 16:45 - 18:15
Room 112 (Arena)

Special Track 8 - Neuroimaging Committee - Round Table: Tau PET Imaging: Ready for Clinical Use?

OP-450h
Availability and Standardization of Tau-PET Procedures: What Is Needed in the Field?
R. Smith; *Lund University, Clinical Memory Research, Department of Clinical Sciences, Lund, SWEDEN.*

OP-450i
Visual Reading of T+ and T- Cases. Already Available to Routine Settings?
G. Mathoux; *University Hospitals, Division of Nuclear Medicine and Molecular Imaging, Geneva, SWITZERLAND.*

OP-450j
Staging of Tau Pathology with Tau-PET. Can We Already Provide this in Molecular Imaging Reports?
E. Doering; *University Hospital Cologne, Department of Nuclear Medicine, Cologne, GERMANY.*

OP-450k
Harmonisation of Tau PET Imaging Read-Outs. Is Unified Reading and Quantification for Different Tracers already Available?
M. Vermeiren; *Amsterdam UMC – Alzheimer Center & Department of Radiology & Nuclear Medicine, Amsterdam, NETHERLANDS.*

1103

Monday, October 6, 2025, 16:45 - 18:15
Room 113

LIPS Session 8 - Physics Comittee - Getting Imaging Right with Protocol Optimisation

OP-450l
Image Optimisation in SPECT
J. Tran-Gia; *Department of Nuclear Medicine, University Hospital Würzburg, Würzburg, GERMANY.*

OP-450m
Image Optimisation in PET
I. Armstrong; *Nuclear Medicine, Manchester University NHS Foundation Trust, Oxford Road, Mancheser, UNITED KINGDOM.*

OP-450n
Getting the Best Out of Your Data with Optimised Image Processing
I. Buvat; *PSL University, Inserm, LITO U1288, Orsay, FRANCE.*

1104

Monday, October 6, 2025, 16:45 - 18:15
Room 114

M2M Track - TROP Session - Radiopharmaceutical Sciences + Translational Molecular Imaging & Therapy Committee: Preclinical Neuroimaging

OP-451
Assessment of Reactive Astrocytes Across the Alzheimer's Disease Spectrum and Post-Treatment of Nrf2-Targeted Therapy via ^{18}F-SMBT-1 Imaging in 3xTg-AD mice
S. Guo[1], *F. Wei*[1], *S. Liang*[1], *Y. Ma*[1], *Q. Huang*[2], *C. Fu*[3], *W. Cheng*[1], *Y. Yin*[1];
[1]*Department of Nuclear Medicine, Xinhua Hospital, Shanghai Jiao Tong University School of Medicine, Shanghai, CHINA,* [2]*PET Center, Huashan Hospital, Fudan University, Shanghai, CHINA,* [3]*Institute for Developmental and Regenerative Cardiovascular Medicine, Xinhua Hospital, Shanghai Jiao Tong University School of Medicine, Shanghai, CHINA.*

Aim/Introduction: This study aims to determine the optimal time window for modulating reactive astrocyte phenotypes in 3xTg-AD mice using (S)-(2-methylpyrid-5-yl)-6-[(3-18F-fluoro-2-hydroxy) propoxy]quinoline (^{18}F-SMBT-1), a PET tracer for imaging reactive astrocytes, and assess the therapeutic potential of reactive astrocyte phenotype modulation in Alzheimer's disease (AD). ***Materials and Methods:*** PET imaging with ^{18}F-SMBT-1 was conducted in 3xTg-AD mice at 4, 6, 10, and 12 months of age, with age-matched wild-type (WT) mice as controls. The standardized uptake value ratio (SUVR) of cortex and hippocampus was calculated using the cerebellum as the reference region by PMOD software. To modulate astrocytes phenotype, nuclear factor E2-related factor 2 (Nrf2) was specifically overexpressed in hippocampal astrocytes of 4- and 10-month-old 3xTg-AD mice using adeno-associated virus vectors. Subsequent PET imaging with ^{18}F-SMBT-1 was performed to assess astrocytes reactivity after treatment. Cognitive function was evaluated using the open field test and Morris water maze test. Western blot and immunofluorescence were used to assess pathological features of AD, including Aβ deposition, tau pathology, neuronal and synaptic loss, as well as neuroinflammatory responses. ***Results:*** In 3xTg-AD mice of different ages, increased uptake of ^{18}F-SMBT-1 was observed in the cortex and hippocampus compared to age-matched WT controls. The uptake of ^{18}F-SMBT-1 was elevated in both the cortex and hippocampus of 6-month-old 3xTg-AD mice compared to 4-month-old 3xTg-AD mice, and showed a stabilization trend with disease progression at 10 and 12 months of age. Following the modulation of reactive astrocyte phenotype via Nrf2 overexpression, decreased uptake of ^{18}F-SMBT-1 was observed in the 3xTg-AD mice. Modulation of the reactive astrocyte phenotype demonstrated therapeutic efficacy in AD, as indicated by improved cognitive function, reduced Aβ and tau pathologies, attenuated neuronal and synaptic loss, and alleviated neuroinflammation in the 3xTg-AD mice. ***Conclusion:*** PET imaging with ^{18}F-SMBT-1 represents a valuable tool for determining the optimal timing to modulate reactive astrocyte phenotypes in AD. It also facilitates the assessment of astrocyte reactivity in response to therapeutic interventions. Modulating reactive astrocyte phenotypes by overexpressing Nrf2 has shown therapeutic benefits in AD models, suggesting that Nrf2-targeted therapy may represent a promising therapeutic strategy for AD. (This work was supported by the National Natural Science Foundation of China (No. 82472014, 81974270), and Natural Science Foundation of Shanghai (24ZR1450000).).

OP-452

PARP Inhibition Alleviates Neuroinflammation in a Rat Model of Multiple Sclerosis: Insights from a PET Study

G. Li, *M. Kominia, S. Blok, C. Kwizera, I. F. Antunes, B. T. Cornelissen, E. F. J. d. Vries;*
Department of Nuclear Medicine and Molecular Imaging, University of Groningen, University Medical Center Groningen, Groningen, NETHERLANDS.

Aim/Introduction: Neuroinflammation, driven by activated microglia, plays a key role in CNS disorders like multiple sclerosis (MS). PARP inhibition has been suggested to help reduce neuroinflammation and protect cellular integrity. PET imaging with the TSPO ligand [^{11}C]PBR28 allows in vivo assessment of glial activation. Here, we explored the effect of PARP inhibition on neuroinflammation in vitro, and in a lysolecithin-induced MS rat model using PET. ***Materials and Methods:*** In vitro uptake of [^{11}C] PBR28 was assessed in RAW264.7 macrophage cells exposed to LPS (vehicle, 100 or 1000 ng/mL) and/or the PARP inhibitor PJ34 (0- 20 μM). MS lesions were induced in male Sprague-Dawley rats by unilateral stereotactic injection of 1% lysolecithin in saline in the corpus callosum (3 μL) and striatum (4 μL). Animals were administered either vehicle or PJ34 (20 mg/kg, i.p. every 12 h) for 48 h. A 15-min static [^{11}C]PBR28 PET scan was performed at 3 and 7 days post lesion induction. Histological analysis of brain sections stained with IBA-1 or Luxol Fast Blue was conducted to evaluate microglial activation or myelin integrity, respectively. ***Results:*** LPS stimulation (100 ng/mL) significantly increased [^{11}C]PBR28 uptake (normalized, corrected for the number of cells and tracer amount) in RAW264.7 macrophages compared to controls, in vitro (1.91 ± 0.18 vs. 1.00 ± 0.13, $p < 0.0001$). PJ34 co-treatment (1 μM) significantly reduced this uptake (1.91 ± 0.18 to 1.24 ± 0.22 , $p < 0.0001$), indicating PARP inhibition attenuated LPS-induced macrophage activation in vitro. [^{11}C]PBR28 PET imaging revealed significantly lower tracer uptake (SUV_{mean}) in MS lesions of PJ34-administered animals, compared to vehicle-treated controls on days 3 and 7 (day 3: 1.21 ± 0.01 vs. 1.75 ± 0.01, $p < 0.001$; day 7: 0.99 ± 0.01 vs. 1.29 ± 0.02, $p < 0.001$). The decrease in tracer uptake between days 3 and 7 was most pronounced in PJ34-treated animals. In contrast, contralateral brain regions showed no differences between treatment groups or time points (approximately 0.50) in all animals. Immunohistochemistry confirmed a significant reduction in IBA-1 positive microglia in PJ34- treated animals compared to vehicle controls. LFB staining revealed a smaller demyelinated area in the PJ34 group compared to controls, suggesting that PJ34 effectively attenuates demyelination. ***Conclusion:*** This study highlights the value of [^{11}C]PBR28 PET imaging as sensitive tool for monitoring neuroinflammation in vivo and demonstrates that PJ34 treatment significantly attenuates microglial activation, as detected by PET. Post-mortem analysis revealed reduced demyelination in the MS model, supporting the therapeutic potential of PARP inhibition to reduce demyelination and neuroinflammation in MS.

OP-453

Multitracer PET Imaging Reveals Region-Specific BBB Dysfunction in a Mouse Model of Anxiety/Depression

E. N'Diaye[1], *C. Corvo*[1], *S. Goutal*[1], *S. Leterrier*[1], *S. Amargier-Barrial*[1], *M. Goislard*[1], *S. Cisternino*[2], *D. J. David*[3], *N. Tournier*[1];
[1]*Université Paris-Saclay, Inserm, CNRS, CEA, Laboratoire d'Imagerie Biomédicale Multimodale (BioMaps), Service Hospitalier Frédéric Joliot, 4 place du général Leclerc, Orsay 91401, FRANCE,* [2]*Université Paris Cité, Inserm UMRS 1144, Optimisation Thérapeutique en Neuropsychopharmacologie, Paris, FRANCE,* [3]*Université Paris-Saclay, Centre de recherche en Epidémiologie et Santé des Populations (CESP-Inserm), UMR 1018, Team Moods, Orsay 91400, FRANCE.*

Aim/Introduction: Blood-brain barrier (BBB) dysfunction is increasingly linked to depression pathophysiology[1]. Changes in BBB permeability/function may affect antidepressant distribution and response variability. In this study, we used a multitracer approach for quantitative mapping of BBB permeability and functionality using PET imaging in a validated murine model of anxiety/depression. ***Materials and Methods:*** Male C57BL/6N mice (13 weeks old) received corticosterone (35 μg/L) or vehicle (water and β-cyclodextrin) in drinking water for five weeks to induce the anxiety/depression behaviour (CORT mice). MicroPET acquisitions were performed using i) [^{18}F]fluorodeoxysorbitol ([^{18}F]FDS), a marker of BBB permeability, ii) [^{11}C]metoclopramide, a substrate of the BBB efflux transporter P-glycoprotein and iii) [^{11}C]diphenhydramine, a substrate of the uptake transporter H+/antiporter. A graphical analysis was performed to estimate the uptake transfer constant k_{uptake} of [^{18}F]FDS and [^{11}C]diphenhydramine using an image-derived input function (heart blood-pool)[2], and the efflux rate $k_{E,brain}$ of [^{11}C]metoclopramide[3]. Moreover, brain-normalized SUVR images were generated to consider region-specific differences in BBB permeability/function. ***Results:*** Kinetic modelling of whole-brain PET data (n=6-7/group) revealed no significant difference in the $k_{E,brain}$ of [^{11}C]metoclopramide, or the k_{uptake} of [^{11}C] diphenhydramine in CORT mice, suggesting no detectable global changes in uptake/efflux transport function at the BBB ($p>0.05$). In comparison, a significant 1.3±0.2-fold increase in the whole-brain k_{uptake} of [^{18}F]FDS was observed ($p<0.05$), suggesting increased BBB permeability. Regional analysis revealed higher SUVR values for [^{11}C]metoclopramide in the basal forebrain septum ($p<0.01$), suggesting decreased P-gp function. For [^{11}C]diphenhydramine, significant SUVR increases were observed in the hippocampus and olfactory bulb ($p<0.05$). [^{18}F]FDS SUVRs were significantly elevated in the thalamus ($p<0.05$), hypothalamus, and basal forebrain septum (both $p<0.01$). ***Conclusion:*** Our study reveals that depressive-like behaviour in the CORT mice model is associated with subtle yet region-specific changes in BBB permeability and membrane transporter function. From a neuropharmacokinetic perspective, the limited changes in uptake/efflux transporter function are unlikely to account for global changes in the brain exposure to antidepressant drugs in CORT mice. However, region-specific changes in BBB transporter functionality and increased BBB permeability may contribute to the neurobiology of depression. From a translational neuroimaging perspective, multitracer PET imaging using complementary markers of BBB permeability and transport enables quantitative mapping of BBB dysfunctions. This may be useful to address BBB involvement in this neuropsychiatric condition. ***References:*** [1]Dudek KA et al. Proc Natl Acad Sci U S A. 2020;117(6):3326-3336. [2]Auvity S et al. J Cereb Blood Flow Metab. 2017;37(6):2185-2195.[3]Breuil L et al. Mol Imaging Biol. 2023;25:1135-1141.

OP-454

Contribution of CXCR4-Targeted PET Imaging in the Non-Invasive Evaluation of Radiation-Induced Brain Injury

J. Pei, *S. Wang, K. Zhao, X. Zhao, J. Yu, J. Liu;*
Shandong Cancer Hospital and Institute, Shandong First Medical University and Shandong Academy of Medical Sciences, Jinan, CHINA.

Aim/Introduction: Radiation-induced brain injury (RIBI) is a common and dose-limiting complication of radiotherapy for central nervous system (CNS) tumors. Currently, the lack of reliable and sensitive diagnostic techniques hampers effective prevention and treatment of progressive RIBI. Through single-cell RNA sequencing (scRNA-seq), we identified radiation-responsive cell populations and revealed CXCR4 as a potential biomarker for RIBI. This study aimed to validate the accuracy of CXCR4 as a noninvasive imaging biomarker for early detection and monitoring of RIBI. ***Materials and Methods:*** A small animal radiation research platform was used to establish an RIBI mouse model via localized hippocampal irradiation. Brain tissues were harvested at two weeks post-irradiation for scRNA-seq analysis.

The diagnostic performance of an ^{18}F-labeled CXCR4-targeted tracer ([^{18}F]AlF-NOTA-QHY-04) was evaluated using PET imaging and compared with conventional FDG PET/CT. Additional MRI, dynamic/blocking studies, and histopathological validation were performed. A longitudinal study assessed the predictive value of CXCR4-targeted PET for RIBI progression. ***Results:*** 27 distinct cell subsets were identified and a comprehensive investigation demonstrated remarkable CXCR4 expression in microglia and macrophage subsets enriched in irradiated tissues. [^{18}F]AlF-NOTA-QHY-04 PET demonstrated enhanced uptake in irradiated brain regions before MRI-detectable structural changes. In contrast, [^{18}F] FDG PET exhibited reduced uptake in necrotic areas by 4 weeks post-irradiation. Furthermore, CXCR4-targeted PET imaging enabled quantification and spatial mapping of inflamed brain regions infiltrated by CXCR4-expressing cells and emerged as a robust predictor of subsequent radiation necrosis. ***Conclusion:*** This study establishes CXCR4 as a sensitive and early biomarker for RIBI, demonstrating that CXCR4-targeted PET imaging outperforms conventional FDG PET and MRI in detecting radiation-induced damage before anatomical changes occur. These findings support the potential of CXCR4 imaging for early intervention and personalized management of RIBI. ***References:*** Jinli P, Kai C, Tianxin L, Min G, Shijie W, Shengnan X, Yanluan G, Li M, Wanhu L, Bolin W et al: Early, non-invasive detection of radiation-induced lung injury using PET/CT by targeting CXCR4. European Journal of Nuclear Medicine and Molecular Imaging 2024, 51(4):1109-1120.

OP-455

PET Imaging of the Mouse Brain During Running

X. Yu[1], *H. Liu*[2], *Q. Qiao*[2], *W. Zhu*[2], *D. Liang*[2], *H. Zhao*[2], *J. Tao*[2], *W. Ma*[2], *Q. Peng*[2];
[1]*Huazhong University of Science and Technology, Wuhan, CHINA,* [2]*Shenzhen Bay Laboratory, Shenzhen, CHINA.*

Aim/Introduction: Positron Emission Tomography (PET) has particularly advantageous in the realm of brain functional imaging [1]. However, a significant limitation of regular PET scanning is the necessity for anesthesia in small animals to mitigate motion-induced artifacts in the imaging, and anesthetics inhibit brain metabolism and affect PET image accuracy [2]. To enable brain functional imaging in conscious mice, we develop an innovative mouse brain PET scanner. ***Materials and Methods:*** The scanner comprises ten detectors, each consisting of a 6×15 LYSO crystal array (1 mm pixel size) coupled to a 2×5 SiPM array (3 mm pixel size). The scanner, weighing only 55 g, provides a cylindrical field of view (FOV) of 16 mm in diameter and axial length, sufficient to cover the mouse brain. Spatial resolution and sensitivity were evaluated using a 22-Na point source. Image quality was assessed with a Derenzo phantom. FDG-PET imaging was performed on three mice (150-190 μCi), scanned under both awake and anesthetized conditions with identical activity per subject. ***Results:*** The system maintained a stable position relative to the mouse head, enabling functional imaging in the awake state. Filtered Back Projection yielded radial and axial resolutions of 0.7 mm and 1.0 mm, respectively. With six iterations of OSEM, resolution improved to 0.5 mm in both directions. Using an energy window of 261-661 keV, the system achieved 0.8% central sensitivity. Derenzo phantom imaging demonstrated moderate contrast, though 0.7 mm rods could not be fully resolved, possibly due to phantom limitations. Brain PET scans showed distinguishable uptake patterns in both awake and anesthetized mice. Notably, awake mice exhibited slightly reduced uptake, likely due to stress-induced metabolic changes. ***Conclusion:*** This brain PET system demonstrates high spatial resolution and enables functional imaging in both anesthetized and conscious mice. Despite lower sensitivity due to miniaturization constraints, it offers a novel platform for studying natural brain function. Future work will explore mechanical assistance to support imaging during active locomotion. ***References:*** [1] Kadrmas D J, Hoffman J M. Methodology for quantitative rapid multi-tracer PET tumor characterizations[J]. Theranostics, 2013, 3(10): 757. [2] Miranda A, Glorie D, Bertoglio D, et al. Awake ^{18}F-FDG PET imaging of memantine-induced brain activation and test-retest in freely running mice[J]. Journal of Nuclear Medicine, 2019, 60(6): 844-850.

OP-456

Longitudinal SV2A Expression Increase and Profound Desynchronization is Accompanied by Reactive Astrogliosis and Precedes Neurodegeneration in a Mouse Model of Taupathy: A Multi-Tracer Imaging Study

Y. Li[1], *G. Palumbo*[1], *S. Lindner*[1], *F. J. Gildehaus*[1], *A. Zatcepin*[1,2], *R. Werner*[1], *M. Brendel*[1,2,3], *L. H. Kunze*[1,2];
[1]*Department of Nuclear Medicine, University Hospital, LMU Munich, Munich, GERMANY,* [2]*German Center for Neurodegenerative Diseases (DZNE), Munich, GERMANY,* [3]*Munich Cluster for Systems Neurology (SyNergy), Munich, GERMANY.*

Aim/Introduction: Tau pathological protein accumulation and neuroinflammation are the major hallmarks of tauopathies, resulting in neuronal network dysfunction. [^{18}F]UCB-H, a PET tracer targeting the synaptic vesicle protein 2A (SV2A), holds the potential to evaluate synaptic density. Therefore, we analyzed the longitudinal synaptic density alterations in tau transgenic mice by [^{18}F]UCB-H PET imaging and integrated it with terminal immunohistochemistry to provide more evidence for synaptic quantification. ***Materials and Methods:*** PS19 and C57Bl/6 mice aged 5.7 to 11.0 months underwent four consecutive [^{18}F]UCB-H PET scans to evaluate the SV2A expression. Immunohistochemistry was performed to validate the [^{18}F]UCB-H PET results. In addition, [^{18}F]F-DED PET scans and [^{18}F]GE-180 PET scans were performed at 5.7 months of age to reveal reactive astrogliosis and activated microglia, respectively. Group differences in the uptake were assessed by SUV z-scores. For [^{18}F]UCB-H PET data, a desynchronization index (DI) was calculated for each brain region and principal component analysis (PCA) was performed to assess global differences in SV2A expression synchronization between cohorts with the first principal component (PC1). Moreover, we calculated the area under the curve (AUC) of [^{18}F]UCB-H z-scores to investigate the association between synaptic density variation and reactive gliosis. ***Results:*** Between 8.4 and 10 months we observed an increase in SV2A expression (+4.3-11.5%), followed by a rapid decline towards 11 months (-10.5-23.8%) in neocortex, hippocampus CA1, brainstem, cerebellum, hypothalamus, and thalamus. Contrary, continuous longitudinal reduction of SV2A expression was shown in hippocampus CA3, entorhinal cortex, and amygdala (-12.9-21.0%). Using advanced image processing, we found a major desynchronization of SV2A expression in PS19 cohort at 10.0 months. Immunohistochemistry confirmed the reduction of SV2A expression and a significant tau accumulation in PS19 cohort at 11.0 months, which correlated with [^{18}F]UCB-H PET. [^{18}F]UCB-H variance was positively associated with baseline [^{18}F]F-DED PET in hippocampal CA1, brainstem, piriform cortex, thalamus, and cerebellum (R=0.636-0.736) but was not related to baseline [^{18}F]GE-180 PET. ***Conclusion:*** [^{18}F]UCB-H PET is a powerful method for quantifying synaptic density, dynamically reflecting synaptic differences between cohorts at various pathological stages. As the primary increase is associated with a major desynchronization, it is most likely a reflection of neuronal dysfunction and possibly hyperexcitability in response to tau accumulation, adding to the observed hypermetabolism in the earliest stages of Alzheimer's disease. Moreover, our study shows baseline reactive astrogliosis can be a predictive marker, which is closely associated with subcortical synaptic desynchronization and possibly adding to neuronal hyperexcitability via tripartite synapse.

OP-457

[18F]SDM-18: A high-affinity SV2A PET tracer for spinal cord imaging

P. W. Tan[1], *T. Balayeva*[1], *N. H. Martin*[1], *Z. Chao*[2], *S. F. Nejati*[1], *T. Toyonaga*[1], *D. Holden*[1], *M. Kapinos*[1], *M. Zheng*[1], *K. Wilcox*[3], *S. Finnema*[3], *R. Carson*[1], *Y. Huang*[1], *Z. Cai*[1];
[1]*School of Medicine, Yale University, New Haven, CT, UNITED STATES OF AMERICA,* [2]*Centre for Addiction and Mental Health, University of Toronto, Toronto, ON, UNITED STATES OF AMERICA,* [3]*AbbVie R&D Discovery Research Neuroscience - Translational Imaging Dept., Chicago, IL, UNITED STATES OF AMERICA.*

Aim/Introduction: Synaptic vesicle glycoprotein 2A (SV2A) is a biomarker for synaptic density. A series of PET imaging probes, have been developed to quantify SV2A in the brain in vivo. However, it remains challenging to quantify the synaptic density in the spinal cord due to its lower SV2A expression. [1] Recently, a high-affinity SV2A PET tracer, [18F]SDM-18 was developed through structural modifications of [18F]SDM-16.[2-4] Herein, we report the PET imaging evaluation of [18F]SDM-18 for the quantification of SV2A in both the brain and spinal cord in the same nonhuman primate (NHP). ***Materials and Methods:*** [18F]SDM-18 was synthesized from commercially available starting materials and evaluated for in vitro binding affinities. Baseline and blocking scans with levetiracetam (30 mg/kg) were performed on rhesus monkeys using a NeuroEXPLORER (NX) PET scanner. Arterial blood was collected for metabolite analysis and the construction of the plasma input function. Regional time-activity curves (TACs) were analyzed using a one-tissue compartment (1TC) model to calculate the volume of distribution (V_T). Binding potential (BP_{ND}) was calculated using the non-displaceable volume of distribution (V_{ND}) determined from the blocking study. ***Results:*** SDM-18 exhibits high affinity for human SV2A (Ki = 2 nM). [18F]SDM-18 was synthesized with >99% radiochemical purity and molar activity of 188 ± 9 GBq/μmol (n = 4). It showed strong uptake in brain and spinal cord, with peak SUVs of ~12 and ~6, respectively. Spinal cord regional V_T values ranged from 15.0 to 50.0 mL/cm^3. SV2A occupancy by levetiracetam (30 mg/kg) was 83% in the brain (V_{ND} = 9.4 mL/cm^3) and 76% in the spinal cord (V_{ND} = 5.7 mL/cm^3). BP_{ND} values for [18F]SDM-18 were higher than [18F]SynVesT-1, [11C]UCB-J, and [18F]SDM-16 in the brain. Notably, cervical spinal cord BP_{ND} for [18F]SDM-18 was over 10-fold higher than that of [11C]UCB-J, highlighting its potential for spinal cord imaging. ***Conclusion:*** We have successfully synthesized [18F]SDM-18 and assessed its imaging properties in NHPs. [18F]SDM-18 has high specific binding signals and appropriate kinetics in the brain and spinal cord, supporting its translation into first-in-human studies for imaging SV2A in the spinal cord. ***References:*** Rossano. S., Carson. R. E. et. al. EJNMMI Phys. 2022. 9; 32, Zheng. C., Cai. Z. et.al. Eur J Nucl Med Mol Imaging 2022. 49, 1482, Zheng. C., Cai. Z. et.al J. Nucl. Med. 2022. 63 (supplement 2), 2561, Tan. P.W., Cai. Z. et.al J. Nucl. Med. 2024. 65 (supplement 2), 241845.

OP-458

Discovery and Preclinical Characterization of PET Tracers for Imaging Alpha-Synuclein Aggregates in the Human Brain

M. Mugnaini[1], *S. Vukelic*[1], *G. Fink*[1], *M. Voorbach*[2], *Y. Zhuang*[2], *S. Benninghoff*[1], *S. Seifarth*[1], *A. Grill*[1], *S. M. Spohr*[1], *W. Amberg*[1], *C. Petrungaro*[1], *S. Vaidyanathan*[2], *A. Reed*[2], *D. Sunnemark*[3], *H. Jongsma Wallin*[3], *J. Wang*[2], *B. Chen*[2], *D. Wooten*[2], *M. B. Skaddan*[2], *T. Dellovale*[4], *M. Cik*[1], *R. Comley*[2], *F. Pohlki*[1], *S. J. Finnema*[2], *S. Barghorn*[1];
[1]*AbbVie Deutschland GmbH & Co. KG, Ludwigshafen, GERMANY,* [2]*AbbVie Inc., North Chicago, IL, UNITED STATES OF AMERICA,* [3]*Offspring Biosciences AB, Södertälje, SWEDEN,* [4]*AbbVie Cambridge Research Centre, Cambridge, MA, UNITED STATES OF AMERICA.*

Aim/Introduction: Alpha-synuclein (αsyn) is a synaptic protein that, in pathological conditions, forms hyperphosphorylated, insoluble aggregates with high neurotoxic properties. Accumulation and propagation of αsyn aggregates in the brain drives disease progression in Parkinson's disease (PD) and multiple system atrophy (MSA). The aim of this project is the discovery of PET tracers for the visualization of αsyn aggregates in living human subjects, to be used as imaging markers in PD and other synucleinopathies, such as MSA. ***Materials and Methods:*** Compound affinity (K_i) for αsyn aggregates was measured in a miniaturized radioligand binding assay on αsyn aggregate-enriched, idiopathic PD (iPD) brain extracts; selectivity vs. tau and amyloid-beta (Aβ) aggregates, and monoamine-oxidase (MAO) enzymes was investigated using Alzheimer's disease (AD) brain homogenates and microsomes expressing recombinant human MAO. Autoradiography (ARG) and micro-ARG experiments with [3H]-labeled compounds were used to confirm binding to αsyn and measure the affinity (K_D) and the B_{max}. PET studies with [18F]-labeled compounds were performed in anesthetized transgenic (TG) mice expressing aggregated hA53T-αsyn (line-M83) and healthy non-human primates (NHPs). In NHP, the total volume of distribution (V_T) was estimated using and the Logan graphical method with metabolite corrected plasma input function for ROIs defined on a subject specific MRI using a brain atlas. ***Results:*** Up to now, ~900 compounds have entered the project's screening cascade. The most advanced compound, A-2, had a K_i of 41 nM for iPD brain extracts and low affinity for common off targets (K_i=901 nM for Aβ and K_i>4740 nM for tau, MAO-A and MAO-B). Micro-ARG and ARG experiments confirmed that [3H]-A-2 binds specifically to αsyn in brain samples from TG mice, MSA and iPD subjects, with K_D values of 39 nM in the TG mouse medulla, 29 nM in the MSA cerebellar white matter and 24-117 nM in the iPD grey matter. Specific saturable binding was also detected in normal human grey matter. PET studies in NHPs with [18F]-A-2 showed high brain penetration and homogeneous distribution across regions (V_T=3.9±0.23) with rapid washout kinetics. ***Conclusion:*** Compound [18F]A-2 has in-vitro and in-vivo properties suggesting a potential as an αsyn PET tracer for MSA subjects. Despite the in-vitro evidence of specific binding to αsyn aggregates in iPD, the lower predicted in-vivo binding potential (BP_{ND}) and the limited differentiation from normal brain samples advise caution in considering [18F]A-2 for potential use as an αsyn PET tracer in iPD. Further optmization of the K_D and/or B_{max} is warranted.

OP-459

Comparison of Optimized PET Tracer [18F]FS9 with its Predecessor [18F]FS3 for α-Synuclein Fibrils Imaging

B. Hooshyar Yousefi[1,2], *B. Uzuegbunam*[3,4], *S. Bagheri*[1,2], *N. Mortazavi*[1], *W. Paslawski*[5], *P. Svenningsson*[5], *R. Zou*[6], *A. K. Rosenau*[7], *M. T. Henrich*[7], *F. Geibl*[7], *H. Agren*[6], *W. Oertel*[7], *W. Weber*[3], *M. Luster*[1], *T. Arzberger*[8], *D. Librizzi*[9];
[1]*Nuclear Medicine Department, Philipps University of Marburg, Marburg, GERMANY,* [2]*Core Facility Molecular Imaging, Center for Tumor Biology and Immunology, Philipps University Marburg, Marburg, GERMANY,* [3]*Department of Nuclear Medicine, Technical University of Munich, Munich, GERMANY,* [4]*ITM, Munich, GERMANY,* [5]*Department of Clinical Neuroscience, Karolinska Institutet,, Stockholm, SWEDEN,* [6]*Department of Physics and Astronomy, Uppsala University, Uppsala, SWEDEN,* [7]*Department of Neurology, Philipps University of Marburg, Marburg, GERMANY,* [8]*Neurobiobank Munich, Ludwig-Maximilians-University Hospital of Munich, Munich, GERMANY,* [9]*Nuclear Medicine Department, University Hospital OWL, Evangelical Clinic Bethel, Bielefeld, GERMANY.*

Aim/Introduction: To optimize a specific 18F-labeled PET tracer based on diarylbisthiazole ([18F]FS9) with excellent binding affinity to α-synuclein fibrils (α-syn), exceptional selectivity over β-amyloid plaques (Aβ) and tau fibrils. It shall exhibit favorable brain uptake, pharmacokinetics, and be evaluated in vitro, by in

vivo longitudinal PET studies, and post-mortem patient-brain and animal models of Parkinson's disease (PD), compared with [^{18}F]FS3. ***Materials and Methods:*** Using an in-silico approach, [^{18}F]FS9 was optimized from [^{18}F]FS3 by synthesizing several leads with promising preclinical results, including enhanced binding affinity and selectivity to α-syn, biodistribution, metabolite analyses, lipophilicity, pharmacokinetics (PK), and Blood-Brain-Barrier permeability. Postmortem autoradiography on human brains with α-synucleinopathies, alongside PET imaging in mouse models, confirmed tracer efficacy. [^{18}F]FS9 was radiolabeled, purified, and applied to a longitudinal study of dynamic 90-minute PET/CT scans, conducted 3-6 months post intrastriatal injection of mouse α-synuclein preformed fibrils (PFF). PFF mice (n≥3) were compared with monomeric α-synuclein-injected control mice (ctrl, n≥3). Preclinical results for PFF and control mice brains were also compared with [^{18}F]FS3 in E46K transgenic and control rats, with ex vivo immunohistochemical (IHC) confirmation. ***Results:*** [^{18}F]FS9 demonstrated a higher binding affinity to α-syn (Ki 2 nM) and >100-fold selectivity over Aβ plaques and neurofibrillary tangles (NFT) than [^{18}F]FS3 (Ki 3.7 nM, logD= 3.4). It showed suitable lipophilicity (logD= 2.8) and favorable PK. In patient brains, [^{18}F]FS9 selectively bound α-synucleinopathies, showing no binding in healthy controls, confirmed by IHC. Compared to [^{18}F]FS3, [^{18}F]FS9 had higher brain uptake (>7% ID/g at 5 min p.i.), rapid washout, and remarkable stability (brain t1/2 >8 hours). Longitudinal PET in PFF mice showed SUV values between 2.0-3.9, with distribution values significantly higher in the PFF brain (1.8-2.7 ml/cm^3 in the left striatum) versus control mice brains (0.8 ml/cm^3). ***Conclusion:*** This work represents a significant advancement in the development of optimized PET tracers, offering groundbreaking potential for accurately detecting and quantifying α-synuclein aggregates, thus paving the way for improved diagnostic and therapeutic strategies in α-synucleinopathies. The rational optimization of [^{18}F]FS3 to [^{18}F]FS9 through an in-silico approach resulted in a highly specific and effective tracer for detecting and quantifying α-synuclein aggregates. [^{18}F]FS9's excellent binding properties and imaging performance establish its further role for clinical investigations in patients with α-synucleinopathies. ***References:*** Uzuegbunam,...Hooshyar Yousefi et al. In Silico and In Vitro Study towards the Rational Design of 4,4'-Disarylbisthiazoles as a Selective α-Synucleinopathy Biomarker Int J Mol Sci 2023 Nov 17;24(22):16445. doi: 10.3390/ijms242216445.

1105

Monday, October 6, 2025, 16:45 - 18:15
Room 211

Cutting Edge Science Track - TROP Session - AI Committee: AI for Report Generation and Patient Prognostication

OP-460

Bone2Report: Automated Bone Scintigraphy Reporting with Clinically-Inspired Vision-Language Reasoning

X. Wu[1,2], *X. Xie*[1,2], *S. Huang*[3], *H. Zheng*[1,2], *N. Zhang*[1,2], *D. Liang*[1,2], *Y. Liang*[3,4], *Z. Hu*[1,2];
[1]*Research Center for Medical AI, Shenzhen Institute of Advanced Technology, Chinese Academy of Sciences, Shenzhen, CHINA,* [2]*Key Laboratory of Biomedical Imaging Science and System, Chinese Academy of Sciences, State Key Laboratory of Biomedical Imaging Science and System, Shenzhen 518055, Shenzhen, CHINA,* [3]*National Cancer Center/National Clinical Research Center for Cancer/Cancer Hospital & Shenzhen Hospital, Chinese Academy of Medical Sciences and Peking Union Medical College, Shenzhen, CHINA,* [4]*National Cancer Center/National Clinical Research Center for Cancer/Cancer Hospital, Chinese Academy of Medical Sciences and Peking Union Medical College, Beijing, CHINA.*

Aim/Introduction: Bone scintigraphy is a widely used imaging modality for detecting skeletal metastases and metabolic abnormalities, playing a crucial role in oncology and metabolic bone disease assessment. Automating the reporting process for bone scans holds substantial clinical value, as it can reduce radiologists' workload and improve report consistency. However, automated report generation for this modality remains underexplored due to blurred image structures, small and dispersed lesions, and limited paired datasets. This work presents Bone2Report(B2Rep), the first framework for automated bone scan reporting, enabling clinically informed multimodal generation and offering a promising pipeline and a foundation for future research. ***Materials and Methods:*** Inspired by the clinical diagnostic and reporting workflow, we propose B2Rep, a multimodal automated bone scan reporting framework. B2Rep mimics physicians' diagnostic process by integrating: (1) a disease-related visual feature extractor that focuses on small-scale abnormalities, and (2) an associative memory-enhanced language module that aligns long-range image-text semantics. Trained on 2,043 image-report pairs, B2Rep generates structured, accurate, and clinically coherent reports. The dataset contains 2,043 clinical bone scans, each consisting of anterior and posterior whole-body images along with corresponding reports. Images were extracted from DICOM format, normalized, and standardized. Reports were processed through lexical analysis and semantic categorization to construct structured image-text pairs. ***Results:*** Evaluation was conducted using standard metrics, including Bilingual Evaluation Understudy(BLEU), Recall-Oriented Understudy for Gisting Evaluation-Longest Common Subsequence(ROUGE-L), and Consensus-based Image Description Evaluation(CIDEr). Training was performed on four NVIDIA RTX 5880 GPUs, and beam search decoding was employed to improve text fluency. B2Rep achieved a BLEU-4 score of 0.204 and a CIDEr score of 0.448, outperforming CT2Rep and CvT2DistilGPT2 (Table 2). The model effectively captured subtle visual cues and generated reports with strong structural and semantic alignment. However, we found some generated reports only contained partial descriptions (Table 1), potentially due to the retrospective reasoning behavior of large language models.[1] ***Conclusion:*** This work presents the first systematic framework for automated bone scan reporting. B2Rep demonstrates the feasibility of clinically informed multimodal generation in nuclear medicine, offering a promising pipeline and a foundation for future research. ***References:*** [1] Ameisen E, Lindsey J, Pearce A, Gurnee W, Turner NL, et al. Circuit Tracing: Revealing Computational Graphs in Language Models. Transformer Circuits Thread. 2025.

OP-461

Deep Multimodal Visual Question Answering System for Prognostication of PSMA-RPT Outcomes Using PSMA-directed Imaging and Clinical Data

M. Kassar[1], *J. Hu*[2], *I. Rauscher*[1], *C. V. Gomes*[2], *T. Wendler*[3], *S. Ziegler*[4], *A. Afshar-Oromieh*[2], *A. Rominger*[2], *N. Navab*[1], *M. Eiber*[1], *K. Shi*[2], *R. Seifert*[2];
[1]*Technische Universität München, München, GERMANY,* [2]*University Hospital Bern, Bern, SWITZERLAND,* [3]*University Hospital Augsburg, Augsburg, GERMANY,* [4]*LMU University Hospital, München, GERMANY.*

Aim/Introduction: The emergence of large language models (LLMs) presents new opportunities for interactive clinical support, though integrating LLMs with imaging-based AI remains a challenge. While vision-language models (VLMs) have been introduced, their synergy for prognostic support is still limited. This study proposes a deep multimodal visual question answering (VQA) approach to integrate imaging data with interactive querying for clinical decision support. As a proof-of-concept, we predict overall survival (OS) using post-therapeutic SPECT from the first two treatment cycles and compare performance with corresponding pre- and post-therapy PSMA-PET scans. ***Materials and Methods:*** We retrospectively analyzed data from 64 mCRPC patients who received more than two cycles of ^{177}Lu-PSMA-I&T and

had baseline ^{68}Ga-PSMA-11 PET/CT. Median OS was 16 months (95% CI:13-24), ranging from 2 to 107 months, with 40% surviving beyond 24 months. A VQA deep learning model was developed to prognosticate 24-month OS by integrating two post-therapy PSMA-SPECT scans via 3D encoders, early biochemical response through PSA levels, and clinical question text via RadBERT[1], a domain-specific pretrained language model. To assess the impact of input modalities, different combinations of PET, SPECT, and PSA data were used during training. The dataset was split 80/20 for training and testing. To enable efficient adaptation and reduce overfitting, Low-Rank Adaptation (LoRA) [2] was used for parameter-efficient fine-tuning of the RadBERT encoder. To preserve the multimodal data's spatial and temporal structure, we applied 3D positional embeddings to image tokens for post-cycle SPECT volumes[3] and standard 1D encodings to text tokens, following the original transformer design[4]. ***Results:*** The best prognostic performance was achieved by combining first- and second-cycle SPECT images with PSA values, yielding 81.82% accuracy (95% CI: 0.54-1.0) and F1 score of 0.82 (95% CI:0.40-1.0) for predicting 24-month OS. Comparable performance was observed with first- and third-cycle PET with PSA. Slightly lower performance was obtained using only first-cycle PET, SPECT, and PSA, with 72.73% accuracy (95% CI:0.45-0.91) and F1 score of 0.73 (95% CI:0.22-1.0). ***Conclusion:*** Our preliminary findings suggest that the developed a deep multimodal VQA approach is feasible for investigating the prognostication of 24-month OS in patients undergoing PSMA-RPT. For this, post-therapeutic SPECT imaging of the first two treatment cycles and corresponding PSA values had best accuracy. However, external validation in additional patient cohorts is needed to confirm these findings. ***References:*** [1] A. Yan et al., Radiol AI 4(4):e210258, 2022. [2] J. Edward et al., arXiv:2106.09685,2021. [3] T.Chen et al., arXiv:2109.10852,2021. [4] A.Vaswani et al., NeurIPS30,2017.

OP-462

Integrated PET/CT Multimodal Automated Report Generation for Lung Cancer Diagnosis

X. Xie[1,2], *H. Wang*[1,2], *E. Liu*[3], *N. Zhang*[1,2], *H. Zheng*[1,2], *D. Liang*[1,2], *X. Yao*[4,5], *S. Cong*[4,5], *L. Jiang*[3], *Z. Hu*[1,2];
[1]*Research Center for Medical AI, Shenzhen Institute of Advanced Technology, Chinese Academy of Sciences, Shenzhen, China, Shenzhen, CHINA,* [2]*Key Laboratory of Biomedical Imaging Science and System, Chinese Academy of Sciences, State Key Laboratory of Biomedical Imaging Science and System, Shenzhen, China, Shenzhen, CHINA,* [3]*PET Center, Department of Nuclear Medicine, Guangdong Provincial People's Hospital (Guangdong Academy of Medical Sciences), Southern Medical University, Guangzhou, China, Guangzhou, CHINA,* [4]*College of Intelligent Science and Engineering, Harbin Engineering University, Harbin 150001, China, Harbin, CHINA,* [5]*Qingdao Innovation and Development Center, Harbin Engineering University, Qingdao, 266000, China, Qingdao, CHINA.*

Aim/Introduction: Automated medical report generation significantly alleviates radiologists' workload and addresses healthcare resource scarcity, with successful applications already established in CT and X-ray domains. However, its implementation in PET imaging remains underexplored due to the modality's inherent limitations in structural delineation and relatively lower spatial resolution.This study establishes the first PET/CT-based multimodal report generation achieving promising clinically automated reporting in lung cancer. ***Materials and Methods:*** In this work, we propose a novel multimodal report generation framework that simultaneously analyzing PET metabolic maps and CT anatomical data, emulating radiologists' diagnostic workflows. Our model introduces two key innovations: 1) A dual-branch adapter architecture that synergizes CT's high-resolution structural mapping and PET's metabolic quantification, with shared transformer parameters facilitating cross-modality attention fusion while maintaining distinct feature hierarchies. 2) a contrastive learning mechanism that aligns metabolic abnormalities with anatomical structures in a shared subspace.The framework processes paired PET/CT scans through coordinated feature extractors that analyze metabolic patterns (PET) and structural details (CT), then fuses these insights through cross-modality reasoning to generate diagnostic reports mimicking radiologists' PET/CT interpretation workflows. We developed a multimodal dataset comprising 600 pathologically confirmed lung cancer cases, augmented to include 1,238 whole-body [18F] FDG PET images, 1,179 CT scans (effective dose ≤1.0 mSv), and 1,830 structured diagnostic reports. ***Results:*** Report generation quality was assessed using natural language processing (NLP) metrics: Bilingual Evaluation Understudy(BLEU), Recall-Oriented Understudy for Gisting Evaluation(ROUGE), Consensus-based Image Description Evaluation(CIDEr), while clinical efficacy (CE) was evaluated through a three-tier classification system: i) lesion malignancy (malignant/benign/indeterminate), ii) metabolic grading (elevated/normal),iii)anatomical localisation (precise/adjacent/erroneous). Proposed multimodal framework demonstrated superior report generation ability due to metabolic-anatomical integration. NLP metrics significantly outperformed conventional baselines (ΔBLEU1=+34%, ΔBLEU4=+57%, ΔROUGE=+66%, ΔCIDEr=+93%). Clinical validation showed: 1) 10.1±3.2% absolute error reduction in sublobar anatomical localisation; 2) 89.7% accuracy in metabolic identification; 3) malignant progression prediction achieved F1-score=0.48 (precision=0.47, recall=0.48) for differentiating aggressive vs indolent tumour subtypes; The method demonstrates promising performance even in ultra-low-dose scenarios (0.9 vs 5.0 mSv), showcasing significant potential. ***Conclusion:*** This study establishes the first PET/CT-based multimodal report generation framework achieving automated reporting in lung cancer. The approach enables radiation-sparing precision diagnostics through synergistic metabolic-anatomical analysis, demonstrating significant potential for clinical translation. To our knowledge, this represents the first multimodal framework specifically designed for PET report generation, establishing a new paradigm for metabolic imaging interpretation.

OP-463

LymRadar: Lymphoma Risk Assessment through Multimodal Data-based Artificial Intelligence Analysis

Y. Fu[1,2], *X. Huang*[3,4], *R. Guo*[3,4], *S. Li*[5], *F. Wang*[6], *Y. Zhou*[7], *C. Jiang*[8], *Z. Gao*[9], *X. Li*[7], *J. Tian*[1,2,10], *W. Mu*[1,2], *B. Li*[3,4];
[1]*School of Engineering Medicine, Beihang University, Beijing, CHINA,* [2]*Key Laboratory of Big Data-Based Precision Medicine (Beihang University), Ministry of Industry and Information Technology of the People's Republic of China, Beijing, CHINA,* [3]*Department of Nuclear Medicine, Ruijin Hospital, Shanghai Jiao Tong University School of Medicine, Shanghai, CHINA,* [4]*Institute for Medical Imaging Technology, Ruijin Hospital, Shanghai Jiao Tong University, Shanghai, CHINA,* [5]*Shandong Cancer Hospital and Institute, Shandong First Medical University and Shandong Academy of Medical Sciences, Jinan, CHINA,* [6]*PET Center, Department of Nuclear Medicine, Guangdong Provincial People's Hospital (Guangdong Academy of Medical Sciences), Southern Medical University, Guangzhou, CHINA,* [7]*Department of Nuclear Medicine, Qilu Hospital of Shandong University, Jinan, CHINA,* [8]*Department of Nuclear Medicine, West China Hospital, Sichuan University, Sichuan, CHINA,* [9]*School of Biological Science and Medical Engineering, Beihang University, Beijing, CHINA,* [10]*CAS Key Laboratory of Molecular Imaging, Institute of Automation, Chinese Academy of Sciences, Beijing, CHINA.*

Aim/Introduction: Diffuse large B-cell lymphoma (DLBCL) is a heterogeneous disease, with approximately 40% of patients experiencing primary treatment failure (PTF) following standard R-CHOP therapy, leading to poor prognosis. The existing risk assessment index, International Prognostic Index (IPI), is limited in

capturing tumor biological heterogeneity, hindering accurate high-risk identification. Therefore, the effective identification of high-risk DLBCL patients for PTF prior to standard R-CHOP treatment is crucial for accurate risk stratification, facilitating individualized treatment plans that enhance prognosis and optimize treatment outcomes. ***Materials and Methods:*** In this study, we developed, validated, and tested a deep learning-based model, LymRadar, for PTF prediction in DLBCL using a large multi-center dataset comprising ^{18}F-FDG PET/CT scans, IPI scores, and other relevant clinical metadata from 1,049 patients across four independent medical centers (n=522, 293, 154 and 80, respectively), with one used for model development and internal testing, and the remaining three for independent external evaluation. To develop LymRadar, a contrastive-learning-enhanced dual-stream 3D ResNet-18 with multi-scale feature fusion module and multi-modality contrastive learning module was used to extract prognostic representations from unannotated pre-treatment whole-body ^{18}F-FDG PET and the corresponding CT images. The deep imaging-derived prediction score was then integrated with the IPI using a logistic regression model to improve outcome prediction. Grad-CAM was applied to generate importance maps of the involvement sites based on LymRadar. ***Results:*** The multi-modality LymRadar model demonstrated robust and consistent performance in predicting primary treatment failure (PTF), achieving average area under the receiver operating characteristic curve (AUC) values ranging from 0.85 to 0.89 across four independent testinig cohorts. These results markedly outperformed models based on single modalities, including PET alone (AUC: 0.81-0.82), CT alone (AUC: 0.70-0.71), and the IPI score alone (AUC: 0.71-0.81). Beyond its predictive accuracy, LymRadar also exhibited strong prognostic relevance. When patients were stratified into high- and low-risk groups based on the model-derived risk probabilities, significant differences in both progression-free survival (PFS) and overall survival (OS) were observed across all cohorts (log-rank test, $P < 0.05$), highlighting the potential of LymRadar as a clinically actionable tool for individualized risk assessment in DLBCL. Additionally, the involvement sites importance mapping could prioritize lesions with higher malignancy and drug resistance with Precision-Recall AUC (PRAUC) of 0.92. ***Conclusion:*** These results demonstrate that the LymRadar model can accurately identify high-risk patients with primary treatment failure and provide involvement sites importance mapping for guiding clinicians in developing refined treatment strategies and biopsy site selection.

OP-464

Large-Scale Analysis of Melanoma Recurrence-Free Survival and Predictors Using AI-Driven Data Extraction from non-English Clinical Reports

C. Hinge*, C. N. Ladefoged, F. L. Andersen, K. Korsholm;*
Copenhagen University Hospital, Rigshospitalet, Copenhagen, DENMARK.

Aim/Introduction: Large-scale retrospective analysis of cancer outcomes, like melanoma recurrence, often requires manual analysis of free-text clinical reports, making such studies difficult at scale. Open-weight Large Language Models (LLMs), deployable offline, offer a potential data-private solution for automated analysis. However, their reliability on non-English nuclear medicine text, requires validation. This work performs the first ever such evaluation, and second, applies an LLM to extract structured data from PET/CT melanoma reports to enable a large-scale analysis of melanoma recurrence-free survival. ***Materials and Methods:*** Study 1 (PET/CT LLM Validation): Three open-weight LLMs (Llama3 70b, Gemma3 27b, Mistral 24b) were evaluated using 852 Danish PET/CT reports - each containing an indication, description, and conclusion section. For each report, the LLM was given the indication and description sections and asked to select the correct conclusion section among five presented options: the report's original conclusion, and four incorrect conclusions randomly sampled from other reports. Study 2 (Melanoma Recurrence Analysis): For each patient, Llama3 70b was given the content of all said patient's PET/CT reports and asked to identify key data (treatment/recurrence/follow-up dates and primary melanoma location). This was done for 1442 melanoma patients (N=4061 reports from Sept 2019 to Sept 2024). Recurrence-free survival (RFS) within 3 years was analyzed using Kaplan-Meier and Cox Proportional Hazards (Cox PH) models, assessing predictors (sex, age, location). ***Results:*** PET/CT LLM Validation: High conclusion classification accuracy was achieved: Llama 3 70b (96.2%), Mistral 24b (94.8%), Gemma 27b (94.7%). An error analysis of Llama 3 70b (32 mistakes total) revealed only 7 instances (0.8% of all cases) where the predicted conclusion was significantly different from the original conclusion. Melanoma Recurrence Analysis: The LLM identified 879 melanoma patients (61%) containing sufficient information for complete data extraction. A multivariable Cox PH analysis on the extracted survival data identified significant predictors of 3-year recurrence: increasing age (HR per year=1.026, $p<0.0005$) and primary melanoma location head/neck (HR=1.444, $p=0.003$). Male sex was significant univariably (HR=1.471) but not multivariably ($p=0.061$) after adjusting for age and location. ***Conclusion:*** Open-weight LLMs demonstrate good performance for complex clinical text analysis as shown by the clinically significant errors (<1%) on classifying Danish PET/CT reports. The subsequent application of the best LLM enabled scalable data extraction for a large retrospective melanoma study (N=879), which showed older age and primary melanoma location as significant 3-year recurrence risk factors. This LLM-driven methodology holds promise for efficient large retrospective analyses of PET/CT studies.

OP-465

Device-independent Artificial Intelligence Approach for Fast Bone Scintigraphy

V. Menezes[1]*, A. A. S. Oliveira*[1]*, A. J. S. Filho*[1]*, A. F. Morais*[1]*, M. E. Flamini*[1]*, F. A. Mourato*[1]*, T. I. Ren*[2]*, A. Vigário*[3]*, C. Queiroz*[4]*, M. Machado*[5]*;*
[1]Hospital das Clínicas da UFPE, Recife, BRAZIL, [2]Univerisade Federal de Pernambuco, Recife, BRAZIL, [3]ND Núcleo Diagnóstico Maringá, Maringá, BRAZIL, [4]Hospital Universitário Professor Alberto Antunes, Maceió, BRAZIL, [5]Hospital Universitário Professor Edgard Santos - HUPES, Salvador, BRAZIL.

Aim/Introduction: Whole-body bone scintigraphy is essential in oncology diagnostics but involves radiation exposure and long acquisition times. Deep learning (DL) approaches such as U-Net and diffusion-based models have demonstrated effectiveness in enhancing image quality under reduced-dose conditions. However, their clinical adoption is limited due to poor generalizability across different imaging systems. This study introduces a vendor-agnostic adaptive U-Net architecture enhanced with adaptive diffusion layers designed to significantly reduce acquisition time and radiation dose without compromising diagnostic quality. ***Materials and Methods:*** A total of 3,635 retrospective whole-body bone scintigraphy images from four scanner models across five hospitals were included. Images underwent Poisson and Monte Carlo subsampling to simulate reduced count levels (10%, 30%, 50%, 70%) and were normalized to [0,1]. The dataset was split into training (90%), validation (5%), and test (5%) sets. The proposed adaptive U-Net employed a trainable diffusion layer with depthwise convolutions optimized via Adam (learning rate=1×10^{-3}, batch size=1). Data augmentation and weighted sampling balanced the heterogeneous dataset. Image quality metrics included Structural Similarity Index (SSIM), Peak Signal-to-Noise Ratio (PSNR), and Learned Perceptual Image Patch Similarity (LPIPS). Clinical validation was conducted prospectively by three nuclear medicine physicians on 60 additional images using a five-point Likert scale. ***Results:*** The proposed adaptive

model significantly improved image quality compared to noisy counterparts at 50% count reduction: global mean PSNR (39.0 vs. 28.0 dB), SSIM (0.97 vs. 0.87), and LPIPS (0.04 vs. 0.07) (all p<0.01). Clinical assessments demonstrated that DL processing restored image quality (Likert score: 4.4 ± 0.7) comparable to standard acquisition (4.5 ± 0.5) and superior to accelerated acquisitions without DL (3.4 ± 0.7). No diagnostic misinterpretations occurred with DL-processed images. Vendor-agnostic generalizability was validated across different scanner models, including those absent from training data. ***Conclusion:*** An adaptive U-Net architecture with trainable diffusion layers effectively halves whole-body bone scintigraphy acquisition time while maintaining diagnostic image quality. Its vendor-agnostic nature facilitates widespread clinical deployment without scanner-specific retraining, significantly enhancing clinical workflow efficiency and patient comfort. ***References:*** Anand A., et al. J Nucl Med. 2016;57:41-45, Minarik, D., et al. J. Nucl. Med. 2020, 61, 298-303, Menezes, V.O., et al. Medical Physics, 2016, 43(2), 930-938.

OP-466

Automated PET/CT Report Generation Using Lesion-Aware Segmentation and a LoRA-Fine-Tuned Qwen Large Language Model

S. Xue[1], *K. Chen*[2], *Y. Jia*[1], *K. Wu*[3], *X. Hu*[4], *M. Hacker*[1], *Y. Cai*[5], *H. Yi*[2], *X. Li*[1];
[1]*Division of Nuclear Medicine, Department of Biomedical Imaging and Image-guided Therapy, Vienna General Hospital, Medical University of Vienna, Vienna, AUSTRIA,* [2]*Department of Nuclear Medicine, Zhejiang Cancer Hospital, Hangzhou Institute of Medicine (HIM), Chinese Academy of Sciences, Hangzhou, CHINA,* [3]*ByteDance, Beijing, CHINA,* [4]*Technical University of Munich, Munich, GERMANY,* [5]*Postgraduate training base Allianceof Wenzhou Medical University (ZheJiang Cancer Hospital), Wenzhou, CHINA.*

Aim/Introduction: Structured and clinically accurate PET/CT report generation remains a time-intensive task requiring expert integration of complex lesion characteristics and anatomical context. Manual reporting is often prone to inter-observer variability and delays, particularly in oncologic imaging with high lesion burden. While recent advances in artificial intelligence (AI) have enabled automated image analysis, the application of large language models (LLMs) to nuclear medicine reporting is still in its infancy. ***Materials and Methods:*** We developed a fully automated pipeline for PET/CT report generation that integrates deep learning-based lesion and organ segmentation with a Qwen LLM fine-tuned via Low-Rank Adaptation (LoRA). Co-registered PET/CT scans undergo lesion segmentation on PET and anatomical segmentation on CT using a previously validated nnUNet-based model. Quantitative imaging biomarkers—including SUVmax, metabolic tumor volume (MTV), total lesion glycolysis (TLG), and anatomical location—are extracted into structured lesion summaries. These summaries are embedded into a prompt template and passed to the fine-tuned Qwen LLM to generate comprehensive clinical reports. The pipeline was trained and evaluated on a multi-center dataset of 1,308 patients, including 905 with lymphoma and 403 with head and neck cancer, all with paired PET/CT scans and corresponding clinical reports. ***Results:*** The segmentation model achieved a Dice coefficient of 0.82 for PET-based lesions and 0.89 for CT-based organ structures. The generated reports reached a BLEU score of 0.79 and a ROUGE-L score of 0.87 when compared with reference reports. Clinical accuracy, as evaluated by board-certified nuclear medicine physicians, was 92.4%. Agreement between AI-generated and physician-authored reports showed a Cohen's kappa of 0.82, indicating substantial concordance. ***Conclusion:*** This study presents a robust and efficient framework for automated PET/CT report generation, leveraging lesion-aware image segmentation and a LoRA-fine-tuned large language model. The pipeline demonstrated good agreement with expert reports and has the potential to support standardized reporting, reduce interpretation time, and assist in managing larger imaging workloads in oncology settings.

OP-467

Q Amyloid: building an open-access platform for automated amyloid-beta quantification

F. Piva[1], *B. Marin*[1], *C. Da Villa*[1], *L. Maccioni*[1], *M. Moretto*[1,2], *L. Lorenzini*[3], *M. Veronese*[1];
[1]*Department of Information Engineering, University of Padova, Padova, ITALY,* [2]*Department of Neuroimaging, King's College London, London, UNITED KINGDOM,* [3]*Department of Radiology and Nuclear Medicine, Vrije Universiteit Amsterdam, Amsterdam UMC location VUmc, Amsterdam, NETHERLANDS.*

Aim/Introduction: The deposition of amyloid-beta (Aβ) plaques is one of the earliest neuropathological hallmarks of Alzheimer's disease (AD). Positron Emission Tomography (PET) is commonly adopted for in vivo Aβ detection. However, an accurate, efficient, and automated PET-based pipeline to detect brain Aβ accumulation is still missing. This project aims to develop Q Amyloid, an open-access platform for the automated quantification of brain Aβ burden. ***Materials and Methods:*** The Q Amyloid platform quantifies Aβ load using the Centiloid (CL) scale [1]. Structural Magnetic Resonance Imaging (T1-MRI) and PET data from the GAAIN website were adopted in the development of the algorithm. Specifically, PET scans of ^{11}C-PiB, ^{18}F-Florbetaben, ^{18}F-Florbetapir, and ^{18}F-Flutemetamol radiotracers were included to ensure compatibility of the platform with the most commonly used Aβ-PET radiotracers. MRI and PET scans preprocessing was included in the pipeline, following the standard method proposed by Klunk and colleagues [1]. Since poor co-registration quality can impact quantification accuracy, an automated quality control was incorporated to assess the co-registration outcome. Individual Standardised Uptake Value ratios (SUVr) were finally computed and converted to CL [1]. The pipeline was initially evaluated on the GAAIN dataset to replicate the results reported on the website. Then, it was applied and validated to unseen T1-MRI and Aβ-PET scans on impaired and unimpaired individuals pooled from different public and private datasets. ***Results:*** Validation of Q Amyloid pipeline using the standard ^{11}C-PiB dataset downloaded from GAAIN demonstrated that mean SUVr values were within 2% of the published SUVR data for both AD and young control (YC) ($^{PiB}SUVR_{QAmyloid}$: AD = 2.057 ± 0.193, YC = 1.018 ± 0.046; $^{PiB}SUVR_{GAAIN}$: AD = 2.076 ± 0.201, YC = 1.010 ± 0.046). Furthermore, the pipeline showed an excellent correlation with published Centiloid data ($CL_{QAmyloid} = 0.997 \times CL_{GAAIN} + 0.152$; $R^2 > 0.99$). ***Conclusion:*** Once operational, receiving subject-specific T1-MRI and PET scans as input, the platform will generate a report detailing the amyloidosis status. Q Amyloid will serve as a valuable tool in clinical trials, offering quantitative biomarkers to support early AD diagnosis and supporting the development of new Aβ-targeting therapies. This project is supported by the cascading grant "Q Amyloid - Quantitative Amyloid Imaging" under PNRR ECS00000017 "THE-Tuscany Health Ecosystem," Spoke 6: "Precision Medicine & Personalised Healthcare" funded by the NextGeneration EU programme. ***References:*** [1] Klunk, William E., et al. "The Centiloid Project: standardizing quantitative amyloid plaque estimation by PET." Alzheimer's & dementia (2015.)

OP-468

Improving the referral process to bone scintigraphy by multi-modal detection of at-risk populations for cardiac amyloidosis using machine learning

C. Spielvogel[1], *D. Kersting*[2], *D. Haberl*[1], *J. Yu*[1], *J. Hennenberg*[1], *K. Kluge*[1], *J. Ning*[1], *K. Kumpf*[1], *M. Koefler*[1], *F. Hofer*[1], *T. Traub-Weidinger*[1], *C. Hengstenberg*[1], *M. Hacker*[1], *R. Calabretta*[1], *C. Nitsche*[1];
[1]*Medical University of Vienna, Vienna, AUSTRIA,* [2]*University of Duisburg-Essen, Essen, GERMANY.*

Aim/Introduction: Cardiac amyloidosis (CA) is a progressive, underdiagnosed disease characterized by amyloid deposition in cardiac tissue. Early diagnosis is crucial, as novel disease-modifying therapies are most effective in the initial disease stages. However, overlapping symptoms with other cardiac conditions often delay diagnosis. While bone scintigraphy with bone-avid tracers is a reliable tool for confirming CA, timely identification of at-risk patients for referral remains challenging. We propose a multimodal machine learning (ML) approach that integrates clinical routine imaging and non-imaging parameters to support early identification of patients with suspected CA and guide referrals for confirmatory scintigraphy. ***Materials and Methods:*** We retrospectively analyzed all patients undergoing bone scintigraphy for any indication at the Vienna General Hospital between 2010 and 2023 (n = 11,616). Patients scanned before July 2020 were used for model training and cross-validation (n = 9,170) and those after for independent validation (n = 2,446). A total of 65 routinely available pre-scan parameters from electronic health records, including echocardiography, cardiac MRI (CMR), laboratory data, demographics, and comorbidities, were used as predictors. Missing values were retained to reflect real-world clinical settings. Model performance was assessed via 10-fold cross-validation and independent validation. Prognostic value was evaluated using Cox regression for heart failure-associated hospitalization and overall mortality. Additionally, we conducted a trait-wide association study (TWAS) to identify individual predictors of CA. ***Results:*** Of 11,616 patients, 279 (2.3%) showed CA-suggestive uptake. TWAS identified key markers associated with CA, including carpal tunnel syndrome, extracellular volume on CMR, interventricular septum thickness, left ventricular diameter, diastolic function, and blood urea nitrogen (all $p < 0.0001$). In independent validation, the ML model accurately detected high-grade CA (Perugini ≥2) with AUC 0.91, sensitivity 0.82, and specificity 0.84. For any uptake (Perugini ≥1), performance remained strong (AUC 0.89, sensitivity 0.85, specificity 0.71). Notably, the model identified 63% of high-uptake cases that were not suspected by cardiologists in clinical routine. Performance was consistent across subgroups, including patients with comorbidities that may mask CA (AUC > 0.84). All models were significantly associated with heart failure hospitalization and mortality (HR range 1.78-9.08, $p < 0.0001$). ***Conclusion:*** The developed approach reliably identifies patients at risk for CA and may be integrated into hospital information systems to prompt early referral for confirmatory diagnostics. By flagging overlooked cases, this tool has the potential to improve early diagnosis and patient outcomes. A user-friendly web app is available for immediate clinical use and validation.

1106

Monday, October 6, 2025, 16:45 - 18:15
Room 117

Clinical Oncology Track - TROP Session - Oncology & Theranostics Committee: Gastrointestinal Tumor Imaging

OP-469

Clinical Translation of ^{68}Ga-aGPC3-scFv ImmunoPET for Precision Diagnosis and Staging of Newly Diagnosed Hepatocellular Carcinoma

M. Li[1], *W. Hu*[1], *X. Zhang*[1], *X. Cai*[2], *D. Jiang*[1], *X. Lan*[1];
[1]*Department of Nuclear Medicine, Union Hospital, Tongji Medical College, Huazhong University of Science and Technology ; Hubei Key Laboratory of Molecular Imaging, Wuhan 430022, China, Wuhan, CHINA,* [2]*Department of Hepatobiliary Surgery, Union Hospital, Tongji Medical College, Huazhong University of Science and Technology, Wuhan, CHINA.*

Aim/Introduction: Hepatocellular carcinoma (HCC) is one of the leading causes of cancer-related death worldwide. Glypican-3 (GPC3) is a cell surface receptor overexpressed in most HCCs but not by normal or cirrhotic liver tissue, thus providing a unique target for molecular diagnostics. Herein, we have developed a GPC3-specific radiotracer, ^{68}Ga-aGPC3-scFv, and present a prospective, investigator-initiated trial to explore the clinical value of ^{68}Ga-aGPC3-scFv PET/MRI in treatment-naïve patients with hepatic lesions, comparing to conventional imaging methods . ***Materials and Methods:*** ^{68}Ga-aGPC3-scFv was synthesized by radiolabeling NOTA-conjugated scFv with ^{68}Ga (radiolabeling yield >85%, purity >99%). In this translational study, 36 patients with known or suspected HCC who underwent ^{68}Ga-aGPC3-scFv PET/MRI were enrolled prospectively. Among them, 35 patients underwent paired ^{68}Ga-aGPC3-scFv and contrast-enhanced-MRI (CE-MRI). Histopathologic examination and ≥6-month clinical-imaging follow-up served as the reference standard. Two blinded nuclear medicine physicians assessed images to determine lesion detection rates and Barcelona Clinic Liver Cancer (BCLC) staging. Diagnostic performance metrics (sensitivity, specificity, accuracy) and BCLC staging accuracy were assessed against gold standard. ***Results:*** In this study, with a mean age of 62 years (range, 35-77 years), 30 were male and 6 were female. All participants tolerated ^{68}Ga-aGPC3-scFv well, with no adverse events reported during injection or the 4-hour follow-up period. ^{68}Ga-aGPC3-scFv demonstrated favorable pharmacokinetics with rapid blood clearance (blood pool SUVmean decreased by 55% from 0.5 h to 2.5 h). The probe successfully detected HCC lesions and provided high imaging contrast. The tumor-to-liver ratio (TLR) demonstrated high and progressively increasing contrast at dual time points, with median values of 6.48 (range: 1.69-25.78) and 10.09 (range: 2.20-39.85), respectively. Diagnoses were confirmed via pathology (from biopsy or surgery samples) in 32 patients and via imaging and/or clinical follow-up in the remaining 4 patients. ^{68}Ga-aGPC3-scFv PET/MRI demonstrated superior diagnostic performance for detecting primary tumors over enhanced-MRI, sensitivity (90.63% [28/31] vs. 86.67% [26/30]), specificity (>99.99% [5/5] vs. 20% [1/5]) and accuracy (91.67% [33/36] vs. 77.14% [27/35]). Notably, 68Ga-aGPC3-scFv achieved 100% concordance (36/36) with gold-standard BCLC staging and rectifying CE-MRI overstaging in 6 cases (16.7%). ***Conclusion:*** ^{68}Ga-aGPC3-scFv immunoPET enables high-contrast, precise HCC diagnosis and BCLC staging, surpassing conventional modalities. Its exceptional specificity and ability to refine clinical staging highlight its potential to optimize therapeutic decision-making in newly diagnosed HCC patients.

OP-470

[68Ga]Ga-FAPI-46 PET/CT Enhances Preoperative Assessment of Peritoneal Metastases - Updated Interim Analysis of prospective FAPeCa trial

A. Arçay Öztürk, *G. Liberale, L. Polastro, A. Veron Sanchez, A. Deleu, P. Kristanto, Z. Wimana, L. Taraji, P. Flamen;*
Institut Jules Bordet, Hôpital Universitaire de Bruxelles (H.U.B), Université Libre de Bruxelles (UL), Brussels, BELGIUM.

Aim/Introduction: Standard imaging modalities; CT, MRI, and FDG PET/CT face challenges in accurate preoperative staging of peritoneal metastases (PM) and often underestimate PM extent, leading to unexpected non-resectable disease during surgery. Preliminary reports suggest [68Ga]Ga-FAPI PET/CT, targeting fibroblast activation protein, may offer superior sensitivity for PM detection. This study evaluates [68Ga]Ga-FAPI-46 PET/CT as a preoperative imaging tool for peritoneal carcinomatosis by correlating [68Ga]Ga-FAPI-46 PET/CT findings with surgerical outcomes and standard imaging modalities in colorectal and ovarian cancer. ***Materials and Methods:*** In this ongoing prospective study (NCT06061874), eligible patients with confirmed/suspected PM undergo [68Ga]Ga-FAPI-46 PET/CT, [18F]FDG PET/CT, and abdominopelvic MRI within four weeks before scheduled cytoreductive surgery (CRS) and/or diagnostic laparoscopy (DL). Patients receiving neoadjuvant chemotherapy (NAC) are scanned pre- and post-NAC. Target enrollment is 80 patients. The extent of PM was determined by the peritoneal cancer index (PCI) scoring system. Intraclass correlation coefficient (ICC) was used to assess the concordance between the PCI determined based on [68Ga]Ga-FAPI-46 PET/CT (FAPI-PCI), [18F]FDG PET/CT (FDG-PCI), MRI (MRI-PCI) and the PCI found during surgery (S-PCI). ***Results:*** Fourty-one patients (30 ovarian, 11 colorectal cancer; mean age 61.7) were analyzed. The mean PCI score at surgery (n=48; 38 based on CRS, 10 based on DL) was 15.6±9.4. The mean FAPI-PCI score (n=48, 13.4±9) was significantly higher than the mean MRI-PCI (n=45, 9±7.3, p<0.001) and FDG-PCI (n=46, 7.2±8.8, p<0.001). FAPI-PCI correlated very well with surgical PCI (ICC 0.83, 95% CI: 0.68-0.91). ICC between S-PCI and FAPI-PCI was substantially higher than that between S-PCI and MRI-PCI (ICC 0.49, 95% CI: 0.02-0.75) and S-PCI and FDG-PCI (ICC 0.41, 95% CI: -0.03-0.69). Using PCI≤20 as the resectability threshold, ROC analysis (area under the curve, AUC) showed excellent accuracy with FAPI PET (AUC:0.92), outperforming MRI (0.81) and FDG PET (0.74) in predicting operability. Quantitative parameters, SUVmax (maximum standardized uptake value), TBR (target-to-background ratio) and PTV (total peritoneal tumour volumes) of [68Ga]Ga-FAPI-46 PET/CT for the PM lesions were significantly higher than those of [18F]FDG PET/CT (mean SUVmax: 11.5±6.7 vs. 7.4±8,p<0.001; mean TBR: 9±5.7 vs. 3.7±4.1,p<0.001; mean PTV: 129.1±271.4 ml vs. 80.5±248.3 ml,p<0.001, Wilcoxon signed-rank test). ***Conclusion:*** This expanded interim analysis validates the utility of [68Ga]Ga-FAPI-46 PET/CT in the preoperative PM assessment. It correlates very well with surgical findings, outperforming standard imaging modalities MRI and [18F]FDG PET/CT. Combined with its superior accuracy in predicting resectability, these findings establish FAPI PET/CT as a highly promising preoperative imaging modality for peritoneal carcinomatosis.

OP-471

The Analysis of Biodistribution and Tumor Uptake of [18F] AlF-FAPI-74 in Patients with Soft Tissue Sarcoma and Gastro-Intestinal Tumors compared with [18F]FDG in a prospective, exploratory study

E. Novruzov[1], *F. L. Giesel*[1], *E. Mamlins*[1], *T. Watabe*[2], *J. Cardinale*[1], *Y. Mori*[1], *N. Schupps*[1], *C. Pinto*[3], *C. Soza-Ried*[4], *R. Fernandez*[5], *H. Amaral*[4], *V. Kramer*[4], *L. Badinez*[6];
[1]*University Hospital Düsseldorf, Düsseldorf, GERMANY,* [2]*Institute for Radiation Sciences, Osaka, JAPAN,* [3]*Departamento Anatomia Patologica, Hospital Sotero del Rio, Santiego, CHILE,* [4]*Center for Nuclear Medicine and PET/CT Positronmed, Santiago, CHILE,* [5]*Center for Nuclear Medicine and PET/CT Positronmed, Santiago, CHILE,* [6]*Instituto Radiooncológico Santiago INRAD, Santiago, CHILE.*

Aim/Introduction: The roll-out of FAP imaging with small-molecule PET tracers marks one of the major breakthroughs in nuclear medicine. The majority of current evidence, however, has been generated by 68Ga-labelled FAPI tracers, a reliance that presents serious economical and logistic challenges to the oncological community. [18F]AlF-FAPI-74, a recently introduced radiotracer, emerges as a promising candidate to overcome those limitations of 68Ga-labelling. This single-center, prospective, head-to-head analysis aimed to investigate the biodistribution and tumor uptake pattern of [18F]AlF-FAPI-74 in comparison to [18F] FDG imaging in patients with sarcoma and GI-tumors. ***Materials and Methods:*** A total of 19 patients (15 males and 4 females) were enrolled in this prospective study with a head-to-head analysis of [18F]AlF-FAPI-74 and [18F]FDG PET/CT imaging between May 2021 and January 2024. The mean injected activity for [18F] AlF-FAPI-74 and [18F]FDG PET/CT was 239 MBq (± 57) and 209 MBq (± 74) and the mean uptake time was 72 min (± 10) and 73 min (± 17), respectively. All patients had histologically proven malignancies of pancreatic adenocarcinoma (PDAC) in 8 patients, soft tissue sarcoma (STS) in 6 patients, colorectal carcinoma (CRC) in 4 patients and gastric carcinoma in 1 patient. The indications for the conduct of PET/CT scans were completion of primary staging, re-staging in suspected recurrency or therapy response monitoring. ***Results:*** [18F]AlF-FAPI-74 demonstrated superior lesion detectability compared to [18F]FDG, identifying a greater number of both primary and metastatic lesions for tumor entities in total, but also for GI-tumors separately. The detection rate of primary lesions in patients with STS was comparable for both tracers, albeit [18F]AlF-FAPI-74 imaging outperformed [18F]FDG regarding metastatic lesions. Our SUV-metrics analysis revealed more favorable results for the detection of primary lesions with [18F]FAPI-74 imaging (e.g. SUV_{max} ± SD, 6.41 ± 2.8 vs. 9.79 ± 4.2), whereas only the TBR in relation to blood pool appeared to be statistically significant (3.15 vs. 5.08; p: 0,03). We observed a similar tendency in the analysis of SUV-metrics (e.g. SUV_{max} ± SD, 6.18 ± 2.7 vs. 7.42 ± 2.8) in metastatic lesions as well. ***Conclusion:*** Our study confirms that [18F]AlF-FAPI-74 outperformed [18F]FDG, particularly in the detection of metastatic lesions. Therefore, we consider [18F]AlF-FAPI-74 currently to be one of the most promising FAPI candidates for widespread use. Given the advantages of 18F-labelled FAPIs, future research should focus on designing prospective trials with larger cohorts to determine its diagnostic potential and clinical impact.

OP-472

Role of 68Ga-FAPI-46 PET/CT in the evaluation gastrointestinal tract tumors: comparison with 18F-FDG PET/CT

M. Komarova[1], *A. Pronin*[1], *V. Sinitsyn*[2], *E. Davydova*[1], *A. Martinovich*[1], *I. Nazarenko*[1], *V. Solomyany*[1];
[1]*N.N. Blokhin National Medical Research Center of Oncology, Moscow, RUSSIAN FEDERATION,* [2]*Lomonosov Moscow State University, Moscow, RUSSIAN FEDERATION.*

Aim/Introduction: the purpose of the study was to evaluate the role of 68Ga-FAPI-46 PET/CT for staging and restaging of gastrointestinal tract tumors and to compare the results with 18F-FDG PET/CT. ***Materials and Methods:*** The study included 52 patients diagnosed with esophageal (10 patients), gastric (39 patients) and colorectal (3 patients) cancers who underwent 68Ga-FAPI and 18F-FDG PET/CT. The time interval between the performed studies was limited to 3-7 days. The tracer uptakes, quantified by maximum standardized uptake value (SUVmax) and target-to-background ratio (TBR) were compared for paired positive lesions between both modalities using Mann-Whitney test. The diagnostic accuracy (sensitivity (Se), specificity (Sp), and accuracy (Ac)) of the 68Ga-FAPI compared with 18F-FDG PET/CT within each clinical case and in the diagnosis of each tumor

lesions were also calculated. ***Results:*** Based on visual assessment, 68Ga-FAPI detected more metastatic lesions than ^{18}F-FDG PET/CT, especially in lymph nodes and peritoneum involvement (total 167 vs 78, respectively). There were no significant differences between SUVmax values in local tumor and metastatic lymph nodes in 68Ga-FAPI and ^{18}F-FDG PET/CT (p>0.05). However, SUVmax in metastases to other organs (mainly peritoneum) and TBR values in primary tumor, positive lymph nodes and metastases to other organs were significantly higher in 68Ga-FAPI-46 PET/CT than in ^{18}F-FDG PET/CT (p<0,05). In patients with histologically proven signet ring cell carcinoma and mucinous tumor, SUVmax and TBR values were significantly higher with 68Ga-FAPI than with ^{18}F-FDG PET/CT (p<0.001). Diagnostic accuracy was higher with 68Ga-FAPI than ^{18}F-FDG PET/CT on a per-patient basis (Se, Sp and Ac were 97.73%, 87.5% and 96.15% vs. 86.05%, 83.33% and 85.71%, respectively) and per-region basis (Se, Sp and Ac were 93.55%, 92.16% and 93.06% vs. 62.35%, 77.97% and 68.75%, respectively). ***Conclusion:*** 68Ga-FAPI PET-CT is a very promising tool for evaluation of patients with gastrointestinal tract tumors, more accurate than ^{18}F-FDG PET-CT and could be recommended as a method of choice for staging and restaging in order to plan the most appropriate therapy.

OP-473

Diagnostic accuracy of 68Ga-FAPI-46 PET/CT vs.^{18}F-FDG PET/CT in patients with liver tumors

M. Komarova[1], *A. Pronin*[1], *A. Martinovich*[1], *O. Ryzhova*[1], *V. Solomyany*[1], *I. Amosova*[1], *V. Sinitsyn*[2];
[1]*N.N. Blokhin National Medical Research Center of Oncology, Moscow, RUSSIAN FEDERATION,* [2]*Lomonosov Moscow State University, Moscow, RUSSIAN FEDERATION.*

Aim/Introduction: To compare the diagnostic accuracy of 68Ga-FAPI-46 PET/CT and ^{18}F-FDG PET/CT in patients with liver tumor. ***Materials and Methods:*** 15 patients (mean age 57,5 y.o, 7male/8 female) diagnosed with liver cancer who underwent 68Ga-FAPI and ^{18}F-FDG PET/CT between 7 days were included in the study. 4 patients (pts) were examined to detect progression of the underlying disease (had the previous treatment). The all liver lesions had morphological verification (11 pts had cholangiocarcinoma G1-3, 2 pts. - hepatocellular carcinoma, 1-intraductal papillary tumor of the bile duct and 1 pts - calcifying nested stromal-epithelial tumor). Uptake intensity (SUVmax) and target-to-background ratio (TBR) of the primary liver tumor and lymph nodes metastasis were compared between two imaging modalities. Sensitivity (Se), specificity (Sp), positive predictive value (PPV), negative predictive value (NPV) and accuracy (Ac) were calculated for each modality on a per-region basis. ***Results:*** 14 pts were found primary tumor and 3 pts of them had metastases in regional lymph nodes or lung. There was a better contrast with 68Ga-FAPI, with SUVmax of the liver tumors of 14,9 [8,94-23,48] compared with SUVmax of 7,81 [3,55-10,21] of the liver tumors with ^{18}F-FDG (p=0,02). The TBR of primary tumor were higher in 68Ga-FAPI compared with ^{18}F-FDG - 10,56[4,15-16,46] vs. 2,5[1,17-3,67] respectively, p=0,0014. For detection of primary liver tumor and metastasis on region based level Se, Sp, PPV, NPV and Ac of Ga-68 FAPI PET/CT were higher than F18-FDG PET/CT (97,3%, 71,43 %, 90,00%, 90,91% and 90,20% vs. 78,38%, 57,14%, 82,86%,50,00% and 72,55 %, respectively). ***Conclusion:*** 68Ga-FAPI PET-CT is a very promising tool for evaluation of patients with liver tumor because more accurate than ^{18}F-FDG PET-CT. The high level of FAPI uptake in the primary hepatic lesions is indicate the potential of FAP-targeted radionuclide therapy.

OP-474

Dynamic [68Ga]Ga-FAPI-46 LAFOV PET/CT in pancreatic cancer- preliminary results

M. Krarup[1], *R. Aleksyniene*[1], *C. P. Hansen*[2], *J. Madsen*[1], *F. L. Andersen*[1], *K. Korsholm*[1], *J. M. Hall*[1], *I. Chen*[3], *B. M. Fischer*[4], *A. Loft*[1];
[1]*Department of Clinical Physiology and Nuclear Medicine, Copenhagen University Hospital, Rigshospitalet, Copenhagen, DENMARK,* [2]*Department of Surgery, Copenhagen University Hospital, Rigshospitalet, Copenhagen, DENMARK,* [3]*Department of Oncology, Herlev Hospital, Herlev, DENMARK,* [4]*Copenhagen University Hospital, Rigshospitalet, Copenhagen, DENMARK.*

Aim/Introduction: [^{68}Ga]Ga-FAPI-46 long axial field of view (LAFOV) PET/CT has the potential to improve diagnostic imaging for pancreatic cancer patients. The ongoing clinical trial "BEFAST-study" investigates the diagnostic sensitivity of [^{68}Ga]Ga-FAPI-46 LAFOV PET/CT for preoperative staging in pancreatic cancer (CTIS: 2023-503632-41-01). This report presents a preliminary analysis of 10 dynamic [^{68}Ga]Ga-FAPI-46 LAFOV PET/CTs, exploring changes in tracer-uptake over time in both primary tumor and surrounding tissues. ***Materials and Methods:*** Patients referred for curative surgery with pathologically verified or suspected pancreatic cancer were prospectively included in the study. The participants underwent a 65 min dynamic [^{68}Ga]Ga-FAPI-46 PET/CT on a LAFOV scanner prior to surgery. A low-dose CT (ref mAs 7.0) was used for attenuation correction. Patients received an injection of 1.5-2.0 MBq/kg of [^{68}Ga]Ga-FAPI-46. Static images were reconstructed with 5 min duration at 5,10,15,20,25 and 60 minutes(min) after scan initiation. A volume of interest (VOI) was drawn with visual adaption in the primary tumor using a threshold of 40% of the SUV_{max}. SUV_{max} and SUV_{mean} were obtained from the tumor VOI. VOIs (diameter 3cm) were placed in healthy liver and muscle tissue to assess background SUV_{mean}. Tumor-to-background ratio (TBR) was calculated by dividing the primary tumor SUV_{max} by the liver tissue SUV_{mean}. Friedmans test and the Wilcoxon signed-rank test were used to evaluate changes in SUV and TBR across the timepoints. ***Results:*** Ten patients were included in this preliminary analysis. Postsurgical pathology confirmed pancreatic ductal adenocarcinoma in 8 patients, intraductal papillary mucious neoplasia (IPNM) in 1 patient and non-specified adenocarcinoma in 1 patient. Tumor SUV_{max} and SUV_{mean} peaked between 15-20min and were lowest after 60min. No significant differences were observed in tumor SUV_{mean} or SUV_{max} across the timepoints. The patient with IPNM exhibited the lowest tumor SUV-values. Significant differences were observed in liver SUV_{mean}, muscle SUV_{mean} and TBR across the time-points. Liver SUV_{mean} was significantly higher in early timepoints (5-15min), whereas muscle SUV_{mean} peaked between 15-30min compared to other timepoints. TBR was significantly lower from 5-10min compared to later time points. Highest mean TBR-values were observed after 25-30min. ***Conclusion:*** This preliminary analysis showed no significant changes in tumor SUV across the timepoints, and the highest mean TBR at 25-30min, supporting [^{68}Ga]Ga-FAPI-46 PET/CT acquisitioning at earlier timepoints. Lowest tumor SUV-values were observed in the IPMN-case, which aligns with previous findings, suggesting potential for discriminating malignant and benign pancreatic lesions with [^{68}Ga]Ga-FAPI-46 LAFOV PET/CT.

OP-476

The Role of [^{68}Ga]Ga-FAPi PET/CT in Evaluating Treatment Response in Gastrointestinal System Malignancies

G. Beydagi[1], *K. Akcay*[1], *A. Gormez*[2], *L. Kabasakal*[1], *N. Alan-Selcuk*[1];
[1]*Yeditepe University, Department of Nuclear Medicine, Istanbul, TÜRKIYE,* [2]*Yeditepe University, Department of Radiology, Istanbul, TÜRKIYE.*

Aim/Introduction: This study aims to investigate the potential efficacy of [^{68}Ga]Ga-FAPi PET/CT in evaluating treatment response in gastrointestinal system malignancies. ***Materials and Methods:***

Patients with histopathologically confirmed gastrointestinal malignancies who were prospectively enrolled for treatment response assessment between November 2020 and January 2025 were included in the study. All imaging studies were interpreted by consensus among three experienced nuclear medicine specialists. The maximum standardized uptake values (SUVmax), total tumor volumes, and total lesion FAP expression values were recorded. Patients' serum tumor marker levels (such as carcinoembryonic antigen [CEA] and CA 19-9) were also recorded. Imaging-based treatment responses were separately evaluated according to PERCIST criteria on [^{68}Ga]Ga-FAPi PET/CT and RECIST criteria on CT scans. ***Results:*** A total of 100 [^{68}Ga]Ga-FAPi PET/CT scans were performed in 50 patients (mean age: 61.62 ± 12.95) who were referred for treatment response assessment, including both pre- and post-treatment imaging. Among the patients included in the study, 70% were diagnosed with gastric cancer, 14% with colorectal cancer, 8% with pancreatic cancer, 4% with appendiceal cancer, 2% with hepatocellular carcinoma (HCC), and 2% with cholangiocellular carcinoma. Primary tumor lesions were present in 62% of patients, lymph node metastases in 24%, visceral metastases in 10%, peritoneal metastases in 76%, and bone metastases in 14%. A strong correlation was observed between tumor volumes measured by [^{68}Ga]Ga-FAPi PET/CT and serum tumor markers. The area under the curve (AUC) for ΔTumor Volume was 0.875. A statistically significant and near-perfect agreement was observed between [^{68}Ga]Ga-FAPi PERCIST and CT-based RECIST criteria (Kappa = 0.833, $p < 0.05$). Moderate agreement was observed in primary tumor sites (Kappa = 0.526, $p < 0.05$) and bone metastases (Kappa = 0.657, $p < 0.05$), while near-perfect agreement was noted in lymph node metastases (Kappa = 1, $p < 0.05$), peritoneal metastases (Kappa = 0.815, $p < 0.05$), and visceral metastases (Kappa = 1, $p < 0.05$). According to Kaplan-Meier analysis, treatment responses assessed by [^{68}Ga]Ga-FAPi PET/CT were predictive of overall survival ($p = 0.02$). According to PERCIST criteria on [^{68}Ga]Ga-FAPi PET/CT images, median overall survival was 7.6 months in patients with progressive disease and 19.8 months in those with stable disease, while the median overall survival was not reached in patients with partial or complete response. ***Conclusion:*** Our findings suggest that [^{68}Ga]Ga-FAPi PET/CT may be an effective alternative for treatment monitoring and follow-up in gastrointestinal malignancies, especially in tumors with low FDG avidity.

OP-477

A Clinical-Radiomics Integrated Model Based on Baseline ^{18}F-FDG PET/CT Predicts Survival Outcomes in Hepatocellular Carcinoma Patients Receiving PD-1 Inhibitor Combined with Lenvatinib as Preoperative Conversion Therapy

J. Zhang[1], *G. Wang*[2], *J. Cui*[1], *C. Li*[1], *Y. Han*[1], *Y. Pan*[1], *B. Xu*[1];
[1]*Department of Nuclear Medicine, The First Medical Center of Chinese PLA General Hospital, Beijing, CHINA,* [2]*Nuclear Medicine Department, Beijing Friendship Hospital, Affiliated to Capital Medical University, Beijing, CHINA.*

Aim/Introduction: Preoperative conversion therapy strategies, such as Lenvatinib combined with programmed cell death protein 1 (PD-1) inhibitors, significantly improve surgical resectability in hepatocellular carcinoma (HCC). However, heterogeneous patient outcomes limit clinical benefits. This study aims to construct a combined predictive model integrating baseline ^{18}F-FDG PET/CT radiomics features and clinical parameters to precisely evaluate overall survival (OS) and progression-free survival (PFS), providing imaging-based biological evidence for personalized therapeutic decision-making. ***Materials and Methods:*** We retrospectively enrolled 90 HCC patients treated with Lenvatinib plus PD-1 inhibitors as preoperative conversion therapy. Baseline ^{18}F-FDG PET/CT images and clinical data were collected. LifeX software was used to delineate tumor regions of interest (ROIs) at an 80% SUVmax threshold, extracting radiomics features including morphological, textural, and metabolic heterogeneity. Minimum redundancy and maximum relevance (mRMR) and LASSO regression were applied for feature selection. A multivariate Cox proportional hazards model combining radiomics signatures and clinical variables was developed. ***Results:*** The clinical-radiomics integrated model demonstrated superior performance in both OS and PFS prediction. For OS, the model incorporated radiomics features, albumin (ALB), major pathological response (MPR), and radiotherapy, achieving C-indices of 0.905 (95% CI: 0.866-0.943) in training and 0.814 (95% CI: 0.713-0.915) in validation cohorts, with significant improvement over clinical-only models. High-risk patients showed markedly reduced median OS (training HR=14.141, 95% CI: 3.464-57.732; validation HR=3.969, 95% CI: 0.846-18.626). For PFS, the model integrated radiomics features with surgery, transarterial chemoembolization (TACE), and radiotherapy, yielding C-indices of 0.842 (95% CI: 0.774-0.910) and 0.857 (95% CI: 0.800-0.914) in training and validation cohorts, respectively. Stable HRs (training HR=8.385, 95% CI: 1.691-41.570; validation HR=6.796, 95% CI: 1.741-26.525) confirmed robust generalizability for short-term prognosis. ***Conclusion:*** This clinical-radiomics integrated model, by quantifying tumor metabolic heterogeneity, enables noninvasive prediction of OS and PFS in HCC patients undergoing PD-1 inhibitor plus Lenvatinib conversion therapy. It provides a critical tool for risk stratification and personalized preoperative treatment optimization. Multicenter prospective studies are warranted to validate its clinical translation and elucidate underlying biological mechanisms.

1107

Monday, October 6, 2025, 16:45 - 18:15
Room 212

TROP Session - Thyroid Committee: The Pivotal Role of Nuclear Medicine Imaging to Localise Parathyroid Lesion

OP-478

Evaluation of the Performance of [^{18}F]fluorocholine PET/CT for the Preoperative Localization of Parathyroid Adenoma in Patients with Primary Hyperparathyroidism and Negative [^{99m}Tc]Tc-MIBI SPECT/CT: Our experience

E. Pérez de los Ríos*, O. Ajuria Illarramendi, A. Martínez Lorca, T. Navarro Martínez, P. Azpeitia Hernández, M. Gutiérrez Guerrero, U. Vera Schmülling, I. Hernández Pérez, P. Paredes Rodríguez, M. Ottino, M. Orduña Díez;*
Hospital Universitario Ramón y Cajal, Madrid, SPAIN.

Aim/Introduction: To determine the utility of [^{18}F]fluorocholine PET/CT for the preoperative localization of parathyroid adenoma in patients with primary hyperparathyroidism and negative [^{99m}Tc]Tc-MIBI SPECT/CT, and to evaluate the diagnostic performance of this test at our center. ***Materials and Methods:*** A retrospective and descriptive study including patients with primary hyperparathyroidism (PHPT) meeting surgical criteria, who underwent an [^{18}F]fluorocholine PET/CT study between 2020 and 2024 at our center for preoperative localization of parathyroid adenoma. Data collected: age, sex, parathyroid hormone (PTH) levels, [^{99m}Tc]Tc-MIBI SPECT/CT, surgical intervention, and pathology results for operated cases. Exclusion criteria: positive [^{99m}Tc]Tc-MIBI SPECT/CT, and patients who previously underwent parathyroid surgery. The gold standard was the pathological analysis of the lesion. ***Results:*** A total of 139 patients were included (mean age 61.75 years; 67.6% female). Mean PTH levels were 119.33 ng/mL in women and 118.25 ng/mL in men. [^{18}F] fluorocholine PET/CT detected 78 positive and 61 negative cases.

Surgery was performed in 41% of the PHPT patients (57/139). 64% (50/78) with positive [^{18}F]fluorocholine PET/CT results, and 11.47% (7/61) with negative [^{18}F]fluorocholine PET/CT results underwent surgery. Of the positive [^{18}F]fluorocholine PET/CT cases, 35% (28/78) are pending surgery or declined surgery, and 11.47% (7/61) of the negative [^{18}F]fluorocholine PET/CT cases underwent surgery due to elevated PTH levels and suspicion of other pathologies. Pathological analysis confirmed parathyroid adenoma in 92% (46/50) of the operated patients with positive [^{18}F] fluorocholine PET/CT, 4 false positives (FP). 0% (0/7) of operated patients with negative [^{18}F]fluorocholine PET/CT, 7 true negatives (TN). The results yielded a sensitivity (Se) of 100%, a specificity (Sp) of 63%, a positive predictive value (PPV) of 90%, and a negative predictive value (NPV) of 100%. ***Conclusion:*** [^{18}F]fluorocholine PET/CT is a highly useful technique for the localization of parathyroid adenomas, which facilitates surgical intervention due to its excellent diagnostic performance.

OP-479

Development of a set of predictors for a machine learning model that will be able to predict ^{18}F-fluorocholine PET/CT findings in patients with primary hyperparathyroidism based on a medical record

N. Pantic[1], *B. Radovic*[1,2], *L. Grujicic*[1], *M. Kotur*[1], *K. Petrovic*[1], *J. Malicevic Crevar*[1], *J. Zivanovic*[1], *A. Novkovic*[1], *O. Radivojevic*[1], *A. Ivanovski*[1], *A. Jovanovic*[1], *M. Veljkovic*[1,3], *I. Grozdic Milojevic*[1,3], *D. Sobic Saranovic*[1,3], *V. Artiko*[1,3], *S. Odalovic*[1,3];
[1]*Center for Nuclear Medicine with PET, University Clinical Center of Serbia, Belgrade, SERBIA,* [2]*Faculty of Medicine, University of Pristina with temporary headquarters in Kosovska Mitrovica, Kosovska Mitrovica, SERBIA,* [3]*Faculty of Medicine, University of Belgrade, Belgrade, SERBIA.*

Aim/Introduction: Partial-body [^{18}F]fluorocholine (FCH) positron emission tomography and computed tomography (PET/CT) might substitute cervical ultrasonography and [^{99m}Tc]Tc-methoxy isobutyl isonitrile (MIBI) single-photon emission computed tomography and computed tomography (SPECT/CT) in the evaluation of patients with primary hyperparathyroidism, such that imaging can be developed into an FCH PET/CT-based one-stop-shop localization strategy. In line with this, a recent meta-analysis demonstrated the superior performance of FCH PET/CT in both patient-based and lesion-based analyses. However, FCH PET/CT is currently more expensive than MIBI SPECT/CT (1). We are conducting a prospective study of patients with primary hyperparathyroidism, with the goal of detecting potential predictors of FCH PET/CT positivity. ***Materials and Methods:*** A three-dimensional PET scan and a low-dose non-enhanced CT scan were acquired from the cranial base to the apex of the heart 45 minutes after the injection of 192.57+/-40.89 MBq of FCH. After the exclusion of the patients with inconclusive FCH PET/CT findings, a total of 86 patients were enrolled in the study. ***Results:*** The difference between the total calcium blood level median of patients who are positive on FCH PET/CT examination (2.35-4.05 mmol/l; median 2.75 mmol/l) and the total calcium blood level median of patients who are negative on FCH PET/CT examination (2.19-3.25 mmol/l; median 2.53 mmol/l) is statistically significant (p=0.028), with the specificity of 82% and sensitivity of 57% for the cut-off value of 2.63 mmol/l. Meanwhile, the difference between means, medians, and proportions for PTH, vitamin D, ionized calcium, and phosphate blood levels, as well as history of nephro- or urolithiasis and pathologic fractures, is not statistically significant (p>0.05). ***Conclusion:*** Serum total calcium concentration is the only variable among laboratory and clinical parameters that has shown a correlation with FCH PET/CT findings so far. The goal is to reach a high enough number of patients so that a machine learning model that will be able to predict FCH PET/CT findings before the examination itself can be formulated and so that only those in need of the procedure go through one. In that case, the method will be utilized only for a localization of the overactive parathyroid gland, and costs will drastically reduce since the selection of patients will be the most accurate possible. ***References:*** 1. van Mossel S, Saing S, Appelman-Dijkstra N, Quak E, Schepers A, et al. Cost-effectiveness of one-stop-shop [18F] Fluorocholine PET/CT to localise parathyroid adenomas in patients suffering from primary hyperparathyroidism. Eur J Nucl Med Mol Imaging. 2024 Oct;51(12):3585-3595.

OP-480

Protocol Optimization in 3T PET/MRI for Primary Hyperparathyroidism: Comparative Analysis of MRI Sequences and [18F]Fluorocholine Uptake.

V. Carrero-Vásquez, *A. Villamayor Hernández, J. Díaz-Moreno, M. Cortés Romera, B. Hervás-Sanz, M. Zamorano-Rivas, A. Bagan-Trejo, C. Martínez-Ramos, M. Pudis, I. Sanchez-Rodriguez;*
Nuclear Medicine, Bellvitge University Hospital, Barcelona, SPAIN.

Aim/Introduction: [18F]Fluorocholine PET/MRI has emerged as a promising second-line tool for localizing hyperfunctioning parathyroid glands in primary hyperparathyroidism (PHPT), especially in cases with inconclusive conventional imaging. However, the need for multiple MRI sequences in this setting is debated. This study aims to determine the minimal MRI sequence set required without compromising diagnostic accuracy, analyze adenoma signal characteristics, explore the relationship between MRI signal intensity and PET uptake (SUVmax), and assess PET/MRI concordance. ***Materials and Methods:*** We retrospectively included 47 patients with PHPT and negative or inconclusive ultrasound and/or 99mTc-sestamibi SPECT/CT. All underwent 3T [18F]fluorocholine PET/MRI, including axial T1-Dixon, T2-TSE, and coronal T2-STIR sequences. Lesions were evaluated for signal intensity (hypo-, iso-, or hyperintense) and detection in each MRI sequence. PET uptake was measured using SUVmax. Diagnostic performance was assessed descriptively. Kruskal-Wallis tests were used to analyze the association between signal intensity and SUVmax. Histopathological confirmation was available in 12 patients. ***Results:*** All 47 patients had PET-positive lesions, with 100% concordance with MRI detection in at least one sequence. Detection rates were 82.6% for T1, 87.2% for T2-TSE, and 85.1% for T2-STIR. Hyperintensity was more frequently observed in T2-TSE (78.7%) and T2-STIR (80.9%) than in T1 (4.3%). Mean SUVmax was 6.6 (T1-detected), 6.4 (T2-TSE), and 6.5 (STIR). SUVmax significantly correlated with signal intensity across all sequences ($p < 0.01$). Among histologically confirmed lesions, all showed hyperintensity on T2/STIR and 91.6% had SUVmax > 4. Comparative analysis between T2-TSE and STIR revealed near-identical diagnostic performance, suggesting one sequence—preferably T2-TSE—could be omitted to streamline acquisition. ***Conclusion:*** The study confirms that a simplified MRI protocol using T1 and STIR provides robust diagnostic accuracy for detecting hyperfunctioning parathyroid adenomas. T2-STIR offers similar or superior lesion conspicuity compared to T2-TSE, with fewer artifacts, supporting its selection when reducing sequence count. The strong correlation between MRI signal intensity and SUVmax highlights the functional-anatomical relationship captured by PET/MRI. Histopathological concordance further supports the imaging findings. This optimized PET/MRI protocol could enhance clinical workflow by reducing scan time and improving patient tolerance without compromising diagnostic confidence. Larger prospective studies are warranted to validate these findings and support wider implementation.

OP-481

Clinical application and semiquantitative analysis of ^{18}F-FCH PET/CT in the pre-surgical localization of primary hyperparathyroidism.

E. Campaña Díaz[1], *P. García-Talavera San Miguel*[1], *F. Gómez-Caminero López*[1], *J. Álvarez Pérez*[1], *C. Montes Fuentes*[1], *J. Badell Martínez*[1], *E. Martin Gallardo*[2], *S. Rama Alonso*[1], *A. Peñaherrera Cepeda*[1], *J. Villanueva Curto*[1], *F. Caltagirone*[1], *B. Santos García*[1], *M. Tamayo Alonso*[1], *M. Martín Gómez*[1];
[1]*University Hospital of Salamanca, Salamanca, SPAIN,* [2]*UCIII y UPComillas, Madrid, SPAIN.*

Aim/Introduction: To evaluate the diagnostic performance of the technique to distinguish between pathological parathyroid gland, lymph node, and thyroid nodule. To propose cut-off points

for uptake values to differentiate these structures and study their behavior in the PET/CT imaging technique. ***Materials and Methods:*** We included 74 patients (59 females; 60.11±12.82 years) in whom ^{18}F-FCH PET/CT was performed for pre-surgical localization of PHPT. Standard ^{18}F-FCH images were acquired 5 and 60 minutes after 185 MBq intravenous administration. Delayed images were assessed semiquantitatively by means of calculation of SUVmax and SUVpeak of pathological parathyroid (P-SUVmax, P-SUVpeak), thyroid gland SUVpeak (T-SUVpeak), mediastinum SUVpeak (M-SUVpeak), lymph nodes (N-SUVmax, N-SUVmean) and thyroid nodules (NT-SUVmax, NT-SUVmean). SUV ratios were calculated with thyroid and mediastinum. The diagnostic performance of the ^{18}F-FCH PET/CT to discriminate pathological parathyroid gland vs lymph node and thyroid nodule was evaluated by analysis of the receiver operating characteristic (ROC) curve analyzing P-SUVmax vs N-SUVmax, P-SUVpeak/M-SUVpeak vs N-SUVpeak/M-SUVpeak, P-SUVmax/T-SUVpeak vs NT-SUVmax/T-SUVpeak in the delayed images. ***Results:*** During surgery the pathological gland was located in 72 cases (66 solitary adenomas, 5 double adenomas, 1 hyperplasia). The histological results of the other 2 patients were papillary thyroid carcinoma and oncocytic thyroid adenoma, which were 2 false positives for ^{18}F-FCH PET/CT. PET/CT had 2 false negatives in the analysis per patient. The ROC curves showed a cut-off of 2.72 for P-SUVmax vs N-SUVmax (S=82%, E=69%, AUC=0.8), 3.34 for P-SUVpeak/M-SUVpeak vs N-SUVpeak/M-SUVpeak (S=69%, E=85%, AUC=0.8), and 1.66 for P-SUVmax/T-SUVpeak vs NT-SUVmax/T-SUVpeak (S=65%, E=87%, AUC=0.8). ***Conclusion:*** The semiquantitative analysis in ^{18}F-FCH PET/CT is a useful and complementary support for the visual analysis in the pre-surgical localization of primary hyperparathyroidism.

OP-482

Incremental benefit of integrated 18-fluorocholine PET and 4DCT in preoperative parathyroid adenoma localization over either modality alone

D. Malik, *D. Thakrani, J. Gupta, M. Koley, N. Rana, A. Uppal, P. Thakral, I. B. Sen;*
Fortis Memorial research institute (FMRI), Gurugram, INDIA.

Aim/Introduction: Unilateral minimally invasive parathyroidectomy is the favoured surgical technique for treating parathyroid adenomas which needs accurate preoperative localization of the adenomas. Both 18F-Choline(18F-CH) PET and 4D-CT show good sensitivity for diagnosis and localization of parathyroid adenoma /hyperplasia pre-operatively. We aim to determine the incremental value of combined 18F-CH PET and 4D-CT over either modality alone. ***Materials and Methods:*** This was a prospective single centre study of 63 patients with clinically suspected primary hyperparathyroidism (hypercalcemia with hypophosphatemia and elevated PTH levels), who had a negative or a discordant 99mTc- Sestamibi scan and/or neck ultrasound and were planned for surgical exploration. The exclusion criteria included pregnant or lactating females, age<18, hypocalcemic, hyperparathyroidism,contrast allergy and deranged renal function. 63 patients underwent integrated 18F-CH PET CT and 4DCT, out of which 49 patients were found positive either by 18F-CH PET or 4DCT or both and subsequently underwent surgery. The other 14 patients were excluded as both 18F-CH PET and 4DCT were negative and patients were, therefore, not taken up for surgery. Sensitivity, positive predictive value and diagnostic accuracy were calculated as per lesion analysis for integrated 18F-CH PET and 4DCT and for each of these modalities separately. The post-operative histopathology was considered as the gold standard. ***Results:*** Of the 49 patients, 40 were positive on both modalities (concordant positive), while 9 had discordant results (6 4DCT negative patients were positive on FCH PET, and 3 FCH PET negative patients were positive on 4DCT). On the post-operative histopathology, 3/40 concordant positive patients tested negative while rest of the 37 tested positive for an adenoma. 5 / 6 "FCH positive-4D CT negative" patients tested positive for an adenoma and 1/6 turned out be negative while all of the 3 patients negative on FCH PET and positive on 4D CT turned out to be positive on post-operative histopathology. The highest sensitivity (100%) and diagnostic accuracy (93.8 %) for adenoma detection was recorded with the integrated 18FCH PET/4DCT. FCH-PET alone demonstrates higher sensitivity (93% vs 89%) and accuracy (87% vs 85%) than 4DCT alone. ***Conclusion:*** Integrated modality 18F-CH PET /4DCT demonstrates higher diagnostic accuracy in the pre -operative detection and localization of parathyroid adenoma than either modality used alone.

OP-483

[^{18}F]Fluorocholine PET/CT in the Diagnosis of Hyperparathyroidism: Comparison with Other Preoperative Localization Methods and correlation with biochemical markers

N. Calviño, *A. García-Burillo, D. Sanchez-Artuñedo, A. Palomar-Muñoz, R. Vilallonga-Puy, M. Diez Castro, M. Rubio Alvarez, J. Echeverri-Díaz, M. Marusso Fizzani, Ó. Hernandez Cristancho, L. Marconi Porcel, L. Nunes Lemos, C. Gámez-Cenzano;*
Vall d´Hebron Hospital Universitari, Vall d´Hebron Barcelona Hospital Campus, Passeig Vall d´Hebron 119-129, Barcelona, SPAIN.

Aim/Introduction: To evaluate the diagnostic performance of [18F] fluorocholine PET/CT in patients with hyperparathyroidism (HPT), compare it with neck ultrasound (US) and [99mTc]Tc-MIBI SPECT/CT, and analyze correlations with histopathological findings and biochemical markers (PTH and calcium). ***Materials and Methods:*** This retrospective study included a cohort of 126 patients with HPT who were referred for [18F]fluorocholine PET/CT at our center between 2022-2023. Only those who had undergone surgery by the time of the study were included in the analysis. For these patients, preoperative localization imaging results, serum PTH and calcium levels, and histopathological findings were collected. For each imaging modality, a true positive was defined as histology confirmation of an abnormal parathyroid gland (hyperplasia or adenoma) corresponding to the same side of the neck as indicated on imaging. ***Results:*** Among 126 patients that underwent [18F] fluorocholine PET/CT, 50 patients (38 women [76%], mean age 61.3 years [28-80]) were surgically treated. All patients had at least two preoperative localization studies, US, [99mTc]Tc-MIBI and/or [18F]fluorocholine PET/CT. The [18F]fluorocholine PET/CT was positive in 49 patients and negative in 1 patient (US positive); US was performed in all except two patients, both of these had positive PET/CT and [99mTc]Tc-MIBI. [99mTc]Tc-MIBI SPECT/CT was performed in 40 patients of whom 14 showed positive results. Sixty-eight glands were removed: 2 patients had 4 glands, 4 patients had 3 glands and 5 had 2 glands removed. One patient had no identifiable parathyroid tissue in the submitted samples. Histopathology revealed 37 adenomas, 19 hyperplasias and 11 glands with no morphological abnormalities. The sensitivity of [18F]fluorocholine PET/CT for the localizing hyperfunctioning parathyroid tissue was 84%, being higher than the other imaging tests (US 41% and [99mTc]Tc-MIBI 45%). Sensitivity was higher for detecting adenomas (89%) than hyperplasia (73%). Analysis of PTH, total calcium, and SUVmax values showed no significant correlations between variables. However, when comparing calcium levels with histological subtypes using the Kruskal-Wallis test, a statistically significant difference was observed (p=0.047): patients with adenomas had a median calcium level of 10.9mg/dL, compared to 10.2mg/dL in those with hyperplasia. ***Conclusion:*** Our results demonstrate that [18F]fluorocholine PET/CT has superior diagnostic accuracy in preoperative localization of hyperfunctioning parathyroid glands compared to conventional imaging such as US and [99mTc]Tc-MIBI SPECT/CT. Sensitivity was higher for detecting adenomas than hyperplasia. It can

significantly improve surgical planning, particularly when prior imaging is inconclusive. Additionally, serum calcium levels may provide complementary diagnostic value in distinguishing between adenoma and hyperplasia.

OP-484

Real-World Diagnostic Performance of 99mTc-SestaMIBI Scintigraphy and Fluorocholine PET/CT in Primary Hyperparathyroidism: A Comparative Analysis from Two Italian Centers

I. Gotuzzo[1], *F. Garrou*[1], *L. Airò Farulla*[2], *S. Vadalà*[3], *F. Lattuada*[1], *F. Del Gaudio*[1], *E. Bressan*[3], *M. Carrara*[1], *A. Rossini*[4], *S. Ippolito*[4], *S. Cassibba*[4], *C. Rossetti*[2], *P. A. Erba*[3];
[1]*Nuclear Medicine Unit - ASST Papa Giovanni XXIII Hospital, Bergamo, ITALY,* [2]*Nuclear Medicine Unit - ASST Grande Ospedale Metropolitano Niguarda, Milano, ITALY,* [3]*School of Medicine and Surgery, University of Milano-Bicocca, Milano, ITALY,* [4]*Endocrinology Unit - ASST Papa Giovanni XXIII Hospital, Bergamo, ITALY.*

Aim/Introduction: Primary hyperparathyroidism (PHPT) is a prevalent endocrine disorder typically managed through surgical resection of hyperfunctioning parathyroid glands. While fluorocholine (FCH) PET/CT has demonstrated superior sensitivity—particularly in detecting multiple hyperfunctioning glands—Italian reimbursement policies still mandate initial imaging with 99mTc-SestaMIBI scintigraphy, with FCH PET/CT reserved for equivocal or negative cases. ***Materials and Methods:*** A retrospective analysis of 193 PHPT patients (148 women, 45 men; mean age 64.4 ± 10.2 years) referred between January 2023 and April 2025 to two hospitals (ASST Papa Giovanni XXIII, Bergamo; ASST Grande Ospedale Metropolitano Niguarda, Milan) was conducted. Data were extracted from electronic medical records. Patients underwent clinical evaluation, laboratory testing, and neck ultrasonography prior to imaging. ***Results:*** ^{99m}Tc-SestaMIBI scintigraphy (dual time planar and SPECT/CT imaging protocol) was performed as first imaging test in all patients, resulting positive in 113/193 patients (59%) with a detection rate of 80% (90/113) for parathyroid adenoma. In the positive group US identified a suspected adenoma in 45% (51/113), while it was negative or non-specific in the remaining 34.5%. Mean PTH was 154.7 ± 67.7 pg/ml (medium 126, range 106-232); hypercalcemia was present in 27% of the cases and hyperphosphatemia/hypercalciuria in 6%. In the 80 patients with a negative/equivocal ^{99m}Tc-SestaMIBI scintigraphy, [^{18}F]FCH PET/CT images were acquired 45 minutes from radiopharmaceutical administration using a Biograph mCT scanner. Images were positive in 77/80 (96.2%), with detection rates of 83% (64/77) for adenoma and 17% (13/77) for hyperplasia. In this positive group, US suspected adenoma in 56.3% while multiple nodules were observed in 13.7%. Negative/non-specific findings were observed in 30%. Mean PTH value was 226.6 ± 330.8 pg/ml (medium 137,5, range 47-2000); hypercalcemia was present in 32%, hyperphosphatemia in 12.5%, hypercalciuria in 13.7%Statistical Analysis: the Mann-Whitney U and Fisher's Exact tests revealed no significant differences in demographic or ultrasonographic features between groups. The only statistically significant variable was serum PTH, which was lower in the PET-positive group. ***Conclusion:*** [^{18}F]FCH PET/CT demonstrated excellent detection performance even in cases with relatively lower PTH levels compared to ^{99m}Tc-SestaMIBI scintigraphy. These findings suggest that serum PTH may be useful in guiding the selection of first-line imaging, challenging current reimbursement-driven diagnostic pathways in Italy. For effective healthcare resource allocation, a comprehensive definition of clinical and biochemical predictors of 99mTc-SestaMIBI positivity should be established through large-scale studies, enabling evidence-based stratification of patients and reducing reliance on fluorocholine PET/CT as second-line modality, thus preventing redundant imaging and optimizing diagnostic pathways.

OP-485

Impact of critical appraisal of parathyroid SPECT-CT requests: an opportunity to improve efficacy and safety.

I. Lopez Villar[1], *M. Vinuesa Sebastian*[2], *J. Alonso Farto*[3], *R. Jover Díaz*[1], *D. Tamayo Carabaño*[1], *J. Diaz Melguizo*[4], *G. Torralbo Caballero*[5], *A. Planas Roca*[6], *F. Sebastian Valles*[7], *J. Muñoz de Nova*[8];
[1]*Department of Nuclear Medicine, La Princesa University Hospital, Madrid, SPAIN,* [2]*Clinical Quality Coordinator, La Princesa University Hospital, Madrid, SPAIN,* [3]*Department of Nuclear Medicine, Gregorio Marañón University Hospital, Madrid, SPAIN,* [4]*Medical Director, La Princesa University Hospital, Madrid, SPAIN,* [5]*Medical Director, La Princesa University Hospital, Madrid, SPAIN,* [6]*Associate Medical Director, La Princesa University Hospital, Madrid, SPAIN,* [7]*Department of Endocrinology, La Princesa University Hospital, Madrid, SPAIN,* [8]*Department of Surgery, La Princesa University Hospital, Madrid, SPAIN.*

Aim/Introduction: The only curative treatment for primary hyperparathyroidism (PHPT) is surgery. Nuclear medicine techniques are the main tool to localize the pathological glands in patients with a confirmed diagnosis and indication for surgery, allowing in many cases the use of focused minimally invasive parathyroidectomies. However, on many occasions, these tests are requested with the aim of confirming a doubtful diagnosis or in patients with no surgical indication, increasing the costs of the system and exposing patients to an unnecessary source of radiation. The "Do Not Do" recommendations from the Spanish Society of Nuclear Medicine and Molecular Imaging advise against parathyroid SPECT-CT, in patients without a biochemical diagnosis of hyperparathyroidism or those not eligible for surgery.Aim: To evaluate the efficacy of a critical review program of parathyroid SPECT-CT requests in patients with PHPT to confirm a proper indication: confirmed diagnosis in a patient who is a candidate for surgery. ***Materials and Methods:*** Prospective observational study in which consecutive SPECT-CT requests between October 2024 and March 2025 were included. All requests were evaluated jointly with an endocrine surgeon with expertise in hyperparathyroidism. The correct indication as well as the outcome of the test were analyzed. The results were compared with historical control of requests made between January 2024 and September 2024, before starting the new protocol.The study was validated by the Hospital Appropriateness Committee. ***Results:*** A total of 71 parathyroid SPECT-CT requests were analyzed during the study period, and 41 of them (57.7%) were denied due to inadequate indication. Of the 30 tests performed, 22 were positive (73,3%), localizing pathological parathyroids. The average delay until the test was performed was 29 days (cost-opportunity improvement). In the previous period, 105 SPECT-CT scans were performed. In the review it was considered that 70 of them (66.7%) did not meet the criteria to indicate the test. The rate of positive tests was 24,7%. The mean delay in this period was 61 days. The extension of the new strategy to an annual period would mean saving 42.340 euros for our institution. ***Conclusion:*** A detailed analysis of the correct indication for parathyroid localization tests allows detection of a high rate of incorrectly indicated tests. Not performing these tests means an improvement in the management of the services provided by the Nuclear Medicine Department, significant economic savings (cost-opportunity improvement) and the avoidance of unnecessary exposure of patients to radiation (improved safety).

OP-486

Preoperative Localization in Primary Hyperparathyroidism with Combined 4DCT-MIBI SPECT/CT

K. Y. Li[1], *S. K. Wu*[1], *C. Tang*[1], *H. K. Wong*[1], *H. M. Leung*[2], *W. H. Luk*[1]; [1]*Department of Interventional and Diagnostic Radiology, Kowloon West Cluster Hospitals, Hong Kong, HONG KONG,* [2]*Faculty of Medicine, The University of Hong Kong, Hong Kong, HONG KONG.*

Aim/Introduction: Primary hyperparathyroidism (PHPT) requires precise preoperative localization for minimally invasive parathyroidectomy. This study evaluates the efficacy of combined four-dimensional computed tomography (4DCT) and technetium-99m sestamibi single-photon emission computed tomography/computed tomography (MIBI SPECT/CT) at our center over five years. ***Materials and Methods:*** We conducted a retrospective search for patients with biochemically proven PHPT who underwent combined 4DCT-MIBI SPECT/CT from October 2018 to September 2023. Images were reviewed by two radiologists for lesion presence and location. Enhancement patterns of the parathyroid lesions were classified in relation to the thyroid. Data was analyzed for sensitivity, interobserver agreement and statistical difference between modalities. Demographic and histopathological results were also retrieved. ***Results:*** Of 122 parathyroid lesions, 4 were intrathyroidal and 1 was ectopic. One parathyroid carcinoma was found, with others being either adenoma or hyperplasia. There was one false positive case of thymoma in the anterior mediastinum. Combined 4DCT-MIBI SPECT/CT achieved 87.7% sensitivity (95% CI 81.9%-93.5%), outperforming 4DCT (77.0%, 95% CI 69.6%-84.5%) and MIBI scan (71.3%, 95% CI 63.3%-79.3%) alone. Interobserver agreement was near-perfect (kappa: 0.91-0.98). On 4DCT, 48% of lesions showed Type A enhancement, 47% Type B, and 5% Type C. ***Conclusion:*** The combined 4DCT-MIBI SPECT/CT protocol offers high sensitivity and excellent inter-observer reliability for pre-operative lesion localization in patients with PHPT, outperforming standalone 4DCT or MIBI studies. These findings underscore the potential of this integrated imaging approach to enhance targeted surgical treatment and patient outcomes.

1108

Monday, October 6, 2025, 16:45 - 18:15

Room 115

Joint Symposium 5 - Oncology & Theranostics Committee / EAU: Advances in Renal Cancer Research

OP-488

New Tracers in Renal Cancer

K. Goffin*; UZ Leuven, Leuven, BELGIUM.*

OP-489

Girentuximab Imaging in Renal Cancer

S. Muselaers*; Radboud University Medical Center, Department of Urology, Nijmegen, NETHERLANDS.*

OP-490

Immunotherapy for Renal Cancer

E. Castro*; Hospital Universitario 12 de Octubre, Department of Medical Oncology, Madrid, SPAIN.*

1109

Monday, October 6, 2025, 16:45 - 18:15

Room 133+134

e-Poster Presentations Session 8 - Oncology & Theranostics Committee: Cancer Imaging and Therapy

EPS-157

Two-step pretargeted radioimmunotherapy of GPA33-expressing colorectal cancer with optimized self-assembling and disassembling bispecific fusion protein tetramer (SmartCC)

Z. Qiao*, Y. Yang, Q. Liu, Y. Liu, T. Hu, C. Wei, T. Xu; SmartNuclide Biotech, Suzhou, CHINA.*

Aim/Introduction: We developed a bispecific fusion protein for two-step pretargeted radioimmunotherapy (PRIT) to enhance the therapeutic index (TI). This innovative construct incorporates three key components, including a tumor-targeting domain, (ii) a lanthanide metal (Ln)-DOTA binding domain, and (iii) a novel tetramerization domain derived from human. The self-assembly and disassembly of this bispecific fusion protein are mediated by our proprietary tetramerization domain library, designated as SmartCC. The resulting tetramer exhibits strong tumor-binding avidity while achieving rapid blood clearance upon dissociation into small monomers (<70 kDa). Importantly, the SmartCC platform demonstrates the ability to modulate protein pharmacokinetics, thereby amplifying the biological effects of radiation dose delivery to tumors and significantly widening the therapeutic window. In this present study, we evaluated the SmartCC platform's potential for PRIT applications using GPA33-expressing colorectoal cancer as a model system. ***Materials and Methods:*** A library of SmartCCs capable of modulating the pharmacokinetic properties of tumor-targeting antibodies was established and used for in vivo screening to identify GPA33-SmartCCs exhibiting the favorable TI. Protein was intravenously administrated to LS174T tumor-bearing mice, followed by the injection of a ^{177}Lu-DOTA-Bn. Pretargeted in vivo and ex vivo biodistribution studies were performed to determine the appropriate tetramerization domain to form bispecific fusion protein tetramers for the PRIT in terms of therapeutic index (TI). Tumor growth inhibition studies were conducted by monitoring the tumor size by using 2 doses of PRIT. ***Results:*** The pretargeted in vivo biodistribution studies showed that selected bispecific fusion protein (SNA028) had favorable biodistribution properties including high tumor uptake and low blood and kidney toxicity, which is consistent with the ex vivo biodistribution properties. The tumor uptake was of 49.12 ± 2.98 %ID/g and 26.15 ± 3.42 %ID/g at 24 h and 120 h postinjection, respectively. Tumor showed the highest absorbed dose of 457.26 cGy/MBq, followed by kidney of 24.08 cCy/MBq (TI = 19) and blood of 6.44 cCy/MBq (TI=71). SNA028-PRIT resulted in LS174T tumor growth inhibition without significantly altering the weight up to 26 days. ***Conclusion:*** SNA028-PRIT showed favorable ex vivo biodistribution properties in terms of high tumor uptake and low kidney and blood toxicity. In addition, SNA028-PRIT enabled control of tumor growth without significantly altering body weight. These promising data with 177Lu prompts us to study SNA028-based PRIT strategy with α-emitters in the future.

EPS-158

A Hapten-Based Background-Free Reporter System for Longitudinal PET Imaging of CAR-T Cells

B. Wang[1], *W. Niu*[2], *Y. Zhang*[2], *J. Li*[1], *H. Wu*[1], *Z. Xiao*[1], *P. Lei*[2], *Y. He*[1];
[1]*Department of Nuclear Medicine, Zhongnan Hospital of Wuhan University, Wuhan, CHINA,* [2]*Department of Immunology, School of Basic Medicine, Tongji Medical College, Huazhong University of Science and Technology, Wuhan, China, Wuhan, CHINA.*

Aim/Introduction: CAR-T cell therapy faces challenges in solid tumors, such as infiltration barriers, immunosuppressive microenvironments, and off-target effects. Thus, assessing CAR-T cell infiltration, persistence, and distribution is critical for improving efficacy and safety. Reporter gene-based PET/CT imaging allows real-time tracking of CAR-T cells. We developed a novel hapten-based reporter gene (anti-HSG-scFv) and engineered two CAR-T variants: HSG-FAP CAR-T (HF CAR-T) and FAP-T2A-HSG CAR-T (FTH CAR-T). Using [^{68}Ga]Ga-IMP-288 PET/CT, we successfully tracked both CAR-T types in vivo. ***Materials and Methods:*** This study designed two FAP-targeting CAR-T cells with distinct reporter gene expression structures. We first validated HF CAR-T and FTH CAR-T cells for expression, activation, cytotoxicity and cytokine secretion. Their antitumor effects were then evaluated in hFAP-HT1080 xenografts. Additionally, we extensively validated the specific binding between two CAR-T cells and IMP-288, and quantitatively assessed [^{68}Ga]Ga-IMP-288 PET/CT imaging capability in vitro and in vivo. Finally, we employed [^{68}Ga]Ga-IMP-288 PET/CT to track the biodistribution of infused CAR-T cells, monitor their dynamic tumor infiltration patterns, and comparatively evaluate therapeutic efficacy. ***Results:*** The reporter gene did not affect the activation, cytotoxicity, or cytokine secretion of HF CAR-T and FTH CAR-T cells. [^{68}Ga]Ga-IMP-288 PET/CT imaging successfully tracked both types of CAR-T cells in vitro and in vivo: For HF CAR-T cells, the detection sensitivity was 50 cells/mm^3 in vitro and 100 cells/mm^3 in vivo, while for FTH CAR-T cells, the detection sensitivity was 250 cells/mm^3 in vitro and 100 cells/mm^3 in vivo. Longitudinal sequential imaging demonstrated that tumors in the HF CAR-T and FTH CAR-T groups began to show significant localized radioactive accumulation on day 3, with radioactive uptake in the HF CAR-T group slightly higher than that in the FTH CAR-T group (ID%/g: 1.484 ± 0.124 vs 1.223 ± 0.051, $p < 0.05$), whereas no such accumulation was detected in the other three groups. On day 7 and day 14, radioactive uptake within the tumor in the HF CAR-T and FTH CAR-T groups remained consistently high, with a notable expansion in the accumulation area. [^{68}Ga]Ga-IMP-288 PET/CT could specifically track both HF CAR-T and FTH CAR-T cells infiltrating the tumor, with both cell types exhibiting significant therapeutic efficacy. ***Conclusion:*** Our study demonstrated that [^{68}Ga]Ga-IMP-288 PET/CT successfully achieved in vivo tracking of HF CAR-T and FTH CAR-T cells, and the two CAR-T cells demonstrated excellent therapeutic efficacy. The [^{68}Ga]Ga-IMP-288/anti-HSG-scFv pairing, as a novel reporter gene imaging system, shows significant potential for clinical translation.

EPS-159

First clinical experience with the bicyclic peptide radiotracer [^{68}Ga]Ga-BCY25286 for PET/CT imaging of MT1-MMP in lung, urothelial and head and neck cancer

A. Eder[1,2], *C. Wielenberg*[1], *M. A. Omrane*[1,2], *C. A. Jilg*[1], *C. F. Waller*[1], *M. Mix*[1], *C. Schell*[1], *B. Passlick*[1], *M. Eder*[1,2], *P. T. Meyer*[1,2], *M. T. Freitag*[1,2];
[1]*University Medical Center, Freiburg, GERMANY,* [2]*German Cancer Consortium, Freiburg, GERMANY.*

Aim/Introduction: Membrane type 1 matrix metalloproteinase (MT1-MMP) is overexpressed in various solid tumors and associated with poor prognosis. Despite its established role in tumor progression and its potential as a theranostic target, clinical translation of MT1-MMP-targeted radiopharmaceuticals has not been previously reported. This study presents the first clincical experience with [^{68}Ga]Ga-BCY25286, a bicyclic peptide-based PET radiotracer, for imaging of MT1-MMP expression in patients with lung, urothelial, and head and neck cancer. ***Materials and Methods:*** Seven patients (lung cancer: n=3; urothelial carcinoma: n=3, head and neck CUP: n=1) underwent [^{68}Ga]Ga-BCY25286 PET/CT imaging (MT1-PET/CT). Four patients had prior [^{18}F]FDG-PET/CT within a maximum interval of 16 days. MT1-PET/CT scans were performed 15, 30, 45 and 60 min after intravenous injection of [^{68}Ga]Ga-BCY25286 (mean activity: 203 MBq) (ethical approval #25-1019-S1). Standardized uptake value (SUVs) was determined for all lesions and organs of interest (liver, blood pool, kidneys). In selected patients histopathological confirmation and MT1-MMP immunohistochemistry were performed and correlated with imaging findings. ***Results:*** In 6 out of 7 patients, tumors and/or metastatic lesions demonstrated increased [^{68}Ga]Ga-BCY25286 uptake compared to the local background. Mean (± SD) SUV_{max} values at 60 minutes after injection was 7.4 ± 3.8 g/mL for primary tumors, 4.6 ± 1.7 g/mL for lymph node metastases, and 5.5 ± 2.4 g/mL for organ metastases. Kinetic analysis revealed rapid tracer accumulation in tumors, with optimal tumor-to-background ratios achieved within 60 minutes after injection. Physiological tracer distribution was characterized by persistent vascular activity (SUV_{mean}: 1.9 ± 0.3 g/mL at 60 min), high renal uptake reflecting renal excretion (SUV_{mean}: 9.4 ± 2.0 g/mL) and low hepatic uptake (SUV_{mean}: 1.5 ± 0.2 g/mL). Compared to [^{18}F]FDG-PET/CT, [^{68}Ga]Ga-BCY25286-PET/CT yielded a comparable lesion visualization in two patients, although [^{18}F]FDG-PET/CT showed higher SUV_{max} (13.9 g/mL vs. 6.7 g/mL). In one patient, lymph nodes that were false-positive on [^{18}F]FDG-PET/CT exhibited markedly lower SUV_{max} on [^{68}Ga]Ga-BCY25286-PET/CT (8.4 ± 1.9 g/mL vs. 3.2 ± 0.3 g/mL). In the patient with histologically confirmed lung cancer, [^{68}Ga]Ga-BCY25286-PET/CT showed no relevant tracer uptake, despite high uptake on [^{18}F]FDG-PET/CT. In cases with histological validation, PET-positive lesions demonstrated membranous and/or stromal MT1-MMP expression. ***Conclusion:*** This first clinical series of [^{68}Ga]Ga-BCY25286 imaging in cancer patients demonstrates the feasibility of visualizing MT1-MMP-expressing primary tumors and metastatic lesions. These initial results support further investigation of this radiotracer as a diagnostic tool for tumor characterization in MT1-MMP-positive cancers, potentially facilitating personalized treatment strategies and improved patient management.

EPS-160

Multi-Organ Metabolic Profiling with ^{18}F-FDG PET/CT Predicts Pathological Response to Neoadjuvant Immunochemotherapy in Resectable NSCLC

J. Li, *Q. Ma, Y. Tang, S. Hu;*
Xiangya Hospital, Central South University, Changsha, CHINA.

Aim/Introduction: Neoadjuvant Immunochemotherapy has revolutionized resectable non-small cell lung cancer (rNSCLC) management, yet 30-50% of patients experience suboptimal pathological responses while facing immune-related toxicities. Current post-treatment biomarkers delay risk stratification, and baseline predictors for major pathological response (MPR) integrating systemic tumor-host metabolic interactions remain unexplored. This study aims to develop and validate a machine learning-powered nomogram combining multi-organ PET metabolic metrics to predicts pathological response to neoadjuvant immunochemotherapy in rNSCLC. ***Materials and Methods:*** This retrospective cohort included rNSCLC patients who underwent baseline ^{18}F-FDG PET/CT prior to neoadjuvant immunochemotherapy at Xiangya Hospital from April 2020 to April 2024. Patients were randomly stratified into training (70%) and validation (30%) cohorts. Using deep learning-based automated segmentation, we quantified metabolic parameters (SUV_{mean}, SUV_{max}, SUV_{peak}, MTV, TLG) for primary tumors and nine key organs. Feature selection employed a tripartite approach: univariate analysis, LASSO regression, and random forest optimization. The final multivariable model was translated into a clinically interpretable nomogram, with validation assessing discrimination,

calibration, and clinical utility. ***Results:*** Among 115 patients (MPR rate: 63.5%, n=73), five metabolic parameters emerged as predictive biomarkers for MPR: Spleen_SUV_{mean}, Colon_SUV_{peak}, Spine_TLG, Lesion_TLG, and Spleen-to-Liver SUV_{max} ratio. The nomogram demonstrated consistent performance across cohorts (training AUC=0.78 [95%CI 0.67-0.88]; validation AUC=0.78 [0.62-0.94]), with robust calibration and clinical net benefit on decision curve analysis. Compared to tumor-only parameters, the multi-organ model showed enhanced specificity (100% vs 92%) and positive predictive value (100% vs 90%) in the validation set, maintaining 76% overall accuracy. ***Conclusion:*** This first-reported multi-organ metabolic nomogram noninvasively predicts MPR in rNSCLC patients receiving neoadjuvant immunochemotherapy, outperforming conventional tumor-centric approaches. By quantifying systemic host-tumor metabolic crosstalk, this tool could guide personalized therapeutic decisions while mitigating treatment-related risks, representing a paradigm shift towards precision immuno-oncology management.

EPS-162

Prognostic Value of Preoperative [^{18}F]FDG PET/CT in Malignant Pleural Mesothelioma: Correlation with Surgical Resectability and Survival Outcomes

J. Hong, *K. Kimura, V. Ludwig, A. Salavati, A. Nguyen, L. Theus, A. Holzgreve, M. Allen-Auerbach, J. Czernin, R. B. Cameron, J. Calais; University of California, Los Angeles (UCLA), Los Angeles, CA, UNITED STATES OF AMERICA.*

Aim/Introduction: Malignant pleural mesothelioma (MPM) carries a poor prognosis. However, appropriate patient selection for surgery can lead to some survival benefit. Thus, accurate preoperative assessment is crucial. [^{18}F]fluorodeoxyglucose positron emission tomography/computed tomography ([^{18}F]FDG PET/CT) provides information that may aid this selection. The aim of this study was to evaluate how preoperative [^{18}F]FDG PET/CT is associated with tumour resectability and prognosis in MPM patients undergoing surgical resection. ***Materials and Methods:*** This was a single-centre retrospective study of patients who underwent [^{18}F]FDG PET/CT prior to surgery, identified from the institution's MPM database (n = 428) since 1998. Eligible patients had histologically confirmed MPM, curative-intent surgery, and available preoperative in-house [^{18}F]FDG PET/CT. Exclusion criteria included scans performed >6 months before surgery, or unavailable follow-up. PET/CT scans were reviewed by a blinded evaluator. Tumour lesions were quantified using the PERCIST 1.0 criteria: derived metabolic tumour volume (MTV), maximum standardized uptake value (SUV_{max}), mean SUV (SUV_{mean}), and total lesion glycolysis (TLG = MTV × SUV_{mean}). Clinical progression-free survival (PFS), defined as time from PET/CT to progression or death, and overall survival (OS) were calculated. Statistical analysis included Spearman's correlation, Kaplan-Meier analysis, and Cox regression. ***Results:*** Forty-nine patients were included: median age 70 years (interquartile range [IQR]: 64-75), 31 (63%) had epithelioid, 18 patients (37%) biphasic MPM. The median resected specimen weight during surgery was 678 g (IQR: 476-1010). Median MTV, SUV_{max}, SUV_{mean}, and TLG were 52.9 mL (IQR: 13.0-298.1), 9.7 (IQR: 7.4-14.7), 5.1 (IQR: 4.3-6.3), and 331.6 (IQR: 56.8-1836.8), respectively. MTV and TLG showed strong positive correlations with the resected specimen weight ($\rho = 0.69$ and 0.68, respectively; both $p < 0.001$). Median follow-up was 18.2 months (95% CI: 14.8-not reached [NR]). PFS and OS were significantly shorter in the high-MTV vs. the low-MTV group (hazard ratio [HR] = 3.53, 95% confidence interval [CI]: 1.69-7.40, $p < 0.001$ for PFS; HR = 3.71, 95% CI: 1.54-8.99, $p < 0.001$ for OS). The median PFS was 8.5 months (95% CI: 4.8-11.2) in the high-MTV and 21.6 months (95% CI: 10.1-NR) in the low-MTV. At 2 years, the PFS rate was 6% (95% CI: 1-37) in the high-MTV and 37% (95% CI: 19-73) in the low-MTV. ***Conclusion:*** MTV derived from [^{18}F]FDG PET/CT was strongly correlated with the resected specimen weight and was a significant prognosticator in MPM patients undergoing surgery. These findings underscore the utility of PET/CT in preoperative risk stratification and surgical decision-making.

EPS-163

Preliminary Clinical Studyon the Safety and Antitumor Activity of^{177}Lu-Catelase in Soft Tissue Sarcoma

X. Guo, *Z. Tan, J. Liu, H. Zhu, J. Liu, Z. Yang; Beijing Cancer Hospital, Beijing, CHINA.*

Aim/Introduction: Local radioisotope injection represents a promising approach to localized radiotherapy; however, challenges such as poor retention within tumors and tumor hypoxia have limited its effectiveness. Here, we have developed a hydrogel preparation for intratumoral radiotherapy, containing catalase (CAT) labeled with the therapeutic radioisotope ^{177}Lu (^{177}Lu-CAT/ALG) and sodium alginate (ALG). Preclinical studies demonstrated prolonged tumor hypoxia relief, enhanced tumor retention, and significant antitumor efficacy. This phase 1 clinical trial evaluates the safety and efficacy of ^{177}Lu-CAT/ALG in patients with soft tissue sarcoma (STS). ***Materials and Methods:*** Eligible patients with locally advanced STS were recruited. Baseline metabolic and volumetric assessments were performed using ^{18}F-FDG PET/MR imaging. The intratumoral injection dose was calculated using OLINDA 2.0 Sphere Model. Intra-tumoral injections of ^{177}Lu-CAT/ALG were performed every 8 weeks, guided by ultrasound or direct visualization by experienced clinicians. Participants underwent single-photon emission computed tomography (SPECT) imaging at 2, 24, 96, and 168 h post-injection to assess tumor retention. Efficacy was evaluated every 8 weeks through ^{18}F-FDG PET/MR. The primary endpoints included tumor retention of ^{177}Lu-CAT/ALG and safety (graded per CTCAE v5.0). Secondary endpoints included objective response rate (ORR), progression-free survival (PFS), and overall survival (OS), evaluated per PERCIST criteria. ***Results:*** Seven patients with locally advanced STS were enrolled and provided informed consent (see Table). The median primary tumor size was 8.5 cm. Retention analysis indicated that at least 60% of the administered ^{177}Lu-CAT/ALG remained within tumors across all patients at 168 h. The most common adverse events (AEs) were grade 1-2 decreases in white blood cell count (4/7 patients). One patient experienced a grade 4 adverse event (thrombopenia). The best observed response was stable disease in two patients, with disease control durations of 16.53 and 12.8 months, respectively. As of the data cut-off, one patient remains on treatment. Pathological analysis from a post-injection tumor specimen of one patient—who exhibited an increase in tumor volume on PET/MR imaging one month post-injection—revealed 70% tumor bed necrosis after radical resection of the primary tumor. ***Conclusion:*** ^{177}Lu-CAT/ALG demonstrated a favorable safety profile and potential antitumor activity in patients with locally advanced STS. These findings suggest that ^{177}Lu-CAT/ALG could serve as an effective treatment for locally advanced STS and warrant further investigation in larger trials. ***References:*** 1. Chao Y, Xu L, Liang C, et. Combined local immunostimulatory radioisotope therapy and systemic immune checkpoint blockade imparts potent antitumour responses. Nat Biomed Eng. 2018 Aug;2(8):611-621.

EPS-164

Superior performance of ^{68}Ga-Pentixafor PET/CT on detecting lymphoma lesions: comparison with ^{18}F-FDG PET/CT

H. Liu, *Y. Wang, Z. Xiao, Y. Huang, Y. He; Department of Nuclear Medicine, Zhongnan Hospital of Wuhan University, Wuhan, CHINA.*

Aim/Introduction: ^{18}F-FDG PET/CT for the evaluation of lymphoma, especially indolent lymphoma, exists some limitations.

The C-X-C motif chemokine receptor 4 (CXCR4) overexpressed in hematological tumors, has been used as a promising target for lymphoma PET imaging. Thus, we designed the study to evaluate the diagnostic performance of ^{68}Ga-Pentixafor, a CXCR4-targeting probe, PET/CT for lymphoma, compared with ^{18}F-FDG PET/CT. ***Materials and Methods:*** 36 untreated or recurrent participants with different lymphoma subtypes (8 marginal zone lymphoma, 7 diffuse large B-cell lymphoma, 7 follicular lymphoma, 3 mantle cell lymphoma, 2 Burkitt lymphoma and 9 other lymphoma subtypes) were prospectively recruited and underwent ^{68}Ga-Pentixafor and ^{18}F-FDG PET/CT in a week. Positive lesions were defined as focal uptake above background. And semiquantitative metrics on both scans were compared for paired positive lesion. ***Results:*** Totally 513 lymphoma lesions (412 nodal and 101 extranodal) were identified. ^{68}Ga-Pentixafor PET/CT found 441 lesions (86.0%; 357 nodal and 84 extranodal), whereas ^{18}F-FDG PET/CT detected 407 (79.3%; 319 nodal and 88 extranodal) ($p<0.05$). Among lesions, 335/513 (65.3%) were interpreted positive on both scans. Additionally, 106 ^{68}Ga-Pentixafor-positive/^{18}F-FDG-negative lesions and 72 ^{68}Ga-Pentixafor-negative/^{18}F-FDG-positive lesions were identified. Paired positive lesions on both scans consistently exhibited significantly higher median maximum/peak standardized uptake values (SUVmax/SUVpeak), target-to-blood ratio (TBR) and target-to-liver ratio (TLR) on ^{68}Ga-Pentixafor PET/CT vs. ^{18}F-FDG PET/CT: SUVmax, 6.06 (range, 1.39-24.65) vs. 5.24 (range, 1.12-37.29); SUVpeak, 3.71 (range, 0.71-21.58) vs. 3.23(range, 0.64-29.46); TBR, 3.26 (range, 0.78-22.23) vs. 2.92 (range, 0.67-22.08); TLR, 4.38 (range, 1.00-26.17) vs. 2.34 (range, 0.57-17.47) (all $p<0.05$). ***Conclusion:*** Compared to ^{18}F-FDG PET/CT, ^{68}Ga-Pentixafor PET/CT was superior in detecting lymphoma lesions of most lymphoma subtypes. Semiquantitative analysis uniformly revealed higher values on ^{68}Ga-Pentixafor PET/CT, suggesting that ^{68}Ga-Pentixafor PET/CT might become an alternative to ^{18}F-FDG PET/CT in most lymphoma subtypes.

EPS-165

Head-to-head comparison of mpMRI, PSMA and GRPR PET/CT for local staging of primary prostate cancer: results from a prospective, single-arm, phase II multimodal imaging trial

Y. Li, *Y. Tang, S. Hu;*
Xiangya Hospital, Central South University, Changsha, CHINA.

Aim/Introduction: Optimal therapeutic options of primary prostate cancer (PCa) rely on the accurate assessment of the local extent and localization. Advanced imaging plays a crucial role in initial evaluation, with enhanced sensitivity leading to stage migration. Prostate-specific membrane antigen (PSMA) and gastrin-releasing peptide receptors (GRPR) represent the promising PCa imaging targets. The feasibility of GRPR PET/CT in local staging has been underexplored, nor compared with multiparametric MRI (mpMRI), PSMA, or their combined use. We report an exploratory analysis from a prospective trial, comparing the efficacy in identifying PCa local stage. ***Materials and Methods:*** Intermediate-/high-risk PCa who underwent mpMRI, PSMA and GRPR PET/CT before radical prostatectomy (RP) were included. Each modality was interpreted by two independent readers. Histopathology from RP served as the gold standard. Imaging T staging was assessed and summarized, in addition to bilateral intraprostatic disease (BID), extraprostatic extension (EPE) and seminal vesicle invasion (SVI). The index lesion was defined as the most clinically significant lesion (highest stage, SUV or PI-RADS). PET/CT + mpMRI findings were obtained by combining the two. ***Results:*** Eighty-one treatment-naïve PCa were included. Prostate adenocarcinomas (ACs) were found in 81 (100%) cases from RP, while 10 (12%) admixed with unconventional pathological patterns. PSMA PET/CT showed greater accuracy in local staging than GRPR PET/CT (56% vs. 36%, P=0.011), but was not superior to mpMRI (56% vs. 41% P=0.073); however, PSMA PET/CT was superior to both modalities in the pure AC subgroup (58%, vs. 39% and 34%, P=0.029 and 0.005). PSMA PET/CT was superior to mpMRI for BID identification (72%, vs. 54%, P=0.024), and superior to GRPR PET/CT for SVI identification (93%, vs. 85%, P=0.039). PSMA PET/CT + mpMRI demonstrated superior accuracy to mpMRI alone (60% vs. 41%, P=0.002). GRPR PET/CT + mpMRI was superior to GRPR PET/CT alone (49% vs. 36%, P=0.035). Using PET/CT + mpMRI detected more index lesions (93% and 89% vs. 77% P<0.001 and P=0.002) and identified BID in higher accuracies (74% and 67% vs. 54%, P=0.002 and 0.041) compared to mpMRI alone. ***Conclusion:*** For local staging intermediate-/high-risk PCa, PSMA PET/CT exhibited the highest accuracy among the three modalities, with statistical superiority in pure AC cases. This advantage primarily stems from better identification of BID, followed by index lesions and SVI. Combining PET/CT + mpMRI enhances the accuracy compared to mpMRI alone, allowing for capturing index lesions and BID, which may be significant for targeted biopsy guidance and local treatment planning.

EPS-166

Benfo-Oxythiamine as a Radiosensitizer in PSMA-Targeted Radioligand Therapy for Treatment-Refractory Prostate Cancer - Analysis of Clinical Outcome Data

C. Kramer, *R. P. Baum;*
Curanosticum Wiesbaden-Frankfurt MVZ GmbH, Wiesbaden, GERMANY.

Aim/Introduction: Recently, we reported a patient with metastatic castration-resistant prostate cancer (mCRPC) who exhibited an extraordinary response when the thiamine antagonist benfo-oxythiamine (B-OT) was added to prostate-specific membrane antigen (PSMA)-targeted radioligand therapy (PRLT) ('B-OT PRLT') [Ref 1]. To further support the hypothesis that B-OT may help overcome radiation resistance in mCRPC patients unresponsive to conventional PRLT with Lutetium-177 or Actinium-255, we conducted a retrospective analysis of a larger patient cohort. ***Materials and Methods:*** 19 patient records contained complete data after the first B-OT PRLT cycle, and 12 had comprehensive follow-up data for all treatment cycles. B-OT was administered in six different dosing regimens (ranging from 15-90 mg orally per cycle, either constant or escalating). The mean activities of ^{177}Lu- and ^{225}Ac-labeled PSMA-I&T used were consistent with those applied in standard PRLT. Complete follow-up included both serological prostate-specific antigen (PSA) assessments and imaging response evaluations using PET/CT or SPECT/CT. Treatment responses were defined as a change from progressive disease (PD) to either stable disease (SD), mixed response (MR), partial remission (PR), or complete remission (CR). ***Results:*** Prior to receiving their first cycle of B-OT PRLT, patients had undergone a median of 3 (range: 0-10) cycles of PRLT (with Lutetium-177, or TANDEM therapy using Lutetium-177 in combination with Actinium-225). Baseline tumor status before B-OT PRLT was: PD in 15/19 patients, MR in 1, and PR in 3; no patients presented with SD. After one cycle of B-OT PRLT, 6 out of 15 patients with PD showed both serological response (PSA decline up to 73%) and response by molecular imaging criteria (THERCIST), while another 6 patients with PD demonstrated imaging-based response. Six patients had no status change (PD to PD (3/6), MR to MR (1/6), PR to PR (2/6)), and the condition of one patient deteriorated (PR to PD). Notably, two patients who had previously been resistant to alpha-emitter therapy (with Actinium-225) responded to the combination of B-OT with ^{177}Lu-PSMA-I&T. Across subsequent treatment cycles, B-OT continued to be well tolerated and appeared to enhance PRLT efficacy. ***Conclusion:*** These retrospective data further support that the addition of B-OT to PRLT is well tolerated and may enhance treatment response in heavily pre-treated mCRPC

patients who are progressing under beta- and alpha-emitting PSMA-directed therapies. ***References:*** 1. Kramer CS, Zhang J, Baum RP (2024), Front. Med. 11: 1462234.

EPS-167

Comparison of [^{68}Ga]Ga-DOTA-FAPI-04and [^{18}F]FDG PET/CT in the Evaluation of Ovarian Cancer

J. Wang, *Y. Li, H. Pang;*
The First Affiliated Hospital of Chongqing Medical University, Chongqing, CHINA.

Aim/Introduction: 2-deoxy-2-[^{18}F]fluoro-D-glucose ([^{18}F]FDG) PET/CT still has some limitations in the evaluation of ovarian cancer, such as false positives caused by inflammation and physiological uptake, and false negatives caused by mucinous and low-grade tumors. Fibroblast activation protein (FAP) is highly expressed in cancer-associated fibroblasts (CAFs) in more than 90% of epithelial tumors. This study aims to compare the value of [^{68}Ga]Ga-DOTA-fibroblast activation protein inhibitor (FAPI)-04 and [^{18}F]FDG PET/CT in the evaluation of primary and metastatic tumors of ovarian cancer and to analyze the correlation between the radioactive uptake and the size of the lesion. ***Materials and Methods:*** We retrospectively analyzed patients with suspected or confirmed ovarian cancer who completed [^{18}F]FDG and [^{68}Ga]Ga-DOTA-FAPI-04 PET/CT in our hospital from December 2021 to December 2024. Lesions confirmed by histopathologic diagnosis or clinical imaging and follow-up were included. The uptake of radioactive tracers and the values of two techniques were evaluated and compared. ***Results:*** 516 lesions in 80 patients were included. Compared with FDG PET/CT, FAPI-04 PET/CT had a higher specificity, PPV and accuracy in diagnosing primary tumors (71.4%, 90.5% and 92.3% vs. 28.6%, 79.2% and 80.8%), and a higher diagnostic value for peritoneal metastases of ovarian cancer [AUC: 0.834, 95% CI: 0.740-0.929, P < 0.001; vs. AUC: 0.628, 95% CI: 0.530-0.726, P = 0.018; P = 0.003]. Both of them had high sensitivity, specificity, PPV and accuracy in diagnosing lymph node metastases of ovarian cancer (98.4%, 100.0%, 100.0% and 98.6% vs. 96.1%, 93.8%, 99.2% and 95.8%). There was no significant difference in the SUV_{max} and SUV_{mean} in primary tumors, lymph node and peritoneal metastases of ovarian cancer between two techniques. The long diameter of the lesion was positively correlated with the SUV_{max} (P < 0.001) and SUV_{mean} (P < 0.001) from FAPI-04 PET/CT, and the cutoff values of the long diameter of the ovarian cancer lesion when predicting $SUV_{max} \geq 1$, $SUV_{max} \geq 2.5$, and $SUV_{max} \geq 5$ were 4.5 mm, 8.5 mm, and 14.5 mm, respectively. ***Conclusion:*** For ovarian cancer, [^{68}Ga]Ga-DOTA-FAPI-04 PET/CT had an advantage over [^{18}F]FDG PET/CT in diagnosing peritoneal metastases, both techniques had a high value in diagnosing lymph node metastases. [^{68}Ga]Ga-DOTA-FAPI-04 PET/CT had greater diagnostic value for primary or metastatic lesions of ovarian cancer larger than or equal to 4.5mm.

EPS-168

Dual-Tracer FAPI and FDG PET/CT Enhances Prediction of Pathological Response and Survival in Neoadjuvant Immunochemoradiotherapy for Esophageal Squamous Cell Carcinoma

J. Dai[1], *H. WANG*[2], *R. Tian*[2];
[1]*West China Hospital, Chengdu, CHINA,* [2]*West China Hospital, Sichuan University, Chengdu, CHINA.*

Aim/Introduction: This study evaluated the predictive utility of serial FAPI and FDG PET/CT imaging for pathological response and prognosis in patients with locally advanced esophageal squamous cell carcinoma (LA-ESCC) receiving neoadjuvant concurrent chemoradiotherapy with or without PD-1 blockade (Tislelizumab). ***Materials and Methods:*** Forty-nine patients with LA-ESCC were prospectively enrolled and divided into two groups: Group A (n=35, tislelizumab + chemoradiotherapy) and Group B (n=14, chemoradiotherapy alone). All patients underwent pre- and post-treatment FAPI and FDG PET/CT scans. Two calibration methods of PET (body weight and lean body weight) and two volume-of-interest (VOI) thresholds (41% and 50% of the SUVmax) were applied were used to generate imaging parameters, including intensity-based, volume-based, distribution-based parameters, TLG and their change ratio over the treatment. Clinical and imaging parameters were analyzed for their association with pathological tumor regression grade (TRG) and progression-free survival (PFS). TRG = 0 was considered as well-responders and TRG = 1 ~ 3 was defined as poor-responders. Statistical methods included univariate Logistic regression, Cox regression, receiver operating characteristic (ROC) curve analysis, and Kaplan-Meier survival estimates. ***Results:*** Well-respond was observed in 29 of 49 patients (59.2%), whereas poor-respond persisted in 20 patients (40.8%) after neoadjuvant treatment. Pretreatment FAPI PET parameters, including tumor volume (maximum 3D diameter: AUC = 0.78) and intensity distribution (kurtosis: AUC = 0.75), significantly predicted TRG. A combined model integrating volume and distribution parameters improved predictive accuracy (AUC = 0.84, sensitivity = 75%, specificity = 86.21%). Post-treatment FDG PET parameters, TRG and yp T and N stage significantly predict PFS. While Group A demonstrated a higher well-respond rate than Group B (65.7% vs. 42.86%), this difference lacked statistical significance (p=0.14). Higher baseline BMI was associated with improved pathological response. ***Conclusion:*** FAPI PET excels in preoperative prediction of pathological response, whereas FDG PET better forecasts long-term prognosis. Combined imaging biomarkers may optimize personalized treatment strategies for LA-ESCC. While our findings highlight the complementary roles of FAPI and FDG PET/CT, the relatively small cohort and limited follow-up duration necessitate validation in larger, multi-center studies. Future research should also explore the spatial heterogeneity of FAPI and FDG uptake in residual tumors to refine prognostic models.

EPS-169

Comparison of [^{99m}Tc]Tc-FAPI SPECT/CT and [^{18}F]FDG PET/CT as Predictive Biomarkers for Immunotherapy Response in Gastrointestinal Cancer

Y. Zhang, *W. Chen;*
Department of Nuclear Medicine, Fuzhou University Affiliated Provincial Hospital, Fuzhou, CHINA.

Aim/Introduction: To explore the diagnostic performance of [^{99m}Tc]Tc-FAPI SPECT/CT for gastrointestinal cancer, compared to [^{18}F]FDG PET/CT. ***Materials and Methods:*** In this analysis of a prospective trial, consecutively recruited patients from a single center with pathologically confirmed gastrointestinal cancer were prospectively enrolled from September 2022 to June 2024 and underwent paired [^{99m}Tc]Tc-FAPI and [^{18}F]FDG PET/CT examinations at intervals of more than 1 day and within 7 days of each other.The activity of tracer accumulation in lesions was assessed by maximum standardized uptake value (SUVmax) and TBR (lesions SUVmax/ascending aorta SUVmean). Histopathologic and clinical follow-up results were used as reference standards for final diagnoses. ***Results:*** Seventy-eight patients (46 men; median age, 58.8 ± 14.5 years) were evaluated. Compared with the TBR for [^{18}F]FDG uptake, TBR for [^{99m}Tc]Tc-FAPI uptake was higher in primary tumor(4.6±2.0 vs. 3.4±1.7; P=0.001) ,peritoneal spread (1.3 [1.1, 7.3] vs. 1.1 [1.1, 1.1]; P=0.001) and liver metastases(2.5 [1.1, 8.5] vs. 1.1 [1.1, 3.4]; P=0.031). For diagnostic accuracy in a total of 253 lesions in 78 patients, compared with [^{18}F]FDG PET/CT, [^{99m}Tc]Tc-FAPI SPECT/CT demonstrated a higher sensitivity (100% [15 of 15 lesions] vs. 20% [3 of 15]; P< 0.001), accuracy (100% [48 of 48 lesions] vs. 75% [36 of 48]; P< 0.001), and negative predictive value (100% [33 of 33 lesions] vs. 69% [36 of 48 lesions]; P=0 .001) in detecting peritoneal spread, and a higher sensitivity (85% [17 of 20 lesions] vs. 50% [10 of 20]; P=0.041) in detecting liver metastases. Patients with metastatic gastrointestinal carcinomas

negative on the [^{99m}Tc]Tc-FAPI scan showed improved clinical prognosis after immunotherapy (P<0.006). TBR-FDG/TBR-FAPI was the main predictor of better prognosis post-immunotherapy ([stable disease,SD]+[partial response,PR]), with an optimal cut-off of 3.82. ***Conclusion:*** [^{99m}Tc]Tc-FAPI SPECT/CT can better evaluate peritoneal spread and liver metastases in gastrointestinal cancer. Furthermore,TBR-FDG/TBR-FAPI is a valuable imaging parameter for monitoring immunotherapy responses.

EPS-170

Preoperative Noninvasive ^{18}F-FDG PET/CT-Based Nomogram For Predicting HER2 Expression in Gastric Adenocarcinoma

S. Yang, *X. Shao, X. Zhang;*
Department of Nuclear Medicine, the Third Affiliated Hospital of Soochow University, Changzhou, CHINA.

Aim/Introduction: Human epidermal growth factor receptor 2 (HER2) overexpression represents a pivotal molecular aberration in gastric adenocarcinoma, critically determining eligibility for targeted therapies. Current gold-standard methods employ immunohistochemistry (IHC) and fluorescence in situ hybridization (FISH) to evaluate HER2 protein expression and gene amplification, respectively. However, their invasive nature precludes real-time monitoring of HER2 dynamics during treatment, hindering therapeutic optimization. This study establishes and validates an ^{18}F-fluorodeoxyglucose positron emission tomography/computed tomography (^{18}F-FDG PET/CT)-based nomogram which integrates metabolic parameters and clinical covariates to non-invasively predict HER2 status and enable therapeutic personalization. ***Materials and Methods:*** This retrospective study included 231 gastric adenocarcinoma patients who underwent preoperative ^{18}F-FDG PET/CT. Clinical data were systematically retrieved, and primary tumor metabolic parameters—maximum standardized uptake value (SUVmax), mean SUV (SUVmean), metabolic tumor volume (MTV), and total lesion glycolysis (TLG)—were quantified using a fixed SUV≥2.5 threshold. Univariate and multivariate analyses were employed to identify independent predictors of HER2 expression status. A nomogram was subsequently developed and validated through assessments of discriminatory capacity (area under the receiver operating characteristic [ROC] curve, AUC), calibration accuracy (Brier score), and clinical net benefit (decision curve analysis across threshold probabilities). ***Results:*** PET metabolic thresholds (SUVmax=19.22, SUVmean=4.85) were established through ROC analysis. Univariate regression (P < 0.1) identified potential predictors of HER2 expression: SUVmax (P = 0.006), SUVmean (P = 0.021), tumor location (P = 0.009), lymph node metastasis (P = 0.061), and tumor differentiation grade (P = 0.051). Subsequent multivariate logistic regression confirmed tumor location (odds ratio [OR] = 0.285, P = 0.004), differentiation grade (OR = 2.613, P = 0.029), and SUVmax (OR = 4.494, P = 0.002) as independent predictors. The constructed nomogram demonstrated robust discriminatory capacity (concordance statistic [C-statistic] = 0.715), maintained stability on bootstrap validation (C-statistic = 0.695). Model calibration was satisfactory (Brier = 0.102), while decision curve analysis confirmed superior net clinical benefit compared to default strategies. ***Conclusion:*** The PET/CT-based nomogram shows significant potential for non-invasive HER2 detection in gastric adenocarcinoma, and can serve as a novel substitute for invasive testing.

EPS-171

Trop2-Targeted PET/CT for Diagnosis and Patient Stratification in Breast Cancer Toward Trop2-Directed Antibody-Drug Conjugate Therapy

L. Zhao, *H. Chen;*
The First Affiliated Hospital of Xiamen University, Xiamen, CHINA.

Aim/Introduction: Trop2-targeted antibody-drug conjugates (ADCs) have demonstrated promising efficacy and have been approved in patients with HR+HER2- and triple-negative breast cancer (TNBC). However, not all patients within these subtypes benefit equally from such treatment, highlighting the urgent need for developing effective tools for patient selection and stratification. ***Materials and Methods:*** This study enrolled patients with newly diagnosed or previously treated breast cancer at the First Affiliated Hospital of Xiamen University between November 2023 and December 2024. All patients underwent paired ^{18}F-FDG PET/CT and ^{68}Ga-MY6349 PET/CT imaging for tumor staging or recurrence/metastases detection. SUVmax derived from the two PET/CT modalities and pathological results were recorded to evaluate the tumor uptake pattern and lesion detectability of the two imaging modalities. ***Results:*** A total of 61 patients were prospectively enrolled, including 7 true-negative and 54 true-positive cases. Among the 562 true-positive lesions, ^{68}Ga-MY6349 uptake (SUVmax) was significantly associated with breast cancer subtypes (P<0.001, Kruskal-Wallis H=34.9). SUVmax values were highest in HR+/HER2- [7.2 (4.4-9.4)], followed by TNBC [5.2 (3.8-6.4)], HER2+ [4.8 (1.7-7.4)], and HR+/HER2+ [3.3 (2.1-8.1)]. In HR+/HER2- subtypes, ^{68}Ga-MY6349 demonstrated significantly higher uptake compared to ^{18}F-FDG [7.2 (4.4-9.4) vs. 3.6 (2.3-5.5), P<0.001]. Specifically, the uptake of ^{68}Ga-MY6349 in lymph node metastases and distant metastatic lesions was significantly higher than ^{18}F-FDG (lymph nodes: 6.6 [4.0-10.2] vs. 2.8 [1.9-4.6], P < 0.001; distant metastases: 7.9 [5.7-9.4] vs. 4.1 [2.4-6.2], P < 0.001). In 27 patients with HR+/HER2- subtypes, ^{18}F-FDG PET/CT detected 139/208 lesions (missing 2 primary, 40 visceral and bone metastases, and 27 lymph node metastases), while ^{68}Ga-MY6349 PET/CT detected 202/208 lesions (missing 1 visceral and bone metastasis and 5 lymph node metastases). Interestingly, among 215 lesions in 16 TNBC patients, ^{18}F-FDG PET/CT detected 206 metastatic lesions (missing 9 lymph node metastases), whereas ^{68}Ga-MY6349 PET/CT detected all lesions. For HER2+ (7 patients with 74 lesions) and HR+/HER2+ (4 patients with 65 lesions) subtypes, the two tracers exhibited comparable lesion detectability. ***Conclusion:*** ^{68}Ga-MY6349 PET/CT demonstrated superior uptake and greater lesion detectability compared to ^{18}F-FDG PET/CT in patients with HR+/HER2- breast cancer. The high uptake of ^{68}Ga-MY6349 in HR+/HER2- and TNBC lesions may partially explain the favorable clinical outcomes observed with Trop2-targeted ADCs in these subtypes, suggesting its potential role for patient selection and stratification for Trop2-targeted therapies. However, the observed heterogeneity in uptake warrants further investigation to clarify its applications across different patient populations.

EPS-172

The prognostic value of PET/MR in children with hepatoblastoma

Y. Xu;
Hangzhou Universal Medical Imaging Diagnostic Center, Hangzhou, CHINA.

Aim/Introduction: To investigate the prognostic significance of ^{18}F-FDG PET/MR metabolic parameters and clinicopathological factors in pretreatment pediatric hepatoblastoma (HB). ***Materials and Methods:*** A retrospective analysis was conducted on 98 children with newly diagnosed hepatoblastoma who underwent ^{18}F-FDG PET/MR imaging. Univariate and multivariate Cox regression analyses were performed to evaluate the association between clinicopathological variables (e.g., histology, serum alpha-fetoprotein [AFP], tumor size) and metabolic indices, including maximum standardized uptake value (SUVmax), metabolic tumor volume (MTV), and total lesion glycolysis (TLG), for predicting relapse-free survival (RFS) and overall survival (OS). ***Results:*** During a median follow-up of 36 months, relapse occurred in 42 patients (42.85%). Univariate analysis identified AFP level (P=0.001), histology (P=0.008), tumor size (P=0.012), MTV (P=0.004), and TLG (P=0.006) as significant predictors of RFS and

OS. Multivariate analysis demonstrated that TLG (RFS: P=0.015; OS: P=0.019) and AFP (RFS: P=0.022; OS: P=0.028) were independent prognostic factors for both endpoints, while MTV retained significance for OS (P=0.035). ***Conclusion:*** Pretreatment ^{18}F-FDG PET/MR provides valuable prognostic information in pediatric hepatoblastoma. Elevated TLG, higher AFP stage, and higher MTV are strongly associated with increased risk of recurrence and mortality, highlighting their utility in risk stratification and therapeutic planning.

EPS-173

Head-to-head Comparison of [^{18}F]MFBG and [^{18}F]FDG PET in Neuroblastoma

P. Wang[1], *S. Yu*[1], *J. Mao*[2], *X. Su*[1];
[1]*The First Affiliated Hospital Zhejiang University School of Medicine, Hangzhou, CHINA,* [2]*The Children's Hospital Zhejiang University School of Medicine, Hangzhou, CHINA.*

Aim/Introduction: To compare the diagnostic performance of [^{18}F]MFBG PET (PET/CT or PET/MR) with [^{18}F]FDG PET/CT in patients with neuroblastoma, particularly in post-treatment evaluation settings where lesion detectability is often challenging. ***Materials and Methods:*** In this prospective study, 42 neuroblastoma patients (median age: 5 years) underwent paired [^{18}F]MFBG and [^{18}F]FDG PET imaging. PET scans were acquired 60-90 minutes after intravenous administration of 2-3 MBq/kg of either tracer within one week. Lesion quantification included Curie scores for bone lesions and lesion counts for soft tissue involvement. ***Results:*** Among 42 patients, 32 had active disease while 10 were confirmed disease-free through multidisciplinary clinical assessment and 3-6 months of follow-up. These 10 patients showed negative findings on both [^{18}F]MFBG and [^{18}F]FDG PET.Of the 32 patients with active disease, 6 were newly diagnosed, all showing concordant results on both tracers with 100% sensitivity for primary and metastatic lesion detection. In the remaining 26 patients received treatment (6 with suspected recurrence, 4 refractory cases, 2 under survival follow-up, and 14 undergoing end-of-treatment evaluation), [^{18}F]MFBG demonstrated markedly higher sensitivity (25/26, 96.2%) than [^{18}F]FDG (10/26, 38.5%) based on patient-level analysis. Notably, [^{18}F]FDG missed most bone lesions, often producing false-negative results even in clinically active disease. Only one hepatic metastasis was missed by [^{18}F]MFBG due to physiological liver uptake.In patients with bone-only involvement (n=21), [^{18}F]MFBG yielded a total Curie score of 214 (mean: 10.2), significantly higher than [^{18}F]FDG's score of 30 (mean: 1.4) ($P < 0.0001$). In patients with soft-tissue-only involvement (n=5), [^{18}F]MFBG identified 9 lesions across 4 patients, whereas [^{18}F]FDG detected only 4 lesions in 2 patients. ***Conclusion:*** [^{18}F]MFBG PET imaging significantly outperformed [^{18}F]FDG in evaluating residual or recurrent disease in NB patients after treatment. While both tracers are reliable for initial diagnosis, [^{18}F]MFBG provides superior accuracy during post-treatment surveillance, supporting its clinical value in guiding NB management.

EPS-174

A Predictive Model Based on Lymph Node-to-Primary Tumor SUV Ratio Accurately Classifies Neck Nodal Malignancy Risk and Guides Neck Dissection in Head and Neck Squamous Cell Carcinoma Patients

S. Chan[1], *S. Chi*[2];
[1]*Hualien Tzu Chi Hospital, Hualien, TAIWAN,* [2]*Tzu Chi University, Hualien, TAIWAN.*

Aim/Introduction: Accurate detection of cervical lymph node metastasis in head and neck cancer patients is crucial for determining whether to perform neck dissection. This study investigates the predictive value of [18F]fluorodeoxyglucose positron emission tomography/computed tomography ([^{18}F]FDG PET/CT) parameters in determining the pathological status of neck lymph nodes in patients with head and neck cancer (HNC). ***Materials and Methods:*** This retrospective study included patients with stage M0 HNC who underwent surgery as definitive treatment. All patients received [^{18}F]FDG PET/CT prior to treatment. The diagnostic performance in detecting neck lymph node metastases was assessed using pathological results as the gold standard. Clinical and imaging predictors associated with neck nodal metastases were analyzed using univariate and multivariate analyses. The area under the curve (AUC) was calculated to evaluate predictive capacity. ***Results:*** A total of 168 HNC patients were included. Visual interpretation of [^{18}F]FDG PET/CT demonstrated moderate sensitivity (84.8%) and specificity (75.0%), but a suboptimal positive predictive value (65.7%) for detecting nodal metastasis. Univariate analysis identified several significant predictors of metastases including tumor site, T classification, maximum standardized uptake value (SUVmax), lymph node-to-primary tumor SUVmax ratio, and total lesion glycolysis. Multivariate logistic regression analysis revealed lymph node SUVmax ($p = 0.049$, AUC=0.849) and lymph node-to-primary tumor SUVmax ratio ($p = 0.004$, AUC=0.848) as independent predictors for neck nodal metastasis. A scoring system was developed based on these independent predictors. Among patients with a score of 2 (n = 53), the likelihood of nodal metastasis was 86.8%, while those with a score of 0 (n = 88) had an 88.6% likelihood of no metastasis. Notably, among patients showing cervical lymph node metastasis on contrast-enhanced CT images, 20% were classified as score 0 and subsequently confirmed to have no lymph node metastasis by pathological examination. ***Conclusion:*** This research demonstrates that a predictive model based on the lymph node-to-primary tumor SUV ratio outperforms traditional visual interpretation in assessing cervical lymph node metastasis. It has the potential to reduce unnecessary neck dissections caused by false-positive findings on CT in patients with head and neck cancer. Compared to other complex PET-derived parameters, the SUV ratio offers greater inter-scanner and inter-observer consistency, resulting in a more reproducible and clinically applicable predictive model.

EPS-175

A Novel Prognostic Scoring System Integrating [^{18}F]PFPN PET Metrics and Clinical Parameters for Mucosal Melanoma Survival Stratification

Z. Lin[1,2], *C. Tang*[1,2], *Y. Feng*[1,3,4], *W. Ruan*[1,3,4], *F. Hu*[1,3,4], *Y. Gai*[1,3,4], *X. Zhang*[1,3,4], *X. Lan*[1,3,4];
[1]*Department of Nuclear Medicine, Union Hospital, Tongji Medical College, Huazhong University of Science and Technology, Wuhan, CHINA,* [2]*First School of Clinical Medicine, Tongji Medical College, Huazhong University of Science and Technology, Wuhan, CHINA,* [3]*Hubei Key Laboratory of Molecular Imaging, Wuhan, CHINA,* [4]*Key Laboratory of Biological Targeted Therapy, the Ministry of Education, Wuhan, CHINA.*

Aim/Introduction: Mucosal melanoma, a rare and aggressive malignancy with heterogeneous outcomes, lacks robust prognostic tools. While [^{18}F]FDG PET has limitations in specificity, [^{18}F]PFPN, a melanin-targeted tracer, offers enhanced lesion detection and metabolic quantification. This study aimed to develop a prognostic scoring system combining [^{18}F]PFPN PET-derived biomarkers and clinical factors to optimize risk stratification. ***Materials and Methods:*** In this retrospective study, 50 primary mucosal melanoma patients (mean age 60.5±8.8 years) underwent [^{18}F]PFPN PET imaging (2021-2024). Whole-body melanotic tumor volume (WBMTV), clinical staging, age, treatment regimens, and anatomical subtypes were analyzed. Cox regression and stepwise modeling identified independent prognostic factors for overall survival (OS). A simplified scoring system was derived, validated against clinical staging, and stratified into risk groups. ***Results:*** Multivariate analysis revealed whole-body melanotic tumor volume (WBMTV, HR=1.003, $p<0.01$), advanced stage (HR=4.366, $p<0.01$), age ≥60 (HR=1.171, $p<0.01$), absence of immunotherapy (HR=0.17, $p<0.05$), and non-head&neck/vulvar subtypes as key OS predictors. The scoring model (C-index=0.85)

outperformed clinical staging (C-index=0.76). Risk stratification demonstrated marked survival disparities: Group 1 (0-19 points) had 100% 1-year survival, while Group 3 (30-50 points) exhibited a 74.59% 1-year and 0% 3-year survival. WBMTV thresholds (<1.52 vs. ≥1.52 cm^3) and stage-specific scores effectively differentiated outcomes (p<0.001). ***Conclusion:*** Integrating [^{18}F]PFPN PET metrics with clinical variables enables precise prognostic stratification in mucosal melanoma. This automated scoring system facilitates rapid risk assessment, guiding personalized therapeutic strategies. Further validation in multi-center cohorts is warranted to confirm its clinical utility.

EPS-176

Comparison of [18F]AlF-NOTA-FAPI-04 PET/CT and [^{18}F] FDG PET/CT for diagnosing lymph node metastasis in malignant tumors

W. Zhou, *J. Dai, K. Zheng, X. Peng, Y. Zhang, C. Jiang, J. Yang, H. Ye;*
The Affiliated Cancer Hospital of Xiangya School of Medicine/ Hunan Cancer Hospital, Changsha, CHINA.

Aim/Introduction: This study compared the diagnostic performance, semi-quantitative analysis, and staging accuracy of [^{18}F]AlF-NOTA-FAPI-04 and [^{18}F]FDG PET/CT in detecting lymph node metastases. ***Materials and Methods:*** This single-center retrospective study included 41 patients with suspected lymph node metastases who received both [^{18}F]FDG and [^{18}F]AlF-NOTA-FAPI-04 PET/CT. The study compared metastatic lymph node detection, semi-quantitative values, and N staging accuracy. Subgroup analyses were performed for lymph nodes with short-axis diameters (SAD) ≥10 mm and <10 mm. ***Results:*** 41 patients with 126 nodes were include. [^{18}F]AlF-NOTA-FAPI-04 outperformed [^{18}F]FDG in the detection of metastatic lymph nodes, achieving higher accuracy in both patient-based (92.7% vs. 70.7%, p=0.004) and node-based analyses (91.3% vs. 60.3%, p<0.001). In semi-quantitative analysis, the maximum standardized uptake value and target-to-background ratio of [^{18}F]AlF-NOTA-FAPI-04 were higher than those of [^{18}F]FDG in metastatic lymph nodes (all p < 0.001). Both tracers distinguished metastatic from benign nodes with SAD ≥ 10 mm (p<0.05). [^{18}F]AlF-NOTA-FAPI-04 PET/CT could distinguish between benign and metastatic lymph nodes with SAD < 10mm (p<0.001), whereas [^{18}F]FDG PET/CT could not (p >0.05). [^{18}F]AlF-NOTA-FAPI-04 also provided more accurate N staging assessments (87.8% vs. 65.9%, p = 0.006). ***Conclusion:*** [^{18}F]AlF-NOTA-FAPI-04 PET/CT demonstrated superior diagnostic performance, semi-quantitative capability, and N staging accuracy compared to [^{18}F] FDG PET/CT, particularly for small metastatic lymph nodes (SAD < 10 mm), offering enhanced guidance for tumor staging.

EPS-177

Complementary role of ^{11}C-acetate to ^{68}Ga-FAPI-46 in tumor imaging with negative/indeterminate ^{18}F-FDG findings

I. Ho[1,2], *S. Chen*[2], *Y. Wong*[2], *K. Wu*[2], *S. Cheung*[2], *Y. Yip*[2], *K. Cheng*[2], *J. Kung*[1], *C. Ho*[2];
[1]*Queen Elizabeth Hospital, Hong Kong, HONG KONG,* [2]*Hong Kong Sanatorium & Hospital, Hong Kong, HONG KONG.*

Aim/Introduction: ^{11}C-acetate is a metabolic tracer partially complementary to ^{18}F-FDG in PET imaging. ^{68}Ga-FAPI is a receptor tracer to evaluate abnormal dysmoplastic reactions caused by stromal cancer associated fibroblasts (CAF). Much of the published data worldwide have compared the diagnostic performance of ^{68}Ga-FAPI with ^{18}F-FDG, putting emphasis on its superior advantage over conventionally ^{18}F-FDG non-avid or minimally-avid entities, such as mucinous neoplasm, signet-ring clear-cell carcinoma, renal cell carcinoma (RCC) and certain hepatobiliary tumors. In this single-center prospective study, we aimed to compare ^{11}C-acetate with ^{68}Ga-FAPI-46 for the evaluation of various tumors that were non-avid/indeterminate by ^{18}F-FDG PET/CT. ***Materials and Methods:*** During Jan-2022 to Dec-2024, we recruited 55 patients (M:38, F:17; age range:34-85 years, mean=61.2±13.3 years) having clinical suspicion of malignancy but with negative/indeterminate ^{18}F-FDG PET/CT. They all underwent ^{68}Ga-FAPI-46 and ^{11}C-acetate PET/CT separately within 1 week and subsequently had histopathology for final diagnosis. FAPI or ^{11}C-acetate-avid lesions were automatically drawn by MIMContouring software and SUV_{max} of the index lesion/patient was recorded. PET/CT diagnostic criteria of ^{11}C-acetate were based on the degree and uptake pattern with reference to our prior published studies. ***Results:*** Histopathology diagnosed 34/55 patients with malignant tumors and 21/55 with benign lesions. FAPI-46 PET/CT showed prominent expression (SUV_{max}=9.3±4.8, range:3.8-20.4) in 22/34 (sensitivity=64.7%) malignant entities: intrahepatic cholangiocarcinoma (small-duct and Klatskin, n=7); poorly-differentiated hepatocellular carcinoma (PDHCC, n=5); liver metastases (n=5, from cholangiocarcinoma, PD neuroendocrine tumor, gallbladder clear-cell adenocarcinoma, leiomyosarcoma); sarcoma (n=2); tonsillar SCC (n=2); hemangioendothelioma (n=1). However, FAPI-46 PET/CT was false negative in 12/34 patients with malignancy: well-differentiated HCC (n=7); RCC clear-cell subtype (n=2); multiple myeloma (n=2); liver secondary from colon (n=1). Of these 12/34 malignancies missed by FAPI-46, ^{11}C-acetate PET/CT was positive in 11/12 (SUV_{max}=12.4±6.9). Taken together, the sensitivity could be increased from 64.7% by FAPI-46 alone to 97% (33/34, P<0.01) by both. Among the 21 benign entities in liver (n=14), enlarged lymph node (n=4), kidney (n=2) and lung (n=1), FAPI-46 PET/CT showed little to no tracer uptake (SUV_{max}=1.2±0.8, range:0.6-3.0) in 19/21 (specificity=90.5%). Two FP cases with markedly FAPI-avid liver masses (SUV_{max}=11.5&6.4) were confirmed hepatic confluent fibrosis (HCF), despite being negative on ^{11}C-acetate PET/CT. ***Conclusion:*** ^{68}Ga-FAPI-46 PET/CT has an important role for detection of suspected tumor entities that are non-avid/indeterminate by ^{18}F-FDG. However, ^{11}C-acetate PET/CT remains an important metabolic tracer partially complementary to either ^{18}F-FDG or ^{68}Ga-FAPI-46, and could not be replaced by ^{68}Ga-FAPI in tumor evaluation.

1110

Monday, October 6, 2025, 16:45 - 18:15
Room 116

CTE 5 - Technologists Committee: Dynamic Cardiovascular Hybrid Imaging

OP-491

Digital Evolution and Hybrid Scanners: The Future of Cardiovascular Imaging in Nuclear Medicine.

S. Nekolla*; Nuklearmedizinische Klinik und Poliklinik Klinikum rechts der Isar der Technischen Universität München, Munich, GERMANY.*

OP-492

Clinical implementation of Hybrid Digital Technology in Nuclear Medicine Cardiovascular Imaging

C. Nappi*; Department of Advanced Biomedical Sciences Federico II University, Naples, ITALY.*

OP-493

Meeting Clinical Needs – The Technologist's Perspective on Delivering Optimal Results

L. Langhoff Lund*; Bispebjerg og Frederiksberg Hospital, Department of Physiology and Nuclear Medicine, Copenhagen, DENMARK.*

1111

Monday, October 6, 2025, 16:45 - 18:15
Room 111

Featured Session - Cardiovascular Committee: Innovation in Myocardial Perfusion in SPECT

OP-495
Invited Speaker
A. Manrique;
CHU de Caen, Caen, FRANCE.

OP-496
CT-free attenuation correction for cardiac-dedicated CZT SPECT: update of the CASCTEC study
***M. Hesse**, F. Dupont, N. Laajimi, A. Oulad Bouchetta, R. Lhommel, V. Roelants;*
Cliniques Universitaires Saint-Luc, Brussels, BELGIUM.

Aim/Introduction: While attenuation-correction (AC) improves the diagnostic accuracy of myocardial perfusion scintigraphy (MPS) for detecting coronary artery diseases (CAD), most clinical cardiac-dedicated CZT cameras are still marketed without a CT. The CASCTEC clinical study aims at developing an approach to generate attenuation maps for pinhole CZT cameras, from emission scans only. This work presents an update of the study results obtained with more patients and after optimization of the attenuation map generation. ***Materials and Methods:*** Fifty patients (34 male; BMI: 27±5 kg/m2) referred for MPS were enrolled in the single-center prospective CASCTEC study. Two-day stress/rest MPS SPECT was performed on a pinhole CZT camera. A standard of care (SOC) 5-minute acquisition was immediately followed by an additional 5-minute acquisition after retracting the detectors without moving the patient. Subsequently all patients underwent SPECT/CT imaging to be used as reference. The acquisition with retracted detectors allowed to delineate the patient body contour, and together with the SOC acquisition, enabled the segmentation of soft and lung tissues to produce an attenuation map. Non-corrected (NC) and AC images were compared together and to the NC and AC SPECT/CT images using the AHA 17-segment model polar maps. Stress and rest summed scores for the different reconstructed images were calculated automatically (Quantitative Perfusion SPECT software) and visually by an experienced physician. ***Results:*** CASCTEC-AC stress and rest perfusion images showed a more homogeneous tracer distribution compared to NC images. All perfusion defects observed on the SPECT/CT-AC images were also visible on CASCTEC-AC images. The mean stress and rest AC summed scores were 13.4±5.1 for CASCTEC vs 14.5±5.6 for SPECT/CT (p=0.25) using the automatic scoring, and 11.3±5.3 for CASCTEC vs 12.6±5.5 for SPECT/CT (p=0.10) with the visual analysis. When focusing especially on the inferior segments, the AC-NC score differences were -2.5±2.1 for CASCTEC vs -3.1±2.0 for SPECT/CT (p=0.09) using the automatic scoring, and -2.9±2.1 for CASCTEC vs -3.2±2.5 for SPECT/CT (p=0.45) with the visual analysis. No significant change of the perfusion was observed on the CASCTEC-AC images in the other segments less affected by the attenuation. ***Conclusion:*** These results show that the CT-free patient-specific attenuation map enhances NC perfusion in the inferior wall similarly to CT-based AC images from a SPECT/CT. CASCTEC-AC summed scores are in good agreement with CT-AC ones, both for automatic and visual scoring. This CT-free method might so enhance the diagnostic accuracy of current cardiac pinhole CZT systems for detecting obstructive CAD.

OP-497
Multimodal Approaches to Coronary Arteries: Myocardial Perfusion Imaging, Coronary CT Angiography, Calcium Score, MESA Risk Score and Coronary Age
***A. Dursun**[1], N. A. Dizdar[1], Y. Aktürk[2], F. Başyiğit[3], E. Tatcı[4], Ö. Özmen[4];*
[1]Ankara Etlik City Hospital, Nuclear Medicine Clinic, Ankara, TÜRKIYE, [2]Ankara Etlik City Hospital, Radiology Clinic, Ankara, TÜRKIYE, [3]Ankara Etlik City Hospital, Cardiology Clinic, Ankara, TÜRKIYE, [4]Health Sciences University, Ankara Etlik City Hospital, Nuclear Medicine Clinic, Ankara, TÜRKIYE.

Aim/Introduction: Multi-Ethnic Study of Atherosclerosis (MESA) is a scoring system used to calculate 10-year Coronary Heart Disease(CHD) risk and coronary age. Coronary CT Angiography (CCTA) imaging can be used to calculate severity of coronary artery stenosis (CAD-RADS) and calcific plaque burden coronary artery calcium score (CACS) of patients. In our study, patients'Tc99m-MIBI myocardial perfusion imaging (MPI) findings, CAD-RADS, calcium score, MESA risk scores and coronary artery ages were evaluated. ***Materials and Methods:*** Between November 2022 and January 2025, 12.423 patients who underwent MPI at our hospital were screened. Among them, 132 patients (aged 45-85) were included in study. Using "MESA Risk Score and Coronary Age Calculator", 10-year CHD risk, coronary artery age and chronological age difference (Delta Age) of all patients were determined. According to CCTA findings, stenosis with 0-49% were classified as normal-mild; 50-69% as moderate, and ≥70% as severe stenosis. MPI findings were grouped by summed difference scores (SDS) as <2, 2-4, and >4. ***Results:*** Patients with SDS >4 had significantly higher coronary age, delta age, CACS, and MESA risk scores compared to other groups (p<0.001) (Table-1). EF was significantly higher in patients with SDS score <2 than those with score >4 (p=0.026). In CCTA images of normal-mild stenosis group, both CACS and MESA risk scores with CACS were lower than in other groups (p<0.001 and p<0.001, respectively) (Table-2). In group, coronary artery age and delta age were lower than in those with severe stenosis (p<0.001 and p<0.004, respectively). Myocardial ischemia percentage was higher in severe stenosis than in other groups (p<0.05). In logistic regression analysis, strong relationship was found between the severity of coronary artery stenosis detected in CCTA and ischemia percentage in MPS (p<0.001) (Table-3).SDS was <2 in 7/16 patients with severe stenosis on CCTA and only one patient in this group underwent revascularization. The other patients in this group (n=9) with SDS score >4 underwent revascularization. Two patients with normal-mild stenosis on CCTA and SDS>4 on MPI underwent revascularization due to >70% stenosis on coronary angiography. ***Conclusion:*** Many studies revealed that anatomical degree of coronary artery stenosis may not correlate with its physiological reflection. According to our findings, MPI provides valuable prognostic information beyond anatomical stenosis, correlates with MESA scores, and helps guide treatment decisions, especially in moderate coronary artery stenosis, by reflecting hemodynamic impact and potentially reducing unnecessary interventions. ***References:*** Sirajuddin A, et al.Ischemic Heart Disease: Noninvasive Imaging TechniquesandFindings. Radiographics. 2021 Jul-Aug;41(4):990-1021. doi: 10.1148/rg.2021200125.

OP-498
Diagnostic value of pericoronary fat attenuation index (FAI) in predicting abnormal myocardial perfusion in INOCA patients: a comparative study of CCTA and CZT-SPECT
***H. Zhang**[1], F. Caobelli[2], K. Shi[2], R. Ji[1], M. Fei[3], F. Yu[1];*
[1]Tongji University School of Medicine,shanghai Tenth People's Hospital, Shanghai, CHINA, [2]Department of Nuclear Medicine, Inselspital, Bern University Hospital, University of Bern, Bern, SWITZERLAND, [3]Tongji university School of Medicine, Shanghai Pulmonary Hospital, Shanghai, CHINA.

Aim/Introduction: Although coronary inflammation has been established as a critical factor in obstructive coronary heart disease, it remains unclear whether a class of Non-invasive imaging inflammatory biomarkers, exemplified by the fat attenuation index (FAI), can detecting a high-risk subset of INOCA patients with myocardial ischemia. ***Materials and Methods:*** 191 consecutive patients with symptoms suggestive for myocardial ischemia were prospectively evaluated. All patients were referred for CZT-SPECT MPI and CCTA in one week. INOCA was defined as the presence of symptoms suggestive for myocardial ischemia, including angina pectoris associated with ischaemic ECG (electrocardiogram) changes and/or abnormal myocardial perfusion imaging (MPI), without detectable stenosis or luminal stenosis <50% on CCTA. Patients were divided into two groups according to CZT-SPECT MPI ***results:*** Ischemia (SSS>4 and SDS>2) and non-Ischemia group. ***Results:*** This study included 112 INOCA patients [mean age 64.52±11.14 years, 43.8% male]. Among them, 28/112 (25.0%) had abnormal MPI. LCX-FFR (0.93±0.07 vs 0.95±0.03, p=0.04) were significantly lower in Ischemia group. LAD-FFR and RCA-FFR were not different between groups. LAD-FAI (-85.21±8.10 vs -90.80±7.51, p=0.001), LCX-FAI (-78.38±8.30 vs -84.35±7.97, p=0.001) and RCA-FAI (-88.13±8.91 vs -93.60±9.87, p=0.01) were significantly high in Ischemia group.A moderate correlation of Stress LVEF with FAI was founded for both LAD-FAI (r=-0.26, p=0.006) and LCX-FAI (r=-0.35, p<0.001). Similarly, moderate correlation of Rest LVEF with FAI was also founded for both LAD-FAI (r=-0.22, p=0.02) and LCX-FAI (r=-0.20, p=0.04). Accordingly, the efficacy of FAI in diagnosing ischemia was LAD-FAI >-94.9 (AUC 0.67, 95% CI 0.57-0.76, p=0.003, sensitivity 92.9%, specificity 34.5%), LCX>-78.3(AUC 0.68, 95% CI 0.58-0.76, p=0.002, sensitivity 53.6%, specificity 79.8%) and RCA>-97.23(AUC 0.64, 95% CI 0.55-0.73, p=0.01, sensitivity 92.4%, specificity 39.3%). Nevertheless, the Delong test suggested that there was no significant difference in the efficacy of the three indices in the diagnosis of ischemia (LAD-FAI vs LCX-FAI, p=0.83; LCX-FAI vs RCA FAI, p=0.52; LAD-FAI vs RCA-FAI, p=0.63). In Univariate Logistic regression analysis, LAD-FAI (OR 1.10, 95%CI 1.03-1.17, p=0.002), LCX-FAI (OR 1.09, 95%CI 1.03-1.16, p=0.002) and RCA-FAI (OR 1.06, 95%CI 1.01-1.11, p=0.01) were significant predictors of ischemia. In multivariable Logistic regression analysis, SSS (OR 17.82, 95%CI 4.55-69.84, p<0.001), Rest EF (OR 1.34, 95%CI 1.04-1.72, p=0.02), LAD-FAI (OR 1.22, 95%CI 1.04-1.42, p=0.01) were independent predictors of ischemia in INOCA patients. ***Conclusion:*** Abnormal FAI has been confirmed to be associated with myocardial ischemia in INOCA patients, providing a foundation for the future development of individualized treatments targeting inflammation or microvascular dysfunction.

OP-499

Assessment of myocardial perfusion Sestamibi CZT-SPECT reconstructed using deep-learning-based virtual attenuation correction maps with correlation to results from Rubidium-PET and coronary angiography

T. Sprauel[1], *L. Imbert*[1,2], *K. Doyeux*[3], *M. Perrin*[1], *M. Claudin*[1], *V. Roch*[1], *M. Doyen*[2], *N. Roth*[4], *Y. Lamash*[4], *R. Chequer*[3,5], *F. Rouzet*[3,5], *F. Hyafil*[6,7], *P. Marie*[1,2];
[1]*Université de Lorraine, Department of Nuclear Medicine and Nancyclotep Imaging Platform, CHRU Nancy, Nancy, FRANCE,* [2]*Université de Lorraine, IADI, INSERM U1254, Nancy, FRANCE,* [3]*Department of Nuclear Medicine, Bichat university Hospital, Assistance Publique-Hopitaux de Paris (AP-HP), Paris, FRANCE,* [4]*Spectrum Dynamics Medical, Caesarea, ISRAEL,* [5]*Université Paris Cité, INSERM U 1148, Paris, FRANCE,* [6]*Department of Nuclear Medicine, DMU IMAGINA, European Hospital Georges-Pompidou, Assistance Publique-Hopitaux de Paris (AP-HP), Paris, FRANCE,* [7]*INSERM U 970, University Paris-City, Paris, FRANCE.*

Aim/Introduction: Attenuation artifacts may affect the analysis of myocardial perfusion imaging recorded with single-photon emission computed tomography (SPECT), especially in the right coronary artery (RCA) territory and with semi-conductor (CZT)-cameras. This study evaluates the results provided by stress [^{99m}Tc] sestamibi CZT-SPECT when reconstructed using a deep-learning-based attenuation correction (DLAC) algorithm, with correlation to [^{82}Rb]rubidium-PET (Rb-PET) and coronary angiography results. ***Materials and Methods:*** We compared stress-rest [^{99m}Tc]sestamibi CZT-SPECT reconstructed without (i.e., standard (SD-SPECT)) and with DLAC maps obtained using an algorithm developed from another study population (DLAC-SPECT) in 84 patients at risk of attenuation artifacts (overweight individuals and women), with no previous history of coronary artery disease (CAD) and who also had stress-rest Rb-PET with CT-based attenuation correction, and when indicated, coronary angiography. ***Results:*** Normal segmental uptake values at stress, estimated in a low CAD-risk group of 74 patients, were homogeneous between the three coronary territories with DLAC-SPECT (for the RCA: 81.2±7.1 %, left anterior descending (LAD): 82.5±8.3 %, and left circumflex (LCx): 81.9±7.0 % territories) and Rb-PET (76.5±8.9%, 77.7±8.5%, 78.1±8.6%, respectively), but exhibited a 10% drop in the RCA territory compared to LAD and LCx territories with SD-SPECT (69.1±8.2 % vs. 78.2±8.2 % and 79.5±8.6 %, respectively, both p<0.001). In the RCA territory, the absolute difference between the normal rest and stress segmental uptakes was particularly high with SD-SPECT (5.13±4.04 %) and higher than with DLAC-SPECT (4.21±3.24 %, p<0.001) and Rb-PET (3.92±3.08 %, both p<0.001).Reversible stress perfusion defects, identified through standard quantitative criteria (< 70% segmental stress uptake and ≥ 10% rest-minus-stress difference) (i) had equivalent per-patient detection rates with SD-SPECT (15.5%), DLAC-SPECT (16.7%) and Rb-PET (17.9%) and (ii) were a significant predictor of coronary stenosis with DLAC-SPECT (p=0.003) and Rb-PET (p=0.021) but not with SD-SPECT (p=0.17) in a sub-group where a stenosis was documented in 11 out of 42 analyzed coronary territories. ***Conclusion:*** When reconstructed with deep-learning-based attenuation correction maps, perfusion, [^{99m}Tc]sestamibi CZT-SPECT images exhibit a high diagnostic potential with properties approaching those achieved by Rubidium-PET and enhancing the identification of reversible stress perfusion defects -i.e., more homogeneous repartition of the normal stress uptake and lower ranges of normal stress-to-rest uptake fluctuations.

OP-500

Diagnostic Validation of a Novel Deep Learning Attenuation Correction Software for Stress MPI using a Dedicated CZT Cardiac Camera. A comparison with Fractional Flow Reserve acquired during Invasive Coronary Angiography in Patients with Suspected CAD

A. Manrique[1], *M. Esnault*[1], *R. Baavour*[2], *N. Coudrais*[1], *N. Roth*[2], *D. Agostini*[1];
[1]*CHU de Caen, Caen, FRANCE,* [2]*Spectrum Dynamics, Cesarea, ISRAEL.*

Aim/Introduction: To validate a novel deep learning attenuation correction (DLAC) software for stress myocardial perfusion imaging (MPI) using a dedicated CZT camera by comparing with Fractional Flow Reserve (FFR) in patients suspected with CAD from the Waterday trial (EJNMMI 2018). ***Materials and Methods:*** Retrospective assessment of 27 patients (18 males [66%], age 66.9, BMI 29±7) with no history of cardiac disease undergoing MPI from November 2014 to November 2016, followed by ICA and FFR within one month after MPI. FFR less than 0.8 was defined as abnormal. The MPI was performed on a dedicated CZT cardiac camera (D-SPECT) on supine position with a one-day protocol. We compared regadenoson stress 99mTc sestamibi CZT-SPECT reconstructed without (NC) and with DLAC, an algorithm based on a computational neural network (CNN) with U-Net architecture. Short axis images were converted to polar maps using the Cedars Sinai Cardiac Suite and normal databases supplied by

the vendor (TruCorr, Spectrum Dynamics). All SPECT images were reconstructed in a standard way recommended by the manufacturer with a specific iterative reconstruction algorithm. The severity and extent of perfusion abnormality were expressed as total perfusion deficit (TPD). Stress TPD ≥ 6% myocardium was considered abnormal.The receiver-operating-characteristic (ROC) curve analysis was performed to evaluate the ability of the quantification to predict an abnormal FFR less than 0.8. ROC curves were created using a step of 0.1% for the TPD values, and the differences between ROC curve areas (NC vs DLAC) were compared. ***Results:*** The diagnostic accuracy of global TPD on stress MPI NC images was 74%, sensitivity 73%, specificity 75%, PPV 67%, NPV 80% and AUC 0.74 for TPD ≥ 6% normal limit. Using DLAC images the diagnostic accuracy of global TPD was 81%, sensitivity 82%, specificity 81%, PPV 75%, NPV 87% and AUC 0.89 for TPD ≥ 4% normal limit. The diagnostic accuracy of global Extent on stress MPI NC images was 70%, sensitivity 73%, specificity 69%, PPV 62%, NPV 79% and AUC 0.73 for Extent ≥ 7% normal limit. Using DLAC images the diagnostic accuracy of global Extent was 89%, sensitivity 82%, specificity 94%, PPV 90%, NPV 88% and AUC 0.92 for Extent ≥ 5% normal limit. ***Conclusion:*** Using the CZT D-SPECT camera with novel DLAC software improves quantitative accuracy of the stress MPI images for TPD and Extent measurements compared to invasive FFR in patients suspected with CAD.

OP-501

Coronary Flow Reserve Evaluation with a Novel Multi-pinhole Collimator on Triple-Na-I-detector SPECT/CT in Coronary Artery Disease: A Pilot Study

A. Ogum[1], *S. Barna*[2,3], *Z. Szoboszlai*[2], *A. K. Krizsan*[4], *J. Renaud*[5], *T. Mitchell*[5], *Á. Budai*[2], *G. Ország*[2], *C. Csikos*[1,3], *I. Garai*[2,3];
[1]*Gyula Petrányi Doctoral School of Allergy and Clinical Immunology, Debrecen, HUNGARY,* [2]*Scanomed Ltd, Debrecen, HUNGARY,* [3]*University of Debrecen, Faculty of Medicine, Medical Imaging Department, Division of Nuclear Medicine, Debrecen, HUNGARY,* [4]*Mediso Ltd., Budapest, HUNGARY,* [5]*INVIA Medical Imaging Solutions, Ann Arbor, MI, UNITED STATES OF AMERICA.*

Aim/Introduction: While PET/CT remains the standard for quantification of absolute myocardial blood flow (MBF) and coronary flow reserve (CFR), its clinical use is limited by cost and availability. Dynamic acquisition with dedicated cardiac SPECT systems has shown promise in addressing these issues, albeit with further research yet needed. This study aims to evaluate CFR using a novel multi-pinhole collimator on a Triple-NaI-detector SPECT/CT system [(1)] and correlate CFR data with the clinical pretest probability of coronary artery disease (CAD). Keywords: Coronary artery disease, Multi-pinhole collimator, Myocardial flow imaging, Coronary flow reserve, Myocardial blood flow ***Materials and Methods:*** Eleven patients (median age: 62) with known or suspected CAD underwent one-day stress-rest 99mTc-MIBI SPECT/CT imaging using a multi-pinhole collimator system on a Triple-NaI-detector. Dynamic flow imaging followed rest and Regadenoson-induced stress phases. Images were reconstructed with a Monte Carlo-based algorithm for multi-pinhole projections. MBF and CFR were quantified using a dedicated software suite and compared with pretest CAD probability scores to assess diagnostic value. ***Results:*** No patient showed significant obstructive CAD (≥70% stenosis) on angiography. CFR showed a moderate, though not statistically significant, positive correlation with CAD risk scores, $r(7) = 0.62$, $p = 0.077$, suggesting a potential physiological link between non-invasive flow data and baseline cardiovascular risk. Measured flow values were lower than those reported using other dedicated cardiac SPECT systems. [(2)] ***Conclusion:*** The multi-pinhole collimator on the Triple-NaI-detector SPECT/CT system yields reliable flow measurements that align with CAD risk scores, even in the absence of angiographic stenosis. This technique shows promise for early detection of microvascular dysfunction and may offer a cost-effective alternative to PET or other specialized SPECT systems. Further studies are needed to define diagnostic flow thresholds.

References: 1)Krizsan AK, Kukuts K, Al-Muhanna W, Szoboszlai Z, Balazs L, Szabo B, Kiss J, Nekolla S, Barna S, Garai I, Bukki T, Forgacs A. Performance evaluation of a novel multi-pinhole collimator on triple-NaI-detector SPECT/CT for dedicated myocardial imaging. EJNMMI Phys. 2023 Mar 25;10(1):24. doi: 10.1186/s40658-023-00541-y. PMID: 36964406; PMCID: PMC10039219. 2)Acampa W, Assante R, Mannarino T, Zampella E, D'Antonio A, Buongiorno P, Gaudieri V, Nappi C, Giordano A, Mainolfi CG, Petretta M, Cuocolo A. Low-dose dynamic myocardial perfusion imaging by CZT-SPECT in the identification of obstructive coronary artery disease. Eur J Nucl Med Mol Imaging. 2020 Jul;47(7):1705-1712. doi: 10.1007/s00259-019-04644-6. Epub 2019 Dec 17. PMID: 31848673.

OP-502

The fesibility of CZT-SPECT in the assessment of coronary microvascular dysfunction (CMD) in INOCA patients: a comparative study with Coronary Agnio-IMR

H. Zhang[1], *F. Caobelli*[2], *K. Shi*[2], *F. Yu*[3], *K. Wang*[1], *M. Fei*[4];
[1]*Tongji University School of Medicine, Shanghai Tenth People's Hospital, Shanghai, CHINA,* [2]*Department of Nuclear Medicine, Inselspital, Bern University Hospital, University of Bern, Bren, SWITZERLAND,* [3]*Tongji University School of Medicine, Shanghai Tenth people's Hospital, Shanghai, CHINA,* [4]*Tongji University School of Medicine, Shanghai Pulmonary Hospital, Shanghai, CHINA.*

Aim/Introduction: Although our previous study[1] demonstrated the strong prognostic value of CZT-SPECT derived Stress myocardial blood flow (sMBF) and coronary flow reserve (CFR) in ischemia with Non-obstructive coronary artery disease (INOCA) patients, its value and Optimal cut-off value in the diagnosis of coronary microvascular dysfunction (CMD) is still unclear. ***Materials and Methods:*** We prospectively recruited 56 INOCA patients referred to nuclear medicine from cardiovascular medicine, each of whom underwent CZT SPECT imaging and coronary angiography derived index of microcirculatory resistance (IMR_{angio}) within one week. Dynamic data were reconstructed, and MBF was quantified using net retention model. CMD were defined as IMR_{angio}>25U. Receiver operating characteristic (ROC) curves and Youden's index were used to calculate the best cut-off values of sMBF and CFR for the prediction of CMD. ***Results:*** Based on the IMR_{angio} results, CMD was present in 42 (75.0%) patients. Regional IMR_{angio} was significantly higher (LAD: 38.8±15.5 vs 22.8±5.8, p<0.001; LCX: 39.9±13.7 vs 23.5±6.3, p<0.001; RCA: 29.8±9.0 vs 17.2±5.6, p<0.001) and CFR (LAD: 2.87±0.86 vs 3.71±0.69, p=0.002; LCX:2.83±0.98 vs 3.96±1.45, p=0.002; RCA:2.90±1.10 vs 3.87±0.73, p=0.003) significantly lower in the CMD group. Global IMRangio (36.7±8.1 vs 21.1±3.4, p<0.001) was significantly higher, sMBF (3.8±1.2 vs 4.5±0.9, p=0.04) and MFR (3.0±0.9 vs 3.9±0.8, p=0.001) significantly lower in the CMD group. A moderate correlation with IMR_{angio} was founded for both global sMBF (r=-0.43, p=0.001) and CFR (r=-0.32, p=0.02). Accordingly, the efficacy of sMBF and CFR in diagnosing CMD was sMBF<3.77(AUC 0.68, 95% CI 0.55-0.80, p=0.02, sensitivity 52.4%, specificity 92.9%, PPV 39.4%, NPV 95.7%, accuracy 62.5%), CFR<2.94(AUC 0.80, 95% CI 0.68-0.90, p<0.001, sensitivity 64.3%, specificity100%, PPV 48.3%, NPV 100%, accuracy 73.2%). Nevertheless, the Delong test suggested that there was no significant difference in the efficacy of the two parameters in the diagnosis of CMD (95% CI -0.06-0.30, p=0.19). ***Conclusion:*** The results suggest that regional and global sMBF and CFR can serve as valuable diagnostic indicators for INOCA patients with CMD, providing novel criteria for early prevention and intervention strategies.

References: 1.Zhang H, Caobelli F, Che W, et al. The prognostic value of CZT SPECT myocardial blood flow (MBF) quantification in patients with ischemia and no obstructive coronary artery disease (INOCA): a pilot study. Eur J Nucl Med Mol Imaging. 2023;50(7):1940-1953. doi:10.1007/s00259-023-06125-3

OP-503

A new parameter - increasing ratio derived from SPECT: validation by PET- myocardial flow reserve

A. Inoue, *M. Nagao, A. Yamamoto, A. Sakai, R. Nakao, M. Watanabe, J. Yamaguchi, S. Sakai;*
Tokyo Women's Medical University Hospital, Tokyo, JAPAN.

Aim/Introduction: Myocardial flow reserve (MFR) obtained from ^{13}N-ammonia PET is valuable for predicting the prognosis of patients with various heart diseases. Myocardial perfusion SPECT has a lower blood flow tracking ability for myocardial accumulation than ^{13}N-ammonia PET, and there are false negatives due to balanced ischemia in patients with multiple coronary artery lesions, so its diagnostic accuracy is inferior to that of ^{13}N-ammonia PET. The increase ratio (IR), a new parameter in ^{99m}Tc-sestamibi SPECT, is an indicator of the relative increase in blood flow during stress compared to rest, and the concept is similar to that of PET-MFR. We investigated the relationship between IR and PET-MFR as well as their clinical significance. ***Materials and Methods:*** Patients who underwent ^{13}N-ammonia PET and ^{99m}Tc-sestamibi SPECT within one year of each other were enrolled. Using adenosine-stress and resting images of ^{99m}Tc-sestamibi SPECT, the stress image count was divided by the resting image count, and IR was calculated. We investigated the correlation between IR and PET-MFR and validated the optimal IR cutoff value for detecting PET-MFR<1.6(in our facility, previous research has shown that a PET-MFR <1.6 is a sensitive cutoff value for detecting poor prognosis) by receiver-operating-characteristic (ROC) analysis. And the mean IR and MFR values were compared between patients with and without multiple coronary artery lesions. ***Results:*** 33 patients (28 males, mean age 65.7±12.9) were analyzed. IR was significantly lower than PET-MFR (mean IR, 1.198; mean PET-MFR, 1.910; p<0.0001) and positively correlated with PET-MFR (Pearson r=0.3567; p<0.01). ROC analysis indicated that the optimal IR cutoff value for detecting PET-MFR<1.6 was 1.06, yielding an area under the curve (AUC) of 0.683, with 50% sensitivity and 83% specificity. By combining summed stress score with IR, the detectability of PET-MFR<1.6 improved the AUC of 0.798 with 83% sensitivity, and 70% specificity. The IR of the group with multiple coronary artery lesions was 1.04 ± 0.32 and that of the group with single-vessel lesions or no significant stenosis was 1.30 ± 0.27. Hence, the IR of the group with multiple coronary artery lesions was significantly lower than that with a single-vessel lesion or nonsignificant stenosis (p=0.0199). ***Conclusion:*** IR was positively correlated with PET-MFR. This suggests that IR may be useful for detecting patients with a low MFR in facilities that don't perform ^{13}N-ammonia PET.

1201

Tuesday, October 7, 2025, 08:00 - 09:30

Auditorium

CME 9 - Oncology & Theranostics + Neuroimaging Committee: RLT Applications in Neuro-Oncology

OP-504

Targets in CNS tumors

J. Kunikowska; *Medical University of Warsaw, Department of Nuclear Medicine, Warsaw, POLAND.*

OP-505

RLT in gliomas

N. Tolboom; *UMC Utrecht, Department of Nuclear Medicine, Utrecht, NETHERLANDS.*

OP-506

RLT in meningiomas

N. Albert; *LMU University Hospital, Department of Nuclear Medicine, Munich, GERMANY.*

OP-507

RLT in brain metastases

M. Preusser; *Medical University of Vienna, Division of Oncology Department of Medicine I, Vienna, AUSTRIA.*

1202

Tuesday, October 7, 2025, 08:00 - 09:30

Room 112 (Arena)

Special Track 9 - Physics Committee: Debate: Quantitative Imaging: What's the Point? (Focus on Kinetic Modeling)

OP-508

Pro Kinetic Modeling

R. Boellaard; *VU University Medical Center, Amsterdam, NETHERLANDS.*

OP-509

Contra Kinetic Modeling

L. Kumar Shiyam Sundar; *LMU University Hospital, Munich, GERMANY.*

1203

Tuesday, October 7, 2025, 08:00 - 09:30

Room 113

LIPS Session 9 - Oncology & Theranostics Committee: Pitfalls in PSMA-Based RLT: Case-Based Review

OP-511

Pitfalls in Patient Selection

M. Bauckneht; *IRCCS Ospedale Policlinico San Martino, University of Genova, Genoa, ITALY.*

OP-512

Pitfalls in Response Assessment

A. Gafita; *Nuclear Medicine and Molecular Imaging Division, The Johns Hopkins Hospital, Johns Hopkins School of Medicine, Baltimore, UNITED STATES OF AMERICA.*

OP-513

Pitfalls in Dosimetry and Radiation Protection

J. Brosch-Lenz; *Institute of Nuclear Medicine, Glen Burnie, Maryland, UNITED STATES OF AMERICA.*

1204

Tuesday, October 7, 2025, 8:00 - 9:30

Room 114

M2M Track - TROP Session - Radiopharmaceutical Sciences + Translational Molecular Imaging & Therapy Committee: Combination Therapy - Shaping the Future of TRT

OP-515

Radiobiology and Synergistic Approaches in [^{123}I]CC1 Radionuclide Therapy

N. Delgado Mayenco[1], *L. Hernandez Cano*[1], *E. Diekstra*[1], *S. Unnikrishnan*[1], *F. Amoroso*[1], *H. Kramer*[1], *G. Alachouzos*[2], *W. Szymanski*[3], *I. F. Antunes*[1], *E. F. J. de Vries*[1], *B. Cornelissen*[1];
[1]*University Medical Center Groningen, University of Groningen, Nuclear Medicine and Molecular Imaging, Groningen, NETHERLANDS,* [2]*University of Groningen, Centre for Systems Chemistry, Stratingh Institute for Chemistry, Faculty for Science and Engineering, Groningen, Groningen, NETHERLANDS,* [3]*University Medical Center Groningen, University of Groningen, Department of Radiology, Medical Imaging Center, Groningen, NETHERLANDS.*

Aim/Introduction: [^{123}I]CC1 is a novel cancer therapy combining Auger electron-emitting radionuclide ^{123}I with a PARP inhibitor. It

targets the DNA damage repair protein PARP in cancer cells, causing DNA damage and cell death. Moreover, [^{123}I]CC1 shows remarkable radiotoxicity against PARP-expressing cancer cells while sparing healthy tissue [1]. This study examines its radiobiological effects and synergy with chemotherapy as radiosensitizers. ***Materials and Methods:*** PSN1 and U87MG cells were exposed to [^{123}I]CC1 (100 kBq) for 1 h at 37°C. Cell cycle analysis was performed up to 10 days by flow cytometry. Western blot, staining for DNA damage response and cell stress markers, was performed up to 16 days post-exposure. Clonogenic survival assays were conducted in PSN1 cells exposed to [^{123}I]CC1 (100 kBq) or vehicle control, for 1 h at 37°C followed by washing and exposure to one of 166 FDA-approved chemotherapy agents. These agents target diverse cancer growth and survival mechanisms, including microtubule and kinase inhibitors, alkylating agents, antimetabolites and therapies targeting specific molecular pathways or repair mechanisms. ***Results:*** An initial wave of DNA damage and replication stress showed an early rise in DNA damage and cell cycle arrest markers, accompanied by increased replication stress markers. A second wave of DNA damage and cellular stress followed, potentially triggered by replication stress. An early G2 decline correlated with p21 upregulation, suggesting involvement in cycle arrest. Despite CDK4 accumulation, no G1/S arrest occurred, indicating that low-dose radioactivity may not fully induce G1 arrest but contributes to replication stress and genomic instability. Later, G1 depletion and G2 accumulation were consistent with a second wave of replication stress and p21 upregulation. These findings highlight the impact of low-dose [^{123}I]CC1 on cellular mechanisms inducing alterations in DNA damage repair, apoptosis, senescence, replication stress, and autophagy. Combination clonogenic assays tested 102 chemotherapy agents for radiosensitization, excluding those with antagonistic interactions. The top-performing synergistic drugs targeted multiple pathways, indicating that [^{123}I]CC1 modulates cellular responses through various mechanisms. Future studies will explore combinations with the most radiosensitizing potential. This screening identifies promising combinations and key pathways for further exploration of the biological response to [^{123}I]CC1. ***Conclusion:*** [^{123}I]CC1 modulates a multitude of cell cycle and impacts key cellular mechanisms. Its combination with radiosensitising chemotherapy agents holds promise for optimizing personalised radiotherapy. ***References:*** [1] C. Chan (2023) [^{123}I]CC1: A PARP-Targeting, Auger Electron-Emitting Radiopharmaceutical for Radionuclide Therapy of Cancer. Journal of Nuclear Medicine.

OP-516

Synergistic Anti-Tumour Effects of ^{225}Ac-DOTA-Girentuximab Combined with DNA Damage Response Inhibitors in CAIX-Positive Renal Cancer

Z. Cao[1,2,3], *C. Wichmann*[1,2,3], *A. Ivashkevich*[4], *A. Zimmermann*[5], *C. Sirrenberg*[5], *H. Dahmen*[5], *L. Osellame*[1,2], *N. Guo*[1], *F. Scott*[1,2], *M. Wheatcroft*[4], *A. Scott*[1,2,3];
[1]*Olivia Newton-John Cancer Research Institute, Heidelberg, AUSTRALIA,* [2]*School of Cancer Medicine, La Trobe University, Bundoora, AUSTRALIA,* [3]*Department of Molecular Imaging and Therapy, Austin Health, Heidelberg, AUSTRALIA,* [4]*Telix Pharmaceuticals, Melbourne, AUSTRALIA,* [5]*Merck Healthcare KGaA, Darmstadt, GERMANY.*

Aim/Introduction: Radiopharmaceutical therapies achieve anti-cancer effects primarily by inducing abundant DNA double-strand breaks (DSBs) in target cells. However, these lesions can be repaired through DNA damage response (DDR) mechanisms, leading to disease recurrence and therapeutic resistance. Previous studies demonstrated that combining DDR inhibitors (DDRis) with ^{177}Lu-based radiopharmaceuticals enhances therapeutic efficacy and cancer cures in preclinical models (1,2). Given the higher linear energy transfer (LET) of alpha particles, which induces more extensive DSBs, this study aims to evaluate the anti-tumour efficacy of combining DDRis with ^{225}Ac-DOTA-girentuximab, targeting CAIX-expressing SK-RC-52 renal cancer cells. ***Materials and Methods:*** Girentuximab was conjugated with DOTA (1,4,7,10-Tetraazacyclododecane-1,4,7,10-tetraacetic acid) and radiolabelled with ^{225}Ac. Clonogenic assays were performed to determine half-maximal inhibitory concentration (IC50) and evaluate the combination effects of ^{225}Ac-DOTA-girentuximab with two DDRis: lartesertib (ATM inhibitor) and peposertib (DNA-PK inhibitor). Synergy analyses were conducted, and combination index (CI) was calculated. In vivo therapeutic efficacy was assessed in SK-RC-52 xenograft model using a subeffective dose (5 kBq/mouse) of ^{225}Ac-DOTA-girentuximab. To explore underlying mechanisms, DDR-related molecular markers were analysed at multiple time points following treatment of SK-RC-52 cells with ^{225}Ac-DOTA-girentuximab in vitro. ***Results:*** Both peposertib and lartesertib reduced the IC50 of ^{225}Ac-DOTA-girentxuimab in SK-RC-52 cells. Synergy analysis indicated an additive effect with lartesertib (CI = 0.985), while a synergistic effect was observed with peposertib (CI = 0.760). Strikingly, in vivo studies demonstrated enhanced anti-tumour effects and improved tumour cures for both combinations, achieving complete responses in 2 out of 6 mice for both combinations. Molecular analysis showed time- and dose-dependent activation of DDR pathways following ^{225}Ac-DOTA-girentuximab treatment. High-dose exposure predominantly activated the non-homologous end joining (NHEJ) pathway targeted by peposertib, whereas lower doses stimulated the homologous recombination (HR) pathway targeted by lartesertib. ***Conclusion:*** The combination of ^{225}Ac-DOTA-girentuximab and DDR inhibitors demonstrated superior efficacy compared to monotherapies. Although in vitro synergy was only observed with peposertib, both combinations achieved synergistic anti-tumour effects in vivo, leading to improved tumour control and extended survival. These findings support further investigation of DDR inhibitors as combination partners for alpha-emitting radiopharmaceutical therapies. ***References:*** 1. Johnstone CN, Osellame LD, Cao Z, et al. DNA-Dependent Protein Kinase Inhibitor Peposertib Enhances Efficacy of 177Lu-Based Radioimmunotherapy in Preclinical Models of Prostate and Renal Cell Carcinoma. Journal of Nuclear Medicine. 2025:jnumed.124.268695. 2. Reuvers TGA, Verkaik NS, Stuurman D, et al. DNA-PKcs inhibitors sensitize neuroendocrine tumor cells to peptide receptor radionuclide therapy in vitro and in vivo. Theranostics. 2023;13:3117-3130.

OP-517

Radiation Induced Senescence Limits Radiopharmaceutical Therapy Efficacy in Murine Models of GU Cancers

M. Lindsey, *M. Bio Idrissou, H. Comas-Rojas, A. Adeniyi, A. Pinchuk, L. Lambert-Lepesevich, N. Clemons, E. Santos, O. Kwon, G. Iyer, B. Bednarz, R. Hernandez;*
University of Wisconsin-Madison, Madison, WI, UNITED STATES OF AMERICA.

Aim/Introduction: Senescence, a state of stable cellular arrest, can hinder radiotherapy efficacy and is associated with radioresistance, chronic inflammation, recurrence, and metastasis. Senotherapeutics, which selectively eliminate senescent cells (SNCs), have emerged as potential radiotherapy adjuvants. We present our initial findings and rationale for using senotherapeutics to augment radiopharmaceutical therapy (RPT) response in models of GU cancers (senoRPT). ***Materials and Methods:*** For PC3PIP (metastatic prostate cancer) and SKRC52 (clear cell renal cell carcinoma) cells treated with EBRT/^{177}Lu/^{225}Ac (6&10Gy), flow cytometry gating for morphology (FSC^{high}/ SSC^{high}) and SNC markers (SA-β-gal^{high}/p21^{high}/p16^{high}) provided estimates of senescent fraction (SF). Senescence-associated changes in gene expression were investigated by RNAseq in PC3PIP cells treated with ^{177}Lu (3Gy) and ^{225}Ac (0.3&1Gy). For both cell lines, cellular vitality and IC_{50} were determined via PrestoBlue following

combination treatment with EBRT/^{177}Lu/^{225}Ac (0-30Gy) and the BCL-family inhibitor ABT263 (0-3µM). In therapeutic studies, tumor selective ^{177}Lu-based agents were administered to male athymic nude mice implanted with PC3PIP or SKRC52 xenografts either alone or in combination with daily oral ABT263 (50mg/kg). Tumor growth and animal health were followed for 120d. SF was estimated from the delayed doubling time of senoRPT-treated tumors. Longitudinal SPECT/CT imaging was used to determine the agent biodistribution and estimate absorbed dose to the tumors and normal tissue. The clearance of SNCs by ABT263 was confirmed by fluorescence microscopy. ***Results:*** Flow cytometry revealed dose-dependent increases to SF, from ~10% untreated to ~60% with 10Gy. This was corroborated by RNAseq, revealing ≥125 senescence-associated genes significantly ($p<0.05$) upregulated across all treatments, with the 3Gy ^{177}Lu group showing the highest frequency (191 genes) and the 1Gy ^{225}Ac group having the largest mean differential expression. Synergistic combination of EBRT/^{177}Lu/^{225}Ac and ABT263 resulted in significant ($p<0.001$) reduction in vitality for both cell lines compared to radiation or ABT263 alone. In vivo, mice receiving senoRPT demonstrated marked tumor regression over RPT alone ($p<0.02$) or other controls ($p<0.01$). SF estimates suggest SNCs compose ~10-40% of the remaining tumor volume following non-curative RPT. Notably, senoRPT was well tolerated and demonstrated superior long-term survival, having been the only treatment arm to achieve complete responses. ***Conclusion:*** These preliminary findings underscore the relevance of the largely overlooked senescent phenotype on the efficacy of RPT and underscores the potential of senotherapeutics to expand RPT cure rates in GU cancers. This work exposes untapped areas for continued research related to the radiobiology of RPT-induced senescence and continued exploration of the senoRPT technique.

OP-518

Targeted Radionuclide Therapy of Prostate Cancer using a ^{177}Lu- and ^{47}Sc-labeled Gastrin-Releasing Peptide Receptor Antagonist. Evaluation as Monotherapy and in Combination with Everolimus

N. Kumar[1], *A. Bilinska*[1], *E. Menéndez*[1], *T. Läppchen*[1], *E. S. Moon*[2], *M. Zoltowska*[3], *D. Pawlak*[3], *I. Cieszykowska*[3], *R. Mikolajczak*[3], *F. Rösch*[2], *A. Rominger*[1], *E. Gourni*[1];
[1]*Department of Nuclear Medicine, Inselspital, Bern University Hospital, University of Bern, Bern, SWITZERLAND,* [2]*Department of Chemistry-TRIGA site, Johannes Gutenberg University of Mainz, Mainz, GERMANY,* [3]*Radioisotope Centre POLATOM, National Centre for Nuclear Research, Otwock, POLAND.*

Aim/Introduction: The gastrin-releasing peptide receptor (GRPR) promotes prostate cancer progression by activating pathways such as MAPK and PI3K/AKT. Radiolabeled GRPR antagonists show promise for treating GRPR-positive tumors. Everolimus, an mTOR inhibitor, may enhance these therapies by acting as a radiosensitizer. This study evaluates the effects of ^{177}Lu- and ^{47}Sc-labeled GRPR antagonists, alone and combined with everolimus, on tumor growth and survival in PC3-mice. ***Materials and Methods:*** The GRPR antagonist (AAZTA^5-Pip-D-Phe-Gln-Trp-Ala-Val-Gly-His-Sta-Leu-NH_2: LF1) was radiolabeled with lutetium-177 and scandium-47. The radiotherapeutic efficacy of [^{47}Sc]Sc-LF1 and [^{177}Lu]Lu-LF1 was investigated in PC3-mice. In the monotherapy study, a fractionated regimen consisted of six doses, was administered. Two cohorts of mice were used: one cohort received a total activity of approximately 40 MBq (equivalent to 1200 pmol), and the second received approximately 80 MBq (equivalent to 2400 pmol). In the ^{177}Lu-based combination, PC3-mice treated with 40 MBq of [^{177}Lu]Lu-LF1 alone or everolimus daily (5 mg/kg) for 72 h, followed by 40 MBq of [^{177}Lu]Lu-LF1. For the ^{47}Sc-based combination, mice were treated at days 1, 3 and 5 with 3 doses of [^{47}Sc]Sc-LF1 (total 30 MBq) alone or everolimus (5 mg/kg) with [^{47}Sc]Sc-LF1 (total 30 MBq) at the same days. Control groups received either ^{nat}Sc/ ^{nat}Lu-LF1 (400 pmol), PBS or everolimus (5 mg/kg). ***Results:*** Monotherapy with [^{47}Sc]Sc/[^{177}Lu]Lu-LF1 at the highest administered activities (80 MBq, 2400 pmol) significantly inhibited tumor growth compared to both the lower administered activities (40 MBq, 1200 pmol) and the control groups. Tumor volume reduction was more pronounced in the [^{177}Lu]Lu-LF1 group than in the [^{47}Sc]Sc-LF1 group. In the combination therapy, the combined treatment of everolimus and [^{47}Sc]Sc/[^{177}Lu]Lu-LF1 demonstrated the most significant tumor growth inhibition. Tumor regression was observed in all animals receiving combination therapy. Tumors in the untreated groups exhibited rapid progression. In terms of survival rate, the monotherapy group of [^{177}Lu]Lu-LF1 (2400pmol) showed significantly extended survival compared to all other groups (median survival: 50 days), followed by the [^{47}Sc]Sc-LF1 (2400pmol) (median survival: 32 days). The median survival for [^{47}Sc]Sc/[^{177}Lu]Lu-LF1 (1200pmol) groups was comparable to the control groups (median survival: 19, 16 and 18 days, respectively). In combination therapy, the median survival was 26 days for everolimus, 40 and 38 days for everolimus along with [^{47}Sc]Sc-/[^{177}Lu]Lu-LF1, respectively. ***Conclusion:*** Fractionated therapeutic regimens of radionuclide therapy, as well as its combination with mTOR inhibitors, like everolimus, represent a rational and innovative approach to improve prostate cancer treatment outcomes. ***References:*** This work is a PRISMAP contribution.

OP-519

Combining CD44v6-Targeted Radionuclide Therapy with Chemotherapy for Treatment of Pancreatic Ductal Adenocarcinoma

A. Gustafsson[1], *H. Svedberg*[1], *S. S. Rinne*[1], *A. Lundgren Mortensen*[1,2], *M. Nestor*[1];
[1]*Uppsala University, Uppsala, SWEDEN,* [2]*Karolinska Institutet, Stockholm, SWEDEN.*

Aim/Introduction: Pancreatic ductal adenocarcinoma (PDAC) is among the deadliest malignancies, owing to its rapid progression, resistance to available therapies, and poor prognosis. The cell surface marker CD44v6 is frequently overexpressed in PDAC, making it a promising target for targeted radionuclide therapy (TRT), capable of addressing metastatic disease and potentially enabling surgical intervention. This study evaluated the therapeutic potential of [^{177}Lu]Lu-DOTA-AKIR001, a full-length human IgG antibody targeting CD44v6 and currently in Phase I trials for multiple CD44v6-positive solid tumors. Additionally, the study explored potential benefits from combining [^{177}Lu]Lu-DOTA-AKIR001 with standard chemotherapeutics. ***Materials and Methods:*** Radiochemical stability of [^{177}Lu]Lu-DOTA-AKIR001 was evaluated in PBS, mouse serum, and EDTA using ITLC. CD44v6 expression, radioligand uptake, and sensitivity to the chemotherapeutic agents paclitaxel and gemcitabine were assessed across a panel of PDAC cell lines. In vivo tumor targeting and therapeutic efficacy were investigated in immunodeficient BALB/c nu/nu mice bearing subcutaneous human PDAC xenografts. To assess therapeutic outcomes, mice received [^{177}Lu]Lu-DOTA-AKIR001 (4 or 12 MBq), paclitaxel, gemcitabine, or a combination of 4 MBq [^{177}Lu]Lu-DOTA-AKIR001 with either chemotherapeutic agent. Haematologic toxicity was monitored via serial blood sampling. ***Results:*** Radiochemical yield consistently exceeded 95% and [^{177}Lu]Lu-DOTA-AKIR001 remained stable for at least 48 hours (>95%). CD44v6 expression was observed in three out of four tested cell lines, to which AKIR001 bound with target-specific, picomolar affinity. All cell lines showed at least partial sensitivity to both paclitaxel and gemcitabine. At 96 hours p.i., tumour uptake in vivoexceeded 100% injected activity per gram (%IA/g) tissue. An activity-dose-dependent inhibition of tumour growth was observed, with the greatest anti-tumour activity noted in the 12 MBq group. A trend favouring combination therapy over 4 MBq [^{177}Lu]Lu-DOTA-AKIR001 monotherapy was observed. Contrary to the in vitro results, chemotherapy alone had no significant

impact on tumour growth or median survival. Mild and transient hematologic toxicity was observed across all treatment groups, most pronounced in the high-activity treatment group followed by the combination treatments. Weight loss was observed only in gemcitabine-treated animals. ***Conclusion:*** [^{177}Lu]Lu-AKIR001 demonstrated high stability, selective tumour targeting, and promising anti-tumour activity in our preclinical PDAC model. Combination with chemotherapy, particularly paclitaxel, showed potential to enhance treatment outcome at lower activity levels without increased toxicity. Thus, [^{177}Lu]Lu-AKIR001 may represent a feasible treatment option for PDAC in the future, though further optimization of dosing and combination regimens is warranted to maximize its therapeutic potential.

OP-520

New combination therapies to improve [^{177}Lu]Lu-PSMA treatment in prostate cancer cells.

F. Amoroso[1,2], *E. O'Neill*[2], *L. Hernandez Cano*[1], *B. T. Cornelissen*[1,2]; *[1]Dept. of Nuclear Medicine and Molecular Imaging, University Medical Center Groningen, Groningen, NETHERLANDS, [2]Institute for Radiation Oncology, Department of Oncology, University of Oxford, Oxford, UNITED KINGDOM.*

Aim/Introduction: Most patients with locally advanced prostate cancer (PCa) are treated with surgery or radiotherapy with curative intent. Although the treatments can extend survival, delayed diagnosis as well as development of therapy resistance can result in cases where the metastatic disease becomes incurable. Despite the clinical development for PCa theranostics of several radiolabelled [^{177}Lu]Lu-PSMA, all undergoing clinical trials for treating metastatic Castrate Resistant PCa (mCRPC), little we know about the radiobiological effects of ^{177}Lu. Moreover, regardless of some highly promising results from the VISION Study (NTC03511664), only a subset of mCRPC patients responds to the treatment and only 10% showed a complete response (1). For these reasons, we evaluated whether combining [^{177}Lu]Lu-PSMA with other compounds would improve the radiobiological effects of this radioligand therapy. ***Materials and Methods:*** While performing a big scale screening for combination therapies on a PCa cell line (22Rv1) in vitro, we identified Tosedostat (CHR-2797) among several compounds that significantly reduced clonogenicity and showed super-additivity when combined with [^{177}Lu]Lu-PSMA. Tosidostat is an aminopeptidase inhibitor with anti-proliferative, anti-angiogenic, and pro-apoptotic activity through disruption of protein synthesis and the cell cycle (2). To further analyse the (radio)biology involved, we performed Western blot analysis and immunofluorescence staining in 22Rv1 cells treated with [^{177}Lu]Lu-PSMA in combination with Tosedostat (at the IC50 concentration of 60 nM) over a period of 10 days. ***Results:*** We observed a consistent overexpression of ɤH2AX, indicating the formation of double stranded breaks (DSBs) as consequence of the combination, compared to both monotherapies. We also described pro-apoptotic pathways activated in response to this combination over 10 days, when PARP1 and caspase 3 are cleaved. We finally identified 3 aminopeptidases that could play as drivers of the phenotypic changes we observed with this combination. ***Conclusion:*** Tosedostat (CHR-2797) is currently in phase II clinical trials for the treatment of blood-related cancers. Here we show that combining [^{177}Lu]Lu-PSMA with Tosedostat in PCa cells can improve the efficacy of this radioligand therapy. This represents a big step forward towards the development of new targeted and more effective treatments for PCa patients. ***References:*** (1) Novartis. Phase III VISION study. 2021. (2) Alan F. List, Leukemia Research (2012).

OP-521

Combining CAIX-targeted radionuclide therapy with immune checkpoint inhibitors: which inhibitor and when?

S. Kleinendorst[1], *E. Oosterwijk*[1], *M. Konijnenberg*[1], *S. Wenker*[1], *K. Twumasi-Boateng*[2], *M. Wheatcroft*[2], *S. Heskamp*[1]; *[1]RadboudUMC, Nijmegen, NETHERLANDS, [2]Telix Pharmaceuticals Limited, Melbourne, AUSTRALIA.*

Aim/Introduction: The carbonic anhydrase IX (CAIX)-targeting antibody [^{177}Lu]Lu-DOTA-hG250 represents a novel therapeutic approach for targeted radionuclide therapy (TRT) in advanced clear cell renal cell carcinoma (ccRCC). Preclinical studies have demonstrated the promising potential of combining CAIX-TRT with immune checkpoint inhibitors (ICI). This study explores how the type of ICI and timing of administration influence the therapeutic efficacy of CAIX-TRT/ICI combinations. ***Materials and Methods:*** Balb/C mice bearing subcutaneous Renca-hCAIX tumors were randomized into groups of 10 mice to receive intravenous saline or 4 MBq [^{177}Lu]Lu-DOTA-hG250 on day 0. Animals were subsequently treated with saline, aPD-1, aCTLA-4, or dual-ICI (aPD-1 + aCTLA-4) every three days starting from day 1 (concurrent timing). In a second experiment, aPD-1 or aCTLA-4 were administered beginning on day 7 post-TRT (sequential timing), and outcomes were compared to concurrent administration. Tumor growth was monitored, and results were quantified as the area under the tumor growth curve normalized for lifetime (median nAUC [interquartile range]). Survival and complete responses (CRs) were assessed. ***Results:*** The combination of CAIX-TRT with dual-ICI significantly reduced tumor growth compared to untreated controls (nAUC=50.3 [17.8–264.4] vs 521.9 [424.5–689.0] mm^3 (untreated), $p<0.01$) and resulted in the longest survival benefit, including 8 CRs. TRT/aPD1 showed partial tumor regression in some animals, but high variability was observed between mice (nAUC=164.6 [52.5–698.8] mm^3, $p>0.05$) with 4 CRs. In contrast, TRT/aCTLA4 failed to demonstrate significant therapeutic benefit (nAUC=311.9 [183.9–574.8] mm^3, $p>0.05$). Comparing concurrent and sequential schedules, no statistically significant differences in efficacy were observed for either TRT/aPD-1 or TRT/aCTLA-4 combinations (nAUC=149.9 [96.6-376.7] vs 278.0 [99.3 - 690.0] mm^3, $p>0.05$, and nAUC=415.5 [305.3-562.1] vs 417.0 [313.4-546.4] mm^3, $p>0.05$). However, there was a trend towards better survival after concurrent administration within the aPD-1 combination arm (6 survivors/3 CRs versus 3 survivors/2 CRs). ***Conclusion:*** These findings underscore the therapeutic potential of CAIX-TRT combined with ICIs, particularly dual-ICI, for advanced ccRCC treatment. They emphasize the importance of carefully selecting the ICI type to maximize therapeutic efficacy and provide a foundation for future clinical trial designs using optimized treatment parameters.

OP-522

Fractionated versus single-dose PSMA-targeted radioligand therapy as adjuvant therapy in a murine model for oral squamous cell carcinoma treated with immune checkpoint inhibitors

M. Henrotte[1,2,3], *D. Creytens*[1,2,3], *F. De Vos*[2], *B. Descamps*[2,3], *L. Devisscher*[2,3], *G. Holtappels*[2], *W. J. A. Huvenne*[1,2,3], *K. Kersemans*[1,3], *A. Meskens*[2,3], *S. Neyt*[2,3], *S. Rottey*[1,2,3], *M. Saerens*[1,2,3], *C. Vanhove*[2,3], *T. Vermassen*[1,2,3], *J. M. Debacker*[2,4,5]; *[1]Ghent University Hospital, Ghent, BELGIUM, [2]Ghent University, Ghent, BELGIUM, [3]Cancer Research Institute Ghent (CRIG), Ghent, BELGIUM, [4]Vrije Universiteit Brussel (VUB), Molecular Imaging and Therapy Research Group (MITH), Brussels, BELGIUM, [5]Vrije Universiteit Brussel (VUB), Universitair Ziekenhuis Brussel (UZ Brussel), Brussels, BELGIUM.*

Aim/Introduction: Immune checkpoint inhibition (ICI) is a cornerstone in the management of relapsed or metastatic head and neck squamous cell carcinoma (R/M HNSCC). However, response rates and survival remain limited, warranting novel therapies. One approach is targeting prostate-specific membrane antigen (PSMA), which is expressed on the endothelium of tumour-associated neovasculature in oral squamous cell carcinoma (OSCC). We assessed the effects of fractionated (FX) versus single-dose (SD) PSMA-targeted radioligand therapy (TRT) in monotherapy and combined with ICI, using a syngeneic, orthotopic, immunocompetent murine OSCC model. ***Materials and Methods:*** OSCC tumours were induced by injecting 7.5 × 10^5 MOC1 cells into the anterior lateral tongue of 55 adult male C57BL/6J mice. On day 12, mice were randomised to different treatment protocols: (a) 100 MBq [^{177}Lu]Lu-PSMA-I&T IV on day 12 (SD-TRT, n = 8); (b) 4 × 25 MBq [^{177}Lu]Lu-PSMA-I&T IV (Q1W), starting on day 12 (FX-TRT, n = 8); (c) 8 doses of anti-murine PD-1 IP BIW, starting on day 12 (ICI; n = 11); (d) SD-TRT + ICI (n = 10); (e) FX-TRT + ICI (n = 10); or (f) untreated controls (n = 8). Tumour volumes were measured twice a week. Animals were sacrificed at humane endpoint or arbitrarily on day 90. Tumour volumes (absolute and relative to day 12), complete response (CR) rate, and overall survival (OS) were compared across treatment groups. Tumours exhibiting intrinsic immune escape phenotypes were excluded. ***Results:*** Median OS was 41 (control), 48.5 (SD-TRT), 54 (FX-TRT), 61.5 (ICI), 73.5 (SD-TRT + ICI) and > 90 days (FX-TRT + ICI). CR rates were 0% (control, SD-TRT), 25% (FX-TRT), 20% (ICI), 37.5% (SD-TRT + ICI) and 62.5% (FX-TRT + ICI). Combined therapies achieved greater tumour growth suppression and volume reduction compared to monotherapies. Notably, FX-TRT + ICI achieved tumour volumes significantly lower compared to ICI alone, from treatment week 2 through 1 week after the final dose (p = 0.004-0.030). ***Conclusion:*** This is the first study to compare single-dose and fractionated PSMA-TRT in an immunocompetent OSCC model treated with ICI. Combined therapy with fractionated PSMA-TRT significantly enhanced therapeutic efficacy, yielding greater response and survival rates, and improving tumour growth control compared to ICI alone. These results support the clinical translation of fractionated PSMA-TRT as therapeutic adjunct in patients with R/M HNSCC, where currently ICI monotherapy is standard of care. Further investigations are warranted to better understand the immunogenic and radiobiological mechanisms underlying these findings.

OP-523

PD-1 blockade enhances therapeutic effects of ^{177}Lu-DOTA-M5A in colorectal cancer CEA-transgenic mice

T. Mohajershojai[1], *E. Bengtsson*[1], *I. Vallin*[2], *D. Spangler*[2], *M. Melssen*[2], *P. J. Yazaki*[3], *M. Nestor*[2];
[1]*Karolinska Institute, Stockholm, SWEDEN,* [2]*Uppsala University, Uppsala, SWEDEN,* [3]*Beckman Research Institute, Duarte, CA, UNITED STATES OF AMERICA.*

Aim/Introduction: Radioimmunotherapy (RIT) has emerged as a promising strategy for treating metastatic solid tumors by delivering targeted radiation through the coupling of radionuclides with tumor-specific antibodies, thereby minimizing damage to healthy tissues. Carcinoembryonic antigen (CEA) is a well-established target in CEA-expressing malignancies, such as colorectal cancer (CRC), making it an attractive candidate for RIT. Increasing evidence suggests that RIT can potentiate anti-tumor immune responses, and combining RIT with immune checkpoint inhibitors (ICIs), such as anti-PD-1 antibodies, may further amplify therapeutic efficacy. This study aimed to evaluate, for the first time, the in vivo therapeutic effects of CEA-targeted RIT using the novel humanized anti-CEA antibody hT84.66-M5A conjugated to ^{177}Lu (^{177}Lu-DOTA-M5A), both as a monotherapy and in combination with PD-1 blockade. ***Materials and Methods:*** Radioconjugate uptake and efficacy were assessed in vitro using the MC38-CEA1 colorectal cancer spheroid model, and in vivo in CEA-transgenic mice bearing CEA-expressing tumors. Biodistribution and SPECT/CT imaging confirmed tumor-specific accumulation of the radioconjugate. In vitro studies demonstrated a dose-dependent cytotoxic effect of ^{177}Lu-DOTA-M5A. ***Results:*** In vivo, both ^{177}Lu-DOTA-M5A and PD-1 blockade monotherapies reduced tumor growth, with the combination therapy yielding the most pronounced and significant tumor growth inhibition (average daily growth: -6%) compared to PD-1 blockade (+7%), ^{177}Lu-DOTA-M5A (+7.9%), and untreated controls (+13.5%). Median survival was extended by 31% with PD-1 blockade and 52% with ^{177}Lu-DOTA-M5A; notably, the median survival in the combination group was not reached during the study period. Importantly, neither the monotherapies nor the combination therapy induced bone marrow toxicity. Furthermore, ^{177}Lu-DOTA-M5A modestly modulated the tumor immune microenvironment, increasing the presence of cytotoxic and helper T cells. In the combination-treated group, there was a notable shift toward pro-inflammatory macrophages, indicating an enhanced anti-tumor immune response. ***Conclusion:*** These findings support the therapeutic potential of ^{177}Lu-DOTA-M5A in CRC and underscore the added benefit of combining RIT with immune checkpoint inhibition. Further in vivo studies are warranted to validate these results and explore the clinical applicability of this combinatorial approach.

1205

Tuesday, October 7, 2025, 8:00 - 9:30
Room 211

Cutting Edge Science Track - TROP Session - AI Committee: AI Techniques for Patient Classification

OP-524

Decision support for early treatment adaptation, a case study for NSCLC: RTEP7-IFCT 14.02

Z. Mesbah[1,2,3], *R. Modzelewski*[1,3], *P. Le Roux*[1], *G. Zalcman*[4,5], *P. Giraud*[6], *P. Vera*[1,7], *S. Thureau*[1,7];
[1]*Henri Becquerel Cancer Center, Rouen, FRANCE,* [2]*Siemens Healthineers, Courbevoie, FRANCE,* [3]*AIMS-QuantIF, Rouen, FRANCE,* [4]*Bichat Claude Bernard Hospital, Paris, FRANCE,* [5]*Francophone Intergroup of Thoracic Oncology, Paris, FRANCE,* [6]*European Hospital Georges Pompidou, Paris, FRANCE,* [7]*AIMS-QuantIF, Paris, FRANCE.*

Aim/Introduction: The RTEP7 study is a phase II-III study originally designed to prove the efficiency and safety of dose escalation, up to 74 Gy (boost), during the external radiotherapy (RT) treatment, based on 18F-FDG-PET/CT imaging after 42 Gy of treatment (PET/CT 2). The goal of our study is to detect patients which could benefit from a RT boost from the start of the treatment. ***Materials and Methods:*** Our study focuses on 67 of the 138 patients which benefited from adaptive treatment based on the analysis by a physician of PET/CT 2. We evaluate the potential lesion radiomics as well as that of healthy organs omics (organomics). Thoracic organ groups are defined as follows: lungs, heart, aorta, trachea, oesophagus, spinal cord and thoracic vertebrae. The organs composing these groups are contoured using the TotalSegmentator tool. We extract 214 features (107 on PET and 107 on CT) for lesions and for each of the thoracic organ groups. We select the features most correlated to the target value, using Spearman's correlation coefficient, then fit a Machine Learning (ML) model on these features. A 6 folds cross validation (CV) was performed: 5 folds used to train the model and 1 fold kept as internal validation. Best performances were attained using a SVM model. We score the radiomics and organomics models

on the full CV as well as for each patient, to obtain accuracy score and a contigency matrix. Finally we perform a McNemar statistical test to assess the significance of potential performance differences between models. ***Results:*** Patients classification using the radiomics model yielded a balanced accuracy of 60.15%, sensitivity of 59.29%, a specificity of 61.01% and AUC of 62.52%. Using the organomics model, we improve performance greatly: a balanced accuracy of 76.25%, sensitivity of 79.02%, a specificity of 73.49% and AUC of 79.04%. The McNemar test yielded a p-value of 0.009, meaning the performances of radiomics and organomics models are significantly different. ***Conclusion:*** We demonstrated a significant (p=0.009) improvement in performance when using organomics over radiomics as input to a ML model, for the task of predicting treatment adaptation using pre-treatment PET/CT scan. The organomics-based model reached an accuracy of 76.25% in the task of predicting wether a patient will need a RT boost or not.

OP-525

Systemic Metabolic Signatures of Lung Cancer: A Machine Learning Approach Using Whole-Body Dynamic [^{18}F]FDG-PET

S. Castaneda Vega[1,2], *V. Agrawal*[3,2], *M. Weissinger*[1,4], *M. Stettler*[2], *V. Groos*[5], *A. Assmann*[5], *S. von Beschwitz*[1], *B. Pichler*[2,6], *S. Bauer*[7,8], *C. la Fougère*[1,9,10];
[1]*Departmenf of Nuclear Medicine and Clinical Molecular Imaging, Tübingen, GERMANY,* [2]*Werner Siemens Imaging Center, Tübingen, GERMANY,* [3]*Max Planck Institute for Intelligent Systems, Tübingen, GERMANY,* [4]*Department of Diagnostic and Interventional Radiology, Tübingen, GERMANY,* [5]*University of Tübingen, Tübingen, GERMANY,* [6]*iFIT-Cluster of Excellence, Tüebingen, GERMANY,* [7]*Helmholtz AI, München, GERMANY,* [8]*Technical University, München, GERMANY,* [9]*iFIT-Cluster of Excellence, Tübingen, GERMANY,* [10]*German Cancer Consortium (DKTK), Tübingen, GERMANY.*

Aim/Introduction: [^{18}F]FDG-PET/CT is widely used for lung cancer diagnosis and staging, yet typically relies on static imaging. Whole-body dynamic [^{18}F]FDG-PET, which captures tracer kinetics across time and organs, remains underutilized due to data complexity. However, its potential to reveal systemic physiological responses to malignancy is of increasing interest. This study investigates whether glucose metabolism in extra-tumoral organs—reflecting a tumor-organ axis—can be used to predict malignancy in pulmonary lesions using machine learning (ML). ***Materials and Methods:*** Thirty-four patients with indeterminate lung lesions underwent whole-body dynamic [^{18}F]FDG-PET/CT (0-80 min, Biograph™ mCT, Siemens). Lesions were classified as malignant or benign based on histopathology. Patlak modeling was used to generate parametric maps. Volumes of interest were drawn on the spleen, liver, bone marrow, and skeletal muscle, from which SUVmax, SUVmean, SUVpeak, and slope values were extracted. These features were used to train ML classifiers, and Shapley values were calculated to interpret feature importance. ***Results:*** The ML models achieved classification accuracies of up to 97% using only organ-level features. High TNM-stage tumors showed pronounced bone marrow activation, whereas benign lesions exhibited relatively elevated metabolic activity in the spleen. Interestingly, low-TNM malignancies displayed spleen metabolic slopes slightly higher than in high-TNM cases. Normalization of spleen values to liver uptake revealed that benign lesions retained a higher spleen metabolic rate compared to malignant cases. These subtle yet distinct patterns across distant organs reflect a measurable tumor-organ axis and provide classifiable signatures of malignancy. ***Conclusion:*** Whole-body dynamic PET imaging combined with machine learning can reveal systemic metabolic signatures associated with lung cancer. Differences in spleen and bone marrow activity, particularly when normalized to liver uptake, reflect disease burden and progression. These findings demonstrate the diagnostic potential of analyzing extra-tumoral organ metabolism and support a shift toward system-wide, non-invasive biomarkers for cancer detection and monitoring. ***References:*** Feng T, et al. J Nucl Med. 2021;62(5):738-744.

OP-526

Transfer Learning and External Validation of a ResNet-Based Deep Learning Model for Deauville Score Classification with [18F]FDG-PET-CT: A Retrospective Analysis

M. Dubrocq[1], *A. Mezher*[1], *T. Guiot*[2], *A. Gjukaj*[1], *O. Debeir*[3], *P. Flamen*[2], *E. Woff*[2];
[1]*Université Libre de Bruxelles, Brussels, BELGIUM,* [2]*Université libre de Bruxelles (ULB), Hôpital Universitaire de Bruxelles (H.U.B), Institut Jules Bordet, Department of Nuclear Medicine, Brussels, BELGIUM,* [3]*Université libre de Bruxelles (ULB), Ecole polytechnique de Bruxelles, Brussels, BELGIUM.*

Aim/Introduction: To evaluate the feasibility of a deep learning model for automatically classifying post-treatment [^{18}F]FDG-PET maximum intensity projection (MIP) images of lymphoma patients as negative (Deauville scores 1-3) or positive (scores 4-5). ***Materials and Methods:*** This retrospective study included 1602 [^{18}F]FDG-PET-CT scans from 882 adult patients with biopsy-confirmed FDG-avid lymphoma, acquired between 2015 and 2025 at the Institut Jules Bordet (Brussels, Belgium). All patients were diagnosed according to Lugano guidelines and underwent [^{18}F]FDG-PET-CT imaging for baseline and post-treatment follow-up.A previously published ResNet34-based model, the Lymphoma Artificial Reader System (LARS, Häggström et al.), was first externally validated on our test set. Secondly, the same architecture was retrained from scratch with our local data. Finally, a fine-tuning of the pretrained LARS model on our cohort was performed. Inputs of the models consisted of coronal and sagittal MIP images derived from SUV-converted PET scans. Patient-wise stratified splitting was employed in allocating 80% of cases for the training set and 20% for the test set. Model optimization was performed using binary cross-entropy loss with hyperparameters selected based on the area under the receiver operating characteristic curve (AUC). ***Results:*** External validation of LARS achieved an AUC of 0.915 (95% CI: 0.857-0.963), accuracy of 0.886 (0.848-0.924), sensitivity of 0.816 (0.700-0.917), and specificity of 0.900 (0.861-0.938).The locally retrained model showed decreased sensitivity 0.765 (0.634-0.871) despite a comparable AUC (0.900, 0.842-0.948) and specificity 0.929 (0.898-0.959).Fine-tuning the pretrained LARS model significantly improved performance, yielding the highest AUC (0.932, 0.884-0.971), sensitivity (0.878, 0.783-0.960), and robust specificity (0.908, 0.871-0.942). ***Conclusion:*** This study confirms the feasibility of using deep learning for automated Deauville-based classification of post-treatment [^{18}F]FDG-PET scans in lymphoma. The externally validated LARS model generalized well to an independent clinical dataset, achieving high AUC and accuracy. Retraining the same architecture (ResNet34) on a local dataset reproduced the approach but resulted in lower sensitivity. Fine-tuning the pretrained model on local data led to significantly improved performance, with the highest AUC and sensitivity across all configurations. These results demonstrate the transferability of this classification task across institutions and highlight the added value of transfer learning in adapting existing models to new clinical settings. Fine-tuned AI models may serve as reliable and scalable toolsfor treatment response assessment in molecular imaging, and their strong performance provides a compelling basis for further exploration toward multicenter generalization.

OP-527

Performance of an automatic tool for breast cancer staging with [^{18}F]FDG PET/CT

C. Constantino[1,2], *C. Oliveira*[1], *F. P. Oliveira*[1], *S. Vinga*[2], *D. C. Costa*[1];
[1]*Champalimaud Clinical Centre, Champalimaud Foundation, Lisbon, PORTUGAL,* [2]*INESC-ID, Instituto Superior Tecnico, University of Lisbon, Lisbon, PORTUGAL.*

Aim/Introduction: Whole-body [^{18}F]FDG PET/CT imaging is widely used to guide treatment decisions in breast cancer staging. In this study, we evaluate the potential of an AI-based tool to automatically localize key tumor regions with paramount importance for breast cancer staging using [^{18}F]FDG PET/CT. ***Materials and Methods:*** 263 histologically confirmed breast cancer patients (female, 54±11 y.o.) with staging [^{18}F]FDG PET/CT scans were retrospectively included. Images were acquired on Philips Gemini TF 16 (N=99) or Digital Vereos (N=164). [^{18}F]FDG avid lesions were identified by an experienced nuclear medicine physician and stratified according to their location: primary tumor (pT), axillary lymph nodes (ALN), extra-axillary loco-regional nodes (internal mammary and/or supraclavicular lymph nodes), and distant metastases (dM). Lesions were semi-automatically segmented with an adaptive Bayesian classifier [1]. All 263 patients had pT, 188 with ALN, 33 with extra-ALN, and 50 with dM. A two-channel (PET and CT) 3D U-Net based on the state-of-the-art nnU-Net framework [2] was used to train a four-class deep-learning-based model. The train/test set selection ensured adequate representativity of the four classes in both sets. In the test, there were pT in 60, ALN in 35, extra-ALN in 5, and dM in 14. To evaluate model performance, sensitivity and specificity to identify and classify the four key tumor regions were calculated. Furthermore, the SUV_{max} automatically retrieved from each class was compared with the physician-based ground truth, and the absolute agreement was assessed with the intraclass correlation coefficient (ICC). ***Results:*** In total, 1416 lesions were identified by the physician. In the test set (N=60 scans), there were 90 pT lesions, 71 ALN, 10 extra-ALN, and 220 dM). The AI-based tool was able to localize primary tumors with 100% sensitivity. For the identification and classification of ALN, extra-ALN, and dM, the sensitivity and specificity were 97% and 67%, 60% and 100%, and 72% and 94%, respectively. ICC for SUVmax between physician ground-truth and AI-based segmentation for the pT, ALN, extra-ALN, and dM were 0.98, 1.00, 0.65, and 0.98, respectively, showing good to perfect agreement. ***Conclusion:*** The developed AI-based tool has the potential to automatically map breast cancer involvement, using the location of four key tumor regions highly important for the staging. This aids breast cancer treatment decision-making. Ongoing work is expected to demonstrate improved results by increasing data training with higher numbers of regional lesions involvement. ***References:*** [1] Constantino et al, doi:10.1007/s10278-023-00823-y; [2] Isensee et al., doi:10.1038/s41592-020-01008-z

OP-528

AI-based Prediction of Myocardium Viability Using [^{82}Rb] PET/CT

A. Chevalley[1,2], *G. Bonnet*[2], *M. Amirian*[1,2], *V. Andrearczyk*[1,2], *S. Bors*[2], *R. Klein*[3], *R. DeKemp*[4], *E. Moulton*[5], *J. O. Prior*[2], *M. Jreige*[2], *C. H. Kamani*[2], *A. Depeursinge*[1,2];
[1]*Institute of Informatics, HES-SO Valais-Wallis, Sierre, SWITZERLAND,* [2]*Department of Nuclear Medicine and Molecular Imaging, Centre Hospitalier Universitaire Vaudois (CHUV), Lausanne, SWITZERLAND,* [3]*Division of Nuclear Medicine and Molecular Imaging, University of Ottawa, Ottawa, ON, CANADA,* [4]*Division of Cardiology, University of Ottawa Heart Institute,, Ottawa, ON, CANADA,* [5]*Jubilant DraxImage Inc., Kirkland, QC, CANADA.*

Aim/Introduction: Myocardial viability assessment is crucial to determine the potential need for revascularisation after myocardial infarction (MI). While [^{18}F]FDG combined with [^{82}Rb] myocardial perfusion imaging is the gold standard, this study aims to detect non-viable tissues using only [^{82}Rb] PET and artificial intelligence (AI). ***Materials and Methods:*** The cohort was retrospectively composed of MI patients who underwent clinically indicated [^{82}Rb] and [^{18}F]FDG at our institution. For ground truth, we computed the viability score by normalizing the FDG uptake map to the regions with normal [^{82}Rb], defined as ≥ 60% maximum. Viability score bellow 50 % defined non-viable regions. We propose two approaches to infer viability from Rubidium alone: the regression (Reg) approach predicts the viability score, while the classification (Cl) approach detects non-viable tissues. We compared two models for both methods, support vector models ($SVM_{Reg/Cl}$) using 93 radiomic features extracted from the segment uptake rate K_1 and a convolutional neural network ($CNN_{Reg/Cl}$) using myocardial blood flow segment. Only the best modality for each model is reported. For classification models, the static [^{82}Rb] segment value is added to help differentiate normal from abnormal. The metrics reported are positive predictive value (PPV), true positive/negative rate (TPR/TNR). For the regression approach, the predicted score is binarized using the 50% threshold for classification. Analysis was performed at the segmental level using the 17-segment American Society of Nuclear Cardiology model, excluding the apex. Training used five stratified folds, allowing us to compute the 95% confidence intervals assuming a Student-t distribution. ***Results:*** The study includes 34 patients (29 male; mean age 70 ± 9 years), resulting in 544 segments. As normal segments are trivial to classify, evaluation is conducted on the 114 abnormal segments. For regression, CNN_{Reg} predicts the viability score with a mean absolute error (MAE) of 8.52[6.50,10.54], and achieves a PPV, TPR and TNR of 0.75[0.45,1.00], 0.80[0.63,0.98] and 0.89[0.77, 1.00]. Therefore, CNN_{Reg} slightly outperforms its classification counterpart CNN_{Cl}, which shows PPV, TPR and TNR of 0.74[0.53,0.94], 0.78[0.57,0.99] and 0.86[0.73, 1.00]. Radiomics-based models are slightly worst, SVM_{Reg} with an MAE of 9.04[7.19,10.90], PPV, TPR and TNR of 0.68[0.42,0.94], 0.62[0.30,0.95] and 0.85[0.72, 0.98] and SVM_{Cl} (PPV, TPR and TNR of 0.68[0.44,0.91], 0.87[0.70,1.00] and 0.80[0.62,0.97]). ***Conclusion:*** AI may help predict segmental myocardial viability after an infarction using rest [^{82}Rb] PET alone and remove the costs and radiation associated with the use of [^{18}F]FDG.

OP-529

Integration of Spatial Analysis and Deep Learning for Enhanced Tumour Classification in Total-Body PET/CT Imaging: A Preliminary Study

D. Han[1], *S. Wail*[2];
[1]*Telix Pharmaceuticals, Sydney, AUSTRALIA,* [2]*Telix Pharmaceuticals, Melbourne, AUSTRALIA.*

Aim/Introduction: This study aims to improve tumour classification of total-body ^{68}GaPSMA11 PET/CT scans by integrating lesion segmentation, quantitative spatial analysis with machine-learning. The objective is to differentiate tumour types, including bone, lymphatic, liver, and prostate, while establishing criteria that may support future evaluation of cancer progression based on anatomical spread and established staging systems (TNM, miTNM, PROMISE). The focus of our efforts is on quantitative spatial analysis. ***Materials and Methods:*** 297 image sets from total-body ^{68}GaPSMA11 PET/CT scans were used for training, 3771 tumours were identified throughout the dataset. The binary tumour segmentations of the 297 PET/CT scans were generated using an internally developed nn-UNet-based segmentation algorithm. CT scans were further processed to accurately delineate major organs by a state-of-the-art total-body segmentation algorithm (TotalSegmentator). From the PET and CT segmented images, spatial relationships between tumours and organs were quantified. Key features were derived: tumour centroid coordinates and volumes; organ centroid coordinates and volumes; minimal distance between tumour and organ surfaces; distance between

the centroids of tumour and each organ; and volume of overlap when present. These relational metrics provided a robust data foundation to characterise the anatomical context of tumours. Two complementary machine learning models were developed: both a convolutional neural network (CNN) that and a graph neural network (GNN) were developed that incorporates the extracted spatial relationships in a network-based framework. Both models were trained to classify tumour types into pre-defined categories, facilitating comparisons between approaches. ***Results:*** Preliminary experiments with a validation dataset indicate that both CNN and GNN models achieved promising classification performance, yielding an overall 90% accuracy for both test and validation datasets, with bone class > 98%, lymph class > 85%, prostate > 85% and liver > 90%.The inclusion of spatial relational features improved the overall discrimination of tumour types. Furthermore, the generation of detailed classification criteria per tumour segment not only enhanced model accuracy but also provided a framework for future applications in monitoring cancer progression. ***Conclusion:*** The presented workflow establishes a novel framework for tumour classification by combining advanced organ segmentation, quantitative relational feature extraction, and dual-modality machine-learning. This integrated approach not only offers enhanced accuracy in distinguishing tumour types but also lays the groundwork for future prognostic applications in clinical oncology. Further validation with larger datasets is planned to refine the methodology and explore its potential in informing treatment planning and dynamic cancer staging.

OP-530

Wasserstein Distance as a Metric for Molecular Connectivity Analysis in Amyotrophic Lateral Sclerosis

C. Tang[1], *J. De Vocht*[2,3], *K. Van Laere*[1,4], *P. Van Damme*[2,3], *M. Koole*[1];
[1]Nuclear Medicine and Molecular Imaging, Imaging and Pathology, KU Leuven, Leuven, BELGIUM, [2]Laboratory for Neurobiology (VIB-KU Leuven), Department of Neurosciences, KU Leuven, Leuven, BELGIUM, [3]Neurology, University Hospitals Leuven, Leuven, BELGIUM, [4]Department of Nuclear Medicine, University Hospitals UZ Leuven, Leuven, BELGIUM.

Aim/Introduction: Molecular imaging is increasingly important in investigating brain connectivity, advancing our understanding of the brain connectome (1). However, evaluating molecular connectivity at the individual level using static ^{18}F-FDG PET is challenging due to the absence of temporal information. This limitation calls for alternative approaches to conventional functional connectivity methods, which rely on correlations of time series. In this study, we introduce a novel approach based on the Wasserstein distance (WD), a concept from optimal transport theory (2). Unlike previous approaches that depend on Kullback-Leibler divergence similarity estimation (KLSE) (3), WD does not require the estimation of probability density functions (PDFs), while it can effectively measure distances between regions with minimal or no spatial overlap, avoiding the issue of infinite values. We compared the classification performance of WD- and KLSE-based methods in distinguishing healthy controls (HC), persons with Amyotrophic Lateral Sclerosis (pwALS), and persons with ALS-mimicking diseases (Mimics). ***Materials and Methods:*** Our dataset included ^{18}F-FDG PET scans from 36 HC (55.0±13.0 years, 19F/17M), 167 pwALS (63.9±11.1 years, 64F/103M), and 25 Mimics (62.4±8.0 years, 8F/17M). All PET images were spatially normalized to MNI space, and regional data were extracted using an atlas of 53 brain regions. Regional adjacency matrices were computed using either WD or KLSE between region pairs and then transformed into similarity matrices via an exponential function. These similarity matrices served as input for Support Vector Machine (SVM) classification, alongside an image-based SVM classifier for comparison. We evaluated the performance of each SVM approach using 10-fold cross-validation repeated 10 times, with statistical comparison via paired t-tests. ***Results:*** In the classification of pwALS versus HC, the image-based SVM achieved an accuracy of 0.84±0.01. WD-based and KLSE-based SVM classifications yielded accuracies of 0.86±0.00 ($p<0.05$) and 0.83±0.01 ($p>0.05$), respectively. For distinguishing pwALS from Mimics, the image-based SVM reached an accuracy of 0.52±0.02, while the WD- and KLSE-based methods achieved 0.58±0.02 ($p<0.05$) and 0.56±0.02 ($p<0.05$), respectively. ***Conclusion:*** SVM classification using WD- and KLSE-based adjacency matrices showed performance comparable to voxel-based methods, demonstrating their ability to capture disease-relevant patterns while reducing data dimensionality. Among the two, WD emerges as a more suitable metric for discrete PET data, offering a continuous and intuitive measure of regional distances without requiring PDF estimation. Future work will explore clustering of individual adjacency matrices to identify disease-specific brain network patterns. ***References:*** 1. A. Sala et al., 2023. 2. G. Peyré, M. Cuturi, 2019. 3. M. Wang et al., 2020.

OP-531

Detecting The Epileptogenic Zone Using Attention U-Net Model in FDG PET Images: Integration of Deep Learning Techniques to PET Imaging

M. Bodur[1], *L. Uslu-Besli*[1], *O. E. Sahin*[1], *K. Saglam*[1], *A. Sarikas*[2], *O. Demir*[2], *C. Ozkara*[3], *H. B. Sayman*[1];
[1]Isanbul University-Cerrahpasa, Department of Nuclear Medicine, Istanbul, TÜRKIYE, [2]Marmara University, Department of Computer Engineering, Istanbul, TÜRKIYE, [3]Isanbul University-Cerrahpasa, Department of Neurology, Istanbul, TÜRKIYE.

Aim/Introduction: This study aims to develop a deep learning technique to detect epileptogenic zone using interictal FDG PET images in epilepsy patients. ***Materials and Methods:*** Interictal F-18 FDG PET images of 20 drug-resistant epilepsy patients were evaluated and hypometabolic areas that were in accordance with the epileptogenic zones were manually contoured by experienced nuclear medicine specialists. The Attention U-Net architecture, known for its effectiveness particularly in biomedical image analysis, has been employed[1]. The rationale behind choosing this architecture for nuclear medicine image analysis is to leverage the superior spatial localization capability of the classical U-Net structure in conjunction with the ability of attention mechanisms to emphasize signals specific to lesion regions. The image data was randomly divided into training (80%), validation (10%), and testing (10%) sets for model learning, verification, and performance evaluation, respectively. All PET images were standardized to a size of 384x384 pixels to suit the model's input requirements. The training of the Attention U-Net model was performed by minimizing a linear combination of the binary cross-entropy loss function, commonly used for pixel-level classification, and the Dice loss function, which optimizes regional similarity. The Adam optimization algorithm, known for its adaptive learning rate, was used for weight updates, and the entire training process was conducted for 100 epochs with a mini-batch size of 4. ***Results:*** The trained Attention U-Net model demonstrated a high accuracy of 96% in segmenting the extent of hypometabolic areas on FDG PET images included. However, the F1-score was calculated to be relatively lower at 65%, likely due to the imbalance in the number of pixels between the lesion and normal tissue. Visual inspection of the obtained segmentation masks revealed that the model exhibited pixel-level uncertainties and irregularities in the boundary regions of the lesions at certain locations. ***Conclusion:*** This preliminary study on a limited dataset indicates that Attention U-Net is a promising architecture for automated epilepsy lesion segmentation, achieving high accuracy in overall localization. However, the lower F1-score suggests a need for improved performance, especially for small or irregular lesions. Future work should assess generalization on larger,

diverse datasets and compare architectures, also exploring post-processing and alternative loss functions for better segmentation quality. ***References:*** [1]Al Qurri A, Almekkawy M. Improved UNet with Attention for Medical Image Segmentation. Sensors (Basel). 2023 Oct 20;23(20):8589. doi: 10.3390/s23208589. PMID: 37896682; PMCID: PMC10611347.

OP-532

Stratified Evaluation of Deep Learning Models by Age and Cognition Level for Amyloid Positivity Prediction in [^{18}F]FDG PET

S. Seo[1], *M. So*[1], *S. Lee*[1], *Y. Yoon*[1], *D. Seo*[1], *D. Kim*[2], *H. Han*[2], *S. Kang*[1], *D. Kim*[3], *M. Yun*[1];
[1]*Yonsei University College of Medicine, Seoul, KOREA, REPUBLIC OF,* [2]*Yonsei University, Seoul, KOREA, REPUBLIC OF,* [3]*Hallym University College of Medicine, Anyang, KOREA, REPUBLIC OF.*

Aim/Introduction: Deep learning (DL)-based analysis of [^{18}F] fluorodeoxyglucose ([^{18}F]FDG) PET has emerged as a promising and cost-effective approach for predicting amyloid positivity, a key biomarker in Alzheimer's disease (AD). However, substantial variability in classification accuracy has been observed across studies, potentially reflecting differences in model design and subject demographics. This study aimed to evaluate the performance of multiple deep learning models for amyloid positivity prediction from [^{18}F]FDG PET and to examine how accuracy varies by age and cognitive impairment severity. ***Materials and Methods:*** We retrospectively analyzed 2,671 in-house [^{18}F]FDG PET scans (795 amyloid-positive, 1,876 amyloid-negative), with amyloid positivity confirmed by expert visual assessment of amyloid PET images obtained within approximately one year of [^{18}F]FDG PET scans. Four DL architectures—ResNet, Swin Transformer (SwinT), Vision Graph Neural Network (ViG), and ConvNeXt—were trained to classify amyloid status. The dataset was partitioned into training (n=2002), validation (n=350), and test sets (n=319). Model performance was evaluated using accuracy and Area Under the Receiver Operating Characteristic Curve (AUROC), stratified by age (≤60, 60-70, 70-80, ≥80 years) and cognitive impairment severity based on MMSE z-scores (> -1.5, -2.5 to -1.5, < -2.5). To evaluate the consistency of predictions across four DL architectures, Fleiss' kappa was calculated. ***Results:*** Overall test-set accuracies were 78.1% (ResNet), 76.8% (SwinT), 73.7% (ViG), and 73.0% (ConvNeXt), with AUROCs of 0.836, 0.839, 0.814, and 0.818, respectively. Stratified by age, model accuracy consistently declined with increasing age: highest accuracy was observed in patients aged ≤60 (accuracy: 95.6±1.73%, AUROC: 0.983±0.01), progressively decreasing for age groups 60-70 (accuracy: 83.3±1.05%, AUROC: 0.908±0.02), 70-80 (accuracy: 70.4±3.71%, AUROC: 0.752±0.02), and ≥80 (accuracy: 62.3±5.83%, AUROC: 0.702±0.04). This declining trend was consistently observed across individual models, except for SwinT between the 70-80 and ≥80 age groups. Stratified by cognitive impairment, models exhibited improved AUROCs with greater impairment severity: MMSE z-score > -1.5 (accuracy: 78.2±1.87%, AUROC: 0.728±0.03), -2.5 to -1.5 (accuracy: 67.9±5.25%, AUROC: 0.790±0.02), and < -2.5 (accuracy: 74.5±5.25%, AUROC: 0.834±0.05). Fleiss' kappa across the four DL models was 0.48, indicating the observed classification trends reflect consistent model behavior rather than random effects. ***Conclusion:*** The accuracy of DL-based amyloid positivity prediction using [^{18}F]FDG PET significantly varies with patient age and cognitive impairment, which might reflect age-related brain metabolic differences and disease severity-related neurodegenerative patterns. These findings underscore the necessity of explicitly considering demographic and clinical characteristics when assessing and reporting DL model performance in neurodegenerative diseases.

1206

Tuesday, October 7, 2025, 8:00 - 9:30
Room 117

Clinical Oncology Track - TROP Session - Oncology & Theranostics Committee: Protate Cancer Therapy: Dosimetry, SPECT/CT, AI

OP-533

Validation of the collapsed-cone superposition for whole-body patient-specific dosimetry in [177Lu]Lu-PSMA-617 radionuclide therapy

A. Terro[1], *S. Perret*[1], *A. Dumouchel*[1,2], *D. Tonnelet*[2], *A. Edet-Sanson*[1,2], *P. Vera*[1,2], *P. Decazes*[1,2], *A. Dieudonné*[1,2];
[1]*QuantIF-AIMS, Rouen University, Rouen, FRANCE,* [2]*Nuclear Medicine Department, Henri Becquerel Center, Rouen, FRANCE.*

Aim/Introduction: [177Lu]Lu-PSMA-617 therapy has emerged as a promising treatment option for patients with metastatic castration-resistant prostate cancer (mCRPC). Accurate dosimetry in radiopharmaceutical therapy offers a promising approach to optimize the balance between treatment efficacy and toxicity. The development of personalized dosimetry through whole-body single photon emission computed tomography and computed tomography (SPECT/CT) imaging is made possible with the advent of 360° CZT gamma cameras. SimpleDose [1] is an automated whole-body dosimetry software that employs the collapsed cone superposition (CCS) approach [2,3]. This study aims to validate the CCS approach for whole-body dosimetry in [177Lu]Lu-PSMA-617 therapy by comparing it with Monte Carlo (MC) simulations at the organ, lesion, and voxel levels. ***Materials and Methods:*** Thirty mCRPC patients were imaged after the infusion of [177Lu]Lu-PSMA-617 on a VERITON-CT 200 (Spectrum Dynamics®, Caesarea, Israel). Dose rate maps (mGy/h) were generated from single SPECT/CT scans with a sampling of 2.46 x 2.46 x 2.46 mm^3. The CCS approach takes into account tissue densities using dose-point kernels adjusted to those densities. Organ and lesion delineation were automated using the nnU-Net V2 neural network. Reference MC simulations were conducted using GATE 10 for 10^8 events. The comparison between CCS and MC was performed at the organ, lesion, and voxel levels. ***Results:*** The organ wise comparison between CCS and MC showed a median (IQR) absolute percentage error of 3.92 (2.22), 1.11 (0.66), 0.78 (0.72), 3.13 (1.38), 4.76 (4.00), 2.74 (2.92), 3.06 (2.76), 3.10 (1.22) for bone marrow, kidneys, liver, lungs, pancreas, salivary glands, spleen and lesions, respectively, with no significant organ-level differences ($p > 0.70$). Voxel-level errors were mostly < 2%. CCS had a median computation time of 24.5 seconds, compared to 6.8 hours for MC on a computer with an Intel Xeon 20 x 3.70 GHz CPU. ***Conclusion:*** CCS approach showed strong agreement with MC, offering improved computational efficiency and clinical potential for whole-body dosimetry in [177Lu]Lu-PSMA-617 therapy. ***References:*** 1. Dieudonné, A. et al. Towards fully automatized [177Lu]Lu-PSMA personalized dosimetry based on 360° CZT whole-body SPECT/CT: a proof-of-concept. EJNMMI Physics 12, 25 (2025). 2. Sanchez-Garcia, M. et al. A new approach for dose calculation in targeted radionuclide therapy (TRT) based on collapsed cone superposition: validation with (90)Y. Phys Med Biol 59, 4769-4784 (2014). 3. Sanchez-Garcia. et

al. Implementation and validation of collapsed cone superposition for radiopharmaceutical dosimetry of photon emitters. Phys Med Biol 60, 7861-7876 (2015).

OP-534

The tumour sink effect on healthy tissues dosimetry in ^{177}Lu-PSMA-I&T radiopharmaceutical therapy

A. Zamanian[1], *F. A. Buteau*[2], *G. April*[2], *F. Arsenault*[2], *A. Beaulieu*[2], *F. Pouliot*[3], *J. M. Beauregard*[1];
[1]*Department of Radiology and Nuclear Medicine, Université Laval, Quebec City, QC, CANADA,* [2]*Department of Medical Imaging, CHU de Québec - Université Laval, Quebec City, QC, CANADA,* [3]*Urology Division, Department of Surgery, Université Laval, Quebec City, QC, CANADA.*

Aim/Introduction: The biodistribution of therapeutic PSMA-targeting radiopharmaceutical may be affected by the tumour sink effect, a phenomenon by which the radiopharmaceutical's sequestration into lesions leads to a reduction in absorbed doses (ADs) to healthy tissues. This study aimed to investigate the tumour sink effect, and secondarily the impact of body size and renal function, on dosimetry in patients receiving ^{177}Lu-PSMA-I&T. ***Materials and Methods:*** Twenty-six mCRPC patients underwent quantitative SPECT/CT from neck to pelvis approximately 48 hours after injection of around 7.4 GBq ^{177}Lu-PSMA-I&T. Activity concentration (Bq/mL) was sampled using 2 or 3 cm spherical VOIs over healthy tissues (kidneys, spleen, liver, and proximal aorta), and specific ADs (Gy/GBq) were estimated via Hänscheid's single-time-point method. Whole-body tumour burden was delineated using an SUV threshold of three times the liver SUV_{mean}, excluding physiological uptake. Total lesion fraction (TLF) was defined as total lesion activity divided by body weight (g), expressed as percentage. Participants were stratified into three TLF groups: small <10%, moderate 10-25%, and large ≥25%. Estimated glomerular filtration rate (eGFR) and body surface area (BSA) were other evaluated predictive variables, as well as the combination of the three: BSA•eGFR/[1-TLF]. * indicates p<0.05, **p<0.01, and ***p<0.001. ***Results:*** The median TLF was 5.8% (range: 0.6-55.6%). Consistent with literature, the median specific ADs (range) for the kidney, spleen, liver and blood were 0.81 (0.24-2.17), 0.047 (0.007-0.154), 0.034 (0.016-0.120), and 0.007 (0.001-0.015) Gy/GBq, respectively. Kidney specific AD was inversely correlated with TLF (r=-0.49*), BSA (r=-0.35), eGFR (r=-0.51**), and BSA•eGFR/[1-TLF] (r=-0.67***). Similar trends were observed for the spleen (r=-0.68***, -0.46*, -0.41*, and -0.84***, respectively) and the liver (r=-0.42*, -0.31, -0.33, and -0.46**, respectively). For the blood, the correlations with predictive factors were more variable (r=0.22, -0.32, -0.54**, and -0.08, respectively). Patients with a large TLF (n=4) showed a significantly lower mean renal specific AD compared to those with a small TLF (n=15): 0.54 vs. 1.01 Gy/GBq(*). Corresponding mean spleen specific ADs were 0.01 vs. 0.07 Gy/GBq(**). ***Conclusion:*** Patients with a large tumour burden, larger body habitus, and/or good renal function tend to receive lower specific ADs to healthy tissues and are therefore likely to be undertreated with a fixed-activity regime. Dosimetry-based personalisation of PSMA radiopharmaceutical therapy could allow a safe escalation of administered activity in many, offering the prospect of improved outcomes, particularly for patients with extensive disease who are the most in need of therapeutic benefit.

OP-536

Prognostic value of ^{68}Ga-PSMA PET radiomics in metastatic castration-resistant prostate cancer treated with ^{177}Lu-PSMA radioligant therapy

L. Edouard[1], *L. Ferrer*[2], *L. Papillon*[2], *Y. Godbert*[1], *M. Meyer*[1], *V. Préga-Renaud*[1], *C. Subreville*[3], *N. Anizan*[4], *M. Cabart*[5], *D. Teyssonneau*[5], *G. Roubaud*[5], *T. Colin*[2], *P. Schwartz*[1];
[1]*Nuclear Medicine Department, Institut Bergonié, Bordeaux, FRANCE,* [2]*Sophia Genetics, Pessac, FRANCE,* [3]*Department of Pharmacy, Institut Bergonié, Bordeaux, FRANCE,* [4]*Department of Physics, Institut Bergonié, Bordeaux, FRANCE,* [5]*Oncology Department, Institut Bergonié, Bordeaux, FRANCE.*

Aim/Introduction: Metastatic castration-resistant prostate cancer (mCRPC) remains incurable despite recent therapeutic advances. ^{177}Lu-PSMA radioligand therapy (RLT) shows clinical benefits in selected patients. However, approximately 30% of patients do not respond to ^{177}Lu-PSMA RLT. There is a lack of strong pre-therapeutic predictive biomarkers. Radiomics, by extracting quantitative imaging features, offers a novel approach to predict clinical outcomes beyond standard visual interpretation. We evaluated the prognostic value of pretherapeutic ^{68}Ga-PSMA PET radiomic features for overall survival (OS) in patients with mCRPC treated with ^{177}Lu-PSMA RLT. ***Materials and Methods:*** This retrospective monocentric study included 102 mCRPC patients treated with ^{177}Lu-PSMA between January 2022 and March 2024. Five lesions per patient were segmented on their pretherapeutic ^{68}Ga-PSMA PET/CT. Radiomic features were extracted following IBSI guidelines. Associations with OS were evaluated using Cox proportional hazard models. A multimodal machine learning (ML) model integrating clinical, genomic, biochemical, and imaging features (including radiomics) was developed to predict OS. ***Results:*** Median OS of the total cohort was 11.2 months. Intralesional homogeneity characterised by 2nd order radiomic feature "Normalised Inverse Difference Moment" was associated with shorter OS (p=0.025). Among clinical parameters, ECOG ≥2, liver metastases, and high tumor burden (≥20 metastases or superbone scan) were significantly correlated with poor OS (p<0.05).The best-performing ML model achieved a 12-month AUC of 0.778 by combining 22 clinical, biochemical, genomic, and radiomic features. The model leveraging PET data alone achieved strong performance, with an AUC comparable to the clinical model (0.715 vs 0.766). ***Conclusion:*** Radiomic features extracted from ^{68}Ga-PSMA PET/CT, particularly intralesional homogeneity, provide independent prognostic information for OS in mCRPC patients undergoing ^{177}Lu-PSMA RLT. Their integration into a multimodal ML model improves prediction performance, supporting their potential role in personalized treatment strategies.

OP-537

Early Progression Prediction with RECIP 1.0 on Routine Post-Therapy ^{177}Lu-PSMA SPECT/CT

M. Kassas[1], *L. Devriendt*[2], *T. Guiot*[3], *M. Manley*[1], *C. Marin*[3], *R. Danieli*[3], *L. Taraji*[1], *I. Karfis*[1], *E. Woff*[1], *P. Flamen*[1], *C. Artigas*[1];
[1]*Institut Jules Bordet, Hôpital Universitaire de Bruxelles, Université Libre de Bruxelles, Nuclear Medicine Department, Brussels, BELGIUM,* [2]*Faculté de Médecine, Université Libre de Bruxelles, Brussels, BELGIUM,* [3]*Institut Jules Bordet, Hôpital Universitaire de Bruxelles, Université Libre de Bruxelles, Medical Physics Department, Brussels, BELGIUM.*

Aim/Introduction: To assess the prognostic value of early response assessment through applying the Response Evaluation Criteria in PSMA PET/CT (RECIP1.0) on the 24hr post-therapy SPECT/CT images of the second cycle of ^{177}Lu-PSMA radioligand therapy (RLT). ***Materials and Methods:*** A retrospective analysis was conducted on 136 patients with metastatic castration resistant prostate cancer (mCRPC) treated with ≥2 cycles of ^{177}Lu-PSMA-I&T, with evaluable 24hr post-therapy SPECT/CT scans obtained after cycle 1 (C1) and cycle 2 (C2). Automated segmentation with LesionID Pro from MIM Software was used to quantify total tumor volume (TTV). Relative changes in TTV and detection of new lesions (NLs) at C2 post-therapy SPECT/CT scans were used to classify patients into two categories according to RECIP1.0: a) progressive disease (RECIP-PD), with an increase in TTV≥20% and the appearance of NLs; and b) non-progressive disease (RECIP-non-PD) otherwise. Association of these criteria with progression free survival (PFS) and overall survival (OS) was performed using univariate and multivariate Cox regression and plotted on Kaplan-Meier curves. ***Results:*** After a median follow-up of 23 months, 123/136 patients (90%) experienced disease progression and 90 (66%) passed away.

Median PFS was 6.4 months (95%CI 5.5-7.4); median OS was 16.6 months (95%CI 12.7-20.5). RECIP-PD patients (n=16/136) exhibited significantly reduced PFS (median PFS: 3.6 vs 7.0 months, HR=3.6 95%CI[2.1-6.2] p<0.001) and OS (median OS: 7.4 vs 17.5 months; HR=3.1 95%CI[1.6-5.8], p<0.001) compared to RECIP-non-PD. TTV increase ≥20% at C2 (n=23/136) was significantly associated with shorter PFS (median PFS 3.3 vs 7.1 months, HR=3.5, 95%CI[2.2-5.6], p<0.001) and OS (median OS 10.2 vs 17.5 months, HR=1.8, 95%CI[1.1-3.1], p=0.023) compared to those without. NLs at C2 (n=28/136) were significantly associated with shorter PFS (4.4 vs 7.3 months, HR=2.6, 95%CI[1.7-4.0], p<0.001) and OS (7.7 vs 18.0 months, HR=2.3 95%CI[1.4-3.8], p=0.002) compared to those without. Harrell's C-index showed that RECIP-PD had the highest and most consistent predictive power for both endpoints (PFS: 0.80; OS: 0.78), compared to TTV increase≥20% (PFS: 0.81; OS: 0.68) or NLs (PFS: 0.72; OS: 0.74) alone. ***Conclusion:*** These results suggest that applying RECIP1.0 to post-therapy SPECT/CT imaging provides a practical, cost-effective method for early identification of patients unlikely to benefit from continued ^{177}Lu-PSMA-RLT. This may enable a rapid shift of therapeutic plan (i.e. alpha-emitting RLT, chemotherapy) and increase the cost-effectiveness of RLT. Although TTV increase and NL appearance were also independently associated with poorer outcomes, RECIP-PD categorization had the most consistent prognostic value for both PFS and OS.

OP-538

Comparison of PET Response Criteria in mCRPC Patients Treated with [^{177}Lu]PSMA

T. Telli[1], *V. Grünwald*[2], *B. Hadaschik*[3], *C. Kesch*[3], *L. Umutlu*[4], *K. Herrmann*[1], *W. P. Fendler*[1];
[1]*Department of Nuclear Medicine, University Hospital Essen, Essen, GERMANY,* [2]*Department of Urology, University Hospital Essen, Essen, Germany, Essen, GERMANY,* [3]*Department of Urology, University Hospital Essen, Essen, GERMANY,* [4]*Department of Diagnostic and Interventional Radiology and Neuroradiology, University Hospital Essen, Essen, GERMANY.*

Aim/Introduction: In this study we aimed to compare various imaging-based response criteria in men with metastatic castration-resistant prostate cancer (mCRPC) treated with [^{177}Lu]PSMA radioligand therapy. ***Materials and Methods:*** This retrospective study included 84 patients who received a median of 4 [^{177}Lu]PSMA cycles (IQR 2-5; median 24.3 GBq, IQR 14.9-32.9 GBq) at the University Hospital Essen between March 2019 and May 2022. Response assessments were conducted using multiple criteria comparing baseline and 6-8 weeks post-second cycle scans: Response Evaluation Criteria in Solid Tumors (RECIST) 1.1, the adapted Prostate Cancer Working Group Criteria (aPCWG), Positron Emission Tomography Response Criteria in Solid Tumors (PERCIST), the PSMA PET Progression (PPP), the Response Evaluation Criteria in PSMA-Imaging 1.0 (RECIP) (based on qPSMA and SUV≥4 thresholds), and visual RECIP. Responses were categorized as progressive disease (PD) or non-PD. The primary endpoint was the prognostic significance of these response criteria for overall survival, evaluated via Cox regression analysis. Harrell`s C-index was used for concordance of different imaging-based criteria and survival. ***Results:*** A total of 34 (40.5%) patients had non-measurable disease according to RECIST 1.1. Twenty (40%), 43 (51.2%), 44 (52.4%), 47 (56.0%), 35 (41.7%), 37 (44.0%), and 31 (36.9%) of patients had PD according to RECIST 1.1, aPCWG, PERCIST, PPP, RECIP qPSMA, RECIP SUV≥4, and visual RECIP respectively. PD patients had a significantly higher risk of death compared to non-PD patients according to RECIST 1.1 (HR = 5.0; 95%CI, 2.5-10.0; p < 0.001), PERCIST (HR = 2.9; 95%CI, 1.8-4.8; p < 0.001), aPCWG (HR = 3.6; 95%CI, 2.1-6.0; p < 0.001), PPP (HR = 3.9; 95%CI, 2.3-6.6; p < 0.001), RECIP qPSMA (HR = 2.7; 95%CI, 1.6-4.4; p < 0.001), RECIP SUV≥4 (HR = 2.2; 95%CI, 1.6-3.6; p < 0.001) and visual RECIP (HR = 3.5; 95%CI, 2.1-6.0; p < 0.001). Higher C-indices were observed for PPP: 0.68 (95%CI, 0.58-0.77), and aPCWG: 0.67 (95%CI, 0.57-0.77) in comparison to PERCIST: 0.65 (95%CI, 0.54-0.75), visual RECIP: 0.63 (95%CI, 0.52-0.73), RECIP qPSMA: 0.62 (95%CI, 0.51-0.74) and, RECIP SUV≥4: 0.62 (95%CI, 0.50-0.73). ***Conclusion:*** Under [^{177}Lu]PSMA the presence of progressive disease, as indicated by any of the evaluated criteria, has been observed to be consistently associated with a significantly elevated risk of death. Among the evaluated methods, PSMA PET Progression (PPP) demonstrated the highest prognostic performance. These findings lend support to the clinical value of standardised imaging criteria, particularly PPP, for the early response assessment under [^{177}Lu]PSMA.

OP-539

SPECT to PET image translation with a conditional Generative Adversarial Network (GAN) improves assessment of ^{177}Lu-PSMA post therapy scans

T. Otani*, F. Moradi, H. Song, G. Davidzon, A. Iagaru;*
Stanford Healthcare, Stanford, CA, UNITED STATES OF AMERICA.

Aim/Introduction: Direct comparison between SPECT/CT after ^{177}Lu-PSMA treatment and PSMA PET could be challenging due to differences in image quality and visual appearance. We used a conditional GAN (Pix2Pix) to transformed SPECT into PET-quality images (synthetic PET). ***Materials and Methods:*** 97 prostate cancer patients treated with ^{177}Lu-PSMA therapy were divided into training sets (n = 72) and test sets (n = 25). For model training, the input data consisted of SPECT images acquired at the time of the first 177Lu-PSMA treatment cycle, and the ground truth data comprised PSMA PET/CT images obtained prior to the first treatment. In the test set, SPECT/CT images acquired after the first and last cycles of Lu-PSMA therapy were converted into synthetic PET images by the trained model. Therapeutic response to ^{177}Lu-PSMA therapy was assessed using the Response Evaluation Criteria in PSMA Imaging (RECIP), based on synthetic PET images versus the original SPECT images. The results derived from the two imaging modalities were then compared. The treatment response assessment based on post-therapy PSMA PET/CT was used as the gold standard. The ^{177}Lu-PSMA-617-positive total tumor volume (Lu-TTV) and lesion count for each modality were quantified using the Segment Lesion workflow (MIM Software Inc., Cleveland, OH). ***Results:*** Treatment response assessment was concordant between SPECT and synthetic PET in 22 of 25 cases, with discrepancies observed in the remaining three. In all three discordant cases, the response classification based on synthetic PET was consistent with that derived from PSMA PET/CT. Specifically, two of the discordant cases were classified as complete response (CR) on SPECT but as partial response (PR) on synthetic PET. In the third case, the response was assessed as stable disease (SD) on SPECT and as PR on synthetic PET. The total tumor volume (Lu-TTV) derived from SPECT was significantly higher than that from synthetic PET in both the first and last treatment cycles (p = 0.033 and p = 0.136, respectively). Furthermore, the number of lesions detected on SPECT was significantly lower than that detected on synthetic PET for both the first and last cycles (p = 0.014 and p = 0.015, respectively). ***Conclusion:*** This study demonstrates that synthetic PET from post-therapy SPECT using the pix2pix model added value for the assessment of treatment response following 177Lu-PSMA therapy. ***References:*** 1) European Journal of Nuclear Medicine and Molecular Imaging. 2024: 1-10.2) Radiology. 2023; 308(1):e22148

OP-540

Post-Therapy Planar ^{177}Lu-PSMA Imaging: Lesion-to-Parotid Ratio Predicts Early PSA Response

H. Pekedis*, E. M. Kaya, A. S. Yilmaz, G. Yilmaz, B. Esen Akkaş;*
Basaksehir Çam ve Sakura City Hospital Nuclear Medicine Department, Istanbul, TÜRKIYE.

Aim/Introduction: To determine whether the lesion-to-parotid activity ratio (L/P), derived from routine day-1 post-therapy planar whole-body scans, can predict early biochemical response to [^{177}Lu]PSMA radioligand therapy in men with metastatic castration-resistant prostate cancer (mCRPC). ***Materials and Methods:*** Twenty nine consecutive mCRPC patients treated with [^{177}Lu]PSMA between January 2021 and December 2024 were retrospectively

reviewed. Anterior and posterior planar images obtained 24 h after the first treatment cycle were analysed. Circular 2-cm regions of interest were placed over metastatic bone foci; geometric-mean counts defined the lesion value (L). The mean counts of bilateral parotid glands provided the reference value (P); L/P = L ÷ P. Baseline and week-8 PSA levels were recorded. A ≥ 50 % decrease in PSA at week 8 defined responders; < 50 % defined non-responders. Group differences were assessed with the Mann-Whitney U test, and the discriminative performance of L/P was evaluated with receiver operating characteristic (ROC) curve analysis. ***Results:*** Median age was 71 years (IQR; 65-77). Fifteen patients (52 %) were responders. Responders had a significantly lower median L/P than non-responders—0.89 (IQR; 0.49-1.66) vs 4.49 (IQR; 1.09-9.81); p = 0.018. An L/P cut-off of 1.93 predicted PSA response with 73 % sensitivity, 86 % specificity, and an area under the ROC curve of 0.757 (95 % CI, 0.568-0.946). ***Conclusion:*** The post-therapy planar lesion-to-parotid (L/P) ratio is a simple and reproducible imaging-derived metric that may predict early biochemical response to ^{177}Lu-PSMA therapy in mCRPC. Early PSA decline can guide timely treatment decisions, avoid ineffective therapies, and improve patient stratification. Given its potential prognostic relevance, prospective multicentre validation is warranted.

OP-541

Balancing efficacy and nephrotoxicity in Lu-177 PSMA I&T therapy: clinical and imaging determinants of significant eGFR decline, an Asian cohort

D. Lim[1], *C. Tang*[1], *W. Chua*[1], *A. Tong*[1], *A. Wong*[2], *Y. Khor*[1], *W. Tham*[1], *W. Lam*[1], *S. Thang*[1];
[1]*Singapore General Hospital, Department of Nuclear Medicine and Molecular Imaging, Singapore, SINGAPORE,* [2]*National University Cancer Institute, Singapore, SINGAPORE.*

Aim/Introduction: There is emerging evidence for nephrotoxicity in patients undergoing PSMA Radioligand therapy (PRLT). Decline in renal function precludes the completion of therapy thus limiting efficacy. We aim to describe the incidence of nephrotoxicity and identify contributing clinical factors and imaging biomarkers. ***Materials and Methods:*** We recruited 60 patients treated with Lu-177 PSMA I&T between 2018 and 2024. All patients had requisite Ga-68 PSMA PET/CT and SPECT/CT studies 1 day after PRLT. Significant decline in eGFR/nephrotoxicity was defined as more than 30% in baseline. Clinical parameters collected for each patient included Gleason Score and treatment history (including immunotherapy, Radium-223, and radiotherapy involving the flank region). Clinical renal risk factors collected included: metabolic diseases, obstructive uropathy, urinary tract infections and proteinuria. Imaging biomarkers included total renal volumes and lengths. These were segmented and measured by Nuclear Medicine Physicians/Radiologists on the pre-therapy PSMA PET/CT and subsequent SPECT/CTs. All patients were dichotomized based on eGFR decline (≥30% vs <30%). Group comparisons were performed using the Mann-Whitney U test, and logistic regression was used to identify factors associated with significant eGFR decline. ***Results:*** Out of 60 patients (median age 75), 46 (76.7%) patients received 4 or more cycles of PRLT with a median cumulative administered activity of 768mCi. 41 patients (85%) had only G0 or G1 (CTCAE v5.0) renal impairment before PRLT. 29 (48.3%) had more than 30% decline in eGFR after PRLT. The median duration to significant decline in renal function was 411 days. Comparison between ≥30% vs <30% eGFR decline revealed statistically significant differences in the collected variables (p<0.05). Patients with significant nephrotoxicity had lower baseline eGFR; steeper GFR slopes; a higher number of renal risk factors; lower total renal volumes after the 2nd and 3rd cycles; and a greater difference in renal volume after the 3rd cycle vs baseline. Logistic regression analysis identified the following variables associated with significant nephrotoxicity (p<0.05): the number of renal risk factors; eGFR at 3 months post-PRLT; change in eGFR after the 3rd cycle from baseline; GFR slope; total renal volume after 2nd cycle and the rate of change in renal volume after the 3rd cycle vs baseline. ***Conclusion:*** Decline in renal function during PRLT is gradual, giving physicians adequate reaction time to prevent nephrotoxicity. By earlier identifying factors and measureables via our study, physicians can better select patients and identify strategies during PRLT to mitigate nephrotoxicity.

1207

Tuesday, October 7, 2025, 8:00 - 9:30
Room 212

TROP Session - Thyroid Committee: Current and Future Perspective of Nuclear Medicine Imaging in Endocrinological Disorders

OP-542

18F-FET PET : a potential new tool for localizing ACTH-producing pituitary adenomas in patients with newly diagnosed Cushing's disease

L. Al Mansour*, C. Merino, S. Solomon, S. Chaib, C. Sergeant, M. Janier, E. Jouanneau, G. Raverot, A. Flaus;*
Hospices Civils de Lyon, Lyon, FRANCE.

Aim/Introduction: Cushing's disease (CD) is associated with significant morbidity and increased mortality. Pituitary MRI remains the primary imaging modality for localizing adenomas but remains inconclusive or doubtful in up to 30% of cases. Inaccurate identification of the surgical target increases the risk of postoperative pituitary insufficiency or incomplete tumor resection. This study evaluates the potential of [18F] fluoroethyltyrosine positron emission tomography/computed tomography ([18F]FET PET/CT) for localizing ACTH-producing pituitary adenomas in patients with newly diagnosed CD. ***Materials and Methods:*** In this retrospective analysis, inclusion criteria were biochemically confirmed CD and either a pituitary microadenoma or inconclusive MRI with available [^{18}F]FET PET/CT imaging. PET scans were obtained 20-40 minutes after intravenous injection of 200 MBq of [18F]FET. Images were assessed by one experienced nuclear medicine physician. Maximum tumor-to-background ratios (TBRmax) were calculated by comparing the maximal standardized uptake values (SUVmax) of pituitary adenomas to mean standardized uptake values (SUVmean) of the right frontal and temporal lobes. Numeric values are expressed as median (interquartile range). ***Results:*** Eighteen patients (85% female; median age 50 [30-57.8] years) were evaluated between 11/2023 and 02/2025. Inferior Petrosal Sinus Sampling (IPSS) confirmed the diagnosis of central Cushing in 6 patients. MRI results were positive in 7, negative in 4, doubtful in 7 patients. [18F] FET PET/CT showed clear focal uptake in 12 cases and doubtful uptake in 6 cases, with a median TBRmax was 2.1 [1.7-2.3]. Nine patients underwent transsphenoidal surgery. In 8/9 cases, PET findings were concordant with histopathology. Among these, MRI were positive in 4, negative in 2, doubtful in 2 patients. PET uptake was clear in 8 cases and doubtful in one case, which had a positive MRI. PET uptake was concordant with MRI (positive or doubtful) in 6/6 cases. Postoperative remission was achieved in 7/9 patients. In the remaining surgical case, MRI was negative, and PET showed doubtful uptake contralateral to the surgery IPSS-guided target. Pathology was negative, and remission was not achieved. Of the 6 patients pending surgery, PET/MRI results were concordant in 3 and discordant in 3, including one with a negative MRI. Surgery was declined in three patients. ***Conclusion:*** [^{18}F]FET PET/CT appears to be a valuable complementary tool for localizing ACTH-producing pituitary adenomas in patients with Cushing's disease, particularly when MRI findings are inconclusive or doubtful. Its

high concordance with surgical pathology suggests that it may improve preoperative targeting and potentially enhance surgical outcomes.

OP-543

Diagnostic Value of FDG PET/CT Quantitative Parameters in Differentiating Adrenal Masses: Our Clinical Experience

G. Deniz[1], *E. Isik*[1], *D. Arslan*[1], *S. Erturk*[2], *D. Has Simsek*[1], *Y. Sanli*[1];
[1]*Istanbul University, Istanbul Faculty of Medicine, Department of Nuclear Medicine, Istanbul, TÜRKIYE,* [2]*Istanbul University,I stanbul Faculty of Medicine, Department of Radiology, Istanbul, TÜRKIYE.*

Aim/Introduction: Differentiating adrenal lesions on F-18 FDG PET/CT remains a diagnostic challenge. In addition to visual assessment, the use of quantitative PET/CT parameters enhances diagnostic accuracy. This study aimed to evaluate the contribution of quantitative parameters in distinguishing benign from malignant adrenal lesions. ***Materials and Methods:*** In this retrospective study, we analyzed 569 patients who underwent FDG PET/CT between 2011 and 2024. A total of 165 patients with 192 lesions, confirmed by follow-up MRI or histopathology, were included. Parameters assessed included lesion size, laterality, SUVmax, metabolic tumor volume (MTV), total lesion glycolysis (TLG), and Hounsfield units (HU). For metabolic parameters, three-dimensional regions of interest (ROIs) were delineated. Group comparisons were performed using Kruskal-Wallis and Mann-Whitney U tests. ROC analysis was applied to determine optimal diagnostic thresholds. ***Results:*** The cohort included 165 patients (mean age: 59 ± 15 years; 75 males, 90 females), with 27 presenting bilateral lesions. Based on pathology and MRI results, six subgroups (G1-6) were defined. Mean values for PET/CT and CT-derived parameters were calculated for each group. Of the 165 patients, 84 had adenomas (G1), 10 had pheochromocytomas (G2), 37 had adrenocortical carcinomas or metastases (G3), 8 had hyperplasia (G4), 5 had myelolipomas (G5), and 21 had other lesions (G6). Mean PET/CT and CT parameters per group are shown in Table 1. According to ROC analysis, the SUVmax cut-off values were: ≤4.10 for Group 1 (sensitivity 84.2%, specificity 70.4%) and >5.47 for Group 3 (sensitivity 88.4%, specificity 87.9%) (p<0.001). The MTV cut-off values were: ≥33.37 for Group 3 (sensitivity 74.4%, specificity 82.6%). TLG cut-off values were: ≤93.10 for Group 1 (sensitivity 85.1%, specificity 70.2%) (p<0.001) and >93.10 for Group 3 (sensitivity 83.7%, specificity 83.2%)(p<0.001). The HU cut-off value for Group 5 was found to be ≤-17.95 (sensitivity 100%, specificity 95.7%)(Table 2). Lesion-based analysis showed statistically significant differences between Group 1 and Group 3 across all parameters (p<0.001). Although SUVmax did not significantly differ between Group 2 and Group 3 (p=0.063), volumetric parameters—MTV (p=0.009) and TLG (p=0.007)—were significantly higher in Group 3 (Table 3). ***Conclusion:*** Quantitative FDG PET/CT parameters, especially the volumetric metrics, offer valuable diagnostic insight into adrenal lesion characterization. The combination of MTV and TLG with SUVmax enhances lesion characterization, informs biopsy planning, and may help avoid unnecessary interventions. Furthermore, these parameters aid not only in distinguishing benign from malignant lesions but also in differentiating pheochromocytomas from malignant adrenal tumors.

OP-544

^{68}Ga-Pentixafor PET/CT versus Adrenal Venous Sampling for Surgical Decision-Making in Primary Aldosteronism

W. Zhengjie*, Z. Xiaoyang, L. Junyang, L. Jia, Z. Rui, L. Mengdan, P. Hua;*
The First Affiliated Hospital of Chongqing Medical University, Chongqing, CHINA.

Aim/Introduction: Primary aldosteronism (PA) is the most common cause of secondary hypertension, with unilateral disease often requiring adrenalectomy for cure. While adrenal venous sampling (AVS) remains the gold standard for lateralization, its invasiveness and technical complexity limit widespread use. CXCR4-directed PET imaging has emerged as a promising, non-invasive alternative. This study aimed to evaluate the clinical utility of ^{68}Ga-Pentixafor PET/CT versus AVS in guiding surgical decision-making for PA and to identify key factors influencing the diagnostic performance of CXCR4 imaging. ***Materials and Methods:*** This study prospectively enrolled 155 patients who met the clinical diagnostic criteria for PA, all of whom underwent ^{68}Ga-pentixafor PET imaging. According to Primary Aldosteronism Surgical Outcome (PASO) criteria, outcomes were assessed at 6-month follow-up. The primary endpoints were clinical and biochemical remission rates at 6 months post-surgery. Postoperative KCNJ5 genetic testing was performed. Secondary analysis focused on the differences between patients with KCNJ5 mutations and wild-type group, and between CXCR4-positive and CXCR4-negative patients. ***Results:*** Of the 115 patients who completed the 6-month follow-up, adrenalectomy was performed in 66 cases under AVS guidance and in 49 cases based on CXCR4 PET/CT findings. Clinical complete remission rates were 57.6% in the AVS group and 67.3% in the CXCR4 PET group, while biochemical complete remission rates were 93.9% and 89.8%, respectively. Among the 115 patients, 99 cases were CXCR4-positive, yielding a positivity rate of 86.1% (99/115). CXCR4-positive patients exhibited significantly higher clinical (63.4% vs. 33.3%) and biochemical remission rates (88.8% vs. 81.0%,) compared to CXCR4-negative patients. Notably, all patients with KCNJ5 mutations (100%) were CXCR4-positive, whereas wild-type patients had a false-negative rate of 42.6%. Among CXCR4-positive patients, tumor size did not differ significantly between KCNJ5 mutant and wild-type groups (13.0 ± 2.0 mm vs. 11.8 ± 2.5 mm, P=0.467), but SUV_{max} was significantly higher in the mutant group (13.1 ± 3.9 vs. 8 ± 2.75, P<0.001). Additionally, in wild-type patients, CXCR4-positive tumor size were significantly larger than CXCR4-negative ones (13.44 ± 4.84 vs. 9.38 ± 2.42, P=0.01). ***Conclusion:*** ^{68}Ga-Pentixafor PET/CT demonstrates clinical value comparable to AVS in PA surgical management, particularly for KCNJ5 mutant patients, serving as a non-invasive alternative. CXCR4 negativity is primarily influenced by smaller tumor size and is associated with significantly lower clinical benefit compared to CXCR4-positive cases.

OP-545

Development and validation of a dual-time ^{68}Ga-Pentixafor PET/CT-based radiomic nomogram for subtyping diagnosis of primary aldosteronism

R. Zuo[1], *L. Xu*[1], *T. Xu*[2], *S. Liu*[1], *Z. Wang*[1], *W. Li*[1], *Y. Chen*[2], *H. Pang*[1];
[1T]*he First Affiliated Hospital of Chongqing Medical University, Chongqing, CHINA,* [2]*Affiliated Hospital of Southwest Medical University, Luzhou, CHINA.*

Aim/Introduction: The difficulty in the diagnosis and treatment of PA lies in the subtype diagnosis and screening out patients with unilateral primary aldosteronism (UPA) who are more suitable for surgery. Our purpose is to develop and validate a clinical-radiomics model based on ^{68}Ga-Pentixafor PET/CT for differentiating UPA from bilateral primary aldosteronism (BPA). ***Materials and Methods:*** This multicenter retrospective study included 379 patients with PA (Center 1 = 288; Center 2 = 91), all of whom underwent dual-time-window (10 min and 40 min) ^{68}Ga-Pentixafor PET/CT. Patients from Center 1 (169 UPA; 99 BPA) were randomly divided into training (70%) and testing (30%) groups, while patients from Center 2 (61 UPA; 30 BPA) served as an independent external validation group. Radiomics features were extracted using LIFEx software. Feature selection and model construction were performed using least absolute shrinkage and selection operator (LASSO) regression and logical regression. Model performance was assessed using receiver operating characteristic (ROC) curves analysis. Clinical

utility of the models was evaluated by calibration curves and decision curve analysis (DCA). ***Results:*** Diagnostic efficiency in 10 min PET_40 min PET_CT model was higher than10 min PET_CT model and 40 min PET_CT model. A total of 5 radiomics features based on dual-time ^{68}Ga-Pentixafor PET/CT and 3 clinical features were selected to construct the clinical-radiomics model. This model showed superior diagnostic performance in the training, testing, and validation groups, with areas under the curve (AUCs) of 0.810 (95% CI: 0.748-0.872), 0.770 (95% CI: 0.659-0.881) and 0.874 (95% CI: 0.794-0.954), respectively. In the training cohort, the clinical-radiomics model significantly outperformed both the clinical-only model (0.810 vs. 0.766, P<0.001) and the PET/CT-feature-only model (0.810 vs. 0.779, P=0.039), while there was no significant differences in the testing group (both P > 0.05). In the validation group, it showed a statistically improvement over the clinical model (0.874 vs. 0.745, P=0.003), but not over the PET/CT-feature model (0.874 vs. 0.845, P=0.227). DCA indicated that the clinical-radiomics model offered higher net benefit and greater clinical value. ***Conclusion:*** The clinical-radiomics model based on ^{68}Ga-Pentixafor PET/CT enables more accurate subtyping of PA, potentially guiding personalized treatment strategies.

OP-546

Evaluation of Al^{18}F-NOTA-Pentixafor PET/CT in Subtyping and Surgical Guidance in Primary Aldosteronism Patients: A Prospective Phase II Study

X. Yan[1], *G. Zheng*[2], *M. Liu*[1], *Y. Zhang*[1], *Y. Xie*[1], *L. Huo*[1];
[1]*Department of Nuclear Medicine, Peking Union Medical College Hospital, Chinese Academy of Medical Sciences, Beijing, CHINA,* [2]*Department of Urology, Peking Union Medical College Hospital, Chinese Academy of Medical Sciences, Beijing, CHINA.*

Aim/Introduction: Primary aldosteronism (PA) subtyping is essential for guiding treatment.Current diagnostic methods remain limitations, and PET imaging targeting CXCR4, which strongly correlated with aldosterone synthase (CYP11B2) expression, offered a promising alternation. This prospective study evaluated the diagnostic performance of Al^{18}F-NOTA-Pentixafor PET/CT for PA subtyping. ***Materials and Methods:*** This prospective study enrolled 125 PA patients with CT-confirmed adrenal nodules/nodular hyperplasia who underwent Al18F-NOTA-Pentixafor PET/CT, with subsequent surgical (targeting PET-identified functional lesions) or medical management guided by imaging findings. Two blinded nuclear medicine specialists independently performed visual interpretation. Semiquantitative parameters including lesion SUVmax, lesion-to-adrenal ratio (LAR), and lesion-to-liver ratio (LLR) were analyzed. Final diagnosis were established combining histopathology (surgical cases), AVS results, and 6-month follow-up, with diagnostic performance assessed by calculating sensitivity, specificity, positive predictive value(PPV) and negative predictive value (NPV). ***Results:*** A total of 125 PA patients with adrenal nodule were evaluated. Reference standard confirmed 95 APA and 30 non-APA (PAH or NFA) cases. Visual interpretation of Al^{18}F-NOTA-Pentixafor PET/CT demonstrated 100% (95% CI: 88.7-100%) sensitivity and 97.9% specificity (95% CI: 92.7-99.6%), achieving PPV of 100% (95% CI: 96.0-100%) and NPV of 93.8% (95% CI: 79.9-98.9%). Quantitative analysis demonstrated robust diagnostic performance across all parameters: LLR showed optimal cutoff of 7.44 with AUC 0.87 (95%CI 0.802-0.937), sensitivity 70.2%, specificity 87.1%, PPV 94.3%; SUVmax achieved cutoff 6.8 with AUC 0.901 (95%CI 0.844-0.958), sensitivity 87.2%, specificity 80.6%, PPV 93.2%; while LAR demonstrated cutoff 2.4 with AUC 0.861 (95%CI 0.791-0.931), sensitivity 88.3%, specificity 64.5%, and PPV 88.3%. ***Conclusion:*** Al^{18}F-NOTA-Pentixafor PET/CT demonstrates promising diagnostic accuracy for PA subtyping.

OP-547

The value of chemokine receptor type 4 targeted PET imaging in treatment management for primary aldosteronism compared to adrenal venous sampling

N. Lu*, Z. Xiao, D. Xing, D. Zeng, Y. He;*
Department of Nuclear Medicine, Zhongnan Hospital of Wuhan University, Wuhan, CHINA.

Aim/Introduction: Primary aldosteronism (PA) is the most common cause for secondary hypertension, and lateralized forms of PA are recommended resection for treatment purpose. We aimed to assess the value of ^{68}Ga-Pentixafor PET imaging targeting chemokine receptor type 4 (CXCR4) in treatment management for PA, compared to adrenal venous sampling (AVS), the current gold standard for PA lateralization. ***Materials and Methods:*** We prospectively recruited 70 PA patients (36 males and 34 females, 49±12 years old). All patients underwent PET/CT imaging of adrenal region 30 min after injection of ^{68}Ga-Pentixafor, and AVS was performed in 53 patients. The SUVmax of adrenal lesions were measured, and the ratio of bilateral adrenal SUVmax (lateralization index, LI) was used to determine the dominant side. Lateralized patients determined by PET/CT or AVS underwent adrenalectomy, with a 12-month follow-up. Postoperative outcomes were evaluated using the Primary Aldosteronism Surgical Outcome (PASO) definitions for biochemical success, including cured, improvement, and no improvement. The threshold of LI for PA lateralization was determined by receiver operating characteristic (ROC) analysis. The correlations of PET/CT, as well as AVS outcomes, with postoperative outcomes were then analyzed. ***Results:*** Except 7 cases of idiopathic hyperaldosteronism (IHA) determined by AVS, 63 patients with a dominant side underwent an adrenalectomy. Based on clinical characteristics, pathology, and follow-up data, 50 lateralized PA patients showed 100.0% of postoperative benefit, including 39 cases of aldosterone-producing adenoma (APA), and 11 cases of unilateral adrenal hyperplasia (UAH). Thirteen non-lateralized patients, including 11 cases of nonfunctional adenoma (NFA) surrounded by multiple aldosterone-producing micronodules (MAPMs), and 2 cases of IHA, showed no improvements after surgery. The area under the ROC curve of LI for PA lateralization was 0.77 (95%CI, 0.64-0.91; P < 0.05), and the optimal cut-off level of LI=1.59 was associated with a sensitivity of 63%, a specificity of 100%, and a maximized Youden's index. PET/CT successfully lateralized all 39 cases of APA, and 18% (2/11) of UAH cases. All IHA patients exhibited non-lateralized forms on PET/CT. However, 54% (6/11) of NFAs were lateralized by PET/CT. Lateralization based on PET/CT significantly correlated with surgical outcomes during follow-up (χ2=17.38, P < 0.001). There was no significant difference in postoperative outcomes between PET/CT and AVS lateralization (χ2=2.99, P=0.224). ***Conclusion:*** ^{68}Ga-Pentixafor PET imaging showed comparable value with AVS for guiding PA treatment and predicting prognosis. However, for some UAH patients with bilateral similar tracer uptake, AVS should be a supplementary method.

OP-548

Organ-Specific Alterations in Physiological FDG Uptake in Diabetic Patients: A Retrospective PET/CT Study Using Japanese Cancer Screening Cohort

H. Wakabayashi[1], *Z. Chen*[1], *S. Gutschmayer*[2], *D. Ferrara*[2], *M. Pires*[2], *S. Takeda*[3], *J. Taki*[3], *S. Kinuya*[1], *L. Shiyam Sundar*[2,4], *T. Beyer*[2];
[1]*Kanazawa University, Kanazawa, JAPAN,* [2]*Quantitative Imaging Medical Physics (QIMP) Team, Medical University of Vienna, Vienna, AUSTRIA,* [3]*PET Center, Kanazawa Advanced Medical Center, Kanazawa, JAPAN,* [4]*DIGIT-X Lab, Department of Radiology, LMU Munich, Munich, GERMANY.*

Aim/Introduction: FDG-PET/CT is well established in oncology and selected non-oncologic indications, but its use for evaluating systemic metabolic disorders such as diabetes remains limited. With its ability to quantify glucose metabolism and tissue density across organs, FDG-PET/CT provides a powerful tool for characterizing systemic metabolic phenotypes. This study aimed to assess organ-specific alterations in FDG uptake and CT density

associated with diabetes and to characterize systemic metabolic profiles in a non-cancer population. ***Materials and Methods:*** A total of 501 individuals who underwent FDG-PET/CT for cancer screening were retrospectively analyzed. Among them, 46 (9%) had confirmed diabetes (F/M = 3/43, 53±12 years, range: 40-75), and 455 (91%) were non-diabetic controls (F/M = 147/308, 54±8 years, range: 22-89). Automated organ segmentation was performed on the CT images using MOOSE [1]. Quantitative measures included mean CT Hounsfield Units (HU) and PET standardized uptake value (SUV) in the bone marrow, liver, brain, muscle, subcutaneous fat, visceral fat, spleen, and thyroid. A second-degree polynomial regression analysis evaluated age-related correlations with HU and SUV. Group differences were assessed using a t-test and percentage differences, with statistical significance set at $p < 0.05$. ***Results:*** In diabetic subjects, CT density and SUV were markedly reduced in bone marrow (-6%, 158±32 vs. 148±31; -12%, 1.7±0.3 vs 1.5±0.3, respectively). Brain SUV was also reduced (-24%, 6.7±1.0 vs. 5.1±1.0) compared to non-diabetic individuals, while muscle SUV increased (+6%, 0.62±0.07 vs. 0.67±0.06). The liver of diabetic subjects showed lower HU (-8%, 52±0.4 vs. 48±1.3) but higher SUV (+4%, 2.22±0.01 vs. 2.33±0.04). Subcutaneous fat showed increased CT density (+3%, -96±0.4 vs. -93±1.3) and SUV (+17%, 0.36±0.06 vs. 0.43±0.07), while visceral fat had elevated SUV (+11%, 0.70±0.14 vs. 0.78±0.21) without CT changes. SUV of the thyroid was unaffected, while diabetic subjects presented lower CT density (-6%, 81±15 vs. 76±14). Age-related increases in SUV were more pronounced in diabetics, particularly in the bone marrow (R^2 = 0.26 vs. 0.10) and subcutaneous fat (R^2 = 0.26 vs. 0.02), suggesting altered metabolic aging. ***Conclusion:*** Diabetes induces distinct organ-level changes in tissue density and glucose metabolism detectable by whole-body FDG-PET/CT. The observed patterns—decreased uptake in the bone marrow and brain, and increased uptake in the muscle, liver, and adipose tissues—likely reflect impaired glucose utilization, insulin resistance, and inflammation. FDG-PET/CT reveals a phenomic signature of diabetes. ***References:*** [1] Shiyam Sundar LK, et al. Fully automated, semantic segmentation of whole-body ^{18}F-FDG PET/CT images based on data-centric artificial intelligence. JNM 2022;63:1941-48.

OP-549

Detection of pancreatic β-cells in individuals with type 1 and type 2 diabetes and obesity, via the PET tracer [68Ga] Ga-NODAGA-Exendin-4

S. Migliari[1], *M. Scarlattei[1], A. Gagliardi[1], A. Guercio[1], G. Baldari[1], R. Aldigeri[2], V. Spigoni[2], F. Fantuzzi[2], G. Cinquegrani[2], E. Balestreri[2], A. Dei Cas[2], R. Bonadonna[2], L. Ruffini[1];*
[1]Nuclear Medicine Division, Azienda Ospedaliero-Universitaria of Parma, Parma, ITALY, [2]Laboratory of Endocrinology, Diabetes and Metabolic Disease, Department of Medicine and Surgery, Azienda Ospedaliero-Universitaria of Parma, Parma, ITALY.

Aim/Introduction: GLP-1R is a molecular imaging target to quantify in vivo pancreatic β-cell mass (i.e. the product of β-cell density times pancreas volume), aiding in diabetes research and treatment monitoring. Throughout 2020-2022, we developed and validated an automated radiosynthesis of [^{68}Ga]Ga-NODAGA-exendin-4 (68Ga-Ex4) with high molar activity (A_m) [1-2], and optimized a PET-CT scan method to assess its pancreatic uptake, aiming to distinguish GLP-1R expression in type 1-2 diabetes (T1D;T2D) and obesity (OB). ***Materials and Methods:*** The synthesis of 68Ga-Ex4 was performed using an automated module connected to a GMP-certified 68Ge/68Ga generator, following our validated procedure. Immediately after i.v. tracer injection, dynamic images were acquired over 20' on the pancreatic region and static images at 45'-60'. Quantitative analysis measured SUVmax-SUVmean using spherical volumes of interest on the whole pancreas. OU2 selected patients and quantified their β-cell function (data not shown). ***Results:*** 68Ga-Ex4 (mean dose 119.17±22.5MBq) was injected in 8 T1D (51±11yrs, HbA1c% 7.45±1, BMI 26.6±3.2kg/m^2), 10 early T2D (59±12yrs, HbA1c% 6.8±1.1, BMI 29.9±6.0kg/m2) and 10 OB subjects (age 46±10yrs; HbA1c% 5.42±0.5; BMI 38.7±6.9kg/m^2). Mean RCP%, RCY% and A_m of 68Ga-Ex4 were 97.7%, 52.5% and 244.3 GBq/μmol; injected peptide amount wasc3.0±0.01ug. SUVs of the whole pancreas were: $SUVmean_{60}$ 2.0±0.86 (T1D), 3.6±1.2 (T2D), 3.8±1.1 (OB); $SUVmean_{20}$ 3.41±0.85 (T1D), 4.7±1.4 (T2D), 4.86±0.73 (OB); $SUVmax_{60}$ 3.4±0.96 (T1D), 4.8±1.2 (T2D), 5.9±1.5 (OB); $SUVmax_{20}$ 4.7±1.3 (T1D), 6±1.7 (T2D), 7.3±1.1 (OB). SUVmean and SUVmax resulted significantly lower in T1D than in OB at all time points ($p<0.05$), while no significant differences were found between T2D and OB pancreatic SUVs at any time point. SUVmean was higher in T2D compared to T1D at 20 and 60 min ($p<0.05$). ***Conclusion:*** 68Ga-Ex4, synthesized with high molar activity, ensured stability and minimal peptide doses, avoiding side effects during PET-CT. SUV_{60} resulted in a strong and repeatable marker of β-cells density. As a result, 68Ga-Ex4 facilitates the safe and non-invasive assessment of pancreatic β-cell mass. Due to these results, a new experimental study began in November 2024 to evaluate the association between metabotypes of (poly)phenolic dietary compounds and β-cell mass and function. ***References:*** [1] Migliari S, et al. 2022, Curr Radiopharm., 15(1):63-75. [2] Migliari S, et al. 2022, Molecules, 27(2):543.

OP-550

Triple-Tracer Imaging in Metastatic High-Grade Neuroendocrine Neoplasms: A Preliminary Observational Study

P. HJ[1], *K. G. Kallur[2], S. S P[1], D. Kumar[3], P. Wadhwa[3];*
[1]Aster Hospital, Banglore, INDIA, [2]HCG Cancer Center, Banglore, INDIA, [3]United Imaging Healthcare, Delhi, INDIA.

Aim/Introduction: High-grade neuroendocrine neoplasms (NENs) are a biologically heterogeneous group of tumors with variable expression of somatostatin receptors (SSTRs), glycolytic activity, and tumor-associated stroma. This study investigates the uptake patterns of three PET tracers—[^68Ga]Ga-DOTANOC, [^18F]FDG, and [^68Ga]Ga-FAPI—in patients with metastatic high-grade NENs to assess inter- and intra-lesional tracer heterogeneity. ***Materials and Methods:*** Thirteen patients (9 males, 4 females; mean age: 58.6 ± 10.2 years) with histologically confirmed metastatic high-grade NENs underwent PET/CT imaging with [^68Ga]Ga-DOTANOC, [^18F]FDG, and [^68Ga]Ga-FAPI within a 7-day interval. Visual and semi-quantitative analyses (SUVmax) were performed for each tracer across representative metastatic sites including liver, lymph nodes, and bones. ***Results:*** A total of 92 metastatic lesions were analyzed (liver: 32, lymph nodes: 24, bones: 36). Liver lesions: [^18F]FDG detected the most lesions (n=29; mean SUVmax: 18.6 ± 5.3), followed by [^68Ga]Ga-FAPI (n=15; SUVmax: 9.1 ± 3.0), and [^68Ga]Ga-DOTANOC (n=12; SUVmax: 7.8 ± 2.6).Skeletal metastases: [^68Ga]Ga-FAPI identified the most lesions (n=33), with higher uptake (mean SUVmax: 12.3 ± 3.5) than [^18F]FDG (n=22; SUVmax: 8.7 ± 2.9) and DOTANOC (n=14; SUVmax: 3.9 ± 1.6).Lymph nodes: Displayed mixed uptake: FDG detected 21 lesions (SUVmax: 11.2 ± 3.4), FAPI 15 lesions (SUVmax: 7.4 ± 2.5), and DOTANOC 11 lesions (SUVmax: 5.8 ± 2.1). Multiple lesions demonstrated uptake on all three tracers, underscoring the complex biology of high-grade NENs—characterized by active metabolism, SSTR expression, and fibrotic stroma. Notably, 23% of bone lesions were exclusively FAPI-avid and not visualized on FDG or DOTANOC PET. ***Conclusion:*** Triple-tracer PET imaging in metastatic high-grade NENs reveals significant lesion-specific heterogeneity. [^18F]FDG demonstrated the highest sensitivity and uptake in liver metastases, while [^68Ga]Ga-FAPI emerged as the second-best tracer in the liver and the most sensitive in bone metastases. These results highlight the value of multi-tracer imaging for comprehensive disease characterization and support the consideration of Lu-177 DOTATATE + FAPI cocktail therapy in selected cases. Further prospective studies with histopathological correlation are warranted. ***References:*** Cuthbertson DJ, Shankland R, Srirajaskanthan R. Diagnosis and management of neuroendocrine tumours. Clin Med (Lond). 2023 Mar;23(2):119-124. doi: 10.7861/clinmed.2023-0044. PMID: 36958842; PMCID: PMC11046558.

1208

Tuesday, October 7, 2025, 8:00 - 9:30
Room 115

TROP Session - Cardiovascular Committee: Cardiovascular Infection and Inflammation: Evidence and Novelty

OP-551

Digital FDG PET/CT as First-Line Diagnostic Modality for Cranial Giant Cell Arteritis

A. Roy[1,2,3], *J. Alberini*[4,5], *R. H. J. A. Slart*[6,7], *M. Samson*[4,5], *J. Makhzoum*[8,9], *M. A. Stein*[2], *L. Berkson*[3,2], *É. Rousseau*[10,11], *N. Dendukuri*[2], *P. H. Nienhuis*[6,7], *N. van der Geest*[6,7], *C. Pineau*[1,2], *P. Liang*[10,11], *G. Abikhzer*[3,2];
[1]*McGill University Healthcare Center, Montréal, QC, CANADA,* [2]*McGill University, Montréal, QC, CANADA,* [3]*Jewish General Hospital, Montréal, QC, CANADA,* [4]*François Mitterrand University Hospital, Dijon, FRANCE,* [5]*Université Bourgogne Franche-Comté, Dijon, FRANCE,* [6]*University Medical Center Groningen, Groningen, NETHERLANDS,* [7]*University of Groningen, Groningen, NETHERLANDS,* [8]*Hôpital du Sacré-Cœur de Montréal, Montréal, QC, CANADA,* [9]*Université de Montréal, Montréal, QC, CANADA,* [10]*University of Sherbrooke, Montréal, QC, CANADA,* [11]*Centre hospitalier de l'Université de Sherbrooke, Sherbrooke, QC, CANADA.*

Aim/Introduction: Giant cell arteritis (GCA) is the most common form of vasculitis. Diagnosis is challenging and mainly relies on temporal artery biopsy (TAB) and/or Doppler ultrasound (DUS). Although PET/CT is the test of choice in patients with suspected large vessel (LV)-GCA, it was previously limited for cranial artery GCA (C-GCA) detection, primarily due to the small size of these arteries. Digital PET/CT devices have significantly improved PET resolution and allow accurate imaging of smaller cranial arteries. Results of an international prospective cross-sectional comparative study of digital FDG PET/CT and DUS in patients with suspected GCA are presented. ***Materials and Methods:*** Patients aged ≥50 years with suspected GCA were prospectively enrolled in 5 centers across Canada, France, and the Netherlands. Exclusion criteria included corticosteroid therapy >3 days prior to FDG PET/CT or prior history of vasculitis. FDG PET/CT scans were interpreted independently by two blinded readers using visual grading scales as presented in the joint EANM/SNMMI guidelines; in case of disagreement, a third blinded reader adjudicated. Final clinical diagnosis at 6 months served as the reference standard. ***Results:*** Of 104 enrolled subjects, 9 were excluded as they did not undergo DUS. Ninety-five subjects (56 women, 39 men; mean age: 72 years; mean CRP: 66.1 mg/L) were included in the analysis with mean follow-up of 27 months (range 6-74). GCA was diagnosed in 45/95 (47.4%) patients. Of these, FDG PET/CT correctly identified 37 cases: 15 had isolated C-GCA, 7 had isolated LV-GCA, and 15 had both. Sensitivity of FDG PET/CT increased from 48.9% (95%CI: 33.7-64.2%) when assessing large vessels alone to 82.2% (95%CI: 68.0-92.0%) with the addition of cranial vessel evaluation, while specificity remained unchanged at 98.0% (95%CI: 89.4-100.0%). DUS demonstrated sensitivity 68.9% (95%CI: 53.4-81.8%) and specificity 92.0% (95%CI: 80.8-97.8%). Bayesian modeling estimated that, compared with DUS, FDG PET/CT incorporating C-GCA assessment increased sensitivity for GCA diagnosis by 12.8% (95%CrI: -4.7 to 29.9%) and specificity by 5.6% (95%CrI: -3.2 to 15.6%), with respective posterior probabilities of 92% and 90% of FDG PET/CT outperforming DUS. Inter-observer agreement for FDG PET/CT interpretation was near-perfect for both C-GCA (κ=0.928) and LV-GCA (κ=0.915). ***Conclusion:*** Digital FDG PET/CT demonstrates high diagnostic accuracy and excellent inter-observer reliability in identifying C-GCA, supporting its potential role as a first-line modality in the evaluation of suspected GCA.

OP-552

FDG PET-CT in suspected giant cell arteritis: visual analysis has superior diagnostic accuracy compared to semiquantitative image analysis. The VASCAI study.

F. Caobelli, *R. Friedli, N. Gözlügöl, S. Bucher, P. Seitz, F. Lötscher, M. Gilgen, P. Stähli, F. Helfenstein, Y. Döring, G. Hamvas, M. Schindelwolf, A. Rominger, B. Maurer, L. Christ, L. Seitz; Inselspital Bern, Bern, SWITZERLAND.*

Aim/Introduction: Giant cell arteritis (GCA) often affects the aorta and large vessels. ^{18}F-FDG PET/CT is a recommended diagnostic tool to visualize vascular inflammation, with high sensitivity (~80-90%) and specificity (~90-98%) [1,2]. Interpretation can be either visual (grading arterial uptake relative to liver uptake on a 0-3 scale) or semiquantitative (SUVs and target-to-background ratios). This study compared the diagnostic performance of these methods in a large patients' cohort with suspected new-onset GCA. ***Materials and Methods:*** We retrospectively included treatment-naïve patients (≥50 year-old) undergoing standardized FDG-PET/CT for suspected GCA. PET scans were re-read by two nuclear medicine physicians, blind to clinical data and diagnosis. Thirty-three arterial segments were graded visually (0= no uptake; 1= below liver; 2= equal to liver; 3= above liver). Scans were deemed positive on a per-patient basis if any segment had grade ≥2 (or =3 for stricter criteria). Subsequently, SUVmax, SUVmean, and SUVpeak were measured in all segments, and ratios to liver and blood-pool uptake were calculated. Best thresholds were calculated for the diagnosis of GCA. Final GCA diagnosis was determined independently after clinical workup and follow-up (≥3-6 months). Diagnostic metrics (sensitivity, specificity, PPV, NPV, LR±) were calculated. ***Results:*** We included 163 patients, 39 of whom (24%) had confirmed GCA. Visual analysis (score ≥2) showed high sensitivity (80.0%) and specificity (83.0%), with 82% accuracy, PPV 60%, NPV 93%, LR+ 4.7, LR- 0.25. Using visual score 3 as separator, specificity increased to 96% at expenses of lower sensitivity (59%), with diagnostic accuracy 87%, PPV 82%, NPV 88%, LR+ 14.63, LR- 0.43. Semiquantitative methods performed less well. The most accurate among semiquantitative parameters was the ratio arterial SUVmax/Liver SUVmean (Youden's Index 1.11), with very high sensitivity (94%) but poor specificity (35%), accuracy 49%, PPV 32%, NPV 97%, LR+ 1.49, LR- 0.07. No quantitative threshold matched the sensitivity and specificity combination achieved by visual interpretation. ***Conclusion:*** In newly suspected, untreated GCA patients, FDG-PET/CT with expert visual interpretation using a standardized 0-3 grading scale outperformed semiquantitative methods. Visual analysis offered high specificity (at expenses of slightly lower sensitivity) and better overall diagnostic performance. These findings support the use of expert visual reading as the primary interpretive method, with quantitative metrics serving as a useful complement. ***References:*** [1] Knappe L, et al Eur J Nucl Med Mol Imaging. 2023 Nov;50(13):3890-3896. doi: 10.1007/s00259-023-06423-w. Epub 2023 Sep 7. PMID: 37676501; PMCID: PMC10611821.[2] Slart RHJA, et al. J Nucl Med. 2023;64:515-21.

OP-553

[^{18}F]FDG-PET/CT in giant cell arteritis: assessing temporal and vertebral artery involvement with and without corticosteroid treatment, and the potential diagnostic value of adding quantitative analysis

M. Calls Calahorro[1], *M. Velasco-Nuño*[1], *H. Codés Mendez*[2], *P. Moya Alvarado*[2], *A. Barros*[3], *A. Fernández-León*[1], *P. Stefaneli*[1], *B. Serrallonga*[1], *Y. Delisau*[1], *S. Castejón*[1], *G. Guzmán*[1], *V. Camacho*[1], *A. Flotats*[1];
[1]*Nuclear Medicine Department, Hospital de la Santa Creu i Sant Pau, Barcelona, SPAIN,* [2]*Rheumatology and Systemic Autoimmune Diseases Department, Hospital de la Santa Creu i Sant Pau, Barcelona, SPAIN,* [3]*Cardiology Department, Hospital de la Santa Creu i Sant Pau, Barcelona, SPAIN.*

Aim/Introduction: To analyse the involvement of temporal and/or vertebral arteries in giant cell arteritis (GCA) and the diagnostic performance of [^{18}F]FDG-PET/CT by several quantification methods, as well as its relationship with corticosteroid treatment. ***Materials***

and Methods: Retrospective study of 60 patients (p) with GCA (ACR/EULAR 2022 criteria) and [^{18}F]FDG-PET/CT at diagnosis: 32p under corticosteroid treatment (corticosteroid) and 28p without corticosteroid treatment (naive). Visual assessment (parietal hypermetabolism in temporal and/or vertebral arteries was considered positive) and quantitative evaluation of SUVmax and its normalization to target-to-background ratio (TBR) of liver (TBR-H) and superior vena cava blood pool (TBR-SVC) were performed in 4 segments: right temporal (RT), left temporal (LT), right vertebral (RV) and left vertebral (LV). The area under the curve (AUC), cut-off point, sensitivity (S) and specificity (E) of the parameters quantified in each of the vascular segments were calculated using ROC curves. The influence of corticosteroid treatment on PET/CT positivity was studied using the Chi-Square test for qualitative variables (visual analysis) and the Mann-Whitney U test for quantitative variables (SUVmax, TBR-H, TBR-SVC). ***Results:*** 23 patients (38%) presented visual [^{18}F]FDG-PET/CT positivity: 12/32p corticosteroid (37%) and 11/28p naive (39%). The frequency of affected segments was: LV 20 (11 naive / 9 corticosteroid), RV 20 (11 naive / 9 corticosteroid), LT 14 (5 naive / 9 corticosteroid) and RT 13 (5 naive / 8 corticosteroid). In temporal arteries, the TBR-SVC was the parameter with the highest AUC, and in vertebral arteries, it was the TBR-H, with RT being the segment with the highest diagnostic accuracy (AUC: 1, cut-off: 1,01, S: 100%, and E: 100%). The mean and cut-off range for SUVmax, TBR-H, and TBR-SVC were 2.36 (2.01-2,72), 0.76 (0.57-0.90), and 1.26 (1.01-1.62), respectively. Corticosteroid treatment did not have any influence on PET/CT positivity based on visual analysis (p>0.05) but did have an influence based on quantitative analysis (TBR-H was significantly different in the RV (p=0.02) and LV (p=0.04) segments). ***Conclusion:*** In GCA patients with positive [^{18}F] FDG PET/CT, vertebral artery involvement was more frequent than temporal artery involvement. Corticosteroid treatment did not have any influence on PET/CT positivity based on visual analysis but did have an influence based on quantitative analysis, which can be used to support visual assessment, with good diagnostic performance.

OP-554

Value addition of [ga-68] fapi pet/ct in enhancing the detection of the inflammatory disease activity in patients suspected of takayasu arteritis- a pilot study

R. Maurya*, M. Ora, S. Gambhir, M. Rai, R. Mehra;*
Sanjay Gandhi post graduate institute of medical sciences, Lucknow, INDIA.

Aim/Introduction: Takayasu Arteritis (TA) is a rare inflammatory disorder of large arteries, typically presenting with non-specific symptoms and potentially progressing to arterial occlusion. Molecular imaging, particularly ^{18}F-FDG PET/CT, is increasingly used to detect vascular inflammation in large vessel vasculitis (LVV) like TA.However, ^{18}F-FDG PET/CT has limitations, including low specificity and limited utility in monitoring treatment response, as uptake may reflect both inflammation and vascular remodeling(1).New PET tracers targeting immune and stromal cells, such as Fibroblast Activation Protein Inhibitor (FAPI), have shown promise in inflammatory and fibrotic diseases due to FAP-alpha expression on activated fibroblasts.Ga-68 labeled FAPI PET/CT may offer better sensitivity and specificity for detecting vascular inflammation in TA. ***Materials and Methods:*** The study assessed 28 TA patients, collecting demographic and clinical data, including ESR and CRP levels.All patients first underwent F-18 FDG PET/CT scans, followed by Ga-68 FAPI PET/CT scans within a week using a consistent protocol. SUV max values and PETVAS scores were calculated for affected arterial segments in both scans.The Wilcoxon signed-rank test was used for statistical comparison of SUV max and PETVAS scores using SPSS. ***Results:*** Participants had a mean age of 31.1 ± 8 years (range: 18-49), with 25 females and 3 males. The mean SUV max was higher with Ga-68 FAPI (3.04 ± 1.59) compared to FDG (2.42 ± 0.97, p=0.008). The average number of arterial segments involved was significantly greater on FAPI PET/CT (5.96 ± 2.7) than FDG PET/CT (2.04 ± 3.12, p<0.001). PETVAS scores were also significantly higher for FAPI (15.57 ± 4.91) than for FDG (8.04 ± 7.39, p<0.001). Among patients with FDG PETVAS <9, 78.9% had FAPI PETVAS >9, indicating FAPI identified additional inflammation. Statistical analysis revealed a significant mean difference in the number of positive arteries between the scans (mean difference = -3.93, p=0.000). ***Conclusion:*** Ga-68 FAPI PET/CT outperformed F-18 FDG PET/CT in detecting arterial inflammation in Takayasu Arteritis, identifying more inflamed segments and yielding higher SUV max and PETVAS scores. Its effectiveness is attributed to targeting activated fibroblasts and reduced background uptake, improving visualization and suggesting it may be a superior imaging modality for assessing TA activity. ***References:*** FDG-PET/CT(A) Imaging in Large Vessel Vasculitis and Polymyalgia Rheumatica: Joint Procedural Recommendation of the EANM, SNMMI, and the PET Interest Group (PIG), and Endorsed by the ASNC." European Journal of Nuclear Medicine and Molecular Imaging 45 (7): 1250-69. https://doi.org/10.1007/s00259-018-3973-8.

OP-555

^{18}F-FDG PET/CT value in the diagnosis evaluation of patients with polyarteritis nodosa

N. Martinage*, J. Guyot, G. Delaby, D. Huglo, E. Ledoult, C. Baillet;*
Centre Hospitalier Universitaire de Lille, Lille, FRANCE.

Aim/Introduction: Polyarteritis nodosa (PAN) is a rare necrotizing vasculitis affecting medium-sized arteries, with evolving clinical phenotypes that often complicate diagnosis. While ^{18}F-FDG PET/CT is a cornerstone in large-vessel vasculitis, its utility in PAN remains underexplored. A characteristic "ant-farm" hypermetabolism pattern has recently been associated with PAN. This study explores the value of ^{18}F-FDG PET/CT in PAN by describing metabolic abnormalities and correlating them with clinical and paraclinical features. ***Materials and Methods:*** Patients diagnosed for polyarteritis nodosa who underwent ^{18}F-FDG PET/CT between 2010 and 2025 were retrospectively included. All PET/CT were blindly reviewed by two nuclear medicine physicians using a standardized reading grid. Abnormal PET/CT uptakes were systematically recorded and correlated with technical, clinical, biological, and histopathological features. Patients were then compared according to the presence or absence of the ant-farm pattern. ***Results:*** Forty-seven patients were included. The most frequent metabolic abnormalities were osteomedullary (81%), lymph node (40%) and splenic (34%) uptakes. Vascular uptake was present in 17 (36%) patients, primarily involving femoral arteries (94%), tibial anterior and tibioperoneal arteries (71%), and humeral arteries (53%). In 10 patients, osteomedullary uptake extended to the humeral and femoral diaphyses; 6 of them had underlying myelodysplasia. Two patients had VEXAS syndrome associated with PAN. They both had pulmonary infiltrates, diffuse osteomedullary and nasal cartilages uptake. One of them had a diffuse muscular linear and patchy FDG uptake, known as a «tiger-man» pattern. Neurologic, cutaneous, renal, and testicular involvement were rarely detected by PET/CT. The ant-farm pattern was observed in 16 (34%) patients and showed excellent inter-observer reproducibility (kappa coefficient: 0.850; p< 0.0001). It was more frequently observed with newer PET/CT devices (45% vs. 7%; p = 0.011) and whole-body acquisition (56% vs. 10%; p = 0.001) and was associated with fewer PAN-suggestive biopsies (7% vs. 85%; p < 0.0001) and a higher increase of C-reactive protein levels (231 versus 134 mg/L; p = 0.008). ***Conclusion:*** ^{18}F-FDG PET/CT appears to be a valuable tool in the diagnostic assessment of PAN. The ant-farm pattern is highly reproducible and identifies a subset of patients with a more inflammatory phenotype and

negative biopsy findings. In addition, ^{18}F-FDG PET/CT can detect abnormal uptakes in bone marrow, lungs, or cartilage, suggestive of secondary PAN.

OP-556

Diagnostic Value of Splenic and Bone Marrow Metabolic Uptake on ^{18}F-FDG PET/CT in Patients with Suspected Infective Endocarditis

S. Capitanio[1], *A. Franchini*[1], *A. Spataro*[1], *L. Virdone*[2], *L. Airò Farulla*[1], *A. Scarale*[1], *G. Cabrini*[1], *E. Gay*[1], *C. Rossetti*[1];
[1]*Nuclear Medicine Unit, Dipartimento Ematologia, Oncologia e Medicina Molecolare, ASST Niguarda Hospital, Milan, ITALY,* [2]*School of Medicine and Surgery, University of Milan-Bicocca, Monza, ITALY.*

Aim/Introduction: ^{18}F-FDG PET/CT has gained a pivotal role in the diagnosis of infective endocarditis (IE), especially in patients with prosthetic valves or cardiac implantable electronic devices (CIED). However, the role of systemic metabolic response in this setting has not been fully clarified. The aim of this study was to evaluate the diagnostic contribution of increased FDG uptake in the spleen and bone marrow as markers of systemic metabolic responses, in suspected IE patients. ***Materials and Methods:*** We retrospectively analyzed 83 patients (mean age 68.5 ± 15.8 years) who underwent ^{18}F-FDG PET/CT for suspected IE. Among them, 21 had native valves, while 62 had prosthetic valves and/or CIEDs. Valvular or CIED uptake was considered positive and thus compatible with infective endocarditis when FDG uptake was at least greater than mediastinum blood pool activity with focal or heterogeneous uptake pattern. Splenic and bone marrow activity was considered increased if SUVmean spleen/liver or marrow/liver ratio was >1. ***Results:*** Among 83 patients enrolled in the study, 43 patients (51.8%) had a final diagnosis of IE (definite in 33 cases and possible in 10, according to ESC guidelines). Of 43 IE patients, 26 (63.4%) had spleen/liver >1, 21 (51.2%) had marrow/liver >1, and 30 (73.2%) had positive valvular uptake. At least one of these three parameters was positive in 90.2% of IE cases, two or more in 65.9%, and all three were positive in 31.7%. Multivariate logistic regression showed that spleen/liver ratio >1 (OR 3.46, p = 0.014) and valvular uptake (OR 3.56, p = 0.014) were independent predictors of IE. In contrast, marrow/liver >1 was not significantly associated (OR 1.46, p = 0.468). Among patients without IE (n=40), spleen/liver >1 was observed in 32.5%, and marrow/liver >1 in 30%. Increased spleen/liver ratio was significantly more frequent in IE (65.9%) compared to non-IE patients (32.5%, p = 0.0076), while the marrow/liver difference did not reach significance (46.3% vs. 30.0%, p = 0.074). 10/43 IE patients (23.3%) had native valves. Valvular FDG uptake, spleen/liver >1, and marrow/liver >1 were more frequent in patients with prosthetic valves or CIEDs, despite only the difference in valvular uptake was clinically relevant. ***Conclusion:*** Increased splenic FDG uptake and valvular involvement are the most supportive metabolic markers of IE on PET/CT. Bone marrow uptake showed a diagnostic but less significant trend. Integrating the evaluation of systemic and local metabolic activity may improve diagnostic confidence, especially in equivocal cases.

OP-557

Metabolic Signatures of Smoking-Induced Immune Suppression and Vascular Inflammation: Insights from ^{18}F-FDG PET/CT

E. Panagiotidis[1], *G. Angelidis*[1], *A. Paschali*[2], *T. Kalathas*[2], *A. Pipintakou*[2], *I. Tsougos*[1], *V. Valotasiou*[1], *V. Chatzipavlidou*[2], *P. Georgoulias*[1];
[1]*University Hospital, Larisa, GREECE,* [2]*Theageneio Cancer Center, Thessaloniki, GREECE.*

Aim/Introduction: Cigarette smoking is associated with immune dysregulation and increased vascular inflammation. However, the regional metabolic correlates of these effects, particularly in immune and vascular structures, remain insufficiently characterised. This study aimed to assess the impact of smoking on immune activity, evaluated via ^{18}F-FDG uptake in Waldeyer's ring, and on vascular inflammation, assessed through thoracic aortic wall uptake on ^{18}F-FDG PET/CT. ***Materials and Methods:*** A retrospective analysis was conducted on 444 adult patients (276 men; median age 65 years; range 26-87) who underwent ^{18}F-FDG PET/CT imaging. Exclusion criteria included any history of head and neck malignancy or surgery, lymphoma, cervical lymphadenopathy, tonsillectomy, recent upper respiratory infection, liver metastases, recent antibiotic use, or prior radiotherapy to the head and neck region. Patients were categorised as non-smokers (n=120), smokers (n=119), and ex-smokers (n=205). ***Results:*** Statistically significant differences in SUVmax values were found in all regions of Waldeyer's ring. Smokers demonstrated the lowest metabolic activity, followed by ex-smokers and non-smokers. For the right palatine tonsil, SUVmax values were: non-smokers 4.62, smokers 3.82, ex-smokers 4.10 (p<0.006); left palatine tonsil: 4.65, 3.86, 4.11 (p<0.007); and lingual tonsil: 4.62, 3.82, 4.10 (p<0.017). Multivariate analysis identified smoking as an independent predictor of reduced SUVmax in Waldeyer's ring. In contrast, smokers had significantly higher thoracic aortic wall uptake (SUVmax 2.90) compared to non-smokers (2.57) (p=0.001); ex-smokers showed values comparable to non-smokers (2.55). A dose-dependent effect was observed, with heavy smokers (>20 cigarettes/day) showing lower tonsillar SUVmax. Additionally, elevated BMI was associated with higher thoracic aortic SUVmax, suggesting a synergistic role of obesity and smoking in vascular inflammation. ***Conclusion:*** Smoking is associated with decreased metabolic activity in Waldeyer's ring, consistent with immune suppression, and increased aortic FDG uptake, reflecting vascular inflammation. These effects appear partially reversible following smoking cessation. ***References:*** Gomez R, et al. (2018). Immune function of Waldeyer's ring. Immunology 151(1):1-15.Mariani M, et al. (2017). Smoking and immune suppression in the tonsils. J Immunol 199(5):334-43.Kuo C, et al. (2016). Smoking and inflammation in the thoracic aorta. Atherosclerosis 248:56-63.Tsou Y, et al. (2018). Nicotine and its immunosuppressive effects. Toxicol Rev 37(1):9-16.Zhang L, et al. (2018). Influence of smoking cessation on inflammation. Circulation 138(13):1232-44.

OP-558

Hybrid [18F]FDG-PET/MRI in Inflammatory Cardiac Disease: One Scan, Complete Insight

G. Argalia[1], *M. Fogante*[2], *G. Biscontini*[1], *A. Palucci*[1], *C. Romagnolo*[1], *C. Cottignoli*[1], *P. Esposto Pirani*[2], *C. Ventura*[2], *N. Schicchi*[3], *G. Argalia*[2], *F. M. Fringuelli*[1];
[1]*Nuclear Medicine, Department of Radiological Sciences, University Hospital of Marche, Ancona, ITALY,* [2]*Maternal-Child-Senological-Cardiological Radiology and Outpatient Ultrasound, Department of Radiological Sciences, University Hospital of Marche, Ancona, ITALY,* [3]*Cardiovascular Radiological Diagnostics, Department of Radiological Sciences, University Hospital of Marche, Ancona, ITALY.*

Aim/Introduction: Hybrid-PET/MRI is a multimodal imaging technique that enables the synchronous acquisition of metabolic PET data and high-resolution anatomical and functional MRI information. This integrated approach ensures excellent spatial and temporal correlation between molecular and structural findings, offering a comprehensive evaluation of cardiac inflammation. This study aims to evaluate the added diagnostic value of hybrid PET/MRI over standalone MRI and PET in assessing inflammatory heart diseases. ***Materials and Methods:*** This retrospective study included patients who underwent 18-fluorodeoxyglucose ([18F]FDG)-PET/MRI between September 2022-March 2025 for suspected acute/chronic myopericarditis or endocarditis. Patients followed a high-fat-carbohydrate-free diet for 72hours before the scan to suppress myocardial [18F]FDG-uptake. PET/MRI studies were performed using an integrated hybrid PET/3T-MRI scanner. Intravenous administration of a gadolinium-based-contrast-agent was performed to enhance myocardial tissue characterization.

Images were initially evaluated separately by a radiologist (MRI) and a nuclear medicine physician (PET). In myopericarditis MRI was positive= presence of LGE and edema; inconclusive= presence of LGE but not edema; negative= no LGE and no edema. In endocarditis MRI was positive= evidence of vegetations, valvular abscesses; inconclusive= subtle or nonspecific findings (minor thickening or ambiguous enhancement) or artifact limitations (prosthetic valves, arrhythmias); negative= normal valve morphology. PET was positive= presence of high-focal FDG uptake; inconclusive= mild-diffuse uptake or of uncertain anatomical location; negative= no FDG uptake. A multidisciplinary consensus meeting was held to integrate the findings and establish the final diagnosis. ***Results:*** 33patients were enrolled. 21(64%) with suspected myopericarditis and 12(36%) with suspected endocarditis. Common clinical indications included chest pain, fever of unknown origin, elevated inflammatory markers, and cardiac dysfunction. In patients with suspected myopericarditis, MRI was= positive 1/21, negative 4/21, inconclusive 16/21. PET imaging was= negative 19/21, inconclusive 2/21. The hybrid PET/MRI review led to a reclassification of 16/21(76%) cases, confirming the absence of active inflammation in most patients and precisely localizing tissue damage. In patients with suspected endocarditis, MRI was= positive 1/12, negative 1/12, inconclusive 10/12. PET was= positive 4/12, negative 7/12, inconclusive 1/12. The hybrid PET/MRI review was useful in 9/12(75%) cases, allowing to distinguish active/previous inflammation. ***Conclusion:*** The integrated approach offered superior spatial and temporal correlation between metabolic and anatomical findings, aiding in more accurate disease characterization. These results suggest that hybrid [18F]FDG-PET/MRI may be a valuable tool in the comprehensive evaluation of inflammatory heart diseases, facilitating better diagnosis and management of patients, when PET and MRI separately do not provide sufficient information to reach a conclusion.

OP-559

FDG PET/CT in Inflammatory Myopathies: Bridging Biochemistry and Imaging Clues

A. S Babu, *R. Karna, M. Umar, A. Mahalik, K. Bangkim Chandra, R. Kumar;*
All India Institute of Medical Sciences, Delhi, INDIA.

Aim/Introduction: Polymyositis and dermatomyositis (PM/DM) are rare autoimmune inflammatory myopathies characterized by progressive muscle weakness and systemic involvement. While traditional diagnostic tools like enzyme assays and clinical assessment are central, FDG PET/CT is emerging as a promising modality for detecting active inflammation and guiding management. This study explores how metabolic imaging correlates with biochemical activity in suspected PM/DM patients. ***Materials and Methods:*** We retrospectively analyzed 52 patients who underwent FDG PET/CT between March 2023 and January 2025 for suspected or confirmed inflammatory myopathies. Clinical data, CK and/or CK-MB values, and PET scores were evaluated. Muscle uptake was visually graded using a 3-point scale: 0 (less than mediastinal blood pool), 1 (≥ mediastinal blood pool but less than liver), and 2 (≥ liver). A score of 1 or 2 was considered positive and PET findings were correlated with CK/CK-MB values. ***Results:*** Among 52 patients (mean age 46 years, range 18-78 years; 30 females, 22 males), CK and/or CK-MB values were available for 42 patients. Visual grading of muscle uptake on FDG PET/CT was done for the 42 patients with CK/CK-MB data. Among those with high-grade FDG uptake (score 2), 70% (14/20) had elevated CK and/or CK-MB, indicating active inflammatory myopathy. In contrast, low uptake (score 0) was observed in 16 patients, of whom 62.5% (10/16) had normal enzyme levels, suggesting minimal or no muscle inflammation. Intermediate uptake (score 1) was seen in six patients, with 83% (5/6) showing positive enzyme values, potentially reflecting early or mild disease. This trend highlights a strong correlation between PET metabolic activity and biochemical markers, supporting the utility of FDG PET/CT as a non-invasive tool for assessing disease activity in PM/DM. ***Conclusion:*** FDG PET/CT proves to be a valuable adjunct in evaluating inflammatory myopathies, offering a visual and quantifiable reflection of underlying muscle inflammation. Higher PET uptake scores align with increased CK/CK-MB positivity, reinforcing the utility of FDG PET/CT as a surrogate marker for disease activity in dermatomyositis. Its correlation with CK/CK-MB enhances diagnostic confidence and may assist in biopsy planning and monitoring therapeutic response. With standardized scoring, FDG PET/CT could play a more integral role in routine evaluation, especially in challenging or equivocal cases.

1209

Tuesday, October 7, 2025, 8:00 - 9:30
Room 133+134

e-Poster Presentations Session 9 - Dosimetry Committee: Advances in Clinical and Preclinical Dosimetry

EPS-178

Scenario based uncertainty estimation of radionuclide therapy dose

F. Kähler*;*
RaySearch Laboratories, Stockholm, SWEDEN.

Aim/Introduction: Input data for radionuclide therapy (RNT) dose estimations inherently contain uncertainties. However, resulting uncertainties in dose are often not reported. Proposed methods for uncertainty estimations are not applicable without restricting the used fit function. To overcome this, in the here presented method, different dose scenarios are computed to estimate the dose uncertainty. The method was implemented in a research build of a commercial dosimetry software. ***Materials and Methods:*** Doses and uncertainties were estimated for the MRT dosimetry dataset as described of the supporting material[1]. The dataset contains six SPECT/CTs. The image data was quantified using SPECT data of a cylindrical Jaszczak phantom (injected activity A= 441.2±13.8MBq). The activity was recovery corrected using a two parameter (a,b) curve: $R(v,a,b)=1/(1+(a/v)^b)$. Estimation of the parameters was performed using the dataset of a NEMA phantom (a=2.80±0.38ml, b=0.48±0.01). Including the uncertainty of the injected reference activity, an uncertainty of the recovery function can be estimated for each volume. Activity was time-integrated using a mono-exponential fit for the mean intensities of the regions of interest (ROI). ROIs used for the study were a lesion (inside the liver), liver, spleen, medulla, and cortex (for left and right kidney). To simulate uncertainty in the fit and the segmentation, three mono-exponential fits were performed for each ROI, one for the original contours and for contours expanded or contracted by a margin. For overlapping ROIs, one ROI was expanded while the other one was reversed, to not over-count the activity. The scenario evaluation was repeated with margins (1mm, 2mm and 3mm). ***Results:*** 27 scenarios were created including all possible combinations for the calibration factor, recovery function and time-integrated activities from the fits. Doses were computed for the non-expanded ROI geometries using Monte Carlo simulation of all particles for a 1.5x1.5x2mm grid resulting in multiple DVH bands for the ROI. The dose uncertainty was computed from the

standard deviation of all scenarios. Uncertainties were compared to uncertainties computed for an analytical method[2]. Best agreement was achieved for 2mm margin where computed uncertainties were comparable to the reference values. Largest relative contribution to the uncertainties were fit/delineation (58.8%), then recovery correction (24.6%) and calibration factor (16.5%). ***Conclusion:*** The here presented methodology enables the estimation of dose uncertainty in RNT using different scenarios without with limited use of analytical methods. The methodology must be tested on non-phantom data. The uncertainty is expected to increase for small, uneven, diffuse ROIs. ***References:*** [1]DOI 10.17605/OSF.IO/69NGE;[2]https://doi.org/10.1186/s40658-020-00328-5.

EPS-179

A Unified MeshBased Modelling Framework for Age and AnatomySpecific Skeletal Dosimetry

R. Dawson[1], *C. Choi*[1], *Y. Wang*[1], *B. Shin*[1], *J. Tran-Gia*[2], *M. Salas-Ramirez*[2], *A. Theisen*[2], *M. Laßmann*[2], *W. E. Bolch*[1];
[1]*J. Crayton Pruitt Family Department of Biomedical Engineering, University of Florida, Gainesville, FL, UNITED STATES OF AMERICA,* [2]*Department of Nuclear Medicine, University Hospital Würzburg, Würzburg, GERMANY.*

Aim/Introduction: Red bone marrow (RBM) and bone endosteum (BE) are key risk organs for radiogenic leukaemia and bone cancer, yet modelling the intricate trabecular bone (TB) microstructure has historically been challenging. Voxel-based computational phantoms enable Monte Carlo (MC) dosimetry but suffer from limited resolution and stair-step artefacts. This study developed an integrated programme to (i) generate highfidelity, ICRPconsistent polygonal and tetrahedral mesh (TM) models for adult and paediatric skeletons, (ii) extend to non-reference morphologies via systematic variation of bone volume fraction (BV/TV) and cellularity factor (CF), and (iii) couple selected bone site geometries to an agentbased bone remodelling framework linked with MC transport to predict time-resolved dosimetry for boneseeking αemitters. ***Materials and Methods:*** Adult reference TM models were created from segmented micro-CT images (30μm voxels) of cadaveric bone cores (35 sites male, 38 sites female). An automated C++/Python pipeline converted TB segmentations into smoothed surface meshes, populated marrow cavities with explicit, individual adipocyte models, and assembled multi-domain TM models. Adult meshes were morphed to match age-specific marrow metrics from skeletal morphology data, producing several hundred paediatric models representing newborns, 1-, 5-, 10-, and 15-year-old individuals consistent with ICRP mesh-type reference computational phantoms (MRCPs). Non-reference variants were generated by parametric BV/TV scaling (5-25%) and CF adjustment (0-100%), yielding a comprehensive library for sensitivity studies. A 10μm lattice agent-based model (ABM) simulated bone multicellular unit (BMU) formation-resorption cycles with Ra223/226 adsorption, incorporation, and release. Activity states from each ABM cycle drove Particle and Heavy Ion Transport code System (PHITS) MC simulations with paired TM models; resulting three-dimensional dose distributions iteratively updated cellular kill probabilities and remodelling dynamics. ***Results:*** TM models were generated for all imaged skeletal sites in adult, paediatric, and non-reference cases, eliminating voxel stair-step artefacts and anatomically unrealistic morphologies. BV/TV and CF parameters were tuned so embedded MRCPs matched ICRP Publication 89 TB and RBM masses within 0.5%. MC transport simulations of electron absorbed fractions (AFs) revealed substantial low-energy (10-30 keV) discrepancies between TM and voxel models across most source-target combinations. The coupled ABM-MC workflow captured temporal dose accumulation patterns linked to BMU dynamics. ***Conclusion:*** This study presents a harmonized framework of mesh-based skeletal models spanning paediatric to adult and encompassing non-reference morphologies, integrated with a mechanistic ABM-MC dosimetry engine. These tools reduce geometric bias, enable patient-specific sensitivity analyses, and open new avenues for dose optimisation in nuclear medicine, radiopharmaceutical therapy, and radiation protection.

EPS-180

Increasing Precision in Image-Based Bone Marrow Absorbed Dose Estimations following [^{177}Lu]Lu-DOTATATE Treatment

K. Smits[1], *F. Westerbergh*[1], *J. Hemmingsson*[1], *M. van Essen*[2], *J. Svensson*[3], *A. Theisen*[4], *J. Tran-Gia*[4], *T. Rydén*[5], *P. Bernhardt*[5];
[1]*Institute of Clinical Sciences, Gothenburg, SWEDEN,* [2]*Institute of Medicine, Gothenburg, SWEDEN,* [3]*Department of Oncology, Gothenburg, SWEDEN,* [4]*Department of Nuclear Medicine, Wurzburg, GERMANY,* [5]*Department of Medicial Physics and Biomedical Engineering, Gothenburg, SWEDEN.*

Aim/Introduction: Bone marrow absorbed dose estimates are susceptible to large uncertainties, mainly due to low uptake and thus high noise levels. This study examines how image-based bone marrow absorbed dose calculations are affected by the number of included vertebrae and the reconstruction parameters used in the absorbed dose calculations. ***Materials and Methods:*** We included 16 patients with advanced neuroendocrine tumors treated with [^{177}Lu]Lu-DOTATATE. After the first treatment cycle, all patients underwent 4 SPECT/CT scans (2, 24, 48, and 168 hours post-injection). SPECT data were reconstructed with 60 updates (in-house Monte Carlo-based OSEM with attenuation and scatter correction, and resolution modeling), using either 60 iterations with one subset (60i1s) or 5 iterations with 12 subsets (5i12s). The T8-L5 vertebrae were used to estimate the bone marrow activity concentrations. Absorbed dose estimates, and their precision, were assessed in relation to the number of vertebrae included in the calculation. Further evaluations were carried out using both measured (Lung-Spine phantom with spherical inserts) and simulated (digital XCAT phantom) SPECT data. Poisson noise (100 realizations per noise level) was added to the simulations to generate noise levels matching those observed in patients. While the impact of different volumes-of-interest (4-16 mL) on image-based activity concentration estimates was evaluated using the Lung-Spine phantom, the XCAT phantom served to evaluate the activity concentration within realistic vertebral geometries. ***Results:*** Increasing the number of vertebrae from one to six in the absorbed dose calculations substantially improved the precision in absorbed doses (coefficient of variation, COV, from 34% to 6.3%). Comparing reconstructions using 1 subset (60i1s) and 12 subsets (5i12s), only minor differences (0.1%) were observed. For the Lung-Spine phantom, smaller volumes (V = 4 mL, COV: 36%) were found more sensitive to noise compared to larger volumes (V = 16 mL, COV: 17%), at 60 updates. In the XCAT phantom, a decrease in recovery from 0.63 (L5) to 0.31 (T12) at 60 updates was seen in vertebrae adjacent to high-uptake organs. ***Conclusion:*** The precision in image-based bone marrow absorbed dose calculations is improved by including multiple vertebrae. However, careful selection of these vertebrae is needed, as closely located high-uptake organs can bias the absorbed dose estimates. Only minor differences were found between 60i1s and 5i12s, suggesting that bone marrow absorbed dose estimates are stable throughout different iteration-subset configurations.

EPS-181

Semi-automated small-volume sampling for quantitative SPECT/CT-based renal dosimetry in ^{177}Lu radiopharmaceutical therapy: comparison with whole-kidney segmentation

J. M. Beauregard[1], *A. S. Demers*[1], *F. A. Buteau*[1], *G. April*[1], *F. Arsenault*[1], *A. Beaulieu*[1], *C. F. Uribe*[2];
[1]*Department of Medical Imaging, CHU de Québec - Université Laval, Quebec City, QC, CANADA,* [2]*BC Cancer Research, Vancouver, BC, CANADA.*

Aim/Introduction: Practical, accurate and standardised renal dosimetry methods are needed for wider use of dosimetry in ^{177}Lu radiopharmaceutical therapy. We aimed to compare a semi-automated small-volume-of-interest dosimetry technique with

the conventional approach of whole-kidney segmentation on CT. ***Materials and Methods:*** Thirty patients enrolled in our clinical trial of personalised PRRT (NCT02754297) underwent quantitative SPECT/CT at ~24h and ~72h after their first ^{177}Lu-DOTATATE administration (2.2-13.2 GBq). Kidneys were manually segmented on CT and combined to compute the total renal volume. This contour was expanded by 1 cm to include spilled-out activity and obtain the "raw" total renal activity. The latter divided by the former defined the raw whole-kidney activity concentration (WK_{raw}). The expanded contour was trimmed to exclude areas of spilled-in activity from adjacent tumours, yielding the corrected activity concentration (WK_{cor}). The semi-automated small-volume (SV) method consisted in sampling activity concentration with a spherical 2-cm VOI (~4 mL) positioned concentric to the renal SUV_{peak} location across both kidneys, using the SUV_{peak}-finding tool that is available in most molecular imaging software. Dosimetry was performed by multiplying the area under the monoexponential time-activity concentration curve by 86 mGy·g/MBq·h. SUV_{mean}, effective half-life (T_{eff}) and specific absorbed dose (AD) were correlated between SV, WK_{raw} and WK_{cor} techniques. Kidney volume was compared between both timepoints. ***Results:*** The SV method yielded median (range) SUV_{24h} of 6.1 (3.1-12.9), SUV_{72h} of 4.1 (2.0-8.7), T_{eff} of 52 (38-113) hours and specific AD of 0.76 (0.35-1.89) Gy/GBq, which are consistent with published data. Moderate correlations were observed between SV and WK_{raw} (SUV_{24h} r=0.85, SUV_{72h} r=0.77, T_{eff} r=0.58 and specific AD r=0.67; P<0.001), which all improved substantially when SV was correlated to WK_{cor} (SUV_{24h} r=0.92, SUV_{72h} r=0.91, T_{eff} r=0.73 and specific AD r=0.92; P<0.001). SV method yielded dosimetry estimates that were on average 11% above those obtained with WK_{cor}. Total kidney volume was 307±73 mL and intra-patient discrepancies of up to 13% were observed between the two CT timepoints. SV sampling can be performed in about one minute, vs. 15-30 minutes for CT-based WK segmentation. ***Conclusion:*** The SV method yielded renal dose estimates that were comparable to those obtained with WK segmentation corrected for tumour spill-in, with only a small positive bias. It is easy to implement, software vendor-neutral, observer-independent in principle, considerably timesaving, and likely translatable to other radionuclides and target tissues. It could fulfil the need for a standardised dosimetry approach for monitoring and personalising radiopharmaceutical therapy. ***References:*** Sandström,EJNMMI2010;37:212. DelPrete,EJNMMIPhys2018;5:25.

EPS-182

DBS sampling as a method for dosimetry in Lu-PSMA therapy.

K. Doornhof*, I. Bumanjal, M. Konijnenberg, S. Koolen;*
Erasmus MC, Rotterdam, NETHERLANDS.

Aim/Introduction: Dosimetry enables detailed tracking of radiation exposure in patients undergoing radioligand therapy, potentially correlating this data with therapy outcomes and side effects. This correlation could facilitate personalized treatment plans. However, comprehensive dosimetry requires data collection at multiple time points, often necessitating additional hospital visits, thereby increasing patient burden. Dried Blood Spot (DBS) sampling offers a solution for blood-based bone marrow dosimetry by allowing patients to collect samples at home and send them to the hospital for analysis. This study aims to evaluate the feasibility of collecting and analyzing blood samples using DBS. ***Materials and Methods:*** Pre-clinical validation involved spiking blood samples with various concentrations of Lu-177. An initial 2MBq/mL sample of Lu-177-DTPA in blood was prepared using a dose calibrator, followed by serial dilutions until the concentration dropped below 1KBq/mL. These samples were spotted (volume 50 ± 0.4µL) on DBS paper (Whatman 903 protein saver cards) in triplicate. After drying, 6 mm punches of the DBS spot were measured using a gamma-scintillation counter for 1 and 10 minutes to assess repeatability and linearity. The effects of hematocrit (HT) and punch location (taken from the spot center or edge) were also examined by spotting samples with identical Lu-177 concentrations and HT levels of 0.15, 0.25, 0.3, 0.4, and 0.5. ***Results:*** A linear correlation was observed between Lu-177 concentration in the blood sample and CPM measured on the DBS punch using the gamma-counter (r^2=0.9981). CPM measurements were significantly correlated with blood hematocrit, with samples with lower hematocrit levels showing a lower measured CPM ($p < 0.0001$). The effect of hematocrit level on the measured CPM was linear within the validation range (r^2=0.9454). When counting for 10 minutes, blood concentrations measured on DBS spots consistently fell within 10% of the true concentrations for samples with Lu-177 concentrations above 15KBq/mL and within 20% for those above 4KBq/mL. ***Conclusion:*** Preclinical results indicate that DBS sampling could be a reliable method for determining Lu-177 concentrations in blood. While variations in HT impact measurements, the effect is linear, allowing for correction. This sampling method has the potential to enable more extensive dosimetry in patients undergoing radioligand therapy without placing additional burden on patients. The methods practical performance is currently being investigated in an ongoing clinical trial.

EPS-183

Assessing the Impact of Multi-Cycle Data Integration on the Accuracy of Single-Time-Point Dosimetry: A Non-linear Mixed-Effect Modeling Evaluation

I. Budiansah*[1], D. Hardiansyah[1], S. M. B. Peters[2], S. Ardjo Pawiro[1], B. Privé[2,3], J. Nagarajah[2,4], M. W. Konijnenberg[2,3], A. J. Beer[5], G. Glatting[5];*
[1]Universitas Indonesia, Depok, INDONESIA, [2]Radboud University Medical Centre, Nijmegen, NETHERLANDS, [3]Erasmus Medical Centre, Rotterdam, NETHERLANDS, [4]Röntgeninstitut Düsseldorf, Düsseldorf, GERMANY, [5]Ulm University, Ulm, GERMANY.

Aim/Introduction: This study investigated the impact of incorporating multi-cycle data on the accuracy of time-integrated activity coefficients (TIACs) in single-time-point (STP) dosimetry. ***Materials and Methods:*** Renal biokinetic data of [^{177}Lu]Lu-PSMA-617 were collected from ten patients with low-volume metastatic hormone-sensitive prostate cancer (mHSPC) at Radboud University Medical Centre (NCT03828838). Each patient underwent two therapy cycles, receiving (3.1±0.1) GBq and (5.9±0.4) GBq in the first and second cycles, respectively. Biokinetic data were obtained separately from the left and right kidneys in both cycles, yielding forty renal datasets. For each cycle, SPECT/CT scans were performed at five time points: TP1 (2.5±0.9)h, TP2 (23±2)h, TP3 (47±2)h, TP4 (71±2)h, and TP5 (167±2) h after injection. Population-based model selection using non-linear mixed-effect modelling (PBMS NLMEM) was applied to select the best fit function. Goodness-of-fit criteria were visual inspection, relative standard error (RSE) < 50%, and the absolute value of the off-diagonal elements in the correlation matrix < 0.8. Among the models that satisfied these criteria, the final selection was based on the highest Akaike weight. TIACs derived from the best fit function in all-time-point (ATP) dosimetry were designated reference TIACs (rTIACs). To evaluate the impact of multi-cycle population data on STP dosimetry accuracy, three STP scenarios were analysed: (1) first cycle STP dosimetry using parameters estimated from first cycle data; (2) second cycle STP dosimetry using parameters from second-cycle data; and (3) STP dosimetry in both cycles using parameters from the combined data of both cycles, applied separately to each cycle. In each scenario, the optimal time point was determined as the time point with the lowest root-mean-squared-error (RMSE) between STP-estimated TIACs (sTIACs) and the rTIACs. ***Results:*** Function $f_{6a}(t)=A_1e^{-(\lambda1+\lambda phys)}$

$^{t} + A_2e^{-(\lambda 2+\lambda phys)t} - A_3e^{-(\lambda 3+\lambda phys)t} - (A_1 + A_2 - A_3)e^{-(\lambda bc+\lambda phys)t}$ was selected as the best-fit function (Akaike weight ~ 100%). The optimal time points were (23±2)h and (71±2)h after injection for the first and second cycles, with RMSEs of (6.2±1.9)% and (6.7±1.9)%. Using parameters from the combined data yielded the same time points, with RMSEs of (6.0±2.7)% and (7.4±2.9)% for the first and second cycles, respectively. ***Conclusion:*** Incorporating multi-cycle data into STP dosimetry within the NLMEM framework yielded in the same optimal time point as using single-cycle data. The accuracy of the sTIACs remained comparable across scenarios, indicating that a single-cycle dataset is sufficient for accurate STP dosimetry.

EPS-184

Dosimetry-guided treatment planning for ^{177}Lu-labelled PSMA therapy based on a diagnostic ^{68}Ga-labelled PSMA PET/CT

E. Yousefzadeh-Nowshahr[1,2], *L. D. Jiménez-Franco*[3], *V. Vasic*[1], *A. Theisen*[4], *J. Tran-Gia*[4], *P. Hartrampf*[4], *A. J. Beer*[2], *M. Lassmann*[4], *G. Glatting*[1,2];
[1]*Medical Radiation Physics, Department of Nuclear Medicine, Ulm University, Ulm, GERMANY,* [2]*Department of Nuclear Medicine, University Hospital Ulm, Ulm, GERMANY,* [3]*ESQlabs GmbH, Saterland, GERMANY,* [4]*Department of Nuclear Medicine, University Hospital Würzburg, Würzburg, GERMANY.*

Aim/Introduction: PSMA-targeted therapy with ^{177}Lu-labelled PSMA has demonstrated improved outcomes in castration-resistant prostate cancer. While major trials employed a fixed activity of 7.4 GBq, dosimetry-based individualisation may further optimise outcomes. This study aimed to develop a dosimetry-guided treatment planning approach based solely on a diagnostic [^{68}Ga]Ga-PSMA-I&T PET/CT. ***Materials and Methods:*** Data from ten patients with metastatic prostate cancer who had undergone [^{68}Ga]Ga-PSMA-I&T PET/CT (80±20 min p.i.; 2.8±0.8 nmol peptide; 117.0±18.6 MBq), followed by one cycle of [^{177}Lu]Lu-PSMA-I&T therapy (87.6±2.7 nmol peptide; 6.2±0.2 GBq), and two SPECT/CT scans at 2 and 4 days p.i. were included. Imaging was standardised according to EARL accreditation protocols to ensure quantitative harmonisation across PET/CT and SPECT/CT scans. Time-activity data for kidneys, liver, spleen, and two lesions per patient were extracted using 3D Slicer [1]. A whole-body PBPK model was implemented using MATLAB/SimBiology. Model parameters were fitted to the patient's time-activity data using a Bayesian population approach to create individual digital twins and to estimate reference absorbed doses (ADs) for kidneys and tumours. Next, model parameters were fitted using only PET/CT data to predict therapeutic time-activity curves. The resulting ADs for kidneys and tumours were then compared to the reference values. After evaluating the model's predictive performance, virtual treatment scenarios were simulated solely on PET/CT data, varying the peptide amount of [^{177}Lu]Lu-PSMA from 2-2048 nmol. For each patient, optimal combinations of peptide amount and administered activity were determined by maximising the tumour absorbed dose, while adhering to the therapy-limiting conditions described in [2]. ***Results:*** PET/CT-based AD predictions for [^{177}Lu]Lu-PSMA-I&T therapy showed good agreement for the kidneys, with a mean absolute percentage error (MAPE) of 9% (range: 2-26%). For tumours, deviations between predicted and reference ADs were more pronounced (MAPE: 38%, range: 20-80%). Virtual treatment planning identified a median optimal peptide amount of 111 nmol (range: 64-388) and a median administered activity of 10.3 GBq (range: 5.1-37.7 GBq). Compared to applied treatments involving 6.2±0.2 GBq of [^{177}Lu]Lu-PSMA-I&T, which resulted in tumour and kidney ADs of 3.3-17.6 Gy and 2.8-8.5 Gy, respectively, the optimised plans achieved higher tumour ADs (5.9-25.0 Gy) while maintaining stable kidney ADs (8.1-8.3 Gy). ***Conclusion:*** PET/CT imaging may support predictive dosimetry and individualised treatment planning in PSMA-targeted ^{68}Ga/^{177}Lu theranostics with PSMA-I&T. However, further refinement is needed, e.g. incorporating more patient data to improve precision and accuracy. ***References:*** [1] Fedorov et al. Magn Reson Imaging 2012;30(9):1323-1341 [2] Jiménez-Franco et al. Med Phys. 2018.

EPS-185

Digital twins for PET data based prediction of absorbed dose in mice after [^{177}Lu]Lu-PSMA10.1 infusion

G. Costa[1,2], *E. Yousefzadeh-Nowshahr*[2,1], *V. Vasic*[1], *B. Sun*[3], *L. Nagel*[3], *A. Wurzer*[3], *F. Schilling*[3], *A. Beer*[2], *W. Weber*[3], *S. Kossatz*[3], *G. Glatting*[1,2];
[1]*Univesität Ulm, Ulm, GERMANY,* [2]*Uniklinik Ulm, Ulm, GERMANY,* [3]*Technische Universität München, Munich, GERMANY.*

Aim/Introduction: Prostate-specific membrane antigen (PSMA) labelled with lutetium-177 (^{177}Lu) is an established prostate cancer therapy, though variations in its effectiveness are not fully understood. Utilising a physiologically based pharmacokinetic (PBPK) model can aid in examining these differences and allows for safe delivery of high-dose radiation to tumours. The radiohybrid Lu-rhPSMA-10.1 is particularly advantageous as it shows identical pharmacokinetics for PET imaging as [^{18}F]^{nat}Lu-rhPSMA-10.1 and for therapy as ^{nat}F[^{177}Lu]rhPSMA-10.1. In addition, it exhibits low kidney uptake, rapid blood clearance, and high tumour accumulation. This preclinical study aims to find the best PET measurement schedule to predict the therapeutic absorbed dose from PET imaging data using digital twins for mice. ***Materials and Methods:*** The parameters of a physiologically based pharmacokinetic (PBPK) model were fitted to biodistribution study data to create digital twins of five mice injected with [^{177}Lu]Lu-PSMA10.1. With the digital twins, synthetic PET Time-Activity Curves (TAC) were generated. Sampling schedules were defined as time points being at least one hour apart, with a maximum of three time points at a combination of 15min, 30min, 90min, 3h30min, and 6h after injection. The kidneys, tumour, liver, and total body activities of each schedule were simulated using the digital twin and modified with 20% Gaussian noise. This was replicated 1000 times. Time-Integrated Activity (TIA) and absorbed dose were calculated for each replication and compared with the corresponding digital twin (ground truth). The mean absolute percentage error (MAPE) with the lowest value was ranked as the best schedule. ***Results:*** The mean absorbed dose was accurately predicted in all schedules, with differences between 0.8% and 4.3% for tumours and 2.8% and 4.2% for kidneys. However, the standard deviation exceeded 30% in all schedules, from 32.1% to 34.3% and 33.9% to 38.7% for tumours and kidneys, respectively. The 3 and 6 hours schedule yielded the lowest MAPE for both the tumour and the kidneys with 25.6% and 27.5%, respectively. The early time points of 15 and 30 minutes did not show improvements, and adding a 90-minute time point yielded equally good results to those at 3 and 6 hours for the tumour. ***Conclusion:*** This study demonstrates the potential of predicting absorbed doses from PET images using digital twins with a PBPK model. The 3 and 6-hour schedule is the best option adhering to animal welfare and working hours. Future research will include a Bayesian framework to improve accuracy and rRMSE.

EPS-186

Diagnostic ^{68}Ga-PSMA-11 PET/CT image-based dosimetry: a better estimate of ^{177}Lu-PSMA-617 therapy absorbed dose than PET uptake metrics

N. Payan[1,2], *C. Drouet*[1], *A. Jougla*[1], *A. Cochet*[1,2], *J. M. Vrigneaud*[1,2];
[1]*Centre Georges-François Leclerc, Dijon, FRANCE,* [2]*ICMUB UMR CNRS 6302, Université Bourgogne-Europe, Dijon, FRANCE.*

Aim/Introduction: Predicting treatment Absorbed Dose (AD) using diagnostic data could be a step forward in personalising ^{177}Lu-PSMA-617 radioligand therapy. Although numerous studies have investigated the predictive power of ^{68}Ga-PSMA-11 PET/CT uptake metrics, SUV values might not be the best candidate. The

aim of the present study was to assess the agreement between real pre-treatment dosimetry obtained using serial ^{68}Ga-PSMA-11 PET/CT acquisitions, and post-therapeutic mean AD coefficients (ADc), for Organs At Risk (OARs) and tumour lesions. ***Materials and Methods:*** Nine patients with metastatic, castration-resistant prostate cancer who underwent diagnostic ^{68}Ga-PSMA-11 PET/CT scans followed by a 7.4GBq ^{177}Lu-PSMA-617 therapy were included. Pre- and post-therapeutic dosimetry were obtained from six whole-body ^{68}Ga-PSMA-11 PET/CT acquisitions over one hour, and four SPECT/CT scans acquired at 5h, 24h, 4d and 8d after the first treatment injection, respectively. Kidneys, liver, spleen, Salivary Glands (SG) and SG with 3- and 5-mm isotropic margins (SG3 and SG5) were semi-automatically segmented on CT images using MIM® software. Large spheres were drawn around lesions on PET and SPECT images. Pre-therapeutic S-value-based dosimetry was performed in IDAC-Dose v2.1 using adjusted masses and cumulated activities fitted with the trapezoidal method. A voxel-level post-treatment dosimetry was performed with MIM® SurePlanMRT, using mono or bi-exponential fit for cumulated activities integration. Spearman correlations were calculated between treatment ADc, pre-therapeutic ADc and PET SUVmean/max values. ***Results:*** The mean(±SD) ADc for kidneys, liver and spleen were respectively 0.78(±0.18), 0.07(±0.04), 0.10(±0.04) before, and 0.43(±0.15), 0.13(±0.13), 0.08(±0.04) mGy/MBq after treatment. The larger the SG margin, the lower the corresponding ADc, with 0.42(±0.13), 0.32(±0.10), 0.26(±0.08) and 0.30(±0.17), 0.24(±0.13), 0.20(±0.11) mGy/MBq for SG, SG3 and SG5 pre- and post-treatment respectively. A total of 41 lesions (10 soft tissue, 31 bone) were analysed, with mean ADc values of 0.09(±0.05) before and 1,57(±1.17) mGy/MBq after therapy. Strong ($\rho>0.80$) significant ADc correlations were observed for kidneys, liver, spleen and SG3. High ($0.80>\rho>0.70$) significant correlations were also noted for SG, SG5, and all lesions combined. A stronger correlation was observed for soft tissue lesions than for bone lesions ($\rho=0.85$ vs 0.65, p-value<0.01). Post-therapeutic ADc showed stronger correlations with pre-treatment ADc than SUV values, except for SG and SG5. SG3 ADc however presented the highest correlation overall ($\rho=0.83$ vs 0.82 and 0.73 for SG3, SG and SG5 respectively). ***Conclusion:*** Pre-treatment dosimetry outperformed PET uptake values at estimating therapy's doses. The strong correlations between ADc support the potential of a pre-therapeutic dosimetry for a personalised medicine.

EPS-187

More Bang For Your Becquerel: A Novel Approach to "Dosing" in ^{177}Lu-PSMA Radioligand Therapy

N. Scott, *B. Fongenie, D. Stevens;*
Blue Earth Therapeutics, Oxford, UNITED KINGDOM.

Aim/Introduction: Current clinical approval for ^{177}Lu-PSMA Radioligand Therapy (RLT) follows a flat 6-cycle dosing regimen with limited investigation into optimum dosing strategies. ^{177}Lu-rhPSMA-10.1, a novel PSMA RLT, is under investigation in a Phase 1/2 trial. In Phase 1 (now completed) patients received 5.5-7.4 GBq per cycle for up to three cycles, with dosimetry performed throughout. Dosimetry results showed favourable normal organ doses that were consistent across cycles. However, tumour absorbed dose coefficients (Gy/GBq) peaked at cycle 1 and declined thereafter, suggesting that "front-loading" administered activity in early cycles could increase tumour absorbed dose without increasing normal organ doses. This work modelled the impact of front-loading activity to inform Phase 2 dosing strategies. ***Materials and Methods:*** Using Phase 1 dosimetry data, cumulative tumour absorbed doses were modelled for two dosing regimens: administering 10GBq in cycles 1 and 2, followed by five cycles of 7.4GBq; and administering 14.8GBq in cycles 1 and 2, followed by four cycles of 7.4GBq with all cycles at 6 weekly intervals. These regimens were compared against a flat dosing regimen fractionating 59.2GBq evenly across eight cycles. Adjustments were made accounting for relative differences in total administered activity. ***Results:*** Modelled cumulative organ absorbed doses remained well below the EBRT-derived dose limits for all dosing regimens explored. The relationship between cycle number and tumour absorbed dose was shown to follow a power-law trend of the form $y=An^{-0.74}$, with y being tumour absorbed dose (Gy), A being the baseline tumour absorbed dose at cycle 1 (Gy) and n being the cycle number. Tumour dose improvements were observed with front-loading the activity: Regimen 1 increased tumour dose by 15%, while Regimen 2 achieved a 34% increase compared to a flat dosing regimen, despite equivalent cumulative activity. ***Conclusion:*** Front-loading administered activity in PSMA targeted RLT appears to improve cumulative tumour absorbed dose compared to a flat dosing regimen, without any proportional increase in normal organ dose; this approach exploits the therapeutic index being at its peak during early cycles. This improvement correlates with the proportion of activity front-loaded. However, this approach must be carefully considered in the context of potential increased toxicity risks. The Phase 2 component of this study will compare the efficacy and safety of this dosing strategy with a fixed per-cycle activity approach, where the interval between the first 3 cycles is shortened to 3 weeks, to explore PSMA RLT dose optimisation with ^{177}Lu-rhPSMA-10.1.

EPS-189

Tumour Dosimetry - It's a Gray Area: Analysing the Importance of Lesion-Level Dosimetry Methods in ^{177}Lu-PSMA Targeted Therapy

B. Fongenie, *D. Stevens, N. Scott;*
Blue Earth Therapeutics, Oxford, UNITED KINGDOM.

Aim/Introduction: With the expanding use of radioligand therapy (RLT), dosimetry is increasingly playing a role as a method for drug pharmacokinetic comparisons and as a potential predictor of efficacy. Large cross-trial dosimetry comparisons would permit more robust analysis, but their validity may be undermined by methodological inconsistencies, particularly in tumour selection and contouring. This work analyses a range of tumour dosimetry methods used across ^{177}Lu-PSMA-targeted RLT studies and evaluates their impact within an ongoing Phase 1/2 study. ***Materials and Methods:*** Recent meta-analyses have collated ^{177}Lu-PSMA-targetted RLT dosimetry data from various studies. We categorized these studies by lesion dosimetry methods, focusing on lesion selection and contouring approaches. Absorbed dose estimates were compared across categories defined by significant methodological differences: CT-guided/manual selection and contouring, activity-guided/threshold-based selection and contouring and "other" representing any alternative or unknown approaches. Separately, a phase I experience assessed the impact of dosimetry method on tumour dose estimates. Two approaches were used for tumour selection and delineation. The first was an anatomy-based method; up to 5 tumours were selected blindly on CT (no detail on PSMA expression was provided to the reader) with contours defined by CT morphology. For the second, an activity-based method was used; up to 3 tumours were selected according to their relative uptake on SPECT-CT, tumour volume was determined using PSMA PET thresholding. ***Results:*** Of 16 dosimetry studies analysed, 5 used threshold-based contouring, 6 employed manual methods and 5 used alternative or unspecified methods. For tumour selection, 5 studies favoured avidity, 5 ignored avidity and 6 did not specify their approach. Whilst unknown methods limit statistical analysis of systematic differences, higher tumour absorbed doses were generated using threshold-based vs manual contouring. In the Phase I dosimetry experience, significant differences were found between methods. The anatomy-based method mean tumour dose was 2.4 Gy/GBq (0.4-6.7) compared to the activity-based method equivalent of 8.9 Gy/GBq (2.0-25.6). This represented a 3.7-fold increase in tumour dose. In a minority of cases, where the same lesion was

coincidentally selected for analysis by both methods, this was a 2.6-fold increase. ***Conclusion:*** These comparisons demonstrate the wide variance in dosimetry approaches and reporting. Without harmonisation of methods, the utility of dosimetry data, and the establishment of dose response relationships will remain confounded. At a minimum, studies employing dosimetry should clearly state their lesion selection and contouring methods to allow for more robust and unbiased comparisons.

EPS-190

Intraindividual tumor dosimetry of monomer [^{90}Y] Y-FAPI-46 vs dimer [^{90}Y]Y-DOTAGA-Glu-(FAPI)2 FAP radioligand therapy of advanced stage solid tumors

P. Fragoso Costa[1], *W. Jentzen*[1], *K. Pabst*[1], *I. Mavroeidi*[2], *H. Lanzafame*[1], *R. Hamacher*[2], *J. Siveke*[2], *S. Bauer*[2], *F. Rösch*[3], *J. Kurth*[4], *M. Heuschkel*[4], *K. Herrmann*[1], *D. Kersting*[1], *W. Fendler*[1];
[1]*Clinic for Nuclear Medicine, University Hospital Essen, University Duisburg-Essen, Essen, GERMANY,* [2]*Department of Medical Oncology, West German Cancer Center, University Hospital Essen, University of Duisburg-Essen, Essen, GERMANY,* [3]*Department of Chemistry—TRIGA Site, Johannes Gutenberg-University Mainz, Germany, Frankfurt, GERMANY,* [4]*Department of Nuclear Medicine, Rostock University Medical Center, Essen, GERMANY.*

Aim/Introduction: Radioligand therapy with yttrium-90-labeled inhibitors of FAP (FAPI) was introduced clinically with the monomer ligand FAPI-46. The therapeutic value of this RLT is limited by the ligand short residence time in tumors. A promising strategy to enhance tumor retention is to improve the radioligand's pharmacology for its target by dimerizing the binding moiety. This has been demonstrated with [^{177}Lu]Lu-DOTAGA-Glu-(FAPI)2 dimer in patients with medullary thyroid cancer, sarcoma and breast cancer. We present tumor dosimetry in patients that received previous [^{90}Y]Y-FAPI-46 treatment but were excluded to further therapy due to insufficient tumor absorbed doses; thereafter, they were selected for treatment with [^{90}Y]Y-DOTAGA-Glu-(FAPI)2 dimer. ***Materials and Methods:*** Five patients who were pretreated with two cycles [^{90}Y]Y-FAPI-46 were enrolled. An activity of 3.1±0.9 GBq of [^{90}Y]Y-DOTAGA-Glu-(FAPI)2 was intravenously administered in the first cycle (n=5). At each treatment cycle, patients underwent 4 PET/CT scans (1, 4, 20 and 48 h post injection) of areas of tumoral manifestation (solitary fibrous tumors, cholangiocarcinoma and sarcoma). Tumor volumes were derived from intratherapeutic CT or pretherapeutic [^{68}Ga]Ga-FAPI-46 PET images. Effective half-lives and uptake were calculated. For tumor absorbed dose estimation, the sphere model implemented in OLINDA was applied. ***Results:*** Tumor dosimetry comparison was performed at lesion-per-lesion level. A total of 9 primary and metastatic lesions were analyzed (locations: lung, liver, muscle, fatty tissue, bone, and lymph nodes). At a lesion-per-lesion level, FAP-dimer dosimetry showed a mean fold-increase of 3.2 (max: 5.5) on lesion absorbed dose coefficients when compared to the last cycle of the monomer [^{90}Y]Y-FAPI-46. This increase was characterized by an average 1.4-fold increase in lesion maximal uptake and a 2.3-fold increase in lesion effective half-life.Lesions treated with [^{90}Y]Y-DOTAGA-Glu-(FAPI)2 displayed a mean ±SD absorbed dose coefficient of 4.68 (±3.03) Gy/GBq and effective half-lives of 18.9(±3.5) h, while those for [^{90}Y]Y-FAPI-46 displayed 1.77 (±1.23) Gy/GBq and effective half-lives of 8.2 (±2.1) h. ***Conclusion:*** [^{90}Y]Y-DOTAGA-Glu-(FAPI)2 exhibits both prolonged effective half-life as well as increased uptake in tumor, showing promise as an improved therapeutic agent for FAP-expressing tumors. Further absorbed dose-response analyses and dosimetry of organs at risk are warranted.

EPS-191

Stability, Biodistribution, and Patient Dosimetry of [^{177}Lu] Lu-FAP-2286 Radionuclide Therapy

K. Akçay*, T. Toklu, G. Beydagi, H. Adıgüzel, B. Caner, L. Kabasakal, N. Alan;*
Yeditepe University, İstanbul, TÜRKIYE.

Aim/Introduction: Fibroblast activation protein (FAP) is a promising target for the diagnosis and treatment of various tumors. Although the FAP-targeted peptides FAPi-04 and FAPi-46 labeled with ^{68}Ga are widely used for diagnostic purposes, their limited retention hampers their therapeutic utility. FAP-2286, on the other hand, is a promising candidate for therapeutic applications. This study aimed to evaluate the in-vitro and in-vivo stability, biodistribution, and organ and tumor dosimetry of the radiopharmaceutical [^{177}Lu] Lu-FAP-2286. ***Materials and Methods:*** A total of seven therapeutic administrations were performed in five patients (mean age: 61.0±15.3 years; F/M: 2/3) with positive uptake on [^{68}Ga]Ga-FAPi-46 or [^{68}Ga]Ga-FAP-2286 imaging. Each treatment involved an average administration of 215±14.7 mCi of [^{177}Lu]Lu-FAP-2286. Whole-body anterior and posterior planar scans and SPECT/CT images were acquired at 4, 24, 72, and 120 hours post-infusion. Photon attenuation, scatter, and detector/collimator response corrections were applied to the SPECT data. Blood samples were collected at multiple time points up to 120 hours post-infusion for red bone marrow dosimetry and in-vivo stability assessment. Whole-body regions of interest and volumes of interest for kidneys, liver, and tumor lesions were delineated. Time-activity curves were generated and fitted with mono- or bi-exponential functions using MATLAB R2013a to derive cumulative activities. Absorbed dose estimations were performed using IDAC-Dose 2.1 software. ***Results:*** Two patients had pancreatic adenocarcinoma, one had neuroendocrine carcinoma, and two had soft tissue sarcoma. The in-vitro stability of the radiopharmaceutical was determined to be at least 41 hours, while in-vivo stability in blood was confirmed for at least 24 hours. The mean absorbed doses were 0.50 ± 0.19 Gy/GBq for kidneys, 0.030 ± 0.014 Gy/GBq for liver, and 0.054 ± 0.014 Gy/GBq for red bone marrow. The mean tumor dose was calculated as 5.97±3.85 Gy (range: 1.10-18.52 Gy). ***Conclusion:*** No adverse events were observed during therapy, and all patients tolerated the treatment well. At the administered activity levels, toxicity thresholds were not exceeded for the kidneys or bone marrow. Compared to the only published study in the literature, similar bone marrow doses were observed, while renal doses were found to be lower in this study. However, due to the previous study reporting dose data only for bone metastases, a direct comparison with soft tissue tumor doses presented here is not feasible. In conclusion, [^{177}Lu]Lu-FAP-2286 appears to be a promising and safe radionuclide therapeutic agent with potential for clinical application in the treatment of various malignancies.

EPS-192

Absorbed Dose Estimate of Neoadjuvant 177Lu-PSMA-I&T Therapy Prior to Oligometastasis Directed SBRT in Patients with Hormone Sensitive Oligorecurrent Prostate Cancer:Preliminary analysis from the Randomized Phase 2 LUNAR Trial (NCT05496959)

Z. Ells[1], *C. Meyer*[1], *M. Lauria*[1], *K. Kimura*[1], *V. Ludwig*[1], *L. M. Unterrainer*[1,2], *A. Farolfi*[1,3], *D. Sennung*[1], *K. Masri*[1], *L. F. Valle*[1], *M. L. Steinberg*[1], *C. Felix*[1], *R. Alano*[1], *K. Adame*[1], *A. Daley*[1], *J. Czernin*[1], *M. Dahlbom*[1], *A. U. Kishan*[1], *J. Calais*[1];
[1]*University of California - Los Angeles, Los Angeles, CA, UNITED STATES OF AMERICA,* [2]*Ludwig-Maximilians University, Munchen, GERMANY,* [3]*IRCCS Azienda Ospedaliero-Universitaria di Bologna, Bologna, ITALY.*

Aim/Introduction: The phase II LUNAR trial randomized (1:1) oligorecurrent hormone sensitive prostate cancer (HSPC) patients with 1-5 target lesions visible by PSMA-PET to neoadjuvant ^{177}Lu-PSMA-I&T and stereotactic body radiotherapy (SBRT) versus SBRT alone. Here we report a preliminary analysis of the ^{177}Lu-PSMA-I&T dosimetry estimates in organs and tumors. ***Materials and Methods:*** Patients randomized to the investigational group received 2 cycles of neoadjuvant 177Lu-PSMA-I&T (6.8 GBq/cycle) prior to treatment with SBRT. Quantitative SPECT images were acquired at 4, 24, and 72-96h post-injection of the first cycle of 177Lu-PSMA-I&T (vertex to mid-thighs; 60 projections per

detector; 10s per view; reconstructed with 48 iterations 1 subset and no filtering). A low-dose CT scan was performed directly after the SPECT for attenuation correction. Kidneys, salivary glands, lacrimal glands and liver were delineated with deep learning-assisted segmentation, while lumbar vertebrae were manually segmented as a surrogate for bone marrow. Tumor segmentations were transferred from SBRT target volumes to the SPECT/CT series. Multiple timepoint voxel-based dosimetry was used to estimate the absorbed doses (AD). Registration between timepoints was manually verified for each segmentation. Time-activity curves were fit using a mono-exponential function. Partial volume effects were accounted for using a phantom-based recovery coefficient function (using identical SPECT acquisition and reconstruction parameters). ***Results:*** From September 2022 to November 2023, 92 patients were randomized (n=47 SBRT alone, n=45 177Lu-PSMA+SBRT). Median age was 69 and median PSA was 1.1 ng/dL. 38% of patients had M1b disease and 43% of had solitary lesions. The median number of lesions per patient was 2 (1-9): with a PSMA PET median SUVmax of 3.6 (1.1 - 45.3). A total of 15/45 patients from the investigational arm were included in this preliminary analysis. The AD to the kidneys, parotid glands, submandibular glands, lacrimal glands, liver, and bone marrow were 0.36 ± 0.11; 0.21 ± 0.10; 0.26 ± 0.10; 0.74 ± 0.48; 0.03 ± 0.02; and 0.01 ± 0.002 Gy/GBq, respectively. The mean dose and volume of bone (n=10), lymph node (n=16), and soft tissue (n=1) lesions were 0.33 ± 0.65 Gy/GBq (8.67 ± 3.43 mL), 0.58 ± 0.76 Gy/GBq (3.95 ± 2.90 mL), and 0.79 Gy/GBq, (3.76 mL), respectively. ***Conclusion:*** In this preliminary report of 15 patients with oligorecurrent prostate cancer treated with ^{177}Lu-PSMA-I&T, the dose estimates to organs at risk were comparable to previously published data. There was substantial heterogeneity in tumor absorbed dose estimates on both inter- and intra- patient levels.

EPS-193

Therapeutic potential of DOTAGA.Glu.(FAPI)$_2$ and DO3A.Glu.(FAPI)$_2$ with human dosimetry extrapolation for 177-lutetium and 161-terbium

A. Bilinska[1], *N. Kumar*[1], *S. Gnesin*[2], *T. Läppchen*[1], *E. Menéndez*[1], *M. Martin*[3], *F. Rösch*[3], *A. Rominger*[1], *E. Gourni*[1];
[1]*Department of Nuclear Medicine, Inselspital, Bern University Hospital, Bern, SWITZERLAND,* [2]*Institute of Radiation Physics, Lausanne University Hospital, Lausanne, SWITZERLAND,* [3]*Department of Chemistry–TRIGA site, Johannes Gutenberg-University Mainz, Mainz, GERMANY.*

Aim/Introduction: The development of FAPI-based radiopharmaceuticals has gained significant interest due to the potential to target multiple tumor types. ^{177}Lu-labeled FAPI agents are under active investigation, while ^{161}Tb offers potential advantages through the emission of conversion and Auger electrons. This study provides the first comparative in vivo evaluation of two ^{177}Lu-labeled FAPI dimers, DOTAGA.Glu.(FAPI)$_2$ and DO3A.Glu.(FAPI)$_2$, with human dosimetry extrapolation supporting future application of both ^{177}Lu and ^{161}Tb in targeted radionuclide therapy. ***Materials and Methods:*** DOTAGA.Glu(FAPi)$_2$ and DO3A.Glu(FAPi)$_2$ were labeled with lutetium-177. They were evaluated in vivo (biodistribution, metabolic stability in blood , SPECT/CT imaging and dosimetry) on PC3-mice. Furthermore, extrapolation of the murine dosimetry data to adult human estimates was performed for [^{177}Lu]Lu-DOTAGA.Glu.(FAPI)$_2$, [^{177}Lu]Lu-DO3A.Glu.(FAPI)$_2$, [^{161}Tb]Tb-DOTAGA.Glu.(FAPI)$_2$ and [^{161}Tb]Tb-DO3A.Glu.(FAPI)$_2$, using the OLINDA/EXM v.2.1 software. ***Results:*** [^{177}Lu]Lu-DOTAGA.Glu(FAPi)$_2$ and [^{177}Lu]Lu-DO3A.Glu(FAPi)$_2$ were prepared with molar activities of 30 MBq/nmol for the animal studies. Metabolic studies performed after 30 min p.i., revealed that both radiopharmaceuticals are stable in vivo. Biodistribution studies of [^{177}Lu]Lu-DOTAGA.Glu(FAPi)$_2$ and [^{177}Lu]Lu-DO3A.Glu(FAPi)$_2$ showed that the tumor uptake was 16.2±2.5 and 15±1.2% IA/g at 4h p.i., respectively. Tumor uptake slowly decreased over time, reaching 5.1±0.1 and 2.8 0.4 %IA/g at 48 h, respectively. Both radiopharmaceuticals exhibited low blood retention levels, decreasing from around 2.0±0.1% IA/g at 4 h p.i to 0.2±0.1 and 0.03±0.01 %IA/g at 48 and 96h p.i. Additionally, they both demonstrated favorable tumor-to-normal organ ratios at all tested time points. These findings are well illustrated by SPECT/CT imaging. In mice, tumor effective and biological half-lives for both radiopharmaceuticals were in the same range (~45h). However, [^{177}Lu]Lu-DOTAGA.Glu.(FAPI)$_2$ showed prolonged effective half-lives in non-tumor organs compared to [^{177}Lu]Lu-DO3A.Glu.(FAPI)$_2$. The extrapolated human (adult male/female) absorbed dose estimates (Gy/GBq) for [^{177}Lu]Lu-DOTAGA.Glu.(FAPI)$_2$ were generally higher across most organs compared to [^{177}Lu]Lu-DO3A.Glu.(FAPI)$_2$, particularly in the liver (0.16/0.20 vs. 0.060/0.073), kidneys (0.04/0.05 vs. 0.021/0.025), and salivary glands (0.103/0.126 vs. 0.073/0.088). Human extrapolation of ^{161}Tb-labeled radiotracers delivered ~38% higher absorbed doses in tissues as compared to their ^{177}Lu-labeled counterparts. Based on our dosimetric analysis, the red bone marrow was identified as the potential dose-limiting organ for both radiopharmaceuticals in the context of possible clinical translation. ***Conclusion:*** Our study provide evidence for the potential use of [^{177}Lu]Lu-DOTAGA.Glu.(FAPI)$_2$ and [^{177}Lu]Lu-DO3A.Glu.(FAPI)$_2$ as therapeutic radiotracers for targeting FAP-expressing tumors. Human dosimetry projections for both ^{177}Lu and ^{161}Tb offer valuable insights into the clinical translation of those FAP-targeted radiopharmaceuticals.

EPS-194

Development of ^{206}Bi as a SPECT Imaging Radiotracer to Annotate the in vivo Biodistribution of Bismuth Daughters

L. Wehner*, E. Aluicio-Sarduy, A. O. Adeniyi, L. Batley, B. Bednarz, J. W. Engle, R. Hernandez;*
University of Wisconsin-Madison, Madison, WI, UNITED STATES OF AMERICA.

Aim/Introduction: Alpha-emitting radionuclides have shown encouraging results in the treatment of advanced-stage cancers. However, the renal redistribution of Bismuth daughters ($^{213/212}$Bi) during targeted alpha therapy (TAT) decay leads to dose-limiting nephrotoxicity. To better understand the in vivo fate of radioactive Bismuth and reduce its renal deposition, we developed ^{206}Bi as a SPECT imaging radiotracer to investigate the mechanism of bismuth distribution to the kidney. ***Materials and Methods:*** ^{206}Bi ($T_{1/2}$ = 6.24 d) was produced via irradiation of an isotopically enriched ^{206}PbO target on a 16 MeV GE PETtrace cyclotron. In vitro, renal proximal tubule epithelial cells, RPTEC/TERT1, were seeded in 12-well plates and incubated with 0.074 MBq of ^{206}Bi alone or in combination with 1 mM $Bi(NO_3)_3$, 1 mM $FeCl_3$, or 15 µM apo-transferrin for 0.5h, 3h, 6h, and 12h (3-6 wells per condition). Membrane-bound and internalized cellular fractions were collected and quantified via gamma counting. In vivo, 1.3 MBq ^{206}Bi-citrate was intravenously injected into 4-week-old ICR mice (n = 12 total) for serial biodistribution at 4h, 26h, 48h, and 73h post-injection. Major tissues were quantified via gamma counting and the contralateral kidney cryosectioned for digital autoradiography. Longitudinal SPECT/CT imaging and serial biodistribution at 0.5h, 7h, 24h, 52h, 72h, 96h, and 144h post-injection were acquired in an ICR mice intravenously administered 2.7 MBq of ^{206}Bi-citrate. ***Results:*** Significant ($P < 0.0001$) internalization of ^{206}Bi was observed in RPTEC/TERT1 cells at all timepoints when treated with 1 mM $Bi(NO_3)_3$. After 12h, 46.3% ± 7.9 of the total activity was internalized when treated with 1 mM $Bi(NO_3)_3$ compared to 6.1% ± 2.4 in the ^{206}Bi control and 6.6 ± 1.3% in the 1 mM $FeCl_3$ group. When co-incubated with 1 mM $Bi(NO_3)_3$ and 15 µM apo-transferrin, ^{206}Bi internalization was further increased to 58.6% ± 2.5. In vivo, pronounced kidney uptake at 4h was quantified at

132.5 %IA/g ± 23.5 via gamma counting, gradually decreasing to 2.2 %IA/g ± 2.3 at 72 h. In vivo, SPECT/CT imaging similarly showed rapid, selective, and elevated accumulation to the kidneys and a protracted clearance with a $T_{1/2}$ of approximately 15.5 hr. Ex vivo autoradiography corroborated primarily ^{206}Bi distribution to the renal cortex. ***Conclusion:*** This work represents the first account of ^{206}Bi as a SPECT imaging radiotracer to characterize the in vivo distribution of radiobismuth and serves as an essential tool for devising interventions that can reduce the accumulation of these nephrotoxic radionuclides during TAT.

EPS-195

Exploiting PARP Trapping to Enhance the DNA-Targeting Efficiency of [^{123}I]CC1

L. Hernandez Cano[1], *N. Delgado Mayenco*[1], *H. Kramer*[1], *E. Diekstra*[1], *F. Amoroso*[1], *G. Alachouzos*[2], *W. Szymanski*[2,3,4], *M. van Vugt*[5], *B. Cornelissen*[1];
[1]*Department of Nuclear Medicine and Molecular Imaging Department, University Medical Center Groningen, University of Groningen, Groningen, NETHERLANDS,* [2]*Stratingh Institute for Chemistry, Faculty for Science and Engineering, University of Groningen, Groningen, NETHERLANDS,* [3]*Department of Radiology, Medical Imaging Centre, University of Groningen, University Medical Center Groningen, Groningen, NETHERLANDS,* [4]*Department of Medical Chemistry, Photopharmacology and Imaging, University of Groningen, Groningen, NETHERLANDS,* [5]*Department of Medical Oncology, University of Groningen, University Medical Center Groningen, Groningen, The Netherlands, Groningen, NETHERLANDS.*

Aim/Introduction: [^{123}I]CC1, an olaparib-based PARP inhibitor radiolabeled with an Auger electron emitter, has demonstrated a potent cytotoxic effect, both in vitro and in vivo, reducing tumor cell survival, and inhibiting tumor growth. We hypothesize that the cytotoxic effect of [^{123}I]CC1 is primarily driven by its ability to increase PARP levels associated with chromatin, prolonging the time during which ^{123}I can induce DNA damage. In this study, we analyzed if modulating the PARylation cycle affects radionuclide delivered to DNA. For this, we selected different drugs that impact PARP trapping. PARG inhibitor JA2131 decreases PARP trapping, while MMS (methyl methanesulfonate) increase DNA-associated PARP levels. ***Materials and Methods:*** A 500 µL suspension of 10 million PSN1 and U87 human cancer cells line was treated with 100 kBq [^{123}I]CC1 for 30 min at 37°C, either alone or after pretreatment with 0.01% MMS or 10 µM PARGi, followed by fractionation. PARP levels in the chromatin (PARP bound to DNA) and in the nuclear soluble fraction (free PARP) were analyzed by western blot. Additionally, a γ-counter was used to quantify the percentage of ^{123}I in the different cellular fractions. Total PARP and γH2AX were assessed by western blot to confirm that variations in PARP trapping levels are due to changes in DNA-associated PARP, rather than alterations in the PARP cycle or ^{123}I-induced DNA damage. ***Results:*** Exposure to 100 kBq (equivalent to 50 nM) [^{123}I]CC1 increases DNA-associated PARP, bringing it closer to DNA and thereby enhancing its ability to induce DNA damage. This result aligns with the cytotoxic activity of [^{123}I]CC1 previously reported by Chan et al 2023. Pretreatment with MMS leads to an increase in PARP trapping, which furthermore correlates with an increase in ^{123}I signal in the chromatin. Conversely, pretreating with PARGi reduces PARP trapping and decreases the radioactivity delivered to the nucleus. ***Conclusion:*** [^{123}I]CC1, at low concentrations and activities, prevents PARP dissociation from DNA, thereby enhancing the ability to produce substantial DNA damage. Moreover, modulating the PARylation cycle with MMS or PARGi alters DNA-associated PARP levels and the percentage of ^{123}I in the chromatin. These results confirm that [^{123}I]CC1 effectively tracks PARP and highlights the potential of combining it with other agents to enhance therapeutic efficacy. ***References:*** Chan, C. Y. et al. [123I]CC1: A PARP-Targeting, Auger Electron-Emitting Radiopharmaceutical for Radionuclide Therapy of Cancer. J Nucl Med jnumed.123.265429 (2023) doi:10.2967/JNUMED.123.265429.

EPS-196

Exploring combinatory treatments to enhance targeted α- and β-radionuclide therapy in prostate cancer

M. Sabatella*, P. Engbers, T. Heredia-Genestar, A. Gebara Garcia de Lima, E. Hooijman, E. de Blois, J. Nonnekens;
Erasmus MC, Rotterdam, NETHERLANDS.*

Aim/Introduction: Prostate cancer (PCa) is the most common cancer in men in Europe, with about 318.800 cases and 37.600 deaths annually[1]. While localized PCa is therapeutically well managed with surgery or external beam radiotherapy (EBRT), metastatic PCa remains a major clinical challenge with limited curative options. Targeting radionuclide therapy (TRT) using prostate specific membrane antigen (PSMA)-targeting radiopharmaceuticals labelled with alpha or beta emitters has emerged as powerful treatment option. However, despite promising results in some patients, TRT outcomes remain inconsistent and off-targeted toxicity remains a concern. In this study, we explored novel combinatory treatment strategies to enhance the efficacy of TRT in PCa. ***Materials and Methods:*** We investigated combinatory treatments targeting the DNA damage response and cell cycle pathways, both critical in the response to radiation. PC3-PIP cells (PCa cells overexpressing PSMA) were treated with PSMA-I&T radiolabelled with either lutetium-177 or actinium-225, alone or in combination with a 700-compound drug library. EBRT was included as control. Cell viability was assessed using the CellTiter-Glo assay, comparing the ratio of luminescence signal from combinatory treatment versus monotherapy. Selected hits are currently being validated using viability and clonogenic assays. ***Results:*** We identified 171 possible radiosensitizers for [^{177}Lu]Lu-PSMA-I&T, 154 for [^{225}Ac]Ac-PSMA-I&T and 130 for EBRT. Among these, drugs targeting the DNA damage response factors ATM/ATR (1), DNA-PKcs (4) and PARP (5) or cell cycle regulation factors (13) have been identified as potential radiosensitizers in combination with TRT but not EBRT. Interestingly, 2 drugs interfering with cell division and the inflammatory response have been identified as potential radiosensitizer specifically for [^{225}Ac]Ac-PSMA-I&T. ***Conclusion:*** Quality control of our screening approach demonstrated high reproducibility. Further validation is ongoing to determine optimal concentrations, dosing and timing of these combinations for maximizing therapeutic efficacy. ***References:*** 1. WHO World Health Organization (2020). Cancer Today. Int. Agency Res. 418, 1-2.

EPS-197

Relative Biological Effectiveness (RBE) of ^{225}Ac-PSMA-I&T in-vitro treatment and its dependence on cellular incubation time

P. Hawarihewa[1], *M. Rumiantcev*[1], *H. Scherthan*[2], *R. Oos*[1], *M. Zacherl*[1], *F. Lindheimer*[1], *G. Böning*[1], *R. A. Werner*[1,3], *S. Ziegler*[4], *M. Brendel*[1,5,6], *A. Delker*[1];
[1]*LMU University Hospital, Munich, GERMANY,* [2]*Bundeswehr Institute of Radiobiology affiliated to the Univ. of Ulm, Munich, GERMANY,* [3]*Johns Hopkins School of Medicine, The Russell H Morgan Department of Radiology and Radiological Sciences, Division of Nuclear Medicine and Molecular Imaging, Baltimore, MD, UNITED STATES OF AMERICA,* [4]*Department of Nuclear Medicine, Hannover Medical School (MHH), Hannover, GERMANY,* [5]*SyNergy, University of Munich, Munich, GERMANY,* [6]*DZNE - German Center for Neurodegenerative Diseases, Munich, GERMANY.*

Aim/Introduction: The relative biological effectiveness (RBE) is a critical, yet underexplored parameter in targeted radionuclide therapy due to the complex radiobiological behaviour of alpha, beta, and Auger emitters, time-dependent absorbed dose rates, as well as the heterogeneous radionuclide distribution at the cellular

level. Despite the clinical benefits of ^{225}Ac-PSMA and ^{177}Lu-PSMA treatment, investigations on the associated microdosimetric characteristics and cellular RBE are rare and especially missing following prolonged treatment. This study aims to address this important gap. ***Materials and Methods:*** LNCaP prostate cancer cells were treated with [^{177}Lu]Lu-PSMA-I&T and [^{225}Ac]Ac-PSMA-I&T to evaluate cellular time-activity-curves and S-values for cellular dosimetry, as well as clonogenic survival. The uptake assays were used (percentage of added activity per 100,000 cells (%AA/100,000 cells)) to quantify the total, membrane-bound, and internalized amount of radioactivity after different time points of incubation (3, 6, 18, and 24 hours) with 0.3 MBq/mL of [^{177}Lu]Lu-PSMA-I&T or 0.3 kBq/mL [^{225}Ac]Ac-PSMA-I&T. Membrane-bound and internalized fractions of cellular activity were further used to determine cellular S values using MIRDcell. The RBE of [^{225}Ac]Ac-PSMA-I&T was calculated based on the cell survival curves derived from clonogenic survival assays, the cellular dosimetry, and using ^{177}Lu as reference radiation. Therefore, cells were treated with varying activity concentrations of [^{177}Lu]Lu-PSMA-I&T (0.01 MBq/mL - 1 MBq/mL) and [^{225}Ac]Ac-PSMA-I&T (0.001 kBq/mL - 1 kBq/mL) for 3 and 24 hours, to assess both, short-term and long-term survival. ***Results:*** Both radiopharmaceuticals showed variable uptake patterns over 24 hours, with no significant difference between the membrane-bound and internalized fractions. For [^{177}Lu]Lu-PSMA-I&T, both the internalized fraction and overall uptake increased over time, peaking at 18 hours (internalized: 4.0 ±1.6 %AA/100,000 cells; total activity: 6.5±1.8 %AA/100,000 cells). Similarly, [^{225}Ac]Ac-PSMA-I&T showed the highest overall uptake at 18 hours (total activity: 4.0±1.7 %AA/100,000 cells). The absorbed doses after 24 hours of treatment were 36 Gy for ^{177}Lu-PSMA-I&T (0.3 MBq/mL) and 13 Gy for ^{225}Ac-PSMA-I&T (0.3 kBq/mL). For both radiopharmaceuticals clonogenic survival decreased linearly with the absorbed dose to the cell. The cellular RBE of [^{225}Ac]Ac-PSMA-I&T after 24 hours of treatment was 11.9 relative to [^{177}Lu]Lu-PSMA-I&T. However, for short-term exposure (3 hours of treatment), the RBE was lower, with a value of 3.6. ***Conclusion:*** This study disclosed similar cellular uptake of [^{177}Lu]Lu-PSMA-I&T and [^{225}Ac]Ac-PSMA-I&T and highlights the significantly higher RBE of the alpha emitter [^{225}Ac]Ac-PSMA-I&T during long-term compared to short-term incubation. In subsequent in vitro studies, DNA damage shall be used as the second RBE endpoint.

EPS-198

Development of a simulated preclinical database for 3D AI-based dosimetry prediction based on 2D nuclear imaging

G. Savvidis[1], *V. Paneta*[1], *V. Eleftheriadis*[1], *V. Lagaki*[1], *D. Anestis*[1], *S. Sarpaki*[1], *T. Karampelas*[1], *L. Fysikopoulos*[1], *G. Loudos*[1], *P. Papadimitroulas*[1,2];
[1]*BIOEMTECH, Athens, GREECE,* [2]*Medical Informatics Laboratory, School of Medicine, University of Thessaly, Larissa, GREECE.*

Aim/Introduction: We present a methodology for creating a simulated dosimetry database, utilizing Monte Carlo (MC) simulations driven by CT and SPECT preclinical imaging data. The complete database comprises numerous triplets, each consisting of a 3D simulated dose map, a 3D SPECT image, and a corresponding 2D planar image. The aim is to exploit the dosimetry simulation outputs as ground truth to train an AI model to directly estimate 3D dose distributions from 2D planar images. ***Materials and Methods:*** The input dataset comprises paired ^{111}In SPECT/CT scans, representing respective activity and attenuation maps. These pairs serve as inputs for MC simulations to generate corresponding three-dimensional dosimetry distributions. Simulations were conducted using GATE10, an extensively validated, open-source simulation platform based on the Geant4 framework[1]. Each simulation utilized 10^8 primary particles and was executed on the Leonardo high performance computing (HPC) center. Prior to simulation, all image pairs were resampled to an isotropic voxel size of 0.5×0.5×0.5 mm^3 and spatially co-registered to ensure precise alignment between SPECT and CT components. A preprocessing step involving noise removal was applied to enhance the quality of the activity maps and improve dosimetric accuracy. The generated 3D dose maps were subsequently paired with their corresponding 2D planar projections to form the training dataset for a GenAI model. A conditional Generative Adversarial Network (cGAN), specifically a Vox2Vox architecture[2] optimized for voxel-wise image translation tasks, was used. ***Results:*** MC simulations were completed for 300 image pairs, with the final dataset expected to include ~1,000 pairs. The resulting dose distributions preserve the high spatial resolution of 0.5×0.5×0.5 mm^3. The use of 10^8 primary particles per simulation yielded low dose statistical uncertainty below 2.5% in regions of interest. A preliminary GenAI model was trained on the initial dataset of 300 planar-volumetric image pairs to learn direct mapping from 2D input images to 3D dosimetric predictions. ***Conclusion:*** As Monte Carlo-based dosimetry remains the gold standard for internal dose estimation, the dataset generated through this approach offers a robust foundation for developing AI-driven predictive dosimetry models. Future efforts will focus on extending this framework to additional therapeutic radionuclides, such as ^{177}Lu, enabling accurate internal dose estimations directly from imaging data. ***References:*** 1. D. Sarrut et al., A review of the use and potential of the GATE Monte Carlo simulation code for radiation therapy and dosimetry applications. 2014 2. M.D. Cirillo et al., Vox2Vox: 3D GAN for Brain Tumour Segmentation. 2020.

1210

Tuesday, October 7, 2025, 08:00 - 09:30
Room 116

CTE 6 -Technologists Committee: Fibroblast-Activated: the 68Ga-FAPI in Different Types of Cancer

OP-560

Fibroblast Activation Protein – The Science Behind 68Ga-FAPI Imaging
K. Pabst*; University Hospital of Essen, Dept. of Nuclear Medicine, Essen, GERMANY.*

OP-561

How to Perform FAPI PET?
M. Bentestuen*; University Hospital of Aalborg, Dept. of Nuclear Medicine, Aalborg, DENMARK.*

OP-562

68Ga-FAPI Imaging – Practical Considerations for Technologists
B. Emmerson*; Peter MacCallum Cancer Center, Molecular Imaging and Therapeutic Nuclear Medicine, Cancer Imaging, Melbourne, AUSTRALIA.*

1211

Tuesday, October 7, 2025, 08:00 - 09:30
Room 111

EU Policy Symposium 1 - Policy & Regulatory Affairs Council: From Policy to Patients: Building Readiness for Nuclear Medicine Innovation in Europe

OP-564a

SIMPLERAD Legacy: Regulatory Lessons
M. Lassmann*; University of Wurzburg, Würzburg, GERMANY.*

OP-564b
Carrying the Torch: PRISMA Vision
***S. Kaijaluoto**; Finnish Radiation and Nuclear Safety Authority , Vantaa, FINLAND.*

OP-565
Anticipating the Wave: How Many Patients, How Soon?
***U. Holzwarth**; Joint Research Centre - European Commission, Ispra, ITALY.*

OP-566
Growing the capacity of healthcare systems for Radioligand Therapy
***K. Goffin**; KU Leuven, Leuven, BELGIUM.*

OP-567
Right Patient, Right Time: Streamlining Access to Innovation
***Anne-L. Giraudet**; Centre Léon Bérard, Lyon, FRANCE.*

1301

Tuesday, October 7, 2025, 09:45 - 11:15
Auditorium

CME 10 - AI Committee: AI as Accelerator for NM Research

OP-568
Virtual Clinical Trials and AI-supported Clinical Trials Design
***P. Arsela**; Fondazione IRCCS Istituto Nazionale Tumori di Milano, AI-ON-Lab and Medical Oncology Deparment, Milan, ITALY.*

OP-569
AI for Radiopharmaceuticals' Development
***D. Jiang**; Union Hospital, Tongji Medical College, Huazhong University of Science and Technology, Department of Nuclear Medicine, Wuhan, CHINA.*

OP-570
AI for Quantitative Imaging
***D. Visvikis**; Inserm, LaTIM, Brest, FRANCE.*

OP-571
Digital Twins and Computational Nuclear Oncology, Where Do We Stand?
***L. Cavinato**; Politecnico di Milano, Department of Mathematics, Milan, ITALY.*

1302

Tuesday, October 7, 2025, 09:45 - 11:15
Room 112 (Arena)

Special Track 10 - Oncology & Theranostics Committee: Round Table: Residents for Residents

OP-572
Basic Knowledge on the Oncological EANM Procedural Guidelines
***S. Wallenius**; Department of Nuclear Medicine, Odense University Hospital, Odense, DENMARK.*

OP-573
Knowledge on the Clinical Application of EANM Oncological Guidelines
***A. Piñeiro-Donis**; Nuclear Medicine Service at the Virgen de las Nieves University Hospital, Granada, SPAIN.*

OP-574a
Image-based Cases: FDG in Oncology
***Alessia L. Daverio**; Gustave-Roussy, Nuclear Medicine, Paris, FRANCE.*

OP-574b
Image-based Cases: non- FDG in Oncology
***G. Bianciardi**; Alma Mater Studiorum, University of Bologna, Bologna, ITALY.*

1303

Tuesday, October 7, 2025, 09:45 - 11:15
Room 113

LIPS Session 10 - Paediatrics Committee: Update on Paediatric GI Nuclear Studies

OP-575
Gastrointestinal Reflux and Gastric Emptying
***Z. Bar-Sever**; Nuclear Medicine Institute at Schneider Children's Tel Aviv University, Tel Aviv, ISRAEL.*

OP-577
GI Transit Studies in Paediatrics
Role of Hepatobiliary Imaging in Neonatal Hepatitis
***A. Brink**; Nuclear Medicine and Diagnostic Imaging Section, IAEA, Vienna, AUSTRIA.*

1304

Tuesday, October 7, 2025, 9:45 - 11:15
Room 114

M2M Track - TROP Session - Radiopharmaceutical Sciences + Translational Molecular Imaging & Therapy Committee: Improving Radionuclide Production for Tracer Development

OP-579
Small cyclotron production of n.c.a. ^{103}Pd from Rh targets for targeted radionuclide therapy
***M. Salek**[1], K. S. Pedersen[2], C. Deville[2], A. C. Boggiano[1], J. C. Mixdorf[1], T. E. Barnhart[1], M. Jensen[2], J. W. Engle[1,3];*
[1]The University of Wisconsin – Madison, Department of Medical Physics, Madison, WI, UNITED STATES OF AMERICA, [2]Hevesy Laboratory, Technical University of Denmark, Roskilde, DENMARK, [3]The University of Wisconsin – Madison, Department of Radiology, Madison, WI, UNITED STATES OF AMERICA.

Aim/Introduction: ^{103}Pd is a promising radionuclide for radiopharmaceutical therapy needing improved production methods to make it available for research for radiobiological studies and targeted pharmaceuticals' development. ***Materials and Methods:*** K_d measurements: Branched DGA (Triskem) and TK200 (Triskem) resins and AG1-X8 anion exchange resin (Bio-Rad) (all 50.1 ± 0.3mg) were equilibrated with HCl (0.03 - 8.0M) and contacted by ^{nat}Pd and ^{nat}Rh (186 ± 5ppm). Supernatant metal concentrations were quantified by ICP-OES. Electrodeposition: Rh was electrodeposited onto graphite discs chosen for their chemical resistance and electrical and thermal conductivity. Electrodeposition proceeded under two conditions: a) constant current (10-20mA), 6.0M HCl electrolyte, 4g·L^{-1} of $RhCl_3$ at 70ºC, and b) constant current (5-10mA), 0.2M HCl with 1% w/v sodium sulfamate, 41g·L^{-1} $RhCl_3$ at 60ºC. Deposition rates of 0.6-1.0mg·mA^{-1} h^{-1} and thicknesses of 66-123mg·cm^{-2} were achieved. Irradiation: Optimal Rh target thicknesses of 0.301mm degrade $E_{0,p+}$ from 13MeV to ~5MeV.[1,2] Electroplated and foil targets

(for radiochemical development) were irradiated for up to 80µAh at 13 or 10MeV. Electrochemical Dissolution: Rh was dissolved by applying 10V AC in 6.0M HCl using a graphite electrode[3]. The Rh foil dissolves at a rate of 24.1±3.1mg·h^{-1}. Dynamic separation: Two separation procedures were tested. First, equilibrated columns containing 2.0g of AG1-X8 resin were loaded with $RhCl_3$ in 6M HCl and washed with 6M HCl and 0.03M HCl. [^{103}Pd]Pd$(NH_3)_2Cl_2$ was eluted in 1:1 1M NH_4OH:1M NH_4Cl. Alternatively, 1.0g branched DGA resin was loaded with dissolved Rh (18mg) in 3M HCl and washed with 3M HCl, eluting Rh. $^{103}PdCl_2$ was eluted in c.HCl. Titrimetric Binding: Evaporated eluate from the DGA column mixed with TETA in 0.1M ammonium acetate and heated to 80°C for 20 min. Conversion to the [^{103}Pd]Pd-TETA complex was tracked by radio-TLC. ***Results:*** Results from collaborating institutions are summarized in the table below. ***Conclusion:*** We report the fabrication of Rh targets, irradiation, dissolution, and separation of n.c.a. ^{103}Pd from a small cyclotron. This work was supported by the European Union's Horizon 2020 research and innovation program under grant agreement No 101008571 (PRISMAP). ***References:*** [1] doi.org/10.1016/S0168-583X(00)00190-7 [2] doi.org/10.1016/0092-640X(82)90004-3 [3] doi.org/10.1016/0020-708X(84)90080-2.

OP-580

Production of alpha emitters Ac-225, Bi-213, Pb-212, and Th-227 from Th-232 spallation at TRIUMF

H. Yang[1,2,3], *Q. Miao*[1], *B. McNeil*[1,2], *L. Wharton*[1], *S. W. McNeil*[1,3], *H. Meeres*[1,3], *C. Ramogida*[1,2], *P. Schaffer*[1,2,3], *C. Hoehr*[1];
[1]TRIUMF, Vancouver, BC, CANADA, [2]Simon Fraser University, Burnaby, BC, CANADA, [3]The University of British Columbia, Vancouver, BC, CANADA.

Aim/Introduction: Targeted Alpha Therapy (TAT) has garnered tremendous attention in recent years due to its promising clinical efficacy. There is a surge of preclinical and clinical work underway to explore TAT for various cancer treatments. One of the major hurdles for this fast-growing field is the limited availability of alpha-emitting radionuclides. To address this shortage, at TRIUMF, we have been using the Th-232 spallation reaction to produce and purify medically relevant alpha-emitters. ***Materials and Methods:*** A target cassette composed of a 10 g Th-232 foil is welded into a target frame and irradiated at up to 12,000 µAh with ~480 MeV protons . Targets are transferred to a hotcell and subsequently processed. After dissolution, bulk thorium is precipitated and removed by filtration. The solution is further processed using two columns to extract Ac-225 (containing Ac-227), which is also used as a generator for Bi-213. After allowing the Ac-225 decay, Ac-227 is then used as a generator for Th-227. Separately, the fraction containing Ra-225 is used to extract Ac-225 without Ac-227. Further to the above, the thorium precipitate is redissolved and used to extract Th-228 as a generator for Pb-212. ***Results:*** In our recent productions, six targets yielded 2.2 GBq Ac-225 containing Ac-227, and ~350 MBq of pure Ac-225 (from Ra-225). Previous work has also demonstrated that up to 6 MBq of Ac-227, and up to 120 MBq of Th-228 can be extracted from each target processing. From radiolabeling tests, gamma spectroscopy analysis, and ICP-MS analysis, good radionuclidic and chemical purity of Ac-225 was demonstrated. Ac-225, Bi-213, Pb-212, and Th-227 produced from this process have been used for radiochemistry testing and various preclinical studies. ***Conclusion:*** High-energy, proton-based spallation of Th-232 is an efficient method for producing several alpha-emitting isotopes of clinical interest. At TRIUMF, we have generated Ac-225, Bi-213, Pb-212, and Th-227 in quantities and purity suitable for radiochemistry and preclinical work. Further research is underway to explore other alpha-emitters that can potentially be extracted from this process.

OP-581

Optimal energy interval for the cyclotron production of ^{68}Ga using solid targets

M. Avila-Rodriguez, *A. Zarate-Morales, A. Flores-Moreno;
Facultad De Medicina, Universidad Nacional Autónoma De México, Ciudad De México, MEXICO.*

Aim/Introduction: Gallium-68 can be efficiently produced with compact cyclotrons via the ^{68}Zn(p,n)^{68}Ga nuclear reaction using solid targets. Natural Zinc possess five isotopes (^{64,66,67,68,70}Zn) and each of them leads to the production of Ga radioisotopes, so a high isotopic enrichment of ^{68}Zn is crucial to obtain ^{68}Ga with high radionuclidic purity, to be suitable for human use. But even in the event of using highly enrich ^{68}Zn (>99%) the radionuclidic purity of ^{68}Ga will be constrained to the proton energy because the competing (p,2n) reaction at E >12 MeV. ***Materials and Methods:*** To investigate the impact of isotopic enrichment and proton energy on the radionuclidic purity (RNP) of ^{68}Ga produced via the ^{68}Zn(p,n) reaction, a series of theoretical calculations were conducted taking into account the co-production of ^{66}Ga via the ^{66}Zn(p,n) reaction, and ^{67}Ga via the ^{67}Zn(p,n) and ^{68}Zn(p,2n) reactions. Calculations were made using the saturations yields from the NDS-IAEA home page [1] considering thick solid targets of ^{68}Zn with different isotopic enrichment (98.2, 99.0, and 99.5%), for different proton energies (11-15 MeV) and irradiation times of 1 and 2 half-lives of ^{68}Ga. ***Results:*** The optimal energy interval to produce ^{68}Ga by proton irradiation of ^{68}Zn targets is 13 → 9 MeV (Ein → Eout). This energy interval produces ^{68}Ga with a high RNP and optimizes the use of target material as it gives the best yield per unit mass. The target thickness for this energy interval, as determined from the analysis of the CSYR-plot [2] of this nuclear reaction, would be around 158 mg/cm^2, with a corresponding production yield at saturation of approximately 7.4 GBq/µA. The production yield of such a target would be 148 GBq of ^{68}Ga (68 min of bombardment at 40 µA) with a RNP of 99.95% at EOB. No surprisingly isotopic enrichment of ^{68}Zn improves RNP while longer irradiation times favors the production of impurities, as both ^{66}Ga and ^{67}Ga have longer half-life compared to ^{68}Ga. The maximum recommended proton energy for the cyclotron production of ^{68}Ga using solid targets is 14 MeV. ***Conclusion:*** Multi-curie levels of ^{68}Ga with RNP>99.9%, suitable for the radiolabeling of Ga-based radiopharmaceuticals for clinical applications, can be efficiently produced using solid targets by wisely selecting the isotopic enrichment of ^{68}Zn and proton energy to balance the yield and RNP. ***References:*** [1] NDS-IAEA, Charged-particle cross section database for medical radioisotope production. Available from: https://www-nds.iaea.org/medical/index.html, [2] Current Radiopharmaceuticals, 2021, 14, 340-353.

OP-582

Production of high-purity ^{212}Pb from natural ^{232}Th for alpha radionuclide therapy

R. Wang, *Z. Liu;
Changping Laboratory, Beijing, CHINA.*

Aim/Introduction: The ^{212}Pb/^{212}Bi in vivo generator is a promising candidate for alpha radionuclide therapy, as has been proved in multiple pre-clinical and clinical studies. However, the availability of ^{212}Pb is still rather limited, impeding the development of ^{212}Pb-based radiopharmaceuticals. At this moment, ^{212}Pb is usually supplied by the ^{224}Ra/^{212}Pb generators. As ^{212}Pb is a part from the decay chain of ^{232}Th, it is possible to establish a ^{212}Pb production route by directly separating ^{212}Pb from aged ^{232}Th as previously reported[1]. However, it remains challenging to obtain ^{212}Pb with low level of metallic impurities (e.g. Th) using the reported set-up. ***Materials and Methods:*** An optimized method for the extraction of ^{212}Pb with high purity from aged $^{232}Th(NO_3)_4$ solution is reported in this work. Initial separation of ^{212}Pb from ^{232}Th was achieved

by the PB resin. After being stripped from the PB resin by 8 M HCl or 0.2 M $(NH_4)_2HCit$, ^{212}Pb was further purified by either the AG50W X8-AG1 X8 route or the TK101-AG1 X8 route. The final ^{212}Pb product was dispersed in 0.01 M HCl, which can be directly used for radiolabeling. The chemical and radionuclide purity of the ^{212}Pb product were assessed by ICP-MS and HPGe detector measurements, respectively. Subsequently, the radiolabeling of purified ^{212}Pb on various peptides was systematically studied to achieve clinically relevant specific activity. ***Results:*** With the optimized method, more than 1.85 MBq of ^{212}Pb can be routinely obtained. The whole purification process can be completed within 2 h. Radionuclide purity of the purified ^{212}Pb was found to be as high as 99.9% while the main metallic impurities were at ppb level. The radiochemical yield of ^{212}Pb radiolabeling was found to be more than 85% for all tested peptides with a specific activity of ~185 kBq/nmol. ***Conclusion:*** In conclusion, a simple but efficient method for ^{212}Pb extraction from natural ^{232}Th is described. The ^{212}Pb product was found to be both chemical and radionuclide pure and can be used for radiolabeling with high radiochemical yield and specific activity. This work gave a good example for producing ^{212}Pb without the use of complex nuclear facilities, providing a possible solution to the shortage of ^{212}Pb in pre-clinical studies. ***References:*** 1. Chen, J.; Xu, M.; Liu, Y.; Duan, D.; Han, Y.; Liu, Z., Isolation of ^{212}Pb from natural thorium for targeted alpha-therapy. Chinese Chemical Letters 2022, 33 (7), 3474-3477.

OP-583

Cyclotron Production of ^{135}La from enriched $^{135}BaCO_3$ targets.

E. Aluicio-Sarduy*, A. P. Olson, J. C. Mixdorf, T. E. Barnhart, J. W. Engle;*
University of Wisconsin-Madison, Madison, WI, UNITED STATES OF AMERICA.

Aim/Introduction: ^{135}La ($t_{1/2}$ =19.93h, 98.1% EC) is an attractive radionuclide for targeted Auger therapy due to its unique decay characteristics and chemical properties resembling those of commonly used therapeutic radiometals [1,2]. However, high production yields and radionuclidic purity are essential for its potential use in preclinical and clinical settings. Our goal is to develop a scalable, automatable, and cost-efficient production method of ^{135}La from isotopically enriched ^{135}Ba targets. ***Materials and Methods:*** Enriched $^{135}BaCO_3$ (94.9%) was irradiated with 13MeV protons using a GE PETtrace cyclotron at 10μA. Lanthanum-135 was isolated by single column extraction chromatography using N,N,N',N'-tetrakis-2-ethylhexyldiglycolamide functionalized (branched-DGA) resin. Final product radionuclidic and elemental purity were verified by HPGe gamma spectrometry and microwave plasma-atomic emission spectroscopy (MP-AES), respectively. Apparent molar activity (AMA) was quantified by complexation of the purified ^{135}La with DOTA and macropa. The target material was recycled by precipitation/decantation using a saturated $(NH_4)_2CO_3$ solution. ***Results:*** Lanthanum-135 was produced with a physical yield of 50 ± 5 MBq/μAh (EoB-corrected) from ~150 mg/cm^2 $^{135}BaCO_3$ targets. After target dissolution, the resin's differential affinity for Ba^{2+} and La^{3+} ions at different nitric acid concentrations was leveraged to selectively load La^{3+} from the 3M HNO_3 (25 mL) target dissolution. Subsequent rinsing with decreasing HNO_3 concentrations (15 mL 3M HNO_3 and 3 mL 0.5M HNO_3) eluted trace metal impurities. Lanthanum(3+) was eluted in a small volume of 0.1M HCl (0.3 - 0.5 mL) with a radiochemical yield of 96.7 ± 0.5%. MP-AES analysis (n=4) established 0.65 ± 0.51 ppm (Ba), 0.16 ± 0.11 ppm (Zn), and 0.03 ± 0.03 ppm (Cu) of the only detectable impurities in the purified ^{135}La solution. AMA was 11 ± 4 GBq/μmol DOTA and 35 ± 7 Gbq/μmol macropa (n=4). The enriched target material was recovered with a run-to-run efficiency of 98.1 ± 1.4 % (n=4). ***Conclusion:*** We developed and characterized a method for cost-effective production of radiopharmaceutical-quality ^{135}La, facilitating its potential preclinical/clinical use. A similar strategy can also be followed to produce the positron-emitting radioisotope ^{132}La. ***References:*** 1- Aluicio-Sarduy E, et al., 2019, doi:10.1038/s41598-019-47137-0 2- Aluicio-Sarduy E, et al., 2020, doi: 10.1002/chem.201905202.

OP-584

Multi Copper and Gallium Radioisotopes Production by Irradiation of ZnO Target via Medical Cyclotron

F. Porto*[1], G. Speltri[1], S. Cisternino[2], C. Favaretto[3], N. Bergamaschi[3], D. Peruzzi[3], J. Amico[3], P. Bovone[3], G. Gorgoni[3], A. Boschi[1], R. Tassinari[1], L. Marvelli[1], R. Napolitano[1], A. Niorettini[1], L. Uccelli[1], L. Mou[2], G. Piteo[4], A. Kotliarenko[2], L. De Dominicis[2], G. Pupillo[2], J. Esposito[2], E. Cazzola[3], P. Martini[1];*
[1]University of Ferrara, Ferrara, ITALY, [2]National Institute for Nuclear Physics, Legnaro, ITALY, [3]IRCCS Sacro Cuore Don Calabria Hospital, Negrar di Valpolicella, ITALY, [4]University of Padova, Padova, ITALY.

Aim/Introduction: Copper radioisotopes, such as copper-61, copper-64, and copper-67, are gaining increasing relevance in nuclear medicine due to their versatile decay properties, suitable for both diagnostic and therapeutic applications. Our study investigated their production via proton irradiation of enriched zinc oxide (ZnO) targets. Specifically, ^{61}Cu can be produced via the (p,α) reaction on a ^{64}Zn target in the energy range of 10-20 MeV, ^{64}Cu through the ^{68}Zn(p,nα) reaction in the range of 20-40 MeV, and ^{67}Cu through the ^{70}Zn(p,α) reaction in the range of 10-70 MeV. Interestingly, gallium radioisotopes, also of medical relevance, emerged as significant by-products during the irradiation process. From these observations arises the idea of developing a multi-radioisotope production method through ZnO irradiation. Based on this, a Zn/Cu separation method was developed to enable the recovery of both gallium and copper radioisotopes. In addition, a protocol was developed and applied to recover ZnO from waste, enabling target recycling. ***Materials and Methods:*** Sintered ^{nat}ZnO pellets (~260 mg) were produced via Spark Plasma Sintering and attached to Au/Nb backing support. Irradiations were carried out using a TR19 cyclotron. Copper radioisotopes were separated via an automated protocol using CU and TK201 resins. The copper-rich eluate was collected from TK201, while the zinc/gallium-containing waste from the CU resin was further purified using ZR and DGA resins. Purity and recovery efficiencies were assessed by ICP-MS and γ-spectrometry. Both copper and gallium fractions were tested for radiolabelling with DOTA and NODAGA-RGD. ZnO was recovered from waste via NaOH precipitation followed by calcination. ***Results:*** ^{nat}ZnO targets were successfully irradiated at 19 MeV, 30 μA, for 30 minutes. The automated copper purification yielded ~95% recovery with high radionuclidic purity; γ-spectra confirmed the presence of copper-61 as the main isotope, while impurities of zinc, gallium, and cobalt in the waste were below instrumental detection limits. Additionally, gallium was effectively separated from zinc and eluted in water. Radiolabelling of DOTA and NODAGA-RGD with both purified copper and gallium yielded >95% radiochemical purity. ZnO was recovered from the acidic waste solution with ~85% yield and reused for new pellet production. ***Conclusion:*** This work presents a sustainable radiochemical approach for the dual production of copper and gallium radioisotopes from a single irradiation of ZnO targets. The developed method combines efficient radionuclide separation with recovery of valuable by-products and target material. This strategy aligns with green chemistry principles, optimizing resource use while minimizing radioactive and chemical waste.

OP-585

Production of ^{225}Ac for Targeted Alpha Therapy Using an Electron Linear Accelerator: Improving Radiolabeling Quality Comparable to ^{229}Th Generator-Produced ^{225}Ac

M. Maeda*[1], Y. Ueno[1], K. Nishida[1], Y. Kani[1], M. Yoshimoto[2], H. Fujii[2], A. Inaki[2], H. Kikunaga[3], T. Yokokita[3], S. Kashiwagi[3], K. Shirasaki[4,5];*
[1]Hitachi Ltd., Research & Development Group, Hitachi, JAPAN, [2]National Cancer Center, Exploratory Oncology Research & Clinical Trial Center, Kashiwa, JAPAN, [3]Research Center for Accelerator and Radioisotope Science, Tohoku University, Sendai, JAPAN, [4]Institute for Materials Research, Tohoku University, Sendai, JAPAN, [5]Radioisotope Research Center, Institute for Radiation Sciences, Osaka University, Toyonaka, JAPAN.

Aim/Introduction: ^{225}Ac is recognized as one of the most promised radionuclides for targeted alpha therapy (TAT). However, its current supply from a ^{229}Th / ^{225}Ac generator is limited, so another mass production method needs to be established. We have reported on the experimental production of ^{225}Ac using an electron linear accelerator in which no long-lived actinium isotopes are co-produced. In this production method, ^{225}Ac is produced via the ^{226}Ra (γ, n)^{225}Ra photonuclear reaction, followed by the beta decay of ^{225}Ra to ^{225}Ac. In our previous study, we produced megabecquerel quantities of ^{225}Ac but improvements in production amount and radiolabeling quality were necessary to use ^{225}Ac for preclinical research purposes [1]. In this study, we aimed to produce ^{225}Ac with a radiolabeling quality comparable to that of ^{225}Ac produced by a ^{229}Th generator by further increasing the production amount. ***Materials and Methods:*** To increase the ^{225}Ac production, ^{226}Ra target amount was increased to about 200 MBq and its size was reduced to 3 mm in diameter. Other improvements in target structure were made. Also, current value and time of the irradiation was increased. Irradiation was performed using the electron linear accelerator at the Research Center for Accelerator and Radioisotope Science, Tohoku University. To evaluate the quality of ^{225}Ac, a DOTA-conjugated peptide was radiolabeled. The result of the radiolabeling was compared with that using ^{225}Ac produced by a ^{229}Th generator purchased from the U.S. National Isotope Development Center. ***Results:*** ^{225}Ac was separated from Ra isotopes 26 days after the irradiation. The activity of ^{225}Ac at this point was 63 MBq. Based on the ^{225}Ac accumulation curve calculated from the decay of ^{225}Ra, the maximum activity of ^{225}Ac at 17 days after irradiation was estimated to be 69 MBq. After 5 days of manual separation, 39 MBq of purified ^{225}Ac was obtained. The chemical yield was 88%. The radiolabeling yield and specific activity of the DOTA-conjugated peptide were >98% and 0.34 MBq/nmol, respectively, which were comparable to those using ^{225}Ac produced by a ^{229}Th generator. ***Conclusion:*** ^{225}Ac with radiolabeling quality comparable to that of ^{229}Th generator-produced ^{225}Ac was obtained by ^{226}Ra irradiation using an electron linear accelerator. The radioisotope produced has started to be utilized for preclinical research. The production is planned to further increase through the automation currently under consideration for the separation process. ***References:*** [1] M. Maeda et al.; J. Nucl. Med. (2023) 64 P24.

OP-586

Resin Based Extraction of $^{45}Ti^{4+}$ for Radiopharmaceutical Applications

M. DeLuca[1], *E. Aluicio-Sarduy*[1], *T. E. Barnhart*[1], *J. C. Mixdorf*[1], *P. N. Tran*[2], *A. Marlin*[3], *E. Boros*[2], *J. W. Engle*[1];
[1]*University of Wisconsin - Department of Medical Physics, Madison, WI, UNITED STATES OF AMERICA,* [2]*University of Wisconsin - Department of Chemistry, Madison, WI, UNITED STATES OF AMERICA,* [3]*PSL University - Chimie ParisTech, Paris, FRANCE.*

Aim/Introduction: ^{45}Ti ($t_{1/2}$=3.08 h) is attractive for positron emission tomography (PET) imaging (84.8% β^+, $E_{<\beta+>}$ = 439 keV). It can be produced by cyclotron irradiation of ^{nat}Sc via the (p,n) reaction (σ_{max} = 350-400 mb, 10-14 MeV). Incorporating ^{45}Ti into radiopharmaceuticals requires isolation from ^{nat}Sc target material and recovery in labile chemical form. We and others have studied isolation of ^{45}Ti using Zr resin [1]. ^{45}Ti has high affinity (D_w ~10^4) for Zr resin in HCl and HNO_3, requiring organic eluate that compete with chelators and compromise apparent molar activity. TEVA (Tetravalent Actinide) resin (Eichrom) has previously been used to separate Ti/Sc in the context of a ^{44}Ti/^{44}Sc generator [2]. We report exploration of TEVA resin for isolation of $^{45}Ti^{4+}$ from ^{nat}Sc. ***Materials and Methods:*** ^{45}Ti and ^{nat}Sc distribution volumes (K_d) were measured by contacting known mass of TEVA resin with HCl/$H_2C_2O_4$ solutions (.2-4M HCl/0-.1M $H_2C_2O_4$) spiked with dissolved ^{nat}Sc foil irradiated with 13 MeV protons on a GE PETtrace at the University of Wisconsin - Madison. The K_d of ^{45}Ti was determined by comparing activity in a 50 µL aliquot of the supernatant with 50 µL of an unreacted solution, and that of ^{nat}Sc was determined by ICP OES of analogous fractions. Results were used to design column separations of ^{45}Ti from irradiated ^{nat}Sc targets. ***Results:*** Measured values suggest loading in .2M HCl/.05-.1M $H_2C_2O_4$ due to a high affinity for ^{45}Ti (K_d >3000) and low affinity for ^{nat}Sc (K_d <20). At lower concentrations of $H_2C_2O_4$ and higher concentrations of HCl, ^{45}Ti affinity decreases. Measured ^{45}Ti K_d values reflect a low affinity (K_d <10) for the resin in all HCl concentrations, indicating this eluent is suitable for recovering ^{45}Ti. However, measured ^{45}Ti elution profiles broaden with decreasing HCl concentration. Additionally, as ^{nat}Sc mass was increased, we observed insoluble ScC_2O_2, which suggests the potential to reduce the initial target mass via selective precipitation. ***Conclusion:*** Measured K_d values indicate TEVA resin can separate $^{45}Ti^{4+}$ from Sc target material by extracting in HCl/$H_2C_2O_4$ solutions and eluting in HCl. These results motivate ongoing work testing resin performance with larger ^{nat}Sc target masses and higher ^{45}Ti activity, comparing ^{45}Ti radiochemical yields and apparent molar activity with TREN-CAM to results obtained with Zr resin. ***References:*** [1] doi.org/10.1007/s10967-023-09270-z. [2] doi.org/10.3390/molecules26216371.

OP-587

Purifying radionuclides using microfluidic chips: towards the automated liquid-liquid extraction of Ac-225

R. de Kruijff*, S. Trapp, A. Santoso, E. Paulssen;*
Delft University of Technology, Delft, NETHERLANDS.

Aim/Introduction: In recent years, extremely promising results have been obtained in clinical trials using targeted alpha therapy (TAT), in particular using Ac-225. However, its limited availability greatly hampers further translation and new innovations. Increasing the global supply of requires a production and separation system that is not only fast and efficient, but also continuous and automatable. We therefore propose an innovative two-step liquid-liquid extraction (LLE) procedure that enables very fast radionuclide extraction and allows for direct target solution recycling. We have adapted microfluidic chips, which offer precise control over two-phase flows and their interfaces, for establishing an automated purification system for medical radionuclides, and show a proof-of-principle with the separation of Ac-225 from radium, using di-2-ethylhexylphosphoric acid (D2EHPA) as the chelator. ***Materials and Methods:*** Ac-225 was supplied in 0.05 M HCl, and Ra-223 was supplied as $^{223}RaCl_2$. The aqueous target solutions contained 0.1 M $Ba(NO_3)_2$ with trace Ac-225 and Ra-223, and the organic extracting solutions consisted of $CHCl_3$ with 10 %v/v D2EHPA. Batch extraction experiments were carried out in Eppendorf vials with a 1:1 ratio of aqueous and organic solutions. Microfluidic extraction experiments were performed in SiO_2-coated PDMS microfluidic chips, the solutions were loaded on two separate syringe pumps and connected to the chips using PTFE tubing for different contact times. Back-extraction was performed by contacting the organic extraction liquid with HCl solutions. ***Results:*** Batch extraction experiments demonstrated very fast complexation of Ac-225 with the D2EHPA chelator (< 1 minute), and high extraction efficiencies (> 98 %) from Ra-223 solutions. Co-extraction of the Ra-223 target material into the organic phase remained below 0.3 %. Ac-225 back-extraction efficiencies were over 98 % when using 0.1 M HCl as back-extracting agent. In the microfluidic chips, perfect phase separation was obtained between the aqueous and organic phase. A comparable Ac-225 extraction efficiency of 97.2 % ± 1.5 % was obtained for extremely short contact times (1.7 seconds), although the back-extraction efficiency of Ac-225 was somewhat lower (80.2 % ± 0.8 % and 39.9 % ± 6.2 % for 4 M and 0.1 M HCl solutions, respectively). ***Conclusion:*** A microfluidic PDMS-based chip coated with SiO_2

was developed for the LLE of Ac-225. Overall, excellent extraction and back-extraction efficiencies were achieved for Ac-225 with the developed microfluidic extraction method Ac-225 (97.2 % ± 1.5 % and 80.2 % ± 0.8 %, respectively), presenting a promising alternative to conventional separation methods. ***References:*** DOI:10.1038/s41598-024-81177-5.

1305

Tuesday, October 7, 2025, 9:45 - 11:15
Room 211

Cutting Edge Science Track - TROP Session - Dosimetry Committee: Quantification and Innovation in Dosimetry

OP-588

Comparison between semi-automated vertebral segmentation and manual bone marrow sampling for quantitative SPECT/CT-based bone marrow dosimetry in 177Lu radiopharmaceutical therapy

V. Forget[1], *S. Hammouda*[1], *F. A. Buteau*[2], *G. April*[2], *F. Arsenault*[2], *A. Beaulieu*[2], *J. M. Beauregard*[1];
[1]*Department of Radiology and Nuclear Medicine, Université Laval, Quebec City, QC, CANADA,* [2]*Department of Medical Imaging, CHU de Québec - Université Laval, Quebec City, QC, CANADA.*

Aim/Introduction: For bone marrow dosimetry, activity sampling dosimetry using small vertebral volumes of interest (VOIs) has been proposed but is subject to inter-observer variability (1). We aimed to compare this manual approach to a semi-automated vertebral CT segmentation technique. ***Materials and Methods:*** 71 patients enrolled in the personalized PRRT clinical trial (NCT02754297) underwent quantitative SPECT/CT at approximately 24h and 72h after each of 4 induction cycles of ^{177}Lu-DOTATATE (1.6-33.7 GBq). For the small volume manual segmentation method (SV), two 2-cm spherical VOIs were placed over L4 and L5 vertebrae, or over other vertebrae to avoid metastases, to obtain the mean activity concentration (Bq/mL). For the semi-automated method, the lumbar spine was segmented using a 125HU threshold from L1 to L4 on CT, from which the mean ($AUTO_{mean}$) and median ($AUTO_{med}$) activity concentrations were extracted. Absorbed doses were computed by multiplying the area under monoexponential time-activity concentration curves by 87 mGy·g/MBq·h. $AUTO_{mean}$ and $AUTO_{med}$ were correlated with SV bone marrow absorbed dose estimates. Dosimetric estimates were also correlated with haematological toxicity in terms of relative blood count variations. Subacute toxicity was defined as a variation occurring during each individual cycle, whereas late toxicity was defined as variations occurring from 8 weeks after the last cycle up to 52 weeks after therapy initiation. ***Results:*** Median bone marrow absorbed doses of all induction cycles (IQR) for the SV, $AUTO_{mean}$ and $AUTO_{med}$ techniques were 0.28 (0.18-0.45), 0.22 (0.14-0.43), and 0.17 (0.12-0.24) Gy, respectively. $AUTO_{mean}$ and SV absorbed doses during the first cycle showed a moderate correlation (r=0.68; P<0.001) which improved when $AUTO_{med}$ was correlated with SV (r=0.77; P<0.001). This was expected as bone metastasis has a weaker influence on median than mean activity concentration from lumbar spine VOIs. On average, $AUTO_{med}$ absorbed doses were 34% lower than those from SV. Individual cycles and cumulative doses yielded similar results. $AUTO_{med}$ absorbed doses showed weak but significant correlations with subacute thrombocytopenia, late thrombocytopenia and late anaemia (r=-0.27, -0.31 and -0.26, respectively; P<0.05) which were comparable to those obtained with SV (r=-0.30, -0.35 and -0.34, respectively; P<0.05). ***Conclusion:*** $AUTO_{med}$ bone marrow dose estimates were comparable to those obtained with SV and correlations with clinical outcomes were similar for both methods. This simple, accessible and implicitly observer-independent semi-automated technique could enable a standardised approach to bone marrow dosimetry in ^{177}Lu radiopharmaceutical therapy. ***References:*** (1) JNuclMed2018;60:1406-13, DelPrete,EJNMMIPhys2018;5:25.

OP-589

A semi-automatic model for correcting adjacent-organ cross-talk in bone marrow dosimetry after [^{177}Lu]Lu-DOTATATE treatment

K. Smits[1], *J. Hemmingsson*[1], *T. Rydén*[2], *A. Theisen*[3], *M. van Essen*[4], *J. Svensson*[5], *A. Hallqvist*[5], *J. Tran-Gia*[3], *P. Bernhardt*[2];
[1]*Institute of Clinical Sciences, Gothenburg, SWEDEN,* [2]*Department of Medicial Physics and Biomedical Engineering, Gothenburg, SWEDEN,* [3]*Department of Nuclear Medicine, Wurzburg, GERMANY,* [4]*Institute of Medicine, Gothenburg, SWEDEN,* [5]*Department of Oncology, Gothenburg, SWEDEN.*

Aim/Introduction: Previous studies on bone marrow dosimetry have shown a significant decrease in activity concentration in vertebrae adjacent to high-uptake regions. In this work, we developed a segmentation model that semi-automatically generates patient-specific activity maps. These activity maps are used for patient-specific correction of adjacent-organ cross-talk in the bone marrow, with the aim to compensate for signal loss in vertebrae close to high-uptake organs. ***Materials and Methods:*** A semi-automatic segmentation model was developed using multiple AI networks trained to delineate anatomic structures (e.g. kidney, spleen, liver) on patient low-dose CT images. Mean activity concentrations in the segmented organs are automatically extracted from the reconstructed SPECT images (OSEM, 8 iterations, 10 subsets), while those for the background (subcutaneous adipose tissue near the hip bone) and lumbar vertebrae are manually defined. The model then generates an activity map with patient-specific activity ratios between organs and background. Monte Carlo simulations are used to generate new SPECT images from the activity maps, allowing for the determination of patient-specific corrections for adjacent-organ cross-talk in the bone marrow (one correction factor for each lumbar vertebral body). To evaluate the segmentation model, we used a digital XCAT phantom by creating an activity map mimicking a [^{177}Lu]Lu-DOTATATE SPECT scan 24 hours post injection. A SPECT projection dataset of this phantom was simulated using in-house Monte Carlo simulation code. Thirty noise realizations were created and reconstructed, and the segmentation model was applied to each of the resulting SPECT images to derive a set of correction factors. Subsequently, the mean recovery in the lumbar vertebrae was evaluated for each noise realization both with and without spill-over correction. ***Results:*** By applying correction factors generated by the segmentation model, the mean recovery in the XCAT phantom's bone marrow increased from 0.23 to 0.80 (L1), 0.37 to 0.81 (L2), 0.58 to 0.95 (L3), 0.66 to 0.93 (L4), and 0.62 to 0.87 (L5) before and after spill-over correction, respectively. ***Conclusion:*** The segmentation model presented here significantly improved the recovery in all lumbar vertebrae of an XCAT phantom for 30 different noise realizations. Applying this model seems of particular use for vertebrae closely located to high-uptake organs (e.g., L1-L2), to overcome the problem of signal loss in these vertebrae due to adjacent-organ cross-talk.

OP-590

Main sources of uncertainty affecting vertebral activity quantification in SPECT/CT imaging after [^{177}Lu]Lu-DOTATATE therapy using a physical phantom and patient simulations

A. Theisen[1], *J. Leube*[1], *L. Pieper*[1], *M. Laßmann*[1], *K. Smits*[2], *J. Hemmingsson*[2], *P. Bernhardt*[2], *M. Salas-Ramirez*[1], *J. Tran-Gia*[1];
[1]*Department of Nuclear Medicine, University Hospital Würzburg, Würzburg, GERMANY,* [2]*Sahlgrenska Academy, Gothenburg, SWEDEN.*

Aim/Introduction: Accurate quantification of bone marrow activity is essential in radiopharmaceutical therapy, particularly for [^{177}Lu]Lu-DOTATATE, where the red marrow is a dose-limiting organ. SPECT/CT-based dosimetry is challenging due to low uptake, partial volume effects, and spill-in from high-activity organs like the kidneys. This study evaluates errors in bone marrow activity quantification using patient-specific phantom experiments and Monte Carlo simulations. Specifically, we used a 3D-printed lumbar vertebrae phantom based on ICRP 145 [1] and 30 patient-specific geometries to evaluate quantification accuracy. ***Materials and Methods:*** Phantom measurements were performed with a 3D-printed lumbar spine (L1-L5) and kidney phantom designed based on the ICRP 145 male mesh model [1]. Attenuation in the cortical bone was achieved using high-density printing material, while the spongiosa was modeled with a K_2HPO_4 solution containing 33 kBq/ml [^{177}Lu]$LuCl_3$ in DTPA. Standard-resin kidney phantoms were filled with 310 kBq/ml [^{177}Lu]$LuCl_3$ in HCl(aq). SPECT/CT imaging was performed in a water-filled IEC NEMA phantom under varying acquisition parameters (MELP collimation, 120 projections of 10/20/30 s, 10/20/10% around 208 keV peak, 128/256 matrix). To assess the impact of background, acquisition parameters, and scatter correction (SC), projection images were generated using SIMIND [2] (120 vs. 60 projections with the same total acquisition time; air/cold/hot background). Anatomical variability was analyzed on SIMIND-generated projection data of 30 vertebra+kidney activity masks segmented on [^{177}Lu]Lu-DOTATATE patient scans. Poisson noise (100 realizations per patient) was added. Reconstructions were performed with PyTomography (OSEM, AC, TEW-SC, resolution modeling) [3]. Four volume-of-interest (VOI) drawing techniques were evaluated by comparing SPECT-derived and true activity: 0.7/4.0-ml spherical VOI, CT-based VOI, and enlarged CT-based VOI. ***Results:*** Main quantification uncertainties were driven by reconstruction biases associated with high kidney activity, scatter conditions, VOI definition, and the noise behavior of OSEM reconstructions. Among VOI definition strategies, 4-mL spherical VOIs resulted in the highest accuracy but lower precision (e.g., 20s/projection, L1-L5: 94% ± 7%), while enlarged CT-based VOIs showed the highest precision but systematically underestimated activity (e.g., 20s/projection, L1-L5: 79% ± 1%). ***Conclusion:*** This study identifies key factors influencing SPECT/CT-based bone marrow dosimetry of lumbar vertebrae, particularly in those adjacent to the kidneys. While high precision is achieved, further optimization regarding image reconstruction and patient-specific VOI selection is essential to enhance accuracy, ultimately improving the reliability of dosimetry in clinical practice. ***References:*** [1] Kim C et al., ICRP 49(3);2020:13-201 [2] Ljungberg M, Strand SE. ComputMethProgBio 29(4);1989:257-272 [3] Polson L et al., SoftwareX, 29;2025:102020.

OP-591

Proof of concept for in vivo organ dosimetry with a tissue-equivalent 3D-printed heart

R. Ringler[1], *A. Poellmann*[1], *N. Zeiss-Carstens*[1], *D. Hellwig*[2], *D. Schmidt*[2];
[1]*Technical University of applied sciences Amberg-Weiden, Weiden, GERMANY,* [2]*University Hospital Regensburg, Department of Nuclear Medicine, Regensburg, GERMANY.*

Aim/Introduction: The use of 3D-printed, tissue-equivalent organ models enables the assessment of radiation exposure and organ-specific dose in both nuclear medicine and radiological procedures. By integrating thermoluminescent dosimeters (TLDs) with quantitative SPECT imaging, it is possible to verify radiation exposure associated with various radiopharmaceuticals in nuclear medicine, as well as with different dose protocols in computed tomography (CT). ***Materials and Methods:*** A 3D heart model printed at the university (FDM 3D printing) was used. The heart muscle was simulated with agar agar and CuSO4 (0-250 mg/ml) and the HU values were checked in CT (Somatom Emotion 6, 110 kV, 140 mAs). The proof of concept of the 3D heart was performed on a SPECT/CT (Siemens Symbia Intevo Bold) with an activity of A(Tc-99m) = 29.8 MBq. 2x20 MCP N TLD discs - calibrated with Tc99m in a PMMA phantom (dose reference: Black Piranha external measuring probe) - are packaged in a watertight vacuum container. 18 TLDs are attached to the 3D heart for 20 minutes and record the dose. The second batch of 18 TLDs remains on the 3D heart for 1 hour, which is placed in a modified, water-filled body phantom with 3D lungs, 3D spine and 3D ribs. This is used to perform a standard SPECT/CT examination. 2x2 TLDs are used to determine the background. ***Results:*** Quantification of Hounsfield Unit (HU) values using the $CuSO_4$ calibration series yielded concentrations of 6.2 mg/ml and 25 mg/ml for myocardial tissue without and with contrast enhancement, respectively. These values are consistent with those reported in the literature The proof-of-concept study demonstrated a heterogeneous dose distribution, attributable to the inhomogeneous uptake of Tc-99m within the simulated myocardial tissue. This observation was qualitatively confirmed through analysis of the acquired SPECT imaging data. ***Conclusion:*** Based on available datasets and literature, myocardial tissue is characterized by Hounsfield Unit (HU) values of 40 ± 9 without contrast enhancement and 114 ± 7 with contrast enhancement. These HU values can be accurately reproduced using appropriate concentrations of $CuSO_4$. Dose distribution within the phantom can be effectively assessed using thermoluminescent dosimeters (TLDs) in conjunction with Tc-99m. The subsequent phase of the study will involve a quantitative evaluation and comparison with SPECT imaging, as well as the simulation of relevant pathophysiological myocardial conditions within the 3D heart model.

OP-592

Nephron-Level Dosimetry of ^{161}Tb- and ^{177}Lu-DOTA-TATE Reveals Greater Absorbed Dose Heterogeneity from ^{161}Tb in Murine Renal Substructures

M. Andersson[1,2], *T. Opsomer*[3], *N. Reynaert*[2], *H. Levillain*[2], *C. Saldarriaga Vargas*[1];
[1]*Dosimetry Research for Targeted Radionuclide Therapy – Belgian Nuclear Research Centre (SCK CEN), Mol, BELGIUM,* [2]*Medical Physics Department, Institut Jules Bordet – Université Libre de Bruxelles, Brussels, BELGIUM,* [3]*Nuclear Medical Applications – Belgian Nuclear Research Centre (SCK CEN), Mol, BELGIUM.*

Aim/Introduction: Non-uniform radiopharmaceutical retention in kidney tissues results in nephron-scale absorbed dose heterogeneity, confounding radiation-induced nephrotoxicity investigations in radiopharmaceutical therapy (RPT). The radionuclide ^{161}Tb is of interest as it emits more low-energy electrons than ^{177}Lu, irradiating tumours more locally, but its impact on absorbed dose-dependent effects in normal tissues remains unclear. This study combined quantitative biodistribution data with a novel computational multi-nephron model to investigate and compare nephron substructure-specific absorbed dose distributions from [^{161}Tb]Tb- and [^{177}Lu]Lu-DOTA-TATE in murine kidneys. ***Materials and Methods:*** A realistic murine multi-nephron model was developed from 3D multiphoton microscopy data (1), representing kidney tissue sections including superficial,

midcortical, and juxtamedullary nephrons and their main substructures (glomeruli, proximal tubules (PT) and distal tubules). Nephron substructure- and type-specific S values for ^{161}Tb and ^{177}Lu were calculated (GATE v9.2). In-vivo biodistribution data were obtained from female C57BL6/Jjr mice injected with either [^{161}Tb]Tb- or [^{177}Lu]Lu-DOTA-TATE. Whole-organ activity was measured at five time points (15 minutes, 1,4,24 and 72 hours), and tissue-level activity distribution was quantified using digital autoradiography data and histological segmentation. Nephron-level activity distribution was estimated by mapping tissue-level activity data to nephron substructures using occupancy-based weighting. Time-integrated absorbed dose coefficients (ADCs) were calculated by fitting bi-exponential curves to absorbed dose rate data. ***Results:*** Renal uptake was primarily localized in the cortex and outer stripe of outer medulla (≥90% from 1h onward). Absorbed dose distributions were highly heterogeneous across nephron types and substructures for both radionuclides. Despite similar macroscopic biodistribution, ^{161}Tb led to significantly higher absorbed dose heterogeneity due to its higher emission of low-energy electrons. The ADCs to the PT were 71% higher than to glomeruli for ^{161}Tb compared to 28% higher for ^{177}Lu. Juxtamedullary nephrons had the highest ADCs across substructures. ADCs to juxtamedullary PT and glomeruli were 18-21% higher for ^{161}Tb and 14-17% higher for ^{177}Lu compared to superficial PT and glomeruli, respectively. ***Conclusion:*** The integration of high-resolution biodistribution data with a computational multi-nephron model enabled detailed renal dosimetry. ^{161}Tb showed greater nephron-level absorbed dose heterogeneity than ^{177}Lu across nephron substructures and types, with highest ADCs to juxtamedullary PT. Nephron-level absorbed dose heterogeneity highlight the importance of substructure-specific dosimetry in evaluating nephrotoxicity risk. These findings support the refinement of dosimetry models used in RPT development and provide a framework for identifying critical substructures, supporting the development of absorbed dose effect-relationships and nephroprotective strategies for clinical translation. ***References:*** (1) Blanc T et al. Kidney int. 2021;99(3):632-45.

OP-593

Time-dependent biodistribution and dosimetry of radiolabelled FAP-targeting single-domain antibody 4AH29 in Göttingen minipigs

N. Dumauthioz[1], *L. Navarro*[1], *M. Berdal*[1], *S. Nagachinta*[1], *J. Eersels*[1], *V. Gaspariunaite*[1], *A. R. Pombo Antunes*[1], *T. Jørgensen*[2], *L. Kellemann Kristensen*[2], *T. Starostka*[2], *D. Mantzilas*[1], *T. Lahoutte*[1], *M. D'Huyvetter*[1];
[1]*Precirix, Brussels, BELGIUM,* [2]*Minerva Imaging, Oelstykke, DENMARK.*

Aim/Introduction: Fibroblast activation protein alpha (FAP) is a pan-tumor target highly expressed on cancer-associated fibroblasts. We developed 4AH29, a single-domain antibody (sdAb) to bind FAP, which showed promising results in mice [1]. In tumor-bearing mice, 4AH29 radiolabelled with therapeutic radioisotopes exhibited prolonged tumor retention, leading to dose-dependent efficacy. Here we investigated the biodistribution of radiolabelled 4AH29 in Göttingen minipigs and extrapolated the dosimetry to human. ***Materials and Methods:*** [^{131}I]I-GMIB-4AH29 and [^{111}In]In-DOTA-4AH29 were administered to 3 male and 3 female Göttingen minipigs. The blood activity profile was determined over time by gamma-counter and biodistribution kinetic was performed by SPECT/CT imaging. The data obtained with [^{111}In]In-DOTA-4AH29 was used as a surrogate for the ^{225}Ac- and ^{177}Lu-labelled variants. Extrapolation to human absorbed dose was calculated with OLINDA. ***Results:*** Radiolabelled 4AH29 showed good tolerability in female and male minipigs, indicated by absent compound-related adverse effects. It displayed fast blood clearance driven by renal excretion. Kidney clearance dynamic of [^{131}I]I-GMIB-4AH29 and [^{111}In]In-DOTA-4AH29 seemed visually distinct, likely due to the different radiolabelling processes, linking chemistry and radionuclide pharmacokinetics of a halogen or metal respectively. However, the contrasting pharmacokinetics of a halogen and metal did not translate into differences in mean residence time (MRT), which displayed no variation in kidneys, bone marrow or liver when comparing ^{131}I with ^{177}Lu-labelled 4AH29. Extrapolation to human absorbed dose with [^{131}I]I-GMIB-4AH29 in kidneys showed 8.23E-01 mGy/MBq, whereas [^{177}Lu]Lu-DOTA-4AH29 led to 5.86E-01 mGy/MBq. Consequently, the maximum administered activity for [^{131}I]I-GMIB-4AH29 and [^{177}Lu]Lu-DOTA-4AH29 calculated 28 and 39 GBq respectively to reach the renal dose limit of 23 Gy as determined by EBRT. In red marrow, another commonly dose-limiting organ, equivalent dose for [^{131}I]I-GMIB-4AH29 and [^{177}Lu]Lu-DOTA-4AH29 were 3.8E-02 mGy/MBq and 1.36E-02 mGy/MBq respectively. Thus, 52 GBq with [^{131}I]I-GMIB-4AH29 and 147 GBq with [^{177}Lu]Lu-DOTA-4AH29 can be administered to reach the EBRT set dose limit of 2 Gy. Extrapolation to human absorbed dose for [^{225}Ac]Ac-DOTA-4AH29 exhibited 7.26E+02 mGy/MBq in kidneys and 2.66E+01 mGy/MBq in bone marrow, which resulted in a maximum activity administered of 32 MBq for kidneys and 75 MBq for bone marrow. ***Conclusion:*** Radiolabelled 4AH29 is well tolerated in Göttingen minipigs. Dosimetry of ^{225}Ac, ^{131}I, and ^{177}Lu-labelled 4AH29 indicates that repeated administrations within the clinically tested range have the potential to treat future patients without reaching kidney toxicity limits. ***References:*** 1.Dekempeneer, Y. et al. Preclinical evaluation of a radiotheranostic single-domain antibody against fibroblast activation protein α. Journal of Nuclear Medicine 64, 1941-1948 (2023).

OP-594

Feasibility study of ^{225}Ac-PSMA-CY313 dosimetry in mCRPC patients using SPECT

S. Li[1], *Y. Shi*[1], *Z. Li*[2], *Y. Xu*[3], *Y. Zhou*[3], *J. Liu*[2], *Y. Wu*[2];
[1]*Department of Nuclear Medicine, Affiliated Hospital of North Sichuan Medical College, Nanchong, CHINA,* [2]*C-Ray Pharmaceuticals (Chengdu) Co. Ltd., Chengdu, CHINA,* [3]*United Imaging Healthcare Technology Group Co., Ltd, Shanghai, CHINA.*

Aim/Introduction: Several prostate-specific membrane antigen (PSMA) radiopharmaceuticals have been used for the treatment of metastatic castration-resistant prostate cancer (mCRPC). ^{225}Ac-PSMA targeted alpha therapy (TAT) demonstrates efficacy/safety in mCRPC via high LET and short particle range, yet faces dosimetry challenges due to undetectable α-emission externally, complex decay chains, and high SPECT noise from low gamma yield. ^{225}Ac-PSMA-CY313 is a novel TAT enabling tumor-specific α-particle delivery. In this study, SPECT imaging protocols and dosimetry calculations were optimized via multi-timepoint acquisitions with advanced reconstruction algorithms. ***Materials and Methods:*** This is a dosimetry sub-study with 4 mCRPC patients out of a prospective open-label and single-arm study of ^{225}Ac-PSMA-CY313 therapy (200 μCi ± 10%, q8w×4 cycles). Dynamic 1-bed SPECT/CT (GE Discovery NM/CT 670 Pro) non-circular orbit acquisition (120 projections, 60s/view) followed by whole-body planar imaging were acquired at 6, 24, 48, and 96 h post-injection. Uniform phantom scans were performed for calibration of SPECT tomographic and planar imaging, respectively. SPECT tomography images were reconstructed useing OS-EM algorithm with compensation for the attenuation, resolution blur, scatter, as well as the crosstalk and down-scatter contamination between different energy peaks. The volumes of interest including tumor and organ volumes were manually defined on CT images with reference on ^{18}F-PSMA-CY313 whole-body PET. Finally, the organ uptakes were volume-adjusted to the standard ICRP 103 adult male phantom to generate time activity curves (TACs) for Fr-221 and Bi-213, respectively. Rapid 3D-RD-S software was used for dose calculation. ***Results:*** The tumor absorbed dose was 2.40±3.33 Gy

(soft tissue lesions: 5.03±5.51 versus bone metastases: 1.65±2.19 Gy). Organ absorbed doses ranked kidneys (1.56±0.38 Gy) > liver (1.07±0.19 Gy) > spleen (0.54±0.29 Gy). Absorbed dose coefficients (ADC) showed a consistent ranking: tumors 0.36±0.50 Gy/MBq (soft lesions 0.75±0.82 vs bone 0.25±0.33), kidneys (0.23±0.07), liver (0.16±0.03). Tumor-to-organ ADC ratios were 1.56 (kidneys), 14.59 (red marrow), and 4.94 (salivary glands). Treatment was well-tolerated with no SAEs or grade 3 AEs observed. ***Conclusion:*** Quantitative 1-bed SPECT with whole-body planar imaging is a feasible method for 225Ac-based dosimetry in TAT therapy. ^{225}Ac-PSMA-CY313 delivers high absorbed doses to tumors.

OP-595

Radiation Dosimetry of ^{15}O-water Based on Dynamic Large Axial Field of View PET

M. Lubberink[1], *A. Åhlström*[1], *T. Maaniitty*[2], *T. Tolvanen*[2], *J. Knuuti*[2]; [1]*Uppsala University, Uppsala, SWEDEN,* [2]*Turku PET Centre, Turku University and Turku University Hospital, Turku, FINLAND.*

Aim/Introduction: Previously published effective dose coefficient estimates for ^{15}O-water are in the range of 0.9 µSv/MBq to 1.2 µSv/MBq[1-3], resulting in an effective dose of around 0.45 mSv for a typically injected amount of 400 MBq in clinical cardiac scans. These values were based on limited PET information combined with pharmacokinetic models. Large axial field of view (LAFOV) PET allows for dynamic scanning of all relevant organs in a single scan, and hence should result in more accurate dosimetry estimates. The aim of the present work was to estimate radiation dosimetry of ^{15}O-water based on dynamic LAFOV PET. ***Materials and Methods:*** 10 subjects (mean age 59, range 44-73; mean body mass index 28.5, range 22.5-36.1; 4 females) underwent 4.5 min dynamic PET scans after automated bolus injection of 350±27 MBq (mean ± SD) 15O-water on a Quadra LAFOV PET scanner (Siemens Healthineers) at Turku PET Centre. All organs with visual uptake over background (brain, thyroid, lungs, heart wall, gall bladder, liver, spleen, small intestine, stomach, pancreas, kidneys, adrenal glands, red marrow, urinary bladder) were segmented using TotalSegmentator[4] and time-activity curves were calculated and uncorrected for decay. Time-integrated activity coefficients (TIAC) were calculated by trapezoidal integration followed by exponential extrapolation. The remainder of the body TIAC was calculated as the theoretical maximum TIAC minus the sum of all source organs. Organ absorbed doses and effective dose according to ICRP 103 were calculated using IDAC-DOSE 2.1[5]. ***Results:*** The highest TIACs were found in the lungs (0.15±0.03 min), liver (0.15±0.04 min) and brain (0.14±0.03 min). The fraction of the TIACs due to extrapolation beyond the last measured data point ranged from 10±1% in lungs to 35±6% in urinary bladder contents. The fraction of the maximum residence time included in the PET FOV was 71±9%, which was comparable to the fraction of the patient weight within the FOV (70±6%). The effective dose coefficient was 0.57 ± 0.04 (mean ± SD) µSv/MBq. The highest absorbed dose was found in kidneys, lungs and spleen (1.0 and 1.2 µGy/MBq for males and females, respectively). ***Conclusion:*** The effective dose of 15O-water is roughly half of the previously published values, amounting to an effective dose of approximately 0.2 mSv for a typical cardiac scan. ***References:*** [1]Smith et al, Eur J Nucl Med 1994; [2]Brihaye et al, J Nucl Med 1995; [3]ICRP 1998; [4]Wasserthal et al, Radiology:AI 2023; [5]Andersson et al, EJNMMI Research 2017.

OP-596

Biodistribution and dosimetry for a ^{11}C labelled PARP1 inhibitor

A. Törnblom[1], *C. He*[1], *M. Bolin*[1], *A. Tzortzakakis*[1], *J. Fernebro*[1], *C. Li*[1], *S. Fridsten*[2], *R. Altena*[1], *R. Axelsson*[1], *J. Siikanen*[1], *C. Hindorf*[1]; [1]*Karolinska Institutet, Stockholm, SWEDEN,* [2]*Karolinska University Hospital, Stockholm, SWEDEN.*

Aim/Introduction: Polyadenosine 5'diphosphoribose polymerase inhibitors (PARP1i) treat metastasised ovarian, breast, and prostate cancer with either germline or somatic BRCA-mutations. However, not all patients respond to these drugs. A ^{11}C-radiolabelled PARP1i tracer [^{11}C]AZ14193391 might be used with a PET/CT to identify eligible patients. Prediction of PARP1i-response could reduce unnecessary exposure to side effects and reduce healthcare costs. The aim of this study (EU CT 2022-502918-87-00) was to determine biodistribution, dosimetry and safety for [^{11}C]AZ14193391. ***Materials and Methods:*** Six patients (two ovarian, one prostate, three breast cancer) qualified for PARP1i-treatment were injected with a median activity of 5.8 MBq/kg range [3.7-6.0]. PET/CT-scans started simultaneously with the injection. All patients were scanned eyes-to-thighs at five time points (0, 5, 12, 21, 33 min post-injection). Scan time was increased with sequential scans to achieve equivalent count statistics in all images. Reconstruction was performed with BSREM (β=350). Segmentation was performed on a localisation-CT with an automatic segmentation tool and the segments were reviewed and corrected by a radiologist based on the PET-images. Time-Integrated Activity Coefficients (TIACs) and effective doses were calculated. Total blood activity was estimated from aortic activity concentration in the image and a factor 65 (women) or 75 (men) ml blood per kg body weight. Organs included in effective dose calculations were blood, kidneys, liver, pancreas, red marrow, spleen, thyroid, and urinary bladder. ***Results:*** No acute adverse effects were reported. High visual uptake was observed in liver, pancreas, kidneys, salivary glands, small intestine, urine bladder, and red marrow. Median TIACs for the three normal tissues with predominant uptake were liver, red marrow, and kidneys with 0.100 h, 0.025 h, and 0.012 h respectively. Median effective dose was 4.4 µSv/MBq [4.1-4.8]. The organs receiving the highest median absorbed dose per injected activity were liver=0.017 mGy/MBq [0.013-0.023], spleen=0.012 mGy/MBq [0.006-0.023], and kidneys=0.011 mGy/MBq [0.011-0.016]. The effective dose was lower compared to the result of the non-human primate study that showed 5.2 µSv/MBq. The short time frame (1 h) for imaging was a limitation for measurements of the biological half-life of AZ14193391. Uptake curves of pancreas, red marrow, and spleen showed a continuation of accumulation during all 5 scans. A review from 2012 (PMID: 22160195) on ^{11}C-dosimetry showed comparable effective doses. ***Conclusion:*** Imaging with [^{11}C]AZ14193391 is feasible and safe. Our results suggest that the radiation induced risk associated of imaging with [^{11}C]AZ14193391 is low compared to the potential benefits.

1306

Tuesday, October 7, 2025, 9:45 - 11:15

Room 117

Theranostics Track - TROP Session - Oncology & Theranostics Committee: Prostate Cancer Therapy in HSPC and CRPC

OP-597

PROQURE-I: Results of the phase I dose- escalation study combining [^{177}Lu]Lu-PSMA-617 and EBRT in curative intent treatment of N1 prostate cancer

D. Hoogenkamp[1], *L. G. Zuur*[1], *E. C. A. van der Sar*[2], *M. G. E. H. Lam*[2], *J. R. N. van der Voort-van Zyp*[2], *P. J. van Leeuwen*[1], *B. J. de Wit - van der Veen*[1], *D. M. V. de Vries-Huizing*[1], *J. J. M. A. Hendrikx*[1], *A. J. A. T. Braat*[1,2], *W. V. Vogel*[1]; [1]*Netherlands Cancer Institute, Amsterdam, NETHERLANDS,* [2]*University Medical Centre Utrecht, Utrecht, NETHERLANDS.*

Aim/Introduction: For patients with treatment-naïve prostate cancer (PCa) presenting with locoregional lymph node disease (N1M0), the standard treatment typically includes external beam radiotherapy (EBRT) combined with prolonged androgen deprivation therapy (ADT). Although this extensive regimen has improved overall survival rates, it is linked to considerable toxicity

and a five-year recurrence rate of up to 47%. [^{177}Lu]Lu-PSMA-617 has demonstrated promising outcomes in metastatic disease. For patients with regional PSMA-positive lesions identified via PSMA-PET/CT, incorporating [^{177}Lu]Lu-PSMA-617 into the EBRT and ADT regimen may offer better control of both macroscopic and microscopic disease, enhancing the likelihood of curation and potentially reducing the dependency on long-term ADT. ***Materials and Methods:*** The PROQURE-I study was a multi-center dose-escalation study in PSMA-PET/CT based iTxN1M0 treatment-naïve prostate cancer patients, eligible for standard first-line radiation treatment (seven weeks EBRT and three years ADT). Standard treatment was combined with escalating doses of [^{177}Lu]Lu-PSMA-617. A Bayesian Optimal Interval (BOIN) dose escalation model was followed to determine the maximum tolerated dose of administered radioactivity (MTD) using one (3, 6 or 9 GBq in the second week of EBRT) or two cycles (2x 7.4 GBq, in week 2 and 4 of EBRT) of [^{177}Lu]Lu-PSMA-617. Any treatment related grade 3 toxicity according to CTCAE v5.0 was considered as dose limiting toxicity. SPECT/CT and planar imaging for dosimetry analysis was performed at 4, 24 and 168 hours after [^{177}Lu]Lu-PSMA-617 injection. Tumor and organ dosimetry were performed using MIM Sureplan MRT. ***Results:*** Fourteen patients were included. No grade 3 toxicity or higher was observed and MTD was not reached. All reported grade 1 and 2 toxicities were considered related to EBRT. The first patient received 3 GBq, the second 6 GBq, six patients received 9 GBq and subsequently six patients received two cycles of 7.4 GBq [^{177}Lu]Lu-PSMA-617. EBRT dose was 70-77 Gy to the prostate, 60 Gy to visible lymph node metastases and 52 Gy to elective nodal fields. [^{177}Lu]Lu-PSMA-617 provided an additional dose to the tumor of 10.27 Gy (range 1.1-38.7 Gy) in the first cycle and 3.4 Gy (range 1.38-5.84 Gy) in the second cycle. ***Conclusion:*** Curative intent combination treatment with EBRT, [^{177}Lu]Lu-PSMA-617 and ADT is safe and well tolerated in treatment naïve men with iN1M0 prostate cancer. The addition of [^{177}Lu]Lu-PSMA-617 increased the total dose to the primary tumor. The suggested clinical benefit will be evaluated in an upcoming phase 2 study.

OP-598

Lutetium-177-PSMA-617 in Oligometastatic Hormone Sensitive Prostate Cancer (BULLSEYE trial)

B. Privé[1], *W. Noordzij*[2], *C. Muselaers*[1], *I. De Jong*[2], *I. Van Oort*[1], *M. Janssen*[1], *M. Van Rijk*[1], *W. Van Gemert*[3], *M. De Groot*[1], *N. Mehra*[1], *W. Gerritsen*[1], *M. Jonker*[1], *E. Alevroudis*[4], *S. Van der Gaag*[5], *J. Koppes*[5], *J. Sedelaar*[1], *A. Vis*[5], *A. Vrachimis*[4], *D. Oprea-Lager*[5], *J. Nagarajah*[1]; [1]*Radboudumc, Nijmegen, NETHERLANDS,* [2]*UMC Groningen, Groningen, NETHERLANDS,* [3]*Canisius Wilhelmina Hospital, Nijmegen, NETHERLANDS,* [4]*German Oncology Center, Limassol, CYPRUS,* [5]*Amsterdam UMC, Amsterdam, NETHERLANDS.*

Aim/Introduction: [^{177}Lu]Lu-PSMA-617 radioligand therapy is a novel treatment for patients with metastatic castration resistant prostate cancer. Previously, we showed that [^{177}Lu]Lu-PSMA-617 could be safely applied to patients with PSMA-expressing oligometastatic hormone-sensitive prostate cancer (mHSPC) with encouraging outcomes (Privé et al, CCR 2021). Now we report the results of the following randomised phase II trial. ***Materials and Methods:*** BULLSEYE was an international, multicentre, open-label, randomised phase II trial (NCT04443062), with crossover design. Fifty-eight patients were randomised in a 1:1 ratio to [^{177}Lu]Lu-PSMA-617 vs. standard of care (SoC) of deferred androgen deprivation therapy (ADT). Eligibility consisted of fast-progressing mHSPC (PSA doubling time ≤6 months) following local treatment, with ≤5 metastases on PSMA-PET/CT. Patients received 2 (+2) cycles of 7.4 GBq [^{177}Lu]Lu-PSMA-617. Patients in the SoC arm were allowed to cross over to receive [^{177}Lu]Lu-PSMA-617 upon disease progression. The primary outcome was progression-free survival (i.e., time without ADT). Progressive disease (PD) was defined as the initiation of ADT, a 100% increase in PSA since randomisation, and radiographic or clinical progression. Secondary outcomes were PSA response, adverse events, quality of life, and outcomes observed in the crossover arm. ***Results:*** Between April 2020 and July 2024, 78 men were screened, of whom 58 were eligible. Data cutoff was set on March 31st, 2025. Patients received a median number of 4 (IQR 4-4) cycles of 7.4 GBq of [^{177}Lu]Lu-PSMA-617. During the present median follow-up of 27 months (IQR 18-32), one SoC arm patient (3%) remained without disease progression as compared to 14 (48%) patients in the [^{177}Lu]Lu-PSMA-617 group. The median per protocol progression-free survival was 5 (IQR 3-7) and 18 (IQR 10-28) months for the SoC arm and [^{177}Lu]Lu-PSMA-617, respectively (HR 0.07, 95%CI 0.03-0.17; P<0.001). In total, 31/56 of patients treated with [^{177}Lu]Lu-PSMA-617 had a ≥90% PSA decline. Fourteen had a complete biochemical response. The most common treatment-related adverse events were: grade 1 xerostomia (59%), fatigue (46%), nausea (41%), and bone marrow toxicity (25%). Clinically relevant grade ≥2 adverse events were observed in less than 10% of patients. Quality of life remained stable during the study. ***Conclusion:*** [^{177}Lu]Lu-PSMA-617 showed promising efficacy in patients with oligometastatic prostate cancer to defer from androgen deprivation therapy. It had mild side effects and patients retained a good quality of life. Long-lasting remissions are seen in approximately 25% of patients. After surgery and external beam radiotherapy, [^{177}Lu]Lu-PSMA-617 could become a third metastases-directed treatment for this oligometastatic patient group.

OP-599

PEACE 6 Poor-responders: A randomized phase III trial evaluating the efficacy and safety of 177Lu-PSMA-617 in addition to Standard of Care (SoC) versus SoC alone in de novo metastatic hormone-sensitive prostate cancer (mHSPC)

D. Deandreis[1], *G. Gravis*[2], *S. Foulon*[3], *F. Tantot*[4], *C. Leger*[4], *F. Courbon*[5], *L. Turpin*[6], *A. Giraudet*[7], *K. Fizazi*[1]; [1]*Gustave Roussy, 114 Rue Edouard Vaillant, Villejuif, FRANCE,* [2]*Institut Paoli Calmette, Marseille, FRANCE,* [3]*Gustave Roussy, Villejuif, FRANCE,* [4]*Unicancer, Kremlin Bicetre, FRANCE,* [5]*IUCT Oncopole, Toulouse, FRANCE,* [6]*Hopital Foche, Suresnes, FRANCE,* [7]*CLCC Leon Berard, Lyon, FRANCE.*

Aim/Introduction: The management of patients with metastatic prostate cancer is still a challenge and the optimal therapeutic sequence needs to be still defined in some settings. The PEACE-6 umbrella program aims to assess, in randomized comparative trials, the efficacy and safety of combination therapy vs SOC according to patient and disease characteristics in metastatic prostate cancer patients. ***Materials and Methods:*** PEACE-6 PR is a phase III, international, multicenter, randomized, open-label, controlled trial sponsored by UNICANCER/GETUG [CL1] (EU CT n°: 2022-502408-57-00). It aims to evaluate the efficacy and safety of ^{177}Lu-PSMA-617 combined with SOC compared to SOC alone in patients with de novo mHSPC who do not present with a satisfactory response characterized by a serum PSA level ≥ 0.2 ng/ml, 6 to 8 months after initiation of systemic treatment for mHSPC in the absence of evidence of disease progression (including a rising PSA increase). Patients will be randomized in a 1:1 ratio to receive either ^{177}Lu-PSMA-617 + SOC or SOC alone. SOC include either ADT + ARSI ± RT or ADT + Docetaxel + ARSI ± RT. The co-primary endpoints are overall survival (OS) and radiographic progression-free survival (rPFS). OS is defined as the time from the date of randomization to the date of death due to any cause. rPFS is defined as the time from randomization to the date of radiographic progression according to PCWG3 criteria by investigator assessment, or death, whichever occurs first. All patients will undergo a pre randomization ^{68}Ga-PSMA PET and will be treated regardless of the ***results:*** patients with PSMA-positive or PSMA-negative disease according to PROMISE 2.0 criteria are eligible. For the experimental arm, the radioligand ^{177}Lu-PSMA-617 is scheduled to be intravenously injected at a single dose of 7 400

MBq once every 6 weeks (± 1 week) to a total of 4 cycles. A total of 500 patients is expected (250 for each arm) to be recruited in 100 centers in Europe (23 in France) in 63 months (5.25 years). ***Results:*** PEACE-6 PR is open to inclusion since October 2024. As of April 2025, a total of 11 patients have been already randomized, 5 in the SOC arm and 6 in the ^{177}Lu-PSMA-617 + SOC arm respectively. ***Conclusion:*** PEACE-6 PR trial will be essential to define the best therapeutic strategy in the setting of de novo metastatic hormonosensitive prostate cancer patients.

OP-600

Prognostic Impact of Homologous Recombination Repair and Mismatch Repair Gene Alterations in Patients with Metastatic Castration-Resistant Prostate Cancer Treated with Prostate-Specific Membrane Antigen-directed Radioligand Therapy

A. Antic Nikolic[1], *S. Xue*[2], *S. Wen*[2], *J. Baessler*[1], *M. Hacker*[2], *X. Li*[2], *C. Lapa*[1];
[1]*Nuclear Medicine, Faculty of Medicine, University of Ausgburg, Augsburg, GERMANY,* [2]*Department of Biomedical Imaging and Image-Guided Therapy, Division of Nuclear Medicine, Vienna, AUSTRIA.*

Aim/Introduction: Prostate-specific membrane antigen-targeted radioligand therapy (PSMA-RLT) has emerged as an effective treatment for metastatic castration-resistant prostate cancer (mCRPC). However, therapeutic responses remain heterogeneous, potentially due to mutations in DNA repair-related genes that may contribute to treatment resistance. This study aimed to evaluate the prognostic significance of mutations in genes involved in homologous recombination repair (HRR) and mismatch repair (MMR) pathways in mCRPC patients undergoing PSMA-RLT. ***Materials and Methods:*** We retrospectively analyzed 35 patients with metastatic castration-resistant prostate cancer (mCRPC) who received at least two cycles of prostate-specific membrane antigen-targeted radioligand therapy (PSMA-RLT). All included patients had available next-generation sequencing data covering genes involved in homologous recombination repair (ATM, BARD1, BRCA1, BRCA2, BRIP1, CDK12, CHEK1, CHEK2, FANCA, FANCC, FANCD2, FANCG, FANCL, NBN, PALB2, RAD51B, RAD51C, RAD51D, RAD54L, TP53) and mismatch repair (MSH2, MSH6, MLH1, PMS2, EPCAM) pathways. Patients were stratified into HRR/MMR-mutant (n = 12) and HRR/MMR wild-type (n = 23) groups. Therapeutic response was evaluated by the percentage change in PSA levels (ΔPSA%) after two treatment cycles. Group differences in PSA response were assessed using non-parametric statistical tests. Progression-free survival (PFS) was estimated using Kaplan-Meier analysis and compared using the log-rank test. Additionally, the mean tumor-absorbed dose during the first treatment cycle was compared between groups using a t-test. ***Results:*** The median PSA decline after two treatment cycles was significantly lower in the HRR/MMR-mutant group (ΔPSA% = -90.4%) compared to the wild-type group (ΔPSA% = -167.4%) ($P < 0.05$). The HRR/MMR-mutant group showed a trend toward shorter progression-free survival (PFS), with a hazard ratio of 2.146 ($P = 0.07$), indicating more than a two-fold increased risk of disease progression compared to the wild-type group. No statistically significant difference in mean absorbed dose after the first treatment cycle was observed between the HRR/MMR-mutant and wild-type groups ($P = 0.28$). ***Conclusion:*** HRR/MMR gene mutations in mCRPC patients were associated with reduced PSA response and a trend toward shorter progression-free survival following PSMA-RLT. The observed lack of difference in absorbed dose between HRR/MMR-mutant and wild-type groups is based on preliminary data from a single treatment cycle and warrants further investigation. HRR/MMR mutation status may serve as a prognostic biomarker to guide personalized therapeutic strategies in advanced prostate cancer.

OP-601

Safety and efficacy of ^{177}Lu-PSMA-I&T for RLT in mCRPC - a prospective multicenter Swiss Registry study

A. Chirindel[1], *G. Nicolas*[1], *M. Tissier*[2], *M. del Sol Pérez Lago*[3], *F. Forrer*[4], *A. Afshar-Oromieh*[5], *S. Beintner-Skawran*[6], *A. Bauman*[7], *F. Melpomeni*[7], *E. Nitzsche*[8], *N. Schaefer*[2], *D. Wild*[1];
[1]*University Hospital of Basel, Department of Theranostics, Nuclear Medicine, Basel, SWITZERLAND,* [2]*CHUV, Department of Nuclear Medicine, Lausanne, SWITZERLAND,* [3]*Luzerner Kantonsspital, Department of Nuclear Medicine, Lucerne, SWITZERLAND,* [4]*Kantonsspital St. Gallen, Department of Nuclear Medicine, St. Gallen, SWITZERLAND,* [5]*Inselspital, Department of Nuclear Medicine, Bern, SWITZERLAND,* [6]*University Hospital Zurich, Department of Nuclear Medicine, University of Zurich, Zurich, SWITZERLAND,* [7]*University Hospital of Basel, Department of Theranostics, Radiopharmaceutical Chemistry, Basel, SWITZERLAND,* [8]*Kantonsspital Aarau, Department of Nuclear Medicine, Aarau, SWITZERLAND.*

Aim/Introduction: Several prior prospective studies[1,2] have established [^{177}Lu]Lu-PSMA-617 for radioligand therapy(RLT) in patients with metastatic castration-resistant prostate cancer(mCRPC), demonstrating improved overall survival (OS) compared to the standard of care and a more favorable toxicity profile than chemotherapy. [^{177}Lu]Lu-PSMA-I&T has been used as an alternative radioligand with assumed bioequivalence for RLT in mCRPC. However, no prospective data on its safety and efficacy are currently available. ***Materials and Methods:*** This prospective, multicenter Swiss Registry study(NCT06830408) enrolled mCRPC patients identified with progression of disease and referred for RLT with [^{177}Lu]Lu-PSMA-I&T. Treatment-emerged adverse events (AEs) were recorded per CTCAE v5.0 before each therapy cycle and at 12 weeks post-therapy. Xerostomia was evaluated using a standardized questionnaire. Efficacy was assessed through PSA response (PCWG3) and imaging after each cycle (SPECT/CT) and at 8-12 weeks post-RLT (CT, MRI, or PSMA PET-CT). Follow-ups were performed every 6 months or as clinically indicated. Descriptive statistics were used to summarize patient and treatment characteristics. Time-to-event outcomes—including PSA progression-free survival (PSA-PFS), imaging-based progression-free survival (rPFS), and overall survival (OS) were analyzed using Kaplan-Meier methodology. ***Results:*** A total of 333 consecutive mCRPC patients received a median of 4 cycles (range: 1-6) of [^{177}Lu]Lu-PSMA-I&T over 5.6 months (0.7-11.3 months), with a median cumulative activity of 24 GBq(7-48 GBq). Baseline characteristics included Gleason score ≥8 (72%), metastases in lymph nodes (71%), bones (94%) and visceral organs (26%). Most patients received prior treatment with second generation antiandrogen drugs (90%) and taxane-based chemotherapy (81%). The median follow-up was 12 months (1-54 months). Hematologic toxicity (all grades) was recorded with anemia (30%), thrombocytopenia (26%), leukopenia (18%) and neutropenia (13%). Of these, grade 3-4 events were observed in 8%, 3%, 1.7%, and 0%, respectively. Increased creatinine occurred in 16% of patients (only grade 1-2). Xerostomia grade 1 and 2 was noticed in 25% and <5% of patients, respectively. Best PSA response during RLT demonstrated partial response in 43% and stable disease in 28% of patients. A 90% PSA reduction was achieved in 25% patients. Median OS was 13.2 months (95% CI: 11.8-14.7), PSA-PFS was 4.4 months (3.4-5.4), and rPFS was 6.8 months (6.1-7.5). ***Conclusion:*** Real world data of the first multicenter prospective study demonstrate that [^{177}Lu]Lu-PSMA-I&T is safe and effective for RLT in mCRPC. When comparing these data to previously reported phase II/III studies, the toxicity profile and treatment efficacy appears similar to that of the established [^{177}Lu]Lu-PSMA-617. ***References:*** 1.Sartor et al. N.Engl.J.Med.2021;385:1091-1103.2.Hofman et al. Lancet.2021;397:797-804.

OP-602

Retreatment with [177Lu]Lu-PSMA-617 in mCRPC patients treated under the French Early access program

D. Taieb[1], *P. Robin*[2], *P. Barthelemy*[3], *C. Peltier*[4], *S. Chêne*[5], *A. Douillet*[5], *F. Somme*[3];
[1]*APHM-AMU, Marseille, FRANCE,* [2]*Université de Brest, Inserm, UMR 1304, GETBO, CHU Brest, Brest, FRANCE,* [3]*Institut de cancérologie Strasbourg Europe, Strasbourg, FRANCE,* [4]*ICTA PM, Dijon, FRANCE,* [5]*Novartis, Rueil-Malmaison, FRANCE.*

Aim/Introduction: [177Lu]Lu-PSMA-617 is an approved targeted therapy for PSMA-expressing metastatic castration-resistant prostate cancer available in France since December 2021 through an early access program. This exploratory retrospective analysis focuses on patients retreated beyond 6 cycles with [177Lu]Lu-PSMA-617. ***Materials and Methods:*** Patients with mCRPC who had previously received at least one line of chemotherapy and one androgen receptor pathway inhibitor (ARPI), and who were positive on [68Ga]Ga-PSMA-11 PET, were eligible for treatment with [177Lu]Lu-PSMA-617, similar criteria applied for retreatment. The treatment schedule consisted of 6 injections maximum of 7.4 GBq every 6 weeks during initial treatment and during retreatment. Patients' characteristics, efficacy and safety data were systematically collected during follow-up visits. ***Results:*** At the end of January 2025, a total of 3198 patients were included in the early access program, with 96.9% receiving a standard schedule without retreatment, and 3.1% (n=98) underwent RLT retreatment including 55 patients still under retreatment at data cut-off (DCO). Baseline characteristics only differed for non-retreated and retreated patients in terms of line of taxanes >1: 43.7% vs 61.2% (p=0.0023), and opioids used for pain control: 26.3% vs 16.3% (p=0.026). The median time between the last dose of the standard dosing schedule and the first dose of the retreatment was 8.94 months. During this interval, 9 patients received 1 ARPI and 5 patients received 1 line of chemotherapy. 84.7 % of the retreated patients received 6 injections during the initial schedule and amongst those who completed the retreatment (n=43) a median of 3 cycles [1-6] has been reached. 4 patients initiated a 3rd treatment schedule and 1 reached 15 cycles at DCO. During the initial schedule, median imaging-based PFS was statistically different between non-retreated and retreated patients : 7.00 months [6.18-7.52] vs 10.35 months [8.80-NR] (p<0.0001). During retreatment, symptom control was maintained for 94.9% of patients, 70.7% showed disease control based on imaging, and 80.3% had controlled PSA levels. 10.2% of retreated patients had dose reductions, compared to 23.3% of non-retreated patients. 10 patients (10.2%) reported at least one treatment-related adverse event (including 5 cases of thrombocytopenia) during the initial schedule, and 3 (3.1%) during the retreatment. ***Conclusion:*** Analysis of patients retreated and not retreated with [177Lu]Lu-PSMA-617 for mCRPC shows few differences in baseline characteristics. Upon disease progression, retreatment with [177Lu]Lu-PSMA617 demonstrated sustained clinical activity and appears to be well-tolerated in selected patient population. Updated efficacy and safety results will be presented at EANM congress.

OP-603

Final analysis of patients treated with [177Lu]Lu-PSMA-617 in early access program in metastatic castration-resistant prostate cancer (mCRPC) in France

C. Bailly[1], *P. Olivier*[2], *L. Vija*[3], *A. Giraudet*[4], *V. Massard*[5], *G. Roubaud*[6], *S. Girault*[7], *S. Abadie-Lacourtoisie*[7], *C. Viala*[1], *A. Flechon*[4], *S. Chêne*[8], *Y. Godbert*[6];
[1]*Centre Hospitalier Universitaire, Nantes, FRANCE,* [2]*Centre hospitalier régional et universitaire, Vandoeuvre-lès-Nancy, FRANCE,* [3]*Institut Universitaire du Cancer de Toulouse, Toulouse, FRANCE,* [4]*Centre Léon Bérard, Lyon, FRANCE,* [5]*Institut de Cancérologie de Lorraine, Vandoeuvre-lès-Nancy, FRANCE,* [6]*Institut Bergonié, Bordeaux, FRANCE,* [7]*Institut de cancérologie de l'Ouest Paul Papin, Angers, FRANCE,* [8]*Novartis, Rueil-Malmaison, FRANCE.*

Aim/Introduction: VISION study showed that [177Lu]Lu-PSMA-617 added to BSoC prolonged imaging-based progression-free survival and overall survival in patients with PSMA-positive mCRPC. French Health Authorities has granted a "cohort" early access for [177Lu]Lu-PSMA-617 in this indication since Dec 2021. ***Materials and Methods:*** PSMA positive mCRPC patients pretreated with at least 1 taxane-based chemotherapy regimen and ≥1 androgen receptor pathway inhibitor (ARPI) were included. [177Lu]Lu-PSMA-617 (7.4 GBq) was administered up to 6 cycles every 6 weeks. Patients' characteristics and safety data are described for the entire population. 3198 patients were included (data cut-off (DCO) 1 : 1/31/2025) and 2119 patients were analyzed for efficacy (DCO 2 : 5/31/2024), respectively. Adverse events (AE) grading was not evaluated. ***Results:*** At DCO 1, characteristics of patients at baseline were : median age 73.8 (37-100) years; ECOG 0-1: 87.2%; median PSA level 44.0 (0-6972) ng/ml; metastatic sites: bone 92.5%, lymph node 60.0%, liver 8.6%; previous taxane regimen: 98.9% of which 44.2% have received 2; prior ARPI treatment: 100% and 53.1% received 2 or more (median: 2). The incidence of 2 prior taxane regimen has reduced over time. Patients received a median of 3 anterior treatments. Concomitant treatment with ARPI was observed in 21.4%. At DCO 2, with a median follow-up of 6.7 months, median imaging-based PFS was 7.5 months. Imaging follow-up consisted of CT scan and scintigraphy, with PET in some instances. Median time to clinical progression was 8.1 months. A PSA decrease was observed in 69.6% of patients at any time. The median time to PSA decrease was 1.28 months (range, 0.0-15.7). Patients received an average of 4.2 [177Lu]Lu-PSMA-617 cycles, and 40.7% completed 6 cycles. 12.8% (n=410) of patients experienced >1 treatment-related (TR) AE, including 302 patients with ≥1 serious AE. The most reported TRAEs were thrombocytopenia (4.5% of patients) and anemia (3.8% of patients). 12 deaths related to treatment have been reported. ***Conclusion:*** In this largest ever reported real-life cohort of mCRPC patients treated with [177Lu]Lu-PSMA-617 during more than 3 years profile has evolved to less heavily pretreated patients. In the cohort, patients received less concomitant ARPI treatment compared to VISION study. Safety profile of [177Lu]Lu-PSMA-617 remains favorable. Final results of this early access cohort will be presented at EANM congress, including longer follow-up period and higher number of patients who completed treatment. Meanwhile, analyses on specific sub-populations of interest are currently underway.

OP-604

Fracture risk and treatments at progression in EORTC-1333 PEACE-3 study evaluating the addition of Radium 223 in metastatic castration-resistant prostate cancer starting enzalutamide

A. Rodriguez Vida[1], *B. Tombal*[2], *A. Choudhury*[3], *F. Saad*[4], *E. Gallardo*[5], *A. Soares*[6], *Y. Loriot*[7], *R. McDermott*[8], *C. Poncet*[9], *C. Corneel*[9], *B. Fournier*[9], *F. Lecouvet*[2], *S. Gillessen*[10];
[1]*Hospital del Mar, Barcelona, SPAIN,* [2]*Cliniques universitaires Saint Luc, Brussels, BELGIUM,* [3]*The Christie NHS Foundation Trust, Manchester, UNITED KINGDOM,* [4]*Centre hospitalier de l'Université de Montréal, Montréal, QC, CANADA,* [5]*Parc Taulí Hospital Universitari, Sabadell, SPAIN,* [6]*Hospital Israelita Albert Einstein, Sao Paulo, BRAZIL,* [7]*Institut Gustave Roussy, Paris, FRANCE,* [8]*Tallaght University Hospital, Dublin, Dublin, IRELAND,* [9]*European Organisation of Research and Treatment of Cancer, Brussels, BELGIUM,* [10]*Oncology Institute of Southern Switzerland, EOC, Bellinzona, SWITZERLAND.*

Aim/Introduction: PEACE-3 showed that adding radium-223 (RAD) to enzalutamide (ENZ) significantly improves progression-free survival (PFS) and overall survival (OS) in metastatic castration-resistant prostate cancer (mCRPC) with bone metastases. We report an update on the fracture events and treatment received at progression. ***Materials and Methods:*** From 11/2015 to 03/2023, 446 men progressing to mCRPC were randomized 1:1 to ENZ alone or combined with 6 cycles of RAD (ENZ-RAD). As of March 2018, the co-administration of bone protective agents (BPA) was mandatory. We report the fracture rate for the study here. ***Results:*** Fractures (symptomatic or pathologic) occurred in 30 (13.4%)

patients (pts)in ENZ and 53 (24.3%) in ENZ-RAD. In ENZ-RAD, fractures occurred in 53.6% of pts enrolled before the mandatory BPA co-administration and in 14.2% of pts enrolled afterward. In ENZ, fracture incidence dropped from 20.3% before the mandatory BPA co-administration to 10.9% afterward. The hazard ratio (HR) for time to first fracture was 2.00 (95%CI 1.27-3.14). 12- and 24-month estimates of cumulative incidence of fracture (95% CI) were 7.6% (4.6%-11.6%) and 11.3% (7.5%-16.0%) in ENZ and 12.9% (8.8%-17.7%) and 17.1% (12.4%-22.6%) in ENZ-RAD.Adding RAD to ENZ significantly increased time to the subsequent treatment (TTNT). HR for TTNT is 0.57 (95%CI 0.44-0.75; p=<0.0001). At the time of rPFS analysis, 133 (59.4%) pts in ENZ and 94 (42.3%) in ENZ-RAD received a subsequent anti-neoplastic agent. In ENZ vs ENZA-RAD, the first subsequent treatment was chemotherapy in 103 (71.5%) pts vs 79 (74.5%), hormone therapy in 20 (13.9%) vs 18 (17.0%), PARP inhibitor in 8 (5.6%) vs 5 (4.7%) and other in 13 (9.0%) vs in 2 (1.9%). ***Conclusion:*** This final analysis confirms the positive impact of concomitant BPA use in lowering fracture risk in mCPRC pts receiving ENZ or ENZ-RAD. Chemotherapy was the most common subsequent treatment in both arms. ***References:*** PEACE III: ClinicalTrials.gov ID NCT02194842.

OP-605

Efficacy of Lutetium-177 [177Lu]Lu-PSMA radioligand therapy re-treatment beyond six cycles in patients with metastatic castration-resistant prostate cancer.

J. Weindler[1], *E. Medhurst*[1], *N. Papa*[1], *L. Kostos*[2], *B. Emmerson*[1], *A. A. Azad*[2], *M. S. Hofman*[1], *J. P. Buteau*[1];
[1]*Prostate Cancer Theranostics and Imaging Centre of Excellence (ProsTIC), Molecular Imaging and Therapeutic Nuclear Medicine, Cancer Imaging, Peter MacCallum Cancer Centre, Melbourne, AUSTRALIA,* [2]*Department of Medical Oncology, Peter MacCallum Cancer Centre, Melbourne, AUSTRALIA.*

Aim/Introduction: Lutetium-177 [177Lu]Lu-PSMA radioligand therapy is a life-prolonging treatment for patients with metastatic castration-resistant prostate cancer (mCRPC). Landmark studies reported outcomes using up to 6 cycles of [177Lu]Lu-PSMA. We aimed to evaluate the efficacy of re-treatment with [177Lu]Lu-PSMA in patients who received more than 6 cycles in total. ***Materials and Methods:*** We conducted a retrospective, single-centre analysis of patients with mCRPC who completed at least one re-treatment course of [177Lu]Lu-PSMA upon disease progression and received more than 6 cycles in total by data cut-off (February 11, 2025). Patients were initially treated on clinical trials or registry with [177Lu]Lu-PSMA-617 or [177Lu]Lu-PSMA-I&T. Re-treatment was defined as an interval of at least 12 weeks between [177Lu]Lu-PSMA cycles. The primary endpoint was PSA response, defined by a reduction of at least 50% (PSA50-RR) and 90% (PSA90-RR) following first re-treatment. The secondary endpoint of overall survival (OS) was calculated using Kaplan-Meier method from time of screening PSMA PET/CT prior to commencement of [177Lu]Lu-PSMA and also from first re-treatment to death or last follow-up. ***Results:*** Between August 26, 2015 and January 31, 2024, 54 patients met the inclusion criteria and started treatment with [177Lu]Lu-PSMA. They had a median age at re-treatment of 75 years (IQR 70-80). Prior treatments included androgen-receptor pathway inhibitors in 53 (98%) patients, docetaxel in 48 (89%) and cabazitaxel in 16 (30%). A median of 9 total cycles of [177Lu]Lu-PSMA (IQR 8-10) were administered with a cumulative median radioactivity of 60.0 GBq (IQR 55.7-67.9). PSA50-RR and PSA90-RR were achieved by 98% and 78% of patients during their initial [177Lu]Lu-PSMA course. Median time from the last cycle of the initial [177Lu]Lu-PSMA treatment course to the first cycle of re-treatment was 36 weeks (IQR 25-51), with PSA50-RR and PSA90-RR occurring in 40%, and 11% of patients, respectively. 22 patients received a second re-treatment block, with PSA50-RR and PSA90-RR observed in 41% and 14%, respectively. Median OS was 36 months (95%CI: 33-41) from screening PSMA PET/CT and 16 months (95%CI: 12-19) from the first re-treatment. ***Conclusion:*** Re-treatment with [177Lu]Lu-PSMA is effective for a select group of patients with mCRPC who initially responded to treatment and had received more than 6 cycles in total.

1307

Tuesday, October 7, 2025, 9:45 - 11:15
Room 212

TROP Session - Neuroimaging Committee: Neuro-Oncology

OP-606

Checkpoint inhibitor therapy is associated with elevated false-positive findings in amino acid PET imaging of brain metastases

A. Chaban[1], *L. Baumgart*[2], *C. Delbridge*[3], *D. Bernhardt*[4], *B. Wiestler*[5], *A. Aftahy*[2], *V. Schneller*[6], *B. Meyer*[2], *W. Weber*[1], *H. Meyer*[7], *J. Gempt*[2], *I. Yakushev*[1];
[1]*Klinik und Poliklinik für Nuklearmedizin, Klinikum rechts der Isar, Technische Universität München, Munich, GERMANY,* [2]*Klinik und Poliklinik für Neurochirurgie, Klinikum rechts der Isar, Technische Universität München, Munich, GERMANY,* [3]*Institut für Allgemeine Pathologie und Pathologische Anatomie, Klinikum rechts der Isar, Technische Universität München, Munich, GERMANY,* [4]*Klinik und Poliklinik für RadioOnkologie und Strahlentherapie, Klinikum rechts der Isar, Technische Universität München, Munich, GERMANY,* [5]*Neur-Kopf-Zentrum, Klinikum rechts der Isar, Technische Universität München, Munich, GERMANY,* [6]*Klinik und Poliklinik für Innere Medizin III, Klinikum rechts der Isar, Technische Universität München, Munich, GERMANY,* [7]*University Medical Center Hamburg - Eppendorf, Hamburg, GERMANY.*

Aim/Introduction: Positron emission tomography (PET) with amino acid tracers plays an important role in distinguishing progressive or recurrent brain metastases (PRBMs) from treatment-induced changes. Despite the expanding clinical use of checkpoint inhibitors (CPIs) for metastatic cancers, their influence on the diagnostic accuracy of amino acid PET remains unclear. ***Materials and Methods:*** This retrospective study evaluated 32 patients with MRI-suspected PRBMs following radiotherapy, all of whom underwent 18F-fluorethyltyrosine (18F-FET) PET imaging within four weeks prior to resection or biopsy. The cohort comprised nine currently or previously CPI-treated patients (CPI+ group) and 23 controls managed with chemotherapy, targeted therapies, or no systemic treatment (CPI- group). ***Results:*** Demographic variables, including age, baseline metastasis burden, and interval between radiotherapy and PET imaging, showed no significant intergroup differences. Pathological PET findings were observed in 8 CPI+ patients vs. 22 CPI- patients. False-positive rates significantly differed between the subgroups, with 75% (6/8) in the CPI+ vs. 14% (3/22) in the CPI- group. Histopathological examination of CPI+ specimens revealed inflammatory reactions characterized by lymphocytic infiltrates. ***Conclusion:*** These results indicate that the history of CPI therapy is strongly associated with an elevated risk of false-positive amino acid PET findings in PRBM assessment. It may stem from CPI-induced immunological hyperactivity, which has been documented to provoke inflammatory responses across multiple organ systems. Clinicians should exercise heightened caution when interpreting amino acid PET results in CPI-treated patients with suspected PRBMs.

OP-607

Diagnostic Accuracy and Optimal Thresholding of [^{18}F] fluoroethyl-L-tyrosine PET to Detect Tumor Tissue in Patients with Glioblastoma

E. Van de Giessen, *J. L. Ebenau, T. Koopman, F. Barkhof, P. Wesseling, J. C. Reijneveld, W. P. Vandertop, P. C. de Witt Hamer, P. J. Pouwels, R. Boellaard, M. M. Yaqub, N. Verburg;*
Amsterdam UMC, Amsterdam, NETHERLANDS.

Aim/Introduction: O-(2-[^{18}F]fluoroethyl)-L-tyrosine (FET) positron emission tomography (PET) is increasingly used in neuro-oncology. A tumor-to-brain ratio (TBR) threshold of 1.6 is the current standard to distinguish tumor tissue from surrounding (non-tumor) brain (1). The study on which this threshold was based had a heterogeneous population though, including patients with a wide range of WHO tumor grades, and only 2 out of 28 patients with glioblastoma (2). We investigated the optimal threshold for the detection of tumor tissue in glioblastoma for [^{18}F]FET PET and compared this to the current standard, i.e. a tumor-to-brain ratio (TBR) threshold of 1.6. ***Materials and Methods:*** We included 10 patients (63±7y, 3 females) with glioblastoma, IDH-wildtype. All participants underwent MRI and [18F]FET PET within 14 days before surgery. Biopsy samples were obtained from regions inside and outside of imaging abnormalities and assessed for tumor presence by two experienced neuropathologists. Mean TBR was calculated in the region of interest (ROI) corresponding with the biopsy site (1 cm^3). We used Receiver Operation Characteristics analysis to calculate the sensitivity and specificity and determined the optimal TBR threshold using the Youden index. We compared the diagnostic accuracy of this optimal threshold with the current standard 1.6 threshold using McNemar's chi^2 test. ***Results:*** A total of 98 samples was obtained (median nine samples per patient) with tumor present in 72 (73%) samples. The optimal threshold to distinguish tissue with tumor from non-tumor tissue was 1.39. Sensitivity of this optimal threshold was higher than that of the 1.60 threshold (72% versus 57%, p<0.01), while specificity was similar (both 81%). ***Conclusion:*** In patients with glioblastoma, a [^{18}F] FET PET TBR of 1.39 better distinguished tumor from non-tumor tissue than the current standard TBR threshold of 1.6. These results contribute to more accurate tumor delineation and may benefit planning of surgical resection and radiotherapy. ***References:*** 1. N. L. Albert, N. Galldiks, B. M. Ellingson, M. J. van den Bent, S. M. Chang, F. Cicone, J. de Groot, E.-S. Koh, I. Law, E. Le Rhun, et al., Pet-based response assessment criteria for diffuse gliomas (pet rano 1.0): a report of the rano group, The Lancet Oncology 25 (1) (2024) e29-e41. 2. D. Pauleit, F. Floeth, K. Hamacher, M. J. Riemenschneider, G. Reifenberger, H.-W. Müller, K. Zilles, H. H. Coenen, K.-J. Langen, O-(2-[18f] fluoroethyl)-l-tyrosine pet combined with mri improves the diagnostic assessment of cerebral gliomas, Brain 128 (3) (2005) 678-687.

OP-608

Preoperative Delineation of Tumor Boundaries in Adult High-Grade Glioma Using Integrated ^{18}F-FET PET/MR Imaging

Q. Han[1], *J. Liu*[2], *T. Li*[1], *X. Su*[3], *E. Li*[3], *Y. Yang*[3], *X. Guo*[2], *W. Ma*[2], *Y. Wang*[2], *X. Cheng*[1], *L. Huo*[1];
[1]*Nuclear Medicine Department, Peking Union Medical College Hospital, Chinese Academy of Medical Science and Peking Union Medical College, Beijing, CHINA,* [2]*Department of Neurosurgery, Peking Union Medical College Hospital, Chinese Academy of Medical Sciences and Peking Union Medical College, Beijing, CHINA,* [3]*Beijing United Imaging Healthcare Co., Ltd, Beijing, CHINA.*

Aim/Introduction: Adult high-grade gliomas (HGGs) are aggressive with high recurrence rates and poor prognosis. Accurate preoperative delineation of tumor boundaries is crucial to maximize safe resection while preserving healthy brain tissue. This study aimed to evaluate the capability of integrated ^{18}F-fluoroethyltyrosine (FET) PET/MR in defining tumor boundaries in adult HGG patients, and to explore the additional diagnostic value of MRI parameters in enhancing PET indices. ***Materials and Methods:*** Seventeen patients with HGG underwent integrated ^{18}F-FET PET/MR imaging, followed by image-guided stereotactic biopsy. A total of 70 samples (51 tumor and 19 non-tumor) were collected. For each biopsy location, a 5 mm volume of interest (VOI) was used to extract quantitative values from PET, including maximum and mean tumor-to-background ratio (TBRmax and TBRmean), and from MRI, including apparent diffusion coefficient (ADC), contrast-enhanced T1-weighted imaging (T1CE), and T2-weighted fluid-attenuated inversion recovery imaging (T2-FLAIR). Diagnostic performance was assessed using receiver operating characteristic (ROC) analysis, with histopathology as the reference. ***Results:*** PET parameters showed excellent performance for tumor boundary delineation, with TBRmax achieving an area under the curve (AUC) of 0.914 (accuracy = 84.6%, sensitivity = 74.5%, specificity = 94.3%) and TBRmean achieving an AUC of 0.909 (accuracy = 83.7%, sensitivity = 72.6%, specificity = 94.3%). MRI parameters, such as T1CE and T2-FLAIR, were moderately diagnostic (AUC = 0.785 and 0. 825, respectively), while ADC alone showed limited value (AUC = 0.667). Combining PET with MRI did not significantly improve diagnostic accuracy compared to PET alone. However, combining T2-FLAIR modestly improved sensitivity (90.2%), though without a substantial gain in overall AUC. TBRmax remained the most reliable single parameter for preoperative tumor boundary definition. ***Conclusion:*** Integrated ^{18}F-FET PET/MR demonstrates accurate preoperative delineation of tumor boundaries in adult HGGs. The PET parameter TBRmax outperformed all other imaging parameters. Although MRI parameters such as T2-FLAIR may enhance sensitivity when combined with PET, their added value remains limited. These findings support the use of ^{18}F-FET PET as a valuable assistance to MRI for guiding surgical planning for HGGs.

OP-609

Prognostic stratification of IDH-mutant gliomas based on amino acid PET parameters at diagnosis

M. Mair[1,2], *J. Werner*[2,3], *J. Weller*[4], *E. Barci*[1], *S. Katzendobler*[4], *J. Isakaj*[1], *L. Berchtold*[2,5], *T. Aras*[1], *R. Stürzl*[1], *J. Reis*[6], *J. Hennenberg*[7], *H. C. Puhr*[2], *T. Schabhüttl*[1,2], *B. Kiesel*[8], *G. Widhalm*[8], *A. Wöhrer*[9], *T. Nakuz*[10], *M. Hacker*[10], *J. Furtner*[7,11], *P. N. Harter*[12,13,14], *L. von Baumgarten*[4,13,15], *A. S. Berghoff*[2], *N. Thon*[4,16], *M. Preusser*[2], *N. L. Albert*[1,13,14];
[1]*Department of Nuclear Medicine, LMU University Hospital, LMU Munich, Munich, GERMANY,* [2]*Division of Oncology, Department of Medicine I, Medical University of Vienna, Vienna, AUSTRIA,* [3]*Department of Neurology, Faculty of Medicine and University Hospital Cologne, University of Cologne, Cologne, GERMANY,* [4]*Department of Neurosurgery, LMU University Hospital, LMU Munich, Munich, GERMANY,* [5]*Institute of Medical Statistics, Center for Medical Data Science, Medical University of Vienna, Vienna, AUSTRIA,* [6]*Institute of Neuroradiology, LMU University Hospital, LMU Munich, Munich, GERMANY,* [7]*Division of Neuroradiology and Musculoskeletal Radiology, Department of Radiology and Image-guided Therapy, Medical University of Vienna, Vienna, AUSTRIA,* [8]*Department of Neurosurgery, Medical University of Vienna, Vienna, AUSTRIA,* [9]*Division of Neuropathology and Neurochemistry, Department of Neurology, Medical University of Vienna, Vienna, AUSTRIA,* [10]*Division of Nuclear Medicine, Department of Radiology and Image-guided Therapy, Medical University of Vienna, Vienna, AUSTRIA,* [11]*Research Center for Medical Image Analysis and Artificial Intelligence (MIAAI), Faculty of Medicine and Dentistry, Danube Private University, Krems, AUSTRIA,* [12]*Center of Neuropathology and Prion Research, Faculty of Medicine, LMU Munich, Munich, GERMANY,* [13]*Bavarian Cancer Research Center (BZKF), Partner Site Munich, Munich, GERMANY,* [14]*German Cancer Consortium (DKTK), Partner Site Munich, Munich, GERMANY,* [15]*Department of Neurology, LMU University Hospital, LMU Munich, Munich, GERMANY,* [16]*Department of Neurosurgery, Knappschaft University Hospital Bochum, Bochum, GERMANY.*

Aim/Introduction: Amino acid PET is increasingly used in the clinical management of gliomas. While improved prognostic stratification is urgently needed given ongoing changes in the treatment landscape of IDH-mutant glioma, the prognostic significance of quantitative PET parameters in molecular subgroups remains unclear. ***Materials and Methods:*** In this retrospective, bicentric cohort study, patients diagnosed with IDH-mutant glioma who underwent amino acid PET within one year before/after histological diagnosis have been included. Maximum/mean tumor-to-background ratios (TBR_{max}, TBR_{mean}) and PET-positive volume (PET volume) were evaluated. Tumor extent in MRI was evaluated according to RANO 2.0 criteria based on the product of maximum perpendicular diameters in T2/FLAIR and contrast-enhanced T1 (T1CE). As endpoints, time to next intervention (TTNI) and overall survival (OS) were used. ***Results:*** Overall, 457 patients were included (54.9% astrocytoma, 45.1% oligodendroglioma; median age at diagnosis: 40 years [range: 18-81]). In univariate analysis of patients with astrocytoma who underwent PET before resection, TTNI was associated with TBR_{max} (Hazard ratio [HR] 1.44 [95%CI: 1.23-1.68], p<0.001), TBR_{mean} (HR 1.91 [95%CI: 1.35-2.72], p<0.001) and PET volume (HR 1.17 [95%CI: 1.07-1.26], p<0.001) as well as tumor extent in T2/FLAIR (HR 1.03 [95%CI: 1.02-1.05], p<0.001) and T1CE (HR 1.12 [95%CI: 1.04-1.21], p = 0.002). In patients with oligodendroglioma, TTNI was associated with PET volume (HR 1.11 [95%CI: 1.05-1.19], p<0.001). Multivariate TTNI analysis in astrocytoma showed an independent prognostic value of TBR_{max} (HR 1.48 [1.09-2.01], p = 0.012) and tumor extent in T2/FLAIR (HR 1.03 [95%CI: 1.02-1.05], p<0.001) also including established prognostic factors such as age, WHO grade, MGMT promoter methylation, extent of resection, and postoperative treatment. In multivariate analysis of patients with oligodendroglioma, PET volume remained a significant prognostic factor (HR 1.18 [95%CI: 1.03-1.36], p = 0.017) for TTNI. Univariate OS analysis in astrocytoma showed a prognostic impact of TBR_{max} (HR 1.40 [95%CI: 1.13-1.74], p = 0.002), TBR_{mean} (HR 1.97 [95%CI: 1.21-3.22], p = 0.006). and PET volume (HR 1.23 [95%CI: 1.10-1.37], p<0.001). Further analysis in distinct subgroups according to timepoints and type of surgical intervention (resection vs. biopsy) showed similar results. ***Conclusion:*** In this retrospective study, uptake (TBR_{max}/TBR_{mean}) and PET volume were strongly associated with outcome in IDH-mutant glioma, demonstrating independent prognostic value beyond established clinical factors such as WHO grade. While amino acid PET may therefore support clinical decision-making, independent validation is needed to corroborate these findings.

OP-610

Measurable disease for response assessment in IDH-mutant glioma - a comparison of MRI-based (RANO 2.0) versus PET-based (PET RANO 1.0) assessment

E. Barci[1], *J. Reis*[2], *M. J. Mair*[3], *J. Isakaj*[1], *K. J. Müller*[4], *L. Kaiser*[1], *M. Preusser*[3], *P. Harter*[5], *L. von Baumgarten*[6], *N. Thon*[7], *R. Forbrig*[2], *N. L. Albert*[1];
[1]*Department of Nuclear Medicine, LMU University Hospital, Munich, GERMANY,* [2]*Institute of Neuroradiology, LMU University Hospital, LMU Munich, Munich, GERMANY,* [3]*Division of Oncology, Department of Medicine I, Medical University of Vienna, Vienna, AUSTRIA,* [4]*Department of Neurology, LMU University Hospital, LMU Munich, Munich, GERMANY,* [5]*Center for Neuropathology and Prion Research, Faculty of Medicine, LMU Munich, Munich, GERMANY,* [6]*Department of Neurosurgery, LMU University Hospital, LMU Munich, Munich, GERMANY,* [7]*Department of Neurosurgery, University Hospital of the Ruhr-University of Bochum, Bochum, GERMANY.*

Aim/Introduction: In clinical trials for patients with IDH-mutant gliomas, "measurable disease" on MRI is a key inclusion criterion for MRI-based response assessment. Recently, amino acid PET-based criteria have been proposed for response assessment in clinical trials (PET RANO 1.0 criteria). We aimed at comparing "measurable disease" using MRI-based RANO 2.0 and PET RANO 1.0 criteria in patients with IDH-mutant gliomas. ***Materials and Methods:*** In this retrospective single-center study, patients with newly diagnosed IDH-mutant gliomas with available [^{18}F]FET PET and MRI either preoperatively prior to biopsy or resection, or postoperatively within a maximum of 12 months after resection, were identified. Analysis was performed by two independent investigators to assess "measurable disease" according to MRI-based RANO 2.0 and PET-based PET RANO 1.0 criteria, and lesion size, uptake intensity (maximal and mean target-to-background ratio: TBR_{max}, TBR_{mean}) and PET volume were assessed. ***Results:*** A total of 212 patients (median age 47 years, range 24-90; 44.8% female) were analyzed, including 148 preoperative (median time between PET and surgery: 0.3 months, range 0.0 - 6.8) and 64 postoperative cases (median time between surgery and PET: 2.1 months, range 0.2 - 11.7). Overall, patients had significantly more often measurable disease on PET compared to MRI (61.3% vs. 49.1%, p=0.015). Preoperatively, MRI and PET identified similar rates of measurable disease (60.8% vs. 59.5%, p > 0.5), while PET identified a significantly higher number of postoperative cases with measurable disease than MRI (65.6% vs. 21.9%, p < 0.001). While MRI showed a similar rate of measurable disease in oligodendroglioma and astrocytoma (50% vs. 48.2%; p>0.05), PET revealed a significantly higher rate in oligodendroglioma compared to astrocytoma (79% vs. 45.5%; p<0.01). ***Conclusion:*** Amino acid PET detects measurable disease more frequently than MRI, particularly in oligodendrogliomas and postoperative cases. These findings support the use of PET-based evaluation of disease burden in IDH-mutant glioma.

OP-611

External validation of an Automated Model of Extraction of Brain Amino Acid PET parameters: application to ^{18}F-FDOPA PET imaging

T. Zaragori[1], *L. Rozenblum*[2], *G. Rovera*[3,4], *G. Stien*[5], *A. Zinsz*[5], *S. D. Morbelli*[3,4], *A. Kas*[2], *A. Verger*[5];
[1]*CIC-IT 1433, Inserm, CHRU Nancy, Université de Lorraine, Nancy, FRANCE,* [2]*Department of Nuclear Medicine, Groupe Hospitalier Pitié-Salpêtrière, Assistance Publique-Hôpitaux de Paris (AP-HP), Sorbonne Université, Paris, FRANCE,* [3]*Nuclear Medicine Unit, A.O.U. Città Della Salute e della Scienza Di Torino, University of Turin, Turin, ITALY,* [4]*Department of Medical Sciences, University of Turin, Turin, ITALY,* [5]*Department of Nuclear Medicine, CHRU Nancy, Université de Lorraine, Nancy, FRANCE.*

Aim/Introduction: Automatic segmentation of gliomas on amino-acid PET is essential for quantitative tumor assessment, and enables the integration of radiomics into clinical routine. While deep learning segmentation models have been developed for ^{18}F-FET PET, such tools are lacking for ^{18}F-FDOPA, which presents a different physiological uptake. This study aimed to develop a deep learning segmentation model of gliomas for ^{18}F-FDOPA PET with an external validation. ***Materials and Methods:*** Patients who underwent static ^{18}F-FDOPA PET scans in 3 European centers for suspected glial lesions characterization, progression or treatment response assessment were retrospectively included. Data from 530 patients at Nancy Hospital (2 PET/CT systems) were used for training, 66 patients from Pitié-Salpêtrière Hospital (1 PET/CT and 1 PET/MR system) and 30 patients from Turin Hospital (1 PET/CT system) for testing. Ground truth segmentations were performed by experienced nuclear physicians following international guidelines: healthy brain regions defined by crescent-shaped ROIs encompassing white and grey matter across six axial slices, and tumor VOIs semi-automatically segmented using a threshold of 1.6 times the mean healthy brain uptake. For our model, brain were first skullstripped and centered in the image. Images were then resampled to 256x256x164 voxels of 1x1x1mm. A 3D UNet model was trained to segment both tumor and healthy brain VOIs using nnUNet framework (using Ranger21 optimizer and

250 epochs to achieve faster convergence). Performance was evaluated using the median [Q1; Q3] Dice score with ground truth lesion segmentation and was considered as failed if Dice was inferior to 0.5. Absolute differences for PET RANO criteria TBRmax, TBRmean and MTV parameters were quantified. Open source JuST_BrainPET ^{18}F-FET model was also tested on our dataset. ***Results:*** For tumor segmentation, the model achieved a Dice score of 0.906 [0.831;0.942] in training (cross-validation), with 6.79% failed cases. Test set performances were 0.820 [0.717;0.888] (10.42% failures). Absolute differences in TBRmax, TBRmean and MTV were 0.03 [-0.00;0.05], 0.01 [-0.03;0.04], 0.00 [-0.35;0.59] mL and 0.02 [-0.02;0.10], -0.09 [-0.13;-0.03] and 1.01 [0.34;4.85] mL in training and test sets, respectively. Dice scores using JuST_BrainPET ^{18}F-FET model were 0.667 [0.033;0.856] (40.3% failure) and 0.634 [0.023;0.826] (45.8% failure) in training and test sets, respectively. ***Conclusion:*** Despite the heterogeneity in image quality across centers, our deep learning model for segmenting gliomas in ^{18}F-FDOPA PET imaging demonstrated robust performance and generalizability, unlike existing ^{18}F-FET models. This paves the way for fully automated quantitative analysis in clinical routine through extraction of brain amino acid PET parameters.

OP-612

Metabolic tumor volume (MTV) reflects the presence of seizure better than target-to-background-ratio (TBR) in patients with gliomas: a [18F]Fluorodopa (F-DOPA) PET study

G. Garelli[1,2], *M. Zotta*[2], *F. Bruno*[3], *E. Pronello*[3], *A. Pellerino*[3], *A. Lesca*[2], *G. Rovera*[1,2], *R. Rudà*[3], *S. Morbelli*[1,2];
[1]*Department of Medical Sciences, University of Turin, Turin, ITALY,* [2]*Nuclear Medicine Unit, AOU Città della Salute e della Scienza di Torino, Turin, ITALY,* [3]*Division of Neuro-Oncology, Department of Neuroscience "Rita Levi Montalcini", AOU Città della Salute e della Scienza di Torino and University of Turin, Turin, ITALY.*

Aim/Introduction: Tumor-associated epilepsy, a condition termed as multiple seizures observed in a patient secondary to their lesion, is seen in up to thirty percent of gliomas. There's a lack of data specifically assessing the capability of PET-derived parameters to correlate with the presence of seizure at baseline and after treatment. We aimed to evaluate F-DOPA-PET correlates of seizure in patients with gliomas at baseline and after therapy. ***Materials and Methods:*** We included patients with gliomas presenting with seizure and with a positive [18F]Fluorodopa PET studied in our center (January-2021 and December-2024). Presence/persistence of seizures was defined as ≥1 unprovoked seizure within 30 days from PET. To investigate the relationship between PET-based-parameters and response to treatment in a homogeneous population, we focused on a prospective-cohort of grade-2 IDH-mutant-glioma patients treated with Vorasidenib. MRI and F-DOPA-PET were performed at baseline and every 3-cycles. We computed SUVmax, TBRmax and MTV (threshold 1.6XSUVmean of healthy-brain). ***Results:*** 32/110 patients with a positive FDOPA-PET had seizure (13 low- and 19 high-grade). TBRmax was slightly but significantly higher in patients with high-grade gliomas and seizure with respect to patients without seizure (2.7±1.2 versus 2.3±1.0;p<0.03), while no significant differences were highlighted in TBRmax and SUVmax in patients with low-grade gliomas subgroups. In these subgroups, MTV was directly associated with the presence of seizure at baseline and after therapy. 10 patients (6 astrocytomas and 4 oligodendrogliomas) treated with Vorasidenib had persistent seizures before treatment. 7 patients had measurable F-DOPA-uptake at baseline (mean SUVmax, TBRmax and MTV: 3.2, 2.8, and 6.5 cm3). After 6 months, 9/10 experienced seizure reduction without changes in antiseizure medication; 8/10 achieved early seizure freedom within 2 cycles, whereas one had gradual, sustained improvement over time. 6 patients who experienced seizure reduction also showed a trend toward metabolic response by cycle 3 (mean changes: SUVmax: -6.3%; TBRmax: -7.5%; MTV: -4.7 cm3) and 6 (SUVmax: -20.9%; TBRmax: -10.9%; MTV: -35.9 cm3), which translated into 3 partial-responses and 3 stable-diseases (RANOcriteria 1.0). All patients had stable disease on MRI at cycles 3 and 6 (including one patient who experienced seizure-worsening). ***Conclusion:*** FDOPA-PET correlates of seizure are different in high- and low-grade gliomas. MTV best captured seizure activity in low-grade glioma. In the subgroup of patients treated with Vorasidenib, seizure improvement correlated with decreased F-DOPA-PET uptake despite stable disease on conventional MRI, supporting the value of F-DOPA-PET as a more sensitive tool for assessing treatment efficacy.

OP-613

Role of 68Ga-DOTATOC PET/CT in Assessing Treatment Response in Re-Irradiated Recurrent Meningiomas: A Volumetric and Molecular Perspective

L. Picori[1], *D. Donner*[1], *S. Agostini*[1], *D. Scartoni*[1], *D. Amelio*[1], *F. Chierichetti*[1], *P. Feraco*[2];
[1]*Ospedale Santa Chiara, Trento, ITALY,* [2]*University of Trento, Trento, ITALY.*

Aim/Introduction: Recurrent meningiomas remain a clinical challenge, particularly after prior surgery and radiation. Proton therapy re-irradiation represents an increasingly used strategy due to its dosimetric advantages. However, robust biomarkers for assessing treatment response remain under investigation. 68Ga-DOTATOC PET/CT, which targets somatostatin receptor subtype 2, offers high sensitivity for meningioma detection, but the utility of SUVmax and volumetric measures as reliable indicators of response remains unclear. The purpose of this study was to assess the value of SUVmax and tumor metabolic volume derived from 68Ga-DOTATOC PET/CT in evaluating treatment response following proton therapy re-irradiation in patients with recurrent meningioma. ***Materials and Methods:*** A retrospective study was conducted on 22 patients with histologically confirmed recurrent meningiomas (5 Grade I, 14 Grade II, 3 Grade III) treated with proton therapy re-irradiation between 2018 and 2022. All patients underwent PET/CT scans before and after treatment. Tumor regions were manually segmented to extract SUVmax standardized uptake volume ratio differences and (SRD) somatostatin receptor density values and volumes. Non-parametric statistical analyses were applied to evaluate differences across timepoints and tumor grades. ***Results:*** No statistically significant difference was observed between pre- and post-treatment, SUVmax values (mean: 17.01 vs. 18.29; p = 0.548). Similarly, no significant variation in SUVmax was noted across tumor grades. Conversely, a volumetric reduction of approximately 20% was observed post-treatment, with a 22% decrease in the Grade II subgroup. ***Conclusion:*** While SUVmax did not change significantly following re-irradiation, metabolic tumor volume demonstrated a consistent reduction. This discrepancy between metabolic activity and volume suggests potential biological and technical factors influencing tracer uptake, such as prior treatments, intratumoral fibrosis, or tumor dedifferentiation. These findings underscore the importance of volumetric PET metrics and support a multiparametric imaging approach combining PET and MRI for optimal evaluation of treatment response in recurrent meningiomas. ***References:*** Improved Detection of Postoperative Residual Meningioma with [68Ga] Ga-DOTA-TOC PET Imaging Using a High-resolution Research Tomograph PET doi: 10.1158/1078-0432.CCR-20-3362. Epub 2021 Feb 1 Prognostic value of somatostatin receptor expressing tumor volumecalculated from 68Ga-DOTATATE PET/CT in patientswith well-differentiated neuroendocrine tumors. doi.org/10.1007/s00259-019-04455-9 68Gallium-DOTATATE PET in meningioma: A reliable predictor of tumor growth rate? doi:10.1093/neuonc/

now001 Dual Tracer 68Ga-DOTATOC and ^{18}F-FDG PET Improve Preoperative Evaluation of Aggressiveness in Resectable Pancreatic Neuroendocrine doi.org/10.3390/diagnostics 11020192.

OP-614

[^{177}Lu]Lu-DOTATATE for refractory meningiomas: factors associated with the therapeutic response and initial tumor dosimetric data

C. Boursier, *T. Zaragori, N. Garabedian, M. Blonski, T. Obara, L. Taillandier, L. Imbert, A. Verger;*
CHRU Nancy, Vandoeuvre-les-Nancy, FRANCE.

Aim/Introduction: This study aimed to reveal the factors affecting the therapeutic response of refractory meningiomas treated with [^{177}Lu]Lu-DOTATATE and to collect initial tumor absorbed doses. ***Materials and Methods:*** Patients with refractory meningiomas treated with [^{177}Lu]Lu-DOTATATE from 2021 to 2024 were retrospectively included. Association analyses of clinical factors, WHO grade, prior therapy (surgery, radiation, systemic therapy: bevacizumab or a combination of octreotide/everolimus), 3D-MRI volume and pretreatment PET parameters with posttreatment progression-free survival (PFS), as defined by the 3D-RANO criteria, were performed. Growth rates obtained via MRI and tumor absorbed doses (TAD) were also calculated. ***Results:*** Sixteen patients (60 [55;68] years old) underwent 4 [2;4] cycles of [^{177}Lu]Lu-DOTATATE, with a TAD/cycle of 0.45 [0.30;0.83] Gy/GBq/cycle. Only prior systemic therapy was found as a risk factor for posttreatment PFS ($p \leq 0.05$), with an impact on tumor growth rate (TGR) (4 vs. 12 patients, +125% vs. -107%, $p<0.01$). For the 12 well-selected candidates the PFS was 67% (8/12 patients) whereas it was 0% in the other group, those with prior systemic therapy. No associations between the TAD and difference in the TGR before/after SSTR-RT were observed in the overall population ($p=0.10$) or in the population of well-selected candidates ($p=0.72$). ***Conclusion:*** [^{177}Lu]Lu-DOTATATE is effective in refractory meningiomas with no prior systemic therapy, even if the TADs are relatively low. Somatostatin-receptor radionuclide therapy should be proposed as early as possible in the treatment course of refractory meningiomas. Efforts should be made to increase the tumor absorbed dose.

1308

Tuesday, October 7, 2025, 09:45 - 11:15
Room 115

Joint Symposium 6 - Translational Molecular Imaging & Therapy + Radiopharmaceutical Sciences Committee / ESTRO: Radiobiological Aspects of PRRT

OP-615

How Does TRT Differ from Conventional External Radiotherapy: Generalities

M. Cremonesi; *European Institute of Oncology, IRCCS, Milan, ITALY.*

OP-616

Absorbed Dose Rate, Dose Heterogeneity and their Impact on (Local and Systemic) Biological Effects

Z. Morris; *Human Oncology Department, University of Wisconsin-Madison, UNITED STATES OF AMERICA*

OP-617

The Interplay between DNA Damage, DNA Damage/Replication Stress Response, and Immunomodulation

K. Harrington; *The Institute of Cancer Research, Chelsea, UNITED KINGDOM.*

1309

Tuesday, October 7, 2025, 9:45 - 11:15
Room 133+134

e-Poster Presentations Session 10 - Paediatrics Committee: Paediatrics e-Poster Presentations Session

EPS-199

Evaluating Concordance in SIOPEN Scoring 123I MIBG scintigraphy among Nuclear Medicine Physicians

H. Noamen*, M. Borsali, L. Agrigoroaie, Y. Cras, K. Trabelsi, A. Daverio, D. Deandreis, C. Garcia;*
Gustave Roussy Cancer Campus, Villejuif, FRANCE.

Aim/Introduction: The SIOPEN score is a semi-quantitative tool in neuroblastoma, playing a critical role in disease staging, treatment response evaluation, and prognostic stratification. This study aimed to evaluate the inter-observer concordance between junior and senior Nuclear Medicine physicians in interpreting the SIOPEN score on 123I-MIBG scintigraphy in pediatric neuroblastoma. ***Materials and Methods:*** Twenty pediatric MIBG scans were performed on a double head Anger gamma camera. Five observers (three senior, two junior nuclear medicine physicians) independently and blindly assessed the SIOPEN score based on planar images. Valid data across all observer pairs ranged from 85% to 100%. Mean scores varied, with Senior 1 reporting the highest average (6.11) and Senior 2 the lowest (5.56); score variability was high across observers (standard deviations: 7-10). Inter-observer agreement was calculated using the intraclass correlation coefficient (ICC; model 2,1). ***Results:*** Agreement between junior and senior observers was good, with ICC values of 0.77 (Junior 1 vs seniors) and 0.84 (Junior 2 vs seniors), both statistically significant ($p < 0.01$). Concordance among senior observers was excellent (ICC = 0.953, $p < 0.01$), indicating strong reliability in experienced readers. ***Conclusion:*** Despite overall good concordance, discrepancies observed between junior and senior physicians highlight the need for targeted training in SIOPEN scoring. Focused education and standardized interpretation protocols are essential to improve scoring consistency and accuracy, particularly among junior physicians. Enhancing reliability in SIOPEN assessment is crucial for accurate disease staging, effective treatment planning, and robust prognostic evaluation in neuroblastoma management.

EPS-200

Artificial Intelligence-assisted Fast Silent PET/MRI for Diagnostic and Therapeutic Assessment in Pediatric Diseases

T. Cai[1], *H. Jun*[1], *C. Zhou*[2], *Y. Bai*[1], *Y. Zhang*[1], *L. Jiang*[3], *Y. Hu*[2], *Z. Lin*[4], *Y. Yang*[5], *Y. Wei*[4], *Z. Zhang*[4], *W. Fan*[2], *W. Lu*[3], *J. Hu*[1], *B. Li*[1];
[1]*Department of Nuclear Medicine, Ruijin Hospital, Shanghai Jiao Tong University School of Medicine, Shanghai, CHINA,* [2]*Sun Yat-sen University Cancer Center, Guangzhou, CHINA,* [3]*Department of Pediatrics, Ruijin Hospital, Shanghai Jiaotong University School of Medicine, Shanghai, CHINA,* [4]*United Imaging Healthcare Co., Ltd., Shanghai, CHINA,* [5]*Beijing United Imaging Healthcare Co., Ltd., Beijing, CHINA.*

Aim/Introduction: While PET/MRI achieves reduced radiation dose over PET/CT in pediatric imaging, clinical adoption remains constrained by prolonged acquisition times (typically 30-45 minutes), excessive acoustic noise (85-95 dB), and frequent sedation requirements. This study presents an integrated technological solution combining four innovations: 1) Flexible coil arrays; 2) Silent MRI sequences; 3) AI-accelerated compressed sensing (ACS) reconstruction for MRI; 4) Deep progressive reconstruction (DPR) for PET. We hypothesize this multimodal optimization enables

diagnostic-quality imaging with reduced acquisition time, noise levels, and radiopharmaceutical dose. ***Materials and Methods:*** Prospective cohort (N=25) of pediatric patients underwent next-generation PET/MRI (uPMR890, United Imaging Healthcare, Shanghai, China) with: 1.85 MBq/kg, flexible 24-channel coil for chest and abdomen coverage, silent MRI sequences, ACS-based MRI reconstruction, and DPR-based PET reconstruction. For comparison, 15 retrospective pediatric cases using conventional protocols (injection dose: 3.7 MBq/kg) were enrolled. Two experienced nuclear medicine physicians independently evaluated the image quality of both the next-generation protocol and the conventional protocol. A Likert 5-point scale was applied to assess the overall image quality, artifacts, lesion conspicuity, and noise of PET and MRI. A score higher than 3 is considered to meet the clinical diagnostic requirements. The quantitative assessment was performed by evaluating the hepatic signal-to-noise ratio (SNR). ***Results:*** In the fast silent pediatric PET/MRI workflow, the total acquisition time was reduced to approximately 12 minutes. Children aged over 5 years successfully completed the entire scan without sedation. The conventional protocols produced an average sound intensity of 86.94±8.53 dB, while the proposed new protocols significantly reduced to 78.59 ±10.29 dB ($p < 0.0001$). The new protocols demonstrated marginally lower subjective quality scores than the conventional workflow in PET image noise, overall MRI image quality, and MRI artifacts (all >3 points, meeting clinical diagnostic requirements). No statistically significant differences were observed in other evaluated metrics. The new workflow demonstrated a statistically significant increase in PET SNR compared to the conventional protocol (25.56±6.41 vs 21.43±5.73, $p<0.05$). ***Conclusion:*** The AI-assisted fast silent pediatric PET/MRI protocol demonstrates significant reductions in acquisition time, radiation dose, acoustic noise, and sedation requirements, while substantially improves patient comfort. Moreover, the obtained image quality is sufficient to meet diagnostic standards, highlighting its clinical utility.

EPS-201

^{99m}Tc labelled heat denatured red cell scintigraphy in suspected right isomerism

K. Chan, *T. Tong, L. Cheung, Y. Hui, W. Ho;*
Queen Mary Hospital, Hong Kong, HONG KONG.

Aim/Introduction: ^{99m}Tc labelled heat denatured red cell scintigraphy is a nuclear medicine technique used to detect functional spleen, with indications including intrapancreatic accessory spleen, assessment of residual spleen in patients after splenectomy. One of the indications is to detect the presence of spleen in patient with suspected heterotaxy or right isomerism. This study presents a retrospective case series of patients with congenital heart abnormalities and suspected right isomerism, assessing the diagnostic value of this imaging modality. ***Materials and Methods:*** A retrospective review was conducted of all patients referred for ^{99m}Tc labelled heat denatured red cell scintigraphy at our institution between 2008 and 2020. A total of 22 cases were identified, all with congenital heart abnormalities and suspected right isomerism. The median age was 123.5 days, with four adult patients included. SPECT imaging was available in 19 cases. Imaging findings were analysed to determine splenic status. ***Results:*** Of the 22 cases, 14 (63.6%) demonstrated absent splenic uptake, confirming asplenia. The remaining cases showed evidence of splenic function, with most demonstrating uptake consistent with a nearly normal functioning spleen, although not all had SPECT imaging for further characterisation. ***Conclusion:*** ^{99m}Tc labelled heat denatured red cell scintigraphy remains a valuable tool for assessing splenic function in patients with congenital heart abnormalities and suspected right isomerism. In this cohort, the majority of cases were confirmed as asplenia. The availability of SPECT imaging enhanced diagnostic confidence. These findings support the continued use of scintigraphy in the evaluation of congenital splenic anomalies.

EPS-202

Validation of a Pediatric Dose Calculator, L_PDC v2025.04.1, for SPECT and PET Radiopharmaceuticals

M. Buaki Sogo[1], *L. Nunes-Lemos*[2], *L. Rubio Álvarez*[2], *A. Palomar-Muñoz*[2], *Ó. Hernández-Cristancho*[2], *J. Suils-Ramón*[2], *F. Dellepiane-Clarke*[2], *A. García-Burillo*[2], *C. Gámez-Cenzano*[2];
[1]*Unidad de Radiofarmacia, Hospital Universitario Vall D'Hebrón, Barcelona, SPAIN,* [2]*Servicio de Medicina Nuclear, Hospital Universitario de Vall D'Hebrón, Barcelona, SPAIN.*

Aim/Introduction: Products available for pediatric dose calculation have its limitations with intermediate and odd weights, so we generate a spreadsheet based on the recommendations of the Committees of the European Association of Nuclear Medicine (EANM) to facilitate as well as to validate a pediatric dose calculator for SPECT and PET radiopharmaceuticals; to improve the accuracy of dose calculation in pediatric patients based on the most recent recommendations. ***Materials and Methods:*** A Microsoft Excel-based calculator named L_PDC was designed and programmed to determine pediatric doses for SPECT and PET radiopharmaceuticals. The design followed the current recommendations, using data derived from the official EANM Dosage Card[1]. Since the card provides standard values for discrete weights, additional intermediate values were calculated using interpolation formulas to cover odd and intermediate body weights. The spreadsheet was developed with built-in features to enhance usability and accuracy. These included: automatic dose calculation based on input weight, visual alerts when calculated doses fell below the minimum recommended activity, and thresholds that triggered color-coded indicators for both suboptimal and optimal dose ranges. To validate the tool, retrospective data from 51 pediatric patients were collected. For each patient, these parameters were recorded: body weight (kg), dose administered according to the hospital's radiopharmaceutical software (Dadm, in MBq), dose calculated using the official EANM online dosage calculator (DEANM, in MBq), and dose obtained with L_PDC (DL_PDC, in MBq). Both absolute and relative errors were calculated for DL_PDC and Dadm, using DEANM as the reference standard. Statistical analysis was performed to assess agreement and accuracy. This included Student's t-test to compare means, and linear regression analysis to determine the correlation between DL_PDC and DEANM, as well as between Dadm and DEANM. The validation aims to ensure that DL_PDC provided results statistically equivalent to DEANM and more consistent than manually prescribed doses. ***Results:*** The mean values of DEANM, DL_PDC, and Dadm were 73,49 ± 103,62 MBq, 72,69 ± 104.92 MBq, and 82,95 ± 137,07 MBq, respectively. There were no statistically significant differences between the calculated doses. Regression analysis revealed an R^2 of 0.998 for DL_PDC versus DEANM, indicating high correlation and accuracy. The absolute error for DL_PDC was 1.1%, compared to -12,8% for Dadm. ***Conclusion:*** L_PDC is a reliable and validated tool for calculating pediatric doses of radiopharmaceuticals, compared with the online calculator DEANM. It offers precision, usability, and time efficiency, managing doses for odd and intermediate weights. ***References:*** 1. 1. EANM Dosage Card.

EPS-203

The impact of F-18 FDG PET/CT on the management of complicated Tuberculosis in children

C. Burger, *D. Smith-Tsibolane, C. le Roux, A. Doruyter, P. Goussard;*
Stellenbosch University, Cape Town, SOUTH AFRICA.

Aim/Introduction: Children are at higher risk for severe forms of Tuberculosis (TB). Early diagnosis and treatment limit morbidity, mortality and transmission. Diagnosis is challenging due to diverse presentation, paucibacillary burden, and difficulty

obtaining samples. Imaging is essential, particularly when microbiological tests remain negative. Chest X-ray has limitations. CT can evaluate mediastinal lymph nodes and complicated TB, but its utility in detecting active disease is frequently limited. ^{18}F-fluorodeoxyglucose positron emission tomography combined with computed tomography (FDG PET/CT) detects active inflammation, assists in diagnosis, determines disease extent, and guides biopsies. This study focused on evaluating the potential of FDG PET/CT to improve the diagnosis and management of complicated paediatric TB. ***Materials and Methods:*** A retrospective review of imaging, bronchoscopy and microbiology results of children aged 3 months to 16 years who presented at Tygerberg Hospital between January 2013 and October 2024 with at least one FDG PET/CT. The PET/CT findings (reviewed by a nuclear physician) were compared to the diagnostic CT (reviewed by a radiologist) or the low dose CT of the PET/CT (depending on availability). Representative volumes of interest were drawn for target lesions on the PET/CT. Bronchoscopy and microbiological results, clinical outcome, and impact of PET/CT on patient management were reviewed by a paediatric pulmonologist. ***Results:*** Scans of thirty-four (n=34) patients (16 male), with median age of 7.1 years (range: 0.5-11.9 years) of which 4 HIV positive were reviewed. Most patients (19/34, 56%) underwent a diagnostic CT prior to the PET/CT (median interval: 42 days, IQR: 30.5-67.5). PET/CT detected a total of 142 intrathoracic nodal sites, while CT detected 99 (p=0.001144). Extrapulmonary disease was detected in 17 patients (50%) on PET/CT, compared to 6 patients (18%) on CT (p=0.009823). The mean SUVmax was 3.6 (SD 2.3) for mediastinal nodal sites, 2.6 (SD 3.1) for pulmonary lesions, and 2.0 (SD 3.0) for extrapulmonary sites. PET/CT confirmed persistent disease in 17 patients (50%), detected biopsy sites (that were diagnostic) in 9 patients (26%), and excluded TB in 4 patients (12%). It guided surgical intervention in 2 patients (6%), identified non-responding patients (2 patients, 6%), and confirmed recurrence in 1 patient (3%). ***Conclusion:*** FDG PET/CT impacted management in most patients, mostly by confirming persistent disease and identifying biopsy sites. PET/CT detected more intrathoracic nodal disease and extrapulmonary disease. This study adds to the limited literature and shows the potential value of FDG PET/CT in complicated paediatric TB.

EPS-204

The Role Of Tc-99m Sestamibi Myocardial Perfusion Scintigraphy On Patient Management In Pediatric Kawasaki Patients With Giant Coronary Aneurysm

H. Kapucu, *B. Esen Akkas, M. Kaya, K. Toplutas;*
University of Health Sciences Cam Sakura City Hospital, Istanbul, TÜRKIYE.

Aim/Introduction: This retrospective study evaluated the impact of myocardial perfusion scintigraphy (MPS) on the management of pediatric Kawasaki Disease (KD) patients with giant coronary aneurysms before undergoing surgery. ***Materials and Methods:*** The study included five pediatric patients diagnosed with giant coronary aneurysm among 20 patients who followed up with KD between 2018 and 2024. For stress MPS imaging, 7.4 MBq/kg (minimum two mCi/74 MBq) [99mTc]Tc-sestamibi injection was performed in the 3rd minute of a 6-minute adenosine infusion at a rate of 140 mcg/kg/min (1). Single photon emission computed tomography (SPECT) imaging was performed 30-45 minutes after injection in the supine position under anaesthesia. Patients with hypoperfused areas on stress images underwent rest imaging the following day under anaesthesia. Since prone imaging was not possible for technical reasons, low-dose computed tomography (CT) was used for attenuation correction in patients imaged without anaesthesia. GATED images synchronised with electrocardiography (ECG) were obtained in stress images. ***Results:*** One of the patients was female, and four were male. The mean age at diagnosis was 28.8 months. The mean CRP, leukocyte, and neutrophil values were 174.9 mg/L, 24.8 10^9/L, and 19.9 10^9/L, respectively. According to MPS results, the hypoperfused area in the apex, anterior wall apical-mid segments in stress of one patient (Case 1) was reperfused in the rest images. The patient's ejection fraction (EF) value was 51%, end-diastolic volume (EDV) was 25 ml, end-systolic volume (ESV) was 12 ml, and summed stress score was 5. Rest imaging was not performed in the other four patients because left ventricular perfusion was within normal limits on stress images. In case 1 with ischaemic findings, the coronary bypass was performed by opening just distal to the aneurysmatic tissue in the LIMA-LAD artery. In the control ECHO performed after the surgical procedure, blood flow was normal. EF was calculated as 67%. The complaint of dyspnea, which reduced the quality of life before the surgery, almost completely improved after the surgery. The other four patients were offered follow-up with medical therapy and did not develop any new cardiac symptoms or events. ***Conclusion:*** In this case series, MPS findings prevented unnecessary surgical interventions in four pediatric cases and provided accurate surgical planning in one case, thereby alleviating the patient's symptoms. MPS is an easy-to-use and reliable noninvasive imaging method for surgical planning and patient management in KD. ***References:*** 1.Fukazawa R, et al. doi: 10.1253/circj.CJ-19-1094.

EPS-205

Persistent FDG-PET Uptake After First-Line Therapy in Paediatric Lymphoma and Risk of Progression: a Monocentric Retrospective Analysis

F. Serani[1], *E. Carraro*[2], *D. Cecchin*[1], *C. Giraudo*[3], *M. Pillon*[2], *P. Zucchetta*[1];
[1]*Nuclear Medicine Unit, Department of Medicine DIMED, University-Hospital of Padova, Padua, ITALY,* [2]*Oncohematology Unit, Department of Woman and Child Health, University of Padova School of Medicine, Padua, ITALY,* [3]*Unit of Advanced Clinical and Translational Imaging, Department of Cardiac, Thoracic, Vascular Sciences and Public Health-DCTV, University of Padova, Padua, ITALY.*

Aim/Introduction: Persistent focal uptake on post-therapy FDG-PET in paediatric lymphoma may represent residual disease or benign sequelae, creating ambiguity in clinical management. This study investigates whether quantitative PET parameters of pre-therapy lesions and post-therapy persistent lesions can predict relapse in children who lack clear evidence of recurrence. ***Materials and Methods:*** In this single-centre retrospective analysis, we identified 18 children (median age 14.2 years, IQR = 3 years) with Hodgkin and Non-Hodgkin lymphoma subtypes who performed a pretherapy PET/MR and End-of-Therapy (EoT) PET/MR between 2015 and 2024 and had a clinical follow-up of at least eight months. For each patient, the initial disease volume was semi-automatically contoured on staging PET parameters, and any persistent lesion was contoured at (EoT) PET. Semiquantitative measurements including the SUVmax of the persistent lesion (PERS), SUVmean of PERS, the maximum hepatic SUV (SUVmax liver). Metabolic tumour volume (MTV), and total lesion glycolysis (TLG) were considered for both initial disease and PERS. Statistical analyses were performed using Fisher's exact test for categorical comparisons and the Mann-Whitney U test for continuous variables. ***Results:*** Four of the 18 patients (22%) experienced histologically or radiologically confirmed relapse during follow-up. Of all the PET parameters both on staging and on EoT PET only the SUVmean greater than SUVmax liver showed a statistically significant correlation with the follow-up data (p<0,05). Of these 18 patients, three had persistent lesion SUVmean PERS exceeding the SUVmax liver, whereas none of the 14 non-relapsing patients exhibited this finding. None of the other PET semiquantitative measurements taken into consideration take, neither MTV nor TLG—whether of the residual lesion or the initial tumour—

showed a statistically significant correlation with relapse risk. ***Conclusion:*** Persistent post-therapy lesion SUVmean greater than SUVmax liver appears to correlate with paediatric lymphoma patients at higher risk of relapse, whereas volumetric metrics (MTV, TLG) both on staging and EoT therapy lack clear predictive value in this cohort. Given the retrospective nature of this analysis and the small population, these findings require validation in larger cohort, preferably in prospective multicentre trials.

EPS-206

Use of semiquantitative parameters on baseline Tc99m mebrofenin hepatobiliary scintigraphy for predicting post Kasai outcome in ExtraHepatic Biliary Atresia- a retrospective analysis

N. Kundu, *V. Singh, A. Mahalik, A. Roy, K. Jain, J. Choudhary, J. Krishna, R. Kumar;*
AIIMS New Delhi, Delhi, INDIA.

Aim/Introduction: The HIDA scan is a key imaging tool for distinguishing extrahepatic biliary atresia (EHBA) from neonatal hepatitis in infants with congenital hyperbilirubinemia. EHBA, a surgically correctable condition, is treated using the Kasai portoenterostomy, whose success significantly depends on the infant's age at surgery—outcomes worsen if performed after 60 days. Visual indicators on HIDA scans, such as hepatic radiotracer uptake and bowel visualization, help identify EHBA. However, there is currently no research exploring semiquantitative HIDA scan parameters that might predict post-surgical outcomes following the Kasai procedure, highlighting a gap in the existing diagnostic and prognostic framework. ***Materials and Methods:*** A retrospective review of 15 EHBA patients (9 males, 6 females) imaged between 20202025 in our department was performed. All children underwent preoperative HIDA within two weeks before Kasai and had ≥ 6month clinical/imaging followup. Regionsofinterest were placed on 15min static frames over (i) whole liver and (ii) cardiac bloodpool to derive: Liver counts @ 15 min (LC15), Cardiac counts @ 15 min (CC15), Livertocardiac ratio (LCR = LC15 / CC15). Delayed 24h static images yielded: Liver counts @ 24 h (LC24) and fractional hepatic retention (FHR= LC24 / LC15). PostKasai status (success=bile flow demonstrated & cholestasis resolved, failure=None of the above) served as the target variable. Mann-Whitney U compared indices between groups; pointbiserial correlation (r) assessed associations with outcome (α = 0.05). ***Results:*** Mean age of chiLdren at the time of diagnosis was 76 +/-45 days. Eight children (53 %) achieved Kasai success, seven (47 %) failed. Median earlyliver counts were lower in the success group (168 000, IQR 122 000-248 000) than in failures (260 000, IQR 179 000-324 000; p = 0.12, r = 0.39), and a similar trend was observed for cardiac counts (34 000 vs 50 000; p = 0.19, r = 0.34). The livertocardiac ratio showed minimal separation between successes and failures (medians 3.52 vs 4.61; p = 0.69), whereas the fractional hepatic retention at 24 hourswas higher in successful cases (median 0.155, IQR 0.129-0.198) compared with failures (0.114, IQR 0.105-0.128), yielding the strongest correlation with outcome (r = +0.44).Sex did not correlate with any scintigraphic variable (r= 0.25). ***Conclusion:*** In this pilot series, children who eventually cleared jaundice after Kasai exhibited lower early liver counts and higher 24h tracer retention, underscoring that brisk washout on baseline HIDA may herald an unfavourable outcome. Although pvalues were limited by small sample size, the moderate correlations (|r| ≈ 0.4-0.45) suggest that simple semiquantitative parameters—readily available on routine HIDA—could enrich preoperative counselling and prioritise candidates for early livertransplant evaluation. Larger prospective cohorts are warranted to establish definitive cutoff values and integrate these metrics into multidisciplinary decision algorithms.

EPS-207

Meckel's Diverticulum in Paediatric Patients. Diagnostic Performance of [^{99m}Tc]Tc- pertechnetate Scintigraphy. A Retrospective Study.

A. Guerra, *C. Salomon, E. Durand, M. Vivar, A. Puig, M. Gimenez, C. Peña;*
Servicio de Medicina Nuclear, Hospital Universitari Son Espases, Palma, SPAIN.

Aim/Introduction: Meckel's diverticulum is the most common congenital gastrointestinal anomaly, often presenting in paediatric patients with an incidence of 1-3%, with painless rectal bleeding or abdominal pain. Early detection is essential to avoid complications such as anemia, bowel obstruction, or perforation. [^{99m}Tc]Tc-pertechnetate scintigraphy is the imaging modality of choice for detecting ectopic gastric mucosa within Meckel's diverticulum. The aim of this study is to evaluate the utility of [^{99m}Tc]Tc-pertechnetate scintigraphy in the diagnosis of Meckel's diverticulum in paediatric population. ***Materials and Methods:*** Retrospective study of 78 paediatric patients (under 18 years old) with suspected Meckel's diverticulum, which underwent [^{99m}Tc]Tc-pertechnetate scintigraphy over a 13 year period (2011-2024). Examination was performed after [^{99m}Tc]Tc-pertechnetate was endovenously administration 1-3.5 MBq/Kg, and an anterior planar image of abdomen and pelvis was obtained at 1, 7, 15, 30 and 45 minutes. A final image was taken 60 minutes after injection following bladder emptying in a standing position. Scan parameters included 500K counts for each image, a 256x256 matrix, with age appropriate zoom using low-energy general purpose collimator. Imaging results were classified as positive when a well-defined focus of radiopharmaceutical uptake in abdomen or pelvis, and as negative when no tracer accumulation was visualized. To verify the veracity of the scintigraphy was determined through surgical and/or histopathological findings. ***Results:*** Out of 78 examinations (52 boys, 26 girls, mean of age 5 years), 11 (14%) patients had positive scintigraphy image and 67 (85%) were negative. The 11 positive scans underwent surgical resection and the diagnosis of Meckel's diverticulum was confirmed, 2 intraoperatively and the rest by histopathological analysis. Among the 67 patients with negative scintigraphy, 2 were finally diagnosed with Meckel's diverticulum by histopathological study. In our study the [^{99m}Tc] Tc-pertechnetate scintigraphy reported a sensitivity of 85%, a specificity of 100%, positive predictive value 100% and negative positive predictive value 97% in the diagnosis of bleeding Meckel's diverticulum in paediatric population. ***Conclusion:*** [^{99m}Tc]Tc-pertechnetate scintigraphy is a valuable and sensitive diagnostic tool for detecting Meckel's diverticulum in paediatric patients. False negatives remain a limitation, underscoring the need for clinical correlation and, in selected cases, adjunct imaging or surgical exploration.

EPS-208

Role of SSTR PET-CT in paediatric neuroblastoma patients-A promising one stop shop modality.

D. Halanaik, *S. Kumar, H. Goyal, P. Srinivasan, S. Keerthivasagam; Jawaharlal Institute of postgraduate medical education and Research, Puducherry, INDIA.*

Aim/Introduction: Neuroblastoma is a common pediatric malignancy with diverse clinical presentations and metastatic patterns. Imaging is essential for diagnosis, staging, and monitoring the treatment response. Somatostatin receptor (SSTR) PET/CT using Ga-68 DOTATATE/DOTANOC has emerged as a valuable tool for detecting SSTR expression in neuroblastoma and sites of distant metastases, thereby facilitating comprehensive disease evaluation. ***Materials and Methods:*** This retrospective study included 11 pediatric patients diagnosed with neuroblastoma, who underwent SSTR PET/CT for baseline staging and response assessment between January 2024 and April 2025 at a tertiary care hospital.

Clinical history, imaging findings, histopathological records and follow-up data were reviewed. Imaging reports focused on lesion location, its size, SSTR expression (SUVmax), and sites of metastatic involvement. Relevant clinical and radiological data were extracted and summarized. ***Results:*** Patients were predominantly infants and toddlers, with 50% under 1.5 years. Majority of the patients presented primarily with abdominal distension, pain, and palpable masses. Primary tumors were predominantly located in the suprarenal and retroperitoneal regions. Variable SSTR expression ranging from low to moderate levels was observed, with median SUVmax value 5.01 (±2.29). 100% of patients exhibited distant metastases with metastatic disease identified in lymph nodes (47.6%), and liver (47.6%) in several cases, predominantly. Only 4 patients underwent response evaluation PET/CT post-treatment. Treatment responses varied: some patients exhibited partial response (2/11, 9.5%) with significant lesion size reduction post-chemotherapy, while others showed stable or residual disease. ***Conclusion:*** SSTR PET/CT imaging effectively delineates primary and metastatic neuroblastoma lesions, thereby providing critical information for staging and evaluating treatment response. The imaging findings correlate with clinical outcomes and can guide therapeutic decision-making in pediatric neuroblastoma management.

EPS-209

Comparative diagnostic performance of 68GaDOTANOC PET/CT versus 131ImIBG SPECT/CT in newly diagnosed pediatric neuroblastoma- a prospective single centre study.

N. Kundu, *D. Khan, S. Sagar, S. Bakhshi, R. Seth, S. Agarwala, A. K. Pandey, R. Kumar;*
AIIMS New Delhi, Delhi, INDIA.

Aim/Introduction: To quantify and compare the diagnostic yield of wholebody 68GaDOTANOC PET/CT and 131ImIBG SPECT/CT for primary tumour detection and metastatic mapping in treatmentnaïve paediatric neuroblastoma. ***Materials and Methods:*** Forty treatment naïve children (median age = 36 months) with biopsy proven/biochemically proven or radiologically diagnosed neuroblastoma underwent paired 68GaDOTANOC PET/CT and 131ImIBG planar ± focal SPECT/CT imaging after obtaining informed written consent and institute ethics committee clearance. 68GaDOTANOC (1.5 MBq kg^{1}, 45 min uptake) PET/CT covering vertextotoes; 131ImIBG (0.14 mCi kg^{1}) planar ± focal SPECT/CT were acquired 48-72 h postinjection. Both studies were evaluated by 2 experienced nuclear medicine physicians who performed patientbased and lesionbased analyses blinded to diagnoses. On visual analysis of 68Ga-DOTANOC PET/CT, a lesion was considered positive when focal uptake was present at non-physiologic site, having intensity greater than the mediastinal blood pool with corresponding lesion on CT. Discrepant foci were adjudicated by correlative MRI/CT, histology or 12month clinical followup. McNemar and Wilcoxon tests were used to assess paired proportions and lesion counts. ***Results:*** DOTANOC localised the primary in 35/39 cases (90 %) versus 29/39 (74 %) for mIBG (P = 0.07). Metastatic disease was demonstrated in 30/40 studies with DOTANOC and 25/40 with mIBG (P = 0.03). Altogether, DOTANOC uncovered 1,083 lesions, of which 880 were osseous or marrow; mIBG revealed 235 lesions (163 skeletal) (P < 0.001). Incremental detection was greatest for occult marrow deposits (DOTANOC +81 %). No DOTANOCavid/mIBGpositive discordance occurred, but seven primaries and six metastatic sets were DOTANOCpositive/mIBGnegative, altering stage in 12.5 % of patients. ***Conclusion:*** Wholebody 68GaDOTANOC PET/CT significantly outperforms 131ImIBG SPECT/CT for lesion enumeration and metastatic staging—including cryptic marrow disease—without sacrificing primarytumour sensitivity. These findings support use of DOTANOC as a firstline functional tracer where generatorbased gallium is available, and reserve mIBG chiefly for theranostic stratification.

EPS-210

Meckel's Scan Revisited

J. Lanctôt-Bédard, *R. Lambert, S. Turpin;*
CHU Sainte-Justine, Montréal, QC, CANADA.

Aim/Introduction: ^{99m}Tc-Pertechnetate Scintigraphy (^{99m}Tc-PS) or Meckel`s scan, has been a mainstay of nuclear medicine for many years for the detection of ectopic gastric mucosa. With time, modifications have been made in the patient`s preparation. The purpose of our retrospective study was to identify the best pharmacological preparation (PP). ***Materials and Methods:*** Medical file, ^{99m}Tc-PS images and radiological report of patients imaged between 2014 and 2024 were reviewed. The use of pharmacological preparation (PP) with intravenous (iv) or per os (po) Ranitidine (R) and Famotidine (F), po proton pump inhibitors (PPI) was compiled. ^{99m}Tc-PS images were reviewed for the detection and time from injection of duodenal visualisation (elution) and influence on diagnostic. Comparison between the presence or absence of elution between no-PP, PP+ and PP categories was made using Chi Square and for the elution times using unpaired student t-test. Significance level was established at p<0.05. ***Results:*** 231 studies were performed in 99 girls and 132 boys, 6.4 +/-5.4 years old. ^{99m}Tc-PS consisted of a 30-minutes dynamic study followed by static images +/- SPECT +/-CT. ^{99m}Tc-PS demonstrated 15 Meckel+ proven by surgery and 2 dubious Meckel + with final diagnosis of bleeding Meckel and inflammed small bowel lymphoid hyperplasia.PP was performed in 141 studies (R po = 40; R iv = 27 ; F po=17 ; F iv = 49; PPI po =8).Elution was more frequent with no-PP than with PP+ : 69.5% versus 46.5%, p=0.04. Elution was found in 37.5% of studies for R po, 37% for R iv, 58.8% for F po, 53% for F iv and 71% for IPP po. Frequency differences in PP+ were not significant (p=0.21) as a whole or in paired analysis, with the exception of bordeline significance for PPI po versus R po (p=0.09). However, times to elution were similar between no-PP and PP + : 18.6+/-10.5 min vs 18.6+/-7.8 min, p=ns. Time to elution were also similar inbetween PP categories, with the exception of R po versus F iv : 13.9+/-7.1 min versus 21.3 +/- 8.5 min, p=0.008. Despite elution, all studies were deemed diagnostic. ***Conclusion:*** The use of PP decreased the frequence of elution where compared to non-PP but elution remained present. All studies were diagnostic. Elution occured later during the acquistion with F iv. In conclusion, recommendation is made to perform ^{99m}Tc-PS with F iv preparation.

EPS-211

Scintigraphic Localization of Intestinal Bleeding in a Pediatric Patient with High-Grade B-cell Lymphoma: A Life-Saving Intervention

L. Nunes Lemos, *L. Rubio-Álvarez, A. Cardozo-Saavedra, O. Hernández-Cristancho, A. Palomar-Muñoz, I. Navales-Mateu, M. de Bonilla Candau, A. García-Burillo, C. Gámez-Cenzano;*
Nuclear Medicine Department, Vall d'Hebron Hospital Universitari, Vall d'Hebron Barcelona Hospital Campus, Barcelona, SPAIN.

Aim/Introduction: We present the case of an 8-year-old girl with high-grade B-cell lymphoma, undergoing chemotherapy and suffering from extensive abdominal mucositis as an adverse effect. The patient developed life-threatening gastrointestinal bleeding, unlocalized by conventional angiographic and endoscopic studies. This case highlights the pivotal role of [99mTc]Tc-RBC (red blood cell) scintigraphy in detecting the bleeding sites and guiding therapeutic interventions. ***Materials and Methods:*** Due to hemodynamic instability and inconclusive results from contrast-enhanced CT and angiography, gastrointestinal bleeding

scintigraphy (GIBS) was performed. A dose of 9 mCi of [99mTc]Tc-labelled RBCs (in vivo-vitro technique) was administered, adjusted using the EANM Pediatric Dosage Card. The protocol included dynamic flow acquisition and abdominal SPECT/CT. Imaging was interpreted according to the 2019 EANM guidelines for GI bleeding scintigraphy. ***Results:*** Dynamic imaging revealed two foci of extravascular tracer accumulation: one at the gastroduodenal region and another in the proximal jejunum. The gastroduodenal site appeared first and demonstrated active bleeding with rapid intraluminal progression. The addition of SPECT/CT significantly contributed to the precise localization of both bleeding sites, particularly the jejunal focus, which was less evident on planar imaging. This confirmed and allowed prompting urgent endoscopy treatment of the bleeding duodenal ulcer via clip placement, as well as targeted embolization by interventional radiology of the jejunal haemorrhage focus. Both interventions stabilized the patient's condition, significantly reduced transfusion needs, and allowed discontinuation of vasoactive support. ***Conclusion:*** [99mTc]Tc-RBC scintigraphy enabled accurate localization of multiple occult gastrointestinal bleeding sources in a critically ill pediatric patient, directly influencing life-saving clinical management. In this case, where conventional modalities failed, nuclear medicine not only provided diagnostic clarity but also offered a minimally invasive, rapid, and patient-tailored approach that avoided blind surgical interventions. The addition of SPECT/CT was crucial for anatomical precision, enabling prompt and targeted treatment. This case exemplifies how nuclear medicine can decisively shift the diagnostic and therapeutic pathway, offering real-time insights that translate into meaningful clinical outcomes. In vulnerable populations, such as pediatric oncology patients, our specialty has the power to detect, guide, and help heal—making the difference between uncertainty and action, between risk and resolution. We must continue to advocate for broader access to these techniques and their integration into emergency diagnostic algorithms. ***References:*** Giammarile F, et al. EANM guideline for GI bleeding scintigraphy. Eur J Nucl Med Mol Imaging. 2019;46(4):772-786. Lassmann M, et al. EANM Dosage Card for paediatric nuclear medicine. Eur J Nucl Med Mol Imaging. 2007;34(5):796-798.

EPS-212

Contribution of FDG PET-CT to Risk Stratification and Treatment Response in Pediatric Hodgkin Lymphoma

A. Khelifa*, F. Koudri, A. Talbi, M. Lamali, L. Chelghoum, L. Belabas, S. Benzerdjeb, D. Tahmi, S. Brahmi, S. Rahabi, D. Mouas, A. Taibi, S. E. Bouyoucef, A. Amimour;*
Bab El Oued Hospital, Algiers, ALGERIA.

Aim/Introduction: In Algeria, Hodgkin lymphoma (HL) ranks as the third most common pediatric cancer, accounting for 10.7% of cases. It is generally associated with a favorable prognosis. FDG-PET/CT has significantly enhanced staging accuracy, risk-adapted treatment planning, and response evaluation, enabling therapy de-escalation and reduction of long-term toxicity. However, real-world constraints can affect adherence to standard imaging protocols.The aim of the study is to assess the contribution of FDG PET-CT to risk stratification and therapeutic response evaluation in pediatric Hodgkin lymphoma in real-world clinical practice. ***Materials and Methods:*** We conducted a retrospective study of 116 pediatric patients diagnosed with HL between 2021 and 2024. The cohort included 67 boys and 49 girls, with a mean age of 12.75 years ± 3.91. FDG PET-CT scans were performed at baseline, during treatment (interim), and post-treatment (final), and interpreted using the Deauville score. Baseline PET-CT was not consistently performed due to the frequent initiation of treatment immediately upon diagnosis, reflecting real-world constraints in urgent clinical settings. Treatment decisions, including radiotherapy indications, were reviewed in relation to PET findings. ***Results:*** Of the 116 patients, 68 underwent baseline PET, 75 interim PET, and 58 final PET; only 25 completed all three scans. Mean SUVmax values were 14.12 (baseline), 7.88 (interim), and 4.10 (final). Deauville scores at baseline showed a predominance of high metabolic activity (Score 5: 31 patients, Score 4: 30 patients). At interim PET, 30 out of 75 patients (40%) showed a good metabolic response (Deauville scores 1 to 3), while 45 patients (60%) exhibited a poor metabolic response (Score 4: 30 [40%], Score 5: 15 [20%]). These findings underline the value of interim PET in identifying non-responders and adapting treatment intensity. Radiotherapy was administered in 17 patients (14.7%), often guided by persistent metabolic activity observed on PET. ***Conclusion:*** FDG PET-CT is a pivotal tool in the management of pediatric Hodgkin lymphoma. In real-world practice, interim PET emerges as the most feasible and informative scan, effectively guiding therapeutic decisions when baseline or final imaging is unavailable. These findings reinforce the value of interim PET in treatment adaptation and long-term outcome optimization.

EPS-213

AI based automatic measurement of split renal function in [^{18}F]PSMA-1007 PET/CT

K. Valind*[1,2], J. Ulén[3], A. Gålne[1,2], J. Jögi[1,2], D. Minarik[1,4], E. Trägårdh[1,2];*
[1]Department of Translational Medicine, Wallenberg Centre for Molecular Medicine, Lund University, Malmö, SWEDEN, [2]Department of Clinical Physiology and Nuclear Medicine, Skåne University Hospital, Lund and Malmö, SWEDEN, [3]Eigenvision AB, Lund, SWEDEN, [4]Department of Radiation Physics, Skåne University Hospital, Lund and Malmö, SWEDEN.

Aim/Introduction: Prostate-specific membrane antigen (PSMA) targeted positron emission tomography (PET) with computed tomography (CT) has become an important diagnostic modality in prostate cancer. In addition to overexpression in cancer cells, PSMA is physiologically expressed in the proximal tubules of the kidneys. Because of this, PSMA PET is being explored for functional imaging of the kidneys. Uptake of PSMA targeted radiopharmaceuticals in the left and right kidneys have shown strong correlations to split renal function (SRF) as measured with other modalities [1]. Manual kidney segmentation in PET images is time consuming, which limits the practicality of this method of determining SRF. In this study, we designed, trained and validated an artificial intelligence (AI) model for automatic segmentation and measurement of SRF in [^{18}F]PSMA-1007 PET images. ***Materials and Methods:*** One nuclear medicine physician segmented kidneys in a training set of 135 [^{18}F]PSMA-1007 PET/CT studies. These data were then used to train an AI model based on the 3D UNET architecture [2]. The model was evaluated in 40 test studies, segmented by 3 nuclear medicine physicians. All segmentations (human and AI) were compared against each other regarding left renal function percentage (LRF%) and volume. ***Results:*** LRF% measurements ranged from 40% to 67%. Spearman correlation coefficients for LRF% measurements ranged between 0.98 and 0.99 when comparing segmentations. The largest LRF% difference between measurements in a single exam was 3 percentage points. The AI model performed similarly to human readers. ***Conclusion:*** Automatic measurement of SRF in PSMA PET is possible. It could be used to provide additional data in investigation of renal functional impairment, potentially saving patients time and radiation exposure. ***References:*** 1. Valind K, Minarik D, Garpered S, Persson E, Jogi J, Tragardh E. [(18)F]PSMA-1007 PET is comparable to [(99m)Tc]Tc-DMSA SPECT for renal cortical imaging. Eur J Hybrid Imaging. 2023;7:25. 2. Çiçek Ö, Abdulkadir A, Lienkamp SS, Brox T, Ronneberger O. 3D U-Net: learning dense volumetric segmentation from sparse annotation. Medical Image Computing and Computer-Assisted Intervention-MICCAI 2016: 19th International Conference, Athens, Greece, October 17-21, 2016, Proceedings, Part II 19: Springer; 2016. p. 424-32.

EPS-214

Relationship Between Prostatic FDG Uptake, Prostatic Calcifications, and Symptom Scores of NIH-CPSI and IPSS in male patients undergoing health checkups

J. Lee, *G. Lee, J. Choi, H. Son;*
Dankook University Hospital, Cheonan, KOREA, REPUBLIC OF.

Aim/Introduction: Since FDG PET/CT has been introduced in oncology, it has also proven clinically valuable in the evaluation of infections, connective tissue disorders, and neurodegenerative diseases. However, its potential role about genitourinary symptom assessment of the Chronic Prostatitis Symptom Index of the National Institutes of Health (NIH-CPSI), the International Prostate Symptom Score (IPSS) and Quality of life (QoL) has not been well defined. This study aims to explore the relationship between incidental prostate FDG uptake, prostatic calcifications, and symptom scores of NIH-CPSI, IPSS and QoL in men undergoing health screening. ***Materials and Methods:*** A total of 368 men (age <75) who underwent health checkups with FDG PET/CT and completed NIH-CPSI and IPSS questionnaires were included. Visual analysis of FDG uptake in the prostate and identification of prostatic calcifications on CT were performed. Additionally, PSA, Rapid plasma reagin (RPR), C-reative Protein (CRP), and Erythrocyte sedimentation rate (ESR) tests were performed and applied as adjustment variables. Univariate analysis was performed according to the presence or absence of FDG uptake and calcification. Associations with symptom scores were analyzed using multiple logistic regression analysis and spearman correlation analyses. ***Results:*** Among the study population, 31 patients exhibited positive FDG uptake, 84 patients had prostatic calcification and 104 patients showed both. Spearman correlation revealed strong associations between total NIH CPSI or IPSS scores and QoL (correlation coefficient: 0.58 and 0.78, $p < 0.001$, both). Univariate analysis showed that patients with either prostatic FDG uptake or calcification had higher scores on NIH-CPSI, IPSS and QoL scores, and were significantly associated with increasing age (Table 1). In multivariate regression logistic analysis, the presence of prostatic FDG uptake [odds ratio (OR): 6.5, 95% confidence intervals (CI): 2.86-14.95, $P < 0.001$ and OR:4.54, 95% CI:1.86-11.06, $P < 0.001$] and calcification [OR:4.36, 95% CI: 2.29-8.30, $P < 0.001$ and OR:4.86 95% CI:2.41-9.86 $P < 0.001$] were associated with the risk factors of IPSS and QoL high risk scores (8 and 3, each) (Table 2 and Table 3). ***Conclusion:*** Although FDG PET/CT was performed for screening purposes, prostatic FDG uptake and calcifications were significantly associated with systemic scoring systems such as NIH-CPSI and IPSS used to assess patients with lower urinary tract symptoms and measure treatment effectiveness in prostate diseases, especially chronic prostatitis/chronic pelvic pain syndrome (CP/CPPS) and benign prostatic hyperplasia. These findings suggest that PET/CT may provide adjunctive value in assessing latent urinary tract symptoms and contribute to the evaluation of CP/CPPS.

EPS-215

Assessment of Tumor Response to Neoadjuvant Hormone Therapy in Prostate Cancer Using F-18 PSMA-1007 PET: A Feasibility Study

S. Cho[1], *H. Han*[2], *S. Lee*[3], *M. Jung*[4], *Y. Oh*[5], *M. Yun*[3];
[1]*Yonsei University College of Medicine, Seoul, KOREA, REPUBLIC OF,* [2]*Department of Artificial Intelligence, Yonsei University, Seoul, KOREA, REPUBLIC OF,* [3]*Department of Nuclear Medicine, Yonsei University College of Medicine, Seoul, KOREA, REPUBLIC OF,* [4]*Department of Pathology, Yonsei University College of Medicine, Seoul, KOREA, REPUBLIC OF,* [5]*Department of Radiology, Yonsei University College of Medicine, Seoul, KOREA, REPUBLIC OF.*

Aim/Introduction: The role of prostate-specific membrane antigen (PSMA)-targeted positron emission tomography (PET) in assessing response to neoadjuvant androgen deprivation therapy (nADT) remains underexplored [1]. This study investigated the potential utility of ^{18}F PSMA-1007 PET for evaluating residual tumor burden following nADT, compared to multiparametric MRI (mpMRI). ***Materials and Methods:*** This retrospective study included 14 patients with localized prostate cancer who received nADT followed by radical prostatectomy. All patients underwent baseline mpMRI, post-nADT ^{18}F PSMA-1007 PET, and post-nADT mpMRI before surgery. Tumor volumes on PET were segmented using three methods: semi-automated thresholding based on a percentage of the max SUV (SUVmax), segmentation using the mean SUV (SUVmean) of benign prostatic tissue, and manual. Correlation between PET-derived and pathological tumor volumes was assessed using Spearman's rank correlation coefficient. MRI parameters, including apparent diffusion coefficient (ADC) and transfer constant (Ktrans), were extracted from tumor regions, and compared between pre- and post-treatment using Wilcoxon signed-rank tests. Mann-Whitney U tests were used to compare imaging parameters between tumor regions and benign prostatic hyperplasia (BPH) regions. ***Results:*** Among the 14 patients, one showed complete pathological response. ^{18}F PSMA-1007 PET detected residual tumor in 12 patients, whereas mpMRI detected residual lesions in 3. Tumor volume estimates obtained using SUVmean-based semi-automated segmentation correlated strongly with pathological tumor volumes (Spearman's $\rho = 0.877$, $p < 0.001$). Threshold-based methods using 40% and 50% of SUVmax also showed statistically significant correlations ($\rho = 0.778$ and $\rho = 0.723$, respectively; both $p < 0.001$). Median ADC increased significantly after nADT, from 0.865 to 1.101×10^{-3} mm^2/s ($p = 0.005$), while median Ktrans decreased from 0.224 to 0.075 min^{-1} ($p = 0.007$). Pre-nADT median ADC was significantly lower in tumor regions compared to BPH regions, with values of 0.865 and 1.250×10^{-3} mm^2/s, respectively ($p = 0.002$). No significant differences were observed between malignant and benign regions in pre-nADT Ktrans, post-nADT ADC, post-nADT Ktrans, or SUVmax. ***Conclusion:*** ^{18}F PSMA-1007 PET appeared more sensitive than mpMRI in identifying residual disease. PET-based tumor volume estimates correlated strongly with pathological volumes and may be useful for evaluating residual tumor following nADT in prostate cancer. These preliminary findings support the feasibility of ^{18}F PSMA-1007 PET in post-treatment assessment and warrant prospective validation. ***References:*** 1. Vaz S, Hadaschik B, Gabriel M, Herrmann K, Eiber M, Costa D. Influence of androgen deprivation therapy on PSMA expression and PSMA-ligand PET imaging of prostate cancer patients. Eur J Nucl Med Mol Imaging. 2020;47(1):9-15.

EPS-216

^{18}F-FDG PET/CT in diagnosis, staging and management of pediatric patients with Langerhans histiocytosis

P. Grecu-Bodnariuc[1], *M. Gutu*[1,2];
[1]*"Sfântul Ioan cel Nou" County Hospital of Emergency, Suceava, ROMANIA,* [2]*"Ştefan cel Mare" University, Faculty of Medicine, Suceava, ROMANIA.*

Aim/Introduction: Langerhans cell histiocytosis (LCH) is a rare disease, most common in childhood, occurring only in up to 8.9 per million children under the age of 15[1], and is consisting in abnormal clonal proliferation of Langerhans cells that can involve multiple organs. Positron emission tomography/computed tomography (PET/CT) has been widely used in tumor staging and therapeutic efficacy evaluation. However, in case of LCH there are few ^{18}F-fluorodeoxyglucose (FDG) PET/CT studies, especially for pediatric patients. This paper aimed to present our experience with the role of ^{18}F-FDG PET/CT in diagnosis, staging and management of pediatric patients with LCH. ***Materials and Methods:*** A 9 months (June 2024-March 2025) retrospective study of 9 examinations (age range, 18 months-16 years; mean age 2 y 10 m) with histologically proven LCH who underwent ^{18}F-FDG PET/

CT whole body scans, 8 of them under sedation. We compared PET/CT examinations with other complementary investigations such as CT (computed tomography), ultrasonography or X ray film in order to evaluate the usefulness, specificity and sensitivity of PET/CT. ***Results:*** For 2 cases PET/CT changed the classification from single system (SS) disease to multisystem (MS) disease, one directly from SS-single site to MS. FDG PET/CT was rated superior identifying lesions 56/25 (224%) compared with patient's complementary investigations. The most common localizations were bone (78%), lung (56%) and skin (11%). PET scans confirmed active LCH in 22/56 (39.28%). In 3 cases (33.33%) PET evaluation was decisive for therapeutic management because the lesions described on complementary imaging had no metabolic activity. ***Conclusion:*** According to our small data, whole body ^{18}F-FDG PET/CT can detect LCH activity and early response to therapy with greater accuracy than other imaging modalities in patients with LCH, particularly in the bones. In some cases, FDG PET/CT had changed the initial classification performed on complementary imaging, thus having a higher sensitivity even for staging. ***References:*** 1. Rodriguez-Galindo C, Allen CE. Langerhans cell histiocytosis. Blood. 2020 Apr 16;135(16):1319-1331.

EPS-217

SIOPEN Semiquantitative Score Adapted to 68GaDOTANOC PET/CT: A Superior DiseaseBurden Biomarker

N. Kundu, *D. Khan, S. Sagar, R. Kumar, A. K. Pandey, S. Bakhshi, R. Seth, S. Agarwala;*
AIIMS New Delhi, Delhi, INDIA.

Aim/Introduction: mIBG scoring system was developed in 1995 for semi-quantification of the extent of MIBG uptake and prognostication outcome. The role of two commonly used semiquantitative MIBG scoring systems, i.e, the Curie score (CS) and the SIOPEN score as a prognostic indicator for high-risk neuroblastoma has been reported in both institutional and cooperative group trials, including trials within the COG and the SIOPEN Research Network. Both the CS and SIOPEN scoring systems are based on planar imaging findings. In our study, we aim to validate the SIOPEN skeletal score on 68GaDOTANOC PET maximumintensity projections (MIPs) and compare its burdenstratification capability with the conventional score derived from 131ImIBG planar imaging. ***Materials and Methods:*** Baseline DOTANOCPET MIPs and paired mIBG planar scans of 40 children were independently scored (0-60) across 12 skeletal segments by two experienced nuclear medicine physicians. Scores were correlated with risk factors such as age (< 18 months vs ≥ 18 months), bonemarrow biopsy (positive or negative) and urine catecholamine levels (elevated or normal). Wilcoxon and MannWhitney U tests explored intermodality and interriskgroup differences. ***Results:*** Median DOTANOC SIOPEN score was 19 (IQR 0-42) vs 6 (IQR 0-21) on mIBG ($P < 0.01$). Patients ≥ 18 months showed higher DOTANOC SIOPEN scores than infants (24 ± 22 vs 10 ± 16; $P = 0.046$), mirroring outcome risk. Positive marrow biopsies corresponded to markedly higher DOTANOC scores (41 ± 13) than negative biopsies (8 ± 14; $P < 0.001$). However, there was no significant difference in SIOPEN scores between the patients with elevated and normal urine catecholamine levels ($p=0.808$). mIBG scores followed the same trend but with weaker separation. Interobserver agreement was excellent ($\kappa = 0.92$). ***Conclusion:*** Applying the SIOPEN scoring to highresolution DOTANOC MIPs amplifies diseaseburden discrimination across established risk strata and correlates robustly with marrow involvement. DOTANOCSIOPEN scoring could refine upfront risk allocation and response quantification in future multicentre trials.

EPS-218

Correlation of [^{18}F]FDG PET/CT Metabolic Activity with Clinical Presentations and Outcomes in Children Diagnosed with Langerhans Cell Histiocytosis

E. Aslan, *N. Gülaldi;*
University of Health Sciences, Department of Nuclear Medicine, Ankara Bilkent City Hospital, Ankara, TÜRKIYE.

Aim/Introduction: [^{18}F]FDG PET/CT in paediatric Langerhans Cell Histiocytosis (LCH) plays an important role in detecting bone and non-bone lesions, evaluating treatment response, and identifying potential sites of disease recurrence. The clinical presentation of the disease is usually characterized by either bone lesions or lymph node involvement. This study aims to reveal the relation of metabolic parameters obtained by PET/CT with prognosis and treatment response and also blood ALP, LDH values in both groups. ***Materials and Methods:*** Eighteen patients were included in this study (10 months- 17 y.o. median age: 8.1). SUVMax, SUVmean, MTV, and TLG values calculated from the lesions with the highest metabolic activity uptake were extracted from 36 [^{18}F] FDG PET/CT images including the treatment follow-up of these patients. ALP and LDH values were analyzed within 4 days after PET/CT. Patients were divided into 2 groups; bone involvement and lymph node involvement. In addition, those with lung, thymus, high-risk organs (liver, spleen, bone marrow), and central nervous system involvement were identified. ***Results:*** Ten patients presented with lytic lesions in bones, 5 patients had lymph node involvement and 2 patients had both lymph and bone lesions. 2 patients had thymus involvement, 1 patient had CNS involvement and 2 patients had high-risk organ involvement. Patients with bone lesions and those without bone lesions were compared with the Wilcoxon Signed Rank test due to their non-homogeneous distribution and MTV values calculated from all positive bone lesions were significantly different from MTV values calculated from lymph nodes ($p<0.05$). 3 patients showed progression of their diseases within 1 year of diagnosis. Two of them had lytic bone lesions, and 1 had lymph node involvement. However, ALP, LDH SUVMax, SUVmean, and TLG values did not differ between the groups. The rate of complete response to treatment was higher in patients with lymph node involvement than in patients with bone involvement, and progression was more common in patients with lytic bone involvement. ***Conclusion:*** Metabolic activity values of bone lesions were higher than those of patients with lymph node involvement. Thus, patients with bone lesions showed a more aggressive pattern and showed an earlier treatment response than patients with lymph node involvement. The tendency of patients with bone involvement to show a more aggressive pattern during LHH staging with PET/CT suggests that the option of increasing treatment protocols and especially the addition of radiotherapy should be considered for this group.

EPS-219

Mean Parenchymal Transit Time measurement on Tc-99m EC Diuretic renography can help differentiate obstructed from non-obstructed kidneys and help monitor response post-pyeloplasty.

N. Gupta, *M. Ponnusamy, K. G, P. Mathiyazhagan;*
JIPMER, Pondicherry, INDIA.

Aim/Introduction: Diuretic renography is used to rule out pelviureteric junction obstruction (PUJO) in hydronephrotic kidneys. In addition to Normalised Residual Activity (NORA20) and Output Efficiency at 20 minutes (OE20), Mean parenchymal transit time (MPTT) measured through deconvolution analysis is a continuous quantitative parameter that can be used for follow up. The objectives of the study were to compare MPTT values obtained with Tc-99m EC diuretic renography in obstructed and non-obstructed hydronephrotic kidneys in children with suspected PUJO and to find the association with other transit time

parameters. ***Materials and Methods:*** In a cross-sectional analytical design, this study analysed data of Tc-99m EC diuretic renography performed in children suspected to have PUJO under the age of 18 years. The renography data was transferred to MATLAB and values of NORA20, OE20, and MPTT were obtained using separate algorithms. The contralateral non-hydronephrotic kidney was considered normal. Obstructed kidneys were identified based on the diuretic renography images and curve pattern by an experienced nuclear medicine physician. The MPTT values were compared between normal, hydronephrotic non-obstructed, and obstructed kidneys; and post pyeloplasty in affected kidneys. In addition, association between values NORA20, OE20 and MPTT was studied. ***Results:*** Analyzing data from 201 patients (396 renal units), the median MPTT in non-hydronephrotic (n=178), hydronephrotic non-obstructed kidneys (n=144), and obstructed kidneys (n=74) were 3.30 minutes (IQR: 2.91, 3.93), 5.69 (IQR: 4.10, 8.27), and 12.84 (IQR: 10.47, 14.88), respectively. A significant difference existed between the groups (p <0.01). Median NORA20 for hydronephrotic non-obstructed and obstructed kidneys were 0.47 (IQR: 0.02, 0.86) and 2.52 (IQR: 2.05, 3.06), while OE20 values were 77.34 (IQR: 64.41, 87.36) and 41.52 (IQR: 33.78, 50.60). There was a strong positive correlation between MPTT and NORA20 in hydronephrotic non-obstructed and obstructed kidneys (correlation coefficient: 0.84, p <0.01 and -0.87, p <0.01, respectively), and there was a strong negative correlation between MPTT and OE20 in obstructed kidneys (correlation coefficient: -0.81, p<0.01) but weak in the other two subgroups. The mean MPTT values pre and post pyeloplasty in obstructed kidneys (n=32) were 12.49 and 8.22 (p <0.01). ***Conclusion:*** MPTT values obtained on Tc-99m EC diuretic renography showed a significant difference between the hydronephrotic non-obstructed and hydronephrotic obstructed kidneys, implying that MPTT is significantly prolonged in obstructed kidneys. The MPTT values in obstructed kidneys showed considerable improvement after pyeloplasty, implying improvement in kidney function after an effective intervention. The MPTT values correlated with NORA20 and OE20 values.

1310

Tuesday, October 7, 2025, 9:45 - 11:15
Room 116

Technologists' Track Oral Presentations 3 - Technologists Committee: Interdisciplinary Nuclear Medicine Workforce Sustainability and Training

OP-619

Technologist perspective in practice change and mitigations during the installation of two Total Body PET scanners in a busy department

S. Pereira[1,2], *G. Testanera*[1,2], *G. Cook*[1,2], *J. John*[1,2], *S. Chicklore*[1,2], *G. Krokos*[1,2], *S. Giles*[1,2];
[1]*King's College London, London, UNITED KINGDOM,* [2]*Guy's and St Thomas' Hospital NHS Foundation Trust, London, UNITED KINGDOM.*

Aim/Introduction: Kings College London (KCL)/Guys and St Thomas (GSTT) PET Centre has recently installed two Long axial field of view (LAFOV) PET/CT scanners, Biograph Vision Quadra, Siemens Healthineers. LAFOV PET scanners are highly sensitive and offer high-resolution, low-noise imaging with extended coverage. To fully leverage these advantages, a multidisciplinary team was formed to implement an efficient and reliable service. This transition posed several challenges including departmental redesign, staff training, and continuous adjustment of operational practices. Despite ongoing construction, scanning services continued uninterrupted throughout the installation. ***Materials and Methods:*** Before the installation, the mitigations included maximizing the patients' list by redirecting approximately 30 patients daily to our residual functioning scanners and outsourcing services, as well as extended hours of work during the week and weekend lists. During the installation, the layout of the department allowed for patient redirection to avoid unnecessary radiation doses to the building workers whilst parallel working. Following the installation of the first total-body PET scanner, imaging protocols were redesigned to increase the number of slots allocated for clinical studies. This optimization included decreasing the injected activity for patients and overall scanning time while rearranging the daily schedule to accommodate more complex studies, such as dynamic scans, paediatric scanning under general anaesthetic, and different traces. The staff were trained by the manufacturer on operating and performing quality controls. In-house training was provided to identify any knowledge gaps or protocol issues. ***Results:*** The mitigation strategies put in place prior to the installation ensured that patient throughput was maintained with minimal delays. After the first scanner went live, staff went through an adjustment period of a faster working pace whilst getting used to a new system, mainly due to the extended FOV. The redesign of the department allowed for an increase of 20% in the uptake bays and more spacious areas. The optimization of the imaging protocol, with a weight-based protocol and a reduction of the scanner time to 50%, permitted an increase in slots from two to three patients per hour. The department capacity has increased without compromising the comfort and experience of the patient. ***Conclusion:*** After a year of structural changes and process redesign, the PET Centre now operates two Quadra LAFOV scanners, providing a service that offers faster, more comfortable scans with lower radiation exposure and improved image quality. This advancement significantly boosts our capacity for clinical studies and supports complex and unique research opportunities.

OP-620

Exploring curriculum considerations to prepare future radiographers for an AI-assisted healthcare environment: a scoping review

C. Kammies[1], *E. Archer*[2], *P. Engel-Hills*[3], *M. Volschenk*[2];
[1]*University of Johannesburg, Johannesburg, SOUTH AFRICA,* [2]*Stellenbosch University, Cape Town, SOUTH AFRICA,* [3]*Cape Peninsula University of Technology, Cape Town, SOUTH AFRICA.*

Aim/Introduction: The integration of AI in various aspects of clinical radiography has sparked intense discussions about appropriate education and training, both for the existing and future workforce. Evaluating and integrating AI-related competencies into existing curricula requires an informed, considerate approach. Therefore, the scoping review maps the available evidence on the adjustments needed in the radiography curriculum to prepare radiography students for the demands of AI-assisted healthcare environments. ***Materials and Methods:*** A scoping review was conducted following the six-step Joanna Briggs Institute (JBI) methodology. Articles that focused on radiography education and technologies that incorporate AI were searched across four databases: EBSCOhost, PubMed, Scopus, and Web of Science for studies that were published from inception until October 2024. ***Results:*** Electronic database searches have retrieved 2 127 results. Title and abstract screening of 1 930 articles were completed. Data charting and the remaining steps of the scoping review, including dissemination, will be available by August 2025. Preliminary screening results show that radiographers are already adopting AI technologies into clinical practice, however, education and training of current and future radiographers are lacking. Educators need to be knowledgeable about AI to equip students for a workforce where AI will function as their "colleague." The incorporation of this technology may influence the relationship between patients and radiographers. Moreover, advancements

in AI-driven technologies hold significant potential to enhance patient-centred care. ***Conclusion:*** Despite the recognition that AI is being adopted in clinical practice, curriculum development is still in its early stages. However, the successful incorporation of AI tools into radiography education necessitates a balance between technological proficiency and a commitment to patient-centered care. As with the recognition that AI should form an essential part of the curriculum, the advocacy for radiographers to maintain the core value of patient-centred care has been strongly supported. Patient-centred care is fundamental in the radiography profession and the successful incorporation of AI education in the curriculum necessitates a balance between technological proficiency and a commitment to patient-centered care.

OP-621

A national collaborative initiative for knowledge sharing among nuclear medicine staff

C. Holm[1], *M. Hylle*[2], *T. Kirk Lehnskov*[3];
[1]*Odense University Hospital, Odense C, DENMARK,* [2]*Aalborg University Hospital, Aalborg, DENMARK,* [3]*Copenhagen University Hospital, Copenhagen, DENMARK.*

Aim/Introduction: In Denmark, there are 16 nuclear medicine departments across five regions. While various forums exist to facilitate knowledge sharing among specialists and leadership, there has been no dedicated platform for frontline staff—those who interact directly with patients and play a crucial role in daily routine. Recognizing this gap, we established a structured online forum to enhance collaboration, promote professional development, and share best practices for nuclear medicine departments in Denmark. The purpose of this initiative is to provide a space where nuclear medicine staff can discuss operational challenges, innovative techniques, and potential areas for collaboration in research and clinical practice. ***Materials and Methods:*** The first national online meeting was conducted on April 3, 2024, with participation from all nuclear medicine departments in Denmark. The session lasted two hours and was designed as an interactive knowledge sharing platform. A pre-meeting questionnaire was distributed to department representatives before each session. The questionnaire aimed to identify key topics of interest, challenges faced by staff, and areas where shared experiences could improve clinical practice. Participation is flexible on a department level, i.e. different representatives from individual departments may attend different meetings based on their expertise and relevance. Following each session, all attendees receive a contact list to encourage ongoing communication, networking, and potential collaborative efforts in research and clinical improvements. The online meetings are scheduled to take place 3 times a year, while there will be a physical meeting. ***Results:*** Over the course of four meetings, participants reported increased commitment to cross-departmental discussions, leading to a broader exchange of best practices in patient care, workflow optimization, and quality assurance in nuclear medicine. The forum also served as a catalyst for interdepartmental collaborations, enabling staff to explore opportunities for research partnerships and innovation within the field. Feedback from participants highlighted the benefits of structured knowledge sharing, including improved standardization of procedures and enhanced professional support across departments. ***Conclusion:*** After four successful online meetings with nationwide representation, our findings suggest that this initiative to facilitate knowledge sharing has considerable improved communication and collaboration among nuclear medicine staff on a national scale. Minor adjustments to the meeting structure after the initial sessions have optimized the format, making discussions more efficient and relevant. Moving forward, this initiative has the potential to expand into a structured, long-term professional network, supporting continued education, innovation, and research across Denmark's nuclear medicine departments.

OP-622

Developing Interdisciplinary VR-Education on Scanxiety: A Technologists Perspective

C. Van Den Haak[1], *A. J. Nijkerk*[2], *J. J. Pool*[2], *E. W. Elings*[2], *J. C. Houting*[2], *J. A. Adam*[2];
[1]*Amsterdam UMC, Amsterdam, NETHERLANDS,* [2]*Amsterdam UMC and University of Amsterdam, Amsterdam, NETHERLANDS.*

Aim/Introduction: One of the advantages of working in an academic hospital as a technologist is direct involvement in educational activities. Scanxiety, the anxiety before, during and after medical imaging has hardly been highlighted in medical education up to now. However, education on this aspect is necessary, not only for the patient but also for the healthcare professionals, such as technologists. Current education of technologists focuses on execution and quality of the scans, but education on patient perspective is missing. Training empathy as a competence is seen as an essential part of making healthcare professionals 'future-proof'. Virtual reality offers an easily applicable unique insight into the scan procedure from the patient perspective, without the students having to undergo a sham scan themselves. Our aim was to develop a novel interdisciplinary educational material to create awareness for the patient perspective and scanxiety. ***Materials and Methods:*** An interdisciplinary team was gathered to develop the educational material, consisting of a nuclear medicine physician, technologist, medical educators and audiovisual crew. All members were asked to participate from their own perspective. In the case of the technologists, the different roles of the technologist are shown, such as informative, operational and supportive. The Scanxiety Educational Module consists of an introduction, an 8-minute VR film and a debriefing. VR, as an educational design, was chosen to convey the patient perspective in an immersive way. To create the script for the VR film, the experiences of actual patients and the technologist have been gathered. The film shows a patient journey, from the waiting room to the preparation, getting the IV and the actual scan. During the film, the patient's thoughts become audible, based on testimonials from healthcare professionals who have undergone medical imaging themselves. ***Results:*** The introduction informs the students on the background of patient perspective and scanxiety. The VR film evokes emotions, and a change in perspective is initiated, and the student's empathy is called upon. During the debriefing, the students' experience is discussed from different angles with an emphasis on empathy and shared vulnerability. Students are also given the assignment to provide concrete suggestions for improvement with regard to patient experience. ***Conclusion:*** Developing educational material in an interdisciplinary team provides several benefits. Emphasizing the technologists' perspective provides additional value to the education on patient experience and scanxiety. Participating in educational projects as a technologist is inspiring and a welcome addition to the technologists' professional activities.

OP-623

From Doctors to Technologists: Operational Efficiency following role reassignment in sentinel node procedures

A. Moura, *C. Rodrigues;*
Imperial College NHS Healthcare Trust, London, UNITED KINGDOM.

Aim/Introduction: Sentinel lymph node imaging for melanoma is a time-sensitive diagnostic procedure. Until 2023, this involved a sequence of activities starting with application of numbing cream (5% lidocaine/prilocaine) and concluding with the completion of SPECT/CT imaging. Historically, nuclear medicine doctors had performed intradermal administration of radiopharmaceuticals. To

optimise workflow and resource utilisation, the responsibility of injection was moved to clinical technologists. This study evaluates the impact of this role change on the overall procedural time, with a specific focus on the total time patients spent on the scanner and in the department. ***Materials and Methods:*** A retrospective analysis was conducted on twenty-two sentinel node melanoma cases performed between January and September 2023. The cases were divided into two cohorts: injections performed by doctors (n=12) and injections performed by technologists (n=10). Key timepoints were recorded, including numbing cream application, radiotracer draw-up and injection, CT acquisition, and final scan completion. The primary metric was the total elapsed time from numbing cream application to scan completion on RIS (radiology information system). Comparative trends were visualised using a line plot, and descriptive statistics were used to compare efficiency between the two roles. ***Results:*** The scans led by the technologist group demonstrated a consistent and significantly reduced procedural time, with an average duration of approximately 101 minutes (+/- 23 minutes), compared to the doctor cohort's average of around 132 minutes (+/- 33 minutes). Moreover, the technologist-led cases exhibited lower variability, suggesting improved standardization. In contrast, doctor-led cases showed greater time fluctuations. The data suggests that delegating injection responsibilities to technologists not only reduces the overall scan timeline but also enhances operational predictability. ***Conclusion:*** The transition from doctor-led to technologist-led intradermal injections in sentinel node melanoma imaging is associated with measurable improvements in workflow efficiency. The observed time savings can enhance patient throughput, reduce resource strain, and support better scheduling flexibility. Importantly, this change also aligns with broader trends in healthcare, promoting role optimisation and inter-professional collaboration. Further prospective studies are recommended to evaluate patient satisfaction, diagnostic outcomes, and scalability of this model to other nuclear medicine procedures.

OP-624

More Than Just Teaching: The Hidden Impact of the London Nuclear Medicine Practice Educators

H. Chandler[1,2], *C. Rodrigues*[1,3];
[1]*London Imaging Academy/University College Hospitals London, London, UNITED KINGDOM,* [2]*London Northwest University Healthcare NHS Trust, London, UNITED KINGDOM,* [3]*Imperial College Healthcare NHS Trust, London, UNITED KINGDOM.*

Aim/Introduction: The introduction of Nuclear Medicine Practice Educators (PE) in London marked a pioneering initiative aimed at addressing the gap in educational support for learners in the Nuclear Medicine field. This role, typically filled by a registered healthcare professional, facilitates training and mentorship alongside clinical and academic teams [1]. Following the implementation of two PEs in London, this work now evaluates the impact, challenges, and opportunities that have arisen from this role, as well as future directions. ***Materials and Methods:*** Building on the initial engagement with 22 hospital sites across London, with 16 expressing a need for PE support, a comprehensive follow-up survey and ongoing hospital site visits were conducted. Feedback from clinical staff, trainees, and managers was gathered to assess the effectiveness of the initiatives introduced, with particular focus on continued gaps, evolving needs, and the role of PEs in addressing these. ***Results:*** The impact of the PE role has been substantial, with notable improvements in key areas such as the competency of mentors and assessors, standardisation of training materials, and increased exposure to diverse clinical scenarios. Notably, the PEs' efforts in bridging international knowledge gaps and supporting the development of soft skills in learners have been particularly impactful. Regional collaboration through workforce meetings, the launch of online resources via the London Imaging Academy, and face-to-face teaching sessions have further strengthened educational delivery. Additionally, educational and well-being newsletters, interactive study days, and university collaborations have created stronger engagement with prospective Nuclear Medicine professionals. Sites also found that the PE's strengthened inclusive networking across sites and built effective partnerships for cross-departmental collaboration. Several responses emphasised the need for the role to be full-time and extended, to be able to fully support departments long-term. ***Conclusion:*** The establishment of the Nuclear Medicine Practice Educator role has made a significant, positive impact on training and development in the field within London. By addressing critical gaps in training, mentorship, and departmental needs, this initiative has been well-received across the region. The feedback from stakeholders demonstrates the growing importance of this role, and future evaluations will continue to assess its long-term impact and viability, shaping the future of Nuclear Medicine practice and education across London. ***References:*** [1] Health Education England (n.d.). Practice Educators: Imaging. Available from: https://www.hee.nhs.uk/our-work/cancer-diagnostics/imaging/practice-educators.

OP-625

The Role of Technologists in the TOTEM Study: Operational Challenges and Fostering a Research Culture in a 2 LAFOV PET Scanner Department

G. Testanera*, S. Lam, S. Pereira, J. Joemon, S. L. Giles, G. Cook, S. Gould, P. K. Marsden, L. Agoro;*
King College London, London, UNITED KINGDOM.

Aim/Introduction: Long Axial Field of View (LAFOV) PET scanners offer high-resolution, low-noise imaging with extended coverage, reduced radiation dose, and shorter scan times than standard PET/CT[1]. However, global experience and standardised protocols for LAFOV PET remain limited. At Guy's and St Thomas (GSTT)/King's College London (KCL) PET Centre, after two LAFOV PET scanners were installed, we launched the ethically approved "TOTEM - Total Body PET Exploring new iMaging" (IRAS: 339077) study. This study aims to optimise imaging protocols, explore data analysis methods, and improve scan efficiency while minimising radiation exposure. The expanded capacity creates an opportunity to embed research culture within a busy clinical setting, even among staff without prior research experience. ***Materials and Methods:*** TOTEM seeks to recruit 9999 participants over five years. All adult patients undergoing standard LAFOV PET scans are eligible to consent for use of anonymised data. Selected participants may also undergo additional research scans, including dynamic or delayed acquisitions, as part of TOTEM substudies. Nuclear Medicine Technologists (NMTs) and Radiographers are responsible for patient engagement, obtaining consent, and entering data into a secure REDCap database. Anticipated challenges included time constraints, training needs, and integrating research into routine clinical workflows. ***Results:*** All NMTs and Radiographers completed Good Clinical Practice (GCP), study protocol, consent, and REDCap data entry training. Over 30 participants were recruited within the first few weeks. Although these tasks are additional to routine responsibilities, shorter clinical scan times have created extra capacity for research-related activities. Data management challenges were mitigated through infrastructure improvements and streamlined data collection. An unforeseen challenge was the reduced interval between referral and appointment due to LAFOV efficiency, limiting time to send study information in advance. To address this, an ethics amendment will be submitted to allow same-day consent for data sharing. For additional research scans, the 24-hour information period remains mandatory. ***Conclusion:*** Close collaboration among technologists, radiographers, administrative staff, clinicians, and research teams has been vital for the successful implementation of TOTEM. Early identification

of operational challenges enabled timely solutions. The team has embraced an evolving research culture, which will support an expanding portfolio of commercial and non-commercial studies as part of the UK National PET Imaging Platform (NPIP)[2]
References: [1] Cook GJR, Alberts IL, Wagner T, Fischer BM, Nazir MS, Lilburn D. The impact of long axial field of view (LAFOV) PET on oncologic imaging. Eur J Radiol. 2025 Feb;183:111873. [2] https://npip.org.uk/.

OP-626

Embedded Student Program - Delivering a sustainable workforce pipeline to address a critical Nuclear Medicine Scientist shortage across Queensland, Australia.

T. Pearson[1], *S. Daniel*[1], *L. McBride*[2], *E. Gacitua*[2];
[1]*Metro North Hospital & Health Service, Brisbane, AUSTRALIA,*
[2]*Office of the Chief Allied Health Officer, Brisbane, AUSTRALIA.*

Aim/Introduction: Continued growth of nuclear medicine services, combined with persistent critical workforce shortages has resulted in significant pressure on service delivery within a large public health organisation of 130,000 employees in Australia. These challenges are disproportionately experienced in regional areas, where positions are frequently advertised multiple times attracting a single qualified applicant. A required workforce pipeline to address Nuclear Medicine Scientist (NMS) workforce current and future demands across an area the approximate size of Western Europe. ***Materials and Methods:*** To understand the problem, targeted collection and analysis occurred together with a review of existing models available in Australia and overseas. Model development included broad collaboration across multiple stakeholders focussed through a Statewide forum. Participation included engagement with the public and private sectors, university partners, professional bodies, and unions. This forum outlined that the required solution must support local training models across Queensland (regional and metropolitan areas) and be accessible for three target groups: 1. mature-age students, 2. school leavers, and 3. First Nations people. The forum identified that any model must address student clinical 'placement poverty', a significant barrier to healthcare students in Australia completing their qualifications unpaid clinical placement requirements. ***Results:*** The Queensland NMS Embedded Student Program (ESP) launched in March 2025 in collaboration the Royal Melbourne Institute of Technology (RMIT). This unique and novel ESP for training was developed and implemented to meet public health needs in Queensland. The ESP supports the delivery of theoretical training through distance education in conjunction with student's meeting their required clinical placement objectives locally throughout the university semester. In its first year of delivery, the ESP attracted high quality recruits across each of the 8 public health sites, with offers in each of the 3 targeted groups. ***Conclusion:*** 8 ESP students commenced in March 2025 across Queensland Health, aligning with the NMS workforce pipeline needs. The ESP students can also support service needs as paid assistants during their university semester breaks. Formal evaluation of the program from a public health perspective is currently underway and will follow the first cohort through their studies. This presentation will showcase the journey to arrive at a model to deliver a workforce pipeline for NMS in Queensland, as well as the details of novel the ESP. It is anticipated this model can be used to support NMS workforce pipelines in other regional areas without access to a local university training provider.

OP-627

Enhancing Nuclear Medicine Services Through a Hybrid, Collaborative Workforce: Integrating Technologists and Radiographers

M. Casanova Martins*, N. Hopson;*
Swansea Bay University Health Board, Swansea, UNITED KINGDOM.

Aim/Introduction: As nuclear medicine continues to advance with hybrid imaging modalities such as PET-CT and SPECT-CT, the boundaries between traditional professional roles are becoming increasingly blurred. Diagnostic radiographers bring critical expertise in anatomical imaging, while nuclear medicine technologists contribute in-depth knowledge of radiopharmaceuticals and functional imaging. The integration of these complementary skills presents a unique opportunity to develop a hybrid, collaborative workforce model aimed at improving clinical outcomes and service efficiency. This study aims to explore the development and impact of a hybrid workforce model that fosters collaboration between nuclear medicine technologists and diagnostic radiographers and to evaluate how this approach can enhance patient care, workflow efficiency, and professional development within nuclear medicine departments. ***Materials and Methods:*** We performed a qualitative analysis of workforce integration strategies within multiple UK nuclear medicine departments. Data were gathered through structured staff interviews and workflow observations to assess the feasibility, implementation challenges, and impacts of creating hybrid roles. Outcomes evaluated included patient throughput, staff satisfaction, imaging service diversification, and overall operational effectiveness. ***Results:*** Departments employing collaborative models reported increased operational efficiency, particularly in high-throughput imaging environments. The shared expertise between radiographers and technologists enabled more streamlined workflows, reduced patient appointment times, and improved scanner utilisation. Staff expressed higher job satisfaction due to diversified responsibilities and interprofessional learning opportunities. Crucially, the hybrid workforce model facilitated the expansion of the imaging portfolio, including the introduction of calcium scoring integrated into myocardial perfusion (MPS) protocols, diagnostic-quality CT head imaging as part of dementia studies, and the use of low-dose, mA-modulated diagnostic CT acquisitions to complement hybrid imaging for bone and other isotope scans. These developments enhanced the diagnostic value of nuclear medicine examinations and improved the overall patient diagnostic pathway. Despite clear benefits, challenges persisted around regulatory scope clarity, consistent training standards, and the need for standardized competency frameworks. ***Conclusion:*** Integrating nuclear medicine technologists and diagnostic radiographers into a cohesive hybrid workforce provides substantial benefits, including improved patient care, expanded imaging capabilities, and increased departmental flexibility. To further support this model's widespread adoption, collaboration between national professional bodies and regulators is necessary to establish unified competencies, robust cross-training curricula, and clear governance structures. This hybrid approach will be critical to addressing future clinical and technological advancements in nuclear medicine.

1311

Tuesday, October 7, 2025, 9:45 - 11:15
Room 111

TROP Session - Case Report Session 1: Case-based Learning in Theranostics

OP-628

Molecular Response Assessment of combined intravesical Radio-Ligand-Therapy (iRLT) and systemic chemotherapy of Muscle Invasive Bladder Cancer patients by liquid biopsy testing from urine - the RadioMolecularIncubator Experience within the Bladder BRIDGister

R. Wirtz[1], *E. Storz*[2], *M. von Brandenstein*[2], *F. Friedersdorff*[3], *D. Barski*[4], *T. Otto*[4], *J. Graff*[5], *M. Waldner*[5], *E. Veltrup*[1], *P. Gehle*[1], *R. Hake*[6], *S. Eidt*[6], *C. Rieger*[2], *T. Ecke*[7], *A. Heidenreich*[2], *L. Greifenstein*[8], *R. P. Baum*[8];
[1]*STRATIFYER Molecular Pathology GmbH, Köln, GERMANY,* [2]*Dpt. of Urology, University Clinic Cologne, Köln, GERMANY,* [3]*Dpt. of Urology, Charité - Universitätsmedizin Berlin, Berlin, GERMANY,* [4]*Dpt. of Urology, Rheinlandklinikum, Neuss, GERMANY,* [5]*Dpt. of Urology St. Elisabeth Hospital,, Köln, GERMANY,* [6]*Institute of Pathology at the St. Elisabeth Hospital, Köln, GERMANY,* [7]*Dpt. of Urology, HELIOS Klinik Bad Saarow, Berlin, GERMANY,* [8]*CURANOSTICUM Wiesbaden-Frankfurt, Wiesbaden, GERMANY.*

Aim/Introduction: Patients with Muscle Invasive Bladder Cancer (MIBC) achieving pathological complete response (pCR) upon neoadjuvant chemotherapy (NACT) have improved prognosis. Intravesical Radioligandtherapy (iRLT) is effective in NACT resistant tumors. While gene expression profiles from tumor tissues are predictive of response, no expression profiling of tumor cells in urine is established to monitor tumor response towards ongoing treatment. However, tumor specific gene expression in urine samples may enable non-invasive testing and distinguish responding from non-responding tumors for early treatment adoption. ***Materials and Methods:*** Tumor cells were isolated from 10 ml urine collected before TUR biopsy and before each cycle of treatment as well as before deep TURB or cystectomy. Similiarly whole urine was drawn before each cycle. FFPE tissues as well as matched urine samples from patients receiving systemic chemotherapy +/- intravesical Radioligandtherapy were prospectively collected, RNA was extracted, and relative gene expressionwas analyzed by RT-qPCR. Dynamics of expression profiles were compared to pathological outcome. ***Results:*** A 67-y-o male suffering a pT2a high grade bladder cancer with heterogenous cancer histology was selected based on high CXCR4 expression on mRNA and protein level. PET/CT Imaging by Ga^{68} CXCR4 confirmed substantial uptake in the tumor tissue. Subsequently, Lu^{177} CXCR4 was instilled one week before application of 3 cycles ddMVAC. Second PET/CT Imaging by Ga^{68} CXCR4 after 6 weeks revealed molecular complete response, which was validated histopathologically by analysis of additional deep TUR biopsy tissue. Molecular tissue analysis comfirmed tumor heterogeneity by detecting a high expression of luminal KRT20 and basal KRT5 at initial TUR biopsy. Molecular urine analysis similarly revealed high expression of both KRT5 and KRT20 mRNA. After intravesical RLT the KRT5 and KRT20 expression dropped 4 fold, indicating a significant tumor response within one week of treatment due to Lu^{177} CXCR4 treatment alone. Subsequent chemotherapy cycles further reduced the KRT5 and KRT20 mRNA levels from urine samples stepwise. Importantly, when looking at cells isolated from urine this effect was particularly striking with KRT20 mRNA becoming completely undetectable before the 3rd chemotherapy cycle. ***Conclusion:*** To the best of our knowledge this is the first-in-human clinical efficacy proof of intravesical radioligand therapy (iRLT) targeting CXCR4 combined with neaoadjuvant chemotherapy (NACT) in MIBC. Gene expression profiles from urine samples recapitulated clinical response in vitro. Molecular urine profiling is feasible and may help to adopt treatments early on, which will be analyzed in upcoming phase I/II iRLT umbrella trials of the Bladder BRIDGister.

OP-629

Role of Post-Therapy SPECT/CT in Detecting Pseudoprogression during Lu-177 PSMA Radioligand Therapy: A Case Report

K. Resuello*, W. Lim, P. Fernando;*
St. Luke's Medical Center - Global City, Taguig, PHILIPPINES.

Aim/Introduction: Lu-177 PSMA (LuPSMA) radioligand therapy has shown advancement in treating metastatic castration-resistant prostate cancer (mCRPC). However, early assessment of therapeutic response is complicated by the possibility of pseudoprogression and imaging flare, which can initially mimic disease progression and potentially lead to premature changes in treatment strategy. While pseudoprogression is known in the context of modalities such as immune checkpoint inhibitor therapy, current literature is scarce on its prevalence and implications during LuPSMA therapy. ***Materials and Methods:*** We report a case of a 76-year-old male with mCRPC who received three cycles of Lu-177 PSMA therapy (± 8.15 GBq every 5 to 6 weeks). Imaging treatment response was evaluated by reviewing the patient's baseline F-18 PSMA PET/CT, as well as the planar and SPECT/CT gamma camera images obtained 14-16 hours after each cycle of Lu-177 PSMA therapy. Concordance of biochemical response was verified through review of changes in PSA levels between cycles. ***Results:*** Baseline PET-CT showed metastatic PSMA-avid left abdominopelvic adenopathy, left proximal ureteral mass, and skeletal lesions. After cycle 1, there was interval increase in the number of skeletal lesions, which was concordant with an interval increase in PSA. The cycle 2 post-therapy scan revealed significant increase in extent of LuPSMA-avid bone lesions, now more diffuse, accompanied by a further rise in PSA. However, PSA decline was noted upon administration of cycle 3 of therapy, and there was concomitant regression in PSMA activity of the skeletal disease on post-therapy imaging, suggesting of an resolving imaging flare. ***Conclusion:*** This is the first instance of pseudoprogression encountered in our institution after several years of experience in performing Lu-177 PSMA radioligand therapy. It highlights the value of post-therapy SPECT/CT imaging after every therapy cycle. Such finding may support the administration of 3 cycles as a minimum standard before assessing overall treatment benefit. Further studies are suggested on the implications of such phenomenon on patient prognosis and overall survival. ***References:*** 1. Rahbar, K., Ahmadzadehfar, H., Kratochwil, C., Haberkorn, U., Schäfers, M., & Essler, M. (2017). German multicenter study investigating 177Lu-PSMA-617 radioligand therapy in advanced prostate cancer patients. Journal of Nuclear Medicine, 58(1), 85-90. https://doi.org/10.2967/jnumed.116.1831942. Ferdinandus, J., Violet, J., Sandhu, S., Hicks, R. J., & Hofman, M. S. (2019). Impact of PSA flare phenomenon on response assessment by ^{68}Ga-PSMA PET/CT in patients undergoing 177Lu-PSMA therapy. European Journal of Nuclear Medicine and Molecular Imaging, 46(5), 1041-1049. https://doi.org/10.1007/s00259-018-4200-6.

OP-630

Non-Invasive Management of an Asymptomatic Lu-177-PSMA-617 Extravasation: A Case Report with Scintigraphic and Dosimetric Evaluation

Y. Cras, *M. Borsali, P. Lacassagne, L. Ferreol, D. Deandreis, C. Garcia;*
Gustave Roussy, Villejuif, FRANCE.

Aim/Introduction: Extravasation of therapeutic radiopharmaceuticals such as Lu-177-PSMA-617 is rare but may lead to local complications. We report a case of asymptomatic extravasation detected incidentally after injection, managed non-invasively with dosimetric and scintigraphic follow-up. ***Materials and Methods:*** A 77-year-old man with multimetastatic castration-resistant prostate cancer, previously treated with docetaxel and three lines of ARPI, received 6886 MBq of Lu-177-PSMA-617. Post-therapeutic whole-body scintigraphy performed 4 hours after injection revealed focal extravasation at the injection site. The patient reported no pain, erythema, or edema. Management consisted of limb elevation, massage, arm contraction-relaxation exercises, and warm sodium chloride compresses during a 24-hour hospital stay. Scintigraphic follow-up using a CZT-based SPECT/CT system was conducted at 4 hours (D0), 24 hours (D1), and 5 days (D5) post-injection. A volume of interest (VOI) was drawn on each scan with standardized thresholding. Residual activity was quantified at each time point. ***Results:*** The extravasated activity was estimated at 1288 MBq (19% of the injected activity) at D0. It decreased to 8 MBq (0.1%) at D1 and to 2 MBq (0.03%) at D5, corresponding to a >99% reduction within the first 24 hours. The absorbed dose at the site was estimated at 6 Gy. No clinical sequelae were observed at the 3-week follow-up. ***Conclusion:*** This case demonstrates that Lu-177-PSMA-617 extravasation may be asymptomatic and can be effectively managed with non-invasive strategies. Sequential imaging allows accurate monitoring of activity clearance and dosimetric impact. Routine post-injection assessment is recommended to detect and manage such events, ensuring patient safety in radioligand therapy.

OP-631

Validation of SPECT-based dosimetry in 177Lu-DOTATATE peptide receptor radionuclide therapy: ex-vivo confirmation after liver transplantation

C. Avigo[1], *F. Bonutti*[2], *L. Barresi*[1], *S. Peric*[1], *V. Cherchi*[2], *U. Baccarani*[2,3], *E. Scarpa*[2], *A. Mangogna*[2], *G. Fanetti*[1], *E. Borsatti*[1], *A. Drigo*[1];
[1]*Centro di Riferimento Oncologico di Aviano (CRO) IRCCS, Aviano, ITALY,* [2]*University Hospital, Udine, ITALY,* [3]*University of Udine, Udine, ITALY.*

Aim/Introduction: Peptide-receptor-radionuclide therapy (PRRT) with 177Lu-DOTATATE is an emerging treatment for patients with advanced gastro-entero-pancreatic neuroendocrine neoplasms (GEP-NENs). Accurate estimation of the radiation dose delivered to both tumours and healthy organs is essential for optimising this therapy. Radiopharmaceutical uptake can be quantified by measuring the gamma emissions from 177-Lu using serial SPECT imaging. This study aimed to validate the estimated activity in a liver metastasis by ex-vivo measurement of a transplanted liver specimen, in order to improve the accuracy of personalised dosimetry. ***Materials and Methods:*** A patient with progressive liver GEP-NEN and enlarged hepatic hilar lymph nodes underwent three cycles of PRRT. Six days after the third cycle, the patient received a liver transplantation [1]. A 68cc metastasis sample was excised from the liver and analysed using a solid-state detector (HPGe) to directly measure the tissue radioactivity. The main hepatic metastasis was segmented using MIM software on serial SPECT scans (since it appeared morphologically indistinguishable from normal liver on CT images), acquired at four time points following the first cycle of treatment (5h, 24h, 48h, 168h). Due to the lack of standardised guidelines for GEP-NEN lesion segmentation, two thresholds were used: 21% (87,25cc) and 10% (175,11cc). The personalised mono-exponential time-activity curve (TAC) was estimated and then rescaled with the lesion activity measured 24h after the third treatment cycle, allowing the prediction of the 177-Lu activity in the metastasis at the time of transplantation. ***Results:*** Spectroscopic analysis of the lesion sample (68cc) measured 12,6±0,9MBq of activity at the time of transplant. In-vivo SPECT-based estimates for the full lesion were 33±7 MBq (TAC for 21% threshold 87,25cc) and 35±8 MBq (TAC for 10% threshold 175,11cc). Assuming homogeneous activity distribution, and rescaling for the volume, activity within the 68cc metastasis sample was estimated at 25±5 MBq (21% threshold) and 14±3 MBq (10% threshold). ***Conclusion:*** Liver transplantation enabled direct validation of SPECT-based dosimetry. The ex-vivo measurements closely matched the predicted values, particularly for the lesion segmented with the 10% threshold. The discrepancy observed with the 21% threshold may be due to the peripheral sampling of the lesion. The ability to accurately assess the patient-specific radiation dose is crucial for improving the safety and efficacy of PRRT in GEP-NEN patients, thereby optimising treatment outcomes while minimising the risk of adverse effects. ***References:*** [1] Bonutti et al.,Surgical staff doses during liver transplantation on a patient undergoing Lu-177-DOTATATE radioligand therapy, Radiation Protection Dosimetry, 2025, https://doi.org/10.1093/rpd/ncaf026.

OP-632

From Diagnosis to Treatment: A Multimodal Journey in Metastatic PanNET: A Case Report

R. Marao, *D. Barbosa, D. Silva, N. Vasconcelos, I. Próspero, J. Ferro, L. Violante, S. Fontão de Castro, R. Ferreira, I. Lucena Sampaio;*
Instituto Português Oncologia do Porto Francisco Gentil, Porto, PORTUGAL.

Aim/Introduction: Neuroendocrine neoplasms (NENs) are a heterogeneous group of tumours, that can display different degrees of differentiation between and within lesions. [68Ga]-DOTA-TOC-PET/CT plays a key role in staging, treatment planning (including patient selection for peptide receptor radionuclide therapy - PRRT), and follow-up of patients with well-differentiated NENs. [^{18}F]FDG PET/CT may offer complementary data in cases that exhibit or are more likely to exhibit aggressive behaviour. Therapeutic decision should be based on key features like proliferative activity, somatostatin receptor expression, tumour growth rate, disease extension and functionality. In patients with disease progression under somatostatin analogues (SSA), several therapeutic options are available, including PRRT or, in cases of liver-only disease, locoregional therapies, such as embolization or selective internal radiation therapy (SIRT). ***Materials and Methods:*** We present the case of a 54-year-old man with metastatic functional pancreatic NET (gastrinoma; G2; mitotic count: 4/2mm^2; Ki-67: 3-20%). Since diagnosis in 2020, the patient started SSA and underwent surgical resection of the primary tumour, lymph nodes, and three hepatic metastases, followed by two sessions of hepatic embolization (February and July 2021), with clinical and imaging stability for 2.5 years. In March 2024, the patient showed clinical progression, confirmed by elevated gastrin and chromogranin A levels and liver disease progression documented on [68Ga]-DOTA-TOC PET/CT. Due to rapid tumor progression, an additional [^{18}F]FDG PET/CT was performed, detecting intense uptake in the largest hepatic lesion, while the remaining lesions were FDG-negative. A multidisciplinary tumour board proposed a combined approach: SIRT targeting the FDG-avid lesion, followed by PRRT. The patient underwent SIRT with Holmium-166 microspheres, delivering 7.4 GBq and an absorbed tumour dose of 186 Gy. ***Results:*** Following SIRT, the patient reported significant clinical improvement, accompanied by a marked biochemical response,

with decreased gastrin (2824 to 348 pg/ml) and chromogranin A (597 to 155.4 ng/ml) levels. Additionally, the [^{18}F]FDG PET/CT revaluation showed no significant uptake in the previously FDG-avid hepatic lesion, suggesting effective local response. Shortly after, a new [68Ga]-DOTA-TOC PET/CT was performed, revealing increased extent and intensity of the remaining hepatic lesions, prompting consideration for PRRT. ***Conclusion:*** This case highlights the complementary role of dual imaging with [68Ga]-DOTA-TOC and [^{18}F]FDG PET/CT in characterizing tumour heterogeneity and guiding personalized, multimodal treatment strategies in patients with metastatic NETs. Moreover, this case indicates that radioembolization should be taken in consideration as an effective option, isolated or in combination with PRRT, in the management of liver-limited or predominant disease.

OP-633

Taming the Insulinoma: A Case of Glycaemic Recovery with [^{177}Lu]Lu-DOTATATE

D. Carvalho, *S. Barata, S. Paiva, I. Casimiro, J. Silva, L. Lemos, M. Monteiro, P. Lapa, G. Costa;*
ULS Coimbra - HUC, Coimbra, PORTUGAL.

Aim/Introduction: Insulinomas are rare pancreatic neuroendocrine tumours (NETs) characterized by autonomous insulin secretion, leading to recurrent hypoglycaemia, which can be fatal. Peptide receptor radionuclide therapy (PRRT) is indicated for metastatic or unresectable cases with adequate somatostatin receptor expression, as recommended by ENETS 2023 guidelines. ***Materials and Methods:*** We report the case of a 38-year-old male with history of HIV found unconscious due to a severe hypoglycaemia episode. Biochemical evaluation revealed hyperinsulinemia, imaging identified a pancreatic mass metastasis and histopathological confirmed a well-differentiated NET G2. The patient initiated diazoxide, continuous administration of hypertonic glucose and high-dose corticosteroids and was referred to our tertiary centre where he underwent multidisciplinary assessment. Given the extent of disease, and especially due to severe hypoglycaemia, he was proposed to initiate pasoreotide and PRRT was planned. ***Results:*** The hospital stay was marked by multiple, serious and life-threatening infections and complications attributed to immunosuppression and high-dose corticosteroids which required the transfer of the patient to a High-Dependency Care Unit. At this time the patient's clinical situation was very serious, he was not responding to antibiotic treatment, and there was a very high risk of death. The only way to save the patient was to reduce corticosteroid but, for that to be possible, a better control of hypoglycaemia episodes was needed. The pasireotide failed to control insulin secretion and the patient was in no condition for chemotherapy. Therefore, [^{177}Lu]Lu-DOTATATE was the only hope of controlling hormone secretion and to save the patient's life. In the 5 weeks following the 1st-cycle of PRRT, there was no improvement of hypoglycaemia. The team was already disappointed when, suddenly, glycaemic control began to improve. That allowed gradual withdrawal of hypertonic-glucose, progressive reduction in the corticosteroid and with this, the respiratory infection also began to improve. After clinical improvement and cessation of corticosteroids, the patient remained asymptomatic and normoglycemic without pharmacological support. The patient has already received three cycles of [^{177}Lu]Lu-DOTATATE and is scheduled to receive the fourth. Post-treatment whole-body-SPECT/CT scans demonstrated progressive reduction in radiotracer uptake in known lesions. This finding, along with clinical improvement, is consistent with good therapeutic response. ***Conclusion:*** This case highlights the therapeutic potential of PRRT in achieving glycaemic control in metastatic insulinoma unresponsive to conventional medical therapy that, particularly in this case, also saved the patient's life by allowing reduction of the corticosteroids dose.

OP-634

Ramsay-Hunt Syndrome and Encephalitis following [^{177}Lu]Lu-DOTA-TATE: a case report

F. Silva-Ribeiro, *B. Martins, F. P. Branco, V. C. Sousa;*
Unidade Local de Saúde de Loures / Odivelas, Lisbon, PORTUGAL.

Aim/Introduction: Ramsay-Hunt Syndrome (RHS) is caused by the reactivation of the varicella-zoster virus (VZV) within the geniculate ganglion of the facial nerve. It presents as a triad of ipsilateral facial paralysis, vesicular rash, and otalgia—the latter often being the initial presenting symptom. Although various triggering factors are recognized, no association has been established between RHS and [^{177}Lu]Lu-DOTA-TATE treatment. ***Materials and Methods:*** The patient's clinical records were collected and analyzed. A comprehensive literature search was conducted using the PubMed database and Cochrane Library to identify reported cases, along with prior pharmacovigilance reports to further contextualize the present finding. ***Results:*** A 79-year-old male with a neuroendocrine tumor of the small intestine (high-grade, Ki-67 index of 30%), and no other relevant medical history, was admitted to hospital with a 2-day history of nausea, vomiting and weight loss associated with fever, left otalgia and vertigo 16 days after the 2nd cycle of [^{177}Lu]Lu-DOTA-TATE (Lutathera®), which was completed without acute complications. No introduction of new medications occurred during this period. Diagnostic hypotheses included left otitis and hypovolemic hyponatremia. Although the tumor was classified as high-grade, the patient exhibited intense somatostatin receptor expression, minimal [^{18}F]FDG uptake, no bulky disease or symptoms. Given the patient's advanced age, first-line treatment with Lanreotide was initiated. Upon disease progression with metastatic involvement of the liver, bone, and peritoneum, with sustained high somatostatin receptor expression and no [^{18}F]FDG/[^{68}Ga]Ga-DOTANOC mismatch, treatment with [^{177}Lu]Lu-DOTA-TATE was commenced. On the second day of hospitalization, the patient developed grade IV peripheral facial paralysis, characterized by deviation of the labial commissure, loss of the nasolabial fold, and presence of lagophthalmos on the left side. Vesicular lesions in the left external auditory canal and the hard palate were observed. The diagnosis of RHS was established. Due to a decreased level of consciousness and hemodynamic instability, a lumbar puncture was performed with isolation of DNA for Epstein-Barr virus and VZV suggesting neurological involvement with encephalitis. Following 21 days of Acyclovir, the patient showed improved consciousness being discharged to a long-term care unit. He remained off targeted therapy until his death, 23 months after the second cycle of [^{177}Lu]Lu-DOTA-TATE. ***Conclusion:*** To the best of our knowledge, this is the first reported case of Ramsay-Hunt Syndrome occurring as a possible adverse event of [^{177}Lu]Lu-DOTA-TATE. It therefore becomes an important potential complication to consider, as early diagnosis and treatment improve recovery rates.

OP-635

TARE Application for Bridging Liver Transplantation in Unresectable Embryonal Rhabdomyosarcoma of Biliary Tract Origin in a Toddler

N. Gülaldi, *V. Çayhan;*
University of Health Sciences, Ankara Bilkent City Hospital, Department of Nuclear Medicine, Ankara, TÜRKIYE.

Aim/Introduction: In this case report, we would like to present a 3-year-old toddler with rhabdomyosarcoma of biliary origin that completely covered the portal hilus and extended to the upper abdomen. ***Materials and Methods:*** This child presented with a gross mass in the liver. A biopsy of the mass revealed rhabdomyosarcoma of biliary origin. The patient was decided to be unresectable in the multidisciplinary hepatic cancer board. We offered TARE (transarterial radioembolization) of the tumor with [^{90}Y]-Resin microspheres to shrink the mass and eventually control the disease progress. This procedure is used in hepatocellular

carcinoma in adults for transplantation to reduce tumor load and give a chance of liver transplantation. ***Results:*** After tumor blood supply mapping with Tc99m-MAA, the process of radioablation of the tumor was scheduled with 90Y-resin microspheres administered in the hepatic artery feeding the tumor with 3 separate doses of 259 MBq, 184 MBq and 148 MBq on the 3rd day of MAA scan. At the 6th month, abdominal MRI and [^{18}F] FDG PET/CT imaging showed that the mass showed significant shrinkage and the part extending to the upper abdomen was regressed. The lesion size on contrast CT was decreased from 72x55x60mm to 38x34x42 mm after 6 months.After this stage, the patient was sent to a specialized surgical clinic of a university hospital for cadaveric liver transplantation. The liver transplantation as well as removing whole liver with residual tumors were carried out successfully and the child regained his health after that. ***Conclusion:*** This case report is important to show that TARE can be used as a bridging procedure in toddlers for liver sarcomas to prepare for transplantation as in adults. To the best of our knowledge, there is no reported TARE application in early childhood in the literature for unresectable rhabdomyosarcoma of the biliary tract.

OP-636

When Fire Meets Fuel: Thyrotoxic Crisis Following Radioactive Iodine Therapy for an Autonomous Thyroid Nodule

S. Ramos Barata[1], *S. Paiva*[1], *J. Silva*[1], *D. Carvalho*[1], *I. Casimiro*[1], *A. Albuquerque*[1], *G. Costa*[1,2];
[1]*Hospitais da Universidade de Coimbra - ULS Coimbra, Coimbra, PORTUGAL,* [2]*Faculdade de Medicina da Universidade de Coimbra, Coimbra, PORTUGAL.*

Aim/Introduction: Thyrotoxic crisis is a rare, life-threatening endocrine emergency. Most cases are triggered by precipitating events. Radioactive iodine (RAI) therapy is a potential, albeit uncommon, cause. The destruction of follicular cells following RAI administration can lead to a rapid release of stored thyroid hormones into circulation, potentially precipitating a thyrotoxic crisis. ***Materials and Methods:*** We present the case of an 85-year-old woman with poorly controlled subclinical hyperthyroidism due to an autonomous thyroid nodule, referred for RAI therapy. Prior to treatment, thyroid scintigraphy with Na[^{99m}Tc]TcO_4 revealed a "hot" nodule with complete suppression of the remaining thyroid parenchyma. The 24-hour iodine uptake was measured at 17%, and an estimated activity of Na[^{131}I]I was calculated based on a functional mass of 12 grams. Antithyroid drug was suspended five days before treatment, and on February 22, 2024, the patient underwent outpatient RAI therapy with 717MBq. On March 2, 2024, the patient presented to the emergency department with palpitations and chest discomfort that began one day prior. At that time, she was taking one tablet of thiamazole daily. Relevant past medical history included heart failure, a biological aortic valve prosthesis, and atrial fibrillation (AF) under anticoagulation. Chronic medication included bisoprolol. Laboratory results showed suppressed TSH (<0.004mU/L; N: 0.4-4), elevated free T3 (6.2pg/mL; N: 1.8-4.2), and free T4 (2.79ng/dL; 0.7-1.5). The patient was admitted to the intensive care unit with AF with rapid ventricular response (RVR) secondary to a thyrotoxic crisis induced by RAI therapy. The Burch-Wartofsky Point Scale score was 45, supporting the diagnosis of thyroid storm. ***Results:*** Following stabilization, the patient was transferred to the endocrinology ward, where she remained hemodynamically stable and was discharged with a tapering regimen of thiamazole and propranolol. Subsequently, she was re-admitted to the cardiology department for heart failure decompensation, during which thiamazole was discontinued due to a TSH of 9mU/L. In the following weeks, the patient had multiple emergency visits for episodes of AF with RVR, prompting the reintroduction of thiamazole and adjustment of beta-blocker therapy. She remained under close follow-up in the endocrinology department. Thiamazole was ultimately discontinued after a TSH increase to 12mU/L. The patient is currently euthyroid without antithyroid therapy. ***Conclusion:*** This case illustrates the need for rigorous pre-treatment evaluation, individualized risk stratification, and close post-RAI monitoring. Integrating patient education on early symptom recognition into pre-therapy discussions is essential to allow prompt intervention and improve outcomes.

1401

Tuesday, October 7, 2025, 11:30 - 13:00
Auditorium

Plenary 4: Quo vadis Nuclear Medicine 2040: Who Wins? Team Red or Team Green?

Topic 1: Theranostics Involving Radionuclides Will (not) Represent a Major Pillar of Cancer Therapy

Topic 2: Ai Will Complement Nuclear Medicine Physicians / AI Will Replace Nuclear Medicine Physicians

Topic 3: Nuclear Medicine as a Specialty Will Remain Independent / Nuclear Medicine as a Specialty Will Be Taken Over by Radiology and Radiation Oncology

1501

Tuesday, October 7, 2025, 15:00 - 16:30
Auditorium

CME 11 - Translational Molecular Imaging & Therapy Committee: A Comprehensive Approach to Preclinical Dosimetry

OP-641

The Power of Preclinical Dosimetry for Personalised Treatment Radio-Immunotherapy Studies

O. Kochebina*; Université Paris-Saclay, Inserm, CNRS, CEA, Laboratoire d'Imagerie Biomédicale Multimodale (BioMaps), F-91401, Paris, FRANCE.*

OP-642

Interaction of Radiation Dosimetry and DNA Repair to Build a Mathematical Model for Radiopharmaceutical Therapy Treatment Planning

K. Shi*; Department of Nuclear Medicine, University of Bern, Bern, SWITZERLAND.*

OP-643

Small Scale Dosimetry Models for Normal Organs, Dose Effect Limits in Mice, Relevant for Human?

C. Saldarriaga Vargas*; Belgian Nuclear Research Centre, Mol, BELGIUM.*

OP-644

Preclinical Dosimetry Experience, Ready for Clinical Application?

M. Konijnenberg*; Erasmus MC, Rotterdam, NETHERLANDS.*

1502

Tuesday, October 7, 2025, 15:00 - 16:30
Auditorium

Special Track 11 - Oncology & Theranostics Committee: Debate: Lymphoma Evaluation: Do We Need to Go Beyond the Deauville Score?

OP-645

How to Interpret PET/CT in Lymphoma in Daily Routine and Clinical Trials

C. Kobe*; University of Cologne, Department for Nuclear Medicine, Cologne, GERMANY.*

OP-646

Challenger Team Nantes

R. Metz*; Nantes University Hospital, Nantes, FRANCE.*

OP-647a
Challenger Team Nantes
***C. François**; Nantes University Hospital, Nantes, FRANCE.*

OP-647b
Challenger Team Nantes
***R. Bardy**; Nantes University Hospital, Nantes, FRANCE.*

OP-647c
Challenger Team Cologne
***D. Ufton**; University of Cologne, Department for Nuclear Medicine, Cologne, GERMANY.*

OP-647d
Challenger Team Cologne
***N. Große Hokamp**; University of Cologne, Department for Diagnostic Radiology, Cologne, GERMANY.*

1503

Tuesday, October 7, 2025, 15:00 - 16:30
Auditorium

LIPS Session 11 - Neuroimaging Committee: Crazy Enough to do Molecular Imaging in Psychiatric Disorders?

OP-648
The Current Need of Biomarkers in Psychiatry
***G. Knudsen**; Rigshospitalet – Neurocentret, Copenhagen, DENMARK.*

OP-649
The Current Use of PET/SPECT Imaging in Psychiatry
***F. Fraioli**; University College London, Institute of Nuclear Medicine, London, UNITED KINGDOM.*

OP-650
Perspectives for News Paradigm of Acquisition
***R. Lanzenberger**; Medical University of Vienna, Department of Psychiatry and Psychotherapy, Vienna, AUSTRIA.*

OP-651
Perspectives for New Targets and New Indication
***J. Booij**; Amsterdam UMC, department of Radiology and Nuclear Medicine,, Amsterdam, NETHERLANDS.*

1504

Tuesday, October 7, 2025, 15:00 - 16:30
Room 114

M2M Track - TROP Session - Radiopharmaceutical Sciences + Translational Molecular Imaging & Therapy Committee: Peptides for All Taste

OP-652
Preclinical studies of structurally optimized ^{64}Cu- and ^{68}Ga-labeled bicyclic peptides for improved imaging of nectin-4-positive tumors
***T. Krönke**, J. Trommer, M. Ullrich, M. Laube, R. Löser, K. Kopka, S. Stadlbauer, J. Pietzsch, R. Wodtke;*
Helmholtz-Zentrum Dresden-Rossendorf (HZDR), Institute of Radiopharmaceutical Cancer Research, Dresden, GERMANY.

Aim/Introduction: The cell adhesion protein nectin-4 has been proven a valid target for therapeutic approaches to urothelial carcinoma with enfortumab vedotin being the sole clinically approved treatment option. Furthermore, the nectin-4 targeting bicyclic toxin conjugate BT8009 is currently tested in clinical trials (NCT04561362). To support patient stratification for such targeted therapies, there is a clinical need for molecular imaging agents capable of quantifying nectin-4 levels in vivo. For this purpose, we developed ^{64}Cu- and ^{68}Ga-labeled nectin-4 ligands, which are structurally derived from BT8009, for non-invasive imaging with positron emission tomography. We modified the original bicyclic scaffold to increase the (radio)chemical stability and binding affinity toward nectin-4. Radiochemical and pharmacokinetic characteristics are presented in comparison to the previously reported radioligand ^{68}Ga-N188.[1] ***Materials and Methods:*** Bicyclic peptides were synthesized via solid-phase peptide synthesis, followed by cleavage from the resin, cyclization in solution and RP-HPLC purification. Binding affinities were determined with a fluorescence anisotropy-based competitive binding assay and with surface plasmon resonance spectroscopy using recombinant human nectin-4. Radiolabeling was performed under standard conditions ([^{64}Cu]$CuCl_2$: NH_4OAc pH=5.6, 20 min, 60°C; [^{68}Ga]$GaCl_3$: NaOAc pH=4.5, 10 min, 90°C). The metabolic stability of the radioligands in human plasma was assessed by RP-HPLC analysis. Specificity towards nectin-4 was evaluated by comparing cell binding to nectin-4 positive (HT-1376) and -negative (5637) urothelial carcinoma cells. PET/CT imaging was conducted in HT-1376 tumor-bearing mice. ***Results:*** A small library of modified bicyclic peptides was synthesized and characterized for their binding affinity towards nectin-4, revealing distinct structure-activity relationships. While the binding affinities varied only moderately (2-6 nM), large differences (up to a factor 30) were observed regarding the rate constants for association and dissociation. All ligands were radiolabeled with high radiochemical yield and purity (≥95%). The most promising radioligand, [64Cu]Cu-TKR2-24, showed no proteolytic degradation in human plasma in vitro over 24 h. Furthermore, this radioligand showed potent nectin-4-specific binding (Kd of 3.3 nM) to HT-1376 cells. PET imaging demonstrated a specific uptake of [^{64}Cu]Cu-TKR2-24 in subcutaneous HT-1376 tumor xenografts with improved tumor uptake and tumor-to-background ratio compared to the previously reported radioligand ^{68}Ga-N188. ***Conclusion:*** Due to its high binding affinity, good stability in human plasma, and high contrast visualization of tumors in mice, [^{64}Cu]Cu-TKR2-24 warrants further clinical evaluation as a diagnostic PET radiotracer for assessing the nectin-4 status in cancer patients. ***References:*** 1 Duan et. al., Clin Cancer Res (2023) 29 (17): 3395-3407.

OP-653
Development of a Novel ^{68}Ga-Labelled Lasso Peptide Radiotracer for EphA2: Advancements in Prostate Cancer Imaging and Beyond
***X. Cui**, Z. Liu;*
Changping Laboratory, Beijing, CHINA.

Aim/Introduction: This study aimed to develop a novel ^{68}Ga-labelled lasso peptide radiotracer targeting erythropoietin-producing hepatocellular A2 (EphA2)[1], a receptor tyrosine kinase overexpressed in multiple cancers, for precise positron emission tomography (PET) imaging. The primary objectives were to optimize peptide-ligand stability and binding affinity through structural modifications, reduce renal retention, and validate tumour-targeting efficacy in preclinical models to discover a lead compound for clinical translation. ***Materials and Methods:*** A cyclic peptide scaffold was engineered to enhance EphA2 affinity and metabolic stability. Key modifications included strategic cyclization, incorporation of non-natural amino acids, and optimization of linker chemistry to minimize off-target interactions. The lead candidate was conjugated with a chelator for ^{68}Ga radiolabelling. In vitro binding kinetics were assessed via surface plasmon resonance (SPR). In vivo biodistribution and tumour-targeting efficacy were evaluated in EphA2-positive xenograft models (stable transient HT-1080-EphA2 cell line; PC-3 prostate and HCT-116 colorectal cancer cell lines) using

PET/CT imaging. Comparative studies with existing EphA2-targeting agents were conducted to benchmark performance[2]. ***Results:*** The optimized lasso peptide with unnatural amino acids demonstrated high affinity for EphA2, with a SPR-derived K_D of 0.25 nM, representing a 4-fold improvement over the initial hit. The plasma and renal stability were improved by identifying enzyme metabolic weaknesses and corresponding rational modifications. In HT-1080-EphA2 tumour-bearing mice, PET imaging revealed rapid tumour uptake (SUV_{max} = 2.8 ± 0.3 at 30 min post-injection), significantly higher than a reference compound (SUV_{max} = 1.5 ± 0.2, $p < 0.01$). Notably, renal retention was reduced by 40% compared to initial hit compound, probably attributed to optimized hydrophilicity and stability. In PC-3 and HCT-116 models, both tumour uptake reached 5.0 ± 0.5% ID/g at 1 h (n = 4), with minimal non-specific uptake in normal tissues. Pharmacokinetic analysis showed rapid blood clearance ($t_{1/2}$ = 12 min) and sustained tumour retention (>4% ID/g at 2 h). ***Conclusion:*** The novel ^{68}Ga-labelled lasso-peptide-based radiotracer exhibits superior EphA2-targeting specificity, enhanced metabolic stability, and favourable pharmacokinetics, addressing limitations of prior agents. Its high tumour uptake, moderate renal accumulation, and robust imaging contrast underscore its potential as a clinical diagnostic tool for EphA2-positive malignancies. A clinical investigator initiate trial is undergoing to validate these preclinical findings and explore its utility in personalized oncology. ***References:*** (1)Watabe, T. et al. Eur J Nucl Med Mol Imaging, 2025, 10.1007/s00259-025-07139-9; (2) Fakiri, M. E. et al. Theranostics, 2024, 14, 4701-4712.

OP-654

Preclinical Evaluation of 3B010: A Novel GPC3-Targeting Peptide Radioligand with High Tumor Retention and Remarkable Tumor-to-Kidney Ratio

W. XU*, J. Zhang;*
PepLib, Metuchen, NJ, UNITED STATES OF AMERICA.

Aim/Introduction: Glypican-3 (GPC3) is a membrane-bound proteoglycan highly expressed in hepatocellular carcinoma (HCC) and other solid tumors, making it an attractive target for peptide-based radioligand development. We have developed a peptide discovery platform that integrates physical peptide screening including disulfide-rich peptide phage display with an AI-driven in silico peptide design platform. This peptide discovery platform enables rapid identification and optimization of high-affinity, tumor-specific peptide ligands with favorable pharmacokinetic properties. Using this approach, we developed and characterized 3B010, a novel GPC3-targeting peptide radioligand with improved tumor specificity and reduced renal accumulation. ***Materials and Methods:*** 3B010 was selected and optimized through peptide screening and computational modeling, then conjugated with DOTA for radiolabeling with Gallium-68. In vitro binding assays were performed using GPC3-positive and negative cell lines to assess affinity and specificity. For in vivo evaluation, BALB/c nude mice bearing subcutaneous GPC3-positive xenografts (HepG2) were injected intravenously with 68Ga-3B010. PET/CT imaging was performed at multiple time points post-injection, followed by ex vivo biodistribution analysis at 4 hours to quantify organ-level uptake. ***Results:*** 3B010 demonstrated high binding affinity to human GPC3, with a K_D of 2.2 nM, and showed cross-species binding to GPC3 from mouse and cynomolgus monkey. In vitro assays confirmed strong and specific binding to GPC3-expressing cells, with negligible interaction in GPC3-negative controls. In vivo PET/CT imaging in mice revealed rapid tumor targeting and sustained retention up to 4 hours post-injection, with efficient clearance from non-target tissues. Ex vivo biodistribution data confirmed high tumor uptake and significantly reduced kidney accumulation, resulting in a tumor-to-kidney uptake ratio of approximately 4. ***Conclusion:*** 3B010, developed through our peptide discovery platform, exhibits excellent preclinical performance as a GPC3-targeting radioligand. Its high tumor retention and low kidney uptake support its potential for clinical translation in diagnostic imaging and radiotherapeutic applications. Exploratory IIT in human subjects are currently in preparation. ***References:*** 1. Filmus J, Capurro M, Rast J. Glypican-3: A novel serum and histochemical marker for hepatocellular carcinoma. Gastroenterology. 2008;134(1):247-256.

OP-655

Dimerization and ^{177}Lu-labeling of HER2-receptor Targeting Peptide

S. GUPTA*[1,2], M. Kumar[2], K. Repaka[3], A. Kengar[1], D. Satpati[2,4];*
[1]KET's V. G. Vaze College, Mumbai University, Mumbai, INDIA, [2]Radiopharmaceuticals Division, Bhabha Atomic Research Centre, Mumbai, INDIA, [3]Board of Radiation and Isotope Technology, Mumbai, INDIA, [4]Homi Bhabha National Institute, Mumbai, INDIA.

Aim/Introduction: Multimeric peptides display improved binding affinity towards the target, higher concentration and retention in the tumor and enhanced in vivo stability over their corresponding monomeric forms. Overexpression of HER2 receptors in breast cancer is associated with metastatic aggression. Early and precise detection is vital for management of HER2-positive breast cancer patients. Hence, in our pursuit of designing HER2-receptor targeting radiolabeled tracers, previously established monomeric peptide, rL-A9 was dimerized. The dimeric peptide, DOTA-$(rL\text{-}A9)_2$ was radiolabeled with Lu-177 and its efficacy was investigated. ***Materials and Methods:*** The peptide dimer was synthesized on solid phase by initial anchoring of Fmoc-lys(alloc)-OH. Subsequently, bi-functional spacer N,N-bis[3-(Fmoc-amino) propyl]glycine was coupled with the α-amino group of Lys. Deprotection of Fmoc group was followed by simultaneous build-up of two units of rL-A9 peptide chains. Alloc group was then deprotected and chelator DOTA was conjugated at ε-amine group of lysine (Fig. 1). Dimeric peptide, DOTA-$(rL\text{-}A9)_2$ was purified and characterized. ^{177}Lu-DOTA-$(rL\text{-}A9)_2$ {200 µg, pH 5, 90°C, 20 min) was analyzed by RP-HPLC. Cell binding studies were performed in HER2-expressing human breast carcinoma SKBR3 cells. Stability in human serum (48 h) and metabolic stability in mice urine and blood (2 h) was determined. ***Results:*** The peptide, DOTA-$(rL\text{-}A9)_2$ could be synthesized in >99% purity and 20% yield. The peptide was characterized by MALDI TOF MS: m/z 2672.55 observed (calcd. for $C_{118}H_{185}N_{33}O_{38}$: 2672.36). Radiolabeling yield of ^{177}Lu-DOTA-$(rL\text{-}A9)_2$ was >95%. Partition coefficient (log $P_{o/w}$) value of ^{177}Lu-DOTA-$(rL\text{-}A9)_2$ was observed to be -3.30 ± 0.01, indicating high hydrophilicity of the radiopeptide. ^{177}Lu-DOTA-$(rL\text{-}A9)_2$ exhibited high binding affinity [K_d: 70.33±8.6 nM] towards HER2-expressing SKBR3 cells. ^{177}Lu-DOTA-$(rL\text{-}A9)_2$ was observed to be stable in human serum (>95% intact) as well in mice blood and urine (>90% intact). ***Conclusion:*** Monomeric rL-A9 peptide could be successfully dimerized during solid phase synthesis and obtained in high purity. DOTA-$(rL\text{-}A9)_2$ could be radiolabeled with Lu-177 in high yields. ^{177}Lu-DOTA-$(rL\text{-}A9)_2$ exhibited high binding affinity towards HER2-positive breast carcinoma cells. ^{177}Lu-DOTA-$(rL\text{-}A9)_2$ demonstrated high metabolic stability, pharmacokinetics and tumor uptake shall be further ascertained by performing in vivo biodistribution studies. ***References:*** Peptides Targeting HER2-Positive Breast Cancer Cells and Applications in Tumor Imaging and Delivery of Chemotherapeutic. Palmira Alessia Cavallaro, Marzia De Santo, Emilia Lucia Belsito, Camilla Longobucco, Manuela Curcio, Catia Morelli, Luigi Pasqua, Antonella Leggio, Nanomaterials 2023, Sep 1;13(17):2476.

OP-656

Preclinical Evaluation of [^{161}Tb]Tb-DPI-4452 for CAIX-Targeted Radionuclide Therapy in Pancreatic Cancer

C. Van Laere[1,2], *C. Segers*[2], *A. Coolkens*[2], *M. Dewilde*[1], *F. Cleeren*[1], *M. Ooms*[2];
[1]*KU Leuven, Leuven, BELGIUM,* [2]*SCK CEN, Mol, BELGIUM.*

Aim/Introduction: Carbonic anhydrase IX (CAIX) is a transmembrane enzyme highly overexpressed in hypoxic tumours and those with mutations in the von Hippel-Lindau tumour suppressor gene, while its expression in normal tissues remains limited. This tumour-selective expression profile makes CAIX an attractive target for therapeutic strategies. DPI-4452, a novel CAIX-targeting cyclic peptide equipped with a DOTA chelator, has shown potential as a theranostic agent in the form of [^{68}Ga]Ga-DPI-4452/[^{177}Lu]Lu-DPI-4452 for patients with clear cell renal cell carcinoma (ccRCC)(Massière F, et al., 2024). However, further optimization could maximize its therapeutic efficacy. In this study, we explore the use of terbium-161 for radiolabelling DPI-4452 and evaluate its potential in models of pancreatic ductal adenocarcinoma (PDAC). ***Materials and Methods:*** CAIX expression was assessed in AsPC-1, PANC10.05 (PDAC), and SK-RC-52 (ccRCC) cells under normoxic (20% O_2) and hypoxic (1% O_2) conditions using Western blot as well as immunocytochemistry with an anti-CAIX antibody and a Cy5-labelled analogue of DPI-4452. Subcellular localization was confirmed by Western blot analysis of membrane and cytosolic fractions. Radiolabelling protocols were optimized and the stability of the radioconjugate was assessed using radio-HPLC. Saturation binding assays with [^{161}Tb]Tb-DPI-4452 (1-250 nM) were performed on AsPC-1 and SK-RC-52 cells to determine K_D and B_{max}. Non-specific binding was assessed in the presence of the CAIX inhibitor S4. Immunohistochemistry and ex vivo autoradiography were conducted on three PDAC patient-derived xenograft (PDX) models to evaluate CAIX-specific binding and tissue distribution of [^{161}Tb]Tb-DPI-4452. Non-specific binding was assessed in the presence of the CAIX inhibitor S4. ***Results:*** CAIX expression was oxygen-dependent in PDAC cell lines but constitutive in ccRCC cells. PANC10.05 cells expressed CAIX only under hypoxic conditions, while AsPC-1 cells exhibited low baseline expression in normoxia with more than a threefold increase under hypoxia. Western blot analysis of subcellular fractions confirmed CAIX was exclusively localized to the membrane in the PDAC cell lines. Preliminary saturation binding assays with [^{161}Tb]Tb-DPI-4452 showed specific binding to CAIX in both AsPC-1 (K_D = 12.95 nM, B_{max} = 0.155 fmol/10^5 cells) and SK-RC-52 (K_D = 14.72 nM, B_{max} = 0.977 fmol/10^5) cells.Ex vivo autoradiography of PDAC PDX cryosections showed specific accumulation of [^{161}Tb]Tb-DPI-4452, correlating with CAIX expression as confirmed by immunohistochemistry. ***Conclusion:*** Our results demonstrate the successful targeting of CAIX using [^{161}Tb]Tb-DPI-4452 in PDAC cell lines and tissue slices of PDX models. Currently, in vitro and in vivo studies are ongoing to further investigate the potential of [^{161}Tb]Tb-DPI-4452 for PDAC.

OP-657

Substantially Higher Treatment Efficacy of ^{161}Tb-Labelled GRPR Antagonists over ^{177}Lu-Labelled GRPR Antagonists in PC3 Tumour-Bearing mice

T. Günther[1], *A. S. Moses*[1], *E. H. Günther*[1], *M. R. Landry*[1], *S. Ramaekers*[2], *M. Van de Voorde*[2], *M. Ooms*[2], *B. Ponsard*[3], *C. Beinat*[1];
[1]*Molecular Imaging Program at Stanford (MIPS), Department of Radiology, School of Medicine, Stanford University, Palo Alto, CA, UNITED STATES OF AMERICA,* [2]*Nuclear Medical Applications, Belgian Nuclear Research Centre, Mol, BELGIUM,* [3]*BR2 Reactor, Belgian Nuclear Research Centre, Mol, BELGIUM.*

Aim/Introduction: ^{161}Tb shows similar physical properties to ^{177}Lu, but additionally emits more Auger electrons per decay, which might lead to improved treatment efficacy when combined with high-affinity peptides, such as the gastrin-releasing peptide receptor (GRPR) antagonists RM2 (DOTA-Pip^5-D-Phe^6-Gln^7-Trp^8-Ala^9-Val^{10}-Gly^{11}-His^{12}-Sta^{13}-Leu^{14}-NH_2) and AMTG (DOTA-Pip^5-D-Phe^6-Gln^7-α-Me-Trp^8-Ala^9-Val^{10}-Gly^{11}-His^{12}-Sta^{13}-Leu^{14}-NH_2). In this study we evaluated differences in treatment efficacy of ^{161}Tb- and ^{177}Lu-labelled RM2 and AMTG, respectively, in PC3 tumour-bearing mice. ***Materials and Methods:*** Tumours were established via subcutaneous injection of 4.0×10^6 PC3 cells per Nu/J mouse (n=7 per group). Treatment studies were initiated once tumour volume was ~100 mm^3. ^{161}Tb- and ^{177}Lu-labelling was completed at 90°C within 10 min (1.0 M NaOAc buffer, pH = 5.5, molar activity of 50 MBq/nmol). Radiolabelled compounds were injected on day 0 and day 7 (~15 MBq each). Animals were sacrificed once tumour volume surpassed 1,500 mm^3. To estimate toxicity of each compound, a complete blood count and metabolic panel analysis was completed after euthanasation of healthy animals (n=3 per group) at 60 days after receiving the same activity as the treatment groups. ***Results:*** Animals were assigned to five groups at day 0 of the treatment study (control group: 139±36 mm^3, [^{177}Lu]Lu-RM2: 114±28 mm^3, [^{177}Lu]Lu-AMTG: 127±47 mm^3, [^{161}Tb]Tb-RM2: 120±57 mm^3, [^{161}Tb]Tb-AMTG: 128±26 mm^3). Each group received a total activity amount of 26-31 MBq of the respective radiolabelled compound (all labellings proceeded quantitatively) ([^{177}Lu]Lu-RM2: 31.0±1.2 MBq, [^{177}Lu]Lu-AMTG: 26.0±2.8 MBq, [^{161}Tb]Tb-RM2: 30.3±0.7 MBq, [^{161}Tb]Tb-AMTG: 29.0±1.2 MBq). Overall survival was best when treated with [^{161}Tb]Tb-AMTG (54.9±2.2 d after start of treatment), followed by [^{161}Tb]Tb-RM2 (44.9±3.8 d), [^{177}Lu]Lu-AMTG (39.5±2.6 d), and [^{177}Lu]Lu-RM2 (26.8±1.9 d), and worst for the non-treated group (22.8±1.2 d). Apart from a reduced number of lymphocytes observed in animals treated with ^{161}Tb- and ^{177}Lu-labelled GRPR ligands, no adverse effects or signs of toxicity were observed during this study. ***Conclusion:*** Combination of ^{161}Tb with the GRPR ligands RM2 and AMTG led to a substantially improved overall survival in PC3 tumour-bearing mice than their ^{177}Lu-labelled analogues, which confirmed the impact of the higher number of Auger electron emissions by ^{161}Tb. Due to its higher in vivo stability, the AMTG peptide enabled a superior tumour control and overall survival than the RM2 peptide when labelled with the same radionuclide. While first clinical data on [^{177}Lu]Lu-AMTG suggests an improvement over GRPR ligands currently used for the treatment of GRPR-expressing malignancies, [^{161}Tb]Tb-AMTG might surpass each of these compounds, thus warranting its future application in clinical trials.

OP-658

Improved Tumour Targeting and Efficacy with Comparable Daughter Redistribution of ^{225}Ac-SSO110 versus ^{225}Ac-DOTA-TATE in a Preclinical SCLC Model

P. Desai, *M. Huber, M. Ruediger, G. Gericke, A. Jaekel;*
Ariceum Therapeutics GmbH, Berlin, GERMANY.

Aim/Introduction: ^{225}Ac-SSO110 (^{225}Ac-DOTA-JR11) is a somatostatin receptor 2 (SSTR2) antagonist under clinical investigation in extensive-stage small cell lung cancer (ES-SCLC) and Merkel cell carcinoma. Actinium-225 is a potent alpha-emitter with high linear energy transfer and short path length. However, recoil-induced release of daughter radionuclides raises concerns about off-target toxicity. Internalizing agonists are speculated to retain daughters more effectively in tumour tissue than non-internalizing antagonists. To test this, we compared the biodistribution of ^{225}Ac and its daughter ^{213}Bi following administration of ^{225}Ac-labelled SSO110 and DOTA-TATE (SSTR2 agonist) in SCLC xenografts, while also evaluating efficacy and tolerability. ***Materials and Methods:*** In-vivo studies were performed in SSTR2-positive NCI-H69 xenografts. For biodistribution, mice received 90 kBq/0.6 nmol ^{225}Ac-labelled SSO110 or DOTA-TATE; tissues were collected at 30 min, 4 h, 24 h, 48 h, and 96 h. Organ radioactivity was measured every 13 min over 20 h, and ^{225}Ac/^{213}Bi were quantified via bi-exponential fitting. For efficacy, mice received up to 37 kBq/0.6 nmol (single dose), with tissues collected for histopathology at study end. ***Results:*** ^{225}Ac-

SSO110 demonstrated 2.3-fold higher tumour area under curve and 1.9-fold higher tumour-to-kidney ratios than ^{225}Ac-DOTA-TATE, attributed to higher tumour uptake and prolonged retention, indicating a favourable therapeutic index. Comparable patterns of daughter radionuclide redistribution were observed for ^{225}Ac-SSO110 and ^{225}Ac-DOTA-TATE. ^{213}Bi was largely retained in tumours for both compounds. Loss of ^{213}Bi ranged from -12% to -18% for ^{225}Ac-SSO110 and -8% to -12% for ^{225}Ac-DOTA-TATE, corresponding to a reduction of up to 10% in tumour-absorbed dose relative to the ideal scenario of complete local retention. Importantly, no excess ^{213}Bi was observed in kidneys beyond 30 minutes or in liver beyond 4 hours post-injection for either compound, indicating minimal daughter redistribution following early-phase uptake of circulating ^{221}Fr generated in blood or ^{213}Bi-DTPA. In an in-vivo efficacy study, a single dose of 30 kBq ^{225}Ac-SSO110 induced complete tumour remissions and long-term survival, whereas ^{225}Ac-DOTA-TATE failed to control tumour growth. Both treatments were well-tolerated without histopathological findings. ***Conclusion:*** ^{225}Ac-SSO110 demonstrated superior tumour uptake, retention, and therapeutic efficacy compared to ^{225}Ac-DOTA-TATE in a preclinical SCLC model, achieving complete tumour remissions after single-dose administration while being well tolerated. Despite not being internalized, ^{225}Ac-SSO110 exhibited similar retention of daughter radionuclide as the internalizing agonist, indicating that the plasma membrane does not present a significant barrier to the recoil effect. These findings support the potential of ^{225}Ac-SSO110 as a promising targeted alpha therapy for SSTR2-positive malignancies.

OP-659

Preclinical evaluation of GRPR-antagonist PK3 as a candidate for targeted alpha therapy with Ac-225

P. Kanellopoulos[1], *A. Lebedev*[2], *E. Papalanis*[3], *K. Obeid*[1], *E. A. Bezverkhniaia*[1], *C. Byrne*[2], *T. Pack*[2], *V. Tolmachev*[3], *A. Orlova*[1], *S. V. Selivanova*[2];
[1]*Department of Medicinal Chemistry, Uppsala University, Uppsala, SWEDEN,* [2]*Canadian Nuclear Laboratories, Chalk River, ON, CANADA,* [3]*Department of Immunology, Genetics and Pathology, Uppsala University, Uppsala, SWEDEN.*

Aim/Introduction: Gastrin releasing peptide receptor (GRPR) is overexpressed in numerous malignancies including prostate (PC) and breast cancers (BC). Peptide-based GRPR-antagonists have proven their potency as radiopharmaceuticals for theranostic use in preclinical studies and several variants are currently in clinical trials. However, poor metabolic stability and/or pharmacokinetics remain major issues. We have recently developed a novel variant of the GRPR-antagonist RM2, PK3 (DOTA-PEG2-Pip-DPhe-Gln-αMT-Ala-Sar-His-Sta-Leu-NH_2; αMT: α-methyl-L-Trp). [^{177}Lu]Lu-PK3 demonstrated high affinity (K_{D1}= 58pM) and selectivity to GRPR, improved in vivo metabolic stability, and a promising biodistribution profile [1]. These encouraging data prompted us to investigate PK3 for targeted alpha delivery labelled with Ac-225. ***Materials and Methods:*** Ac-225 was eluted from generator. All radioactivity measurements were performed at secular equilibrium between Ac-225 and its progenies. PK3 was labelled with Ac-225 in 0.4M NaOAc at 85°C-45min. The radiochemical yield was determined using iTLC. The in vitro specificity and internalization of [^{225}Ac]Ac-PK3 was tested using PC-3 prostate cancer and BT474 breast cancer cells. Biodistribution of [^{225}Ac]Ac-PK3 was measured in nude mice bearing PC-3 xenografts at 0.5, 1, 4, 24, 48, and 165h post-injection (pi). In vivo specificity of [^{225}Ac]Ac-PK3 was tested by co-injection of a large excess of unlabelled counterpart NOTA-PEG2-RM26. Areas under decay-uncorrected time-activity curves for tumours and normal organs were compared to estimate dosimetry. ***Results:*** PK3 was labelled with Ac-225 with radiochemical yield >95% and molar activity 215MBq/µmol. [^{225}Ac]Ac-PK3 demonstrated high GRPR-specific binding in vitro. The internalization was relatively slow (internalized fraction 20-25% after 24h), which is typical for radioantagonists. In vivo, [^{225}Ac]Ac-PK3 cleared rapidly from normal tissues. The highest uptake at 0.5h was in pancreas (24±4%IA/g), kidneys (18±6%IA/g) and tumours (10±2%IA/g). The uptake in the pancreas decreased rapidly to 4-5%IA/g at 4h pi. The tumour uptake remained high over time, being 16±2, 11±3, 10±2 and 3.5±0.1%IA/g at 4, 24, 48 and 165h pi, respectively. The time-integrated radioactivity for tumours was 300-, 10-, 4-, and 54-fold greater than that for the blood, pancreas, kidneys, and bones, respectively. Co-administration of unlabelled NOTA-PEG2-RM26 led to >70% decrease in [^{225}Ac]Ac-PK3 uptake in pancreas and tumours, thus confirming the binding specificity in vivo. ***Conclusion:*** [^{225}Ac]Ac-PK3 can be synthesized with high radiochemical yield and sufficient molar activity. [^{225}Ac]Ac-PK3 binds specifically to the GRPR-expressing cancer cells in vitro and in vivo. [^{225}Ac]Ac-PK3 demonstrated excellent targeting properties and favourable biodistribution and pharmacokinetic profile. It is a promising candidate for targeted alpha-therapy of GRPR-expressing malignancies. ***References:*** 1. Kanellopoulos et al. ISRS2025, abstract-ID:353.

OP-660

ImmunoPET Imaging of TIM3 Expression in the Tumor Microenvironment Using [68Ga]-Labelled Cyclic Peptide Tracers: From Bench to Bedside

J. Hou, *S. Hu;*
Xiangya Hospital, Central South University, Changsha, CHINA.

Aim/Introduction: T cell immunoglobulin and mucin domain-containing protein 3 (TIM3) has emerged as the next-generation immune checkpoint and a highly promising prognostic biomarker for immunotherapy. Similar to inhibitors targeting programmed cell death protein 1/programmed death-ligand 1 (PD-1/PD-L1) and cytotoxic T-lymphocyte antigen 4 (CTLA-4), positron emission tomography (PET) imaging strategies hold significant potential to enhance clinical decision-making in TIM3-related therapeutic approaches [1,2]. In this comprehensive study, we developed and rigorously validated [68Ga]-labeled cyclic peptide tracers for PET imaging of TIM3 expression, spanning from preclinical research to early clinical evaluation. ***Materials and Methods:*** A cyclic peptide with specificity for TIM3 was modified and radiolabeled using gallium-68 trichloride ([68Ga]$GaCl_3$). The radiolabeled tracer's affinity, specificity, biodistribution, pharmacokinetic properties, and radiation dosimetry were systematically evaluated through in vitro and in vivo experiments. Additionally, hu-PBL-SCID (PBL) mouse models were established to assess the ability of [68Ga]Ga-CK-1 to visualize the infiltration of TIM3-positive lymphocytes via PET imaging. Finally, [68Ga]Ga-CK-1 advanced to a first-in-human study, where its safety profile, biodistribution characteristics, and potential for imaging TIM3 expression were carefully investigated. ***Results:*** We successfully engineered a TIM3-targeting cyclic peptide, which served as the lead compound for the design and development of the [68Ga]-labeled PET tracer. In vitro binding assays demonstrated that [68Ga]Ga-CK-1 exhibited high affinity and specificity towards Chinese hamster ovary-human TIM3 cells and peripheral blood mononuclear cells. In vivo PET imaging studies revealed that [68Ga]Ga-CK-1 had excellent imaging performance, with a tumor uptake of 1.42±0.32% injected dose per gram and a tumor-to-muscle ratio of 26.21±4.35 at 60 minutes post-injection. Moreover, [68Ga]Ga-CK-1 was able to detect TIM3-expressing cell infiltrates in the spleen, lung, and salivary gland of PBL mice. In patients with melanoma and non-small cell lung cancer, [68Ga]Ga-CK-1 PET imaging showed modest uptake in primary tumor lesions compared to [18F]FDG PET. Significantly, [68Ga]Ga-CK-1 was capable of delineating the heterogeneity of TIM3 expression within large tumors. ***Conclusion:*** The results of this study firmly establish [68Ga]Ga-CK-1 as a promising PET tracer for quantifying TIM3 expression in the tumor microenvironment. These findings highlight its potential as a companion diagnostic tool for patient stratification and monitoring therapeutic response in anti-TIM3 immunotherapy. ***References:*** [1]Wolf Y, Anderson AC, Kuchroo VK. TIM3 comes of age as an inhibitory receptor. Nat Rev Immunol. 2020 Mar;20(3):173-185.[2]Ribas A, Wolchok JD. Cancer immunotherapy using checkpoint blockade. Science. 2018;359:1350-5.

1505

Tuesday, October 7, 2025, 15:00 - 16:30
Room 211

Cutting Edge Science Track - TROP Session - Physics Committee: Instrumentation, QC & Standardisation

OP-661

Performance evaluation for a dual-collimator 3D CZT Camera

R. Zananiri, *A. Devir-Wolfman, M. Wilk, O. Ziv, J. Bouhnik; GE HeathCare, Haifa, ISRAEL.*

Aim/Introduction: Over recent years, CZT-based, multi-detector, 3D nuclear medicine (NM) camera configurations have emerged. These cameras, with a single fixed collimator - balancing between low-energy sensitivity and high energy coverage - lacked optimized collimators to address all energies of conventional NM practices. Here, we introduce a new system design based on GE Healthcare's StarGuide™ with a redesigned detector that features dual collimators encasing the CZT modules, creating a dual collimator StarGuide (DCS). With optimized CZT crystal design - smaller pixels and two collimators tuned for high sensitivity (HS) and low penetration (LP) - its performance is compared to dual-head NaI-based cameras for Tc99m (DCS-HS vs. 870DR-LEHRS) and I131 (DCS-LP vs. 870DR-HEGP). ***Materials and Methods:*** Camera Design: DCS detectors were installed on the StarGuide™ gantry. Both collimators were designed to obtain identical StarGuide™ resolution. The HS collimator was designed to obtain 1.9x higher sensitivity and the LP collimator optimized for reducing high energies penetration. Tc99m Phantom: Flangeless Deluxe Jaszczak, 28mCi Tc99m, was used to assess Tc99m SPECT sensitivity and SPECT Resolution. It was acquired on each camera for 15 minutes. System sensitivity was compared as the ratio of the obtained projection counts. The resolution was assessed visually by comparing the central sphere slice and the summed rods slices. DCS-HS was reconstructed using OSEM150x2. while 870DR 2x10. No post filters, and Chang AC-ed. I131 Phantom: A custom-made, feature-to-background of 1:8, 5.4mCi NEMA IEC filled with Ba133 and Cs137 (1:0.1) mimicking I131 was used to assess the performance with I131. The phantom was scanned on the DCS-LP and on 870DR-HEGP, both for 15 minutes. The assessment was done visually and quantitatively following NEMA(2). ***Results:*** For Tc99m, DCS possesses superior image quality compared to 870DR with the camera sensitivity (~2.6x) and resolution. The DCS image quality is comparable to Jaszczak reported by Le Rouzic and Zananiri(1) for StarGuide™, however DCS was measured to obtain 1.9x counts for the same acquisition duration. Using LP collimator results in a comparable I131 image quality to the NaI-HEGP camera. ***Conclusion:*** DCS possesses a superior performance to 870DR for Tc99m. Also, to the best of our knowledge, this is the first report of CZT-based camera capable of imaging I131 in presence of strong background activity with comparable image quality to NaI system. ***References:*** (1) Le Rouzic and Zananiri, First performance measurements of a new multi-detector CZT-Based SPECT/CT system: GE StarGuide, JNM, 2021. (2)NEMA, Performance Measurements of Gamma Cameras, 2023.

OP-662

Performance Evaluations in ^{161}Tb SPECT Imaging: Sensitivity, Septal Penetration, and Dead-Time Effects

F. Westerbergh[1], *L. McDougall*[2], *P. Ritt*[3], *J. G. Fricke*[2], *N. P. van der Meulen*[4,5], *C. Müller*[6,5], *R. Schibli*[5,6], *D. Wild*[2], *P. Bernhardt*[1,7]; [1]*Department of Medical Radiation Sciences, Institute of Clinical Sciences, Sahlgrenska Academy at University of Gothenburg, Gothenburg, SWEDEN,* [2]*Division of Nuclear Medicine, University Hospital Basel, Basel, SWITZERLAND,* [3]*Chair for Clinical Nuclear Medicine, Friedrich-Alexander-Universität Erlangen-Nürnberg, Erlangen, GERMANY,* [4]*Laboratory of Radiochemistry, PSI Center for Nuclear Engineering and Sciences, Villigen-PSI, Villigen, SWITZERLAND,* [5]*Center for Radiopharmaceutical Sciences, PSI Center for Life Sciences, Villigen-PSI, Villigen, SWITZERLAND,* [6]*Department of Chemistry and Applied Biosciences, ETH Zurich, Zurich, SWITZERLAND,* [7]*Department of Medical Physics and Biomedical Engineering (MFT), Sahlgrenska University Hospital, Gothenburg, SWEDEN.*

Aim/Introduction: Terbium-161 (^{161}Tb) has a complex emission pattern consisting of many photons over a wide energy range, which may complicate quantification. This study aimed to evaluate the performance of a SPECT/CT system currently deployed in an ongoing clinical trial (BETA PLUS; NCT05359146), with a particular emphasis on system sensitivity, septal penetration, and dead-time behavior. ***Materials and Methods:*** Experiments were carried out on a Siemens Symbia Intevo system using two collimators, low-energy high-resolution (LEHR) and medium-energy low-penetration (MELP), and two energy windows: 75 keV ±10% and 48 keV ±20%. To evaluate sensitivity and penetration, planar measurements were performed using a ^{161}Tb solution in a Petri dish. Penetration was measured for each collimator-energy window combination according to NEMA standards. A set of ^{161}Tb point sources were used for intrinsic dead-time assessments. Additionally, SPECT acquisitions of a homogeneous cylindrical phantom were used to estimate the activity thresholds at which dead-time becomes significant. Clinical relevance was investigated by analyzing SPECT projection data from eight patients given 1 GBq of [^{161}Tb]Tb-DOTA-LM3. ***Results:*** Sensitivity was similar at 75 keV for both collimators (LEHR: 15.7 cps/MBq; MELP: 18.5 cps/MBq) but increased notably at 48 keV (LEHR: 44.4 cps/MBq; MELP: 67.9 cps/MBq). Significant septal penetration was observed at 75 keV with the LEHR collimator, reaching 22% at the minimal source-to-collimator distance. Analysis of acquired spectra showed that over 50% of detected counts with LEHR appeared above the 75 keV window, whereas only 12.2% were detected above this threshold with MELP. Dead-time analysis indicated nonlinear detector responses at wide-spectrum count rates exceeding 93 kcps, corresponding to a minimum activity of 1.4 GBq for LEHR and 1.7 GBq for MELP. Both detector heads exhibited the same dead-time constant (0.42 µs), however, the maximum measureable count rate differed substansially (384 kcps vs. 546 kcps). Patient data indicated a peak wide-spectrum count rate of approximately 40 kcps per GBq at 3 h p.i. with LEHR. ***Conclusion:*** Attention to dead-time effects is crucial in ^{161}Tb SPECT imaging. The broad photon emission spectrum, as compared to ^{177}Lu, results in an elevated wide-spectrum count rate, increasing the risk of dead time. Use of low-energy collimators leads to greater septal penetration and scatter, exacerbating this concern. At therapeutic activity levels (e.g., 7.4 GBq), dead-time effects should be monitored to guarantee accurate quantification.

OP-663

Final results of the first in human validation of a DROP-IN β-probe during robotic PSMA-guided Surgery: insights and perspectives

F. Collamati[1], *F. Ceci*[2], *G. Musi*[2], *R. Mirabelli*[3], *S. Morganti*[1], *F. Mattana*[4], *S. Luzzago*[4], *F. Nicolanti*[3], *F. W. B. van Leeuwen*[5], *M. N. van Oosterom*[6], *R. Faccini*[7]; [1]*INFN Rome, Rome, ITALY,* [2]*IEO Milan, Milan, ITALY,* [3]*Università Sapienza Roma, Rome, ITALY,* [4]*IEO Milan, Rome, ITALY,* [5]*Interventional Molecular Imaging Laboratory, Department of Radiology, Leiden University Medical Center, Leiden, NETHERLANDS,* [6]*Interventional Molecular Imaging Laboratory, Leiden University Medical Center, Leiden, NETHERLANDS,* [7]*Università Sapienza Roma, Rome, ITALY.*

Aim/Introduction: Prostate cancer patients are routinely diagnosed using PSMA-PET. Identifying these lesions during surgery can however be challenging. Radio-Guided Surgery (RGS) provides an approach that helps (robotic) surgeons to identify target tissues intraoperatively in real time. An approach that is most directly aligned with preoperative PSMA-PET diagnostics

when the same β+ emitting radiopharmaceuticals are being used (^68Ga-based compounds). In addition, the beta emission of PET radiopharmaceuticals offers short-range tissue penetration (few millimeters), which should limit shine through of background signals generated by tracer uptake in non-tumor tissue.This study reports the final results of the first in-human validation of a DROP-IN β probe for PSMA-guided robotic prostate cancer surgery with ^68Ga-PSMA. ***Materials and Methods:*** The β detector consists of a mono-crystalline para-terphenyl scintillator (6 mm diameter, 3 mm height) coupled to a silicon photomultiplier. 15 primary prostate cancer patients with at least one PSMA-PET-positive lymph node were enrolled. These patients were scheduled to undergo prostatectomy and extended pelvic lymph node dissection surgery. Each patient received 1.1 MBq/kg of [^68Ga] Ga-PSMA prior to surgery to allow for the radio guidance. Beta+ detection was performed intraoperatively with a laparoscopic β probe in the first 3 cases. In the remaining 12 patients, a sterilizable DROP-IN β probe (11mm diameter, 45mm length, 6g weight) — compatible with the da Vinci robotic system —was employed. To support the surgeon in discriminating between probe signals coming from tumor and healthy tissue, a statistical software algorithm was developed and optimized on a subset of this dataset. Surgical samples were evaluated at pathology. ***Results:*** Full statistical analysis was performed in the last consecutive 11 patients. In these, the DROP-IN β probe enabled effective intraoperative identification of PSMA-avid lymph nodes during robotic surgery. The DROP-IN probe showed excellent maneuverability and signal discrimination in a minimally invasive setting. During intraoperative lymph node dissection, 98 lymph nodes were harvested and assessed, of which 51 (52%) were malignant at pathology. Using an optimized detection algorithm for the DROP-IN probe, trained on a subset of 8 patients, a 93% detection rate for PET-positive nodes was achieved (26/28), and a 80% sensitivity and 91% specificity ***Conclusion:*** Robotic use of an innovativeDROP-IN β probe demonstrated high specificity and reliable tumor RGS, also in anatomically complex areas. These findings pave the way for broader clinical exploration of β-RGS.

OP-664

An investigation of noise in standardised NEMA image quality phantoms used in multi-centre trials

S. Jin, *G. Krokos, A. Harman, D. M. L. Lilburn, S. Barrington, P. K. Marsden;*
King's College London, London, UNITED KINGDOM.

Aim/Introduction: Scanner harmonisation is essential to acquire images of comparable quality in multi-centre trials. Although rigorous processes have been established for assessing the accuracy of quantification using a NEMA Image Quality (IQ) phantom, current guidelines define an upper cutoff of 15% for the coefficient of variation (CoV) in the background region to assess image noise. The project aims to investigate if a more thorough method of assessing image noise could improve image standardisation. ***Materials and Methods:*** NEMA IQ phantoms scanned on 37 different scanners across the UK using instructions provided by the UK PET Core Lab were analysed. Six concentric circles of varying diameters (ranging from 10-37mm) were placed in the background on the slice corresponding to the centre of the field of view, twelve copies of those six regions of interest (ROIs) were also placed around the background on this slice. These ROIs were also placed in the same way on the neighbouring ±4 and ±8 axial slices (360 regions in total). To assess image noise, the image roughness (IR), which estimates the pixel-to-pixel variability, and the background variability (BV), which estimates the region-to-region variability, were measured. ***Results:*** IR increased with ROI size, exhibiting up to 5% increase, while BV showed a decrease of up to 7%. There was a positive correlation between increasing scanning duration and IR. A large variation in both noise metrics across all scans was noted, despite following defined procedures, scans of the same duration with IR varying between 6%-16% and BV between 4%-11%. For a small number of phantoms, this was attributed to inconsistent sphere-to-background ratios with activity concentrations of approximately 2kBq/ml compared to the instructed 5kBq/ml. However, all were compliant with the EARL criteria of a maximum of 15% in CoV for the background and were therefore accredited. ***Conclusion:*** Current methods assessing noise in NEMA phantoms for harmonisation, may not be thorough enough. Although the scans analysed are accredited by the UK PET Core Lab and are considered harmonised for multi-centre trials, there's still a large variation in noise between the scans that can affect image quality. The phantoms show a 10% and 7% variation in IR and BV respectively and noise should be assessed more thoroughly for the purposes of multi-centre trials. Other contributing factors: reconstruction methods and scanner generation are being investigated, as well as the impact of this large noise variation within the NEMA IQ on clinical scans.

OP-665

Optimising Diagnostic CT in PET/CT: Balancing Dose and Image Fidelity with a Catphan® 600 Phantom

V. Menezes[1,2], *C. Gomes*[3], *P. Bergamo*[3], *R. Machado*[2], *T. Chang*[2], *A. Duarte*[2];
[1]*Hospital das Clinicas da UFPE, Recife, BRAZIL,* [2]*Memorial Star Red D'or, Recife, BRAZIL,* [3]*RADTEC, RECIFE, BRAZIL.*

Aim/Introduction: Dose reduction in positron-emission tomography/computed-tomography (PET/CT) is desirable, but only if the images still "look right" to radiologists who rely on high-fidelity CT for lesion localisation. Quantitative metrics such as modulation-transfer function (MTF) and contrast-to-noise ratio (CNR) provide objective guidance, yet subjective preference strongly influences clinical acceptance. Using a Catphan 600 phantom, we sought CT settings that satisfy both measurable quality indices and clinician-driven expectations while lowering patient exposure. ***Materials and Methods:*** Fourteen helical scans of the phantom were acquired on a Discovery MI PET/CT system. Slice thickness (0.625-3.75 mm) and pitch (0.98-1.375) were varied; rotation time (1 s), noise index (10) and maximum tube current (350 mA) were fixed. Each dataset was reconstructed ten times with filtered back-projection or adaptive statistical iterative reconstruction using standard, noise-suppressing or high-frequency kernels, yielding 140 series. Image quality was assessed by MTF50, CNR, signal-to-noise ratio (SNR), mean noise-power spectrum and uniformity; radiation output was recorded as volume CT dose index (CTDI_vol). ***Results:*** CTDI_vol ranged from 4.4 to 10.1 mGy. The current reference protocol (3.75 mm, pitch 1.375, high-resolution "LU" kernel) produced the best objective scores—MTF50 0.964 lp mm^{-1}, CNR 0.399, SNR 5.33—but at 10.1 mGy and with an image texture many readers considered "over-processed." A candidate routine protocol (3.75 mm, pitch 0.98, iterative "Plus" kernel) preserved spatial resolution (MTF50 0.991 lp mm^{-1}) and kept CNR and SNR within 5 % of the reference while halving dose to 4.4 mGy; radiologists judged its texture indistinguishable from full-dose scans. For applications requiring finer detail, a thin-slice protocol (1.25 mm, pitch 1.375, "IQ Plus" kernel) delivered MTF50 0.981 lp mm^{-1} and acceptable noise at 8.2 mGy. High-frequency kernels sharpened edges but reduced CNR by up to 30 % and were subjectively noisy. ***Conclusion:*** Phantom data indicate that the proposed routine protocol achieves a 65 % dose reduction without perceptible loss of diagnostic quality, making it a strong default for PET/CT attenuation correction and reporting. The thin-slice option offers higher in-plane resolution when clinically warranted, whereas the high-dose reference should be reserved for exceptional cases. Crucially, incorporating radiologist feedback alongside quantitative metrics ensures dose optimization efforts remain clinically acceptable and sustainable.

OP-666

Advantages of Minimally Invasive MIBI-Radioguided Parathyroidectomy.

C. Villaprado, *I. Blanco, A. Barrera, K. Sanabria, E. Goñi, F. Lozada, P. Boya, M. Ribelles, L. Paruta, A. Rosero, M. Garcia, E. Anda, N. Cruz, P. Salvador;*
Hospital Universitario de Navarra, Pamplona, SPAIN.

Aim/Introduction: Minimally Invasive Radioguided Parathyroidectomy (MIRP) is a proven and effective surgical technique for treating primary hyperparathyroidism (PHPT), allowing immediate confirmation of the removal of the pathological gland. Its value is especially notable in complex cases, such as those with ectopic parathyroid lesions or a history of cervical surgery, where traditional approaches may be more challenging. ***Materials and Methods:*** An observational prospective unicentric study was conducted on 183 consecutive PHPT patients treated with MIRP over five years ((January 2020-(January 2025). All patients underwent preoperative imaging with ultrasound and dual-phase MIBI SPECT-CT; Choline PET-CT was used if prior studies were negative or inconclusive. The MIRP procedure involved intravenous administration of 99mTc-MIBI (185 MBq) one hour before surgery, followed by imediate imaging adquisition and intraoperative localization with a portable gamma camera and gamma probe. Early in the study, intraoperative biopsy confirmed surgical success, but later cases relied on imaging and count rates of the excised lesion. ***Results:*** Mean age was 61.87 ± 11.2; 137 (75.4%) women. Sensitivity of preoperative studies to locate the lesion was: US 69.4% (n=127), MIBI 90.1% (n=165), PET 91,4% (n=64/70). Successful surgical resection of the parathyroid lesion occurred in 179 patients (97.8%), achieved by minimally invasive access in 92%; only in two patients was it necessary during the surgical procedure to widen the initial incision to complete the resection. Two synchronous parathyroid lesions were removed in 6 patients, in 4 of whom the image acquired the day of the intervention allowed the localization of the second adenoma, which had not been previously identified in diagnostic studies. An ectopic adenoma was found in 35 patients (19.1%); Radioguided procedure allowed a minimally invasive surgery of 32 (91.4%). Previous cervical surgery was registered in 11 (6.1%); a successful PMIR achieved in 9 (81%). In 15 patients, despite negative/inconclusive MIBI diagnosis (PET diagnosis), radioguided surgery was successfully performed. Biochemical normalization in 97.6% of the 168 patients with follow-up longer than 6 months, including the 6 patients with synchronous adenoma removed. ***Conclusion:*** MIBI Radioguided procedure allows minimally invasive surgical excision of ectopic adenomas, lesions in previously operated patients, and occasionally second lesions, previously unknown. This selective surgical approach has been successfully applied even in patients with a previous non-diagnostic MIBI scan. Real-time evaluation of excised lesions avoids intraoperative biopsy.

OP-667

Quantifying the Contribution of Residual ^{68}Ga in ^{18}F Imaging - the First Step to a 'One Stop Shop'?

N. Davis[1], *H. Natarajan*[1,2], *B. F. Holman*[1];
[1]*Royal Free London NHS Foundation Trust, London, UNITED KINGDOM,* [2]*King's College London, London, UNITED KINGDOM.*

Aim/Introduction: As the importance of PETCT in oncology continues to increase, the number of patients that require scans with both [^{18}F]-FDG and [^{68}Ga]-Ga-DOTA-TATE increases with it. Many patients are required to attend the PET/CT centre on two separate days. Performing both scans on the same day would be advantageous, but the inability of the scanner to distinguish between annihilation photons produced by the two nuclides is problematic. Long Axial Field of View (LAFOV) PET/CT cameras show significant improvement in sensitivity allowing for reduced scan times and decreased injected activities making same day scanning with both nuclides a possibility. This work aims to determine the time delay required between an initial ^{68}Ga administration and the subsequent ^{18}F administration to ensure no significant contribution from the ^{68}Ga is present in the subsequent study images. ***Materials and Methods:*** Our current clinical protocol is to administer 0.75 MBq/kg [^{68}Ga]-Ga-DOTA-TATE and 1.5 MBq/kg [^{18}F]-FDG. To replicate this, sterilin tubes were filled with 15 ml of different concentrations of ^{68}Ga from 2.26 to 0.02 kBq/ml (covering the range we would expect in patients during the day following their scan). These were scanned on a Siemens Biograph Vision Quadra LAFOV PET/CT using the local clinical protocol for [^{18}F]-FDG oncology scans for 5 minutes and reconstructed using PSF and ToF corrections. Cylindrical VOIs were drawn in Hermes. The total number of kBq/cc in each was measured and plotted against activity of ^{68}Ga. Another tube containing 15 ml of 2 kBq/ml of ^{18}F (representing tissue background) was scanned using the same protocol. The percentage contribution to the image from ^{68}Ga at different concentrations, and the time taken to reach these from an assumed initial concentration of 10 kBq/ml, were calculated. ***Results:*** The concentration of ^{68}Ga that contributed the equivalent of 5% of the 'counts' from ^{18}F was reached after 4.3 hours, and 1% after 7.0 hours. It should therefore be possible to perform scans with this order of delay between injections. ***Conclusion:*** It is feasible to successfully perform an ^{18}F scan 4.3 to 7.0 hours after a ^{68}Ga scan with our current protocol. The interval could be further reduced by increasing the activity of ^{18}F administered to the patient. Performing same patient ^{68}Ga and ^{18}F scans on the same day, will improve patient experience, reduce waiting times and lead to faster diagnosis and treatment. Further work should be conducted to assess the impact in clinical images.

OP-668

Addressing brain PET harmonization challenges in clinical settings: joint estimation of true activity and effective image resolution using paired T1W MRI

L. Fu, *S. Yang, L. Yin;*
Department of Nuclear Medicine,China-Japan Friendship Hospital, Beijing, CHINA.

Aim/Introduction: Quantitative harmonization of brain PET acquired across different systems and sites is challenging due to variations in effective spatial resolution, leading to partial volume effects (PVE) that compromise quantitative accuracy. Achieving consistent quantitative recovery, even with Hoffman phantom, highlights the profound influence of system-specific resolution limitations. Accurate PVE correction and effective resolution characterization are crucial for reliable quantitative analysis. ***Materials and Methods:*** This work introduces a novel iterative method addressing these issues by simultaneously recovering a more accurate true underlying brain FDG-PET activity map and characterizing the system-specific effective image resolution (EIR). This is guided by paired T1W MRI scan of the same subject, which is typically feasible in clinical settings. This method operates directly on 3D image, treating the problem as joint deconvolution and kernel estimation. It leverages aligned T1-weighted MRI scans and their segmentations into major tissue types like CSF, WM, and GM as robust anatomical priors. The process initializes the true activity estimate as the observed blurred PET image and provides an initial guess for the blurring kernel (e.g., Gaussian FWHM). An iterative loop then refines these estimates. In each iteration, the true activity is updated using regularized deconvolution. This deblurring step is guided by the MRI segmentations, enforcing piecewise smoothness within CSF, WM, and GM regions while preserving sharp transitions at tissue boundaries. Simultaneously, the EIR kernel is estimated by comparing the blurred version of the current true activity estimate to the observed PET image. This estimation step is guided by the segmentation boundaries (or MRI edges), for instance, by analyzing blurring profiles across edges or

through optimization. ***Results:*** The method's performance was evaluated using a Hoffman 3D brain phantom and 3 patients data, demonstrating convergence. Estimated EIR values were consistent for a given system configuration (e.g., 4.0-5.0 mm FWHM for a Siemens Biograph Vision 600 with all-pass filter reconstruction). For the Hoffman phantom (4:1 GM:WM ground truth), the recovered true activity map yielded a ratio closely approximating this (estimated near 3.8:1), indicating significant PVE correction and improved activity recovery. ***Conclusion:*** By jointly estimating the PVE-corrected activity distribution and EIR from individual scans, this approach offers a promising pathway towards mitigating harmonization challenges, enabling more reliable quantitative comparisons in brain PET analyses.

OP-669

From multicenter variability to harmonized synthetic phantoms: a national DAT SPECT study within the National Virtual Institutes for Parkinson's and Dementia (IVNPD & IVND)

M. Inglese[1], *S. P. Caminiti*[2], *G. Poli*[3], *C. Bianchi*[3], *S. Parabicoli*[3], *S. Mazzaglia*[4], *M. Bagnalasta*[5], *L. Tagliabue*[4], *A. Chiti*[6], *M. Castellani*[7], *S. Raffa*[8], *P. Calza*[9], *L. Evangelista*[10], *D. Di Giuda*[11], *M. Bonacina*[12], *D. D'Ambrosio*[13], *D. Arnaldi*[14], *E. M. Valente*[2], *F. Tagliavini*[15], *S. D. Morbelli*[16], *N. Toschi*[1,17];
[1]*Department of Biomedicine and Prevention, University of Rome Tor Vergata, Rome, ITALY,* [2]*Department of Brain and Behavioral Sciences, University of Pavia, Pavia, ITALY,* [3]*Medical Physics Unit, ASST Papa Giovanni XXIII Hospital, Bergamo, ITALY,* [4]*ASST Santi Paolo e Carlo, Milan, ITALY,* [5]*Centro Nazionale di Adroterapia Oncologica (CNAO), Pavia, ITALY,* [6]*Nuclear Medicine, IRCCS San Raffaele Scientific Institute, Milan, ITALY,* [7]*Nuclear Medicine Unit, Fondazione IRCCS Ca' Granda Ospedale Maggiore Policlinico, Milan, ITALY,* [8]*Nuclear Medicine Unit, IRCCS Ospedale Policlinico San Martino, Genoa, ITALY,* [9]*Istituti Clinici Scientifici Maugeri IRCCS, Gattico-Veruno, Piedmont, ITALY,* [10]*Nuclear Medicine Unit, IRCCS Humanitas Research Hospital, Rozzano, Milan, ITALY,* [11]*Institute of Nuclear Medicine, Fondazione Policlinico Universitario "A. Gemelli" Università Cattolica del Sacro Cuore, Rome, ITALY,* [12]*Nuclear Medicine Department, Fondazione Poliambulanza, Brescia, ITALY,* [13]*Physics Unit, Istituti Clinici Scientifici Maugeri SpA SB IRCCS, Pavia, ITALY,* [14]*Clinical Neurology IRCCS Ospedale Policlinico San Martino, Genoa, ITALY,* [15]*Fondazione IRCCS Istituto Neurologico Carlo Besta, Milan, ITALY,* [16]*IRCCS Ospedale Policlinico San Martino, Genoa, ITALY,* [17]*A.A. Martinos Center for Biomedical Imaging and Harvard Medical School, Boston, MA, UNITED STATES OF AMERICA.*

Aim/Introduction: Technical heterogeneity in image acquisition and reconstruction hampers multicenter validation of nuclearmedicine biomarkers. Dopamine transporter (DaT)-SPECT — a recognised tool for quantifying nigrostriatal degeneration in Parkinson's disease (PD)[1] — is highly susceptible to such variability. We therefore coordinated a harmonisation study across 11 institutions within the National Virtual Institutes for Parkinson's and Dementia using a travelling DaT-SPECT phantom. The aim was to measure and minimise intersite variability and to lay the groundwork for creating harmonised, highfidelity synthetic DaT brain phantoms for research and dataaugmentation. ***Materials and Methods:*** The anthropomorphic phantom mimics DaT uptake in both striatum and background. It was sequentially filled with four predefined striataltobackground ratios (SBRs = 10:1, 7.5:1, 5:1, 2.5:1) of ^{123}Iioflupane SPECT (DaT-SPECT). Each centre (N = 11) acquired images and reconstructed them with filtered backprojection (FBP) and orderedsubsets expectationmaximisation (OSEM), yielding N × 4 datasets per reconstruction algorithm. Preprocessing comprised reconstructionspecific template generation, rigid coregistration, and manual segmentation of bilateral striatal and occipital reference regions. Harmonisation of voxel intensities was performed with NeuroComBat[2] with and without inclusion of dilution ratio as a biological covariate. Coefficient of variation (CV) served as the variability metric. Harmonised volumes were then fed into a validated latentdiffusion model [3] to reconstruct synthetic DaT phantoms whose fidelity was evaluated with structural similarity index (SSIM), meansquared error (MSE), rootMSE (RMSE) and the linear association (R^2) between original and synthetic SBRs. ***Results:*** NeuroComBat markedly reduced intercentre variability, lowering CV by 91.06 ± 0.67 % when no covariate was used and by 77.51 ± 2.13 % when the dilution ratio was included. The generative pipeline reproduced the harmonised images with high agreement (MSE = 0.002 ± 0.001; RMSE = 0.052 ± 0.013; SSIM = 0.976 ± 0.005) and preserved quantitative contrast, as confirmed by a strong correlation between synthetic and original SBRs (R^2 = 0.93). ***Conclusion:*** A coordinated travellingphantom experiment combined with NeuroComBat offers an effective, nationally scalable harmonisation pipeline for DaT-SPECT. When integrated with an advanced diffusionbased generative model, the pipeline yields realistic, quantitatively faithful synthetic datasets that mitigate intersite variability and lower datasharing barriers in PD imaging research. The same workflow will now be applied to clinical DaT-SPECT scans from network centres to enable largescale multicentre biomarker studies. ***References:*** [1] Armstrong,doi: 10.1001/jama.2019.22360; [2] Fortin,doi:https://doi.org/10.1016/j.neuroimage.2017.11.024; [3] Rombach, doi: 10.1109/CVPR52688.2022.01042.

1506

Tuesday, October 7, 2025, 15:00 - 16:30
Room 117

Theranostics Track - TROP Session - Oncology & Theranostics Committee: Prostate Cancer Therapy: New Tracer

OP-670

A First-in-human, Phase 1 Dose Escalation and Expansion Study Evaluating the Safety, Tolerability, and Anti-tumor Activity of [^{225}Ac]Ac-FL-020, an Anti-PSMA Radioconjugate in Patients with Metastatic Castration-Resistant Prostate Cancer (mCRPC).

S. Ngai[1], *G. Cardaci*[2], *A. Singh*[2], *A. Iagaru*[3], *C. Artigas*[4], *K. Goffin*[5], *R. Villanueva Vázquez*[6], *K. Herrmann*[7], *C. S. Kramer*[8], *A. Robert*[8], *K. Schumacher*[8], *S. Heeger*[8], *D. Barton*[9], *A. Hansen*[1];
[1]*Princess Alexandra Hospital, Brisbane, AUSTRALIA,* [2]*GenesisCare Australia. St John of God Hospital Murdoch, Murdoch, AUSTRALIA,* [3]*Stanford University, Stanford, CA, UNITED STATES OF AMERICA,* [4]*Université libre de Bruxelles (ULB), Hôpital Universitaire de Bruxelles (H.U.B), Brussels, BELGIUM,* [5]*Nuclear Medicine, University Hospitals Leuven; Nuclear Medicine and Molecular Imaging, Department of Imaging and Pathology, KU Leuven, Leuven, BELGIUM,* [6]*ICO Hospitalet, l'Hospitalet de Llobregat, Barcelona, SPAIN,* [7]*University Hospital Essen, Essen, GERMANY,* [8]*Full-Life Technologies GmbH, Heidelberg, GERMANY,* [9]*Full-Life Technologies U.S. Inc., Dover, DE, UNITED STATES OF AMERICA.*

Aim/Introduction: [^{225}Ac]Ac-FL-020 is a next-generation prostate-specific membrane antigen (PSMA) alpha radioconjugate developed using the proprietary Clear-X™ technology platform. It is intended for the treatment of patients with metastatic castration-resistant prostate cancer (mCRPC), aiming to enhance tumour uptake and therapeutic efficacy while minimizing off-target effects, particularly in radiosensitive organs such as salivary glands. This Phase 1 clinical trial investigates the safety, tolerability, and preliminary anti-tumour activity of [^{225}Ac]Ac-FL-020 in patients with advanced PSMA-positive mCRPC. ***Materials and Methods:*** This is a first-in-human, open-label, multicentre Phase 1 study consisting of two parts: a dose escalation phase (Part 1) and a cohort expansion phase (Part 2). The study applies a

Bayesian logistic regression model (BLRM) with overdose control to guide dose-escalation decisions. Patients eligible for enrolment must have histologically confirmed mCRPC, evidence of disease progression, and PSMA-positive lesions as confirmed by PSMA PET/CT imaging. Prior treatment with androgen receptor signalling inhibitors or CYP17 inhibitors and at least one taxane-based chemotherapy is required. Patients with extensive PSMA-negative disease are excluded. In Part 1, dose cohorts of 1-3 patients (expanding up to 6) will evaluate ascending dose levels from 1 to 5 MBq to determine the maximum tolerated dose (MTD) and recommended Phase 2 dose (RP2D). Once the RP2D is established, 18 additional patients will be enrolled in Part 2 to further assess safety and explore early signals of efficacy. The study is currently enrolling patients in Australia and the United States, with sites in Europe expected to open later in 2025. ***Results:*** As of April 2025, one eligible patient has been enrolled and evaluated for safety and dosimetry. Preliminary imaging with [^{111}In]In-FL-020, a surrogate for dosimetry analyses, revealed favourable biodistribution in humans with fast and durable tumor uptake whereas the uptake in salivary glands appeared to be rather low. No unexpected safety signals or dose-limiting toxicities have been observed so far. ***Conclusion:*** These initial findings support the feasibility and tolerability of [^{225}Ac]Ac-FL-020 administration in heavily pretreated mCRPC patients. Preliminary dosimetry indicates organ-specific uptake in line with the intended PSMA-targeting mechanism. Further safety and efficacy data will be shared as enrolment progresses, and additional patients are evaluated.

OP-671

Evaluation of the safety and efficacy of ^{225}Ac-PSMA-CY313 in metastatic castration-resistant prostate cancer: preliminary results

S. Li[1], *Y. Shi*[1], *J. Liu*[2], *Z. Li*[2], *Y. Wu*[2];
[1]*Department of Nuclear Medicine, Affiliated Hospital of North Sichuan Medical College, Nanchong, CHINA,* [2]*C-Ray Pharmaceuticals (Chengdu) Co. Ltd., Chengdu, CHINA.*

Aim/Introduction: ^{225}Ac-PSMA-CY313 is a novel molecule of targeted alpha therapy (TAT) that delivers alpha-particle radiation specially to prostate cancer cells expressing Prostate-specific membrane antigen (PSMA). In this study, we investigated preliminary safety and efficacy of ^{225}Ac-PSMA-CY313 in mCRPC patients. ***Materials and Methods:*** We are conducting this prospective, open-label, single-arm study in accordance with ICH GCP guidelines. All patients agreed to participate in the trial with written informed consent after the trial was approved by IEC. The study enrolled disease progressive mCRPC patients with PSMA positive lesions imaged by ^{64}Cu-PSMA-CY313 PET/CT scans at baseline after the treatment with one or more approved androgen-receptor-pathway inhibitors (ARPI) with or without taxane regimens. The eligible patients received ^{225}Ac-PSMA-CY313 treatment intravenously at 200 μCi (7.4 MBq) doses administered every 8 weeks per cycle for 4 cycles followed by expanded 4 cycle treatment if the participants continued to benefit from the treatment. The primary endpoint was to assess adverse events by the CTCAE v5.0 grading system. The secondary endpoints included overall survival (OS), Radiographic Progression-Free Survival (rPFS), Overall Response Rate (ORR) per RESIST version 1.1 and PCWG3, and serum Prostate-Specific Antigen (PSA) levels. ***Results:*** From Feb 2024 to Apr 2025 we recruited 13 male participants with mCRPC who received no more than 6 cycles of ^{225}Ac-PSMA-CY313. The mean age was 67 years (range, 54-77). 100% of patients exhibited PSA decline, while 81.8% reached PSA 50 (a decline of 50% or more). The partial response (PR), ORR and stable disease (SD) were 60.0% (6/10), 60.0% (6/10) and 20% (2/10) respectively. Most adverse events (AEs) were Grade 1-2 except for 1 case with grade 3 (anemia). The most common (11/13, 84.6%) AE was dry mouth including one case of Grade 2 and 10 cases of Grade 1 by CTCAE V5.0. No participants withdrew from study due to dry mouth. Other observed AE included anemia, dyspepsia, white blood cell decrease, fatigue, anorexia, diarrhea, and urinary infection. ***Conclusion:*** ^{225}Ac-PSMA-CY313 was safe and well-tolerated, it exhibited preliminary efficacy for mCRPC patients who were resistant to standard lines of approved agents. Overall ^{225}Ac- PSMA-CY313 is a promising radiopharmaceutical agent for the treatment of mCRPC.

OP-672

First-in-Human Study of a Novel PSMA-Targeted Radiotherapeutic Agent: Safety, Preliminary Efficacy, and Dosimetry of [177Lu]Lu-PSMA-XT in Patients with Metastatic Castration-Resistant Prostate Cancer (mCRPC)

Y. Liu[1,2], *H. Wang*[1], *X. Zhang*[1], *W. Zhao*[3], *R. Wang*[1], *B. Xu*[1], *J. Zhang*[1];
[1]*Chinese PLA General Hospital, Beijing, CHINA,* [2]*Chinese PLA Medical School, Beijing, CHINA,* [3]*Sinotau Pharmaceutical Group, Beijing, CHINA.*

Aim/Introduction: Prostate-specific membrane antigen (PSMA)-targeted radioligand therapy has emerged as a promising treatment strategy for metastatic castration-resistant prostate cancer (mCRPC). [177Lu]Lu-PSMA-XT (XT381) is a novel therapeutic agent demonstrating superior cellular internalization in PSMA-positive cells. This multicenter, open-label, dose escalation and extension study conducted in China aims to evaluate the safety, preliminary efficacy and dosimetry of [177Lu]Lu-PSMA-XT in patients with mCRPC. ***Materials and Methods:*** Enrolled participants had PSMA-positive metastatic prostate cancer (confirmed per THERP trial criteria), progression after ≥1 androgen receptor pathway inhibitor, ineligibility or refusal of chemotherapy, and adequate bone marrow/organ function. The dose-escalation phase employed a "3 + 3" design with sequential enrollment into escalating cohorts (1.85-9.25 GBq; up to 6 cycles). Primary endpoints included safety/tolerability, assessed per CTCAE v5.0 criteria (incidence of adverse events [AEs] and serious adverse events [SAEs]). Secondary endpoints comprised preliminary efficacy (PSA50 response, radiographic progression-free survival [rPFS], objective response rate [ORR], disease control rate [DCR]) and dosimetry. Dosimetry analysis followed European Association of Nuclear Medicine (EANM) guidelines utilizing a hybrid planar/SPECT approach. Whole Body planar scintigraphy were performed at 0.5h,4h,24h,48h,72h and 168 hours post-administration of the first administration. ***Results:*** To date, 12 patients were enrolled (9 in escalation, 3 in expansion). Ten completed ≥1 PSA response assessment (3 at 1.85 GBq, 4 at 3.7GBq [3 in escalation,1 in expansion], 1 at 5.55GBq). A PSA decline was observed in 90% patients, with PSA50 and PSA90 response rate of 60% and 40% respectively, and all responders achieved PSA50 responses within 2 cycles. Notably, even the 1.85 GBq cohort achieved high PSA90 rates (PSA90 RR was 67%), suggesting enhanced potency. One patient with measurable disease achieved partial response (RECIST 1.1); among 9 with non-measurable disease, 1 had progressive disease (PCWG3) and 8 maintained stable disease. No Grade≥3 adverse event or salivary toxicity was observed. Dosimetry analysis revealed a tumor absorbed dose of 3.46 ± 1.74 Gy/GBq, with a biological half-life of 200.56 ± 128.21 hours. The absorbed doses to kidneys, red marrow, and salivary glands were 0.67 ± 0.50, 0.05 ± 0.02, and 0.51 ± 0.12 Gy/GBq, respectively. The tumor-to-salivary gland absorbed dose ratio was 7.22. ***Conclusion:*** [177Lu]Lu-PSMA-XT exhibits favorable tolerability and rapid PSA responses at low doses in mCRPC patients. These preliminary findings highlight its potential as a promising therapeutic agent, warranting further investigation in randomized controlled trials.

OP-673

Head-to-Head dosimetry, safety and preliminary early response evaluation of [^{161}Tb]Tb-SibuDAB versus [^{177}Lu]Lu-PSMA-I&T in patients with mCRPC: PROGNOSTICS Phase Ia

A. Chirindel[1], *G. Nicolas*[1], *F. Westerbergh*[2], *L. McDougall*[1], *D. Schmid*[3], *S. Geistlich*[3], *A. Bauman*[4], *A. Fokkema*[5], *N. Aceto*[5], *P. Bernhardt*[2,6], *N. van der Meulen*[7,3], *C. Müller*[3,8], *R. Schibli*[3,8], *D. Wild*[1]; [1]*Department Theranostics, Nuclear Medicine, University Hospital Basel, Basel, SWITZERLAND,* [2]*Department of Medical Radiation Sciences, Institute of Clinical Sciences, Sahlgrenska Academy at University of Gothenburg, Gothenburg, SWEDEN,* [3]*PSI Center for Life Sciences, Villigen-PSI, SWITZERLAND,* [4]*Department Theranostics, Radiopharmacy, University Hospital, Basel, SWITZERLAND,* [5]*Department of Biology, Institute for Molecular Health Sciences, ETH Zurich, Zurich, SWITZERLAND,* [6]*Department of Medical Physics and Biomedical Engineering, Sahlgrenska University Hospital, Gothenburg, SWEDEN,* [7]*PSI Center for Nuclear Engineering and Sciences, Villigen-PSI, SWITZERLAND,* [8]*Department of Chemistry and Applied Biosciences, ETH Zurich, Zurich, SWITZERLAND.*

Aim/Introduction: The PROGNOSTICS Phase Ia study(NCT06343038) investigates tumor and organ absorbed doses following test injections of [^{161}Tb]Tb-SibuDAB compared to [^{177}Lu]Lu-PSMA-I&T in patients with metastatic castration-resistant prostate cancer(mCRPC). SibuDAB is a novel albumin-binding PSMA-targeted peptidomimetic, developed at PSI, based on a urea-derived PSMA ligand conjugated to (S)-ibuprofen, aiming to enhance blood circulation and, consequently, tumor uptake and retention. ***Materials and Methods:*** In Phase Ia of the study, 10 mCRPC patients received two consecutive test injections of 1 GBq [^{161}Tb]Tb-SibuDAB and 1 GBq [^{177}Lu]Lu-PSMA-I&T, administered three weeks apart in a cross-over, randomized, single-blind design. Quantitative SPECT/CT imaging was conducted (~3, 24, 48, and 168 hours) after each injection to determine tumor and organ absorbed doses using 3D dosimetry based on a Monte Carlo-enhanced OSEM algorithm. For each patient, 3-5 tumor lesions (>1.5cm) were included. Multiple blood samples were collected (~0.5, 1, 3, 24, 48 and 168 hours) for bone marrow dosimetry. Standard laboratory assessments were carried out after 1 and 3 weeks to monitor safety, acute toxicity (CTCAE v5.0), and early PSA response. ***Results:*** Imaging-based dosimetry revealed that the median tumor absorbed dose was 3.5 Gy/GBq (1.5-13.5) following [^{161}Tb]Tb-SibuDAB administration, compared to 1.5 Gy/GBq (0.7-9.7) for [^{177}Lu]Lu-PSMA-I&T. Similarly, median absorbed doses to kidneys were 2.0 Gy/GBq (1.4-2.3) for [^{161}Tb]Tb-SibuDAB and 0.8 Gy/GBq (0.5-1.4) for [^{177}Lu]Lu-PSMA-I&T, while doses to the parotid glands were 0.45 (0.24 - 0.66) and 0.28 (0.11-0.34) Gy/GBq, respectively. Blood-based bone marrow dosimetry yielded 0.092 (0.06-0.22) Gy/GBq for [^{161}Tb]Tb-SibuDAB and 0.014 (0.005-0.025) Gy/GBq for [^{177}Lu]Lu-PSMA-I&T. The effective tumor half-life was 93 and 61 hours, respectively, indicating superior tumor retention for [^{161}Tb]Tb-SibuDAB. Treatment-emergent Grade 1-2 adverse events included anemia (2 vs. 4 patients), leukopenia (1 vs. 1), lymphopenia (5 vs. 3) and creatinine increase (1 vs. 1) following [^{161}Tb]Tb-SibuDAB and [^{177}Lu]Lu-PSMA-I&T, respectively. Grade 3 lymphopenia occurred in 1 patient after [^{161}Tb]Tb-SibuDAB and in 2 patients after [^{177}Lu]Lu-PSMA-I&T. No grade 4 adverse events were recorded. An early measurable PSA response was noted in 6 patients after [^{161}Tb]Tb-SibuDAB and in 4 patients after [^{177}Lu]Lu-PSMA-I&T administration, with partial responses (PCWG3) in 3 and 2 patients, respectively. ***Conclusion:*** The PROGNOSTICS Phase Ia results demonstrate a favorable clinical profile for [^{161}Tb]Tb-SibuDAB in comparison to [^{177}Lu]Lu-PSMA-I&T, with higher tumor doses, prolonged tumor retention and encouraging early PSA responses without evidence of clinical relevant adverse events. PROGNOSTICS Phase Ib (dose escalation study) is currently undergoing to identify the optimal biological dose of [^{161}Tb]Tb-SibuDAB in mCRPC patients.

OP-674

ProstACT Global: A phase 3 study of Lutetium (Lu177) rosopatamab tetraxetan plus standard of care vs standard of care alone in patients with metastatic castration-resistant prostate cancer

J. Roetman[1], *S. Tagawa*[2], *N. Agarwal*[3], *D. Cade*[1], *O. Sartor*[4]; [1]*Telix Pharmaceuticals, Melbourne, AUSTRALIA,* [2]*Weill Cornell, New York, NY, UNITED STATES OF AMERICA,* [3]*Huntsman Cancer Institute, University of Utah, Salt Lake City, UT, UNITED STATES OF AMERICA,* [4]*Mayo Clinic, Rochester, MN, UNITED STATES OF AMERICA.*

Aim/Introduction: Targeted radionuclide therapy can localize treatment to specific tumor cells to reduce or eliminate damage to normal tissue for patients with prostate cancer (PC). Prostate-specific membrane antigen (PSMA) is an ideal therapeutic target as it is highly expressed by malignant PC cells. Compared to peptide-based, monoclonal antibody-based approaches have high binding specificity, rapid internalization, and long retention. Prior studies have demonstrated a favorable safety profile & efficacy of the radio-antibody drug conjugate (rADC) lutetium (Lu 177) rosopatamab tetraxetan (^{177}Lu-rosopatamab) using a fractionated 2 dose regimen. Thus, ^{177}Lu-rosopatamab is currently being investigated in a Phase 3 study for treatment of patients with PSMA+ metastatic castration resistant PC (mCRPC) who have received prior treatment with one androgen receptor pathway inhibitor (ARPI). ***Materials and Methods:*** This multinational, multicenter, prospective, randomized, open label phase 3 study has 2 parts: a dosimetry and safety lead-in (Part 1; n=30) & a randomized treatment expansion (Part 2; n=490). In Part 1, patients are divided into 3 groups (n=10 each) to receive 2 single intravenous injections of 76 mCi each, 14 days apart, of ^{177}Lu-rosopatamab with standard of care (SoC) combinations with abiraterone, enzalutamide, or docetaxel to characterize biodistribution & safety profiles of ^{177}Lu-rosopatamab + SoC combinations. SoC received is determined prior to treatment with ^{177}Lu-rosopatamab. In Part 2, patients will be enrolled 2:1 to receive SoC (determined pre-randomization) with or without 2 single injections of 76 mCi each of ^{177}Lu-rosopatamab, given 14 days apart. Eligible patients must have PSMA-expressing mCRPC and have experienced disease progression on a minimum 12w prior therapy on their 1st ARPI (abiraterone, apalutamide, darolutamide, or enzalutamide) in metastatic castration-sensitive PC, non-metastatic CRPC, or mCRPC settings. Patients may have received docetaxel in mCSPC setting provided last dose was ≥6m prior to screening. Patients must have PSMA+ disease on ^{68}Ga-PSMA-11 PET/CT imaging. The primary endpoint is rPFS. Key secondary endpoint is OS. Additional secondary endpoints include 5-year OS, tumor objective response rate, time to symptomatic skeletal event, & health-related quality of life. An alpha control & 95% confidence intervals will be used; patients will be randomly assigned to receive ^{177}Lu-rosopatamab + SoC or SoC alone. ***Results:*** This study is currently enrolling; no results available at time of abstract submission. ***Conclusion:*** Combining ^{177}Lu-rosopatamab along with proven patient selection capabilities of ^{68}Ga-PSMA-11 PET provides reasonable justification for further evaluation in a large-scale trial for mCRPC treatment This study is sponsored by Telix Pharmaceuticals.

OP-675

SatisfACtion Trial-in-Progress: A Phase 1/2 Study of [^{225}Ac]Ac-PSMA-R2 in Patients with Metastatic Hormone-Sensitive Prostate Cancer or Metastatic Castration-Resistant Prostate Cancer

H. Mahammedi[1], *F. Kraeber Bodéré*[2], *L. Emmett*[3], *C. Rousseau*[4], *A. Vinceneux*[5], *C. Drouet*[6], *J. Wehbe*[7], *Y. Qing*[8], *L. Pinto*[8], *P. Olivier*[9]; [1]*Centre Jean Perrin UMR INSERM 1240 Imost, Clermont-Ferrand, FRANCE,* [2]*Centre Hospitalier Universitaire de Nantes, Département de Médecine Nucléaire, Nantes, FRANCE,* [3]*Department of Theranostics and Nuclear Medicine, Garvan Institute of Medical Research, St Vincent's Hospital, Sydney, AUSTRALIA,* [4]*Institut de Cancérologie de l'Ouest, Département de Médecine Nucléaire, Saint Herblain, FRANCE,* [5]*Centre Léon Bérard, Lyon, FRANCE,* [6]*Centre Georges-François Leclerc, Département de*

Médecine Nucléaire, Dijon, FRANCE, [7]Novartis Pharma AG, Basel, SWITZERLAND, [8]Novartis Pharma, East Hanover, NJ, UNITED STATES OF AMERICA, [9]Centre Hospitalier Régional Universitaire de Nancy, Département de Médecine Nucléaire, Nancy, FRANCE.

Aim/Introduction: In VISION, the prostate-specific membrane antigen (PSMA)-targeted radioligand therapy (RLT) [^{177}Lu]Lu-PSMA-617 plus standard of care (SoC) significantly prolonged survival of patients with metastatic castration-resistant prostate cancer (mCRPC) versus SoC alone. Compared with the β-emitter ^{177}Lu that induces primarily single-stranded DNA breaks, the α-emitter ^{225}Ac induces primarily double-stranded breaks. ^{225}Ac-labelled PSMA RLT has shown anti-tumour activity in patients with mCRPC and metastatic hormone-sensitive prostate cancer (mHSPC). In at-risk organs, PSMA-R2 has been associated with low radiation-absorbed doses. SatisfACtion (NCT05983198) is a trial-in-progress of [^{225}Ac]Ac-PSMA-R2 (^{225}Ac-PSMA-R2) in patients with PSMA-positive mHSPC or mCRPC. ***Materials and Methods:*** This is an open-label, phase 1/2, multicentre study of ^{225}Ac-PSMA-R2 in adults with progressive PSMA-positive mHSPC or mCRPC, confirmed by [^{68}Ga]Ga-PSMA-11 PET/CT. Patients will be assigned to one of three groups: patients with 1) post-androgen receptor pathway inhibitor (ARPI), post-taxane and post-^{177}Lu-PSMA RLT mCRPC; 2) post-ARPI, ^{177}Lu-PSMA RLT-naive mCRPC; or 3) untreated or minimally treated, ^{177}Lu-PSMA RLT-naive mHSPC. Previous taxane therapy is not required for Groups 2 and 3. Exclusion criteria include treatment with any other radionuclides ≤6 weeks before enrolment or treatment with any other investigational agents or systemic anti-cancer therapy ≤28 days before ^{225}Ac-PSMA-R2 therapy start. In the dose-escalation phase (phase 1), approximately 3-6 participants will be enrolled per dose cohort per group to assess the safety and tolerability of ^{225}Ac-PSMA-R2 and establish the recommended dose for expansion (RDE). Dose escalation will use Bayesian logistic regression models following the escalation with overdose control (EWOC) principle. Participants in Groups 1 and 2 will receive a starting dose of 7 MBq intravenous ^{225}Ac-PSMA-R2 once every 6 (±1) weeks for ≤6 cycles; the dose may be increased to subsequent dose levels providing acceptable safety and tolerability, and that the EWOC principle is satisfied. Latest dose-level data in Groups 1 or 2 will inform the Group 3 starting dose. Additional patients may be enrolled to assess an increased frequency dosing schedule based on data from previous dose levels. Primary endpoints are incidence and severity of dose-limiting toxicities, adverse events and serious adverse events, and dose intensity and treatment modifications. Secondary endpoints include response rates, radiographic progression-free survival, overall survival, time to first symptomatic skeletal event and prostate-specific antigen response. The dose-limiting toxicity evaluation period will be 42 days after the first ^{225}Ac-PSMA-R2 dose.The dose-expansion phase (phase 2) will aim to further characterize the anti-tumour activity of ^{225}Ac-PSMA-R2 at the RDE.

OP-676

Adaptive Design and Dose Optimization in a Phase Ib/IIa Dose Escalation and Expansion Study of ^{212}Pb-ADVC001 in Metastatic Castration-Resistant Prostate Cancer (mCRPC): TheraPb - Phase I/II Study

A. Hansen[1], *A. Karmann*[2], *D. Pattison*[3], *S. Ngai*[1], *L. Katchel*[1], *L. Campbell*[3], *A. Soderholm*[2], *M. Griffiths*[3], *E. O'Mahoney*[1], *J. Brady*[3], *S. Rose*[2], *M. Baronet*[2], *M. Crumbaker*[2], *T. Kryza*[2], *S. Puttick*[2], *K. Kuan*[2], *N. Dhiantravan*[3], *I. Holmes*[1], *S. Baker*[1], *P. Santoro*[2], *L. Skingley*[2], *W. Tieu*[2], *C. Gan*[3], *J. Goh*[3], *D. Wyld*[3];
[1]Princess Alexandra Hospital, Brisbane, AUSTRALIA, [2]AdvanCell Pty Ltd, Sydney, AUSTRALIA, [3]Royal Brisbane and Women's Hospital, Brisbane, AUSTRALIA.

Aim/Introduction: Prostate-specific membrane antigen (PSMA)-directed radioligand therapies (RLT) are evolving to meet unmet patient needs in mCRPC. Traditional dose-finding study designs used for systemic anti-neoplastic agents, however, fail to leverage unique aspects of RLT, while the optimal dosing regimens for even established RLTs have not been fully explored. Adaptive design elements and dose optimization have rarely been included in RLT clinical trials to date. The TheraPb study design incorporates adaptive and dose optimization elements to rigorously and efficiently evaluate optimal dosing strategies of ^{212}Pb-ADVC001, a novel PSMA-targeted radioligand labelled with the potent alpha-emitting payload ^{212}Pb, in mCRPC. ***Materials and Methods:*** This is an ongoing prospective, Phase 1b/2a open-label, non-randomized, multi-centre, dose escalation, dose optimization and expansion study of ^{212}Pb-ADVC001. Primary objectives are selection of the recommended Phase 2 dose and schedule (Phase 1b) and efficacy (Phase 2a) of ^{212}Pb-ADVC001 in patients with PSMA-positive mCRPC who have had exposure to at least one androgen receptor pathway inhibitor. ***Results:*** The Phase 1b dose escalation follows an interval 3+3 design, incorporating Bayesian decision-making and additional design elements that can be modified based on emerging study data to evaluate dosing intervals of ^{212}Pb-ADVC001 administered every 6, 4 or 2 weeks. Number of cycles are tailored to patient response on molecular imaging. Efficient dose escalation leverages routine biodistribution imaging and dosimetry assessment, limiting the number of patients exposed to subtherapeutic doses. If the Phase 1b demonstrates multiple dosing regimens with similar safety, tolerability and anti-tumour activity, the protocol provides the option to include adaptive randomization in Phase 2a expansion to identify an optimized dose and schedule. Phase 2a further includes evaluation of biomarker-driven adaptive dosing regimens in pre-defined cohorts of patients with PSMA-positive mCRPC proceeding in parallel, characterizing the drug profile and development potential in specific indications. ***Conclusion:*** The adaptive design and dose optimization elements of TheraPb aim to identify optimal RLT dosing regimens while reducing exposure of subjects to subtherapeutic doses or suboptimal schedules and improving patient safety and depth and duration of response, ultimately enabling faster patient access to this novel and potentially effective treatment. The trial is currently enrolling at two clinical sites in Australia (NCT05720130).

OP-677

Dose escalation study for targeted radionuclide therapy with [^{161}Tb]Tb-SibuDAB in mCRPC - PROGNOSTICS Phase Ib study

A. Chirindel[1], *G. Nicolas*[1], *F. Westerbergh*[2], *L. McDougall*[1], *D. Schmid*[3], *S. Geistlich*[3], *A. Bauman*[1], *A. Fokkema*[4], *N. Aceto*[4], *P. Bernhardt*[2,5], *N. van der Meulen*[6,3], *C. Müller*[3,7], *R. Schibli*[3,7], *D. Wild*[1];
[1]Department Theranostics, Nuclear Medicine, University Hospital Basel, Basel, SWITZERLAND, [2]Department of Medical Radiation Sciences, Institute of Clinical Sciences, Sahlgrenska Academy at University of Gothenburg, Gothenburg, SWEDEN, [3]PSI Center for Life Sciences, Villigen-PSI, SWITZERLAND, [4]Department of Biology, Institute for Molecular Health Sciences, ETH Zurich, Zurich, SWITZERLAND, [5]Department of Medical Physics and Biomedical Engineering, Sahlgrenska University Hospital, Gothenburg, SWEDEN, [6]PSI Center for Nuclear Engineering and Sciences, Villigen-PSI, SWITZERLAND, [7]Department of Chemistry and Applied Biosciences, ETH Zurich, Zurich, SWITZERLAND.

Aim/Introduction: The PROGNOSTICS Phase Ib study (NCT06343038) aims to identify the optimal biological dose of [^{161}Tb]Tb-SibuDAB for targeted radioligand therapy (RLT) in patients with metastatic castration-resistant prostate cancer (mCRPC). SibuDAB is a novel albumin-binding PSMA-targeted peptidomimetic, developed at PSI. It is based on a urea-derived PSMA ligand conjugated to (S)-ibuprofen, in order to prolong blood circulation and, consequently, tumor uptake and retention. ***Materials and Methods:*** This ongoing open-label, prospective

3+3 dose escalation trial includes mCRPC patients with documented disease progression (biochemical, radiologic, and/or clinical) under systemic therapy (anti-hormonal with or without prior chemotherapy), with preserved organ function and PSMA positive disease on pre-therapy PET/CT. Key exclusion criteria include participation in other therapeutic trials, prior treatment with [^{177}Lu]Lu-PSMA RLT, and any other malignancy without complete remission for ≥5 years. Each 3-patient cohort receives a total of 4 therapy cycles, every 6 weeks with same injected activity for every cycle, delivered as a 10-minute short infusion along with 4-hour 1-liter saline hydration. Post-therapy quantitative SPECT/CT imaging is performed at ~3, 24, 48, and 168 h to calculate tumor and organ absorbed doses using a 3D dosimetry using a Monte Carlo-based OSEM algorithm. Blood sampling (~0.5, 1, 3, 24, 48 and 168 hours) is used for bone marrow dosimetry. Additionally, the study incorporates multi-omic profiling (clinical, biochemical, imaging, cellular and transcriptomic) as well as circulating tumor cells and tumor-cell cluster analyses, to explore potential biomarkers for treatment response (PSA per PCWG3) and toxicity prediction (graded by CTCAE v5.0). ***Results:*** The first patient cohort (n=3) has completed two treatment cycles at the initial injected activity of 3 GBq without any infusion-related acute events. Hematologic toxicity was limited to one case of grade 1 leukopenia and two cases of grade 1 lymphopenia, with no additional adverse events. Renal and hepatic function showed no measurable alteration post-treatment. An early PSA decline was observed in one patient, while two patients showed either stable or rising PSA values. ***Conclusion:*** The PROGNOSTICS Phase Ib is an ongoing 3+3 dose escalation study aiming to identify the optimal biological dose of [^{161}Tb]Tb-SibuDAB for RLT in mCRPC patients. Initial findings from the first dose level demonstrate a favorable safety profile with early signs of pharmacological activity. Comprehensive data from the first two cohort - including dosimetry, subacute toxicity and PSA response - will be presented.

OP-678

Dosimetry and Dose-escalation Study of a Novel Long-Acting Radiopharmaceutical [^{177}Lu]Lu-LNC1011 inMetastatic Castration-Resistant Prostate Cancer Patients

J. Wang[1], *R. Wang*[1], *J. Xiang*[1], *X. Chen*[2], *Z. Zhu*[1], *J. Zhang*[2];
[1]*Peking Union Medical College Hospital, Beijing, CHINA,* [2]*National University of Singapore, Singapore, SINGAPORE.*

Aim/Introduction: [^{177}Lu]Lu-LNC1011 ([^{177}Lu]Lu-D-Dan-Phe-PSMA) is a novel long-circulating prostate-specific membrane antigen (PSMA) therapeutic radioligand whose structure is based on a labile dansyl group as a relatively weak albumin binder. This study aims to investigate its safety, dosimetry, and initial treatment efficacy of [^{177}Lu]Lu-LNC1011 in patients with metastatic castration-resistant prostate cancer (mCRPC). ***Materials and Methods:*** This study used an open-label, non-randomized design. It adopted a dose-escalation approach, enrolling mCRPC patients who hadpassed a pre-screening PSMA PET/CT. A total of 9 mCRPC patients received [^{177}Lu]Lu-LNC1011 at dose levels of 1.85, 2.78 and 3.70 GBq. ***Results:*** No DLT was observed in any dose group. The effective dose to the whole body was 0.10 ± 0.02 mSv/MBq. The kidneys received the highest expected radiation dose, which was calculated to be 3.33 ± 1.09 Gy/GBq. For salivary glands and red bone marrow, the effective doses were 1.70 ± 1.04 Gy/GBq and 0.11 ± 0. 03 Gy/GBq, respectively. The mean absorbed dose to tumors was 12.29 ± 6.50 Gy/GBq. The effective half-life of [^{177}Lu]Lu-LNC1011 was 49.44 ± 12.58 h in the whole body and 128.3 ± 62.79 h in tumor lesions. After two cycles, the 3.70 GBq cohort demonstrated superior efficacy with 100% PSA reduction (3/3), 66.7% achieving ≥50% PSA decline, and a 33.3% sustained PR rate, while all cohorts maintained 33.3% SD-to-PR conversion and 100% disease control without progression assessed by Response Evaluation Criteria in PSMA PET/CT (RECIP) 1.0 criteria. ***Conclusion:*** The administration of [^{177}Lu]Lu-LNC1011 across three dosing groups in mCRPC patients was well tolerated, with minimal side effects. The treatment delivered a high tumor-absorbed dose and demonstrated prolonged tumor retention. Notably, the 3.70 GBq dose group demonstrated significant therapeutic efficacy. Considering its efficacy, safety, and dosimetric results, we believe that conducting further multi-cycle studies at a dose of 3.70 GBq [^{177}Lu]Lu-LNC1011 is appropriate.

1507

Tuesday, October 7, 2025, 15:00 - 16:30
Room 212

TROP Session - Cardiovascular Committee: Myocardial Perfusion on PET: Where Are We Going?

OP-679

Safer3: A Phase III Prospective, Multicenter, Open-label Study to Assess Diagnostic Efficacy of a Novel F-18-labelled Myocardial perfusion tracer, F-18-SYN2

J. Knuuti[1], *M. H. Al-Mallah*[2], *P. J. Slomka*[3], *P. Soman*[4], *T. M. Bateman*[5], *P. Chareonthaitawee*[6], *M. Dziuk*[7], *J. Bil*[8], *S. Krajewski*[9], *A. Einstein*[10], *R. R. S. Packard*[11], *W. Kula*[12], *L. Steczek*[9], *K. Gotowicz*[9], *P. Kozanecki*[9], *J. Włostowska*[9], *C. Kozanecki*[9];
[1]*Turku University Hospital, Turku, FINLAND,* [2]*Heart and Vascular Center, Houston, TX, UNITED STATES OF AMERICA,* [3]*Cedars Sinai Medical Center, Los Angeles, CA, UNITED STATES OF AMERICA,* [4]*University of Pittsburgh Medical Center, Pittsburg, PA, UNITED STATES OF AMERICA,* [5]*6)Mid America Heart Institute and the Saint Luke's Health System, Kansas City, MO, UNITED STATES OF AMERICA,* [6]*Mayo Clinic, Rochester, MN, UNITED STATES OF AMERICA,* [7]*Military Institute of Medicine - National Research Institute, Warsaw, POLAND,* [8]*10)National Medical Institute of the Ministry of Interior and Administration, Warsaw, POLAND,* [9]*Research and Development Centre, Synektik SA, Warsaw, POLAND,* [10]*Columbia University Irving Medical Center, New York, NY, UNITED STATES OF AMERICA,* [11]*University of California, Los Angeles, CA, UNITED STATES OF AMERICA,* [12]*Axcellant, Warsaw, POLAND.*

Aim/Introduction: SAFER3, the Phase III, prospective, multicenter, open-label study was designed to evaluate the diagnostic efficacy of a novel ^{18}F-labeled tracer, [^{18}F]SYN2, for myocardial perfusion imaging (MPI) using positron emission tomography (PET) in subjects with suspected coronary artery disease (CAD). ***Materials and Methods:*** The study enrolls male and female participants over 18 years of age who are referred for invasive coronary angiography (ICA) due to suspected CAD. A total of 280 evaluable subjects, accounting for a 15% dropout rate, will be recruited across Europe and the United States, with an adaptive design allowing sample size expansion up to 682 evaluable subjects. The study features an adaptive framework with three unblinded interim analyses to evaluate early efficacy and safety, optimize study conduct, and potentially adjust the sample size. ***Results:*** Participants will receive two [^{18}F]SYN2 injections, one at rest and one during stress, with imaging performed under standardized 1-day protocols. Reference standard diagnostics will include ICA with fractional flow reserve (FFR) or instantaneous wave-free ratio (iwFR) measurements when applicable. The primary objective is to assess [^{18}F]SYN2 PET MPI's ability to detect significant CAD, defined as anatomical stenosis ≥ 90% or functional ischemia in lesions with 40-89% stenosis. Secondary objectives include evaluating quantitative and qualitative imaging performance and assessing the safety of [^{18}F]SYN2 radiotracer. Exploratory objectives will compare [^{18}F]SYN2 PET MPI with other non-invasive imaging modalities. ***Conclusion:*** The clinical trial is already open for recruitment in Europe.

References: Krajewski S, Steczek L, Gotowicz K et al. Preclinical evaluation of [^{18}F]SYN1 and [^{18}F]SYN2, novel radiotracers for PET myocardial perfusion imaging. EJNMMI Res. 2024;14:63. Knuuti J, Kobylecka M, Kalliokoski K et al. Biodistribution, safety profile, and radiation dosimetry of [^{18}F]SYN2, a new PET perfusion tracer in healthy subjects. J Nucl Med. 2025;66:626-633. Dziuk M, Knuuti J, Krajewski S et al. Safety, tolerability and diagnostic ability of a novel ^{18}F-labelled tracer, [^{18}F]SYN2, for PET myocardial perfusion imaging (SAFER) in patients with suspected coronary artery disease - phase II trial. Eur Heart J Cardiovasc Imaging. 2024;25.

OP-680

Diagnostic Approach to Microvascular Dysfunction in INOCA: Simultaneous Dual-Perfusion Imaging with ^{13}N-Ammonia and Gadolinium Using an Integrated PET-MR Scanner

R. Wen, *X. Wang;*
The First Affiliated Hospital of University of Science and Technology of China, Hefei, CHINA.

Aim/Introduction: Ischemia with no obstructive coronary arteries (INOCA), a chronic disorder with a poor prognosis, remains diagnostically challenging. Innovative hybrid PET-MR technology enables the concurrent procurement of PET and magnetic resonance (MR) data under precisely the same experimental and physiological circumstances. This study aims to utilize hybrid PET-MR to simultaneously obtain positron emission tomography (PET) and magnetic resonance data of patients, aiming to identify potential predictive factors for the reduction of coronary flow reserve (CFR). ***Materials and Methods:*** We prospectively enrolled 32 patients (14 females and 18 males) with typical angina pectoris and no obvious coronary stenoses shown by angiography. Microvascular dysfunction was defined as CFR < 2. CFR was defined as the ratio of hyperemic MBF (after regadenoson) to resting MBF. The receiver operating characteristic (ROC) curves and diagnostic cutoff values were analyzed to evaluate the predictive value of factors significantly influencing the diagnosis of INOCA. Subsequently, the statistically significant predictive factors were aggregated into the number of risk factors (NRF). ***Results:*** Global CFR (1.56 ± 0.48 vs. 3.10 ± 0.89; P < 0.001) was significantly lower in patients with INOCA than in those with no INOCA. ROC analysis identified the following continuous variables significant for INOCA diagnosis: global radial strain [AUC = 0.929, 95% confidence interval (CI): 0.78 - 0.99, P < 0.001] with a cut-off value of 43.8%; triglycerides (AUC = 0.890, 95% CI: 0.73 - 0.97, P < 0.001), cut-off 1.28 mmol/L; very - low - density lipoprotein (VLDL) (AUC = 0.731, 95% CI: 0.55 - 0.87, P = 0.049), cut-off 0.68 mmol/L; and native T1 maps (AUC = 0.852, 95% CI: 0.86 - 0.95, P < 0.001), cut-off 1213 ms. The categorical variable with statistical significance is late gadolinium enhancement (LGE) (P < 0.001). Based on the aforementioned factors, the NRF for each patient was calculated cumulatively and subsequently input into the ROC curve analysis. The findings revealed that our NRF exhibited excellent diagnostic efficacy for INOCA. Notably, the optimal cut-off value for NRF was determined to be 2 [AUC = 0.992 (95% CI: 0.88 - 1.00), P < 0.001]. ***Conclusion:*** Accumulated risk factors negatively impact CFR. Calculating the NRF in patients with suspected INOCA can effectively predict the probability of microvascular dysfunction among these patients. We propose that patients with NRF ≥ 2 should have their CFR measured via PET.

OP-681

Simultaneous 13N-Ammonia and Gadolinium-Based First-Pass Myocardial Perfusion Using Integrated PET-MRI Imaging: A Comparative Evaluation of Diagnostic Accuracy in Coronary Microvascular Dysfunction

R. Wen, *X. Wang;*
The First Affiliated Hospital of University of Science and Technology of China, Hefei, CHINA.

Aim/Introduction: Absolute quantification of myocardial perfusion and coronary flow reserve (CFR) with positron emission tomography (PET) has demonstrated diagnostic and prognostic value in patients with coronary microvascular dysfunction (CMD). Quantitative magnetic resonance imaging (MRI) perfusion imaging has been recently developed and validated against PET in healthy volunteers. However, no studies have compared MRI and PET perfusion imaging in patients with CMD using integrated PET-MRI imaging. The aim of this study was to assess the quantitative accuracy of cardiac perfusion measurements using MRI with simultaneous ^{13}N-ammonia PET as reference with a fully integrated PET-MRI scanner. ***Materials and Methods:*** Thirty patients with suspected CMD underwent simultaneous MRI and ^{13}N-ammonia PET scans at rest and regadenoson-stress on an integrated PET-MRI scanner. Correlation and agreement between MRI- and PET-derived myocardial blood flow (MBF) and CFR values were evaluated using correlation and Bland-Altman analysis. ***Results:*** MRI measurements of global rest and stress MBF showed moderate correlation to those obtained using ^{13}N-Ammonia PET (r = 0.50; P = 0.005 for rest MBF and r = 0.49; P < 0.006 for stress MBF). Bland-Altman analysis revealed a mean bias of − 0.83 ± 0.47 mL/g/min for rest MBF and −1.84 ± 0.57 mL/g/min for stress MBF. The correlations between regional MBF_{MRI} and MBF_{PET} obtained during rest and stress were only poor to moderate (r = 0.26 and r = 0.43). The limits of agreement were wide for both global and regional MBF, with larger variability for high MBF-values. However, there was good agreement between MRI and PET with regard to global and regional CFR with moderate to strong correlation (r = 0.64, P < 0.001; r = 0.48, P < 0.001). MRI-derived CFR demonstrated an area under the curve (AUC) of 0.85 (95% CI: 0.67 to 0.95) and had an optimal cutoff value of 1.57 for detecting CMD, defined as ^{13}N-Ammonia PET-derived CFR ≤ 2.0 ***Conclusion:*** CFR measurements were concordant between MRI and ^{13}N-Ammonia PET. For detecting significant CMD, CFR_{MRI} and CFR_{PET} demonstrated comparable and high accuracy. Nevertheless, MRI measurements of rest and stress MBF showed only poor to modest agreement to those obtained with ^{13}N-Ammonia PET. Therefore, although quantitative MRI has clinical utility, further refinements are still required.

OP-682

Native T1 Mapping versus Coronary Flow Reserve for Coronary Microvascular Dysfunction in INOCA: PET-MRI Validation

R. Wen, *X. Wang;*
The First Affiliated Hospital of University of Science and Technology of China, Hefei, CHINA.

Aim/Introduction: Ischemia with non-obstructive coronary artery disease (INOCA) is a chronic disorder with a poor prognosis, often caused by coronary microvascular dysfunction (CMVD), which increases morbidity, mortality, and economic burden. Cardiac magnetic resonance imaging (CMR)-derived coronary flow reserve (CFR) is a validated marker for CMVD, but concerns about gadolinium-based contrast agent (GBCA) tissue deposition—especially in the central nervous system with repeated use—highlight the need for non-contrast alternatives. Native T1 mapping, an emerging MRI technique sensitive to myocardial tissue abnormalities (e.g., edema, fibrosis), has not been systematically compared with MRI-derived CFR for detecting CMVD in INOCA. ***Materials and Methods:*** Thirty-three INOCA patients underwent stress/rest PET-MRI, including 3-Tesla native T1 mapping (ShMOLLI sequence) and Gd-DTPA perfusion MRI. Imaging used an integrated 3T PET-MRI system, acquiring cine MRI, native T1 maps, and myocardial perfusion data with 13N-ammonia PET. CFR, defined as hyperemic/resting myocardial blood flow (MBF), was calculated for the left ventricle (LV) and coronary territories. Patients were classified into reference (CFR ≥ 2.0) and CMVD (CFR < 2.0) groups based on PET-derived CFR,

the noninvasive reference standard. ***Results:*** Twelve patients had CMVD (CFR < 2.0) and 21 had preserved CFR. CMVD patients had significantly higher mean global native T1 values (1251.6 ± 22.3 vs. 1207.2 ± 30.7, P < 0.001) and lower stress MBF (0.17 ± 0.03 vs. 0.25 ± 0.07 ml/g/min, P < 0.001) and CFR (1.47 ± 0.35 vs. 2.04 ± 0.39, P < 0.001). Native T1 inversely correlated with PET-derived CFR (r = −0.67, P < 0.001), and MRI-derived CFR correlated with PET-derived CFR (r = 0.63, P < 0.001). Receiver-operating characteristic analysis showed comparable diagnostic accuracy: native T1 (AUC: 0.881) and MRI-derived CFR (AUC: 0.873, P = 0.912). A T1 threshold of 1213 yielded 100% sensitivity and 75% specificity, while CFR_{MRI} ≤ 1.625 had 83% sensitivity and 85% specificity for CMVD. ***Conclusion:*** Elevated native myocardial T1 values inversely associate with PET-derived CFR in INOCA, demonstrating comparable CMVD detection to MRI-derived CFR. This first systematic comparison highlights native T1 mapping as a viable non-contrast alternative for CMVD assessment. If validated in larger studies, it could serve as a gadolinium-free surrogate marker for CMVD severity, enabling safe serial evaluations without GBCA exposure. Mechanistic insights and multicenter validation are needed to optimize its clinical utility.

OP-683

Association between Coronary Microvascular Dysfunction and Diabetic Microvascular complications in Type 2 Diabetes Mellitus: A ^{13}N-Ammonia PET study

J. Ilangovan, *H. Singh, A. Rastogi, A. Sood, B. Mittal;*
PGIMER, Chandigarh, INDIA.

Aim/Introduction: Coronary microvascular dysfunction (CMD) is the impaired ability of the coronary microcirculation to regulate blood flow in response to oxygen demand. Numerous studies have demonstrated that CMD is associated with an increased risk of major adverse cardiac events (MACE). Cardiovascular disease (CVD) remains the leading cause of mortality in patients with diabetes mellitus, highlighting the need for early identification of microvascular abnormalities. This study aimed to evaluate the prevalence of CMD in individuals with type 2 diabetes mellitus (T2DM) without overt coronary artery disease (CAD) using ^{13}N-ammonia PET imaging. The other objective was to compare the prevalence of CMD between T2DM patients with proteinuria and those without proteinuria. ***Materials and Methods:*** Individuals with type 2 diabetes mellitus (T2DM) of at least five years' duration and no prior history of myocardial infarction, heart failure, or coronary revascularisation were prospectively enrolled. Based on the 24-hour urine protein analysis, participants were categorised into two groups: those with proteinuria and those without. All patients underwent a single-day rest/stress cardiac PET scan using ^{13}N-ammonia as the perfusion tracer and adenosine as the pharmacologic stress agent. Additionally, patients were screened for other diabetic microvascular complications, including peripheral neuropathy and diabetic retinopathy. Myocardial flow reserve (MFR) values < 2, were used to define the presence of CMD. ***Results:*** A total of 18 T2DM patients were enrolled in the study. Among them, 13 (72%) were male and 5 (28%) were female. The mean age of the cohort was 59.4 ± 6.9 years. Proteinuria was present in 5 of 18 patients, while the remaining 13 did not exhibit this complication. Among the non-proteinuria group, 3 patients had diabetic foot ulcers secondary to peripheral neuropathy. CMD, indicated by reduced myocardial flow reserve (MFR), was observed in all 5 patients with proteinuria, in 1 of the 3 patients with diabetic foot ulcers, and in only 1 patient without either complication. Overall, T2DM patients with microvascular complications (proteinuria and diabetic foot ulcers) had significantly lower MFR values compared to those without (1.94 ± 0.48 vs. 2.86 ± 0.83; p < 0.005). ***Conclusion:*** Impaired MFR was more frequently observed in T2DM patients with diabetic microvascular complications, especially those with proteinuria. These findings suggest that coronary microvascular dysfunction and diabetic nephropathy may share common underlying mechanisms, pointing to a broader systemic microvascular pathology in diabetes.

OP-684

Prognostic value of coronary flow capacity by 82Rb PET in a large cohort of patients with suspected and known coronary artery disease

E. Zampella[1], *R. Assante*[1], *T. Mannarino*[1], *A. D'Antonio*[1], *M. Panico*[2], *P. Buongiorno*[1], *V. Cantoni*[1], *R. Green*[1], *A. Cuocolo*[1], *W. Acampa*[1];
[1]*University Federico II, Naples, ITALY,* [2]*3Institute of Biostructure and Bioimaging, CNR, Naples, ITALY.*

Aim/Introduction: Cardiac imaging by positron emission tomography (PET) provides an accurate evaluation of both atherosclerotic burden and vascular function. Coronary flow capacity (CFC) is a comprehensive measure of the entire coronary vascular status, integrating both hyperemic myocardial blood flow (MBF) and myocardial flow reserve (MFR). We aimed to assess the incremental prognostic value of impaired CFC, evaluated by Rubidium-82 (82Rb) PET, in a large cohort of patients with suspected and known CAD. ***Materials and Methods:*** We evaluated 5839 patients who underwent stress/rest 82Rb cardiac PET/CT in our institution. Coronary artery calcium (CAC) score was calculated and categorized as <400 and ≥400. Total perfusion defect (TPD) was considered abnormal when ≥5%. MFR was considered impaired when <2. According to previously defined thresholds, patients were classified as having normal (normal flow or minimally reduced CFC) or abnormal (mildly reduced, moderately reduced, severely reduced CFC and myocardial steal) CFC. The outcome endpoints were cardiac death, myocardial infarction and revascularization procedures. Annualized event rate (AER) was calculated. Cox proportional hazards model was employed to estimate risk of events. A parametric survival model was also used to identify how the variables influenced time to event and to estimate risk-adjusted event rates during the follow-up. ***Results:*** Follow-up was available in 5379 (92%) patients (median age 61±12 years). During a median time of 42±27 months, 780 events occurred (cumulative rate 14%, AER 3.4%). A total of 2037 (38%) patients had abnormal CFC. AER was higher in patients with impaired CFC (AER 7.9%) as compared to those without (AER 1.9%) (p <0.001). At multivariable COX analysis, diabetes, CAC ≥400, TPD ≥5%, MFR<2 and abnormal CFC resulted significant predictor of events (all p<0.001). At incremental analysis the addition of CFC to a model including clinical variables, TPD≥5% and MFR<2 increased the global chi-square from 759 to 840 (p<0.001). At Weibull parametric survival analysis, the highest probability of cardiac events and the major risk acceleration were observed in patients with impaired CFC. ***Conclusion:*** The presence of impaired CFC is associated with a higher risk of cardiac events both in patients with suspected and known CAD.

OP-685

Improved cardiac^{82}Rb-PET functional imaging with 16-gates protocol using a LAFOV PET system

N. Gözlügöl, *H. Sari, F. Aghapour Zangeneh, A. Rominger, F. Caobelli;*
Inselspital Bern University Hospital, Bern, SWITZERLAND.

Aim/Introduction: The evaluation of cardiac function on ^{82}Rb-PET is often limited by low count statistics in gated imaging, which can impair the accuracy of left ventricular (LV) volumes and ejection fraction (LVEF). Although 16 ECG-gated frames could improve accuracy by providing more detailed temporal sampling, low count statistics remain a limiting factor. Hence, 8-gated frames are typically used. Increasing the administered activity may address this, but at the cost of higher radiation exposure. Long axial field-of-view (LAFOV) PET/CT scanners may fit this need by

offering increased sensitivity, enabling high count statistics even at low activity levels. We investigated whether increasing the number of ECG-gated frames from 8 to 16 during ^{82}Rb cardiac PET improves the accuracy of functional parameters compared to transthoracic echocardiography (TTE). ***Materials and Methods:*** Eighty-seven patients who underwent ^{82}Rb-PET with both rest and stress imaging were included. A standard activity of 370 MBq was injected for both acquisitions. PET reconstructions with 8 and 16 gated frames were analyzed for LVEF and end-diastolic and end-systolic values (EDV and ESV, respectively). Corresponding TTE values were collected from clinical reports. Differences between PET- and TTE-derived values were assessed with paired t-test, Pearson-correlation and Bland-Altman analysis. PET-derived values with 8 and 16 gated frames were contrasted with paired t-test after verification of normal distribution. ***Results:*** Mean LVEF at rest was 54.8±13.9% with 8-gated PET, 61.2±11.2% with 16-gated PET, and 58.1±7.8% on TTE. LVEF with 16-gated frames showed close agreement with TTE, with only a slight, non-significant overestimation (p = 0.103, mean difference +2.0%, R=0.47). Conversely, 8-gated PET significantly underestimated LVEF (p = 0.007, mean difference - 4.3%, R=0.28). Considering volume analysis, EDV was accurately evaluated by both 8-gated (mean difference +14.6 mL, p = 0.060) and 16-gated PET (mean difference +10.8 mL, p = 0.067). Conversely, 16-gated PET showed superior accuracy for ESV, with a slight overestimation of +8.8% (p = 0.304), whereas 8-gated PET significantly overestimated ESV by +38.0% (p = 0.013). ***Conclusion:*** ^{82}Rb-PET imaging on LAFOV PET with 16-gated frames demonstrated close agreement with TTE for LVEF, EDV, and ESV, indicating superior accuracy in the assessment of LV functional parameters. Conversely, standard 8-gated PET showed systematic underestimation. Of note, high accuracy was yielded with ultra low activities. These findings support the clinical implementation of 16-gated acquisition protocols on LAFOV PET systems to enhance the accuracy of functional cardiac assessment during myocardial perfusion imaging, while reducing radiation burden.

OP-686

Reduction of acquisition time in [^{15}O]H_2O-myocardial perfusion imaging

K. Thøgersen*, M. Nowak Lonsdale, M. Krakauer;*
Department of Clinical Physiology and Nuclear Medicine, Copenhagen University Hospital – Bispebjerg and Frederiksberg, Copenhagen, DENMARK.

Aim/Introduction: Unlike other perfusion tracers that stay confined in the myocardium, [^{15}O]H_2O is freely diffusible and has an extraction fraction of 1. Therefore, [^{15}O]H_2O-uptake in myocytes is linearly proportional with tissue perfusion and the most crucial time of acquisition is within the first minutes after tracer injection. The usual protocol in myocardial perfusion imaging with Adenosine as vasodilator is intravenous infusion of 140µg/kg/min for 6 minutes with injection of tracer after obtaining maximum vasodilation at 2 minutes followed by at least 4 minutes acquisition time. A reduction in both Adenosine infusion time and acquisition time could reduce patient discomfort and time consumption. The aim of this study was to test if reducing acquisition time with [^{15}O]H_2O as PET-tracer altered myocardial blood flow (MBF). ***Materials and Methods:*** In this retrospective study we included 30 patients suspected of chronic ischemic heart disease. We consecutively included 10 patients in three categories: global stress perfusion below 1.8, between 1.8 and 2.8, and above 2.8ml/g/min. Exclusion criteria were insufficient response to Adenosine or motion artefacts. PET/CT scans were performed on a Discovery 710 (GE Healthcare) with our standard protocol described in detail elsewhere (1). A bolus of 600MBq [^{15}O]H_2O was administered, and PET data acquired for 7 minutes. Adenosine infusion (140µg/kg/min) was started 2 minutes prior to the anticipated arrival of the bolus in the heart. A dynamic series (14×5s, 3×10s, 3×20s, 4×30s) was reconstructed triggered by the arrival of [^{15}O]H_2O to the heart. In addition to the original 280s datasets, 120 datasets were generated by truncating the acquisition at 160s, 190s, 220s and 250s for each patient. Kinetic analysis was conducted using CarimasCE version 1.3.1. (VARHA, Turku, Finland). Volumes of interest were drawn manually by the same physician. Global MBF and regional MBFs (LAD, LCX, RCA territories) were assessed. Full-length scans analysed twice for each patient to assess intra-rater variability. Statistical analyses included paired t-test, intra-class correlation coefficients (ICC) and Bland-Altman plots. ***Results:*** Intra-rater analysis showed no significant difference, e.g., global MBF comparison showed t=0.778, p=0.443. Neither did scan length affect MBF significantly, e.g., global full length versus the shortest showed t=0.402, p=0.691 with high reliability ICC(95%) 0.995(0.991-0.997). Bland Altman plots showed no biases. ***Conclusion:*** Shortening acquisition time by 2 minutes, thus also reducing Adenosine infusion duration, did not affect MBF. This could reduce patient discomfort and time consumption without compromising diagnostic performance. ***References:*** (1) Krakauer M et al. J Nucl Cardiol. 2023 Dec;30(6):2790-2802.

OP-687

Reproducibility of splenic blood flow and splenic switch-off in ^{15}O-water positron emission tomography myocardial perfusion imaging

J. Jou*[1], J. Nordström[2], J. Sörensen[3], M. Lubberink[3], T. Kero[3];*
[1]Department of Medical Sciences, Clinical Physiology, Uppsala University, Uppsala, SWEDEN, [2]Center for Research and Development Uppsala/Gävleborg Country, Gävle, SWEDEN, [3]Molecular Imaging and Medical Physics, Department of Surgical Sciences, Uppsala University, Uppsala, SWEDEN.

Aim/Introduction: Myocardial perfusion imaging (MPI) with adenosine stress is widely used to diagnose ischemia in coronary artery disease (CAD). However, confirming adequate myocardial vasodilation remains a challenge. Splenic switch-off (SSO) — the reduction in splenic blood flow during adenosine stress— is considered an indirect marker of systemic and coronary vasodilation. A spleen stress/rest ratio (SSR-ratio) below 0.9 has been proposed as a threshold of adequate adenosine effect. Despite its potential, the reproducibility of quantitative splenic perfusion measures is not well established. This study aimed to evaluate the reproducibility of splenic blood flow and SSR-ratio using ^{15}O-water PET. ***Materials and Methods:*** Twenty-one patients with suspected CAD underwent same-day test-retest ^{15}O-water PET MPI at rest and during adenosine stress. All subjects were asked to abstain from caffeine for 24 hours before imaging. Splenic blood flow was quantified at rest and stress using 2D regions of interest (ROIs) in the spleen in full field-of-view parametric blood flow (K1) images. The SSR-ratio was calculated as stress/rest splenic blood flow. Reproducibility was assessed using the repeatability coefficient (RC = 1.96 × SD of differences), mean test-retest differences, and within-subject coefficient of variation (wCV). ***Results:*** Three subjects were excluded from the analysis: two subjects due to suspected caffeine intake between test and retest (a SSO effect and increase in stress myocardial blood flow (MBF) was observed during test, but not during retest); and one subject due to suspected caffeine intake prior to the test (a paradoxical splenic perfusion response —higher splenic blood flow during stress— and low stress MBF and myocardial flow reserve was observed during both test and retest). Eighteen patients (44% female) were thus included in the final analysis. Mean splenic blood flow was 1.13 ± 0.33 and 1.08 ± 0.33 mL/min/g at rest , and 0.20 ± 0.19 and 0.18 ± 0.17 mL/min/g during stress, for test and retest respectively. Mean SSR-ratio was 0.16 ± 0.13 and 0.18 ± 0.16 for test and retest, respectively. SSR-ratios were <0.6 in all patients. The RC of SSR-ratio was 0.38, corresponding to 221% of the mean, with a mean absolute relative difference of 76%, and wCV of 80%. ***Conclusion:*** Splenic blood flow during adenosine stress demonstrates high variability. Nevertheless, SSR-ratios

were <0.6 in all subjects, indicating consistent and optimal SSO and supporting its use as a quantitative biomarker of adequate adenosine response.

1508

Tuesday, October 7, 2025, 15:00 - 16:30
Room 115

Joint Symposium 7 - Inflammation & Infection Committee / EUSEM: The Role of Nuclear Medicine Imaging in Intensive Care Unit (ICU) Patients

OP-688
Infection and Inflammation in ICU Patients
H. Bracht; *Department of Anesthesiology, Intensive Care, Emergency Medicine, Transfusion Medicine, and Pain Therapy, University Hospital of Bielefeld, Campus Bielefeld-Bethel, Bielefeld, GERMANY.*

OP-689
Patient Preparation, Transport Logistics and Safety
J. Pillay; *Department of Critical Care, University Medical Center Groningen, University of Groningen, Groningen, NETHERLANDS.*

OP-690
Diagnostic Performance of FDG PET/CT in ICU Patients
E. Romano Gargarella; *Institute of Nuclear Medicine, Università Cattolica del Sacro Cuore, Rome, ITALY.*

1509

Tuesday, October 7, 2025, 15:00 - 16:30
Room 133+134

e-Poster Presentations Session 11 - AI Committee: AI e-Poster Presentations Session

EPS-220
SuPro-MPI: Deep Learning-based Supine-to-Prone Transformation of ^{99m}Tc-MIBI SPECT MPI
G. Hajianfar[1], *P. Mohammadi Kazaj*[2], *Y. Salimi*[1], *S. Bagheri*[3], *Z. Mansouri*[1], *A. Aghaee*[4], *M. Mogharrabi*[5], *M. Ghodsirad*[6], *A. Khorasanchi*[7], *E. Askari*[4], *M. Sehati*[8], *F. Shirdel*[7], *A. Sanaat*[1], *I. Shiri*[2], *H. Zaidi*[1];
[1]*Division of Nuclear Medicine and Molecular Imaging, Geneva University Hospital, Genève, SWITZERLAND,* [2]*Department of Cardiology, Inselspital, Bern University Hospital, University of Bern, Bern, SWITZERLAND,* [3]*Department of Nuclear Medicine, Children Medical Center, Tehran University of Medical Sciences, Tehran, IRAN, ISLAMIC REPUBLIC OF,* [4]*Department of Nuclear Medicine Research Center, Mashhad University of Medical Sciences, Mashhad, IRAN, ISLAMIC REPUBLIC OF,* [5]*Nuclear Medicine department, 5 Azar Hospital, Golestan University of Medical Sciences, Gorgan, IRAN, ISLAMIC REPUBLIC OF,* [6]*Department of Nuclear Medicine, Shohada Tajrish Hospital, Shahid Beheshti University of Medical Science, Tehran, IRAN, ISLAMIC REPUBLIC OF,* [7]*Razavi Cancer Research Center, Razavi Hospital, Imam Reza International University, Mashhad, IRAN, ISLAMIC REPUBLIC OF,* [8]*Comprehensive Cancer Center, Hashemi Rafsanjani Hospital, Tehran, IRAN, ISLAMIC REPUBLIC OF.*

Aim/Introduction: Prone positioning in SPECT myocardial perfusion imaging (MPI) is used to reduce attenuation artifacts caused by the diaphragm in the inferior wall and the breast tissue in the anterior and anteroseptal walls. SPECT/CT-based attenuation correction may introduce some artifacts and is not available in all centers. Due to the limitations of prone image acquisition in patients with physical limitations (obesity or large breasts), this technique is not feasible for all patients. Artificial intelligence (AI) has shown promising results in attenuation correction for SPECT MPI. The aim of this study is to use a deep learning model to synthesize prone-position images from supine acquisitions, thereby eliminating the need for acquiring prone images. ***Materials and Methods:*** We employed 7,472 paired supine and prone SPECT MPI scans with ^{99m}Tc-MIBI collected from five centers. Two centers (1,140 cases) were reserved for external test set, while the remaining 6,332 cases were used for model training and validation. PyTomography was used for image reconstruction. A nnUNetv2 model was used for automatic segmentation of the left ventricle (LV), trained on an independent dataset consisting of 540 SPECT MPI scans using 5-fold cross-validation. The trained model was applied to all images for LV delineation, after which each image was cropped to a bounding box surrounding the LV based on the segmentation output. Rigid registration was subsequently performed to align supine images with their corresponding prone images. For model training, we employed SwinUNETR architecture. The synthetic prone images and supine images were compared to the prone images as standard of reference using structural similarity index (SSIM), peak signal-to-noise ratio (PSNR), mean relative error (MRE%), and mean absolute relative error (MARE%) metrics. ***Results:*** The mean Dice and IoU for LV segmentation were 0.91 and 0.84, respectively. The quantitative evaluation demonstrated that the synthetic prone images were more similar to the ground truth prone images in comparison with the original supine images, achieving higher SSIM (90.49 ± 8.46 vs. 87.40 ± 8.23) and PSNR (24.17 ± 2.43 vs. 22.88 ± 2.37), lower MRE% (2.80 ± 19.14 vs. 7.31 ± 21.46) and MARE% (27.58 ± 15.17 vs. 44.23 ± 19.24). ***Conclusion:*** This study demonstrates the feasibility of synthesizing prone SPECT MPI from supine acquisitions. The synthetic prone images have the potential to eliminate the need for additional prone image acquisition, particularly in patients with physical limitations, obesity, or large breasts and providing complementary diagnostic information using only supine imaging.

EPS-221
Evaluation of histo-image based Fast PET reconstruction method in whole-body 82-Rubidium blood-flow studies with a LAFOV PET scanner
I. Brovedani[1,2], *M. Morini*[1,2], *M. Millardet*[3,4], *M. De Francisci*[2], *Y. Zheng*[3], *D. Bharkhada*[3], *M. Conti*[3], *L. Mercolli*[1], *M. Castellaro*[2], *M. Veronese*[2,5], *A. Rominger*[1], *F. Caobelli*[1], *H. Sari*[1,6];
[1]*Department of Nuclear Medicine, Bern University Hospital, Bern, SWITZERLAND,* [2]*Department of Information Engineering, University of Padova, Padua, ITALY,* [3]*Siemens Medical Solutions, USA Inc., Knoxville, TN, UNITED STATES OF AMERICA,* [4]*Department of Radiology, University of Pennsylvania, Philadelphia, PA, UNITED STATES OF AMERICA,* [5]*Department of Neuroimaging, Kings College London, London, UNITED KINGDOM,* [6]*Siemens Healthineers International AG, Zurich, SWITZERLAND.*

Aim/Introduction: Deep learning-based PET image reconstruction has gained increasing attention due to its fast reconstruction times and low-count imaging capabilities. Fast reconstruction is particularly valuable for dynamic PET imaging, where multiple frames are needed to capture tracer kinetics. Long axial field-of-view PET scanners enable total-body quantitative blood-flow imaging, allowing measurements across multiple organs of interest beyond the myocardium. This study provides the first systematic evaluation of FastPET(1,2), which uses multi-angular histo-images and attenuation correction factors as inputs to a 3D-UNET to reconstruct PET images in approximately 20 seconds(2), in whole-body 82-Rubidium blood flow imaging. ***Materials and Methods:*** Twenty patients underwent whole-body rest/stress 82-Rubidium PET scans using a LAFOV PET/CT system. List-mode PET data were acquired for 7 minutes at both rest and stress conditions, starting just before administration of 370 MBq of 82-Rubidium. PET data were reconstructed into 35 frames using FastPET and using OSEM to serve as reference reconstructions. Furthermore, static images were reconstructed using FastPET and OSEM

from the last 3.5 minutes. Volumes of interest were segmented semi-automatically in lungs, kidneys, spleen, aorta, liver, and myocardium. Time activity curves (TACs) and mean uptake values were computed using dynamic and static images reconstructed with both methods. Signal-to-noise (SNR) was computed in aorta. TACs were fitted with 1-tissue-compartment model to extract K_1 values. Pearson correlation and paired t-tests were used for statistical comparison. ***Results:*** FastPET and OSEM static images showed close visual resemblance, with FastPET images appearing smoother. The mean SNR was higher in FastPET (6±2 at rest and 5±2 at stress) than in OSEM (3±1 at rest and stress). Uptake value measurements from FastPET static images correlated strongly with OSEM across all organs ($r>0.97, p<0.05$). The mean percentage differences in organ uptake values measured with Fast PET, using OSEM as the reference, ranged from -1.95±1.95 % to 3.08±3.33%. A strong agreement was particularly observed in myocardium values, where the percentage difference in uptake values was -0.65±2.58%(rest) and -0.55±2.41%(stress) with no statistically significant difference (r=0.15 and 0.22 respectively). K_1 estimates with FastPET demonstrated strong correlation with (r=0.97 at rest and r=0.92 at stress, with mean percentage differences of -4.07±7.03% (rest) and -8.51±13.38% (stress). ***Conclusion:*** FastPET reconstruction yields higher SNR and comparable quantitative accuracy to OSEM in dynamic 82-Rubidium PET imaging. Uptake and kinetic parameter (K_1) estimates from FastPET showed strong agreement with OSEM, supporting its potential use for dynamic 82-Rubidium studies. ***References:*** 1)Whiteley W.et al.,IEEE NSS&MIC,2020, 2)Millardet M.et al.,IEEE NSS&MIC,2023.

EPS-222

Feasibility Study of Deep Learning-Based Low-Dose PET and Accelerated MR Imaging in PET/MR

Y. Xu;
Hangzhou Universal Medical Imaging Diagnostic Center, Hangzhou, CHINA.

Aim/Introduction: Positron Emission Tomography/Magnetic Resonance (PET/MR) imaging requires high doses of radioactive tracers for PET and prolonged MR scanning times to ensure diagnostic accuracy, which raises concerns about radiation exposure risks and patient discomfort. While reducing PET tracer doses shortens radiation exposure, low-dose PET (L-PET) images suffer from increased noise and artifacts. Similarly, accelerated MR scans introduce motion artifacts and reduced spatial resolution, further compromising image quality. Reconstructing high-quality full-dose PET (F-PET) images from L-PET and enhancing accelerated MR scans using deep learning presents a promising solution to address both challenges. ***Materials and Methods:*** In this study, L-PET data were simulated by retaining 10% of the original tracer dose, while accelerated MR data were generated by subsampling 20% of k-space data. A dual-branch deep learning framework, **FusionNet-DSR**, was proposed to simultaneously reconstruct F-PET (100% dose) from L-PET (10% dose) and restore high-resolution MR images from accelerated scans. FusionNet-DSR integrates a transformer-enhanced generative adversarial network (GAN) for PET reconstruction and a deformable convolutional network with spatial-frequency attention for MR super-resolution. The framework was trained on 12,000 paired PET/MR slices from 50 oncology patients and validated on 30 independent cases. Performance was evaluated using peak signal-to-noise ratio (PSNR), structural similarity index (SSIM), and normalized root mean square error (NRMSE) for PET, alongside edge sharpness (ES) and artifact suppression ratio (ASR) for MR. Six state-of-the-art models—ResGAN, U-Net++, 3D-RCAN, CyclePET-MR, and two task-specific networks—were compared. Two radiologists blindly assessed diagnostic consistency between original and reconstructed images. ***Results:*** FusionNet-DSR achieved superior results: PET reconstruction yielded the highest PSNR (31.2±2.9) and SSIM (0.945±0.04), with the lowest NRMSE (0.039±0.011), while MR enhancement attained an ES of 92.4%±3.1 and ASR of 88.7%±2.8, outperforming all competitors. Bland-Altman analysis confirmed narrow limits of agreement (−0.18 to 0.19 for PET SUV; −1.2% to 1.1% for MR spatial accuracy), and paired t-tests revealed no significant differences in radiologists' diagnostic scores ($p > 0.05$) between reconstructed and original images. The dual-branch design effectively preserved metabolic details in PET and anatomical structures in MR, with 40% faster inference than cascaded single-task models. ***Conclusion:*** FusionNet-DSR demonstrates the feasibility of jointly reducing PET tracer doses and shortening MR scan times without compromising diagnostic quality. This approach holds potential to enhance patient safety and operational efficiency in clinical PET/MR workflows.

EPS-223

MlPET: A Fast Localized Machine Learning Approach for Probabilistic PET Image Reconstruction Using Informed Priors - Application to Phantom data

T. M. Hansen[1], *N. L. Christensen*[2], *M. H. Vendelbo*[3,2];
[1]*Department of Geoscience, Aarhus University, Aarhus, DENMARK,* [2]*Department of Nuclear Medicine & PET, Aarhus university Hospital, Aarhus, DENMARK,* [3]*Department of Biomedicine, Aarhus University, Aarhus, DENMARK.*

Aim/Introduction: Positron Emission Tomography (PET) imaging faces inherent limitations in noise and resolution that affect clinical diagnosis, particularly for small lesion detection. This study aims to develop and evaluate MlPET, a novel fast localized machine learning approach for probabilistic PET image reconstruction that addresses these limitations by integrating Point Spread Function (PSF) modeling, spatially correlated noise characterization, and informed Priors. ***Materials and Methods:*** We implemented a neural network-based method that transforms the traditional inverse sampling problem [1] into a computationally efficient local approach. The method incorporates a local neighborhood analysis strategy where posterior statistics are considered for subsets of model parameters using reconstructed PET data around central pixels. This approach was evaluated using phantom data across three different PET scanners (Vision Quadra, Biograph Vision 600, and Discovery MI) with acquisition times ranging from 1 to 900 seconds. Performance was assessed using quantitative metrics including Contrast Recovery Coefficient (CRC), Coefficient of Variation (COV), spatial resolution (FWHM), and visual assessment of lesion detectability. ***Results:*** MlPET achieved substantially improved quantitative performance compared to conventional reconstruction methods. For the smallest spheres (10mm), MlPET reached CRC values approaching 1.0 (0.99 at 900 seconds) compared to 0.56 for conventional PET. Noise characteristics showed approximately tenfold reduction in COV at extended acquisition times. Spatial resolution improved from approximately 2mm FWHM with conventional methods to 0.6mm FWHM with MlPET, representing a 3.5-fold improvement. Most significantly, MlPET at 40-80 seconds acquisition time outperformed conventional PET at 900 seconds across key image quality metrics, suggesting a potential 10-20 fold reduction in required scan time while maintaining or improving diagnostic quality. ***Conclusion:*** The MlPET approach demonstrates significant potential for enhancing PET image quality, particularly for small lesion detection, while enabling shorter scan times or reduced radiation exposure. By integrating PSF modeling, noise characterization, and informed priors through a localized neural network approach, this methodology addresses the traditional trade-off between noise reduction and resolution enhancement. While these phantom-based results represent an idealized scenario with well-matched prior information that may not fully translate to clinical applications, they clearly demonstrate the theoretical boundaries of what could be achieved. These findings suggest MlPET could

improve diagnostic capabilities in oncology applications requiring detection of small lesions, potentially transforming clinical workflows through more efficient scanner utilization. ***References:*** [1] Hansen, T.M., et al. "Probabilistic deconvolution of PET images using informed priors." Frontiers in Nuclear Medicine 2 (2023): 1028928.

EPS-224

Assessment of Deep Learning Attenuation Correction for Myocardial Perfusion Scintigraphy on a Dedicated Cardiac CZT-SPECT Camera: Comparison with [^{82}Rb] PET-CT

M. Westerman[1], *P. Bharadwaj*[1], *G. Keramida*[1], *L. Munemo*[2], *K. Wechalekar*[1], *L. Hossen*[1];
[1]*Royal Brompton Hospital, London, UNITED KINGDOM,* [2]*Auckland City Hospital, Auckland, NEW ZEALAND.*

Aim/Introduction: TruCorr, a deep learning-based attenuation correction method developed for the D-SPECT CZT cardiac camera for Myocardial Perfusion Scintigraphy (MPS), offers potential for attenuation correction (AC) utilising patient emission data. Traditionally 2 imaging positions are acquired, upright and supine, to mitigate attenuation artefacts. This study compares performance of D-SPECT supine [^{99m}Tc]Tetrofosmin MPS data including TruCorr-AC against [^{82}Rb] PET-CT MPS to explore its effectiveness and potential to support single-position D-SPECT imaging. ***Materials and Methods:*** Nineteen patients (15/19 males, age: 48-91, BMI: 20-39.8 kg/m^2) with SPECT and PET-CT scans within one year without major clinical events were selected. Most patients had underlying coronary artery disease. A blinded assessment was performed by two experts comparing D-SPECT stress and rest supine images without AC (Set-1) to D-SPECT stress and rest supine images with TruCorr-AC (Set-2), and to PET dynamic, stress and rest supine images with CT-AC (Set-3). Assessed parameters included image quality, presence, location, and correction of attenuation artefacts, vascular distribution, summed perfusion and reversibility percentages for stress, rest and difference respectively (SS%, SR%, SD%). Statistical analysis included two-tailed sign test, Wilcoxon signed-rank test, and McNemar's test. ***Results:*** Image quality was comparable between Set-2 and Set-3 ($p>0.05$). Attenuation artefacts could be identified in 5/19 Set-1, 14/19 Set-2, and 18/19 Set-3 cases. In absence of AC data, experts faced challenges determining attenuation artefacts in 13/19 cases, resulting in significant differences between Set-1 vs Set-2 ($p=0.0117$) and Set-1 vs Set-3 ($p=0.0005$). This also affected artefact location interpretation between Set-1 and Set-3 ($p=0.0024$). Most artefacts were in the inferior wall, extending to the septum, lateral walls, and some anterior walls. In 4/12 cases, Set-3 appeared to fully correct attenuation artefacts that Set-2 only partially corrected. Although there were observable differences in vascular distribution (e.g. RCA, LAD, CX), no significant statistical differences were found. RCA and LAD were abnormal on Set-1 (RCA: 7/19; LAD: 6/19) and Set-2 (6/19 in both, RCA & LAD) but normal on Set-3. No significant differences were found in SD%, and SS%. However, SR% differed significantly: Set-1 vs Set-3 ($p=0.0093$) and Set-2 vs Set-3 ($p=0.0048$), with PET-CT producing minimal defects. ***Conclusion:*** D-SPECT MPS imaging in supine position with TruCorr-AC improves image quality and confidence compared to SPECT alone for attenuation artifacts. TruCorr-AC gives a conservative correction for attenuation compared to PET-CT. It has the potential for achieving outcomes closer to [^{82}Rb] PET-CT. Further development could support moving to single position supine imaging.

EPS-225

Feasibility Study of Deep Learning-Based Low-Dose PET and CT Imaging in PET/CT

Y. Xu;
Hangzhou Universal Medical Imaging Diagnostic Center, Hangzhou, CHINA.

Aim/Introduction: Positron Emission Tomography/Computed Tomography (PET/CT) imaging necessitates high doses of radioactive tracers for PET and elevated radiation exposure from CT scans, raising concerns about cumulative radiation risks and patient safety. While reducing PET tracer doses decreases radiation burden, low-dose PET (L-PET) images exhibit amplified noise and quantitative inaccuracies. Similarly, lowering CT radiation doses (L-CT) introduces noise, streak artifacts, and compromised contrast resolution, further degrading diagnostic utility. Reconstructing high-quality full-dose PET (F-PET) images from L-PET and enhancing L-CT scans using deep learning offers a synergistic strategy to mitigate these dual challenges. ***Materials and Methods:*** In this study, L-PET data were simulated by retaining 10% of the original tracer dose, while L-CT data were generated by reducing tube current to 20% of standard protocols. A hybrid deep learning framework, **DualResNet-CTR**, was developed to jointly reconstruct F-PET (100% dose) from L-PET and restore high-fidelity CT images from L-CT. DualResNet-CTR combines a multi-scale residual network with channel attention for PET denoising and a transformer-based U-Net with edge-preserving constraints for CT artifact suppression. The model was trained on 15,000 paired PET/CT slices from 60 oncology patients and validated on 40 independent cases. Performance was evaluated using peak signal-to-noise ratio (PSNR), structural similarity index (SSIM), and standardized uptake value (SUV) error for PET, alongside Hounsfield unit (HU) accuracy, noise reduction rate (NRR), and artifact index (AI) for CT. Five state-of-the-art models—DeepPET, CT-GAN, DenseUNet, JointRecon-Net, and a cascaded single-task network—were benchmarked. Two radiologists performed blinded assessments of diagnostic concordance between original and reconstructed images. ***Results:*** DualResNet-CTR achieved superior performance: PET reconstruction yielded the highest PSNR (32.1±2.5) and SSIM (0.953±0.03), with minimal SUV error (3.8%±1.2), while CT enhancement demonstrated HU accuracy of 98.6%±1.4, NRR of 85.3%±4.1, and AI reduction of 79.5%±3.6, surpassing all competitors. Bland-Altman analysis showed narrow limits of agreement (−0.22 to 0.25 for PET SUV; −2.1% to 1.9% for CT HU values), and Wilcoxon signed-rank tests confirmed no significant differences in radiologists' diagnostic confidence scores ($p > 0.05$) between reconstructed and original images. The integrated architecture effectively preserved metabolic quantification in PET and anatomical fidelity in CT, with 35% faster inference than sequential single-modality models. ***Conclusion:*** DualResNet-CTR validates the feasibility of concurrently reducing PET tracer doses and CT radiation exposure without sacrificing diagnostic accuracy. This approach may significantly enhance patient safety and streamline clinical PET/CT workflows.

EPS-226

Cross-Modal Synthesis of Tau-PET Images from Amyloid-PET Scans Using Deep Learning

Y. Hu[1], *D. E. Peretti*[2], *V. Garibotto*[1], *A. Sanaat*[1], *H. Zaidi*[1];
[1]*Division of Nuclear Medicine and Molecular Imaging, Geneva University Hospital, Geneva, SWITZERLAND,* [2]*Laboratory of Neuroimaging and Innovative Molecular Tracers (NIMTlab), Geneva University Neurocenter and Faculty of Medicine, University of Geneva, Geneva, SWITZERLAND.*

Aim/Introduction: The deposition of amyloid-β plaques and the accumulation of neurofibrillary tau tangles are two primary pathological hallmarks of Alzheimer's disease (AD). Studies suggest a complex interplay between tau protein and amyloid plaques. Flortaucipir (FTP) PET imaging is crucial for

understanding AD progression and surpasses Amyloid-PET in predicting cognitive decline. However, the clinical application of FTP-PET is hindered by high costs and limited availability. This study proposes a deep learning framework leveraging SwinUnetR to synthesize FTP-PET images from Amyloid-PET scans, aiming at reducing patient burden, minimize radiation exposure, and improve diagnostic efficiency. ***Materials and Methods:*** A dataset from the Alzheimer's Disease Neuroimaging Initiative (ADNI) and hospital university Geneva (HUG) memory center comprising 415 patients with Amyloid-PET tracers including ^{18}F-Florebetaben (FBB), ^{18}F-Florbetapir (FBP), and ^{18}F-Flutemetamol (FMM) was used to develop a cross-modal synthesis model. The model was trained using five-fold cross-validation with mean squared error loss. Given the regional accumulation patterns of tau protein, a CenTauR mask including relevant regions was generated and multiplied by PET images to focus the model on these regions. The synthesized FTP-PET images were evaluated using quantitative metrics, including peak signal-to-noise ratio (PSNR), structural similarity index (SSIM), mean relative error (MRE), mean relative absolute error and absolute error. ***Results:*** The model successfully synthesized realistic FTP-PET images for all tracers (FBB, FBP, FMM) (Figure 1). As shown in Table 1, the MRE for FTP generated using FBB images was 0.23 ± 1.02%, 0.2 ± 1.27% for FTP generated using FBP, and 0.28 ± 1.11% for FTP generated using FMM. Figure 2 presents regional error analyses, demonstrating minimal error values: FTP from FBB had errors ranging from -0.025 to 0.005 standardized uptake value ratio (SUVR), FTP from FBP had errors ranging from -0.005 to 0.005 SUVR, and FTP from FMM had errors ranging from -0.03 to 0.01 SUVR. ***Conclusion:*** This study proposes and validates a cross-modal image generation method that synthesizes accurate FTP-PET from Amyloid-PET images without requiring additional PET scans, thus simplifying AD diagnostic workflows.

EPS-227

Deep Learning Model for Denoising and Positron Range Correction for Clinical Gallium-68 PET/CT Scanning

P. Gavriilidis[1,2,3], *R. Wierts*[1], *F. M. Mottaghy*[1,4], *M. Koole*[3];
[1]*Maastricht UMC+, Maastricht, NETHERLANDS,* [2]*Maastricht University, Maastricht, NETHERLANDS,* [3]*KU Leuven, Leuven, BELGIUM,* [4]*RWTH Aachen University Hospital, Aachen, GERMANY.*

Aim/Introduction: Gallium-68 (^{68}Ga) features larger positron range than Fluorine-18 (^{18}F), which can be compensated via positron range correction (PRC), as was demonstrated in a previous patient study [1]. Meanwhile, deep learning models (DLMs) have been employed to denoise PET images, thus enabling a reduction in scan time or injected activity. In this study, a DLM was developed to perform both ^{68}Ga-specific PRC and denoising on clinical ^{68}Ga-PET/CT data. ***Materials and Methods:*** List-mode PET/CT data from 76 patients scanned with ^{68}Ga-DOTATOC (1.5 MBq/kg) were split into 50% count subsets. High-count data were reconstructed using Q.Clear including Point-Spread-Function (PSF) modeling and Time-of-Flight (ToF) information, both with and without a tissue-independent PRC (β=600 and β=700, respectively) [1]. Low-count data were reconstructed with Q.Clear, including PSF and ToF but without PRC (β=700). A DLM based on U-Net was trained to map reconstructed low-count PET data without PRC to their corresponding high-count PET data with PRC. The scans were divided into training (54), validation (10), and test (12) sets. Model performance was evaluated by comparing the coefficient of variation (COV) in liver, as a measure for noise levels between the low-count, DLM and high-count PET data. Additionally, the maximum standardized uptake value (SUV_{max}) and contrast-to-noise ratio (CNR) of corresponding tumor lesions between low-count, DLM and high-count PET images were compared. Statistical analysis was performed using the Wilcoxon signed-rank test (α=0.05), with Bonferroni correction for multiple comparisons. ***Results:*** The low-count PET data without PRC demonstrated significantly higher noise levels (28.2%, p=0.002), reduced SUV_{max} (-10.6%, p=0.002), and lower CNR (-20.5%, p<0.001) compared to the high-count PET images with PRC. The DLM achieved noise levels comparable to high-count PET data with and without PRC, as no statistically significant COV differences were observed (p=1). For soft tissue lesions (23), the DLM resulted in a reduced SUV_{max} (-8.7%, p<0.001) and similar CNR (p=0.5) compared to high-count PET data with PRC. When compared to high-count PET data without PRC, the DLM increased the CNR (7.6%, p=0.005), while no statistically significant difference was observed for SUV_{max} (p=1). ***Conclusion:*** The DLM provided sufficient denoising performance to enable a 50% reduction in acquisition time for clinical ^{68}Ga PET/CT imaging while maintaining image quality. However, addressing simultaneously the longer positron range of ^{68}Ga with a DLM appears to be less effective than incorporating a PRC directly into the high-count ^{68}Ga-specific PET reconstruction of patient scans. ***References:*** [1] Gavriilidis P, et al., EJNMMI, 2025.

EPS-228

Image quality and lung nodule detectability in LAFOV PET: quantitative and qualitative evaluation

A. Spataro*, A. Franchini, S. Capitanio, A. Scarale, L. Airo' Farulla, G. Cabrini, E. Gay, C. Rossetti;*
Nuclear Medicine Unit, Dipartimento Ematologia, Oncologia e Medicina Molecolare, ASST Niguarda, Milan, ITALY.

Aim/Introduction: Large Axial Field-of-View (LAFOV) PET/CT systems offer increased sensitivity and enable ultra-fast acquisitions with lower injected activity. This opens new possibilities for faster, lower-dose protocols, especially relevant in the evaluation of solitary pulmonary nodules, where lesion detectability and image quality are essential. In this study, we aimed to assess how different reconstruction methods, including both standard and AI-based techniques, perform in a LAFOV PET setting, using various acquisition durations. ***Materials and Methods:*** In this retrospective study, data were collected from 40 patients (21 men and 19 women; mean age 67.6 years) who underwent [^{18}F]FDG PET/CT for characterization of indeterminate pulmonary nodules between January 1 and March 31 2025. Patients were all scanned 60 minutes after FDG injection on a LAFOV PET/CT system featuring 148 cm Axial Field of View. A 3-minute acquisition was performed on each patient, and 4 image sets were reconstructed: standard OSEM algorithm at 3 minutes, a new iterative algorithm (Hyper iterative) at 30 seconds, a deep learning-based algorithm (DPR) at 3 minutes and the same DPR algorithm at 30 seconds. For every reconstruction, we analyzed SUVmax, SUVmean, SUVpeak, signal-to-noise ratio (SNR), and tumor-to-background ratio (TBR). A total of three nuclear medicine physicians analyzed all sets of images, blinded to reconstruction method, scoring overall image quality, background noise, and nodule definition on a four-point scale. Inter-reader agreement was determined using Fleiss' kappa. We further examined the relationship between visual scores and quantitative imaging metrics using Pearson's correlation coefficient. ***Results:*** DPR at 30 seconds provided the best TBR and SNR results, significantly outperformed standard OSEM at 3 min reconstruction ($p < 0.001$) and showed statistically and clinically significant improvements, enhancing lesion visibility, visual scores and interpretability, especially in small nodules. The visual assessment also favored the DPR reconstructions, during which the DPR 3 minutes and DPR 30 seconds demonstrated the highest average scores. Inter-reader agreement was very good for all visual criteria (kappa: 0.77-0.94). Of the visual features, nodule definition correlated the most with quantitative parameters, particularly SUVmax ($R = 0.70$), SUVpeak ($R = 0.58$), and TBR ($R = 0.66$). SUVpeak values showed excellent consistency across all reconstruction methods ($R > 0.99$). ***Conclusion:*** DPR-based reconstruction, even with just 30 seconds of acquisition, provides excellent image quality and

lesion detectability, outperforming standard protocols. SUVpeak and nodule definition proved to be the most reliable indicators. These results support the clinical adoption of AI-based methods, enabling faster, lower-dose PET imaging without compromising diagnostic performance.

EPS-229

Study of Different Partial Volume Correction Methods in Tau PET Imaging for Alzheimer's Disease

A. Rohmah[1], *K. Lin*[2], *I. Hsiao*[1,2];
[1]*Chang Gung University, Taoyuan, TAIWAN,* [2]*Department of Nuclear Medicine, Chang Gung Memorial Hospital, Taoyuan, TAIWAN.*

Aim/Introduction: Partial volume effect (PVE) leads to the degradation of the quantitative accuracy of the PET imaging. This study compares different partial volume correction (PVC) methods in [18F] APN-1607 ([18F]-Florzolotau) to assess their impact on image quantification for Alzheimer's Disease. ***Materials and Methods:*** A total of 149 subjects, including 42 normal control (NC), 43 mild cognitive impairment (MCI), and 64 Alzheimer's disease (AD), underwent [18F] APN-1607 tau PET and MRI imaging. The T1 MRI images were co-registered with the corresponding PET images, segmented using FastSurfer, and merged into 48 regions. All PET images were corrected by Muller-Gartner (MG), Multi-Target Correction (MTC), Region-Based Voxel-Wise Correction (RBV), Iterative Yang (IY), Richardson-Lucy (RL), and Van-Cittert (VC) methods using the PETPVC toolbox. The crus was used as the reference region to generate the standardized uptake value ratio (SUVR). The percentage of group differences between uncorrected and corrected SUVR and Cohen's d-effect sizes of the Braak stage VOIs were evaluated. ***Results:*** The result showed increasing in SUVR values after PVC in all groups. MG led the highest percentage, with increased SUVR by 9%, 14%, and 18% in NC; 19%, 26%, and 30% in MCI; and 28%, 41%, and 46% in AD for Braak stage I/II, III/IV, and V/VI, respectively. A similar trend in the MTC, with increases of 5%, 10%, and 11% in NC; 12%, 20%, and 21% in MCI; and 19%, 33%, and 32% in AD. In MCI vs NC, the effect sizes before PVC were 0.66, 0.74, and 0.60 for Braak stage I/II, III/IV, and V/VI, respectively. After PVC, MG led the largest effect size in Braak stage I/II (0.86), Braak stage III/IV (0.92), and Braak stage V/VI (0.86). In AD vs NC, the effect sizes before PVC were 1.13, 1.50, and 1.40 for Braak stage I/II, III/IV, and V/VI, respectively. The MG led the largest effect size in Braak stage I/II (1.43), while the methods of MTC, RBV, and IY showed the same effect size of 1.62 in Braak stage III/IV and 1.60 in Braak stage V/VI. ***Conclusion:*** The application of the PVC methods contributes to improving the clinical group differentiation in the Braak stages between disease and non-disease. The selection of an appropriate PVC method is important for accurate quantification of the tau burden in tau PET imaging.

EPS-230

Independent external validation of NSCLC Pro Score, a clinico-radiomic predictive signature of survival for NSCLC patients treated with immunotherapy.

R. Abgral[1,2], *D. Bourhis*[1,2], *V. Bourbonne*[3], *K. Amrane*[4], *C. Le Meur*[3], *M. Geier*[5,2], *R. Floch*[1], *K. Kerleguer*[1], *P. Salaün*[1,2], *C. Nioche*[6], *I. Buvat*[6], *F. Orlhac*[6];
[1]*Molecular Imaging and Radiotheranostic Department, University Hospital of Brest, Brest, FRANCE,* [2]*UMR 1304 Inserm GETBO, Brest, FRANCE,* [3]*Radiotherapy Department, University Hospital of Brest, Brest, FRANCE,* [4]*Oncology Department, Regional Hospital of Morlaix, Morlaix, FRANCE,* [5]*Thoracic Oncology Department, University Hospital of Brest, Brest, FRANCE,* [6]*Institut Curie, Université PSL, Inserm, U1288, LITO, Orsay, FRANCE.*

Aim/Introduction: The management of patients with non-small cell lung cancer (NSCLC) treated with immune checkpoint inhibitors (ICIs) remains challenging. To help identify patients likely to benefit from ICIs, NSCLC Pro Score was developed using a cohort of 197 patients and validated on an external cohort of 86 patients [1]. This signature, which combines five [18F]FDG PET radiomic features with age, enables the classification of patients into two survival profiles. We evaluated whether the predictive power of the NSCLC Pro Score could be confirmed in a larger external cohort from a third center. ***Materials and Methods:*** A retrospective database of 264 patients with advanced NSCLC (without EGFR mutations or ALK rearrangements and ineligible for surgery) treated with first- or second-line ICIs in combination with chemotherapy was collected. The analysis of [^{18}F]FDG PET/CT images acquired before ICI initiation was performed by the team from this third center using the NSCLC Pro Score module in LIFEx [2] (www.lifexsoft.org, version 7.8.0) as follows: 1) All metabolically active lesions on baseline [18F]FDG-PET images were segmented (threshold = 4 SUV), and two spherical regions of interest were respectively drawn in the liver (14ml) and in the spleen (4ml); 2) The user provided the patient's height, weight, and age; 3) The NSCLC Pro Score combining the patient's age with the Total Metabolic Tumor Volume (TMTV), the TMTV of pleural metastases, the spleen-to-liver uptake ratio, the maximum distance between lesions (SDmax), and the standard deviation of sphericity across all lesions was automatically calculated by a dedicated module in LIFEx; 4) That module classified each patient into one of two survival profiles (low-risk or high-risk) based on the previously determined cut-off [1]. Performance was evaluated using Kaplan-Meier analysis and a log-rank test. ***Results:*** In this external validation dataset, overall survival (OS) was significantly different between low-risk (n=187) and high-risk patients (n=77), using the discrimination cut-off previously established (log-rank test: p<0.0001). One-year OS rates were 72% for low-risk patients versus 47% for high-risk patients, and 54% versus 30% at two years. ***Conclusion:*** NSCLC Pro Score was validated on an external cohort by an independent team using the dedicated module in LIFEx, demonstrating the robustness and predictive capability of this six-feature signature for NSCLC patients treated by ICI, without modifying the model parameters or the discrimination threshold between low- and high-risk patients. ***References:*** [1] Comte et al. J Nucl Med 2024. 65(suppl 2):241256. [2] Nioche et al. Cancer Res 2018;78:4786-4789.

EPS-231

Refining Prognostic Models in Metastatic Breast Cancer Patients Using Whole-Body Radiomic Features

J. Auriac[1], *N. Hovhannisyan-Baghdasarian*[1], *C. Nioche*[1], *R. Seban*[1,2], *N. Jehanno*[1,2], *M. Luporsi*[1], *F. Bidard*[3], *I. Buvat*[1], *F. Orlhac*[1];
[1]*Institut Curie, Université Paris-Saclay, Inserm LITO U1288, Orsay, FRANCE,* [2]*Institut Curie, Department of Nuclear Medicine, Paris-St-Cloud, FRANCE,* [3]*Institut Curie, Department of Medical Oncology, Paris-St-Cloud, FRANCE.*

Aim/Introduction: To determine whether whole-body PET features contribute to stratifying patients with metastatic breast cancer according to their Progression Free Survival (PFS). ***Materials and Methods:*** Baseline FDG-PET/CT images and clinical data, including molecular subtype, were retrospectively collected for 516 women with metastatic breast cancer before any treatment, chronologically divided into discovery/test sets according to the PET/CT date. All lesions were manually segmented with a threshold of 4 SUV. Based on these delineations, the number of organs including metastases (N-Organs) was calculated and four whole-body PET-radiomic features were automatically measured using LIFEx (www.lifexsoft.org, v.7.7.16 [1]): Total Metabolic Tumor Volume (TMTV), maximum distance between two lesions (Dmax), maximum uptake (maxSULmax) or average uptake (TSULmean) normalized by lean body mass across all tumor lesions. Based on these imaging features and clinical data, univariable analysis was performed using the Cox proportional hazard model. Features with p<0.05 were selected to build models combining clinical and

radiomic features. A risk score was derived and binarized by the median in the discovery set to stratify patients in two risk groups. An analysis of variance (ANOVA) was conducted to compare model performance using the χ2 test. Survival analyses were performed using the Kaplan-Meier method and log-rank test. ***Results:*** The discovery and test sets included 321 and 195 patients respectively. In univariable analysis, Age (HR=1.01; Wald test: p=.02), Negative HER2 Status (HR=1.90; p<0.001), Dmax (HR=1.17; p<0.001), TMTV (HR=1.08; p<0.001) and N-Organs (HR=1.36; p<0.001) were statistically associated with PFS. These five features were combined into four incremental multivariate models developed on the discovery set and then applied on the test set. The addition of TMTV (=M2), followed by Dmax (=M3), and then N-organs (=M4) to the clinical model (=M1) systematically improved performance (χ^2 test: p≤0.01). M4 achieved the best discrimination with a difference in the two-year progression rates between the two groups of 37% in discovery and 41% in test sets compared to M1 (discovery=21%, test=7%), M2 (29%, 19%) and M3 (26%, 32%). ***Conclusion:*** In addition to clinical data, TMTV, Dmax and the number of involved organs further improve patient stratification in metastatic breast cancer and could therefore enhance patient management. ***References:*** [1] Nioche et al. Cancer Res 2018.

EPS-232

[^{11}C]PIB Uptake in Lateral Ventricles is Associated with Neuroinflammation: A PET Imaging Study in Down Syndrome and Normal Aging

D. Mantovani, *L. C. Oliveira, O. V. Forlenza, C. A. Buchpiguel, D. de Paula Faria;*
University of São Paulo, São Paulo, BRAZIL.

Aim/Introduction: Positron emission tomography (PET) imaging studies with [^{11}C]PIB suggest that lateral ventricle uptake is a potential indicator of cerebrospinal fluid (CSF) clearance efficiency. In this study, we investigated whether [^{11}C]PIB uptake in the lateral ventricles is associated with cortical and subcortical neuroinflammation, as measured by [^{11}C]PK11195, in individuals with Down syndrome (DS), a genetically determined form of Alzheimer's disease (AD), and neurotypical (NT) controls. ***Materials and Methods:*** Age-matched DS (n=29, 41.2±12.7 years) and NT (n=35, 41.3±12.7 years) individuals underwent [^{11}C]PIB (349±29 MBq) and [^{11}C]PK11195 (336±21 MBq) PET scans during different visits (maximum 1 month between visits). PET list mode data was reconstructed into a 60 minute [^{11}C]PK11195 dynamic image and 30 minute [^{11}C]PIB static image (40-70 minute post injection). Magnetic resonance T1-weighted images were acquired simultaneously and used for brain parcellation and partial volume correction of PET images. Binding potential (BP_{ND}) and standard uptake value ratio (SUVR) parametric maps were generated for [^{11}C]PK11195 and [^{11}C]PIB, respectively, using supervised clustering and the cerebellum cortex as reference regions. Correlation analyses between regional [^{11}C]PK11195 BP_{ND} and the lateral ventricle [^{11}C]PIB SUVR were performed using Pearson and Spearman coefficients for linear and monotonic associations. ***Results:*** Lower [^{11}C]PIB SUVR in the lateral ventricles was associated with higher [^{11}C]PK11195 BP_{ND} values across multiple cortical and subcortical regions of both DS and NT individuals. In the NT group, significant negative correlations were observed in the posterior cingulate cortex (Pearson r=-0.60, p<0.001), temporal cortex (r=-0.57, p<0.001), orbitofrontal cortex (r=-0.57, p<0.001), and striatum (r=-0.56, p<0.001). In the DS group, a similar but less consistent pattern was observed, with significant negative correlations detected in the amygdala (r =-0.50, p=0.006) and fusiform cortex (r=-0.44, p=0.018). No positive correlations were observed. Spearman analyses confirmed similar monotonic associations. ***Conclusion:*** Our results demonstrate that ventricular [^{11}C]PIB uptake, as an indirect marker of CSF clearance efficiency, is inversely associated with [^{11}C]PK11195 uptake in both DS and NT individuals. The observed associations highlight a possible link between glial cell activation and CSF clearance mechanisms, suggesting a potential assessment of alterations in the glymphatic system through in vivo and non-invasive PET imaging. Our study is an indication that future investigations need to be performed on CSF clearance and its role in brain aging and AD pathogenesis.

EPS-233

Metabolic Brain Network and "Imaging-Protein" Association Analysis of Cognitive Function Recovery in Aging Rats Based on STT3A/ALG5

Z. Yang[1], *L. Chen*[1], *K. Pandya*[2], *T. Wang*[1], *B. Nie*[3], *B. Shan*[3], *Q. Liu*[4], *T. Wang*[5], *S. H. Bossmann*[6], *K. Shi*[2], *G. Zhu*[1];
[1]*Department of Nuclear Medicine, First Affiliated Hospital of Kunming Medical University, Kunming, CHINA,* [2]*Department of Nuclear Medicine, Inselspital, University of Bern, Bern, SWITZERLAND,* [3]*Beijing Engineering Research Center of Radiographic Techniques and Equipment, Institute of High Energy Physics, Beijing, CHINA,* [4]*Department of Library, First Affiliated Hospital of Kunming Medical University, Kunming, CHINA,* [5]*Institute of Neurological Disease, Translational Neuroscience Center, West China Hospital, Chengdu, CHINA,* [6]*The University of Kansas Medical Center, Department of Cancer Biology, Kansas city, KS, UNITED STATES OF AMERICA.*

Aim/Introduction: Aging populations are rapidly increasing, yet the "imaging-protein" associations or mechanisms underlying cognitive impairment in aging remain unexplored. This study integrated [^{18}F]FDG PET imaging and multi-proteomics to investigate metabolic brain networks and molecular mechanisms of cognitive recovery in aging rats. This study aimed to identify diagnostic and therapeutic targets for age-related neurodegenerative diseases impacted by aging and provide interpretable data to support AI-driven medical imaging. ***Materials and Methods:*** Eighteen 22-month-old female Sprague-Dawley rats were randomized into three groups: short-hairpin-STT3A and short-hairpin-ALG5 as experimental groups for cognitive recovery, and a control group for aging-related cognitive decline. Viral-mediated gene knockdown targeted the hippocampus, with PET imaging and multi-proteomics data collected after 8 weeks. Metabolic brain networks were built using regional SUVR and analyzed for network properties and modularity. Differential proteins and modification sites were screened from multi-proteomics data and functionally assessed. The MT-SCCALR algorithm integrated both modalities to construct an "imaging-protein" association functional matrix, validated for diagnostic potential via SVM. ***Results:*** The experimental groups enhance cognition by streamlining metabolic brain networks and optimizing modularity. Knockdown of key genes regulated recovery mainly through post-translational modifications, not total protein levels, with glycosylation sites showing common traits and phosphorylation sites indicating distinct features. The matrix pinpointed Sept8 and Grin1 as potential targets, with imaging-protein links offering diagnostic value, enabling non-invasive protein detection, and providing a molecular basis for imaging feature interpretation. ***Conclusion:*** This study advances our understanding of cognitive recovery in aging and provides a high-quality, interpretable data foundation and a data mining framework for AI-driven medical imaging.

EPS-234

Novel approach for simultaneous quantitative parametric imaging in Large Axial field-of-view PET

H. Iida[1], *N. Ono*[2], *H. Merisaari*[1], *A. E. Latva-Rasku*[1], *J. Tuisku*[1], *N. Tuomola*[1], *N. Tuomola*[1], *R. Siekkinen*[1], *V. Saunavaara*[1], *J. Knuuti*[1], *L. Nummenmaa*[1], *K. Virtanen*[1], *P. Nuutila*[1];
[1]*Turku PET Centre, Turku University Hospital and University of Turku, Turku, JAPAN,* [2]*Nara Institute of Information Science and Technology, Ikoma, FINLAND.*

Aim/Introduction: We aimed to develop novel software that calculates parametric K_1-flow images for the total body using ^{15}O-labelled water ($[^{15}O]H_2O$) and a Large Axial Field-Of-View (LAFOV) PET and investigate the administration dose dependency, the inter-scan reproducibility, and the among-organ consistency. ***Materials and Methods:*** Seven volunteers, including two lean, four mildly obese, and one severely obese, participated in the $[^{15}O]H_2O$ PET imaging with eight sequential PET scans at four different administration doses ranging from 20 to 700 MBq at 15-minute intervals. The novel parametric image calculation employed a single-tissue compartment model with the arterial blood volume fraction [1]. Calculating K_1-flow images was done with the acceleration of the fit using a PC with a graphics processing unit (GPU). The fit was then carried out on the logarithmic domain with the tolerance in the Euclidean space for further acceleration. Volumes of interest (VOIs) were selected from sixteen regions that covered an extensive range of K_1-flow. The bootstrap analysis was conducted [2] to evaluate the statistical error propagation using four scan data sets from a single volunteer, at four administration doses. The administration dose dependency and inter-scan variation were investigated using all paired data with the same administration dose. ***Results:*** Seven volunteers, including two lean, four mildly obese, and one severely obese, participated in the $[^{15}O]H_2O$ PET imaging with eight sequential PET scans at four different administration doses ranging from 20 to 700 MBq at 15-minute intervals. The novel parametric image calculation employed a single-tissue compartment model with the arterial blood volume fraction [1]. Calculating K_1-flow images was done by accelerating the fit using a PC with a graphics processing unit (GPU). The fit was then carried out on the logarithmic domain with tolerance in the Euclidean space to ensure the fit convergence. Volumes of interest (VOIs) were selected from sixteen regions that covered an extensive range of K_1-flow. The bootstrap analysis was conducted first [2] to evaluate the statistical error propagation using four scan data sets from a single volunteer, at four administration doses. The administration dose dependency and inter-scan variation were investigated using paired data with the same administration dose. ***Conclusion:*** K_1-flow values were consistent across a wide range of administration doses, with pixel-by-pixel and VOI-based fits. LAFOV PET allows a reduced administration dose of 20 MBq in the $[^{15}O]H_2O$ K_1-flow assessment in major organs. ***References:*** [1] Knuuti et al., J Nucl Med, 2024. [2] Dahlbom, et al., IEEE TNS, 2001.

EPS-235

AI-Based 3D Diffusion Model Enables High-Fidelity, Quantitatively Accurate Ultra-Low-Dose Whole-Body PET Imaging

V. Menezes[1], *M. Machado*[2], *C. Queiroz*[3], *B. Anjos*[4], *E. Almeida*[4], *A. Oliveira*[1], *M. Flamini*[1], *F. Mourato*[1], *T. Ren*[5];
[1]*Hospitals Das Clinicas Da UFPE, Recife, BRAZIL,* [2]*Hospital Universitário Professor Edgard Santos - HUPES, Salvador, BRAZIL,* [3]*Hospital Universitário Professor Alberto Antunes, Maceió, BRAZIL,* [4]*Nuclearis, Recife, BRAZIL,* [5]*Univerisade Federal de Pernambuco, Recife, BRAZIL.*

Aim/Introduction: Whole-body FDG-PET/CT is indispensable for cancer diagnosing and staging. Lowering injected activity or shortening scan duration reduces radiation burden but amplifies noise, degrading image quality. Conventional 3D AI models demand prohibitive computational memory. We present a novel AI-based 3D U-Net that restores image fidelity and quantitative accuracy in ultra-low-dose whole-body PET while remaining computationally efficient. ***Materials and Methods:*** A retrospective multicentre dataset of 2738 whole-body PET/CT examinations from scanners Siemens Biograph mCT, Siemens Biograph Horizon and GE Discovery 710 were simulated to 10%, 25 %, 50 % and 75 % of original counts, using Noise Power Spectrum simulation. In addition, 40 prospective studies were list-mode re-binned with 10% injected activity for validation. The AI-3D-U-Net couples a ResNet-50 encoder with a three-level U-Net decoder and an adaptive diffusion layer. The network was trained using mixed-precision optimization. A composite loss was used: mean-squared error, 3D gradient consistency and perceptual error. Performance was assessed on held-out 10 %-count scans using peak signal-to-noise ratio (PSNR), structural similarity index measure (SSIM), Learned Perceptual Image Patch Similarity (LPIPS) and SUVmax bias in the liver. Two blinded nuclear-medicine specialists rated diagnostic quality on a five-point Likert scale. ***Results:*** The AI-3D-U-Net achieved PSNR = 47 dB, SSIM = 0.98 and LPIPS = 0.01 on denoised volumes, against ≤37 dB, ≤0.95, ≥0.12 in the noisy data. Whole-body SUVs exhibited a mean bias of +0.10 and 95 % limits of agreement of ± 0.12 SUV. Reader evaluation confirmed non-inferior image quality versus full-count images (Likert 4.6 ± 0.4 vs. 3,5 ± 0.4; p = 0.03). End-to-end inference required 17 s per examination on a single NVIDIA RTX 3090 graphics processing unit. ***Conclusion:*** The proposed AI-3D-U-Net delivers artefact-free, quantitatively reliable reconstructions for whole-body PET acquired with as little as 1/10 of standard 5,2 MBq/Kg dose, independent of scanner vendor. Its short inference time, reader reliability and tight SUV agreement support adoption in routine clinical practice, enabling substantial reductions in dose or scan duration without compromising image quality. ***References:*** Menezes, V.O., et al. Medical Physics, 2016, 43(2), 930-938.

EPS-236

Improving the Generalization of PET Image-Enhancing Deep Learning Algorithms Through Domain Randomization. A Monte Carlo Study.

J. Poveda[1,2], *J. Gómez*[2], *F. López*[3], *G. Webber*[4], *M. Dassanayake*[4], *B. Pan*[4], *A. Reader*[4], *P. Aguiar*[1], *J. Silva*[3];
[1]*Universidad Santiago de Compostela, Santiago de Compostela, SPAIN,* [2]*Qubiotech Health Intelligence, A Coruña, SPAIN,* [3]*Reina Sofia Alzheimer Centre, CIEN Foundation, Madrid, SPAIN,* [4]*King's College London, London, UNITED KINGDOM.*

Aim/Introduction: Deep learning (DL) models for PET image enhancement are often constrained by limited variability within datasets, resulting in overfitting and poor generalization when applied to domains outside the training distribution, such as data from different scanners/centers. In this study, we propose a Monte Carlo (MC) simulation-based domain randomization (DR) strategy consisting of introducing controlled randomization of scanner characteristics, thereby expanding coverage across the domain space. We assessed the impact of this increased domain coverage by training a DL model on datasets with varying levels of diversity, thus evaluating the resulting impact on model performance. ***Materials and Methods:*** An initial dataset of 273 realistic activity maps for MC simulation was generated using a previously validated methodology[1, 2]. DR of the scanner domain was achieved by stochastically varying a curated subset of acquisition and scanner parameters, selected based on theoretical and empirical knowledge, producing a unique yet plausible scanner configuration for each case. Simulation and reconstruction were performed using SimPET[1], then both the simulated PET images and corresponding activity maps (ground truths) underwent preprocessing before DL. Five datasets with training subsets of increasing size (n = 15, 30, 60, 120, 240) were constructed, while maintaining the same validation and test sets for all the datasets. Subsequently, a separated Attention U-Net was trained for each training subset to estimate axial slices of the activity map from the corresponding simulated PET image slices, representing an idealized image enhancement task. Model performance was evaluated quantitatively using the Structural Similarity Index Measure (SSIM) and Mean Squared Error (MSE). Potential bias was assessed through voxel-wise paired t-tests between predicted and ground truth activity maps. ***Results:*** Increasing the training

set size (and thus, the number of scanners in the training dataset) from n=15 to n=240 led to approximately linear performance improvements. Compared to n=15, there were notable gains in both slice-wise metrics (SSIM +17.4%, MSE -35.3%) and volume-wise metrics (SSIM +5.3%, MSE -33.3%). Qualitatively, spatial resolution and signal-to-noise ratio (SNR) consistently improved with larger datasets. However, voxel-wise analysis highlighted localized biases in the left temporal/frontal lobes, right insula, and corpus callosum. ***Conclusion:*** Expanding domain coverage via scanner space DR led to improved model performance, indicating that this strategy constitutes a feasible and cost-efficient approach to increase PET dataset diversity and enhance generalization capabilities of DL models. ***References:*** [1]J. Paredes-Pacheco et al. Med Phys 2021; 48, 5, 2482-2493, [2]F. J. López-González et al., NeuroImage 2020; 222, 117229.

EPS-237

AI denoising enhances centiloid analysis in count-poor amyloid brain PET/CT scans

K. Knesaurek;
Icahn School of Medicine at Mount Sinai, New York, NY, UNITED STATES OF AMERICA.

Aim/Introduction: The aim of this study is to enhance centiloid analysis of count-poor amyloid brain PET/CT studies using AI-based denoising. ***Materials and Methods:*** Amyloid brain PET/CT scans were acquired in list mode using a time-of-flight (TOF) PET/CT system. Alongside the standard 10-minute acquisition, the list mode enabled reconstruction of shorter 2 min scans. Image reconstruction employed a 3D iterative Poisson-OSEM algorithm with 8 iterations and 5 subsets (8i5s), incorporating an all-pass filter, point spread function correction, and TOF correction. Low-dose CT (80 kV, 120 mAs) was used for PET attenuation correction. The reconstruction matrix was 440 × 440, yielding a pixel size of 1.65 × 1.65 mm and a slice thickness of 3.0 mm. Both the original 2-minute scan and the 2-minute scan enhanced with AI-based denoising software were visually and quantitatively compared to the gold-standard 10-minute scan. Quantitative comparisons utilized centiloid analysis and standardized uptake value ratios (SUVr), calculated for six cortical regions (anterior cingulate gyrus, inferior medial frontal gyrus, lateral temporal lobe, posterior cingulate gyrus, precuneus, and superior parietal lobule) relative to the cerebellum. Centiloid analysis standardizes amyloid PET quantification by scaling measurements to a 0-100 scale, anchored to data from young controls (≤45 years) and patients with typical Alzheimer's disease. ***Results:*** In an exemplary case, the 2-minute, AI-corrected 2-minute, and 10-minute amyloid PET scans show strong visual similarity between the AI-corrected 2-minute scan and the 10-minute scan. The centiloid value for the 10-minute scan was 47.59, with regional SUVr values of 1.36, 1.33, 1.40, 1.14, 1.20, and 1.19, respectively. The AI-denoised 2-minute scan yielded a centiloid value of 47.86, with corresponding SUVr values of 1.37, 1.35, 1.38, 1.13, 1.20, and 1.17. In both cases, the average SUVr across the six cortical ROIs was 1.27, indicating an amyloid-positive case. Z-score analysis of the 10-minute and AI-corrected 2-minute scans revealed near-identical results. ***Conclusion:*** Centiloid analysis indicates that AI-denoised 2-minute PET amyloid scans are quantitatively equivalent to standard 10-minute scans. These findings support the clinical viability of AI-enhanced denoising in improving diagnostic quality in count-poor amyloid PET/CT studies.

EPS-238

Partial Volume Correction Enables Feasible Kinetic Analysis of Brain Tumours on Short Axial Field-of-View PET Scanners: A Preliminary Study

A. Lazar[1], *P. Scifo*[2], *A. Chiti*[1,2];
[1]*Vita-Salute San Raffaele University, Milan, ITALY,* [2]*Department of Nuclear Medicine, IRCCS San Raffaele Hospital, Milan, ITALY.*

Aim/Introduction: Dynamic PET imaging plays a pivotal role in assessing tumour physiology, particularly in gliomas. However, the analysis of dynamic images is usually based on time-activity curve (TAC)'s aspect rather than kinetic parameters. Short axial field-of-view (SAFOV) scanners present a challenge in parametric imaging due to the inability to sample the image derived input function (IDIF) from large vessels like the aorta, which is achievable on long axial field-of-view scanners. This study investigates the use of partial volume correction (PVC) to enable IDIF sampling from the carotid arteries in brain tumour patients, assessing the feasibility of performing parametric imaging on SAFOV scanners. ***Materials and Methods:*** Dynamic [^{18}F]F-FET PET images were acquired on a 32-cm axial field-of-view PET scanner over 40 minutes and reconstructed using a 35-frame protocol. Two iterative deconvolution PVC methods were employed: Lucy-Richardson with 10 iterations (LR10i), and reblurred Van Cittert with 8 (VC8i) and 12 iterations (VC12i). IDIF was extracted from the carotid arteries by averaging TACs obtained from each artery using the 5 hottest connected pixels within a 2×7mm cylindrical VOI placed in each lumen. Brain tumours were segmented using isocontour, while a 7-cm diameter sphere was placed in the frontoparietal cortex for normal tissue(NT) assessment. Quantification was performed using PMOD software investigating the following kinetic models: irreversible and reversible two-tissue compartment models, MLAIR, RE-GP, and Patlak analysis. Goodness-of-fit was evaluated using R^2 and Akaike Information Criterion(AIC) in tumour and NT. Friedman and Wilcoxon signed-rank tests assessed statistical significance across reconstructions. ***Results:*** 12 patients (13 brain lesions) were included in the analysis. Patlak analysis provided the best model fit across all reconstruction methods. Friedman test showed no significant differences in AIC or R^2 values across PVC reconstructions for tumour or NT (AIC p: tumour=0.212, NT=0.117; R^2p: tumour=0.066, NT=0.469). Pairwise comparisons revealed that VC8i provided superior R^2 over both LR10i (p=0.028) and VC12i (p=0.034). In tumours, LR10i and VC12i significantly increased Patlak intercepts relative to noPVC (p<0.05), while VC8i showed no significant bias(p=0.225); Ki remained stable across all methods (p>0.05). In NT, all PVC methods significantly increased Ki (p<0.05) and trended toward higher intercepts(p=0.068), indicating potential overcorrection. ***Conclusion:*** Our preliminary findings suggest that PVC can improve Patlak analysis, but its utility depends on the parameter, tissue type, and algorithm choice. For [^{18}F]F-FET PET, VC8i emerges as a promising compromise, enhancing model fit quality without biasing Ki, though further validation against gold-standard vascular measures is needed.

EPS-239

Partial Volume Correction Improves Kinetic Modelling in Dynamic [^{18}F]FET PET: A Simulation-Based Validation Study

S. Raju[1,2], *T. Schmidt*[1], *A. J. Zounek*[1], *Y. Beqqali*[2], *E. Barci*[1], *E. Istrefi*[1], *J. Isakaj*[1], *N. L. Albert*[1], *S. Ziegler*[3,1], *L. Kaiser*[1];
[1]*Department of Nuclear Medicine, LMU University Hospital, LMU Munich, Munich, GERMANY,* [2]*Department of Physics, Technical University of Munich, Munich, GERMANY,* [3]*Department of Nuclear Medicine, Hannover Medical School (MHH), Hannover, GERMANY.*

Aim/Introduction: Dynamic PET imaging with [^{18}F]FET enables advanced tumour characterisation through pharmacokinetic modelling, but its accuracy is hindered by limited spatial resolution and noise-induced partial volume effects (PVE). This

study investigates whether partial volume correction (PVC) enhances the reliability of kinetic parameter estimation. ***Materials and Methods:*** A simulation framework based on clinical [^{18}F]FET PET scans from 21 glioma patients was developed. Time-activity curves (TACs) were extracted from segmented brain regions and used to generate ground truth parametric maps via a one-tissue compartment model (1TCM). These parametric maps were then used to generate voxel-wise dynamic PET data using the dPETSTEP (Dynamic PET Simulator of Tracers via Emission Projection) tool [1], simulating various scanner resolutions (2, 5, 8 mm FWHM) and noise levels (scale factor for number of true counts 200 000, 500 000, 1 000 000). Kinetic parameters were re-estimated from the degraded images both with and without PVC using the geometric transfer matrix (GTM) method and compared to ground truth. ***Results:*** Median differences in kinetic parameters (K1, k2, Vb) between estimated and ground truth values revealed substantial improvements after applying GTM-based PVC. At clinical resolution (5 mm), grey matter showed a median underestimation in K1 of 18% without correction, which was reduced to 1.4% post-PVC. In tumour regions, K1 underestimation decreased from 12% to 3% after correction. Similar trends were observed for k2 and Vb across all regions. At high resolution (2 mm), differences to ground truth were minimal even without correction, but PVC further improved accuracy. Variations in noise levels had only minor effects on parameter estimation compared to the dominant influence of spatial resolution and partial volume effects. ***Conclusion:*** Partial volume correction markedly improved the accuracy of kinetic modelling in dynamic [^{18}F]FET PET. This simulation-based analysis underscores the necessity of incorporating PVC into dynamic PET quantification pipelines for reliable evaluation of pharmacokinetic properties. These findings support future clinical applications aiming to enhance PET-based neuro-oncological diagnostics. ***References:*** 1. Haggstrom, I., B.J. Beattie, and C.R. Schmidtlein, Dynamic PET simulator via tomographic emission projection for kinetic modeling and parametric image studies. Med Phys, 2016. ***43***(6): p. 3104-3116.

EPS-240

Patient-specific reinforcement learning for planar-based 3D SPECT imaging synthesis

A. Lopez Montes[1], *R. Seifert*[1], *A. Delker*[2], *G. Boening*[2], *J. Wang*[1], *A. Afshar-Oromieh*[1], *A. Rominger*[1], *K. Shi*[1];
[1]*University of Bern, Bern, SWITZERLAND,* [2]*Ludwig-Maximilians-Universität in Munich, Munich, GERMANY.*

Aim/Introduction: SPECT dosimetry imaging remains as a burden in clinical practice. On the other side, 2D-planar dosimetry imaging is fast, economic and widely applied. However, it has limited accuracy and capability for tumor dosimetry assessment. Producing synthetic 3D SPECT from planar scans would provide a desired solution. However, the problem is highly ill-posed and remains unpractical even using standard AI methods. In this work we proposed a patient-specific reinforcement learning leveraging pre-therapy PET/CT data in the AI model for planar-based 3D SPECT imaging synthesis. For proof of concept, we focused on the dosimetry of ^{177}Lu-PSMA radiopharmaceutical therapy. ***Materials and Methods:*** We trained two 3DResUNet networks: one from a population dataset and another with our model using a patient-specific reinforcement learning. The inputs consisted of two (anterior and posterior) planar images (128x175x2) and the outputs were 3D maps (128x128x175; 5.7 mm) obtained from 52 total-body ^{18}F-PSMA PET/CT scans. Planar images for training were simulated from the 3D-PET to ensure matching. For the patient-specific reinforced network, we generated a dataset of 100 possible 3D uptake maps for individualized patients: first we segmented the organs from pre-therapy PET, then we applied random scaling factors to the activity in each organ (0.5-2 times the original activity) and random 3D rigid transformations, finally we simulated the corresponding planar images and the network was re-trained exclusively for patient-specific data. We validated our method on 5 simulated cases with planar images obtained from a post-therapy PET (thus knowing the ground truth 3D) and in 5 real cases from full body planar ^{177}Lu-PSMA acquisitions. In all cases the personalized network was trained from the pre-therapy PET as described above. ***Results:*** In simulations, the relative Mean Absolute Error (MAE) between the images and the ground truth was 0.92±0.33 for generic population training, which was reduced to 0.59±0.21 with our method. We computed the difference for every organ, yielding an average difference 0.97±0.97 for population-based training and 0.45±0.51 for our model. For the real cases (without a ground truth 3D activity for comparison), visual inspection exhibited better delineation of the organs for the patient specific network when compared with the generic population training. ***Conclusion:*** We have demonstrated viability of the generation of 3D maps from only two 2D planar images using patient-specific reinforcement learning. Future work is focused on improving the generative models and the 3D maps of the patients used for training with special attention to lesions.

EPS-241

Integration of Deep Learning and Radiomics for Predicting the Histologoical Classification of Peripheral Neuroblastic Tumor Base on ^{18}F-FDG PET/CT Imaging

Z. Zhou*;*
Capital Medical University, Beijing Friendship Hospital, Beijing, CHINA.

Aim/Introduction: To evaluate the performance of the clinical model, two-dimensional deep learning model (2D DL), radiomics model, and the fusion model for predicting the histological type of peripheral neuroblastic tumors (pNTs). ***Materials and Methods:*** In this retrospective study, a total of 196 pediatric patients newly diagnosed with neuroblastoma between June 2018 and December 2020 at Beijing friendship hospital were included. The cohort was divided into a training set (n=137) and a test set (n=59). The clinical model was constructed based on clinical data. The 2D DL, radiomics model were developed using 18F-fluorodeoxyglucose positron emission tomography/computed tomography (^{18}F-FDG PET/CT). Two fusion strategies were employed to constructed the fusion model: the feature based DLRad_FB model and the decision based DLRad_DB model. The receiver operating characteristic (ROC) and decision curve analysis (DCA) curves were used to evaluate the performance of the model. ***Results:*** The 2D DL features demonstrated superior diagnostic effectiveness compared to clinical model and radiomics model. The DLRad_FB model achieved the highest are under the curve (AUC) of 0.918 (95%CI: 0.866, 0.970) and 0.874 (95%CI: 0.777, 0.972) among all models in the training and test sets. Compared to the DLRad_FB model, the AUC values for the clinical, radiomics, 2D DL and DLRad_DB models were 0.733 (95%CI: 0.646, 0.819), 0.781 (95%CI: 0.700, 0.862), 0.860 (95%CI: 0.794, 0.927), 0.878 (95%CI: 0.815, 0.940) in the training set respectively. ***Conclusion:*** The Feature Based Model DLRad_FB, which combines clinical, radiomics and 2D DL date, can predict the histological type of pNTs and assist in early therapeutic strategies.

1510

Tuesday, October 7, 2025, 15:00 - 16:30
Room 116

CTE 7 - Technologists Committee - Hybrid Imaging in Differentiated Thyroid Cancer (DTC) Diagnosis and Treatment

OP-691a
Differentiated Thyroid Cancer Diagnosis and Treatment - The Current and Future Challenges
***R. Czepczyński**; Dept. of Endocrinology, Metabolism and Internal Diseases, Poznan University of Medical Sciences, Poznan, POLAND.*

OP-691b
Clinical Impact of Radioiodine Hybrid Imaging in the Management Of DTC Patients
***A. Campenni**; Unit of Nuclear Medicine, Department of Biomedical and Dental Sciences and Morpho-Functional Imaging, University Hospital of Messina, Messina, ITALY.*

OP-691c
Nuclear Medicine in Thyroid Cancer Diagnosis – An Overview
***C. Nielsen**; Nuclear Medicine educator, Gurnick Academy of Medical Arts, Concord, California, UNITED STATES OF AMERICA.*

1511

Tuesday, October 7, 2025, 15:00 - 16:30
Room 111

EU Policy Symposium 2

OP-691d
Setting the Stage: The Future of HTA in Nuclear Medicine
***N. Withofs;** Liège University Hospital, Liège, BELGIUM.*

OP-691e
The EU Regulation on Health Technology Assessment (HTAR) Applying from January 2025
***J. Spony;** Policy officer, European Commission, Directorate-General for Health and Food Safety, Unit C2 Health Technology Assessment, BELGIUM.*

OP-691f
The Impact of EU HTAR on National HTA Bodies: The Case of Belgium
***M. Neyt;** Belgian Health Care Knowledge Centre, BELGIUM.*

OP-691g
Patient-Centred Perspectives: Implications for Radioligand Therapy in Light of the New EU HTAR
***E. Briers;** Patient Representative, Europa Uomo, BELGIUM.*

OP-691h
Positioning Imaging in the HTA Process
***M. Beck;** European Society of Radiology, SWITZERLAND.*

1601

Tuesday, October 7, 2025, 16:45 - 18:15
Auditorium

CME 12 - Oncology & Theranostics Committee - Improving Breast Cancer Care: Highlights from Focus Meeting 6: Staging

OP-691i
Loco-Regional (T&N) Staging with Imaging
***T. van Nijnatten**; Maastricht University Medical Center+, Department of Radiology and Nuclear Medicine, Maastricht, NETHERLANDS.*

OP-691j
Systemic (M) Staging with Imaging
***S. Carrilho Vaz**; Champalimaud Clinical Center, Nuclear Medicine-Radiopharmacoloy, Lisbon, PORTUGAL.*

OP-691k
Expectations Towards Emerging New PET Tracers
***P. Backhaus**; Hospital Münster, Department of Nuclear Medicine, Münster, GERMANY.*

OP-691l
Nuclear Medicine Toolkit - The Answers the Oncologist Is Looking for in Clinical Practice
***A. Gennari**; University of Piemonte Orientale, Department of Oncology, Maggiore University Hospital, Novara, ITALY.*

1602

Tuesday, October 7, 2025, 16:45 - 18:15
Room 112 (Arena)

Special Track 12 - Dosimetry Committee - Round Table: Unlocking the Potential: Can Total Body PET Revolutionise Dosimetry?

OP-691m
Y-90 SIRT and Conventional PET Imaging – Technical Challenges and Quantitative Potential
***S. Gnesin**; Lausanne University Hospital and University of Lausanne, Institute of Radiation Physics, Lausanne, SWITZERLAND.*

OP-691n
Total-Body PET for Y-90 SIRT – New Opportunities for Pre- and Post-Therapy Dosimetry
***R. Abgral**; CHU of Brest, Nuclear Medicine Department, Brest, FRANCE.*

OP-691o
Future of Y-90-based Therapies: FAPI, CXCR4 and I-124 Dosimetry with TB-PET
***P. Fragoso Costa**; University Hospital Essen, Nuclear Medicine, Essen, GERMANY.*

OP-691p
Kinetic Modelling with TB-PET – Towards Quantitative Therapy Guidance
***C. Tsoumpas**; Medical Center Groningen, Nuclear Medicine and Molecular Imaging, Groningen, NETHERLANDS.*

OP-691q
Young Perspective on Dosimetry with Total-Body PET – The New Normal?
***P. Lindner**; University Hospital Tuebingen, Nuclear Medicine and Molecular Imaging, Tuebingen, GERMANY.*

1603

Tuesday, October 7, 2025, 16:45 - 18:15
Room 113

LIPS Session 12 - Inflammation & Infection Committee - Interpretation of FDG PET/CT in Common Infectious-Inflammatory Diseases

OP-691r
FDG PET Pattern Recognition in the Main Inflammatory and Infectious Diseases
G. Treglia; *Imaging Institute of Southern Switzerland, Ente Ospedaliero Cantonale, Division of Nuclear Medicine, Bellinzona, SWITZERLAND.*

OP-691s
Visual vs Semiquantitative Assessment in Cardiovascular Infections
L. Leccisotti; *Fondazione Policlinico Universitario A. Gemelli IRCCS, Department of Nuclear Medicine, Rome, ITALY.*

OP-691t
Pitfalls of FDG PET/CT in Inflammation and Infection in Adults
R. Slart; *University Medical Center Groningen, Department of Nuclear Medicine and Molecular Imaging, Groningen, NETHERLANDS.*

OP-691u
Pitfalls of FDG PET/CT in Inflammation and Infection in Paediatrics
M. Øbro Fosbøl; *Copenhagen University Hospital, Rigshospitalet Hospital/Institute, Department of Clinical Physiology and Nuclear Medicine, Copenhagen, DENMARK.*

1604

Tuesday, October 7, 2025, 16:45 - 18:15
Room 114

M2M Track - TROP Session - Radiopharmaceutical Sciences + Translational Molecular Imaging & Therapy Committee: Imaging of Non-oncological Targets

OP-692
Stabilin-2 receptorspecific radioligand ^{18}FS2P for atherosclerotic plaque PET imaging
D. Adili, *D. Zhang, Z. Li, X. Su;*
First Affiliated Hospital of Zhejiang University, School of Medicine, Zhejiang University, Hangzhou, CHINA.

Aim/Introduction: Stabilin-2 receptor overexpression on plaque macrophages represents a promising molecular target for atherosclerosis imaging. The S2P peptide (Cys-Arg-Leu-Thr-Leu-Thr-Val-Arg-Lys-Cys, CRTLTVRKC) exhibits specific binding to stabilin-2, a receptor overexpressed on macrophages within atherosclerotic plaques. This study aims to evaluate the feasibility of using the stabilin-2-targeted ^{18}F-labeled tracer (^{18}F-S2P) for positron emission tomography (PET) imaging to identify atherosclerotic plaques. ***Materials and Methods:*** ^{18}F-S2P was synthesized via standard radiochemical procedures with quality control validation. Experimental design included: 1) In vitro stability assessment in NaCl and fetal bovine serum; 2) Longitudinal micro-PET/CT imaging (0.5 h post-injection) in LDLR$^{-/-}$ mice (high-fat diet 3-12 weeks) versus chow-fed littermate controls; 3) Comparative analysis with ^{18}F-Pentixafor (CXCR4-targeted) imaging; 4) Ex vivo biodistribution studies with gamma counting and autoradiography; 5) Safety evaluation through hematological profiling (complete blood count, liver enzymes) and histopathological examination (H&E staining) of major organs. Plaque characterization employed Oil Red O lipid staining and H&E morphology analysis. ***Results:*** ^{18}F-S2P demonstrated >95% radiochemical purity and stable tracer integrity under physiological conditions (PBS: 100%; FBS: 95% at 2h). In vivo PET quantification revealed disease duration-dependent uptake (SUVmax = 0.37 ± 0.15 at 3 weeks vs. SUVmax = 0.77 ±0.15 at 12 weeks, $p<0.05$), correlating strongly with histological plaque burden. Notably, ^{18}F-S2P showed 2.7-fold higher aortic arch uptake versus controls (SUVmax = 0.77 ± 0.15 vs. SUVmax = 0.29 ± 0.25), outperforming ^{18}F-Pentixafor (SUVmax = 0.85 ± 0.07 vs. SUVmax = 0.47 ± 0.10, $p<0.05$) in lesion contrast. No significant hematotoxicity or organ damage was observed. ***Conclusion:*** This study introduces a novel stabilin-2-targeted PET probe (^{18}F-S2P) for non-invasive imaging of atherosclerotic plaques, enabling the detection of atherosclerotic inflammation.

OP-693
Superiority of αvβ6 Integrin-Targeted 68 Ga-Trivehexin over ^{18}F-FDG in Diagnosis and Therapeutic Efficacy Monitoring of Idiopathic Pulmonary Fibrosis: A Translational Study from Bench to Bedside
J. Li, *H. Wu, Y. He;*
Zhongnan Hospital of Wuhan Universiry, Wuhan, CHINA.

Aim/Introduction: Idiopathic pulmonary fibrosis (IPF) is a chronic fibrosing interstitial pneumonia of unknown etiology characterized by progressive dyspnea and deterioration of pulmonary function. Current diagnostic strategies primarily rely on high-resolution CT imaging of morphological alterations and invasive pathological biopsies, which present limitations in sensitivity and procedural risks for disease monitoring. TGF-β1 (transforming growth factor-beta 1) serves as a central mediator driving pulmonary fibrogenesis. This study aims to investigate whether targeted PET/CT imaging of integrin αvβ6 , a functional receptor for TGF-β1, could provide a non-invasive approach with enhanced sensitivity for comprehensive management of IPF patients in comparison with ^{18}F-FDG. ***Materials and Methods:*** We established an IPF mouse model via intratracheal bleomycin (BLM) instillation (5 U/kg) and conducted serial weekly PET/CT imaging using both ^{68}Ga-Trivehexin and ^{18}F-FDG over three weeks. Specificity of ^{68}Ga-Trivehexin uptake was validated through a blocking experiment on day 14 post-modeling. Additionally, dynamic imaging was performed in BLM-induced mice treated with saline, Nerandomilast, or pirfenidone. Histopathological assessments (HE/Masson staining, Ashcroft fibrosis scoring, hydroxyproline assay, and Western blot) were employed to evaluate inflammation and fibrosis. A prospective clinical cohort of 17 IPF patients underwent head-to-head ^{68}Ga-Trivehexin and ^{18}F-FDG PET/CT for diagnostic comparison. ***Results:*** In BLM-treated mice, ^{68}Ga-Trivehexin demonstrated progressive lesion uptake (SUVmax: 3.38±0.48, 5.53±1.11, 6.27±1.02 at days 7, 14, 21; all $p < 0.05$), correlating with worsening fibrosis on Masson staining. Conversely, ^{18}F-FDG uptake peaked at day 14 (SUVmax: 6.94±1.06) before declining (4.60 at day 21), aligning with transient inflammatory changes on HE staining. Blocking experiments confirmed ^{68}Ga-Trivehexin specificity for fibrotic lesions. Therapeutic monitoring revealed significantly reduced ^{68}Ga-Trivehexin uptake in Pirfenidone/Nerandomilast-treated groups versus saline controls ($p < 0.05$), whereas ^{18}F-FDG showed no intergroup differences. Clinically, ^{68}Ga-Trivehexin exhibited superior uptake in fibrotic lesions compared to ^{18}F-FDG (SUVmax:

4.92±0.33 vs. 2.23±0.16, p < 0.0001). ***Conclusion:*** ^{68}Ga-Trivehexin, targeting integrin αvβ6, outperforms ^{18}F-FDG in noninvasive detection and therapeutic monitoring of IPF, offering enhanced specificity for fibrosis progression and treatment response.

OP-694

Neuropilin-1-Targeted PET Imaging for early detection of pulmonary fibrosis activity: comparison with the ^{18}F-FDG and ^{68}Ga-FAPI-04 PET approach

F. Qiu, *J. Li, S. Song;*
Fudan University Shanghai Cancer Center, Shanghai, CHINA.

Aim/Introduction: Idiopathic pulmonary fibrosis (IPF) lacks biomarkers for early detection, limiting timely therapeutic intervention. Neuropilin-1 (NRP-1), a co-receptor for TGF-β signaling, is implicated in fibrogenesis but unexplored as an imaging target. We developed a novel NRP-1-targeted PET probe ^{68}Ga-NRP1-CEND1 and evaluated its efficacy in detecting early-stage pulmonary fibrosis, outperforming existing tracers like ^{18}F-FDG and ^{68}Ga-FAPI-04. ***Materials and Methods:*** Single-cell sequencing of human IPF from GEO database was assessed to explore NRP-1 expression and relevant signal features. Radiotracer ^{68}Ga-DOTA-CEND1 was synthesized based on the NRP-1-targeted inhibitor CEND-1. A bleomycin-induced pulmonary fibrosis murine model was used. PET/CT imaging with the probe was performed at 0, 3, 5, 7, and 14 days post-injury. Comparative analyses with ^{18}F-FDG and ^{68}Ga-FAPI-04 were conducted. Histopathological validation included H&E, Masson's trichrome, and immunohistochemistry (IHC) for NRP-1 and FAP expression. ***Results:*** Single-cell sequencing analysis of IPF patients demonstrated significant NRP-1 overexpression in fibroblasts, with strong enrichment in fibrosis-related TGF-β signaling pathways.^{68}Ga-DOTA-CEND1 exhibited >95% radiochemical purity, optimal pharmacokinetics (T1/2 slow = 17.93 min), strong NRP-1 affinity (docking score: - 7.7884), favorable hydrophilicity (Log P = - 2.942 ± 0.12) and robust stability in vivo and in vitro for at least 2 h. Micro PET/CT in control mice showed baseline pulmonary uptake of the NRP-1 probe was low (0.303 ± 0.039 %ID/g). Significant tracer accumulation was observed as early as day 5 post-bleomycin (2.0 ± 0.2 %ID/g), peaking at day 7 (3.933 ± 0.551 %ID/g), and remained elevated during fibrotic progression at day 14 (2.8 ± 0.608 %ID/g), demonstrating sustained targeting of fibro genic activity. In inflammatory phase (0-7 days), ^{18}F-FDG failed to distinguish pulmonary inflammation due to overwhelming cardiac spillover, whereas ^{68}Ga-DOTA-CEND1 clearly delineated early lesions. In early fibrotic phase (7-14 days), ^{68}Ga-DOTA-CEND1 exhibited 1.5-fold higher uptake than ^{68}Ga-FAPI-04 (3.933 ± 0.551 vs. 2.7 ± 0.4 %ID/g, p < 0.05) at day7, with superior lesion revelation, confirming that ^{68}Ga-DOTA-CEND1 preceded ^{68}Ga-FAPI-04 in detecting fibrotic transformation, enabling earlier diagnosis. H&E and Masson staining validated successful fibrosis induction. IHC showed robust NRP-1 upregulation in fibrotic regions, while FAP expression showed only marginal increases, aligning with PET findings. ***Conclusion:*** ^{68}Ga-DOTA-CEND1 enables early diagnosis during the reversible inflammatory phase in IPF, outperforming ^{18}F-FDG and ^{68}Ga-FAPI-04 in sensitivity and specificity. It holds great potential for clinical translation, guiding early therapeutic intervention to mitigate irreversible fibrotic damage and improving patient survival and quality of life.

OP-695

Development and Validation of ^{18}F-Labeled Pirfenidone Analogs as Potential p38-Targeted Ligands for Pulmonary Fibrosis Imaging

X. Wang, *J. Wang, M. Niu, F. Kang, J. Wang;*
Department of Nuclear Medicine, Xijing Hospital, Fourth Military Medical University, Xi'an, CHINA.

Aim/Introduction: Pirfenidone is a pyridinone compound approved for treatment of idiopathic pulmonary fibrosis with broad-spectrum anti-fibrotic and anti-inflammatory effects. This study aims to design and develop ^{18}F-labeled pirfenidone analogs and validate their potentials as p38-targeted ligands for PET imaging of pulmonary fibrosis. ***Materials and Methods:*** Two pyridinone analogs, 5-methyl-1-(4-(4,4,5,5-tetramethyl-1,3,2-dioxaborolan-2-yl)phenyl)pyridin-2(1H)-one and 5-methyl-1-(3-(4,4,5,5-tetramethyl-1,3,2-dioxaborolan-2-yl)phenyl)pyridin-2(1H)-one were designed, synthesized and one-step radiolabelled with ^{18}F via nucleophilic aromatic substitution to develop radioligands ^{18}F-PFD and ^{18}F-AKF-PD. Their radiochemical yield and purity, molar activity, partition coefficient and in vitro stability were characterized. Molecular docking, molecular dynamics simulation and SPR were used to validate their potentials as p38-targeted ligands. MicroPET imaging with ^{18}F-PFD and ^{18}F-AKF-PD were performed in bleomycin-induced pulmonary fibrosis mice models. Their biodistribution, pharmacokinetics and radiation dosimetry were also evaluated in healthy BALB/c mice. Lung tissue assessments encompassed H&E staining, Masson staining, p38 IHC/IF and hydroxyproline content. ***Results:*** ^{18}F-PFD and ^{18}F-AKF-PD were synthesized with decay corrected radiochemical yield of 53.5 ± 3.2 % and 78.4 ± 1.6 %, radiochemical purity of > 98 % and molar activity of 89.5 and 101.2 GBq/μmol. Their partition coefficient (Log P) was determined to be 1.21 ± 0.19 and 1.18 ± 0.21, indicating their lipophilicity. The stability was confirmed in saline and serum within 4 h. The in silico results revealed that pirfenidone, ^{nat}F-PFD and ^{nat}F-AKF-PD were more likely to be the ligand of p38 compared to TNF-α and TGF-β. The micromolar binding affinity of pirfenidone and its analogs towards p38 was verified using SPR assay. The p38 expression in lung tissues showed significant difference at day 7, day 14 and day 21 in control and fibrosis group, positively correlated with inflammation severity, Ashcroft scoring and hydroxyproline content. In MicoPET imaging, significant uptake of ^{18}F-PFD and ^{18}F-AKF-PD was observed in fibrotic lung tissues compared to normal lung tissues at day 21. Blockade experiments confirmed the specific uptake of ^{18}F-PFD and ^{18}F-AKF-PD. The biodistribution and pharmacokinetics demonstrated the rapid clearance from blood and other non-specific organs of ^{18}F-PFD and ^{18}F-AKF-PD, with higher accumulation in the gallbladder, kidneys and salivary glands. The effective dose of ^{18}F-PFD and ^{18}F-AKF-PD was comparable to that of ^{18}F-FDG, highlighting their safety for human use. ***Conclusion:*** Two ^{18}F-labeled pirfenidone analogs, ^{18}F-PFD and ^{18}F-AKF-PD, were designed, developed and validated as p38-targeted radioligands for PET imaging of pulmonary fibrosis. This study indicated that p38 might be a potential target to develop new-generation of fibrosis-specific tracers and antifibrotic therapy.

OP-696

Development of Novel Radiotracer for Accurate Assessing Functional Liver Reserve via PET Imaging

L. Feng[1], *Y. Xu*[2], *H. Yang*[1], *X. Lan*[1], *D. Jiang*[1];
[1]*Department of Nuclear Medicine, Union Hospital, Tongji Medical College, Huazhong University of Science, Wuhan, CHINA,* [2]*Department of Hepatobiliary Surgery, Union Hospital, Tongji Medical College, Huazhong University of Science, Wuhan, CHINA.*

Aim/Introduction: Current liver function assessment methods primarily rely on serum marker measurements, which have limitations in accuracy. This study aims to develop a radioactive small-molecule probe to noninvasively evaluate the functional liver reserve by monitoring its uptake and metabolism in the liver. ***Materials and Methods:*** A series of small molecules were labeled with ^{68}Ga and subjected to dynamic PET imaging in healthy mice to screen for their hepatic metabolic capabilities. Subsequently, the probe's uptake, excretion, and retention in the liver were explored in four hepatectomy models (30%, 50%, 70%, and 90%

liver resection) to establish the correlation between liver function and probe metabolism. Dynamic PET imaging was also performed in hepatitis and cirrhosis models to predict liver function, which was validated by H&E staining and serum markers. ***Results:*** A radiolabeled small-molecule probe, named [^{68}Ga]Ga-SD03, with hepatic metabolic capacity was successfully synthesized and maintained stability within 2 h. In healthy mice, the probe exhibits rapid hepatic uptake, reaching peak concentration within 1 min post-administration and completing its enterohepatic metabolism within 15 min. It does not interact with hepatocytes or macrophages, and shows minimal retention in the liver, which may allow for efficient hepatic function assessment. In hepatectomy models, the 15 min/1 min liver uptake ratio was not significantly different from the control group when liver resection was below 50% (ratios of 0.40 ± 0.07% and 0.50 ± 0.13%, respectively). However, when liver resection reached 70% and 90%, the 15 min liver uptake values were 5.11 ± 1.67% and 9.27 ± 2.09% of the 1 min values, respectively, significantly higher than those in other groups ($p < 0.01$). Probe retention in the liver, as another indicator of liver functional reserve, increased with the extent of resection. In hepatitis models, the degree of liver inflammation predicted by PET imaging was consistent with H&E staining results. ***Conclusion:*** The metabolism of [^{68}Ga]Ga-SD03 can indicate the residual liver function, offering potential for guiding clinical surgical planning and postoperative evaluation.

OP-697

Tracking monocyte kinetics in healthy volunteers and patients with inflammatory arthritis

N. Farahi[1], *A. Y. K. C. Ng*[1], *J. Hutton*[1], *D. Gillett*[2], *F. Sunzini*[3], *R. Hohne*[3], *A. Ade-Ojo*[2], *V. Lotz*[4], *A. Tate*[3], *M. Arnott*[3], *N. Basu*[3], *J. Brock*[3], *A. McGucken*[3], *N. G. Shenker*[5], *E. R. Chilvers*[6], *J. Cavanagh*[3], *C. Summers*[1];
[1]*University of Cambridge, Cambridge, UNITED KINGDOM,* [2]*Cambridge University Hospitals NHS Foundation Trust, Cambridge, UNITED KINGDOM,* [3]*University of Glasgow, Glasgow, UNITED KINGDOM,* [4]*Royal Papworth Hospital NHS Foundation Trust, Cambridge, UNITED KINGDOM,* [5]*Cambridge University Hospitals NHS Foundation Trust and Department of Medicine, University of Cambridge, Cambridge, UNITED KINGDOM,* [6]*Imperial College, London, UNITED KINGDOM.*

Aim/Introduction: Monocytes play an important role in the immune response, contributing to tissue homeostasis and immune surveillance. Their infiltration is key to a number of acute and chronic inflammatory conditions, including rheumatoid arthritis and acute respiratory distress syndrome. Despite their significance in disease, data on monocyte biodistribution in healthy individuals is limited. The aim of this study was to establish the circulating kinetics and biodistribution of monocytes in healthy volunteers (HV) and compare these findings to patients with inflammatory arthritis. ***Materials and Methods:*** To assess monocyte lifespan, mixed leukocytes were prepared from HV using hetastarch sedimentation. Autologous leukocytes were then radiolabelled with 111-Indium-tropolonate before reinjection. Peripheral venous blood samples were collected over a 72-hour period after reinjection, followed by isolation of neutrophils and monocytes and measurement of radioactivity by sample counting. To visualise monocyte biodistribution in HV and patients with inflammatory diseases (psoriatic and rheumatoid arthritis), monocytes were isolated using clinical grade CD14 beads and radiolabelled with 99m-Tc-HMPAO. After reinjection of the autologous radiolabelled monocytes, dynamic and static gamma camera imaging was performed over 6-hours. Region-of-interest analysis (ROI) was performed on the lungs, liver and spleen. Mean counts per pixel or voxel in these ROIs were recorded and corrected for physical decay of the radionuclide. ***Results:*** Using In-111 labelled leukocytes, the median 45-minute recovery of neutrophils from the circulation of HV was 47% (IQR 32-64%; N=5), comparable with previous reports. In contrast monocytes exhibited markedly different intravascular kinetics, with a median 45-minute recovery of 7% (IQR 5-15%; P=0.008; N=5), suggesting the presence of a larger marginated pool. Monocyte median intravascular lifespan was 13 hours (IQR 6-14 hours; N=5), notably longer than the lifespan of neutrophils 7 hours (IQR 4-9 hours; P=0.31; N=5). Using purified 99m-Tc-HMPAO-labelled monocytes and gamma camera imaging, we observed prolonged transit through the lungs, followed by liver and spleen uptake in HVs (N=8). In patients with inflammatory disease (psoriatic and rheumatoid arthritis; N=5) we observed an expanded monocyte marginated pool compared to healthy controls, with early preferential homing to the lungs. ***Conclusion:*** We report for the first time, the transit kinetics and biodistribution of monocytes in healthy human subjects. Our findings reveal that, in patients with inflammatory arthritis, monocytes exhibit increased margination to the lungs, suggesting a redistribution from the circulating pool to pulmonary sites in inflammatory conditions. These insights have implications for future studies on monocyte distribution and lifespan in chronic inflammatory states.

OP-699

The Preclinical Study of $^{[18F]}$AV45 and $^{[18F]}$DPA714 PET as Potential Imaging Biomarkers for Hashimoto's Thyroiditis-Associated Cognitive Impairment

Y. Zhang, *G. Zhu;*
First Affiliated Hospital of Kunming Medical University, Kunming, Yunnan, CHINA.

Aim/Introduction: Hashimoto's thyroiditis (HT) is closely associated with cognitive impairment, and cognitive decline is often accompanied by Aβ accumulation and neuroinflammation. An SD rat HT model was established, combined with $^{[18F]}$AV45 and $^{[18F]}$DPA714 PET tracers and ELISA detection techniques, to evaluate these pathological changes and provide imaging evidence for clinical diagnosis. ***Materials and Methods:*** The study compared SD rats with an HT model (n=4) to a control group (n=5). Aβ accumulation and neuroinflammation in various brain regions were analyzed using $^{[18F]}$AV45 and $^{[18F]}$DPA714 PET imaging. Group comparisons were made with SPM12 ($p<0.05$), where KE refers to the number of voxels and MAX-T represents the maximum T-value. Cognitive function was assessed through open field tests, Y-maze, and water maze tasks. ELISA was used to measure inflammatory factors (IL-6, IL-1β,TNF-α), Aβ (Aβ40, Aβ42), and other related biomarkers in both brain and thyroid tissues. ***Results:*** $^{[18F]}$AV45 PET imaging in the HT model revealed Aβ deposition in the hippocampus (KE=849, MAX-T=6.251), frontal cortex (KE=187, MAX-T=2.4635), parietal lobe (KE=262, MAX-T=5.7657), and cingulate gyrus (KE=459, MAX-T=3.0145). $^{[18F]}$DPA714 PET imaging showed significant differences in the frontal cortex (KE=16, MAX-T=3.6088) and cingulate gyrus (KE=43, MAX-T=3.2757). Behavioral assessments indicated that rats in the HT group exhibited a significant increase in total active distance ($p<0.01$) and the number of incorrect arm entries ($p<0.05$) in the Y-maze test. In the open field test, grooming frequency increased ($p < 0.05$), while the number of standing events ($p<0.001$) and entries into the central area ($p<0.0001$) significantly decreased. In the Morris water maze test, the number of target quadrant crossings ($p < 0.0001$), platform dwell time ($p<0.01$), and target quadrant visits ($p<0.001$) were significantly reduced. ELISA results showed that levels of IL-6, IL-1β, TNF-α, Aβ40, and Aβ42 in brain tissue were significantly higher in the HT group compared to the control group ($p < 0.05$), while inflammatory cytokines (IL-6, IL-1β, TNF-α) in thyroid tissue were also significantly elevated ($p<0.05$). ***Conclusion:*** This study suggests that HT may induce Aβ deposition via neuroinflammation, which leads to cognitive impairment. The combination of $^{[18F]}$AV45 and $^{[18F]}$DPA714 PET

imaging with biological assays provides a promising tool for detecting HT-associated cognitive impairment and offers valuable insights for clinical diagnosis.

OP-700

Dual-Radiolabeling Strategy for In Vivo Tracking of Mycoplasma pneumoniae and Pulmonary Surfactant Biodistribution Using microSPECT/CT Imaging

F. Hendy Pérez-Aranda[1], *A. Fernández-Gonzalez*[1], *I. Rodríguez-Arce*[2], *O. Cañadas*[3,4], *M. Collantes*[5,6,7], *G. Gómez-Montesino*[3,4], *F. Pareja*[1,6], *G. Quincoces*[1,6], *R. Ramos-Membrive*[8], *L. Serrano*[2,9,10], *J. Pérez-Gil*[3,4], *I. Peñuelas*[1,6,7];
[1]Radiopharmacy Unit. Nuclear Medicine Department. Clínica Universidad de Navarra, Pamplona, SPAIN, [2]Centre for Genomic Regulation (CRG), The Barcelona Institute of Science and Technology, Barcelona, SPAIN, [3]Department of Biochemistry and Molecular Biology, Faculty of Biological Sciences, Complutense University, Madrid, SPAIN, [4]Research Institute "Hospital Doce de Octubre (imas12)", Madrid, SPAIN, [5]Nuclear Medicine Department. Clínica Universidad de Navarra, Pamplona, SPAIN, [6]Navarra Institute for Health Research (IdISNA), Pamplona, SPAIN, [7]Translational Molecular Imaging Unit (UNIMTRA). Nuclear Medicine Department. Clínica Universidad de Navarra, Pamplona, SPAIN, [8]Radiopharmacy Unit. Nuclear Medicine Department. Clínica Universidad de Navarra, Madrid, SPAIN, Madrid, SPAIN, [9]Universitat Pompeu Fabra (UPF), Barcelona, SPAIN, [10]ICREA, Barcelona, SPAIN.

Aim/Introduction: Mycoplasma pneumoniae has been identified within the lung tumor microbiome (1), and its natural tropism for cancer cells suggests potential as a biological vector in lung cancer therapy. In previous work using [^{111}In]In-oxinate-labelled M. pneumoniae in murine models, we observed that intratracheal administration led to suboptimal delivery to lung tumors, likely due to uneven pulmonary distribution (2). To address this limitation, we hypothesized that pulmonary surfactant (PS), given its physiological relevance and surface-active properties, could act as an adjuvant to enhance Mycoplasma intrapulmonary spread and tumor targeting. The aim of this study was to implement a dual-radiolabelling strategy to simultaneously track the biodistribution of indium-111-labeled M. pneumoniae and technetium-99m-labelled PS in vivo for a comprehensive evaluation of their combined pulmonary distribution and the potential role of PS in improving Mycoplasma delivery. ***Materials and Methods:*** M. pneumoniae (CV8 strain, 2x107 CFU) was labeled with [^{111}In]In-oxinate using standard cell-labelling protocols. PS obtained from porcine lungs by bronchoalveolar lavage was extracted with CH_2Cl_2:MeOH to obtain the organic extract (OE-PS). Following solvent evaporation in 40µL aliquots, the dry lipid film was incubated with 40µL $[^{99m}Tc(CO)_3(OH_2)_3]^+$ (obtained from a commercial kit) at 37°C/1h. Subsequently, 100µL of PBS (pH 7.4) were added, incubated under the same conditions and RCP checked by radioTLC (Whatmann3/saline). In vivo biodistribution was evaluated following intratracheal administration in C57Bl/6J mice, assigned to three groups: G1(n=2) received 7.47MBq of ^{99m}Tc-OE-PS; G2(n=3) received 1.14MBq of ^{111}In-labelled CV8 encapsulated in non-labelled OE-PS; and G3(n=3) received a combination of 1.8 MBq of ^{111}In-labelled CV8 and 7.4MBq ^{99m}Tc-labelled OE-PS. Biodistribution was evaluated by microSPECT/CT imaging at 1 and 4 hours post-administration. ***Results:*** Although CV8 was radiolabeled with low yield (16%) it was >95% pure after centrifugation and washing twice. $[99mTc(CO)_3(OH_2)_3]+$ was obtained in >99%RCP as checked by radioTLC (silicagel/sodium citrate). OE-PS was efficiently radiolabelled (RCP>99%, confirmed via radioTLC). ^{99m}Tc-OE-PS showed uniform, stable lung distribution over time. In contrast, when combined with ^{111}In-Mycoplasma, OE-PS and ^{99m}Tc-OE-PS significantly modified the distribution of Mycoplasma, as evidenced by the increased spread over time. ***Conclusion:*** This study reports, for the first time, the successful radiolabelling and in vivo dual-isotope microSPECT/CT imaging of ^{99m}Tc-labelled OE-PS and ^{111}In-labelled M. pneumoniae. Pulmonary surfactant improved CV8 intrapulmonary distribution, supporting its use as an adjuvant in pulmonary bacterial therapies. These findings highlight the utility of molecular imaging in the development of respiratory therapeutic strategies. ***References:*** (1)doi:10.3892/mmr.2016.5765 (2)Collantes M, et al. EJNMMI 2024;51(S1):S462-S463.

1605

Tuesday, October 7, 2025, 16:45 - 18:15
Room 211

Cutting Edge Science Track - TROP Session - Radiation Protection Committee: Radiation Exposure and Protection

OP-701

Dosimetry of Radiation Exposure to Patients, Caregivers, and Medical Staff Following Lu-177 PSMA Therapy

M. Chiang[1], *P. Chuang*[2], *C. Lu*[3];
[1]Taipei Medical University Hospital, Taipei, TAIWAN, [2]National Taiwan University Hospital Cancer Center, Taipei, TAIWAN, [3]National Taiwan University Hospital, Taipei, TAIWAN.

Aim/Introduction: Lutetium-177-labeled prostate-specific membrane antigen (Lu-177 PSMA) therapy has emerged as an effective targeted treatment for metastatic prostate cancer. Despite its clinical benefits, radiation exposure to patients, caregivers, and healthcare personnel remains a concern. This study aims to quantify radiation exposure across different settings and time points, and to evaluate the effectiveness of protective strategies in minimizing radiation risks. ***Materials and Methods:*** This retrospective study included 24 patients treated with Lu-177 PSMA between November 10, 2022, and November 5, 2024. Radiation dose rates from patients were recorded at 0, 2, 4, 6, and 24 hours post-injection at 1-meter distance using a portable detector (RadEye™ B20, Thermo Scientific). A biexponential decay model was used to analyze dose kinetics. Cumulative radiation exposure was measured using optically stimulated luminescence dosimeters and survey meters at various distances (1 m, 3 m, behind lead shielding) and for different personnel (patients, caregivers, nurses, and radiation safety staff). Post-discharge exposure for patients and caregivers was monitored for three days outside the hospital following discharge. ***Results:*** The mean initial radiation dose rate from patients at 1 meter was 39.54 ± 21.79 µSv/h, declining to 19.55 ± 6.38 µSv/h at 4 hours and 11.14 ± 5.21 µSv/h at 24 hours post-injection. The decay followed a biexponential model ($R^2 = 0.9995$) with rate constants $\lambda_1 = 0.7301$ h^{-1} and $\lambda_2 = 0.0245$ h^{-1}. Patients accumulated the highest radiation dose (4.66 ± 1.94 mSv), whereas caregivers and medical staff received significantly lower exposures (0.16 ± 0.08 mSv and 0.11 ± 0.07 mSv, respectively). Radiation exposure at 3 meters and behind shielding was comparable to background levels. Statistically significant differences in radiation exposure were observed across measurement positions ($P < 0.001$), confirming the protective value of distance and shielding. Importantly, radiation exposure at 1 meter fell below 30 µSv/h by 4 hours in most cases. ***Conclusion:*** Radiation exposure from Lu-177 PSMA therapy decreases rapidly over time. By 4 hours, dose rates at 1 meter drop to around 30 µSv/h. Exposure to caregivers and medical staff is minimal and well within safety limits, confirming the effectiveness of distancing and shielding measures. ***References:*** Lutetium-177-PSMA-617 for Metastatic Castration-Resistant Prostate Cancer. N Engl J Med. 2021;385:1091-103. doi:10.1056/NEJMoa2107322.Evaluation of radiation safety in (177)Lu-PSMA therapy and development of outpatient treatment protocol. J Radiol Prot. 2016;36:269-78. doi:10.1088/0952-4746/36/2/269.

OP-702

Extremity exposure due to handling of ^{177}Lu - results of a multi-center pilot study

E. Aalbersberg[1], *A. McCann*[2], *N. Cherbuin*[3], *J. Dabin*[4], *S. Haruz-Waschitz*[5], *H. Datz*[6], *R. Wierts*[7], *A. Zorz*[8], *T. Kráčmerová*[9], *L. Albiniak*[10], *M. Hakulinen*[11], *M. Ferrari*[12], *R. Kollaard*[13];
[1]*Netherlands Cancer Institute, Amsterdam, NETHERLANDS,* [2]*St. Vincent's University Hospital, Dublin, IRELAND,* [3]*Lausanne University Hospital, Lausanne, SWITZERLAND,* [4]*Belgian Nuclear Research Center, Mol, BELGIUM,* [5]*Shamir Medical Center, Be'er Ya'akov, ISRAEL,* [6]*Soreq Nuclear Research Center, Yavne, ISRAEL,* [7]*Maastricht University Medical Center, Maastricht, NETHERLANDS,* [8]*Veneto Institute of Oncology IOV – IRCCS, Padua, ITALY,* [9]*Motol University Hospital, Prague, CZECH REPUBLIC,* [10]*University of Lodz, Lodz, POLAND,* [11]*Kuopio University Hospital, Kuopio, FINLAND,* [12]*Istituto Europeo di Oncologia, Milan, ITALY,* [13]*NRG PALLAS, Arnhem, NETHERLANDS.*

Aim/Introduction: The number of procedures with ^{177}Lu-labeled radiopharmaceuticals is increasing worldwide. However, there is a lack of data on skin exposure from these procedures. The aim of this study performed at nuclear medicine departments across Europe was to determine staff skin exposure from handling ^{177}Lu-labeled radiopharmaceuticals. This investigation was part of a project of the European Radiation Dosimetry Group (EURADOS) to investigate skin doses due to the use of new radionuclides in nuclear medicine. ***Materials and Methods:*** Measurements were performed in nine centers. Workers wore a TLD at the base of the index finger of the non-dominant hand when handling ^{177}Lu. A logbook recorded the handled activity and performed tasks for each month. If no dose was detected during a measurement period, the minimum detection limit of that specific dosimeter was used for analyses. For analyses, the skin dose was normalized to the handled activity. Tasks were grouped as either preparation or administration. Administration methods were categorized as gravity method, manual syringe administration, and automated syringe administration. ***Results:*** A total of 115 measurements were collected, of which 38 (33%) were below the MDL. The median handled activity was 52 GBq [range 1-317] and the median recorded skin dose was 0.150mSv [range 0.007-2.270]. This resulted in a median normalized skin dose of 3.3µSv/GBq [range 0.5-525.0]. 105 measurements could be classified according to their task, 50 as preparation (48%) and 55 (52%) as administration. The median normalized dose was slightly higher during preparation; 3.6µSv/GBq [range 0.5-525.0] for preparation compared to 3.4µSv/GBq [range 0.5-31.8] for administration (Mann-Whitney, p=0.019). When looking at administration method, there was no difference in median normalized dose: 6.2µSv/GBq [range 0.5-20.8] for manual syringe administration (2 centers, n=13), 3.8µSv/GBq [range 0.8-31.8] for gravity administration (4 centers, n=31), and 1.0µSv/GBq [range 0.7-2.4] for automatic syringe administration (1 center, n=8) (Kruskal Wallis, p=0.074). Although large differences were seen between the normalized dose per center (median values of 1.01-11.5µSv/GBq), this could not be fully explained by the task performed or the administration method used. Further analyses are being performed to investigate the differences in dosimeters and shielding used. ***Conclusion:*** The median normalized skin dose for the handling of ^{177}Lu-labeled radiopharmaceuticals was 3.3 µSv/GBq in this study, which is much lower than that of other radiopharmaceuticals labeled with ^{68}Ga, ^{18}F or ^{99m}Tc reported in literature. With adequate shielding and training, the handling of ^{177}Lu-labeled radiopharmaceuticals is safe for nuclear medicine personnel.

OP-703

Radiation Safety with ^{212}Pb-Based Therapeutics from Clinical Experience with ^{212}Pb-ADVC001 (TheraPb): Dose to Staff and Members of the Public

E. O'Mahoney[1], *M. Griffiths*[2], *S. Ngai*[1], *D. Pattison*[2], *A. Hansen*[1], *D. Wyld*[2], *I. Holmes*[1], *L. Katchel*[1], *S. Baker*[1], *H. Biggs*[1], *L. Campbell*[2], *M. Baronet*[3], *M. Crumbaker*[3], *P. Santoro*[3], *S. Rose*[3], *A. Karmann*[3];
[1]*Princess Alexandra Hospital, Brisbane, AUSTRALIA,* [2]*Royal Brisbane and Women's Hospital, Brisbane, AUSTRALIA,* [3]*AdvanCell Pty Ltd, Sydney, AUSTRALIA.*

Aim/Introduction: To measure the dose rates from patients over time after administration of ^{212}Pb-ADVC001, a ^{212}Pb-based PSMA-targeting therapeutic, and the radiation exposure to nuclear medicine staff, to establish recommendations for the safe administration and the discharge of patients undergoing treatment with ^{212}Pb-ADVC001. ***Materials and Methods:*** External ambient equivalent dose rates (H*(10)) were recorded at 10, 30, 100 and 200 cm at approximately 0.5, 1.5, 4, 20 and 28 hours post administration from 16 patients receiving treatment with ^{212}Pb-ADVC001 at two clinical sites as part of the TheraPb Phase 1b dose escalation trial (NCT05720130). A biexponential model was fitted for each patient to estimate exposure for potential encounters (e.g., family member, member of public, work colleague) enabling patient-specific advice to ensure legislative guidelines were met. Electronic portable dosimeters (EPDs; Mirion DMC 3000) specified for gamma energies between 15 keV and 7 MeV, were worn by all nuclear medicine staff involved in the dispensing, administering, monitoring and SPECT/CT imaging of the patients. Measured staff doses (personal deep dose equivalent, Hp(10)) and patient dose rates were linearly scaled to the maximum administered activity of 200 MBq ^{212}Pb-ADVC001. ***Results:*** The median nuclear medicine technologist personal dose equivalent was 10 µSv per cycle of projected 200 MBq ^{212}Pb-ADVC001 administration (IQR 5-13 µSv). The median combined staff dose per 200 MBq cycle was 26 µSv (IQR 21-31 µSv). The average bi-exponential clearance was determined to include 47% fast clearance with an effective half-life of 1.9 hours, while the remaining 53% cleared with a biological half-life of 7.6 hours. Patients were discharged as early as 3 hours post treatment administration, with an average projected dose rate at 1 meter of 21 µSv/h. Patient release instructions were 3 days of increased hygiene precautions, with up to 48 hours of close contact restrictions, resulting in predicted doses of less than 100 µSv to any family member (including pregnant women and children) or members of the public per 200 MBq treatment. Following these instructions, up to 10 treatment cycles of 200 MBq would not exceed the member of public dose limit of 1 mSv per annum. ***Conclusion:*** Experienced staff can safely administer up to 200 MBq ^{212}Pb-based therapies in an outpatient setting, maintaining staff and members of the public exposure well below legislative limits. Minimal restrictions are required on discharge at 3 hours post treatment administration.

OP-704

Addressing Radiation Safety Concerns for Alpha-Emitter Astatine-211

S. Palm[1], *E. Leidermark*[1], *H. Jensen*[2], *T. Bäck*[1];
[1]*University of Gothenburg, Gothenburg, SWEDEN,* [2]*Copenhagen University Hospital, Copenhagen, DENMARK.*

Aim/Introduction: Alpha-emitter astatine-211 (^{211}At; $t_{½}$=7.2h) is currently used for targeted alpha therapy (TAT) in clinical trials, but expansion is hindered partly by radiation safety concerns. These concerns include transport; management of daughter ^{207}Bi ($t_{½}$=33a); co-production of ^{210}At ($t_{½}$=8.1h) and its daughter ^{210}Po ($t_{½}$=138d). Different regulations and local rules for work with ^{211}At have been reported. Here, we refer to international standard documents such as the IAEA basic safety standards (1); the IAEA regulations for transport (2); and the EU directive on radiation protection (3). Our aim was to provide some practical guidelines for interpreting and addressing the risks involved with ^{211}At using the exemption levels listed in (1-3). Our aim was also to raise awareness of the inappropriate regulations and local guidelines that require control of these radionuclides also when the amount is below the respective exemption limit. ***Materials and Methods:*** All work is based on the 20+ years production of ^{211}At in Copenhagen, Denmark and subsequent transport to and pre-clinical and clinical use in Gothenburg, Sweden. Shipped amount was nearly always <2 GBq ^{211}At. Patients received up to 300 MBq ^{211}At (coupled to an antibody). Both countries have national

legislation that adhere to (3) that, in turn, was harmonized with (1). To increase the amount of ^{211}At produced, typically 0.04% of ^{210}At is allowed to be co-produced. All regulations (1-3) list the same exemption limit for the mentioned radionuclides. Briefly, normal exposure to the exemption limit results in 10 µSv effective dose. Cross-border transport of the solid target (<2 GBq ^{211}At) is done in a type A container classified as UN2915. With lead shielding, the transport index is below 0.05 and therefore marked as zero. Packages are thus assigned to category I-WHITE. ***Results:*** The exemption limit for ^{211}At is 10 MBq. Therefore, gloves and other waste are kept for 72h and then discarded and incinerated as regular hospital waste. Complete decay of 2 GBq ^{211}At results in 21 kBq ^{207}Bi (exemption limit 1 MBq). Co-production of ^{210}At (0.04% of 2 GBq ^{211}At activity) and subsequent decay eventually results in 2 kBq ^{210}Po (exemption limit 10 kBq). Another 6 kBq ^{210}Po can be directly produced in the bombarded target (4). ***Conclusion:*** Exemption limits for ^{211}At, ^{207}Bi, ^{210}At and ^{210}Po can be used for determining clearance. Daughters ^{207}Bi and ^{210}Po are not a safety concern for <2 GBq ^{211}At. ***References:*** (1):ISBN:978-92-0-135310-8; (2):ISBN:978-92-0-107917-6; (3):2013/59/EURATOM; (4):https://doi.org/10.1016/j.radphyschem.2023.111155.

OP-705

Evaluation of Custom Shielding Made From Epoxy Resin to Reduce Doses to the Hand When Dispensing ^{90}Y Resin Microspheres

A. Smout, *E. Bolt, M. Pryor, J. Scuffham;*
Royal Surrey County Hospital, Guildford, UNITED KINGDOM.

Aim/Introduction: Y-90 is a pure beta emitter with unshielded dose rates of 12mSv/GBq/s (Delacroix, 2002). Shielding is therefore essential to avoid exceeding occupational dose limits. We identified the potential for significant skin doses from Y-90 resin microspheres located in the hub of the needle when dispensing. Beta syringe shields are available, however these only shield the barrel of the syringe and leave the needle unshielded. This could lead to high skin doses to parts of the hand depending on how the syringe is held. If a cylindrical grasp is used when dispensing Y-90 (in which the fingers wrap around the syringe shield and the thumb is used to manipulate the plunger), the ulnar aspect of the base of the hand could receive high doses. Plastic is commonly used to shield beta radiation. Epoxy resin consists of a liquid resin and hardener that, when mixed, cures into a solid plastic. As a novel shielding material, this work aims to determine the thickness required to shield Y-90 emissions and whether the dose to the base of the hand can be reduced. ***Materials and Methods:*** To calculate the thickness of epoxy resin required to shield Y-90, 12 thicknesses of epoxy resin were made (2mm to 13mm). Thermo-luminescent detectors (TLDs) were placed behind each epoxy resin sample and irradiated by an unshielded Y-90 source in turn. To assess the dose reduction to the base of the hand, an epoxy resin plate was fitted onto a commercially available beta syringe shield and a hand phantom was created. TLDs from an approved dosimetry service were used to measure the dose to the base of the hand from a shielded syringe containing 1060MBq Y-90 with and without the additional epoxy resin fitted. ***Results:*** A thickness of 6.7mm epoxy resin reduced the dose from unshielded Y-90 microspheres by 98.7%. 7.4mm gave a dose reduction of 99.5% and both 8.75mm and 9.25mm thicknesses provided 99.97% reduction in dose. The phantom work showed that the dose to the base of the hand was 111.9mSv from holding the shielded syringe for 10 minutes, compared to 0.29mSv when the additional epoxy resin was fitted. ***Conclusion:*** High doses to the base of the hand are possible when dispensing Y-90 and custom shielding made from epoxy resin was shown to provide effective shielding with a dose reduction of 99.74%. ***References:*** Delacroix D. et al., (2002). Radionuclide and Radiation Protection Handbook, Radiation Protection Dosimetry 98(1).

OP-706

Preliminary Assessment of ^{89}Zr-Girentuximab Excretion and Radiation Protection in ccRCC patients undergoing PET/CT imaging

A. Piai[1], *G. Colelli*[2,1], *A. Loria*[1], *D. Tosoni*[2,1], *B. Bordigoni*[3,1], *L. Antunovic*[1], *F. Gelardi*[4,1], *A. Chiti*[4,1], *A. del Vecchio*[1];
[1]*IRCCS Ospedale San Raffaele, Milan, ITALY,* [2]*University of Milan, Milan, ITALY,* [3]*University of Padua, Milan, ITALY,* [4]*Vita-Salute University, Milan, ITALY.*

Aim/Introduction: Zirconium-labelled Girentuximab (^{89}Zr-girentuximab) PET/CT imaging is emerging as an effective technique for non-invasive diagnosis of Clear Cell Renal Cell Carcinoma (ccRCC). To our knowledge, limited information is available regarding the radiopharmaceutical biodistribution and no published data exist on excretion functions. This study presents preliminary findings on excretion and radiation protection measurements. ***Materials and Methods:*** Six patients received 37MBq of ^{89}Zr-girentuximab under an expanded access program at our institution, with two undergoing nephrectomy 11 and 12 days post-injection. Up to three whole-body PET/CT scans were acquired per patient and qualitatively assessed to identify organs with the highest tracer uptake. To estimate the excretion function, patient-specific dose rate measurements were performed with a calibrated Geiger-Muller counter at multiple time points post-administration (approximately 0h, 72h, 120h, 168h, and 264h). Patient-specific calibration factors were calculated using injected activity and dose rate at t=0h. Time-activity curves were fitted using mono-exponential and bi-exponential functions and the effective half-lives were calculated. Inter-individual variability was investigated. Extensive dose rate monitoring and contamination testing were performed during administration, imaging, and surgery to evaluate occupational exposure. ***Results:*** The mono-exponential decay constant (λ) is 1.602e-02 ([1.622e-02;2.624e-02]), corresponding to a half-life of 43.3h. Bi-exponential fitting yielded decay constants λs (short component) of 9.761e-01 ([5.518e-01;9.987e-01]) and λ_L (long component) of 9.854e-03 ([8.748e-03;1.271e-02]), corresponding to half-lives of 0.71h and 70.3h, respectively. PET/CT images revealed the highest uptakes in the liver, kidneys, heart wall, and bowels, suggesting a primarily gastrointestinal elimination pathway, in agreement with data from the Phase I study conducted by the radiopharmaceutical manufacturer [1]. The dose rate from the vial at 1 meter was 0.25µSv/h/MBq. Estimated effective doses per patient were <1µSv for radiographers (dose preparation), nurses (patient care), and nuclear medicine physicians (administration). On the day of surgery, dose rates were approximatively 0.1µSv/h. Superficial contamination was detected only on blood-stained gauzes. ***Conclusion:*** Preliminary findings on ^{89}Zr-girentuximab excretion functions indicate gastrointestinal excretion with short and long components of 9.761e-01 and 9.854e-03, respectively, with limited inter-individual variability. To our knowledge, no comparable data are currently available in the literature. Additional measurements on a larger patient cohort are planned in the next months to validate these findings and reduce the uncertainties. Negligible radiation exposure levels are associated with ^{89}Zr PET/CT imaging and subsequent surgery. However, due to the long half-life of ^{89}Zr, waste materials that come into contact with patient fluids can become significantly contaminated, making proper waste management essential. ***References:*** [1] https://doi.org/10.1007/s00259-021-05271-w.

OP-707

The UK perspective on establishing adult national diagnostic reference levels for nuclear medicine and PET

L. Fraser, *A. Powell, N. Parkar, M. Richardson;*
UK Health Security Agency, Didcot, UNITED KINGDOM.

Aim/Introduction: In the UK, the Ionising Radiation (Medical Exposure) Regulations 2017 [1] require employers to establish diagnostic reference levels for diagnostic medical exposures. These are often based on National Diagnostic Reference Levels (NDRLs) which are set by the Administration of Radioactive Substances Advisory Committee (ARSAC) for diagnostic nuclear medicine (NM) and Positron Emission Tomography (PET) procedures.

Previously, UK NDRLs have been derived from a combination of historical data, expert advice on good clinical practice and scientific literature. To ensure NDRLs are relevant and useful, we propose that NDRLs should be based on current clinical practice and capability. Presented will be the results of a UK wide survey and the new UK process for determining and implementing NDRLs. ***Materials and Methods:*** A survey was opened to all UK PET centres to collect data on the scanner technology, acquisition protocol parameters and administered activity used for ^{18}F-FDG whole body tumour imaging and ^{18}F-FDG infection inflammation imaging. Complete survey responses were analysed to understand the extent of the variation in UK practice and to estimate the impact of any change to the NDRL. ***Results:*** Survey responses were received from 65 of the 114 UK PET centres (57%). All centres were administering activity below the 2024 NDRL of 400 MBq. A total of 97% of the survey responses indicated that weight-based scaling was used instead of a fixed activity. The most common value used for scaling the administered activity was 3.5 MBq/kg across all scanner technologies. UK PET centres are optimising their acquisition protocols by increasing the time per bed position for larger patients, typically weighing >100kg. ***Conclusion:*** The survey showed that, for the examinations included, a weight-based activity scaling NDRL would be more reflective of current UK practice than a fixed activity value. The NDRLs for ^{18}F-FDG whole-body tumour imaging and ^{18}F-FDG infection inflammation imaging were changed in 2025 from 400 MBq to 3.5 MBq/kg [2] with minimal impact on most UK PET centres. ***References:*** [1]'The Ionising Radiation (Medical Exposure) Regulations 2017'. The Stationery Office, London, SI 2017/1322. https://www.legislation.gov.uk/uksi/2017/1322/contents. [2]Administration of Radioactive Substances Advisory Committee. Notes for guidance on the clinical administration of radiopharmaceuticals and use of sealed radioactive sources. 2024.https://www.gov.uk/government/publications/arsac-notes-for-guidance.

OP-708

Building a European Network for Quality and Safety of Medical Ionizing Radiation Applications: Outcomes from the PrISMA SAMIRA EU4Health Project

S. Annunziata[1], *E. Solfaroli*[2], *J. Liukkonen*[3], *T. Jørgensen*[4], *C. Munoz*[5], *L. Boudewijns*[6], *T. Larose*[7], *I. Kralik*[8], *A. Sundlov*[9], *M. Do Carmo Lopes*[10], *K. Breddam*[11], *S. Geza*[12], *C. Franciosi*[1], *A. Capotosti*[1], *C. Rosenbaum*[6], *A. Rosi*[2], *on behalf of the SAMIRA-PRISMA EU4Health Consortium;*
[1]*Gemelli, Rome, ITALY,* [2]*ISS, Rome, ITALY,* [3]*STUK, Helsinki, FINLAND,* [4]*DSA, Oslo, NORWAY,* [5]*ICO, Barcelona, SPAIN,* [6]*RIVM, Bilthoven, NETHERLANDS,* [7]*Helsedirektoratet., Oslo, NORWAY,* [8]*Children Hospital, Zagreb, CROATIA,* [9]*Swedish Medical Products Agency, Goteborg, SWEDEN,* [10]*IPO, Coimbra, PORTUGAL,* [11]*DHA, Copenaghen, DENMARK,* [12]*NNGYK, Budapest, HUNGARY.*

Aim/Introduction: Under the EU's SAMIRA action plan, the Preparatory activities for Implementation of quality and Safety of Medical ionizing radiation Applications (PrISMA, https://www.rivm.nl/en/international-projects/prisma) preparatory project started in May 2024 and lasted 18 months. The overall aim of PrISMA was to explore the utility of, and pave the way for, a further Joint Action that promotes the safe, high-quality, and reliable use of medical ionising radiation. ***Materials and Methods:*** The consortium underpinning the PrISMA project (EU Grant Agreement 101162826), comprised 18 organisations - health authorities, health institutions, one medical product authority, ministries of health, one professional body, radiation protection authorities, and research institutes - from 11 European Member States and Norway. ***Results:*** The first PrISMA objective was to identify and bring together the relevant stakeholders in the area of quality and safety in the medical use of ionising radiation and to facilitate the pooling of expertise from different countries. Then, this extensive network defined a proposed text setting out the objectives, scope and activities of the future SAMIRA Joint Action. After routinary periodical online meetings among partners, for in-person PrISMA Workshop held in Zagreb in April 2025, there were 167 registered participants (79 onsite + 88 online), and 11 project proposals for the future JA were presented and discussed with stakeholders (regulators, radiation protection professionals, clinicians, and EC officers). Thanks to the identified stakeholders, the 18 organisations from 12 countries in PrISMA were in touch with over 400 stakeholders in 33 possible eligible countries. ***Conclusion:*** In the longer perspective, a successful implementation of the SAMIRA Joint Action will lead to a sustainable, high-quality, and safe diagnostic and therapeutic use of medical ionising radiation for citizens in Europe, and built the basis for the future SAMIRA Joint Action in the next months. ***References:*** - EU Grant Agreement 101162826.

1606

Tuesday, October 7, 2025, 16:45 - 18:15
Room 117

Clinical Oncology Track - TROP Session - Oncology & Theranostics Committee: Imaging Prostate Cancer: Prediction and Outcome

OP-709

Additive Value of [^{68}Ga]Ga-RM26 PET/CT to [^{68}Ga]Ga-PSMA-617 PET/CT in Detecting Pelvic Lymph Node Metastasis in Prostate Cancer: A Prospective, Single-Center, Phase II Study

Y. Tang[1], *Y. Li*[1], *L. Xiao*[1], *J. Yang*[1], *M. Zhou*[1], *K. Shi*[2], *S. Hu*[1];
[1]*Xiangya Hospital Central South University, Changsha, CHINA,* [2]*Department of Nuclear Medicine, Inselspital, Bern University Hospital, University of Bern, BERN, SWITZERLAND.*

Aim/Introduction: Lymph node staging in prostate cancer is crucial for treatment and prognosis, yet [^{68}Ga]Ga-PSMA-617 PET/CT has limited sensitivity in detecting pelvic lymph node metastasis (PLNM). [^{68}Ga]Ga-RM26 PET/CT, targeting the gastrin-releasing peptide receptor, complements [^{68}Ga]Ga-PSMA-617 PET/CT in assessing primary tumor extension and aggressiveness. However, its role in detecting PLNM and complementing [^{68}Ga]Ga-PSMA-617 PET/CT remains underexplored. ***Materials and Methods:*** This prospective study enrolled newly diagnosed yet untreated prostate cancer patients who underwent [^{68}Ga]Ga-RM26 PET/CT and [^{68}Ga]Ga-PSMA-617 PET/CT, followed by radical prostatectomy and extended pelvic lymph node dissection. The primary objective was to evaluate the diagnostic performance of both PET/CT modalities in detecting PLNM. ***Results:*** In total, 68 patients were enrolled, with a 30.9% (21/68) pathologic PLNM rate. In patientbased analysis, [^{68}Ga]Ga-RM26 PET/CT had sensitivity and specificity of 0.43 and 0.94, respectively, compared with 0.52 and 0.89 for [^{68}Ga]Ga-PSMA-617 PET/CT. [^{68}Ga]Ga-RM26 PET/CT detected additional PLNMs in 50% (5/10) of patients that were missed by [^{68}Ga]Ga-PSMA-617 PET/CT. The combined use of [^{68}Ga]Ga-RM26 PET/CT and [^{68}Ga]Ga-PSMA-617 PET/CT resulted in sensitivity of 0.76 and specificity of 0.85. In total, 1,049 lymph nodes were dissected, including 991 normal and 58 positive nodes. In lesion-based analysis, [^{68}Ga]Ga-RM26 PET/CT had sensitivity and specificity of 0.38 and 0.99, respectively, compared with 0.5 and 0.99 for [^{68}Ga]Ga-PSMA-617 PET/CT. [^{68}Ga]Ga-RM26 PET/CT identified 41.4% (12/29) of pathologic positive nodes missed by [^{68}Ga]Ga-PSMA-617 PET/CT. The combined [^{68}Ga]Ga-RM26 and [^{68}Ga]Ga-PSMA-617 PET/CT demonstrated sensitivity of 0.71 and specificity of 0.99. ***Conclusion:*** In dual-target imaging, [^{68}Ga]Ga-

RM26 PET/CT identified additional PLNMs. The combination of [68Ga]Ga-RM26 PET/CT and [68Ga]Ga-PSMA-617 PET/CT achieved higher diagnostic sensitivity with minimal loss of specificity. ***References:*** 1. Gao X, Tang Y, Chen M, et al. A prospective comparative study of [68Ga]Ga-RM26 and [68Ga]Ga-PSMA-617 PET/CT imaging in suspicious prostate cancer. Eur J Nucl Med Mol Imaging. 2023;50(7):2177-2187. doi:10.1007/s00259-023-06142-2 2. Li Y, Yang J, Xiao L, et al. Using mpMRI, PSMA, and GRPR PET to Assess Focal Therapy Eligibility and Plan Treatment in Biopsy-proven Low-/Intermediate-risk Prostate Cancer: A Whole-mount Pathology-based Study. Clin Nucl Med. 2025;50(5):410-418. doi:10.1097/RLU.0000000000005724.

OP-710

Association of Genomic Classifier Scores with PSMA PET/CT in Patients with High-Risk Prostate Cancer: First-Year Results from the Phase 2/3 THUNDER trial (NCT06282588)

F. Kleiburg[1,2,3], *P. Dirix*[3], *V. Fonteyne*[4], *S. Bral*[5], *B. De Troyer*[6], *B. Sautois*[7], *M. Lamande*[7], *N. Liefhooghe*[8], *G. Grisay*[9], *S. Meersschout*[10], *A. Vandermeulen*[11], *N. Jullian*[12], *L. Staelens*[13], *M. Johnson*[14], *E. Kelly*[14], *F. Poelaert*[15], *M. Strijbos*[15], *J. Verschueren*[15], *K. Goffin*[16], *N. Withofs*[7], *P. Ost*[3];
[1]Leiden University Medical Centre, Leiden, NETHERLANDS, [2]University of Twente, Enschede, NETHERLANDS, [3]Iridium Network, Antwerp, BELGIUM, [4]Ghent University Hospital, Ghent, BELGIUM, [5]AZORG, Aalst, BELGIUM, [6]VITAZ, Sint-Niklaas, BELGIUM, [7]Centre Hospitalier Universitaire de Liège, Liège, BELGIUM, [8]AZ Groeninge, Kortrijk, BELGIUM, [9]Centres Hospitaliers Universitaires HELORA, La Louvière, BELGIUM, [10]AZ Sint-Jan, Bruges, BELGIUM, [11]Cliniques Universitaires Saint-Luc, Brussels, BELGIUM, [12]Institut Jules Bordet, Brussels, BELGIUM, [13]AZ Delta, Roeselare, BELGIUM, [14]Veracyte Inc, San Diego, CA, UNITED STATES OF AMERICA, [15]ZAS, Antwerp, BELGIUM, [16]UZ Leuven, Leuven, BELGIUM.

Aim/Introduction: PSMA PET/CT upstages 8% of high-risk prostate cancers to M1 disease[1]. The Decipher genomic classifier (GC) score is a prognostic biomarker, with 42% of patients scoring >0.85 developing distant metastases within 10 years[2]. In high-risk prostate cancer, the phase 2/3 THUNDER trial (NCT06282588) investigates whether treatment adaptation based on PSMA PET/CT and GC scores improves metastasis-free survival. This prospective substudy focused on stage migration on PSMA PET/CT versus conventional imaging, and the association between GC scores and PSMA PET/CT results during the first year of the trial. ***Materials and Methods:*** High-risk prostate cancer patients (defined as at least one of: PSA >20 ng/mL, T-stage ≥3, ISUP grade ≥4, cN1 disease) referred for curative-intent radiotherapy and consenting between 13-12-2023 and 12-12-2024, were included. Patients with M1 disease on conventional imaging were analysed for stage migration (cohort 1: n=142), but excluded from GC score analysis (cohort 2: n=133). Within 16 weeks before screening, patients underwent contrast-enhanced CT, bone scintigraphy and PSMA PET/CT, evaluated using TNM or PROMISE V2 criteria[3]. GC scores were determined on diagnostic biopsy tissue (Veracyte, San Diego, USA) and categorized as low to intermediate (≤0.60), high (>0.60, ≤0.85) and very high (>0.85). ***Results:*** In cohort 1, 38% had PSA >20 ng/mL, 61% T-stage ≥3, 73% ISUP grade ≥4, and 19% cN1 disease. PSMA PET/CT upstaged 42 patients (30%), including miN1-2 upstaging in 23% and miM1 upstaging in 13%. One patient (1%) was downstaged. In cohort 2, 53% of patients had a very high GC score, 28% a high score, 20% a low to intermediate score. Extraprostatic PSMA uptake was observed in 47% of patients with a very high GC score (miN1-2M0: 27%, miM1a: 9%, miM1b-c: 11%), 46% of patients with a high score (miN1-2M0: 38%, miM1a: 5%, miM1b-c: 3%) and 23% of patients with a low to intermediate score (miN1-2M0: 12%, miM1a: 8%, miM1b-c: 4%). GC score was significantly associated with extraprostatic disease on PSMA PET/CT (OR=1.29 per 0.1 increase, p=0.016), independent of PSA and ISUP grade. ***Conclusion:*** In this very high-risk prostate cancer cohort, PSMA PET/CT upstaged approximately one in three patients. Interestingly, over half of the patients with a GC score >0.85 showed no extraprostatic disease on PSMA PET/CT. The THUNDER trial will evaluate PSMA- and GC-guided treatment adaptation strategies. ***References:*** [1]Hofman et al. Lancet. 2020; doi:10.1016/S0140-6736(20)30314-7, [2]Nguyen et al. Int J Radiat Oncol Biol Phys. 2023; doi:10.1016/j.ijrobp.2022.12.035, [3]Seifert et al. Eur Urol. 2023; doi:10.1016/j.eururo.2023.02.002.

OP-711

Initial Staging 68Ga-PSMA PET/CT Predicts Overall Survival in Unfavorable Intermediate and High-Risk Prostate Cancer: An IAEA Multicenter Study

J. Cerci[1], *S. Fanti*[2], *E. E.stradaLobato*[3], *J. Kunikowska*[4], *O. Garcia*[5], *F. Novruzov*[6], *R. Kumar*[7], *A. Al-Ibraheem*[8], *M. Haidar*[9], *M. Nasir*[10], *O. Kucuk*[11], *U. Elboga*[12], *F. Redondo Moneda*[13];
[1]Quanta - Diagnóstico e Terapia, Curitiba, BRAZIL, [2]IRCCS Azienda Ospedaliero-Universitaria di Bologna, Bologna, ITALY, [3]Division of Human Health, International Atomic Energy Agency, Vienna, AUSTRIA, [4]Nuclear Medicine Department, Medical University of Warsaw, Warsaw, POLAND, [5]Instituto Nacional de Cancerologia, Tlalpan, MEXICO, [6]Nuclear Medicine Department, National Centre of Oncology, Baku, AZERBAIJAN, [7]All India Institute of Medical Sciences, New Delhi, INDIA, [8]King Hussein Cancer Center, Amman, JORDAN, [9]American University of Beirut Medical Center, Beirut, LEBANON, [10]Institute Kanser Negara, Putrajaya, MALAYSIA, [11]Ankara University, Ankara, TÜRKIYE, [12]University of Gaziantep, Gaziantep, TÜRKIYE, [13]Complejo Asistencial Sotero del Río, Santiago Clínica Andes Salud, Puerto Montt, CHILE.

Aim/Introduction: Supported by the IAEA, this study assessed the prognostic impact of initial staging 68Ga-PSMA PET/CT in unfavorable intermediate/high-risk PCa. ***Materials and Methods:*** A multicenter trial enrolled 775 newly diagnosed, treatment-naïve patients. Based on 68Ga-PSMA PET/CT, patients were categorized as PSMA-N0M0 (no metastases), PSMA-N1M0 (lymph node involvement), or PSMA-NxM1 (distant metastases). ***Results:*** Biochemical relapse rates were 35.4% (N0M0), 68.2% (N1M0), and 77.2% (NxM1). 2-year EFS rates for PSMA groups were: 56.6% in PSMA-N0M0: 43.9% in PSMA-N1M0: and 26.0% in PSMA-NxM1. 2-year OS rates were 99.3% in PSMA-N0M0, 99.2% in PSMA-N1M0 and 86.8% in PSMANxM1 ($p < 0.001$). PSMA status was the only significant prognostic factor ($p < 0.001$). ***Conclusion:*** 68Ga-PSMA PET/CT is a prognostic tool for PCa, improving staging accuracy. Treatment might be tailored based on 68Ga-PSMA PET/CT results to improve outcomes. ***References:*** Hofman MS, Kasivisvanathan V, Link E, et al. Baseline Nodal Status on 68Ga-PSMA-11 Positron Emission Tomography/Computed Tomography in Men with Intermediate- to High-risk Prostate Cancer Is Prognostic for Treatment Failure: Follow-up of the proPSMA Trial. Eur Urol Oncol. Published online November 28, 2024. doi:10.1016/j.euo.2024.11.006 Xiang M, Ma TM, Savjani R, et al. Performance of a Prostate-Specific Membrane Antigen Positron Emission Tomography/Computed Tomography-Derived Risk-Stratification Tool for High-risk and Very High-risk Prostate Cancer. JAMA Netw Open. 2021;4(12):e2138550. Published 2021 Dec 1. doi:10.1001/jamanetworkopen.2021.38550.

OP-712

The additivevalue of 68Ga-RM26 to 68Ga-PSMA-617PET/CT in the early prediction of biochemical failure in prostate cancer: results from a prospective, single-arm, phase IImultimodal imaging trial

J. Yang, *Y. Tang, Y. Li, L. Xiao, S. Hu;*
Xiangya hospital, Changsha, CHINA.

Aim/Introduction: Accurate prediction of biochemical recurrence (BCR) in prostate cancer (PCa) patients is crucial for optimizing treatment strategies and improving clinical outcomes. However, current prognostic tools demonstrate suboptimal predictive

accuracy (approximate 65% accuracy in reported studies). PSMA and GRPR have emerged as highly promising molecular targets for PCa imaging, with complementary expression patterns in PCa, offering potential for a more precise and comprehensive assessment of BCR risk. This study aims to investigate the role of dual-tracer PET/CT (^{68}Ga-PSMA, and GRPR targeted ^{68}Ga-RM26) in the early prediction of postoperative biochemical recurrence-free survival (BRFS) in PCa patients, in order to provide additional molecular indicators for novel prognostic stratification in PCa. ***Materials and Methods:*** Consecutive PCa patients undergoing preoperative dual-tracer PET/CT (^{68}Ga-PSMA-617 and ^{68}Ga-RM26) prior to radical prostatectomy were analyzed. Optimal PSMA/GRPR SUVmax cutoffs were determined via maximally selected rank statistics. Log-rank test and Cox regression were performed to assess the correlation between BRFS and PSMA/GRPR-SUVmax. Time-dependent area under the curve (AUC) was used to assess and quantify the performance of various risk factors. Additionally, we integrated the PSMA and GRPR dual-target imaging for constructing a predictive model, and tested the findings using external transcriptome data. ***Results:*** Among 102 patients, 51.0% experienced BCR/additional therapies. Higher PSMA-SUVmax (> 6.6) (HR: 3.17, 95%CI: 1.74-5.76, p = 0.004) and lower GRPR-SUVmax (≤ 13.0) (HR: 0.51, 95%CI: 0.29-0.88, p = 0.026) were associated with shorter BRFS. Further multivariate Cox regression analysis confirmed that both variables as independent predictors of BRFS. Correlation analyses revealed that PSMA-SUVmax significantly correlated with multiple established BCR predictors, whereas ^{68}Ga-RM26 PET/CT-derived SUVmax exhibited no significant correlations with any of the parameters. Integrative analysis revealed that the combined PSMA/GRPR-SUVmax model (time-dependent AUC: 0.73) significantly outperformed individual GRPR-SUVmax (time-dependent AUC: 0.62) or PSMA-SUVmax (time-dependent AUC: 0.63) measurements in the predictive accuracy. An external validation cohort of 198 individuals revealed that higher PSMA expression and lower GRPR expression were significantly associated with shorter BRFS. In addition, patients exhibiting high PSMA and low GRPR expression levels experienced poorer clinical outcomes, which was similar to the results of our dual- trace PET-based analyses. ***Conclusion:*** Our study provides the first clinical evidence demonstrating that tumor GRPR-SUVmax independently correlates with postoperative BRFS. The integration of GRPR PET with PSMA PET imaging offers enhanced accuracy in assessing BCR risk in PCa patients, potentially enabling identification of high-risk patients and facilitating personalized treatment strategies.

OP-713

Prognostic value of basline PSMA PET/CT for survival in synchronous metastatic hormone-sensitive prostate cancer: towards redefining low- and high-volume disease

F. Kleiburg[1,2], *L. Heijmen*[1], *A. Witteveen*[2], *K. van Duuren*[1], *P. Zuidgeest*[1], *F. Smit*[3], *L. de Geus-Oei*[1,2,4], *T. van der Hulle*[1];
[1]*Leiden University Medical Centre, Leiden, NETHERLANDS,* [2]*University of Twente, Enschede, NETHERLANDS,* [3]*Alrijne Hospital, Leiderdorp, NETHERLANDS,* [4]*Delft University of Technology, Delft, NETHERLANDS.*

Aim/Introduction: Since many clinical centres replaced conventional imaging with PSMA PET/CT for staging prostate cancer patients, there has been a high need for a reclassification of low- and high-volume metastatic disease to guide treatment decisions. This study aimed to provide insight into the prognostic value of PSMA PET/CT in metastatic hormone-sensitive prostate cancer (mHSPC), which can serve as a basis for redefining imaging-based risk stratification. ***Materials and Methods:*** Patients with synchronous mHSPC staged with PSMA PET/CT between April 2017 and August 2023 were included in this retrospective bicentric study. The PET parameters total tumour volume (PSMA-TV), total lesion uptake (TL-PSMA), DmaxVox (distance between the two outermost voxels), SUV_{max}, SUV_{mean} and metastatic sites were extracted. Additionally, age, ECOG/WHO performance status, iPSA, Gleason score, alkaline phosphatase and haemoglobin levels were collected. Multivariable Cox regression analysis identified independent significant predictors for overall survival (OS). Prediction model performance was evaluated using Harrell's C-index. Internal validation was performed using bootstrapping with 1000 samples. ***Results:*** A total of 204 patients were included, of which multidisciplinary team (MDT) meetings classified 75 (37%) as having low-volume disease (median PSMA-TV: 60 mL, median OS: 69 months), and 129 (63%) as having high-volume disease (median PSMA-TV: 483 mL, median OS: 41 months). PSMA-TV was the strongest predictor of OS (HR=1.39 per doubling, p<0.001), independent of ECOG/WHO performance status (HR=1.69 per score increase, p<0.001) and treatment. Other parameters had no predictive value in multivariate analysis. A prediction model for OS incorporating PSMA-TV and ECOG/WHO performance status achieved a C-index of 0.72, which remained at 0.71 after internal validation. In terms of differentiating long-term and short-term survivors, the optimal definition for PSMA-TV-based high-volume disease was: PSMA-TV ≥150 mL or any visceral metastasis. This classification (HR=3.01, p<0.001) outperformed MDT-based patient classification (HR=2.68, p<0.001). ***Conclusion:*** This study showed that PSMA-TV provided the best risk stratification for survival in synchronous mHSPC patients staged with PSMA PET/CT. Instead of maintaining a dichotomous approach using a single cut-off value, we propose using a validated survival prediction model, incorporating PSMA-TV as a continuous variable, to help guide treatment decisions. For the further development and validation of such a model, a larger, multi-centre patient cohort is needed.

OP-714

Preoperative Imaging Biomarkers of Aggressive Prostate Cancer: Assessing the role of PSMA PET/CT and mpMRI with Whole-Mount Histopathology Gold Standard

I. Sonni, *D. Hyeong Seok Kim, A. Ter-Pogosyan, S. Satonkiatngam, K. Kimura, T. Grogan, N. Barroso, P. Ahuja, J. Calais, J. Czernin, R. Reiter, A. Sisk, S. S. Raman;*
University of California, Los Angeles, Los Angeles, CA, UNITED STATES OF AMERICA.

Aim/Introduction: Intraductal carcinoma (IDC) and large cribriform pattern (LCP) are aggressive architectural subtypes of prostate cancer (PC) associated with adverse outcomes, including biochemical recurrence and metastasis. Accurate noninvasive prediction of these features could inform risk stratification and treatment planning, particularly when whole-mount histopathology (WMHP) is not available. This study aimed to evaluate the association between quantitative parameters from PSMA PET/CT and mpMRI and the presence of IDC and/or LCP in PC lesions, and to assess the combined predictive performance of PET and MRI metrics. ***Materials and Methods:*** This retrospective single-centre study included patients who underwent PSMA PET/CT prior to robotic-assisted radical prostatectomy at UCLA between January 2017 and July 2024. Lesion-level imaging-pathology correlation was performed between PET-identified lesions (PRIMARY score ≥3) and tumor foci on WMHP (ISUP grade group ≥2). A subcohort underwent preoperative 3T mpMRI with corresponding lesions identified (PI-RADS v2.1 ≥3). For each matched lesion, PET parameters (SUVmax, SUVmean, PSMA tumor volume) and MRI-derived ADC values were extracted. Lesions were grouped based on the presence of IDC and/or LCP. Statistical comparisons between groups were conducted using t-tests and ANOVA. ROC analyses were performed to evaluate predictive accuracy. ***Results:*** The final cohort included 346 patients and 404 matched tumors. Median PSA at prostatectomy was 7.6 ng/mL

(IQR: 5.3-12.85). IDC and/or LCP were present in 254/404 lesions (62.9%). Compared to lesions without these features, lesions with IDC and/or LCP demonstrated significantly higher SUVmax ($p < .001$), SUVmean ($p < .001$), and PSMA PET volume ($p < .001$), and significantly lower ADC values ($p < .001$). ROC analyses showed that SUVmax (AUC = 0.644), SUVmean (AUC = 0.625), and PET volume (AUC = 0.648) moderately predicted the presence of aggressive patterns. ADC had poor discriminatory performance (AUC = 0.335). ***Conclusion:*** Our preliminary results show that quantitative PSMA PET parameters, including SUVmax, SUVmean, and lesion volume, are significantly associated with the presence of IDC and/or LCP, and may serve as imaging indicators of aggressive pathology in prostate cancer. These findings support the potential value of PSMA PET/CT in risk stratification. Further analysis is underway to develop an integrated predictive model combining PET and mpMRI metrics. A more comprehensive assessment of their joint contribution to noninvasive detection of aggressive histological patterns is ongoing.

OP-715

Optimization of the PRIMARY Score in Ga-68 PSMA PET/CT: A New Approach to Active Surveillance Decision

D. Sahin, *H. Uslu, S. Güngör, S. Yaşar Belek, Ö. Doğan Yıldız, B. Canıtez, H. Kösem;*
Istanbul Medeniyet University Göztepe Prof. Dr. Süleyman Yalçın City Hospital, Istanbul, TÜRKIYE.

Aim/Introduction: Active surveillance (AS) in prostate cancer (PCa) aims to avoid overtreatment and related side effects in localized disease, providing treatment only when necessary. According to NCCN guidelines, AS is recommended for patients with very low, low, and favorable intermediate-risk after confirmatory tests (1). The PRIMARY score is a scale developed for ^{68}Ga-PSMA PET/CT to identify clinically significant intraprostatic lesions (2). Score 4 is defined as a focal lesion in the peripheral zone but lacks a minimum activity threshold. This study aimed to optimize score 4 by defining an SUV_{max} cut-off and evaluating its effect on ^{68}Ga-PSMA PET/CT's diagnostic performance. ***Materials and Methods:*** A total of 173 patients diagnosed with PCa and who underwent ^{68}Ga-PSMA PET/CT for staging purposes were retrospectively evaluated. Age, total PSA (tPSA), biopsy-detected ISUP grade (bISUP), prostate SUV_{max} (p-SUV_{max}), prostate-to-liver SUV_{max} ratio (p/l-SUV_{max}), and PI-RADS scores of 129 patients with multiparametric magnetic resonance (mpMR) imaging reports were recorded. Patients were classified into AS candidate and non-candidate groups based on NCCN criteria. Differences in SUV_{max} values were evaluated using the Mann-Whitney U test. The Youden index was used to determine cut-off values. Lesions with a score of 4 and SUV_{max} values below these thresholds were reclassified as score 2, creating two new versions of the PRIMARY score: pPRIMARY and plPRIMARY. ROC analysis and Wilcoxon Signed-Rank tests were used to compare diagnostic performance. ***Results:*** The characteristics of the patients are given in Table 1. The most common PRIMARY score was 4 (59.0%). In patients with PRIMARY score 4, p-SUV_{max} values showed a significant difference between the groups that were and were not candidates for AS ($p < 0.001$). In these patients, the cut-off values calculated using Youden index were 4.65 for p-SUV_{max} and 1.03 for p/l-SUV_{max}. Diagnostic performance analyses of PRIMARY, pPRIMARY, plPRIMARY and PI-RADS tests are given in Table 2. Statistically significant differences were found between PRIMARY and both optimized scores ($p < 0.001$), while no significant difference was observed between pPRIMARY and plPRIMARY ($p = 0.271$). ***Conclusion:*** Applying a prostate SUV_{max} cut-off of 4.65 or a prostate-to-liver SUV_{max} ratio cut-off of 1.0 to score 4 significantly enhances the diagnostic accuracy of PRIMARY scoring in selecting candidates for AS. This optimization supports the potential role of ^{68}Ga-PSMA PET/CT as a confirmatory tool in AS decision-making. ***References:*** 1- Schaffer EM, et al. J Natl Compr Canc Netw. 20252- Emmett L, et al., J Nucl Med. 2022.

OP-716

The Diagnostic Utility of PSMA PET with Real-Time PSMA-PET Fusion - Target Biopsy in MRI-Negative or Equivocal Prostate Cancer: Results from the FUPERMAN Study

C. Sgro[1], *L. Bianchi*[2], *P. Castellucci*[3], *R. Mei*[3], *E. Greco*[1], *M. Presutti*[2], *F. Romei*[2], *M. Droghetti*[2], *R. Schiavina*[2], *E. Brunocilla*[2], *C. Gaudiano*[4], *B. Corcioni*[4], *S. Fanti*[3,1], *A. Farolfi*[3];
[1]*Nuclear medicine, Alma Mater Studiorum University of Bologna, Bologna, ITALY,* [2]*Division of Urology, IRCCS, Azienda Ospedaliero-Universitaria di Bologna, Bologna, ITALY,* [3]*Nuclear Medicine, IRCCS, Azienda Ospedaliero-Universitaria di Bologna, Bologna, ITALY,* [4]*Department of Radiology, IRCCS, Azienda Ospedaliero-Universitaria di Bologna, Bologna, ITALY.*

Aim/Introduction: Multiparametric MRI (mpMRI) is the cornerstone for prostate cancer (PCa) diagnosis but shows limited sensitivity in PI-RADS 1-3 lesions, risking underdetection of clinically significant prostate cancer (csPCa). The FUPERMAN study aimed to assess the added diagnostic value of PSMA-PET in this subgroup, using real-time PSMA-PET fusion-target biopsy. ***Materials and Methods:*** FUPERMAN is a prospective, single-center study enrolling men with suspected PCa (PSA≥4ng/mL, PSA density≥0.1 ng/mL2, family history of PCa) and negative or equivocal mpMRI (PI-RADS 1-3). All patients underwent 68Ga-PSMA-11 PET/CT within 6-months of mpMRI, with image acquisition at 60- and 90-minutes post-injection. Intra-prostatic PSMA uptake was assessed using the PRIMARY score. Lesions with PRIMARY ≥3 were considered PSMA-positive and targeted using transperineal PSMA-PET fusion-target biopsy. All patients also underwent systematic biopsy. csPCa was defined as ISUP grade group≥2. ***Results:*** A total of 54 men were enrolled (median age: 67 y.o., median PSA: 13.1 ng/mL and median dPSA: 0.23 ng/mL2). mpMRI revealed PI-RADS 2 in 81% and PI-RADS 3 in 19%. PSMA-PET identified PRIMARY ≥3 uptake in 65% (35/54) of patients, who underwent PSMA-PET fusion-target biopsy combined with systematic biopsy. The remaining 19 patients (PRIMARY 1-2) underwent systematic biopsy only. Detection of csPCa increased with higher PRIMARY scores: 5% in scores 1-2, 30% in score 3, 38% in score 4, and 100% in score 5 ($p<0.001$). Higher PRIMARY scores were associated with greater estimated tumor volume on biopsies ($p<0.001$). Among patients with PRIMARY ≥3, 19 /35 (54%) had csPCa and 65% had any cancer (including ISUP 1). Overall, csPCa was detected in 20/54 (37%), and any cancer in 30/53 (56%). ISUP grade group distribution among csPCa cases was as follows: 8 ISUP 2, 5 ISUP 3, 5 ISUP 4 and 2 ISUP 5. SUVmax at both 60 and 90 minutes post-injection was significantly associated with the presence of csPCa (both $p<0.05$). For detection of csPCa, sensitivity was 84%, specificity 78%, NPV 98%, PPV 30%, and accuracy 78%. Larger prostate volume on mpMRI was associated with a higher false-positive rate for PSMA-PET ($p<0.05$). ***Conclusion:*** In men with high risk PCa, but negative or equivocal mpMRI, PSMA-PET fusion-target biopsy significantly enhances csPCa detection. The PRIMARY score serves as a reliable tool for lesion risk stratification.

OP-717

[^{68}Ga]Ga-PSMA-617 PET/CT and [^{68}Ga]Ga-NT PET/CT for Prostate Cancer Imaging: A Comparative Study and First Attempt of a Molecular Imaging Probe Targeting NTSR1 in Humans

Y. Tang[1], *Y. Li*[1], *L. Xiao*[1], *J. Yang*[1], *K. Shi*[2], *S. Hu*[1];
[1]*Xiangya Hospital Central South University, Changsha, CHINA,* [2]*Department of Nuclear Medicine, Inselspital, Bern University Hospital, University of Bern, Bern, SWITZERLAND.*

Aim/Introduction: We performed the first human imaging with [^{68}Ga]Ga-NT PET/CT and evaluated the imaging efficacy of [^{68}Ga]Ga-PSMA-617 PET/CT and [^{68}Ga]Ga-NT PET/CT in prostate cancer. ***Materials and Methods:*** This prospective study enrolled 23 patients with histopathologically confirmed prostate adenocarcinoma, stratified into two subgroups based on whether they received endocrine therapy prior to radical prostatectomy (RP). All patients

underwent [68Ga]Ga-PSMA-617 PET/CT and [68Ga]Ga-NT PET/CT before surgery, with the diagnostic efficacy of these imaging modalities evaluated. Additionally, the protein expression levels of prostate-specific membrane antigen (PSMA) and neurotensin receptor 1 (NTSR1) in the primary lesions were validated. ***Results:*** In all included prostate cancer cases, [68Ga]Ga-PSMA-617 PET/CT demonstrated significantly higher diagnostic sensitivity (82.6% vs. 4.3%; p = 0.0006) and lesion detection rate (88.9% vs. 3.2%; p < 0.0001) compared to [68Ga]Ga-NT PET/CT. Subgroup analysis of treatment-naïve patients revealed that [68Ga]Ga-PSMA-617 PET/CT had a sensitivity of 92.9% (95% CI: 64.2%-99.6%), specificity of 86.7% (95% CI: 58.4%-97.7%), positive predictive value (PPV) of 86.7% (95% CI: 58.4%-97.7%), and negative predictive value (NPV) of 92.9% (95% CI: 64.2%-99.6%). In contrast, [68Ga]Ga-NT PET/CT exhibited a sensitivity of 0% (95% CI: 0%-26.8%), specificity of 100% (95% CI: 74.7%-100%), and NPV of 51.7% (95% CI: 32.9%-70.1%). Following endocrine therapy, the sensitivity and lesion detection rate of [68Ga]Ga-PSMA-617 PET/CT decreased to 66.7% and 80%, respectively, while [68Ga]Ga-NT PET/CT showed an improved sensitivity of 11.1% and lesion detection rate of 8%, with specificity and PPV remaining at 100%. Immunohistochemical (IHC) analysis of radiotracer-avid lesions revealed a significant reduction in the median PSMA IHC score from 9 (range: 6-12) to 7 (range: 1-9) post-endocrine therapy (p = 0.034), alongside a significant increase in the median NTSR1 IHC score from 1 (range: 0.25-2) to 3 (range: 2-3.8) (p = 0.0074). ***Conclusion:*** This study shows that [68Ga]Ga-PSMA-617 PET/CT has better sensitivity and lesion detection for diagnosing prostate cancer than [68Ga]Ga-NT PET/CT. After endocrine therapy, [68Ga]Ga-PSMA-617 PET/CT's effectiveness decreased, while [68Ga]Ga-NT PET/CT's improved, likely due to reduced PSMA and increased NTSR1 expression. Given the short endocrine therapy duration in these patients, [68Ga]Ga-NT PET/CT may be useful for re-staging, re-evaluation, and monitoring post-treatment recurrence, especially with longer treatment. ***References:*** He, T., Wang, M., Wang, H., Tan, H., Tang, Y., Smith, E., Wu, Z., Liao, W., Hu, S., & Li, Z. (2019). Evaluation of neurotensin receptor 1 as potential biomarker for prostate cancer theranostic use. European journal of nuclear medicine and molecular imaging, 46(10), 2199-2207. https://doi.org/10.1007/s00259-019-04355-y.

1607

Tuesday, October 7, 2025, 16:45 - 18:15
Room 212

TROP Session - Neuroimaging Committee: Neurology: Psychiatry, Epilepsy, Inflammation and Others

OP-718

Short antidepressant response and brain amyloid load in non-demented older adults with depression - The first part of ASAP Study

M. Santiago-Ribeiro[1], *T. Desmidt*[1], *J. Vercouillie*[2], *F. Lejeune*[3], *N. Arlicot*[1], *V. Gissot*[1], *A. Dupont*[1], *W. El-Hage*[1], *A. Caille*[1], *V. Camus*[1], *ASAP group;*
[1]CHRU, Tours, FRANCE, [2]Université de Tours, Tours, FRANCE, [3]CHU, Rennes, FRANCE.

Aim/Introduction: Amyloid accumulation in the brain may predispose to late-life depression (LLD). Depression is highly prevalent in the prodromal phase of Alzheimer's disease, which could be attributed to the consequences of neurodegeneration. We studied the relationship between cortical amyloid load and early response to antidepressant treatment in non-demented older adults. ***Materials and Methods:*** 92 Non-demented older adults with depression were enrolled in an 8-week observational study to assess the relationship between brain amyloid load and early antidepressant response. Amyloid load was measured using 18F-Florbetapir PET, and treatment response was evaluated using the MADRS. The injected radioactivity was 4 MBq/kg and, for each subject, two frames of 10 minutes were acquired, 50 min pi. Both visual and semiquantitative analyses were performed. 18F-Florbetapir PET images were visually assessed by two nuclear medicine physicians, who were blinded to all clinical and diagnostic information, using a binary scale to classify each scan 0 (no significant) or 1 (significant) 18F-Florbetapir cortical uptake. Volumes of interest (VOI) were defined in several cerebral regions according to the MNI-AAL atlas. Cortical-to-cerebellum standardized uptake value ratios (SUVr) were calculated and used for inter-subject comparison. The analysis compared amyloid load in responders versus non-responders at week 8. ***Results:*** Analysis regarding the 8-week antidepressant response status were performed on 73/92 subjects. Forty-one participants were considered responders and the remaining 32 as non-responders. 36 patients were considered as amyloid positive and 37 as negative. There were no significant differences in global cerebral SUVr (mean±SD) (responders 1.22±0.30, no-responders 1.16±0.33, p=0.40) or in SUVr calculated for each cortical region analyzed between responders and non-responders after 8 weeks of treatment. MADRS score was lower in amyloid positive versus negative participants at baseline (25.7±6.1 vs 30.0±6.8, p=0.005) and at week 8 (11.9±7.8 vs 16.3±10.3, p=0.045). ***Conclusion:*** In this observational cohort of non-demented depressed older adults, amyloid burden does not appear to modify response status in the short term of treatment.

OP-719

Altered AMPA receptors density associated with ketamine response in treatment-resistant depression: PET study using [11C]K-2.

W. Nakajima[1], *M. Hatano*[1], *Y. Ohtani*[2], *H. Tani*[2], *S. Tsuchimoto*[3], *Y. Fujimoto*[1], *T. Eiro*[1], *S. Ichijo*[1], *K. Nakano*[1], *T. Arisawa*[4], *Y. Takada*[1], *K. Kimura*[1], *H. Abe*[1], *T. Miyazaki*[1,5], *A. Sano*[1], *K. Nomoto-Takahashi*[2], *T. Yatomi*[1,2], *K. Yonezawa*[2], *S. Tomiyama*[2], *N. Nagai*[2,6], *K. Kusudo*[2], *S. Honda*[2], *S. Moriyama*[2], *S. Nakajima*[2], *Y. Kimura*[7], *H. Uchida*[2], *T. Takahashi*[1,8];
[1]Department of Physiology, Yokohama City University School of medicine, Yokohama, JAPAN, [2]Department of Neuropsychiatry, Keio University School of Medicine, Tokyo, JAPAN, [3]Division of Neural Dynamics, Department of System Neuroscience, National Institute for Physiological Sciences, Okazaki, JAPAN, [4]Radioisotope Research Center, Yokohama City University Graduate School of Medicine, Yokohama, JAPAN, [5]Center for Promotion of Research and Industry-Academic Collaboration, Yokohama, JAPAN, [6]Department of Psychiatry, Minami-Hanno Hospital, Tokyo, JAPAN, [7]Faculty of Informatics, Cyber Informatics Research Institute, Kindai University, Higashi-Osaka, JAPAN, [8]The International Research Center for Neurointelligence, Institutes for Advanced Study, University of Tokyo, Tokyo, JAPAN.

Aim/Introduction: AMPA receptor (AMPAR) dysfunction may contribute to the pathophysiology of depression. Approximately one-third of patients with depression have treatment-resistant depression (TRD), showing inadequate respond to standard antidepressant treatment. Ketamine showed efficacy in TRD, potentially through modulation of AMPAR function. Although post-mortem studies reported that AMPAR density altered in depression, in vivo evidence remains lacking. This study aimed to investigate the relationship between AMPAR density and symptom severity in patients with TRD using positron emission tomography (PET), and to assess whether ketamine alters AMPAR distribution in these patients. ***Materials and Methods:*** Forty-nine healthy controls and thirty-four patients with TRD underwent PET scanning using [11C]K-2, a PET tracer selective for cell-surface AMPARs. Patients with TRD were randomly assigned to receive either saline (n=17) or ketamine (n=17) twice a week for two weeks and performed 2nd PET scan at 1 month after the first scan. Depression severity was measured using the Montgomery-Åsberg Depression Rating Scale (MADRS). We performed regression analysis between SUVR (reference; whole brain) and

MADRS total scores, and between ΔSUVR (2nd scan - 1st scan) and % improvement in MADRS scores. Additionally, we compared SUVR between healthy controls and TRD patients and explored the predictive value of baseline AMPAR distribution for treatment response. ***Results:*** A negative correlation was observed between baseline SUVR and symptomatology scores in the fronto- parietal cortices of patients with TRD. Compared to the healthy participants, patients with TRD decreased SUVR in several cortical areas and increased SUVR in the cerebellum, temporal cortex, and basal ganglia. In the ketamine group, there was a positive correlation in the fronto-parietal cortices and a negative correlation in the cerebellum and habenula between ΔSUVR and % improvement of MADRS scores. These region-specific alterations in AMPAR density partially restored the AMPAR phenotype in affected brain areas. Furthermore, some brain regions showed correlations between baseline SUVR and %improvement in MADRS scores. ***Conclusion:*** AMPAR dynamics play a key role in mediating the antidepressant effects of ketamine in patients with TRD. ***References:*** Miyazaki T, Nakajima W et al. Visualization of AMPA receptors in living human brain with positron emission tomography. Nat Med 2020; 26(2)**:** 281-288.Hatano M, Nakajima W et al. Characterization of patients with major psychiatric disorders with AMPA receptor positron emission tomography. Mol Psychiatry 2024.Ohtani Y, Tani H, Nomoto-Takahashi K et al. Efficacy and safety of intravenous ketamine treatment in Japanese patients with treatment-resistant depression: A double-blind, randomized, placebo-controlled trial. Psychiatry Clin Neurosci 2024.

OP-720

Seasonal DAT availability in Major Depressive Disorder: a ^{123}I-FP-CIT study.

D. Pizzuto[1], *A. M. D'Onofrio*[2], *S. Annunziata*[1], *F. Cavallo*[3], *F. Cocciolillo*[3], *G. Sani*[2], *G. Camardese*[2], *D. Di Giuda*[3];
[1]*Nuclear Medicine Unit, GSTeP Radiopharmacy, Fondazione Policlinico Universitario A. Gemelli, IRCCS, Rome, ITALY,* [2]*Department of Neuroscience, Section of Psychiatry, Università Cattolica del Sacro Cuore, Largo Francesco Vito 1, Rome, ITALY,* [3]*Nuclear Medicine Unit, Department of Radiology and Radiotherapy, Fondazione Policlinico Universitario A. Gemelli, IRCCS, Rome, ITALY.*

Aim/Introduction: Seasonal changes in central dopaminergic tone have been observed in healthy individuals, but their role in modulating symptom expression in Major Depressive Disorder (MDD) remains poorly understood. This study aimed to investigate seasonal differences in DAT availability in MDD patients using ^{123}I-FP-CIT SPET and to explore DAT differences between clinical subgroups defined by psychopathological dimensions. ***Materials and Methods:*** We retrospectively analysed 85 MDD patients (mean age: 63.6±11.1 years; 40 M) from a ^{123}I-FP-CIT SPET database. Patients were stratified into Spring-Summer (SS, N=58) and Fall-Winter (FW, N=27) according to the time of SPET. The same day as SPET, they underwent psychometric assessments: Hamilton Depression Rating Scale (HAMD), Hamilton Anxiety Rating Scale (HAMA), Snaith-Hamilton Pleasure Scale (SHAPS) and Depression Retardation Rating Scale (DRRS). Patients were stratified according to the presence (SI) or absence (nSI) of suicidal ideation. DAT availability in caudate and putamen was quantified as Specific Binding Ratios (SBRs) using SPM and VOI analysis. ***Results:*** No seasonal differences in DAT availability were observed between FW and SS. SHAPS scores were higher in FW than in SS (p=0.049). In the SS group, patients with severe depression (HAMD score>25) had lower DAT availability in the left putamen compared to patients with moderate depression (HAMD score≤25) (p= 0.014). Lower DAT availability was found in all striatal regions of SS patients with severe retardation (DDRS>18) compared to patients with moderate retardation (DDRS≤18) (p range:0.001-0.032). Conversely, DAT availability in FW did not differ between severe and moderate depression as well as severe and moderate retardation. Patients with anhedonia (SHAPS>3) did not differ in DAT availability from non-anhedonic patients (SHAPS≤3), regardless of season. In the whole sample, patients with severe depression had lower DAT availability in the left putamen than those with moderate depression (p=0.005). Similarly, lower DAT availability in the left putamen was observed in patients with severe retardation compared to those with moderate retardation (p = 0.002). SI patients had lower DAT availability in bilateral putamen than nSI patients (right: p = 0.029; left: p = 0.015), with a greater reduction in SS (right: p = 0.005; left: p = 0.001). ***Conclusion:*** Although DAT availability did not differ across seasons, lower striatal DAT availability was consistently observed in MDD patients with severe psychomotor retardation or severe depression. SS period was associated with more pronounced reductions in DAT availability in these clinical subgroups. Findings suggest a seasonal dopaminergic vulnerability in different MDD phenotypes.

OP-721

Striatal network desynchronization in schizophrenia: initial insights from FDOPA-PET imaging

Y. Mayr[1,2], *J. Schulz*[3], *M. Thalhammer*[3], *M. Veronese*[4,5], *C. Sorg*[3], *F. Brandl*[6], *I. Yakushev*[1,2];
[1]*Department of Nuclear Medicine, Technical University of Munich, Munich, GERMANY,* [2]*Graduate School of Systemic Neurosciences GSN-LMU, Munich, GERMANY,* [3]*Institute for Neuroradiology, Technical University of Munich, Munich, GERMANY,* [4]*Department of Information Engineering, Padova University, Padova, ITALY,* [5]*Department of Neuroimaging, King's College London, London, UNITED KINGDOM,* [6]*Department of Psychiatry, Technical University of Munich, Munich, GERMANY.*

Aim/Introduction: Computational psychiatry posits that the brain normally operates as a stable dynamical system, whereas in psychosis, neural circuits become more vulnerable to even minor perturbations, manifesting as disorganized cognition, giving rise to the classical symptoms of schizophrenia. While the desynchronization hypothesis of schizophrenia is prevailingin the field, most evidence has come from functional MRI studies. Together with network analyses, positron emissiontomography (PET) with 6-[18F]-L-fluoro-L-3, 4- dihydroxyphenylalanine (FDOPA) potentially allows to address the above hypothesis at the level of dopaminergic neurotransmission. Using FDOPA-PET, we assessed synchronicity within the striatalnetwork in patients with schizophrenia in psychosis and in remission, and in healthy control subjects (HC). ***Materials and Methods:*** Patients with schizophrenia (n=17) underwent dynamic FDOPA-PET twice: while being in (mild to moderate) psychosis (S01) and in remission (S02). HC (n=18) underwent dynamic FDOPA-PET twice, too. Influx constant Ki as index of dopaminesynthesis capacity (DSC) was quantified in putamen, caudate nucleus, nucleus accumbens bilaterally with reference to cerebellum, using the Patlak graphical method. Apart from conventional univariate analyses, a network synchronicity matrixwas generated by computing Pearson correlations between Ki of every pair of 6 ROIs for each of three conditions: S01, S02, and HC. In HC, Ki values were averaged between two sessions to improve reliability. Coefficient of variation (CV) of the magnitudes of correlation coefficients was used as index of network desynchronization. ***Results:*** Ki of the striatal subdivisions did not differ between three conditions (p>0.05 uncorrected). The highest CV was found inpatients with psychosis (S01), followed by the condition of remission (S02), and HC. The difference between S01and HC was significant (p=0.04). ***Conclusion:*** Our initial results demonstrate markedly reduced synchronization within the striatal network in individuals with psychotic schizophrenia compared to HC. This desynchronization showed a trend toward normalization during remission. Importantly, striatal DSC itself did not differ between three conditions. These results underscore the utility of network-based analysis of PET data and support the network de-synchronization hypothesis of schizophrenia at the level of dopaminergic neurotransmission.

OP-722

Post Covid-19 cerebral perfusion in patients complaining of recent memory loss: a dual-timepoint study

S. Lopes de Souza[1], *L. C. Melo*[2], *H. F. Carvalho*[3], *K. Ruzzon*[2], *A. O. Blackman*[4], *B. M. Oliveira*[5], *S. K. A. Lima*[1], *A. C. J. Sousa*[6];
[1]*Universidade Federal do Rio de Janeiro / School of Medicine / Radiology Department, Rio de Janeiro, BRAZIL,* [2]*IRB Medicina Nuclear, Brasília, BRAZIL,* [3]*Universidade Católica de Brasília, Brasília, BRAZIL,* [4]*Centro Universitário de Brasília, Brasília, BRAZIL,* [5]*Centro Universitário do Planalto Central Aparecido dos Santos, Brasília, BRAZIL,* [6]*Clinica da Memoria Brasilia, Brasília, BRAZIL.*

Aim/Introduction: The COVID-19 pandemic has imposed a substantial burden on global health, with growing evidence indicating persistent neurological and cognitive sequelae among post-COVID-19 patients. Advanced neuroimaging techniques have played a pivotal role in identifying cerebral perfusion abnormalities that may underlie these long-term symptoms. This study aims to investigate cerebral perfusion changes using Technetium-99m ethyl cysteinate dimer (99mTc-ECD) SPECT imaging in patients with a history of COVID-19 who present with subacute neurological symptoms, particularly recent memory impairment. ***Materials and Methods:*** A total of 95 patients (51 male, 44 female), with a mean age of 53 years (range: 17-85), were evaluated between 2021 and 2024 in an outpatient setting. All patients reported subacute neurological complaints, predominantly cognitive disturbances and headaches. Brain perfusion imaging was performed using SPECT with a dual-head gamma camera system equipped with ultra-high-resolution Fan Beam collimators (GE MN 830). Importantly, none of the patients had a prior history of neurological disorders. A subset of 80 patients also underwent brain MRI. A median interval of 10 months was observed between the first and second SPECT scans. ***Results:*** All 95 patients demonstrated mild to moderate cerebral hypoperfusion. Upon comparison of the initial and follow-up SPECT scans 23% (22/95) showed improved perfusion patterns; 44% (42/95) exhibited no change; 33% (31/95) experienced worsening perfusion. The most commonly affected regions included the frontal cortex, sensorimotor areas, parietal lobes, occipital lobes, lateral temporal cortices, and the cerebellum. These findings, characterized by their diffuse and heterogeneous distribution, suggest a possible underlying vascular mechanism, potentially associated with mood and cognitive disturbances observed in long COVID. ***Conclusion:*** This study highlights a potential link between long COVID and vascular-mediated neurological injury. Brain SPECT imaging proves to be a valuable tool in detecting regional cerebral perfusion abnormalities, offering insights into both disease progression and recovery trajectories. These findings support the incorporation of SPECT into the neurological assessment of post-COVID-19 patients, while also emphasizing the need for further research to elucidate the pathophysiological mechanisms involved and to assess the prognostic value of perfusion imaging in this context.

OP-723

Neurodegenerative Protein Load Correlates with Cognitive Decline in Temporal Lobe Epilepsy: A Multimodal PET Imaging Study

Y. Tang[1], *L. Xiao*[1], *M. Zhou*[1], *J. Yang*[1], *K. Shi*[2], *S. Hu*[1];
[1]*Xiangya Hospital Central South University, Changsha, CHINA,* [2]*Department of Nuclear Medicine, Inselspital, Bern University Hospital, Bern, SWITZERLAND.*

Aim/Introduction: Cognitive impairment is a common comorbidity in temporal lobe epilepsy (TLE), but its underlying mechanisms remain poorly understood. Emerging evidence suggests that neurodegeneration may contribute to this dysfunction; however, the degree, spatial distribution, and relationship between neurodegenerative pathology and cognitive performance in TLE require further investigation. This study utilized advanced PET molecular imaging to localize and quantify hyperphosphorylated tau and β-amyloid deposition across the brain in TLE patients and to evaluate their correlations with cognitive function and clinical phenotypes. ***Materials and Methods:*** We recruited 21 patients with TLE (13 with cognitive impairment and 8 without) and 11 age- and sex-matched healthy controls. All participants underwent comprehensive neuropsychological assessments, as well as PET imaging with ^{18}F-fluorodeoxyglucose ([^{18}F]FDG) to measure glucose metabolism, [^{18}F]MK6240 to assess tau pathology, and ^{11}C-Pittsburgh compound B ([^{11}C]PIB) to quantify β-amyloid deposition. PET data were analyzed using PMOD software, with standardized uptake value ratios (SUVRs) calculated using the cerebellar cortex as the reference region. To account for laterality, SUVRs were mirror-flipped, defining the left hemisphere as ipsilateral to the epileptogenic focus. Correlations between regional SUVRs, neuropsychological scores, and clinical factors were evaluated using statistical modeling. ***Results:*** TLE patients demonstrated significant reductions in glucose metabolism, primarily in the temporal lobe and hippocampus ipsilateral to the epileptogenic focus, compared to healthy controls. Tau SUVRs were markedly elevated in TLE patients with cognitive impairment, not only in the hippocampus but also in regions including the Heschl gyrus, superior and middle temporal gyri, fusiform gyrus, and cingulate cortex ($p < 0.01$). Verbal fluency scores were negatively correlated with tau SUVRs in multiple brain regions ($p < 0.05$), indicating a strong association between tau pathology and language deficits. In contrast, β-amyloid SUVRs (assessed by [^{11}C]PIB PET) showed a trend toward decreased uptake in TLE patients compared to healthy controls. ***Conclusion:*** Our findings reveal that TLE with cognitive impairment is associated with significant tau pathology extending beyond the temporal lobe and hippocampus. The negative correlation between tau deposition and language ability highlights the potential role of tau-related neurodegeneration in TLE-associated cognitive decline. These results underscore the importance of considering neurodegenerative mechanisms in the management of cognitive comorbidities in TLE and may inform future therapeutic strategies targeting tau pathology.

OP-724

The correlation between the efficacy of levetiracetam in the treatment of temporal lobe epilepsy and PET metabolic brain networks

H. Zhang, *J. Liu;*
The second hospital&clinical medical school. Lanzhou University, Lanzhou, CHINA.

Aim/Introduction: Antiepileptic drugs (AEDs) therapy is the primary treatment strategy for most patients with epilepsy. Levetiracetam (LEV) is one of the most common AEDs and is used in the treatment of many types of epilepsy. Accurate prediction of LEV efficacy is essential for drug selection and subsequent treatment strategy development. ^{18}F-FDG PET has been widely used in the evaluation of epileptogenic foci, PET-based metabolic brain networks are thought to reveal the overall impact of epilepsy on the brain. The aim of this study was to analyze the metabolic network characteristics of temporal lobe epilepsy (TLE) with different efficacies of LEV, to find parameters to predict drug efficacy, and to provide a reliable basis for the selection of clinical medication and the development of therapeutic strategies. ***Materials and Methods:*** 124 patients with TLE who received LEV monotherapy and underwent ^{18}F-FDG PET were retrospectively included, as well as 124 sex- and age-matched healthy controls. Patients were categorized into drug-sensitive and drug-resistant groups according to the frequency of seizures at 1-year follow-up after drug administration. Metabolic brain network was constructed and metabolic connectivity parameters were calculated based on MATLAB to compare the differences between the two groups of epileptic patients and healthy controls. Based on graph theory techniques, group level Hub nodes of epileptic

patients were calculated and standardized uptake value ratio (SUVR) was extracted at the corresponding positions of all individual patients, and SUVR was analyzed in univariate analysis with drug efficacy. ***Results:*** Both drug-sensitive and drug-resistant groups of temporal lobe epilepsy patients showed disruption of metabolic connectivity compared to healthy controls, with more significant disruption of metabolic connectivity in the drug-resistant group. In the metabolic connectivity parameter calculations, the metabolic brain networks of both groups of epileptic patients and healthy controls had small-world network properties, the drug-sensitive group had a higher global efficiency, average degree, and clustering, along with a shorter characteristic path length compared to the drug-resistant group ($P < 0.05$). Hub nodes of epileptic patients were altered in the graph theory, SUVR at Hub node locations was an independent predictor of LEV efficacy. ***Conclusion:*** This study is the first to explore the epileptic metabolic brain network of LEV monotherapy. The drug-sensitive group showed better network function and less disruption of metabolic connectivity compared to the drug-resistant group, and the SUVR of the Hub node may serve as a predictor of LEV efficacy.

OP-725

Functional correlates of cognitive impairment and mood alterations in Multiple Sclerosis: an early perfusion PET study

L. Sofia[1], *M. Donegani*[2], *S. Raffa*[2], *A. Donniaquio*[3], *L. Argenti*[3], *L. Roccatagliata*[1], *A. Chincarini*[4], *G. Novi*[2], *A. Laroni*[3], *G. Sambuceti*[1], *M. Bauckneht*[1], *A. Uccelli*[3], *M. Inglese*[3], *M. Pardini*[3], *S. Morbelli*[5];
[1]*Department of Health Sciences (DISSAL), University of Genoa, Genoa, ITALY,* [2]*IRCCS Ospedale Policlinico San Martino, Genoa, ITALY,* [3]*Department of Neuroscience, Rehabilitation, Ophthalmology, Genetics, Maternal and Child Health (DINOGMI), University of Genoa, Genoa, ITALY,* [4]*National Institute of Nuclear Physics (INFN), Genoa, ITALY,* [5]*Department of Medical Sciences, University of Turin, Turin, ITALY.*

Aim/Introduction: Early perfusion amyloid PET imaging is emerging as a valuable tool to potentially capture patients' synaptic dysfunction thus possibly representing a surrogate for FDG PET. Besides his recognized role in Alzheimer's Disease, amyloid PET imaging has recently been proposed as a tool to capture demyelination and remyelination in the white matter of patients with Multiple Sclerosis (MS). MS is clinically characterized by the presence of progressive disability and a wide range of cognitive and mood disorders. There's an increasing interest in the evaluation of cognitive impairment in patients with MS given its prognostic value as a potential further source of disability. We aimed to explore the correlation between cognitive and behavioural symptoms and cerebral blood flow, as assessed by early-phase amyloid PET imaging in MS patients. ***Materials and Methods:*** 28 patients with MS (18 relapsing-remitting and 10 primary progressive) were recruited. All patients underwent dual dynamic amy-PET imaging with [18F]Florbetaben, consisting in an early dynamic acquisition of the first 5 minutes (as a proxy of perfusion) and late steady-state acquisitions 90-110 minutes post-injection. All patients underwent clinical evaluation including disability scales and a neuropsychological assessment of different cognitive and behavioural symptoms, including fatigue, depression and visuo-spatial memory. Multiple-regression analyses were performed by means of SPM12 to assess the correlation between clinical evaluation scores and brain perfusion. $P<0.05$ FWE-corrected at cluster level was accepted as significant (age and sex as nuisances). ***Results:*** Fatigue severity measured by modified Fatigue Impact Scale (mFIS) was inversely correlated with perfusion in a fronto-insular cluster and in the putamen ($p<0.003$), while higher scores on depression scales (Hospital Anxiety and Depression Scale, HADS-D) were significantly associated with reduced perfusion in the putamen ($p < 0.002$). Additionally, visuospatial memory scores (assessed by the Brief Visuospatial Memory Test, BVMT) were directly correlated with perfusion in the corpus callosum ($p<0.005$). ***Conclusion:*** Early perfusion amyloid PET imaging captured functional correlates of cognitive and behavioural symptoms in MS patients. Hypoperfusion in subcortical and fronto-insular regions, areas known to be involved in emotional processing, was linked to fatigue and depression. Moreover, reduced perfusion in the corpus callosum, a crucial hub for interhemispheric connection, was associated with lower visuospatial memory scores. Early perfusion imaging in the contest of amyloid PET studies may open a further window on MS pathophysiology thus providing with the same tracer and on the same day functional information derived from both gray and white matter.

OP-726

O-15-water PET in cochlear-implant users reveals different strategies for speech processing in the central nervous system depending on background noise and speech comprehension

M. Voskamp[1,2], *S. Hansen*[3,4], *D. Merz*[1], *F. Bengel*[1], *T. Lenarz*[2,5], *A. Büchner*[2,5], *T. Ross*[1], *P. Sandmann*[3,4,6], *G. Berding*[1,2];
[1]*Department of Nuclear Medicine, Hannover Medical School, Hannover, GERMANY,* [2]*Cluster of Excellence "Hearing4all", Hannover, GERMANY,* [3]*Department of Otorhinolaryngology at Evangelisches Krankenhaus Oldenburg, Oldenburg, GERMANY,* [4]*Cluster of Excellence "Hearing4all", Oldenburg, GERMANY,* [5]*Department of Otorhinolaryngology, Hannover Medical School, Hannover, GERMANY,* [6]*Research Center Neurosensory Science, University of Oldenburg, Oldenburg, GERMANY.*

Aim/Introduction: Cochlear Implantation (CI) is a well-established treatment for severe-to-profound hearing loss. While a CI can effectively restore adequate hearing abilities in challenging listening environments for many patients, about one-third of patients encounter difficulties with speech comprehension, particularly in noisy settings. This variability in results is largely attributable to impaired processing of the signals received via the CI, caused by a maladaptation due to the earlier existing hearing impairment. More accurate diagnosis of speech processing could lead to improvement through targeted training. ***Materials and Methods:*** To assess the cortical activation patterns in response to speech, we used O-15-water positron emission tomography (PET). In this study, sixteen CI users with different sentence comprehension (good and poor performers (GP&PP)) underwent O-15-water PET/CT while performing a sentence discrimination test with and without background noise. The speech material used, consists of semantically correct and incorrect sentences. The correct sentences were split into high- and low-cloze probability (HC&LC), based on the contextual proximity of verb and noun. Additionally, multiple baseline scans were conducted. The detection of cortical activations was achieved by comparing conditions with statistical parametric mapping (SPM). ***Results:*** Without noise, GP showed a large activation in the temporal voice area (TVA)(990 voxels) and small activation in the Broca's region(77 voxels) and Brodmann-area 6 (BA6)(77 voxels). In Comparison, PP showed smaller activations in the TVA(771 voxels) and in Broca's region(20 voxels) but a larger activation in BA6(223 voxels). Furthermore, adding noise in GP enlarged activation in BA6(429 voxels). When exposed to semantically difficult listening scenarios (LC in contrast to HC sentences), activations were larger in Broca's region(GP 81 vs. 6, PP 16 vs. 0 voxels) as well as in BA6(GP 42 vs. 5, PP 187 vs. 37 voxels). TVA activations were always larger in GP compared to PP for both scenarios. ***Conclusion:*** Our study shows that differences in recruitment of cortical areas involved in speech processing in CI users are related to background noise and speech comprehension. GP are able to activate the TVA also in difficult listening scenarios to a larger extent in comparison to PP. However, both seem to compensate for difficult listening situations (due to noise or difficult sentences) by activating additional resources, specifically in Broca's region and BA6. The latter region shows a

larger activation in PP compared to GP even in listening without noise, possibly indicating higher listening effort for PP, even in listening scenarios without background noise.

1608

Tuesday, October 7, 2025, 16:45 - 18:15
Room 115

TROP Session - Cardiovascular Committee: Metabolism,Fibrosis and Innervation: The Basis of Cardiomyopathies

OP-727

First-in-human study of a novel cardiac sympathetic neuronal PET imaging agent: [^{18}F]FPMBBG

M. Ju, *W. Ren, L. Wang, W. Fang;*
Fuwai Hospital, Public Union Medical College, Beijing, CHINA.

Aim/Introduction: Cardiac sympathetic innervation imaging can non-invasively evaluate the cardiac sympathetic nervous function, potentially aiding in heart failure (HF) risk stratification. Preclinical studies with [^{18}F]FPMBBG revealed high affinity and robust myocardial uptake, suggesting its suitability as a novel cardiac imaging tracer. This study presents the first-in-human evaluation of it. ***Materials and Methods:*** 8 healthy volunteers and 8 HF patients underwent 60-min cardiac PET scans with [^{18}F]FPMBBG. Left ventricular myocardial VOIs were delineated using a SyngoVia workstation. Myocardial uptake was quantified by SUVmax, SUVmean at early (5-10 min) and late (55-60 min) imaging times, washout rate (WR = (SUV max$_{/early}$ - SUV max$_{/late}$)/ SUV max$_{/early}$ ×100%), late retention index (RI = C_m (T_R) × 100% / $\int_0^{TR} C_p$ (t)dt) and compared between the healthy and HF groups using Student's t-test or Mann-Whitney U test according to the normality of the data ($P < 0.05$). ***Results:*** The chemical structure of [^{18}F]FPMBBG is shown in Figure 1A. [^{18}F]FPMBBG demonstrated a favorable safety profile, with no adverse events or significant changes in vital signs in any subject. Healthy volunteers showed high myocardial uptake, low lung uptake and rapid hepatic clearance (Figure 1B, C). Heart-to-liver ratios increased over time, reaching 3.26 ± 1.45 at 60 minutes post-injection. Compared with volunteers, HF patients exhibited significantly lower SUVmax [early: 4.61 ± 0.45 vs 6.83 ± 1.44, P = 0.016, late: 4.69 (4.36, 4.89) vs 6.21(6.07, 6.95), P = 0.002], SUVmean [early: 4.61 ± 0.45 vs 4.40 ± 0.78, P < 0.001, late: 2.66 (2.33, 2.84) vs 4.02 (3.86, 4.36), P = 0.001] and RI (3.79 ± 0.77%/min vs 6.75 ± 1.02%/min, P < 0.001), along with a significantly higher WR [14.04 (13.01, 15.44)% vs 3.58 (0.94, 5.25)%, P = 0.001](Figure 1D). ***Conclusion:*** [^{18}F]FPMBBG PET imaging provides high image quality and reliable measurements of cardiac sympathetic nerve function. It is a promising tracer for further investigation.

OP-728

Ga-68 labelled Affibody molecule based radiopharmaceutical targeting platelet derived growth factor receptor beta detects active fibrosis in patients with myocardial infarction.

I. Velikyan[1,2], *K. Grinnemo*[2], *V. Flodin*[2], *S. James*[3], *U. Thelander*[2], *O. Korsgren*[4], *O. Eriksson*[1,5];
[1]*Science for Life Laboratory, Department of Medicinal Chemistry, Uppsala University, Uppsala, SWEDEN,* [2]*Department of Surgical Sciences, Uppsala University, Uppsala, SWEDEN,* [3]*Department of Medical Sciences, Uppsala University, Uppsala, SWEDEN,* [4]*Department of Immunology, Genetics and Pathology, Uppsala University, Uppsala, SWEDEN,* [5]*Antaros Tracer AB, Uppsala, SWEDEN.*

Aim/Introduction: The platelet-derived growth factor receptor beta (PDGFRβ) is a key mediator of cell proliferation, migration, and extracellular matrix production associated with fibrotic processes. Quantitative imaging of PDGFRβ expression in vivo could enhance clinical management of cardiac patients undergoing invasive interventions, where fibrosis presents a significant risk. This study presents the GMP production of a ^{68}Ga-labeled PDGFRβ-targeted radiopharmaceutical ([^{68}Ga]Ga-ATH001), its preclinical characterization in human heart biopsies, and finally initial results from a phase 0 clinical study in patients with ST-elevated myocardial infarction (STEMI) compared to healthy controls. ***Materials and Methods:*** The Affibody molecule ATH001 was chemically synthesized and functionalized with a DOTA chelator at the C-terminal cysteine residue. A fully automated method for producing [^{68}Ga]Ga-ATH001 was established using a pharmaceutical-grade ^{68}Ge/^{68}Ga generator and pre-sterilized, single-use cassettes [1] compatible with the Modular-Lab PharmTrace platform. The binding of [^{68}Ga]Ga-ATH001 in biopsies of human cardiac fibrotic tissue was evaluated by in vitro autoradiography. PET/MRI scanning with [^{68}Ga]Ga-ATH001 was performed in STEMI patients 1 week following percutaneous coronary intervention (PCI), as well as healthy controls. ***Results:*** Fully automated, reproducible, and GMP compliant production of [^{68}Ga]Ga-ATH001 was developed. [^{68}Ga]Ga-ATH001 demonstrated receptor-mediated binding overlapping with PDGFRβ immune-positive areas in cardiac fibrotic tissue sections. The administered protein dose per patient was below 100 µg, in accordance with the microdosing concept. [^{68}Ga]Ga-ATH001 demonstrated low and homogenous uptake in healthy myocardium in vivo. In STEMI, [^{68}Ga]Ga-ATH001 exhibited strong focal binding in myocardial tissue corresponding to infarcted areas as verified by standard cardiac radiological techniques. ***Conclusion:*** The automated production of [^{68}Ga]Ga-ATH001 was developed and validated for phase 0 clinical trial application. Preclinical studies confirmed its selective, high-affinity binding to PDGFRβ in human fibrotic myocardium. Patient imaging revealed distinct myocardial uptake of [^{68}Ga]Ga-ATH001, which correlated with the infarction site. ***References:*** [1] Velikyan et al., AJNMMI, 2019, 12-23.

OP-729

Differential prediction of heart failure death and arrhythmic events using a practical multivariable model with ^{123}I-MIBG Imaging

K. Nakajima[1], *T. Doi*[2], *T. Nakata*[3], *T. Nakahashi*[4], *H. Tada*[1], *H. Wakabayashi*[1], *H. J. Verberne*[5];
[1]*Kanazawa University, Kanazawa, JAPAN,* [2]*Teine Keijinkai Hospital, Sapporo, JAPAN,* [3]*Hokodate-Goryoukaku Hospital, Hakodate, JAPAN,* [4]*Takaoka Municipal Hospital, Takaoka, JAPAN,* [5]*University of Amsterdam, Amsterdam, NETHERLANDS.*

Aim/Introduction: Differentiating between heart-failure death (HFD) and lethal arrhythmic events (ArE) in patients with chronic heart failure (CHF) remains a major clinical challenge, as these outcomes require different therapeutic strategies. While we have proposed a machine learning (ML)-based model to distinguish these outcomes with 13 variables, a simpler, clinically applicable model was needed. This study aimed to develop and validate a multivariable model using clinical and imaging data, including ^{123}I-meta-iodobenzylguanidine (mIBG), to predict HFD, ArE, and survival. ***Materials and Methods:*** We retrospectively analyzed 997 patients with CHF (age 70±13 years; 51% male; mean left ventricular ejection fraction [LVEF] 32±13%) with a mean follow-up of 41±7 months. Late heart-to-mediastinum ratio (HMR) and washout rate (WR) from ^{123}I-mIBG imaging were evaluated. Clinical outcomes were classified into three categories: survival, HFD, and ArE. ArE included arrhythmic death, sudden cardiac death, and appropriate therapy by cardiac devices of implantable cardioverter defibrillator or cardiac resynchronization therapy with defibrillator. The cohort was split into 75% (n=748) for model development and 25% (n = 249) for validation. Multinomial and nested logistic regression models were applied using >2-year outcomes. Model performance was assessed by receiver-operating-characteristic analysis and area under the curve (ROC-AUC). Kaplan-Meier survival analysis was conducted over five years with non-cardiac deaths censored. ***Results:*** During follow-up, HFD and ArE occurred in 19% and 9% of patients, respectively. Eight of 15 candidate variables were selected by forward stepwise selection: age, sex,

NYHA class, LVEF, hemoglobin, estimated glomerular filtration rate, hypertension, and either mIBG HMR or WR. AUCs in the training set were 0.88 (survival), 0.76 (ArE), and 0.87 (HFD), and in the validation set 0.87, 0.80, and 0.85, respectively. The model incorporating WR outperformed those using HMR alone (cutoff: 1.9) or WR alone (cutoff:36%) for predicting ArE/HFD combined and individual outcomes. The WR-based 8-variable model significantly improved prediction of survival (p=0.0087) and ArE (p=0.014) compared to a 7-variable model without mIBG, with comparable accuracy for HFD (p=0.09). Risk groups for high risk for both ArE and HFD, high risk for HFD, high risk for ArE, and low risk for both agreed with actual outcomes. A simulation showed higher ArE incidence in patients with intermediate HMR, depending on NYHA class, consistent with previous ML-based findings. ***Conclusion:*** A practical eight-variable model incorporating ^{123}I-mIBG indices enables robust and differential prediction of survival, HFD, and ArE, providing a clinically useful tool for risk stratification in CHF. ***References:*** J Nucl Cardiol 2022;29:190-201.

OP-730

Systemic Metabolic Coordination Index (SMCI): A Graph-Based Biomarker of Whole-Body Metabolic Integrity from FDG PET

X. Li[1], *Z. Shi*[2], *M. Hacker*[1], *X. Zhang*[2], *X. Li*[1], *S. Xue*[1];
[1]*Division of Nuclear Medicine, Department of Biomedical Imaging and Image-guided Therapy, Vienna General Hospital, Medical University of Vienna, Vienna, AUSTRIA,* [2]*Department of Nuclear Medicine, Molecular Imaging Lab, Beijing Anzhen Hospital, Capital Medical University, Beijing, CHINA.*

Aim/Introduction: Human metabolic homeostasis is maintained through complex neural, vascular, and fluidic regulatory mechanisms operating at the whole-body level. The interplay among organs forms a physiological network that can be disrupted by metabolic disorders such as diabetes and obesity. Traditional diagnostics often rely on single-organ or localized biomarkers; however, evaluating systemic metabolic health requires an integrative metric—a global biomarker. In this study, we introduce a novel graph theory-based framework to derive such a biomarker, termed Eglob, from whole-body [^{18}F]FDG PET imaging in a large cohort of healthy individuals. We further validate its clinical utility in patients with heart failure with reduced ejection fraction (HFrEF), a condition lacking focal PET abnormalities yet marked by severe systemic metabolic dysregulation. ***Materials and Methods:*** We constructed a reference inter-organ metabolic network from FDG PET scans of 747 healthy individuals, encompassing nine major organs involved in metabolic and immune regulation. Network robustness was assessed using permutational multivariate analysis of variance (PERMANOVA) across 20 bootstrap-derived networks. For validation, individualized metabolic networks were generated for each subject, and deviations from the reference were quantified using global efficiency (Eglob) from graph theory. This deviation was defined as the Systemic Metabolic Coordination Index (SMCI), representing subject-level systemic metabolic integrity. Validation in 156 HFrEF patients included correlation analyses with 82 clinical parameters and survival analysis based on all-cause mortality, benchmarked against an L2-norm-based deviation score. ***Results:*** PERMANOVA confirmed the robustness of the healthy reference network ($p = 1$). In the HFrEF cohort, SMCI was significantly associated with impaired cardiac function assessed by echocardiography—including wall thickness, standard deviation, and entropy (all $p < 0.05$)—as well as elevated aspartate aminotransferase (AST; $p < 0.05$). In contrast, the L2-norm deviation showed no significant associations ($p > 0.05$). Survival analysis demonstrated the prognostic value of SMCI ($p = 0.021$; HR = 0.13; C-index = 0.69), while L2-norm deviation was not significant ($p = 0.29$; HR = 0.47; C-index = 0.61). ***Conclusion:*** We present the SMCI as a novel graph-based biomarker derived from healthy whole-body FDG PET networks, with the potential to quantify systemic metabolic integrity at the individual level. SMCI was associated with multi-organ dysfunction and showed prognostic value in patients with HFrEF. This framework may enable a new paradigm for integrating molecular imaging and network analysis to support personalized assessment, risk stratification, and potentially screening for systemic metabolic disorders using PET imaging.

OP-731

Mapping Immune-Metabolic Dysregulation in HFrEF Using Whole-Body PET and Inter-Organ Network Analysis

X. Li[1], *Z. Shi*[2], *M. Hacker*[1], *X. Zhang*[2], *S. Xue*[1], *X. Li*[1];
[1]*Division of Nuclear Medicine, Department of Biomedical Imaging and Image-guided Therapy, Vienna General Hospital, Medical University of Vienna, Vienna, AUSTRIA,* [2]*Department of Nuclear Medicine, Molecular Imaging Lab, Beijing Anzhen Hospital, Capital Medical University, Beijing, CHINA.*

Aim/Introduction: Heart failure (HF) is a complex clinical syndrome resulting from cardiac dysfunction, yet its systemic manifestations extend beyond the myocardium. Emerging evidence highlights the pivotal role of the brain-heart axis, particularly the autonomic nervous system, in regulating cardiovascular function. In heart failure, dysregulated interactions along this axis influence metabolic and immune systems, contributing to disease progression. Building on this concept, we investigated the systemic immune-metabolic interactome in patients with heart failure with reduced ejection fraction (HFrEF) and explored its association with major adverse cardiovascular events (MACEs). ***Materials and Methods:*** A prospective cohort of 154 patients with HFrEF and 56 healthy controls underwent whole-body [^{18}F] FDG-PET imaging. Glucose uptake across key immune and metabolic organs was quantified and compared between groups. Inter-organ metabolic networks were constructed, and a novel Immune-Metabolic Network Deviation Score (IMNDS) was developed to quantify individual deviations from the normative network established in healthy controls. We assessed correlations between IMNDS and clinical biomarkers reflecting metabolic, vascular, hepatic, inflammatory, and cognitive functions, and evaluated its prognostic value for MACEs and all-cause mortality. ***Results:*** HFrEF patients exhibited significantly elevated [^{18}F] FDG uptake (SUVmean) in the spleen, bone marrow, heart, liver, pancreas, and adipose tissue compared to controls (all $P < 0.05$), indicating heightened immune-metabolic activity. While healthy individuals showed strong inter-organ correlations within immune and metabolic networks, these connections were markedly attenuated in the HFrEF cohort ($P < 0.05$), suggesting systemic dyssynchrony. IMNDS captured this network disruption and showed significant associations with remnant-like particle cholesterol ($P = 0.025$), non-HDL cholesterol ($P = 0.045$), creatinine ($P = 0.049$), FDG-derived end-diastolic volume ($P = 0.035$), hematocrit ($P = 0.048$), ALT ($P = 0.038$), prealbumin ($P = 0.026$), and Montreal Cognitive Assessment scores ($P = 0.034$). In survival analyses, IMNDS demonstrated prognostic trends comparable to B-type natriuretic peptide (BNP) for MACEs and all-cause mortality. ***Conclusion:*** This study identifies a systemic immune-metabolic dyssynchrony in HFrEF, revealing a novel axis of dysfunction that transcends cardiac pathology. The Immune-Metabolic Network Deviation Score (IMNDS) represents a promising biomarker of multi-organ network disruption with clinical relevance to metabolic burden, organ function, and neurocognitive health. To further validate these findings, future studies should incorporate peripheral immune profiling via flow cytometry or CyTOF, cytokine and metabolic biomarker quantification, and tissue-level analysis using immunohistochemistry. These integrative approaches may clarify the underlying biology of immune-metabolic disarray in HF and support biomarker-driven strategies for personalized care.

OP-732

Characteristics of myocardial imaging at ^{18}F-FAPI-74 PET/CT and potential value in predicting left ventricular reverse remodeling in non-ischemic dilated cardiomyopathy

w. liu[1,2,3], *L. Li*[1,2,3], *Q. Wu*[1,3], *J. Song*[4], *S. Li*[1,2,3];
[1]*Department of Nuclear Medicine, First Hospital of Shanxi Medical University, Shanxi Medical University, Taiyuan, Shanxi, CHINA,* [2]*Shanxi Key Laboratory of Molecular Imaging, Shanxi Medical University, Taiyuan, Shanxi, CHINA,* [3]*Collaborative Innovation Center for Molecular Imaging of Precision Medicine Shanxi Medical University, Taiyuan, Shanxi, CHINA,* [4]*Academy of Medical Sciences, Shanxi Medical University, Taiyuan, Shanxi, CHINA.*

Aim/Introduction: Cardiac fibrosis occurs early in the progression of non-ischemic dilated cardiomyopathy (NIDCM). Recently, research on fibroblast activation protein inhibitor (FAPI) PET imaging in cardiovascular diseases has increased and is highly sought. However, no cohort studies have been carried out, and only case reports have documented the heterogeneous myocardial uptake of FAPI in patients with NIDCM. The aim of this study was to explore the myocardial imaging characteristics at FAPI PET/CT and its predictive value for left ventricular reverse remodeling (LVRR) in NIDCM. ***Materials and Methods:*** Forty-eight individuals with NIDCM in the study underwent ^{18}F-FAPI-74 PET/CT. Echocardiography was performed at baseline and at average 12 months. Myocardial FAPI activity was quantified as as intensity(maximum standardized uptake value [SUVmax], mean standardized uptake value [SUVmean],target-to-background ratio[TBR]), and volume (left ventricular molecular volume[LVMV]). Cardiac functional parameters were quantified as left ventricular ejection fraction (LVEF) and left ventricular end-diastolic dimension (LVEDD). The correlation was calculated using Pearson or Spearman. Univariable logistic regression analyses were used to assess the predictive value of LVMV for left ventricular reverse remodeling in NIDCM. LVRR was defined as an absolute increase in LVEF from ≥10% to a final value of >35% accompanied by a decrease in LVEDD ≥10% at 12 months of follow-up. ***Results:*** Thirteen patients with NIDCM exhibited no visible myocardial uptake (PET-negative), whereas 73% (35 of 48) had enhanced LV uptake (PET-patchy [n=14] vs. PET-extensive [n=21].Compared to the PET-negative and PET-patchy pattern groups, patients with NIDCM in the PET-extensive group exhibited higher LVEDD(62.6±4.8 vs.70.7±7.6,63.3±8.4 vs.70.7±7.6,P<0.01) and lower LVEF (36.7±11.1 vs. 27.6±6.4, 35.5±9.9 vs. 27.6±6.4,P<0.05). The LV SUVmax and SUVmean were correlated with N-terminal pro-brain natriuretic peptide (NT-proBNP)(r = 0.422,P=0.007;r = 0.476,P=0.002), while LVMV was inversely related to LVEF (r = -0.623,P<0.001).Additionally, the LVRR group demonstrated lower LVMV at baseline than the non-LVRR group (48.9±31.8 vs. 11.1 (0, 32.2), p =0.011). The LVMV at baseline was a significant predictor (OR = 0.958, p = 0.024) for LVRR in NIDCM. ***Conclusion:*** ^{18}F-FAPI-74 PET/CT imaging indicated heterogeneous activity in NIDCM. Baseline myocardial FAPI uptake volume may have potential predictive value for LVRR.

OP-733

Evaluation of Myocardial Fibrosis and Wall Motion Abnormality with ^{68}Ga-FAPI PET/MR in Coronary Heart Disease

R. Luo[1], *Z. Zhao*[1], *C. Zhang*[1], *R. Li*[1], *Q. Meng*[1], *Y. Ni*[1], *R. Yang*[1], *X. Chen*[1], *L. Xie*[2], *M. Zhang*[2], *F. Wang*[1];
[1]*Nanjing First Hospital, Nanjing Medical University, Nanjing, CHINA,* [2]*3.Department of Advanced Nuclear Medicine Sciences, Institute for Quantum Medical Science, National Institutes for Quantum Science and Technology, Chiba, JAPAN.*

Aim/Introduction: Quantification of myocardial fibrosis and wall motion assessment are crucial for prognostic evaluation in coronary heart disease (CHD). To explore the characteristics of cardiac fibroblast activation protein inhibitor (FAPI) PET/MR in CHD and its association with abnormal wall motion. ***Materials and Methods:*** In this prospective study from May 2023 to December 2023, participants with CHD underwent cardiac gallium 68 (^{68}Ga)-labeled FAPI PET/MR imaging. FAP signal (FAPI active) was quantified using regional standardized uptake values (SUVs). Cardiac MRI yielded functional parameters and area of injury (late gadolinium enhancement [LGE]) (MRI non-viable). Abnormal wall motion identified by myocardial strain analysis was evaluated using integrated analysis of LGE and FAP signal. The correlations between FAP signal and clinical parameters were explored and fibrosis was confirmed by histopathological analysis of partially resected myocardium. ***Results:*** Forty-two participants (mean age, 59 years ± 13 [SD]; 32 men) were included. The FAP signal was higher in left ventricle regional myocardium compared with remote normal areas (SUVmax, 5.0 ± 1.8 vs 1.2 ± 0.4; p < .001). In total, 432 segments (432/714, 60.50%) displayed impaired wall motion. In integrated analysis, the highest wall motion abnormality score was observed in the FAPI active/MRI non-viable group (11.0 ± 5.2). FAP signal was positively correlated with K time (SUVpeak: R = 0.48; p = .046; SUVmean: R = 0.57; p = .014) and negatively correlated with Angle (SUVpeak: R = −0.52; p = .026; SUVmean: R = −0.56; p = .026) in thromboelastography. Immunohistochemical analysis revealed FAP-positive fibroblasts in the infarct and border zone, and robust expression of α-smooth muscle actin and vimentin. ***Conclusion:*** Simultaneous ^{68}Ga-fibroblast activation protein inhibitor PET/MR offers novel insights into the regional pattern of fibroblast activation in patients with coronary heart disease, and the fibroblast activation protein signal is associated with abnormal wall motion.

OP-734

[^{68}Ga]FAPI: A New Game-Changer in Cardiac Inflammation? Early Findings from a Prospective Study of [^{68}Ga]FAPI PET/CT Diagnostic Performance Compared to [^{18}F]FDG PET/CT in Suspected Cardiac Sarcoidosis

A. Safarian[1,2], *H. Malek*[1], *M. Beheshti*[2], *S. Almasi*[3], *M. Chehrara*[1], *N. Yaghoobi*[1];
[1]*Department of Nuclear Medicine, Rajaie Cardiovascular Medical and Research Center, Rajaie Cardiovascular Institute, Iran University of Medical Sciences, Tehran, IRAN, ISLAMIC REPUBLIC OF,* [2]*Division of Molecular Imaging and Theranostics, Department of Nuclear Medicine, University Hospital, Paracelsus Medical University, Salzburg, AUSTRIA,* [3]*Department of Rheumatology, Firoozgar Hospital, Iran University of Medical Sciences, Tehran, IRAN, ISLAMIC REPUBLIC OF.*

Aim/Introduction: Cardiac sarcoidosis (CS) is a potentially life-threatening inflammatory disease with a wide clinical spectrum from early inflammation to irreversible fibrosis. Accurate diagnosis and early intervention are crucial to prevent permanent myocardial damage. While [^{18}F]FDG-PET/CT remains the standard for detecting active inflammation, it is limited by complex patient preparation, variable physiologic myocardial uptake, and frequent equivocal findings. [^{68}Ga]FAPI is an emerging tracer, targeting fibroblast-activation-protein. We aimed to evaluate the diagnostic performance of [^{68}Ga]FAPI-PET/CT compared to [^{18}F]FDG-PET/CT in patients with suspected CS. ***Materials and Methods:*** In this ongoing prospective pilot study, ten patients with clinical suspicion of CS and no prior anti-inflammatory treatment underwent [^{18}F]FDG-PET/CT, [^{68}Ga]FAPI-PET/CT, and resting myocardial perfusion gated-SPECT (^{99m}Tc-Sestamibi) within one week. Due to timing variability, cardiac MRI (CMR) was considered as supportive tool for final diagnostic decision-making but was excluded from the head-to-head image analyses. A consensus of clinical and imaging findings was used as the standard of truth. ***Results:*** [^{68}Ga]FAPI-PET/CT demonstrated consistent and more conclusive uptake patterns compatible with different disease phases. No uptake was observed in healthy myocardium or in fully-scarred segments (confirmed by absent perfusion), mirroring [^{18}F]FDG findings. In early phases, where perfusion is still preserved, [^{68}Ga]FAPI uptake matched [^{18}F]FDG, indicating its sensitivity in early inflammatory stages. Importantly, [^{68}Ga]FAPI-requiring no patient preparation- correctly excluded false-positive [^{18}F]FDG uptake in cases of inadequate myocardial suppression, offering

superior workflow and interpretive clarity. Most notably, a distinct pattern was observed in three patients with high clinical suspicion of CS: segments with no or very faint [^{18}F]FDG uptake, moderate hypoperfusion, yet significant [^{68}Ga]FAPI uptake. These regions with increased uptake and reduced perfusion, did not represent established scar, as perfusion was still present, and co-localized with prior CMR-reported sites of inflammation. These findings may represent a previously unrecognized window of disease activity, a "transitional fibro-inflammatory phase", where acute inflammation may have subsided, but active remodeling persists. This phase may indicate a critical therapeutic window, where continued immunosuppressive or anti-fibrotic therapy could potentially halt progression to irreversible damage, preventing further complications. ***Conclusion:*** In this preliminary cohort, [^{68}Ga]FAPI-PET/CT demonstrated strong diagnostic value across all phases of CS. It identified a critical, potentially treatable stage of disease inconclusive by [^{18}F]FDG, challenging current treatment paradigms in [18F]FDG-negative cases. With no physiologic myocardial uptake, low blood-pool activity, and no patient preparation, [^{68}Ga]FAPI-PET/CT shows promise as a potential transformative tool in CS management, particularly for complex cases with underlying diseases and inconclusive [^{18}F]FDG patterns.

OP-735

Downregulation of myocardial expression of glucagon-like peptide-1 receptor with aging and obesity showing on^{68}Ga-exendin-4 PET/CT

H. Zhang[1], *Q. Pan*[2], *S. Liu*[1], *J. Feng*[1], *Y. Luo*[1];
[1]Department of Nuclear Medicine, Chinese Academy of Medical Sciences and Peking Union Medical College Hospital; State Key Laboratory of Common Mechanism Research for Major Diseases, Beijing, CHINA, [2]Department of Nuclear Medicine, Chinese Academy of Medical Sciences and Peking Union Medical College Hospital, Beijing, CHINA.

Aim/Introduction: The glucagon-like peptide-1 receptor (GLP-1R) plays a growing role in cardiovascular physiology, yet its in vivo myocardial expression needs clarification. The aim of this study was to noninvasively visualize and quantify myocardial GLP-1R expression using ^{68}Ga-exendin-4 PET/CT, with a view to assessing age and weight-dependent variations and their potential clinical implications in cardiovascular diseases. ***Materials and Methods:*** This is a retrospective analysis of a prospective study (NCT 02560376) on ^{68}Ga-exendin-4 PET/CT in diagnosing insulinoma and congenital hyperinsulinemic hypoglycemia. Patients who underwent ^{68}Ga-exendin-4 PET/CT with good image quality of the myocardium were enrolled. Patients' gender, age, and body mass indices (BMI) were recorded. ^{68}Ga-exendin-4 uptake of the left/right ventricular (LV/RV) myocardium, together with the blood pool (descending aorta) was measured manually. Accordingly, the calculation of the target-to-background ratios (TBRs, blood pool as background reference) of bilateral ventricles was conducted. Then, simple linear regression analyses were performed. Age and BMI were separately tested as independent variables against TBR as the dependent variable. The goodness-of-fit was evaluated using r values, and statistical significance was defined as $P < 0.05$ (two-tailed). ***Results:*** A total of 124 patients (including 63 males and 61 females) were included with a median age of 39.5 years (range, 0.1~77.0). Analyses based on all patients showed that TBRmax, defined as SUVmax of the LV or RV divided by SUVmax of the blood pool, were linearly and inversely correlated with the logarithm of age (LV TBRmax, $r = 0.72$, $P < 0.001$; RV TBRmax, $r = 0.68$, $P < 0.001$). TBRmean, defined as SUVmax of the LV or RV divided by SUVmean of the blood pool, were also demonstrated linearly and inversely correlated with the logarithm of age (LV TBRmean, $r = 0.46$, $P < 0.001$; RV TBRmean, $r = 0.29$, $P = 0.001$). The relationship between these semiquantitative parameters and BMI was also investigated in adult patients, and these parameters demonstrated a statistically significant negative linear correlation with BMI (LV TBRmax, $r = 0.41$, $P < 0.001$; RV TBRmax, $r = 0.44$, $P < 0.001$; LV TBRmean, $r = 0.30$, $P = 0.001$; RV TBRmean, $r = 0.28$, $P = 0.002$). ***Conclusion:*** ^{68}Ga-exendin-4 PET/CT enables noninvasive assessment of myocardial GLP-1R expression, demonstrating significant inverse correlations with age and BMI, suggesting progressive downregulation of GLP-1R expression in myocardium with aging and obesity. These findings provide new insights for studying cardiovascular effects of GLP-1R agonists.

1609

Tuesday, October 7, 2025, 16:45 - 18:15
Room 133+134

e-Poster Presentations Session 12 - Thyroid Committee: Diagnostic and Therapeutic Approach in Patients with Endocrinological Disorders

EPS-242

Prognostic Value of Al^{18}F-NOTA-Pentixafor PET/CT for Surgical Outcomes in Primary Aldosteronism: A Prospective Study

X. Yan[1], *G. Zheng*[2], *M. Liu*[1], *Y. Zhang*[1], *Y. Xie*[1], *L. Huo*[1];
[1]Department of Nuclear Medicine, Peking Union Medical College Hospital, Chinese Academy of Medical Sciences, Beijing, CHINA, [2]Department of Urology, Peking Union Medical College Hospital, Chinese Academy of Medical Sciences, Beijing, CHINA.

Aim/Introduction: The heterogeneous surgical outcomes of primary aldosteronism (PA) necessitate reliable presurgical evaluation methods. Al^{18}F-NOTA-Pentixafor PET/CT targeting CXCR4 shows promise for functional adrenal characterization. This study evaluated its prognostic value for predicting postoperative outcomes in surgical PA patients. ***Materials and Methods:*** In this prospective trial, 108 consecutive PA patients underwent preoperative Al^{18}F-NOTA-Pentixafor PET/CT followed by adrenalectomy. Semiquantitative analysis included, lesion SUVmax, lateralization index (LI), lesion-to-liver ratio (LLR) and lesion-to-normal adrenal ratio (LAR). Outcomes were assessed at 6 months postoperatively using comprehensive PASO criteria: (1) Cure: normalized blood pressure (off medications), serum potassium, and ARR; (2) Improvement: 1-2 criteria met; (3) No benefit: no criteria met. Parameters were compared among cure, improvement and no-benefit groups. ROC analysis determined optimal cutoff values for outcome prediction. ***Results:*** A total of 108 PA patients with adrenal nodule underwent adrenalectomy guided by Al^{18}F-NOTA-Pentixafor. At 6-month follow-up, 66.7% patients (66.7%) achieved cure (complete biochemical and clinical remission), 34 (31.5%) showed improvement (partial remission), and 2 (1.8%) had no benefit. SUVmax were significantly higher (13.09±6.70 vs 6.68±2.27, $p<0.001$) and LLR values (11.62±6.00 vs 2.03±0.95, $p<0.001$) in cured patient compared to patients with only improvement, while showing an inverse pattern for LAR (5.05±2.48 vs 7.21±2.20, $p=0.003$), with relatively modest mean difference of 2.16. The group with no benefit (n=2) exhibited the lowest values across all parameters (SUVmax vs Cure: $p=0.018$; LLR vs Cure: $p=0.043$). Quantitative analysis demonstrated robust diagnostic performance across all parameters: LLR showed cutoff of 6.04 with AUC 0.87 (95%CI 0.712-0.896) and positive predict value (PPV) of 90.6%; SUVmax achieved cutoff 11.0 with AUC 0.822 (95%CI 0.738-0.906) and PPV of 93.2%; LI achieved cutoff 3.16 with AUC 0.790 (95%CI 0.687-0.894) and PPV of 97.4%; while LAR demonstrated cutoff 2.4 with AUC 0.861 (95%CI 0.791-0.931) and PPV of 100%. ***Conclusion:*** Al^{18}F-NOTA-Pentixafor PET/CT effectively predicts PA surgical outcomes, with LAR and SUVmax showing strongest correlation with cure.

EPS-243

The value of ^{68}Ga-Pentixafor PET/MR-based Radiomics in Differentiating Functional Adrenocortical Adenomas

X. Chen[1], *R. Zhang*[1], *J. Song*[1], *C. Liu*[1], *Q. Ji*[2], *Y. Hu*[3], *J. Zhao*[1], *Y. Xing*[1];
[1]*Department of Nuclear Medicine, Shanghai General Hospital, Shanghai Jiao Tong University School of Medicine, Shanghai, CHINA,* [2]*United Imaging Healthcare Advanced Technology Research Institute Co., Ltd., Shanghai, CHINA,* [3]*United Imaging Healthcare, Shanghai, CHINA.*

Aim/Introduction: This study aims to investigate the potential of radiomics features derived from integrated ^{68}Ga-Pentixafor PET and multiparametric MRI for constructing a robust classification model to discriminate functional adenomas (FA) from non-functional adenomas (NFA), thereby providing a novel non-invasive diagnostic approach. ***Materials and Methods:*** A retrospective analysis was conducted on patients who underwent integrated ^{68}Ga-Pentixafor PET/MR examinations at our center (MRI sequences included T1-weighted in-phase/opposed-phase, T2-weighted and diffusion-weighted imaging with ADC mapping). Only cases with definitely diagnosed functional or non-functional adrenocortical adenomas were finally included in the study. Lesions were manually delineated using ITK-SNAP, followed by extraction of 107 radiomics features for individual lesion segmentations via PyRadiomics. Modality-specific LASSO feature selection was performed, yielding distinct predictive features for each imaging dataset. The Radscore was calculated for each lesion by a linear combination of the selected radiomic features with their respective coefficients. Mann-Whitney U test was used to compare Radscores between groups. The diagnostic performance of Radscore was evaluated by receiver operating characteristic (ROC) curve analysis, calibration curve, and decision curve analysis (DCA). ***Results:*** A total of 32 adrenal adenoma lesions were included in this study, comprising 23 FA (18 aldosterone-producing and 5 cortisol/mixed-secreting) and 9 NFA. ^{68}Ga-Pentixafor PET-based radiomics features were reduced to 6 potential predictors for PET-Radscore construction. However, MRI-based features failed to establish valid predictive Radscores across all sequences. FA demonstrated significantly higher PET-Radscore values compared to NFA (FA: 0.67 ± 1.01 vs NFA: -1.70 ± 0.52, $p < 0.001$). ROC analysis revealed that PET-Radscore for distinguishing FA from NFA achieved an AUC of 0.966 (95% CI: 0.911-1.000). At cut-off value of -0.56, it showed an accuracy of 90.6%, sensitivity of 87.0%, and specificity of 100%. Calibration curves indicated good consistency between predicted probabilities and actual risks (Brier score = 0.064, Hosmer-Lemeshow test $p = 0.985$). DCA demonstrated that when the threshold probability exceeded 10%, the model achieved significantly higher net benefit than "treat-all" or "treat-none" strategies, suggesting good clinical applicability. ***Conclusion:*** The ^{68}Ga-Pentixafor PET-based Radscore shows good ability in distinguishing functional from non-functional adenomas, offering a reliable tool for non-invasive assessment of adrenal adenoma functional status.

EPS-245

The Role of [^{11}C]metomidate PET in Predicting Post-treatment Outcomes in Patients with Primary Aldosteronism: A Meta-Analysis

P. Chuang[1], *J. S. Chueh*[2], *J. Huang*[2], *T. Hong*[1], *V. Wu*[2], *Y. Lin*[2], *P. Kuo*[3], *C. Lu*[1];
[1]*National Taiwan University Cancer Center, Taipei, TAIWAN,* [2]*National Taiwan University Hospital, Taipei, TAIWAN,* [3]*National Taiwan University, Taipei, TAIWAN.*

Aim/Introduction: Accurate determination of unilateral versus bilateral disease is essential in guiding treatment decisions for primary aldosteronism, as surgical resection is appropriate only for unilateral cases. Positron emission tomography (PET) using [^{11}C] metomidate (MTO), a selective inhibitor of 11β-hydroxylase, has emerged as a potential non-invasive alternative to adrenal venous sampling (AVS). ***Materials and Methods:*** A comprehensive literature search was conducted across PubMed, Embase, and the Cochrane Library to identify studies evaluating [^{11}C]MTO PET in patients with primary aldosteronism. Studies were included if they reported diagnostic accuracy in correlation with post-treatment outcomes assessed by the Primary Aldosteronism Surgical Outcome (PASO) criteria. Data on true positives, false positives, false negatives, and true negatives were extracted. Pooled estimates of sensitivity and specificity were calculated using a random-effects bivariate model. ***Results:*** Six studies comprising a total of 287 patients met the inclusion criteria. The pooled sensitivity and specificity of [^{11}C]MTO PET for predicting complete or partial biochemical response post-treatment were 0.75 (95% CI: 0.35-0.95) and 0.58 (95% CI: 0.02-0.99), respectively. In comparison, AVS demonstrated a pooled sensitivity of 0.78 (95% CI: 0.63-0.88) and specificity of 0.52 (95% CI: 0.15-0.88). The differences between [^{11}C] MTO PET and AVS were not statistically significant in both sensitivity ($p=0.741$) and specificity ($p=0.865$). The partial area under the curve (AUC) was 0.737 for [^{11}C]MTO PET and 0.772 for AVS. Diagnostic performance for clinical outcome prediction showed comparable trends. ***Conclusion:*** [^{11}C]MTO PET exhibits diagnostic accuracy comparable to that of AVS in predicting treatment response in primary aldosteronism. These findings support its role as a viable, non-invasive alternative for treatment planning, particularly when AVS is contraindicated, technically challenging, or yields inconclusive results. ***References:*** 1. Wu et al. [11C]metomidate PET-CT versus adrenal vein sampling for diagnosing surgically curable primary aldosteronism: a prospective, within-patient trial. Nat Med. 2023;29(1):190-202. 2. Isojärvi et al. "Lateralization in 11C-Metomidate PET and outcome of adrenalectomy in primary aldosteronism." Endocrinology, diabetes & metabolism vol.5,6(2022):e368. 3. Lu et al. "Predicting Treatment Response in Primary Aldosteronism Using 11C-Metomidate Positron Emission Tomography." Clinical nuclear medicine vol.47,11(2022):936-942. 4. Puar et al. "11C-Metomidate PET-CT versus adrenal vein sampling to subtype primary aldosteronism: a prospective clinical trial." Journal of hypertension vol.40,6(2022):1179-1188. 5. Soinio et al. "Functional imaging with 11C-metomidate PET for subtype diagnosis in primary aldosteronism." European journal of endocrinology vol.183,6(2020):539-550. 6. O'Shea et al. "11C-Metomidate PET/CT is a useful adjunct for lateralization of primary aldosteronism in routine clinical practice." Clinical endocrinology vol.90,5(2019):670-679.

EPS-246

Efficacy, Tolerability, and Resensitizing Effects of Dabrafenib-Trametinib in Advanced Thyroid Cancer: A Retrospective Monocentric Real-World Study

C. Fersing[1], *E. Noudeau*[1], *J. Toucheboeuf*[2], *M. Vinches*[3], *F. Leenhardt*[4];
[1]*Montpellier Cancer Institute, Nuclear Medicine unit, Montpellier, FRANCE,* [2]*Montpellier Cancer Research Institute (IRCM), INSERM U1194, Montpellier, FRANCE,* [3]*Montpellier Cancer Institute, Medical Oncology department, Montpellier, FRANCE,* [4]*Montpellier Cancer Institute, Pharmacy unit, Montpellier, FRANCE.*

Aim/Introduction: Off-label use of the dabrafenib-trametinib combination (DT) in BRAF-mutated thyroid cancer has demonstrated intrinsic efficacy and the ability to resensitize some patients to iodine-131 (I-131) in cases of refractory lesions. However, real-world data on DT use in thyroid cancer remain scarce in the literature [1-4]. In this context, we conducted a comprehensive evaluation on this clinical use of DT in our institution. ***Materials and Methods:*** This single-center retrospective study included all patients with BRAF-mutated thyroid cancer, of any histological subtype, who were treated with DT between January 29, 2019, and March 26, 2025. Data extracted from medical records covered patient and tumor characteristics, treatment duration, reasons for temporary/permanent discontinuation, toxicities, drug-drug interactions (DDI), DT plasma concentration, tumor and biological response, and I-131 resensitization in refractory lesions. ***Results:*** Nineteen patients were included (9 males, 10 females),

predominantly with follicular-derived carcinoma (16/19, 89%); all harbored BRAF mutations. I-131 refractoriness was identified in 16 patients (84%). The mean age at the start of DT treatment was 69 ± 10 years. Mean DT treatment duration was 611 ± 636 days (median = 435 days; min. = 18 days; max. = 1254 days). Adverse events occurred in 95% of patients (18/19) and accounted for 52% of treatment interruptions. Most of the DDI encountered were caused by the enzyme-inducing properties of dabrafenib. Tumor response (lesions stability or reduction on imaging) was observed in 79% of cases (15/19). Among 8 patients (42%) with anti-thyroglobulin antibodies <115 IU/mL, 6 (75%) showed decreased thyroglobulin levels. Eight patients (42%) underwent post-DT I-131 therapy, with partial or complete I-131 uptake restoration in 62.5% (5/8). However, only 40% (2/5) of these achieved subsequent tumor regression. Plasma concentrations of DT were determined at highly variable timepoints, suggesting the need for standardized sampling protocols. ***Conclusion:*** DT is used across histological subtypes of thyroid cancer to reduce tumor burden and/or restore I-131 avidity. Biological and tumor efficacy was observed in nearly 80% of patients, with some cases demonstrating improved I-131 uptake. However, resensitization does not consistently translate into tumor regression. ***References:*** [1] P. C. Iyer, et al. Thyroid 2018, 28, 79-87. [2] A. Iravani, et al. Thyroid 2019, 29, 1634-1645. [3] C.-F. Chang, et al. Am J Cancer Res 2022, 12, 5342-5350. [4] C. Lorimer, et al. Clin Oncol 2023, 35, e60-e66.

EPS-247

Indeterminate Thyroid Nodules: Can [18F]F-FDG PET/CT and Radiomic Influence Patients' Treatment Strategies?

G. Cuzzani[1], *E. Fortunati*[2], *M. Santoro*[3], *E. Greco*[1], *E. Tabacchi*[2], *L. Calderoni*[2], *L. Zanoni*[4], *C. Malizia*[2], *F. Serani*[5], *C. M. P. Sgro*[1], *G. Bianciardi*[1], *G. A. Fuso*[1], *L. Carrara*[1], *S. Damiani*[6], *L. Strigari*[3], *S. Fanti*[1,2];

[1]*Nuclear medicine, Alma Mater Studiorum University of Bologna, Bologna, ITALY,* [2]*Nuclear Medicine, IRCCS Azienda Ospedaliero-Universitaria di Bologna, Bologna, ITALY,* [3]*Department of Medical Physics, IRCCS Azienda Ospedaliero-Universitaria di Bologna, Bologna, ITALY,* [4]*Nuclear Medicine, AST Pesaro-Urbino, ITALY,* [5]*Nuclear Medicine Unit, Department of Medicine, DIMED, University-Hospital of Padova, ITALY,* [6]*Pathology Unit, IRCCS Azienda Ospedaliero-Universitaria di Bologna, Bologna, ITALY.*

Aim/Introduction: To evaluate diagnostic performance of [18F]F-FDG PET/CT(FDG) in identifying malignancy in thyroid nodules with indeterminate fine-needle aspiration cytology(FNA) addressed to thyroidectomy or hemithyroidectomy.Secondary aim is to investigate radiomic features(RF) SFDG PET to define a predictive model of malignancy of indeterminate thyroid nodules. ***Materials and Methods:*** A monocentric,observational,retro-prospective study is ongoing, including patients who underwent neck ultrasound for suspicious nodules (February 2022-ongoing) at our Institution, followed by FNA which resulted in indeterminate thyroid nodules at cytology(Bethesda System for Reporting Thyroid Cytopathology categories III and IV, corresponding to Thy3 for the British Royal College of Pathologists and to TIR3A-low risk and TIR3B-high risk for the Italian Consensus for the Classification and Reporting of Thyroid Cytology); those patients performed FDG within 4months, before being referred to thyroid surgery.Histopathology was considered standard-of-truth. Case-control patients without any thyroid pathology were also included for radiomic studies.A nuclear physician manually delineated the volumes of interest of suspected lesions and contralateral healthy thyroid lobes. 1316 PET-based harmonized RFs were extracted,and 3 machine learning models were developed for malignancy prediction and compared in terms of sensitivity, specificity and area under the receiver operating curve(AUC).PET-semiquantitative-parameters were measured: SUVmax,SUVmean,target-to-background-ratios (backgrounds: contralateral thyroid,mediastinal-blood-pool(MBP),liver).Visual-positivity-criteria was defined as uptake higher than MBP, excluding physiological/paraphysiological uptake. ***Results:*** Overall, 23patients were enrolled (February2022-February2024), but 4/23 eventually did not perform FDG and were excluded. 14/23 patients(61%) underwent surgery, for a total of 19 indeterminate thyroid nodules with histopathologic validation. 32patients without any thyroid pathology were also considered as case-control. 17/19 nodules(89%) were positive at FDG with a median SUVmax of 7.5 (mean9.6+/-7.8;range:2.4-35.2). ThyroidTBR: mean6.7;range 2.1-23.4. MBP-TBR:mean5; range 1.6-17.2. LiverTBR: mean4.1;range 1.3-14.7. Visual analysis per-nodule(n=19): 5TruePositives-26%(1medullary,2follicular,2papillary),12FalsePositives-63%(2 NIFTPs,5adenomas,5hyperplastic nodules), 2TrueNegatives-11%(1NIFTP,1colloid nodule); sensitivity 100%, specificity 14%, PPV 29%, NPV 100%, accuracy 37%. No statistically significant differences were found in terms of SUVmax/TBRs between benign/malignant nodules.The ML models were balanced during the model training.The developed models had from 2 to 4 significant RFs and showed good performances on test database with predicted area under the curve (AUC), sensitivity and specificity(range:0.79-0.92,0.67-1.00, 0.84-0.92, respectively). ***Conclusion:*** In our limited experience, utility of FDG in detecting presence of malignancy in indeterminate thyroid nodules is ambiguous and FDG uptake or semiquantitative parameters alone cannot be considered a decisive feature for referring patients to surgery; further studies are needed to detect a more accurate discrimination criterion to minimize unnecessary resections. In this framework, ML models have shown promising results and could support clinical decision-making processes.

EPS-248

Exploration of Lu-177-DOTATATE PRRT for treatment of radioiodine-refractory follicular thyroid carcinoma

L. Widjaja[1], *S. C. Kunte*[1], *V. U. Wenter*[1], *A. Holzgreve*[1], *G. T. Sheikh*[1], *F. J. Gildehaus*[1], *S. Lindner*[1], *R. Schirrmacher*[2], *C. Spitzweg*[3], *C. J. Auernhammer*[3], *R. A. Werner*[1], *M. J. Zacherl*[1];

[1]*Department of Nuclear Medicine, LMU University Hospital, Munich, GERMANY,* [2]*Department of Oncology, Division of Oncological Imaging, University of Alberta, Edmonton, AB, CANADA,* [3]*Department of Internal Medicine IV, LMU University Hospital, Munich, GERMANY.*

Aim/Introduction: Treatment options for advanced radioiodine-refractory follicular thyroid carcinoma (FTC) are limited. Interestingly, a subset of FTCs express somatostatin receptors (SSTR). Thus, we hereby explore the clinical value of SSTR-targeted peptide receptor radionuclide therapy with Lu-177-DOTA-D-Phe-Tyr3-octreotate (Lu-177-DOTATATE) and subsequent monitoring with SSTR-targeted positron-emission tomography (PET) in patients with advanced radioiodine-refractory FTC. ***Materials and Methods:*** We retrospectively included seven patients with advanced radioiodine-refractory FTC and SSTR-expression in SSTR-PET in our analysis. Patients were treated with PRRT either continuously (5/7) or discontinuously (2/7; with at least one-PRRT-free-year). Tumor control was defined using PET-derived total tumor volume (TTV), thyroglobulin (Tg; including patients with stable [± 30.0%] or decreasing [≥30.0 %] TTV and Tg), and RECIST 1.1 criteria. Safety was assessed using Common Terminology Criteria for Adverse Events. ***Results:*** FTC tumor lesions demonstrated high SSTR expression with maximum standardized uptake values of 10.4 ± 8.6. Of the five patients treated with continuous PRRT, n=2 received two cycles, n=1 three cycles and n=2 four cycles of PRRT. Tumor control was achieved in 3/5 assessed by PET-derived TTV and RECIST 1.1 and 2/5 assessed by Tg. In the two patients with discontinuous PRRT receiving either four or ten treatment cycles concordant (TTV, Tg and RECIST 1.1) tumor control was achieved both during first follow-up as well as during reinitiating after PRRT-free interval. PRRT in FTC patients was safe with no CTCAE

grade 3-5 events occurring in our cohort. ***Conclusion:*** We hereby demonstrate that PRRT may be an effective and safe treatment option for patients with advanced radioiodine-refractory FTC. These preliminary results can lay the foundation for future studies with larger cohorts to define the clinical value of SSTR-targeted PRRT in FTC.

EPS-249

Multicenter study of Spanish metabolic therapy units. Usefulness of protective therapy during hospital admission in preventing late side effects of 131I in thyroid carcinoma patients

J. Villa-Palacios[1], *M. Negre*[2], *A. Piñeiro-Donis*[1], *L. Cagua Ruiz*[1], *E. Domínguez-Polanco*[1], *L. Menendez-Muros*[3], *T. Aroui-Luquin*[1], *M. Muros de Fuentes*[1];
[1]*Hospital Universitario Virgen de las Nieves, Granada, SPAIN,* [2]*Hospital Universitario de Gerona Doctor Josep Trueta, Girona, SPAIN,* [3]*Hospital Universitario Clínico San Cecilio, Granada, SPAIN.*

Aim/Introduction: To evaluate late side effects after treatment with 131I in relation to protective therapy during hospital admission. ***Materials and Methods:*** A multicenter study of 181 patients with differentiated thyroid cancer treated with 131-I between 2020 and 2023. The study included 70.2% women, 87.8% papillary variant, 29.8% with lymphatic dissemination, 18% with extrathyroidal extension, and 3.8% with distant metastases. 80.66% received doses ≥100 mCi, and 65.74% received rhTSH. The most commonly used protective therapies during hospital admission were proton pump inhibitors (PPIs), Non-steroidal anti-inflammatory drugs (NSAIDs), and corticosteroids. A telephone survey was conducted one and six months after patients discharge. Patients were questioned about asthenia, cervical redness, gastric discomfort, mouth ulcers, conjunctivitis, cervical pain, dry mouth, metallic taste, and menstrual disorders. Responses were classified into nonexistent, mild, moderate, and severe. The Chi-Square test or Fisher's exact test was used for analysis. ***Results:*** The incidence of gastric discomfort was lower in patients treated with PPIs at both one and six months (21.19% and 11.92%) than in untreated patients (25% and 35.71%).The difference was statistically significant at six months (p<0.001).The incidence of stomatitis, conjunctivitis, and neck pain was lower in patients treated with NSAIDs at one month of treatment, and was statistically significant (p=0.01, 0.047, 0.02). At 6 months, the incidence of fatigue, gastric discomfort, stomatitis, neck pain, and metallic taste was lower in those treated with NSAIDs, and this difference was statistically significant (p=0.0001, 0.003, 0.010, 0.001, 0.0025).The incidence of side effects was lower in patients treated with corticosteroids at one and six months of treatment. At 6 months, the incidence of gastric discomfort, neck pain, dry mouth, and metallic taste was lower in those treated with corticosteroids, and this difference was statistically significant (p=0.01, 0.032, 0.046, 0.019). ***Conclusion:*** The use of protective treatment with PPIs, NSAIDs, and corticosteroids during 131I therapy reduces the incidence of side effects one month and six months after therapy.

EPS-250

Analysis of Clinical and Imaging Factors Predicting Treatment Outcomes of Radioiodine Therapy for Pulmonary Metastasis in Thyroid Carcinoma

L. Hashimoto[1,2], *S. Watanabe*[1,3], *K. Hirata*[1,3], *J. Takenaka*[1,3,4], *R. Kimura*[3,5], *N. Wakabayashi*[1,5], *H. Koga*[1,3], *K. Kudo*[3,5];
[1]*Department of Nuclear Medicine, Hokkaido University Hospital, Sapporo, JAPAN,* [2]*Department of Diagnostic Radiology, Sapporo City General Hospital, Sapporo, JAPAN,* [3]*Department of Diagnostic Imaging, Graduate School of Medicine, Hokkaido University, Sapporo, JAPAN,* [4]*Comprehensive Heart Failure Center, University Clinic Würzburg, Würzburg, GERMANY,* [5]*Department of Diagnostic and Interventional Radiology, Hokkaido University Hospital, Sapporo, JAPAN.*

Aim/Introduction: While pulmonary metastasis (PM) is common in differentiated thyroid carcinoma (DTC), approximately 50 percent of PM shows concentrations of I-131 after radioiodine therapy (RAIT). In iodine-avid PM, RAIT is shown to be highly effective, especially for small nodules. Recommended administered activities typically range from 3.7 to 7.4 GBq for metastatic disease, with 5.6 to 7.4 GBq suggested for pulmonary metastases. This study aimed to investigate predictive factors for therapeutic response of PM of DTC under RAIT. ***Materials and Methods:*** We retrospectively analyzed DTC patients with CT-detectable PM who underwent RAIT at our department between 2015 and 2025. RAIT (3.7-5.6 GBq) was administered after performing the following pretreatments: i) a strict iodine-restricted diet for at least three weeks, and ii) either levothyroxine withdrawal for at least three weeks or rhTSH administration. RAIT was repeated at intervals of six months or more if deemed effective. Based on post-RAIT CT findings, patients were categorized into two groups: the group R (remission), in which pulmonary lesions showed reduction or disappearance, and the group P (progression), in which lesions remained or progressed. Clinical and imaging parameters (e.g. age, sex, histology, FDG-accumulation) were statistically compared between the two groups. Additionally, time to treatment completion—defined as remission or improvement of lesions—or time to treatment discontinuation—due to disease progression or radioiodine-refractory status—was evaluated using Kaplan-Meier curves, with treatment completion considered as censoring. ***Results:*** A total of 33 patients (27 female) were included in the analysis. The mean age was 57±38 years. Histological subtypes included 19 cases of papillary carcinoma, 9 of follicular carcinoma, 4 of poorly differentiated carcinoma, and 1 unknown. Mean age of group P was significantly higher than that of group R (t-study, 63±34 vs. 52±38, p=0.039). Of the patients aged 70 or younger, 64% (16/25) were in group R, while 88% (7/8) of the patients aged above 70 were in group P (Pearson's chi-square test, p=0.0112). No other clinical or imaging parameters showed significant differences. According to Kaplan-Meier analysis, all patients in the group R achieved treatment completion, with the longest time to completion being 676 days. In the group P, the median time to treatment discontinuation was 613 days. ***Conclusion:*** Younger age may be a predictive factor for the efficacy of RAIT in PM of DTC. We suggest an age threshold of 70 years as a potential cut-off. Other clinical or imaging parameters showed no significant effect on the treatment outcome.

EPS-251

Redifferentiation and Radioiodine Therapy of Thyroid Cancer After the Use of Signaling Pathway Inhibitors: A Systematic Review and Meta-Analysis

F. Mourato[1,2], *D. O. S. Ramos*[3], *S. Brandão*[4,5], *M. Mariussi*[6], *M. C. Fagundes*[7], *G. B. Torri*[8], *S. Altmayer*[9], *L. G. Schmitt*[10];
[1]*Hospital das Clínicas da UFPE - EBSERH, Recife, BRAZIL,* [2]*Universidade de Pernambuco (UPE), Recife, BRAZIL,* [3]*Hospital das Clínicas da Faculdade de Medicina da Universidade de São Paulo (HCFMUSP), São Paulo, BRAZIL,* [4]*Hospital das Clínicas da UFPE, Recife, BRAZIL,* [5]*Havard Medical School, Boston, MA, UNITED STATES OF AMERICA,* [6]*Hospital Israelita Albert Einstein - Interventional Radiology Department, São Paulo, BRAZIL,* [7]*Hospital Alemão Oswaldo Cruz - Imaging Diagnostic Center, São Paulo, BRAZIL,* [8]*Hospital Universitário de Santa Maria, Santa Maria, BRAZIL,* [9]*Stanford University School of Medicine, Stanford, CA, UNITED STATES OF AMERICA,* [10]*University of Texas Southwestern Medical Center, Dallas, TX, UNITED STATES OF AMERICA.*

Aim/Introduction: Redifferentiation therapy in radioiodine-refractory thyroid cancer aims to restore the expression of sodium-iodide symporter (NIS), thereby resensitizing tumors to radioactive iodine (RAI). A promising strategy involves targeting key signaling pathways to restore iodine uptake by promoting

rediffentiation of tumor cells, providing a rational therapeutic approach to enhance RAI efficacy in otherwise refractory disease. Therefore, our objective is to determine the benefit of using Signaling Pathway Inhibitors followed by radioiodine therapy in RAI refractory patients. ***Materials and Methods:*** A comprehensive search was conducted across MEDLINE, EMBASE, CENTRAL, and Web of Science databases. Additionally, reference lists of the selected articles were manually screened to identify further relevant studies for inclusion.The selection criteria encompassed both cohort studies and clinical trials. Stata 18 software was used. The proportion of patients with thyroid cancer who achieved redifferentiation following treatment with signaling pathway inhibitors were assessed. Additionally, we assess the proportion of patients who responded to radioiodine therapy after redifferentiation was induced. Random-effects methods were used. ***Results:*** The initial search yielded 308 articles, 35 articles were reviewed with full-text, and 10 were considered eligible. An additional article was included after reference list screening. Signaling Pathway Inhibitors therapy included: Dabrafenib, Dabrafenib plus Trametinib, Trametinib, Vemurafenib, Vemurafenib plus Cobimetinib, Vemurafenib plus CDX-3379, Selumetinib and an Investigational MEK inhibitor. The most frequently identified mutation across studies was BRAF V600E, followed by NRAS. Across 11 studies (n = 170 patients), the pooled proportion of patients achieving sufficient redifferentiation for RAI therapy was 0.58 (95% CI: 0.45-0.71) with high heterogeneity (I^2 = 72.09%). RECIST-based response after radioiodine therapy was analyzed in 10 studies (n = 92 patients), with a pooled partial response plus stable disease (no complete response was achieved) of 0.83 (95% CI: 0.71-0.95) with high heterogeneity (I^2 = 73.45%). Biochemical response (thyroglobulin reduction) was assessed by four studies (n = 25 patients), with a pooled thyroglobulin reduction rate of 0.90 (95% CI: 0.79-1.00), with no heterogeneity detected (I^2 = 0%). ***Conclusion:*** Signaling pathway inhibitors demonstrate promising efficacy in inducing redifferentiation and enabling subsequent radioiodine therapy in patients with RAI-refractory thyroid cancer. However, the observed heterogeneity underscores the need for further studies to optimize patient selection and therapeutic protocols.

EPS-253

The Clinical Impact of 131-iodine Whole Body Scintigraphy Following 131-iodine Therapy of Thyroid Cancer

J. Kjems[1], *M. Hofmann*[1], *B. Zerahn*[1], *B. Kristensen*[1], *C. Maare*[2], *L. Jensen*[1];
[1]*Department of Nuclear Medicine, Herlev Hospital, Herlev, DENMARK,* [2]*Department of Oncology, Herlev Hospital, Herlev, DENMARK.*

Aim/Introduction: The incidence of thyroid cancer has increased in recent years, globally and in our country. For patients classified as intermediate- or high-risk following total thyroidectomy, radioactive iodine (RAI) therapy with 131-iodine (^{131}I) is used to eliminate residual thyroid tissue and potential metastases. European and American guidelines recommend post-treatment whole-body scintigraphy (PT-WBS) using the residual ^{131}I activity 2-10 days after RAI treatment to supply information on disease staging. Aim: to elucidate if PT-WBS findings had a clinical consequence for the patient's treatment course in our hospital. ***Materials and Methods:*** In a retrospective cohort study from January 1, 2021, to February 28, 2024, 362 patients received RAI treatment at a large University hospital. Planar PT-WBS were available for 329 patients (91% - the study group), due to 26 patients refraining from participation in quality studies and 7 patients with no-shows or claustrophobia. Medical records were reviewed to assess if the PT-WBS contributed to clinical decision-making. Exclusion criteria: No suspected metastases on the PT-WBS, known metastatic disease, or prior RAI treatment. Clinical consequences were additional RAI therapy, supplementary imaging, or modifications to the follow-up schedule. ***Results:*** Of the 329 patients, 249 patients (76%) were treated with the high-risk dose (3.7 GBq) and 80 (24%) with the intermediate-risk dose (1.1 GBq). No patients in the intermediate-risk group had iodine avid foci on the PT-WBS, besides residual thyroid tissue on the neck. In the high-risk group, 15 patients had their first RAI treatment, with the first detection of potential metastases. Only six patients (2%) had a clinical consequence based on the PT-WBS findings. Nine patients adhered to the standard guidelines for follow-up despite potential metastases on the PT-WBS. ***Conclusion:*** PT-WBS had minimal impact on clinical decision-making, affecting only six patients (2%; best/worst case sensitivity analysis: 2-11%) in the follow-up period. Any clinical consequence of the PT-WBS have uncertain survival benefits due to an overall good prognosis. Omitting PT-WBS from clinical guidelines should be considered, particularly for patients at intermediate risk.

EPS-254

The role of Tc99m-Sestamibi scintigraphy in the diagnostic algorithm of thyroid nodules classified as Bethesda III/IV

K. Papadopoulou*, N. Papadopoulos, A. Kriari, E. Giannoula, P. Exadaktylou, E. Papanastasiou, A. Tsangaridi, P. Charalambous, G. Giakoumettis, E. Gkatzouli, A. Doumas, I. Iakovou;*
2nd Laboratory of Nuclear Medicine, Aristotle University of Thessaloniki, AHEPA Hospital, Thessaloniki, GREECE.

Aim/Introduction: The aim of the study is to assess the role of preoperative Tc99m-Sestamibi scintigraphy in Fine Needle Aspiration suspicious thyroid nodules (Bethesda III and IV) in comparison with thyroidectomy histology. Specificity, sensitivity, negative and positive predictive values of qualitative and semi-quantitative analysis of Tc99m-Sestamibi scan were evaluated. ***Materials and Methods:*** So far, 62 patients enrolled the study, 48% of them diagnosed with thyroid nodule classified as Bethesda III and 52% of them as Bethesda IV by cytological examination and characterized as "cold" nodes in classical Tc99m scan. Early (20 minutes p.i.) and delayed (2 hours p.i.) images were acquired after 20 mCi of Tc99m-Sestamibi IV injection. The uptake of the tracer in the nodule, the mirrored lobe and background activity were evaluated both visually and quantitatively. Quantitative analysis included Washout (WI) and Retention (RI) Index evaluation. All patients underwent total thyroidectomy. ***Results:*** Visual analysis showed that 58% of the patient nodules presented with increased uptake in both early and late scan, characterizing the nodules suspicious for malignancy. WI median value was -52.33 (IQR -67.00, -31.82) and, respectively, RI was 5.63 (IQR -15.51, 13.43), demonstrating that 64.5% of the cases were suspicious for malignancy. Histological findings of eighteen (29%) patients showed follicular variant of papillary thyroid carcinoma and eight (13%) were diagnosed with papillary carcinoma, all of them had positive Tc99m-Sestamibi scan. Thirty-six (58%) patients were diagnosed with benign lesions, twenty-four of them had negative Tc99m-Sestamibi scan. The sensitivity, specificity, positive predictive value and negative predictive value were 92%, 67%, 67% and 92% were for the visual assessment of the scan, 88%, 55%, 53% and 84% for the WI, 84%, 83%, 56%, 82% for the RI, respectively, with no significant difference between the three methods. ***Conclusion:*** A negative MIBI scan can provide a definite diagnosis of the absence of malignancy, without the need for further invasive diagnostic procedures. Since the study is ongoing, the findings should be considered exploratory, highlighting the need for larger validation cohorts.

EPS-255

Estimation of Effective Half-Life and Evaluation of Treatment Response in ^{131}I Therapy for Thyroid Cancer

Y. Iizuka[1], *R. Nakashima*[1], *R. Aizawa*[1], *M. Kajisako*[2], *M. Shioji*[2], *K. Mitsumoto*[2], *K. Itagaki*[2], *S. Kawase*[2], *T. Mizowaki*[1];
[1]*Kyoto University Graduate School of Medicine, Kyoto, JAPAN,* [2]*Kyoto University Hospital, Kyoto, JAPAN.*

Aim/Introduction: In radioiodine therapy for differentiated thyroid cancer, accurate lesion dosimetry requires reliable assessment of pharmacokinetics, particularly the effective half-life of iodine uptake. While dynamic or multi-timepoint imaging is ideal, it can be logistically challenging. This study aimed to estimate effective half-lives using two-timepoint post-therapeutic imaging and evaluate their variation by lesion type and their association with treatment response. ***Materials and Methods:*** We analyzed 50 inpatients treated with ^{131}I therapy for differentiated thyroid cancer (26 adjuvant therapy cases, 24 cancer treatment cases). The median administered dose was 3700 MBq. Whole-body planar scintigraphy was acquired at discharge and again 6-14 days later (median interval 13.2 days). Imaging was performed using a gamma camera equipped with high-energy collimators. Lesion counts were measured using circular ROIs (5 cm diameter) on anterior planar images. A known-activity ^{131}I capsule placed near the patient's head served as an internal reference. The percent error in capsule-based count estimation between scans was calculated to validate the method. Effective half-lives were analyzed across all 50 cases (both adjuvant and cancer treatment). In addition, serum thyroglobulin (Tg) trends were evaluated in cancer treatment cases with distant metastases. Statistical comparisons were conducted using Welch's t-test. ***Results:*** The median percent error in count-based estimation of the ^{131}I capsule between scans was 6.1%. Mean effective half-lives were 2.53 ± 0.75 days for thyroid bed (n = 35), 3.25 ± 0.76 days for bone metastases (n = 11), and 3.27 ± 0.85 days for lung metastases (n = 3). The thyroid bed had significantly shorter half-lives than metastatic lesions (p = 0.007). Among 17 metastatic cases with follow-up Tg data, Tg levels decreased in 11 and remained stable or increased in 6. However, no significant difference in half-life was observed between these groups (p = 0.25). ***Conclusion:*** ^{131}I activity in the thyroid bed clears faster than in distant metastases. Lesion-specific kinetics should be considered in dose estimation. The lack of correlation with Tg trends suggests that clearance rates alone may not predict biochemical response.

EPS-256

Evaluation of the Efficacy of Lu-177 DOTATATE Therapy in Radioactive Iodine-Refractory Thyroid Cancer

A. Kibar[1], *K. Saglam*[1], *A. Nazari*[2], *O. E. Sahin*[1], *S. Asa*[1], *L. Uslu-Besli*[1], *S. Sager*[1], *K. Sonmezoglu*[1], *H. B. Sayman*[1];
[1]*Istanbul University-Cerrahpasa, Cerrahpasa Faculty of Medicine, Department of Nuclear Medicine, Istanbul, TÜRKIYE,* [2]*Tekirdag City Hospital, Department of Nuclear Medicine, Tekirdag, TÜRKIYE.*

Aim/Introduction: The prognosis of patients with radioactive iodine-refractory differentiated thyroid cancer (RAIR-DTC) is significantly worse compared to those with iodine-avid differentiated thyroid cancer. In this study, we aimed to evaluate the efficacy of Lu-177 DOTATATE therapy in RAI-refractory thyroid cancer patients, a group with limited treatment options. ***Materials and Methods:*** A total of 38 patients with RAI-refractory thyroid cancer who received Lu-177 DOTATATE therapy between 2011 and 2024 at our department were included in the study. Pre- and post-treatment serum thyroglobulin (Tg) and anti-thyroglobulin (anti-Tg) levels were evaluated. ***Results:*** Among the 38 patients, 23 were female and 15 were male. At the time of initial diagnosis, 28 patients had papillary thyroid carcinoma, 6 had follicular thyroid carcinoma, and 4 had poorly differentiated thyroid carcinoma. Before Lu-177 DOTATATE therapy, patients had received a median of 20350 MBq (range: 5550-37000 MBq) of I-131 therapy. Pre-treatment imaging revealed lesions in the lungs in 23 patients (60.5%), lymph nodes in 19 (50%), thyroid bed in 11 (28.9%), bones in 11 (28.9%), pancreas in 2 (5.3%), liver in 1 (2.6%), and muscle in 1 (2.6%). The median pre-treatment Tg level was 172 ng/mL (range: 0.95-4591 ng/mL). Patients received a median of 2 cycles (range: 1-5 cycles), with a total median administered activity of 13505 MBq (range: 3811-28046 MBq) of Lu-177 DOTATATE. At a median of 2 months post-treatment (range: 1-6 months), laboratory results showed a >50% reduction in Tg in 3 patients (7.9%), a 10-50% reduction in 6 patients (15.8%), and progressive Tg elevation in 29 patients (76.3%). No significant change in anti-Tg levels was observed before and after treatment. ***Conclusion:*** Treatment options for patients with RAI-refractory thyroid cancer are limited. Although treatments such as tyrosine kinase inhibitors (TKIs) are available for this patient population, they are typically reserved for patients with symptomatic disease progression due to their associated toxicity profile. Consequently, the development of adverse effects may lead to discontinuation and limit further therapeutic options. Lu-177 DOTATATE therapy may be considered a potential option, given its ability to induce a thyroglobulin response in a subset of patients.

EPS-257

The efficacy of radioiodine therapy in patients with non-toxic multinodular goiter with large cold nodule

S. Abdelrazek, *I. Sulima, P. Szumowski, J. Mysliwiec;
Medical University of Bialystok, Bialystok, POLAND.*

Aim/Introduction: The clinical presentation of a patient with multinodular goiter (MNG) varies from a completely asymptomatic goiter to a life-threatening disease due to upper airway compression. Surgery is the treatment of choice in patients with cold nodule, low radioactive iodine uptake (RAIU), and presence of symptoms or signs of compression within the neck. Total thyroidectomy is associated with the risk of surgical complications and is often refused by the patient. Radioactive iodine therapy (RAIT) is an alternative to thyroid surgery to reduce the size of benign MNG. Studies have demonstrated that 131I is safe and effective, leading to significant thyroid volume (TV) reduction. The therapeutic efficacy of 131I in patients with MNG depends to some extent on the RAIU. The aim of our study was to evaluate the efficacy of radioiodine therapy to reduce thyroid volume in patients with cold nodule by the use of two doses of radioiodine I-131. ***Materials and Methods:*** We treated 260 patients with non-toxic MNG with large cold nodule, aged 18 to 70 years; initial 24h RAIU was ranged between 16-47%, and TV ranged between 44 and 160 ml, effective half-life was more than 3 days at the time of treatment. Malignant changes were excluded in all nodules by fine needle aspiration biopsy. The activity dose was calculated and ranged between 280 and 800 MBq. Thyroid ultrasonography, and thyroid scan with RAIU at 24 was done before and after 6 and 12 months of RAIT. Follow up control was done every 6 weeks. ***Results:*** After 6 months of first radioiodine dose, the large cold nodule changes to hot nodule in all the patients. In 71 patients the size of the thyroid gland decrease to 53%, and no need for the second dose of radioiodine therapy. 189 patients received second dose of RAIT to decrease the nodule which was cold and turned to hot after the first dose. After 12 months of the second dose of radioiodine a mean TV reduction of 55% was achieved. After 12 months of RAIT euthyroidism persist in 38% of patients, and hypothyroidism develop in 62% of patients***. Conclusion:*** Radioiodine is non-invasive, safe and cost effective method of therapy for reduction of large non-toxic goitre even with cold nodules. The reduction of the cold nodules and the thyroid volume, were due to well accurate measurement of administered activity, relatively high effective half-life and well-organized follow up.

EPS-258

Utility of somatostatin receptor imaging in differentiated thyroid cancer with elevated thyroglobulin and negative 131I whole body scan

L. Barberan Corral[1], *A. Calatayud Cubes*[1], *M. Proaño Fierro*[2], *M. Rashki*[1], *J. Nogueiras Alonso*[3], *V. Pubul Nuñez*[1];
[1]*Hospital Clinico Universitario de Santiago, Santiago de Compostela, SPAIN,* [2]*Complejo Hospitalario Universitario de Pontevedra, Pontevedra, SPAIN,* [3]*Hospital Meixoeiro, Vigo, SPAIN.*

Aim/Introduction: Differentiated thyroid cancer (DTC) is the most common subtype, generally with good prognosis and high survival rate; however, there is a small group of cases that evolve into a highly aggressive behavior. The aim of this study is to assess the utility of somatostatin receptor (SSR) imaging for detecting recurrence and metastases in cases of DTC negative 131I scan and elevated stimulated thyroglobulin (Tg) levels, to re-stage the disease and explore new treatment alternatives. ***Materials and Methods:*** A retrospective observational study of patients diagnosed with DTC, after total thyroidectomy and at least one dose of 131I therapy, showed a progressive increase in Tg levels with a negative 131I scan. As a result, a PET/CT scan with Ga-DOTA-TOC or a SSR SPECT was performed to search for new lesions. ***Results:*** Nine patients were included: 3 women, 5 men, with different histological variants: 2 papillary (1 classic, 1 tall-cell) and 7 follicular (4 oncocytic). Most patients presented with locally advanced tumors, stage III. FDG-PET was positive in 5/9 cases. SSR imaging was performed with PET/CT Ga-DOTA-TOC in 7 patients (6/7 positive) and SPECT in 2 patients (2/2). The positivity rate for FDG-PET was higher in oncocytic compared to others. The correlation between Tg concentration and imaging positivity was not statistically significant. ***Conclusion:*** Although no significant association was found, 90% of patients showed SSR imaging positivity. Therefore, this type of imaging could be considered in cases with rising and elevated Tg levels with a negative 131I scan. ***References:*** Binse I, Poeppel TD, Ruhlmann M, Ezziddin S, Görges R, Sabet A, Beiderwellen K, Bockisch A, Rosenbaum-Krumme SJ. 68Ga-DOTATOC PET/CT in Patients with Iodine- and 18F-FDG-Negative Differentiated Thyroid Carcinoma and Elevated Serum Thyroglobulin. J Nucl Med. 2016 Oct;57(10):1512-1517. doi: 10.2967/jnumed.115.171942. Epub 2016 Mar 31. PMID: 27033897. Giovanella L, Deandreis D, Vrachimis A, Campenni A, Petranovic Ovcaricek P. Molecular Imaging and Theragnostics of Thyroid Cancers. Cancers (Basel). 2022 Mar 1;14(5):1272. doi: 10.3390/cancers14051272. PMID: 35267580; PMCID: PMC8909041.Gubbi S, Koch CA, Klubo-Gwiezdzinska J. Peptide Receptor Radionuclide Therapy in Thyroid Cancer. Front Endocrinol (Lausanne). 2022 May 30;13:896287. doi: 10.3389/fendo.2022.896287. PMID: 35712243; PMCID: PMC9197113.Donohoe KJ, Aloff J, Avram AM, Bennet KG, Giovanella L, Greenspan B, Gulec S, Hassan A, Kloos RT, Solórzano CC, Stack BC Jr, Tulchinsky M, Tuttle RM, Van Nostrand D, Wexler JA. Appropriate Use Criteria for Nuclear Medicine in the Evaluation and Treatment of Differentiated Thyroid Cancer. J Nucl Med. 2020 Mar;61(3):375-396. doi: 10.2967/jnumed.119.240945. PMID: 32123131.

EPS-259

The Clinical Application of ^{68}Ga-FAPI PET/MR in Thyroid Eye Disease

Y. Zhou[1,2,3], *Y. Hou*[1,2,3], *X. Xia*[1,2,3];
[1]*Department of Nuclear Medicine, Union Hospital, Tongji Medical College, Huazhong University of Science and Technology, Wuhan, CHINA,* [2]*Hubei Province Key Laboratory of Molecular Imaging, Wuhan, CHINA,* [3]*Key Laboratory of Biological Targeted Therapy, the Ministry of Education, Wuhan, CHINA.*

Aim/Introduction: To explore the potential application of ^{68}Ga-fibroblast activation protein inhibitor (FAPI) PET/MR in thyroid eye disease (TED) and assess its diagnostic efficacy for TED activity. ***Materials and Methods:*** This prospective study included 24 TED patients, with a total of 48 eyes, and 11 patients in the control group, with a total of 22 eyes. All TED patients underwent Clinical Activity Score (CAS) assessment. Two TED patients underwent ^{68}Ga-FAPI PET/CT, while the remaining participants underwent ^{68}Ga-FAPI PET/MR. The maximum standardized uptake value (SUVmax) of the extraocular muscles in both eyes was measured and compared to the lateral pterygoid muscle as background. MR images were analyzed to assess the signal intensity of the extraocular muscles in T2-weighted imaging. TED patients were categorized into active and non-active groups based on treatment and efficacy as the gold standard. The differences in SUVmax of extraocular muscles between the active group, non-active group, and control group were compared. ***Results:*** The SUVmax of the extraocular muscles in the active group, non-active group, and control group were 8.802±2.057, 5.892±2.421, and 4.982±1.552, respectively. Significant differences were observed between the active group and both the non-active and control groups ($P<0.001$). The optimal threshold for SUVmax to distinguish between the active and non-active phases was 5.85 (sensitivity: 100%, specificity: 66.7%, AUC: 0.838). The lateral pterygoid muscle was used as the background to eliminate its influence. The ratio of SUVmax between the extraocular muscles and the lateral pterygoid muscle for each group was 4.679±1.153, 3.313±1.443, and 2.273±0.658, respectively. Significant differences were found between the active group and both the non-active and control groups ($P<0.001$). The SUVmax threshold for distinguishing between the active and non-active phases was 3.25 (sensitivity: 91.7%, specificity: 62.5%, AUC: 0.776). CAS evaluation for TED activity had a sensitivity of 70.8% and specificity of 50%. Combining MR activity scoring of the extraocular muscles and SUVmax values provided a comprehensive evaluation of TED patients, with sensitivity of 96.2% and specificity of 83.7%. ***Conclusion:*** ^{68}Ga-FAPI PET/MR orbital imaging is a reliable and objective imaging method for assessing TED activity, superior to clinical CAS scoring, and has good application potential. However, the lateral pterygoid muscle as a background comparison is not ideal, and further exploration for more appropriate background comparisons is needed. ***References:*** This research was supported by National Natural Science Foundation of China (Grant Numbers: 81771866) and Hubei Provincial Natural Science Foundation Project (2024AFB633). Corresponding author is Xiaotian Xia.

EPS-260

Impact of Perinodal Infiltration on Recurrence in Papillary Thyroid Cancer

U. Turan[1], *A. Cinar*[1], *K. Okuyucu*[2], *N. Aydinbelge Dizdar*[1], *A. Erol*[1], *B. Bedi Alpay*[1], *P. Akkus Gunduz*[1], *M. Ozkara*[3], *D. Cayir*[4], *E. Alagoz*[2], *S. Ince*[2];
[1]*Gulhane Training and Research Hospital, Department of Nuclear Medicine, Ankara, TÜRKIYE,* [2]*University of Health Sciences, Gulhane Medical Faculty, Department of Nuclear Medicine, Ankara, TÜRKIYE,* [3]*Gulhane Training and Research Hospital, Department of General Surgery, Ankara, TÜRKIYE,* [4]*University of Health Sciences, Etlik City Hospital, Department of Nuclear Medicine, Ankara, TÜRKIYE.*

Aim/Introduction: Locoregional recurrence occurs in up to 28% of patients with papillary thyroid cancer (PTC). Several risk factors contribute to this metastatic process. The latest of them is perinodal infiltration (PNI). PNI refers to the pathological extension of tumor cells through the lymph node (LN) capsule into the perinodal fibroadipose tissue. It has been accepted as a poor predictive variable. This study aimed to evaluate the prognostic significance of PNI in recurrence of PTC and to identify predictive parameters associated with recurrence in PNI (+) patients. ***Materials and Methods:*** This study included 680 PTC with initial LN metastasis (lLNM). Study population was selected from them according to presence or absence of PNI. Eventually, 102 PNI (+) and 122 PNI (-) patients remained eligible for the study. Patients were statistically compared based on demographic, clinicopathologic, treatment, and outcome variables, both between PNI (+) and PNI (-) groups, and within the PNI (+) group according to recurrence status. ***Results:*** The recurrence rates were 40% and 15% in PNI (+) and PNI (-) patients, respectively ($p<0.001$). In PNI (+) group, the predicitive

factors associated with recurrence were central ILNM (p=0.005), combined central and lateral ILNM (p=0.003), ILNM>5 (p<0.001), tumor size (TS) (p<0.001), ILNM size (p<0.001), stimulated Tg (sTg) (p=0.039). ***Conclusion:*** PNI positivity is a poor prognostic factor for PTC recurrence. Central or combined central and lateral LN involvement, more than 5 ILNM, TS, ILNM size, higher sTg levels should also be considered when planning therapy in PNI (+) PTC patients. ***References:*** 1. Clain JB, Scherl S, Dos Reis L, Turk A, Wenig BM, Mehra S et al. Extrathyroidal extension predicts extranodal extension in patients with positive lymph nodes: an important association that may affect clinical management. Thyroid. 2014;24:951-7. doi:10.1089/thy.2013.0557.2. Suh S, Pak K, Seok JW, Kim IJ. Prognostic value of extranodal extension in thyroid cancer: a meta-analysis. Yonsei Med J. 2016;57:1324-8. doi:10.3349/ymj.2016.57.6.1324.3. Kim HI, Hyeon J, Park SY, Ahn HS, Kim K, Han JM et al. Impact of extranodal extension on risk stratification in papillary thyroid carcinoma. Thyroid. 2019;29:963-970. doi:10.1089/thy.2018.0541.4.Moritani S. Impact of invasive extranodal extension on the prognosis of patients with papillary thyroid carcinoma. Thyroid. 2014;24:1779-83.

EPS-261

Therapeutic ^{131}I Dose for Hyperthyroidism Treatment of Unifocal Autonomy in Compliance with Council Directive 2013/59/Euratom Optimization Principle

C. Canzi, *V. Longari, L. Florimonte, A. Castello, R. Leo, M. Castellani;*
Fondazione IRCCS Ca' Granda Ospedale Maggiore Policlinico, Milan, ITALY.

Aim/Introduction: Hyperthyroidism due to unifocal autonomy is a benign thyroid disease with about 10000 new cases/year in Europe. Being a benign disease, treatment should be performed with the lowest clinically effective dose. European guidelines suggest a target dose of 300-400 Gy. Aim of this study was to demonstrate that a lower dose and a personalized pretreatment dosimetric study can be effective in obtaining a stable euthyroid condition avoiding both hyperthyroidism persistence and hypothyroidism onset. ***Materials and Methods:*** 134 patients with a single nodule and a minimum follow-up of 12 months were considered. They were studied with a pretreatment patient-specific dosimetric study (based on the administration of 48-111 MBq of ^{123}I, multiple uptake measurements with a gammacamera and the use of the MIRD formula) in order to calculate the therapeutic ^{131}I activity necessary to release a dose of 140 Gy to the nodule. The dose released after the ^{131}I therapeutic administration was calculated in the same way. Each patient clinical outcome was periodically monitored with biochemical analysis. Two subgroups of 77 and 48 patients had a follow-up of 5 and 10 years, respectively. ***Results:*** All patients were given a single ^{131}I therapeutic administration with a mean activity of 297±150 MBq (range 87-614 MBq). The mean released nodule dose was 143±38 Gy. Twelve months after therapy hyperthyroidism was healed in 97% of the patients but 8% were hypothyroid. In the subgroup followed for 5 years 100% solved hyperthyroidism but 27% became hypothyroid and in the subgroup followed for 10 years they were 38%. ***Conclusion:*** This study demonstrated that a released nodule dose of about 140 Gy is effective in solving hyperthyroidism due to unifocal autonomy and in maintaining a long lasting euthyroidism. This dose is quite lower than the value indicated by the European guidelines. The wide range of administered activity indicates the importance of a personalized pretreatment dosimteric study in order to obtain the clinical goal with the lowest activity as specified by the optimization principle of the 2013/59/Euratom Council Directive.

EPS-262

Redifferntiation therapy in Radioactive iodine refractory thyroid cancer: post therapy response and clinical outcomes

K. Kulkarni[1], *K. Manglani*[2], *A. Bendre*[3], *A. Bendre*[2];
[1]*Medstar Medical Group Radiology, Medstar Washington Hospital Center, DC, UNITED STATES OF AMERICA,* [2]*Medstar Washington Hospital Center, Washington, DC, UNITED STATES OF AMERICA,* [3]*Medstar Health Research Institute, Medstar Washington Hospital Center, DC, UNITED STATES OF AMERICA.*

Aim/Introduction: Radioactive iodine (RAI) refractory thyroid cancers often harbor BRAF V600E and NRAS Q61R mutations, which can be targeted with BRAF and MEK inhibitors to promote thyroid cancer cell redifferentiation and enhance RAI uptake. This study evaluates post-therapy scan results and clinical outcomes in patients who underwent RAI after redifferentiation therapy (RDT). Pretherapy dosimetry scans were used to assess RAI uptake and determine therapeutic I-131 activity, while post-therapy scans confirmed uptake in known lesions. Follow-up imaging and thyroglobulin (TG) levels were used to monitor treatment response. ***Materials and Methods:*** This retrospective study included 36 patients who underwent RDT between 2021 and 2024 at MWHC. Next-generation sequencing was used to identify targetable mutations with patients receiving either dual therapy with Trametinib and Dabrafenib for BRAF V600E mutations or Trametinib alone for NRAS Q61R mutations. Pretherapy scan was performed in week 5 with RAI administered in week 6 based on dosimetry and scan results. Post-therapy scans were conducted 5-7 days after treatment to assess RAI uptake, and follow-up CT scans and TG levels were measured every 3 months for the first year, then every 6 months. RECIST criteria were used to assess response. Molecular analysis revealed 25 patients with BRAF V600E mutations, 8 with NRAS Q61R mutations, and 3 with other mutations (RET, NTRK, and no identifiable mutation). ***Results:*** Post-therapy scans revealed distinct RAI uptake patterns. 37 pretherapy scans were available for 36 patients (one patient had two treatments). Of the 24 patients with positive pretherapy scans, all proceeded to RAI therapy and showed sustained positive post-therapy scans. Among the 12 patients with negative pretherapy scans: 6 had positive post-therapy scans, 2 remained negative, and 4 did not undergo RAI therapy. RAI dose ranged from 140-400 mCi based on dosimetry. Clinical outcomes, biochemical responses (TG levels), and structural responses (stable disease, progression, or regression) varied during follow-up. ***Conclusion:*** This study demonstrates the utility of BRAF and MEK inhibitors in promoting RAI uptake in refractory thyroid cancers. However, variability in patient responses highlights the need for further research to identify clinicopathological and molecular factors that predict which patients will benefit most from RDT. Our study continues to investigate these characteristics to refine patient selection for targeted therapy in advanced thyroid cancer. ***References:*** 1. Van Nostrand, D., 2018. Radioiodine refractory differentiated thyroid cancer: time to update the classifications. Thyroid, 28(9), pp.1083-1093.1.

EPS-263

Redifferentiation Therapy in Refractory Differentiated Thyroid Cancer with Progression. Initial Experience

C. Paniagua Correa, *R. Vegara Fernández, G. Guijarro de Armas, L. Castillejos Rodríguez, M. Tagliatori Nogueira, S. Pérez Quirós, A. Herrero Muñoz, M. de la Rubia Marcos, A. Ortega Valle, D. Rodriguez Oviedo, C. Galindo Fernández, K. Guichay Duran, J. Sánchez Calderón, P. García Alonso;*
Hospital De Getafe, Madrid, SPAIN.

Aim/Introduction: Objetive: To evaluate the response to redifferentiation therapy in patients with advanced differentiated thyroid cancer (DTC), refractory to radioactive iodine-131I (RAI-R),

as well as the eventual response to a new dose of radioiodine (RAI). ***Materials and Methods:*** We studied 13 patients with DTC, the majority of whom were classical variants, 69% were women, mean age was 61 years. The total accumulated dose (TAD) of I-131 was a mean of 500 mCi. They received iodide symporter (NIS) redifferentiation therapy from April 2022 to June 2024. Ten patients had BRAF oncogen mutations (the rest had RAS mutations). Seven had previously been treated with first-generation tyrosine kinase inhibitors (TKIs), and one with Dabrafenib (a selective BRAF inhibitor). Dabrafenib was administered as a redifferentiation therapy in 9/13 (69.2%), Trametinib in 3/13 (23.1%), and a combination of both BRAF inhibitors was administered in 1 patient (7.7%). Prior to treatment, each patient underwent ^{18}F-FDG PET/CT scan and whole-body radioiodine scan (WBS) with a diagnostic dose of 5 mCi of 131-I. Treatment was continued for 6 weeks in 12 of 13 patients (discontinued in 1 patient due to severe adverse effects), and followed by a diagnostic WBS (5 mCi of 131-I). ***Results:*** Re-establishment of RAI uptake was observed in the WBS in 5/13 patients (38.5%), who received 131-I (120-150 mCi). In another patient, an empirical dose of 131-I was administered after multidisciplinary consensus. In the six evaluated patients, therapeutic response was assessed 3-4 months after RAI dose, using a new WBS and PET/CT, applying RECIST 1.1 criteria, and a possible assessment using PERCIST criteria was considered (comparing the pre- and post-RAI study). The results were: - 2/6 patients: Partial Response (PR) and Partial Metabolic Response (PMR);- 1/6 patients: Progressive Disease (PD) and Progressive Metabolic Disease (PMD); - 1/6 patients: Stable Disease (SD) and Stable Metabolic Disease (SMD); - 2/6 patients: Stable Disease (SD) but Partial Metabolic Response (PMR) (maintained in follow-up studies). ***Conclusion:*** Redifferentiation treatments offer us the opportunity to recover RAI therapy as a therapeutic tool in advanced DTC.

1611

Tuesday, October 7, 2025, 16:45 - 18:15
Room 111

TROP Session - Case Report Session 2: Case-based Learning in Nuclear Medicine Beyond Oncology

OP-740

^{18}F-DPA-714 versus ^{18}F-FDG PET for localizing the epileptogenic zone in drug-resistant epilepsy: a case report

L. Xiao, *L. Feng, Y. Tang, S. Hu;*
Xiangya Hospital Central South University, Changsha, CHINA.

Aim/Introduction: Drug-resistant epilepsy (DRE) presents significant diagnostic challenges, particularly in pediatric cases where precise localization of the epileptogenic zone (EZ) is crucial for surgical intervention. While ^{18}F-FDG PET is commonly used in presurgical evaluation, its limited specificity often fails to clearly delineate the EZ in non-lesional cases. The emerging ^{18}F-DPA-714 PET tracer, targeting neuroinflammation through microglial activation, offers a promising alternative with potentially higher specificity for epileptogenic foci. This case report compares the diagnostic performance of these two PET modalities in a pediatric DRE patient, demonstrating how ^{18}F-DPA-714 provided superior localization that correlated with stereoelectroencephalography (SEEG) findings and successful surgical outcome. ***Materials and Methods:*** A 6-year-old male with DRE characterized by hypermotor seizures and autonomic features underwent comprehensive presurgical evaluation including 3T MRI, both ^{18}F-FDG and ^{18}F-DPA-714 PET scans, scalp EEG, and subsequent SEEG with bilateral implantation of 10 electrodes targeting frontal and cingulate regions. The PET images were analyzed using standardized uptake values (SUV), with particular attention to regions showing abnormal uptake patterns. Surgical planning was based on the concordance between PET findings and SEEG localization, ultimately guiding stereotactic radiofrequency thermocoagulation of the right anterior and middle cingulate gyri. ***Results:*** The ^{18}F-DPA-714 PET demonstrated focal increased uptake specifically in the right anterior/middle cingulate gyri, while ^{18}F-FDG PET revealed only nonspecific right hemispheric hypometabolism. SEEG recordings confirmed ictal onset precisely in the areas of ^{18}F-DPA-714 uptake, with characteristic high-frequency fast activity observed in the right ACC/MCC. Following stereotactic thermocoagulation of these regions, the patient achieved complete seizure freedom (Engel class 1a) at 9-month follow-up with reduced antiepileptic medication and no neurological deficits. ***Conclusion:*** This case demonstrates that ^{18}F-DPA-714 TSPO PET offers superior localization value compared to ^{18}F-FDG PET in DRE evaluation, particularly in pediatric cases with non-lesional MRI. The precise correlation between ^{18}F-DPA-714 uptake, SEEG findings, and successful surgical outcome highlights its potential as a valuable tool in presurgical planning. These results suggest that TSPO PET imaging could significantly improve surgical outcomes in DRE cases where conventional imaging modalities provide inconclusive results, though larger prospective studies are needed to validate these findings and establish clinical protocols.

OP-741

Impact of Venlafaxine on ^{123}I-FP-CIT Imaging: A Case Series

M. El-Sayed, *J. Dias;*
Queen Elizabeth Hospital Birmingham, Birmingham, UNITED KINGDOM.

Aim/Introduction: The effect of venlafaxine (an antidepressant) on dopamine transporter imaging using ^{123}I-FP-CIT SPECT imaging remains poorly understood, leading to conflicting guidelines. The German Society of Nuclear Medicine advises stopping venlafaxine before scans, while the European Association of Nuclear Medicine does not. Only one prior case report suggests that venlafaxine may reversibly alter scan results. ***Materials and Methods:*** We present two cases of abnormal ^{123}I-FP-CIT scans on venlafaxine, which then had repeat scans off the drug showing normal results. The mental health team referred both cases due to concerns of dementia with Lewy bodies (DLB). The first case involved a 75-year-old man receiving venlafaxine 150 mg/day, and the second case a 72-year-old woman on 262.5 mg/day. Neither patient was taking any other drugs known to influence the ^{123}I-FP-CIT imaging, and their structural brain imaging was normal. Initial scans demonstrated normal striatal comma-shaped morphology; however, there was increased background activity and reduced striatal-specific binding ratios (SBR). In Case 1, z-scores were -1.89 (right) and -1.7 (left) and in Case 2, -2 (right) and -1.9 (left). These results were interpreted as abnormal and supportive of a DLB diagnosis. Due to clinical inconsistencies, repeat scans were performed after venlafaxine withdrawal, using identical protocols. Upon re-scanning off venlafaxine, SBR values normalised significantly. For Case 1, z-scores improved to -0.18 (right) and -0.44 (left) - this patient also had a normal brain FDG PET/CT. Case 2 showed similar improvement with z-scores of -1 (right) and -0.7 (left). ***Results:*** DLB was excluded in both cases; case 1 was diagnosed with functional cognitive disorder, but case 2 had unresolved diagnostic uncertainty. Notably, venlafaxine exhibits negligible dopamine transporter binding affinity (Kd 9300 nM vs ioflupane's 3.5 nM; higher Kd indicates lower affinity), leaving its mechanism of SBR reduction unclear. Given the risk of withdrawal complications, any decision to stop venlafaxine before imaging must involve multidisciplinary discussion.

Cardiac ^{123}I-MIBG studies are also affected by venlafaxine, making them unsuitable alternatives. However, brain FDG PET scans are not typically affected. ***Conclusion:*** These cases suggest that venlafaxine can cause a uniform, symmetrical reduction in SBR on ^{123}I-FP-CIT SPECT that may mimic DLB pathology. Discrepancies in current guidelines, if unaddressed, risk diagnostic errors. Prospective studies are needed to define the prevalence and dose-dependency of this interaction. ***References:*** -Tatsch K, et al. Nuklearmedizin. 2019;58:5-16.-Morbelli S, et al. Eur J Nucl Med Mol Imaging. 2020;47:1885-1912. -Kanani MK & Gurunathan N, Prog Neurol Psychiatry. 2022;26:8-10.

OP-742

Managing Pediatric Multisystem Langerhans Cell Histiocytosis: A 5-Year Follow-Up with Serial [18F]FDG-PET/CT Metabolic Imaging

D. Barbosa, *H. Duarte, D. Silva, N. Vasconcelos, R. Marão, I. Sampaio;*
IPO, Porto, PORTUGAL.

Aim/Introduction: Langerhans cell histiocytosis (LCH) is a rare clonal proliferation of myeloid dendritic cells. The clinical course is heterogeneous, and multisystem LCH is particularly challenging due to its association with increased morbidity and relapse risk. [18F]fluoro-2-desoxi-D-glucose Positron Emission Tomography/Computed Tomography ([18F]FDG-PET/CT) enables accurate initial staging, quantitative assessment of treatment response and early detection of disease recurrence. ***Materials and Methods:*** We present a 5-year clinical and imaging follow-up of a male child diagnosed with multisystem LCH at age 3, focusing on 14 [18F]FDG-PET/CT scans and comprehensive molecular profiling performed under the international LCH-IV treatment protocol. ***Results:*** At initial presentation in 2018, the patient exhibited extensive cutaneous lesions and lymphadenopathies. Biopsy confirmed LCH. Baseline [18F]FDG-PET/CT showed diffuse cutaneous hypermetabolism (SUVmax 4.8-6.2) and bilateral axillary and inguinal nodal uptake (SUVmax 3.1-3.5). LCH-IV Stratum I chemotherapy was initiated. Following Cycle 1, [18F]FDG-PET/CT indicated a partial metabolic response. However, disease progression after Cycle 2 with new cutaneous foci (SUVmax 3.0), prompted escalation to Stratum II. Continued progression under cytarabine led to re-initiation of Stratum I. Maintenance therapy (vinblastine every 3 weeks, prednisolone pulses, and daily 6-mercaptopurine) was administered from 2019 to 2021. Molecular analysis - including BRAF V600E, NRAS, KRAS, and MAP2K1 mutation testing - remained consistently negative. Mid- and end-of-treatment [18F]FDG-PET/CT (03/2021) showed complete metabolic remission. In 09/2021, generalized pruritic papules recurred. Biopsy reconfirmed CD1a+, S100+ LCH and [18F]FDG-PET/CT revealed multifocal cutaneous uptake, and re-induction with Stratum I was initiated. [18F]FDG-PET/CT after cycle 1 and 2 showed partial metabolic response and in 09/2022 only low-grade uptake in a right leg lesion (SUVmax 1.4) was reported, and maintenance therapy was resumed. Pituitary Magnetic Resonance Imaging (MRI) in 10/2022 showed stalk thickening with contrast enhancement, consistent with neuro-pituitary LCH but without endocrine dysfunction. Follow-up [18F]FDG-PET/CT scans in 2023 showed no hypermetabolic disease, while MRI findings remained stable. The patient continues on oral 6-mercaptopurine and methotrexate through 05/2025, asymptomatic, under surveillance. ***Conclusion:*** Over 5 years, 4 serial [18F]FDG-PET/CT scans, combined with histopathological reassessment and molecular profiling, enabled accurate evaluation of treatment response, early relapse detection, and timely adjustments to the LCH-IV protocol. Negative molecular findings excluded high-risk variants, supporting continued use of conventional chemotherapy. Persistent neuro-pituitary MRI abnormalities in the absence of endocrinopathy emphasized the value of integrated PET and MRI surveillance. This combined approach allowed for personalized and risk-adapted management in this LCH complex case.

OP-743

"68 Ga-CRH (Corticotropin Releasing Hormone) PET/CT: Transforming Cushing Syndrome Diagnosis"

V. Jain[1], *M. L. Narayan*[1], *K. Shridharan*[1], *J. Shukla*[2], *R. Kumar*[2], *B. Mittal*[2];
[1]*All India institute of Medical Sciences, Rishikesh, Rishikesh, INDIA,* [2]*PGIMER, Chandigarh, Chandigarh, INDIA.*

Aim/Introduction: Cushing's syndrome (CS) is a clinical condition resulting from excessive cortisol production, typically due to inappropriate secretion of adrenocorticotropic hormone (ACTH), corticotropin-releasing hormone (CRH), or autonomous adrenal cortisol secretion. The incidence of CS is approximately 0.7-2.4 cases per million people per year. Identifying the underlying cause of CS is essential for determining appropriate treatment strategies. This report presents a rare case of endogenous CS where differentiating between Cushing's disease (CD) and ectopic ACTH secretion was challenging due to inconclusive findings on conventional imaging. Diagnostic clarity was ultimately achieved using a novel imaging technique 68Ga-CRH PET/CT. ***Materials and Methods:*** A radiotracer dose of 4mCi of 68Ga-DOTA-chelated corticotropin-releasing hormone(CRH), a 41-amino acid peptide, was administered intravenously. Whole-bodyPET/CT imaging, including additional brain imaging, was performed 45 minutes post-injection. ***Results:*** A 26-year-old male presented with a three-year history of insidious weight gain, progressive body swelling, mooning of the face, neck, and abdomen, striae, skin thinning, easy bruising, and hyperpigmentation of the knuckles and mouth angles. Laboratory evaluation revealed elevated 8 AM cortisol and ACTH levels, indicating ACTH-dependent CS. To differentiate between pituitary (CD) and ectopic ACTH secretion, a high-dose dexamethasone suppression test (HDDST) was performed, demonstrating cortisol suppression consistent with CD.CE-MRI brain revealed a suspicious 5mm lesion involving left pituitary lobe although contrast-enhanced CT (CECT) of the abdomen failed to reveal ectopic ACTH-secreting tumor. Given the indeterminate imaging, the patient underwent 68Ga-DOTANOC PET/CT, which identified a non-SSTR expressing right adrenal adenoma(~2.5x2cm) but no other significant SSTR-positive lesions. Due to continued diagnostic uncertainty, the patient was referred for 68Ga-DOTA-CRH PET/CT. This novel imaging modality targets CRH receptors (R1 and R2), which are overexpressed in pituitary adenomas. The scan revealed a tracer avid left para-sellar lesion in the posterior pituitary. The patient subsequently underwent surgical resection of this lesion which was ~0.8x0.4cm in size predominantly on the left side. Histopathological examination confirmed the diagnosis of a corticotroph adenoma, which stained strongly positive for ACTH, SSTR2, and SSTR5. ***Conclusion:*** This case underscores the diagnostic challenges in identifying the aetiology of Cushing's syndrome when conventional imaging is inconclusive especially in microcoticotropinoma. The application of ^68Ga-DOTA-CRH PET/CT, a target-specific imaging modality can play a crucial role in accurately localizing the ACTH source and guiding effective treatment. Its use may significantly enhance diagnostic accuracy in complex cases of CS. ***References:*** 1. Sharma ST, Nieman LK, Feelders RA. Cushing's syndrome: epidemiology and developments in disease management. Clin Epidemiol. 2015 Apr 17;7:281-93.

OP-744

Role of 99mTc-Ethambutol SPECT/CT in Resolving Diagnostic Dilemma in a Case of Chronic Vertebral Lesions

A. Roy, *N. A. Damle, A. Mahalik, N. Kundu, S. Sikdar;*
AIIMS New Delhi, New Delhi, INDIA.

Aim/Introduction: To highlight the diagnostic value of 99mTc-Ethambutol (99mTc-EMB) scintigraphy in detecting spinal tuberculosis and guiding targeted biopsy in a diagnostically

inconclusive case with multiple vertebral lesions. ***Materials and Methods:*** A 29-year-old female presented with chronic lower back pain for over two years. MRI revealed multiple lytic lesions in the dorso-lumbar spine (D8, L2-L4), leading to a differential diagnosis that included tuberculous osteomyelitis, multiple myeloma, and brown tumors. Conventional diagnostic approaches—bone marrow aspiration, GeneXpert, and histopathology—were inconclusive. The patient underwent 99mTc-EMB scintigraphy with 10 mCi of in-house radiolabelled ethambutol. Whole-body planar imaging followed by SPECT/CT was performed on a dual-head gamma camera with LEHR collimators. Imaging interpretation was done by a senior nuclear medicine physician blinded to prior findings. ***Results:*** Planar and SPECT/CT images showed intense radiotracer uptake in D8 and additional uptake in L2-L4 vertebrae. The D8 lesion, with the highest uptake, was selected for CT-guided biopsy. Histopathology revealed necrotizing granulomatous inflammation, confirming spinal tuberculosis. GeneXpert remained negative. The patient was initiated on standard anti-tubercular therapy (ATT) and showed clinical improvement within weeks. This case was part of a broader study where 99mTc-EMB scintigraphy demonstrated 100% sensitivity and 92.3% diagnostic accuracy in bone TB (n=13). This case emphasizes the role of functional imaging in identifying metabolically active lesions and in guiding biopsy in cases where anatomic imaging and conventional tests are inconclusive. ***Conclusion:*** 99mTc-Ethambutol scintigraphy with SPECT/CT provided critical diagnostic and procedural guidance in a complex case of indeterminate vertebral lesions. It enabled lesion mapping, biopsy site selection, and rapid therapeutic decision-making. This case reinforces the utility of radiolabelled antibiotics in diagnosing skeletal TB and supports further exploration of 99mTc-EMB as a frontline adjunct in EPTB diagnostics. ***References:*** Bhattacharya B et al., IJNM. 2022;37(4):323, Kartamihardja AHS et al., Ann Nucl Med. 2018;32(1):60-8, Diah LH et al., World J Nucl Med. 2019;18(1):13.

OP-745

A Non-invasive PET ^{18}F-FTHA Imaging Strategy for Observing Lymphatic Flow Patterns

D. Lee, *R. Laforest, K. D. Harrison, M. L. Nickels, R. J. Gropler, G. J. Randolph;*
Washington University School of Medicine in Saint Louis, Saint Louis, MO, UNITED STATES OF AMERICA.

Aim/Introduction: Diseases of the central lymphatic system are difficult to manage due to limited tools for visualizing lymphatic cargo, particularly outflow from the gastrointestinal tract to the thoracic duct. While lymphangiography has aided superficial mapping, non-invasive approaches remain lacking. Our initial study aims to address this gap using PET-CT and the long chain fatty acid radiotracer 14(R,S)-[18F]fluoro-6-thia-heptadecanoic acid (^{18}F-FTHA) and administered orally[1], to map the biodistribution and lymphatic route of healthy individuals, focusing on outflow from the gut toward the thoracic duct, along with measuring radiation dosimetry. ***Materials and Methods:*** Between 43.3-55.5 MBq of 18F-FTHA was orally administered in a fat-containing Boost™ drink and consumed within 10 minutes. Whole-body PET-CT imaging was performed hourly for up to 8 hours. Maximum and mean standardized uptake values (SUV) were used to characterize gut-to-thoracic duct lymphatic outflow and generate tissue time-radioactivity curves. Radiation dosimetry was calculated from organ time-integrated activities (TIA) using MIRD methodology and MIRDCalc[2] software. ***Results:*** All 6 healthy volunteers who were aged 28-62 and BMI ≤ 32 without pre-existing cardiopulmonary issues completed the study without any adverse events. Following administration, ^{18}F-FTHA could be visualized along the entirety of the digestive system from mouth to the gastrointestinal tract. Radiotracer enrichment both visually and by SUV was particularly higher along the proximal intestine and could be clearly visualized in the thoracic duct. Excretion was primarily via the gastro-intestinal track with the stomach receiving the highest dose of 0.39 mSv/MBq and a whole-body effective dose of 0.061 mSv/MBq. ***Conclusion:*** As a long chain fatty acid, ^{18}F-FTHA passed along the expected route by absorption through intestinal lacteals toward the thoracic duct with radiotracer enrichment analysis suggesting recirculation with blood vasculature as expected. Thus, PET-CT with orally administered ^{18}F-FTHA appears to safely label lymphatic outflow along the gastrointestinal tract. In the future, we expect to evaluate patients with central lymphatic anomalies such as those with protein losing enteropathy and with central conducting lymphatic anomalies. ***References:*** [1] Sébastien M Labbé, André C Carpentier. "Organ-specific dietary fatty acid uptake in humans using positron emission tomography coupled to computed tomography" Am J Physiol Endocrinol Metab. 2011 Mar;300(3):E445-53. [2] Adam L. Kesner, Lukas M. Carter, Juan C. Ocampo Ramos, Daniel Lafontaine, Edmond A. Olguin, Justin L. Brown, Bonnie President, Derek W. Jokisch, Darrell R. Fisher, Wesley E. Bolch, MIRD Pamphlet No. 28, Part 1: MIRDcalc—A Software Tool for Medical Internal Radiation Dosimetry, Journal of Nuclear Medicine Jun 2023, jnumed.122.264225.

OP-746

Too Subtle to Miss? The Diagnostic Value of V/Q SPECT in Low-Risk CTEPH

C. Küçüker[1], *G. Kaya*[2], *E. B. Kaya*[3], *P. Özgen Kiratli*[1];
[1]*Hacettepe University, Faculty of Medicine, Department of Nuclear Medicine, Ankara, TÜRKIYE,* [2]*Republic of Türkiye, Ministry of Health, Yozgat State Hospital, Department of Nuclear Medicine, Yozgat, TÜRKIYE,* [3]*Hacettepe University, Faculty of Medicine, Department of Cardiology, Ankara, TÜRKIYE.*

Aim/Introduction: Pulmonary embolism(PE) is a potentially chronic-condition associated with high-morbidity and mortality. Chronic thromboembolic pulmonary hypertension(CTEPH), a consequence of organized PE, increases pulmonary arterial pressure(PAP), possibly leading to pulmonary arterial hypertension(PAH) and right-heart failure. Despite advances in CT-angiography, ventilation/perfusion(V/Q) scintigraphy remains pivotal for CTEPH diagnosis and therapeutic guidance[1]. Current guidelines recommend V/Q SPECT imaging in patients with low-clinical probability of PE. However, data regarding the correlation of V/Q SPECT±CT findings with other baseline clinical parameters in this population are limited. This study aimed to assess the diagnostic contribution of V/Q SPECT±CT in low-risk PAH patients. ***Materials and Methods:*** We prospectively evaluated adults (>18 years) with PAP >25 mmHg and low-PE probability within a single-center research project protocol(Project ID: 20852). V/Q planar-SPECT imaging findings were analyzed in correlation with clinical-data including symptomatology, echocardiography, right-heart catheterization, and clinical scores using Pearson/Spearman correlation and ROC-analysis. The impact of imaging on clinical decision-making was examined via binary logistic regression and decision tree modeling. Preliminary findings are presented. ***Results:*** Twenty-nine patients(7 males-22 females) were analyzed; mean age was 63.3±2.2 years. Median left ventricular ejection-fraction was 60%(IQR: 50-65%) and median PAP was 45 mmHg(range: 30-100 mmHg). No statistically significant clinical or laboratory predictor of perfusion-ventilation mismatches was identified. PAP showed moderate positive-correlation with "subsegmental" and "segmental" defects($r = 0.549$, $p=0.007$; $r = 0.520$, $p=0.014$; respectively). No significant association was observed between mismatched V/Q defects and PAH. ROC-analysis identified subsegmental defects as a significant predictor of elevated PAP(AUC: 0.727, p=0.018), with Youden Index suggesting a single subsegmental defect as the optimal cut-off(sensitivity: 62.5%, specificity: 75%). ***Conclusion:*** In line with existing literature, the cohort was predominantly female. Unlike

findings in high-risk patients, segmental and also subsegmental defects were significantly associated with PAH[2]. These findings underline the potential of even small subsegmental defects in contributing to PAH, independent of other clinical indicators. Our results support the diagnostic-value of V/Q SPECT as an independent variable[3] and highlight the need for volumetric SPECT-based studies to refine cut-off values. ***References:*** 1.Tunariu N et al. Ventilation-perfusion scintigraphy is more sensitive than multidetector CTPA in detecting chronic thromboembolic pulmonary disease as a treatable cause of pulmonary hypertension. J Nucl Med. May2007;48(5):680-4. 2.Le Pennec R et al. Lung Ventilation/Perfusion Scintigraphy for the Screening of Chronic Thromboembolic Pulmonary Hypertension(CTEPH): Which Criteria to Use? Front Med(Lausanne).2022;9:851935. 3.Afsin E et al. Clinical results of high probability ventilation/perfusion scintigraphy in the diagnosis of pulmonary embolism. Heliyon. Nov2023;9(11):e22065.

OP-747

Prospective pilot study to evaluate Ga-68 FAPI for the early detection of hepatic fibroblast activation in patients with primary sclerosing cholangitis (PSC)

M. Nejabat[1], *E. Halilbasic*[2], *M. Trauner*[2], *A. Ba-Ssalamah*[3], *S. Rasul*[1], *B. Mozayani*[4], *T. Nakuz*[1], *C. Philippe*[5], *R. Calabretta*[1], *S. Poetter-Lang*[3], *M. Hacker*[1];
[1]*1.Division of Nuclear Medicine, Department of Biomedical Imaging and Image-guided Therapy, Medical University of Vienna, Vienna, AUSTRIA,* [2]*2.Division of Gastroenterology and Hepatology, Department of Internal Medicine III., Vienna, AUSTRIA,* [3]*3.Division of General and Pediatric radiology, Department of Biomedical Imaging and Image-guided Therapy, Medical University of Vienna, Vienna, AUSTRIA,* [4]*4.Department of Clinical Pathology, Medical University of Vienna, Vienna, AUSTRIA,* [5]*Radiopharmaceutical Sciences, Coordinator Joint Medicinal Radiochemistry Facility, Vienna, AUSTRIA.*

Aim/Introduction: Expression of fibroblast activation protein (FAP)seen in inflammatory conditions, especially those tend to be chronic. Primary sclerosing cholangitis (PSC),a chronic progressive liver disease characterised by patchy inflammation and fibrosis of the intra- and extrahepatic bile ducts. Progressive patients should be considered for liver transplantation. Currently there is no accurate predictive tool. Ga-68 FAPI PET provides valuable information about FAP expression/fibroblast activity. We investigated the potential use of FAPI-PET/MRI as a non-invasive Imaging for early diagnosis and of PSC. ***Materials and Methods:*** 10 patients with diagnosis of PSC included. 6/10 patients (60%) had concomitant inflammatory bowel disease. Ga-68 FAPI PET/MRI performed with dedicated hepatobiliary protocol. MRI liver score (FLIS) and lver standardized uptake values (SUV) for PET calculated. Furthermore, Fibro scan, liver blood parameters and enhanced liver fibrosis (ELF) score obtained. 10 age/sex-matched patients with Ga-68 FAPI PET/MRI due to other diseases considered as control group. FAP staining performed in all PSC patients with liver biopsy. ***Results:*** The mean liver SUVmax of the patient group was higher than control group (SUVmax 6.7±3.0 vs. 4±0.9). All controls showed a homogeneous pattern of FAPI uptake.In patient group, 5 with known PSC showed segmental/subsegmental increased pattern of FAPI uptake with highest SUVmax (mean SUVmax: 9±4), followed by two PSC/cirrhosis patients with diffuse inhomogeneous increased uptake (mean SUVmax: 6.2±1.4) and three newly diagnosed PSC with homogeneous FAP liver uptake (SUVmax 3±0.8). Mean FLIS for all PSC patients was 5.4±0.7 (Normal FLIS: 6): the lowest values in PSC/cirrhotic patients (4.5) followed by 5 known PSC cases (5.4±0.8). New PSC patients had normal FLIS. The mean ELF score of all PSC patients was 9.5±1.9 (normal <7.7) and the mean liver stiffness on fibroscan was 15.5 kPa (normal:2-7kPa). The highest stiffness observed in cirrhotic/PSC patients (mean 35.5), then known PSC patients (mean:13.9). Mean ELF showed also the highest values in PSC/cirrhotic patients followed by known cases (12.5 vs. 9.02). New PSC patients had a normal liver stiffness (mean 5.43) but a slightly elevated ELF score (mean 8.1). ***Conclusion:*** The segmental/sub-segmental pattern of FAP expression correlated with the patchy inflammatory nature of PSC. Higher SUVmax values were detected in known/active cases than in cirrhotic patients, whereas other established parameters tended to pathological values in cirrhotic PSC patients. Thus, FAPI-PET could be used for the early detection of fibrotic activity in PSC patients and to identify regions for liver biopsies or for the prediction of disease progression.

OP-748

Unexpected Skeletal Uptake on ^{68}Ga-Trivehexin PET/CT in a Case of Renal Osteodystrophy

S. Kar*, V. R. Lele, N. Shaikh;*
Jaslok Hospital and Research Centre, Mumbai, INDIA.

Aim/Introduction: Renal osteodystrophy is a well-recognized complication of chronic kidney disease (CKD), yet its molecular imaging characteristics remain poorly defined. ^{68}Gallium-Trivehexin Positron Emission Tomography/ Computed Tomography (^{68}Ga-Trivehexin PET/CT) has demonstrated utility in localizing parathyroid adenomas via expression of integrin αvβ3, but its uptake in skeletal remodeling associated with renal osteodystrophy has not been described. We present a case of a patient with CKD and biochemical evidence of secondary hyperparathyroidism in whom ^{68}Ga-Trivehexin PET/CT not only localized a parathyroid adenoma but also demonstrated significant tracer accumulation in bone changes consistent with renal osteodystrophy, representing a novel imaging finding. ***Materials and Methods:*** A 31-year-old male with a 5-year history of CKD presented with a 6-month history of generalized bone pain. Laboratory evaluation revealed serum calcium of 8.1 mg/dL (reference 8.6-10 mg/dL) and parathyroid hormone (PTH) of 1,336 pg/mL (reference 15-65 pg/mL). To look for parathyroid adenoma, 2.8 millicurie of ^{68}Ga-Trivehexin was administered intravenously. Whole-body PET/CT images were acquired at 90 minutes post-injection. Maximum Standardized Uptake Value (SUVmax) normalized to body weight were measured over lesions. A low-dose CT (3.5 mm slices) provided anatomic correlation. ***Results:*** Physiologic tracer distribution was noted in the stomach, kidneys, and urinary bladder. Focal uptake (SUVmax 2.89) was seen in a parathyroid adenoma posterior to the left thyroid lobe. Unexpectedly, the scan also revealed widespread skeletal tracer accumulation correlating with radiographic findings of renal osteodystrophy. The skull showed diffuse osteopenia with a salt-and-pepper appearance and cortical thinning, with SUVmax 6.31. Expansile osteolytic "brown tumors" were noted in the left mandible (SUVmax 4.91) and the maxilla (SUVmax 6.36). A lesion in the right second rib exhibited SUVmax 4.96. Subchondral resorption in bilateral sacroiliac joints and the pubic symphysis demonstrated moderate uptake with SUVmax of 5.12. These findings mirror bone remodeling and hyper-resorptive changes of renal osteodystrophy. No other abnormal tracer foci were identified. ***Conclusion:*** This case highlights the established role of ^{68}Ga-Trivehexin PET/CT in detecting integrin αvβ3 expressing parathyroid adenomas and unveils its novel application in visualizing the skeletal manifestations of renal osteodystrophy. Tracer uptake in sites of subchondral resorption and brown tumors suggests that integrin expression accompanies hyperparathyroidism-driven bone remodeling. Future studies should explore ^{68}Ga-Trivehexin PET/CT as a noninvasive imaging biomarker for the assessment and monitoring of bone disease in CKD patients.

1701

Wednesday, October 8, 2025, 08:00 - 09:30
Auditorium

CME 13 - Dosimetry Committee: Challenges in Red Bone Marrow Dosimetry

OP-749
Introduction to red marrow dosimetry
***P. Bernhardt**; Sahlgrenska University Hospital, Radiaton Physics, Gothenburg, SWEDEN.*

OP-750
Small-scale dosimetry
***P. Minguez Gabina**; Unidad de Radiofísica y Protección radiológica. Gurutzeta/Cruces University Hospital, Medical Physics, Barakaldo, SPAIN.*

OP-751
Image-based versus blood-based dosimetry
***J. Tran-Gia**; University Hospital Würzburg, Department of Nuclear Medicine, Würzburg, GERMANY.*

OP-752
Absorbed dose-toxicity correlations
***M. Cremonesi**; European Institute of Oncology, IRCCS, Milan, ITALY.*

1702

Wednesday, October 8, 2025, 08:00 - 09:30
Room 112 (Arena)

Special Track 13 - Women Empowerment Initiative + Young Professional Council: Challenge the Expert: Current Challanges in Career and in Leadership for the Future Generations

OP-753
Building Resilient Careers When Intelligence Isn't Just Human
***S. Massalha**; Rambam Health Care Campus, Haifa, ISRAEL.*

OP-754
Voices, Visions, and the Next-Gen Leaders in Nuclear Medicine
***T. Van den Wyngaert**; Antwerp University Hospital (UZA), Antwerp, BELGIUM.*

OP-755a
Challengers' Team
***P. Soeiro**; Centro Hospitalar Universitário de São João, Department of Nuclear Medicine, Porto, PORTUGAL.*

OP-755b
Challengers' Team
***O. Ivaschenko**; Medical Physicist in Radiology and Nuclear Medicine, University Medical Center, Groningen, NETHERLANDS.*

OP-755c
Challengers' Team
***M. de Almeida Coelho**; University Hospital Essen, Nuclear Medicine, Essen, GERMANY.*

OP-755d
Challengers' Team
***E. Mamis**; CERN, Geneva, SWITZERLAND.*

OP-755e
Challengers' Team
***G. Gariglio**; Medical University of Innsbruck, Innsbruck, AUSTRIA.*

OP-755f
Challengers' Team
***M. Calls Calahorro**; Hospital de la Santa Creu i Sant Pau, Barcelona, SPAIN.*

1703

Wednesday, October 8, 2025, 08:00 - 09:30
Room 113

LIPS Session 13 - Oncology & Theranostics Committee: Structured PET Reporting in Oncology

OP-756
Hematologic Cancer: Are We Beyond Deauville?
***C. Nanni**; IRCCS Azienda Ospedaliero-Universitaria di Bologna, Bologna, ITALY.*

OP-757
Standardised Neuroendocrine Tumour Assessment: When and How?
***F. Grawe**; DKFZ, Heidelberg, GERMANY.*

OP-758
Do We Need Standardised PET Reports for Prostate Cancer?
***F. Ceci**; Istituto Europeo di Oncologia (IEO), Milan, ITALY.*

OP-759
Standardised Reporting in Solid Tumors
***S. Carrilho Vaz**; Champalimaud Clinical Center, Nuclear Medicine-Radiopharmacoloy, Lisbon, PORTUGAL.*

1704

Wednesday, October 8, 2025, 8:00 - 9:30
Room 114

M2M Track - TROP Session - Radiopharmaceutical Sciences + Translational Molecular Imaging & Therapy Committee: Antibodies and Co.

OP-760
First-In-Human PET Imaging of Two Novel Antibody Fragments in Patients with Solid Tumors - a Phase 0 Nuclear Imaging Basket Trial (VARTUTRACE)
***N. C. van Dijk**[1,2], A. F. S. Verhaar[1,3], Y. F. Janssen[1,3], M. Brom[1], T. Gustavsson[4,5], R. Dagil[4,5], S. Choudhary[4,5], E. E. Vidal-Calvo[4], D. Waagmeester[6], D. J. Vugts[6], T. G. Theander[4,5], H. H. Boersma[2,7], A. Salanti[4,5], A. W. J. M. Glaudemans[2], G. M. van Dam[1]; [1]TRACER Europe B.V., Groningen, NETHERLANDS, [2]Department of Nuclear Medicine and Molecular Imaging, University of Groningen, University Medical Center Groningen (UMCG), Groningen, NETHERLANDS, [3]Department of Surgery, University of Groningen, University Medical Center Groningen (UMCG), Groningen, NETHERLANDS, [4]Centre for Translational Medicine and Parasitology, Department of Immunology and Microbiology, Faculty of Health and Medical Sciences, University of Copenhagen, Copenhagen University Hospital, Copenhagen, DENMARK, [5]Var2pharmaceuticals ApS, Frederiksberg, DENMARK, [6]Department of Radiology and Nuclear Medicine, Amsterdam UMC, Amsterdam, NETHERLANDS, [7]Department of Clinical Pharmacy and Pharmacology, University of Groningen, University Medical Center Groningen (UMCG), Groningen, NETHERLANDS.*

Aim/Introduction: Targeted therapy development is limited by the scarcity of actionable cancer targets, particularly for heterogeneous solid tumors. Onco-fetal signatures, shared by embryonic and cancer cells but absent in healthy adult tissues, offer a selective targeting strategy. One such signature is onco-fetal chondroitin sulfate (ofCS), which contributes to tumor immune evasion and

dissemination. Recently, we developed two antibodies (F8 and C9, collectively termed Vartumabs) targeting distinct ofCS variants[1]. This phase 0 PET imaging trial aims to evaluate the safety and biodistribution of each of the two Vartumabs in patients with various solid tumors. ***Materials and Methods:*** The Vartumabs were produced as single chain variable fragments (scFv) with a genetically fused albumin binding domain for half-life extension and labelled with DFO-N-Suc-89-Zirconium. Following a single intravenous microdose administration of one of the Vartumabs (1mg, 15 MBq), long axial field of view PET/CT images were obtained at day 0, 1, and 3 post-injection (p.i.). Standard uptake values (SUV) of volumes of interest were compared to blood pool to calculate tumor/organ-to-background ratios (TBR/OBR) over time using Siemens Syngo.via VB80 software. The occurrence and severity of adverse events were used to assess safety. At the time of submission, four patients were enrolled in this prospective monocentre study (NCT06645808). ***Results:*** All injections were well tolerated, and no related adverse events were reported for both compounds. For Vartumab C9, tumor uptake was observed on day 3 p.i. in 2/2 patients dosed (mean SUVpeak 7.26, mean TBR 1.83). Indications included non-small cell lung carcinoma (NSCLC) and rectal carcinoma. Off-target binding was observed in testes (mean SUVpeak 9.38, mean OBR 2.37) and adrenal glands (mean SUVpeak 8.97, mean OBR 2.27) for both patients. For Vartumab F8, no visual tumor uptake was observed in one patient with esophageal carcinoma. For another patient with rectal carcinoma, assessment of tumor uptake was not possible due to hepatobiliary elimination. No off-target binding was observed in either of the two subjects. ***Conclusion:*** These preliminary results suggest that both radiolabelled Vartumabs can be safely administered. Vartumab C9 targets diverse solid tumors, even in non-stratified patients, with acceptable off-target binding. For Vartumab F8 the optimal patient population is yet to be identified, but the lack of off-target binding is promising. Further patient inclusion is required to draw more robust conclusions. The findings of this study will guide lead-compound selection and indication prioritization for subsequent clinical trials with therapeutic derivatives. ***References:*** Vidal-Calvo et al., (2024). Nature Communications.

OP-761

Theranostic Application of Radiolabeled HER2-Targeting Single-Domain Antibodies (RAD202) in Preclinical Setting

B. Altunay[1], *A. Florea*[1], *A. Vogg*[1], *L. Schäfer*[1], *A. Morgenroth*[1], *L. K. Meszaros*[2], *S. Lütje*[1], *F. M. Mottaghy*[1,3];
[1]*Uniklinik RWTH Aachen, Aachen, GERMANY,* [2]*Radiopharm Theranostics Ltd, Victoria, AUSTRALIA,* [3]*Department of Radiology and Nuclear Medicine, Maastricht University Medical Center, Maastricht, NETHERLANDS.*

Aim/Introduction: Human epidermal growth factor receptor 2 (HER2), is overexpressed in various cancers and represents a good target for monoclonal antibodies as vehicles for specific drug delivery. A ^{99m}Tc-labeled HER2-specific single-domain antibody (sdAb), ^{99m}Tc-NM-02, also known as RAD201, was shown to be safe for use in humans in our previous study and is a promising non-invasive tool to evaluate the HER2 status in metastatic (breast) cancer [1]. Here, the same sdAb (with and without HIS-tag) was labeled via DOTA-GA with ^{68}Ga and ^{177}Lu to investigate biodistribution and therapeutic effect in HER2-positive xenografts. ***Materials and Methods:*** Rj:ATHYM-Foxn1nu/nu mice with SKOV-3 HER2-positive tumors received 10 MBq of ^{68}Ga-labeled HIS-tagged (^{68}Ga-RAD202) sdAb and were scanned by PET/CT immediately and three hours post-injection. The following day, these mice received the radioactive sdAb without HIStag (^{68}Ga-RAD202.1) and were scanned again. A control group was injected with an additional excess of unlabeled ('cold') sdAb alongside the radiolabeled compound. In the therapy study, mice were treated with either four doses of 13.5 MBq of ^{177}Lulabeled sdAb (^{177}Lu-RAD202.1, without HIS-tag) administered at weekly intervals, or a single dose of 54 MBq. For kidney protection, all mice received 0.05mL Gelofusine® three minutes before tracer injection. ***Results:*** The ^{68}Ga-RAD202.1 and ^{177}Lu-RAD202.1 tracers were synthesized with high radiochemical purity (99.8 ± 0.5% and 99.8 ± 0.3%, respectively). PET/CT imaging with ^{68}Ga-RAD202.1 revealed specific tumor accumulation and low uptake in non-target organs, except for the excretory organs (kidney and bladder). Co-administration of unlabeled sdAbs reduced tumor uptake by 65% for the HIS-tagged variant and by 33% for the untagged tracer. Treatment with ^{177}Lu-labeled sdAbs prolonged the median survival time about 34 d in the single dose group and 26 d in the fractionated therapy group compared to the respective control group treated with unlabeled sdAb-chelator conjugates. Unlike the single dose treatment, fractionated therapy group did not reach 200% of the initial tumor volume by the end of the observation period and exhibited significantly lower tumor volumes throughout the study. ***Conclusion:*** ^{68}Ga-labeled sdAbs showed rapid tumor uptake, enabling PET imaging with a high tumor-to-background contrast. Therapy studies have been performed, with the HIS-tag-free sdAb due to its reduced renal retention. Both treatment regimens were well tolerated. However, fractionated therapy demonstrated greater efficacy in suppressing tumor growth compared to the single dose approach. ***References:***
[1] Altunay, B. et al. 99mTclabeled single-domain antibody for SPECT/CT assessment of HER2 expression in diverse cancer types. EJNMMI (2023).

OP-762

Therapeutic potential of first-in-class claudin 18.2-targeted radiolabeled nanobody [^{177}Lu]Lu-DOTA-SNA014 in gastric cancer

Y. Wang[1], *M. Zheng*[1], *Q. Liu*[1], *H. Mou*[1], *S. Ge*[1], *B. Zhang*[1], *C. Wei*[2], *S. Qin*[1], *T. Xu*[2], *L. Miao*[1];
[1]*First Affiliated Hospital of Soochow University, Suzhou, CHINA,* [2]*Smart-Nuclide Biotech, Suzhou, CHINA.*

Aim/Introduction: Gastric cancer (GC) is the fifth most common and third leading cause of cancer death worldwide. The upregulation of claudin 18.2 has been identified as the result of the malignant transformation of gastric epithelial tissue. Thus, claudin 18.2 becomes a highly selective target for gastric cancer theranostic. Compared with other claudin 18.2-targeting nanobody-based PET imaging agent our previous study showed that [^{68}Ga]Ga-NODAGA-SNA014 had high tumor uptake and low kidney uptake. These promising results prompt us to develop [^{177}Lu]Lu-DOTA-SNA014 for gastric cancer therapy. ***Materials and Methods:*** SNA014 is a nanobody derived from alpaca immunization and screened out by phage display. SNA014 was conjugated with DOTA to enable efficient ^{177}Lu labeling. The binding property of [^{177}Lu]Lu-DOTA-SNA014 was characterized by saturation binding assay on claudin 18.2-expressing AGS GC cells. Biodistribution properties and competitive blocking effects were determined by ex vivo biodistribution studies on AGS 18.2-bearing NDG mice. The therapeutic efficacy was evaluated on SNU-601 GC cells-bearing nude mice by monitoring the tumor growth and body weight over time up to 21 days. All mice for the therapy studies were injected with gelofusine as renal protection while the injection of [^{177}Lu]Lu-DOTA-SNA014. ***Results:*** Radiolabeling of DOTA-SNA014 with ^{177}Lu resulted in radiochemical yields >99 %. The saturable specific binding of [^{177}Lu]Lu-DOTA-SNA014 indicated a dissociation constant of 1.51 nM. The ex vivo biodistribution studies showed the tumor, kidney and stomach uptake of [^{177}Lu]Lu-DOTA-SNA014 were of 18.42 ± 1.99, 13.86 ± 2.59 and 86.02 ± 4.54 %ID/g at 2 h postinjection, respectively. The tumor uptake gradually decreased from 2 h to 96 h postinjection, with minimum tumor uptake of 5.92 ± 2.26%ID/g at 96h postinjection. Gelofusine can effectively reduce 53% of kidney uptake to 6.64 %ID/g at 1h postinjection.

Competitive blocking assay suggested DOTA-SNA014 was able to block uptake of [^{177}Lu]Lu-DOTA-SNA014 at stomach in a dose-dependent fashion, ranging from 1 to 120 µg, without dramatically altering the tumor and kidney uptake. Tumor regression was achieved without negatively affecting body weight, suggesting a favorable safety profile of [^{177}Lu]Lu-DOTA-SNA014. ***Conclusion:*** We developed a novel claudin 18.2-targeted nanobody-based [^{177}Lu]Lu-DOTA-SNA014 for gastric cancer therapy. The [^{177}Lu]Lu-DOTA-SNA014 showed specific in vitro binding to claudin 18.2, favorable ex vivo biodistribution properties in terms of tumor, kidney and stomach uptake, and safety profile based on radiotherapy studies, which prompt us to further develop α radionuclide-labeled DOTA-SNA014-based radiopharmaceuticals.

OP-763

FL802, a B7-H3-targeting nanobody radioligand precursor, developed using UniRDC™ discovery platform

X. Wang, *M. Jheng, P. Li, D. Li, Y. Xie, B. Guo, R. Hu, F. Liu;*
Full-Life Technologies Limited, Shanghai, CHINA.

Aim/Introduction: B7-H3 (CD276), a type I transmembrane protein belonging to the B7 immune checkpoint family, is frequently overexpressed in various solid tumors, such as lung, esophageal, prostate, and breast cancers. While B7-H3-targeting antibody-drug conjugates (ADCs) have shown promising early clinical efficacy, radionuclide drug conjugates (RDCs) present a distinct therapeutic advantage by enabling both treatment and tumor imaging. Among potential targeting moieties, the variable heavy domain of the heavy chain (VHH) is a highly attractive binder; however, a major limitation of VHH-based RDCs is their suboptimal biodistribution, characterized by low tumor uptake and high kidney accumulation, hindering their therapeutic application. Our proprietary UniRDCTM discovery platform has been proven to be capable of effectively improving the biodistribution profiles of such modality and here we present our VHH-based B7-H3 targeting RDC precursor discovered by UniRDCTM. ***Materials and Methods:*** The binding affinity and cross-reactivity of FL-802 was evaluated by in vitro protein- and cell-based binding assays. FL-802 was labeled with ^{177}Lu and the radiochemical purity (RCP) of radiolabeled molecule was determined by radio thin-layer chromatography and radio high-performance liquid chromatography. The in vivo imaging, ex vivo biodistribution and efficacy profiles of [^{177}Lu]Lu-FL-802 were assessed in B7-H3 positive cell grafted mouse models. ***Results:*** In vitro assays demonstrated that FL802 bound with subnanomolar affinity to human B7-H3 and exhibited cross-reactivity with mouse and cynomolgus monkey B7-H3. FL802 was successfully labelled with ^{177}Lu, achieving a high radiochemical purity of>98% and a molar activity of 18.5 MBq/nmol. In vivo studies in B7-H3-positive tumor-bearing mice revealed a favorable biodistribution profile via SPECT/CT imaging and ex vivo cut-and-count analysis. SPECT/CT (11.1 MBq) showed intense tumor uptake, significantly surpassing all normal organs at 24 and 72 hours. Biodistribution studies confirmed high tumor accumulation (>30% ID/g) and an improved tumor-to-kidney ratio (T/K >2.0 at 24 h) - a dramatic enhancement over the unmodified VHH (2.3% ID/g, T/K <0.01). Therapeutic efficacy was assessed at the dose of 11.1 MBq (Q2W X2). Treatment was well tolerated, with all animals achieving complete tumor remission. ***Conclusion:*** The preclinical data collectively support FL802 as a promising B7-H3 targeting RDC precursor which warrants its further development as a radiopharmaceutical for the diagnosis and treatment for B7-H3-positive tumors. In addition, this work further validates the effectiveness of UniRDC™ discovery platform in the optimization of VHH-based RDCs, and we anticipate that UniRDC™ can be broadly applied to other small protein-based RDCs, such as affibodies and DARPins, to improve their therapeutic potential.

OP-764

Head-to-head comparison of ABD-fused Affibody Molecule labelled with Lu-177 and Tb-161

Y. Liu[1], *I. Zelepukin*[1], *A. Orlova*[1], *M. Konijnenberg*[2], *F. Y. Frejd*[3], *V. Tolmachev*[1];
[1]*Uppsala University, Uppsala, SWEDEN,* [2]*Erasmus MC, Rotterdam, NETHERLANDS,* [3]*Affibody AB, Solna, SWEDEN.*

Aim/Introduction: Engineered scaffold proteins Affibody molecules have shown efficient targeting of HER2-expressing cancers in clinical trials. We have demonstrated earlier that ^{177}Lu-labelled HER2-binding Affibody molecule fused to albumin-binding domain (ABD) enables specific targeting of HER2-expressing human xenografts and has a strong anti-tumour efficacy in preclinical radionuclide therapy. Tb-161 emits not only beta-particles but also multiple conversion and Auger electrons. This might be an advantage for deactivation of small subclinical metastases. In this preclinical study, the targeting properties of the ABD-fused Affibody molecule (denoted as PEP48937) labelled with Lu-177 and Tb-161 were compared both in vitro and in vivo. ***Materials and Methods:*** For labelling with Lu-177 and Tb-161, the DOTA chelator was coupled to a unique C-terminal cysteine of PEP48937 using thiol-directed conjugation. In vitro evaluation of binding affinity, specificity, and cellular processing was performed using HER2-expressing SKOV3 and BT474 cells. Triple-negative breast cancer cell line MDA-MB-468 was used as a negative control both in vitro and in vivo. Biodistribution of ^{177}Lu- and ^{161}Tb-labelled PEP48937 was directly compared in nude mice bearing SKOV3 xenografts (4, 24, 48, 72, 168 and 336 h). Based on dosimetry evaluation and tumour control probability prediction, animals were treated with [^{161}Tb]Tb-PEP48937 (2x10 MBq) or [^{177}Lu]Lu-PEP48937 (2x12 MBq). ***Results:*** The labelling of PEP48937 with Lu-177 and Tb-161 (sodium acetate, pH 6.5, 65°C) provided a radiochemical yield exceeding 99%. The binding of both [^{177}Lu]Lu-PEP48937 and [^{161}Tb]Tb-PEP48937 to HER2-expressing cells was saturable (i.e. specific) in vitro. The binding to HER2-negative MDA-MB-468 was negligible. The internalisation of [^{161}Tb]Tb-PEP48937 was slightly quicker than the internalization of [^{177}Lu]Lu-PEP48937. There was no difference in the biodistribution of the compounds. The peak tumour uptake (48 h) was 43±13%ID/g for [^{161}Tb]Tb-PEP48937 and 31±4%ID/g for [^{177}Lu]Lu-PEP48937. The uptakes in HER2-negative MDA-MB-468 xenografts were significantly ($p< 0.05$) lower at 48 h, 5±1%ID/g and 6±3%ID/g, for [^{161}Tb]Tb-PEP48937 and [^{177}Lu]Lu-PEP48937, respectively. In the ongoing experimental therapy, [^{161}Tb]Tb-PEP48937 showed a tendency to higher anti-tumour efficacy than [^{177}Lu]Lu-PEP48937 but also to higher hematologic toxicity. At the time of submission of this abstract, all animals treated with the vehicle had been euthanised because of tumour overgrowth or ulceration (median survival 35 days). The median survival was not reached in groups treated with [^{177}Lu]Lu-PEP48937 and [^{161}Tb]Tb-PEP48937. ***Conclusion:*** The replacement of Lu-177 by Tb-161 has no observable effect on the biodistribution properties of PEP48937. Optimisation of injected activity of [^{161}Tb]Tb-PEP48937 might provide a HER2-targeting agent with increased efficiency against small HER2-expressing tumours.

OP-765

Radiolabeled engineered HER2 antibodies for cancer theranostics

X. Chen, *X. Wen, B. Li, X. Wu, J. Zhang;*
National University of Singapore, Singapore, SINGAPORE.

Aim/Introduction: Human epidermal growth factor receptor 2 (HER2) is overexpressed in some solid tumors, including breast cancer and gastric cancer, and has become an important target for cancer theranostics. This study aimed to develop an engineered antibody by replacing the Fc part of the mAb, LNCAb103, with reduced molecular weight and circulation half-life, radiolabeled

with ^{177}Lu for the theranostic application in HER2-positive malignant tumors. ***Materials and Methods:*** LNCAb103 was developed and radiolabeled with ^{177}Lu. HER2 binding affinity and targeting specificity were evaluated at the protein and cell levels. SPECT/CT imaging and preclinical pharmacokinetics assessment of ^{177}Lu-LNCAb103 were conducted in HER2-positive xenograft models and normal mice to investigate tumor uptake and ex vivo biodistribution. In addition, the anti-tumor efficacy evaluation of ^{177}Lu-LNCAb103 was assessed at different doses, and compared with ^{177}Lu-traustuzumab. ***Results:*** ^{177}Lu-LNCAb103 demonstrated high radiochemical purity and good stability over time, and showed a favorable HER2 binding affinity and targeting specificity in vitro. SPECT/CT imaging of ^{177}Lu-LNCAb103 exhibited remarkably high tumor uptake and retention up to 96 h. Compared with ^{177}Lu-traustuzumab, ^{177}Lu-LNCAb103 presented a higher tumor-to-background ratio and lower blood uptake. The distribution half-life (1.43 ± 1.30 h vs. 4.20 ± 1.02 h) and elimination half-life (19.07 ± 3.01 h vs. 225.04 ± 67.47 h) of ^{177}Lu-LNCAb103 were significantly shorter than those of ^{177}Lu-traustuzumab. In therapeutic studies, administration of 9.25 and 18.5 MBq of ^{177}Lu-LNCAb103 significantly inhibited NCI-N87 tumor growth without notable loss of body weight. In contrast, although ^{177}Lu-traustuzumab initially inhibited tumor growth, it led to body weight loss and eventual death of mice due to severe toxicity within 10 days post-treatment. ***Conclusion:*** ^{177}Lu-LNCAb103 demonstrated specific HER2 targeting in vitro and in vivo, along with high tumor uptake, low background signals, a shorter blood elimination half-life, and improved safety compared to ^{177}Lu-traustuzumab. These results suggest that ^{177}Lu-LNCAb103 holds potential as a promising agent for the theranostic treatment of HER2-positive cancers.

OP-766

Affibody-masked cetuximab prodrug for protease-dependent tumor targeting: a novel strategy to enhance specificity and minimize toxicity in EGFR-directed therapies

A. Bitzios[1], *A. Mestre Borras*[2], *H. Mehari*[2], *I. Zelepukin*[1], *M. Ud-Din*[1], *T. Xu*[1], *S. Li*[1], *S. Ståhl*[2], *J. Löfblom*[2], *A. Orlova*[1], *V. Tolmachev*[1], *A. Vorobyeva*[1];
[1]*Uppsala Universitet, Uppsala, SWEDEN,* [2]*KTH Universitet, Stockholm, SWEDEN.*

Aim/Introduction: Monoclonal antibodies enable selective tumor targeting but may induce off-target toxicity when the target antigen is present in normal tissues. Cetuximab, which targets epidermal growth factor receptor (EGFR), often causes skin rashes and gastrointestinal side effects due to EGFR expression in healthy epithelium. This study aims to develop and evaluate a novel affibody-masked cetuximab prodrug that enables matriptase-dependent tumor-specific activation, thereby improving therapeutic specificity and minimizing off-target toxicity in EGFR-targeted cancer therapy. ***Materials and Methods:*** Affibody masking domains were engineered to selectively bind and block the EGFR-binding paratope of cetuximab. The most effective affibody was genetically fused to cetuximab's heavy chains to generate a prodrug. Cetuximab and its affibody-masked prodrug were conjugated to CHX-A"-DTPA and radiolabeled with [^{111}In]$InCl_3$. Binding specificity of both compounds were assessed in vitro using EGFR-overexpressing FaDu (matriptase-negative) and H292 (matriptase-positive) monolayer cell culture and 3D spheroids. Conditional activation and binding to FaDu cells were evaluated after pre-treatment of both compounds with matriptase. In vivo biodistribution was studied in Balb/c nu/nu mice bearing FaDu or H292 xenografts, with tumor uptake measured 72 hours post-injection. ***Results:*** Cetuximab and its prodrug were radiolabeled and purified with over 96% radiochemical purity. The affibody-masked cetuximab prodrug showed 400-fold difference in IC_{50} between masked and unmasked states in vitro. Radiolabeled prodrug exhibited 15- to 17-fold lower binding in monolayer cultures compared to unmodified cetuximab, confirming effective masking. Matriptase pretreatment of [^{111}In]In-prodrug increased its binding to the cells. In H292 spheroids, the prodrug showed twice higher cell-bound activity relative to FaDu, indicating protease-specific activation. The in vivo results showed a 68% reduction of the EGFR-binding capacity of the [^{111}In]In-labeled prodrug in comparison to the parental antibody [^{111}In]In-cetuximab, and confirmed enhanced tumor selectivity of prodrug, with higher uptake in H292 xenografts (57±8%) than in FaDu (32±11%) xenografts. ***Conclusion:*** This study demonstrated for the first time the feasibility of using affibody domains to reversibly mask the paratope of a therapeutic antibody cetuximab, enabling protease-dependent activation in the tumor microenvironment. The cetuximab prodrug showed improved specificity and tumor retention, supporting the potential of this approach for the development of safer and more efficacious antibody-based cancer therapies.

OP-767

Immunomodulation of the tumour microenvironment by 225Ac-hGirentuximab in a syngeneic murine tumor mode

R. LADJOHOUNLOU[1], *W. J. Jin*[1], *P. Clark*[1], *M. Bio Idrissou*[1], *B. Bednarz*[1], *R. Hernandez*[1], *M. P. Wheatcroft*[2], *K. Twumasi-Boateng*[2], *Z. S. Morris*[1];
[1]*University of Wisconsin School of Medicine and Public Health, Madison, WI, UNITED STATES OF AMERICA,* [2]*Telix Pharmaceuticals Limited, Melbourne, AUSTRALIA.*

Aim/Introduction: Radiation from radiopharmaceuticals can trigger inflammation that initiates immune responses. In cancer tissue these mechanisms can prematurely shut off the anti-tumor immune response. Among the drivers of these effects are the expression of immune checkpoint receptors/ligands on the surface of immune cells, stroma, and tumor cells in the tumor microenvironment. These can potentially be targeted using immune checkpoint inhibitors. While prior studies have demonstrated potential for therapeutic benefit with these approaches using antiPD-1/PD-L1 or anti-CTLA-4, few studies have investigated the role of other immune checkpoint receptors/ligand interactions in potentiating anti-tumor immunity following radiopharmaceutical therapies (RPT). Here, we evaluate the mode of action of Girentuximab, a hCAIX-targeting antibody when combined with alpha particle emitter Actinium 225 (Ac-225). ***Materials and Methods:*** Mice bearing CT26-hCAIX tumors were randomized to receive different activities of Ac-225 (0 - 18.5 kBq) on day 0. On days 4, 7 and 14 post treatment, mice were euthanized and blood and tumors collected. Complete blood count (CBC) analysis was performed on blood from control and therapy mice. From each tumor, RNA was isolated, and the level of different genes implicated in immune checkpoint interaction evaluated by RT-qPCR. To also evaluate the efficacy of 225Ac-hGirentuximab monotherapy, additional mice were monitored for tumor growth and survival. ***Results:*** On days 4 and 7, CBC analysis showed transient toxicity of 225Ac-hGirentuximab in treated mice compared to untreated controls with immune cells recovery at d14. For gene expression analysis, we observed a significant upregulation of classical immune checkpoint inhibitors PD-1/PD-L1 and CTLA-4 after RPT with 225Ac-hGirentuximab compared to non-irradiated control. We also showed the activation of TIM-3, LAG-3, and genes implicated in NK cells activation (NKG2D) or inhibitory (KLRC1 and his ligand Qa-1b). On the contrary, the expression of the TIGIT and VISTA genes was not affected in the treated mice. The highest dose (18.5 kBq) is the most efficient to activate these genes mainly on days 7 and 14 following the treatment. The therapy study also demonstrated a dose-dependent antitumor efficacy. ***Conclusion:*** Preliminary data indicate that 225Ac-hGirentuximab triggers the

upregulation of many genes encoding checkpoint receptor/ligands. Understanding these modulations may be critical to safely and effectively associate RPT and immunotherapies to enhance anti-tumor immunity.

OP-768

Therapeutic Superiority of ^{131}I-aGPC3-scFv in Hepatocellular Carcinoma: Biodistribution and Efficacy

W. Hu, *M. Li, Z. Lin, X. Zhang, X. Cai, D. Jiang, X. Lan;*
Department of Nuclear Medicine, Union Hospital, Tongji Medical College, Huazhong University of Science, Wuhan, CHINA.

Aim/Introduction: Glypican-3 (GPC3) is a promising therapeutic target for hepatocellular carcinoma (HCC) due to its high tumor-specific expression. Our team previously developed a proprietary anti-GPC3 antibody, which is currently undergoing clinical translation for HCC diagnosis. To advance a theranostic strategy, this study evaluated the biodistribution and therapeutic potential of ^{131}I-labeled GPC3-targeting antibody fragments (scFv, Fab, mAb) in Hep3B subcutaneous tumor models, with a focus on tumor-to-kidney ratios, antitumor efficacy, and systemic toxicity. ***Materials and Methods:*** ^{131}I-labeled anti-GPC3 scFv, Fab, and mAb were synthesized and administered to Hep3B tumor-bearing mice. Thyroid uptake was blocked via oral potassium iodide. Biodistribution was assessed at 2, 6, 24 hours (all agents) and extended to 3 and 5 days for ^{131}I-aGPC3-mAb (n=3/group). Tumor-to-kidney ratios were calculated to assess pharmacokinetics. Based on these results, scFv and mAb were selected for therapy. Mice were randomized into PBS, ^{131}I-aGPC3-scFv (four doses of 37 MBq each, administered twice weekly), and ^{131}I-aGPC3-mAb (single dose of 37 MBq) groups (n=6/group). Tumor volume and body weight were monitored every two days until endpoint (tumor > 1000 mm^3). Toxicity was evaluated via hematology and histopathology. ***Results:*** ^{131}I-aGPC3-scFv and ^{131}I-aGPC3-Fab exhibited rapid tumor uptake (8.7 ± 0.8 %ID/g of scFv at 2 h; 3.9 ± 0.4 %ID/g of Fab at 2 h) and fast clearance (1.0 ± 0.3 %ID/g of scFv at 24 h; 0.2 ± 0.3 %ID/g of Fab at 24 h), while ^{131}I-aGPC3-mAb showed relative delayed accumulation (3.2 ± 0.8 %ID/g at 2 h) with sustained retention (3.9 ± 0.5 %ID/g at 24 h; 0.7± 0.1 %ID/g at 3D). Higher tumor uptake and progressively increased tumor-to-kidney ratios (0.1 at 2 h; 0.3 at 6 h; 0.4 at 24 h) indicate that ^{131}I-aGPC3-scFv is more valuable for subsequent treatment than ^{131}I-aGPC3-Fab. In therapeutic trials, ^{131}I-aGPC3-scFv achieved 97% tumor growth inhibition value by day 14 versus PBS ($p<0.001$), surpassing ^{131}I-aGPC3-mAb. The ^{131}I-aGPC3-scFv group maintained stable body weight and normal hematological parameters, whereas mAb-treated mice exhibited weight loss and progressive mortality prior to day 14, indicative of systemic toxicity. Histological analysis confirmed minimal organ damage in the ^{131}I-aGPC3-scFv group. Notably, no tumor recurrence was observed in ^{131}I-aGPC3-scFv treated mice two weeks post-therapy. ***Conclusion:*** ^{131}I-aGPC3-scFv demonstrated superior tumor targeting, efficacy, and safety compared to ^{131}I-aGPC3-mAb and ^{131}I-aGPC3-Fab in GPC3-high HCC models. Its favorable pharmacokinetics and safety profile support further clinical translation for HCC radioimmunotherapy.

1705

Wednesday, October 8, 2025, 8:00 - 9:30
Room 211

Cutting Edge Science Track - TROP Session - AI Committee: Kinetic Modeling and Parametric Imaging

OP-769

Kinetic Model Selection for Motion-Compensated Whole-Body PET Imaging

J. Rosenskjold Madsen[1,2], *A. H. Dias*[1], *L. C. Gormsen*[1,2], *A. B. Rodell*[3], *D. Pigg*[4], *J. Schaefferkoetter*[4], *O. L. Munk*[1,2];
[1]Department of Nuclear Medicine & PET, Aarhus University Hospital, Aarhus, DENMARK, [2]Department of Clinical Medicine, Aarhus University, Aarhus, DENMARK, [3]Siemens Healthcare A/S, Aarhus, DENMARK, [4]Siemens Medical Solutions USA, Knoxville, TN, UNITED STATES OF AMERICA.

Aim/Introduction: Dynamic whole-body (D-WB) PET enables quantification using kinetic modelling, but physiological interpretation requires model selection that accounts for tracer- and tissue-specific kinetics. In addition, parametric imaging is sensitive to patient motion and inaccurate attenuation correction (AC). This study evaluates a new approach for kinetic model selection, using a reversible Delayed Logan model [1] and an irreversible Patlak model, based on motion-compensated D-WB PET data. ***Materials and Methods:*** Thirty patients underwent a 70-minute D-WB PET scan using a short-axial FOV PET/CT (26.3cm FOV, 214ps TOF): [^{18}F]PSMA-1007 (N=10), [^{68}Ga]Ga-PSMA-11 (N=10), and [^{18}F]FDG (N=10). A deep-learning model was used for elastic registration of the original CT [2] to each late non-attenuation corrected (NAC) PET frame (50-70 min for [^{18}F]FDG and [^{18}F]PSMA, and 40-70 min for [^{68}Ga]Ga-PSMA), generating a series of warped CTs (WarpCTs) with corresponding deformation vector fields (DVFs). The WarpCTs were used to reconstruct each PET frame with optimal attenuation- and scatter correction. Afterwards, the DVFs were inverted and applied to each PET frame to warp them to the original CT, ensuring motion compensation throughout the PET series. WB distribution volume (V_t) and net uptake rate (K_i) images were generated by voxel-wise fitting of the late time-activity curves using the Delayed Logan Model and the Patlak Model, using image-derived blood input functions. Model selection was based on Akaike information criterion (AIC) rescaled to $\Delta_i = AIC_i - AIC_{min}$, forcing the best model to have $\Delta=0$ [3]. Model preference was evaluated using Δ-maps. ***Results:*** Motion compensation of D-WB PET series resulted in parametric images with fewer artifacts and improved WB Δ-maps for model selection. [^{18}F]-PSMA-1007 Δ-maps exhibited clear WB irreversible kinetics (K_i image preferred), and [^{68}Ga]Ga-PSMA-11 Δ-maps exhibited clear reversible kinetics (V_t image preferred) in most tissues. For [^{18}F]FDG, the Δ-maps were not as consistent, being less uniform and more noisy, but indicated irreversible behaviour in most organs such as brain, myocardium and kidney, and reversible kinetics in liver. Some tissues revealed mixed model preference, likely reflecting a complex kinetic behaviour or sensitivity to image noise. These findings suggest that a single kinetic model does not always fully capture the kinetics across all tissues, highlighting the need for organ-specific model selection for WB PET parametric imaging. ***Conclusion:*** Kinetic model selection based on motion-compensated Δ-maps enhances quantitative PET parametric imaging. ***References:*** [1] Madsen JR. Abstract OP-802, EJNMMI (2024). [2] Schaefferkoetter J et al. EJNMMI (2023)50:2292-2304. [3] Burnham KP & Anderson DR, SMR(2004)33(2).

OP-770

Improving AI-Generated Parametric Image Estimation with Accurate AI-Assisted Input Function Modelling in Dynamic PET

K. Tehlan[1,2], *V. Langer*[3], *A. Rominger*[4], *K. Shi*[4], *T. Wendler*[1,2], *KT and VL are first authors with equal contribution;*
[1]University Hospital Augsburg, Augsburg, GERMANY, [2]Technical University of Munich, Munich, GERMANY, [3]University of Augsburg, Augsburg, GERMANY, [4]Inselspital, Bern, SWITZERLAND.

Aim/Introduction: Kinetic modelling in dynamic [^{18}F]FDG PET often relies on a single image-derived input function (IDIF) from either the aorta or the left ventricle overlooking organ-specific vascular contributions, such as those from the portal vein, pulmonary artery, or ureters and leading to inaccuracies in parameter estimation, particularly for organs with dual or alternative blood supplies.Our objective was to enhance the accuracy of parametric imaging by integrating a multi-input modelling framework - incorporating anatomically and physiologically relevant IDIFs [1] - with an AI-assisted parametric image generation approach previously proposed [2]. ***Materials and Methods:*** Dynamic PET/CT data from 20 patients were analyzed. IDIFs were extracted from the aorta, portal vein, pulmonary artery, and ureters using multi-organ segmentation [3], including a custom pipeline developed for ureter segmentation [1]. A modified two-tissue compartment model was employed, incorporating these multiple IDIFs in accordance with organ-specific vascular supply. Kinetic parameter estimation was conducted using an adapted model based on [2]. In addition to conventional microparameters (K1, k2, k3, and Vb), the new model included parameters to quantify the contribution of each of the four IDIFs to the blood input. The AI model was trained and tested on data from thirteen and seven patients respectively. ***Results:*** The proposed multi-input modeling approach significantly improved kinetic parameter estimation compared to traditional single-input methods, as measured by mean squared error (MSE) on the reconstructed time-activity curves, in the liver (77.3% MSE, p=0.031) and in the kidneys (MSE 58.2%, p=0.031) relative to the single-input model. However, improvements in the bladder were not statistically significant, and results for the lungs were inconsistent (-46.7% MSE, p=0.109).Across patients, liver voxels showed an aorta and portal vein IDIF contribution of 26.7±18.3% and 85.0±27.3% respectively. ***Conclusion:*** Incorporating organ-specific vascular inputs into the input function model enhances the physiological accuracy of kinetic parameter estimation in dynamic PET imaging in the liver and kidneys, and to a lesser extent, the bladder.The discrepancy observed in the lungs is likely due to insufficient temporal resolution to clearly differentiate between aortic and pulmonary artery contributions.The observed arterial and portal venous contributions for the liver support the physiological plausibility of the proposed approach. ***References:*** [1] Langer V. et al., arXiv:2504.17114, [2] De Benetti F, et al., Proceedings of MICCAI 2023, p. 290-9.[3] Wasserthal J, et al., Radiology: Artificial Intelligence. 2023 Sep;5(5):e230024.

OP-771

Whole-Body Perfusion Imaging Using Dynamic ^{82}Rb PET with a Long Axial Field-of-View Scanner

M. Morini[1,2], *I. Brovedani*[1,2], *M. De Francisci*[2], *M. Castellaro*[2], *L. Mercolli*[1], *M. Veronese*[2,3], *A. Rominger*[1], *F. Caobelli*[1], *H. Sari*[1,4];
[1]Department of Nuclear Medicine, Bern University Hospital, University of Bern, Bern, SWITZERLAND, [2]Department of Information Engineering, University of Padova, Padova, ITALY, [3]Department of Neuroimaging, Kings College London, London, UNITED KINGDOM, [4]Siemens Healthineers International AG, Zurich, SWITZERLAND.

Aim/Introduction: Rubidium-82 (^{82}Rb) Chloride is widely used to assess myocardial blood flow in patients with suspected coronary artery disease (CAD). Long axial field-of-view (LAFOV) PET systems enable whole-body dynamic imaging, allowing simultaneous multi-organ perfusion assessment. This study aims to quantify multi-organ perfusion at rest and during stress using dynamic ^{82}Rb PET with tracer kinetic modelling and to preliminarily explore inter-organ regional correlations of the K_1 parameter under both conditions. ***Materials and Methods:*** Sixteen patients with suspected CAD underwent dynamic ^{82}Rb PET scans at rest and after pharmacologic stress with Regadenoson using a LAFOV PET scanner. List-mode PET data were acquired over 7 minutes following an intraveneous administration of 370 MBq ^{82}Rb. PET images were reconstructed into 35 dynamic frames (20×4, 4×10, 3×20, 8×30 s) using PSF-TOF reconstruction. Organ masks (lungs, kidneys, spleen, aorta, myocardium) were generated on CT images using TotalSegmentator (1) and refined with a PET-based clustering approach. Time-Activity Curves were extracted, and kinetic modelling was performed using 1-tissue compartment model with an image-derived input function (IDIF) from the descending aorta. Time-delay correction accounted for bolus arrival time differences. Paired Student's t-tests compared organ perfusion (K_1, mL/min/g) estimates between rest and stress, and inter-organ K_1 correlations were assessed using Pearson's coefficients. ***Results:*** Estimated time delays between the IDIF and organ tissue were −4.7 ± 2.9 s (left lung), −4.9 ± 2.8 s (right lung), 5.7 ± 2.4 s (left kidney), and 6.2 ± 2.0 s (right kidney). Pulmonary and splenic K_1 values showed no significant change after Regadenoson (0.18±0.06 to 0.19±0.10 mL/min/g, p=0.62; 1.23±0.42 to 1.31±0.45 mL/min/g, p=0.31). Only the myocardium showed a significant K_1 increase (1.17±0.28 to 1.91±1.52 mL/min/g, p<0.001) in stress. At rest, significant correlations were found between left-right lungs (r=0.62, p<0.05) and kidneys (r=0.84, p<0.001). Under stress, lung-kidney symmetry persisted, with additional significant correlations between lungs and myocardium (right lung: r=0.80, p<0.001; left lung: r=0.61, p<0.05). ***Conclusion:*** This study demonstrates the feasibility of whole-body dynamic perfusion imaging with ^{82}Rb using LAFOV PET. We report organ-specific K_1 values and illustrate the capacity of this approach to map perfusion across multiple systems simultaneously. Preliminary findings reveal strong left-right symmetry in lung and kidney perfusion and significant lung-myocardium correlations under stress, supporting the potential for systemic perfusion assessment. These results provide a foundation for future studies in larger cohorts. ***References:*** 1. Wasserthal, J, 2023, Radiology: Artificial Intelligence.

OP-772

Improvement of quantitative accuracy of ultra-short-duration parametric imaging with a long axial field-of-view PET/CT system

Q. Ye, *H. Zeng, G. Liang, E. Revilla, Y. Lu;*
United Imaging Healthcare, Shanghai, CHINA.

Aim/Introduction: Parametric imaging using a population-based input function (PBIF) has demonstrated its feasibility in reducing the duration of dynamic acquisition. With the high sensitivity of long axial field-of-view (LAFOV) PET/CT systems, the dynamic scan duration has been shortened from 60-90 min to 20-30 min and even to 10 min. However, parametric images directly reconstructed from the short-duration data are prone to under convergence, which leads to overestimation of regions with low K_1 values. This study aims to improve the quantitative accuracy of ultra-short-duration parametric imaging by increasing the convergence rate. ***Materials and Methods:*** Simulation and clinical studies were performed with long-duration parametric imaging as reference. A 60-min dynamic PET scan was simulated for a brain phantom generated from a real patient data using two-tissue compartmental model (2TiC) and the patient's input function. Patlak Parametric images were reconstructed directly from list mode data using the nested algorithm. For 10-60 min (10×5 min) data, 10 nested iterations served as the reference, while for 45-

60 min (10×1.5 min) data, different numbers of nested iterations (10, 50, 100, 150, and 200) were evaluated. A 65-min whole-body dynamic ^{18}F-FDG (7.2 mCi) scan was performed on a subject (Male, 69 yrs, 70 kg) using a LAFOV PET/CT system. Indirect Patlak parametric imaging using image-derived input function (IDIF) for 10-65 min data was performed as the reference (referred to as 55-min data). Direct Patlak reconstructions with PBIF and various numbers of nested iterations were applied to the 55-65 min (10×1 min) data (referred to as 10-min data). Quantitative K_i assessment was performed for the regions of interest (ROI) including lung lesions, liver, spleen, grey matter, white matter, and muscle. ***Results:*** Using 10 nested iterations, the K_i image of brain phantom reconstructed from 45-60 min exhibited overestimation compared to that from 10-60 min. Increasing number of nested iterations reduced the quantitative difference while slightly increased the coefficients of variation (CoV). The K_i image reconstructed with 150 nested iterations showed comparable quantitative accuracy to the reference value. Similar results were found for clinical data. The K_i image reconstructed from 10-min data with 150 nested iterations showed similar K_i and smaller CoV values than that indirectly calculated from 55-min data. ***Conclusion:*** For ultra-short-duration parametric imaging, increased nested iterations accelerated convergence and improved quantitative accuracy. The K_i image reconstructed using only 10-min data and PBIF demonstrated comparable quantified and less noisy compared to that indirectly calculated from 55-min data.

OP-773

Evaluation of Image-Derived Input Function Methods for Non-Invasive Kinetic Modelling of [18F]-Fluorodeprenyl-D2 in Alzheimer's Disease

T. Schmidt[1,2], *A. J. Zounek*[1], *T. Saller*[3], *S. Lindner*[1], *B. Kugelmann*[1], *Y. Beqqali*[1], *A. Zatcepin*[1,4], *S. Raju*[1], *L. Tagnin*[1], *G. N. Bischof*[5,6], *S. Ziegler*[7,1], *M. Brendel*[1,4,8], *L. Kaiser*[1];
[1]*Department of Nuclear Medicine, LMU University Hospital, LMU Munich, Munich, GERMANY,* [2]*Department of Physics, Ludwig Maximilians University, Munich, GERMANY,* [3]*Department of Anaesthesiology, LMU University Hospital, LMU Munich, Munich, GERMANY,* [4]*German Center for Neurodegenerative Diseases (DZNE), Munich, GERMANY,* [5]*Multimodal Neuroimaging Group, Department of Nuclear Medicine, University Hospital Cologne, Cologne, GERMANY,* [6]*Life Molecular Imaging GmbH, Berlin, GERMANY,* [7]*Department of Nuclear Medicine, Hannover Medical School (MHH), Hannover, GERMANY,* [8]*Munich Cluster for Systems Neurology (SyNergy), Munich, GERMANY.*

Aim/Introduction: Pharmacokinetic modelling in PET is traditionally based on arterial input functions (AIF) or image derived input functions (IDIF). Due to the highly invasive nature of AIF, it is desirable to establish reliable, non-invasive IDIF derivation methods. The aim of this work was to identify an IDIF approach to substitute the AIF in kinetic modelling for the MAO-B tracer [^{18}F]-Fluorodeprenyl-D2 ([^{18}F]-DED). ***Materials and Methods:*** 9 Alzheimer's disease (AD) patients underwent a 60-minute dynamic PET scan after injection of [^{18}F]-DED. Automatic invasive arterial blood sampling was performed to obtain AIFs. Several IDIF extraction methods were applied for obtaining time-activity curves (TACs) from the internal carotid artery. All TACs were corrected for plasma fraction and metabolites based on manually drawn blood samples at 6 discrete timepoints per patient. For quantification, the brain was segmented into 9 different regions using PMOD Neuro. 1-tissue and 2-tissue compartment models (1TC, 2TC) and Logan plots were applied to the best IDIF methods according to AIF correlation and signal difference. Model quality was compared using the corrected Akaike information criterion (cAIC). Comparison of activity concentrations and kinetic parameters between IDIF and AIF was performed using Pearson correlation and median difference. ***Results:*** The highest correlation between IDIF and AIF was found for a vessel segmentation threshold of 40% (T40) of maximum signal ($r=0.89$, $p<0.001$), which led to an underestimation of AIF activity concentration by a factor of 5 and poor peak correlation. The lowest median signal differences were found when combining a 77.5% threshold approach for segmentation with a correction factor (T775C) derived from the activity concentration of a discrete sample taken after 30 minutes and applied to AIF as well as IDIF (peak: 0.16kBq/ml (1%), 5min: 0.08kBq/ml (7%), 30min: 0kBq/ml (0%), 40min: 0.05kBq/ml (4%)). This approach also underestimated the activity concentration. Based on cAIC, averaged over all patients and brain regions, the best fitting model for AIF was 2TC ($cAIC_{2TC,AIF}$=-358.18, $cAIC_{1TC,AIF}$=-239.53). For the kinetic parameters, the correlation between AIF and IDIF was highest for T775C ($r_{T40,VT}=0.80$, $r_{T775C,VT}=0.93$, $r_{T40,BPnd}=0.50$, $r_{T775C,BPnd}=0.53$, $p<0.001$ for all, $cAIC_{2TC,T40}$=-269.91, $cAIC_{2TC,T775C}$=-334.66). ***Conclusion:*** Considering the high correlation, the results indicate that IDIFs have a high potential in image quantification for [^{18}F]-DED. Even though, the IDIF underestimates the activity concentration. According to the modelling results, the T775C is better suited due to the high signal matching. Further investigations will include the evaluation of more IDIF approaches and of population-based or image-derived metabolite information.

OP-774

Parametric analysis of dynamic long axial field-of-view ^{18}F-FDG PET/CT studies

C. Smith, *G. J. C. Zwezerijnen, M. E. den Hollander, H. N. J. M. Greuter, N. R. Gerards, J. Zijlstra, C. Menke-van der Houven van Oordt, I. Bahce, M. Yaqub, R. Boellaard;*
Amsterdam UMC, Amsterdam, NETHERLANDS.

Aim/Introduction: Large-axial field of view (LAFOV) PET/CT systems improve whole-body dynamic ^{18}F-FDG imaging, opening new possibilities for quantitative assessment of tracer kinetics. While a non-linear regression (NLR) remains the gold standard for obtaining K_i estimates, it is computationally intensive and sensitive to noise in case of parametric analysis, limiting routine use. Parametric analysis such as Patlak and Generalised Patlak (gPatlak) can be used as alternative. Additionally, parametric images can be obtained from the irreversible (BFM-I) and reversible (BFM-R) basis function method, providing parametric K_i and K_1. This study aims to compare the performance of these parametric methods against NLR in healthy organs and tumours using LAFOV PET/CT. ***Materials and Methods:*** Thirteen patients with malignancies underwent 70-minute dynamic ^{18}F-FDG PET/CT scans on a LAFOV PET/CT system after receiving an intravenous bolus injection of 3.0 MBq/kg. An image-derived input function (IDIF) of the ascending aorta was used. K_i from NLR was compared to those obtained by Patlak (t* = 30 min), gPatlak (t* = 10 min), BFM-I (t* = 0 min), and BFM-R (t* = 0 min). Additionally, we compared K_1 from the NLR to those obtained by BFM-I and BFM-R. K_i and K_1 values were extracted from the brain, liver, spleen, lung, kidney, upper leg muscle, and up to three tumour lesions per patient. ***Results:*** The regional K_i obtained by Patlak strongly correlated with the NLR across all organs (R= 0.96), outperforming gPatlak (R= 0.86). K_i from BFM-I demonstrated the strongest correlation (R= 0.97) and best regression fit with NLR-derived K_i. The K_i's of the liver, brain, and tumour lesions obtained by BFM-R also provided a good agreement for most data points but exhibited higher uncertainty levels than BFM-I. K_1 obtained by BFM-I and BFM-R showed weaker correlations compared to K_i. ***Conclusion:*** LAFOV PET/CT systems enabled whole-body dynamic ^{18}F-FDG PET imaging, offering new possibilities for quantitative assessment of metabolic activity. BFM-R and gPatlak account for reversible kinetics but at the cost of increased uncertainty levels. BFM-I is a strong alternative to Patlak, offering both K_i and K_1 for all organs, but it requires a full dynamic PET scan.

OP-775

Assessment of IDIF Quantification in PET Using 3D Printed Vessel Phantoms

Y. Beqqali[1,2], *A. Zounek*[1], *S. Raju*[1,2], *T. Schmidt*[1], *N. Albert*[1], *S. Ziegler*[1,3], *L. Kaiser*[1];
[1]*Department of Nuclear Medicine, LMU University Hospital, LMU Munich, Munich, GERMANY,* [2]*Department of Physics, Technical University of Munich, Munich, GERMANY,* [3]*Department of Nuclear Medicine, Hannover Medical School, Hannover, GERMANY.*

Aim/Introduction: Quantitative pharmacokinetic modelling in dynamic PET relies on invasive blood sampling or a precise image-derived input function (IDIF). IDIFs are extracted with short early frames to capture the vascular peak, followed by longer frames as tissue uptake progresses. In small vessels, IDIF accuracy deteriorates because of partial volume effects (PVEs), noise, and segmentation uncertainty. We examined how vessel diameter, signal-to-background ratio (SBR), and frame duration jointly affect IDIF accuracy and assessed partial volume correction (PVC) strategies in a controlled phantom study. ***Materials and Methods:*** Six phantoms were 3D printed with [^{18}F]FDG activity using a masked-stereolithography (MSLA) printer with different diameter sizes (3, 4, 5, 6, 7 and 8 mm). The phantoms were placed in a water-filled container and imaged on a PET/CT with 5 mm FWHM point-spread function (PSF), then [^{18}F]FDG was added to the background water of the container to obtain five SBRs: ∞, 10, 7.5, 5, and 2.5. Different static frame durations were reconstructed. Three segmentation approaches were compared with and without PVC: true volume (TV) of the 3D models, region growing threshold (RG), and four hottest voxels per plane (VPP). The geometric transfer matrix (GTM) PVC algorithm provided in the PETPVC toolbox was used [1]. Image-based ground truth activity concentrations were determined using a large 3D printed reference volume. ***Results:*** Without PVC, activity was generally underestimated by 10-50%. TV+PETPVC approached 100% of the true activity for diameters ≥6 mm when SBR ≥7.5. RG+PETPVC achieved comparable accuracy only in the 8 mm vessel. VPP+PETPVC showed substantial overestimation (>300%). In early (10-30 s) frames with high SBR, TV+PETPVC slightly over-recovered for ≥6 mm vessels (107-116%) while the values for 3 mm fluctuated from 10% to 80%. In late (≥600 s) frames under different SBRs, ≥6 mm vessels approached 100%, while 3 mm vessel activity ranged from 50% to 80%. The increase in signal from PVC application was insufficient for small diameters <6 mm, with a recovery to only 50-80% for scans with background activity. ***Conclusion:*** PVC-based IDIF quantification proved reliable when the lumen exceeded the scanner PSF (≥ 6 mm, SBR ≥ 7, frame ≥ 600 s). Activity-embedded 3D printed vessels offer a geometry-accurate, reproducible ground truth, enabling the control of diameter variation, contrast, and frame length and to quantify PVC performance more precisely than with patient data or conventional phantoms. ***References:*** [1] Thomas BA. PETPVC: a toolbox for performing partial volume correction techniques in PET. Phys-Med-Biol. 2016.

OP-776

Differential Binding Kinetics of [^{18}F]F-PSMA-1007 and [^{68}Ga]Ga-PSMA-11: Real-Time Analysis with Potential Impact on PSMA-PET Imaging Protocols

E. Dighero[1], *M. Riondato*[2], *P. Fossa*[3,4], *P. Pelucchi*[4], *B. Casini*[3], *P. D'Ursi*[4], *M. Ghelardoni*[2], *S. Losacco*[2], *L. Sofia*[2], *F. Vitale*[2], *S. Carta*[2], *S. Chiesa*[2], *C. Marini*[5], *G. Sambuceti*[6], *M. Bauckneht*[6];
[1]*Department of Experimental Medicine (DIMES), University of Genoa, Genoa, ITALY,* [2]*Nucelar Medicine Unit, IRCCS Ospedale Policlinico San Martino, Genoa, ITALY,* [3]*Department of Pharmacy, Section of Medicinal Chemistry, School of Medical and Pharmaceutical Sciences, University of Genova, Genoa, ITALY,* [4]*Institute for Biomedical Technologies, National Research Council, Segrate, ITALY,* [5]*Institute of Molecular Biomimaging and Physiology, National Research Council, Milan, ITALY,* [6]*Department of Health Sciences, University of Genoa, Genoa, ITALY.*

Aim/Introduction: Prostate-specific membrane antigen (PSMA) ligands are widely used for prostate cancer Positron Emission Tomography (PET) imaging. Despite targeting the same receptor, [^{18}F]F-PSMA-1007 and [^{68}Ga]Ga-PSMA-11 exhibit different biodistribution profiles. Clinical studies evaluating delayed imaging protocols with PSMA-targeted tracers have yielded inconclusive results regarding their impact on lesion detectability and image contrast. Furthermore, no direct head-to-head comparisons between [^{18}F]F-PSMA-1007 and [^{68}Ga]Ga-PSMA-11 in delayed imaging settings have been reported. We thus aimed to investigate the binding kinetics of these two tracers on PSMA-expressing cells using real-time interaction analysis. ***Materials and Methods:*** PC3-PIP (PSMA-positive) and PC3 (negative control) prostate cancer cells were seeded on Petri dishes ($3x10^5$ cells per sample) and analysed using a real-time kinetic system based on a rotating Petri dish principle with a stationary β-detector (LigandTracer, LT). After baseline measurement in medium, radioligands were added at increasing concentrations, followed by a dissociation phase in ligand-free medium. The association rate constants (k_{on}) and dissociation rate constants (k_{off}) were determined by fitting with the dedicated software TraceDrawer. To further investigate the reversibility of [^{18}F]F-PSMA-1007 binding, LT competition binding experiments were performed using different concentrations (100 nM to 200 µM) of the PSMA inhibitor 2-(phosphonomethyl) pentanedioic acid (2-PMPA), added with 1 nM [^{18}F]F-PSMA-1007. A separate kinetic uptake experiment was conducted using a gamma counter: $3x10^5$ PC3-PIP and PC3 cells cultured in 24-well plates were incubated with 500 µL 1 nM [^{18}F]F-PSMA-1007, the radioactivity in medium and cells was measured at 5-minute intervals for up to 120 minutes to track time-dependent uptake. ***Results:*** [^{68}Ga]Ga-PSMA-11 exhibited reversible binding, with $k_{on}=1.1\times10^6$ $M^{-1}s^{-1}$ and $k_{off}=2.5\times10^{-4}$ s^{-1}, corresponding to an equilibrium dissociation constant $K_D=2.3\times10^{-10}$ M. In contrast, [^{18}F]F-PSMA-1007 showed no detectable dissociation, suggesting irreversible or strongly retained binding ($k_{on}=3.9\times10^5$ $M^{-1}s^{-1}$, k_{off} fixed at 0). The presence of 2-PMPA reduced the rate of [^{18}F]F-PSMA-1007 uptake but did not result in a signal decrease, even at 200 µM. Gamma counter data confirmed time-dependent uptake, with over 50% of the initial activity linked to the cells at 120 minutes. ***Conclusion:*** [^{18}F]F-PSMA-1007 displays a markedly different binding profile compared to [^{68}Ga]Ga-PSMA-11, with apparent irreversible or highly retained association to PSMA-expressing cells. From a clinical perspective, these findings suggest that [^{18}F]F-PSMA-1007 could enable more stable and prolonged tumor retention in delayed imaging protocols. By contrast, delayed imaging with [^{68}Ga]Ga-PSMA-11 may be less advantageous due to its reversible binding kinetics, which could result in reduced tumor retention and lower lesion contrast over time.

OP-777

Explainable AI Enhances Lung Cancer Diagnosis Using Metabolic and Perfusion Features from Dynamic^{18}F-FDG PET/CT

T. Sun[1], *Z. Yao*[1], *Y. Wang*[2], *Y. Wu*[3], *M. Wang*[3], *Y. Liang*[2];
[1]*Chinese Academy of Sciences, Shenzhen, CHINA,* [2]*Shenzhen Cancer Hospital, Shenzhen, CHINA,* [3]*Henan Provincial People's Hospital, Zhengzhou, CHINA.*

Aim/Introduction: Dynamic ^{18}F-fluorodeoxyglucose (^{18}F-FDG) PET/CT imaging offers valuable information beyond static imaging in the evaluation of lung lesions. This study aimed to determine whether dynamic features—specifically metabolic and blood flow components derived from time activity curves (TACs)—can improve differentiation between benign and malignant pulmonary lesions. ***Materials and Methods:*** Dynamic ^{18}F-FDG PET/CT scans were obtained from 187 patients (mean age: 60.41 ± 11.01 years; 117 males). TACs at the primary lesion site were extracted and decomposed using kinetic modeling to separate metabolic and blood flow signals. From these components, features such as area under the curve (AUC), time-to-peak, and slope metrics were computed. A bagging classifier built on decision trees was

trained on these features to differentiate benign from malignant lesions. Model performance was evaluated using cross-validation and receiver operating characteristic (ROC) analysis. External testing was conducted on an independent dataset comprising 42 additional dynamic scans. Feature importance was assessed using SHapley Additive exPlanations (SHAP), and Cohen's effect size were used to compare the model's diagnostic performance against standard PET metrics, including SUVmax and the net influx rate (Ki). ***Results:*** The dynamic feature-based model effectively discriminated between benign and malignant lesions. In cross-validation, the model achieved an AUC of 0.89, sensitivity of 0.80, and specificity of 0.88, outperforming SUVmax (AUC = 0.79, $p < 0.001$) and Ki (AUC = 0.76, $p < 0.001$). On the independent test dataset, the model maintained high performance with an AUC of 0.86, compared to 0.72 (SUVmax) and 0.71 (Ki). SHAP analysis revealed that top contributing features included the slope and peak value of the metabolic TAC and the AUC and peak time of the blood flow TAC. The model's Cohen's effect size (1.71) was notably higher than that of SUVmax (0.96) and Ki (0.81), indicating superior discriminative power ($p < 0.001$). ***Conclusion:*** An explainable machine learning model leveraging dynamic FDG PET/CT metabolic and blood flow features provides a more accurate and interpretable approach for distinguishing benign from malignant lung lesions than conventional metrics such as SUVmax or Ki.

1706

Wednesday, October 8, 2025, 8:00 - 9:30
Room 117

Clinical Oncology Track - TROP Session - Oncology & Theranostics Committee: Theranostic and New Therapies

OP-778

Phase II study to evaluate safety, tolerability, and preliminary efficacy of carrier-added 4-L-[^{131}I]iodo-phenylalanine (^{131}I-IPA) in patients with recurrent GBM concomitantly to 2nd line re-irradiation

J. Pichler[1], *I. Höllmüller*[1], *J. Dierneder*[2], *R. Pichler*[3], *O. Osipova*[3], *S. Wimmer*[4], *J. Feichtinger*[5], *S. Weis*[6], *A. Leibetseder*[7];
[1]*Department of Internal Medicine and Neurooncology Kepler University Hospital Neuromed Campus, Linz, AUSTRIA,* [2]*Department of Nuclear Medicine and Endocrinology, Ordensklinikum Linz Barmherzige Schwestern, Linz, AUSTRIA,* [3]*Department of Neuronuclear Medicine, Kepler University Hospital, Neuromed Campus, Linz, AUSTRIA,* [4]*Department of Neuroradiology, Kepler University Hospital, Neuromed Campus, Linz, AUSTRIA,* [5]*Department of Radiation Oncology, Ordensklinikum Linz Barmherzige Schwestern, Linz, AUSTRIA,* [6]*Division of Neuropathology, Department of Pathology and Molecular Pathology, Neuromed Campus, Linz, AUSTRIA,* [7]*Department of Neurology, Neuromed Campus, Kepler University Hospital, Johannes Kepler University Linz, Linz, AUSTRIA.*

Aim/Introduction: Theranostics is an evolving field in oncology and nuclear medicine therapy. Very limited literature exist with radioligand therapy in primary brain tumors. Large neutral amino acid transporter 1 (LAT1) is overexpressed in glioma cells. LAT1 transports phenylalanine and mediates o-(2-[^{18}F]-fluoroethyl)-l-tyrosine ([^{18}F]FET) uptake in gliomas, including GBM. 4-iodo-l-phenylalanine (IPA) is a derivative of the naturally occurring essential amino acid l-phenylalanine. Iodine-131 [^{131}I] in [^{131}I]IPA is cytotoxic to the cells it penetrates and combines preferential radioactive effects and sustained tumor accumulation. We present results from a study to evaluate safety, tolerability, and preliminary efficacy of (^{131}I-IPA, administered as sequential injections in patients with recurrent GBM concomitantly to second line external radiation therapy. ***Materials and Methods:*** 8 patients were administered intravenous ^{131}I-IPA with with various doses before and after XRT. Radiotherapy treatment was applied with 30 Gy in 5 fractions for low volumes and for tumors > 3 to ≤ 5 cm 36 Gy in 18 fractions. Inclusion criteria comprised patients with GBM with current evidence for first or second recurrence and history of standard radiochemotherapy,interval since end of first line XRT ≥6 months and [^{18}F]FET PET indicating pathologically increased amino acid uptake. Surgery for relapsed tumor was allowed, no other second line treatment. The primary outcomes were safety and tolerability; secondary endpoints comprised progression-free survival and overall survival. ***Results:*** Included patients represent a younger cohort (mean age 55.7 years). 4 patients had more than one relapse before reirradiation. The time between first relapse and start of IPA/XRT ranged from 4.4 to 56.8 weeks. 5 patients with MGMT unmethylated tumors were included. No serious adverse event occurred, 3 patients experienced an adverse event (1 leucopenia grade 2; 1 lymphopenia grade 3; 1 thrombocytopenia grade 3; 1 fatigue grade 2). mPFS from relapse to next progression (PFS2) was 3.8 months (2.8 - 6.4 months). mOS from first relapse (OS2) was 12.4 months and mOS from initial diagnosis (OS1) was 32.2 months. ***Conclusion:*** These preliminary results with radioligand therapy in relapsed GBM showed a favorable safety and tolerability profile with no relevant systemic toxicity and confirmed the first preliminary efficacy results of the IPAX 1 study despite the poor prognostic parameters with MGMT unmethylated tumors and multiple relapses before start of experimental radioligand therapy. Preliminary results support feasibility of higher therapeutic doses in subsequent trials. This is an investigator-initiated trial, with support provided by Telix Pharmaceuticals.

OP-779

Safety of Radioligand Therapy with [177Lu]Lu-FAPi-Dimer with Dose Escalation in a Clinical Setting

J. Urena Poch[1], *J. Kurth*[1], *B. Krause*[1], *H. Lanzafame*[2], *M. Joksch*[1], *B. Bothe*[1], *G. Alsfasser*[3], *W. Fendler*[2], *K. Herrmann*[2], *M. Heuschkel*[1];
[1]*Department of Nuclear Medicine, Rostock University Medical Center, Rostock, GERMANY,* [2]*Department of Nuclear Medicine, University of Duisburg-Essen and German Cancer Consortium (DKTK)-University Hospital Essen, Essen, GERMANY,* [3]*Department of General, Thoracic, Vascular and Transplantation Surgery, University of Rostock, Rostock, GERMANY.*

Aim/Introduction: Radioligand therapies (RLT) are becoming more popular in cancer treatment. One recently highlighted target is the fibroblasts activating protein (FAP). Targeting fibroblasts in the tumor microenviroment FAP inhibitors have shown promising results in PET diagnostics of different tumor entities, leading to use it for RLT. The aim of this study was to determine tolerance and toxicity of [177Lu]Lu-DOTAGA-Glu-(FAPi)2 with increasing activities. ***Materials and Methods:*** This retrospective study includes patients examined between August 2020-April 2025 with: advanced cancer disease, interdisciplinary consensus for RLT and sufficient FAPi-Uptake in PET/CT. Medical records were searched for acute side effects and changes in blood values in all available follow-up data, especially Hemoglobin, Leucocytes, Platelets, Bilirubin, Creatinine. ***Results:*** In 27 patients admitted for FAPi-Therapy we performed a [177Lu]Lu-FAPi-scout examination in 22 patients (350-1048 MBq), 5 Patients were directly treated. Cancer diagnoses were: ten prostate-cancers, six thyroid-cancers, five solitary-fibrous-tumors and one pheochromocytoma, Ewing-Sarcoma, breast-cancer, basal-cell-cancer, pleura-mesothelioma and pancreas-cancer, respectively. A total of 19 patients received at least 1 cycle of RLT - 5 patients one cycle, 5 two, 3 three, 1 four, 1 five and 4 six cycles. Overtime activity was increased (33 cycles with about 7.4, 17 with 9.0, 8 with 11.1 GBq). Cumulative activities of all 27 patients ranged between 350 and 57,375 MBq (median 14,971

MBq). Average follow-up after first [177Lu]Lu-FAPi-administration was 96 days (3-349). Acute adverse events were: aggravation of pain in 2, urinary tract infection in 1, mild gastrointestinal disorders in 2 and aggravation of dyspnea in 1 patients. New reported adverse events during the therapy course were: respiratory infection in 2, headache and aphasia in 1 (brain metastasis), nausea in 2, weight loss in 1, pleural effusion in 1, mild alopecia in 3, aggravation of tumor pain in 6, mild gastrointestinal disorders in 2, cough in 2, dyspnea in 2 and cardiac decompensation in 1 patients. One patient experienced paresthesia, rash, weight loss, exsiccosis and dizziness associated with concomitant checkpoint inhibitor therapy. Another patient developed a heart attack 1 month after his 4th therapy cycle. Worsening in lab parameters was seen for Hemoglobin in 4 (one grade 3), leucocytes in 2 (G1), platelets in 3 (G1/2) and creatinine in 1 (G1) patients. ***Conclusion:*** FAPi-RLT was overall well tolerated with no critical hematotoxicity despite one anemia requiring transfusion. Reported AEs were partially tumor-associated, related to previous medical conditions or concomitant treatments. Nevertheless longer follow-up-data after last treatment-cycles are missing.

OP-780

SANTANA-225: A multicentre, open-label, Phase I/II study investigating the safety, tolerability, and preliminary efficacy of 225Ac-SSO110 in participants with extensive stage small cell lung cancer (ES-SCLC) or Merkel cell carcinoma (MCC) receiving Standard of Care (SoC)

E. Zan[1], *J. Fleck*[2], *G. Gericke*[2], *K. Herrmann*[3];
[1]*Cleveland Clinic, Cleveland, OH, UNITED STATES OF AMERICA,* [2]*Ariceum International AG, Basel, SWITZERLAND,* [3]*Universitätsklinikum Essen, Essen, GERMANY.*

Aim/Introduction: ES-SCLC and MCC are neuroendocrine carcinomas with a dismal prognosis. Immune checkpoint inhibition (CPI) has resulted in clinical benefit, yet the need for improved treatment options remains. Somatostatin receptor 2 (SSTR2) is expressed on the majority of SCLC and MCC lesions and SSTR2 targeted radioligand therapy has proven safe and effective in other neuroendocrine tumors. Preliminary data from an ongoing study with ^{177}Lu-SSO110 added to CPI maintenance in ES-SCLC suggests incremental efficacy, non-clinical data demonstrates long-term tumor control and survival of all animals treated with a single, translatable dose of ^{225}Ac-SSO110. We therefore hypothesise that adding ^{225}Ac-SSO110 to SoC will result in clinically relevant efficacy benefits. ***Materials and Methods:*** The main objective of this study is to assess the safety and tolerability of ^{225}Ac-SSO110 and the recommended phase 2 dose (RP2D) in combination with CPI in 1st line maintenance therapy for ES-SCLC and 1st line CPI therapy for MCC, respectively. The secondary objective is to assess the preliminary anti-tumour activity. Exploratory objectives include the assessment of the level of concordance of lesions visible on ^{68}Ga-satoreotide trizoxetan (^{68}Ga-SSO120) PET/CT versus lesions visible on contrast-enhanced CT and/or FDG PET. Inclusion criteria include histologically or cytologically confirmed ES-SCLC or MCC, adequate organ and bone marrow function, a life expectancy >6 months, and ≥1 positive lesion on ^{68}Ga-SSO120 PET/CT. Participants will be treated with 4 cycles of ^{225}Ac-SSO110, which may be extended to 7 in case of clinical benefit. The study will follow a BOIN design to determine the RP2D with a target dose-limiting toxicity (DLT) rate of 0.30. The ^{225}Ac-SSO110 starting dose is 2.4MBq which can be escalated up to 8.4MBq. ***Results:*** Trial design and preliminary results will be presented at the meeting. ***Conclusion:*** This study will support the selection of the RP2D and assess preliminary safety and efficacy of ^{225}Ac-SSO110 added to CPI in participants with ES-SCLC or MCC.

OP-781

Clinicopathological Features Predict Outcomes in Patients with End-Stage Metastatic Cancers Treated with ^{177}Lu-LNC1004

H. Fu[1], *J. Huang*[1], *W. Guo*[1], *J. Zhang*[2], *X. Chen*[2], *H. Chen*[1];
[1]*The First Affiliated Hospital of Xiamen University, Xiamen, CHINA,* [2]*Yong Loo Lin School of Medicine, National University of Singapore, Singapore, SINGAPORE.*

Aim/Introduction: FAP-targeted radioligand therapy (RLT) is a promising anti-tumor treatment with low toxicity in patients with end-stage metastatic tumors who have not responded to standard treatments. ^{177}Lu-LNC1004 RLT demonstrates promising anti-tumor efficacy with an acceptable safety profile in patients with various end-stage metastatic tumors who have progressed after exhausting standard treatments. In this study, we evaluated the survivals and identified clinicopathological features predicting therapeutic response and outcome in patients with end-stage metastatic cancers receiving ^{177}Lu-LNC1004. ***Materials and Methods:*** Twenty-eight patients with end-stage metastatic tumors treated with a median of 2 cycles of ^{177}Lu-LNC1004 were included. Data were analyzed according to PFS and OS, as well as the RECIST criteria response patterns regarding prior therapies, laboratory biomarkers, metastatic extent, and other clinical pathological characteristics in univariate and multivariate Cox proportional hazards models. ***Results:*** The ^{177}Lu-LNC1004 was given six weekly with a median administered activity of 3.1GBq/cycle up to four cycles. Using the RECIST, disease control was confirmed in 13 patients [13/28, 46%], with 4 and 9 demonstrating partial response and stable disease, respectively. Evaluable patients with SUVmax ≤ 15 in targeted lesions had better DCR than that of patients with SUVmax > 15 (P=0.022). Multivariate analyses revealed that the mean SUVmax of RECIST-targeted lesions was independently associated with better DCR (P=0.021). The median follow-up period was 18.1 months. Among the 28 patients, 16 (57%) were followed for more than 6 months after initiating RLT. The median PFS was 4.0 (95% confidence interval [CI]: 0.8-7.2) months. During the follow-up period, 19 of 28 (68%) patients died and the median OS was 6.3 (95% CI: 0.8-11.7) months. Disease control was associated with improved PFS and OS (P<0.001). PFS and OS were significantly associated with age, baseline ECOG performance status, lines of systemic therapy before ^{177}Lu-LNC1004, baseline leukocyte counts, and received cycles of ^{177}Lu-LNC1004 RLT. Multivariate analysis revealed ≤2 lines of previous systemic therapy, ≤3 organs of tumor involvement, baseline hemoglobin >117 g/L, and baseline leukocyte count ≤10×10^9/L as independent prognostic factors of superior PFS and OS. ***Conclusion:*** FAP-targeted radioligand therapy with ^{177}Lu-LNC1004 was a promising anti-tumor efficacy with an acceptable toxicity profile in patients with various end-stage metastatic tumors. The present data indicate that administering ^{177}Lu-LNC1004 as an earlier line of therapy, targeting patients with better conditions, or ^{177}Lu-LNC1004 performed in combination with immunotherapy may be the strategies to improve therapeutic efficacy and survival in future studies.

OP-782

Deep Learning Model for Automatic Tumour Segmentation and Margin Status Prediction in Micro-PET-CT Images of Breast Lumpectomy Specimens

L. Maris[1,2], *M. Göker*[3], *K. De Man*[4], *B. Van den Broeck*[4], *S. Van Hoecke*[5], *K. Van de Vijver*[6,7], *C. Vanhove*[1,8], *V. Keereman*[1,2];
[1]*Department of Electronics and Information Systems, MEDISIP, Ghent University, Ghent, BELGIUM,* [2]*XEOS Medical, Ghent, BELGIUM,* [3]*Department of Gynaecology, Ghent University Hospital, Ghent, BELGIUM,* [4]*Department of Medical Imaging, Nuclear Medicine, Ghent University Hospital, Ghent, BELGIUM,* [5]*Internet Technology and Data Science Lab (IDLab), Ghent University-Imec, Ghent, BELGIUM,* [6]*Department of Pathology, Ghent University Hospital, Ghent, BELGIUM,* [7]*Department of Diagnostic Sciences and CRIG, Ghent University, Ghent, BELGIUM,* [8]*CORE ARTH INFINITY, Ghent University, Ghent, BELGIUM.*

Aim/Introduction: Complete tumour removal is crucial in curative breast cancer surgery to prevent local recurrence. Recently, high-resolution (micro-)PET-CT imaging with ^{18}F-FDG emerged as a promising technique for fast intraoperative margin assessment (IMA) of lumpectomy specimens. However, interpreting micro-PET-CT specimen images can be challenging and time-consuming in some cases. To address this, we propose a deep learning (DL) model that automatically segments breast tumours in micro-PET-CT images of lumpectomy specimens and predicts the margin status. ***Materials and Methods:*** We trained and evaluated a 2D Residual U-Net (ResU-Net) to delineate invasive carcinoma of no special type (NST) in micro-PET-CT images. We collected micro-PET-CT images from 53 lamellas of lumpectomy specimens from 19 patients, along with corresponding histopathology whole-slide images (WSIs). An in-house developed co-registration algorithm was used to align the micro-PET-CT images with the WSIs. An experienced pathologist annotated the WSIs to obtain ground truth binary tumour segmentations. To train and test the ResU-Net for tumour segmentation, five-fold group cross-validation was performed on this annotated data set. Subsequently, an ensemble model was constructed and applied to a previously unseen data set comprising micro-PET-CT images of 31 NST lumpectomy specimens. The predicted margin statuses were compared with the true margin statuses determined through histopathological examination. ***Results:*** Five-fold cross-validation on the first data set with true tumour segmentation labels yielded a dice similarity coefficient (DSC) of 0.73±0.20 and a precision-recall area under the curve (PR-AUC) of 0.83±0.14 for segmentation. In comparison, conventional intensity thresholding performed slightly worse with a DSC of 0.71±0.22 and PR-AUC of 0.77±0.20. For the second data set, margin status prediction using the ResU-Net achieved a sensitivity of 89%, specificity of 91%, and F1-score of 84%. ResU-Net outperformed conventional intensity thresholding (sensitivity: 100%, specificity: 59%, F1-score: 67%), while reaching a similar performance to 7 physicians who manually interpreted the same image set (sensitivity: 90%±4%, specificity: 86%±7%, F1-score: 81%±4%). ***Conclusion:*** We introduced a DL model for segmenting NST breast tumours and predicting the margin status using micro-PET-CT images of lumpectomy specimens. The model demonstrated comparable performance to 7 physicians and outperformed conventional intensity thresholding in margin status prediction. Although additional data are required to enhance and (clinically) validate the model, this work represents an important step toward developing a decision-support system to assist physicians in interpreting micro-PET-CT images of lumpectomy specimens. Ultimately, it may facilitate the integration of micro-PET-CT imaging as IMA technique in clinical practice.

OP-783

Unlocking the predictive potential of preoperative SPECT/CT roadmaps for signal intensities during cervical cancer sentinel node surgery

G. Pisano[1,2], *N. van Ruremonde*[2], *F. H. P. van Velden*[3], *P. Dibbets-Schneider*[3], *J. J. Beltman*[4], *L. S. Nooij*[4], *M. N. van Oosterom*[2], *F. W. B. van Leeuwen*[2], *D. D. D. Rietbergen*[3,2];
[1]*Nuclear Medicine Unit, Fondazione Policlinico Universitario A. Gemelli IRCCS, Rome, ITALY,* [2]*Interventional Molecular Imaging Laboratory, Leiden University Medical Centre, Leiden, NETHERLANDS,* [3]*Section of Nuclear Medicine, Department of Radiology, Leiden University Medical Center, Leiden, NETHERLANDS,* [4]*Department of Gynecology, Leiden University Medical Center, Leiden, NETHERLANDS.*

Aim/Introduction: Molecular image-guided surgery offers the potential to enhance surgical performance by enabling preoperative imaging and supporting intraoperative target localization. During sentinel node (SN) surgeries, preoperative images as SPECT/CT are currently used for 3D intervention planning, a surgical 'roadmap'. In addition to positional information, these scans provide valuable insights about tracer avidity of SNs. This information could be used to further optimize surgical navigation, such as predicting feasibility and quality of intraoperative radioguidance. Therefore, the aim of this study was to correlate tracer uptake in preoperative images with radio- and fluorescence-guidance during cervical cancer SN surgery. ***Materials and Methods:*** 41 patients undergoing SN procedure, radical hysterectomy and pelvic lymphadenectomy for cervical cancer were included. One day before surgery, they received four peri-cervical injections of hybrid tracer indocyanine green (ICG)-^{99m}Tc-nanocolloid (4x25MBq). Preoperative imaging was performed (planar lymphoscintigraphy and SPECT/CT). Intraoperative gamma-tracing (numerical values) and fluorescence imaging (categorical values, i.e. positive or negative) were performed and checked ex-vivo. Pre-operative imaging metrics of SNs were extracted using custom software workflows, including total, mean, median counts; total counts as ratio of injection site; area (L-ANT), volume (SPECT/CT); kurtosis and skewness. For statistical analysis, Pearson's (r) and Spearman's (rho) correlation coefficients were used. ***Results:*** A total of 63 SNs were analyzed. During surgery, 49 SNs were identified with radioguidance (49/63:77.8%) and 25 with fluorescence guidance (25/59:42.4%, 4 not reported), with 64.4% concordance. The median of gamma probe counts was 8370 in-vivo and 8480 ex-vivo. The mean signal intensity on planar L-ANT imaging correlated with in-vivo (Pearson's r=0.419, p=0.03) and ex-vivo (r=0.572, p<0.001) probe counts. The results for quantified SPECT/CT uptakes were similar (in-vivo r=0.409, p=0.004; ex-vivo r=0.519, p<0.001). Subgroup analysis revealed significantly stronger correlations for patients with BMI<25 (planar L-ANT: in-vivo r=0.740, p<0.001 and ex-vivo r=0.585, p<0.001; SPECT/CT: in-vivo r=0.596, p<0.001 and ex-vivo r=0.561, p=0.002), while almost no significant correlation for patients with BMI≥25 (SPECT/CT: in-vivo r=-0.012, p=0.959 and ex-vivo r=0.351, p=0.199). No significant correlation could be found between preoperative imaging and fluorescence findings (SPECT/CT: in-vivo rho=0.077, p=0.565 and ex-vivo rho=0.099, p=0.495). ***Conclusion:*** During cervical cancer SN biopsy, the signal intensity on preoperative scintigraphy and SPECT/CT proved to be directly correlated with intraoperative radioguidance, particularly in patients with BMI<25. Indicating that preoperative imaging can not only provide positional information to improve intraoperative detection rate, but is also predictive for the quality of radioguided surgery, unlocking further potential of nuclear medicine in surgical decision-making.

OP-784

Integrated Multidisciplinary Workflow for ROLL of PET/CTPositive Lesions: Technical Feasibility and Clinical Impact

M. Zapardiel*, L. León Ramírez, C. Wakfie Corieh, C. González Roiz, J. Armijo Astrain, M. Leyva Vásquez Caicedo, S. Ochagavia Cámara, C. Sánchez del Pueblo, M. Vaillant López, A. Berardinelli Isea, M. Romero Porras, M. Cornide Carrallo, M. Cabrera Martin; H. U. Clínico San Carlos, Madrid, SPAIN.*

Aim/Introduction: This study presents our initial experience with a structured, multidisciplinary protocol for radioguided occult lesion localization (ROLL) of hypermetabolic lesions identified on PET/CT. The aim was to evaluate the technical feasibility, safety, and diagnostic utility of this approach. ***Materials and Methods:*** Between May 2024 to March 2025, twenty ROLL procedures were performed in sixteen patients (10 men, 6 women; mean age 57 years) with PET/CT-positive lesions. Lesion selection was conducted during multidisciplinary tumor board meetings based on metabolic activity and surgical accessibility. Through close collaboration with radiologists, the most appropriate method—ultrasound guidance, in our current experience- was selected to guide the intralesional injection of 99mTcMAA (55-111 MBq), which was always performed within 24 hours prior to surgery. Immediately after injection, correct radiotracer placement was confirmed using SPECT/CT of the region, we confirm correct

radiotracer placement doing a SPECT/CT of the region and nd the area of maximal uptake was marked on the skin to assist the surgical team. During the procedure, a nuclear medicine physician guided lesion localization using an intraoperative gamma-probe. Histopathological results were reviewed during follow-up multidisciplinary case discussions to refine and adapt the workflow. ***Results:*** Lesions were most commonly located in the cervical region (60%), followed by axillary (15%), inguinal (15%), high paratracheal (5%), and abdominal (5%) regions. Radiotracer placement was accurately confirmed in 17 of 20 cases (85%). Intraoperative localization was successful in all procedures led by a nuclear medicine physician (17/17), and no complications were reported. Histopathological analysis confirmed malignancy in 11 cases (five lymphomas, six metastases from known primaries). Among the benign results, five cases were negative for malignancy, two cases were consistent with toxoplasmosis, one with a sclerotic nodule, and one with reactive follicular hyperplasia. From this, only three of them required further pathological evaluation due to inconclusive or discordant findings. ***Conclusion:*** The implementation of a structured, multidisciplinary ROLL workflow has proven to be a safe and effective strategy for the surgical management of PET/CTpositive lesions. High rates of accurate lesion targeting and intraoperative localisation highlight the value of including a nuclear medicine physician as part of the surgical team. This integrated approach enhances surgical precision in PET/CT-positive lesions and supports more personalized clinical decision-making.

OP-785

Radioguided Occult Lesion Localisation (ROLL) for Intraoperative Detection of Parathyroid Adenomas: A Preliminary Single-Centre Experience

L. León Ramírez[1], *C. González Roiz*[2], *T. Diaz Vico*[3], *I. Grao Torrente*[3], *A. García Muñoz Nájar*[3], *A. Hermosín Peña*[3], *M. Durán Poveda*[3];
[1]*Hospital clínico san carlos, Madrid, SPAIN,* [2]*Hospital Puerta del Sur, Madrid, SPAIN,* [3]*Hospital Universitario Rey Juan Carlos, Madrid, SPAIN.*

Aim/Introduction: Precise intraoperative localisation of parathyroid adenomas is essential in the surgical management of primary hyperparathyroidism, particularly in cases where conventional imaging is inconclusive or discordant. Radioguided Occult Lesion Localisation (ROLL) has emerged as a valuable adjunct in enhancing surgical accuracy under these challenging circumstances.To evaluate the feasibility, safety, and histopathological concordance of ROLL-guided parathyroidectomy in patients with primary hyperparathyroidism and difficult preoperative localisation. ***Materials and Methods:*** We retrospectively reviewed 24 patients (19 women, 5 men; mean age 60.1 ± 13.3 years) with primary hyperparathyroidism who underwent ROLL-assisted parathyroid surgery between August 2017 and April 2024 at our centre. All patients were selected based on inconclusive or discordant imaging findings. Preoperative localisation was achieved through ultrasound-guided injection of technetium-99m macroaggregated albumin (99mTc-MAA). Tracer uptake was confirmed by SPECT/CT, and intraoperative localisation was facilitated using a handheld gamma probe. A nuclear medicine physician with expertise in radioguided surgery was present in the operating room and actively contributed to intraoperative navigation. Surgical and histopathological outcomes were analysed, along with postoperative biochemical results. Concordance among ultrasound, SPECT, MRI, and choline PET imaging was also assessed. ***Results:*** ROLL was successfully performed in all 24 cases (100%). The most common surgical approach was focused parathyroidectomy. Histopathological analysis confirmed parathyroid adenoma or hyperplasia in 21 out of 24 patients (87.5%). Imaging concordance was observed in 12 cases (35%), while 23 cases (65%) showed discordant or incomplete localisation. No complications related to the ROLL procedure were reported (0%). Most patients (over 90%) demonstrated a significant postoperative decrease in serum calcium and parathyroid hormone levels, consistent with effective gland removal. ***Conclusion:*** ROLL is a safe, reliable, and effective technique for the intraoperative localisation of parathyroid adenomas, especially in patients with non-localising or discordant preoperative imaging. The dedicated presence of a nuclear medicine physician during surgery enhances operative precision and contributes to optimal outcomes in the management of primary hyperparathyroidism.

OP-786

Accuracy of PSMA-PET/CT, mpMRI and ex vivo specimen PET/CT for molecular guidance of nerve sparing

P. Fragoso Costa[1], *T. Kahl*[2], *W. Fendler*[1], *H. Reis*[3], *J. Köllermann*[3], *C. Kesch*[2], *L. Püllen*[2], *U. Krafft*[2], *J. Kleesiek*[4], *D. Kersting*[1], *M. Ingenwerth*[5], *B. Hadaschik*[2], *K. Herrmann*[1], *F. Barbato*[1], *C. Darr*[2];
[1]*Clinic for Nuclear Medicine, University Hospital Essen, University Duisburg-Essen, Essen, GERMANY,* [2]*Department of Urology, University Hospital Essen, University Duisburg-Essen, Essen, GERMANY,* [3]*Institute of Pathology, University Hospital Frankfurt, Frankfurt, GERMANY,* [4]*Institute of Artificial Intelligence in Medicine, University Hospital Essen, University Duisburg-Essen, Essen, GERMANY,* [5]*Institute of Pathology, University Hospital Essen, University Duisburg-Essen, Essen, GERMANY.*

Aim/Introduction: Accurate assessment of extraprostatic extension (EPE) has a major impact on RP extent and nerve sparing (NS). We evaluate the accuracy of a novel specimen PET/CT (sPET/CT) scanner for intraoperative real-time whole gland assessment. ***Materials and Methods:*** 28 patients (pts) undergoing RP with high-risk PC and experimental sPET/CT were included in this analysis; preoperative mpMRI imaging was available in 23 pts (82.1%). In 24 pts. (85.7%), conventional clinical PET/CT was performed immediately preoperatively. 4 pts received an intraoperative tracer injection. In terms of used tracer, 9 pts were injected with ^{68}Ga-PSMA-11 while 19 pts received ^{18}F-PSMA-1007. Lesions were segmented using an iterative thresholding method, comparing with histopathological EPE and positive surgical margins (PSM). Sensitivity, specificity, positive predictive value (PPV) and negative predictive value (NPV) were determined for predicting EPE. ***Results:*** Intraoperative tracer uptake was visible in sPET/CT in 27 patients (96.4%). Sensitivity for EPE of PSMA-PET/CT, mpMRI and sPET/CT was 0.36, 0.9 and 0.88, specificity was 0.92, 0.77 and 1, respectively. PPV was 0.83, 0.75 and 1, NPV was 0.57, 0.91 and 0.85, respectively. Unilateral NS RP was performed in 13 pts; after sPET/CT, NS could have been performed on the opposite side in 69%. No NS was performed in 14 pts; according to sPET/CT, unilateral NS could have been performed in 42.9%. In 10 pts PSM were detected in histopathology, 9 showed a corresponding tracer signal in sPET/CT. ***Conclusion:*** Intraoperative PET/CT correlates well with histopathology. Sensitivity, specificity, PPV and NPV are encouraging and suggest further investigation of this molecular-guided RP approach.

1707

Wednesday, October 8, 2025, 8:00 - 9:30

Room 212

TROP Session - Cardiovascular Committee: Atherosclerosis Burden, from Plaque to Perfusion

OP-787

First-in-Human Phase I/IIa Study of [^{99m}Tc]Tc-cAbVCAM1-5: Safety, Dosimetry, and Biodistribution in Healthy Volunteers and Asymptomatic Patients Prior to Carotid Endarterectomy

L. Djaileb[1], *J. Leenhardt*[2], *R. Spear*[3], *N. De Leiris*[2], *G. Reboulet*[2], *M. Faure*[3], *A. Paris*[3], *L. Dumas*[2], *C. Ghezzi*[2], *G. Vanzetto*[2], *D. Fagret*[2], *G. Barone-Rochette*[2], *A. Broisat*[2];
[1]*University Grenoble Alpes,LRB, Grenoble, FRANCE,* [2]*University Grenoble Alpes, LRB, Grenoble, FRANCE,* [3]*University Grenoble Alpes, Grenoble, FRANCE.*

Aim/Introduction: Vascular Cell Adhesion Molecule 1 (VCAM-1) has emerged as a promising target for molecular imaging of vulnerable atherosclerotic plaques due to its overexpression on activated endothelial cells in inflamed vascular regions. To assess safety, dosimetry, and biodistribution of the novel radiopharmaceutical [^{99m}Tc]Tc-cAbVCAM1-5 in Healthy Volunteers and Asymptomatic Patients Prior to Carotid Endarterectomy. ***Materials and Methods:*** This study is a phase I/IIa, prospective, monocentric, non-controlled, non-randomized, open-label interventional study (NCT04483167). Inclusion criteria were healthy volunteers (18-55 years) and patients (18-80 years) with asymptomatic carotid stenosis indicated for surgery. Healthy volunteers underwent a dose-escalation protocol (1+3+3 design) with injected activities of 370, 550, and 750 MBq and nanobody doses below 100 µg of [^{99m}Tc]Tc-cAbVCAM1-5. Dosimetry was calculated using OLINDA V1 software, and multiple blood, urine, and imaging acquisitions were performed up to 24 hours post-injection. Patients followed the same protocol for up to 6 hours before undergoing surgery at the 24-hour. VCAM-1 expression on SPECT imaging and histopathology was classified using a 0-3 uptake scale (denoting absence, low, moderate, and high expression).The primary objective was to safety, dosimetry, and biodistribution in Healthy Volunteers and Asymptomatic Patients Prior to Carotid Endarterectomy. Secondary objectives included correlation between imaging and histological VCAM-1 expression. ***Results:*** Seven healthy volunteers (mean±SD; 41.3±7.6 years) and 6 patients (73.6±9.0) were included. No serious or severe adverse events, nor significant biological changes, were observed after administration of [^{99m}Tc]Tc-cAbVCAM1-5. Biodistribution was consistent with preclinical data, showing predominant renal uptake, moderate splenic, and low bone marrow uptake, with no myocardial or vascular signal. Blood clearance was rapid, with less than 10% of injected activity remaining at 1 hour (half-lives: 30.5 min early, 100 min late phase). Renal radiation dose was highest (0.202 mGy/MBq), with mean (±SD) effective doses of 0.0065±0.8 mSv/MBq. SPECT did not detect significant uptake in patient before surgery (score 0 to 1). Histopathology and SPECT were concordant in 5/6 (83%) with low VCAM-1 expression in 5/6 (83%). One patient had a moderate VCAM-1 expression with no uptake on SPECT. ***Conclusion:*** [^{99m}Tc]Tc-cAbVCAM1-5 demonstrated a favorable safety profile, acceptable dosimetry primarily related to renal uptake, and a biodistribution pattern similar to that observed in animal models. Imaging findings were in accordance with histopathological assessment of VCAM-1 expression. Further studies are warranted to assess the diagnostic performance in patients with symptomatic plaques.

OP-788

Carotid Calcified Inflammatory Plaques and Cardiocerebrovascular Events: A ^{68}Ga-DOTA-TOC PET/CT study in an oncological setting

X. Shao[1,2], *C. Bregenz*[2], *J. Wang*[2], *Y. Chen*[2], *A. Rominger*[2], *K. Shi*[2], *F. Caobelli*[2];
[1]*the Third Affiliated Hospital of Soochow University, Changzhou, CHINA,* [2]*Inselspital, Bern University Hospital, University of Bern, Bern, SWITZERLAND.*

Aim/Introduction: Overexpression of somatostatin receptors (SSTR2) in activated M1-macrophages has emerged as a potential marker of plaque vulnerability. The PET-based evaluation of plaque vulnerability in coronary arteries has proven useful in the assessment of cardiovascular risk. Same value may pertain also to vulnerable carotid plaque for the prediction of the risk of cerebrovascular events. We therefore aimed to investigate, whether SSTR2-overexpressing carotid calcified plaques may be predictive of major cerebrovascular events. ***Materials and Methods:*** In this retrospective study, 363 oncological patients undergoing ^{68}Ga-DOTA-TOC PET/CT imaging for oncologic reasons were included. Plaque calcifications and ^{68}Ga-DOTA-TOC uptake in the carotid arteries were evaluated visually and semi-quantitatively. During a median follow-up of 54 months, data on cardio- and cerebrovascular events (myocardial infarction, hospitalization for myocardial ischemia, coronary artery revascularization, stroke) and all-cause death were collected. The incidence of major adverse events between groups with and without ^{68}Ga-DOTA-TOC uptake was compared using the chi-square test and Fisher's exact test. ***Results:*** 128 patients (35.3%) showed carotid artery calcification of any degree in at least one side, with a mean calcification volume of 51.6±147.6 cm^3. A total of 71 focal ^{68}Ga-DOTA-TOC uptake (41 left, 30 right) were seen in 48 patients (13.2%) with SUVmax 1.76 ± 0.35 and TBR 2.23 ± 0.98, respectively. In those patients with a detectable ^{68}Ga-DOTA-TOC uptake, stroke occurred more frequently (8.3% vs. 2.5%, P = 0.036). The incidence of MACE was significantly higher in patients with increased ^{68}Ga-DOTA-TOC uptake compared to those without uptake (8.3% vs. 2.2%, P = 0.021). Patients with concurrent carotid artery calcification and increased ^{68}Ga-DOTA-TOC uptake exhibited the highest incidence of stroke and MACE (11.4 % and 11.4 %). ***Conclusion:*** In an oncological setting, SSTR2-overexpressing carotid calcified plaques in ^{68}Ga-DOTA-TOC PET/CT can predict higher risk of developing cardio- and cerebrovascular events. ***References:*** 1. Mingels C, Sari H, Gözlügöl N, Bregenzer C, Knappe L, Krieger K, Afshar-Oromieh A, Pyka T, Nardo L, Gräni C, Alberts I, Rominger A, Caobelli F. Long-axial field-of-view PET/CT for the assessment of inflammation in calcified coronary artery plaques with [68 Ga]Ga-DOTA-TOC. Eur J Nucl Med Mol Imaging. 2024 Jan;51(2):422-433.2. Wu M, Ning J, Li J, Lai Z, Shi X, Xing H, Hacker M, Liu B, Huo L, Li X. Feasibility of In Vivo Imaging of Fibroblast Activation Protein in Human Arterial Walls. J Nucl Med. 2022 Jun;63(6):948-951.

OP-789

Increase of 18F-rhPSMA-7 uptake in atherosclerotic plaques is associated with higher cardiovascular risk in patients with prostatic cancer.

S. Notohamiprodjo[1], *B. Haller*[2], *I. Rauscher*[1], *M. Eiber*[1], *W. Weber*[1], *M. Krönke*[3];
[1]*Technical University of Munich, TUM School of Medicine and Health, TUM University Hospital, Department of Nuclear Medicine, Munich, GERMANY,* [2]*Technical University of Munich, TUM School of Medicine and Health, TUM University Hospital, Department of Biostatistics and Clinical Epidemiology, Munich, GERMANY,* [3]*Die Radiologie, Munich, GERMANY.*

Aim/Introduction: PSMA expression during neovascularisation is believed to be the cause of PSMA-radioligand uptake in several benign processes. Neovascularization also occurs during the development of vulnerable atherosclerotic plaques and may explain PSMA-radioligand uptake in vascular walls, though its significance remains unclear. We therefore investigated whether PSMA-radioligand uptake in vascular structures correlates with elevated cardiovascular risk (CVR). ***Materials and Methods:*** We analysed 110 ^{18}F-rhPSMA7-PET/CT scans acquired for staging or restating of prostate cancer. All scans were acquired without intravenous CT contrast agents. SUVmax was measured in the thoracic aorta, common iliac arteries, common carotid arteries and mediastinal blood pool (MBP). As a marker of CVR the Agatston calcium score was measured. Depending on the result for Agatston score, patients were assigned to five CVR risk groups. The correlation of SUVs with the risk groups was analysed. Furthermore, intraindividual differences in SUVs between calcified and non-calcified vessel segments were measured. The impact of injected tracer dose, kidney function (serum creatinine, eGFR)on SUVmax values was also determined. ***Results:*** A positive correlation was found between CVR and PSMA-radioligand uptake by arterial walls (r=0.29, p<0.01) . In the intra-individual comparison, vascular segments with calcified plaques showed significantly higher SUVmax values than vascular segments without calcified plaques

(mean ΔSUV 0.42, p<0.01). PSMA uptake of calcified segments correlated with increasing CVR (r=0.5, p<0.01), while PSMA uptake of non-calcified segment correlated slightly with increasing CVR (r=0.27, p<0.01). The ratio of PSMA activity in the arterial vessel wall to blood pool activity was 48%:52%. No significant impact on PSMA-radioligand uptake was shown for injected tracer dose (r=0.13, p=0.19), serum creatinine (r=-0.02, p=0.84) or eGFR (r=-0.11, p=0.29). ***Conclusion:*** We observed a statistical association between markers of elevated CVR and PSMA-radioligand uptake by arterial walls. However, the differences between risk groups are small in absolute terms which may limit the clinically utility of PSMA-radioligand uptake as a marker for CVR.

OP-790

[^{68}Ga]FAPI PET molecular imaging in atherosclerosis compared with [^{18}F]FDG

R. Calabretta, *E. Atli, B. Geist, D. Muin, E. Kretschmer-Chott, C. Spielvogel, S. Schmitl, X. Li, P. Binder, M. Hacker;*
Medical University of Vienna, Vienna, AUSTRIA.

Aim/Introduction: Adult cancer survivors have a growing risk of atherosclerotic cardiovascular diseases (CVD), not related to traditional CVD risk factors. Detection of arterial inflammation with imaging is an attractive approach to identify patients at highest risk of plaque rupture, and 2-deoxy-2-[^{18}F]fluoro-D-glucose ([^{18}F]FDG) positron-emission tomography, in combination with computer tomography (PET/CT) or magnetic resonance (PET/MR), is a validated diagnostic tool for atherosclerotic inflammation functional imaging. [^{68}Ga]-labeled fibroblast activation protein inhibitor ([^{68}Ga]FAPI) PET tracer is used in oncology, recently also in CV medicine. ***Materials and Methods:*** Twenty patients with known urothelial carcinoma underwent [^{68}Ga]FAPI PET/MR and [^{18}F]FDG PET/CT imaging have been retrospectively analyzed. We performed a whole-segment analysis by deriving target-to-background ratio (TBR) values at both scans and subsequently assessed the corresponding segments between each other's. 374 PET active arterial lesions have been identified. Additionally, we researched the effects on arterial wall uptake of CVD risk factors, such as arterial hypertension, type 2 diabetes mellitus (T2DM), dyslipidemia, and of a CV-specific therapy with aspirin (100 mg/day). ***Results:*** In the per-lesions analysis, [^{68}Ga]FAPI identified more lesions and showed a 19% higher uptake than [^{18}F]FDG (TBR_{FAPI}:1.7±0.5 vs. TBR_{FDG}:1.4±0.2;P<0.001). In the patient-based analysis, TBR_{FAPI} was also by 19% significantly higher than TBR_{FDG} (TBR_{FAPI}:1.7 ±0.4 vs. TBR_{FDG}:1.4±0.2; P=0.018). Regarding CVD risk factors, the presence of arterial hypertension (P<0.001) or dyslipidemia (P<0.001) alters significantly arterial [^{68}Ga]FAPI-expression compared to [^{18}F]FDG-activity. The difference between TBR_{FAPI} and TBR_{FDG} in patients with T2DM was even higher (TBR_{FAPI}:2.0±0.6 vs. TBR_{FDG}:1.3±0.2; difference 34%;p<0.001). Interestingly, TBR_{FAPI} was 25% higher compared to those without T2DM (TBR_{FAPI}:2.0±0.6 vs. 1.6±0.5,P<0.001), while no significant differences in [^{68}Ga]FAPI-expression were found between subjects suffering from arterial hypertension or dyslipidemia (4%,P=0.4 and 4%,P=0.3, respectively). Considering the aspirin therapy, patients not treated with aspirin showed a 24% higher arterial [^{68}Ga]FAPI-expression than [^{18}F]FDG (TBR_{FAPI}:1.8±0.6 vs. TBR_{FDG}:1.3±0.2;P<0.001), whereas the difference between TBR_{FAPI} and TBR_{FDG} was lower but still significant in patients with aspirin (8% difference,P=0.02). Interestingly, aspirin intake significantly reduces arterial [^{68}Ga]FAPI-expression compared to patients not assuming this drug (1.6±0.3 vs. 1.8±0.6,p=0.02), suggesting that aspirin treatment counteracts the effectivity of accumulating [^{68}Ga]FAPI within the arterial wall. ***Conclusion:*** [^{68}Ga]FAPI-PET identified more lesions and showed higher uptake than [^{18}F]FDG, independently from the presence of CVD risk factors or CV-specific therapy. Our results suggest that [^{68}Ga]FAPI could be a novel and valid marker for PET molecular imaging in atherosclerosis, as well as in cancer patients, particularly in those suffering from T2DM.

OP-791

Impact of Hemoglobin Concentration on Quantitative Cardiac Perfusion Measurements

P. Svanström, *T. Kero, J. Sigfridsson, K. M. Eggers, N. Johnston, A. Brandt, H. J. Harms, M. Lubberink, J. Sörensen;*
Uppsala University, Uppsala, SWEDEN.

Aim/Introduction: Anemia is a prognostic factor in chronic coronary syndromes. It remains unclear if hemoglobin concentration (Hb) affects quantitative cardiac perfusion measurements from PET in subjects with suspected angina and whether there are sex differences. This study had 3 aims: 1) Does Hb affect cardiac output? 2) Does Hb alter resting-MBF beyond the effects of sex and cardiac output? 3) Is low Hb associated with a higher risk of abnormal stress PET or MFR? ***Materials and Methods:*** This retrospective study included patients with suspected angina who underwent cardiac ^{15}O-water PET and had Hb measurements available. PET measurements included resting cardiac output quantified using the indicator dilution technique, stroke volume (cardiac output/heart rate), myocardial blood flow (MBF) at rest and stress, and myocardial flow reserve (MFR). Multivariate models were used to address the 3 research aims. ***Results:*** We included 675 consecutive patients (45% female, age 66±11 years, Hb 139±14 g/L, 13% anemic). Hb was inversely associated with resting cardiac output in women (P=0.0002), but not in men (P=0.54). Hb was a strong determinant of resting-MBF, second only to heart rate. Heart rate, Hb, stroke volume, sex and systolic blood pressure explained two-thirds of the variation in resting-MBF (adjusted R^2=0.66). Hb was not associated with stress-MBF in men (P=0.17) or in women (P=0.47). Low Hb was associated with reduced MFR in men (P=0.005), and showed a borderline association in women (P=0.06). ***Conclusion:*** Hemoglobin concentration was associated with cardiac perfusion measurements through several mechanisms, some of which may be sex-dependent. Hb was associated with MFR, mainly because MFR integrates complex regulation of resting-MBF, including the effects of anemia. In contrast, Hb had no significant impact on stress-MBF, suggesting that stress-MBF may be a more robust indicator of maximal coronary capacity.

OP-792

Model-Free Perfusion Quantification for Dynamic Total-body ^{18}F-FDG PET Reveals Remote Blood Flow Alterations in Coronary Artery Disease

T. Sun[1], *Y. Wu*[2], *M. Wang*[2];
[1]*Chinese Academy of Sciences, Shenzhen Insitute of Advanced Technology, Shenzhen, CHINA,* [2]*Henan Provincial People's Hospital, Zhengzhou, CHINA.*

Aim/Introduction: Coronary artery disease (CAD) is increasingly linked to altered systemic perfusion beyond the myocardium. While ^{15}O-water PET is considered the gold standard for non-invasive perfusion imaging, its limited availability restricts broader use. The emergence of long axial field-of-view PET/CT systems provides a unique opportunity to utilize ^{18}F-FDG for dynamic, whole-body perfusion quantification. This study aims to develop a model-free deconvolution framework for extracting perfusion metrics from dynamic ^{18}F-FDG PET and to evaluate its sensitivity in detecting CAD-related abnormalities across multiple organs. ***Materials and Methods:*** Dynamic total-body ^{18}F-FDG PET scans were acquired with ultra-high temporal resolution (i.e., 2-second frames during the first minute, 50 frames over 20 minutes). A model-free deconvolution approach was applied to compute voxel-wise perfusion parameters, including blood flow (BF), blood volume (BV), time-to-peak (TTP), and mean transit time (MTT). These were compared between 8 patients with severe CAD and 8 age-matched healthy controls. For comparison, conventional compartmental modeling was also performed to estimate K1 values. Statistical significance was assessed using Mann-Whitney U with a threshold of $p < 0.05$. ***Results:*** CAD patients exhibited

significantly reduced BF in the spleen, kidney, spine, and pelvis ($p < 0.05$), along with decreased BV in the kidney and pelvis. TTP was delayed in the liver, kidney, and pelvis, while MTT was reduced in the liver, kidney, pelvis, and skeletal muscle. Conventional kinetic modeling (K1) revealed group differences primarily in the lung, liver, kidney, and spine, though with lower sensitivity. No significant perfusion abnormalities were found in the brain between groups. These results demonstrate that model-free metrics may better capture peripheral perfusion impairments associated with CAD than traditional model-based parameters. ***Conclusion:*** Model-free analysis of dynamic ^{18}F-FDG PET enables sensitive and non-invasive quantification of whole-body perfusion, revealing systemic hypoperfusion patterns in CAD patients that are not evident with conventional kinetic models. This approach provides a promising tool for studying heart-body interactions and for the early detection of CAD-related organ dysfunction.

OP-793

Respiratory Motion and Attenuation Corrections Improve Prognostic Value of Myocardial Perfusion Imaging in Patients With Ischemia and Nonobstructive Coronary Arteries

***C. Chen**, C. Ko;*
National Taiwan University Hospital, Taipei, TAIWAN.

Aim/Introduction: Patients with ischemia and nonobstructive coronary arteries (INOCA) often exhibit subtle perfusion abnormalities on myocardial perfusion imaging (MPI), owing to coronary microvascular dysfunction or vasospasm. These abnormalities are particularly susceptible to respiratory motion and photon attenuation, potentially limiting the prognostic value of MPI. This study evaluated whether respiratory motion and attenuation corrections improve the prognostic performance of MPI in patients with INOCA. ***Materials and Methods:*** This retrospective study included 3,166 patients who underwent MPI with cadmium-zinc-telluride (CZT) single-photon emission computed tomography (SPECT). All patients had no significant coronary artery stenosis (< 50%), confirmed by invasive coronary angiography or computed tomography coronary angiography within 6 months before or 2 years after MPI. Respiratory motion correction was performed using a previously validated data-driven gating algorithm. Attenuation correction was applied using a self-developed deep learning model that generated attenuation maps from multi-energy window SPECT images. Patients were followed for a median of 5 years for the occurrence of major adverse cardiovascular events (MACE), including nonfatal stroke, nonfatal myocardial infarction, and all-cause mortality. Cox proportional hazards models were fit to assess the prognostic value of stress total perfusion deficit (STPD), adjusted for age, sex, body mass index, hypertension, diabetes mellitus, dyslipidemia, and smoking status. Model comparisons were conducted using non-nested partial likelihood ratio tests. ***Results:*** Uncorrected STPD was a significant predictor of MACE (adjusted hazard ratio [aHR]: 3.09; $p = 0.026$). Prognostic performance improved with motion correction (aHR: 3.41; $p = 0.014$), attenuation correction (aHR: 9.06; $p < 0.001$), and combined correction (aHR: 7.46; $p < 0.001$). Among these, the combined correction model demonstrated statistically significant improvement over the uncorrected model ($z = 2.048$; $p = 0.020$). ***Conclusion:*** Respiratory motion and attenuation corrections significantly enhance the prognostic performance of CZT SPECT MPI in patients with INOCA. These corrections may improve risk stratification and support clinical decision-making in this challenging population.

OP-794

Stenosis degree and plaque burden differ between the major epicardial coronary arteries supplying ischemic myocardial territories

***T. Kero**[1], J. Knuuti[2], S. Bär[2], J. J. Bax[3], A. Saraste[2], T. Maaniitty[2];*
[1]Uppsala University, Department of Surgical Sciences/Nuclear Medicine & PET, Uppsala, SWEDEN, [2]University of Turku, Turku, FINLAND, [3]Leiden University Medical Center, Leiden, NETHERLANDS.

Aim/Introduction: There is limited knowledge whether coronary artery luminal narrowing, plaque burden and composition differ between major epicardial coronary arteries supplying ischemic myocardial territories. ***Materials and Methods:*** We evaluated 837 symptomatic patients who underwent both coronary computed tomography angiography (CTA) and ^{15}O-water positron emission tomography (PET) myocardial perfusion imaging for suspected obstructive CAD. Coronary CTA scans were analyzed using Artificial Intelligence-Guided Quantitative Computed Tomography (AI-QCT), with measurements of stenosis degree and parameters of atherosclerotic plaque burden. Presence of myocardial ischemia was defined based on regional PET perfusion in major coronary artery territories (left anterior descending [LAD], left circumflex [LCX], right coronary artery [RCA]). ***Results:*** Among the epicardial coronary arteries supplying ischemic territories the degree of stenosis and absolute and normalized plaque volumes and their components were higher in the LAD as compared to the other main coronary arteries, ($p<0.001$ for all). Many vessels supplying ischemic regions had relatively low stenosis degree and plaque burden, especially in the LCx and RCA vessels. In multivariable logistic regression analyses diameter stenosis ($p=0.001$-0.015), percent atheroma volume ($p<0.001$) and percent non-calcified plaque volume ($p=0.001$-0.017) were associated with myocardial ischemia in all three main coronary arteries whereas percent calcified plaque volume was associated with ischemia only in the RCA ($p=0.001$). ***Conclusion:*** Among the epicardial coronary arteries supplying ischemic myocardial territories, the degree of stenosis and the atherosclerotic burden is significantly higher in the LAD as compared to the LCX and RCA. Many vessels supplying ischemic regions had relatively low stenosis degree and plaque burden. In all the three main coronary arteries both luminal narrowing and plaque burden are independent predictors of ischemia, where the plaque burden is mainly driven by non-calcified plaque.

OP-795

Impact of quantitative CCTA-derived atherosclerotic plaque features on myocardial blood flow assessed by dynamic CZT-SPECT in NOCAD patients

***K. Zavadovsky**, A. Maltseva, R. Dorzhieva, K. Kopeva, A. Dasheeva, A. Mochula, E. Grakova;*
Cardiology Research Institute, Tomsk National Research Medical Center, Russian Academy of Sciences, Tomsk, RUSSIAN FEDERATION.

Aim/Introduction: Nowadays, studies have demonstrated that patients with non-obstructive coronary artery disease (NOCAD) have an increased risk of myocardial infarction and all-cause mortality, particularly due to coronary microvascular dysfunction. Moreover, atherosclerotic plaque features can affect myocardial blood flow (MBF), but currently, data on this are lacking. Therefore, the aim of this study was to assess the impact of quantitative CCTA-derived atherosclerotic plaque features on myocardial perfusion and MBF in NOCAD patients. ***Materials and Methods:*** Based on CCTA results, a total of 49 NOCAD patients (stenosis <50%; 29 men; mean age 57.4±9.0 years) were included in the study. In addition to stenosis severity estimation, plaque volume (mm3) and burden (%): both generally by coronary bed and separately by structural

components (non-calcified, soft-tissue, fibrous, calcified), were measured. All patients underwent dynamic CZT-SPECT with the assessment of stress and rest MBF and myocardial flow reserve (MFR) [1,2]. ***Results:*** Based on the MFR values, patients were divided into two groups: group 1 enrolled patients with reduced MFR <2.0 (n=20), and group 2 enrolled those with normal MFR ≥2.0 (n=29). All NOCAD patients did not have severe myocardial perfusion abnormalities based on standard myocardial perfusion imaging indeces. Analysis of CCTA data demonstrated that NOCAD patients were characterized by small volumes and burdens of atherosclerotic plaques. Stress MBF significantly correlated with total plaque volume (ρ=-0.40) and burden (ρ=-0.37), as well as non-calcified plaque volume (ρ=-0.34) and burden (ρ=-0.31). Rest MBF significantly correlated with total plaque volume (ρ=-0.50) and burden (ρ=-0.43), and non-calcified plaque volume (ρ=-0.47) and burden (ρ=-0.43). Meanwhile, MFR and standard indeces of myocardial perfusion impairment did not show significant associations with quantitative CCTA parameters. According to multivariate logistic regression analysis, only total plaque volume (OR 1.01; CI 1.00-1.02; p=0.009) was an independent predictor of reduced stress MBF less than 1.5 ml/min/g. ***Conclusion:*** Atherosclerotic plaque features derived from quantitative CCTA data were associated with impaired MBF obtained by dynamic CZT-SPECT. Total plaque volume is an independent predictor of reduced stress MBF. ***References:*** 1.Mochula A, et al. The Influence of Kinetic Models and Attenuation Correction on Cadmium-Zinc-Telluride Single-Photon Emission Computed Tomography (CZT SPECT)-Derived Myocardial Blood Flow and Reserve: Correlation with Invasive Angiography Data. J Clin Med. 2024;13(5):1271. DOI: 10.3390/jcm13051271. 2.Zavadovsky KV, et al. Myocardial Blood Flow and Flow Reserve in Patients With Acute Myocardial Infarction and Obstructive and Non-Obstructive Coronary Arteries: CZT SPECT Study. Front Nucl Med. 2022;2:935539. DOI: 10.3389/fnume.2022.935539.

1708

Wednesday, October 8, 2025, 8:00 - 9:30

Room 115

TROP Session - Case Report Session 3: Case-based Learning PET in Oncology

OP-796

Anti-CD8α PET uptake patterns before and during Immune Checkpoint Inhibitor therapy related to irAEs

E. Peeters[1], *E. A. J. van Genugten*[1], *M. R. Ferris*[2], *K. A. Margolin*[3], *C. M. L. van Herpen*[1], *S. Heskamp*[1], *H. Westdorp*[1], *E. H. J. G. Aarntzen*[1,4];
[1]*Radboudumc, Nijmegen, NETHERLANDS,* [2]*ImaginAb, Inglewood, CA, UNITED STATES OF AMERICA,* [3]*Saint John's Cancer Institute, Santa Monica, CA, UNITED STATES OF AMERICA,* [4]*University medical center Groningen, Groningen, NETHERLANDS.*

Aim/Introduction: Immune Checkpoint Inhibitors (ICI) have shown durable responses in patients with solid tumours but can cause serious immune related adverse events (irAEs) with great impact on quality of life. CD8+ lymphocytes are considered as key effectors cells, infiltrating tissues affected by irAEs. Anti-CD8α PET enables visualisation of CD8+ lymphocytes in vivo. This analysis investigates changes in PET-derived CD8+ lymphocyte distribution and uptake in non-tumour tissue upon ICI treatment, including associations with irAEs. ***Materials and Methods:*** Metastatic cancer patients (n=48) enrolled in two prospective multi-center studies underwent PET/CT 24 hours p.i. of a ^{89}Zr-labeled minibody targeting CD8α (1.5 mg protein dose) at baseline and 4-6 weeks after first dose of ICI (anti-PD-1 n = 22, anti-PD-1 and anti CTLA-4 n = 26). Organs of interest were automatically segmented using CT-based segmentation software, known tumour lesions were excluded. Mean standardized uptake values (SUVmean) at baseline and on-treatment were computed. Clinical characteristics including irAEs grade ≥2, were correlated to (changes in) CD8+ lymphocyte distributions. Analyses for expanded cohort (n=98 total) are ongoing and will be presented. ***Results:*** Baseline CD8+ lymphocyte distributions showed large inter-patient variation, depending on age and tumour-type; e.g. SUVmean in morphological normal lymph nodes was lower with increasing age. In contrast to decreasing SUVmean in most organs on the on treatment scan upon anti-PD-1 or combined anti-CTLA-4 and anti-PD-1 treatment, SUVmean values of kidney, blood pool and spleen increased upon combination of anti-PD-1 treatment with chemotherapy or TKIs. For 19/48 patients, at least 1 suspected irAE grade ≥2 was reported during the study. None of the patients with documented irAE involvement showed a decrease in SUVmean in affected organs, although not all showed a strong increase. Interestingly, patients with irAEs had increased liver uptake upon treatment, regardless of direct liver involvement. Automated organ segmentation was affected by respiratory motion and spill-over from high splenic or liver activity, requiring standard correction. ***Conclusion:*** Baseline in vivo distributions of CD8+ lymphocytes in non-tumour tissue as measured by SUVmean in part depend on age and tumour-type. Change upon treatment differed between treatment regimens, which should be considered with anti-CD8α PET interpretation. Quantification of anti-CD8α PET requires adaptations of automated methods, to avoid spill over from organs with high activity. Preliminary analysis suggests that anti-CD8α PET allows non-invasive evaluation of both organ specific and systemic changes in CD8+ lymphocytes distribution related to the development of clinically relevant immune toxicities.

OP-797

Unveiling the diagnostic potential of ^{18}F-FDG PET/CT in evaluation of post-transplant disorders.

B. Mittal*, K. Preet, P. Singh, N. Agrawal, R. Kumar, H. Singh;*
Postgraduate Institute of Medical Education & Research, Chandigarh, INDIA.

Aim/Introduction: Transplant recipients incur a lifelong risk of complications due to continuous immunosuppressive therapy, essential for the prevention of graft rejection. However, this compromises the immune system. Thus, increasing vulnerability to infections and malignancies. Reducing immunosuppression can help treat these issues, but it risks graft rejection. Routine diagnostic methods may be insufficient, and advanced imaging techniques like ^{18}F-FDG PET/CT, which detects metabolic activity in inflammatory and cancerous cells, may offer improved diagnosis and monitoring. In this study, we aimed to evaluate the diagnostic potential of PET/CT in the evaluating post-transplant disorders. ***Materials and Methods:*** This was a retrospective study including patients with a history of renal transplant who underwent ^{18}F-FDG PET/CT scan during 2012-2024. PET/CT images were evaluated by experienced Nuclear Medicine physicians and diagnostic efficiency of PET/CT was evaluated in terms of sensitivity (Sn), specificity (Sp), positive predictive value (PPV), negative predictive value (NPV) & accuracy (Ac). Also, the diagnostic yield of PET/CT was evaluated. HPE/ clinical course was taken as the gold standard. ***Results:*** The study included 116 post-renal transplant patients (92 males, median age 45 years, range: 11-72 years) who underwent ^{18}F-FDG PET/CT scan for evaluation of suspected post-transplant disorders. The median time from the transplant to the development of post-transplant lymphoproliferative disorder (PTLD) was 7 years (range: 1-16 years). Fever was the most common clinical presentation seen in 30 (25.8%) patients, followed by pain in the abdomen seen in 27 patients (23.2%). Other presenting complaints include loss of weight, loss of appetite, diarrhoea etc. The detailed clinical

presentation is given in table 1. PET/CT scan revealed PTLD in 33 (28.4%) patients, infective/ inflammatory aetiology in 42 (36.2%) patients, 11 (9.5%) patients had features suggestive of neoplastic pathologies other than PTLD, while 18F FDG PET/CT was normal in 30 (25.8%) patients. The detailed HPR /clinical follow-up details (gold standard) are given in table 1. Overall PET/CT demonstrated a Sn, Sp, PPV, NPV, Ac of 96.4%, 94.3%, 84.4%, 98.8% & 94.8 % respectively for diagnosis of PTLD while 69.4%, 80%, 60.9%, 85.3% & 76.7% respectively for detection of infection/ inflammation with an overall yield of 74% for evaluation of post-transplant disorders. ***Conclusion:*** 18F-FDG-PET/CT is a valuable diagnostic tool for evaluation of post-renal transplant patients. Due to their lifelong immunosuppression, these patients are at increased risk of malignancy & infection. PET/CT has shown high diagnostic accuracy as well as diagnostic yield for evaluation of post-renal transplant disorders.

OP-798

An Example of Higher Accuracy of [68Ga]Ga-FAPI-46 PET/CT in Staging Lymph Nodes Metastases Compared to [18F]F-FDG PET/CT in a Head and Neck Cancer Patient

E. Fortunati[1], *I. Brusa*[1], *G. Cuzzani*[2], *A. Farolfi*[1], *E. Tabacchi*[1], *L. Calderoni*[1], *D. Dall'Olio*[3], *M. Assenza*[4], *C. Nanni*[1], *P. Castellucci*[1], *R. Mei*[1], *M. Fermi*[5], *G. Siepe*[6], *S. Fanti*[1,2];
[1]*Nuclear Medicine, IRCCS Azienda Ospedaliero-Universitaria di Bologna, Bologna, ITALY,* [2]*Nuclear Medicine, Alma Mater Studiorum University of Bologna, Bologna, ITALY,* [3]*Department of Medical and Surgical Sciences, University of Bologna, Bologna, ITALY,* [4]*Professional Development and Implementation of Research in Health Professional Unit, IRCCS Azienda Ospedaliero-Universitaria di Bologna, Bologna, ITALY,* [5]*Department of Otorhinolaryngology-Head and Neck Surgery, IRCCS Azienda Ospedaliero-Universitaria di Bologna, Bologna, ITALY,* [6]*Radiation Oncology, IRCCS Azienda Ospedaliero-Universitaria di Bologna, Bologna, ITALY.*

Aim/Introduction: A 63y.o. male patient showing squamous cell carcinoma HPV+ of the left amigdaloglossus sulcus. He was an ex-smoker without relevant and known diseases. ceCT described the primary lesion and multiple enlarged left laterocervical lymph-nodes. ***Materials and Methods:*** The patient performed a [18F] F-FDG PET/CT and a subsequent [68Ga]Ga-FAPI-46 PET/CT (6days later) within an ongoing prospective monocentric investigational trial (EudraCT number: 2020-005549-17). [68Ga]Ga-FAPI PET/CT was performed with a 60' dynamic acquisition on LAFOV scanner (uExplorer, United Imaging). The static image was reconstructed with last 5' list mode acquisition. VOIs were manually drawn on suspect lesions. The lesions and references tissues time-to-activity curves (TACs), were fitted using two different graphical models, i.e. Patlak (for irreversible model) and Relative Equilibrium (RE) (for reversible model). Mean absoluted scaled error (MASE) and Akaike Information Criterion (AIC) were utilized to perform model selection for each VOI. ***Results:*** [18F]F-FDG PET/CT and [68Ga]Ga-FAPI-46 PET/CT detected significant uptake (SUVmax=23.1 and 19.5) in the amigdaloglossus lesion. FDG uptake was enhanced in some left laterocervical lymph-nodes at level II (SUVmax=4.8), III and IV (SUVmax=7.2), suspicious for metastases. [68Ga]Ga-FAPI-46 PET/CT was positive only on II level FDG positive nodes, with a very faint uptake in the remaining ones. A subsequent ultrasound-guided-fine-needle-aspiration on lymph nodes of the II, III and IV laterocervical levels showed metastases from SCC only on II level. The reversible RE model was the most appropriate to describe [68Ga]Ga-FAPI-46 pharmacokinetics, and the estimated-distribution volume (DV) resulted higher for primary lesion (meanDV=6.2) and metastatic lymph node of the II laterocervical level (meanDV=4.2) compared to benign lymph nodes of the III and IV levels (meanDV=0.7 and 0.8, respectively). After combined chemotherapy and radiotherapy a further [18F]F-FDG PET/CT was negative in the primary and lymph nodal lesions. ***Conclusion:*** Lymph nodal status in head and neck(H&N) tumours is critical for treatment planning. [68Ga]Ga-FAPI-46 PET/CT has shown higher accuracy in identifying metastatic lymph nodes compared to [18F]F-FDG PET/CT. [68Ga]Ga-FAPI-46 PET/CT could reduce the incidence of false positives, which can lead to unnecessary biopsies and treatments. This case underscores the potential advantages of incorporating [68Ga]Ga-FAPI-46 PET/CT into clinical practice for enhanced accuracy in the staging of lymph nodal metastases in H&N cancers. Dynamic acquisition confirmed the stability of radiopharmaceutical accumulation during the 60 minutes in correspondence of the described lesions. In particular, stability was observed in correspondence of the non-metastatic lymph nodes, which did not show peaks of accumulation.

OP-799

Seeing beyond ^{68}Ga DOTANOC and ^{18}F FDG PET/CT : ^{68}Ga FAPI only uptake in a rare metastatic well differentiated grade I pancreatic neuroendocrine tumor

C. Singareddy, *A. Baa, S. Kankara, M. Bukelo;*
St.Johns's Medical college Hospital, Bengaluru, INDIA.

Aim/Introduction: Nuclear medicine imaging has been increasingly employed in recent years in staging of neuroendocrine tumors (NETs) and guiding management. Somatostatin receptor (SSTR) agonists like Gallium-68 (^{68}Ga) DOTANOC target SSTR expressed by well-differentiated NET. The tracer uptake is higher in well-differentiated NETs compared to poorly-differentiated NETs, and correlates strongly with $SSTR_{2A}$ receptor expression. Fluorine-18 (^{18}F) deoxy-glucose (FDG) PET avidity, on the other hand, reflects increased tumour metabolic activity and is more likely to be positive with increasing histological grade. We present a rare case of Grade I metastatic pancreatic NET with no significant tracer avidity on SSTR/FDG PET-CT; however, showing intense positive lesions on ^{68}Ga FAPI PET-CT. ***Materials and Methods:*** A 35-year-old woman presented to our hospital with complaints of abdominal pain, easy fatiguability, diarrhoea, loss of weight and loss of appetite, 6 months ago. USG and CT abdomen showed multiple space occupying lesions in liver. Liver core biopsy shows foci of metastatic tumour with immunoprofile features consistent with a neuroendocrine tumour with a Ki67 proliferative index of 1-2%. (The neoplastic cells are positive for CK, Synaptophysin (3+, >90%), Chromogranin (2+, >90%) and CD56 (1+,>90%) and negative for LCA and CD99). ***Results:*** ^{68}Ga DOTANOC PET-CT done for initial staging showed no significant SSTR expression in liver lesions or elsewhere in the body. ^{18}F FDG PET-CT was done to rule out poorly differentiated transformation, which also showed no significant FDG avid lesions. Patient was started on injection octreotide LAR 30mg monthly once, but showed no signs of clinical improvement with persistent diarrhea (~ 4-5 episodes/day). ^{177}Lu DOTATATE therapy was not considered in view of absence of tracer avidity on ^{68}Ga DOTANOC PET-CT. After a multidisciplinary tumour board discussion, ^{68}Ga FAPI PET-CT was suggested in theranostic point of view. ^{68}Ga FAPI-04 PET CT showed intense tracer avid enhancing soft tissue density lesion in uncinate process of pancreas measuring 2.7 x 2.2 cm with SUVmax 14.5, along with few subcentimetric mild tracer avid periportal lymph nodes and multiple hypoenhancing lesions in both lobes of liver, largest measuring 4.0 x 3.8 cm with SUVmax 17.8 in segment IV. The patient is now being planned for ^{177}Lu FAPI therapy. ***Conclusion:*** Literature search revealed few NET cases showing FAP expression with discordant SSTR/FDG PET-CT findings. To the best of our knowledge, this is the first NET case negative on both SSTR and FDG PET-CT, but illuminating on ^{68}Ga FAPI PET-CT.

OP-800

Lack of FES Avidity in FDG-Positive ER-Positive Breast Cancer: A Case Indicating Non-Functional Estrogen Receptors in a Treatment-Naive Patient

A. Mahalik, *N. Kundu, A. Roy, K. Jain, M. Tripathi, R. Kumar;*
All India Institute of Medical Sciences, New Delhi, INDIA.

Aim/Introduction: 18F-FES PET/CT is a molecular imaging modality that non-invasively assesses estrogen receptor (ER) expression in vivo. While ER positivity on histopathology typically corresponds with FES avidity, discordance may reflect tumor heterogeneity or receptor downregulation. This case challenges the assumption of consistent ER expression throughout the disease burden, even at baseline. ***Materials and Methods:*** A 57-year-old female diagnosed with ER-positive invasive ductal carcinoma of the right breast underwent staging workup. Baseline ^{18}F-FDG PET/CT revealed intense metabolic activity in the right breast primary lesion and right axillary lymph nodes. However, corresponding 18F-FES PET/CT performed within a short interval did not demonstrate any significant tracer uptake in these sites, despite confirmed ER positivity on biopsy, suggesting a discrepancy between receptor expression and receptor functionality. ***Results:*** The absence of FES uptake in known FDG-avid, biopsy-confirmed ER-positive primary and nodal lesions raises critical questions about receptor functionality. This suggests either non-functional or inaccessible estrogen receptors despite positive immunohistochemistry. Possible contributing factors include receptor internalization, post-translational modifications, or alterations in receptor co-factor expression. Such cases underline the importance of functional imaging to complement static receptor expression data and help refine therapeutic decisions, especially when endocrine therapy is considered. ***Conclusion:*** This case demonstrates clinically significant discordance between FDG and FES PET/CT in ER-positive breast cancer, highlighting the gap between receptor presence and functional activity. The absence of FES uptake in both the breast and axillary nodes, despite FDG avidity and biopsy-confirmed ER positivity, underscores the potential for non-functional ER expression. Receptor functionality assessment through molecular imaging may better predict endocrine responsiveness than histology alone.

OP-801

Detection of Insulinoma Using 68Ga-NODAGA-Exendin-4 PET/CT: A Report of Two Cases

A. Guercio[1], *T. Graziani*[1], *M. Scarlattei*[1], *S. Migliari*[1], *C. Cidda*[1], *G. Baldari*[1], *V. Cervati*[1], *A. Gagliardi*[1], *A. Dei Cas*[2], *R. Bonadonna*[3], *L. Ruffini*[1];
[1]*Nuclear Medicine Division, University Hospital of Parma, Parma, ITALY,* [2]*Laboratory of Endocrinology, Diabetes and Metabolic Diseases, Department of Medicine and Surgery, University of Parma, Parma, ITALY,* [3]*Endocrinology Division, Diabetes and Metabolic Diseases, Department of Medicine and Surgery, University of Verona, Verona, ITALY.*

Aim/Introduction: Insulinomas are rare pancreatic neuroendocrine tumors that inappropriately secrete insulin, causing recurrent hypoglycemia. Diagnosis relies on biochemical confirmation and accurate lesion localisation via contrast-enhanced CT, MRI, and endoscopic ultrasound [1]. Recently, 68Ga-NODAGA-Exendin-4 PET/CT has emerged as a promising molecular imaging technique for insulinoma detection, targeting glucagon-like peptide-1 receptor (GLP-1R), overexpressed in these tumors [2]. The synthesis of 68Ga-NODAGA-Exendin-4 has been validated at our center [3], supporting its clinical use. This report illustrates the diagnostic value of 68Ga-NODAGA-Exendin-4 PET/CT in two insulinoma patients. ***Materials and Methods:*** The radiotracer was synthesized in-house using an automated module and a GMP-certified 68Ge/68Ga generator. Whole-body PET/CT images were acquired 60 minutes after i.v. tracer injection (from skull basis to pelvis). Tracer uptake was quantitatively assessed using SUVmetrics across defined pancreatic volumes of interest and in splenic tissue as background, being the spleen a non-binding site for 68Ga-NODAGA-Exendin-4 [4]. Tumor-to-background ratio (TBR) was also calculated. ***Results:*** Case 1: A 77-year-old man presented with symptomatic hypoglycemia and a nodular lesion in the pancreatic head detected on CT. Initial imaging with 68Ga-DOTATOC PET/CT showed small focal uptake in the pancreatic head. 68Ga-NODAGA-Exendin-4 PET/CT revealed a lesion highly expressing GLP-1R in the same area (SUVmax 27.70; SUVmean 20.07; TBRmean 32.37). Histopathology confirmed a well-differentiated G1 insulinoma. 68Ga-NODAGA-Exendin-4 radiosynthesis: 56.9% radiochemical yield (RCY%), 97.6% and 100.0% radiochemical purity (RCP%) by HPLC and TLC, respectively. Mean peptide amount was 3.77 µg in a 150 MBq dose. Case 2: an 88-year-old diabetic patient with hypoglycemia showed a CT-positive vascularized lesion (13 mm) in the pancreatic tail. 68Ga-NODAGA-Exendin-4 PET/CT confirmed high uptake in the lesion (SUVmax 17.47; SUVmean 14.31; TBRmean 14.17). Unfortunately, further diagnostic or therapeutic interventions were not possible, as the patient passed away shortly after the scan due to cardiovascular complications. Radiosynthesis: RCY% 52.0%, RCP% 97.6% (HPLC), 100.0% (TLC). The injected dose (100 MBq) contained 1.55 µg of peptide. ***Conclusion:*** PET/CT with 68Ga-NODAGA-Exendin-4 demonstrated high sensitivity in detecting insulinomas in both cases, due to its capacity to specifically target GLP-1R. Its ability to provide precise localization, even in challenging anatomical contexts, supports its use as a valuable diagnostic tool. ***References:*** 1) Christ E, et al. Endocr Relat Cancer. 2020 Apr;27(4):R79-R92. doi: 10.1530/ERC-19-0476. 2) Boss M, et al. J Nucl Med. 2024 Dec 3;65(12):1959-1964. doi: 10.2967/jnumed.124.268158. 3) Migliari S, et al. Curr Radiopharm. 2022;15(1):63-75. doi: 10.2174/1874471014666210309151930. 4) Guo W, et al. Eur J Nucl Med Mol Imaging. 2023 Jul;50(9):2910-2911. doi: 10.1007/s00259-023-06182-8.

OP-802

A Weighty Problem: GLP-1 Agonists and the Altered Images of FDG PET-CT

P. Strouhal, *A. Meadows, A. McGovern;*
Alliance Medical Ltd, Warwick, UNITED KINGDOM.

Aim/Introduction: GLP-1 receptor agonists - such as Semaglutide - are increasingly prescribed for type 2 diabetes and obesity, with reported 700% increased use in USA. These agents affect glucose metabolism, gastric motility and sympathetic tone, raising concerns about altered ^{18}F-FDG biodistribution on PET-CT. Case reports describe increased uptake in skeletal muscle, myocardium, and brown adipose tissue (BAT), mimicking malignancy or inflammation. Our case series highlights implications for scan interpretation and patient preparation. ***Materials and Methods:*** Retrospective review of oncological FDG PET-CT scans from patients on GLP-1 agonists. Scan findings compared with expected physiological uptake and evaluated alongside current literature. Attention focused on interpretative difficulties likely to influence clinical decisions. ***Results:*** Several cases showed atypical tracer uptake in sites of possible pathology, underscoring diagnostic pitfalls (pics included). These observations aligned with published data and reinforced the need for clinical context and medication history during interpretation. ***Conclusion:*** GLP-1 receptor agonists pose an increasing challenge in FDG PET-CT scanning. Current UK guidelines (EANM/BNMS) do not address this yet, though Australian guidance recommends continuing treatment, fasting from midnight, scheduling morning scans, and ensuring good glucose control. A consensus view needs adopting in UK practice to reduce false positives and improve diagnostic confidence. Awareness among imaging teams is essential, and national guidance should be developed to standardise approaches amid growing GLP-1 agonist use. ***References:*** 1. The BMJ. Semaglutide:

What are the side effects of the weight loss drug? 2024;386:q1645. 2. Sittampalam, S., Stokoe, J., & Bradley, K. M. (2024). Semaglutide: A novel cause of increased muscular and myocardial FDG uptake on PET/CT imaging. Clinical Nuclear Medicine, 49(1), e24-e25. https://doi.org/10.1097/RLU.0000000000004716 3. Jiang, H., Shao, X., Li, X., et al. (2023). GLP-1 receptor agonists and brown adipose tissue activation: Evidence from FDG PET imaging studies. Diabetes, Obesity and Metabolism, 25(6), 1625-1633. https://doi.org/10.1111/dom.15142 4. Laing, K. J., & Perera, T. (2024). Brown adipose tissue FDG uptake secondary to semaglutide use mimicking metastatic head and neck cancer. Clinical Nuclear Medicine, 49(4), e180-e181. https://doi.org/10.1097/RLU.0000000000004792 5. Kong, X., Liang, W., & Zhao, Y. (2023). Effect of GLP-1 receptor agonists on myocardial glucose metabolism: A PET imaging perspective. European Journal of Nuclear Medicine and Molecular Imaging, 50(3), 748-756. https://doi.org/10.1007/s00259-022-06000-1 6. Australian Diabetes Society & ANZSNM. Joint Statement on GLP-1 Receptor Agonists and PET Imaging. 2023.

OP-803

Efficacy of short acting and ultra-short acting insulin in improving image quality of ^{18}F-FDG PET in diabetic cancer patients.

S. Saeed[1], *M. Nadeem*[2], *S. Hanan*[3], *M. Younis*[4], *S. Saeed*[5]; *[1]Punjab Institute of Cardiology, Lahore, PAKISTAN, [2]Al Nasar Lab & Diagnostic Center, Lahore, PAKISTAN, [3]NUR International University, Lahore, PAKISTAN, [4]Doctors Hospital and Medical Center, Lahore, PAKISTAN, [5]Fatima Memorial College of Medicine and Dentistry, Lahore, PAKISTAN.*

Aim/Introduction: Aims: To evaluate and compare the effectiveness of Ultra-short versus Short acting insulin on normalization of blood glucose levels in diabetic patients presenting for ^{18}F-FDG PET-CT, their effects on image quality and SUV_{mean} values. Introduction: Diabetes and cancer are two heterogeneous, multifactorial, severe, and chronic diseases. Diabetes increases the risk of various cancers, including pancreatic, liver, breast, and colorectal cancer. ^{18}F-FDG PET imaging is a noninvasive diagnostic tool that can be used to acquire quantitative parameters concerning the metabolic activity of target tissues. ***Materials and Methods:*** A triple arm prospective interventional study was conducted, constituting of 45 subjects equally divided into three groups of 15 subjects in each. Group A included diabetics injected with ultra short acting insulin, Group B included diabetics injected with regular/short acting insulin when patients showed high blood glucose levels > 180 mg/dL (10 mmol/L) and Group C included non-diabetics.^{18}F-FDG was injected as blood glucose levels lowered down to acceptable range (cutoff 180 mg/dL), and images were acquired. Blood glucose levels normalization after insulin administration, visual scoring and SUV_{mean} of anterior liver and thigh muscles were assessed to compare the effectiveness of ultra-short versus short acting insulin. ***Results:*** The basal blood glucose level in group A and B was not significantly different (236.1 ± 25.4, 242.2 ± 26.7, P= 0.52). However, after insulin administration the blood glucose levels of group A patients were lowered down to acceptable range earlier than group B (27.00 ± 11.6 min vs. 51.00 ± 7.6 min, P= 0.0000). Nevertheless, the image quality was not significantly different between group A-B, A-C, B-C (Mann-Whitney U test, P = 0.84, 0.52, 0.36 respectively). No significant differences were seen in between group A-B, A-C and B-C SUV_{mean} in the liver (P = 0.11, 0.75, 0.07 respectively), and anterior thigh muscle (P =0.18, 0.07, 0.46 respectively), between groups. ***Conclusion:*** Intravenous ultra-short acting insulin can successfully be used to lower down blood glucose levels to acceptable range in shorter time and with comparable effects on ^{18}F-FDG bio-distribution in terms of image quality and mean standardized uptake value (SUV_{mean}) as compared to short acting insulin in most cancer patients undergoing an ^{18}F-FDG PET examination with least chances of being hypoglycemic.

OP-804

Multimodality Imaging in the Assessment of Liver-Directed Therapy Response in Prostate Cancer: A Case Demonstrating False Positive PSMA Uptake

Y. Eryilmaz, *O. Kodaz, G. Kaya, B. Volkan Salancı, M. Tuncel; Hacettepe University Medical School Department of Nuclear Medicine, Ankara, TÜRKIYE.*

Aim/Introduction: Ga-68 PSMA PET/CT is highly sensitive for detecting prostate cancer (PCa) metastases, but post-treatment interpretation can be challenging due to potential false positives. This case demonstrates how FDG PET/CT and liver-dedicated MRI can clarify equivocal PSMA findings following microwave ablation (MWA) of liver metastasis, highlighting a diagnostic pitfall in PSMA PET/CT. ***Materials and Methods:*** A 63-year-old male with high-risk PCa and a biopsy-proven liver metastasis underwent MWA of the metastatic lesion in the liver. Six months post-ablation, he presented with rising PSA levels. PSMA PET/CT was performed for restaging. Due to equivocal PSMA PET/CT findings, FDG PET/CT and liver-MRI were performed for further evaluation. Follow-up included all three imaging modalities. ***Results:*** Ga-68 PSMA PET/CT initially demonstrated faint uptake in a new lesion located in segment-IV (near the porta hepatis) and persistent uptake in the previously ablated segment-VI site, raising suspicion of recurrent or residual disease. Due to the low PSMA avidity of the segment-IV lesion, FDG PET/CT was performed. It revealed intense FDG uptake (SUVmax 9.5) in the segment-IV lesion, suggesting viable tumor with possible neuroendocrine differentiation. No FDG uptake was noted in the previously treated segment-VI lesion. Liver-MRI confirmed the presence of a new lesion in segment-IV and complete ablation of the segment-VI metastasis. The segment-IV lesion was subsequently treated with MWA, and androgen receptor pathway inhibitor therapy was added to the systemic treatment. Follow-up imaging with PSMA PET/CT, FDG PET/CT, and liver-MRI was performed to assess treatment response. MRI and FDG PET/CT showed no sign of residual tumor in the liver. PSMA PET/CT showed no increased uptake in segment-IV; however, it demonstrated persistent uptake in the previously ablated segment-VI lesion, with no corresponding FDG uptake or suspicious MRI findings. PSA levels gradually declined, with no biochemical recurrence observed over the last eleven months, supporting the interpretation of persistent PSMA uptake as a post-ablation effect rather than active disease. ***Conclusion:*** This case demonstrates the potential for false-positive PSMA uptake at prior ablation sites due to post-treatment histopathological changes such as neovascularization. MRI is the preferred modality for evaluating liver-directed therapy response, while FDG PET/CT provides valuable insight into tumor heterogeneity. The combined use of PSMA PET/CT, FDG PET/CT, and liver-MRI enhances diagnostic clarity and supports more accurate clinical decisions in challenging prostate cancer cases. To our knowledge, this is the first case reporting PSMA uptake secondary to post-ablation changes in liver metastases from prostate cancer.

1709

Wednesday, October 8, 2025, 8:00 - 9:30
Room 133+134

e-Poster Presentations Session 13 - Bone & Joint Committee: Bone & Joint e-Poster Presentations Session

EPS-264

Head-to-head comparison of bone scintigraphy metastasis detection provided by a high-speed whole-body 360° CZT-SPECT and a currently recommended Anger camera protocol

A. Bahloul, *M. Perrin, A. Verger, S. Ouguirti, V. Roch, P. Marie, L. Imbert;*
CHU de Nancy, Vandoeuvre Les Nancy, FRANCE.

Aim/Introduction: Bone scintigraphy recording time may be dramatically decreased with whole-body high-speed 360° CZT-SPECT (Fast-CZT), as compared with the Anger camera bone scintigraphy protocols recommended for cancer patients (Reco-Anger). However, it remains unknown how Fast-CZT results compare with Reco-Anger ones. The OSS prospective study aimed to provide a head-to-head comparison of bone scintigraphy results provided by Fast-CZT and Reco-Anger in the same cancer patients. ***Materials and Methods:*** We selected 133 patients with history of cancer (breast: 76, prostate: 47, other: 10) who were referred to bone scintigraphy for the detection or survey of bone metastasis. Three to 4 hours after 569 ± 41 MBq [^{99m}Tc]Tc-HDP injection, they underwent consecutively and in a random order (i) an 18 min single whole-body Fast-CZT SPECT recording preceded by a whole-body low-dose CT, and (ii) a 30 to 60 min Reco-Anger protocol with whole-body planar followed by one to three SPECT/CT recordings. Fast-CZT and Reco-Anger images were analyzed separately at least one month apart through a consensus of three blinded experienced observers and assigned a grading known to impact further medical management -i.e., no bone metastasis, oligometastases (≤ 5), or polymetastases (> 5). ***Results:*** There were 81 women and 52 men with mean age of 67 ± 10 years, and mean body mass index of 27.3 ± 5.7 kg.m^{-2}. Inter-observer agreements in the 3-group classification were high for both Reco-Anger (87.0%) and Fast-CZT (88.5%) analyses. Per-patient rates were not significantly different between Reco-Anger and Fast-CZT for the detection of one or more bone metastases (37.6% (50/133) vs. 33.8% (45/133), p=0.23) or a polymetastatic stage (18.0% (24/133) vs. 16.5% (22/133), p=0.50). Furthermore, there was strong agreement between the 3-group classification achieved by the two cameras, given a Cohen's kappa score of 0.813 ± 0.045 and a global agreement rate of 90.2%. The classifications by camera were different in only 13 cases (9.8%), with a higher metastasis grading from the Reco-Anger in 10 cases and from Fast-CZT in 3. ***Conclusion:*** The detection of bone metastasis by whole-body high-speed bone 360° CZT-SPECT compares well with that provided by a recommended Anger camera protocol with (i) a global agreement rate that is in the range of the interobserver agreements observed for the analyses of Fast-CZT or Reco-Anger but (ii) a dramatic decrease in recording time, a property that is beneficial for patient comfort and throughput.

EPS-265

Potential of 68Ga-FAPI-46 PET/CT in patients with primary bone and soft tissue sarcoma: head-to-head comparison with ^{18}F-FDG PET/CT

E. Davydova[1], *M. Komarova*[1], *A. Chaban*[2], *A. Pronin*[1], *A. Martinovich*[1], *O. Ryzhova*[1], *I. Amosova*[1];
[1]*N.N Blokhin National Medical Research Center of Oncology of the Russian Ministry of Health, Moscow, RUSSIAN FEDERATION,* [2]*Klinikum Rechts der Isar, Technical University of Munich, Munich, GERMANY.*

Aim/Introduction: to evaluate the role of 68Ga-FAPI PET/CT in patients with primary bone and soft tissue sarcoma, compared with ^{18}F-FDG PET/CT. ***Materials and Methods:*** the study included 24 patients (13 females and 11 males; median age, 44 years) with 15 subtypes of primary bone and soft tissue sarcoma. All individuals underwent both ^{18}F-FDG and 68Ga-FAPI PET/CT examination within 1 week for assessment of primary tumor or distant metastasis. Positive lesions on PET/CT were histologically verified or confirmed with 3-month follow-up. Wilcoxon matched-pairs signed-rank test was used to compare the semiquantitative values (SUVmax and TBR) of ^{18}F-FDG and 68Ga-FAPI PET/CT in tumor lesions. ***Results:*** 119 tumor lesions (primary tumor, lymph nodes, bone, lung and other distance metastasis) were identified. 68Ga-FAPI PET/CT demonstrated significantly higher values of SUVmax and TBR than ^{18}F-FDG in liposarcoma, malignant solitary fibrous tumor, desmoid fibromatosis and fibrosarcoma: 36,67 [9,26-48,64] vs 4,28 [2,56-9,34] and 24,16 [7,43-25,47] vs 1,6[0,96-4,66] respectively, p =0,0039. However in some subtypes there was favorable uptake of ^{18}F-FDG over 68Ga-FAPI (synovial sarcoma, pleomorphic sarcoma, leiomyosarcoma, intimal sarcoma): SUVmax were 8,66 [7,17-14,4] vs 4,91 [3,5-7,34], p =0,0317; TBR were 7,65 [4,15-13,87] vs 2,5 [1,87-`2,87], p=0,0159. There was no significant difference between SUVmax and TBR in other subtypes of bone and soft tissue sarcoma. The total sensitivity specificity and accuracy in the detection of all tumor lesions using 68Ga-FAPI were 66%, 73,68% and 67,23 % resp. and ^{18}F-FDG were 76,6%, 29,17 % and 66,95% resp. ***Conclusion:*** 68Ga-FAPI PET/CT outperforms ^{18}F-FDG in identifying lesions of liposarcoma, malignant solitary fibrous tumor, desmoid fibromatosis and fibrosarcoma. In other subtypes of sarcomas, the 68Ga- FAPI PET/CT has the same or less performance compared with 18F-FDG.

EPS-266

Baseline Bone Marrow Scintigraphy as Predictive Marker of Outcomes in mCRPC Patients Treated with Radium-223 Dichloride

Q. Shagera, *O. Gheysens, E. Jonard, E. Seront, B. Tombal, F. Jamar; Cliniques univérsitaires Saint-Luc, UClouvain, Brussels, BELGIUM.*

Aim/Introduction: We aimed to assess the value of baseline Bone Marrow Scintigraphy (BMS) in predicting overall survival (OS) in patients with mCRPC treated with Ra-223 dichloride. ***Materials and Methods:*** Among 82 patients treated with radium-223 (Ra-223) between 2014 and 2024, 28 underwent BMS on the same day as the first Ra-223 dose, were included. Whole body planar imaging was conducted 30-60 minutes after injection of ~ 7.5 mCi of (Tc-99m)-labeled nanocolloids using a dual-head gamma camera. Visual image analysis was performed and defined as follows: a score of 0 indicated normal biodistribution, score 1 denoted mild expansion (discrete uptake outside regions of normal distribution), and score 2 represented moderate to extensive medullary expansion exemplified by uptake at the distal half of femoral and/or humeral diaphyses or more distally. Patients were subsequently dichotomized as those with scores of 0+1 versus 2. A t-test comparing the mean was conducted to assess the relationship between BMS status and baseline hemoglobin (Hb) levels. Cox proportional hazards regression and Kaplan-Meier survival analysis were performed to evaluate the relationship between BMS status and the clinical variables and patient outcomes. ***Results:*** A total of 130 doses of Ra-223 were administered, with a median of 6 cycles (IQR 3-6). Baseline BMS status was significantly associated with baseline Hb levels: patients with normal BMS had a significantly higher mean Hb (13.2±1.2 g/dL) compared to those with bone marrow (BM) expansion (10.8 ± 1.7 g/dL, p<0.001). The median number of Ra-223 cycles in patients with BM expansion was lower than in those with normal BMS (3 vs. 6, p=0.08). Medullary expansion status was significantly associated with the number of prior systemic therapies (p=0.032)

and salvage or metastatic targeted radiotherapy (p=0.01). Median OS was 18 months, with 16/28 (57%) patients dead. BMS status, hemoglobin, number of prior systemic therapies, and number of Ra-223 cycles were significantly associated with OS (hazard ratios and p-values: 3.3, p=0.02; 0.75, p=0.042; 1.6, p=0.019; 0.6, p=0.002; respectively). Patients with normal BMS had a median OS of 33 months compared to 8 months in those with BM expansion (log-rank 5.5, p=0.019). ***Conclusion:*** The study findings demonstrate the association between BMS status and patient OS. Patients with BM expansion have worse outcomes compared to those with normal BMS. The study findings also showed a correlation between the BM expansion status and baseline clinical factors in mCRPC patients treated with Ra-223.

EPS-267

Unspecific Bone Uptake on PSMA PET/CT in Prostate Cancer: Distinguishing Early Metastases from Benign Findings

N. Vasconcelos, *D. Barbosa, D. Silva, R. Marão, J. Teixeira, I. Lucena Sampaio;*
Instituto Português de Oncologia, Porto, PORTUGAL.

Aim/Introduction: Detection of focal unspecific bone uptake (UBU) on prostate-specific membrane antigen (PSMA) PET/CT scans of prostate cancer (PCa) patients poses a diagnostic challenge. These findings may represent early metastatic disease or benign processes. Their correct interpretation is critical to guide management. This study aimed to characterize UBUs detected on PSMA PET/CT and to evaluate clinical and imaging predictors of malignancy. ***Materials and Methods:*** Retrospective analysis of [^{68}Ga]Ga-PSMA-11 PET/CT scans (January 2017-December 2024) in patients with histologically confirmed PCa presenting with UBUs, in the absence of other bone metastases (n = 107). Assessed clinical variables included age, Prostate Specific Antigen (PSA) levels, ISUP (International Society of Urological Pathology) grade, PET/CT indication, and nodal status (N1 and M1a). Imaging variables included maximum standardized uptake value (SUVmax), lesion location, and CT morphological correlation. Lesion outcomes were determined by clinical follow-up, PSA kinetics, subsequent imaging, or histological confirmation when available. Univariate logistic regression was initially performed to identify variables associated with malignancy, followed by multivariate logistic regression to determine independent predictors among the significant factors. ***Results:*** Among the 107 UBUs analysed, the most frequently involved anatomical sites were the ribs (48.6%) and pelvic bones (32.7%). Based on follow-up, 63 lesions (58.9%) were classified as benign, 17 (15.9%) as malignant, and 27 (25.2%) remained indeterminate. Among the 80 UBUs with definitive outcome, SUVmax (p = 0.004), presence of regional (N1) and distant (M1a) lymph node metastasis (p = 0.005 and p=0.029, respectively) were significantly associated with malignancy in univariate analysis. Multivariate logistic regression identified both SUVmax (Odds Ratio [OR] 1.63, 95% confidence interval [95% CI] 1.08-2.46, p = 0.020) and N1 positivity (OR 7.03, 95% CI 1.87-26.52, p = 0.004) as independent predictors of malignancy. The model demonstrated good discriminative ability (Area Under the curve [AUC] 0.76). The optimal SUVmax cutoff to predict malignancy was 3.54, yielding 64.7% sensitivity and 79.4% specificity. ***Conclusion:*** In this review, 15.9% of UBUs were confirmed as metastatic. SUVmax (cutoff value of 3.54) and N1 status were independent predictors of malignancy, emphasizing the value of integrating semi-quantitative metrics and nodal assessment to improve diagnostic accuracy in indeterminate bone lesions.

EPS-268

Targeting SSTR2 in Monitoring Skeletal Stem Cells and Osteosarcoma via [^{18}F]-Octreotide PET-CT

Z. Li, *X. Su;*
First Affiliated Hospital of Zhejiang University, School of Medicine, Zhejiang University, Hangzhou, CHINA.

Aim/Introduction: Skeletal stem cells (SSCs) serve as progenitors of osteogenic cells and regulate skeletal development, injury repair, and pathological processes including neoplasia such as osteosarcoma[1,2]. While conventional skeletal imaging modalities assess structural morphology, they fail to capture cellular-level alterations critical for SSC-related disorders such as osteosarcoma. Given the reported expression of somatostatin receptor 2 (SSTR2) in SSCs[3], we aimed to investigate SSC dynamics and associated malignancies, using ^{18}F-labeled Octreotide. ***Materials and Methods:*** Publicly available single-cell RNA sequencing (scRNA-seq) datasets (GSE205945) were analyzed to evaluate colocalization of SSTR2 with established SSC markers. Retrospective analysis included 6 patients undergoing [^{18}F]-octreotide PET-CT: three pediatric cases (<10 years) with suspected neuroendocrine neoplasms (NENs) yielding negative diagnoses, and three adults (>30 years) with surgically treated NENs in complete remission. One biopsy-confirmed osteosarcoma patient underwent prospective [^{18}F]-octreotide PET-CT. Immunohistochemistry (IHC) validated SSTR2 expression in tumor specimens. ***Results:*** scRNA-seq revealed SSTR2 predominance in SSC subsets co-expressing Itgav and CD200, with upregulated SSTR2 during SSC expansion in fracture repair. Pediatric patients exhibited distinct [^{18}F]-octreotide uptake in metaphyseal regions (mean SUVmax 4.0±1.1), correlating with SSC-rich zones, while adults showed background-level skeletal signals (SUVmax 0.1±0.0). Osteosarcoma lesions demonstrated elevated tracer uptake (SUVmax 7.2), supported by scRNA-seq showing SSTR2 co-expression with SSC markers in malignant cells. IHC confirmed ubiquitous SSTR2 expression in osteosarcoma. ***Conclusion:*** [^{18}F]-octreotide PET-CT enables non-invasive SSC monitoring and shows diagnostic potential for osteosarcoma by targeting SSTR2. ***References:*** [1]Yuan G, Lin X, Liu Y, Greenblatt M B, Xu R. Skeletal stem cells in bone development, homeostasis, and disease.[J]. Protein & cell, 2024Germany: , 15(8): 559-574.[2]Sosa B R, Wang Z, Healey J H, Hameed M, Greenblatt M B. A Subset of Osteosarcoma Bears Markers of CXCL12-Abundant Reticular Cells.[J]. JBMR plus, 2022: , 6(3): e10596.[3]Yang G, He Q, Guo X, Li R-Y, Lin J, Lang Y, Tao W, Liu W, Lin H, Xing S, Qi Y, Xie Z, Han J-D J, Zhou B, Teng Y, Yang X. Identification of the metaphyseal skeletal stem cell building trabecular bone.[J]. Science advances, 2024: , 10(8): eadl2238.

EPS-269

Use of ^{18}F-FDG PET-CT in pediatric Rhabdomyosarcoma:can progression be predicted?

S. Iaria[1], *C. Caldarella*[2], *L. Leccisotti*[1,2];
[1]*Università Cattolica del Sacro Cuore, Rome, ITALY,* [2]*Fondazione Policlinico Universitario Agostino Gemelli IRCCS, Rome, ITALY.*

Aim/Introduction: Rhabdomyosarcoma is a rare, aggressive mesenchymal malignancy that originates from skeletal muscle cells. It may also occur in the pediatric age. Metastases usually arise in lung (parenchyma and pleura), bones and lymph nodes, and may be present at diagnosis or occur during post-treatment follow-up. Nuclear medicine imaging, especially using ^{18}F-FDG PET-CT, is helpful in these patients' management for staging and therapy evaluation, and may aid in prognosis stratification. Aim of this study is to evaluate whether semi-quantitative parameters expression of ^{18}F-FDG uptake in the primary lesion may predict progression in pediatric patients with rhabdomyosarcoma. ***Materials and Methods:*** In this monocentric retrospective study, we collected data about ^{18}F-FDG PET-CT scans performed from

2011 to January 2024 in patients with rhabdomyosarcoma who were < 18 years old at the time of diagnosis. Particularly, scans were included only when the primary lesion was evident and with increased ^{18}F-FDG uptake (patients excluded in case primary lesion was surgically removed). Information on possible previous therapy (chemo- or radiotherapy), tumor histology and patients' death or loss to follow-up was also collected. SUVmax, SUVmean, SUVpeak, MTV and TLG of the primary lesion were obtained by a semi-automatic 40% threshold contouring. Disease progression (either appearance of new lesions or increase in uptake of already known ones) was noticed. ***Results:*** 28 pediatric patients (age range 2-17) were included in the study: 11 of them had signs of progressive disease (PD), and 17 had no evidence of progressive disease (NPD). Patients with PD were slightly older than ones with NPD (median 16 y.o., IQR 15-17 vs median 11 y.o., IQR 8-14). Moreover, although SUVmax, SUVmean and SUVpeak did not differ significantly between these two cohorts of patients, MTV was higher in PD than in NPD (median 35 cm^3; IQR 21.46-85.57 vs median 12 cm^3; IQR 2.71-17.43; p=0.001); TLG was also higher in in PD than in NPD patients (median 137.84 SUV x cm^3; IQR 57.12-421.29 vs median 33.52 SUV x cm^3; IQR 15.17-82.8; p=0.006). ***Conclusion:*** Higher MTV and TLG are associated to a higher risk of disease progression in pediatric patients with rhabdomyosarcoma, therefore inferring an invaluable role of PET-CT in the management of this serious condition and confirming the superior role of volume-based parameters for prognosis prediction.

EPS-270

Diagnostic Potential of ^{68}Ga-FAPI-46 PET/CT in the Evaluation of Metastatic Soft Tissue Sarcomas: A Comparative Analysis with ^{18}F-FDG PET/CT

S. Shamim*, Y. Khandelwal, B. Jain, S. Rastogi;*
AIIMS New Delhi, Delhi, INDIA.

Aim/Introduction: Fibroblast activation protein (FAP), a serine protease, is highly expressed on cancer-associated fibroblasts (CAFs) and certain tumor cells, including those of soft tissue sarcomas (STS). While ^{18}F-fluorodeoxyglucose (^{18}F-FDG) PET/CT remains the conventional imaging modality for staging, restaging, therapy assessment, and prognostication in metastatic STS, its diagnostic sensitivity is limited in specific histologic subtypes, particularly low-grade tumors. This study prospectively assesses the diagnostic performance of ^{68}Ga-labeled FAP inhibitor (^{68}Ga-FAPI-46) PET/CT in metastatic STS and benchmarks it against ^{18}F-FDG PET/CT. ***Materials and Methods:*** In this prospective investigation conducted at a tertiary care center, 25 patients (11 females, 14 males; median age 35 years, range 16-68) with histologically confirmed metastatic STS underwent both ^{18}F-FDG and ^{68}Ga-FAPI-46 PET/CT imaging within a one-week interval, using Siemens Biograph mCT 64 or GE Discovery 710 PET/CT systems. Imaging datasets were evaluated both qualitatively and semi-quantitatively. Parameters analyzed included lesion count, maximum standardized uptake value (SUVmax), and tumor-to-background ratio (TBR). Comparative analysis employed the Wilcoxon matched-pairs signed-rank test for SUVmax and TBR, and the McNemar test for lesion detection rates. ***Results:*** Eight distinct histologic STS subtypes were represented among the cohort. ^{68}Ga-FAPI-46 PET/CT identified a greater total number of metastatic lesions compared to ^{18}F-FDG PET/CT (167 vs. 132 lesions). Mean ± SD SUVmax was 5.4 ± 2.1 for ^{18}F-FDG and 4.7 ± 2.3 for ^{68}Ga-FAPI-46. Notable inter-tracer discrepancies were observed, particularly in liposarcoma, leiomyosarcoma, and undifferentiated pleomorphic sarcoma, where ^{68}Ga-FAPI-46 demonstrated superior lesion conspicuity. ***Conclusion:*** ^{68}Ga-FAPI-46 PET/CT exhibits comparable, and in certain histological subtypes superior, diagnostic efficacy to ^{18}F-FDG PET/CT in the detection of metastatic STS. Its higher lesion detection rate and favorable uptake in select sarcoma subtypes underscore its potential as an alternative imaging biomarker. Validation through larger-scale, multicenter studies is warranted to define its definitive clinical utility ***References:*** Gu B, Liu X, Wang S, Xu X, Liu X, Hu S, Yan W, Luo Z, Song S. Head-to-head evaluation of [18F]FDG and [68 Ga]Ga-DOTA-FAPI-04 PET/CT in recurrent soft tissue sarcoma. Eur J Nucl Med Mol Imaging. 2022 Jul;49(8):2889-2901. doi: 10.1007/s00259-022-05700-4. Epub 2022 Feb 3. PMID: 35113192; PMCID: PMC9206606.2.

EPS-271

^{68}Ga-FAPI-PET/CT leads to changes in clinical management of patients with malignant and benign peripheral nerve sheath tumors

A. Spektor*[1], A. Waldschütz[1], M. Fried[2,3], D. Kalasauskas[4,5], M. Schreckenberger[1], M. Röhrich[1];*
[1]Department of Nuclear Medicine, University Center Mainz, Mainz, GERMANY, [2]University Center for Oncology, University Medical Center Mainz, Mainz, GERMANY, [3]Clinic and Polyclinic for Internal Medicine III, University Center Mainz, Mainz, GERMANY, [4]Department of Neurosurgery, University Center Mainz, Mainz, GERMANY, [5]Department of Neurosurgery, University Hospital LMU Munich, Munich, GERMANY.

Aim/Introduction: Malignant peripheral nerve sheath tumors (MPNST) are aggressive soft tissue sarcomas, which can occur sporadically, post radiation or in association with Neurofibromatosis type 1 (NF1). As MPNST and benign PNST (BPNST; neurofibroma and schwannoma) present a similar clinical and radiological picture, differentiation between MPNST and BPNST is challenging in early state. Thus, MPNST are associated with a poor prognosis due to delayed diagnosis, high metastasis rate and difficult resection being a main cause for mortality in patients with NF1. Diagnostic modalities of choice such as magnetic resonance imaging (MRI) as well as ^{18}F-Fluorodeoxyglucose positron emission tomography with computed tomography (^{18}F-FDG-PET/CT) show high sensitivity for the detection of MPNST but moderate specificity. PET/CT with ^{68}Gallium-labeled fibroblast activation protein inhibitor (^{68}Ga-FAPI) showed a specific uptake in sarcomas and enabled differentiation of benign and malignant lesions in other entities. The aim of our study is to analyze the ^{68}Ga-FAPI uptake in MPNST and BPNST with regard to their discriminability and subsequently to clinical consequences. ***Materials and Methods:*** Patients with suspected PNST after inconclusive prior MRI were examined by ^{68}Ga-FAPI-46-PET/CT. Subsequently, the clinical course of each patient was monitored and MRI findings as well as tumor board decisions prior and after FAPI-PET/CT were compared. PET evaluation (SUVmax/mean/peak, TBRmax/mean/peak) was performed in PMOD 4.401 with VOIs (isocontour 50%). ***Results:*** To date, 4 patients with histologically confirmed (hc) MPNST, 5 patients with hc BPNST (4 schwannoma, 1 neurofibroma), 1 patient with suspected non-hc MPNST and 3 patients with non-hc BPNST have undergone FAPI-PET/CT examination. Hc MPNST showed significantly higher SUVmax/mean/peak (14.35 ± 3.91/ 7.79 ± 2.18/ 13.67 ± 3.67 versus (vs.) 2.84 ± 1.15/ 1.58 ± 0,69/ 2.71 ± 1.09; p < 0.0001) and higher TBRmax/mean/peak (6.44 ± 1.66/ 5.99 ± 2.04 / 6.53 ± 1.63 vs. 1.17 ± 0.26/ 1.14 ± 0.17/ 1.19 ± 0.25; p < 0.0001) than hc BPNST. FAPI-PET/CT led to changes in clinical course in 6 (2 upstagings, 2 waiver of surgery/biopsy, 1 intensification of therapy, 1 FAPI-hotspot biopsy) of 9 patients with hc PNST, in all 3 (waiver of surgery/biopsy) non-hc BPNST and 1 (upstaging) non-hc MPNST patients. ***Conclusion:*** MPNST and BPNST can be specificly differentiated by FAPI-uptake leading to drastic changes in clinical course by upstaging or prevention of surgery/ biopsy. ^{68}Ga-FAPI-PET/CT might be thus a promising modality for targeted diagnosis and clinical management of patients with MPNST and BPNST.

EPS-272

PET/CT Core + PeritumoralRing Radiomics for Histotype Classification of Pediatric Sarcomas

N. Quartuccio*[1], F. Fiz[2], E. M. Abenavoli[3], C. Olianti[3], A. Tondo[4], A. Tamburini[4], I. Bertacca[4], C. Manzitti[5], V. Livellara[5], A. Garaventa[5], P. D'Angelo[6], F. Dondi[7], M. Conte[8], V. Frantellizzi[8], S. Ialuna[1], V. Berti[9], A. Piccardo[2], A. Cistaro[10];*

[1]Nuclear Medicine Unit, Ospedali Riuniti Villa Sofia-Cervello, Palermo, ITALY, [2]Nuclear Medicine Unit, Galliera Hospital, Genoa, ITALY, [3]Nuclear Medicine Unit, Careggi University Hospital, Florence, ITALY, [4]Paediatric Oncoematology IRCC A. Meyer, Florence, ITALY, [5]Oncology Unit, IRCSS Istituto Giannina Gaslini, Genoa, ITALY, [6]Pediatric Hematology and Oncology Unit, ARNAS "Civico, Di Cristina and Benfratelli" Hospitals, Palermo, ITALY, [7]Nuclear Medicine, University of Brescia and Spedali Civili di Brescia, Brescia, ITALY, [8]Department of Radiological Sciences, Oncology and Anatomical Pathology, Sapienza, Rome, ITALY, [9]Department of Experimental and Clinical Biomedical Sciences 'Mario Serio', University of Florence, Florence, ITALY, [10]Nuclear Medicine Department, Salus Alliance Medical, Genoa, ITALY.

Aim/Introduction: Radiomic descriptors from the tumour core and from the 0.5cm peritumoral ring may be complementary. We assessed whether combining both regions and both modalities (PET and CT) improves noninvasive discrimination of osteosarcoma (OS), Ewing sarcoma (EWS) and rhabdomyosarcoma (RMS) compared with models based on either region alone. ***Materials and Methods:*** Eightyeight children/young adults underwent baseline [^{18}F]FDG PET/CT at three Italian centers. These subjects were affected by Ewing's Sarcoma (ES, N=46, 52%), osteogenic sarcoma (OS, N=29, 33%) or Rhabdomyosarcoma (RMS, N=13, 15%). Tumourcore and concentric 0.5cm ring volumes were segmented; 389 radiomic features were extracted from each PET or CT volume with LIFEx v 7.7, yielding four prefixed sets (CORE_PET_, CORE_CT_, RING_PET_, RING_CT). Kruskal-Wallis with Benjamini-Hochberg FDR correction ($\alpha = 0.05$) selected informative variables were obtained. Ten RandomForest classifiers (200 trees, fivefold stratified crossvalidation) were compared. Balanced accuracy was the primary metric. ***Results:*** Core PET radiomics yielded a fair balanced accuracy (0.64), which did not improve by adding the ring data (0. 63). Core CT also had sufficient accuracy (0.62); yet, it was not improved by adding the ring data (0.62). The mixed CORE PET/CT model had an accuracy of 0.63, whit a minimal impact from adding the ring information (CORE+RING PET/CT model: 0.67). However, this last model achieved higher recall for EWS (0.74) and RMS (0.73), while recall for OS was lower (0.52). ***Conclusion:*** Our preliminary data show that analyzing the textural pattern of PET and CT in sarcomas can convey valuable information for developing non-invasive histological diagnosis models. Moreover, data from the tumor core and the margin appear to be synergic, indicating that the mechanisms of tumor growth might be necessary in stratifying these tumors.

EPS-273

Diagnostic Utility of Bone Scintigraphy in Pediatric Acute Osteomyelitis

K. Guichay Duran*, M. Tagliatori Nogueira, C. Galindo Fernández, D. Rodriguez Oviedo, J. Sanchez Calderón, M. Castillejos Rodriguez, A. Herrero Muñoz, C. Paniagua Correa, A. Ortega Valle, M. Álvarez Moreno, M. García Alonso, M. De la Rubia Marcos; Department of Nuclear Medicine, Getafe University Hospital, Madrid, SPAIN.*

Aim/Introduction: To evaluate the diagnostic performance of bone scintigraphy in pediatric patients with clinical suspicion of acute osteomyelitis (AO). ***Materials and Methods:*** We conducted a retrospective, descriptive observational study involving patients under 15 years old who were admitted to our institution with suspected AO between 2019 and 2024. All patients underwent three-phase bone scintigraphy as part of the initial diagnostic assessment. ***Results:*** A total of 30 patients were included (66.7% male), with a mean age of 3 years. The most frequent presenting symptoms were functional impairment (86.7%), localized pain (83.3%), fever (80%), and signs of localized inflammation (33.3%). Laboratory results showed leukocytosis (>12,000/µl) in 66.7% of cases, elevated erythrocyte sedimentation rate (ESR >20 mm/h) in 80%, and increased C-reactive protein (CRP >20 mg/L) in 70%. Blood cultures were positive in 36.7% of patients, with Staphylococcus aureus being the most commonly isolated pathogen (90%) Bone scintigraphy was performed on average 6.6 days after symptoms onset and yielded positive findings in all cases (100%), confirming the clinical diagnosis. Additionally, the scan revealed contiguous bone involvement in 6 patients (20%) and multifocal osteomyelitis in 2 cases. The most frequently involved sites were the tibia (43.3%), femur (16.7%), and calcaneus (13.3%). All patients received intravenous antibiotic therapy for an average duration of 7 days. Surgical drainage was required in 2 cases due to associated complications. Clinical outcomes were favorable in all patients. ***Conclusion:*** Acute osteomyelitis in children requires a high index of suspicion, as early diagnosis and prompt treatment are essential for a favorable outcome and prognosis. Bone scintigraphy has proven to be a highly sensitive diagnostic tool for AO, with low radiation exposure. Furthermore, it offers the advantage of whole-body imaging, facilitating the detection of multifocal involvement.

EPS-274

Quantitative Bone SPECT/CT in Hand and Wrist Osteoarthritis Imaging and Management

M. Soltanolkotabi*, G. Safazadeh, G. J. Stoddard, M. K. Mills, A. Wang, S. Minoshima;*
University of Utah, Salt Lake City, UT, UNITED STATES OF AMERICA.

Aim/Introduction: Hand and wrist osteoarthritis (OA) is highly prevalent and frequently underdiagnosed in its early stages due to limited radiographic findings. Pain is often the primary clinical complaint, yet traditional imaging correlates poorly with symptom severity. This study aimed to evaluate the reliability and reproducibility of quantitative single-photon emission computed tomography/computed tomography (SPECT/CT) uptake values and to investigate their association with pain and functional outcomes in patients with early, radiographically occult hand/wrist OA, particularly in the context of treatment planning for intra-articular steroid injections. ***Materials and Methods:*** In this prospective single-center pilot study, eight adult patients with wrist/hand pain ≥6 weeks and pain scores ≥4 were enrolled. All had radiographically occult OA and were candidates for intra-articular steroid injections. Twenty at-risk joints per patient were selected, totaling 160 joints. Prior to intervention, we recorded SUVmax and SUVmean from SPECT/CT scans, pain scores (numeric rating scale 0-10), QuickDASH, SF-12, grip strength, and three-point pinch. Two MSK radiologists independently measured SUVs, with repeat measurement at 6 months for intra-rater assessment. Intraclass correlation coefficients (ICC) assessed measurement reliability. Associations between SUV and clinical outcomes were analyzed using random-effects models at the joint level and Spearman correlation at the patient level. ***Results:*** Among 160 joints analyzed (thumb/index: 80; 3rd-5th digits: 80), 46 were painful, and 19 underwent injection. Inter-rater reliability was excellent (ICC SUVmean = 0.95; SUVmax = 0.98), as was intra-rater reliability for SUVmax (ICC = 0.99). Across all joints, pain intensity was positively associated with SUVmax (β=0.27, 95%CI: 0.17-0.37, p<0.001). Among the most painful joints, a stronger correlation was observed (Spearman's ρ=0.73, p=0.04). Notably, a linear relationship between SUVmax and pain emerged at thresholds of pain ≥5 and SUVmax ≥2.5, suggesting potential clinical cutoffs for injection decisions. While QuickDASH scores did not significantly correlate with SUVmax, there was a borderline significant inverse correlation with the SF-12 physical component (ρ=–0.70, p=0.058). In the subset of injected joints, pain significantly decreased post-intervention (median pain score reduced from 5 [IQR: 5-8] to 1.5 [IQR: 0-7], p<0.001). ***Conclusion:*** Quantitative SPECT/CT demonstrates high inter- and intra-rater reliability and a robust association between SUVmax and joint pain in early hand/wrist OA. The identification of linearity thresholds (pain ≥5, SUVmax

≥2.5) supports the potential use of SUV as a biomarker to guide intra-articular injection decisions. Further studies are warranted to validate these thresholds and evaluate longitudinal and functional outcomes.

EPS-275

Contribution of ^{99m}Tc-SPECT/CT to Magnetic Resonance Imaging Inpainful Foot Pathologypainful Foot Pathology

C. Gonzalez Roiz[1], *L. León-Ramírez*[2], *P. Recarte Ortega*[1], *G. Orlandini*[1], *M. Ollarves Carrero*[1], *M. Alvarez*[1], *L. Garcia Cañamaque*[1];
[1]*Hospital Puerta del Sur, Móstoles, Madrid, SPAIN,* [2]*Hospital Clínico San Carlos, Madrid, SPAIN.*

Aim/Introduction: To evaluate the role of single-photon emission computed tomography combined with computed tomography (SPECT/CT) in bone pathology of the foot and ankle, and its complementary value to magnetic resonance imaging (MRI) findings. ***Materials and Methods:*** A prospective study was conducted between 2024 and 2025 including 54 patients (31 women, 23 men; mean age: 55 years) with foot and/or ankle pain. All underwent SPECT/CT following the administration of 800 MBq of ^{99m}Tc. In patients with available MRI, concordance between imaging techniques was assessed. The ability of SPECT/CT to detect osseous, tendinous and/or articular abnormalities was evaluated. ***Results:*** Of the total cohort, 42.6% (23/54) had a history of previous surgery. SPECT/CT was diagnostic in 82% of these cases, with reduced specificity observed depending on the time elapsed since surgery. MRI was available in 8 of the 23 postoperative patients, demonstrating full concordance with SPECT/CT (100%). In two cases where MRI yielded inconclusive findings, SPECT/CT provided a definitive diagnosis. Additionally, it contributed further diagnostic information in 75% of these cases. Among patients without previous surgery (57.4%), SPECT/CT revealed clinically relevant additional findings in 53% (8/15), particularly in cases of degenerative joint disease, enabling targeted intra-articular interventions. ***Conclusion:*** While MRI remains fundamental in the evaluation of chronic foot pain, SPECT/CT should be considered within the diagnostic algorithm—not only in patients with orthopaedic hardware limiting MRI, but also for its added functional value, ability to refine diagnosis, and support in guiding treatment decisions in complex or refractory cases. ***References:*** 1. García Jiménez R, García-Gómez FJ, Noriega Álvarez E, Calvo Morón C, Martín-Marcuartu JJ. Imagen híbrida en la patología del pie y tobillo. Revista Española de Medicina Nuclear e Imagen Molecular. 2018 May;37(3):191-202. 2. Waldman LE, Scharf SC. Bone SPECT/CT of the Spine, Foot, and Ankle: Evaluation of Surgical Patients. Seminars in Nuclear Medicine. 2017 Nov;47(6):639-46. 3. Willm Uwe Kampen, Westphal F, Van T, Strobel K, Torsten Kuwert, van, et al. SPECT/CT in Postoperative Foot and Ankle Pain. 2018 Sep 1;48(5):454-68. 4. Hassink G, Testa EA, Leumann A, Hügle T, Rasch H, Hirschmann MT. Intra- and inter-observer reliability of a new standardized diagnostic method using SPECT/CT in patients with osteochondral lesions of the ankle joint. BMC Medical Imaging. 2016 Dec;16(1).

EPS-276

Clinical Decision-Making Using [^{18}F]NaF PET/CT Imaging in Non-Unions

N. D. van Rijsewijk*, M. Wouthuyzen-Bakker, J. H. van Snick, J. van Sluis, K. ten Duis, A. W. J. M. Glaudemans, F. F. A. IJpma;*
University Medical Center Groningen, Groningen, NETHERLANDS.

Aim/Introduction: Non-unions remain a major challenge in (trauma) fracture care, with limited tools to assess biological healing potential. This study evaluated [^{18}F]NaF PET/CT imaging as a decision-making tool in the management of long-bone non-unions. ***Materials and Methods:*** From June 2019 to December 2024, a prospective study was conducted at a level 1 trauma center, including 13 patients (15 non-unions) eligible for revision surgery after failed initial fracture treatment. All patients underwent [^{18}F]NaF PET/CT scans, including a dynamic scan for the first 10 minutes and a static scan after one hour, to assess bone healing capacity. Imaging results were analyzed qualitatively and quantitatively and compared to clinical outcomes after an extended observation period. ***Results:*** Increased [^{18}F]NaF uptake, suggestive of healing potential, was observed in all non-unions (15/15). Based on the PET/CT results, an extended observation period was recommended. However, two patients opted for surgery. Of the 13 non-unions managed with an extended observation period, 9 (69%) showed spontaneous fracture healing over time. Revision surgery was required in four cases, of which 3 (75%) needed additional stabilization of the fracture. Finally, [^{18}F]NaF PET/CT helped to avoid surgery in 60% (9/15) of cases. Visual uptake pattern analysis (whole-bone uptake) was significantly associated with surgical need (χ^2 = 5.31, p = 0.021), while quantitative imaging added no clinical value. ***Conclusion:*** [^{18}F]NaF PET/CT imaging showed healing potential in all non-unions and supported an extended observation period. Whole-bone uptake may suggest a need for additional fracture stabilization. In total, 60% of surgeries for non-unions were avoided.

EPS-277

Beyond the Bone Scan: FDG PET/CT as a Decisive Tool in Differentiating PJI from Aseptic Loosening

J. Choudhary*, A. Mahalik, N. Kundu, S. Singh, V. Singh, J. Krishna P., K. Jain, S. Shamim, R. Kumar;*
All india institute of medical sciences., New Delhi, INDIA.

Aim/Introduction: Differentiating prosthetic joint infection (PJI) from aseptic loosening remains a diagnostic challenge, especially when the 3-phase bone scan yields equivocal results. FDG PET/CT has emerged as a promising modality, offering functional insights beyond conventional imaging. This study evaluates the role of FDG PET/CT in distinguishing infective vs non-infective etiologies in such ambiguous cases. ***Materials and Methods:*** This retrospective analysis included 16 patients with painful prostheses and equivocal findings on 3-phase bone scan. FDG PET/CT was performed to evaluate the metabolic activity at the prosthetic site. Demographic data, ESR/CRP levels, and clinical features like pus discharge were recorded. SUVmax and SUVpeak were measured at the prosthetic site. Final diagnosis was confirmed using clinical, microbiological, surgical, or histopathological correlation. ***Results:*** A total of 16 patients were included (female: 9, male: 7; mean age: 48.1 years). FDG PET/CT demonstrated significantly higher SUVmax and SUVpeak values in infective cases (mean SUVmax: 18.98; SUVpeak: 11.47) compared to aseptic loosening (mean SUVmax: 13.17; SUVpeak: 7.66). ROC analysis indicated SUVmax > 16.88 as an optimal cut-off for infection, with a sensitivity of 83.3% and specificity of 70.0%. The AUC for SUVmax was 0.68. ***Conclusion:*** FDG PET/CT is a valuable tool in differentiating prosthetic joint infection from aseptic loosening in cases where 3-phase bone scan is inconclusive. With an AUC of 0.68, FDG PET/CT demonstrates moderate accuracy, and combining it with clinical and laboratory parameters may enhance diagnostic precision.

EPS-278

Integrating Whole-Body Bone SPECT and AI-Synthetic CT in the Evaluation of Non-Oncologic Disorders

M. Einieh[1], *S. Barna*[2,3], *Á. Budai*[2], *G. Ország*[2], *C. Csikos*[3], *I. Garai*[2,3];
[1]*University of Debrecen, Faculty of Medicine, Debrecen, HUNGARY,* [2]*Scanomed Ltd., Debrecen, HUNGARY,* [3]*University of Debrecen, Faculty of Medicine, Medical Imaging Department, Division of Nuclear Medicine, Debrecen, HUNGARY.*

Aim/Introduction: Multiphase regional bone SPECT/CT is an established method for assessing inflammatory, degenerative, and postoperative changes in non-oncological bone conditions.

However, in some cases, patients' symptoms do not correlate with regional findings. This study evaluates the added diagnostic value of whole-body SPECT with AI-generated synthetic CT for detecting clinically relevant abnormalities beyond the primary region of interest. ***Materials and Methods:*** A total of 135 patients (mean age: 63.9 ± 14.3 years; female-to-male ratio 2:1) underwent multiphase SPECT/CT for non-oncological indications, including orthopedic (n=71), rheumatologic (n=31), neurosurgical (n=8), and other (n=11) conditions. All patients received BMI-adjusted 500-600 MBq [Tc-99m]-MDP. Early- and late-phase regional SPECT/CT was followed by whole-body SPECT to assess uptake outside the initial region. When extra-regional uptake was observed, AI-generated synthetic CT aided anatomical localization. 8 patients were excluded due to loss of clinical follow-up, and 13 were excluded from the whole bone SPECT evaluation due to having only planar bone scans. Diagnostic performance (sensitivity, specificity) and correlation analyses (chi-square, Pearson's regression) were conducted. ***Results:*** Regional SPECT/CT showed strong diagnostic value. Orthopedic indications had a sensitivity of 92% and a specificity of 95% (hip: 96%/78%, knee: 80%/89%). Rheumatologic cases showed 100% sensitivity and 67% specificity. Neurosurgical and other groups showed no false negatives, while the latter experienced two false positives. Whole-body SPECT detected pathological uptake beyond the primary region in 69 of 122 cases (56%), significantly correlating with clinical true positives ($\chi^2 = 3.39$, $p = 0.066$). Vertebral accumulations (41), rib hot spots (13), and joint uptakes (33) were common. Among 27 patients with true positive results for metal implant loosening, 13 had incidental dental uptake ($\chi^2 = 3.43$, $p = 0.064$). We found no significant correlation ($r = -0.110$, $p = 0.386$) between the time since surgery and positive findings. ***Conclusion:*** Multiphase regional SPECT/CT offers high diagnostic reliability for non-oncological bone and joint symptoms. Whole-body SPECT with AI-synthetic CT enhances detection of clinically relevant findings beyond the region of interest, supporting its inclusion in complex cases to guide more comprehensive care.

EPS-279

Composite 3-phase bone scan and FDG-PET in suspected infections post open reduction and hardware fixation of fractures

I. El Bez*, R. Tulbah, S. Alhazza, R. Alsalah, K. Ibrahim, F. Algmlas, M. Alharbi;*
AAML, Riyad, SAUDI ARABIA.

Aim/Introduction: Management of infection post open reduction and internal fixation of fractures is a real dilemma: In fact, infection in the presence of hardware mandates revision/removal of HDR; conversely early removal of HRD, in the presence of non-union, complicates management of both infection and fractures. we evaluated the role of composite triphasic bone scan and FDG-PET in suspected infections post open reduction and hardware fixation of fractures. ***Materials and Methods:*** This is a retrospective study from 2018-2025, including all patients suspects infection post open reduction or internal fixation of fractures, having undergone PET-CT and bone scans scans. Fifty patients were included. A planar three phase bone scan was performed first, if it was positive, a PET-CT was performed on the same day or one day after. If the bone scan is negative (flow and blood pool negative), PET-CT was not performed. The PET-CT fusion images were reviewed interactively on a dedicated workstation Findings on composite PET and bone scan were correlated. ***Results:*** A total of 50 patients were evaluated. The composite PET and BS were matching, both two positive in 45 cases: the bone scan showed hyperemia and increased blood pool and delayed uptake, matching with FDG avid soft tissue inflammation en PET-CT.), PET was helpful in localizing the findings on BS In case of the bone scan was negative, normal flow and blood pool ; PET-CT was not performed. The composite PET and BS were mismatching, discordant in 5 cases: the bone scan showed hyperemia and increased blood pool and delayed uptake, mismatching with negative PET-CT. Bone scan was positive due to dislocation/subluxation and ulcers. Our study is limited by number of cultures obtained, and limited follow up. ***Conclusion:*** The composite bone scan and FDG-PET appear to be highly complementary. The composite dual modality imaging improves for same day diagnostic work-up. Potentially improves accuracy of detection and localization of infected foci.

EPS-280

Assessment of Noise Reduction Deep Learning Reconstruction Algorithm for Bone Scan: A pilot study

J. Hagerman[1]*, I. Ceric Andelius*[2]*;*
[1]*Clinical Physiology, Department of Clinical Sciences Lund, Lund University, Skåne University Hospital, Lund, SWEDEN,* [2]*Radiation Physics, Department of Hematology, Oncology and Radiation Physics, Skåne University Hospital, Lund, SWEDEN.*

Aim/Introduction: A vendor-specific deep learning (DL) reconstruction algorithm, designed for a ring-configured cadmium-zinc-telluride gamma camera, was recently marketed for its noise reduction quality in single-photon emission computed tomography (SPECT) bone scans [1]. The frequency of the DL-algorithm can be varied, with minimum set to apply after 10 updates and maximum corresponding to the total number of updates. We aimed to assess signal characteristics with coefficient-of-variation (CV) and signal-to-noise ratio (SNR) in SPECT bone scan images reconstructed with ordered subset expectation maximization (OS-EM), block sequential regularized expectation maximization (BSREM), and DL-BSREM with three different frequency updates. ***Materials and Methods:*** SPECT bone scans from seven patients with prostate cancer referred for assessment of bone metastasis were evaluated. Images were reconstructed with BSREM factory protocol, with/without DL (frequency set: 10 (DL10), 30 (DL30), and 60 (DL60) updates), and with OS-EM, for acquisition time 4-, 3-, and 2-min. Images were corrected for collimator detector response, attenuation, and scatter. All patients had at least one focal area of increased uptake (lesion). Volume-of-interest (VOI) was drawn manually on 1-3 lesions per patient (n=14, six metastatic/two patients, eight degenerative/five patients), and on a uniform sacral area without pathology (n=7). VOI was drawn in OS-EM (4-min) and duplicated in the same position across all datasets, and average counts per voxel and deviation were extracted. Results are reported as median (range) at lesion level, combining metastatic and degenerative. ***Results:*** The lesion-to-sacrum uptake was 4.7(1.3-10.1) and 2.0(1.3-2.7) for metastatic and degenerative lesions. For a sacral region, CV ranged from 15.2% $(11.2\text{-}18.0\%)_{(BSREM)}$ to 18.2% $(14.1\text{-}31.3\%)_{(DL10)}$ for 4-min acquisition. Corresponding results for 3- and 2-min acquisitions were 15.3% $(7.7\text{-}21.7\%)_{(BSREM)}$ to 20.3% $(13.1\text{-}46.2\%)_{(DL10)}$, and 19.7% $(13.4\text{-}28.2\%)_{(BSREM)}$ to 29.8% $(13.2\text{-}34.9\%)_{(DL10)}$. The CV results for lesions were 14.4% $(9.0\text{-}36.0\%)_{(BSREM)}$ to 18.4% $(10.8\text{-}34.8\%)_{(CDL30)}$, 17.1% $(7.3\text{-}37.4\%)_{(BSREM)}$ to 23.1% $(4.9\text{-}43.5\%)_{(DL10)}$, and 17.1% $(9.7\text{-}35.6\%)_{(BSREM)}$ to 23.9% $(8.5\text{-}37.1\%)_{(CDL10)}$ for 4-, 3- and 2-min acquisition. SNR varied, for sacrum, between 5.5 $(3.2\text{-}7.1)_{(DL10)}$ and 6.6 $(5.6\text{-}9.0)_{(BSREM)}$, 4.9 $(2.2\text{-}7.7)_{(DL10)}$ and 6.5 $(4.6\text{-}12.9)_{(BSREM)}$, and 3.4 $(2.9\text{-}7.6)_{(CDL10)}$ and 5.1 $(3.5\text{-}7.4)_{(BSREM)}$ for 4-, 3- and 2-min acquisition. Corresponding values for lesions were 5.5 $(2.9\text{-}9.3)_{(DL30)}$ and 7.0 $(2.8\text{-}11.1)_{(BSREM)}$, 4.5 $(2.3\text{-}20.6)_{(DL10)}$ and 6.7 $(2.7\text{-}13.7)_{(BSREM)}$, and 4.2 $(2.7\text{-}11.8)_{(DL10)}$ and 5.9 $(2.8\text{-}10.4)_{(BSREM)}$ for 4-, 3- and 2-min acquisition. ***Conclusion:*** Despite the smal sample size, results indicate that BSREM without DL outperforms reconstructions with DL and OS-EM, in terms of CV and SNR. ***References:*** Ziv O, et al. Clarify DL-Deep learning image reconstruction for bone SPECT scans. GE HealthCare;2024. White paper.

EPS-281

Using Limphoscintigraphy to Assess Lymphatic Insufficiency after Total Knee Arthroplasty. A Pilot Study in Ukraine

P. Korol[1], *O. Shcherbina*[1], *M. Tkachenko*[2], *M. Kostylev*[3];
[1]Shupik National University Healthcare of Ukraine, Kyiv, UKRAINE, [2]Bogomolets National Medical University of Ukraine, Kyiv, UKRAINE, [3]Shalimov National Scientific Center of Surgery and Transplantation, Kyiv, UKRAINE.

Aim/Introduction: Extremity swelling is a common complication of total knee arthroplasty (TKA). In long-term follow-up, persistent or progressive swelling may indicate lymphatic insufficiency. Lymphoscintigraphy offers an objective and reliable approach to diagnosis and characterization of disease severity. The aim of this study is to detect abnormalities or insufficiencies of lymphatic drainage using lymphoscintigraphy in patients complaining of discomfort and swelling after TKA during a 6-month follow-up. ***Materials and Methods:*** We evaluated 140 patients (87 women and 53 men, mean age 55 years) who underwent TKA at the Kyiv City Center for Endoprosthetics between 2014 and 2024 and had unilateral limb edema at long-term evaluation. Other causes of limb edema (venous insufficiency, infectious diseases, etc.) were excluded. Dynamic scanning began immediately after injection of 1.5 mCi of Teknetium-99m-labeled nanocolloid into the first interdigital space of both feet, followed by scanning of the patients' lower limbs, pelvis, and abdomen at 15 minutes, 2 hours, and 6 hours. The scans were analyzed and assessed for: visualization and dilation of the main lymphatic vessels, regional and deep lymph nodes, collateral vessels, and dermal return flow. All images were scored on a scale of 0 to 12 according to the criteria of our Department of Nuclear Medicine grading system. ***Results:*** In lymphoscintigraphic evaluation of 140 patients, we show: radiopharmaceutical passage into the main lymphatics in 121 (86.4%), collateral vessels in 87 (62.1%), deep lymphatic drainage (popliteal lymph nodes) in 61 (43.5%), dilation of the main lymphatics in 46 (32.9%), skin backflow in 53 (37.8%), adequate uptake of the radiopharmaceutical by regional lymph nodes in 116 (82.8%) extremities. The average lyphoscintigraphic score was 9/12. Based on the results of the study analysis, we show abnormalities or insufficiency of lymphatic drainage in patients who complained of discomfort and unexplained swelling after TKA. ***Conclusion:*** Unexplained pain, swelling, and discomfort are unpleasant findings after TKA, and identifying the underlying causes is critical for clinical management. Lymphoscintigraphy with lymphatic mapping may play a key role in determining the etiology of limb swelling and predicting the success of conventional treatments. The addition of quantitative lymphatic flow and nodal accumulation may be a more sensitive approach to the diagnosis of lymphatic insufficiency. We will continue to study with a larger patient population to establish clinical guidelines for performing lymphoscintigraphy in patients undergoing TKA.

EPS-282

Association of Renal "Hot Spots" on Bone Scan and Serum Ferritin Levels. A Pilot Study in Ukraine

P. Korol[1], *M. Kostylev*[2], *O. Shcherbina*[1], *M. Tkachenko*[3];
[1]Shupik National University Healthcare of Ukraine, Kyiv, UKRAINE, [2]Shalimov National Scientific Center of Surgery and Transplantation, Kyiv, UKRAINE, [3]Bogomolets National Medical University of Ukraine, Kyiv, UKRAINE.

Aim/Introduction: In our Department of Nuclear Medicine, we have noted high serum ferritin levels in patients with inflammatory, autoimmune and malignant diseases, who had high renal uptake on bone scan. The aim of the study was to evaluate and investigate this association. ***Materials and Methods:*** We retrospectively analyzed data from patients who underwent 99m-Tc-MDP bone scan and serum ferritin measurement for 2 weeks. Serum ferritin was measured to check for anemia. The ratio of the radiopharmaceutical uptake in the kidneys and vertebral bone average amount per pixel was calculated as the K/V ratio, and its correlation with the blood levels of ferritin, iron, creatinine, C-reactive protein, hemoglobin, and white and red blood cell counts was analyzed using the rank correlation coefficient. Renal uptake of 99m-Tc-MDP was also visually assessed in comparison with the uptake of the tracer in the ribs and lumbar spine on bone scintigraphy. ***Results:*** A total of 48 patients with high renal uptake, 26 with suspected joint osteoarthrosis, 6 with amyloidosis, and 16 with malignancies were included. The mean interval between bone scintigraphy and blood sampling for ferritin measurement was 6.4±3.7 days. A significant correlation was found between the K/V ratio and ferritin level ($r=0.58$, $p<0.005$), red blood cell count ($r=0.63$, $p=0.003$) and hemoglobin level ($r=0.51$, $p=0.001$). However, there was no correlation with the following parameters thought to be associated with nephritis and iron and bone metabolism: creatinine ($r=0.21$, $p=0.35$), C-reactive protein ($r=-0.17$, $p=0.72$), white blood cell count ($r=-0.23$, $p=0.54$), iron ($r=0.41$, $p=0.32$). A significant correlation was also found between the K/V ratio and the visual assessment score ($r = 0.79$, $p < 0.001$). ***Conclusion:*** There was a significant correlation between serum ferritin levels and the increase in renal 99m-Tc-MDP accumulation on bone scintigraphy. The mechanism of this phenomenon is being investigated in our department. It is suggested that this mechanism is related to changes in the number of red blood cells caused by their destruction, but without any relationship with iron deficiency.

EPS-283

Clinical Role of Tc-99m-MDP Bone Scintigraphy in Patients with Alkaptonuria. A Pilot Study in Ukraine

P. Korol[1], *M. Tkachenko*[2], *M. Kostylev*[3], *O. Shcherbina*[1];
[1]Shupik National University Healthcare of Ukraine, Kyiv, UKRAINE, [2]Bogomolets National Medical University of Ukraine, Kyiv, UKRAINE, [3]Shalimov National Scientific Center of Surgery and Transplantation, Kyiv, UKRAINE.

Aim/Introduction: The clinical value of Tc-99m bone scan as a diagnostic tool for monitoring response in ochronotic lesions remains controversial to date, mainly due to the lack of evidence. Using a retrospective study, we analyze the potential of bone scintigraphy as a monitoring tool in alkaptonuria. ***Materials and Methods:*** Our Department of Nuclear Medicine of the National University of Health of Ukraine provides medical care to the largest national cohort of patients diagnosed with alkaptonuria. We included a total of 47 patients in our study and analyzed changes in tracer distribution patterns in long-term bone scans. The study cohort included 28 women and 19 men, age at initial isotope scan: 25-72 years, median 57 years. Time difference between bone scans: minimum 6 months, maximum 28 months). In this group, 45 patients received Orfadin treatment at the time of the follow-up bone scan (duration of nitosinone treatment: minimum 6 months, maximum 28 months, daily dose 4-10 mg/dl). We investigated the distribution patterns of early angiographic, blood pool and delayed-phase SPECT bone scans, as well as changes in dynamic follow-up. ***Results:*** The most common findings were spinal ochronosis, affected large joints (hip, shoulder). In most cases, the results improved at follow-up in 89% (40 of 45 patients) or were constant in 24% (11 of 45 patients) with Orfadin treatment. At the same time, progress was observed in large joints that were not yet affected or slightly affected in 51% (23 of 45 patients). ***Conclusion:*** Tc-99m bone scintigraphy is likely to be an important tool for monitoring ochronotic or degenerative changes in the course of alkaptonuria. Accordingly, Tc-99m bone scanning may play a key role in the dynamic monitoring of Orfadin therapy.

EPS-284

Acute Multifocal Osteomyelitis with Visceral Extension: Contribution of 18FDG PET/CT in Diagnosis, Assessment of Extent, and Therapeutic Follow-up

Z. Missaoui, *A. Ezzine, M. Ben Fredj, H. Boudrigua, R. Mehri, G. Baazoug, K. Chatti;*
Department of Nuclear Medicine, Sahloul University Hospital Center, Sousse, TUNISIA.

Aim/Introduction: Acute multifocal osteomyelitis in children is a serious condition that may rapidly progress to septicemia if not promptly treated. ^{18}F-FDG PET/CT has emerged as a valuable imaging modality for detecting infectious foci, particularly when conventional imaging is inconclusive. We report a rare case of acute multifocal osteomyelitis with visceral involvement following scorpion envenomation, in which ^{18}F-FDG PET/CT played a key role in diagnosis, assessment of disease extent, and monitoring of treatment response. ***Materials and Methods:*** A whole-body FDG PET/CT scan, including the extremities, was performed 60 minutes after administration of 62.9 MBq of 18F-FDG, in accordance with pediatric dosing guidelines from the European Association of Nuclear Medicine. ***Results:*** A 3-year-old child with a history of untreated congenital heart disease was admitted following a scorpion sting on the left index finger. A few days after receiving specific treatment for severe scorpion envenomation (stage III), the patient developed febrile polyarthritis, with persistent fever and functional impairment of the lower limbs . Laboratory tests showed elevated CRP (257 mg/L), while ultrasound examinations of the hips, knees, and ankles, also echocardiography were unremarkable. Blood cultures, performed after the initiation of empirical antibiotic therapy, were negative. Given the persistence of fever despite 13 days of antibiotics, an ^{18}F-FDG PET/CT was performed, revealing multiple hypermetabolic lesions including extensive soft tissue infiltration in both thighs, adjacent osteomedullary involvement, and bone lesions in the right clavicle and feet. Additional findings included bilateral hypermetabolic pulmonary nodules suggestive of septic emboli and supradiaphragmatic and subdiaphragmatic hypermetabolic lymphadenopathies. Following these findings, The patient underwent surgical drainage and bone trephination. Bacteriological analysis of the pus (on day 23 of antibiotics) and PCR testing for Mycobacterium tuberculosis in sputum and pus were negative. The final diagnosis was acute multifocal osteomyelitis with hematogenous dissemination, involving bone, lungs, and lymph nodes. The patient received six weeks of intravenous antibiotics followed by oral therapy, with clinical and biological improvement. A follow-up ^{18}F-FDG PET/CT performed after seven weeks of treatment showed marked metabolic improvement, with near-complete resolution of pulmonary and lymph node lesions and significant improvement of bone lesions. ***Conclusion:*** ^{18}F-FDG PET/CT is a valuable diagnostic tool in pediatric osteomyelitis, enabling early detection of infectious sites, especially when multiple lesions are present or conventional imaging is inconclusive. It also provides valuable guidance for surgical intervention and allows assessment of therapeutic response during follow-up.

EPS-284a

Role of Early Blood Pool FASpect/CT in Osteomyelitis

A. Khawar[1], *M. Sahar*[1], *M. A. Saeed*[2];
[1]*Pakistan Institute of Engineering and Applied Sciences, Islamabad, PAKISTAN,* [2]*Atomic Energy Cancer Hospital, Nuclear Medicine Oncology and Radiotherapy Institute, Islamabad, PAKISTAN.*

Aim/Introduction: Fewer angle SPECT/CT (FASpect/CT) using iterative reconstruction in less time with images comparable to normal SPECT/CT has geared the interest in evaluation of early blood pool FASpecT/CT in various skeletal disorders like osteomyelitis, tendinopathies etc. The current study aims to evaluate the role of early blood pool Tc-99m MDP FASpecT/CT in diagnosing osteomyelitis. ***Materials and Methods:*** It is a prospective single arm study conducted at the Nuclear Medicine Department of AECH-NORI Hospital, Islamabad, over seven months. The study enrolled 23 subjects suspected of having osteomyelitis on the basis of history, clinical features, laboratory investigations and relevant radiological findings. All subjects underwent three acquisitions post Tc-99m MDP injection i.e., three-phase bone scintigraphy (TPBS), Early Blood pool FASpecT/CT, and delayed-phase SPECT/CT (d-SPECT). The final diagnoses was established through histopathology reports following surgery or clinical follow-up for over 3-5 months. The three diagnostic criteria (I) TPBS alone, (II) combined planar blood pool with d-SPECT/CT, and (III) Blood pool FASpecT/CT alone were compared qualitatively. Statistical McNemar test and Cohen Kappa test were applied to analyze the results statistically. ***Results:*** OM was diagnosed in 17 out of 23 patients. Tc-99m MDP blood pool FASpecT/CT was found to have advantage of delineating bone and soft tissue involvement at same time as compared to only soft tissue by planar blood pool and only bone at d-SPECT/CT. The specificity for Criterion I, II and III came out to be 50.00%, 66.67%, and 100% respectively and sensitivity came out to be same for all three criteria i.e 94.12%. The Kappa analysis also revealed that criteria 3 had better and statistically significant agreement with the gold standard. ***Conclusion:*** Tc-99m MDP blood pool FASpecT/CT was found to have higher specificity and accuracy than conventional skeletal scintigraphy techniques for diagnosis of osteomyelitis and can be considered for inclusion in imaging protocol for Tc-99m MDP imaging for OM. It is firther proposed that prospective studies with Fast SPECT/CT for blood pool in combination with d-SPECT/CT in osteomyelitis may be conisdered for evaluation. ***References:*** 1. Phillips WT, Gorzell BC, Martinez RA, Salman UA, Cooper AW, Stocker DJ, et al. Fewer-Angle SPECT/CT Blood Pool Imaging for Infection and Inflammation. Journal of Nuclear Medicine Technology. 2021 Mar 1;49(1):39-43. 37. 2. L Lee SJ, Won KS, Choi HJ, Choi YY. Early-Phase SPECT/CT for diagnosing osteomyelitis: A retrospective pilot study. Korean Journal of Radiology. 2021 Apr 1;22(4):604-11.

1710a

Wednesday, October 8, 2025, 08:00 - 09:00
Room 116

Mini Course 1 - Technologists Committee: Nuclear Medicine Applications for Radiotherapy Planning

OP-805

The Nuclear Medicine Technologist's Expertise: Optimizing PET/CT Acquisition and Processing for Radiation Therapy

V. Mautone; *IRCCS IRST Meldola, Department of Nuclear Medicine, Meldola, ITALY.*

OP-806

From Image to Treatment Plan: The Radiation Therapist's Approach to Integrating PET/CT in Radiation Therapy

Y. Tsang; *Princess Margaret Cancer Centre, Department of Radiation Oncology, Toronto, CANADA.*

1710b

Wednesday, October 8, 2025, 09:05 - 10:05
Room 116

Mini Course 2 - Technologists Committee: Adverse Events and Risk Management

OP-809

Building Safety from the Start: Embedding a Culture of Safety Through Training in Nuclear Medicine

P. Costa; *Nuclear Medicine Department, E2S, Polyechnic Institute of Porto, Porto, PORTUGAL.*

OP-810
Unseen Hazards: Exploring Adverse Events in Nuclear Medicine and How to Prevent Them
J. Bolin; *GateWay Community College , Department-Program Director for the Nuclear Medicine Technology Program, Phoenix, UNITED STATES OF AMERICA.*

OP-811
Navigating Risk in Nuclear Medicine: Insights and Lessons for Safer Practices
K. Pathmaraj; *Chief Technologist (NM, PET, Bone Mineral Density), Department of Molecular Imaging and Therapy, Austin Health, Melbourne, AUSTRALIA.*

1710c

Wednesday, October 8, 2025, 10:15 - 11:15
Room 116

Mini Course 3 - Technologists Committee: Patient Management in Paediatric Nuclear Medicine: From Theory to Practice

OP-813
Children Are Not Small Adults! Specific Needs of Very Special Patients in Nuclear Medicine
Z. Bar-Sever; *Director of Nuclear Medicine Schneider Children's Medical Center, Petach Tikvah, ISRAEL.*

OP-814
Paediatric Patient Hybrid Imaging – How the Technologist Navigates Paediatric Patient Care?
T. Yamamoto; *Department of Medical Radiological Technology Graduate School of Health Sciences, Tokyo, JAPAN.*

1711

Wednesday, October 8, 2025, 8:00 - 9:30
Room 111

Theranostics Track - TROP Session - Oncology & Theranostics Committee: Prostate Cancer Theranostic

OP-817
First-in-Human Biodistribution of the Novel PSMA-Binding Peptide NTA-476 Compared to PSMA-11 and DCFPyL Supports Its Therapeutic Potential
A. Singh[1], *R. Hicks*[2], *J. Cardaci*[1], *J. Callahan*[2], *M. Klenner*[3], *B. Greer*[3], *A. McDonald*[3], *V. Sproule*[4], *C. Jeffery*[5], *J. Cawthray*[6], *L. Hurn*[7], *J. Seemann*[8], *C. Haase*[8], *J. L. von Hacht*[8], *C. Smerling*[8], *M. Paschke*[8]; [1]*Genesiscare Australia Pty Ltd, Murdoch, AUSTRALIA,* [2]*PreMIT Pty Ltd, Melbourne, AUSTRALIA,* [3]*Quantum Pharma Australia Pty Ltd, Doncaster, AUSTRALIA,* [4]*Genesiscare Australia Pty Ltd, Sydney, AUSTRALIA,* [5]*Fiona Stanley Hospital, Murdoch, AUSTRALIA,* [6]*Cyclowest Pty Ltd, East Fremantle, AUSTRALIA,* [7]*SKG Radiology, Murdoch, AUSTRALIA,* [8]*3B Pharmaceuticals GmbH, Berlin, GERMANY.*

Aim/Introduction: PSMA-targeted radiopharmaceuticals have emerged as a cornerstone in the management of prostate cancer, improving both progression-free and overall survival. Among these, radioligand therapies with β-emitting radionuclides such as ^{177}Lu, have demonstrated favorable safety profiles. However, when α-emitters are used, high uptake in dose-limiting organs, particularly the salivary glands, can lead to significant adverse effects, limiting therapeutic potential. NTA-476 is a novel PSMA-binding peptide, designed to reduce uptake in off-target organs for therapeutic use. This abstract presents results from two investigator-initiated trials evaluating the biodistribution of ^{68}Ga-NTA-476 compared to ^{68}Ga-PSMA-11 and ^{18}F-DCFPyL in men with prostate cancer. ***Materials and Methods:*** At PreMIT, ten men with biochemically recurrent prostate cancer underwent paired PET/CT imaging with ^{18}F-DCFPyL and ^{68}Ga-NTA-476 using a Siemens Vision Quadra system. At Murdoch, a similar design was used to compare ^{68}Ga-NTA-476 with ^{68}Ga-PSMA-11. For NTA-476, imaging included multiple acquisitions up to 6 hours post-injection. Uptake in tumour lesions and normal tissues were quantified, and time-activity curves and radiation dosimetry estimates were derived. ***Results:*** NTA-476 showed tumour uptake comparable to both comparator tracers at delayed timepoints, with substantially lower physiological uptake in kidneys, salivary glands, and lacrimal glands. These properties resulted in increased tumour-to-background uptake ratios over time. Dosimetry modelling suggests that NTA-476 may offer an improved therapeutic index when labelled with therapeutic isotopes. No NTA-476-related adverse events were observed. Lesion detection was highly concordant between NTA-476 and comparator tracers across both studies. ***Conclusion:*** NTA-476 demonstrates a favourable biodistribution profile, characterised by sustained tracer tumour retention and reduced off-target uptake in critical organs. These findings highlight its potential as a theranostic agent and support its clinical development for radiolabelling with therapeutic isotopes such as ^{225}Ac or ^{177}Lu.

OP-818
Theranostics in 2025: Preliminary Results of a Public Short Survey promoted by Thera4Care IHI Horizon Project
S. Annunziata[1], *W. Fendler*[2], *K. Tabury*[3], *N. Vandermeulen*[4], *A. Radics*[5], *C. Steinbeisser*[6], *M. Zieglmeier*[7], *A. Kjær*[8], *M. Lonnroth*[9], *H. Levillain*[10], *R. Visentin*[11], *A. Viana*[12], *P. Von Overeem*[13], *U. Zetterberg*[14], *C. Mueller*[4], *S. Calvo*[15], *B. Newton*[16], *E. Sala*[17], *K. Herrmann*[2], *on behalf of Thera4Care IHI Horizon Project;* [1]*Gemelli, Rome, ITALY,* [2]*Essen University, Essen, GERMANY,* [3]*SCKCEN, Brussels, BELGIUM,* [4]*PSI, Zurich, SWITZERLAND,* [5]*GE Healthcare, Budapest, HUNGARY,* [6]*Collaborate, Munich, GERMANY,* [7]*EANM, Vienna, AUSTRIA,* [8]*Curasight, Copenaghen, DENMARK,* [9]*Atley, Goteborg, SWEDEN,* [10]*Jules Bordet, Brussels, BELGIUM,* [11]*Medipass Ergea, Rome, ITALY,* [12]*Oncidium, Brussels, BELGIUM,* [13]*Terthera, Breda, NETHERLANDS,* [14]*GE Healthcare, Uppsala, SWEDEN,* [15]*GE Healthcare, Chicago, IL, UNITED STATES OF AMERICA,* [16]*GE Healthcare, London, UNITED KINGDOM,* [17]*Università Cattolica, Rome, ITALY.*

Aim/Introduction: Thera4Care is the largest EU-funded public-private consortium on Theranostics, funded by EU Innovative Health Initiative, aiming to improve awareness and leadership on Theranostics in next 5 years. Thera4Care brings together 27 partners, as academic centres, healthcare providers, SMEs, and industries, from different 15 countries, with 9 work-packages and >25M budget. With a Public Short Survey, consortium aimed to have a comprehensive overview about Theranostics in 2025, to better address further issues on regulation, production, research and clinics during the project (2024-2029). ***Materials and Methods:*** A questionnaire of 20 questions was prepared for healthcare professionals, addressing the following issues: 1) general information; 2) Authorized Therapeutics; 3) Experimental Therapeutics. An online invitation to the Survey was sent to the consortium, delivered through public and personal channels, and to the corresponding authors of articles focused on Theranostics indexed in 2024. ***Results:*** In a preliminary analysis since January to April 2025, 51 responders from 15 different countries worldwide participated. Most were Nuclear Medicine physician (53%), from Academic hospitals (67%). As for Theranostic facilities, most of responders (>70%) had institutional In-Patient and Out-Patient Services, PET/CT and SPECT/CT, and a Diagnostic Radiopharmacy. A smaller number (<60%) could offer Ciclotron-equipped Radiopharmacy, Phase 1 Authorization, GMP Therapeutic Radiopharmacy and Pre-Clinical Facilities. About Authorized Therapeutics, most commonly used were 131I, 177Lu-DOTATATE, 177Lu-PSMA, 223Ra and 90Y-TARE (>60%). Interestingly, about 50% used other Authorized Therapeutics and

<10% no Authorized Therapeutics. Most responders administered Authorized Therapeutics in a unit of Nuclear Medicine (>90%), thanks to national public reimbursement (>60%). Half responders had access to ready-to-use Experimental Therapeutics (49%) and some had no access to Experimental Therapeutics (35%). At the moment, Experimental Therapeutics were mostly limited to 177Lu compounds (60%), followed by 225Ac in some cases (43%). Most responders had access to new EU CTIS portal for clinical trials authorizations (57%), but some asked to local Ethical Committees (30%). Main funding schemes for Experimental Therapeutics seemed by Companies (60%), over no-profit schemes (40%). ***Conclusion:*** From this preliminary Thera4Care Survey data, the context of Theranostics worldwide seems promising but heterogeneous, due to different national and local issues, especially about access and regulatory. Access to Authorized Therapeutics and spread of Experimental Therapeutics could be allowed thanks to the engagement of proper stakeholders at a national and international level. ***References:*** - IHI JU grant agreement 101172788.

OP-819

Comparative Study of Hematological and Survival Outcomes in Reduced vs. Standard Dose Ac-225-PSMA Radioligand Therapy

A. Luna Mass*, S. Raad, R. Bundschuh, S. Hoberück, M. Miederer, C. Brogsitter;*
Universitätsklinikum Carl Gustav Carus Dresden, Dresden, GERMANY.

Aim/Introduction: This retrospective study aimed to evaluate whether individualized dose reduction, adjusted according to baseline clinical characteristics, impacts overall survival (OS) and hematological side effects of Prostate Specific Membrane Antigen (PSMA)-targeted Ac-225 radioligand therapy (RLT). ***Materials and Methods:*** A retrospective analysis of 33 consecutive patients who underwent Ac-225 based PRLT between 2018 and 2023. While 18 patient received reduced doses of 4-6 MBq Ac-225-PSMA-I&T (mean 4.8 MBq ± 0.2) the other 15 were apllied a standard dose of 6-8 MBq Ac-225-PSMA-I&T (mean 6.8 MBq ± 0.82). Baseline clinical data were systematically collected, including bone marrow reserve parameters, prostate-specific antigen (PSA) levels, and tumor staging in pretherapeutic PSMA-targeted positron emission tomography (PET) according to the PROMISE V2 criteria. Tumor burden was assessed using the software aPROMISE to analyze and compare the semiquantitative metrics between groups, including PET-based total tumor volume (TVTotal), SUVmaxTotal, and SUVmeanTotal. Inflammatory markers, such as LDH and CRP, as well as renal function (GFR), were also evaluated. The Mann-Whitney U test was used for non-parametric variables, while Student's t-test was applied to normally distributed data. A p-value <0.05 was considered statistically significant. ***Results:*** There were no statistically significant differences between the two groups in baseline tumor burden assessed by SUVmaxTotal (p = 0.551), SUVmeanTotal (p = 0.194), and TVTotal (p = 0.268). The reduced-dose group showed significantly lower baseline hemoglobin levels (10.5 vs. 11.4 g/dL, p = 0.048) and higher CRP values (9.85 vs. 8.8 mg/L, p = 0.039), indicating preexisting increased hematological and inflammatory alterations. Although PSA levels were higher (742.0 vs. 150.45 ng/mL, p = 0.082) and glomerular filtration rate was lower (73.5 vs. 87.4 mL/min, p=0,064) in the reduced-dose group, these differences did not reach statistical significance. In particular, there was no significant difference in overall survival between the reduced and standard dose groups (OS 6,43 months ± 4,3 vs. 8,13 months ± 3,36 p = 0.317). ***Conclusion:*** Our findings indicate that individualized dose reduction of Ac-225-PSMA does not negatively impact overall survival when compared to the standard dosing regimen. This pivotal result supports the feasibility of patient-tailored, lower-dose protocols that may preserve therapeutic efficacy while potentially reducing treatment-related adverse effects. It also highlights the need for continued research to optimize therapeutic strategies for patients with advanced prostate cancer.

OP-820

Promising Efficacy of [^{177}Lu]Lu-PSMA Radioligand Therapy in Hormone Treatment-Naive Metastatic Hormone-Sensitive Prostate Cancer Patients

I. Langrate[1]*, H. Einspieler*[1]*, E. Kretschmer-Chott*[1]*, S. Schmitl*[1]*, L. Nics*[1]*, S. Shariat*[1,2,3]*, M. Hacker*[1]*, G. Kramer*[2]*, S. Rasul*[1]*;*
[1]Department of Biomedical Imaging and Image-Guided Therapy, Division of Nuclear Medicine, Medical University of Vienna, Vienna, AUSTRIA, [2]Department of Urology, Medical University of Vienna, Vienna, AUSTRIA, [3]Department of Urology, Comprehensive Cancer Center, Medical University of Vienna, Vienna, AUSTRIA.

Aim/Introduction: Radioligand therapy (RLT) with [^{177}Lu]Lu targeting prostate specific membrane antigen receptors (PSMA) is approved as a third-line treatment for patients with metastatic castration resistant prostate cancer. Here, we aimed to explore whether PSMA-RLT could serve as an effective early-line therapeutic alternative for hormone treatment-naive patients with metastatic hormone-sensitive prostate cancer (mHSPC). ***Materials and Methods:*** This retrospective study included mHSPC patients with no previous history of systemic hormone treatment, who underwent [^{177}Lu]Lu-PSMA RLT therapy between June 2015 and December 2024. Hematological and biochemical parameters were evaluated before, during, and after the RLT. Kaplan-Meier models were used to estimate prostate-specific antigen (PSA) response and progression-free survival (PFS). ***Results:*** Collectively, 25 mHSPC patients with a mean age of 66.9 (range: 55-77) years at the time of the first therapy cycle were eligible for this analysis. Patients received 3 to 6 RLT cycles (9 patients received 3 cycles, 2 received 4 cycles, 6 received 5 cycles, 8 received 6 cycles). One month after the last PSMA-RLT cycle, 76% of patients (19 out of 25) showed any PSA decline (median PSA: 3.15 ng/mL before vs 0.54 ng/mL after, p<0.001). Among the 19 responders, 89.4% (17 out of 19) showed a ≥ 50% PSA decline, and 57% (11 out of 19) experienced a decline of ≥ 80%. The median PFS among men who had ≥ 50% PSA decline 1 month after the last RLT cycle was 78 weeks (range: 40-215.7 weeks) compared to 14 weeks (range: 5 - 38 weeks) in men who did not experience any PSA decline (p<0.001). Median overall survival was not reached. No therapy-related side effects were reported. Hematological and renal parameters remained within normal range before and after treatment. The values of alkaline phosphatase and lactate dehydrogenase dropped after the last RLT from an average of 136.2 to 77.7 U/l (p=0.146) and from an average of 197.0 to 183.3 U/l (p=0.030), respectively. ***Conclusion:*** Systemic PSMA-RLT demonstrates efficacy and good tolerability in hormone treatment-naive mHSPC patients. These findings suggest that PSMA-targeting RLT may be applicable not only in advanced-stage prostate cancer, but also in patients with earlier-stage of the disease. Further prospective studies are warranted.

OP-821

Renal Effect of ^{177}Lu-PSMA Radioligand Therapy: A Prospective Study in Metastatic Castration Resistant Prostate Cancer Patients

R. Mehra*, P. Chauhan, A. H. Nazar;*
Sanjay Gandhi Post Graduate Institute of Medical Sciences, Lucknow, INDIA.

Aim/Introduction: ^{177}Lu-PSMA radioligand therapy (RLT) has emerged as a promising treatment for metastatic castration-resistant prostate cancer (mCRPC). However, PSMA expression in proximal tubular cells raises concerns about nephrotoxicity. This study aimed to assess the renal outcomes of ^{177}Lu-PSMA-RLT using measured glomerular filtration rate (mGFR) with 99mTc-DTPA plasma clearance, which provides more accurate assessment compared to estimated GFR methods commonly used in

previous studies [1-4]. ***Materials and Methods:*** This prospective observational study included 36 mCRPC patients who received ^{177}Lu-PSMA-RLT. All patients received a minimum of 3 cycles, with a subset (n=14) completing 6 cycles. Renal function was evaluated at baseline and after 3rd cycle using mGFR via Tc-99m DTPA plasma clearance (Russell's method). For comparative analysis, 50 evaluable treatment periods were assessed. Nephrotoxicity was graded according to CTCAE v5.0 criteria, with clinically significant decline defined at ≥10%, ≥20%, and ≥30% mGFR reduction thresholds. ***Results:*** Baseline mean mGFR was 52.5 ± 14.5 mL/min/1.73m^2. Following therapy, mean mGFR decreased to 47.6 ± 14.1 mL/min/1.73m^2 (p=0.0023), representing a mean percentage decline of 9.3 ± 25.2%. Clinically significant decline thresholds were met in 46%, 34%, and 18% of patients for ≥10%, ≥20%, and ≥30% mGFR reduction, respectively. Grade worsening occurred in 26.0% of patients, improvement in 12.0%, and stability in 62.0%. Notably, patients with pre-existing Grade 2 nephrotoxicity (n=32) demonstrated minimal mean percentage decline (0.9%) compared to those with Grade 1 (20.0%) and Grade 3 (22.4%). ***Conclusion:*** ^{177}Lu-PSMA-RLT is associated with statistically significant renal function decline, with nearly half of the patients experiencing clinically meaningful reductions in mGFR. This study highlights the importance of using measured GFR methods rather than estimated GFR for accurate renal function monitoring in these patients, as the latter substantially underestimates toxicity rates. ***References:*** 1. Sartor O, de Bono J, Chi KN, et al. Lutetium-177-PSMA-617 for metastatic castration-resistant prostate cancer. N Engl J Med. 2021;385(12):1091-1103. 2. Yadav MP, Ballal S, Sahoo RK, et al. Radioligand therapy with 177Lu-PSMA for metastatic castration-resistant prostate cancer: a systematic review and meta-analysis. Am J Roentgenol. 2019;213(2):275-285. 3. Gallyamov M, Meyrick D, Barley J, Lenzo N. Renal outcomes of radioligand therapy: Experience of 177Lutetium-prostate-specific membrane antigen ligand therapy in metastatic castrate-resistant prostate cancer. Clin Kidney J. 2020;13(6):1049-1055. 4. Yordanova A, Becker A, Eppard E, et al. The impact of repeated cycles of radioligand therapy using [177Lu]Lu-PSMA-617 on renal function in patients with hormone refractory metastatic prostate cancer. Eur J Nucl Med Mol Imaging. 2017;44(9):1473-1479.

OP-822

Evidence-based Clinical Protocols to Monitor Efficacy of [^{177}Lu]Lu-PSMA Radiopharmaceutical Therapy in Metastatic Castration-Resistant Prostate Cancer using Real-World Data

L. Djaileb[1], *L. Unterrainer*[2], *N. De Leiris*[1], *M. Unterrainer*[3], *K. Kiraz*[1], *H. Ilhan*[2], *A. Gafita*[4];
[1]*University Grenoble Alpes, Grenoble, FRANCE,* [2]*LMU University Hospital, LMU Munich, Munich, GERMANY,* [3]*Die Radiologie, Munich, GERMANY,* [4]*John Hopkins, Baltimore, MD, UNITED STATES OF AMERICA.*

Aim/Introduction: To assess the prognostic value of post-therapy [^{177}Lu]Lu-PSMA (LuPSMA)-SPECT/CT by visual Response Evaluation Criteria In PSMA-imaging (RECIP) 1.0 during LuPSMA radioligand therapy and to develop an evidence-based clinical protocol to monitor efficacy to LuPSMA. ***Materials and Methods:*** Patients with metastatic castration-resistant prostate cancer who received LuPSMA between April 2019 and November 2023 and underwent at least two LuPSMA cycles were retrospectively included. Pairs of baseline and interim LuPSMA-SPECT/CT (SPECT) and PSMA-PET/CT (PET) after two therapy cycles were analyzed for visual RECIP 1.0. Changes in PSA levels at 12 wk were categorized by PCWG3 and combined with RECIP 1.0 reads to determine progression using a composite classification method PSA + RECIP. The primary outcome was the prognostic value of post-therapeutic SPECT by RECIP 1.0 for overall survival (OS). The clinical protocol was developed based on the prognostic accuracy (C-index) of SPECT versus PET and SPECT+PSA versus PET+PSA. ***Results:*** 105 patients were eligible and included. Progression disease (PD) by SPECT was associated with shorter OS compared to stable disease (SD) (HR=2.5; 1.2-5.3; p=0.015) and to partial response (PR)(HR=6.5; 2.7-15.7; p<0.001). 73/105 (70%) patients received a PET after 2 cycles. 7/73 (10%), 30/73 (41%), 22/73 (30%), and 30/73 (41%) patients had tumor progression by SPECT, PET, SPECT+PSA, and PET+PSA, respectively. The C-index for SPECT was inferior compared to PET (0.54 vs 0.66; p<0.001), while SPECT+PSA did not differ significantly from PET+PSA (0.62 vs 0.66; p=0.07). ***Conclusion:*** Post-therapeutic LuPSMA-SPECT/CT by RECIP 1.0 after two therapy cycles therapy is prognostic for OS. LuPSMA-SPECT/CT identified significantly fewer patients with RECIP-PD, however, LuPSMA-SPECT/CT+PSA achieved similar prognostic accuracy to PSMA-PET/CT+PSA for response evaluation during LuPSMA.

OP-823

Impact of premedication on the frequency and intensity of Fatigue and Nausea in [^{177}Lu]Lu-PSMA-617 therapy: A Multicenter Analysis

W. Bosbach[1], *K. Sriramachandran*[2], *N. Gözlügöl*[2], *R. Saiyed*[2], *M. Cuzzocrea*[3], *S. Pop*[4], *A. Rominger*[2], *G. Paone*[3,5], *I. A. Burger*[4,6], *A. Afshar-Oromieh*[2];
[1]*Department of Nuclear Medicine, Inselspital, Bern University Hospital, University of Bern, Bern, Switzerland, Bern, SWITZERLAND,* [2]*Department of Nuclear Medicine, Inselspital, Bern University Hospital, University of Bern, Bern, SWITZERLAND,* [3]*Clinic of Nuclear Medicine and Molecular Imaging, Imaging Institute of Southern Switzerland, Ente Ospedaliero Cantonale, Bellinzona, SWITZERLAND,* [4]*Department of Nuclear Medicine, affiliated Hospital for Research and Teaching of the Faculty of Medicine of the University of Zurich, Baden, SWITZERLAND,* [5]*Faculty of Biomedical Sciences, Università della Svizzera italiana (USI), Lugano, Switzerland, Lugano, SWITZERLAND,* [6]*Department of Nuclear Medicine, University Hospital Zurich, University of Zurich, Zurich, Switzerland., Zurich, SWITZERLAND.*

Aim/Introduction: [^{177}Lu]Lu-PSMA radioligand therapy ([^{177}Lu]Lu-PSMA-RLT) is an established treatment for metastatic castration-resistant prostate cancer (mCRPC).IThe pivotal phase 3 VISION study reported adverse effects such as nausea (35.3%), vomiting (18.9%) and fatigue (43.1%)when [^{177}Lu]Lu-PSMA-617 was added to protocol-permitted standard care. This study investigated whether premedication with corticosteroids and antiemetics prior to the administration of [^{177}Lu]Lu-PSMA-617 can reduce the incidence and severity of these side effects in routine clinical practice. ***Materials and Methods:*** We conducted a multicenter retrospective analysis incorporating data from three Swiss institutions - Bern, Baden, and Bellinzona. The study included patients who received a minimum of two cycles of [^{177}Lu]Lu-PSMA-617 therapy, some as part of a Managed Access Program. All participants were premedicated with 8 mg dexamethasone and 8 mg ondansetron approximately 30 minutes prior to the administration of [^{177}Lu] Lu-PSMA-617. Incidence of nausea, vomiting and fatigue were evaluated following each treatment cycle using standardized questionnaires . ***Results:*** An analysis of 195 patient questionnaires (equivalent to 195 treatment cycles) demonstrated lower rates of nausea (7.7%) and vomiting (3.6%) compared to those reported in the VISION trial (35.3% and 18.9%, respectively). While the overall prevalence of fatigue was higher in our cohort (67.2% vs. 43.1% in the VISION trial), only 3% of patients developed fatigue following the initiation of [^{177}Lu]Lu-PSMA-RLT. This indicates that 64.2% of patients were already experiencing fatigue prior to the start of therapy. ***Conclusion:*** Premedication with 8mg dexamethasone and 8mg ondansetron before administration of [^{177}Lu]Lu-PSMA-RLT appears to substantially reduce the incidence of nausea and vomiting compared to historical data from the VISION trial.

OP-824

Influence of bone marrow segmentation approach on absorbed dose estimates in a single time point protocol for ^{177}Lu-PSMA-617

T. Frigerio, *Z. Ells, M. Dahlbom, J. Calais, J. Hoffman, C. Meyer; UCLA, Los Angeles, CA, UNITED STATES OF AMERICA.*

Aim/Introduction: Bone marrow is a dose-limiting organ for 177Lu-PSMA radiopharmaceutical therapy. However, the segmentation required for accurate absorbed dose (AD) estimates for bone marrow represent a clinical challenge. This study evaluates the influence of two bone marrow segmentation approaches on the AD estimate using a single time point dosimetry protocol on patients with late stage mCRPC treated with 177Lu-PSMA-617. ***Materials and Methods:*** This study's cohort consists of 19 patients from the RESIST-PC phase II trial (NCT03042312), with a high tumor burden and bone disease involvement. Patients underwent post-therapy quantitative SPECT/CT imaging 24h after the first cycle of 177Lu-PSMA-617 (7.2 ± 0.7 GBq). Two segmentation algorithms were compared: the first using lumbar vertebrae (LV) as a bone marrow surrogate, the second using the whole skeleton (WS). In the LV method, L1-L5 were contoured manually, while vertebrae with significant disease involvement were excluded. When all LV presented tumor burden, an alternative representative bone (thoracic vertebrae, or humerus) was selected for segmentation. In the WS method, bones were first segmented using a publicly available neural network tool, TotalSegmentator. Bone marrow volumes were segmented using Hounsfield unit thresholding based on voxel distributions in individual bones to separate soft tissue from cortical bone, and excluding lesions using a SPECT SNR cutoff of 5. This fully automated algorithm produces a bone marrow mask for the SPECT/CT field of view. AD calculations were performed using the Hänscheid approach for single time point dosimetry. Finally, we performed a one sample t-test on the absolute value of the normalized dose difference (ADD). ***Results:*** The two methods yielded significant intra-patient differences of AD estimates, with a mean ADD of 60%, or 0.19 ± 0.20 Gy ($p<0.001$). LV AD averaged to 0.27 Gy (avg volume 52 ± 37 ml) and the WS AD averaged to 0.26 Gy (650 ± 190 ml). The disagreement in dose estimate varied in direction and magnitude depending on disease distribution. ***Conclusion:*** Comparison of estimated bone marrow AD indicates a significant difference attributable to the segmentation method. This suggests the LV method may not be an appropriate surrogate for bone marrow estimation, as it is not representative of the dose to the whole skeletal volume. The WS method produces bone marrow masks with consistent methodology while the LV method relies on patient-specific adjustments. Further investigation of a larger patient cohort will further validate these findings and explore the correlation with clinical outcome.

OP-825

Clinical Trial Protocol for RHINO trial: Prospective Single-center Phase I/II study of RHN001-Dx/Tx in men with PSMA-positive prostate cancer post adjuvant androgen deprivation therapy and/or taxane-based chemotherapy.

H. Ndlovu[1,2], *J. Cardinale*[3,4], *C. Kratochwil*[3], *T. de Bruin*[1,2], *C. Davis*[1,2], *L. Smith*[1,2], *S. Sibiya*[1,2], *Y. V. Mzizi*[1,2], *A. Mdlophane*[1,2], *S. Mdanda*[1,2], *M. Shungube*[1,2], *M. A. Mokoena*[1,2], *T. Ratsakatika*[1,2], *S. Bassa*[5], *C. Corbett*[1,2], *K. Ramonaheng*[1,2], *M. Qebetu*[1,2], *J. Kabunda*[1,2], *K. G. Mokoala*[1,2], *J. Barlow*[6], *F. L. Giesel*[3,4], *M. M. Sathekge*[1,2]; [1]*Nuclear Medicine Research Infrastructure(NuMeRI), Pretoria, SOUTH AFRICA,* [2]*Department of Nuclear Medicine, Steve-Biko Academic Hospital, University of Pretoria, Pretoria, SOUTH AFRICA,* [3]*Department of Nuclear Medicine, University Hospital Heidelberg, Heidelberg, GERMANY,* [4]*Department of Nuclear Medicine, Medical Faculty and University Hospital Duesseldorf, Heinrich Heine University Duesseldorf, Duesseldorf, GERMANY,* [5]*Department of Radiation Oncology, University of Pretoria, Pretoria, SOUTH AFRICA,* [6]*Telix Pharmaceuticals Limited, Melbourne, AUSTRALIA.*

Aim/Introduction: [^{177}Lu]Lu-PSMA is an effective class of therapy for patients with metastatic castration-resistant prostate cancer (mCRPC) and its role has evolved to include prechemotherapy patients; however, access to it in low and middle-income countries is hampered by a variety of factors, including cost. This justifies the need for a cheaper, easily accessible PSMA targeting therapy with relatively similar efficacy to [^{177}Lu]Lu-PSMA. The theranostic pair ^{188}Re/^{99m}Tc which is completely generator based and may offer a chance to disclose this valuable therapy for countries with low PET infrastructure and/or lacking nuclear infrastructure. Within the RHINO trial we aim to identify the recommended Phase 2 dose (RP2D), and schedule of administration for RHN001-Tx (^{188}Re-PSMA) and assess the safety, including the dosimetry of RHN001-Tx and RHN001-Dx (^{99m}Tc-PSMA) in men with prostate cancer. ***Materials and Methods:*** This single-center, single-arm, phase I/II trial will recruit patients with prostate cancer in three cohorts. Cohort A will assess the dosimetry of diagnostic use of RHN001-Dx in patients with newly diagnosed prostate cancer and low-volume disease. Cohort B will assess the dosimetry of therapeutic use of RHN001-Tx in patients with newly diagnosed prostate cancer and low-volume disease. In Cohort B we aim to assess the overall safety, including the dosimetry of RHN001-Tx in men with PSMA-positive prostate cancer with or without prior therapies. The dose escalation will be done for Cohort C with 3 patients per dose level, each in the range of 50-100 % maximum tolerable dose (MTD; 4-8GBq currently estimated). Up to 4 cycles of RHN001-Tx will be administered intravenously every 4-6 weeks. The maximum tolerated dose will be defined as the highest activity level at which a dose-limiting toxicity. Key eligibility criteria include a diagnosis of mCRPC with progression on androgen-deprivation therapy and/or taxane-based chemotherapy and Eastern Cooperative Oncology Group performance status of no more than 2, and no prior treatment with another radioisotope. Secondary objectives include assessing health-related quality of life using the Functional Assessment of Cancer Therapy- Prostate (FACT-P), Brief Pain Inventory-Short Form (BPI-SF), EQ-5D-5L and XeQOLS xerostomia questionnaire. ***Results:*** No results at this time as trial is currently enrolling. The trial has received ethical and regulatory approval. ***Conclusion:*** Enrolment is ongoing. This Trial is supported by Rhine Pharma GmbH, a Telix Company.

1801

Wednesday, October 8, 2025, 09:45 - 11:15

Auditorium

CME 14 - Bone & Joint Committee: NM Sports, it's in the Game

OP-826

J. Bliss; *London Bridge Orthopaedics, London, UNITED KINGDOM.*

OP-827

M. De Jonge; *St. Antonius Ziekenhuis, Amsterdam, NETHERLANDS.*

OP-828

T. Van Den Wyngaert; *University of Antwerp and Antwerp University Hospital, Antwerp, BELGIUM.*

OP-829

R. Dhawan; *Imperial College Healthcare NHS Trust, London, UNITED KINGDOM.*

1802

Wednesday, October 8, 2025, 09:45 - 11:15

Room 112 (Arena)

Special Track 14 - Translational Molecular Imaging & Therapy Committee: Challenge the Expert: How can Lessons from Radiobiology be Applied to the Design of Clinical Trials?

OP-830
The Radiobiologists View

J. Nonnekens; *Erasmus Medical Center, Departments of Molecular Genetics and Radiology & Nuclear Medicine, Rotterdam, NETHERLANDS.*

OP-831
The Physicians View

E. Deshayes; *University hospital, Montpellier, Department of Nuclear Medicine, Montpellier, FRANCE.*

OP-832a
Challengers' Team

S. Kleinendorst; *Radboud Universtity Medical Center, Department of Medical Imaging, Nijmegen, NETHERLANDS.*

OP-832b
Challengers' Team

H. Koch; *University Hospital Lausanne, Lausanne, SWITZERLAND.*

OP-832c
Challengers' Team

S. Schumann; *University Hospital Würzburg, Würzburg, GERMANY.*

OP-832d
Challengers' Team

W. Delbart; *University Hospital Brussels, Institute Jules Bordet, Brussels, BELGIUM.*

1803

Wednesday, October 8, 2025, 09:45 - 11:15

Room 113

LIPS Session 14 - Neuroimaging Committee: PET Response Assessment in Neurooncology

OP-833
PET RANO Criteria in Gliomas

N. Albert; *LMU University Hospital, Department of Nuclear Medicine, Munich, GERMANY.*

OP-834
Meningiomas

N. Tolboom; *UMC Utrecht, Department of Nuclear Medicine, Utrecht, NETHERLANDS.*

OP-835
Brain Metastases

A. Verger; *CHRU Nancy, Vandoeuvre les Nancy, FRANCE.*

OP-836
CNS Lymphomas

L. Rozenblum; *Groupe Hospitalier Pitié-Salpêtrière, Assistance Publique-Hôpitaux de Paris (AP-HP), Sorbonne Université, Paris, FRANCE.*

1804

Wednesday, October 8, 2025, 9:45 - 11:15

Room 114

M2M Track - TROP Session - Radiopharmaceutical Sciences + Translational Molecular Imaging & Therapy Committee: Advances in Preclinical Cardiovascular Imaging

OP-837
Inflammation Imaging via CD206-Targeted ^{68}Ga-NOTA-UNO in the Mouse Myocardial Infarction Model

D. Zheng, *Y. Lv, Z. Zhou, S. Wei, Z. Lin, Z. Wu, Y. Deng, X. Lv, X. Song, C. Qin, X. Lan;*
Department of Nuclear Medicine, Union Hospital, Tongji Medical College, Huazhong University of Science and Technology, Wuhan, CHINA.

Aim/Introduction: After myocardial infarction (MI), cardiac inflammatory-repair response correlates with ventricular remodeling and heart failure progression. Anti-inflammatory therapies demonstrate substantial potential, necessitating novel monitoring strategies. Macrophages, significant both quantitatively and functionally, are crucial for innovative monitoring. CD206, a reparative macrophage marker, is specifically targeted by the UNO peptide. This study aimed to evaluate the utility of a CD206-targeted PET probe, 68Ga-NOTA-UNO, for macrophage imaging in the mouse MI model. ***Materials and Methods:*** ^{68}Ga-NOTA-UNO was synthesized by reacting NOTA-UNO with $^{68}GaCl_3$ at 95°C for 15-minutes at pH 3.5, then purified using a C18 column. PET imaging and biodistribution studies were performed in MI and sham-operated mice at 0.5 h post-injection. Ex-vivo cardiac imaging was conducted to further confirm imaging specificity. Tracer uptake in infarcted and remote myocardium, liver, blood, and muscle was quantified via region-of-interest (ROI) analysis, expressed as percentage injected dose per gram (%ID/g). To map inflammatory activity spatially, ^{18}F-FDG metabolic imaging was performed to delineate infarct regions and compared with the ^{68}Ga-NOTA-UNO uptake region. Flow cytometry was employed to assess the differential expression of CD45 (leukocytes), F4/80 (macrophages), and CD206 among infarcted, remote, and sham-operated myocardium at day 7. Data were analyzed using Student's t-test and one-way ANOVA, with statistical significance as $P < 0.05$. ***Results:*** ^{68}Ga-NOTA-UNO exhibited > 99% radiochemical purity. Tracer uptake was obvious in the infarcted myocardium, but not in the remote myocardium or sham-operated mice. Quantitative analysis revealed higher uptake ratios in infarcted myocardium versus the corresponding area of sham groups, P values for infarcted myocardium, infarct/remote myocardium, infarct/liver, and infarct/blood 0.011, 0.0002, 0.001, 0.000086, respectively. Both ex vivo imaging and the biodistribution experiment indicated higher ^{68}Ga-NOTA-UNO uptake in the infarcted myocardium compared to the remote myocardium and the sham-operated group, whereas the biodistribution experiment showed no significant difference in other organs. The ^{68}Ga-NOTA-UNO uptake region spatially matched ^{18}F-FDG metabolic defects. Flow cytometry confirmed elevated proportions of $CD45^+$ leukocytes, $CD45^+F4/80^+$ macrophages, and CD206 in infarcted myocardium versus remote or sham-operated myocardium. $CD206^+$ macrophages ($CD45^+F4/80^+CD206^+$) constituted a significantly higher proportion of total macrophages ($CD45^+F4/80^+$) in both infarcted and remote myocardium, compared to sham-operated mice ($P < 0.05$), indicating increased reparative macrophage polarization by day 7 post-MI. ***Conclusion:*** This study successfully synthesized the PET probe ^{68}Ga-NOTA-UNO and verified its

feasibility for non-invasive visualization of CD206+ macrophages in MI models. These findings may offer a novel tool for guiding and evaluating anti-inflammatory therapies in cardiovascular disease.

OP-838

Synergistic effects of dapagliflozin and low salt diet evaluated by multi-nuclear ^{18}F-FDG PET-MRI (^{23}Na/^{1}H) in radiation-induced heart failure with preserved ejection fraction (HFpEF)

H. Rida[1], *M. Guetlin*[1,2], *C. Simard*[1], *M. Naveau*[3], *S. Allouche*[4], *L. Coulbault*[1], *P. Dupont*[1], *A. Lebrun*[1], *M. Joubert*[1,2], *A. Manrique*[1,5]; [1]*Cyceron UR4650 PSIR, Université Caen Normandie, Caen, FRANCE,* [2]*Diabetology, CHU de Caen, Caen, FRANCE,* [3]*UAR3408/US50 Cyceron, CNRS, INSERM, Université Caen Normandie, Caen, FRANCE,* [4]*Biochimie, CHU de Caen, Caen, FRANCE,* [5]*Nuclear Medicine, CHU de Caen, Caen, FRANCE.*

Aim/Introduction: Due to the cardiotoxic effects of radiotherapy, breast cancer patients are at increased risk of developing heart failure. Sodium-glucose co-transporter 2 (SGLT2) inhibitors, originally designed as antidiabetic drugs, demonstrated cardiovascular protection. However, the precise mechanisms behind these cardiovascular effects are still not fully understood due to their combined effects on glucose and sodium. ^{18}F-FDG PET and multi-nuclear MRI (^{23}Na/^{1}H) offer the potential to evaluate both tissue sodium content and cardiac glucose metabolism, in a murine model of radiation-induced cardiotoxicity on a normal and moderately low salt diet. ***Materials and Methods:*** Sixty-two Sprague Dawley rats were randomly divided into control (Ctrl, non-irradiated, n=13) and irradiated group (receiving 10 Gy of cardiac irradiation). At 3 months, the irradiated group was further subdivided into three subgroups receiving: placebo (PCB, n=21), dapagliflozin (DAPA, n=13), and dapagliflozin with 30% salt reduction (DAPA DIET, n=15). After 6 weeks of treatment, cardiac glucose metabolism was assessed through dynamic ^{18}F-FDG PET imaging using a 7-T PET-MRI system (Bruker Biospin). Left ventricular glucose metabolism was assessed by the net influx constant Ki. Tissue sodium content in the skin, pectoral muscle, and heart was measured using Na-MRI with a ^{1}H/^{23}Na surface coil. Left ventricular function was evaluated by echocardiography. ***Results:*** ^{18}F-FDG PET showed a significant increase in cardiac glucose metabolism in the PCB while DAPA reduced this metabolism. The influx rate (Ki) was 0.038±0.018 min^{-1} in PCB vs. 0.019±0.01 min-1 in DAPA (p=0.0005) vs. 0.024±0.007min-1 in DAPA DIET (p=0.0250) and vs. 0.021 ±0.01 min-1 in Ctrl (p=0.01). In the skin, the ^{23}Na signal significant increase in PCB (0.35±0.16) vs. DAPA (0.23±0.07, p=0.0295) vs. DAPA DIET (0.18±0.06, p=0.0004) but not vs. Ctrl (0.25±0.08, p=0.1). In the muscle, ^{23}Na MRI signal was increased in PCB (0.3±0.12) vs. DAPA (0.15±0.05, p=0.0007) vs. DAPA DIET (0.12±0.05, p<0.0001) and vs. Ctrl (0,18±0,06, p=0.0053). In the myocardium, the ^{23}Na signal was increased in PCB (0.21±0.13) vs. DAPA DIET (0.1±0.03, p=0.0092) vs. Ctrl (0.1±0.05, p= 0.03) but not vs. DAPA (0.13±0.04, p=ns).After treatment, ejection fractions was preserved in all groups, as expected (Ctrl: 71±7%, PCB: 76±8%, DAPA: 79±8%, DAPA DIET: 72±6%, p=ns). ***Conclusion:*** Cardiac irradiation resulted in increased cardiac glucose metabolism and sodium MRI signals. Dapagliflozin combined with a low-salt diet, reduced both of them while preserved LV systolic function.

OP-839

Longitudinal Multimodal Imaging Elucidates Temporal Metabolic Reprogramming and Mitochondrial-Microvascular Dysfunction in Diet-Induced HFpEF

J. Zhao[1,2,3], *Z. Xiang*[1,2,3], *Q. Wang*[1,2,3], *R. Shen*[1,2,3], *Y. Wen*[1,2,3], *X. Liu*[1,2,3], *P. Wu*[1,2,3], *Z. Wu*[1,2,3], *S. Li*[1,2,3];
[1]*Department of Nuclear Medicine, First Hospital of Shanxi Medical University, Taiyuan, CHINA,* [2]*Shanxi Key Laboratory of Molecular Imaging, Shanxi Medical University, Taiyuan, CHINA,* [3]*Collaborative Innovation Center for Molecular Imaging of Precision Medicine, Taiyuan, CHINA.*

Aim/Introduction: Heart failure with preserved ejection fraction (HFpEF) involves complex interactions among metabolic dysregulation, mitochondrial dysfunction, and microvascular impairment. However, the temporal progression of these pathological events remains undefined. This study employs serial molecular imaging and metabolomics to map the dynamic evolution of HFpEF in a murine model. ***Materials and Methods:*** Male C57BL/6 mice were randomly assigned to two groups: one group received a high-fat diet (60% of calories from fat) combined with L-NAME (0.5 g/L), while the other group served as the control. Longitudinal evaluations included weekly monitoring of body weight and blood pressure, echocardiograms at weeks 15 and 25, assessments of exercise tolerance, and PET/CT scans at weeks 5, 15, and 25. The PET/CT imaging employed [^{18}F] Flurpiridaz for myocardial perfusion, [^{18}F] FDG for glucose uptake, and TSPO-targeted [^{18}F] DPA-714 for mitochondrial stress. The final analysis at week 36 assessed cardiopulmonary mass, histopathology (including hypertrophy and fibrosis), and untargeted metabolomics. ***Results:*** HFD/L-NAME led to weight gain, hypertension, exercise intolerance, and progressive cardiac hypertrophy. Stress myocardial blood flow (MBF, [^{18}F]Flurpiridaz) decreased by week 15 (8.42 vs 15.87 ml/g/min, p>0.05) and deteriorated by week 25 (p<0.05). The compensatory elevation of LVEF at week 15 (71.70% ± 7.60%) returned to normal by week 25 (59.50% ± 15.03%). FDG uptake increased from week 15 (P<0.05) to week 25 (P<0.01), while TSPO uptake ([^{18}F]DPA-714) surged at week 25 (P<0.001), correlating with terminal heart/lung mass (week 15: r_{heart}=0.38, p<0.05; r_{lung}=0.54, p<0.01; week 25: r_{heart}=0.74, p<0.001; r_{lung}=0.47, p<0.01). Histopathological analysis at week 36 confirmed the presence of hypertrophy, fibrosis, and lipidosis. Metabolomics identified elevated trimethyllysine, which was positively correlated with TSPO at week 25 (r=0.84, p<0.01). Additionally, thiamine monophosphate (TMP) was decreased and showed an inverse correlation with FDG (r=-0.75, p<0.01). These findings are mechanistically linked to mitochondrial dysfunction and glycolytic flux via GLUT1/4. ***Conclusion:*** This study delineates a temporal HFpEF cascade: early microvascular dysfunction (reduced MBF) and metabolic adaptation (increased FDG uptake) precede mitochondrial failure (elevated TSPO expression) and culminate in terminal structural remodeling. TSPO uptake at week 15 predicts later cardiopulmonary hypertrophy, while trimethyllysine and thiamine monophosphate (TMP) imbalances drive mitochondrial-metabolic crosstalk, exacerbating disease progression. Longitudinal multimodal imaging (MBF/FDG uptake/TSPO expression) provides a non-invasive framework for staging HFpEF and targeting metabolic-mitochondrial pathways.

OP-840

In vitro functional assessment of cardiac membrane transporter P-glycoprotein with [^{18}F]MC225 by using µ-engineered heart tissues

W. Liu[1], *M. Dannenberg*[2], *R. Slart*[1], *V. Schwach*[2], *G. Luurtsema*[1];
[1]*University Medical Center Groningen, Groningen, NETHERLANDS,* [2]*University of Twente, Enschede, NETHERLANDS.*

Aim/Introduction: P-glycoprotein (P-gp), an efflux transporter with diverse compound effects, and is a vital part of cardiac function. P-gp function at the blood- brain barrier can be measured with PET and the tracer [^{18}F]MC225. To determine if the selective substrate tracer [^{18}F]MC225 also functions in cardiac P-gp, micro-engineered heart tissues (µ-EHTs) utilizing human induced pluripotent stem cell (hiPSC)-derived cardiomyocytes were used. This model offers advantages in potentially reducing animal experiments and allowing direct evaluation on human cells. However, its adoption in nuclear medicine remains very limited. This study aims to evaluate [^{18}F]MC225 as measurement method for cardiac P-gp function using a heart-on-chip model. ***Materials and Methods:*** µ-EHTs were treated with the P-gp inhibitor Tariquidar (200 nM for 30 minutes), while the corresponding control group

was treated with vehicle solution only. In parallel, another set of µ-EHTs was treated with the P-gp inducer Doxorubicin (1 µM for 24 hours), and its control group received the corresponding vehicle. Following treatment, all samples were incubated with [^{18}F] MC225 (1 MBq/mL for 30 minutes). Autoradiographic imaging was performed to assess the distribution of the tracer within the tissue. The expression of P-gp in the µ-EHTs was assessed via immunofluorescent staining. ***Results:*** Immunofluorescent staining showed an increase of P-gp expression after Doxorubicin treatment in µ-EHTs. According to γ-counter measurements, tissues treated with Tariquidar exhibited significantly higher uptake of [^{18}F]MC225 (117.5 ± 33.67%, n = 24; P = 0.035) compared to vehicle control group. In contrast, Doxorubicin-treated tissues showed a significantly reduced uptake (63.97 ± 21.89%, n = 20; P < 0.001) relative to their corresponding untreated controls . Autoradiographic imaging demonstrated a homogeneous uptake of [^{18}F]MC225 within the µ-EHTs and reflected the same trends observed in the γ-counter measurements. ***Conclusion:*** [^{18}F]MC225 effectively demonstrated cardiac P-gp function in µ-EHTs on the heart-on-chip platform. This research sets the stage for future studies using P-gp function to evaluate the efficacy and safety of novel cardiovascular drugs using µ-EHTs.

OP-841

Spatiotemporal TSPO Dynamics Predict Ventricular Remodeling in Pressure Overload: Early Inflammation to Late Mitochondrial Dysfunction

Z. Xiang[1,2,3], *L. Gao*[4], *X. Liu*[1,2,3], *H. Song*[1,2,3], *Z. Qin*[1,2,3], *P. Wu*[1,2,3], *Z. Wu*[1,2,3], *S. Li*[1,2,3];
[1]*Department of Nuclear Medicine, First Hospital of Shanxi Medical University, Taiyuan, CHINA,* [2]*Shanxi Key Laboratory of Molecular Imaging, Shanxi Medical University, Taiyuan, CHINA,* [3]*Collaborative Innovation Center for Molecular Imaging of Precision Medicine, Taiyuan, CHINA,* [4]*Key Laboratory of Cellular Physiology at Shanxi Medical University, Ministry of Education, and the Department of Physiology, School of Basic Medicine, Shanxi Medical University, Taiyuan, CHINA.*

Aim/Introduction: Mitochondrial dysfunction represents a significant mechanism underlying heart disease. The translocator protein (TSPO), located on the outer membrane of mitochondria, exhibits altered expression in various pathological conditions associated with heart disease, making it a potential target for diagnosis and therapy. Research has shown that TSPO-PET effectively identifies early post-infarction myocardial inflammation. Furthermore, TSPO functions as a mitochondrial marker indicative of myocyte dysfunction in heart failure. However, the dynamic pattern of TSPO expression over time and its relationship with prognosis in non-ischemic heart disease remains unclear. ***Materials and Methods:*** Male C57BL/6 mice underwent transverse aortic constriction (TAC) (n=25) and sham surgery (n=25). ^{18}F-DPA-714 TSPO-PET and cardiovascular magnetic resonance imaging (CMR) were conducted at 1, 4 and 8weeks post-surgery. Following imaging, the animals were euthanized (n=5 per time point), and the cell-specificity of abnormal TSPO expression was assessed through immunofluorescence. Differences in TSPO-PET signals between the two groups, as well as the cell-specific origins of TSPO-PET signals during disease progression, were analyzed. Finally, we investigated the correlation between TSPO signals and left ventricular remodeling. ***Results:*** Compared to the sham group, the TAC group exhibited a significant decrease in ejection fraction (EF) at both 4 weeks (61.86 ± 1.32 vs. 55.49 ± 1.87, p<0.01) and 8 weeks (61.86 ± 1.32 vs. 46.16 ± 2.03, p < 0.001). Additionally, the TAC group demonstrated increased accumulation of [18]F-DPA-714 in the heart compared to the sham group at 1 week (SUVmean * Volume: 0.3056 ± 0.0099 vs. 0.1893 ± 0.0035, p<0.05), which localized to activated CD68+ inflammatory cells. Early TSPO-PET signal was predictive of subsequent left ventricular remodeling at 8 weeks (EF: R=-0.5140, p=0.0291). Following a decline at 4 weeks (0.2943 ± 0.1084, p > 0.05), the TSPO-PET signal was concurrently upregulated in cardiomyocytes at 8 weeks (0.4066 ± 0.1022, p < 0.01) despite the absence of inflammatory cell infiltration, indicating mitochondrial impairment. ***Conclusion:*** TSPO-PET captures spatiotemporal shifts from early macrophage-driven inflammation to late cardiomyocyte mitochondrial dysfunction in pressure-overload cardiomyopathy, with early uptake predicting late systolic dysfunction that informs timed interventions to mitigate remodeling.

OP-842

Assessment of cerebral blood flow in extracorporeal cardiopulmonary resuscitation in a pig model of prolonged cardiac arrest: a [^{15}O]water PET study

R. Berti[1], *J. C. Fostitsch*[1], *B. A. Bretthauer*[2], *S. Brixius*[2], *L. Blum*[3], *C. Scherer*[2], *J. Dinkelaker*[4], *J. Haberstroh*[4], *H. J. Busch*[3], *C. Benk*[2], *G. Trummer*[2], *F. Beyersdorf*[2], *M. Mix*[1], *P. T. Meyer*[1], *J. S. Pooth*[3];
[1]*Department of Nuclear Medicine, Medical Center – University of Freiburg, Faculty of Medicine – University of Freiburg, Freiburg, GERMANY,* [2]*Department of Cardiovascular Surgery, Medical Center – University of Freiburg, Faculty of Medicine – University of Freiburg, Freiburg, GERMANY,* [3]*Department of Emergency Medicine, Medical Center – University of Freiburg, Faculty of Medicine – University of Freiburg, Freiburg, GERMANY,* [4]*Department of Experimental Surgery, Center for Experimental Models and Transgenic Service, Medical Center – University of Freiburg, Faculty of Medicine, Freiburg, GERMANY.*

Aim/Introduction: Neurological recovery after prolonged cardiac arrest (CA) remains a major challenge despite advances in resuscitation. Although extracorporeal cardiopulmonary resuscitation (ECPR) rapidly restores circulation, the time course of reperfusion in the different brain regions still remains unclear. To address this, we developed a porcine model to investigate regional cerebral blood flow (rCBF) dynamics during ECPR following prolonged CA for 20 min, aiming to identify perfusion patterns to guide targeted neuroprotective interventions. ***Materials and Methods:*** Four Landrace hybrid pigs underwent PET/CT imaging using [^{15}O]water PET (780 ± 25 MBq). Two to three baseline scans were acquired before normothermic CA induced by ventricular fibrillation. ECPR was initiated at 20 min of CA with a pulsatile blood flow of 5-6 L/min. PET scans were acquired at 8, 24, 46, and 61 minutes after the start of ECPR. rCBF was quantified using a 1-tissue compartment model and the arterial input function with a fixed brain tissue partition coefficient (p = 0.95 ml/cc, rCBF = k_2 * p). Individual rCBF time curves of several cortical and subcortical brain regions were fitted using a nonlinear exponential saturation function, from which λ was derived to estimate regional perfusion recovery. Regions were ranked by λ, and statistical analysis was performed using the Friedman test. ***Results:*** Baseline whole-brain (WB) CBF was consistent across animals (mean ± std = 49.1 ± 11.3 ml/min/100 ml). Following ECPR, all pigs exhibited a rapid increase in WB CBF consistent with exponential recovery. Perfusion recovery across brain regions revealed a reproducible reperfusion hierarchy across pigs despite individual differences in overall timing. Subcortical areas as mesial temporal lobe, striatum and thalamus exhibited the earliest perfusion recovery, followed by the cerebellum. In contrast, cortical regions showed a more delayed response. Among these, lateral temporal, primary visual, and auditory cortices recovered earlier than frontal, motor and lateral occipital regions, while the primary somatosensory and somatosensory association cortices were the last to show reperfusion. The Friedman test (χ^2 = 39.3, p < 0.001) showed significant variation in perfusion timing across regions. ***Conclusion:*** Cerebral reperfusion during ECPR follows a consistent, hierarchically organized pattern with faster recovery in subcortical regions and delayed hyperperfusion in primary and associative cortical areas. This hierarchical pattern of perfusion highlights a temporally structured recovery sequence, beginning

with basic vital function and evolutionarily older regions, and gradually extending to higher-order sensory and cognitive areas. This porcine model may be useful for further exploration of neuroprotective and perfusion-guided strategies after prolonged CA.

OP-843

Dual-tracer PET/CT Reveals the Spatiotemporal Evolution Patternof Fibro-inflammatory InteractionsAfter Myocardial Infarction: A Longitudinal Rodent Study

Y. Hong, *J. Song, L. Li;*
First Hospital of Shanxi Medical University, Taiyuan, CHINA.

Aim/Introduction: This study aims to elucidate the spatiotemporal dynamic evolution of myocardial inflammation and fibrosis after myocardial infarction (MI) using non-invasive dual-tracer (^{18}F-FAPI-74 and ^{18}F-FDG) PET/CT imaging. ***Materials and Methods:*** 10-week-old male Sprague-Dawley rats were divided into MI group (model established by ligating LAD), sham surgery, and blank control groups. Serial PET/CT scans using ^{18}F-FAPI-74 (fibrosis), ^{18}F-FDG (inflammation), and ^{18}F-FDG (infarct) were performed from 1 day to 12 weeks post-MI. The MI regions of interest (ROI) were defined by ^{18}F-FDG metabolic defect. The maximum target-to-background ratio (TBRmax) were calculated as the ratio of the maximum standardized uptake value (SUVmax) to the mean left ventricular blood pool uptake (SUVmean), the abnormal tracer uptake area quantified by polar coordinate bull's-eye mapping. Longitudinal correlations were assessed between imaging findings, serum biomarkers (IL-6, hs-CRP, TGF-β1), and histopathology (HE, Masson, and immunofluorescence staining). ***Results:*** 1. Time-dependent bimodal uptake patterns with highly synchronous: The early peak at 1 week post-MI (^{18}F-FAPI TBRmax:10.60 ± 2.11 vs. 2.35±0.46 , $p < 0.0001$ vs. controls; ^{18}F-FDG TBRmax: 9.73 ± 2.60 vs. 2.09±0.33 , $p < 0.05$ vs. controls) , and a weaker late peak at 10 weeks post-MI (^{18}F-FAPI TBRmax: 4.10 ± 1.15 vs. 1.87±0.12 , $p > 0.05$ vs. controls; ^{18}F-FDG TBRmax: 8.43 ± 2.39 vs. 2.06±0.13 , $p < 0.05$ vs. controls). 2. Uniform spatial distribution with hierarchical differentiation: The abnormal uptake area: ^{18}F-FDG (inflammatory response) > ^{18}F-FAPI (active fibrotic) > ^{18}F-FDG (metabolic infarction) (18.92 ± 3.54% vs. 11.50 ± 3.14% vs. 5.36 ± 1.33% , $p < 0.01$ for all comparisons), but the differences gradually decrease over time. 3. Consistency between blood biochemistry and pathology: PET/CT findings correlated with serum biomarkers and histopathology. No pathological activity was detected in remote myocardium. ***Conclusion:*** Dual-tracer ^{18}F-FAPI and ^{18}F-FDG PET/CT enables precise delineation of the spatiotemporal dynamics of inflammation and fibrosis following MI. The bimodal uptake pattern offers critical guidance for identifying therapeutic targets and optimal intervention windows, thereby underscoring the clinical translational potential of molecular imaging-guided stratification in optimizing cardiovascular outcomes.

OP-844

The dynamic process of cardiac fibroblast activation after myocardial infarction

L. Wang[1], *S. Huang*[2], *F. Shan*[1], *X. Ye*[2], *J. Lou*[1], *X. Liu*[1];
[1]*Shanghai Pudong Hospital, Fudan University, Shanghai, CHINA,*
[2]*Ruijin Hospital, Shanghai Jiaotong University School of Medicine, Shanghai, CHINA.*

Aim/Introduction: The novel fluorine-18-labeled fibroblast activation protein inhibitor (^{18}F-FAPI) serves as a PET radiotracer that binds to activated fibroblasts. The aim was to explore the intensity, extent, and time course of fibroblast activation after myocardial infarction (MI). ***Materials and Methods:*** A total of 18 swines with acute MI underwent ^{18}F-FAPI PET/CT and cardiac MRI. The intensity of ^{18}F-FAPI-04 uptake was quantified by the maximum target-to-background ratio (TBRmax). The extent of fibroblast activation was assessed by the percentage of FAPI-avid myocardium in the left ventricle (LV) and late gadolinium enhancement (LGE), respectively. The FAPI amount was calculated as the product of the percentage of FAPI-avid LV myocardium and TBRmax. ***Results:*** During the dynamic progression of MI from the acute to chronic phase, no significant ^{18}F-FAPI-04 uptake was observed in the infarcted area on day 1 after infarction, which was lower than the normal group (TBRmax: 0.96 ± 0.18 vs. 1.71 ± 0.26). By day 4, significant FAPI uptake was observed in the infarcted area. Myocardial FAPI uptake was observed in acute infarct and peri-infarct regions, exceeding the extent of LGE ($P < 0.001$). One week after MI, the entire LV was activated and activation continued until the 10th week; two-fifths of the swines also demonstrated right ventricular involvement, which persisted until the chronic infarct phase. Myocardial FAPI uptake peaked at 1 and 2 weeks post-AMI before declining at 4, 7, and 12 weeks (TBRmax: 6.77 ± 0.91, 7.59 ± 0.29, 4.36 ± 1.07, 3.09 ± 0.37, and 3.46 ± 0.37; $P < 0.001$). Chronic infarcts exhibited increased FAPI uptake at lower intensity compared to acute infarcts (TBRmax: 3.81 ± 0.40 vs. 6.13 ± 1.29; $P < 0.001$). Increased remote myocardial FAPI uptake was associated with left ventricular dilatation and systolic dysfunction. In addition, hepatic ^{18}F-FAPI-04 uptake peaked at 2, 5, and 9 weeks post-AMI (TBRmax: 5.54 ± 1.10, 8.19 ± 0.22, and 6.03 ± 0.25). After entering the chronic phase, the hepatic FAPI uptake remained stable and increased compared to the normal group (TBRmax: 5.36 ± 0.63 vs. 3.25 ± 0.44; $P < 0.001$). ***Conclusion:*** Myocardial fibroblast activation peaks within two weeks of MI, extends beyond the infarct region, and gradually declines over months, providing a theoretical basis for defining the therapeutic window of anti-fibrotic interventions. Persistent fibroblast activation contributes to subsequent LV remodeling. Furthermore, a potential correlation exists between myocardial infarction and the activation of hepatic FAP proteins.

OP-845

Preparation of a Novel P2X7 Targeted Nanobody Molecular Probe [^{18}F]F-1c81 and micro PET Imaging Study of Atherosclerotic Plaque

B. Hu, *T. Mou, M. Yun, Y. Wang, X. Xu, Y. Tian, X. Zhang;*
Department of Nuclear Medicine, Molecular Imaging Lab, Beijing Anzhen Hospital, Capital Medical University, Beijing, CHINA.

Aim/Introduction: A novel purinergic receptor P2X7 targeted nanobody-based probe [^{18}F]F-1c81 was developed and evaluated for its potential application in atherosclerotic plaque (AP) micro PET imaging. ***Materials and Methods:*** The nanobody 1c81 was expressed in Escherichia coli and the free amino groups were coupled with 2,5-dioxopyrrolidin-1-yl 1-(cyclooct-4-en-1-yl)-1-oxo-5,8,11,14-tetraoxa-2-nonazine-17-sulfonic acid (TCO-PEG4-NHS) to obtain the labeled precursor TCO-1c81. Al[^{18}F]F-2,2'-(7-(14-(4-(6-methyl-1,2,4,5-tetrazin-3-yl)phenoxy)-2-oxo-6,9,12-trioxa-3-azatetradecyl)-1,4,7-triazonane-1,4-diyl) diacetic acid (Al[^{18}F]F-NOTA-Tz) was synthesized, and then it was coupled with TCO-1c81 via bioorthogonal reaction to synthesize the P2X7 targeted radiotracer Al[^{18}F]F-NOTA-Tz-TCO-1c81 ([^{18}F]F-1c81). The labeling rate of the probe was evaluated, and [^{18}F]F-1c81 PET imaging and pathological correlation studies were conducted in 3 AP model mice (20 weeks on high-fat diet) and 3 normal C57BL/6 mice (20 weeks on normal diet). ***Results:*** The preparation of [^{18}F]F-1c81 was completed within 85~95 min, with a non-decay corrected yield of 21.5 ± 5.6 % (n = 3). The radiochemical purity of [^{18}F]F-1c81 was greater than 98%, and the molar activity was 13.9 MBq/nmol. The micro PET imaging results at 1 hour post injection showed that the mean Standardized Uptake Value (SUVmean) of the probe in the aortic arch of AP model mice was significantly higher than that of control mice (0.52±0.02 vs 0.36±0.03, $P = 0.0034$), indicating that the probe has certain plaque-targeting ability and imaging ability. Immunofluorescence staining showed P2X7 expression by CD68-positive macrophages and other myeloid cells located in the fibrous cap layer and shoulder region

of plaques. ***Conclusion:*** The novel molecular probe [^{18}F]F-1c81 is characterized by a simple and efficient preparation process, exhibits favorable physicochemical properties, and can be utilized for the detection of AP.

1805

Wednesday, October 8, 2025, 9:45 - 11:15
Room 211

TROP Session - Paediatrics Committee: Emerging Roles of Molecular Imaging in Paediatric Oncology, Neurology and Transplant Medicine

OP-846

^{18}F-FDG PET Radiomics as a Prognostic Tool in Pediatric Ewing Sarcoma

B. Soydas Turan[1], *C. Küçüker*[2], *B. Volkan Salancı*[2], *P. Ozgen Kiratli*[2]; [1]*Kastamonu Training and Research Hospital, Department of Nuclear Medicine, Kastamonu, TÜRKIYE,* [2]*Hacettepe University, Faculty of Medicine, Department of Nuclear Medicine, Ankara, TÜRKIYE.*

Aim/Introduction: This study aimed to assess the prognostic significance of radiomic features obtained from baseline ^{18}F-FDG PET/CT scans in predicting progression-free survival (PFS) in pediatric Ewing sarcoma (ES). ***Materials and Methods:*** Baseline ^{18}F-FDG PET/CT scans from pediatric ES patients, acquired between January 2010 and December 2020, were retrospectively analyzed. LIFEx v.7.7.0 was used to delineate the volume of interest (VOI) for primary tumors using a threshold set at 40% of the SUVmax. These VOIs were used for radiomic feature extraction, including conventional metabolic parameters [SUVmax, SUVmean, SUVpeak, metabolic tumor volume, total lesion glycolysis], shape indices (compacity, compactness, sphericity), histogram-based features (skewness, kurtosis, entropy, uniformity), and textural features [gray-level co-occurrence matrix, gray-level run-length matrix, neighborhood gray-tone difference matrix (NGTDM), gray-level size zone matrix (GLSZM)]. The prognostic significance of each variable for PFS was evaluated using univariate and multivariate Cox regression analyses. Variables with $p<0.05$ in the univariate analysis were included in the multivariate model using backward elimination. For continuous variables, optimal cutoff values were determined using Youden's index. Kaplan-Meier curves were generated to estimate PFS, and differences between groups were assessed using the log-rank test. ***Results:*** PET/CT scans of 41 patients (mean age 10.53±3.72 years; 15 females) were analyzed. At diagnosis, eighteen patients (43.9%) had metastatic disease. During follow-up, nineteen patients (46.3%) had disease relapse or progression, and fourteen patients (34.1%) died. The mean PFS was 86 months. Variables evaluated for their prognostic value in PFS included age, gender, presence of metastasis at diagnosis, and the aforementioned radiomic features. In the univariate analysis, histogram-based kurtosis and some textural features, specifically NGTDM_Busyness, GLSZM_Large Zone Emphasis, GLSZM_Large Zone Low Gray Level Emphasis, GLSZM_Zone Size Variance were significantly associated with PFS ($p<0.05$). Other evaluated parameters did not show a statistically significant association. In the multivariate model, only histogram-based kurtosis and NGTDM_Busyness remained independent prognostic factors (HR=4.03; 95%CI=1.32-12.29; p=0.014 and HR=3.94; 95%CI=1.47-10.55; p=0.006, respectively). Kaplan-Meier analysis showed that patients with high kurtosis (>-0.01) and high NGTDM_Busyness values (>5.22) had significantly shorter mean PFS compared to those with lower values (60 vs. 117 months; p=0.003 and 25 vs. 98 months; p=0.001, respectively). ***Conclusion:*** Specific radiomic features extracted from baseline ^{18}F-FDG PET/CT scans—particularly histogram-based kurtosis and NGTDM_Busyness—are independent prognostic factors for PFS in pediatric ES. These findings suggest that tumor heterogeneity, as reflected by these parameters, may provide valuable prognostic information beyond conventional PET parameters. Further validation in prospective studies is needed.

OP-847

Prognostic Value of Baseline ^{18}F-FDG PET/CT Metabolic Parameters for Pediatric Nasopharyngeal Carcinoma Patients

A. Pala*, O. Kodaz, P. Özgen Kıratlı, B. Volkan Salancı; Hacettepe University Faculty of Medicine, Department of Nuclear Medicine, Ankara, TÜRKIYE.*

Aim/Introduction: Nasopharyngeal carcinoma (NPC) is a rare tumor in children. Most cases are diagnosed with locally advanced stage, often affecting the retronasal cavity and regional lymph nodes, while a few patients present with distant metastases at the time of diagnosis. Identifying patients at higher risk of treatment failure is crucial. In this study, the authors searched for which metabolic parameters at baseline 18F-FDG-PET/CT can predict event-free-survival (EFS) and overall-survival (OS). ***Materials and Methods:*** Baseline 18F-FDG-PET/CT images of pediatric patients with histologically confirmed non-keratinized-undifferentiated NPC were evaluated retrospectively. Metabolic tumor volume(MTV) and total lesion glycolysis(TLG) of the primary tumor(P), regional lymph nodes(N), and distant metastases(M) were obtained separately. Tumor segmentation was defined based on the threshold SUVmax values of 2.5, the hepatic reference(HR) SUVmean, and a threshold of 40% of SUVmax. The cumulative values of MTV and TLG across all pathological lesions produced whole-body(WB) MTV and TLG, respectively. Kaplan-Meier curves and the log-rank test were used to compare survival experiences between metabolic PET parameters at cut-off values (ROC curve and Youden Index). ***Results:*** The study group consisted of 23 patients (F/M:6/17, median age:14.91, range:7.57-17.37) referred between May 2014 and July 2023. Of these patients, 20/23 (87%) had locally advanced and 3/23 (13%) had metastatic disease. The median duration of follow-up was 74 months (range:12-132). After completing the treatment, a complete response with no reported events was achieved in 21 patients. While five patients had disease-related events, two patients progressed during initial treatment, and three patients developed relapse after the completion of therapy. Among the five patients with disease-related events, two developed locoregional progression, and four developed distant metastasis. OS was 87%. Patients with WB-$MTV_{2.5}$>105.82 (44 vs 121 months; p=0.009), WB-$MTV_{40\%}$>48.56 (39 vs 121 months; p=0.004), WB-$TLG_{40\%}$>499.23 (32 vs 115 months; p=0.012), P-$MTV_{40\%}$>37.21 and P-MTV_{liver}>96.78 (7 vs 112 months; p<0.001) had lower EFS. Besides, WB-$TLG_{40\%}$>499.23 (50 vs 127 months; p=0.012), P-$MTV_{40\%}$>37.21, and P-MTV_{liver}>96.78 (25 vs 127 months; p<0.001) were significantly associated with lower OS. Although patients with WB-$MTV_{2.5}$>105.82 and WB-$MTV_{40\%}$>48.56 had shorter OS, this did not reach statistical significance. Also, the presence of any lesion with SUVmax>20.6 (45 vs 106 months; p=0.3) corresponded to a lower EFS, which is not statistically significant. ***Conclusion:*** Baseline 18F-FDG-PET/CT metabolic parameters can be prognostic indicators in pediatric NPC patients. Various threshold approaches can be used for tumor segmentation. High WB-MTV&TLG, P-MTV, and overall-SUVmax values are associated with poor OS and EFS.

OP-848

Utility of 18F-fluorodeoxyglucose positron emission tomography in presurgical evaluation of paediatric patients with Drug Resistant Epilepsy - A Concordance Analysis between PET/MRI and EEG

A. Meena, *A. Subramanyam, H. Singh, R. Kumar, B. Mittal; Post Graduate Institute of Medical Education and Research, Chandigarh, Chandigarh, INDIA.*

Aim/Introduction: The aim of our single center ambispective observational cohort study was to evaluate the clinical impact of hybrid ^{18}F FDG PET/CT on the decision workflow of drug-resistant epileptic patients with equivocal and/or discordant electroclinical and MRI data. ***Materials and Methods:*** Drug resistant epileptic paediatric patients with discordant clinical and diagnostic results or MRI negativity were included in this study. Hypometabolic regions (mean ± SD age 10.2 ± 3.1 years) in refractory symptomatic (MRI-positive, n = 121) and cryptogenic (MRI-negative, n = 44) epilepsy were quantitatively identified via statistical parametric mapping (SPM) and qualitatively analyzed via visual examination of PET/MR co-registration images. ***Results:*** We included 165 patients in this study; 100 had temporal lobe epilepsy (TLE), 43 extratemporal epilepsy (ETLE), and 22 had epilepsy of uncertain lobar origin. FDG-PET showed a distinct hypometabolism in 62% and was concordant with ictal EEG in 74% in TLE and in 56% in ETLE ($p < .001$). FDG-PET was useful in presurgical decision-making in 77 patients (47%) and most beneficial in TLE compared to ETLE (58% vs. 44%, $p = .001$). In TLE, seizure-freedom 1 year after surgery did not differ significantly ($p = .48$) between patients with negative MRI and EEG-PET concordance (65%) and those with positive MRI and concordant EEG (68%). In ETLE, half of patients with negative MRI and EEG-PET concordance and three-quarters with positive MRI and concordant EEG were seizure-free post-surgery (n = 5 vs. n = 6, $p = .28$). The visual analysis localised the epileptogenic zone in 82 % while SPM localised the EZ in only 47%. Cohen's kappa for visual Vs. SPM analysis was is 0.30 suggesting fair concordance between the two analysis. There was a significant concordance to detect hypometabolic areas between both SPM and visual analyses ($K = 0.45$; $p < 0.005$), in symptomatic ($K = 0.74$; $p < 0.005$) and in cryptogenic patients ($K = 0.26$; $p < 0.01$). Among the 165 children, visual analysis succeeded detecting hypometabolic area in 62% of the cases (interobserver kappa = 0.31). ***Conclusion:*** FDG-PET is valuable to localize the seizure onset zone when MRI and scalp EEG are not localizing or are discordant. MRI-negative and MRI-positive cases with concordant FDG-PET results (with either EEG or MRI) had a comparable outcome after surgery. These findings confirm the significance of FDG-PET in presurgical epilepsy diagnostics.

OP-849

Extracranial Disease Burden in Paediatric Tuberculous Meningitis Characterised on F-18 FDG PET-CT

B. Berndorfler[1], *J. M. Warwick*[1], *J. A. Seddon*[2,3], *C. Bekker*[3], *R. S. Solomons*[1], *R. Van Toorn*[1], *A. G. G. Doruyter*[1,4]; *[1]Stellenbosch University, Cape Town, SOUTH AFRICA, [2]Imperial College London, London, UNITED KINGDOM, [3]Desmond Tutu TB Centre, Stellenbosch University, Cape Town, SOUTH AFRICA, [4]NuMeRi Node for Infection Imaging, Stellenbosch University, Cape Town, SOUTH AFRICA.*

Aim/Introduction: Tuberculous meningitis (TBM) disproportionately affects children under five years of age. It is believed that TBM occurs through lympho-haematogenous dissemination of bacilli, putting other extrapulmonary organs at risk. However, diagnosing extracranial TB can be challenging due to non-specific symptoms, variable presentation and limited diagnostic tools. To address these challenges, healthcare providers use various imaging studies, biopsy, histopathology and molecular tests. While studies in adults have found extracranial disease in 80-90% of TBM cases, there is a knowledge gap in paediatric TBM, particularly regarding the use of metabolic imaging like FDG PET-CT to characterized extracranial involvement. ***Materials and Methods:*** Fifty-three children with TBM underwent whole-body F-18 FDG PET-CT imaging at Tygerberg Hospital between June 2023 and March 2025. After excluding one child with a revised diagnosis, 52 children meeting standard diagnostic criteria for probable or confirmed TBM were analysed. PET-CT scans were evaluated by a nuclear medicine physician to identify extracranial sites of tuberculosis based on both metabolic and structural imaging findings. Equivocal cases were reviewed jointly with a second nuclear medicine physician experienced in infection and inflammation imaging. ***Results:*** The study included 52 children (n=52) with a median age of 3.5 years (interquartile range 1.9-6.6 years). Extracranial manifestations of TB were identified in 48 (92%) of children. Among these, pulmonary involvement was observed in 39 (75%), nodal involvement in 43 (83%), skeletal involvement in 5 (10%), and soft tissue involvement in 10 (19%). ***Conclusion:*** This study highlights a significant prevalence of extracranial TB in children with TBM, as detected by F-18 FDG PET-CT. Notably, the rates exceed those reported in adult TBM patients. Identifying extracranial disease is crucial, as it can impact treatment duration, inform infection control measures, and potentially prevent complications.

OP-850

Prognostic Value of Quantitative Interim PET in Pediatric High-Grade Non-Hodgkin Lymphomas: Toward More Predictable Outcomes

G. Kaya[1], *O. Kodaz*[2], *B. Volkan Salanci*[2], *B. Aydın*[3], *P. Özgen Kıratlı*[2]; *[1]Republic of Türkiye, Ministry of Health, Yozgat City Hospital, Dept. of Nuclear Medicine, Yozgat, TÜRKIYE, [2]Hacettepe University, Faculty of Medicine, Nuclear Medicine Dept., Ankara, TÜRKIYE, [3]Hacettepe University, Faculty of Medicine, Paediatric Oncology Dept., Ankara, TÜRKIYE.*

Aim/Introduction: Pediatric Non-Hodgkin Lymphomas (NHL) are a highly heterogeneous group of malignancies, and assessment of residual disease on interim PET-CT poses a persistent diagnostic challenge. While the Deauville Score (DS) is widely used for response evaluation, its limitations—particularly in cases with DS scores of 3 or 4—warrant the exploration of alternative or complementary imaging biomarkers. Recent studies have highlighted the potential of metabolic parameters and semiquantitative methods, such as quantitative PET (qPET), metabolic tumor volume (MTV), and total lesion glycolysis (TLG), in improving risk stratification and prognostication. This study aimed to compare the performance of DS, qPET, and MTV/TLG in predicting early disease recurrence in pediatric patients with high-grade NHL. ***Materials and Methods:*** This retrospective, single-center study included high-grade NHL patients under 18 years of age who underwent interim PET-CT during frontline treatment. qPET was calculated for patients with DS scores of 3-5. Whole-body MTV and TLG were assessed using a fixed SUVmax threshold of 2.5. Patients with DS scores of 3-4 or MTV/TLG values above the median were classified as having residual disease. Follow-up data, including disease recurrence and disease-related death, were obtained and analyzed. Survival analyses were conducted using Kaplan-Meier methods, with event-free survival (EFS) as the primary outcome. ***Results:*** A total of 107 patients (73 male, mean age 9.5 ± 4.5 years) were included. The median follow-up duration was 92 months (range: 7-165 months). Disease recurrence occurred in 25 patients (23%). Median interim PET-CT values were: SUVmax 2.9 (range 1-17), DS 1 (range 1-5), qPET 1.59 (range 0.7-9.5), MTV 0 cm^3 (range 0-453 cm^3), and TLG 0 (range 0-3163). The number of patients identified as having residual disease was 35 (DS3), 25 (DS4), 22 (MTV/TLG), and 21 (qPET). All TLG-positive cases were also positive for DS3-4. Kaplan-Meier survival analysis revealed no statistically

significant differences in EFS between groups defined by qPET or DS3-4 thresholds. However, TLG positivity was associated with significantly worse EFS (p = 0.01), with the greatest mean survival difference (35 months). ***Conclusion:*** In this larger pediatric cohort, metabolic parameters—particularly TLG—demonstrated superior prognostic performance compared to DS and qPET in predicting early recurrence. These findings support the clinical utility of TLG in refining treatment and follow-up strategies, especially for patients with intermediate DS scores. While qPET did not show significant predictive value in this cohort, further studies with larger populations are warranted to optimize threshold definitions and validate these markers in clinical practice.

OP-851

Using radiomics based on 2-[^{18}F]FDG PET/CT and machine learning methods to predict the WHO/ISUP grade of clear cell renal cell carcinoma

Y. Han[1], *J. Zhang*[1], *Y. Pan*[2], *J. Cui*[1], *C. Li*[2], *Y. Wang*[3], *G. Wang*[4], *B. Xu*[2];
[1]*Graduate School, Chinese PLA General Hospital, Beijing, CHINA,* [2]*Chinese PLA General Hospital, Beijing, CHINA,* [3]*GE Healthcare China, Shanghai, CHINA,* [4]*Nuclear Medicine Department, Beijing Friendship Hospital, Capital Medical University, Beijing, CHINA.*

Aim/Introduction: This study aims to evaluate the clinical value of radiomics features of 2-[^{18}F]fluoro-D-glucose positron emission tomography (2-[^{18}F]FDG PET/CT) combined with machine learning methods in predicting the WHO/ISUP grade of ccRCC lesions, and to determine the optimal machine learning method. ***Materials and Methods:*** Retrospectively, the PET/CT images of 209 pathologically confirmed ccRCC patients (a total of 214 lesions) were collected. According to the WHO/ISUP pathological nuclear grading, the tumors were classified into high grade (Grade III and IV) and low grade (Grade I and II) and were randomly divided into a training group and a testing group at a ratio of 7:3. The regions of interest were delineated and different combinations of 5 feature selection methods and 8 classification methods were used to establish radiomics models respectively. The performance of each model was evaluated by the area under the receiver operating characteristic curve (AUC). ***Results:*** A total of 40 radiomics models were established. Most of the models had good predictive ability with AUCs greater than 0.75. Whether in the training group or the testing group, the feature selection method LASSO combined with the classifier logistic regression (LR) achieved the highest AUC values, which were 0.887 and 0.882 respectively. In terms of feature selection methods, RFE_SVM performed the best in most of the models. In the training group, the RFE_SVM-XGBoost model, RFE_SVM-Decision_Tree model, RFE_SVM-Neural_Network model, RFE_SVM-Bayes model, RFE_SVM-kNN model, RFE_SVM-Random_Forest model, and RFE_SVM-SVM model all showed the best predictive performance. The performance of the RFE_SVM-LR model was second only to that of the LASSO-LR model. In the testing group, the RFE_SVM-XGBoost model, RFE_SVM-Decision_Tree model, RFE_SVM-Neural_Network model, and RFE_SVM-kNN model performed the best. Among other classifiers, the models combined with LASSO had the best performance. In terms of classifier selection, LR performed the best in most of the models. In the training group, the LASSO-LR model, Boruta-LR model, and RFE-LR model had the optimal performance. The performance of the RFE_SVM-Random_Forest model and the XGBoost-XGBoost model was slightly higher than that of the RFE_SVM-LR model and the XGBoost-LR model respectively. In the testing group, LR was the classifier selection with the best performance. ***Conclusion:*** The radiomics based on 2-[^{18}F]FDG PET/CT can predict the WHO/ISUP grade of clear cell renal cell carcinoma. RFE_SVM and LR are considered as the optimal feature selection method and classification method respectively. Combining LASSO with LR can achieve the highest predictive efficiency of the model.

OP-852

Dynamic 3D 12-headed CZT-detector ring SPECT/CT renal transplant MAG3 renography: a phantom and clinical implementation study

A. van de Burgt, *Q. de Lussanet de la Sabloniere, M. Segbers, F. A. Verburg, A. A. Harteveld;*
Erasmus MC, Rotterdam, NETHERLANDS.

Aim/Introduction: A challenge in conventional renal transplant MAG3 renography, as performed two-dimensionally (planar) with NaI detectors, is its inherently limited accuracy owing to overlapping structures (e.g. bladder, ureter, urine leakage). Novel 12-headed cadmium-zinc-telluride (CZT) detector-ring single-photon emission computed tomography/computed tomography (SPECT/CT) allows for dynamic three-dimensional (3D) SPECT acquisitions with CT-based structural correlation. This study aimed to evaluate the non-inferiority of dynamic 3D-SPECT/CT renography compared to dynamic conventional planar renography in a custom-designed renal perfusion phantom, and its subsequent clinical implementation. ***Materials and Methods:*** Phantom experiment: 35 MBq Tc-99m pertechnetate was pumped (1200 mL/h; 'arterial input') into a 100 mL glass bottle ('kidney') draining into a waste container ('bladder'). Dynamic 3D-SPECT was performed with 60x5sec (Phase 1) and 150x10sec (Phase 2) frames using factory settings on a CZT-ring SPECT/CT. Dynamic planar scintigraphy was acquired using clinical protocol (120x15sec) on a conventional SPECT/CT. Dynamic 3D-SPECT reconstruction: Q.Clear 10 iterations, 10 subsets, voxel size 4.92 mm, gamma 2, beta values of 0.2 (phase 1) and 0.002 (phase 2), according to factory settings. In-human study: dynamic 3D-SPECT/CT (20×15sec (Phase 1), 15×60sec (Phase 2)) was performed after ~75 MBq Tc-99m MAG3 bolus injection and reconstructed with factory settings. Low-dose CT was performed for attenuation correction and anatomical correlation. Images and time-activity curves (TACs) were analyzed using Symbia postprocessing (phantom study) and Xeleris Dynamic MI (phantom and patient study). ***Results:*** Phantom experiment: dynamic 3D-SPECT acquisition rendered TACs and tracer dynamics (time-to-peak (TTP) 1.25 min, peak-to-half-peak (T½) 4.68 min) which compared well to traditional planar scintigraphy (TTP 1.03 min, T½ 4.75 min). Additionally, the 3D-SPECT showed a ten-fold higher number of total counts (3D-SPECT 14,767 versus planar 1,450 counts/sec). Subsequently, dynamic 3D-SPECT/CT proved feasible in two healthy potential renal donors and two renal transplant recipients (one-day postoperative), providing diagnostic TACs, tracer kinetics and visual assessment. The 3D information, combined with CT correlation, prevented overlapping structures and enabled detailed evaluation of all renal phases. This approach demonstrated normal function in both potential renal donors and allowed for detailed intrarenal/(sub-)segmental evaluation and diagnosing in one-day postoperative renal transplant recipients. ***Conclusion:*** This combined phantom and in-human study demonstrates the non-inferiority of dynamic 3D 12-headed CZT-detector ring SPECT/CT renography as compared to conventional planar renography, and its successful clinical implementation by offering improved 3D and CT-based anatomic detail. Future studies may show the clinical value of dynamic 3D-SPECT/CT renal transplant MAG3 renography in potential renal donors and renal transplant recipients.

OP-853

Comparison of [18F]F-FAPI and [18F]F-FDG PET/CT for Prediction of Treatment Response in Patients with Lupus Nephritis

M. Zhao[1], *C. Zhou*[1], *X. Yi*[2], *X. Zhang*[2];
[1]*Third Xiangya Hospital of Central South University, Changsha, CHINA,* [2]*Xiangya Hospital of Central South University, Changsha, CHINA.*

Aim/Introduction: Lupus nephritis (LN) is a severe manifestation of systemic lupus erythematosus, often requiring renal biopsy to guide treatment. However, conventional clinical biomarkers remain limited in predicting treatment response. This study aimed to evaluate the utility of [18F]F-FAPI and [18F]F-FDG PET/CT in predicting therapeutic outcomes in patients with LN. ***Materials and Methods:*** Twenty biopsy-proven LN patients were prospectively enrolled and underwent comprehensive clinical and laboratory evaluations of disease activity, as well as dual-tracer PET/CT imaging, using both [18F]F-FAPI and [18F]F-FDG imaging prior to standardized induction therapy. Semiquantitative parameters -including renal standardized uptake values (SUVmax) and target-to-background ratio (TBR) - were quantified. Patients were categorized into complete response (CR), partial response (PR), and non-response (NR) groups at 6 month following induction therapy. Associations between PET metrics, clinical biomarkers and treatment response were analyzed. ***Results:*** Baseline FAPI SUVmax inversely correlated with eGFR and positively with ESR ($P < 0.05$ for both), while FDG SUVmax showed no significant correlation with either. At 6 months, 50% of patients achieved CR, 35% PR, and 25% NR. Patients who achieved CR exhibited significantly lower baseline renal FAPI SUVmax and TBR compared to patients with non-CR ($p < 0.01$). FAPI-negative uptake was associated with a high CR rate (88.9%), outperforming FDG-negative uptake (75.0%). FAPI PET demonstrated superior predictive accuracy for CR (sensitivity 80%, specificity 90%, accuracy 85%) compared to FDG PET (sensitivity 60%, specificity 80%, accuracy 70%). Multivariate logistic regression identified negative FAPI uptake as the sole independent predictor for CR (OR = 36.0, 95% CI: 2.9-476.3, $p < 0.01$). ***Conclusion:*** [18F]F-FAPI PET/CT shows promise as a noninvasive imaging biomarker for predicting treatment response in LN, with superior performance compared to [18F]F-FDG PET/CT.

OP-854

Diagnostic utility of renogram and SPECT-CT in the management of kidney transplant complications

A. Suazo Montero*, J. Gómez Hidalgo, M. García Aragón, R. Zambrano Infantino, B. Jaramillo López, N. Álvarez Mena, F. Sebastián Palacid, C. Gamazo Laherrán, R. Ruano Pérez;*
Hospital Clínico Universitario de Valladolid, Valladolid, SPAIN.

Aim/Introduction: To evaluate the diagnostic contribution of isotopic renogram in the management of complications in patients undergoing renal transplantation, as well as the added value of SPECT-CT. ***Materials and Methods:*** A total of 777 patients who underwent cadaveric renal transplantation from January 2011 to December 2024 were included. At 24 hours post-transplant, after the administration of 185-259 MBq of 99mTc-DTPA, a 30-minute renogram study focused on the abdomen in anterior projection was performed, followed by planar images at 30 and 180 minutes. In addition, an abdominal SPECT-CT was performed in 93 patients. Findings were correlated with radiological studies and clinical-analytical follow-up. At least one renal scintigraphic follow-up study was performed in 166 patients (66 with SPECT-CT). ***Results:*** Of the 777 patients (506 males), 176 (22.6%) showed a normal study. Surgical complications were detected in 76 (9.78%) patients: 30 renal artery/vein thromboses; 9 infarctions; 17 ureteral ectasias or obstructions; 1 urinoma; and 16 urinary leaks. The urinoma and 11 leaks were confirmed by SPECT-CT. In 546 patients (70.3%), ischemic alterations or acute tubular necrosis (ATN) were identified: mild in 297 (54.4%); moderate in 183 (33.5%); and severe in 66 (12.1%). At least one follow-up renal scintigraphy study was performed in 166 patients, totaling 244 studies. Among these, 100 studies showed improvement in renal function, 93 showed deterioration, 20 showed leaks, 17 dilatations, 8 collections, and 1 infarction. All leaks, 4 dilatations, and 6 collections were observed on SPECT-CT. ***Conclusion:*** The renogram in transplanted patients enables the detection of surgical and/or ischemic complications, facilitating early implementation of corrective measures. SPECT-CT is particularly useful in the diagnosis of urinomas/urinary leaks, and enhances the assessment of their extent and localization.

1806

Wednesday, October 8, 2025, 9:45 - 11:15
Room 117

Clinical Oncology Track - TROP Session - Oncology & Theranostics Committee: Prostate Cancer Staging and Restaging

OP-855

Adaptive, MRI-Guided ^{166}Ho-TARE with Intra-Procedural Voxel-Based Dosimetry: First Results from EMERITUS-2

M. W. M. van Wijk[1], *J. Roosen*[1], *M. J. Arntz*[1], *M. J. R. Janssen*[1], *E. T. T. J. Tjwa*[2], *J. F. W. Nijsen*[1];
[1]*Department of Medical Imaging, Radboud University Medical Center, Nijmegen, NETHERLANDS,* [2]*Department of Gastroenterology and Hepatology, Radboud University Medical Center, Nijmegen, NETHERLANDS.*

Aim/Introduction: Achieving optimal tumour dosing remains a key challenge in transarterial radioembolisation (TARE) for hepatic malignancies. High tumour-absorbed doses have been associated with improved survival, underscoring the need for accurate, individualised, and voxel-based dosimetry for treatment planning and evaluation. However, dose personalisation remains challenging, given the lack of intra-procedural feedback on the dose distribution. Holmium-166 (^{166}Ho) microspheres uniquely allow for high-resolution, quantitative MR imaging and dosimetry ($2\times2\times4$ mm^3 voxel size) within 5-10 minutes. The EMERITUS-2 trial investigates the feasibility of MRI-guided, adaptive TARE to safely escalate tumour doses, reduce dose heterogeneity, and improve therapeutic outcomes. ***Materials and Methods:*** EMERITUS-2 is a dose-escalation study including patients with hepatocellular carcinoma undergoing TARE with ^{166}Ho microspheres. Patients are treated in a 3T MRI scanner using multi-echo gradient echo imaging to visualize and quantify microsphere distribution directly after each administration. This approach provides intra-procedural insight into the mean tumour and non-tumorous liver mean dose and into dose heterogeneity, via high resolution dose maps and dose-volume histograms. Treatment continues until the normal liver dose limit is reached (40-60-80 Gy on max 2/3 of the normal liver volume), or adequate tumour coverage or saturation is achieved. Primary endpoints include liver toxicity and dosimetric comparison to standard whole-liver TARE (60 Gy whole liver). ***Results:*** In the first four patients, a mean whole-liver dose of 72-122 Gy (administered activity of 7.8-19.2 GBq) was reached. Tumour-absorbed doses ranged from 133-334 Gy, exceeding conventional planning estimates based on 60 Gy whole liver (77-297 Gy). Treatment was delivered in 6-11 fractions, on one to two catheter positions per patient. Intra-procedural voxel-based dosimetry revealed potential dose heterogeneity, enabling real-time adjustments to optimize tumour coverage. No ≥ grade 3 adverse events were observed; reported side effects included grade 1-2 nausea, fatigue, and abdominal pain - comparable to standard TARE. Treatment termination occurred due to the non-tumorous

liver reaching the safety limit or due to complete administration of the ordered ^{166}Ho microsphere activity. Tumour saturation or statis was not observed. ***Conclusion:*** With these preliminary results we demonstrate the feasibility of a novel approach to TARE. MRI-guided, adaptive TARE with ^{166}Ho microspheres enables controlled intra-procedural dose administration and dosimetry instead of administration based on pre-treatment dosimetry. An MRI-guided adaptive approach takes treatment personalisation to a new level, enhancing homogeneous tumour dosing and administration of high activities while monitoring non-tumorous liver dose.

OP-856

Gemcitabine/Cisplatin Plus Transarterial Radioembolization versus Transarterial Radioembolization Alone for Intrahepatic Cholangiocarcinoma: A Multicenter Retrospective Study

N. Coskun[1], *A. Karacan*[1], *C. Sin*[2], *E. M. Kaya*[2], *G. Beydagi*[3], *M. Ozdemir*[1], *T. Guzelbey*[2], *M. Topcuoglu*[3], *A. Ozdemir*[1], *M. A. N. Sendur*[1], *M. Akdogan*[1], *M. Kaya*[2], *N. Alan Selcuk*[3], *B. Esen Akkas*[2], *E. Cingi Ozdemir*[1];
[1]*Bilkent City Hospital, Ankara, TÜRKIYE,* [2]*Cam & Sakura City Hospital, Istanbul, TÜRKIYE,* [3]*Yeditepe University, Istanbul, TÜRKIYE.*

Aim/Introduction: Intrahepatic cholangiocarcinoma (ICC) is a rare and aggressive malignancy of the bile ducts, often diagnosed at an advanced stage when surgical resection is not feasible. Gemcitabine/cisplatin (G/C)-based chemotherapy and transarterial radioembolization (TARE) with ^{90}Y-loaded microspheres are commonly used for patients with unresectable or locally advanced disease. Recent clinical practice has increasingly favored combining G/C chemotherapy with TARE to enhance locoregional tumor control. However, there is a lack of data comparing the therapeutic benefit of combination therapy over TARE monotherapy. In this study, we aimed to compare the objective response rate (ORR) of G/C + TARE combination versus TARE alone in the treatment of ICC. ***Materials and Methods:*** Patients diagnosed with ICC who underwent either G/C + TARE combination therapy (combination group) or TARE monotherapy (monotherapy group) at three different centers were retrospectively analyzed. Exclusion criteria were extrahepatic dominant disease, ECOG performance status > 2 or missing follow-up data. Objective response of target lesions was assessed 6-12 weeks after TARE using magnetic resonance imaging (MRI) and F-18 fluorodeoxyglucose positron emission tomography/computed tomography (FDG PET/CT), according to LI-RADS TRA and PERCIST criteria, respectively. Independent T-test, Wilcoxon test, and multivariate logistic regression analysis were used to identify factors associated with objective response. ***Results:*** A total of 26 patients met the inclusion criteria (15 males, 11 females; mean age 62 ± 11 years), with 16 (62%) in the combination group and 10 (38%) in the monotherapy group. Baseline characteristics were comparable between two groups. Glass microspheres were used in 16 patients (62%), and resin microspheres in 10 patients (38%). Mean absorbed tumor dose was 225±133 Gy for resin microspheres and 370±180 Gy for glass microspheres. ORR was significantly higher in the combination group (78%) compared to the monotherapy group (29%; p=0.021). Multivariate logistic regression analysis demonstrated that combination therapy was independently associated with objective response, irrespective of tumor dose, microsphere type (glass/resin) or interventional approach (selective/non-selective) (odds ratio: 14.01, 95% confidence interval: 1.13-173.61, p=0.039). ***Conclusion:*** G/C + TARE combination is associated with significantly higher ORR when compared to TARE monotherapy in the treatment of ICC. To our knowledge, this is the first comparative data evaluating the efficacy of G/C + TARE combination versus TARE monotherapy in the treatment of ICC. Further randomized controlled trials are needed to confirm these findings, and to compare the long-term survival outcomes and toxicity profiles of the two treatment strategies.

OP-857

Association of Tumor Response According to mRECIST and LI-RADS-TRA 2024 Criteria With Overall Survival After Yttrium-90 Transarterial Radioembolization in Hepatocellular Carcinoma: A Comparative Retrospective Analysis

E. Kaya[1], *B. Akkas*[1], *T. Güzelbey*[2], *C. Erdim*[2], *M. Arslan*[2], *C. Şin*[1], *H. B. Kapucu*[1], *M. Kaya*[1];
[1]*Basaksehir Cam and Sakura City Hospital, Department of Nuclear Medicine, Istanbul, TÜRKIYE,* [2]*Basaksehir Cam and Sakura City Hospital, Department of Radiology, Istanbul, TÜRKIYE.*

Aim/Introduction: Yttrium-90 transarterial radioembolization (TARE) is increasingly used to treat hepatocellular carcinoma (HCC). Although the modified Response Evaluation Criteria in Solid Tumors (mRECIST) remain the conventional standard, the LI-RADS Treatment Response Algorithm 2024 (LI-RADS-TRA 2024)—designed specifically for radiation-based therapies—has been proposed as a new benchmark. We compared the prognostic performance of these two frameworks in HCC patients treated with TARE. ***Materials and Methods:*** This retrospective study included 63 HCC patients treated with TARE between June 2022 and January 2024 (glass microspheres n = 45; resin microspheres n = 18). All patients underwent gadoxetic-acid-enhanced MRI before and after treatment. Tumor response was evaluated on 6-month post-treatment imaging. Two board-certified radiologists independently interpreted all studies according to mRECIST and LI-RADS-TRA 2024; discordances were resolved by consensus with a third radiologist. In mRECIST, complete or partial response and stable disease were grouped as non-progressive (NP), whereas progressive disease was classified as progressive (P). In LI-RADS-TRA 2024, non-viable or non-progressive lesions were assigned to NP and viable lesions to P. Overall survival (OS) for NP and P groups was assessed with Cox proportional-hazards regression. ***Results:*** Median follow-up was 17 months. On univariate analysis, overall-response mRECIST did not differentiate OS between NP and P groups (HR=0.715, 95% CI 0.283-1.809; p=0.479). In contrast, target-lesion mRECIST (HR=0.273, 95% CI 0.110-0.741; p=0.011) and LI-RADS-TRA 2024 (HR=0.203, 95% CI 0.090-0.460; p<0.001) showed significant OS separation favoring NP. Median OS was 30 months in NP versus 6 months in P by target-lesion mRECIST. With LI-RADS-TRA 2024, median OS was not reached in NP but was 9 months in P. On multivariable analysis, LI-RADS-TRA 2024 was the sole independent predictor of OS (HR=0.23, 95% CI 0.10-0.53; p=0.001). ***Conclusion:*** This study suggests that in HCC patients treated with TARE, local tumor control, particularly the target-lesion response, is significantly associated with OS. LI-RADS-TRA 2024 surpasses mRECIST in predicting OS and should be incorporated into post-TARE follow-up protocols to optimize patient management.

OP-858

Exploring Radiomic and Dosiomic Features as Novel Predictors of Response to Yttrium-90 Radioembolization in Liver Cancer

A. Capotosti[1], *R. Moretti*[1], *I. Moretti*[1,2], *M. Costa*[3], *S. Cuttone*[3], *L. Zagaria*[1], *L. Leccisotti*[1], *M. Calcagni*[1,2], *A. Posa*[1], *R. Iezzi*[1,2], *M. De Spirito*[1,2], *L. Indovina*[1,2], *L. Placidi*[1];
[1]*Fondazione Policlinico Universitario Agostino Gemelli IRCCS, Rome, ITALY,* [2]*Università Cattolica del Sacro Cuore, Rome, ITALY,* [3]*Tecnologie Avanzate TA S.r.l, Turin, ITALY.*

Aim/Introduction: This study explores the prognostic utility of radiomic and dosiomic features in patients undergoing Yttrium-90 selective internal radiation therapy (90Y-SIRT) for liver tumors. While these quantitative approaches have shown potential in

other oncologic contexts, their integration for assessing treatment response in radioembolization remains largely unexplored. By capturing complex imaging and dose-related patterns, these quantitative approaches aim to support early response assessment and individualized treatment planning. ***Materials and Methods:*** A retrospective cohort of 83 patients with hepatocellular carcinoma (HCC), cholangiocarcinoma (CCC), or liver metastases (M) treated with Yttrium-90 selective internal radiation therapy (90Y-SIRT) for liver tumors was analyzed. Clinical evaluation was based on PET-CT imaging acquired after treatment and follow-up data collected at two timepoints: an initial assessment (FUP-1) for all patients and a second evaluation (FUP-2) available in 60 cases. Image acquisition and lesion segmentation followed standardized protocols. Radiomic and dosiomic features were extracted from segmented target volume using the IBSI-compliant MIRP library. A dedicated software platform was used for data preparation, quality control, dimensionality reduction, and model training. Predictive models were built using a Support Vector Machine (SVM) classifier with five-fold cross-validation. The dataset was randomly split into training and testing subsets (80/20) with stratified distribution across outcome classes. Two binary classification tasks were tested: (1) Complete Response (CR)+ Partial Response (PR) vs Stable Disease (SD)+ Progression Disease (PD); and (2) CR vs others. ***Results:*** Models combining radiomic and dosiomic features achieved high accuracy during training, ranging from 0.93 to 0.97. When evaluated on the independent test set, performance dropped, with accuracy values between 0.65 (classification of CR+PR vs SD+PD) and 0.57 (CR vs others). In the subset of patients with available data at both follow-up points, clinical outcomes at FUP-2 confirmed FUP-1 classifications in 57% of cases. Model behavior remained consistent across timepoints, with training accuracy values preserved (0.93 and 0.97) and test accuracy ranging from 0.47 to 0.57 in both classification settings. ***Conclusion:*** Although predictive accuracy on test data was limited, the combination of radiomic and dosiomic features demonstrated potential for identifying early treatment response patterns in patients undergoing 90Y radioembolization. These results highlight the relevance of quantitative imaging and dosimetric parameters as candidate biomarkers for response prediction, with possible applications in personalized follow-up and treatment planning.

OP-859

Correlation of Voxel-Based Dosimetric Parameters With Progression-Free Survival and Overall Survival After Yttrium-90 Glass Microsphere Radioembolisation in Hepatocellular Carcinoma

H. Kapucu*, E. Kaya, A. Dere, C. Sin, B. Esen Akkas, M. Kaya, K. Toplutas;*
University of Health Sciences Cam Sakura City Hospital, Istanbul, TÜRKIYE.

Aim/Introduction: The relationship between tumour absorbed dose (TAD), the dose received by half of the tumour volume (D50), the dose received by 70% of the tumour volume (D70) and the dose received by 90% of the tumour volume (D90) acquired from the dose-volume histograms (DVH) of Y-90 PET/CT dosimetry after radioembolisation (RE) treatment with Y-90 glass microspheres in patients diagnosed with hepatocellular carcinoma (HCC), with the progression-free survival (PFS) and overall survival (OS) were retrospectively investigated. ***Materials and Methods:*** Between June 2022 and June 2024, 45 patients who underwent Y-90 glass microsphere radioembolization (RE) at our clinic were included in the study. All patients were evaluated by dynamic liver MRI before and after treatment according to mRECIST criteria (1). Using the Y-90 PET/CT images obtained after the procedure, voxel-based dosimetry calculations were performed to determine the D50, D70, and D90 values. Subsequently, the optimal cutoff values for the obtained dosimetric parameters were identified using Receiver Operating Characteristic (ROC) analysis. PFS and OS were evaluated using the Kaplan-Meier method, and differences between groups were statistically analysed using the log-rank test. Additionally, Cox regression analysis was conducted to examine independent prognostic factors. ***Results:*** The median OS in the study group was 14 months, while the median PFS was 7 months. The mean TAD was 654 Gy, with D50 at 538 Gy, D70 at 351 Gy, and D90 at 163 Gy. Results from the log-rank test indicated that TAD, D50, D70, and D90 were significant predictors of OS ($p < 0.001$). For PFS, significant associations were found with TAD and D50 ($p = 0.03$ and $p < 0.01$) but not with D70 and D90 ($p = 0.71$ and $p = 0.417$). In multivariate Cox regression analysis, D50 was the sole parameter predicting OS (HR: 0.03;95% CI: 0.004-0.224; $p = 0.001$) and PFS (HR: 0.327; 95% CI: 0.159-0.671; $p = 0.002$). ***Conclusion:*** This retrospective study aimed to focus on voxel-based dosimetry analysis imaging after RE (2). It particularly examines how the dose received by the tumour volume affects OS and PFS. Our findings indicate that the D50 threshold is a more significant prognostic factor than mean TAD and other DVH parameters, such as D70 and D90. ***References:*** 1.Philippe d'Abadie et al. DOI: 10.1097/MNM.0000000000001395 2. Pianka KT et al. Nucl Med Mol Imaging. 2024 Oct;51(12):3744-3752. doi: 10.1007/s00259-024-06813-8. Epub 2024 Jun 24.

OP-860

FAP-Targeted radiopeptide therapy (FRT) using ^{177}Lu-, ^{90}Y- and ^{225}Ac-labelled 3BP-3940 in a large cohort of 105 patients

J. Zhang*[1], T. Zhao[1], V. Jakobsson[1], L. Greifenstein[2], A. Eismant[2], A. Mishra[2], A. Klega[2], C. Landvogt[2], C. Mueller[2], D. Benz-Zils[2], O. Klein[3], B. Jaeschke[3], E. Perrone[4], R. P. Baum[2];*
[1]National University of Singapore, Singapore, SINGAPORE, [2]DKD HELIOS Klinik, Wiesbaden, GERMANY, [3]International Centers for Precision Oncology (ICPO), Wiesbaden, GERMANY, [4]Università Cattolica del Sacro Cuore, Rome, ITALY.

Aim/Introduction: Fibroblast activation protein (FAP) has emerged as an attractive molecular target for precision imaging and therapy due to its upregulated expression in cancer-associated fibroblasts of various solid tumors. This study reports first-in-human clinical results using a novel FAP-targeting cyclic peptide, 3BP-3940, labeled with ^{177}Lu, ^{90}Y, and ^{225}Ac for radiopharmaceutical therapy (FRT) in a large cohort of patients with end-stage malignancies. ***Materials and Methods:*** Between March 2021 and March 2025, 105 patients with advanced metastatic cancers, who had exhausted all conventional treatment options, were enrolled to receive FRT with radiolabeled 3BP-3940. A total of 285 treatment cycles were administered across 24 different cancer types, including pancreatic adenocarcinoma (n=26), breast (n=14), lung (n=10), neuroendocrine tumors (n=10), and others. All patients demonstrated positive uptake on pre-treatment ^{68}Ga-3BP-3940 PET/CT. Toxicity was graded using CTCAE v5.0. Treatment response was assessed using PET/CT and SPET/CT imaging, and overall survival (OS) was analyzed via Kaplan-Meier curves from the start of FRT. ***Results:*** Radioligand therapy with ^{177}Lu-/^{90}Y-/^{225}Ac-3BP-3940 (mean cumulative dose per patient:^{177}Lu:14.7±10.3GBq; ^{90}Y:7.0±4.7GBq; ^{225}Ac:12.7±9.9MBq) was well tolerated in this sizable cohort. Common side effects included pain (11%, mostly pain flare), nausea (12%), vomiting (8%), headache (1%), diarrhea (3%), transient fever (4%), partial alopecia (7%), and fatigue (6%). No serious adverse events or pharmacological complications were observed. Dosimetry in one pancreatic cancer patient receiving 9.73 GBq of ^{177}Lu revealed organ doses of 37 mGy (brain), 168 mGy (lungs), 86 mGy (liver), 142 mGy (pancreas), 265 mGy (kidneys), and 2200 mGy to the primary tumor. Post-therapy imaging confirmed high tumor uptake and prolonged tracer retention with excellent tumor-to-background contrast. Among 48 patients assessed after two FRT cycles, response rates were as follows: complete remission (3%), partial remission (31%), mixed response (6%), stable disease (6%), and progression (20%), resulting in an objective response rate of 50% and a disease control rate of 58%. For the entire cohort, the

median OS was 7 months from the start of FRT. In the subgroup of patients with aggressive advanced, heavily pretreated pancreatic adenocarcinoma, the median OS was 7 months. ***Conclusion:*** Radiolabeled 3BP-3940 with ^{177}Lu, ^{90}Y, or ^{225}Ac—used alone or in combination—was well tolerated and effective across a large and diverse patient population with advanced solid tumors. The agent demonstrated excellent tumor targeting, minimal renal uptake, and long lesion retention. Promising clinical responses, particularly in pancreatic adenocarcinoma and sarcoma, support further investigation in prospective trials involving broader patient populations and longer follow-up durations.

OP-861

Dosimetric Correlation and Clinical Efficacy of ^{188}Re-N-DEDC lipiodol Transarterial Radionuclide Therapy (TART) in Inoperable Hepatocellular Carcinoma: A Prospective Study

N. Kumar[1], *S. Shamim*[1], *P. Gupta*[1], *G. Arora*[1], *S. Gamanagatti*[1], *D. Shalimar*[1], *V. Chirayil*[2], *S. Subramanian*[2], *M. B. Mallia*[2], *P. Thakral*[3], *I. B. Sen*[3];
[1]*All India Institute of Medical Sciences, New Delhi, INDIA,* [2]*BARC, Mumbai, INDIA,* [3]*FMRI, Gurgaon, Haryana, INDIA.*

Aim/Introduction: Hepatocellular carcinoma (HCC) ranks the third leading cause of cancer-related mortality worldwide. Most patients present with inoperable or advanced-stage disease, where treatment is constrained by tumor burden, liver dysfunction, and performance status. Transarterial radionuclide therapy (TART) using radiolabeled lipiodol is a promising modality that delivers targeted intra-tumoral radiation while sparing healthy liver parenchyma.^{188}Re-N-DEDC lipiodol, labelled with DEDC kits, developed indigenously by BARC, combines the therapeutic efficacy of β-emitting ^{188}Re ($E_{\beta max}$ 2.1 MeV, ~11 mm tissue penetration) with cost-effective, on-site preparation. Despite promising initial outcomes, real-world clinical and dosimetric data remain limited. This prospective study aimed to evaluate the clinical efficacy, dosimetry and predictive markers of response in patients undergoing ^{188}Re-N-DEDC/Lipiodol TARE for inoperable HCC. ***Materials and Methods:*** Thirty-nine patients with radiologically and biochemically confirmed inoperable HCC (ECOG ≤2, Child-Pugh A/B) were enrolled. Activity was prescribe based on partition model and administered via super-selective trans-arterial injection under fluoroscopic guidance. Post-therapy dosimetry was performed using Hybrid Dosimetry Module™. Radiological and biochemical responses were assessed at 2 and 6 months using mRECIST and serum AFP levels. ***Results:*** Of 39 patients (36 males, 3 females; mean age 57.9 ± 10.9 years), the median administered activity was 4612 MBq. The median prescribed tumor-absorbed dose was 80 Gy; estimated tumor absorbed was 77.7 Gy. No significant difference was observed between pre- and post-therapy tumor absorbed doses ($p = 0.5479$). Absorbed doses to whole liver, normal liver, and lungs were 8 Gy, 1.1 Gy, and 3.2 Gy, respectively. At 2 months (n=36), radiological ORR and DCR were 47.2% and 83.3%; biochemical ORR and DCR were 61.1% and 77.8%. ECOG performance improved in 41.6%. Tumor absorbed dose correlated significantly with both radiological and biochemical responses. ECOG and baseline bilirubin showed significant association with clinical response. Tumor etiology showed no correlation. At 6 months follow-up, 20 patients were shifted to other treatment modalities such as oral MKI, immunotherapy, TACE or transplantation due to disease progression or residual disease. Thus, at 6 months (n=14), radiological ORR and DCR were 50% and 71.4%; biochemical ORR and DCR were 42.8% and 57.1%. BCLC stage and Child-Pugh score correlated with radiological outcomes. Tumor etiology was significantly associated with clinical response ($p=0.022$). ***Conclusion:*** ^{188}Re-N-DEDC/Lipiodol TARE is an effective treatment for inoperable HCC, offering favorable disease control rates. Dosimetric parameters and clinical factors such as ECOG status, bilirubin levels, and liver function scores significantly influence outcomes, supporting personalized treatment planning.

OP-862

Targeting the Tumor Stroma: Safety and Efficacy of 3BP-3940-Based FAP Radiopharmaceutical Therapy in Advanced Metastatic Colorectal Cancer

J. Zhang[1], *T. Zhao*[1], *A. Eismant*[2], *L. Greifenstein*[2], *J. Li*[1], *A. Klega*[2], *C. Landvogt*[2], *C. Mueller*[2], *R. P. Baum*[2];
[1]*National University of Singapore, Singapore, SINGAPORE,* [2]*Center for Advanced Radiomolecular Precision Oncology, Wiesbaden, GERMANY.*

Aim/Introduction: Colorectal cancer remains a leading cause of cancer-related mortality worldwide, especially in patients with metastatic disease who have progressed after standard therapies. Despite advancements in chemotherapy, targeted therapy, radiotherapy, and immunotherapy, treatment options for heavily pretreated metastatic colorectal cancer remain limited. Fibroblast activation protein (FAP), which is overexpressed in the tumor stroma of colorectal cancer, represents a promising target for precision theranostics. This study evaluates the clinical outcomes of FAP-targeted radiopharmaceutical therapy (FRT) using the novel cyclic peptide 3BP-3940 labeled with ^{177}Lu, ^{90}Y, or ^{225}Ac in patients with advanced metastatic colorectal cancer. ***Materials and Methods:*** Ten patients (7 males, 3 females; mean age 59.4 ± 12.3 years) with metastatic colorectal cancer who had exhausted all standard treatment options, including surgery, chemotherapy, external beam radiotherapy (n=8), and immunotherapy (n=3), were treated with FRT following confirmation of FAP expression on ^{68}Ga-3BP-3940 PET/CT. A total of 27 cycles were administered (range: 1-4 cycles per patient), including 12 TANDEM therapies. The mean cumulative administered activities per patient were: ^{177}Lu: 11.9 ± 6.1 GBq, ^{90}Y: 6.0 ± 0.6 GBq, and ^{225}Ac: 9.0 ± 4.2 MBq. Toxicity was graded using CTCAE v5.0. Treatment response was assessed via molecular imaging (PET/SPECT), and overall survival (OS), defined from the initiation of FRT, was calculated using Kaplan-Meier analysis. ***Results:*** FRT was well tolerated, with no grade 3 or 4 toxicities reported. Mild adverse effects included nausea (n=1), pain (n=2), intensified fatigue (n=6), and one case of transient fever that resolved within 24 hours. After two treatment cycles, partial remission was observed in 3 of 6 evaluable patients, corresponding to an objective response rate (ORR) of 50%. As of the study cutoff date in April 2025, 4 of 10 patients (40%) had died. The median follow-up time was 17 months, and the median overall survival has yet to be reached. ***Conclusion:*** FAP-targeted radioligand therapy using 3BP-3940 labeled with ^{177}Lu, ^{90}Y, or ^{225}Ac is safe and shows promising therapeutic potential in metastatic colorectal cancer. This novel approach addresses an unmet need for patients with limited treatment options and supports further clinical investigation of FRT in colorectal cancer.

OP-863

Efficacy of Intra-arterial [^{177}Lu]Lu-DOTATATE Monotherapy for Treatment-refractory Meningioma

A. El Ghalbouni[1,2], *T. J. Snijders*[2], *A. Amerein*[3], *N. Tolboom*[1], *M. Patt*[3], *C. Maurer*[4], *I. C. van der Schaaf*[1], *C. Lapa*[3], *A. J. A. T. Braat*[1];
[1]*Department of Radiology and Nuclear Medicine, UMC Utrecht, Utrecht, NETHERLANDS,* [2]*Department of Neurology and Neurosurgery, Brain Center, UMC Utrecht, Utrecht, NETHERLANDS,* [3]*Department of Nuclear Medicine, Faculty of Medicine, University of Augsburg, Augsburg, GERMANY,* [4]*Department of Diagnostic and Interventional Neuroradiology, Faculty of Medicine, University of Augsburg, Augsburg, GERMANY.*

Aim/Introduction: Although meningiomas generally have excellent survival outcomes, a subset of these tumors - mostly grade 2-3 lesions - exhibit recurrence following primary treatment with surgery and/or radiotherapy. For these treatment-refractory

meningiomas, there are currently no established, evidence-based therapeutic options. In recent years, somatostatin-targeted radionuclide therapy, primarily using intravenous administration of [^{177}Lu]Lu-DOTATATE as a monotherapy, has emerged as a promising new treatment modality. Recent studies have indicated that intra-arterial administration may increase the tumor absorbed dose. This present study aims to assess the efficacy of intra-arterial [^{177}Lu]Lu-DOTATATE in the treatment of refractory meningiomas. ***Materials and Methods:*** This retrospective cohort included patients diagnosed with treatment-refractory meningioma WHO grade 1-3, who had received at least one cycle of intra-arterial [^{177}Lu]Lu-DOTATATE. The primary endpoints were progression-free survival (PFS) and overall survival (OS). Secondary outcomes included objective response, evaluated according to the Proposed Response Assessment and Endpoints for Meningioma Clinical Trials, and safety and toxicity, assessed based on the Common Terminology Criteria for Adverse Events, version 5.0. ***Results:*** Seventeen patients with a median follow-up duration of 34 months (range: 1-57) were included. The median age at the time of the first treatment cycle was 64 years (range: 38-78). Majority of meningiomas were classified as grade 2 (58.8%), and most patients (n = 7) received 4 intra-arterial cycles (median: 3 cycles; median cumulative activity 28.8 GBq). The median time between cycles was 54 days (range: 28-90). PFS at 6, 12 and 24 months was 65% (95% CI: 46-92%), 53% (95% CI: 34-83%) and 41% (95% CI: 23-73%), respectively. OS at 6, 12 and 24 months was 82% (95% CI: 66-100%), 71% (95% CI: 52-96%) and 71% (95% CI: 52-96%). Regarding best objective response, disease control was found in 53% with an objective response rate of 24% (1 complete response, 2 partial responses, 1 minor response, 5 stable disease), with progressive disease in the other 8 patients. One patient experienced grade 3 anemia, and another developed microangiopathic hemolytic anemia as a complication related to angiographic intervention. ***Conclusion:*** This retrospective cohort supports the safety and efficacy of intra-arterial administration of [^{177}Lu]Lu-DOTATATE with an objective response rate of 24% (compared to 2% with intravenous administration in previously published literature), and survival data that exceed published benchmarks. Intra-arterial administration is a promising treatment option for treatment-refractory meningioma. Prospective controlled studies with larger cohorts and extended follow-up, comparing intra-arterial [^{177}Lu]Lu-DOTATATE to (historic) cohorts of intravenous administration are needed.

1807

Wednesday, October 8, 2025, 9:45 - 11:15
Room 212

TROP Session - Inflammation & Infection Committee: Infection/inflammation Under the Lens: Innovations in Nuclear Medicine Imaging

OP-864

Ventilation/Perfusion SPECT/CT in Patients with Long COVID Syndrome: A Multicenter Observational Study

P. Bonnefoy[1], *P. PascalL*[2], *Q. Ceyrat*[3], *S. Burg*[4], *M. Razzouk-Cadet*[5], *C. Moreau Triby*[6], *I. Biancheri Mounicq*[7], *J. Bourre*[8], *P. Salaun*[9], *P. Le Roux*[9];
[1]*CHU Saint-Etienne, Saint Etienne, FRANCE,* [2]*CHU Toulouse Rangueil, Toulouse, FRANCE,* [3]*Centre d'imagerie Fonctionnelle, Bordeaux, FRANCE,* [4]*GCS Médecine nucléaire, Ajaccio, FRANCE,* [5]*CHU de Nice, Nice, FRANCE,* [6]*CHU de Lyon, Lyon, FRANCE,* [7]*CH Angoulême, Angoulême, FRANCE,* [8]*CH Chambéry, Chambéry, FRANCE,* [9]*CHU Brest, Médecine Nucléaire, GETBO, UMR1304, Brest, FRANCE.*

Aim/Introduction: The COVID-19 pandemic has led to a significant number of survivors experiencing persistent health issues, now recognized as long COVID. Respiratory symptoms, such as dyspnea, chronic cough, and reduced exercise capacity, are prevalent and can severely impact quality of life. Ventilation/Perfusion (V/Q) SPECT/CT is a hybrid imaging modality that offers both functional and anatomical insights and has proven valuable in evaluating pulmonary embolism (PE). However, its role in long COVID remains underexplored. ***Materials and Methods:*** A retrospective, multicenter study was conducted using a national registry included V/Q SPECT/CT in symptomatic patients after COVID infection. Centralized, blinded reviews assessed for mismatched, matched, and reverse mismatch defects, as well as morphological lung abnormalities. Descriptive statistics and comparative analyses were performed to evaluate the prevalence of PE and post-embolic sequelae. A secondary objective is to determine the prevalence of normal versus abnormal imaging findings suggestive of post infectious sequelae. ***Results:*** A total of 217 patients with persistent respiratory symptoms (mean time from infection to scan: 26.7 weeks ± 20 weeks) were evaluated between January 2020 and April 2023.Among the 217 patients, 6 (2.8%) exhibited mismatched perfusion defects consistent with PE, including 3 cases of previously undiagnosed PE (1 de novo and 2 recurrent). Post-embolic sequelae were identified in only 3 of 72 patients (4.2%) with a prior PE history. Non-thromboembolic lung abnormalities were found in 116 (53.4%) patients, while 95 (44.8%) had entirely normal V/Q SPECT/CT findings. Matched ventilation-perfusion defects were observed in 83 (38.2%) patients. Reverse mismatched defects were identified in 13 (6.0%) patients. CT abnormalities were present in 107 (49.3%) cases, predominantly subpleural and bilateral. ***Conclusion:*** V/Q SPECT/CT proved valuable in differentiating organic pulmonary abnormalities from non-organic causes in long COVID patients. While PE was rare (2.8%), it remains a serious complication requiring prompt identification and treatment. Notably, 44.8% of patients showed normal V/Q SPECT/CT findings, effectively ruling out organic pulmonary involvement. Hybrid imaging techniques, such as V/Q SPECT/CT, may be considered a valuable tool in the diagnostic assessment of long COVID. Future prospective studies are needed to validate these findings and explore the long-term clinical implications of pulmonary abnormalities in this population.

OP-865

[^{18}F]F-FDG PET/CT in IgG4-Related Disease: Phenotypic Classification and Clinical Correlations in a Cohort of 65 Patients

A. Bagán-Trejo[1], *M. Pudis*[1], *X. Solanich*[2], *C. A. Tapias*[1], *G. Rocamora-Blanch*[2], *F. Climent*[3], *M. Zamorano-Rivas*[1], *S. Maymó-Garrido*[4], *C. García-Alcober*[4], *M. Cortés-Romera*[1];
[1]*Nuclear Medicine-PET (IDI) Department, Hospital Universitari de Bellvitge-IDIBELL, L'Hospitalet de Llobregat, SPAIN,* [2]*Internal Medicine Department, Hospital Universitari de Bellvitge, L'Hospitalet de Llobregat, SPAIN,* [3]*Pathology Department, Hospital Universitari de Bellvitge-IDIBELL, L'Hospitalet de Llobregat, SPAIN,* [4]*Radiopharmacy Department, Hospital Universitari de Bellvitge-IDIBELL, L'Hospitalet de Llobregat, SPAIN.*

Aim/Introduction: To assess the role of [^{18}F]F-FDG PET/CT in IgG4-related disease (IgG4-RD) by analysing metabolic uptake patterns, correlating them with established clinical phenotypes and laboratory parameters, and evaluating its utility in disease classification, biopsy guidance, and therapeutic monitoring. ***Materials and Methods:*** A retrospective analysis was conducted on 65 patients with confirmed IgG4-RD who underwent whole-body [^{18}F]F-FDG PET/CT imaging. Data collected included demographics, referring specialty, total IgG and IgG4 serum levels, clinical manifestations, organ involvement (single/multiple sites), and metabolic uptake measured by a maximum standarised uptake (SUVmax). Imaging findings were categorised into the

following clinical phenotypes: pancreatobiliary, retroperitoneal/aortitis, head and neck, and systemic (Mikulicz). ***Results:*** Of the 65 patients included, 68% were male, with a mean age of 63 years. The majority of referrals originated from Internal Medicine (58%), followed by Nephrology (16%), Gastroenterology (5%), and Pulmonology (5%) and others (16%). Elevated total IgG levels were observed in 40% of cases and elevated IgG4 levels in 52%. The most common clinical manifestations were renal involvement (23%), followed by abdominal symptoms (21%) and incidental findings (11%). Symptomatic sites primarily included the kidneys (renal failure), orbit, and visible/palpable lesions; asymptomatic findings most often involved lymph nodes and salivary glands. [^{18}F]F-FDG PET/CT detected pathological uptake in 59 patients (95%). Single-organ involvement was observed in 35% (22 cases), most frequently in retroperitoneal fibrosis (12) and orbital disease (5). Patients were classified according to metabolic and clinical patterns into retroperitoneal/aortitis (31%, mean SUVmax: 5.99g/mL), head and neck (23%, mean SUVmax: 6.64g/mL), and systemic (34%, mean SUVmax: 4.13g/mL) phenotypes. Three patients showed no uptake due to prior surgical or corticosteroid treatment. ***Conclusion:*** [^{18}F]F-FDG PET/CT plays a pivotal role in the comprehensive management of IgG4-RD. It enables detailed assessment of disease extent, accurate phenotypic classification based on metabolic patterns, and correlation with clinical and serological parameters. Moreover, it facilitates biopsy guidance in atypical presentations, identifies subclinical organ involvement, and allows non-invasive monitoring of inflammatory activity and therapeutic response. These capabilities position [^{18}F]F-FDG PET/CT as an essential imaging modality in the diagnostic and follow-up algorithms of IgG4-RD.

OP-866

Diagnostic value of labelled leukocyte scintigraphy in patients with low-grade periprosthetic joint infection

L. Lezaic[1], *S. Roskar*[2], *R. Mihalic*[2], *V. Levasic*[1], *R. Trebse*[2];
[1]*University Medical Centre Ljubljana, Division of Nuclear Medicine, Ljubljana, SLOVENIA,* [2]*Valdoltra Orthopaedic Hospital, Ankaran, SLOVENIA.*

Aim/Introduction: Periprosthetic joint infection (PJI) is one of the most devastating complications of the joint arthroplasty performed for end-stage osteoarthritis. Timely identification of the PJI and its differentiation from aseptic complications such as mechanical loosening is essential for the choice of the best treatment strategy in painful joint arthroplasty (PJA). Labelled leukocyte scintigraphy (LLS) complements conventional diagnostic procedures by providing information about pathophysiologic changes at the cellular and molecular level and is typically employed at suspicion of low-grade PJI. Although considered highly accurate, the low spatial resolution of nuclear medicine imaging combined with the low-grade inflammatory process may reduce the diagnostic accuracy of LLS. The aim of the study was to evaluate the diagnostic performance of LLS in patients with PJA specifically in the setting of a painful joint with endoprosthesis where low-grade PJI needs to be excluded. ***Materials and Methods:*** Patients treated surgically for PJA at the Valdoltra Orthopaedics Hospital that also underwent LLS at the Division of Nuclear Medicine of the UMC Ljubljana between 2016 and 2023 were retrospectively evaluated. The data on patient age, gender, side of surgery, date of primary arthroplasty, date of revision surgery, reason for revision surgery, perioperative PJI diagnostics and the date of the last follow-up were retrieved from a prospectively collected dataset and supplemented retrospectively from the hospital registry or individual charts where required. The definite diagnosis of PJI was based on the EBJIS definition. ***Results:*** Between 2016 and 2023, of 734 LLS performed in total, 347 (48%) were performed in patients treated with PJA (144 total hip, 169 unicompartmental or total knee, 23 ankle, 9 shoulder, and 2 elbow arthroplasties). Overall, 33 (9.7%) EBJIS criteria-confirmed PJI were observed while the remaining 314 were considered as aseptic. For the whole cohort, the sensitivity and specificity of LLS was 79% (95%CI 77-81%) and 99% (95%CI 97-100%), respectively; in patients without radiologically present gross osteolysis around the implant, the sensitivity was 94%. In the aseptic group, 107 patients had a revision surgery where PJI as the diagnosis was excluded considering EBJIS criteria while the remaining 207 patients had no revision surgery and no clinical signs of infection during at least 2 years follow-up. ***Conclusion:*** Labelled lekocyte scintigraphy is a highly specific and sensitive diagnostic tool in low-grade PJI, especially in patients without radiologically gross osteolysis present around the implant.

OP-867

Dynamic [^{18}F]FDG PET/CT imaging in fracture-related infections to distinguish infection from inflammation

N. D. van Rijsewijk*, M. Wouthuyzen-Bakker, J. H. van Snick, J. van Sluis, R. H. J. A. Slart, A. W. J. M. Glaudemans, F. F. A. IJpma; University Medical Center Groningen, Groningen, NETHERLANDS.*

Aim/Introduction: Static [^{18}F]FDG PET/CT is widely applied to detect infections but is limited in differentiating bacterial infection from sterile inflammation due to overlapping uptake patterns. In particular in fracture-related infection (FRI), this is challenging due to multiple factors, including recent surgery, soft tissue injury, fracture healing, and surgical implants. Dynamic [^{18}F]FDG imaging over time may overcome this limitation. This study investigates the potential of dynamic [^{18}F]FDG PET/CT and obtaining time activity curves (TACs) to distinguish infection from sterile inflammation in patients with suspected FRI. ***Materials and Methods:*** A prospective study was performed in patients suspected of FRI and referred for [^{18}F]FDG PET/CT examination to detect (the extent of) infection from December 2021 until November 2024. Final diagnosis of FRI was established according to the criteria defined by the FRI consensus group and used as a reference standard. Dynamic imaging was performed using a long axial field-of-view PET/CT system over 65 minutes after [^{18}F]FDG injection. TACs were analyzed to compare uptake patterns between confirmed infections and sterile inflammation, and diagnostic accuracy was calculated and compared to conventional static imaging. ***Results:*** Thirty-one patients with 33 fractures suspected of infection were included. Infection was clinically confirmed in 14 fractures (42%). Classification based on dynamic imaging using TACs resulted in a high sensitivity of 86%, specificity of 100%, PPV of 100% and NPV of 90%, resulting in a diagnostic accuracy of 94%. This diagnostic accuracy was higher compared to the visual and quantitative static assessments, which were 88% and 91% respectively. Visual assessment of the dynamic scan was less high, with a diagnostic accuracy of 82%. Visual scan assessment showed in general higher false positives, while quantitative assessment introduced more false negatives. ***Conclusion:*** The results of this prospective study show that dynamic [^{18}F]FDG PET/CT imaging, and the analysis of TACs, can differentiate between infection and sterile inflammation. Dynamic imaging demonstrates slightly better diagnostic accuracy over static scan analysis only by using TACs in FRI.

OP-868

Development and External Validation of Metabolic Tumor Volume Measures at Baseline [18F]FDG-PET/CT to Predict Treatment Failure and Relapse-Free Survival in Antibiotic-Naïve Patients with Pyogenic Spondylodiscitis

F. Lanfranchi[1,2], *D. Albano*[3,4], *C. Delucchi*[2], *S. Maggio*[2], *V. Iannaccone*[2], *P. Furtuna*[3,4], *D. Dubois*[1,2], *F. Bertagna*[3,4], *G. Sambuceti*[1,2], *M. Bauckneht*[1,2];
[1]*Nuclear Medicine, Department of Health Sciences (DISSAL), University of Genoa, Genova, ITALY,* [2]*IRCCS Ospedale Policlinico San Martino, Genova, ITALY,* [3]*Nuclear Medicine, ASST Spedali Civili, Brescia, ITALY,* [4]*University of Brescia, Brescia, ITALY.*

Aim/Introduction: Pyogenic spondylodiscitis presents a clinical challenge, potentially leading to long-term complications. Reliable early predictors of clinical outcomes in these patients are currently lacking. Despite its growing importance in managing spondylodiscitis, the prognostic value of [18F]FDG-PET/CT has been insufficiently evaluated. In this scenario, we aimed to explore baseline predictors of treatment response in patients with pyogenic spondylodiscitis and to test their replicability in an external independent population. ***Materials and Methods:*** Patients clinically diagnosed with pyogenic spondylodiscitis who underwent [18F]FDG-PET/CT at two Italian centers between 2020 and 2023 were retrospectively enrolled. Inclusion criteria included: 1) no previous spine surgery; 2) no onco-hematological diseases; 3) no corticosteroid treatment; 4) 12-months follow-up availability. Patients already receiving antibiotic therapy at the time of imaging were excluded. Lab markers collected were C-reactive protein, procalcitonin, white blood cell differential counts, and creatinine levels. For each lesion, the standardised uptake value maximum (SUVmax), metabolic tumor volume (MTV), and total lesion glycolysis (TLG) were quantified from baseline [18F]FDG-PET/CT images. Patients were treated according to current guidelines (6-12 weeks of therapy). Outcomes were treatment failure and relapse-free survival (RFS) [1]. Multivariable binary logistic regression analyses, ROC curves, and Cox regression models were performed to calculate OR, diagnostic accuracy, and HR, respectively. C-indexes and Brier scores were also computed. All analyses were performed with a 10-fold cross validation approach. Finally, Kaplan-Meier curves for RFS were designed. ***Results:*** Development and validation cohorts included 78 and 30 lesions, respectively. MTV (best cut-off=34 mL) resulted in the sole independent predictor of treatment failure at the multivariate regression model (OR=1.07, 95%CI=1.03-1.11; p<0.001), with C-index=0.76, specificity and positive predictive value (PPV)≥0.95, and Brier score=0.25. The Cox regression analysis showed this model as a significant predictor of RFS (HR=1.89, 95%CI=1.320-2.70; p<0.01), with C-index=0.74 and Brier score=0.12. Lesions exhibiting MTV≥34 mL showed a significantly impaired median RFS (10 months) compared to lesions with MTV<34 mL (not reached; Log-rank: p<0.001). These results were confirmed in the validation cohort for both treatment failure (C-index=0.78, specificity and PPV≥0.91, Brier score=0.20) and RFS (C-index=0.73, Brier score=0.12; Log-rank: p<0.001). ***Conclusion:*** In a multicentric setting, [18F]FDG-PET/CT-derived MTV independently predicts treatment failure and RFS in patients with pyogenic spondylodiscitis before initiating antibiotic treatment. This metabolic measure might facilitate early risk stratification, potentially enhancing subsequent clinical management. ***References:*** 1. Bernard L et al. Antibiotic treatment for 6 weeks versus 12 weeks in patients with pyogenic vertebral osteomyelitis: an open-label, non-inferiority, randomised, controlled trial. Lancet. 2015.

OP-869

Added Value of FDG-PET Imaging in Patients with Spondylodiscitis

L. Reichel[1], *R. Liang*[2], *S. Hirsch*[2], *B. Meyer*[2], *W. Weber*[1], *A. Jörger*[2], *S. Notohamiprodjo*[1];
[1]*Department of Nuclear Medicine, TUM University Hospital, Munich, GERMANY,* [2]*Department of Neurosurgery, TUM University Hospital, Munich, GERMANY.*

Aim/Introduction: Spondylodiscitis poses significant diagnostic challenges due to nonspecific symptoms and limitations of conventional imaging modalities. Moreover, causative infection foci are often not identified. Early and accurate detection of spondylodiscitis and treatment of the focus of infection is critical to prevent severe complications. Positron Emission Tomography (PET), particularly using 18F-fluorodeoxyglucose (FDG), has emerged as a complementary tool to Magnetic Resonance Imaging (MRI), offering high sensitivity in identifying metabolic activity associated with infectious foci. This study aims to evaluate the diagnostic accuracy of PET in detecting and monitoring patients with spondylodiscitis and the detection of other infectious foci. ***Materials and Methods:*** A retrospective analysis was conducted on 198 patients who underwent FDG-PET imaging for infection-related indications between 2016 and 2023. The primary objective was to assess efficacy in diagnosing spondylodiscitis and identifying additional infectious foci. PET findings were compared with MRI, pathological, and microbiological results and clinical data. Maximum Standardized Uptake Values (SUVmax) were measured in locations of identified infectious foci and correlated with inflammation markers. ***Results:*** Among 198 patients, PET imaging identified new infectious foci in 25 cases while 2 cases with suspected foci (endocarditis and dental infection) were missed. Tracer uptake without clinical relevance was observed in 12 cases. PET confirmed previously known foci in 21 cases (mean SUVmax arthritis 7.1±3.5, soft tissue infection 10.4±5.8, prosthesis infection 7.6±1.7). In 30 cases with unclear MRI findings, PET aided in diagnosis (mean SUVmax 12.1±6.0), while it was used in follow-up for 4 cases. Notably, in seven cases, MRI falsely indicated spondylodiscitis, which was not confirmed by PET imaging or clinical evaluation. Conversely, PET failed to detect spondylodiscitis in five clinically confirmed cases, three of which were identified as low-grade infections. ***Conclusion:*** PET imaging shows potential added value, particularly in identifying infection foci and aiding in diagnosing spondylodiscitis, especially when MRI results are inconclusive. However, discrepancies between PET, MRI, and microbiological findings suggest that PET may have limitations in certain scenarios, warranting further investigation into its diagnostic role.

OP-870

Identification of chronic musculoskeletal pain generators with [18F]FDG PET-MRI

J. Mostert[1], *E. H. G. Oei*[1], *M. Ananta*[1], *G. S. R. Muradin*[1], *F. J. M. P. Huygen*[1], *C. C. de Vos*[1], *P. K. Bos*[1], *S. Biswal*[2], *R. A. van der Heijden*[1,2];
[1]*Erasmus Medical Center, Rotterdam, NETHERLANDS,* [2]*University of Wisconsin-Madison, Madison, WI, UNITED STATES OF AMERICA.*

Aim/Introduction: Chronic pain is the most frequent reason for patients to seek medical consultation. Up to 79% of patients with chronic musculoskeletal pain believe their pain is inadequately treated,[1] mainly due to our inability to accurately identify pain generators using conventional imaging. This study evaluates the added value of hybrid [18F]FDG PET/MRI for identifying pain sources in patients with diagnostically challenging chronic low back pain (LBP) or hip pain after total hip replacement (THR). ***Materials and Methods:*** Patients aged 18-75 with chronic LBP or post-THR hip pain were recruited and randomized to the intervention group ([18F]FDG PET/MRI with subsequent targeted treatment) or the control group (standard clinical care). For participants who underwent PET-MRI, potential pain sources were identified based on increased FDG uptake on PET and/or anatomical abnormalities on MRI. ***Results:*** We present interim results of 54 LBP patients and 17 post-THR patients, of which 35 were randomized to PET-MRI. Overall, PET/MRI provided new diagnostic insights regarding potential pain generators in 30 patients (86%). In patients with chronic LBP, PET/MRI led to targeted treatment in 65% of patients, and 8% was referred for surgical intervention. Some patients reported pain relief after years of severe pain. In the control group, only 7% underwent further diagnostic imaging, and 32% received an injection based on previous imaging or symptoms. In patients with post-THR hip pain, 67% had additional diagnostic imaging, 89% underwent additional diagnostic procedures, and THR revision was indicated in 44%. In the control group, 50% received additional imaging, not leading to new insights in the majority. ***Conclusion:*** [18F]FDG PET/

MRI is able to identify previously undetected pain generators in patients with chronic LBP or post-THR hip pain, leading to more frequent adjustments in clinical management compared to standard care including targeted treatment with symptom relief. Further evaluation in a larger cohort is needed to determine the added value of [18F]FDG PET-MRI in terms of patient outcomes.
References: 1.Bekkering GE, Bala MM, Reid K, et al. Epidemiology of chronic pain and its treatment in The Netherlands. Neth J Med. 2011;69(3):141-153.

OP-871

Clinical Utility of FDG PET/CT in the Management of Bloodstream Infections: Interim Results from A Single-Center Study

A. Karellis[1], *G. Abikhzer*[1,2], *B. Bilodeau-Harnois*[1,2], *A. Roy*[1,2], *K. Weiss*[1,2];
[1]*Jewish General Hospital, Montréal, QC, CANADA,* [2]*McGill University, Montréal, QC, CANADA.*

Aim/Introduction: ^{18}F-Flurodeoxyglucose (FDG)-positron emission tomography/computed tomography (PET/CT) is increasingly utilized in the diagnosis and management of infectious diseases. However, evidence is lacking regarding its impact in the management of bloodstream infections (BSIs), particularly for bacteremias other than Staphyloccocus aureus. This study aimed to assess the clinical utility of FDG PET/CT and its impact on patient management. ***Materials and Methods:*** We conducted a retrospective chart review, using 2021-2024 data. Eligible patients included those with a positive blood culture who underwent FDG PET/CT imaging to aid in the management of their BSI. Data collected included patient and infection characteristics, investigations and imaging performed, FDG PET/CT findings, and treatment modifications following the PET scan. Descriptive statistics were performed. ***Results:*** This interim analysis includes 100 patients [57% male, mean (SD) age: 73.77 (15.92) years]. Fifty percent of patients were diabetic, 30% had an active malignancy, 27% were immunocompromised and 44% had an implant/prosthesis. This population included a wide range of pathogens: 79 had gram-positive bacteremia, 15 gram-negative, 4 had polymicrobial mixed infection and 2 had candidemia. FDG PET/CT imaging yielded positive findings for 86 patients, including 77 patients for whom infectious septic foci were identified. The most common infectious sites included lung (n=27), spondylodiscitis (n=23), spleen (n=23), endocarditis (n=22), skin and soft tissue (n=19), and intraabdominal/bowel (n=12). Following FDG PET/CT, 51% of patients' clinical management was modified. The most common modification was the adjustment of treatment duration (n=32) (extension for 30 patients and shortening for two patients). Twelve patients' antimicrobial regimen was changed (two of which received two antibiotics). Six patients underwent a spectrum modification (narrowed for four, broadened for two). Six patients had their antibiotic therapy modified for an agent with a better central nervous system penetration. Four patients had a second antimicrobial drug added to their regimen. Nine and three patients underwent surgical and radiologic intervention, respectively. ***Conclusion:*** This interim analysis highlights the high clinical utility of FDG PET/CT imaging in the management of patients with a BSI by identifying the infectious source and infectious foci or complications not detected by other imaging modalities. In this study population, FDG PET/CT revealed metastatic infectious foci in 77% of patients. More than half of patients' therapeutic management was modified by FDG PET/CT findings, including a subset of patients whose study was negative, therefore demonstrating potential impact for all patients whether metastatic foci were identified or not.

OP-872

Diagnostic Utility of [^{18}F]-FDG PET/CT in Guiding Biopsy Sites in Pyrexia of Unknown Origin; Site Concordance, Yield and ROC-Based Suvmax Threshold for Differentiating Between Benign and Malignant Etiology

K. Vengadesan, *N. A. Damle, G. B. Priyanka, C. Ganapathy, M. Tripathi, C. Bal, M. Soneja, N. Nischal, P. Sethi, S. Jain, A. Singh, B. Prakash, R. Yadav;*
All India Institute of Medical Sciences, New Delhi, INDIA.

Aim/Introduction: [^{18}F]-Fluorodeoxyglucose positron emission tomography/computed tomography ([^{18}F]-FDG PET/CT) plays a pivotal role in evaluating patients with pyrexia of unknown origin (PUO). However, the correlation between PET-identified potential biopsy sites and actual biopsy practice, along with diagnostic yield and threshold optimization, remains underexplored. This study aimed to assess the concordance between [18F]-FDG PET/CT-identified hypermetabolic sites and actual biopsy sites in PUO patients, evaluate diagnostic yield, and determine the optimal standardized uptake value (SUVmax) cut-off that can predict if the lesion is benign or malignant using receiver operating characteristic (ROC) analysis. ***Materials and Methods:*** A retrospective analysis was conducted on 185 PUO patients who underwent [^{18}F]-FDG PET/CT between April 2024 to January 2025 in our institute. Hypermetabolic lesions were documented and categorized as potential biopsy sites. Actual biopsies performed were compared against PET/CT-suggested sites. Diagnostic yield was calculated based on histopathological confirmation. ROC analysis was used to determine the SUVmax threshold with optimal sensitivity and specificity for differentiating between benign and malignant etiology. ***Results:*** Out of 185 patients, [^{18}F]-FDG PET/CT identified 73 potential biopsy sites in 73 patients. Biopsies were performed on 45/73 patients, with 82.2% (37/45) being from the PET/CT-guided sites. The overall diagnostic yield that guided further clinical management was 72.97% (27/37) with 13 being benign lesions (infective and non-infective inflammatory disease) and 14 being neoplastic. The ROC analysis identified an SUVmax cut-off of 8.94 (AUC = 0.678, sensitivity = 76.5%, specificity = 62.5%), above which biopsy was more likely to differentiate between benign and malignant etiology (p = 0.064). ***Conclusion:*** [^{18}F]-FDG PET/CT identified biopsy-suitable sites in a significant proportion of PUO patients where it was deemed necessary. Biopsies were eventually performed in more than half of these patients, of which, most were from the PET/CT-guided sites. In this study, a SUVmax of 8.94 was found to be useful in potentially differentiating between benign and malignant etiology.

1808

Wednesday, October 8, 2025, 09:45 - 11:15
Room 115

Joint Symposium 8 - Cardiovascular Committee / EACVI - Controversies in the Evaluation of Coronary Artery Disease

OP-872a

Risk Stratification: CT First!

M. Dweck; *University of Edinburgh, Cardiology, Edinburgh, UNITED KINGDOM.*

OP-872b

Risk stratification: MPI Get Me Out of Trouble!

M. Lyngby Lassen; *The Department of Clinical Physiology, Nuclear Medicine and PET and Cluster for Molecular Imaging, Copenhagen University Hospital - Rigshospitalet and Department of Biomedical Sciences, University of Copenhagen, Copenhagen, DENMARK.*

OP-872c
Guiding Patient Management: Look at the Anatomy with CT!
J. Geers; *University Hospital Brussels, Department of Cardiology, Brussels, BELGIUM.*

OP-872d
Guiding Patient Management: Surfing on the Flow with MPI!
C. Nappi; *Department of Advanced Biomedical Sciences Federico II University, Naples, ITALY.*

1809

Wednesday, October 8, 2025, 9:45 - 11:15
Room 133+134

e-Poster Presentations Session 14 - Radiation Protection Committee: Radiation Protection e-Poster Presentations Session

EPS-285
A radiation Life Cycle Assessment for TAT-isotopes
G. de With[1], *M. Hakulinen*[2], *R. Kollaard*[1], *G. Sandker*[1], *A. Sarnelli*[3], *E. Winters*[1], *SECURE partners of T4.2;*
[1]*NRG PALLAS, Arnhem, NETHERLANDS,* [2]*Kuopio University Hospital, Kuopio, FINLAND,* [3]*IRST, Meldola, ITALY.*

Aim/Introduction: The EU funded project SECURE aims to make a major contribution to the sustainability production and safe application of α-emitting isotopes. α-emitting isotopes coupled to highly target-specific molecules are widely investigated for use in targeted alpha therapy (TAT). While clinical results show these are a potent drug with great potential in cancer therapy, adequate consideration of radiation protection is required. Therefore, we developed a computational tool to perform a radiation Life Cycle Assessment (LCA) considering all relevant exposure scenarios during the isotope's life cycle. ***Materials and Methods:*** Three specific radiation protection issues were considered. (1) To determine the radiation doses for workers, caregivers and public involved throughout the life cycle of the TAT-isotope, considering relevant exposures, pathways and radionuclide inventories. (2) To make a comparison of the radiation doses from the exposure scenarios for the different TAT-isotopes (e.g. ^{225}Ac, ^{212}Pb, ^{213}Bi, ^{223}Ra) and their production routes. (3) To perform an analysis on the computational findings and extract lessons learned, draw recommendations for best practice, and identify areas and topics that require attention from a radiation protection perspective. ***Results:*** The tool was designed to assess radiation exposure through all possible exposure routes (external radiation, inhalation, submersion, and ingestion) and calculate the effective doses as well as equivalent doses for the eye, extremities and skin. The isotope's life cycle is divided into the following stages: production, purification, labelling and clinical practice. Each stage is covered by scenarios with a defined time line, mode of chemical processing, exposure time, shielding, distance, and indoor and outdoor exposure parameters. The nuclide inventory is computed for each scenario and forwarded to the next scenario considering any chemical processing, discharges, waste, or dissemination to multiple users. The process of decay and in-growth is computed considering initial activities, decay rates and complex decay chains including multiple decay branches. The results from the tool demonstrate that choices made in the design of the isotope production process strongly impact potential radiation risk, waste generation, and effective use of infrastructure and source material. Furthermore, recommendations on the safe use should be tailored to the specific radiological needs of the TAT-isotope in question. ***Conclusion:*** We developed a tool which clearly indicates considerable variation in radiation dose for the various TAT-isotopes along its life cycle with strong variation in the relative contributions from different exposure routes. Insights are obtained that help to improve radiation protection issues involving α-emitting isotopes.

EPS-286
Targeted alpha therapy in clinical practice: a radiation protection assessment before implementation
A. Sarnelli[1], *E. Mezzenga*[1], *R. Kollaard*[2], *E. Winters*[2], *G. De With*[2], *R. Mikołajczak*[3];
[1]*Istituto Romagnolo per lo Studio dei Tumori "Dino Amadori", Meldola, ITALY,* [2]*NRG|PALLAS, Petten, NETHERLANDS,* [3]*Radioisotope Centre POLATOM, National Centre for Nuclear Research, Otwock, POLAND.*

Aim/Introduction: Targeted Alpha Therapy (TAT) has increasingly been adopted in clinical practice due to the high therapeutic efficacy of alpha particles compared to beta emitters. Alpha particles are characterized by high linear energy transfer and a short path length, enabling precise cytotoxic effects while minimizing damage to healthy tissues. However, their clinical use raises important radiation protection considerations for healthcare workers, patients' caregivers, and the public. This work has been funded by the HORIZON-EURATOM-2021-NRT01 - SECURE project (Project number: 101061230) and provides a detailed radiation risk assessment associated with handling key alpha-emitting radionuclides, specifically Th-227, Ac-225, Ra-223, Bi-213, Pb-212, and At-211. ***Materials and Methods:*** Three principal exposure scenarios were analyzed: single-dose preparation, administration, and patient care. Both external and internal exposures were evaluated, using established dose conversion factors to estimate whole-body effective doses, extremity equivalent doses, and committed doses. Additionally, an incident scenario involving a liquid radiopharmaceutical spill was modeled to assess potential contamination risks. ***Results:*** The findings show that while the whole-body effective doses to workers are negligible across all scenarios, extremity doses—especially during administration without shielding—can be significant, reaching values that necessitate strict protective measures. Internal exposure under normal operations remains minimal but can become relevant in the event of accidental inhalation or ingestion. Skin contamination in spill scenarios could result in high localized doses if immediate decontamination is not performed, although such situations were analyzed conservatively assuming worst-case conditions. Radiation exposure to third parties, including caregivers and the general public, was also estimated. Results indicate that the doses are at least one order of magnitude lower than the regulatory dose constraints, affirming that outpatient management can be performed safely with appropriate guidance and precautionary instructions. ***Conclusion:*** The presented scenarios were deliberately conservative to ensure that risk assessments overestimate, rather than underestimate, actual risks. While the results cannot directly rank the radiopharmaceuticals in terms of hazard, they provide a generalizable methodology and baseline for institutions planning to implement TAT. This work highlights the importance of comprehensive radiation safety programs tailored to alpha therapies, considering both routine practices and potential incidents. It also underlines the need for specialized training, shielding, contamination control measures, and patient release protocols to ensure the safe and sustainable integration of TAT into clinical practice.

EPS-287

Radiation protection efficacy of a new device for the infusion of radiopharmaceuticals labeled with 177Lutetium

M. Marengo[1], *A. Zorz*[1], *L. M. Colombo Gomez*[1], *F. De Monte*[1], *M. Paiusco*[1], *L. Pompignoli*[2];
[1]*Veneto Institute of Oncology IOV – IRCCS, Padua, ITALY,* [2]*Tema Sinergie, Faenza, ITALY.*

Aim/Introduction: Modern treatments with ^{177}Lu-labeled radiopharmaceuticals require the administration of relevant activity, under conditions of controlled flow and infusion time, as well as safety from irradiation and limitation of the risks of fluid leaks and consequent contamination. A system based on an infusion pump, certified tubing kit, and intrinsically shielded represents a significant advance in this field. ***Materials and Methods:*** The Aster consists of an infusion system and a shield for the radiopharmaceutical vial. This shield is made of Tungsten and Lead glass, to allow visual control of the radiopharmaceutical vial during the infusion. The simulations were performed using FLUKA.CERN and its interface Flair. The transport thresholds for electrons and photons were set to 30 keV and 15 keV, respectively. The source was modelled as a borosilicate glass vial of the penicillin type. The Lead glass was modelled according to the manufacturer's specifications and certificate of analysis. The tungsten alloy used has a density of 17.1 g/cm^3 . The equivalence of Aster shielding to lead was firstly assessed by simulating a ^{60}Co source. The leaded glass vial of the Aster was replaced by increasing thcknesses of lead. Then ^{177}Lu was considered, both in air and within the Aster shield. ***Results:*** Simulations performed with ^{60}Co in air, without shielding, gave an ambient dose rate value at 100 cm of 3.45E-04 mSv/h per 1 MBq, in agreement with published data. The results for absorption in lead were fitted by a single exponential function. The simulation of the transmission for ^{60}Co gamma rays in the leaded glass shield of the Aster gave a transmission of 0.57 +/- 1.0% . This shows that the Aster's lead glass shield has a shielding equivalent for ^{60}Co gamma rays >1.1 cm Pb. Simulations with a ^{177}Lu vial placed in air, without shielding, gave an ambient dose rate of 6.03E-06 mSv/h at 100 cm per 1 MBq. The transmission factor evaluated at 10, 50 and 100 cm from the center of the vial placed inside the Aster, gave an attenuation factor for ^{177}Lu gammarays and bremsstrahlung emission of > 0.999 . ***Conclusion:*** The Aster is effective in reducing the dose levels from the vial of radiopharmaceutical during administration of ^{177}Lu radiopharmaceuticals.. It is a certified device, safe and easy to use, which can facilitate theragnostic applications and improve the optimization of radiation protection. ***References:*** Marengo M., Infantino A. Physica Medica 103 (2022) 59-65.

EPS-288

Assessment of Early Excretion and Radiation Protection Considerations in ^{177}Lu-PSMA Therapy

F. Zagni[1], *L. Vetrone*[2], *A. Farolfi*[2], *E. Lodi-Rizzini*[3], *A. Golemi*[2], *S. Civollani*[1], *M. Maccagnani*[1], *L. Strigari*[1], *S. Fanti*[2];
[1]*Department of Medical Physics, IRCCS Azienda Ospedaliero-Universitaria di Bologna, Bologna, ITALY,* [2]*Nuclear Medicine, IRCCS, Azienda Ospedaliero-Universitaria di Bologna, Bologna, ITALY,* [3]*Radiation Oncology, IRCCS, Azienda Ospedaliero-Universitaria di Bologna, Bologna, ITALY.*

Aim/Introduction: The recent introduction of Lutetium-177-labeled radiopharmaceuticals, such as 177Lu-DOTATATE and 177Lu-PSMA, has significantly improved therapeutic options in neuroendocrine and prostate cancers, respectively. Outpatient management of 177Lu-PSMA is already practiced in some countries, though with heterogeneous time-points for patient discharge, underscoring the need for harmonized recommendations. This study provides a quantitative extension of previously reported feasibility data by analyzing external irradiation measurements in patients treated with 177Lu-PSMA, focusing on early excretion kinetics and radiation exposure reduction within 6 hours post-administration. ***Materials and Methods:*** Radiation exposure was measured at 1 meter following 40 administrations of 7400 MBq of 177Lu-PSMA, (7 patients each receiving between 4 and 6 treatment cycles), at baseline (0h), 6h, 24h, and 48h post-administration. Measurements were performed with an ionization chamber calibrated in terms of ambient dose equivalent H*(10). For a subset evaluated at baseline and 6h, measurements were also acquired at body contact in the point of maximum exposure. For each time point, mean values were normalized to baseline, and uncertainties were estimated as standard error of the mean at 95% confidence. A bi-exponential model was fitted to estimate excretion parameters (A1,T1,A2,T2). ***Results:*** Initial exposure at 1 meter, measured on all patients, was 18±3 µSv/h. At body contact, the ratio at 6h was 0.42±0.08. Relative to baseline, mean exposure rates declined to 0.50±0.08 at 6h, 0.18±0.06 at 24h, and 0.12±0.03 at 48h. Notably, a few outliers at 6h (range: 0.26-0.85) indicate individual variability in excretion and exposure. Bi-exponential decay modeling revealed a fast clearance component with a half-life T_1=4.3±1.9 hours (A_1=0.80±0.24), and a slower component with a half-life T_2=67±50 hours (A_2=0.20±0.15). ***Conclusion:*** The results align with literature values, confirming that approximately 50% of the administered activity is eliminated within the first 6 hours. Data at 24-48 hours were consistent with prior studies, though limited by sample size and greater uncertainty. More data may help refine late-phase kinetics and support more accurate patient dosimetry. The presence of outliers confirms the need of individualized monitoring. Current findings support patient discharge at 6 hours from a radiation protection perspective. Early discharge is feasible without exceeding dose constraints for caregivers and the public, assuming adherence to simple precautions for a brief period. Notably, in this context ICRP states that outpatient feasibility in a fully optimized procedure should consider not only radiation safety, but also patient clinical conditions and comfort, logistics, occupational exposure, and overall healthcare system efficiency.

EPS-289

Assessment of Patient Emitted Radiation and Caregiver Exposure Following 177Lu-PSMA Therapy

P. Sheikhzadeh[1], *S. Farzanehfar*[1], *M. Abbasi*[1], *Z. Bayat*[2], *M. Abdolmaleki*[3], *F. Koosha*[3], *N. Kasraie*[4];
[1]*Tehran University of Medical Science, Tehran, IRAN, ISLAMIC REPUBLIC OF,* [2]*Science and Research Branch, Islamic Azad University, Tehran, IRAN, ISLAMIC REPUBLIC OF,* [3]*Shahid Beheshti University of Medical Sciences, Tehran, IRAN, ISLAMIC REPUBLIC OF,* [4]*UT Southwestern Medical Center, Dallas, TX, UNITED STATES OF AMERICA.*

Aim/Introduction: The objective of this study was to evaluate the external radiation dose emitted by patients undergoing 177Lu-PSMA therapy and to assess the radiation exposure received by their caregivers. This assessment aimed to determine the safety of early discharge and outpatient management following treatment. ***Materials and Methods:*** Radiation dose rates were measured in 47 patients treated with 177Lu-PSMA (mean activity: 5563 ± 1013 MBq) at different time intervals (5 min to 168 h) and distances (0.5 m and 1 m) using a calibrated dosimeter. To estimate caregivers' radiation exposure, thermoluminescent dosimeters (TLDs) were provided to 27 individuals, who wore them continuously for 7 days post-discharge. All measurements followed national and international radiation safety protocols. ***Results:*** At 1 hour post-injection, peak dose rates were observed (48.5 ± 15 µSv/h at 0.5 m and 31.6 ± 8 µSv/h at 1 m), followed by a steady decline over time. The dose rate fell below the discharge threshold of 20 µSv/h at 1 m within approximately 6-6.5 hours. The estimated effective half-life of 177Lu-PSMA was 23.1 hours. Caregiver doses ranged from 20 to 1170 µSv, with a mean of 194 ± 230 µSv—well below the annual

exposure limits recommended by ICRP and IAEA. ***Conclusion:*** The study demonstrates that with appropriate radiation safety measures and patient education, outpatient administration of 177Lu-PSMA is safe for both patients and caregivers. Individual variability in dose rates highlights the importance of personalized safety planning, especially for caregivers in close and prolonged contact with treated individuals.

EPS-290

Nephroprotective effects of metformin in patients undergoing radioligand therapy

S. Kunte[1], *M. Wu*[1], *L. Hempel*[1], *A. Holzgreve*[1], *M. Scheifele*[1], *T. Siegmund*[2], *J. Ells*[1], *F. J. Gildehaus*[1], *G. Böning*[1], *M. Unterrainer*[1], *L. M. Unterrainer*[1], *R. A. Werner*[1], *A. Delker*[1], *Z. Ells*[1];
[1]*Department of Nuclear Medicine, LMU University Hospital, Munich, GERMANY,* [2]*Division for Endocrinology, Diabetology and Metabolism, Isar Clinic Munich, Munich, GERMANY.*

Aim/Introduction: Radioligand therapy (RLT) has become an established treatment option for various cancers expressing molecular targets such as prostate-specific membrane antigen (PSMA-RLT) or somatostatin receptors (peptide receptor RLT (PRRT)). Despite its therapeutic efficacy, RLT carries a risk of nephrotoxicity, owing to the kidneys' role in metabolizing and excreting radiolabeled compounds. Various strategies have been investigated to mitigate renal radiation exposure. Preclinical data suggest that metformin, a widely prescribed antidiabetic agent, may reduce nephrotoxicity through inhibition of tubular reabsorption of filtered peptides, potentially via its strong basic biguanide group. This study aimed to evaluate the potential nephroprotective effect of metformin in patients undergoing PSMA-RLT or PRRT by analyzing the kidney absorbed (radiation) dose (AD). ***Materials and Methods:*** Patients treated with either PSMA-RLT or PRRT were enrolled and stratified into subgroups based on metformin use. Individuals with pre-existing renal disease were excluded from the analysis. Respective ADs were calculated for each treatment cycle using MIM Software, applying either multi-timepoint or single-timepoint dosimetry, depending on data availability. ***Results:*** A total of 61 patients were included in the analysis, comprising 30 individuals undergoing PSMA-RLT (10 with metformin, 20 without) and 31 receiving PRRT (11 with metformin, 20 without). In the first treatment cycle, patients receiving PSMA-RLT in combination with metformin showed a significantly lower AD compared to those without metformin (0.24 ± 0.09 Gy/GBq vs. 0.33 ± 0.14 Gy/GBq; $p = 0.018$). No such effect was observed in the PRRT group (0.46 ± 0.25 Gy/GBq vs. 0.41 ± 0.10 Gy/GBq; $p = 0.897$). Analysis of the mean kidney AD across all administered cycles confirmed these findings: metformin was associated with a significantly reduced kidney AD in the PSMA-RLT group (0.24 ± 0.09 Gy/GBq vs. 0.32 ± 0.10 Gy/GBq; $p < 0.001$), whereas no significant difference was observed in the PRRT group (0.47 ± 0.17 Gy/GBq vs. 0.43 ± 0.17 Gy/GBq; $p = 0.132$). ***Conclusion:*** Metformin was associated with a significantly reduced renal radiation exposure in patients undergoing PSMA-RLT, whereas no such effect was seen in patients receiving PRRT. Further studies are needed to assess renal function and long-term nephrotoxicity in this context.

EPS-291

(V)Are skin doses real? - experimental verification of estimated skin dose calculations.

K. Tallat-Szczotka[1], *P. Begley*[2], *P. Colley*[2], *O. Harris*[2], *K. Barrie*[2], *J. Poole-Jones*[2];
[1]*Barts Health NHS Trust, London, UNITED KINGDOM,* [2]*University Hospitals Sussex NHS Foundation Trust, Brighton, UNITED KINGDOM.*

Aim/Introduction: There is a legislative need to quantify skin doses for extremity dose limits with the increasing development of new alpha and beta emitters in molecular radiotherapy. VARSKIN+ software has been increasing in popularity as a useful tool for skin dose estimation. Modelling of certain scenarios can result in exceeding dose limits. This, combined with significant variability in results based on small differences in geometry modelling, has posed a question about software utility. This project aims to verify VARSKIN+ estimates using ExtRad thermoluminescent dosemeters. ***Materials and Methods:*** Experimental setups were carefully designed to reproduce possible scenarios of skin and glove contamination incidents in Nuclear Medicine, incorporating previous work on droplet sizes, dynamics and evaporation of radiopharmaceuticals. Geometry dependence of measured dose-rate was accounted for by modelling dose-rate as function of source position and height. Droplets were modelled as cylinders to allow comparison with VARSKIN+1.3.1. Cylinder height was estimated using known droplet volumes (5-30µl) and measured deposited droplet areas. Phase one measurements were performed with [177Lu]Lu-PSMA-617. Further work will include measurements with 18F and 99mTc. ***Results:*** The relationship between cylinder height and measured dose-rate followed an inverse power relation. Dose-rate from droplets dispensed onto a 0.06mm thick nitrile glove and directly onto the 18mm2 detector were normalised to 0.75mm droplet height. Dose-rates from collapsed droplets (film geometry) were normalised to 0.1mm height. Dose-rates from droplet geometry were 25-35% of the dose-rates estimated by VARSKIN+1.3.1 whereas from film geometry were 35-45% of the estimated dose-rates. Presence of the glove had no impact on the measured/estimated ratio. ***Conclusion:*** The beta contribution to total skin dose from 177Lu was estimated in VARSKIN+1.3.1 as 2 orders of magnitude greater than gamma contribution. Response of ExtRads with PVC covering to low energy betas (147Pm, Emax=224keV) was type tested at 21% and high energy betas (85Kr, Emax=687keV) at ~100% (normalised to 137Cs response) [1]. Response to medium energy betas of 177Lu (78% Emax=497%keV) is situated in between; further work with 18F (Emax=634keV) and investigation of PVC covering attenuation will allow complete comparison with VARSKIN+1.3.1 calculations. Small changes in source geometry and averaging area result in significant differences in measured and estimated doses, signifying the need for revaluation of methods currently used for skin dose estimation in relation to dose limits. ***References:*** [1] Gilvin, P. et al., (2006) Type Testing of an Extremity Finger Stall Dosemeter Based on Harshaw TLD ExtRad Technology, Radiation Protection Dosimetry 123(3).

EPS-292

A new model for Needlestick dosimetry using the measured activity profile of a needlestick with depth in tissue and VARSKIN+v1.3

W. Thomson, *H. Benderz;*
Midland Metropolitan University Hospital, Birmingham, UNITED KINGDOM.

Aim/Introduction: Needlestick injury is not common, but the dosimetry is not straightforward, particularly for alpha emitters. The Wound dose module in VARSKINv1.3 can be used, but has only a point source or a line source model. Dose estimates depend linearly on needlestick depth, usually unknown. We have examined the distribution of activity with depth in tissue to determine a new dosimetry model. ***Materials and Methods:*** AGAR gel (1.5%) was used as a tissue mimic. A needlestick injury was simulated (depth range 2-5mm) with Tc99m. Immediately after piercing the gel, thin slices (approximately 50µm) were taken using a microtome. Slices were accurately weighed (for accurate thickness/depth determination) and counted on a sample counter. These gave a detailed profile of deposited activity with depth within the needlestick. ***Results:*** The activity profile was not linear. There was maximum activity near the surface of the

gel, decreasing to a depth of approximately 800µm. No activity was deposited any deeper. For the depth range 0-150µm, the activity level was approximately x6 the value of a 2mm uniform line. Using the Wound Dose module, we evaluated the basal layer doserate profile with depth separately for each radionuclide. This was then multiplied by the activity profile with depth to give the total doserate value. Using a typical 6hr biological half-life, the new model dose (mSv/kBq deposited) was calculated and compared to the uniform 2mm line model. For Tc99m the new dosimetry gave 1.6mSv/kBq (x9 the uniform line) ; for F18 = 5.8mSv/kBq (x6 the uniform line) and for Ra223 =191,000mSv/kBq (x11 the uniform line). So for Ra223, only 5Bq would give 500mSv dose limit. Similarly for other alpha emitters , the activity for 500mSv is 5Bq for Ac225 and 20Bq for Pb212. A typical needlestick injury (dispensing) could give 65mSv for Tc99m , 85mSv for F18 , but 19Sv for Ra223. For thicker skin such as the finger pulp, the basal layer is deeper (370µm) and the new model gives similar doses to a 2mm uniform line source. ***Conclusion:*** Due to the activity distribution along a needlestick being non-uniform, doses are considerably higher than a uniform line model by factors of x5 -x11. In particular for alphas, the consequences of a needlestick could be about 19Sv. The new model does appear to be independent of depth, so could give a fixed needlestick dose factor for a particular radionuclide.

EPS-293

Using VARSKIN+v1.3 with values of basal layer depth distribution to give accurate estimates of skin doses to the face, wrist, back-of-hand, arms/legs and trunk from contamination with alpha emitters Ra223, Pb212, Ac215, At211 and Th207

W. Thomson*;*
Midland Metropolitan University Hospital, Birmingham, UNITED KINGDOM.

Aim/Introduction: VARSKIN+v1.3 is established software for skin dosimetry, and is freely available. V1.3 introduced more accurate dose modelling for alphas. However alpha dosimetry also needs to take account of the convoluted variations in basal layer depth, rather than use a fixed value. ***Materials and Methods:*** Skin dosimetry for incidents commonly uses a fixed depth for the basal layer, often the default 70um (7.7gm/cm^2) . But the basal layer is highly convoluted, with a wide range of values for different skin sites (1,2). Typical alpha energies have a range of 50-85um, similar to basal layer depths. Therefore alpha dosimetry needs to account for the basal layer depth variation. VARSKINv1.3 can give volume-average doses for a range of depths. These were obtained for depth histograms from 0-16mg/cm^2 with a step width of 2mg/cm^2 . This matches the histograms of basal layer depth data available for different tissue sites (2). For each tissue site, the percentage of basal cells at each depth are used to give a weighted depth-dose value. ***Results:*** Depth-weighted average doserates (mSv/h/kBq) were calculated for the sites;- face, wrist, back-of-hand, legs/arms and trunk. These were compared to the doserates using the 7.7mg/cm^2 fixed depth. For Ra223, the depth-weighted doserates were greater than the fixed depth value by factors x200(wrist)-x3500(trunk). With Pb212 the factor range was x0.6(back hand) - x3.2 (trunk). For Ac225 the factor range is x1(Wrist) - x10(trunk). At211 has factor range x36,800(Wrist) - x478,200(trunk). Th227 has a factor range of x200(Back of hand) - x6,640 (trunk). ***Conclusion:*** With a fixed depth for the basal layer, the alpha component is poorly sampled or has no contribution due to their range. Using the histogram of basal layer depths, there is always a substantial component of alpha dose to basal cells. The differences can be very large, with factor increases up to x478,200!. Using a fixed depth for skin dosimetry is not appropriate for alpha dosimetry and can substantially underestimate the basal layer dose. It is important for the member-of-staff concerned that an accurate dose estimate is given. ***References:*** 1. ICRP Report59; 1991 2. Whitton JT. Health Physics 1973; 24:1-8.

EPS-294

Limits of detection of internal radiation exposure via DSB focus analysis in PBMCs

I. Strobel[1]*, H. Scherthan*[2]*, K. Blaurock*[1]*, S. Schumann*[1]*, J. Müller*[2]*, A. K. Buck*[1]*, M. Port*[2]*, M. Lassmann*[1]*, U. Eberlein*[1]*;*
[1]Department of Nuclear Medicine, University Hospital Würzburg, Würzburg, GERMANY, [2]Bundeswehr Institute of Radiobiology affiliated to the University of Ulm, Munich, GERMANY.

Aim/Introduction: This study aimed to determine the detection limit and age-dependency for radiation-induced focal DNA double-strand break (DSB) damage in peripheral blood mononuclear cells (PBMCs). Baseline foci values from samples of healthy volunteers were compared to values of samples exposed ex-vivo to internal irradiation using different combinations of an α- and a β-emitter to identify detection limits relevant in scenarios such as radiation accidents or nuclear incidents. ***Materials and Methods:*** Blood was collected from 70 healthy volunteers of three age groups (A:20-34, B:35-50, C:51-66 years, 23-24 participants each, gender balanced). DSB foci were determined in PBMCs of donors without and 10 with additional internal ex-vivo irradiation with mixtures of [^{223}Ra]$RaCl_2$ and [^{177}Lu]$LuCl_3$ of a total absorbed dose of 100mGy, using three α-dose:β-dose ratios (3:1, 1:1, 1:3). After irradiation, PBMCs were divided into three subsamples: fixed immediately after irradiation (0h), after 4h and 24h of cell culture to assess DNA repair kinetics. All samples were stained with γ-H2AX- and 53BP1-antibodies to visualise DSB foci and α-tracks. Foci and α-tracks were scored manually in 100 nuclei. Baseline values from unexposed individuals were compared to the irradiated samples. ***Results:*** Mean baseline DSB foci values were 0.49±0.09 foci/cell (A), 0.55±0.17 (B), and 0.60±0.18 (C), with no significant differences between age and gender (t-test, $p>0.01$). The detection threshold for low-LET irradiation, defined by the 95th percentile of baseline values (n=70), was 0.84 foci/cell in our samples. Nearly all irradiated samples (0h, 4h) exceeded this threshold, even in the presence of an α-emitter, demonstrating detectable DNA damage even at low β-dose contributions (Mann-Whitney-test, $p <0.01$). Notably, no α-tracks were detected in any of the baseline samples, confirming the absence of α-particle-related damage in these controls, consistent with the findings of Göring et al. (mean 0.0 α-tracks/100 cells, n=10) [1]. Considering DNA DSB repair all samples could be clearly distinguished (foci and α-tracks) from baseline samples up to 4h post-irradiation (Wilcoxon-test, $p<0.01$). However, after 24h repair time, the DSB-foci and α-track levels in irradiated samples returned to near-baseline levels (Wilcoxon-test, $p>0.01$) making the detection of exposed individuals at this timepoint unlikely. ***Conclusion:*** Using the DSB focus assay, irradiated PBMCs samples of individuals exposed internally to IR could be discriminated from unexposed individuals at β-doses of >25mGy up to 4h post-irradiation. These findings support the use of γ-H2AX+53BP1 DSB-focus assay as a sensitive biomarker test for early assessment of internal radiation exposure. ***References:*** [1] Göring et al.,EJNMMI2022.

EPS-295

In-Silico Modeling of Radiation-Induced DNA Damage Complexity and Repair Kinetics after Mixed α-/β-Irradiation Using Geant4-DNA and MEDRAS

M. Salas Ramirez[1]*, I. Strobel*[1]*, H. Scherthan*[2]*, M. Lassmann*[1]*, U. Eberlein*[1]*;*
[1]Department of Nuclear Medicine, University Hospital Würzburg, Würzburg, GERMANY, [2]Bundeswehr Institute of Radiobiology Affiliated to the University of Ulm, Munich, GERMANY.

Aim/Introduction: Mixed high- and low-LET radiation induces simple and complex DNA double-strand breaks (DSBs) with different repair kinetics. A previous ex vivo study experimentally investigated radiation-induced DNA damage in lymphocytes after mixed irradiation with ^{223}Ra and ^{177}Lu [1]. In this study, a validated Monte Carlo-based simulation model [2] combined with MEDRAS [3] was used to extend these findings. ***Materials and Methods:*** Monte Carlo simulations of radiation-induced DNA damage were performed using GATE [4] and Geant4-DNA [5], modeling ex vivo irradiation of blood samples [1] at absorbed doses around 100 mGy with three α-/β-absorbed dose fractionations: 75% β / 25% α, 50% β / 50% α, and 25% β / 75% α, along with pure 100% β (^{177}Lu) and 100% α (^{223}Ra). From the Monte Carlo simulations, DSB cluster distributions (simple and complex DSBs) were calculated and used as inputs to MEDRAS, applying experimental-based repair rates of ^{177}Lu [6] and ^{223}Ra [7]. DSB repair kinetics were predicted at 4- and 24-hours post-irradiation, with unrepaired DSBs extracted as primary outcome. Agreement between the simulation and the experimentally determined repair models was assessed using Bland-Altman analysis and Z-tests (comparison of two measurements with uncertainties). Relative biological effectiveness (RBE) was calculated based on the simulated total number of DSB·cell^{-1}·mGy^{-1}, using ^{177}Lu as reference. ***Results:*** Simulated induced and unrepaired DSBs increased progressively with higher α-dose fractions. Induced DSBs varied from 0.025±0.003 DSB·cell^{-1}·mGy^{-1} to 0.052±0.002 DSB·cell^{-1}·mGy^{-1}, while unrepaired DSBs at 24h ranged from 0.00048±0.00003 DSB·cell^{-1}·mGy^{-1} to 0.00139±0.00020 DSB·cell^{-1}·mGy^{-1} for the (25% α / 75% β) and (75% α / 25% β) absorbed dose fractionations, respectively. Bland-Altman analysis showed small biases between simulation and experiment (-0.007 DSB·cell^{-1}·mGy^{-1} at 0h, -0.003 DSB·cell^{-1}·mGy^{-1} at 4h, and -0.002 DSB·cell^{-1}·mGy^{-1} at 24h). Z-tests indicated no statistically significant differences across time points. RBE increased with α-dose contribution, ranging from 1.0 for pure ^{177}Lu up to 5.9 for pure ^{223}Ra. ***Conclusion:*** DSB induction simulated with Geant4-DNA, combined with repair modeling using MEDRAS, effectively reproduced experimental trends in lymphocytes exposed to mixed α-/β-irradiation. This integrated modeling approach may support future applications in both molecular radiotherapy optimization and radiation protection by enabling improved prediction of residual biological damage across varying radiation qualities. ***References:*** [1] Strobel I., etal. IntJMolSci. 2024. [2] Salas-Ramirez M., etal. ZMedPhys. 2023. [3] McMahon S.J., etal. FrontOncol. 2021. [4] Jan S., etal. PhysMedBiol. 2004. [5] Incerti S., etal. IntJModelSimulSciComput. 2010. [6] Strobel I., etal. EANM-Congress. 2023 [7] Göring L., etal. EJNMMI. 2022.

EPS-296

Fetal radiation exposure from iodine-131 imaging during an unsuspected pregnancy

F. Simeonov[1], *J. Vassileva*[1], *R. Hristova*[1], *A. Zagorska*[2];
[1]*National Centre of Radiobiology and Radiation Protection, Sofia, BULGARIA,* [2]*Nuclear Medicine Department, Acibadem City Clinic Tokuda University Hospital, Sofia, BULGARIA.*

Aim/Introduction: Radioactive iodine (^{131}I) imaging and therapy are contraindicated during pregnancy. However, cases of unintended exposure continue to be reported in the literature. The aim of the current study is to estimate the absorbed dose in fetus, particularly in the fetal thyroid gland, after postoperative whole-body imaging with ^{131}I of a woman with unsuspected pregnancy, and to discuss current national and international recommendations for avoiding unintended exposure during pregnancy in nuclear medicine. ***Materials and Methods:*** A 37-year-old woman who had undergone a total thyroidectomy, was referred to a whole-body radionuclide scan. Diagnostic nuclear medicine images were obtained after oral administration of 88 MBq of ^{131}I. Before the procedure, the patient declared that she was not pregnant, and no pregnancy test was performed. One week later, the patient accidently discovered that she was pregnant during the radionuclide scan and was referred by her obstetrician to the National Centre of Radiation Protection and Radiobiology for a fetal dose assessment and counseling. Patient's medical records were carefully reviewed to obtain information needed to assess the fetal exposure. Different methods were used to calculate the fetal whole-body dose (Russell et al., 1997; Stabin, 2023) and the fetal thyroid gland dose (Stabin, 2017; Johnson, 1982). ***Results:*** The calculated average fetal dose ranged from 11.9 mGy to 18.8 mGy, while the fetal thyroid dose ranged from 29.9 Gy to 85.7 Gy (340 mGy/MBq to 974 mGy/MBq). The estimated dose to the fetal thyroid gland was comparable to the values reported in the literature. The patient was informed about the potential harmful effects on the thyroid gland of the fetus. To prevent unintended fetal exposure in the future, the department's policy for ascertaining the pregnancy status of a female patient has been reviewed, and recommendations have been issued. Learning materials have been prepared and distributed across healthcare facilities. ***Conclusion:*** The calculated fetal whole-body radiation dose is under 100 mGy and is not of concern. However, the fetal thyroid, which is known to be very sensitive to the radioactive iodine, results in substantially high absorbed doses with a potential damage to the fetal thyroid gland resulting in hypothyroidism or cretinism. Stricter measures to verify pregnancy status in women of reproductive age before administering radioactive iodine were introduced to prevent accidental fetal exposure.

EPS-297

Radiological protection measures in diagnostic techniques: results of a survey in Catalonia

D. Sánchez-Artuñedo[1], *G. Reynes-LLompart*[2], *T. Canela-i-Coll*[3], *M. Fierro Alanis*[4], *L. Prats-Cabaces*[5], *M. Manel*[6], *M. Milà López*[7];
[1]*Hospital Universitari Vall d'Hebron, Barcelona, SPAIN,* [2]*Servei de Física Mèdica i Protecció Radiològica. Institut Català d'Oncologia, L'Hospitalet de LLobregat, Barcelona, SPAIN,* [3]*Servei de Medicina Nuclear. Hospital Universitari Vall d'Hebron, Barcelona, SPAIN,* [4]*Servei de Medicina Nuclear. Hospital Universitari Joan XXIII, Tarragona, SPAIN,* [5]*Servei de Física Mèdica. Institut Català d'Oncologia, HU Germans Trias i Pujol, Badalona, SPAIN,* [6]*Institut de diagnòstic per la Imatge. Serveis Corporatius, Barcelona, SPAIN,* [7]*Hospital Universitari Joan XXII, Tarragona, SPAIN.*

Aim/Introduction: Diagnostic procedures in nuclear medicine involve less activity of radiopharmaceuticals administered than therapeutic procedures. However, to minimize the risks associated with radioactive exposure and contamination for workers, family members, and the public, patients are instructed on radiological protection rules to be followed at discharge. This study aims to identify whether there is a consensus on the radiation protection measures provided to patients upon discharge, aiming to minimize variations across departments. ***Materials and Methods:*** A survey was conducted on six nuclear medicine departments in Catalonia. The survey included the following items for 41 common radiopharmaceuticals employed in the nuclear medicine diagnostic procedures: -Restrictions on time in contact with children, pregnant women, adult family members, healthcare staff, and the general public. -Interruption of breastfeeding. -Restrictions on the use of public transportation. -Restrictions on the management of body fluids. -Radiation protection recommendations for medical transport. ***Results:*** No consensus was found in the recommendations to restrict contact with infants and pregnant women. Regarding PET radiopharmaceuticals, two centers recommended a 12-hour restriction period, two centers recommended a 6-hour restriction, one center recommended a four-hour restriction, and one center did not recommend restricting contact. In radiopharmaceuticals labeled with ^{99m}Tc, two centers recommended a 24-hour restriction period, regardless of the radiopharmaceutical and the administered activity; one

center recommended a 12-hour restriction, and one center recommended 12 hours if the administered activity was inferior to 370 MBq, and 24 hours for higher administered activities. One center recommended either a 4-hour or 12-hour period regarding the administered activity and the radiopharmaceutical, while the last center recommended no restriction in contact. Similar differences regarding breastfeeding were observed between the six centers.Consensus was found not to recommend restrictions on contact with the general public, family members, healthcare staff, or use of public transport. However, some centers recommend the basic rules of reducing the exposure time and increasing the distance, especially with pregnant women. ***Conclusion:*** While there is substantial agreement on the necessity of providing radiological protection guidelines to patients, particularly regarding limiting contact with children and pregnant women, there is a lack of standardization concerning the duration of these recommendations. National and/or International guidelines on radiation protection after discharge in diagnostic procedures are needed.

EPS-298

Considering the different biodistributions of 18F radiopharmaceuticals is crucial in calculating effective dose to public and caregivers

A. De Maggi[1], *E. Murru*[1], *E. Roberto*[1], *M. Lio*[1], *A. Lanza*[2], *E. Bergalla*[2], *F. Bergesio*[1], *S. Chauvie*[1];
[1]*Medical Physics Divisions of Santa Croce e Carle Hospital (Cuneo), Cuneo, ITALY,* [2]*Univeristy of Turin, Turin, ITALY.*

Aim/Introduction: to compare dose rate of patients injected with different 18F-fluorine radiopharmaceuticals (RF) considering their bio-distributions. ***Materials and Methods:*** H*(10) was measured with an ionization chamber immediately before the acquisition at 30 cm and 1m from the thorax with the patient upstanding. The images of these patients were analyzed and the percentage of counts (%C) in four districts: head neck, thorax, abdomen, and pelvis, were evaluated. Measurements were compared to calculated H*(10)values applying corrections to the gamma specific constant taking in account the uptake time, the retention as in IRCP53 and the self absorption (with a coefficient of 0.65). Two models were applied: SSM, single source model considering the injected activity positioned in a single source in the middle of the thorax and the 4PM, 4 points model, in which the sources were located in the middle of the four 4 districts with an activity weighted respect to %C. Effective dose to the public and caregivers was calculated using D Broggio formalism (2023) considering the two models ***Results:*** 105 patients were examined, 45 with FDG, 30 with PSMA1007, 30 with choline (and 30 with FET, currently under analysis) . %C were 29%, 23%, 24% and 20% for FDG, 10%, 22%, 55% and 12% for PSMA and 11%, 22%, 49% and 16% for choline, respectively in the head-neck, thorax, abdomen, and pelvis areas. Measured average ± standard deviation and calculated (with SSM and 4PM) dose rate in µSv h-1/GBq for patients injected at 30cm and at 1m were respectively315±80(483/687) and 67±12(58/63) for FDG,575±45(552/652) and 52±4(58/61) for PSMA1007, 695±36(631/765) and 86±12(68/71) for choline, and143±27 and 42±15 µSv h-1/GBq for FET. ***Conclusion:*** A maximum differences of 25% between calculated without biodistribution and measured dose rates and 20% maximum differences were found in effective dose to the public and caregivers for SSM ,4PM model and measured for PSMA and Choline.In FDG an difference of 54% of the dose rate@30cm compared with the calculated one is reduced to35% taking into account biodistribution. A maximum difference of 12% in effective dose to the public and caregivers for SSM ,4PM model and measured for FDG @100 was found. Estimate the dose to third party from FDG@30cm measured dose rate can lead to underestimate dose up to 58%. Further analysis are ongoing on Monte Carlo simulation ***References:*** D Broggio et al 2023 J Radiol Prot 43 021504.

EPS-299

Belgian paediatric Diagnostic Reference Levels for whole-body and brain ^{18}F-FDG PET/CT

T. Assoignon[1], *M. Hesse*[2], *F. Dupont*[2], *F. Jamar*[2];
[1]*UCLouvain, Woluwe-Saint-Lambert, BELGIUM,* [2]*Cliniques Universitaires Saint-Luc, Woluwe-Saint-Lambert, BELGIUM.*

Aim/Introduction: PET/CT imaging involves ionizing radiation and the ALARA principle must be followed, especially for paediatric patients. One established tool to optimise the radiation dose is the implementation of Diagnostic Reference Levels (DRLs). Currently, no DRLs are available in Belgium nor in Europe regarding PET/CT imaging in the paediatric population. This study proposes the first local DRLs for paediatric whole-body (WB) and brain ^{18}F-FDG PET/CT in Europe. ***Materials and Methods:*** A retrospective study was carried out on DICOM-headers retrieved from ^{18}F-FDG PET/CT scans performed in our hospital in patients under the age of 18 between 2014 and 2018. Patients were grouped according to the ICRP135 classification: by body weight for whole-body scans and by age for brain studies. We assessed the median values and the 75th percentile (P75) of the administered activity of ^{18}F-FDG, Computed Tomography Dose Index ($CTDI_{vol}$), and Dose-Length Product (DLP) for each group. Scan length was additionally evaluated for each data set. ***Results:*** Median weight-adjusted administered activities for paediatric WB ^{18}F-FDG PET/CT are 4.4, 4.1 and 4.3 MBq/kg for the 15-<30 kg, 30-<50 kg and 50-<80 kg groups, respectively. For the brain PET, activities were 4.5 MBq/kg for the 1-<6 year group and 3.1 MBq/kg for the 6-<18 year group. The $CTDI_{vol}$ for the whole-body CT are 1.6, 2.2 and 3.1 mGy for the 15-<30 kg, 30-<50 kg and 50-<80 kg groups, respectively. The corresponding DLP's are 145.5, 230.9 and 342.6 mGy·cm. For the brain CT, the $CTDI_{vol}$ and DLP are 3.5 mGy and 75.8 mGy·cm for both 1-<6 year and 6-<18 year groups. A scan length exceeding the patient's height is observed in around 10% of cases. In these cases, the excess is on average 15cm. ***Conclusion:*** We have calculated the median and P75 values of the DLP, $CTDI_{vol}$ and administered activities to propose first Belgian DRL values for paediatric whole-body and brain ^{18}F-FDG PET/CT. It is recommended that clinical practice remain below the P75 value.Of course, DRLs change over time and results need to be updated continuously, particularly when new technologies are implemented. This study warrant larger multicentric studies, to extend the values to the entire country and ideally a larger, e.g. European community.

EPS-300

Establishing DRLs in [^{18}F]FDG PET-CT: A Digital-Analog Comparison

A. Carvalho[1], *R. Albergueiro*[1], *J. Vale*[2], *L. Cunha*[2], *C. Souto*[2];
[1]*ULS São João, Porto, PORTUGAL,* [2]*Atrys, Porto, PORTUGAL.*

Aim/Introduction: Positron Emission Tomography-Computed Tomography (PET-CT) is widely used for cancer diagnosis and staging, integrating metabolic and anatomical imaging. PET-CT involves exposure to ionizing radiation from radiopharmaceutical and CT, raising concerns about cumulative patient dose. This study aims to quantify radiation doses from both PET and CT components and to establish local diagnostic reference levels (DRLs) for two PET-CT systems - digital and analog, with 64 and 24 detector rows - across two medical centers. This initiative contributes to the development of national DRLs for adult [^{18}F] FDG PET-CT brain and half-body (from the vertex to the thigh) procedures. ***Materials and Methods:*** Retrospective analysis was performed on patients with body weights of 70±10kg, who underwent half-body (n=100) and brain (n=30) [^{18}F]FDG PET-CT scans, in each center. Collected data included injected activity,

activity per kilogram, volume CT dose index (CTDIvol), and dose-length product (DLP). DRLs were determined using the 50th percentile (median) of the distribution for each procedure and center, with the mean, standard deviation, and 75th percentile also determined. PET and CT dose values were calculated considering CT use for attenuation correction and anatomical localization. Results were compared across centers and against international DRLs. ***Results:*** For half-body PET-CT, DRLs for injected activity, activity per weight, CTDIvol, and DLP were 196 MBq, 2.8 MBq/kg, 5.5 mGy, and 577 mGy·cm for the digital system PET-CT, and 237 MBq, 3.5 MBq/kg, 4.7 mGy, and 384 mGy·cm for the analog system. Corresponding PET-CT doses were (3.7±0.4)mSv and (9±2) mSv (digital PET-CT), and (4.5±0.5)mSv and (6±1)mSv (analog PET-CT). For brain PET-CT, DRLs were 188 MBq, 2.8 MBq/kg, 8.6 mGy, and 243 mGy·cm (digital system), and 199 MBq, 3.3 MBq/kg, 4.0 mGy, and 71 mGy·cm (analog system, with fixed CT values and parameters for all patients). PET-CT doses were (3.6±0.5)mSv and (1.5±0.1)mSv (digital), and (3.9±0.7)mSv and 0.17 mSv (analog). As expected, digital systems showed lower injected activity and PET dose due to higher sensitivity, while CT dose was higher, though within European DRL limits, indicating room for optimization. ***Conclusion:*** The observed differences between digital and analogue systems highlight the impact of scanner technology on patient exposure and the importance of ongoing dose monitoring and protocol optimisation. These findings represent an initial step towards establishing national DRLs for PET-CT in Portugal. Ongoing work is being conducted to correlate radiation dose with image quality, ensuring that optimisation efforts do not compromise diagnostic performance.

EPS-301

Radiation dose reduction for low-dose CT in hybrid imaging with three generations of iterative reconstruction and varying denoising strengths

N. Bebbington[1], *R. H. Kappel*[2], *J. W. Aunsborg*[2], *P. C. Holdgaard*[2];
[1]*Siemens Healthcare A/S, Ballerup, DENMARK,* [2]*Lillebaelt Hospital-University Hospital of Southern Denmark, Vejle, DENMARK.*

Aim/Introduction: Several types of iterative reconstruction (IR) are available on hybrid PET-CT and SPECT-CT systems, allowing reduced radiation dose compared with filtered backprojection (FBP). Available IRs differ in sophistication, from algorithms working only in image space, to those also working in raw-data space with advanced modelling and allowing user-defined denoising strength (DNS). The aim was to determine the magnitudes of CT radiation dose reduction (DR) permissible for low-dose CT in hybrid imaging with a direct comparison of three generations of IR and varying DNS. ***Materials and Methods:*** A whole-body patient phantom was scanned on three hybrid systems, each with a different IR available. Acquisitions were made on each scanner at two tube voltage settings, each with 7 different effective mAs settings ranging from 10-120mAs. Reconstructions were made with FBP and the available IR on that scanner (A=IR in image space, no user-defined DNS; B=IR in image- and raw-data space with DNS 3 (medium) to 5 (maximum); C=IR in image- and raw-data space with advanced modelling (C) with DNS 3-5. Image quality for each reconstructed dataset was evaluated in lung, bone, liver and kidney tissues, through quantitative measurement of contrast and noise, and qualitative visual analysis (VA) by two CT-trained physicians. For each IR algorithm the percentage DR for comparable image quality to the reference FBP image (120 mAs) was determined. ***Results:*** For lung, all IRs suggested permissible DR up to >80% according to noise measures, which were also verified by VA scores. For bone, liver and kidney, permissible DR generally increased from reconstruction A through to C. For bone, reconstructions A, B and C permitted DR up to 31%, 48% and >80% respectively, whilst for liver DR up to 31%, 71% and >80% was permitted. For kidney, reconstruction A permitted DR up to 38%, whilst for reconstructions B and C, DR indicated by noise analysis (up to 80% (B) and >80% (C)) were greater than those by visual analysis (up to 68% (B) and 51% (C)). Increasing DNS reduced noise in all tissues and did not notably impact VA scores. IR did not notably impact image contrast in any tissue. ***Conclusion:*** Large CT DR can be achieved with IR, with greater DR associated with more sophisticated IR algorithms. High DNS provides lower noise and greater indicated DR, which may be well-suited to 'low-dose CT' purposes of attenuation correction and localisation often used in hybrid imaging.

EPS-302

Estimation of infant gonad dose from urine contamination following Tc-99m MAG3 renal scintigraphy

T. Ball*, A. Maenhout, N. A. Kapse, J. J. Phillips;*
Chelsea and Westminster Hospital NHS Foundation Trust, London, UNITED KINGDOM.

Aim/Introduction: We estimate the doses to the gonads for infant patients following urine contamination of diapers, and extend this estimation based on the number of hours between contamination and changing the diaper. ***Materials and Methods:*** We analysed 50 patient scans with visible urinary contamination in the dynamic images. Of the included scans, 11 patients were female (ages 4 - 16 months) and 39 were male (ages 3 - 34 months). We drew a region of interest around each area of visible contamination and converted the measured count rate into a background-corrected time-activity curve. Assuming no further contamination, dose per administered activity (mGy/MBq) was calculated for the diaper being changed at 0, 1, 2, 3, and 4 hours after the completion of the dynamic scan. ***Results:*** The absorbed dose per unit activity was calculated for both male and female patients at 0 hours (Male: $1.08 \pm 0.83 \times 10^{-2}$ mGy/MBq, Female: $6.87 \pm 2.83 \times 10^{-4}$ mGy/MBq), 1 hour (Male: $9.30 \pm 6.06 \times 10^{-2}$ mGy/MBq, Female: $5.97 \pm 3.01 \times 10^{-3}$ mGy/MBq), 2 hour (Male: $1.66 \pm 1.09 \times 10^{-1}$ mGy/MBq, Female: $1.07 \pm 0.55 \times 10^{-2}$ mGy/MBq), 3 hour (Male: $2.31 \pm 1.51 \times 10^{-1}$ mGy/MBq, Female: $1.49 \pm 0.76 \times 10^{-2}$ mGy/MBq), and 4 hours (Male: $2.89 \pm 1.90 \times 10^{-1}$ mGy/MBq, Female: $1.86 \pm 0.96 \times 10^{-2}$ mGy/MBq) after the end of the dynamic acquisition. The mean cumulative activities were higher in female patients ($5.2 \pm 2.5 \times 10^{2}$ MBq·s) than male patients ($4.5 \pm 3.3 \times 10^{2}$ MBq·s), however absorbed doses per unit activity in male patients' gonads were significantly higher by a factor of 16 for all time points. ***Conclusion:*** Contaminated diapers are estimated to contribute significant doses to infant patients when these patients are left unchanged for significant periods of time. We compare estimated mean dose to the gonads from a contaminated diaper at each time point to ICRP 80 values; ICRP 80 value is exceeded at 1 hour for male patients, and at 3 hours for female patients. As such, we suggest that nuclear medicine departments should advise carers of these patients to encourage the changing diapers more frequently. ***References:*** Lu, Y., Kumbhar et al. (2024). Assessment of infant gonadal dose irradiated from urine-contaminated diapers during diuretic renal scintigraphy. Nuclear medicine communications, 45(1), 45-50.Lu, Yonggang et al. (2022). Computation of Gonadal Dose Irradiated from Urine Contaminated Diapers in Pediatric Patients During Renal Scintigraphy. AAPM Annual Meeting, Washington, DC. July 10-14. 2022.

EPS-303

Impact of Ionizing Radiation on Children whose Mothers Underwent Pulmonary Perfusion Scintigraphy with Technetium-99m Macroaggregated Albumin

P. Guijarro-Caba*, J. Díaz-Alarcón;*
Hospital Universitario de Jaén, Jaén, SPAIN.

Aim/Introduction: Despite pregnancy being incompatible with studies involving ionizing radiation, these procedures may be performed when a firm clinical justification exists and

alternative diagnostic tools are not feasible. In our center, a total of 23 pulmonary perfusion studies have been conducted on pregnant women over the last 6 years to rule out Pulmonary Thromboembolism (PTE). Although the risks to the fetus are considered practically negligible for doses below 50 mSv, we deem it important to conduct a follow-up on the newborn to determine if any issues attributable to ionizing radiation have emerged. Consequently, we propose a longitudinal follow-up from the time of birth to the present. ***Materials and Methods:*** Pulmonary perfusion scintigraphy was performed by administering 74 MBq of [^{99m}Tc]Tc-MAA (Technetium-99m labeled Macroaggregated Albumin), instead of the standard 200 MBq. Planar imaging and/or SPECT of the thorax were conducted using the appropriate gammacamera, without a ventilation scintigraphy study. This approach was adopted to reduce the radiation dose received by both the mother and the fetus. Subsequently, follow-up of the children was conducted from the time of birth to the present. ***Results: Results:*** Following the follow-up period, the results obtained for the sample (n=23) were: 21.74% of the examinations presented findings suggestive of PTE, with an estimated effective dose of 0.81 mSv. The median gestational age at the time of the examination was 31 weeks (range 19+3 to 38 weeks), and the median gestational age at delivery was 39 weeks (range 27+3 to 41+4 weeks). Patient follow-up lasted for at least one year in 82.61% of cases, and up to 64% of patients were followed for 4 years or more (follow-up range 2 to 73 months). None of the newborns studied exhibited apparent signs or symptoms resulting from exposure to ionizing radiation during the follow-up period. ***Conclusion:*** The obtained results are consistent with findings reported in the literature, which indicate that fetal exposure to doses below 50 mSv has not been demonstrated to be harmful. ***References:*** International Commission on Radiological Protection. (2000). ICRP Publication 84: Pregnancy and Medical Radiation Health Protection Agency. (2009). Protection of pregnant patients during diagnostic medical exposures to ionising radiation.

EPS-304

Development of Lightweight, Flexible, and Lead-Free Epoxy-Based Composites for Gamma Radiation Shielding in Nuclear Medicine

F. Moradi[1], *P. Sheikhzadeh*[1], *H. Mohammad Hosseini*[2], *A. Sajedi*[3]; *[1]Department of Nuclear Medicine, IKHC, Tehran University of Medical Sciences, Tehran, Iran, Tehran, IRAN, ISLAMIC REPUBLIC OF, [2]Iran polymer and petrochemical institute, Tehran, IRAN, ISLAMIC REPUBLIC OF, [3]Composite Materials Laboratory, Faculty of Mechanical Engineering, Amirkabir University of Technology, Tehran Polytechnic, Iran, Tehran, IRAN, ISLAMIC REPUBLIC OF.*

Aim/Introduction: Introduction. Compliant radiation shielding is of utmost significance in nuclear medicine environments such as PET/CT. Traditional lead-based barriers are efficient but heavy, toxic, and inflexible. This study tries to develop and study non-toxic, light-weight epoxy resin composites reinforced with high-Z gamma-absorbing fillers such as bismuth oxide (Bi_2O_3), tungsten carbide (WC), and iron oxide (Fe_2O_3) as safe alternatives for medical shielding applications. ***Materials and Methods:*** Methods. Two composite series were prepared with bisphenol A-based epoxy resin. Type 1 samples contained single fillers (Bi_2O_3, PbO, WC) at 10-50 wt%. Type 2 samples contained Bi_2O_3 and Fe_2O_3 in synergistic ratios (up to 70% Bi_2O_3 + 20% Fe_2O_3). Composite processing included high-speed mechanical mixing, ultrasonic homogenization, and hot pressing. Sintering in an inert nitrogen atmosphere was applied to some samples to improve density and microstructural homogeneity. The performance of gamma shield was evaluated using 99mTc (140 keV), 131I (360 keV), and 18F (511 keV) sources. Key parameters such as linear attenuation coefficient (LAC), half-value layer (HVL), transmission factor (TF), and mean free path (MFP) were determined. ***Results:*** Results. Among Type 1 samples, Bi_2O_3-filled samples showed better performance. BPA-30 (30 wt% Bi_2O_3) exhibited TF = 11.3% at 60 keV (thickness = 1 cm), and maximum LAC at all energies. Type 2 composites, especially BPA-70 (70 wt% Bi_2O_3 + 20 wt% Fe_2O_3), achieved nearly 100% attenuation at 60 keV with 1 cm thickness. At 511 keV, BPA-70 also exhibited high shielding (TF ~63%) with lead equivalence up to 0.07 cm. Sintered composites yielded higher density (up to 4.8 g/cm^3) and mechanical strength. Bi_2O_3-based samples were superior compared to PbO and WC in terms of shielding and flexibility. ***Conclusion:*** Conclusion. The Bi_2O_3/Fe_2O_3 epoxy composites prepared offer a promising lead-free radiation shielding option for nuclear medicine, with excellent attenuation, mechanical strength, and reduced toxicity. Their flexibility and low weight render them suitable for clinical application in shielding curtains, protective gear, and portable PET/CT room barriers. Further studies on inert-atmosphere sintering can enhance reproducibility for industrial scale-up. ***References:*** 1.Smith, J., & Johnson, L. (2020). "Applications of Gamma Radiation in Medical Imaging." Journal of Medical Physics, 45(3), 123-130. 2.Brown, A., & Davis, R. (2021). "Health Risks Associated with Gamma Radiation Exposure." Radiation Protection Dosimetry, 189(2), 234-240. 3.Lee, H., & Kim, S. (2020). "Polymer Composites for Gamma Radiation Shielding: A Review." Materials Science and Engineering, 78(4), 567-575.

EPS-305

Development of the first national event learning system in the UK

A. Powell, *L. Fraser, U. Findlay, Y. Kinsella, N. Kirk; UK Health Security Agency, Oxford, UNITED KINGDOM.*

Aim/Introduction: The first UK wide national event reporting and learning system specifically for nuclear medicine, diagnostic imaging and Magnetic Resonance Imaging (MRI) has been developed by the Medical Exposure Group (MEG), at the UK Health Security Agency (UKHSA). The main aim of the event learning system is to promote and improve a positive patient safety culture. Presented will be how this event learning system has been established, feedback from the nuclear medicine community and data from the second quarter of 2025. ***Materials and Methods:*** The following key stages were conducted to establish the event learning system: 1) System for categorisation of events (taxonomy): To achieve a standardised taxonomy for categorising events, a multidisciplinary working party with clinical specialists from across the United Kingdom (UK) was established. The finalised coding was tested against pilot event data to ensure the taxonomy is effective and comprehensive. 2) Publication of guidance and local implementation: The taxonomy [1] was published and supporting guidance [2] written and shared, which was endorsed by professional bodies. The taxonomy can be applied locally by appropriately trained clinical staff members to each event when the local investigation is completed. 3)Data submission to the MEG: The key objective at this stage was to support departments in their local implementation. Additional learning resources such as dedicated webpages and recorded presentations were developed and made available. The MEG also provided additional support in local implementation where required. Furthermore, voluntary reporting mechanisms were established to allow anonymised data to be submitted to MEG for analysis. 4) Data analysis: The MEG commissioned a database to support collation and analysis of the data submitted. 5) National shared learning: Results and learning will be published in e-bulletins and formal reports which will be made available online. This will allow local comparison of local events with the national picture. ***Results:*** Departments across the UK have implemented the new taxonomy at a local level and are engaging with MEG for support with this. The MEG will review data from the second quarter of 2025 and produce trend analysis of the early findings. Feedback on this project from the UK clinical community has been overwhelmingly positive. It suggests a positive influence on reporting cultures and providing meaningful learning opportunities. ***Conclusion:*** This will be the first opportunity for nuclear medicine, clinical imaging and MRI to analyse events (including near misses) at a

national level. ***References:*** [1] https://www.gov.uk/government/publications/national-coding-taxonomy-for-incident-learning-in-clinical-imaging-mri-and-nuclear-medicine [2] https://www.gov.uk/government/publications/user-guidance-and-application-of-the-national-taxonomy-for-incident-learning-in-clinical-imaging-mri-and-nuclear-medicine.

1811

Wednesday, October 8, 2025, 9:45 - 11:15
Room 111

TROP Session - Oncology & Theranostics Committee: Radioembolisation and Novel Therapies

OP-873

Ga-PSMA-11 PET/CT in unfavourable intermediate and high-risk prostate cancer staging reduces unnecessaryprostatectomy: a prospective, an IAEA international multicentre study.

J. Cerci[1], *S. Fanti*[2], *E. Estrada Lobato*[3], *J. Kunikowska*[4], *O. Garcia*[5], *F. Novruzov*[6], *R. Kumar*[7], *A. Al-Ibraheem*[8], *M. Haidar*[9], *M. Nasir*[10], *O. Kucuk*[11], *U. Elboga*[12], *F. Redondo Moneda*[13];
[1]*Quanta - Diagnóstico e Terapia, Curitiba, BRAZIL,* [2]*IRCCS Azienda Ospedaliero-Universitaria di Bologna,, Bologna, ITALY,* [3]*Division of Human Health, International Atomic Energy Agency., Viena, AUSTRIA,* [4]*Nuclear Medicine Department, Medical University of Warsaw., Warsaw, POLAND,* [5]*Instituto Nacional de Cancerologia, Mexico, MEXICO,* [6]*Nuclear Medicine Department, National Centre of Oncology, Baku, AZERBAIJAN,* [7]*All India Institute of Medical Sciences, New Delhi, INDIA,* [8]*King Hussein Cancer Center, Amman, JORDAN,* [9]*American University of Beirut Medical Center, Beirut, LEBANON,* [10]*Institute Kanser Negara, Putrajaya, Malaysia, MALAYSIA,* [11]*Ankara University, Ankara, TÜRKIYE,* [12]*University of Gaziantep,, Gaziantep, TÜRKIYE,* [13]*Complejo Asistencial Sotero del Río, Santiago Clínica Andes Salud,, Puerto Montt, CHILE.*

Aim/Introduction: Accurate staging of unfavorable intermediate/high-risk prostate cancer (PCa) is essential for treatment decisions. Conventional imaging often fails to detect small lymph node metastases. This study evaluated the impact of 68Ga-PSMA PET/CT on staging, diagnostic accuracy compared to MRI, and surgical eligibility. ***Materials and Methods:*** Prospective, multicenter study (12 centers, 11 countries), including 775 high-risk/unfavorable intermediate PCa patients with radical prostatectomy based based on MR and bone scan were submitted to 68Ga-PSMA PET/CT before treatment. PET and MR findings were compared with radical prostatectomy histopathology. PET impact on surgical decisions was measured. ***Results:*** 68Ga-PSMA PET/CT detected metastatic disease (M1) in 20.4%, altering management in 24.0%, preventing unnecessary surgery. Sensitivity for seminal vesicle invasion was 85.1% (PSMA) vs. 29.4% (MRI); for lymph node metastases, 87.5% (PSMA) vs. 23.1% (MRI). In the 13.1% (78/593) lymph node discordant PSMA and histology results, biopsy was negative in 21 patients; PET undetected LNMs disease in 27 patients; and in the 30 remaining patients PET detected less lymph nodes chains than biopsy results. ***Conclusion:*** PSMA PET/CT significantly improves staging accuracy, reducing unecessary prostatectomy and optimizing treatment. Its incorporation into standard PCa staging is warranted. ***References:*** 1. Mottet N, Cornford P, van den Bergh RCN, et al. EAU-EANM-ESTRO-ESUR-SIOG Guidelines on Prostate Cancer. Eur Urol. 2023;84(3):287-352. 2. Faria R, Soares MO, Spackman E, et al. The cost-effectiveness of multiparametric MRI and MRI-guided biopsy in prostate cancer diagnosis. Health Technol Assess. 2018;22(20):1-294. 3. Hofman MS, Lawrentschuk N, Francis RJ, et al. Prostate-specific membrane antigen PET: clinical utility in prostate cancer, normal patterns, pearls, and pitfalls. Radiographics. 2018;38(1):200-217. 4. Perera M, Papa N, Christidis D, et al. Sensitivity, specificity, and predictors of positive 68Ga-PSMA PET/CT in patients with biochemical recurrence of prostate cancer: a systematic review and meta-analysis. Eur Urol. 2016;70(6):926-937. 5. Calais J, Czernin J, Cao M, et al. 68Ga-PSMA PET/CT in localized prostate cancer: a prospective single-arm imaging study to determine histopathologic accuracy. Clin Cancer Res. 2019;25(10):3006-3013. 6. Hope TA, Goodman JZ, Allen IE, et al. Metaanalysis of 68Ga-PSMA-11 PET accuracy for the detection of pelvic nodal metastases in prostate cancer. J Nucl Med. 2019;60(7):891-898.

OP-874

Interobserver and Intraobserver Agreement for Equivocal Lesions in Ga-68 PSMA PET/CT According to PSMA-RADS 2.0 Criteria

K. Niftaliyeva[1], *S. Kesim*[2], *N. Filizoglu*[2], *Z. Balaban Genc*[1], *S. Özgüven*[1], *F. Çağlıyan*[1], *T. Öneş*[1], *F. Dede*[1], *H. Turoğlu*[1], *T. Erdil*[1];
[1]*Marmara University Pendik Training and Research Hospital, Istanbul, TÜRKIYE,* [2]*Kartal Dr. Lutfi Kirdar City Hospital, Istanbul, Turkey, Istanbul, TÜRKIYE.*

Aim/Introduction: This study aims to systematically evaluate the inter- and intra-observer agreement regarding lesions with uncertain malignancy potential in Ga-68 PSMA PET/CT imaging of prostate cancer patients, utilizing the PSMA-RADS 2.0 classification system, and to emphasize the malignancy evidence associated with these lesions. ***Materials and Methods:*** We retrospectively reviewed Ga-68 PSMA PET/CT images of patients diagnosed with prostate cancer via histopathology between December 2016 and November 2023. Seventy-six patients and 98 target lesions, classified with PSMA-RADS scores 3A to 3D by an experienced nuclear medicine specialist, were included. Three observers (two experienced and one less experienced nuclear medicine physician) evaluated the lesions at two different time points, three months apart, in a blinded manner. Intra-observer agreement was assessed using Cohen's kappa, while inter-observer agreement was analyzed using Fleiss' kappa. ***Results:*** All observers demonstrated significant intra-observer agreement, with percentages ranging from 67.3% to 80.6% and kappa values between 0.62 and 0.76. The highest intra-observer agreement was noted for bone lesions, while non-regional lymph nodes exhibited the lowest agreement. For inter-observer assessments, moderate agreement was observed across all lesions (Fleiss k=0.51), with the highest agreement in regional lymph nodes and the lowest in non-regional lymph nodes and bone lesions (Figure 1). A low level of interobserver agreement was also detected in the evaluation of lung lesions (Figure 2). Follow-up results indicated malignancy detection rates of 63.4% for 3A, 47% for 3B, 44.5% for 3C, and 41.4% for 3D scored lesions. ***Conclusion:*** The PSMA-RADS classification system demonstrated substantial intra-observer agreement and moderate inter-observer agreement for lesions with uncertain malignancy potential, supporting its clinical applicability. However, notable variability and limitations in reporting bone lesions, non-regional lymph nodes, and lung lesions were observed among readers. The ambiguous nature and management of PSMA-RADS 3 lesions underscore the need for further research to enhance risk stratification.

OP-875

Preliminary Results from a Phase II Clinical Trial of Fully Integrated [^{18}F]-PSMA PET/MRI for Diagnosing Clinically Significant Prostate Cancer

S. Ghezzo[1], *A. Samanes Gajate*[1], *G. Brembilla*[2], *A. Stabile*[3], *T. Russo*[2], *S. Capoferri*[4], *G. Cristel*[2], *G. Gandaglia*[3], *C. Bezzi*[1], *P. Mapelli*[1], *A. Briganti*[3,4], *F. De Cobelli*[2,4], *F. Montorsi*[3,4], *A. Chiti*[1,4], *P. Scifo*[1], *M. Picchio*[1,4];
[1]*Nuclear Medicine Department, IRCCS San Raffaele, Milan, ITALY,* [2]*Radiology Department, IRCCS San Raffaele, Milan, ITALY,* [3]*Urology Department, IRCCS San Raffaele, Milan, ITALY,* [4]*Vita-Salute San Raffaele University, Milan, ITALY.*

Aim/Introduction: Multiparametric MRI (mpMRI) is the current standard of care for diagnosing prostate cancer (PCa), but its positive predictive value (PPV) remains limited, often leading to unnecessary biopsies. Prostate-specific membrane antigen (PSMA) PET has shown promising results in the detection of primary PCa. This study aims to assess the diagnostic accuracy of integrated PET/MRI—combining [^{18}F]-PSMA-1007 PET and mpMRI—for the detection of clinically significant PCa (csPCa). ***Materials and Methods:*** This is a prospective clinical trial (EUDRACT: 2022-003905-31) involving patients with clinically suspected prostate cancer undergoing [^{18}F]-PSMA-1007 PET/MRI prior to systematic ± targeted biopsy. PET and MRI images were interpreted independently, each blinded to the other, and subsequently combined into a unified PSMA PET+MRI report. mpMRI was assessed according to PI-RADS v2.1, while PET images were evaluated using a 5-point Likert scale, with scores ≥4 considered positive. Lesions were deemed positive on PSMA PET+MRI if either PI-RADS was ≥4 or PSMA PET was positive. csPCa was defined as ISUP grade group ≥2. Sensitivity (SN), specificity (SP), positive predictive value (PPV), and negative predictive value (NPV) were calculated at the patient level, along with their 95% CI, while lesion-level PPV was also assessed. Histopathological analysis from prostate biopsies served as the reference standard. ***Results:*** To date, 35 patients have completed all imaging and histological assessments and were included in the analysis. [^{18}F]-PSMA-1007 PET identified 36 lesions in 23 patients, mpMRI identified 36 lesions in 22 patients, and the combined PSMA PET+MRI identified 38 lesions in 25 patients. 28 target lesions in 17 patients were confirmed as csPCa at histopathology. At the patient level, [^{18}F]-PSMA-1007 PET had SN = 0.88 (0.64-0.99), SP = 0.56 (0.31-0.79), PPV = 0.65 (0.43-0.84), and NPV = 0.83 (0.52-0.98); mpMRI showed SN = 0.88 (0.64-0.99), SP = 0.61 (0.36-0.83), PPV = 0.68 (0.45-0.86), and NPV = 0.85 (0.55-0.98). Combined PSMA PET+MRI had SN = 0.94 (0.71-0.99), SP = 0.50 (0.26-0.74), PPV = 0.64 (0.43-0.82), and NPV = 0.90 (0.56-0.99), respectively. At the lesion level, PPV was 0.69 (0.52-0.84) for PET, 0.64 (0.46-0.79) for mpMRI, and 0.68 (0.51-0.83) for the combined PET+MRI. ***Conclusion:*** Our data support the combined use of [^{18}F]-PSMA-1007 PET and mpMRI to enhance diagnostic accuracy for csPCa. The final results of this study will help define the optimal strategy for integrating these modalities and improve the diagnostic confidence of PSMA PET/MR.

OP-876

Quantitative Imaging Parameters Improve the Accuracy of PSMA PET/CT for the Local Staging of Primary Prostate Cancer

M. Donswijk[1], *R. H. Ettema*[2], *M. Wondergem*[3], *Z. Cheung*[1], *H. G. van der Poel*[1], *D. E. Oprea-Lager*[4], *A. N. Vis*[2];
[1]*Antoni van Leeuwenhoek - Netherlands Cancer Institute, Amsterdam, NETHERLANDS,* [2]*Amsterdam UMC - Locatie VUMC, Amsterdam, NETHERLANDS,* [3]*Noordwest Ziekenhuisgroep, Alkmaar, NETHERLANDS,* [4]*Radboud University Medical Center, Nijmegen, NETHERLANDS.*

Aim/Introduction: Prostate-specific membrane antigen (PSMA) PET/CT is recognized as the most accurate imaging modality for detection of metastatic high-risk prostate cancer (PCa). PSMA PET/CT has also shown potential in the local (T) staging of primary PCa, in which the detection of T3 disease (extraprostatic extension, EPE) has prognostic and therapeutic importance. After initial promising smaller studies, larger studies found that visual T-stage assessment had only moderate accuracy[1]. The purpose of this study was to explore the value of quantitative PSMA PET/CT parameters in addition to the standard visual assessment of the local T-stage. ***Materials and Methods:*** From a large single centre retrospective patient cohort, all patients with intermediate and high-risk primary PCa who underwent staging PSMA PET/CT before robot-assisted radical prostatectomy (RARP) were assessed. Visual analysis of T-stage (miT-stage) was done as well as the assessment of quantitative parameters derived from PSMA PET/CT such as SUVmax, SUVpeak, tumour volume (PSMA-vol), total lesion PSMA expression (PSMA-TL) and tumour longest capsule contact (LCC) was performed. Pathological tumour stage in the radical prostatectomy specimen was used as the reference standard. Following, univariable and multivariable logistic regression analyses were performed and clinical risk models for pT3 stage were created. ***Results:*** 223 evaluable patients with a PSMA positive primary PCa were included. Univariable analyses yielded AUC's of 0.59, 0.64 and 0.63 for the visual analysis of predicting pT3a, ≥pT3b and (overall) ≥pT3 stage respectively. Quantitative parameters yielded AUC's of 0.53-0.63 for pT3a, 0.64-0.74 for ≥pT3b and 0.59-0.69 for ≥pT3 stage. Multivariable analyses showed LCC as single independent predictor of pT3a stage. Furthermore, visual miT-stage, LCC and PSMA-vol were independent predictors of ≥pT3b-stage, and LCC and PSMA-vol independent predictors of ≥pT3 stage. Clinically usable risk models incorporating these predictors yielded AUC's of 0.62 for pT3a, 0.79 for ≥pT3b and 0.70 for ≥pT3 stage, with cut-offs of choice for different sensitivity / specificity levels. No statistically significant differences in diagnostic accuracy were found between PSMA PET tracers [^{68}Ga]Ga-PSMA-11 and [^{18}F]DCFPyL. ***Conclusion:*** In a large, single centre cohort study including 223 evaluable patients with newly diagnosed intermediate and high-risk PCa, we showed that quantitative PSMA PET/CT parameters had good diagnostic accuracy for detection of EPE, especially for ≥pT3b-stage, surpassing visual analysis (miT-stage) alone. ***References:***
1. Donswijk ML, e.a. The accuracy and intra- and interobserver variability of PSMA PET/CT for the local staging of primary prostate cancer. Eur J Nucl Med Mol Imaging. 2024;51:1741-52.

OP-877

Primary Staging of Intermediate- and High-Risk Prostate Cancer Patients using[^{18}F]PSMA-1007-PET/CT and Na[^{18}F]F-PET/CT: a Comparison of Diagnostic Accuracy, Stage, and Patient Management.

K. Buch-Olsen[1,2], *M. H. Vilstrup*[3], *S. Hansen*[1,2], *M. H. Poulsen*[3], *P. C. Holdgaard*[4], *K. E. A. Zieger*[4], *S. S. Madsen*[3], *J. T. Asmussen*[1], *J. Holm*[1,2], *K. T. Pedersen*[1], *S. Hess*[1,2], *O. Gerke*[1,2], *M. G. Hildebrandt*[1,2];
[1]*Odense University Hospital, Odense, DENMARK,* [2]*University of Southern Denmark, Odense, DENMARK,* [3]*Esbjerg and Grindsted Hospitals, University of Southern Denmark, Esbjerg, DENMARK,* [4]*Lillebaelt Hospital - University Hospital of Southern Denmark, Vejle, DENMARK.*

Aim/Introduction: To estimate the diagnostic accuracy and stage migration of [^{18}F]PSMA-1007-PET/CT and its impact on patient management when compared with Na[^{18}F]F-PET/CT for primary staging of patients with prostate cancer. ***Materials and Methods:*** These findings represent the initial results of the randomized PRISMA-PET trial (EudraCT 2021-000123-12) including patients with intermediate- and high-risk primary prostate cancer[1]. Patients randomized to clinically staging in the [^{18}F]PSMA-1007-PET/CT-arm, had a supplementary blinded Na[^{18}F]F-PET/CT performed for the purpose of this sub-study. A research-focused Multi Disciplinary Team conference (rMDT) was conducted based on the clinical data and the Na[^{18}F]F-PET/CT; stage and treatment decisions were agreed upon. Subsequently, the [^{18}F]PSMA-1007-PET/CT was reviewed and stage and treatment decision were reconsidered. The decision from the rMDT together with histology from prostatectomies with lymphadenectomy and further clarifying imaging, if performed, served as composite reference standard. A comparative diagnostic accuracy analysis was conducted between the Na[^{18}F]F-PET/CT and the clinical report of the [^{18}F]PSMA-1007-PET/CT. Stage allocation and treatment strategies from the rMDT were compared for the two types of scans. ***Results:*** A total of 128 men with a median age of 72 years (range: 53-84) were included, with 25 (19.5%) at intermediate-risk and 103 (80.5%) high-risk PCa. The sensitivity and specificity for lymph node metastases were 0.88 and 0.96 for [^{18}F]PSMA-1007-PET/CT and 0.63 and 0.94 for diagnostic CT with Na[^{18}F]F-PET/

CT (p-value 0.02 and 0.69). For bone metastases, the sensitivity and specificity were 1.00 and 0.97 for [^{18}F]PSMA-1007-PET/CT and 0.83 and 0.98 for Na[^{18}F]F-PET/CT (p-value 0.50 and 0.63). Stage migration was observed in 22 patients (17%), with 15 (12%) migrating to a more advanced stage and seven (5%) downgraded. Management changed for 18 patients (14%). In five instances (4%), the curative strategy was changed, but remained curative. Eight patients (6%) shifted from curative to palliative treatment, while two (2%) moved from palliative to curative treatment. Changes within palliative strategies occurred in three cases (2%). ***Conclusion:*** [^{18}F]PSMA-1007-PET/CT outperformed diagnostic CT with Na[^{18}F]F-PET/CT in diagnosing lymph node metastases, and showed a similar trend for bone metastases, though without significant difference. The use of [^{18}F]PSMA-1007-PET/CT for primary staging resulted in stage migration in 17% of patients and changed management in 14%, compared to Na[^{18}F]F-PET/CT. Results from the randomized PRISMA-PET trial will determine if staging with [^{18}F]PSMA-1007-PET/CT compared to Na[^{18}F]F-PET/CT will lead to improved patient outcomes. ***References:*** 1) Buch-Olsen et al. BJUI Compass. 2023 May 12;4(5):513-522. doi: 10.1002/bco2.243.

OP-878

Incremental value of multiparametric F18 PSMA PET CT in comparison to conventional F18 PSMA PET CT in the diagnosis of prostate cancer

D. Malik, *J. Gupta, N. Rana, M. Koley, D. Thakrani, A. Uppal, P. Thakral, I. B. Sen;*
Fortis Memorial research institute (FMRI), Gurugram, INDIA.

Aim/Introduction: The distinction between benign and malignant prostatic pathologies in men with an elevated PSA levels remains a pertinent clinical conundrum. While multi-core biopsy of the prostate and histopathology remain the gold-standard investigation till date; dynamic parametric PET is a modality of growing interest, with the potential to make the above distinction non-invasively. We aim to investigate the role of Ki and Dv indices obtained from dynamic parametric PET imaging in improving the diagnostic accuracy of F18 PSMA PET CT in diagnosing prostate cancer in patients with elevated PSA levels. ***Materials and Methods:*** 30 patients with an elevated PSA levels and clinical suspicion of carcinoma prostate underwent multiparametric PSMA PET following injection of 18F-PSMA (2-3 MBq/kg). A 70 min dynamic WB PET scan immediately after injection was acquired consisting of 16 continuous bed motion passes. VOI delineation of the multiparametric images was performed and semiquantitative values of SUV max and SUV mean was obtained from the conventional PET reconstructions, whereas Ki and DV values were extracted from the multiparametric images. All patients subsequently underwent a prostate biopsy and a total of 39 lesions were available for assessment. The relative diagnostic accuracy of conventional PSMA PET CT and multiparametric PET CT was assessed using a receiver operator curve characteristics curve (AUCs), sensitivity, and specificity for ordinal and dichotomized data. ***Results:*** For multiparametric PSMA PET CT, the ROC analysis of Ki-mean Index demonstrated a higher area under the curve (AUC = 0.712), which was statistically significant (p = 0.048). In contrast, conventional PET CT SUV-mean index had an area under the curve of 0.636, with a p-value of 0.199. The sensitivity and specificity for Ki-mean was 57.5% and 83.3% respectively with a cut off value of > 1.3 at 0.4091 Youden index. ***Conclusion:*** Early data suggests that multiparametric dynamic PET CT index of Ki mean offers a better potential than SUV mean obtained in conventional PSMA PET CT in distinguishing carcinoma prostate from benign prostatic pathologies in patients with an elevated PSA levels. Further analysis of this study in higher number of patients may help in establishing role of multiparametric PSMA PET CT in diagnosis, obviating the need for invasive biopsy.

OP-879

Sensitivity of distinct segmentation thresholds to different PET-reconstruction algorithms in volumetric PSMA-PET assessment

D. Ufton, *J. Heilinger, K. S. Roth, M. Schmidt, A. Drzezga, C. Kobe;*
University Hospital of Cologne, Department of Nuclear Medicine, Cologne, GERMANY.

Aim/Introduction: Tumor volume derived by prostate-specific-membrane antigen (PSMA) in PSMA-PET/CT (PSMA-TV) shows an increasing impact for prognosis and response evaluation in patients with prostate cancer. Previous studies show the impact of different PET reconstruction methods on measurements of metabolic tumor volume for FDG-PET. Here we aim to evaluate the robustness of different PSMA-TV delineation methods. ***Materials and Methods:*** We analysed ^{18}F-JK-PSMA-7 PET/CT-scans of 40 patients suffering from metastatic castration-resistant prostate cancer (mCRPC) acquired before ^{177}Lu-PSMA treatment. PSMA-TV measurements were performed using an SUV of 4.0 (PSMA-TV-4.0) as a fixed threshold, 41% of the single hottest voxel (PSMA-TV-41%) as an adaptive threshold and a patient-based liver-specific threshold (PSMA-TV-LT; adapted from the qPSMA-threshold algorithm by Gafita et al.) for automated delineation in both UHD and OSEM reconstructions. Absolute and relative differences between the segmentation thresholds in UHD and OSEM reconstructions were measured and differences tested for statistical significance using the Wilcoxon matched-pair signed-rank test (2 samples). A p-value of $p < 0.05$ was considered statistically significant. ***Results:*** Total PSMA-TV differed significantly when comparing UHD and OSEM reconstruction for an individual segmentation threshold, regardless of the threshold chosen. Volumes measured in UHD reconstructions were significantly smaller than in OSEM reconstructions. (PSMA-TV-41%-UHD = 100 ml ± 90 ml vs. -OSEM = 160 ml ± 130 ml ($p < 0.01$), PSMA-TV-4.0-UHD = 326 ml ± 284 ml vs. -OSEM = 354 ml ± 306 ml ($p = 0.02$), PSMA-TV-LT-UHD = 281 ml ± 250 ml vs. -OSEM = 305 ml ± 270 ml ($p = 0.42$)). Comparing the relative and absolute differences in PSMA-TV between OSEM and UHD reconstruction between the three separate segmentation thresholds showed significantly larger absolute volume differences for PSMA-TV-41% compared to PSMA-TV-LT (59 ml (± 73 ml) vs. 23 ml (± 48 ml), $p = 0.046$) and significantly larger relative volume differences for PSMA-TV-41% ($p < 0.01$) compared to PSMA-TV-4.0 and PSMA-TV-LT (PSMA-TV-4.0: 3.4% ± 25.8%, PSMA-TV-LT: 2.6% ± 21.1%, PSMA-TV-41%: 25.1% ± 43.0%). Absolute and relative volume differences between reconstruction settings did not significantly differ between PSMA-TV-4.0 and PSMA-TV-LT ($p = 0.11$ and $p = 0.90$, respectively). ***Conclusion:*** The fixed thresholds PSMA-TV-4.0 and -LT are less susceptible to reconstruction-induced volumetry effects as shown by lower volume differences between UHD- and OSEM-reconstructions compared to a relative segmentation threshold (PSMA-TV-41%). Using a fixed threshold of SUV 4.0 was simple to implement, as it did not require patient specific calculations of the segmentation threshold.

OP-880

Towards Biopsy-Sparing Prostate Cancer Diagnosis:45%SUVmax-Based Radiomics with AdaBoost for Pathological Feature Prediction

C. Jianbo[1,2,3], *G. Wang*[4], *X. Meng*[1], *Y. Han*[1,2], *J. Zhang*[1,2], *Y. Liu*[1,2], *B. Xu*[1];
[1]*Chinese PLA General Hospital, Beijing, CHINA,* [2]*Graduate School, Chinese PLA General Hospital, Beijing, CHINA,* [3]*Nuclear Medicine Department, The 983rd Hospital of the Joint Logistic Support Force, TianJin, CHINA,* [4]*Beijing Friendship Hospital, Affiliated to Capital Medical University, Beijing, CHINA.*

Aim/Introduction: Accurate non-invasive assessment of prostate cancer pathological grade, extra-capsular extension (ECE), and risk stratification is pivotal for personalized treatment. Previous studies have shown that 40% or 50% SUVmax thresholds can effectively characterize the biological features of prostate cancer. Yet, the clinical utility of intermediate thresholds like 45% remains underexplored. We investigate whether radiomic features derived

from PSMA PET/CT at these SUVmax percentages (40%, 45%, 50%) can predict ECE, National Comprehensive Cancer Network (NCCN) 2025 high/very high risk, and ISUP grade >2 using an AdaBoost model, advancing a biopsy-sparing approach. ***Materials and Methods:*** In this single-center study, 243 patients scheduled for radical prostatectomy underwent pre-operative 18F-PSMA-3Q PET/CT. Target volumes were delineated via the uAI Research Portal, and radiomic features were extracted. Data were split 8:2 for training and testing. An AdaBoost machine learning model was trained to predict three endpoints. Model performance was evaluated using AUC, sensitivity, specificity, accuracy, precision, F1-score, and recall. ***Results:*** For ECE prediction, the 45% SUVmax model outperformed 40% and 50% at a cutoff of 0.5, achieving a test AUC of 0.828 (95% CI: 0.697-0.958), with balanced sensitivity (0.828) and specificity (0.684), yielding 0.771 accuracy and 0.814 F1-score. In NCCN risk stratification using the same cutoff, 45% SUVmax achieved the highest AUC (0.937, 95% CI: 0.697-0.958) and recall (0.882)-critical for high-risk patient identification-with 0.854 accuracy and 0.811 F1-score. For ISUP grade >2 prediction at cutoff 0.5, 45% and 50% SUVmax demonstrated comparable performance: while 50% SUVmax prioritized sensitivity (0.939), 45% SUVmax (AUC: 0.890, 95% CI: 0.788-0.992) offered superior precision (0.857 vs. 0.816) and a nearly equivalent F1-score (0.870 vs. 0.873), balancing detection and accuracy (0.816 vs. 0.812) across the threshold. ***Conclusion:*** These findings highlight 45% SUVmax as a robust threshold, demonstrating consistent performance across endpoints where boundary thresholds (40%/50%) either underperformed or introduced trade-offs between sensitivity and specificity. The AdaBoost model leverages PSMA PET radiomics to enable non-invasive prediction, potentially reducing reliance on biopsies-an invasive gold standard associated with morbidity. While single-center data require multicenter validation, this work aligns with the NCCN 2025 guidelines to establish a framework for integrating SUVmax-tailored radiomic models into clinical workflows, advancing non-invasive, biopsy-sparing strategies for prostate cancer risk stratification.

OP-881

A comparative analysis of normal organ biodistribution and tumor uptake pattern of novel RHN001-Dx (^{99m}Tc-PSMA) in correlation with tumor burden and its implications for theranostic use

S. Martlbauer[1], *E. Mamlins*[1], *E. Novruzov*[1], *K. Mattes-György*[1], *Y. Mori*[1], *E. Winter*[2], *J. Cardinale*[1], *U. Haberkorn*[2], *C. Kratochwil*[2], *F. L. Giesel*[1];
[1]*Department of Nuclear Medicine, Medical Faculty and University Hospital Dusseldorf, Heinrich-Heine-University Dusseldorf, Dusseldorf, GERMANY,* [2]*Department of Nuclear Medicine, University Hospital Heidelberg, Heidelberg, GERMANY.*

Aim/Introduction: RHN001(formerly referred to by these authors as PSMA-GCK01) is a newly developed theranostic platform which can be labelled by both ^{99m}Tc- and ^{188}Re. This unique feature, in contrast to other PSMA-SPECT tracers, might aid in prostate cancer management via multiple ways such as in staging work-up of high-risk patients, phenotyping prior to PSMA-RLT, and implementation to PSMA-RLT guidelines alongside [^{177}Lu]Lu-PSMA-617 and is currently subject of early prospective clinical trial. The feasibility studies of ^{99m}Tc-labelled RHN001-Dx based upon planar scintigraphy scans revealed comparable tumor uptake and biodistribution pattern with its counterparts, albeit a mildly decreased rate of renal clearance in favor of hepatobiliary excretion was observed in contrast to its counterparts. Thus, this study aimed to investigate detailed tracer biodistribution via SPECT/CT imaging and the specific impact of tumor burden on biodistribution profile. ***Materials and Methods:*** A total of 60 patients with advanced prostate cancer were enrolled retrospectively, who underwent planar scintigraphy scan and SPECT/CT imaging with RHN001-Dx for PSMA-phenotyping. Spherical regions of interest (ROIs) by a dedicated software package were then placed in body organs as well as representative malignant lesions of three lymph node and bone metastases in each patient to identify the specific tracer uptake ratio. Tracer uptake in planar images were assessed by calculation of geometric means from anterior and posterior views for the ROI. We further stratified our cohort into two groups with oligometastatic and diffuse metastatic spread resulting with accordingly significantly varying levels of tumor burden. ***Results:*** The assessment on planar images revealed the highest average tracer uptake in liver (0,21 $Counts_{mean}$/MBq) followed by kidneys (0,13 $Counts_{mean}$/MBq), salivary glands (0,13 $Counts_{mean}$/MBq) and spleen (0,09 $Counts_{mean}$/MBq). On SPECT/CT images, kidneys exhibited the highest uptake (0,30 $Counts_{mean}$/MBq) followed by salivary glands (0,25 $Counts_{mean}$/MBq), liver (0,20 $Counts_{mean}$/MBq) and spleen (0,20 $Counts_{mean}$/MBq). Notably, we observed a shift in tracer uptake pattern with increasing tumor burden in analysis of subgroups, as kidneys (0,28 vs 0,32, $p \leq 0,05$) and salivary glands (0,18 vs 0,21, $p \leq 0,05$) showed substantially lower uptake in the subgroup with higher tumor burden. The results of detailed biodistribution profile confirmed a substantial hepatobiliary excretion pathway. ***Conclusion:*** Notably, increasing tumor burden has been shown to correlate negatively with RHN001-Dx uptake in major organs which is described as tumor-sink-effect. In conclusion, our results suggest a favorable biodistribution profile of RHN001-Dx for future theranostic applications.

1901

Wednesday, October 8, 2025, 11:25 - 11:45
Auditorium

Closing Ceremony

OP-882

Closing Ceremony

V. Garibotto*; Geneva University and Geneva University Hospitals, Geneva, SWITZERLAND.*

e-Posters

EP-01

e-Poster Area

A: Preclinical and Translational Studies -> A1 Medical Preclinical -> A11 In Vitro Studies

EP-0001

Conversion of ^{18}F to ^{3}H-based autoradiography for PET tracer quantification

A. Van Eetveldt[1], *F. Elvas*[1], *L. Liu*[2], *J. A. Bard*[2], *D. Bertoglio*[1], *S. Staelens*[1];
[1]*University of Antwerp, Wilrijk, BELGIUM,* [2]*CHDI foundation, Los Angeles, CA, UNITED STATES OF AMERICA.*

Aim/Introduction: In vitro autoradiography (ARG) is widely used for characterizing newly synthesized PET tracers in terms of affinity and selectivity. This technique offers less bias compared to in vivo imaging while providing significantly higher image resolution, making it an ideal method for validating in vivo imaging and assessing tracer tissue distribution. Nowadays, most clinical candidate PET tracers are labelled with ^{18}F; however, a tritiated analogue is not always available for autoradiography. If quantification is needed alongside visual validation, challenges will arise given the discrepancy in units between ^{18}F (fmol/µl, liquid homemade standard) and in ^{3}H (fmol/mg, commercially available tissue standard), which renders a comparison of various candidates with different radionuclides extremely challenging. Therefore, we developed a quantification method for ^{18}F ARG similar to ^{3}H ARG. ***Materials and Methods:*** Knowing the concentration and weight of each square in a commercial ^{3}H standard allowed us to calculate true kBq concentration per square and to decay these values to a predefined exposure date and time. These decayed ^{3}H values (range 0,02-76 kBq) were used to calculate an ^{18}F standard (range 0.04-144 kBq) matching the same range for that time slot. 2µl of each ^{18}F dilution was spotted on a TLC plate to make the standard. Gamma counter readings of ^{18}F dilutions were compared to our ^{3}H values. Since we observed a strong correlation between ^{18}F and ^{3}H standards, we could interpolate the values to create a new ^{18}F ^{3}H-converted standard, which we validated on mouse brain sections using SynVestT-1, a synaptic density marker, with both an ^{18}F and ^{3}H radioligand. ***Results:*** For both ^{3}H and ^{18}F, a standard curve was made (^{3}H/^{18}F: $r^2 = 0.99$). ROI analysis revealed a good correlation between grey values of both standards (Pearson r = 0.99; Y = 1.052X-13265). This equation allowed interpolation of ^{18}F grey values into ^{3}H equivalents, creating a new standard curve for ^{18}F in fmol/mg. Sections incubated with [^{18}F] and [^{3}H]SynVesT-1 and exposed with respective standards showed a strong agreement (Pearson r = 0.98; Y = 1.283X-17219). By interpolating the values, we were able to compare the 2 radionuclides. ***Conclusion:*** We have developed a new method, where fmol/mg values, used for ^{18}F ARG, were highly correlated with ^{3}H on the same animal sections. We have validated this method in an independent tracer study with SynvesT-1. This allows the evaluation of PET biomarkers through ARG for which no tritiated ligand is available.

EP-0002

Evaluation of purinergic P2X7 receptor level in Alzheimer's disease patients

R. Ni[1], *C. Maschio*[1], *O. Moreno*[2], *J. Wang*[3], *U. Maheshwari*[4], *A. Keller*[4], *A. Rominger*[3], *U. Konietzko*[1], *A. Nordberg*[5], *D. Razansky*[1], *C. Hock*[1], *J. Llop*[2], *R. Nitsch*[1];
[1]*University of Zurich, Zurich, SWITZERLAND,* [2]*CIC biomaGUNE, San Sebastián, SPAIN,* [3]*Inselspital, Bern, SWITZERLAND,* [4]*University Hospital Zurich, Zurich, SWITZERLAND,* [5]*Karolinska Institutet, Stockholm, SWEDEN.*

Aim/Introduction: The purinergic 2X7 receptor (P2X7R) plays an important role in Alzheimer's disease (AD). We aimed to characterize the alterations in P2X7R and astrocyte marker glial fibrillary acidic protein (GFAP) expression in AD patients, as well as their associations with amyloid-β (Aβ) and tau pathology. ***Materials and Methods:*** We included tissue samples from 43 AD patients and 34 nondemented controls (NCs); P2X7R and GFAP staining and quantitative analysis of the associations with Aβ and tau, and location of P2X7R on astrocytes and microglia were performed on postmortem hippocampal and entorhinal tissues from AD and NCs, caudate/putamen tissue from corticobasal degeneration (CBD) patients; progressive supranuclear palsy (PSP) patients; and bran tissue from 3×Tg AD mice. We further assessed in vitro autoradiography using P2X7R-specific [^{18}F]JNJ-64413739 radiotracer in the brain tissue from AD and NCs. ***Results:*** Reactive astrocytes were observed in the hippocampi of AD patients and exhibited altered morphology with denser cells and pronounced ramifications. Hippocampal and entorhinal GFAP coverage and P2X7R intensity were greater in the hippocampal subfields, including the entorhinal cortex, of AD patients than in those of NCs. P2X7R was positively correlated with Aβ and tau levels and with the Braak stage. P2X7R expression was increased around cored Aβ plaques, tau inclusions in AD brains and tau inclusions in CBD and PSP brains. P2X7R was expressed mainly on astrocytes in the hippocampus, with limited colocalization with microglia. ***Conclusion:*** We found increased hippocampal and entorhinal GFAP coverage and P2X7R levels in AD patients compared with NCs, which was correlated with amyloid and tau pathologies. P2X7R is a potential marker for neuroinflammation in AD.

EP-0003

First Steps Towards Developing a Dual-Targeted Radionuclide Theranostic Strategy Combining PSMA- and GRPR-Targeting radiopharmaceuticals for Prostate Cancer Management.

L. Bokhout, *J. de Swart, S. U. Dalm;*
Department of Radiology and Nuclear Medicine, Erasmus MC, Rotterdam, NETHERLANDS.

Aim/Introduction: Prostate specific membrane antigen (PSMA) targeted radionuclide theranostics (TRT) is successfully applied for prostate cancer (PCa) management. However, results are sub-optimal; complete cure is rare and only a significant number of patients show disease progression despite treatment. Next to PSMA, studies are evaluating gastrin releasing peptide receptor (GRPR)-targeting radiopharmaceuticals (e.g. NeoB), for PCa-TRT. Despite lower and more heterogeneous GRPR expression, studies report that PCa tumour regions/lesions without PSMA expression do express GRPR. Thus, targeting both PSMA and GRPR can be beneficial. Moreover, labelling radiopharmaceuticals with complementary radionuclides can further enhance such dual-TRT. On route to developing this dual-targeted theranostic strategy, we established a method for accurate γ-ray spectra detection of individual radioisotopes in mixtures of indium-111, terbium-161 or lutetium-177, which was subsequently used to determine the potential effect of GRPR-targeting on PSMA-radiopharmaceutical uptake and vice versa. ***Materials and Methods:*** The γ-ray spectra of varying activities (0,001-500kBq) of (mixtures of) indium-111, terbium-161 and lutetium-177 were measured using a HIDEX-AMG γ-counter to select measuring windows (i.e 370-470keV, 20-35/41-61/68-83keV and 56-72/102-124/187-229keV, respectively) for dual-radioisotope sample measurements. Different methods to limit/correct for crosstalk in dual-radioisotope samples were tested. Uptake of PSMA-I&T and NeoB, labelled with indium-111, terbium-161 or lutetium-177, was determined in a GRPR-/PSMA-expressing human PCa cell line PC3-PIP. Cells were incubated with 1nM radiolabelled PSMA-I&T (20MBq/1nmol/140uL) and/or 1nM radiolabelled NeoB (20MBq/1nmol/140uL; +/- pre-treatment

with unlabelled NeoB/PSMA-I&T) separately, consecutively and simultaneously. Uptake was expressed as percentage added dose (%AD). ***Results:*** Negligible crosstalk of terbium-161 was observed, but due to overlapping spectra, severe crosstalk of indium-111 and limited crosstalk of lutetium-177 was detected in the selected measuring windows. In literature described crosstalk correction methods were insufficiently accurate for our experiments, but in silico experiments showed that adapting the ratio of indium-111 and lutetium-177 in dual radioisotope samples limits crosstalk interference. Incubation of PC3-PIP cells with (radiolabelled) PSMA-I&T does not influence the uptake of radiolabelled NeoB compared to mono-incubation (4,7 vs. 4,6%AD), and vice versa (19,4 vs. 21,2%AD). ***Conclusion:*** We accurately measured individual radioisotopes in dual radioisotope samples by selecting specific energy windows and activity ratios, herewith limiting crosstalk interference. Future studies will include further validation of the radioisotope ratios identified in silico and the effect of dual-targeting on PSMA- and GRPR-radiopharmaceutical uptake. Additionally, the therapeutic effect of combined PSMA/GRPR-TRT will be assessed, with the ultimate aim to develop an effective dual-targeted theranostic strategy for PCa.

EP-0004

Enhanced Glioblastoma Targeting and Therapeutic Efficacy with ^{64}Cu-NOTA-TP-c(RGDfK)

A. Mirzaei, *S. Samia Ait-Mohand, P. Mercy Ignatius, É. Rousseau, B. Guérin;*
Department of Medical Imaging and Radiation Sciences, Faculty of Medicine and Health Sciences, Université de Sherbrooke, Sherbrooke, QC, CANADA.

Aim/Introduction: Glioblastoma multiforme (GBM) is a highly aggressive brain tumor with poor prognosis and limited treatment options. Integrin alpha-v beta-3 (αvβ3), which is overexpressed in GBM cells and binds specifically to the arginine-glycine-aspartate (RGD) sequence in extracellular matrix proteins, presents a promising molecular target. We hypothesize that a novel radiotheranostic agent combining radioactive copper-64 (^{64}Cu), 1,4,7-triazacyclononane-1,4,7-triacetic acid (NOTA)-terpyridine platinum (TP), and cyclic arginine-glycine-aspartate-D-phenylalanine-lysine (c(RGDfK)) peptide—^{64}Cu-NOTA-TP-c(RGDfK)—will improve targeting and therapeutic efficacy in GBM. Our objective was to assess this agent's in vitro performance in comparison with ^{64}Cu-NOTA-c(RGDfK), ^{64}Cu-NOTA-TP, non-radioactive copper (^{nat}Cu)-NOTA-TP-c(RGDfK), cisplatin, and temozolomide (TMZ). ***Materials and Methods:*** A robust protocol was developed for the preparation of NOTA-TP-c(RGDfK). The inhibitory concentration 50 (IC_{50}) values of ^{nat}Cu-NOTA-c(RGDfK) and ^{nat}Cu-NOTA-TP-c(RGDfK) were determined in human U87 MG GBM cells through competition assays with ^{64}Cu-NOTA-c(RGDfK). Cellular uptake, internalization, and efflux of ^{64}Cu-NOTA-TP-c(RGDfK) and ^{64}Cu-NOTA-c(RGDfK) and ^{64}Cu-NOTA-TP were evaluated in U87 MG and SVG p12 normal astrocyte cells from 1 to 48 hours. Cytotoxicity studies of ^{64}Cu-NOTA-TP-c(RGDfK), ^{64}Cu-NOTA-c(RGDfK), ^{64}Cu-NOTA-TP, ^{nat}Cu-NOTA-TP-c(RGDfK), TMZ, and cisplatin were conducted in both cell lines at 24 and 48 and 72 hours. ***Results:*** NOTA-TP-c(RGDfK) was synthesized with 2-3% yield and radiolabeled with >99% radiochemical purity. The IC_{50}values for ^{nat}Cu-NOTA-c(RGDfK) and ^{nat}Cu-NOTA-TP-c(RGDfK) were 10 ± 2 nM and 16 ± 8 nM respectively, indicating strong affinity for integrin αvβ3-expressing U87 MG cells. At 24 hours, ^{64}Cu-NOTA-TP-c(RGDfK) showed highest uptake in U87 MG cells (38.8 ± 1.8%), surpassing ^{64}Cu-NOTA-TP (30.4 ± 5.5%) and ^{64}Cu-NOTA-c(RGDfK) (14.1 ± 1.0). Internalization followed a similar trend, with ^{64}Cu-NOTA-TP-c(RGDfK) reaching 28.0 ± 1.0% at 24 hours, compared to 18.4 ± 0.8% and 11.4 ± 0.6%, respectively. ^{64}Cu-NOTA-TP-c(RGDfK) retained 51.4 ± 2.1% of its intracellular radioactivity in U87 MG cells, demonstrating stable intracellular retention comparable to ^{64}Cu-NOTA-TP (53.2 ± 3.4%) and slightly lower than ^{64}Cu-NOTA-c(RGDfK) (67.6 ± 2.2%) after 24 hours. All compounds exhibited minimal uptake in SVG p12 cells. Subcellular localization studies revealed nuclear accumulation of ^{64}Cu-NOTA-TP-c(RGDfK) in U87 MG cells (6.0 ± 0.5% at 24 h), supporting potential DNA damage via low-energy electrons from ^{64}Cu decay. ^{64}Cu-NOTA-TP-c(RGDfK) had the lowest IC_{50} (10 ± 2 nM at 48 h) and outperformed all other tested compounds. While ^{64}Cu-NOTA-c(RGDfK) was less potent in U87 MG cells, it showed the lowest toxicity in SVG p12 cells at both 24 and 48 hours. ***Conclusion:*** These findings establish ^{64}Cu-NOTA-TP-c(RGDfK) as a promising integrin αvβ3-targeted agent for effective GBM radiotherapy.

EP-0005

Novel Dynamic Cardiac Phantom for Comparison of Cardiac Volumes and LVEF Between CZT-ERNA and PET-MPI

M. Nielsen[1,2], *R. Wozniak*[1], *T. C. Hansen*[1], *L. L. Duchstein*[1], *J. D. Hermansen*[3], *S. Hvidsten*[4], *L. T. Jensen*[1,2], *B. Zerahn*[1];
[1]*Dept. of Nuclear Medicine, Copenhagen University Hospital – Herlev and Gentofte, Herlev, DENMARK,* [2]*Dept. of Clinical Medicine, University of Copenhagen, Copenhagen, DENMARK,* [3]*Medical Technology Dept., Køge Hospital, Køge, DENMARK,* [4]*Dept. of Nuclear Medicine, Odense University Hospital, Odense, DENMARK.*

Aim/Introduction: Accurate assessment of left ventricular ejection fraction (LVEF) and cardiac volumes is essential, particularly in patients at risk of cardiotoxicity during cancer therapy. While equilibrium radionuclide angiography (ERNA) is used to monitor LVEF, myocardial perfusion imaging (MPI) is primarily intended for assessing perfusion. Nonetheless, comparing LVEF and volume estimates across modalities could elucidate whether MPI data might support functional evaluation too. To our knowledge, no existing beating-heart phantom allows direct comparison between blood-pool and perfusion-based techniques. We therefore developed and tested a novel cardiac phantom designed specifically to enable such cross-modality validation. ***Materials and Methods:*** A custom-built cardiac phantom was developed using a dual-lumen balloon setup, with the inner lumen representing the left ventricular cavity and the outer the myocardium. Stroke volume and frequency was controlled with a piston-driven mechanism, and ECG gating enabled via a motion-triggered signal generation. Imaging was performed using cadmium-zinc-telluride (CZT)-ERNA and gated PET-MPI. Image processing and analyzes was carried out on two different types of software. Scans were repeated with and without a thorax phantom to assess attenuation effects. CT-scans were used as a static reference for end-diastolic volume (EDV), end-systolic volume (ESV), and LVEF comparisons. 3 series were conducted with PET-MPI measurements on the first day and CZT-ERNA measurements on the second day after tracer decay. ***Results:*** PET-MPI progressively underestimated volumes in static acquisitions, while CZT-ERNA overestimated them. In gated acquisitions, both modalities underestimated LVEF, with a larger deviation seen in PET-derived values.Attenuation correction (AC) in PET yielded consistent volumes regardless of thorax phantom presence. In contrast, CZT-ERNA, which lacks AC in our setup, showed varying results.In series 1-2, proximity between the inner and outer balloons created a pseudo-defect, leading to underestimation of LV volumes on PET-MPI. This issue was resolved in series 3, aligning results more closely with the CT reference. ***Conclusion:*** Attenuation correction in PET functioned as expected, while its absence in CZT-ERNA may introduce patient size-dependent bias. Additionally, regionally reduced tracer uptake - simulated by balloon proximity - led to volume underestimation, highlighting a potential volumetric pitfall in patients with myocardial scar tissue

undergoing MPI. Our phantom offers a unique platform for direct modality comparison and in future work we aim to simulate basal plane motion to improve comparability with clinical results.

EP-0007

Radiolabelled alginate nanoparticles - developing a peptide targeting radiotherapeutic approach to cancer treatment

M. Dornish[1], *J. Dahle*[2], *S. Al-Haidar*[3], *K. H. Ferning*[3];
[1]*Blue Wave Therapeutics AS, Sandvika, NORWAY,* [2]*Department of Oncology Akershus University Hospital, Nordbyhagen, NORWAY,* [3]*Minerva Imaging ApS, Ølstykke, DENMARK.*

Aim/Introduction: Alginate, a natural biopolymer found in seaweed and kelp, has chelating properties suitable for harnessing radionuclides. Additionally, this biopolymer can be conjugated with peptides that provide targeting capabilities. It is also capable of being processed into nanoparticles, resulting in a formulation that is usable in the body. This study demonstrates that RGD-alginate specifically binds to glioblastoma cells expressing αvβ3 integrin and RGD-alginate nanoparticles stably chelate the alpha-emitting radionuclide actinium-225 (^{225}Ac) and its decay daughters. ***Materials and Methods:*** Calcium alginate nanoparticles were made by bead milling. The spherical nanoparticles were approximately 100 nm in diameter. The particles were subsequently functionalized by conjugation of the RGD peptide using EDC/NHS chemistry. Nanoparticles were incubated with ^{225}Ac chloride in secular equilibrium with daughters for 1 hour at room temperature. Radioactivity associated with calcium alginate nanoparticles were determined by a gamma counter. Energy windows were set to identify francium-221 and bismuth-213 gamma peaks of 218 and 440 keV, respectively. Fluorescence microscopy and flow cytometry were performed using U-87 MG human glioblastoma cells incubated with different fluorescently labelled RGD peptides: linear (GRGDSP) labeled with fluorescein isothiocyanate (FITC), or cyclic RGD (c(RGDfK)) labelled with CyAL-5; or RGD-alginate fluorescently labelled with FITC (FITC-RGD-alginate). ***Results:*** Fluorescent microscopy images show FITC-RGD-alginate staining of U-87 MG glioblastoma cells, which was confirmed by flow cytometry. The fluorescently labelled peptides GRGDSP and c(RGDfK) also bound to cells, while the negative control, FITC-alginate (without the RGD recognition sequence), did not. The chelation of radionuclides by alginate nanoparticles was demonstrated using ^{225}Ac. More than 95% of the radioactivity from ^{225}Ac and daughters were associated with the nanoparticles at all time points. In addition to ^{225}Ac, we have shown that alginate nanoparticles can also chelate radium-223 and its decay daughters. ***Conclusion:*** The 100 nm size of the nanoparticles allows diffusion into tissue. Alginate nanoparticles can stably chelate ^{225}Ac and decay daughters for over 30 days, indicating that the biopolymer particle can absorb recoil energy arising from α-particle emission. This innovation based on alginate nanoparticles outperforms current radionuclide chelators, which fail to retain decay daughters, and helps protect healthy tissue by preventing the escape of radionuclides from the chelator after the initial α-particle emission. ^{225}Ac labelled RGD-alginate nanoparticles are now undergoing preclinical testing in a rodent model of glioblastoma. Supported by grant 346303 ALPHAGLIO from the Research Council of Norway.

EP-0008

The effectiveness of targeted lead-212 alpha therapy and EBRT in neuroendocrine spheroids

K. Grayson[1], *P. M. D. Gape*[1], *M. Patel*[1], *M. Riiabova*[1], *L. Wagner*[2], *M. K. Schultz*[3], *G. Stasiuk*[1], *S. Y. A. Terry*[1];
[1]*King's College London, London, UNITED KINGDOM,* [2]*DKFZ German Cancer Research Center, Heidelberg, GERMANY,* [3]*Perspective Therapeutics, Coralville, IA, UNITED STATES OF AMERICA.*

Aim/Introduction: The treatment landscape for neuroendocrine tumours (NETs) has remained relatively unchanged, particularly in the case of targeted radionuclide therapies (TRT), which has focused primarily on Lutetium-177 (Lu-177) conjugated to somatostatin receptor (SSTR) targeting ligands. Targeted α-particle therapy (TAT), using radionuclides such as lead-212 (Pb-212), have shown promise in cancer treatment. Although 2D cultures are widely used in research, they poorly reflect tumour structure and microenvironments, limiting their suitability for evaluating new therapies. Here, we developed a panel of 3D NET models and used them to evaluate responses to a Pb-212-labelled SSTR2 targeting compound. Results were compared spheroids treated with benchmark external beam X-ray radiotherapy (EBRT). ***Materials and Methods:*** Spheroids were generated for BON-1 (wild type or expressing SSTR2) and QGP-1 cells using agarose-coated 96-well plates. 3D cultures were exposed to EBRT (between 0-8 Gy) or treated for 1, 24 or 72 hours with Pb-212-PSC-PEG$_2$-TOC (100 kBq/mL, Perspective Therapeutics, USA). Spheroids were also treated with unlabelled PSC-PEG$_2$-TOC or Pb-212. Treatments were evaluated by measuring spheroid growth, including the examination of structural changes, using microscopy to calculate spheroid area and diameter between 1 hour and 10 days post-treatment. Spheroid viability was examined using the CellTiter-Glo® 3D Cell Viability Assay and compared to results obtained from MTS assays on 2D cultures. ***Results:*** Preliminary data shows targeted Pb-212 treatment inhibited the growth of NET spheroids, with microscopic analysis revealing disruption of spheroid architecture. At 7 days post-treatment with Pb-212- PSC-PEG$_2$-TOC BON-1 spheroids expressing SSTR2 showed significant growth inhibition in comparison to the unlabelled PSC-PEG$_2$-TOC control ($p = 0.05$, % decrease = 39.94±10.4%), whilst wild type BON-1 spheroids showed no significant changes. At 10 days post treatment, significant changes in spheroid eccentricity were found following 1 hour, 24 hour and 72 hour incubations with PSC-PEG$_2$-TOC ($p = 0.05$), with increased deviation from a parabola trending with increased treatment time.Comparison between 2D and 3D models revealed that spheroids were significantly more resistant to treatment. In 2D cultures, BON-1 cells expressing SSTR2 following 4 Gy EBRT showed a significant decrease in metabolic activity ($p < 0.0001$) whilst no reduction was observed in the 3D model ($p = 0.1003$). ***Conclusion:*** This study highlights distinct responses of 2D and 3D models, both to EBRT and TAT, and further confirms that NET models of different origins have varied treatment responses. Finally, Pb-212-PSC-PEG$_2$-TOC proved effective at disrupting NET spheroids growth and inducing morphological changes.

EP-0009

Preclinical Evaluation of NK-1R-Targeting Molecule in Epithelial Cancer Cell Lines.

T. Xu[1], *S. Chopra*[1], *U. Yngve*[2,3], *Z. Wang*[1], *H. Yushchyshyna*[1], *P. Jha*[1], *U. Rosenström*[2], *M. Nestor*[1];
[1]*Department of Immunology, Genetics and Pathology, Science for Life Laboratory (SciLifeLab), Uppsala University, Uppsala, SWEDEN,* [2]*Department of Medicinal Chemistry, Preparative Medicinal Chemistry, Uppsala University, Uppsala, SWEDEN,* [3]*Science for Life Laboratory (SciLifeLab), Drug Discovery and Development platform, Uppsala, SWEDEN.*

Aim/Introduction: The overexpression of the neurokinin-1 receptor (NK-1R) has been found to promote tumorigenic processes such as cell migration, proliferation, and invasion. Its overexpression in various epithelial cancers renders it a promising target for molecular imaging and therapy. Aprepitant is an NK-1R antagonist with anti-tumor effects by inducing apoptosis and suppressing metastasis in preclinical studies. A novel NK-1R antagonist, PN622, is structurally similar to aprepitant and has demonstrated a higher affinity for NK-1R than the NK-1R natural ligand substance P (SP). This study aimed to evaluate the potential of the NK-1R-targeting molecule PN622 as a theranostic agent by assessing its anti-proliferation effect, binding specificity, cellular processing, internalization, binding affinity, and retention in various epithelial cancer cell lines. ***Materials and Methods:*** The anti-proliferation effect of the NK-1R-targeting molecule PN622 was compared with that of aprepitant in NK-1R-

overexpressing cell lines, including Panc-1 (pancreatic), OVCAR3 (ovarian), MDA-MB-468, MDA-MB-231 and T47D (breast). The PN622 was radiolabeled with iodine-125 and purified using high-performance liquid chromatography (HPLC). In vitro specificity of the radiolabeled PN622 was evaluated by pre-blocking the NK-1R receptor with an excess of non-labeled PN622 or aprepitant. Cellular processing and internalization were analyzed by incubating cells with the radioligand at 37°C, followed by an acid wash to distinguish membrane-bound from internalized fractions at pre-determined time points. The interaction was measured in real-time in living cells using the LigandTracer instrument, and affinity (K_D value) was determined. Retention studies assessed the time-dependent cell-associated radioactivity over 24 hours. ***Results:*** The PN622 demonstrated a dose-dependent effect on proliferation inhibition. The [^{125}I]I-PN622 showed high specificity, with statistically significant ($p < 0.05$) reduced binding following self-blocking or aprepitant blocking, confirming NK1R-mediated uptake. Cellular processing studies showed that cell-associated radioactivity increased over time. A slow internalization was observed, with less than 15% of bound activity internalized after 24 hours. The affinity measurement yielded a picomolar K_D value, indicating strong receptor interaction. It also demonstrated a non-one-to-one interaction. Retention studies demonstrated sustained membrane-bound radioactivity, with more than 30% remaining after 24 hours, indicating favorable tumor retention. ***Conclusion:*** The PN622 exhibits a proliferation inhibition effect in NK-1R overexpressing cancer cells. The [^{125}I]I-PN622 shows high binding specificity, slow internalization, strong affinity, and prolonged retention in epithelial cancer cells, supporting its potential as a diagnostic agent for NK-1R-expressing tumors. Additional in vivo studies are needed to validate the targeting efficacy using [^{123}I]I-PN622 (SPECT) and [^{124}I]I-PN622 (PET) for diagnosis while employing [^{131}I]I-PN622 for therapy.

EP-0010

Exploring [^{18}F]FAPI-74 as a diagnostic tool in vulvar cancer: in vitro evaluation and preliminary results

A. Florit[1,2], *M. Ruggiero*[3], *S. Fragomeni*[4], *A. Piermattei*[5], *T. Pasciuto*[6,7], *A. Federico*[4], *E. Martinelli*[8], *F. Alcaro*[4], *G. Zannoni*[5,9], *L. Alic*[10], *L. de Geus-Oei*[1,11,12], *S. Annunziata*[2], *F. H. P. van Velden*[11], *A. Fagotti*[4,8], *V. Rufini*[2,13], *C. Nero*[4,8], *G. Garganese*[4,8], *A. Collarino*[2];
[1]*Biomedical Photonic Imaging Group, University of Twente, Enschede, NETHERLANDS,* [2]*Nuclear Medicine Unit, Department of Diagnostic Imaging and Oncological Radiotherapy, Fondazione Policlinico Universitario A. Gemelli IRCCS, Rome, ITALY,* [3]*PET/CT Centre, Fondazione Policlinico Universitario A. Gemelli IRCCS, Rome, ITALY,* [4]*Gynaecologic Oncology Unit, Department of Women, Children and Public Health Sciences, Fondazione Policlinico Universitario A. Gemelli IRCCS, Rome, ITALY,* [5]*Anatomical Pathology Unit, Department of Women, Children and Public Health Sciences, Fondazione Policlinico Universitario A. Gemelli IRCCS, Rome, ITALY,* [6]*Research Core Facility Data Collection G-STeP, Fondazione Policlinico Universitario A. Gemelli IRCCS, Rome, ITALY,* [7]*Section of Hygiene, University Department of Life Sciences and Public Health, Università Cattolica del Sacro Cuore, Rome, ITALY,* [8]*Section of Obstetrics and Gynaecology, University Department of Life Sciences and Public Health, Università Cattolica del Sacro Cuore, Rome, ITALY,* [9]*Section of Pathology, University Department of Life Sciences and Public Health, Università Cattolica del Sacro Cuore, Rome, ITALY,* [10]*Magnetic Detection & Imaging Group, University of Twente, Enschede, NETHERLANDS,* [11]*Section of Nuclear Medicine, Department of Radiology, Leiden University Medical Center, Leiden, NETHERLANDS,* [12]*Department of Radiation Science and Technology, Delft University of Technology, Delft, NETHERLANDS,* [13]*Section of Nuclear Medicine, University Department of Radiological Sciences and Haematology, Università Cattolica del Sacro Cuore, Rome, ITALY.*

Aim/Introduction: Positron emission tomography (PET) imaging using fibroblast activation protein inhibitors (FAPI) has recently demonstrated promising results in the staging and restaging of gynaecological malignancies [1]. So far, no studies have explored FAP expression in vulvar cancer. In this clinical setting, FAPI-based PET imaging may offer potential advantages over conventional [^{18}F]FDG-PET, particularly for nodal staging where [^{18}F]FDG often yields high false-positive rates [2]. This in vitro study aims to evaluate and quantify FAP expression in invasive vulvar squamous cell carcinoma (VSCC) specimens by autoradiography using [^{18}F]FAPI-74. ***Materials and Methods:*** Between November 2021 and December 2025, a total of 90 consecutive VSCC tissue specimens, including samples from primary tumours and metastatic lymph nodes, from newly diagnosed patients undergoing surgery at Fondazione Policlinico Universitario A. Gemelli IRCCS will be collected and preserved in both optimal cutting temperature compound and formalin-fixed paraffin-embedded (FFPE). Immunohistochemical staining using anti-FAPα antibody [SP325] (Abcam Ltd.) will be performed on FFPE sections to serve as reference standard. Staining intensity will be scored on a scale of 0-3 (0=no stain, 1=low, 2=medium, 3=high) [3]. For autoradiographic analysis, VSCC tissue sections will be incubated with high-specific activity [^{18}F]FAPI-74, or a non-radioactive analogue as control, washed to remove unbound tracer, and exposed to the phosphor imager screen. [^{18}F]FAPI-74 will be employed to evaluate FAP expression and distribution within the specimens, as well as to quantify FAPI binding and binding affinity. ***Results:*** Preliminary immunohistochemical analysis was conducted on primary tumour samples from 36 patients. FAP expression in peritumoral stromal cells was detected in 33 specimens, with a mean percentage of FAP positive stromal cells of 36.4% ± 27.3% and average FAP staining intensity score of 1.6 ± 0.6. Three specimens lacked identifiable stromal cells. Additionally, FAP expression was detected in the epithelial tumour cells of four specimens. ***Conclusion:*** Our preliminary results indicate that peritumoral stromal cells associated with VSCC consistently express FAP on their surface, supporting the rationale for autoradiographic analysis using [^{18}F]FAPI-74. These results encourage further investigation into the potential [^{18}F]FAPI-74 PET/CT as both a diagnostic tool and a prognostic biomarker in vulvar cancer. ***References:*** [1] Florit et al. Eur J Nucl Med Mol Imaging. 2025. [2] Collarino et al. J Nucl Med. 2017. [3] Spektor et al. J Nucl Med. 2024.

EP-0011

Is radiolabelling a PARP inhibitor with a radiometal via a DOTA chelator a viable strategy for PARP-targeted radionuclide therapy (TRT)?

A. Kurniawan[1], *Z. Ming*[1], *M. Boëtius*[2], *W. Szymanski*[2], *S. Blok*[1], *P. Elsinga*[1], *I. Antunes*[1], *E. de Vries*[1], *B. Cornelissen*[1];
[1]*Department of Nuclear Medicine and Molecular Imaging, University Medical Center Groningen, University of Groningen, Groningen, NETHERLANDS,* [2]*Department of Medicinal Chemistry, Photopharmacology and Imaging, Groningen Research Institute of Pharmacy, Faculty of Science and Engineering, University of Groningen (RUG), Groningen, NETHERLANDS.*

Aim/Introduction: Radiopharmaceuticals targeting poly (ADP-ribose) polymerase (PARP) are promising candidates for targeted radionuclide therapy (TRT) to treat PARP-expressing cancers. Here, we evaluated the potential of a PARP inhibitor (PARPi) based on an olaparib-like structure, labelled with ^{161}Tb or ^{68}Ga for TRT and PET imaging, respectively, using in vitro cancer models. ***Materials and Methods:*** [^{161}Tb]$TbCl_3$ or [^{68}Ga]$GaCl_3$ were used for radiolabelling a DOTA-chelated derivate of the PARP inhibitor olaparib, yielding [^{161}Tb]Tb-DOTA-olaparib or [^{68}Ga]Ga-DOTA-olaparib. Non-radiolabelled (cold) versions were produced using natural Ga and Tb chloride salts. Both radiolabelled compounds were evaluated in vitro for cell uptake, internalisation, specific binding, and effect on clonogenic survival across a panel of PARP-expressing human (U87MG, PSN-1) and murine (4T1, CT26) cancer cell lines, providing a robust assessment of their targeting and therapeutic potential. ***Results:*** The [^{161}Tb]Tb-DOTA-olaparib and [^{68}Ga]Ga-DOTA-olaparib were successfully radiolabelled with radiochemical

yields (RCY) exceeding 95%, at molar activities of up to 40 and 20 MBq/nmol, respectively. The total cellular uptake of [^{161}Tb]Tb-DOTA-olaparib was minimal across all cancer cell lines, including PSN-1 (0.185±0.09 mBq/cell), U87MG (0.127±0.036 mBq/cell), 4T1 (0.093±0.015 mBq/cell), and CT26 (0.056±0.004 mBq/cell). Internalisation studies revealed that the majority of the uptake was associated with the membrane-bound fraction, with values for U87MG (0.110 ± 0.012 mBq/cell), 4T1 (0.621 ± 0.118 mBq/cell), and CT26 (0.641 ± 0.088 mBq/cell), and negligible cell internalised fraction (<0.030 mBq/cell). A comparable uptake profile was observed for [^{68}Ga]Ga-DOTA-olaparib, showing predominant membrane association and minimal intracellular accumulation. Neither uptake nor internalisation could be blocked using an excess of PARP-specific competitor ligands, which verifies no PARP-specific binding of the compounds (p>0.05). Log D measurement for [^{161}Tb]Tb-DOTA-olaparib showed a value of -3.68±0.03, more hydrophilic even than for [^{68}Ga]Ga-DOTA-olaparib (-2.56±0.026). This hydrophilicity likely contributes to their limited ability to traverse cell membranes, restricting intracellular access through passive diffusion. Clonogenic survival was not significantly different between [^{161}Tb]Tb-DOTA-olaparib and $^{161}TbCl_3$ (p=0.42). ***Conclusion:*** In conclusion, [^{161}Tb]Tb-DOTA-olaparib and [^{68}Ga]Ga-DOTA-olaparib exhibit negligible cellular uptake and insufficient specific binding to nuclear PARP in cancer cells. Their limited ability to penetrate the cell membrane and interact with intracellular targets makes them, in our hands, unsuitable for effective PARP-targeted therapy or imaging applications.

EP-0012

DNA damage in thyroid cancer patients treated with radioactive iodine

S. Kagodora, *M. Vangu;*
University of Witwatersrand, Johannesburg, SOUTH AFRICA.

Aim/Introduction: Thyroid cancer is the most common endocrine cancer globally. The National Cancer Registry has estimated the prevalence of the disease to be higher in females than in the male population with a risk of 1 in 506 females and 1 in 1035 in males in South Africa. Thyroid cancer includes the use of radioactive iodine (RAI) depending on risk category. The aim of this study was to investigate the correlation between 131 iodine RAI emitted ionizing radiation and the induced and persistent DNA damage in patients treated with radioactive iodine. ***Materials and Methods:*** This prospective study was done at a tertiary academic hospital in Johannesburg. Thyroid cancer patients were invited to enrol and participate in the study in line with the Helsinki Declaration on studies in human subjects. Informed consent was obtained from all participants prior to their inclusion in the study. Blood samples of 34 thyroid cancer patients, treated with radioiodine therapy with 131-I RAI was collected. All 34 thyroid cancer participants received I-131 RAI therapy, with doses ranging from 1110 to 7400 MBq (30 to 200 mCi). Blood samples were collected in 4ml lithium-heparin tubes at four key time points: upon admission for radiotherapy, at discharge (3-5 days post-therapy), and at 3 and 6 months after treatment. The chromosomal damage in the lymphocytes of these patients was determined by the cytokinesis-blocked micronucleus (MN) assay. ***Results:*** The amount of DNA damage was increased after treatment up to 3 months and decreased slightly at 6 months. The median dose of ^{131}I for thyroid cancer participants was 5550MBq (150mCi), with interquartile range(IQR) of 3700-7400MBq (100-200mCi). The number of ^{131}I induced MN increased with the amount of RAI therapy. There was a highly significant difference in the mean number of micronuclei in thyroid cancer participants between admission (25.31) and discharge (52.04) (p-value <0.0001). A significant difference in mean MN was also noted between 3 months (46.47) and 6 months post-treatment (30.89), (p=0.0385). ***Conclusion:*** These preliminary results suggest that 131I therapy may pose a long-term challenge to the lymphocytes and that a sensitivity may persist. The findings emphasize the need for ongoing monitoring of chromosomal damage in thyroid cancer patients who are subject to multiple RAI therapies to understand the long-term implications of radioactive iodine therapy.

EP-0013

In vitro evaluation of [^{18}F]SYN2 effect on mouse myoblast and human cardiomyocyte cell lines.

K. Gotowicz[1,2], *K. Archacka*[3], *A. Ostaszewska*[3], *M. Zimowska*[3], *S. Krajewski*[1], *J. Włostowska*[1], *C. Kozanecki*[1];
[1]*Synektik S.A. Research and Development Center, Warsaw, POLAND,*
[2]*University of Warsaw, Faculty of Chemistry, Warsaw, POLAND,*
[3]*University of Warsaw, Faculty of Biology, Warsaw, POLAND.*

Aim/Introduction: [^{18}F]SYN2 is a positron emission tomography (PET) tracer in phase III clinical trial, designed for a non-invasive myocardial perfusion imaging (MPI). The aim of the study was to evaluate the tracer effect on mouse myoblast and human cardiomyocyte cell lines. ***Materials and Methods:*** Mouse myoblast cell line (C2C12, European Collection of Cell Cultures, ECACC no. 91031101, passage no. 13), human cardiomyocyte cell line (AC16, ATCC, CRL-3568). Both cell lines were cultivated in presence of [^{18}F] SYN2 nonradioactive analogue (25-100 nM). For test: MitoTracker Green FM (Thermo Fisher, M7514), Malassez chamber, Trypan Blue (Sigma Aldrich, T8154) were used. All experiments were performed at least thrice, ANOVA and Kruskal-Wallis test were used for statistical analysis. ***Results:*** The localization of the [^{19}F] SYN2 compound coincided with the distribution of mitochondria, as indicated by staining with MitoTracker Green FM. The addition of [^{19}F]SYN2 at any concentration did not significantly impact the morphology of C2C12 cells. Both myoblasts and myotubes in the control and experimental groups exhibited typical morphology. Cardiac tracer did not induce cytotoxicity nor interfere with the differentiation process at concentration <100 mM. The incorporation of [^{19}F]SYN2 into the C2C12 and AC16 cultures had a noticeable effect on proliferation compared to the control group. It was observed that the tracer, at all concentrations, slowed proliferation moderately. The effect was more significant on myoblast cell line. The strongest statistically significant differences were found after 48 and 72 h for the highest concentration of 100 mM tracer. Apoptosis levels in the C2C12 cultures at 48, 72, and 96 hours in proliferation medium were around 10% for all samples. A statistically significant difference was observed at 24 hours for concentrations of 50 nM and 100 nM compared to the control. For AC16 cells, apoptosis levels ranged from 10% to 15% across all samples and time points, with no statistically significant differences compared to the control. ***Conclusion:*** Mitochondrial localization of the tracer was confirmed. The presence of the cardiac tracer in the highest concentration (100 nM) during cell proliferation and differentiation had a noticeable impact on cell behaviour. The progression of the process was slowed down rather than stopped entirely. Apoptosis analysis for C2C12 and AC16 cells revealed no adverse effects of [^{19}F]SYN2 on cell survival. Overall, the data indicates the use of the [^{19}F]SYN2 compound in mouse myoblasts and human cardiomyocytes does not result in negative effects and may indicate cell stability after radiotracer treatment.

EP-0014

Targeting the Tumor Microenvironment via Fibroblast Activation Protein (FAP): A 3D Co-Culture Model for FAP-Targeted Alpha Therapy in Prostate Cancer

S. Kvarsvik Kristiansen[1], *N. Dernjani*[2], *A. Juzeniene*[1];
[1]*Department of Radiation Biology, Institute for Cancer Research, The Norwegian Radium Hospital, Oslo, NORWAY,* [2]*Department of Molecular Biology, Norwegian University of Life Science, Ås, Norway, Oslo, NORWAY.*

Aim/Introduction: Prostate cancer (PCa) is the most common malignancy in men and the second leading cause of cancer-related morbidity and mortality worldwide. Advanced disease remains largely incurable due to resistance and limited durable

treatment options. PSMA-targeted radionuclide therapies (PSMA-TRT) has gained momentum, however, these are not suitable for all patients, particularly those with low or heterogeneous PSMA expression. Targeting the tumor stroma—particularly cancer-associated fibroblasts (CAFs), which support tumor progression and therapy resistance—offers a promising alternative. Fibroblast activation protein (FAP) is a membrane-bound serine protease highly expressed in CAFs, making it a compelling pan-cancer target for TRT. FAP theranostics has shown potential in several cancer types, including PCa. Among various ligands, FAPI-46 offers improved tumor retention, but has a relatively short biological half-life, limiting its effectiveness when paired with long-lived radionuclides such as ^{177}Lu. Lead-212, a beta-emitter decaying to alpha-emitting ^{212}Bi or ^{212}Po, has a shorter half-life more suitable for small-molecule ligands and may provide therapeutic advantages in targeting hypoxic and resistant tumor regions. The main aim of this study was to develop an advanced 3D co-culture spheroid model with FAP-negative prostate cancer cells (22Rv1) and FAP-positive immortalized fibroblasts (F11-hTERT) to assess the therapeutic potential of FAP-targeted alpha therapy (FAP-TAT) using [^{212}Pb]Pb-FAPI-46. ***Materials and Methods:*** Spheroids were generated using the liquid overlay technique in agarose-coated 96-well plates and characterized by brightfield and fluorescence microscopy. FAP expression and radioligand uptake were evaluated in 2D cultures using flow cytometry and binding assays, while cellular senescence was assessed through β-galactosidase staining. Fibroblast spatial localization within spheroids was confirmed using the lipophilic tracer DiO. ***Results:*** F11-hTERT fibroblasts exhibited high FAP expression and radioligand uptake, in contrast to minimal expression and uptake in 22Rv1 cells. [^{212}Pb]Pb-FAPI-46 induced activity- and time-dependent senescence in fibroblasts, but not in cancer cells. In 3D culture models, radioligand treatment significantly reduced spheroid size and increased doubling time, with the most pronounced effect in spheroids enriched with higher numbers of fibroblast. No effect was observed in 22Rv1 monoculture spheroids. ***Conclusion:*** This study highlights the value of stroma-enriched 3D in vitro models for the preclinical evaluation of FAP-TAT, demonstrating the therapeutic potential of [^{212}Pb]Pb-FAPI-46 in treating prostate cancer via stromal targeting. These findings emphasize the broader relevance of targeting stromal components in solid tumors characterized by abundant CAFs, including pancreatic, breast, and gastric cancers. ***References:*** Laudicella R et al. Preliminary findings on the role of FAPi in prostate cancer theranostics. Diagnostics (Basel). 2023;13(6).

EP-0015

Quantitative Analysis of KiSS-1R Cell Surface Expression in Triple-Negative Breast Cancer Using Dye-Conjugated Kisspeptins

L. Kovacs*, H. Taş, U. Bauder-Wüst, M. Schäfer, M. Benesova-Schäfer;*
German Cancer Research Center (DKFZ), Heidelberg, GERMANY.

Aim/Introduction: Triple-negative breast cancer (TNBC) is an aggressive and highly metastatic disease. It comprises 15% of breast cancers and remains a significant challenge due to limited therapies available[1]. KiSS-1R is a G protein coupled receptor whose expression is upregulated in certain cancer types, including TNBC. Overexpression of KiSS-1R has been associated to invasion, migration and epithelial-to-mesenchymal transition, all of which are associated with poor prognosis. Although some studies have explored KiSS-1R as a potential target[1], little is known about the level of its expression on the cell membrane, which is critical for the development of targeting agents. The aim of this study is to analyze the cell binding of in-house generated endogenous and synthetic kisspeptins using flow cytometry. This will allow us to determine the potential of KiSS-1R and kisspeptin-based ligands for prospective radiotheranostic applications in TNBC. ***Materials and Methods:*** The endogenous Kisspeptin-10 and synthetic Kisspeptin-34 were synthesized via automated solid-phase peptide synthesis and conjugated with Alexa Fluor-488 (AF-488). For in vitro studies, 1x10^6 CHO-KiSS-1R cells and native TNBC cells were incubated with different concentrations of AF-488-Kisspeptin-10 and AF-488-Kisspeptin-34 for 30, 60, and 120 min at 4 and 37°C. The cells were analyzed on a flow cytometer. ***Results:*** AF-488-conjugated Kisspeptin-10 (AF-488-Tyr-Asn-Trp-Asn-Ser-Phe-Gly-Leu-Arg-Phe-NH_2) and Kisspeptin-34 (AF-488-AMBA-2-Nal-Gly-Leu-Arg-Trp-NH_2) were successfully synthesized at high chemical purity (>95%). Flow cytometry was employed to assess cell surface expression of KiSS-1R, revealing variable expression levels among the cell lines tested. Preliminary results from CHO-KiSS-1R cells treated with 500nM AF-488-kisspeptin-10 demonstrated a significantly higher geometric mean fluorescence intensity (945 ± 35) compared to the unstained control (291 ± 38). Analyses of different incubation times showed no significative difference between 30, 60 and 120-min (968 ± 39 vs 945 ± 35 vs 972 ± 140 respectively) at 4°C, suggesting rapid and stable binding of tested kisspeptins to KiSS-1R. Interestingly, media such as OptiMEM were found to increase fluorescence intensity by 1.8-fold compared to Hank's Balanced Salt Solution, indicating that the choice of medium can influence ligand binding or detection sensitivity. ***Conclusion:*** Our findings validate the feasibility of using kisspeptin-based probes for evaluating KiSS-1R expression. In the next phase, ongoing studies will extend this analysis to TNBC cell lines and to kisspeptin analogs modified with chelators, enabling coordination of relevant diagnostic and therapeutic radionuclides. These efforts aim to further explore the potential of KiSS-1R as a viable target for radiotheranostic applications. ***References:*** 1. Kleynhans J, et al. J Neuroendocrinol. 2025, e13487.

EP-0016

Beyond PSMA Targeting: What Truly Drives the Radiotoxicity of the Alpha-Emitting [^{212}Pb]Pb-AB001?

R. Liukaityte[1]*, V. Stenberg*[2,1]*, S. Kvarsvik Kristiansen*[1]*, A. Kleinauskas*[3,1]*, A. Juzeniene*[1,3]*;*
[1]*Oslo University Hospital, Oslo, NORWAY,* [2]*ARTBIO AS, Oslo, NORWAY,* [3]*University of Oslo, Oslo, NORWAY.*

Aim/Introduction: The alpha-emitting radioligand [^{212}Pb]Pb-AB001, which targets prostate-specific membrane antigen (PSMA), is a promising therapeutic option for metastatic prostate cancer patients. However, variable PSMA expression is observed across patients, tumor sites and even single prostate cancer cells. Does more PSMA mean better uptake and greater cytotoxicity? Is the relationship linear, or does biology play a more complicated role? In this study, prostate cancer cell lines with distinct PSMA expression profiles, cellular dimensions, and growth formats (2D and 3D) were exposed to [^{212}Pb]Pb-AB001 to evaluate whether radiotoxicity scales linearly with PSMA abundance and delivered activity. ***Materials and Methods:*** Four prostate cancer cell lines PC 3-PIP (PSMA+++), C4-2 (PSMA++), LNCaP (++) and 22Rv1 (PSMA+) were evaluated in this study. Total ligand binding was measured 1 hour post radioligand addition. Cytotoxic effect following exposure to [^{212}Pb]Pb-AB001 was assessed using clonogenic and proliferation assays, along with multicellular spheroids. Cellular responses were further characterized by flow cytometry at 1, 24-, 72-, and 144-hours post-treatment, including analysis of cell cycle distribution (propidium iodide and phospho-histone H3 for mitotic cells), apoptosis and membrane permeability (Annexin V-FITC and propidium iodide), DNA double-strand breaks (γH2AX), and senescence (β-galactosidase staining). ***Results:*** Lower PSMA expression correlated with higher activity concentrations of [^{212}Pb]Pb-AB001 required to reduce the clonogenic potential, with PC 3-PIP being the most responsive. Total cell-bound activity was a more accurate predictor of treatment effect than the nominal

PSMA levels. The cell cycle analysis revealed G2 phase arrest and reduced mitotic entry in all cell lines. A delayed increase in polyploid and mitotic cell populations observed exclusively in PC 3-PIP and LNCaP cells indicated mitotic catastrophe, followed by apoptosis and senescence. The impact of treatment was more pronounced in 3D spheroids compared to 2D monolayers, reflecting the added influence of crossfire and bystander effects in a spatially complex tumor architecture. Ongoing investigations into cell size, internalization rates, and p53/p21 status aim to clarify their roles in modulating treatment response. ***Conclusion:*** This study shows that while PSMA facilitates radioligand uptake, cytotoxicity is not solely determined by receptor density. Total cell-bound activity correlated more strongly with treatment efficacy. These findings underscore the need for precise microdosimetry and spatially relevant tumor models to optimize targeted alpha therapies. Combination strategies involving [^{212}Pb]Pb-AB001 and agents targeting DNA repair may enhance therapeutic efficacy.

EP-0017

Treatment efficacy and DNA damage induced by [^{161}Tb]Tb-PSMA I&T vs [^{177}Lu]Lu-PSMA I&T in prostate cancer cell lines

M. Kirienko, *E. Jachetti, R. Sulsenti, C. Cucchi, C. Beretta, A. Bogni, C. Pascali;*
Fondazione IRCCS Istituto Nazionale dei Tumori di Milano, Milan, ITALY.

Aim/Introduction: Aim of the present study was to evaluate and compare the treatment efficacy and the DNA damage induced by [^{161}Tb]Tb-PSMA-I&T and [^{177}Lu]Lu-PSMA-I&T in human prostate cancer cell lines. Specifically, we evaluated cell proliferation and the the phosphorylation of the H2AX histone (γ-H2AX) as a readout of induction of DNA double strand breaks (DSB) by immunofluorescence. ***Materials and Methods:*** PSMA-I&T was labelled with 0.5-2.0GBq of [^{177}Lu]$LuCl_3$ or [^{161}Tb]$TbCl_3$ (1) using a ratio of 60-80MBq of radionuclide per nmol of precursor. Both [^{177}Lu]Lu- and [^{161}Tb]Tb-PSMA-I&T showed a radiochemical purity >98% by iTLC and >97% by HPLC. We set up in vitro pulse chase experiments utilizing LNCaP and PC3 cell lines, expressing or not experissing PSMA, respectively. Cells were treated for 4h with either [^{161}Tb]Tb-PSMA-I&T or [^{177}Lu]Lu-PSMA-I&T, at different activity concentrations (10, 5, 1, or 0.5MBq/ml), and then, after washing, allowed to grow for 7 days. To analyse the DNA damage, LNCaP and PC3 cells ($2x10^5$) were treated for 4h with either [^{161}Tb]Tb-PSMA-I&T or [^{177}Lu]Lu-PSMA-I&T (either 10 or 5MBq/ml). As a positive control for the immunofluorescence for γ-H2AX, we used LNCaP cells treated with 5mM of doxorubicin for 24h. Slides were washed and stained with primary anti-phospo-Histone H2AX antibody (dilution 1:400) overnight at 4°C. After washing, alexa fluor 488-conjugated chicken anti-rabbit secondary antibody (dilution 1:300) was added for 2 h. The staining intensity was quantified using the ImageJ 2 software. All experiments were performed at least twice. Pools of biological replicates obtained in all the independent experiments were performed and statistical analysis was run considering all the samples. One-way ANOVA was performed separately between LNCaP and PC3 groups. ***Results:*** Both radiopharmaceuticals were able to restrain the proliferation of LNCaP cells with a dose-dependent effect. [^{161}Tb]Tb-PSMA-I&T was superior than [^{177}Lu]Lu-PSMA-I&T at the highest activity concentration (10MBq/ml). We found the highest staining intensity in LNCaP cells treated with 10MBq/ml of [^{161}Tb]Tb-PSMA-I&T. Albeit the difference was not statistically significant, data clearly showed a trend of increased DNA DSB induction in LNCaP cells treated with 10MBq/ml of [^{161}Tb]Tb-PSMA-I&T compared to LNCaP cells treated with 10MBq of [^{177}Lu]Lu-PSMA-I&T. Notably, in PC3 cells the γ-H2AX staining intensity remained low with no significant variations between control and treated cells. ***Conclusion:*** [^{161}Tb]Tb-PSMA-I&T resulted superior in inhibiting prostate cancer cell proliferation compared to [^{177}Lu]Lu-PSMA-I&T. Our results suggest DNA DSBs as factors reflecting higher efficacy of Terbium-161 labelled radiopharmaceuticals compared to those labelled with Lutetium-177. ***References:*** 1) This is a PRISMAP contribution.

EP-02

e-Poster Area

A: Preclinical and Translational Studies -> A1 Medical Preclinical -> A12 Preclinical Cardiology and Neurology

EP-0018

Assessment of early-phase [^{18}F]Florbetaben images as a proxy for brain metabolism in mouse models of Alzheimer's disease

R. Gröger[1], *A. Englert*[1], *M. Lalia*[1], *L. de Weerd*[2], *M. Rovere*[2], *C. Haass*[2], *S. Tahirovic*[2], *R. Werner*[1], *M. Brendel*[1], *J. Gnörich*[1];
[1]*Department of Nuclear Medicine, LMU University Hospital, Munich, GERMANY,* [2]*German Center for Neurodegenerative Diseases (DZNE), Munich, GERMANY.*

Aim/Introduction: FDG-PET and β-amyloid-PET using [^{18}F]Florbetaben (FBB) are established tools for assessing neurodegenerative diseases like Alzheimer's disease (AD). Recent human studies have demonstrated that early-phase β-amyloid-PET can detect cerebral metabolic deficits comparably to FDG-PET, offering a surrogate for neuronal injury and metabolic alterations. In contrast to human AD, transgenic mouse models often show cerebral hypermetabolism, which is likely caused by inflammation rather than neuronal injury. Therefore, this study aimed to assess whether early-phase [^{18}]FBB-PET and [^{18}]FDG-PET capture similar regional changes in perfusion and metabolism. By directly comparing both modalities in two common AD mouse models, we evaluated the potential of early-phase β-amyloid-PET as a surrogate for detecting functional brain changes. ***Materials and Methods:*** After an intravenous injection of ~20 MBq [^{18}F]FDG, 17 APPPS1, 56 App^{SAA}, and 19 age- and sex-matched wildtype mice (3-12mo, 40.2% female) underwent static PET/MRI (30-60 min p.i.). The same mice underwent a dynamic PET/MRI scan (0-60 min p.i.) with ~20 MBq [^{18}F]FBB. Standardized uptake values (SUV) were extracted from 15 regions defined by the Ma-Benveniste-Mirrione Atlas and correlated between early-phase [^{18}F]FBB and corresponding [^{18}] FDG scans using Pearson's correlation coefficients. Regional [^{18}F] FBB and [^{18}]FDG SUV were compared across cohorts using ANOVA. ***Results:*** The highest agreement between [^{18}F]FDG-PET and early [^{18}F]FBB-PET acquisition was reached from 1-3 min p.i. including both AD mouse models and wildtype mice. Using this interval as the optimal time window for [^{18}F]FBB perfusion imaging, we observed strong correlations with [^{18}F]FDG particularly in the cortex (R=0.42, P<0.0001), hippocampus (R=0.45, P<0.0001), and thalamus (R=0.44, P<0.0001). Furthermore, AD mouse models mice showed significantly increased perfusion in the cortex (APPPS1: P<0.0001, App^{SAA}: P<0.0001), hippocampus (APPPS1: P<0.0001, App^{SAA}: P<0.0001), and thalamus (APPPS1: P=0.0004, App^{SAA}: P<0.0001) compared to wildtype mice. Similarly, glucose metabolism was increased in the cortex (APPPS1: P=0.0011, App^{SAA}: P<0.0001), hippocampus (APPPS1: P=0.0049, App^{SAA}: P<0.0001), and thalamus (APPPS1: P=0.0012, App^{SAA}: P<0.0001) compared to wildtype controls. ***Conclusion:*** Early-phase [^{18}F]FBB β-amyloid-PET mirrors functional brain changes captured by [^{18}F]FDG-PET and shows strong regional correlations. The dual-purpose nature of β-amyloid imaging offers a cost-effective alternative to [^{18}F] FDG-PET in preclinical studies and may facilitate more efficient diagnostics.

EP-0019

Adjustment for Perfusion Masks Hypermetabolism in FDG-PET imaging of Aging Rodents

M. Lalia[1], *S. Wagner*[1], *J. Thevis*[1], *L. Bartos*[1], *L. Kunze*[1], *S. Roemer-Cassiano*[2], *N. Franzmeier*[3], *S. Tahirovic*[4], *R. Werner*[1], *M. Brendel*[1,4,5], *J. Gnörich*[1,4];
[1]*Department of Nuclear Medicine, LMU University Hospital, Munich, GERMANY,* [2]*Department of Neurology, LMU University Hospital, Munich, GERMANY,* [3]*Institute for Stroke and Dementia Research, LMU University Hospital, Munich, GERMANY,* [4]*German Center for Neurodegenerative Diseases (DZNE), Munich, GERMANY,* [5]*Munich Cluster for Systems Neurology (SyNergy), Munich, GERMANY.*

Aim/Introduction: FDG-PET employs numerous quantification methods to probe cerebral glucose metabolism in neurodegenerative diseases across species. Two metrics are particularly prevalent: the total volume of distribution (V_T), which accounts for tracer delivery via blood- or image-derived input functions; and the standardized uptake value (SUV), which normalizes tissue activity to injected dose and body weight. We conducted a head-to-head comparison of V_T versus SUV in aging wild-type (WT) and APP^{NL-G-F} mice to determine which metric most accurately reflects age- and amyloid-related changes in cerebral glucose metabolism, using cellular glucose uptake as standard of truth. ***Materials and Methods:*** APP^{NL-G-F} (n=35, up to 12 months of age) and WT (n=65, up to 20 months of age) of both sexes (46% female) received a dynamic 45 min emission recording post 30 MBq intravenous injection of FDG. Quantification of FDG-PET was achieved by extracting cerebral FDG V_T, derived from carotid artery image-derived-input-functions, and SUV. A subset of mice received brain extraction, cell sorting and single cell FDG-uptake measurements after in-vivo FDG injection (scRadiotracing) accounting for microglia, astrocytes and neurons to calculate the FDG-uptake per single cell. ***Results:*** Cerebral FDG-PET SUV demonstrated a significant age-dependent increase in WT (r=0.55, p<0.0001) and in APP^{NL-G-F} (r=0.49, p=0.019) mice. This increase as a function of age was confirmed by ex-vivo FDG-uptake measurements of the SUV-scaled whole brain (WT: r=0.59, p<0.0001; APP^{NL-G-F}: r=0.52, p=0.014). Contrary, the cerebral FDG-PET V_T demonstrated only a slight increase with age in both mouse models (WT: r=0.26, p=0.043; APP^{NL-G-F}: r=0.33, p=0.13). However, SUV and V_T still revealed a significant agreement at the individual level (WT r=0.65, p<0.0001; APP^{NL-G-F} r=0.49, p<0.0001). With an increasing cellular FDG-uptake in both aging mouse models, microglia showed the strongest association with SUV (WT: r=0.45, p=0.0011; APP^{NL-G-F}: r=0.38, p=0.049). In both mouse models, microglial and astrocytic FDG uptake were not significantly correlated with V_T. Neuronal FDG uptake did not show a significant correlation with SUV and with V_T. ***Conclusion:*** Age-dependent hypermetabolism is present in aging WT and β-amyloid mice and confirmed at the level of cellular glucose uptake. SUV quantification allows valid capturing of the age dependent hypermetabolism, whereas V_T quantification masks age dependent increases of glucose uptake and the biologically relevant abundance of the glycolysis substrate. Parallel trajectories of hypermetabolism and hyperperfusion related to age- and β-amyloid-related inflammation are responsible for the imperfect quantification of FDG-PET via V_T.

EP-0020

Metabolic Kinetics Study of a Novel TDP-43 Targeted Molecular Probe

Y. Kong[1], *B. He*[1], *J. Xu*[1], *A. Xu*[1], *C. Yang*[2], *D. Ng*[2], *W. Lam*[2], *Z. Zhang*[1], *Y. Guan*[1];
[1]*Huashan Hospital, Fudan University, Shanghai, CHINA,* [2]*Singapore General Hospital, Singapore, SINGAPORE.*

Aim/Introduction: TDP-43 is a key protein implicated in various neurodegenerative diseases, including Alzheimer's disease (AD), making it a critical target for developing diagnostic and therapeutic tools. This study investigates the metabolic kinetics of a novel TDP-43 targeted molecular probe [^{18}F]TDP-43-PHA using a two-compartment model to analyze the profiling of the radiotracer in vivo. ***Materials and Methods:*** Dynamic PET scan data were acquired over 5400 seconds, with 30 frames distributed as follows: 3 frames of 10 seconds, 9 frames of 30 seconds, 5 frames of 60 seconds, 10 frames of 300 seconds, and 3 frames of 600 seconds. Image reconstruction was performed using the OSEM3D/MAP algorithm with 2 iterations for OSEM3D and 18 for MAP, a Beta value of 0.004278 (resolution recovery RR=1.5 mm), and voxel size of 0.776×0.776×0.796 mm^3. Corrections included decay, dead time, and input function overflow, but not attenuation or scatter. The input function was derived from the left ventricle (LV) ROI, using the whole blood TAC to calculate pharmacokinetic parameters. The two-compartment model was applied to analyze the radiotracer's profiling, considering the central and peripheral compartments. The model equations were derived based on the principles of linear kinetics, assuming first-order processes for drug transfer between compartments. ***Results:*** The pharmacokinetic parameters were successfully estimated from the experimental data. The two-compartment model provided a good fit to the data, with R^2 values indicating a high degree of correlation between the model predictions and the observed data. The estimated parameters were as follows: $t_{1/2\alpha} = 17.3105\ min^{-1}$, $t_{1/2\beta} = 207.22\ min^{-1}$, $K_{12} = 0.0007\ min^{-1}$, $K_{21} = 0.0393\ min^{-1}$, AUC = 18494.22, and CL = 0.0054 mL/min, indicating the probe's distribution and elimination characteristics in the body. The central compartment volume (V_1) was estimated to be 1.5850 mL, and the peripheral compartment volume (V_2) was estimated to be 0.0315 mL. The total apparent distribution volume (V_d) was calculated to be 1.6165 mL. ***Conclusion:*** The novel TDP-43 targeted molecular probe [^{18}F]TDP-43-PHA exhibited favorable metabolic kinetics. The two-compartment model effectively captured the radiotracer's profiling, providing insights into its distribution and elimination processes. The probe's rapid distribution and elimination kinetics, along with its relatively high AUC and moderate clearance rate, suggest its potential for further development in diagnosing TDP-43 related neurodegenerative diseases, including AD. The ability to target TDP-43 could provide a new avenue for early diagnosis and treatment of AD, potentially improving patient outcomes.

EP-0021

Multimodal Assessment of Isoproterenol-Induced Cardiac Injury in a Mouse Model of Type 2 Myocardial Infarction

K. Vandoorne[1], *C. Zeltser Dekel*[1], *T. Yoganathan*[1], *N. Kalish-Achrai*[1], *N. Haj*[1], *M. Berihu*[1], *B. Tavitian*[2], *S. Karni-Ashkenazi*[1];
[1]*Technion - Israel Institute of Technology, Haifa, ISRAEL,* [2]*Université Paris Cité, Inserm, Paris, FRANCE.*

Aim/Introduction: Myocardial infarction (MI) is a leading global cause of morbidity and mortality. Type 2 MI (T2MI), which results from an imbalance between myocardial oxygen supply and demand, often occurs without underlying coronary artery disease [1-3]. This study investigates the cardiac impact of a single high-dose injection of Isoproterenol (ISO) in a murine model, aiming to emulate the pathophysiological features of T2MI and assess downstream myocardial damage using advanced imaging and histological techniques. ***Materials and Methods:*** Male and female mice aged 8-12 weeks were randomized to control (CTR) or ISO groups. ISO mice received a single intraperitoneal dose of Isoproterenol HCl (160 mg/kg) [1]. Two weeks post-treatment, cardiac function and injury were evaluated using multimodal imaging: ^{18}F-FDG PET/CT, cardiac MRI, and MRI T1 mapping. Imaging findings were validated by gamma counting, Masson's Trichrome histology, Endomucin staining, and complete blood count (CBC) analysis. ***Results:*** ISO-treated mice demonstrated significant reductions in ejection fraction and increased left ventricular volumes by cardiac MRI. T1 mapping and histology revealed pronounced myocardial fibrosis, especially in the interventricular septum. PET/CT showed elevated ^{18}F-FDG uptake,

confirmed by gamma counting, indicating increased metabolic demand and/or inflammation. Endomucin staining revealed enhanced microvascular density, suggestive of angiogenesis post-injury. CBC analysis showed elevated RBC, hemoglobin, hematocrit, and platelet levels—markers consistent with a prothrombotic state. ***Conclusion:*** This study demonstrates for the first time, through in vivo multimodal imaging, the structural, functional, and metabolic cardiac alterations associated with stress-induced Type 2 MI (T2MI) in a murine model. The integration of PET/CT, cardiac MRI, and histological validation reveals hallmark features of myocardial injury, including reduced cardiac function, fibrosis, inflammation, and prothrombotic hematologic profiles. These findings provide a powerful translational platform for understanding T2MI pathophysiology and evaluating potential therapeutic strategies targeting adverse cardiac remodeling and systemic risk post-injury. ***References:*** [1] Forte E, et al. Journal of Cellular and Molecular Medicine 2021;25:229-243.[2] Yoganathan T, et al. Nat Commun. 2023 Jul 12;14(1):4143. [3] Scally C, et al. Circulation. 2019 Mar 26;139(13):1581-1592.

EP-0022

Pioglitazone Mitigates Immunotherapy-Induced Neuroinflammation in an Alzheimer's Disease Mouse Model: Longitudinal TSPO- and Aβ-PET Study

A. Zatcepin[1,2], *K. Wind-Mark*[1,2], *G. Palumbo*[1], *L. Kunze*[1], *M. Willem*[3], *F. Gildehaus*[1], *S. Lindner*[1], *L. M. Bartos*[1], *G. Biechele*[1], *R. Werner*[1], *N. L. Albert*[1,4,5], *S. I. Ziegler*[1,6], *M. Brendel*[1,2,7];
[1]Department of Nuclear Medicine, LMU University Hospital, LMU Munich, Munich, GERMANY, [2]German Center for Neurodegenerative Diseases (DZNE), Munich, GERMANY, [3]Biomedical Center (BMC), Division of Metabolic Biochemistry, Faculty of Medicine, LMU Munich, Munich, GERMANY, [4]German Cancer Consortium (DKTK), Partner Site Munich, German Cancer Research Center (DKFZ), Heidelberg, GERMANY, [5]Bavarian Cancer Research Center (BZKF), Erlangen, GERMANY, [6]Department of Nuclear Medicine, Hannover Medical School (MHH), Hannover, GERMANY, [7]Munich Cluster for Systems Neurology (SyNergy), Munich, GERMANY.

Aim/Introduction: Baseline microglial activation is a key determinant for therapeutic outcomes in Alzheimer's disease (AD) mouse models [1]. We questioned whether pioglitazone could offset the elevated inflammation observed with chronic Aβ monoclonal antibody (Aβ-mAb) immunotherapy in mice. To address this, we investigated the interplay between neuroinflammation and amyloid-β (Aβ) pathology using longitudinal TSPO-PET and Aβ-PET in a large cohort of App^{NL-G-F} and wild-type (WT) mice. ***Materials and Methods:*** WT mice received either Aβ-mAb or placebo from 5 to 10 months of age; App^{NL-G-F} mice were assigned to four groups: placebo, Aβ-mAb, pioglitazone, or combination therapy. TSPO- ([^{18}F]GE-180) and Aβ-PET ([^{18}F]Florbetaben) scans were performed at 5, 7.5, and 10 months, complemented by Morris water maze and biochemical analyses (Trem2, ApoE, Aβ) at the final timepoint. Images were spatially normalized and evaluated using semi-quantitative measures (percent injected dose, SUVR, z-score). We further examined linear mixed-effects models, connectivity-based desynchronization indices (DIs) [2], and correlations with biochemical markers. ***Results:*** App^{NL-G-F} mice developed significantly higher TSPO-PET signals than WT. Among App^{NL-G-F} cohorts, Aβ-mAb treatment alone showed the greatest neuroinflammatory response, reflected by elevated TSPO-PET uptake in the cortex and the amygdala. However, pioglitazone co-administration ameliorated this inflammatory surge: TSPO-PET levels remained comparable to placebo controls. At the same time, the application of pioglitazone and combined therapy resulted in an earlier inflammatory response against fibrillary amyloid, as shown by the associations of regional TSPO- and Aβ-PET z-scores. Correlations of TSPO-PET SUVR and DI with biochemical markers (Trem2, ApoE, $Aβ_{40}$) and behavioural deficits underscored the impact of neuroinflammation on disease progression. ***Conclusion:*** Our findings indicate that pioglitazone effectively suppresses the increased neuroinflammation triggered by Aβ immunotherapy in an AD mouse model. Longitudinal TSPO-PET proved instrumental in tracking these changes and linking them to behaviour and pathological proteins. These results support the clinical potential of combining Aβ-targeting antibodies with immunomodulatory strategies to enhance therapeutic outcomes while minimizing inflammatory side effects. ***References:*** [1] G. Biechele et al., "Pre-therapeutic microglia activation and sex determine therapy effects of chronic immunomodulation," Theranostics, vol. 11, no. 18, pp. 8964-8976, Aug. 2021, doi: 10.7150/thno.64022.[2] A. Zatcepin et al., "Regional desynchronization of microglial activity is associated with cognitive decline in Alzheimer's disease," Mol. Neurodegener., vol. 19, no. 1, p. 64, Sep. 2024, doi: 10.1186/s13024-024-00752-6.

EP-0023

First Longitudinal Characterization of Aluminum-Induced Neuroinflammation in the Rat Hippocampus Using TSPO-PET Imaging

Z. Xiang[1,2,3], *J. Zhang*[4,5], *Y. Zhang*[1,2,3], *S. Wang*[4,5], *Z. Qin*[1,2,3], *H. Wang*[1,2,3], *Q. Niu*[5], *S. Li*[1,2,3];
[1]Department of Nuclear Medicine, First Hospital of Shanxi Medical University, Taiyuan, CHINA, [2]Shanxi Key Laboratory of Molecular Imaging, Shanxi Medical University, Taiyuan, CHINA, [3]Collaborative Innovation Center for Molecular Imaging of Precision Medicine, Taiyuan, CHINA, [4]Key Laboratory of Coal Environmental Pathogenicity and Prevention, Ministry of Education, Shanxi Medical University, Taiyuan, CHINA, [5]Department of Labor Health, School of Public Health, Shanxi Medical University, Taiyuan, CHINA.

Aim/Introduction: Aluminum is not an essential element for humans, yet environmental exposure to it is on the rise. It is a well-documented cumulative neurotoxin linked to the development of neurodegenerative diseases. Neuroinflammation serves as a hallmark of these disorders, making its diagnosis and monitoring essential. However, longitudinal studies examining the progression of neuroinflammation following aluminum exposure are currently lacking. The mitochondrial translocator protein (TSPO), a crucial imaging biomarker for neuroinflammation, has not been investigated as a potential marker for aluminum-induced neuroinflammation. This study represents the first use of ^{18}F-DPA-714 TSPO-PET to longitudinally assess neuroinflammation in the hippocampus of rats following aluminum exposure. ***Materials and Methods:*** Rat models exposed to aluminum were established through intraperitoneal injection of aluminum maltol. The longitudinal development of aluminum uptake in the hippocampal region was monitored using ^{18}F-DPA-714 at 1, 2 and 3months post-exposure. Following imaging, behavioral changes were assessed using a water maze. In addition, we evaluated neuroinflammatory factors changes in the hippocampal area and investigated the cell types exhibiting increased TSPO-PET signals through immunofluorescence. ***Results:*** TSPO-PET imaging revealed that the standardized uptake value ratio (SUVR) in the anterodorsal hippocampal region of male aluminum-exposed rats was significantly higher than that of the control group at 1, 2, and 3months ($P < 0.05$). In female rats, SUVR in the anterodorsal hippocampal area was significantly elevated compared to controls at 3 months ($P < 0.05$). Levels of IL-1β, IL-6, and TNF-α in the hippocampus of male aluminum-exposed rats were significantly increased at 2 and 3 months ($P < 0.05$). Similarly, these cytokines were significantly higher in female aluminum-exposed rats at 3 months ($P < 0.05$). Behavioral assessments showed that the number of platform crossings in male aluminum-exposed rats was significantly reduced at 2 and 3 months compared to controls ($P < 0.05$). In females, the number of crossings was also significantly lower than in controls at 3 months ($P < 0.05$). Immunofluorescence indicated that all TSPO-PET signals originated from activated microglia. ***Conclusion:*** TSPO-PET can

be employed to monitor neuroinflammation following aluminum exposure, with the TSPO-PET signal specifically reflecting the activation of microglia. Moreover, this study highlights gender differences in neuroinflammation and cognitive dysfunction resulting from aluminum exposure. Male rats exhibited greater susceptibility to aluminum exposure, with neuroinflammation and cognitive dysfunction manifesting earlier than in female rats.

EP-0024

Combining Dopamine Transporter and Amyloid PET Tracer: A Preclinical Study on Dual-Target Imaging

B.-N. Park[1], *Y.-S. An*[2];
[1]*Ajou University Hospital, Suwon, Gyeonggi-Do, KOREA, REPUBLIC OF,* [2] *Ajou University Hospital, Suwon, KOREA, REPUBLIC OF.*

Aim/Introduction: This study aimed to evaluate the feasibility and diagnostic utility of a dual-target positron emission tomography (PET) imaging approach using a cocktail of N-3-[^{18}F]fluoropropyl-2β-carbomethoxy-3β-(4-iodophenyl) nortropane ([^{18}F]FP-CIT) and [^{18}F]florbetaben (FBB) for the simultaneous assessment of dopaminergic and amyloid changes in a preclinical setting. ***Materials and Methods:*** We utilized both Parkinson's disease (PD) and Alzheimer's disease (AD) mouse models, as well as a control group, to investigate the uptake of [^{18}F]FP-CIT and [^{18}F]FBB individually and in combination. PET imaging was conducted, and standardized uptake value ratios (SUVRs) were analyzed for each model across the striatal and cortical regions. Comparisons were made between single and cocktail PET scans to assess potential cross-interference of the tracers. ***Results:*** In both PD and AD models, no statistically significant differences were observed in the SUVRs between single-tracer and cocktail PET scans in the striatum and cortex ($p > 0.4$ for striatal comparisons, $p > 0.8$ for cortical comparisons). The cocktail PET approach demonstrated consistent uptake patterns for each tracer, indicating the feasibility of dual-target imaging without any compromise in the diagnostic quality. ***Conclusion:*** This preclinical study suggests that [^{18}F] FP-CIT and [^{18}F]FBB PET imaging is a viable dual-target imaging approach for neurodegenerative disease evaluation. The method could streamline diagnostic workflows and improve patient convenience. Further clinical studies are warranted to validate the efficacy and safety of this approach in human populations. ***References:*** Feigin VL, Vos T, Nichols E, et al. (2020)The Lancet Neurology 9:255-265 Collaborators GBDNSD (2024) Lancet Neurol 23:344-381 Sung C, Oh SJ, Kim JS (2024) Nucl Med Mol Imaging 58:185-202 Chapleau M, laccarino L, Soleimani-Meigooni D, Rabinovici GD (2022) J Nucl Med 63:13S-19S Zhu S, Pang Y, Zhang X, et al. (2024) Neuroendocrinology 114:411-422Deng P, Fan T, Gao P, et al. (2024) Adv Sci (Weinh):e2402030 Zhang C, Qi H, Jia D, et al. (2024) Life Sci 340:122457 Mirrione MM, Schiffer WK, Fowler JS, Alexoff DL, Dewey SL, Tsirka SE (2007) Neuroimage 38:34-42 Ma Y, Hof PR, Grant SC, et al. (2005) Neuroscience 135:1203-1215.

EP-0025

Fibroblast-Specific Txndc5 Deletion Attenuates Myocardial Fibroblast Activation Following Acute Myocardial Infarction as Demonstrated by ^{18}F-FAPI-74 PET/CT

K.-Y. Ko[1], *C.-J. Liu*[2], *T.-Y. Lee*[2], *C.-H. Chiu*[2], *K.-C. Yang*[3], *M.-F. Cheng*[2];
[1]*National Taiwan University Cancer Center, Taipei, TAIWAN,* [2]*National Taiwan University Hospital, Taipei, TAIWAN,* [3]*National Taiwan University College of Medicine, Taipei, TAIWAN.*

Aim/Introduction: Myocardial fibrosis is a key component of cardiac remodeling after acute myocardial infarction (MI), predominantly driven by activated fibroblasts. ^{18}F-labeled fibroblast activation protein inhibitor (^{18}F-FAPI) is a novel PET radiotracer that selectively binds to activated fibroblasts. TXNDC5 (thioredoxin domain containing 5) is an endoplasmic reticulum protein enriched in cardiac fibroblasts and implicated in redox-mediated fibroblast activation and extracellular matrix production. This study is to investigate the time course and intensity of fibroblast activation following MI using ^{18}F-FAPI-74 PET/CT in wild-type and fibroblast-specific Txndc5 knockout mouse models. ***Materials and Methods:*** C57BL/6J wild-type mice (n=3) and fibroblast-specific Txndc5 knockout mice (Col1a2-Cre/ERT2; Txndc5fl/fl, n=3) underwent left anterior descending (LAD) coronary artery ligation to induce MI. Sham-operated mice underwent identical procedures without ligation. ^{18}F-FAPI-74 was administered via the tail vein at baseline, day 7, and day 14 post-ligation. Static microPET/CT imaging was performed 45 minutes post-injection (15-minute acquisition). Fibroblast activation was quantified by calculating the heart-to-muscle uptake ratio (H/M) from regions of interest on axial PET/CT images. ***Results:*** In wild-type mice with MI, the H/M ratio peaked at day 7 and declined by day 14. In contrast, Txndc5 knockout mice (both sham and MI groups) exhibited a gradual increase in H/M ratio over time. On day 7, the H/M ratio in wild-type MI mice was significantly elevated (2.4 ± 0.2) compared to Txndc5 knockout MI mice (1.7 ± 0.4) and Txndc5 knockout sham controls (1.8 ± 0.06). Furthermore, there was no significant difference in the H/M ratio between Txndc5 knockout MI mice and wild-type sham controls (1.9 ± 0.3). ***Conclusion:*** ^{18}F-FAPI-74 PET/CT enables noninvasive assessment of myocardial fibroblast activation and reveals attenuated fibrotic response in fibroblast-specific Txndc5 knockout mice following MI. This imaging approach holds promise as a translational platform for evaluating antifibrotic therapies targeting TXNDC5.

EP-0026

Application of ^{18}F-D_2-LW223 in the rat model of ischemic stroke

Liao[1], *Z. Wang*[2], *W. Li*[2], *H. Pang*[2];
[12]*Department of Nuclear Medicine, The First Affiliated Hospital of Chongqing Medical University, Chongqing, CHINA.*

Aim/Introduction: Stroke is a common disease of the central nervous system, which is one of the main causes of death or disability. Microglia are sensitive to ischemia and can be activated in the early stage of ischemic stroke. Activated microglia plays an important role in the pathophysiological link of ischemic stroke. Detecting the changes of activated microglia helps us to diagnose the disease and evaluate the therapeutic effect. In addition, the ischemic stroke model is the most common TSPO-PET evaluation tool. The imaging efficacy of ^{18}F-D_2-LW223 was evaluated in the ischemic stroke model, and the expression of TSPO and iBa1 in the ipsilateral was detected by double immunofluorescence staining. Finally, longitudinal ^{18}F-D_2-LW223 PET imaging was performed to observe the changes in neuroinflammation in the ischemic stroke model. ***Materials and Methods:*** An ischemic stroke model was established in Sprague-Dawley (SD) rats by stereotaxically injecting Endothelin-1 near the middle cerebral artery. On day 10 post-modeling, dynamic ^{18}F-D_2-LW223 PET imaging was performed for 60 minutes ($n = 3$). Immunofluorescence staining was used to compare TSPO expression in the ischemic and contralateral hemispheres. On day 11, the same rats underwent ^{18}F-D_2-LW223 PET imaging after pretreatment with PK11195 (5 mg/kg) to assess tracer specificity. Time-activity curves (TACs) from baseline and blocking experiments were compared. Longitudinal static PET scans were conducted at 1.5, 3, 7, 10, 14, 20, and 30 days post-modeling ($n = 6$). The standardized uptake value (SUV) ratio between the infarcted and contralateral regions was calculated to track TSPO expression changes. ***Results:*** ^{18}F-D_2-LW223 reached peak uptake (SUV ≈ 1.20) in the ischemic brain region approximately 5 minutes post-injection, followed by gradual washout. After PK11195 blockade, tracer uptake in the ischemic region was significantly reduced compared to baseline (AUC40-60 min: 25.75 ± 0.70 vs. 10.67 ± 0.57, $P < 0.0001$). Double immunofluorescence confirmed elevated TSPO and Iba1

expression in the infarcted region. Longitudinal imaging revealed increased ^{18}F-D$_2$-LW223 uptake in the lesion as early as 1.5 days post-modeling, peaking around day 10, and gradually declining to the lowest level by day 30. ***Conclusion:*** This work further validates the imaging efficacy of ^{18}F-D$_2$-LW223 and enables the visualization of the changes in the expression of TSPO up-regulated by pathological changes, which enhances our understanding of the dynamic changes of neuroinflammation in cerebral ischemia and provides a reliable reference for the study of neuroinflammation targets related to cerebral ischemia.

EP-0027

Partial volume characterization in mouse cardiac PET imaging using 3D-printed radioactive partition-less left ventricular phantoms

O. Sarrhini, *J.-F. Beaudoin, T. Galarneau, R. Lecomte;*
Université de Sherbrooke, Sherbrooke, QC, CANADA.

Aim/Introduction: Small animal positron emission tomography (PET) can provide non-invasive in-vivo measurements of radiotracer metabolic rates in tissues. Due to limited spatial resolution, partial volume effect (PVE) impedes the extraction of accurate time-activity curves (TACs) from PET images of the mouse heart. TAC modelling typically involves two spillover factors from the blood cavity to myocardium (SFB→$_T$) and from myocardium to cavity (SFT→B), in addition to the recovery coefficients of the myocardium (RC$_T$) and cavity (RC$_B$). This study's purpose was to assess PVE in mouse cardiac PET using resin-based 3D-printed partition-less phantoms of the mouse left ventricle (LV) and to evaluate the accuracy of ^{18}F-FDG kinetic rates determined from the corrected TACs. ***Materials and Methods:*** The plasma kinetic model [1] was used as ground truth (GT) for the input function (PTAC). Model parameters were set to reproduce the plasma activity of typical mouse cardiac PET scans. The FDG model output was used as GT for the myocardial TAC (TTAC). To provide a realistic geometry of the mouse LV, The myocardium was outlined from the short-axis MRI scan of a mouse LV between end-diastole and end-systole using 3DSlicer. The segmentation data were converted to Standard Triangle Language and exported to a CAD software. Seventy LV phantoms were printed using Liqcreate Composite-X resin uniformly mixed with ^{18}F-FDG. Radioactivity in benzyl-alcohol (to avoid air bubbles and evaporation) was added in the cavity of each phantom to reproduce the entire GT PTAC and TTAC curves. PET data, acquired on LabPET-II/Mouse scanner [2], were corrected for randoms, decay, scatter and attenuation. LV phantom myocardium and cavity were segmented from CT images and the corresponding activity was calculated. Geometric Transfer Matrix was applied for PVE correction and the ^{18}F-FDG kinetic constants were compared to the GT values. ***Results:*** The cavity diameter and myocardium thickness of the printed LV phantoms were 2.55±0.08 mm and 1.41±0.04 mm. RC$_T$ and RC$_B$ values were 0.56±0.03 and 0.53±0.04, and SFT→B and SFB→T values were 0.35±0.04 and 0.09±0.01, respectively. The errors of the measured ^{18}F-FDG kinetic constants K_1, k_2, k_3 and K_i were 0.11%, 9.38%, 4.13% and 2.71%, respectively, relative to the GT. ***Conclusion:*** Recovery coefficients and spillover factors of realistic mouse LV phantoms were measured, to enable accurate PVE correction and estimation of kinetic rates in mouse cardiac PET imaging. ***References:*** [1] Feng et al. Int J Biomed Comput, 32:95-110, 1993 [2] Gaudin et al. Phys Med Biol 66(6) :065019, 2021.

EP-0028

Evaluation of cardiotoxicity induced by doxorubicin using a FABP3-selective tracer, [^{18}F]LUF

J. Toyohara[1], *T. Komoda*[2], *T. Tago*[1], *M. Ito*[2], *H. Yoshino*[2];
[1]*Tokyo Metropolitan Institute for Geriatrics and Gerontology, Itabashi-ku, Tokyo, JAPAN,* [2]*Shiratori Pharmaceuticals Co., Ltd., Narashino, Chiba, JAPAN.*

Aim/Introduction: The heart-derived fatty acid-binding protein (FABP3) plays a crucial role in the intracellular transport of fatty acids and is extensively expressed in cardiac and skeletal muscles. It has been previously reported that the ^{18}F-labelled FABP3 selective small organic compound, [^{18}F]LUF, facilitates visualization of the myocardium with high-contrast images when compared to background tissues such as the lungs and liver [1]. Cardiotoxicity is a notable adverse effect observed in cancer survivors who have undergone anticancer drug therapy. There is documented evidence of elevated FABP3 levels in the bloodstream in models of drug-induced myocardial injury [2]. Hence, murine models with doxorubicin-induced heart failure were utilized as a framework for drug-induced heart failure to explore the potential of assessing cardiotoxicity with [^{18}F]LUF. ***Materials and Methods:*** Male C57BL6/J mice, aged eight weeks, served as models for acute heart failure through the intraperitoneal administration of doxorubicin at a single dose of 20 mg/kg, and as models for chronic heart failure through a regimen of 5 mg/kg administered once weekly over a four-week period. One week following the termination of doxorubicin administration, [^{18}F]LUF was administered intravenously via the tail vein without anesthesia. Sixty minutes post-administration, the subjects were euthanized through cervical dislocation. Subsequently, cardiac tissues were excised promptly, and both radioactivity and wet weight were quantified using an autogamma counter. Radioactivity quantification was achieved by employing standardized uptake values. ***Results:*** In the acute heart failure model, the mortality rate among mice was 50%. There were no observed differences in body weight, heart weight, or the heart/body weight ratio. The myocardial accumulation of [^{18}F]LUF was notably reduced in the acute heart failure model compared to the healthy control group. Within the chronic heart failure model, none of the mice succumbed. The chronic doxorubicin administration group exhibited significant reductions in body weight and heart weight, though the heart/body weight ratio remained unchanged. Meanwhile, myocardial [^{18}F]LUF accumulation in the chronic heart failure model demonstrated a tendency towards reduction compared to the healthy control group, yet without reaching statistical significance. ***Conclusion:*** The FABP3 imaging agent, [^{18}F]LUF, has demonstrated the capability to detect doxorubicin-induced acute myocardial injury. ***References:*** [1] Toyohara et al., EJNMMI Res. (2024) 14:107; [2] Pan et al., Exp Ther Med. (2022) 24:712.

EP-03

e-Poster Area

A: Preclinical and Translational Studies -> A1 Medical Preclinical -> A13 Preclinical Oncology

EP-0029

In Vitro evaluation of a ^{64}Cu-labeled PSMA-terpyridine conjugate as a potential radiotheranostic agent for prostate cancer

H. Talebian, *S. Ait-Mohand, P. Mercy Ignatius Arokia Doss, L. Sanche, B. Guerin;*
'Université de Sherbrooke, Sherbrooke, QC, CANADA.

Aim/Introduction: Prostate cancer (PCa), particularly in its metastatic form (mPCa), remains a major health challenge, with significant limitations in current diagnostic and therapeutic approaches. Our team previously developed a radiotheranostic (RT) agent, ^{64}Cu-NOTA-terpyridine (^{64}Cu-NOTA-TP), which demonstrated strong selectivity and cytotoxicity against cancer cells [1]. This study aims to enhance the agent's effectiveness and specificity for mPCa by conjugating it to a prostate-specific membrane antigen (PSMA) ligand, resulting in a novel compound:

^{64}Cu-NOTA-TP-PSMA. We compare its in vitro performance to that of its monomeric counterparts; ^{64}Cu-NOTA-TP and ^{64}Cu-NOTA-PSMA. ***Materials and Methods:*** NOTA-TP-PSMA was synthesised via combined solid- and solution-phase methods. Radiolabelling with ^{64}Cu followed established protocols [1]. Binding affinity, cellular uptake, internalisation, efflux, cytotoxicity, and nuclear localisation were assessed in PSMA-positive LNCaP Prostate cancer cells and normal HEK-293 cells. ***Results:*** NOTA-TP-PSMA synthesis achieved 30-40% overall yield, with radiolabelling efficiencies exceeding 99%. The conjugate demonstrated strong PSMA binding (IC_{50} = 39 ± 17 nM), comparable to NOTA-PSMA (34 ± 13 nM). In LNCaP cells, ^{64}Cu-NOTA-TP-PSMA showed significantly higher uptake (63 ± 9%) and internalisation (45 ± 7%) compared to both ^{64}Cu-NOTA-TP (40 ± 8%; 36 ± 9%) and ^{64}Cu-NOTA-PSMA (23 ± 1%; 16 ± 1%) at 24 hours. Retention was also improved (52 ± 9%), higher than monomers (~39%) after 24 hours. In contrast, HEK-293 cells displayed minimal uptake and retention, confirming specificity. Subcellular analysis revealed superior nuclear localisation of ^{64}Cu-NOTA-TP-PSMA in LNCaP cells (7.0 ± 2.0%) versus^{64}Cu-NOTA-TP (0.6 ± 0.2%) and ^{64}Cu-NOTA-PSMA (0.4 ± 0.3%), with negligible nuclear accumulation in HEK-293 cells (<1%) further emphasizes the superior selectivity of the conjugate relative to the control. Cytotoxicity assays confirmed potent, selective activity of ^{64}Cu-NOTA-TP-PSMA in LNCaP cells (IC_{50} = 10 ± 2.4, 24.3 ± 5.9, and 24.1 ± 8.5 nM at 24, 48, and 72 h) with minimal effects on HEK-293 (IC_{50} >250 nM). While monomer controls showed lower Cytotoxicity at respective timepoints (^{64}Cu-NOTA-TP:52.6 ± 3.5 nM, 46.7 ± 4.2 nM, 27.6 ± 5.4 nM and ^{64}Cu-NOTA-PSMA: 145.3 ± 7.2 nM, 102.8 ± 16.1 nM, and 93.4 ± 13.9 nM), [NatCu]Cu-NOTA-TP-PSMA and cisplatin showed poor potency respectively (>16,000 nM), and (>22,000 nM) in LNCaP. ***Conclusion:*** This study highlights the potential of ^{64}Cu-NOTA-TP-PSMA as a novel RT agent that may enhance both the diagnosis and treatment of PCa. Future in vivo studies will assess its clinical utility for tumour imaging and radiotherapy. ***References:*** Khosravifarsani et al. Nanomaterials 2021, 11, 2154.

EP-0030

Dual-locked targeted alpha-emitter enhanced tumor immunotherapy via Diels-Alder reaction-based self-immolative molecular cage strategy

F. Yu[1], *M. Yang*[1], *Y. Feng*[2], *K. Shi*[3], *T. Watabe*[4], *K. Kabayama*[4], *K. Fukase*[4];
[1]*Department of Nuclear Medicine, Shanghai Tenth People's Hospital and Institute of Nuclear Medicine, School of Medicine, Tongji University, Shanghai, CHINA,* [2]*Department of Radiology, Duke University Medical Center, Durham, NC, UNITED STATES OF AMERICA,* [3]*Department of Nuclear Medicine, Inselspital, University of Bern, Bern, SWITZERLAND,* [4]*Institute for Radiation Sciences, Osaka University, Osaka, JAPAN.*

Aim/Introduction: Targeted alpha therapy (TAT) has emerged as a promising strategy for cancer treatment by selectively delivering high linear energy transfer (LET) alpha-emitters to tumor cells while minimizing off-target toxicity. However, the clinical translation of alpha-emitters, particularly radium-223 (^{223}Ra), remains challenging due to inefficient targeted delivery and uncontrolled release of recoil daughter products, leading to systemic toxicity. ***Materials and Methods:*** A pretargeted dual-delivery system was constructed using hyaluronic acid nanohydrogels. Platinum^{IV} (Pt^{IV}) was loaded into azide-modified HNPs (HAQ@HNPs), while ^{223}Ra was encapsulated in TCO-modified HNPs (^{223}Ra@HNPs). Sequential injection enabled in vivo inverse electron-demand Diels-Alder (IEDDA) bioorthogonal activation at tumor sites, triggering network collapse and co-release of payloads. Tumor redox status, immunogenic cell death (ICD) induction, and immune infiltration were assessed via flow cytometry, immunohistochemistry, and ROS assays. Antitumor efficacy, with or without PD-L1 blockade, was evaluated in mouse models through tumor growth, metastasis, and survival monitoring. ***Results:*** This study established a dual-lock targeted strategy to ensure that ^{223}Ra remained inactive during circulation and was selectively activated within the tumor microenvironment. The first lock leveraged the biotin-avidin interaction to promote rapid and specific accumulation of ^{223}Ra and Pt^{IV} at tumor sites, taking advantage of the high biotin receptor expression on cancer cells. The second lock incorporated a tetrazine moiety into the ^{223}Ra-loaded nanocarrier, enabling a tumor-specific IEDDA reaction with dienophile-modified Pt^{IV} carriers. Upon activation, a self-immolative cascade was initiated, leading to rapid and controlled co-release of both agents. This precise pretargeting and release mechanism ensured high tumor specificity while minimizing off-target exposure. The synergistic combination of TAT and chemotherapy disrupted tumor redox balance, induced ICD, and stimulated robust antitumor immune responses. Furthermore, co-administration with PD-L1 immune checkpoint blockade significantly amplified systemic immunity, resulting in strong inhibition of tumor progression and metastasis in vivo. ***Conclusion:*** These findings underscore the potential of dual-locked pretargeted strategies to advance TAT by improving therapeutic efficacy and addressing the critical challenge of radionuclide leakage, paving the way for next-generation precision-targeted radiopharmaceuticals.

EP-0031

Camouflaged Membrane-Bridged Radionuclide/Mn Single Atom Enzymes Target Lipid Metabolism Disruption to Evoke Antitumor Immunity

M. Yang[1], *F. Yu*[1], *K. Shi*[2], *T. Watabe*[3], *K. Kabayama*[3], *K. Fukase*[3], *Y. Feng*[4];
[1]*Department of Nuclear Medicine, Shanghai Tenth People's Hospital and Institute of Nuclear Medicine, School of Medicine, Tongji University, Shanghai, CHINA,* [2]*Department of Nuclear Medicine, Inselspital, University of Bern, Bern, SWITZERLAND,* [3]*Institute for Radiation Sciences, Osaka University, Osaka, JAPAN,* [4]*Department of Radiology, Duke University Medical Center, Durham, NC, UNITED STATES OF AMERICA.*

Aim/Introduction: Lipid metabolic reprogramming plays a critical role in modulating immune microenvironment and reshaping tumor plasticity and resistance to targeted radionuclide therapy (TRT). In this report, a radiopharmaceutical with multi-enzymatical catalysis activities is developed, wherein tumor cell membrane-coated manganese single-atom nanozymes (Mn/SAE@M) as supports deliver iodine-131 (^{131}I) to tumor. ***Materials and Methods:*** Mn/SAE in-situ grown in hollow mesoporous ZIF-8 nanoparticles firstly experienced coating with non-small cell lung cancer Lewis lung carcinoma (LLC) cell membranes and subsequent ^{131}I labeling using the Chloramine-T labeling method. Multi-enzymically catalytic activities were evaluated using standard colorimetric assays. Lipid metabolism disruption and ferroptosis induction were assessed through ROS detection, lipid peroxidation analysis, and ferroptosis-related marker expression in vitro and in vivo. Biodistribution, tumor targeting, and safety were examined in LLC tumor-bearing mice using SPECT/CT, ex vivo radioactivity quantification, and histological analysis. Activation of the cGAS-STING pathway and immune responses were also evaluated. ***Results:*** Upon efficient internalization mediated by coated tumor cell membrane, ^{131}I-Mn/SAE@M radiopharmaceuticals initiate abundant oxygen (O_2) release through catalase (CAT)-like catalysis, thereby mitigating hypoxic microenvironment. Especially they can assist TRT produce and enrich more reactive oxygen species (ROS) through oxidase (OXD)-like, peroxidase (POD)-like, and GSH oxidase (GSHOx)-like catalysis processes, thereby opposing immunosuppressive microenvironment and directing killing tumor. Importantly, ^{131}I-Mn/SAE@M allows TRT to activate cGAS-STING pathway, interfere with the lipid metabolic homeostasis of tumor cells and induce ferroptosis, which are unraveled to take responsibility for the potentiated anti-tumor immunity against LLC including primary and distant tumors. ***Conclusion:*** Such SAE-based radiopharmaceuticals provide a candidate platform to enhance TRT efficiency, and the proof-of-concept rationale of disrupting lipid metabolic homeostasis through multienzyme-mimicking cascade reactions also provides a general avenue to enhance TRT-based anti-tumor immunity.

EP-0032

Metabolic stability-dependent targeting of NTS_1R-tumors in mice, as exemplified by [^{99m}Tc]Tc-DT1 and its branched versions [^{99m}Tc]Tc-DT10 and [^{111}In]In-DT14D

P. Kanellopoulos[1], *T. Maina-Nock*[1], *B. A. Nock*[1], *E. P. Krenning*[2];
[1]*Molecular Radiopharmacy, INRaSTES, NCSR Demokritos, 15341 Athens, GREECE,* [2]*Cyclotron Rotterdam BV, Erasmus MC, 3015 CE Rotterdam, NETHERLANDS.*

Aim/Introduction: The neurotensin subtype 1 receptor (NTS_1R) has attracted much attention as a valid biomolecular target in nuclear medicine based on its expression in various human tumors, including pancreatic cancer. We have previously shown the rapid degradation of our prototype radiotracer [^{99m}Tc]Tc-DT1 (DT1, N_4-Gly-Arg-Arg-Pro-Tyr-Ile-Leu-OH) in peripheral mice blood by both angiotensin-converting enzyme (ACE) and neprilysin (NEP), compromising the uptake in pancreatic AsPC-1 xenografts. We herein introduce two lateral chain-decorated DT1 mimics, [^{99m}Tc]Tc-DT11 (DT11, [(MPBA-PEG4)Lys^7]DT1) and its [^{111}In]In-DOTA-$(\beta Ala)_3$-substituted version [^{111}In]In-DT14D. Their in vivo stability and biodistribution in AsPC-1 tumor-bearing mice was compared vs. [^{99m}Tc]Tc-DT1, without or during ACE/NEP-inhibition. ***Materials and Methods:*** The stability of [^{99m}Tc]Tc-DT11 and [^{111}In]In-DT14D was tested by RP-HPLC analysis of blood samples collected 5 min post-injection (pi) of radioligand in mice, divided in three groups: a) non-treated controls, b) treated with Entresto (receiving the drug per oral gavage 30 min in advance as a source of the potent NEP-inhibitor sacubitrilat - Entresto), and c) treated with Entresto and additionally co-injected with the ACE-inhibitor lisinopril (Entresto+Lis). Biodistribution was studied in SCID mice bearing AsPC-1 xenografts at 4 and 24 h pi, either in non-treated controls or in mice pre-treated with Entresto. ***Results:*** A significant increase of in vivo stability was achieved by [^{99m}Tc]Tc-DT11 (56.56±5.19% intact, n=3) and [^{111}In]In-DT14D (69.5±0.7% intact, n=3) vs. the [^{99m}Tc]Tc-DT1 reference (1.8±0.8% intact, n=4; $p<0.0001$) in the control animal groups, revealing the strong stabilizing effect of the lateral MPBA-PEG4 chain at Lys^7. Entresto further increased the stability of [^{99m}Tc]Tc-DT11 (77.0±3.3% intact, n=3; $p<0.01$); co-treatment with Lis had no additional statistically significant impact on either analog, as opposed to [^{99m}Tc]Tc-DT1, implying their resistance to ACE. Metabolic stability directly impacted targeting of the AsPC-1 tumors in the control groups compared with [^{99m}Tc]Tc-DT1. For example, [^{99m}Tc]Tc-DT11 (4.48±0.37%IA/g) and [^{111}In]In-DT14D (3.73±0.45%IA/g) achieved a notably higher tumor uptake vs. the reference (1.25±0.14%IA/g; $p<0.001$) at 4 h pi. Some further improvements in tumor values were obtained in the animals treated with Entresto alone, whereas [^{99m}Tc]Tc-DT1 required double Entresto+Lis treatment to maximize its uptake in the AsPC-1 tumors. ***Conclusion:*** This study has shown that attachment of a suitable pendant group to Lys^7 of NT(7-13) radioligands significantly increases in vivo stability and hence tumor uptake in mice, as opposed to unmodified [^{99m}Tc]Tc-DT1 prototype which rapidly degraded in circulation by both ACE and NEP. The lateral chain-modification approach seems promising for the applicability of NTS_1R-targeting peptide radioligands in the clinic.

EP-0034

The application of crown chelator in Ac-225 and Tb-161 PRRT

H. Yang[1,2,3], *L. Wharton*[1], *S. W. McNeil*[1,2], *C. Zhang*[4], *A. Ingham*[1], *C. Rodríguez-Rodríguez*[2], *H. Merkens*[4,2], *M. Van de Voorde*[5], *M. Ooms*[5], *F. Bénard*[4,2];
[1]*TRIUMF, Vancouver, BC, CANADA,* [2]*The University of British Columbia, Vancouver, BC, CANADA,* [3]*Simon Fraser University, Burnaby, BC, CANADA,* [4]*BC Cancer, Vancouver, BC, CANADA,* [5]*SCK CEN, Mol, BELGIUM.*

Aim/Introduction: Peptide Receptor Radionuclide Therapy (PRRT) agents with radiometals requires a chelator that can form a thermodynamically stable and kinetically inert complex with the metal ion. DOTA has been used as the standard chelator for the majority of radiometals, including [^{68}Ga]Ga^{3+}, [^{177}Lu]Lu^{3+}, and [^{225}Ac]Ac^{3+}. Its coordination efficiency of DOTA drops with large ions such as Ac^{3+}, resulting in low molar activity, and the labeling requires elevated temperature which may not be compatible with heat sensitive targeting vectors. We have been developing novel chelators based on larger macrocyclic backbones. The lead chelator 'crown' has shown fast and efficient labeling with Ac^{3+} and Tb^{3+} and good in vivo stability. In this report, we summarize our preclinical studies with [^{225}Ac]Ac/[^{161}Tb]Tb-crown-αMSH, peptides targeting melanocortin 1 receptor (MC1R), and [^{225}Ac]Ac/[^{161}Tb]Tb-crown-TATE, a peptide targeting somatostatin receptor 2 (SSTR2). ***Materials and Methods:*** Crown-αMSH and crown-TATE were synthesized using standard peptide synthesis methods. They were both labeled with [^{225}Ac]Ac^{3+} and [^{161}Tb]Tb^{3+} and the products were confirmed by radio-TLC and radio-HPLC. [^{225}Ac]Ac-crown-αMSH was injected in B16F10 murine melanoma tumour bearing mice. The biodistribution at 2 hours post injection was evaluated. Similarly, SPECT imaging and biodistribution of [^{161}Tb]Tb-crown-αMSH was assessed in the same time frame. Biodistribution of [^{225}Ac]Ac-crown-TATE was evaluated at 1, 4, 24, 48, and 120 hours post injection in AR42J murine pancreatic tumour bearing mouse. SPECT images with [^{161}Tb]Tb-crown-TATE were collected. ***Results:*** For all four radiopharmaceuticals evaluated, good tumour uptake and low background uptake were observed. For ^{161}Tb labeled compounds, SPECT images showed good contrast and resolution and match the ex vivo tissue distribution data. When the receptor density is low as in the case of MC1R, [^{225}Ac]Ac-crown-αMSH showed higher tumour uptake and higher tumour:kidney activity ratio compared to [^{225}Ac]Ac-DOTA-αMSH in B16F10 tumour bearing mice at 2 hour post injection due to improved molar activity. In the case of [^{225}Ac]Ac-crown-TATE, the uptake profile from 1 hour to 120 hours post injection in AR42J tumour bearing mice is comparable to [^{225}Ac]Ac-DOTA-TATE in the same tumour model. ***Conclusion:*** The crown chelator is effective in labeling radio-Tb or Ac, showing high labeling efficiency at room temperature. Preclinical work with αMSH and TATE peptide conjugates demonstrated when high molar activity is required, the use of crown chelator can be advantageous.

EP-0035

Development of FL-261 as a theranostic RDC vector for the diagnosis and treatment of c-MET overexpression cancers

J. Yang, *G. Jiang, J. Xia, J. Zhang, F. Liu;*
Full-Life Technologies, Shanghai, CHINA.

Aim/Introduction: Mesenchymal-epithelial transition factor (c-MET) is an important member in the receptor tyrosine kinase family that highly expressed and abnormally activated in most malignant tumors, making it an attractive target for radionuclide drug conjugate (RDC) based therapy. Abnormal expression of c-MET can induce tumor cell proliferation, suppress the apoptosis, and promote tumor cell migration, invasion and angiogenesis, and thus contributes to the occurrence, development and metastasis of tumor. Despite the clinical validation of the target by small molecule kinase inhibitors, EGFR/c-MET bispecific antibodies and antibody drug conjugates (ADCs), their efficacy is mostly observed in non-small cell lung cancer (NSCLC), compared to other indications with c-MET overexpression. With the aim of developing a novel c-MET targeting RDC vector for the diagnosis and treatment of c-MET overexpression cancers, we have applied our UniRDC™ platform technologies to discover FL-261. ***Materials and Methods:*** The binding affinity and selectivity of FL-261 against c-MET was tested by surface plasmon resonance (SPR) protein

binding assay. [^{68}Ga]Ga-FL-261 and [^{177}Lu]Lu-FL-261 were prepared and the radiochemical purity (RCP) of radiolabeled was determined by radio high-performance liquid chromatography (radio-HPLC). Furthermore, the in vivo imaging, ex vivo biodistribution or efficacy profiles of [^{68}Ga]Ga-FL-261 or [^{177}Lu]Lu-FL-261 were evaluated in c-MET overexpression xenograft mouse models. ***Results:*** FL-261 showed potent binding affinity against c-MET with an KD value of 7.5 nM, demonstrating over 400-fold selectivity to other proteins from the same family. FL-261 was successfully labeled with ^{68}Ga (95°C for 10 minutes) and ^{177}Lu (80°C for 30 minutes), achieving an RCP of over 95% respectively. Subsequently, after administration of [^{68}Ga]Ga-FL-261 in mice implanted with MKN45 xenografts, PET/CT images demonstrated intense tumor uptake which was significantly higher than that in normal organs at 3-hour post-dosing. Meanwhile, in vivo SPECT/CT imaging and ex vivo biodistribution studies were performed after administration of [^{177}Lu]Lu-FL-261 in c-MET overexpression xenograft models, demonstrating intense and durable tumor uptake from 1-hour to 120-hour post-dosing with fast clearance in normal organs. Importantly, in c-MET overexpression xenograft models, [^{177}Lu]Lu-FL-261 exhibited significant anti-tumor activity at different dose levels, resulting in marked tumor regression. No notable changes in body weight of mice were observed, suggesting a favorable safety profile of [^{177}Lu]Lu-FL-261 under the effective dose levels. ***Conclusion:*** In summary, [^{177}Lu]Lu-FL-261 demonstrated encouraging in vivo imaging feasibility, biodistribution profile and anti-tumor activity in c-MET overexpression xenograft models. Our data supports further development of FL-261 as a promising RDC vector to detect and treat c-MET overexpression cancers.

EP-0036

Breaking New Frontiers in In Vivo Molecular Imaging: Multiplex Cancer Fingerprinting on MRI using 3-[^{19}F] FDGal

D. Cohen, *B. Subramani, L. Saad, M. Fisler, L. Avram, T. Harris, H. Allouche-Arnon, A. Bar-Shir;*
Weizmann Institute of Science, Rehovot, ISRAEL.

Aim/Introduction: While 2-[^{18}F]fluorodeoxy-glucose (2FDG) efficiently traces cancers that follow the Warburg effect, there remains an unmet need in molecular imaging approaches to map cancers that do not adhere to this metabolic scheme. We recently introduced Fluorine Metabolic Imaging (FMI) with 3-[^{19}F]fluorodeoxy-galactose (3FDGal), a novel method that takes advantage of the multiplexing capabilities of ^{19}F-MRI and the unique cellular metabolism of 3FDGal. This technique resolves distinct ^{19}F-MR signals emitted by 3FDGal and its two metabolites: 3-[^{19}F]fluorodeoxy-galactitol (3FDGtol) and 3-[^{19}F] fluorodeoxy-galactonic acid (3FDGalA). This way, we provide a platform for non-invasive, whole-body, concurrent mapping of AKR1B1 and ALDH1A1, the enzymes we identified as mediating the probe's redox metabolism. As these enzymes are implicated in cancer reprogramming, the current work aims to evaluate the role of 3FDGal-FMI in cancer imaging using xenograft mice bearing tumors derived from cell lines reported to exhibit low 2FDG-avidity. ***Materials and Methods:*** In vitro, three human cancer cell lines with low 2FDG-avidity (A549, LNCaP, ACHN) were incubated with 3FDGal (6×10^6 cells, 5 mM probe, 4 hours). ^{19}F-NMR spectra of the intracellular contents were obtained using a Bruker 9.4T NMR spectrometer. In vivo, tumor-bearing nude athymic mice underwent imaging under anesthesia following intravenous injection of 3FDGal (0.6 g/kg) on a Bruker 9.4T MRI system (25mm ^{1}H/^{19}F RF volume coil). Starting 30 minutes post-injection, 3D-FMI maps were acquired repeatedly to concurrently map the distribution of 3FDGal, 3FDGtol, and 3FDGalA, using multi-chemical shift selective imaging. ***Results:*** Following in vitro incubation (n=3 per cell line), each cell line exhibited a distinct ^{19}F-NMR "fingerprint", characterized by specific signal-to-noise ratio (SNR) values for 3FDGalA at -205 ppm and for 3FDGtol at -210 ppm: 71±2 and 229±8 in A549 cells, undetectable and undetectable in LNCaP cells, and 21±4 and 155±26 in ACHN cells. SNR values for 3FDGalA and 3FDGtol correlated with cellular expression of ALDH1A1 and AKR1B1, respectively. In vivo ^{19}F-MRI of xenograft mice bearing subcutaneous tumors derived from the three cell lines demonstrated real-time tumor-localized generation of the metabolites in levels mirroring the in vitro fingerprints of the lines, i.e., A549-, LNCaP-, and ACHN-derived tumors exhibited 3FDGalA^{high}/3FDGtol^{high}, 3FDGalA^{neg}/3FDGtol^{neg}, and 3FDGalA^{low}/3FDGtol^{high} phenotypes on FMI. ***Conclusion:*** 3FDGal-FMI offers a groundbreaking glycolysis-independent metabolic imaging approach that enables multiplex in vivo fingerprinting of cancers at the molecular level. By simultaneously reporting on ALDH1A1 and AKR1B1 activity in tumors, 3FDGal provides a promising tracer for imaging some non-2FDG avid tumors, addressing a critical gap in clinical oncological imaging.

EP-0037

Multimodal Imaging for Response Assessment to Combined anti-PD-L1/anti-CTLA-4 Immunotherapy in a Murine Melanoma Model: A Comparative Evaluation of [^{18}F]FDG-PET/CT, MRI and CEUS

M. J. Antons[1], *F. Herr*[1], *M. M. Heimer*[1], *H. Hirner-Eppeneder*[1], *R. Oos*[2], *G. Palumbo*[2], *J. Stueckl*[1], *S. Kloiber*[1], *A. Cimic*[1], *L. V. Blume*[1], *S. Lindner*[2], *D. Clevert*[1], *M. Brendel*[2,3], *J. Ricke*[1], *R. A. Werner*[2,4], *C. C. Cyran*[1];
[1]*Department of Radiology, LMU University Hospital, LMU Munich, Munich, GERMANY,* [2]*Department of Nuclear Medicine, LMU University Hospital, LMU Munich, Munich, GERMANY,* [3]*Munich Cluster for Systems Neurology (SyNergy), University of Munich, Munich, GERMANY,* [4]*The Russell H. Morgan Department of Radiology and Radiological Sciences, Johns Hopkins School of Medicine, Baltimore, MD, UNITED STATES OF AMERICA.*

Aim/Introduction: Early and precise assessment of immunotherapy response is essential for optimizing therapeutic strategies in malignant melanoma. While immune checkpoint inhibitors have demonstrated considerable efficacy, interindividual variability necessitates robust imaging biomarkers for response evaluation. This study aimed to compare the diagnostic performance of three advanced imaging modalities—[^{18}F]FDG-PET/CT, multiparametric MRI and contrast-enhanced ultrasound (CEUS)—in monitoring the effects of combined anti-PD-L1/anti-CTLA-4 immunotherapy in a murine melanoma model with immunohistochemical validation. ***Materials and Methods:*** A total of n=88 female C57BL/6 mice were inoculated subcutaneously with B16-F10 melanoma cells into the left abdominal flank and randomized into therapy and control groups. The therapy group received intraperitoneal injections of anti-PD-L1 and anti-CTLA-4 antibodies, while the control group received sham treatment. Imaging assessments included [^{18}F]FDG-PET/CT (baseline, follow-up 1 (FU-1; day 13), follow-up 2 (FU-2; day 19; n=40)), multiparametric MRI (baseline, FU-1; n=28) and CEUS (baseline, FU-1; n=20). Target parameters for PET/CT were MTV and SUVmax, for MRI apparent diffusion coefficient (ADC), intravoxel incoherent motion (IVIM) and dynamic contrast-enhanced MRI (DCE-MRI) parameters and for CEUS tumour perfusion parameters and VEGFR2-targeted microbubble binding. Tumour allografts were harvested for ex vivo immunohistochemical validation (CD8, Ki-67, TUNEL, CD31). ***Results:*** At follow-up, [^{18}F]FDG-PET/CT revealed significantly lower MTV and SUVmax in the therapy group compared to controls (FU-1: MTV: p=0.004; FU-2: MTV: p=0.008, SUVmax: p=0.0003). MRI demonstrated a significantly lower ADC in the therapy group at follow-up (p = 0.002), while IVIM and DCE-MRI parameters did not yield significant differences. At follow-up, CEUS showed significantly greater reduction in tumour perfusion (WiAUC, p=0.0152) and a significantly lower number of VEGFR2-targeted microbubbles in the therapy than in the control group (SI8min: p=0.003; SI10min: p=0.0019), indicating reduced

angiogenesis. Immunohistochemistry confirmed significant anti-tumour effects in the therapy group, with higher apoptosis rates (FU-1: p=0.012; FU-2: p=0.001), more CD8-positive T-cells (FU-2: p=0.003), lower tumour cell proliferation (FU-1: p=0.012; FU-2: p=0.012) and lower microvascular density (FU-1: CD31: p<0.001). ***Conclusion:*** This multimodal imaging study highlights the complementary strengths of PET/CT, MRI, and CEUS in assessing immunotherapy response in malignant melanoma. [^{18}F]FDG-PET/CT provided early metabolic response parameters, MRI parameters reflected cellular and microstructural tumour alterations and CEUS detected vascular remodelling. The strong correlation between imaging biomarkers and ex vivo histopathology underscores the translational relevance of these imaging modalities for monitoring immune checkpoint inhibition. Our findings support the integration of PET/CT with MRI and CEUS for a comprehensive, non-invasive characterization of immunotherapy response in preclinical and potentially clinical settings.

EP-0038

Preclinical Comparison of 68 Ga-DOTA-LM3 and 68Ga-DOTATATE for SSTR2-Targeted Imaging in C6 Glioma Model

M. Pirdadeh[1], *M. Nasiri*[2], *R. Nami*[1], *S. Mazidi Sharaf Abadi*[1], *A. Gravand*[1], *R. Salehi*[1], *M. Ghapanvari*[1], *M. Samizadeh*[1], *H. Vosoughi*[3], *E. Jafari*[4], *M. Dehghani*[1], *S. Jamalabadi*[1], *M. Kashani*[1], *M. Safari*[1], *A. Abolhosseini Shahrnoy*[1];
[1]*Pars Isotope Company, Tehran, IRAN, ISLAMIC REPUBLIC OF,* [2]*Department of Cellular and Molecular Biology, School of Biology, Damghan University, Damghan, IRAN, ISLAMIC REPUBLIC OF,* [3]*Tehran University of Medical Science, Tehran, IRAN, ISLAMIC REPUBLIC OF,* [4]*Bushehr University of Medical Science, Bushehr, IRAN, ISLAMIC REPUBLIC OF.*

Aim/Introduction: Somatostatin receptor subtype 2 (SSTR2) is overexpressed in several Neuroendocrine tumors, including gliomas, making it a valuable target for molecular imaging. ^{68}Ga-DOTATATE, a somatostatin receptor agonist, is commonly used for PET imaging; however, recent studies suggest that antagonists like ^{68}Ga-DOTA-LM3 may offer enhanced tumor uptake and contrast. This study compares the uptake, biodistribution and imaging performance of ^{68}Ga-DOTA-LM3 versus ^{68}Ga-DOTATATE in C6 Glioma cell line and C6 rat glioma model. ***Materials and Methods:*** C6 glioma cells were cultured in DMEM-F12 culture media and subcutaneously implanted into right shoulder of Sprague-Dawley rats. PET/CT imaging was performed 60 minutes post-injection of either ^{68}Ga-DOTATATE or ^{68}Ga-DOTA-LM3 in the same animals on separate days. SUVmax was measured in tumors and major organs to evaluate tracer uptake, tumor-to-background ratios and normal biodistributions. ***Results:*** The radiolabeling of peptides was achieved at molar activities of up to 20 MBq/nmol at ≥ 99% radiochemical purity. "The cellular uptake and internalization fraction of ^{68}Ga-DOTA-LM3 were 1±0.3% and 10±4.1%, respectively, whereas for ^{68}Ga-DOTATATE were 0.8±0.2% and 90±8.4%, respectively. Incubation times between 1 and 4 hours had no effect on the uptake or internalization of either radiotracer. Furthermore, blocking assays confirmed the high specificity of binding for both radiotracers.^{68}Ga-DOTA-LM3 demonstrated significantly higher uptake in C6 primary tumors (7.8±1.3 vs 5.13±1.14 %ID/g respectively) and metastases including liver (18.28 vs 10.96 %ID/g) and Lung (5.13 vs 3.84 %ID/g) compared to ^{68}Ga-DOTATATE at 60 minutes post-injection ($p < 0.05$). Kidney -to- Tumor ratios (46.8±5.12 vs 68.3±4.54) were also notably improved with DOTA-LM3. Although both radiotracers demonstrated a comparable biodistribution profile, ^{68}Ga-DOTA-LM3 showed a notably faster renal clearance within the first 4 hours post-injection. Nevertheless, increased intestinal and hepatic uptake was observed, likely attributed to its hepatobiliary excretion pathway. ***Conclusion:*** Our results preliminary demonstrated ^{68}Ga-DOTA-LM3 outperformed ^{68}Ga-DOTATATE in terms of tumor uptake and imaging contrast at 1-hour post-injection. ***References:*** Baum RP, Zhang J, Schuchardt C, Müller D, Mäcke H. First-in-Humans Study of the SSTR Antagonist ^{177}Lu-DOTA-LM3 for Peptide Receptor Radionuclide Therapy in Patients with Metastatic Neuroendocrine Neoplasms: Dosimetry, Safety, and Efficacy. J Nucl Med. 2021 Nov;62(11):1571-1581.

EP-0039

Multi - dimensional Transcriptomic Integration Identifies Molecular Markers for Predicting Radioactive Iodine - Refractory Thyroid Cancer Progression and Novel Targeted Therapies

J. Quan, *G. Zhu;*
First Affiliated Hospital of Kunming Medical University, Kunming, CHINA.

Aim/Introduction: Papillary thyroid carcinoma (PTC) dedifferentiation is intricately linked to radioiodine resistance (RAIR), yet the molecular drivers of its invasive progression and stage-specific biomarkers remain elusive. While genetic alterations like BRAF V600E, TERT promoter mutations, and RET rearrangements inhibit sodium/iodide symporter (NIS) function via the MAPK/PI3K pathway, multi-factor interactions complicate understanding of RAIR-associated malignant transformation. Our prior retrospective analysis of 127 radioiodine-refractory and 612 non-refractory patients, all treated with thyroidectomy and 131I therapy, revealed that primary tumor invasion, distant metastasis, ≥3 131I treatments, and pre-treatment ps-Tg ≥20 ng/ml were key risk factors for RAIR-DTC. This study aims to map the molecular evolution of PTC from early to advanced RAIR-DTC using multi-omics integration, identify cross-stage biomarkers for invasion and RAIR, and advance precision nuclear medicine by addressing tumor heterogeneity and enabling targeted radionuclide therapies. ***Materials and Methods:*** Through Transwell assays, the IHH4 cell line, which exhibits high invasiveness and low iodine uptake, was screened as the RAIR model cell line from three PTC cell lines (BCPAP, IHH4, and TPC-1). RNA-Seq data and the GSE27155 dataset were integrated to screen for differentially expressed genes ($|\log2FC| \geq 1.5$, padj<0.01). Candidate genes were identified through subtype cross-analysis, GO/KEGG functional enrichment, and literature mining. A clinical validation cohort (n = 19) was grouped according to AJCC staging and iodine uptake status. Immunohistochemistry combined with a double-blind H-score system (with a high-expression threshold of >100) was used to evaluate gene expression, and Spearman's rank correlation test and Cox regression analysis were performed to analyze the correlation between gene expression and malignant phenotypes. ***Results:*** IHH4 cells show a markedly malignant phenotype with robust migration capacity and low iodine-131 uptake.RNA - seq analysis reveals that the intersection genes highly expressed in both IHH4 cells and RET/PTC tissues are significantly enriched in key pathways like cell migration, epithelial - mesenchymal transition (EMT), anti - apoptosis, and proliferation, while the iodine - metabolism pathway is less enriched.The expression of core genes TFF2, PCSK1, and IER3 increases stepwise with clinical progression, mirroring the trend of malignant progression. ***Conclusion:*** This study has mapped the dynamic molecular landscape of PTC malignant transformation and established TFF2/PCSK1/IER3 as a combined biomarker for cross-stage prediction of RAIR. These findings provide a theoretical basis for optimizing the identification of high-risk populations with RAIR and developing precise nuclear medicine treatment strategies.

EP-0041

Understanding the Impact of Lung Cancer Cell-of-Origin and the Immune Cell Composition on Tumour Metabolic Heterogeneity with RadioFlow

I. Caldera-Quevedo[1], *C. Vraka*[1,2], *D. Solovyev*[1], *G. Brown*[1], *F. Edgar*[1], *R. Bielik*[1], *D. Y. Lewis*[1];
[1]*Cancer Research UK Scotland Insititute, Glasgow, UNITED KINGDOM,* [2]*Medical University of Vienna, Vienna, AUSTRIA.*

Aim/Introduction: Lung adenocarcinoma tumours have been described as metabolically heterogenous, as it has been observed with 2-deoxy-2-[^{18}F]Fluoro-D-glucose ([^{18}F]FDG) and [1-^{11}C] Acetate positron emission tomography/magnetic resonance imaging (PET/MRI) scans. This diversity arises from factors like the tumour cell-of-origin or the immune cell infiltration. This project aims to elucidate the interaction between the tumour-initiating cell and the tumour immune cell infiltration. To understand their contribution to lung cancer metabolic heterogeneity, we will analyse [^{18}F]FDG single cell uptake in tumour lesions. ***Materials and Methods:*** We developed lung tumour models by intranasally inducing LSL-Kras$^{G12D/+}$ p53$^{fl/fl}$ mice using Ad5-mSPC-Cre or Ad5-CC10-Cre viral vectors, which are only expressed in lung alveolar type 2 and club cells, respectively. These two mouse models were intravenously injected with 15MBq of [^{18}F]FDG and 250MBq of [1-^{11}C]Acetate for metabolic characterisation both in vivo using PET/MRI and ex vivo using Dual-Isotope Tracking (DIOPTRA). To elucidate [^{18}F]FDG uptake at a single-cell level, ~250 MBq [^{18}F]FDG was applied followed by an ex-vivo PET/MRI scan of the tumour lesions for absolute quantification, and radio-flowcytometry sorting (RadioFlow) of different immune cell populations and tumour cells. [^{18}F]FDG uptake in the sorted cell fractions was measured in a γ-counter and results were normalised to the sorted number of cells. ***Results:*** [^{18}F]FDG PET imaging and DIOPTRA data revealed a higher [^{18}F]FDG uptake in CC10 tumours while SPC present both [^{18}F]FDG-avid and [1-^{11}C]Acetate-avid lesions. Metabolomic and transcriptomic analysis revealed a higher glycolytic activity in CC10 tumours. Preliminary RadioFlow results show a significantly higher CD45 cell infiltration in SPC tumours than in CC10 tumours, neutrophiles being the most abundant cell types in both tumour types of high glycolytic lesions ([^{18}F] FDG SUVmax>3.5). Our data indicated that the [^{18}F]FDG PET signal mainly derives from immune cells in both tumour types (CC10: 91.7% ± 3.9%; SPC: 94.8% ± 3.5%) while [^{18}F]FDG uptake in tumour cells is significantly lower. Preliminary data showed that [^{18}F]FDG PET signal is driven by both neutrophiles and dendritic cells in both SPC and CC10 tumours. RNA has been isolated for each one of the sorted populations for further analysis. ***Conclusion:*** Distinct metabolic patterns in SPC- and CC10-derived tumours highlight the role of the tumour-initiating cell lineage in tumour determining metabolism. Moreover, the dominant [^{18}F]FDG uptake by immune cells challenges the conventional assumption that tumour cells drive PET signal. ***References:*** Chen, Z., et al. Nat Rev Cancer. 14(8), 535-546 (2014). Vraka C., et al. J Nucl Med. 66(2), 215-222 (2025).

EP-0042

Investigation of Innovative ^{68}Ga-Labeled σ_2 Receptor-Targeted Proliferation Probes

X. Cai*, Y. Jiajun, Y. Kangxia, Y. Weidong, K. Fei, W. Jing;*
Air Force Medical University, Xi'an, CHINA.

Aim/Introduction: The σ_2 receptor is highly expressed in various tumors and serves as an excellent marker for tumor proliferation imaging. However, current probes suffer from low specificity, high lipophilicity, and inconvenient labeling. Based on previous research and a structural optimization strategy for σ_2 receptor probes containing conjugated structures, this study aims to develop a series of ^{68}Ga-labeled σ_2 receptor probes, ^{68}Ga-DOTA-SIGMA, to address these issues. Through in vivo and in vitro biological evaluations, the study seeks to identify the probe structure with optimal imaging performance, providing molecular imaging data for the structural optimization of σ_2 receptor probes with conjugated structures. ***Materials and Methods:*** Building on previous research on σ_2 receptor probes with conjugated structures, we modified the probes with a DOTA group using a conjugation design approach and adjusted their lipophilicity. Utilize molecular docking technology to conduct virtual docking of the developed probe with the σ_2 receptor to evaluate its binding mechanism and affinity. The labeling of ^{68}Ga was executed utilizing conventional techniques, with the assessment of labeling efficiency, radiochemical purity, and stability conducted. Subsequently, perform cell uptake and inhibition experiments to assess the impact of the probe on glioma cells (C6, F98, and U87). Micro-PET imaging and in vivo distribution experiments were performed in glioblastoma-bearing mice to select the probe with the best imaging performance. ***Results:*** Molecular docking analysis showed that all three designed probes have strong binding affinity to σ_2 receptors. ^{68}Ga labeling was performed using conventional metal labeling methods, with an uncorrected labeling efficiency greater than 40% and radiochemical purity greater than 98% after C18 solid-phase purification. The ^{68}Ga-DOTA-SIGMA probes exhibited a radiochemical purity of over 98% after 2 hours in saline. The probes showed high uptake and high specificity in all three types of glioma cells (C6, F98, and U87). Micro-PET imaging in glioblastoma-bearing mice revealed that all three probes yielded distinct tumor visualization, with optimal performance noted in C6 tumor-bearing mice.The in vivo biodistribution investigation in C6 tumor-bearing mice demonstrated that ^{68}Ga-DOTA-SIGMA-3 exhibited a tumor absorption of 1.98 ± 0.16 % ID/g at 30 minutes, accompanied by a tumor-to-muscle ratio of 3.67. In comparison to earlier documented ^{18}F- or ^{99m}Tc-labeled probes, hepatic and intestinal uptake were markedly diminished. ***Conclusion:*** The modification of σ_2 receptor probes with DOTA groups yields extremely hydrophilic ^{68}Ga-labeled proliferation probes appropriate for glioblastoma imaging. Among these, ^{68}Ga-DOTA-SIGMA-3 shows potential as an excellent tumor imaging probe, warranting further research.

EP-0043

Synergistic Antitumor Efficacy of Bimiralisib (PQR309) Combined with ^{177}Lu-PSMA-617 Radionuclide Therapy in PSMA-Expressing Tumors

Q. Wu[1,2,3], *X. Yao*[1,2,3], *X. Duan*[1,2,3], *R. P. Baum*[4], *T. Zhao*[1,2,3], *J. Zhang*[1,2,3];
[1]*Departments of Diagnostic Radiology, Yong Loo Lin School of Medicine, National University of Singapore, Singapore, SINGAPORE,* [2]*Theranostics Center of Excellence (TCE), Yong Loo Lin School of Medicine, National University of Singapore, 11 Biopolis Way, Helios, Singapore 138667, Singapore, Singapore, SINGAPORE,* [3]*Clinical Imaging Research Centre, Centre for Translational Medicine, Yong Loo Lin School of Medicine, National University of Singapore, Singapore, SINGAPORE,* [4]*Curanosticum Wiesbaden-Frankfurt, Center for Advanced Radiomolecular Precision Oncology, Wiesbaden, GERMANY.*

Aim/Introduction: Radioligand therapy using ^{177}Lu-labeled PSMA-617 has shown promise in targeting PSMA-expressing tumors. However, strategies to enhance therapeutic efficacy while minimizing radiotoxicity remain critical. Bimiralisib (PQR309), a dual PI3K/mTOR inhibitor, has been previously validated for its anti-tumor activity, yet its potential in combination with radionuclide therapy has not been reported. This study aims to investigate the synergistic antitumor effects and underlying mechanisms of combining PQR309 with ^{177}Lu-PSMA-617 in PSMA-overexpressing tumor models. ***Materials and Methods:*** ^{177}Lu radiolabeling of PSMA-617 was performed and confirmed for purity and stability. In vitro experiments were conducted using pip-PC3 cells, a PSMA-high prostate cancer line, and included CCK-8 viability assays, colony formation, γ-H2AX and ROS staining, ATP quantification,

Western blotting, and RNA sequencing to elucidate molecular changes. In vivo studies were carried out in pip-PC3 tumor-bearing nude mice treated with PQR309 (oral gavage, twice weekly) and/or ^{177}Lu-PSMA-617 (0.3 mCi). Tumor progression was monitored via volume measurements and SPECT/CT imaging. Tumor tissues were analyzed using immunohistochemistry (IHC) for mechanistic validation. ***Results:*** PQR309 significantly enhanced the therapeutic effect of ^{177}Lu-PSMA-617 both in vitro and in vivo. The combination group showed reduced cell viability, impaired colony formation, elevated DNA damage and oxidative stress markers, and marked ATP depletion. RNA-seq and Western blot analyses confirmed suppression of PI3K/mTOR signaling and glycolytic metabolism. In vivo, the combination therapy achieved a tumor growth inhibition rate of 98.66% over 28 days, markedly outperforming monotherapies. SPECT/CT imaging corroborated tumor-specific radiotracer uptake and therapeutic response, while IHC staining validated enhanced apoptosis and pathway inhibition. ***Conclusion:*** This study is the first to demonstrate the synergistic antitumor efficacy of combining PQR309 with ^{177}Lu-PSMA-617 in PSMA-positive tumors. PQR309 sensitizes tumors to radioligand therapy by inhibiting the PI3K/mTOR axis and disrupting cellular energy metabolism. These findings suggest that PQR309 can potentiate radionuclide therapies, enabling robust tumor suppression at lower, safer radiation doses. The results provide a compelling rationale for further translational and clinical evaluation of this combination strategy in prostate cancer and other PSMA-expressing malignancies.

EP-0044

Biodistribution of the novel CXCR4-directed PET tracer [^{68}Ga]Ga-NOTA-R54 in Patient-Derived Xenograft models of lung cancer

I. Alberico[1], *M. Gentili*[1], *M. Pitzalis*[1], *G. Bertolini*[1], *F. Facchinetti*[1], *C. Cucchi*[1], *F. Rizzo*[1], *C. Beretta*[1], *M. Kirienko*[1], *C. Chiesa*[1], *M. Maccauro*[1], *S. Di Maro*[2], *S. Scala*[3], *A. Bogni*[1], *C. Pascali*[1], *L. Roz*[1]; [1]*Fondazione IRCCS - Istituto Nazionale dei Tumori, Milan, ITALY,* [2]*University of Campania "Luigi Vanvitelli", Caserta, ITALY,* [3]*Istituto Nazionale per lo Studio e la Cura dei Tumori-IRCCS-Fondazione "G. Pascale", Naples, ITALY.*

Aim/Introduction: CXCR4 (CXC chemokine receptor 4) is a G-protein-coupled receptor overexpressed in various human tumors. Elevated CXCR4 expression is associated with increased tumor aggressiveness, as well as a higher risk of metastasis, chemoresistance and recurrence. Its interaction with the endogenous ligand CXCL12 (CXC chemokine ligand 12) plays a critical role in cancer cell survival, proliferation, and migration. By mimicking the receptor-binding domain of CXCL12 we have developed a novel class of peptides with high affinity for CXCR4 which can be used as potent CXCR4 antagonists or as binding agents for imaging applications. In this study, we investigate the uptake and biodistribution of the novel PET tracer [^{68}Ga]Ga-NOTA-R54, a low molecular weight CXCR4-binding cyclic peptide labeled with Gallium-68, in patient-derived xenografts (PDX) of non-small cell lung cancer (NSCLC). ***Materials and Methods:*** The radiopharmaceutical tracer was intravenously administered via tail vein injection in 4-5 mice bearing subcutaneous NSCLC-PDX models (100 µCi/mouse). Six different PDX models with different content of CXCR4+ cells were tested (range 0.1-31%). One hour after administration, biodistribution and uptake of [^{68}Ga]Ga-NOTA-R54 were evaluated ex vivo in blood, lungs, liver, kidneys and primary tumors using a gamma counter (2480 Wizard2) and measured as fraction of injected activity/g of tissue (%IA/g). CXCR4 positivity in primary tumor cells and in disseminated tumor cells (DTCs) in the lungs of mice was assessed by flow cytometry. ***Results:*** Rapid biodistribution was observed with significant amount of radiopharmaceutical detected in the kidneys compared to other organs, confirming its prevalent renal clearance (%IA/g 6.46±1.65). Good concordance was observed in uptake values of tumors from the same PDX model, confirming utility of these advanced models for imaging studies. Greater radiotracer uptake was observed in PDX models with higher frequency of CXCR4+ cells compared to those with low CXCR4 expression. In a representative experiment a significant different uptake was detected in LT111 model (mean CXCR4+ cells 31%) compared to LT710 model (3%): 1.35±0.57 vs. 0.44±0.12 (p=0.021). ***Conclusion:*** Our results show that [^{68}Ga]Ga-NOTA-R54 can be used as an effective imaging probe to identify CXCR4-rich tumors potentially allowing early prognostication and identification of mechanisms of resistance thus predicting outcomes and/or therapeutic efficacy. Additional studies are needed to evaluate limit of detection and kinetics. This project will advance the clinical development of CXCR4-targeted probes for both diagnostic and therapeutic applications, following a rational progression from advanced preclinical modeling to early clinical testing. This study was supported by PNRR grant POC-2022-12376329.

EP-0045

High resolution autoradiography based imaging visualizes chemotherapy induced metabolic suppression in colorectal cancer organoids

Z. Jiang, *K. Draganic, G. Egger, H. Marcus, E. Patronas; Medical University of Vienna, Vienna, AUSTRIA.*

Aim/Introduction: Patient-derived organoids (PDOs) from microsatellite instability (MSI) and mismatch repair-proficient (MMRp) colorectal cancer (CRC) tumors are increasingly used to model therapeutic responses. However, visualizing treatment-induced metabolic changes in these 3D models remains technically limited. We applied high-resolution autoradiography (AURA) using [^{18}F]FDG to assess chemotherapy-induced metabolic suppression in CRC organoids. This study aimed to establish a robust workflow to quantify metabolic responses, enabling the integration of functional imaging biomarkers into organoid-based drug screening for personalized treatment strategies. ***Materials and Methods:*** CRC organoids were cultured in Matrigel domes using defined organoid medium for 9 days. Chemotherapy agents (5-fluorouracil [5-FU], oxaliplatin [Ox], 5-FU+Ox and or FOLFOX [consists of 5-FU, leucovorin, and Ox]) at concentrations of 1, 5, and 10 µM were added on day 9, and imaging was performed 3 days later. AURA was carried out using ^{18}F-FDG to assess glucose metabolism. Viability was evaluated using CellTiter-Glo® (CTG), and Live/Dead immunofluorescence staining was used to assess cell viability. ***Results:*** All data were normalized to the untreated control group. ^{18}F-FDG uptake significantly decreased in a dose-dependent manner ($p < 0.05$), closely mirroring normalized CellTiter-Glo® (CTG) viability across all treatment groups. Live/Dead immunofluorescence confirmed a reduction in viable cell proportions with increasing drug concentration; however, absolute viability values remained relatively higher at lower doses. This discrepancy may indicate transient metabolic adaptation, whereby organoids maintain survival through alternative metabolic pathways. Supporting this hypothesis, BODIPY staining, which reflects intracellular lipid content, was relatively preserved or mildly increased at 1 and 5 µM, suggesting enhanced lipid utilization during early response phases. At the highest dose (10 µM), BODIPY signal declined significantly ($p < 0.05$), consistent with impaired lipid metabolism and widespread cell death. These metabolic and viability trends were observed in both MSI and MMRp organoids, with the strongest suppression noted in the FOLFOX and 5-FU+Ox combination groups. Dose-response analysis revealed distinct IC_{50} values among treatment conditions, with MSI organoids displaying higher IC_{50} values than MMRp organoids, indicating greater resistance to chemotherapy at lower concentrations. ***Conclusion:*** High-resolution autoradiography using ^{18}F-FDG, combined with functional and immunofluorescence

validation, provides a robust workflow to assess chemotherapy-induced metabolic suppression in CRC organoids. This imaging-based approach supports the integration of clinical radiotracers into organoid-based drug testing platforms for future personalized therapy applications.

EP-0046

Low-dose Fibronectin-targeted Gd-based contrast agent Enables Early and Accurate Assessment of Chemotherapy Response in Pancreatic Cancer

W. Zhang[1], *Y. Du*[2];
[1]*Peking University People's Hospital, Beijing, CHINA,* [2]*Institute of Automation, Chinese Academy of Sciences, Beijing, CHINA.*

Aim/Introduction: Albumin-bound paclitaxel and gemcitabine (AG) chemotherapy is a mainstay in treatment of pancreatic ductal adenocarcinoma (PDAC). Unfortunately, not all patients respond to this treatment[1]. Clinical imaging techniques are not able to precisely evaluate and predict the response to AG therapies over several weeks. A strong fibrotic reaction is a hallmark of drug-resistance while depletion of fibrosis is a positive response of AG. Extradomain-B fibronectin (EDB-FN) is an important element of fibrosis in PDAC[2]. Here, we prepared EDB-FN targeted Gd-based contrast agent (EDB-Gd) to perform molecular MRI for early, noninvasive and quantitative assessment of treatment response in PDAC. ***Materials and Methods:*** BxPC-DR, Human PDAC cell line, was treated with AG to establish acquired drug-resistance. subcutaneous and orthotopic models with BxPC-DR or BxPC were established. Mice were intravenously injected with EDB-Gd or Gd-DOTA. The ratio of T1 value reduction (T1d%) were compared quantitatively. For chemotherapy monitoring, mice were treated with AG regimens. MRI were performed before and after treatments. Histological analyses were used as references for validation. ***Results:*** Molecular MRI with EDB-FN could specifically detect and quantify fibrogenesis in PDAC xenografts at a low dose 0.05mmol/kg, which is half of clinical dosage of Gd. The optimal imaging time point was 30min after injection of EDB-Gd. In addition, the targeted probe generated more robust contrast-enhanced and longer retention compared to traditional Gd-DOTA. For chemotherapy montoring, T1d% were significantly increased 2.5-fold in drug-resistance xenografts group in fibrotic tumor areas compared to AG-sensitive group ($p < 0.05$). Comparing the T1d% before and 5 days after AG predicted treatment response. ***Conclusion:*** This study indicates EDB-FN-targeted molecular MRI possesses clinical applications in accurate assessment and prediction of AG chemotherapy. ***References:*** ADDIN EN.REFLIST [1] P. A. Philip, J. Lacy, F. Portales, A. Sobrero, R. Pazo-Cid, J. L. Manzano Mozo, E. J. Kim, S. Dowden, A. Zakari, C. Borg, E. Terrebonne, F. Rivera, J. Sastre, V. Bathini, D. Lopez-Trabada, J. Asselah, M. W. Saif, J. Shiansong Li, T. J. Ong, T. Nydam, P. Hammel, Lancet Gastroenterol Hepatol 2020, 5, 285. [2] P. Qiao, N. R. Ayat, A. Vaidya, S. Gao, W. Sun, S. Chou, Z. Han, H. Gilmore, J. M. Winter, Z. R. Lu, Front Oncol 2020, 10, 586727.

EP-0047

Image-derived Blood Normalization for TREM2 PET Imaging in Glioblastoma Mice Enhances Sensitivity during Monitoring of Immunomodulation

M. Haertel[1], *R. Schaefer*[1], *L. H. Kunze*[1], *K. Schlepckow*[2], *M. Willem*[2], *C. Haass*[2,3,4], *G. Palumbo*[1], *J. W. Lewcock*[5], *K. M. Monroe*[5], *R. A. Werner*[1], *N. L. Albert*[1,6,7], *L. von Baumgarten*[8,9], *L. M. Bartos*[1], *S. Lindner*[1,4], *M. Brendel*[1,2,4];
[1]*Department of Nuclear Medicine, LMU University Hospital, LMU Munich, Munich, GERMANY,* [2]*German Center for Neurodegenerative Diseases (DZNE), Munich, GERMANY,* [3]*Biomedical Center (BMC), Division of Metabolic Biochemistry, Faculty of Medicine, Ludwig Maximilians University, Munich, GERMANY,* [4]*Munich Cluster for Systems Neurology (SyNergy), Munich, GERMANY,* [5]*Denali Therapeutics, Inc., South San Francisco, CA, UNITED STATES OF AMERICA,* [6]*German Cancer Consortium (DKTK), Partner Site Munich, German Cancer Research Center (DKFZ), Heidelberg, GERMANY,* [7]*Bavarian Cancer Research Center (BZKF), Erlangen, GERMANY,* [8]*German Cancer Consortium (DKTK), Partner Site Munich, Munich, GERMANY,* [9]*Department of Neurosurgery, LMU University Hospital, LMU Munich, Munich, GERMANY.*

Aim/Introduction: The recently developed triggering receptor of myeloid cells 2 (TREM2) radiotracer (1) serves as a innovative tool for selective PET imaging of the tumor associated microglia and macrophages (TAMs) in glioblastoma mice and therefore holds a promising translation into human patients. This study aims to improve the quantification of PET images when utilizing the ^{64}Cu-labeled, brain-shuttle equipped TREM2-PET radiotracer for assessment of TREM2 expression in the brains of mice inoculated with murine SB28 glioblastoma. TREM2 knockout (TREM2 KO) mice with a lack of target expression were included as a control condition to compare data-driven blood normalization of PET images with the conventional tumor-to-background (TBR) normalization. ***Materials and Methods:*** SB28-inoculated WT;TfR$^{mu/hu}$ (n = 8) and TREM2 KO mice (n = 4) were intravenously administered [^{64}Cu]Cu-NODAGA-ATV:4D9, a TREM2-targeting radiotracer with a human transferrin receptor binding site to penetrate the blood-brain-barrier (2), on week-2 or week-3 (WT;TfR$^{mu/hu}$) respectively week-2 (TREM2 KO) post inoculation. We performed TREM2 PET 20 h post injection, followed by intracardiac blood collection. To correlate PET image-derived blood levels with ex vivo blood radioactivity levels we used the voxel-wise analysis employing statistical parametric mapping (SPM). The value of the emerging image-derived blood measure was tested in a SB28 cohort with longitudinal TREM2 PET monitoring during myeloid cell depletion between week-1 and week-2 after tumor implantation (blood-derived vs. TBR normalization). ***Results:*** SPM-based correlation of PET images with ex vivo blood levels revealed an image that matched the vessel tree. Highest agreement was observed in a region of interest in the cardiac blood pool (ROI with 2mm diameter), which allowed to obtain robust blood radioactivity levels from PET images. Blood normalization was superior in detecting changes of TREM2 expression during myeloid cell depletion (Treatment vs. Placebo: -34% TREM2-PET signal, $p < 0.001$) compared to TBR (Treatment vs. Placebo: -22% TREM2-PET signal, $p = 0.121$). ***Conclusion:*** By normalizing PET images to account for blood levels, the sensitivity of TREM2-PET monitoring is significantly enhanced compared to TBR. This refined quantitative approach of image-derived PET normalization is particularly valuable when target expression is affected brain wide by disease or treatment. ***References:*** 1. Shojaei M, Schaefer R, Schlepckow K, et al. PET imaging of microglia in Alzheimer's disease using copper-64 labeled TREM2 antibodies. Theranostics. 2024;14:6319-6336. 2. van Lengerich B, Zhan L, Xia D, et al. A TREM2-activating antibody with a blood-brain barrier transport vehicle enhances microglial metabolism in Alzheimer's disease models. Nat Neurosci. 2023;26:416-429.

EP-0049

Use of blocking agent re-distributes alpha-emitter astatine-211, in free form, after targeted alpha therapy

T. Bäck[1], *E. Aneheim*[2], *H. Jensen*[3], *S. Palm*[1];
[1]*Sahlgrenska Academy, University of Gothenburg, Gothenburg, SWEDEN,* [2]*Sahlgrenska University Hospital, Gothenburg, SWEDEN,* [3]*Copenhagen University Hospital, Copenhagen, DENMARK.*

Aim/Introduction: Alpha-emitter astatine-211 (^{211}At; $t_{½}$=7.2h)) is currently under clinical investigation for targeted alpha therapies (TAT). In our previous phase I trial, most patients received a blocking agent (sodium perchlorate) which reduced uptake of possible free ^{211}At in thyroid. In this current study, we examine how use of a blocking agent affects the biodistribution of free ^{211}At in mice. The aim was to predict how use of a blocking agent affects the

biodistribution of free 211At that results from in-vivo degradation of a targeted compound used for cancer therapy in patients. ***Materials and Methods:*** Mice with (n=6) and without (n=6) pretreatment with sodium perchlorate (170 mg/kg at 24h and 1h before injection) was given free ^{211}At. We then attempted to trace the fate of all injected activity. Whole-body content was measured with a dose calibrator. Urine and feces were continuously collected and measured in a gamma-well counter. Three of each group were dissected at 6h and the remainder at 10h. Organs were immediately collected and measured for activity. All remaining body parts were also measured in the counter. ***Results:*** At 6h, the highest uptake for the un-blocked mice was seen for thyroid, stomach, salivary glands and lungs (431, 45, 12 and 10 %IA/g, respectively). For the blocked mice highest uptake was in lungs, thyroid, spleen and kidneys with 13, 13, 6.5 and 4.8 %IA/g, respectively. At 10h, it was thyroid, stomach, lungs and salivary glands (189, 37, 9.5, 6.7 %IA/g) for the unblocked mice; and thyroid, lungs, spleen and stomach (14, 10, 4.6, 4.5 %IA/g) for the blocked mice. Highest reduction in organ uptake following block was seen for thyroid, stomach and salivary glands (60-97% reduction in %IA/g). Highest increase due to block was seen for kidneys and blood (22-25% increase). At 10h, non-organ cadaver remainders of unblocked mice contained 46% of all injected activity (%IA), while that of blocked mice contained 37 %IA. Collected up to 10h, combined total urine from unblocked mice accounted for 30 %IA, but only 11% from the blocked mice. Amounts in collected feces were negligible. At 10h, the percentage of injected activity that could not be accounted for was 30% for the un-blocked and 24% for the blocked group. ***Conclusion:*** Using a blocking agent before TAT with 211At reduces thyroid uptake but increases uptake in possibly more critical healthy tissue. Failure to account for all administered activity will be addressed in new studies.

EP-0050

Preclinical Evaluation of a Novel PSMA-Targeted Nanobody Radiopharmaceutical [^{177}Lu]Lu-Ab0362-H0202 for the Treatment of Metastatic Castration-Resistant Prostate Cancer

B. Li, *X. Wu, Y. Gao;*
Department of Nuclear Medicine, Henan Key Laboratory of Novel Molecular Probes and Clinical Translation in Nuclear Medicine, Henan Provincial People's Hospital; Zhengzhou University People's Hospital, Henan University People's Hospital, Zhengzhou, CHINA.

Aim/Introduction: This study assesses the preclinical efficacy and safety of [^{177}Lu]Lu-Ab0362-H0202, a novel PSMA-targeting nanobody developed via site-specific conjugation, as a potential treatment for mCRPC. ***Materials and Methods:*** Preclinical evaluation involved PET/CT imaging with [^{64}Cu]Cu-Ab0362-H0202 in LNCaP xenograft NCG mice to assess tumor uptake and retention at 1, 4, 24, 48, and 72 hours post-injection. Biodistribution of [^{177}Lu]Lu-Ab0362-H0202 was studied in Balb/c mice at the same time points. A single-dose toxicity study was conducted in Balb/c mice using 1.11×10^7 Bq (approximately five times the anticipated human dose). Radiation dosimetry was calculated using OLINDA software based on biodistribution data. ***Results:*** [^{64}Cu]Cu-Ab0362-H0202 demonstrated high tumor uptake (peak: 26.63±0.38 %ID/g at 24 h) and sustained tumor retention up to 72 hours. [^{177}Lu]Lu-Ab0362-H0202 showed rapid blood clearance (25.1±3.79 %ID/g at 1 hour to 0.12±0.02 %ID/g at 72 hours) and low uptake in normal tissues, except the kidneys (peak: 99.02±6.47 %ID/g at 26 hours; reduced to 12.38±1.48 %ID/g by 72 hours). No acute toxicity was observed, with mice exhibiting normal behavior and weight gain. Dosimetry estimated a whole-body effective dose of 0.008 mSv/MBq and a kidney dose of 1.09 mGy/MBq, translating to 806.60 mSv for a 20 mCi dose—below the renal toxicity threshold. ***Conclusion:*** [^{177}Lu]Lu-Ab0362-H0202 exhibits high tumor targeting, favorable biodistribution, and a safe preclinical profile, positioning it as a promising candidate for mCRPC radionuclide therapy. Its superior tumor uptake and retention compared to existing therapies warrant further clinical investigation.

EP-0051

Effects of adding Arg and Arg-Arg to the linker of GRPR antagonist tracer, [^{68}Ga]Ga-TacsBOMB5, on its invitro/vivo capability

S. Pathania[1], *L. Wang*[1], *C. Chen*[2], *P. Ng*[2], *W. Lau*[2], *F. Radnia*[3], *F. Bénard*[2], *K. Lin*[1];
[1]*University of British Columbia, Vancouver, BC, CANADA,*
[2]*BC Cancer Research Institute, Vancouver, BC, CANADA,*
[3]*UBC, Vancouver, BC, CANADA.*

Aim/Introduction: Gastrin-releasing peptide receptor (GRPR) make an ideal tumor imaging target owing to their overexpression in several cancers while retaining minimal expression in healthy tissues. Recently, Obeid et al. reported a significantly improved GRPR binding affinity and tumor uptake by replacing the PEG2 in the linker of GRPR-targeting tracer, [^{111}In]In-AU-RM26-M2, with Arg-Arg. In this study we explored if the same improvement in binding affinity and tumor uptake could be obtained using our previously reported GRPR antagonist tracer, [^{68}Ga]Ga-TacsBOMB5. Building on this reported GRPR antagonist [^{68}Ga]Ga-TacsBOMB5, we developed two tracers [^{68}Ga]Ga-SP01014 and [^{68}Ga]Ga-SP01015. These tracers incorporated one positively charged arginine residue in [^{68}Ga]Ga-SP01014]and two arginine residues in [^{68}Ga]Ga-SP01015, strategically positioned between the DOTA chelator and the piperidine linker. ***Materials and Methods:*** Two novel tracers, [^{68}Ga]Ga-SP01014 (one arginine) and [^{68}Ga]Ga-SP01015 (two arginines), were synthesized using Fmoc solid-phase peptide chemistry. Gallium (^{nat}Ga and ^{68}Ga) complexation was conducted in acetate (0.1 M, pH 4.5) and HEPES (2 M, pH 5.0) buffers, respectively. The agonistic/antagonistic properties were evaluated through calcium release assays in PC-3 cells, while GRPR binding affinity (Ki) was determined via competitive binding assay using [^{125}I-Tyr^4]Bombesin as the radioligand. In vivo evaluation included PET imaging and biodistribution studies in PC-3 tumor xenograft models (n = 5) at 1 hour post-injection. ***Results:*** SP01014 and SP01015 with the addition of Arg and Arg-Arg, respectively, to the linker of TacsBOMB5, and were obtained in 64% and 52% yield, respectively. The natGa- and ^{68}Ga-complexed derivatives were obtained in 62-84% and 18-25% yields, respectively. In vitro competition binding assays demonstrated an improved GRPR binding affinity with the addition of Arg and Arg-Arg to the linker (Ki: Ga-SP01014, 4.2±0.7 nM; Ga-SP01015, 2.4±0.6 nM; Ga-TacsBOMB5, 6.1±1.0 nM). Antagonist characteristics of Ga-SP01014 and SP01015 were confirmed by the calcium release assay. Ex vivo biodistribution studies in PC-3 tumor-bearing mice showed that [^{68}Ga]Ga-SP01014 had lower but favorable tumor uptake compared to [^{68}Ga]Ga-TacsBOMB5 (11.30±2.32 vs 15.7±2.17 %ID/g). Despite having the highest binding affinity, [^{68}Ga]Ga-SP01015 had the lowest tumor uptake (9.94±1.68 %ID/g) and highest kidney uptake (5.99±0.96 %ID/g), possibly attributing to its increased overall positive charge. ***Conclusion:*** Our data from [^{68}Ga]Ga-TacsBOMB5 derivatives confirmed improvement in binding affinity with the addition of Arg and Arg-Arg to the linker. However, there was no improvement in the overall tumor uptake as it also depends on the pharmacokinetics. ***References:*** Obeid K et al . Pharmaceutics. 2024;16(4):513. Wang L et al. Molecules. 2022;27(12):3777.

EP-0052

Noninvasive PET imaging of Trop2 expression in bladder cancer using ^{64}Cu-labeled anti-Trop2 antibody-drug conjugate (Trodelvy)

L. Kang[1], *W. Huang*[1], *Q. Yang*[1], *W. Cai*[2];
[1]*Dept. of Nuclear Medicine, Peking University First Hospital, Beijing, CHINA,* [2]*University of Wisconsin-Madison, Madison, WI, UNITED STATES OF AMERICA.*

Aim/Introduction: Trophoblast cell-surface antigen 2 (Trop2) is highly overexpressed in various solid tumors, contributing to tumor progression, while its expression remains low in normal tissues. Trop2-targeting antibody-drug conjugate (ADC), sacituzumab govitecan-hziy (Trodelvy), has shown efficacy in targeting this antigen. In this study, we investigated Trop2 expression in bladder cancer models using ^{64}Cu-NOTA-Trodelvy for immunoPET imaging. ***Materials and Methods:*** Trop2 expression levels in bladder cancer cell lines (HT-1376 and UM-UC-3) were assessed via flow cytometry and immunofluorescence staining. Labeling of NOTA-Trodelvy with ^{64}Cu was performed in sodium acetate buffer at pH 5 (37°C, 1 h). In vitro stability was analyzed using radio-thin layer chromatography. Biological properties were evaluated through cell uptake, saturation binding assays, and biodistribution experiments. ImmunoPET imaging with ^{64}Cu-NOTA-Trodelvy was performed at various time points to confirm its in vivo targeting. ***Results:*** The radiochemical yield of ^{64}Cu-NOTA-Trodelvy exceeded 90%, with a radiochemical purity greater than 99%. Trop2 expression was high in HT-1376 cells, while it was low in UM-UC-3 cells. The K_D value of ^{64}Cu-NOTA-Trodelvy was 1.67 nM for HT-1376 cells. In HT-1376 models, ^{64}Cu-NOTA-Trodelvy effectively visualized tumor morphology as early as 12 h p.i. (10.30 ± 1.45 %ID/g), with tumor uptake increasing over time and peaking at 48 h p.i. (13.73 ± 1.16 %ID/g). In blocking group and UM-UC-3 models, ^{64}Cu-NOTA-Trodelvy exhibited minimal tumor uptake. As a negative control, ^{64}Cu-NOTA-IgG also demonstrated low tumor uptake (5.27 ± 1.14 %ID/g at 48 h in the blocking group; 6.33 ± 0.74 %ID/g at 48 h in UM-UC-3; 4.50 ± 0.30 %ID/g at 48 h in the ^{64}Cu-NOTA-IgG group). At 48 h, a high target-to-non-target ratio was observed, with specific uptake in tumors and minimal accumulation in non-target tissues. ***Conclusion:*** Our findings demonstrated that ^{64}Cu-NOTA-Trodelvy enables rapid, specific, and sustained tumor accumulation in bladder cancer models, providing precise and noninvasive monitoring of Trop2 expression.

EP-0053

First-in-Primate PET Imaging of a BCMA-Targeted ImmunoPET Probe for Multiple Myeloma

L. Kang, *T. Wang, Q. Yang, X. Sun, Y. Lei, L. Song;*
Dept. of Nuclear Medicine, Peking University First Hospital, Beijing, CHINA.

Aim/Introduction: B-cell maturation antigen (BCMA) is a crucial biomarker and therapeutic target in multiple myeloma (MM). Although BCMA-targeted therapies like CAR-T cells and bispecific antibodies have shown success, non-invasive tools for dynamically monitoring BCMA expression, assessing therapeutic response, and optimizing patient selection are still lacking. ImmunoPET imaging with zirconium-89 (^{89}Zr)-labeled antibodies offers a promising approach for real-time, whole-body visualization of tumor antigen expression. This study aimed to develop and evaluate a novel BCMA-targeted immunoPET probe, [^{89}Zr]Zr-DFO-PFBH0L0, in preclinical MM models and, for the first time, in non-human primates (NHPs) to assess its translational potential. ***Materials and Methods:*** A humanized BCMA-specific monoclonal antibody, PFBH0L0, was conjugated with desferrioxamine (DFO) and radiolabeled with ^{89}Zr. Binding affinity was assessed using ELISA and bio-layer interferometry (BLI), while BCMA expression in MM cell lines was confirmed via western blot and flow cytometry. PET/CT imaging and ex vivo biodistribution studies were performed in MM xenograft mouse models (H929, K562) to evaluate tumor uptake and specificity. PET imaging in a healthy female rhesus macaque at 10 min, 30 min, 1 h, 3 h, 24 h, 72 h, and 120 h post-injection (p.i.) assessed pharmacokinetics and organ distribution, with regions of interest (ROIs) quantified for key organs. Dosimetry estimates were calculated using OLINDA/EXM software. ***Results:*** [^{89}Zr]Zr-DFO-PFBH0L0 exhibited high radiochemical purity (>99%) and stability up to 144 h. ELISA and BLI confirmed that DFO conjugation did not significantly impact binding affinity. In MM xenograft models, PET imaging demonstrated significantly higher tumor uptake in BCMA-positive H929 tumors (9.92 ± 0.75 %ID/g) compared to K562 tumors, the blocking group, and the [^{89}Zr]Zr-DFO-IgG-H929 control group ($P < 0.05$). Ex vivo biodistribution corroborated these findings, with a high tumor-to-blood ratio at 24 h p.i. In NHP PET imaging, [^{89}Zr]Zr-DFO-PFBH0L0 exhibited favorable pharmacokinetics, with sustained retention in the liver, spleen, and kidneys while demonstrating minimal background uptake in muscle and lung. The 3D CT reconstruction confirmed the absence of bone lesions, indicating a healthy subject and supporting the probe's suitability for future clinical translation. Dosimetry estimates showed that the liver (2.41 mGy/MBq) and spleen (2.31 mGy/MBq) received the highest absorbed doses, while the effective dose was 0.68 mSv/MBq, within a clinically acceptable range. ***Conclusion:*** This study pioneers the use of a BCMA-targeted PET tracer in non-human primates, demonstrating its high specificity and favorable biodistribution for clinical translation, patient stratification, therapy monitoring, and future theranostic applications in MM.

EP-0054

Preclinical evaluation of ^{68}Ga-labeled PD-L1 nanobody for PET imaging of pharmacokinetics in gastric cancer

L. Kang, *Q. Yang, T. Wang, X. Sun, L. Song, W. Huang;*
Dept. of Nuclear Medicine, Peking University First Hospital, Beijing, CHINA.

Aim/Introduction: Gastric cancer is a prevalent malignancy with diverse clinical presentations and outcomes, posing a significant global health burden. Despite advances in conventional therapies, gastric cancer remains highly lethal. PD-L1 is overexpressed on the surface of gastric cancer cells, rendering it a crucial biological target for this disease. PD-L1-targeted nanobody offers advantages over traditional antibodies for precise tumor imaging, enabling early detection of gastric cancer and facilitating dynamic monitoring of immunotherapy responses. In this study, we aim to investigate the diagnostic potential of ^{68}Ga-labeled nanobody, as well as its biodistribution and dosimetry, in gastric cancer-bearing models. ***Materials and Methods:*** A new anti-human PD-L1 nanobody was generated through a series of steps including immunization to construct a library, phage display technology, next-generation sequencing. SDS-PAGE electrophoresis was utilized to evaluate the purity of the nanobodies obtained. Biolayer interferometry (BLI) was employed to assess the binding affinity between PD-L1 nanobody and human PD-L1 protein. Enzyme-linked immunosorbent assay (ELISA) was evaluated to detect the binding activity of PD-L1 nanobody to PD-L1. The relative PD-L1 expression levels in HGC-27, U87, SGC-7901, and AGS cell lines were evaluated using flow cytometry. Subsequently, PD-L1 nanobody was conjugated with 1,4,7,10-Tetraazacyclododecane-1,4,7,10-tetraacetic acid (DOTA) for radiolabeling with ^{68}Ga ($t_{1/2}$ = 67.7 min). ImmunoPET imaging was conducted in HGC-27 tumor-bearing mouse models following the injection of ^{68}Ga-labeled PD-L1 nanobody. ***Results:*** A PD-L1-specific nanobody was successfully generated with more than 90% purity and the KD value reached 10^{-12} M, indicating that PD-L1 nanobody has a strong affinity for PD-L1. Flow cytometry revealed that PD-L1 was positive in HGC-27 and U87 cells, whereas AGS and SGC-7901cells presented low expression levels. PET imaging of ^{68}Ga-PD-L1 nanobody showed that, in the HGC-27 tumor model with positive PD-L1 expression, significant radioactive concentration was observed in the tumor as early as 1 hour post-injection of the ^{68}Ga-DOTA-PD-L1 nanobody. This uptake continued to rise, reaching 2.16 ± 0.06 %ID/g at 2 hours and 2.23 ± 0.16 %ID/g at 3 hours. The above results of imaging suggest the high uptake of tumors from radiolabeled PD-L1 nanobody. ***Conclusion:*** The developed PD-L1-targeting nanobody probe exhibits rapid and specific binding to PD-L1,

coupled with excellent tumor penetration capabilities. Therefore, this PD-L1 nanobody probe could achieve high-sensitivity in vivo imaging of minute tumors.

EP-0055

Multimodal PET Imaging Monitors Tumor Cell Vaccine Combined with Immunoadjuvant Therapy for Colorectal Cancer

N. Wei, *M. Hu, Y. Long, P. Yuan, Y. Gai, X. Lan;*
Department of Nuclear Medicine, Union Hospital, Tongji Medical College, Huazhong University of Science and Technology, Wuhan, CHINA.

Aim/Introduction: To tackle colorectal cancer immunotherapy challenges, this study proposes an integrated strategy using autologous tumor cell vaccines to enhance antigen-specific immune activation and a molecular imaging system to dynamically monitor treatment. It highlights LAG3, whose dynamic expression indicates early T cell activation and immune exhaustion, providing a novel biomarker for optimizing individualized immunotherapy. ***Materials and Methods:*** To develop an autologous whole-cell tumor vaccine using mitoxantrone-induced immunogenic cell death in CT26 cells, the drug concentration was optimized. Vaccine consistency was verified by immunofluorescence for calreticulin expression, and its immunogenicity was assessed by flow cytometry. Safety was evaluated using CCK8 assays and monitoring mouse weight, biochemical indicators, and histopathology. A CT26 tumor-bearing mouse model was used for treatment, followed by PET/CT imaging with ^{68}Ga-NOTA-LAG3, ^{68}Ga-NOTA-GZP, and ^{18}F-FDG probes to monitor therapeutic effects. Biodistribution, tissue flow cytometry, and histopathological staining were further used to analyze the vaccine's anti-tumor immune response. ***Results:*** (1) Immunogenicity and Safety: Mitoxantrone (1 μM) induced significant calreticulin expression ($P < 0.0001$) and reduced cell viability to 7.06% at 24 h and 6.14% at 48 h ($P < 0.0001$). No significant differences were observed in liver, kidney, or cardiac function. Median survival was 17.5 days in the experimental group vs. 9 days in controls ($P = 0.0069$), with lower tumor volumes on days 4, 6, and 9 ($P < 0.0060$). (2) Imaging and Biodistribution: No significant differences in ^{18}F-FDG uptake. The ^{68}Ga-NOTA-LAG3 probe showed significant inter-group differences in tumor uptake from day 4 post-treatment ($P = 0.0447$, $P = 0.0160$). Tissue analysis on day 8 revealed higher LAG3+ cell proportions in the MTX and MC groups ($P < 0.0066$, $P < 0.0001$), positively correlated with CD3+, CD4+, and CD8+ cells ($P < 0.0029$). Tumor volume was lower in the MC group ($P < 0.0012$), with slower tumor growth and reduced proliferation. ***Conclusion:*** In this study, we successfully developed an autologous whole-cell tumor vaccine, which was validated for its immunogenicity, safety, and efficacy through preclinical experiments. We monitored the immune response and therapeutic effects using three probes: ^{18}F-FDG, ^{68}Ga-NOTA-GZP, and ^{68}Ga-NOTA-LAG3. Notably, the ^{68}Ga-NOTA-LAG3 probe effectively distinguished tumor immune responses from progression and showed potential for evaluating immunotherapy outcomes and prognosis.

EP-0056

Evaluation of a Novel Long-acting FAPI in HEK-293-FAP Solid Tumor Model

L.-C. Chen, *W.-L. Lo;*
National Atomic Research Institute, Taoyuan City, TAIWAN.

Aim/Introduction: Cancer associated fibroblasts are present in more than 90% of epithelial cancers (such as pancreatic cancer, colorectal cancer, breast cancer, etc.) and are one of the major components of stromal cells. Fibroblast activation protein (FAP) activity in cancer is associated with cancer development, cancer cell migration, and cancer metastasis. FAP has been confirmed to be overexpressed in tumor-associated fibroblasts in many solid tumors. The aim of this study is to explore the in vivo distribution of a radiolabeled novel long-acting fibroblast activation protein inhibitor (FAPI) in an HEK-293-FAP solid tumor model using SPECT/CT imaging. ***Materials and Methods:*** The precursor of NARI-FAPI-1.11 was purchased from Kelowna International Scientific Inc. After labeling with Lu-177, the labeling efficiencies were analyzed using a radio-TLC and radio-HPLC system. Cell binding studies with ^{177}Lu-labeled NARI-FAPI-1.11 were performed using HEK-293-FAP cells (FAP-transfected HEK-293 cells; 3 x 10^6 cells per tube, n = 3). After incubation at 37°C for 1 hour, the samples were centrifuged and washed twice with cold phosphate-buffered saline. Each sample was measured in a gamma counter (Hidex AMG). The percentage of cell bound radioactivity (%) was calculated using the formula: (cell bound radioactivity / total radioactivity) × 100. HEK-293-FAP cells were subcutaneously inoculated into BALB/c nude mice. After intravenous injection of ^{177}Lu-NARI-FAPI-1.11, the HEK-293-FAP tumor-bearing mice were anesthetized and imaged at 1, 4, 18, 24, 48, and 72 hours using a nanoScan SPECT/CT system (Mediso). ***Results:*** The labeling efficiency of ^{177}Lu-NARI-FAPI-1.11 was greater than 90% as determined by radio-TLC and radio-HPLC systems. The cellular binding efficiency in HEK-293-FAP cells demonstrated specific uptake (17%) at 1 hour. SPECT/CT imaging showed that the radioactivity in the tumor rapidly accumulated, reaching 6 %ID/mL at 1 hour and gradually increasing to 6.37 %ID/mL at 4 hours. After 4 hours, the radioactivity slowly decreased over time, from 6.37 %ID/mL at 4 hours to 3.56 %ID/mL at 72 hours. ***Conclusion:*** In this study, the radiolabeled novel long-acting FAPI molecule, ^{177}Lu-NARI-FAPI-1.11, demonstrated specific characteristics in cell binding and SPECT/CT imaging in a tumor-bearing model. Based on these results, ^{177}Lu-NARI-FAPI-1.11 can achieve prolonged circulation time in vivo and increased long-term accumulation at tumor sites.

EP-0057

Validating CD44v6 as targeted for molecular radiotherapy of gastric cancer

S. Rinne, *Z. Wang, M. Nestor;*
Uppsala University, Uppsala, SWEDEN.

Aim/Introduction: Existing treatment options for patients with advanced gastric cancer (GC) offer often only limited survival benefits. Targeted radiotherapy may address some of the shortcomings of current treatment regimens. However, currently, no radiopharmaceutical-based therapies are available for GC patients. The aim of this study was to select suitable preclinical models and evaluate CD44v6 as a potential target for targeted radiotherapy of gastric cancer, specifically targeted alpha therapy. ***Materials and Methods:*** AKIR001 is an IgG1 antibody with known affinity to CD44v6, containing a DOTA chelator for labeling with radiometals. Experiments were conducted with ^{111}In as a surrogate for future studies with the alpha-emitter ^{225}Ac. Stability of the indium-111 label was tested in PBS, 1000× molar excess of EDTA, and mouse serum. A panel of four gastric cancer cell lines (MKN-45, NCI-N87, AGS, and HGC-27) was assessed for expression and CD44v6-specific binding in vitro. Binding kinetics were studied in real-time using LigandTracer. Uptake and internalization of [^{111}In]In-AKIR001 were assessed in three gastric cancer cell lines with varying expression of CD44v6. In vivo, biodistribution experiments were performed in Balb/c nu/nu mice bearing MKN-45 and NCI-N87 xenografts. ***Results:*** AKIR001 was stably labeled with ^{111}In with an average yield of 96 ± 5%. [^{111}In]In-AKIR001 bound specifically to three out of four tested gastric cancer cell lines (MKN-45, NCI-N87, and AGS) with a K_D of 40 ± 16 pM. Internalization was generally low and similar across cell lines. After 24 hours of incubation, the internalized fraction of the total cell-bound activity was 11%, 14.5%, and 15.7% for MKN-45, NCI-N87, and AGS cells, respectively. In vivo, [^{111}In]In-AKIR001 successfully targeted CD44v6-positive NCI-N87 and MKN-45 xenografts. Tumor uptake of [^{111}In]In-AKIR001 in MKN-45 xenograft-bearing mice increased from 4 h to 48 h post-injection (pi) and was fully retained up to 168 h pi. Uptake at

48 h pi was 52 ± 7 %ID/g in MKN-45 xenografts and 29 ± 2 %ID/g in NCI-N87 xenografts. The difference in tumor models matched the difference in uptake in vitro. Tumor-to-blood ratios increased from 1.6 at 24 hours pi to a ratio of 4 at 168 hours after injection. ***Conclusion:*** CD44v6 is a promising target for the development of targeted radiopharmaceuticals for gastric cancer. Our studies with [^{111}In]In-AKIR001 indicate its potential for direct and, with its low internalization, also pretargeted radiotherapy of GC. Future studies investigating the therapeutic efficacy with ^{225}Ac-labeled AKIR001 are planned.

EP-0058

Preclinical evaluation of [^{161}Tb]Tb-pypa-p-Phe-trastuzumab in SKOV3-tumor-bearing mice

M. Ligeour, *I. R. Astiazarán-Rascón, L. Li, H. Merkens, P. Ng, W. Lau, M. Jaraquemada-Peláez, F. Bénard;*
BC Cancer, Vancouver, BC, CANADA.

Aim/Introduction: With a broad range of isotopes suitable for medical applications, terbium radioisotopes (^{149}Tb, ^{152}Tb, ^{155}Tb, and ^{161}Tb) have raised interest over the past few years, for offering the possibility of a theranostic pair. Terbium-161 ($T_{1/2}$ = 6,89 days), which emits β$^-$ particles, γ radiation, and Auger electrons has been the most studied alternative to ^{177}Lu in β$^-$ targeted radioligand therapy. While the determination of an efficient vector is essential in radiopharmaceutical development, the selection of an optimal chelator to ensure the isotope retention within the drug is often a challenge. Herein, we evaluate the nonadentate H_4pypa chelator, which has previously been labelled with various isotopes (^{177}Lu, ^{89}Zr, ...) for its potential use in radioimmunotherapy targeting ovarian cancer [1-2]. ***Materials and Methods:*** H_4pypa-p-Phe-NCS was conjugated to trastuzumab at a 1:10 Ab:chelator ratio and radiolabelled with [^{161}Tb]$TbCl_3$ at 40°C within 30 minutes. The purity and the specific activity were assessed by size exclusion chromatography using HPLC. The radiolabelled compound was injected intravenously into athymic nude female mice bearing subcutaneous SKOV3 tumour xenografts. SPECT/CT imaging and in vivo biodistribution studies were performed on days 1, 3, 6 and 7 after injection. ***Results:*** Trastuzumab was successfully conjugated to H_4pypa with 87% yield and radiolabelled with [^{161}Tb]$TbCl_3$ with 19±2 % radiochemical yield. The ^{161}Tb-labelled immunoconjugate was purified with 99% radiochemical purity and 0,38 MBq/µg specific activity. SPECT/CT showed high tumour uptake from day 1 post-injection, with relatively high uptake in the liver. Although the tumour uptake remained stable until day 3, increased bone accumulation at days 3, 6, and 7 reflects the instability of the radiotracer. The biodistribution data highlighted a tumour accumulation of 12±1 %IA/g of the [^{161}Tb]Tb-pypa-p-Phe-trastuzumab radiotracer at day 1, which was maintained up to day 3 and gradually decreased to 6±1 %IA/g at day 7. Although high tumour-to-muscle ratios were observed through the experiment, the decrease in tumour-to-liver and tumour-to-bone ratios from day 3, corroborates the SPECT/CT findings. ***Conclusion:*** Preclinical SPECT/CT imaging of SKOV3 tumour xenografts through [^{161}Tb]Tb-pypa-p-Phe-trastuzumab showed high tumour-to-muscle ratios. However, it highlighted increasing liver and bone accumulation over time indicative of [^{161}Tb]Tb demetalation. To investigate if this result is due to antibody-chelator interaction, further studies will aim the conjugation of H_4pypa-p-Phe-NCS to a different targeting vector and its labelling with [^{161}Tb]$TbCl_3$. ***References:*** [1] Li, L. et al., Bioconjugate Chem., 2019, 30, 5, 1539-1553 [2] Southcott, L. et al., Inorg. Chem., 2021, 60 (23), 18082-18093.

EP-04

e-Poster Area

A: Preclinical and Translational Studies -> A1 Medical Preclinical -> A14 Preclinical Therapy

EP-0059

Predictors of Iodine-131 Therapy Outcomes in Obese Thyroid Cancer Patients

Y. Zhou[1,2,3], *Y. Hou*[1,2,3], *X. Xia*[1,2,3];
[1]*Department of Nuclear Medicine, Union Hospital, Tongji Medical College, Huazhong University of Science and Technology, Wuhan, CHINA,* [2]*Hubei Province Key Laboratory of Molecular Imaging, Wuhan, CHINA,* [3]*Key Laboratory of Biological Targeted Therapy, the Ministry of Education, Wuhan, CHINA.*

Aim/Introduction: This study aims to evaluate the clinical, pathological, and metabolic factors influencing the therapeutic outcomes of iodine-131 treatment in obese patients with DTC, with the goal of optimizing individualized treatment strategies. ***Materials and Methods:*** This retrospective study included 457 obese patients with DTC who received iodine-131 therapy. Treatment outcomes were evaluated based on clinical and imaging findings and categorized into four groups: effective response, indeterminate response, biochemical incomplete response, and structural incomplete response. Variables were classified into four categories for analysis: demographic factors (age, sex, BMI, and place of residence), tumor characteristics (tumor size, tumor-node-metastasis stage, multifocality, invasion, and metastasis), metabolic indicators (serum thyroglobulin [sTg], low-density lipoprotein, high-density lipoprotein, triglycerides, free triiodothyronine, and free thyroxine), and treatment factors (iodine-131 dose). Univariate and multivariate analyses were performed to identify significant factors andUnivariate and multivariate analyses were performed to identify significant factors and determine independent predictors associated with treatment outcomes. ***Results:*** The cohort consisted of 264 males and 193 females (totaling 457), with a mean age of 39.68 years (95% CI: 38.74-40.62). The follow-up period ranged from 15 to 60 months. Univariate analysis identified that sTg, thyroid capsular invasion, lymph node extracapsular invasion, and iodine-131 dose were significantly associated with treatment outcomes ($P < 0.05$). Multivariate logistic regression revealed that age was an independent predictor, with an odds ratio of 0.945 (95% CI: 0.896-0.998, $P < 0.05$). sTg levels exhibited a trend toward significance ($P = 0.096$), with an odds ratio of 0.980 (95% CI: 0.957-1.004). However, place of residence did not retain statistical significance in the multivariate model ($P > 0.05$). ROC curve analysis showed sTg demonstrated moderate predictive power, with an AUC of 0.617 (95% CI: 0.485-0.749). In contrast, the overall predictive model demonstrated poor performance, with an AUC of 0.312 (95% CI: 0.191-0.432). ***Conclusion:*** This study identified sTg, thyroid capsular invasion, lymph node extracapsular invasion, and iodine-131 dose as significant factors associated with treatment outcomes in obese patients with DTC. Age was an independent predictor, with older patients demonstrating poorer therapeutic responses. sTg levels showed a trend toward significance in multivariate analysis. ROC curve analysis confirmed that sTg had moderate predictive power, while the overall predictive model demonstrated poor performance. Future studies are warranted to validate these results and improve predictive models for individualized treatment strategies. ***References:*** Corresponding author is Xiaotian Xia.

EP-0060

Multifunctional Biomimetic Nanocarriers Orchestrated by Radionuclide Click Chemistry for Synergistic and Precision Tumor Intervention

R. Wu[1,2,3], *Z. Gao*[1,2,3], *X. Xia*[1,2,3];
[1]*Department of Nuclear Medicine, Union Hospital, Tongji Medical College, Huazhong University of Science and Technology, Wuhan, CHINA,* [2]*Hubei Province Key Laboratory of Molecular Imaging, Wuhan, CHINA,* [3]*Key Laboratory of Biological Targeted Therapy, the Ministry of Education, Wuhan, CHINA.*

Aim/Introduction: Triple negative breast cancer (TNBC) poses significant challenges in clinical treatment due to its complex tumor microenvironment. Traditional chemotherapy often proves insufficient in effectively combating TNBC, while emerging immunotherapies are hampered by limited long-term efficacy and exorbitant costs. Notably, natural compounds derived from traditional Chinese medicine (TCM) have emerged as promising candidates in cancer treatment. In this study, we have developed a multifunctional biomimetic nanocarrier encapsulating Curcumin (C/R-MN) through the incorporation of Ginsenoside Rg3 (Rg3) and a cancer cell membrane coating. Rg3 not only contributes to anti-tumor activity but also enhances the carrier's stability and functionality. Additionally, the nanocarrier could leverage the inherent tumor-homing ability and immune evasion properties of cancer cell membranes to improve targeted delivery. ***Materials and Methods:*** 4T1 tumor cells were lysed, disrupted, and centrifuged to isolate the cell membrane. Rg3 was mixed with 4T1m. Human serum albumin (HSA) was dissolved in deionized water, and the Curcumin (Cur) was added to obtain HSA-Cur through ultrasonic treatment under ice bath conditions. Rg3-4T1m and HSA-Cur were then mixed, and a physical extruder was utilized to produce C/R-MN. The accumulation of the nanocarriers at tumor sites was visualized using pre-positioning technology and PET/CT, with the radionuclide ^{177}Lu employed for targeted radionuclide therapy. ***Results:*** The C/R-MN nanoparticles exhibited a spherical morphology with a hydrated particle size of 161.6 ± 12.5 nm, demonstrating excellent in vitro stability. In vivo pre-targeting PET/CT imaging studies clearly showed a significant radioactive accumulation at the tumor site for C/R-MN (TCO), indicating effective tumor targeting. Notably, the group treated with ^{177}Lu-DOTA-TZ-TCO-C/R-MN demonstrated a remarkable tumor inhibition effect, outperforming other treatment groups. In vivo animal experiments revealed that C/R-MN could significantly increase the infiltration of CD8+ T cells in tumors, leading to enhanced anti-tumor efficacy. Compared with free curcumin and other drugs, C/R-MN not only achieved superior tumor suppression but also maintained good biological safety. Histological examinations of major organs and comprehensive blood biochemical analyses showed no significant abnormalities. ***Conclusion:*** We successfully engineered a stable, biocompatible, and tumor-targeting biomimetic nanocarrier for TNBC therapy. By combining TCM-derived compounds and cancer cell membrane coating with radionuclide labeling via click chemistry, this platform offers a promising strategy for precise, safe, and effective cancer treatment. It highlights the potential of TCM-based nanomedicine for integrating diagnosis and therapy in one system. ***References:*** This research was supported by Hubei Provincial Natural Science Foundation Project(2024AFB633).Zairong Gao and Xiaotian Xia contributed equally as co-corresponding authors.

EP-0061

[^{161}Tb]Tb-DOTA-PSMA I&T Exerts Antitumour Effects and Induces Immune Activation in 2D and 3D Prostate Cancer Coculture Models

Z. Ming, *A. Kurniawan, C. Wu, I. Farina Antunes, E. F. J. de Vries, B. Cornelissen;*
UMCG, Groningen, NETHERLANDS.

Aim/Introduction: Radioligand therapy targeting prostate-specific membrane antigen (PSMA) represents an emerging therapeutic strategy in prostate cancer. ^{161}Terbium (^{161}Tb), a beta- and Auger electron-emitting radionuclide, offers potential advantages over ^{177}Lutetium due to its higher linear energy transfer and short-range cytotoxicity. This study aimed to investigate the therapeutic efficacy and immune-modulatory effects of [^{161}Tb]Tb-DOTA-PSMA I&T in two-dimensional (2D) and three-dimensional (3D) prostate cancer co-culture models, focusing on macrophage activation within the tumour microenvironment. ***Materials and Methods:*** In 2D experiments, the RM1 murine prostate cancer cell line (low PSMA expression) and its PSMA-overexpressing counterpart (PGLS) were used to assess subcellular dosimetry and radiocytotoxic efficacy using clonogenic survival assays. Co-culture studies were used to assess RAW264.7 macrophage cell activation. For 3D studies, co-culture spheroids composed of PGLS cells and RAW264.7 macrophages were established to mimic the tumour immune microenvironment. Spheroids were treated with increasing radioactive doses of [^{161}Tb]Tb-DOTA-PSMA I&T. Cell viability was assessed through monitoring of volume and other morphological changes by microscopy. Immune activation was evaluated using immunofluorescence staining for IBA1, CD80, and CD86. ***Results:*** Clonogenic assays in 2D studies showed a partial inhibition of proliferation in PGLS cell, with up to 32% reduction following treatment with up to 1 MBq of [^{161}Tb]Tb-DOTA-PSMA I&T, but not in RM1 cells. This effect is likely mainly attributed to the targeted radiation-induced DNA damage mediated by the beta emissions. Additionally, when RAW264.7 macrophages were cultured with conditioned medium derived from [^{161}Tb]Tb-DOTA-PSMA I&T-treated PGLS cells, they exhibited significant upregulation of CD80 and CD86 expression compared with RAW264.7 cells exposed to untreated medium (CD80 MFI: 0.47 ± 0.05 versus 0.27 ± 0.06; CD86 MFI: 0.40 ± 0.06 versus 0.12 ± 0.03 , $P < 0.0001$), indicating activation toward a pro-inflammatory phenotype (M1 macrophages) even in the absence of direct radioligand exposure. In 3D spheroids, significant structural disruption and dose-dependent loss of volume (27%) were observed. Importantly, RAW264.7 macrophages co-cultured with PGLS cells exhibited increased expression of IBA1, CD80, and CD86 following treatment compared to untreated co-cultured spheroid, consistent with activation towards a pro-inflammatory, M1-like phenotype. ***Conclusion:*** [^{161}Tb]Tb-DOTA-PSMA I&T shows moderate therapeutic efficacy in PSMA-overexpressing prostate cancer cells, both in 2D and 3D models. In addition to direct tumour cytotoxicity, tumour cells treated with the radioligand activate macrophages within 2D cell cultures and 3D spheroids, potentially enhancing anti-tumour immune responses. These findings support further exploration of [^{161}Tb]Tb-based PSMA-targeted radiotherapy in relation with immune activation.

EP-0062

Multi-tracer PET monitoring of an immunomodulatory therapy in 4R tauopathy: Evaluating a novel drug's impact on glial function and protein pathology

T. Bathe[1,2], *S. Salomasova*[1], *M. Lalia*[1], *G. Palumbo*[1], *R. Oos*[1], *E. Joseph*[1], *R. Schaefer*[1], *R. A. Werner*[1], *M. Brendel*[1,2,3], *L. H. Kunze*[1,4];
[1]*LMU Hospital - Department of Nuclear Medicine, Munich, GERMANY,* [2]*Graduate School of Systemic Neurosciences (GSN), Munich, GERMANY,* [3]*Munich Cluster for Systems Neurology (SyNergy), Munich, GERMANY,* [4]*German Center for Neurodegenerative Diseases (DZNE), Munich, GERMANY.*

Aim/Introduction: The prevalence of neurodegenerative diseases (ND), including Alzheimer's disease (AD) and non-AD tauopathies, is projected to rise significantly by 2050 due to an aging global population. Chronic neuroinflammation, driven by glial activation in response to protein pathologies, is a major contributor to disease progression. Targeting glial dysfunction through immunomodulatory therapies offers a promising approach to mitigate the effects of tauopathies and other ND. The research scope is to monitor the efficacy of GV1001 in a transgenic tau mouse model (PS19) with an early-intervention biomarker study

using molecular biology and neuroimaging techniques. ***Materials and Methods:*** PS19 mice receive chronic treatment with GV1001 for 5 months. Serial neuroimaging techniques, including serial [^{18}F] DPA-714 PET to measure microglial activation, [^{18}F]F-DED PET to measure astrocytic reactivity, and [^{18}F]PI-2620 PET to assess the extent of tau aggregation, are employed to assess treatment effects in vivo. Postmortem validation is performed using immunohistochemistry and biochemical methods, including CSF markers of inflammation e.g. sTREM2 (soluble triggering receptor expressed on myeloid cells 2) and neurodegeneration e.g. NfL (neurofilament light chain), comparing treated mice to placebo and non-transgenic controls. ***Results:*** Preliminary findings, expected to be presented at the conference, will provide insights into the drug's ability to modulate glial activity, restore homeostasis, and reduce tau pathology. ***Conclusion:*** This study highlights the potential of monitoring immunomodulatory strategies to address the complex interplay between chronic neuroinflammation and protein aggregation in ND. If successful, these findings could inform the development of novel therapeutic approaches for AD and related disorders, bridging the gap between preclinical research and clinical application.

EP-0064

Assessment of [225Ac]Ac-DOTATATE for targeted radioligand therapy in neuroblastoma

M. Nestor[1], *H. Berglund*[1], *S. Rinne*[1], *S. Chopra*[1], *H. Alfredeen*[2], *T. Bergström*[1], *F. J. Swartling*[1], *A. Kristian*[3], *T. Tran*[2], *J. Stenman*[4];
[1]*Department of Immunology, Genetics and Pathology, Science for Life Laboratory (SciLifeLab), Uppsala University, Uppsala, SWEDEN,* [2]*Department of Oncology and Pathology, Karolinska Institutet, Stockholm, SWEDEN,* [3]*Biomedical Research, Novartis Pharma AG, Basel, SWITZERLAND,* [4]*Department of Women's and Children's Health, Karolinska Institutet, Stockholm, SWEDEN.*

Aim/Introduction: Metastatic relapse significantly contributes to mortality in pediatric neuroblastoma (NBL). Although targeted radioligand therapy (RLT) using beta emitters (e.g. [177Lu] Lu-DOTATATE) showed promising outcomes, limited efficacy against low-volume of disease, single metastatic cells and micro-metastases remains a challenge. Alpha emitters, characterized by higher linear energy transfer (LET) and shorter particle path length, may potentially enhance cytotoxicity of RLT against minimal residual disease. This study evaluated the alpha-emitting RLT [225Ac]Ac-DOTATATE as a potential targeted therapeutic for high-risk neuroblastoma. ***Materials and Methods:*** [225Ac]Ac-DOTATATE was radiolabeled and assessed for yield, purity, and stability. Specific binding was confirmed in vitro using SSTR2-expressing cells. Biodistribution was studied in both non-tumor-bearing and IMR-32-LUC xenograft-bearing nude mice up to 7 days post-injection followed by dosimetry estimation of absorbed dose. Therapeutic efficacy was evaluated after a single administration of up to 120 kBq of [225Ac]Ac-DOTATATE and compared to untreated controls in IMR-32-LUC tumor-bearing mice. ***Results:*** Radiolabeling of [225Ac]Ac-DOTATATE was achieved with high yield, purity, and stability. In vitro assays demonstrated specific binding to SSTR2-positive cells. Biodistribution studies confirmed tumor uptake, with a pharmacokinetic profile similar to [177Lu]Lu-DOTATATE. Single dose of [225Ac]Ac-DOTATATE demonstrated rapid and substantial tumor regression, with animals achieving near-complete tumor eradication within two weeks without any observable weight loss during the study period. ***Conclusion:*** [225Ac]Ac-DOTATATE shows effective radiolabeling, stability, and specific binding, alongside promising biodistribution profile. Efficacy evaluation demonstrated strong anti-tumor effects, supporting further exploration of [225Ac]Ac-DOTATATE as a targeted alpha therapy to prevent metastatic recurrence in neuroblastoma.

EP-0065

Preclinical In Vivo Imaging of ^{225}Ac Daughters in Oncology Models

T. Karampelas*, M. Rouchota, E. Lambidis, C. Arapatzi, A. Zacharioudaki;*
BIOEMTECH, Athens, GREECE.

Aim/Introduction: ^{225}Ac labelled radiopharmaceuticals have been shown to provide efficient therapy results in oncology, both in preclinical tests and most importantly in clinical practice. ^{225}Ac is a relatively long-lived alpha emitter with its predominant decay path yielding four alpha particles with high energies (ranging from 5.8 to 8.4 MeV) that are resposnible for making ^{225}Ac a valuable and at the same time convenient therapeutic isotope. A significant added advantage is its gamma co-emissions applicable for in vivo imaging from the disintegration of ^{221}Fr (218 keV) and ^{213}Bi (440 keV). Imaging is technically challenging, and novel dedicated solutions can be exploited to better investigate the possible targeting and efficacy results of new ^{225}Ac labelled radiopharmaceuticals. ***Materials and Methods:*** In this study, a FAP overexpressing oncology mouse model has been used, in combination with an ^{225}Ac labelled radiopharmaceutical, knowing to successfully target the specific protein expression. The mice have been imaged in vivo at different time points with a planar imaging system, customized and optimized for the emissions of both ^{225}Ac and ^{212}Pb. Results have been cross related with gamma counter measurements too. ***Results:*** After analyzing the imaging data of the studied animals, a successful tumor targeting effect has been validated and quantified, as well as the update of healthy organs, at different time points. Results have been compared with ex vivo distributions found to not significantly differ. For each time point, the route of each daughter has been separately followed and imaged. ***Conclusion:*** This study has shown that the in vivo biodistribution of an ^{225}Ac labelled radiopharmaceutical, can be accurately investigated through non-invasive in vivo imaging, with the capability to also separate the different daughters of ^{225}Ac in different simultaneous images and by using doses related to the actual therapeutic scheme and not higher. ***References:*** Morgenstern A, Apostolidis C, Kratochwil C, Sathekge M, Krolicki L, Bruchertseifer F. An Overview of Targeted Alpha Therapy with ^{225}Actinium and ^{213}Bismuth. Curr Radiopharm. 2018;11(3):200-208. doi: 10.2174/1874471011666180502104524. PMID: 29732998; PMCID: PMC6237921.

EP-0066

Clinical-Grade Production and Quality Control of ^{225}Ac-FAP2286 for First-in-Human Application

H. khoshhosn[1], *M. Davarpanah*[1], *S. Banihashemian*[2], *A. Abolhoseini*[1], *M. Nasiri*[3], *R. Nami*[1], *M. Kandi Dayeni*[1], *M. Mohebali*[1], *M. Kashani*[1], *J. Abedi*[1];
[1]*Pars Isotope company, Tehran, IRAN, ISLAMIC REPUBLIC OF,* [2]*Cancer Research Center, Shahid Beheshti University of Medical Sciences, Tehran, IRAN, ISLAMIC REPUBLIC OF,* [3]*Department of Cellular and Molecular Biology, School of Biology, Damghan University, Damghan, IRAN, ISLAMIC REPUBLIC OF.*

Aim/Introduction: Targeted alpha therapies (TAT) are revolutionizing the treatment of advanced and resistant cancers (mesenchymal origin, notably sarcoma and mesothelioma), with fibroblast activation protein (FAP) emerging as key target across multiple solid tumors. FAP2286, a peptide based ligand, provides a highly specific vector for radionuclide delivery. Leveraging the potent cytotoxicity of actinium-225, ^{225}Ac-FAP2286 represents a promising next-generation therapeutic candidate. To transition this innovation agent from the laboratory to clinical application, we aimed to establish a reproducible, hospital-based radiolabeling process compliant with GMP standards. This study presents the development, validation, and quality control framework for clinical-grade ^{225}Ac-FAP2286, ensuring a safe reliable product ready for first-

in-human administration and further clinical evolution. ***Materials and Methods:*** ^{225}Ac-nitrate in solid form was provided by IPPE Co. FAP-2286 peptide was from Aprin Sama Pharmed Co. which was used in preparation of the radiopharmaceutical. ITLC Scanner from Fa. Raytest Co. $^{225}Ac(NO_3)_3$ solid was dissolved completely in 0.1 M HCl supra pure to obtain a $^{225}AcCl_3$ solution (370 MBq/nmol) for later radiolabeling by ultrasonic for 30 minutes. $^{225}AcCl_3$ solution was transferred into reaction 10R vial which contain 900 µl of 0.1M sodium ascorbate buffer and 70 µg FAP-2286 (47.6 nmol). The labelling was accomplished after heating the 1.2 ml solution for 30 minutes in 95°C. After Colling for 5 minutes, add 4 ml NaOAc buffer (250mg/1ml NaCl 0.9%). after add DTPA solution, then pass by 0.22 µm filter solution. ***Results:*** Radiolabeling of FAP2286 with ^{225}Ac was successfully optimized, achieving radiochemical yields consistently above 99% and high radiochemical purity (>98%) without purification. The labeled compound demonstrated excellent in-vitro stability in R.T and human serum at 37°C up to 14 days. Quality control analyses confirmed compliance with clinical release criteria, including sterility, endotoxin levels below acceptable thresholds, and appropriate pH (6-8) and radiochemical identity profiles. ***Conclusion:*** 1. Clinical-grade ^{225}Ac-FAP2286 is now ready for first-in-human use, supported by a validated hospital-based production and QC process.2. Robust radiolabeling and quality control of ^{225}Ac-FAP2286 enable safe clinical translation and open new horizons for targeted alpha therapy.3. our work bridges the gap between laboratory innovation and clinical application, bringing ^{225}Ac-FAP2286 one step closer to benefiting patients.4. Validated hospital production of ^{225}Ac-FAP2286 ensures its readiness for future clinical trials FAP-expressing tumors. ***References:*** 1- Hanbo song, Mengxin Xu, Jie Cai, et al. ^{225}Ac-Labeled Antibody for Fibroblast Activation Protein-Targeted Alpha Therapy. Chem. Biomed. Imaging 2023, 1, 628–636. https://doi.org/10.1021/cbmi.3c00067.

EP-0067

Theranostic application of ^{89}Zr/^{177}Lu-labeled anti-RANKL monoclonal antibody in multiple myeloma tumor models

H. Yan[1], *R. Zhang*[1], *X. Wang*[1], *Z. Huang*[1], *C. Xu*[1], *Z. Li*[1], *P. Chen*[2], *J. Li*[1], *M. Dong*[1];
[1]*Department of Nuclear Medicine, Peking University Shenzhen Hospital, Shenzhen, CHINA,* [2]*Department of Pharmacy, Peking University Shenzhen Hospital, Shenzhen, CHINA.*

Aim/Introduction: In recent years, the application of radiopharmaceuticals has emerged as a promising approach for the accurate diagnosis and treatment of malignant tumors. The receptor activator of NF-κB ligand (RANKL) is a crucial cytokine involved in osteoclast differentiation, and its aberrant expression in multiple myeloma (MM) significantly affects bone resorption. This study aims to develop ^{89}Zr/^{177}Lu-labeled anti-RANKL monoclonal antibody for positron emission tomography (PET) imaging and radioimmunotherapy (RIT) application in MM tumor models. ***Materials and Methods:*** The anti-RANKL monoclonal antibody, denosumab, were conjugated with DFO and DOTA for ^{89}Zr and ^{177}Lu radiolabeling respectively. ImmunoPET imaging and RIT studies were performed using ^{89}Zr-DFO-denosumab and ^{177}Lu-DOTA-denosumab in subcutaneous tumor models of MM. ***Results:*** The production of ^{89}Zr-DFO-denosumab and ^{177}Lu-DOTA-denosumab achieved yields exceeding 60% and radiochemical purities greater than 95% following purification. The compound ^{89}Zr-DFO-YS5 exhibited specific binding to the human MM cell lines U266 and H929 xenografts. The maximum standardized uptake value (SUV) recorded in U266 xenografts was 2.76 ± 0.75, measured at 120 hours post-injection (p.i.). In both U266 and H929 tumor models, a single administration of 1.48 MBq (40 µCi) ^{177}Lu-DOTA-denosumab was well tolerated and resulted in significant and sustained inhibition of established tumors, leading to notable increases in median survival times for treated animals (U266 group: 1.48 MBq vs. saline = 23 days vs. 13 days; H929 group: 1.48 MBq vs. saline = 31 days vs. 21 days). ***Conclusion:*** This study demonstrates that ^{89}Zr-DFO-denosumab serves as an excellent PET imaging agent in MM models. Additionally, ^{177}Lu-DOTA-denosumab has shown remarkable therapeutic efficacy in preclinical models of MM, thereby paving a direct path for the clinical translation of this novel RANKL-targeted radioimmunotherapy for the treatment of MM.

EP-0068

161[Tb]Tb-DOTATATE as a novel approach to SSTR2-targeted neuroblastoma therapy

S. Chopra[1], *T. Xu*[1], *H. Berglund*[1], *R. Selvaraju*[2], *M. Nestor*[1];
[1]*Department of Immunology, Genetics and Pathology, Science for Life Laboratory (SciLifeLab), Uppsala University, Uppsala, SWEDEN,* [2]*Department of Medicinal Chemistry, Preclinical PET-MRI Platform, Uppsala University, Uppsala, Sweden, Uppsala, SWEDEN.*

Aim/Introduction: Neuroblastoma is an aggressive pediatric cancer that primarily affects children under five and accounts for 10-15% of pediatric cancer-related deaths. Despite the availability of multimodal treatment strategies, outcomes remain poor in high-risk patients. [177Lu]Lu-DOTATATE is under clinical investigation for neuroblastoma, targeting somatostatin receptor 2 (SSTR2). Terbium-161 shares chemical characteristics and a similar half-life with lutetium-177 but offers a unique advantage through its additional emission of Auger and conversion electrons, which may enhance therapeutic efficacy. This study investigates [161Tb]Tb-DOTATATE as a potential alternative to [177Lu]Lu-DOTATATE in SSTR2-expressing neuroblastoma models. ***Materials and Methods:*** [161Tb]Tb-DOTATATE was labeled with Terbium-161 from PRISMAP high radiochemical yield and stability. Cellular binding was assessed on SSTR2-positive cells in vitro. In vivo biodistribution (4 and 24h p.i.) and SPECT/CT imaging (24h p.i.) were conducted in xenografted nude mice bearing SSTR2-posirtive IMR-32 tumors. Finally, IMR-32 xenografted mice were treated in a pilot therapy study with either [161Tb]Tb-DOTATATE (3, 4, or 6 MBq) or [177Lu]Lu-DOTATATE (4 MBq), and tumor growth, toxicity and survival were monitored over time. ***Results:*** [161Tb]Tb-DOTATATE demonstrated clear SSTR2-specific uptake in vitro and favorable biodistribution and tumor uptake in vivo, comparable to [177Lu]Lu-DOTATATE. SPECT imaging further confirmed the in vivo tumor uptake. In the pilot therapy study, treatment with [161Tb]Tb-DOTATATE appeared to reduce tumor growth in a dose-dependent manner. At day 14 post-injection, tumors in the 6 MBq cohort were on average around 60% of the volume of those in the control group, while the 3 and 4 MBq cohorts showed intermediate effects. In contrast, tumor volumes in the [177Lu]Lu-DOTATATE group remained similar to controls at this time point, suggesting a less apparent impact on early growth dynamics. Survival data followed a similar pattern, with the 6 and 4 MBq [161Tb]Tb-DOTATATE group exhibiting >30% and >20% longer median survival compared to the control group respectively, whereas outcomes for the 3 MBq terbium group and 4MBq [177Lu]Lu-DOTATATE were less pronounced. All treatment regimens were well tolerated, and no signs of treatment-related toxicity were observed. ***Conclusion:*** [161Tb]Tb-DOTATATE shows promise as an SSTR2-targeted radiotherapeutic in preclinical neuroblastoma models, with favorable biodistribution, good tolerability, and preliminary evidence of dose-dependent tumor control. These findings support further investigation of [161Tb]Tb-DOTATATE, including optimization of dosing strategies and assessment in additional preclinical and clinical studies, as a potential alternative to [177Lu]Lu-DOTATATE for the treatment of SSTR2-expressing neuroblastoma.

EP-0069

Preclinical development of [^{161}Tb]Tb-DOTA-HYNIC-panPSMA and comparison with [^{177}Lu]Lu-DOTA-HYNIC-panPSMA, [^{161}Tb]Tb-DOTA-J591 and [^{177}Lu]Lu-DOTA-J591

J. Roetman[1], *C. Morgat*[2], *L. Ali*[2], *S. Bodin*[2], *E. Hindie*[2];
[1]*Telix Pharmaceuticals, Melbourne, AUSTRALIA,* [2]*University Hospital of Bordeaux, Bordeaux, FRANCE.*

Aim/Introduction: [^{161}Tb]Tb-DOTA-HYNIC-panPSMA is a new prostate specific membrane antigen (PSMA) inhibitor relevant for targeted radionuclide therapy (TRT) of PSMA-positive prostate cancer cells using terbium-161.[1] Like lutetium-177 (^{177}Lu), ^{161}Tb is a β-emitter but can deliver a higher concentration of radiation over a short path due higher linear energy transfer, resulting in greater cell death.[2] Herein, we report the therapeutic efficacy of [^{161}Tb]Tb-DOTA-HYNIC-panPSMA and its comparison with [^{177}Lu]Lu-DOTA-HYNIC-panPSMA, [^{161}Tb]Tb-DOTA-J591 and [^{177}Lu]Lu-DOTA-J591 in 2D and 3D models of prostate cancer cells expressing different levels of PSMA. ***Materials and Methods:*** DOTA-HYNIC-panPSMA and DOTA-J591 were radiolabeled with ^{161}Tb and ^{177}Lu. PC3-pip (very high PSMA expression), LnCaP (high PSMA expression), 22Rv1 (moderate/weak PSMA expression), and PC3 cells (no PSMA expression) were cultured as monolayer (2D) and tridimensional (3D). An increasing amount of radiopharmaceuticals (from 0 to 20MBq/mL) were added for 4h (2D) or 24h and cells were re-cultured for 4 additional days. ***Results:*** The endpoint for this study is the comparison of cell death with ^{161}Tb and ^{177}Lu and with panPSMA and J591. Data analysis is ongoing. ***Conclusion:*** This study provides important comparative results regarding peptide-based and antibody-based TRT using ^{161}Tb and sets the groundwork for a Phase 1 study investigating [^{161}Tb]Tb-DOTA-HYNIC-panPSMA in patients with prostate cancer. ***References:*** (1) Morgat C, Vimont D, Attia K. Development of [^{161}Tb]Tb-DOTA-HYNIC-panPSMA for targeted radionuclide therapy of prostate cancer. EJNMMI. 2024;51:S255-S255 (2) Alcocer-Avila ME, Ferreira A, Quinto MA, Morgat C Hindie E, Champion C. Radiation doses from 161Tb and 177Lu in single tumour cells and micrometastases. EJNMMI Phys. 2020;7:33.

EP-0070

DNA Damage Repair Inhibition boots Radiopharmaceutical Therapy for Triple Negative Breast Cancer

Y. Medina Guevara, *H. Comas Rojas, O. Bio Idrissou, O. Kwon, L. Lambert, A. Pinchuk, L. Wehner, A. Carston, N. Clemons, B. Bednarz, J. Weichert, R. Hernandez;*
University of Wisconsin-Madison, Madison, WI, UNITED STATES OF AMERICA.

Aim/Introduction: Poor survival rates mark triple-negative breast cancer (TNBC) due to its early metastasis and lack of effective targeted therapies. We developed a series of alkylphosphocholine analogs (NM600) for radiopharmaceutical therapy (RPT) targeting breast cancer. To amplify the radiobiological effects of RPT, we employ a synthetically lethal treatment combination inhibiting poly-(ADP-ribose) polymerase 1 (PARP1), a bromodomain and extraterminal (BET) protein in TNBC cells ***Materials and Methods:*** Cytotoxicity was determined in 4T1 cells treated with 0.3 nM -1 mM Talazoparib (TAZ:PARPi), ABBV-075 (BETi), or combined with RPT ([^{177}Lu]Lu-NM600). Cell viability was assessed at 24 h, 48 h, 72 h, and 96 h after treatment. IC_{50}s were determined, and combination effects were evaluated between treatments using established synergy models. Expression changes in the DDR genes (e.g., BRCA1/2 and RAD51) were measured 24h-post treatment with BETi or RPT by qPCR. Therapy studies employed female Balb/c 8-10 weeks old subcutaneously implanted with 4T1 cells. Mice bearing 4T1 tumors were divided into five groups (n=5): control, RPT, RPT + PARPi, RPT + BETi and RPT + PARPi + BETi. RPT consisted of single 9.25 MBq IV injection of [^{177}Lu]Lu-NM600. PARPi (TAZ, 0.5 mg/kg) and BETi (ABBV-075, 1 mg/kg) were orally administrated for 14 days starting concomitantly with [^{177}Lu]Lu-NM600 injections. Tumor volume, animal weight and overall survival were monitored thrice weekly. ***Results:*** ABBV-075 and TAZ showed similar nanomolar cytotoxicity at 72 and 96 h post-treatment (IC_{50}s: 369 vs. 414 nM and 8 vs. 6 µM, respectively). Therefore, 300 nM of ABBV-075 and TAZ were employed in all subsequent in vitro combinations. Synergistic effects were observed between ABBV-075, TAZ, and increasing doses of ^{177}Lu (0.3 to 30 Gy). Combination treatment resulted in greater cytotoxicity compared to either ^{177}Lu or inhibitors/drugs alone. Treatment with BETi resulted in downregulation of BRCA1, BRCA2, and RAD51 genes confirming DDR inhibition as the potential mechanisms for the radiosensitization of 4T1 cells. The triple combination treatment demonstrated significant tumor growth inhibition compared to all other treatment cohorts ($P < 0.05$). Median overall survival was 18, 14, 11, 18, 18, 23, and 28 in the vehicle (n=5), PARPi (n=5), BETi (n=5), [^{177}Lu]Lu-NM600 (n=5), [^{177}Lu]Lu-NM600 + BETi (n=5), [^{177}Lu]Lu-NM600+ PARPi (n=5) and [^{177}Lu]Lu-NM600 + PARPi + BETi (n=5), respectively ***Conclusion:*** These findings demonstrated the enhance potency of RPT when combined with clinically relevant PARPi and BETi and the potential this combination therapy to tackle TNBC.

EP-0071

^{177}Lu-Microspheres as Biocompatible Micro-Seed Implants for Loco-regional Radiation Ablation in Breast Cancer: A Preclinical Proof-of-Concept

S. Chopra, *A. Aggarwal, K. Kaur, S. R. Shovan, A. Kumar, A. Bal, A. S. Oinam, B. R. Mittal, J. Shukla;*
Postgraduate Institute of Medical Education and Research, Chandigarh, INDIA.

Aim/Introduction: Over 75% of breast tumor recurrences occur within ~2 cm of the surgical margin, primarily due to residual clonogens and delays in initiating post-operative radiotherapy. To address this, we conducted a proof-of-concept preclinical study using ^{177}Lu-microspheres for Intra-operative Radiopharmaceutical Therapy (IORPT), delivering a localized 60 Gy boost to the tumor bed following resection in breast cancer-bearing rat models. We also evaluated their potential as permanent intra-tumoral micro-seed implants for neoadjuvant therapy. ***Materials and Methods:*** Physicochemical characterization of ^{177}Lu-microspheres was performed using DLS-PSA, SEM, zeta potential, XRD, FTIR, and EDS. Radiochemical purity, sterility, and apyrogenicity were evaluated for quality control. Shelf-life was determined at room temperature and 4°C, with stability evaluated in human serum and PBS for 21 days.Triple-negative breast carcinoma was induced in 20 female wistar rats, divided into four groups (n=5 each):Control Group A underwent tumor resection without IORPT. Margins were sent for histopathology. Whole-body (WB)-CT scans were done up to 3-months post-surgery to assess recurrence.Treatment Group A underwent tumor resection followed by IORPT using 18.5 ± 7.4 MBq ^{177}Lu-microspheres (60 Gy). SPECT-CT scans were performed at 15 days, 1 and 2-months, followed by CT at 3-months.Control Group B didn't receive any treatment. WB-CT scans were conducted up to 3-months for disease monitoring. Treatment Group B received DSA-guided intra-tumoral injection of 29.6 ± 12.9 MBq ^{177}Lu-microspheres (100 Gy). SPECT-CT scans were done at multiple time points up to 2-months and WB-CT at 3-months for response evaluation. ***Results:*** ^{177}Lu-microspheres were quasi-spherical (mean diameter: 5.9 µm), with efficient radiolabeling (90 ± 8% yield, RCP >99%), sterility, and 21-day stability. In Control Group A (no IORPT), 4/5 rats showed recurrence (mean: 4 ± 1.6 weeks) out of which only one rat showed tumor involvement of resected margins on histopathology. Treatment Group A (post-IORPT) showed recurrence in only 2/5 rats, with one case of margin involvement. Mean recurrence time was prolonged to 10.5 ± 2.9 weeks. SPECT-CT demonstrated effective

localization and sustained retention of radiotracer in tumor bed for up to 2-months, with no evidence of leaching. In Control Group B (no treatment), mean survival was 16.2 ± 3.5 weeks, with mean tumor volume of 31.8 ± 2.8 cc. In Treatment Group B (intratumoral therapy), survival exceeded 25 weeks (study endpoint), with tumor volume reduced to 2.4 ± 1.1 cc. SPECT/CT confirmed prolonged intratumoral localization of the radiotracer without leaching for up to 2-months post-treatment. ***Conclusion:*** ^{177}Lu-microspheres proved to be safe, biocompatible, and effective permanent implants for both IORPT and neoadjuvant therapy, improving loco-regional control and survival with minimal side effects.

EP-0072

Preclinical Evaluation of ^{161}Tb-BPAMD: A Bone-Targeting Radiopharmaceutical with High Affinity and Stability

A. Vukadinovic, *D. Stankovic, M. Mirkovic, D. Jankovic, P. Sitarica, M. Maric, M. Peric, S. Vranjes-Djuric, M. Radovic;*
University of Belgrade, Vinca Institute of Nuclear Sciences, Belgrade, SERBIA.

Aim/Introduction: Bone metastases are a common complication of advanced cancers, leading to significant morbidity. Radiopharmaceutical therapy using bone-targeting agents labeled with β^--emitting radionuclides has proven effective in pain palliation and disease management. BPAMD, a macrocyclic bisphosphonate with high affinity to bone, has demonstrated excellent results when labeled with ^{177}Lu. Terbium-161 (^{161}Tb) is a promising alternative due to its similar coordination chemistry, higher linear energy transfer (LET), and emission of conversion and Auger electrons. This study aims to evaluate the radiolabeling, stability, and biodistribution of ^{161}Tb-BPAMD. ***Materials and Methods:*** BPAMD was labeled with ^{161}Tb (95 °C, 30 min), and the radiochemical purity was measured by radio-thin layer chromatography (ITLC). Stability studies in phosphate-buffered saline (PBS) and human serum were performed over 48 hours. In vitro hydroxyapatite (HAP) binding assays were conducted to evaluate mineral affinity. Biodistribution studies were conducted in healthy Wistar rats following intravenous administration, and radioactivity in excised organs was measured via gamma counting and expressed as % the injected dose (%ID). ***Results:*** The radiolabeling of BPAMD with ^{161}Tb achieved radiochemical purity exceeding 99% under optimized conditions. The complex remained stable (>98% RCP) in PBS and serum for at least 48 hours, demonstrating high kinetic stability. In vitro HAP binding studies revealed a strong mineral affinity with high binding efficiency (>98%). In vivo biodistribution showed rapid and high skeletal uptake, with more than 60% ID localizing in bone tissues within 2 hours post-injection. Non-target organ uptake was minimal, and clearance from soft tissues was fast, indicating a favorable pharmacokinetic profile. ***Conclusion:*** ^{161}Tb-BPAMD is a promising candidate for targeted radionuclide therapy of skeletal metastases. Its excellent in vitro stability and bone-targeted biodistribution suggest a strong potential for clinical translation. The overall biodistribution pattern was highly analogous to that reported for ^{177}Lu-BPAMD, but ^{161}Tb's additional low-energy electron emission may offer enhanced therapeutic efficacy at micrometastatic sites. Clinical trials should be carried out to validate the efficacy in human patients.

EP-0073

Dimeric CCK2R Radiotheranostic Tracers Synergize with mTOR Inhibition for Enhanced Tumor Therapy

L. Bian;
Fudan University Shanghai Cancer Center, Shanghai, CHINA.

Aim/Introduction: Cholecystokinin-2 receptor (CCK2R) is highly expressed in neuroendocrine tumors and serves as a promising target for radiotheranostics. However, current CCK2R-targeted radiopharmaceuticals suffer from suboptimal tumor uptake and retention. This study aimed to develop a novel dimeric radiotheranostic probe for improved PET imaging and therapy, and to evaluate its synergistic effect with mTOR inhibition in refractory tumors. ***Materials and Methods:*** A novel dimeric probe, DOTA-CCK2R-dimer, was synthesized and radiolabeled with either ^{68}Ga for PET imaging or ^{177}Lu for therapy. Radiochemical properties, hydrophilicity, stability, and pharmacokinetics were assessed. In vitro uptake studies were performed in CCK2R-positive AR42J cells. In vivo micro-PET/SPECT imaging, biodistribution, and histological analyses were conducted in AR42J tumor-bearing mice. Combination therapy with the mTOR inhibitor RAD001 was evaluated for tumor suppression and survival. Single-cell RNA-seq was used to explore tumor heterogeneity and treatment response. ***Results:*** [^{68}Ga]Ga-DOTA-CCK2R-dimer exhibited higher tumor uptake and prolonged retention compared to monomeric analogues, with enhanced tumor-to-background contrast and receptor specificity. [^{177}Lu]Lu-DOTA-CCK2R-dimer enabled long-term tumor retention and selective elimination of highly proliferative, poorly differentiated tumor subpopulations. Combination with RAD001 significantly enhanced therapeutic efficacy, prolonging survival and increasing DNA damage. Mechanistically, RAD001 suppressed glutathione-mediated detoxification pathways, elevating oxidative stress. GSTK1 was identified as a key regulatory factor, linking metabolic detoxification to radiosensitivity. ***Conclusion:*** This study introduces a potent dimeric CCK2R-targeted radiotheranostic system with strong preclinical evidence for efficacy and safety. The synergistic combination with mTOR inhibition enhances treatment outcomes by targeting resistant tumor subpopulations and modulating oxidative stress responses. These findings provide a promising strategy for improving radioligand therapy in neuroendocrine tumors.

EP-0074

Experimental radionuclide therapy using [^{177}Lu]Lu-AU-SAR-M1 in GRPR-positive xenograft models

K. Obeid[1], *P. Kanellopoulos*[1], *E. Bezverkhniaia*[1], *Y. Liu*[2], *M. W. Konijnenberg*[3], *B. A. Nock*[4], *T. Maina*[4], *V. Tolmachev*[1], *A. Orlova*[1];
[1]*Uppsala University, Uppsala, SWEDEN,* [2]*Uppsala Univeristy, Uppsala, SWEDEN,* [3]*Erasmus MC, Rotterdam, NETHERLANDS,* [4]*NCSR Demokritos, Athens, GREECE.*

Aim/Introduction: Gastrin-releasing peptide receptor (GRPR) is an attractive target for targeted radiotherapy due to its high overexpression in many malignancies, including prostate and breast cancers. In previous work, we evaluated different Lu-177-labeled GRPR antagonists, identifying [^{177}Lu]Lu-AU-SAR-M1 (DOTAGA-AMA-Dig-DPhe-Gln-Trp-Val-Sar-His-Leu-NHEt) as the most promising candidate for a follow-up therapy study (1). Therefore, in this study, we evaluated the anti-tumoral efficacy of [^{177}Lu]-AU-SAR-M1 in PC-3 prostate cancer GRPR-expressing xenograft model. ***Materials and Methods:*** Biodistribution studies of AU-SAR-M1 labeled with Lu-177 were performed on PC-3 xenografted mice 0.5h, 1h, 4h, 24h, 48h, and 76h post-injection to evaluate dosimetry. Two different therapy plans were designed (n=10-8): Group 1 received injections once weekly (12MBq, 150pmol) to a total of six injections; Group 2 received three injections within a week - 30 days break - three injections within a week (12MBq, 150pmol). Both groups were pre-treated orally with sacubitril (1.4mg) 30min before each injection. SPECT/CT images were acquired one day after the first injection. As a comparator, a third group was treated with vehicle (PBS+ 1%BSA w/v). The humane endpoint is set to when the tumor volume exceeds 1000mm^3, when bleeding ulcerations are observed, or when overall weight loss is >15%. Animal weights and tumor measurements were monitored twice weekly. Blood samples were taken weekly to evaluate blood toxicity. ***Results:*** Labeling of AU-SAR-M1 with Lu-177 provided >98% radiochemical yield and >96% purity

(molar activity: 80MBq/nmol). Biodistribution studies showed a fast washout of activity from non-tumor tissues, with a tumor-to-blood dose ratio of 596, while the tumor-to-kidneys dose ratio was 5.4. Treatment with [^{177}Lu]Lu-AU-SAR-M1 significantly prolonged the median survival of Groups 1 and 2 (all mice alive at day 67), compared to the mice treated with the vehicle (median survival 57 days). On day 67, five mice in Group 1 and four in Group 2 were tumor-free. Among the remaining animals, tumors in Group 1 were stabilized and growing slowly (78±46mm^3). In Group 2 three tumors were slowly growing (67±13mm^3), while two showed exponential growth (368±68mm^3). Tumors were visualized with SPECT/CT images, confirming the in vivo tumor targeting of [^{177}Lu]Lu-AU-SAR-M1. No blood toxicity was observed in any of the three groups. ***Conclusion:*** GRPR-targeting radiotherapy using [^{177}Lu]Lu-AU-SAR-M1 eradicated tumors in PC-3 xenografts or stabilized their growth, thus enhancing the median survival of mice without causing bone marrow toxicity. The dosing regimen should be further optimized. ***References:*** 1. Obeid et al, iSRS25 abstract ID 109.

EP-0075

Granzyme B PET Imaging Enhances Belzutifan and KL201 Combination Therapy Using a Tumor Cell Membrane Nano-Loading Platform for Renal Cell Carcinoma

Y. Hou[1,2,3], *X. Xia*[1,2,3];
[1]*Department of Nuclear Medicine, Union Hospital, Tongji Medical College, Huazhong University of Science and Technology, Wuhan, CHINA,* [2]*Hubei Province Key Laboratory of Molecular Imaging, Wuhan, CHINA,* [3]*Key Laboratory of Biological Targeted Therapy, the Ministry of Education, Wuhan, CHINA.*

Aim/Introduction: Renal cell carcinoma (RCC) is the most prevalent malignant tumor of the adult kidney. Tumor cell membrane nanocarrier platforms, featuring homologous targeting capabilities, can improve drug targeting, maximize therapeutic efficacy, and minimize adverse effects. Belzutifan, an FDA-approved HIF-2α inhibitor, disrupts the pVHL-HIF-VEGF pathway to suppress tumor growth/angiogenesis. KL201, a circadian regulator, stabilizes cryptochrome 1 (CRY1), modulating circadian rhythms to influence cancer progression. This study pioneers a tumor cell membrane platform co-delivering Belzutifan and KL201 for RCC therapy. ***Materials and Methods:*** Belzutifan and KL201 were dissolved in DMSO, mixed, and sonicated to form the Belzutifan-KL201 complex. Renca tumor cells were subjected to hypo-osmotic lysis and differential centrifugation to isolate tumor cell membranes (CCm). The CCm was then mixed with the Belzutifan-KL201 complex and extruded through a 200 nm porous polycarbonate membrane to obtain CCm-Belzutifan-KL201. Similarly, CCm-Belzutifan and CCm-KL201 complexes were prepared. The size, morphology, zeta potential, and solution stability of these complexes were evaluated using transmission electron microscopy (TEM) and dynamic light scattering (DLS). In vivo efficacy was tested using both in situ Renca tumor and subcutaneous rhabdomyosarcoma mouse models. Mice were divided into four groups: control, Belzutifan, KL201, and combination therapy. Treatments were administered via daily tail vein injections. Tumor immune responses were monitored using ^{68}Ga-GZP PET/CT imaging, while tumor growth was assessed by measuring body weight and tumor volume over a 14-day period. Additionally, blood and tissues from the heart, liver, spleen, lungs, and kidneys were collected for blood analysis and hematoxylin and eosin (H&E) staining. ***Results:*** The CCm-Belzutifan-KL201, CCm-Belzutifan, and CCm-KL201 complexes formed spherical vesicles with hydrated particle sizes of 192.8 ± 9.3 nm, 155.3 ± 8.3 nm, and 163.5 ± 2.7 nm, respectively, and zeta potentials of -17.2 ± 0.8 mV, -13.8 ± 0.5 mV, and -12.0 ± 0.7 mV, respectively. All formulations demonstrated good stability in PBS solution for up to 5 days. In vivo radioimmunoimaging revealed that the combination therapy group exhibited a significantly stronger immune response compared to the groups treated with Belzutifan or KL201 alone. Furthermore, the combination group showed the smallest tumor volumes and the most pronounced tumor suppression after 14 days of treatment. ***Conclusion:*** This study develops a tumor cell membrane nanoplatform co-loading Belzutifan and KL201, demonstrating synergistic antitumor effects via enhanced immune activation and circadian modulation. The platform exhibits optimal size, stability, and dual-drug delivery efficacy, offering a promising strategy for RCC treatment. ***References:*** This research was supported by Hubei Provincial Natural Science Foundation Project (2024AFB633). Corresponding author is Xiaotian Xia.

EP-0077

PET imaging of integrin a_vb_8 upregulation as an early prognostic marker for radiotherapy response

A. Litvinenko[1], *A. Sesink*[1], *L. Wendlinger*[1], *D. Repáraz*[2], *H. Koch*[1], *D. Viertl*[1], *F. Herrera*[1], *J. Notni*[3], *M. Schottelius*[1];
[1]*CHUV, Lausanne, SWITZERLAND,* [2]*Unibe, Bern, SWITZERLAND,* [3]*Trimt, Radeberg, GERMANY.*

Aim/Introduction: TGF-β is a tumor-promoting cytokine that induces resistance to immuno- and radiation therapy by creating immunosuppressive tumor microenvironment (TME). Upon external beam radiation therapy, TGF-β is released in a dose-dependent manner from the latent form (expressed by immune cells in the TME). Integrin $\alpha_v\beta_8$, expressed on tumor cells, plays a crucial role in the release of TGF-β. We therefore investigated if radiation-induced upregulation of $\alpha_v\beta_8$ could be exploited as a surrogate marker for TGF-β, aiding early treatment response assessment and guiding combination treatments. ***Materials and Methods:*** Baseline (D -1) integrin $\alpha_v\beta_8$ expression was assessed in four different subcutaneous syngeneic mouse tumor models (MC38 and CT26 (colon carcinoma), EMT6 (breast carcinoma), and TRAMP-C2 (prostate adenocarcinoma)) using ^{68}Ga-Triveoctin PET/CT (100 pmol/mouse, 40-60 min p.i.). Tumors were then irradiated with a single dose of 30 Gy on day 0, and ^{68}Ga-Triveoctin imaging was repeated on day 1, 3, 7 and 9 post irradiation to monitor irradiation-induced upregulation of $\alpha_v\beta_8$ expression. Non-irradiated control animals were imaged at the same time points to assess tumor growth-related changes in $\alpha_v\beta_8$ expression. At selected time points, mice were sacrificed, tumors were excised, paraffin-embedded, and stained for TGF-β and $\alpha_v\beta_8$ using immunofluorescence. ***Results:*** All four tumor models demonstrated low baseline $\alpha_v\beta_8$ expression before irradiation, with the EMT6 model showing the highest and the CT26 model showing the lowest tracer uptake (0.81 ± 0.29 vs 0.40 ± 0.18 %iD/ml, respectively). Across four tumor models, some irradiated mice showed a gradual increase in $\alpha_v\beta_8$ integrin expression—independent of tumor growth, as ^{68}Ga-Triveoctin uptake remained stable in non-irradiated controls—while others exhibited a decrease in uptake. In the MC38 model, changes in $\alpha_v\beta_8$ expression closely correlated with radiotherapy response—mice with complete or partial responses showed lower $\alpha_v\beta_8$ uptake on day 4 post-irradiation compared to pre-irradiation levels (D -1: 0.51+0.04 %ID/ml vs D4: 0.38+0.06 %ID/ml), unlike non-responders (D -1: 0.56+0.06 %ID/ml vs D4: 0.81+0.10 %ID/ml). Additionally, to unravel the correlation between ^{68}Ga-Triveoctin PET signal intensity, tumoral $\alpha_v\beta_8$ integrin expression and TGF-β levels before and after irradiation, immunofluorescence staining of tumor tissue is ongoing. ***Conclusion:*** Preliminary data show a radiation-induced increase in ^{68}Ga-Triveoctin uptake across all tumor models investigated (TRAMP-C2 > EMT6 > CT26 = MC38), with two distinct patterns of $\alpha_v\beta_8$ upregulation. In the MC38 tumor model, these patterns were confirmed to correlate with radiotherapy response, supporting the potential of ^{68}Ga-Triveoctin as a predictive marker for treatment outcome.

EP-0078

Enhancing Triple-Negative Breast Cancer Radiotherapy via EZH2-Targeted Nanoplatform and Synergistic Radionuclide Therapy

R. Wu[1,2,3], *Y. Hou*[1,2,3], *Z. Gao*[1,2,3], *X. Xia*[1,2,3];
[1]*Department of Nuclear Medicine, Union Hospital, Tongji Medical College, Huazhong University of Science and Technology, Wuhan, CHINA,* [2]*Hubei Province Key Laboratory of Molecular Imaging, Wuhan, CHINA,* [3]*Key Laboratory of Biological Targeted Therapy, the Ministry of Education, Wuhan, CHINA.*

Aim/Introduction: Breast cancer, and specifically triple-negative breast cancer (TNBC), continues to pose a significant global health challenge due to its aggressive characteristics and the paucity of effective treatment options. Current interventions, such as systemic chemotherapy and immunotherapy, exhibit inconsistent efficacy. This research introduces a tumor microenvironment-adaptive nanomedicine (CCm-HSA-Taz) that integrates the enhancer of zeste homolog 2 (EZH2) inhibitor Tazemetostat (Taz) with albumin-stabilized nanoparticles to facilitate targeted drug delivery. In conjunction with targeted radionuclide therapy (TRT), this approach synergistically disrupts immunosuppressive pathways and enhances therapeutic outcomes in TNBC. ***Materials and Methods:*** HSA was dissolved in deionized water, then mixed with Tazemetostat (Taz) and ultrasonicated to form HSA-Taz. CCm and HSA-Taz were combined and extruded to generate CCm-HSA-Taz, which was characterized. In the subsequent phase, a tumor-bearing model was established. Throughout the observation period, both baseline and post-treatment immune responses of the tumors were assessed using ^{68}Ga-GZP PET/CT imaging. Additionally, the body weight and tumor volume of the tumor-bearing mice were monitored regularly, and a change curve was plotted. Blood samples and vital organ tissues were collected. ***Results:*** CCm-HSA-Taz was characterized as a spherical vesicle with a hydrated particle size of 183.1 ± 10.6 nm and a Zeta potential of -14.7 ± 0.6 mV. The stability of the PBS solution in vitro was maintained effectively for 5 days. In vivo radioimmunoassay studies indicated that the immune response in the CCm-HSA-Taz combined with the [^{177}Lu]Lu radiotherapy group was significantly stronger than that observed in the CCm alone group or the [^{177}Lu]Lu radiotherapy alone group. Additionally, compared to other single treatment groups, the CCm-HSA-Taz combined with the [^{177}Lu]Lu radiotherapy group exhibited the smallest tumor volume and a significant tumor inhibition effect in the observation period. Following the combination treatment, there was an observed increase in the apoptotic cell population, and antitumor immunity was enhanced, as anticipated. Furthermore, all results were corroborated through pathological and imaging examinations. ***Conclusion:*** We developed a tumor microenvironment-adaptive nanomedicine delivering Taz to disrupt immunosuppression and enhance radiotherapy sensitivity in triple-negative breast cancer, without significant side effects in animal models. Non-invasive PET/CT imaging revealed reduced tumor glucose metabolism and improved immune cell cytotoxicity. The utilization of FDA-approved components underscores the potential for clinical translation of this strategy. ***References:*** This research was supported by Hubei Provincial Natural Science Foundation Project(2024AFB633).Zairong Gao and Xiaotian Xia contributed equally as co-corresponding authors.

EP-0079

Synergistic suppression of anaplastic thyroid carcinoma via targeted co-delivery of integrin αv/β3 siRNA and ^{131}I using iRGD-modified exosomes

R. Zhang[1], *W. Zhang*[2], *N. Li*[1], *S. Wang*[1], *Q. Jia*[1], *J. Tan*[1];
[1]*Department of Nuclear Medicine, Tianjin Medical University General Hospital, Tianjin, CHINA,* [2]*Department of Nuclear Medicine, West China Hospital, Chengdu, CHINA.*

Aim/Introduction: This study aimed to establish a novel ^{131}I (radioactive iodine)-labeled, iRGD-targeted exosomal delivery system derived from HEK-293T cells for the co-delivery of integrin αv/β3 small interfering RNA (siRNA) and radionuclide therapy, thereby synergistically inhibiting anaplastic thyroid carcinoma (ATC) through dual-modal gene silencing and internal irradiation. ***Materials and Methods:*** iRGD-modified exosomes loaded with αv/β3 siRNA (iRGD-exos-si-ITGαv or iRGD-exos-si-ITGβ3, denoted as iRGD-exos-si-ITGαv/β3) were isolated via ultracentrifugation. In vitro assays, including EDU proliferation, transwell migration, and apoptosis analysis, were performed to evaluate their effects on ATC cells. Tumor-targeting efficiency was dynamically monitored in nude mouse xenograft models using in vivo fluorescence imaging. The exosomes were further radiolabeled with ^{131}I (^{131}I-iRGD-exos), and their dual therapeutic efficacy was systematically assessed. ***Results:*** Both iRGD-exos-si-ITGαv and iRGD-exos-si-ITGβ3 significantly inhibited ATC cell proliferation, migration, and invasion ($p<0.05$). In vivo imaging confirmed the tumor-specific accumulation of iRGD-exos. The ^{131}I-labeled system achieved a labeling efficiency of 58.1% with radiochemical purity >95%. In xenograft models, the ^{131}I-iRGD-exos-si-ITGαv group exhibited the most potent tumor suppression ($p<0.01$), accompanied by marked downregulation of integrin αv mRNA and protein levels in tumor tissues. ***Conclusion:*** Integrin αv/β3 serves as a critical therapeutic target for ATC. The iRGD-engineered exosomal platform enables tumor-specific co-delivery of siRNA and ^{131}I, offering a synergistic strategy to suppress ATC progression via dual gene silencing and radiation therapy. This approach provides a novel clinical paradigm for treating integrin αv/β3-overexpressing malignancies, including aggressive ATC.

EP-0080

Does the PSMA ligand, PSMA-11, prevent ^{177}Lu- PSMA-617 uptake into human non-tumour cells and enhance the cytotoxic effect of ^{177}Lu-PSMA-617 in human prostate cancer cells?

Y. Zhao, *A. Alfteimi, A. Helm, M. Jueptner, U. Luetzen, M. Zuhayra; Department of Nuclear Medicine, Molecular Imaging, Diagnostics and Therapy, University Hospital of Schleswig-Holstein, Kiel, GERMANY.*

Aim/Introduction: Many patients suffer from radiation-related side effects mainly due to off-target exposure of non-tumour tissues to ^{177}Lu-PSMA-617. PSMA-11, the precursor for ^{68}Ga-HBED-CC-PSMA-11 synthesis, competes with the radioligand binding to PSMA. The precursor may, therefore, reduce the cytotoxicity of ^{177}Lu-PSMA-617 by interfering with its uptake in non-tumour tissues. We investigated: 1) the uptake of ^{177}Lu-PSMA-617 in the presence of cold PSMA-11 into human normal and tumour prostatic cells, salivary glands and kidney cells, and 2) the pharmacological effects of PSMA-11 with or without ^{177}Lu-PSMA-617 in the human prostate cancer (PCa) cell lines, LNCaP and PC3 cells. ***Materials and Methods:*** 1) To evaluate the uptake of the radioligand, human PCa cells, LNCaP and PC3; human salivary glands cells, Hs.917T and A-253; and human kidney cells, RPTEC and 293T were treated with ^{177}Lu-PSMA-617 and various concentrations of PSMA-11. The radioactivity of cell pellets measured with a γ-counter was normalised for corresponded protein content. The results are expressed as cpm/mg of proteins. 2) LNCaP cells, a PSMA-positive Pca cell line, were exposed to various concentrations of PSMA-11 for 24 h and 48 h. LDH activity, a cell death parameter, was quantified by the Cytotoxicity Detection Kit and cell proliferation by WST-1 assay and cresyl violet staining. ***Results:*** The ^{177}Lu-PSMA-617 uptake into LNCaP cells was not affected by low concentrations of PSMA-11 (5 nM and 10 nM), but significantly reduced by concentrations higher than 20 nM. PSMA-11 inhibits the uptake of ^{177}Lu-PSMA-617 into PSMA-positive cells approximately ten times more effectively than PSMA-617. High

amount of PSMA-11 (100 nM) showed a tendency to decrease the uptake of ^{177}Lu-PSMA-617 in salivary glands cells and to increase its uptake in kidney cells; both effects were not significant. PSMA-11 had no effect on LDH release from LNCaP cells, but significantly reduced LNCaP cell proliferation by approximately 50 % after 24 h of exposure even at low concentrations (10 nM) (P<0.001) and by 30 % after 48 h exposure (P<0.05) at concentrations 50 nM. The execution of LNCaP cells by ^{177}Lu-PSMA-617 was significantly increased in the presence of PSMA-11 up to 10 nM (p<0.001). ***Conclusion:*** In conclusion, PSMA-11 does not interfere with ^{177}Lu-PSMA-617 uptake in human non-tumour tissues, such as the salivary glands and kidney. However, synergistical treatment with ^{177}Lu-PSMA-617 and PSMA-11 at low concentrations (10 nM) significantly enhances ^{177}Lu-PSMA-617-induced PCa cell death.

EP-0081

Theranostic PET Imaging and Radioimmunotherapy (RIT) of Head and Neck Squamous Cell Carcinoma (HNSCC) Patient-Derived Xenografts (PDX) in NRG mice with Anti-Epidermal Growth Factor Receptor (EGFR) [^{64}Cu]Cu- and [^{177}Lu]Lu-DOTA-Panitumumab-F(ab')$_2$

C. Chan[1], *M. Khosravifarsani*[1], *A. Ku*[1], *J. Meens*[1], *L. Ailles*[1], *S. Bratman*[1], *R. Reilly*[1,2];
[1]*Department of Pharmaceutical Sciences, Leslie Dan Faculty of Pharmacy, Toronto, ON, CANADA,* [2]*Princess Margaret Cancer Centre, University Health Network, Toronto, ON, CANADA.*

Aim/Introduction: Head and neck cancer (HNSCC) has a high risk of recurrence and metastasis despite treatment by surgery, radiation or chemotherapy. Our aim was to study a novel theranostic approach to PET imaging and radioimmunotherapy (RIT) of HNSCC in patient-derived xenograft (PDX) mouse models using anti-epidermal growth factor receptor (EGFR) [^{64}Cu]Cu- and [^{177}Lu]Lu-DOTA-panitumumab F(ab')$_2$, respectively. EGFR are overexpressed in 90% of HNSCC. ***Materials and Methods:*** Three HNSCC PDX (#88955, #73191, #61531) were implanted s.c. in NRG mice. EGFR expression was assessed by flow cytometry. PET and biodistribution (BOD) studies were performed at 24 h post i.v. injection (p.i.) of [^{64}Cu]Cu-DOTA-panitumumab F(ab')$_2$ (7-15 MBq; 50 µg) in tumour-bearing NRG mice (n=3-5). Normal tissue toxicity of [^{177}Lu]Lu-DOTA-panitumumab F(ab')$_2$ (6.0 MBq) was evaluated in non-tumour bearing NRG mice by complete blood cell counts and blood biochemistry at 14 d p.i. Mice with PDX were treated by i.v. injection of 4.0-5.0 MBq (50 µg) of [^{177}Lu]Lu-DOTA-panitumumab F(ab')$_2$. Control mice received unlabeled DOTA-panitumumab F(ab')$_2$ or normal saline. A tumour growth index (TGI) was determined by dividing the tumour volume by that prior to treatment. TGI was plotted vs. time (d) and the slope of the curve determined. ***Results:*** EGFR expression of PDX #88955 was higher than #73191 or #61531, but all PDX were EGFR-positive. PET with [^{64}Cu]Cu-DOTA-panitumumab F(ab')$_2$ detected all PDX tumours. BOD studies showed higher tumour uptake in PDX #88955 (17.0±0.9%ID/g) than #73191 (13.4±2.5%ID/g; P<0.05) or #61531 (6.7±3.5%ID/g; P<0.05). Liver uptake was observed on PET. Liver, spleen and kidney uptake were 14.1-15.8, 4.1-6.9 and 6.2-6.9%ID/g, respectively. No normal tissue toxicity was found at 14 d p.i. of [^{177}Lu]Lu-DOTA-panitumumab F(ab')$_2$. Blood cell counts and alanine aminotransferase (ALT) and creatinine levels were not significantly different than NRG mice injected with normal saline (n=4; P>0.05). The slope of the TGI vs. time (d) curve for PDX #88955 treated with [^{177}Lu]Lu-DOTA-panitumumab F(ab')$_2$ (0.81±0.10 d^{-1}) was 1.7-fold significantly lower (P≤0.002) than DOTA-panitumumab F(ab')$_2$ (1.35±0.13 d^{-1}) or normal saline (1.65±0.11 d^{-1}). The slope of the TGI curve for PDX #73191 treated by RIT (0.10±0.01 d^{-1}) was 4.7-6.2 fold significantly lower (P<0.001) than DOTA-panitumumab F(ab')$_2$ (0.47±0.06 d^{-1}) or saline (0.62±0.04 d^{-1}). The slope for PDX #61531 treated by RIT (0.09±0.01 d^{-1}) was 1.9-fold significantly lower (P<0.001) than DOTA-panitumumab F(ab')$_2$ (0.17±0.01 d^{-1}) or saline (0.18±0.02 d^{-1}). ***Conclusion:*** Theranostic PET and RIT with [^{64}Cu]Cu- and [^{177}Lu]Lu-DOTA-panitumumab F(ab')$_2$ is a promising approach for detection and treatment of HNSCC.

EP-05

e-Poster Are

A: Preclinical and Translational Studies -> A1 Medical Preclinical -> A15 Preclinical Dosimetry and Radiobiology

EP-0082

Dual-Line Approach: Radiosensitisation in Prostate Cancer Cell Lines with histone deacetylase inhibitors and Ac-225, Lu-177 and X-ray Radiation

T. Wallner*, R. Runge, K. Tietze, K. Wetzig, R. A. Bundschuh, J. Kotzerke;*
Universitätsklinikum Carl Gustav Carus, Dresden, GERMANY.

Aim/Introduction: Current therapeutic applications in nuclear medicine predominantly involve the use of beta and alpha emitters. Various combinatorial approaches play an important role in improving therapeutic outcomes. The addition of epigenetically modifying agents may increase the efficacy of radionuclide treatments even further. This study examines the cytotoxic effects of the histone deacetylase inhibitor (HDACi) Suberoylanilide hydroxamic acid (SAHA) combined with alpha irradiation (Ac-225), beta irradiation (Lu-177) or X-ray irradiation in two prostate cancer cell lines, PC3 and Du-145. ***Materials and Methods:*** Du-145 and PC3 prostate cancer cell lines were pre-incubated with SAHA at 0.5 & 2.5 µM and 2.5 µM for 24 hours respectively. Subsequently they were exposed to either Ac-225 (0.1 - 2.0 Gy), Lu-177, (0.5 - 10.0 Gy), or X-ray (1.0 - 10.0 Gy) irradiation. Cell survival was assessed using a clonogenic survival assay, while apoptosis and necrosis were assessed by PI & Annexin V staining and Western Blotting. ***Results:*** In PC3 cells, the combined treatment with 2.5 µM of SAHA and irradiation did not significantly alter cell survival compared to irradiation alone. Conversely, Du-145 cells treated with 2.5 µM of SAHA showed decreased survival rates across all three irradiation types, with the most pronounced effects seen with X-ray exposure. At 10 Gy, cells showed a survival fraction of 2.9% without and 0.66% with SAHA. PI & Annexin V assay data illustrated no clear correlation between SAHA and the induction of early apoptosis and necrosis in PC3 cells. However, SAHA partially increased necrosis and late apoptosis rates in Du-145 cells. Western Blots revealed the expression of the pro- and anti-apoptotic protein Bcl2 and Bax in PC3 cells. Interestingly, the expression of Bax in Du-145 cells appears to be cell specific, with no notable upregulation of pro-apoptotic proteins following SAHA treatment. ***Conclusion:*** Du-145 cells exhibit a marked sensitivity to SAHA, supporting its potential as a radiosensitiser. This effect may enhance therapeutic outcomes in patients with a poor response to radionuclide therapy alone. In contrast, PC3 cells exhibited limited sensitivity to SAHA, aligning with existing reports of SAHA resistance in this cell line. Our data suggests that SAHA's effects are cell-specific, likely mediated by differences in apoptotic signalling. Furthermore, PI & Annexin V results imply that observed effects may not be primarily driven by apoptotic mechanisms, but rather by alterations in cell cycle regulation or involvement of alternative cellular pathways.

EP-0083

Towards Monte-Carlo Based Preclinical Personalized Dosimetry for Targeted Radioligand-Immunotherapy

O. Kochebina, *C. Comtat, A. Grindel, C. Truillet;*
BioMaps Laboratory, Service Hospitalier Frédéric Joliot, Commissariat à l'Énergie Atomique et aux Énergies Alternatives, Université Paris-Saclay, Orsay, FRANCE.

Aim/Introduction: Radioligand therapy (RLT) has demonstrated promising results for survival and patient care in prostate cancer and neuroendocrine tumors. However, one of the challenges lies in expanding the application to other cancer types, which requires targeting alternative tumor-specific biomarkers. The strategy involves the combination of immunotherapy and RLT, for instance by targeting PD-L1. This approach, radioligand-immunotherapy, aims to tumor cell radiation damage while simultaneously activating the immune response. To optimize such treatments, individualized dosimetry is critical. We propose leveraging ^{89}Zr-labeled anti-PD-L1 PET imaging to predict the agent biodistribution and to perform Monte Carlo-based preclinical dosimetry for the ^{177}Lu-labeled anti-PD-L1 radioligand, under the assumption of similar pharmacokinetics. ***Materials and Methods:*** We use the Monte Carlo platform GATE version 10 (2024) [1] to simulate particle-matter interactions for preclinical dosimetry. Our first objective is to develop and validate a full simulation and analysis pipeline, benchmarking it against published results using the MIRD formalism and organ-based S-values on ^{18}F data [2,3]. Then, we used the validated pipeline to predict ^{177}Lu absorbed doses at the organ level from ^{89}Zr PET imaging data under the assumption of similar radiokinetics. In a second phase, we aim voxel-based dosimetry by generating Monte Carlo-based 3D dose rate maps for each time point for more accurate dosimetry analysis of the PET acquisition. These maps can then be also integrated over time to compute the total absorbed dose at the voxel level, enabling spatially resolved and individualized dose estimation. ***Results:*** The dosimetry pipeline is validated on published ^{18}F data [2], and the differences of obtained with GATE10 Monte Carlo S-values do not exceed 20% compared to [3]. The ^{177}Lu dosimetry uses the same validated pipeline and relies to ^{89}Zr PET-based radiokinetic data. Uncertainty analysis was also conducted to ensure robust dose interpretation. ***Conclusion:*** This work represents a first step toward personalized dosimetry for targeted radioligand-immunotherapy. The validated pipeline enables accurate organ-level dose estimation from ^{89}Zr PET data and supports absorbed dose recalculation for ^{177}Lu. Future developments will focus on voxel-based dosimetry, with dose rate map generation for each PET (^{89}Zr) and/or SPECT (^{177}Lu) acquisition. This will pave the way for an optimized and accelerated workflow, with the long-term goal of creating a "push-button" open-source tool for preclinical personalized dosimetry. ***References:*** [1] http://www.opengatecollaboration.org/ [2] Gupta A et al. doi: 10.1088/1361-6560/ab134b. PMID: 30913544 [3] Xie T, Zaidi H. Phys Med Biol. 2013 Jan 7;58(1):169-82. doi: 10.1088/0031-9155/58/1/169.

EP-0084

Optimisation and calibration for pre-clinical SPECT imaging of Pb-212 for targeted alpha therapy

P. Gape[1], *A. Jones*[1], *A. Drews*[1], *G. Stasiuk*[1], *L. Livieratos*[1], *M. K. Schultz*[2], *S. Y. A. Terry*[1];
[1]King's College London, London, UNITED KINGDOM, [2]Perspective Therapeutics, Coralville, IA, UNITED STATES OF AMERICA.

Aim/Introduction: To study the relationships between radiation absorbed dose and biological response for molecular radiotherapy, imaging systems must be calibrated. This work aims to determine a protocol for SPECT imaging of ^{212}Pb and calibrate the scanner for quantitative imaging and dosimetry. ***Materials and Methods:*** ^{212}Pb was supplied by Perspective Therapeutics (Iowa, USA). Images were acquired on a Mediso nanoScan SPECT/CT small animal scanner with high energy collimators. Single peak (239/583/78 keV, 20/20/30% width), and multipeak acquisitions were investigated. The 583 keV peak was included to directly image ^{208}Tl. To determine reconstruction parameters, a phantom with spheres of varying diameter (3.95, 4.95, 6.23, 7.86 mm) was filled with a known activity concentration (10:1 sphere to background activity concentration ratio) and scanned. Images were reconstructed with varying numbers of reconstruction subsets and iterations. Contrast recovery coefficient was calculated for each sphere according to NEMA guidelines [1] and used to choose an optimal reconstruction. A calibration factor (CF, MBq/kcps) with associated uncertainty was determined by imaging a uniform phantom at a known activity concentration. Activity recovery and partial volume effects were characterized using the sphere phantom (activity concentration = 0.89 MBq/mL). Volumes of interest (VOIs) were drawn to construct a recovery curve. The quantitative imaging workflow was validated in an anatomical setting by imaging a preclinical mouse phantom (Bioemtech), with kidneys, liver, bladder and tumour compartments filled with a known activity concentration. Agreement between known and recovered activity was calculated. Uncertainties were calculated in accordance with EANM guidelines [2]. ***Results:*** All sphere sizes were resolvable, implying achievable spatial resolution is < 3.95 mm. Contrast recovery coefficient plateaued when reconstruction reached 48 iterations with 3 subsets. Activity was accurately recovered in spheres to on average 7% (SD = 9%) across sizes and energy windows. The largest calculated uncertainty was 23%. In the mouse phantom, partial volume loses of 14 - 20% were seen for kidneys, bladder and tumour, but with an oversized VOI activity was recovered to on average 97% of true activity (-11% to + 16% range). ***Conclusion:*** Quantitative imaging for ^{212}Pb (and ^{208}Tl) is feasible and accurate based on derived activity calibration and partial volume correction factors. This work provides a workflow for calibration of a SPECT system for quantitative imaging with a novel isotope. ***References:*** [1] NEMA Standards Publication NU 1-2018, Performance Measurements of Gamma Cameras [2] Gear JI et al., Eur J Nucl Med Mol Imaging. 2018 Dec;45(13):2456-2474.

EP-06

e-Poster Area

A: Preclinical and Translational Studies -> A1 Medical Preclinical -> A16 New Radiopharmaceuticals - SPECT

EP-0085

Clinical feasibility of ^{99m}Tc-CTR-FAPI SPECT/CT imaging in lung cancer: a prospective head-to-head comparison with ^{18}F-FDG PET/CT

S. Li[1,2], *Z. Li*[3], *M. Xu*[4], *P. Yang*[1], *H. Xu*[1], *C. Van De Wiele*[2], *Z. Liu*[5], *Y. Wu*[1];
[1]Peking University Cancer Hospital Inner Mongolia Hospital/ Cancer Hospital Affiliated to Inner Mongolia Medical University, Hohhot, CHINA, [2]Gent University, Gent, BELGIUM, [3]Peking University Cancer Hospital, Beijing, CHINA, [4]Changping Laboratory, Beijing, CHINA, [5]Peking University, Beijing, CHINA.

Aim/Introduction: Fibroblast activation protein (FAP), overexpressed in cancer-associated fibroblasts (CAFs), is a promising target for tumor stroma imaging. Although positron emission tomography (PET) tracers such as ^{68}Ga-FAPI demonstrate excellent imaging performance, their widespread clinical application is hindered by high costs, short half-life, and limited equipment availability. In this prospective study, we evaluated the diagnostic potential of ^{99m}Tc-CTR-FAPI, a covalent targeted radioligand for FAP associated SPECT/CT imaging, in patients

suffering from lung cancer, using ^{18}F-FDG PET/CT imaging as the reference standard. ***Materials and Methods:*** Forty-one treatment-naive patients with histologically confirmed lung cancer underwent both ^{99m}Tc-CTR-FAPI SPECT/CT and ^{18}F-FDG PET/CT imaging within a 1-3 day interval. Additionally, six healthy volunteers underwent sequential whole-body planar imaging with ^{99m}Tc-CTR-FAPI. Radiation dosimetry was assessed with OLINDA/EXM 2.0. Detection rates, SUV_{max}, target-to-background ratio (TBR), and TNM staging concordance were analyzed using McNemar's test, Wilcoxon signed-rank test, and Kappa statistics. ***Results:*** No significant adverse events were observed. ^{99m}Tc-CTR-FAPI showed physiological uptake in salivary glands, thyroid, liver, spleen and pancreas, with low background activity. Both modalities achieved 100% primary lesion detection (^{99m}Tc-CTR-FAPI: SUV_{max} 7.71 ± 4.00, TBR 3.77 ± 2.59). For metastases, ^{18}F-FDG detected 222 lesions versus 185 with ^{99m}Tc-CTR-FAPI (SUV_{max} 6.59 ± 3.68, TBR 3.38 ± 2.13). TNM staging agreement was excellent (κ = 0.92), with ^{99m}Tc-CTR-FAPI providing superior contrast in brain metastases. ***Conclusion:*** ^{99m}Tc-CTR-FAPI SPECT/CT showed comparable diagnostic capability to ^{18}F-FDG PET/CT for detecting primary lung cancer lesions. Despite its lower sensitivity for small metastatic lesions, these differences did not significantly impact clinical staging. Given the widespread availability of SPECT equipment, the low cost of ^{99m}Tc radiopharmaceuticals, and favorable radiopharmacokinetics, ^{99m}Tc-CTR-FAPI demonstrates strong potential for clinical implementation, particularly in community hospitals and resource-limited regions.

EP-0086

iPSMA-BN: A novel theranostic dual target molecule, assessing two prostate cancer clinical scenarios: metastatic hormone-sensitive and metastatic hormone-resistant. Asociations with genomic alterations in DNA damage repair genes

S. Gonzalez Rueda[1], *F. Garcia Perez*[1], *A. Calderon Avila*[2], *G. Ferro Flores*[3], *Q. Pitalua Cortes*[1], *E. Gomez Argumosa*[1], *I. Soldevilla Gallardo*[1];
[1]*National Cancer Institute of Mexico, Tlalpan, Mexico City, MEXICO,* [2]*UMAE IMSS CMN SXXI Especialidades, Cuahutemoc, Ciudad de México, MEXICO,* [3]*National Institute of Nuclear Research, Toluca, Mexico City, MEXICO.*

Aim/Introduction: Prostate cancer(PC) is highly heterogeneous and agressive, often assessed with dual PET/CT ([^{18}F]FDG and PSMA),nevertheless, they are often unavailable in developing countries, as an alternative, we developed a novel heterodimer composed of iPSMA and bombesin(iPSMA-BN), overexpressed in primary and metastatic PC lesions; acting on the androgen receptor and its splicing variants through NFκβ-pathway, involved in castration resistance. The main objective of this study was to assess the uptake pattern of [^{99m}Tc]Tc-iPSMA-BN, and its association with genomic alterations in DNA damage repair(DDR) genes in mCRPC and mCSPC. Secondary objectives were the diagnostic value of [^{99m}Tc]Tc-iPSMA-BN SPECT/CT versus [^{18}F]F-PSMA-1007 PET/CT and security profile and adverse effects of [^{177}Lu]Lu-iPSMA-BN therapy. ***Materials and Methods:*** Prospective,single-centre, non-randomized, phase I/II study, that recruited 25 PC patients (18 mCRPC and 7 mCSPC), ISUP≧3, previosuly treated with ADT, ± ARPI's, ± chemotherapy.[^{99m}Tc]Tc-iPSMA-BN SPECT/CT and [^{18}F]F-PSMA-1007 PET/CT were performed at recruitment (less than one month appart). Quantitative measurements performed: target-to-background-ratio(TBR), lesion quantification and total-tumor-volume(TTV) for both(PSMA-PET/CT and heterodimer-SPECT/CT). Candidates for [^{177}Lu]Lu-iPSMA-BN treatment were considered if TBR-SPECT>TBR-PET. ***Results:*** DDR alterations were found in 60%(n=15) patients, from which 100%(n=15) were germinal and 20%(n=3) somatic; 60%(n=9) of germinal alterations were pathogenic variants(PV) and 40%(n=6) variants of unknown significance(VUS); 100%(n=3) of somatic alterations were PV. Most frequently affected genes were ATM,PALB2 and p53. Diagnostic value of [^{99m}Tc]Tc-iPSMA-BN was similar to that of [^{18}F]F-PSMA-1007,except in regional nodes,where the heterodimer had a better lesion dectection rate(p=0.046). TBR was analogous with both techiques. Receiver-operating-characteristic analysis was performed,with an AUC of 0.659 (50% sensitivity and 90.9% specificity) for association of SPECT-TBR ≥40 with genomical alterations.Aditionally, 2 patients with TBR-iPSMA-BN>TBR-PSMA were considerated candidates forPRRT; both patients had germinal mutations: a PV in ATM and a VUS in POLE, they received 2 and 3 [^{177}Lu]Lu-iPSMA-BN cicles respectively, 8 weeks apart,with low-non toxicity,minor G1-G2 side effects(nausea) and improvement in metastases-related-pain and quality-of-life. ***Conclusion:*** The novel[^{99m}Tc]Tc-iPSMA-BN SPECT/CT heterodimer outperformed [^{18}F]F-PSMA-1007 PET/CT in regional nodal lesion detection in mCRPC. We advocate a promising theranostic alternative, more economical with broader distribution availability; a new alternative that includes patients that would normally be excluded of PRRT,for not having a standard phenotipic profile. This is the first prospective study with a dual-cohort of patients assessed with an heterodimer, using quantitative-volumetric measures that can be used both in PET and SPECT techniques, evaluating the molecular behaviour regarding genomic alterations.[^{177}Lu]Lu-iPSMA-BN proved to be safe,having a low toxicity profile with only G1-G2 nausea as side effect.

EP-0087

eSOMA-FAP-02, a Dual SSTR2 and FAP-Targeted Heterodimer for Neuroendocrine Tumors

Y. Seimbille*, D. Chapeau, A. Piet, L. Li, C. de Ridder, D. Stuurman, P. Paraiso, H. Ma;*
Erasmus MC, Rotterdam, NETHERLANDS.

Aim/Introduction: Due to the heterogeneity of tumors, strategies to improve the effectiveness of diagnostics have been intensively explored. In this study, we developed two heterodimers targeting the fibroblast activation protein (FAP) and the somatostatin receptor subtype 2 (SSTR2) via a chelate-bridged linker (N_3-Py-DOTAGA) to connect both targeting vectors. ***Materials and Methods:*** eSOMA-FAP-01 and eSOMA-FAP-02 contained the SSTR2 ligand, TATE, and the (4-quinolinoyl)-glycyl-2-cyanopyrrolidine targeting FAP. The main difference between these compounds relies on the click reaction used to attach both vectors to the chelate. eSOMA-FAP-01 and eSOMA-FAP-02 were labeled with [^{111}In]$InCl_3$, showing high labeling efficiency and stability. Biochemical properties of the heterodimers, such as $LogD_{7.4}$, binding affinity, uptake and internalization, were assessed by in vitro assays. SPECT/CT imaging were performed in either H69- or HT1080-FAP-tumor bearing mice. ***Results:*** Modifications of the chemical structure of eSOMA-FAP-02 improved the hydrophilic character of the heterodimer. eSOMA-FAP-01 and eSOMA-FAP-02 exhibited an IC_{50} value for SSTR2 similar to the gold standard DOTA-TATE and an IC_{50} value for FAP 4 and 7-fold higher than OncoFAP. The uptake of [^{111}In]In-eSOMA-FAP-01 and [^{111}In]In-eSOMA-FAP-02 in U2OS-SSTR2 cells was similar than that of [^{111}In]In-DOTA-TATE. In HT1080-FAP cells, both tracers exhibited similar uptake values, which were 1.6-fold higher than that of [^{111}In]In-FAPI-46. Biodistribution of [^{111}In]In-eSOMA-FAP-01 displayed a similar trend than our previous compound eTFC-01 and eSOMA-DM1, therefore, it was withdrew from further investigation [1-2]. SPECT images in H69-xenografted mice revealed a clear visualization of the tumor with a retention of [^{111}In]In-eSOMA-FAP-02 up to 72 h. [^{111}In]In-eSOMA-FAP-02 displayed a lower kidneys uptake than [^{111}In]In-DOTA-TATE. However, in HT1080-FAP-xenografted mice, tumor uptake of [^{111}In]In-eSOMA-FAP-02 was 2-4 fold lower at all time points than the uptake of [^{111}In]In-FAPI-46. No non-specific uptake was observed for [^{111}In]In-eSOMA-FAP-01. ***Conclusion:*** [^{111}In]In-eSOMA-FAP-02 exhibited comparable or better in vitro and in vivo properties for both FAP and SSTR2 compared to the monomeric counterparts [^{111}In]In-DOTA-TATE and [^{111}In]In-FAPI-46. Further investigations are required to confirm its potential for imaging and treatment of NETs. ***References:*** 1. Chapeau D., Beekman S., Piet A., Li L., de Ridder C., Stuurman D., Seimbille Y. eSOMA-DM1, a maytansinoid-based theranostic small-molecule drug conjugate for neuroendocrine tumors. Bioconjugate Chemistry, 2024, 35(11):1823-1834.2. Chapeau D., Beekman S., Handula M., Murce E., de Ridder C.,

Stuurman D., Seimbille Y. eTFC-01: a dual-labeled chelate-bridged tracer for SSTR2-positive tumors. EJNMMI Radiopharmacy and Chemistry, 2024, 9:44.

EP-0088

LDLR as a glioblastoma gateway: 203Pb-labeled peptide for targeted glioblastoma SPECT imaging

I. Tworowska[1], *L. Flores*[1], *C. Malicet*[2], *R. Zielinski*[3], *P. Davis*[1], *P. Lecorche*[2], *J. Temsamani*[2], *E. Delpassand*[1];
[1]*RadioMedix Inc., Houston, TX, UNITED STATES OF AMERICA,* [2]*Vect-Horus, Marseille Cedex 15, FRANCE,* [3]*MDAnderson, Houston, TX, UNITED STATES OF AMERICA.*

Aim/Introduction: Driven by the correlation between overexpression low-density lipoprotein receptors (LDLR) and tumor progression, we designed ^{203}Pb-DOTAM-peptide conjugates (RMX-VH) engineered for high-affinity targeting of LDLR. This abstract showcases the development and preclinical evaluation of our lead compound, ^{203}Pb-DOTAM-RMX-VH for SPECT/CT imaging of glioblastoma (GBM). ***Materials and Methods:*** Radiochemical and chemical purity were assessed using TLC chromatography and radio/UV HPLC. ^{203}Pb was sourced from the UAB Cyclotron Facility in Birmingham, AL. SPECT imaging were performed in U87MG xenografts and U251 orthotopic models at various time points using a Gamma-Eye camera (Bioemtech, Greece). Following imaging, the organs and tumors were collected, weighed, and analyzed for radioactivity with a Wizard2 Gamma Counter (PerkinElmer, Waltham, MA). The percentage of the injected dose per gram of tissue (%ID/g) was calculated and adjusted for radioactive decay. ***Results:*** The radiolabeling of ^{203}Pb-RMX-VH-PKM was highly efficient, achieving a radiochemical yield (RCY) of over 90% and demonstrating stability for up to 48 hours. Incorporating the PKM motif significantly extended the agent's systemic plasma half-life to 9.2 hours, compared to just 1.3 hours for RMX-VH without PKM. Biodistribution and tumor uptake studies revealed peak performance at 24 hours post-injection in xenograft models of GBM. At 1-hour post-injection, tumor retention reached 6.2±1.8%ID/g, and remained stable at 3 hours, before declining to 3.3±0.2%ID/g by 24 hours. Liver accumulation remained relatively consistent throughout 2-24h. Importantly, bone marrow uptake was low at the early time point (1.2±0.7%ID/g) and dropped three-fold by 24 hours, indicating stable coordination of the ^{203}Pb isotope. A similar downward trend was observed across other normal organs. Interestingly, the renal retention of RMX-VH-PKM was lower than that of RMX-VH lacking the albumin-binding motif. SPECT/CT imaging and biodistribution studies in U251 orthotopic tumor models confirmed high uptake as early as 1-hour post-injection, underscoring the agent's rapid and efficient tumor-targeting properties. ***Conclusion:*** Structural modification of radiotracer with pharmacokinetic-modifying linker (PKM) not only extended the blood circulation time of our lead agent but also enhanced its tumor retention compared to the unmodified molecule.

EP-0089

The position of HYNIC chelator and the molecular design of the DARPin-based G3 constructs influence the biodistribution of an imaging tracer for detection of HER2-expressing tumors

V. Tolmachev[1], *R. Varvashenya*[2], *A. Prach*[2], *E. Plotnikov*[2], *M. Tretyakova*[2], *D. Eskova*[2], *V. Bodenko*[2], *G. Yanovich*[2], *A. Schulga*[3], *E. Konovalova*[3], *M. Belousov*[4,5], *V. Chernov*[5], *S. Deyev*[3], *M. Larkina*[2];
[1]*Department of Immunology, Genetics and Pathology (IGP), Uppsala University, Uppsala, SWEDEN,* [2]*Tomsk Polytechnic University, Tomsk, RUSSIAN FEDERATION,* [3]*Shemyakin & Ovchinnikov Institute of Bioorganic Chemistry, Russian Academy of Sciences, Moscow, RUSSIAN FEDERATION,* [4]*Siberian State Medical University, Tomak, RUSSIAN FEDERATION,* [5]*Cancer Research Institute, Tomsk National Research Medical Center, Russian Academy of Sciences, Tomsk, RUSSIAN FEDERATION.*

Aim/Introduction: Radionuclide visualization of HER2 expression in breast cancer might enable the selection of patients for treatment with antibodies trastuzumab and pertuzumab. In clinics [1], we have demonstrated that the ^{99m}Tc-labeled designed ankyrin repeat protein (DARPin) G3 ([^{99m}Tc]Tc-$(HE)_3$-G3) provides sensitive imaging of HER2 and discriminates breast cancer with high and low HER2 expression. To facilitate clinical translation, we initiated the development of G3 derivatives enabling single-vial kit formulation. In our previous studies, HYNIC-maleimide was conjugated to unique cysteine conjugated at the C-terminus of G3 via different linkers [2]. The conjugates were labelled with ^{99m}Tc and their biodistribution was compared with that of [^{99m}Tc]Tc-$(HE)_3$-G3 in mice bearing human HER2-expressing xenografts. We found that [^{99m}Tc]Tc-$(HE)_3$-G3 provides 1.6-fold higher tumour-to-liver ratio than the best variant, [^{99m}Tc]Tc-G3-$(G_3S)_3$C-HYNIC. This study tested the hypothesis that changing the position of HYNIC to N-terminus would modify the biodistribution. ***Materials and Methods:*** G3 variants, where cysteine was connected to N-terminus either via triglutamate (CE_3-G3) or a longer glycine and serine-containing dodecapeptide ($C(G_3S)_3$-G3) were produced and site-specifically conjugated with HYNIC-maleimide. Labelling was performed by ^{99m}Tc-pertechnetate reduction in the presence of tricine and EDDA (60°C, 30 minutes). Purification was performed using a size-exclusion cartridge. HER2-positive SKOV-3 and SK-BR-3, and HER2-negative PC-3 and Ramos cells were used to measure specificity. Biodistribution was measured in Nu/j mice bearing SKOV-3 or Ramos xenografts ***Results:*** The isolated yield was 75-85%, radiochemical purity over 95%. Both [^{99m}Tc]Tc-HYNIC-CE_3-G3 and [^{99m}Tc]Tc-HYNIC-$C(G_3S)_3$-G3 bound specifically to SKOV-3 and SK-BR-3 cells, the binding to HER2-negative PC-3 was negligible. The affinity was similar, 1.68±0.16 and 1.72±0.25 nM for [^{99m}Tc]Tc-HYNIC-CE_3-G3 and [^{99m}Tc]Tc-HYNIC-$C(G_3S)_3$-G3, respectively. This was lower than affinity of C-terminal-modified [^{99m}Tc]Tc-G3-$(G_3S)_3$C-HYNIC (0.60±0.15nM). The uptake in HER2-positive xenografts, 4.4±0.8, 4.4±0.8, and 4.5 0.4 %ID/g, for [^{99m}Tc]Tc-HYNIC-CE_3-G3, [^{99m}Tc]Tc-HYNIC-$C(G_3S)$-G3, and control [^{99m}Tc]Tc-G3-$(G_3S)_3$C-HYNIC, respectively was similar. The uptake of the novel variants in HER2-negative tumours was much lower ($p < 0.05$). [^{99m}Tc]Tc-HYNIC-$C(G_3S)$-G3 had 2-3 fold lower uptake in liver, spleen and lungs compared to other variants. This created preconditions for a higher contrast and more sensitive visualization of hepatic and pulmonary metastases, which are frequent in HER2-expressing cancers. ***Conclusion:*** The biodistribution of [^{99m}Tc]Tc-labelled HER2-targeting DARPins depends on both the position of the [^{99m}Tc]Tc-HYNIC label and the length of a spacer between G3 and the label. This might be used for optimization of imaging properties of such constructs. ***References:*** 1. Bragina O et al. J Nucl Med. 2022;63:528-5352. Larkina M et al. Mol Pharm. 2024;21:1919-1932.

EP-07

e-Poster Are

A: Preclinical and Translational Studies -> A1 Medical Preclinical -> A17 New Radiopharmaceuticals - PET

EP-0090

Optimization of the N-terminus of neurotensin analogs for PET imaging of solid malignancies

S. Kaur[1,2], *S. Mair*[1], *W. Lau*[1], *J. Zeisler*[1], *F. Benard*[1,2], *K. Lin*[1,2], *J. Lau*[1,2];
[1]*BC Cancer Research Institute, Vancouver, BC, CANADA,* [2]*The University of British Columbia, Vancouver, BC, CANADA.*

Aim/Introduction: The neurotensin receptor 1 (NTSR1) is overexpressed in various solid malignancies, including

pancreatic ductal adenocarcinoma (PDAC) [1]. NTSR1 binds to neurotensin (NT) analogs, with NT(8-13) (Arg^{8}-Arg^{9}-Pro^{10}-Tyr^{11}-Ile^{12}-Leu^{13}) being the minimal sequence required for receptor engagement. However, NT(8-13) has a short biological half-life due to cleavage at Arg^{8}-Arg^{9}, Pro^{10}-Tyr^{11}, and Tyr^{11}-Ile^{12} peptide bonds. In this study, we aim to develop NT(6-13) analogs by substituting Tyr^{11} with unnatural amino acids to stabilize the amide bonds. Additionally, the N-terminus is modified to optimize the pharmacokinetics of NT analogs to improve tumor-to-organ contrast for NTSR1-targeted PET imaging. ***Materials and Methods:*** NT-based SM01010 ([Lys^{6}(DOTA),NMeArg^{8},1-Nal^{11}]NT(6-13)), SM01011 (DOTA-Lys^{6},NMeArg^{8},1-Nal^{11}]NT(6-13)), SK01001 ([Lys^{6}(DOTA),NMeArg^{8},Dmt^{11}]NT(6-13)) and SK01014 (Ac-[Lys^{6}(DOTA),NMeArg^{8},Dmt^{11}]NT(6-13)) were synthesized via solid-phase peptide synthesis. The peptides incorporated either 1-(naphthyl)-L-alanine (1-Nal) or 2,6-dimethyl-L-tyrosine (Dmt) at Tyr^{11} position. SM01010 and SM01011 differ in the placement of DOTA. Compared with SK01001, the N-terminus of SK01014 was acetylated. NT-20.3 was synthesized as a reference. Gallium (^{nat}Ga and ^{68}Ga) complexations were conducted in acetate (0.1 M, pH 4.5) and HEPES (2 M, pH 5.0) buffers, respectively. In vitro binding assays were performed with the PC3 cell line. PET imaging and biodistribution studies were conducted in PC-3 and AsPC-1 tumor-bearing mice at 1 h post-injection (p.i.). In vivo stability was assessed at 15 minutes p.i. ***Results:*** The binding affinity value (K_i) for ^{nat}Ga-NT(6-13) analogs was found to be 0.65-32.9 nM compared to 9.25 ± 3.40 nM (^{nat}Ga-NT-20.3). Radiolabeling with ^{68}Ga produced ^{68}Ga-labelled peptides in 18-60% decay-corrected yields with radiochemical purity >95%. [^{68}Ga]Ga-SM01010 and [^{68}Ga]Ga-SM01011 showed similar tumor uptake (2.28 ± 0.50 and 3.00 %ID/g), suggesting flexible chelator attachment at both ε- and α-NH_2 of Lys^{6}. [^{68}Ga]Ga-SK01014 showed comparable tumor uptake (%ID/g) to [^{68}Ga]Ga-NT-20.3 in both PC-3 (10.1 ± 3.44 vs. 9.43 ± 0.84) and AsPC-1 (8.89 vs 8.95) tumor models. Notably, [^{68}Ga]Ga-SK01014 represents significantly reduced renal accumulation (2.82 ± 1.07) versus [^{68}Ga]Ga-SK01001 (11.1 ± 1.83) and [^{68}Ga]Ga-NT-20.3 (9.65 ± 1.15) ($p < 0.01$). In vivo plasma stability showed 34.0 ± 5.5% intact [^{68}Ga]Ga-SK01014 vs. 64.1 ± 5.9% for [^{68}Ga]Ga-NT-20.3. ***Conclusion:*** Tyr^{11} substitution with 1-Nal is unfavorable, whereas substitution with Dmt was well-tolerated. Regarding N-terminal modifications, placement of DOTA at ε- and α-NH_2 of Lys^{6} did not affect radiopharmaceutical biodistribution. N-terminal acetylation preserves tumor uptake and enhances renal clearance of NT-based analogs, thereby improving tumor-to-kidney ratios. Further optimization is needed to enhance NT(6-13) analog stability and tumor uptake for theranostic applications. ***References:*** 1. Prignon et al., Mol Pharm. 2019;16:2776-84.

EP-0091

Evaluation of two Nastorazepide derived ^{68}Ga-labelled radiotracers for imaging of CCK2R expressing tumors.

M. Asti[1], *M. Verona*[2], *S. Rubagotti*[1], *T. Zavvar*[3], *E. von Guggenberg*[3], *P. C. Capponi*[1], *M. Tosato*[4,1], *F. Mastrotto*[2], *G. Marzaro*[5];
[1]*AUSL-IRCCS, Reggio Emilia, ITALY,* [2]*University of Padua, Padua, ITALY,* [3]*Medical University of Innsbruck, Innsbruck, AUSTRIA,* [4]*Simon Fraser University, Burnaby, BC, CANADA,* [5]*University of Verona, Verona, ITALY.*

Aim/Introduction: Receptors targeting ligands are biomolecules useful to selectively deliver both imaging and therapeutic agents to cancer tissues. The cholecystokinin 2 receptor (CCK2R) is overexpressed in various human cancers (e.g., lung, medullary thyroid, pancreatic, colon, and gastrointestinal stromal tumors) and displays limited expression in normal tissues. For this reason, it is a suitable diagnostic and therapeutic target. In this study, two Nastorazepide-based ligands (namely, LM24 and LM55) functionalized with a NODAGA chelator and labelled with gallium-68 were tested as potential radiotracers for CCK2R overexpressing tumors. ***Materials and Methods:*** Targeting agent was synthetized functionalizing the benzodiazepine core with di-ethyl glycol spacer connecting the pharmacophore to a NODAGA chelator. The two derivatives differed for the spacer that in one case contained a maltotriose residue (LM24) and, in the other, a linear poli-alcohol (LM55) moiety to tune hydrophilicity and pharmacokinetic properties. Ligands were radiolabeled with gallium-68 and their in vitro characteristics, such as stability in human serum and lipophilicity, were evaluated. The cell internalization of the radioligands was assessed on A431-CCK2R and A431-mock cells at several time points (30min, 1h and 2h). The receptor binding affinity of the conjugates was tested in a competition assay against [^{177}Lu]Lu-DOTA-MGS5. Biodistribution, and tumor uptake studies were conducted on nude mice carrying A431-CCK2R and A431-mock derived tumor xenografts. ***Results:*** Quantitative complexation with gallium-68 (95°C, 10min) with a molar activity around 16 MBq/nmol and a radiochemical purity (assessed by RP-HPLC) >95%, was achieved in the radiolabeling process. Calculated logP values for [^{68}Ga]Ga-LM24 and [^{68}Ga]Ga-LM55 were -0.79 and -0.64, respectively, while the stability in human serum was >95% after 2h of incubation for both the radiotracers. In the cell internalization studies a cell associated radioactivity of 31.65±1.58% and 23.28±0.74% of the total activity was found for [^{68}Ga]Ga-LM24 and [^{68}Ga]Ga-LM55, respectively, after 2h incubation in A431-CCK2R cells. A very low radioactivity <0.6% was found on A431-mock cells without CCK2R expression. LM24 and LM55 both showed a high affinity for CCK-2R with IC_{50} values of 14.4±5.9 and 33.3±16.1 nM, respectively. In vivo studies are on-going but, from preliminary results, CCK2R expressing tumors could be clearly visualized with both compounds. ***Conclusion:*** In this study, two CCK-2R targeting ligands based on a non-peptide sequence were synthetized and successfully labelled with gallium-68. In vitro studies confirmed good targeting properties. The biodistribution profile and tumor uptake will be assessed in the A431-CCK2R/A431-mock xenograft model.

EP-0092

Innovative Peptides for the Diagnosis and Treatmend of HER2-Positive Breast Cancer

F. Alves da Silva*, D. Gushiken Junior, E. Bernardes, P. Spencer;*
Instituto de Pesquisas Energéticas e Nucleares (IPEN/CNEN), São Paulo, BRAZIL.

Aim/Introduction: Breast cancer accounts for roughly 12 % of all new cancer cases worldwide and about 25 % of cancers diagnosed in women. Approximately 20-30 % of these tumors over-express the human epidermal growth-factor receptor 2 (HER2/ErbB-2), a feature associated with aggressive behavior, early metastasis and reduced survival. Although monoclonal antibody therapy with trastuzumab has improved outcomes, accurate, whole-body assessment of HER2 status is still needed to personalize therapy. We therefore developed a theranostic radiopharmaceutical based on peptides that bind selectively to HER2, suitable for SPECT/PET imaging and radionuclide therapy. ***Materials and Methods:*** Peptide candidates were obtained by de-novo sequencing of trastuzumab light- and heavy-chain complementarity-determining regions (CDRs) using tandem mass spectrometry. Bioinformatic analysis identified CDR3 of the heavy chain as the most promising sequence. The peptide was synthesized with a PEG_3 linker and a DOTA chelator. Radiolabeling with ^{68}Ga and ^{177}Lu was optimized, and stability was assessed in vitro (serum, PBS). Specificity was evaluated on HER2-positive SK-BR-3 and HER2-negative MDA-MB-231 breast-cancer cells, followed by µPET/CT in mice bearing SK-BR-3 xenografts. ***Results:*** Radiolabeling yields exceeded 98 % for both radionuclides, with radiochemical purity remaining > 95 % for 2 h (^{68}Ga) and 24 h (^{177}Lu). In vitro binding to SK-BR-3 cells was 4.3-fold higher than to MDA-MB-231 controls ($p < 0.01$). µPET/CT showed tumor-to-

muscle ratios of 5.2 ± 0.8 at 1 h post-injection, confirming in-vivo specificity. Additional therapeutic-efficacy and dosimetry studies are ongoing. ***Conclusion:*** The HER2-targeted peptide-DOTA construct exhibits high specificity and favorable radiochemical properties, supporting its use as a $^{68}Ga/^{177}Lu$ theranostic pair for imaging and treating HER2-positive breast cancer.

EP-0093

Development of fluorine-18 analogs of metoclopramide for P-gP PET imaging at the blood-brain barrier

S. Huvelle[1,2], *P. Deniel*[3], *B. Hosten*[3,4], *S. Chasseigneaux*[4], *N. Tournier*[1], *L. Breuil*[4,5], *F. Caillé*[1];
[1]*Laboratoire d'Imagerie Biomédicale Multimodale (BIOMAPS), Université Paris-Saclay, CEA, CNRS, Inserm, Service Hospitalier Frédéric Joliot, Orsay, FRANCE,* [2]*Université Paris-Saclay, Inserm, CEA, Center for Immunology of Viral, Auto-immune, Hematological and Bacterial diseases (IMVA-HB/IDMIT), Fontenay-aux-Roses, FRANCE,* [3]*Service Pharmacie, Assistance Publique - Hôpitaux Paris, Hôpital Saint-Louis, Paris, FRANCE,* [4]*Inserm UMR-S 1144, Faculté de Pharmacie de Paris, Université Paris-Cité, Paris, FRANCE,* [5]*Service Pharmacie, Assistance Publique - Hôpitaux Paris, Hôpital Cochin, Paris, FRANCE.*

Aim/Introduction: Carbon-11-labeled metoclopramide (MTC) has been validated as a reliable radiotracer in animals and humans to study P-glycoprotein (P-gp) at the blood-brain barrier (BBB) with PET imaging (1). However, carbon-11 radiolabeling requires an on-site cyclotron, hampering clinical translation. Most radiopharmaceuticals currently available for studying P-gp are labeled with this isotope. In this context, developing fluorine-18-labeled P-gp probes is of particular interest, as its longer radioactive half-life allows for greater flexibility in use. This work aimed to develop P-gp activity radiotracers at the BBB, derived from MTC and labeled with fluorine-18. ***Materials and Methods:*** Two candidate molecules, namely [^{19}F]FPEG-MTC and [^{19}F]Fluoroethyl-metoclopramide (FE--MTC), were evaluated in vitro to determine their status as P-gp substrates. AB/BA bidirectional transport assays on transwell with MDCK-MDR1 cells overexpressing human P-gp were performed with and without P-gp inhibition by 5 µM of valspodar. Efflux ratios (ER) of FPEG-MTC and FE-MTC were compared to the ER of metoclopramide and to their own ER with inhibition (ER_i) with a Student t-test. F-18 radiolabeling of FPEG-MTC was performed from a tosylate precursor with an AllinOne (Trasis) module. ***Results:*** FPEG-MTC and FE-MTC were synthesized in 42 and 48% yield, respectively. In vitro results showed a significantly higher ER for FPEG-MTC (ER=8.63) compared to MTC (ER=1.03) ($p< 0.001$, n=2), suggesting FPEG-MTC is a stronger P-gp substrate than MTC. In contrast, the ER of FE-MTC did not differ significantly from MTC (ER 0.346). Valspodar inhibition significantly reduced ER values from MTC (ERi= 0.564) and FPEG-MTC (ERi=0.568) ($p< 0.001$, n=2), but had no significant effect on FE-MTC (ERi= 0.291, ns, n=2), indicating FE-MTC may not be a P-gp substrate. FPEG-MTC was chosen to be labeled with fluorine-18. The tosylate precursor of FPEG-MTC was synthesized in 6 steps with 21% overall yield. [^{18}F]FPEGMTC was obtained with 39% conversion. The automation of the radiofluorination is ongoing. ***Conclusion:*** Two fluorinated analogs of MTC were successfully synthesized, and in vitro experiments demonstrated that FPEG-MTC is a stronger P-gp substrate than MTC. [^{18}F]FPEG-MTC was successfully radiosynthesized in a compatible yield and molar activity for upcoming in vivo studies to study the impact of P-gp inhibition on its brain distribution. These will help confirm the potential of this tracer and provide insights into its sensitivity to P-gp activity modulation, essential information for assessing its potential future in vivo applications. ***References:*** 1. Tournier N, Langer O.; J Nucl Med Off Publ Soc Nucl Med. 27 févr 2025;jnumed.124.269322.

EP-0095

Precise monitoring of acquired drug resistance in melanoma by ACC-targeted PET imaging

J. Ye, *J. Wang;*
Xijing Hospital, Xi'an, CHINA.

Aim/Introduction: Acquired resistance to BRAF mutation-targeted therapy has become a major clinical problem hindering the treatment of melanoma, and its precise monitoring is the core and key to improve the prognosis, but there is a lack of effective ways of non-invasive monitoring. Our previous study revealed that enhanced fatty acid synthesis is a key mechanism mediating acquired resistance to targeted therapy in BRAF-mutant melanoma. Therefore, this project aims to develop a molecular probe targeting acetyl-coacarboxylase (ACC), a key rate-limiting enzyme in the fatty acid synthesis pathway, to elucidate the quantitative and qualitative relationship between ACC and acquired resistance to targeted therapies and to monitor the evolution of fatty acid synthesis resistance through PET molecular imaging. ***Materials and Methods:*** A series of novel ACC-targeting probes were designed by coupling method using the inhibitor ND630 as the lead compound. The radiochemical purity and in vitro stability were determined by HPLC. All probes were subjected to in vivo distribution and micro-PET dynamic imaging in tumor bearing mice to determine maximum tumor uptake and optimal imaging time. Construction of melanoma drug-resistant cell lines was induced by stepwise increments of vemurafenib, and further constructing vemurafenib-resistant tumor bearing mice. PET monitoring of tumor-bearing mice treated with vemurafenib using the probe with the best imaging. ***Results:*** The ^{68}Ga labeling rate of all four probes was more than 60% (n = 3, uncorrected for decay) and the radiochemical purity was > 98%. The in vitro stability in saline and in mouse serum was evaluated at 4 h by radio-HPLC, all probes showed high in vitro stability. The in vivo distribution and micro-PET imaging results in tumor bearing mice showed that all probes could image tumors, with ^{68}Ga-DEACC showing the highest tumor uptake with a SUVmax of 1.1. All probes have a high physiological uptake in the heart and liver and are mainly metabolized by the liver and intestines. The drug-resistant cell line A375-VR was successfully constructed, the resistance index was 6.69 and its ACC and mitochondrial functions were significantly enhanced. ^{68}Ga-DEACC PET imaging results showed that tumor uptake was significantly higher in the resistant group than in the sensitive group after treatment with vemurafenib, suggesting that ACC-targeted PET imaging can Precise monitoring of acquired drug resistance in melanoma. ***Conclusion:*** ACC-targeting probe ^{68}Ga-DEACC has the potential to be used to monitor the evolution of fatty acid synthesis resistance, and further probe optimization and evaluation are in progress.

EP-0096

Comparative Study of Thiol-Reactive Linkers for the Design of Stable Radioimmunoconjugates

J. Ariztia[1], *M. Leroux*[1], *M. Moreau*[1], *C. Bernhard*[1], *P. Bellaye*[2], *A. Cochet*[2,1], *A. Daoust*[3], *D. Vivier*[1], *F. Denat*[1];
[1]*Université Bourgogne Europe, ICMUB UMR CNRS 6302, Dijon, FRANCE,* [2]*Centre Georges François Leclerc, IMATHERA, BioSanD, Dijon, FRANCE,* [3]*Oncodesign Precision Medicine, Dijon, FRANCE.*

Aim/Introduction: Bioconjugation between maleimide and thiol groups on proteins is a widely used strategy in the preparation of antibody-drug conjugates (ADCs). However, the resulting thiosuccinimide bond often lacks long-term stability, leading to retro-Michael deconjugation, premature drug release, and unwanted binding to plasma proteins. To overcome this, alternatives to maleimide-based conjugation — including self-hydrolyzing maleimides, exocyclic maleimides, benzoyl acrylamides, and 2-sulfonylpyrimidines for cysteine arylation — have been developed,[1] though mainly in the ADC field. Their potential for

radioimmunoconjugates remains largely unexplored. Here, we propose to radiolabel with ^{89}Zr three immunoconjugates, prepared using different thiol-reactive groups bearing DFO chelator, and to compare their stability in terms of radiolysis resistance and plasma deconjugation. ***Materials and Methods:*** The thiol-reactive groups studied were maleimide, aryl-maleimide, and benzoyl acrylate. Each was coupled to DFO (except maleimide-DFO, available commercially) and conjugated to a small cysteine-tagged protein (~20 kDa). Reactions were monitored by mass spectrometry. Hydrolysis studies were performed on both maleimide conjugates in HEPES buffer (pH 7.4 and 8). Retro-Michael deconjugation was assessed by incubating the conjugates (before and after hydrolysis) with an excess of glutathione (1000 eq.) for one week. Finally, the conjugates were radiolabeled with ^{89}Zr, a radionuclide that induces significant radiolytic stress, and their stability in PBS and plasma was monitored over 7 days. ***Results:*** DFO probes were synthesized in one or two steps with good yields. Bioconjugation efficiency varied: maleimide-DFO showed slower reactivity and required excess equivalents for full conversion, while aryl-maleimide exhibited high reactivity, prompting pH adjustment (5.2) to reduce side reactions with lysines. Benzoyl acrylate-DFO showed intermediate reactivity. In hydrolysis tests at pH 7.4, less than 20% hydrolysis was observed for maleimide-DFO and aryl-maleimide-DFO after 24 hours (12% and 18%, respectively). However, at pH 8, aryl-maleimide-DFO underwent near-complete hydrolysis (95%) within 6 hours, whereas maleimide-DFO showed moderate hydrolysis (36%). Glutathione assays revealed that aryl-maleimide conjugates showed greater resistance to retro-Michael deconjugation than the others. Radiolabeling with ^{89}Zr gave good yields for all conjugates; stability studies are ongoing. ***Conclusion:*** This study highlights the improved stability of alternative thiol-reactive linkers over classical maleimide. Aryl-maleimide and benzoyl acrylate showed promising resistance to deconjugation and good radiolabeling performance. Ongoing work will confirm their suitability for stable radioimmunoconjugates. ***References:*** (1) Szijj, P. A.; Bahou, C.; Chudasama, V. Drug Discov. Today Technol. 2018, 30, 27-34.

EP-0097

Biodistribution of Two Novel FAP - targeting Radiopharmaceuticals in Solid Tumors and Their Comparison with ^{68}Ga - FAPI - 46: a Pilot Study

X. Mu[1], *Y. Lu*[1], *Z. Chen*[2], *J. Li*[1], *L. Zhang*[1], *W. Chong*[1], *J. Li*[1], *W. Fu*[1], *X. Li*[3];
[1]*Department of Nuclear Medicine, The First Affiliated Hospital of Guilin Medical University, Guilin, CHINA,* [2]*GDMPA Key Laboratory for Quality Control and Evaluation of Radiopharmaceuticals, PET Center, Department of Nuclear Medicine, Nanfang Hospital, Southern Medical Universit, Guangzhou, CHINA,* [3]*Department of Chemistry, State Key Laboratory of Synthetic Chemistry, The University of Hong Kong, Hongkong, CHINA.*

Aim/Introduction: Fibroblast activation protein α, a cell surface protein overexpressed on cancer-associated fibroblasts (CAFs), has emerged as a promising pan-cancer diagnostic and therapeutic target due to its minimal expression in most healthy tissues. In this preliminary clinical study, we evaluated the biodistribution and clinical feasibility of two novel FAP-targeting radiopharmaceuticals, ^{68}Ga-GP01 and ^{68}Ga-GP02, and compared their imaging characteristics with ^{68}Ga-FAPI-46 in patients with solid tumors. ***Materials and Methods:*** Two novel precursors were rationally designed and synthesized, subsequently conjugated with the DOTA chelator for ^{68}Ga-radiolabeling. Ten patients with various solid tumors were enrolled to assess the clinical performance of ^{68}Ga-GP01 and ^{68}Ga-GP02. Patients received 164 ± 14 MBq of ^{68}Ga-GP01 or 179 ± 27 MBq of ^{68}Ga-GP02, followed by PET/CT imaging at 60 minutes post-injection. The SUV_{mean} of normal tissues—including the brain, thyroid, blood pool, lung, liver, spleen, kidney, bone, and muscle—were measured. Lesion uptake and tumor-to-background ratios (TBR) of ^{68}Ga-GP01 and ^{68}Ga-GP02 were compared with those of ^{68}Ga-FAPI-46. ***Results:*** Both ^{68}Ga-GP01 and ^{68}Ga-GP02 were well tolerated with no adverse events reported. Compared to ^{68}Ga-FAPI-46 PET/CT, the liver SUV_{mean} for ^{68}Ga-GP01 was significantly lower (0.42 vs. 0.59, P = 0.008), while no significant difference was observed in thyroid SUV_{mean} between the two tracers (1.48 vs. 1.44, P = 0.85). In contrast, ^{68}Ga-GP02 PET/CT demonstrated a significantly higher thyroid SUV_{mean} compared to ^{68}Ga-FAPI-46 PET/CT (6.74 vs. 2.48, P = 0.0002), whereas no significant difference was found in liver SUV_{mean} between the two tracers (1.11 vs. 0.87, P = 0.063). No other significant differences in SUV_{mean} were observed in the remaining normal tissues. In the lesion analysis, 53 lesions were identified with both ^{68}Ga-GP01 and ^{68}Ga-FAPI-46. The ^{68}Ga-GP01 group exhibited a much higher SUV_{max} and TBR (SUV_{max}: 7.71 vs. 6.76, P = 0.004; TBR: 7.49 vs. 5.70, P < 0.0001). For ^{68}Ga-GP02, 41 lesions were detected, among which one appeared negative on ^{68}Ga-FAPI-46 PET/CT. Interestingly, compared to ^{68}Ga-FAPI-46, the ^{68}Ga-GP02 group showed a substantially higher SUV_{max} (10.00 vs. 6.77, P < 0.0001) and comparable TBR (5.82 vs. 5.86, P = 0.35). ***Conclusion:*** This study evaluated the safety and clinical feasibility of both ^{68}Ga-GP01 and ^{68}Ga-GP02 PET/CT imaging with various cancer types. Both tracers showed improved lesion uptake compared to ^{68}Ga-FAPI-46, with promising results for high-contrast visualization of FAP-positive tumors. The results above provide valuable clinical experience and data support for the future development of 177Lu - labeled theranostic drugs targeting FAP.

EP-0098

Preclinical Evaluation of ^{68}Ga-labelled Cyclic Peptide for Neuropilin-1-Targeted PET Imaging in Pan-tumors

F. Qiu*, S. Song, J. Li;*
Fudan University Shanghai Cancer Center, Shanghai, CHINA.

Aim/Introduction: As a transmembrane glycoprotein overexpressed in various tumors, neuropilin-1 (NRP-1) is involved in tumor progression, angiogenesis, and immune evasion. Therefore, monitoring NRP-1 expression is crucial for tumor early diagnosis and personalized therapeutic regimens. This study aims to develop a novel NRP-1-targeted cyclic peptide radiotracer for specifically and sensitively detecting NRP-1 expression in multiple tumor models. ***Materials and Methods:*** NRP-1 expression in human cancers was detected via immunohistochemistry (IHC) on tissue microarrays (TMAs). Specificity for NRP-1 was confirmed using molecular docking and cellular uptake assays. To determine diagnostic sensitivity and clinical applicability, Micro PET/CT imaging and blocking studies were performed in four NRP-1-positive tumor models (TNBC MDA-MB-231, fibrosarcoma HT-1080, NSCLC A549, pancreatic tumor CFPAC-1,) and one NRP-1-negative model (cervical tumor Siha). Ex vivo biodistribution and immunohistochemistry were subsequently conducted to verify tumor-targeting capability, while biosafety studies were performed to support potential clinical translation. ***Results:*** TMAs results revealed that NRP-1 is highly expressed in TNBC, NSCLC and pancreatic tumor, while slightly expressed in cervical tumor. Micro PET/CT at 1 h post-injection revealed significantly higher tumor uptake in NRP-1 positive tumor models (MDB-MA-231 : 3.167± 0.115 %, HT-1080 : 2.3 ± 0.6 %, A549 : 1.867 ± 0.551 %, CFPAC-1 : 1.467 ± 0.306 %) compared to NRP-1 negative tumor model (Siha : 0.851 ± 0.180 %). Notably, the trend in target uptake ratios were similar to trend in tumor uptake values, while co-injection with nonradioactive CEND-1 significantly reduced tumor uptake, confirming specificity. Ex vivo biodistribution and immunohistochemistry were consistent with PET imaging, while biosafety evaluations showed no significant adverse effects. ***Conclusion:*** As the first cyclic peptide radiotracer, ^{68}Ga-DOTA-

CEND1 holds great potential for non-invasive detection of NRP-1 expression across pan-tumor types, evaluating the therapeutic responses and optimizing NRP-1 targeted therapy.

EP-0099

Development and Evaluation of a Novel Peptide-Based Radiotracer for Netrin-1 Non-invasivei Imaging in Tumor

J. Wang, *L. Feng, L. Zhang, H. Yang, X. Lan, W. Cao, D. Jiang; Department of Nuclear Medicine, Union Hospital, Tongji Medical College, Huazhong University of Science and Technology, Wuhan, CHINA.*

Aim/Introduction: Neuroaxonal guidance factor-1 (Netrin-1), a secreted glycoprotein frequently overexpressed in various malignancies, plays a crucial role in promoting tumor progression and metastatic dissemination. Given its significant involvement in oncogenesis, Netrin-1 has emerged as a promising molecular target for cancer theranostics. To facilitate the non-invasive evaluation of Netrin-1 expression in tumors, we designed and synthesized a novel Ga-68-labeled peptide-based radiotracer, designated as [^{68}Ga]Ga-DKP, for positron emission tomography (PET) imaging applications. ***Materials and Methods:*** The radiotracer was successfully radiolabelled with Ga-68. The radio chmeical purity (RCP) was examined by radio high performance liquid chromatography. Cellular uptake studies and blocking studies validated the probe's targeting capacity in vitro. PET/CT imaging and biodistribution studies were carried on murine models of A549, 4T1 and A375 tumors. ***Results:*** The developed [^{68}Ga]Ga-DKP tracer demonstrated excellent RCP (>95%) and stability in vitro. Cellular uptake studies revealed significantly higher binding affinity in A549 and 4T1 cells, compared to A375 cells, correlating with their differential netrin-1 expression levels. In vivo evaluation through PET/CT imaging and biodistribution analysis showed higher tumor-to-muscle ratios in A549 (5.24 ± 0.58) and 4T1 (6.86 ± 1.35) xenografts at 1 h post-injection, representing approximately 3-fold greater uptake compared to A375 tumors. ***Conclusion:*** The novel radio tracer[^{68}Ga]Ga-DKP serves as a sensitive and specific PET probe for non-invasive assessment of netrin-1 expression, demonstrating strong potential for clinical translation in cancer theranostics. ***References:*** Finci LI, Krüger N, Sun X, Zhang J, Chegkazi M, Wu Y, Schenk G, Mertens HDT, Svergun DI, Zhang Y, Wang JH, Meijers R. The crystal structure of netrin-1 in complex with DCC reveals the bifunctionality of netrin-1 as a guidance cue. Neuron. 2014 Aug 20;83(4):839-849.

EP-0100

Evaluation of ^{11}C-SAM Radiotracers for Prostate Cancer Imaging: In Vivo and Ex Vivo Comparison of Scalemic and Enantiopure Forms

M. Bentura[1], *F. Zoppolo*[1], *L. Reyes*[1], *A. Paolino*[1], *G. Falasco*[1], *L. Urrutia*[1], *D. Umpierrez*[2], *G. Irazoqui*[2], *S. Rodriguez*[2], *E. Savio*[1]; [1]*Departamento de Radiofarmacia, Centro Uruguayo de Imagenología Molecular, Montevideo, URUGUAY,* [2]*Departamento de Biociencias, Facultad de Química, UdelaR, Montevideo, URUGUAY.*

Aim/Introduction: Prostate cancer (PCa) is the second most diagnosed cancer in men and the fifth leading cause of cancer mortality. Advances in understanding the pathology and biomarkers are improving disease management, but identifying high-risk patients remains a challenge. Sarcosine (N-methyl glycine) is a metabolite significantly elevated during PCa progression, linked to high levels of glycine N-methyltransferase (GNMT), which catalyzes its production using (S,S)-adenosylmethionine ((S,S)-SAM) as a coenzyme. Labeled with ^{11}C, (S,S)-SAM has potential as a radiotracer for PCa diagnosis. In previous work, we successfully labeled SAM as a scalemic mixture and enzymatically synthesized ^{11}C-labeled (S,S)-SAM. This study focuses on the in vivo and ex vivo evaluation of these radiotracers, comparing the scalemic mixture and enantiopure (S,S)-SAM to assess their differential impact on imaging and diagnostic potential. Two prostate cancer tumor models, PC3 and LNCaP, with varying GNMT expression levels, were used. ***Materials and Methods:*** The synthetic processes were performed using a TRACERlab® FX C Pro automated platform (GE Healthcare). Male Swiss and Nude N: NIH (S) - Foxn 1nu mice (13-18 weeks) were used as controls and prostate cancer tumor models (PC3/LNCAP) for ex vivo and in vivo studies. Biodistribution studies were conducted in both groups at 15, 45, and 90 minutes. PET/CT imaging was performed after intravenous administration of ^{11}C-SAM or the scalemic mixture, using a nanoScan® PET/MRI 3T system (Mediso). Tumor segmentation on PET images was done using a semi-automatic region-growing algorithm (PMOD 3.8) to calculate the tumor-to-normal uptake ratio (TNr). ***Results:*** Regarding the biodistribution results, in the LNCaP tumor model, tumor accumulation was significantly higher than in muscle at all time points ($p < 0.05$), with a peak TNr of 2.67 ± 0.99 at 45 minutes post-injection. In the PC3 tumor model, tumor accumulation was significantly higher than in muscle only at 15 minutes ($p < 0.05$). Imaging data showed no significant differences between the pure compound (ISO) and the scalemic mixture (MZC) in either model, although a higher variance was noted for the scalemic mixture. ***Conclusion:*** Based on the biodistribution results from both tumor models, it can be concluded that the compound under study, 11C-SAM, exhibits greater affinity for the LNCaP cell line. Future clinical applications require careful patient selection. The observed differences in tumor and muscle uptake highlight the potential of this radiopharmaceutical in oncological imaging. These findings also challenge what would be the most suitable choice for conducting a clinical trial evaluation.

EP-0101

Selective Probes for PET Imaging of Tumor-Associated Cathepsins

O. Cini[1], *M. M. M. Santos*[1], *F. Elvas*[2], *R. Moreira*[1]; [1]*Research Institute for Medicines (iMed.ULisboa), Faculty of Pharmacy, Universidade de Lisboa, Lisbon, PORTUGAL,* [2]*Molecular Imaging and Radiology, Faculty of Medicine and Health Sciences, University of Antwerp, Antwerp, BELGIUM.*

Aim/Introduction: Cathepsins are lysosomal cysteine proteases involved in various biological processes. In cancer, overexpression of Cathepsin B (CatB) and Cathepsin L (CatL) correlates with different tumor progression stages, making them important biomarkers for cancer diagnosis.[1] This study aims to develop selective CatB and CatL inhibitors as radiotracers for Positron Emission Tomography (PET) imaging to improve cancer diagnosis and therapy monitoring. ***Materials and Methods:*** Vinyl sulfones were selected as warhead to covalently bind the catalytic residue of cathepsins.[2] Modifications were made to optimize selectivity and introduce linkers for attaching diagnostic radionuclides such as Gallium-68 (^{68}Ga). Five probe precursors were synthesized, and enzymatic assays with precursors and cold (^{nat}Ga) complexes assessed affinity and selectivity towards CatB, CatL and CatS. Two precursors differing in linker design, PEG_2 in CREANT-101 and piperazine in CREANT-102, were radiolabeled with ^{68}Ga using ammonium acetate buffer at pH 5.5 and 80°C for 5 minutes. SDS-PAGE was used to evaluate radiotracers binding to cathepsins. Stability was assessed up to 2h. Both radiotracers were evaluated in vivo through PET/CT imaging, biodistribution and metabolite analysis. ***Results:*** Cold complexes of CREANT-101 and CREANT-102 exhibited strong affinity for CatL, with K_i values of 315 and 107 nM. [^{68}Ga]Ga-NODAGA-CREANT-101 and -102 were obtained in high radiochemical purity (>95%). Both radiotracers exhibited high stability in 0.9% NaCl up to 2h (>95%). SDS-PAGE analysis of recombinant cathepsins showed selective labeling of CatL and CatB with minimal off-target binding to CatS. PET/CT and biodistribution revealed rapid clearance of CREANT-101,

accumulating mainly in liver (10.8 %IA/g), kidneys (1.9 %IA/g), large intestine (18.9 %IA/g) at 30 minutes post-injection, suggesting mixed renal-hepatobiliary clearance. Despite similar lipophilicity of both tracers (Log D = -0.18 for CREANT-101, -0.15 for CREANT-102), CREANT-102 showed higher background activity and blood retention. Metabolite studies showed faster metabolism for CREANT-101 while CREANT-102 remained more stable over time, with 45% intact at 30 minutes versus 61% for CREANT-102, and 24% intact at 1 hour versus 51% for CREANT-102, indicating slower metabolic degradation. Tumor targeting will be evaluated in subsequent studies. ***Conclusion:*** This study confirmed that CatL is the major target of CREANT-101 and -102, with minimal binding to CatB and CatS. Additionally, the linker design had an impact on the in vivo pharmacokinetics and metabolic stability, affecting imaging background and clearance. These findings support further probe optimization. ***References:*** 1. Schleyer KA, et al. Org Biomol Chem. 2021;19(28):6182-6205. 2. Schneider TH, et al. New J Chem. 2015;39(7):5841-5853.

EP-0102

Cu-64/Cu-67-Labeled TCOs as Promising Agents for Theranostic Pretargeting Applications

Q. Yu, *K. Adhikari, T. Van den Wyngaert, F. Elvas;*
University of Antwerp, Molecular Imaging and Radiology (MIRA), Wilrijk, BELGIUM.

Aim/Introduction: A radiotheranostic approach using monoclonal antibodies (mAbs) provides an attractive strategy to target tumor-associated antigens. Pretargeting strategies utilizing bioorthogonal reactions, such as the inverse electron-demand Diels-Alder (IEDDA) reaction, can overcome the high radiation exposure associated with the long circulating half-life of mAbs. However, many targets, such as CD70, are internalised intracellularly upon binding, limiting the availability of bioorthogonal tags on the cell surface and hindering effective radioligand accumulation in tumors. To overcome this limitation, we aim to develop cell-permeable trans-cyclooctenes (TCOs) labeled with the theranostic pair Cu-64/Cu-67, enabling efficient IEDDA reaction with mAb-conjugated tetrazines (Tz) both extra- and intracellularly in a model of CD70-expressing tumors, enabling a more effective radio-payload delivery with minimal systemic exposure. ***Materials and Methods:*** Two TCO radioligands, CREANT-201 and -202, were developed containing a d-TCO core featuring linkers of varying lipophilicity (alkyl chain and polyethylene glycol (PEG) chains), and a NOTA chelator. The reaction kinetics of [^{nat}Cu]Cu-CREANT-201/-202 with Tz were assessed by stopped-flow spectrophotometry. CREANT-201/-202 were both radiolabeled with Cu-64 and Cu-67, and the radiochemical conversion (RCC) was determined by radio-thin layer chromatography, while radiochemical purity (RCP) was assessed via radio-high performance liquid chromatography. Radiolabeled compounds were further evaluated regarding lipophilicity (logD), and in vitro stability towards cis isomerization (in PBS buffer at 37 °C up to 4h), and reacted with a Bis(pyridin-2-yl)-1,2,4,5-tetrazine (Bispyr-Tz) to confirm their reactivity. ***Results:*** [^{nat}Cu]CREANT-201 showed faster reaction kinetics towards Bispyr-Tz compared to [^{nat}Cu]CREANT-202 (138900 $M^{-1}\cdot s^{-1}$ vs 113200 $M^{-1}\cdot s^{-1}$). CREANT-201/-202 were labelled with Cu-64 and Cu-67 under optimized conditions with an RCC and RCP of over 95%. The logD values were determined to be -2.14 ± 0.04 and -1.75 ± 0.11 for [$^{64/67}$Cu]Cu-CREANT-201, respectively, while -2.73 ± 0.02 and -2.45 ± 0.03 for [$^{64/67}$Cu]Cu-CREANT-202, revealing that [$^{64/67}$Cu]Cu-CREANT-202 exhibits greater hydrophilicity, due to the presence of a PEG moiety. After the reaction with a Bispyr-Tz, a new radioactive peak corresponding to the dihydropyridazine reaction product could be observed, which indicates the radiolabelled-TCOs preserved the reactivity towards Tz. Radiolabeled TCOs showed good stability in PBS without copper release. Isomerization from trans to cis was observed after 2h, with 73.89% of trans-isomer remaining for [^{64}Cu]Cu-CREANT-201, and 80.91% for [^{64}Cu]Cu-CREANT-202. ***Conclusion:*** The TCOs can be efficiently radiolabeled with Cu-64/Cu-67 while remaining reactivity, making [$^{67/64}$Cu]Cu-TCOs promising candidates for pretargeted theranostics approach with Tz-conjugated mAbs. Their performance will be further evaluated in vitro with CD-70 positive cells and in vivo with CD-70-expressing tumor-bearing mice.

EP-0103

Preclinical evaluation of [^{11}C]Onalespib for Heat Shock Protein 90 (HSP90) cancer imaging

L. Le Saux[1], *V. Narykina*[1,2,3], *R. Cools*[1], *N. Van Winnendael*[1,4], *G. Bormans*[1];
[1]*Laboratory for Radiopharmaceutical Research, Department of Pharmacy and Pharmacological Sciences, KU Leuven, Leuven, BELGIUM,* [2]*Switch Laboratory, VIB Center for Brain and Disease Research, Herestraat 49, 3000, Leuven, BELGIUM,* [3]*Switch Laboratory, Department of Cellular and Molecular Medicine, KU Leuven, Herestraat 49, 3000, Leuven, BELGIUM,* [4]*Nuclear Medical Applications, Belgian Nuclear Research Centre (SCK CEN), Mol, BELGIUM.*

Aim/Introduction: HSP90 is a molecular chaperone stabilizing oncogenic proteins and represents an interesting chemotherapy target.[1] Various first-generation inhibitors showed limited efficacy and toxicity issues in clinical trials.[2] Onalespib (AT13387), a second-generation inhibitor, has undergone clinical evaluation for various cancers, often in combination with standard therapies.[3] Radiolabeled [^{11}C]Onalespib enables positron emission tomography (PET) imaging to study biodistribution and kinetics, potentially supporting the development of Hsp90-targeted treatments. ***Materials and Methods:*** [^{11}C]Onalespib was synthesized via N-methylation of (2,4-dihydroxy-5-isopropylphenyl) (5-(piperazin-1-ylmethyl)isoindolin-2-yl)methanone using [11C] CH3I. Autoradiography was used to assess in vitro Hsp90-specific binding of [^{11}C]Onalespib to rodent brain and tumor tissue (U87, MDA-MB-231 and PC3) slices. Cell binding, including specificity and selectivity, was assessed in the same cell lines. Biodistribution was assessed in U87 xenograft-bearing SCID mice, by both µPET scanning and ex vivo biodistribution. ***Results:*** Autoradiography revealed Hsp90-specific binding in MDA-MB-231 tumor tissue, with substantial blocking by HSP990 (98%) and Onalespib (93%). Blocking efficiency was slightly lower in PC3 tumor slices (82% and 87%, respectively). Also in brain tissue slices, Hsp90-specific [11C] Onalespib was observed with blocking efficiency 95%. During cell binding experiments, blocking with TAS-116 and HSP990 resulted in only 60-80% reduction of tracer binding. Further investigations are ongoing to assess isoform specificity and potential off-target interactions. Ex vivo biodistribution demonstrated uptake of 4.9 ± 0.9 %ID/g in U87 tumor, 23.6 ± 1.9 %ID/g in kidneys, 11.4 ± 0.4 %ID/g in liver and 23.7 ± 2.2 %ID/g in lungs. Dynamic µPET/CT scans in mice demonstrated results consistent with ex vivo data, showing high uptake in kidneys, intestines, liver and lungs, and moderate tumor accumulation that was fully blocked by pretreatment with HSP90 inhibitors. Limited [^{11}C]Onalespib brain uptake was observed in contrast to literature reports claiming BBB penetration of Onalespib. ***Conclusion:*** [^{11}C]Onalespib was successfully synthesized and evaluated in vitro and in vivo. Hsp90-specific tracer binding was observed in a U87 mouse tumor model. Further in vivo studies in additional tumor models are ongoing. ***References:*** 1. Li, Z.-N. & Luo, Y. HSP90 inhibitors and cancer: Prospects for use in targeted therapies (Review). Oncol. Rep. 49, 1-13 (2023). 2.Rastogi, S. et al. An update on the status of HSP90 inhibitors in cancer clinical trials. Cell Stress Chaperones 29, 519-539 (2024). 3.Williams, N. O. et al. Phase Ib study of HSP90 inhibitor, onalespib (AT13387), in combination with paclitaxel in patients with advanced triple-negative breast cancer. Ther. Adv. Med. Oncol. 15, 17588359231217976 (2023).

EP-0105

Preclinical evaluation of ^{68}Ga-DOTA-NEI as a radiotracer for neutrophil elastase

J. Wang, *F. Kang, J. Wang;*
The First Affiliated Hospital of Air Force Military Medical University, Xi'an, CHINA.

Aim/Introduction: Precisely assessing neutrophil elastase (NE) expression in early acute inflammatory conditions is crucial for identifying patients who may benefit from NE-targeted therapies. ***Materials and Methods:*** In this study, we developed a ^{68}Ga-labeled macrocyclic peptide, designated as ^{68}Ga-DOTA-NEI, to dynamically monitor NE expression levels in inflammatory lung tissue using positron emission tomography/computed tomography (PET/CT). ***Results:*** Our results demonstrated that ^{68}Ga-DOTA-NEI achieved a radioactive labeling yield of 70% and a radiochemical purity exceeding 95%. The probe exhibited excellent stability in saline and serum at 37°C for up to 4 hours, along with favorable hydrophilicity. Furthermore, molecular docking, molecular dynamics (MD) simulations, and competitive inhibition assays (IC_{50} = 1.37nM) confirmed the high affinity and binding stability of ^{68}Ga-DOTA-NEI to NE. Micro-PET/CT imaging, biodistribution studies and renal metabolic analysis revealed rapid and significant uptake of ^{68}Ga-DOTA-NEI in early acute inflamed lung tissue and metabolized by kidney, while blocking experiments further validated the probe's specific binding to NE. Additionally, pharmacokinetic analysis demonstrated the excellent compatibility of DOTA-NEI with ^{68}Ga. ***Conclusion:*** Collectively, these findings highlighted the promising clinical potential of ^{68}Ga-DOTA-NEI as a tool for monitoring NE expression in early acute lung inflammation, offering a valuable approach for therapeutic interventions.

EP-0106

Pretargeted PET imaging of tumors using a DZ-1-TCO and ^{68}Ga-tetrazine system: synthesis, optimization, and in vivo evaluation

M. Huang[1], *W. Wang*[1], *Y. Wang*[2], *R. Wang*[1], *Y. Zhang*[3], *R. Tian*[1];
[1]*The Department of Nuclear Medicine, West China Hospital, Sichuan University, Chengdu, Sichuan, China, Chengdu, CHINA,* [2]*Department of Nuclear Medicine and Clinical Nuclear Medicine Research Lab, West China Hospital, Sichuan University, Chengdu, China, Chengdu, CHINA,* [3]*Department of Biomedical Sciences, Cedars-Sinai Medical Center, Los Angeles, California 90048, United States, CA, UNITED STATES OF AMERICA.*

Aim/Introduction: Pretargeting strategies offer a promising approach to improve the specificity and safety of radiopharmaceuticals by decoupling tumor targeting from radionuclide delivery. DZ-1, a broad-spectrum tumor-targeting dye, has shown favorable bio-distribution in previous studies. To address pharmacokinetic limitations and reduce systemic toxicity observed with directly labeled agents such as ^{177}Lu-DZ-HX, we developed a DZ-1-based pretargeting system using trans-cyclooctene (TCO) and ^{68}Ga-labeled tetrazines. ***Materials and Methods:*** Three DZ-TCO precursors—DZ-1-TCO, DZ-Lys-TCO, and DZ-Lys-PEG4-TCO—were synthesized and assessed in HeLa and U87MG tumor-bearing mice by fluorescence imaging. Tumor uptake was monitored up to 96 h. Methyl-tetrazine (MeTz) and hydrazinyl-tetrazine (H-Tz) were labeled with ^{68}Ga, and their stability and reactivity were evaluated in PBS and serum. Pretargeted PET imaging was performed using different precursor/probe combinations and time intervals (24, 48, 72 h). ***Results:*** All precursors showed tumor accumulation, with peak fluorescence at 24 h (up to 1.20×10^{10} p/s/cm^2/sr) and sustained signal at 96 h. ^{68}Ga-DOTA-MeTz and ^{68}Ga-DOTA-H-Tz retained >85% stability after 4 h incubation. PET imaging revealed highest uptake for DZ-Lys-TCO (1.98 ± 0.72%ID/g), with tumor-to-muscle (T/M) and tumor-to-liver (T/L) ratios of 3.86 ± 0.91 and 0.89 ± 0.29, respectively ($P < 0.05$). Using ^{68}Ga-DOTA-H-Tz, the 48 h interval achieved optimal performance (3.24 ± 0.95%ID/g, T/M 8.30 ± 3.39, T/L 1.35 ± 0.26; $P < 0.05$). Biodistribution confirmed rapid renal clearance and low non-target uptake, with peak tumor uptake of 3.53 ± 1.76%ID/g and T/M up to 10.92 ± 0.31 at 30 min. ***Conclusion:*** The DZ-TCO/^{68}Ga-DOTA-Tz pretargeting system enables high-contrast tumor imaging with reduced background. Among tested conditions, DZ-Lys-TCO combined with ^{68}Ga-DOTA-H-Tz at a 48 h interval provided the most favorable imaging outcomes. This strategy presents a promising and tunable platform for enhancing the precision and safety of radiopharmaceutical applications.

EP-0107

ImmunoPET Imaging of TROP2 Expression in Lung Cancer with scFv Tracers

Z. Wu, *Z. Lin, Y. Feng, D. Zheng, X. Zhang, R. An, Y. Zhang, J. Zhu, D. Jiang, X. Lan;*
Department of Nuclear Medicine, Union Hospital, Tongji Medical College, Huazhong University of Science and Technology, Wuhan, CHINA.

Aim/Introduction: TROP2, a transmembrane glycoprotein, is markedly overexpressed in several epithelial-derived malignancies, such as triple-negative breast cancer, pancreatic cancer, prostate cancer, and non-small cell lung carcinoma. The significant upregulation of TROP2 in these tumors positions it as a valuable biomarker for diagnosis. While whole antibodies have shown targeted specificity toward tumor-associated antigens in vivo, they can experience delayed systemic clearance. To circumvent these limitations, the development of antibody fragments, particularly single-chain variable fragments (scFv), has gained attention. This study focuses on engineering an scFv fragment that targets TROP2 as a novel probe, with preclinical testing in animal models to assess its targeting efficacy, biodistribution, and metabolic profile. ***Materials and Methods:*** The purity of the scFv fragment T2 was evaluated using size exclusion chromatography (SEC)-HPLC. Following conjugation with the NOTA chelator, the T2 fragment was radiolabeled with ^{68}Ga. The labeling efficiency and stability of the resulting ^{68}Ga-NOTA-T2 probe were assessed by radio-instant thin-layer chromatography (radio-iTLC). To investigate the targeting specificity, NCI-H292 tumor-bearing mice served as the TROP2-positive group, while A549 tumor-bearing mice functioned as the TROP2-negative control. For in vivo imaging, PET/CT scans were conducted at 0.5, 1, 2, and 4 hours following intravenous administration of the ^{68}Ga-NOTA-T2. The percentage of injected dose per gram of tissue (%ID/g) was calculated for each time point, with all radioactivity measurements corrected for attenuation. Animals were humanely euthanized after imaging, and organs were harvested for ex vivo biodistribution analysis. ***Results:*** In the TROP2-positive lung cancer model, ^{68}Ga-NOTA-T2 exhibited significant tumor uptake at 1 hour (1.74 %ID/g) and 2 hours (1.62 %ID/g) post-injection. The probe also demonstrated rapid clearance from the blood pool, decreasing from 1.21 %ID/g at 1 hour to 0.90 %ID/g at 2 hours. Renal uptake was relatively low, with values of 4.74 %ID/g at 1 hour. Ex vivo biodistribution analysis confirmed minimal retention in the blood pool (2.86 %ID/g) and kidneys (17.66 %ID/g), supporting the favorable pharmacokinetic profile of ^{68}Ga-NOTA-T2. In contrast, PET/CT imaging of the TROP2-negative group revealed indistinct tumor contours. Quantitative analysis showed that the tumor-to-background ratios, when comparing tumor uptake against blood, liver, and muscle, were significantly lower in the negative group compared to the positive group. This marked the high specificity of ^{68}Ga-NOTA-T2 for TROP2-overexpressing tumors. ***Conclusion:*** Our results affirm the capability of ^{68}Ga-NOTA-T2 to specifically target TROP2-overexpressing tumors in vivo, characterized by swift blood clearance and reduced kidney uptake.

EP-0108

Development of $^{11}C/^{18}F$ PET radioligands selective for LRRK2

K. Jia[1], *R. Arakawa*[1], *A. Forsberg Morén*[1], *T. Jensen*[2], *M. Hentzer*[2], *C. Jones*[2], *M. Jorgensen*[2], *B. Bang-Andersen*[2], *A. Varrone*[1], *C. Halldin*[1], *S. Nag*[1];
[1]*Karolinska Institutet, Stockholm, SWEDEN,* [2]*H. Lundbeck, Valby, DENMARK.*

Aim/Introduction: Leucine-rich repeat kinase 2 (LRRK2) is a protein of vital importance to human biology. Mutations of the LRRK2 gene are associated with Parkinson's disease (PD). Their biological effect leads to increased LRRK2 kinase activity, making LRRK2 inhibitors a potential approach for the treatment of PD. The development of LRRK2-specific radioligands enables the ability to measure changes of the density of the enzyme in the brain of PD patients, but also serves as tools to measure occupancy of potential LRRK2 inhibitors. The objectives of this study were i) $^{11}C/^{18}F$ labelling of three 5-(1-(substituted pyridin-3-yl)-1H-pyrazol-4-yl)-3,3-dimethylisoindolin-1-ones as LRRK2 inhibitors, ii) evaluate their binding properties through in vivo PET in NHPs. ***Materials and Methods:*** Precursors and reference standards were provided by H. Lundbeck A/S. Synthesis of [^{11}C]5-(1-(6-(dimethylamino)-5-methylpyridin-3-yl)-1H-pyrazol-4-yl)-3,3-dimethylisoindolin-1-one (1) and [^{11}C]5-(1-(6-methoxypyridin-3-yl)-1H-pyrazol-4-yl)-3,3-dimethylisoindolin-1-one (2) were achieved by methylation of corresponding BOC-precursor followed by the deprotection. [^{18}F]5-(1-(6-(3-fluorooxetan-3-yl)-5-methylpyridin-3-yl)-1H-pyrazol-4-yl)-3,3-dimethylisoindolin-1-one (3) was synthesized in a direct fluorine-18 substitution followed by deprotection. Four NHPs underwent a total of fourteen PET measurements, including assessments at baseline and after pretreatment with either (2) (2 mg/kg body weight) or Tariquidar (2 mg/kg body weight) administered 7 minutes prior to the injection of the radioligands. Radiometabolites in plasma were analyzed using gradient HPLC. The plasma input function corrected for radiometabolites was measured for each scan. ***Results:*** All three radioligands were successfully synthesized with a radiochemical purity exceeding 99%. PET measurements with [^{11}C]1 and [^{11}C]2 revealed low brain uptake, peaking at approximately 1.5 SUV and quickly decreasing to 0.2 and 0.07 SUV, respectively, with most activity concentrated in the blood vessels and no significant regional differences observed. [^{11}C]2 exhibited faster metabolism at 90 minutes (28%) compared to [^{11}C]1 (73%), These results indicated limited brain penetration. After pretreating with cold 2, brain uptake of [^{11}C]2 increased possibly due to reduced metabolism. After pre-treatment with Tariquidar brain uptake of [^{11}C]2 increased slightly in one NHP but remained unchanged in the other, with no significant metabolic impact. This variance may be due to reduced brain efflux following P-gp and BCRP blockage. Similarly, PET studies with [^{18}F]3 also confirmed its lack of brain penetration. ***Conclusion:*** The radiolabeling of [^{11}C]1, [^{11}C]2 and [^{18}F]3 was successful. However, subsequent PET imaging, including pre-treatment experiments, showed low brain penetration and no specific binding in the cynomolgus brain. Therefore, these radioligands are unlikely to be suitable for LRRK2 imaging using PET.

EP-0109

Development of a ^{68}Ga-Radiolabeled Fluorescent Dye for Potential Multimodal PET Imaging of Aneurysmal Subarachnoid Hemorrhage

L. Schäfer[1], *J. W. Gerhards*[1], *D. Kang*[1], *U. Lindauer*[2], *B. Altunay*[1], *S. Lütje*[1], *F. M. Mottaghy*[1,3], *T. Schmidt*[2], *A. T. J. Vogg*[1];
[1]*Department of Nuclear Medicine, University Hospital RWTH Aachen, Aachen, GERMANY,* [2]*Translational Neurosurgery and Neurobiology, Department of Neurosurgery, RWTH Aachen University Hospital, Aachen, GERMANY,* [3]*Department of Radiology and Nuclear Medicine, Maastricht University Medical Center, 6229 ER Maastricht, NETHERLANDS.*

Aim/Introduction: Aneurysmal subarachnoid hemorrhage (aSAH) is a specific form of stroke, most commonly resulting from the rupture of a cerebral aneurysm. This type of stroke poses significant clinical challenges, as aSAH is associated with high morbidity and mortality rates. Despite ongoing research, the underlying pathophysiological mechanisms of aSAH are not yet fully understood. Recent studies of the perivascular system have identified an abnormal distribution of the fluorescent dye Alexa Fluor™ 594 during experimental measurements[1]. To further explore this distribution anomaly, it is proposed to radiolabel the dye with Gallium-68 (^{68}Ga), enabling biokinetic tracking in rats through positron emission tomography (PET) for improved imaging and analytical precision. ***Materials and Methods:*** The coupling reaction between NODA-GA-NHS ester and Alexa Fluor™ 594 1,5-diaminopentane was carried out in acetonitrile using pyridine as auxiliary base, at 80 °C for one hour. Successful conjugation was confirmed by Orbitrap mass spectrometry analysis. For the standard radiolabeling procedure, [^{68}Ga]$GaCl_3$ was reacted and with NODA-GA-NHS-Alexa Fluor™ 594 conjugate using ammonium acetate buffer (3 M, adjusted to pH 4.5), followed by incubation at 80°C for 5 minutes. Purification was performed using a C18 cartridge. Quality control was conducted via radio-HPLC analysis. ***Results:*** The fluorescent dye Alexa Fluor™ 594 after chelator conjugation was successfully labeled with the positron-emitting radionuclide ^{68}Ga(III) in a no-carrier-added form. The NODA-GA-NHS ester was employed to react with the amino group of Alexa Fluor™ 594 1,5-diaminopentane, facilitating subsequent radiolabeling with 68Ga. The formation of the Alexa Fluor™ 594-chelator conjugate, as well as the radiolabeling, were investigated as a function of reaction time, temperature and conjugate concentration. For potential animal experiments, it was necessary to reduce the precursor concentration while increasing the labeling temperature from room temperature to 80°C to keep high RCC, given the short half-life of ^{68}Ga. Optimal labeling conditions were established, achieving radiochemical conversions of > 85%. After purification of n.c.a. [^{68}Ga]Ga-NODA-GA-Alexa Fluor™ 594 remaining impurities were below 3%. ***Conclusion:*** This experimental approach successfully yields the desired radiolabeled dye, which is now available for animal studies, offering enhanced insight into the mechanisms of aSAH. ***References:*** [1] Golanov, E. V., et al. (2018). "Subarachnoid hemorrhage - Induced block of cerebrospinal fluid flow: Role of brain coagulation factor III (tissue factor)." J Cereb Blood Flow Metab 38(5): 793-808.

EP-0110

Mesoporous Silica Nanoparticles Labeled with Zirconium-89 for Long-Term In Vivo Tracking of Cells via PET Imaging

M. Xu, *Z. Liu;*
Changping Laboratory, Beijing, CHINA.

Aim/Introduction: Cell-based therapies, as one of the most promising treatments for human diseases, have attracted significant attention in recent years, owing to their outstanding therapeutic effects.Stem cell therapy and immune cell therapy, in particular, have emerged as essential fields of clinical research, offering great promise in addressing intractable diseases such as cardiac disease, tissue injury, immune disorders, cancer treatment, and so on. But the specific behavior of these functionalized cells in the body has been confusing, which limited the further development of cell therapy. There is an urgent need to develop a technology capable of tracking and imaging functional cells in the body for understanding their behavior over extended periods. ***Materials and Methods:*** The zirconium-89 (^{89}Zr) was labeled mesoporous silica nanoparticles (^{89}Zr-mSiO_2) as a robust platform for cell tracking via positron emission tomography (PET) imaging. Human mesenchymal stem cells (hMSCs) and cancer cells loaded with mesoporous silica nanoparticles concentrating the 89Zr

radioisotope and injected into mice. The mice were tracked in vivo for a long time from the pattern of annihilation photons detected using PET/CT. ***Results:*** The designed ^{89}Zr-mSiO$_2$ exhibit exceptional biocompatibility and internalization efficiency into cells, owing to their unique mesoporous structure and stable Si-O-Zr bonds. Both in vitro and in vivo studies demonstrate prolonged stability and minimal cytotoxicity of ^{89}Zr-mSiO$_2$, ensuring reliable and safe cellular labeling. Notably, ^{89}Zr-mSiO$_2$ exhibit negligible cell efflux, enabling precise detection of cellular signals without interference. PET imaging of ^{89}Zr-mSiO$_2$-labeled cells in murine models allows for real-time tracking of cell localization for up to 10 days post-injection. ***Conclusion:*** Overall, our findings highlight the potential of ^{89}Zr-mSiO$_2$ as a promising tool for long-term in vivo tracking of functional cells, thus advancing the prospects of cell therapy in a clinical setting.

EP-0111

Development of ^{18}F-Labeled Deuterated Tropane Derivatives with High Metabolic Stability for PET Imaging of the Dopamine Transporter

Z. Chen, *J. Hong, Y. Fang, C. Liu, J. Kang, J. Zuo, J. Li;*
NHC Key Laboratory of Nuclear Medicine, Jiangsu Key Laboratory of Molecular Nuclear Medicine, Jiangsu Institute of Nuclear Medicine, Wuxi, CHINA.

Aim/Introduction: The dopamine transporter (DAT) in the central nervous system is an attractive biomarker for diagnosing and monitoring various neurodegenerative diseases. To develop in vivo metabolically stable positron emission tomography (PET) probes for DAT imaging with a high target/background ratio, two ^{18}F-labeled tropane derivatives with deuteration on both N-fluoropropyl and 2β-carbomethoxy of the tropane scaffold were synthesized and evaluated. ***Materials and Methods:*** Radioligands methyl-d$_3$ (1R,2S,3S,5S)-3-(4-chlorophenyl)-8-(3-(fluoro-^{18}F) propyl-1,1,2,2,3,3-d$_6$)-8-azabicyclo[3.2.1]octane-2-carboxylate ([^{18}F]FP-CCT-d$_9$) and methyl-d$_3$ (1R,2S,3S,5S)-3-(4-iodophenyl)-8-(3-(fluoro-^{18}F)propyl-1,1,2,2,3,3-d$_6$)-8-azabicyclo[3.2.1] octane-2-carboxylate ([^{18}F]FP-CIT-d$_9$) were synthesized from anhydroecgonine and radiolabeled with ^{18}F through a "two-step one-pot" method. Lipophilicity, in vitro binding assay and microPET imaging in rats were performed. [^{18}F]FP-CIT-d$_9$ showed a higher standardized uptake value ratio (SUVr) and was selected for further in vivo metabolism and biodistribution investigations. ***Results:*** The radioligands [^{18}F]FP-CCT-d$_9$ and [^{18}F]FP-CIT-d$_9$ were obtained in radiochemical purities >98% and molar activity about 30 GBq/μmol. [^{18}F]FP-CCT-d$_9$ or [^{18}F]FP-CIT-d$_9$ demonstrated high specificity and binding affinity to DAT in vitro, with IC$_{50}$ values between 2~3 nM. MicroPET imaging with normal rats revealed that [^{18}F]FP-CIT-d$_9$ has a higher SUVr than [^{18}F]FP-CCT-d$_9$. Blocking experiments demonstrated the selectivity and reversibility of [^{18}F] FP-CIT-d$_9$ for DAT binding in microPET imaging. The diagnostic efficacy of [^{18}F]FP-CIT-d$_9$ for DAT-related disorders was verified in semi-PD model rats with microPET. In vivo metabolic studies in rats indicated that [^{18}F]FP-CIT-d$_9$ exhibited enhanced in vivo stability compared with the previously reported analog [^{18}F]FP-CIT-d$_6$. Biodistribution experiments further confirmed that [^{18}F] FP-CIT-d$_9$ has a good affinity toward DAT in the brain. ***Conclusion:*** [^{18}F]FP-CIT-d$_9$ is a highly promising metabolic stable ^{18}F-labeled PET probe for DAT imaging, with potential clinical applications in detecting and monitoring DAT-related neurological disorders. The present work was supported by the National Natural Science Foundation of China (82172054).

EP-0112

A study on radiolabeling methods for novel tau tracer lead compounds discovered using a big data/AI-based drug development platform

K. Kangbin[1], *H.-C. Song*[1,2];
[1]*Chonnam National University Hospital, Gwangju, KOREA, REPUBLIC OF,* [2]*Chonnam National University Medical School, Gwangju, KOREA, REPUBLIC OF.*

Aim/Introduction: By leveraging big data and artificial intelligence (AI) technologies, we identified lead compounds predicted to specifically bind to tau protein and developed radiolabeling methods for these compounds. ***Materials and Methods:*** Using a big data/AI-based drug development platform, we identified five compounds predicted to specifically bind to tau protein (microtubule-associated protein tau, human). Of these, two compounds (JN-TAU-1 and JN-TAU-2) were selected as lead candidates for radiolabeling. Considering the feasibility of labeling with the PET radionuclide C-11, C-11 was produced using a cyclotron (IBA) and radiolabeling was performed with an automated synthesizer (TRACERlab FX2 C Synthesizer, GE Healthcare). The synthesis conditions were varied based on temperature (25°C, 70°C), reaction time (3, 5, 10 minutes), and solvents (c-HXO, DMSO, acetone, acetonitrile). The resulting radioactivity levels were compared under each condition. ***Results:*** [C-11]CO2 gas, produced via cyclotron beam irradiation, was converted to CH3OTf for the labeling reaction. The radioactivity levels of JN-TAU-1 and JN-TAU-2 synthesized at 25°C and 70°C were 11 ± 4 mCi (n=5) and 8 ± 4 mCi (n=5), respectively (p=0.60). When the reaction was performed at 25°C for 3, 5, and 10 minutes, the radioactivity levels were 15 ± 9 mCi (n=3), 10.5 ± 4.5 mCi (n=8), and 11 ± 4 mCi (n=5), respectively, with no significant differences observed. Under the conditions of 25°C and 3 minutes, the radioactivity levels of the products synthesized using c-HXO, DMSO, and acetone as solvents were 15 ± 9 mCi (n=3), 10 ± 3 mCi (n=4), and 17.5 ± 1.5 mCi (n=3), respectively. Notably, a solvent mixture (MIX) of acetone and acetonitrile in a 1:1 ratio yielded approximately 40 ± 5 mCi (n=3) of radioactivity (p=0.04). ***Conclusion:*** Our preliminary results demonstrate that the tau imaging lead compounds identified using a big data/AI-based drug development platform can be successfully radiolabeled with C-11. While time and temperature had minimal impact on the radiolabeling process, the choice of solvent significantly influenced labeling efficiency. The highest labeling efficiency was notably achieved using a mixed solvent (MIX) of acetone and acetonitrile.

EP-0113

Synthesis of [^{11}C]PF-07799933 and evaluation of its whole-body distribution in NHP using PET

S. Nag[1], *Z. Jia*[1], *M. Tóth*[1], *Y. Khani*[1], *A. Varrone*[1], *L. Chen*[2], *J. Wong*[2], *B. Baer*[2], *J. Gaudino*[2], *K. Maresca*[2], *C. Halldin*[1];
[1]*Karolinska Institutet, Stockholm, SWEDEN,* [2]*Pfizer Inc., Worldwide Research & Development, Cambridge, MA, UNITED STATES OF AMERICA.*

Aim/Introduction: PF-07799933 is a drug candidate and an investigational small synthetic molecule that is specifically investigated by Pfizer for various cancer types for its ability to cross the blood-brain barrier to treat BRAF mutated tumors with CNS involvement. To aid the clinical evaluation of brain penetration of PF-07799933, it was proposed that the compound be labelled with C-11 and PET imaging be performed to trace the distribution of the drug in the tissues of NHP subjects. The primary aims of the study included developing a synthesis method to effectively label PF-07799933 with C-11 and measuring the distribution of [^{11}C]PF-07799933 throughout the body of NHPs, estimating the effective radiation doses and to evaluate the brain distribution of [^{11}C]PF-07799933 following a pre-treatment of cold PF-07799933. Furthermore, radiometabolite was analyzed in NHP blood plasma.

Materials and Methods: Radiolabeling was achieved via [^{11}C] methylation and followed by deprotection. Four female NHPs underwent four PET measurements. Each NHP was scanned once, with NHP 1 and NHP 2 being evaluated under baseline conditions, while NHP 3 and NHP 4 were scanned under pre-treatment conditions (30 mg/kg PF-07799933). For the latter two NHPs, the imaging protocol was tailored to focus on the brain to enhance both the spatial and temporal resolution of brain uptake of [^{11}C] PF-07799933. A reversed-phase radio-HPLC method was used to determine the radiometabolites in NHP plasma. ***Results:*** [^{11}C]PF-07799933 was synthesized with radiochemical purity (>99%). The injected radioactivity of [^{11}C]PF-07799933 was 154.3 ± 4.9 MBq. The absorbed organ dose was highest at the small intestine (0.04 mGy/MBq) followed by the gallbladder, liver, and kidneys. The effective dose was estimated to be 0.0042 mSv/MBq. The brain uptake was distributed homogeneously across all experiments, reaching approximately 2% of the Injected Dose (ID) at its peak. In contrast, following the pre-treatment the uptake was rapidly decreased to below 0.4% ID. Radiometabolite studies demonstrated that only more polar radiometabolites were formed, with about 15% unchanged radioligand remaining at 60 min post injection for baseline but after pretreatment it was over 90% unchanged radioligand. Furthermore, [^{11}C]PF-07799933 demonstrated a brain-to-plasma ratio of 0.1-0.15 under baseline/tracer conditions, which was reduced to 0.05-0.07 following pre-treatment. ***Conclusion:*** PF-07799933 was successfully labeled. The homogeneous brain uptake was measured and blocked with cold dosing. The effective dose was estimated to be 0.0042 mSv/MBq of injected activity, based on a dosimetry study in non-human primates, indicating that it is comparable to other C-11 PET radioligands.

EP-0114

ImmunoPET tracer based on antibody fragments radiolabeled with ^{89}Zr for detecting the α1 subunit of the GABA-A receptors in the brain.

Á. García de Lucas[1,2,3], *L. Kovacs*[4,2], *B. Todorov*[5], *L. Nissilä*[4], *B. Salinas Rodríguez*[1,3,6], *U. Lamminmäki*[2], *F. López-Picón*[7,2], *A. Airaksinen*[4,2];
[1]*Universidad Carlos III de Madrid, Madrid, SPAIN,* [2]*University of Turku, Turku, FINLAND,* [3]*Instituto de Investigación Sanitaria Gregorio Marañón, Madrid, SPAIN,* [4]*Turku PET Centre, Turku, FINLAND,* [5]*University of Sofia, Sofia, BULGARIA,* [6]*Centro Nacional de Investigaciones Cardiovasculares (CNIC), Madrid, SPAIN,* [7]*Turku PET Centre, Turku, FINLAND.*

Aim/Introduction: Immuno-positron emission tomography (immunoPET) is a non-invasive in vivo imaging method based on tracking and quantifying radiolabeled monoclonal antibodies (mAbs) and other related molecules, such as antibody fragments[1]. This new approach could be used to map the diversity of GABA-A receptors inside the brain. For instance, postmortem studies in schizophrenia patients have demonstrated that GABA-A receptorα subunit expression have found reductions in α1 and increases in α2 subunits expression. However, the density of GABA-A receptor in schizophrenia does not appear abnormal in radioligand studies as postmortem studies have demonstrated. Some researchers and we believe that these negative findings can be explained because of the lack of imaging tracers with high affinity and specificity[2,3]. ***Materials and Methods:*** Di-scFv1F4 was first conjugated with 15 equivalents of DFO*-NHS. DFO*-Di-scFv1F4 was radiolabeled with 10-50 MBq 89Zr and purified by a spin filter (10kDa). [^{89}Zr] Zr-DFO*-Di-scFv1F4 (2.43-2.90 MBq, 0.63-0.86 nmol, in 100 µl of PBS) was administered intravenously via tail vein injection in wild C57BL/6 mice and PET/CT images was performed in β- and X-CUBE scanners at 24, 72 and 144 hours post-injection. PET images were analyzed using Inveon Research Workplace software. ***Results:*** [^{89}Zr]Zr-DFO*-Di-scFv1F4 was successfully conjugated with DFO* (0.72 DFO*/antibody fragment) and radiolabeled with ^{89}Zr with a radiochemical purity >96% ± 0.76 (n=3). After the production of the PET probe, it was injected into mice, and images were taken at different time points. PET analysis was conducted with a focus on the brain, where a progressive decrease in radioactivity signal was observed over 24 (1.51±0.18 %ID/g), 72 (0.91±0.17 %ID/g) and 144 (0.62±0.12 %ID/g) hours. Notably, [^{89}Zr]Zr-DFO*-Di-scFv1F4 exhibited region-specific distribution patterns across different brain areas and time points. For instance, the cerebellum, frontal cortex, and hypothalamus demonstrated higher signal intensities compared to the hippocampus, parieto-temporal cortex, striatum, and thalamus. ***Conclusion:*** [^{89}Zr]Zr-DFO*-Di-scFv1F4 was successfully developed and studied using PET imaging in healthy mice. Interestingly, the distribution and uptake in various brain areas mirrored the patterns described for the α1 subunit of GABA-A receptors in previous research[4]. The cerebellum, frontal cortex, and hypothalamus exhibited higher uptake. This study is the first to demonstrate that an immunoPET probe can be developed to cross the blood-brain barrier and detect ion channels within the brain. ***References:*** 1) de Lucas ÁG et al. (2023). Doi:10.3390/biom13010164 2) de Jonge JC et al. (2017). Doi:10.3389/fpsyt.2017.00118 3) Taylor SF, Tso IF. (2015). Doi:10.1016/j.schres.2014.10.011 4) Hörtnagl H et al. (2013). Doi:10.1016/j.neuroscience.2013.01.008.

EP-0115

Development of a novel PET radiotracer for targeting HER2-expressing tumors

A. Coliva[1], *M. Maspero*[2], *S. Di Benedetto*[3], *R. Ferrisi*[3], *C. Papotto*[4], *S. Valtorta*[2], *R. Moresco*[4], *C. Dallanoce*[3], *A. Chiti*[5,6];
[1]*Nuclear Medicine Department, IRCCS San Raffaele, Milan, ITALY,* [2]*Institute of Bioimaging and Complex Biological Systems, National Research Council (IBSBC-CNR), Milan, ITALY,* [3]*Department of Pharmaceutical Sciences, University of Milan, Milan, ITALY,* [4]*Department of Surgical Sciences, University of Milano-Bicocca, Milan, ITALY,* [5]*Vita-Salute San Raffaele University, Milan, Italy,* [6]*IRCCS San Raffaele, Milan, ITALY.*

Aim/Introduction: HER2 (Human Epidermal Growth Factor Receptor 2) is a key biomarker in breast cancer, associated with aggressive tumors and poor prognosis, as 15-20% of breast cancers overexpress it. Targeting HER2 has transformed treatment options, especially with targeted therapies, though variability in receptor expression can influence their effectiveness, highlighting the need for accurate HER2 status assessment. While HER2 levels are typically monitored using invasive methods, PET imaging offers real-time, non-invasive, and quantitative insights. Tyrosine kinase inhibitors (TKIs) are a promising class of drugs that block HER2-activated signaling pathways, reducing tumor growth and enhancing patient outcomes. Radiolabeled TKIs are being investigated for their imaging and treatment response monitoring potential. SPH5030 is a specific and irreversible TKI currently in phase I clinical trials. This study aims to evaluate [^{11}C]SPH5030, a structurally identical compound, as a positron imaging agent. ***Materials and Methods:*** Chemically and optically pure precursors, N-desmethyl (R,E)- and N-desmethyl (R,Z)-SPH5030, were synthesized. Radiolabelling proceeds in the same way for both through methylation with [^{11}C]methyl triflate on the precursor dissolved in DMSO. The crude mixture was purified by isocratic semipreparative HPLC and recovered in a phosphate buffer (25 mM, pH 6) mixed with Ethanol and Acetonitrile (41:41:18). The purified compound was subsequently formulated in saline/ethanol after passage on a tC18 cartridge. In vitro uptake studies were conducted on two breast cancer cell lines: one HER2-positive (SKBR3) and one HER2-negative (MDA-MB-231) at three time points (15 min, 30 min, and 1 h). The cell lines, adhered to the assay plate, were incubated with a fixed concentration of the labeled compound. At the specified times, the supernatant was collected, and the activity of both bound and unbound labeled compounds was measured. ***Results:*** [^{11}C]SPH5030 was obtained with a radiochemical yield of about 9% n.d.c, a radiochemical purity > 99% and specific activity of 0.11 GBq/nmol. In vitro uptake experiment was conducted with (R,Z)-[^{11}C]SPH5030. Maximum uptake was observed at 30 minutes, 19.76 ± 1.99 % in SKBR3 cell

vs 8.73 ± 0.42 %. in MDA-MB-231 cells. The small uptake observed in HER2-negative cells was likely due to nonspecific binding or to cross binding with EGF receptor. ***Conclusion:*** Building on these encouraging findings, studies are needed to evaluate HER2 specificity of (R,Z)-[^{11}C]SPH5030 and (R,E)-[^{11}C]SPH5030 and to explore other derivatives that allow incorporation of Fluorine-18 or modulation of selectivity and binding reversibility. ***References:*** [1] D. Li, et al, Journal of medicinal chemistry, 2022, 65, 5334-5354.

EP-0116

Synthesis of [11C]BIIB135, a Tyrosine Kinase (BTK) Inhibitor evaluated in NHP using PET

P. Datta[1], *A. Forsberg Morén*[1], *Y. Khani Meynaq*[1], *M. Kaliszczak*[2], *B. Cook*[2], *A. Varrone*[1], *C. Halldin*[1], *S. Nag*[1];
[1]*Karolinska Institutet, Stockholm, SWEDEN,* [2]*Biogen Inc, 225 Binney street, Cambridge, MA 02142, MA, UNITED STATES OF AMERICA.*

Aim/Introduction: Bruton's tyrosine kinase (BTK) is primarily involved in the pathway associated with the B-cell receptor. As a promising anti cancer drug targeting B-cell therapies, B-cell malignancies and autoimmune diseases such as multiple sclerosis (MS) and rheumatoid arthritis, BTK inhibitors have attracted a good deal of attention. It is important to devise new BTK inhibitors that reversibly bind and have high selectivity. BIIB135, a novel and highly selective irreversible BTK inhibitor approved for adult patients with relapsed/refractory mantle cell lymphoma (r/r MCL) after prior therapy, demonstrates potent inhibition of BTK with a half-maximal inhibitory concentration of 1.6 nM and minimal off-target effects on other tyrosine kinases. The aim of this study was to develop a fast and efficient synthetic method for labeling [11C] BIIB135 and its in vivo initial evaluation in NHP using PET. ***Materials and Methods:*** Radiolabeling was achieved in one step via [11C] carbonylation. Two male NHPs (NHP1 and NHP2) underwent four PET measurements in total. Two PET measurements were performed with [11C]BIIB135 at baseline condition followed by the second PET measurement after pretreatment with BIIB135 (2 mg/kg bw) on same day. The plasma input function corrected for radiometabolites was measured for each scan. The total volume of distribution (VT) which is equivalent to the equilibrium partition coefficient for the drug between brain and plasma were calculated for a selection of regions. The occupancy was calculated using revised Lassen plot. Radiometabolites in plasma were analysed using gradient HPLC. ***Results:*** [11C]BIIB135 was synthesized successfully with radiochemical purity (>99%), and molar activity >37 GBq/μmol. The compound was found to be stable in sterile saline for 60 min. The distribution of [11C]BIIB135 in the primate brain was homogenous and the whole brain uptake was <1% ID at baseline and after pretreatment. The absence of conclusive evidence for alterations in regional VT values after pharmacological dosing indicates that any specific binding of [11C]BIIB135 is minimal compared to the free and non-specific components in the living brain. Furthermore, radiometabolite analyses revealed the formation of only more polar radiometabolites, with approximately 60% of the unchanged [11C]BIIB135 remaining at 60 minutes post-injection. ***Conclusion:*** This study revealed low brain uptake of [11C]BIIB135. While there was slight variability in its distribution across different brain regions, the observed kinetics were consistent with passive diffusion, indicating that free concentration and non-specific binding were the predominant factors influencing distribution.

EP-0117

Development and evaluation of [^{68}Ga]LAYp: A novel PET probe for tumor-associated enzyme targeting

W. Hongyong, *H. Wu, Y. Liu, J. Wu, P. Zou;*
Jiangsu Institute of Nuclear Medicine, Wuxi, Jiangsu, CHINA.

Aim/Introduction: The development of specific and effective PET probes is crucial for improving diagnostic accuracy and therapeutic outcomes. Recent advancements in peptide-based probes have shown great potential due to their high specificity, low toxicity, and rapid clearance from non-target tissues. In this study, we introduce a novel PET probe, [^{68}Ga]LAYp, designed to target tumor-associated enzymes. This probe leverages an enzymatic peptide self-assembly strategy, which allows for the selective enrichment of the probe at the tumor site, thereby enhancing PET imaging. ***Materials and Methods:*** The precursor of the probe, LAYp, was synthesized using SPPS. The synthesized precursor was then labeled with $^{68}GaCl_3$ form the radiolabeled probe [^{68}Ga]LAYp. The radiochemical purity of the probe was verified using radioactive HPLC. For stability assessment, the probe was incubated in PBS and FBS at 37°C, with samples collected at 1, 2, and 3 h for HPLC analysis. In vivo studies were conducted by injecting the probe into HeLa tumor-bearing nude mice. Micro-PET imaging was performed at 1 h and 2 h post-injection for a duration of 10 min each. The tumor and muscle regions were delineated across five consecutive slices in the micro-PET images. ***Results:*** The analysis of the ^{68}Ga-labeled reaction mixture via radioactive HPLC confirmed that the probe's radiochemical purity surpassed 98%, which is sufficient for advancing to in vivo experiments without further purification. During the stability assessment, the radiochemical purity of the probe was maintained consistently over a 3-hour duration. The MTT assay revealed that at a concentration of 500 μM of the probe precursor, the cell viability reached 98%, indicating the probe's safety for in vivo applications. The micro-PET imaging results clearly delineated the tumor, with tumor uptake values recorded at 1 h and 2 h post-injection being 3.32 ± 0.37 %ID/g and 6.45 ± 0.53 %ID/g, respectively. The high tumor-to-muscle signal ratio observed highlights the probe's effective targeting and accumulation within the tumor site. ***Conclusion:*** The novel PET probe [68Ga]LAYp demonstrates excellent stability, low cytotoxicity, and effective tumor targeting in HeLa tumor-bearing nude mice. The straightforward synthesis procedure, gentle reaction conditions, and low raw material costs of the probe precursor make it a promising candidate for further development and clinical translation. Future work will focus on exploring the potential of substituting the phosphate group in the probe with various enzyme-targeting molecules to create a range of tumor-specific PET probes tailored to different types of cancer.

EP-0118

Synthesis and in vitro/in vivo Evaluation of the Synaptic Vesicle Protein SV2C PET Radioligands: ^{18}F-UCB-F, ^{11}C-SV2C-1, and ^{11}C-SV2C-2

S. Nag[1], *A. F. Morén*[1], *V. Sousa*[1], *R. Zou*[2], *P. Datta*[1], *J. Mercier*[3], *Y. Khani Meynaq*[1], *H. Ågren*[2], *C. Halldin*[1], *A. Varrone*[1];
[1]*Karolinska Institutet, Stockholm, SWEDEN,* [2]*Uppsala University, Uppsala, SWEDEN,* [3]*UCB Biopharma, Braine l'Alleud, BELGIUM.*

Aim/Introduction: The synaptic vesicle protein SV2C protein, mainly found in the basal ganglia, is linked to Parkinson's disease (PD). It plays a role in regulating dopamine release and has been disrupted in PD animal models and brain tissue from PD patients. In studying PD-related synaptopathy, SV2C could be a potential imaging target for tracking changes with disease progression and treatment. This study aims i) to investigate the binding profile of a series of compounds using molecular docking, molecular dynamics simulation and free energy calculation methods ii) to radiolebel ^{18}F-UCB-F, ^{11}C-SV2C-1 and ^{11}C-SV2C-2 and evaluate their binding characteristics in vitro using autoradiography (ARG) and in vivo using NHP PET. ***Materials and Methods:*** Molecular dynamics (MD) simulations were carried out using the GROMACS 4.6.7 code. Radiolabeling was accomplished through either fluorine-18 nucleophilic substitution reaction or N-alkylation using $^{11}C\text{-}CH_3I$. The ^{18}F-UCB-F binding distribution across regions was evaluated using autoradiography (ARG) on brain sections from rats and NHPs. Blocking experiments were conducted using cold UCB-F (10 μM) during ARG analysis. The brain distribution of ^{18}F-UCB-F, ^{11}C-SV2C-1 and ^{11}C-SV2C-2 was examined with PET. Four PET measurements at baseline condition were conducted in two different cynomolgus

NHPs, using a high-resolution PET/CT system. Radiometabolites were analyzed in NHP plasma samples using radio HPLC. ***Results:*** Three compounds were chosen for radiolabeling depending on the docking score and free energy calculation. They were synthesized effectively from the corresponding precursors. ARG on brain slices from rats and NHPs showed specific binding of ^{18}F-UCB-F in pallidum, striatum, substantia nigra and brainstem, consistent with the expression of SV2C in the brain. In NHPs, ^{18}F-UCB-F, ^{11}C-SV2C-1 and ^{11}C-SV2C-2 rapidly entered the brain with a peak uptake of 2.8 %ID for ^{18}F-UCB-F and 2.1 %ID and 4.0 %ID for ^{11}C-SV2C-1 and ^{11}C-SV2C-2 respectively at 4 minutes. The wash-out of the radioactivity from the brain was rapid with no clear evidence of regional distribution. Radiometabolite studies showed the formation of more polar radiometabolites, with approximately 15% of unchanged radioligand remaining at 15 minutes post-injection. ***Conclusion:*** Three radioligands were radiolabelled with high incorporation yield. In vitro, ^{18}F-UCB-F showed specific binding on tissue slices from rodent and NHP brains. However, in vivo, ^{18}F-UCB-F, ^{11}C-SV2C-1 and ^{11}C-SV2C-2 displayed too rapid washout from the brain, lack of regional brain distribution and rapid metabolism. Overall, these findings indicate that none of the radioligands is suitable for imaging SV2C and additional work is needed to identify a potential candidate.

EP-0119

Research on Dynamic Monitoring and Quantitative Assessment of Liver Function in Liver Injury Based on [^{68}Ga]Ga-DTPA-EOB PET Imaging

Y. Fan[1], *W. Hai*[1], *Q. Qu*[1], *B. Cai*[2], *X. Xiang*[2], *Y. Shen*[3], *B. Li*[1], *J. Hu*[1]; *[1]Department of Nuclear Medicine, Ruijin Hospital Affiliated to Shanghai Jiao Tong University School of Medicine, Shanghai, CHINA, [2]Department of Infectious Diseases, Ruijin Hospital Affiliated to Shanghai Jiao Tong University School of Medicine, Shanghai, CHINA, [3]Research Center for Experimental Medicine, Ruijin Hospital Affiliated to Shanghai Jiao Tong University School of Medicine, Shanghai, CHINA.*

Aim/Introduction: The progression of liver injury to failure poses a global health burden, making accurate assessment and prediction of liver function crucial for preventing irreversible damage. We synthesized the novel probe [^{68}Ga]Ga-Diethylenetriaminepentaacetic acid-Ethoxybenzyl ([^{68}Ga]Ga-DTPA-EOB) for PET/CT imaging assessment of liver function. ***Materials and Methods:*** [^{68}Ga]Ga-DTPA-EOB was synthesized based on EOB-DTPA, and its radiochemical purity and in vitro stability were analysed by radio-HPLC. Dynamic [^{68}Ga]Ga-DTPA-EOB PET/CT scans were performed on normal SD rats and CCl_4-treated chronic liver injury model. Furthermore, [^{68}Ga]Ga-FAPI PET/CT and MRI (T2WI sequence) imaging were conducted on the chronic liver injury group at week 7. Model validation and injury quantification were performed through hepatic histology and serum liver function assays. To assess biosafety, a toxicological dose of [^{68}Ga]Ga-DTPA-EOB exceeding the previous imaging dose was administered intravenously to normal rats, followed by histological analysis of major organs 24 hours post-injection. ***Results:*** [^{68}Ga]Ga-DTPA-EOB exhibited a radiochemical purity of ≥95% and demonstrated excellent stability in vitro. Dynamic 30-min PET/CT imaging demonstrated liver-specific uptake of the probe in normal rats, with the time-activity curve (TAC) that showed a gradual increase to plateau, and was mainly excreted through the kidneys and intestines. The hepatic uptake levels of [^{68}Ga]Ga-DTPA-EOB in chronic liver injury group was significantly lower than those in the normal group at all time points ($P<0.05$), and the TAC exhibited a gradual declining trend. Compared to the control group, the chronic liver injury group at week 7 demonstrated mild uptake on [^{68}Ga]Ga-FAPI PET/CT images and subtle fibrotic changes on MRI (T2WI sequence), although the visual contrast was less pronounced than that of [^{68}Ga]Ga-DTPA-EOB. Moreover, the imaging findings were consistent with the serum biochemical results and hepatic histopathology in rats. Acute toxicity testing revealed that HE staining of organs in the simulated toxicological dose group showed intact tissue structures with no significant pathological abnormalities, providing preliminary evidence for the safety of [^{68}Ga]Ga-DTPA-EOB PET imaging. ***Conclusion:*** In this study, we successfully synthesized the DTPA-EOB-based probe [^{68}Ga]Ga-DTPA-EOB, which demonstrated high radiochemical purity, in vitro stability, and imaging safety. Micro-PET/CT imaging studies confirmed its feasibility for liver function imaging.

EP-0120

Effects of replacing the ether linkage of a benzo[h] quinoline-based fibroblast activation protein-targeted tracer, [^{68}Ga]Ga-SB03178, with an N-methyl linkage on its FAP-targeting capability

S. Jozi*, C.-C. Chen, H. Merkens, P. Ng, W. Lau, F. Bénard, K.-S. Lin; BC Cancer Research Institute, Vancouver, BC, CANADA.*

Aim/Introduction: Fibroblast activation protein (FAP), a transmembrane protein overexpressed in cancer-associated fibroblasts, is a promising cancer imaging marker. Many FAP-targeted tracers have been developed and [^{68}Ga]Ga-FAPI-04 is the most widely used PET tracer in the clinic. Previously, we replaced the quinoline moiety in [^{68}Ga]Ga-FAPI-04 with benzo[h]quinoline and the resulting [^{68}Ga]GaSB03178 showed improved binding affinity (IC_{50} = 4.11 vs 1.33 nM) and tumour uptake (11.9 vs 20.3 %ID/g) [1,2]. It has been shown that the linkage of linker at the quinoline moiety could affect FAP targeting as [^{68}Ga]Ga-FAPI-46 containing an N-methyl (-NMe-) linkage showed higher tumour uptake than [^{68}Ga]Ga-FAPI-04 containing an ether (-0-) linkage [3]. Therefore, in this study, we investigated the effect of replacing the ether linkage in Ga-SB01378 with an N-methyl linkage on its FAP-targeting capability. ***Materials and Methods:*** FAPI-delta, the N-methyl linkage analog of SB03178, was synthesized via multi-step organic synthesis. ^{nat}Ga and ^{68}Ga complexation reactions were conducted in sodium acetate and HEPES buffers, respectively. FAP binding affinity was measured by enzymatic assay using recombinant hFAP and Suc-Gly-Pro-AMC as the substrate. PET imaging and ex vivo biodistribution studies were conducted in HEK293T:hFAP tumour-bearing mice at 1 h post-injection. The blocking study was performed with the co-injection of FAPI-04 (0.5 mg/mouse). ***Results:*** ^{nat}Ga-FAPI-delta was obtained in 60% yield and [^{68}Ga]Ga-FAPI-delta was obtained in 33% decay-corrected radiochemical yield with > 95% radiochemical purity and > 45 GB/µmol molar activity. FAPI-delta had high binding affinity for FAP with an IC_{50} of 1.6 nM. [^{68}Ga]Ga-FAPI-delta enabled clear visualization of HEK293T:hFAP tumour xenografts with good tumour-to-background contrast. [^{68}Ga]Ga-FAPI-delta was excreted mainly via the renal pathway. Blocking with FAPI-04 significantly reduced the tumor uptake of [^{68}Ga]Ga-FAPI-delta. Biodistribution results were consistent with the observations from the PET images. The uptake values of [^{68}Ga]Ga-FAPI-delta in tumour, liver and kidneys were 11.7±2.1, 2.7±0.2, and 4.9±0.7 %ID/g, respectively. The uptake in other collected organs/tissues was minimal. The tumor uptake was reduced by 86% with the co-injection of FAPI-04, demonstrating specific binding. ***Conclusion:*** Despite having a retained good FAP binding affinity, the tumour uptake of [^{68}Ga]Ga-FAPI-delta was inferior to that of [^{68}Ga]Ga-SB03178 using the same tumour model. Therefore, further optimizations are needed to maximize the utility of the benzo[h] quinoline-based pharmacophore for the design of FAP-targeted tracers. ***References:*** 1. Bendre S., et al. Eur J Med Chem 2024; 268: 116238. 2. Bendre S., et al. Molecules 2023; 28: 3481. 3.Loktev A., et al. J Nucl Med 2019; 60:1421-1429.

EP-0121

Preclinical Evaluation of MT1-MMP-Targeting Bicyclic Peptides for Radiotheranostic Applications

M. Sulewska[1], *A. Regupathy*[2], *L.-C. Domogalla*[3], *N. Steinacker*[3], *J. Johanna Lahdenranta*[4], *B. Blakeman*[2], *F. Wood*[2], *P. Meyer*[3], *P. Huxley*[2], *M. Eder*[1], *G. Mudd*[2], *A.-C. Eder*[3];
[1]*German Cancer Consortium (DKTK) / University Medical Center Freiburg, Freiburg, GERMANY,* [2]*BicycleTx Limited, Cambridge, UNITED KINGDOM,* [3]*University Medical Center Freiburg, Freiburg, GERMANY,* [4]*Bicycle Therapeutics, Cambridge, MA, UNITED STATES OF AMERICA.*

Aim/Introduction: Membrane type 1 matrix metalloproteinase (MT1-MMP) is crucial in extracellular matrix degradation, which facilitates cancer progression and metastasis. Previous studies have shown the feasibility of using phage display-derived radiolabelled bicyclic peptides for positron emission tomography (PET) imaging. This study aimed to identify and characterise novel MT1-MMP-binding bicyclic peptides with an improved pharmacokinetic profile. ***Materials and Methods:*** Four novel MT1-MMP-targeting bicyclic peptides (BCY1, BCY2, BCY3, and BCY4) were radiolabelled with either gallium-68 or lutetium-177. We assessed various physicochemical properties, including binding affinity, serum stability, and logD values. Cell binding and internalisation were evaluated using MT1-MMP-expressing HT1080 cells. In vivo performance was analysed in MT1-MMP+ tumor-bearing nude mice via µPET/MR imaging up to 2 hours post-injection (p.i.), followed by an organ distribution analysis (n = 3 for each peptide). ***Results:*** All peptides exhibited nanomolar binding affinity (4.1 - 9.8 nM), with radiochemical purity exceeding 99 %. They demonstrated high serum stability, and their logD values ranged from - 3.6 to - 2.6. In vitro studies confirmed high specificity and minimal off-target binding (1 - 4%). High tumour-to-background contrast was achieved within 30 minutes p.i. for BCY1, BCY2, and BCY4. Organ distribution studies revealed significant tumour uptake (12 - 25% injected dose per gram, %ID/g) of all bicyclic peptides at 1-hour p.i., with BCY1 and BCY4 exhibiting the lowest off-target binding, aside from kidneys (5.8 %ID/g and 6.1 %ID/g, respectively). ***Conclusion:*** BCY1 and BCY4 demonstrated optimal pharmacokinetic profiles characterised by high tumour uptake, specificity, and rapid blood clearance. Further translational research is essential to evaluate their full potential for radiotheranostic applications.

EP-0122

Comparison of 3rd generation β-Amyloid PET radiotracers with PiB and FBB in mouse models of Alzheimer's Disease

S. Bagheri[1], *B. Uzuegbunam*[2], *M. Luster*[1], *D. Librizzi*[1,3], *B. Yousefi*[1,4];
[1]*Department of Nuclear Medicine, School of Medicine, Philipps University Marburg, Marburg, GERMANY,* [2]*Department of Nuclear Medicine, Technical University of Munich, and Isotope Technologies Munich (ITM), Munich, GERMANY,* [3]*Department of Nuclear Medicine, University Hospital OWL, Evangelical Hospital Bethel, Bielefeld, GERMANY,* [4]*Preclinical Imaging Core Facility, Center for Tumor Biology and Immunology (ZTI), Philipps University Marburg, Marburg, GERMANY.*

Aim/Introduction: Early diagnosis of Alzheimer's disease (AD) and the accurate quantification of β-amyloid plaques (Aβ) using PET imaging are critical for managing dementia patients. This study evaluates two novel ^{18}F-labelled Aβ tracers, [^{18}F]FIBT-TEG and [^{18}F]FIBT, developed from a library of over 600 compounds. These tracers are compared with the established tracers [^{18}F]Florbetaben (FBB) and [^{11}C]PiB in two transgenic mouse models of AD to assess their potential for clinical application. ***Materials and Methods:*** [^{18}F]FIBT-TEG and [^{18}F]FIBT were chosen for their high affinity to Aβ (Ki/Kd = 0.7 nM), >1000-fold selectivity over tau aggregates, low off-target binding, and favourable lipophilicity. PET scans (60 minutes) were performed in Arctic APP transgenic mice (tg), APP/PS1 double transgenic mice (tgtg), and age-matched control mice. PET analysis was conducted using PMOD software (ver 4.3) with cross-validation through autoradiography, biodistribution studies, and stability tests in brain and plasma. ***Results:*** [^{18}F]FIBT-TEG displayed excellent Aβ binding affinity (Ki = 0.7 nM), comparable to [^{18}F]FIBT and superior to [^{18}F]Florbetaben (Kd = 6.7 nM) and [^{11}C]PiB (Kd = 1.5 nM). Brain uptake of [^{18}F]FIBT-TEG was 8% ID/g at 5 min p.i., surpassing [^{11}C]PiB and [^{18}F]FIBT (7% ID/g), with rapid clearance (1.5% ID/g at 30 min). Cortex/cerebellum SUVRs for [^{18}F]FIBT-TEG were 1.67 (tg mice) and 1.85 (tgtg mice), higher than [^{18}F]FIBT (1.35) and comparable to [^{11}C]PiB (2.08) and [^{18}F]Florbetaben (1.68). Autoradiography confirmed selective binding to Aβ-rich regions with minimal off-target uptake. [^{18}F]FIBT-TEG also showed superior plasma protein binding (0.47 ± 0.12%) and high in vivo stability (brain: 90% ± 4% at 30 min, plasma: 8% ± 2%). ***Conclusion:*** [^{18}F]FIBT-TEG demonstrates excellent preclinical performance, combining high specificity, favourable pharmacokinetics, and minimal non-specific binding. These findings highlight its translational potential for clinical PET imaging applications in AD diagnosis and management.

EP-0123

FAPI-DyeMER: a Novel Dual-Modality Agent for Image-Guided Cancer Surgery

G. Gariglio[1], *C. Rangger*[1], *K. Bendová*[2], *Z. Novy*[2], *M. Petřík*[2], *C. Decristoforo*[1];
[1]*Department of Nuclear Medicine, Medical University Innsbruck, Innsbruck, AUSTRIA,* [2]*Institute of Molecular and Translational Medicine, Palacky University, Olomouc, CZECH REPUBLIC.*

Aim/Introduction: The complete and minimally invasive resection of solid tumours remains challenging. As a Swiss Army Knife, dual-modality probes combine several functionalities in one single tool and have the potential to enhance surgical outcomes through the integration of preoperative imaging and intraoperative real-time fluorescence guidance [1]. Here, we investigated the potential of FAPI-DyeMER, the first dimeric candidate targeting the fibroblast activation protein (FAP). ***Materials and Methods:*** The precursor was successfully labelled with Gallium-68/67 and Zirconium-89. In vitro, we investigated the binding and retention with HT1080hFAP cells. Tumour targeting and biodistribution of the ^{67}Ga-labelled compound were evaluated in xenografted mice up to 1 day p.i. In the same model, the in vivo imaging potential was evaluated at early time points via PET and up to 2 days p.i via SPECT and fluorescence imaging (FI). ***Results:*** Cell binding assays revealed that ^{68}Ga-FAPI-DyeMER exhibited higher cellular uptake (28.01±2.54 % after 1h of incubation) than the control compound lacking the fluorophore (18.91±2.53 %), demonstrating the advantageous impact of the fluorophore. The incorporation of the dye improved also the overall biodistribution profile, as evidenced by lower accumulation in most organs when comparing ^{68}Ga-FAPI-DyeMER to the control compound. The efflux study showed a significant enhancement in cellular retention for this candidate (with 97% internalised 2h after incubation) when compared to the established ^{68}Ga-FAPI-46 (22%). Ex vivo experiments and in vivo PET, SPECT and FI studies in HT1080hFAP/HT1080 xenografted mice demonstrated sustained tumour uptake (7.57±1.06 and 5.44±0.23 % ID/g at 1 h and 1 day p.i. respectively). A satisfactory tumour-to-background contrast was maintained even at later time points, with the signal intensity ratio between FAP-positive and FAP-negative tumour at 1 day post-injection measured at 3.4 for radioactivity and 4.1 for fluorescence. ***Conclusion:*** This study introduced FAPI-DyeMER, a novel dual-modality imaging agent. Following a single administration in a mouse model, FAPI-DyeMER enabled tumour visualisation with satisfactory background contrast over a prolonged period highlighting its potential for preoperative nuclear imaging and subsequent fluorescence-guided surgery. ***References:*** [1] Buckle, Tessa , 'Lessons learned

in application driven imaging agent design for image-guided surgery', European Journal of Nuclear Medicine and Molecular Imaging, 20 June 2024 /(51), 3040-3054.

EP-08

e-Poster Area

A: Preclinical and Translational Studies -> A1 Medical Preclinical -> A18 New Radiopharmaceuticals - Therapy

EP-0124

***C. Lu**, M. Zhou, P. Liu, S. Hu;*
Xiangya Hospital, Central South University, Changsha, CHINA.

Aim/Introduction: To develop a novel PSMA-targeted theranostic probe integrating ^{68}Ga/^{177}Lu and indocyanine green (ICG) for PET/NIRF imaging-guided radioisotope-photothermal therapy (RIT+PTT) in prostate cancer (PCa). ***Materials and Methods:*** First, computer-aided drug design was employed to construct and optimize the molecular structure of the probe PSI, and molecular docking was used to analyze its binding mode and affinity with PSMA. The targeting capability of the probe was verified through cellular uptake assays in human prostate cancer cells PC3-PIP (PSMA$^+$) and PC3 (PSMA$^-$); the cytotoxicity and DNA damage induced by the combined photothermal-radioligand therapy were assessed using Cell Counting Kit-8 (CCK-8), live/dead cell staining, and γH2AX staining. Next, a PCa xenograft mouse model was established to evaluate the tumor-targeting ability and diagnostic value of the probe via PET/CT and NIRF imaging, along with analysis of its biodistribution and pharmacokinetics. Subsequently, mice were treated with RIT, PTT, or combined PTT+RIT, and therapeutic efficacy was assessed by monitoring tumor volume changes; treatment safety was evaluated through histopathological and biochemical analyses. Finally, transcriptomic sequencing and bioinformatics analyses were conducted to investigate the potential molecular mechanisms of different treatment modalities. ***Results:*** (1) Molecular docking revealed superior PSMA-binding affinity compared to conventional PSMA ligands. (2) Cellular experiments showed that probe uptake positively correlated with PSMA expression, confirming its high specificity; CCK-8, live/dead staining, and γH2AX staining indicated that the combined photothermal-radioligand treatment significantly enhanced cytotoxicity and induced more severe DNA damage. (3) PET/CT and NIRF imaging clearly visualized tumors, with tumor-to-muscle ratios exceeding 10. (4) Biodistribution studies suggested prolonged tumor retention of ^{177}Lu-PSI, enabling sustained radiation damage; Combined RIT and PTT achieved 87.4% tumor inhibition in PC3-PIP xenograft model, significantly surpassing monotherapies; no significant systemic toxicity was observed in treated mice. (5) Transcriptomic sequencing analysis revealed that the combined therapy enhanced antitumor efficacy through the inhibition of oxidative phosphorylation metabolism and synergistic activation of dual cell death pathways (apoptosis and autophagy). ***Conclusion:*** This study successfully developed a novel PSMA-targeted probe, ^{68}Ga/^{177}Lu-PSI, for theranostic applications in PCa. Integrating PET/NIRF dual-modality imaging with photothermal-radioligand combination therapy, the probe supports full-process precision management of "accurate diagnosis-intraoperative navigation-targeted therapy". This work lays a theoretical and technical foundation for the clinical translation of ^{68}Ga/^{177}Lu-PSI in personalized theranostics and PSMA-targeted combination therapy for prostate cancer.

EP-0125

Optimization of theMolar Dose of Dimeric FAP-Targeted Radioligandsfor TherapeuticApplications

***L. Li**, H. Ma, D. Stuurman, C. d. Ridder, A. Piet, Y. Seimbille;*
Erasmus Medical Central, Rotterdam, NETHERLANDS.

Aim/Introduction: Overexpression of fibroblast activation protein (FAP) in cancer-associated fibroblasts enables selective tumor targeting using FAP inhibitors. Although radiolabeled small-molecule FAP inhibitors are widely used for imaging, their short tumor retention limits therapeutic efficacy. To overcome this limitation, we developed two dimeric FAP-targeted radioligands, eFAP-51 and eFAP-52, which exhibit enhanced tumor accumulation and prolonged retention. In this study, we systematically investigated the effect of molar dose on the in vivo biodistribution of [^{177}Lu]Lu-eFAP-51 and [^{177}Lu]Lu-eFAP-52 in FAP-expressing xenografts to optimize therapeutic dosing. ***Materials and Methods:*** In vivo imaging and biodistribution studies were performed using NMRI-Foxn1 nu/nu mice bearing subcutaneous HT-1080.hFAP tumors and wild-type HT-1080 (WT) tumors as controls. Mice received intravenous injection of [^{177}Lu]Lu-eFAP-51 or [^{177}Lu]Lu-eFAP-52 at molar doses of 4, 12, 24, or 96 nmol/kg. Small-animal SPECT/CT imaging was conducted at 1, 4, 24 and 48 hours post-injection, followed by ex vivo biodistribution at 48 hours. Uptake values in tumor and non-target tissues, as well as tumor-to-background (T/B) ratios, were analyzed to evaluate FAP specificity, dose dependency, and pharmacokinetics. ***Results:*** Both dimers exhibited dose-dependent tumor uptake in HT-1080.hFAP xenografts, while showing minimal accumulation in WT tumors and nontarget organs across all tested doses, confirming FAP-mediated specificity. [^{177}Lu]Lu-eFAP-51 exhibited optimal tumor retention (2.49 ± 0.32% ID/g at 4 nmol/kg) with dose-dependent reduction in normal tissue uptake (liver: 0.49 to 0.18% ID/g; spleen: 0.58 to 0.11% ID/g; kidney: 0.16 to 0.06% ID/g from 4 to 96 nmol/kg) while target saturation at 96 nmol/kg was observed by a 60% reduction in tumor uptake. Remarkably, the therapeutic window of [^{177}Lu]Lu-eFAP-51 was defined between 12 and 24 nmol/kg with maintained tumor uptake (>85% of maximum) and optimal T/B ratio. In contrast, [^{177}Lu]Lu-eFAP-52 achieved peak tumor uptake (3.41 ± 1.84% ID/g at 4 nmol/kg), but exhibited paradoxical dose-response with 74% decreased tumor retention and significantly increased kidney (0.32 to 1.35% ID/g) uptake at 96 nmol/kg, along with 30% slower blood clearance compared to eFAP-51 at equivalent doses. ***Conclusion:*** [^{177}Lu]Lu-eFAP-51 emerged as a lead candidate with its favorable biodistribution and therapeutic dose window (12-24 nmol/kg). The superior performance of [^{177}Lu]Lu-eFAP-51 underscores the importance of hydrophilicity in achieving optimal balance between tumor avidity and systemic clearance. These findings provide critical insights for the clinical translation of [^{177}Lu]Lu-eFAP-51, and highlighted the need for comprehensive preclinical dose optimization. Future studies will evaluate its therapeutic efficacy at the identified optimal dose in preclinical tumor models.

EP-0127

In-Vivo Evaluation of a Novel Fibroblast Activation Protein (FAP) Inhibitor as a Targeted Therapeutic Agent in Oncology

***M. Rezaeianpour**[1,2], M. Mosayebnia[2], A. Gravand[1], R. Nami[1], M. Ghapanvari[1], S. Mazidi[1], M. Dehghani[1];*
[1]PARS ISOTOPE Co., Tehran, IRAN, ISLAMIC REPUBLIC OF,
[2]Department of Pharmaceutical Chemistry and Radiopharmacy, School of Pharmacy, Shahid Beheshti University of Medical Sciences, Tehran, IRAN, ISLAMIC REPUBLIC OF.

Aim/Introduction: Due to the widespread incidence of cancer globally, early diagnosis and effective treatment of tumors are essential for improving patient outcomes. The tumor microenvironment, which makes up over 90% of solid tumors, is

rich in fibroblast activation protein (FAP), absent in normal tissues. This selective overexpression of FAP has attracted attention for its potential as a therapeutic target. FAP is involved in crucial tumor processes, including growth, waste removal, and immune evasion (1,2). This study aims to present a novel approach using FAP-targeted radiopharmaceuticals labeled with Lutetium-177 (Lu-177), offering promising prospects for targeted treatment in cancers. ***Materials and Methods:*** A novel cyclic peptide designed to target FAP was synthesized using solid-phase peptide synthesis techniques. The peptide conjugated to the DOTA chelator was radiolabeled with Lutetium-177 (Lu-177). After checking the quality of the resulting compound using TLC and HPLC, its stability in saline and human plasma were studied. To evaluate the pharmacokinetics, the labeled peptide was tested in a preclinical setting using HEK-293 xenograft nude mice. A biodistribution analysis was performed alongside SPECT/CT imaging to assess the distributions of the tracer in different tissues. ***Results:*** The radiolabeling of the FAPI peptide with Lutetium-177 resulted in a product with high radiochemical purity (RCP > 99%) and remarkable stability in both saline and human plasma for up to 14 days. Significant tumor uptake of the radiotracer was observed at the HEK-293 tumor sites, which was increased over the first 14 days following injection. Concurrently, the radioactivity in non-target tissues decreased, leading to five-fold tumor-to-blood and tumor-to-liver ratio 24 h post-injection. Notably, the tumor's radioactivity remained relatively stable for up to 14 days, indicating its long-term retention. In-vivo SPECT/CT imaging of the HEK-293 tumor-bearing mice demonstrated excellent tracer retention at the tumor sites. ***Conclusion:*** The new ^{177}Lu-FAPI radiopharmaceutical demonstrates superior kinetic behavior and extended tumor retention properties compared to the existing Lutetium-177-based FAPI agents. So, this tracer can be a promising candidate for targeted tumor therapy across various cancer types. Ongoing investigations are focused on further evaluating its therapeutic potential in diverse clinical applications. ***References:*** 1. Anastasia Loktev, Thomas Lindner, Eva Maria Burger, et al. Development of Fibroblast Activation Protein Targeted Radiotracers with Improved Tumors: A Narrative Review. Front Oncol.2021; 11:6448187.2. Lei Xin , Jinfang Gao , Ziliang Zheng , et al. Fibroblast Activation Protein-α as a Target in the Bench-to-Bedside Diagnosis and Treatment of Tumors: A Narrative Review. Front Oncol. 2021; 11:648187.

EP-0128

Preliminary theranostic candidates for Glioblastoma tumors based on Substance P derivatives.

S. Mozaffari[1], *J. Abedi*[1], *H. A. Khoshhosn*[1], *N. Soltani*[1], *A. Tavakoli*[1], *Y. H. Tavakoli*[1], *M. Davarpanah*[1], *S. M. Mazidi*[1], *R. Nami*[1], *F. Johari Daha*[2], *M. Erfani*[2];
[1]*PARS ISOTOPE Co., Tehran, IRAN, ISLAMIC REPUBLIC OF,* [2]*Nuclear Science and Technology Research Institute (NSTRI), Atomic Energy Organization of Iran (AEOI), Tehran, IRAN, ISLAMIC REPUBLIC OF.*

Aim/Introduction: Substance P (SP) is a neuropeptide with high-affinity to neurokinin 1 receptor (NK1R). It is involved in angiogenesis, mitosis and the progression of some tumors especially Glioblastoma multiforme (GBM) by overexpression of NK1Rs. The distribution density of NK1Rs correlates with the degree of malignancy. SP analogues could be developing radiopharmaceuticals for specific targeting of GBM via NK1Rs. ***Materials and Methods:*** In our previous studies two derivatives of SP were synthesized and labeled with Tc99m and I131 radioisotope for theranostic application in GBM. The stability, protein binding and partition coefficient were examined. They were evaluated by docking software and then the in vitro tests on human U373MG cell line and in vivo bio distribution studies on normal mice were done. After that some new small ligands were designed and evaluated by docking software and MD simulations. They are capable of radiolabeling with Ga68 for PET and radiolabeling with I131, Lu177, Bi213 and Ac225 for Therapy. ***Results:*** The proposed radioligands were interacted with crystal structure of NK1R acquired from PDB and displayed binding energies around -8 to -9 kcal/mol. The previously radiolabeled peptides showed an average radiochemical yield of 95% and 73% respectively. Protein binding to human serum was 44 % for Tc99m and about 60% for I131. The stability was up to 12 h for Tc99m compound at 37 ºC in saline and human serum. Furthermore, the stability was up to 3 days for I131compound at -4 ºC just in saline. A value of -3.75 log P was calculated for radiolabeled Tc99m-peptide but it was calculated -1.6 for I131-peptide. Biodistribution studies showed high accumulation in kidneys and salivary glands regions 1 h and 4 h post-injection of radiopeptide. ***Conclusion:*** These derivatives could be theranostic candidates for GBM and other NK1R positive tumors. Design and further evaluations of new derivatives by I131 and F18 are ongoing.

EP-0129

A Phase I Clinical Trial to Evaluate the Safety and Tolerability of ^{68}Ga-NRT6020 Injection and ^{177}Lu-NRT6020 Injection in FAP-positive Participants with Advanced Solid Tumors

X. Zhang*, X. Li, Q. Liu, J. Liu, X. Xu, Q. Kong, Y. Wu, C. Huang, S. Cao, J. Cai;*
Chengdu New Radiomedicine Technology Co. LTD., Chengdu, CHINA.

Aim/Introduction: Fibroblast activation proteins (FAP) are type II integral membrane proteins with both intracellular and extracellular soluble truncated forms, which present in the membranes of normal cells and tumor stroma.[1-2] The novel theranostic pair ^{68}Ga-NRT6020 (diagnostic PET tracer) and ^{177}Lu-NRT6020 (therapeutic) target FAP for radiotherapeutic aim. ^{68}Ga-NRT6020 serves as a FAP-targeted PET imaging agent to select eligible patients with various cancers for ^{177}Lu-NRT6020 treatment. The ongoing phase I study is a dose escalation/expansion clinical trial on the integrated diagnostic and therapeutic product of ^{68}Ga/ ^{177}Lu-NRT6020 injection, which aims to evaluate the tolerability, safety, preliminary efficacy, pharmacokinetic characteristics, and radiation dosimetry of ^{68}Ga/ ^{177}Lu-NRT6020 injection in patients with advanced malignant solid tumors. ***Materials and Methods:*** 1. Binding affinity of NRT6020 was determined by Surface Plasmon Resonance (SPR) and Enzymatic inhibition Assay. 2. In vivo PET/MR Imaging determined the tissue biodistribution using NOG mice bearing HEK293-FAP tumor cells after ^{68}Ga-NRT6020 administration. 3. Lung patient PET/CT scan: PET/CT imaging was performed from the head to the upper thighs at different timepoints after injection of ^{68}Ga-NRT6020.[3] 4. In vivo biodistribution was assessed by SPECT/CT of ^{177}Lu-NRT6020 using HEK293-FAP xenograft model.5. In vivo efficacy was determined with ^{177}Lu-NRT6020 in HEK293-FAP tumor-bearing nude mice. ***Results:*** Preclinical data show high FAP affinity, strong tumor uptake, and superior anti-tumoral efficacy of ^{68}Ga/ ^{177}Lu-NRT6020 . Binding affinity of NRT6020 presents good potent FAP inhibition activity, binding affinity and target selectivity. ^{68}Ga-NRT6020 PET/CT imaging in lung cancer patients that exhibits sustained and progressively increased retention within the tumor over time. In vivo efficacy assay shows ^{177}Lu-NRT6020 has significant anti-tumor effects. ***Conclusion:*** ^{68}Ga-NRT6020 and ^{177}Lu-NRT6020 is expected to demonstrate broad clinical application prospects in the field of theranostics. ***References:*** 1. CHEN X, SONG E. Turning foes to friends: targeting cancer-associated fibroblasts[J]. Nat Rev Drug Discov, 2019,18(2):99-115. 2. FITZGERALD A A, WEINER L M. The role of fibroblast activation protein in health and malignancy[J]. Cancer Metastasis Rev, 2020,39(3):783-803. 3. WANG R, TIAN R. Preclinical Evaluation of 68Ga/177Lu-Labeled FAP-Targeted Peptide for Tumor Radiopharmaceutical Imaging and Therapy. J Nucl Med. 2025 Feb 3;66(2):250-256.

EP-0130

Carbonic Anhydrase IX-Targeting for Radioimmunotherapy in Triple-Negative Breast Cancer

A. Ivashkevich[1], *A. Elz*[2,3], *V. Liapis*[2,3,4], *M. P. Wheatcroft*[1], *M. P. Brown*[2,4,3], *A. H. Staudacher*[2,1,3];
[1]*Telix Pharmaceuticals Ltd Pty, Melbourne, AUSTRALIA,* [2]*Central Adelaide Local Health Network, Adelaide, AUSTRALIA,* [3]*Translational Oncology Laboratory, Centre for Cancer Biology, SA Pathology and University of South Australia, Adelaide, AUSTRALIA,* [4]*Adelaide Medical School, The University of Adelaide, Adelaide, AUSTRALIA.*

Aim/Introduction: The chimeric IgG1 monoclonal antibody Girentuximab (TLX250) binds to carbonic anhydrase IX (CAIX), a cell surface protein highly expressed by most renal cancer cells and in the hypoxic tumour microenvironment of other solid tumours, such as aggressive triple-negative breast cancer (TNBC) cells. The objective of this study was to evaluate Girentuximab as (i) a diagnostic tool to identify tumour-specific targeting in TNBC, and (ii) a radioimmunotherapeutic tool to treat TNBC when given as a single agent or combined with conventional chemotherapy. ***Materials and Methods:*** The expression level of CAIX in the TNBC cell line MDA-MB-468 was examined by flow cytometry and immunofluorescent staining using Girentuximab. Tumour uptake of Zirconium-89-labelled Girentuximab (^{89}Zr-DFO-TLX250) in female nude mice bearing MDA-MB-468 xenografts was examined by live-animal PET imaging followed by tissue biodistribution analysis. The therapeutic effect of TLX250 radioimmunotherapy (RIT) was evaluated by labelling the antibody with the β-emitting radioisotope Lutetium-177 (^{177}Lu) and administering it alone or co-dosed with chemotherapy (capecitabine) in the TNBC xenograft model. Ongoing experiments are now investigating and comparing the therapeutic effect and the time course of DNA damage in the tumour matrix after treatment with ^{117}Lu- or other radionuclides radiolabelled TLX250, when administered alone or with chemotherapy. ***Results:*** High expression of CAIX by MDA-MB-468 cancer cells was confirmed by flow cytometry and immunofluorescent staining under normoxic culture conditions, which increased further under hypoxia. Live-animal PET imaging of TNBC xenografts using ^{89}Zr-DFO-TLX250 revealed sufficient tumour uptake of the antibody, with no difference in tumour uptake when co-administered with chemotherapy, while uptake in healthy tissues remained low. Radioimmunotherapy (^{177}Lu-DOTA-TLX250), administered as a single dose up to 10MBq, was well-tolerated and resulted in effective control of tumour growth, which was improved further when co-administered with conventional chemotherapy. Current experiments investigate the time course of DNA damage following ^{177}Lu-labelled Girentuximab-based RIT, alone or combined with capecitabine, as well as other therapeutic radionuclides, and results will be presented at the EANM 2025 meeting. ***Conclusion:*** CAIX-targeting Girentuximab is a promising diagnostic and therapeutic modality with high potential for expansion of its clinical use to other types of cancers besides kidney cancer. The presented results give first evidence of its ability to effectively target and control tumour growth in a TNBC xenograft model, particularly when combined with chemotherapy. Additional studies are now being conducted to further expand on the therapeutic application of Girentuximab-based RIT in TNBC, including the use of other therapeutic radionuclides.

EP-0131

Fibroblast Activation Protein (FAP)-Targeted Theranostic Application of [^{161}Tb]Tb-FAPI-04: Radiolabelling, Qualilty Control and Scintigraphic Imaging in Wistar Rats

C. Sezgin[1], *E. Uygur*[2], *B. Ozel*[3], *R. Celik*[3], *G. Gumuser*[4], *F. Z. Biber Muftuler*[3], *Y. Parlak*[4];
[1]*Manisa City Hospital, Manisa, TÜRKIYE,* [2]*Manisa Celal Bayar University, Biomedical Device Technologies, Manisa, TÜRKIYE,* [3]*Ege University, Izmır, TÜRKIYE,* [4]*Manisa Celal Bayar University, Manisa, TÜRKIYE.*

Aim/Introduction: Fibroblast activation protein (FAP) is overexpressed in cancer-associated fibroblasts in various malignancies, making it a promising target for pan-tumour imaging and therapy. FAPI-04, a quinoline-based FAP inhibitor, has demonstrated suitability for theranostic applications when radiolabelled with diagnostic and therapeutic radionuclides. Terbium-161 (^{161}Tb) is a β$^-$emitter with decay properties similar to those of ^{177}Lu. Still, it offers the additional advantage of emitting short-range conversion and Auger electrons, potentially enhancing the tumour-absorbed dose. This study aimed to evaluate the feasibility, radiochemical quality, and biodistribution of [^{161}Tb]Tb-FAPI-04 in vivo. ***Materials and Methods:*** ^{161}Tb was conjugated with FAPI-04 via DOTA chelation and radiolabelled with carrier-free ^{161}Tb (half-life: 6.9 days), achieving a radiochemical purity >95% (n=3). Radiochemical yield was confirmed using high-performance liquid radiochromatography (HPLRC) and thin-layer radiochromatography (TLRC). In vivo planar scintigraphic imaging was performed in 8-to 10-week-old Wistar albino rats (n = 3). Each rat received an intravenous injection of 37 MBq of [^{161}Tb]Tb-FAPI-04. Imaging was performed under anaesthesia at 1, 4, 24, 48, and 96 hours post-injection (p.i.) using a dual-head gamma camera equipped with a high-resolution parallel-hole collimator. Energy windows were centred around the gamma (74 keV) emissions of ^{161}Tb. Region-of-interest (ROI) analysis was used to evaluate tracer uptake in major organs. ***Results:*** [^{161}Tb]Tb-FAPI-04 demonstrated high in vivo stability and favourable biodistribution, with strong and persistent uptake in FAP-expressing tissues and minimal non-specific background signal. The high-resolution scintigraphic images showed distinct tracer accumulation, supporting the suitability of the radioligand for tumour targeting. Clearance was predominantly renal, and no unexpected accumulation of the tracer was observed. ***Conclusion:*** The results demonstrate the feasibility of using [^{161}Tb]Tb-FAPI-04 as a theranostic agent with promising properties for targeted radionuclide therapy. The enhanced radiation properties of ^{161}Tb, combined with the broad tumour affinity of FAPI-04, highlight its potential for pan-tumour treatment strategies.

EP-09

e-Poster Area

A: Preclinical and Translational Studies -> A1 Medical Preclinical -> A19 New Biological Targets and Ligands

EP-0132

Development and characterisation of peptide-based agents targeting HER2 receptor for breast cancer radiotheranostics

L. Wagner[1], *M. Amghar*[1], *U. Bauder-Wüst*[1], *Y. Remde*[2], *M. Schäfer*[2], *M. Benešová-Schäfer*[1];
[1]*Research Group Translational Radiotheranostics, German Cancer Research Center, Heidelberg, GERMANY,* [2]*Service Unit for Radiopharmaceuticals and Preclinical Studies, German Cancer Research Center, Heidelberg, GERMANY.*

Aim/Introduction: Breast cancer (BCa) is a highly heterogeneous disease, primarily due to the considerable variation in surface receptor expression. Four molecular subtypes have been identified, each presenting significant challenges for early detection and treatment. Among these, HER2-positive BCa, characterised by the overexpression of the human epidermal growth factor receptor 2 (HER2), accounts for approximately 15-25% of all cases and is typically associated with poor prognosis. HER2 is primarily targeted by the dimeric monoclonal antibody trastuzumab and its derivatives. However, some drawbacks such as cardiotoxicity, immunogenicity and high costs have been reported. Several peptidic structures have been described to have high affinity to HER2, notably the peptide A9 (QDVNTAVAW-NH_2) which corresponds to the Fab fragment of trastuzumab. This

project aims to develop A9-based ligands for HER2-expressing BCa radiotheranostics. Furthermore, reversed and D-amino acid versions of the sequence were designed to improve the stability. Most of all, to mimic the dimeric structure of trastuzumab, A9 homodimers were assessed. ***Materials and Methods:*** A9-based HER2-targeting ligands such as their reverse-, D-, D-reverse- and scrambled-sequences have been synthetised using solid phase peptide synthesis and coupled to a DOTA chelator. Multimerisation was achieved by Copper(I)-catalysed Azide-Alkyne Cycloaddition (CuAAC) between propargyl derivatives of the peptidic library and azidolysine-based multimerisation scaffold, prior to DOTA coupling. The resulting DOTA-conjugates have been radiolabelled with [^{177}Lu]$LuCl_3$ (~5 MBq) in 0.4 M NaOAc (pH 5), at 95°C, for 15-30 min. Internalisation assays of ^{177}Lu-labeled conjugates have been performed on HER2-positive and -negative cell lines. ***Results:*** A9-based HER2-targeting ligands have been successfully synthesised with high chemical purities (>95%) and radiolabelled with [^{177}Lu]$LuCl_3$, achieving radiochemical yields (RCY) of >99%. These high RCYs confirm the robustness and efficiency of the radiolabelling protocols, supporting their suitability for radiotheranostic applications. Notably, significantly higher cellular uptake has been observed for the dimeric constructs (4.5-22.2%) compared to their monomer equivalents. HER2 specificity has been confirmed by the markedly lower uptake of scrambled sequence controls (<0.65%). ***Conclusion:*** A diverse library of A9-based monomeric and homodimeric ligands targeting HER2 has been successfully synthesised and radiolabelled with lutetium-177. Preliminary in vitro studies on HER2-expressing cell lines have demonstrated encouraging uptake, particularly for the homodimeric constructs, highlighting their potential for HER2-targeted radiotheranostic applications. Ongoing biological evaluations are expected to further validate the therapeutic and diagnostic value of these novel radioligands and will be reported in due course.

EP-0133

Preclinical Evaluation of Novel ^{68}Ga/^{177}Lu-labeled Minigastrin Analogs as CCK2R targeted radiotheranostics

X. Chen, *H. Yang, X. Wen, Z. Qiao, X. Wu, J. Zhang;*
National University of Singapore, Singapore, SINGAPORE.

Aim/Introduction: The gastrin/cholecystokinin-2 (CCK-2) receptor has been identified as a possible target for peptide receptor radionuclide imaging and therapy. Several radiolabeled peptides binding to this receptor have been explored in animal models but with low tumor uptake. The aim of this study was to identify a peptide with improved tumor uptake and prolonged tumor retention compared with the current candidates. ***Materials and Methods:*** A small peptide-chelator library based on the C-terminal sequences of CCK-8 or minigastrin was constructed. The peptides were radiolabeled with ^{68}Ga and ^{177}Lu, as determined by high-performance liquid chromatographic analysis. The peptides were screened by assessing tumor and kidney uptake in 293T-CCK2R tumor xenograft model and compared with ^{177}Lu-MGS5. ***Results:*** All peptides were radiolabeled with ^{68}Ga and ^{177}Lu with high labeling efficiency (>95%). PET studies of ^{68}Ga-K000-31 293T-CCK2R tumor xenograft model demonstrated the highest tumor uptake (19.3 ± 2.6 %ID/g at 4 h), which was 3-fold higher than that of ^{68}Ga-MGS5 (6.4 ± 1.1 %ID/g at 4 h). Kidneys had the highest uptake of ^{177}Lu-K000-31 in healthy tissue suggesting that the major route of elimination was renal excretion. SPECT imaging showed that the tumor uptake of ^{177}Lu-K000-31 gradually increased, peaked around 4 h (16.3 ± 1.3 %ID/g), and remained high over time (7.0 ± 0.5 %ID/g at 72 h). Conversely, ^{177}Lu-MGS5 exhibited significantly lower tumor uptake at 1 h (7.3 ± 3.0 %ID/g) and 72 h (2.5 ± 0.4 %ID/g at 72 h). ***Conclusion:*** ^{68}Ga/^{177}Lu-K000-31, characterized by high tumor uptake and retention along with timely clearance from normal organs and tissues are highly promising CCK2R targeted radiotheranostics.

EP-0134

Development and primary evaluation of[^{99m}Tc]Tc$(CO)_3$-(H_2O)-Erlotinib as a potential radiopharmaceutical for molecular imaging in triple negative breast cancer

A. Rey[1], *J. Afonso*[1], *D. Gamenara*[2], *G. Carrau*[2], *M. Tejería*[1];
[1]*Area Radioquimica, Facultad de Química, Udelar, Montevideo, URUGUAY,* [2]*Departamento de Química Orgánica, Facultad de Química, Udelar, Montevideo, URUGUAY.*

Aim/Introduction: Triple negative breast cancer is a global public health problem since it occurs at an early age and has a high recurrence and mortality rate. the epidermal growth factor receptor (EGFR) is overexpressed In 60% of the cases . Consequently, we have prepared and evaluated a ^{99m}Tc labelled derivative of Erlotinib, a reversible inhibitor of EGFR with the objective of developing a potential molecular imaging agent for this disease. ***Materials and Methods:*** The Erlotinib derivative methyl 2-amino-4-(4-(3-((6,7-bis(2-methoxyethoxy)quinazolin-4-yl)amino)phenyl)-1H-1,2,3-triazol-1-yl)butanoate (L) was obtained through a "click chemistry" reaction between the triple bond of Erlotinib and the azide group of the esterified N-Boc-3-azido-L-alanine. The structure was confirmed by spectroscopic methods. Compound L was labeled in 2 steps: preparation of the tricarbonyl precursor fac-[[^{99m}Tc]Tc (I)$(CO)_3(H_2O)_3]^+$ (30-50 mCi) followed by substitution with L (0.7 mg) and incubation for 30 min at 75°C (3-6 mCi). Radiochemical purity (RCP) was evaluated by high efficiency liquid chromatography (HPLC). Stability was evaluated by HPLC up to 4 hours post labelling. Lipophilicity was determined through partition coefficient (P) between octanol and phosphate buffer 0.1M, pH = 7.4 and protein binding was evaluated by molecular exclusion at 30 and 60 minutes. ***Results:*** The labelling strategy used was the formation of a [^{99m}Tc]Tc tricarbonyl complex. L acts as bidentate towards the tricarbonyl core. The Tc atom coordinates through the N atom in position 3 of the triazole ring and the amino group of the alanine substituent and a water molecule from the precursor remains in the coordination sphere. HPLC analysis showed a main species with RCP of 85%, which was purified by HPLC and remained stable for at least 4 hours (RCP≥95%). Lipophilicity expressed as log P was 1.3±0.1. The average protein binding was 66± 9 %. ***Conclusion:*** A [^{99m}Tc]Tc tricarbonyl complex bearing a EGFR binding moiety was obtained with high RCP after purification. The complex showed high stability. Lipophilicity was adequate to ensure penetration through biological membranes. Protein binding was high, probably due to the presence of a water molecule in the final compound. Although no evidence of instability was observed the inclusion of a monodentate coligand to complete the Tc coordination sphere could improve the physicochemical properties. Biological evaluation including in vitro studies in MDA-MB-231 cells will be performed to evaluate the specific binding to the receptor and the internalisation. Acknowledgements: Agencia Nacional de Investigación e Innovación (ANII) (POS_NAC_2022_1_173941), Centro de Medicina Nuclear, Hospital de Clínicas, Pedeciba-Química.

EP-0135

SPAAC-Enhanced Puromycin Linker optimizes cDNA-Dispaly for Targeted Peptide Selection

S. Schneider[1,2,3], *M. Boll*[1,2], *M. Eder*[1,2], *A. Eder*[1,2];
[1]*Division of Radiopharmaceutical Development, German Cancer Consortium (DKTK), Partner Site Freiburg and German Cancer Research Center (DKFZ), Heidelberg and Freiburg, GERMANY,* [2]*Department of Nuclear Medicine, University Medical Center Freiburg, Faculty of Medicine, University of Freiburg, Freiburg, GERMANY,* [3]*Faculty of Biology, University of Freiburg, Freiburg, GERMANY.*

Aim/Introduction: Display techniques like cDNA-display are powerful techniques for the identification of tumor binding peptides. Our aim was to improve key features of cDNA-display

to develop a new strategy for the discovery of novel cyclic peptides serving as binding motifs for highly affine and specific radiopharmaceuticals. ***Materials and Methods:*** The branched puromycin linker was fused from two building blocks using strain-promoted azide-alkyne cycloaddition (SPAAC). The efficiency of the reaction was quantified by HPLC. In addition, the optimization of the efficiency of the puromycin linker trapping the nascent peptide during translation was studied by varying combinations of 365 nm UV irradiation doses during crosslinking between mRNA and PuL and $MgCL_2$ and KCl concentrations during translation. To achieve post-translational peptide cyclization, the peptide-bearing puromycin linker was immobilized on magnetic beads and treated with tris-bromomethylbenzene (TBMB) to incorporate between the cysteine residues of the peptides by forming covalent bonds to generate bicyclic peptides. The examination of the bicyclization process was conducted by MALDI-TOF. ***Results:*** HPLC analysis revealed a median 97% reaction yield for the puromycin linker, a significant improvement over previous methods that reached yields of 15 - 20%[1]. The mean efficiency in puromycin trapping of the nascent peptides, reaching 42%, was achieved using 1200 mJ cm^{-2} UV irradiation and 750 mM KCl and 65 mM $MgCl_2$. Furthermore, MALDI-TOF mass spectrometry after the in-display peptide cyclization and cleavage from the magnetic beads, revealed the accurate incorporation of TBMB into the peptide structure during the display procedure, by detecting exactly the theoretical mass of a bicyclic test-peptide. ***Conclusion:*** The novel SPAAC-based strategy for the synthesis of branched puromycin linkers significantly improves reaction efficiency and reduces the overall cost of the display approach. Furthermore, puromycin-bound peptides were modified into bicyclic peptides and proven as biyclic during the display protocol. This approach provides a powerful tool for cDNA display applications, enabling the generation of structurally robust peptides with potential in anticancer and radiopharmaceutical developments. ***References:*** (1) Arai, H.; Kumachi, S.; Nemoto, N. CDNA Display: A Stable and Simple Genotype-Phenotype Coupling Using a Cell-Free Translation System. In Methods in Molecular Biology; Humana Press Inc., 2020; Vol. 2070, pp 43-56. https://doi.org/10.1007/978-1-4939-9853-1_3.

EP-0136

Development and characterisation of a novel peptide-based tracer targeting proteoglycans overexpressed in triple-negative breast cancer

J. D. Campeiro[1], *C. Morgat*[2], *S. U. Dalm*[1];
[1]*Erasmus University Medical Centre, Rotterdam, NETHERLANDS,* [2]*University Hospital of Bordeaux, Bordeaux, FRANCE.*

Aim/Introduction: Triple-negative breast cancer (TNBC) is an aggressive subtype urgently requiring novel treatments but lacking cancer-specific biomarkers. Proteoglycans (PGs) play key roles in cancer and are often upregulated. Amongst other, TNBCs show aberrant PG expression. Accordingly, multiple strategies have been explored to inhibit PGs' function in other cancers, unfortunately without success. Rather than inhibiting PGs'function, we propose exploiting their aberrant expression for delivering diagnostics and/or cytotoxic radionuclides. Crotamine, a positively charged cell-penetrating peptide, exhibits high affinity for PGs (e.g., syndecan-1), making it the ideal vehicle for this approach. We aim to develop a novel crotamine-based radiopharmaceutical and study its potential for targeting TNBC. ***Materials and Methods:*** PGs' gene expression level was analysed in a published dataset (55 TNBC vs. 14 normal tissues). In vitro studies using the human TNBC cell lines (MDA-MB-231, MDA-MB-468, and HCC-1806) were performed. First, the importance of the cyclic structure of crotamine for PG binding was explored. For this, non-linearized and linearized (using 5 mM DTT for 15 min at 95°C) fluorescently labelled peptide (crotamine-Cy3) were compared. Cells were incubated with 5 µM of either form at 37°C for 15 min. Peptide binding and expression of the PG syndecan-1 were evaluated by immunofluorescence by incubation with mouse anti-human syndecan-1-Cy5 (1:100) at 4 °C, 30 min, followed by incubation with 5 µM crotamine-Cy3, 4 °C, 15 min. Fluorescence intensity was then calculated. ***Results:*** Gene expression analysis showed that specific PGS are significantly upregulated in TNBC vs healthy tissues. PCA/clustering analysis with the top 8 upregulated genes (Fold-change: VCAN:7.7; COL12A1:5.0; SRGN:4.4; COL9A3:3.7; BGN:3.7; SDC1:3.6; CD44:2.7; EPYC: 2.3) accurately distinguished TNBC from healthy tissues (ROC curve AUC: 0.997). Furthermore, upregulated EPYC, VCAN, and COL12A1 show a strong correlation with a reduced time-to-relapse. Preliminary peptide characterization shows that the linearized crotamine-Cy3 exhibited a 76.2% decrease in binding versus its non-linearized counterpart. MDA-MB-468 exhibited higher syndecan-1 expression (24.8±7.5 arbitrary unit(a.u.)) and higher crotamine binding (33.3±5.8a.u.) compared to MDA-MB-231 (15.5±4.9/9.1±2.3) and HCC-1806 (9.9±2.4/10.0±2.8). ***Conclusion:*** These findings suggest the top 8 upregulated PGs may serve as a gene signature capable of distinguishing TNBC and healthy samples with high accuracy (99.7%). Moreover, the tertiary structure of crotamine is critical for PG interaction. Additionally, crotamine binding positively correlates with syndecan-1 expression. This initial characterization is crucial for the development of a crotamine-based radiopharmaceutical, which will be developed in the near future.

EP-0137

Optimization of an Affibody molecule construct for PDGFRb-targeted theranostics

H. Mallapura[1], *A. Abouzayed*[1,2], *H. Olsson*[3], *M. Xiong*[1], *O. Korsgren*[4], *J. Löfblom*[3], *M. Wagner*[2], *O. Eriksson*[1,2];
[1]*Science for Life Laboratory, Department of Medicinal Chemistry, Uppsala University, Uppsala, SWEDEN,* [2]*Antaros Tracer AB, Uppsala, SWEDEN,* [3]*Department of Protein Science, Division of Protein Engineering, KTH Royal Institute of Technology, Stockholm, SWEDEN,* [4]*Department of Immunology, Genetics and Pathology, Uppsala University, Uppsala, SWEDEN.*

Aim/Introduction: Platelet Derived Growth Factor Receptor Beta (PDGFRb) is strongly expressed on cancer-associated fibroblasts (CAFs) and has been extensively investigated as a therapeutic target for anti-cancer drugs[1]. Targeting of tumor stroma for molecular imaging and radioligand therapy (RLT) has recently been shown to be a promising strategy. Affibody molecule ATH001 is in clinical development for Positron Emission Tomography (PET) imaging of PDGFRb (NCT06562361), but its high renal uptake limits its suitability as a RLT agent[2]. This study aimed to improve the biodistribution of ATH001 by conjugating albumin-binding fatty acid moieties with varying chain lengths to enable longer circulation and thereby therapeutic applications. ***Materials and Methods:*** Modified ATH001 constructs were synthesized by conjugating fatty acids of different chain lengths via a multifunctional linker including a DOTA chelator. Binding affinity to human PDGFRb and human and murine albumin was assessed by Surface plasmon resonance (SPR). The constructs were radiolabeled with gallium-68 (^{68}Ga) and indium-111 (^{111}In) for PET imaging and biodistribution studies. In-vitro binding was evaluated by tissue autoradiography and in a U87 glioblastoma cell line with and without blocking. In vivo biodistribution and dosimetry were evaluated for up to 7 days post-injection in healthy rats and U87 xenografted mice. ***Results:*** SPR analysis confirmed that conjugation of fatty acid moieties to ATH001 increased the affinity for albumin, indicating potential for extended circulation half-life. Longer fatty acids exhibited higher affinity to albumin. LogD7.4 measurements revealed a shift toward greater lipophilicity with increasing fatty acid chain length, compared to the reference molecule ATH001. Autoradiography demonstrated binding to PDGFRb positive tissues and cells for all fatty acid conjugated ATH001 constructs. Biodistribution studies in healthy rats and U87 xenografted mice confirmed that fatty acid

conjugated ATH001 exhibited superior tumor uptake and lower kidney retention and dosimetry compared to reference molecule ATH001. The longest fatty acid conjugate showed favorable pharmacokinetics, with prolonged tumor uptake and circulation, and reduced kidney retention. ***Conclusion:*** Fatty acid conjugation to ATH001 increased albumin binding, thereby improving tumor uptake and reduced renal retention. Longer fatty acid chains were associated to stronger albumin binding, resulting in superior tracer circulation time and improved biodistribution profiles. Thus, fatty acid-conjugated ATH001 constructs are promising theranostic agents for PDGFRb-targeted RLT. Further studies will evaluate the therapeutic efficacy of the longer fatty acid-conjugated ATH001 construct labeled with therapeutic radionuclides. ***References:*** 1. Zou, X., et al., Int J Biol Macromol, 2022. 2. Wegrzyniak, O., et al., ISCIENCE, 2024.

EP-0138

Comparative Biodistribution and Stability Assessment of [^{68}Ga]Ga-labeled Kisspeptins: Implications for Design of KiSS-1R Targeting Radioligands

H. Taş[1], *M. Schäfer*[2], *U. Bauder-Wüst*[1], *Z. Nový*[3], *M. Petřík*[3], *M. Benešová-Schäfer*[1];
[1]*DKFZ (Research Group Translational Radiotheranostics), Heidelberg, GERMANY,* [2]*DKFZ (Service Unit for Radiopharmaceuticals and Preclinical Studies), Heidelberg, GERMANY,* [3]*Institute of Molecular and Translational Medicine, Faculty of Medicine and Dentistry, Palacký University (UPOL) and University Hospital Olomouc, Olomouc, CZECH REPUBLIC.*

Aim/Introduction: Breast cancer remains a leading cause of cancer mortality in women, with triple-negative breast cancer (TNBC) accounting for ~15% of cases. With limited treatment options, the reported KiSS-1R overexpression in TNBC [1] highlights its strong potential as a theranostic target. Kisspeptin (KP)-based radioligands, such as [^{68}Ga]Ga-NODAGA-KiSS-54 [2] and [^{68}Ga/^{177}Lu]Ga/Lu-KiSS-10 [3], have shown promise in imaging and therapy. However, the susceptibility of endogenous KPs to proteolytic degradation remains a significant challenge. To address this limitation, we conducted a comparative study on DOTA-conjugates based on endogenous and reported synthetic KPs regarding their biodistribution and ex vivo stabilities in BALB/c mice. We aimed to identify structural modifications that enhance stability and optimize pharmacokinetic profiles for the design of improved KiSS-1R-targeting radioligands for potential theranostic applications against TNBC. ***Materials and Methods:*** Endogenous (KiSS-10,-15,-54) and synthetic KPs (KiSS-10-EEE, p354, p356, TAK-448, KiSS-34) were N-terminally conjugated to respective DOTA derivatives. Following in vitro validation, these DOTA-KPs were ^{68}Ga-radiolabeled (sodium acetate buffer, 95 °C, 15 min) and their in vivo biodistribution was evaluated in positron emission tomography (PET) imaging in healthy BALB/c mice. Compound stabilities were assessed with ex vivo HPLC urine analysis at 30- and 90-min post-injection (p.i.). ***Results:*** DOTA-KPs were synthesized (>99% purity) using active ester routes and subsequently ^{68}Ga-radiolabeled at high efficiencies (>95%). Static PET/CT imaging (30 min p.i.) revealed notable biodistribution variations among [^{68}Ga]Ga-labeled DOTA-KPs, particularly in kidney uptake and liver accumulation. Ex vivo HPLC urine analysis demonstrated that [^{68}Ga]Ga-DOTA-KiSS-34 (AMBA-2Nal-Gly-Leu-Arg-Trp) exhibited superior metabolic stability likely attributable to its AMBA-2Nal substitution, showing minimal degradation at 30- and 90-min p.i. The remaining DOTA-KPs displayed varying degrees of instability and metabolite formation. ***Conclusion:*** Our findings indicate that DOTA-conjugates of several reported KPs exhibit suboptimal biodistribution and stability profiles. Despite partial liver accumulation, the inclusion of the non-natural amino acids, AMBA-2Nal, in [^{68}Ga]Ga-DOTA-KiSS-34 correlates with its notable stability and rapid renal clearance, positioning it as a promising lead for further development. The remaining KPs need further structural modifications - e.g. via non-natural amino acid substitutions - to increase their potential for preclinical evaluation for KiSS-1R-based imaging and therapy in TNBC. ***References:*** [1] A. Blake, M. Dragan, R. G. Tirona, et al. Sci. Rep. 2017, 7, 46525. [2] I. Israel, G. Riehl, E. Butt, et al. Pharmaceuticals (Basel, Switzerland) 2024, 17. [3] J. Kleynhans, R. Reeve, C. H. S. Driver, et al. J. Neuroendocrinol. 2025, e13487.

EP-0139

Basic Comparative Study of $^{64}Cu^{2+}$ complexes with tripodal amine ligands using the extrahepatic bile duct carcinoma cell line TFK-1

M. Shinada[1,2], *M. Takahashi*[1,2], *C. Igarashi*[2], *H. Matsumoto*[2], *F. Hihara*[2], *T. Tachibana*[2,1], *M. Oikawa*[2], *H. Suzuki*[2], *M.-R. Zhang*[2], *T. Higashi*[2], *H. Kurihara*[3], *Y. Yoshii*[2], *Y. Doi*[1];
[1]*TOHO University, Funabashi, JAPAN,* [2]*Institute for Quantum Medical Science, National Institutes for Quantum Science and Technology, Chiba, JAPAN,* [3]*Kanagawa Cancer Center, Yokohama, JAPAN.*

Aim/Introduction: Cu accumulates in the nuclei of cancer cells and plays an important role in transcription-related tumor proliferation and metastasis. While several studies have been conducted to investigate the potential of $^{64}Cu^{2+}$ ions as antitumor radiotherapeutic drugs, intravenously administered $^{64}Cu^{2+}$ is known to primarily accumulate in the liver. To enhance tumor-targeting efficiency and reduce liver uptake, ligand complexation of $^{64}Cu^{2+}$ is a promising strategy. This study investigated the effect of three tripodal amine ligands, diethylenetriamine (Dien), tris(2-aminoethyl)amine (Tren), and tris(2-pyridylmethyl)amine (TPMA), on the in vivo distribution and in vitro cellular uptake using the extrahepatic bile duct carcinoma cell line TFK-1. ***Materials and Methods:*** The in vivo tissue biodistribution of $^{64}Cu^{2+}$-Tren, $^{64}Cu^{2+}$-Dien, $^{64}Cu^{2+}$-TPMA, and unchelated $^{64}Cu^{2+}$ were assessed in a xenograft mouse model bearing TFK-1 tumors. The in vitro intracellular Cu localization was analyzed using micro-PIXE (particle-induced X-ray emission) analysis. The correlation between in vivo tumor uptake and in vitro cellular uptake was evaluated and the physicochemical properties were calculated with in silico software (SwissADME). ***Results:*** $^{64}Cu^{2+}$-Tren and $^{64}Cu^{2+}$-Dien showed significantly higher tumor uptake than $^{64}Cu^{2+}$-TPMA and unchelated $^{64}Cu^{2+}$ in TFK-1 tumors. An inverse relationship was observed between liver and tumor uptake among these $^{64}Cu^{2+}$ complexes and unchelated $^{64}Cu^{2+}$. Micro-PIXE analysis showed that in vitro cellular uptake was similar to in vivo tumor uptake, and nuclear delivery was the highest for $^{64}Cu^{2+}$-Tren. $^{64}Cu^{2+}$-Tren, $^{64}Cu^{2+}$-Dien, and $^{64}Cu^{2+}$-TPMA were found to satisfy the following conditions respectively: (I) less than 5 hydrogen bond donors, (II) less than 10 hydrogen bond acceptors, (III) molecular weight less than 500 Da, and (IV) partition coefficient (logP) less than 5, not exceeding Lipinski's "rule of five". ***Conclusion:*** $^{64}Cu^{2+}$-Tren and $^{64}Cu^{2+}$-Dien demonstrated higher in vivo tumor uptake and in vitro cellular and nuclear uptake than $^{64}Cu^{2+}$-TPMA and $^{64}Cu^{2+}$ in TFK-1 cells. These findings suggest that $^{64}Cu^{2+}$-Tren and $^{64}Cu^{2+}$-Dien are promising candidates for the development of ^{64}Cu-based anticancer radiotherapeutics. This study also provides useful methods for the future development of ^{64}Cu radiopharmaceuticals.

EP-0140

Technetium-99m radiolabeling of HYIGSR peptide for in vivo and ex vivo assessment as a biomarker in breast cancer

F. Ferreira Mendonça[1], *M. Tejeria*[2], *P. Decuadra*[2], *M. Zeni*[2], *A. Rey*[2], *S. Nogueira*[3], *J. Mejia*[3], *M. Barboza*[3], *L. Fuscaldi*[1], *L. Malavolta*[1];
[1]*Faculty of Medical Sciences of Santa Casa de São Paulo, São Paulo, BRAZIL,* [2]*Faculty of Chemistry at the University of the Republic, Montevideo, URUGUAY,* [3]*Hospital Israelita Albert Einstein, São Paulo, BRAZIL.*

Aim/Introduction: According to the World Health Organization, over 14 million people are diagnosed with breast cancer annually, and this number is projected to rise to 21 million by 2030, underscoring the need for improved diagnostic and therapeutic

strategies. Biologically active peptides derived from laminin-111, such as YIGSR, have been shown to regulate gene expression in breast cancer cells. This study aimed to synthesize the HYIGSR analogue, radiolabel it with technetium-99m (^{99m}Tc), and evaluate its in vitro and ex vivo properties as a potential biomarker for breast cancer. ***Materials and Methods:*** The peptide was synthesized via solid-phase peptide synthesis. Radiolabeling was performed using the tricarbonyl method. The $[^{99m}Tc(CO)_3]^+$ was formed with [^{99m}Tc] TcO_4^- (~148 MBq) and subsequently incubated with HYIGSR (0.25 mg) at 85 °C for 30 min. Stability studies were conducted at 1, 2, 3, and 4 h after radiolabeling, while serum protein binding was assessed at 30 and 60 min. Cellular binding and internalization assays using MCF-7 breast cancer cells were performed at 1 and 4 h. For biodistribution analysis, the radiopeptide was administered to both healthy and tumor-bearing female Balb/c nude mice. The tumor model was established by subcutaneously inoculation 1 × 10^7 MDA-MB-231 breast cancer cells with in vivo and ex vivo evaluations at 1 and 3 h post-injection. Scintigraphic images were obtained using a Discovery VH gamma camera with a pinhole collimator, with a 5-minute acquisition time and 9× geometric magnification. ***Results:*** The HYIGSR was successfully characterized and radiolabeled, achieving a radiochemical yield of 95.53%±1.19 (n=5) with stability maintained for up to 4 hours in both reaction and serum media. Physicochemical analysis indicated a hydrophilic nature and a serum protein binding of 46.08%±3.75 at 60 min, n=3). In vitro studies of [^{99m}Tc]Tc-HYIGSR with MCF-7 cells exhibited a binding and internalization 3.39% and 22.18% at 4 h, respectively. Ex vivo biodistribution in Balb/c nude mice (n=4) demonstrated rapid blood clearance and low accumulation of the radiopeptide in non-target organs and tumors (<5% ID). In tumor-bearing mice, increased uptake was observed in the liver, stomach, intestine, and thyroid. Scintigraphic imaging correlated with biodistribution data, confirming hepatic and intestinal accumulation. ***Conclusion:*** HYIGSR demonstrated good radiolabeling efficiency and stability. However, in vivo and ex vivo biodistribution indicated low tumor uptake, suggesting that further modifications may be necessary to enhance the tumor-targeting capability of radiopeptide. Additionally, the imaging results were consistent with the biodistribution data. Grant FAPESP #2021/10265-8, CancerThera/CEPID.

EP-0141

[^{18}F]4-(3-(4-(4-fluorophenyl)piperidine-1-carbonyl) phenoxy)benzamide, a promising PET agent to investigate PARP10

M. Riondato[1,2], *G. Destro*[3], *M. Nemati*[3], *J. Martinelli*[2], *F. Vitale*[1], *S. Morbelli*[4], *G. Sambuceti*[2], *E. Terreno*[3];
[1]*IRCCS Policlinic Hospital of Genoa, Genoa, ITALY,* [2]*Dept. Health Sciences, University of Genoa, Genoa, ITALY,* [3]*University of Torino, Department of Molecular Biotechnology and Health Sciences, Turin, ITALY,* [4]*University of Torino, Department of Medical Sciences, Turin, ITALY.*

Aim/Introduction: Poly-ADP-ribose polymerases (PARP) are an enzyme family of 17 members catalysing the attachment of poly- or mono- ADP-ribose units on different targets.[1] While the research of PARP 1 inhibitors is widely pursued in clinic, the development of mono-ADP ribose transferases inhibitors is still in the early stages. PARP10 overexpression is observed in various cancers leading to the hypothesis that this enzyme promotes cancer proliferation and acts as oncogene. [2] We aim to develop a PET tracer for studying PARP10 role in different cancer models, paving the way for novel PET agents. ***Materials and Methods:*** The boronic pinacol ester precursor was chemically synthesized in 5 steps. [^{18}F]Fluorine was produced using an Eclypse HP cyclotron (Siemens, Germany). The radiolabelling protocol was developed on a AllInOne36 synthesizer platform (Trasis, Belgium) able to carry out Cu-mediated 18F-fluorodeboronation using the precursor, including deprotection and semipreparative purification before reformulation. Cell uptake and blocking experiments were carried out in the MCF7 cell line expressing PARP10 enzyme, and A549 cell line as a negative control using a gamma counter (Perkin Elmer) to measure the radioactivity in cell lysates. The time-dependent uptake was evaluated for 30 minutes since the plateau was rapidly reached. ***Results:*** SEM-protected boronic pinacol ester precursor, obtained with high purity and an overall yield of 12.3%, was reacted with 10-15 GBq of [^{18}F]Fluorine using an automated radiosynthesis performed on radiosynthesiser using a copper-mediated 18F-fluorodeboronation. At the end of the process, [^{18}F]4-(3-(4-(4-fluorophenyl)piperidine-1-carbonyl) phenoxy)benzamide was obtained with an activity yield (AY) of 15% non-decay corrected and a molar activity (Am) up to 220GBq/mmol. The uptake study showed how the tracer reached a plateau over 30 minutes fastly in the cell line expressing PARP10. On the other hand, there was almost a 3-fold lower uptake in the A549 cell line. The blocking experiment showed a diminishment in the radioactive signal in MCF7 cell line. More investigations are needed to understand the tracer binding kinetics. ***Conclusion:*** Given the challenges for PARP inhibitor therapy such as patient staging and resistance to PARP therapy, the development of new tracers able to target other PARP isoforms may offer a way to overcome these problems and improve treatment outcomes for patients. These preliminary results show the potential of this tracer to start interrogating PARP10 expressions. We will move further to more in vitro evaluation. ***References:*** [1]Nizi MG, et al. J Med. Chem. 2022; 65:7532-7560 [2]Yu M, et al. Oncogene. 2005; 24:1982-1993.

EP-10

e-Poster Area

A: Preclinical and Translational Studies -> A1 Medical Preclinical -> A20 Radiopharmacokinetics and Drug Development

EP-0143

First-in-Monkey SPECT Imaging of ^{131}I-Labeled Aging Targeted Extracellular Vesicles

K. Yu*, J. Ye, F. Kang, J. Wang;*
The First Affiliated Hospital of Air Force Medical University, Shaanxi, Xi'an, CHINA.

Aim/Introduction: Extracellular vesicles (EVs) are tiny vesicles released by cells that can transport bioactive molecules. After being released into the extracellular matrix, EVs can travel through the blood-body fluid circulation to distant organs and tissues, where they are taken up by receptor cells and then affect their biological functions. Therefore, EVs are widely involved in the physiological and pathological processes of the human body and have shown great potential in the field of disease diagnosis and treatment. In this study, an in vivo tracer study of an EVs targeting aging by SPECT imaging will be performed with ^{131}ILabeling. The safety, biodistribution and pharmacokinetics of ^{131}I-labeled EVs were also evaluated. ***Materials and Methods:*** Firstly, Iodogen was used as an oxidant to label EVs with ^{131}I, and in vivo distribution experiments were conducted on normal mice to track and calculate pharmacokinetics. Subsequently, SPECT imaging of ^{131}I-EVs was performed in a normal monkey model to monitor the distribution of the tracer in vivo. ***Results:*** ^{131}I-EVs were successfully prepared using the Iodogen method, the radiochemical yield was about 70% and the radiochemical purity was > 98%. The in vitro stability in saline and in mouse serum was evaluated at 48 h by radio-TLC and showed that ^{131}I-EVs have high in vitro stability. The in vivo distribution of ^{131}I-EVs is consistent with other extracellular vesicles. The results of the in vivo biological

distribution experiment in normal mice showed that the highest uptake of ^{131}I-EVs was found in the blood. The lung had high intake and was also distributed in the heart, liver, kidneys, and bones. The pharmacokinetic results showed a distribution half-life ($T_{1/2\alpha}$) of 2.473 hours and an elimination half-life ($T_{1/2\beta}$) of 16.69 hours. Due to the high uptake in the blood, its cardiac blood pool is clearly visible from in the SPECT/CT imaging of monkey. Also a very high physiologic uptake of ^{131}I-EVs was seen in the liver due to the EPR effect. In addition, a high uptake of ^{131}I-EVs was observed in the nasal cavity. ***Conclusion:*** First-in-Monkey SPECT imaging of ^{131}Ilabeled aging targeted extracellular vesicles was performed in this study. And the safety, biodistribution and pharmacokinetics of the ^{131}I-labeled EVs were also evaluated. The results will play a promoting role in advancing the clinical translation of EVs. And further evaluation is in progress.

EP-0144

Clinical Pharmacology and Dose Optimization Considerations applied to Radioligand Therapies (RLTs)

A. Manon[1], *D. Imbs*[1], *D. Heller*[2], *H. Stephens*[2], *M. Trame*[2];
[1]*Certara, Paris, FRANCE,* [2]*Certara, Radnor, PA, UNITED STATES OF AMERICA.*

Aim/Introduction: While therapeutic radiopharmaceuticals also known as Radioligand therapies (RLTs) are raising more and more interest in the oncology space, the regulatory landscape continues to evolve leaving clinical development teams without clear regulatory guidance on clinical pharmacology requirements for RLTs. Dose optimization is also a key challenge since the optimal dosing (radioactivity or dosing interval) is still debated, even for the approved drugs such as PSMA-targeting RLT. ***Materials and Methods:*** The available FDA and EMA regulatory guidelines focus on non-clinical testing requirements, labeling recommendations, or CMC considerations. But no clinical regulatory guideline is currently available for RLTs. We propose clinical pharmacology recommendations for RLTs that are based on our experience, FDA/EMA feedback received by our clients, and regulatory guidelines relevant to the specific targeting moiety. ***Results:*** The clinical pharmacology package should be defined early in the clinical development. Sponsors can perform most clinical pharmacology assessments in the First in Human (FIH) study in patients. 1/ Characterize Absorption Distribution Metabolism and Excretion (ADME) data by collecting blood and urine radioactivity PK, targeting moiety PK and dosimetry data. These data will enable drug developers to characterize the RLTs' biodistribution, absorbed dose in critical organs, elimination pathways, and effective half-life. 2/ Assess potential drug-drug interactions (DDI): evaluation of in vivo plasma and metabolic stability of the RLT and full in vitro DDI assessments depends on the targeting moiety nature. 3/ Assess QT prolongation: integrated non-clinical and clinical QTc risk assessment is based on the nature of the targeting moiety. Collection of time-matched PK and ECG data is highly recommended during the FIH study. 4/ Special populations: leverage ADME data to identify early significant covariates impacting PK and obtain a potential waiver from regulatory agencies for Clinical Pharmacology studies. 5/ Immunogenicity: The nature of the targeting moiety defines the need to characterize whether anti-drug antibodies could impact PK/safety/efficacy 6/ Dose optimization: in the context of Project Optimus, PK and dosimetry/biodistribution data are key to support dose selection. Population PK model and Exposure-Response analyses can be used to correlate exposure and organ absorbed doses to clinical efficacy endpoints or safety events to guide dose selection and therapeutic index definition. ***Conclusion:*** FIH studies for RLTs are key to guiding the clinical pharmacology strategy for later-phase trials and dose justification for labeling. ***References:*** Guideline on the non-clinical requirements for radiopharmaceuticals. EMA/CHMP/SWP/686140/2018 Oncology Therapeutic Radiopharmaceuticals: Nonclinical Studies and Labeling Recommendations. FDA Guidance for Industry 2019.

EP-0145

Dynamic Total Body PET imaging unfolds [11C]-choline kinetics and dosimetry

G. Fuso[1], *I. Brusa*[2], *M. Santoro*[2], *D. Dall'Olio*[3], *F. Zagni*[2], *M. Assenza*[2], *E. Fortunati*[2], *E. Tabacchi*[2], *A. Farolfi*[2], *R. Mei*[2], *C. Nanni*[2], *P. Castellucci*[2], *L. Calderoni*[2], *L. Strigari*[2], *G. Castellani*[3], *S. Fanti*[1,2];
[1]*Policlinico Sant'Orsola-Malpighi, University of Bologna, Bologna, ITALY,* [2]*IRCCS Azienda Ospedaliero-Universitaria di Bologna, Bologna, ITALY,* [3]*University of Bologna, Bologna, ITALY.*

Aim/Introduction: Choline is a precursor of membrane phospholipids and preferentially accumulates in tissues with high coline-kinase activity, a hallmark of rapidly proliferating malignant cells. Compared to other PET radiotracers, [^{11}C]-choline has high sensitivity, low radiation dose and can detect small lesions. Yet, the physiology underlying [^{11}C]-choline uptake in reference organs remain unclear. Since static PET imaging snapshots the [^{11}C]-choline uptake within a limited-time window, dynamic PET (dPET) imaging can represent a solution over this limitation, as it can characterize the full tracer-uptake process. Here, we harness the Total Body (TB) PET/CT scanner to evaluate the biodistribution, dosimetry and kinetics of [11C]-choline in reference organs, which may provide a reference for future dPET imaging. ***Materials and Methods:*** A 50-min dPET scanning followed by a 20-min static TB PET/CT acquisition using a Long Axial Field of View scanner (LAFOV) at 100±10 min after injection was performed on 4 patients referred to our Centre for presurgical parathyroid adenoma detection. Whole body [^{11}C]-choline distribution and pharmacokinetics were evaluated by Standardized Uptake Value (SUV), tissue uptake, organ-absorbed doses and, finally, multi-time graphical analysis (MTGA) and kinetic modelling with compartment models (2TCM). ***Results:*** Rapid blood clearance was detected (<10 seconds) and only gallbladder, gluteus, liver, parotids and prostate showed a gradual rising uptake with no early uptake peak. Average uptake values after 50 minutes for liver (17.61±2.82%) and bowel (5.77±1.80%) compared to kidneys (2.77±0.24%) and urinary bladder (0.21±0.16%) suggested alternative excretion pathways for [11C]-choline other than renal clearance. Gallbladder (0.0192±0.0039 mGy/MBq), liver (0.0372±0.0084 mGy/MBq), pancreas (0.0222±0.0051 mGy/MBq), kidneys (0.0160±0.0048 mGy/MBq), and spleen (0.0229±0.0085 mGy/MBq) were the organs with the highest observed effective doses. These organs also showcased extreme values among K1, k2, k3 and k4, which provide them with the most distinctive kinetic patterns. ***Conclusion:*** Our study suggests that [11C]-choline is rapidly cleared from blood circulation and its biodistribution changes very slowly from 5 minutes onwards. The TB dynamic approach highlighted the pivotal role of liver metabolism, minimal renal excretion, and unique kinetic behaviors of gallbladder, pancreas, kidneys, and spleen. These data advance our understanding of [^{11}C]-choline's physiological uptake and support its continued use as a safe and highly informative tracer.

EP-0146

Design of Heterodimeric Radiopharmaceuticals Targeting FAP and SSTR2 Receptors Using Theoretical Affinity Profiling and Biodistribution Correlation

A. Abolhosseini Shahrnoy[1], *M. Pirdadeh*[1], *M. Safari*[1], *M. Dehghani*[1], *Z. Karimi*[1], *R. Salehi-Moratab*[1], *M. Nasiri*[2], *R. Nami*[1], *S. Mazidi*[1];
[1]*PARS ISOTOPE Company, Tehran, IRAN, ISLAMIC REPUBLIC OF,* [2]*Department of Cellular and Molecular Biology, School of Biology, Damghan University, Damghan, IRAN, ISLAMIC REPUBLIC OF.*

Aim/Introduction: Fibroblast activation protein (FAP) and somatostatin receptor subtype 2 (SSTR2) are widely expressed in various tumors and represent attractive targets for diagnostic and therapeutic radiopharmaceuticals. This study aimed to design novel heterodimeric compounds targeting both FAP and SSTR2 by analyzing the molecular characteristics of previously reported ligands and correlating them with their biodistribution profiles. ***Materials and Methods:*** A total of 125 radiopharmaceuticals, including 60 SSTR2-targeted and 65 FAP-targeted compounds, were selected from existing preclinical studies. Molecular structures were optimized, and their theoretical binding affinities to FAP and SSTR2 were evaluated using molecular docking and computational modeling. Key physicochemical parameters such as lipophilicity, molecular weight, and hydrogen bond donors/acceptors were calculated and correlated with reported biodistribution data to identify favorable traits. Based on these analyses, two dual-targeting heterodimers named PIC-6888 and PIC-2188 were designed to exhibit optimal binding and biodistribution characteristics. ***Results:*** Theoretical modeling identified specific structural motifs and physicochemical profiles that contributed to enhanced receptor affinity and favorable biodistribution. PIC-6888 and PIC-2188 were selected as lead compounds due to their predicted high affinity for both FAP and SSTR2 and favorable pharmacokinetic properties. These heterodimers are currently under synthesis for further in vitro and in vivo evaluation. ***Conclusion:*** This study demonstrates the utility of integrative computational approaches in designing heterodimeric radiopharmaceuticals with dual-target affinity. PIC-6888 and PIC-2188 are promising candidates for future preclinical studies and may offer improved tumor targeting in cancers co-expressing FAP and SSTR2.

EP-0147

Decoding Fluorine-18 PET Tracers: Integrated Pharmacokinetics and Molecular Design

V. Trusova*, U. Malovytsia, P. Kuznietsov, I. Yakymenko, G. Gorbenko;*
V.N. Karazin Kharkiv National University, Kharkiv, UKRAINE.

Aim/Introduction: Fluorine-18-labeled PET tracers are central to oncology imaging, yet their comparative evaluation across pharmacokinetic and molecular dimensions remains fragmented. Current studies often focus on isolated tracers or rely on modality-specific metrics. To address this gap, we aimed to develop a multidimensional in silico framework integrating kinetic simulation, ADME profiling, and clustering analysis to systematically characterize and stratify five widely used ^{18}F-labeled radiopharmaceuticals: [^{18}F]FDG, [^{18}F]FET, [^{18}F]DOPA, [^{18}F]FMISO, and [^{18}F]FLT. ***Materials and Methods:*** Each tracer was simulated in COPASI using a harmonized three-compartment model, capturing uptake under normal and pathological conditions. Pharmacokinetic metrics—area under the curve ($AUC_{0\text{-}60}$), tumor-to-normal ratios (TNR_{30}, TNR_{60}), and early-phase uptake slope (0-20 min)—were extracted. Sensitivity analysis was performed by perturbing kinetic rate constants (k_1, k_2, k_3) by ±20% to assess model robustness. In parallel, ADMETlab 3.0 was employed to predict structural descriptors, including lipophilicity (logP), topological polar surface area (TPSA), volume of distribution (VDss), plasma clearance, blood-brain barrier permeability, and CYP3A4 metabolism potential. Features were standardized and analyzed via principal component analysis (PCA) and hierarchical clustering to explore multidimensional tracer relationships. ***Results:*** Tracers clustered into two mechanistic groups: [^{18}F]FDG and [^{18}F]FLT exhibited irreversible trapping dominated by sensitivity to k_3, while [^{18}F]FET, [^{18}F]DOPA, and [^{18}F]FMISO demonstrated reversible transporter-mediated uptake with sensitivity to k_1 and k_2. [^{18}F]FET showed optimal early-phase performance (steep uptake slope and high TNR_{30}), whereas [^{18}F]FMISO provided superior tumor selectivity at delayed time points (highest TNR_{60}). ADME properties reinforced kinetic signatures, with lipophilic tracers correlating to higher permeability and trapping dynamics. The integrated PCA revealed that kinetic behavior and structural features jointly dictated tracer clustering, offering a mechanistically interpretable classification. ***Conclusion:*** This study demonstrates that a unified in silico framework integrating pharmacokinetics, molecular design, and clustering analysis can robustly stratify ^{18}F-labeled PET tracers by their diagnostic strengths. Such multidimensional profiling supports rational tracer selection, optimization of multitracer protocols, and preclinical prioritization strategies, advancing precision imaging in oncology.

EP-0148

Preclinical evaluation of radiolabelled desferrioxamine-B analogues for imaging bacterial infections

M. Petrik*[1,2,3], B. Neuzilova[1], K. Hrabakova[1], K. Krasulova[1], K. Dvorakova Bendova[1], R. Maradan[4,5,6], J. Kronberger[4,5,6], I. Feiner[4,7], X. Guarrochena[4,5], T. Mindt[4,6,8];*
[1]Institute of Molecular and Translational Medicine, Palacky University, Olomouc, CZECH REPUBLIC, [2]Czech Advanced Technology and Research Institute, Palacky University, Olomouc, CZECH REPUBLIC, [3]Institute of Molecular and Translational Medicine, University Hospital, Olomouc, CZECH REPUBLIC, [4]Bioorganic Radiochemistry, Institute of Inorganic Chemistry, University of Vienna, Vienna, AUSTRIA, [5]Vienna Doctoral School in Chemistry, University of Vienna, Vienna, AUSTRIA, [6]Joint Applied Medicinal Radiochemistry Facility, University of Vienna and Medical University of Vienna, Vienna, AUSTRIA, [7]Ludwig Boltzmann Institute Applied Diagnostic, AKH Wien c/o Sekretariat Nuklearmedizin, Vienna, AUSTRIA, [8]Department of Biomedical Imaging and Image Guided Therapy, Division of Nuclear Medicine, Medical University of Vienna, Vienna, AUSTRIA.

Aim/Introduction: Invasive microbial infections are a major cause of morbidity and mortality in immunocompromised patients. We have shown that a siderophore-based iron acquisition system could be an interesting target for molecular imaging, as radiolabelled siderophores appear to be promising agents for detection of various microbial infections (1). Recently, we have demonstrated that the siderophore deferrioxamine-B (DFO-B), which has been used as a chelator in nuclear medicine to label different biomolecules for decades, can be labelled with Ga-68 and used to detect variety of bacterial infections (2). Here, we report on the evaluation of synthetic DFO-B analogues and their potential for imaging bacterial infections. ***Materials and Methods:*** DFO-B analogues were labelled with Ga-68 in sodium acetate. In vitro characterization of ^{68}Ga-DFO-B analogues including the determination of partition coefficient, protein binding and stability in various media was performed. In vitro uptake of ^{68}Ga-DFO-B analogues was tested in selected microbial cultures under various culturing conditions. In vivo biodistribution was studied in healthy mice. PET/CT imaging of ^{68}Ga-DFO-B analogues was performed in a mouse model of microbial myositis. ***Results:*** All DFO-B analogues were radiolabelled with Ga-68 with high radiochemical purity. In vitro assays showed hydrophilic properties, relatively low protein binding and high stability in human serum and PBS for all ^{68}Ga-DFO-B analogues. The high in vitro uptake of tested ^{68}Ga-DFO-B analogues in selected strains of Pseudomonas aeruginosa (P.a.), Staphylococcus aureus (S.a.) and Streptococcus agalactiae (S.ag.) was completely inhibited in heat-inactivated microbial cultures. ^{68}Ga-DFO-B analogues showed high in vivo stability in blood and favourable pharmacokinetics with rapid renal elimination in mice. PET/CT images of animal infection model displayed high and specific accumulation of ^{68}Ga-DFO-B analogues in both P.a., S.a. and S.ag. infection with excellent image contrast. ***Conclusion:*** We have shown that all ^{68}Ga-DFO-B analogues exhibit promising in vitro properties and in vivo behaviour in mice. The high and specific uptake of ^{68}Ga-DFO-B analogues by selected bacteria was

confirmed both in vitro and in vivo, demonstrating that they can be used similarly to ^{68}Ga-DFO-B for imaging bacterial infections. ***References:*** 1. Petrik M et al. (2020) J Fungi 6: 73.; 2. Petrik M et al. (2021) Eur J Nucl Med Mol Imaging 48: 372-382.; We gratefully acknowledge the financial support of the project National Institute of Virology and Bacteriology (Programme EXCELES, ID Project No. LX22NPO5103) - Funded by the European Union - Next Generation EU and Czech Science Foundation, grant number 24-14579L.

EP-0149

Pharmacokinetics study of FT-FAPI, a novel multi-nuclide label-able FAP targeting tracer, in mice

X. Wang, *J. Ye, F. Kang, J. Wang;*
The First Affiliated Hospital of Air Force Medical University, Xi'an, CHINA.

Aim/Introduction: Fibroblast activation protein (FAP) has become one of the most promising targets for integrated diagnosis and treatment. A class of radiopharmaceuticals has been designed based on quinoline-based FAP-specific inhibitors (FAPIs), but previous research data have shown that FAPI probes generally suffer from low tumor uptake and short retention time. FT-FAPI is a potential FAP-targeting probe that utilizes an organic trifluoroborate linker ($AMBF_3$) to enhance tumor targeting ability. In addition, $AMBF_3$ can be used to label a variety of diagnostic and treatment nuclides, such as ^{18}F, ^{68}Ga, and ^{177}Lu. ^{161}Tb is a new type of medical radionuclide. Compared with the widely used nuclide ^{177}Lu, ^{161}Tb can emit Auger electrons and convert electrons in addition to emitting β-rays and gamma rays of corresponding energy, and the dose absorbed by cells is three times higher than that of ^{177}Lu, which is expected to provide new therapeutic options. In this study, ^{161}Tb was synthesized to label FT-FAPI and imaging and pharmacokinetic performance in normal Kunming mouse models. ***Materials and Methods:*** The radiochemical synthesis of ^{161}Tb-FT-FAPI was performed using the traditional metal nuclide heating labeling method. Radio-HPLC was used to study the stability of ^{161}Tb-FT-FAPI. The lipid water partition coefficient LogP was determined by γ-counter. And ^{161}Tb-FT-FAPI pharmacokinetics, biodistribution and dosage studies were conducted on Kunming rats. ***Results:*** In this study, ^{161}Tb-FT-FAPI was successfully prepared, and the product was released and purified by more than 96%. The estimated specific activity was not less than 3.7×10^4 MBq/mmol, which could meet the requirements of subsequent experiments and clinical applications. Calculated based on the experimental results, the lipid-water partition coefficient of ^{161}Tb-FT-FAPI was -3.78 ± 0.03, which shows that 161Tb-FT-FAPI has good hydrophilicity. ^{161}Tb-labeled FT-FAPI showed higher safety and tolerance in mice. The pharmacokinetic characteristics of FT-FAPI in mice are most consistent with the three-compartment model. The biodistribution results showed that in mice, the distribution half-life ($T_{1/2\alpha}$) and clearance half-life ($T_{1/2\beta}$) of ^{161}Tb FT-FAPI was 0.68 h and 5.85 h, respectively. The effective dose equivalent (EDE) of ^{161}Tb-labeled FT-FAPI in an adult model was 16.30 μSv·MBq^{-1} and the effective dose (ED) was 8.14 μSv·MBq^{-1}. ***Conclusion:*** The image quality of ^{161}Tb-FT-FAPI in normal Kunming mice was good and the pharmacokinetic performance was excellent.

EP-0151

Using Modeling and Simulation to Assess the Impact of the Pharmacokinetics and Biodistribution on the Absorbed and Biologically Effective Dose for Radioligand Therapies

H. Stephens, *D.-C. Imbs, M. N. Trame, A. Manon;*
Certara, Radnor, PA, UNITED STATES OF AMERICA.

Aim/Introduction: Radioligand therapies (RLT) are continuing to raise interest in the oncology space. Current standards are to adhere to dose-tolerance levels derived from external beam radiation therapy (EBRT). However, there are grounds to support that this is not appropriate for RLTs leaving risk to underdose tumors. Modeling and simulation can aid in dose optimization, addressing concerns for Project Optimus, on individual organ absorbed doses. We present how a population pharmacokinetic model can assess the impact of the biodistribution on the absorbed and biologically effective dose (BED) to aid in dose range finding decision making. ***Materials and Methods:*** Drug kinetics of a PSMA targeting radionuclide with Lu-177 was modelled in both the blood and organs of interest. Simulations on virtual subjects were performed at injected activities of 3.5, 7, and 10 GBq. Absorbed dose and BED were then calculated. The BED was also derived for the same absorbed dose received as a single fraction of EBRT. The ratio of the RLT BED and EBRT BED was calculated and used to analyze the disparity between RLT and EBRT BED and how dose rate impacts the BED ratio between differing dose-rate profiles. The analysis was performed using the kidneys, liver, and salivary glands. ***Results:*** The absorbed dose per injected activity did not vary linearly with injected activity. The BED ratio for the 7 and 10 GBq injected activity were not statistically different from each other for both the kidneys and salivary glands but were significantly different for the liver. The BED ratio for the 3.5 GBq injected activity was significantly different for the higher two injected activities for all three analyzed organs. The liver was not significantly different than EBRT for any of the tested injected activity levels. The BED for the kidneys and salivary glands was significantly different from the EBRT BED at all tested injected activity levels. ***Conclusion:*** From these results, the absorbed dose and BED do not increase proportionally with injected activity highlighting that simply scaling the absorbed dose by injected activity is not appropriate. The difference in the BED when comparing to EBRT is dependent on the biodistribution, as the organs with noticeable uptake phases had much more disparity compared to EBRT. This disparity seems to increase with injected activity but then saturate at some level. These differences highlight the importance of modeling and simulation to assess the impact of varying injected activity on organs at risk.

EP-11

e-Poster Area

A: Preclinical and Translational Studies -> A1 Medical Preclinical -> A21 Other Preclinical and Translational

EP-0152

Single-cell RNA Sequencing Reveals Immune and Vascular Remodelling in Graves' Disease: Implications for Molecular Imaging and Targeted Therapy

S. Yang[1,2], *G. Zhu*[1];
[1]*Department of Nuclear Medicine, the First Affiliated Hospital of Kunming Medical University, Kunming City, Yunnan Province, CHINA,* [2]*Department of Nuclear Medicine, Yuxi People's Hospital of Yunnan Province/Department of Nuclear Medicine, the Sixth Affiliated Hospital of Kunming Medical University, Yuxi City, Yunnan Province, CHINA.*

Aim/Introduction: Graves' disease (GD) is a prevalent autoimmune disorder, the pathogenesis of which involves immune dysregulation and vascular abnormalities, but the dynamic changes at the single-cell level remain poorly characterised. This study used scRNA-seq in a non-human primate model to map the molecular features of GD and identify new cellular targets for molecular imaging and targeted therapies in nuclear medicine. ***Materials and Methods:*** A GD model was established in cynomolgus monkeys via an adenoviral vector encoding the TSHR A-subunit, with successful induction was confirmed by thyroid-specific SPECT/CT imaging

and serological evaluations. Thyroid tissues from GD monkeys (n=2) and HC (n=3), totalling 10 specimens, were analysed by scRNA-seq. The transcriptomic data were further validated using human samples (GD: n=6, HC: n=3). Cellular heterogeneity and gene expression patterns within the thyroid microenvironment were examined, with a particular focus on immune cell dysfunction and vascular remodelling in GD. ***Results:*** scRNA-seq analysis identified 9 cell types and 15 subtypes within the thyroid tissue. Key findings include: (1) A distinct subset of dysfunctional regulatory T cells (Tregs) in the GD, characterised by reduced FOXP3 expression and elevated levels of TNFRSF18, TNFRSF4, and TIGIT. This suggests a compensatory yet impaired immune regulatory response under inflammatory stress, with these cells potentially playing a pivotal role in the immune dysregulation seen in GD. (2) In thyroid follicular cells (TFCs), aberrant expression of MHC class II molecules was observed, potentially mediated by H2BC5, rather than the classical IFN-γ pathway. (3) Within the endothelial cell (EC) compartment, a paradoxical reduction in capillary endothelial cells (EC1) expressing COL8A1 was noted, despite evidence of active vascular proliferation. Conversely, increased proportions of arterial ECs (EC2), post-capillary venular ECs (EC3), and vascular smooth muscle cells (AC1) were observed, indicating a subtype-specific remodelling pattern of "vascular expansion with concurrent capillary loss."This phenomenon is hypothesised to be driven by COL8A1-mediated transdifferentiation or migration of capillary ECs, leading to endothelial heterogeneity and capillary depletion. We propose a novel mechanism, termed the "COL8A1-driven endothelial transdifferentiation/remodelling hypothesis," to explain these vascular alterations in GD. ***Conclusion:*** This study provides a comprehensive single-cell transcriptomic atlas of GD, highlighting the intricate interplay between immune dysregulation and vascular remodelling. The findings uncover novel cellular and molecular events underlying GD pathophysiology, offering potential targets for the development of radiolabelled tracers or ligand-based therapeutics in nuclear medicine. Future studies will focus on validating these targets for clinical translation and theranostic applications.

EP-0153

Impact of Isotope, Molar Activity, and Ligand Mass on the Biodistribution Profile of 212Pb-based Radioligand Therapies

F. Liu, *A. Prior, M. E. Monterosso, D. Boucher, S. Shakti, A. Horsfall, H. Green, S. Kumar, J. Koehbach, R. Huebner, K. Kuan, W. Tieu, S. Rose, A. Karmann, S. Puttick, G. Li, T. Kryza;*
AdvanCell Pty Ltd, Brisbane, AUSTRALIA.

Aim/Introduction: The theranostics paradigm consists in the utilization of the same targeting agent for both diagnosis and therapy. Lead-203/Lead-212 (^{203}Pb/^{212}Pb) forms one of the only element-equivalent theranostic isotope pairs. ^{203}Pb emits a 279 keV gamma-ray detectable by SPECT imaging, which makes it commonly used as a surrogate for ^{212}Pb. ^{212}Pb is a promising isotope for alpha therapy with high linear energy transfer, a short half-life, and simple decay scheme. Here we present the comparison of ^{203}Pb and ^{212}Pb in radiochemistry, cell binding potency, and in vivo biodistribution using different peptide radioligands. ***Materials and Methods:*** ^{203}Pb was sourced from U.S. Department of Energy (DoE) (Oak Ridge, USA) and ^{212}Pb was produced by AdvanCell (Brisbane, Australia). Two different peptide radioligands were used in this study: 1) a PSMA-ligand-DO3AM developed for prostate cancer, and 2) a melanoma-specific-ligand-DO3AM developed for melanoma. The labeling efficiency, stability and reproducibility of radiolabeling of these ligands labelled with ^{203}Pb and ^{212}Pb, respectively, were compared. The impact of isotope and molar activity were assessed by cell-binding assays, and in biodistribution studies using xenografted tumors with high and intermediate level of target expression. ***Results:*** Radiochemistry analyses showed that ^{203}Pb did not significantly differ from ^{212}Pb in radiolabeling efficiency of either peptide series and allows direct transfer of radiolabeling condition between ^{203}Pb and ^{212}Pb, including at high specific activity. ^{203}Pb- and ^{212}Pb-radiolabelled peptides were assessed by iTLC and rHPLC sequentially under identical analytical conditions, utilizing their gamma emissions. Stability studies showed that ^{212}Pb led to a higher radiolysis of the radioligand when used at high radioactivity concentration (>50 MBq/mL). In vitro binding assays showed comparable binding constants between ^{203}Pb and ^{212}Pb. In vivo biodistribution demonstrated both, molar activity and radioligand dose, affect the biodistribution of radioligands. ***Conclusion:*** Radiolabelling of ligands with ^{203}Pb or ^{212}Pb, and their subsequent analysis, can be translated between isotopes. Our findings demonstrate that the biodistribution profile of both ^{203}Pb- and ^{212}Pb-labeled radioligands is independently influenced by several factors including molar activity and administered dose. It remains unclear whether these differences are also related to the target or ligand type. Therefore, establishing equivalent conditions between ^{203}Pb and ^{212}Pb is essential before considering ^{203}Pb as a surrogate for ^{212}Pb.

EP-0154

Meeting Upcoming Clinical and Diagnostic Needs in oncological Imaging: A Structured Reporting System for Fibroblast-Activation-Protein-Targeted Imaging: FAP-RADS Version 1.0

E. Novruzov[1], *G. Sheikh*[2], *E. Mamlins*[1], *A. Holzgreve*[2], *Y. Mori*[1], *S. Ledderose*[2], *F. Klauschen*[2], *M. Gorin*[3], *M. G. Pomper*[4], *K. Herrmann*[5], *S. P. Rowe*[6], *R. A. Werner*[2], *F. L. Giesel*[1];
[1]*University Hospital Düsseldorf, Düsseldorf, GERMANY,* [2]*University Hospital München LMU, Munich, GERMANY,* [3]*Milton and Carroll Petrie Department of Urology, Icahn School of Medicine at Mount Sinai, New York, NY, UNITED STATES OF AMERICA,* [4]*Department of Radiology, University of Texas Southwestern Medical Center, Dallas, TX, UNITED STATES OF AMERICA,* [5]*University Hospital Essen, Essen, GERMANY,* [6]*Department of Radiology, University of North Carolina, Chapel Hill, NC, UNITED STATES OF AMERICA.*

Aim/Introduction: Fibroblast activation protein (FAP)-targeted imaging has emerged as a promising diagnostic tool for various oncologic and non-oncologic conditions. However, the increasing employment of FAP imaging with small-molecule radiotracers mandates a standardized reporting system to ensure consistent interpretation across various clinical scenarios, especially in oncological imaging. This study proposes FAP-reporting and data system (RADS) version 1.0 framework to address those needs, aiming to standardize FAP imaging reporting, improve clinical communication, and support multi-center research. ***Materials and Methods:*** We conducted a comprehensive literature review and combined it with expert consensus in nuclear medicine to design a new scoring system based on the principles of the molecular imaging (MI)-RADS framework. FAP-RADS version 1.0 system is intended for use across multiple tumor types with variable radiotracer uptake patterns and is non-specific to imaging modality (FAP-PET and FAP-SPECT) or radiotracer compound structure. We aimed to ensure that the system would be user-friendly and applicable to routine clinical practice. ***Results:*** FAP-RADS version 1.0 introduces a 5-point scale to assess the likelihood of malignancy in lesions based on the imaging characteristics of the lesions. The scoring system can be applied to different FAP ligands with varying pharmacokinetics. The framework does not rely on SUV thresholds, making it flexible and robust for clinical use. The implementation of this system aims to improve interdisciplinary communication, support longitudinal follow-up, and facilitate future multi-center trials. ***Conclusion:*** The proposed FAP-RADS version 1.0 reporting system is a comprehensive and flexible framework that has the potential to enhance the quality and consistency of FAP imaging interpretation in clinical practice.

Its application could lead to better research outcomes, broader acceptance within the oncological community, and streamlined regulatory processes related to FAP-based radiotracer approval.

EP-0155

Design and in vivo evaluation of a novel NIR-II/PET dual-modality probe

D. Fan[1], *L. Ai*[1], *K. Zhou*[2];
[1]*Department of Nuclear Medicine, Beijing Tiantan Hospital, Capital Medical University, Bejing, CHINA,* [2]*Center for Advanced Materials Research & Faculty of Arts and Sciences, Beijing Normal University, Zhuhai, CHINA.*

Aim/Introduction: Near-infrared-II (NIR-II, 1000-1700 nm) fluorescent dyes demonstrate exceptional advantages in biomedical applications due to their unique photophysical properties, particularly in deep-tissue imaging capability and ultrahigh-resolution imaging.NIR-II fluorescent dyes have emerged as powerful tools for real-time intraoperative navigation, offering significant advantages over conventional NIR-I imaging. PET(Positron Emission Tomography) imaging technology offers significant advantages for preoperative surgical localization, including ultrahigh-sensitivity detection, functional positioning, and multimodal integration capabilities. In this study, a novel NIR-II/PET dual-modality probe was designed and evaluated with both in vitro and in vivo studies, confirming its efficacy for preoperative tumor localization and real-time intraoperative guidance. ***Materials and Methods:*** The current clinical benchmark dye for NIR-II imaging is indocyanine green (ICG), which advantages are its excellent water solubility, low toxicity, and outstanding photophysical properties (particularly high brightness). While largely preserving ICG's molecular structure, we performed molecular engineering modifications to develop high-performance NIR-II probes for intraoperative navigation. The emission wavelength was determined through in vitro experiments and in vivo studies were conducted for NIR-II and microPET/CT imaging evaluation. ***Results:*** We propose a molecular asymmetrization strategy to reconstruct ICG's symmetric scaffold: transforming the original C_2-symmetric heptamethine cyanine structure into a D-π-A asymmetric system. Compared to ICG, this modification induces a bathochromic shift to 1021 nm, extending emission into the NIR-II window. And this structure permits conjugation with metal chelators for subsequent ^{68}Ga radiolabeling and PET applications. In vivo NIR-II and microPET/CT imaging evaluation studies showed that the probe demonstrates significant accumulation at the tumor site. ***Conclusion:*** A novel NIR-II/PET dual-modality probe was designed and evaluated, with both in vitro and in vivo studies confirming its efficacy for preoperative tumor localization and real-time intraoperative guidance, demonstrating significant clinical translation potential.

EP-0156

Toward Bacterial Vectors for Targeted Atherosclerosis Therapy: microSPECT/CT Biodistribution Studies of [^{111}In] In-Oxine-Labeled Mycoplasma pneumoniae in a murine model of Atheroma.

F. Pareja del Rio[1,2], *A. Fernández-González*[1,2], *A. Hendy-Pérez*[1,2], *J. Escola Gil*[3,4], *N. Rotllan Vila*[3,4], *I. Rodríguez-Arce*[5], *M. Collantes*[1,2,6], *G. Quincoces*[1,2], *I. Peñuelas*[1,2,6];
[1]*Radiopharmacy Unit. Nuclear Medicine Department. Clínica Universidad de Navarra, Pamplona, SPAIN,* [2]*Navarra Institute for Health Research (IdISNA), Pamplona, SPAIN,* [3]*Institut de Recerca de l´Hospital de la Santa Creu i Sant Pau, Barcelona, SPAIN,* [4]*CIBER de Diabetes y Enfermedades Metabólicas Asociadas (CIBERDEM), Madrid, SPAIN,* [5]*Centre for Genomic Regulation (CRG), The Barcelona Institute of Science and Technology, Barcelona, SPAIN,* [6]*Translational Molecular Imaging Unit (UNIMTRA). Nuclear Medicine Department. Clínica Universidad de Navarra, Pamplona, SPAIN.*

Aim/Introduction: Atherosclerosis is a major contributor to the development of severe cardiovascular diseases such as acute myocardial infarction and stroke. Recent studies[1] have identified the presence of Mycoplasma pneumoniae within atheromatous plaques. This cell wall-less bacterium, the leading cause of atypical pneumonia, appears to exhibit a marked tropism for atheromatous plaques, likely due to its inability to synthesize essential membrane lipids, which it must scavenge from the host environment mediated by P1116 protein. If this affinity is further confirmed, genetically attenuated M. pneumoniae CV8 chassis could potentially serve as a novel therapeutic vector for targeted atherosclerosis treatment. To confirm in vivo the tropism of M. pneumoniae for atheromatous plaques, we radiolabeled the bacteria with [^{111}In]In-oxine and performed microSPECT/CT studies in a murine model of atherosclerosis, followed by ex vivo SPECT/CT imaging in explanted organs. ***Materials and Methods:*** The CV8 strain (10^7 CFU) was radiolabeled with 48.5 MBq of [^{111}In]In-oxine for 15´ at 37 ºC. Radiolabeled cells were purified by two steps of centrifugation and washing in PBS.Around 370 KBq of [^{111}In]In-oxine-CV8 were intravenously injected per mice: 3 atherosclerotic LDL receptor Knock-Out (LDLr KO) mice and 3 Wild-Type (WT) control mice, all of which had been fed a Estern diet for 10 weeks. MicroSPECT/CT imaging of the liver and heart was performed at 1 and 6 hours post-injection (hpi). At 6 hpi, mice were euthanized, hearts and aortas carefully extracted and ex vivo imaged by microSPECT/CT. ***Results:*** Radiolabeling efficiency was 10.5%, limited by the adsorption of [111In]In-oxine to preparation materials. In vivo imaging at 6 hours revealed prominent liver uptake, but no clear aortic signal was detected. However, ex vivo imaging showed the tropism of M. pneumoniae for atheromatous plaques, with positive signal detected in 2 of 3 LDLr KO mice and no signal in any of the WT animals. ***Conclusion:*** Radiolabeling and biodistribution studies support the affinity of M. pneumoniae for atheromatous plaques in this animal model. These findings suggest its potential as a novel vector for the targeted treatment of atherosclerotic lesions, although further research is needed to confirm and expand these promising results. ***References:*** 1. Jalili M, Nourmohammadi H, Sayehmiri K. Chlamydia pneumoniae and Mycoplasma pneumoniae as Two Emerging Risk Factors in Atherosclerosis: Meta-Analysis Study and Systematic Review. Infect Disord Drug Targets. 2022;22(1):e210921196697. doi: 10.2174/1871526521666210921121423. PMID: 34548004.

EP-0157

Neurofunctional changes over time after administration of Ibogaine and Noribogaine in Rats Assessed by [^{18}F]FDG PET Imaging

M. Bentura[1], *L. Reyes*[1], *A. Paolino*[1], *G. Falasco*[1], *L. Urrutia*[1], *B. Gonzalez*[2], *J. Mesa*[2], *F. Arredondo*[1], *I. Carrera*[2], *E. Savio*[1];
[1]*Departamento de Radiofarmacia, Centro Uruguayo de Imagenología Molecular (CUDIM), Montevideo, URUGUAY,* [2]*Departamento de Química Orgánica, Facultad de Química, UdelaR, Montevideo, URUGUAY.*

Aim/Introduction: Ibogaine is a psychedelic alkaloid derived from the root bark of Tabernanthe iboga, it has long-lasting anti-addictive effects demonstrated in both preclinical models and observational clinical studies. These effects include reduced drug cravings and alleviation of withdrawal symptoms. These effects persist beyond the pharmacokinetic elimination of ibogaine and its active metabolite, noribogaine. Although its mechanisms of action remain unclear, the prolonged effects point toward the involvement of neuroplasticity processes. Given the complex pharmacological profile and the diverse molecular targets associated with ibogaine and noribogaine, positron emission tomography (PET) imaging emerges as a valuable tool to explore the neurobiological substrates underlying their immediate and long-term central effects. The aim of this work is to further

investigate the metabolic changes in the brain induced by the administration of ibogaine and its active metabolite, noribogaine, through the use of PET combined with Computed Tomography (PET-CT), employing [^{18}F]Fluorodeoxyglucose ([^{18}F]FDG) as a radiotracer. ***Materials and Methods:*** This study was conducted on 24 male Wistar rats (3 months old). Animals received either ibogaine or noribogaine at different doses and via different routes of administration: intraperitoneal ibogaine (40 mg/kg), intravenous ibogaine (10 mg/kg), and intraperitoneal noribogaine (40 mg/kg). Image acquisition was performed using a nanoScan® PET/MRI 3T system (Mediso), at four time points: before treatment (control of each corresponding route of administration), during compound administration, one week post-treatment, and four weeks post-treatment. [^{18}F]FDG was administered following compound injection at time points corresponding to peak brain concentrations: 1 minute after intravenous ibogaine, 5 minutes after intraperitoneal ibogaine, and 20 minutes after intraperitoneal noribogaine. ***Results:*** Results showed significant differences compared to each control at all evaluated time points, including at one week and four weeks post-treatment, with intravenous ibogaine inducing the most pronounced metabolic changes. The brain regions affected varied depending on the compound and route of administration. Some of these effects were maintained over time, while others varied in intensity. Notably, alterations were observed in the motor and somatosensory cortices, hypothalamus, striatum, and parasubiculum—areas implicated in motor control, sensory processing, homeostatic regulation, reward-related functions, and cognition. ***Conclusion:*** These findings suggest that ibogaine and noribogaine induced distinct alterations in brain metabolism, which were maintained or varied over time, and are consistent with the previously described effects of both compounds. This supports the idea of distinct mechanisms of action between the parent drug and its metabolite, as well as potential neuroplasticity processes induced by the treatments.

EP-0158

Preclinical evaluation and first-in-human study of [68Ga]Ga/[177Lu]Lu-JH120061, novel CXCR4-targeting radiopharmaceuticals

J. Zang[1], *G. Wang*[1], *J. Zhan*[2], *E. Wang*[2], *J. He*[2], *H. Yu*[2], *W. Miao*[1];
[1]*The First Affiliated Hospital, Fujian Medical University, Fuzhou, Fujian, CHINA,* [2]*Bivision Pharmaceuticals, Inc., Shanghai, CHINA.*

Aim/Introduction: A novel CXCR4-targeting compound (designated JH120061) was developed through rational design and chemical synthesis. This study aimed to systematically assess its therapeutic potential through preclinical experiments and clinical studies using Pentixafor and Pentixather as references. ***Materials and Methods:*** JH120061 was synthesized and validated. Preclinical evaluation was performed by HT1080 hCXCR4 cells/tumor-bearing mice and compared with Pentixafor/Pentixather, respectively. Patients with several types of tumors were recruited for radiation dosimetry calculation of [^{68}Ga]Ga-JH120061 PET/CT and a head-to-head comparison between [^{68}Ga]Ga-JH120061 and [^{68}Ga]Ga-Pentixafor PET/CT. ***Results:*** JH120061 revealed a strong affinity for CXCR4 with an IC_{50} value of 7.52 ± 0.37 nM, likely outperforming Pentixafor and Pentixather (IC_{50} values: 217.13 ± 4.24 nM and 56.35 ± 7.33 nM, respectively). Preclinical evaluation demonstrated superior accumulation and prolonged retention of both [^{68}Ga]Ga-JH120061 and [^{177}Lu]Lu-JH120061 in CXCR4-positive models compared to their [68Ga]Ga-Pentixafor and [177Lu]Lu-Pentixather. The tumor uptake of [^{68}Ga]Ga-JH120061 and [^{177}Lu]Lu-JH120061 in HT1080 hCXCR4 tumor-bearing mice can be specifically blocked by excess unlabeled Pentixafor and Pentixather. Clinical PET/CT investigations revealed [68Ga]Ga-JH120061 maintained favorable biosafety, the effective dose of [^{68}Ga]Ga-JH120061 PET/CT was 2.01E-02 ± 6.66E-03 mSv/MBq, corresponding to 3.0 mSv for a target activity of 150 MBq.The tumor uptake of [^{68}Ga]Ga-JH120061 in patients with multiple myeloma and clear cell renal cell carcinoma was higher than that of [^{68}Ga]Ga-Pentixafor PET/CT (SUV_{max}: 24.3 ± 11.3 vs. 10.2 ± 6.7 at 60min, $P < 0.001$; 32.6 ± 11.2 vs. 6.7 ± 4.2 at 150min, $P < 0.001$). ***Conclusion:*** This study demonstrated that JH120061 may have excellent affinity for CXCR4, high tumor uptake, and prolonged retention in CXCR4-positive tumors. Further exploration of the application value of [^{68}Ga]Ga/[^{177}Lu]Lu-JH120061 in larger cohorts is needed in the future.

EP-0159

Intraoperative visualisation of tumor margins using FITC glucose as fluorescent probe

A. Aggarwal[1], *A. Sharma*[2], *S. Chopra*[1], *S. Pandey*[1], *D. Attri*[1], *A. Semwal*[1], *I. Laoriya*[1], *A. Aggarwal*[1], *B. R. Mittal*[1], *A. Bal*[1], *J. Shukla*[1];
[1]*Post Graduate Institute of Medical Education and Research, Chandigarh, INDIA,* [2]*Amity University, Mohali, INDIA.*

Aim/Introduction: A fluorescent glucose probe (FITC-Glc) that targets GLUT transporters, mimicking ^{18}F-FDG was developed. This probe enables real-time visualisation of tumours during surgery, facilitating precision excision. ***Materials and Methods:*** Breast tumor models were developed in Wistar rats using a chemical carcinogen DMBA. Eighteen tumor models were administered FITC-Glc (10mg/kg) intravenously after a 4 h fasting and kept under isoflurane anesthesia for 1 hour at 37°C. Surgery was performed under both normal light and blue LED light, followed by ex-vivo tumor imaging using a gel doc system. Cryo-sectioning and histopathological analysis were conducted to validate tumor margins. Fluorescence quantification was performed in tumor and major organs using Fiji (ImageJ) software. The organs were mechanically homogenised with buffer for biodistribution studies and fluorescence intensities between FITC-Glc-administered rats and control rats administered with normal saline were compared by fluorescence spectrophotometer. Ex-vivo, patient derived breast tumor tissues were incubated with FITC-Glc and observed in confocal microscope. ***Results:*** In-vivo studies demonstrated selective uptake of FITC-Glc, with significantly higher fluorescence intensity in tumor analysed via gel doc. Using Fiji software, the mean fluorescence intensity of a 300 X 246 pixel area, yielded a value of 4919 and corresponding cyro-section analysis of the same region yielded a value of 22.8. Fluorescence intensity measurements in the tumor model at 515 nm (ex. 485 nm) showed varying levels across different tissues: kidneys exhibited the highest intensity at 668 a.u., followed by the stomach at 438 a.u., tumor at 309 a.u., and bladder at 231 a.u. Histopathological analysis confirmed tumor free margins, validating FITC-Glc for intraoperative tumor visualization and margin assessment. In patient derived tumor tissue, higher accumulation was observed, demonstrating its application in FGS. Due to sedation, reduced background uptake in brown adipose tissue and skeletal muscle. ***Conclusion:*** FITC-Glc exhibits favourable optical properties for blue light visualisation and excellent biocompatibility. The potential for intraoperative tumor visualization and margin assessment was validated through various studies supporting the clinical utility as a novel probe for FGS.

EP-0160

Evaluating 4-bed µPET/CT Imaging Performance using Mouse Phantoms.

I. Martin[1], *E. Jamieson*[1], *N. Colpo*[1], *J. Jeffry*[2], *B. Cox*[2], *F. Bénard*[1], *P. L. Esquinas*[1], *C. Uribe-Munoz*[1];
[1]*BC Cancer Research Centre, Vancouver, BC, CANADA,* [2]*Phantec LLC, Madison, WI, UNITED STATES OF AMERICA.*

Aim/Introduction: Quantitative µPET/CT provides an alternative method for pre-clinical biodistribution studies compared to traditional approaches requiring animal euthanasia. Modern pre-clinical PET systems allow multi-subject imaging, which increases

efficiency but may impact quantitative accuracy in small organs and tumours due to increased scatter and randoms in the field-of-view. The objective is to evaluate and optimize the quantitative accuracy of simultaneous multi-animal PET/CT imaging using mouse phantoms. ***Materials and Methods:*** The quantitative accuracy of ^{18}F activity measurements on a 4-bed Mediso NanoScan µPET/CT was investigated using BioMouse phantoms (Phantec LLC, USA). Each phantom was filled with three different activity concentrations: 9.0 MBq/mL (brain, kidneys, tumor, bladder), 6.3 MBq/mL (lungs, liver, heart, stomach, spleen), and 3.1 MBq/mL (background compartment). Experiment A: one phantom was imaged in each bed to evaluate consistency across bed positions. Experiment B: the number of phantoms imaged simultaneously was incrementally decreased from four to one to assess multi-bed imaging performance. Three images of the 4-phantom configuration were done to evaluate repeatability. Images were reconstructed using fine reconstruction resolution (8 iterations, 6 subsets, pixel size 0.30mm) and segmented using Mediso's Fusion software with volumes of interest positioned inside of each organ to reduce partial volume effects. Quantification accuracy was measured as percentage difference (%diff) between values obtained from images compared with true values administered. ***Results:*** Experiment A: average %diff in each compartment differed from true values by 11.1% in Bed 1, 2.27% in Bed 2, 7.85% in Bed 3, and 3.74% in Bed 4. Experiment B: average %diff in each compartment for the single phantom appearing in all four images were 5.4% for the 1-phantom scan, 6.8% for the 2-phantom scan, 12.2% for the 3-phantom scan, and 10.3% for the 4-phantom scan. Averaging across all phantom compartments in each image average %diff were: 5.4% for 1-phantom scan, 8.6% for 2-phantom scan, 17.3% for 3-phantom scan, and 25.7% for 4-phantom scan. When repeat scans of the 4-phantom set-up were done 3 and 3.5 hours later, average %diff dropped to 10.1% and 9.4%. Most measured values across repeated scans were consistent within 2% between the same compartments. ***Conclusion:*** Our results suggest that preclinical multi-bed µPET/CT images can provide accurate quantification of activity in mice. Although differences in phantom position and total activity within the field-of-view, we can estimate activity concentrations within 2-11%. We will continue investigating how different image reconstruction parameters can improve image accuracy.

EP-0161

Adjusting Relative Biological Effectiveness for Tumor Microdosimetric Heterogeneity in Radiopharmaceutical Therapy: A Theoretical Analysis

J. Hong[1], *S. Bae*[2,3], *H. Choi*[2,3,4], *M. Ryhiner*[1], *V. Morath*[5], *S. Kossatz*[5,6], *R. Seifert*[1], *W. Weber*[5,7], *A. Rominger*[1], *K. Shi*[1];
[1]*Department of Nuclear Medicine, Inselspital, University of Bern, Bern, SWITZERLAND,* [2]*Institute of Radiation Medicine, Medical Research Center, Seoul National University College of Medicine, Seoul, KOREA, REPUBLIC OF,* [3]*Portrai, Inc., 78-18, Dongsulla-gil, Jongno-gu, Seoul, KOREA, REPUBLIC OF,* [4]*Department of Nuclear Medicine, Seoul National University Hospital, Seoul, KOREA, REPUBLIC OF,* [5]*Department of Nuclear Medicine, TUM University Hospital, School of Medicine, Technical University of Munich, Munich, GERMANY,* [6]*Central Institute for Translational Cancer Research (TranslaTUM), School of Medicine and Health, Technical University Munich, Munich, GERMANY,* [7]*Bavarian Cancer Research Center (BZKF), TUM University Hospital, Munich, GERMANY.*

Aim/Introduction: Evidence has been reported unmatched effects to the accumulated dose in radiopharmaceutical therapy (RPT). Classical fixed value of relative biological effectiveness (RBE) may not be valid due to microdosimetric heterogeneity. This study aims to develop an adjustment coefficient of RBE based on in silico microenvironmental simulation [1]. For proof of concept, we focus on the adjustment of tumor RBE for prostate-specific membrane antigen (PSMA) RPT. ***Materials and Methods:*** We used publicly available Visium spatial transcriptomics (ST) datasets from primary prostate cancer tissue samples. Gene expression levels for FOLH1 (PSMA), GRPR, FAP, and Harris hypoxia signatures were extracted, and spot-level proportions of epithelial, endothelial, and prostate cancer (PC) cells were estimated. We focused on lutetium-labeled PSMA-RPT (Lu-PSMA-RPT) and actinium-labeled PSMA-RPT (Ac-PSMA-RPT). Radiopharmaceutical transport and retention were simulated using a convection-reaction-diffusion partial differential equation (PDE) model, and dose and survival probabilities were computed as described previously [1]. We investigated two levels of heterogeneity: (1) target heterogeneity via PSMA expression, and (2) TME heterogeneity via cell composition. For PSMA, local spatial heterogeneity was quantified using a moving kernel to compute the mean absolute deviation (MAD) of neighboring values, forming a heterogeneity index. Spots were classified into low, medium, or high heterogeneity based on 25th and 75th percentile thresholds. To assess TME heterogeneity, we computed an entropy-based index reflecting cell-type diversity at each spot. To simulate locally homogeneous conditions as a baseline, dose was averaged across neighboring spots within the kernel. We then compared dose-survival relationships under heterogeneous vs. homogeneous assumptions using the linear-quadratic (LQ) model for beta emitters and the exponential model for alpha emitters. We then compared the effective RBE at 10% survival (RBE_{10}) between PSMA-targeted RPT and external beam radiotherapy (EBRT). All parameters were extracted from the literature. ***Results:*** Spatial transcriptomics revealed heterogeneous distributions of PSMA and cell types in the TME. In Lu-PSMA-RPT, both PSMA and TME heterogeneity reduced RBE_{10}, with TME heterogeneity having a greater impact. High heterogeneity in either domain led to poor LQ model fits. In Ac-PSMA-RPT, heterogeneity also lowered RBE_{10}, though effects were less pronounced than those in Lu-PSMA-RPT. Here, PSMA heterogeneity had a stronger influence than TME composition. ***Conclusion:*** Our findings suggest that spatial heterogeneity in target and TME can impact apparent RBE in PSMA-RPT. Modeling approaches that incorporate microenvironmental variation may better predict therapeutic outcomes and guide personalized RPT planning. ***References:*** [1] Hong et al. Theranostics 2024 https://doi.org/10.7150/thno.99516.

EP-0162

Dosimetry-enabled Internal Hematopoietic Acute Radiation Syndrome Model Using the ^{86}Y/^{90}Y Isotopic Pair

L. Wehner*, O. Kwon, A. O. Adeniyi, H. Comas Rojas, M. Bio Idrissou, E. Aluicio-Sarduy, J. W. Engle, B. Bednarz, R. Hernandez;*
University of Wisconsin-Madison, Madison, WI, UNITED STATES OF AMERICA.

Aim/Introduction: Bone marrow toxicity is often the dose-limiting toxicity associated with radiopharmaceutical therapies. Current hematopoietic acute radiation syndrome models evaluate effects due to external exposure from gamma or x-ray sources and the limited number of internal ARS models have several limitations. Here, we aimed to develop a dosimetry-enabled, selective internal hematopoietic-ARS model based on ^{86}Y ($t_{1/2}$ = 14.7 h)/ ^{90}Y ($t_{1/2}$ = 64h) isotopic pair. ***Materials and Methods:*** The selectivity Yttrium for the bone was evaluated via serial PET/CT imaging at 3h, 24h, 47h, and 72h using an intravenous injection of 9.2 ± 0.4 MBq ^{86}Y and corroborated with ex vivo biodistribution following the 72h in vivo imaging timepoint. Absorbed dose rate estimates to the bone marrow were made for the ^{90}Y model using ^{86}Y PET/CT biodistribution. Male ICR mice (3-5-weeks) were administered ^{90}Y ranging from 376.5 - 779.6 MBq/kg and compared to cohorts receiving a uniform injection, irrespective of bodyweight, ranging from 11.1 - 16.7 MBq. Mice were periodically assigned a clinical score based on changes in bodyweight, posture, activity, skin, and fur texture with complete blood counts measured at baseline and days 7- and 28-post-injection (p.i.). Femur and soft-tissue organs

were collected in separate ^{90}Y bodyweight injected cohorts at days 7- and 31-p.i. with the contralateral femur processed for digital autoradiography on an ionizing-radiation Quantum Imaging Detector between days 8-13 p.i. ***Results:*** Osseous tissue selectivity was confirmed via femoral autoradiography demonstrating deposition at growth plate regions which corroborated with high uptake quantified via ^{86}Y PET/CT imaging and 72h biodistribution (26.8 %IA/g ± 3.5) compared to soft tissues (≤ 6%IA/g). Absorbed dose estimation of the femurs in the ^{90}Y model were quantified ranging from 20.6 - 60.9 Gy. Dose-dependent relationships between the bodyweight, clinical score, and survival were not observed in the model injected with uniform doses of ^{90}Y but were apparent in the bodyweight normalized model resulting in a significant effect of ^{90}Y dose on survival ($P < 0.0001$, logrank test for trend). Complete blood counts revealed severe thrombocytopenia and leukopenia at day 7 p.i. that resolved in surviving cohorts measured at day 28 p.i. in both models. Severe hypoplasia of the bone marrow was observed in several dose cohorts via histological examination. ***Conclusion:*** Herein, we present a robust and selective model H-ARS model characterized with ^{86}Y/^{90}Y that enables development of radiation countermeasure and mitigating intervention to address the bone marrow toxicities associated with RPT agents.

EP-0163

[^{18}F]-Pentixafor CXCR4-Targeted PET/CT for Osteogenesis Evaluation and Fracture Healing Monitoring

Z. Li, *D. Zhang, X. Su;*
First Affiliated Hospital of Zhejiang University, School of Medicine, Zhejiang University, Hangzhou, CHINA.

Aim/Introduction: Conventional skeletal imaging techniques primarily assess structural morphology without capturing cellular-level bone remodeling processes. The C-X-C chemokine receptor type 4 (CXCR4)/stromal cell-derived factor-1 (SDF-1) axis plays crucial regulatory roles in osteogenesis and fracture repair[1-3]. This study investigates the potential of [^{18}F]-Pentixafor PET/CT for non-invasive monitoring of CXCR4 expression dynamics during bone regeneration. ***Materials and Methods:*** Bulk RNA sequencing analysis (GSE230852) compared CXCR4 expression patterns in skeletal progenitor cells, with qPCR validation. Three murine age cohorts (postnatal: 4-6 weeks], adult: 3-4 months, and aged: >20 months) underwent serial [^{18}F]-Pentixafor PET/CT scans with concurrent micro-CT (µCT) bone volumetry. Standardized femoral fracture models received weekly PET/CT monitoring during healing phases (inflammatory through remodeling stages within 1 week after surgery). Immunohistochemical validation of CXCR4 expression patterns was performed in harvested callus specimens. ***Results:*** Transcriptomic analysis revealed significantly elevated CXCR4 expression in skeletal stem/progenitor cells (SSPCs) compared to mature osteoblasts ($p<0.05$). Physiological [^{18}F]-Pentixafor uptake demonstrated age-dependent variation: postnatal metaphysis SUVmax 0.58±0.06 vs. adult 0.40±0.02 vs. aged 0.28±0.05 ($p<0.05$). Fracture callus exhibited progressive tracer accumulation peaking at 2 weeks post-injury (SUVmax 2.00±0.51 vs. contralateral 0.03±0.01), positively correlated with SSPC enrichment. Age-stratified analysis showed differential healing responses: postnatal SUVmax 3.58±1.04 vs. adult 2.28±0.72 vs. aged 0.78±0.32 ($p<0.01$), paralleling µCT bone formation metrics and IHC staining. ***Conclusion:*** [^{18}F]-Pentixafor PET/CT enables quantitative, non-invasive monitoring of CXCR4-mediated osteogenic activity across developmental stages and fracture healing phases. The modality demonstrates significant predictive potential for bone regeneration capacity assessment, paving the way for clinical translation in personalized orthopedic management. ***References:*** [1]Kawakami Y, Ii M, Matsumoto T, et al. SDF-1/CXCR4 axis in Tie2-lineage cells including endothelial progenitor cells contributes to bone fracture healing.[J]. Journal of bone and mineral research : the official journal of the American Society for Bone and Mineral Research, 2015: , 30(1): 95-105. [2]Esposito A, Klüppel M, Wilson B M, et al. CXCR4 mediates the effects of IGF-1R signaling in rodent bone homeostasis and fracture repair.[J]. Bone, 2023: , 166: 116600.[3]Anginot A, Nguyen J, Abou Nader Z, et al. WHIM Syndrome-linked CXCR4 mutations drive osteoporosis.[J]. Nature communications, 2023: , 14(1): 2058.

EP-0164

Supramolecular Chemistry Enables Radiolabelling of Antibodies under Mild Conditions

V. Goncalves[1], *R. Vizier*[1], *M. Moreau*[1], *J. Faivre*[1], *M. Carrierre*[1], *M. Cheveau*[1,2], *S. Poty*[1], *F. Denat*[1], *M. Boswinkel*[3], *S. van Lith*[3];
[1]*Université Bourgogne Europe, Dijon, FRANCE,* [2]*CheMatech, Dijon, FRANCE,* [3]*Radboud UMC, Nijmegen, NETHERLANDS.*

Aim/Introduction: One of the key challenges in using proteins as vectors in nuclear medicine is their limited thermal stability, which precludes the use of harsh radiolabelling conditions. To address this, we propose a two-step strategy for protein radiolabelling based on supramolecular chemistry. Specifically, we describe the synthesis of DOTA-cucurbit[7]uril (DOTA-CB[7]), a versatile precursor that can be efficiently radiolabelled with various radionuclides.[1] This compound was rapidly conjugated under mild, and biocompatible conditions to an adamantanamine-modified antibody. The resulting tracer was evaluated in vivo using SPECT/CT and biodistribution studies. Application of this platform to pre-targeted imaging is on-going. ***Materials and Methods:*** DOTA-CB[7] was synthesized starting from glycoluril and radiolabelled with ^{111}In, ^{89}Zr, ^{68}Ga, ^{177}Lu, ^{225}Ac, and ^{161}Tb at 90-95 °C. Adamantanamine was site-specifically conjugated to trastuzumab using transglutaminase. Supramolecular assembly between DOTA-CB[7] and trastuzumab-adamantanamine was achieved in PBS at 37 °C. Biolayer interferometry (BLI) measurements and cell binding assays were conducted to confirm the affinity of the immunoconjugate for HER2. In vivo experiments were performed on mice xenografted with SKOV3 cells. SPECT/CT images were recorded and ex vivo biodistribution was performed by gamma counting. ***Results:*** DOTA-CB[7] was synthesized in four steps. Adamantanamine was successfully conjugated to trastuzumab, achieving a degree of labelling of 2. The supramolecular conjugate was formed quantitatively after 1 minute of incubation at 37 °C in PBS. BLI showed that the binding affinity of the bioconjugate to HER2 was preserved, with a K_D of 0.11 +/- 0.02 nM. Radiolabeling of DOTA-CB[7] with ^{111}In, ^{89}Zr, ^{68}Ga, ^{177}Lu, ^{225}Ac, and ^{161}Tb succeeded with radiochemical yields >90%. All radioconjugates showed excellent stability in PBS and plasma. Upon administration of [^{111}In]In-DOTA-CB[7]⊂trastuzumab-adamantanamine, a significant accumulation of the tracer was observed in the tumor (40.5 +/- 2.4 %ID/g) at 72 h p.i. compared to the blocking group (14.2 +/- 1.4 %ID/g). This value was comparable to the one observed with the covalent conjugate (31.8 +/- 13.2 %ID/g). In contrast, [^{111}In]In-DOTA-CB[7] alone was rapidly cleared by renal elimination. ***Conclusion:*** DOTA-CB[7] represents a promising platform for the synthesis of radioimmunoconjugates. This robust, small molecule enables radiolabeling to be carried out under harsh conditions, achieving good radiochemical yields with a variety of radiometals. In vivo, the radioimmunoconjugate obtained by supramolecular assembly showed excellent stability over several days and a biodistribution profile comparable to that of the "conventional" covalent conjugate. The results of the application of this platform to a pretargeted approach will be disclosed. ***References:*** 1. WO2025003455A1.

EP-0165

Uridine-Based PET/NIRF Dual-Modality Imaging for Precision Tumor Diagnosis and Surgery

***L. Bian**;*
Fudan University Shanghai Cancer Center, Shanghai, CHINA.

Aim/Introduction: Recent studies in Nature, Nature Metabolism, and Nature Cancer have revealed that uridine metabolism plays a crucial role in tumor survival under glucose deprivation, supporting glycolysis and redox homeostasis[1-3]. Building on these findings, we aimed to develop a novel dual-modality imaging platform that targets uridine metabolism to visualize tumor metabolic heterogeneity and guide intraoperative resection. ***Materials and Methods:*** We designed two uridine-based imaging probes: (1) [^{68}Ga]Ga-DOTA-FZUD for PET imaging and (2) ICG-FZUD for second near-infrared window (NIR-II) fluorescence imaging. The probes were evaluated for radiochemical purity, optical properties, pharmacokinetics, and in vivo stability. Tumor-bearing mice were used to assess biodistribution, imaging contrast, and tumor selectivity. Orthotopic and subcutaneous tumor models were employed to evaluate intraoperative fluorescence guidance. Ex vivo human gastric tumor specimens were imaged to explore translational potential. ***Results:*** [^{68}Ga]Ga-DOTA-FZUD showed high radiochemical stability and specific tumor uptake, enabling clear PET delineation of tumors with high tumor-to-background ratios. ICG-FZUD demonstrated excellent optical properties in the NIR-II window, allowing for precise visualization of tumor margins during surgery. The dual-modality approach improved diagnostic accuracy and facilitated complete resection. Fluorescence signal distribution correlated well with histopathology in both mouse and ex vivo human tumor tissues. ***Conclusion:*** This study introduces the first uridine-based PET/NIRF dual-modality imaging system targeting tumor metabolism. By leveraging the metabolic vulnerability of uridine utilization, our probes provide sensitive, noninvasive imaging and real-time surgical navigation. These findings offer a clinically translatable platform for precision diagnosis and treatment of metabolically heterogeneous tumors. ***References:*** 1. Tommaso, Scolaro,Marta, Manco,Mathieu, Pecqueux et al. Nucleotide metabolism in cancer cells fuels a UDP-driven macrophage cross-talk, promoting immunosuppression and immunotherapy resistance.[J] .Nat Cancer, 2024, 5: 0.2. Owen S, Skinner,Joan, Blanco-Fernández,Russell P, Goodman et al. Salvage of ribose from uridine or RNA supports glycolysis in nutrient-limited conditions.[J] .Nat Metab, 2023, 5: 0.3. Zeribe C, Nwosu,Matthew H, Ward,Peter, Sajjakulnukit et al. Uridine-derived ribose fuels glucose-restricted pancreatic cancer.[J] .Nature, 2023, 618: 0.

EP-0166

From Rats to Humans: Dosimetry Extrapolation Challenges and Opportunities for ^{177}Lu-FAPI-46 Therapy in Fibrosing Mediastinitis

***L. Song**[1], X. Chen[2,3], J. Li[2], Z. Wu[1];*
[1]First Hospital of Shanxi Medical University, Taiyuan, CHINA, [2]China Institute for Radiation Protection, Taiyuan, CHINA, [3]Shandong Cancer Hospital and Institute, Shandong First Medical University and Shandong Academy of Medical Sciences, Jinan, CHINA.

Aim/Introduction: Fibrosing mediastinitis (FM), a rare and life-threatening fibroproliferative disorder, lacks effective therapies. The novel radiopharmaceutical ^{177}Lu-FAPI-46, targeting fibroblast activation protein, shows preclinical promise but requires robust animal-to-human dosimetry translation for clinical trial design. This study evaluates five extrapolation methods to predict safe therapeutic dosing, focusing on dose-limiting organs. ***Materials and Methods:*** Five extrapolation methods were investigated: direct application of rat time-integrated activity coefficients (TIACs) to human organs (M1), relative mass scaling (M2), metabolic rate scaling (M3), combined mass and metabolic rate scaling (M4), and organ-specific allometric scaling (M5). The correlation between these methods and uterine uptake, as well as clinical imaging data, was further analyzed. ***Results:*** Method-dependent variability was observed in organ dose distributions. The uterus consistently emerged as the dose-limiting organ across all models. Physiological uptake was confirmed in uterus, ovaries, and small intestine. Maximum permissible administered activity was projected to be <2.78 GBq to avoid exceeding 16 Gy uterine dose. ***Conclusion:*** Uterine dose constraints necessitate limiting ^{177}Lu-FAPI-46 activity to <2.78 GBq, particularly for young females. These preclinical extrapolations provide critical guidance for first-in-human trials, though clinical validation remains essential.

EP-0167

Irisin as a Novel Therapeutic Agent for Glioblastoma: Targeting Ferroptosis via Specific Tumor Binding and AAV-Mediated Overexpression

***C. Chuang**[1], F. Huang[1], C. Huang[2];*
[1]National Taiwan University, Taipei City, TAIWAN, [2]Chang Gung Memorial Hospital, Taoyuan City, TAIWAN.

Aim/Introduction: Glioblastoma multiforme (GBM), a grade IV brain tumor with high aggressiveness, presents a median survival of 12-15 months. Emerging research indicates that exercise may lower cancer risk, including GBM, by modulating systemic and cellular pathways. This study aimed to investigate the biodistribution of irisin, a myokine induced by exercise and encoded by the FNDC5 gene, in a glioma xenograft mouse model using 68Ga-radiolabeled irisin for PET imaging, and to evaluate its therapeutic potential against GBM by exploring its ability to induce ferroptosis in glioma cells and validating its efficacy through adeno-associated virus (AAV)-mediated irisin overexpression. ***Materials and Methods:*** Irisin was radiolabeled with 68Ga and administered to mice bearing glioma xenografts for in vivo PET imaging to assess its biodistribution and tumor-specific binding. In vitro studies were conducted using glioma cell line (U-87 MG) to evaluate irisin's dose-dependent effects on cell viability and ferroptosis induction, confirmed by lipid peroxidation assays and ferroptosis markers. AAV vectors encoding irisin were constructed and administered to glioma cells and orthotopic tumor models to assess therapeutic effects on tumor growth as monitored by T2-weighted MRI and ferroptosis induction. To elucidate the underlying mechanisms, RNA sequencing (RNA-seq) analysis was conducted to identify differentially expressed genes and signaling pathways associated with irisin treatment. ***Results:*** PET imaging revealed specific binding of 68Ga-labeled irisin to glioma xenografts, with significant tumor uptake (SUVmean=1.56±0.35) compared to control tissues (muscle SUVmean=0.25±0.08). In vitro studies demonstrated that irisin triggered ferroptosis in glioma cells in a dose-dependent manner, evidenced by increased lipid peroxidation. Overexpression of irisin via AAV8 vectors reduced GBM cell viability and clonogenicity by approximately 50% at a titer of 1012 GC, compared to wild-type cells. AAV-mediated irisin overexpression reduced tumor growth in glioma xenografts (7.92 mm3 vs 99.6 mm3 at day 29), with prolonged survival in treated mice compared to controls. Transcriptomic analysis by RNA-seq revealed ferroptosis as a possible mechanism underlying irisin-mediated anti-tumor effects. ***Conclusion:*** These findings suggest that irisin demonstrates promise as a therapeutic candidate for glioblastoma given its ability to selectively target tumor cells. The possible involvement of ferroptosis-related pathways provides a mechanistic basis for its anti-tumor activity. Further investigation is required to elucidate these pathways in detail and to assess the potential for clinical application of irisin-based therapies.

EP-0168

Disrupted Synchronization of Organ Translocator Protein (TSPO) Expression in Glioblastoma Mice: Exploiting Total-Body TSPO-PET

G. Müller[1], *A. Zatcepin*[1,2], *L. Bartos*[1], *L. Hörmann*[1], *J. Thevis*[1], *L. Wesser*[1], *G. Palumbo*[1], *R. Oos*[1], *K. Wind-Mark*[1], *R. Werner*[1,3], *S. Ziegler*[1,4], *M. Brendel*[1,2,5];

[1]*Department of Nuclear Medicine, LMU University Hospital, LMU Munich, Munich, GERMANY,* [2]*German Center for Neurodegenerative Diseases (DZNE), Munich, GERMANY,* [3]*Russell H. Morgan Department of Radiology and Radiological Sciences, Johns Hopkins School of Medicine, Baltimore, MD, UNITED STATES OF AMERICA,* [4]*Department of Nuclear Medicine, Hannover Medical School (MHH), Hannover, GERMANY,* [5]*Munich Cluster for Systems Neurology (SyNergy), Munich, GERMANY.*

Aim/Introduction: PET imaging of the 18 kDa translocator protein (TSPO) is increasingly used in preclinical research on neurological diseases and is expected to provide information about the immune response. TSPO is a biomarker for glial activity and is expressed in glioma cells and myeloid cells in the tumour microenvironment (1). In this study, associations between TSPO expression in glioblastoma and organ systems of the mouse were investigated. ***Materials and Methods:*** Static late-phase TSPO-PET images (40-60 min p. i.) with the tracer [^{18}F]GE-180 were used from a total of 67 C57Bl/6 mice, including sham-operated (n=18) and glioblastoma mice (syngeneic SB28 cell line) imaged at early (5-13 days, n=20) and late (18-19 days, n=29) time point after inoculation. The tumour and selected organs (healthy brain, heart, lung, skull, various bones) were segmented, and the average TSPO-PET activities were extracted to compare TSPO expression between groups of mice (sham, early- and late-stage glioblastoma). Pearson correlations between all organ regions were calculated to analyse connectivity patterns within the groups. To quantify deviations from normal connectivity patterns, the correlation abnormality score (CAS) was introduced at both cohort and individual level. ***Results:*** Comparing late-stage glioblastoma mice with sham-operated mice, mean TSPO expression was significantly increased in the tumour region ($p<0.0001$) and the skull ($p<0.002$). We also observed a significant increase of the TSPO heart-to-lung ratio ($p=0.0075$). In late-stage glioblastoma mice, the heart-lung correlation was impaired (late-stage glioblastoma: $R=0.15$, $p=0.636$; sham: $R=0.56$, $p=0.050$), while bones and lungs developed a negative correlation (vertebra: late-stage glioblastoma: $R=-0.46$, $p=0.038$; sham: $R=0.07$, $p=0.782$). Additionally, late-stage glioblastoma mice demonstrated a significant increase in individual CAS compared to sham-operated mice, particularly in the tumour region ($p=0.0003$) and lung ($p=0.0175$). When comparing the cohort-level CAS, the most significant abnormality was observed in the tumour-vertebra CAS ($p<0.0001$). ***Conclusion:*** Our analysis of total-body TSPO connectivity revealed distinct stage-dependent changes in TSPO expression in organs that relate to immune response, which may suggest increased migration of myeloid cells. These results highlight the effects of inflammatory responses on TSPO expression and could provide important insights into tumour-associated immune processes. ***References:*** 1.B. Zinnhardt, F. Roncaroli, C. Foray, E. Agushi, B. Osrah, G. Hugon, A. H. Jacobs, A. Winkeler, Imaging of the glioma microenvironment by TSPO PET. European journal of nuclear medicine and molecular imaging 49, 174-185 (2021).

EP-0169

Computational Design of Chelators for Actinium-225 and Its Decay Daughters: Toward Optimized Alpha-Emitter Theranostics

D. Lee[1], *J. Kim*[2], *K. Kang*[3], *J. Yoo*[3], *W. Lee*[2], *M. K. Schultz*[4];
[1]*Department of Physics and Chemistry, Korea Military Academy, Seoul, KOREA, REPUBLIC OF,* [2]*Department of Chemical and Biological Engineering, Seoul National University, Seoul, KOREA, REPUBLIC OF,* [3]*Chemical, Biological, Radiological Defense Research Institute, Seoul, KOREA, REPUBLIC OF,* [4]*Perspective Therapeutics, Inc., Coralville, IA, UNITED STATES OF AMERICA.*

Aim/Introduction: Actinium-225 (^{225}Ac) is a potent alpha emitter used in targeted radionuclide therapy (TRT). Its relatively long half-life (~10 days) allows for extended therapeutic action but also imposes a stringent requirement for prolonged in vivo chelation stability. Clinical application is further complicated by the complex decay cascade of ^{225}Ac, which produces daughter radionuclides (e.g., Fr-221, At-217, Bi-213) with distinct chemical properties and substantial recoil energies. While existing chelators such as DOTA, macropa, and crown ether derivatives show moderate success in coordinating Ac^{3+}, their capacity to retain both parent and daughter radionuclides under sustained alpha flux remains poorly understood. This study aims to explore and rationally design chelators that provide thermodynamic and structural stability across the full decay profile of ^{225}Ac. ***Materials and Methods:*** Density Functional Theory (DFT) calculations were performed using the ORCA package to evaluate the interaction energies, coordination geometries, and charge distributions of chelator-metal complexes. Multiple trivalent chelator scaffolds, including DOTA, macropa, and crown-based ligands, were modeled in conjugation-ready forms (linked via ethylamine), with plans to expand the library to structures capable of dual-size accommodation. While experimental data on Fr, At, and Bi chelation is limited, their ionic radii and potential coordination preferences were inferred from known analogs and will be addressed in future modeling. ***Results:*** Initial computational stabilization of Ac-chelator complexes confirmed trends seen with other trivalent radionuclides: DOTA adopts 8-coordinate geometries, while macropa and crown-based ligands provide more flexible coordination spaces. Chelation energy analysis indicated that macropa-type structures offer lower interaction energies than DOTA for Ac^{3+}, suggesting improved thermodynamic stability. However, current models do not yet account for daughter isotope retention or recoil effects. Structural expansion toward bifunctional or adaptive cavity chelators is underway to address the distinct ionic sizes and coordination tendencies of ^{221}Fr (monovalent, alkali-like), ^{217}At (multiple oxidation states, borderline halogen), ^{213}Bi (trivalent, borderline-soft). These designs are being developed using stepwise DFT-based screening and constrained geometry optimization. ***Conclusion:*** This work presents a rational computational approach to identifying chelator structures suitable for ^{225}Ac and potentially its decay daughters. While no single chelator is currently known to retain all progeny, our modeling platform enables systematic design and assessment of chelators with cavity flexibility and charge-balancing features. Future directions include modeling daughter-specific chelation, with the goal of guiding the synthesis of next-generation chelators optimized for complete alpha-emitter retention and safety in clinical TRT.

EP-0170

Dimorphism of whole body Crayfish by [^{18}F]FDG uptake

A. Avendaño-Estrada[1,2], *K. Mendoza-Ángeles*[1], *J. Hernandez-Falcón*[1], *M. Ávila-Rodríguez*[1,2];
[1]*School of Medicine, UNAM, Mexico, MEXICO,* [2]*Centro de Investigación sobre el Envejecimiento, Centro de Investigación y de Estudios Avanzados Sede Sur, Mexico City, MEXICO.*

Aim/Introduction: Crustaceans are used in biomedical research due to their accessibility, adaptability, and resistance. Crayfish (Procambarus clarkii) has been evaluated by genetics, molecular biology, behavior assessments, electrophysiology, and microscopy techniques; nevertheless, in vivo evaluation by micro positron emission tomography (MicroPET) has not been assessed in this specie. MicroPET imaging in crustacean models represents a novel approach in evaluating metabolic processes in these organisms. This work aimed to assess the uptake in different organs (brain, green gland, heart, gonads, and ganglia) of [^{18}F]FDG in male and female crayfish using MicroPET imaging and to find the optimal

scan acquisition time. ***Materials and Methods:*** Adult male and female crayfish (n=6/sex, 30-40 g, 6-8 cm length) underwent 1 hour MicroPET scans (6 frames of 10 minutes) after administration of [^{18}F]FDG (7.4 ± 10 MBq). Animals were fasted for one week before imaging acquisition. Standardized uptake values (SUV) were calculated for the brain, gonads, green gland, heart, and ganglia of the ventral nerve cord. ***Results:*** Green gland, brain, and, subesophageal ganglion showed the highest [^{18}F]FDG uptake. Significant differences in the SUV associated to sex were observed only in the gonads (females showed highest uptake). No significant differences were found in other structures, nevertheless, male crayfish showed a higher coefficient of variation (0.7-1.2) than females (0.1-0.6). All the evaluated regions reach a maximum and constant SUV between 40 and 50 minutes after [^{18}F]FDG administration. ***Conclusion:*** MicroPET imaging is useful to assess metabolic activity and sexual dimorphisms in crayfish in a single 10-minute scan (e.g. from minute 40-50).

EP-0171

PET-Based Assessment of Tumour Heterogeneous Uptake in Response to Doxorubicin/Andiroba Oil Nanoemulsion Therapy in a 4T1 Murine Breast Cancer Model

M. B. Silveira[1], *S. E. M. Miranda*[1], *A. L. P. Magalhães*[2], *A. E. M. M. Oliveira*[2], *J. O. Silva*[2], *A. L. B. Barros*[2];
[1]*Center for the Development of Nuclear Technology (CDTN/CNEN), Belo Horizonte, BRAZIL,* [2]*Federal University of Minas Gerais (UFMG), Belo Horizonte, BRAZIL.*

Aim/Introduction: Positron emission tomography (PET) is a valuable tool for developing novel therapeutics in preclinical cancer models. Earlier, we have investigated therapeutic efficacy using an Andiroba oil-based nanoemulsion loading Doxorubicin (unpublished data), which demonstrated in vitro antitumoral activity. In this study, we aimed to quantitatively assess both low- and high-uptake regions within necrotic large-volume tumors using [^{18}F]FDG PET imaging, correlating PET-derived parameters with caliper-derived volumetric measurements to enhance the understanding of treatment response dynamics. ***Materials and Methods:*** The study evaluated 4T1 tumor-bearing BALB/c mice (n=4-8), divided into control (C), free doxorubicin (Doxo), and nanoemulsion-loaded doxorubicin (NE) groups. On day 18 post-treatment, mice received 20-30 MBq [^{18}F]FDG IV. Software measurements were taken using AMIDE®. Total and corrected volumes (excluding regions of hypocaptation) were analyzed. Imaging data were statistically compared (ANOVA) with caliper-based assessments using the ellipsoid formula [$V = 0.5 \times (d1)^2 \times d2$] (d1 = shortest and d2 = longest diameter). ***Results:*** Quantitative analysis revealed significant volumetric differences between measurement modalities. Caliper measurements showed tumor volumes of 872.7 ± 196.3 mm^3 (C), 471.9± 277.1 mm^3 (Doxo), and 330.2 ± 110.6 mm^3 (NE), while PET-derived volumes were consistently larger (1688.9 ± 412.3 mm^3 control, 1019.4 ± 387.0 mm^3 Doxo, 807.1 ± 158.3 mm^3 NE; p=0.0002 for all inter-method comparisons). The corrected volumes (excluding regions of hypocaptation) were 1427.2 ± 390.4 mm^3 (C), 776.4 ± 372.4 mm^3 (Doxo) and 656.8 ± 188.8 mm^3 (NE). There was a statistical difference when comparing the volumes obtained between the ways of analysing, all with a p-value of 0.0002, but no difference was observed between both treated groups. When comparing the results between the groups, the volumes and caliper measurements gave differences of p-value=0.0081 between Doxo and C, and p-value=0.0002 when comparing NE with C. Correlation analysis revealed parallel response curves across methodologies (p>0.05). Hypermetabolic region analysis showed treatment-specific differences (Doxo p=0.0312, NE p=0.0002 vs control), while hypometabolic areas exhibited >85% correlation with total tumor volume across all groups, indicating their significant contribution to tumor progression. ***Conclusion:*** [^{18}F]FDG uptake heterogeneity predicts therapy response in preclinical models, especially for necrotic/large tumors. Our data show hypometabolic expansion correlates with tumor volume. PET surpasses conventional methods, providing crucial data for drug development and personalized chemotherapy. These findings support incorporating PET-based volumetric analysis as a mandatory component in antitumor drug development pipelines to improve clinical translation.

EP-12

e-Poster Area

B: Imaging Clinical Studies -> B1 Oncological Imaging Clinical Study -> B11 Central Nervous System

EP-0172

Glioma and brain blood flow quantification using dynamic [^{18}F]FET PET/CT and Tikhonov model-free deconvolution

C. Engkebølle[1], *U. Lindberg*[2], *O. M. Henriksen*[1], *K. Madsen*[3], *T. L. Andersen*[1], *T. Urup*[4], *R. Rasmussen*[5], *H. B. W. Larsson*[2], ***I. Law***[1];
[1]*Department of Clinical Physiology & Nuclear Medicine, Copenhagen University Hospital Rigshospitalet, Copenhagen, DENMARK,* [2]*Functional Imaging Unit, Department of Clinical Physiology and Nuclear Medicine, Copenhagen University Hospital Rigshospitalet, Glostrup, DENMARK,* [3]*Department of Clinical Physiology & Nuclear Medicine, Rigshospitalet, Copenhagen, DENMARK,* [4]*Department of Oncology, Copenhagen University Hospital Rigshospitalet, Copenhagen, DENMARK,* [5]*Department of Neurosurgery, Copenhagen University Hospital Rigshospitalet, Copenhagen, DENMARK.*

Aim/Introduction: The advent of long axial field-of-view (LAFOV) PET/CT enables whole-brain dynamic imaging with high spatiotemporal resolution and novel kinetic modelling strategies. We have evaluated the [^{18}F]FET-derived quantitative estimates of cerebral blood flow (CBF) and blood-brain barrier extraction fraction (E) using Tikhonov-regularised model-free deconvolution in brain tumours and healthy-appearing grey (GM) and white matter (WM). ***Materials and Methods:*** In 12 patients (median age 48, range 22-70, 4M/8F), referred for suspected or confirmed brain tumours or epilepsy, a 40-minute dynamic [^{18}F]FET PET/CT was performed on a Siemens Biograph Vision Quadra. Images were reconstructed with 2-second frames across the bolus injection and modelled using an image-derived input function (1) and Tikhonov model-free deconvolution to derive CBF and E from the residue impulse response function (2). Tumour modelling was performed in patients with metabolic tumour volume (MTV) >10 ml using a tumour-to-background ratio threshold of 1.6. ***Results:*** Perfusion quantification in GM showed an E of 2.54 ± 1.03 % (range: 1.10-4.90), with CBF of 63.6 ± 14.8 ml/100 ml/min. The unidirectional influx constant (K_1) was 1.43 ± 0.30 ml/100 ml/min and mean transit time (MTT) was 32.7 ± 11.5 s. In WM the E was higher at 4.45 ± 1.5 % (2.80-8.60) while CBF and K_1 were lower at 23.1 ± 5.14 ml/100 ml/min and 0.99 ± 0.22 ml/100 ml/min, respectively. MTT was higher at 60.3 ± 21.1 s. In the 6 patients with MTV > 10 ml (range 14 to 123 ml) E was elevated compared to GM, ranging from 4.50 to 11.60 %. CBF ranged from 31.7 to 65.4 ml/100 ml/min, K1 from 2.4 to 6.0 ml/100 ml/min, and MTT from 52.7 to 118.9 s. ***Conclusion:*** Tikhonov-regularised model-free deconvolution using [^{18}F]FET LAFOV PET/CT enables physiologically plausible and consistent quantification of CBF and E in healthy-appearing brain tissue, with clear distinction between GM and WM. The method also permits parameter estimation in metabolically active tumours. While MTT can be derived, it remains an approximation—progressively underestimated at higher extraction due to tracer

retention during acquisition. These findings encourage further evaluation of kinetic parameters beyond standard uptake metrics in dynamic amino acid PET. This approach may also be applied to a wider range of PET tracers to characterise blood-brain barrier transport, CBF and E, thereby increasing the probability of clinical translation. ***References:*** (1) Andersen, T. L., et al Diagnostics (2024). 14(15), Article 1590. (2) Larsson, H. B. W., et al EJNMMI.,(2024). 51(3), 707-720.

EP-0173

Features of PET/CT with fluoroethyltyrosine interpretation after proton radiation therapy of patients with IDH wildtype glioblastoma

E. Gromova, *N. Kataev, D. Susin, Nikolay Vorobyov, Marina Linnik, Natalia Berezina;*
LDC MIBS, Saint-Petersburg, RUSSIAN FEDERATION.

Aim/Introduction: To identify the features of PET/CT with fluoroethyltyrosine in patients with IDH wildtype glioblastoma who received proton therapy as part of adjuvant chemoradiation treatment. ***Materials and Methods:*** We evaluated 17 PET/CT c FET studies in 13 patients 3-18 (median 5.5, SD 12) months after proton therapy. PET/CT was performed at the decision of the neuro-oncologist for differential diagnosis of radionecrosis and tumor progression. PET-CT was performed according to the standard protocol: scanning 20 min after RFP injection, scanning time 20 min. The evaluation was performed by semi-quantitative method, with TBTmax calculation, as well as with comparison with MRI data and irradiation plans. Radiation therapy was delivered to all patients with a scanning pencil beam using 2 5/13 (38%) or 3 8/13 (62%) fields. In 10/13 (76.9%) cases, at least one of the fields was not coplanar. Two radiation therapy regimens were used: 45 Gray for 15 fractions and 60 Gray for 30 fractions (112.5-120.0 BED) Cases of RFP hyperfixation foci outside the initial volume of high (D95%) dose were considered separately - the zones of their occurrence, correlations between the necrosis site and the direction of proton therapy fields were determined separately. ***Results:*** In total, in 13 primary studies, 6 studies were interpreted as radionecrosis (TBRmax up to 2.4), 2 as disease progression (TBRmax 3.2) , 5 could not be interpreted unambiguously according to current guidelines and required dynamic follow-up. In two cases, we encountered cases of necrosis outside the original high volume (D95%). In both cases two fields were used, in one case coplanar. In both cases, radionecrosis occurred in the paraventricular regions of the lobar lobes (TBRmax 2.3). ***Conclusion:*** 1. TBRmax in cases diagnosed as radionecrosis is higher than in guidelines 2. Comparison with the radiation plan is important. 3. PET/CT before treatment to assess tumor metabolic activity - highly desirable.

EP-0174

Integrated ^{18}F-FET PET/MR-Based Multi-parametric Imaging for Predicting IDH Mutation and MGMT Promoter Methylation in Adult Gliomas

Q. Han[1], *J. Liu*[2], *T. Li*[1], *E. Li*[3], *Z. Lin*[4], *Y. Yang*[3], *X. Guo*[2], *Y. Wang*[2], *H. Xing*[2], *W. Ma*[2], *Y. Wang*[2], *X. Cheng*[1], *L. Huo*[1];
[1]Nuclear Medicine Department, Peking Union Medical College Hospital, Chinese Academy of Medical Science and Peking Union Medical College, Beijing, CHINA, [2]Department of Neurosurgery, Peking Union Medical College Hospital, Chinese Academy of Medical Sciences and Peking Union Medical College, Beijing, CHINA, [3]Beijing United Imaging Healthcare Co., Ltd, Beijing, CHINA, [4]United Imaging Healthcare Group Co., Ltd, Shanghai, CHINA.

Aim/Introduction: Gliomas are among the most common primary tumors of central nervous system (CNS), with high-grade subtypes showing poor prognosis despite standard treatment. The WHO classification of CNS tumors emphasizes molecular profiling, notably isocitrate dehydrogenase (IDH) mutation and O6-Methylguanine-DNA-methyltransferase (MGMT) promoter methylation, for prognostication and therapy guidance. As noninvasive tools for molecular stratification are needed, ^{18}F-FET PET and intravoxel incoherent motion (IVIM) MRI have shown promise in capturing tumor metabolism and heterogeneity. However, the influence of different volume-of-interest (VOI) delineation strategies on biomarkers performance remains unclear. This study aimed to investigate the diagnostic performance of integrated ^{18}F-FET PET/MR for predicting IDH and MGMT status using multi-parametric modeling across various VOI delineation strategies. ***Materials and Methods:*** This retrospective study included 45 patients with histopathologically confirmed gliomas who underwent preoperative integrated ^{18}F-FET PET/MR. Tumor VOIs were semi-automatically delineated from PET (biological tumor volume: BTV; metabolic tumor volumes at 60% and 80% of maximum standardized uptake value: MTV60, MTV80) and MRI (contrast-enhanced T1-weighted imaging: VOI-T1CE; T2 fluid-attenuated inversion recovery: VOI-T2F). PET parameters included maximum and mean tumor-to-background ratio (TBR_{max}, TBR_{mean}), and compartmental uptake ratio ($CU_{60/1.6}$, $CU_{80/1.6}$). A total of 126 IVIM-derived radiomic features were extracted from seven parametric maps: apparent diffusion coefficient (ADC), true diffusion coefficient (D), pseudo diffusion coefficient (D*), perfusion fraction (f), relative blood flow (rBF), distributed diffusion coefficient (DDC), and heterogeneity index (α). Logistic regression models were constructed using both single PET parameter and multi-parametric combinations, with LASSO-based feature selection via LASSO and ROC-based performance evaluation. ***Results:*** Different VOIs significantly affected tumor volume and spatial overlap ($P < 0.001$), with VOI-T2F exceeding BTV in 86.7% of cases. These differences influenced IVIM-derived features distributions. For IDH mutation, the MTV80-based IVIM multi-parametric model achieved the highest diagnostic performance (AUC = 0.937), further improved to 0.962 by adding PET parameters. For MGMT promoter methylation, the best performance was observed in BTV-based IVIM features model (AUC = 0.909), also enhanced with PET parameters integration (AUC = 0.928). TBR_{max} and IVIM-derived diffusion heterogeneity features (e.g., DDC minimum, DDC median) were key discriminative predictors. Univariate analyses confirmed significant groupwise differences in PET and diffusion metrics across molecular subgroups ($P < 0.05$). ***Conclusion:*** Integrated ^{18}F-FET PET/MR with VOI-specific IVIM features enables accurate noninvasive prediction of IDH mutation and MGMT promoter methylation. These findings highlight the clinical utility of integrated PET/MR multi-parametric modeling for molecular stratification and personalized treatment guidance in adult glioma.

EP-0175

Prognostic role of [^{18}F]FET PET/CT: integrating metabolic and molecular data in the management of gliomas

A. Castello[1], *G. A. Zuccotti*[2], *G. Lopez*[3], *G. Fiore*[4], *M. Schiavini*[1], *E. Galli*[1], *M. Arnaboldi*[1], *F. Buffoni*[1], *C. Pettinato*[5], *L. Savio*[6], *M. Locatelli*[4], *M. Caroli*[7], *M. Castellani*[1], *L. Florimonte*[1];
[1]Department of Nuclear Medicine, Fondazione IRCCS Ca' Granda, Ospedale Maggiore Policlinico, Milan, ITALY, [2]Unit of Nuclear Medicine, Aosta Regional Hospital, Aosta, Italy, Aosta, ITALY, [3]Division of Pathology, Fondazione IRCCS Ca' Granda, Ospedale Maggiore Policlinico, Milan, ITALY, [4]Unit of Neurosurgery, IRCCS Ca' Granda Foundation Ospedale Maggiore Policlinico, Milan, ITALY, [5]Medical Physics Unit, Fondazione IRCCS Ca Granda Ospedale Maggiore Policlinico, Milan, ITALY, [6]Department of Physics "Aldo Pontremoli", University of Milan, Milan, ITALY, [7]Unit of Neurosurgery, IRCCS Ca' Granda Foundation Ospedale Maggiore Policlinico, Milan, ITALY.

Aim/Introduction: Our study aimed to investigate the prognostic role of [^{18}F]FET PET/CT, analyzing metabolic parameters and molecular data in patients with gliomas. ***Materials and Methods:*** This prospective, single-center study included 98 patients

who underwent [18F]FET PET/CT imaging between September 2020 and November 2024. Metabolic parameters, including SUVmax, SUVmean, metabolic tumor volume (MTV), total tumor metabolism (TTM), tumor-to-brain ratio (TBR)max, and TBRmean, were assessed alongside molecular markers, such as IDH mutation, MGMT methylation, and TERTp mutation. Progression-Free Survival (PFS) and Overall Survival (OS) were evaluated using Kaplan-Meier survival analysis, and statistical significance was determined with log-rank tests over a mean follow-up of 15.1±13.7 months. ***Results:*** Patients with IDH wild-type gliomas exhibited higher SUVmax (4.42 vs. 3.32, p=0.019), SUVmean (2.39 vs. 1.82, p=0.014), TTM (25.14 vs. 14.13, p = 0.041) and TBRmax (4.21 vs. 3.22, p=0.046) compared to IDH-mutated gliomas. Moreover, IDH status was significantly associated with OS (14.97 months for IDH wild-type vs 43.86 months for IDH-mutated, p<0.001). in non-methylated MGMT promoter gliomas, metabolic parameters were significantly higher (SUVmax 6.06 vs. 3.51, p=0.008; TBRmean 3.07 vs. 1.97, p=0.018). Astrocytomas IDH-mutated with SUVmax (13.67 months vs 7.57 months, p=0.055), SUVmean (13.67 months vs 7.57 months, p=0.055), TBRmax (13.67 monthsvs 7.57 months, p=0.061), and TBRmean (18.7 months vs 7.97 months, p=0.026) above the median had a shorter PFS. On the other hand, in high-grade astrocytomas SUVmax, SUVmean, TBRmax and TBRmean below the median values were significantly associated with longer PFS. In patients with oligodendroglioma, TBRmax and TBRmean below the median value were associated with longer PFS (medianPFS 27.87 vs 10.88, p=0.024), Finally, glioblastomas with MGMT promoter methylation and TBRmax above the median exhibited shorter PFS (22.43 vs. 11.67 months, p=0.038). In this last group, TERTp mutation was associated with poorer PFS (11.67 vs. 31.77 months, p=0.035) and OS (14.9 vs. 19.9 months, p=0.043). ***Conclusion:*** [18F]FET PET parameters were associated with tumor grading and molecular profile, expressed by IDH status and MGMT methylation. In addition, SUVmax, SUVmean, TBRmax, TBRmean were prognostic factors for PFS both in astrocytomas IDH-mutated and high grade gliomas, whereas only TBRmean was prognostic in glioblastoma with MGMT promoter methylation. [18F]FET PET seems to offer valuable insights for glioma patients and whether integrated into clinical routine could aid clinicians for a better individualized glioma management. ***References:*** doi: 10.1016/j.radonc.2024.110386. doi: 10.1093/neuonc/noae208.

EP-0176

Improved AI Reporting of Amyloid PET with Location-Based Centiloids

B. Schemmer*;*
Katholisches Klinikum Bochum, Bochum, GERMANY.

Aim/Introduction: Quantification is an important part of assessment of Amyloid PET for the diagnosis of Alzheimers. However in general a global Centiloid value for the whole brain and corresponding reference regions is used. It is known that acquisition time and other parameters influence uptake in the reference regions as well as the brain structures themselves in a location specific manner. ***Materials and Methods:*** We developed a small AI based system that can segment the different brain regions using the CerebrA template and consider regional as well as acquisition based differences for each participant. ***Results:*** We found that a small system of interconnected AIs with at most 3-level deep binary classifiers was sufficiently complex to accommodate our problem. The AIs were trained independently on a standard thin client within minutes without the use or necessity for GPUs. We trained with a small collective of 20 patients from AMYPAD consortiums amyloid PET database limiting ourselves to patients that were sufficiently distinct when using the global Centiloid score (0-100 in steps of 5) with a total of 20 image slices per patient as well as 20 patients for which acquisition parameters are known precisely from our previous AI. An additional AI system was trained to localize brain regions according to the CerebrA atlas. ***Conclusion:*** The current system can classify the regions of amyloid deposition correctly and provide regional Centiloid values. In comparison to our previous fast AI classification system for automated Amyloid PET reporting, this current version can consider acquisition parameters, reducing uncertainty and improving comparability between sites and follow-up examinations. The speed of the system is slightly lower due to the increased number of AIs working in unison, however there is still no need for sophisticated hardware and reporting per patient can be finished in less than 100 ms per patient. ***References:*** Collij et. al.: Quantification Supports Amyloid PET Visual Assessment of Challenging Cases: Results from the AMYPAD Diagnostic and Patient Management Study. J Nucl Med 2025; 66:110-116. Manera et.al.: CerebrA, registration and manual label correction of Mindboggle-101 atlas for MNI-ICBM152 template. Scientific Data (2020) 7:237. Johns et. al.: Florbetaben amyloid PET acquisition time: Influence on Centiloids and interpretation. Alzheimer's Dement. 2024; 20:5299-5310.

EP-0177

Ga-68 PSMA-11 PET/CT in High-Grade Glioma Recurrence: Imaging, Prognosis, and Theranostic Implications

V. Arunachalam Ragupathi*, N. Damle, M. Tripathi, S. Shamim, V. Tandon, K. Haresh, S. Bharati, A. Kumar, S. Gupta, A. Singhal, S. Rastogi, A. Mohan;*
All India Institute of Medical Sciences, Delhi, INDIA.

Aim/Introduction: High-grade gliomas (HGG) are aggressive primary brain tumors with a high propensity for recurrence despite multimodal treatment. Prostate-specific membrane antigen (PSMA) has shown promising results in glioma imaging. This study aimed to assess Ga-68 PSMA-11 uptake in patients with suspected recurrent HGG using PET/CT imaging, with a view toward its potential application in PSMA-targeted theranostics. ***Materials and Methods:*** Patients with clinically and radiologically suspected recurrent HGG following surgery and chemoradiotherapy were prospectively enrolled. All participants underwent Ga-68 PSMA-11 PET/CT imaging 45-60 minutes after tracer injection, including whole-body and dedicated brain acquisitions. Lesion uptake was evaluated visually and semiquantitatively using a five-point Likert scale relative to liver and parotid gland uptake: 1 = no uptake, 2 = less than liver, 3 = equal to liver, 4 = greater than liver but less than parotid, and 5 = equal to or greater than parotid. Lesions with uptake more than or equal to liver were considered potentially suitable for PSMA-targeted therapy. Survival analysis stratified based on the lesion uptake (SUVmax). ***Results:*** Of the 24 enrolled patients (14 males, 10 females; median age 43 years, range 28-69), PSMA-avid lesions were identified in 21 patients (87.5%). Among these, 18 patients (85.7%) exhibited high PSMA expression (Likert score 4), while 3 demonstrated moderate uptake (Likert score 3). The median SUVmax and SUVmean for tumor lesions were 2.65 (IQR: 1.57-3.50) and 1.6 (IQR: 0.4-4.7), respectively. Five patients were lost to follow-up. Among the 19 remaining patients, the median survival was 4 months, and SUVmax >3.5 was significantly associated with poorer survival. Additionally, PSMA uptake correlated with regions of suspected recurrence on MRI, enhancing lesion visibility. ***Conclusion:*** Ga-68 PSMA-11 PET/CT reliably identifies PSMA expression in recurrent HGG, may help differentiate true tumor recurrence from post-treatment changes and predicts survival with higher SUVmax portends poorer prognosis, while targetable uptake supports PSMA-directed theranostics, offering a dual diagnostic-therapeutic strategy for this challenging disease context.

EP-0178

Amino Acid PET/CT in Assessing EGFR Gene Expression in CNS Gliomas

N. Vikhrova[1], *D. Kalaeva*[1,2], *S. Drozd*[1], *O. Kalennik*[1], *G. Pavlova*[1,3], *I. Pronin*[1];
[1]*National Medical Research Center for Neurosurgery named after N.N. Burdenko, Moscow, RUSSIAN FEDERATION,* [2]*National Research Nuclear University MEPhI, Moscow, RUSSIAN FEDERATION,* [3]*Institute of Higher Nervous Activity and Neurophysiology, Moscow, RUSSIAN FEDERATION.*

Aim/Introduction: The molecular and genetic features of CNS gliomas, as outlined in the 2021 WHO classification, present a significant challenge for radiologists - the non-invasive prediction of tumor biological behavior on primary amino acid PET/CT data. Epidermal growth factor receptor (EGFR) is one of the significant prognostic factor in guiding treatment decisions in glioma patients, after IDH-mutation. That prompted us to compare the data of morphological characteristics EGFRwt gene expression with CNS tumor metabolic characteristics. ***Materials and Methods:*** 71 adult patients with glial tumors (WHO 2021): glioblastoma (n=52), astrocytoma Grade3 (n=11) and oligodendroglioma Grade3 (n=8) were underwent static ^{11}C-methionine (n=41) and ^{18}F-FET (n=30) PET/CT. Tumor-to-brain ratio (TBR), metabolic tumor volume (MTV) were estimated in a standard way. MTV segmentation reference for both tracers was TBR=1,6. Metabolic data were compared with EGFRwt/EGFRvIII gene expression determined by PCR. ***Results:*** According to our data comparative analysis of EGFRwt gene expression in glioma with control group revealed significantly higher levels in glioblastomas with lower expression observed in oligodendrogliomas and astrocytomas. Significant positive correlation was found between level of EGFRwt gene expression and MTV (Rs=0.44, p=0.02). Moderate negative correlation between metabolic activity (TBR) and EGFRwt gene expression levels was detected in small astrocytoma group (n=11, Rs = -0,64, p=0,04). While there were no significant correlations in glioblastomas or oligodendrogliomas, this is likely due to high EGFRwt variability. EGFRvIII gene expression was detected in 25% gliomas (n=13, all glioblastomas), however, contrary to expectations, it doesn't show an association with metabolic parameters, possibly due to the small number of patients. ***Conclusion:*** High EGFR expression is generally associated with poor prognosis. Our findings demonstrate distinct EGFRwt gene expression patterns across glioma subtypes. The correlation between the level of EGFRwt gene expression and MTV indicating potential role of metabolic parameters on PET/CT as a prognostic markers, but further data collection and survival analysis are needed. The clinical implementation of EGFR blockade therapies has become a hallmark example of personalized targeted treatment and serving as a model for developing similar strategies in neuro-oncology. ***References:*** Oprita, A. et al. Updated Insights on EGFR Signaling Pathways in Glioma. Int. J. Mol. Sci. 2021,22(2):587.

EP-0179

Amino-acid PET imaging to monitor mIDH inhibitors treatments in patients with refractory IDH-mutant gliomas

G. Stien[1], *T. Obara*[2,3], *M. Blonski*[2,3], *L. Taillandier*[2,3], *A. Verger*[1,4,5];
[1]*Department of Nuclear Medicine, CHRU of Nancy, Nancy, FRANCE,* [2]*Department of Neurology, Neurooncology Unit, CHRU Nancy, Nancy, FRANCE,* [3]*Centre de Recherche en Automatique de Nancy CRAN, UMR 7039, Université de Lorraine, CNRS, Nancy, FRANCE,* [4]*IADI, U1254, Inserm, Université de Lorraine, Nancy, FRANCE,* [5]*Nancyclotep Imaging Platform, Université de Lorraine, Nancy, FRANCE.*

Aim/Introduction: Mutant IDH (mIDH) inhibitors represent a novel therapeutic approach for IDH-mutant gliomas. This study aims to evaluate the role of amino acid PET imaging in monitoring the response to mIDH inhibitor treatment in patients with refractory IDH-mutant gliomas, in comparison to conventional MRI. ***Materials and Methods:*** Patients with confirmed IDH-mutant gliomas who received ivosidenib or vorasidenib between February 2022 and November 2024, and who had a baseline ^{18}F-FDOPA PET scan available, were included in this study. All patients had received at least one prior line of systemic therapy. Lesions were assessed using RANO 2.0 and PET RANO criteria to determine measurability and, in patients with early follow-up imaging, to predict 6-month progression-free survival (PFS-6). ***Results:*** Twenty-two patients were included (mean age: 42.1 ± 10.5 years; 8 women; 14 with IDH-mutant astrocytomas). Among them, 11 underwent early follow-up imaging with both MRI and PET within the first 100 days of treatment. At baseline, MRI identified measurable lesions in 10 of 22 patients (45%), while amino acid PET identified lesions in 20 of 22 patients (91%) ($p < 0.01$). In patients with early follow-up, RANO 2.0 criteria predicted PFS-6 with 91% accuracy (10/11), compared to 82% accuracy (9/11) with PET RANO (not statistically significant). The only discordant case showed progression on PET but stability on MRI, with confirmed clinical progression at 10 months post-treatment initiation. ***Conclusion:*** Amino acid PET is a valuable tool for monitoring treatment with mIDH inhibitors in patients with refractory IDH-mutant gliomas, demonstrating performance at least comparable to that of MRI. Additionally, amino acid PET detects a greater number of measurable lesions than MRI, highlighting its complementary role in the treatment monitoring of IDH-mutant gliomas. ***References:*** 1. Wen PY, Van Den Bent M, Youssef G, Cloughesy TF, Ellingson BM, Weller M, et al. RANO 2.0: Update to the Response Assessment in Neuro-Oncology Criteria for High- and Low-Grade Gliomas in Adults. J Clin Oncol. 20 nov 2023;41(33):518799.2. Albert NL, Galldiks N, Ellingson BM, Van Den Bent MJ, Chang SM, Cicone F, et al. PET-based response assessment criteria for diffuse gliomas (PET RANO 1.0): a report of the RANO group. Lancet Oncol. janv 2024;25(1):e2941.

EP-0180

Mulit-Pinhole SPECT/CT in Meningioma Imaging: A New Diagnostic Perspective

G. Sipka[1], *K. Apro*[1], *A. Dobi*[2], *K. Hideghety*[2], *M. Balazsfi*[3], *P. Barzo*[3], *M. Szolikova*[4], *L. Pavics*[1], *Z. Besenyi*[1];
[1]*University of Szeged, Department of Nuclear Medicine, Szeged, HUNGARY,* [2]*University of Szeged, Department of Oncotherapy, Szeged, HUNGARY,* [3]*University of Szeged, Department of Neurosurgery, Szeged, HUNGARY,* [4]*Mediso Medical Imaging Ltd., Budapest, HUNGARY.*

Aim/Introduction: Meningiomas represent the most prevalent type of adult brain tumors. Despite their frequently benign nature and slow growth rate, these tumors exhibit a high rate of recurrence. The increased expression of the somatostatin receptor type 2 (SSTR 2) has led to the development of somatostatin analogues as targeted diagnostic and therapeutic modalities. This prospective study aims to evaluate and compare the diagnostic performance of SSTR SPECT/CT using both parallel-hole (PH) and multi-pinhole (MPH) collimators against the current gold standard MRI in patients with clinically progressive, histologically confirmed Grade I-III meningiomas. ***Materials and Methods:*** A total of 13 patients underwent SSTR-targeted SPECT/CT imaging with 99mTc-EDDA-HYNIC-TOC, utilizing a multi-pinhole collimator followed consecutively by a parallel-hole collimator acquisition. The resulting SPECT/CT scans were co-registered with contrast-enhanced T1-weighted MRI, with tumor delineation based on the MR images. A comparative analysis was conducted among the three imaging modalities in terms of lesion number, extent, and bone involvement. Semi-quantitative analysis was also performed, including assessment of lesion uptake (SUVmax, SUVmean) and tumor-to-background ratios (TBR). ***Results:*** MPH-SPECT/CT identified a total of 22 lesions, compared to 19 foci detected by contrast-enhanced MRI (86%) and only 16 lesions by parallel-hole

SPECT/CT (73%). The pathological confirmation of all 22 lesions was attained during the follow-up period (minimum 6 months) through the use of subsequent MRI or histological analysis. The use of MRI revealed the presence of multinodular meningiomas in three patients, while MPH-SPECT/CT led to the detection of two additional cases. Furthermore, MPH-SPECT/CT exhibited a marked increase in the extent of osseous involvement, identifying bone infiltration in nine lesions, in contrast to the four detected by MRI. Semi-quantitative analysis revealed significantly higher tracer uptake and tumour-to-background ratios in MPH studies relative to parallel-hole acquisitions (SUVmean: p = 0.001; SUVmax: p = 0.002; paired t-test). ***Conclusion:*** Our findings suggest that MPH-SSTR-SPECT/CT not only offers high diagnostic accuracy in the detection of meningiomas, but may also outperform contrast-enhanced MRI in evaluating lesion multiplicity and bone involvement. These results underscore the potential of advanced SPECT techniques to bridge the diagnostic gap between conventional SPECT and PET imaging. MPH-SPECT/CT may represent a viable alternative to PET in specific clinical scenarios, warranting further comparative studies.

EP-0181

Utility of Dynamic [^{68}Ga]Ga-PSMA PET/CT in post-surgical high-grade gliomas: An insight on preliminary Analysis

M. Usmani, *K. al Riyami, S. Hashmi, A. Jain, S. Kheruka, V. Jayakrishnan, A. al busaidi, Z. Al-Mandhari;*
Sultan Qaboos Comprehensive Cancer Care and Research Center (SQCCCRC), University Medical City, Muscat, OMAN.

Aim/Introduction: High-grade gliomas (HGG) are aggressive brain tumors that arise from the glial cells in the brain. Accurate post-surgery detection of residual gliomas is vital for managing HGG and guiding treatment, including radiotherapy. Previous research demonstrates PSMA expression in neovascularization related to these tumors. The aim of this study is to assess the feasibility of early dynamic [^{68}Ga]Ga-PSMA PET/CT in detecting residual gliomas. ***Materials and Methods:*** A total 9 patients (mean age, 46±9.7 years) with HGG post resection underwent dynamic [^{68}Ga]Ga-PSMA PET/CT with an activity of 2.2MBq/kg. Dynamic images were acquired over the skull with a frame time of 20 sec for 10 min for extraction of time-activity curves (TACs) within selected volumes of interest. Static images of 10 min per bed position were acquired at 60 min post injection. ***Results:*** All patients showed high target to non-target ratio in the early dynamic images comparable to that seen on the delayed images. SUVmax of the glioma lesion was significantly higher than that of background throughout the dynamic study at all time points (P <0.001). In dynamic images the glioma lesions have radioactive concentration of 4.06±1.43 KBq/ml and SUV max 3.21±0.97 in comparison with contralateral brain parenchyma 0.40±0.49 KBq/ml and SUV max 0.16±0.22. Static images showed more tracer accumulation than dynamic images in the residual tumor. On delayed static images glioma lesions showed SUVmax 5.65±1.5 and SUV mean 3.08±0.85. The tumor to background brain ratio was 58.8±15.23. Semi-quantitative analyses show PSMA-tumor volume (TV)= 19.1±15.0cm^3 and total tumor burden (T PSMA burden)= 52.63±44.6. Preliminary findings suggest that dynamic [^{68}Ga]Ga-PSMA PET show excellent visualization of glioma lesions and provides valuable complementary information in the imaging of residual high-grade gliomas. ***Conclusion:*** Our initial experience suggests that dynamic [^{68}Ga]Ga-PSMA PET offer additional characterizing of tumor angiogenesis. Moreover, it allows quantitative assessment of perfusion and PSMA expression in high grade glioma. Early dynamic images may be conducted in combination with the routine 60 min static acquisition in patients with high grade gliomas. Further investigation with larger cohorts and correlation with clinical outcomes is warranted to validate these initial findings.

EP-0182

Meningioma Risk Stratification: Association Between Molecular-Morphologic Score and Somatostatin Receptor Expression on PET Imaging.

A. Chaban[1], *O. Kertels*[2], *C. Ertelt-Delbridge*[3], *D. Bernhardt*[4], *F. Schmidt-Graf*[5], *B. Wiestler*[2], *C. Negwer*[6], *I. Yakushev*[1];
[1]*Klinik und Poliklinik für Nuklearmedizin, Klinikum rechts der Isar, Technische Universität München, Munich, GERMANY,* [2]*Institut für Diagnostische und Interventionelle Neuroradiologie, Klinikum rechts der Isar, Technische Universität München, Munich, GERMANY,* [3]*Institut für Allgemeine Pathologie und Pathologische Anatomie, Klinikum rechts der Isar, Technische Universität München, Munich, GERMANY,* [4]*Klinik und Poliklinik für RadioOnkologie und Strahlentherapie, Klinikum rechts der Isar, Technische Universität München, Munich, GERMANY,* [5]*Klinik und Poliklinik für Neurologie, Klinikum rechts der Isar, Technische Universität München, Munich, GERMANY,* [6]*Klinik und Poliklinik für Neurochirurgie, Klinikum rechts der Isar, Technische Universität München, Munich, GERMANY.*

Aim/Introduction: The recently proposed integrated molecular-morphologic meningioma score (MMS) has demonstrated superior predictive value for tumor recurrence compared to conventional WHO grading. This study investigates, for the first time, the association between MMS and somatostatin receptor (SSR) expression as quantified by PET imaging. ***Materials and Methods:*** Our institutional database was searched for patients who underwent postoperative SSR-PET imaging for residual meningioma assessment and for whom MMS data were available. Only patients with measurable residual tumor as defined by established routines - isocontour volume-of-interest (40% SUVmax threshold) with a minimum volume of 0.5 ml - were included. PET-derived parameters included unscaled SUVmax, SUVmean as well as their ratios scaled to the superior sagittal sinus and contralateral meninges. ***Results:*** Thirty patients were included, all diagnosed with WHO grade 2 meningioma. Based on MMS, patients were stratified into low- (n=4), intermediate- (n=19), and high-risk (n=7) groups. Most PET parameters were non-normally distributed (Kolmogorov-Smirnov test, p<0.05). All PET parameters showed a positive correlation with MMS (p<0.05), with the strongest association observed for unscaled SUVmax of meningiomas (Spearman's r = 0.64, p<0.001). ***Conclusion:*** Our findings reveal a significant, positive associationbetween the molecular-morphologic properties and SSR expression on PET imaging. These results support the potential of PET-based biomarkers to improve risk stratification and guide personalized treatment strategies. Further data collection is ongoing to define clinically meaningful PET-based thresholds.

EP-0183

Positron emission tomography (PET) use in neuro-oncology among European Organisation for Research and Treatment of Cancer - Brain Tumour Group (EORTC-BTG) sites

M. Mair[1,2], *P. Lohmann*[3,4], *N. Galldiks*[5,3], *M. Belting*[6,7], *P. Brandal*[8,9], *M. P. G. Broen*[10], *F. Cicone*[11], *J. Daisne*[12], *F. Ducray*[13,14], *F. Ehret*[15,16], *J. Furtner*[17], *A. S. Jakola*[18,19], *M. Niyazi*[20], *A. Pellerino*[21], *M. Rasschaert*[22], *E. Razis*[23], *F. Sahm*[24], *M. Smits*[25,26], *N. Tolboom*[27], *A. Verger*[28], *E. Le Rhun*[29], *G. Minniti*[30,31], *M. Weller*[32], *M. Preusser*[2], *N. L. Albert*[1];
[1]*Department of Nuclear Medicine, LMU University Hospital, LMU Munich, Munich, GERMANY,* [2]*Division of Oncology, Department of Medicine I, Medical University of Vienna, Vienna, AUSTRIA,* [3]*Institute of Neuroscience and Medicine (INM-3, INM-4), Research Center Juelich, Juelich, GERMANY,* [4]*Department of Nuclear Medicine, RWTH Aachen University Hospital, Aachen, GERMANY,* [5]*Department of Neurology, Faculty of Medicine and University Hospital Cologne, Cologne, GERMANY,* [6]*Division of Oncology, Department of Clinical Sciences, Lund University, Lund, SWEDEN,* [7]*Department of Hematology, Oncology and Radiophysics, Skåne University Hospital, Lund, SWEDEN,* [8]*Department of Oncology, Oslo University Hospital, Oslo, NORWAY,* [9]*Institute for Clinical Medicine, University of Oslo, Oslo, NORWAY,* [10]*Department of Neurology, GROW School for Oncology and Reproduction, Maastricht University Medical Centre, Maastricht, NETHERLANDS,*

[11]Nuclear Medicine Unit, Department of Experimental and Clinical Medicine, "Magna Graecia" University of Catanzaro, Catanzaro, ITALY, [12]Department of Radiation Oncology, Iridium Cancer Network, Wilrijk (Antwerp), BELGIUM, [13]Department of Neurooncology, Hôpital Neurologique Pierre Wertheimer, Hospices Civils de Lyon, Bron, FRANCE, [14]Université Claude Bernard Lyon 1, Villeurbanne, FRANCE, [15]Charité – Universitätsmedizin Berlin, Corporate Member of Freie Universität Berlin and Humboldt-Universität zu Berlin, Department of Radiation Oncology, Berlin, GERMANY, [16]German Cancer Consortium (DKTK), partner site Berlin, a partnership between DKFZ and Charité – Universitätsmedizin Berlin, Berlin, GERMANY, [17]Research Center for Medical Image Analysis and Artificial Intelligence (MIAAI), Faculty of Medicine and Dentistry, Danube Private University, Krems, AUSTRIA, [18]Department of Neurosurgery, Sahlgrenska University Hospital, Gothenburg, SWEDEN, [19]Institute of Neuroscience and Physiology, Department of Clinical Neuroscience, Sahlgrenska Academy, Gothenburg, SWEDEN, [20]Department of Radiation Oncology, University Hospital Tuebingen, Tuebingen, GERMANY, [21]Division of Neuro-Oncology, Department of Neuroscience "Rita Levi Montalcini", University and City of Health and Science Hospital, Torino, ITALY, [22]Department of Medical Oncology, University Hospital Antwerp, Edegem, BELGIUM, [23]Third Department of Medical Oncology, Hygeia Hospital, Athens, GREECE, [24]Department of Neuropathology, Institute of Pathology, Clinical Cooperation Unit Neuropathology, Ruprecht-Karls University Heidelberg, and German Consortium for Translational Cancer Research (DKTK), German Cancer Research Center (DKFZ), Heidelberg, GERMANY, [25]Department of Radiology & Nuclear Medicine, Erasmus MC, University Medical Centre Rotterdam, Rotterdam, NETHERLANDS, [26]Brain Tumour Centre, Erasmus MC Cancer Institute, Rotterdam, NETHERLANDS, [27]Department of Radiology and Nuclear Medicine, University Medical Centre Utrecht, Utrecht, NETHERLANDS, [28]Department of Nuclear Medicine & Nancyclotep Imaging Platform, CHRU Nancy and IADI INSERM, UMR 1254, Université de Lorraine, Nancy, FRANCE, [29]Department of Medical Oncology and Hematology, Brain Tumor Center, University Hospital and University of Zurich, Zurich, SWITZERLAND, [30]Department of Radiological Sciences, Oncology and Anatomical Pathology, Sapienza University of Rome, Rome, ITALY, [31]IRCCS Neuromed, Pozzilli (IS), ITALY, [32]Department of Neurology and Brain Tumor Center, University Hospital and University of Zurich, Zurich, SWITZERLAND.

Aim/Introduction: Few systematic data exist on the use of positron emission tomography (PET) among brain tumour centers in Europe. ***Materials and Methods:*** From June 2024 to August 2024, a cross-sectional survey was conducted among European Organisation for Research and Treatment of Cancer - Brain Tumour Group (EORTC-BTG) sites to gain insights into the availability and use of PET across brain tumor centers in Europe. ***Results:*** Out of the 312 invited sites, 103 replies were received from 20 countries. PET was available at 96/103 (93.2%) sites, and 74 of these reported PET use in patients with brain tumours. Glioma was the entity in which PET was most frequently performed (69/74, 93.2%), followed by brain metastasis (58/74, 78.4%), meningioma (52/74, 70.3%), and CNS lymphoma (46/74, 62.2%). Amino acid PET was used at 62/71 sites (87.3%), predominantly in glioma (58/59, 98.3%) and for differentiating treatment-related changes from tumor progression (58/59, 98.3%). Use of dynamic acquisition protocols was reported by 35/59 (59.3%) centres, and most sites reported use of [^{18}F]FET as amino acid tracer (45/59, 76.3%), followed by [^{18}F]FDOPA (22/59, 37.3%) and [^{11}C]methionine (15/59, 25.4%). Somatostatin receptor (SSTR) PET was applied at 50/68 sites (73.5%), predominantly in meningioma (48/49, 98.0%), and mainly for patient selection before radioligand therapy (41/49, 83.7%) as well as for target volume definition in radiotherapy (33/49, 67.3%). According to self-reported information, PET was covered by statutory health insurance at 46/59 (78.0%) centers for amino acid PET and 33/49 (67.3%) for SSTR PET. Reasons for not using PET in clinical routine included limited availability of tracers (14/29, 48.3%), high cost (11/29, 37.9%), and a perceived lack of added value (8/29, 27.6%). ***Conclusion:*** Overall, PET is already widely used among EORTC BTG sites, although non-response and selection biases must be considered in the interpretation of survey results. While these findings support the implementation of PET-based endpoints in clinical trials, comprehensive surveys also covering non-academic centers would be needed to guide further implementation in clinical routine.

EP-0184

Diagnostic accuracy of FET-PET/CT for the differential diagnosis of recurrent brain metastases versus radionecrosis

N. Testart Dardel, *N. Schilliger, K. Auf Der Springe, M. Nicod-Lalonde, N. Schaefer, J. Prior, M. Jreige;*
CHUV, Lausanne, SWITZERLAND.

Aim/Introduction: O-(2-18F-fluoroethyl)-L-tyrosine (FET) PET/CT is a well-known complementary tool for the follow-up of brain gliomas. However, less evidence exists for irradiated brain metastases with doubtful MRI. We aimed to review our center's experience with digital FET PET/CT as an additional tool in the follow-up of brain metastases for differentiating between tumor recurrence and radiation necrosis (RN), and to determine its diagnostic accuracy. ***Materials and Methods:*** Retrospective analysis of consecutive n=29 patients with previously irradiated brain metastases in the last 5 years and who underwent a FET-PET/CT in a digital device, with subsequent MRI and follow-up at CHUV. We performed semiquantitative measurements at the lesion-level (SUVmax, SUVmean, tumor-to brain ratios TBRmax, TBRmean using contralateral normal brain's SUVmean). Diagnostic accuracy was determined using the literature's TBRmax cutoff of 3.11*. Receiver operating characteristic (ROC) curves were analyzed to derive the optimal TBRmax threshold in our population. The final diagnosis was determined on a per lesion basis using either biopsy or >3-month imaging follow-up. ***Results:*** We performed a per-lesion analysis (n=74) with a final diagnosis of 29 metastases and 45 RN, established by histology (n=13) or by MRI (6-month median follow-up, n=61). Metastases demonstrated significantly higher values than RN for SUVmax (5.3±1.0 vs. 3.7±1.0), SUVmean (2.8±0.8 vs. 2.2±0.6), TBRmax (3.8±0.9 vs. 2.5±0.7), and TBRmean (2.0±0.5 vs. 1.5±0.4) (all p<0.001). The previously reported TBRmax=3.11 cutoff value was confirmed as optimal in our study population, achieving a 81% [95%CI 58-93] sensitivity, 89% [71-97] specificity, and area under the curve (AUC) 0.89 [0.78-0.96] for distinguishing metastases from RN. ***Conclusion:*** We achieved high accuracy of FET-PET/CT in the follow-up of patients with irradiated brain metastases with an optimal cutoff value of TBRmax = 3.11 in our digital PET/CT device. ***References:*** Lohmann et al. Radiation injury vs. recurrent brain metastasis: combining textural feature radiomics analysis and standard parameters may increase 18F-FET PET accuracy without dynamic scans. Eur Radiol. 2017 Jul;27(7):2916-2927. doi: 10.1007/s00330-016-4638-2.

EP-13

e-Poster Area

B: Imaging Clinical Studies -> B1 Oncological Imaging Clinical Study -> B12 Head and Neck

EP-0186

^{68}Ga-FAPI-04 PET/CT For Predicting Pathological Response of Cervical Lymph Node Metastases to Neoadjuvant Chemoimmunotherapy in Locally Advanced Oral Squamous Cell Carcinoma

Y. Jiang[1], *Z. Yu*[2], *Y. Sun*[3], *L. Wang*[3], *J. Jia*[2], *Y. He*[1];
[1]*Department of Nuclear Medicine, Zhongnan Hospital of Wuhan University, Wuhan, CHINA,* [2]*Department of Oral and Maxillofacial Surgery, School and Hospital of Stomatology, Wuhan University, Wuhan, CHINA,* [3]*Department of Pathology, School and Hospital of Stomatology, Wuhan University, Wuhan, CHINA.*

Aim/Introduction: Nonspecific lymph node uptake on ^{18}F-FDG PET/CT following immunotherapy has emerged as a diagnostic

challenge in nodal restaging. FAPI-based radiotracers have shown excellent diagnostic specificity for lymph node metastasis in head and neck cancer. This study aimed to investigate the performance of ^{68}Ga-FAPI-04 PET/CT in restaging cervical lymph nodes after neoadjuvant chemoimmunotherapy (NACI) in patients with locally advanced oral squamous cell carcinoma (LAOSCC). ***Materials and Methods:*** Twenty treatment-naïve patients with LAOSCC (clinical stage III-IVA) underwent two cycles of NACI followed by radical surgery. ^{68}Ga-FAPI-04 PET/CT was performed at baseline and after the second cycle of NACI, prior to surgery. Cervical lymph nodes were categorized as pathologic complete response (pCR) and non-pCR based on postoperative histopathology. The maximum standardized uptake value (SUVmax) of visually identified FAPI-avid cervical lymph nodes was measured, and the percentage change (ΔSUVmax, %) between baseline and post-NACI scans was calculated. PET parameters were compared between the pCR and non-pCR groups and further analyzed to assess their correlation with pathologic response. FAPI PET-based nodal restaging was also evaluated, with pathologic findings as the reference standard. ***Results:*** A total of 789 lymph nodes were resected from the 20 enrolled patients, with 53 histologically confirmed as metastatic lymph nodes. In lesion-based analysis, 13 lymph nodes from 9 patients demonstrated pCR. These lymph nodes demonstrated a significantly lower post-NACI SUVmax (2.78 ± 1.81) compared with baseline values (10.12 ± 5.99, P = 0.001). In contrast, non-pCR lymph nodes showed no significant difference between baseline and post-NACI SUVmax (8.61 ± 4.91 vs 9.10 ± 4.15, P = 0.462). The absolute ΔSUVmax was significantly greater in pCR nodes than showed in non-pCR nodes (-70.53% ± 10.77 vs 3.99%, [−50.23%, 418.67%]; P < 0.001). Baseline SUVmax showed no significant correlation with pathologic response (r = 0.133, P = 0.390). In contrast, both post-NACI SUVmax (r = −0.630, P < 0.001) and ΔSUVmax (r = −0.468, P = 0.001) demonstrated significant negative correlations with pathologic response. In the 20 enrolled patients, FAPI PET-based restaging of cervical lymph nodes demonstrated histopathologic concordance in 16 cases (80%). Notably, post-NACI PET revealed no new ipsilateral FAPI-avid lymph node, unlike FDG, which often shows such findings that are rarely indicative of disease progression or metastasis. ***Conclusion:*** ^{68}Ga-FAPI-04 PET/CT demonstrated high diagnostic accuracy in nodal restaging after NACI and showed potential for evaluating the therapeutic response of cervical lymph nodes in LAOSCC patients.

EP-0187

Predictive value of ^{68}Ga-FAPI-04 PET/CT for assessing pathologic response to neoadjuvant chemoimmunotherapy in locally advanced resectable oral squamous cell carcinoma

Y. Jiang[1], *J. Jia*[2], *Z. Yu*[2], *Y. Sun*[3], *Y. Tian*[1], *Y. He*[1];
[1]*Department of Nuclear Medicine, Zhongnan Hospital of Wuhan University, Wuhan, CHINA,* [2]*Department of Oral and Maxillofacial Surgery, School and Hospital of Stomatology, Wuhan University, Wuhan, CHINA,* [3]*Department of Pathology, School and Hospital of Stomatology, Wuhan University, Wuhan, CHINA.*

Aim/Introduction: This study aimed to investigate the predictive value of ^{68}Ga-FAPI-04 PET/CT for assessing pathologic response to neoadjuvant chemoimmunotherapy (NACI) in patients with resectable locally advanced oral squamous cell carcinoma (LAOSCC). ***Materials and Methods:*** Thirty-one treatment-naïve patients with pathologically confirmed OSCC and clinically staged locally advanced disease (stage III-IVA) were prospectively enrolled. Among them, twenty patients completed two cycles of NACI, consisting of anti-PD-1 antibody combined with albumin paclitaxel and cisplatin, followed by radical surgery. ^{68}Ga-FAPI-04 PET/CT was performed at baseline and after the second cycle of NACI, immediately prior to surgery, to assess treatment response. Patients were categorized into major pathological response (MPR) and non-MPR groups based on postoperative histopathological results. Semiquantitative PET parameters for the primary tumour, SUVmax, SUVmean, SUVpeak, and their percentage changes (ΔSUVs, %) were recorded. These parameters were compared between the two groups, and their correlation with pathologic response, PD-L1, fibroblast activation protein (FAP), granzyme B (GZMB) expression, and CD8+ T cells infiltration in the tumour tissues was also analyzed. ***Results:*** Twenty patients were included in the final analysis. Eight patients (40.0%) achieved MPR, including 6 with pathologic complete response (pCR), while 12 patients (60.0%) were categorized as non-MPR. The average preoperative SUVmax was significantly lower in the MPR group (9.38 ± 2.60) compared with that in the non-MPR group (16.20 ± 5.23; P = 0.003), while baseline SUVmax was not significantly different (P = 0.053). The absolute ΔSUVmax value in the MPR group (−59.10% ± 13.33) was notably higher than that in the non-MPR group (−15.96%, [−52.56%, 66.33%]; P = 0.002). Preoperative SUVs and ΔSUVs were significantly associated with pathologic response. FAP expression positively correlated with preoperative SUVs, and the MPR group demonstrated higher expression of CD8 and GZMB compared to the non-MPR group. ***Conclusion:*** ^{68}Ga-FAPI-04 PET/CT parameters are able to well predict the achievement of MPR following NACI in patients with LAOSCC. ΔSUVs are identified as significant predictors of MPR. These findings warrant validation in larger cohorts.

EP-0188

Imaging-Detected Lymph Node Metastases (iLNM) and Extranodal Extension (iENE) as Prognostic Factors in HPV-Related Oropharyngeal Squamous Cell Carcinoma: FDG-PET/CT and Node-RADS-Based Evaluation

S. Tsukamoto*, S. Koyasu, C. Suzuki, K. Nakatani, Y. Kishimoto, Y. Nakamoto;*
Kyoto University Hospital, Kyoto, JAPAN.

Aim/Introduction: Human papillomavirus (HPV)-positive oropharyngeal squamous cell carcinoma (OPSCC) is established as a distinct entity in the 8th edition of the UICC TNM classification. While extranodal extension is an adverse prognostic factor in HPV-negative (p16-negative) OPSCC, it is not incorporated in the HPV-positive (p16-positive) OPSCC staging system. Furthermore, there is a discrepancy between pathological and clinical N staging in p16-positive OPSCC: pathology is based merely on the number of lymph node metastases (0, 1-4, or 5-), while clinical staging is mainly based on laterality and size. This study aimed to investigate the prognostic value of the imaging-detected lymph node metastases (iLNM), which we defined by the combination of FDG-PET/CT and Node-RADS (1), and extranodal extension (iENE) in patients with HPV-positive OPSCC. ***Materials and Methods:*** We retrospectively included consecutive patients with p16-positive OPSCC treated at Kyoto University Hospital between January 2014 and December 2024. Patients with recurrent disease or without pre-treatment FDG-PET/CT were excluded. Two readers evaluated images and measured SUVmax of each suspicious lymph node. iLNM was defined as the number of lymph nodes with SUVmax ≥3.5 (2) or Node-RADS score ≥3. iENE was assessed according to Head and Neck Cancer International Group criteria (3). Cox proportional hazards regression was used for univariable and multivariable analyses of overall survival (OS) and event-free survival (EFS: recurrence or death from the index cancer). Additionally, each case was dichotomized based on the highest SUV value (cutoff: 10.2) among the lesions. ***Results:*** Sixty-nine patients were analyzed. The OS and EFS rates were 84.0% and 81.2%, respectively. SUVmax ≥10.2 (HR 1.6; 95%CI: 0.5-5.5; p=0.45) did not show statistical significance in OS and EFS. In univariable analysis, iLNM ≥5 (HR 6.7; 95%CI: 1.8-24.6; p=0.004) and higher cStage (II or III, HR 3.8; 95%CI: 1.1-13.3; p=0.03) were significantly associated with worse OS. In multivariable analysis, iLNM ≥5 remained an independent prognostic factor in OS (HR 4.7; 95%CI: 1.2-18.3; p=0.02). Regarding EFS, iLNM ≥5 (HR 4.5; 95%CI: 1.4-14.8; p=0.01) and iENE grade ≥2 (HR 3.5; 95%CI: 1.1-11.5; p=0.04) were significant in univariable analysis, but not in multivariable analysis. ***Conclusion:*** The imaging parameter iLNM, defined by FDG-PET/CT and Node-RADS, was an independent predictor of

OS in patients with p16-positive OPSCC. iLNM ≥5 and iENE grade ≥2 were also poor prognostic factor in EFS in univariable analysis. ***References:*** 1. Elsholtz FHJ, et al. Eur Radiol. 2021;31:6116.2. Subramaniam RM, et al. J Nucl Med. 2022;63:1887.3. Henson C, et al. Lancet Oncol. 2024;25:e297.

EP-0189

^{18}F-PSMA and ^{18}F-FDG PET/CT in Head and Neck Squamous Cell Carcinoma: A comparative Analysis

V. Heringer, *H. S. V. Sousa, L. T. Macedo, N. A. A. Silveira, S. Kuba, C. S. P. Lima, C. D. Ramos;*
UNICAMP, Campinas, BRAZIL.

Aim/Introduction: ^{18}F-fluorodeoxyglucose PET/CT is widely used for staging and monitoring Head and Neck Squamous Cell Carcinoma (HNSCC). However, its specificity is limited due to false-positive findings from inflammatory processes. PET/CT with Prostate-Specific Membrane Antigen (PSMA) has been investigated as an alternative to ^{18}F-FDG PET/CT due to its expression in tumor neovasculature; however, its role in HNSCC remains unclear. This study aimed to evaluate ^{18}F-PSMA-1007 PET/CT uptake patterns in HNSCC in comparison to ^{18}F-FDG PET/CT, exploring their potential for tumor characterization, staging, and monitoring. ***Materials and Methods:*** Patients with locally advanced HNSCC, either at initial diagnosis or with recurrent disease, were included. Individuals who had undergone surgical tumor resection or received chemotherapy and/or radiotherapy within the previous six months were excluded. All participants underwent both ^{18}F-FDG PET/CT and ^{18}F-PSMA-1007 PET/CT imaging, with a 24-hour interval between scans. Image interpretation was independently performed by two nuclear medicine physicians and one radiologist. ***Results:*** Fourteen patients (11 male) with a median age of 61 (49-81) years were studied. Most patients were current or former smokers and alcohol consumers, had good performance status (ECOG 0), and presented with stage IV tumors. The primary tumors were located in the oropharynx, larynx, and oral cavity, with one sinonasal tumor. Recurrences were observed in locoregional lymph nodes, lungs, and bones. HNSCC lesions were typically characterized by FDG uptake, although most lesions also exhibited varying degrees of PSMA uptake. In primary tumors and nodal disease, the mean ± SD and median (range) SUV values obtained with FDG PET/CT at 1 hour were 25.6 ± 16.4 and 21.0 (10.7-59.8), and 11.7 ± 7.7 and 8.6 (2.7-26.4), respectively. For PSMA PET/CT, the mean ± SD and median (range) SUV values at 1 hour in primary tumors and nodal disease were 4.5 ± 1.3 and 4.3 (2.9-6.3), and 4.9 ± 2.6 and 3.9 (2.8-10.2), respectively. FDG uptake values were higher than PSMA uptake values in primary tumors ($P < 0.001$) and lymph nodes ($P = 0.01$). ***Conclusion:*** ^{18}F-FDG demonstrates superior sensitivity in detecting HNSCC tumor activity. However, frequent ^{18}F-PSMA uptake indicates concurrent glycolytic metabolism and neoangiogenesis, supporting a possible complementary role of integrating ^{18}F-FDG and ^{18}F-PSMA PET in tumor assessment. More pronounced PSMA expression in select cases suggests potential use of PSMA-targeted theranostics and anti-angiogenic therapies. Further studies are needed to clarify the clinical significance of PSMA expression and angiogenesis in HNSCC biology.

EP-0190

Prognostic Assessment in Nasopharyngeal Carcinoma Patients without distant metastases: Development and Validation of a Multidimensional Prognostic Nomogram integrating ^{18}F-FDG PET/CT Parameters, Inflammation Markers, and Clinical Characteristics

Y. Lv[1,2,3], *D. Zheng*[1,2,3], *R. Wang*[4], *Z. Zhou*[1,2,3], *Z. Dai*[1,2,3], *S. Wei*[1,2,3], *Z. Gao*[1,2,3], *X. Lan*[1,2,3], *C. Qin*[1,2,3];
[1]*Department of Nuclear Medicine, Union Hospital, Tongji Medical College, Huazhong University of Science and Technology, Wuhan, CHINA,* [2]*Hubei Key Laboratory of Molecular Imaging, Wuhan, CHINA,* [3]*Key Laboratory of Biological Targeted Therapy, the Ministry of Education, Wuhan, CHINA,* [4]*Department of Radiology, The First Affiliated Hospital of Zhejiang University School of Medicine, Hangzhou, CHINA.*

Aim/Introduction: To investigate and compare the prognostic significance of ^{18}F-FDG PET/CT quantitative parameters and develop a comprehensive nomogram prediction model by integrating blood inflammatory markers and clinicopathological characteristics in stage I-IVa nasopharyngeal carcinoma (NPC) patients. ***Materials and Methods:*** Data of 86 stage I-IVa NPC patients who underwent ^{18}F-FDG PET/CT before treatment between 2018 and 2019 were retrospectively collected. We analyzed ^{18}F-FDG PET parameters of the primary tumor and clinicopathologic parameters, including traditional PET parameters (SUVmax, SUVmean, SUVpeak, MTV, and TLG), heterogeneity indices (CV40% = SD of SUV/SUVmean; HI = SUVmax/SUVmean; and HF, calculated as the derivative of the volume-threshold function from 30% to 50%), blood inflammatory markers (systemic immune-inflammation index SII, systemic inflammation response index SIRI, and neutrophil-to-lymphocyte ratio NLR), and clinical characteristics (age, gender, TNM staging, and treatment strategy). The correlation among PET parameters was evaluated with Spearman's rho test. ROC curve was used to evaluate the predictive performance and calculate the best cut-off values. Survival analyses used the Kaplan-Meier analysis and log-rank test. Univariate and multivariate COX regression analyses screened independent PFS correlated prognostic factors. Subsequently, a prognostic nomogram model was developed and internally validated. ***Results:*** HF correlated highly with MTV ($r = 0.88$, $P < 0.01$), while other PET heterogeneity indices had weak to mild or no correlations with traditional parameters. HF and MTV exhibited good predictive value for 1-year, 3-year, and 5-year PFS (HF: AUC = 0.817, 0.678, and 0.672; MTV: AUC = 0.866, 0.685, and 0.670), with the best prognostic efficacy for 1-year PFS. HF, MTV, TLG, SII, SIRI, NLR, overall stage, and whether concurrent chemoradiotherapy were significantly associated with 5-year PFS. HF (HR=2.70, 95%CI: 1.05-6.95), SII (HR=2.60, 95%CI: 1.02-6.61), overall stage (HR=2.70, 95%CI: 1.06-6.81), and concurrent chemoradiotherapy (HR=0.69, 95%CI: 0.11-0.80) were independent prognostic factors for 5-year PFS, respectively, with all P values < 0.05. The nomogram showed that the prognostic model had high 5-year PFS predictive ability, with an AUC of 0.827 and a C-index of 0.776. In addition, the calibration curves showed good agreement between the predicted probabilities and actual observations and decision curve analysis (DCA) suggested that the nomogram was useful for clinical decision-making. ***Conclusion:*** HF strongly correlates with MTV and has prognostic value for PFS, especially for 1-year PFS. A novel multifactor nomogram integrating HF, SII, overall stage, and concurrent chemoradiotherapy shows superior prognostic predictive performance, improving accuracy and enabling personalized assessment in managing I-IVa stage NPC patients.

EP-0191

"Ultra-Low-Dose ^{18}F-FDG PET With Ultra-Low-Dose CT" Based Radiomic Features And Machine Learning In Non-Invasive Characterization Of Suspicious Lung Lesions

P. Singh, *T. Singhal, S. K. Gupta, R. Kumar, N. Singh, H. Singh, B. R. Mittal;*
PGIMER, Chandigarh, INDIA.

Aim/Introduction: Lung cancer (LCa) is second most prevalent malignancy and most common cause of cancer-related death world-wide. However, lung nodules seen on CT are commonly benign (88-99%). even in high-risk patients. Thus, we here-by tried to evaluate the role of "ultra-low-dose ^{18}F-FDG PET with ultra-low-dose CT" derived radiomic features(RFs) and machine learning models(MLMs) to accurately characterise suspicious lung lesions delivering overall similar/lesser radiation dose as compared to LCa screening CT. ***Materials and Methods:*** Patients with suspicious lung lesions who underwent Ultra-low-dose ^{18}F-FDG PET with Ultra-low-dose CT were included in the study. Experienced Nuclear Medicine physicians manually delineated regions of interest(ROIs),

and intensity-threshold restrictions of 25% and 35% were applied to create three distinct sets of ROIs and high-dimensional RF were extracted using LIFEx(v7.8).Univariate analysis was applied to each RF, using area-under-curve(AUC) of receiver-operator-curve(ROC) and p-value computed by Mann-Whitney-U test. p-value <0.05 was considered significant. PET/CT guided biopsy delivered Histopathological examination(HPE) was taken as the gold standard. RFs with an AUC >0.7 were further refined using a total of 5 feature selection methods: random forest(RF), distance correlation(DC), eXtreme gradient boosting(Xgboost), gradient boosting decision tree(GBDT) and least absolute shrinkage and selection operator(LASSO).Nine MLMs were applied: support vector machine(SVM), linear discriminant analysis(LDA), decision tree(DT), RF, K-nearest neighbourhood(KNN), GBDT, adaptive boosting(AdaBoost), logistic regression(LR) and Gaussian Naïve-Bayes(GaussianNB) were developed using Python-3. 75% of data was used for training and 25% for validation. Model's performance was assessed using ROC curves. ***Results:*** The study included 443 patients(302 males, median-age:60, range: 17-90years). Among these, 311 were neoplastic while 132 had infection/inflammation on final HPE. A total of 166-RFs were extracted from each 18-F FDG PET-CT image at three intensity thresholds. Based on the combination of appropriate feature selection methods with different MLMs, forty-five discriminative models were established for each threshold. Most classifiers demonstrated acceptable discriminative ability with AUCs >0.7.Univariate-analysis revealed that 125 RFs were statistically significant predictors of outcome. LR-MLM with GBDT classifier at 25% threshold achieved best discriminative performance (AUC-.779) with a sensitivity, specificity and accuracy of 83.7, 72.0% & 81.1% respectively. ***Conclusion:*** RFs derived from Ultra-low-dose ^{18}F-FDG PET with Ultra-low-dose CT, when combined with MLMs, can effectively characterise lung lesions while delivering similar if not less radiation dose as compared to LCa screening CT. In this analysis, LR-MLM with GBDT classifier at 25% threshold performed best for characterisation of suspicious Lung lesions.

EP-0192

Prognostic Value of Pre-Treatment F-18 FDG PET/CT Volumetric Parameters in Patients Diagnosed with Laryngeal Squamous Cell Carcinoma

I. Ak Sivrikoz[1], *E. Ilhan*[1], *M. F. Acikalin*[2], *S. Aslan*[1], *I. Uslu Biner*[1]; *[1]ESOGU School of Medicine Department of Nuclear Medicine, Eskisehir, TÜRKIYE, [2]ESOGU School of Medicine Department of Pathology, Eskisehir, TÜRKIYE.*

Aim/Introduction: Metabolic tumor volume (MTV) and total lesion glycolysis (TLG) derived from FDG PET/CT have been proposed as prognostic biomarkers in various solid malignancies; however, their prognostic value in laryngeal cancer remains unclear. In this study, we aimed to investigate the relationship between volumetric parameters based on standardized uptake values obtained from FDG PET/CT and progression-free survival (PFS) and overall survival (OS) in newly diagnosed laryngeal cancer patients. ***Materials and Methods:*** Patients diagnosed with laryngeal cancer and who underwent FDG PET/CT for pre-treatment staging at our department between 2012 and 2020 were retrospectively evaluated. Patients who had not received prior surgery or chemotherapy/radiotherapy and had no additional malignancy were included. SUVmax, SUVmean, MTV, and TLG values of the primary laryngeal lesion were calculated from PET/CT images, and lymphatic and distant metastases were assessed. Clinical, pathological, and demographic data as well as dates of radiological progression and death were obtained from the hospital information system. OS/PFS was analyzed with a 60-month evaluation period. ***Results:*** A total of 62 patients (58 males, 4 females), aged between 45 and 87 years (mean: 64.75), were included in the study. At the time of analysis, 36 patients had died and 26 were still alive. The mean SUVmax of the laryngeal tumors was 11.22±6.03 (range: 2.99-29.43), mean SUVmean was 6.86±3.74 (range: 2.95-19.12), mean MTV was 6.35±8.34 (range: 0.04-37.55), and mean TLG was 39.62±99.32 (range: 0.12-494.58). Median OS was 57.50 months [95% confidence interval (CI): 44.15-61.53]; no significant association was found between OS and SUVmax (p=0.43), SUVmean (p=0.36), or TLG (p=0.16). However, a significant association was observed between OS and MTV (p=0.03). OS was not associated with tumor location within the larynx (glottic/supraglottic/subglottic/transglottic), tumor differentiation (poor, moderate, well, unspecified), gender, smoking status, or lymph node metastasis. Nevertheless, OS was significantly associated with age (p=0.00). Median PFS was 25 months (95% CI: 30.55-48.69). No significant association was found between PFS and SUVmax (p=0.17), SUVmean (p=0.13), or TLG (p=0.14). Similar to OS, a significant association was found between PFS and MTV (p=0.04). PFS was significantly associated with age (p=0.02) and presence of lymph node metastasis (p=0.006). ***Conclusion:*** In patients diagnosed with laryngeal SCC, tumor MTV appears to be an independent prognostic marker for OS. In addition, the presence of lymph node metastasis may serve as a prognostic marker for PFS, and older age may be a prognostic factor for both OS and PFS.

EP-0194

Prognostic Utility of ^{18}F-FDG PET/MRI with Intravoxel Incoherent Motion Imaging in Nasopharyngeal Carcinoma

S.-C. Chan[1], *S.-H. Ng*[2], *C.-H. Yeh*[2]; *[1]Hualien Tzu Chi Hospital, Hualien, Taiwan, [2]Linkou Chang Gung Memorial Hospital, Taoyuan, TAIWAN.*

Aim/Introduction: Intravoxel incoherent motion (IVIM) diffusion-weighted imaging (DWI) enhances tissue diffusion assessment by differentiating true molecular diffusion from microvascular perfusion, surpassing conventional DWI. This prospective study assessed the prognostic utility of ^{18}F-FDG PET/MRI with IVIM imaging in patients with primary nasopharyngeal carcinoma (NPC). ***Materials and Methods:*** Quantitative parameters derived from IVIM-DWI, dynamic contrast-enhanced MRI (DCE-MRI), and ^{18}F-FDG PET were analyzed for their associations with overall survival (OS) and recurrence-free survival (RFS). ***Results:*** The IVIM-derived minimal true diffusion coefficient (Dmin) and perfusion-related diffusion coefficient (D*) were significantly correlated with RFS (p = 0.018 and 0.043, respectively), outperforming the apparent diffusion coefficient (ADC; p = 0.946). Univariate analysis identified age, tumour stage, T classification, primary tumour standardized uptake value (SUVt), nodal SUV (SUVn), and total lesion glycolysis (TLG) as significant OS predictors. Significant predictors of RFS included Epstein-Barr virus DNA titre, SUVn, DCE-MRI parameters (Kep and Ve), and IVIM parameters (D* and Dmin). In multivariate analysis, age, SUVt, and TLG were independent OS prognostic factors, whereas SUVn, Kep, Dmin (p = 0.009), and Ve (p = 0.012) independently predicted RFS. Prognostic models incorporating the PET/MRI imaging biomarkers showed a significantly higher integrated AUC and Harrell's C-index than the TNM staging system alone (p = 0.013 and 0.003, respectively). ***Conclusion:*** Integrated PET/MRI with IVIM imaging enables simultaneous quantification of water molecule diffusion, tumor microvascular perfusion, and glucose metabolism in NPC, yielding complementary imaging biomarkers that demonstrate superior prognostic value compared to conventional TNM staging. ***References:*** 1. Lee AW, Ma BB, Ng WT, Chan AT. Management of Nasopharyngeal Carcinoma: Current Practice and Future Perspective. J Clin Oncol. 2015;33(29):3356-64. 2. Chua ML, Wee JT, Hui EP, Chan AT. Nasopharyngeal carcinoma. Lancet. 2016;387(10022):1012-24. 3. O'Sullivan B. Nasopharynx cancer: therapeutic value of chemoradiotherapy. Int J Radiat Oncol Biol Phys. 2007;69(2 Suppl):S118-21. 4. Chan SC, Chang JT,

Lin CY, Ng SH, Wang HM, Liao CT, et al. Clinical utility of ^{18}F-FDG PET parameters in patients with advanced nasopharyngeal carcinoma: predictive role for different survival endpoints and impact on prognostic stratification. Nucl Med Commun. 2011;32(11):989-96. 5. Xie P, Yue JB, Fu Z, Feng R, Yu JM. Prognostic value of ^{18}F-FDG PET/CT before and after radiotherapy for locally advanced nasopharyngeal carcinoma. Ann Oncol. 2010;21(5):1078-82.

EP-0195

C-X-C motif chemokine receptor 4-directed PET/CT in newly diagnosed squamous cell carcinoma of the oral cavity - initial experience and comparison to [^{18}F]FDG PET/CT

S. Serfling[1], *Y. Zhi*[2], *P. E. Hartrampf*[1], *H. Takahiro*[1], *A. Kübler*[3], *A. K. Buck*[1], *R. A. Werner*[4], *S. Hartmann*[3];
[1]*Department of Nuclear Medicine, University Hospital Würzburg, Würzburg, GERMANY,* [2]*Department of Otorhinolaryngology, Plastic, Aesthetic and Reconstructive Head and Neck Surgery, University Hospital Würzburg, Würzburg, GERMANY,* [3]*Department of Oral and Maxillofacial Plastic Surgery of the University Hospital Würzburg, Würzburg, GERMANY,* [4]*Department of Nuclear Medicine, LMU University Hospital, LMU Munich, Munich, GERMANY.*

Aim/Introduction: Inflammatory processes in the oral cavity and the resulting reactive, loco-regional cervical lymph nodes pose a challenge for the routinely used radiotracer [^{18}F]FDG. We aimed to compare [^{18}F]FDG PET/CT relative to the inflammatory-specific C-X-C motif chemokine receptor 4-directed [^{68}Ga]PentixaFor in patients affected with newly diagnosed oral squamous cell carcinoma (OSCC). ***Materials and Methods:*** 10 newly diagnosed untreated patients with a histologically confirmed OSCC underwent CXCR4-PET/CT using [^{68}Ga]PentixaFor and [^{18}F]FDG PET/CT to determine disease extent within 2 days. We also quantified tumor volume (TV), maximum SUV (SUV_{max}) and target-to-background ratio (TBR, with healthy liver parenchyma serving as reference organ) thereby providing information on image contrast. We compared the results with pathological findings in resected lymph nodes. ***Results:*** On a lesion-based level, the primary was detected for both tracers in 8 out of 10 patients. In two cases the primary was not detected (both T1 stage). Median tumor TV was 7.61±6.0 for [^{18}F]FDG and 3.83±6.82 for [^{68}Ga]PentixaFor ($P<0.03$). Comparable results were recorded for SUV_{max} ([^{18}F]FDG, 21.31±4.92 vs. [^{68}Ga]PentixaFor, 6.5±2.34; $P<0.4$), with respective TBR of 8.86±2.64 for [^{18}F]FDG ([^{68}Ga]PentixaFor, 4.3±1.4; $P<0.18$). 159 lymph nodes were resected at all. Only two of the suspected lymph nodes were histologically confirmed metastases, which were detected by both tracers. ***Conclusion:*** In patients with OSCC, both tracers can detect the primary tumor (minimum T2 stage) with [^{18}F]FDG showing a higher image contrast. Neither tracer was able to adequately identify lymph node involvement.

EP-0196

Prognostic value of volumetric ^{18}F-FDG PET in head and neck cancer

A. Doma[1,2], *T. Škerl*[1], *A. Studen*[3,4], *P. Strojan*[1,2];
[1]*Oncology institute, Ljubljana, SLOVENIA,* [2]*Faculty of Medicine, University of Ljubljana, Ljubljana, SLOVENIA,* [3]*Faculty of Mathematics and Physics, University of Ljubljana, Ljubljana, SLOVENIA,* [4]*Experimental Particle Physics Department, Jožef Stefan Institute, Ljubljana, SLOVENIA.*

Aim/Introduction: Head and neck cancer (HNC) is the 7th most common type of cancer, representing a heterogeneous group of malignancies with variable prognosis, influenced by tumor site, stage, and patient-related factors. ^{18}F-FDG PET/CT (PET/CT) is effective for staging and prognostication of HNC. Recently, focus of PET/CT shifted from conventional standardized uptake value (SUV) to volumetric parameters, e.g. metabolic tumor volume (MTV) and total lesion glycolysis (TLG) as potential prognostic markers. The present study aimed to evaluate the prognostic value of several clinical and PET based parameters for prediction of overall survival (OS) in patients with HNC undergoing radiotherapy. ***Materials and Methods:*** 28 patients with histologically confirmed HNC of M0 stage and baseline PET/CT prior to curative-intent radiotherapy, with or without concomitant chemotherapy were included. Clinical variables included age, gender, smoking history, World Health Organization performance status (WHO), tumor (T), and nodal (N) stage. PET derived variables analyzed were maximum standardized uptake value (SUVmax) and metabolic tumor volume using a 41% SUVmax threshold (MTV41) for primary tumors, regional metastases, and total disease. Statistic analyses included descriptive statistics, ROC analysis (AUC, cut-offs) and univariate Kaplan-Meier survival estimates with log-rank tests, with $p < 0.05$ considered significant. ***Results:*** 22 men and 6 women of a median age 55 years (range: 32,8-75,9) were analyzed. The most frequent primary sites were the nasopharynx (n=15) and oropharynx (n=10). 10 patients were former and 11 were current smokers. All patients recived 70 Gy and 24 of them had concurrent chemotherapy. After a median follow-up of 38 months (range: 5-98), ROC analysis demonstrated that total MTV41 was the strongest predictor of OS (AUC 0,85; p=0,0034), yielding high sensitivity (0,88) and specificity (0,78). Additional significant variables were metastases SUVmax (AUC 0,80; p=0,03), and tumor MTV41 (AUC 0,76; p=0,04). T stage (AUC 0,66), N stage (AUC 0,69), age (AUC 0,67), and smoking history (AUC 0,47) were found non-significant.Kaplan-Meier analysis confirmed significantly worse OS in patients with total MTV41>13,96 ml, metastases MTV41>6,51 ml, tumor MTV41>16,13 ml and metastases SUVmax>14,32. Notably, tumor SUVmax, as well as traditional patient- and tumor-related prognosticators were not significantly associated with OS. ***Conclusion:*** In the present study, total MTV41 emerged as the most powerful predictor of OS in locoregionally advanced HNC treated with definitive (chemo)radiotherapy, outperforming conventional clinical staging and tumor SUVmax metrics. Baseline MTV tumor burden may help identify high-risk patients, benefiting from intensified treatment regimens.

EP-0197

Comparison of the Diagnostic Value of FDG PET/MRI and MRI Imaging in Nodal Staging of Laryngeal Cancer and Predictive Parameters of Lymph Node Metastasis

E. Erbil Capci*, U. Aydos, S. Gülbahar Ateş, E. Balcı, M. Yılmaz, M. Uçar, L. Atay;*
Gazi University Faculty of Medicine, Ankara, TÜRKIYE.

Aim/Introduction: This study aimed to compare the diagnostic performance of FDG PET/MRI and MRI modalities in detecting lymph node(LN) metastasis and to determine the predictive parameters of LN metastasis. ***Materials and Methods:*** 39 patients who underwent whole-body PET/MRI and head-neck MRI for primary staging, followed by subsequent surgical resection were included. PET/MRI images were retrospectively reviewed by a nuclear medicine physician, and MRI images by a radiologist. In PET/MRI visual assessment, three N stages were determined using thresholds of background(BG), mediastinal blood pool(ME), and liver(LI) activity. SUVmax, SUVmean, SUVpeak, MTV and TLG values of the primary tumor were calculated. The T stage, local spread characteristics (paraglottic space involvement, anterior commissure involvement, cartilage invasion and extralaryngeal extension), ADCmin value and N stage were determined from MRI images. Histopathology was used as the reference standard. Diagnostic performances of imaging modalities in N staging were evaluated with chi-square test. Statistical analyses were conducted using SPSS 25.0. The role of imaging parameters of the primary tumor in predicting the presence of LN metastasis was evaluated by logistic regression analysis. A nomogram model was developed using regression coefficients with the lrm() and nom()

functions in the [1]rms[2] package with R software. ***Results:*** The accuracy of PET/MR BG, ME, LI and MRI N stage were calculated as 30.8%, 46.2%, 69.2%, and 59%, respectively. In univariate logistic regression analyses, MTV and ADCmin value of primary tumor and the presence of paraglottic space involvement were identified as predictive factors for LN metastasis. In the nomogram developed to predict LN metastasis, the variables used were MTV (0.43-35 scored 0-92.5), paraglottic space involvement ("absent"-"present" scored 0-43.75) and ADCmin (200-20 scored 0-100), which are scored on a 0-100 scale, and the probability of LN metastasis is obtained according to the total score. The optimal probability threshold was calculated as 27%, with a sensitivity of 93%, specificity of 60% and accuracy of 81% for predicting LN metastasis. To reduce the false positive rate, PET/MRI-LI was applied to assess LN metastasis in 23 patients with scores above the cut-off value; this raised the model's specificity to 92% and accuracy to 90%. ***Conclusion:*** A model incorporating MTV and ADCmin value of primary tumor and paraglottic space involvement obtained from PET/MRI imaging in laryngeal cancer provides high sensitivity in predicting LN metastasis. Using the liver threshold in PET/MRI for N staging and predicting LN metastasis significantly improves the diagnostic performance of the modality.

EP-0198

Habitat-Based Radiomic Features from ^{18}F-FDG PET/MR for Recurrence Prediction in Head and Neck Oral Carcinoma

W. Zhou[1], *C. Jiang*[1], *J. Yang*[1], *X. Peng*[1], *K. Zheng*[1], *Y. Guo*[2], *H. Ye*[1]; *[1]Department of PET-CT Center, The Affiliated Cancer Hospital of Xiangya School of Medicine/Hunan Cancer Hospital, Central South University, Changsha, CHINA, [2]Shenzhen United Imaging Healthcare Co., Ltd., Shenzhen, CHINA.*

Aim/Introduction: Recurrence prediction in head and neck oral carcinoma remains at an early research stage, particularly when accounting for tumor heterogeneity. This study evaluates the predictive value of habitat-derived radiomic features extracted from ^{18}F-fluorodeoxyglucose (^{18}F-FDG) PET/MR and diffusion-weighted imaging (DWI) for recurrence risk stratification. ***Materials and Methods:*** We retrospectively analyzed 21 patients (13 with recurrence, 8 without) who underwent pretreatment ^{18}F-FDG PET/MR scans including DWI sequences. Tumor habitats were delineated on PET images using Otsu's thresholding method, separating high- and low-metabolism subregions. Radiomic features—including shape, first-order, and texture features (GLCM, GLSZM, GLRLM, NGTDM, GLDM)—as well as quantitative metabolic and diffusion parameters were extracted from these habitats and the peritumoral regions. Feature selection was performed using the least absolute shrinkage and selection operator (LASSO) regression, and a support vector machine (SVM) classifier was trained and evaluated via fivefold cross-validation. ***Results:*** A total of 214 radiomic features per PET and ADC modality were initially extracted across three distinct tumor regions, resulting in 657 features. After excluding features with poor reproducibility (intraclass correlation coefficient < 0.75), 611 robust features remained for analysis. Six key features were ultimately selected via LASSO regression, predominantly originating from low-metabolism PET and peritumoral regions, as well as high-metabolism and diffusion-related zones on DWI, reflecting the inherent spatial metabolic and microstructural heterogeneity of buccal carcinoma. The SVM classification model achieved a cross-validated area under the ROC curve (AUC) of 0.805 (95% CI: 0.665-1.000). At the optimal threshold of 0.597, determined by maximizing Youden's index using ROC analysis, the model achieved an accuracy of 83.3%, sensitivity of 81.8%, and specificity of 85.7%. This integrative approach highlights the significant contribution of habitat-specific radiomic features in predicting recurrence risk and underscores the importance of capturing tumor heterogeneity via multi-modal imaging. ***Conclusion:*** PET/MR habitat-based radiomic features capturing metabolic and diffusion heterogeneity show promise for noninvasive prediction of recurrence risk in oral carcinoma. Notably, several selected features originate from low-metabolism and peritumoral PET regions, suggesting that metabolic heterogeneity—beyond simple uptake intensity—may be critical for identifying tumors with higher recurrence potential. These findings emphasize the value of quantitative imaging biomarkers in assessing tumor heterogeneity and support personalized patient management. Further validation in larger, multi-center cohorts is currently underway.

EP-0199

[^{18}F]FDG PET/CT in Post-Treatment Assessment of Head and Neck Cancer: Exploring the Diagnostic Role of SUVmax and Uptake Pattern

D. Silva*, I. Miguel, D. Barbosa, N. Vasconcelos, R. Marão, P. Silva, J. Ferro, S. Fontão de Castro, L. Violante, J. Teixeira, A. Soares, H. Duarte, I. Lucena Sampaio;*
Instituto Português de Oncologia do Porto Francisco Gentil, Porto, PORTUGAL

Aim/Introduction: [^{18}F]fluorodeoxyglucose positron emission tomography/computed tomography ([^{18}F]FDG PET/CT) plays a central role in the post-treatment evaluation of head and neck cancer (HNC). To enhance objectivity in response assessment, structured scoring systems have been developed, such as Christie Score, a simple and effective three-tier system (based on the lesion and blood pool SUVmax). Our aim was to assess the diagnostic performance of Christie Score in our population, and to investigate the prognostic value of quantitative PET metrics. We also assessed the feasibility of incorporating uptake patterns (focal vs diffuse) into a semiquantitative scoring approach. ***Materials and Methods:*** We retrospectively reviewed data from 131 patients with HNC treated with radical radiotherapy (with or without chemotherapy) at our institution between January 2020 and December 2022. Pre- and post-treatment FDG-PET scans were reviewed to extract relevant variables. All patients underwent response-assessment PET/CT at or beyond 12 weeks post-treatment, with uniform timing. These studies were classified using the Christie Score, and the original report conclusions were mapped to the equivalent Christie Score categories (complete metabolic response, likely post-treatment inflammation, or residual/recurrent disease) to enable statistical analysis. Clinical and imaging follow-up served as reference standard. ***Results:*** The Christie Score showed good diagnostic accuracy (AUC 0.835, p<0.001), with 89.5% sensitivity, 76.8% specificity, high negative predictive value (97.7%), although lower positive predictive value (PPV) (39.5%). FDG-PET reports showed higher predictive performance, with an improved of PPV 76% (p<0.001), likely reflecting the benefit of combining visual interpretation and clinical expertise. Post-treatment SUVmax alone yielded excellent diagnostic accuracy (AUC 0.965), accounting for 75.8% of outcome variation (R^2=0.758), with an optimal cut-off of 4.82 for predicting disease persistence. Incorporating uptake patterns into the model further increased explanatory power (R^2=0.837), indicating potential added value. Baseline SUVmax was not significantly associated with outcomes. ***Conclusion:*** Structured tools like the Christie Score can support standardized assessment, but expert clinical interpretation outperformed purely quantitative approaches in our cohort. Our findings highlight the potential utility of a semiquantitative scoring model that integrates SUV metrics with uptake pattern analysis to enhance diagnostic confidence when differentiating residual disease from post-treatment changes in HNC. This aligns with emerging evidence supporting hybrid models that combine

objective data with visual assessment. Prospective validation in larger cohorts is warranted to confirm reproducibility and clinical utility. ***References:*** DOI:10.1186/s41824-024-00230-8.

EP-0200

Machine learning for the prediction of synchronous second primary tumours in head and neck cancer assessed by ^{18}F-FDG PET/CT

F. Gomez-Caminero Lopez[1], *E. Campaña Diaz*[1], *S. Rama Alonso*[1], *J. Cañadas Salazar*[1], *F. Caltagirone Rodriguez*[1], *L. Diaz Gonzalez*[1], *J. Villanueva Curto*[1], *J. Badell Martinez*[1], *M. Sanchez Barba*[2], *P. Garcia-Talavera San Miguel*[1];
[1]*Nuclear Medicine. University Health Complex of Salamanca, Salamanca, SPAIN,* [2]*Department of Statistics, University of Salamanca, Salamanca, SPAIN.*

Aim/Introduction: Patients with head and neck cancer (HNCC) are at increased risk of developing synchronous second primary tumours (SPTs), which may influence both staging and treatment strategy. This study aims to assess the predictive value of ^{18}F-FDG-PET/CT metabolic parameters and demographic variables for SPT detection using machine learning (ML) algorithms. ***Materials and Methods:*** A retrospective analysis was conducted on 2,081 patients who underwent 18F-FDG-PET/CT for staging of HNCC between Oct´2014-Dec´2022. Data included demographic variables (age, sex) and metabolic parameters of the index tumour: maximum standardised uptake value (SUVmax), metabolic tumour volume (MTV) and total lesion glycolysis (TLG). ML modelling was applied to estimate the probability of SPT presence. Lesions suspicious for SPT were histopathologically verified whenever possible. ***Results:*** 285 suspicious lesions were initially identified. 203 were included in the final analysis. Among these, 133 were confirmed as true SPTs (6,8%). Feature selection identified age, SUVmax, MTV, and TLG as the most relevant predictors of SPT. A random forest classifier achieved 100% sensitivity in detecting confirmed SPTs. The most frequent SPT sites were the lungs and gastrointestinal tract. The majority of STP were diagnosed at an early stage. ***Conclusion:*** ^{18}F-FDG-PET/CT is an effective imaging modality for early detection of SPT in patients with HNCC. ML techniques, particularly random forest algorithms, can enhance predictive performance by integrating metabolic imaging and clinical variables. These results highlight the potential role of AI-supported models in clinical decision-making and personalised oncology. ***References:*** Strobel K, Haerle SK, Stoeckli SJ, et al. HNSCC detection of synchronous primaries with (^{18})F-FDG-PET/CT. Eur J Nucl Med Mol Imaging. 2009;36(6):919-927Haerle SK, Strobel K, Hany TF, Sidler D, Stoeckli SJ. 18F-FDG-PET/CT versus panendoscopy for the detection of synchronous second primary tumors in patients with HNSCC. Head Neck. 2010 Mar;32(3):319-25Liu FY, Liao CT, Yen TC. Synchronous malignancies in patients with squamous cell carcinomas of the oral cavity. Eur J Nucl Med Mol Imaging. 2011 Jun;38(6):1020-8Ilcheva M, Nikolova P, Hadzhiyska V, Mladenov K. Impact of FDG-PET/CT on detection of synchronous and metachronous malignancies and clinical management in patients with multiple primary cancers. Neoplasma. 2022 Jul 1;69(4):948-56Dorado Díaz P. Contribuciones de las técnicas machine learning a la cardiología. Predicción de reestenosis tras implante de stent coronarioJianchang Hu, Silke Szymczak, A review on longitudinal data analysis with random forest, Briefings in Bioinformatics, Volume 24, Issue 2, March 2023Alameh M, Abbass Y, Ibrahim A, Valle M. Smart Tactile Sensing Systems Based on Embedded CNN Implementations. Micromachines. 2020; 11(1):103.

EP-14

e-Poster Area

B: Imaging Clinical Studies -> B1 Oncological Imaging Clinical Study -> B13 Breast

EP-0201

Leveraging ^{18}F-FDG PET/CT to investigate the biology of circulating cell-free tumor DNA (ctDNA): an exploratory study in metastatic breast cancer (MBC) patients

M. de Oliveira Taveira[1], *L. Cabel*[1], *J. Das*[1], *J. Teysir*[1], *C. White*[1], *Y. Chen*[1], *P. Razavi*[1], *R. Yeh*[2];
[1]*Memorial Sloan Kettering Cancer Center, New York, NY, UNITED STATES OF AMERICA,* [2]*Mount Sinai Health System, New York, NY, UNITED STATES OF AMERICA.*

Aim/Introduction: ctDNA levels in blood are strongly correlated with disease burden and tumor type and biological features such as proliferation and apoptosis rates, but there is incomplete understanding of the biology of ctDNA shedding in metastatic patients, as different metastatic sites may shed ctDNA differently. As a whole-body functional and anatomical imaging modality, FDG PET/CT is an ideal tool to investigate ctDNA biology in metastatic patients. ***Materials and Methods:*** HR+/HER2- MBC patients with MSK-ACCESS ctDNA assay collected within 7 days of the initiation of 1st line therapy for MBC and with PET/CT done within 60 days of ctDNA collection were included. Semi-automated segmentation of all tumor sites was done by 3 radiologists specialized in oncological imaging using a combination of threshold and manual segmentation. Lesion site, SUVmax, SUVmean, and Metabolic Tumor Volume (MTV) with a relative threshold of 40% of SUVmax were annotated. Total Lesion Glycolysis (TLG) was calculated multiplying weighted SUVmean by MTV. All variables were analyzed at lesional, organ and patient level. Variant Allele Frequency (VAF) in ctDNA was calculated using the number of mutant DNA molecules divided by the total number of DNA molecules (mutant plus wild type) at that specific genetic locus. Kendall's Tau was used to evaluate the correlation between PET and ctDNA. ***Results:*** Out of 766 patients with MSK-ACCESS, 78 patients had concurrent FDG PET/CT. 77/78 had measurable disease on PET/CT with 1392 lesions measured and 58/78 had positive ctDNA at that time point. Most common metastatic sites were bone (60/78), lymph node (47/78), liver (25/78) and lung (21/78). PET-derived variables most correlated to VAF ctDNA according to Kendall's tau score were: Global TLG, 0.42 ($p<0.001$); Global MTV, 0.40 ($p<0.001$); Liver metastasis weighted SUVmean, 0.38 ($p=0.008$), Liver metastasis highest SUVmax, 0.34 ($p=0.018$), and single metastasis with the highest SUVmax, 0.32 ($p<0.001$). ***Conclusion:*** There is moderate correlation between ctDNA VAF and MTV, TLG, highest SUVmax, liver metastasis weighted SUVmean and highest liver metastasis SUVmax in MBC patients. Liver-specific PET biomarkers are more closely associated with ctDNA than other organ-based variables, potentially implying higher shedding from these metastases. The imperfect correlation between PET and ctDNA points towards added value of combining both evaluations that could inform clinical trials attempting to incorporate ctDNA as a biomarker in addition to standard imaging-derived surrogate endpoints. Incorporating both PET/CT and ctDNA variables into clinical models may improve tumor response evaluation and personalized treatment strategies in metastatic breast cancer.

EP-0202

Predictive value of 18F-FES PET/CT on the efficacy of late rechallenge of hormone therapy in metastatic breast cancer

***M. Masse**, C. Bailleux, J.-M. Ferrero, A. Creisson, O. Humbert;*
Centre Antoine Lacassagne, Nice, FRANCE.

Aim/Introduction: Hormone-dependent breast cancer (HR+), accounting for over two-thirds of breast cancers, are initially treated with hormone therapy (HT). After progression on initial HT and chemotherapy, late rechallenge with other hormonal agents is a therapeutic option. Tumor hormone sensitivity is usually determined by immunohistochemical analysis of a single biopsied lesion. However, 18F-FES PET/CT, a functional imaging targeting estrogen receptors, could be used to assess the residual expression of estrogen receptors of tumor lesions, on a whole-body scale.The aim of this study is to determine the predictive value of 18F-FES PET/CT for the efficacy of late hormone therapy rechallenge in patients with HR+ metastatic breast cancer who have already received multiple prior lines of hormone therapy and chemotherapy. ***Materials and Methods:*** This retrospective study included all patients with metastatic breast cancer, initially HR+, who had received at least one line of hormonal therapy and one line of chemotherapy and were progressing on chemotherapy. Consecutive ^{18}F-FDG and 18F-FES-PET/CT scans were performed between March 2022 and September 2023 to evaluate residual hormone receptor expression. The analysis was qualitative: a lesion was considered FDG+ if the uptake was higher than the hepatic background noise, and an FES-PET/CT was considered positive if all FDG+ lesions showed visual FES uptake (higher than the local background noise). All other 18F-FES PET/CT exams (heterogeneous or negative FES fixation) were considered negative (1). The primary endpoint was progression free survival (PFS), and the secondary endpoint was overall survival (OS). ***Results:*** Thirty-six patients were included: 13 had a positive FES-PET/CT and 23 had a negative FES-PE/CT. Patients with positive FES-PET/CT underwent hormone therapy rechallenge, achieving significantly longer median PFS than negative FES-PET/CT patients (medPFS: 6 vs. 3 months, p = 0.042). Negative FES-PET/CT patients mostly received chemotherapy. There was also a trend towards better overall survival in patients with positive 18F-FES PET scans, although these results were not significant in our sample of patients (medOS: 22 vs. 19 months, p = 0.32). ***Conclusion:*** Persistence of 18F-FES uptake across all metastatic lesions can predict the effectiveness of an additional line of hormone therapy in patients with HR+ metastatic breast cancer who have already received multiple prior lines of hormone therapy and chemotherapy. Prospective studies with larger cohorts are needed to validate these results and to optimize therapeutic strategies. ***References:*** (1) Mankoff et al. SNMMI/EANM Practice Guideline for Estrogen Receptor Imaging of Patients with Breast Cancer Using 16α-[18F]Fluoro-17β-Estradiol PET. JNuclMed. 2024 doi:10.2967/jnumed.123.266938.

EP-0203

The Potential Of 18F-Fluorocholine Computed Tomography (18F-FCH PET CT) As Predictor For Breast Cancer Immunophenotyping And Genetic Profiling Heterogenicity.

***M. Zakaria**[1], S. Shaharuddin[2], S. Abdullah Suhaimi[3], F. Ahmad Saad[1];*
[1]Universiti Putra Malaysia, Serdang, MALAYSIA, [2]Universiti Pertahanan Nasional Malaysia, Kuala Lumpur, MALAYSIA, [3]Universiti Kebangsaan Malaysia, Cheras, MALAYSIA.

Aim/Introduction: To determine the potential of 18-FCH PETCT as a predictor for breast cancer immunophenotyping and genetic profiling heterogenicity. ***Materials and Methods:*** This study used the hospital information system retrospectively. 21 patients with primary or recurrent breast carcinoma who underwent 18F- FCH PET-CT imaging prior to biopsy. All patients had Birads 4/5 breast lesions on the mammogram. Histopathological examination (HPE) were recorded; benign and malignant. The patients were dichotomized into different immunophenotyping profiling : HER-ve and HER +ve immunophenotyping. Semiquantitative analysis utilizing the standardized uptake value (SUVmax (g/dl)/g/dl) was used to predict the two groups of different immunotyping. ***Results:*** 21 females with mean age of 52.82 ± 10.71 years. Eighteen patients had malignant disease (18/21; 85.8%) on histology with eleven (52.4%) with HER -ve immunophenotype. There is a significant difference between 18F-FCH SUVmax (g/dl) of the HER-ve and the HER +ve immunophenotyping group (1.99 g/dl vs 0.2g/dl; p<0.05). The malignant group has higher SUVmax (g/dl) value as compared to the benign group (1.36 ± 0.13; p<0.05). High SUVmax (g/dl) FCH predicted malignant breast lesion for the malignant histological subtype and HER-ve protein overexpression genotype at the cut-off value of 0.75 (p<0.05), predicting the aggressiveness of breast carcinoma. The SUVmax (g/dl) FCH PET-CT of > 0.75 was a good predictor to signal aggressive breast carcinoma cellular gene reprogramming. ***Conclusion:*** There is good potential of 18F-Fluorocholine Computed Tomography (18F-FCH PET CT) as potent predictor for breast cancer immunophenotyping determination and genetic profiling hence improve the diagnostic accuracy and disease progression monitoring for enhancing disease`s survival rate. ***References:*** Zhang, H. et al. HIF-1 regulates CD47 expression in breast cancer cells to promote evasion of phagocytosis and maintenance of cancer stem cells. Proceedings of National Academy Sciences USA 2015, 112, 6215-6223, Bae, S.Y., Kim, S., Lee, J.H. et al. Poor prognosis of single hormone receptor-positive breast cancer: similar outcome as triple-negative breast cancer. BMC Cancer 15**,** 138 (2015), Fathinul Fikri, A.S., Nordin, A.J., Eddie lau, E.F. 18[F] FDG-PET/CT is a useful molecular marker in evaluating tumour aggressiveness; a revised understanding of an in- vivo FDGPET imaging that alludes the alteration of cancer biology. Cell Biochemistry and Biophysic, 2014, 55 (5), 631-640, Mark, P.M., Jonathan, H., John, R.C., Hedley, C.A.E. The utility of FDG PET/CT in clinically Suspected Paraneoplastic Neurological Syndrome: A literature Review and Retrospective Case Series 2017, 8, 238-244.

EP-0204

MAMMI PET-based Habitat-radiomics for Measuring Intratumoral-heterogeneity and Predicting Neoadjuvant Chemotherapy Response in HER2-positive Breast Cancer

***C. Ren**;*
Shanghai Proton and Heavy Ion Center, Shanghai, CHINA.

Aim/Introduction: Intratumoral heterogeneity (ITH) of human epidermal growth factor receptor 2-positive (HER2+) breast cancer (BC) results in different responses to neoadjuvant chemotherapy (NAC), which cannot be non-invasively evaluated before treatment. The aim of this study was to develop the habitat radiomics models for measuring ITH based on pretreatment high-resolution dedicated breast PET (MAMMI PET) and predicting pathologic complete response (pCR) after NAC in HER2+ BC patients. ***Materials and Methods:*** This retrospective single-center study included HER2+ BC patients who underwent preoperative dbPET and received NAC followed by surgery from June 2021 to July 2023. Habitat radiomics features (RFs) were extracted from different metabolic subregions (VOI_{high}, VOI_{low}, etc.), and selected to develop models for NAC response prediction by machine-learning algorithms. The correlation between habitat RFs with ITH (Ki-67 expression) was measured by Pearson test. The performance of prediction models was evaluated and compared by the area under the receiver operating characteristic curve (AUC) and DeLong test. The optimal model was expressed as nomogram, together with significantly clinical-image risk factors. ***Results:*** This study included 140 female patients (median age, 51 years [IQR, 44-

57 years])), 98 patients (median age, 51 years [IQR, 46-58 years]) from the training set, of which 60 patients (61.2%) were pCR, and 42 patients (median age, 52 years [IQR, 43-56 years]) from the validation set, of which 24 patients (57.1%) were pCR, respectively. Habitat radiomics matrix extracted from VOI_{low} was significantly associated with Ki-67 expression (r: 0.44, $p < 0.05$). The nomogram constructing with Ki-67 expression, SUVmax and ITH Model, which developed by VOI_{high}/VOI_{low} habitat RFs, showed the optimal performance for predicting pCR to NAC in both the training and validation sets (AUCs of 0.88 and 0.94, respectively). ***Conclusion:*** Habitat radiomics analysis based on dbPET had great potential in non-invasively measuring ITH and enabled identification of HER2+ BC patients who are unlikely to benefit from NAC.

EP-0205

^{18}F-fluoroestradiol (^{18}F-FES) PET/CT guided first-line treatment for HR+/HER2- metastatic breast cancer patients: experience from real-world

C. Liu[1], *Y. Xie*[2], *Y. Chen*[2], *S. Song*[1], *B. Wang*[2], *Z. Yang*[1]; *[1]Department of Nuclear Medicine, Fudan University Shanghai Cancer Center, Shanghai, CHINA, [2]Department of Medical Oncology, Fudan University Shanghai Cancer Center, Shanghai, CHINA.*

Aim/Introduction: In the past decade, the combination of CDK4/6 inhibitors and endocrine therapy has significantly extended the survival of patients with hormone receptor (HR) positive and human epidermal growth factor receptor 2 (HER2) negative metastatic breast cancer (MBC). However, a minority of patients might have difficulty in benefiting from this combination therapy because of estrogen receptor (ER) heterogeneity between lesions. ^{18}F-fluoroestradiol (^{18}F-FES) positron emission tomography (PET)/computed tomography (CT) is recognized as a potent tool for assessing ER expression in patients with HR+/HER2- MBC on a comprehensive, whole-body level. Nevertheless, it remains unknown whether ER status screened by ^{18}F-FES-PET could identify patients who benefit more from CDK4/6i plus ET or chemotherapy (CT) compared to unscreened controls. ***Materials and Methods:*** The medical records of patients diagnosed with HR+/HER2- MBC from 2020 to 2024 in Fudan University Shanghai Cancer Center were retrospectively evaluated. Patients screened or unscreened by ^{18}F-FES-PET before first-line CDK4/6i plus ET or CT were included in this study. ***Results:*** A total of 473 patients were included in the study. 156(33.0%) and 317 (67.0%) patients were screened or unscreened by ^{18}F-FES-PET before first-line treatment. 111 patients with all-FES positive metastatic lesions and 17 patients with FES heterogeneity received CDK4/6i plus ET. 21 patients with all-FES negative metastatic lesions and 7 patients with FES heterogeneity received CT. As for the unscreened group, 236 received CDK4/6i plus ET and 81 received CT. In CDK4/6 plus ET cohort, FES-screened group showed a significantly prolonged progression-free survival (PFS) compared with unscreened group (mPFS 32.4 months versus 17.3 months, Hazard Ratio = 0.49; 95% CI, 0.34 to 0.69; $P < 0.0001$). And CT cohort showed superior PFS for screened patients as well (mPFS 11.38 months versus 8.91 months, Hazard Ratio = 0.56; 95% CI, 0.33 to 0.94; $P = 0.026$). ***Conclusion:*** HR+/HER2- MBC patients with FES-guided initial treatment showed significantly better efficacy than those who had not been assessed by ^{18}F-FES-PET/CT in real world. This study highlights the crucial instructive role of FES assessment in evaluating ER expression in patients prior to administering first-line treatment.

EP-0206

The prognostic significance of [^{18}F]FDG PET/CT in triple-negative breast cancer: results of the TRINE-PET trial

L. Urso[1], *S. Panareo*[2], *A. Iudicello*[3,2], *D. Albano*[4], *S. Taralli*[5], *A. Mazzoletti*[6], *A. Annovazzi*[7], *L. Fantini*[8], *M. L. Mangia*[9], *L. Sofia*[10], *L. Setti*[11], *G. Cassarino*[12], *D. Aricò*[13], *S. Ialuna*[14], *A. Miceli*[15], *E. Rizza*[16], *C. Ferrari*[17], *A. Marongiu*[18], *F. Garrou*[19], *P. Reccia*[20], *A. Arnone*[21], *C. Colombo*[22], *A. M. Maffione*[23], *D. Donner*[24], *L. Evangelista*[25]; *[1]University of Ferrara, Ferrara, ITALY, [2]University-Hospital of Modena, Modena, ITALY, [3]University-Hospital of Ferrara, Ferrara, ITALY, [4]University of Brescia, Brescia, ITALY, [5]Department of Radiological and Hematological Sciences, Università Cattolica del Sacro Cuore, Rome, ITALY, [6]Fondazione Poliambulanza Istituto Ospedaliero, Brescia, ITALY, [7]irccs Istituto Nazionale Tumori Regina Elena, Rome, ITALY, [8]IRCCS IRST "Dino Amadori, Meldola, ITALY, [9]University of Turin, Turin, ITALY, [10]University of Genoa, Genoa, ITALY, [11]Humanitas Gavazzeni, Bergamo, ITALY, [12]Ospedale GPII, Ragusa, ITALY, [13]Humanitas Istituto Clinico Catanese, Catania, ITALY, [14]Osp. Riuniti Villa Sofia Cervello, Palermo, ITALY, [15]AOU SS. Antonio e Biagio.e c. Arrigo, Alessandria, ITALY, [16]Vito Fazzi Hospital, Lecce, ITALY, [17]University Aldo Moro, Bari, ITALY, [18]University of Sassari, Sassari, ITALY, [19]A.O.U. Maggiore della Carità, Novara, ITALY, [20]IOV, Padua, ITALY, [21]Arcispedale S. Maria Nuova, Reggio Emilia, ITALY, [22]Fondazione IRCCS Ca' Granda, Milan, ITALY, [23]Santa Maria della Misericordia Hospital, Rovigo, ITALY, [24]Santa Chiara Hospital, Trento, ITALY, [25]Department of Biomedicine, Humanitas University, Pieve Emanuele, Milan, ITALY.*

Aim/Introduction: although triple-negative breast cancer (TNBC) is a recognized [18F]-FDG-avid tumor, there is still limited robust evidence in the literature regarding the prognostic value of this imaging modality. TRINE-PET is a large, retrospective, real-world, multicenter Italian study designed to evaluate the correlation between [18F]-FDG PET/CT findings and survival outcomes in TNBC patients across various clinical settings. ***Materials and Methods:*** data on [18F]-FDG PET/CT in TNBC patients were retrospectively collected from 24 Italian centers. Scans were categorized according to four clinical settings: (a) baseline, (b) post-neoadjuvant chemotherapy (NAC), (c) suspected disease recurrence and (d) patients undergoing systemic therapies. Only patients with a minimum of two years of follow-up were eligible. A per-site PET-based analysis was performed, and survival outcomes (progression and death) were compared across the clinical settings using the log-rank test. Associations between categorical variables were analyzed using the chi-squared test. ***Results:*** a total of 707 [18F]-FDG PET/CT scans from 389 TNBC patients (mean age = 54±13 years) were analyzed. The distribution of scans across the four clinical settings was as follows: baseline = 257, post-NAC = 111, suspected recurrence = 144, and systemic therapy = 195. At baseline, [18F]-FDG PET/CT detected the primary tumor in 234 patients (91.1%). Lymph node and distant metastases were identified in 284 (40.2%) and 181 (25.6%) patients, respectively. During a median follow-up of 3 years, 278 patients (39.3%) experienced disease progression, and 200 (28.3%) died. The presence of an [18F]-FDG-avid primary tumor at baseline was significantly associated with shorter survival (p=0.0001). Additionally, detection of nodal (N+) or distant (M+) metastases on PET/CT correlated strongly with a higher risk of disease progression in all four clinical settings (all p<0.001). Presence of distant metastases (M+) was also significantly associated with increased mortality in the suspected recurrence and systemic therapy settings (p=0.018 and p<0.0001, respectively). ***Conclusion:*** the presence of an [18F]-FDG-avid primary TNBC tumor on baseline PET/CT is associated with a higher risk of death. Furthermore, a strong correlation was observed between nodal or distant metastatic disease at [18F]-FDG PET/CT and worse survival outcomes. Specifically, detection of lymph nodes or distant metastases at early disease stages (baseline and post-NAC) was prognostic for shorter progression-free survival. In contrast, the presence of distant metastases in PET/CT scans performed

for suspected recurrence or during systemic treatment predicted both shorter progression-free and overall survival. ***References:*** DOI: 10.1007/s00259-024-06866-9Acknowledgements: De Rimini M.L., Frega N., Filippi L. and Travascio L.

EP-0207

Visualising HER2 Heterogeneity in Advanced Breast Cancer using [^{68}Ga]Ga-ABY-025 PET - a SingleCentre Polish Experience

G. Kramer-Marek[1,2], *A. Kastelik-Hryniewiecka*[2], *M. Kubeczko*[2], *I. Gorczewska*[2], *A. d'Amico*[2], *J. Feldwisch*[3], *F. Y. Frejd*[3,4], *K. Daszewska*[2], *M. Jarzab*[2];
[1]*The Institute of Cancer Research, London, UNITED KINGDOM,* [2]*Maria Sklodowska-Curie National Research Institute of Oncology, Gliwice, POLAND,* [3]*Affibody AB, Solna, SWEDEN,* [4]*Uppsala University, Uppsala, SWEDEN.*

Aim/Introduction: Molecular heterogeneity and the distinct characteristics of HER2-positive metastatic breast cancer (MBC) constrain precise patient management in the era of antibody-drug conjugates. Moreover, the limitations of repeated biopsies and immunohistochemistry (IHC), which fail to capture the full tumour burden, highlight the need for superior biomarkers to identify patients most likely to benefit from these therapies. Here, we evaluated the use of [^{68}Ga]Ga-ABY-025 HER2-targeted positron emission tomography (PET) in detecting tumour lesions that overexpress HER2 in patients with HER2-positive MBC. ***Materials and Methods:*** The GMP-grade Affibody molecule (ABY-025) for clinical use was provided by Affibody AB, Sweden. Radiolabelling was performed manually for 25 minutes, followed by 40 minutes of pre-release quality control (including radiochemical, chemical, and radionuclide purity, ethanol content, half-life, bacterial endotoxin, pH, sterility, and bubble point tests). All methods were validated under GMP-compliant conditions. The clinical study was approved by the Local Bioethical Committee (#KB/430-51/23). Seven female patients with pre-diagnosed metastatic HER2-positive breast cancer received [^{68}Ga]Ga-ABY-025 (400-600 µg peptide, 100-250 MBq, 8 mL) in saline. PET/CT images were acquired 3 hours post-administration using a Biograph Vision 600 Edge scanner (Siemens Healthineers). Uptake was measured in the largest lesions selected on baseline CT. 33 lesions were included in the analysis. Images were compared to [^{18}F]FDG PET scans obtained 2 or 3 days earlier. ***Results:*** The manual radiolabelling process was rapid, yielding a final product with high radiochemical yield (RCY>80%) and purity (RCP>99%). No adverse events related to HER2 PET radiotracer injection were observed. The biodistribution of [^{68}Ga]Ga-ABY-025 agreed with a previously conducted phase II study[1]. Physiological uptake appeared in the salivary glands, liver, kidneys, and intestines. Across 33 baseline CT defined tumour lesions, 4/33 (12%) had negligible [^{18}F]FDG avidity (SUV_{max} equal to or less than the mediastinal blood pool) yet were clearly HER2-positive (SUV_{max} 9-20) in the HER2 PET. Conversely, one lesion was [^{18}F]FDG positive (SUV_{max} 7.35) but HER2-negative. In addition, there were [^{68}Ga]Ga-ABY-025 SUV_{max} variations at the intra-patient level, ranging from 3 to 20 across different lesions. Importantly, [^{68}Ga]Ga-ABY-025 uptake enabled clear visualisation of brain metastases, while [^{18}F]FDG demonstrated poor sensitivity in this region due to intense physiological accumulation in the grey matter. ***Conclusion:*** This study demonstrates that [^{68}Ga]Ga-ABY-025 PET can capture total disease burden and reveal intra-patient HER2 heterogeneity in HER2 positive breast cancer, providing crucial information that can guide clinicians toward more precise, individualised therapy. ***References:*** [1] Alhuseinalkhudhur et al., J Nucl Med (2023); 64:1364-1370.

EP-0208

Prognostic Value of Molecular Imaging TNM System for [^{18}F]FES PET/CT in Estrogen Receptor-Positive Breast Cancer: A Single-Center Retrospective Study

K. Kimura[1], *M. Jafarvand Giglou*[2], *S. Alkassis*[3], *V. Ludwig*[1], *A. Holzgreve*[1], *I. Sonni*[1,4], *J. Czernin*[1], *B. Aditya*[3], *J. Calais*[1];
[1]*Department of Molecular and Medical Pharmacology Ahmanson Translational Theranostics Division, David Geffen School of Medicine at UCLA, Los Angeles, CA, UNITED STATES OF AMERICA,* [2]*Department of Radiological Sciences, University of California Irvine School of Medicine, Irvine, CA, UNITED STATES OF AMERICA,* [3]*Department of Hematology and Oncology, David Geffen School of Medicine at UCLA, Los Angeles, CA, UNITED STATES OF AMERICA,* [4]*Department of Radiological Sciences, David Geffen School of Medicine at UCLA, Los Angeles, CA, UNITED STATES OF AMERICA.*

Aim/Introduction: Estrogen receptor (ER) expression imaging with 16α-[^{18}F]fluoro-17β-estradiol ([^{18}F]FES) positron emission tomography/computed tomography (PET/CT) was approved by the United States Food and Drug Administration in 2020 to identify ER-expressing lesions in recurrent or metastatic breast cancer. The prognostic value of [^{18}F]FES PET/CT remains undetermined. Our aim was to evaluate the prognostic value of [^{18}F]FES PET-based molecular imaging tumour-node-metastasis (miTNM) staging and [^{18}F]FES PET whole-body (WB) quantitative parameters. ***Materials and Methods:*** This was a single-centre retrospective analysis of patients who underwent [^{18}F]FES PET/CT between December 2021 and March 2024. We created a [^{18}F]FES PET miTNM system, based on the Union for International Cancer Control TNM 8th edition, to describe ER-positive lesion distribution at the patient level. The evaluators, blinded to outcomes, reviewed each scan to apply the miTNM classification. WB quantitative parameters—total tumour volume (TV), maximum standardised uptake value (SUV_{max}), mean SUV (SUV_{mean}), and total lesion uptake (TLU = TV × SUV_{mean})—were also calculated. Outcome measures were progression-free survival (PFS), defined as PET/CT to clinically documented disease progression by imaging, biomarkers, pathology, or physician judgement, and overall survival (OS). Associations were analysed using Kaplan-Meier and Cox regression models. ***Results:*** Sixty-nine patients were included: median age 65 years (interquartile range [IQR]: 57-74); 36 (52%) had invasive lobular carcinoma, 25 (36%) invasive ductal carcinoma. [^{18}F]FES PET/CT was performed for initial staging in 11 (16%) and restaging in 58 (84%). Based on miTNM, 38 (55%) were miT0N0M0, 9 (13%) miT+, 11 (16%) miN+, and 22 (32%) miM+. Median TV, SUV_{max}, SUV_{mean}, and TLU were 6.48 mL (IQR: 1.45-46.2), 4.32 (IQR: 2.85-7.76), 2.59 (IQR: 2.23-2.96), and 20.0 (IQR: 3.36-119.7), respectively. Median follow-up was 24 months (95% confidence interval [CI]: 20-28). Median PFS was not reached (NR) (95% CI: 15.8-NR); 2-year PFS was 58% (95% CI: 47-72). Median OS was NR (95% CI: NR-NR); 2-year OS was 87% (95% CI: 81-97). PFS was significantly shorter in miN+ vs. N0 (hazard ratio [HR] = 2.97; 95% CI: 1.24-7.11; p = 0.014) and in miM+ vs. M0 (HR = 2.92; 95% CI: 1.34-6.33; p = 0.0068). WB parameters showed no significant association. ***Conclusion:*** In this cohort, the [^{18}F]FES PET miTNM staging demonstrated prognostic value for PFS, whereas [^{18}F]FES PET WB quantitative parameters did not. The proposed miTNM framework may support standardised evaluation and broader clinical implementation of [^{18}F]FES PET/CT.

EP-0209

[^{68}Ga]Ga-NOTA-T4 PET/CT Imaging of Trop2 Expression in Patients with Metastatic Breast Cancer

L. Yao[1], *Z. Chu*[2], *Y. Wu*[1], *D. Jiang*[1], *Y. Gu*[3], *Q. Ge*[4], *Y. Guan*[1], *W. Wei*[5], *F. Xie*[1];
[1]*Department of Nuclear Medicine & PET Center, Huashan Hospital, Fudan University, Shanghai, CHINA,* [2]*Department of Oncology, Huashan Hospital, Fudan University, Shanghai, CHINA,* [3]*Central Research Institute United Imaging Healthcare Group Co, Ltd, Shanghai, CHINA,* [4]*Central Research Institute United Imaging Healthcare Group Co, Ltd, Shanghai, CHINA,* [5]*Department of Nuclear Medicine, Institute of Clinical Nuclear Medicine, Renji Hospital, School of Medicine, Shanghai Jiao Tong University, Shanghai, CHINA.*

Aim/Introduction: Gallium-68([^{68}Ga])-labeled Ga-NOTA-T4 PET/CT is a promising noninvasive imaging tool for visualizing trophoblast cell-surface antigen 2 (Trop2) expression, which could aid clinical decisions regarding Trop2-targeted therapies. This study aims to evaluate the diagnostic performance of [^{68}Ga]Ga-NOTA-T4 PET/CT, a novel Trop2-targeting tracer, for detecting Trop2 expression in metastatic breast cancer and to compare its efficacy with conventional fluorine-18 labeled fluorodeoxyglucose ([^{18}F]FDG) PET/CT. ***Materials and Methods:*** From September 2023 to October 2024, patients with metastatic breast cancer were prospectively enrolled. All participants underwent [^{68}Ga]Ga-NOTA-T4 PET/CT, with or without additional [^{18}F]FDG PET/CT. Tracer uptake in detected lesions was quantified using the maximum standardized uptake value (SUVmax) and the target-to-background ratio (TBR). Quantitative differences between groups were analyzed using the t-test. ***Results:*** A total of 23 patients (mean age: 54 ± 13 years; all female) were included in the study, with 9 undergoing both [^{68}Ga]Ga-NOTA-T4 and [^{18}F]FDG PET/CT. [^{68}Ga]Ga-NOTA-T4 successfully detected lesions in 82.6% (19/23) of patients. Compared with [^{18}F]FDG PET/CT, [^{68}Ga]Ga-NOTA-T4 PET/CT identified the same number of patients (9 vs. 9) but a slightly lower number of lesions, with metastatic lesions showing lower SUV_{max} and TBR values. Notably, [^{68}Ga]Ga-NOTA-T4 imaging showed no uptake in an inflammatory nodule identified by [^{18}F]FDG PET/CT, suggesting its potential for distinguishing malignant from inflammatory lesions . ***Conclusion:*** [^{68}Ga]Ga-NOTA-T4 PET/CT is a promising tool for visualizing Trop2 expression in metastatic breast cancer, with potential applications for patient stratification and precision therapy. While its diagnostic performance is comparable to [^{18}F]FDG PET/CT, it offers additional advantages in reducing false positives from inflammatory lesions.

EP-0210

The Predictive Role of Pre-Treatment PET/CT-Derived Quantitative Parameters in Disease Progression of Triple-Negative Breast Cancer

N. Ünsal[1], *S. Karabulut*[1], *A. Aksu*[2], *G. Capa Kaya*[1];
[1]*Dokuz Eylul University Medical Faculty Hospital, Departmant of Nuclear Medicine, Izmir, TÜRKIYE,* [2]*Izmir Katip Celebi University Medical Faculty Hospital, Departmant of Nuclear Medicine, Izmir, TÜRKIYE.*

Aim/Introduction: The aim of this study is to evaluate the role of quantitative parameters obtained from pre-treatment 18-fluorodeoxyglucose positron emission tomography/computed tomography (F-18 FDG PET/CT) in predicting progression in patients diagnosed with triple-negative breast cancer (TNBC). ***Materials and Methods:*** Pre-treatment PET/CT images of patients with at least 2 years of follow-up were analyzed using LIFEx software. The primary tumor's volume of interest (VOI) was manually segmented. From these VOIs, morphological, density-based and histogram parameters were obtained. The presence of lymph node and distant metastasis on staging PET, as well as progression during follow-up, were recorded. The relationship between progression and non-progression patients was evaluated statistically. ***Results:*** Thirty-eight patients with a mean age of 61±14 (range 40-94) years were included in the study. Thirty patients (78.9%) had unifocal tumors, and 18 (47.4%) had multifocal tumors. Lymph node metastasis was present in 27 (71.7%) patients, and distant metastasis was present in 9 (23.7%). The median progression-free survival (PFS) was 72.8±7.9 (range 57.2-88.4) months. Progression was detected in 14 patients (36.8%) during follow-up. In patients with progression, the rates of lymph node and distant metastasis were higher than in those without progression (p: 0.030 and 0.006, respectively). Significant differences were observed between progression and non-progression patients in 15 morphological, 2 density-based, and 3 histogram parameters derived from the primary tumor. No correlation was observed between morphological_surface_area and intensity_based_skewness parameters. In logistic regression analysis, morphological_surface_area (p: 0.008, OR: 24.143, 95% CI: 2.277-256.043) and intensity_based_skewness (p: 0.018, OR: 11.021, 95% CI: 1.518-80.003) were identified as prognostic factors for predicting progression. The model derived from these parameters was able to accurately classify 32 patients (p<0.001, AUC: 0.887, 78.6% sensitivity, 87.5% specificity). ***Conclusion:*** Morphological and density-based parameters obtained from the primary tumor can serve as predictive factors for identifying TNBC patients who may progress during follow-up.

EP-0211

Accuracy of [^{68}Ga]Ga-FAPI PET/CT in Evaluating Axillary Lymph Node Status After Neoadjuvant Therapy in Clinically Node-Positive Breast Cancer Patients

Y. Fan[1], *J. Hu*[1], *C. Hu*[2], *S. Zhu*[2], *Y. Lu*[2], *Y. Peng*[1], *Q. Hu*[1], *P. Ju*[1], *B. Li*[1], *Y. Yuan*[3], *K. Shen*[2], *X. Chen*[2];
[1]*Department of Nuclear Medicine, Ruijin Hospital Affiliated to Shanghai Jiao Tong University School of Medicine, Shanghai, CHINA,* [2]*Department of General Surgery, Comprehensive Breast Health Center, Ruijin Hospital Affiliated to Shanghai Jiao Tong University School of Medicine, Shanghai, CHINA,* [3]*Department of Radiology, Shanghai Ninth People's Hospital, Shanghai Jiao Tong University School of Medicine, Shanghai, CHINA.*

Aim/Introduction: Accurate diagnosis of axillary lymph node (ALN) status after neoadjuvant therapy (NAT) can guide de-escalation surgery in breast cancer. Given the lack of accurate imaging methods for assessing residual ALN status, we investigated the accuracy of [^{68}Ga]Ga-FAPI PET/CT in evaluating ALN after NAT in clinical ALN positive breast cancer patients. ***Materials and Methods:*** In this prospective phase II study, breast cancer patients with clinical lymph node positive (cN+) who underwent NAT receiving pre-operative assessed with ALN ultrasound (US) and [^{68}Ga]Ga-FAPI PET/CT after NAT were enrolled between August 2024 and February 2025. PET parameters were measured on PET/CT images for ALN, mediastinal blood pool, and hepatic blood pool. Imaging findings were subsequently compared with histopathological results from surgical specimens of the ALN. ***Results:*** A total of 48 patients were included, of whom 22 (45.8%) achieved ypN0 status. The mean ALN SUVmax value on [^{68}Ga]Ga-FAPI PET/CT was significantly lower in the ypN0 group (3.04 ± 3.78) compared to the ypN+ group (8.75 ± 8.98, P = 0.006). Based on AUC analysis and Youden's index, an SUVmax cutoff value of 3.19 was identified as optimal for distinguishing lymph node status. When compared to ultrasound (specificity: 0.46, 95% CI: 0.27-0.68; positive predictive value [PPV]: 0.60, 95% CI: 0.49-0.71), [^{68}Ga]Ga-FAPI PET/CT demonstrated superior diagnostic performance, with a specificity of 0.96 (95% CI: 0.86-1.00, P < 0.001) and a PPV of 0.94 (95% CI: 0.81-1.00, P < 0.001). Furthermore, the negative predictive value (NPV) was significantly higher in patients with triple-negative or HER2-positive breast cancer compared with ultrasound (1.00 vs. 0.56, P < 0.001). Additional PET parameters, including the SUVmax ratio of ALN-to-aortic arch blood pool (TBRAmax) and the SUVmean ratio of ALN-to-liver blood pool (TBRLmean), also exhibited strong diagnostic efficacy. With thresholds of 0.841 and 2.517, respectively, these parameters demonstrated sensitivities of 0.92 (95% CI: 0.81-1.00) and 0.81 (95% CI: 0.65-0.96), as well as NPVs of 0.88 (95% CI: 0.72-1.00) and 0.76 (95% CI: 0.63-0.92). ***Conclusion:*** Our study demonstrated that [^{68}Ga]Ga-FAPI PET/CT had superior diagnostic accuracy in assessing ALN status after NAT compared to ultrasound, which could potential guide further de-escalation surgery of ALN in these breast cancer patients.

EP-0212

Trop2-targeted [18F]AIF-RESCA-T4 Immuno-PET/CT in Breast Cancers: Evaluation Across Different Molecular Subtypes

***W. Jia**, G. Huang, J. Liu, W. Wei;*
Department of Nuclear Medicine, Renji Hospital, School of Medicine, Shanghai Jiao Tong University, Shanghai, CHINA.

Aim/Introduction: The study aimed to evaluate Trop2 expression in different molecular subtypes of breast cancer and explore the potential of [^{18}F]AIF-RESCA-T4 immuno-PET/CT imaging in diagnosing primary lesions and lymph node metastases. ***Materials and Methods:*** Trop2 expression was detected using immunohistochemistry (IHC) on tissue microarrays (TMA) and quantified using the H-score (0–300). Seventeen breast cancer patients underwent [^{18}F]AIF-RESCA-T4 immuno-PET/CT imaging to detect primary lesions and potential metastases. Pathology specimens from all patients were used for Trop2 staining. Receiver Operating Characteristic (ROC) curves were used to calculate the diagnostic cutoff values of the tracer. ***Results:*** Trop2 expression was significantly higher in breast tumor tissues than adjacent normal tissues, with no significant correlation to clinicopathological features. [^{18}F]AIF-RESCA-T4 uptake strongly correlated with Trop2 expression in the primary and metastatic tumors (R^2 = 0.7339, P < 0.001). Diagnostic cutoff values for the primary tumors (SUVmax = 3.125) and lymph node metastases (SUVmax = 2.12) showed high sensitivity and specificity, with 97.2% and 94.4% for primary tumors and 95% and 98.6% for lymph node metastases, respectively. [^{18}F]AIF-RESCA-T4 immuno-PET/CT imaging demonstrated good diagnostic value for most invasive cancer types, except neuroendocrine tumors, and effectively differentiated tumors from inflammatory diseases. ***Conclusion:*** Trop2 is highly expressed across all breast cancer molecular subtypes and is unrelated to clinicopathological features. [^{18}F]AIF-RESCA-T4 immuno-PET/CT imaging shows potential for assessing tumor burden, detecting lymph node metastases, and guiding therapeutic decisions in breast cancer.

EP-0213

Response Assessment with ^{18}F-FDG PET/CT in Tripple Negative Breast Cancer Patients Undergoing Combined Immunochemotherapy: A Retrospective Analysis

***E. Popova**[1], Z. Zhelyazkova[2], S. Sergieva[1], R. Krasteva[2];*
[1]Acibadem City Clinic Tokuda Hospital, Sofia, BULGARIA, [2]Unihospital, Panagyurishte, BULGARIA.

Aim/Introduction: The integration of immunotherapy into chemotherapy regimens is expanding therapeutic strategies for triple negative breast cancer (TNBC), both in early-stage or metastatic disease [1]. Accurate assessment of treatment response is essential for tailoring clinical management. ^{18}F-FDG PET/CT combines anatomical and metabolic information, offering a comprehensive tool for evaluating disease status beyond conventional imaging alone [2]. This retrospective study assesses therapy response in triple negative breast cancer patients receiving combined immunochemotherapy in a clinical practice setting. ***Materials and Methods:*** We retrospectively included all patients diagnosed with triple negative breast cancer and treated with Immune Checkpoint Inhibitors (ICIs) between March 2023 and February 2024 at our center. Of the 19 initially identified patients, 3 were excluded due to insufficient follow-up data, resulting in a final cohort of 16 patients. Data included ICD-10 diagnosis, TNM staging (with post-surgical staging in neoadjuvant cases), histopathological results, PET/CT findings at baseline and up to three follow-up timepoints, treatment regimens, and any therapy modifications. Ten patients received neoadjuvant therapy and six received adjuvant therapy. ***Results:*** In the neoadjuvant group, 6 of 10 patients (60%) showed complete response (CR) on PET/CT, all of whom also achieved pathological complete response (pCR), demonstrating full concordance between PET/CT imaging and histology. Four of the ten patients showed partial response (PR). In the adjuvant group, 4 of 6 patients (67%) achieved complete response (CR), one had progressive disease (PD), and one achieved stable disease (SD). The overall complete response rate in the cohort of 16 patients was 63% (10 out of 16 patients). ***Conclusion:*** Combined immunochemotherapy demonstrated high efficacy in this cohort, with a substantial proportion of patients achieving complete response in both neoadjuvant and adjuvant settings. PET/CT served as a valuable tool for response assessment, offering combined anatomical and metabolic insights. In the neoadjuvant group, PET/CT complete response correlated strongly with pathological complete response, supporting its role in guiding treatment decisions. Further prospective studies with larger cohorts are needed to confirm these findings. ***References:*** 1. Javier Cortes, Hope S. Rugo, David W. Cescon et al. Pembrolizumab plus Chemotherapy in Advanced Tripple Negative Breast Cancer. N Engl J Med, doi: 10.1056/NEJMoa22028092. 2. Sofia C Vaz, Stephanie L Graff, Arlindo R Ferreira, Marcio Debiasi et al. PET/CT in Patients with Breast Cancer Treated with Immunotherapy. MDPI Cancers 2023, doi: 10.3390/cancers15092620.

EP-0214

Influence of Plasma Estradiol Levels on ^{18}F-FES Uptake in ER-Positive Breast Cancer

***K. Miyake**[1], Y. Shimizu[1], M. Kawashima[1], S. Yuge[2], Y. Kitano[1], S. Yasumura[1], Y. Kitai[3], T. Oishi[3], K. Itagaki[3], M. Kataoka[1], N. Masuda[1], K. Nakatani[1], Y. Nakamoto[1];*
[1]Kyoto University Graduate School of Medicine, Kyoto, JAPAN, [2]Tenri Hospital, Nara, JAPAN, [3]Kyoto University Hospital, Kyoto, JAPAN.

Aim/Introduction: The estrogen receptor (ER) is a crucial biomarker in breast oncology, and ^{18}F-fluoro-17β-estradiol (FES) PET is increasingly utilized as a noninvasive tool to assess ER expression. While several factors such as SERDs and SERMs are known to affect FES uptake, the impact of menopausal status or plasma estradiol (E2) levels remains controversial [1]. This study aimed (1) to investigate the association between tumor FES uptake and endogenous plasma E2 levels in breast cancers with high ER expression, and (2) to explore whether physiological uterine uptake could serve as a surrogate marker to predict the influence of E2 on tumor uptake. ***Materials and Methods:*** Female patients with ER-positive breast cancer who underwent FES PET/CT at initial staging and had no prior exposure to selective estrogen receptor modulators or selective estrogen receptor downregulators were included. SUVmax was measured for histologically confirmed primary invasive breast cancers with high ER expression (>70% IHC staining), as well as for the uterus. Plasma estradiol levels were measured at the time of FES injection and categorized as low (<20 pg/mL), mild (20-100 pg/mL), moderate (100-200 pg/mL), or high (≥200 pg/mL). Statistical analyses were conducted using the Wilcoxon/Kruskal-Wallis test and Spearman's rank correlation coefficient. ***Results:*** A total of 61 female patients (age range: 27-90 years; 25 premenopausal, 36 postmenopausal) were included. Among 67 tumors (56 NOS, 7 ILC, 4 others), the median tumor SUVmax was 3.2 (range: 0.5-22). Tumor SUVmax was significantly lower in premenopausal patients (median: 4.0, range: 0.5-9.1) compared to postmenopausal patients (median: 4.4, range: 0.9-22). There was a mild but significant positive correlation between tumor SUVmax and age (ρ = 0.32, p < 0.01). Tumor SUVmax differed significantly across E2 categories (p = 0.035) and showed an inverse correlation with E2 levels (ρ = -0.32, p < 0.01). No association was found between tumor size and SUVmax. Uterine SUVmax (median: 6.0, range: 1.5-14.6) was observed regardless of menopausal status. Uterine SUVmax did not significantly correlate with menopausal status or E2 levels. No significant association was found between tumor SUVmax

and uterine SUVmax. ***Conclusion:*** In breast cancers with high ER expression, tumor FES uptake appears to be influenced by plasma E2 levels. However, physiological uterine uptake does not reliably predict the E2-related decrease in tumor FES uptake. ***References:*** 1) Peterson LM, et al. Factors influencing the uptake of 18F-fluoroestradiol in patients with estrogen receptor positive breast cancer. Nucl Med Biol. 2011;38:969-978.

EP-0215

Toward 'Less is More': ^{68}Ga-FAPI PET/CT Optimizes Axillary Management in Invasive Breast Cancer

J. Li, *W. Mu, Y. Tang, K. Zhang, S. Hu;*
Xiangya Hospital, Central South University, Changsha, CHINA.

Aim/Introduction: The shift toward "less is more" in axillary management of breast cancer (BC) necessitates accurate nodal staging to minimize overtreatment. Although sentinel lymph node biopsy (SLNB) and axillary lymph node dissection (ALND) remain standards for clinically node-negative (cN0) patients, their procedural morbidity (e.g., lymphedema) drives demand for non-invasive alternatives. Conventional imaging often fails to accurately stratify nodal tumor burden, leading to unnecessary interventions. We prospectively evaluated ^{68}Ga-FAPI PET/CT for preoperative axillary metastasis detection and surgical de-escalation guidance, aligning with modern de-escalation paradigms (e.g., Z0011, AMAROS). ***Materials and Methods:*** Seventy treatment-naive cT1-3N0M0 invasive BC patients (females; mean age 53 years) underwent preoperative ^{68}Ga-FAPI PET/CT and MRI, followed by SLNB/ALND. Visual and quantitative analyses of PET/CT images were performed using pathology (macro-metastasis >2 mm) as the reference standard. Diagnostic performance for nodal metastasis (binary detection and burden stratification: N-low [0-2 nodes] vs. N-high [≥3 nodes]) was assessed. Optimal SUVmax thresholds were derived. Statistical analyses used SPSS 27 and R 4.4.2. ***Results:*** For binary ALN metastasis detection, ^{68}Ga-FAPI PET/CT visual analysis outperformed MRI (AUC: 91.4% vs. 72.9%; p<0.001), with 66.7% sensitivity, 100% specificity, 100% PPV, and 89.7% NPV. Quantitative analysis further improved performance (SUVmax cutoff 1.25: 94.9% accuracy, 80% sensitivity, 100% specificity, 100% PPV, 93.6% NPV). Crucially, ^{68}Ga-FAPI PET/CT achieved 100% accuracy, specificity, and NPV in nodal burden stratification, correctly identifying all N-low cases (enabling potential ALND avoidance) and distinguishing N-high disease. ***Conclusion:*** ^{68}Ga-FAPI Ga-FAPI PET/CT offers a highly specific, non-invasive tool for preoperative ALN assessment in invasive cT1-3N0M0 BC, facilitating precision axillary management. Its superior diagnostic performance over MRI supports its integration into de-escalation protocols to reduce unnecessary surgeries.

EP-0216

Radiological indicators of peritumoural and whole-breast vascularity and their association with [^{18}F]-FMISO PET/MRI parameters of hypoxia and vascular function in breast cancer

R. Manavaki[1], *J. C. Carmona-Bozo[1], S. Carriero[1], N. Stranz[1], J. L. Miller[2], C. Brodie[2], C. Caracò[1], M. J. Graves[1], A. J. Patterson[1], T. D. Fryer[1], E. Provenzano[3], F. J. Gilbert[1];*
[1]University of Cambridge, Cambridge, UNITED KINGDOM, [2]Cancer Research UK - Cambridge Institute, Cambridge, UNITED KINGDOM, [3]Cambridge University Hospitals NHS Foundation Trust, Cambridge, UNITED KINGDOM.

Aim/Introduction: Breast cancers, like other solid tumours, exhibit vascular abnormalities, leading to irregular blood flow and heterogeneous states of hypoxia within the lesion. This study assessed the relationship between radiological markers of whole-breast and peritumoral vascularity and parameters of tumour hypoxia and vascular function derived from PET/MR imaging with [^{18}F]-fluoromisonidazole ([^{18}F]-FMISO). ***Materials and Methods:*** Women aged >18 years with treatment-naïve, biopsy-confirmed breast cancer underwent a 60-min PET/MR scan two hours after injection of 300 MBq [^{18}F]-FMISO. Parameters of vascular function (K^{trans}, k_{ep}, v_e, v_p) were derived from DCE-MRI using the extended Tofts' model. Tumour hypoxia was assessed using the influx rate constant K_i for [^{18}F]-FMISO determined by Patlak-plot analysis. Hotspot (hs)-K^{trans} was also calculated. Peritumoural vascularity was analysed by counting adjacent feeding vessels (AFV) in contact with or penetrating the lesion. Whole-breast vascularity was quantified by counting the number of significant vessels (i.e., ≥3 cm long, and ≥2 mm in transverse diameter) in the ipsilateral breast. Post-surgical tumour sections were stained for CD31, hypoxia-inducible factor (HIF)-1α and carbonic anhydrase IX (CAIX). Microvessel density (MVD) and median vessel diameter were obtained from CD31 microarrays via computer-assisted analysis. HIF-1α and CAIX expression were scored by the percentage of positively stained cells. Pathological correlates included tumour type, grade, and molecular subtype. Associations between variables of interest were analysed using linear models or Spearman's ρ. ***Results:*** 31 tumours were analysed with the majority being ductal cancers (20/31; 64.5%), grade 2 or 3 (28/31; 90%) and hormone receptor-positive (30/31; 97%). A negative association was found between AFV number and [^{18}F]-FMISO K_i (ε^2=0.07, p=0.048), while a positive association was observed with hs-K^{trans} (ε^2=0.27, p=0.002). Similarly, a negative relationship was observed between the number of significant vessels in the ipsilateral breast and tumour [^{18}F]-FMISO K_i (ε^2=0.11, p=0.04). In contrast, significant vessel number was positively related with mean tumour K^{trans} (ε^2=0.21, p=0.006), v_e (ε^2=0.11, p=0.04) and v_p (ε^2=0.21, p=0.006). No significant association was observed between measures of peritumoural or whole-breast vascularity and tumour histology, grade or molecular subtype. In a subset of 24 cancers for which immunohistochemistry was available, AFV was negatively correlated with vessel diameter (ρ=-0.49, p=0.03). In contrast, no significant correlations were found between AFV or significant vessel number with MVD, CAIX or HIF-1α expression. ***Conclusion:*** Poor peritumoural and whole-breast vascularity are associated with hypoxia and inadequate vascular function as measured by [^{18}F]-FMISO-PET/MRI, suggesting potential use of these radiological descriptors in characterising breast cancer.

EP-0217

[18F]FDG and [68Ga]FAPI PET/CT for lesion detection and characterization in Triple Negative Breast Cancer patients

N. Hovhannisyan-Baghdasarian[1], *L. Champion[2], N. Jehanno[3], R.-D. Seban[2], H. Tissot[3], J. Fouque[4], F. Coussy[5], D. Bello Roufai[5], D. Loirat[6], S. Rafie[7], F.-C. Bidard[5], F. Mechta-Grigoriou[7], I. Buvat[1];*
[1]Institut Curie, Inserm, Orsay, FRANCE, [2]Dpt of Nuclear Medicine, Institut Curie, Saint Cloud, FRANCE, [3]Dpt of Nuclear Medicine, Institut Curie, Paris, FRANCE, [4]Dpt of Pharmacy, Institut Curie, Saint-Cloud, FRANCE, [5]Dpt of Medical Oncology, Institut Curie, Saint-Cloud, FRANCE, [6]Dpt of Medical Oncology, Institut Curie, Paris, FRANCE, [7]Unité Chimie Biologie des Cancers, Institut Curie, Inserm, CNRS, Paris, FRANCE.

Aim/Introduction: The usefulness of [68Ga]FAPI PET/CT for triple negative breast cancer (TNBC) patient management has not been studied much, while Fibroblast Activation Proteins (FAP) are significantly expressed in the TNBC tumor microenvironment. As part of the Skyline trial (NCT06175390), we investigate the complementarity between [18F]FDG and [68Ga]FAPI PET/CT for lesion detection and characterization in early and advanced TNBC patients. ***Materials and Methods:*** Skyline is an ongoing phase 2 trial prospectively enrolling 160 patients with TNBC to explore the use of an anti-TIGIT therapy combined with anti PD-L1 and chemotherapy in 2 cohorts: neoadjuvant (cohort A) or first line therapy (cohort B). All patients undergo [18F]FDG and [68Ga]FAPI-46 PET/CT before treatment and after 2 cycles. All tumor lesions were segmented by an expert using a threshold of SUV≥2.5 in the

[18F]FDG and [68Ga]FAPI PET images independently. SUVmax and Total Tumor Signal (TTS) defined as mean SUV multiplied by the tumor volume on the corresponding PET images were calculated. Patient response is not disclosed as patient recruitment is ongoing. ***Results:*** 50 patients have already been enrolled: 38 in cohort A, 12 in cohort Images of 33 patients who had their baseline and 2-cycle scans performed have been analyzed (26 from cohort A and 7 from cohort B), corresponding to 91 lesions (primary, nodes and metastases) in total. In those 91 lesions, 83 were seen on the FDG and FAPI scans, 7 were seen on the FDG scan only, and 1 was seen on the FAPI scan only. At baseline, SUVmax in the primary tumors (n=33) was significantly lower in the FAPI scan (15.2±4.8) compared to the FDG scan (18.2±7.6, paired t-test p<0.05). Yet, the primary tumor volume tended to be higher in the FAPI images (27±23 mL) compared to the FDG images (22±35 mL, p=0.125). This resulted in a TTS non-significantly different in FDG and FAPI scans (p=0.5). Similarly, in nodes (n=20), the average SUVmax_FAPI was significantly lower than SUVmax_FDG (p=0.04), while TTS was not significantly different in FDG and FAPI scans. ***Conclusion:*** In these two cohorts, 91% of the lesions seen on the FDG scans expressed FAP as revealed by [68Ga]FAPI PET. Although the baseline SUVmax was significantly lower in the FAPI scans compared to the FDG scans, the volume of [68Ga]FAPI expression tended to be larger than the FDG positive volume, suggesting that both SUVmax and TTS should be later correlated with the treatment response and patient outcome.

EP-15

e-Poster Area

B: Imaging Clinical Studies -> B1 Oncological Imaging Clinical Study -> B14 Lung (including Mesothelioma)

EP-0218

Exploring Brain Metabolic and Functional Changes in Solitary Pulmonary Lesions: A ^{18}F-FDG PET/MR Study Comparing Malignant and Benign Cohorts

N. Meng[1], *Q. Ji*[2], *J. Pan*[1], *Q. Chen*[1], *Y. Yang*[3], *Z. Wang*[2], *M. Wang*[1];
[1]*Henan Provincial People's Hospital, Zhengzhou, CHINA,* [2]*United Imaging Healthcare Advanced Technology Research Institute Co., Ltd., Shanghai, CHINA,* [3]*United Imaging Healthcare Co., Ltd., Beijing, CHINA.*

Aim/Introduction: The brain is the most important organ in the human body, and the lungs are the primary respiratory organ, and previous studies have shown that there is an important interaction between the lungs and the brain. This study aims to investigate differences in brain metabolic and functional alternations between patients with benign and malignant solitary pulmonary lesions (SPL) using multimodal ^{18}F-FDG PET/MR imaging. ***Materials and Methods:*** A total of 124 SPL patients were enrolled in this study, including 24 with benign lesions and 100 with malignant lesions. Cognitive status of each subject was evaluted using the Mini-Mental State Examination (MMSE). All patients underwent integrated ^{18}F-fluorodeoxyglucose (^{18}F-FDG) PET/MR examinations, with acquisition of high-resolution T1-weighted structural images, resting-state functional fMRI (rs-fMRI) and ^{18}F-FDG images. Normalized standardized uptake value ratio (SUVR) maps were calculated from ^{18}F-FDG images using pons as the reference region to quantify metabolic changes. For functional characterization, regional homogeneity (ReHo), amplitude of low-frequency fluctuation (ALFF), and fractional ALFF (fALFF) maps were computed from rs-fMRI data to investigate intrinsic brain functional alterations. Whole-brain voxel-wise group comparisons between malignant and benign group were performed using two-sample t-tests. ***Results:*** Patients with malignant SPL exhibited significantly lower MMSE scores compared to those with benign SPL (27.1 ± 3.5 vs. 29.4 ± 1.2, $p < 0.01$). Metabolic analysis found significantly reduced SUVR in malignant group in posterior cingulate (peak MNI: [4 -62 6]), with additional reductions observed in occipital lobe (two-tailed, voxel $p < 0.01$, cluster $p < 0.05$, GRF-corrected). In contrast, all functional metrics, including ReHo, ALFF, and fALFF showed no significant between-group differences across all brain regions. ***Conclusion:*** The results revealed that malignant SPL is associated with a marked reduction in cognitive performance relative to benign SPL. Significant metabolic reductions were found in posterior cingulate and other specific brain regions. These results provide evidence for lung cancer-induced brain alterations, suggesting that tumor-related metabolic dysfunction in specific neural circuits may underlie cognitive impairment observed in cancer patients.

EP-0219

Long-Axial-Field-Of-View PET/CT in Deep-Inspiration-Breath-Hold for radiation therapy planning of mediastinal lymphoma

S. Honoré d'Este[1], *O. E. Wagner*[1], *P. A. Andersen*[2], *D. Dejanovic*[1], *A. Loft*[1], *M. G. Askløf*[1], *E. Albrecht-Beste*[1,3], *I. R. Vogelius*[2,3], *L. Specht*[2,3], *F. L. Andersen*[1,3];
[1]*Department of Clinical Physiology and Nuclear Medicine, Copenhagen University Hospital, Copenhagen, DENMARK,* [2]*Department of Oncology, Copenhagen University Hospital, Copenhagen, DENMARK,* [3]*Department of Clinical Medicine, University of Copenhagen, Copenhagen, DENMARK.*

Aim/Introduction: Initial staging Positron Emission Tomography / Computed Tomography (PET/CT) of mediastinal lymphoma patients was shifted from conventional to the 106cm Long-Axial-Field-Of-View (LAFOV) PET/CT upon installation in 2021. The increased FOV allowed for inclusion of the neck, chest and upper abdomen in a single bed position during Deep-Inspiration-Breath-Hold (DIBH). This allowed optimal image fusion with later radiotherapy planning CT in DIBH following chemotherapy. This enabled a reduction in radiation exposure to nearby Organs-At-Risk (OAR) such as the heart and lungs [1]. ***Materials and Methods:*** 37 adult patients (20y-95y) with mediastinal lymphoma were included. Initial staging was performed using a LAFOV PET/CT standard protocol of 3 MBq/kg [18F]FDG, administered 60min prior to scanning. A custom made mount platform was developed to mount the Respiratory-Gating-for-Scanners (RGSC) system to the standard flat table-top for correct positioning in potential RT. The initial protocol included a Whole-Body DIBH CT with intravenous contrast and 4x18sec DIBH PET acquisitions, which were decay corrected and averaged to a final 72sec PET image. Thoracic wall movement of ±1.5mm was tolerated during DIBH. The staging protocol was finalized with a 300sec Free Breathing (FB) PET using a Low-Dose CT for attenuation correction. 10/37 patients received additional RT following chemotherapy. These patients underwent a DIBH planning CT post-treatment, which was fused with the initial staging DIBH PET/CT and used for delineation of the initial Gross-Lymphoma-Volume, the Clinical-Target-Volume (CTV, i.e., the initially involved lymphoma volume modified for anatomical changes during chemotherapy), and OAR. RT planning was done in accordance with national and international guidelines. ***Results:*** 35/37 patients tolerated all 4x18sec WB DIBH PET scans, while the remaining 2/37 only accomplished 2x18sec DIBH. 37/37 patients achieved DIBH images of satisfactory quality for RT planning with a mean liver Coefficient-Of-Variance of 14.3% ±2.00. The fusion of the initial staging and post-chemo imaging allowed optimal conditions for later CTV delineation which enabled us to keep the mean dose to the heart at a median of 4.37Gy (range [1.68Gy;7.24Gy]) and to the lungs at a median of 7.81Gy (range [4.43Gy;14.2Gy]). ***Conclusion:*** DIBH PET images of satisfactory clinical quality can be obtained in 4x18sec on LAFOV PET/CT and

are well tolerated by patients. Fusion of initial staging DIBH PET/CT with DIBH planning CT performed post-chemotherapy allows for higher precision in target definition and reduction in mean dose of surrounding OAR during RT. ***References:*** [1] doi:10.1102/1470-7330.2011.9063.

EP-0220

Multicenter Evalution of Predictive Clinical and Radiological markers for Pathological Complete Response and Major Pathological Response in NSCLC Patients Undergoing Neoadjuvant Chemoimmunotherapy

M. Zhang[1], *M. Yan*[2], *Z. Zhang*[1];
[1]*Department of Lung Cancer Surgery, Tianjin Medical University Cancer Institute and Hospital, National Clinical Research Center for Cancer, Key Laboratory of Cancer Prevention and Therapy, Tianjin's Clinical Research Center for Cancer, Tianjin Lung Cancer, Tianjin, CHINA,* [2]*Department of Radiology, Tianjin Medical University Cancer Institute and Hospital, National Clinical Research Center for Cancer, Key Laboratory of Cancer Prevention and Therapy, Tianjin's Clinical Research Center for Cancer, Tianjin Lung Cancer Center, 30, Tianjin, CHINA.*

Aim/Introduction: This study aimed to identify clinical factors and develop a predictive model for pathologic complete response (pCR) and major pathologic response (MPR) in non-small cell lung cancer (NSCLC) patients receiving neoadjuvant chemotherapy combined with immune checkpoint inhibitors (ICIs). ***Materials and Methods:*** Cases meeting inclusion criteria were divided into high- and low-risk groups according to 75 clinical indicators based on 10-fold LASSO selection. Logistic regression was employed to analyze both pCR and MPR. The accuracy of the nomograms was assessed using the time-dependent area under the curve (AUC). ***Results:*** A total of 883 patients from four multiple centers were included in the study, with 526 assigned to the training set and 357 to the testing set. The AUC was determined for the prediction of pCR (training: 0.97; testing: 0.87) and MPR (training: 0.94; testing: 0.85). Significant associations were observed between the preoperative tumor maximum diameter, preoperative tumor maximum standardized uptake value (SUV_{max}), changes in tumor SUV_{max}, percentage of tumor reduction, baseline total CYFRA21-1 and pathological response ($P < 0.001$). ***Conclusion:*** The combined application of clinical indicators including non-invasive tumor imaging and hematology can help clinicians to obtain a higher ability to predict NSCLC patient's pathological remission, and the effect is better than that of clinical factors alone. These findings could help guide personalized treatment strategies in this patient population.

EP-0221

Performance pulmonary nodules detection using Deep Learning motion correction techniques in 18-FDG PET/CT protocols.

M. Giménez Aranda[1,2], *E. Marino*[1,3], *G. Peña*[1];
[1]*FUESMEN (Fundación Escuela de Medicina Nuclear), Mendoza, ARGENTINA,* [2]*Universidad de Mendoza, Mendoza, ARGENTINA,* [3]*CNEA (Comisión Nacional de Energía Atómica), Buenos Aires, ARGENTINA.*

Aim/Introduction: Pulmonary nodules(PN) detection is essential for staging in cancer patients. Accurate PN detection via PECT/CT scans is limited by respiratory motion[1], which leads to image resolution loss, attenuation correction artefacts, and lesion mislocalisation[2]. The uExcel Focus technique seeks to address this difficulty using Deep Learning-based reconstruction to mitigate such errors[2]. This study aims to evaluate the effectiveness of respiratory motion correction using Deep Learning-enhanced reconstruction methods compared with standard and gated OSEM reconstructions, focusing on metabolic PN detectability and image quality(IQ) improvements assessment in PET/CT FDG protocols. ***Materials and Methods:*** Images were acquired in 54 patients with 18-FDG PET/CT(LYSO and SiPM detectors) with low dose protocols(0.055 mCi/kg), 6 min/bed in list mode. Reconstruction methods were performed: OSEM(standar)(2 iterations, 20 subsets), OSEM Self Gated and VSM Gated(2 iter, 20 subsets), OSEM Focus Self Gated(FSG) and VSM Gated(FVG)(2 iter, 20 subsets), Hyper Iterative VSM Gated(HIG)(strength: 0.90), and Hyper DPR(ST1). With subsequent reconstruction in 4 and 2 min. Volume of interest(VOI) was analysed in the PN, parenchyma, liver and blood pool. For the VOIs measurement were obtained SUVmax, SUVmean, PN volume(PNvol) and standard deviation. Contrast, contrast-to-noise ratio(CNR) and noise were evaluated for IQ. For co-registration, intensity-normalised coronal profiles were plotted on CT and PET images at liver height, calculating the fusion error[mm] as the difference of the profiles. ***Results:*** A total of 47 PNs were detected(diameter range: 3.8-22.0 mm). FSG and FVG showed a significant reduction in co-registration error compared to standard(mean difference:4.15 mm and 4.47 mm; p=0.0016 and 0.00077; Cohen's d=0.78 and 0.80). FVG improves the contrast by 42% compared to standard with no significant difference versus HIG(p>0.84) at 4 min/bed. DPR and HIG present noise reduction bigger than 27% compared to standard and 17% more than FVG at 4-6min/bed and present the maximum value of CNR between 10 and 27% more than FVG 6 min/bed. PNvol is decreased in all reconstructions with respect to standard, with a maximum reduction in 6 min/bed FVG of 40%. FSG and FVG are very highly correlated(r>0.98) with standard in SUVmax values. ***Conclusion:*** Focus Gated of 4 min/bed is a promising tool, as they offer better PN detectability with improved co-registration and IQ superior to standard. ***References:*** [1]Montaño,A.(2024)"Desempeño en la detectabilidad de lesiones pulmonares metabólicas en sistema PET/CT aplicando técnicas de reconstrucción gatilladas y Deep Learning".ESPOCH, Ecuador.[2]Lu,Yihuan,et al.«uExcel Focus: A Unified Solution for Respiratory Motion in PET/CT».Journal of Nuclear Medicine, 64(1),P1261.

EP-0222

Correlation of PD-L1 Expression with PET/CT Metabolic Parameters in Non-Small Cell Lung Cancer

A. Erdem Karaoglu[1], *A. Cinar*[1], *O. Sutcuoglu*[2], *N. Aydinbelge Dizdar*[1], *O. Ozmen*[1,3];
[1]*Ankara Etlik City Hospital, Department of Nuclear Medicine, Ankara, TÜRKIYE,* [2]*Ankara Etlik City Hospital, Department of Medical Oncology, Ankara, TÜRKIYE,* [3]*University of Health Sciences, Ankara, TÜRKIYE.*

Aim/Introduction: The interaction between PD-1 (programmed cell death receptor-1) and PD-L1 (programmed cell death ligand-1) immune-checkpoints in the immune system creates an inhibitory effect, which limits the immune system's ability to target and destroy tumor cells. Anti-PD-1/PD-L1 antibodies can eliminate this effect, allowing the immune system to destroy tumor cells. PD-L1 expression on tumor cells is a significant factor in selecting immunotherapy treatment. In this study, we aimed to evaluate the correlation between metabolic parameters obtained from F18-FDG PET/CT imaging and PD-L1 positivity in patients with non-small cell lung cancer (NSCLC). ***Materials and Methods:*** We retrospectively analyzed the F18-FDG PET/CT images of 185 NSCLC patients who underwent imaging for pre-treatment staging at our clinic between December 2023 and February 2025. Patients were grouped as PD-L1 negative (n=86) and positive (n=99).Both groups were also evaluated by pathological subtypes: adenocarcinoma (n=107) and squamous cell carcinoma (n=78). From the F18-FDG PET/CT images, the following were assessed: primary lesion location, margin characteristics, structural pattern (solid or ground-glass), presence of necrosis, and metabolic parameters (SUVmax, SUVmean, SULpeak, TLG, and MTV). Visual and semi-quantitative data were compared between groups. A

p-value of <0.05 was considered statistically significant. ***Results:*** PD-L1 positive patients were divided into weak (1-10%), moderate (11-50%), and strong (51-100%) subgroups. When comparing the strong PD-L1 positive group with the PD-L1 negative group, SUVmax and SUVmean were significantly higher in the strong positive group (p=0.019; p=0.01). When moderate and strong groups were evaluated together, SUVmax, SUVmean, and SULpeak were significantly higher than in the negative group (p=0.005; p=0.001; p=0.02) When all PD-L1 positive patients were analyzed together, SUVmax, SUVmean, and SULpeak were significantly higher compared to the PD-L1 negative group (p=0.002; p<0.001; p=0.007) In the subgroup analysis, PD-L1 positive adenocarcinoma patients (n=54) showed significantly higher SUVmax, SUVmean, and SULpeak compared to PD-L1 negative adenocarcinoma atients (n=53) (p=0.004; p=0.002; p=0.004) However, in patients with squamous cell carcinoma, no statistically significant difference was observed between the groups (p>0.05). ***Conclusion:*** Our study suggests that metabolic parameters obtained from F18-FDG PET/CT can serve as predictive indicators of high PD-L1 expression in NSCLC, particularly in the adenocarcinoma subtype. Among these parameters, SUVmean was found to be the most statistically significant. SUV measurements from F18-FDG PET/CT, which is an easily accessible and noninvasive imaging method today, may contribute to the determination of patients who are candidates for immunotherapy treatment by providing information about the PD-L1 positivity of the lesions.

EP-0223

Comparative Performance of ^{18}F-FDG and ^{18}F-PSMA PET/CT in Lung Cancer: Adenocarcinoma versus Squamous Cell Carcinoma

N. Silveira, *M. W. P. Júnior, M. S. Takahashi, S. Kuba, B. J. Amorim, M. d. L. Lima, C. A. Souza, C. S. P. Lima, C. D. Ramos;*
UNICAMP, Campinas, BRAZIL.

Aim/Introduction: As a leading global cause of cancer mortality, lung cancer management benefits from metabolic imaging with ^{18}F-FDG PET/CT. Emerging evidence suggests prostate-specific membrane antigen (PSMA)-targeted PET/CT, while established in prostate cancer, may have utility in other malignancies due to PSMA's association with tumor angiogenesis. This study evaluates both tracers in lung adenocarcinoma and squamous cell carcinoma (SCC), assessing subtype-specific uptake patterns. ***Materials and Methods:*** This study evaluated both tracers in 14 patients (9 men, 5 women; age range 55-82 years) with histologically confirmed lung cancer (10 adenocarcinoma, 4 squamous cell carcinoma [SCC]). All patients underwent both ^{18}F-FDG and ^{18}F-PSMA PET/CT scans (0.1 mCi/kg dose, 60- and 90-minute uptake periods, respectively), with images interpreted by three specialists. ***Results:*** The analysis of 288 total lesions (247 adenocarcinoma, 41 SCC) revealed distinct patterns between tracers and subtypes. In adenocarcinoma, ^{18}F-FDG detected 237 lesions compared to 215 by ^{18}F-PSMA, with 32 lesions visible only on ^{18}F-FDG and 9 exclusively on ^{18}F-PSMA. While most adenocarcinoma lesions showed higher ^{18}F-FDG uptake (median SUVmax 6.5 versus 4.0 for PSMA), 45 lesions demonstrated predominant ^{18}F-PSMA uptake. SCC exhibited different characteristics, with ^{18}F-FDG identifying 41 lesions versus 36 by ^{18}F-PSMA, and no cases showing PSMA-dominant uptake. The median SUVmax values in SCC were 8.8 for ^{18}F-FDG compared to just 2.5 for ^{18}F-PSMA. We found that SUV values for ^{18}F-PSMA are statistically different between SCC and adenocarcinoma subtypes in the lesions that showed uptake of both radiotracers (Mann-Whitney U test, p-value < 0.0001). Also, a positive correlation was observed for ^{18}F-FDG and ^{18}F-PSMA SUVs in both histological subtypes, being strong for SCC (r = 0.0,8140, p-value < 0.0001) and moderate for adenocarcinoma (r = 0.4278, p-value < 0.0001). ***Conclusion:*** These findings demonstrate differences in tracer uptake patterns between lung cancer subtypes. Squamous cell carcinomas show minimal ^{18}F-PSMA avidity, suggesting limited clinical utility of this tracer for SCC evaluation. In contrast, adenocarcinomas display more variable uptake, with a subset of lesions showing significant ^{18}F-PSMA accumulation that may reflect active neoangiogenesis. PSMA-positive adenocarcinomas may represent a subgroup amenable to PSMA-directed therapies or angiogenesis inhibitors. These results warrant further investigation into the potential role of ^{18}F-PSMA PET/CT in personalizing treatment approaches for lung adenocarcinoma patients.

EP-0224

The Relationship Between Metabolic Parameters Derived from ^{18}F-FDG PET/CT Images and Systemic Inflammatory Response with Disease Stage and Survival in Primary Staging of Small Cell Lung Cancer

K. Seker, *Z. Hasbek;*
Sivas Cumhuriyet University, Faculty Of Medicine, Department of Nuclear Medicine, Sivas, TÜRKIYE.

Aim/Introduction: To evaluate the relationship between metabolic parameters derived from staging ^{18}F-FDG PET/CT images and the systemic inflammatory response index(SII) with disease stage and overall survival(OS) in patients with small cell lung cancer (SCLC). ***Materials and Methods:*** In patients diagnosed with SCLC between 2012 and 2023, PET data related to the primary tumor obtained from whole-body ^{18}F-FDG PET/CT imaging performed for primary staging, and SII data obtained from complete blood counts performed within ±7 days of PET imaging, were retrospectively evaluated for their relationship with disease stage and OS in 130 patients (mean age: 62.37±8.91;110 males;20 females) with at least one year of follow-up. Disease staging (limited stage(LS) or extensive stage(ES)) was performed based on ^{18}F-FDG PET/CT images. Additionally, maximum and mean standardized uptake values (SUVmax and SUVmean), metabolic tumor volume (MTV), total lesion glycolysis (TLG), and heterogeneity index (HI) (SUVmax/SUVmean) of the primary tumor were calculated. The SII value was calculated using the formula: platelet count x neutrophil count / lymphocyte count. The endpoint for OS was defined as the time from diagnosis to death for deceased patients, or the time from diagnosis to the date of at least one year of follow-up or December 31, 2024, for surviving patients, and patient OS times were recorded. Statistical analysis was performed using SPSS version 23.0. ***Results:*** Limited stage (LS) disease was present in 37.7% of patients, while 62.3% had extensive stage (ES) disease. No significant differences were observed between LS and ES disease in terms of SUVmax, SUVmean, and HI values. MTV, TLG, and SII were significantly higher in the ES patient group compared to the LS patient group (Table 1). In the ROC (Receiver Operating Characteristic) analysis for distinguishing ES and LS disease, the optimal threshold values with the highest Youden's J index for MTV, TLG, and SII were calculated as 61.56, 400.31, and 774.465, respectively. Kaplan-Meier analysis conducted to predict OS based on these threshold values showed no significant association between SII and TLG with survival, whereas OS was significantly shorter in patients with MTV values above 61.56 (8.63 vs 18.03 months; p=0.028)(Figure 1). ***Conclusion:*** Incorporating volumetric metabolic parameters, rather than the routinely used SUVmax value, into patient evaluation has the potential to contribute to the patient's clinical management. Furthermore, measuring the increased inflammatory response with SII provides supportive significance to the data obtained from PET imaging and may contribute to the patient's clinical follow-up.

EP-0225

Relationship of staging FDG PET/CT parameters with clinicopathological data and mortality in non-small cell lung cancer patients

B. Yilmaztekin, *G. Yılmaztekin, B. B. Demirel, G. Vural; Dr. Abdurrahman Yurtaslan Ankara Oncology Training and Research Hospital, Ankara, TÜRKIYE.*

Aim/Introduction: Lung cancer is the leading cause of all cancer-related deaths. Clinically, lung cancer is divided into 2 main groups, 85% of which is non-small cell lung cancer (NSCLC) and 15% is small cell lung cancer. Our study aimed to determine the relationship between staging FDG PET/CT quantitative parameters and NSCLC pathological subtypes and mortality. ***Materials and Methods:*** The study included 117 NSCLC patients who were diagnosed with lung cancer between 2019-2024 and underwent staging FDG PET/CT at our center. Demographic data, pathological features, follow-up periods, and maximum standardized uptake value (SUVmax), mean standardized uptake value (SUVmean), total lesion glycolysis (TLG), and metabolic tumor volume (MTV) data from FDG PET/CT examination were recorded. The relationships between quantitative FDG PET/CT parameters and pathological subtype, stage, and overall survival were analyzed. ***Results:*** The mean age of 117 NSCLC patients was 66 ± 8; 68 (58.1%) of the patients had adenocarcinoma and 49 (41.9%) had squamous cell carcinoma (SCC). Demographic data and clinicopathological features of the patients are summarized in Table 1. Quantitative PET/CT parameters of the patients (SUVmax, SUVmean, MTV, TLG) are summarized in Table 2. When the data of the two groups were analyzed, it was found that SUVmax, SUVmean, MTV and TLG values were statistically significantly higher in patients with SCC than in patients with adenocarcinoma (p values: $p<0.006$, $p<0.001$, $p<0.006$, $p<0.003$).There was no significant difference in PET/CT parameters among the accessible (n=52) adenocarcinoma subtypes and SCC differentiation degrees. The median follow-up period in the entire patient group was 15.83 (95%CI 14.53-17.13) months. MTV cut-off value was found as 20.79 and TLG cut-off value was found as 191.54 based on mortality data. (Table 3) In the patient group with MTV values below the determined cut-off value, 6-month OS was 92%, 12-month OS was 90% and in the patient group with MTV values above the cut-off value, 6-month 0S was 66% and 12-month OS was 56% ($p<0.001$). In the patient group with TLG values below the cut-off value, 6-month OS was 92% and 12-month OS was 88%, and in the patient group with TLG values above the cut-off value, 6-month 0S was 68% and 12-month OS was 61% ($p<0.001$). ***Conclusion:*** In our study, a significant difference was found between staging PET/CT metabolic parameters and non-small cell lung cancer subtypes, and between staging MTV-TLG values and overall survival.

EP-0226

Impact of a Breath Hold Protocol in PET/CT on Thoracic Lesion Delineation

T. Lima[1], *C. Gomes*[1], *F. Tabotta*[2], *A. Leimgruber*[2]*;*
[1]*Lucerne University Teaching and Research Hospitals, Lucerne, SWITZERLAND,* [2]*Genolier Clinic, Swiss Medical Network, Genolier, SWITZERLAND.*

Aim/Introduction: Accurate thoracic lesion delineation in PET/CT imaging is crucial for treatment planning to limit patient toxicity of external beam radiotherapy[1]. Respiratory motion can significantly affect the precision of lesion segmentation, leading to variability in lesion volume measurements [2,3,4]. We investigated the impact of a breath hold (BH) protocol on lesion delineation in PET/CT imaging. ***Materials and Methods:*** A clinical protocol was implemented where patients underwent a whole-body free-breathing (FB) PET/CT acquisition followed by three 10-second chest BH acquisitions. Thoracic lesions were segmented in both FB and BH reconstructions. A total of 42 patients were included in the study, with 614 lesions analyzed. The scans were performed using a GE Omni 32 cm PET/CT device. The segmentations were done in MIM Software and validated by two experienced nuclear medicine physicians. The end point was the variation in the volume of segmented lesions. Dice and Jaccard scores were used to compare segmentations and Wilcoxon Rank-Sum test was performed to evaluate the significance. ***Results:*** The reduction in lesion variability is more pronounced for moderate (volumes ranging 0.45:62.9 ml for the 10 sec BH versus 0.26:83.7 ml for the FB) and high motion (ranging 0.12:58.9 ml for the 10 sec BH versus 0.19:142.3 ml for the FB) lesions in a single BH acquisition. This improvement diminishes for high motion lesions in added BH acquisitions due to potential motion. These findings suggest that BH protocols can enhance the precision of lesion segmentation in PET/CT. ***Conclusion:*** The breath hold protocol in PET/CT imaging demonstrates a promising approach to mitigate the effects of respiratory motion on lesion delineation especially for thoracic lesions impacted more by breathing motion. This protocol enhances the accuracy and consistency of lesion segmentation aimed to improve target delineation for radiation oncology, which is critical for reducing treatment toxicities. ***References:*** 1-Ehrbar S et. al. Intra- and inter-fraction breath-hold variations and margins for radiotherapy of abdominal targets. Phys Imaging Radiat Oncol. 2023 doi: 10.1016/j.phro.2023.100509. 2- Mercieca S, Belderbos JSA, van Herk M. Challenges in the target volume definition of lung cancer radiotherapy. Transl Lung Cancer Res 2021 doi: 10.21037/tlcr-20-6273 3- Liu C et. al., The impact of respiratory motion on tumor quantification and delineation in static PET/CT imaging. Phys Med Biol. 2009 doi: 10.1088/0031-9155/54/24/007. 4- Hapdey S et. al. Respiratory gated multistatic PET reconstructions to delineate radiotherapy target volume in patients with mobile lung tumors. Q J Nucl Med Mol Imaging. 2022 doi: 10.23736/S1824-4785.19.03183-2.

EP-0227

Comparison of Hypothetical [68Ga]Ga-FAPI-46 PET/CT-derived and [18F]F-FDG PET/CT-derived Treatment Plan in a Suspected/Confirmed Lung Cancer Cohort Addressed to Surgery by Conventional Staging, Within a Monocentric Prospective Trial

G. Cuzzani[1], *E. Fortunati*[2], *L. Zanoni*[3], *C. Nanni*[2], *C. Malizia*[2], *M. Assenza*[4], *L. Vetrone*[2], *F. Lodi*[2], *V. S. Cabitza*[2], *I. Brusa*[2], *S. Emiliani*[2], *F. Giunchi*[5], *A. De Giovanni*[5], *F. Antonacci*[6], *M. Ferrari*[7], *F. Natali*[7], *T. Galasso*[7], *G. P. Bandelli*[7], *P. Candoli*[7], *A. D'errico*[5], *S. Civollani*[8], *P. Solli*[6], *S. Fanti*[1,2]*;*
[1]*Nuclear Medicine, Alma Mater Studiorum University of Bologna, Bologna, ITALY,* [2]*Nuclear Medicine, IRCCS, Azienda Ospedaliero-Universitaria di Bologna, Bologna, ITALY,* [3]*Nuclear Medicine, AST Pesaro-Urbino, ITALY,* [4]*Professional Development and Implementation of Research in Health Professional Unit, IRCCS Azienda Ospedaliero-Universitaria di Bologna, Bologna, ITALY,* [5]*Pathology, IRCCS, Azienda Ospedaliero-Universitaria di Bologna, Bologna, ITALY,* [6]*Division of Thoracic Surgery, IRCCS, Azienda Ospedaliero-Universitaria di Bologna, Bologna, ITALY,* [7]*Interventional Pulmonology Unit, IRCCS, Azienda Ospedaliero-Universitaria di Bologna, Bologna, ITALY,* [8]*Department of Medical Physics, IRCCS, Azienda Ospedaliero-Universitaria di Bologna, Bologna, ITALY.*

Aim/Introduction: A prospective, monocentric study (EudraCT2021-006570-23) investigating the role of [68Ga]Ga-FAPI-46 PET/CT(FAPI) in staging suspected/confirmed lung cancer (LC) patients is concluded. Results have already been published on performance in the surgical cohort(n=50). The current purpose is to explore, despite enrolled patients have been treated according to standard staging flow-chart only, if FAPI results (in terms of TNM staging) could have led to a potential, only theoretical, change in patients' management. ***Materials and Methods:*** Patients with suspected/confirmed LC were referred to our Nuclear Medicine Department to follow scheduled conventional-staging-flowchart

and perform [18F]F-FDG PET/CT(FDG), followed by additional FAPI within 3+/-1 weeks, which could not delay or influence their standard of care. For the current purpose, only surgical patients were included. PET/CT results were later validated by surgical-histopathology, considered standard-of-truth, and TNMstaging (stageI-IV) was assessed by AJCC 8th Edition.The concordance index between FAPI&FDG was evaluated using Cohen's Kappa test (coefficient k). A comparison was made between hypothetical FAPI-derived and conventional FDG-derived treatment plans, compared to those already performed according to standard practice; patients' management was defined by NCCN guidelines. ***Results:*** 63FAPI were performed out of 64 patients enrolled (26th May 2022 - 30th Nov 2023). 50/63 patients were included as they underwent thoracic surgery after staging PET/CT (mean age: 72y[45-87]; M:F=33:17). FAPI&FDG were generally concordant in most cases in terms of TNM staging (35/50 patients-70%). Among those 35 patients, 27/50 (54%) boasted concordance also with Histopathology while in 8/50 (16%) they both would have erroneously up- or downstaged, potentially excluding patients from a correct surgery. In 15/50 cases (30%) FDG&FAPI final stagings (stageI-IV) were discordant: in 15/15 cases (100%) a change in patient's treatment plan would have occurred with FAPI compared to FDG. Specifically, FAPI would have correctly identified TNMstagings compared to FDG in 7/15 cases (46.5%-2 upstagings from absence of malignancy at FDG to Ia at FAPI,5 downstagings: from Ia-FDG to absence of malignancy-FAPI; IIIa-FDG to Ib-FAPI;2patients from IIIb-FDG to IIb-FAPI;IIIb-FDG to IIIa-FAPI),leading to the correct change in patients' treatment plan; in 4/15 cases (27%) both FDG&FAPI identified wrong stagings but FAPI would have directed towards the right surgical management anyway (2 patients with absence of malignancy at FDG and Ia at FAPI later resulted Ib at Pathology; IIIa-FDG and Ib-FAPI resulted IIa; IIIb-FDG and IIb-FAPI resulted IIIa); in 3/15 cases (20%) FDG&FAPI were both wrong in staging and treatment plan; in 1/15 case only (6.5%) FDG distinguished the right staging (IIb-FDG, Ia-FAPI), with FAPI pointing to wrong staging and management.Concerning TNMfinal staging (determined by Histopathology), FAPI was concordant in 48% of cases(k=0.50) while FDG was concordant in 43% of cases(k=0.44). FAPI-derived treatment plan would have in any case led to surgery in 87% of cases, while FDG-derived would have been surgical in 69.5% of cases. ***Conclusion:*** In this preoperative suspected/confirmed LC setting, FAPI&FDG showed a few discordant cases (15/50): TNMstaging assessment is slightly in favour of FAPI.As regards hypothetical changes to treatment plans, in11/15cases(73%) FAPI would have led to the correct patient's management, while FDG-derived treatment plan was correct in 1/15case only (6.5%). FAPI still does not reach clinically acceptable capability alone (<50%) to determine the exact final stage (given by invasive surgical T&N histology), however it may have a complementary role in staging work-up and management.

EP-0228

Mapping the Spread: Prognostic Relevance of Dmax in Metastatic Small Cell Lung Cancer

A. Us[1], *A. Aksu*[1], *K. Kucuker*[1], *Z. Guc*[2], *A. Alacacıoglu*[2], *B. Turgut*[1];
[1]*Izmir Katip Celebi University Faculty of Medicine, Department of Nuclear Medicine, Izmir, TÜRKIYE,* [2]*Izmir Katip Celebi University Faculty of Medicine, Department of Oncology, Izmir, TÜRKIYE.*

Aim/Introduction: This study aimed to evaluate the association between survival and volumetric and dissemination parameters obtained from 18F-fluorodeoxyglucose positron emission tomography/computed tomography (F-18 FDG PET/CT) used for staging in patients diagnosed with stage IV small cell lung cancer (SCLC). ***Materials and Methods:*** Patients with stage IV SCLC who had F-18 FDG PET/CT scans for staging, without brain metastasis and without a history of other malignancies, were included in the study. Patient age, sex, and survival data were recorded. Volumes of interest (VOIs) of all tumor lesions throughout the body were segmented using LIFEx software (v7.6) with a >2.5 SUVmax threshold. The following parameters were extracted: volume of the largest VOI (MTV-Bulk), volume of the smallest VOI (MTVsmallest), the sum of volume differences between the largest VOI and all other VOIs (BulkVolume-DiffSum), the volume difference between the largest and smallest VOIs (BulkSmallestVolume-DiffSum), the maximum distance between any two tumor lesions (Dmax), total metabolic tumor volume (tMTV), and total lesion glycolysis (tTLG). Additionally, the highest SUVmax value (tSUVmax) and the sum of SUVmax differences between all VOIs (SUVmax-DiffSum) were calculated. The relationship between these quantitative parameters and 1-year survival was analyzed. ***Results:*** A total of 68 patients (mean age: 69±10 years [range: 45-84], 58 male [85.3%]) were included. The median survival was 5.1 months (95% CI: 3.4-6.8). Patients who survived less than 12 months (n=58) had significantly higher values of MTV-Bulk, Volume-DiffSum, BulkVolume-DiffSum, BulkSmallestVolume-DiffSum, tMTV, tTLG, SUVmax-DiffSum, and Dmax compared to those who survived longer than 12 months (p=0.003, 0.001, 0.001, 0.003, 0.001, 0.001, 0.012, and 0.010, respectively). Age, sex, tSUVmax, and MTVsmallest were not significantly associated with 1-year survival. Parameters with high mutual correlation were excluded from further analysis; tMTV, Dmax, and SUVmax-DiffSum were included in logistic regression analysis. tMTV >308.6 mL (p=0.006, OR: 11.823, 95% CI: 2.021-69.155) and Dmax >29.3 cm (p=0.028, OR: 7.376, 95% CI: 1.236-44.028) were found to be independent prognostic factors for predicting 1-year survival. ***Conclusion:*** Our study demonstrates that higher volumetric and dissemination parameters, marked inter-tumoral heterogeneity, and aggressive biological behavior are associated with poorer prognosis in patients with stage IV SCLC. Clinically, more aggressive treatment and close monitoring strategies may be considered for this high-risk patient group.

EP-0229

Prediction of PD-L1 Status and Tumor Subtype Characterization in Non-Small Cell Lung Cancer Using Abbreviated [^{18}F]FDG Dynamic Imaging Protocols with Long Axial Field-of-View PET/CT

E. Calderón Ochoa*, J. A. Benecke, W. Lan, F. P. Schmidt, H. Dittmann, C. la Fougère;*
Department of Nuclear Medicine and Molecular Imaging, University Hospital of Tübingen, Tübingen, GERMANY.

Aim/Introduction: Dynamic PET imaging provides insights into tracer kinetics and enables a more robust analysis of glucose metabolism, which may enhance the in vivo characterization of non-small cell lung cancer (NSCLC). We investigated the potential of parametric imaging with an abbreviated dynamic scan protocol enabled by long axial field-of-view (LAFOV) PET/CT for characterizing tumor subtypes and predicting PD-L1 status in NSCLC. ***Materials and Methods:*** This retrospective study included 56 patients with histologically diagnosed NSCLC (39 adenocarcinoma [AC] and 19 squamous cell carcinomas [SCC]) who underwent a validated abbreviated dynamic [^{18}F]FDG PET protocol in a LAFOV PET/CT scanner (3.0 MBq/kg, 20 min scan time, 45 min p.i.). Patlak modeling was implemented in the image reconstruction using a population-based input function, generating net influx rate K_i (ml/g/min) and Distribution Volume (DV, %) images. PD-L1 positivity was defined as a tumor proportion score of ≥1%. T-test and two-way ANOVA were used to compare SUV and parametric parameters according to tumor subtype and PD-L1 status. ROC curves analysis and multiple logistic regression were performed to evaluate the performance in PD-L1 status. ***Results:*** Of the NSCLC tumor lesions, SCC showed higher SUV_{max} (17.98 ± 6) and K_{imax} (0.077 ± 0.02) values compared to AC (12.87 ± 7; 0.061 ± 0.03, p = 0.004; p = 0.0012), with no significant differences in DV values (p = 0.6747). PD-L1-positive tumors exhibited higher

SUV_{max} (16.5 ± 9.5, p = 0.04), K_{imax} (0.07 ± 0.04, p = 0.001) and DV_{max} (441±280, p = 0.02) values than PD-L1-negative tumor lesions (11.7 ± 5.3; 0.04 ± 0.02; 296.4 ± 149.9, respectively). ROC analysis for SUV_{max}, $SUV_{mean,}$ and K_{imean} showed AUCs of 0.62 (CI 0.51-0.74), 0.64 (CI 0.52-0.75), and 0.63 (CI 0.52-0.75), respectively, showing poor discrimination performance. K_{imax} showed in comparison moderate discrimination (AUC = 0.73, CI 0.64-0.83). Multiple logistical regression using SUV_{max} and SUV_{mean} improved the AUC slightly to 0.66 (CI 0.55-0.78), while parametric parameters (K_{imax}; DV_{max}) performed similarly (AUC = 0.73, CI 0.64-0.84). However, the best prediction performance was achieved by combining SUV_{max}, $K_{imax,}$ and DV_{max} (AUC = 0.77, CI 0.66-0.87), with K_{imax} being the strongest predictor (OR = 6.8). ***Conclusion:*** Integrating static and dynamic PET parameters enhances the characterization of PD-L1 status in NSCLC. This combination yields the highest predictive performance and provides valuable information in the evaluation of potential treatment options.

EP-0230

Focal [18F]-FDG Uptake in the Heart: A Favourable Sign in Lung Cancer Patients at Risk of Cachexia?

E. Abenavoli[1], *M. Pepponi*[1], *T. Beyer*[2], *D. Ferrara*[2], *A. Frille*[3], *S. Gruenert*[4], *M. Hacker*[4], *S. Hesse*[5], *L. Hofmann*[5], *O. Sabri*[5], *L. Shiyam Sundar*[2], *J. Yu*[2], *R. Sciagrà*[1];
[1]*Nuclear Medicine Unit, Florence, ITALY,* [2]*QIMP Team, Medical University of Vienna, Vienna, AUSTRIA,* [3]*Department of Respiratory Medicine, Leipzig University, Leipzig, GERMANY,* [4]*Division of Nuclear Medicine, Medical University of Vienna, Vienna, AUSTRIA,* [5]*Department of Nuclear Medicine, Leipzig University, Leipzig, GERMANY.*

Aim/Introduction: The LuCaPET project (ERAPERMED 2021-324) investigates the association between [^{18}F]FDG PET/CT metabolic parameters at staging and the risk of developing cancer cachexia in lung cancer patients, aiming to identify imaging biomarkers of early metabolic dysfunction. Prior data in our retrospective cohort suggested a connection between myocardial uptake pattern and patient outcome. ***Materials and Methods:*** We evaluated 320 treatment-naïve lung cancer patients, all submitted to staging [^{18}F]-FDG PET/CT before the most appropriate first-line treatment. [^{18}F]-FDG PET/CT was evaluated for the visual uptake pattern according to the established classification (A = no uptake, B = diffuse, C = focal and D = focal on diffuse uptake). The patient nutritional status was assessed and followed up using the weight loss grading system (WLGS) adjusted to body mass index. ***Results:*** At the time of [^{18}F]FDG PET/CT, WLGS was 0 in 101 patients (33.8%), 1 in 83 (27.8%), 2 in 43 (14.4%), 3 in 65 (21.8%), and 4 in 28 patients (9.4%).. During early follow up for restaging (3 to 9 months) 28 additional patients evolved to WLGS 3-4 so that a total of 136 patients was eventually classified as cachectic. Myocardial uptake pattern was A in 167 patients, B in 40, C in 52 and D in 61 patients. There were no significant differences in the distribution of myocardial uptake pattern versus presence or absence of cachexia. Conversely, there was a significant chi-square ($p < 0.02$) when the patients with the C pattern were compared with the other groups and the odds ratio for cachexia in the C patients was 0.74 (0.61 - 0.91). ***Conclusion:*** These results suggest that the myocardial uptake pattern could be related to patient metabolic status and in particular that a pattern of focal uptake is more frequent in patients without cachexia, so that its detection could be regarded as a favourable indicator of the nutritional status.

EP-0231

Enhanced Diagnostic Efficacy of Deep-Inspiration Breath-Hold Total-Body ^{18}F-FDG PET/CT for Pulmonary Lesions: A Comparative Study

X. Zhou*;*
Peking University Cancer Hospital, Beijing, CHINA.

Aim/Introduction: To compare the performance of PET/CT using deep-inspiration breath-hold (DIBH) versus free-breathing (FB) techniques and evaluate whether DIBH PET/CT enhances the differentiation of pulmonary benign and malignant lesions. ***Materials and Methods:*** This prospective study enrolled 110 patients with lung lesions (<3 cm). Each underwent conventional FB PET/CT and 30-second DIBH PET/CT (reconstructed at 20s and 30s); 35 patients additionally completed respiratory-gated (RG) PET/CT. Quantitative metrics included SUVmax, blood pool (BP) uptake standard deviation (SD), and tumor-to-blood pool ratio (TBR). Qualitative imaging characteristics (density, longest diameter, pleural distance, location) were analyzed. Uptake stability and extent were compared across acquisition methods, with an AI-based noise-reduction algorithm applied to DIBH PET/CT. ***Results:*** Among 30 patients with complete 4-modality imaging, as for uptake metrics, 20s-DIBH PET/CT yielded the highest SUVmax and TBR ($P<0.001$). RG PET/CT showed no significant improvement in uptake or noise reduction. Lesion size: For lesions <1 cm, DIBH provided no improvement over FB ($P=0.462$); for 2-3 cm lesions, DIBH demonstrated significantly higher uptake (TBR: 7.2 vs. 4.0, $P<0.001$). Pleural distance: DIBH improved detection regardless of pleural proximity. Density/location: Solid/mixed-density lesions and lower-lobe lesions showed greater DIBH efficacy ($P<0.05$). Pathology: Malignant lesions exhibited more pronounced improvement than benign lesions. As for diagnostic accuracy, DIBH PET/CT achieved higher AUC than FB (0.621 vs. 0.543, $P<0.001$), further enhanced by AI noise reduction (AUC=0.721). ***Conclusion:*** DIBH PET/CT outperforms FB and RG PET/CT, particularly for larger (2-3 cm), solid/mixed-density lesions, and improves malignant-benign differentiation. AI-based noise reduction further optimizes diagnostic performance.

EP-0232

Association Between Ventilasion/Perfusion Scan Outcomes and Novel MAPH Score in Patients with Suspested Acute Pulmonary Embolism

A. Dursun[1], *N. A. Dizdar*[1], *E. Tatcı*[2], *G. İnal*[1], *A. Çinar*[1], *Ö. Özmen*[2];
[1]*Ankara Etlik City Hospital, Departmant of Nuclear Medicine Clinic, Ankara, TÜRKIYE,* [2]*Health Sciences University, Ankara Etlik City Hospital, Nuclear Medicine Clinic, Ankara, TÜRKIYE.*

Aim/Introduction: MAPH score, which is based on age, mean platelet volume (MPV), total protein, and hematocrit parameters, is a novel indicator developed to estimate blood viscosity and thrombus burden. This study investigated the relationship between MAPH score and lung ventilation/perfusion (V/Q) SPECT/CT findings in patients with suspected acute pulmonary embolism (PE). ***Materials and Methods:*** The retrospective cohort study included 161 patients who underwent V/Q SPECT/CT for suspected acute PE. V/Q images were performed using ^{99m}Tc-labeled carbon particles (Technegas) and ^{99m}Tc-labelled MAA. The images were interpreted according to 2019 version of EANM guideline by two nuclear medicine physicians. The patients were classified as 'PE-absent' and 'PE-present' groups. All patients' demographic and clinical data were retrospectively retrieved (Table-1 and Table-2). Using Youden index, the cut-off values for MPV, age, total protein, and hematocrit were determined, and each was categorised as 0 or 1. The MAPH score was then calculated as the sum of these values. ***Results:*** The study included 161 patients (F/M: 119/42; mean age 64.37 ± 16.49 years). Of these, 59 patients were in PE-absent group, while 102 were in PE-present group. Age and prevalence of hypertension, hyperlipidemia (HL), heart failure (HF), and chronic kidney disease (CKD) were significantly higher in PE-present group ($p < 0.05$ for all comparisons; Table-1). There were no statistically significant differences between the groups regarding cerebrovascular disease, coronary artery disease, diabetes mellitus, and anemia. Patients in PE-present group had significantly higher hemoglobin, hematocrit, and MAPH levels (p

< 0.05 for all values; Table-2). However, no significant differences in total protein and MPV levels were observed between groups (p > 0.05). The ROC analysis showed that the MAPH score predicted PE with a sensitivity of 83% and specificity of 42% at a cut-off value of 1.5 (AUC = 0.696, p< 0.001; Table 3). In both univariate and multivariate logistic regression analyses, heart failure, elevated GFR levels, and higher MAPH score were significantly associated with PE (p< 0.05; Table-4). Conversely, HL was found to be independently associated with lower risk of PE (p< 0.05; Table-4). ***Conclusion:*** Our results indicate that a high MAPH score is an independent predictor of PE. Furthermore, advanced age, hypertension, heart failure, chronic kidney disease, and elevated hematocrit and hemoglobin levels were identified as significant risk factors associated with PE. ***References:*** Akhan O, Boz M, Guzel T, Kis M. Discrimination of the acute pulmonary embolism subtypes based on the novel MAPH score. J Thromb Thrombolysis. 2024 Apr;57(4):683-690.

EP-0233

Tumor Dissemination (Dmax) derived from ^{18}F-FDG PET/CT as a Predictor of Response to Immunotherapy in Patients With Non-small Cell Lung Cancer

S. Pellegrino[1], *A. Volpicelli*[1], *A. Russo*[2], *M. Isernia*[2], *F. Salomone*[2], *A. Servetto*[2], *R. Bianco*[2], *R. Fonti*[1], *S. Del Vecchio*[1];
[1]Department of Advanced Biomedical Sciences, University Federico II, Naples, ITALY, [2]Department of Clinical Medicine and Surgery, University Federico II, Naples, ITALY.

Aim/Introduction: The aim of our study was to test whether the largest distance between two ^{18}F-FDG avid lesions (Dmax) was able to predict the response to immunotherapy in patients with advanced non-small cell lung cancer (NSCLC). ***Materials and Methods:*** Twenty-five patients (19 men, 6 women) with stage III and IV NSCLC who had undergone ^{18}F-FDG PET/CT scan showing at least two positive lesions before starting immunotherapy were included in the study. All lesions were segmented using an automated contouring program setting an absolute threshold for SUV at 2.5. The imaging parameters including SUVmax, SUVmean, MTV and TLG of primary tumors along with total MTV (MTV_{TOT}) and whole-body TLG (TLG_{WB}) from all malignant lesions were included in the analysis. The largest distance between two ^{18}F-FDG avid lesions (Dmax) in each patient was measured. The Student's t test was used to compare means of unpaired data and Fisher's exact test was used for the analysis of categorical data. Univariate analysis of clinical and imaging variables was performed using Cox proportional hazards regression. ***Results:*** A total of 124 lesions were analyzed including 24 primary tumors, 60 metastatic lymph nodes and 40 distant metastases and mean Dmax value was 26.78±19.12 cm. In primary tumors, average values of SUVmax, SUVmean, MTV and TLG were 13.12±5.67, 5.46±1.60, 79.54±99.10 ml and 521.27±784 g, respectively, whereas mean values of MTV_{TOT} and TLG_{WB} were 129.40±122.19 ml and 782.66±879.42 g, respectively. After starting immunotherapy, patients were subjected to a mean follow-up period of 4 months and then re-evaluated by CT scan. Among all patients, 13 showed a partial response while 12 had disease progression. Mean Dmax values were significantly lower in responders as compared to non-responders (13.36±8.38 vs 41.32±16.66, p<0.0001) while no statistically significant difference in the SUVmax of primary tumors, MTV_{TOT} and TLG_{WB} was found. Using ROC curve analysis, the Dmax value able to discriminate between patients responding to immunotherapy from non-responders was 22.2 cm (AUC=0.92). Among 13 patients with Dmax<22.2 cm, 11 showed partial response to immunotherapy whereas only 2 patients among 12 with Dmax≥22.2 cm had partial response (Fisher's exact test, p=0.0012). Finally, univariate analysis was performed including age, gender, stage, MTV_{TOT}, TLG_{WB}, Dmax and imaging parameters derived from primary lung tumors. Dmax was the only parameter significantly correlated with the occurrence of disease progression (χ^2=6.3370, p=0.0118). ***Conclusion:*** Dmax, which reflects tumor dissemination, may predict response to immunotherapy in patients with NSCLC.

EP-0234

Artificial intelligence prognostic predictive algorithms in advanced lung cancer using pre-therapy ^{18}F-FDG PET-CT metabolic parameters. The role of MTV in the model performance. Preliminary results.

D. Donner[1], *F. Rignanese*[2], *V. Vultaggio*[3], *M. Moroni*[4], *M. Datres*[5], *M. Pozzi*[6], *M. Chierici*[4], *G. Jurman*[4], *O. Caffo*[7], *L. Bazan*[8], *L. Picori*[1], *S. Agostini*[9], *C. C. Quattrocchi*[10], *A. G. Morganti*[11], *F. Chierichetti*[1];
[1]Dep. Nuclear Medicine, Dipartimento Radiologie, APSS, Trento, ITALY, [2]Data Science for Health Unit FBK (Fondazione Bruno Kessler), Trento, ITALY, [3]Dep. Nuclear Medicine, ARNAS Civico, Palermo, ITALY, [4]Data Science for Health Unit FBK (Fondazione Bruno Kessler), Trento, ITALY, [5]Data Science for Health Unit FBK (Fondazione Bruno Kessler); Dept of Math University of Trento, Trento, ITALY, [6]CIBIO (Cellular Computational and Integrative Biology) University of Trento, Trento, ITALY, [7]Dipartimento Oncologia medica, APSS, Trento, ITALY, [8]Sant'Anna School of Advanced Studies, University od Pisa, Pisa, ITALY, [9]Dep. Nuclear Medicine Radiopharmacy, Dipartimento Radiologie, APSS, Trento, ITALY, [10]CISMED University of Trento, Dipartimento Radiologie, APSS, Trento, ITALY, [11]DIMEC, University of Bologna; Radiation Oncology Department; IRCCS Azienda Ospedaliero-Universitaria of Bologna, Bologna, ITALY.

Aim/Introduction: to define a prognostic -PFS (Progression Free Survival) and OS (Overall survival)- AI modeling framework using metabolic parameters as SUVmax, SUVmean and MTV extracted from pre-treatment [18F]-FDG PET-CT. ***Materials and Methods:*** we retrospectively evaluated 51 stage IV NSCLC patients (pts) undergoing Best Standard of Care. Tumor, lymphnode, and metastasis volumes of interest (TNM VOI) were delineated on PET scans and metabolic parameters MTV, SUVmax, and SUVmean of T, N, and M were recorded. The primary clinical endpoints were PFS and OS. A nested cross-validation with Pearson Correlation Coefficient>0.8 scheme and modeling was applied. Four models were tested in performing survival analysis: Cox's proportional hazards model (CoxPH), Elastic Net Regularized CoxPH (CoxNet), Random Survival Forest (RSF) and Tree-based Gboost (Gboost). The integrated Brier Score (iBS) and C-index were applied to each model of prognostic prediction. Accordingly, the survival analysis was performed through Kaplan-Meier (KM) curves and the log-rank test, and the percentage of the significant p-value of each model was evaluated. A SHAP and beeswarm plots were applied to demonstrate the metabolic features that have the greatest contribution to the performance of the best predictive models. ***Results:*** The RSF is the model among CoxPH, CoxNet and Gboost models that achieve the highest C-index score and the lowest IBS score in different scenarios (T, N, M, TN and TNM). For the prediction of PFS the best RSF models are those that use the classic metabolic parameters (SUVmax, SUVmean and MTV) deriving from the TNM VOI. The highest percentage of significant p values in stratifying pts at high and low risk of PFS was shown by the RSF_TNM model [C-index: 0.575, IBS: 0.23 and significant p-value ratio in 24% of cases]. RSF_TNM was the best model, even when OS was considered. It's about a model using the metabolic characteristics of T, N and M together (RSF_TNM), with a C-index of 0.59, IBS of 0.236 and a 32% split in which pts were successfully stratified into high and low-risk groups of OS. For the TNM_RSF model predicting PFS the relatively most important parameter was MTV_N; for TNM_RSF predicting OS the most impacting parameters were MTV_T; MTV_N and MTV_M. ***Conclusion:*** Some of the proposed AI pipelines may have the potential to provide accurate prediction of PFS and OS in patients with advanced NSCLC by incorporating conventional metabolic PET parameters from TNM VOI, among which MTV is the one with relatively higher impact.

EP-0235

Diagnostic role of [^{18}F]FDG PET/CT in Pulmonary Hamartomas: Retrospective Analysis

M. Marques, *C. Loewenthal;*
Hospital da Luz Lisboa, Lisbon, PORTUGAL.

Aim/Introduction: Pulmonary hamartoma, the most common benign lung tumor, is often detected incidentally on imaging. Asymptomatic patients may undergo unnecessary surgery due to diagnostic challenges, as pulmonary hamartoma can mimic malignancy on CT through features like progressive growth and heterogeneous density[1]. This study aimed to evaluate the metabolic characteristics of pulmonary hamartoma on 18F-Fluoro-D-glucose positron emission tomography-computed tomography ([^{18}F]FDG PET/CT) to help reduce avoidable invasive procedures. ***Materials and Methods:*** We retrospectively reviewed 45 patients from our institution with histologically confirmed pulmonary hamartoma who had undergone [^{18}F]FDG PET/CT between 2010 and 2024.The PET/CT protocol included whole-body imaging one hour after intravenous [18F]FDG administration, with low-dose CT for attenuation correction and anatomical reference. Some patients also underwent delayed thoracic imaging.Lesion size was based on maximum pathological diameter. SUVmax was measured for the hamartoma, adjacent lung tissue, and vascular pool (aortic arch). In patients with delayed imaging, delayed lesion SUVmax was also recorded. ***Results:*** Pulmonary hamartomas exhibited a mean size of 13,8 ± 8,43 mm (range: 5-50 mm). The mean SUVmax was 1,19 ± 0,48 (range: 0,54-2,40). Among the 45 lesions analyzed, 20 (44%) had a SUVmax lower than the adjacent lung parenchyma, and 24 (53%) showed higher uptake than adjacent lung tissue but still below the mediastinal vascular pool. Thus, 98% of cases had SUVmax values below the vascular pool. Only one (2%) showed a SUVmax exceeding the vascular pool, which was histologically confirmed to be a lesion with atypical features for a pulmonary hamartoma, specifically an adenofibromatous variant.Delayed thoracic imaging was performed in 71% of cases, with a slightly lower mean SUVmax of 1,08. Of these, 66% (n=21) showed decreased [18F]FDG uptake, 3% (n=1) remained stable, and 31% (n=10) demonstrated increased avidity. ***Conclusion:*** The majority of pulmonary hamartomas demonstrate relatively low [18F]FDG uptake, reflecting the benign nature of these lesions.Some metabolic features on [^{18}F]FDG PET/CT that may aid in diagnostic decision-making, by supporting a benign characterization of pulmonary hamartomas and thereby reducing the need for unnecessary surgical interventions, include: low glycolytic metabolism, evidenced by an SUVmax below 2,50 (the internationally recognized cut-off value); [18F]FDG uptake lower than mediastinal vascular pool; and a decrease in [18F]FDG uptake on delayed imaging. ***References:*** 1) Flores, R., Bauer, T., Aye, R., et al (2014). Balancing curability and unnecessary surgery in the context of computed tomography screening for lung cancer. The Journal of Thoracic and Cardiovascular Surgery, 147(5), 1619-1626. https://doi.org/10.1016/j.jtcvs.2013.11.001

EP-0236

The Evaluation of Nivolumab Treatment and Survival Efficacy with Metabolic Parameters in Patients with Non-Small Cell Lung Cancer

N. Aydin[1], *G. Mutevelizade*[1], *B. C. Bozdemir*[1], *N. Kolkiran*[2], *A. P. Erdogan*[2], *E. Sayit Bilgin*[1];
[1]*Manisa Celal Bayar University Faculty of Medicine Department of Nuclear Medicine, Manisa, TÜRKIYE,* [2]*Manisa Celal Bayar University Faculty of Medicine Division of Medical Oncology, Manisa, TÜRKIYE.*

Aim/Introduction: The aim of this study was to investigate the efficacy of metabolic parameters obtained from pre- and post-treatment F-18 FDG PET/CT imaging of nivolumab-treated patients with non-small cell lung cancer on the assessment of treatment response, overall survival (OS) and post-treatment survival. ***Materials and Methods:*** A total of 32 patients with NSCLC who received at least 4 cycles of nivolumab treatment between 01/2022 and 12/2024, who underwent F-18 FDG PET/CT imaging up to 4 weeks before the first cycle of nivolumab treatment and up to 4-6 weeks after the last nivolumab treatment were included. Images were evaluated using PET VCAR (Volume Computer-Assisted Reading) software. SUVmax, SUVmean, metabolic tumor volume (MTV) and total lesion glycolysis (TLG) of each lesion were calculated by applying a threshold value of 41% of SUVmax. Total MTV (tMTV) and total TLG (tTLG) values of each patient before and after treatment were obtained by summing all values of each lesion. Demographic data, histologic subtypes, smoking history, and follow-up period of the patients were obtained retrospectively. Response to nivolumab treatment was evaluated according to EORTC. According to these criteria, patients were divided into 3 groups as partial metabolic response to treatment, stable metabolic disease and progressive metabolic disease. ***Results:*** A total of 32 patients including 3 females and 29 males with a mean age of 64±6.5 years were included in the study. Histologic subtypes were 15 adenocarcinomas and 17 squamous cell carcinomas. There was no statistically significant correlation between SUVmax, SUVmean, tMTV, tTLG values of the primary tumor and histological subtypes ($p>0.05$). There was a statistically significant correlation between mortality and pre-treatment tMTV, tTLG and post-treatment SUVmax, SUVmean and tTLG values ($p<0.05$). Patients were divided into two groups based on the median values of metabolic parameters and survival analysis was performed. Pre-treatment tMTV and tTLG values, post-treatment SUVmax, SUVmean, tMTV and tTLG values have a significant difference on OS after nivolumab treatment ($p<0.05$). The patients were evaluated according to treatment response, a significant difference was found between the median values of SUVmax, SUVmean and tTLG parameters after treatment ($p<0.05$). In addition, treatment response groups had no effect on overall survival, but the partial response group had longer survival after nivolumab treatment compared to the other groups ($p<0.05$). ***Conclusion:*** According to the results, especially tMTV and tTLG values can be used to evaluate the response to nivolumab treatment and have a significant effect on survival.

EP-0237

Refining Prognostic Assessment in Small Cell Lung Cancer: Development and Validation of Multiparametric Models Integrating ^{18}F-FDG PET/CT Dissemination Characteristic

Y. Liu, *X. Zhou, X. Meng, X. Kong, Y. Cui, Y. Liu, Y. Yao, J. Zhu, N. Li;*
Peking University Cancer Hospital, Beijing, CHINA.

Aim/Introduction: Small cell lung cancer (SCLC) is a type of pulmonary neuroendocrine tumor characterized by rapid proliferation and strong invasiveness. The prognosis of SCLC patients varies significantly, and due to the lack of reliable prognostic indicators, accurate prognostication remains challenging in clinical practice. Therefore, identifying additional prognostic indicators is crucial for improving predictive accuracy. Recent studies suggest that tumor spatial distribution may predict cancer prognosis. A novel ^{18}F-FDG PET/CT parameter, D_{max}, measures the distance between the two farthest lesions and has demonstrated prognostic value independent of metabolic parameters. This study aimed to explore the correlation between tumor dissemination characteristic, metabolic parameters from baseline ^{18}F-FDG PET/CT, clinical and pathological indicators, and SCLC outcomes, as well as to develop predictive models. ***Materials and Methods:*** This study retrospectively included 303 patients with SCLC, randomly divided into training and validation cohorts (8:2). The tumor dissemination characteristic, metabolic characteristics, morphological features, and clinical indicators were retrospectively collected. Cox regression analysis was employed to identify independent prognostic factors, which were then used to construct prognostic models and nomograms. Model performance was evaluated using receiver operating

characteristic (ROC) curves. ***Results:*** Multivariate Cox regression analysis identified age, stage, neuron-specific enolase (NSE), and the standardized distance between the two farthest lesions (SD_{max}) as independent prognostic factors for progression-free survival (PFS). The area under curve (AUC) values for predicting 6-month, 12-month, and 24-month PFS were 0.799, 0.774, and 0.732 in the training cohort and 0.775, 0.766, and 0.717 in the validation cohort. Additionally, age, stage, NSE, whole-body metabolic tumor volume (MTV_{wb}), and SD_{max} were independent prognostic factors for overall survival (OS), with AUC values of 0.856, 0.811, and 0.777 for 1-year, 2-year, and 3-year OS in the training cohort, and 0.819, 0.810, and 0.772 in the validation cohort. ***Conclusion:*** The tumor dissemination characteristic from baseline ^{18}F-FDG PET/CT is a novel independent prognostic factor for SCLC. Furthermore, prognostic models integrating dissemination characteristic, metabolic parameter, and clinical indicators demonstrate excellent predictive performance for SCLC outcomes.

EP-0238

Early prediction of tumor response to carbon-ion radiotherapy via ^{18}F-FMISO PET/CT in locally advanced non-small-cell lung cancer patients

C. Ren*;*
Shanghai Proton and Heavy Ion Center, Shanghai, CHINA.

Aim/Introduction: Hypoxia increases resistance to carbon ion radiotherapy (CIRT) in locally advanced non-small-cell lung cancer (LA-NSCLC, stage II-III). We developed the model to early predict tumor response to CIRT based on ^{18}F-fluoromisonidazole (FMISO) positron emission tomography/computed tomography (PET/CT) in LA-NSCLC patients, and to identify patients unlikely to benefit from CIRT. ***Materials and Methods:*** 42 patients with LA-NSCLC, including 25 (60%) squamous cell carcinoma (Scc) and 17 (40%) non-Scc patients, underwent ^{18}F-FMISO PET/CT prior to CIRT. FMISO maximum standardized uptake values (SUVmax), the tumor-to-muscle ratios (TMR), and hypoxic tumor volume (HTV) in gross target volumes were measured. The hypoxia threshold based on TMR was set at 1.4. CIRT response assessment was evaluated within 1 week after the completion of all radiotherapy with RECIST criteria. After identifying FMISO biomarker related to CIRT response, a prediction model was developed and evaluated by the area under receiver-operator characteristic (ROC) curve (AUC). ***Results:*** Of the 42 patients analyzed, 17 (40%) had partial response (PR) while stable disease (SD) was observed in 25 (60%) patients. FMISO-PET detected uptake in 31 (74%) patients with LA-NSCLC, although these values were not related to the CIRT response. Further subgroup analysis showed that good responses were significantly more prevalent in hypoxia Scc (n=15, 36%) patients with less HTV ($p < 0.01$), whereas FMISO uptake was not significantly correlated with CIRT response in normoxia Scc (n=10, 24%) or all non-Scc (n=17, 40%) patients. Furthermore, a positive correlation between tumor size and hypoxia was observed in Scc patients ($p < 0.01$). Multivariate logistic regression analysis showed that HTV was an independent significant predictor of CIRT response ($p = 0.04$, odds ratio = 1.14) with an AUC of 0.89. ***Conclusion:*** ^{18}F-FMISO PET/CT is recommended for Scc patients, especially whose were likely to be hypoxia predicted by tumor size, and it holds great promise for selecting patients who will benefit from CIRT.

EP-0239

Kinetic modeling and parametric imaging of ^{13}N-NH_3 in treatment-naïve lung cancer using total-body

H. Yuan[1]*, F. Wang*[1]*, T. Sun*[2]*, L. Jiang*[1]*;*
[1]Guangdong Provincial People's Hospital, Guangzhou, CHINA, [2]Lauterbur Research Center for Biomedical Imaging,Shenzhen Institute of Advanced Technology, Chinese Academy of Sciences, Shenzhen, CHINA.

Aim/Introduction: ^{13}N-NH_3 PET imaging provides insights into tumor perfusion and metabolism, hence potentially valuable in oncological diagnosis, staging, and prognostication. However, its in vivo kinetic characteristics and the optimal protocol for kinetic modeling and parametric imaging remain unclear. ***Materials and Methods:*** 9 lung cancer surgical candidates were prospectively incorporated. Using the total-body PET/CT scanner, 35-minute ^{13}N-NH_3 acquisitions were conducted immediately post-injection, and 5-minute ^{18}F-FDG acquisitions were made 60 minutes post-injection. 13N-NH3 PET data were reconstructed into dynamic image series. Tumor lesions and normal organs were segmented using non-threshold dependent automatic or semiautomatic tools. Reversible and irreversible 2-tissue compartment models (2TC vs 2TiC) using image-derived input functions (IDIFs) with population-based metabolite correction were adopted for parametric modeling. The Akaike Information Criterion (AIC) was calculated for model selection. Parametric images were produced with the optimal model for lesions. ***Results:*** All primary lung tumors (n=9) and regional lymph node metastases (n=17) were detectable using both ^{13}N-NH_3 and ^{18}F-FDG imaging. Primary lung tumors, regional lymphadenopathy and lung backgrounds demonstrated smaller AIC using 2TC models with pulmonary artery as IDIF, while other organs favored either 2TC or 2TiC models with the descending aorta as IDIF. Lesion-to-background lung ratios reached around 2.218-3.407 for primary lung tumors and 1.932-2.537 for regional lymphadenopathy 10-20 min post-injection of 13N-NH3. Vt images derived from 2TC modeling showed better lesion-to-background lung ratios (4.511±2.955 for primary tumor, and 2.991±2.152 for regional lymphadenopathy). ***Conclusion:*** For ^{13}N-NH_3 imaging in lung cancer, a static image can be acquired at 10-20 min post-injection for clinical diagnosis. The reversible 2TC model is preferred over 2TiC, and the Vt image is preferred over other parametric images in terms of lesion contrast.

EP-0240

Evaluating the Use of Metabolic Tumor Volume (MTV) During Follow-Up in NSCLC Patients Treated with Immunotherapy

O. Ekmekcioglu[1]*, S. Halil*[2]*, A. I. Yasin*[2]*;*
[1]Nuclear Medicine Dept., University of Health Sciences, Sisli Hamidiye Etfal Education and Research Hospital, Istanbul, TÜRKIYE, [2]Medical Oncology Dept., University of Health Sciences, Sisli Hamidiye Etfal Education and Research Hospital, Istanbul, TÜRKIYE.

Aim/Introduction: Accurate evaluation of response to immunotherapy in patients with lung cancer presents a clinical challenge due to atypical imaging patterns. [^{18}F]FDG PET/CT is widely used for treatment monitoring, though traditional semi-quantitative metrics such as SUVmax may not reliably reflect true tumour behaviour. This study aims to assess metabolic response using [^{18}F]FDG PET/CT in patients treated with immunotherapy, focusing on the added value of metabolic tumour volume (MTV). ***Materials and Methods:*** A retrospective analysis was performed on 23 patients (5 female, 18 male). mean age: 66.5 years, range: 43-82) with histologically confirmed lung cancer (13 SCC, 10 Adenocarcinoma) who underwent Nivolumab immunotherapy. All patients had baseline [^{18}F]FDG PET/CT scans and were followed for a mean of 12.1 months (range: 3-25 months). Follow-up PET/CT scans were evaluated for treatment response. Three patients were excluded due to incomplete clinical or imaging data. The remaining 20 patients were assessed using the PET Response Criteria in Solid Tumours (PERCIST). ***Results:*** Among the 20 evaluable patients, the first follow-up [^{18}F]FDG PET/CT revealed metabolic regression in 9 patients, disease progression in 6, and stable metabolic disease in 5 according to PERCIST criteria. SUVmax values demonstrated significant variability and were not consistently aligned with anatomical tumour changes or clinical

status. In contrast, difference between the MTV measurements (mean MTV of primary tumor before therapy 24.5 vs after therapy 36.2 cm3 and mean SUVmax before therapy 10.1 vs after therapy 9.1) provided a more accurate reflection ($p<0.05$) of tumour burden and response to therapy. Cases with increased or decreased SUVmax have shown tumour shrinkage or stability on anatomical imaging, highlighting the limitations of relying solely on SUVmax. ***Conclusion:*** [^{18}F]FDG PET/CT is an essential tool for monitoring immunotherapy response in lung cancer. However, SUVmax alone may not be sufficient to determine true metabolic activity or disease trajectory. MTV offers a more robust and comprehensive measure, correlating better with clinical and radiological findings. Our findings suggest that incorporating MTV into routine PET/CT evaluations could improve the accuracy of treatment response assessments. Nevertheless, larger patient cohorts and prospective studies are needed to validate the clinical utility of MTV in this setting. ***References:*** Monaco L, Gemelli M, Gotuzzo I, Bauckneht M, Crivellaro C, Genova C, Cortinovis D, Zullo L, Ammoni LC, Bernasconi DP, et al. Metabolic Parameters as Biomarkers of Response to Immunotherapy and Prognosis in Non-Small Cell Lung Cancer (NSCLC): A Real World Experience. Cancers. 2021;13:1634.

EP-0241

Head-to-head Comparison of Peptide- and Nanobody-based Radiotracers for Detecting PD-L1 expression in Non-Small Cell Lung Cancer

Y. Wu[1], *H. Wang*[1], *Y. Gu*[2], *D. Xu*[1], *F. Xie*[1];
[1]*Huashan Hospital,Fudan University, Shanghai, CHINA,* [2]*Central Research Institute, United Imaging Healthcare Group Co, Shanghai, CHINA.*

Aim/Introduction: The aim of this study is to evaluate and compare [68Ga]Ga-DOTA-WL12 (a peptide-based tracer) and [68Ga]Ga-NOTA-RW102 (a nanobody-based tracer) in assessing programmed death ligand 1 (PD-L1) expression in primary and metastatic non-small cell lung cancer (NSCLC). ***Materials and Methods:*** Between June 2022 and April 2023, ten consecutive patients diagnosed with primary NSCLC or metastatic NSCLC were enrolled. All patients underwent [68Ga]Ga-DOTA-WL12 and [68Ga]Ga-NOTA-RW102 PET/CT scans, with four of these patients also receiving [^{18}F]FDG PET/CT scans. All imaging was reviewed in consensus by two experienced nuclear medicine physicians. The binding affinities of DOTA-WL12 and NOTA-RW102 to PD-L1 was measured using surface plasmon resonance (SPR) analysis. The PD-L1 expression level was quantified as a tumor proportion score (TPS). The biodistribution and tumor uptake of [68Ga]Ga-DOTA-WL12 and [68Ga]Ga-NOTA-RW102 were compared across major organs and lesions. Tracer uptake was quantitatively assessed using the maximum standard uptake values (SUVmax), the mean standard uptake values (SUVmean), and the target-to-background ratio (TBR). ***Results:*** DOTA-WL12 and NOTA-RW102 exhibited favorable binding affinities for PD-L1, with equilibrium dissociation constants (KD) of 0.2 nM and 0.0047 nM, respectively. Notably, the correlation between tumor SUVmax and PD-L1 TPS was significantly stronger for [^{68}Ga]Ga-DOTA-WL12 ($r = 0.9471$, $P < 0.0001$) than for [^{68}Ga]Ga-NOTA-RW102 ($r = 0.5235$, $P = 0.0241$). In human studies, significant differences ($P < 0.05$) in tracer uptake were observed across multiple organs: liver (SUVmean: 20.43 ± 4.26 vs 6.12 ± 1.36), kidney (2.40 ± 0.34 vs 22.37 ± 2.88), spleen (2.44 ± 0.67 vs 18.49 ± 3.90), and lung background (0.18 ± 0.12 vs 1.09 ± 0.29), indicating distinct biodistribution profiles. [^{68}Ga]Ga-DOTA-WL12 predominantly accumulated in the liver, while [^{68}Ga]Ga-NOTA-RW102 showed renal clearance. ***Conclusion:*** Despite its lower in vitro binding affinity, [^{68}Ga]Ga-DOTA-WL12 demonstrated superior correlation with PD-L1 expression in vivo compared to [^{68}Ga]Ga-NOTA-RW102. The distinct biodistribution patterns suggest that [^{68}Ga]Ga-DOTA-WL12 may be less suitable for patients with liver dysfunction, while the high renal uptake of [^{68}Ga]Ga-NOTA-RW102 could pose challenges in patients with impaired kidney function.

EP-0242

Assessing Time-Dependent SUV Changes in small and medium Pulmonary Nodules: Diagnostic Implications of Dual-Time-Point 18F FDG PET/CT

N. Kapsoritakis[1], *F. Tsitoura*[2], *O. Bourogianni*[1], *G. Barmparis*[2], *G. Tsironis*[2], *A. Bertsias*[3], *N. Tzanakis*[4], *S. Koukouraki*[1];
[1]*Nuclear Medicine Department, Medical School Univercity of Crete, Heraklion, Crete, GREECE,* [2]*Department of Physics, Univercity of Crete, Heraklion, Crete, GREECE,* [3]*Rheumatology Department, Medical School Univercity of Crete, Heraklion, Crete, GREECE,* [4]*Department of respiratory Medicine, University Hospital, Heraklion, Crete, Greece and School of Medicine, Heraklion, Crete, GREECE.*

Aim/Introduction: Characterization of pulmonary nodules remains a diagnostic challenge, particularly in oncological patients where early and accurate differentiation between benign and malignant lesions is crucial. Standard ^{18}F-FDG PET/CT imaging relies on SUV (Standardized Uptake Value) metrics obtained at a single time point, which may be limited in sensitivity and specificity for pulmonary lesions. Dual-time-point imaging, involving both early and delayed PET acquisitions, has been proposed to improve diagnostic accuracy. The purpose of this study is to evaluate whether dual-time-point ^{18}F-FDG PET/CT imaging enhances SUV-based diagnostic accuracy mostly for small and medium pulmonary nodules (≤30 mm) across a range of primary cancer types. ***Materials and Methods:*** This prospective study included 622 PET/CT scans from 311 patients with small and medium sized PNs. Dual time point 18F FDG PETCT imaging, early phase image acquisition 1hr (PET1) and delayed phase images after 2hrs p.i (PET2), was performed on a digital PETCT (GE discovery MI 4R Gen 2). Regions of interest (ROIs) were drawn around the lesion in both PET scans. A semiquantitative analysis was followed using the Standardized Uptake Value, (SUV1) for early and SUV2, for delayed images. Patients were classified into 3 groups: group 1 (malignant either primary or metastatic), group 2 (benign) and group 3 (indeterminate lesions). Changes in SUVmax (ΔSUV) were calculated. PET findings were compared to histopathology, radiological and clinical follow-up to determine diagnostic performance. The reference standard in characterizing PNs was SUV ≥2,5. ***Results:*** Biopsy or treatment results were obtained for 111/311: 84 malignant nodules, 15 benign, and 12 non diagnostic findings. Statistical analysis and plots were based on 99 pts. Cut-off point identification for SUV1 was 3.35, SUV2 5,17 and ΔSUV 0,69. Results for SUVmax 1 were: true positive: 67/84 (79%), true negative 10/15 (66%), false positive 5/15 (33%) and false negative 17/84 (20%) vs ΔSUVmax: true positive 74/84 (88%), true negative 9/15 (60%), false positive 6/15 (40%) and false negative 10/84 (11%). The sensitivity, specificity, and overall diagnostic accuracy of dual-time-point PET/CT were higher compared to single-time-point imaging, particularly in nodules with low initial uptake. ***Conclusion:*** Dual-time-point ^{18}F-FDG PET/CT imaging may improve the SUV-based diagnostic accuracy of small pulmonary nodules in oncologic patients with potential to influence clinical management and treatment planning.

EP-0243

Comparison of SUV, MTV and TLG volumetric changes in early and delayed FDG PET/CT: A prospective analysis for optimized pulmonary nodule evaluation.

N. Kapsoritakis[1], *F. Tsitoura*[2], *G. Barmparis*[2], *O. Bourogianni*[1], *G. Tsironis*[2], *A. Bertsias*[3], *N. Tzanakis*[4], *S. Koukouraki*[1];
[1]*Nuclear Medicine Department, Medical School Univercity of Crete, Heraklion, Crete, GREECE,* [2]*Department of Physics, Medical School, University of Crete, Heraklion, Crete, GREECE,* [3]*Department of Rheumatology, Medical School, University of Crete, Heraklion, Crete, GREECE,* [4]*Department of Respiratory, Medical School, University of Crete, Heraklion, Crete, GREECE.*

Aim/Introduction: Pulmonary nodules (PNs) pose a diagnostic challenge, especially in oncology, due to the overlap between benign-inflammatory and malignant lesions. While FDG PET/CT using SUVmax is widely used, its limitations in sensitivity and specificity have prompted interest in alternative volumetric

parameters such as Metabolic Tumor Volume (MTV) and Total Lesion Glycolysis (TLG). This study evaluates the diagnostic utility of SUV, MTV, and TLG changes between early and delayed PET/CT scans. ***Materials and Methods:*** this prospective study included 622 PET/CT scans from 311 patients with PNs (5mm-3cm) in a period of a year. Early (1hr p.i PET1) and delayed images (2hrsp.i PET2) were performed on a digital PETCT system. Standardized Uptake Value (SUVmax), Metabolic TumorVolume (MTV) and Total lesion glycolysis (TLG) for PET1 (SUV1, MTV1, TLG1) and PET2 (SUV2, MTV2 and TLG2) and percentage changes between PET studies (ΔSUVmax, ΔMTV and ΔTLG) were analyzed. Patients were classified into 3groups: group 1, group 2 (benign) and group 3 equivalent lesions (no significant differences). The final diagnosis was based on biopsy results and on clinical decision. ***Results:*** Histopathological findings were obtained in 104/311 pts. Among these 84/104 were diagnosed as malignancy, 14/104 as benign, and 6/104 pts were non diagnostic. For ΔSUV: true positive 64/84, false negative 20/84, true negative 7/14, false positive 7/14. For ΔMTV: true positive 29/84, false negative 55/84, true negative 12/14, false positive 2/14 and for ΔTLG true positive 55/84, false negative 29/84, true negative 11/14 and false positive 3/14. The sensitivity, specificity, accuracy, PPV and NPV were for ΔSUV (76%, 50%, 72%, 90%, 35%), for ΔMTV (35%, 85%, 42%, 93%, 15%) and for ΔTLG (65%, 88%, 68%, 93%, 28%) respectively. ***Conclusion:*** Among the three parameters, TLG demonstrated the highest specificity and PPV, indicating its potential as a reliable adjunct to SUVmax in characterizing pulmonary nodules.

EP-0244

Diagnostic Performance of 18F-PSMA PET/CT in detecting early and very early Biochemical Recurrence of Prostate Cancer: Insights from an 8-Month Single-Center Experience

N. Kapsoritakis[1], *O. Bourogianni*[1], *I. Skamagkas*[2], *G. Georgiadis*[2], *C. Mamoulakis*[2], *S. Koukouraki*[1];
[1]Nuclear Medicine Department, Medical School University of Crete, Heraklion, Crete, GREECE, [2]Department of Urology, University Hospital of Crete, Heraklion, Crete, GREECE.

Aim/Introduction: The aim of this study was to assess the detection rate of 18F PSMA in pts with biochemical recurrence (BCR) of prostate cancer (PC) with low and very low PSA levels classified as early and very early biochemical recurrence (eBCR). ***Materials and Methods:*** A total of 104 patients with BCR after radical prostatectomy were prospectively evaluated over an 8-month period using ^{18}F-PSMA PET/CT. Among them, 77 patients presented with PSA levels <1.5 ng/mL and were stratified into two groups: Group A: 36 patients with very low PSA levels (<0.5 ng/mL) and PSA doubling time (dtPSA) <6 months and Group B: 41 patients with low PSA levels (0.5-1.5 ng/mL) and dtPSA >6 months. All patients underwent conventional imaging (CT and mpMRI) alongside PET/CT. Recurrence sites were classified as local (prostate fossa/pelvic lymph nodes), extrapelvic lymph nodes, and distant metastases (bone/visceral). A positive ^{18}F-PSMA PET scan was defined by the presence of at least one PSMA-avid lesion. Lesions were considered true-positive if a >50% PSA decline was observed post-treatment or confirmed by histopathology, primarily in bone lesions. ***Results:*** Out of 77 patients, 44 (57.1%) had at least one PSMA-avid lesion. Group A (n=36): 16 patients (44.4%) had positive findings: Local recurrence: 8/16 (50%) | SUVmax range: 7.2-15.2, Bone metastases: 6/16 (37,5%), Lung metastases: 2/16 (12,5%). No PSMA-avid lesions in 20/36 (55.5%). Group B (n=41): 28 patients (68.3%) had positive findings: Local recurrence: 15/28 (53.6%), Bone metastases: 10/28 (35.7%), Visceral metastases (all lung): 3/28 (10.7%). Therapeutic management changed in 44% of Group A and 68% of Group B based on PSMA PET/CT results. ***Conclusion:*** ^{18}F-PSMA PET/CT demonstrates high diagnostic accuracy in detecting recurrent disease even at very low PSA levels, significantly influencing clinical decision-making and enabling personalized treatment approaches. However, the clinical implications of negative PSMA scans in patients with very low PSA remain an area of uncertainty and warrant further investigation.

EP-0245

Is M1c1 a Distinct Prognostic Entity? Survival Impact of Single-Organ Extrathoracic Metastasis in the Proposed TNM-9 Lung-Cancer Classification

D. Nak[1], *O. Bülbül*[1], *B. Demir*[2], *M. H. Baltacioğlu*[3];
[1]Recep Tayyip Erdoğan University Training and Research Hospital, Rize, TÜRKIYE, [2]Mehmet Akif İnan Training and Research Hospital, Şanlıurfa, TÜRKIYE, [3]Trabzon University Faculty of Medicine Trabzon Kanuni Research and Training Hospital, Trabzon, TÜRKIYE.

Aim/Introduction: The 9th edition AJCC/IASLC TNM classification subdivides extrathoracic spread into M1b (single metastasis in a single organ), M1c1 (multiple metastases limited to a single organ) and M1c2 (multiple organs). It remains unclear whether M1c1 adds prognostic detail over M1b. We compared overall (OS) and progression-free survival (PFS) between these subcategories and explored organ-specific outcomes within M1c1. ***Materials and Methods:*** We retrospectively restaged 823 consecutive stage IV lung cancer patients (mean age 68 ± 10 years) with baseline ^{18}F-FDG PET/CT between 2016 and 2023. Extrathoracic disease was classified as M1b, M1c1 or M1c2 according to TNM-9. Log-rank tests and Kaplan-Meier curves assessed OS and PFS; subgroup analyses assessed bone, brain, adrenal, liver and distant lymph node involvement. The median follow-up was 11 ± 12 months (range 0.1-97). ***Results:*** In the cohort of 823 stage-IV lung cancer patients restaged according to the proposed 9th edition TNM classification system, median overall survival (OS) was 21.7 months for M1a, 17.0 months for M1b, 13.5 months for M1c1, and 9.8 months for M1c2; global comparison between the M1a, M1b, and M1c1 groups was not statistically significant ($p = 0.167$), with the worst prognosis observed in M1c2. Median progression-free survival (PFS) showed a similar pattern-11.40, 13.07 and 8.80 months for M1a, M1b and M1c1, respectively-and there was no significant difference between these three groups ($p = 0.278$). Organ-specific analyses reinforced the relative advantage of M1b: in patients with bone metastases, median OS was 15.4 months in M1b vs 12.8 months in M1c1 and 9.5 months in M1c2 ($p = 0.010$ for M1b-M1c2 comparison; $p = 0.404$ for M1b-M1c1); PFS was similarly longer in M1b than in M1c2 (12.3 vs 6.7 months; $p = 0.012$). A similar picture was observed in patients with brain metastases: Mean OS was 15.6 months in M1b, 17.6 months in M1c1, and only 10.0 months in M1c2 ($p = 0.025$ for M1b-M1c2 comparison; $p = 0.702$ for M1b-M1c1). In the M1c1 subgroup, the specific organ involved (brain, adrenal, liver, distant lymph node or bone) did not affect survival. ***Conclusion:*** These results suggest that M1c1 represents a distinct prognostic category, with outcomes closer to M1b than M1c2, reinforcing the clinical relevance of the new TNM subclassification. Further validation is needed to optimize treatment strategies for this subgroup. ***References:*** Detterbeck, F. C., Woodard, G. A., Bader, A. S., et al. (2024). The proposed ninth edition TNM classification of lung cancer. Chest, 166(4), 882-895.

EP-0246

Can F-18 FDG PET/CT Metabolic Parameters Predict STAS in Non-Small Cell Lung Cancer Patients?

B. Kocabeyoglu, *R. H. Tokac, A. Akgun;*
Ege University Nuclear Medicine Department, Izmir, TÜRKIYE.

Aim/Introduction: In patients with Non-Small Cell Lung Cancer (NSCLC), STAS (spread through air spaces) is a histological term describing the spread of cancer cells through airways outside the main tumor borders. In this study, we aimed to preoperatively

predict STAS, which is a prognostic factor for local recurrence and considered as an invasive pattern for NSCLC, using metabolic parameters obtained by F-18 FDG PET/CT imaging. ***Materials and Methods:*** The pathological data and F-18 FDG PET/CT findings of 75 patients who underwent F-18 FDG PET/CT imaging for metabolic characterization of solitary pulmonary nodules and NSCLC staging in our clinic between 2019 and 2024 were retrospectively included in the study. Metabolic tumor volume (MTV) and total lesion glycolysis (TLG), which are classical fixed threshold (42%) volumetric parameters with SUVmax values showing the highest uptake in the primary lesion area on PET/CT images, were calculated. In addition, different threshold values (lower limit SUVmax 2.5) were determined according to the primary lesion SUVmax value of each patient and maximum MTV and TLG values were calculated. Then, peripheral zonal MTV and TLG values, which are the difference of these values around the borders of the primary tumor, were obtained in accordance with the STAS term. ***Results:*** The patient age group was between 47-88 years (mean: 67) at the time of diagnosis, 14 were female and 61 were male. Lobectomy was performed in 43 patients, wedge resection in 29 patients and pneumonectomy in 3 patients. 38 patients were diagnosed with NSCLC including adenocarcinoma (20 acinar dominant, 7 solid dominant, 7 micropapillary dominant, 4 lepidic dominant subtypes), 24 squamous cell carcinoma, 3 large cell carcinoma and 10 other subtypes. According to histopathologic results, 55 patients were STAS positive and 20 patients were STAS negative. Primary tumor diameter (p=0.016), SUVmax (p=0.019) and peripheral zonal TLG (p=0.042) were statistically significantly correlated with STAS. On the other hand, no significant correlation was found between MTV, TLG, maximum MTV, TLG and peripheral zonal MTV values and STAS. ***Conclusion:*** It was concluded that STAS, which has an important role in lung cancer treatment management and prognosis prediction, can be predicted by SUVmax and peripheral zonal TLG values obtained in preoperative F-18 FDG PET/CT imaging and may be helpful in operation preferences.

EP-0247

Predicting PD-L1 expression status in NSCLC using radiomic analysis of FDG-PET/CT images

F. Kiss, *I. Járó, K. Szigeti, T. Györke;*
Semmelweis University, Budapest, HUNGARY.

Aim/Introduction: Lung cancer is the most common form of malignancy worldwide; its prognosis and treatment depend significantly on the results of histological and molecular analysis. Some molecular pathological features, such as PD-L1 positivity, provide an opportunity for immunotherapy. Taking histological samples is often problematic. Radiomic analysis of the imaging data is promising in the non-invasive determination of tumor phenotype by characterizing tumor heterogeneity and capturing complex patterns complementary to other clinical information. This study aims to investigate the potential of radiomics for predicting PD-L1 expression status in NSCLC patients based on FDG-PET/CT images. ***Materials and Methods:*** In this retrospective study, the staging FDG-PET/CT scans of 105 patients with NSCLC of different phenotypes (72 ACC, 33 SCC, 64 PD-L1 positive, 41 PD-L1 negative) were analysed. Different types of segmentation schemes were assessed. Radiomic features were obtained from the original and transformed images using the PyRadiomics package. After splitting the records into training and test sets in a 7:3 ratio, Mann-Whitney U test, LASSO regression, and Spearman correlation analysis were applied to reduce the number of examined features. A logistic regression model was trained using the selected features under different settings. The performance of the model was evaluated on the test set using ROC curve, AUC score, and various other performance metrics. ***Results:*** The extensive comparison of the tested models revealed that the best-performing one, which utilized translated masks and original and transformed images, achieved an AUC of 0.783 (95% confidence interval: 0.625, 0.942) and demonstrated high accuracy (81.25%), sensitivity (90.00%) and notably high NPV of 80.00%. These results indicate the reliability of the model in predicting the minority class, PD-L1 negative status in the imbalanced dataset. ***Conclusion:*** The results indicate that models built from radiomic features extracted from FDG-PET/CT images can distinguish between PD-L1 positive and PD-L1 negative NSCLC. Thus, radiomics with multimodal imaging holds significant potential for predicting the phenotype of NSCLC, providing a non-invasive alternative for selecting patients benefiting from targeted immunotherapy. ***References:*** Li B, Su J, Liu K, et al. Deep learning radiomics model based on PET/CT predicts PD-L1 expression in non-small cell lung cancer.

EP-0248

Baseline PET/MR Imaging for Lung Cancer Patients with Immunotherapy: A Correlation and Prognostic Study of IVIM, CTRW Diffusion and PET Metabolic Parameters

Y. Jiang[1], *S. Xie*[1], *C. Zhou*[1], *C. Sun*[2], *Y. Guo*[3], *Y. Wu*[1], *W. Fan*[1];
[1]*Sun Yat-sen University Cancer Center, Guangzhou, CHINA,*
[2]*United Imaging Healthcare Group Co., Ltd, Shanghai, CHINA,*
[3]*Shenzhen United Imaging Healthcare Co., Ltd., Shenzhen, CHINA.*

Aim/Introduction: This study aimed to investigate the baseline chest PET/MR imaging with multi-b value sequences in lung cancer patients undergoing immunotherapy, focusing on the correlation between intravoxel incoherent motion (IVIM) [1] and continuous time random walk (CTRW) models[2]with PET metabolic parameters, and their prognostic significance. ***Materials and Methods:*** Forty-five lung cancer patients were included, with baseline PET/MR imaging acquired, including multi-b value MR sequences. Following the scan, biopsy was performed for pathological confirmation. Patients subsequently underwent chemotherapy combined with immunotherapy. The biopsy lesions were semi-automatically contoured on PET images, and the corresponding mask was registered to diffusion-weighted imaging (DWI). The IVIM and CTRW diffusion models were fitted to obtain the parameters: α_CTRW, β_CTRW, D_CTRW, ADC, D_ivim, D_star_ivim, and f_ivim. PET metabolic parameters, including SUVmax, SUVmean, total lesion glycolysis (TLG), and metabolic tumor volume (MTV), were also calculated. Median values for these parameters were used for binary categorization, and univariate and multivariate analyses were performed to evaluate their prognostic value. The median survival time for the cohort was 5.03 [2.767-9.200] months. ***Results:*** Univariate and multivariate analyses revealed that the high and low of SUVmean and β_CTRW depending on median values were identified as independent prognostic risk factors for survival in lung cancer patients undergoing immunotherapy. Kaplan-Meier survival analysis showed that both high SUVmean ($p = 0.0084$) and low β_CTRW ($p = 0.044$) were associated with better survival outcomes. These results suggest that SUVmean and β_CTRW are significant independent prognostic factors for survival. ***Conclusion:*** Baseline chest PET/MR imaging, incorporating IVIM and CTRW diffusion models, can provide valuable information regarding tumor microenvironmental characteristics and is predictive of immunotherapy prognosis. SUVmean and β_CTRW were identified as independent prognostic factors, potentially aiding in personalized treatment strategies. ***References:*** 1. Bao X, Bian D, Yang X, Wang Z, Shang M, Jiang G, et al. Multiparametric MRI for evaluation of pathological response to the neoadjuvant chemo-immunotherapy in resectable non-small-cell lung cancer. Eur Radiol. 2023;33:9182-93.2. Karaman MM, Sui Y, Wang H, Magin RL, Li Y, Zhou XJ. Differentiating low- and high-grade pediatric brain tumors using a continuous-time random-walk diffusion model at high b -values. Magn Reson Med. 2016;76:1149-57.

EP-0249

^{18}F-FAPI PET/CT Imaging in Pneumoconiosis:a new tool for early diagnosis and guiding treatment of pulmonary fibrosis

C. Liu, *S. Li;*
First hospital of shanxi medical university, Taiyuan, CHINA.

Aim/Introduction: Pneumoconiosis is characterized by pulmonary fibrosis. The activation of fibroblasts play an important role in the pathological development of pulmonary fibrosis. Chest CT, as a conventional examination to diagnose pulmonary fibrosis of pneumoconiosis, cannot evaluate the fibrosis activity. The application value of ^{18}F-FAPI in pneumoconiosis is unclear. This study aimed to clarify the feasibility of ^{18}F-FAPI PET/CT in non-invasively monitoring the activity evolution of pulmonary fibrosis in pneumoconiosis and the anti-fibrotic treatment. ***Materials and Methods:*** A preliminary clinical study was conducted on 6 pneumoconiosis patients and 4 healthy control individuals, correlation analysis was performed between the ^{18}F-FAPI uptake in pulmonary fibrosis areas and the pulmonary diffusing function. Sprague-Dawley rat experiments were performed on three groups concluding pneumoconiosis model, pirfenidone-treated, and normal control groups. ^{18}F-FAPI and ^{18}F-FDG PET/CT, histopathologic, and hematological analysis were assessed monthly from modeling until 6 months. ***Results:*** ^{18}F-FAPI uptake in fibrotic areas was found in the pneumoconiosis patients, and negatively correlated with the diffusing function ($r = -0.929$, $P = 0.022$). In the pneumoconiosis model, ^{18}F-FAPI activity preceded one month earlier than relative collagen content (%) in Masson trichrome staining and the level of connective tissue growth factor in plasma, an indicator reflecting the fibroblast activation. The uptake of ^{18}F-FAPI, rather than ^{18}F-FDG, significantly decreased in the pirfenidone-treated group compared to the pneumoconiosis group ($P < 0.05$). ***Conclusion:*** ^{18}F-FAPI PET/CT imaging holds promise for the early identification of pulmonary fibrosis activity and monitoring its evolution in pneumoconiosis, offering a precise clinical opportunity for targeted anti-fibrotic treatment.

EP-0250

Comparative Evaluation of 68-Gallium-Fibroblast Activation Protein Inhibitor (FAPI) PET/CT and 18-F-Fluorodeoxyglucose (FDG) PET/CT in Non-Small Cell Lung Cancer: Insights from an Expanded Cohort

S. Sathoo, *D. Halanaik, R. Manju, S. Pradeep;*
Jawaharlal Institute of Postgraduate Medical Education & Research, Puducherry, INDIA.

Aim/Introduction: Lung cancer remains a major global health challenge, where precise staging is essential for guiding treatment. Although ^{18}F-FDG PET/CT is well established in clinical imaging, the newer 68Ga-FAPI PET/CT, which targets cancer-associated fibroblasts, has shown potential advantages. This study compares the effectiveness of ^{18}F-FDG and 68Ga-FAPI PET/CT in assessing non-small cell lung cancer (NSCLC). ***Materials and Methods:*** This single-centre study included 31 patients with newly diagnosed, treatment-naive NSCLC. Each patient underwent both 68Ga-FAPI and ^{18}F-FDG PET/CT scans within one week for baseline staging. Primary lesions, lymph nodes, and distant metastases were evaluated and compared across both imaging methods. Semi-quantitative metrics, including SUVmax (adjusted for body surface area) and Tumour-to-Background Ratio (TBRmax), were calculated and analysed using Paired T-tests. The tumours were staged according to the 9th edition of the TNM classification for lung cancer. ***Results:*** Among the participants (mean age 58.5 ± 9.4 years; 23 males, 8 females), 68Ga-FAPI PET/CT identified more metastases: lymph nodes (157 vs 124), bone (154 vs 135), liver (7 vs 5), pleura (39 vs 33), lung (42 vs 37), adrenal (8 vs 7) and brain (1 vs 0). SUVmax was higher for 68Ga-FAPI in primary lesions (5.1±1.8 vs 3.9±1.7, p<0.001), lymph nodes (3.3±1.4 vs 2.3±1.2, p<0.001), bone (3.8±1.7 vs 2.1±0.9, p<0.001), liver (5.3±2.5 vs 2.5±0.6, p=0.04) and pleural (2.7±1.1 vs 1.6±0.6, p<0.001) metastases. The TBRmax was significantly higher in 68Ga-FAPI scans across all these lesions (p<0.05). 68Ga-FAPI improved metastasis visualisation in bone, brain, and liver compared to ^{18}F-FDG due to reduced background uptake. No significant differences were found in SUVmax or TBRmax for lung (SUVmax: 2.0 ± 1.0 vs 1.8 ± 0.9, p>0.05; TBRmax: 3.8 ±2.1 vs 3.3 ±1.7, p>0.05) or adrenal metastases (SUVmax: 3.0 ± 1.1 vs 2.5 ± 1.5, p>0.05; TBRmax: 4.5 ±1.9 vs 3.3 ± 3.4, p>0.05). The 68Ga-FAPI PET/CT scan led to N-stage upstaging in 16% of patients (5 out of 31) and resulted in an overall TNM stage upstaging in approximately 10% (3 out of 31). ***Conclusion:*** 68Ga-FAPI PET/CT demonstrates superior performance compared to ^{18}F-FDG PET/CT in detecting metastatic lesions in lymph nodes, bone, liver, pleura, lung, adrenal and brain among patients with non-small cell lung cancer (NSCLC). Its higher SUVmax values and improved tumour-to-background ratios contribute to more accurate staging and may enhance therapeutic planning for metastatic disease.

EP-0251

Prognostic Value of Cerebral Metabolic Activity in Metastatic Non-Small Cell Lung Cancer (NSCLC) Patients

J. Auriac[1], *G. Lemoudda*[1], *N. Hovhannisyan-Baghdasarian*[1], *M. Pires*[2], *L. K. Shiyam Sundar*[3], *P. Salamoun-Feghali*[4], *R.-D. Seban*[1,5], *N. Jehanno*[1,5], *C. Nioche*[1], *M. Luporsi*[1], *T. Beyer*[2], *N. Girard*[4], *I. Buvat*[1], *F. Orlhac*[1];
[1]*Institut Curie, Université Paris-Saclay, Inserm LITO U1288, Orsay, FRANCE,* [2]*Quantitative Imaging and Medical Physics (QIMP) Team, Medical University of Vienna, Vienna, AUSTRIA,* [3]*DIGIT-X Lab, Department of Radiology, LMU University Hospital, Munich, GERMANY,* [4]*Institut Curie, Institut du Thorax Curie-Montsouris, Paris, FRANCE,* [5]*Institut Curie, Department of Nuclear Medicine, Paris-St-Cloud, FRANCE.*

Aim/Introduction: Whole-body PET/CT images associated with automated segmentation tools offer new opportunities to investigate inter-organ metabolic connections. Doing so, we identified an unexpected relationship between brain FDG uptake and overall survival (OS) in metastatic Non-Small Cell Lung Cancer (NSCLC) patients that we thoroughly investigated in this study. ***Materials and Methods:*** Whole-body FDG-PET/CT images were retrospectively collected for 380 metastatic NSCLC patients before treatment, chronologically divided into discovery/test sets according to the scan date. All lesions were automatically segmented on PET using LION[1] followed by SUV>4. The whole brain was segmented using TotalSegmentator[2] based on CT. Maximum distance between two lesions (Dmax), maximum uptake (maxSUVmax) and average uptake (TSUVmean) across all lesions, Total Metabolic Tumor Volume (TMTV) and whole-brain average FDG uptake ($SUVmean_{brain}$) were extracted using LIFEx[3]. Univariable analysis was performed using the Cox proportional hazard model. Features with p<0.05 were included in a Cox multivariable model without (Model1) and with $SUVmean_{brain}$ (Model2). A risk score was derived and binarized by the median in the discovery set to stratify patients into two groups. Survival analyses were performed using the Kaplan Meier method. The relationship between $SUVmean_{brain}$ and clinical/imaging features was investigated using Spearman coefficients (rS) and Wilcoxon tests. ***Results:*** The discovery and test sets included 234 and 146 patients respectively. In univariable analysis, ECOG Performance Status ≥2 (Hazard Ratio=2.20, Wald test: p<0.001), smoking history (HR=1.63, p=0.01), Dmax (HR=1.07, p=0.009), TMTV (HR=1.12, p<0.001) and $SUVmean_{brain}$ (HR=0.83, p<0.001) were associated with OS. In multivariable analysis, $SUVmean_{brain}$ remained an independent prognostic factor (HR=0.88; 95%CI: [0.80-0.98]; p=0.02). Model2 outperformed Model1 (χ^2 test: p=0.02). The median survival gap between low- and high-risk patients with Model2 (Log-rank test: p<0.001) was larger than with Model1 in the discovery (14.9 vs. 14.4 months) and test sets

(13.5 vs. 7.3 months). $SUVmean_{brain}$ was lower in patients who died within one year (Wilcoxon test: p<0.001). $SUVmean_{brain}$ was significantly correlated with CRP (rS=-0.44), neutrophils (rS=-0.44) and albumin (rS=0.39) and was neither correlated with radiomic features (rS<0.24) nor associated with brain metastases (p=0.68). ***Conclusion:*** $SUVmean_{brain}$ was an independent prognostic factor in metastatic NSCLC patients. Low-cerebral metabolism might be associated with immune response and systemic inflammation, which warrants further evaluation. ***References:*** 1.Pires et al. EJNMMI 2024. 2.Wasserthal et al. Radiology: AI 2023. 3.Nioche et al. Cancer Res 2018.

EP-0252

Spatial radiomics features derived from SUVmax location in resectable NSCLC are associated with tumor aggressiveness

Z. Jiang, *D. Haberl, C. P Spielvogel, J. Yu, K. Lukas, H. Marcus;*
Medical University of Vienna, Vienna, AUSTRIA.

Aim/Introduction: Accurate non-invasive prediction of histopathologic invasiveness and recurrence risk remains a clinical challenge in resectable non-small cell lung cancer (NSCLC). Radiomics has shown promise in extracting biologically meaningful information from imaging. In this study, we developed and validated the Edge Proximity Score, a novel spatial PET radiomic feature that quantifies the displacement of metabolic activity from the tumor center, to predict invasive histopathologic features and progression-free survival (PFS). ***Materials and Methods:*** We retrospectively analyzed 244 NSCLC patients with baseline ^{18}F-FDG PET/CT and complete clinical-pathological data. The Edge Proximity Score was calculated based on the normalized distance between the SUVmax and both the tumor centroid and perimeter. PET-derived radiomics features (n = 105) were extracted. The dataset was randomly split 80:20 into training and validation cohorts, and models were trained using 10-fold cross-validation. Eight machine learning classifiers were developed to predict lymphovascular invasion (LVI), visceral pleural invasion (VPI), and spread through air spaces (STAS). Feature selection was conducted using minimum redundancy maximum relevance (mRMR), and SHAP was used to visulize feature contributions. Cox regression and Kaplan-Meier analyses were performed to assess the prognostic value of the Edge Proximity Score. RNA sequencing data from 76 TCIA patients were used for biology analysis. ***Results:*** The Edge Proximity Score was significantly elevated in STAS-positive ($P = 6.7\times10^{-12}$), VPI-positive ($P = 8.3\times10^{-5}$), and LVI-positive ($P = 9.9\times10^{-5}$) tumors. Logistic regression achieved the best predictive performance (AUC = 0.74 for STAS, 0.69 for LVI, and 0.66 for VPI), with the Edge Proximity Score ranking among the top five features in SHAP analysis. In multivariable Cox regression, the Edge Proximity Score was an independent predictor of PFS (HR = 2.629, 95% CI: 1.178-5.870; P = 0.018), along with TNM stage (P = 0.014), VPI (P = 0.037), and age (P = 0.009). Patients with high Edge Proximity Scores showed significantly worse PFS in both the internal cohort (P = 1e−4) and external TCIA cohort (P = 0.0045). Transcriptomic analysis revealed upregulation of cell cycle and metabolic pathways in high-risk tumors, while immune-related pathways (e.g., interferon responses, IL6-JAK-STAT3) were enriched in the low-risk group. Immune cell deconvolution confirmed higher infiltration of neutrophils, monocytic lineages, and myeloid dendritic cells in low-risk tumors ($P < 0.005$). ***Conclusion:*** The Edge Proximity Score is a non-invasive, interpretable biomarker associated with tumor invasiveness, recurrence, and immune activity in NSCLC, with potential to enhance preoperative risk stratification.

EP-0253

Performance of [18F] FDG PET/CT versus FAPI PET/CT for lung cancer assessment

M. Komarova, *N. Meshcheryakova, I. Nazarenko, O. Ryzhova, A. Pronin, V. Solomyany;*
N.N. Blokhin National Medical Research Center of Oncology, Moscow, RUSSIAN FEDERATION.

Aim/Introduction: to compare the diagnostic performance of 18-fluorodeoxyglucose (FDG) PET/CT and fibroblast activating protein inhibitor (FAPI) PET/CT in the assessment of primary tumors, lymph nodes and distant metastases in lung cancer patients. ***Materials and Methods:*** In this retrospective study, patients (pts) with lung cancer who underwent FAPI PET/CT and FDG PET/CT between 2022-2024 were analyzed. Lesion uptake was converted to SUVmax. Mann-Whitney test was used to compare the SUVmax and the number of positive lesions detected by the two methods was recorded. We calculated the diagnostic efficiency (sensitivity (Se), specificity (Sp), positive predictive value (PPV), negative predictive value (NPV) and accuracy (Ac)) for each modality on a per-region basis and for lymph nodes metastasis detection. Positive tumor lesions on PET/CT images were verified by biopsy or follow-up. ***Results:*** In total 20 participants (median age: 66,5 years; 3 females/ 17 males; histopathologic findings: adenocarcinoma 12 pts, squamous cell carcinoma 5 pts, neuroendocrine tumor 2pts and non-small-cell lung cancer 1 pts) were assessed. There were no significant differences between uptake of FAPI and of FDG in both primary lesions, metastatic lymph nodes and other metastases. The mean SUVmax in primary lesions were 11,01 [8,98-14,69] for FDG PET/CT and 12,11[5,69-15,51] for FAPI PET/CT, p=0,98; in lymph nodes were 4,93 [3,77-7,53] vs. 7,25 [0,78-15,06] respectively, p= 0,69. The detection of lymph nodes lesions using FAPI PET/CT was superior to that with FDG PET/CT (total number of lesions were 73 vs. 53, respectively). However, the detection sensitivity for primary tumors using both modalities was comparable. The diagnostic capabilities were higher with FAPI PET/CT than FDG PET/CT on a per-region basis (Se 98,67% vs. 73,33%, Sp 87,80% vs. 63,41% and Ac 94,83% vs. 76,83%, respectively) and in the diagnosis of lymph nodes metastasis (Se 97,78% vs. 66,67%, Sp 96,97% vs. 60,61% and Ac 97,44 % vs. 64,10%, respectively). ***Conclusion:*** Compared to FDG PET/CT, FAPI PET/CT demonstrated better lesion detection capabilities for patients with lung cancer, particularly of metastasis to lymph nodes.

EP-0254

Towards Personalised Lung Cancer Screening: A Prospective Multicentre Study Integrating LDCT, [^{18}F] FDG-PET/CT and AI-Driven Risk Stratification

F. Gelardi[1], *P. Muriana*[1], *L. Antunovic*[1], *M. Sollini*[2,1], *D. Palumbo*[1], *R. Ferrara*[2,1], *R. Petrelli*[1], *R. Di Donato*[1], *R. Cuocolo*[3], *P. Veltri*[4], *P. Soda*[5], *G. Veronesi*[2,1], *A. Chiti*[2,1];
[1]*IRCCS Ospedale San Raffaele, Milan, ITALY,* [2]*Università Vita-Salute San Raffaele, Milan, ITALY,* [3]*Università di Salerno, Baronissi (SA), ITALY,* [4]*DIMES, Università della Calabria, Rende (CS), ITALY,* [5]*Università Campus Bio-Medico di Roma, Rome, ITALY.*

Aim/Introduction: Low-dose CT (LDCT) screening significantly increases the early detection of lung cancer and improves survival. However, its clinical utility is limited by high false-positive rates, overdiagnosis and a lack of consensus on optimal screening intervals. There is an urgent need to move from one-size-fits-all screening protocols to personalised strategies that improve diagnostic accuracy while minimising unnecessary interventions. This study investigates a comprehensive screening model that integrates individual risk factors, clinical data and advanced imaging - LDCT and [^{18}F]FDG PET/CT - augmented by artificial intelligence (AI) to improve the accuracy and efficiency of lung cancer detection. ***Materials and Methods:*** In this prospective, multicentre study, 334 high-risk patients (age>50yrs; PLCOm2012>4%) will be enrolled and assigned to one of two cohorts: Cohort 1 will receive combined LDCT and [^{18}F]FDG PET/CT; Cohort 2 will receive LDCT alone. LDCT findings will be classified according to Lung-RADS 2022 criteria, while PET/CT will be considered positive if significant FDG uptake is detected in lung nodules or extra thoracic sites. AI algorithms will synthesise patient-specific clinical and imaging data to refine nodule classification,

identify high-risk individuals and personalise screening intervals and modalities. ***Results:*** Recruitment began in January 2025 and is ongoing. To date, 17 participants have been enrolled in Cohort 1 (median age 66 years; 8 females, 9 males), all with a history of heavy smoking and no known occupational or environmental exposures. One patient presented with a Lung-RADS 4a nodule on LDCT, with no corresponding FDG uptake; 6-months follow-up CT was recommended. No significant nodules were identified in the remaining participants. PET/CT revealed incidental findings in three participants: FDG-avid colonic polyps, FDG-avid Warthin tumours, and an adrenal adenoma. ***Conclusion:*** This study aims to demonstrate that the integration of [^{18}F]FDG-PET/CT with LDCT improves screening specificity, reduces false positive rates and allows more accurate staging of regional and distant disease. In addition, PET/CT can detect clinically relevant smoking-related extrapulmonary malignancies not detected by chest LDCT alone. The AI-driven approach is expected to refine screening protocols by individualising the timing and imaging modalities based on patient risk profiles, thereby reducing unnecessary follow-up and procedures. Overall, this integrative approach has the potential to transform lung cancer screening into a more targeted, efficient and patient-centred practice. Acknowledgements: The Italian Ministry of Health and the European Union support the project "Advancing Lung Cancer Screening: Artificial Intelligence, Multimodal Imaging and Cutting-Edge Technologies for Early Detection and Characterization" (PNRR-MCNT2-2023-12377755).

EP-16

e-Poster Area

B: Imaging Clinical Studies -> B1 Oncological Imaging Clinical Study -> B15 Gastro-Intestinal (including Liver and Non-Endocrine Pancreas)

EP-0255

Early tumor response following transarterial radioembolization (TARE): preliminary data from 30 patients with primary and secondary liver tumors

A. Moretti*, A. Vizzuso, M. Renzulli, E. Giampalma, E. Del Giudice, D. Tirotta, R. Galassi, G. Pontone, F. Di Mauro, F. Matteucci;*
Ospedale Morgagni Forli, Forli, ITALY.

Aim/Introduction: Transarterial radioembolization (TARE) with Yttrium-90 microspheres is an established locoregional treatment for hepatocellular carcinoma (HCC) and selected liver metastases. However, its short-term efficacy and potential to downstage tumors for surgery remain areas of active investigation. This study aims to describe the early radiological response and clinical outcomes of patients treated with TARE at our institution. ***Materials and Methods:*** A retrospective analysis was conducted on 30 consecutive patients treated with TARE between April 2024 and April 2025. Diagnoses included hepatocellular carcinoma (HCC), intrahepatic cholangiocarcinoma, neuroendocrine tumors (NETs), and secondary liver metastases from colon cancer. For each patient, data were collected on tumor histology, treatment date, administered activity (GBq), radiological response at 1, 3, and 6 months (according to RECIST criteria: PR, partial response; CR, complete response; PD, progressive disease, SD, stabile disease), surgery after TARE, and vital status. ***Results:*** Histological distribution: HCC (73.3%), cholangiocarcinoma (13.3%), NETs (6.7%), and metastases (6.7%). Radiological response at 1 month (n = 18):- PR: 11 patients (61.1%)- CR: 3 patients (16.7%)- PD: 2 patients (11.1%)- Not assessable: 2 patients (11.1%). At 3 months (n = 8):- PR: 5 (62.5%)- CR: 2 (25.0%)- PD: 1 (12.5%). At 6 months (n = 3):- PR: 2 (66.7%)- CR: 1 (33.3%). Surgery post-TARE was performed in one patient (3.3%). At the time of data collection, 96.7% of patients were alive. ***Conclusion:*** Preliminary findings suggest that TARE achieves a high rate of tumor control in the early months following treatment, with over 60% of patients showing partial response and up to 25% complete response by 3 months. Although conversion to surgery was limited, possibly due to disease extent or comorbidities, the therapy appears to offer promising short-term outcomes. Further studies with longer follow-up and larger cohorts are warranted to confirm these results and better define TARE's role in integrated treatment strategies.

EP-0256

Fibroblast activation protein-targeted PET/CT with ^{18}F-Fibroblast activation protein inhibitor-74 for evaluating the staging and guiding clinical management of gastrointestinal cancers: comparison with contrast-enhanced CT

L. Ma*[1], Z. Quan[1], H. Chen[2], F. Kang[1], J. Wang[1];*
[1]Xijing Hospital, Fourth Military Medical University, Xi'an, Shaanxi, CHINA, [2]The First Affiliated Hospital of Xiamen University, School of Medicine, Xiamen University, Xiamen, CHINA.

Aim/Introduction: The aim of this study is to compare the efficacy of ^{18}F-FAPI-74 PET/CT targeting fibroblast activation protein (FAP) labeled with ^{18}F and enhanced CT (Ce-CT) in the staging and clinical management of gastrointestinal cancer. ***Materials and Methods:*** A prospective dual-center study included 38 patients with pathologically confirmed gastrointestinal cancers (including gastric, colorectal and pancreatic). All patients underwent both ^{18}F-FAPI-74 PET/CT and Ce-CT within two weeks, with surgical or biopsy pathology as the reference standard.Compare the diagnostic performance of Ce CT and^{18}F-FAPI-74 PET/CT using the McNemar test, and compare them with the gold standard. ***Results:*** Finally, 38 patients were included in the analysis. In terms of lymph node metastasis detection, the sensitivity (60% vs. 32%), specificity (98% vs. 96.1%), and accuracy (92% vs. 85%) of ^{18}F-FAPI-74 PET/CT were significantly better than CE-CT (all P<0.05). The sensitivity (94% vs. 19%) and accuracy (97% vs. 58%) of 18F-FAPI-74 PET/CT in detecting distant metastases were significantly higher than those of CE-CT (all P<0.001), especially in the detection of peritoneal metastases. In terms of clinical management, 37% of patients changed their treatment decisions due to ^{18}F-FAPI-74 PET/CT (18% made significant adjustments, such as transitioning from direct surgery to neoadjuvant therapy or palliative care). ***Conclusion:*** ^{18}F-FAPI-74 PET/CT is significantly better than CE-CT in staging gastrointestinal cancer, especially in detecting small distant metastases (such as peritoneal metastases), which can more accurately guide personalized clinical management.

EP-0258

Multicentre Study Comparing [^{68}Ga] FAPI-04 PET/CT and [^{18}F]FDG PET/CT for Staging Gastrointestinal Tumours

P. Hj*[1], H. Nagaraj[2,3], K. G. Kallur[4,3], S. S P[1], M. Saini[2], P. Saini[2], R. Krishnappa[3], P. G. Ramachandra[3], D. Kumar[5], P. Wadhwa[5];*
[1]Aster Hospital, Banglore, INDIA, [2]The Nairobi West Hospital, Nairobi, KENYA, [3]HCG CCK Cancer Centre, Nairobi, KENYA, [4]HCG Cancer Center, Banglore, INDIA, [5]United Imaging Healthcare, Delhi, INDIA.

Aim/Introduction: [^{18}F] FDG PET/CT remains a widely adopted modality for assessing tumour metabolism, its diagnostic utility can be limited in certain GI malignancies due to variable glucose uptake and reduced sensitivity in tumours with low metabolic activity or mucinous components. In contrast, [^{68}Ga] FAPI-04 PET/CT has emerged as a promising alternative. This study aims to compare the diagnostic performance of FAPI-04 PET/CT and FDG PET/CT for staging GI tumours in a cohort of 75 patients, excluding those with gastrointestinal lymphomas. ***Materials and Methods:*** This retrospective, multi-center study was conducted across Aster Whitefield Hospital in Bangalore, India, The Nairobi

West Hospital, and HCG CCK Cancer Center in Nairobi, Kenya. It included 75 patients with either suspected or histologically confirmed gastrointestinal (GI) malignancies who were referred to these centers for diagnostic evaluation and staging. Each patient underwent both [^{18}F]FDG PET/CT and [^{68}Ga]FAPI-04 PET/CT within a 7-day interval. In India, both the scans were done at Aster Whitefield Hospital, Banglore, India, whereas, in Kenya FDG scans for the patients were conducted at The Nairobi West Hospital, whereas FAPI was conducted at HCG CCK Cancer Center. Across the cohort, 145 lesions were detected, encompassing colorectal, gastric, pancreatic, and esophageal cancers. Comparative analysis was performed between the two imaging modalities based on lesion localization, size, and tracer uptake characteristics. Diagnostic performance metrics—sensitivity, specificity, and overall accuracy—were determined using histopathological findings as the reference standard. ***Results:*** FAPI O4 PET/CT showed a higher sensitivity (92%) in detecting gastrointestinal tumors compared to FDG PET/CT (84%), particularly excelling in cases of pancreatic and colorectal cancers, where fibrotic stroma and low metabolic activity can limit FDG uptake. The specificity of FAPI O4 PET/CT was also greater (95%) than that of FDG PET/CT (88%), likely due to its reduced uptake in non-cancerous tissues. Lesion detection was more effective with FAPI O4 PET/CT, identifying 142 out of 145 lesions, whereas FDG PET/CT identified 124 ($p = 0.02$). Overall diagnostic accuracy favoured FAPI O4 PET/CT at 94%, compared to 86% for FDG PET/CT. FAPI O4 PET/CT also had superior performance in identifying metastatic spread to the liver, peritoneum, and lymph nodes. ***Conclusion:*** FAPI O4 PET/CT demonstrates superior performance over FDG PET/CT in staging gastrointestinal cancers, showing higher sensitivity, specificity, and overall diagnostic accuracy—especially in tumours with significant stromal components. ***References:*** 1. Giesel, F. L., et. al. (2021). JNM

EP-0259

Evaluating Protein-Losing Enteropathy Using 99mTc-MDP Scintigraphy: A Non-Invasive Diagnostic Approach

K. Vidhya[1], *S. K. Jha*[2], *P. Palanivel*[3], *S. L S*[4], *R. Mishra*[5], *V. K. Dhingra*[1]; *[1]AIIMS, Rishikesh, Rishikesh, INDIA, [2]Ranchi Cancer Hospital and Research Centre, Ranchi, INDIA, [3]American Oncology Institute, Coimbatore, INDIA, [4]AIIMS, Delhi, Delhi, INDIA, [5]Hope and Heal Cancer Hospital, Siliguri, INDIA.*

Aim/Introduction: Protein-losing enteropathy (PLE) is a rare disorder characterized by excessive loss of plasma proteins through the gastrointestinal tract, often presenting with diarrhoea, hypoalbuminemia, and peripheral edema. Etiologies include lymphatic obstruction, mucosal inflammation, or erosion. While 99mTc-labeled human serum albumin (HSA) scintigraphy is traditionally used, limited availability necessitates alternative tracers. 99mTc-methylene diphosphonate (MDP), commonly used for bone imaging, has emerged as a potential alternative for detecting intestinal protein loss and is a rarely-utilized yet readily available tracer for this pathology. ***Materials and Methods:*** Patients with clinical features of PLE—hypoalbuminemia, peripheral edema, and chronic diarrhea—underwent 99mTc-MDP scintigraphy. Each received 740 MBq (20 mCi) of 99mTc-MDP intravenously. Dynamic, blood pool, delayed planar whole-body, and SPECT/CT images were acquired using a dual-head gamma camera. Radiochemical purity was confirmed at 98% via chromatography, and physiological tracer biodistribution was evaluated to rule out free pertechnetate or contamination. ***Results:*** Here we present two female patients with symptoms of PLE and how MDP scintigraphy helped in their diagnosis. In Case 1, a 66-year-old woman demonstrated focal tracer accumulation in the ascending and transverse colon. Stool counts were elevated, and biopsy confirmed colitis as the site of protein loss. In Case 2, a 53-year-old woman showed diffuse uptake throughout the colon, with SPECT/CT localizing pooling in the caecum and proximal ascending colon. Elevated stool counts supported active protein loss. Previous biopsies from unrelated bowel segments were normal; based on imaging, targeted biopsy from the caecum was recommended. In both cases, physiological skeletal and renal excretion was observed without abnormal uptake in the thyroid, stomach, or liver, ruling out tracer impurities. ***Conclusion:*** 99mTc-MDP scintigraphy successfully localized intestinal protein loss in both patients, guiding further diagnostic biopsies and clinical management. As a widely available, cost-effective, and non-invasive alternative to 99mTc-HSA, 99mTc-MDP shows promising utility in evaluating PLE. These cases underscore its potential role in diagnosis and biopsy guidance, especially in resource-limited settings.

EP-0260

Timing is Everything: Unmasking Pancreatic Cancer with Multiple-Time-Point [^{68}Ga]Ga-FAPI-46 PET Imaging

P. Rasinski[1,2], *T. Nilsson*[1,2], *A. Gebremariam*[2], *M. Holstensson*[1,2], *E. Sparrelid*[1,3], *M. Löhr*[1,3], *T. Tran*[2,4], *R. Axelsson*[2,5]; *[1]Department of Clinical Science, Intervention, and Technology, Karolinska Institutet, Stockholm, SWEDEN, [2]Department of Nuclear Medicine and Medical Physics, Karolinska University Hospital, Stockholm, SWEDEN, [3]Department of Upper Gastrointestinal Diseases, Karolinska University Hospital, Stockholm, SWEDEN, [4]Department of Oncology-Pathology, Karolinska Institutet, Stockholm, SWEDEN, [5]Department of Molecular Medicine and Surgery, Karolinska Institutet, Stockholm, SWEDEN.*

Aim/Introduction: FAPI-PET imaging is a promising imaging technique, particularly in the assessment of pancreatic cancer (PC). However, differentiating between malignant and non-malignant lesions that are FAPI-positive remains a challenge. It has been suggested that multiple-time-point imaging could enhance the distinction between malignant and benign pancreatic tracer uptake when compared to single time-point imaging. The aim of this study was to establish whether multiple-time-point PET acquisition can improve the differentiation of PC in patients with concomitant pancreatitis. ***Materials and Methods:*** In an ongoing prospective clinical trial (EU2024-514967-25-00; NCT05172310), the diagnostic value of [68Ga]Ga-FAPI-46 PET/CT imaging in patients with suspected PC is investigated. Prior to surgery patients undergo FAPI PET imaging. A preliminary analysis was conducted of ten patients with histopathologically confirmed concomitant PC and pancreatitis. The patients were administered with [68Ga]Ga-FAPI-46 (mean activity 195±47 MBq), followed by a 45-minute dynamic PET acquisition with list mode, centred over the lesion in the pancreas. At 60 minutes post-injection, a whole-body static PET acquisition was performed (4 minutes per bed position). At 180 minutes post-injection, an additional static acquisition (14 minutes per bed position), centred over the pancreatic lesion was carried out. The dynamic PET raw data were statistically truncated and reconstructed to produce images of 4-minute acquisition duration, at 10, 20, 30, and 40 minutes post-injection. The images were co-registered, and lesion segmentation was conducted using Affinity (version 4.0.2) on the 40-minute images. Volumes of interest technique, with a 40% threshold, were drawn, and the volumes were copied to the other time-point images. ***Results:*** The mean SUVmax, SUVmean, and SUVpeak in PC remained relatively stable up to the 60-minute imaging and decreased slightly at 180-minute imaging. In pancreatitis lesions, the mean of all SUV parameters decreased relatively steadily between the subsequent time points. Notably, there were significant differences in SUVmax and SUVmean between PC and pancreatitis at both 60-minute and 180-minute imaging, as well as in SUVpeak at 180-minute imaging. ***Conclusion:*** Preliminary findings indicate that imaging at 60 and 180 minutes post-injection enhances the differentiation of PC in patients with concomitant pancreatitis compared to

earlier time-point imaging. Although the clinical value of repeated imaging at various time points was not clearly established in these results, further analyses are ongoing to determine its potential.

EP-0261

Prognostic Value of Preoperative Staging ^{18}F-FDG PET/MRI Findings in Surgically Resected Gastric Cancer Patients

R. Kalkan, *S. Gülbahar Ateş, U. Aydos, Ü. Ö. Akdemir, L. Ö. Atay;*
Gazi University Faculty of Medicine, Ankara, TÜRKIYE.

Aim/Introduction: Our aim was to investigate the prognostic value of staging ^{18}F-FDG PET/MRI findings related to the primary tumor and lymph nodes (LN) in predicting overall survival in gastric cancer patients undergoing surgical resection. ***Materials and Methods:*** We included 78 patients with gastric cancer who underwent ^{18}F-FDG PET/MRI for primary staging before surgical resection and total/subtotal gastrectomy at follow-up between 2018 and 2024. Demographic characteristics, type of surgery, history of chemotherapy/radiotherapy, histopathological features of the tumor, tumor location, wall thickness, SUVmax, minimum apparent diffusion coefficient (ADCmin) values, SUVmax/liver SUVmean ratio, number and SUVmax of ^{18}F-FDG positive LNs, LN SUVmax/liver SUVmean ratio, the size of largest LN, presence of mortality during follow-up and last follow-up dates were recorded. Continuous variables were categorized by determining the optimum threshold values according to Youden index in ROC analysis. Cox regression analysis was performed with SPSSv27 to determine the factors predicting mortality and Kaplan-Meier analysis to determine survival. ***Results:*** The clinicopathologic characteristics of the patients are summarized in a table. The median follow-up period was 23.7 months and mortality was observed in 39 (50%) of the patients. In the univariate analysis performed to determine the factors predicting overall survival, type of surgery (p=0.002), histopathologic subtype (p=0.021), pT (p=0.025) and pN (p=0.004) stages, ADCmin (p=0.023), presence of lymphovascular (p=0.013) and perineural (p=0. 017) invasion, gastric tumor wall thickness (p=0.031), number of ^{18}F-FDG positive LNs (p=0.027), LN size (p=0.007) and tumor SUVmax/liver SUVmean ratio (p=0.008) were statistically significant. In multivariant analysis, tumor SUVmax/liver SUVmean ratio (p=0.002), and histopathological subtype (p<0.001) were found to be independent risk factors for mortality. A tumor SUVmax/liver SUVmean ratio above 2.6 was associated with an approximately 4.4-fold increased mortality risk at follow-up, while the presence of signet-ring cell carcinoma pathology was associated with an approximately 5.9-fold increased mortality risk. The mean survival of operated gastric cancer patients was calculated as 42.7 ±3.5 months. Overall survival was lower in patients with the histopathologic type of signet-ring cell carcinoma than in those with adenocarcinoma-subtypes (p=0.019). Patients with a high tumor SUVmax/liver SUVmean ratio(>2.6) had a lower survival compared to patients with a low tumor SUVmax/liver SUVmean ratio (p=0.005). ***Conclusion:*** SUVmax/liver SUVmean ratio, which is a measure of the metabolic activity of the primary tumor normalized to the liver in preoperative staging ^{18}F-FDG PET/MR images in operated gastric cancer patients, is an independent risk factor along with histopathology in determining postoperative patient prognosis.

EP-0262

Head-to-Head Comparison of ^{18}F-FDG and ^{18}F-PSMA PET/CT in Hepatocellular Carcinoma

G. Picciola Bordoni, *M. E. S. Takahashi, F. F. Zarpelão, N. A. A Silveira, V. C. C. R Heringer, S. Kuba, N. Tobar, S. Q. Brunetto, C. A. de Souza, J. B. C. Carvalheira, C. Dario Ramos;*
Universidade Estadual de Campinas UNICAMP, Campinas, BRAZIL.

Aim/Introduction: Although ^{18}F-FDG PET/CT is widely used in oncology, its diagnostic performance in hepatocellular carcinoma (HCC) remains suboptimal. Prostate-specific membrane antigen (PSMA), primarily recognized as a biomarker for prostate cancer, has also been linked to tumor neoangiogenesis. Here, we performed a head-to-head comparison of ^{18}F-FDG and ^{18}F-PSMA PET/CT for evaluating hepatic lesions in patients with HCC. ***Materials and Methods:*** Eleven patients with confirmed HCC (six with BCLC stage C and five with stage B) were included (median age: 74 years; range: 59-86). Each patient underwent both ^{18}F-FDG (60 and 120 minutes post-injection) and ^{18}F-PSMA (60 and 120 minutes post-injection) PET/CT images, within a one-day interval. Maximum standardized uptake values (SUVmax) were measured for each hepatic lesion, and changes between early and delayed images (ΔSUVmax) were calculated. Correlation between SUVmax values was assessed using Spearman's rank correlation coefficient, with significance set at $p < 0.05$. ***Results:*** Nine of the 11 patients had multiple hepatic lesions. A median of 3 lesions per patient (1-15) was detected with ^{18}F-FDG, and 2 lesions per patient (1-11) with ^{18}F-PSMA, totaling 75 lesions. Fifty-six lesions were positive for both radiotracers, 16 were only for ^{18}F-FDG, and 3 only for ^{18}F-PSMA. In the BCLC-B group (n = 5), 11 lesions were detected with ^{18}F-FDG, 15 with ^{18}F-PSMA, and 32 with both. The median SUVmax (early images) was 6.3 (3.5-8.5) for ^{18}F-FDG and 17.2 (15.0-25.6) for ^{18}F-PSMA. In the BCLC-C group (n = 6), 34 lesions were detected with ^{18}F-FDG, 14 with ^{18}F-PSMA, and 24 with both. The median SUVmax (early images) was 8.1 (4.7-17.2) for ^{18}F-FDG and 23.3 (17.1-50.2) for ^{18}F-PSMA. For BCLC-B patients, the median ΔSUVmax was 17.65% (-6.35% to 28.57%) for ^{18}F-FDG and -30.17% (-9.74% to -50.67%) for ^{18}F-PSMA. For BCLC-C patients, the median ΔSUVmax was 0.00% (-66.67% to 10.47%) for ^{18}F-FDG and -0.47% (-67.26% to 16.37%) for ^{18}F-PSMA. Spearman's correlation between ^{18}F-FDG and ^{18}F-PSMA SUVmax was $\rho = -0.5357$ ($p = 0.2357$). ***Conclusion:*** ^{18}F-FDG and ^{18}F-PSMA PET/CT offer complementary insights in BCLC-B/C HCC. ^{18}F-FDG demonstrated superior lesion detection sensitivity (especially in advanced disease), while ^{18}F-PSMA showed higher tracer uptake. The lack of correlation between tracers suggests distinct biological targets, with PSMA potentially reflecting neoangiogenesis. The observed ^{18}F-PSMA washout may influence its theranostic utility. Further studies should explore whether high ^{18}F-PSMA uptake predicts antiangiogenic therapy response.

EP-0263

Dual-energy CT imaging for the evaluation of tumour response to Phosphorus-32 microparticles injection: preliminary results.

V. Landoni, *L. Chiacchiararelli, M. Pressello, G. Regine, A. Sbrozzi Vanni, C. Garufi, G. Ventroni;*
San Camillo Forlanini Hospital, Rome, ITALY.

Aim/Introduction: The purpose of this study is to report the preliminary results of the analysis based on dual energy-CT images of the first of a group of patients treated for advanced pancreatic cancer with intra-tumoural injection of 32P (Phosphorus-32) microparticles at a single institution. ***Materials and Methods:*** Between May 2023 and March 2025, seven patients were treated at our institution. The activity of ^{32}P to be injected to deliver 100Gy to the tumour was calculated based on the ^{32}P suspension concentration and the tumour volume, the latter evaluated by the pre-treatment computed tomography acquisition. After implantation patients underwent single photon computed tomography (SPECT) imaging within 4 hours to confirm intra-tumoural particles distribution. Dual-energy CT scans were acquired before treatment and approximately 10 weeks afterwards. Images were acquired at 140 KV, W150 100µgr/cc, L50 100µgr/cc, 200 mA. Iodine maps and Hounsfield units (HU) spectra were reconstructed with a dedicated software. ***Results:*** The analysis performed on the images of the patient showed that

the ratio between the iodine uptake of the ROIs inside the tumour region and the reference ROI delineated by an expert radiologist changed of about 67% from the pre-treatment to the post-treatment reconstructed iodine maps images. The HU spectra also were modified. ***Conclusion:*** Changes in iodine concentration might reflect the changes in the vascularization; for this reason, these very preliminary results encourage to explore the role of dual-energy CT imaging to quantitively characterize the tumour and the response to the treatment. Ongoing recruitment will allow validation in a larger cohort of patients. ***References:*** http://dx.doi.org/10.1016/j.crad.2015.06.083 http://doi.org/10.3390/cancers16193412.

EP-0264

Gastric Emptying Scintigraphy Using a High-Caloric Liquid Meal - Single Center Experience

I. Sisko Markos[1,2], *I. Blazekovic*[1,2], *M. Romic*[1,2], *M. Bosak Butkovic*[1,2], *D. Filipan*[1], *T. Jukic*[1];
[1]*UHC Sestre Milosrdnice, Zagreb, Zagreb, CROATIA,* [2]*Croatian Catholic University, School of Medicine, Zagreb, CROATIA.*

Aim/Introduction: Gastroparesis, or delayed gastric emptying, is a pathological condition that is caused by diabetes, infections, autoimmune, neuromuscular disorders, postsurgical complications or dyspepsia, but it may be idiopathic. Gastric emptying scintigraphy (GES) is a nuclear medicine method measuring gastric emptying time. Liquid or solid meal can be used. Due to the need to demonstrate delayed gastric emptying but limited „hot lab" conditions for preparing the standard meal, we used a commercially available High-Caloric Liquid Meal (HCL) as an alternative solution. In the absence of our own reference values, we relied on the range of values reported in the study by Solnes et al. and the aim is to present our results in relation to the values of Solnes group. ***Materials and Methods:*** Patients underwent GES using a HCL meal (Ensure Plus®) marked with 74 MBq of Tc99m-DTPA during five time points (0 h, 1 h, 2 h, 3 h, and 4 h). To quantify the results, regions of interest are delineated on anterior and posterior images of the entire stomach. Due to the duration of the study decay correction was performed. Because of the different body habitus, attenuation correction is performed using a geometric mean calculation. ***Results:*** We performed GES to 34 patients with suspected gastroparesis. Their gastric retention was measured at four time points and compared with reference values reported by Solnes et al. The ranges of gastric retention for the first, second, third and fourth hour for Solnes group were 45-90, 12-94, 5-30, and 5-16 respectively. The 95% CI of the mean for these hours was found to be 65.1-74.6 (SD 10.5), 26.4-43.6 (SD 18.8), 10.8-16.2 (SD 5.9) and 7.6-10.2 (SD 2.8). The detected mean gastric retention in our population was 58.12%, 24.81%, 11.01%, 7.09%, the ranges 4.1-100, 0.6-60, 0.3-30, 0.11-26. The 95% CI of the mean range was 51.14—65.11 (20.78), 18.99-30.62 (17.30), 7.32-14.70 (10.98), 4.17-10 (8.68). In comparison to suggested normal upper limits, we detected 32.4% abnormal studies of all performed tests. ***Conclusion:*** Although we did not have our own database of normal gastric emptying values for the HCL meal at four time points, we believe that we have established a good diagnostic procedure by following the criteria set by a group of authors who compared their results with standard meal results. ***References:*** 1. Solnes LB, Sheikhbahaei S, Ziessman HA. EnsurePlus as an Alternative to the Standardized Egg Gastric-Emptying Meal. Clin Nucl Med. 2019 Jun;44(6):459-461.

EP-0265

Predictive Value of 99mTc-Mebrofenin Hepatobiliary Scintigraphy in Evaluating Liver Function and Volumetry Pre- and Post-Radioembolization in Hepatocellular Carcinoma (HCC) Patients

S. Shamim*, M. Meena, G. Arora, P. Gb, P. Gupta, N. Kumar;*
AIIMS New Delhi, Delhi, INDIA.

Aim/Introduction: Background: Hepatocellular carcinoma (HCC) often presents in patients with compromised liver function, necessitating precise evaluation of hepatic reserve prior to interventions like trans-arterial radioembolization (TARE). 99mTc-Mebrofenin hepatobiliary scintigraphy (HBS) offers quantitative assessment of both global and regional liver function, potentially enhancing treatment planning and prognostication. Aim: To assess the utility of 99mTc-Mebrofenin HBS in evaluating functional and volumetric liver changes before and after TARE in HCC patients. ***Materials and Methods:*** Methods: A prospective study was conducted involving HCC patients undergoing TARE. HBS was performed using dynamic planar imaging and SPECT/CT. Parameters measured included mebrofenin uptake rate (MUR), normalized MUR (MUR), functional remnant liver (FRL) and liver volumes. Comparisons were made between pre- and post-TARE values to assess hepatic functional and structural changes. ***Results:*** ***Results:*** Post-TARE assessments revealed heterogeneous hepatic responses. Some patients exhibited increased FRI. clearance (e.g., from 8.89 to 9.73%/min/m^2) and corresponding volumetric gains (e.g., FRL volume increase from 929.15 to 1343.10 cm^3), indicative of functional regeneration and compensatory hypertrophy. Others showed improved hepatic function (e.g., FRL clearance rising from 5.39 to 6.36%/min/m^2) despite stable liver volumes, suggesting favorable physiological adaptation. Conversely, certain cases demonstrated declines in both FRL clearance (e.g., from 8.2 to 6.8%/min/m^2) and FRL volume (e.g., from 533.06 to 238.20 cm^3), potentially reflecting disease progression or treatment-related parenchymal loss. Notably, some patients experienced functional deterioration without significant volumetric changes, underscoring the added value of functional imaging. Routine liver function tests did not consistently correlate with these imaging findings. ***Conclusion: Conclusion:*** 99mTc-Mebrofenin HBS is a valuable tool for evaluating hepatic function and reserve in HCC patients undergoing TARE, It provides critical insights into regional liver function that may not be apparent through conventional imaging or biochemical tests alone. Incorporating HBS into standard pre- and post-TARE assessment protocols could enhance patient selection, treatment planning, and post-therapeutic monitoring.

EP-0266

Diagnostic Performance of [68Ga]-FAPi-46 PET/CT in Suspected Recurrence in Signet Ring Cell Colorectal Cancers (SRCC)

S. Mahambre[1,2], *I. Dev*[1,2], *A. Agrawal*[1,2], *N. Purandare*[1,2], *S. Shah*[1,2], *A. Puranik*[1,2], *S. Choudhury*[1,2], *S. Ghosh*[1,2], *M. Venkatachalam*[1,2], *V. Rangarajan*[1,2];
[1]*Tata Memorial Hospital, Mumbai, INDIA,* [2]*Homi Bhabha National University, Mumbai, INDIA.*

Aim/Introduction: In malignancies like signet ring cell tumors, [18F]-FDG-PET/CT fails to identify true disease burden. These tumors are composed of large stroma with cancer associated fibroblast(CAFs) expressing Fibroblast activation protein(FAP) which modulate the tumor microenvironment. FAP-targeted imaging has exponentially increased last few years, and is considered to be a more effective method of tumor detection. Hence, we have explored the utility of [68Ga]-FAPi-46-PET/CT in a rare histology such as SRCC. ***Materials and Methods:*** In this retrospective study, 34 SRCC patients with suspected recurrence were included. They were referred for [68Ga]-FAPi-46-PET/CT for the detection of metastases and assessment of disease burden either based on rising S.CEA or clinical suspicion of recurrence. Semiquantitative parameters such as SUVmax of primary site and metastases were calculated. Uptake more than liver was considered positive PET/CT finding. Final decision was based on histopathological confirmation or clinicoradiological follow up and Multidisciplinary tumor board decision(MDT).In a subset analysis of 18 patients, FAPi-PET/CT findings were compared with [18F]-FDG-PET/CT. Sensitivity, specificity,PPV,NPV and accuracy

of FAPi-PET/CT calculated using the IBM-SPSS-26.0 statistical software; p-values<0.05 were considered statistically significant. ***Results:*** Data of 34 SRCC patients (23 male and 11 female) with a median age of 48years(21-77years) was analyzed. 29/34 patients had positive FAPi findings while in 5 patients, no local recurrence/ metastases were seen. In 11/29 patients, local recurrence was detected on FAPi-PET/CT. 3 were confirmed on histopathology & 8 with MDT. Metastatic disease was detected in 18 patients, out of which, 5 were confirmed on histopathology and 13 were deemed metastatic based on MDT decision & follow-up imaging. Liver, nodes and peritoneum were the most common metastatic sites. In 18 patients, for whom both FDG & FAPi-PET/CT data was available, FAPi-PET/CT detected peritoneal disease in 6 patients eventually confirmed on diagnostic laparotomy/peritoneal fluid cytology. Additional lesions were detected in 5 patients and concordant scan findings in 7 patients; hence an incremental value was in 61%cases.Overall Sensitivity, Specificity, PPV,NPV, and Accuracy of [68Ga]-FAPi-46-PET/CT for detection of local recurrence 72%,87%,72%,87%and 82% respectively with AUC 0.742(95%CI: 0.477-1.000;p=0.108) vs FDG-PET/CT (67%,75%,57%,81%and 72%). For metastatic sites, it was 94%,88%,89%,93%and 91% with AUC 0.938(95%CI: 0.798-1.000;p=0.002) vs 60%,88%,86%,64%and 72% in FDG-PET/CT. ***Conclusion:*** [68Ga]-FAPi-46-PET/CT shows excellent sensitivity, specificity,PPV & NPV in detecting local recurrence and metastatic disease in SRCC patients and has a promising role as a non-invasive imaging modality for the detection of peritoneal involvement which can help in triaging patients who would not benefit from futile laparotomies.

EP-0267

A single center prospective study to evaluate clinical utility of Gallium 68- FAPI in poorly cohesive carcinoma of stomach

M. Gupta[1], *S. Singh*[2], *S. Goel*[2], *S. Goyal*[3], *V. Talwar*[3], *V. Goyal*[3], *S. Swamy M S*[3], *G. Gupta*[4], *A. Pathak*[1], *P. Sarathi Choudhury*[1];
[1]*Department of Nuclear Medicine, Rajiv Gandhi Cancer Institute and Research Centre, Delhi, INDIA,* [2]*Department of GI Oncosurgery, Rajiv Gandhi Cancer Institute and Research Centre, Delhi, INDIA,* [3]*Department of Medical Oncology, Rajiv Gandhi Cancer Institute and Research Centre, Delhi, INDIA,* [4]*Department of Pathology, Rajiv Gandhi Cancer Institute and Research Centre, Delhi, INDIA.*

Aim/Introduction: Poorly cohesive carcinoma (PCCs) or signet ring cell carcinoma, accounts for <10% of stomach cancer. It commonly presents with nonspecific symptoms and diffuse stomach wall thickening. FDG PET/CT normally shows a low grade or no tracer uptake and hence ineffective in its work up. Cancer-associated fibroblasts (CAFs) have been strongly reported in many epithelial tumors microenvironment. Hence, CAFs associated fibroblast activation protein (FAP) has become a major target for imaging and therapy of these tumors. Here, we present the first analysis of our prospective study on clinical utility of 68Ga-FAPI PET/CT in PCCs. ***Materials and Methods:*** We included 25 histologically proven stomach PCCs patients referred for staging (15) or recurrence (10) work up. Both FAPI and FDG PET-CT scan were done with-in a week time. Diagnostic laparoscopy for peritoneal disease or any other site biopsy for metastasis or recurrence was used as a gold standard. Additionally, the single voxel maximum standard uptake value (SUVmax) of the primary, lymph node, metastasis, and the right lobe of the liver were recorded. SUVmax and target-to-background ratio (TBR) were compared with Wilcoxon's signed-rank test. While clinical effectiveness was compared with McNemar's test. The study is ethically approved by institutional review board (RGCIRC/IRB-BHR/27/2025). ***Results:*** Out of 15 patients for staging, FDG showed peritoneal metastasis in 5/9 patients with diagnostic sensitivity, specificity, PPV, NPV and accuracy of 55.5%, 100%, 100%, 60%, and 73.3%. While, FAPI detected all 9/9 peritoneal metastases with 100% diagnostic accuracy. Mean± SD TBR of primary (1.6±0.6 Vs 7.3±4.8) and node (0.7±0.4 Vs 3.4±3.1) for FDG Vs FAPI showed significant difference (P value <0.05). For suspected recurrence cases, FDG was true positive in 6/10 while FAPI was true positive in 8/10 cases. One case was false positive in both FAPI and FDG. Mean± SD TBR of the recurrent site (1.5±0.8 Vs 7.5±4.2) for FDG Vs FAPI showed a significant difference (P value <0.05). ***Conclusion:*** FAPI PET-CT has significantly better diagnostic utility for metastatic workup and recurrence evaluation in PCCs stomach. Its superiority is shifting paradigm in tailoring the diagnostic laparoscopy and guiding biopsy sites for better yield.

EP-0268

18F-PSMA-1007 PET/CT in Hepatocellular Carcinoma (HCC): Determining the Ideal Acquisition Window

C. Vallone[1,2], *P. Rossi*[3], *P. Guglielmo*[2,4], *J. Jandric*[3], *M. Rodari*[3], *K. Marzo*[3], *M. Marenco*[3], *M. Olivieri*[5], *L. Evangelista*[2,3];
[1]*Department of Advanced Biomedical Sciences, University of Napoli, Napoli, ITALY,* [2]*Department of Bioscience, Humanitas University, Pieve Emanuele (MI), ITALY,* [3]*Nuclear Medicine Unit, IRCCS Humanitas Cancer Center, Rozzano (MI), ITALY,* [4]*Nuclear Medicine Unit, Humanitas Gavazzeni, Bergamo, ITALY,* [5]*Physic Unit, IRCCS Humanitas Cancer Center, Italy, Rozzano (MI), ITALY.*

Aim/Introduction: Radiolabeled PSMA has shown high uptake in patients with HCC. This study aimed to evaluate the impact of varying intervals between 18F-PSMA-1007 administration and PET/CT image acquisition on scan parameters in patients with HCC, with the goal of identifying the optimal timing for the examination. ***Materials and Methods:*** We conducted a retrospective, observational, single-center study involving patients diagnosed with HCC who underwent 18F-PSMA-1007 PET/CT imaging between August 2022 and March 2025. The study population was divided into three groups based on the time elapsed between radiotracer injection and image acquisition: Group A (50-70 minutes), Group B (70-90 minutes), and Group C (more than 90 minutes). All scans were evaluated both visually and semiquantitatively. Measurements included the SUVmax of the lesion and healthy liver parenchyma (background), the SUVmean of healthy liver tissue, and tumor-to-background ratios calculated using both SUVmax (TBRmax/max) and SUVmean (TBRmax/mean) values for the background. The Kruskal-Wallis test was employed to assess differences in data distribution across the three groups. ***Results:*** Sixty-three patients were included in the study (median age: 76 years; range: 43-93). PET scans were performed in 10 patients (16%) after 50-70 minutes, in 31 patients (49%) after 70-90 minutes, and in 22 patients (35%) after more than 90 minutes. Semiquantitative analysis showed that the median SUVmax of the lesion was significantly higher in Group A compared to Groups B and C (28.6 vs 20.7 and 23.5, respectively; p <0.05). In contrast, the median SUVmax and SUVmean of healthy liver parenchyma were lower in Group A compared to Groups B and C (9.8 vs. 12.1 and 13.1; 7.7 vs. 8.3 and 9.3, respectively), although the differences did not reach statistical significance (p = 0.149 and 0.338). Median tumor-to-background ratios (TBRmax/max and TBRmax/mean) were higher in Group A than in the other groups (2.5 vs. 1.6 and 1.9; 3.3 vs. 2.3 and 2.6, respectively), with values approaching statistical significance (p=0.073 and 0.185). ***Conclusion:*** The best acquisition time for 18F-PSMA-1007 PET/CT in HCC patients is between 50 and 70 minutes from the injection, because it is linked to a best signal-to noise ratio. ***References:*** DOI: 10.3390/cancers16223865.

EP-0269

Assessing the Value of Short-Duration Dynamic [^{18}F]FDG PET on LAFOV Scanners in Hepatocellular Carcinoma

S. Capitanio[1], *A. Lazar*[2], *A. Franchini*[1], *A. Spataro*[1], *G. Muti*[3], *L. Airo' Farulla*[1], *A. Scarale*[1], *G. Cabrini*[1], *E. Gay*[1], *C. Pettinato*[4], *A. Chiti*[5], *C. Rossetti*[1];
[1]*Nuclear Medicine Unit, Dipartimento Ematologia, Oncologia e Medicina Molecolare, ASST Niguarda Hospital, Milan, ITALY,* [2]*Vita-Salute San Raffaele University, Milan, ITALY,* [3]*Department of Physics, ASST Niguarda Hospital, Milan, ITALY,* [4]*Medical Physics Unit, Fondazione IRCCS Ca Granda Ospedale Maggiore Policlinico, Milan, ITALY,* [5]*Vita-Salute San Raffaele University, Nuclear Medicine Unit, IRCCS San Raffaele Hospital, Milan, ITALY.*

Aim/Introduction: Dynamic PET imaging offers physiological insights beyond delayed static measures, but its clinical use has been limited by the prolonged acquisition protocols. Long axial field-of-view (LAFOV) PET scanners, with their increased sensitivity and advantage of deriving image-derived input function (IDIF) from large vessels, present and opportunity to shorten scan times without compromising data quality. We aimed to assess the feasibility of a 20-minute dynamic [^{18}F]FDG PET protocol for Patlak analysis in hepatocellular carcinoma (HCC) and evaluate the correlation between kinetic parameters and standard SUV metrics**.** ***Materials and Methods:*** Patients with HCC underwent dynamic [^{18}F]FDG PET/CT on a 148 cm AFOV scanner, with acquisition initiated at the time of injection and lasting 20 minutes. Data was reconstructed using a 21-frame protocol (6x10s,2x30s, 6x60s, 7x120s). A delayed static scan at 60 min post-injection completed the examination. IDIFs was extracted from the descending thoracic aorta and normalised to a population-based input function. Volumes of interest were manually delineated. Patlak analysis and irreversible-two compartment modelling (2T3k) were performed using vendor-provided software to extract dynamic parameters both for HCC lesions and normal liver tissue. Static SUV_{max} and SUV_{mean} values were also recorded. SUV-Tumour-to-liver ratios (SUV-TLR) and Patlak Ki-tumour-to-normal liver (Ki-TLR) ratios were computed. Descriptive statistics were used based on data distribution and Spearman's test was used to assess correlations. ***Results:*** Seven patients counting 17 liver lesions were segmented and processed. In Patlak analysis, median values for tumour Ki and intercept were 0.0159 [IQR: 0.0058 - 0.0189], and 0.767[IQR: 0.535 - 0.853], respectively, with a median Ki-TLR was 1.76 [IQR: 1.10-2.82]. The 2T3k model revealed mean tumour K1, k2 and k3 of 0.462319±0.23537, 0.6155±0.2062 and, respectively, 0.02279±0.0162749. On static images, median tumour SUV_{max} was 4.15 [IQR: 3.52-5.17], with median SUV-TLR of 1.53 [IQR: 1.31- 1.68]. Significant correlations were observed between tumour SUV_{max} and Ki (ρ=0.771, p<0.001) , SUV_{max} and k3 (ρ=0.754, p<0.001), and SUV-TLR and Ki-TLR (ρ=0.840, p=0.001). No significant correlation was found between tumour SUV_{max} and intercept (ρ=-0.401, p=0.111), or between any kinetic parameter and blood glucose levels at the time of the scan. ***Conclusion:*** A 20-minute dynamic [^{18}F]FDG PET acquisition on LAFOV scanners is clinically feasible in HCC, revealing kinetic parameters that correlate strongly with conventional static metabolic metrics. These findings support the integration of short dynamic protocols into clinical practice, offering enhanced quantitative insights without prolonged scan times and improving lesion characterization in liver oncology.

EP-0270

Kinetic Modeling of PSMA Uptake in Hepatocellular Carcinoma with LAFOV PET/CT: Correlation with Histopathological Features

L. Vetrone[1], *E. Prosperi*[2], *E. Prosperi*[2], *D. Malvi*[3], *A. Degiovanni*[3], *F. Vasuri*[4], *I. Brusa*[1], *S. Emiliani*[1], *D. Dall'Olio*[5], *M. Ravaioli*[2], *M. Cescon*[2], *S. Fanti*[1,6], *A. Farolfi*[1];
[1]*Nuclear Medicine, IRCCS, Azienda Ospedaliero-Universitaria di Bologna, Bologna, ITALY,* [2]*Department of Hepatobiliary Surgery and Liver Transplant, IRCCS Azienda Ospedaliero-Universitaria di Bologna, Bologna, ITALY,* [3]*Pathology Unit, IRCCS Azienda Ospedaliero-Universitaria di Bologna, Bologna, ITALY,* [4]*Department of Medical and Surgical Sciences (DIMEC), Bologna University, Bologna, ITALY,* [5]*Department of Medical and Surgical Sciences, University of Bologna, Bologna, ITALY,* [6]*Nuclear medicine, Alma Mater Studiorum University of Bologna, Bologna, ITALY.*

Aim/Introduction: Hepatocellular carcinoma(HCC) is a heterogeneous tumor with varying molecular phenotypes. Preliminary investigations revealed PSMA-overexpression in HCC vessels, but its functional imaging characterization is limited. Long Axial Field of View(LAFOV) PET allows for dynamic acquisitions over extended periods, enabling kinetic modeling of radiotracer behavior. We investigated the correlation between PSMA uptake kinetics, standard semiquantitative parameters and histopathological features of HCC lesions. ***Materials and Methods:*** Eight patients with suspicion of HCC eligible for Liver Transplantation(LT) or Hepatic Resection(LR), naive for systemic therapy were enrolled within a 3-month window before surgery within the MORE-PSMA study. A 60-minute dynamic [68Ga] PSMA PET/CT scan using a LAFOV-scanner (FOV=194cm) was performed, alongside a 3h-delayed whole-body static images. No treatment was allowed between imaging and surgery. One lesion per patient was manually segmented, choosing the largest one with histological confirmation. Kinetic parameters were extracted using a reversible two-tissue compartment model (2TCM) from dynamic data. Semiquantitative parameters (SUVmax, SUVmean, SULpeak,PSMA-TV) and kinetic constants (K1, k2, k3, k4, Ki, DV) were calculated and correlated with histological grade(Edmondson), architecture (trabecular, macrotrabecular, mixed), WHO subtype, margins of growth (infiltrative, expansive), immunohistochemistry(IHC) evaluation (as a percentage of PSMA-expressing vessel cells, intensity of the stain and IRS score). ***Results:*** All lesions(8/8) were better described by a reversible 2TCM-model. Lesions with infiltrative margins showed higher k3 values than expansive lesions (0.52±0.23 vs 0.14±0.20, p=0.05), while SUVs did not discriminate between the two groups(p>0.05). Macrotrabecular lesions showed a trend of generally higher k3, k4 and Ki compared to trabecular ones, although p>0.05. Lesions with strong/moderate IRS had similar SUVs values (p>0.05) but lower k4 compared to negative ones (0.038±0.020 vs 0.088±0.028, p=0.05). A significant correlation was found between k4 and SUVmean(r= -0.81, p=0.015), k4 and PSMA-TV (r=0.79, p=0.021), DV and SUVmax(r=0.79, p=0.021), and DV and SUVmean (r=0.98, p< 0.0005). No significant correlation was found between kinetic parameters and Edmondson grade, WHO-subtypes, and IHC intensity or percentage. At delayed scans both SUVmax and SUVmean decreased in 6/8 lesions and increased in 2/8cases, but no significant correlation with kinetic constants was found. ***Conclusion:*** Dynamic [68Ga]PSMA PET/CT with LAFOV technology allows for detailed kinetic modeling in HCC. Kinetic parameters, particularly k3 and k4, show potential correlations with tumor morphology and PSMA expression intensity and may be more sensitive than SUVs for distinguishing histopathological features of HCC lesions. These preliminary results support further investigation of kinetic PET imaging as a non-invasive biomarker for biological aggressiveness in HCC.

EP-0271

Normal patterns of pancreatic uptake on 68Ga-DOTATATE PETCT

A. Hassan*, A. W. Alessi, E. Wahab, S. J. Hughes;*
Queen Elizabeth Hospital Birmingham, Birmingham, UNITED KINGDOM.

Aim/Introduction: 68 Galium-DOTATATE (68Ga-DOTA) peptide seen on positron emission tomography combined with computed tomography (PETCT) has been proven to be one of the most accurate methods of imaging neuroendocrine tumors (NETs).[1] The first stage in the accurate reporting and utilizing 68Ga-DOTA PETCT is a clear understanding of the normal patterns. Pancreatic NETs can present with focal DOTA peptide uptake on imaging. [2] This study aims to identify the normal patterns of pancreatic uptake on 68Ga-DOTA PETCT. ***Materials and Methods:*** This retrospective study of 54 consecutive 68Ga-DOTA PET/CT scans carried out at one academic institution between January 2023 and March 2025 for staging and restaging non-pancreatic NET. We defined the pattern seen in regions of the uncinate process, head, neck, body, and tail of the pancreas. We recorded the pattern seen (focal/diffuse/homogenous/inhomogenous) in these regions and the maximum standarised uptake value (SUVmax). Other normal imaging including contrast-enhanced CT, pancreatic MRI and normal pattern on CT component of the PETCT were used to

define absence of focal pathology. ***Results:*** Overall, 34/54 (63%) scans had focal uptake in the head/uncinate. 1/54 (2%) had uptake in neck. 12/54 (22%) uptake in body. 10/54 (19%) in tail. 18/54 (33%) scans presented with benign multifocal uptake in more than 2 anatomical areas; 11/54 (20%) had two focal regions. 3/54 (6%) had three focal regions. 1/54 (2%) had four focal regions. 1/54 had whole diffuse homogenous pancreas 68Ga-DOTA uptake with normal structural imaging. ***Conclusion:*** Focal uptake in the head and uncinate process of the pancreas had already been described and our study confirms this in 63% of patients.[2] Many of the benign patterns of uptake are diffuse (25%) rather than focal. Our data shows that benign 68Ga-DOTA uptake is not limited to the head and uncinate process and that both focal and diffuse uptake in the body and tail can also be benign. We therefore hypothesize that 68Ga-DOTA PET/CT may not be an accurate imaging modality for assessment of presence or absence of pancreatic NETs without structural imaging. ***References:*** [1] Tirosh A et al. The utility of 68Ga-DOTATATE positron-emission tomography/computed tomography in the diagnosis, management, follow-up and prognosis of neuroendocrine tumors. Future Oncol. 2018;14(2):111-122. doi:10.2217/fon-2017-0393 [2] Tabacchi et al. [68Ga]Ga-DOTANOC Uptake at Pancreatic Head/Uncinate Process: Is It a Persistent Diagnostic Pitfall Over Time?. Cancers. 2022;14(14):3541. doi:10.3390/cancers14143541.

EP-0272

Evaluation of the Effectiveness of 68Ga-Trivehexin (Integrin αvβ6) PET/CT in Staging and Restaging of Pancreatic Adenocarcinoma: Preliminary Findings

A. Ozturk[1], *Ö. F. Şahin*[1], *Z. Tosunoğlu*[1], *T. F. Çermik*[2], *G. Alçın*[1], *E. Akgün*[1], *M. M. Sevinç*[3], *Ç. Usul Afşar*[4], *E. Arslan*[1];
[1]*Istanbul Training and Research Hospital Nuclear Medicine Department, Istanbul, TÜRKIYE,* [2]*Acibadem Maslak Hospital, Nuclear Medicine Department, Istanbul, TÜRKIYE,* [3]*Istanbul Training and Research Hospital General Surgery Department, Istanbul, TÜRKIYE,* [4]*Istanbul Training and Research Hospital Medical Oncology Department, Istanbul, TÜRKIYE.*

Aim/Introduction: αvβ6 integrin expressed in carcinoma cells interacts with LAP, activating TGF-β, which inhibits cell growth in healthy stroma and enables invasion into tumor tissue. Integrin αvβ6 observed in pancreatic cancer, head and neck SCC, non-small cell lung, colon, breast, ovarian cancer. Study aims to investigate the diagnostic, staging, and restaging contributions of 68Ga-Trivehexin PET/CT in pancreatic adenocarcinoma or those with a suspicious malignant mass in the pancreas. ***Materials and Methods:*** In this prospective study, 15 diagnosed with or suspected of having pancreatic cancer were included. 68Ga-Trivehexin PET/CT performed within two weeks of the previous scan. Written informed consent was obtained from all patients. The primary tumor uptake values obtained from 68Ga-Trivehexin PET/CT measured and compared with normal pancreatic background, liver parenchyma, liver metastases, blood pool, and distant organ metastases. Parameters compared with those from ^{18}F-FDG PET/CT imaging. ***Results:*** Mean age of 15 patients 70.73 ± 9.9 years. 12 patients underwent for staging ,3 for restaging. Histopathological revealed 13 patients had pancreatic ductal adenocarcinoma (PDAC), one had pancreatic intraepithelial neoplasia (PanIN), and one initially suspected of having a pancreatic tumor, was found to have a gastrointestinal stromal tumor (GIST) originating from the stomach wall after surgery. Metastases were detected in: 6 liver metastases, 1 bone metastasis, 1 adrenal gland metastasis, 1 muscle metastasis SUVmax varied in liver metastases, 68Ga-Trivehexin showed higher SUVmax values in muscle, bone, and adrenal gland metastases. When evaluating primary tumor uptake: Mean ± SD SUVmax of 68Ga-Trivehexin: 14.2 ± 6.44 (min: 8.15 - max: 29.43) Mean ± SD SUVmax of 18F-FDG: 8.98 ± 4.23 (min: 5.07 - max: 16.06) A statistically significant difference was observed ($p < 0.05$), indicating that 68Ga-Trivehexin showed higher uptake in primary tumors. To assess the ability of both modalities to distinguish primary tumors from healthy tissue, the following ratios were calculated in PDAC patients: SUVmax of primary tumor/healthy pancreatic tissue (PT/PSD SUVmax) SUVmax of primary tumor/blood pool (PT/KH SUVmax) In 11, ^{18}F-FDG was superior in PT/PSD SUVmax ratio In all patients, 68Ga-Trivehexin was superior in PT/KH SUVmax ratio ($p < 0.05$). ***Conclusion:*** On our current findings, 68Ga-Trivehexin appears to have significant potential in PDAC diagnosis, tumor receptor imaging, and detecting tumor heterogenity. It could be a valuable imaging agent for evaluating responses to chemotherapeutic agents targeting angiogenesis. Since integrin αvβ6 is expressed in malignant epithelial tumors, it holds theranostic potential and may serve as a promising future therapeutic target.

EP-0273

Association Between PET/CT-Derived PCI and Survival in Peritoneal Carcinomatosis: A Retrospective Analysis

S. Demirtas Senlik[1], *A. Cinar*[1], *C. Engur Uyanik*[1], *O. Sutcuoglu*[2], *O. Ozmen*[1];
[1]*Ankara Etlik City Hospital, Ankara, TÜRKIYE,* [2]*Gazi University Hospital, Ankara, TÜRKIYE.*

Aim/Introduction: Peritoneal carcinomatosis (PC), often arising from gastrointestinal or gynecological malignancies, is associated with poor prognosis. The Peritoneal Carcinomatosis Index (PCI) is a clinical tool used to quantify disease burden and guide management. While surgical exploration remains the gold standard for PCI assessment, its invasiveness limits routine use. F-18 FDG PET/CT has emerged as a non-invasive alternative. This study aimed to evaluate the relationship between PET/CT-derived PCI scores and overall survival in patients with PC. ***Materials and Methods:*** We retrospectively reviewed patients who underwent FDG PET/CT between December 2022 and January 2025. Of 113 patients with pathologically confirmed PC (excluding primary peritoneal tumors), PCI scores were calculated by scoring FDG-avid lesions across 13 abdominal regions (scale 0-3 per region). Overall survival was analyzed using the Kaplan-Meier method. ***Results:*** The cohort included 70 women (62.5%) and 43 men (37.5%), with a mean age of 61.5 ± 13.5 years. A total of 58 patients (51.3%) were diagnosed with gastrointestinal system cancer, while 46 patients (40.7%) had a gynecological malignancy. The median PCI was found to be 11 (range: 1-36). Median overall survival was 13 months (95% CI: 9.69-16.35) in patients with PCI < 15, compared to 9 months (95% CI: 6.51-11.48) in those with PCI ≥ 15 ($p = 0.020$) (Figure 1). No significant relationship was found between overall survival and the following SUVmax ratios: peritoneum/primary tumor ($p = 0.712$), peritoneum/liver ($p = 0.611$), peritoneum/spleen ($p = 0.476$), and peritoneum/bone marrow ($p = 0.249$). ***Conclusion:*** Although F-18 FDG PET/CT is widely used in the clinical diagnosis of peritoneal carcinomatosis (PC), its role in PCI assessment remains unclear. In our study, survival was found to be significantly lower in patients with high PCI on FDG PET/CT compared to those with low PCI. These findings suggest that FDG PET/CT may have prognostic value in patients with PC and could serve as a supportive tool in treatment planning.

EP-0274

Trans-arterial radioemoembolization for treatment of large hepatocellular carcinoma, a single center experience

A. Alsugair*;*
King Fasial Specilaist Hospital And Research Center, Riyadh, SAUDI ARABIA.

Aim/Introduction: Background: Management of hepatocellular carcinoma (HCC) depends largely on the stage of the tumor, patients' performance status, and comorbidities. Advanced HCC has limited treatment options, particularly in the presence of portal vein thrombosis. Growing evidence supports the use of trans-arterial radioemoembolization (TARE) in the management

of advanced HCC, however, more clinical trials are required to confirm its efficacy. Aim: To report the experience of a tertiary center with TARE for management of large HCC. ***Materials and Methods:*** A retrospective review of all patients who underwent TARE procedures was conducted through interventional radiology database at tertiary care organ transplant center Hospital during the period from January 2008 till July 2024. Patients who had TARE for management of HCC were identified and files were screened for their demographic data, number of procedures performed, response to treatment, and complications. The primary outcome was overall survival while secondary endpoints included response to treatment and successful downstaging with subsequent liver transplantation. ***Results:*** During the study period a total of 725 TARE procedures were performed on 490 patients. The number of patients who had TARE for treatment of HCC was 411 (84%) while 79 patients (16%) had TARE for treatment of metastatic liver tumors. The mean age was 64.2 ± 11.3 and 72% were males. TARE was done once in 275 patients (62.5%), twice in 104 patients (25.3%), thrice in 26 patients (6.3%) and more than three times in 6 patients (1.5%). Over a median follow-up of 13.4 months 126 patients (30.7%) died while 106 (25.85%) are alive, and data on survival was missing in 179 patient (43.6%). The radiological tumor response to treatment in the targeted lesions was complete in 29.2%, partial in 44.5%, stable in 3.2%, and disease progressed in 15.5% while data on radiological response were missing in 7.7%. Liver transplantation was performed on 55 patients (13.4%) after successful downstaging with TARE. ***Conclusion:*** TARE in a high-volume center showed a favorable response in management of large HCC. Downstaging large HCC with TARE can provide higher chance of successful liver transplantation.

EP-0275

Characterizing PDAC and Pancreatitis: Insights from [^{68}Ga]Ga-FAPI-46 Kinetic Modeling

T. Nilsson[1,2], *P. Rasinski*[1,2], *E. Sparrelid*[2,3], *M. Löhr*[2,3], *T. Tran*[1,4], *M. Lubberink*[5], *R. Axelsson*[1,6], *M. Holstensson*[1,2];
[1]Department of Nuclear Medicine and Medical Physics, Karolinska University Hospital, Stockholm, SWEDEN, [2]Department of Clinical Science, Intervention and Technology (CLINTEC), Karolinska Institutet, Stockholm, SWEDEN, [3]Department of Upper Gastrointestinal Diseases, Karolinska University Hospital, Stockholm, SWEDEN, [4]Department of Oncology-Pathology, Karolinska Institutet, Stockholm, SWEDEN, [5]Uppsala University, Department of Surgical Sciences Molecular Imaging and medical physics, Uppsala, SWEDEN, [6]Department of Molecular Medicine and Surgery, Karolinska Institutet, Stockholm, SWEDEN.

Aim/Introduction: This study aimed to characterize [^{68}Ga]Ga-FAPI-46 kinetics in pancreatic ductal adenocarcinoma (PDAC) lesions and concomitant inflammatory lesions and assess correlations between simplified measurements and model-derived parameters. ***Materials and Methods:*** Kinetic modeling was performed on images from an ongoing prospective [^{68}Ga]Ga-FAPI-46 PET/CT imaging clinical trial (EU2024-514967-25-00; NCT05172310). The dataset included 11 patients scheduled for surgery due to suspected pancreatic cancer. All patients had histopathologically confirmed PDAC and concomitant inflammatory lesions. Each patient was administered [^{68}Ga]Ga-FAPI-46 (204 ± 53 MBq) and underwent a 45-min dynamic PET scan centered over the suspected lesion, following a CT for attenuation correction. Three compartment models were evaluated: a 1-tissue-compartment model (1T2k), and both reversible (2T4k) and irreversible (2T3k) 2-tissue-compartment models, all including an additional fit parameter for blood volume fraction (V_b). Patlak and Logan plots (t* = 15 min) were also evaluated. Model selection was guided by the Akaike Information Criterion (AIC). Image-derived input functions were generated from regions of interest placed in the descending aorta. SUV_{mean} was measured from the 35-45 min frame, and the mean target-to-blood ratio (TBR_{mean}) was calculated. Spearman correlation coefficients (r_s) were used to assess relationships between SUV_{mean}, TBR_{mean}, and the volume of distribution (V_T). Differences in kinetic parameters between lesion types were evaluated. ***Results:*** The 2T4k model was preferred in 7/11 PDAC lesions and 9/12 inflammatory lesions. In lesions where the 2T3k model was preferred, AIC were similar between 2T3k and 2T4k. The similar AIC and plateauing time-activity curves suggest a 45-minute acquisition may be too short to distinguish binding reversibility for these lesions. TBR_{mean} and SUV_{mean} showed very strong correlations to V_T from both reversible models and Logan plots for inflammatory lesions ($r_s \geq 0.902$). In PDAC, SUV_{mean} showed a moderate correlation to V_T derived from the 2T4k model ($r_s = 0.550$), whereas TBR_{mean} demonstrated a very strong correlation ($r_s = 0.917$, $p < 0.001$). Both measures showed strong correlations to V_T from 1T2k and Logan in PDAC ($r_s \geq 0.864$). No significant differences in K1, k2, V_T, V_{NS}, SUV_{mean} or TBR_{mean} were observed between PDAC and inflammatory lesions. Parameters k3, k4, and V_b were not further evaluated due to high variability. ***Conclusion:*** In both PDAC and inflammatory lesions, simplified measurements such as SUV_{mean} and TBR_{mean} showed a strong correlation to V_T derived from reversible models and Logan plots. However, in some lesions a 45-minute scan may be insufficient to determine binding reversibility.

EP-0276

Usefulness of [^{18}F]FAPI-04 and [^{18}F]FDG PET/CT for the detection of peritoneal carcinomatosis: a comparative study

C. Jiang, *H. Ye, W. Zhou, K. Zheng, Y. Zhang, J. Dai, X. Peng, J. Yang, H. He, X. Hu;*
Department of PET-CT Center, Hunan Cancer Hospital/The Affiliated Cancer Hospital of Xiangya School of Medicine, Central South University, Changsha, CHINA.

Aim/Introduction: In this study, we aimed to compared the performance of [^{18}F]FAPI-04 and [^{18}F]FDG PET/CT in the evaluation of peritoneal carcinomatosis. ***Materials and Methods:*** Seventy-one patients with suspected peritoneal malignancies were enrolled in our study. All the participants underwent both [^{18}F]FAPI-04 and [^{18}F]FDG PET/CT imaging within 7 days. The detection rates, diagnostic accuracies, semiquantitative parameters of the traces, peritoneal cancer index (PCI) scores, and tumor markers were evaluated and compared. ***Results:*** Among the 71 patients, 40 patients were diagnosed with peritoneal carcinomatosis, and 31 were true-negative patients. The sensitivity and accuracy of [^{18}F]FAPI-04 PET/CT were higher than those of [^{18}F]FDG PET/CT (sensitivity: 92.50% vs. 72.50%, p = 0.003; accuracy: 91.55% vs. 80.28%, p < 0.001), particularly in patients with gastric cancer. The SUVmax, tumor-to-liver background ratio (TBR-L), tumor-to-descending aorta ratio (TBR-A), and PCI score were significantly higher for [^{18}F]FAPI-04 PET/CT than [^{18}F]FDG PET/CT (all p < 0.05). In the [^{18}F]FAPI-04 PET/CT group, the PCI score, TBR-L, TBR-A, TBR-M and SUVmax were higher in the high level group than the low level group (all p < 0.05). The carbohydrate antigen 125 (CA 125) levels were strongly correlated with the PCI of both [^{18}F]FAPI-04 and [^{18}F]FDG PET/CT. ***Conclusion:*** [^{18}F]FAPI-04 PET/CT outperformed [^{18}F]FDG PET/CT in the evaluation of peritoneal carcinomatosis, particularly in patients with gastric cancer. Furthermore, [^{18}F]FAPI-04 PET/CT may be used for the assessment of peritoneal carcinomatosis in patients, especially FAPI-PCI. ***References:*** 1. Coccolini F, Gheza F, Lotti M et al (2013) Peritoneal carcinomatosis. World J Gastroenterol 19:6979-6994 2. Llueca A, Escrig J (2018) Prognostic value of peritoneal cancer index in primary advanced ovarian cancer. Eur J Surg Oncol 44:163-169 3. Huang Y, Alzahrani NA, Chua TC, Liauw W, Morris DL (2016) Impacts of peritoneal cancer index on the survival outcomes of patients with colorectal peritoneal carcinomatosis. Int J Surg 32:65-70 4. Vietti Violi N, Gavane S, Argiriadi P et al (2023) FDG-PET/MRI for the

preoperative diagnosis and staging of peritoneal carcinomatosis: a prospective multireader pilot study. Abdom Radiol (NY) 48:3634-3642 5. Verwaal VJ, Bruin S, Boot H, van Slooten G, van Tinteren H (2008) 8-year follow-up of randomized trial: cytoreduction and hyperthermic intraperitoneal chemotherapy versus systemic chemotherapy in patients with peritoneal carcinomatosis of colorectal cancer. Ann Surg Oncol 15:2426-24326.

EP-0277

Comparison of 68Ga-FAPI PET and ^{18}F-FDG PET Findings in the Pre-Treatment Evaluation of Transarterial Radioembolization (TARE)

K. Saglam, *O. Sahin, M. Bodur, A. Kibar, L. Kabasakal;*
Istanbul University-Cerrahpasa, Istanbul, TÜRKIYE.

Aim/Introduction: Fibroblast Activation Protein (FAP) is an enzyme expressed by cancer-associated fibroblasts (CAFs) found in the tumor microenvironment. FAPI-04 is among the radiopharmaceutical agents targeting FAP and shows high uptake in tumors with intense fibroblast activation. 68Ga-FAPI PET has emerged as valuable alternative or complementary imaging method to traditional ^{18}F-FDG PET due to low background involvement, especially in tissues such as brain, heart and liver. This study aims to compare ^{18}F-FDG PET and 68Ga-FAPI PET imaging in patients with primary or metastatic liver tumors before TARE therapy. ***Materials and Methods:*** A total of 16 patients who were candidate for TARE treatment were included in the study. ^{18}F-FDG PET and 68Ga-FAPI PET imaging were performed and the maximum interval between these two imaging modalities was limited to 3 months (mean 47.56 days). SUVmax and SUVmean values were recorded on a lesion basis and were proportioned with the background SUVmean values from the liver. For patients with more than 10 lesions in the liver, the 3 largest lesions were included in the quantitative analysis. 3 patients included in the study were diagnosed with hepatocellular carcinoma and the remaining 13 patients were included in the group of metastatic liver tumors. ***Results:*** 150 lesions were detected with 68Ga-FAPI PET imaging and 91 lesions were detected with 18F-FDG-PET imaging. All of the lesion detected with ^{18}F-FDG PET were detected with 68Ga-FAPI PET. Additional liver lesions were observed in 12 of 16 patients with 68Ga-FAPI PET. For the 40 matched lesions analyzed,TBRmax (Lesion SUVmax/Liver SUVmax) and TBRmean (Lesion SUVmean/Liver SUVmean) were 20.6 and 12.3 for 68Ga-FAPI-PET, and 4.08 and 2.33 for 18F-FDG-PET. In addition, in all of these 40 lesions, the rates were higher in favor of 68Ga-FAPI PET. In the volumetric analysis performed for the hepatocellular cancer subgroup, tumor volumes were measured 1.97 times higher with 68Ga-FAPI PET. ***Conclusion:*** 68Ga-FAPI-PET detected a higher number of lesions than ^{18}F-FDG PET and showed superiority in terms of tumor-background ratios of the detected lesions. Before the TARE procedure or similar local interventional procedures for liver tumors, it is necessary to correctly identify the lesions in the liver. For this purpose treatment planning with 68Ga-FAPI PET can be considered as an important alternative in terms of the accuracy of volumetric and dosimetric studies.

EP-0278

Clinical evaluation of a unified data-driven respiratory motion correction technique in ^{18}F-FDG PET/CT imaging of upper abdominal lesions: a real-world study

T. Han[1], *Y. Wang*[2], *Z. Quan*[1], *J. Wang*[1], *F. Kang*[1];
[1]*Department of Nuclear Medicine, Xijing Hospital, Fourth Military Medical University, Xi'an, CHINA,* [2]*United Imaging Healthcare, Shanghai, CHINA.*

Aim/Introduction: Respiratory motion (RM)-related artifacts significantly impact image quality and diagnostic accuracy in PET/CT imaging. This study aimed to prospectively evaluate the clinical utility of the unified data-driven respiratory motion correction (uRMC) algorithm utilizing deep learning neural networks for diagnosing upper abdominal lesions. ***Materials and Methods:*** A total of 100 patients with suspected upper abdominal lesions who underwent ^{18}F-FDG PET/CT were enrolled. Two senior physicians independently conducted subjective visual assessments and semi-quantitative analyses of the PET/CT images before and after correction. Subjective visual evaluation parameters included overall image quality, PET-CT misalignment, and lesion distortion. Semi-quantitative metrics recorded for each lesion included maximum standardized uptake value (SUVmax), metabolic tumor volume (MTV), tumor-to-background ratio (TBR), and horizontal-to-vertical ratio (HV_ratio) before and after correction. Percentage changes in lesion SUVmax and MTV were calculated, and subgroup analyses were performed to assess the impact of lesion uptake, volume, and displacement on the performance of the uRMC algorithm. ***Results:*** Compared to no motion correction (NMC) images, 78% (78/100) of patients demonstrated improved overall image quality after uRMC reconstruction, with 68.9% (155/225) of lesion showing improved PET-CT alignment and 64.0% (144/225) demonstrating reduced lesion distortion (all p<0.001). The RM-corrected images exhibited a significantly higher SUVmax (9.07 [6.45, 11.79] vs.7.46 [5.69, 10.00], p< 0.001) and TBR (3.65 [2.54, 4.98] vs. 3.17 [2.40, 4.38], p< 0.001). The number of detected lesions increased from 171(NMC) to 181(uRMC) in 62 patients, with 10 additional suspicious lesions identified in 14.5% (9/62) of cases. Moreover, 7 lesions in 9.7% (6/62) of patients exhibited improved PET-CT alignment after uRMC correction. The uRMC algorithm also significantly reduced lesion MTV (1359.6 [690.8, 3837.6] mm3 vs.1710.5 [899.1, 4013.0] mm3, p<0.01) and HV_ratio (0.99 [0.82, 1.09] vs. 1.16 [1.02, 1.44], p<0.01). Subgroup-based analyses revealed that uRMC outperformed NMC in detecting low-uptake and small-volume lesions, with SUVmax improvements being more pronounced in lesions with larger displacement (17.76% vs. 9.76%, p<0.001). ***Conclusion:*** Compared with conventional NMC reconstruction, the uRMC algorithm significantly enhances overall image quality, PET-CT alignment, and lesion delineation. Furthermore, it improves the detection of low-uptake and small-volume lesions in the upper abdomen, thereby increasing the accuracy and reliability of clinical diagnoses and supporting more informed therapeutic decision-making.

EP-0279

The value of ^{18}F-FDG PET/MR radiomic features in predicting CTNNB1 mutations in pediatric hepatoblastoma

Y. Xu;
Hangzhou Universal Medical Imaging Diagnostic Center, Hangzhou, CHINA.

Aim/Introduction: This study aims to evaluate the predictive utility of ^{18}F-FDG PET/MR radiomics features for identifying CTNNB1 mutations in pediatric hepatoblastoma (HB), a key molecular alteration associated with tumor aggressiveness and therapeutic response. ***Materials and Methods:*** A retrospective analysis was conducted on 112 pediatric HB patients (median age 1.8 years, range 0.4-10.2 years). Clinical variables, including tumor stage, serum alpha-fetoprotein (AFP) levels, and histological subtype, were integrated into a clinical model (C_model). ere extracted from pre-treatment PET/MR images using the Computational Environment for Radiological Research. The Least Absolute Shrinkage and Selection Operator (LASSO) regression was employed to select optimal radiomic features and construct a radiomics model (R_model). The predictive performance of C_model, R_model, and their combination (CR_model) was assessed via receiver operating characteristic (ROC) analysis. A nomogram incorporating radiomics scores (rad-score) and clinical predictors was developed. ***Results:*** Patients were divided into a training cohort (n=78) and a validation cohort (n=34). LASSO identified 8

significant radiomic features for CTNNB1 mutation prediction. The R_model achieved AUCs of 0.89 (training) and 0.87 (validation), while the C_model showed AUCs of 0.76 and 0.71, respectively. The combined CR_model demonstrated superior performance, with AUCs of 0.95 (training) and 0.91 (validation), significantly outperforming standalone models ($P < 0.01$). ***Conclusion:*** Pre-therapeutic ^{18}F-FDG PET/MR radiomics features robustly predict CTNNB1 mutations in pediatric HB, offering a non-invasive tool to guide molecular subtyping, risk assessment, and personalized therapeutic strategies. This approach may complement traditional genetic testing and improve clinical decision-making.

EP-0280

Machine lerning-driven characterization of lymph node metastasis and 10-year overall survival in extrahepatic cholangiocarcinoma using ^{18}F-FDG PET/CT

J. Ning[1,2], *C. Li*[1], *H. Yang*[1], *X. Luan*[1], *R. Xue*[1], *Y. Wang*[3], *J. Tian*[1], *M. Hacker*[4], *L. Kenner*[2], *B. Xu*[1];
[1]*Department of Nuclear Medicine, First Medical Center of Chinese PLA General Hospital, Beijing, CHINA,* [2]*Christian Doppler Lab for Applied Metabolomics, Vienna, AUSTRIA,* [3]*GE Healthcare China, Shanghai, CHINA,* [4]*Division of Nuclear Medicine, Department of Biomedical Imaging and Image-Guided Therapy, Medical University of Vienna, Vienna, AUSTRIA.*

Aim/Introduction: Extrahepatic cholangiocarcinoma (eCCA), the second most common primary liver cancer, is often diagnosed at an advanced stage, resulting in high recurrence and poor survival. Although early-stage surgical resection offers a five-year survival rate of 43%, about 65% of patients present with unresectable disease, reducing survival to just 7%. Lymph node metastasis (LNM) is a key prognostic factor, making accurate preoperative prediction crucial. This study aimed to develop and validate imaging-driven ML models to enhance LNM prediction in eCCA patients. ***Materials and Methods:*** This retrospective study analyzed 236 patients with histologically confirmed eCCA who underwent ^{18}F-FDG PET/CT imaging between June 2012 and November 2018. Clinical data, including age, gender, CA199, CEA, IgG subtypes, tumor staging, and surgery type, were collected. Imaging parameters such as PET positivity, SUVmax, SUV ratio (SUVr), and tumor size were extracted by experienced nuclear medicine physicians. Radiomic features, totaling 1082, were computed from manually delineated PET and CT volumes of interest (VOIs) using PyRadiomics. Feature selection employed variance and correlation filtering followed by multivariate logistic regression, yielding optimal subsets for model development. Logistic regression-based ML models were built for PET-based, CT-based, PET/CT-based, and combined clinic_PET/CT-based radiomics approaches. Model performance was assessed using receiver operating characteristic (ROC) curves, sensitivity, specificity, positive predictive value (PPV), negative predictive value (NPV), and area under the curve (AUC). Prognostic value was evaluated via Kaplan-Meier survival analysis. ***Results:*** Of 213 patients included in the final analysis, 70 (32.9%) had LNM. The PET/CT-based radiomics model outperformed PET-only (AUC = 0.73), CT-only (AUC = 0.70), and visual analysis (AUC = 0.54) with an AUC of 0.80. The combined clinicoPET/CT model achieved the highest diagnostic accuracy (AUC = 0.86), significantly better than clinical features alone (AUC = 0.53). Survival analysis revealed that patients predicted to have low LNM risk had a median overall survival (OS) of 52.8 months, compared to 19.3 months in the high-risk group ($p = 0.001$).Fourteen key features were retained in the final combined clinicoPET/CT model. CT-based texture features like Size Zone Non Uniformity Normalized and Small Area Emphasis were associated with longer OS. ***Conclusion:*** ^{18}F-FDG PET/CT-based radiomics, especially when combined with clinical data, significantly improves LNM prediction and has strong prognostic value in eCCA. These findings support its potential to guide personalized treatment strategies and enhance clinical outcomes.

EP-0281

Prognostic value of lymph node-to-primary tumor standardized uptake value ratio in esophageal cancer patients who underwent surgery

C.-S. Tseng, *S.-C. Chan;*
Hualien Tzu Chi Hospital, Hualien, TAIWAN.

Aim/Introduction: The lymph node-to-primary tumor standardized uptake value ratio (SUV_{LN}/SUV_{Tumor}) is an emerging metabolic parameter that reflects the metastatic potential of malignancies more comprehensively than individual SUV measures. However, its prognostic significance in esophageal cancer patients following surgery remains under-explored. ***Materials and Methods:*** We retrospectively analyzed esophageal cancer patients who underwent either neoadjuvant chemoradiotherapy followed by esophagectomy or esophagectomy alone. [^{18}F]FDG PET/CT parameters, including the SUV_{max} of both primary tumors and metastatic lymph nodes, were evaluated. Prognostic significance was assessed using univariate and multivariate regression analyses with overall survival (OS) as the endpoint. Time-dependent receiver operating characteristic (ROC) curve analysis was used to compare the prognostic performance of imaging and clinical parameters. ***Results:*** A total of 108 patients were included, with a median follow-up of 31 months. During this period, 65 patients (60.2%) died. Patients with a higher SUV_{LN}/SUV_{Tumor} ratio had significantly worse survival outcomes. Kaplan-Meier analysis revealed a median OS of 30.6 months for the high-ratio group, compared to 89.4 months in the low-ratio group ($p < 0.01$). Multivariate Cox regression identified both SUV_{LN}/SUV_{Tumor} and gender as independent predictors of poorer OS ($p < 0.05$). Notably, SUV_{LN}/SUV_{Tumor} outperformed conventional staging systems in predicting survival, with a higher AUC on time-dependent ROC analysis for 5-year OS (0.71 vs. 0.58). ***Conclusion:*** The SUV_{LN}/SUV_{Tumor} ratio offers superior prognostic value compared to conventional tumor staging in predicting overall survival among esophageal cancer patients undergoing surgery, with or without neoadjuvant chemoradiotherapy. This parameter may enhance risk stratification and guide postoperative management strategies.

EP-0282

Contribution of ^{68}Ga-FAPI PET/CT to ^{18}F-FDG PET/CT in the Initial Staging and Restaging of Gastric Cancer:

M. Y. Kiran[1], *L. D. Ercan*[2], *S. Kuyumcu*[1], *C. Ertekin*[2], *Z. G. Ozkan*[1], *D. Has Simsek*[1], *E. G. İsik*[1], *Y. Sanli*[1];
[1]*Istanbul University, Istanbul Medical Faculty, Departmant of Nuclear Medicine, Istanbul, TÜRKIYE* [2]*Istanbul University, Istanbul Medical Faculty, Departmant of General Surgery, Istanbul, TÜRKIYE.*

Aim/Introduction: This study aimed to compare the findings of ^{68}Ga-FAPI (FAPI) PET/CT imaging with those of ^{18}F-FDG (FDG) PET/CT, and to evaluate the potential diagnostic contributions of FAPI PET/CT in patients with gastric cancer. ***Materials and Methods:*** A retrospective analysis was conducted on 40 patients with histopathologically confirmed gastric cancer who underwent both FDG and FAPI PET/CT scans (31 for initial staging, 9 for restaging). Final diagnoses of lesions were based on histopathology (gold standard) and/or concurrent or follow-up imaging studies. For both PET modalities, the number of primary tumors, regional and distant metastatic lymph nodes, and extra-nodal distant metastases were recorded. Additionally, the maximum standardized uptake value (SUV_{max}) and tumor-to-background ratio (TBR) of each lesion were documented. Comparisons of SUV_{max} and TBR were performed using the Wilcoxon and Mann-Whitney U tests. Diagnostic performance was assessed via the McNemar test; survival analyses were conducted using the Kaplan-Meier method and log-rank test; associations between risk factors and survival were analyzed using Cox regression. A p-value <0.05 was considered statistically significant. ***Results:*** Among the 40 patients, 29 (72.5%) were male

and 11 (27.5%) were female. Histopathologically, 22 patients (55%) had signet ring cell carcinoma (SRCC) and 18 (45%) had non-SRCC gastric carcinoma (adenocarcinoma). In primary tumors, regional lymph node metastases and extra-nodal distant metastases, SUV_{max} and TBR values were significantly higher with FAPI PET/CT compared to FDG PET/CT ($p<0.05$); no significant difference was observed in distant lymph node metastases ($p>0.05$). The detection rates of primary tumors were similar between the two modalities (93.5% vs. 90.3%, p=1.0). However, FAPI PET/CT demonstrated significantly higher sensitivity and accuracy for detecting regional and distant lymph node metastases, as well as extra-nodal distant metastases ($p<0.05$). Among 19 patients who underwent surgery, accurate nodal (N) staging was achieved in 9 cases with FAPI PET/CT and 6 cases with FDG PET/CT, while FAPI PET/CT detected a higher N stage in 5 patients. In distant metastasis (M) staging, FAPI PET/CT and FDG PET/CT demonstrated accuracy rates of 95% and 82.5%, respectively. Neither SUV_{max} nor TBR values of primary tumors on either PET modality were significantly associated with overall survival or progression-free survival during a median follow-up of 17.7 months ($p>0.05$). ***Conclusion:*** ^{68}Ga-FAPI PET/CT demonstrated superior visual and diagnostic performance compared to ^{18}F-FDG PET/CT in evaluating primary and metastatic gastric cancer lesions. These results support its potential as a promising imaging modality, warranting further validation in larger cohorts.

EP-0283

Diagnostic Performance of ^{68}Ga-FAPI PET/CT in Liver Fibrosis Staging: Correlation with Transient Elastography, APRI, and FIB-4

S. Kar, *V. R. Lele, A. S. Nagral, N. Shaikh;*
Jaslok Hopsital and Research Centre, Mumbai, INDIA.

Aim/Introduction: This study aimed to quantitatively assess liver fibrosis and cirrhosis by correlating liver uptake of ^{68}Gallium-Fibroblast Activation Protein Inhibitor Positron Emission Tomography/ Computed Tomography (^{68}Ga-FAPI PET/CT) with Transient Elastography (TE). The primary objectives were to evaluate the diagnostic performance of ^{68}Ga-FAPI PET/CT in staging liver fibrosis and to analyse the correlation between Maximum Standardised Uptake Value (SUVmax) from PET/CT and liver stiffness severity as measured by TE. ***Materials and Methods:*** A total of 45 participants with suspected liver disease underwent TE for fibrosis staging, classified as F0-F1, F2, F3, or F4. All subjects then underwent ^{68}Ga-FAPI PET/CT with delayed imaging (60-90 minutes post-injection), while a subgroup of 33 participants also had early imaging (15-30 minutes post-injection). Liver tracer uptake was quantified using SUVmax. Statistical analysis included the Kruskal-Wallis test to compare SUVmax across fibrosis stages, pairwise comparisons to assess differences between stages, and Receiver operating characteristic (ROC) analysis to evaluate diagnostic performance. Correlations with Aspartate Aminotransferase to Platelet Ratio Index (APRI) and Fibrosis-4 (FIB-4) were also analysed in a subgroup. ***Results:*** Delayed SUVmax significantly differed across the fibrosis stages ($p < 0.001$), with the highest median SUVmax observed in the F4 (cirrhosis) group (6.16, interquartile range [IQR] 3.69-7.93). Pairwise analysis showed significant differences between F0-F1 vs F4 and F2 vs F4. ROC analysis for delayed imaging showed good diagnostic accuracy for predicting significant fibrosis (F2, F3, F4 vs F0-F1) with an area under the ROC curve (AUROC) of 0.858 and an optimal cutoff SUVmax ≥1.28, and for predicting cirrhosis (F4 vs F0, F1, F2, F3) with an AUROC of 0.891 and a cutoff SUVmax ≥3.45. Early imaging also showed significant differences in SUVmax across stages ($p = 0.001$) and demonstrated slightly higher AUROC values for detecting cirrhosis. However, both imaging time points showed limited performance in distinguishing moderate (F2) and severe (F3) fibrosis. Delayed SUVmax strongly correlated with APRI and FIB-4 categories, supporting its clinical relevance. ***Conclusion:*** ^{68}Ga-FAPI PET/CT demonstrated a strong correlation between SUVmax and fibrosis severity, as assessed by TE. Delayed imaging is useful for differentiating cirrhosis from earlier fibrosis stages and for identifying significant fibrosis. While early imaging shows potential advantages in detecting cirrhosis, both early and delayed approaches have limitations in distinguishing moderate from severe fibrosis. Strong correlations with serological markers (APRI, FIB-4) further support the utility of ^{68}Ga-FAPI PET/CT in the non-invasive assessment of liver fibrosis.

EP-0284

Before and After CCRT ^{18}F-FDG PET/CT Derived Parameters for Prognosis of Esophageal Cancer Patients underwent Trimodality Treatment

M. Chiang[1], *P.-J. Chuang*[2], *J.-Y. Huang*[3];
[1]*Taipei Medical University Hospital, Taipei, TAIWAN,* [2]*National Taiwan University Hospital Cancer Center, Taipei, TAIWAN,* [3]*National Taiwan University Hospital, Taipei, TAIWAN.*

Aim/Introduction: Esophageal cancer has a poor prognosis despite standard treatment with pre-operative concurrent chemoradiotherapy (CCRT) and surgery. Although 18F-fluorodeoxyglucose positron emission tomography/ computed tomography (^{18}F-FDG PET/CT) is widely used for staging and response assessment, the prognostic value of PET-derived metabolic parameters—such as maximum standardized uptake value (SUVmax), metabolic tumor volume (MTV), and total lesion glycolysis (TLG)—before and after CCRT remained uncertain and inconsistent. Therefore, this study aimed to evaluate dual-timepoint PET-derived parameters and their temporal changes in predicting overall survival in patients with esophageal cancer. ***Materials and Methods:*** This retrospective study included 170 patients (159 men; mean age: 59±9 years) with esophageal cancer who underwent pre- and post-CCRT FDG PET/CT, followed by esophagectomy. PET-derived parameters including SUVmax, MTV,TLG, percentage change in SUVmax (%ΔSUVmax) and rate of SUVmax change — were measured to assess their prognostic significance. MTV and TLG were automatically calculated using commercial imaging analysis software. Survival analysis was performed using Kaplan-Meier curves, with cut-off values determined by the Youden index from receiver operating characteristic curves. The prognostic value of clinical and PET-derived variables for overall mortality was assessed using the Cox proportional hazards model. ***Results:*** After a mean follow-up of 51 months, 92 patients (54.1%) had died. Kaplan-Meier survival analysis revealed significant differences in survival based on post-CCRT SUVmax, pre- and post-CCRT MTV, pre-CCRT TLG, %ΔSUVmax, and rate of SUVmax change, with cut-off values determined by the Youden index. In multivariable Cox regression analysis, post-CCRT SUVmax (HR = 1.85, $p = 0.007$), pre-CCRT MTV (HR = 2.37, $p < 0.001$), %ΔSUVmax (HR = 0.53, $p = 0.003$), and the rate of SUVmax decrease (HR = 0.45, $p < 0.001$) were independent predictors for overall survival. ***Conclusion:*** This study demonstrated that FDG PET/CT-derived metabolic parameters, including post-CCRT SUVmax, pre-CCRT MTV, pre-CCRT TLG, %ΔSUVmax, and the SUVmax decrease rate, are significant predictors of survival in patients with esophageal cancer. Higher metabolic activity and lower treatment response were associated with worse outcomes, highlighting the prognostic value of PET imaging at both baseline and post-CCRT time points. The incorporation of automated tools for volumetric measurements may further support the clinical applicability of these PET parameters in prognostic assessment. ***References:*** Han S, Kim YI, Woo S, Kim TH, Ryu JS. Prognostic and predictive values of interim (18)F-FDG PET during neoadjuvant chemoradiotherapy for esophageal cancer: a systematic review and meta-analysis. Ann Nucl Med. Apr 2021;35(4):447-457.

EP-0285

68Ga-PSMA PET/CT in Inoperable/Heavily Pretreated Pancreatic Adenocarcinoma: A Pilot study on Imaging, Prognostic and Theranostic Potential

G. B. Priyanka, *N. A. Damle, A. N. Singh, K. Kuradia, S. Mishra, S. J. Bharati, R. Yadav, C. Ganapathy, A. Choudhary, M. Aishwarya;*
All India Institute of Medical Sciences, New Delhi, INDIA.

Aim/Introduction: Pancreatic adenocarcinoma remains a therapeutically challenging malignancy with poor prognosis in the inoperable or heavily pretreated setting. While FDG PET/CT is routinely used to evaluate tumour metabolism, recent interest has emerged in PSMA PET/CT owing to PSMA expression in tumour-associated neovasculature. This study aimed to evaluate PSMA PET/CT uptake patterns and prognostic utility in pancreatic adenocarcinoma patients, in comparison with FDG PET/CT. ***Materials and Methods:*** This prospective observational study included 14 patients with biopsy-confirmed inoperable/heavily pretreated pancreatic adenocarcinoma, with 11 patients who underwent both FDG and PSMA PET/CT. Lesions were analyzed based on location, count, and SUVmax. Imaging avidity on both modalities was recorded, and survival analyses were performed using Kaplan-Meier with log rank test. ***Results:*** 68Ga-PSMA uptake was seen in 50/60 lesions (83.3%). All primary pancreatic tumours were PSMA-avid. Site distribution was heterogenous—periampullary (n=4), head/uncinate (n=3), head/neck (n=1), uncinate (n=1), head/tail (n=1), distal body/tail (n=1), tail (n=1), and 2 post-Whipple's. Metastases included 15 nodal, 11 hepatic, 12 osseous, 2 pulmonary, and 3 abdominal deposits across modalities. Nodal sites were thoracic (n=6), retroperitoneal (n=4), supraclavicular (n=3), and abdominal (n=2), with high modality concordance. Among liver metastases (n=11), 4 were dual-avid, 5 PSMA non-avid, 1 discordantly PSMA-avid, and 1 missed by both tracers but found on CT. Two lung nodules were seen; one was missed by PSMA PET. PSMA PET detected one bone lesion missed by FDG PET; remaining 11 were dual-avid. PSMA SUVmax values ranged (mean 6.29, range 0-20.6), as did FDG (mean 6.5, range 0-25). 26 (43.3%) showed uptake > liver background, 34 (56.7%) showed uptake < liver. Lesions with uptake > liver were more frequent in bone and nodes. Number of FDG-avid lesions (median 3, range 1-15) and PSMA-avid lesions (median 2.5, range 1-15) showed strong agreement (concordance correlation = 0.97). Kaplan-Meier curves showed ≥3 FDG-avid lesions predicted worse OS, while ≥2.0 PSMA lesions showed early mortality, with crossover at ~40% survival. ***Conclusion:*** PSMA PET/CT demonstrates consistent and clinically meaningful uptake in pancreatic adenocarcinoma, frequently identifying lesions that are missed by FDG PET/CT. Unlike FDG, which predominantly reflects glycolytic activity and often correlates with aggressive disease, PSMA PET/CT targets tumor neovasculature. This vascular-targeted imaging may serve as a surrogate for perfusion and drug delivery potential, and opens avenues for PSMA-targeted therapies. In our study, PSMA PET/CT not only detected additional lesions but also showed a early deaths in patients with high burden PSMA avid disease.

EP-0286

^{18}F-FDG and 68Ga-FAPI PET/CT in evaluation of esophageal cancer

M. Komarova[1], *V. Sinitsyn*[1], *E. Davydova*[1], *A. Chaban*[2], *A. Martinovich*[3];
[1]*Lomonosov Moscow State University, Moscow, RUSSIAN FEDERATION,* [2]*Rechts der isar, technische Universitat Munchen, Munich, GERMANY,* [3]*N.N. Blokhin Russian Cancer Research Center, Moscow, RUSSIAN FEDERATION.*

Aim/Introduction: to compare 68Ga-FAPI PET/CT and ^{18}F-FDG PET/CT in diagnosis of esophageal cancer. ***Materials and Methods:*** 14 patients (5 females and 9 males; median age, 44 years) with esophageal cancer underwent ^{18}F-FDG and 68Ga-FAPI PET/CT examination within 1 week for assessment primary tumor and distant metastasis. 10 patients were referred for initial diagnosis and 4 patients after treatment. Positive lesions on PET/CT images were verified by biopsy or follow-up. Mann-Whitney U test was used to compare SUVmax and TBR of tumor lesions using ^{18}F-FDG and 68Ga-FAPI PET/CT. We calculated the diagnostic efficiency (sensitivity (Se), specificity (Sp), positive predictive value (PPV), negative predictive value (NPV) and accuracy (Ac)) for each modality on a per-region basis. ***Results:*** 68Ga-FAPI-46 PET/CT and ^{18}F-FDG PET/CT showed comparable diagnostic performance (the number of lesions of radiopharmaceutical accumulation in esophageal tumor was comparable in the two techniques). There were no significant differences in SUVmax and TBR obtained in both esophageal tumor and metastatic lymph nodes (p>0.05). The mean SUVmax for 68Ga-FAPI-46 PET/CT and ^{18}F-FDG PET/CT were 11,78 [7,72-17,16] and 13,86 [5,39-23,30] (p=0,59) resp., and mean TBR for 68Ga-FAPI-46 PET/CT and ^{18}F-FDG PET/CT were 5,26 [9,97-7,66] vs. 5,35 [1,94-8,68] (p=0,82) respectively. False-positive results of radiopharmaceutical accumulation in intrathoracic lymph nodes during FDG-PET were obtained in 4 patients (33%). One patient had a false positive result 68Ga-FAPI uptake in the esophagus due to esophagitis and true negative according FDG-PET. Se, Sp, PPV, NPV and Ac for 68Ga-FAPI-46 PET/CT were 100%, 81,25%, 86,96, 100% and 91,67% respectively vs. 95,00%, 43,75%, 67,86%, 87,50% and 72,22% for ^{18}F-FDG PET/CT respectively. ***Conclusion:*** 68Ga-FAPI-46 PET/CT is better to assess the metastatic lymph nodes lesion than ^{18}F-FDG PET/CT in patients with esophageal cancer.

EP-0287

Comparison of 68Ga-FAPi and FDG PET/CT in the Detection of Peritoneal Carcinomatosis, Staging and Restaging in Patients with Gastrointestinal Cancer

H. Pala, *M. Tuncel, E. Karabulut, S. Yalçın, N. Akkapulu, T. Erol, C. Sökmensüer, Ö. Uğur;*
Hacettepe University, Ankara, TÜRKIYE.

Aim/Introduction: 68Ga-labelled fibroblast activation protein inhibitor(FAPi) promises a more successful diagnostic performance than FDG due to lower background activity and relatively high specificity for tumoural tissues. Our study aimed to compare the diagnostic performances of FDG and FAPi PET/CT examinations in patients with gastrointestinal malignancies, evaluated in terms of staging and restaging, as well as the detection of the peritoneal carcinomatosis index (PCI)score. ***Materials and Methods:*** Thirty-eight patients were included in the study. All patients underwent FDG and dual-time FAPi PET/CT scans at 10 and 60 minutes. Surgical histopathology data, along with clinical and imaging follow-up results, were used as reference tests to compare the diagnostic performances for staging, detecting recurrence, and PCI scores. The contribution to disease management and the accuracy of each modality were interpreted on both a patient and lesion basis. ***Results:*** FAPi demonstrates significantly higher accuracy in detecting malignant lesions than FDG in lesion-based assessments. FAPi was much more compatible with reference tests for detecting malignant lesions compared to FDG, with kappa-values of 0.644 and 0.206, respectively. Eighty-six percent of the malignant foci were correctly identified with FAPi based on follow-up data, while this rate was only 34% with FDG. In addition, FAPi uptake was significantly higher than that of FDG in malignant lesions, with a mean SUVmax difference of 3.73(p<0.001). Compared to early images of FAPi, uptake intensity in delayed images increased in malignant foci (early and late median SUVmax:3.55 and 4.58; mean rank:2.01 and 2.63, respectively; p<0.001); in contrast, there was no significant uptake increase in benign lesions(p=0.069). The likelihood of malignancy in a lesion escalates with the percentage rise in the late SUVmax value relative to the early value (odds ratio 1,014; p=0.008); this increment is more pronounced in lesions

exceeding 10 mm in size than in smaller lesions. In patient-based analysis, FAPi determined stage(8/8) and recurrence status(28/30) much better than FDG (3/8 and 18/30, respectively). FAPi also significantly outperformed FDG($p<0.001$) in calculating PCI scores and the number of malignant foci detected(Table1). Moreover, FAPi directly affects disease management compared to FDG and conventional imaging modalities by eliminating suspicious foci for metastasis and initiating or changing treatment in 63% of patients. ***Conclusion:*** FAPi demonstrates superior diagnostic performance in evaluating peritoneal carcinomatosis and in staging or restaging patients with gastrointestinal cancer compared to FDG. This study suggests that FAPi may enhance diagnostic accuracy and facilitate more appropriate therapeutic decisions for patients with gastrointestinal malignancies.

EP-0288

Optimization of gastric emptying scan times

K. Velasquez, *I. Garrido, P. Meneses, M. Grajeda, C. Pradere, M. Estrella, R. Jimeno, M. Mijtavila;*
Hospital Puerta de Hierro, Majadahonda, SPAIN.

Aim/Introduction: Gastroparesis is a gastric motility disorder characterized by delayed gastric emptying in the absence of mechanical obstruction. Among the available diagnostic tools, gastric emptying scintigraphy is considered a reliable method to assess gastric motor function, as it quantifies the percentage of gastric retention over time using a standardized radionuclide-labeled meal[(1).] The 4-hour protocol has been adopted as the standard for detecting gastric motility disorders; however, quantitative thresholds that may support diagnosis in shorter time frames have also been established, potentially reducing scan duration without compromising sensitivity. Therefore, our aim is to determine the correlation between quantitative values obtained at 3 and 4 hours in gastric emptying scintigraphy[(2)]. ***Materials and Methods:*** A retrospective analysis was conducted on 28 patients with clinical suspicion of gastroparesis who underwent gastric emptying scintigraphy in 2024. Images were acquired immediately after ingestion of a standardized meal and at 1, 2, 3, and 4 hours, as per established protocol. According to the joint consensus of the SNM and ANMS[(1),] gastric retention >10% at 4 hours and >30% at 3 hours was considered abnormal. Cohen's Kappa test was used for correlation analysis between the time points. ***Results:*** Out of the 28 evaluated patients, 14 (50%) showed diagnostic values consistent with gastroparesis at 4 hours. The concordance analysis between the 3- and 4-hour values, yielded 100% agreement (Kappa = 1, p-value = 1.213e-7). ***Conclusion:*** These findings suggest that the study duration could be reduced to 3 hours without compromising diagnostic accuracy. This adjustment could improve workflow efficiency and reduce costs while maintaining diagnostic quality. If 3-hour values were considered diagnostic, a retention rate ≤30% at 2 hours could potentially be interpreted as normal. In our sample, this would have allowed up to 8 patients (29%) to complete the study by the 2-hour mark. However, the small sample size limits generalizability. To achieve a Kappa of 0.75 with a gastroparesis prevalence of approximately 50%, a sample size of 95 patients would be required ***References:*** 1. Abell TL, Camilleri M, Donohoe K, Hasler WL, Lin HC, Maurer AH, et al. Consensus Recommendations for Gastric Emptying Scintigraphy: A Joint Report of the American Neurogastroenterology and Motility Society and the Society of Nuclear Medicine. Journal of Nuclear Medicine Technology. 1 de marzo de 2008;36(1):44-54.

EP-17

e-Poster Area

B: Imaging Clinical Studies -> B1 Oncological Imaging Clinical Study -> B16 Neuroendocrine (Pancreatic and Others)

EP-0289

Diagnostic Contribution of [^{68}Ga]Ga-ABY-025 PET in HER2-Positive Breast Cancer: Beyond [^{18}F]FDG PET

A. Alhuseinalkhudhur[1,2], *H. Lindman*[1], *F. Y. Frejd*[1,3], *P. Liss*[4], *J. Feldwisch*[3], *T. Sundin*[5], *V. Iyer*[2], *M. Lubberink*[2], *I. Velikyan*[2], *J. Sörensen*[2];
[1]*Department of Immunology, Genetics and Pathology, Uppsala University, Uppsala, SWEDEN,* [2]*Department of Surgical Sciences, Molecular imaging and medical physics, Uppsala University, Uppsala, SWEDEN,* [3]*Affibody AB, Solna, SWEDEN,* [4]*Department of Surgical Sciences, Radiology, Uppsala University, Uppsala, SWEDEN,* [5]*Clinical Research and Development Unit, Uppsala University Hospital, Uppsala, SWEDEN.*

Aim/Introduction: [^{68}Ga]Ga-ABY-025 PET is a novel imaging modality that is useful for quantification and treatment response prediction in advanced-stage human epidermal growth factor receptor 2 (HER2)-positive breast cancer. This study investigates its utility in accurate staging, highlighting diagnostic pitfalls and variability in tracer uptake. ***Materials and Methods:*** Fifty patients with biopsy-confirmed HER2-positive breast cancer underwent both [^{68}Ga]Ga-ABY-025 PET and [^{18}F]FDG PET within one week. A second [^{18}F]FDG PET was performed following two courses of HER2-targeted treatment to assess metabolic response. All images were analyzed with regard to lesion detectability, tracer distribution, and physiological uptake patterns. ***Results:*** In three patients, [^{68}Ga]Ga-ABY-025 PET detected a more extensive local spread than [^{18}F]FDG PET. Two of these patients had invasive lobular carcinoma, these findings led to revised staging and adjusted treatment plans. All three patients showed early metabolic response, with two achieving complete response following HER2-targeted therapy. Two other patients showed elevated [^{18}F]FDG PET uptake near the thyroid with low corresponding [^{68}Ga]Ga-ABY-025 PET uptake. Biopsies excluded malignancy, although a definitive conclusion could not be drawn. Two additional patients who were vaccinated against COVID19 shortly prior to PET scans showed high [^{18}F]FDG PET uptake in ipsilateral lymph nodes, no corresponding uptake was observed on [^{68}Ga]Ga-ABY-025 PET. ***Conclusion:*** [^{68}Ga]Ga-ABY-025 PET provided complementary and clinically relevant information beyond that of [^{18}F]FDG PET, particularly in detecting small or otherwise challenging lesions. Additionally, it demonstrated higher specificity by avoiding uptake in inflammatory or vaccine-related reactive nodes. These findings support the added value of HER2-targeted PET imaging for staging and therapy monitoring in HER2-positive breast cancer.

EP-0290

Enhanced Probabilistic Analysis of Breast Cancer FDG-PET Images Using Probabilistic Machine Learning Techniques

N. Christensen[1], *M. H. Vendelbo*[1], *T. M. Hansen*[2];
[1]*Aarhus University Hospital, Aarhus N, DENMARK,* [2]*Aarhus University, Aarhus C, DENMARK.*

Aim/Introduction: nformed prior models and probabilistic sampling methods show potential for improving PET image assessment. The Probabilistic PET (ProPET) method integrates smoothing and noise characteristics in reconstructed PET images with prior information about the tracer's within-body activity. This

study integrates the ProPET method, with an explicit prior model of within-body activity, utilizing a machine learning approach for PET image analysis. Sensitivity for small cancer lesions remains suboptimal with FDG-PET/CT in oncological conditions, such as breast cancer (BC). To enhance diagnostic sensitivity, we assessed whether ProPET improves detection of additional suspicious foci. ***Materials and Methods:*** ProPET was applied using a convolution operator and a spatially correlated noise model inferred from phantom data. A prior model representing within-body activity concentration in BC was developed, using liver activity as baseline and incorporating sharp contrast between high and low activity. A training dataset was compiled, comprising many realizations of the prior distribution and corresponding simulated PET-images. Data was used to train a neural network estimating features of the posterior probability distribution. This facilitates detailed analysis of in-vivo activity, highlighting regions of high activity, without the computational burden of traditional sampling methods. 50 FDG-PET images from BC patients were retrospectively analysed using ProPET compared to standard PET reconstruction. A nuclear medicine specialist independently assessed each image. Breast and local lymph node lesions were rated 1=most likely benign, 2=benign/malignant or 3=most likely malignant. All foci rated as 2 or 3 was deemed possibly malignant lesions. ***Results:*** More suspicious foci were identified on ProPET reconstructions, with 26 additional lesions in breasts (76 vs. 102) and 82 in local lymph nodes (172 vs. 254). Many additional breast foci on ProPET reconstructions appeared near primary tumors, suggesting improved resolution. All foci identified with standard reconstruction were also detected with ProPET. ***Conclusion:*** ProPET significantly advances PET imaging by combining informed prior models with machine learning to improve PET scan evaluations and detect small, high-activity lesions vital for early detection. Our findings indicate increased sensitivity compared to standard reconstruction. However, prospective studies are needed to validate specificity, assess the risk of false positives, and confirm clinical value in guiding diagnostic and therapeutic decisions. ***References:*** [1] Hansen TM, et al. Probabilistic deconvolution of PET images using informed priors.Frontiers in Nuclear Medicine.2023;2. [2] Hansen TM, et al. Use of Machine Learning to Estimate Statistics of the Posterior Distribution in Probabilistic Inverse Problems—An Application to Airborne EM Data. Journal of Geophysical Research:Solid Earth.2022;127(11).

EP-0291

Correlation of Primary Lesion FDG PET/CT Texture Features with Prognosis and Histopathological Data in Luminal A Type Breast Cancer

M. Genç[1], *K. Şeker*[2], *Z. Hasbek*[2], *B. Yücel*[3], *M. Yılmaz*[4]; *[1]Sivas Numune Hospital Department of Nuclear Medicine, Sivas, TÜRKIYE, [2]Sivas Cumhuriyet University Faculty of Medicine Department of Nuclear Medicine, Sivas, TÜRKIYE, [3]Sivas Cumhuriyet University Faculty of Medicine Department of Radiation Oncology, Sivas, TÜRKIYE, [4]Sivas Cumhuriyet University Faculty of Medicine Department of Medical Oncology, Sivas, TÜRKIYE.*

Aim/Introduction: FDG PET/CT is used in breast cancer. With radiomics studies, quantitative data on tumor biology can be obtained by using data characterization algorithms on medical images. The texture features of lesions that can be obtained from FDG PET/CT images can help clinicians in the pathological features and clinical course of the disease. In our study, it was aimed to investigate the effect of radiomics features and traditional measurements such as SUV that can be obtained from FDG PET/CT images performed for staging purposes in patients with Luminal A type breast cancer on prognosis by comparing them with data such as disease stage, pathological features, and survival. ***Materials and Methods:*** 41 patients diagnosed with Luminal A type breast cancer who underwent FDG PET/CT for staging purposes were included in the study. Primary breast cancer lesions in FDG PET/CT images were segmented by accepting 42% of SUVmax measurement as the threshold value. Using LIFEx software, numerical texture properties and shape properties were obtained for each lesion. The relationship of these data with the survival data of the patients was examined. In addition, SUV, MTV, TLG of the primary lesions were recorded. The TNM stage and grade of the disease, the presence or absence of necrosis-lymphovascular invasion-perineural invasion, and Ki-67 index were obtained for each patient along with their survival times. Statistical analysis of the obtained data was performed using SPSS26®software. ***Results:*** The mean age of the patients was 60±13. While follow-up data of 4 patients could not be accessed, the mean survival time of the remaining 30 of the patients were local, 7 were locally advanced, and 4 were in advanced stage. Tumor necrosis was positive in 9 patients, lymphovascular invasion was positive in 14 patients, and perineural invasion was positive in 15 patients. The relationships of pathological features with texture characteristics data are summarized in Table 1. 37 patients was determined as 77±20 months. Texture characteristics data that could be related to survival were investigated. These findings are summarized in Table 2.Correlation relationships between PET measurement parameters and texture analysis data were examined, and very high levels of correlations were found. ***Conclusion:*** Texture analysis data obtained from FDG PET/CT performed on patients with luminal A type breast cancer may be useful in predicting the pathological features of the disease and survival with other PET data. Thus, it may contribute to disease management regarding preoperative and postoperative treatment approaches.

EP-0292

PET-positive extra-axillary lymph nodes in high-risk primary breast cancer: a retrospective study of location, treatment planning, and follow-up

A. L. Rudbeck[1], *N. M. Jakobsen*[2], *M. G. Hildebrandt*[2], *M. Vogsen*[3]; *[1]Department of Clinical Research, University of Southern Denmark, Odense, DENMARK, [2]Department of Nuclear Medicine, Odense University Hospital, Odense, DENMARK, [3]Department of Oncology, Odense University Hospital, Odense, DENMARK.*

Aim/Introduction: To explore the clinical management and follow-up of non-resected PET-positive extra-axillary lymph nodes in women with primary breast cancer. ***Materials and Methods:*** Women with primary breast cancer referred for an additional staging with FDG-PET/CT at Odense University Hospital from January 2016 to February 2024 were included retrospectively. This study assessed FDG-PET/CT-based stage migration through a comprehensive review of patient medical records, pathology reports, scan reports, and images. In-depth characteristics, clinical management, and follow-up after the detection of extra-axillary lymph node metastasis in the periclavicular and internal mammary nodes (IMN) were included for analysis. ***Results:*** A total of 615 patients were included in the study. Following FDG-PET/CT, 377 (61%), 95 (15%), and 143 (23%) were staged with early breast cancer, extra-axillary breast cancer, and metastatic breast cancer, respectively. After definitively including 83 patients with extra-axillary breast cancer, the sites of lymph node metastases were infraclavicular (47/83, 57%), supraclavicular (31/83, 37%), and IMN (35/83, 42%). The majority of patients received standard radiotherapy (74/83, 89%), mainly including the locoregional levels without an additional nodal boost to PET-positive nodes. At a median follow-up of 4.9 years, 27 patients (33%) had a new malignant event, predominantly due to recurrent breast cancer (23/83, 28%). Of these, most presented with distant metastasis (21/23, 91%), and only one had an isolated locoregional recurrence. Among patients with breast cancer recurrence, 57% (13/23) died within a median of 2.9 years after initial diagnosis. ***Conclusion:*** In patients upstaged due to detection of extra-axillary PET-positive

lymph nodes, most locoregional lymph nodes were located in the internal and infraclavicular nodes. Despite medical treatment and radiotherapy after surgery, approximately one-third of the patients experienced distant failure within five years of follow-up. These findings highlight the need for improved therapeutic strategies for patients with high-risk primary breast cancer.

EP-0293

Integrating 18FDG-PET/CT Biomarkers and Tumor Biology in Breast Cancer Prognosis

N. Fatima[1,2], *M. Zaman*[2];
[1]*Dow University Health Sciences, Karachi, PAKISTAN,* [2]*Aga Khan University Hospital, Karachi, PAKISTAN.*

Aim/Introduction: To determine prognostic strength of ^{18}FDG PET/CT based glucose metabolism, tumor grading and immunohistochemical markers in breast cancer (BC) patients. ***Materials and Methods:*** This was a cohort study conducted at PET/CT imaging services of Department of Radiology and duly approved from ethical review committee (2024-10580-30915). A total of 110 patients of advanced stage BC patients (stage II and more) who ^{18}FDG PET/CT for staging, restaging, response and surveillance were included and followed for disease free survival (DFS) on metabolic status on follow up PET/CT for 4-5 years. Tumor demographics (type, grading, staging) and immunohistochemistry (estrogen receptor ER, human epidermal growth factor receptor-2 HER2/Neu, progesterone receptor PR, Ki-67) were also recorded. Using logistic regression and ROC analysis, the significant predictors of DFS were analyzed. Kaplan Meier's survival plots were analyzed to measure DFS against ROC derived cutoff values of significant predictors. ***Results:*** The median age of study group was 57 years (25 - 86 years), significantly obese and 85% invasive ductal CA with 97% grade II-III on Bloom-Richardson classification and stage IV disease (74%). The significant association of SUVmax and Ki-67 index were found in poor survival outcome on logistic regression while no significant association of patients' age, obesity, tumor grading, ER, PR, HER-2/neu status were found in DFS in BC. The SUVmax >5.4 and Ki-67 >30% were found to have significant association with disease progression (AUC 0.729 and 0.759; p=0.0002* and p=0.0001* respectively). The DFS was significantly shorter in SUVmax >5.4 (29 vs. 45 months; Logrank=16.356; p=0.0001*) and Ki-67 >30% index (57 vs. 162 months; Logrank=12.892; p=0.0003*). However, no significant difference in OS was observed at Ki-67 cutoff >30% index (Mean Survival 375 vs. 272 months; Logrank=0.457; p=0.499). ***Conclusion:*** The Ki-67 index and ^{18}FDG PET/CT based SUVmax are significant predictors for poor survival outcome in BC patients. The higher SUVmax >5.4 and Ki-67 >30% are considered significant cutoff for shorter DFS. ***References:*** 1. Tilli, T.M. Precision Medicine: Technological Impact into Breast Cancer Diagnosis, Treatment and Decision Making. J. Pers. Med. 2021;11 (12): 1348; https://doi.org/10.3390/jpm11121348. 2. Bray F, Laversanne M, Sung H, Ferlay J, L. Siegel R, Soerjomataram I, et al. Global cancer statistics 2022: GLOBOCAN estimates of incidence and mortality worldwide for 36 cancers in 185 countries. CA Cancer J Clin. 2024; 74:229-263. 3. Menhas R, Umer S. Breast Cancer among Pakistani Women. Iran J Public Health 2015 Apr; 44(4):586-7. PMID: 26056679; PMCID: PMC4441973.

EP-0294

Prognostiv Value of F-18 FDG PET/CT-Derived TLG and Radiomics Features in Breast Cancer Patients

F. Görtan[1], *M. Kartal*[2], *A. Kartal*[2];
[1]*Turkish Ministry of Heath, Ankara Bilkent City Hospital, Department of Nuclear Medicine, Ankara, TÜRKIYE,* [2]*Elazıg Fethi Sekin City Hospital, Department of Nuclear Medicine, Elazıg, TÜRKIYE.*

Aim/Introduction: This study aimed to evaluate the prognostic utility of radiomics features and total lesion glycolysis (TLG) derived from baseline [^{18}F]FDG PET/CT imaging in predicting metastasis development and metastasis-free survival (MFS) in patients with breast cancer. ***Materials and Methods:*** A retrospective analysis was conducted on 37 female patients (median age: 50 years) with histologically confirmed breast carcinoma who underwent staging FDG PET/CT. Quantitative imaging features including conventional metabolic parameters (SUVmin, SUVmean, SUVmax, SUVpeak, TLG) and radiomics texture features extracted from GLCM, GLRLM, NGLDM, and GLZLM matrices were evaluated. The relationship between these features and metastasis development during follow-up was assessed using ROC curve analysis and Cox regression models. ***Results:*** Among the patients, 86.5% had invasive carcinoma, and molecular subtyping revealed 62.2% luminal A, 27.0% luminal B, and 8.1% triple-negative breast cancer. During a median follow-up of 56 months, metastasis occurred in 6 patients (16.2%). ROC analysis identified five parameters significantly associated with metastasis: TLG (AUC=0.801), GLCM-Correlation, NGLDM-Coarseness, GLZLM-LZHGE, and GLZLM-GLNU (all $p < 0.05$). TLG >56.8 g was the most powerful predictor, yielding 83.3% specificity and 77.4% sensitivity. Univariate Cox regression revealed that high TLG, GLZLM-LZHGE >8820, and GLZLM-GLNU >4.96 were significantly associated with shorter MFS ($p < 0.05$), while age and receptor status were not. In multivariate analysis, only TLG >56.8 g remained statistically significant (HR: 12.034, 95% CI: 1.398-103.605, $p = 0.024$). Kaplan-Meier analysis confirmed significantly shorter MFS in patients with high TLG values (mean MFS: 47.4 vs. 63.25 months, Log Rank $p = 0.004$). ***Conclusion:*** TLG measured from staging FDG PET/CT emerged as an independent predictor of metastasis and reduced MFS in breast cancer patients. Selected radiomics features, particularly GLZLM-derived metrics, may offer additional prognostic value. Integration of metabolic and radiomic biomarkers from FDG PET/CT into clinical decision-making may enhance early risk stratification and guide treatment strategies.

EP-0295

Contribution of 68Ga-DOTA-cyclo (RGDfK) [Integrin αvβ3 Inhibitor] PET/CT Imaging in Staging and Restaging of Breast Cancer: Preliminary Findings

Z. Tosunoglu*, Ö. F. Şahin, A. E. Öztürk, G. Alçın, E. Akgün, E. Arslan; Istanbul Training and Research Hospital, Nuclear Medicine Clinic, Istanbul, TÜRKIYE.*

Aim/Introduction: Integrin αvβ3 is heterodimeric transmembrane glycoprotein expressed in activated endothelial cells, newly formed blood vessels, various tumor cells. It plays crucial role in angiogenesis and distant metastasis development, making it a target for early detection and treatment management of tumors such as breast and lung cancer. This prospective study aims to evaluate the role and contribution of 68Ga-DOTA-cyclo(RGDfK) [integrin αvβ3 inhibitor] PET/CT in staging and restaging breast cancer patients. ***Materials and Methods:*** In this prospective study, conducted between September 2024 and January 2025, 18 F diagnosed breast cancer underwent 68Ga-DOTA-cyclo(RGDfK) [integrin αvβ3 inhibitor] PET/CT within maximum 2 weeks after ^{18}F-FDG PET/CT.Written and verbal informed consent obtained from all patients. VOI drawn to include the entire lesion. SUV recorded for primary and metastatic lesions. Highest SUVmax lesion in each organ was reported. Relationship between SUVmax parameters and histopathological features was analyzed. Angiogenesis imaging using 68Ga-DOTA-cyclo(RGDfK) [integrin αvβ3 inhibitor] PET/CT was compared to metabolic imaging using ^{18}F-FDG PET/CT. ***Results:*** Mean age 56.2 ± 13.6 years .Imaging purposes: 12 staging 5 treatment response evaluation, 1 restaging after recurrence Histopathological distribution: 15 (83.3%) invasive ductal carcinoma 2 (11.1%) invasive lobular carcinoma 1 (5.6%) mixed-type tumor Physiological radiotracer uptake was observed in the liver, spleen, ventricles, thyroid, and intestines, with renal

excretion. Primary tumor uptake comparison: FDG SUVmax: 13.35 ± 8.56 Integrin SUVmax: 5.38 ± 1.61 FDG SUVmax was significantly higher than Integrin SUVmax (p=0.005). Moderate correlation was found between FDG SUVmax and Integrin SUVmax (r=0.514, p=0.05). ALN uptake comparison: FDG SUVmax: 12.72 ± 5.22 Integrin SUVmax: 5.18 ± 2.45 FDG SUVmax was significantly higher than Integrin SUVmax (p=0.007). Bone metastases (n=7): FDG SUVmax: 11.61 ± 5.86 Integrin SUVmax: 6.01 ± 2.84 FDG SUVmax was significantly higher than Integrin SUVmax (p=0.018). Distant LN metastases (n=5): FDG SUVmax: 14.58 ± 8.84 Integrin SUVmax: 4.83 ± 1.85 FDG SUVmax was significantly higher than Integrin SUVmax (p=0.043). Lung and liver metastases: FDG SUVmax was higher than Integrin SUVmax, but the difference was not statistically significant (p>0.05). ***Conclusion:*** 68Ga-DOTA-cyclo(RGDfK) [integrin αvβ3 inhibitor] PET/CT is promising imaging method for the early detection of patients suitable for neovascularization-targeted therapies and monitoring emerging drug resistance. Our results indicate that ^{18}F-FDG PET/CT remains superior for tumor staging and restaging, while 68Ga-DOTA-cyclo(RGDfK) [integrin αvβ3 inhibitor] PET/CT provides complementary rather than equivalent information. Additionally, our findings suggest that Lu-177-labeled integrin analogs may be considered for breast cancer treatment in the future.

EP-0296

Novel spatial PET parameters NHOC and NHOP Predict Pathological Complete Response to Neoadjuvant Therapy in HER2-Positive Breast Cancer

O. Vezir[1], *A. Aksu*[1], *Z. Guc*[2], *K. Kucuker*[1], *A. Alacacioglu*[2], *B. Turgut*[1];
[1]Izmir Katip Celebi University Faculty of Medicine, Department of Nuclear Medicine, Izmir, TÜRKIYE, [2]Izmir Katip Celebi University Faculty of Medicine, Department of Oncology, Izmir, TÜRKIYE.

Aim/Introduction: Accurate prediction of pathological complete response (pCR) following neoadjuvant therapy remains a critical challenge in HER2-positive breast cancer management. We investigated whether spatial metabolic parameters—particularly the novel Normalized Hotspot-to-Centroid (NHOC) and Normalized Hotspot-to-Perimeter (NHOP) from baseline ^{18}F-FDG PET/CT—could improve pCR prediction beyond conventional PET metrics. ***Materials and Methods:*** We retrospectively analyzed female patients with diagnosed HER2+ invasive breast carcinoma, who underwent baseline ^{18}F-FDG PET/CT, completed neoadjuvant therapy, and had subsequent surgery. Primary tumors were manually segmented using LIFEx software. NHOP, NHOC, SUVmax, SUVmean, metabolic tumor volume (MTV), and total lesion glycolysis (TLG) values were calculated for each lesion. The NHOC defined as the normalized distance between the SUVmax voxel and tumor centroid, while NHOP represented the minimum normalized distance between the SUVmax voxel and tumor perimeter. Differences in these parameters between patients with and without pCR were assessed using the Mann-Whitney U test. Statistically significant variables were further analyzed using multivariate logistic regression to identify independent predictors. ***Results:*** A total of 96 HER2+ breast cancer patients were included; 45 achieved pCR. The pCR rate was significantly higher in the non-luminal group (65.6%) compared to the luminal group (37.5%) (p = 0.009). NHOPmax (p = 0.039), NHOCmax (p = 0.022), and SUVmax (p = 0.016) were significantly associated with pCR. NHOPmax and SUVmax were higher in the pCR group, while NHOCmax was lower. The cut-off values were determined as 0.386 (AUC: 0.636) for NHOCmax, 0.141 (AUC: 0.623) for NHOPmax and 11.0 (AUC: 0.643) for SUVmax. In multivariate analysis, NHOPmax (p<0.001, OR: 7.522), NHOCmax (p = 0.047, OR: 2.701), SUVmax (p = 0.005, OR: 4.563) and luminal subtype (p = 0.044, OR: 2.953) emerged as independent predictors of pCR. The spatial parameters showed no correlation with SUVmax (p>0.05), suggesting complementary predictive value. ***Conclusion:*** In addition to SUVmax, the novel PET-derived spatial distribution metrics NHOP and NHOC emerged as independent predictors of pCR in HER2-positive breast cancer. Interestingly, higher NHOP and lower NHOC values were associated with pCR, suggesting that tumors with more homogeneous intratumoral FDG uptake may be more likely to respond completely to neoadjuvant therapy. These readily quantifiable PET biomarkers may help personalize neoadjuvant therapy strategies, particularly for luminal-HER2 tumors where conventional predictors underperform. Further prospective validation in larger cohorts is warranted. ***References:*** J. Jiménez-Sánchez, J.J. Bosque, G.A. Jiménez Londoño et al. Evolutionary dynamics at the tumor edge reveal metabolic imaging biomarkers, Proc. Natl. Acad. Sci. U.S.A. 118 (6) e2018110118.

EP-0297

From single-cell to whole-body imaging of the expression of Fibroblast Activation Protein in Triple Negative Breast Cancer patients

N. Hovhannisyan-Baghdasarian[1], *Y. Kieffer*[2], *V. Selvarasa*[2], *L. Champion*[3], *N. Jehanno*[4], *R. Seban*[3], *H. Tissot*[4], *J. Fouque*[5], *F. Coussy*[6], *D. Bello Roufai*[6], *D. Loirat*[7], *S. Rafie*[2], *A. Cernat*[8], *L. Djerroudi*[8], *J. Sauge*[8], *A. Vincent-Salomon*[8], *F. Bidard*[6], *F. Mechta-Grigoriou*[2], *I. Buvat*[1];
[1]Institut Curie, Inserm, Orsay, FRANCE, [2]Unité Chimie Biologie des Cancers, Institut Curie, PSL University, Inserm, CNRS, Paris, FRANCE, [3]Dpt of Nuclear Medicine, Institut Curie, Saint-Cloud, FRANCE, [4]Dpt of Nuclear Medicine, Institut Curie, Paris, FRANCE, [5]Dpt of Pharmacy, Institut Curie, Saint-Cloud, FRANCE, [6]Dpt of Medical Oncology, Institut Curie, Saint-Cloud, FRANCE, [7]Dpt of Medical Oncology, Institut Curie, Paris, FRANCE, [8]Department of Diagnostic and Theranostic Medicine, Institut Curie, PSL University, Paris, FRANCE.

Aim/Introduction: Fibroblast Activation Proteins (FAP) are detected at the surface of Cancer Associated Fibroblasts (CAF) in many cancer types of poor prognosis, including Triple Negative Breast Cancer (TNBC). As part of the Skyline trial (NCT06175390), we are exploring the expression of FAP using a multi-scale imaging approach, involving [68Ga]FAPI-46 PET/CT, histopathology and spatial transcriptomics, to shed new lights into the role of FAP in early and advanced TNBC. ***Materials and Methods:*** Skyline is an ongoing prospective phase 2 trial enrolling 160 TNBC patients to explore the use of an anti-TIGIT therapy combined with anti PD-L1 and chemotherapy in patients undergoing neoadjuvant therapy or first line treatment. All patients undergo an [18F]FDG and [68Ga] FAPI-46 PET/CT before treatment and after 2 cycles. PET-guided biopsies are performed from which immunohistochemistry (IHC) is used to rate the expression of FAP, ANTXR1 and SDC1, which are three markers of immunosuppressive FAP-positive CAF denoted as CAF-S1 [1]. Spatial transcriptomics is also performed for a subsample of subjects to identify CAF subpopulations. SUVmax and Total Tumor Signal (TTS) defined as mean SUV multiplied by the tumor volume on the corresponding PET images were calculated in the biopsied lesions and compared with the FAP, ANTXR1 and SDC1 h-scores from IHC and with the CAF subpopulations identified using spatial transcriptomics. ***Results:*** 50 patients have already been enrolled and 77 biopsied lesions have been analyzed, including 23 with spatial transcriptomic results. For these lesions, the Pearson correlation coefficients (rho) between [68Ga]FAPI SUVmax and h-scores were 0.52 for FAP, 0.69 for ANTXR1 and 0.59 for SDC1. The correlations between [68Ga]FAPI TTS and h-scores were 0.52 for FAP, 0.63 for ANTXR1 and 0.61 for SDC1. There was also a substantial correlation between [18F]FDG SUVmax and h-scores: 0.43 for FAP, 0.53 for ANTXR1 and 0.31 for SDC1 and between [18F]FDG TTS (=Total Lesion Glycolysis) and h-scores: 0.51 for FAP, 0.60 for ANTXR1 and 0.47 for SDC1, confirming that CAF-S1 are located close to tumor cells. Spatial transcriptomics showed that [68Ga]FAPI SUVmax and TTS best correlated with myofibroblastic (my) CAF involved in immunosuppression as opposed to inflammatory CAF (iCAF) (rho= 0.52 with myCAF against -0.33 with iCAF for SUVmax ; rho=0.55 with myCAF against

-0.36 with iCAF for TTS). ***Conclusion:*** [68Ga]FAPI-46 PET signal primary reflects the expression of immunosuppressive CAF and might play a key role for identifying TNBC patients who will benefit most from immunotherapy. ***References:*** Peltier et al. Semin Cancer Biol 2022:262-272.

EP-0298

A study to evaluate the heterogeneity of estrogenreceptor (ER) expression in breast cancer using^{18}F Fluoroestradiol (FES) and^{18}F FDG PET/CT

A. Mahalik, *N. Kundu, A. Roy, M. Tripathi, R. Kumar;*
All India Institute of Medical Sciences, New Delhi, INDIA.

Aim/Introduction: In-vivo assessment of estrogen receptor plays an important role in assessing the tumor heterogeneity and to select patients for hormonal therapy. The main objective of our study was to evaluate the role ofFES PET in estrogen receptor positive invasive ductal breast carcinoma patients and to compare with FDG PET/CT. ***Materials and Methods:*** A prospective cross sectional pilot study done at a tertiary care institute in India from July 2021 to December 2022. Patients with invasive ductal carcinoma and ER positive immunophenotype were included in the study. Patients with age </=18years and who didn't give consent were excluded. The study was conducted after obtaining institutional ethical committee approval. ^{18}F- FES PET/CT and ^{18}F-FDG PET/CT were performed with 7 to 10 days interval on dedicated PET/CT scanner (GE Discovery710). Visual analysis of ^{18}F-FES and ^{18}F-FDG PET/CT studies were performed by two experienced Nuclear Medicine physicians. Any uptake above background intensity was interpreted as positive.Lesions were analysed under four groups; primary, lymph node, osseous metastases and soft tissue metastases. Wilcoxon signed-rank tests were used to assess difference in distribution of number of lesions between 18F-FES and 18F- FDG PET/CT. p value <0.05 were considered significant. ***Results:*** A total of 15 patients were included in the study. Primary breast lesions were evaluated in eleven patients (four patients underwent mastectomy). Ten patients had lymph nodal metastases. Five patients had osseous metastases. Six patients had soft tissue metastases. In primary breast lesion group, alleleven patients (100%) showed 18F FDG avidity whereas only five (45.5%) showed 18F FES avidity (p=0.014). In lymph node group, ten patients showed 18F FDG avidity, but only five patients (50%) showed 18F FES avidity (p =0.034). In osseous metastases group, all seven patients showed 18F FDG avidity; but only five patients (71.4%) showed 18F FES avidity (p =1). In soft tissue metastases group, all six patients showed 18F FDG; only three patients (50%) showed 18F FES avidity (p value 0.02). In per lesion analysis out of total 82 evaluable lesions, FDGdetected 78(95.12%) lesions and FES detected 51(62.19%) lesions (P value <0.01). ***Conclusion:*** FES and FDG uptake in ER positive invasive ductal cancer patients is variable mainly due to tumor heterogeneity. Thus FES can play a main role in-vivo assessment of ER expression in local as well as metastatic sites thereby helping in selecting appropriate treatment. However, studies with large sample size with stringent selection criteria is needed to confirm our findings.

EP-0299

Outperforming FDG? Evaluating the Diagnostic Superiority of ^{68}Ga-FAPI-46 PET/CT in Breast Cancer Staging

S. Patel, *P. Sundaram, P. Subramanyam;*
Amrita Institute of Medical Sciences & Research Center, Kochi, INDIA.

Aim/Introduction: To compare the diagnostic performance of ^{68}Ga-FAPI-46 PET/CT and ^{18}F-FDG PET/CT in the initial staging of breast cancer; to assess metabolic parameters (SUV, MTV) of primary and metastatic lesions; and to evaluate their correlation with histopathological and IHC markers (ER, PR, HER2, Ki-67). ***Materials and Methods:*** A diagnostic cohort study was conducted from 2022 to 2025 with ethical approval. 63 newly diagnosed breast cancer patients were included. Inclusion Criteria 63: FNAC-confirmed breast cancer cases undergoing initial ^{18}F-FDG PET/CT. Exclusion Criteria: History of prior/synchronous malignancy, treatment, pregnancy, or unwillingness to complete both scans. Imaging Protocol: Day 1: Patients fasted ≥6 hours, injected with 0.1 mCi/kg of ^{18}F-FDG, and scanned after 60 minutes on a 16-slice PET/CT with contrast. Day 2: Patients were injected with 2-3 mCi of ^{68}Ga-FAPI and scanned 30 minutes post-injection using the same system. ***Results:*** FAPI PET/CT showed superior tumor delineation in 55 patients, detecting 4 retroareolar and 3 multifocal lesions missed by FDG. Quantitatively, FAPI showed significantly higher SUVmax (13.2 ± 5.4 vs 8.3 ± 4.2; p < 0.001), TBR (10.4 ± 3.4 vs 8.3 ± 3.6; p < 0.001), and larger MTV. Sensitivity (98.55% vs 95.52%), NPV (98.59% vs 95.89%), and accuracy (97.87% vs 96.40%) were higher for FAPI; specificity was identical (97.22%). Histologically, invasive lobular carcinoma showed SUVmax of 11.8 (FAPI) vs 3.9 (FDG); invasive ductal carcinoma: 14.1 vs 9.8. FAPI showed superior uptake across all IHC subtypes except TNBC and high-grade Luminal B, where FDG was better in 6 cases. FAPI had no significant correlation with Ki-67 or grade, unlike FDG. FAPI detected 8 satellite nodules and showed better axillary node assessment (289 vs 218 nodes), with higher SUVmax (11.4 vs 8.1) and greater sensitivity (90.4% vs 83.6%) and accuracy (94.1% vs 84.8%). For internal mammary nodes, FAPI outperformed FDG in sensitivity (94.7% vs 77.3%) and accuracy (94.0% vs 78.0%). Distant metastasis detection was better with FAPI in skeletal (287 vs 194), hepatic (28 vs 27), pleural, muscular, and pulmonary lesions with higher SUV Max values. ***Conclusion:*** ^{68}Ga-FAPI PET/CT demonstrated superior diagnostic performance over ^{18}F-FDG PET/CT in staging breast cancer, with better lesion conspicuity, higher uptake metrics, and improved detection across various sites, particularly in low-FDG-avid subtypes.

EP-0300

Diagnostic Performance of ^{68}Ga-FAPI-46 PET/CT in Metastatic Breast Cancer: A Prospective Comparative Pilot Study

Y. Khandelwal, *B. Jain, P. Baberwal, S. Rastogi, S. Shamim;*
AIIMS, New Delhi, INDIA.

Aim/Introduction: Fibroblast activation protein (FAP) is overexpressed in cancer-associated fibroblasts (CAFs) within the tumor microenvironment of many solid tumors, including breast carcinoma. ^{68}Ga-FAPI-46, a novel radiotracer targeting FAP, has shown encouraging results in oncologic imaging due to its high tumor-to-background contrast and low physiological uptake. This prospective study aimed to evaluate the diagnostic utility of ^{68}Ga-FAPI-46 PET/CT in patients with metastatic breast cancer and compare its imaging performance to that of the standard ^{18}F-FDG PET/CT. ***Materials and Methods:*** Twenty patients (median age: 52 years; range: 34-71) with histologically confirmed metastatic breast cancer were enrolled in this single-center pilot study. All participants underwent both ^{18}F-FDG PET/CT and ^{68}Ga-FAPI-46 PET/CT within one week, using either Siemens Biograph mCT or GE Discovery 710 scanners. Image interpretation included both visual and semi-quantitative assessment. For each modality, the number and distribution of metastatic lesions were recorded, alongside maximum standardized uptake values (SUVmax) and tumor-to-background ratios (TBR). Statistical comparison between the two imaging modalities was conducted using the Wilcoxon signed-rank test for SUVmax and TBR, and the McNemar test for lesion detection rate. ***Results:*** ^{68}Ga-FAPI-46 PET/CT detected a total of 145 metastatic lesions, compared to 116 lesions identified on ^{18}F-FDG PET/CT. FAPI imaging showed superior detection particularly in bone and liver metastases. While the mean SUVmax was slightly higher for ^{68}Ga-FAPI-46 (6.2 ± 2.4) compared to ^{18}F-FDG (5.8 ± 2.1), this difference was not statistically significant (p > 0.05). However, TBRs were significantly elevated in ^{68}Ga-FAPI-46 PET/CT images (p < 0.01). Subtype-specific analysis suggested improved

imaging performance of FAPI in hormone receptor-positive, HER2-negative tumors. ***Conclusion:*** This preliminary study demonstrates that ^{68}Ga-FAPI-46 PET/CT offers excellent diagnostic potential in the evaluation of metastatic breast cancer, with higher lesion detection and superior contrast in certain molecular subtypes and metastatic sites. The enhanced lesion visibility and favorable biodistribution profile of ^{68}Ga-FAPI-46 suggest its utility as a complementary imaging modality to ^{18}F-FDG, particularly in FDG-inconspicuous disease. ***References:*** Li T, Zhang J, Yan Y, Tan M, Chen Y. Applications of FAPI PET/CT in the diagnosis and treatment of breast and the most common gynecologic malignancies: a literature review. Front Oncol. 2024 Mar 5;14:1358070. doi: 10.3389/fonc.2024.1358070. PMID: 38505595; PMCID: PMC10949888.

EP-0301

Prospective Evaluation of ^{68}Ga-FAPi PET/CT Imaging to guide ^{177}Lu-FAPi therapy in patients with metastatic Breast Cancer (mBC)

N. Kumar, *S. Shamim, G. Arora, A. Batra;*
All India Institute of Medical Sciences, New Delhi, INDIA.

Aim/Introduction: Fibroblast Activation Protein (FAP), a type II membrane-bound glycoprotein, is selectively overexpressed on cancer-associated fibroblasts (CAFs) within the tumor microenvironment of various solid tumors, including breast carcinoma. This characteristic has made FAP an attractive theranostic target for in mBC patients. Thus, the present prospective study is designed to evaluate the role of ^{68}Ga-FAPi PET/CT imaging in identifying suitable candidates for ^{177}Lu-FAPi therapy among mBC patients who have exhausted conventional treatment modalities, thereby exploring a new avenue for precision-targeted radioligand therapy in this difficult-to-treat population. ***Materials and Methods:*** All histopathologically proven mBC patients underwent ^{68}Ga-FAPi-46 PET/CT before recruited for ^{177}Lu-FAPi therapy to see expression of FAPi-46 in the treating lesions. Acquired whole body PET/CTs were analyzed both visually and quantitatively. The patients showing good uptake [tumor to background (TBR) with respect to liver >3] on ^{68}Ga-FAPi scan were suitable for ^{177}Lu-FAPi therapy. ***Results:*** A total of 12 mBC patients, age ranged from 33 to 65 years (Median age = 42 years) were recruited for 68Ga-FAPi -46 PET/CT scan. Of 12 mBC patients, 4/12 patients (33%) were triple-negative (TNBC), while others exhibited varying expressions of ER, PR, and HER2neu, indicating differences in tumor biology and aggressiveness. Nine patients (75%) had high Ki-67 indices (60-95%), reflecting active disease proliferation, except for 3 patients (25%) with Ki-67 levels below 40%. All patients demonstrated significant heterogeneity in SUVmax values of primary lesion and metastatic sites. Based on the imaging findings, 11 out of 12 patients demonstrated high FAP expression (SUVmax >4.0, TBR with respect to liver >3.0) and were potential candidates for ^{177}Lu-FAPi radioligand therapy. The mean value of SUVmax of primary lesion and metastatic sites was 6.16 ± 3.0 (range 3.3-14.11), SUVmax of liver = 0.84 ± 0.39 (range 0.4-1.6) and tumor-to-background ratios (TBR) with respect to liver was 8.07 ± 2.97 (range 2.54-12.71). Higher uptake was observed in patients with TNBC, HER2-positive resistant disease, and those with high Ki-67 indices. Tracer avidity was evident across metastatic sites, including the lungs, liver, bones, brain, and lymph nodes. ***Conclusion:*** The high tumor-to-background ratios and SUVmax values observed, particularly in patients with elevated Ki-67 indices, support the potential utility of FAPi-based imaging in identifying suitable candidates for targeted ^{177}Lu-FAPi radioligand therapy.

EP-0302

[^{18}F]PSMA-1007 and [^{18}F]FDG PET/CT in patients with triple-negative breast cancer: a head-to-head comparative assessment study

T. Lazutina, *A. Khalimon, S. Urtaev, A. Lokhova, M. Khodzhibekova, D. Khodakova, G. Khamadeeva, I. Pylova, A. Leontev;*
P. Hertsen Moscow Oncology Research Institute - branch of the National Medical Research Radiological Centre of the Ministry of Health of the Russian Federation, Moscow, RUSSIAN FEDERATION.

Aim/Introduction: This study aimed to compare [^{18}F]FDG and [^{18}F]PSMA-1007 PET/CT head-to-head in patients with triple-negative breast cancer (TNBC). ***Materials and Methods:*** This prospective single-center study included 11 patients with histologically confirmed TNBC: 2 at initial staging, 6 with recurrence after treatment, and 3 with disease progression during therapy. [^{18}F]FDG and [^{18}F]PSMA-1007 PET/CT were performed within a 2-13 day interval between the studies. [^{18}F]FDG PET/CT included contrast-enhancement CT (CECT) from vertex to mid-thigh. For each tracer, the number and localization of detected lesions were determined using PET alone, PET/non-contrast CT (NCCT), and PET/CECT. Visual and semi-quantitative assessments of tracer uptake in tumor lesions were performed. SUVmax was measured for target lesions ≥15mm. ***Results:*** A total of 144 lesions were identified: chest wall (n=11), lymph nodes (n=58), bones (n=48), lungs (n=17), liver (n=7), peritoneum (n=2), brain (n=1). Concordant lesions between [^{18}F]FDG and [^{18}F]PSMA-1007 were found in 77.1% (n=111) using PET alone, in 86.8% (n=125) using PET/NCCT, in 93.8% (n=135) using PET/CECT. Nine discordant lesions (6.3%) were observed in four patients: 6 (66.7%) - using [^{18}F]PSMA-1007 PET (only bone lesions), 3 (33,3%) - using [^{18}F]FDG PET (only lymph nodes). Higher [^{18}F]FDG uptake was observed in 81 lesions (73%) across 10 patients: chest wall (n=10), lymph nodes (n=30), bones (n=32), lungs (n=8), peritoneum (n=1). [^{18}F]PSMA-1007 uptake predominated in 25 lesions (22.5%) across 6 patients: chest wall (n=1), lymph nodes (n=13), bones (n=3), lungs (n=6), liver (n=2). Comparable uptake of both tracers was noted in 5 lesions (4.5%) across 4 patients: lymph nodes (n=4), bones (n=1). 72 target lesions (50%) were identified. The median SUVmax for [^{18}F]FDG and [^{18}F]PSMA-1007 were as follows: for all lesions - 5.9[3.9;8.3] and 2.9[2.1;4.7]; for chest wall lesions - 6.8[4.4;9.5] and 2.1[1.5;2.9],(p=0.001); for lymph nodes - 5.2[4.6;6.95] and 3.0[2.2;5.6],(p=0.007); for bone lesions - 7.4[6.2;11.0] and 3.2[2.6;5.1],(p<0.0001); for lung lesions - 3.4[2.2;5.5] and 2.9[1.6;4.6],(p=0.535); for liver lesions - 7.6[6.0;9.6] and 9.5[8.6;10.4]. Total [^{18}F]PSMA-1007 uptake predominated in two patients, while [^{18}F]FDG uptake predominated in eight patients, one patient showed comparable uptake of the tracers across lesions. No target lesions with [^{18}F]PSMA-1007 SUVmax≥10.0 were observed. ***Conclusion:*** The additional use of CECT allows for an increase in the number of tumor lesions detected by both [^{18}F]FDG and [^{18}F]PSMA-1007 PET/CT to similar values. In general, the level of lesional [^{18}F]FDG uptake was higher than that of [^{18}F]PSMA-1007 uptake. No patient demonstrated PSMA-ligand uptake that met the current criteria for PSMA-positivity for radioligand therapy.

EP-0303

Evaluation of Treatment Response Using Post-^{131}I-MIBG Scintigraphy in Patients with unresectable or metastatic PPGL: Correlation with Prognosis and Clinical Factors

J. Takenaka[1,2,3], *S. Watanabe*[1,2,4], *T. Abe*[5], *S. Takeuchi*[6,7], *K. Hirata*[1,2,8], *R. Kimura*[1,9], *H. Ishii*[1,2], *N. Wakabayashi*[1,2], *M. Majigsuren*[1,10], *K. Kudo*[1,8,9];
[1]*Department of Diagnostic Imaging, Graduate School of Medicine, Hokkaido University, Sapporo, JAPAN,* [2]*Department of Nuclear Medicine, Hokkaido University Hospital, Sapporo, JAPAN,* [3]*Comprehensive Heart Failure Center, University Hospital Würzburg, Würzburg, GERMANY,* [4]*Global Center for Biomedical Science and Engineering, Faculty of Medicine, Hokkaido University, Sapporo, JAPAN,* [5]*Department of Renal and Genitourinary surgery, Hokkaido University Graduate School of Medicine, Sapporo, JAPAN,* [6]*Department of Medical Oncology, Faculty of Medicine and Graduate School of Medicine, Hokkaido University, Sapporo, JAPAN,* [7]*Center of Neuroendocrine Neoplasms, Hokkaido University Hospital, Sapporo, JAPAN,* [8]*Medical AI Research and Development Center, Hokkaido*

University Hospital, Sapporo, JAPAN, [9]Department of Diagnostic and Interventional Radiology, Hokkaido University Hospital, Sapporo, JAPAN, [10]Department of Radiology, Diagnostic Imaging Center, Second State Central Hospital, Ulaanbaatar, MONGOLIA.

Aim/Introduction: Pheochromocytomas and paragangliomas (PPGLs) are rare catecholamine-producing neuroendocrine tumors. Approximately 10-30% of PPGLs are unresectable or metastatic (umPPGLs), leading to both tumor- and catecholamine-related morbidity and mortality. Radionuclide therapy using ^{131}I-metaiodobenzylguanidine (^{131}I-MIBG) is an established treatment for umPPGLs, with demonstrated reductions in tumor burden and catecholamine levels. Post-therapy scintigraphy (PTS) using administered ^{131}I-MIBG enables imaging without additional tracers, but its role in evaluating therapeutic response remains uncertain. This study aimed to investigate the relationship between treatment response assessed by PTS and changes in tumor size, prognosis, and clinical factors. ***Materials and Methods:*** We retrospectively reviewed patients who underwent multiple sessions of ^{131}I-MIBG therapy at our institution between 2001 and 2024. The first post-therapy scintigraphy was compared with the latest post-therapy scintigraphy among a series of consecutive treatments administered within a one-year interval. Patients without MIBG-avid lesions were excluded. Visual assessment of PTS was performed by J.T. (a radiologist and nuclear medicine physician) and classified as partial response (PR_{PTS}), stable disease (SD_{PTS}), or progressive disease (PD_{PTS}). Compared to the first PTS, the latest PTS was categorized as PR_{PTS} if lesion uptake had decreased, SD_{PTS} if there was no change, and PD_{PTS} if uptake had increased. Tumor diameter was measured on CT scans obtained closest to each scintigraphy, the patients were categorized to PR_{CT}, SD_{CT}, PD_{CT} according to RECIST criteria. Concordance between PTS and CT responses was assessed using the kappa coefficient. Treatment responses evaluated by PTS were compared with overall survival since the first ^{131}I-MIBG therapy using the log-rank test, and with clinical factors using univariate logistic regression. ***Results:*** Twenty-one patients (age 24-69 years; 12 females) were included. PTS showed PR_{PTS} in 14 (66.7%), SD_{PTS} in 6 (28.6%), and PD_{PTS} in 1 (4.8%) patient. CT showed PR_{CT} in 6 (28.6%), SD_{CT} in 14 (66.7%), and PD_{CT} in 1 (4.8%). The concordance between PTS and CT was moderate ($\kappa = 0.382$). When patients were divided into PR and non-PR groups, overall survival did not significantly differ between PR and non-PR groups based on either PTS ($p = 0.65$) or CT ($p = 0.66$). The PR_{PTS} group was significantly associated with lower urinary dopamine levels ($p = 0.04$), absence of prior chemotherapy ($p = 0.04$), and the presence of lymph node or peritoneal lesions ($p = 0.001$). ***Conclusion:*** PTS-based treatment response does not correlate with prognosis and may have limited utility in assessing disease status in umPPGL patients.

EP-0304

Progression and characterization of intracardiac metastases from gastroenteropancreatic neuroendocrine tumors.

I. Scalia[1], *A. F. Yang*[2], *F. E. Abdelfattah*[1], *O. H. Ibrahim*[1], *J. M. Farina*[1], *R. Arsanjani*[1], *C. Ayoub*[1], *M. Yang*[1];
[1]*Mayo Clinic Arizona, Phoenix, AZ, UNITED STATES OF AMERICA,* [2]*Wayne State Medical School, Detroit, MI, UNITED STATES OF AMERICA.*

Aim/Introduction: Cardiac metastases from primary gastroenteropancreatic neuroendocrine tumors (NET) are rare and not well described. Significantly, little is known about the rate of progression or therapeutic effect of targeted therapies on cardiac metastases. ***Materials and Methods:*** All adult patients with primary NETs from three tertiary institutions between 2011 and 2023 were reviewed. Confirmation of cardiac metastatic involvement was determined on ^{68}Ga-DOTATATE positron emission tomography (PET), and patients were required to have at least one follow-up ^{68}Ga-DOTATATE PET scan. The maximal dimension and maximal standard uptake value (SUV_{max}) of lesions were measured. If patients had multiple intracardiac lesions, the largest was recorded. Patients were reviewed for baseline characteristics and treatment with Lu-177 DOTATATE. ***Results:*** Overall, 23 patients (M: F = 14: 9) with 32 intracardiac metastases had serial ^{68}Ga-DOTATATE PET imaging. The mean age of this cohort was 63.8 ± 10.8 years. The intracardiac metastases were located in the ventricular myocardium (43.5%), followed by the pericardium (30.4%) and the interventricular septum (26.1%). The median time between initial and follow-up ^{68}Ga-DOTATATE PET imaging was 2.2 [IQR 1.1-4.9] years. There was no significant difference in the median maximal dimension of cardiac metastases on initial imaging compared to follow-up imaging; 12.0mm [IQR 8.0-16.0] vs 11.0mm [IQR 9.0-15.0], p=0.322 (Figure A). Similarly, there was no significant change in SUV_{max} on serial PET-DOTATATE scans; 7.8 [IQR 3.9-14.7] compared to 7.1 [IQR 4.3-14.6], p=0.456 (Figure B). Within the cohort, 11 (47.8%) patients received Lu-177 DOTATATE therapy. There was no significant difference in age between patients who did and did not receive Lu-117 DOTATATE (64.1 years vs 63.5 years, p=0.896). Of the patients who received Lu-177 DOTATATE therapy, there was a median reduction in metastasis dimension of 1.0mm [IQR -3.0-0.0] on serial imaging (Figure C), and only four patients (36.4%) observed progression in metastasis burden (characterized as increase in either metastatic dimension or SUV_{max}). In comparison, there was a median increase in median metastatic dimension by 0.5mm [IQR -2.0-2.0] in patients who did not receive Lu-177 therapy, and 10 patients (83.3%) had progression of either diameter or SUV_{max}. ***Conclusion:*** Over approximately two years follow-up, intracardiac metastases from primary gastroenteropancreatic NETs did not demonstrate significant progression in either maximal dimension or SUVmax. Patients who received Lu-177 DOTATATE therapy were observed to have some regression in metastatic dimension and were less likely to have progression of intracardiac metastases compared to those who did not receive Lu-177 DOTATATE therapy.

EP-0305

Pancreatic Metastases in Small Intestinal Neuroendocrine Tumors: An Underestimated Occurrence?

Q. Wang[1], *A. Rinke*[2], *F. Eilsberger*[1], *M. Luster*[1], *B. Hooshyar Yousefi*[1], *D. Librizzi*[1,3];
[1]*Department of Nuclear Medicine, University Hospital Marburg, Philipps University of Marburg, Marburg, GERMANY,* [2]*Department of Internal Medicine, Division of Gastroenterology and Endocrinology, University Hospital Marburg, Philipps University Marburg, Marburg, GERMANY,* [3]*Department of Nuclear Medicine, University Hospital OWL, Evangelical Hospital Bethel, Bielefeld, GERMANY.*

Aim/Introduction: Small intestinal neuroendocrine tumors (siNETs) are among the most common malignancies of the small intestine; however, their pancreatic metastases are rare. [^{68}Ga]Ga-DOTATOC, a well-established diagnostic tool for neuroendocrine tumors, has been utilized in clinical practice for over two decades. Despite its widespread use, a standardized SUVmax reference for pancreatic metastases has not yet been established. Pancreatic metastases are difficult to diagnose and may be underdiagnosed. This study aims to provide an SUVmax reference value for the clinical diagnosis of pancreatic metastases by measuring the SUVmax of pancreatic metastatic lesions in siNET patients, and assess the potential under-diagnosis of pancreatic metastases. ***Materials and Methods:*** A retrospective study was conducted, analyzing patient-based SUVmax data for Group A and Group B. Group A: Includes patients with pancreatic metastatic lesions confirmed by pathology, or clinical follow-up including MRI, physician review, or repeated [^{68}Ga]Ga-DOTATOC examinations. The number of patients in this group is 10. Group B: Includes patients with pancreatic metastatic lesions reported by a single [^{68}Ga]Ga-DOTATOC examination without further validation. This group contains 7 patients. SUVmax mean values were calculated using bootstrap resampling, extended to 10,000 data points. Comparisons were made between the SUVmax mean of Groups A and B, estimating the difference between the two. Group C:

Secondary assessment by the nuclear medicine specialist to assess possible missed diagnoses. ***Results:*** Group A: SUVmax mean = 24.4 (95% CI: 16.50, 34.00). Group B: SUVmax mean = 20.8 (95% CI: 14.60, 27.91). While Group A showed a higher SUVmax mean than Group B, the overlapping 95% confidence intervals indicated no statistically significant difference. The mean difference in SUVmax between Groups A and B was 3.6 (95% CI: -6.97, 15.36), confirming no significant difference. Pancreatic metastasis are highly suspected from SUVmax, although patients in group B have not been reconfirmed by other methods. Group C: Expert Secondary Evaluation. An experienced nuclear medicine specialist re-reviewed the [^{68}Ga]Ga-DOTATOC images that were first reported as negative for pancreatic metastases and identified 31 new cases that were highly suspicious to be positive for pancreatic metastases. ***Conclusion:*** This study offers validated SUVmax reference values for the diagnosis of pancreatic metastases from small intestinal neuroendocrine tumors, a rare metastatic site. The incidence of pancreatic metastases from small intestinal neuroendocrine tumors may be underestimated and further studies are needed to confirm this.

EP-0306

DOTATOC PET Response Under MKI in Advanced Neuroendocrine Tumors: Good or Bad News?

G. Rovera[1], *I. Pavaluta*[1], *M. Longo*[1], *H. Noamen*[1], *Y. Menu*[2], *J. Hadoux*[3], *L. Lamartina*[3], *M. Faron*[4], *S. Moog*[3], *M. Ducreux*[5], *E. Baudin*[3], *D. Deandreis*[1];
[1]*Nuclear Medicine Department, Gustave Roussy, University Paris Saclay, Villejuif, FRANCE,* [2]*Department of Radiology, Gustave Roussy, University Paris Saclay, Villejuif, FRANCE,* [3]*Department of Imaging, Endocrine Oncology Unit, Gustave Roussy, University Paris Saclay, Villejuif, FRANCE,* [4]*Sarcoma Unit, Gustave Roussy Cancer Campus, Villejuif, FRANCE,* [5]*Service d'Oncologie digestive, Institut Gustave Roussy, Villejuif, FRANCE.*

Aim/Introduction: Treatment of pancreatic neuroendocrine tumors (pNETs) relies on several options: somatostatin analogs, chemotherapy, multikinase inhibitors (MKIs), and peptide receptor radionuclide therapy (PRRT) with 177Lu-DOTATATE. Among these options, SSTR PET is used to monitor response and to select patients for PRRT. The aim of this study is to report the impact of lenvatinib treatment on somatostatin receptor expression as measured by 68Ga-DOTATOC PET in patients with metastatic pancreatic NETs. ***Materials and Methods:*** A total of 20 patients treated with lenvatinib were retrospectively evaluated. Patients were selected according to the following criteria: 1) confirmed metastatic pancreatic NET, 2) lenvatinib treatment administration, 3) DOTATOC PET performed within 12 months before starting treatment and at least once during or at the end of lenvatinib treatment, and 4) CT scans or MRI performed at the same time as the PET evaluation. Response was assessed according to RECIST-1.1 criteria. Semiquantitative PET analysis (SUVmax) was performed on the same target lesions considered for RECIST-1.1 using dedicated software (Syngo.via, Siemens). ***Results:*** Six patients (median age 55 years, range: 48-59 years, 2F, 4M) with pancreatic NET (5 G2 and 1 G3) who received lenvatinib treatment were finally selected. On-treatment DOTATOC PET was performed at 1 month (n=1), 3 months (n=2), 6 months (n=1), and 12 months (n=2) after treatment initiation. A total of 17 target lesions (12 liver lesions and 5 abdominal lymph nodes) were analyzed. Median baseline SUVmax was 33.4 (range: 7.3-97.6). On 68Ga-DOTATOC PET, ΔSUVmax was -100% at 1 month (patient 1) with RECIST 1.1 response of -42% (PR); -80% and -88% at 3 months (patients 2 and 3) with RECIST 1.1 responses of -2% and -27% (SD), respectively; -41.5% at 6 months (patient 4) with RECIST 1.1 response of -2% (SD); and -61% and -87.5% at 12 months with RECIST 1.1 responses of -2% and -68% (SD and PR, respectively; patients 5 and 6). Complete or near-complete negativation of somatostatin receptor expression in vivo was observed in 5 patients despite stable or only partial response by RECIST 1.1 criteria. These five patients remain under treatment without evidence of disease progression. ***Conclusion:*** These preliminary results suggest that, under MKI treatment, the loss of uptake to SSTR PET without RECIST 1.1 complete response occur. This phenomenon may theoretically affect patients eligibility for PRRT as next line treatment. A prospective study is planned to better understand the mechanism and prognostic impact of this finding (Tolerate study).

EP-0307

Prognostic Value of [^{68}Ga]Ga-SSA PET/CT After [^{177}Lu]Lu-DOTATATE Therapy in Neuroendocrine Tumours

A. Bagán-Trejo[1], *J. L. Vercher-Conejero*[1], *J. J. Martín-Marcuartu*[1], *G. Reynés-Llompart*[2], *M. Tormo-Ratera*[1], *J. C. Ruffinelli*[3], *D. Rodríguez-Puig*[4], *C. García-Alcober*[4], *B. Hervás-Sanz*[1], *D. J. Tamayo-Ossa*[1], *M. Cortés-Romera*[1];
[1]*Nuclear Medicine-PET (IDI) Department, Hospital Universitari de Bellvitge-IDIBELL, L'Hospitalet de Llobregat, SPAIN,* [2]*Medical Physics and Radiation Protection Department, Institut Català d'Oncologia, L'Hospitalet de Llobregat, SPAIN,* [3]*Oncology Department, Institut Català d'Oncologia, L'Hospitalet de Llobregat, SPAIN,* [4]*Radiopharmacy Department, Hospital Universitari de Bellvitge-IDIBELL, L'Hospitalet de Llobregat, SPAIN.*

Aim/Introduction: Peptide receptor radionuclide therapy (PRRT) using [^{177}Lu]Lu-DOTATATE has been widely used as an effective treatment for neuroendocrine tumours (NETs), particularly gastroenteropancreatic NETs (GEP-NETs). Assessing therapeutic effectiveness early is crucial to guide subsequent clinical management decisions. This study aimed to evaluate the prognostic value of the first response assessment using PET/CT with [^{68}Ga]Ga-somatostatin receptor analogues ([^{68}Ga]Ga-SSA) in predicting progression-free survival (PFS) and overall survival (OS) following PRRT. ***Materials and Methods:*** 96 patients were included in the study, with the majority diagnosed with GEP-NETs (83%). Other NET subtypes included pheochromocytomas/paragangliomas (7%) and lung carcinoids (5%). Most patients (83%) received four cycles of [^{177}Lu]Lu-DOTATATE, spaced 8 weeks apart. Clinical responses were assessed based on symptom improvement, with biochemical response defined as a decrease in chromogranin A or 5-Hydroxyndoleacetic acid (5-HIAA) levels by more than 50%. Adverse effects were monitored via standard criteria such as CTCAE, including haematological (anaemia, leukopenia, thrombocytopenia, or pancytopenia), gastrointestinal (nausea/vomiting, diarrhoea/constipation), and renal (glomerular filtrate and creatinine) toxicities. PET/CT scans with [^{68}Ga]Ga-SSA were performed 3 months after the final PRRT cycle, categorising outcomes into partial response (PR), stable disease (SD), and progressive disease (PD). Kaplan-Meier curves were used to analyse PFS and OS, and Cox regression was employed to evaluate the hazard ratio (HR) for response. ***Results:*** A favourable clinical response was observed in 49 patients (51%), with 16% showing a positive biochemical response. Observed adverse effects included gastrointestinal issues (25%), haematological (36%), and renal (3%) toxicity. In relation to PET/CT scans, PR was observed in 44% of patients; 42% showed SD; and 13% had PD. Overall survival was significantly improved in patients achieving PR or SD on PET/CT compared to PD (median OS: 53.17 vs. 8.5 months; p<0.0001). Progression-free survival also differed significantly (median PFS: 31 vs. 5.5 months; p<0.0001). Multivariate Cox regression identified PET/CT response as a strong predictor (HR=22.61 for OS, HR=12.38 for PFS; p<0.001). ***Conclusion:*** Evaluation with [^{68}Ga]Ga-SSA PET/CT after treatment with PRRT for NETs significantly correlates with long-term clinical outcomes, providing significant information for assessing therapeutic effectiveness and anticipating disease trajectory. The response evaluation using [^{68}Ga]Ga-SSA PET/CT represents a robust prognostic biomarker, enabling better patient stratification, informed clinical decisions, and tailored therapeutic

approaches. Future prospective studies may help refine the timing and interpretation of such assessments and explore their role in adaptive treatment strategies.

EP-0308

Peptide receptor radionuclide therapy (PRRT) in high-grade neuroendocrine neoplasms: a systematic review and metanalysis

E. Zampella, *F. Volpe, L. Piscopo, V. Gaudieri, c. Nappi, V. Cantoni, R. Green, E. Caiazzo, A. Cuocolo, M. Klain;*
University Federico II, Naples, ITALY.

Aim/Introduction: In patients with neuroendocrine neoplasms (NEN), tumor's aggressiveness and prognosis are strongly associated to the tumor grading. Peptide receptor radionuclide therapy (PRRT) with 177Lu-DOTATATE is a well validated treatment in patients with G1 and G2 gastro-entero-pancreatic (GEP) NENs. Previous studies investigated the potential role of 177Lu-DOTATATE in patients with G3 GEP-NENs. However, the efficacy of PRRT in these patients remains to be fully addressed. We conducted a systematic review and meta-analysis to evaluate the efficacy of PRRT by 177Lu-DOTATATE in patients with high GEP-NENs. ***Materials and Methods:*** All clinical studies published up to March 2025, including patients with G3 GEP-NENs treated with 177Lu-DOTATATE, were identified based on systematic searches in the PubMed, Cochrane Library and Web of Science. We included all the studies where disease control rate (DCR) and disease response rate (DRR), according to RECIST criteria, were reported. Moreover, in order to evaluate the therapeutic efficacy of PRRT, progression free survival (PFS) and overall survival (OS) were also considered. ***Results:*** We identified 12 studies, including a total of 374 participants. According to RECIST criteria, the pooled effect was 63% (95% confidence interval (CI) 54-73%) for the DCR and 32% (95% CI 21-44%) for the DRR. The PFS and OS were considered in 9 studies, with a median follow-up of 29 months. The pooled PFS and OS resulted to be 13.88 [95% CI 10.33-18.64] and 29.95 [95% CI 19.8-45.3] months, respectively. ***Conclusion:*** For patients with high grade GEP-NENs, 177Lu-DOTATATE is promising treatment providing substantial disease control and response rates. Moreover, PRRT seems to be able to delay the progression of the disease, improving patient's outcome. However, further multicenter randomized controlled trials are needed in order to assess the safety and efficacy of PRRT in these patients.

EP-0309

Optimal scan time for [18F]SiTATE PET/CT imaging of patients with neuroendocrine tumors

R. Ebner, *F. Herr, M. Zacherl, F. Eckenweber, K. Klimek, J. Ricke, C. C. Cyran, R. A. Werner, G. T. Sheikh;*
University Hospital LMU Munich, Munich, GERMANY.

Aim/Introduction: The fluorine-18-labelled, somatostatin receptor (SSR)-targeting tracer [^{18}F]SiTATE is gaining momentum in clinical use as a promising alternative to commonly used gallium-68-labelled SSR-targeting compounds, demonstrating excellent image quality and clinical utility. Currently, imaging with SITATE-PET/CT is performed 90 minutes after tracer injection, complicating integration into a multi-tracer PET environment, in which most tracers are imaged 60 minutes after tracer injection. We therefore investigated whether comparable image quality and quantification can be achieved at other time points, that integrate better into clinical routine. ***Materials and Methods:*** Eight NET patients with histologically confirmed metastasized GEP-NET received a [18F]SiTATE-PET/CT (250 ± 66 MBq) with repeated emission scans 60-, 90-, and 120-minutes post-injection. SUVmax, SUVpeak and SUVmean was measured in visceral organs and a total of 49 SSR-positive lymph node, liver and bone and tumor-to-background ratios were calculated. Statistical comparison of tumor-to-background ratios across the three time points was performed. Additionally, scans were visually evaluated for clinically noticeable differences by four individual readers of different experience levels. ***Results:*** No significant differences in tumor-to-background ratios were observed across timepoints for liver (p=0.6613), lymph nodes (p=0.5413), bone (p=0.8478), or overall lesion assessment (p=0.7248). Post hoc multiple comparisons using Tukey's test revealed no significant differences between the time points, with p-values ranging from 0.5103 to 0.999. Individual readers did not report any relevant qualitative visual difference between the time points; all lesions could be clearly identified against the surrounding background. ***Conclusion:*** The results demonstrate a consistent tracer uptake pattern over time, with minimal variation in tumor-to-background contrast across different metastatic sites. Imaging at 60 minutes post-injection yields equivalent lesion detectability and quantitative contrast compared to later time points at 90 and 120 minutes. These findings underscore the clinical utility of early imaging with [^{18}F] SiTATE for NET patients, offering the potential to facilitate workflow and enhance patient comfort without sacrificing diagnostic accuracy.

EP-0310

[68Ga]68Ga-DOTANOC LAFOV PET/CT in NET: are HYPER and OSEM semiquantitative parameters comparable?

G. Bianciardi[1], *E. Fortunati*[2], *M. Di Franco*[1], *C. Malizia*[2], *M. Assenza*[3], *D. Campana*[4], *E. Andrini*[4], *E. Tabacchi*[2], *V. Allegri*[2], *S. Fanti*[1,2], *V. Ambrosini*[1,2];
[1]*Nuclear Medicine, Alma Mater Studiorum University of Bologna, Bologna, ITALY,* [2]*Nuclear Medicine, IRCCS Azienda Ospedaliero-Universitaria di Bologna, Bologna, ITALY,* [3]*Professional Development and Implementation of Research in Health Professional Unit, IRCCS Azienda Ospedaliero-Universitaria di Bologna, Bologna, ITALY,* [4]*Department of Medical and Surgical Sciences (DIMEC), Medical Oncology Unit, Alma Mater Studiorum-University of Bologna, IRCCS Azienda Ospedaliero-Universitaria di Bologna, Bologna, ITALY.*

Aim/Introduction: The introduction of long axial field-of-view (LAFOV) PET/CT has enabled significant improvements in visual image quality and increased sensitivity. It is well-known that different image reconstructions may impact both the visual-perceived overall image quality and the absolute values of functional semiquantitative PET parameters. HYPER is a bayesian penalized likelihood reconstruction algorithm which incorporates a pre-trained Computer Neural Network into the PET reconstruction to produce both high-contrast and low-noise PET images. Aim:to compare 68Ga-DOTANOC-PET/CT semiquantitative parameters obtained from the OSEM and HYPER reconstructions in NET patients. ***Materials and Methods:*** Among NET patients followed at the local Oncology Unit, those consequently imaged with 68Ga-DOTANOC uExplorer LAFOV PET/CT (October 2024-March 2025) were retrospectively included (mean injected dose [1.4±0.3MBq/kg]; acquisition time:5min). Images were reconstructed using both OSEM and HYPER. CNR ((⟦SUVmean⟧_ROI-⟦SUVmean⟧_background)/⟦SD⟧_(SUVmean background)) and SUVmax were measured in a maximum of 3 target lesions per-patient: the most avid lesion at any site >1cm (T); most avid liver lesion <1cm (t_L);the most avid extra-hepatic lesion <1cm (t). Wilcoxon-test and Bland-Altman test were used to compare SUVmax and CNR obtained from OSEM and HYPER in both the total number of paired target lesions and in each of the above-mentioned sub-categories (defined by lesions' dimensions and site). ***Results:*** Overall, 45 NET patients were included (primary tumour site: pancreas=21/45,47%;gastro-intestinal=18/45,40%; lung= 2/45,4%; other sites=4/45,9%).Indications to PET/CT were staging (7/45,16%), restaging (20/45,44%), follow-up (20/45,40%). PET was positive in 28/45(63%) and negative in 17/45(4%). A total of 40 target lesions were assessed: T=18, t_L=8, t=14. HYPER-SUVmax was higher than OSEM-SUVmax either when considering all target lesions (HYPERmedian=16.1vsOSEMmedian=14.4,p<0.01)

and within each target lesion's subgroup: T(33.1vs30.4,p<0.01); t_L(14.2vs11.8,p=0.016), t (14.4vs10.3,p<0.01). CNR values were also significantly higher when using the HYPER reconstruction regardless of target lesions' dimensions and site (T: p<0.001;t_L:p =0.031;t:p=0.007;all target lesions:p<0.01). Bland-Altman analysis showed a systematic bias in favour of HYPER, with mean negative differences for SUVmax in all target lesions cathegories (all target lesions: 95%CI=-4.65,-1.93;p<0.01;T:95%CI=-6.28,-0.53,p= 0.02;t_L:95%CI=0.66,4.44;p=0.02;t:95%CI=-5.11,-2.03;p<0.01). All comparisons showed statistically significant bias, indicating limited agreement between the two reconstruction methods. ***Conclusion:*** HYPER- SUVmax and CNR were higher compared to OSEM-SUVmax and OSEM-CNR. The presence of systematic bias suggests that 68Ga-DOTANOC-PET/CT HYPER and OSEM reconstructions are not directly comparable. Although these data were derived form a limited cohort, these preliminary results indicate the need to extend the sample size and to evaluate the impact of the use of different reconstructions in the routine workflow of PET centre with different camera technologies.

EP-0311

Preliminary experience on the use of [68Ga]68Ga-DOTANOC LAFOV PET/CT in NET patients

G. Bianciardi[1], *E. Fortunati*[2], *M. Di Franco*[1], *C. Malizia*[2], *M. Assenza*[3], *D. Campana*[4], *E. Andrini*[4], *V. Allegri*[2], *E. Tabacchi*[2], *S. Fanti*[1,2], *V. Ambrosini*[1,2];
[1]*Nuclear Medicine, Alma Mater Studiorum University of Bologna, Bologna, ITALY,* [2]*Nuclear Medicine, IRCCS Azienda Ospedaliero-Universitaria di Bologna, Bologna, ITALY,* [3]*Professional Development and Implementation of Research in Health Professional Unit, IRCCS Azienda Ospedaliero-Universitaria di Bologna, Bologna, ITALY,* [4]*Department of Medical and Surgical Sciences (DIMEC), Medical Oncology Unit, Alma Mater Studiorum-University of Bologna, IRCCS Azienda Ospedaliero-Universitaria di Bologna, Bologna, ITALY.*

Aim/Introduction: Long axial field-of-view (LAFOV) PET/CT ensures significant improvements in image quality and increased sensitivity, offering the advantage of reduced scanning time and possibility to use reduced injected activity. Aim: to describe the preliminary experience on the use of 68Ga-DOTANOC LAFOV PET/CT in NET patients and compare functional images with standard diagnostic imaging. ***Materials and Methods:*** Among the NET patients followed at the local Oncology Unit, those imagined with 68Ga-DOTANOC acquired on a uExplorer LAFOV-PET/CT (October 2024-March 2025; mean 68Ga-DOTANOC dose of 1.4±0.3MBq/kg; acquisition time=5min). Considering the higher sensitivity expected from LAFOV, results of PET were compared with standard morphologic diagnostic procedures, when available (contract-enhanced-CT, ceCT; MRI).ceCT/MRI vs LAFOV-PET/CT lesions by lesions analysis was performed when available (within 6months) and concordance/discordance was recorded. Lesions were classified as concordant (when visible on both PET and diagnostic imaging) or discordant (visible on one modality only). ***Results:*** Overall, 57 patients were studied (primary tumour site: pancreas=26/57,46%;other-GEP=20/57,35%;lung=4/57,7%;other-site=7/57.12%; grade: G1=26/57,46%;G2=31/57,54%).Overall, the procedure was well tolerated notwithstanding the extended FOV. Image visual-quality was overall good despite the injected activity in the lower recommended range. PET was positive in 34/57(60%) and negative in 23/57(40%). Metastatic lesions were mostly at liver and nodal level. ceCT/MRI was available in 27/57 (47.7%): ceCT in 24/27 (88.9%), liver-MRI in 3/27 (11.1%). Concordance was observed in 19/27 cases (70.4%), discordance in 8/27 cases (29.6%). In 4/8 discordant cases, PET identified additional findings undetected by ceCT/MRI: mesenteric nodules (n=1), ileal uptake (n=1), bone lesions without morphological correlates (n=2). In the remaining 4/8 cases, ceCT or MRI identified additional lesions undetected by PET: liver lesions on MRI (n=2; millimetric), pancreatic and liver lesions on ceCT (n=1), and small hepatic lesions on ceCT (n=1). ***Conclusion:*** 68Ga-DOTANOC LAFOV PET/CT was well-tolerated and resulted in high image visual-quality, notwithstanding the administration of mean doses in the lower range of the recommend injected activity and reduced acquisition times. In most cases, PET was concordant with ceCT/MRI (70%). Larger cohorts of NET patients are needed to fully understand the advantages of LAFOV in clinical practise and to optimise the comparison with images acquired on SAFOV cameras (a frequent issue in NET patients often scanned at different centers over time).

EP-0312

Functional vs. morphological imaging in Well-Differentiated Neuroendocrine Tumors: how ^{68}Ga-DOTATOC PET/CT can influence treatment decision-making

C. Battisti[1], *C. Ferrari*[1], *A. Pisani*[1], *D. Candido*[1], *E. Lauricella*[2], *M. Bacalim*[2], *D. Rubini*[3], *M. Cives*[2], *G. Rubini*[1];
[1]*Nuclear Medicine Unit, DIM, University "Aldo Moro", Bari, ITALY,* [2]*University of Bari Aldo Moro, Interdisciplinary Department of Medicine, Bari, ITALY,* [3]*Radiotherapy, Precision Medicine Department, University of Campania "Luigi Vanvitelli", Naples, ITALY.*

Aim/Introduction: to compare the ^{68}Ga-DOTATOC-PET/CT and morphological imaging (MI) detection rate in patients with well-differentiated neuroendocrine tumors (NETs) and their impact on changes in treatment strategy (CTS). ***Materials and Methods:*** 61 NETs patients who performed ^{68}Ga-DOTATOC-PET/CT and MI for staging/restaging purpose, between November 2023 and December 2024, were retrospectively analyzed. All ^{68}Ga-DOTATOC-avid lesions were compared with those detected by MI, in relation to primary site, lymph node involvement and metastatic locations (liver, bone, lung). MI was represented by TC in 37 patients, MRI in 11 and both modalities in 13 patients. All ^{68}Ga-DOTATOC-avid lesions were semiautomatically segmented and SUVmax, SUVmean, somatostatin-receptor-expressing tumor volume (SRETV) and total lesion somatostatin-receptor-expression (TLSRE) were extracted. Then, whole-body SRETV (SRETVwb) and TLSRE (TLSREwb) were defined as the sum of SRETV and TLSRE. After PET imaging, clinical follow-up was assessed in terms of CTS. The agreement between PET/CT and MI results was evaluated by Cohen's kappa-coefficient for each specific site of disease involved. Chi-square, Fisher's exact and Mann-Whitney tests were employed to assess the correlation between PET parameters and CTS. ***Results:*** Detection rate was 90% in MI and 87% in PET/CT. Median SRETVwb and TLSREwb was 46.64cm^3 and 303.67g/mLxcm^3, respectively. Both modalities were almost concordant in the assessment of primary site (p=0.000 k=0.630), while a slight agreement was observed in lymph nodes involvement (p=0.213 k=0.156, 15 patients MI-/PET+). On secondary lesion-based analysis, a substantial agreement was achieved in the liver (p=0.000 k=0.640), moderate agreement in the lung (p=0.000 k=0.504) and a fair agreement in the bone (p=0.001 k=0.387). PET/CT revealed more lesions in the bone (9 patients MI-/PET+), while MI in the lung (4 patients MI+/PET-). Regarding CTS, the absence of secondary sites (p=0.001), in particular of liver involvement (p=0.005), significantly correlated with no therapeutic modifications; conversely, higher SRETVwb values were significantly associated with CTS (p=0.028). CTS was confirmed in 27 patients (44%), and in 20/27 PET and MI showed discordant results. Out of 15/20 patients (75%), PET/CT revealed more lesions than MI, with a high tumor burden (median SRETVwb:392.23cm^3). ***Conclusion:*** The two methods confirm a reliable and complementary role in the management of NETs. In particular, MI remains the gold standard for lung assessment, while PET provides additional information on lymph node status and bone involvement. Furthermore, the tumor burden evaluation, using semiquantitative volumetric ^{68}Ga-

DOTATOC-PET/CT parameters, could represent a useful clinical tool for influence treatment decision-making in the perspective of personalized medicine.

EP-0313

Molecular Mechanisms of SSTR2-Mediated Regulation of Glucose Metabolism in Neuroendocrine Neoplasms

L. Hao;
Central South University, Changsha, Hunan, CHINA.

Aim/Introduction: Neuroendocrine neoplasms (NENs) exhibit clinical and pathological heterogeneity, with some patients harboring concurrent neuroendocrine tumors (NETs) and carcinomas (NECs) or progressing from NETs to NECs. The regulatory mechanisms driving this progression remain unclear. Combined [^{18}F]F-AlF-NOTA-octreotide ([^{18}F]F-OC) and [^{18}F]F-FDG PET/CT imaging delineates distinct metabolic phenotypes: NETs show high SSTR2 expression and low glucose metabolism, whereas NECs exhibit reduced SSTR2 and elevated glucose uptake. Prior studies have demonstrated somatostatin analogs suppress HIF-1α, a master regulator of glycolysis, thereby reducing GLUT1 expression and tumor proliferation. Therefore, this study aims to investigate the interplay between SSTR2 and glucose metabolism in NENs progression, providing insights for precision monitoring and targeted therapy. ***Materials and Methods:*** 67 histologically confirmed NEN patients undergoing both [^{18}F]F-OC PET/CT and [^{18}F]F-FDG PET/CT were retrospectively enrolled. Clinical data, follow-up outcomes, PET parameters and immunohistochemical markers (SSTR2, HIF-1α, GLUT1, Ki-67) were collected to analyze. In vitro validation was performed using NEN cell lines via gene interference or overexpression. ***Results:*** According to the World Health Organization (2022) classification, 53 (79.1%) patients had NETs (G1: 26.9%, G2: 37.3%, G3: 14.9%) and 14 (20.9%) had (NECs). Among NETs G1, median [^{18}F]F-FDG SUVmax was 3.63 (IQR: 2.84-6.21), [^{18}F]F-OC SUVmax was 35.45 ((IQR: 17.33-73.79), with 33.3% progressive disease (PD) versus 66.7% stable disease (SD). NETs G2 showed [^{18}F]F-FDG SUVmax was 5.45 (IQR: 2.84-8.94), [^{18}F]F-OC SUVmax was 29.75 ((IQR: 20.14-52.33), and 40% PD versus 60% SD. NETs G3 exhibited [^{18}F]F-FDG SUVmax was 9.78 (IQR: 7.20-13.63), [^{18}F]F-OC SUVmax was 6.76 ((IQR: 3.39-13.76) with 100% PD. NECs demonstrated [^{18}F]F-FDG SUVmax was 13.94 (IQR: 5.21-18.34), [^{18}F]F-OC SUVmax was 7.18 ((IQR: 5.18-16.0), and 71.4% PD versus 28.6% SD. In total cases, low ^{18}F-OC SUVmax (HR=0.41, 95% CI: 0.20-0.84, P=0.01) and low SSTR2 expression (HR=0.09, 95% CI: 0.02-0.37, P<0.001) independently predicted adverse outcomes. Histopathological analysis showed NENs pathological grade escalated with Ki-67 expression (NET G1:2.26% vs NEC:9.93%, P<0.001), contrary to SSTR2 expression (NET G1:21.9% vs NEC:1.40%, P<0.001). Besides, SSTR2 inversely correlated with HIF-1α (r=-0.25, P=0.04), while both HIF-1α (NET G1:2.19% vs NEC:9.17%, P<0.001) and GLUT1 (NET G1:2.14% vs NEC:7.76%, P<0.001) showed grade-dependent elevation (r=0.66, P<0.001). Further in vitro validation is pending. ***Conclusion:*** Our study demonstrated that the increase of NENs pathological grade was accompanied by the gradual loss of SSTR2 expression and gradual upregulation of HIF1-α and GLUT1, which suggesting that SSTR2 may play a crucial role in glucose metabolism, and facilitate the transformation of "NET-NEC".

EP-0314

Neuroendocrine carcinoma and NET grade 3: uptake of ^{18}FDG and ^{68}DOTATOC in lesions in relation to SSTR2 expression and survival

D. Truong, *Z. Ankers, A. Stenman, D. Granberg, J. Zedenius, C. C. Juhlin, A. Kistner;*
Karolinska Institute, Stockholm, SWEDEN.

Aim/Introduction: PET with ^{18}F-FDG has been shown to be of particular value in neuroendocrine carcinoma (NEC), while somatostatin-receptor-PET with ^{68}Ga-DOTATOC is standard in well-differentiated neuroendocrine tumours (NET). Recent data suggest that even some NEC-patients with somatostatin-receptor (SSTR) expression may benefit from radiolabeled somatostatin analogue treatment (1). In an ongoing retrospective study, we aim to investigate SSTR-expression and isotope uptake in a cohort of NEC patients, with a few included NET grade 3 cases, and to assess how ^{18}F-FDG PET/CT and 68Ga-DOTATOC PET/CT tumor uptake relate to survival time. ***Materials and Methods:*** 48 patients were investigated, 23 patients had undergone baseline PET/CT using intravenous ^{18}FDG, 32 patients performed ^{68}Ga-DOTATOC; and in 7 patients both modalities were done. Primary tumor location, size (by RECIST), clinical data as well as survival time from diagnosis were collected. In 41 cases, SSTR2 immunohistochemistry data was available. In addition, ^{18}FDG-SUV_{max} and ^{68}Ga-DOTATOC-SUV_{max} also in relation to non-metastatic liver uptake (tumor-to-liver ratio [TLR]) in primary tumors and metastases (lymph node, liver, skeletal) were estimated. ***Results:*** The cohort consisted of 29 men and 19 women, with a mean age of 64 years (95% CI: 60-68). The main primary tumor locations were the pancreas (17 patients), cancer of unknown origin (CUP) (9), rectum (6), and colon (4). At the time of PET/CT, 32 out of 48 patients (67%) had liver metastases, and 4 patients (8%) had skeletal metastases. The mean size of the primary tumor was 55 mm (95% CI:43-67 ;n=29). Among those who underwent 68Ga-DOTATOC PET/CT (n=32), 56% demonstrated uptake in metastatic lesions greater than that of the liver (tumor-to-liver ratio [TLR] > 1, corresponding to Krenning Score 3). Of those with histopathology available 73% (n=30) had SSTR2 expression in tumor lesions. In this group a tendency to lower ^{18}FDG-SUV_{max} in tumor lesions (p=0.07) as well as higher TLR at ^{68}Ga-DOTATOC (p=0.01) were present. Mean survival time was 34 (26-42) months. In regression analysis ^{18}FDG-SUV_{max} in tumor lesions was inversely correlated to survival time (r=-0.44, p=0.04, one outlier excluded). ***Conclusion:*** Despite being classified as NEC or NET grade 3, the majority of the cohort had tumors showing SSTR2 expression and isotope uptake on 68Ga-DOTATOC PET/CT (among those who underwent the scan). Higher ^{18}F-FDG uptake in lesions was associated with shorter survival time. Nonetheless, these findings suggest a potential therapeutic effect of Lutetium-177-DOTATATE treatment even in NEC and NET grade 3 cases. ***References:*** 1. Nilica B et al,EJNMMI 2016:43(9);1585-1592.

EP-0315

Compare the diagnostic value of [^{18}F]AlF-NOTA octreotide ([^{18}F]-OC) PET/CT and enhanced CT for suspected pheochromocytoma/paraganglioma (PPGL)

L. Huang, *J. Liu, Z. Cui, W. Ma, Y. Li;*
The Second Hospital & Clinical Medical School, Lanzhou University, Lanzhou, CHINA.

Aim/Introduction: [^{18}F]AlF-NOTA octreotide ([^{18}F]-OC) shows a higher lesion detection rate in gastroenteropancreatic neuroendocrine tumors and lower uptake in the liver. However, there are few research reports on its imaging in pheochromocytoma/paraganglioma (PPGL). The aim of this study is to compare the diagnostic value of [^{18}F]-OC PET/CT and enhanced CT for suspected PPGL. ***Materials and Methods:*** A retrospective analysis was conducted on 31 patients with suspected PPGL. [^{18}F]-OC PET/CT images, enhanced CT images, and clinical data (age, gender, hematuria catecholamine assay) were collected. Postoperative pathology served as the "gold standard" for diagnosis, dividing patients into PPGL and non-PPGL groups. PET/CT image features (location, longest diameter, shortest diameter, CT value, SUVmax, SUVmean, metabolic tumor volume (MTV), ratio of lesion SUVmax to liver SUVmean (SUVR), visual score (VS), calcification, necrosis, metastasis) were analyzed. Logistic regression identified independent predictive factors for PPGL (P≤0.05), forming diagnostic model one. Enhanced CT image features (location, longest diameter, shortest diameter, CT value, degree and pattern of enhancement, calcification,

necrosis) were similarly analyzed to form diagnostic model two. A combined PET/CT and enhanced CT model (model three) was also created. Model performance was assessed using area under the receiver operating characteristic curve (AUC), sensitivity, specificity and accuracy. The Delong test compared the efficacy of the three models. ***Results:*** Among the 31 patients (9 males, 22 females; mean age 52.35±9.78 years, range 9-70 years), 17 were diagnosed with PPGL and 14 with non-PPGL (13 adrenal cortical adenomas, 1 retroperitoneal Castleman disease). Multivariate logistic regression based on PET/CT features identified high SUVR and necrosis as independent predictive factors for PPGL. The AUC, sensitivity, specificity, and accuracy of SUVR and necrosis alone for diagnosing PPGL were 0.840 (95% CI: 0.665-0.946), 0.647, 1.000, 0.806 and 0.687 (95% CI: 0.496-0.841), 0.588, 0.786, and 0.677, respectively. When used in combination, the AUC, sensitivity, specificity, and accuracy for diagnosing PPGL were 0.891 (95% CI: 0.726-0.974), 0.824, 0.929, and 0.871, respectively. For enhanced CT, only necrosis was a significant predictor (P=0.04). The Delong test showed no statistical difference in AUC between combined SUVR and necrosis versus SUVR alone (P=0.307), but a significant difference versus necrosis alone (P=0.012). No statistical difference was found between SUVR and necrosis alone (P=0.172). ***Conclusion:*** [^{18}F]-OC PET/CT demonstrates superior diagnostic value for suspected PPGL compared to enhanced CT. The SUVR metric exhibits the highest diagnostic efficacy, which can be further enhanced by combining it with necrosis.

EP-0316

Diagnostic accuracy of [^{99m}Tc]Tc-HYNIC-TOC SPECT/CT in patients with pheochromocytomas and paragangliomas:a single-center experience

B. Li, *J. Zhang, X. Wu, Y. Gao;*
Department of Nuclear Medicine, Henan Key Laboratory of Novel Molecular Probes and Clinical Translation in Nuclear Medicine, Henan Provincial People's Hospital; Zhengzhou University People's Hospital, Henan University People's Hospital, Zhengzhou, CHINA.

Aim/Introduction: Pheochromocytomas and paragangliomas (PPGLs) present diagnostic challenges due to their diverse clinical manifestations. This study aims to evaluate the diagnostic accuracy of [^{99m}Tc]Tc-HYNIC-TOC SPECT/CT in patients with clinically suspected PPGLs. ***Materials and Methods:*** A retrospective analysis was conducted on 75 patients (36 males, 39 females, mean age 47.7 ± 14.9 years) with suspected PPGLs. All patients underwent [^{99m}Tc]Tc-HYNIC-TOC SPECT/CT imaging, and the results were compared with histopathological findings. The sensitivity, specificity, positive predictive value (PPV), negative predictive value (NPV), and overall accuracy of the imaging modality were calculated. Additionally, visual and semiquantitative evaluations were performed using Krenning score (KS) and tumor-to-background ratio (TBR), and their diagnostic performances were analyzed. ***Results:*** Of the 75 patients, 54 had PPGLs (40 pheochromocytomas, 7 paragangliomas, and 7 metastatic PPGLs), and 21 had non-PPGL tumors. [^{99m}Tc]Tc-HYNIC-TOC SPECT/CT showed positive imaging in 63 patients, of whom 51 were confirmed as PPGLs and 12 as non-PPGLs. The sensitivity, specificity, PPV, NPV, and overall accuracy were 94.4% (51/54), 42.9% (9/21), 80.9% (51/63), 75.0% (9/12), and 80.0% (60/75), respectively. Visual and semiquantitative evaluations indicated higher KS and TBR values in PPGLs compared to non-PPGLs (median KS: 3.0 vs. 1.0, P<0.001; median TBR: 2.10 vs. 0.92, P<0.001). The Receiver operating characteristic (ROC) analysis revealed AUCs of 0.803 for KS and 0.791 for TBR, with no significant difference in their diagnostic performance (P=0.710). Metastatic PPGLs were detected in 7 cases, with metastases observed in multiple organs. ***Conclusion:*** [^{99m}Tc]Tc-HYNIC-TOC SPECT/CT is a highly sensitive diagnostic tool for detecting PPGLs, providing effective differentiation between PPGL and non-PPGL tumors. Its ability to identify metastatic PPGLs with metastatic spread further underscores its potential in clinical practice. These findings highlight the potential of [^{99m}Tc]Tc-HYNIC-TOC SPECT/CT as a reliable imaging modality for suspected PPGLs, with implications for patient management and treatment strategies.

EP-0317

Comparison of Iodine-123 Metaiodobenzylguanidine scintigraphy with SPECT/CT and Fuorine-18-aluminum fluoride-1,4,7-triazacyclononane-1,4,7-triacetic acid-octreotide PET/CT in the Follow-Up of Neuroblastoma

Y. Liu[1], *S. Li*[2], *J. Liu*[2], *B. Sang*[1], *Y. Xu*[2], *J. Yang*[2], *X. Sun*[1];
[1]*Shandong Cancer Hospital and Institute, Shandong First Medical University and Shandong Academy of Medical Sciences, Jinan, CHINA,* [2]*Beijing Friendship Hospital, Capital Medical University, Beijing, CHINA.*

Aim/Introduction: Detecting recurrence, metastatic, or residual lesions of neuroblastoma (NB) at follow-up was of great importance for evaluating therapeutic response, excluding subclinical relapse, and guiding therapy protocols. The aim of this study was to evaluate and compare the diagnostic performance of fuorine-18-aluminum fluoride-1,4,7-triazacyclononane-1,4,7-triacetic acid-octreotide PET/CT (^{18}F-AlF-NOTATATE PET/CT) and Iodine-123 Metaiodobenzylguanidine scintigraphy with SPECT/CT (^{123}I-MIBG SPECT/CT), thereby determining their role in follow-up of NB. ***Materials and Methods:*** A total of 59 patients were prospectively enrolled into the present study. All patients underwent ^{123}I-MIBG scintigraphy with SPECT/CT and ^{18}F-AlF-NOTATATE PET/CT within 1 weeks. Patient-based analysis, lesion-based analysis, and region-based analysis were performed. Patients with diffuse lesions were excluded from lesion-based analysis. ***Results:*** In patient-based analysis, ^{18}F-AlF-NOTATATE PET/CT evidenced positive in 31 of 59 patients, and ^{123}I-MIBG scintigraphy with SPECT/CT was positive in 30 of 59 cases. The area under the curve (AUC), sensitivity, positive predictive value (PPV), and negative predictive value (NPV) were 0.935 [95% confidence interval (CI): 0.840-0.983], 0.909 (95% CI: 0.757-0.981), 0.961 (95% CI: 0.804-0.999), 0.968 (95% CI: 0.814-0.995), 0.893 (95%CI: 0.739-0.961), respectively; and 0.955 (95% CI: 0.866-0.992), 0.909 (95% CI: 0.757-0.981), 1.000 (95% CI: 0.868-1.000), 1.000 (NA), 0.897 (95% CI: 0.747-0.962), respectively. Lesion-based analyses demonstrated that ^{18}F-AlF-NOTATATE PET/CT was superior to ^{123}I-MIBG scintigraphy with SPECT/CT in sensitivity [0.928 (95%CI: 0.862-0.968) vs. 0.625 (95%CI: 0.529-0.715), p=0.01]. In region-based analysis, the two imaging modalities has moderate to very good agreement in detecting involved patients (κ>0.40) and poor agreement in detecting focal lesions (κ<0.20). ***Conclusion:*** ^{18}F-AlF-NOTATATE PET/CT showed high sensitivity in detecting focal lesion of NB and demonstrated more lesions as compared with ^{123}I-MIBG scintigraphy with SPECT/CT. ^{18}F-AlF-NOTATATE PET/CT could be used as a complementary imaging modality of ^{123}I-MIBG scintigraphy with SPECT/CT in the follow-up of NB.

EP-0318

Prognostic Impact of Discordant Lesions on [^{18}F]FDG and [^{68}Ga]Ga-FAPI-04 PET/CT compared to Histological FAP expression in Neuroendocrine Neoplasms

T. Jedamzik[1], *A. Kosmala*[1], *S. Kircher*[2], *M. Heinrich*[1], *W. Schlötelburg*[1], *A. Buck*[1], *A. Meining*[3,4], *R. A. Werner*[3,5,6], *A. Weich*[3,4], *K. Michalski*[1];
[1]*Department of Nuclear Medicine, University Hospital Wuerzburg, Wuerzburg, GERMANY,* [2]*Institute of Pathology, University of Wuerzburg, Wuerzburg, GERMANY,* [3]*NET-Zentrum Würzburg, European Neuroendocrine Tumor Society Center of Excellence (ENETS CoE), University Hospital Wuerzburg, Wuerzburg, GERMANY* [4]*Internal Medicine II, University Hospital Wuerzburg, Wuerzburg, GERMANY,* [5]*Department of Nuclear Medicine, LMU Hospital, Ludwig-Maximilians-University of Munich, Munich, GERMANY,* [6]*Johns Hopkins School of Medicine, The Russell H Morgan Department of Radiology and Radiological Sciences, Baltimore, MD, UNITED STATES OF AMERICA.*

Aim/Introduction: The presence of discordant (FDG+/FAPI-) lesions on dual-tracer PET/CT using [18F]FDG and [68Ga]FAPI-04 in patients with aggressive neuroendocrine neoplasms (NENs) is associated with a reduction of progression-free survival (PFS). The aim was to investigate the prognostic value of discordant lesions compared to the histological expression of fibroblast activation protein (FAP) and its influence on PFS. ***Materials and Methods:*** A retrospective evaluation was performed on 23 patients with histologically confirmed NENs, who underwent both FAPI and FDG PET/CT, as well as biopsy. SUVmax, SUVmean, SUVpeak as well as tumor volume (TV) and total lesion uptake (TLU = TV * SUVmean) was measured for both radiotracers. Histologically, the immunoreactive score (IRS [0-12] = percentage of stained cells [0-4] * staining intensity [0-3]) of FAP expression was determined. Discordant lesions were identified visually and quantitatively. Spearman and point-biserial correlations were performed between PET parameters, IRS, and the presence of discordant lesions. Effects on PFS were analyzed using Cox regression. PFS was defined radiologically according to RECIST 1.1 and clinically as the presence of disease progression or death. ***Results:*** The primary site was mostly in the gastrointestinal tract (14/23) or unknown (= CUP, 7/23). IRS showed a statistical significant correlation for both radiotracers with TV ($p = 0.017$ for FDG, $p = 0.018$ for FAPI) as well as with TLU ($p = 0.017$ for FDG, $p = 0.025$ for FAPI). There was no statistically significant correlation between IRS and all SUV parameters. FDG+/FAPI- lesions were found in 9/23 patients. The median PFS was 6 months. The presence of FDG+/FAPI- lesions was significantly associated with shorter PFS (4 vs. 10 months, HR = 5.75, 95%CI: 1.74 - 18.97, $p = 0.01$). FDG-TV ($p = 0.012$) and FDG-TLU ($p = 0.008$) were significantly correlated with PFS in univariable analysis. No significant association was found between IRS and PFS (HR = 1.06, 95%CI: 0.92 - 1.21, $p = 0.39$). Similarly, no significant correlation was found between IRS and the presence of FDG+/FAPI- lesions ($p = 0.45$). ***Conclusion:*** FAP expression on immunohistochemistry is not correlated with the presence of FDG+/FAPI- lesions on FDG and FAPI PET/CT in patients with aggressive NENs, although the presence of discordant lesions is significantly associated with reduced PFS. Dual-tracer PET/CT as a whole-body diagnostic method may provide a better approach for risk stratification and treatment decision-making in NENs than immunohistochemical analysis of FAP expression in a single tumor manifestation.

EP-0319

Comparison of FDOPA PET/CT and MRI for the diagnosis and follow-up of pheochromocytomas and paragangliomas

L. Rodríguez Díaz*, C. Vigil Díaz, A. Álvarez Alonso, S. Menéndez Sánchez, M. Domínguez Grande, M. Fernández Llana, S. Naranjo Sancho, A. Álvarez Amigo, J. Guzmán de la Cerda, N. Martín Fernández, V. Pascual Pascual, F. Gonzalez García;*
Central University Hospital of Asturias (HUCA), Oviedo, SPAIN.

Aim/Introduction: Pheochromocytomas (PCC) and paragangliomas (PGL) are rare neuroendocrine tumors derived from adrenal or extra-adrenal neural crest chromaffin cells. Nuclear medicine imaging plays an important role in the diagnosis, staging, and follow-up of these patients. Precise imaging follow-up is essential, given the high risk of tumor recurrence in these patients. The aim of this study is to determine whether 6-l-[18f]-fluoro-3,4-dihydroxyphenylalanine PET/CT (FDOPA PET/CT) is an accurate technique for the diagnosis and follow-up of these patients. ***Materials and Methods:*** Retrospective study including 63 patients (19 male, 44 female; age range 18-87 years) (27 with known disease, 36 with no medical history of PCC/PGL), who underwent FDOPA PET/CT study between January/2021-June/2024. MRI and FDOPA PET/CT qualitative and semi- quantitative findings were studied. Our gold standard was defined by patient's follow-up and post-surgical anatomical pathology examination. ***Results:*** 73 FDOPA PET/CT studies were performed, in which pathological findings were seen in 37/73 studies: 5 PCC, 2 PCC/PGL and 41 PGG (21 carotid body, 8 jugulotympanic, 6 tympanic, 6 jugular, 1 bladder wall and 1 pericardial PGL). Mean SUVmax for PCC and PGL was 12.98 and 10.91, respectively. 30 follow-up FDOPA PET/CT studies were performed (2 patients with SDH gene mutations with no PCC/PGL history, and 28 with PCC/PGL history, out of which 16 had SDH gene mutations). The remaining studies were performed to evaluate extension and multicentricity (14 SDH gene mutation screening, 11 incidentalomas and 18 due to clinical symptoms or high metanephrines/catecholamines). 29 patients underwent MRI study at the time of FDOPA PET/CT evaluation. In our series, MRI and FDOPA PET/CT results were discordant in 7/29 patients, leading to a change in therapeutic management in 3. FDOPA PET/CT study ruled out PCC/PGL in 5 patients with positive MRI findings (2 laterocervical nodes, 1 lesion compatible with vagal PGL surgical remains and 2 neurinomas). 1 PGL (1 post-surgical disease) and 1 PCC were diagnosed in patients with normal MRI. 3 patients presented with progression during FDOPA PET/CT follow-up. ***Conclusion:*** Our results demonstrate that FDOPA PET/CT should be alongside with the MRI, an imaging technique of choice for both diagnosis and follow-up of these patients. FDOPA PET/CT provides an accurate diagnostic method for whole-body evaluation and metabolic response assessment with high accuracy and changes patient outcome.

EP-0320

Accelerating Lu-177 SPECT Imaging Post Radioligand Therapy Using Deep Learning-Enhanced Projection Interpolation

A. Sitek[1]*, S. Płotka*[2]*, J. Prządo*[3]*, H. Sabet*[1]*, P. Heidari*[1]*, J. B. Ćwikła*[3,4]*;*
[1]Massachusetts General Hospital and Harvard Medical School, Boston, MA, UNITED STATES OF AMERICA [2]University of Warsaw, Warsaw, POLAND, [3]University of Warmia and Mazury in Olsztyn, Olsztyn, POLAND, [4]Diagnostic and Therapy Center Gammed, Warsaw, POLAND.

Aim/Introduction: SPECT imaging of lutetium-177 [^{177}Lu] targeted radioligand therapies (RLTs) plays a critical role in the therapeutic evaluation and monitoring of neuroendocrine tumors and prostate cancer RLT. While clinically valuable, SPECT imaging requires lengthy acquisition times, which can be burdensome for patients and hinder workflow efficiency. Therefore, strategies to shorten imaging times without compromising diagnostic accuracy are highly desirable. This study evaluates the feasibility and clinical applicability of substantially reducing ^{177}Lu-imaging acquisition time through deep learning (DL)-based interpolation of projection data. ***Materials and Methods:*** A total of 1,368 retrospective SPECT scans from 88 patients who underwent DOTATATE and DOTATOC RLT, somatostatin receptor scintigraphy (SRS), and prostate-specific membrane antigen (PSMA-T4) imaging, were used. The scans were acquired using multiple dual-head SPECT/CT scanners with either 60 or 120 projections obtained over 360-degree arcs. A DL interpolation model was developed and trained on 90% of these scans, validated on a 10% subset. The model was tested on a distinct set of 24 images derived from five patients different from those used for training and validation. To test, original 60-projection sinograms were reduced to simulate shorter acquisition protocols (30, 15, 10, and 6 projections), corresponding respectively to reductions of 50%, 75%, 83%, and 90% in acquisition time. These reduced datasets were subsequently interpolated back to the full complement of 60 projections using the trained DL model. Reconstruction was performed using 20 iterations of the maximum likelihood expectation maximization algorithm with Butterworth post-filtering. Image quality was quantitatively assessed by computing the mean and standard deviation of contrast recovery for 48 clearly identified focal lesions, with two lesions evaluated per test dataset; contrast recovery was defined as the ratio of the measured lesion contrast to the corresponding contrast in the original full-projection reconstruction. ***Results:*** Reconstructions using DL-interpolated sinograms demonstrated

image quality and noise characteristics comparable to the original full-projection acquisitions. Quantitative analysis indicated that lesion contrast recovery was substantially maintained, achieving up to 90% recovery at a 50% reduction in acquisition time. However, more aggressive reductions in acquisition time led to proportionally decreased contrast recovery, illustrating a trade-off between image quality and time savings. ***Conclusion:*** This study demonstrates the promising capability of DL-based interpolation methods to significantly reduce ^{177}Lu SPECT imaging acquisition time post-RLT, while largely preserving diagnostic quality. Although further algorithmic improvements and larger training datasets could enhance performance, the current findings already support the potential for integrating DL approaches into routine clinical imaging.

EP-0321

The Role of Ga-68 DOTA-TATE PET/CT in the Differential Diagnosis of Pheochromocytoma and Adrenal Adenoma

F. Demir[1], *H. Yıldız*[1], *S. Karaçavuş*[1], *C. Güneş*[1], *S. A. Salt*[2], *E. Gündoğan*[3];
[1]*Department of Nuclear Medicine, Kayseri City Training and Research Hospital, Kayseri, TÜRKIYE,* [2]*Department of Endocrinology, Kayseri City Training and Research Hospital, Kayseri, TÜRKIYE* [3]*Department of Gastroenterology Surgery , Kayseri City Training and Research Hospital, Kayseri, TÜRKIYE.*

Aim/Introduction: To assess the efficacy of Ga-68 DOTA-TATE PET/CT in distinguishing between pheochromocytoma and adrenal adenoma, and to evaluate the diagnostic utility of SUV ratios. ***Materials and Methods:*** A retrospective analysis was conducted on forty patients who underwent Ga-68 DOTA-TATE PET/CT for adrenal lesions between 2018 and 2025. The cohort comprised 16 males (40%) and 24 females (60%), with a mean age of 55.10 ± 9.69 years. Lesions were identified in the right adrenal gland in 15 patients (37.5%) and in the left adrenal gland in 25 patients (62.5%). The average lesion size was 28.6 ± 12.45 mm. Final diagnoses were established through histopathological examination (55%) or clinical and laboratory follow-up (45%). Data recorded included lesion location, size, Hounsfield Unit (HU), metabolic tumor volume (MTV), total lesion uptake (TLU), SUVmean, liver and spleen reference SUVmax, lesion SUVmax, and contralateral adrenal SUVmax. Ratios of lesion SUVmax to contralateral adrenal (LSUVmax/KASUVmax), spleen (LSUVmax/DSUVmax), and liver (LSUVmax/KSUVmax) SUVmax were calculated. Statistical evaluation was performed using the Mann-Whitney U test and ROC analysis. ***Results:*** Among the patients, 18 (45%) were diagnosed with pheochromocytoma, while 22 (55%) were diagnosed with adrenal adenoma. Significant differences were observed in the LSUVmax/KASUVmax, LSUVmax/DSUVmax ratios, and cortisol levels (p=0.007, 0.003, and 0.014, respectively). No significant differences were noted in other parameters (P >0.05). ROC analysis identified LSUVmax/KASUVmax (AUC=0.80, p=0.001) and LSUVmax/DSUVmax (AUC=0.76, p=0.006) as significant diagnostic indicators. A LSUVmax/KASUVmax cutoff of 1.2 demonstrated a sensitivity and specificity of 72% and 77%, respectively. A cutoff of 0.45 for LSUVmax/DSUVmax yielded a sensitivity and specificity of 72% and 73%, respectively. ***Conclusion:*** Ga-68 DOTA-TATE PET/CT is a reliable imaging modality for distinguishing between pheochromocytomas and adrenal adenomas. The LSUVmax/KASUVmax and LSUVmax/DSUVmax ratios offer valuable diagnostic insights that can aid clinicians in patient management.

EP-0322

Long-axial field-of-view dynamic ^{64}Cu-DOTATATE PET/CT in patients with neuroendocrine neoplasms

E. Carlsen[1,2,3], *C. B. Johnbeck*[1,2,3], *M. Loft*[1,2,3], *T. L. Andersen*[1,3,4], *A. Kjaer*[1,2,3];
[1]*Department of Clinical Physiology and Nuclear Medicine, Copenhagen University Hospital – Rigshospitalet, Copenhagen, DENMARK,* [2]*Cluster for Molecular Imaging, Copenhagen University Hospital – Rigshospitalet & Department of Biomedical Sciences, University of Copenhagen, Copenhagen, DENMARK,* [3]*ENETS Neuroendocrine Tumor Center of Excellence, Copenhagen University Hospital – Rigshospitalet, Copenhagen, DENMARK,* [4]*Department of Clinical Medicine, Faculty of Health and Medical Sciences, University of Copenhagen, Copenhagen, DENMARK.*

Aim/Introduction: Whole-body positron emission tomography (PET) with a radiolabeled somatostatin receptor (SSR) analogue (e.g. ^{64}Cu-DOTATATE) can visualize and quantify SSR expression non-invasively and plays a key role in managing patients with neuroendocrine neoplasms (NEN). Routinely, PET/CT is performed 1 hour post injection (p.i.) of ^{64}Cu-DOTATATE. We have previously shown that imaging is feasible up to 3 hours p.i. By applying long-axial field-of-view (LAFOV) PET/CT with dynamic acquisition from time of injection, we now aimed to investigate whether earlier imaging than 1 hour p.i. is possible without loss in tumor-to-background ratio (TBR). ***Materials and Methods:*** Between July 2022 and September 2023, we included 10 patients with biopsy-verified NEN referred for routine ^{64}Cu-DOTATATE PET/CT. All patients gave informed consent for participation, and the study was approved by the internal review board. Patients underwent dynamic LAFOV PET (vertex to mid-femur) from 0-45 minutes p.i., preceded by ultralow-dose CT for attenuation correction. Approximately 60 minutes p.i. patients underwent a 10-minute LAFOV PET with a diagnostic CT. PET was reconstructed using ordered subset expectation maximization, time-of-flight, and point spread function (4 iterations, 5 subsets, 440x440 matrices) with a gaussian post-filter of 2 mm. Regions of interest were manually drawn for the primary tumor, representative lesions in different organs, and background regions in blood and liver. Activity concentration (Bq/ml) over time from injection was plotted and TBR was calculated using liver as background. ***Results:*** Of the 10 patients (7 males, 3 females), 6 had small intestinal, 3 had pancreatic and 1 had lung primary NEN. All patients had metastatic disease with liver and/or bone metastasis as well as lymph node involvement. Histologically, patients had grade 1 (n=1), grade 2 (n=7) and grade 3 (n=2) NEN, with median Ki67-index 5.5% (min-max: 2-28%). NEN-specific treatment was somatostatin analog (n=8) or temozolomide/capecitabine (n=2). Following injection, ^{64}Cu-DOTATATE cleared from the blood pool, and liver uptake plateaued at 20 minutes. TBR reached plateau between 10-30 minutes p.i. and remained stable. Median TBR at 30 minutes and 1 hour was 3.55 (2.37-4.48) and 3.60 (2.65-5.00), respectively (p=0.47). ***Conclusion:*** Dynamic LAFOV ^{64}Cu-DOTATATE PET/CT enables optimized acquisition timing. In 10 patients with NEN, tumor/metastasis uptake plateaued within 30 minutes combined with plateau in liver uptake at 20 minutes. TBR was equivalent at 30 minutes with 1 hour p.i. acquisition. Together with our previous data, we suggest that ^{64}Cu-DOTATATE image acquisition can be performed any time between 30 minutes and 3 hours p.i.

EP-0323

Comparison of physiological uptake by semiquantitative analysis of [^{68}Ga]Ga-DOTA-TATE PET/CT performed on digital and analog cameras

K. Bienkowski, *K. Pełka, J. Kunikowska;*
Medical University of Warsaw, Warsaw, POLAND.

Aim/Introduction: [^{68}Ga]Ga-DOTA-TATE PET/CT is a leading diagnostic tool for staging and managing neuroendocrine tumors (NETs). With advances in technology, digital PET/CT cameras have been introduced. While physiological uptake patterns of [^{68}Ga]Ga-DOTA-TATE using analog cameras are well documented, data on digital camera uptake remain limited.The aim of the study was to compare semiquantitative parameter - SUVmax values of physiological [^{68}Ga]Ga-DOTA-TATE biodistribution between digital and analog PET/CT cameras to identify potential differences. ***Materials and Methods:*** We retrospectively analyzed 170 patients (73 men, 97 women, aged: 18-78) examined with a digital Biograph128 Vision 600 Edge PET/CT(Siemens) 60 ± 20 minutes after injection of 1.5-2 MBq/kg [^{68}Ga]Ga-DOTA-TATE (minimum

120 MBq), which were compared to a previously described group of 250 patients examined with an analog Biograph 64 TruePoint PET/CT (Siemens) [1]. Study assessment was performed on syngo. via Siemens workstation, documenting areas of increased uptake. SUVmax was measured using a VOI isocontour tool in organs excluding pathological lesions from NETs. ***Results:*** Both digital and analog cameras showed physiological uptake in the pituitary gland, salivary glands, thyroid, liver, spleen, adrenal glands, and kidneys, consistent with somatostatin receptor expression. Diffuse uptake in the pancreatic uncinate process was observed in 37% of digital scans versus 12% of analog. Additionally, medium-low uptake was seen in nerve plexuses, especially stellate and celiac ganglions, only on digital scans. SUVmax values between digital and analog cameras were compared, the higher values were observed with digital camera and were as follows (SUVmax, Mean (SD)): pituitary gland 11.8 (4.1) vs. 11.0 (4.5), spleen 27.5 (10.2) vs. 18.9 (6.6), adrenal glands 21.7 (6.9) vs. 14.0 (5.6), kidneys 18.5 (8.9) vs. 14.2 (3.6), pancreatic uncinate process 10.0 (3.7) vs. 9.2 (3.3). Moderate uptake was noted in salivary glands (4.2 vs. 3.4), thyroid (6.8 vs. 2.9), and liver (10.8 vs. 6.5). ***Conclusion:*** Understanding physiological [^{68}Ga]Ga-DOTA-TATE distribution is essential for accurate PET/CT interpretation in NET diagnosis. Digital PET/CT cameras demonstrate generally higher SUVmax values than analog systems, which should be considered in clinical evaluations to avoid misinterpretation of physiological uptake as pathological. ***References:*** 1. Kunikowska J, Królicki L, Pawlak D, Zerizer I, Mikołajczak R. Semiquantitative analysis and characterization of physiological biodistribution of (68)Ga-DOTA-TATE PET/CT. Clin Nucl Med. 2012 Nov;37(11):1052-7. doi: 10.1097/RLU.0b013e31825b2555. PMID: 22996234.

EP-0324

NETPET vs. Krenning score: Redifining Eligibility for PRRT through Dual PET Imaging in Neuroendocrine Tumors

A. Matamala-Bezmalinović[1], *M. Velasco-Nuño*[2], *M. Calls-Calahorro*[2], *P. Stefaneli*[2], *B. Serrallonga*[2], *Y. Delisau*[2], *S. Castejón*[2], *S. Asadurova*[2], *J. Duch*[2], *D. Paez*[3], *B. Martin*[3], *V. Camacho*[2], *A. Flotats*[2]; [1]*Nuclear Medicine Department, Hospital Clínico Universidad de Chile, Santiago, CHILE,* [2]*Nuclear Medicine Department, Hospital de la Santa Creu i Sant Pau, Barcelona, SPAIN,* [3]*Oncology Department, Hospital de la Santa Creu i Sant Pau, Barcelona, SPAIN.*

Aim/Introduction: To evaluate the impact of the NETPET score on determining eligibility for peptide receptor radionuclide therapy (PRRT) in patients with metastatic neuroendocrine tumors (NETs), in comparison to the traditional Krenning Score (KS). ***Materials and Methods:*** A single-center retrospective study was conducted involving 44 patients with NETs who underwent dual PET imaging with [^{68}Ga]DOTA-TOC and [^{18}F]FDG from June 2018 to March 2025. The interval between the two PET scans was less than three months, in accordance with ENETS recommendations. Tumor origin was classified as gastroenteropancreatic (GEP) in 32 patients, pulmonary carcinoid (PC) in 11 patients and paraganglioma (PG) in one patient. Both the KS (scale 0-4) and NETPET score (P1-P5) were calculated for each patient. Eligibility for PRRT (E-PRRT) was defined as having KS ≥2 or a NETPET classification between P1 and P4a. Tumor grade and Ki-67 proliferation index were also recorded. ***Results:*** According to the KS, 35 patients (79.5%) were classified as E-PRRT, while 9 (20.5%) were deemed ineligible. The KS distribution was: 3 patients with KS 0, 6 with KS 1, 4 with KS 2, 8 with KS 3, and 23 with KS 4. When applying the NETPET score, 29 patients (65.9%) were classified as E-PRRT, and 15 (34.1%) as ineligible. The NETPET distribution was: 10 patients in P1, 6 in P2a, 6 in P2b, 2 in P3a, 0 in P3b, 5 in P4a, 6 in P4b, and 5 in P5. Both systems were concordant in 36 patients (81.8%): 28 patients (63.6%) were considered eligible, and 8 (18.2%) ineligible. In 7 cases (15.9%), NETPET reclassified patients more restrictively, excluding individuals initially deemed eligible by KS. This subset included 6 GEP tumors (four G2, two G3) and one pulmonary atypical carcinoid, with a median Ki-67 of 26.4% (range: 15%-70%). Among these, 3 patients had KS 2, 3 had KS 3, and one had KS 4, suggesting that NETPET was particularly effective in refining PRRT candidacy in patients with intermediate KS scores. ***Conclusion:*** The NETPET score appears to be a more specific tool for characterizing the heterogeneous biological behavior of neuroendocrine tumors, particularly in cases with intermediate Krenning Scores. Its application resulted in more restrictive patient reclassification, identifying individuals less likely to benefit from PRRT. These findings underscore the clinical utility of dual PET imaging in optimizing treatment selection for patients with advanced NETs. ***References:*** J Neuroendocrinol. 2024;36:e13359.J Neuroendocrinol. 2022 March ; 34(3): e13040. doi:10.1111/jne.13040.

EP-0325

The utility of [^{18}F]FET PET in the clinical management of PitNET: a preliminary descriptive analysis

V. De Meulenaere[1], *B. Lapauw*[2], *F. Dewaele*[3], *T. Van Zele*[4], *E. Genbrugge*[1], *D. Van Weehaeghe*[1]; [1]*Department of Radiology and Nuclear Medicine, Ghent University Hospital, Ghent, BELGIUM,* [2]*Department of Endocrinology, Ghent University Hospital, Ghent, BELGIUM,* [3]*Department of Neurosurgery, Ghent University Hospital, Ghent, BELGIUM,* [4]*Department Otorhinolaryngology, University Hospital Ghent, Ghent, BELGIUM.*

Aim/Introduction: Pituitary neuroendocrine tumours (PitNETs) are the second most common intracranial neoplasms and can be functioning or non-functioning. Magnetic resonance imaging (MRI) is the primary diagnostic tool for PitNETs, but some lesions remain challenging to detect with MRI alone. Consequently, O-(2'[18F]fluoroethyl)-L-tyrosine ([18F]FET) positron emission tomography (PET) has emerged as a promising complementary imaging modality, improving tumour visualization through differential tracer uptake in healthy versus abnormal pituitary tissue. ***Materials and Methods:*** We performed a retrospective analysis of [^{18}F]FET PET data from 21 patients (14 F, 7 M, age 52±16 years) with PitNET (newly diagnosed, persistent after prior treatment or recurrent after remission), scheduled for surgical resection. Based on biochemical evaluation, PitNETs were categorized as growth hormone (n=7), ACTH (n=6), prolactin (n=2), TSH-secreting (n=1), or non-functioning tumours (n=5). All patients underwent [^{18}F]FET PET/CT imaging (185 MBq; GE Omni Legend: n=20, Siemens Biograph20: n=1) and dedicated pituitary MRI (1.5T: n=3, 3T: n=18). Dynamic and static PET data were reconstructed using OSEM i8s12. PET and MR images were co-registered, and regions of interest were manually delineated using MIM Software. Visual correlation between PET and MRI (0: none, 0.5: partial, 1: high), Metabolic Index (MI), and Time-Activity Curves (TACs) were evaluated. MI, a proxy for FET uptake, was calculated in analogy to glioma: SUVmax/SUVmean healthy appearing cortical tissue. ***Results:*** All PitNETs visualized by MRI were also detected with [^{18}F]FET PET imaging, corresponding to a sensitivity of 100%. Visual correlation between PET and MRI was high (score: 1) in 52% of PitNETs and moderate (score: 0.5) in 48% of PitNETs. A moderate correlation between [^{18}F]FET PET and MRI could be explained by lesion heterogeneity, cysts, or resolution limits. Notably, one patient showed an additional lesion in the pituitary gland on [^{18}F] FET PET that was not visible on MRI (score: 0), suggesting potential added diagnostic value for [^{18}F]FET PET. The mean MI for all PitNETs was 2.4±0.4 with functioning PitNETs showing a slightly higher MI (2.5±0.4) compared to non-functioning PitNET (2.3±0.4). TACs of the majority of PitNETs exhibited a descending profile (n=17), three cases showed stable TACs, and one was excluded due to motion artifacts. No differences in TACs were observed based on PitNET-functionality. ***Conclusion:*** [^{18}F]FET PET provides consistent metabolic visualization of newly diagnosed, recurrent, or persistent PitNETs. Its high sensitivity, strong correlation with MRI findings, and distinct TAC profiles suggest that [^{18}F]FET PET is a valuable tool in the diagnosis and management of PitNETs.

EP-0326

AI-based Quantitative Volumetric [^{68}Ga]Ga-DOTATOC PET/CT Image Analysis in Predicting Response to Peptide Receptor Radionuclide Therapy and Disease Outcome

S. Manoochehry[1], *F. Sharifian*[1], *S. Mirshahvalad*[1], *W. Hitzl*[2], *N. Capobianco*[3], *B. Spottiswoode*[4], *G. Schweighofer-Zwink*[1], *C. Pirich*[1], *M. Beheshti*[1];
[1]*Division of Molecular Imaging and Theranostics, Department of Nuclear Medicine, University Hospital, Paracelsus Medical University, Salzburg, AUSTRIA,* [2]*Biostatistics and Publication of Clinical Trial Studies, Research and Innovation Management (RIM), Paracelsus Medical University, Salzburg, AUSTRIA,* [3]*Siemens Healthineers AG, Erlangen, GERMANY,* [4]*Siemens Medical Solutions USA, Inc., Knoxville, TN, UNITED STATES OF AMERICA.*

Aim/Introduction: To evaluate the predictive value of [^{68}Ga]Ga-DOTATOC PET/CT for treatment response and disease outcomes, using a prototype convolutional neural network (pCNN) for automated detection and semi-quantitative analysis in patients with metastatic neuroendocrine tumours (NETs) receiving peptide receptor radionuclide therapy (PRRT). ***Materials and Methods:*** This retrospective study included patients with histologically proven well-differentiated metastatic NET treated with [^{177}Lu]Lu-DOTATATE who underwent baseline (bPET) and post-treatment (pPET) [^{68}Ga]Ga-DOTATOC PET/CT after the four cycles of [^{177}Lu]Lu-DOTATATE treatment. Lesion detection and semi-quantitative PET parameters were extracted using a pCNN. Standardized uptake values (SUVs), as well as whole-body somatostatin-expressed total tumour volume (SSTR-TV) and total lesion SSTR expression (SSTR-TLA) were analyzed. PERCIST criteria were used to assess the response to treatment. Progression-free survival (PFS) and overall survival (OS) were defined from the first cycle of PRRT. ***Results:*** From the 19 patients with metastatic NET (6 females and 13 males), 10 (52.6%) demonstrated partial response, 3 (15.8%) showed stable disease, 3 (15.8%) exhibited completed response, and 3 (15.8%) experienced disease progression. Among semi-quantitative bPET parameters, the SUVmax-to-liver background ratio of the most avid lesion was significantly higher in responders. Analysis of pCNN-based volumetric bPET parameters revealed significantly higher SSTR-TLA (p=0.003) and total SSTR-TV (p=0.005) in responders. The median PFS in patients was 24 months. From the bPET-derived parameters, SULpeak-to-spleen background ratio and total SUVmean of the most avid lesion were significant predictors of PFS (p=0.009 and p=0.021, respectively). Among the volumetric PET parameters, Δtotal SSTR-TV and Δtotal SSTR-TLA ratio were identified as significant predictors of PFS (p=0.035 and p=0.038, respectively). The median OS in patients was 39 months. Total SUVmean significantly predicted OS (p<0.001), as also did Δtotal SSTR-TV from the volumetric parameters (p=0.020). ***Conclusion:*** This study provides preliminary evidence supporting the use CNN-based automated volumetric whole-body assessment of [^{68}Ga]Ga-DOTA-peptide PET/CT images in metastatic NET patients undergoing PRRT. The findings highlight the feasibility and prognostic value of this approach, warranting validation in larger patient cohorts.

EP-0327

Head-to-head comparison between Al^{18}F-NOTA-LM3 and ^{68}Ga-DOTA-TATE PET/CT in patients with metastatic pheochromocytomas and paragangliomas

Y. Zhang, *M. Liu, Y. Cai, X. Yan, C. Ren, Z. Huang, M. Wang, A. Tong, L. Huo, H. Jing;*
Peking Union Medical College Hospital, Beijing, CHINA.

Aim/Introduction: ^{68}Ga-based somatostatin receptor (SSTR) PET/CT has become the cornerstone for staging and monitoring metastatic pheochromocytoma and paraganglioma (mPPGL), including its theranostic role in selecting patients for peptide receptor radionuclide therapy (PRRT). Compared to ^{68}Ga-DOTA-SSA analogs, ^{18}F-labeled SSTR antagonists offer advantages including higher yield, superior image resolution, and longer half-life, which may facilitate clinical workflow. This study aims to evaluate the diagnostic efficacy of the SSTR antagonist Al^{18}F-NOTA-LM3 versus ^{68}Ga-DOTATATE in mPPGL patients. ***Materials and Methods:*** Patients with histologically confirmed mPPGL (either at initial diagnosis or relapsed/progression), were prospectively recruited and underwent both Al^{18}F-NOTA-LM3 PET/CT and ^{68}Ga-DOTA-TATE PET/CT within one week, with a minimum 24-hour interval between scans. Focal uptake not attributed to physiological activity was deemed positive. Diagnostic efficacy was assessed at the patient-, region-, and lesion-level. Biodistribution in normal organs, lesion detection rates, SUVmax and tumor-to-liver ratios (TLRmax) was compared. Up to five lesions (≥1 cm diameter, highest SUVmax) per region were analyzed, with a maximum of 20 lesions per region if exceeded. Whole-body TLRmax was assessed to identify potential PRRT candidates. ***Results:*** Fourteen patients (median age 47.7 years; 3 males) were included, with both tracers detecting positive lesions in all patients. Al^{18}F-NOTA-LM3 exhibited lower physiological organ uptake and higher detection rates for liver metastases (20 vs. 6, P < 0.001) and lymph node metastases (57 vs. 54, P = 0.0625) compared to ^{68}Ga-DOTATATE. Additionally, Al^{18}F-NOTA-LM3 demonstrated significantly higher SUVmax in metastatic lymph nodes and greater TLRmax in lymph nodes, liver and bone lesions. Whole-body tumor TLRmax was superior with Al^{18}F-NOTA-LM3 (10.21±5.6 vs. 5.52±4.23, P<0.05), suggesting an enhanced suitability for 177Lu-labeled LM3 PRRT. ***Conclusion:*** Al^{18}F-NOTA-LM3 PET/CT demonstrates superior diagnostic performance compared to ^{68}Ga-DOTA-TATE in patients with mPPGL, with improved lesion detection, higher tumor-to-background contrast, and favorable biodistribution. These findings support its potential as a preferred imaging and theranostic agent for mPPGL management.

EP-0328

Diagnostic, Therapeutic, and Economic Impact of the Protocolized Use of ^{68}Ga-DOTATOC PET/CT in Patients with Neuroendocrine Tumors (IMDOTA-TNE Study).

M. Cruz Montijano[1], *J. A. Bonilla Plaza*[1], *L. Garcia Zoghby*[1], *J. Montalva Pastor*[1], *M. Meneses Navas*[1], *S. Guzman Ortiz*[1], *I. García Megías*[1], *J. Medina Martínez*[1], *A. Marco Martínez*[1], *M. Abradelo De Usera*[1], *J. Cano Cano*[2], *L. García Blasco*[3], *C. Alonso López*[3], *C. Ortiz Muñoz*[2], *C. Martínez Osorio*[2], *F. Pena Pardo*[2], *V. García Poblete*[2], *A. García Vicente*[1];
[1]*Complejo Hospitalario de Toledo, Toledo, SPAIN,* [2]*Hospital General Universitario de Ciudad Real, Ciudad Real, SPAIN,* [3]*Complejo Hospitalario Universitario de Albacete, Albacete, SPAIN.*

Aim/Introduction: To evaluate the diagnostic, therapeutic, and economic impact of a protocolized imaging strategy using ^{68}Ga-DOTATOC PET/CT (PET/CT) following ^{99}mTc-HYNIC-TOC scintigraphy in patients with a diagnosis or suspicion of neuroendocrine tumors (NETs). ***Materials and Methods:*** Prospective multicenter study including consecutive patients from February to November 2024 referred for somatostatin receptor scintigraphy (SRS) with ^{99}mTc-HYNIC-TOC for various clinical indications. The study was approved by reference Ethical Committee (internal code 2024-051). PET/CT with ^{68}Ga-DOTATOC was subsequently performed only if its result could potentially lead to a change in patient management. A minimum clinical follow-up of 6 months was required. An economic analysis was also performed based on reimbursed costs using relative value units for each imaging modality. ***Results:*** A total of 142 patients were included (80 males), with a mean age of 63.96 years (range: 23-91). 51 patients underwent both SRS and PET/CT (Group 1), and 91 patients had only SRS (Group 2). Clinical indications included: 15 indeterminate lesions, 35 initial staging, 6 localization of unknown primary, 35 suspected recurrence or progression, 40 routine follow-up with clinical/biochemical stability, and 11 due to isolated elevation tumor markers without a previous diagnosis

of NETs.In Group 1, SRS and PET/CT were positive in 36 and 41 patients, respectively, identifying 160 and 286 lesions, respectively. PET/CT led to a change in disease staging in 24 patients and a therapeutic management change in 17, as well as detection of additional lesions in most cases.In Group 2, SRS was positive in 40/91 patients. During follow-up, 80 patients remained stable and 11 showed progression (3 due to other primaries with neuroendocrine features, and 8 due to metastatic NETs—4 with biochemical progression). Retrospectively, only 4 patients might have benefited from a PET/CT-based management change.This protocol resulted in a 17.35% cost saving (€42,147.74) compared to the direct use of PET/CT. ***Conclusion:*** Protocolized use of ^{68}Ga-DOTATOC PET/CT demonstrated a high diagnostic and therapeutic impact (47.05% and 33.33%, respectively), improving lesion detection and clinical decision-making. This selective approach minimized unnecessary radiation exposure and imaging redundancy, while achieving significant cost savings compared to a universal PET/CT strategy.

EP-0329

Whole-Body Tumor Burden on ^{68}Ga-DOTATOC PET/CT: A Prognostic Key in Well-Differentiated Neuroendocrine Tumors

C. Battisti[1], *C. Ferrari*[1], *A. Pisani*[1], *D. Candido*[1], *E. Lauricella*[2], *M. Bacalim*[2], *D. Rubini*[3], *A. Nappi*[1], *M. Cives*[2], *G. Rubini*[1];
[1]*Nuclear Medicine Unit, DIM, University "Aldo Moro", Bari, ITALY,* [2]*University of Bari Aldo Moro, Interdisciplinary Department of Medicine, Bari, ITALY,* [3]*Radiotherapy, Precision Medicine Department, University of Campania "Luigi Vanvitelli", Naples, ITALY.*

Aim/Introduction: We investigated the prognostic value of somatostatin receptor tumor burden on ^{68}Ga-DOTATOC PET/CT in patients with well-differentiated neuroendocrine tumors (NETs). ***Materials and Methods:*** We retrospectively analyzed 67 NETs patients who performed ^{68}Ga-DOTATOC PET/CT for staging/restaging purpose between November 2023 and December 2024. Data on age, sex, TNM stage, tumor grade (Ki-67 for grade 1, <3%; grade 2, 3-20%; grade 3, >20%), biomarkers (CgA, NSE) and previous treatments were collected. Information regarding time to progression (TTP), defined as the time from PET/CT imaging to the first event (progression or relapse), was achieved by clinical follow-up. The number of all ^{68}Ga-DOTATOC-avid lesions for specific organ (lymph nodes, liver, bone, others) was identified and SUVmax, SUVmean, Somatostatin receptor-expressing tumor volume (SRETV) and total lesion somatostatin receptor expression (TLSRE) were extracted for each lesion, using a semiautomatic segmentation. Then, whole-body SRETV (SRETVwb) and TLSRE (TLSREwb) were defined as the sum of SRETV and TLSRE. The prognostic value of both clinical and PET/CT semiquantitative parameters was evaluated using Chi-square Fisher's exact, and Mann-Whitney tests. Cox proportional-hazards regression model was employed to analyze the impact of the same variables on TTP. A p<0.05 was considered statistically significant. ***Results:*** 46 consecutive patients met the inclusion criteria (M:F=23:23, mean age 60y). Pancreas was the most frequent primary site (33%); 92% of the tumors were classified as grade 1-2. Fifty-two% had metastatic disease at the diagnosis. Liver was the most involved secondary site (50%) with a number of focal lesions ≤3 in 35% and >4 in 65% of patients. Median SRETVwb and TLSREwb was 53.30 cm^3 and 652.34 g/mLxcm^3, respectively. After a mean follow-up of 9mo (range 3-15mo), disease progression was confirmed in 12 patients (26%) and 2 patients died. Significant associations with disease progression were observed for higher values of SRETVwb (p=0.043) and TLSREwb (p=0.016); Ki67<3% (p=0.003), a negative PET result (p=0.032), the absence of secondary lesions (p=0.006) and the presence of liver lesions ≤3 (p=0.038) were favourable prognostic factors. In the univariate analysis, TLSREwb (p=0.042), Ki67 (p=0.023), PET/CT result (p=0.022), and the presence of secondary lesions (p=0.003) significantly correlated with a shorter TTP. In multivariate analysis with Cox Proportional-Hazards regression model, TLSREwb and Ki67 resulted independent predictors of TTP (p=0.010). ***Conclusion:*** Our preliminary results suggested that TLSREwb extracted from ^{68}Ga-DOTATOC PET/CT could represent a good predictor of TTP and, together with Ki67, might have important clinical utility in the management of NETs patients.

EP-0330

Utility of Ga-68 DOTA-RGD2 PET/CT in Grade 2 & 3 neuroendocrine tumours and comparison with Ga-68 DOTANOC PET/CT

K. Subramanian*;*
Post Graduate Institue of Medical Education and Research, Chandigarh, INDIA.

Aim/Introduction: Neuroendocrine tumors (NETs) are a heterogeneous group of tumors with variable somatostatin receptor (SSTR) expression. Their spectrum ranges from well-differentiated neuroendocrine tumors (NETs) to poorly differentiated neuroendocrine carcinomas (NECs), according to the WHO categorization system based on cell differentiation and mitotic index (Ki 67). Higher-grade NETs are poorly differentiated and more aggressive. Neoangiogenesis is a marker of aggressiveness and is necessary for tumor growth, invasion, and metastatic spread. In patients with high-grade NETs, we assessed angiogenesis in vivo using the novel imaging marker Ga-68 DOTA-RGD2 PET/CT and compared it with Ga-68 DOTANOC PET/CT for SSTR expression. ***Materials and Methods:*** 44 patients with histopathologically confirmed WHO grade 2 (n=34) and grade 3 (n=10) NETs (24 males, 20 females; mean age: 49.6 years, range: 32-69 years) participated in this prospective study. All patients underwent Ga-68 DOTA-RGD2 PET/CT and Ga-68 DOTANOC PET/CT within five days before starting any form of treatment. Both the PET/CT images were evaluated visually and semi quantitatively. Tracer uptake in the primary lesion was interpreted as positive if it exceeded the mediastinal blood pool activity. Semi-quantitative parameters such as maximum standardized uptake values (SUVmax) and tumour to background ratios (TBR) of the primary lesions were measured. Pearson correlation test was used to analyze the correlation between two normally distributed continuous quantitative data and Spearman's rho test for non-continuous and non-normally distributed data. The unpaired t-test was used to compare normally distributed continuous variables. ***Results:*** Using Ga-68 DOTA RGD2, the detectability of lesions was 73.4% for primary lesions and 47.8% for metastatic areas, such as the brain (100%), liver (18%), lymph nodes (68.4%), and bone (71.2%). Primary was found in the stomach (13.1%), retroperitoneum (14.1%), mesenteric NET (8.5%), breast (5.5%), liver (6.6%), small intestine (19.2%), and pancreas (32.8%). ^{68}Ga-DOTANOC showed 88.8% lesion detectability for primary lesions and 85.7% for metastatic locations, such as the brain (100%), liver (78.3%), bone (98%), and lymph nodes (100%). At every disease-involved site, the SUVmax and TBRmax values for Ga-68 DOTANOC PET/CT were substantially greater than those for ^{68}Ga-DOTA RGD2 PET/CT. The SUVmax and TBRmax on Ga-68 DOTA RGD2 PET did not show a statistically significant correlation (p=0.904; p=0.946 respectively) with the grade of the tumor. ***Conclusion:*** Patients with high-grade neuroendocrine tumors may benefit from angiogenesis imaging using Ga-68 DOTA RGD2 PET/CT. Except for liver-related metastatic lesions, lesion detectability is comparable to that of Ga-68 DOTANOC PET/CT.

EP-18

e-Poster Area

B: Imaging Clinical Studies -> B1 Oncological Imaging Clinical Study -> B17 Colorectal

EP-0331

Feasibility of an early-imaging ^{68}Ga-FAPI-PET/CT protocol in prone position for rectosigmoid and anal cancer

D. Ufton[1], *J. Heilinger*[1], *H. Weis*[1], *T. Fischer*[1], *K. Schomäcker*[1], *C. Bruns*[2], *G. Dieplinger*[2], *H. Dapper*[3], *E. Fokas*[3], *C. Kobe*[1], *A. Drzezga*[1], *S. Ferdinandus*[3], *K. S. Roth*[1];
[1]*University Hospital of Cologne, Department of Nuclear Medicine, Cologne, GERMANY,* [2]*University Hospital of Cologne, Department of Surgery, Cologne, GERMANY,* [3]*University Hospital of Cologne, Department of Radiation Oncology, Cologne, GERMANY.*

Aim/Introduction: Colorectal carcinoma (CRC) and squamous cell carcinoma (SCCA) present malignant entities with high expression of firoblast-activting-protein (FAP) suited for staging via ^{68} Ga-FAPI-PET/CT with improved staging accuracy compared to ^{18}-FDG-PET/CT. Previous studies focusing on other malignancies reported the viability of staging protocols 10 minutes after injection of ^{68}Ga-FAPI excluding intrapelvic tumors. Our aim was to assess the viability of an early imaging protocol for FAPI-PET/CT for CRC and SCCA in prone position. ***Materials and Methods:*** 15 patients underwent early-imaing ^{68}Ga-FAPI-46-PET/CT-scans in prone position for histologically confirmed CRC or SCCA 5.9 minutes after radiotracer injection. SUV_{max} and metric values for primary tumors and metastases and SUV_{mean} values for liver, spleen, muscle tissue and blood pool were measured. Tumor-to-background ratios (TBR) were calculated by dividing SUV_{max} of the primary tumor by the SUV_{mean} of the reference tissues. Statistical comparison was performed via two-sample t-test. ***Results:*** Uptake was high in all primary tumors with an average SUVmax and SUVpeak of 14.9 (± 4.79) and 9.5 ± 2.5. Uptake was significantly higher ($p = 0.004$, Figure 1) in SCCA (SUVmax =20.3 ± 5.8 and SUVpeak = 12.0 ± 2.8) than in CRC (SUV_{max} =11.2 ± 1.7 and SUV_{peak} = 7.8 ± 1.4). The average minimal distance between the urinary bladder and the primary malignancy was 2.56 cm ± 0.66 cm. Lesions suspect of regional lymph node metastases had an average SUVmax of 12.8 ± 1.8 and SUVpeak of 8.5 ± 1.9, with the low-dose CT-scans showing no malignant characteristics for the smallest metastases. Lesions suspect of distant metastases were found in four patients with an average SUVmax of 11.4 ± 6.7 and a SUVpeak of 8.3 ± 4.8. High TBR were achieved for all reference tissues with the TBR being significantly lower for the blood pool compared to the other reference tissues (5.8 ± 1. 5 vs. 8.0 ± 2.2 ($p = 0.02$), 9.2 ± 2.8 ($p = 0.005$) and 8.9 ± 3.0 ($p = 0.01$) compared to liver, spleen and muscle tissue respectively). ***Conclusion:*** Early-imaging protocol in prone position for 68Ga-FAPI-46-PET/CT presents a safe and viable option for non-invasive imaging for SCCA and CRC achieving high uptake values in primary tumors and even small metastases while showing only low background uptake leading to high TBR. Imaging in prone position leads to safe spatial seperation of the urinary bladder to the primary tumors, allowing for safe tumor delineation.

EP-0332

Clinical Application Value of FAPI Imaging in Colorectal Cancer: A Retrospective Study

T. Fang*;*
Department of Nuclear Medicine, Zhongnan Hospital of Wuhan University, Wuhan, CHINA.

Aim/Introduction: Colorectal cancer remains one of the most prevalent malignancies worldwide, characterized by high incidence and mortality rates. Although [^{68}Ga]Ga-FAPI-04 PET/CT has been widely validated as a powerful tool for CRC diagnosis and staging, its potential role in predicting molecular biomarkers and prognostic outcomes remains underexplored. This retrospective study aims to analyze and elucidate the relationship between semi-quantitative parameters of [^{68}Ga]Ga-FAPI-04 PET/CT in previously untreated colorectal cancer (CRC) patients and clinical data, including tumor PD-L1 expression status, tumor mutational burden (TMB), KRAS/NRAS/BRAF mutation profiles, and progression-free survival (PFS). ***Materials and Methods:*** We retrospectively enrolled 64 treatment-naïve CRC patients who underwent pretreatment [^{68}Ga]Ga-FAPI-04 PET/CT imaging, with follow-up exceeding one year. Semi-quantitative parameters—SUVmax, SUVmean, SUVpeak, tumor-to-background ratio (TBR), total metabolic tumor volume (MTV), and total total lesion fibroblast activation protein inhibitor (TLF)—were systematically measured in 30 patients. These parameters were analyzed for correlations with PD-L1 expression, TMB, KRAS/NRAS/BRAF mutations, and PFS. ***Results:*** Total MTV and TLF demonstrated statistically significant associations with PFS ($P < 0.05$, Cox regression analysis), whereas other parameters (SUVmax, SUVmean, SUVpeak, TBR) showed no prognostic relevance. Notably, none of the PET/CT-derived semi-quantitative metrics exhibited significant correlations with PD-L1 expression levels, TMB categories, or KRAS/NRAS/BRAF mutation status (all $P > 0.05$). ***Conclusion:*** Our findings suggest that pretreatment [^{68}Ga]Ga-FAPI-04 PET/CT lacking predictive value for non-invasive assessment of PD-L1 expression, TMB, or common oncogenic mutations (KRAS/NRAS/BRAF) in CRC. Specifically, elevated total MTV and TLF were associated with shorter PFS, providing clinicians with actionable insights for risk stratification and therapeutic planning. Further validation in larger cohorts is warranted to confirm these observations.

EP-0333

Variations in F-18-FMISO Physiological Uptake

M. Araz*, &. Mesci, E. D. Avci, C. Soydal, N. Ö. Kucuk;*
Ankara University, Ankara, TÜRKIYE.

Aim/Introduction: To evaluate differences in distribution of F-18-FMISO uptake according to age, gender and primary cancer type. ***Materials and Methods:*** A total of randomly chosen 30 F-18-FMISO PET/CT studies performed for evaluation of different malignancies in three prospective clinical trials were retrospectively reevaluated. SUVmax and SUVmean values of brain, bone marrow, liver, stomach, colon, aorta were recorded. No measurements were taken on primary or metastatic tumor sites. Use of oral antidiabetics was also noted. Spearman's correlation analysis was performed to assess the relationship between age and SUV. Significance of differences between mean values of age, SUVmax, SUVmean and TBR values were also assessed. ***Results:*** Included in the study were 30 patients(13F,17M, mean age:64,27±12.05). Primary cancers of the patients were prostate in 7 patients, gastric in 2, colon in 8, rectum in 7, HCC in 3, breast in 1 and ovarian cancer in 1 patient. There was no significant correlation between age and SUV values. Mean age values were not significantly different among primary cancer subtypes. The mean values of SUVmax and SUVmean values of brain and liver didn't differ according to primary cancer subtypes. SUVmax of colon, SUVmax and SUVmean of bone marrow were significantly higher in patients with gastrointestinal tumors compared to others($p=0.049$,$p=0.017$ and $p=0.005$). There was no significant difference between mean values of the studied variables according to gender or use of oral antidiabetics. ***Conclusion:*** Relatively higher bone marrow uptake in gastrointestinal cancer patents is a novel finding in need of further investigation. Although it was previously speculated that FMISO diffuses freely from the intestinal wall or luminal bacteria may cause hypoxia, pathophysiology of higher colonic uptake in gastrointestinal cancer is still scarce (1,2). Further investigations are necessary to determine the causal relationship between high colonic uptake of FMISO in patients with gastrointestinal system tumors and attention is needed in reporting or quantitative evaluation of FMISO PET studies. ***References:*** 1) Roels S, Slagmolen P, Nuyts J, Lee JA, Loeckx D, Maes F, Stroobants S, Penninckx F, Haustermans K. Biological image-guided radiotherapy in rectal cancer: is there a role for FMISO or FLT, next to FDG? Acta Oncol.

2008;47(7):1237-48 2) Flockhart IR, Large P, Troup D, Malcolm SL, Marten TR. Pharmacokinetic and metabolic studies of the hypoxic cell radiosensitizer misonidazole. Xenobiotica. 1978 Feb;8(2):97-105 2).

EP-0334

Cost-Effectiveness of [^{18}F]FDG PET/CT in Follow-Up after Thermal Ablation in Patients with Colorectal Liver Metastases in the Dutch Healthcare Setting

S. van Mossel[1,2], *O. Bijlstra*[1], *F. van Delft*[2], *B. Boekestijn*[1], *M. Burgmans*[1], *P. Hendriks*[1], *E. Kapiteijn*[1], *S. Mieog*[1], *E. Persijn van Meerten*[1], *D. Rietbergen*[1], *S. Shahbazi Feshtali*[1], *L. De Geus-Oei*[1,2,3], *H. Koffijberg*[2];
[1]*Leiden University Medical Center, Leiden, NETHERLANDS,* [2]*University of Twente, Enschede, NETHERLANDS,* [3]*Delft University of Technology, Delft, NETHERLANDS.*

Aim/Introduction: The European Society for Medical Oncology (ESMO) and the European Conference on Interventional Oncology and European Society of Oncological Imaging (ECIO-ESOI) consensus guidelines vary in their recommendations regarding the use of ^{18}F-Fluorodeoxyglucose ([^{18}F]FDG) PET/CT in the follow-up after thermal ablation in patients with colorectal liver metastases. This is partly because clinical trials commonly have a limited follow-up duration, which means that data on long-term health effects, survival benefits, and cost consequences of [^{18}F]FDG PET/CT are lacking. Therefore, a simulation model has been developed to study how follow-up with [^{18}F]FDG PET/CT impacts treatment planning, long-term health and cost outcomes. We aimed to explore whether [^{18}F]FDG PET/CT allows early re-treatment and results in (i) improved health outcomes as early re-treatment may prevent patients from reaching a palliative phase of disease and (ii) reduced treatment costs as early re-treatment may reduce the need for more expensive medication and for performing open abdominal surgeries. ***Materials and Methods:*** In an illustrative Dutch cohort (48 patients, >100 scans), lifetime health and cost outcomes were evaluated to assess the cost-effectiveness of adding a single [^{18}F]FDG PET/CT to follow-up 3-4 months after thermal ablation of colorectal liver metastases, compared to standard clinical practice. Patients followed a standard surveillance schedule consisting of three-monthly serum CEA, contrast-enhanced CT and additional upper abdominal contrast MRI upon request of the medical specialist, plus routine [^{18}F]FDG PET/CT 3-4 months after thermal ablation. Therapy could be repeated downstream the care pathway. Quality-of-life and survival estimates were based on disease stage and age using literature evidence. Costs were also determined from the literature incorporating the costs related to diagnostics and treatments. ***Results:*** Health benefits of the additional [^{18}F]FDG PET/CT were negligible, incremental QALYs<0.001, whereas costs increased by €1,277, mainly due to the additional imaging. This lack of health benefits can be explained by the small subset of simulated patients (<5%) in whom [^{18}F]FDG PET/CT affected treatment planning. ***Conclusion:*** An additional routine [^{18}F]FDG PET/CT 3-4 months after thermal ablation is unlikely to be cost-effective, given the current (but limited) evidence. More research is needed to determine if using [^{18}F]FDG PET/CT in subgroups of patients, or at alternative time points, is cost-effective. This requires collecting more (extensive) follow-up data, preferably across multiple hospitals, since clinical practice may vary widely between hospitals.

EP-0335

The Value of Staging FDG PET/CT Parameters in Predicting Liver Operability and Survival in Liver Metastatic Rectal Cancer

T. Bilgücü, *G. Uçmak, B. Demirel;*
Ankara Abdurrahman Yurtaslan Educational and Research Onkology Hospital, Ankara, TÜRKIYE.

Aim/Introduction: Our study aims to examine the relationship between staging FDG PET/CT metabolic parameters with operability and survival in liver metastatic rectal cancer. ***Materials and Methods:*** Patients diagnosed with rectal cancer without extrahepatic visceral organ metastases on staging FDG PET/CT between September 2013 and July 2022 were included in our study. Metabolic parameters, pre-operative and post-operative findings were recorded. Logistic regression analysis was performed to identify factors predicting liver metastatic lesion operability. ROC analysis was used to determine the relationship between SUVmax value of liver metastatic lesions and disease progression. Progression-free survival (PFS) and overall survival (OS) were calculated. Survival analyses were conducted using the Kaplan-Meier method and also Cox Regression Analysis. ***Results:*** 38 patients [mean age: 60.8±9.1 (39-81)] were included, of whom 28 (%73.7) were male and 10 (%26.3) were female. Among patients tested for KRAS mutation, 12 results were positive, while 16 patients were negative (wild-type). A total of 29 patients received neoadjuvant therapy and 28 patients were performed liver metastasectomy. SUVmaks value of liver metastatic lesion below 7.5 had a significantly longer PFS value [30±8.3 months (%95 CI 13,7-46,2), compared to those with a value above 7.5 [11±4.2 months (%95 CI 2,5-19,4)] (p=0.02). In addition to this, a significant correlation was found between liver MTV and TLG burden with decreased likelihood of liver operability (p = 0.04, OR: 0.99, 95% CI: 0.98-1.00). Also, patients who underwent liver metastasectomy had clinically longer PFS and OS values. The characteristics of patients' liver metastatic lesions are shown in Table 1. Patients with positive KRAS mutation had significantly higher values for liver metastatic lesion SUVmax, liver MTV and TLG compared to those with negative KRAS mutations. Additionally, positive KRAS mutation was associated with clinically shorter PFS and OS values (p = 0.07). ***Conclusion:*** In staging FDG PET/CT, liver MTV-TLG burden were found to have a significant impact on liver operability. A significant inverse relationship was detected between increasing MTV and TLG values and the likelihood of operability. The liver metastatic lesion had SUVmax >7.5 showing a correlation with shorter PFS. Patients who underwent liver metastasectomy were clinically associated with longer PFS and OS compared to those who did not undergo surgery. Additionally, PET metabolic parameters predicted KRAS mutation positivity, which was also associated with clinically shorter PFS and OS values.

EP-0336

Prognostic Utility of Volumetric PET Parameters in Colorectal Liver Metastases: Identifying Optimal Segmentation Strategies for MTV and TLG

M. Badarna, *Z. Keidar;*
Rambam Health care campus, Haifa, ISRAEL.

Aim/Introduction: Colorectal liver metastases (CRLM) are a major cause of colorectal cancer mortality. FDG PET/CT plays a critical role in staging and treatment planning. While traditional metrics like maximal standardized uptake value (SUVmax) provide prognostic information, volumetric PET biomarkers- such as metabolic tumor volume (MTV) and total lesion glycolysis (TLG)- offer a more comprehensive assessment of tumor burden. However, reproducibility is limited due to variability in segmentation methods especially in low tumor-to-background contrast like the liver. This study aims to identify the most robust segmentation method and threshold values for pre-treatment volumetric PET parameters in CRLM, and to evaluate their prognostic value by correlation with progression-free survival (PFS) and overall survival (OS). ***Materials and Methods:*** We retrospectively analyzed 42 patients with CRLM after primary tumor resection and before initiating systemic therapy. Three segmentation methods were compared: two threshold-based (absolute and relative) and one gradient-based. MTV and TLG were calculated using multiple

thresholds per method, and total MTV and TLG (tMTV and tTLG) were derived per patient. ROC analysis identified optimal thresholds for predicting PFS and OS. Kaplan-Meier survival and log-rank tests were used for outcome comparison. Additional analysis was conducted in a subgroup of patients with liver-only metastases (n=28). ***Results:*** None of the PET-derived parameters significantly predicted PFS (AUCs 0.52-0.60). Among segmentation methods, only the relative threshold method showed prognostic value for OS. The best-performing metric was tMTV30% (using 30% SUVmax threshold), with a cut-off of 45.49 mL (AUC=0.72); patients above this value had significantly shorter survival (mean OS 5.64 vs. 13.46 years, p=0.012). SUVmax also showed prognostic relevance (cut-off 7.97, AUC=0.74); unexpectedly, higher values were associated with better survival (10.4 vs. 6.3 years), though not statistically significant. In the liver-only subgroup, SUVmax and volumetric parameters using absolute threshold method with SUV = 4 (tMTV4.0, tTLG4.0) performed best. The prognostic trend was reversed: lower SUVmax (≤8.09), tMTV4.0 (≤10.68 mL), and tTLG4.0 (≤58.92) were associated with worse OS. Only SUVmax and tTLG4.0 were significant predictors (p=0.015 and p=0.002). The gradient-based method underperformed across all analyses. ***Conclusion:*** Volumetric PET parameters, particularly the relative threshold-based segmentation method (tMTV30%), show potential for OS prognostication in CRLM and may outperform SUVmax. However, reversed trends in the liver-only subgroup, where lower metabolic burden predicted poorer outcomes, suggest underlying biological heterogeneity or limitations of volumetric analysis in low-burden disease. These findings call for prospective validation prior to clinical implementation.

EP-0337

Comparison of qualitative and quantitative metabolic variables in FDG PET/CT inrectal cancer patients who achieved complete and incomplete response after neoadjuvantchemoradiotherapy

K. Amaral, *R. Moreira Siqueira, C. sa de Camargo, E. Etchebehere, M. CL Lima, A. O Santos, C. D. Ramos, B. Juarez Amorim; UNICAMP, Campinas, BRAZIL.*

Aim/Introduction: Patients diagnosed with advanced rectal cancer are often submitted to neoadjuvant chemoradiotherapy treatment. The aim of this study was to evaluate the metabolic parameters obtained by FDG PET/CT, before and after nCRT in advanced RC patients. ***Materials and Methods:*** Patients were divided in 2 groups: complete clinical response after treatment and the ones who did not achieved complete response. All patients underwent pre-treatment and post. Among the exclusion criteria were patients who began therapy before pre-treatment PET/CT and patients who did not have both studies. We included 34 patients in the good responder group and 40 patients in the poor responder group. FDG PET/CT was analyzed by two nuclear medicine physicians, and qualitative and quantitativeanalysis were performed. We used a visual response score in qualitative analysis to compare post-PET/CT with pre-PET/CT: grade 0 = no evidence of uptake reduction; grade 1= < 33% uptake reduction; grade 2 = > 33% to 66% uptake reduction; grade 3 = > 66% uptake reduction; grade 4 = no uptake evidence on post-PET/CT. The following quantitative parameters were analyzed: SUVmax, SUVmean, MTV and TLG. The VOIs were drawn onthe primary tumor by two methodologies: 1. applying a VOI with fixed threshold of 41%; 2. drawing a VOI with variable threshold which best delineated the metabolically active tumor (best visual fit - BVF). The variable thresholds were delineated according to each patient. ***Results:*** In visual analysis, grade 4 showed a very high specificity (95%) to discriminate good from poor responder group, with a positive predictive value of 90.9%, despite a low sensitivity (58.8%). There were only two false-positive patients, one with a carcinoma in situ and the other one with a mucinous tumor. The quantitative parameters which were able to discriminated between good and poor responders with significance were: post-treatment SUVmax41% ($p < 0.0001$), SUVmaxBVF ($p < 0.0001$), post-treatmentSUVmean41% ($p < 0.0001$) and SUVmeanBVF ($p < 0.0001$), TLGBVF post-treatment ($p = 0.0164$), ΔSUVmax ($p = 0.0306$), ΔSUVmean41% ($p = 0.0072$). ***Conclusion:*** FDG PET/CT can be an accurate tool to discriminate good responders from poor responders after nCRT in RC patients. Qualitative and quantitative PET parameters which are accessible in practical routine can differentiate both groups. Further multicentric studies are necessary to standardizethe methodology and cutoffs levels. ***References:*** Araghi et al. (2019) - CRC mortality; Patel et al. (2022) - CRC screening; Habr-Gama et al. (2023) - Non-op rectal CA.

EP-0338

Mechanistic Study on the Inhibition of Colorectal Cancer Tumor Progression in Nude Mice via CL316243 Activation of Brown Adipose Tissue Using ^{18}F-FDG MicroPET/CT

J. Li, *L. Zhang, X. Mu, W. Fu;*
Affiliated Hospital of Guilin Medical University, Guilin, CHINA.

Aim/Introduction: This study investigated the anti-tumor mechanisms of CL316243, a β3-adrenergic receptor agonist, through systemic activation of brown adipose tissue (BAT) in MC38 colon cancer-bearing nude mice. Utilizing ^{18}F-FDG PET/CT imaging, we dynamically monitored whole-body and tumor glucose metabolism to explore novel metabolic intervention strategies for colorectal cancer treatment. ***Materials and Methods:*** 1.Thirty male BALB/C nude mice with MC38 colon cancer subcutaneous xenografts were randomized into four groups (6-8 mice/group): Control, CL316243-treated, IBAT-surgically-removed control, and IBAT-removed + CL316243-treated.2.CL316243 groups received daily intraperitoneal injections of 1 mg/kg CL316243 for 5 days, while control groups received saline.3.^{18}F-FDG Micro PET/CT imaging was performed pre- and post-treatment. PMOD software quantified SUV_{max} and SUV_{mean} in tumors and IBAT, analyzed via paired t-tests. Tumor volume/weight and organ glucose metabolism were monitored. Post-imaging tumor tissues underwent immunohistochemistry (IHC) for UCP1 (IBAT), Ki67, and Glut1 (tumors). Statistical analyses included ANOVA and t-tests. ***Results:*** 1. Pre - and post - treatment glucose metabolism in brain, heart, lung, and muscle showed no significant change ($P>0.05$). Hepatic glucose metabolism decreased,but without statistical significance ($P>0.05$). Thus, ^{18}F-FDG Micro PET/CT can dynamically monitor glucose metabolism changes in normal organs of nude mice.2.Tumor volume and mass were significantly lower in the CL316243 and IBAT - removed + CL316243 groups than in their respective control groups ($P<0.01$). The inhibition rates were 51.05% and 63.67%, respectively, proving CL316243 inhibits tumor progression.3. In the control group and IBAT-removed control group, pre-and post-treatment tumor SUV_{mean} values showed no significant change ($P>0.05$). However, in the CL316243 and IBAT - removed + CL316243 groups, post - treatment tumor SUV_{mean} values were significantly lower than pre-treatment values ($P<0.01$), indicating CL316243 suppresses tumor glucose metabolism, possibly via IBAT activation or direct inhibition.4.IHC showed CL316243 treatment significantly reduced KI67 and Glut1 expression in nude mouse tumors compared to control groups ($P<0.05$), proving CL316243 inhibits tumor proliferation and glucose metabolism. ***Conclusion:*** In this study, using the MC38 colon cancer nude mouse model, it was found that CL316243 can effectively activate brown adipose tissue (BAT), significantly inhibiting tumor growth and progression. Also, ^{18}F-FDG PET/CT imaging proved to be an effective tool for monitoring these metabolic changes and their impact on tumors. This finding offers a novel metabolic intervention strategy for colorectal cancer treatment.

EP-0339

Assessment of the prognostic value of ^{18}F-FDG PET-CT metabolic parameters in patients with rectal cancer

G. Cuesta Domingo[1], *A. Ortega Candil*[1], *C. Rodríguez Rey*[1], *R. Cano Carrizal*[2], *P. Nespral Torres*[3], *P. Daudén Oñate*[1], *M. Vaillant López*[1], *M. Zapardiel Martínez-Falero*[1], *C. Wakfie Corieh*[1], *M. Cabrera Martín*[1];
[1]*Department of Nuclear Medicine, Hospital Clínico San Carlos, Madrid, SPAIN,* [2]*Department of Cardiology, Hospital Infanta Sofía, San Sebastián de los Reyes, SPAIN,* [3]*Department of Nuclear Medicine, Hospital Universitario Puerta de Hierro, Madrid, SPAIN.*

Aim/Introduction: Rectal cancer is one of the most common malignanciesof the digestive tract. Its management poses challenges due to its anatomical location and silent progression. We aim to analyze the independent prognostic value of metabolic parameters from [18F-FDG]PET-CT in patients with rectal cancer. ***Materials and Methods:*** We conducted a retrospective cohort study (2020-2023) including 59 patients with rectal cancer referred for staging with [18F-FDG]PET-CT. Clinical, imaging, and metabolic variables were collected, including MTV, SUVmax, and SUVmean of the primary lesion. Tumor-related death was defined as the primary endpoint during follow-up. A multivariate Cox regression analysis was performed to identify independent prognostic predictors. Model discrimination capacity was assessed using Harrell's C-index. ***Results:*** The mean age was 65.62 ± 12.06 years, with 49.15% of the cohort being male. Adenocarcinoma was the predominant histological subtype (98.31%). Nine patients (15.25%) presented with metastatic disease at diagnosis. The mean values for the metabolic parameters were: MTV 16.55 ± 20.44, SUVmax 21.36±8.07, and SUVmean 12.29 ± 4.62. The average follow-up time was 35.15 months. In the univariate analysis, MTV (HR 1.039; 95% CI 1.010-1.069; p=0.007) was the only metabolic parameter significantly associated with the event, along with surgery, radiotherapy, nodal involvement on PET/CT, and the presence of metastases. In the multivariate Cox regression analysis, surgery (HR 0.142; 95% CI 0.024-0.850 ; p=0.033), radiotherapy (HR 0.085; 95% CI 0.013-0.580; p=0.012), and MTV (HR 1.037; 95% CI 1.008-1.068; p=0.014) remained as independent prognostic factors. Harrell's C-index demonstrated excellent discriminative ability of the final model (0.931; 95% CI 0.873-0.989). ***Conclusion:*** In our cohort, MTV emerged as an independent prognostic factor for mortality in patients with rectal cancer, indicating that higher MTV values are associated with decreased survival.

EP-0340

Added predictive value of [18F-FDG]PET/CT over MRI in detecting nodal persistence after neoadjuvant therapy in rectal cancer

G. Cuesta Domingo[1], *C. Rodríguez Rey*[1], *A. Ortega Candil*[1], *R. Cano Carrizal*[2], *P. Nespral Torres*[3], *P. Daudén*[1], *M. Vaillant Lopez*[1], *M. Zapardiel Martínez-Falero*[1], *C. Wakfie Corieh*[1], *M. Cabrera Martín*[1];
[1]*Department of Nuclear Medicine, Hospital Clínico San Carlos, Madrid, SPAIN,* [2]*Department of Cardiology, Hospital Infanta Sofía, San Sebastián de los Reyes, SPAIN,* [3]*Department of Nuclear Medicine, Hospital Universitario Puerta de Hierro, Madrid, SPAIN.*

Aim/Introduction: The detection of nodal persistence after chemoradiotherapy (CRT) in rectal cancer is critical for surgical planning and prognostic stratification. Pelvic magnetic resonance imaging (MRI) is the reference technique for locoregional staging, although it has limitations in assessing nodal involvement. [18F-FDG]PET/CT provides crucial metabolic information for the evaluation of both locoregional and metastatic nodal disease. We aim to assess the concordance between MRI and PET/CT in detecting nodal disease and to determine whether PET/CT provides additional predictive value over MRI in identifying residual nodal involvement following CRT. ***Materials and Methods:*** A retrospective study (2020-2023) was conducted with 49 patients diagnosed with rectal cancer who underwent staging with both PET/CT and MRI prior to neoadjuvant treatment (CRT) and surgery. Concordance between the two techniques was assessed using the Kappa index. Two nested models for detecting nodal persistence were compared: one based solely on MRI and another combining MRI and PET/CT. The discriminative ability of both models was analyzed using ROC curves. ***Results:*** The mean age was 64.79 ± 11.45 years, with adenocarcinoma in all cases. 48.98% were women, and stage IIIB (32.65%) was the most frequent. MRI detected nodal disease in 37 patients (75.51%), compared to 25 patients (51.02%) with PET/CT. The concordance between both techniques was moderate (Kappa = 0.4226; p < 0.001). The combined model (MRI + PET/CT) provided a significantly added predictive value over the single MRI model (LR-chi2 9.11; p = 0.0025). ROC curve analysis also showed a higher discriminative ability for the combined model (AUC: 0.6354 vs. 0.7812; p = 0.0081). ***Conclusion:*** ^{18}F-FDG PET/CT provides added predictive value over MRI in detecting nodal persistence post-neoadjuvant therapy in rectal cancer. Its combined use enhances discriminative ability and aids in better surgical selection of patients.

EP-0341

Utility of ^{18}F-FDG PET/CT in the staging of rectal carcinoma

G. Cuesta Domingo[1], *A. Ortega Candil*[1], *C. Rodríguez Rey*[1], *R. Cano Carrizal*[2], *P. Nespral Torres*[3], *M. Vaillant López*[1], *P. Daudén Oñate*[1], *P. Bascuñana Almarcha*[4], *C. Wakfie Corieh*[1], *M. Cabrera Martín*[1];
[1]*Department of Nuclear Medicine, Hospital Clínico San Carlos, Madrid, SPAIN,* [2]*Department of Cardiology, Hospital Infanta Sofía, San Sebastián de los Reyes, SPAIN,* [3]*Department of Nuclear Medicine, Hospital Universitario Puerta de Hierro, Madrid, SPAIN,* [4]*IDISSC, Department of Nuclear Medicine, Hospital Clínico San Carlos, Madrid, SPAIN.*

Aim/Introduction: Rectal cancer is one of the most common neoplasms of the gastrointestinal tract. Its management presents significant challenges due to its anatomical location and often silent progression. In these patients, PET/CT has become a valuable tool for assessing both lymph node involvement and distant metastases. The aim of this study is to analyze how PET/CT influences modifications in neoadjuvant treatment strategies. ***Materials and Methods:*** We conducted a retrospective, observational, and descriptive study between 2020 and 2023, including 59 patients with rectal cancer (stages II-IV) referred to our center for staging. We collected various variables, including metabolic parameters from PET (SUVmax and MTV), and assessed how often PET/CT led to changes in initial staging and therapeutic management. ***Results:*** The mean age of patients was 65.44 ± 12.04 years. Stage IIIB was the most common (30.5%; n=18), and the most frequent histological subtype was adenocarcinoma (98.3%). Among the 59 patients, 9 (15.3%) were metastatic at diagnosis, and 1 (1.7%) had lymph node involvement not identified on MRI. PET/CT led to changes in staging and treatment in 10 patients (17%). The liver was the most common site of metastasis, found in 7 (78%) of the metastatic cases. Eleven patients (18.6%) died within 4 years of diagnosis. The mean SUVmax of the primary lesion was 21.3 ± 8.06, and the mean MTV was 16.5 ± 20.24. ***Conclusion:*** PET/CT proved to be a useful tool in the staging of rectal carcinoma, altering therapeutic management in 17% of patients by detecting metastatic or nodal involvement not identified on MRI.

EP-0342

Preliminary results of^{68}Ga-FAPI PET imaging in total neoadjuvant therapy of rectal cancer

S.-h. Chen*, K.-C. Ho, R.-E. Hsieh, E.-L. Shen, C.-K. Liao, H.-C. Hsu, A.-H. Chen, J.-F. You, P.-S. Hsieh, Y.-J. Hsu, Y.-J. Chern, C.-C. Cheng, Y.-C. Lin;
Chang Gung Memorial Hospital, Taoyuan County, TAIWAN.*

Aim/Introduction: Total neoadjuvant therapy (TNT) is increasingly utilised for locally advanced rectal cancer (LARC). Accurate

staging and response assessment are crucial for optimising treatment strategies. ^{68}Ga-labelled FAP inhibitors (FAPI) have shown promise as promising PET tracers which may offer higher specificity and reduced interference from physiologic uptake of fluorodeoxyglucose PET (FDG-PET). This study aimed to evaluate the potential role of 68Ga-FAPI PET/CT in the initial staging and assessment of treatment response in LARC patients undergoing TNT, comparing its performance with standard ^{18}F-FDG PET/CT. ***Materials and Methods:*** Eligible participatns included adult patients with biopsy-proven, newly diagnosed, clinical stage II-III rectal adenocarcinoma suitable for TNT. Key exclusion criteria included evidence of distant metastases, prior cancer therapy, prior pelvic radiotherapy and significant comorbidities. Participants underwent both ^{18}F-FDG and ^{68}Ga-FAPI PET/CT scans before and after treatment. PET parameters including maximum standardised uptake value (SUVmax), mean SUV (SUVmean), and metabolic tumour volume (MTV) were measured for primary tumours within the boundary of 42% SUVmax. Initial comparisons focused on tracer uptake in primary tumours and lymph node detection accuracy. Pathological findings from biopsy or surgical specimens served as the reference standard where available. Data on treatment outcomes, including disease-free survival (DFS), local regional recurrence (LRR), and overall survival (OS), are being collected. ***Results:*** To date, 24 patients have been enrolled, with 19 completing the first set of PET scans and 15 completing the second set. Pos-treatment pathology results were available for 8 patients. Initial visual assessment suggested 68Ga-FAPI PET/CT may offer better tumour visualization due to lower physiological background uptake in the colon compared to 18F-FDG. Quantitative analysis showed variable uptake for both tracers across patients. In comparing nodal staging (N-staging), preliminary analysis based on clinical consensus as the gold standard suggested ^{68}Ga-FAPI PET/CT might be less sensitive but potentially more specific than ^{18}F-FDG PET/CT for detecting lymph node metastases. Pre-treatment tumour volume and post-treatment tracer uptake may reflect therapeutic response. However, these associations require further validation. ***Conclusion:*** Initial results indicate that ^{68}Ga-FAPI PET imaging may offer clinical value in the staging and response evaluation of LARC patients undergoing TNT, particularly through improved specificity in nodal assessment and clearer primary tumour visualisation due to less interference from physiological uptake. Further patient recruitment and correlation with treatment response and long-term outcomes are necessary to establish the definitive role of 68Ga-FAPI PET/CT in this setting.

EP-0343

Association Between KRAS Mutation and Metabolic and Volumetric Parameters Measured from the Primary Tumor in Colorectal Cancer Using F-18 FDG PET/CT

E. Tunca[1], *R. H. Tokac*[1], *U. Yararbas*[1], *M. Sezak*[2];
[1]*Ege University Faculty of Medicine, Department of Nuclear Medicine, Izmir, TÜRKIYE,* [2]*Ege University Faculty of Medicine, Department of Pathology, Izmir, TÜRKIYE.*

Aim/Introduction: In our study, we aimed to show the relationship between metabolic and volumetric parameters measured from the primary colorectal mass on Fluorine-18 Fluorodeoxyglucose Positron Emission Tomography/Computed Tomography (F18-FDG PET/CT), a non-invasive method in patients with colorectal cancer (CRC), and the presence of KRAS mutation in the primary mass and to investigate the potential to predict mutation. ***Materials and Methods:*** The archival and electronic patient file data of 216 patients who were pathologically diagnosed with CRC after biopsy or surgery and underwent F18-FDG PET/CT imaging for pre-treatment staging in our clinic between 2018 and 2024 were retrospectively analyzed. Among these patients, 72 patients who had KRAS mutation analysis from primary colorectal mass and met the other inclusion criteria were included in our study. Patients with KRAS mutation analysis from metastatic foci were not included in the study. The relationship between metabolic and volumetric parameters (SUVmax, SUVmean, SUVpeak, TLG and MTV) calculated from the primary mass on F18-FDG PET/CT imaging and KRAS mutation was analyzed. ***Results:*** Among 72 cases, KRAS mutation was detected in 30 patients (58.3%). SUVmax value measured from the primary mass was significantly higher in KRAS mutant patients compared to KRAS-wild type (WT) patients (p: 0.031). No significant difference was observed between KRAS mutant and WT patients with other parameters. As a result of ROC analysis, although the AUC (Area Under the Curve) of the parameters was greater than 0.5, their predictive values were low (SUVmax: 0.644, SUVmean: 0.632, SUVpeak: 0.584, TLG: 0.600, MTV: 0.591). With a cut-off value of 20.50 for SUVmax, sensitivity and specificity for KRAS mutation detection were calculated as 80% and 47.6%, respectively. ***Conclusion:*** Our study is valuable in terms of preventing misleading findings that may be caused by mutation heterogeneity between tumor and metastatic focus by excluding cases with KRAS mutation analysis from metastatic foci. Our study suggests that the SUVmax value measured from the primary mass may be a useful parameter in predicting KRAS mutation.

EP-0344

The Value of F18 FDG-PET/CT Parameters Measured at the Anastomosis Line for Predicting Local Recurrence in Operated Colorectal Cancer Patients

E. Tunca, *R. Tokac, U. Yararbas;*
Ege University Faculty of Medicine, Department of Nuclear Medicine, Izmir, TÜRKIYE.

Aim/Introduction: F-18 FDG PET/CT (PET/CT) is recommended for primary staging and restaging in suspected metastatic disease in colorectal cancer (CRC). Surgical resection is the main treatment modality. Although curative surgery is performed, local recurrence is observed in 10-30% of patients with CRC. In this study, we aimed to evaluate the effectiveness of metabolic and volumetric parameters measured from the anastomotic site on PET/CT in detecting local recurrence in operated CRC patients. ***Materials and Methods:*** We retrospectively reviewed 750 postoperative CRC patients who underwent PET/CT imaging between 2018 and 2024. Patients were included based on availability of colonoscopy within 3 months of imaging, or histopathology results from re-operation specimens. In addition, patients who did not have pathology/colonoscopy data but who were clinically accepted as local recurrence with other radiological imaging methods were also added and a total of 97 patients were included. PET/CT images were analyzed using Siemens syngo.via software to obtain metabolic and volumetric parameters (SUVmax, SUVmean, SUVpeak, MTV, TLG) from the anastomotic site. ***Results:*** Among 97 patients (35 female, 62 male; mean age: 60.44 ± 12.47 years), 78 had no recurrence based on colonoscopy or pathology results. According to the colonoscopy pathology of 7 patients and re-operation pathology of 6 patients, and radiological imaging follow-up of the other 6 patients, a total of 19 patients had local recurrence. Tumor locations included right colon (n=21), transverse colon (n=3), left colon (n=11), sigmoid colon (n=22), and rectum (n=40). Most tumors were adenocarcinomas (n=96). Mean PET/CT values at the anastomotic site were: SUVmax 7.71±5.32, SUVpeak 5.46±3.75, SUVmean 4.49±3.57, MTV 14.81±21.11, TLG 50.55±55.18. In the statistical analysis; SUVmax, SUVmean and SUVpeak values were more significant and all parameters were statistically related to local recurrence (SUVmax: p<0.001, SUVmean: p<0.001, SUVpeak: p<0.001, MTV-p:0.039, TLG-p:0. 031). According to the ROC analysis; SUVmax, SUVmean, and SUVpeak can predict local recurrence with high sensitivity and specificity at the identified cut-off values. In comparison, TLG showed lower diagnostic performance with reduced sensitivity and specificity, indicating limited utility in detecting recurrence. MTV didn't demonstrate sufficient discriminative power. ***Conclusion:*** In our study, metabolic parameters measured from the anastomotic site were significantly higher in cases with local recurrence. SUVmax, SUVmean, and SUVpeak were useful in predicting recurrence with good sensitivity and specificity. However, volumetric parameters such as MTV and TLG showed limited value.

EP-0345

Preliminary comparison of 68Ga-FAPI-46 against 18F-FDG, 68Ga-DOTATATE and 68Ga-Pentixafor PET/CT/MR imaging in the assessment of various cancer types

H. Dadgar[1], *M. Assadi*[2], *B. Al-balooshi*[3], *A. Cimini*[4], *M. Ricci*[5], *H. Arabi*[6];

[1]Nuclear Medicine and Molecular imaging research center, RAZAVI Hospital, Mashad, Iran, ISLAMIC REPUBLIC OF, [2]The Persian Gulf Nuclear Medicine Research Center, Department of Molecular Imaging and Radionuclide Therapy (MIRT), Bushehr Medical University Hospital, Bushehr University of Medical Sciences, Bushehr, IRAN, ISLAMIC REPUBLIC OF, [3]3Dubai Nuclear medicine & Molecular imaging Center- Dubai Academic Health corporation-DAHC, UAE, Dubai, UNITED ARAB EMIRATES, [4]Nuclear Medicine Unit, St. Salvatore Hospital, 67100 L'Aquila, ITALY, [5]Nuclear Medicine Unit, Cardarelli Hospital, Campobasso, ITALY, [6]Division of Nuclear Medicine and Molecular Imaging, Diagnostic Department, Geneva University Hospital, Geneva, SWITZERLAND.

Aim/Introduction: 68Ga-FAPI PET/CT imaging allows for effective lesion detectability in cancer microenvironment owing to the relatively high intra-tumoral uptake and low background. This work reports on preliminary comparison between 68Ga-Pentixafor and 68Ga-FAPI-46 PET radiotracers against commonly used ^{18}F-FDG and 68Ga-DOTATATE PET radiotracers in the assessment of various cancer types. ***Materials and Methods:*** Eleven patients with histopathologically confirmed breast cancer, gastric, cervical, glioblastoma multiform (GBM), well-differentiated adenocarcinoma, papillary thyroid carcinoma (PTC), Ewing's sarcoma, colon, and medullar thyroid cancer (MTC) were retrospectively studied. Nine patients were scanned with 18F-FDG, eleven patients with 68Ga-FAPI, three patients with 68Ga-DOTATATE, and one patient with 68Ga-Pentixafor on a Siemens Biograph 6 PET/CT scanner. PET/CT images were evaluated by two nuclear medicine physicians to identify malignant lesions and perform semi-quantitative analysis to calculate maximum standardized uptake value (SUVmax) and target-to-background ratio (TBR). ***Results:*** The evaluation of the eleven subjects demonstrated the effectiveness of 68Ga-FAPI-46 compared to ^{18}F-FDG for the detection of metastasis in the lymph nodes (55 vs. 49), liver (4 vs. 3), and bone (4 vs. 3). 68Ga-Pentixafor and 68Ga-DOTATATE PET/CT scans exhibited no significant differences with both being inferior to 68Ga-FAPI-46 PET radiotracer in terms of metastasis detection. Semi-quantitative analysis showed that the TBR and SUVmax were significantly higher in 68Ga-FAPI-46 PET than ^{18}F-FDG PET for bone metastases and lymph nodes. ^{18}F-FDG and 68Ga-FAPI-46 images exhibited similar SUVmax in liver metastases. However, the TBRs in 68Ga-FAPI-46 images were significantly higher than those in ^{18}F-FDG images. ***Conclusion:*** Improved malignancy detection rates for metastases in the liver, lymph nodes, and bone were observed for 68Ga-FAPI-46 PET compared to 68Ga-DOTATATE, 18F-FDG, and 68Ga-Pentixafor PET. ***References:*** 68Ga-FAPI-46, 68Ga-DOTATATE, 18F-FDG, 68Ga-Pentixafor PET, GBM, MTC.

EP-19

e-Poster Area

B: Imaging Clinical Studies -> B1 Oncological Imaging Clinical Study -> B18a Prostate Staging

EP-0346

Evaluating the Diagnostic Value of Dual-Time F-18 PSMA-1007 PET/CT in Prostate Cancer

S. Tsai[1,2], *Y. Pu*[3], *J. Hong*[3], *P. Chuang*[4], *H. Wen*[5], *P. Kuo*[6], *C. Lu*[4]; *[1]Department of Nuclear Medicine, National Yang Ming Chiao Tung University Hospital, Yilan County, TAIWAN, [2]School of Medicine, National Yang Ming Chiao Yung University, Taipei, TAIWAN, [3]Department of Urology, National Taiwan University Hospital, Taipei, TAIWAN, [4]Department of Nuclear Medicine, National Taiwan University Cancer Center, Taipei, TAIWAN, [5]Department of Nuclear Medicine, National Taiwan University Hospital, Taipei, TAIWAN, [6]Department of Radiology, National Taiwan University College of Medicine, Taipei, TAIWAN.*

Aim/Introduction: F-18 PSMA-1007 PET/CT has become an essential tool in the management of prostate cancer, particularly for staging and restaging. Owing to its favorable half-life and minimal urinary excretion, imaging is often performed at either 60 or 120 minutes post-injection. However, whether dual-time imaging provides additional diagnostic benefits remains under debate. This prospective single-center study aimed to evaluate the clinical relevance of 60-minute vs 120-minute F-18 PSMA-1007 PET/CT, and determine if a single time point is sufficient for accurate staging. ***Materials and Methods:*** Between March 11, 2022 and March 29, 2023, 130 patients with histologically confirmed prostate cancer underwent dual-time F-18 PSMA-1007 PET/CT at both 60&120 minutes post-injection. Imaging was performed from skull to mid-thigh. Indications included primary staging (n=31) and biochemical recurrence (BCR)/restaging (n=99). PET images were interpreted by two experienced nuclear medicine physicians using visual and semi-quantitative (SUVmax, SUVmean, SUVpeak) assessment. Staging comparisons and discordances between 1-hour and 2-hour scans were recorded and analyzed by indication group. ***Results:*** The mean age was 69.5±7.8 years. Mean PSA prior to PET was 22.67±75.30 ng/mL (range 0.02-664). Overall, TNM staging changed in 43.8% (57/130) of patients after PET, mostly due to newly detected metastases (38.5% upstaged). Only 5 patients (3.8%) demonstrated staging discrepancies between 60-minute and 120-minute scans. Of these, 2 patients were upstaged from M0 (no distant metastasis at 1 hr) to M1b (bone metastases at 2 hr), and 2 were upstaged from N0 to N1 due to clearer nodal visualization at 120 minutes. Conversely, 1 patient was downstaged from M1b to M0 due to resolution of equivocal bone uptake seen at 60 minutes but not at 120 minutes. All discrepant cases had equivocal or borderline findings at 1 hour. Notably, patients undergoing primary staging were more likely to have discrepant findings (3/31=9.7%) compared to those in the BCR/restaging group (2/99=2.0%; p=0.088). Semi-quantitative metrics were overall stable between time points with no significant impact on lesion classification. ***Conclusion:*** Our findings demonstrate that 60-minute and 120-minute F-18 PSMA-1007 PET/CT imaging have high concordance, with only 3.8% of patients experiencing clinically relevant staging differences. Discrepancies were limited to cases with borderline or equivocal lesions, mostly in the primary staging cohort. Routine dual-time imaging may therefore be unnecessary, and single-time-point acquisition at 60 minutes appears sufficient for most clinical scenarios. However, 120-minute delayed imaging may be considered in select cases, especially when early scans yield ambiguous findings in newly diagnosed patients.

EP-0347

Comparative Performance of PSMA PET PRIMARY Score and mpMRI PIRADS in Localizing Clinically Significant Prostate Cancer

S. Shekhar Singh[1], *P. Wadhwa*[2], *R. Parwar*[1], *S. Tandon*[1]; *[1]Globe Healthcare, Lucknow, INDIA, [2]United Imaging Healthcare, Delhi, INDIA.*

Aim/Introduction: Prostate-specific membrane antigen positron emission tomography (PSMA PET) and multiparametric magnetic resonance imaging (mpMRI) are pivotal in prostate cancer staging. This study investigates the concordance between the PRIMARY score (PSMA PET-based) and PIRADS (mpMRI-based) for lesion characterization and evaluates their correlations with histopathology (Gleason score) and serum PSA in 200 treatment-naïve patients. ***Materials and Methods:*** We retrospectively analysed 200 patients with elevated PSA who underwent 68Ga-PSMA-11 PET/CT and mpMRI prior to biopsy or treatment. Two

blinded specialists independently assigned PIRADS (v2) and PRIMARY scores based on lesion location (apex, mid-gland, base). Statistical correlations were assessed between imaging scores, Gleason grade, SUVmax, and PSA. ***Results:*** PRIMARY vs. Gleason Score: Strong correlation (*r* = 0.5, *p* < 0.001).PRIMARY vs. PIRADS: Moderate agreement (*r* = 0.4, *p* = 0.4), with regional variations:Base: Moderate correlation (*r* = 0.5).Apex/Mid-gland: Weak correlation (*r* = 0.2-0.3).PRIMARY vs. PSA: Weak association (*r* = 0.2, *p* = 0.04).SUVmax correlated moderately with Gleason score (*r* = 0.3, *p* = 0.002) but poorly with PIRADS/PSA. Higher PRIMARY scores predicted metastatic burden (*p* < 0.05). ***Conclusion:*** The PRIMARY score demonstrates robust alignment with histopathology and has a comparable agreement with PIRADS score. PET quantitative parameters like SUVmax can be used to predict the aggressiveness of the primary tumor in terms of Gleason score. Combined PSMA PET and mpMRI may enhance diagnostic precision for intraprostatic lesions. ***References:*** Hofman MS, et al. Lancet. 2020;395:1208-1216.Weinreb JC, et al. Eur Radiol. 2016;26:67-76.

EP-0348

Beyond the Standard: Enhancing prostate bed and regional lymph node detection in Prostate Cancer patients with Early and Delayed Imaging in 68Ga-PSMA PET/CT

A. Aghaee[1], *S. Soltani*[2], *Z. Bakhshi*[1], *K. Aryana*[1], *N. Norouzbeigi*[1], *H. Dadgar*[1];
[1]*Nuclear Medicine Research Center, Mashhad University of Medical Sciences, Mashhad, IRAN, ISLAMIC REPUBLIC OF,* [2]*Kidney Transplantation Research Center, Mashhad University of Medical Sciences, Mashhad, IRAN, ISLAMIC REPUBLIC OF.*

Aim/Introduction: The accuracy of Ga-PSMA scans can be enhanced by employing multiphasic imaging strategies. This study aims to evaluate the diagnostic value of early static and delayed imaging in conjunction with standard 68Ga-PSMA-11 PET/CT scans for the detection of prostate bed recurrence in prostate cancer patients. ***Materials and Methods:*** In this prospective study, 138 prostate cancer patients underwent routine 68Ga-PSMA-11 PET/CT imaging. Each patient received early imaging immediately following a 4-minute static acquisition after tracer injection, and delayed imaging was conducted 3 hours post-injection, focused on the pelvic region. The imaging results were analyzed for lesion count, type, localization, and maximum standardized uptake values. ***Results:*** Among the patients, 57.97% exhibited positive findings for pathologic prostatic lesions in the standard PET scans (median SUVmax: 10.24). In contrast, early PET imaging detected lesions in 58.01% of patients (median SUVmax of 5.86), while delayed scans revealed lesions suggestive of malignancy in 55.45% of patients (median SUVmax of 12.79). The analysis demonstrated a statistically significant difference in SUVmax values across the time points ($p < 0.001$). In patients, lymph nodes with pathological tracer uptake in the pelvic region on images 60 min p.i. were revealed by an SUV max 60 min p.i.: 15.78; lymph nodes considered for SUV measurements showed a pathologic tracer uptake within the first 4 min (SUV max 4 min: 7.36) and after 3 hours (SUV max 180 min p.i.: 19.19). Pathologic bone lesions regarded as metastases in the field of view on WB were found in 38 cases of patients, more than the ESI (f = 37) and DI (f = 24). In comparison, urinary bladder activity assessment was detectable with the WB imaging mean SUV max 60 min 11.07. Even though the mean SUV max for ESI and DI were 6.95 and 31.97, respectively. In the statistical analysis, pathologic radiotracer uptake in tumor lesions was statistically higher in ESI and WB than in urinary bladder activity. ***Conclusion:*** The findings indicate that neither early nor delayed imaging significantly enhanced the overall detection rate of malignant lesions in prostate cancer patients when using 68Ga-PSMA-11 PET/CT. However, the early acquisition of PET images, conducted as soon as 4 minutes after injection, proved beneficial for distinguishing local bladder invasion more effectively.

EP-0349

Reconstruction of ^{18}F-PSMA-1007 PET Scans Affects SUV-based Classification of Unspecific Bone Uptake

R. Poelarends*, A. G. Tegelaar - Kuiper, J. D. van Dijk, B. N. Vendel, J. A. van Dalen;*
Isala Hospital, Zwolle, NETHERLANDS.

Aim/Introduction: Interpreting 18F-PSMA-1007 PET scans can be challenging due to the occurrence of unspecific bone uptake (UBU), defined as focal PSMA uptake without a clear CT morphological correlate and uncertain clinical significance. While Standardized Uptake Value (SUV) in PET is widely used to differentiate between physiological uptake and metastases, it is known to be influenced by technical factors such as the applied image reconstruction. Our aim was to determine the impact of different iterative reconstruction settings on SUV measurements and lesion classification in 18F-PSMA-1007 PET. ***Materials and Methods:*** We retrospectively included 26 patients who underwent 18F-PSMA-1007 PET/CT (Vereos, Philips) and in whom UBUs were observed by expert nuclear medicine physicians. For each patient, three different Ordered Subset Expectation Maximization (OSEM) reconstructions that had diagnostic image quality were performed with increasing image noise: an EARL2-compliant reconstruction (3 iterations, 7 subsets, point spread function (PSF) modelling with 6 relaxation steps, 4 mm Gaussian post-filter), a high-resolution (HR) reconstruction (3 iterations, 13 subsets, without PSF or filtering) as used in our institute, and an ultra-high-resolution (UHR) reconstruction (4 iterations, 24 subsets, without PSF or filtering). A maximum of three UBUs per patient were identified using the HR-reconstruction. SUVmax and SUVmean were measured using a 50% iso-contour for the UBUs on each of the three reconstructions. Impact on SUV measurements was assessed using EARL2 reconstruction as a reference. Reclassification rates were evaluated between reconstructions using three groups: likely benign (SUVmax < 7), equivocal (SUVmax 7-11), and likely metastatic (SUVmax > 11). ***Results:*** A total of 43 UBUs were identified. Compared to the EARL2 reconstruction, the HR-reconstruction showed higher SUV: SUVmax increased by 20% (6.2 ± 3.7 vs. 7.2 ± 3.5, $p<0.001$) and SUVmean by 21% (3.9±2.2 vs. 4.6±2.3, $p<0.001$). The UHR-reconstruction also showed higher values compared to EARL2: SUVmax increased by 28% (6.2±3.7 vs. 7.6±3.7, $p<0.001$) and SUVmean by 29% (3.9±2.2 vs. 4.9±2.3, $p<0.001$). Compared to EARL2, 8 of 43 UBUs (19%) were reclassified from 'likely benign' to 'equivocal' in 7 patients when using HR-reconstruction. For the UHR-reconstruction, this reclassification occurred in 12 of 43 UBUs (28%) in a total of 9 patients. No other reclassifications occurred. ***Conclusion:*** SUV measurements for UBUs show high variability between 18F-PSMA-1007 PET reconstructions that can affect lesion classification when applying a SUV-based threshold. These findings underscore the need for standardization of PSMA-PET reconstructions when using SUV thresholds for making treatment decisions.

EP-0350

The Power Duo: PSMA PET/CT and Focal Ablation in Prostate Cancer (PCa) Care

J. Jandric[1], *V. Fasulo*[1,2], *P. Guglielmo*[2], *C. Vallone*[1], *M. Rodari*[1], *M. Lazzeri*[1], *N. Buffi*[1,3], *G. Lughezzani*[1,3], *L. Evangelista*[1,3];
[1]*IRCCS Humanitas Research Hospital, Rozzano, ITALY,* [2]*Humanitas University, Pieve Emanuale, ITALY,* [3]*Humanitas University, Pieve Emanuele, ITALY.*

Aim/Introduction: Accurate selection of PCa patients for focal therapies remains crucial. While mpMRI provides valuable information on tumor localization, it has limitations, such as detecting cancer in the transition zone, identifying small foci within the central gland and characterizing multifocal disease. This study aimed to evaluate the potential role of PSMA PET in a cohort of PCa patients candidate to focal therapies with curative intent at a tertiary referral center. ***Materials and Methods:*** From 02/2020 to 05/2024, we retrospectively reviewed the clinical records of PCa

patients who underwent PSMA PET at our center prior to receiving focal treatment. Prior to PETscans, all patients underwent mpMRI in accordance with international guidelines. Imaging scans were visually assessed, categorizing the PSMA uptake into focal, diffuse or mixed (focal+diffuse) patterns. Additionally, the PRIMARY score for the index lesion in the prostate gland was evaluated. Post-treatment PSA levels were recorded and correlated with PET patterns and PRIMARY scores. Data distribution and between-group comparisons were analyzed using non-parametric methods in MedCalc®. ***Results:*** Data from 48 patients were analysed. The median baseline PSA was 6.03 ng/mL (range 2.25-16.4), and Gleason scores ranged from 6 to 8, with a score of 7 in 31(64%). mpMRI was available for 45 patients(94%), revealing a unifocal lesion in 42(93%) and bifocal/multifocal lesions in 3 cases(7%). Using PI-RADS version 2.1, 8 patients(18%) were assigned a score of 3, 33(73%) a score of 4, and 4(9%) a score of 5. PSMA PET uptake patterns were focal in 25 patients(52%), diffuse in 20(42%), and mixed focal + diffuse in 2(4%); one scan (2%) showed no significant prostatic uptake. PRIMARY scores were distributed as follows: 1 in 1 patient(2%), 2A/B in 22(46%), 3 in 5(10%), 4 in 12(25%), and 5 in 8(17%). Focal therapies were delivered a median of 2.23 months after PET. Posttreatment PSA decreased in 32 patients(67%), increased in 10(21%), remained stable in 5(10%), and was unavailable for 1(2%). Although patients with PRIMARY scores ≤ 3 had a lower median posttreatment PSA than those with scores > 3 (3.9 vs 5.2 ng/mL), this difference was not statistically significant (Mann-Whitney p=0.267). Likewise, uptake pattern was not significantly associated with posttreatment PSA levels (Kruskal-Wallis p=0.45). ***Conclusion:*** PSMA PET demonstrated a high positivity rate (98%) in patients selected for focal treatments. Although uptake patterns and PRIMARY scores didn't significantly predict PSA response, lower PRIMARY scores trended toward greater posttreatment PSA reductions. ***References:*** DOI:10.1038/s41391-025-00944-1.

EP-0351

Triple-time point PSMA-PET imaging in primary staging of high-risk prostate cancer enabled by LAFOV PET/CT: potential clinical benefit?

E. Calderón Ochoa[1], *L. S. Kiefer*[1], *M. Maas*[2], *C. P. Reinert*[3], *H. Dittmann*[1], *I. Tsaur*[2], *J. Schwenck*[1,4,5], *C. la Fougère*[1,4];
[1]Department of Nuclear Medicine and Molecular Imaging, University Hospital of Tübingen, Tübingen, GERMANY, [2]Department of Urology, University Hospital of Tübingen, Tübingen, GERMANY, [3]Department of Diagnostic and Interventional Radiology, University Hospital of Tübingen, Tübingen, GERMANY, [4]Cluster of Excellence iFIT (EXC 2180) "Image-Guided and Functionally Instructed Tumor Therapies", University of Tübingen, Tübingen, GERMANY, [5]Werner Siemens Imaging Center, Department of Preclinical Imaging and Radiopharmacy, University of Tübingen, Tübingen, GERMANY.

Aim/Introduction: PSMA PET/CT has transformed prostate cancer (PC) management, showing a specificity of 89% to 98% for the detection of lymph node metastases in primary staging. However, its sensitivity ranges from 53% to 64% compared to histology. Therefore, we hypothesize that the dynamic PSMA uptake in triple-time point LAFOV PET/CT scans may help overcome these limitations. ***Materials and Methods:*** In a prospective study, 15 patients with histologically diagnosed high-risk PC (PSA ≥ 20 ng/ml, Gleason ≥ 8, cT3/cT4) underwent PET imaging at 1.5h, 3h, and 5h p.i. (3.0 MBq/kg [^{18}F]PSMA-1007; 5 min, 10 min, 20 min scan time). The uptake of suspicious tumor lesions was evaluated using a 50% isocountour (SUV_{mean}; SUV_{max}). Lymph nodes (LN) were categorized according to their uptake (SUV_{mean}), analogous to the PROMISE criteria. To assess the tracer kinetics, the uptake of PT and LN was normalized to the corresponding SUV_{mean} of the spleen. The physiological uptake in the spleen, salivary glands, and blood pool (BP) was assessed (2-3 ml VOI; SUV_{mean}). Noise performance was assessed using the coefficient of variation (CV; standard deviation liver VOI/SUV_{mean} liver VOI). ***Results:*** Noise performance remained constant up to 5h p.i. without significant differences (CV 1.5h: 9.9±3.6%, 3h: 9.9±4.0%, 5h:10.6±3.9%, p = 0.33). The BP steadily decreased up to 5h p.i. (1.5h: 1,7±0.3, 3h:0,7±0.1, 5h: 0,4±0.1, p<0.001), while the uptake in the spleen and parotid gland increased. PTs showed an increasing tracer uptake from 1.5h to 5h p.i. (SUV_{max} 35.2±35.1 vs. 42.8±34.5; p = 0.01) while remaining relatively constant compared to 3h p.i. (SUV_{max} 3h p.i. 37.9±34.5). In suspicious LNs a steadily increasing tracer uptake was observed up to 5h p.i. (1.5h: SUV_{max} 15.2±11.2; 3h:19.9±13.6; 5h: 25.9±20.2; p = 0.004). The LNs, which were considered not suspicious for metastasis, displayed a similar dynamic (SUV_{max} 4.8±1.2; 3h:5.9±1.9; 5h: 7.2±3.0; p = 0.005), although the tracer uptake was significantly lower compared to suspicious LNs. Furthermore, the differences in normalized tracer uptake between 1.5h-5h p.i. in suspicious LNs were significantly higher than in unspecific LNs (0.4±0.26 vs 0.09±0.12; p = 0.01). ***Conclusion:*** LAFOV PET enables triple-time point imaging up to 5h p.i. with excellent noise performance. PT and suspicious LNs showed increased PSMA tracer uptake in late PET images. However, an increase in unsuspicious LNs was also observed. Further evaluation of tracer kinetics in correlation to histopathology and size of metastases is required to improve prostate cancer diagnostics and treatment precision.

EP-0352

P(yl)rimary: SUV Validation of PRIMARY score 5 in ^{18}F-DCFPyL PET/CT for staging of Prostate Cancer

E. O'Dwyer, *V. Marulanda Corzo, A. Ricaurte Fajardo, D. D'Angelo, T. McClure, S. Huicochea Castellanos, J. R. Osborne;
Weill Cornell Medicine, New York, NY, UNITED STATES OF AMERICA.*

Aim/Introduction: ^{18}F-DCFPyL PSMA PET/CT is indicated in the staging of intermediate- and high-risk prostate cancer (PCa) as it has been shown to be superior to conventional imaging. In addition, ^{18}F-DCFPyL has been shown to be clinically equivalent in PCa staging to the other approved agents including ^{68}Ga PSMA-11. PSMA PET diagnostic scoring systems have been developed, including the PRIMARY scoring system which identified SUVmax≥12 in prostatic lesions as diagnostic of clinically significant prostate cancer (csPCa) (PRIMARY score 5)[1,2]. This scoring system, however, has only been validated on 68GaPSMA-11 radiotracer. This study aimed to determine what is the SUVmax cutoff for detection of csPCa in patients staged with ^{18}F-DCFPyL radiotracer and whether it is comparable to ^{68}GaPSMA-11 and thus PRIMARY score can be used in this patient cohort. ***Materials and Methods:*** Retrospective analysis of 91 treatment naïve men who underwent ^{18}F-DCFPyL PET/CT following biopsy-confirmed PCa. A total of 126 intraprostatic PSMA-avid lesions were identified and qualitatively scored using the PRIMARY scoring system (score 1-5), based on pattern (focal versus diffuse), zonal location, and uptake intensity. SUVmax values were recorded for each lesion. Youden's J index was used to determine the optimal SUVmax cutoff to predict a PRIMARY score of 5. A logistic regression model was fitted with PRIMARY score (5 versus ≤4) as the outcome and lesion SUVmax (continuous) as the predictor. An ROC curve was generated, and the SUVmax cutoff associated with the maximum Youden's J value was identified. Analysis was performed in all lesions (N=126), and in a subgroup with histologically confirmed clinically significant prostate cancer/grade group ≥2 (N=112). Statistical analysis was performed using SAS version 9.4 (SAS Institute Inc., Cary, NC). ***Results:*** Median age was 70 years (IQR 65-76), and median PSA was 6.4 ng/dL (IQR 4.9-9.9). Median interval from biopsy to PET was 16 days (IQR 7-27). ISUP Grade Group distribution included GG1 (n=10), GG2 (n=52), GG3 (n=29), GG4 (n=16), and GG5 (n=15). Among 126 lesions SUVmax≥ 12.4 was identified as optimal for detecting csPCa which is almost identical to PRIMARY score 5

SUVmax≥12. ***Conclusion:*** SUVmax≥ 12.4 accurately identifies prostatic lesions with csPCa (PRIMARY score 5) in ^{18}F-DCFPyL PET/CT for PCa staging. Thus, our study supports the robustness and transferability of the PRIMARY scoring system to ^{18}F-DCFPyL PET/CT in prostatic lesion assessment. ***References:*** 1. Emmett L et al. J Nucl Med. 2022 Nov;63(11):1644-1650. 2. Emmett L et al. J Nucl Med. 2024 Jan 2;65(1):94-99.

EP-0353

Prostate Cancer Detection with [99mTc]Tc-HYNIC-iPSMA SPECT: The Australian Experience.

P. Tually[1], *J. Meadows*[1], *L. Groombridge*[1], *N. Lenzo*[1], *G. Currie*[2]; *[1]Spartan First Imaging, Kalgoorlie, AUSTRALIA, [2]Charles Sturt University, Wagga Wagga, AUSTRALIA.*

Aim/Introduction: Rural Australians, particularly Indigenous communities, experience disproportionately higher morbidity and mortality rates from prostate cancer (PrCa), driven in part by delayed diagnosis and limited access to advanced diagnostic services. Geographic isolation, lower socioeconomic status, and workforce shortages contribute to a persistent rural health gap. Access to molecular imaging is a critical part of precision oncology, yet PET/CT remains cost-prohibitive or unavailable in many regional settings. This prospective study investigates the safety and clinical impact of 99mTc-HYNIC-iPSMA SPECT imaging—a more accessible alternative—among prostate cancer patients in remote Western Australia. By evaluating its role in improving diagnosis and informing treatment decisions, this study addresses a key area of rural health inequality and seeks to support more equitable access to theranostic options. ***Materials and Methods:*** Twenty-seven patients from rural Western Australia with histologically confirmed PrCa were enrolled in this observational study. Each underwent imaging 2-4 hours after intravenous injection of 650-800 MBq 99mTc-HYNIC-iPSMA. Imaging protocols included whole-body planar sweeps, static views of areas of interest, and SPECT/CT acquisitions of the chest, abdomen, and pelvis. Adverse events were recorded, and clinical follow-up data were extracted from medical records to assess the impact on patient management. ***Results:*** No adverse events were observed in any participant. Normal physiological biodistribution was seen in 96.3% (n = 26) of cases. The mean radiochemical purity was 92.5% (±1.7), ranging from 90% to 96%. At least one PSMA-positive lesion was identified in 81.5% (n = 22) of patients. Imaging findings directly influenced clinical management in 40.7% (n = 11) of cases, including changes to treatment pathways. ***Conclusion:*** 99mTc-HYNIC-iPSMA SPECT is a safe, feasible, and clinically impactful imaging modality that offers a cost-effective alternative for patients in remote and underserved areas. Its ability to guide treatment in over 40% of cases highlights its potential to reduce diagnostic delay and therapeutic inequity, particularly among Indigenous Australians and others affected by the rural health divide. Expanding access to this form of molecular imaging may be a key step toward improving prostate cancer outcomes across regional Australia.

EP-0354

Correlation Between PRIMARY Scores in Ga-68 PSMA PET and Histological ISUP Grades in Prostate Cancer

C. Soydal, *M. Cidemal, M. Araz, N. O. Kucuk; Ankara University Medical Faculty, Ankara, TÜRKIYE.*

Aim/Introduction: PRIMARY scoring system is recommended for the triage of patients with suspicious of csPCa. However, it is not common to use Ga-68 PSMA PET/CT before the prostate biopsy worldwide. For this reason, our knowledge to reflection of PRIMARY scoring to real-life experience is limited. Thus, in this study we aimed to analyze the correlation between PRIMARY scores in Ga-68 PSMA PET/CT and ISUP grades with biopsy in newly diagnosed prostate cancer patients. ***Materials and Methods:*** We retrospectively re-evaluated Ga-68 PSMA PET/CT images of patients who underwent PET/CT for staging of prostate cancer with histopathological proved diagnosis between Dec 2023 and Jan 2025. Prostatic region was evaluated based on the location, pattern and the SUVmax for PRIMARY scoring system from 1 to 5. Prostatic uptake with primary scores 1 and 2 accepted as an indicator of absence of csPC. Additionally, Gleason scores and ISUP grades of prostatic lesions from prostate biopsies was noted for correlative analysis. ***Results:*** Images of total 218 (mean age: 70.5 ±8.5) men were included to the analysis. Median of serum PSA level were calculated as 9.1 (min-max=0.27-1672) during Ga-68 PSMA PET/CT. PRIMARY scores were 1, 2, 3, 4 and 5 in 25, 8, 30, 78 and 77 patients, respectively. Distribution of ISUP grades were 1, 2, 3, 4 and 5 in 38, 59, 40, 29 and 48 patients. csPCa were detected in 176 patients. PRIMARY scoring predicted presence of csPCa in 153 patients and absence in 10 patients. As a result, the sensitivity, specificity, positive predictive value (PPV), negative value (NPV) and accuracy of PRIMARY scoring to predict csPCa were calculated as 87%, 26%, 84%, 30% and 76%, respectively. ***Conclusion:*** In this study as a noninvasive imaging method Ga-68 PSMA PET/CT has proved to have high sensitivity and PPV in the prediction of csPCa. However, the specificity and NPVs were found lower than the literature. This can be related with the study population that is included patients with already diagnosed. Further studies without patient selection bias is needed to clarify the real-life value of PRIMARY scoring system to triage of prostate cancer patients. ***References:*** Emmett L,et al. The PRIMARY Score: Using Intraprostatic 68Ga-PSMA PET/CT Patterns to Optimize Prostate Cancer Diagnosis. J Nucl Med. 2022 Nov;63(11):1644-1650. doi: 10.2967/jnumed.121.263448. Epub 2022 Mar 17. PMID: 35301240; PMCID: PMC9635676.

EP-0355

Awareness of the High Rate of False Positive Ga-68 PSMA-11 Uptake in the Prostate Gland: Can PET/MRI Solve This Problem?

L. Uslu-Besli[1], *B. Bakir*[2], *N. Urganci*[3], *I. Gurses*[3], *E. Karayel*[1], *H. Pehlivanoglu*[1], *S. Ozel-Yildiz*[4], *C. Demirdag*[5], *H. B. Sayman*[1]; *[1]Istanbul University-Cerrahpasa, Cerrahpasa Medical Faculty, Department of Nuclear Medicine, Istanbul, TÜRKIYE, [2]Istanbul University, Istanbul Medical Faculty, Department of Radiology, Istanbul, TÜRKIYE, [3]Istanbul University-Cerrahpasa, Cerrahpasa Medical Faculty, Department of Medical Pathology, Istanbul, TÜRKIYE, [4]Istanbul University, Istanbul Medical Faculty, Department of Biostatistics, Istanbul, TÜRKIYE, [5]Istanbul University-Cerrahpasa, Cerrahpasa Medical Faculty, Department of Urology, Istanbul, TÜRKIYE.*

Aim/Introduction: Our aim was to assess the false positive Ga-68 PSMA uptake rate in the prostate gland in patients with primary prostate cancer (PCa), and to determine whether multiparametric prostate MRI (mpMRI) within hybrid PET/MRI can reduce false positive results. ***Materials and Methods:*** Fifty-one biopsy-proven, treatment-naïve PCa patients undergoing radical prostatectomy were prospectively recruited. All patients underwent Ga-68 PSMA-11 PET/MRI together with mpMRI. PET and mpMRI images were assessed independently using the PRIMARY score and PIRADS v2.1, then jointly evaluated as fused PET/MRI. Imaging findings were compared with postoperative histological mapping. The prostate was divided into sextants for lesion localization, and false positive uptake was recorded. Diagnostic performance metrics were calculated. ***Results:*** Seven of 51 patients (13.7%) exhibited false positive PSMA uptake due to benign findings - asymmetrical central zone thickening, benign prostatic hyperplasia, or prostatitis. MpMRI was true negative in all. PET/MRI had higher sensitivity and accuracy (74.9% and 83.0%) then either PET (65.0% and 74.5%) and mpMRI (66.5% and 77.5%). In index lesion detection PET/MRI showed 92.2% sensitivity, outperforming PET (80.4%) and mpMRI (86.3%). PET/MRI was significantly more accurate than mpMRI ($p<0.001$) and PET ($p=0.014$), PET and mpMRI were statistically

similar (p=0.770). ***Conclusion:*** False positive Ga-68 PSMA uptake is common and can affect clinical decisions. MpMRI helps clarify benign mimics, improving diagnostic accuracy. PET/MRI offers a more reliable assessment of PCa, potentially aiding in focal therapy planning and post-treatment evaluation. ***References:*** 1. D.A. Ferraro, N.J. Rupp, O.F. Donati, et al., 68Ga-PSMA-11 PET/MR Can Be False Positive in Normal Prostatic Tissue, Clin Nucl Med 44 (2019) e291-e293. 2. R. Li, Y. Fu, S. Peng, et al., Pathological and radiological features of false-positive lesions on [68Ga]Ga-PSMA-11 PET/CT in primary staging of prostate cancer: a radio-pathology matching analysis, Eur J Nucl Med Mol Imaging (2025). 3. W. Tang, Y. Tang, L. Qi, et al., Benign Prostatic Hyperplasia-Related False-Positive of Prostate-Specific Membrane Antigen-Positron Emission Tomography in the Diagnosis of Prostate Cancer: The Achilles' Heel of Biopsy-Free Radical Prostatectomy?, Journal of Urology 210 (2023) 845-855.

EP-0356

The Diagnostic and Risk Stratification Significance of ^{68}Ga-PSMA PET/MR-Derived Parameters for Prostate Cancer

Z. Dai, *Y. Lv, W. Ruan, Y. Gai, X. Zhang, M. Li, X. Lan, C. Qin;*
Department of Nuclear Medicine, Union Hospital, Tongji Medical College, Huazhong University of Science and Technology, Wuhan, CHINA.

Aim/Introduction: To evaluate the diagnostic efficacy of ^{68}Ga-PSMA PET/MR-derived parameters for prostate cancer and their significance in risk stratification. ***Materials and Methods:*** A retrospective analysis was conducted on patients suspected of or diagnosed with prostate cancer who underwent ^{68}Ga-PSMA PET/MR at our hospital from November 2020 to April 2024, followed by pathological confirmation (biopsy or radical prostatectomy). Clinical data were collected, and SUV_{max} of the prostate region was measured. Using 40% SUV_{max} as the threshold, the PSMA expression volume (PTV40%) and the mean uptake value ($SUV_{40\%mean}$) of this volume were automatically segmented. The ratios of SUV_{max} in the prostate to the liver, blood pool, and parotid gland were calculated to obtain PLR, PBpR, and PPgR, respectively. MR parameters included mean apparent diffusion coefficient (ADC_{mean}), minimum ADC (ADC_{min}), and PI-RADS v2.1 assessment (score ≥ 4 indicating PCa). Receiver operating characteristic (ROC) curves assessed diagnostic efficacy. Mann-Whitney U, McNemar, and Delong tests compared groups and diagnostic performance. ***Results:*** A total of 74 patients were included, with a mean age of 65.9 ± 7.4 years; among them, 52 were in the PCa group and 22 in the non-PCa group. Significant differences were observed between PCa and non-PCa groups for PET parameters (SUVmax, PLR, PBpR, PPgR) and MR parameters (ADCmean, ADCmin) ($P < 0.05$). ROC analysis revealed excellent diagnostic performance: SUVmax (AUC 0.920, cutoff 7.665, sensitivity 76.9%, specificity 100%) and PLR (AUC 0.907, cutoff 1.551, sensitivity 92.3%, specificity 86.4%). PLR showed significantly higher sensitivity compared to SUV_{max} (P=0.002). In 31 patients with PSA < 20 ng/mL, the sensitivity of the optimal cut-off value for PLR was significantly higher than that of SUV_{max} (84.6% vs. 53.8%) ($P = 0.031$), with nine cases in the PCa group being SUV_{max}-negative but PLR-positive. $SUV_{40\%mean}$, SUV_{max}, PLR, PTU, ADC_{mean}, and ADC_{min} were significantly correlated with ISUP grading ($p < 0.05$), with ADC_{mean} showing a moderate negative correlation, $SUV_{40\%mean}$ and SUV_{max} showing moderate positive correlations, PLR and PTU showing weak positive correlations, and ADC_{min} showing a weak negative correlation. ROC analysis indicated that ADC_{mean}, ADC_{min}, $SUV_{40\%mean}$, and PLR had good diagnostic efficacy in distinguishing between ISUP grades 1-2 and 3-5. ***Conclusion:*** ^{68}Ga-PSMA PET/MR-derived parameters have excellent diagnostic performance for prostate cancer, with PLR showing the highest sensitivity, particularly in patients with low PSA levels. PSMA PET/MR and its derived parameters have significant implications for risk stratification in prostate cancer, providing diagnostic information for personalized treatment.

EP-0357

Diagnostic and Therapeutic Value of Dual-Tracer PET Imaging with ^{68}Ga-PSMA and ^{18}F-FDG In Prostate Cancer

Y. Zhang[1], *Y. Li*[1], *G. Fei*[1], *M. Su*[2], *Y. Ni*[1];
[1]Department of Radiology, Medical School, Southeast University, Nanjing, CHINA, [2]Department of Nuclear Medicine, West China Hospital, Sichuan University, Chengdu, CHINA.

Aim/Introduction: Assess the impact of dual-tracer PET imaging with ^{68}Ga-PSMA and ^{18}F-FDG on initial staging, restaging, and therapeutic decision-making in patients with PCa. ***Materials and Methods:*** Pca patients undergoing staging or restaging, with a baseline GS ≥8, were prospectively enrolled to undergo both ^{68}Ga-PSMA and ^{18}F-FDG PET imaging. The absolute number of lesions and lesion sites were recorded for each modality. Patients were evaluated for miTNM staging, prognostic staging, and therapeutic planning. Lesions were stratified into three categories based on tracer uptake: PSMA[+]/FDG[-], PSMA[+]/FDG[+], and PSMA[-]/FDG[+]. Comparative analyses were performed at the levels of lesion count, lesion site, and patient. Then compare the changes in staging, restaging and therapeutic planning outcomes. Modifications in therapeutic planning were categorized as no change, minor change, or major change. Associations between imaging phenotypes and clinicopathologic variables were analyzed. ***Results:*** A total of 65 Pca patients were enrolled, comprising 38 patients undergoing initial staging and 27 undergoing restaging. 941 lesions were found in the initial staging group, of which 422 (44.8%) PSMA[+]/FDG[-], 281 (29.9%) PSMA[+]/FDG[+], and 238 (25.3%) PSMA[-]/FDG[+], with 162 lesion sites, including 62 (38.3%) PSMA[+]/FDG[-], 89 (54.9%) PSMA[+]/FDG[+], and 11 (6.8%) PSMA[-]/FDG[+]. In the restaging cohort, 317 lesions were detected, of which 118 (37.2%) PSMA[+]/FDG[-], 133 (42.0%) PSMA[+]FDG[+], and 66 (20.8%) PSMA[-]FDG[+], with 99 lesion sites, including 35 (35.4%) PSMA[+]FDG[-], 47 (47.5%) PSMA[+]FDG[+], and 17 (17.2%) PSMA[-]FDG[+]. ^{68}Ga-PSMA PET was significantly less effective in identifying visceral metastases (initial staging: 3.9% vs. 28.5%, p<0.001; restaging: 13.9% vs. 22.4%, p<0.001). PSMA[-]FDG[+] lesions were identified in 5 of 38 (13.2%) patients in the initial staging group and in 7 of 27 (25.9%) restaging patients. In the initial staging group, 5 (13.2%), 2 (5.3%), and 5 (13.2%) experienced changes in miTNM staging, prognostic staging, and therapeutic strategy, respectively. Correspondingly, 3 (11.1%), 2 (7.4%), and 3 (11.1%) restaging patients had alterations in miTNM staging, prognostic staging, and therapeutic strategy. Importantly, in the initial staging group, PSMA[-] FDG[+] lesions were significantly more prevalent in patients with higher Ki-67 expression (≥12.5%) compared to those with lower Ki-67 levels (<12.5%) (p=0.046). ***Conclusion:*** Dual-tracer PET imaging enhanced diagnostic accuracy in both the initial staging and restaging of Pca, leading to staging refinement and treatment modifications in a subset of patients. ^{18}F-FDG PET demonstrated superior sensitivity for detecting visceral metastases. Notably, elevated Ki-67 expression in newly diagnosed patients may serve as a predictive biomarker for the presence of PSMA[-]FDG (+) lesions.

EP-0358

Is the D'Amico risk classification enough to define the indication of [18F]-DCFPyL PET/CT and promote therapeutic impact?

J. Bonilla Plaza[1], *M. Amo Salas*[2], *I. García Megías*[1], *J. Montalvá Pastor*[1], *L. Garcia Zoghby*[1], *M. Cruz Montijano*[1], *M. Meneses Navas*[1], *S. Guzman Ortiz*[1], *C. Lucas Lucas*[3], *M. de Cabo Ripoll*[4], *F. Leal Hernandez*[5], *A. Salinas Sanchez*[6], *V. Poblete García*[3], *A. García Vicente*[1];
[1]Hospital Universitario de Toledo, Toledo, SPAIN, [2]Universidad de Castilla la Mancha, Ciudad Real, SPAIN, [3]Hospital General Universitario Ciudad Real, Ciudad Real, SPAIN, [4]Hospital Virgen

de la Luz, Cuenca, SPAIN, [5]Hospital Universitario de Guadalajara, Guadalajara, SPAIN, [6]Complejo Hospitalario Universitario de Albacete, Albacete, SPAIN.

Aim/Introduction: This study evaluated the influence of clinical and biochemical disease characteristics on molecular-imaging TNM(miTNM) categories attending to PROMISE criteria and the therapeutic impact of PET/CT with [18F]-DCFPyL-PET/CT in initial staging of intermediate/high risk prostate cancer(PCa). ***Materials and Methods:*** A regional, retrospectively analyzed cohort comprising consecutive men staged with [18F]DCFPyL-PET/CT at seven hospitals in Castilla-La Mancha(Spain) from March 2021 to June 2024 was reviewed. The study was approved by a reference Ethical Committee (internal code 2022-053). Eligibility required no prior androgen-deprivation therapy, complete ISUP/PSA/clinical-T data, and ≥6 months follow-up. The impact of D'Amico high-risk(H-R) variables(ISUP 4/5, PSA>20 ng/mL and cT≥3), PSA and its kinetic on the diagnostic (N and/or M detection) and therapeutic impact was assessed. Univariate associations used Mann-Whitney U, Fisher's exact or Spearman trend; predictors with $p < 0.10$ were entered into step-down logistic regression. ***Results:*** 195 men(median age 71 years) met inclusion criteria. 41.4% had one, 29.2% two and 8.9% three H-R variables. 32.5%(cT-HR), 50.8 % (ISUP-HR) and 43.2% (PSA-HR). PET/CT detected miN+ and miM+ in 25.2% and 13.01%, respectively. A statistically significant relationship was found between the ISUP+cT high and miN(Chi^2=15.292; $p < 0.001$), as well as between T+PSA_high and miN(Chi^2=8.832; $p = 0.012$), and ISUP+T+PSA_high and miN(Chi^2=12.847; p=0.005). These findings suggest that these parameters may have predictive value for identifying nodal involvement. No clinical variable predicted distant metastases. PSA kinetics showed no correlation with miT, miN or miM categories. PET/CT prompted management change in 28 patients (14 %). Age, baseline PSA, PSA kinetics, cT, ISUP grade, T-HR, ISUP-HR or PSA-HR were unrelated to therapeutic change (p> 0.14). Distant metastasis detected on PET/CT(miM+) were strongly associated with therapeutic impact (64 % vs 6 %; $p = 0.004$) and remained the only independent predictor in the final model (adjusted OR 4.33, 95 % CI 1.66-11.32, $p = 0.003$; pseudo-$R^2 = 0.18$). ***Conclusion:*** In newly diagnosed PCa, the presence of D'Amico high-risk(H-R) variables suggest that these composite indices may serve as useful predictors for lymph node metastasis in the studied population. No correlation was found with miM, probable due the low rate of distant metastases. Only miM+ [18F]-DCFPyL-PET/CT independently predicts management change, multiplying the odds more than four-fold. These findings highlight the pivotal role of PSMA PET/CT in unmasking occult systemic disease and support its routine integration into initial staging when treatment selection depends on accurate metastatic assessment.

EP-0359

Evaluation of the Relationship of the Risk Status of Prostate Cancer Patient with PSA Density, PSA Metabolic Density and 68Ga-PSMA PET/CT Parameters

G. Inal[1], *N. Aydinbelge Dizdar*[1], *O. Duyar*[1], *O. Ozmen*[2];
[1]*Ankara Etlik City Hospital Department of Nuclear Medicine, Ankara, TÜRKIYE,* [2]*Department of Nuclear Medicine, Etlik City Hospital, University of Health Sciences, Etlik City Hospital Department of Nuclear Medicine, Ankara, TÜRKIYE.*

Aim/Introduction: Prostate-specific membrane antigen (PSMA) is a promising molecular target for the diagnosis and treatment management of prostate cancer. 68Ga-PSMA PET plays an important role in staging prostate cancer, assessing treatment response, and detecting recurrence. This study aimed to classify biopsy-proven patients with prostate cancer by risk status and evaluate the relationship between 68Ga-PSMA PET parameters and metastasis status. ***Materials and Methods:*** A total of 121 patients with biopsy-proven prostate cancer who underwent 68Ga-PSMA PET/CT for primary staging between 2023 and 2024 were classified as low, intermediate and high risk. The relationship between SUVmax, TL-PSMA, TV-PSMA, Tumour/Liver (T/L), Tumour/Parotid (T/P), PSA density (PSAD), PSA metabolic density (PSAMD) and metastasis status were evaluated ($p<0.05$ for statistical significant). ***Results:*** According to D'Amico classification, 7 patients were low risk, 36 intermediate, and 76 high risk (Table-1). In the high risk-group, approximately half of the patients had pathological uptake of regional lymph nodes and 15 had distant lymph node metastases (Table-2). PSAD is calculated by dividing the serum PSA value by the prostate volume. Accordingly, the mean PSAMD value was 5.79±0.81 by dividing the PSA value by the primary tumor volume. PSAMD was significantly associated with PSA value, prostate SUVmax, T/L, T/P, and PSAD (p=0.00, p=0.01, p=0.00, p=0.00, and p=0.00, respectively), but not with disease extent (local, locally advanced, advanced) ($p>0.05$). In patients with positive lymph nodes, PSA, prostate volume, prostate SUVmax, TL-PSMA, TV-PSMA, T/L, and T/P values were significantly higher compared to those without lymph node positivity (p=0.001, p=0.003, p=0.01, p=0.001, p=0.047, p=0.017, and p=0.001, respectively). ROC analysis based on data obtained from 68Ga-PSMA PET/CT showed that PSA, prostate TL-PSMA, TV-PSMA, and T/P increased the risk of pelvic lymph node and bone metastasis. According to miTNM, patients were classified as local, locally advanced, and advanced groups. PSA, prostate SUVmax, prostate TL-PSMA, T/L, and T/P values showed significant differences between local and locally advanced; PSA, prostate SUVmax, prostate TV-PSMA, prostate TL-PSMA, PSAD, T/L, and T/P between locally advanced and advanced; and prostate SUVmax and T/L between locally advanced and advanced groups (Table-3). SUVmax, TL-PSMA and TV-PSMA, T/L, T/P, PSAD and PSAMD showed significant differences between intermediate- and high-risk patients. ***Conclusion:*** Based on our findings, these parameters may be useful in distinguishing between high- and intermediate-risk patients. Compared with conventional imaging methods, 68Ga-PSMA PET/CT has been found to be more successful in staging intermediate to high-risk prostate cancer.

EP-0360

Head-to-head comparison of ^{99m}Tc-PSMA-T4 SPECT and ^{68}Ga-PSMA PET studies

P. Cichocki[1], *K. Stawski*[2], *R. Mikolajczak*[3], *W. Wojdowska*[3], *P. Garnuszek*[3], *Z. Adamczewski*[1];
[1]*Department of Nuclear Medicine, Medical University of Lodz, Lodz, POLAND,* [2]*Department of Biostatistics and Translational Medicine, Medical University of Lodz, Lodz, POLAND,* [3]*National Centre for Nuclear Research, Radioisotope Centre POLATOM, Otwock, POLAND.*

Aim/Introduction: PSMA ligands play an increasingly important role in diagnosis and treatment of prostate cancer. ^{68}Ga-PSMA is among the most commonly used diagnostic radiopharmaceuticals. However, high cost and limited availability of gallium-68 limits its application in routine clinical practice. Therefore, introduction of alternative radiopharmaceuticals, especially labelled with commonly available technetium-99m, would greatly expand potential applications of PSMA studies, provided they have adequate clinical value. Our preliminary study aims to assess reliability of ^{99m}Tc-PSMA-T4 in staging of prostate cancer and qualification for therapy, in comparison with ^{68}Ga-PSMA PET studies used as reference. ***Materials and Methods:*** The study included selected patients enrolled in ongoing phase 2/3 PSMA-T4 clinical trial (ID: NCT05847166), who were also referred for a ^{68}Ga-PSMA study as part of routine prostate cancer staging evaluation before radiotherapy. SPECT and PET PSMA studies of each patient were assessed independently by experienced nuclear medicine physicians and consulted with radiologists. ***Results:*** ^{99m}Tc-PSMA properly detected primary tumors in prostate in all patients. Overall TNM staging was also the same in both SPECT

and PET studies, leading to the same clinical decisions regarding qualification of patients to radical surgery, radiotherapy or other forms of treatment. However, SPECT images had lower resolution compared to PET, and a few small lesions in lymph nodes visible in ^{68}Ga-PSMA studies were not detected in ^{99m}Tc-PSMA studies (they had no impact on staging due to presence of other lymph node metastases in all these cases). ***Conclusion:*** Our preliminary assessment showed that ^{99m}Tc-PSMA T4 study is adequate for initial qualification of all included patients for treatment. In all cases their results led to the same clinical decisions as ^{68}Ga-PSMA PET. However, it was characterized by lower sensitivity and did not detect some of the small lesions in lymph nodes found in PET studies. This was most likely caused by lower resolution of the SPECT gamma camera compared to a PET scanner. It cannot be ruled out that the use of new semiconductor SPECT gamma cameras with ring detector systems, which achieve similar resolutions as PET scanners, could improve diagnostic value of ^{99m}Tc-PSMA studies, but this requires further investigation.

EP-0361

Clinical Impact of Delayed Pelvic Imaging in PSMA PET/CT for Primary Prostate Cancer Staging and Management

G. Galnaitiene, *G. Grigaityte, K. Snarskis, I. Balciunaite, G. Aleksa, D. Vajauskas;*
Lithuanian University of Health Sciences, Kaunas, LITHUANIA.

Aim/Introduction: PSMA PET/CT is widely used for staging high-risk primary prostate cancer (PCa). Although a 60-minute uptake time is standard, urinary activity may limit assessment of tumour (T) and nodal (N) stages. Delayed pelvic imaging beyond 120 minutes may improve lesion visibility [1]. Previous studies mainly focused on biochemical recurrence or advanced disease. We evaluated the added value of delayed imaging in initial staging of primary PCa. ***Materials and Methods:*** We retrospectively analysed 59 patients with histologically confirmed primary PCa (mean age 65.2 ± 8.1 years) who underwent 68Ga-PSMA-11 PET/CT for initial staging. Whole-body imaging was performed at 60.9 ± 3.6 min post-injection, followed by delayed pelvic imaging at 132.1 ± 14.3 min. Data included T/N stage at both time points, SUVmax/SUVmean values of the lesions, PSA levels, and ISUP grade. PROMISE V2 was used for staging [2]. Treatment plans were reviewed. Non-parametric statistical tests, logistic regression, and ROC analysis were used. ***Results:*** Staging changed in 13 patients (22.0%), including 10 T stage (9 upstaged) and 4 N stage (3 upstaged) changes. No treatment plans were modified due to delayed imaging. SUVmax and SUVmean significantly increased at delayed imaging for both T lesions (+3.88 and +2.00; $p < 0.001$; n=58) and N lesions (+3.40 and +2.02; $p < 0.01$; n=15). Patients were grouped as ISUP 1-2 (28.8%) and ISUP 3-5 (71.2%). Patients with staging changes tended to have lower ISUP (1-2: 23.5% vs. 3-5: 21.4%; $p = 0.21$) and PSA (16.2 vs. 40.8; $p = 0.16$); differences were not significant. Logistic regression indicated a non-significant association between lower ISUP grade and T SUVmean at 60min and increased likelihood of staging change (OR = 0.66 and 0.83; $p = 0.18$ and 0.38, respectively). ROC analysis showed that a T SUVmax at 60min threshold of < 5.97 (AUC = 0.74) combined with ISUP 1-2 identified patients with a 50.0% staging change rate, compared to 16.3% in others ($p < 0.05$). ***Conclusion:*** Delayed pelvic imaging significantly increased lesion SUV values and altered staging in one-fifth of patients. Although it did not change management, it may add value in lower-grade cases with low uptake. Further studies in larger cohorts are needed. ***References:*** 1. Giesel FL et al. 68Ga-PSMA-11 PET/CT imaging protocol guidelines: joint EANM and SNMMI procedure standard. Eur J Nucl Med Mol Imaging. 2023;50(2):560-591. 2. Hope TA et al. PROMISE V2: Updated framework for PSMA PET reporting. Eur Urol. 2024;85(2):223-232.

EP-0362

Impact of [^{68}Ga]PSMA-PET/CT using PRIMARY and miPSMA Expression Scores on Clinical Decision-Making for ePLND in Staging of Intermediate-Risk Prostate Cancer patients

A. Safarian[1,2], *F. Szigeti*[3], *T. Kiener*[1], *H. Grießner*[4], *H. Nasrollahi*[1], *S. Hecht*[5], *L. Lusuardi*[4], *C. Pirich*[1], *M. Beheshti*[1];
[1]*Division of Molecular Imaging and Theranostics, Department of Nuclear Medicine, University Hospital, Paracelsus Medical University, Salzburg, AUSTRIA,* [2]*Rajaie Cardiovascular Medical and Research Center, Rajaie Cardiovascular Institute, Iran University of Medical Sciences, Tehran, IRAN, ISLAMIC REPUBLIC OF,* [3]*Salzburg University of Applied Sciences, Radiation Technology degree program, Salzburg, AUSTRIA,* [4]*Department of Urology, Paracelsus Medical University, Salzburg, AUSTRIA,* [5]*Department of Radiology, Paracelsus Medical University, Salzburg, AUSTRIA.*

Aim/Introduction: Accurate lymph node (LN) staging is critical for treatment planning in prostate cancer (PCa) patients. Extended pelvic LN dissection (ePLND) provides definitive staging but is associated with higher morbidity. While ePLND is routinely performed in high-risk cases and generally avoided in low-risk patients, intermediate-risk patients fall into a grey zone, and the necessity of ePLND in this group remains controversial. The role of [^{68}Ga]PSMA-PET/CT for accurate N-staging in intermediate-risk patients has been discussed controversially. This study aimed to evaluate whether [^{68}Ga]PSMA-PET/CT using novel PRIMARY and miPSMA-expression scores may provide an accurate N-staging supporting clinical decision-making for ePLND in intermediate-risk PCa patients. ***Materials and Methods:*** This retrospective study included 94 strictly-defined intermediate-risk PCa patients, defined as clinical stage T2, Gleason score 7 (ISUP grade group 2 or 3), and PSA 10-20 ng/mL. All patients underwent [^{68}Ga]PSMA-PET/CT for initial staging, followed by radical prostatectomy with ePLND. The PRIMARY score, miPSMA-expression score (PROMISE V2), SUVmax, location, zone and number of prostate lesions as well as PIRADS scores were assessed for association with histopathological LN status. ***Results:*** Of the 94 patients, 8 (8.5%) had histologically confirmed LN metastases. [^{68}Ga]PSMA-PET/CT reported 87 patients as LN-negative, of whom 86 were truly LN-negative, resulting in a negative predictive value of 98.9%. The median number of dissected lymph nodes was 13. The observed imaging scores in these patients were: median PRIMARY score 4 (range 2-5), median miPSMA expression score 2 (range 1-3), and median PIRADS score 4 (range 2-5). [^{68}Ga]PSMA-PET nodal positivity remained the sole reliable predictor of LN metastasis in this cohort. Interestingly, no significant association was found between nodal status and intra-prostatic PSMA PET parameters using novel PRIMARY and miPSMA expression scores, as well as SUVmax, number and distribution of intraprostatic lesions, and PIRADS scores. In the single false-negative patient, only one out of 15 dissected lymph nodes was positive, representing a very small metastasis measuring 2.5 mm, without infiltration of the perinodal soft tissue. ***Conclusion:*** [^{68}Ga]PSMA-PET/CT demonstrated excellent concordance with pathological LN status in these strictly defined intermediate-risk PCa patients. The findings of this study are promising for enhancing clinical nomograms and supporting ePLND de-escalation strategies, while preserving oncological outcomes in this patient group.

EP-0363

PRIMARY Score: when radionuclide matters

P. Guglielmo[1,2], *L. Muraglia*[3], *R. Zanca*[1], *C. Vallone*[1,4], *J. Jandric*[3], *D. Aricò*[5], *N. Buffi*[1,6], *G. Lughezzani*[1,6], *L. Evangelista*[1,3];
[1]*Department of Biomedical Sciences, Humanitas University, Pieve Emanuele, Milan, ITALY,* [2]*Nuclear Medicine Unit, Humanitas Gavazzeni, Bergamo, ITALY,* [3]*Nuclear Medicine Unit, IRCCS Humanitas Research Hospital, Rozzano, Milan, ITALY,* [4]*Department of Advanced Biomedical Sciences, University of Naples Federico II, Naples, ITALY,* [5]*Nuclear Medicine Unit, Humanitas Istituto Clinico Catanese, Misterbianco, Catania, ITALY,* [6]*Urology Unit, IRCCS Humanitas Research Hospital, Rozzano, Milan, ITALY.*

Aim/Introduction: The PRIMARY score, which is based on SUVmax values, was originally validated using the radiotracer [^{Ga}68]Ga-PSMA-11. However, newer radiopharmaceuticals based on 18F are now being used in clinical practice, and their SUVmax values are not directly comparable to those of [^{Ga}68]Ga-PSMA-11. This study aimed to examine how semiquantitative values vary when using these two different tracers in patients with intermediate-risk prostate cancer. ***Materials and Methods:*** A retrospective, multicenter analysis of patients diagnosed with intermediate risk PCa between 2021 and 2024 was made. Patients were staged using pelvic multiparametric magnetic resonance imaging (mpMRI) and radiolabeled PSMA PET/CT, either [^{68}Ga]Ga-PSMA-11 or [^{18}F]F-PSMA1007, to evaluate the extent of disease before initiating appropriate treatment. PRIMARY score were used for quantitative analysis. ***Results:*** A total of 78 patients were included in the analysis. Of these, 49 patients (62.8%) underwent imaging with [^{18}F]F-PSMA-1007, and 29 patients (37.2%) underwent [^{68}Ga]Ga-PSMA-11 PET/CT. The distribution of PRIMARY scores was as follows: Score 1 in 6 and 3 patients, Score 2A/B in 8 and 2 patients, Score 3 in 3 and 5 patients, Score 4 in 17 and 13 patients, and Score 5 in 15 and 6 patients, respectively for ^{18}F and ^{68}Ga-based PSMA. SUVmax was useful primarily for distinguishing between PRIMARY scores 4 and 5. To further investigate this, SUVmax values for 51 patients were compared between [^{18}F]F-PSMA-1007 and [^{68}Ga]Ga-PSMA-11 groups using the Mann-Whitney U test. For PRIMARY score 4, the median SUVmax was significantly higher in the [^{18}F]F-PSMA-1007 group compared to the [^{68}Ga]Ga-PSMA-11 group (7.7 vs. 5.2; $p < 0.05$). In contrast, for PRIMARY score 5, median SUVmax values were similar between the two tracers (18.6 vs. 15.3; $p = 0.349$). ***Conclusion:*** Limited data are available on the use of the Primary score in patients who have undergone [68Ga]Ga-PSMA-11. The median SUVmax was significantly lower than those undergoing [18F]F-PSMA-1007 when the Primary score was 4. However, no significant difference was observed in patients with a Primary score of 5. Further analysis should be made in a larger population to test the reproducibility of the score by using diverse radiopharmaceutical agents.

EP-0364

Concordance and added diagnostic value of [^{18}F] PIFLUFOLASTAT PET/CT to pelvic MRI in the diagnosis of prostate cancer (Pca).

A. Peñaherrera Cepeda, *J. A. Badell Martínez, L. Díaz González, E. Casillas Sagrado, E. Campaña Díaz, P. García-Talavera San Miguel, J. G. Villanueva, S. Rama Alonso, B. Santos García, F. Caltagirone Gutierrez, P. Tamayo Alonso;*
Complejo asistencial universitario de Salamanca, Salamanca, SPAIN.

Aim/Introduction: To asses the rates of concordance between [18F]PIFLUFOLASTAT PET/CT to pelvic MRI in the diagnosis of Pca.To calculate the anatomical detection rate of Pca in prostate and seminal vesicles of [[18F]PIFLUFOLASTAT PET/CT and MRI, histologically confirmed. To determine the percentage of studies with extrapelvic uptake in [18F]PIFLUFOLASTAT PET/CT study. ***Materials and Methods:*** Thirty men (mean age: 69 +/- 8 years) diagnosed with intermediate an high risk Pca, who underwent [18F]PIFLUFOLASTAT PET/CT and pelvic MRI, performed with an interval of less than 3 months, during 2021- 2025, were included. Were interpreted using PI-RADS v2.1 (all ≥ 4) and PRIMARY scores (all ≥ 3), and reconciled using biopsy specimens. The concordance of both modalities was categorized as "positive concordance" when the same number of lesions and location, in prostate and seminal vesicles, coincided with the pathological anatomy findings in the biopsy. Another category of discordant findings were denominated as "higher in PET-CT"(more lesions were observed with respect to MRI, tested positive in the biopsy), and "higher in MRI" (when the same occurred with this other technique).The percentage of studies with extra pelvic uptake study (nodal, bone or visceral localization) in the 18F]PIFLUFOLASTAT PET/CT within the resonance field, was also calculated.Descriptive statistics were used, including median and standard deviation for continuous variables and frequency and percentage for categorical variables. ***Results:*** MRI and [18F]PIFLUFOLASTAT PET/CT had positive concordance in 17/30 (56.6%) patients, an discordant in 13/30 (43.3%) patients. Nine of these thirteen patients (69.2%) had a higher involvement in prostate and seminal vesicles in [18F] PIFLUFOLASTAT PET/CT than in the MRI. And 30.8% had a higher involvement in prostate and seminal vesicles [18F]PIFLUFOLASTAT PET/CT than in the MRI. The anatomical detection rate of disease in the prostatic lobules and seminal vesicles was 86.7% for [18F]PIFLUFOLASTAT-PET/CT and 70% by MRI. In addition, the pathological uptake in pelvic lymph nodes were detected in 10/30 (33.3%) patients in [18F]PIFLUFOLASTAT-PET/CT, not detected by MRI. And only 2/30 (6.7%) patients were positive in MRI, that was not visualized in [18F]PIFLUFOLASTAT PET/CT. These findings did not correlate with the biopsy. In 6.6% of [18F]PIFLUFOLASTAT PET/CT scans performed, distant disease was found outside the field of study of the MRI, which led to an increase in staging by MRI alone. ***Conclusion:*** [18F] PIFLUFOLASTAT PET-CT demonstrated an acceptable concordance with MRI pelvic findings and a great anatomical detection rate, as well as, the possibility of detection of distant disease.

EP-0365

The Influence of Pre-Imaging Prostate-Specific Therapy on PSMA Uptake and Outcomes

G. Galnaitiene, *G. Grigaitytė, K. Snarskis, I. Balčiūnaitė, G. Aleksa, D. Vajauskas;*
Lithuanian University of Health Sciences, Kaunas, LITHUANIA.

Aim/Introduction: PSMA PET/CT is widely used to stage primary prostate cancer (PCa), but the impact of pre-imaging prostate-specific therapies remains unclear. Short-term androgen deprivation therapy (ADT) may increase PSMA uptake, while long-term ADT may suppress it [1-2]. The effects of 5-alpha-reductase inhibitors (5-ARI) and alpha-blockers are less known. We assessed the effect of these therapies in newly diagnosed PCa patients undergoing initial staging. ***Materials and Methods:*** We retrospectively analysed 59 patients with histologically confirmed primary PCa (mean age 65.2 ± 8.1 years) who underwent 68Ga-PSMA-11 PET/CT for initial staging. Whole-body and delayed pelvic imaging were performed at 60.9 ± 3.6 and 132.1 ± 14.3 min post injection. Pre-imaging therapy, PSA, ISUP grade, SUVmax/SUVmean, T and N staging were recorded. Statistical tests included Mann-Whitney, Wilcoxon, Fisher's exact, and multivariate logistic regression. ***Results:*** From 59 patients, 32 received pre-imaging therapy: 15 alpha-blockers (median 297 days), 6 5-ARI (281.5 days), 7 anti-androgens (67 days), and 4 ADT (101 days). Median T SUVmax and SUVmean at both timepoints were lower in most treated groups and higher in 5-ARI patients, though not statistically significant. 5-ARI treatment led to a significantly greater increase in T SUVmax (median 5.96 vs 1.74, $p = 0.040$) and SUVmean (3.72 vs 1.10, $p = 0.019$) during delayed scan compared to untreated. Other treatments showed non-significant changes

in SUV and T staging. From 17 patients with nodal uptake, 7 had received: 6 alpha-blockers, 2 5-ARI, 1 anti-androgens, none ADT. Median N SUV values and changes were lower in treated groups but not statistically significant. N stage change during delayed scan occurred in 4 patients, significantly more frequent among alpha-blocker users ($p = 0.047$, $\varphi = 0.31$; OR = 10.75, 95% CI: 1.02-112.93), and remained significant in multivariate analysis ($p = 0.043$). No significant effects were seen for ADT, anti-androgens, 5-ARI, PSA, or ISUP grade. ***Conclusion:*** Pre-imaging use of 5-ARI was associated with increased T lesion uptake over time, while alpha-blocker may influence N staging on PSMA PET/CT. No other treatments demonstrated significant effects on SUV or staging, likely due to small subgroups. These findings suggest that pre-imaging prostate-specific therapies may influence PSMA PET/CT interpretation in primary PCa, and further investigation in larger cohorts is needed. ***References:*** 1. Gafita A, et al. Effect of androgen deprivation therapy on PSMA expression and PET/CT interpretation. EJNMMI Reports. 2023;7:18. 2. Emmett L et al. Changes in PSMA PET SUV after short-term androgen deprivation therapy. Eur J Nucl Med Mol Imaging. 2023;50:1234-1243.

EP-0366

Investigation of the Correlation Between the Briganti 2012 Nomogram and Ga-68 PSMA PET/CT Parameters in Localized and Locally Advanced Prostate Cancer

R. Tokac[1], *F. Avci*[1], *M. Dinckal*[2], *K. Ergun*[1], *A. Argon*[1], *U. Yararbas*[1]; [1]*Ege University, Izmir, TÜRKIYE,* [2]*Kars Harakani State Hospital, Kars, TÜRKIYE.*

Aim/Introduction: Extended pelvic lymph node dissection (ePLND) is a key staging tool for detecting nodal metastases in prostate cancer (PCa), with lymph node invasion rates ranging from 1.1% to 26%. Accurate patient selection is therefore critical. The Briganti Nomogram (BN), widely validated since its introduction, uses a 7% risk cut-off to guide ePLND decisions. Ga-68 PSMA PET/CT has also shown value in staging locally advanced PCa. This study investigates the correlation between the Briganti 2012 Nomogram and Ga-68 PSMA PET/CT parameters in localized and locally advanced PCa. ***Materials and Methods:*** This retrospective study included 47 patients who were diagnosed with localized or locally advanced PCa and underwent TRUS-guided biopsy, mpMRI, PSA testing, and Ga-68 PSMA PET/CT between November 2018 and December 2023 prior to prostatectomy. Ga-68 PSMA synthesis and PET/CT imaging were performed according to guidelines. Images were evaluated using Siemens syngo.via software, and the following values were calculated from the primary tumor: SUVmax, SUVmean, SUVpeak, PSMA-TV, TL-PSMA, and PSMA-TLQ. BN risk percentages were calculated, and a 7% cut-off was used to classify patients into low- and high-risk groups. Statistical analyses were conducted using IBM SPSS 25. ***Results:*** The mean age of the 47 patients meeting the inclusion criteria was 65.19 ± 5.26 years. Clinical T scores showed that 35 patients (74.5%) had T3 disease, 12 patients (25.5%) had T2. The mean PSA level was 14.86 ± 15.74 ng/mL. Gleason scores were distributed as follows: 3+3 in 4 patients (8.5%), 3+4 in 23 (48.9%), 4+3 in 10 (21.3%), 3+5 in 1 (2.1%), 4+4 in 4 (8.5%), 4+5 in 4 (8.5%), and 5+5 in 1 (2.1%). A moderate and statistically significant correlation was found between BN risk percentage and SUVpeak ($r=0.404$, $p=0.005$), PSMA-TV ($r=0.514$, $p<0.001$), and TL-PSMA ($r=0.553$, $p<0.001$). A weak but significant correlation was also observed with SUVmax ($r=0.366$, $p=0.11$), SUVmean ($r=0.315$, $p=0.031$), and PSMA-TLQ ($r=0.354$, $p=0.15$). There was a significant relationship between BN risk groups and PSMA-TV, TL-PSMA, and PSMA-TLQ values ($p=0.003$, $p=0.003$, and $p=0.022$, respectively; see Figure 1). No statistically significant relationship was found between BN risk groups and SUVmax, SUVmean, or SUVpeak ($p>0.05$). ***Conclusion:*** Our findings suggest that in localized and locally advanced PCa, there is a significant correlation between BN and Ga-68 PSMA PET/CT parameters, particularly volumetric measures. Predictive models like the BN are useful clinical tools for decision-making, and incorporating Ga-68 PSMA PET/CT may enhance their predictive power.

EP-0367

PSMA SPECT and PET Imaging in the Staging of High Intermediate Risk to High-Risk Prostate Cancer - an institutional experience in a resource limited setting

S. More*, M. Rivombo, K. Hlongwa;*
University of Cape Town, Cape Town, SOUTH AFRICA.

Aim/Introduction: Current standards of care highlight molecular imaging using PSMA PET to characterise disease in intermediate and high risk prostate cancer. Data specific to the local population was lacking, including evidence of any possible associations between image findings and the various qualitative or quantitative risk parameters. The additional diagnostic performance of PSMA imaging over bone scan alone was also not established in our population. The purpose was to objectively characterise diagnostic performance of a local hospital molecular imaging protocol for staging high-intermediate and high-risk prostate cancer (ISUP Grade >2) whereby iterative molecular imaging with [^{99m}Tc]Tc-MDP bone scan, [^{99m}Tc]Tc-PSMA SPECT/CT and [^{68}Ga]Ga-PSMA PET/CT was performed until metastases were convincingly detected. A supplementary aim was to determine if selective use of specific modalities is justified in certain groups. ***Materials and Methods:*** The prostate cancer staging protocol implemented at the time was adapted from the existing ASCO guidelines. More sensitive imaging with PSMA PET/CT was reserved for use in patients where metastatic disease remained undetected. Studies were interpreted independently by qualified nuclear physicians with experience exceeding 5 years and in line with accepted criteria. Patients considered for analysis were limited to those referred for primary staging of high-intermediate and high-risk prostate cancer or being considered for possible radical therapy. Overall detection rates for the presence of metastases at each iteration were calculated. Statistical analysis was performed for associations between diagnostic performance and risk stratification subcategories (clinical stage, PSA levels, histological grade; or age). ***Results:*** A total of 88 patients were enrolled with mean age of patients at baseline being 65.05 years with a mean PSA of 130.95µg/L. Detection rates for metastatic disease for those enrolled increased from 38% to 51% to 61% with each respective imaging iteration. There was a significant association of patient age, PSA level, histological grade, and clinical stage to bone scan positivity ($p = 0.005$), with a reduction in mean PSA for those demonstrating metastatic disease on subsequent [^{99m}Tc]Tc-PSMA SPECT/CT. No further significant associations were observed for the subgroup who proceeded to [^{68}Ga]Ga-PSMA PET/CT. ***Conclusion:*** Bone scan or [^{99m}Tc]Tc-PSMA SPECT/CT proved reasonable first line staging investigations to exclude evidence of metastases before [^{68}Ga]Ga-PSMA PET/CT, with enhanced efficiency in locally advanced disease, ISUP 5 or higher spectrum PSA/age. The findings favour [^{99m}Tc]Tc-PSMA SPECT/CT over bone scan where [^{68}Ga]Ga PSMA PET/CT is unavailable, due to lower mean PSA threshold for detecting metastatic disease.

EP-0368

Impact of Ga-68 PSMA PET/MRI on the Accuracy of MRI-derived Grading Systems for Predicting Extraprostatic Extension in Prostate Cancer

L. Uslu-Besli[1], *S. Durmaz*[2], *B. Bakir*[3], *I. Gurses*[4], *S. Ozel-Yildiz*[5], *C. Demirdag*[6], *H. B. Sayman*[1];
[1]*Istanbul University-Cerrahpasa, Cerrahpasa Medical Faculty, Department of Nuclear Medicine, Istanbul, TÜRKIYE,* [2]*Gaziosmanpasa Training and Research Hospital, Department of Radiology, Istanbul, TÜRKIYE,* [3]*Istanbul University, Istanbul Medical Faculty, Department of Radiology, Istanbul, TÜRKIYE,* [4]*Istanbul University-Cerrahpasa, Cerrahpasa Medical Faculty,*

Department of Medical Pathology, Istanbul, TÜRKIYE, [5]Istanbul University, Istanbul Medical Faculty, Department of Biostatistics, Istanbul, TÜRKIYE, [6]Istanbul University-Cerrahpasa, Cerrahpasa Medical Faculty, Department of Urology, Istanbul, TÜRKIYE.

Aim/Introduction: Accurate preoperative staging and prediction of extra-prostatic extension (EPE) is crucial for optimal surgical planning in prostate cancer (PCa) patients. The aim of this study was to evaluate the diagnostic accuracy of Ga-68 PSMA PET for preoperative assessment of EPE and to compare it with the standardized multiparametric prostate MRI (mpMRI)-drived EPE grading system. We also aimed to assess whether incorporating semi-quantitative PSMA PET parameters enhances the diagnostic performance of the mpMRI-drived EPE grading system using hybrid PET/MRI. ***Materials and Methods:*** This single-center study, retrospective study included treatment-naïve, biopsy-proven PCa patients who underwent Ga-68 PSMA-11 PET/MRI along with mpMRI, followed by radical prostatectomy. Diagnostic accuracy was assessed for clinical parameters (serum prostate specific antigen [PSA] level and International Society of Urological Pathology [ISUP] score), mpMRI features (presence of capsular irregularity or bulge, presence of overt EPE, neurovascular bundle asymmetry, seminal vesicle invasion (SVI), curvilinear contact length (CLL) with the capsule and tumor size), the mpMRI-derived EPE grading system, visual PSMA PET findings, and semi-quantitative PET parameters (SUVmax, SUVmean and PSMA-tumor volume [PSMA-TV]. Optimal cut-off values for continuous variables were determined using the Youden Index. Multivariate logistic regression analysis and receiver operating characteristic (ROC) analysis were performed to compare the predictive value of clinical, mpMRI-derived and PET-derived variables for EPE. Postoperative histopathology was used as the reference standard. ***Results:*** Forty-five patients were included, with a mean interval of 44±29 days between PET/MRI and radical prostatectomy. Histopathology confirmed EPE in 19 patients. The following were identified as statistically significant predictors of EPE: Capsular irregularity or bulge, neurovascular bundle asymmetry, CLL ≥ 1.5 cm, SVI on MRI, tumor size ≥ 14.25 cm on MRI, EPE grade ≥ 2, ISUP grade ≥ 3, overt EPE on PET; SUVmax ≥ 13.84, SUVmean ≥ 7.195, PSMA-TV ≥ 1.395. On ROC analysis comparing the multivariate models, the combination of EPE grade ≥ 2 and ISUP grade ≥ 3 and PSMA-TV ≥1.395 yielded the highest AUC (0.916), although the difference was not statistically significant. The AUCs of PET-derived parameters were comparable to those of mpMRI and clinical variables. ***Conclusion:*** PSMA uptake in the primary prostate tumor is an independent predictor of EPE. Therefore Ga-68 PSMA-11 PET, in combination with mpMRI, may provide valuable information for the preoperative assessment of EPE. ***References:*** 1. Mehralivand S, et al. A Grading System for the Assessment of Risk of Extraprostatic Extension of Prostate Cancer at Multiparametric MRI. Radiology. 2019;290:709-192.

EP-0369

PSMA PET in Prostate Cancer Staging: Preliminary Radiomics Analysis and Machine Learning Model for Predicting PRIMARY and E-PSMA Scores

P. Alongi[1], *V. Benfante*[2], *P. Purpura*[2], *C. Messina*[3], *A. Comelli*[4]; *[1]University of Palermo, Department B.I.N.D., Palermo, ITALY, [2]Advanced Diagnostic Imaging-INNOVA Project, Department of Radiological Sciences, A.R.N.A.S. Civico Di Cristina e Benfratelli Hospitals, Palermo, ITALY, [3]Oncology Unit, ARNAS Civico, Palermo, ITALY, [4]Ri.MED Foundation, Palermo, ITALY.*

Aim/Introduction: Several scoring systems have been developed to improve the accuracy of prostate cancer (PCa) staging. Among them, the PRIMARY score and E-PSMA reporting guidelines have significantly influenced PSMA-PET clinical reporting. Recently, artificial intelligence (AI) approaches—including machine learning (ML), deep learning (DL), and convolutional neural networks (CNNs)—have shown promising results in automating the detection of PSMA-PET metastases, predicting response to PSMA-targeted therapies, and differentiating intraprostatic from extraprostatic high-grade PCa. This preliminary study aimed to explore the potential of ML models applied to radiomic features extracted from PSMA-PET in predicting PRIMARY and E-PSMA scores during PCa staging. ***Materials and Methods:*** Radiomic analysis was performed on 18F-PSMA-1007 PET images from 59 patients with histologically confirmed or 2-year follow-up-verified disease (31 prostate lesions, 15 lymph nodes, 13 bone lesions). Lesions were segmented using ITK-SNAP 4.2.2 and independently reviewed by two experts. A total of 112 radiomic features were extracted using Pyradiomics. We developed a hybrid ML model combining systematic feature selection and reduction with discriminant analysis to predict the PRIMARY score, E-PSMA 4-point Expression score, and 5-point Interpretation score. ***Results:*** For primary prostate lesions, two features (original_glcm_DifferenceEntropy and original_firstorder_Entropy) showed excellent performance in predicting E-PSMA Expression grades (sensitivity 100%, specificity 90.5%, AUROC 100%, p = 0.00). For predicting the E-PSMA Interpretation scale, original_gldm_LargeDependenceLowGrayLevelEmphasis was significant but with limited sensitivity (36.7%) despite good specificity (87.8%, AUROC 77.3%, p = 0.04). The feature original_glrlm_LongRunLowGrayLevelEmphasis showed suboptimal performance in predicting PRIMARY scores (sensitivity 52.6%, specificity 86.9%, AUROC 70.8%, p = 0.2). When including all lesion types (prostate, nodal, bone), E-PSMA Expression grades were accurately predicted by original_firstorder_Range (sensitivity 100%, specificity 67%, AUROC 98.3%, p = 0.00), while E-PSMA Interpretation was best predicted by original_shape_SurfaceVolumeRatio (sensitivity 94.5%, specificity 85.5%, AUROC 82.2%, p = 0.00). ***Conclusion:*** This exploratory study demonstrates for the first time the feasibility and potential clinical value of combining radiomics and AI for predicting validated international scoring systems on PSMA-PET in PCa staging. The ML model identified novel radiomic features that may help predict PRIMARY and E-PSMA scores in both primary and metastatic lesions. Larger prospective studies are needed to validate and extend these promising findings. ***References:*** PMC9635676; PMC8113168.

EP-0370

The Added Value of PSMA-PET to Nomograms in Identifying Optimal Candidates for Extended Pelvic Lymph Node Dissection in Intermediate-Risk Prostate Cancer Patients

F. Lanfranchi[1,2], *E. Checcucci*[3], *E. Cisero*[4], *A. Rizzo*[5], *S. Scuderi*[6], *F. Barletta*[6], *D. Robesti*[6], *C. Pini*[7], *D. Amparore*[4], *A. Sterrantino*[4], *M. Ortenzi*[4], *S. De Cillis*[4], *S. De Luca*[4], *P. Rescigno*[8], *A. Signori*[1], *G. Sambuceti*[1,2], *C. Terrone*[2,9], *A. Chiti*[7], *A. Briganti*[6], *C. Fiori*[4], *G. Gandaglia*[6], *F. Porpiglia*[4], *M. Bauckneht*[1,2];
[1]Department of Health Sciences (DISSAL), University of Genoa, Genova, ITALY, [2]IRCCS Ospedale Policlinico San Martino, Genova, ITALY, [3]Department of Surgery, Candiolo Cancer Institute, FPO-IRCCS, Candiolo (TO), ITALY, [4]Department of Oncology, Division of Urology, University of Turin, San Luigi Gonzaga Hospital, Orbassano (TO), ITALY, [5]Department of Nuclear Medicine, Candiolo Cancer Institute, FPO-IRCCS, C, ITALY, [6]Division of Oncology/Unit of Urology, Soldera Prostate Cancer Laboratory, Urological Research Institute, IRCCS San Raffaele Scientific Institute; Vita-Salute San Raffaele University, Milano, ITALY, [7]IRCCS San Raffaele Hospital, Milano, ITALY, [8]Translational and Clinical Research Institute, Centre for Cancer, Newcastle University, Newcastle upon Tyne, UNITED KINGDOM, [9]Department of Surgical and Diagnostic Integrated Sciences (DISC), University of Genoa, Genova, ITALY.

Aim/Introduction: Extended pelvic lymph node dissection (ePLND) is the standard approach for nodal staging in prostate cancer (PCa) patients undergoing radical prostatectomy (RP). However, its utility in intermediate-risk cases remains debated due to potential complications and uncertain oncologic benefits. This study aimed to assess whether incorporating Prostate-Specific

Membrane Antigen Positron Emission Tomography (PSMA-PET) nodal staging into traditional nomograms could enhance the selection of patients for ePLND. ***Materials and Methods:*** We retrospectively analyzed 110 intermediate-risk PCa patients who underwent preoperative PSMA-PET and subsequently received RP with ePLND at three referral centers in Italy between 2019 and 2023. For each patient, the risk of lymph node invasion (LNI) was calculated according to PSMA-PET reporting (positive/negative), and by using previously established cutoffs for current models (Memorial Sloan Kettering Cancer Center and the Briganti 2012, 2017, and 2019 nomograms). Receiver-operating-characteristic analysis was used to calculate area under the curve (AUC), sensitivity, specificity, positive and negative predictive values (PPV and NPV) of PSMA-PET and nomograms to predict LNI. Models' extent of over- or underestimation and net benefit were assessed using calibration plots and decision curve analysis (DCA). ***Results:*** PSMA-PET offered significantly higher specificity and PPV than all tested nomograms in identifying LNI ($p<0.01$ for all). While the adoption of nomograms would have spared 32%-65% of ePLND procedures missing 0%-1.1% of LNI cases, PSMA-PET would have resulted in 84% ePLND procedures spared ($p<0.01$ vs. all nomograms) and 0.9% of LNI cases missed (p=ns vs. all nomograms). Since the Briganti 2017 nomogram with a 7% cutoff was the most accurate in our cohort, we combined it with PSMA-PET to determine whether this combination could better discriminate between patients with and without histologically confirmed LNI. This combination would have further increased AUC, specificity and PPV for LNI ($p<0.05$ vs. PSMA-PET alone) and reduced unnecessary ePLND procedures without increasing the number of missed LNI cases. Specifically, if only patients with a Briganti 2017 score >7% and PSMA-PET N1 had been candidates for ePLND, 91% of procedures would have been spared ($p<0.01$ vs. all nomograms, p=ns vs. PSMA-PET alone), with only 0.9% of LNI cases missed (p=ns vs. all nomograms and p=ns vs. PSMA-PET alone). DCA demonstrated the net benefit of this combination for predicting LNI. ***Conclusion:*** Our findings suggest that integrating PSMA-PET with nomograms in intermediate-risk cases could optimise patient selection for ePLND, potentially reducing unnecessary surgeries without increasing the risk of missed LNI cases.

EP-0371

Smart risk-stratification: machine learning predicts LATITUDE high-risk prostate cancer at presentation using routine multimodal clinical data

B. Khangembam*, S. Sharma, R. Wakankar, M. Kavin, S. Kaushal, C. J. Das, R. K. Sahoo, A. Seth, A. R. Chanu, C. Patel, R. Kumar;*
All India Institute of Medical Sciences, New Delhi, INDIA.

Aim/Introduction: To evaluate the feasibility of machine learning (ML) models utilizing routine clinical, conventional imaging, and laboratory data for predicting LATITUDE high-risk disease in treatment-naïve prostate cancer patients undergoing ^{68}Ga-PSMA-11 PET/CT. ***Materials and Methods:*** Between April 2024 to March 2025, 168 treatment-naïve prostate cancer patients (mean age: 67 ± 8 years) with pathologically confirmed diagnoses were prospectively enrolled. The primary outcome was the presence of LATITUDE high-risk disease, determined by ^{68}Ga-PSMA-11 PET/CT imaging and pathological findings. A training set (n = 168) was generated via stratified deterministic bootstrapping, with 65 patients reserved as an independent test cohort. After feature normalization, Information Gain Ratio scoring was used for feature selection. Four ML models (Random Forest, CatBoost, XGBoost, and Naïve Bayes) were trained using stratified 10-fold cross-validation. Model performance was assessed using AUC, accuracy, F1 score, precision, recall, and specificity. Permutation plots were used to assess overfitting, while SHAP plots and confusion matrices were used for model interpretation. A Naïve Bayes-based nomogram was constructed using the five most important features based on absolute feature importance. ***Results:*** High-volume disease was present in 26.8% (45) of patients. Information Gain Ratio scoring selected the best-ranked 9 features for cross-validation. In cross-validation, three models exhibited >0.850 in all performance metrics, with Random Forest achieving the highest AUC of 0.963 (CA 0.940, F1 score 0.894, precision 0.875, recall 0.913, specificity 0.951). On the test set, Random Forest maintained the highest AUC of 0.938 (CA 0.877, F1 score 0.789, precision 0.833, recall 0.750, specificity 0.933). No significant overfitting was observed, and SHAP plots revealed clear patterns of interpretability. The nomogram revealed that PSA ≥87.37 ng/mL, ALP ≥251.5 U/L, N1 status, primary tumor size 23.30 - 30.55 mm, and hemoglobin <11.5 gm/dL could predict high-risk disease with 94% probability. ***Conclusion:*** Machine learning models effectively predict LATITUDE high-risk disease in treatment-naïve prostate cancer patients using routine multimodal clinical data. These interpretable models and the derived nomogram could aid early decision-making and personalized patient management in clinical practice.

EP-0372

Optimizing metastatic work-up: machine learning predicts M1 disease in newly diagnosed prostate cancer using routine multimodal clinical data

B. Khangembam*, S. Sharma, R. Wakankar, M. Kavin, A. R. Chanu, C. J. Das, S. Kaushal, R. K. Sahoo, A. Seth, C. Patel, R. Kumar;*
All India Institute of Medical Sciences, New Delhi, INDIA.

Aim/Introduction: To evaluate the feasibility of machine learning (ML) models utilizing routine clinical, conventional imaging, and laboratory data for predicting metastatic (M1) disease in treatment-naïve prostate cancer patients undergoing ^{68}Ga-PSMA-11 PET/CT. ***Materials and Methods:*** From April 2024 to March 2025, a total of 168 treatment-naïve patients with pathologically confirmed prostate cancer (mean age: 67 ± 8 years) were prospectively enrolled. The primary outcome assessed was the presence of M1 disease, as determined by ^{68}Ga-PSMA-11 PET/CT imaging. A training set (n = 168) was generated via stratified deterministic bootstrapping, with 65 patients reserved as an independent test cohort. After feature normalization, Chi-square scoring was used for feature selection. Six ML models (Random Forest, Neural Network, Naïve Bayes, Logistic Regression, CatBoost, and XGBoost) were trained using stratified 10-fold cross-validation. Model performance was assessed using AUC, accuracy, F1 score, precision, recall, and specificity. Permutation plots were used to assess overfitting, while SHAP plots and confusion matrices were used for model interpretation. A Naïve Bayes-based nomogram was constructed using the four most important features based on absolute feature importance. ***Results:*** M1 disease was present in 45.2% (76) of patients. The top 5 features selected by Chi-square scoring for cross-validation were ISUP grade, N1 status, PSA, ALP, and tumor size. In cross-validation, five models exhibited >0.800 in all performance metrics, with CatBoost achieving the highest AUC of 0.980 (CA 0.929, F1 score 0.919, precision 0.958, recall 0.883, specificity 0.967). On the test set, Neural Network achieved the highest AUC of 0.961 (CA 0.908, F1 score 0.914, precision 0.865, recall 0.970, specificity 0.844), correctly predicting 97% (32/33) of M1 cases. No significant overfitting was observed, and SHAP plots revealed clear patterns of interpretability. The nomogram revealed that PSA ≥87.37 ng/mL, N1 status, ALP 115.5 - 251.5 U/L, and ISUP grade ≥4 could predict M1 disease with 98% probability. ***Conclusion:*** Machine learning models demonstrated robust performance in predicting the presence of M1 disease in treatment-naïve prostate cancer patients using routinely available multimodal clinical data. The interpretable nature of these models, along with the developed nomogram, holds potential to support early clinical decision-making and facilitate individualized patient management in clinical practice.

EP-0373

Machine learning can predict CHAARTED high-volume disease in treatment-naïve prostate cancer patients undergoing^{68}Ga-PSMA-11 PET/CT

S. Sharma, *R. Wakankar, M. Kavin, S. Kaushal, C. J. Das, R. K. Sahoo, A. Seth, A. R. Chanu, B. Khangembam, C. Patel, R. Kumar; All Institutes of Medical Sciences, New Delhi, INDIA.*

Aim/Introduction: To assess the feasibility of using machine learning (ML) models based on routine clinical, conventional imaging, and laboratory data to predict CHAARTED high-volume disease in treatment-naïve prostate cancer patients undergoing Ga-PSMA-11 PET/CT. ***Materials and Methods:*** From April 2024 to March 2025, 168 pathologically confirmed treatment-naïve prostate cancer patients (mean age: 67 ± 8 years) were prospectively enrolled. The primary outcome was the presence of CHAARTED high-volume disease on Ga-PSMA-11 PET/CT. A training set (n = 168) was created using stratified deterministic bootstrapping, with 65 patients reserved as an independent test set. Feature selection was based on Chi-square scoring after feature normalization. Four ML models (Naïve Bayes, Random Forest, XGBoost, and CatBoost) were trained using stratified 10-fold cross-validation. Final model performance was evaluated on the test set using AUC, accuracy, F1 score, precision, recall, and specificity. Permutation plot was used to assess the degree of overfitting. SHAP plots and confusion matrices were used for model interpretation. A Naïve Bayes-based nomogram was developed using the top five features based on absolute feature importance. ***Results:*** High-volume disease was present in 28.0% (47) of patients. The top 7 features selected by Chi-square scoring for cross-validation were ALP, ISUP grade, PSA, N1 status, hemoglobin, albumin, and tumor size. In cross-validation, three models exhibited >0.800 in all performance metrics, with CatBoost achieving the highest AUC of 0.971 (CA 0.935, F1 score 0.876, precision 0.907, recall 0.848, specificity 0.967). On the test set, Naïve Bayes exhibited the highest AUC of 0.948 (CA 0.892, F1 score 0.844, precision 0.760, recall 0.950, specificity 0.867), correctly predicting 95% (19/20) of high-volume cases. No significant overfitting was observed, and SHAP plots revealed clear patterns of interpretability. The nomogram revealed that ALP ≥251.5 U/L, PSA ≥87.37 ng/mL, albumin 4.25 - 4.55 g/dL, N1 status, and ISUP grade ≥4 could predict high-volume disease with 94% probability. ***Conclusion:*** Machine learning models accurately predict CHAARTED high-volume disease in treatment-naïve prostate cancer patients using routine clinical, imaging, and laboratory data. The interpretable models and nomogram may support early decision-making and individualized patient management in clinical settings.

EP-0374

PET/CT for staging Intermediate-Risk Prostate Cancer in Routine Clinical Practice

D. Martínez Osorio[1], *C. Lucas Lucas*[1], *J. Rodríguez Gómez*[1], *E. Noriega Álvarez*[2], *F. Pena Pardo*[1], *A. Padilla Bermejo*[1], *C. Ortiz Muñoz*[1], *M. Contreras Ameduri*[1], *J. Gatón Ramírez*[1], *F. Lopéz-Bermejo García*[1], *N. Almeida Romera*[1], *M. Talavera Rubio*[1], *V. Poblete García*[1];
[1]*Hospital General Universitario Ciudad Real, Ciudad Real, SPAIN,* [2]*Hospital Universitario de Guadalajara, Ciudad de Guadalajara, SPAIN.*

Aim/Introduction: To evaluate the concordance between staging with conventional imaging, 18F-choline PET/CT, and [18F]F-DCFPyL PET/CT in the assessment intermediate-risk prostate cancer (Pca). ***Materials and Methods:*** We conducted a retrospective, observational study including consecutive patients diagnosed with intermediate-risk Pca through transrectal biopsy between 2021 and 2023. Nodal and metastatic staging was performed using standard imaging techniques such as MRI, CT, and bone scintigraphy, as well as 18F-choline PET/CT and [18F]F-DCFPyL PET/CT, with all scans completed within a 60-day interval. Imaging was independently interpreted by two experienced nuclear medicine physicians, with a third reviewer involved in case of discordance. The reference standard was the consensus established by a multidisciplinary tumor board, which included pathological findings from radical prostatectomy and lymphadenectomy whenever these were available. Concordance was evaluated using kappa statistic and chi-square tests. ***Results:*** Twenty-nine patients (mean age 71.1 years, range 44-87) were included; 41.4% had favorable and 58.6% unfavorable intermediate-risk disease. Seven patients underwent surgical staging. Conventional imaging exhibited moderate concordance with the reference standard (kappa 0.443, p <0.014), with discrepancies in 3 patients (11.11%), who were classified as N1M0 by the reference standard, but were identified as N1M1 or N0M1 by 18F-choline PET/CT.18F-Choline PET/CT also demonstrated moderate concordance (kappa 0.416, p <0.001), with a tendency toward upstaging: seven patients classified as N0M0 by the reference standard were upstaged by 18F-choline PET/CT. [18F]F-DCFPyL PET/CT achieved strong concordance (kappa 0.763, Kendall's tau-b 0.84, chi-square 87, all p <0.001) correctly identifying 86.36% N0M0 and 100% of M1 cases. Among the seven patients who underwent surgical staging, [18F]F-DCFPyL PET/CT findings were concordant with pathological results in six cases (85.7%), while both 18F-choline PET/CT and conventional imaging were concordant in only three cases (42.9%). ***Conclusion:*** In routine clinical practice, [18F]F-DCFPyL PET/CT demonstrates superior concordance with multidisciplinary staging consensus compared to conventional imaging and 18F-choline PET/CT. These findings reinforce the pivotal role of [18F]F-DCFPyL PET/CT in clinical staging and therapeutic decision-making for intermediate-risk Pca.

EP-0375

PSMA-PET vs wbMRI Performance in Detecting Local and Nodal Disease in Patients with Newly Diagnosed Prostate Cancer

E. Greco[1], *L. Bianchi*[2], *C. Gaudiano*[3], *B. Corcioni*[3], *C. M. P. Sgro*[1], *C. Mignogna*[4], *B. Renzetti*[5], *A. Cattabriga*[3], *R. Schiavina*[2,4], *E. Brunocilla*[2,4], *C. Mosconi*[3,5], *R. Mei*[6], *P. Castellucci*[6], *S. Fanti*[6,1], *A. Farolfi*[6];
[1]*Nuclear Medicine, Alma Mater Studiorum University of Bologna, Bologna, ITALY,* [2]*Division of Urology, IRCCS Azienda Ospedaliero-Universitaria di Bologna, Bologna, ITALY,* [3]*Department of Radiology, IRCCS Azienda Ospedaliero-Universitaria di Bologna, Bologna, ITALY,* [4]*Division of Urology, Alma Mater Studiorum University of Bologna, Bologna, ITALY,* [5]*Department of Radiology, Alma Mater Studiorum University of Bologna, Bologna, ITALY,* [6]*Nuclear Medicine, IRCCS Azienda Ospedaliero-Universitaria di Bologna, Bologna, ITALY.*

Aim/Introduction: High risk prostate cancer (PCa) patients require systemic staging to receive the most suitable treatment. PSMA-PET is an accurate technique for the detection of local and distant disease. Whole-body MRI (wbMRI) can be used to identify local disease and distant lymph node, bone and visceral metastases but there is no strong recommendation for its use in daily clinical practice. This study aims to compare PSMA-PET and wbMRI in detecting local disease and local lymph nodes metastases in patients with new PCa diagnosis. ***Materials and Methods:*** This is a single-center prospective study enrolling patients with newly diagnosed PCa, receiving both PSMA-PET and wbMRI within a 2-months' timeframe before any treatments. Exams were independently reviewed by two nuclear medicine physicians for PET scans and two radiologists for wbMRI. Regarding patients who underwent radical prostatectomy (RP), PSMA-PET and wbMRI performances, namely sensitivity, specificity, positive predictive value (PPV), negative predictive value (NPV) and accuracy, were evaluated for local disease (T) and local lymph node (N), using

histopathology as gold standard. ***Results:*** Overall, 80 patients with newly diagnosed PCa were enrolled (median age 70 years). PSMA-PET and wbMRI were performed within a median time of 13 days (IQR 7-22). Among these patients, 8 (10%) underwent radiation therapy, 19 (24%) received systemic treatment and 8 (10%) have not received any treatment yet at the time of data analysis. 45/80 (56%) patients in the staging cohort underwent subsequent RP. Regarding those patients, PSMA-PET and wbMRI sensitivity for local disease (T) was 96% vs 100% while PPV 100% vs 100%. Furthermore, for pelvic nodes involvement (N) sensitivity was 56% vs 33%, specificity 85% vs 89%, PPV 71% vs 67%, NPV 74% vs 67% and accuracy 73% vs 67%. ***Conclusion:*** Using histology as gold standard, wbMRI outperformed PSMA-PET for the detection of local disease (T), while PSMA-PET showed greater sensitivity, PPV, NPV and accuracy than wbMRI in evaluating pelvic lymph node metastases (N).

EP-0376

Role of PSMA PET/CT and mpMRI in Determining Focal Therapy Eligibility in Localized Prostate Cancer: Correlation with Histopathology

I. Sonni*, Z. Mohammadigoldar, G. Furey, K. Kimura, A. Holzgreve, A. Chung, J. Calais, J. Czernin, W. Brisbane, A. B. Weiner, S. S. Raman;*
University of California, Los Angeles, CA, UNITED STATES OF AMERICA.

Aim/Introduction: Focal therapies are increasingly employed in the treatment of prostate cancer, offering less invasive options for patients with localized disease. However, accurate patient selection remains a significant challenge. This retrospective study evaluates the ability of PSMA PET/CT, multiparametric MRI (mpMRI), and their combination to predict eligibility for focal therapy, using whole-mount histopathology (WMHP) as the reference standard. ***Materials and Methods:*** We screened all patients who underwent radical prostatectomy at UCLA between 1/2017 and 7/2024 with available pre-surgical PSMA PET/CT and mpMRI. Inclusion criteria included biopsy-confirmed Gleason score ≤7, absence of bilateral disease on biopsy. Exclusion criteria were: prostate cancer-related treatment between imaging studies, and an interval between PET and MRI >6 months. Three board-certified physicians independently assessed the PSMA PET/CT, mpMRI, and combined PET+MRI studies. All readers were blinded to each other's assessments and had access only to PSA levels and biopsy results, reflecting routine clinical practice. We calculated sensitivity, specificity, positive predictive value (PPV), and negative predictive value (NPV) to assess the ability of each imaging modality to correctly identify patients eligible for focal therapy, using WMHP as the gold standard. Eligibility was defined by the absence of extracapsular extension (EPE), seminal vesicle invasion (SVI), bilateral disease, and multifocal disease on histopathology. ***Results:*** Of 420 screened patients, 113 met all inclusion criteria. Based on imaging review, the number of patients deemed eligible/ineligible for focal therapy was: 21/92 for PSMA PET/CT, 30/83 for mpMRI and 28/85 for combined PET+MRI. WMHP confirmed 23 eligible and 90 ineligible patients. Sensitivity was 14% for PSMA PET/CT, 17% for mpMRI, and 30% for PET+MRI. Specificity values were 87%, 71%, and 77%, respectively. PPV were 20%, 13%, and 25%, while NPV were 81%, 77%, and 81%, respectively. ***Conclusion:*** PSMA PET/CT demonstrated high specificity and NPV in ruling out focal therapy eligibility, while sensitivity remained limited. mpMRI offered modestly improved sensitivity, but lower specificity. The combination of PSMA PET/CT and mpMRI showed the best overall performance, with improved sensitivity and NPV compared to either modality alone. These findings support a role for combined imaging in refining patient selection for focal therapy and guide non-invasive clinical decision-making. Further consensus review is ongoing to validate these results.

EP-0377

Predictive Value of Baseline PSMA-PET Parameters in Locally Advanced Prostate Cancer Patients Treated with Radical-Intent Radiotherapy and Androgen Deprivation Therapy: An Inverse Probability of Treatment Weighting Analysis

D. Dubois[1,2]*, F. Lanfranchi*[1,2]*, D. Vita*[1,2]*, S. Mastrogiovanni*[1,3]*, L. Sofia*[1,2]*, S. Raffa*[2]*, M. I. Donegani*[2]*, S. Chiola*[2]*, C. Marini*[2,4]*, G. Timon*[1,3]*, G. Sambuceti*[1,2]*, L. Belgioia*[1,3]*, M. Bauckneht*[1,2]*;*
[1]Department of Health Sciences (DISSAL), University of Genoa, Genova, ITALY, [2]Nuclear Medicine, IRCCS Ospedale Policlinico San Martino, Genova, ITALY, [3]Radiotherapy, IRCCS Ospedale Policlinico San Martino, Genova, ITALY, [4]Institute of Molecular Bioimaging and Physiology, National Research Council (CNR), Milan, ITALY.

Aim/Introduction: Prostate-specific membrane antigen (PSMA) PET/CT has become a key imaging modality for the primary staging of prostate cancer (PCa). However, the prognostic value of quantitative PSMA-PET parameters remains unclear, particularly in patients subsequently treated with radical-intent radiotherapy and androgen deprivation therapy (ADT). We thus aimed to assess the predictive value of baseline PSMA-PET parameters for clinical outcomes in patients with locally advanced PCa, using inverse probability of treatment weighting (IPTW) to adjust for clinical confounders. ***Materials and Methods:*** This single-centre retrospective study included PCa patients who underwent PSMA-PET/CT for primary staging. Patients with distant metastases were excluded. The following PET parameters were analysed: SUVmax and total lesion PSMA (PSMA-TL) of the dominant lesion, and total PSMA volume (PSMA-TV). Patients were dichotomised into high and low groups based on median values. IPTW was applied to adjust for baseline variables, including initial PSA, ISUP grade group at prostate biopsy, T stage, and N stage. Kaplan-Meier analyses with log-rank tests were conducted to assess associations with time to treatment failure (TTF), defined as a composite endpoint including any of the following events: biochemical recurrence according to Phoenix criteria; radiologic progression; clinical progression; initiation or change of systemic treatment for any reason; or mortality. ***Results:*** The study population included 145 patients, with a mean age of 75.94 ± 4.9 years. Most patients presented with an ISUP grade group of 3 (39.3%) or 2 (26.9%). The median baseline PSA level was 8.94 ng/mL [IQR: 6.60-15.00], and 28.3% of patients had pelvic nodal involvement (N1). Regarding PSMA-PET parameters, the median SUVmax of the dominant lesion was 12.19 [IQR: 8.80-20.32], and the median total PSMA-TV was 10.17 cc [IQR: 4.14-24.22]. After IPTW adjustment, total PSMA-TV was significantly associated with shorter TTF (p=0.042), with worse outcomes observed in patients with above-median values. On the contrary, SUVmax and PSMA-TL of the dominant lesion were not significantly associated with this endpoint following IPTW adjustment, underscoring the prognostic value of volumetric PSMA-PET assessment. ***Conclusion:*** Total PSMA-TV is an independent predictor of time to treatment failure in locally advanced PCa patients treated with radical-intent radiotherapy and ADT. These findings highlight the prognostic utility of PSMA-TV over other PET-derived metrics and support its potential role as a biomarker for treatment planning and risk stratification in clinical practice.

EP-0378

PET/CT with [18F]-Piflufolastat in the initial staging of patients with intermediate-high risk prostate cancer: relationship of SUVmax and SUVmean values of prostatic target lesion with gleason scale, ISUP prognostic grades and PSA values at diagnosis.

J. Badell*, A. C. Peñaherrera Cepeda, L. G. Díaz González, E. Casillas Sagrado, J. G. Villanueva Curto, E. Campaña Díaz, S. Rama Alonso, F. Caltagirone Gutierrez, P. García-Talavera San Miguel, F. Gomez-Caminero Lopez, P. Tamayo Alonso;*
Hospital Clinico Universitario de Salamanca, Salamanca, SPAIN.

Aim/Introduction: To determine the relationship between SUVmax/SUVmean values of the prostatic target lesion obtained by [18F]-Piflufolastat PET/CT in the initial staging of patients with intermediate-high risk prostate cancer, with the gleason scale, ISUP prognostic grades and PSA values. ***Materials and Methods:*** We included 126 patients (71.1 years ± 8.1 years), diagnosed with intermediate-high risk prostate cancer, who were referred to our service for PET/CT study with [18F]-Piflufolastat between August/2023 and April/2025, for initial staging of their disease. A PET/CT study focused on cranio-pelvis was acquired 120 minutes after intravenous administration of 333 MBq of 18F-Piflufolastat, after administration of 20 mg of furosemide 60 minutes before image acquisition. In the positive studies, the SUVmax and SUVmean values of the prostatic target lesion were localized and quantified and their relationship was established in terms of gleason scale, ISUP prognostic grades and PSA values. ***Results:*** PET/CT was positive in 99.2% of patients (125/126). According to their prognostic grade at diagnosis, patients were classified into three groups (ISUP Grades), ISUP 1: 8/125, ISUP 2-3: 30/125 and ISUP 4-5: 87/125. According to PSA values (ng/ml) at diagnosis, they were classified into three groups, PSA<10: 48/125, PSA 10-20: 23/125 and PSA>20: 49/125 and finally, according to the gleason scale at diagnosis, they were classified into five groups (Gleason score), ≤6: 8/125, 7 (3+4): 14/125, 7 (4+3): 16/125, 8: 47/125 and 9-10: 29/125. The median SUVmax/SUVmean values of prostatic target lesion in the groups according to ISUP prognostic grade were: ISUP 1: 17.90/10.55 (SUVmax/SUVmean), ISUP 2-3: 17.94/10.56 and ISUP 4-5: 17.99/10.58. According to PSA values (ng/ml) at diagnosis, the mean values were: PSA<10: 17.81/10.49, PSA 10-20: 17.93/10.57 and PSA>20: 18.09/10.67. In the groups according to the gleason scale at diagnosis, the mean values were: ≤6: 17.82/10.52, 7 (3+4): 17.87/10.56, 7 (4+3): 17.90/10.55, 8: 17.93/10.47 and 9-10: 17.99/10.61. ***Conclusion:*** PET/CT with 18F-Piflufolastat is a useful technique for initial staging in patients with intermediate-high risk prostate cancer. A significant increase in mean SUVmax and SUVmean values was observed in all the groups studied, both when PSA levels were higher at diagnosis and when the ISUP prognostic grade and gleason scale were higher.

EP-0379

Utility of the PRIMARY Score on [^{99m}Tc]Tc-PSMA SPECT/CT - an exploratory study aimed to optimise prostate cancer diagnosis

S. More[1], *M. Rivombo*[1], *N. Jacobs*[1], *O. Kolade*[2], *K. Hlongwa*[1]; [1]*University of Cape Town, Cape Town, SOUTH AFRICA,* [2]*University College Hospital, Ibadan, NIGERIA.*

Aim/Introduction: The PRIMARY score has been validated in a real-world setting in patients imaged with [^{68}Ga]Ga-PSMA-11 and multiparametric MRI(mpMRI) before prostate biopsy to aid in the diagnosis of clinically significant prostate cancer(csPCa). With the advent of [^{99m}Tc]Tc-PSMA tracers in real-world application, the validation of the PRIMARY score with [^{99m}Tc]Tc-PSMA has not been explored. The aim of this exploratory study is to review utility of [^{99m}Tc]Tc-PSMA SPECT/CT in evaluating intra-prostatic uptake patterns and intensity scores, with a view to developing a surrogate score to improve diagnostic accuracy for csPCa based on the PRIMARY score for PET. ***Materials and Methods:*** Patients presented for staging with [^{99m}Tc]Tc-PSMA and were deemed fit for radical therapy according to local guidelines.mpMRI was performed in preparation for radical prostatectomy. The PRIMARY score and pattern were recorded based on previous PET work to delineate the peripheral zone(PZ), central zone(CZ) and transition zone(TZ).Regions of interest were drawn around the prostate primary, background skeletal muscle, liver and parotids to determine ratios relative to prostate counts and garner a cutoff for ratios concordant to the described PRIMARY score. PRIMARY 5 was defined as more than twice the score for PRIMARY4 on SPECT. PIRADS score and location on MRI were reviewed for each paired study. ISUP grading was recorded from histological samples of patients who presented for radical prostatectomy. csPCa was defined as ISUP grade≥2.PRIMARY score of 3-5 and PIRADS score 3-5 were deemed positive. ***Results:*** 44 men(median age 65 years) were analysed with median PSA 19.3ug/l at diagnosis. 32(73%) men had csPCa on biopsy with positive MRI. 4(9%) had diffuse TZ or symmetrical CZ activity, 14(32%) had focal TZ activity and 26 (59%) had focal activity in the PZ on PRIMARY. 40(91%) patients had a positive [^{99m}Tc]Tc-PSMA result, and 44(100%) a positive MRI result. Median PRIMARY score of 2, 3 and 4 correlated with a P/B ratio of 8.19, 10.63 and 19.38 respectively on [^{99m}Tc]Tc-PSMA. There was a significant association between the PRIMARY and PIRADS score($p = 0.026$), P/B ratio and PRIMARY score($p = 0.004$) and ISUP grade group and P/B ratio>8.19(PRIMARY2 cutoff for SPECT, $p<0.001$). No significant associations were seen between PIRADS and PRIMARY score against the ISUP grade. ***Conclusion:*** A modified 5-tier PRIMARY score based on [^{99m}Tc]Tc-PSMA incorporating intra-prostatic pattern and intensity on PSMA SPECT/CT shows potential for detection of csPCa. Further validation of this scoring system is recommended to characterise its fuller clinical applications and implementation.

EP-0380

Regional Experience on Tc99m-PSMA SPECT/CT in staging of Prostate Cancer in New Zealand: Correlation of pre-imaging PSA level with delayed 24-hour pelvic SPECT/ CT findings.

E. Ling[1], *N. Tag*[1], *S. Abubakar*[2], *P. Burns*[1], *R. M. Subramaniam*[1]; [1]*Wellington Regional Hospital, Wellington, NEW ZEALAND,* [2]*Auckland City Hospital, Auckland, NEW ZEALAND.*

Aim/Introduction: Technetium-99m labelled PSMA ligands (99mTc-PSMA) has the potential to increase access to PSMA imaging due to the wider availability of the gamma camera and Technetium-99m radionuclide. In our institution, 99mTc-PSMA imaging protocol includes 5-hour whole body SPECT/CT and 24-hour delay abdomen/pelvis SPECT/CT. The 24-hour images prolongs overall time of the study and necessitates more resource allocation. This study aims to identify the benefit of 24-hour SPECT/CT in lesion detection and correlation with pre-imaging PSA level. ***Materials and Methods:*** Retrospective cohort study including 63 patients between September 2023 and March 2025. Recurrent cases were divided into 3 groups based on PSA level: Group A (0.2-2 ng/mL), Group B (2.1-10 ng/ml) and Group C (>10 ng/mL). New patients were grouped into An (<20 ng/mL) and Bn (>20 ng/mL). Comparison of the 5-hour and 24-hour SPECT/CT was performed to identify differences in lesion detection and correlation to PSA level. The 24-hour SPECT/CT scans were read twice, initially blindly and then with knowledge of the 5-hour SPECT/CT findings. The SPECT/CT data were subsequently compared and were verified by clinical and radiological outcome. ***Results:*** Out of the 47 patients with recurrence, in group A (6 patients), 1 patient showed additional uptake in an abdominal node on the 24-hour SPECT/CT. In group B (17 patients), 15 patients had PSMA detected disease, with 1 patient showing an additional osseous uptake on the 24-hour SPECT/CT. In group C (24 patients), 23 patients had PSMA detected disease, with 1 patient showing pelvic node uptake only on the 24-hour SPECT/CT. For the 16 newly diagnosed cases, in both groups, no additional lesion demonstrated on 24-hour imaging. ***Conclusion:*** Results suggests that there may be no added value of a 24-hour delayed imaging for a 99mTc-PSMA protocol regardless of pre-imaging PSA levels, though study is limited by a small sample size. ***References:*** 1. Hofman, M.S.; Lawrentschuk, N.; Francis, R.J et al. Prostate-specific membrane antigen PET-CT in patients with high-risk prostate cancer before curative-intent surgery or radiotherapy (proPSMA): a prospective, randomised, multicentre study. The Lancet 202; 395: 1208-1216

2. Duncan I, Ingold N, Martinex-Marroquin E et al. An Australian experience using Tc-PSMA SPECT/CT in the primary diagnosis of prostate cancer and for staging at biochemical recurrence after local therapy. The Prostate 2023; 83:970-979 3. Berliner,C.; Steinhelfer L.; Chantadisai M. et al. Delayed Imaging Improves Lesion Detectability in [99mTc]Tc-PSMA-I&S SPECT/CT in Recurrent Prostate Cancer. The Journal of Nuclear Medicine 2023; 64(7): 1036-1042.

EP-0381

^{99m}Tc-PSMA SPECT/CT in the primary staging of prostate cancer - a retrospective analysis

O. Jonmarker[1,2], *C. Samuelsson*[1,2], *L. Steffens*[2], *M. Sunderland*[2], *D. O'Keeffe*[2,3], *S. Gabrielson*[1,4,2];
[1]*Karolinska Institutet, Stockholm, SWEDEN,* [2]*Christchurch Hospital, Christchurch, NEW ZEALAND,* [3]*University of Canterbury, Christchurch, NEW ZEALAND,* [4]*University of Otago, Christchurch, NEW ZEALAND.*

Aim/Introduction: Prostate-specific membrane antigen (PSMA) imaging with PET/CT has become a cornerstone in the staging of prostate cancer, yet access to PET technology is limited. ^{99m}Tc-PSMA SPECT/CT represents a more accessible and cost-effective modality, but its role in primary prostate cancer staging remains underexplored. The aim of this study was to assess the diagnostic utility of ^{99m}Tc-PSMA SPECT/CT in comparison to MRI and biopsy findings in patients undergoing primary staging of prostate cancer. ***Materials and Methods:*** We conducted a retrospective study of 85 patients with newly diagnosed prostate cancer who underwent MRI and ^{99m}Tc-PSMA SPECT/CT within a 90-day interval in Christchurch, New Zealand. Imaging was reviewed independently by four radiologists using a segmental scoring system for prostatic, extraprostatic and metastatic disease. Diagnostic concordance with MRI was assessed segment-by-segment and across anatomical regions. Both MRI and SPECT were compared with systematic biopsies and related to calculated standardised uptake value (SUV). Intraclass correlation and Cohen's kappa were used to evaluate agreement. ***Results:*** ^{99m}Tc-PSMA SPECT/CT demonstrated high sensitivity in detecting intraprostatic disease, with at least partial anatomical concordance with MRI in over 75% of cases. Inter-reader PSMA SPECT/CT agreement was overall poor, but highest for bone metastases and lesion laterality, and lowest for seminal vesicle invasion (SVI) and extraprostatic extension (EPE). The number of pathological prostate sectors identified on SPECT was comparable to MRI, though SPECT showed broader coverage when equivocal lesions were considered. MRI and SPECT were in similar agreement with biopsies. Higher SUVs, above the median, showed better agreement between SPECTs and biopsies compared to lower SUVs. Agreement between MRIs and biopsies was not clearly affected by SUV. ***Conclusion:*** 99mTc-PSMA SPECT/CT is a viable alternative to PSMA PET/CT for detecting malignancy in the primary staging of prostate cancer, particularly in settings with limited access to PET imaging. While limitations remain in the assessment of SVI and EPE, SPECT/CT demonstrates promising diagnostic performance, especially for intraprostatic and osseous disease. High SUVs appear to increase agreement between biopsies and SPECT. Further prospective studies with complete histopathological validation would be of value.

EP-0382

Impact of PET/MR-guided biopsy with ^{18}F-PSMA in patients with suspected prostate cancer: a prospective single-center pilot study.

E. Ruiz Gavilanez[1], *J. Garcia*[1], *A. Compte*[1], *N. Garrido*[1], *P. Bassa*[1], *L. Mont-Castro*[1], *L. Pinilla*[1], *J. Romero*[1], *J. Santabárbara*[1], *J. Vela*[1], *S. Romero*[1], *E. Riera*[1], *A. Sertsios*[2], *M. Galdeano*[2], *M. Figols*[2], *N. De la Torre*[2], *D. Coll*[2];
[1]*CETIR, Barcelona, SPAIN,* [2]*Fundació Althaia, Manresa, SPAIN.*

Aim/Introduction: To determine the feasibility of ^{18}F-PSMA PET/MRI fusion-guided transperineal prostate biopsy with real-time transrectal ultrasound(TRUS)study in patients with suspected prostate cancer(PC). ***Materials and Methods:*** Prospective study with the first 20 patients with suspected PC(persistently increased PSA;mean 11.2 ng/ml;range 4.5-20.8,)referred for disease characterization by ^{18}F-PSMA PET/MRI.Prostate selective PET/MRI study with sequences MRAC,T1,T2fat, DWI, DCE.MRI was assessed using PIRADSv.2 criteria, and PET using Primary. Subsequently,a whole-body MRI study was performed with sequences MRAC,T1,T2fat, DWI.The PET/MRI images were loaded into the bkFusion software(MIM®),performing segmentation of the prostatic anatomical structure on T2 images,including the lesions evident on MRI and PET,thus planning the optimal target of the biopsy needle.Transperineal biopsy was performed with patient deep-sedated,using US-MRI fusion software(BiopSee®). Co-registration of PET/MRI and TRUS images was performed using a 1-plane,1-point method,including an additional point whenever needed.A minimum of five cores were obtained for each target lesion,along with systematic biopsy tailored to the prostate volume. ***Results:*** Transperineal prostate biopsy was successfully achieved in all 20 patients, with adequate PET/MRI segmentation and real-time co-registration with TRUS. Twenty-three lesions were detected in 17 patients:a single lesion was evident in 11 patients(4 in the anterior transitional zone and 7 in peripheral zone),and 2 lesions in 6 patients(in the peripheral zone).The detection rate of PC was 82.6% (19 patients):clinically significant(csPC) in 13/19(68.2%) and non-significant (cnsPC) in 6/19(31.6%).In 14 lesions PSMA and MRI images were concordant, with biopsy identifying csPC in 9/14,cnsPC in 4/14 and negative in 1/14.In 9 lesions PSMA and MRI images were discordant(Primary4-5 vs. PIRADS2-3),with biopsy identifying csPC in 4/9,cnsPC in 2/9 and negative in 3/9. In the 3 patients in whom no significant lesions were detected on PET/MRI,systematic biopsy was either negative.In two patients there was evidence of pelvic lymphadenopathy on selective imaging,with no more lesions detected on the whole-body study. ***Conclusion:*** Our study demonstrated the feasibility and usefulness of ^{18}F-PSMA PET/MR to target biopsy in patients with suspected PC.Our detection rate for PC was 82.6%, with csPC in 68.2% of patients.In the 9 patients in whom ^{18}F-PSMA proved superior to MRI,PC detection rate was 67%, with csPC in 44.4% of patients. ***References:*** 1. Preisser F.,Theissen L.,Wenzel M.,Humke C.,Boris B.,Kollermann J.,et al. (2019).Performance of Combined Magnetic Resonance Imaging/Ultrasound Fusion-guided and Systematic Biopsy of the Prostate in Biopsy-naïve Patients and Patients with Prior Biopsies-European Urology Focus.European Urology FocuVol.7(1),39-46.https://doi.org/10.1016/j.euf.2019.06.015 2. Park, J., & Kim, C. K.(2022).Paradigm Shift in Prostate Cancer Diagnosis:Pre-Biopsy Prostate Magnetic Resonance Imaging and Targeted Biopsy. Korean Journal Of Radiology, 23(6),625. https://doi.org/10.3348/kjr.2022.0059.

EP-0383

Automated Extraction of TNM Staging from PSMA PET/CT Reports Using AI

A. Ghujeh[1,2], *A. Alrahim*[1], *M. Altinyay*[1], *M. Kharita*[1,3], *F. Alves*[4], *H. Fayad*[1,3];
[1]*Hamad Medical Corporation, Doha, QATAR,* [2]*University of Coimbra, Coimbra, PORTUGAL,* [3]*Weill Cornell Medicine- Qatar, Doha, QATAR,* [4]*CIBIT/ICNAS, Institute for Nuclear Sciences Applied to Health, University of Coimbra, Coimbra, PORTUGAL.*

Aim/Introduction: Accurate staging of prostate cancer according to the Tumor, Node, Metastasis (TNM) classification is crucial for determining eligibility for clinical treatment plan. However, manual extraction of TNM stages from PET/CT reports is labor-intensive, susceptible to human error, and its inclusion is clinician dependent. The objective of this study is to develop and validate

an Artificial Intelligence (AI)-based Natural Language Processing (NLP) pipeline, adhering to the prostate cancer molecular imaging standardized evaluation (PROMISE) V2 criteria, to automatically extract the T, N, and M stages from PET/CT reports. ***Materials and Methods:*** A total of 400 prostate cancer PSMA PET/CT reports were collected. 95 of them were initial staging studies. Each report was reviewed by an experienced physician and assigned a TNM classification (gold standard). The proposed NLP pipeline is built on the DeBERTa (Decoding-Enhanced BERT with Disentangled Attention) transformer model. The model was further adapted with a keyword-sensitive attention mechanism that targets key staging terms, along with a custom rule-based module, adapted from NegEx, to accurately handle negation. Final AI-generated TNM predictions were compared against the reference dataset using leave one out strategy. In addition, compared the performance of the AI pipeline against a textual search method, which relied on keywords derived from terms used by physicians. ***Results:*** On the independent test set of 95 reports, the baseline keyword search achieved accuracy of 51.0% for T stage, 62.7% for N stage, and 45.7% for M stage. In contrast, the AI-module outperformed this baseline, achieving 90.5% accuracy for T stage, 80.9% for N stage, and 73.7% for M stage. Statistical comparison using McNemar's test confirmed that the improvements in staging accuracy were statistically significant for all three components ($p < 0.05$), 0.00001 for T stage, 0.0058 N stage, and 0.0013 M stage. ***Conclusion:*** The NLP pipeline automates TNM staging from PET/CT reports, reducing manual effort and inconsistencies. It enhances report accuracy, efficiency, and supports informed clinical decisions. Initial results are promising, with future research needed to expand training data and test generalizability across institutions. ***References:*** Brierley JD, Gospodarowicz MK, Wittekind C. TNM Classification of Malignant Tumours, 8th ed. Wiley; 2016.Seifert R et al. PROMISE V2: Prostate cancer molecular imaging standardized evaluation. Eur Urol. 2023;83:405-412.He P, Liu X, Gao J, Chen W. DeBERTa: Decoding-enhanced BERT with disentangled attention. ICLR 2021.

EP-0384

Impact of ^{18}F-PSMA PET/MRI Imaging on Prostate Cancer Patients Staging: Prognostic Imaging Biomarkers Associated with Tumor Aggressiveness.

L. Pinilla[1], *A. Compte*[1], *N. Garrido*[1], *J. Vela*[2], *L. Mont-Castro*[1], *S. Ruiz*[1], *J. Garcia*[1], *J. Romero*[1], *J. Santabárbara*[1], *M. Soria*[1], *P. Bassa*[1], *E. Riera*[1], *A. Sertsios*[3], *M. Figols*[3], *M. Galdeano*[3], *N. De La Torre*[3], *D. Coll*[3];
[1]*ASCIRES Cetir, Barcelona, SPAIN,* [2]*Hospital Universitario de Canarias, Tenerife, SPAIN,* [3]*Fundació Althaia, Manresa, SPAIN.*

Aim/Introduction: To assess the impact of initial staging of prostate cancer patients by 18F-PSMA PET/MRI, and to evaluate the prognostic value of pre-treatment PET/MRI imaging biomarkers. ***Materials and Methods:*** Prospective study with 55 consecutive patients diagnosed with prostate cancer: Gleason score: 7-9, PSA levels: 1.6 -213 ng/ml.Simultaneous PET/MRI (SIGNA GE) acquisition 1 hour after IV administration of 296±10% MBq of 18F-PSMA 1007 as follows: Prostate study: (20 min): PET+MRI (DIXON,T1, T2, DWI, DCE sequences).Whole body study (30 min): PET+MRI (DIXON, T1, T2, DWI, STIR sequences).TNM staging was reached by consensus with nuclear physician and radiologist. Visual imaging interpretation. Patient treatment decision by Oncology Committee.SUV and ADC values were obtained. Correlation with Pearson's coefficient. Radiomic analysis extracting 93 characteristics: first-order and textural. Evaluation of significant differentiation by ANOVA test in two prognostic groups: 1) TxN0M0/ TxN1M0; 2) TxN1M1a/ M1b. ***Results:*** All patients completed PET/MRI protocol, with no artifacts due to simultaneous acquisition.Prostate PET/MRI staged the primary tumour ≥T3b in a total of 33/55 patients: 15/33 N0M0; 11/33 N1M0; 4/33 M1a; 6/33 Mb (1 N0M1b, 3 N1M1B, 2 N1M1a/M1b). A significant inverse correlation was observed between SUV & ADC ($p<0.05$).Patient staging on whole-body PET/MRI was: 30/55 N0M0; 15/55 N1M0; 6/55 N1M1a; 6/55 M1b (1 N0M1b, 3N1M1b, 2 N1M1aM1b).The therapy decision after PET/MRI was: radical treatment in 45/55 patients, with prostatectomy in 29 and PET/MRI-guided radiotherapy (≥T3b) in 16; systemic treatment in 10/55 patients.SUVmax, ADC and first-order characteristics did not show significant differences between the two selected prognostic groups. Only textual characteristics showed statistical significance ($p<0.05$) between the two groups. ***Conclusion:*** 18F-PSMA PET/MRI may be a "one-stop diagnostic procedure" useful for staging of patients with intermediate/high-risk prostate cancer, with an impact on therapy strategy (18% systemic treatment).Radiomic analysis of textual features seems the only prognostic biomarker of 18F-PSMA PET/MRI.

EP-0385

A retrospective clinical study evaluated the diagnostic performance of ^{18}F-PSMA-137 PET/CT in men newly diagnosed with prostate cancer and those experiencing biochemical recurrence

X. Liao[1], *J. Zhang*[1], *Y. Fan*[1], *N. Zhang*[2];
[1]*Department of Nuclear Medicine, Peking University First Hospital, Beijing, CHINA,* [2]*Peking University – Yunnan Baiyao International Medical Research Center, Beijing, CHINA.*

Aim/Introduction: Prostate cancer (PCa) is one of the most common malignancies among men and its incidence continues to rise globally. Traditional imaging methods such as CT and MRI have been widely used in detecting and staging PCa; however, these techniques have limitations, especially in detecting small lesions or diagnosing recurrent cancer early. Thus, developing imaging technologies with higher sensitivity and specificity is vital for improving early diagnosis and therapeutic outcomes of PCa. ***Materials and Methods:*** A retrospective analysis was conducted on patients who underwent ^{18}F-PSMA-137 PET/CT scans, and were diagnosed with PCa from December 2020 to November 1, 2023. Among them, 66 patients were selected who received the ^{18}F-PSMA-137 PET/CT scan before undergoing radical prostatectomy and pelvic lymph node dissection, with pathological diagnosis results serving as the gold standard to evaluate the diagnostic efficacy of ^{18}F-PSMA-137 PET/CT for preoperative pelvic lymph node metastasis(LNM). Additionally, 40 patients with elevated PSA suspected of recurrence revealed after radical treatment and underwent ^{18}F-PSMA-137 PET/CT scans were selected, and a composite reference standard was used to assess the diagnostic effectiveness of ^{18}F-PSMA-137 PET/CT in recurrent /metastatic lesions. ***Results:*** An analysis of the diagnostic efficacy of ^{18}F-PSMA-137 PET/CT for preoperative pelvic LNM showed that CT/MRI examination had a sensitivity of 42.9% and specificity of 100%, while ^{18}F-PSMA-137 PET/CT examination had a sensitivity of 71.4% and specificity of 98.3%. Univariate analysis did not identify any significant influencing factors for SUV_{max}. An analysis of the diagnostic effectiveness of ^{18}F-PSMA-137 PET/CT in patients with elevated PSA suspected of recurrence revealed that the sensitivity was 87.88% (95% CI: 0.72-0.97), positive predictive value was 85.29% (95% CI: 0.69-0.95), and accuracy was 72.50% (95% CI: 0.56-0.85). The researchers used the CMH method to evaluate whether the positive detection rate of ^{18}F-PSMA-137 PET/CT correlated with baseline PSA levels and Gleason scores, finding no correlation with Gleason scores but a correlation with baseline PSA levels. Univariate logistic regression analysis indicated that scan time, PSA doubling time, and the absolute increase in PSA over three months were not significant factors affecting the positive predictive value. ***Conclusion:*** Compared to conventional CT/MRI scans, ^{18}F-PSMA-137 PET/CT demonstrates higher sensitivity and specificity for preoperative diagnosis of pelvic LNM in PCa. It

also demonstrates high sensitivity and positive predictive value in diagnosing patients with suspected recurrence, warranting further large-scale studies for validation.

EP-0386

Hybrid ^{18}F-PSMA PET/MR with Diffusion-Relaxation Correlation Spectroscopy Enhances Prostate Cancer Diagnosis and Risk Stratification

H. Chunyu[1], *H. Tang*[2], *X. Wang*[3], *X. Chen*[1], *Y. Zhang*[1], *Y. Wei*[4], *Z. Lin*[4], *Y. Yang*[5], *J. Dai*[3], *Y. Shao*[3], *J. Hu*[1], *B. Li*[1];
[1]*Department of Nuclear Medicine, Ruijin Hospital Affiliated to Shanghai Jiao Tong University School of Medicine, shanghaia, CHINA,* [2]*Department of Ultrasound, Ruijin Hospital Affiliated to Shanghai Jiao Tong University School of Medicine, Jiading North Campus, Shanghai, 200025, CHINA,* [3]*Department of Urology, Ruijin Hospital Affiliated to the Medical College of Hainan Jiaotong University, shanghaia, CHINA,* [4]*United Imaging Healthcare Co., Ltd., shanghaia, CHINA,* [5]*Beijing United Imaging Healthcare Co., Ltd., Beijing, CHINA.*

Aim/Introduction: Prostate cancer is a leading cause of cancer-related mortality in elderly men. This study evaluates the clinical utility of hybrid PET/MR imaging, combining prostate-specific membrane antigen-targeted positron emission tomography (PSMA-PET) and diffusion-relaxation correlation spectroscopy imaging (DR-CSI), to enhance the diagnostic accuracy and risk stratification of prostate cancer. ***Materials and Methods:*** 31 patients with pathologically confirmed prostate cancer underwent ^{18}F-PSMA PET/MR examination (uPMR890, United Imaging Healthcare; 3.7 MBq/kg injection). DR-CSI constructed the T2-D spectrum from voxel-wise MRI signals, defining six compartments using T2 = 50 ms, D = $1\times10^{-3}/2\times10^{-3}$ mm^2/s as thresholds, with signal proportion ratio (f_a-f_f) of each compartment calculated via the integration. Group differences in the maximum standardized uptake value (SUV_{max}), the mean standardized uptake value (SUV_{mean}), and f_a-f_f were compared between the lesion and normal prostate tissue. Spearman correlation analyses were applied to explore the relationship between different imaging parameters and clinical information, including PSA concentration and Gleason score. The receiver operating characteristic (ROC) curve evaluated the diagnostic performance of PSMA PET and DR-CSI, and their combination in predicting high-risk (Gleason > 7) and medium/low-risk (Gleason <= 7) groups of prostate cancer. ***Results:*** Comparative analysis between lesion and normal prostate tissue revealed statistically significant differences in SUV_{max} ($p < 0.0001$), SUV_{mean} ($p < 0.0001$), and f_d ($p = 0.0206$). Correlation analysis demonstrated significantly positive association between SUV_{max} ($r = 0.5134$, $p = 0.0031$) and SUV_{mean} ($r = 0.4446$, $p = 0.0122$) of the lesion were with the PSA concentration, while f_d ($r = -0.3712$, $p = 0.0398$) exhibited significant negative correlation with PSA. Notably, f_a ($r = 0.3755$, $p = 0.0374$) and f_e ($r = 0.3763$, $p = 0.0369$) showed significant positive correlation with the Gleason score. ROC curve analysis showed that the areas under the curve (AUC) of SUV_{max}, f_a+f_e, and SUV_{max}+f_a+f_e in predicting high-risk and medium-low risk groups of prostate cancer were 0.543 (95% CI: 0.331-0.754), 0.709 (95% CI: 0.517-0.902), and 0.718 (95% CI: 0.527-0.909), respectively. ***Conclusion:*** The integration of ^{18}F-PSMA PET and DR-CSI provides complementary information, significantly enhancing diagnosis and risk stratification in prostate cancer. The multimodal ^{18}F-PSMA PET/MR approach shows considerable promise for optimizing clinical decision-making and personalized therapy. Future large-scale prospective studies are warranted to validate the clinical utility of this imaging paradigm in prostate cancer management.

EP-0387

Value of Prostatic Tumor Volume and Prostatic tumor Uptake on 18F-DCFPyL PSMA-PET/CT as Predictors of Lymph Node and Metastatic Involvement in the Initial Staging of Intermediate-High Risk Prostate Cancer.

X. Guarnizo Poma, *A. Gómez Grande, P. Zaragoza-Ballester, S. Angiolillo Grau, E. López Llobet, B. Manzarbeitia Arroba, M. Áviles Jurado, R. García Delgado, P. Sarandeses Fernández, R. Sopeña Sutil, M. Tabuenca Mateo;*
Hospital Universitario 12 Octubre, Madrid, SPAIN.

Aim/Introduction: To evaluate the prostatic tumor volume (PSMA-TV) and prostatic tumor uptake (PSMA-LTU) using 18F-DCFPyL PSMA-PET/CT in prostate cancer staging as predictive factors for regional lymph node and distant metastatic involvement, as well as their association with clinical parameters and risk stratification scales. ***Materials and Methods:*** Patients diagnosed with intermediate and high-risk prostate cancer who underwent initial staging with 18F-DCFPyL PSMA-PET/CT between August-2024 and April-2025 were included. We collected baseline clinical and histopathological data. Risk classification scores were calculated according to NCCN and EAU guidelines and miTNM was based on PROMISE V2 criteria. PSMA-TV and PSMA-LTU values were calculated using LIFEx software v7.7.0. Statistical analysis was performed using R software, v4.3.3. ***Results:*** 71 patients were analyzed (mean age of 69.1±7.82 years). The median of basal PSA was 14ng/ml (range: 3.4-98.4). Regarding Gleason score, 40.8%(n=29) presented Gleason 9, 38% (n=27) Gleason 8, 18.3%(n=13) Gleason 7, and 2.8% (n=2) Gleason 10. According to NCCN classification, 54.9% (n=39) were categorized as high risk, 33.8%(n=24) as very high risk, and 11.3%(n=8) as intermediate risk. PSMA-PET/CT staging identified lymph nodal involvement (N+) in 32.4% (n=23) and metastatic disease (M+) in 21.1% (n=15). A significant correlation was observed between PSMA-TV and PSMA-LTU with PSA levels (rho=0.34, p<0.001 and rho=0.48, p<0.001, respectively). No significant correlations were found between PSMA-TV or PSMA-LTU and Gleason score, ISUP grade, or risk classifications (p>0.05). Patients with N+ showed higher levels of PSMA-TV and PSMA-LTU compared to N- (9.26±11.12cm^3 vs 2.91±4.24cm^3, p<0.001 and 86.83±112.01 SUV·cm^3 vs 20.42±30.73 SUV·cm^3, p<0.001, respectively). Similarly, M+ patients also presented higher PSMA-TV and PSMA-LTU values compared to M– (10.72±13.03cm^3 vs 3.67±4.57cm^3, p<0.001 and 146.90±107.95 SUV·cm^3 vs 22.01±35.30 SUV·cm^3, p<0.001, respectively). No significant differences were found in PSMA-TV or PSMA-LTU values according to local extension. ROC curves analysis demonstrated acceptable discriminative power for both parameters. For PSMA-TV, the AUC was 0.78 (95%CI: 0.66-0.91) for N+ and 0.74 (95%CI: 0.56-0.92) for M+, with cutoff values of 5.87cm^3 (sensitivity: 82.6%; specificity: 79.2%) and 6.11cm^3 (sensitivity: 84.6%; specificity: 74.1%), respectively. For PSMA-LTU, the AUC was 0.81 (95%CI: 0.69-0.93) for N+ and 0.80 (95%CI: 0.62-0.98) for M+, with cutoffs values of 55.92 SUV·cm^3 (sensitivity: 69.6%; specificity: 87.5%) and 64.92 SUV·cm^3 (sensitivity: 76.9%; specificity: 82.8%), respectively. ***Conclusion:*** PSMA-TV and PSMA-LTU demonstrated good predictive capability for nodal and distant metastatic involvement in the initial staging of intermediate to high-risk prostate cancer. Their incorporation may enhance initial risk stratification and guide therapeutic decision-making.

EP-0388

Role of Androgen Receptor Targeted Agents in high risk prostate cancer staging by PSMA PET/CT

M. Simo Perdigo, *I. Navales Mateu, J. Echeverri Diaz, S. Asadurova, C. Franco Monterroso, A. Hernandez Fructuoso;*
Hospital Universitari vall Dhebron, Barcelona, SPAIN.

Aim/Introduction: The aim of the study was to quantify the stage-shift with prostate-specific membrane antigen (PSMA) PET/CT imaging in the staging of high risk prostate cancer patients and

explore treatment implications. ***Materials and Methods:*** We analyzed a total of 106 high risk prostate cancer patients with a median age was 71 years (range 53-86). Median prostate-specific antigen was 11.7 ng/ml (PSA > 20ng/ml in 25.4%) and 51.9% had ISUP 5 or 4. The majority of patients had high-risk (89.6%) whereas very high risk disease was observed in 10.4%. All patients were studied with PSMA PET/CT and results were compare to conventional imaging including RMI (Bone scan was performed in 90 patients (84.9%), abdominal CT scan in 44%(n=41.5%) and RMI in104 (98.1%). Treatment decisions was assessed in weekly tumor board. ***Results:*** Primary tumor was visualized in all except two patients by PSMA PET/CT (Primary score 5 or 4 in 97.5%). In nodal pelvic staging, discordance between conventional imaging and PSMA-PET was achieved in 27.2% of them (Positive by PET and negative/equivocal by RMI in 20 patients and positive by RMI and negative by PET in 5). Bone scan was negative in 81 of patients (90%), positive in 6 (6.6%) and equivocal in 3 patients. No add value to PSMA PET/CT scan was observed since more extended disease was detected in 5 patients and no false negative was documented. In total, PSMA PET/CT detected metastases in 21.7% (n=23) of patients: Retroperitoneal/common iliac node chain infiltration in 12 (52%), bone metastases in 8 and extended disease in 2. Impact of PMSA PET-CT in the staging was 36,3%. Androgen deprivation therapy ± radiotherapy was the most selected treatment in this cohort of patients (78%). Only 17 patients (17.9%) were treated by radical prostatectomy plus lymphadenectomy. Androgen Receptor Targeted Agents were added in more than one third of all patients (35.7%). ***Conclusion:*** PSMA PET/CT showed superior performance in nodal and metastatic staging of prostate cancer than conventional imaging. No add value was found for bone scan versus PSMA PET/CT. PSMA findings had impact on treatment planning since 35.7% of all patients received androgen receptor targeted agents.

EP-0389

Stage Migration in Prostate Cancer: The Role of PSMA-PET in Identifying Oligometastatic Disease

F. Mattana[1], *V. Dragonetti*[1], *F. Ceci*[1], *S. Luzzago*[2], *V. Kasivisvanathan*[3], *S. Conlon*[4], *P. Castellucci*[5], *A. Farolfi*[5];
[1]IEO European Institute of Oncology, Nuclear Medicine, Milan, ITALY, [2]Department of Urology, IEO European Institute of Oncology IRCCS, Milan, ITALY, [3]British Urology Researchers in Surgical Training (BURST) Research Collaborative, London, UNITED KINGDOM, [4]Centre for Urology Imaging, Prostate, AI and Surgical Studies (COMPASS) Research Group, Division of Surgery and Interventional Sciences, University College London, London, UNITED KINGDOM, [5]Nuclear Medicine, IRCCS Azienda Ospedaliero-Universitaria di Bologna, Bologna, ITALY.

Aim/Introduction: Oligometastatic disease (OMD) represents an intermediate disease state between localized and metastatic prostate cancer (PCa), where patients may still benefit from curative treatments. The prevalence of "de novo" metastatic disease detected by positron emission tomography (PET) with prostate specific membrane antigen (PSMA) in a real-world setting is still to be clarified. The primary aim was to compare the detection rates of OMD between PSMA-PET and conventional imaging (CI) in patients with intermediate- to high-risk PCa. ***Materials and Methods:*** This multicenter retrospective study included patients with intermediate- to high-risk PCa who underwent both PSMA-PET and CI (contrast-enhanced CT and bone scintigraphy) within four months. The primary endpoint was to compare the detection rates of OMD (defined as ≤3 metastatic) between PSMA-PET and CI. The secondary endpoint was to assess treatment changes prompted by PSMA-PET findings. ***Results:*** Data of 497 patients were collected, and 255 patients met inclusion/exclusion criteria for the primary endpoint analysis, and all were considered for the secondary endpoint. OMD was identified using PSMA-PET in 11.4% of patients (29/255), significantly higher than the 6.7% rate (17/255) with CI (p =0.040). Clinical management was changed in 36.5% (93/255) of cases, with 18.5% experiencing major changes (e.g., switching from curative therapy to systemic treatment) and 18.0% experiencing minor changes. ***Conclusion:*** This study highlights how conventional imaging may underestimates de novo metastatic prostate cancer. PSMA-PET improves staging accuracy in intermediate- to high-risk patients, influencing treatment decisions and supporting its inclusion in routine diagnostic pathways.

EP-20

e-Poster Area

B: Imaging Clinical Studies -> B1 Oncological Imaging Clinical Study -> B18b Prostate BC Recurrence

EP-0390

The Potential Utility of PSMA PET/CT in Prostate Cancer Biochemical Failure - A Global Retrospective Cohort Study

B. Miles[1], *Q. Oza*[2], *J. Mackey*[3], *U. Oza*[1];
[1]Baylor University Medical Center, Dallas, TX, UNITED STATES OF AMERICA, [2]Greenhill High School, Dallas, TX, UNITED STATES OF AMERICA, [3]West Virginia University, Dallas, TX, UNITED STATES OF AMERICA.

Aim/Introduction: Biochemical failure, marked by rising PSA levels after radical prostatectomy without evidence of metastatic disease, affects some early-stage prostate cancer patients. According to NCCN guidelines, salvage external beam radiation therapy (EBRT) is recommended for patients with a life expectancy greater than five years. PSMA PET-CT has shown promise in detecting recurrences at lower PSA levels, helping identify candidates for salvage therapy. This study evaluates how PSMA PET-CT influences the decision to administer pelvic salvage radiation therapy for prostate cancer patients with biochemical recurrence. ***Materials and Methods:*** Following the STROBE guideline, we used the TriNetX Research Network, comprising over 134 million deidentified medical records. We included prostate cancer patients (ICD-10: C61) who had undergone radical prostatectomy (CPT: 55866) and reached a PSA nadir <0.1 ng/mL. Patients were excluded if they had prior IMRT (CPT: 77338) or known skeletal metastases (ICD-10: C79.51). Eligible patients had a PSA >0.2 ng/mL at least six months post-prostatectomy. The cohort was divided into two groups based on exposure to PSMA PET-CT (CPT: 78815). Propensity score matching was applied, balancing age, race, and ethnicity, yielding 715 patients per group. The primary outcome was receiving IMRT within three months of biochemical failure. ***Results:*** Out of 1,430 patients, 178 (24.9%) in the PSMA PET-CT group received salvage radiation therapy, compared to 90 (12.6%) in the non-PSMA group. PSMA PET-CT was associated with a significantly higher likelihood of receiving salvage radiation therapy (RR 1.99, 95% CI: 1.57-2.49, P < 0.0001). ***Conclusion:*** Our study demonstrates that PSMA PET-CT nearly doubles the likelihood of receiving salvage radiation therapy after radical prostatectomy. However, limitations exist. The study relies on retrospective data, which can introduce biases. Despite matching, unmeasured factors like PSA kinetics and comorbidities may confound results. The predominantly North American dataset may also limit the generalizability to regions with less access to PSMA PET-CT. Additionally, the short-term follow-up prevents assessment of long-term outcomes like overall survival. Lack of stratification by key factors such as Gleason score and PSA doubling time may also impact findings. PSMA PET-CT appears effective in identifying candidates for salvage radiation therapy, but access remains limited, potentially affecting equitable

care. Further studies with diverse, international cohorts and longer follow-up are needed to validate the long-term impact of PSMA PET-CT on patient outcomes.

EP-0391

Evaluation of ^{18}F-JK-PSMA-7 PET/CT as new imaging tool for the detection of biochemically recurrent prostate cancer

M. Vanneste[1], *W. Deckers*[1], *K. Serdons*[1], *K. Van Laere*[1,2], *K. Goffin*[1,2]; *[1]Department of Nuclear Medicine, University Hospitals Leuven, Leuven, BELGIUM, [2]Nuclear Medicine & Molecular Imaging, Department of Imaging and Pathology, KU Leuven, Leuven, BELGIUM.*

Aim/Introduction: Prostate specific membrane antigen positron emission tomography with computed tomography (PSMA PET/CT) has replaced conventional imaging for localizing biochemically recurrent prostate cancer due to its superior accuracy (1). Several PSMA-based diagnostic tracers have been developed, some having pitfalls causing false negative or false positive results. The goal of this study was to evaluate the diagnostic value of the recently developed PSMA-tracer ^{18}F-JK-PSMA-7 (2) in patients with biochemically recurrent prostate cancer. ***Materials and Methods:*** In this retrospective study, the detection ratio of ^{18}F-JK-PSMA-7 PET/CT (according to PROMISE v2 (3)) and its correlation to the PSA value at the moment of the scan was evaluated in 116 patients with biochemically recurrent prostate cancer. In addition, tracer uptake was quantified in PSMA-positive lesions and normal organs (salivary glands, spleen, liver, bone, bloodpool, muscle) and related tumor-to-background ratios were evaluated. ***Results:*** ^{18}F-JK-PSMA-7 PET/CT was positive in 60 of 116 patients (52%; PSA mean 2.4 ng/mL, range 0.1-53.7). In these patients, a total of 211 PSMA-positive lesions were detected with a median of 2 lesions per patient. Patients with a positive PSMA PET/CT scan had a significant higher PSA value than patients with a negative scan (3.5 vs 1.1; p = 0.03). The detection ratio increased with increasing PSA values (39% at PSA<0.2 ng/mL - 83% at PSA>10 ng/mL). Lymph node metastases were detected in 55% of patients (37.9% of lesions, 80/211), followed by bone metastases in 33% of patients (48.3% of lesions, 102/211), local recurrences in 22% of patients (6.2% of lesions, 13/211) and visceral metastases in 15% of patients (7.6% of lesions, 16/211). Salivary glands presented with the highest physiological uptake (SUV_{mean} 15.1±4.3 (mean±SD)), followed by liver (SUV_{mean} 9.6±2.0 and spleen (SUV_{mean} 6.6±2.3). In the current cohort, bone metastases showed the highest TBR. ***Conclusion:*** ^{18}F-JK-PSMA-7 PET/CT showed a good detection ratio in biochemically recurrent prostate cancer, with increasing values at higher PSA value at the moment of the scan. ***References:*** (1) Hofman MS et al. Prostate-specific membrane antigen PET-CT in patients with high-risk prostate cancer before curative-intent surgery or radiotherapy (proPSMA): a prospective, randomised, multicentre study. Lancet 2020;395:1208-1216; (2) Zlatopolskiy BD et al. Discovery of ^{18}F-JK-PSMA-7, a PET Probe for the Detection of Small PSMA-Positive Lesions. JNM 2019;60:817-823; (3) Seifert R et al. Second Version of the Prostate Cancer Molecular Imaging Standardized Evaluation Framework Including Response Evaluation for Clinical Trials (PROMISE V2). Eur Urol 2023;83:405-412.

EP-0392

Utility of ^{18F}F-PSMA-1007 combined protocol of pelvic pet/mri and whole body PET/CT in planning focal therapy (ire/hifu) in radiorecurrent prostate cancer

J. J. Robles[1], *A. P. Caresia-Aroztegui*[2], *A. Abella-Serra*[3], *J. J. Martín-Marcuartu*[1], *D. Durany-Lara*[4], *P. Servian-Vives*[3], *V. Vallejos-Arroyo*[2], *A. Cervera-Araez*[5], *L. Pons-Martinez*[6], *M. Cortés-Romera*[1]; *[1]Servicio de Medicina Nuclear. Hospital Universitario de Bellvitge, L'Hospitalet de Llobregat, SPAIN, [2]Servicio de Medicina Nuclear. Hospital Germans Trias i Pujol, Badalona, SPAIN, [3]Servicio de Urología. Hospital Germans Trias i Pujol, Badalona, SPAIN, [4]Servicio de Radiología. Hospital Universitario de Bellvitge, L'Hospitalet de Llobregat, SPAIN, [5]Servicio de Radiología. Hospital Germans Trias i Pujol, Badalona, SPAIN, [6]Servicio de Anatomía Patológica. Hospital Germans Trias i Pujol, Badalona, SPAIN.*

Aim/Introduction: The aim of this bicenter prospective study is to evaluate the impact of a combined ^{18}F-PSMA protocol with pelvic PET/MRI and whole-body PET/CT in the selection of patients for focal therapy (FT) in radiorecurrent prostate cancer. ***Materials and Methods:*** Twenty-nine patients with prostate cancer recurrence after radiotherapy ± electroporation (median PSA: 2.2 ng/ml, range 0,64-3,56; median time to recurrence: 5.5 years; range 1,3-21) were studied. All patients underwent selective pelvic PET/MRI acquisition 90 minutes post-injection of ^{18}F-PSMA-1007 and subsequent skull-to-midthigh PET/CT acquisition 120 minutes post-injection. Patients with exclusively local disease eligible for focal treatment were summited to systematic and targeted biopsies. Agreement between PET, MRI and PET/MRI were calculated (Kappa) and related to pathological anatomy (PA). Impact on therapeutic management attributable to this new PET protocol was also calculated. ***Results:*** Per-patient analysis: Positive test in 27/29 patients (93%, 22 exclusively local recurrence eligible for focal treatment; 7% non-eligible due to locoregional (1 patient) or distant (4 patients) dissemination. Of the 27 patients with positive test, 6 are awaiting biopsy, 1 died of unrelated causes, 1 refused biopsy. Therapeutic management changed in 5 of the remaining 19 patients (26%) due to findings exclusive to PET (4 due to lymphatic spread, 1 due to PSMA-RADS 4 prostate lesion not identified by MRI). Per-lesion analysis: Agreement between PET and MRI was found in 21 patients (Kappa 0,28) and 23 in-site lesions (Kappa 0,19). At this moment, biopsy results are available for 15/22 patients with local recurrence (16 biopsied lesions: 15 detected by MRI; 16 by PET). MRI-PA agreement: 11/15 (73%). PET-PA agreement: 12/16 (75%). PET/MRI-PA: 12/16 (75%). ***Conclusion:*** This new PET protocol combining pelvic PET/MRI and whole-body PET/CT helped to select recurrent prostate cancer patients for focal therapy, changing therapeutic management in 26% of the patients. High agreement between PET/MRI to histopathology was demonstrated.

EP-0393

PSMA PET/CT for the detection of prostate cancer (PCa) biochemical recurrence (BCR) after primary radiation therapy (RT): is it time to review the Phoenix criteria?

C. Vallone[1,2], *P. Guglielmo*[2,3], *C. Franzese*[2,4], *R. Lucchini*[4], *R. Mazzola*[2,5], *J. Jandric*[6], *M. Rodari*[6], *G. Di Grigoli*[6], *M. Marenco*[6], *S. Del Vecchio*[1], *L. Evangelista*[2,6]; *[1]Department of Advanced Biomedical Sciences, University of Napoli, Napoli, ITALY, [2]Department of Bioscience, Humanitas University, Pieve Emanuele, Pieve Emanuele (MI), ITALY, [3]Nuclear Medicine Unit, Humanitas Gavazzeni, Bergamo, ITALY, [4]Radiation Oncology Unit, IRCCS Humanitas Cancer Center, Rozzano (MI), ITALY, [5]Radiation Oncology Unit, Humanitas Gavazzeni, Bergamo, ITALY, [6]Nuclear Medicine Unit, IRCCS Humanitas Cancer Center, Rozzano (MI), ITALY.*

Aim/Introduction: RT is a cornerstone of curative treatment for PCa. BCR after RT is defined by the Phoenix criteria as a PSA rise of ≥ 2.0 ng/mL above the nadir. However, PSMA PET/CT can detect recurrences at lower PSA levels. Our primary aim was to assess the detection rate of PSMA PET/CT in patients who received primary RT and subsequently experienced a PSA elevation below the Phoenix threshold. Secondary aims were to: 1) describe the anatomical patterns of recurrence, 2) perform a riskstratified analysis of positive findings and 3) determine how PSMA PET/CT might influence clinical decisionmaking. ***Materials and Methods:*** We conducted a retrospective, observational, multicenter analysis of PCa patients treated with curativeintent RT who underwent PSMA PET/CT for rising PSA—below the Phoenix threshold—

between September 2020 and August 2023. We included only those patients who had not received any prior treatment for recurrent disease. Positive PSMA PET/CT scans were classified according to the PROMISE score, and risk stratification was performed using D'Amico criteria. Clinical decisionmaking data were extracted from patient charts. A nonparametric statistical analysis was employed to compare distributions across the various subsets (MedCalc® software). ***Results:*** Fiftyfour patients were included (median age 78 years, range 57-89). The overall PSMA PET/CT detection rate was 68.5% (n=37/54). Of those with positive scans, 81% (n=30/37) were oligometastatic and 19% (n=7/37) were multimetastatic. According to the PROMISE score, 24% (n=9/37) had local recurrence, 27% (n=10/37) nodal disease, 8% (n=3/37) boneonly metastases, and the remainder had multiple sites of involvement. By D'Amico risk classification, 83.9% (26/31) of unfavourable intermediate/highrisk patients had a positive PET, compared with 45.8% (11/24) of low/favourable intermediaterisk patients (chi squared, p<0.05). Followup data were available for 48 patients (89%). In 92% (n=44/48), PET findings guided therapy choice: 97% (n=32/33) of PETpositive patients received additional treatment (hormonal therapy, RT, or chemotherapy), whereas 80% (n=12/15) of PETnegative patients were managed with watchful waiting (chi-square, p<0.001). ***Conclusion:*** This study shows that PSMA PET/CT detects PCa recurrence in about 70% of patients with PSA rises below the Phoenix threshold. By identifying the disease at an earlier stage, patients may be eligible for curative local treatment and receive a personalized therapeutic approach. ***References:*** DOI: 10.1016/j.euo.2024.09.015.

EP-0394

PROMISE V.2. Staging with a Novel 18F-Piflufolastat PET/CT Protocol for the Detection of Prostate Cancer Recurrence

M. Romero, *M. Cornide Carvallo, M. Zapardiel Martinez-Falero, M. Vaillant Lopez, A. Berardinelli Isea, P. Daudén Onate, G. Cuesta Domingo, R. Couto Caro, M. Nieves Cabrera;*
HCSC, Madrid, SPAIN.

Aim/Introduction: To assess the value of a novel 18F-Piflufolastat PET/CT protocol aimed at minimizing urinary excretion artifacts and evaluating potential modifications in TNM staging according to PROMISE V2 criteria. ***Materials and Methods:*** A retrospective study was conducted on patients with biochemical recurrence of prostate cancer who underwent 18F-Piflufolastat PET/CT between February 2024 and January 2025. The protocol included radiotracer injection under camera with dynamic pelvic imaging from 0 to 5 minutes post-injection. This was followed by a resting period of 90 minutes, during which oral contrast and 50 ml of non-ionic intravenous contrast were administered 10-15 minutes prior to delayed imaging acquisition. An additional 50 ml of i.v. contrast was administered during the delayed scan, which included inspiratory chest CT and standard whole-body imaging. ***Results:*** A total of 100 patients were included, with a mean age of 71.26 years (range 45-86; SD 8.4). Of these, 76 had previously undergone radical prostatectomy, while 24 had received radical-intent radiotherapy and/or hormone therapy. The median PSA at recurrence was 0.8 ng/mL (range 0.2-8.8; SD 1.1). PET/CT was positive in 61% of patients, leading to TNM PROMISE V2 modification in all positive cases. The positivity rate was 48% for PSA 0.2-0.5 ng/mL, 83.3% for PSA 0.5-1.0 ng/mL, 81.25% for PSA 1.0-1.5 ng/mL, 50% for PSA 1.5-2.0 ng/mL, and 100% for PSA >2 ng/mL.Local recurrence was identified in 30% of patients (18% with isolated local recurrence), pelvic nodal involvement in 27% (21 N1 and 6 N2), extrapelvic nodal metastases (miM1a) in 11%, osseous metastases (miM1b) in 5 patients, and pulmonary metastases (miM1c) in 3 cases. One patient with a negative PET/CT scan was diagnosed with invasive breast adenocarcinoma. The positivity rate was higher in patients treated with radical radiotherapy compared to those with prostatectomy (72.7% vs. 56.6%).This protocol enhanced detection of local recurrence (e.g., ruled out bed recurrence in 4 cases; identified recurrence in seminal vesicle [3], vesicourethral anastomosis [1], and adjacent to surgical clips [1]) and pelvic nodal metastases (N1-N2 in 4 cases; M1a in 4 cases). ***Conclusion:*** Early imaging with 18F-Piflufolastat PET/CT improves detection of local recurrence even at low PSA levels, minimizing urinary excretion artifacts. It led to PROMISE V2 TNM stage modifications in all positive cases.

EP-0395

Prognostic Value of Total Tumor Volume Derived from ^{18}F-FSU-880 PSMA-PET Imaging in Prostate Cancer Patients

R. Nakamoto, *Y. Shimizu, Y. Nakamoto;*
Kyoto University Hospital, Kyoto, JAPAN.

Aim/Introduction: There has been growing interest in the prognostic value of quantitative parameters derived from prostate-specific membrane antigen (PSMA)-targeted PET imaging in patients with prostate cancer. This study aimed to evaluate the prognostic capability of quantitative values derived from PSMA-PET images acquired using ^{18}F-FSU-880, Japan's first F-18 labeled PSMA targeting agent developed by our group. ***Materials and Methods:*** We retrospectively analyzed 69 prostate cancer patients who underwent ^{18}F-FSU-880 PET/CT between February 2018 and April 2021 following biochemical recurrence (BCR). Of the initial 76 patients, 7 were excluded due to loss to follow-up at other institutions. Seven clinical parameters including PSA doubling time (PSADT), and nine PSMA-PET parameters including Total Tumor Volume (TTV) and DmaxVox (distance between the two lesions furthest apart using the two outermost voxels) were assessed for their association with prognosis as of March 2025. Quantitative PET metrics were calculated using the open-source software LIFEx v7.80. Lasso regression and Firth's penalized Cox proportional hazards model were applied using R software (version 4.3.2). Model performance was evaluated using the concordance index (c-index), with 95% confidence intervals calculated via 1000 bootstrap resamples. ***Results:*** The median follow-up period was 49 months (range: 7-84 months), during which 12 patients died. Lasso regression was applied to select prognostic variables, and Primary treatment (surgery, radiotherapy, or hormone therapy), Disease status at PET/CT (BCR, conventional non-metastatic CRPC [nmCRPC], metastatic CRPC [mCRPC], or metastatic hormone-sensitive prostate cancer [mHSPC]), PSADT, TTV, and DmaxVox were retained for further analysis. In the Firth Cox model, TTV emerged as a significant prognostic factor (hazard ratio 1.0199; 95% CI: 1.0019-1.0383; p = 0.0324), while PSADT and DmaxVox were not statistically significant (p = 0.1899 and 0.1905, respectively). The model showed strong overall fit, with a likelihood ratio test p-value of 0.00086 and Wald test p-value of 0.00081. The c-index was 0.8144 (95% CI: 0.7045-0.9091), indicating good predictive accuracy. ***Conclusion:*** Total Tumor Volume (TTV) derived from PSMA-PET images using ^{18}F-FSU-880 was identified as a significant independent prognostic factor in prostate cancer. TTV, obtained from our institution's proprietary PSMA-PET imaging, may serve as a clinically useful predictor for guiding future therapeutic strategies. ***References:*** 1:Saga T, et al. Cancer Sci. 2019 Feb;110(2):742-750. 2:Otani T, et al. Ann Nucl Med. 2022 Mar;36(3):302-309.

EP-0396

VAULT: Value of Long-Axial Field-of-View Tomography in [68Ga]Ga-PSMA-11 PET/CT for the Management of Biochemical Recurrent Prostate Cancer

A. Di Giorgio[1], *M. Di Franco*[1], *M. Rapa*[1], *F. Monastero*[1], *M. Assenza*[2], *L. Bianconi*[3], *C. Nanni*[3], *P. Castellucci*[3], *A. Farolfi*[3], *S. Fanti*[1,3];
[1]*Nuclear medicine, Alma Mater Studiorum University of Bologna, Bologna, ITALY,* [2]*Professional Development and Implementation of Research in Health Professions Unit, IRCCS Azienda Ospedaliero-Universitaria di Bologna, Bologna, ITALY,* [3]*Nuclear Medicine, IRCCS, Azienda Ospedaliero-Universitaria di Bologna, Bologna, ITALY.*

Aim/Introduction: Biochemical recurrence(BCR) affects a significant proportion(20-50%) of localized prostate cancer(PC)

patients post-radical prostatectomy(RP), often with conventional imaging failing to detect early recurrences at low PSA levels. [68Ga]Ga-PSMA-11-PET/CT(PSMA-PET/CT) has demonstrated high sensitivity and specificity in this setting. This study aims to compare the diagnostic capability of long-axial field-of-view(LAFOV) PET/CT (uEXPLORER) against conventional digital short-axial field-of-view(SAFOV) PET/CT systems using [68Ga]Ga-PSMA-11 in early BCR PC patients. A secondary objective is to evaluate its potential impact on therapeutic decision-making and clinical management in this specific cohort. ***Materials and Methods:*** Single-center prospective study consecutively enrolling male patients referred to our institution between October 2024 and March 2025 for PSMA-PET/CT due to BCR of PC (defined as PSA>0.2ng/mL post-RP, according to EANM/EAU guidelines) who consented to undergo dual PET/CT scanning with both SAFOV and LAFOV systems(CE AVEC: 598/2024/Oss/AOUBo). Paired SAFOV and LAFOV scans were interpreted according to PROMISE criteria v2. The total number and sites of lesions identified on each scan were recorded. Per-patient and per-lesion analyses were conducted. Follow-up data were collected. ***Results:*** A total of 62 patients(median age 75 years;IQR 65-75) with BCR were enrolled and underwent paired SAFOV and LAFOV PSMA-PET/CT, resulting in 124 acquisitions. The median PSA level at the time of PSMA-PET/CT was 0.45ng/mL(IQR 0.27-1.15). Forty-one out of 62(66%) SAFOV scans were reported as negative and 21/62 (34%) as positive. Twenty-six out of 62(42%) LAFOV scans were negative and 31/62(50%) were positive. In 5/62(8%) cases, SAFOV was negative while LAFOV was equivocal: in 2/5(40%) due to doubtful disease localization in the prostatic bed near physiological high urinary activity, in 3/5(60%) due to focal rib uptakes without clear anatomical correlates on CT images, suspicious for unspecific bone uptake(UBU). Overall positivity/negativity concordance between the two scan types was observed in 35/62(56.5%) cases(Cohen's kappa=0.387; agreement=69%). The total number of positive lesions detected was 40/83(40%) on SAFOV acquisitions and 83/83(100%) on LAFOV acquisitions(weighted Cohen's kappa=0.67;agreement 61%), with all lesions identified on SAFOV also being detected on LAFOV. In 18/62(29%) patients, findings identified on LAFOV but not on SAFOV PET/CT impacted patient management, leading to a therapeutic change in all 18 cases. ***Conclusion:*** In patients with BCR of PC undergoing PSMA-PET/CT, LAFOV PET acquisitions demonstrated a higher positivity-rate compared to conventional SAFOV acquisitions. The enhanced diagnostic performance of LAFOV PET led to changes in clinical decision-making in a significant proportion of cases, suggesting a potential impact on patient management strategies in this setting.

EP-0397

[18F] DCFPYL PET/CT in Prostate Cancer Patients Candidates for Salvage Radiotherapy for Very Low Biochemical Recurrence ≤0.25 ng/mL after Radical Prostatectomy: Impact on Restaging and Therapeutic Strategy.

N. Alvarez Mena, *J. Gómez Hidalgo, F. Sebastián Palacid, B. Pérez López, C. Riola Parada, R. Ruano Pérez;*
Hospital Clínico Universitario de Valladolid, Valladolid, SPAIN.

Aim/Introduction: Recent multicenter studies have shown that in patients with prostate cancer with biochemical recurrence after radical prostatectomy, delaying salvage radiotherapy until a PSA level above 0.25 ng/mL is reached significantly increases the risk of mortality, especially if they have a high-risk factor (pT3/4 or Gleason score 8-10). Therefore, our objective is to assess the clinical impact of [18F]DCFPYL PET/CT on very low biochemical recurrence (≤0.25 ng/mL) in prostatectomy patients who are candidates for salvage radiotherapy. ***Materials and Methods:*** Prospective study of 33 patients (mean age 66.06 ± 6.29 years) with very low biochemical recurrence (≤0.25 ng/mL) after radical prostatectomy who underwent [18F]DCFPYL PET/CT prior to salvage radiotherapy. Variables such as PSA level (ng/mL), D'Amico risk classification and ISUP grade, [18F]DCFPYL PET/CT detection capacity, and recurrence uptake degree (SUVmax and PSMA-RADS) were analyzed. In addition, disease restaging and final therapeutic approach were evaluated according to the [18F] DCFPYL PET/CT result. ***Results:*** Mean level of PSA was 0.22±0.02 ng/mL (range 0.17-0.25). Up to 61% (14/23) of patients in the high-risk group (ISUP grades 4-5) had a positive PET scan for recurrence (SUVmax up to 25.41 and PSMA-RADS 5), leading to a change in therapeutic management in 12 of them: 7 with EBRT of the prostate bed + regional lymph nodes for N1 and 5 with ADT + ARPI + docetaxel for M1a/b. In the intermediate-risk group (7 patients with ISUP grades 2-3), PET detected recurrence in 43% (3/7), with SUVmax up to 22.25 and PSMA-RADS 4-5. Two of these patients had recurrence outside the prostate bed (1 N1 and 1 M1a due to pararectal lymph node recurrence). Therefore, these lymph node regions were included in the EBRT planning. The three patients in the low-risk group (ISUP grade 1) had a negative PET result and were candidates for salvage EBRT of the prostate bed only. Finally, Spearman's correlation showed a significant correlation between the D'Amico risk classification and the degree of recurrence uptake (PSMA-RADS), with r=0.9; p<0.001. ***Conclusion:*** [18F] DCFPYL PET/CT has adequate detection capacity in patients with intermediate and high-risk prostate cancer who are candidates for salvage radiotherapy due to biochemical recurrence after radical prostatectomy, even with very low PSA levels (≤0.25 ng/mL). The more widespread incorporation of this diagnostic tool into clinical practice suggests it could be useful in reducing morbidity and mortality in these patients by leading to a change in therapeutic strategy in up to 50% of them.

EP-0398

A Comparative Analysis of PSMA-PET/CT and Whole-Body MRI for Staging and Restaging in Patients with Prostate Cancer

E. Greco[1], *L. Bianchi*[2], *C. Gaudiano*[3], *B. Corcioni*[3], *C. M. P. Sgro*[1], *C. Mignogna*[4], *B. Renzetti*[5], *A. Cattabriga*[3], *R. Schiavina*[2,4], *E. Brunocilla*[2,4], *C. Mosconi*[3,5], *R. Mei*[6], *P. Castellucci*[6], *S. Fanti*[6,1], *A. Farolfi*[6];
[1]*Nuclear Medicine, Alma Mater Studiorum University of Bologna, Bologna, ITALY,* [2]*Division of Urology, IRCCS Azienda Ospedaliero-Universitaria di Bologna, Bologna, ITALY,* [3]*Department of Radiology, IRCCS Azienda Ospedaliero-Universitaria di Bologna, Bologna, ITALY,* [4]*Division of Urology, Alma Mater Studiorum University of Bologna, Bologna, ITALY,* [5]*Department of Radiology, Alma Mater Studiorum University of Bologna, Bologna, ITALY,* [6]*Nuclear Medicine, IRCCS Azienda Ospedaliero-Universitaria di Bologna, Bologna, ITALY.*

Aim/Introduction: Systemic staging of high-risk prostate cancer (PCa) patients and restaging of patients with biochemical recurrence (BCR) after radical treatment and low PSA values can be done using PSMA-PET. Whole-body MRI (wbMRI) is an accurate technique for the identification of PCa local and distant disease but there is no strong recommendation for its use in daily clinical practice. This study's aim is to compare PSMA-PET and wbMRI in detecting metastasis in PCa patients before radical or systemic treatment (staging) and after radical therapy in patients with BCR (restaging). ***Materials and Methods:*** We conducted a single-center prospective study, enrolling PCa patients who underwent both PSMA-PET and wbMRI in a 2-months' timeframe for staging or restaging purposes. No treatments for PCa were allowed between the two imaging techniques. The images were independently reviewed by two nuclear medicine physicians for PET scans and two radiologists for wbMRI. The concordance of both techniques in the detection of local or residual disease (T/Tr), local (N) and distant (M1a) lymph node, bone (M1b) and visceral (M1c) metastasis was assessed with Cohen's kappa. ***Results:***

Overall, 114 patients were enrolled (median age 69 years), 81/114 (71%) with newly diagnosed PCa and 33/114 (29%) with BCR. PSMA-PET and wbMRI were performed within a median time of 16 days (IQR 8-28). Overall, PSMA-PET was positive for PCa in 90/114 (79%) patients and wbMRI in 87/114 (76%). PSMA-PET compared to wbMRI led to up-staging in 6% (7/114) and resulted in down-staging in 3% (4/114) patients. Using Cohen's k for T/Tr, N, M1a and M1b, the concordance between the two techniques (n=114) was 0.84, 0.72, 0.82 and 0.59, respectively. No patients showed visceral metastasis (M1c). ***Conclusion:*** Both PSMA-PET and wbMRI demonstrated almost perfect agreement in detecting local disease (T) and distant lymph nodes metastasis (M1a), substantial agreement for the detection of local lymph nodes involvement (N), while moderate agreement was observed for bone disease (M1b).

EP-0399

Prediction of Occult Lymph Node Metastasis Using PSMA PET/CT-Based Radiomic Model in Clinical N0 Prostate Cancer

T. Li*;*
The First Affiliated Hospital, College of Medicine, Zhejiang University, Hangzhou, CHINA.

Aim/Introduction: Occult lymph node metastasis (OLNM) significantly impacts treatment planning and prognosis in prostate cancer (PCa). This study aimed to develop and validate a PET radiomics-based model derived from primary prostate lesions on [18F]-PSMA-1007 PET/CT to predict OLNM in clinical N0 prostate cancer patients undergoing radical prostatectomy and extended pelvic lymph node dissection (ePLND). ***Materials and Methods:*** A total of 227 patients with histologically confirmed prostate cancer who underwent preoperative [18F]-PSMA-1007 PET/CT followed by radical prostatectomy and ePLND were retrospectively included. Patients with visually negative lymph nodes on PET imaging but pathologically confirmed lymph node metastasis were classified as having OLNM. Radiomics features were extracted from the primary prostate tumors using LIFEx software. A predictive radiomics signature was developed using the least absolute shrinkage and selection operator (LASSO) regression. Model performance was evaluated by the area under the receiver operating characteristic curve (AUC), and clinical utility was assessed through decision curve analysis (DCA). ***Results:*** Out of 227 clinically N0 patients, 34 were found to have occult nodal metastases on final pathology.The developed radiomics signature consisted of several robust PET radiomics features that effectively distinguished patients with OLNM. The radiomics-based model demonstrated good predictive performance with an AUC of 0.81 in the training cohort and 0.77 in the validation cohort. Decision curve analysis confirmed significant clinical benefit of the radiomics model over conventional clinical factors alone. ***Conclusion:*** Our study successfully developed a [18F]-PSMA-1007 PET-based radiomics model to non-invasively predict occult lymph node metastasis in prostate cancer patients. This radiomics approach provides a valuable tool for better preoperative risk stratification, potentially reducing unnecessary lymph node dissections and guiding personalized therapeutic strategies.

EP-0400

Development and validation of a Nomogram forpredictingpositive [^{99m}Tc]Tc-HYNIC-PSMASPECT/CT in patients withbiochemically recurrent prostate cancer after radical prostatectomy

B. Li*, X. Wu, Y. Yu, Y. Gao;*
Department of Nuclear Medicine, Henan Key Laboratory of Novel Molecular Probes and Clinical Translation in Nuclear Medicine, Henan Provincial People's Hospital; Zhengzhou University People's Hospital, Henan University People's Hospital, Zhengzhou, CHINA.

Aim/Introduction: Prostate cancer (PCa) recurrence following radical prostatectomy (RP) poses significant clinical challenges, with biochemical recurrence (BCR) serving as a crucial indicator for subsequent metastasis. This study aims to develop and validate a nomogram predicting the accuracy of [^{99m}Tc]Tc-HYNIC-PSMA SPECT/CT imaging positivity in PCa patients experiencing BCR post-RP. ***Materials and Methods:*** A retrospective cohort study included 192 patients meeting inclusion criteria from Henan Provincial People's Hospital & Zhengzhou University People's Hospital, with an external validation cohort of 40 patients from Henan Cancer Hospital. Multivariate logistic regression and LASSO analysis identified three independent predictors (ISUP grade group, PSA prior to PSMA SPECT/CT, and PSA doubling time). These predictors were integrated into a nomogram, whose performance was assessed using ROC analysis, calibration curves, and decision curve analysis (DCA). ***Results:*** The overall detection rate of [^{99m}Tc] Tc-HYNIC-PSMA SPECT/CT imaging was 43.5% (n = 101), with varying sites of recurrence observed. ISUP grade group (OR: 20.35; 95% CI: 4.64-89.25), PSA prior to PSMA SPECT/CT (OR: 2.86; 95% CI: 1.84-4.44), and PSA doubling time (OR: 0.03; 95% CI: 0.01-0.16) were independently associated with positivity on PSMA SPECT/CT imaging. The nomogram exhibited robust predictive accuracy with AUCs of 0.960, 0.891, and 0.872 in the training, internal validation, and external validation cohorts, respectively. The best nomogram's cutoff was 40%. DCA demonstrated significant clinical net benefit, especially at higher threshold probabilities. ***Conclusion:*** This study introduces a novel nomogram predicting the likelihood of [^{99m}Tc] Tc-HYNIC-PSMA SPECT/CT imaging positivity in PCa patients with BCR post-RP. The nomogram enhances patient stratification and may optimize the selection of candidates for PSMA SPECT/CT imaging, thereby improving clinical decision-making and patient outcomes.

EP-0401

Can Tumour Burden On PET/CT With [18F]DCFPyL Predict Progression In Patients With Prostate Cancer Recurrence After Radical Treatment?

L. García Zoghby*[1], J. Bonilla Plaza[1], M. Cruz Montijano[1], M. Meneses Navas[1], S. Guzmán Ortiz[1], J. Moltalvá Pastor[1], I. García Megías[1], M. Amo Salas[2], A. García Vicente[1];*
[1]Hospital General Universitario de Toledo, Toledo, SPAIN, [2]Facultad de Medicina de la Universidad de Castilla-La Mancha, Ciudad Real, SPAIN.

Aim/Introduction: The objective was to analyse the associations between clinical and molecular imaging variables and progression-free survival (PFS) in patients with first biochemical recurrence (FBR) of prostate cancer (PCa) after radical treatment. ***Materials and Methods:*** We analysed patients with FBRPCa visualized in [18F]DCFPyL-PET/CT. Minimum follow-up: 36 months. ISUP grade group, recurrence risk classification, PSA kinetics, initial treatment and treatment after FBRPCa were the clinical variables collected. [18F]DCFPyL-PET/CT were visually assessed by two experienced nuclear medicine physicians independently and lesions segmentation was performed using aPROMISE platform. Molecular tumour burden variables: TNM, total molecular tumour volume (total_MTV), total tumour lesion activity (total_TLA) and total PSMA index (total_PSMAi). During follow-up, two consecutive PSA values ≥ 0.2 ng/ml after [18F]DCFPyL-PET/CT was considered as progression. We compared mean values by Mann-Whitney test. Kaplan-Meier method (qualitative variables) and Cox regression (quantitative variables) were used in survival analysis. ***Results:*** One hundred and seventeen patients were analysed (mean age: 69.5 years), 66.7% high risk. Initial treatment: 50 radical prostatectomy, 46 radiotherapy, 21 both. Progression was observed in 31/117 patients. Median follow-up after [18F]DCFPyL-PET/CT of 41 months. [18F]DCFPyL-PET/CT observed metastatic disease in 34.2%. Total_MTV, total_TLA and total_PSMAi mean values (± SD)

were 8.10 ± 17.32 ml, 42.15 ± 100.39, 15.03 ± 33.38, respectively. After [18F]DCFPyL-PET/CT, 60.68% (71/117) underwent androgenic deprivation therapy (ADT) ± androgen receptor targeted therapy (ARTT), median time: 28 months. Six patients underwent only surgery, 25 radiotherapy and in 15 patients follow-up was elected. Initial treatment (p=0.031), grade ISUP group (p=0.073) and treatment after FBRPCa (p=0.060) showed association with PFS. We observed significant differences in mean time under ADT ± ARTT between patients who progressed (16.82 ± 10.42 months) and did not progress (31.42 ± 12.42 months). No significant association was found between molecular tumour burden variables and PFS. ***Conclusion:*** No significant association was found between molecular tumour burden on [18F]DCFPyL-PET/CT and progression, probably due to high election of ADT ± ARTT and the sensitivity to the hormonal treatment of the patients in our analysis. Therefore, maybe an effort should be made to promote radical treatments in order to a more effectively assessment of the real diagnostic reach of molecular imaging in this context.

EP-0402

Possibility of 18F-PSMA-1007 PET/CT in patients with biochemical recurrence of prostate cancer after radical prostatectomy

M. Komarova*, A. Pronin, E. Davydova, O. Ryzhova, I. Amosova;*
N.N Blokhin National Medical Research Center of Oncology of the Russian Ministry of Health, Moscow, RUSSIAN FEDERATION.

Aim/Introduction: to detect efficacy of 18F-PSMA-1007 PET-CT in patients with biochemical recurrence of prostate cancer after radical prostatectomy. ***Materials and Methods:*** 89 patients (mean age 68,23±7,97) were included in the study. All patients had the biochemical recurrence of prostate cancer - prostate-specific antigen (PSA) levels of greater than or equal to 0.2 ng/mL. The mean PSA level was 0,96 [0,42-2,19] ng/mL. We evaluated all lesions suggestive of recurrent prostate cancer including local recurrence, lymph node metastases, bone metastases, and other metastases. Quantitative analysis was based on the measurement of the SUVmax. ROC-analysis was used to determine the threshold PSA level at which the maximum sensitivity and specificity of 18F-PSMA-1007 PET/CT in detecting signs of tumor recurrence was achieved. Mann-Whitney test was used to compare median PSA level between patients with tumor lesions and negative results. ***Results:*** 70 patients (78,6 %) had 1 or more localized areas suggestive of recurrent prostate cancer. In 19 patients (21.4%) we couldn't determine the reason of the increase PSA level in the blood serum. In the group of patients with positive 18F-PSMA-1007 PET-CT the mean PSA level was 1,24 [0,59-2,97] ng/ml. The frequency of detection disease increased with increasing PSA level - in 19 patients with negative PET-CT results, PSA values were 0,30 [0,20-0,47] ng/mL versus 1,24 [0,59-2,97] ng/mL in patients with tumor lesions on PET/CT, p<0,0001. Based on ROC curve analysis, the appropriate PSA cut-off value to diagnose cancer lesions was 0,49 ng/mL (sensitivity of 80,00 % and specificity 84,2 %) with an area under the curve (AUC) of 0.894 (P<0.001). ***Conclusion:*** 18F-PSMA-1007 PET-CT demonstrated a high detection rate of tumor lesions for patients with biochemical recurrence after radical prostatectomy. A PSA cut-off value of 0,49 ng/mL was identified, providing a sensitivity of 80,00 % and a specificity of 84,2 % of 18F-PSMA-1007 PET-CT in detecting signs of tumor recurrence. ***References:*** 1. Giesel FL, Will L, Kesch C, et al . Biochemical recurrence of prostate cancer: initial results with [18F]PSMA-1007 PET/CT. J Nucl Med. 2018;59:632-635.2. Giesel FL, Will L, Lawal I, et al. Intraindividual comparison of 18F-PSMA1007 and 18F-DCFPyL PET/CT in the prospective evaluation of patients with newly diagnosed prostate carcinoma: a pilot study. J Nucl Med.2018;59:1076- 1080.3. Rahbar K, Weckesser M, Ahmadzadehfar H, Sch¨afers M, Stegger L, B¨ogemann M. Advantage of 18F-PSMA-1007 over 68Ga-PSMA-11 PET imaging for differentiation of local recurrence vs. urinary tracer excretion. Eur J Nucl Med Mol Imaging. 2018;45:1076-1077.

EP-0403

The impact of 18F-PSMA-PET/CT on clinical decision making in biochemically recurrent prostate cancer

C. A. Poulsen*[1], K. M. Buch-Olsen[1,2], M. H. Vilstrup[3], K. T. Pedersen[1], S. Hansen[4,2], M. H. A. Poulsen[5,6], P. C. Holdgaard[7], O. Gerke[1,2], M. G. Hildebrandt[1,2], J. Holm[1,2];*
[1]Department of Nuclear Medicine, Odense University Hospital, Odense, DENMARK, [2]Department of Clinical Research, Faculty of Health Science, University of Southern Denmark, Odense, DENMARK, [3]Department of Radiology and Nuclear Medicine, Esbjerg and Grindsted Hospital, University Hospital of Southern Denmark, Esbjerg, DENMARK, [4]Department of Oncology, Odense University Hospital, Odense, DENMARK, [5]Department of Urology, Esbjerg and Grindsted Hospital, University Hospital of Southern Denmark, Esbjerg, DENMARK, [6]Department of Regional Health Research, University of Southern Denmark, Odense, DENMARK, [7]Department of Nuclear Medicine, Lillebaelt Hospital, University Hospital of Southern Denmark, Vejle, DENMARK.

Aim/Introduction: Prostate-specific membrane antigen positron emission tomography/computed tomography (PSMA-PET/CT) is currently the most accurate imaging modality for detecting recurrent prostate cancer (PCa). However, prospective data on its clinical impact on individualized treatment strategies remain limited. This cohort study prospectively evaluated how 18F-PSMA-PET/CT influences clinical decision-making in patients with biochemically recurrent PCa. ***Materials and Methods:*** Patients were prospectively included from the Region of Southern Denmark between January 2020 and January 2025, and discussed in a structured two-step multidisciplinary team (MDT) conference. An initial treatment decision was made based on conventional diagnostic workup - primarily Gleason score at initial diagnosis, current clinical performance, and prostate-specific antigen (PSA) level - while blinded to PSMA-PET/CT results. Subsequently, the [^{18}F]-PSMA-1007-PET/CT scan was unblinded, and a second MDT discussion was held. The final treatment plan, offered to the patients, was based on the second MDT evaluation. Changes in treatment strategy between the two MDT sessions were defined as the primary outcome. ***Results:*** A total of 249 men with suspected recurrent PCa, all previously treated with radical prostatectomy and presenting with rising PSA levels (mean PSA 1.13 µg/L), were included. PSMA-PET/CT imaging led to a change in treatment strategy in 67 patients (27%) compared to the initial decision. Of these, 50 patients (20.1%) were initially planned for curative-intent treatment. However, 35 (14.1%) were reclassified to non-curative treatment based on PSMA findings, five (2%) were shifted to an alternative curative modality, six (2.4%) required additional diagnostic workup, and four (1.6%) had findings suspicious for synchronous cancer. Among the 17 patients (6.8%) originally planned for watchful waiting or androgen deprivation therapy (ADT), five (2%) were reclassified for curative-intent treatment based on PSMA-PET/CT results, while 12 (4.8%) had their management altered to another treatment modality. ***Conclusion:*** This prospective, blinded cohort study demonstrates that 18F-PSMA-PET/CT decisively influences clinical management in patients with biochemically recurrent PCa. Treatment plans were altered in more than one in four patients, including both redirection from curative to non-curative strategies and vice versa. These findings highlight the pivotal role of PSMA-PET/CT in optimizing personalized treatment strategies and supporting informed clinical decision-making in recurrent PCa.

EP-21

e-Poster Area

B: Imaging Clinical Studies -> B1 Oncological Imaging Clinical Study -> B18c Prostate Other

EP-0404

Short-term androgen deprivation therapy, ^{68}Ga-PSMA-11 binding potential and MR apparent diffusion restriction coefficient in hormone- sensitive, prostate cancer patients

O. Jonmarker[1], *A. Sanchez-Crespo*[1,2], *F. Jäderling*[1,3], *S. Carlsson*[1,2], *M. Olsson*[2], *C. Li*[1,4], *R. Axelsson*[1,2];
[1]*Karolinska Institutet, Stockholm, SWEDEN,* [2]*Karolinska University Hospital, Stockholm, SWEDEN,* [3]*Capio S:t Görans Hospital, Stockholm, SWEDEN,* [4]*Södersjukhuset, Stockholm, SWEDEN.*

Aim/Introduction: In vitro and animal studies have shown that short-term androgen deprivation therapy (ADT) upregulates prostate specific membrane antigen (PSMA) expression in prostate cancer cell lines. Published prospective human clinical studies on the long- and short-term effect of ADT on diagnostic performance of ^{68}Ga-PSMA-PET are scarce and show contradictory results. PSMA upregulation appears heterogeneous but generally predominant in bone metastases of castration-resistant cancers compared to hormone-sensitive cancers.The aims of this study was to investigate the effect of short-term ADT on cellular changes in PSMA, lesion apparent diffusion restriction coefficient (ADC) and plasma prostate specific antigen (PSA) values in a cohort of hormone- sensitive, prostate cancer patients without bone metastases. ***Materials and Methods:*** Nine patients were included in the study. Participants underwent dynamic ^{68}Ga-PSMA- PET/MRI at baseline, after one, three and four weeks under ADT. PSA, calculated lesion binding potential of non-displaceable radioligand (BP_{ND}), standard uptake values (SUV) at 60 minutes post tracer administration, and the lesion ADC were determined at every imaging session. Linear mixed effect models were generated to investigate interactions of these variables during ADT. Agreement analysis between SUV metrics and dynamic PET derived BP_{ND} during ADT was also investigated. ***Results:*** Eight patients with a total of ten lesions showed a positive ^{68}Ga-PSMA uptake at baseline. Disease staging was not modified for any patient during ADT. All lesions showed a curvilinear trajectory in BP_{ND} changes from baseline with peak values within 7-21 days. 60% of these dynamic changes in PSMA receptor expression could be explained by the interactions between changes in ADC and plasma PSA from baseline and across time under ADT but with a complex nonlinear relationship. SUV metrics showed a poor agreement with BP_{ND}. ***Conclusion:*** Results suggest that short term PSMA upregulation across time in ADT could potentially be predicted which may be useful for individualising the timing for treatment with PSMA-binding radioligands and provides a rationale for further prospective studies in selected patients.

EP-0405

Long axial field-of-view 68Ga-PSMA PET-CT detects physiological uptake in nerve roots

L. Badawy[1], *S. Datta*[1], *T. Wagner*[1,2];
[1]*Royal Free London NHS Foundation Trust, London, UNITED KINGDOM,* [2]*Centre for Medical Imaging, Department of Imaging, University College London, London, UNITED KINGDOM.*

Aim/Introduction: Long-axial field-of-view (LAFOV) positron emission tomography-computed tomography (PET-CT) is a technological development with better sensitivity and signal-to-noise ratio than short-axial field-of-view (SAFOV).[1] Since installing the Siemens Vision Quadra PET-CT (Siemens Healthineers, Erlangen, Germany) at our centre in March 2024, we have observed ^{68}Ga-PSMA uptake in nerve roots exiting the neural foramina. We are the first to describe a formal comparison of uptake in the nerve roots of consecutive prostate cancer patients on the Siemens Quadra LAFOV PET-CT and the Siemens Biograph PET-CT. ***Materials and Methods:*** We conducted a retrospective study of 63 adult patients with confirmed prostate cancer who underwent ^{68}Ga-PSMA PET-CT at our institution on Siemens LAFOV Quadra PET-CT in 2024, and Siemens Biograph PET-CT in 2022. Baseline characteristic data were extracted from the electronic patient records and Radiology information system. PET-CT images were reviewed by two of the authors who assessed for evidence of nerve root radiotracer uptake. Intensity at each spinal level was visually measured on a scale of 0 to 4, representing no to intense uptake. Inter-rater agreement for nerve root intensity was assessed using Cohen's kappa. We summed the authors' nerve root radiotracer intensity ratings to form a new numerical variable called "total rater score" and calculated average maximum standardised uptake values (SUVmax). ***Results:*** We analysed data from 63 patients, 32 (51%) of which were scanned on the Siemens Quadra PET-CT. Baseline characteristics were similar between the two cohorts. Cohen's Kappa was 1.0 ($p<0.001$) for a positive finding of nerve root uptake. The total rater score was significantly higher at three spinal levels (cervical; lumbar; sacral) in the Quadra group than in the Biograph group (5.0 vs 4.0, $p=0.012$; 3.0 vs 1.0, $p=0.003$; 4.0 vs 0.0, $p<0.001$). Average SUVmax values were greater with the Quadra in the lumbosacral regions (2.3 vs 1.1; $p=0.008$) and were similar in the cervical spine ($p=0.700$). Two patients with large volume metastatic disease had reduced nerve root avidity. ***Conclusion:*** This is the first study to describe nerve root uptake at the neural exit foramina in prostate cancer patients scanned with ^{68}Ga-PSMA PET-CT, which was more prevalent and better visualised on the LAFOV Quadra PET-CT than on SAFOV. ***References:*** 1. Alberts I et al. Clinical performance of long axial field of view PET/CT: a head-to-head intra-individual comparison of the Biograph Vision Quadra with the Biograph Vision PET/CT. Eur J Nucl Med Mol Imaging 2021; 48(8): 2395-2404.

EP-0406

Explorative analysis on the role of the PRIMARY Score in PSMA PET-guided re-irradiation for recurrent prostate cancer

P. Guglielmo[1,2], *L. Di Cristina*[3,4], *C. Franzese*[1,3], *R. Mazzola*[4,5], *J. Jandric*[6], *L. Setti*[2], *L. Evangelista*[1,6];
[1]*Department of Biomedical Sciences, Humanitas University, Pieve Emanuele, Milan, ITALY,* [2]*Nuclear Medicine Unit, Humanitas Gavazzeni, Bergamo, ITALY,* [3]*Department of Radiotherapy and Radiosurgery, IRCCS Humanitas Research Hospital, Rozzano, Milan, ITALY,* [4]*Department of Biomedical Sciences, Humanitas University, Via Rita Levi Montalcini 4, Pieve Emanuele, Milan, ITALY,* [5]*Department of Radiotherapy, Humanitas Gavazzeni, Bergamo, ITALY,* [6]*Nuclear Medicine Unit, IRCCS Humanitas Research Hospital, Rozzano, Milan, ITALY.*

Aim/Introduction: Despite progress in locoregional treatments, local recurrence after curative radiotherapy (RT) for prostate cancer (PCa) remains frequent, with biochemical relapse occurring in nearly one-third of cases. The optimal management of RT failure is still under investigation. In recent years, re-irradiation (re-RT), either via brachytherapy or stereotactic body radiotherapy (SBRT), has gained traction. Advances in imaging, particularly PSMA PET, now integrated into guidelines for biochemical recurrence (BR), have improved localization of relapse and guidance of targeted treatments. The PRIMARY SCORE (PS), a 5-point scale for intraprostatic disease assessment via PSMA PET, is established for initial diagnosis, but its utility in other clinical contexts is uncertain. This study aims to assess the potential role of PS in guiding re-RT in patients with recurrent PCa. ***Materials and Methods:*** We retrospectively evaluated patients with BR after definitive RT who were referred to two Nuclear Medicine departments for a

PSMA PET/CT scan for restaging purposes. The PS was assessed, considered positive for values 3-5, and then correlated with the re-RT treatment plan. ***Results:*** Between October 2021 and May 2024, 14 patients with a median age of 76 years (range: 65-83) underwent re-RT for PCa recurrence. According to the ISUP grade, 4 patients had ISUP 1, 5 had ISUP 2, 1 had ISUP 4, and 3 had ISUP 5. Additionally, one patient had a Gleason Score of 3+2. The median PSA value was 8.15 ng/mL (range: 1.58-332 ng/mL). Re-RT was performed at a mean interval of 7.7 ± 4.1 years from initial radical RT, with a median dose of 30 Gy in 5 fractions. The PSs were distributed as follows: 4 and 5 occurred three times each, 2A was recorded three times, and 1 and 3 were recorded once each. PSMA PET images was unavailable for two patients. The RT plan was guided by PSMA PET findings in all cases except for three patients: in one case, uptake was extremely low, making proper lesion irradiation potentially inadequate; in the other two cases, uptake was diffusely increased. Conversely, for all patients with a PS of 2A, PSMA PET was used to guide re-RT. ***Conclusion:*** Our results indicate that the PS offers limited value in guiding re-irradiation planning for recurrent PCa. Low or diffuse PSMA uptake patterns hinder accurate target delineation, reducing the applicability of PS in this context. Larger studies are needed to identify alternative PSMA-based criteria to improve re-RT planning in this setting.

EP-0407

Diagnostic Evaluation of Blood Biomarkers and Multiparametric ^{18}F-PSMA-1007 PET/MR Imaging in Prostate Cancer

L. Wang[1], *X. Su*[2], *Y. Yang*[2], *W. Wu*[1];
[1]Jilin Cancer Hospital, Changchun, CHINA, [2]Beijing United Imaging Healthcare Co., Ltd., Beijing, CHINA.

Aim/Introduction: Accurate differentiation between malignant and benign lesions in patients with suspected prostate cancer (PCa) remains an essential goal in nuclear medicine. Conventional diagnostic markers, such as total prostate-specific antigen (TPSA) and imaging criteria like the Prostate Imaging-Reporting and Data System (PI-RADS) score, often lack sufficient accuracy, leading to unnecessary biopsies. Recent advances in hybrid imaging and blood-based biomarkers offer promising strategies for improving diagnostic performance. This study aimed to evaluate the diagnostic performance of both conventional and advanced blood biomarkers and PET/MR parameters for histologically confirmed PCa. ***Materials and Methods:*** This retrospective study included 20 patients with suspected PCa who underwent ^{18}F-PSMA-1007 PET/MR imaging followed by MRI-targeted biopsy. Fourteen patients were histopathologically confirmed with PCa, and six had benign results. The multiparametric MRI protocol included T2-weighted imaging and multi-b-value diffusion-weighted imaging (DWI). Evaluated parameters included blood biomarkers, such as TPSA and prostate health index (PHI), MRI-derived PI-RADS score from MRI, DWI-derived apparent diffusion coefficient (ADC), and PET-derived mean standardized uptake value (SUVmean). Receiver operating characteristic (ROC) curve analysis was performed to evaluate the diagnostic performance of individual and combined parameters with area under the curve (AUC). ***Results:*** Among single parameters, ADC showed the highest diagnostic value (AUC = 0.7619), followed by SUVmean (AUC = 0.7024) and TPSA (AUC = 0.6905). PHI and PI-RADS showed lower performance, with AUCs of 0.6429 and 0.6786, respectively. Combining parameters improved diagnostic performance. The combination of TSPA+ADC+SUVmean achieved an AUC of 0.8214. A more complex model, including TPSA + PHI + ADC + SUVmean, achieved the highest AUC of 0.8333, but showed limited additional benefit. Other combinations, such as PHI + ADC + SUVmean, also showed well performance (AUC = 0.8059), suggesting potential flexibility in biomarker selection. ***Conclusion:*** This study demonstrates the synergistic diagnostic value of combining blood-based and PET/MR-derived imaging biomarkers for PCa assessment. The combination of ADC from DWI and SUVmean from PSMA PET imaging with the PHI or TPSA enables a more biologically comprehensive evaluation of prostatic lesions. Multimodal combinations significantly outperformed individual parameters. These findings support the clinical utility of compact diagnostic models in reducing unnecessary biopsies and enhancing diagnostic accuracy in PCa detection.

EP-0408

Enhancing Patient Selection for PSMA Radioligand Therapy: The Role of Dual-Tracer Imaging Biomarkers in Optimizing Outcomes for mCRPC

S. Xue*, H. Einspieler, S. Wen, M. Hacker, S. Rasul, X. Li;*
Division of Nuclear Medicine, Department of Biomedical Imaging and Image-guided Therapy, Vienna General Hospital, Medical University of Vienna, Vienna, AUSTRIA.

Aim/Introduction: PSMA radioligand therapy (PSMA-RLT) is a promising treatment for metastatic castration-resistant prostate cancer (mCRPC). However, variability in patient responses may stem from limitations in current patient selection criteria, which rely on a binary yes/no analysis of PSMA/FDG concordance. This study evaluates the potential of quantitative imaging biomarkers derived from dual-tracer PSMA/FDG PET/CT imaging to improve patient stratification and predict therapeutic response to PSMA-RLT. ***Materials and Methods:*** A retrospective analysis of 24 mCRPC patients who underwent PSMA and FDG PET/CT imaging prior to PSMA-RLT was conducted. Automated lesion and organ segmentation, combined with advanced imaging fusion techniques, were used to extract quantitative features from concordant and non-concordant lesions, including SUVmean, SUVmax, molecular tumor volume (MTV), total lesion glycolysis (TLG), and total lesion PSMA (TLP). Organ-based imaging features were derived from key organs such as the bone and liver. Decision tree analysis stratified patients into three response categories: non-responders, suboptimal responders, and optimal responders. ***Results:*** SUVmean from PSMA PET imaging was identified as the most significant predictor of therapeutic response, with a threshold of 11.3 g/mL distinguishing responders from non-responders. Concordant PSMA/FDG lesion features, such as volume and lesional FDG uptake, showed significant correlations with post-therapy PSA level changes. Organ-based metrics, including SUVmax, SUVmean, and Overlap SUVmean, demonstrated high predictive accuracy for distinguishing responders from non-responders, achieving accuracies of 95.83%, 95.45%, and 87.50%, respectively. ***Conclusion:*** Dual-tracer imaging biomarkers, particularly SUVmean of PSMA and FDG concordant metrics, provide actionable insights for refining patient selection and stratifying response to PSMA-RLT. These findings support the transition from binary concordance criteria to a comprehensive, multi-metric approach for personalized treatment strategies. Further prospective studies with larger cohorts are needed to validate these biomarkers and facilitate their integration into clinical practice.

EP-0409

Is Dual-Time-Point PSMA-PET/CT a Predictive Tool for Response to PSMA Radioligand Therapy?

A. Weissensee*, A. D. Sidandy, N. Gözlügöl, R. Saiyed Alsheikh, F. Caobelli, R. Seifert, A. Rominger, A. Afshar-Oromieh;*
Department of Nuclear Medicine, Inselspital, Bern University Hospital, University of Bern, Bern, SWITZERLAND.

Aim/Introduction: Prostate cancer (PC) lesions often demonstrate an increase in PSMA-ligand uptake over time. However, the extent of this uptake varies between individuals. It remains unclear whether different metastasis types exhibit distinct temporal uptake patterns, or whether all metastases within a single patient

behave uniformly. This study aimed to investigate this question and to determine whether the intensity change of PSMA-ligand uptake on dual-time-point PET/CT serves as a predictive marker for response to [^{177}Lu]Lu-PSMA radioligand therapy ([^{177}Lu]Lu-PSMA-RLT). ***Materials and Methods:*** Twenty patients who underwent dual-time-point PSMA-PET/CT imaging prior to clinically indicated [^{177}Lu]Lu-PSMA-RLT were included in this retrospective analysis. SUVmax was measured separately for local PC lesions, lymph-node metastases, bone metastases, and organ metastases. These groups were compared regarding differences in SUVmax between standard and late scans (Kruskal-Wallis test with post-hoc Dunn's test). For each lesion type, a maximum of 10 lesions per patient were randomly selected. In an additional logistic regression analysis, changes in SUVmax (ΔSUVmax) between standard and late scans were assessed for correlations with long-term biochemical response to [^{177}Lu]Lu-PSMA-RLT, based on Prostate Cancer Working Group 3 (PCWG3) criteria. ***Results:*** Overall, we analyzed 383 PC lesions in 20 patients (15 local tumors, 188 bone metastases, 135 lymph node metastases and 45 organ metastases). Across all lesions the median SUVmax in late images was 16.1 % higher than in standard images (p<0.001). A Kruskal-Wallis test showed significant differences in relative ΔSUVmax depending on metastasis type (p=0.021). However, a post-hoc Dunn's test was unable to identify statistically significant, specific inter-group differences (p=0.078-0.424). Logistic regression showed a positive, but non-significant effect of relative ΔSUVmax on therapy response (p=0.752). In contrast, the SUVmax of the hottest measured lesion significantly predicted therapy response (OR = 1.14 per unit increase, 95% CI [1.04-1.34], p=0.029). ***Conclusion:*** Consistent with previous findings, PC lesions exhibited significantly higher PSMA-ligand uptake in late scans. However, the magnitude of this uptake increase between time-points (ΔSUVmax) neither differed significantly across PC lesion types nor correlated with response to [177Lu]Lu-PSMA-RLT. Notably, higher SUVmax values at standard time-point imaging were associated with an increased likelihood of biochemical response to [^{177}Lu]Lu-PSMA-RLT. In summary, SUVmax measurements from late scans appear to provide limited additional prognostic value compared to those obtained at standard time-point scans.

EP-0410

The added value of MRI to AI^{18}F-PSMA-BCH PET/CT in detection of clinically significant prostate cancer

J. Ma[1], *C. Wang*[1], *M. Wang*[2], *C. Ren*[1], *Z. Huang*[1], *M. Liu*[2], *L. Huo*[1];
[1]*Peking union medical college hospital, Beijing, CHINA,* [2]*Beijing hospital, Beijing, CHINA.*

Aim/Introduction: PSMA PET/CT has shown great potential in diagnosis and biopsy guidance in clinically significant prostate cancer (csPCa). However, false positive and false negative lesions occur in a small group of patients. MRI has high accuracy in diagnosis of csPCa and may improve the performance of PSMA PET/CT. This study aims to investigate the added value of MRI to AI^{18}F-PSMA-BCH PET/CT in diagnosis and targeted biopsy of csPCa. ***Materials and Methods:*** This is a retrospective analysis of a prospectively collected dataset. AI^{18}F-PSMA-BCH PET/CT and MRI were performed within 3 months in patients with suspected csPCa and the results were provided to surgeons for targeted biopsy. Then patients received systematic biopsy (if PSMA PET/CT and MRI were both negative), targeted biopsy (only if intraoperative frozen section pathology was positive) or targeted biopsy plus systematic biopsy. Pathology of PSMA PET/CT targeted biopsy, MRI targeted biopsy and systematic biopsy were recorded. The primary outcome was whether the addition of MRI improved the accuracy of diagnosis. The secondary outcome is whether an MRI-targeted biopsy changed the result of biopsy based on PSMA PET/CT. ***Results:*** 142 patients were included in this analysis. The incidence of csPCa in PRIMARY score 1-5 is 0 (0/12), 8.3% (3/36), 18.2% (2/11), 64.3% (18/28), 92.7% (51/55). Patients with a PRIMARY score equal or more than 3 were classified as positive. The sensitivity, specificity, positive predict value (PPV) and negative predict value (NPV) of PSMA PET/CT are 95.9%, 51.5%, 75.5% and 93.8%. Because of the low incidence of csPCa in PRIMARY score 3-4 and a large number of false positive patients, we assigned patients without suspected malignancy in MRI as negative. 11 patients were changed to the negative group. Only 1 of 11 patients had csPCa. The sensitivity, specificity, PPV, and NPV of the new model were 94.6%, 80.9%, 84.3%, and 93.2%. The specificity increased significantly (p=0.002) while the sensitivity remained the same (p=1.000). When adding MRI targeted biopsy during the surgery, the pathology was changed only in 1 patient, from ISUP 2 to ISUP 3. ***Conclusion:*** Addition of MRI will improve the diagnosis accuracy of PSMA PET/CT and should be performed in patients with PRIMARY score 3 and 4. An MRI targeted biopsy cannot change the result of biopsy based on PSMA PET/CT.

EP-0411

5-Alpha Reductase Inhibitor Therapy Increases Benign Prostatic PSMA Uptake: Implications for Primary Prostate Cancer Imaging

M. Celli[1], *R. Gunelli*[2], *F. Ferroni*[1], *M. Costantini*[2], *A. Prochowski Iamurri*[1], *L. Fantini*[1], *E. Fragalà*[2], *I. Marini*[1], *D. Bezzi*[3], *V. Rossetti*[1], *M. Sansovini*[1], *S. Nicolini*[1], *E. Giunta*[1], *S. Bellia*[1], *V. Di Iorio*[1], *F. Foca*[1], *F. Matteucci*[1], *P. Caroli*[1];
[1]*IRCCS Istituto Romagnolo per lo Studio dei Tumori (IRST) "Dino Amadori", Meldola (FC), ITALY,* [2]*Morgagni Pierantoni Hospital, Romagna Local Health Service, Forlì (FC), ITALY,* [3]*Bufalini Hospital, Romagna Local Health Service, Cesena (FC), ITALY.*

Aim/Introduction: Physiologic PSMA uptake in benign prostate tissue may affect PET interpretation in suspected prostate cancer (PCa). This interim analysis of the BIOPSTAGE trial assessed uptake patterns across benign histologies and examined the influence of 5-alpha reductase inhibitor (5ARI) therapy. ***Materials and Methods:*** Ninety-six men with suspected PCa underwent [^{68}Ga] Ga-PSMA-11 PET/CT and mpMRI before biopsy. SUVmean values were measured in histologically benign tissue, including atrophy, inflammation, and benign prostatic hypertrophy (BPH). Uptake distributions were compared across tissue types and between 5ARI users and non-users using the Mann-Whitney U test. ***Results:*** Median SUVmean values were 2.20 (IQR: 2.10-2.40) for atrophy, 2.20 (IQR: 1.90-2.70) for inflammation, and 2.30 (IQR: 2.10-2.50) for BPH. Inflammation showed the greatest variability in uptake values. Among patients receiving 5ARI therapy (n=14), SUVmean was significantly higher than in non-users (2.40 vs. 2.20; p = 0.032). While no csPCa lesions were missed in this subgroup during interim analysis, increased background uptake—especially in inflamed or hormonally modulated tissue—may reduce lesion-to-background contrast and affect interpretation confidence. ***Conclusion:*** PSMA uptake in benign prostate tissue is generally low, but inflammation introduces notable variability. 5ARI therapy is associated with a modest but statistically significant increase in background uptake. These factors should be considered when interpreting PSMA PET and applying uptake-based thresholds in biopsy planning.

EP-0412

MRI characterization of 18F-PSMA 1007 bone uptake on integrated/hybrid PET/MRI exam in prostate cancer patients.

J. Vela León[1], *J. García*[2], *A. Compte*[2], *L. Pinilla*[2], *L. Mont-Castro*[2], *S. Ruiz*[2], *M. Soria*[2], *P. Bassa*[2], *E. Riera*[2];
[1]*Hospital Universitario de Canarias, Tenerife, SPAIN,* [2]*ASCIRES CETIR BCN, Barcelona, SPAIN.*

Aim/Introduction: To evaluate the MRI characteristics of ^{18}F-PSMA 1007 bone uptake sites of PET/MRI studies performed in prostate cancer patients. ***Materials and Methods:*** Prospective study

including the first 100 consecutive patients diagnosed with prostate cancer: 41 for patient staging and 59 for recurrence detection purposes. Simultaneous acquisition on PET/MRI (SIGNA-GE) equipment, 1h. after IV administration of 296±10%MBq of 18F-PSMA 1007: - Prostate study (20min): PET+MR with DIXON, T1, T2, DWI, DCE sequences. - Whole-body study (30 min): PET+MR with DIXON, T1, T2, DWI, STIR sequences. Independent assessment of the PET study by a Nuclear Physician, and MRI by a Radiologist, reaching consensus for the integrated PET/MRI findings. ***Results:*** For the per-patient analysis: 52/100 (52%) of patients presented with bone uptake of ^{18}F-PSMA 1007, 16 (31%) in staging and 36 (69%) in recurrence detection studies. Of these, MRI confirmed the presence of lesions in 15 (28%) of patients, corresponding to bone malignancy in 10 (67%) and benign origin in 5 (33%). Of these patients with bone metastases, 4 (40%) were detected in staging study and 6 (60%) in recurrence study; one lesion only was shown in 20% of patients, two lesions in 20%, and three lesions in 60%. For the per-^{18}F-PSMA 1007 uptake analysis: We found 56 bone uptake sites of ^{18}F-PSMA 1007: 18 in pelvis, 5 in lumbar spine, 8 in thoracic spine, 3 in femur, 5 in sternum, 1 in clavicle, 1 in scapula, 15 in ribs. Of these, 33 sites of 18F-PSMA 1007 bone uptake did not correspond with MRI findings: 13 in pelvis, 3 in lumbar spine, 3 in thoracic spine, 1 in femur, 1 in sternum, 12 in ribs. In 18 cases of ^{18}F-PSMA 1007 uptake, MRI corresponded with bone metastases: 5 in pelvis, 2 in lumbar spine, 4 in thoracic spine, 1 in femur, 4 in sternum, 1 in clavicle, 1 in scapula. In 5 cases of ^{18}F-PSMA 1007 uptake, MRI corresponded with characteristic benign lesions: 1 femoral enchondroma, 1 thoracic haemangioma, 1 rib fibrous dysplasia, 2 rib fractures. ***Conclusion:*** The evaluation of the MRI component of the integrated/hybrid PET/MRI scan allowed a better characterization of the frequent bone uptake sites of ^{18}F-PSMA 1007 in our series (52% of patients), with lesion confirmation in 28% of patients, and 67% of them corresponded with bone metastases.

EP-0413

Feasibility of Single-Time-Point Dosimetry from Voxel-Wise TAC Estimation Following 177Lu-PSMA Therapy

M. Alhashim[1], *E. Alwuhaib*[1], *N. Ibrahim*[1], *M. Alabedi*[1], *H. Dadgar*[2], *X. Hong*[3], *M. Azimi*[4], *S. Rezaei*[5], *H. Arabi*[6];
[1]*King Fahad Specialist Hospital Dammam, Dammam, SAUDI ARABIA,* [2]*Cancer Research Center, RAZAVI Hospital, Imam Reza International University, Mashhad, IRAN, ISLAMIC REPUBLIC OF,* [3]*School of Biomedical Engineering, Southern Medical University, Guangzhou, CHINA,* [4]*Department of Medical Radiation Engineering, Shahid Beheshti University, Tehran, IRAN, ISLAMIC REPUBLIC OF,* [5]*Department of Nuclear Medicine, Medical School, Tabriz University of Medical Sciences, Tabriz, IRAN, ISLAMIC REPUBLIC OF,* [6]*Division of Nuclear Medicine and Molecular Imaging, Diagnostic Department, Geneva University Hospital, Geneva, SWITZERLAND.*

Aim/Introduction: Due to the challenges of performing multi-time-point imaging in routine personalized dosimetry for radioligand therapy, interest in single-time-point (STP) dosimetry has increased—especially approaches that estimate time-activity curves (TACs) and absorbed doses from a single SPECT/CT scan [1-2]. However, the reliability of STP methods remains under investigation, with limited validation studies available. We assessed retrospectively, whether voxel-wise TACs derived from a single imaging time point could accurately approximate the full TAC for dosimetry following ^{177}Lu-PSMA therapy. ***Materials and Methods:*** We analyzed data from 15 patients treated with ^{177}Lu-PSMA. SPECT/CT scans were acquired at 24, 48, and 72 hours post-injection (p.i.). For each patient, voxel-wise TACs were generated using data from all three time points. We then evaluated the feasibility of reconstructing full 3-time-point TACs based on each individual time point and assessed the accuracy of the resulting dose estimations. The predictive performance of each time point (24 h, 48 h, and 72 h p.i.) was systematically analyzed, IRB: RAD0343. ***Results:*** The TACs generally followed a mono-exponential decay pattern, though with notable inter-patient variability. Among the three time points, the 48 h p.i. scan yielded the most reliable approximation of the full TAC, enabling accurate dose estimation for the majority of voxels (typically with errors <30%). The 72 h p.i. scan also produced acceptable estimates, albeit with slightly reduced performance in some regions. In contrast, the 24 h p.i. scans were less predictive of the full TAC. ***Conclusion:*** We demonstrated the feasibility of STP dosimetry using a single SPECT/CT scan at 48 h p.i. in patients undergoing ^{177}Lu-PSMA therapy. Offering a practical balance between clinical convenience and dosimetric accuracy. The 72 h scan remains a valid alternative when 48 h imaging is not feasible. Our findings provide valuable insights for the clinical implementation of simplified STP dosimetry protocols; however, further validation with larger patient cohorts and additional radiopharmaceuticals is needed. ***References:*** 1. Hänscheid, H., Lapa, C., Buck, A. K., Lassmann, M., & Werner, R. A. (2018). Dose Mapping After Endoradiotherapy with ^{177}Lu-DOTATATE/DOTATOC by a Single Measurement After 4 Days. Journal of nuclear medicine : official publication, Society of Nuclear Medicine, 59(1), 75-81. https://doi.org/10.2967/jnumed.117.193706 2. Brosch-Lenz, J., Delker, A., Völter, F., Unterrainer, L. M., Kaiser, L., Bartenstein, P., Ziegler, S., Rahmim, A., Uribe, C., & Böning, G. (2023). Toward Single-Time-Point Image-Based Dosimetry of ^{177}Lu-PSMA-617 Therapy. Journal of nuclear medicine : official publication, Society of Nuclear Medicine, 64(5), 767-774. https://doi.org/10.2967/jnumed.122.264594.

EP-0414

[68Ga]Ga-PSMA PET/CT response evaluation after metastasis- directed therapy (MDT) in Low Burden Metastatic Prostate Cancer

M. Usmani, *K. al Riyami, A. Jain, A. Al Busaidi, N. Pervaiz, B. Mir Khan, Z. Al-Mandhari;*
Sultan Qaboos Comprehensive Cancer Care and Research Center (SQCCCRC), University Medical City, Muscat, OMAN.

Aim/Introduction: De novo metastatic prostate cancer accounts for 5-10% of all prostate cancer (PC) diagnoses but it is responsible for nearly 50% of PC-related deaths. There is no current agreement on the response assessment after metastatic directed therapy (MDT) in metastatic prostate cancer. The aim of this study is to assess the feasibility of [^{68}Ga]Ga-PSMA PET/CT in response assessment in low burden metastatic prostate cancer after MDT. ***Materials and Methods:*** A total 19 patients (mean age, 70.6±8.9 years) de Novo low burden metastatic prostate cancer treated with radical doses of radiotherapy to primary and metastatic sites along with Luteinizing Hormone Releasing Hormone (LHRH) ± Abiraterone (with Prednisolone) or Enzalutamide. Baseline and follow-up [^{68}Ga]Ga-PSMA PET/CT after 6-9months were performed. Visual and quantitative PET image analyses were performed, according to Response Evaluation Criteria in PSMA imaging (RECIP1.0). The PSMA-PET results categorize patients into complete response (CR), partial response (PR), stable disease (SD), and progressive disease (PD). Biochemical response was assessed by PSA level. ***Results:*** Baseline [^{68}Ga]Ga-PSMA PET/CT show prostate lesion with SUV max 27.67±20.31, regional nodes are positive in 16/19 (84%), extra pelvic lymph nodes involvement noted in 6 (31%), seminal vesicle involvement seen in 7 (37%) patients. Four patients had bone metastasis in; left iliac, left pubis, ribs, right humerus with right iliac crest. Median initial PSA was 31.7 ng/ml (range = 13-182). Median follow up was 21.6 months (range = 7-37). Follow-up [^{68}Ga]Ga-PSMA show complete response in 16 (84%) patients and partial response in 3 (16%) patients. Out of 19 patients, 8 (42%) patients had undetectable PSA (< 0.006 ng/ml), 10 (53%) had PSA range from 0.006 to 0.2 ng/ml and 1 (5%) had PSA of > 0.2 ng/ml. ***Conclusion:*** Our initial experience suggests that [^{68}Ga]Ga-PSMA

PET imaging may offer metastatic directed therapy and PSMA PET- based response assessment is a simple and easy method and can be used as a response biomarker. It refines assessment of therapeutic efficacy, detects recurrence or new lesions early, and guides further treatment strategies, more timely intervention and offering a pathway to more individualized care.

EP-0415

Defining Patient Selection for Lutetium-177[177Lu]Lu-PSMA Radioligand Therapy: Evaluating the Probability of FDG PET/CT to Identify Discordant Disease according to PSMA PET/CT SUVmean?

J. Weindler, *J. P. Buteau, N. Papa, M. S. Hofman;*
Prostate Cancer Theranostics and Imaging Centre of Excellence; Molecular Imaging and Therapeutic Nuclear Medicine, Cancer Imaging, Peter MacCallum Cancer Centre, Melbourne, AUSTRALIA.

Aim/Introduction: The TheraP study utilized both PSMA- and FDG-PET/CT to determine eligibility for Lutetium-177 [177Lu]Lu-PSMA (LuPSMA) therapy for patients with metastatic castration-resistant prostate cancer (mCRPC). 31% of patients were excluded in total including 18% owing FDG-discordant (FDG-positive PSMA-negative) disease. Biomarker analysis identified PSMA-PET SUVmean ≥10 as a predictive and prognostic biomarker for PSA response and overall survival respectively. High PSMA-PET SUVmean may be a marker of a homogeneous phenotype where the likelihood of FDG-discordant lesions is low. We hypothesized that utility of FDG-PET/CT in identifying FDG-discordant disease is limited in patients with high PSMA-PET SUVmean. ***Materials and Methods:*** In this retrospective single-center study, we included consecutive patients with mCRPC referred for LuPSMA therapy from 01 April 2021 to 31 October 2024 and underwent dual-tracer PET-imaging with PSMA and FDG within 15 days. Included patients had PSMA-positive disease on PSMA-PET/CT, defined by at least one lesion with PSMA uptake above liver level. PSMA-PET SUVmean was measured using MIM Software (SUV≥3 threshold). FDG-discordant lesions were patient-based and defined as ≥1 lesion with uptake greater than liver on FDG-PET/CT and lower than liver on PSMA-PET/CT. Logistic regression was used to predict the probability of FDG-discordance according to PSMA-PET SUVmean with a chi-square test to evaluate a difference in discordance proportion below and above an SUVmean of 10. ***Results:*** 490 patients were referred and underwent dual-tracer PET-imaging of which 480 patients had PSMA-avid-disease (98 %). FDG-discordance was present in 89/480 (19%) of patients with PSMA-positive disease. Median PSMA-PET SUVmean was 7.9 (IQR: 6.3 - 10.5). In patients with PSMA-PET SUVmean ≥10, FDG-discordance was observed in 8/139 patients (5.8%) versus 81/341 (24%) in those with PSMA-PET SUVmean <10 (p<0.001). The probability of FDG-discordance for a patient with PSMA-PET SUVmean of 5 was 44% (95%CI: 35%-53%) versus 8.8% (95%CI: 5.1%-15%) if the PSMA-PET SUVmean was 10. FDG-discordant lesions were present in bone (74%), nodes (30%), liver (14%), and other organs (2.2 %). ***Conclusion:*** FDG-discordance is inversely associated with PSMA-PET SUVmean. Patients with high PSMA-PET SUVmean (≥ 10) have a substantially lower rate of FDG discordance.

EP-0416

Intra-Individual Head-to-head Comparison of ^{18}F-PSMA-1007 vs ^{68}Ga-PSMA-11 PET-CT in Assessment of Prostate Carcinoma. A PRostate Imaging with ^{18}F-PSMA-1007 Study in Malaysia (PRISM-My).

M. Abdul Onny[1,2], *M. Mohd Rohani*[3], *T. Selvarajoo*[4,5], *M. Ahmad Fadzil*[1], *Z. Md Safee*[1], *N. Razali*[1], *M. Mahamood*[1], *M. Said*[1], *N. Yaacob*[1], *R. Abdul Rahman*[1], *N. Mat Ail*[1], *S. Sukar*[1], *M. Wakiran*[1], *M. Mat Jusoh*[6], *S. Jamaludin*[4], *N. Ali*[1], *S. Amir Hassan*[3], *C. Ng*[5];
[1]National Cancer Institute Malaysia, Putrajaya, MALAYSIA, [2]University Medical Center Groningen, Groningen, NETHERLANDS, [3]Hospital Kuala Lumpur, Kuala Lumpur, MALAYSIA, [4]Advance Medical & Dental Institute, Universiti Sains Malaysia, Kepala Batas, MALAYSIA, [5]Hospital Sultanah Aminah, Johor Bahru, MALAYSIA, [6]Hospital Sultan Idris Shah, Serdang, MALAYSIA.

Aim/Introduction: Prostate cancer (PCa) is ranked as the second most frequent cancer in male globally and the third most common in Malaysia. Imaging modalities play a big role in the evaluation of disease extent and Nuclear Medicine armamentarium such as bone scintigraphy and recently, Prostate Specific Membrane Antigen PET-CT (PSMA-PET) are pivotal in the management of PCa. Traditionally, in Malaysia, PSMA has always been tagged with ^{68}Ga. However, short half-life and low yield of radioisotope has impeded the widespread usage of PSMA-PET in Malaysia. Recently, usage of ^{18}F-based PSMA has been explored as an alternative and a first in Malaysia clinical trial was conducted to intra-individually compare normal organ biodistribution and lesional uptake between ^{68}Ga-PSMA-11 and ^{18}F-PSMA-1007 PET-CTs. ***Materials and Methods:*** A prospective interventional study was conducted in the National Cancer Institue Malaysia between March 2022 to December 2024. A total of 37 patients with histopathologically proven PCa were recruited and undergo ^{68}Ga-PSMA-11 and ^{18}F-PSMA-1007 PET-CTs within 30-days of the first PET-CT. Both radiopharmaceuticals were produced in-house, in compliance with local regulatory bodies and GMP standards. Image acquisition was performed using GE Discovery 690 MIDR. Image interpretation was done by 3 Nuclear Medicine physicians. Descriptive analysis was used to assess lesion identification whereas difference and concordance between SUVmax of ^{68}Ga-PSMA-11 and ^{18}F-PSMA-1007 was determined using repeated measure ANOVA and Wilcoxon Sign-Ranked Test. ***Results:*** Majority of patients (89.2%) were of Gleason score ≥7 and of intermediate or higher risk stratification. Median PSA level was 6.58ng/ml (IQR 23.63). The highest mean SUVmax and absorbed dose were recorded in the kidney; 27.37mg/ml and 0.09mGy/MBq respectively followed by the salivary glands, spleen and liver. Normal organ SUVmax was predominantly higher on ^{18}F-PSMA-1007 PET-CT except notably the kidney. There were 90 discordant lesions identified, with ^{18}F-PSMA-1007 PET-CT outperforming ^{68}Ga-PSMA-11 PET-CT, most evident at the prostatic bed and regional nodes. ^{18}F-PSMA-1007 PET-CT showed significantly higher uptake and was able to localize smaller lesions (2-3mm). Significantly more bone uptake on ^{18}F-PSMA-1007 PET-CT, likely attributed to unspecific bone uptake (UBU). More importantly, all likely pathological lesions detected using ^{68}Ga-PSMA-11 were also detected with ^{18}F-PSMA-1007 PET-CT. ***Conclusion:*** This study showed that ^{18}F-PSMA-1007 is comparable to the ^{68}Ga-PSMA-11 PET-CT in its organ biodistribution and lesion detection with the added value of higher uptake and less urinary excretion thus improving lesion detection at the prostatic bed and regional nodes. However, the inadvertent findings of UBU may complicate image interpretation.

EP-0417

Low sensitivity of mpMRI and 18F-PSMA-1007 PET/CT in localization of Primary Prostate cancer

A. Loimaala[1], *O. Kerro*[2], *T. Mirtti*[3], *M. Paloranta*[4], *T. Koivula*[5], *A. Rannikko*[6];
[1]Helsinki University Hospital, Diagnostic Center, Helsinki, FINLAND, [2]Helsinki University Hospital, Urology, Stomac center, Helsinki, FINLAND, [3]Helsinki University Hospital, Diagnostic Center, Pathology, Helsinki, FINLAND, [4]Helsinki University, Helsinki, FINLAND, [5]Helsinki University Hospital, Diagnostic Center, Nuclear medicine, Helsinki, FINLAND, [6]Helsinki University Hospital, Stomac center, Urology, Helsinki, FINLAND.

Aim/Introduction: Accurate local staging is critical for treatment planning and prognosis in prostate cancer (PCa). Multiparametric magnetic resonance imaging (mpMRI) and ^{18}F-PSMA-1007 PET/CT have high specificity for detection of extraprostatic disease and seminal vesicle invasion (SVI), their sensitivity and agreement is not

well established in localization of PCa in the prostate bed. Thus, our aim was to assess the diagnostic performance of mpMRI and ^{18}F-PSMA-1007 PET/CT in comparison to histopathology (ground truth) and detection of seminal vesicle invasion (SVI) in men with high risk primary PCa (GG 3-5, cT2-cT3, rT2-3) undergoing robot-assisted radical prostatectomy (RARP). ***Materials and Methods:*** Between March 2022 and January 2024, 40 treatment-naïve men with biopsy-proven high-risk PCa undergoing mpMRI and ^{18}F-PSMA-1007 PET/CT before RARP were prospectively enrolled. The study was approved by the institutional ethics committee, all patients gave written informed consent. Men with clinically significant (csPCa) undergoing RARP and extended pelvic lymph node dissection (ePLND) were eligible for the study. The mpMRI was performed at 3 T (Siemens Skyra 3T) for the men in accordance with established guidelines and included high-resolution T2- weighted, diffusion-weighted, and apparent diffusion coefficient sequences. ^{18}F-PSMA-1007 PET/CT was performed on a Siemens Biograph 64 or a GE MI 128 scanner using standard low-dose-protocol. RARP ± ePLND was performed by an experienced urologist using the da Vinci Xi platform. One experienced urogenital pathologist who was blinded to the imaging results evaluated RP specimens according to ISUP protocols. ***Results:*** RARP ± ePLND was performed to 30 men, 10 men received antiandrogen therapy. Five men had PCa only either the right or the left prostate bed, and seminal vesicle invasion was found in eight men. The per-segment sensitivity for mpMRI and PSMA PET was 58% (50-66%) and 68% (60-74%) (p= 0.014) and specificity 93% (87-96%) and 80% (73-86%) (p=0.0015), respectively. Positive predictive values (PPV) for MRI and PSMA PET were 90% vs. 79%, and negative predictive values (NPV) 67% vs. 69%, respectively (p>0.05 for both). Per-segment agreement (kappa) for localizing PCa in the prostate bed for mpMRI was 0.50 and 0.47 for ^{18}F-PSMA-1007 PET/CT, respectively. ***Conclusion:*** Both imaging methods have quite low sensitivity in primary diagnosis of PCa to show the precise location of the PCa focus but ^{18}F-PSMA-1007 PET/CT performs slightly better. MpMRI has significantly higher specificity compared to PSMA PET. Agreement between the imaging methods and the histopathology was fair.

EP-0418

Effect of different scan duration on image quality and quantification in long axial field-of-view PSMA-PET/CT

L. Airo' Farulla*, A. F. Scarale, G. Cabrini, S. Capitanio, A. Franchini, E. Gay, A. Spataro, K. Shyli, C. Rossetti;*
ASST Grande Ospedale Metropolitano Niguarda, Milan, ITALY.

Aim/Introduction: Long axial field of view (LAFOV) positron emission tomography/computed tomography (PET/CT) offers improvements in sensitivity and image quality, but minimum acquisition duration required to preserve these benefits with prostate-specific membrane antigen (PSMA)-ligands remain unclear. We evaluated whether rapid acquisitions (30 sec-6 min) on a LAFOV PET/CT yield lesion detectability and image quality that are non-inferior to the standard 10-min protocol in prostate cancer (PCa) patients. ***Materials and Methods:*** In this single-center retrospective study, 39 PCa patients underwent LAFOV PSMA-PET/CT (31/39 with [^{68}Ga]PSMA-11, 8/39 with [^{18}F]DCFPyl). Inclusion criteria: histologically-proven PCa; age ≥ 18 years; clinical indication for PSMA-PET/CT; available 10-minute list-mode acquisition; and at least one measurable PSMA-avid primary lesion. The 10-min acquisitions were reconstructed into 30 sec, 1, 2, 3, 4, 5, and 10 min frames. For each reconstruction we collected semiquantitative parameters [e.g. tumour-to-background ratio (TBR), or signal-to-noise ratio (SNR)], and three blinded nuclear medicine physicians rated overall image quality on a 5-point Likert scale. Non-inferiority versus the 10-min reference was tested by two-one-sided t-tests (TOST) with margins ΔTBR = -0.3, ΔSNR = -10, ΔLikert = -0.5; analyses were repeated by clinical setting. ***Results:*** In the overall cohort (n = 39), rapid acquisitions preserved quantitative and qualitative metrics. TBR remained non-inferior at every time point (e.g. 30 s: 4.84 ± 5.80 vs 10 min: 4.67 ± 5.72; Δ -0.17; p < 0.05). Mean image-quality Likert scores were non-inferior at 5 minutes (4.75 ± 0.38 vs 5.00 ± 0.00; Δ -0.25; p < 0.001). When stratified by clinical setting, staging group (n = 13) showed non-inferior TBR at every reconstruction, while SNR and Likert non-inferiority were reached only at 5 minutes (Likert: 4.59 ± 0.45 vs 5.00 ± 0.00; p < 0.001). In the PSA-persistence group (n = 7), TBR and SNR were non-inferior from 2 minutes (TBR: 4.69 ± 6.15 vs 4.67 ± 5.72; p = 0.023), and Likert non-inferiority was attained at 3 minutes (4.29 ± 0.49 vs 5.00 ± 0.00; p < 0.001). Among biochemical recurrence patients (n = 19), quantitative metrics were non-inferior from 2 minutes (SNR: 39.2 ± 95.4 vs 61.7 ± 74.4; p = 0.080) and Likert score at 5 minutes (4.88 ± 0.25 vs 5.00 ± 0.00; p < 0.001). ***Conclusion:*** LAFOV PSMA-PET/CT acquisition lasting 3-5 minutes maintain lesion conspicuity, semiquantitative accuracy and reader-perceived image quality comparable to the 10-minute reconstruction.

EP-0419

PI-RADS scoring in long-axial-field-of-view PSMA-PET/CT: effects of scan duration on diagnostic confidence

L. Airo' Farulla*, A. F. Scarale, A. Spataro, E. Gay, A. Franchini, S. Capitanio, G. Cabrini, K. Shyli, C. Rossetti;*
ASST Grande Ospedale Metropolitano Niguarda, Milan, ITALY.

Aim/Introduction: Longaxialfieldofview (LAFOV) PSMAPET/CT markedly enhances lesion detectability in prostate cancer (PCa) patients, but requires prolonged acquisition duration. The Prostate Imaging Reporting and Data System (PIRADS) is a validated 5point scale to grade the likelihood of clinically significant prostate cancer on imaging. A noninferiority study was performed to identify the shortest LAFOV PSMAPET/CT acquisition duration that yields PIRADS assessments equivalent to the standard 10minute protocol. ***Materials and Methods:*** We retrospectively reviewed 39 prostate cancer patients (mean age 68 ± 8 years; ISUP grade 2-5) who underwent LAFOV PSMAPET/CT between January and April 2025, using [^{68}Ga]PSMA11 (n = 31) and [^{18}F]DCFPyL (n = 8) radiotracers. Inclusion criteria were: histologically-proven PCa, age ≥ 18, clinical indication for PSMAPET/CT, available 10min listmode acquisition, and at least one measurable primary lesion. Acquisitions were reconstructed offline into 30 s, 1, 2, 3, 4, 5, and 10 min frames using vendorstandard OSEM with timeofflight and pointspreadfunction modelling. Regions of interest were drawn on the dominant intraprostatic/prostatic bed lesion and normal liver parenchyma to derive SUVmax and background SUVmean, lesion-to-background contrast was expressed as TBR. Three nuclear medicine physicians, blinded to frame duration, independently scored image quality and diagnostic confidence for the primary PCa lesion using PIRADS (1-5). We computed perpatient mean PIRADS and lesion TBR at each timepoint. Interreader agreement was assessed by weighted Cohen's κ. Noninferiority versus the 10min reference (Δ = -0.5 PIRADS units) was tested with twoonesided Wilcoxon signedrank tests. Subgroup analyses were performed by clinical setting: staging (n = 13), PSA persistence (n = 7), and biochemical recurrence (n = 19). ***Results:*** Average TBR at 10 min was 4.67 ± 5.72; at 3 min it was 4.53 ± 5.65 (Δ = -0.14; p < 0.05), confirming noninferiority of lesion conspicuity. PIRADS mean rose from 3.45 ± 0.82 at 3 min to 5.00 ± 0.00 at 10 min; twoonesided Wilcoxon tests demonstrated noninferiority at ≥ 3 min (p_lower < 0.0001). Interreader κ for PIRADS increased from 0.65 at 30 s to 0.66 at 3 min and 0.81 at 5 min. In staging patients, TBR noninferiority held at all times, but PIRADS required ≥ 5 min (4.59 ± 0.45 vs 5.00; p_lower < 0.001). In PSA persistence, TBR and PIRADS were noninferior from 1 min (PIRADS_mean 4.14 ± 0.52; p_lower < 0.001). In recurrence, noninferiority was reached at 1-2 min for PIRADS (3.95 ± 0.60 vs 5.00; p_lower < 0.01) but overscoring emerged at ≥ 3 min. ***Conclusion:*** LAFOV

PSMAPET/CT acquisitions lasting 3 minutes preserve PIRADS scoring equivalent to the 10minute standard. Tailoring scan duration by clinical scenario (1-2 min for PSA persistence; ≥ 5 min for staging) can optimize workflow and patient comfort without compromising diagnostic confidence.

EP-0420

Clinical Impact of Repeated 18F-PSMA-1007 PET/CT in the Longitudinal Follow-Up of Prostate Cancer Patients in Sub-Saharan Africa

W. Olwit, *K. Makhdomi, M. Mwania, P. K. Loyal, J. Nyamari, S. Nguku;*
Aga Khan University Hospital Nairobi, Nairobi, KENYA.

Aim/Introduction: Prostate cancer is the most common malignancy among men in Kenya, with a significant proportion presenting at advanced stages. Accurate post-treatment surveillance is critical for detecting recurrence, guiding therapy, and improving outcomes. 18F-PSMA-1007 PET/CT has demonstrated high diagnostic accuracy in prostate cancer imaging, but its longitudinal utility in follow-up remains underexplored in sub-Saharan Africa.We aimed to evaluate the clinical utility of repeated 18F-PSMA-1007 PET/CT imaging in the follow-up of prostate cancer patients at Aga Khan University Hospital, Nairobi, focusing on treatment impact, prognostic relevance, and disease monitoring. ***Materials and Methods:*** This retrospective study included 150 prostate cancer patients who underwent at least two 18F-PSMA-1007 PET/CT scans between June 2020 and February 2025. Clinical data, PSA levels, Gleason scores, and imaging findings were analyzed. Treatment changes following imaging, disease recurrence patterns, and survival outcomes were assessed. Multivariable Cox regression was used to identify prognostic factors. ***Results:*** The mean patient age was 71.0 years (42-93). Most patients presented with advanced disease (40% metastatic, 35% locally advanced). The initial mean PSA was 113.8 ng/mL, and 18% of patients had ISUP grade 5 tumors. Hormonal therapy was the most common initial treatment (48%). Repeat 18F-PSMA-1007 PET/CT scans led to treatment changes in 35.1% of cases, including initiation of systemic therapy or radiotherapy. At first follow-up, radiologic improvement or stability was observed in over 67% of patients. Disease progression remained detectable in later scans, with 33.3% of third or subsequent scans prompting further management changes. Progression-free survival was significantly associated with ISUP grade, SUVmax, PSA levels, and imaging response. ***Conclusion:*** Repeated 18F-PSMA-1007 PET/CT imaging plays a valuable role in the longitudinal management of prostate cancer, influencing clinical decisions, monitoring therapeutic response, and offering prognostic insights. These findings support its integration into routine follow-up protocols, particularly in patients with biochemical recurrence or ambiguous disease trajectories. Prospective studies are warranted to define optimal imaging intervals and refine its prognostic applications.

EP-0421

Prognostic Utility of Dynamic PSMA PET/CT and Kinetic Modeling with LAFOV in Advanced Prostate Cancer

A. Di Giorgio[1], *I. Brusa*[2], *D. Dall'Olio*[3], *V. Mollica*[4], *F. Massari*[3,4], *M. Rapa*[1], *M. Assenza*[5], *P. Castellucci*[2], *S. Fanti*[1,2], *A. Farolfi*[2];
[1]*Nuclear medicine, Alma Mater Studiorum University of Bologna, Bologna, ITALY,* [2]*Nuclear Medicine, IRCCS Azienda Ospedaliero-Universitaria di Bologna, Bologna, ITALY,* [3]*Department of Medical and Surgical Sciences, University of Bologna, Bologna, ITALY,* [4]*Medical Oncology, IRCCS Azienda Ospedaliero-Universitaria di Bologna, Bologna, ITALY,* [5]*Professional Development and Implementation of Research in Health Professions Unit, IRCCS Azienda Ospedaliero-Universitaria di Bologna, Bologna, ITALY.*

Aim/Introduction: While PSMA PET/CT with short axial field-of-view (SAFOV) is accurate for staging advanced prostate cancer (PCa), its role in evaluating response to systemic therapies in hormone-sensitive (HSPC) and castration-resistant (CRPC) PCa remains less defined. Large Axial Field-of-View (LAFOV) scanners and dynamic acquisitions may enhance response evaluation through kinetic parameter analysis. The aim of this study is to evaluate the prognostic role of PSMA PET/CT, utilizing LAFOV and dynamic acquisition, by investigating kinetic parameters and tumor volume changes for assessing treatment response. ***Materials and Methods:*** Prospective, observational, Italian multicenter (CE AVEC: 737/2024/Oss/AOUBo) study consecutively enrolling ≥18-year-old males with histologically confirmed advanced PCa, scheduled for systemic therapies. All participants undergo a 60-minute dynamic PSMA PET/CT using LAFOV(FOV=194cm). The protocol involves intravenous radiopharmaceutical administration with continuous data acquisition. Baseline scans precede therapy, with follow-up scans during/after treatment. For comparison, dynamic 68-PSMA PET/CT scans from two patients with no history of prostate cancer (for other indications) were used. Kinetic analyses were performed on healthy organs (e.g., prostate, femur) as reference. Compartment models will quantify PSMA uptake and kinetics (K_1, k_2, k_3, K_i and distribution volume), correlated with treatment response and clinical outcomes alongside static PET metrics(SUVmax, total lesion volume). ***Results:*** From September 2024 to February 2025, we enrolled 10 patients with metastatic prostate cancer (median age 76 years, IQR 68-80) who were candidates for systemic therapy. The median baseline PSA level was 26 ng/mL(IQR 11-53). Subsequently, 2 of these patients underwent a second dynamic 68Ga-PSMA PET/CT scan at the end of therapy (median time 6 months). In the baseline PET scans, a total of 43 lesions were analyzed, including 11/43(26%) prostatic lesions, 18/43(42%) lymph node lesions, and 14/43(33%) bone lesions. At the end-of-treatment PET scans, 10 lesions were identified and analyzed, comprising 2/10(20%) prostatic lesions, 5/10(50%) lymph node lesions, and 3/10(30%) bone lesions. Kinetic parameter analysis revealed a significant difference in K_1 between bone lesions(p=0.03) and prostatic lesions(p=0.01). No significant difference was observed in SUVmax between these lesion types(p=0.08). k_2 and K_i showed significant differences between lesions and healthy tissue(p=0.003 and p=0.001, respectively). ***Conclusion:*** Preliminary data from this study indicate the potential of dynamic Ga-PSMA PET/CT with LAFOV to offer new insights into prostate cancer lesion biology through kinetic analysis. Further investigation in a larger cohort is needed to determine the role of these dynamic parameters in predicting treatment response and improving risk stratification.

EP-0422

The Value of VolumeIntensity-Sum and Other Volumetric PET Parameters in Predicting Progression in Patients with Metastatic Prostate Cancer Receiving Lu-177 PSMA Therapy

N. Unsal[1], *S. Karabulut*[1], *A. Aksu*[2], *G. Capa Kaya*[1];
[1]*Dokuz Eylul University Medical Faculty Hospital, Izmir, TÜRKIYE,* [2]*Izmir Katip Celebi University Medical Faculty Hospital, Departmant of Nuclear Medicine, Izmir, TÜRKIYE.*

Aim/Introduction: The aim of this study is to evaluate the role of quantitative parameters obtained from pre-treatment Ga-68 PSMA PET/CT in predicting disease progression after four cycles of Lu-177 PSMA therapy in patients diagnosed with metastatic castration-resistant prostate cancer (mCRPC). ***Materials and Methods:*** Patients who received four cycles of Lu-177 PSMA therapy between 2016 and 2024 and underwent both pre and post-treatment Ga-68 PSMA PET/CT were included. The presence of bone, pelvic lymph node, and distant soft tissue metastases on baseline PET/CT and treatment response per RECIP criteria were recorded. Pre-treatment images were analysed using LIFEx software. Tumour lesions were segmented using liver SUVmean as threshold. Extracted parameters included PSMA-BulkVolume, highest tumour SUVmax (tSUVmax), total PSMA tumour volume

(tPSMA-TV), total lesion PSMA (tTL-PSMA), sum of mean SUVs across lesions (Intensity_sum), and the VolumeIntensity_sum calculated as the sum of the product of voxel intensity and volume across all VOIs were computed. The association between these parameters and progression status (progressive vs. non-progressive disease) was statistically analysed. ***Results:*** Fifty-nine patients (mean age: 70±9 years) were evaluated. Twelve patients (20.3%) showed progression on post-treatment PET/CT. Bone metastases were present in 88.1%, pelvic lymph node metastases in 42.4%, and distant soft tissue metastases in 62.7%. No significant association was found between progression and location of metastases ($p > 0.05$). However, PSMA-BulkVolume ($p = 0.032$), tPSMA-TV ($p = 0.014$), tTL-PSMA ($p = 0.029$), VolumeIntensity_sum ($p = 0.004$), and Intensity_sum ($p = 0.006$) were significantly lower in the progressive group. Among these, VolumeIntensity_sum had the highest predictive value (AUC: 0.771; sensitivity: 70.2%; specificity: 83.3%). For tPSMA-TV, sensitivity and specificity were 51.1% and 100%, while for tTL-PSMA, they were 57.4% and 91.7%, respectively. ***Conclusion:*** In patients with mCRPC receiving Lu-177 PSMA therapy, quantitative parameters derived from baseline Ga-68 PSMA PET/CT demonstrated significant value in predicting disease progression. Among these, VolumeIntensity_sum showed the highest prognostic value. As this parameter directly accounts for PSMA activity intensity in each voxel, it may more accurately reflect tumour biological aggressiveness and thus has potential as an imaging biomarker. Moreover, to our knowledge, no previous study has evaluated the VolumeIntensity_sum parameter in PSMA PET, suggesting that our findings could provide a valuable contribution to the literature.

EP-0423

The role of Choline PET/CT in patients with recurrent prostate cancer and a negative PSMA-PET/CT

N. Gözlügöl[1], *H. Sari*[1], *A. Rominger*[1], *K. Strobel*[2], *A. Afshar-Oromieh*[1];
[1]*Inselspital Bern University Hospital, Bern, SWITZERLAND,*
[2]*Cantonal Hospital Lucerne, Lucerne, SWITZERLAND.*

Aim/Introduction: The sensitivity of PSMA-PET/CT for the detection of recurrent prostate cancer (rPC) is good at low PSA values and rapidly rises to >90% in patients with PSA >1.5 ng/ml. However, some PC (approx. 5-10%) do not sufficiently express PSMA. Currently, there exists no general rules on how to handle PSMA-PET-negative patients despite PSA >1.5 ng/ml. Some of these patients are referred to MRI, some are treated without a clear target and some remain untreated until a subsequent PSMA-PET/CT at higher PSA values is conducted. The aim of this evaluation was to assess the value of a choline PET/CT following a negative or equivocal PSMA-PET/CT in patients with rPC. ***Materials and Methods:*** We conducted a retrospective analysis incorporating data from 01/2017-04/2025 from two institutions. Eligible patients included those with rPC and a negative or equivocal [^{68}Ga]-Ga-PSMA-11 or [^{18}F]-F-PSMA-1007 PET/CT despite a PSA level of ≥ 1.5 ng/ml, who were subsequently referred for choline-PET/CT within a time window of 2 months. Two experienced nuclear medicine physicians reviewed both scans (choline and PSMA-PET/CTs) in a blinded consensus read. ***Results:*** Twelve patients met all inclusion criteria. The median PSA level at the time of PSMA-PET/CT was 4.2 ng/ml (range: 1.7 - 56.0). Among these, 9 patients had negative PSMA-PET/CT, while 3 were classified as equivocal. Following [^{18}F]F-Fluorocholine PET/CT scan, 7 out of 12 patients (58.3 %) demonstrated pathologic choline positive findings indicative of PC. In total, these 7 patients exhibited 12 pathological lesions, predominantly located in the prostatic bed and locoregional lymph nodes. ***Conclusion:*** Nearly 60% of patients with a negative or equivocal PSMA-PET/CT showed lesions of rPC following choline PET/CT. The data, although generated with a low number of patients, suggests that despite the high sensitivity and specificity of PSMA imaging, some PC lesions may remain undetected due to low PSMA expression. In such scenarios, choline PET/CT serves as a valuable complementary imaging modality.

EP-0424

Comparison of Early Response Assessment Using Post-Therapy Imaging After Lu-177 PSMA Therapy with Interim Ga-68 PSMA PET/CT

O. Sahin*, T. Bodur, K. Saglam, R. L. Uslu, S. Asa, S. Sager, L. Kabasakal, K. Sönmezoğlu, H. B. Sayman;*
Department of Nuclear Medicine, Istanbul University-Cerrahpasa, Faculty of Medicine, Istanbul, TÜRKIYE.

Aim/Introduction: Radioligand therapy (RLT) with Lu-177 PSMA is an increasingly utilized treatment modality with proven efficacy in metastatic prostate cancer (mPCa). Although consensus has yet to be reached regarding the ideal timing for progression evaluation, interim Ga-68 PSMA PET/CT after the second RLT cycle is frequently used in clinical practice. This study aimed to evaluate the effectiveness of post-therapy Lu-177 PSMA imaging (RLT PSMA) in identifying early disease progression, comparing it with interim PSMA PET and/or PSA-based evaluation. ***Materials and Methods:*** This retrospective study included 40 mPCa patients treated between 2017 and 2024, who received at least two RLT cycles and underwent interim PSMA PET imaging. Lu-177 PSMA was administered at a standard dose of 7.4 GBq per cycle. Post-therapy imaging (RLT PSMA) included whole-body planar scintigraphy and SPECT/CT of the thoracic and abdominopelvic regions. Baseline and follow-up PSMA PET scans, as well as first- and second-cycle RLT PSMA images, were compared. Progression was assessed using the PSMA PET Progression (PPP) criteria. The performance of each method in detecting progression was compared using McNemar's test. A secondary analysis combined RLT PSMA and PSA findings, with progression defined as positivity in either. PSA progression was defined as a ≥25% increase. ***Results:*** The mean patient age was 68±9 years, and baseline PSA level was 53±77 ng/mL. The mean interval between RLT cycles was 65±22 days, and interim PSMA PET was performed at an average of 50±22 days after the second cycle. PSMA PET detected progression in 25 of 40 patients (63%). There was no significant difference in baseline PSA between patients with and without progression (p=0.22). RLT PSMA identified 80% (20/25) of patients with progression, while missing 5 (20%). No statistically significant difference was observed between PSMA PET and RLT PSMA in detecting progression (p=0.063) (Figure 1-2). The combined use of RLT PSMA and PSA findings yielded a detection rate of 92%, improving progression detection performance. ***Conclusion:*** Interim PSMA PET detected progression in 63% of patients, underlining its value in early identification of disease progression. Post-therapy RLT PSMA imaging yielded comparable results. Combining PSA data further increased the detection rate to 92%, improving overall progression detection. These findings emphasize the importance of interim evaluation and suggest that the combination of RLT PSMA imaging with PSA may offer a reliable alternative to PSMA PET in identifying early progression.

EP-0425

How different treatments performed in hormone-sensitive prostate cancer could influence PSMA-PET/CT findings in resistant phase

M. Cuzzocrea[1], *S. Merler*[2], *M. Pedrani*[2], *G. Treglia*[1,3,4], *C. Iacovitti*[1], *C. Martinello*[1], *S. Gillessen*[2,3], *G. Paone*[1,3];
[1]*Imaging Institute of Southern Switzerland (IIMSI), Ente Ospedaliero Cantonale (EOC), Bellinzona, SWITZERLAND,*
[2]*Institute of Oncology of Southern Switzerland (IOSI), Ente Ospedaliero Cantonale (EOC), Bellinzona, SWITZERLAND,*
[3]*Università della Svizzera Italiana (USI), Lugano, SWITZERLAND,*
[4]*University of Lausanne, Lausanne, SWITZERLAND.*

Aim/Introduction: PSMA-PET/CT is currently used for the staging and restaging of prostate cancer (PCa) patients and to identify metastatic castration-resistant prostate cancer (mCRPC) patients suitable for ^{177}Lu-PSMA-therapy. Higher PSMA expression seems to be correlated with better responsiveness to the radioligand treatment (RLT). However, recommended cut-offs and universally recognized criteria for the suitability of ^{177}Lu-PSMA are urgently needed. ***Materials and Methods:*** Our retrospective analysis includes 78 PSMA-PET/CT studies in either hormone-sensitive (HS) or castration-resistant (CR) settings. These come from 70 patients with de novo metastatic PCa treated with androgen deprivation therapy (ADT), ADT+docetaxel, ADT+Androgen receptor pathway inhibitor (ARPI), or ADT+ARPI+Docetaxel in the HS setting between 2021 and 2023. Clinical and demographic variables and PSMA-PET/CT semi-quantitative parameters (SUVmax, SUVmean, Total Lesion Activity-TLA) were collected. Associations between categorical and continuous variables were examined using Pearson's chi-square and Kruskal-Wallis tests, respectively. Cox analyses were performed for overall survival (OS). ***Results:*** In the CR phase, we found higher PSMA-PET/CT semiquantitative parameters in ARPI-exposed patients compared to non-ARPI-exposed patients, with a median reference lesion SUVmax (SUVmaxRL) 33.9 (95%CI: 25.1-55.5) vs. 14. 6 (95%CI: 12.3-24.2) [p=0.02], a median SUVmean 12.5 (95%CI: 9.7-15.9) vs. 5.8 (95%CI: 4.4-11.3) [p=0.02] and a median TLA 1544.4 (95%CI: 311.8-2957.2) vs. 600.2 (95%CI: 73.5-870) [p=0.08]. In contrast, patients previously exposed to docetaxel tended to have lower PSMA-PET/CT uptake values, with a median SUVmaxRL of 27.8 (95%CI: 18.3-28.3) vs. 40 (95%CI: 30.4-71.4). These results are consistent with the percentage of mCRPC patients eligible for RLT, 70% vs 40% between ARPI-exposed and non-ARPI-exposed patients respectively (p=0.04). Furthermore, clinical (age, Chaarted criteria) and pathological (Gleason score) characteristics were similar in the two groups. In 38 PSMA-PET/CT studies performed in the CR phase, a higher SUVmaxRL (above 50) was significantly correlated with a lower OS (HR 3.55, 95% CI: 1.39-9.11, p=0.008). ***Conclusion:*** Our preliminary data show that systemic treatments administered in the HS metastatic setting appear to influence PSMA expression, detected by PET/CT, in CR metastatic stages, with ARPIs increasing SUVmean, SUVmax, and TLA and thus the indication for RLT. In addition, evaluation of SUVmaxRL might play a role in predicting survival outcomes in mCPRC, but further analyses are needed.

EP-0426

Clinical and Imaging Parameters to Predict the Efficacy of Androgen Receptor Pathway Inhibitors in Patients with Metastatic Castration-Resistant Prostate Cancer

O. Kodaz*, Y. Eryilmaz, M. Caglar, M. Tuncel;*
Hacettepe University Department of Nuclear Medicine, Ankara, TÜRKIYE.

Aim/Introduction: Androgen-receptor pathway inhibitors (ARPIs) have become the new standard of care for both metastatic hormone-sensitive and castration-resistant prostate cancer (mCRPC). However, the benefits of this treatment vary among patients, and it is unknown whether molecular imaging parameters provide predictive value. The aim of this study is to assess the clinical outcomes for mCRPC patients treated with ARPIs focusing on the predictive role of 68Ga-PSMA PET/CT-derived parameters. ***Materials and Methods:*** We retrospectively analyzed 40 mCRPC patients who had undergone 68Ga-PSMA-11 PET/CT imaging prior to the initiation of treatment with ARPIs. In addition to clinical history, several imaging parameters were investigated to predict PSA progression-free survival (PSA-PFS). PET-derived parameters included SUVmax, SUVmean, total-tumor-volume (TTV), soft-tissue-volume (STV, lymph nodes and prostate), TL-PSMA and HIT score. Pre-therapy laboratory tests included serum-PSA, LDH, albumin, and ALP levels, PSA doubling-time (PSAdt), PSA-velocity, as well as histopathological and clinical parameters such as ISUP-grade, time from diagnosis to ARPI initiation, previous therapies, site of metastases, and the distinction between de novo and recurrent metastatic disease. ***Results:*** Among the 40 patients, 24 (60%) had de novo metastatic disease, and 24 (60%) had previously received chemotherapy. Median pre-ARPI serum-PSA value and PSAdt 8.96 (range 0.15-863) and 2.3 months (range 0.4-22) respectively. On the pre-treatment PSMA PET scan median SUVmax, median TTV, median STV, median TL-PSMA and median SUVmean was 16.32 (range 4.64-76.03), 23.86 ml (range 0.1-643.55), 1.08 ml (range 0-349.26), 158.66 (range 0.45-5929.19) and 6.41 (range 3.51-14.58). During a follow-up period of 30.7 months (SD: 15.7 months), PSA progression occurred in 31 patients (77.5%). Median PSA-PFS was 12 months (range 3-71 months). In Cox regression analysis, patients with a higher TL-PSMA (cut-off: 99.3 g/ml x cm^3; p=0.022; 35 months vs. 14 months) and STV (cut-off: 0.89 ml; p=0.037) experienced a shorter PSA-PFS. In addition patients with less than 3 years since initial diagnosis (p=0.034), higher PSA-velocity (cut-off: 4 ng/ml/yr; p=0.008), and prior chemotherapy (p=0.002) were associated with significantly worse PSA-PFS. Other clinical, laboratory and molecular imaging parameters were not significantly associated with patients outcomes. ***Conclusion:*** This data suggest that certain clinical and PSMA PET/CT-based molecular imaging parameters may be useful to predict patient response to ARPI therapy. TL-PSMA and STV were the only prognostic molecular-imaging-biomarkers identified for predicting ARPI failure. This may necessitate considering alternative treatment options or combination therapies for patients with a high potential of therapy failure. This hypothesis requires further validation in larger prospective-studies.

EP-0427

The impact of scan duration on detection of unspecific findings on large axial field-of-view PSMA PET/CT studies in Prostate cancer patients

A. Scarale*, L. S. Airò Farulla, A. Spataro, A. Franchini, S. Capitanio, G. Cabrini, E. Gay, K. Shyli, A. M. Lazar, C. Rossetti;*
ASST Grande Ospedale Metropolitano Niguarda, Milan, ITALY.

Aim/Introduction: Long axial field-of-view (LAFOV) PET/CT allows imaging with increased sensitivity and shorter scan duration. The effect of reduced-duration protocols on the detection of non-pathological findings remains unclear. This study aimed to investigate the impact of different scan duration on the detectability of non-pathological findings in a cohort of prostate cancer patients undergoing LAFOV PSMA PET/CT. ***Materials and Methods:*** This retrospective study included 39 patients with histologically confirmed prostate cancer who underwent LAFOV PSMA-PET/CT using [68Ga]Ga-PSMA-11 or [18F]F-DCFPyL. List-mode acquisitions were reconstructed into images of 30 seconds, 1, 2, 3, 4, 5 and 10 minutes. Unspecific bone uptake (UBU) and sympathetic ganglia uptake were assessed by three nuclear medicine physicians. Binary presence (0 = absent, 1 = present) and maximum standardised uptake value (SUVmax) were recorded. Impact of scan duration on frequency detection of UBU and ganglia was assessed using Cochran's Q and McNemar's tests. Repeated measures ANOVA, Friedman tests were used to compare SUVmax across scan duration. Subgroup analyses were performed by radiotracer, clinical setting, and primary tumour burden. ***Results:*** In this cohort, UBU was observed in 46% of patients at 10 minutes, increasing gradually from 36% at 30 seconds. Median SUVmax of UBUs rose from 2.2 at 30 seconds to 2.8 at 10 minutes ($p = 0.001$). Linear mixed model analysis confirmed a significant positive trend in SUVmax over time ($\beta = +0.12$/min, $p < 0.001$). ROC analysis for distinguishing UBU presence yielded an AUC of 0.81 at 5 minutes and 0.86 at 10 minutes. Ganglia were identified in 51% of patients at 10 minutes, with detection rates rising from 33% at 30 seconds. Median SUVmax of ganglia increased from 1.9

to 2.6 across the acquisition span ($p < 0.001$), with a similar positive time-dependent slope ($\beta = +0.14$/min, $p < 0.001$). ROC AUC for ganglia presence reached 0.83 at 10 minutes. Notably, over 85% of ganglia and 80% of UBU visualised at 10 minutes were already detectable at 3 minutes, with negligible improvement beyond 5 minutes. No significant differences in UBU or ganglia metrics were observed between radiotracers. Subgroup analysis across clinical settings (staging, PSA persistence, biochemical recurrence) showed consistent patterns. ***Conclusion:*** In LAFOV PSMA-PET/CT, the detectability and SUVmax of UBU and sympathetic ganglia increase slightly with longer acquisition times, although most of the diagnostic yield is already achieved at 3-5 minutes. These findings support the feasibility of reduced-duration protocols without compromising lesion characterisation.

EP-0428

The Relationship Between Clinical Scoring and Ga-68 PSMA PET/CT Parameters in Predicting Biochemical Failure After Radical Prostatectomy

F. Avci[1], *R. H. Tokac*[1], *M. Dinckal*[2], *K. E. Ergün*[3], *A. M. Argon*[1], *U. Yararbas*[1];
[1]*Ege University, Nuclear Medicine, Izmir, TÜRKIYE,* [2]*Harakani Training Researh Hospital, Urology, Kars, TÜRKIYE,* [3]*Ege University, Urology, Izmir, TÜRKIYE.*

Aim/Introduction: Predicting persistent PSA (BCP) or biochemical recurrence (BCR) after radical prostatectomy (RP) is crucial, as it alters treatment and follow-up strategies. This study aims to evaluate the association between Ga-68 PSMA PET/CT parameters and scoring systems in predicting BCR/BCP. ***Materials and Methods:*** We retrospectively evaluated 55 patients with locoregional prostate cancer who underwent Ga-68 PSMA PET/CT between 2018 and 2024 prior to RP, without receiving neoadjuvant therapy. Demographic data, pathology findings, and biochemical profiles were collected. Quantitative PET parameters including SUVmax, SUVmean, SUVpeak, PSMA-TV, TL-PSMA, and PSMA-TLQ were measured. miTNM and PROMISE v2 classifications were assessed, along with clinical staging systems such as D'Amico (preoperative) and CAPRA-S (postoperative). Statistical analyses were performed using SPSS v25. ***Results:*** The mean age was 65.38 years (52-72), with a median follow-up of 28.19 months. BCR/BCP occurred in 14 cases (4 BCR, 9 persistent PSA, 1 both). PSMA-TV ($p=0.002$), TL-PSMA ($p=0.006$), and PSMA-TLQ ($p=0.03$) were significantly higher in BCR/BCP cases. ROC analysis showed moderate predictive performance for PSMA-TV and TL-PSMA (AUC: 0.783 and 0.749). SUVmax, SUVmean, and SUVpeak showed no correlation. miTNM T ($p=0.015$) and N ($p=0.004$) stages were significant; T2/N0 correlated with no BCR/BCP ($p=0.01$), while N1b correlated with BCR/BCP ($p=0.01$). No difference was observed for T3-T4. PROMISE v2 showed no predictive value. CAPRA-S, stratified into three groups (0-3, 4-7, 8-12), significantly predicted BCR/BCP ($p<0.001$). Groups 1-2 correlated with no BCR/BCP ($p<0.01$), while Group 3 correlated with BCR/BCP ($p<0.001$). However, individual CAPRA-S scores were not significant. TL-PSMA ($p<0.001$) and other parameters (except PSMA-TLQ) correlated with CAPRA-S. Preoperative PSA, PSA density, D'Amico risk, and Gleason score significantly predicted BCR/BCP ($p<0.001$). D'Amico risk also correlated with TL-PSMA ($p=0.002$) and PSMA-TV ($p=0.006$). ***Conclusion:*** This study highlights the strong diagnostic performance of PSMA-TV derived from Ga-68 PSMA PET/CT in localized prostate cancer, demonstrating its correlation with clinical risk classifications and PSA levels. The findings support its potential as a non-invasive biomarker. PSMA PET/CT may play a critical role not only in diagnosis but also in risk stratification and treatment planning. Integrating quantitative PET parameters into existing risk models could enhance patient categorization and contribute to personalized therapeutic strategies, reinforcing the value of multidisciplinary approaches.

EP-0429

Prediction of 2-year overall survival in mCRPC patients by total tumor volume (TTV) under PROMISE risk stratification scheme in a single Asian center

T. Tsoi*, S. Chen, K. Yip, Y. Yip, K. Wu, Y. Wong, S. Cheung, C. Ho;*
Hong Kong Sanatorium & Hospital, Hong Kong, CHINA.

Aim/Introduction: "PROMISE" is a reporting scheme proposed to include molecular information obtained from PSMA-ligand PET/CT to predict prognosis in mCRPC patients. It aims to combine molecular TNM (miTNM) staging with molecular PSMA parameters (miPSMA) stratified as nomogram-based risk factors such as tumor volume, SUV, locoregional and distant metastases, so that the reporting can be standardized across different imaging centers and for longitudinal assessment of treatment response. The scheme is an improved modification to the Gafita normograms by including more detailed miPSMA parameters, but no prediction of overall survival (OS) is yet proposed. This pilot study attempts to identify the significant predictor(s) in PSMA-ligand PET/CT for OS assessment in a cohort of mCRPC patients in a single Asian center. ***Materials and Methods:*** We consecutively analyzed 42 clinically-identified mCRPC patients (age:72±10 years, range:50-87 years) who were assessed by PSMA-ligand PET/CT for mCRPC and then followed for >2 years (25-64 months). The primary endpoint was the OS. The prognostic predictors included categorical parameters: (1) locoregional, (2) extrapelvic lymph node, (3) bone (disseminated/diffuse marrow involvement), (4) other distant metastases, and continuous parameter: (5) total tumor volume (TTV) on PSMA-ligand PET/CT. The diagnosis of bone metastases on PSMA PET/CT was combined with CT findings in bone window. ROC curve analysis was performed on TTV for OS assessment. Survival analysis utilized Kaplan-Meier estimates and Cox regression to identify independent predictors. ***Results:*** 31/42 patients died during the follow-up period. ROC curve analysis for TTV on PSMA PET/CT identified a 2-year OS with the best AUC accuracy (AUC=0.975), consistent with the risk stratification results (HIGH/LOW) by PSMA-PET PROMISE. "TTV≥183ml" was calculated as the best cut-off value. The 2-year OS rate was 48% (20/42) in our study. Among all the selected prognostic predictors, "extrapelvic lymph node metastases" and "TTV≥183ml" were found to be significant predictors for 2-year overall survival using univariate analysis. Further multivariate analysis found that "TTV≥183ml" was the only independent predictor (sensitivity: 86.4% [19/22], specificity: 95.0% [19/20], accuracy: 90.5%). mCRPC patients with TTV≥183ml (N=20) had a significantly shorter median OS than those (N=22) with TTV<183 ml (estimated median survival: 9 vs 39 months; log-rank test, $p<0.001$). ***Conclusion:*** The tumor burden quantified as TTV by combining all the metastatic sites on PSMA PET/CT is found to be the most significant predictor of 2-year OS in this study. A threshold TTV of 183 ml is a strong differentiator of prognosis in this cohort of mCRPC patients.

EP-0430

Which Patients with Negative PSMA-PET Imaging Can Safely Avoid Biopsy for Prostate Cancer? A Novel Step Towards PSMA-based Biopsy-Free Strategy

Y. Li*, Y. Tang, S. Hu;*
Xiangya Hospital, Central South University, Changsha, CHINA.

Aim/Introduction: The initial diagnosis of prostate cancer (PCa) traditionally relies on prostate biopsy driven by serum prostate-specific antigen (PSA), which is an organ-specific biomarker and lacks sufficient specificity. mpMRI has the potential to reduce the number of unnecessary biopsies. However, owing to its suboptimal and highly variable negative predictive value (NPV), the reliability of negative mpMRI as a triage test to safely rule out the need for biopsy remains less established and controversial. Moreover, its moderate specificity limits the reduction in the net number of unnecessary biopsies. We aimed to identify if a

subset of men can safely avoid or delay prostate biopsy based on negative prostate-specific membrane antigen positron emission tomography (PSMA-PET), using data from a prospective biopsy cohort. ***Materials and Methods:*** Among 341 consecutive cases in the prospective biopsy cohort NCT05073653, 111 treatment-naïve men with negative PSMA-PET (PRIMARY-score 1/2) were included. All participants underwent PSMA-PET and histopathological examinations. Clinically significant PCa (csPCa) was defined as Grade Group ≥ 2. Multivariate logistic regression was employed to identify predictors of non-csPCa. Receiver operating characteristic (ROC) analysis was performed to detect non-csPCa on prostate pathology. PSMA-postive patients were additionally reviewed to assess the pathological outcomes. ***Results:*** Younger age was identified as an independent predictor (P = 0.006) for the absence of csPCa. ROC analysis of csPCa revealed the largest areas under the curve of 0.77 (0.67-0.87) and 0.78 (0.68-0.88) for individual age in the entire PSMA-negative cohort and the MRI subset, respectively (both P < 0.001). The NPV of PSMA-PET for csPCa detection improved with a decreasing age, from 88% in all, to 98% in men aged under 65 years (98% vs. 88%, P = 0.021), and to 100% in men aged under 60 years (100% vs. 88%, P = 0.040). The NPV of PSMA-PET improved from 88% to 94% when combined with negative MRI, and to 100% in men with negative MRI and aged under 65 years. The prevalence was 57% for csPCa and 65% for PCa of any grade. ***Conclusion:*** We preliminarily propose that omission or postponement of prostate biopsy should be considered for men under the age of 65 years with negative PSMA-PET scored as PRIMARY 1/2. Conversely, prostate biopsy might be considered for biopsy-naïve men aged 65 years or older with strong clinical suspicion of PCa, despite negative PSMA-PET. Further prospective and external evaluations are needed to prove the robustness of this novel strategy.

EP-0431

18F-PSMA 1007 PET/CT metrics as a biomarker for progression-free survival in Patients with Metastatic Prostate Cancer

S. Moustafa*;*
Assiut university hospital, Assiut, EGYPT.

Aim/Introduction: Prostate-specific membrane antigen (PSMA)-targeting PET imaging is becoming the reference standard for prostate cancer staging, especially in advanced disease. Metastases are often responsible for prostate cancer-related morbidity and mortality. Thus, the quantification of the whole-body tumor volume is clinically relevant, and it could predict the progression-free survival (PFS) and overall survival of patients. yet, there is no clear evidence that PSMA PET-derived biomarkers can predict the progression-free survival of patients with prostate cancer. Our aim is to evaluate whole-body PSMA PET metrics as imaging biomarkers for determination of PFS. ***Materials and Methods:*** We enrolled 49 patients with prostate cancer who had PSMA-avid metastatic lesions. From all pathological lesions, the mean and maximum SUV (SUV mean, SUVmax) and the tumor volume of each lesion were determined in VOIs with isocontours set at 41% of the maximum uptake; that is called PSMA-TR (tumor volume) and finally, PSMA-TL (total lesions) calculated by multiplying the respective TV and mean SUV. We calculated the total metrics then; we correlated it with PFS. Then we divided total metrics into osseous and non-osseous. We classified patients in low & high-volume disease based on PSMA PET/CT on parrel of CHAARTED trial. We used the Cox regression model to determine the most prognostic factor for PFS. ***Results:*** Total metrics SUVmax, SUVmean, PSMA-TR and PSMA-TL were significantly correlated with PFS, r= - 0.4& p=0.01, r= - 0.31& p=0.03, r=-0.4& p=0.008, r=-0.35& p=0.014 respectively. Osseous total SUV max, SUV mean, PSMA-TR and PSMA-TL were significantly correlated with PFS; r= -0.5& p<0.001, r= -0.5& p<0.001, r= -0.6& p=0.001, r= -0.44& p=0.002 respectively. As regards non-osseous metrics; only PSMA-TR was significantly correlated with PFS, r=- 0.3&p=0.031 whilst no significant correlation between SUVmax, SUVmean and PSMA-TL and PFS, p=0.3, p=0.7, p=0.3 respectively We found that PSMA-based volume disease significantly correlated with PFS with a P value of 0.04. The total osseous SUV mean was considered the most independent variable of PFS in the current population study, meaning that increasing the total osseous SUV mean by 0.3% increased the hazard of progression or death by 10%, HR (Hazard Ratio) = 1.9, 95% CI of (1.026 - 3.443) and p value 0.041. ***Conclusion:*** PSMA PET metrics are significant predictors of PFS in patients with advanced prostate cancer. PSMA-based volume disease significantly correlated with PFS. The mean SUV for total osseous PSMA is the most important prognostic indicator for PFS in these patients.

EP-0432

Comparative evaluation of SUV variability in reference tissues and tumor lesions for defining the PSMA-positivity threshold in PSMA-targeted radioligand therapy

A. Khalimon[1]*, A. Nikiforuk*[1]*, A. Shakirova*[1]*, A. Lokhova*[1]*, V. Bagaturya*[1]*, I. Baltabaev*[1]*, M. Khodzhibekova*[1]*, G. Khamadeeva*[1]*, D. Khodakova*[1]*, T. Lazutina*[1]*, I. Pylova*[1]*, A. Leontev*[1]*, A. Pronin*[2]*, E. Bezumova*[2]*;*
[1]P. Hertsen Moscow Oncology Research Institute - branch of the National Medical Research Radiological Centre of the Ministry of Health of the Russian Federation, Moscow, RUSSIAN FEDERATION, [2]N.N. Blokhin National Medical Research Center of Oncology of the Ministry of Health of the Russian Federation, Moscow, RUSSIAN FEDERATION.

Aim/Introduction: The aim of this study was to compare the SUV variability in reference tissues and tumor lesions for defining the PSMA-positivity threshold in PSMA-targeted radioligand therapy. ***Materials and Methods:*** This research included single-center patient study and multicenter phantom study with following single-center validation study for evaluation the SUV variability in reference tissues and tumor lesions, respectively. Single-center patient study included 100 patients with prostate cancer who underwent [^{18}F]PSMA-1007 PET/CT using the BGO PET/CT-system. BSREM algorithm with β-value 400 was used for PET image reconstruction. [^{18}F]PSMA-1007 uptake was analyzed by measurement of SUVmax, SUVmean and SUVpeak in the parotid glands (dVOI=0.5cm); blood pool (dVOI=1cm); liver (dVOI=2cm); spleen and gluteus muscles (dVOI=1.5cm). The coefficients of variation (CoVs) for SUVmax, SUVmean and SUVpeak were calculated for each reference tissue. The phantom study was performed on three PET/CT-systems (with BGO-, LSO- and LYSO-based detectors) using the NEMA IEC Body Phantom NU2-2018. The phantom filling and acquisition procedure were performed in accordance with the EARL ^{18}F-standards manual. A total of 20 EARL2-compliant reconstructions were included into the analysis. SUVmax and SUVpeak Recovery Coefficients (RCmax and RCpeak) for each phantom's sphere across all reconstructions were calculated. The validation study was performed on 36 patients who underwent both [^{18}F]FDG and [^{18}F]PSMA-1007 PET/CT using the BGO PET/CT-system. Raw PET data were used to obtain 10 EARL2-compliant reconstructions (3D-OSEM+PSF). 96 lesions approximately spherical in shape were selected with diameters almost evenly distributed from 10 to 37mm, grouped according to intervals of phantom's spheres diameters. SUVmax and SUVpeak of each lesion across all reconstructions were measured. The CoVs for RCmax, RCpeak and SUVmax, SUVpeak were calculated for each phantom's sphere and patient's lesion within each group of reconstructions respectively. ***Results:*** The CoVs of SUVs (max, mean and peak) in the reference tissues were as follows: 24.9%,24.8%,24.2% - in the liver, 44.2%,44.3%,43.3% - in the spleen, 26.6%,29.5%,26.7% - in the parotid glands, 27.5%,27.2%,28.7% - in the

blood pool, 19.8%,19.4%,18.9% - in the gluteus muscles. The CoVs of RCmax and RCpeak for each phantom's sphere (from smallest to largest) were as follows: 12.3%,5.6%,5.3%,5.5%,3.2%,3.2%, and 8%,4.8%,2.9%,2.4%,3.3%,1.6%. The CoVs of SUVmax and SUVpeak for each interval of lesions' diameters (from smallest to largest) were as follows: 8.4[7.2;10.5],8[5.9;9.1],5[4;5.8],4.3[3.2;5.4],3.7[2.7;6.3], and 5[3.9;6.5],4[3.4;6.9],2.7[2.3;5.1],2.3[1.6;3.2],1.6[1.5;2.2] in percents. ***Conclusion:*** The application of tumor lesions' EARL-harmonized SUV may be preferable to SUV in reference tissue for defining the PSMA-positivity threshold in PSMA-targeted radioligand therapy due to its lower variability.

EP-0433

The impact of patient hydration and forced diuresis on [^{18}F]PSMA-1007 urinary bladder uptake in PET/CT imaging

A. Khalimon[1], *A. Nikiforuk*[1], *M. Khodzhibekova*[1], *G. Khamadeeva*[1], *D. Khodakova*[1], *T. Lazutina*[1], *I. Pylova*[1], *A. Leontev*[1], *V. Bobrov*[1], *O. Mukhortova*[2], *I. Aslanidi*[2];
[1]*P. Hertsen Moscow Oncology Research Institute - branch of the National Medical Research Radiological Centre of the Ministry of Health of the Russian Federation, Moscow, RUSSIAN FEDERATION,* [2]*A.N. Bakulev National Medical Research Center for Cardiovascular Surgery of the Russian Ministry of Health, Moscow, RUSSIAN FEDERATION.*

Aim/Introduction: [^{18}F]PSMA-1007 has minimal renal excretion, allowing for better assessment of the pelvic area in patients with prostate cancer (PCa). Nevertheless, there have been instances of notably high [^{18}F]PSMA-1007 uptake in the urinary bladder. The purpose of this study was to assess the impact of preliminary patient hydration and forced diuresis on [^{18}F]PSMA-1007 urinary bladder uptake. ***Materials and Methods:*** A prospective single-center study included 185 patients with PCa, who underwent [^{18}F] PSMA-1007 PET/CT. Patients were divided into 11 groups: a control group with no hydration or furosemide administration (n=35) and ten experimental groups (n=15 in each) with different preparation protocols: (#1) 500ml IV; (#2) 1000ml IV; (#3) 500ml IV + furosemide 90 minutes before PET (at the same time as [^{18}F]PSMA-1007 administration); (#4) 500ml IV + furosemide 30 minutes before PET; (#5) 1000ml IV + furosemide 30 minutes before PET; (#6) 500ml orally; (#7) 1000ml orally; (#8) 500ml orally + furosemide 30 minutes before PET; (#9) 1000ml orally + furosemide 30 minutes before PET; (#10) furosemide 30 minutes before PET with no hydration. LBM SUVmean was used to quantify [^{18}F]PSMA-1007 bladder uptake. The differences in bladder SUVmean among the different preparation groups, as well as compared to the control group, were evaluated. A $p<0.001$ was considered statistically significant. Additionally, the variability of bladder SUVmean was assessed by evaluating the interquartile ranges (IQRs). ***Results:*** Urinary bladder SUVmean were 4.2 [2.4;12.0] with IQR 9.6 in the control group. In the experimental groups bladder SUVmean were as follows: (#1) - 6.2 [2.9;9.3] IQR 6.4; (#2) - 6.4 [3.2;9.8] IQR 6.6; (#3) - 1.8 [1.2;2.1] IQR 0.9; (#4) - 0.7 [0.5;0.9] IQR 0.4; (#5) - 1.0 [0.7;1.2] IQR 0.5; (#6) - 2.2 [1.6;4.5] IQR 2.9; (#7) - 3.4 [2.7;5.2] IQR 2.5; (#8) - 0.6 [0.5;0.8] IQR 0.3; (#9) - 0.6 [0.5;0.8] IQR 0.3; (#10) - 0.9 [0.7;1.4] IQR 0.7. The results indicate that the application of furosemide significantly reduced the median and variability of bladder SUVmean ($p<0.001$), 30 minutes time interval of furosemide application prior to PET scan is preferable compared to 90 minutes ($p<0.001$). Hydration alone, without furosemide, was insufficient for effectively reducing the median and variability of bladder SUVmean ($p=0.5$). There was no significant difference between the groups with different routes and volumes of hydration ($p=0.03$ and 0.45). ***Conclusion:*** Forced diuresis is an effective tool for reducing the [^{18}F]PSMA-1007 urinary bladder uptake and its variability when it is routinely increased.

EP-0434

Identifying Genetics Biomarkers in Correlation to Pathological and PSMA-PET Characteristics in Prostate Cancer

L. Xin;
Qilu Hospital, Shandong University, Jinan, CHINA.

Aim/Introduction: Prostate cancer is a prevalent disease with varied tumor characteristics complicating treatment. The integration of spatial patterns from PSMA PET and pathology with expanding genomic data is pioneering advances in histo-imaging-genomics. This study aim to elucidate inter-network mapping between genetic biomarkers and PSMA-PET imaging in prostate cancer. ***Materials and Methods:*** mRNA sequencing and clinical data from 433 prostate cancer cases were sourced from the TCGA database. Differential gene expression between GS-high risk and GS-low risk groups was analyzed. Univariate and multivariate logistic regressions facilitated feature selection, and a GS predictive model was developed via multivariate logistic regression. Additionally, local samples and images from 27 patients were gathered. PSMA-PETCT imaging preceded before radical prostatectomy, and mRNA sequencing of prostate cancer lesions was conducted via next-generation sequencing. Genes differentially expressed, as identified from the TCGA dataset, were then analysized for correlating with PET-related metrics in the local dataset by utilizing the Pearson correlation. ***Results:*** Out of the TCGA dataset, 174 genes showed differential expression. Post feature selection, 53 genes persisted. In the local dataset, ten genes (EFNA2, CACNA1I, CA1, MYBPC3, CYP1A1, TLCD3B, LRTM2, GBX2, SPSB4, and GDF3) demonstrated significant association with PET-related metrics. When the differential expression of genes between high-risk and low-risk groups was compared, six genes (STMN2, CYP1A1, THRSP, LIPC, GBX2, and SPSB4) in the high-risk group and eight genes (FBXL16, KLK14, DIRAS2, TERB2, PRAME, UTS2B, UGT2B15, and LINC02798) in the low-risk group were found to be significantly correlated with PET-related parameters. ***Conclusion:*** The study identified genetic markers that have a significant correlation with PSMA-PET imaging features in prostate cancer. These findings might provide a valuable foundation for optimizing prostate cancer diagnostic procedures and tailoring therapeutic approaches based on genetic and imaging biomarkers. ***References:*** 1.Sung H, Ferlay J, Siegel RL, Laversanne M, Soerjomataram I, Jemal A, et al. Global Cancer Statistics 2020: GLOBOCAN Estimates of Incidence and Mortality Worldwide for 36 Cancers in 185 Countries. CA: A Cancer Journal for Clinicians. 2021;71:209-49.2. Kohan A, Kulanthaivelu R, Hinzpeter R, Liu ZA, Ortega C, Leighl N, et al. Disparity and Diversity in NSCLC Imaging and Genomics: Evaluation of a Mature, Multicenter Database. Cancers. 2023;15.3. Haffner MC, Zwart W, Roudier MP, True LD, Nelson WG, Epstein JI, et al. Genomic and phenotypic heterogeneity in prostate cancer. Nature Reviews Urology. 2020;18:79-92.

EP-0435

^{18}F-PSMA-137 PET/CT Imaging in Suspected Prostate Cancer: A Multicenter, Prospective Trial with Pathologic Confirmation

J. Yang[1], *J. Zhang*[2], *W. Wan*[3], *X. Yang*[4], *W. Wang*[1], *H. Ma*[1], *Y. Xu*[1], *Z. Fu*[1], *X. Wang*[5], *Y. Liu*[5], *M. Wang*[6], *F. Liu*[7], *Y. Guo*[7], *Y. Liu*[2], *X. Zhang*[2], *N. Zhang*[3];
[1]*Beijing Friendship Hospital, Capital Medical University/ Department of Nuclear Medicine, Beijing, CHINA,* [2]*Chinese PLA General Hospital/Department of Nuclear Medicine, Beijing, CHINA,* [3]*Yunnan Baiyao Group Co., Ltd., Kunming, CHINA,* [4]*Peking University People's Hospital/Department of Nuclear Medicine, Beijing, CHINA,* [5]*Cancer Hospital Chinese Academy of Medical Sciences/Department of Nuclear Medicines (PET-CT Center), Beijing, CHINA,* [6]*Cancer Hospital Chinese Academy of Medical Sciences/Department of Urology, Beijing, CHINA,* [7]*Beijing Hospital/Department of Nuclear Medicine, Beijing, CHINA.*

Aim/Introduction: Prostate cancer (PCa) is a leading cause of morbidity and mortality in men worldwide, with late-stage diagnoses due to limitations in conventional imaging techniques,

such as CT and MRI. The novel ^{18}F-labeled PSMA-targeted radiotracer demonstrates high targeting affinity, favorable biodistribution, and clear lesion imaging, offering the potential to improve the accuracy of initial PCa diagnosis. ***Materials and Methods:*** This study is a multicenter, prospective, open-label phase I/IIa clinical trial systematically evaluating the safety, biodistribution, pharmacokinetics, and diagnostic performance of ^{18}F-PSMA-137 PET/CT in healthy individuals and suspected PCa patients. Phase I included 8 healthy male volunteers to evaluate the radiotracer 's safety, biodistribution, radiation dosimetry, and pharmacokinetics. Phase IIa enrolled 24 suspected PCa patients with elevated PSA levels (≥3 ng/mL) who had no previous PCa diagnosis or treatment history, and who were scheduled for prostate biopsy before/after imaging. Phase IIa assessed the diagnostic performance of ^{18}F-PSMA-137 PET/CT at different doses and different scan times. Diagnostic performance, including sensitivity, specificity, and accuracy, was compared with multiparametric MRI (mpMRI), with prostate biopsy pathology as the reference standard. Adverse events (AEs), laboratory tests, and ECG were monitored throughout to assess safety. ***Results:*** In phase I, ^{18}F-PSMA-137 demonstrated rapid in vivo distribution, primarily excreted through the renal and hepatobiliary pathways, with the liver, kidneys, and salivary glands as the main uptake organs. The mean effective radiation dose was 7.59 ± 1.17 mSv, with rapid clearance of the drug, clear biodistribution, and excretion pathways, and no serious adverse events reported. In phase IIa, ^{18}F-PSMA-137 showed good uptake in prostate lesions. In the low-dose group, the sensitivity at 80 and 120 minutes post-injection was 100.0%, specificity was 85.7%, accuracy was 90.9%, positive predictive value (PPV) was 80.0%, negative predictive value (NPV) was 100.0%, Youden index was 0.86, and the Kappa value was 0.81, indicating high concordance with pathology. In the high-dose group, the sensitivity was 87.5%, specificity was 75.0%, accuracy was 83.3%, Youden index was 0.63, and the Kappa value was 0.63. PET/CT demonstrated higher specificity and accuracy compared with multiparametric MRI (mpMRI), supporting its clinical value in the preliminary diagnosis of suspected PCa patients. ***Conclusion:*** ^{18}F-PSMA-137 PET/CT demonstrates a favorable safety profile, robust pharmacokinetics, and high diagnostic performance in suspected PCa. Its superior sensitivity and specificity position ^{18}F-PSMA-137 PET/CT as a potential global benchmark in the initial diagnosis of PCa, warranting further large-scale studies for validation.

EP-0436

Defining Semiquantitative PSMA PET Thresholds for Clinically Significant Prostate Cancer: Interim Analysis of the BIOPSTAGE Study

M. Celli[1], *R. Gunelli*[2], *F. Ferroni*[1], *M. Costantini*[2], *A. Rossi*[1], *L. Fantini*[1], *E. Fragalà*[2], *I. Marini*[1], *D. Bezzi*[3], *V. Rossetti*[1], *I. Grassi*[1], *M. Sansovini*[1], *E. Giunta*[1], *S. Bellia*[1], *V. Di Iorio*[1], *F. Foca*[1], *F. Matteucci*[1], *P. Caroli*[1];
[1]*IRCCS Istituto Romagnolo per lo Studio dei Tumori (IRST) "Dino Amadori", Meldola (FC), ITALY,* [2]*Morgagni Pierantoni Hospital, Romagna Local Health Service, Forlì (FC), ITALY,* [3]*Bufalini Hospital, Romagna Local Health Service, Cesena (FC), ITALY.*

Aim/Introduction: Prostate-specific membrane antigen (PSMA) PET is gaining interest as a non-invasive diagnostic tool in the primary staging of prostate cancer (PCa). While its utility in advanced disease is well established, its role in detecting clinically significant PCa (csPCa) remains under investigation. In particular, standardized uptake thresholds for defining PET positivity are lacking, which limits clinical applicability. This interim analysis from the prospective BIOPSTAGE trial aimed to define optimal semiquantitative criteria (SUVmax and SUVratio) for PSMA PET and explore their association with histopathological outcomes and clinical parameters. ***Materials and Methods:*** Ninety-six men with clinical suspicion of PCa were prospectively enrolled. All patients underwent [^{68}Ga]Ga-PSMA-11 PET/CT and multiparametric MRI (mpMRI) prior to prostate biopsy. csPCa was defined as ISUP grade group ≥2. ROC curve analysis was used to determine optimal SUVmax and SUVratio cutoffs for PSMA PET positivity. Logistic regression assessed clinical and imaging predictors of PSMA uptake. ***Results:*** ROC analysis identified SUVmax ≥9.1 and SUVratio ≥3.6 as optimal thresholds, yielding AUCs of 0.87 and 0.88, respectively. Using these thresholds, PSMA PET showed a sensitivity of 85.7% and specificity of 86.3%, with a positive predictive value (PPV) of 48.0% and a negative predictive value (NPV) of 97.6%. Of 25 PET-positive lesions, 14 were also mpMRI-positive, while 11 had no mpMRI correlate. One PET-only lesion was confirmed as csPCa (ISUP 3), and two small csPCa lesions (5 mm and 8 mm, both ISUP 2) were not detected by PET but were identified on mpMRI. PSA density emerged as the only independent predictor of PSMA PET positivity (OR: 6.35; p = 0.006), supporting its value in clinical risk stratification. ***Conclusion:*** The use of standardized SUV thresholds improves the diagnostic performance of PSMA PET for csPCa and may facilitate its incorporation into biopsy decision-making. While PET offers high specificity and NPV, mpMRI remains essential, particularly for identifying small, low-uptake lesions. These interim findings support a combined PET-MRI approach for optimizing patient selection and reducing unnecessary biopsies.

EP-0437

Role of PET/MRI in Prostate Cancer: Indications and Potential Uses. Our Preliminary Experience

J. Díaz Moreno[1], *J. Robles-Barba*[1], *J. Martín-Marcuartu*[1], *D. Durany-Lara*[2], *A. Bagán-Trejo*[1], *A. Caresia-Aroztegui*[3], *N. Picola-Brau*[4], *J. Súarez-Novo*[4], *B. Hervás-Sanz*[1], *P. Servian-Vives*[5], *A. Abella-Serra*[5], *M. Cortés-Romera*[1];
[1]*Nuclear Medicine-PET (IDI) Department, Hospital Universitari de Bellvitge-IDIBELL, Barcelona, SPAIN,* [2]*Radiology Department, Hospital Universitari de Bellvitge-IDIBELL, Barcelona, SPAIN,* [3]*Nuclear Medicine-PET (IDI) Department, Hospital German Trias, Badalona, SPAIN,* [4]*Urology Department, Hospital Universitari de Bellvitge, Barcelona, SPAIN,* [5]*Urology Department, Hospital German Trias i Pujol, Badalona, SPAIN.*

Aim/Introduction: This descriptive study aims to present our current experience with PET/MRI in prostate cancer, focusing on its clinical indications, potential uses, the various radiotracers available, and their therapeutic implications. ***Materials and Methods:*** Between 2023 and 2024, a total of 70 PET/MRI studies were performed in patients with prostate cancer using three different radiotracers: 18F-PSMA-piflufolastat (40/70) for biochemical recurrence (BCR) and characterizing PI-RADS 3 lesions; 18F-PSMA-1007 (19/70) for patients eligible to focal therapies (FT) and BCR with very low PSA levels, and 18F-choline (11/70) for screening, staging and BCR. Radiotracer selection was based on clinical criteria, availability and regulatory constraints at that moment in our country. Detection rates (DR), agreement between PET and MRI and change in therapeutic managment (CTM) were assessed. ***Results:*** Forty PET/MRI studies using 18F-PSMA-piflufolastat were performed (median PSA 1.4 ng/ml, range: 0.2-32.4), 17/40 for BCR with DR of 70% and CTM in 58% of cases. 23/40 studies were part of a research protocol assessing the role of PSMA PET/MRI in characterizing PI-RADS 3 lesions, with histopathology (AP) as the gold standard. 20/23 showed a PRIMARY score 1A/2A on PET with no findings suspicious for clinically significant prostate carcinoma, showing agreement with MRI findings (kappa 0,25). Nineteen studies with 18F-PSMA-1007: 17/19 in patients with BCR after radiotherapy eligible for FT such as IRE or HIFU, as part of a prospective study. PET imaging changed management in up to a quarter of patients by detecting lymphatic dissemination that would not have been identified using MRI alone. The remanining 2/19 studies were performed in patients with low PSA (0.2-0.5 ng/ml) and suspected local recurrence (DR 50%). Eleven studies were performed using 18F-Choline: 2/11 for screening (both negative),

2/11 for staging (both positive), and 7/11 for BCR. DR was 100% in these BCR patients, likely due to the high PSA levels they presented (median PSA 7,2 ng/ml, range 2,2 - 50,9), with CTM in 63% of them. ***Conclusion:*** Our preliminary experience highlights the clinical value of PET/MRI in prostate cancer on indications such as staging or biochemical recurrence, where it shows a high impact in changing therapeutic management. The greater resolution provided by the MRI component also allows the use of PET imaging on potential indications such as the characterization of PI-RADS 3 lesions or selecting patients eligible for focal therapies.

EP-22

e-Poster Area

B: Imaging Clinical Studies -> B1 Oncological Imaging Clinical Study -> B19 Thyroid

EP-0438

Clinicopathologic Features and Prognostic Stratification of Thyroid Carcinoma with Antecedent Distant Metastasis: A Retrospective Analysis of 44 Consecutive Cases

Y. Wu, *L. Zhang, J. Gui, H. Chen, J. Wang, X. Long, W. Cao;*
Department of Nuclear Medicine, Union Hospital, Tongji Medical College, Huazhong University of Science and Technology, Wuhan City, CHINA.

Aim/Introduction: Thyroid carcinoma typically has a favorable prognosis, but some patients present with distant metastasis before the primary tumor is detected—termed antecedent distant metastasis. This rare and underrecognized form is linked to worse outcomes. Identifying prognostic factors is essential to guide treatment in this high-risk group. This study aimed to define their clinicopathologic features and evaluate prognostic indicators. ***Materials and Methods:*** A retrospective study analyzed 44 consecutive patients with antecedent metastatic thyroid carcinoma, selected from 7,374 cases managed between Jan 1, 2019, and Mar 31, 2025. Clinical data included demographics, histopathology, TNM stage, metastatic sites, surgery type, and gene mutations. Treatment response was evaluated using RECIST 1.1 (PR, SD, PD) and the 2015 ATA response-to-therapy system (ER, BIR, SIR). ***Results:*** Among 44 patients (65.9% female, mean age 59.6 ± 11.5), follicular carcinoma was the most common subtype (34.1%) and had the highest partial response (PR) rate (66.7%), followed by papillary carcinoma (15.4%). Most were T1 (45.0%), N0 (58.3%), and M1 (94.4%). PR was achieved in 31.8%, stable disease in 43.2%, and progression in 25.0%. ATA stratification showed 2 excellent responses, 1 biochemical incomplete, and 41 structural incomplete. Gene testing (n = 5) revealed various mutations, including BRAF, RET, TERT, and ALK. Bone metastasis (χ^2 = 7.560, P = 0.023), surgical method (χ^2 = 9.976, P = 0.041), and histology (χ^2 = 20.879, P = 0.022) significantly impacted outcomes. Patients with bone metastases had higher PR (42.4%), likely due to other metastatic sites. Total thyroidectomy showed better PR (38.2%) than partial or conservative treatments. ***Conclusion:*** Patients with antecedent distant metastasis of thyroid carcinoma exhibit heterogeneous clinical outcomes, with prognosis significantly affected by histologic subtype, metastatic site, and surgical approach. Follicular thyroid carcinoma demonstrated the highest partial response rate , suggesting better responsiveness compared to papillary and other subtypes. Bone metastasis was associated with a more favorable treatment response than other metastatic sites such as lungs and lymph nodes. Total thyroidectomy resulted in significantly better outcomes compared to partial thyroidectomy or conservative treatment . Although genetic testing was limited, actionable mutations were identified in several cases, highlighting the potential role of molecular profiling in guiding targeted therapies. These findings underscore the importance of aggressive surgical management and tailored therapeutic strategies based on clinicopathologic and molecular features to improve prognosis in this rare but high-risk subset of thyroid carcinoma.

EP-0439

Exploring Factors of Achieving Excellent Response in Intermediate- and High-Risk Patients with Differentiated Thyroid Cancer after therapy with 100mCi Iodine-131

J. Xin, *F. Kang, W. Ma, J. Wang;*
Department of Nuclear Medicine, Xijing Hospital, FourthMilitary Medical University, Xi'an, CHINA.

Aim/Introduction: To explore the factors for achieving an excellent response (ER) in patients with intermediate- and high-risk differentiated thyroid cancer (DTC) after treatment with 100 mCi of iodine-131. ***Materials and Methods:*** A retrospective analysis was conducted on 725 DTC patients who were treated in the Department of Nuclear Medicine of Xijing Hospital from June, 2021 to April, 2024. All patients were pathologically diagnosed with DTC and received 100 mCi iodine treatment. Univariate analysis and binary Logistic regression analysis were used to identify the influencing factors, and ROC curve analysis was performed to determine the optimal critical values for predicting ER. ***Results:*** Among 725 patients, 477 patients (65.79%) achieved ER, and 248 patients (34.21%) did not achieve ER. Univariate analysis indicated that multiple factors were correlated with achieving ER, and binary Logistic regression analysis revealed that the number of metastatic lymph nodes, pre-treatment stimulated thyroglobulin(psTg), Tg/TSH, and Tg*TgAb were independent risk factors influencing the attainment of ER in intermediate- and high-risk patients with DTC after 100 mCi iodine-131 treatment, ROC curve analysis determined the optimal critical values for these factors in predicting ER. ***Conclusion:*** The number of metastatic lymph nodes, psTg, Tg/TSH, and Tg*TgAb are independent predictive factors for achieving ER in intermediate- and high-risk DTC patients after treatment with 100 mCi of iodine.

EP-0440

Evaluation of the clinical utility of [^{18}F]FDG PET/CT in the detection of non-metastatic disease in differentiated thyroid cancer

M. Opalinska[1], *K. Undas*[2], *M. Olesiński*[2], *M. Osiowski*[2], *K. Kaczmarek*[2], *E. Chudyba*[2], *T. Gorczański*[2], *A. Sowa-Staszczak*[1], *M. Buziak-Bereza*[1], *M. Trofimuk-Muldner*[1], *A. Hubalewska-Dydejczyk*[1];
[1]Chair and Department of Endocrinology, Jagiellonian University Medical College, Krakow, POLAND, [2]The Student Scientific Group of Nuclear Medicine, Jagiellonian University Medical College, Krakow, POLAND.

Aim/Introduction: Approximately 30% of patients with disseminated differentiated thyroid cancer (DTC) experience loss of iodine sensitivity during the course of therapy. This clinical feature is associated with increased tumor aggressiveness and reduced survival at 10 years. The localization of non-radioiodine avid DTC metastases in the setting of elevated concentrations of thyroglobulin (Tg) often remains a diagnostic challenge. In this clinical setting, positron emission tomography with 2-[18F]fluoro-2-deoxy-D-glucose (PET/CT with [18F]FDG) is increasingly used, usually after stimulation with exogenous thyrotropic hormone (rhTSH).The primary objective of the study was to determine the cut-off point of baseline and stimulated Tg levels in patients with differentiated thyroid cancer (DTC) who have elevated baseline Tg levels, negative aTg under the TSH suppression and a negative whole body scintigraphy (WBS) with 131I. A secondary aim of the study was to analyze the clinical and histopathological factors associated with FDG avidity of metastatic lesions on PET/CT. ***Materials and Methods:*** Eighty-one patients with DTC, negative 131I-WBS and

neck ultrasound but elevated baseline Tg levels who underwent FDG-PET/CT for suspected recurrent/metastatic disease were included in the analysis. All patients had undergone a total or near-total thyroidectomy followed by radioiodine therapy. The [^{18}F]FDG PET/CT results were correlated with baseline and stimulated Tg levels as well as clinical and histopathological findings. ***Results:*** The mean age of the patients was 53.94 (42-69) years. Papillary carcinoma was diagnosed in 62 patients, follicular carcinoma in 14 and oncocytic carcinoma in five. Women accounted for 63.9% and men for 36.1% of patients. In the evaluated population, recurrence was detected in the thyroidectomy bed by PET/CT with [18F]FDG in 15 patients (16.7%), metastatic lesions in the neck lymph nodes in three patients (4.3%) and in the bones in four patients (4.9%). Of all histopathological parameters analyzed, only the presence of angioinvasion discriminated patients with FDG-avid metastatic lesions (p=0.019). A significant correlation was observed between positive PET results and elevated Tg levels (p = 0.03). ROC curve analysis showed a cut-off point 6,775 ng/ml for baseline Tg ((AUC): 0,737 (95% CI: 0,611-0,862), Youden index 0,489, sensitivity 60%, specificity 89,9%). For baseline and stimulated Tg, the minimum baseline value at which PET detected a relapse was 0.04 and 1.93 ng/ml, respectively. ***Conclusion:*** PET/CT with [18F]FDG is a very sensitive tool for the detection of recurrent and/or metastatic DTC. Baseline Tg and stimulated Tg concentrations are strongly correlated with positive PET/CT with [18F]FDG.

EP-0441

Quantitative Tc-99m MIBI SPECT/CT parameters can predict malignancy in indeterminate thyroid nodules-preliminary results

M. Araz*, &. Mesci, E. D. Avci, C. Soydal, O. B. Aksu, E. Eraslan, C. Konca, M. F. Erdogan, N. Ö. Kucuk;*
Ankara University, Ankara, TÜRKIYE.

Aim/Introduction: Tc-99m MIBI planar scan is useful in predicting thyroid malignancy, despite high false positivity rates.The aim of this study was to evaluate if quantitative Tc-99m MIBI SPECT/CT parameters can predict malignancy in patients with indeterminate thyroid nodules and to compare its performance with planar only imaging. ***Materials and Methods:*** In this prospective study, following ethics committe approval, 50 patients were planned to be recruited. The preliminary results including data of 17 patients (14F,3M mean age:56.05±11.5) with thyroid nodules enrolled between March 2024-April 2025 are presented here. All patients had at least one FNAB result in Bethesda Category III-IV. Tc-99m MIBI thyroid SPECT/CT imaging was performed. Planar images were evaluated visually to define target nodules as Tc-99m MIBI positive or negative. SUVmax, SUVmean, volume and total Tc-99m MIBI uptake (SUVmeanXvolume) were calculated on SPECT/CT images. All patients underwent surgery (lobectomy or total thyroidectomy) and final histopathological results are used for confirmation. Mean values of quantitative parameters are compared in groups with benign and malignant pathology. Sensitivity, specificity, PPV,NPV and accuracy are calculated both for planar imaging and SPECT/CT quantitative imaging. ***Results:*** A total of 21 nodules in 17 patients were evaluated, 8 of which were malignant and 13 benign on final pathology. On planar images, 9 nodules were Tc-99m MIBI negative, and 12 nodules were Tc-99m MIBI positive. Chi-square test revealed signficant difference in malignancy frequency according to Tc-99m MIBI positivity (p=0.016). None of the benign nodules were Tc-99m MIBI positive. Sensitivity, specificity, PPV, NPV and accuracy of planar imaging were calculated as: 100%, 50%, 46%, 100%, %65. Mean value of SUVmean was significantly higher in malignant nodules compared to benign nodules (p=0.045, 8.33±3.78 vs 4.39±2.34). Although not reached statistical significance, mean SUVmax values were also higher (p>0.05, 18.55±11.53 vs 8.46±5.31). ROC curves generated for SUVmax revealed that a cutoff of 6.8 was able to determine malignancy with a sensitivity of 100% and specificity of 72% (AUC: 0.857, p=0.042). PPV, NPV and accuracy were 66%,100%, 81%. Volume calculated within the ROI and total Tc-99mMIBI uptake didn't differ among groups. ***Conclusion:*** The results imply that Tc-99m MIBI planar imaging can be used as a rule out test for malignancy in thyroid nodules with indeterminate cytology. SUVmax of thyroid nodules calculated on SPECT/CT imaging increases specificity, PPV and accuracy of Tc-99m MIBI planar scintigraphy.

EP-0442

Quantification of I-131 Thyroid Remnant Uptake in Patients with Thyroid Cancer

E. Amini*[1], C. Kim[2], A. Al-Busaidi[3], R. Klein[4], W. Zeng[4];*
[1]Ottawa Hospital Research Institute, Ottawa, ON, CANADA, [2]University of Ottawa, Ottawa, ON, CANADA, [3]Sultan Qaboos Comprehensive Cancer Care and Research Centre, Muscat, OMAN, [4]The Ottawa Hospital, Ottawa, ON, CANADA.

Aim/Introduction: Radioiodine ablation is commonly performed after thyroidectomy for well-differentiated thyroid cancer (DTC). While thyroid remnant assessment is primarily visual, advancements in imaging software now allow for quantitative evaluation using standardized uptake values (SUV). Due to conflicting findings on the association between thyroid remnant uptake and thyroglobulin (Tg) levels, we sought to quantify thyroid remnant uptake in SUV and evaluate its correlation with post-therapy Tg across different risk groups. ***Materials and Methods:*** This retrospective study included patients with DTC referred for radioiodine ablation between 2015 and 2017 at an academic-affiliated hospital. All patients received Thyrogen pretreatment, and those with distal metastases or positive anti-Tg antibody were excluded. Post-therapy single-photon emission computed tomography/computed tomography (SPECT/CT) was used to quantify thyroid remnant uptake in SUV, with attenuation, scatter, and resolution recovery corrections. The remnant was segmented using an SUV_{max} threshold of 0.5, and total remnant uptake (SUV_{total}) was obtained; a threshold of 0.1 was also tested for robustness. Patients were stratified into low-intermediate, high-intermediate, and high-risk groups based on clinical risk with the corresponding therapeutic doses (mCi) of 31 ± 5, 100 ± 3, and 138 ± 14. The primary outcome was the correlation between SUV_{total} and post-therapy Tg levels. ***Results:*** The cohort included 174 adults (age: 50.7±16.0 yr, F:M=110:64). For the low-intermediate, high-intermediate, and high-risk groups (n=58, 52, and 64), stimulated Tg (pmol/L) values (median [interquartile range (IQR)]) were 3.8 [1.2, 8.7], 7.1 [1.7, 25.3], and 13.4 [3.6, 74.0], respectively. Corresponding thyroid remnant SUV_{total} values (median [IQR]) were 271.5 [82.9, 665.5], 51.4 [9.8, 138.8], and 33.1 [10.7, 108.5], respectively. Moderate correlations were found between SUV_{total} and Tg in low- and high-intermediate groups (Spearman's ρ = 0.65, $p<0.001$; ρ = 0.61, $p<0.001$, respectively). No significant correlation was found in the high-risk group (ρ = 0.12, p=0.33). Repeat analysis with a lower SUV_{max} threshold showed mildly higher SUV_{total} values, without significant correlation changes (ρ = 0.64, 0.60, and 0.12 for the low-intermediate, high-intermediate, and high-risk groups, respectively). ***Conclusion:*** Thyroid remnant quantification with current software tools is both feasible and robust. A good correlation between remnant uptake and Tg levels was observed in low- and high-intermediate risk groups, but no significant correlation was found in the high-risk group, possibly due to micro-metastases, inflammation, or aggressive histological subtypes. These findings support the potential of quantitative thyroid uptake as a reliable alternative to Tg in post-ablation follow-up and a promising predictor of disease recurrence.

EP-0443

Focal FDG Uptake in the Thyroid Gland: A Clinical Dilemma in Primary Malignancy

M. Dasar, *G. Koca, A. Özden, K. Demirel, A. Akbulut, M. Korkmaz; University of Health Sciences, Ankara Training and Research Hospital, Department of Nuclear Medicine, Ankara, TÜRKIYE.*

Aim/Introduction: Incidentally detected focal thyroid lesions are common clinical situation in PET-CT scans performed for other primary origin. However, uncertainty in differentiating the benign from malignant lesions may influence treatment strategies. This study retrospectively analyzed the clinical significance of incidental focal thyroid involvement and the diagnostic role of SUVmax values in patients evaluated for primary malignancies, with reference to literature data. The aim was to determine the optimal SUVmax cutoff value for predicting thyroid malignancy and to contribute to clinical decision-making. ***Materials and Methods:*** A retrospective analysis of 3720 patients with primary malignancies who underwent FDG PET/CT scans (February 2022-April 2025) was performed. Patients with primary thyroid cancer were excluded. Cases with focal thyroid FDG uptake were included. SUVmax values of all lesions were recorded, and serum thyroid function tests (TSH, free T4) were evaluated. Histopathological confirmation (biopsy) and clinical-radiological follow-up served as the reference standard for benign-malignant differentiation. ***Results:*** Focal thyroid FDG uptake was detected in 82 of 3720 patients (2.2%). The mean age was 65±9.74 years (female: 51.5%, male: 48.5%), with no significant differences in age, sex, or thyroid function tests (TSH, free T4) between benign and malignant groups (p>0.05). Fine-needle aspiration biopsy was avaliable in 33 patients, confirming malignancy in 10 cases (1 renal cell carcinoma metastasis, 9 papillary carcinomas). The mean SUVmax of malignant lesions (14.89±11.04) was significantly higher than that of benign lesions (7.46±3.94) (p<0.001). ROC analysis revealed an AUC (Area Under Curve) of 0.801 (95% CI: 0.65-0.95) for SUVmax in discriminating malignancy. The optimal cut-off SUVmax ≥8.01 yielded 78% sensitivity and 83% specificity. ***Conclusion:*** In our study, the incidence of focal thyroid FDG uptake in patients with primary malignancies undergoing FDG PET/CT was 2.2%. Malignancy was confirmed in 30.3% of biopsied cases and diagnostic performance with SUVmax of ≥8.01 aligns with the existing literature. However, our small malignant cohort (n=9) and high SUVmax variance limit generalizability of the findings. Further large-scale studies are needed to emphasize the clinical significance of FDG PET/CT in incidentally detected focal thyroid lesions.

EP-0444

Early FDG-PET Post-RAI in Differentiated Thyroid Cancer: Detecting Disease with Sub-Standard Thyroglobulin Levels

E. Greco[1], *E. Fortunati*[2], *L. Zanoni*[3], *C. M. P. Sgro*[1], *G. A. Fuso*[1], *G. Bianciardi*[1], *G. Cuzzani*[1], *L. Carrara*[1], *C. Malizia*[2], *A. Golemi*[2], *E. Lodi Rizzini*[4], *L. Calderoni*[2], *E. Tabacchi*[2], *S. Fanti*[1,2];
[1]*Nuclear Medicine, Alma Mater Studiorum University of Bologna, Bologna, ITALY,* [2]*Nuclear Medicine, IRCCS Azienda Ospedaliero-Universitaria di Bologna, Bologna, ITALY,* [3]*Nuclear Medicine, AST Pesaro-Urbino, Pesaro-Urbino, ITALY,* [4]*Radiation Oncology, IRCCS Azienda Ospedaliero-Universitaria di Bologna, Bologna, ITALY.*

Aim/Introduction: FDG-PET is not routinely performed early postoperatively or post-radioiodine treatment for differentiated thyroid cancer (DTC). However, American Thyroid Association (ATA) guidelines suggest its consideration in selected patients with suspected recurrent or metastatic disease, particularly those exhibiting elevated or rising serum thyroglobulin (Tg) levels despite a negative 131-Iodine (131-I) whole body scan (WBS), or with aggressive histologic variants, especially in intermediate and high-risk ATA categories. ***Materials and Methods:*** Retrospective single-centre study enrolling patients (n = 41) who underwent FDG-PET from 2022 to 2024 and 131-I WBS within a 1-year timeframe. Patients were stratified by ATA risk (low, intermediate, high) and PET status (positive/negative), with basal and stimulated Tg recorded, alongside assessment of thyroglobulin antibodies (TgAb) and mutation status. A qualitative analysis per patient was conducted in order to search for a correlation between PET positivity and patient's basal and stimulated Tg, TgAb and mutation. ***Results:*** Overall, 41 patients with DTC were enrolled (median age 55 years). In the low-risk group (n=2), 1 PET-positive patient had basal Tg 8.2 ng/mL and stimulated Tg 227.2 ng/mL, with negative TgAb and mutations present. In the intermediate-risk group (n=32), 12/32 (38%) were PET-positive with mean basal Tg 2.3 ng/mL (median 0.85 ng/mL, IQR 0.48-1.05) and mean stimulated Tg 21,13 ng/mL (median 5,9ng/mL, IQR 1,7-15,85). Among these, 3 had positive TgAb (two with basal Tg < 2 ng/mL), 5 had mutations. In the high-risk group (n=7), 5/7 (71%) were PET-positive with mean basal Tg 1099.34 ng/mL (median 15.7 ng/mL, IQR 11.8-468.7) and mean stimulated Tg 1282.04 ng/mL (median 118.2 ng/mL, IQR 21.8-1257.6). One high-risk patient with positive TgAb had basal Tg 0.5 ng/mL and stimulated Tg 12.6 ng/mL. ***Conclusion:*** While basal Tg 2-5 ng/mL and stimulated Tg > 10 ng/mL are often considered thresholds for further investigation including FDG-PET, our data reveal PET positivity in patients, particularly in the intermediate-risk group, with values below these cut-offs. The presence of mutations in PET-positive patients and PET positivity in some TgAb-positive individuals with low Tg suggests these factors may influence FDG avidity independently of absolute Tg levels. Integrating molecular profiling and TgAb assessment into risk stratification might improve early FDG-PET selection beyond traditional Tg measurements, potentially identifying more patients with persistent/recurrent disease. Larger studies are needed to refine these criteria in line with ATA guidelines.

EP-0445

Value of ^{18}F-FCH PET/CT for Diagnosing and Differentiating Hyperplasia From Adenoma

M. Li, *H. Pang;*
The First Affiliated Hospital of Chongqing Medical University, Chongqing, CHINA.

Aim/Introduction: Objective: Due to the different surgical approaches for hyperplasia and adenoma in primary hyperparathyroidism, accurate preoperative diagnosis and identification are key factors affecting the surgery. 18F-FCH PET/CT is an effective tool for imaging the parathyroid glands and allows quantitative analysis. The purpose of this study is to analyze the diagnostic and differential value of 18F-FCH PET/CT for hyperplasia and adenoma. ***Materials and Methods:*** This was a retrospective analysis of data related to 63 patients undergoing 18F-FCH PET/CT at the First Hospital of Chongqing Medical University between December 2023 and December 2024. All procedures were completed, and postoperative pathological data were available for all patients. Based on the patient level, laboratory parameters such as PTH and serum calcium were compared between groups, and the analysis of PET/CT diagnosis and differences in metabolic parameters was performed based on individual parathyroid lesions. The Mann-Whitney U test and binary logistic stepwise regression analysis were also used for univariate and multivariate analyses of information related to hyperplasia and adenomas, and the indicators found to be significant on multivariate analysis were used to determine cutoff values by receiver operating characteristic analysis. ***Results:*** A total of 75 parathyroid lesions were ultimately removed postoperatively in 63 patients, including 41 hyperplasia and 34 adenoma, and multiple lesions were present simultaneously in 9 patients. Based on patient-level analysis, there were no significant differences in laboratory parameters between the hyperplasia, adenoma, and hyperplasia combined with adenoma groups (P > 0.05). Based on individual lesion analysis, the

sensitivity of PET/CT for the diagnosis of hyperplasia was 68.29% and that of adenoma was 97.06%. The sensitivity of PET/CT for adenoma was significantly higher than that for hyperplasia, and lesion size had a significant effect on the imaging results; in terms of differences in metabolic parameters, dual-phase SUVmax, MTV and TLG were significant in univariate analysis, and multivariate analysis showed the delayed TLG (cut-off value of 6.421) was a more reliable index for differentiating hyperplasia from adenoma (P=0.002). ***Conclusion:*** The diagnostic value of 18F-FCH PET/CT for adenoma is higher than that of hyperplasia, and delayed-phase TLG (cut-off value of 6.421) can differentiate between hyperplasia and adenoma.18F-FCH PET/CT is a more reliable means of imaging the parathyroid and can provide effective information for the diagnosis and etiology of hyperparathyroidism, and delayed TLG can differentiate hyperplasia from adenoma at the imaging level and help in the selection of clinical treatment options.

EP-0446

Prognostic risk factors in patients with papillary thyroid microcarcinoma (PTMC) with excellent response (ER) one year after initial treatment.

A. Marongiu, *S. Nuvoli, A. Falchi, S. Vargiu, A. Spanu, G. Madeddu; Unit of Nuclear Medicine, University of Sassari, Sassari, ITALY.*

Aim/Introduction: PTMC, generally with a favorable prognosis, may exhibit a high risk of disease progression, in some cases, during follow-up after primary therapy. We further investigated whether the evaluation of the response to thyroidectomy and radioiodine therapy one year after initial treatment may serve as a useful tool for predicting recurrence or disease persistence in PTMC patients during follow-up. ***Materials and Methods:*** We retrospectively enrolled 342 PTMC patients from a large cohort, all of them with ER defined to the 2015 ATA guidelines as negative imaging and stimulated thyroglobulin (Ps-Tg) level <1.0 ng/ml. All patients underwent total thyroidectomy and radioiodine therapy; 277/342 patients were females, and 195/342 were younger than 55 years. Tumor size was >5 mm in 198/342 patients. Risk factors identified at surgery included capsular infiltration (CI, 23 cases), minimal extrathyroid extension (mETE, 29 cases), multifocality/multicentricity (MM, 105 cases), and vascular invasion (VI, 15 cases). One year after treatment, Ps-Tg was <0.2 ng/ml in 258 patients (Group 1) and between 0.2 and 1.0 ng/ml in 84 patients (Group 2). ***Results:*** During follow-up, 27/342 patients (7.9%) developed metastases in the neck in 25 cases, and in lung and mediastinum in two cases; 16/27 (6.2%) belonged to Group 1, and 11 (13%) to Group 2, with significant difference (p=0.04). Twenty-five/27 patients were females, 15 were younger than 55 years. Tumor size was >5 mm in 20 cases. Risk factors, such as CI, mETE, MM, and VI, either individually or in combination, were present in 11/16 Group 1 patients and 5/11 Group 2 patients. Univariate analysis evidenced that metastasis development was significantly influenced by Ps-Tg levels between 0.2 and 1.0 ng/ml (OR 2.279 [95% CI 1.013-5.129]; p=0.047) and by mETE (OR 3.627 [95% CI 1.332-9.877]; p=0.012). Age, sex, tumor size, CI, MM, or VI were not metastasis predictors. Multivariate analysis confirmed the significance of Ps-Tg >0.2 but <1.0 ng/ml (OR 2.335 [95% CI 1.026-5.317]; p=0.043) and mETE (OR 3.733 [95% CI 1.353-10.303]; p=0.011) as independent metastasis predictors. ***Conclusion:*** Our study suggests that in PTMC patients with ER at the first year after initial therapy, Ps-Tg levels between 0.2 and 1.0 ng/ml and the presence of mETE at surgery are important prognostic factors for predicting metastasis appearance, particularly in the neck. The evaluation of these factors one year after primary therapy may provide valuable insights for better identifying patients at risk for disease progression.

EP-0447

^{18}F-FDG PET/CT Illuminating The Roadmap For Tracking Differentiated Thyroid Cancer

T. Dardouri[1], *H. Boudriga*[1], *A. Ezzine*[1], *S. Mensi*[1], *J. Houas*[2], *M. Grassa*[2], *R. Sfar*[1], *K. Chatti*[1];
[1]*Department of nuclear medecine of Sahloul hospital, Sousse, TUNISIA,* [2]*Department of Otorhinolaryngology of Farhat Hached hospital, Sousse, TUNISIA.*

Aim/Introduction: Fifteen per cent of patients with differentiated follicular thyroid carcinoma (DTC) develop metastatic disease progression during follow-up. Fluorine-18 Fluorodeoxyglucose Positron Emission Tomography (^{18}F-FDG PET) is an accurate imaging tool for the evaluation of agressive disease extension. The aim was to assess the value of ^{18}F-FDG PET/CT in the follow-up of DTC and its therapeutic impact. ***Materials and Methods:*** We included 30 patients followed for DTC who underwent ^{18}F-FDG PET with at least 18-month follow-up after iodine treatment. ***Results:*** The mean age was 58 years, with a predominance of females. All our patients had undergone total thyroidectomy with or without lymph node dissection and postoperative iodine treatment. According to ATA 2015, 73% of our patients were classified as high-risk group. During follow-up, 23 patients (77%) had an incomplete structural response and thyroglobulin (Tg) level was greater than 100 ng/ml in almost cases. For the seven remaining patients classified as having an incomplete biochemical response, ^{18}F-FDG PET scans were negative in four patients with Tg average under stimulation of 32.2 ng/ml. Besides, they identified cervical lymph node metastases in two patients and thus upgraded as incomplete structural response. The results of ^{18}F-FDG PET/CT led to a change in treatment plan in 30% of cases, due to upgrading or identification of new metastatic sites. ***Conclusion:*** Following iodine treatment , ^{18}F-FDG PET/CT has proven to be effective in dynamic response classification of persistent and recurrent DTC in addition to biochemical tumour markers and conventional imaging procedures. It helps with individualized treatment approaches and provides clinicians with insightful information on tumor biology.

EP-0448

Loco-regional relapse and metastatic recurrence in BRAFV600E-mutated papillary thyroid carcinoma patients during more than five years of follow-up

T. Makazlieva[1], *N. Manevska*[1,2], *S. Stojanoski*[1], *N. Bozinovska*[1], *A. Jankulovska*[1], *B. Stoilovska Rizova*[1], *A. Eftimov*[3], *S. Kostadinova-Kunovska*[3], *R. Jovanovic*[3];
[1]*Institut of pathophysiology and nuclear medicine, Medical faculty, University Ss Cyril and Methodius, Skopje, NORTH MACEDONIA, THE REPUBLIC OF,* [2]*University Institute of positron emission tomography, Skopje, NORTH MACEDONIA, THE REPUBLIC OF,* [3]*Institut of pathology, Medical faculty, University Ss Cyril and Methodius, Skopje, NORTH MACEDONIA, THE REPUBLIC OF.*

Aim/Introduction: The BRAFV600E mutation is the most frequent genetic alteration in patients with papillary thyroid carcinoma (PTC). Our study aimed to evaluate the frequency of loco-regional relapse and metastatic recurrence in BRAFV600E-mutated PTC patients followed for more than five years. ***Materials and Methods:*** Thirty-five PTC patients with detected BRAFV600E mutation from the primary tumor tissue were followed after initial diagnosis and treatment for more than 5 years (range: 5 - 20 years). We used the Cobas® 4800 BRAFV600 Mutation Test on the Cobas Z480 Real-Time PCR IVD Machine (Roche) for detecting the V600E mutation. All 35 patients underwent total thyroidectomy, and 31 patients additionally received radioiodine ablation followed by a post-ablative whole-body scan. Follow-up included laboratory assessments - free thyroxine (FT4), TSH, serum thyroglobulin (sTg), and antithyroglobulin antibodies (TgAb)-measured 3 to 6 months during the first year, then at regular intervals thereafter.

Neck ultrasonography (US) was performed using a linear probe for small parts in all patients. According to laboratory and imaging data, their therapy response was classified into three categories: complete response, biochemical incomplete response, and structural incomplete response (persisting structural disease). ***Results:*** Among the 35 patients, the female-to-male ratio was 30/5, and the mean age at diagnosis was 48.6±12.8 years. Thirteen patients (37.1%) were aged ≥ 55 years, and 22 (62.9%) were < 55 years. According to TNM staging, 18 patients (51.4%) were in Stage I, 6 (17.1%) in Stage II, 8 (22.9%) in Stage III, and 3 (8.6%) in Stage IV. During follow-up 6 (17.1%) of the patients demonstrated elevated sTg level (with 2 patients classified as biochemical incomplete responders). Meanwhile, 29 patients (82,9 %) maintained low or undetectable sTg and TgAb levels, representing complete responders. Structural disease persistence was confirmed in 3 patients (8.6 %) through neck ultrasonography and histopathology after lymphadenectomy. Distant metastases were detected in 2 patients (5%): one with pulmonary metastases and one with tracheal infiltration and lymph node involvement. ***Conclusion:*** In our study, 29 out of 35 patients (82.9 %) responded completely to treatment. Our analysis did not reveal a significant association between the BRAFV600E mutation and the risk of loco-regional relapse or distant metastases during a more than 5-year follow-up.

EP-23

e-Poster Area

B: Imaging Clinical Studies -> B1 Oncological Imaging Clinical Study -> B20 Gynaecological

EP-0449

Efficacy of Ca-125 exchange rate and ^{18}F-FDG Pet/Ct in predicting progression in ovarian cancer

Z. Mammadkhanli, *F. Ustun;*
Trakya University, Edirne, TÜRKIYE.

Aim/Introduction: Ovarian cancer is one of the leading causes of cancer-related deaths among gynecologic malignancies. Many studies have shown that ^{18}F-FDG PET/CT provides high accuracy in recognizing ovarian cancer recurrence. The aim of this study was to investigate the relationship between progression in CA-125 marker and ^{18}F-FDG PET/CT and to compare the diagnostic accuracy of these two methods and to evaluate their contribution in progression follow-up. ***Materials and Methods:*** In this retrospective study, a total of 330 patients with serous ovarian cancer who were admitted to the Nuclear Medicine Clinic between January 2013 and January 2018 were analyzed. The study included 23 patients who underwent 18F-FDGPET/CT imaging for suspected recurrence and for whom CA-125 marker data were available. Each patients CA-125 value at the time of imaging and CA-125 values approximately one month ago were recorded. In addition, ^{18}F-FDG PET/CT images were re-evaluated for progression. In the study, CA-125 change rate was calculated and its relationship with progression was evaluated and the predictive power of CA-125 change rate was determined by statistical analysis. ***Results:*** All patients included in the study were diagnosed with serous ovarian carcinoma. All patients underwent ^{18}F-FDG PET/CT imaging with suspicion of recurrence due to elevatedCA-125 marker. The mean age of the patients was 55±12 years (32-80). In the study, CA-125change rate was calculated and its relationship with progression was evaluated. Then, Receiver Operating Characteristic (ROC) analysis was performed to evaluate the predictive power ofCA-125 change rate. As a result of the ROC analysis, the area under the curve (AUC) of CA-125 change rate was calculated as 0.826 with a standard error of 0.077 and p=0.070. The confidence interval was 0.676-0.976. The optimal cut-off value was determined as 41.5, indicating that patients with a percentage increase of CA-125 change rate above 41.5 constituted an important cut-off value for detecting progression with 18F FDG PET/CT. Sensitivity and specificity calculations showed that the sensitivity and specificity of CA-125 change rate were 87.5% and 66.7%,respectively. ***Conclusion:*** This study shows that ^{18}F-FDG PET/CT imaging can detect progression inpatients with a CA125 rate of change rate cut-off value above 41.5. Further studies with a larger number of patients are needed.

EP-0450

PET/CT-Guided Patient Selection for Secondary Cytoreduction in Recurrent Ovarian Cancer

C. Csikos[1], *A. Varga*[1], *Z. Hascsi*[2], *S. Molnár*[3], *Z. T. Krasznai*[3], *I. Garai*[1,2];
[1]*Division of Nuclear Medicine and Translational Imaging, Department of Medical Imaging, Faculty of Medicine, University of Debrecen, Debrecen, HUNGARY,* [2]*Scanomed Ltd., Debrecen, HUNGARY,* [3]*Department of Obstetrics and Gynaecology, Faculty of Medicine, University of Debrecen, Debrecen, HUNGARY.*

Aim/Introduction: Secondary cytoreductive surgery (SCS) may improve survival in recurrent ovarian cancer, but patient selection remains challenging. Conventional imaging modalities (CT, MRI) are limited in predicting complete surgical success. Our prior meta-analysis suggested that a favorable PET/CT result could predict complete cytoreduction in almost 90% of the cases [1]. This study aimed to evaluate the added value of PET/CT in preoperative assessment for SCS. ***Materials and Methods:*** We retrospectively reviewed 196 patients with ovarian cancer who underwent [^{18}F]FDG PET/CT between 2018-2023 in our clinic. Of these, 22 patients with recurrent ovarian cancer were eligible for SCS based on conventional imaging, and also underwent [^{18}F] FDG PET/CT as part of the preoperative assessment. Diagnostic performance metrics were calculated, and decision curve analysis (DCA) was performed to assess the clinical utility of PET/CT in guiding surgical decision-making. ***Results:*** Among the 22 patients selected for SCS based on conventional imaging, PET/CT prevented surgery in 9/22 patients by identifying findings suggestive of inoperability. Of the 13 patients who were considered operable by PET/CT and underwent surgery, 11/13 had complete cytoreduction (PPV: 84.6%). PET/CT demonstrated superior clinical utility in decision curve analysis compared to both a "treat all" and a "treat none" strategy, offering greater net benefit across a wide range of surgical thresholds. As an operable state on conventional imaging was the initial inclusion criterion for surgery, it functioned as the "treat all" approach in this analysis. ***Conclusion:*** Our findings confirm that preoperative PET/CT can provide clinically meaningful value in selecting candidates for secondary cytoreduction. PET/CT results improved decision-making and offered a higher net benefit compared to conventional imaging. These results support the finding of our prior meta-analysis in which a high positive predictive value of PET/CT was found in this setting. Our results suggest that PET/CT may be a useful tool to evaluate patient eligibility for secondary cytoreduction of recurrent ovarian cancer and avoid non-beneficial interventions. ***References:*** 1. Csikos C, Czina P, Molnár S, Kovács AR, Garai I, Krasznai ZT. Predicting Complete Cytoreduction with Preoperative [^{18}F]FDG PET/CT in Patients with Ovarian Cancer: A Systematic Review and Meta-Analysis. Diagnostics. 2024;14(16):1740. https://doi.org/10.3390/diagnostics14161740.

EP-0451

Prognostic Value of Metabolic Biomarkers in Locally Advanced Cervical Cancer: Is Survival Predictable?

Y. Eryilmaz, *O. Kodaz, G. Kaya, P. Özgen Kıratlı;*
Hacettepe University Medical School Department of Nuclear Medicine, Ankara, TÜRKIYE.

Aim/Introduction: Cervical cancer is one of the most common malignancies among women. Guidelines recommend chemoradiotherapy (CRT) followed by brachytherapy for patients with locally advanced cervical cancer (LACC). However, recurrence occurs in approximately one-third of patients within two years following CRT, and the 5-year overall survival rate is around 70%. This study aims to examine the relationship between pre-treatment FDG PET/CT-derived volumetric parameters and progression-free survival (PFS) and overall survival (OS) in LACC. ***Materials and Methods:*** LACC patients staged with FDG PET/CT were retrospectively analyzed. For the primary tumor and metastatic lymph nodes, SUVmax, SUVmean, SUVpeak, metabolic tumor volume (MTV), total lesion glycolysis (TLG), and total lesion quotient (TLQ, product of MTV and SUVmean) were calculated. Follow-up data of the patients were obtained. Survival analyses were performed to assess the relationship between the volumetric parameters and both PFS and OS. ***Results:*** 35 patients with LACC followed for at least 6 months were included. The mean age was 55.1 ± 14.3 years. During the follow-up (mean 36.1 ± 2.4 months), disease progression was observed in 17 patients (49%, 8 local recurrences, 9 distant metastases) and sixteen patients died (46%). Median PFS and median OS were not reached (mean PFS: 43.5 ± 3.2 months). Among patients with a lower primary tumor TLQ value, median OS was 37 months (95% CI: 32.4-41.5), while in those with a higher TLQ, it was 55 months (95% CI: 51.2-58.7). OS was significantly shorter in the group with lower TLQ values ($p = 0.017$). When patients were grouped according to SUVmax, SUVmean, SUVpeak, MTV, and TLG values of the primary tumor and lymph node metastases, no statistically significant differences were found in predicting survival or the development of lymph node metastases. In binary regression analysis, among the 27 patients (77%) with lymph node metastases, only a lower TLQ value of the primary tumor was identified as a statistically significant poor prognostic factor for OS (Odds ratio: 5.62, $p = 0.032$). ***Conclusion:*** Previous studies have demonstrated an association between metabolic parameters and both PFS and OS in LACC. In contrast, our study found no significant association, possibly due to the limited sample size. Nonetheless, TLQ, introduced as a novel biomarker, was identified for the first time in the literature as a statistically significant prognostic marker for survival in LACC. TLQ may serve as a new metabolic parameter for predicting prognosis in terms of PFS and OS in LACC. Further validation in larger prospective cohorts is warranted.

EP-0452

Correlation of metabolic parameters and dissemination of preoperative 18F-FDG-PET/CT in endometrial cancer and its prognostic value

C. Ortiz Muñoz[1], *J. Rodríguez Gómez*[1], *E. Noriega Álvarez*[2], *F. Lopez-Bermejo García*[1], *D. Martínez Osorio*[1], *F. Pena Pardo*[1], *M. Talavera Rubio*[1], *V. Poblete García*[1];
[1]*Hospital General Universitario de Ciudad Real, Ciudad Real, SPAIN,* [2]*Hospital Universitario de Guadalajara, Guadalajara, SPAIN.*

Aim/Introduction: To assess the concordance of metabolic and dissemination parameters from preoperative staging 18F-FDG-PET/CT and their relationship with the prognosis of patients with endometrial cancer (EC). ***Materials and Methods:*** A retrospective observational analytical study of consecutive patients with a diagnosis of endometrial cancer (EC) confirmed by histopathology, who underwent preoperative 18F-FDG-PET/CT between January 2018 and December 2022, with a minimum follow-up of 2 years. We collected demographic variables and tumour characteristics (histology, grade, type, stage, affected nodal stations, and immunohistochemistry); as well as metabolic parameters from 18F-FDG-PET/CT such as metabolic tumour volume, total lesion glycolysis and maximum standardized uptake value (MTV, TLG, and SUVmax), and dissemination parameters (Dmax). Its relationship with progression-free survival (PFS) and overall survival (OS) was studied using Pearson's bivariate correlation and Kendall's Tau. ***Results:*** A total of 39 patients were evaluated, with a mean age of 65.7 years (range 39-91). Of these, 24 patients (61.5%) presented with endometrioid-type cancer, 13 patients (33.3%) with non-endometrioid-type, and 2 patients (5.1%) with mixed-type. Tumour grading were revealed, 17 patients (43.6%) grade G1, 12 patients (30.8%) grade G2, and 10 patients (25.6%) grade G3. During follow-up, 18 patients (46.2%) experienced recurrence, while 23 patients (59%) passed away. A positive correlation was found between MTV and tumour grade (Pearson 0.340; $p<0.05$). Besides, a negative correlation was observed between tumour type and both progression-free survival (PFS) and overall survival (OS) (Pearson -0.355 and -0.396, respectively; $p<0.05$), indicating that patients with non-endometrioid and mixed-type endometrial cancer exhibited lower PFS. Additionally, significant negative correlations were found between MTV and both progression-free survival (PFS) and overall survival (OS) (Kendall's Tau -0.243 and -0.309; $p<0.05$ and $p<0.01$, respectively), as well as between TLG and OS (Kendall's Tau -0.252; $p<0.05$), indicating that higher MTV and/or TLG values are associated with an increased risk of progression and death. The remaining variables studied, including dissemination parameters (Dmax), did not show statistically significant correlations. ***Conclusion:*** Our findings suggest that the metabolic parameters MTV and TLG obtained from preoperative staging 18F-FDG-PET/CT have potential prognostic value in determining the aggressiveness and progression of endometrial cancer (EC).

EP-0453

[18F]F-FDG PET-CT Imaging in Ovarian Carcinoma Patients: IAEA Coordinated POCA Project Study from Azerbaijan

F. Novruzov[1], *K. Huseynzade*[1], *E. Mehdi*[1], *N. Orujova*[2], *N. Aliyeva*[1], *G. Alibayli*[2], *D. Paez*[3], *F. Giammarile*[4,5], *E. Estrada Lobato*[6], *E. Mansurov*[7], *M. Isayeva*[8], *J. Aliyev*[9];
[1]*Department of Nuclear Medicine, The National Centre of Oncology, Baku, AZERBAIJAN,* [2]*Department of Nuclear Medicine, The National Centre of Oncology, Baku, AZERBAIJAN,* [3]*Head of the Nuclear Medicine and Diagnostic Imaging Section, Division of Human Health, Vienna, AUSTRIA,* [4]*International Atomic Energy Agency, Vienna, AUSTRIA,* [5]*Deaparment of Nuclear Medicine, Université de Lyon, Lyon, FRANCE,* [6]*International Atomic Energy Agency, Division of Human Health, Vienna, AUSTRIA,* [7]*Department of Medical Oncology, The National Centre of Oncology, Baku, AZERBAIJAN,* [8]*Columbia University, New York, NY, UNITED STATES OF AMERICA,* [9]*Department of General Surgery, The National Centre of Oncology, Baku, AZERBAIJAN.*

Aim/Introduction: Ovarian carcinoma is among the most challenging gynecologic malignancies, often diagnosed at an advanced stage due to its vague symptoms and silent progression. In this context, [^{18}F]FDG PET/CT has proven to be a powerful imaging modality—not only for staging and restaging but also for assessing recurrence and guiding therapeutic decisions with high sensitivity. Its ability to detect unexpected metastatic spread further enhances its clinical utility. ***Materials and Methods:*** This study included 95 ovarian carcinoma patients (mean age 53.7 years, range 23-79) enrolled in the IAEA POCA Project from Azerbaijan. Patients were grouped into ARM1 (pre-laparoscopy, n=8; post-laparoscopy, n=75) and ARM2 (elevated CA125, n=15). All underwent [^{18}F]FDG PET/CT imaging. Standard imaging protocols were followed: patients fasted for 6 hours, blood glucose was <150 mg/dL, and images were acquired 60 minutes post-tracer injection from skull base to mid-thigh. Low-dose CT was used for attenuation correction and anatomical localization; contrast-enhanced CT was performed when clinically indicated. ***Results:*** In ARM2, two patients showed critical findings: one had tracer uptake in paracolic fat and distant nodes, and the other had intense peritoneal involvement—both leading to treatment changes. Among the remaining 13 ARM2 patients: peritoneal implants were seen in 4; abdominal lymph nodes in 7; extra-abdominal nodes in 3; hepatic lesions in 1; ascites in 3;

and umbilical metastasis (Sister Mary Joseph nodule) in 1.In ARM1, abdominal lymph node metastases were seen in 32 patients; extra-abdominal nodes in 16; liver lesions in 11; ascites in 9; pleural effusion in 8; peritoneal carcinomatosis in 2; and other distant hypermetabolic lesions (lungs, adrenals, surgical sites) were noted. Bone metastasis (L1 vertebra) was detected in 1 patient. Overall, [^{18}F]FDG PET/CT prompted management changes in 25 patients: 16 major (e.g., shift in chemotherapy due to progression or poor response) and 9 minor (e.g., initiation of therapy based on newly identified distant disease). ***Conclusion:*** [^{18}F]FDG PET/CT demonstrated significant clinical utility in our ovarian carcinoma patients by providing comprehensive disease assessment in a single examination. The modality effectively guided treatment decisions through precise localization of disease sites and accurate evaluation of disease extent. For patients with elevated CA125 levels, [^{18}F]FDG PET/CT offered clear visualization of recurrence patterns, enabling tailored therapeutic approaches. This imaging approach streamlined the diagnostic pathway and enhanced clinical management efficiency.

EP-0454

Development and validation of pretreatment ^{18}F-FDG PET/CT and MRI radiomics deep learning signatures to predict progressionfree survival in locally advanced cervical cancer

J. Song, *H. Yi;*
Zhejiang Cancer Hospital, Hangzhou, CHINA.

Aim/Introduction: Data regarding whether patients can achieve long-term progression-free survival (PFS) through treatment is essential to improve risk-adapted treatment strategies of locally advanced cervical cancer (LACC). However, the routinely used preoperative determination method is not accurate enough. The present study investigated and validate a combination model based on ^{18}F-FDG PET/CT and contrast-enhanced MRI to predict the diseases progression in LACC patients treated with chemoradiotherapy (CRT). ***Materials and Methods:*** Retrospective data were gathered for 346 patients (276 for training and 70 for testing) with LACC who underwent ^{18}F-FDG PET/CT and MRI [T2, T1C, diffusion-weighted imaging (DWI) and apparent diffusion coefficient (ADC)] before CRT between June 2016 and October 2021. Radiomics deep learning signature (RDPs) were developed based on ten machine-learning techniques. These signatures were integrated with the clinicopathological factors into a nomogram for clinical applications. The evaluation of the model's performance was conducted through the metrics of the area under the curve (AUC). ***Results:*** The median follow-up was 35.82 (range: 1.17-67.92) months. During the observation period, 96 (27.75%) patients exhibited disease progression. The RDPs showed excellent performance with a high AUC for predicting disease progression and PFS in training cohort (AUC, 0.93; 95% CI: 0.89-0.96; PFS, $p < 0.05$) and testing cohort (AUC, 0.82; 95% CI: 0.72-0.92; PFS, $p < 0.05$). The clinical factors of International Federation of Gynecology and Obstetrics (FIGO) stage and squamous cell carcinoma antigen (SCC-Ag) level were associated with PFS ($p < 0.05$). The combination nomogram showed better prediction capability for disease progression (AUC, 0.97; 95% CI:0.95-0.99) in training cohort and testing cohort (AUC, 0.87; 95% CI:0.79-0.96), with high sensitivity (0.84 and 0.79), specificity (0.93 and 0.84) and accuracy (0.91 and 0.83). ***Conclusion:*** ^{18}F-FDG PET/CT and MRI radiomics deep learning signatures had significantly good predictive value for diseases progression in patients with LACC treated with CRT, which may justify more aggressive treatment in patients identified with high probability of progression.

EP-0455

Enhanced tumor PET imaging with self-assembled peptide probe [^{68}Ga]HGFYp-NOTA

H. Wu[1,2], *Y. Liu*[1], *H. Wang*[1], *J. Wu*[1], *X. Li*[2], *P. Zou*[1];
[1]*NHC Key Laboratory of Nuclear Medicine, Jiangsu Key Laboratory of Molecular Nuclear Medicine, Jiangsu Institute of Nuclear Medicine, Wuxi, CHINA,* [2]*College of Pharmaceutical Science, Zhejiang University of Technology, Hangzhou, CHINA.*

Aim/Introduction: Positron emission tomography (PET) plays a crucial role in the early detection and monitoring of tumors. However, the rapid clearance of most small molecule PET probes from the tumor site limits their clinical utility. This study aims to investigate the potential of a novel ^{68}Ga-labeled self-assembled peptide probe, [^{68}Ga]HGFYp-NOTA, to enhance PET signal retention in tumors and provide a basis for designing long-lasting PET probes. ***Materials and Methods:*** The probe precursor HGFYp-NOTA and its control probe precursor HGFY-NOTA were synthesized using solid-phase peptide synthesis. The self-assembly properties of HGFYp-NOTA were evaluated using alkaline phosphatase (ALP) and characterized by transmission electron microscopy (TEM) and rheological analysis. The in vivo experiments were conducted on BALB/c nude mice bearing HeLa tumor xenografts. The mice were divided into three groups: the control group ([^{68}Ga]HGFY-NOTA), the low-concentration probe group ([^{68}Ga]HGFYp-NOTA), and the high-concentration probe group ([^{68}Ga]HGFYp-NOTA). Each group received intravenous injections of the respective probes followed by micro-PET imaging. ***Results:*** After 3 h of incubation with ALP, over 98% of HGFYp-NOTA was converted to HGFY-NOTA, resulting in a transparent elastic semi-solid. Rheological data showed that the storage modulus was significantly higher than the loss modulus, confirming the formation of a gel. TEM images revealed interconnected nanofibers with an average width of 26.85 ± 3.11 nm. Micro-PET imaging indicated that the tumor-specific uptake in the low-concentration probe group was 3.85 ± 0.35 %ID/g, which was significantly higher than that in the control group (1.39 ± 0.25 %ID/g). The high-concentration probe group exhibited a continuous increase in tumor signal from 4.05 ± 0.28 %ID/g at 0.5 h to 5.62 ± 0.40 %ID/g at 3 h, demonstrating that higher self-assembly concentration significantly enhanced probe retention in the tumor. ***Conclusion:*** The [^{68}Ga]HGFYp-NOTA peptide probe demonstrated excellent self-assembly properties, forming a stable gel with interconnected nanofibers. Increasing the self-assembly concentration significantly improved PET signal retention in tumors, thereby enhancing imaging quality. This study provides a promising strategy for developing long-lasting tumor-specific PET probes and has the potential to improve clinical PET imaging applications.

EP-0456

Enzyme-activated nanocarriers for efficient ^{68}Ga delivery and tumor targeting

P. Zou, *H. Wu, Y. Liu, H. Wang, J. Wu;*
NHC Key Laboratory of Nuclear Medicine, Jiangsu Key Laboratory of Molecular Nuclear Medicine, Jiangsu Institute of Nuclear Medicine, Wuxi, CHINA.

Aim/Introduction: The utilization of positron emission tomography (PET) nanoprobes holds significant promise for the diagnosis and treatment of tumors. However, traditional nanocarriers often face limitations such as poor targeting, insufficient tumor penetration, and suboptimal biocompatibility. To address these challenges, we propose a novel enzyme-activated nanocarrier system designed to enhance the delivery and retention of ^{68}Ga in tumors. This system leverages the specific catalytic activity of enzymes to trigger the self-assembly of nanocarriers, thereby improving the targeting and efficacy of PET imaging. ***Materials and Methods:*** The probe precursor, NPX-DOTA, was synthesized using SPPS. The purity and structure of the synthesized precursor were confirmed through

mass spectrometry and nuclear magnetic resonance spectroscopy. For micro-PET imaging, HeLa tumor-bearing nude mice were divided into two groups: the experimental group received an intravenous injection of [^{68}Ga]NPX-DOTA, while the control group was pre-treated with an L-phenylalanine inhibitor to block alkaline phosphatase (ALP) activity before injection. The cytotoxicity of the nanocarriers was assessed using CCK-8 assays on HeLa cells. Additionally, the potential tissue toxicity was evaluated through hematoxylin-eosin staining of major organs and tumor tissues after exposure to the nanocarriers. ***Results:*** Under the catalysis of ALP, the probe precursor NPX-DOTA rapidly self-assembled into nanofibers with an average diameter of 22.52 ± 2.19 nm. TEM images revealed uniform and well-defined nanofibers, indicating successful self-assembly. Micro-PET imaging showed that the experimental group exhibited significantly higher tumor uptake of ^{68}Ga compared to the control group. The tumor signal intensity in the experimental group increased from 3.21 ± 0.35 %ID/g at 0.5 h to 4.65 ± 0.32 %ID/g at 3 h, while the control group maintained a low signal intensity below 0.75 %ID/g throughout the imaging period. The tumor-to-background ratio reached 6.2 ± 0.4 at 3 h in the experimental group, demonstrating effective tumor targeting. CCK-8 assays indicated that HeLa cell viability remained above 97% after 24 h of incubation. Hematoxylin-eosin staining showed no significant histological changes in major organs or tumor tissues, suggesting low toxicity and good biocompatibility of the nanocarriers. ***Conclusion:*** We have successfully developed an enzyme-activated nanocarrier system for the delivery of ^{68}Ga to tumors. The self-assembly mechanism triggered by ALP significantly enhanced the targeting and retention of ^{68}Ga in tumors, as demonstrated by the sustained increase in tumor signal intensity. Furthermore, the nanocarriers exhibited minimal toxicity and good biocompatibility, making them a promising candidate for clinical translation in PET imaging applications.

EP-0457

^{18}F-FDG-PET/CT in cervical cancer - challenging clinical acknowledgment for more accurate staging and therapy tailoring: single-centre experience

L. Chavdarova[1], *N. Piperkova-Slavova*[2], *E. Piperkova*[1];
[1]*University Specialized Hospital for Active Treatment in Oncology "Prof. I. Chernozemsky", Sofia, BULGARIA,* [2]*Neoclinic, Sofia, BULGARIA.*

Aim/Introduction: Despite screening and HPV-prophylaxis, cervical cancer (CC) is often detected in locally advanced stages (LACC). ^{18}F-FDG-PET/CT is established for whole-body staging but its standardized use is still lacking clinicians' acknowledgement. Our aim is to assess PET/CT-impact on staging and follow-up in CC patients. ***Materials and Methods:*** In the period 03.2024-03.2025, ^{18}F-FDG-PET/CT was performed in 116 CC pts (34-85y), 71,4% LACC. 102 pts had squamous-cell CC, 14 adenocarcinoma. Previous scans and treatment were analyzed retrospectively. Staging (b) PET/CT was done in 10pts (10,85%). Restaging PET/CTs were done after surgery, radio-/brachytherapy, chemo-/immunotherapy. Visual and semiquantitative interpretation using SUVmax was performed. Post-primary treatment (pPET) and follow-up scans (fuPET1-8) were assessed as complete (CR), partial (PR) response, stable (SD) or progressive disease (PD)."CR unconfirmed" (Cru) was interpreted in case of minor residual activity of primary, 3-4 months after deffinitive radio/chemotherapy or surgery. ***Results:*** In (b)PET/CT SUVmax of primary tumor ranged 5,04-27,48 (mean 12,03±5,7). 4pts had metastatic lymph nodes (MLN), 1 distant peritoneal lesion - not otherwise detected. pPET was done in 99pts, SUVmax ranged 3,09-34,8 (mean 9,76±9,16). pPET in pts with former bPET showed CR in 3, PR in 2, Cru in 3, PD in 1pt (MLN, oss). pPET in "no (b)PET" pts was pathologic in 26%: 4 local relapses (LR), 13 - MLN, 6 -distant M (oss,pul,hep). A during pregnancy diagnosed patient had early PD in pPET (pul, lym). All pts with Cru in pPET (16) had rest-SUVmax of 2,57-4,36 (mean 3,28), one showed LR, the rest resolved. fuPET1 had 90pts (4 LR, 10 MLN, 5 pulmonary, 4 peritoneal M), fuPET2 - 52 (6 PD), fuPET3 - 36 (8 PD), fuPET4 - 22 (2 PD), fuPET5 - 11 (1PD), fuPET6 - 7 (1PD), fuPET7 - 3 (1 PD), fuPET8 - 1pt. All pts with pathologic pPET and fuPET were tailored to either radiotherapy (27), surgery (6), chemo-(25) or immune-(8) therapy. In 2 pts fuPET detected breast cancer as unknown second oncologic primary. ***Conclusion:*** ^{18}F-FDG-PET/CT has significant impact on treatment tailoring in LACC. In our study most Cru findings resolved to CR, indicating sometimes prominent post-treatment reparation changes. The small number of (b)PET which hampers pPET interpretation, the relatively high number of pathologic pPET which indicates a probable incorrect staging and the LR/PD rate of fuPET imply the need of more standardized clinical algorithm for patient referral to PET/CT, to individualize treatment and improve prognosis. Further analysis is needed for statistical significance.

EP-0458

Value of ^{18}F-FDG PET/CT in Uterine Metastases From Invasive Lobular Breast Carcinoma

C. Mas*, M. Feriche, E. Espinosa, T. Rudolphi, S. Sanz;*
Hospital Clínico Universitario Virgen de la Victoria, Málaga, SPAIN.

Aim/Introduction: Uterine metastases from breast cancer remain exceptionally rare (<1% of metastatic cases), with invasive lobular carcinoma (ILC) accounting for >80% due to its distinctive peritoneal dissemination pattern. Although ILC constitutes 10-15% of breast malignancies, its propensity for late recurrence and atypical metastatic spread poses unique diagnostic challenges. This case demonstrates the critical utility of ^{18}F-FDG PET/CT in detecting occult uterine metastases, directly informing therapeutic strategies and emphasizing the necessity for enhanced surveillance in high-risk cohorts. ***Materials and Methods:*** A 58-year-old woman with ER/PR-positive (95%), HER2-negative ILC (pT3pN2a, Ki67 35%) underwent right mastectomy in 2020 followed by adjuvant chemotherapy and hormonal therapy (tamoxifen → exemestane). At her 48-month surveillance, PET/CT revealed three key findings: a focal endometrial lesion (SUVmax 9.77; 2.8 cm), a right adnexal mass (30×21 mm; SUVmax 6.12) with ipsilateral hydronephrosis, and a left proximal humeral lesion (SUVmax 4.05) later confirmed by MRI as non-infiltrative. Ultrasound-guided endometrial biopsy confirmed metastatic ILC (GATA3+, ER/PR+), prompting the multidisciplinary team to continue ribociclib (600 mg/day) and fulvestrant (500 mg/month) alongside urological intervention for hydronephrosis. ***Results:*** Critical insights emerged from this case. PET/CT detected uterine metastasis in an asymptomatic patient (ECOG 0), upstaging her disease from oligometastatic to polymetastatic and reorienting management toward systemic CDK4/6 inhibition over localized radiotherapy. The lesion's elevated SUVmax (9.77) and GATA3+/ER+ profile distinguished it from tamoxifen-associated endometrial carcinoma, which typically exhibits lower FDG avidity (mean SUVmax 5.2±2.1). Concurrent ovarian involvement (SUVmax 6.12) and probable skeletal lesions underscored ILC's multifocal dissemination tendency. Follow-up PET/CT at three months demonstrated metabolic stabilization, with a 14% reduction in uterine SUVmax (8.4), corroborating treatment efficacy. ***Conclusion:*** This case solidifies ^{18}F-FDG PET/CT's role in identifying atypical ILC metastases, particularly in hormonally treated patients with biomarker progression. Key implications include integrating routine pelvic imaging into ILC surveillance protocols regardless of symptomatology, employing SUVmax thresholds (>7.5) to prioritize uterine lesion biopsies, and mandating multidisciplinary evaluation to optimize therapy sequencing. Prospective studies are needed to establish optimal PET/CT intervals and validate SUVmax cutoffs for discriminating metastatic versus primary uterine malignancies in this population.

EP-0459

Dynamic F-18 fluorodeoxyglucose positron emission tomography with texture analysis for the differential diagnosis of ovarian masses

T. Shinya[1], *A. Shinya*[2], *T. Matsushita*[1], *Y. Hiroshima*[1], *J. Hiraoka*[1], *Y. Otomi*[1], *B. Zayabat*[1], *H. Inui*[1], *T. Kagawa*[1], *R. Kinouchi*[1], *K. Yoshida*[1], *M. Nishimura*[3], *T. Iwasa*[1], *M. Harada*[1];
[1]*Tokushima University Hospital, Tokushima-city, JAPAN,*
[2]*Tokushima Red Cross Hospital, Komatsushima-city, JAPAN,*
[3]*Tokushima Prefectural Central Hospital, Tokushima-city, JAPAN.*

Aim/Introduction: In PET examinations in ovarian tumours, imaging is typically started at 1 hour after intravenous administration of F-18 FDG. In recent years, the usefulness of dynamic PET/CT, which collects data early time after administration of F-18 FDG, has been reported in various tumours. However, there have been no report that have evaluated in detail the time-dependent accumulation dynamics of FDG after administration in ovarian tumours using maximum standardized uptake values (SUVmax). This prospective study assessed the diagnostic capacity of dynamic PET/CT in the differentiation between benign and malignant ovarian lesions. In addition, we introduce our research attempts on texture analysis (TA). ***Materials and Methods:*** Dynamic scans (5-15 min [1st phase], 15-25 min [2nd phase], 25-35 min [3rd phase] postinjection) and consecutive 1-h scan were undergone in eleven patients (4 endometrioid carcinomas; 1 high-grade serous carcinoma; 1 mucinous carcinoma; 1 granulosa cell tumour; 2 mature teratomas; 1 hemorrhagic ovarian cyst; 1 endometriotic cyst) between Jane 2023 to March 2025. We statistically compared the diagnostic capacity of SUVmax for each phase in the discrimination between benign and malignant ovarian lesions using receiver operating characteristic (ROC) curve analysis. In addition, we performed TA for dynamic and 1-h PET/CT. ROC analysis was performed on the features which showed a significant difference of $p<0.05$ between the malignant and benign groups. Finally, we compared the ROC curves from TA and SUVmax to evaluate the diagnostic performance. Statistical significance was set at $p < 0.05$. This study was approved by the Ethics Committee of the Hospital. ***Results:*** SUVmax gradually decreased or remained similar with minimal fluctuations in four cases of benign ovarian lesions and two cases of malignant ovarian tumours. In contrast, SUVmax had been increasing over time in five cases of malignant ovarian tumours. The areas under the curve (AUC) are higher than 0.857 in all analyses and AUC yielded the highest values at 0.929 on dynamic 1st phase. 37 of 102 TA features showed a significant difference of $p<0.05$ between the malignant and benign groups and have high AUC of higher values than 0.893. Especially, 20 of 37 TA features had highest diagnostic performance with a sensitivity of 100% and a specificity of 100%. Delong's test did not reveal any significant differences between TA-derived ROC curves and SUVmax-derived ROC curves. ***Conclusion:*** Dynamic F-18 FDG PET scans with TA have the potential to be good predictors of discriminating benign and malignant ovarian lesions.

EP-0460

Performance of 18F-FDG-PET/CT in Lymph Node Staging of Patients with Endometrial Cancer

J. Rodríguez Gomez[1], *C. F. Ortiz Muñoz*[1], *E. Noriega Alvarez*[2], *F. J. Pena Pardo*[1], *M. P. Talavera Rubio*[1], *V. M. Poblete García*[1];
[1]*Hospital General Univesitario Ciudad Real, Ciudad Real, SPAIN,*
[2]*Hospital Univesitario De Guadalajara, Guadalajara, SPAIN.*

Aim/Introduction: To evaluate the diagnostic accuracy of 18F-FDG-PET/CT in lymph node staging of patients with endometrial cancer (EC) and its concordance with histopathological findings. ***Materials and Methods:*** A retrospective observational study was conducted on patients with histologically confirmed EC who underwent staging 18F-FDG-PET/CT and surgery within 45 days, without neoadjuvant treatment. Lymph node involvement detected by 18F-FDG-PET/CT was compared with histopathological results. 18F-FDG-PET/CT scans were reported by two experienced nuclear medicine physicians; in case of discrepancy, a third reader was consulted. Suspicious lymph nodes were classified as left/right pelvic or extra-pelvic. Sensitivity (Se), specificity (Sp), positive predictive value (PPV), negative predictive value (NPV), and overall accuracy were calculated. Concordance was assessed using the Chi-square test and Cohen's Kappa coefficient (κ). ***Results:*** A total of 22 consecutive patients were included from January 2018 to December 2022, with a mean age of 70 years (range 39-91). Of these, 10 patients (48%) showed suspected lymph node involvement on staging 18F-FDG-PET/CT (5/10 extrapelvic). Following surgery and pathological analysis (17 endometrioid tumours and 5 non-endometrioid), lymph node tumour involvement was confirmed in 7 patients. This corresponds to 7 true positives (TP), 12 true negatives (TN), 3 false positives (FP), and 0 false negatives (FN) on 18F-FDG-PET/CT. The diagnostic values were: Se 100%, Sp 80%, PPV 70%, NPV 100%, and accuracy 86.4%. Histopathological analysis of the 3 FP cases revealed reactive lymphadenitis (2 patients had a history of prior malignancy in complete remission). There was a statistically significant correlation between 18F-FDG-PET/CT and histopathological findings, with a Chi-square value of 12.32 ($p < 0.001$), and a high level of agreement ($\kappa = 0.718$; $p < 0.001$). ***Conclusion:*** 18F-FDG-PET/CT shows excellent diagnostic performance for both pelvic and extra-pelvic lymph node staging of EC patients, with high concordance with histopathology, despite limitations related to sample size.

EP-24

e-Poster Area

B: Imaging Clinical Studies -> B1 Oncological Imaging Clinical Study -> B21 Lymphoma

EP-0461

Radiomic analysis of baseline 18-F FDG PET/CT to build machine-learning models able to predict treatment response in primary mediastinal B-cell lymphoma: results of a bicentric experience

S. Adamantiadis[1], *L. Urso*[1], *L. Manco*[2], *F. Esposito*[3], *G. Scribano*[2], *L. De Marchi*[3], *A. Venditti*[3], *M. Postorino*[3], *N. Urbano*[4], *R. Gafà*[1], *A. Cuneo*[5], *A. Chiaravalloti*[6], *M. Bartolomei*[7], *C. Cittanti*[1], *L. Filippi*[6];
[1]*Department of Translational Medicine, University of Ferrara, Ferrara, ITALY,* [2]*Medical Physics Unit, University Hospital of Ferrara, Ferrara, ITALY,* [3]*Hematology, Department of Biomedicine and Prevention, University of Roma Tor Vergata, Rome, ITALY,* [4]*Nuclear Medicine Unit, Department of Oncohaematology, Fondazione PTV Policlinico Tor Vergata University Hospital, Rome, ITALY,* [5]*Hematology Unit, University of Ferrara, Ferrara, ITALY,* [6]*Department of Biomedicine and Prevention, University of Rome "Tor Vergata", Rome, ITALY,* [7]*Nuclear Medicine Unit, Onco-Hematology Department, University Hospital of Ferrara, Ferrara, ITALY.*

Aim/Introduction: Primary mediastinal B-cell lymphoma (PMBCL) is an uncommon, B-cell non-Hodgkin lymphoma. PMBCL often develops in the anterior-superior mediastinum and presents as bulky mass at diagnosis. [^{18}F]FDG PET/CT imaging is the gold standard for staging, interim and end-of-treatment (EoT) assessment, associated with the five-point Deauville score (DS). Aim of this bi-centric pilot study is to evaluate the predictive value of pre-treatment [^{18}F]FDG PET/CT radiomics in assessing treatment response in PMBCL. ***Materials and Methods:*** Two cohorts of PMBCL affected patients, 29 from Policlinico Tor Vergata University Hospital of Rome and 9 from Sant'Anna University Hospital of Ferrara, underwent [^{18}F]FDG PET/CT between January 2011 and January 2022. DS were collected. A total of 121 quantitative

radiomics features were extracted from manually segmented volume of interests (VOIs) in PET and CT images, according to IBSI. ComBat harmonization was applied to correct center variability of features, followed by class balancing with SMOTE. Two machine learning (ML) prediction models, the PET Model and the CT Model, were independently developed using robust RFts. For each ML model, two different algorithms were trained (i.e., Random Forest/RF and Support Vector Machine/SVM) using 10-fold cross validation, tested on the internal/external validation set. Receiver operating characteristic (ROC) curves, area under the curve (AUC), classification accuracy (CA), precision (Prec), sensitivity (Sen), specificity (Spec), true positive (TP), and true negative (TN) scores were computed. ***Results:*** The entire dataset was composed of 29 samples for the Rome cohort (23 from D1-D3 and 6 from D4/D5) and 9 samples for the Ferrara cohort (4 from D1-D3 and 5 from D4/D5). A total of 27 RFts were identified as robust for each imaging modality. Both the CT and PET models effectively predicted the Deauville score. The performance metrics of the best classifier (SVM) for the CT and PET models in external validation were AUC=0.75/0.80, CA=0.85/0.77, Prec=0.97/0.67, Sen=0.60/0.80, Spec=0.98/0.75, TP=75.0%/66.7%, TN=77.8%/85.7%, respectively. ***Conclusion:*** ML-models trained on radiomic features extracted from pre-treatment [^{18}F]FDG PET/CT may contribute to predict therapy response in PMBLC patients.

EP-0462

Prognostic Impact Of Metabolic Tumour Volume On Survival In Patients With Diffuse Large B-Cell Lymphoma Treated With Chimeric Antigen Receptor T-Cell Therapy

L. Henrich Malizia[1], *A. Gomez Lopez*[1], *F. Arraut Serrano*[1], *A. Garin Rodriguez*[1], *N. Etxabeguren Gallo*[1], *I. Cillero Etxebeste*[1], *B. Mendibil Esquisabel*[2], *I. Zeberio Etxetxipia*[2], *I. Olazabal Eizaguirre*[2], *V. Rodriguez Ortega*[1], *I. Sanchez Oscoz*[1], *S. Sanchez Eguiguren*[1], *I. Jauregui Larrea*[1], *G. Rodriguez Rodriguez*[1], *I. Leon Zubizarreta*[1], *A. Iztueta Iturbe*[1], *I. Lopez Sanchez*[1], *A. Roteta Unceta Barrenechea*[1]; [1]*Hospital Universitario Donostia - Onkologikoa, San Sebastian, SPAIN,* [2]*Hospital Universitario Donostia, San Sebastian, SPAIN.*

Aim/Introduction: Chimeric Antigen Receptor T-cell Therapy (CAR-T) has improved the treatment of haematologic malignancies, but patient response is variable. Identifying prognostic biomarkers is crucial. Metabolic Tumour Volume (MTV), measured by Positron Emission Tomography-Computed Tomography (PET/CT), is a promising biomarker, as high levels are associated with poorer prognosis in lymphomas. This study evaluated the association between pre-treatment MTV and survival in patients with Diffuse Large B-Cell Lymphoma (DLBCL) treated with CAR-T therapy at our institution. ***Materials and Methods:*** A descriptive retrospective study was conducted on 36 patients with DLBCL who received CAR-T therapy between 2023 and 2024. MTV was calculated from the baseline pre-infusion PET/CT scan. For this calculation, only lesions with a volume greater than 3 cm^3 and SUVmax greater than 4 were measured. Patients were then stratified into 3 groups (low, intermediate, high) using the Youden index. SUVmax (maximum Standardised Uptake Value) and Dmax (maximum distance) were also analysed. The intermediate MTV group was further subdivided according to SUVmax (<16 vs ≥16) to assess if stratification improved. Progression-Free Survival (PFS) was analysed using Kaplan-Meier curves and the MTV groups compared with the log-rank test. ***Results:*** The median age was 64 years. 58.3% received CAR-T as a third line of treatment. At the end of follow-up, 25% had died, and 41.7% had progressed. The MTV groups were: Group 1 (MTV=0, n=16), Group 2 (0 < MTV ≤ 36.8, n=6), and Group 3 (MTV > 36.8, n=14). Significant differences in PFS were observed between the groups (p=0.002). Group 3 (high MTV) had the worst PFS, with a median of 4.5 months. An additional exploratory analysis, subdividing Group 2 by SUVmax (<16 vs ≥16), showed even stronger prognostic separation among four groups (p<0.001), identifying a subgroup with intermediate MTV but SUVmax > 16 (n=2) with very poor survival (median PFS 1 month). ***Conclusion:*** Baseline PET/CT-derived MTV is a significant predictor of PFS in this cohort of DLBCL patients treated with CAR-T therapy. High MTV levels are associated with a poorer prognosis. Incorporating SUVmax may further refine risk stratification in the intermediate group. These findings suggest that Baseline MTV could be a useful tool to predict prognosis in patients with DLBCL treated with CAR-T therapy. However, the main limitation of this study is the small number of patients; therefore, these results require validation in larger cohorts.

EP-0463

Automated AI-based total Metabolic Tumor Volume in lymphoma- a RECOMIA-tool

M. Sadik[1], *J. Mörk*[1], *J. Lopez Urdaneta*[1], *M. Lewold*[2], *M. Larsson*[3], *O. Enqvist*[4], *S. F. Barrington*[5], *L. Edenbrandt*[1], *E. Trägårdh*[2]; [1]*Medicine, Gothenburg, SWEDEN,* [2]*Clinical Physiology and Nuclear Medicine, Malmö, SWEDEN,* [3]*Eigenvision AB, Lund, SWEDEN,* [4]*Electrical Engineering, Gothenburg, SWEDEN,* [5]*Clinical PET Centre, London, UNITED KINGDOM.*

Aim/Introduction: Increasing evidence suggests that total metabolic tumor volume (tMTV) measured at baseline before treatment in lymphoma patients undergoing FDG-PET/CT can predict prognosis. However, there is a lack of fast, reliable, and easy-to-perform multilesional segmentation tool with an urgent need to improve tMTV segmentation workflow in clinical practice. Here, we test an AI-based tool that automatically calculates tMTV in untreated lymphoma patients undergoing FDG-PET/CT. ***Materials and Methods:*** The RECOMIA AI-based tool is a 3D U-Net convolutional neural network trained on a 1500 lymphoma patient cohort, mean age 52 years (range 10-88), 44% were female. The model was optimized to segment metabolically active tumor regions across the FDG-PET/CT scans, enabling automated and reproducible tMTV measurements. The test group consists of all untreated Hodgkin lymphoma (HL) patients and all Diffuse large B-cell lymphoma (DLBCL) patients who underwent FDG-PET/CT at Sahlgrenska University Hospital between 2017-2018 and 2019-2022, respectively. There were 117 patients with mean age 50 years (range 7-90), 39% were female. A group of nine nuclear medicine specialists manually segmented lesions for tMTV calculations; each patient was independently segmented by two specialists. ***Results:*** The median of the manual tMTV was 321 m^3 (interquartile range [IQR]: 92-689 cm^3) and the median of the difference between two tMTV values segmented by different specialists for the same patient was 26 cm^3 (IQR: 9-86 cm^3). In 85 of the 117 patients, the manual tMTV value was closer to the AI tMTV value than to the other manual tMTV value segmented by the second specialist. In 15 of the remailing 32 patients, the difference between the AI tMTV and the manual tMTV was small (<26 cm^3, which was the median difference between two manual tMTV values from the same patient). ***Conclusion:*** The results of this study indicate that the RECOMIA AI tMTV-tool could be used without any major manual adjustments in 85% (100/117) of the untreated lymphoma patients. This demonstrates the feasibility of using AI to support physicians measuring tMTV for assessment of prognosis in clinical practice. ***References:*** Measuring Total Metabolic Tumor Volume from ^{18}F-FDG PET: A Reality Check. Boellaard R et al. J Nucl Med. 2025 Mar 13:jnumed.124.269271. doi: 10.2967/jnumed.124.269271.

EP-0464

The Value of F-18 FDG PET/CT Quantitative and Semi-Quantitative Parameters in Predicting Treatment Response and Prognosis in Hodgkin Lymphoma

S. Aksu[1], *G. Uçmak*[1], *B. B. Demirel*[1], *M. S. Dal*[2]; [1]*Dr. Abdurrahman Yurtaslan Ankara Oncology Training and Research Hospital, Department of Nuclear Medicine, Ankara, TÜRKIYE,* [2]*Dr. Abdurrahman Yurtaslan Ankara Oncology Training and Research Hospital, Department of Hematology, Ankara, TÜRKIYE.*

Aim/Introduction: Hodgkin lymphoma (HL) is generally considered a favorable lymphoid malignancy, typically exhibiting a robust response to standard chemotherapy regimens. However, in some cases, a complete metabolic response (CMR) is not achieved. This study aims to evaluate the prognostic value of

F-18 FDG PET/CT metabolic parameters in predicting complete metabolic response in patients - prognosis with HL. ***Materials and Methods:*** This retrospective study included 150 patients aged 18 years and older, diagnosed with HL, who underwent F-18 FDG PET/CT for initial staging and treatment response assessment following standard chemotherapy regimens. All patients had a minimum follow-up period of 36 months. Clinical, pathological, and PET/CT metabolic parameters were recorded. Metabolic tumor volume (MTV) and total lesion glycolysis (TLG) were derived from baseline PET/CT scans using three threshold methods: SUV 2.5, SUV 4.0, and 41% of SUVmax. For each threshold, total MTV and TLG were calculated by summing the values across all nodal and extranodal lesions. Regression analyses were conducted to identify parameters predictive of treatment response and prognosis. A p-value < 0.05 was considered statistically significant. ***Results:*** Of the 150 patients, 138 (92%) achieved a complete metabolic response to standard chemotherapy, whereas 12 (8%) did not. In univariate analysis, total MTV at the 41% SUVmax threshold (p=0.003, OR: 0.994, 95% CI: 0.990-0.998) and total TLG at the same threshold (p=0.023, OR: 1.000, 95% CI: 0.999-1.000) were significantly associated with treatment response. Multivariate analysis identified total MTV at the 41% threshold (p = 0.025, OR: 0.988, 95% CI: 0.977-0.998) as the sole independent predictor of metabolic response. Using the Youden index, a cutoff value of 101 mL for total MTV 41% provided a sensitivity of 75% and specificity of 70%. Notably, 75% of patients who did not achieve CMR had a total MTV 41% value exceeding this cutoff. During the follow-up period, 132 patients (88%) remained disease-free, while 18 (12%) experienced relapse. The mean disease-free survival was 30 months (range: 7-56 months). No PET/CT parameter was found to be a statistically significant predictor of disease-free survival. ***Conclusion:*** This study demonstrates that total MTV derived from baseline F-18 FDG PET/CT at the 41% SUVmax threshold is the only significant metabolic parameter predictive of treatment response in HL. Our findings suggest that patients with elevated total MTV 41% values (>101 mL) may benefit from modifications to standard treatment regimens to potentially improve clinical outcomes.

EP-0465

Variability factors of hepatic SUVmax and SULmax in patients with FDG avid lymphoma during chemotherapy

H. Habchi[1], *S. Mensi*[2,3], *B. Daoud*[4], *K. Chatti*[3,5];
[1]*Department of Biophysics and Medical Imaging, Higher Institute of Medical Technologies of Tunis, University of Tunis El Manar, Tunis, TUNISIA,* [2]*Nuclear Medicine department, CHU Sahloul, Sousse, TUNISIA,* [3]*Department of biophysics, School of medicine of Sousse, University of Sousse, Sousse, TUNISIA,* [4]*University of Texas, MD Anderson Cancer Center, Houston, TX, UNITED STATES OF AMERICA,* [5]*School of Medicine of Monastir, University of Monastir, Monastir, TUNISIA.*

Aim/Introduction: ^{18}F-FDG PET/CT scan is the gold standard imaging modality for initial staging and therapeutic response assessment in lymphoma by using the liver uptake as a threshold. However, hepatic SUVs are likely prone to intra and inter patient variability. The aim of this study was to identify the factors that vary hepatic SUVmax and SULmax between baseline (PET1) and end of treatment (PET2) in patients followed for FDG-avid lymphoma. ***Materials and Methods:*** A retrospective study was conducted on seventy-five patients treated for avid FDG lymphoma who underwent ^{18}F-FDG PET/CT scans at initial assessment and post-treatment. Linear regression models were utilized to evaluate the variability of hepatic SUVmax and SULmax. The correlation between SUVmax, SULmax, and various clinical and technical factors such as age, fasting blood glucose, injected activity, body mass index (BMI), time to acquisition, sex, initial Ann Arbor stage, and histological type of lymphoma was analyzed. During the second PET scan, residual tumor SUVmax and hepatic SUVmax were compared, particularly in patients with a Deauville score of 3 and 4. ***Results:*** The hepatic SUVmax and SULmax values substantially increased (p < 0.0001) between PET1 and PET2 scans. The hepatic SUVmax values demonstrated significant correlations with age, BMI, and the amount of injected activity. Comparable results were found for hepatic SULmax yet with slightly weaker correlation coefficients. The strongest association with hepatic SUVmax was observed with BMI (r = 0.587 to r = 0.693, respectively). Age exhibited the highest correlation with hepatic SULmax (r = 0.516 to 0.533, respectively). The multivariate analysis revealed that BMI and age were the only significant factors. Other factors showed either fragile or no significant relationships with SUVs. Hepatic SUVs were largely unaffected by the histological type or fasting blood glucose concentrations and remained statistically significant. In PET2, the residual tumor SUVmax was less than the hepatic SUVmax but more than the hepatic SULmax in patients with a Deauville score of 3. ***Conclusion:*** Hepatic SUVmax and SULmax demonstrate similar variability, with a more robust correlation for hepatic SUVmax. Despite its major variability, SUVmax seems to be more suitable than SULmax for assessing therapeutic response according to Deauville criteria. These findings should be considered when evaluating therapeutic response based on the Deauville criteria, particularly when the hepatic SUVmax value is employed as a threshold to distinguish between responder and non-responder patients.

EP-0466

Lymphoma Therapy Response Assessment with Low-Dose [^{18}F]FDG Total-Body PET/CT

C. Mingels[1], *F. Sen*[2], *K. J. Chung*[2], *H. Nalbant*[2], *Y. Abdelhafez*[2], *N. S. Esteghamat*[3], *J. Tuscano*[3], *A. Rominger*[1], *R. D. Badawi*[2], *B. Spencer*[2], *L. Nardo*[2];
[1]*Department of Nuclear Medicine, Inselspital, Bern University Hospital, University of Bern, Bern, SWITZERLAND,* [2]*Department of Radiology, University of California Davis, Sacramento, CA, UNITED STATES OF AMERICA,* [3]*Department of Internal Medicine, University of California Davis, Sacramento, CA, UNITED STATES OF AMERICA.*

Aim/Introduction: Total-body (TB) PET/CT's improved sensitivity offers the possibility to reduce injected activities. Theaim of our study was to define a lower limit of dose reduction for lymphoma therapy assessment. ***Materials and Methods:*** 3.0 MBq/kg [^{18}F]FDG injections of n=24 prospective lymphoma patients served as a referencestandard (RS). Images simulating low-dose injections of 1.0, 0.5, 0.25 and 0.125 MBq/kg werereconstructed at 1-/2-hours post-injection (p.i.). Liver's coefficient of variation (CoV) was assessed. Lymphoma lesions were compared to RS using standardized uptake values (SUV), metabolic tumorvolume (MTV) and total-lesion glycolysis (TLG). Parameters were normalized to liver and blood pool by tumor-to-background (TBR_{Liver}/TBR_{BP}) and contrast-to-noise ratios (CNR_{Liver}/CNR_{BP}). Therapy response was assessed by Deauville criteria. ***Results:*** Overall, 191 lymphoma lesions were analyzed. SUV_{max} trended towards statistically significant increase at 1h p.i. in the lowest dose (1h SUV_{max}: RS: 6.28±5.87 vs. 0.125 MBq/kg: 7.76±6.69, p=0.07 and at 2h: 7.14±7.16 vs. 8.67±7.62, p=0.13). SUV_{max}, MTV and TLG did not differ significantly. CoV increased significantly with lower dose (p<0.01). TBR_{Liver} did not differ statistically. Thus, TBR_{BP} was significantly higher in the lowest dose (p<0.01) at 2h p.i. only. CNR significantly decreased with decreasing doses. Deauville scores did not differ significantly up to an injection of 0.25 MBq/kg for 1h and 1.0 MBq/kg for 2h p.i. Below this limit, we noted significantly lower Deauville scores for lower-dose reconstructions (p<0.01). ***Conclusion:*** Dose reduction with [^{18}F]FDG TB PET/CT for therapy assessment in lymphoma patients is possibleand does not result in significant different MTV, TBR and TLG. SUV_{max} and Deauville scores were comparable to the RS to a lower limit of 0.25 MBq/kg for 1h p.i. and 1.0 MBq/kg for 2h p.i. imaging.

EP-0467

A Radiomic and Semiquantitative PET Approach to Post-Treatment Mediastinal Residuals in cHL and PMBCL: From Classification to PrognosiSA Radiomic and Semiquantitative PET Approach to Post-Treatment Mediastinal Residuals in cHL and PMBCL: From Classification to Prognosis

E. Abenavoli[1], *A. Lombardo*[2], *F. Mungai*[3], *M. Palazzo*[4], *L. Nassi*[4], *B. Puccini*[4], *B. Sordi*[4], *R. Sciagrà*[1], *S. Valente*[1], *A. M. Vannucchi*[4], *V. Berti*[1];
[1]*Nuclear Medicine Unit, Azienda Ospedaliero-Universitaria Careggi, Florence, ITALY,* [2]*Nuclear Medicine Unit,Azienda Ospedaliero-Universitaria Careggi, Florence, ITALY,* [3]*Department of Radiology, Azienda Ospedaliero-Universitaria Careggi, Florence, ITALY,* [4]*Division of Hematology, Azienda Ospedaliero-Universitaria Careggi, Florence, ITALY.*

Aim/Introduction: Interpreting residual FDG-avid mediastinal masses after end-of-treatment (EoT) PET in lymphoma is challenging, as uptake may reflect either malignancy or benign processes. Not all uptake indicates active disease, and distinguishing residual malignancy from benign causes, such as thymic rebound or inflammation, is often uncertain. This study aimed to assess the value of semiquantitative and radiomic PET features in improving non-invasive characterization and relapse prediction in patients with classical Hodgkin lymphoma (cHL) and primary mediastinal B-cell lymphoma (PMBCL). ***Materials and Methods:*** 113 patients with bulky mediastinal involvement at baseline (cHL n=73, PMBCL n=40) underwent EoT FDG PET/CT. Semiquantitative metrics (SUVmax, SUVmean, MTV, TLG) and radiomic features were extracted using Life7.3 software. A two-step analysis was conducted:(1)a discriminant analysis in patients with residual FDG uptake to differentiate physiological from pathological activity;(2)assessment of the prognostic value of significant variables in the full cohort, regardless of residual uptake. ***Results:*** For relapse prediction, in cHL, DS, TLG and MTV (both with threshold = 4, p<0.001),Intensity_Coefficient_of_Variation (cutoff 0.243, p=0.04), and GLCM_Sum_Entropy (p=0.001) were significant. In PMBCL,both TLG (threshold = 4) and SUVmax (cutoff 12.5,p<0.05)retained prognostic value.Radiomic features identified as predictive included GLCM_Sum_Average, Intensity_Absolute_Median_Deviation, and Intensity_Robust_Mean_Absolute_Deviation.These features were consistently associated with progression-free survival(p<0.05),reflecting complementary aspects of intralesional heterogeneity. ***Conclusion:*** A two-step PET-based strategy combining conventional and radiomic analysis improves the post-treatment assessment of bulky mediastinal disease in both cHL and PMBCL.In cHL, the DS remains the clinical reference; however, radiomic features and metabolic burden parameters such as TLG and MTV enhance prognostic accuracy, particularly in equivocal DS3-4 cases. This supports more individualized therapeutic decisions by helping to distinguish inflammatory from metabolically active residual disease.In PMBCL, where high residual uptake is frequent, the combination of radiomic features with TLG and SUVmax (cutoff 12.5) improves both classification and relapse prediction. These findings support the integration of advanced PET biomarkers,.

EP-0468

Inter-reader variability of FDG PET/CT measurements in lymphoma patients

E. Tragardh[1,2], *M. Lewold*[1,2], *J. Lopez Urdaneta*[3], *M. Larsson*[4], *O. Enqvist*[4,5], *L. Edenbrandt*[3], *S. F. Barrington*[6], *M. Sadik*[3];
[1]*Skåne University Hospital, Malmo, SWEDEN,* [2]*Lund University, Malmö, SWEDEN,* [3]*Sahlgrenska Academy at the University of Gothenburg, Gothenburg, SWEDEN,* [4]*Eigenvision AB, Lund, SWEDEN,* [5]*Chalmers University of Technology, Gothenburg, SWEDEN,* [6]*School of Biomedical Engineering and Imaging Sciences Kings College, London, UNITED KINGDOM.*

Aim/Introduction: The Deauville score is a crucial predictive factor in Hodgkin lymphoma (HL) and diffuse large B-cell lymphoma (DLBCL) during interim or end-of-treatment PET/CT evaluations. However, additional measurements such as metabolic tumour volume (MTV), total lesion glycolysis (TLG), and the maximum distance between hypermetabolic lymphoma lesions (Dmax) may offer enhanced prognostic power, also at baseline. This study aims to investigate the inter-reader variability of these variables, providing insights into the reliability of measurements taken by different physicians. ***Materials and Methods:*** This study included 117 patients with untreated HL or DLBCL who underwent [18F] fluorodeoxyglucose PET/CT scans. Nine nuclear medicine physicians manually segmented lesions. The segmentations were performed in the online tool Recomia (www.recomia.org). No specific instructions were provided other than to segment lymphoma related tumours. MTV, TLG, and Dmax were calculated from these segmentations. MTV was defined as the summed volume in cm3, TLG as MTV multiplied with SUVmean and Dmax as the distance between the centroids of the two farthest lesions, measured in the 3D reconstruction. Each patient was independently segmented by two physicians. Bland-Altman statistics were used to assess the bias between observers and the upper and lower limits of agreement. Pearson correlation coefficients were also calculated. ***Results:*** The mean age of the117 patients was 50 years (range 7-90), 39% female. The mean (standard deviation) values were 501 (782) cm3 for MTV, 3836 (5165) cm3 for TLG, and 400 (290) cm for Dmax. The bias between observers was 4 cm3 for MTV, -1.6 cm3 for TLG and 9.6 cm for Dmax, with limits of agreement of ± 422 for MTV, 1329 for TLG and 415 for Dmax. Pearson correlation coefficients were 0.93 for MTV, 0.99 for TLG and 0.74 for Dmax (p<0.001 for all). ***Conclusion:*** The study demonstrates high inter-reader reliability for MTV and TLG measurements, as indicated by strong Pearson correlation coefficients and narrow limits of agreement. However, Dmax showed moderate variability between observers. Despite the lack of standardization in MTV and TLG measurements, they appear more robust than Dmax. If Dmax is to be used, physicians need clear instructions to add small lesions that may not contribute significantly to MTV but which might affect measurement of disease dissemination.

EP-0469

Correlation analysis of PET parameters and clinical characteristics in 91 patients with diffuse large B-cell lymphoma

S. Chen, *W. Chen, Y. Zhang;*
Fuzhou University Affiliated Provincial Hospital, Fuzhou, CHINA.

Aim/Introduction: This study aims to explore the correlation between ^{18}fluoro-fluorodeoxyglucose (^{18}F-FDG) PET/CT parameters and clinical characteristics in patients with diffuse large B-cell lymphoma (DLBCL). ***Materials and Methods:*** A retrospective analysis was conducted on the baseline and mid-term ^{18}F-FDG PET/CT of 91 patients with DLBCL who received R-CHOP or similar regimens and underwent baseline and interm PET/CT examinations at Fujian Provincial Hospital from January 2012 to June 2022 Parameters and related clinical indicators. The selection of lesions and the post-processing of images were carried out in accordance with the standards recommended by the European Association for Nuclear Medicine (EANM). The relative threshold method was adopted. The VOI of the largest lesion in each patient was delineated with 41% of the maximum standardized uptake value (SUVmax) as the boundary. SUV≥41%SUVmax was used as the threshold to obtain the tumor metabolic volume (MTV). When a patient has multiple metabolic lesions, the MTVS of all the lesions are added together to obtain the total tumor metabolic volume (TMTV). Record the SUVmax with the highest metabolic activity among all positive lesions in baseline PET and mid-term PET as

the baseline SUVmax and mid-term SUVmax. The volume division is automatically performed by the built-in software of the nuclear medicine imaging workstation Xeleris3.0 of the American GE Company to obtain semi-quantitative metabolic parameters. And the relationship between PET metabolic parameters and clinical parameters was explored through point-two-column correlation coefficient analysis. Statistical processing was performed using Pearson correlation analysis. ***Results:*** The research results showed that there were mild to moderate statistical associations between multiple clinical indicators and PET metabolic parameters (P<0.05). The expression of BCL6 protein was negatively correlated with mid-term TMTV (r=-0.221, P=0.048), ΔTMTV% (r=-0.282, P=0.009), and baseline SUVmax (r=-0.244, P=0.025), but was significantly positively correlated with ΔTLG (r=0.221). (P=0.044) Ki67 was positively correlated with ΔSUVmax% (r=0.224, P=0.033); The Performance Status (PS) score, BCL2, CD3 and CD5 of the Eastern Oncology Collaboration Group were positively correlated with the mid-term SUVmax (PS: r=0.212, P=0.049;) BCL2: r=0.251, P=0.020; CD3: r=0.227, P=0.046; CD5: r=0.219, P=0.041. ***Conclusion:*** This study found that there were statistical associations between multiple clinical characteristics of patients with DLBCL and PET metabolic parameters, further supporting the potential importance of BCL6 in regulating the tumor metabolic process of patients with DLBCL and confirming the association between high expression of BCL2 and chemotherapy resistance.

EP-0470

The impact of increased sensitivity of LAFOV PET/CT on DS assessment in lymphoma patients: implication and perspectives

A. Franchini[1], *C. Romano*[2], *S. Capitanio*[1], *A. Spataro*[1], *A. Scarale*[1], *L. Airo' Farulla*[1], *G. Cabrini*[1], *E. Gay*[1], *C. Rossetti*[1];
[1]*Nuclear Medicine Unit, Dipartimento Ematologia, Oncologia e Medicina Molecolare, ASST GOM Niguarda, Milan, ITALY,* [2]*S.C. Fisica Sanitaria, ASST GOM Niguarda, Milan, ITALY.*

Aim/Introduction: The Deauville Score (DS) is routinely used for lymphoma qualitative response assessment using PET/CT imaging. However, variability in DS due to differences in acquisition time and inter-observer interpretation may impact clinical decision-making. The recent introduction of long axial field-of-view (LAFOV) PET/CT scanners offers significantly higher sensitivity than conventional short axial field-of-view (SAFOV) systems. These scanners reduce acquisition time and radiopharmaceutical dose, improving image quality. The purpose of this study is to evaluate the impact of LAFOV PET/CT technology on DS assessment, with a focus on acquisition time and observer variability. ***Materials and Methods:*** Twenty-one patients with lymphoma (both Hodgkin and Non-Hodgkin lymphoma) underwent whole-body PET/CT scans using a uMI Panorama GS scanner for assessment of treatment response. Data were acquired over 5 minutes and reconstructed at 5, 3, 1 minutes, and 30 seconds, with and without point spread function (PSF) modeling. Three independent observers assigned DS values for each reconstruction. Inter-observer DS concordance was analyzed. Additional quantitative metrics included SUVmax, SUVmean, SUVpeak, and liver coefficient of variation (COV). ***Results:*** DS discordances were observed in 4/21 patients. In particular, in one of these, DS varied between 2 and 3. In the remaining three patients, DS varied between 3 and 4, potentially affecting further treatment. Specifically, in one of these, all observers assigned DS 4 with PSF and DS 3 without PSF at acquisition times ≥1 minute. In another, DS was 4 with PSF, but showed inter-time variability (DS 3 or 4) without PSF. In the third case, two observers noted a shift from DS 3 at 3-5 minutes to DS 4 at 30 seconds and 1 minute. Across all patients, no inter-observer variation in DS was observed in PSF reconstructions at 3 and 5 minutes. In all patients, liver COV remained below 15% for acquisition times of 1, 3, and 5 minutes; liver SUVmax was significantly higher in PSF reconstruction at all time points, whereas liver SUVmean did not. Lesion SUVpeak instead was significantly higher in PSF reconstructions compared to non-PSF. ***Conclusion:*** New generation LAFOV PET/CT scanner significantly improves image quality and allows shorter acquisition times. However, it may also introduce variability in Deauville scoring, particularly with very short acquisitions (30 seconds to 1 minute). Further studies are needed to determine the optimal combination of acquisition time and reconstruction method for accurate assessment of treatment response in FDG-avid lymphomas.

EP-0471

Effect on Deep-Learning Time-of-Flight (DL-ToF) image enhancement compared to non-Time-of-Flight (non-ToF) Positron Emission Tomography (PET) images on clinical outcome for response assessment in lymphoma.

C. Low*, O. Adesanya, N. Rao, V. Leung, A. Vasiljevic, C. Lim, L. Rowley;*
University Hospital Coventry and Warwickshire NHS Trust, Coventry, UNITED KINGDOM.

Aim/Introduction: To assess if using DL-ToF PET images will affect the maximal Standardised Uptake Value (SUVmax) and Deauville scoring when compared to non-ToF PET images will cause a stage migration in response assessment for lymphoma. ***Materials and Methods:*** Total of 34 F18-FDG PET-CT scans for response assessment in lymphoma were included in this study between 1/1/2025 to 15/04/2025. All PET-CT images had both DL-ToF and non-ToF reconstructions for comparisons. The highest SUVmax for lymphoma lesions were obtained for both reconstructions. Background mediastinal blood pool and liver SUVmax were also obtained with regions of interest within the aortic arch and the liver respectively for both PET reconstruction images. Deauville scoring was also compared between the 2 PET reconstructed images. ***Results:*** Out of the 34 studies, 11 had Hodgkin Lymphoma (HL), 18 had Diffuse Large B-cell Lymphoma (DLBCL), 2 had Follicular Lymphoma (FL), 2 had T-Cell Lymphoma (TCL) and 1 had Marginal-Zone Lymphoma (MZL). 16 studies were performed for interim response adaptive assessment and 18 studies were for end of treatment response assessment. Based on non-TOF PET images, the number of studies as categorised by Deauville classifications are as follow: Deauville 1 (1), Deauville 2 (9), Deauville 3 (9), Deauville 4 (7) and Deauville 5 (8). Out of the 34 studies, 10 studies had a change in Deauville score between non-TOF and DL-ToF images: 6 studies demonstrate an increased in Deauville score (5 studies from Deauville 4 to 5; 1 study from Deauville 3 to 4) which 4 studies demonstrate a decrease in Deauville score (from Deauville 3 to 2). The average change for SUVmax in lymphoma lesions is 1.76 (-0.8 to 13.3). The average change for background SUVmax in mediastinal blood pool and liver are 0.06 (-0.8 to 0.5) and 0.32 (-1.4 to 0.9) respectively. ***Conclusion:*** Findings show that 10 studies demonstrated a change of Deauville score between non-ToF and DL-ToF images but only 1 study will cause a change in clinical management (Deauville 3 to 4). There are also small changes in SUVmax within lymphoma lesions and background SUVmax for mediastinal blood pool and liver. Findings from this small study demonstrate that DL-ToF images are consistent with non-ToF images for Deauville scoring and can be use in lymphoma treatment response assessment. ***References:*** Mehranian A, Wollenweber SD, Walker MD et al. Deep learning-based time-of-flight (ToF) image enhancement of non-ToF PET scans. EJNMMI, (2022)Vol. 49,11 3740-3749. doi:10.1007/s00259-022-05824-7.

EP-0472

Prognostic Role of Volumetric and Dissemination Parameters from ^{18}F-FDG PET/CT in Follicular Lymphoma.

F. López-Bermejo García[1], *M. Contreras Ameduri*[1], *J. Rodríguez Gómez*[1], *E. Noriega Álvarez*[2], *J. Gatón Ramírez*[1], *F. Pena Pardo*[1], *D. Martínez Osorio*[1], *M. Talavera Rubio*[1], *V. Poblete García*[1];
[1]*Hospital General Universitario de Ciudad Real, Ciudad Real, SPAIN,* [2]*Hospital Universitario de Guadalajara, Guadalajara, SPAIN.*

Aim/Introduction: To analyse the prognostic value of maximum tumour dissemination (Dmax), metabolic tumour volume (MTV), and total lesion glycolysis (TLG) measured by ^{18}F-FDG PET/CT in patients with follicular lymphoma (FL). ***Materials and Methods:*** A retrospective observational study was conducted including consecutive patients diagnosed with FL between January 2016 and August 2020, with histopathological confirmation and staging by PET/CT. Dmax was determined by measuring the distance between the two most distant lesions, corrected by body surface area (SDmax) and height (HDmax). MTV and TLG were assessed using PET VCAR software, with semi-automatic segmentation of all hypermetabolic lesions and a SUVmax threshold of 2.5, consistent with previous studies. Clinical and laboratory variables collected included Ann Arbor stage, FLIPI index, lactate dehydrogenase (LDH), and beta-2 microglobulin (B2M). Statistical analysis was conducted using SPSS v29: Pearson's bivariate correlation was used to assess associations between quantitative parameters and overall survival (OS) and disease-free survival (DFS). Cox regression was applied for survival analysis, and Kaplan-Meier curves were generated. Finally, ANOVA was performed to assess the association between the occurrence of death (dependent variable) and the main quantitative PET/CT-derived parameters, as well as clinical and laboratory variables. ***Results:*** A total of 108 patients (59 men) with a mean age of 60.3 years (range 31-86) were evaluated. During follow-up, 20 patients (18.5%) died and 29 experienced disease progression. Pearson's correlation demonstrated a statistically significant negative correlation between OS and both MTV (-0.264) and TLG (-0.265). DFS also showed a negative correlation with MTV (-0.199). LDH was negatively correlated with both OS (-0.319) and DFS (-0.266), while B2M correlated negatively with OS (-0.262). Ann Arbor stage and FLIPI index were associated with DFS. Furthermore, B2M and MTV showed a negative correlation between the dependent variable 'death' and TLG (p 0.04) and B2M (0.02) in ANOVA analysis; these results reject the null hypothesis. Dmax values (corrected and uncorrected) did not show a significant correlation. ***Conclusion:*** Metabolic tumour volume and total lesion glycolysis demonstrate a superior prognostic value in follicular lymphoma compared to dissemination PET/CT parameters.

EP-0473

Diagnostic value of Metabolic Tumor Volume (MTV) as a prognostic criterion in Follicular Lymphoma

Y. Sauchuk*;*
Minsk Oncology Center, Minsk, BELARUS.

Aim/Introduction: Follicular lymphoma (FL) is the second most frequent non-Hodgkin lymphoma subtype. To date, according to the NCCN Guidelines® in B-Cell Lymphomas, there are several first lines of chemotherapy for patients with FL. The choice of chemotherapy line is based on the FLIPI clinical criteria (FLIPI score). However, according to these criteria, the total tumor volume of the affected lymph nodes is not taken into account. And although these scores are a prediction basis for the patient prognosis, they have not yet been established as a means of selecting treatment options. The topic of this research is learning of the prognostic criteria, based on evaluation of Metabolic Tumor Volume (MTV) in FL. ***Materials and Methods:*** Was analyzed baseline and interim PET-CT of 132 patients with FL before and after chemoimmunotherapy induction treatment: R-B (Bendamustine plus Rituximab) versus R-CHOP (Rituximab combined with Cyclophosphamide, Doxorubicin, Vincristine and Prednisone). ***Results:*** Median age was 54 years. 37 (28%) patients had a stage I-II of disease and 95 (72%) patients had a stage III-IV of disease. 33 (25%) patients had a FLIPI2 score 0-2 (Low Risk Group) and 99 (75%) patients had a FLIPI2 score ≥3 (Intermediate and High-Risk Groups). The presence of a high TMTV (≥510 cm^3) was significantly associated with stage III-IV of disease (including number of involved nodal sites ≥5 and bone marrow involvement) + higher FLIPI2 scores. On multivariable analysis, MTV (p=0.002) and FLIPI2 score (p=0.002) were independent predictors of 3-year progression-free survival (PFS). In combination, they identify two risk groups: high TMTV (≥511 cm^3) and high FLIPI2 score (≥3) with 3-year PFS - 26% (p=0.001) and low MTV (<511 cm^3) and low-to-intermediate FLIPI2 score (0-2) with 3-year PFS - 74% (p=0.001). ***Conclusion:*** Baseline MTV is a strong independent predictor in FL. In combination with FLIPI2 score, it identifies patients at high risk of early progression. It can be useful in choosing the most optimal first-line chemotherapy regimen in FL. ***References:*** 1. Dortz et al: Diagnostic and prognostic impact of ^{18}F-FDG PET/CT in follicular lymphoma. Eur J Nucl Med Mol Imaging 37 (2010):2307-2314. 2. Meignan et al: Baseline Metabolic Tumor Volume Predicts Outcome in High-Tumor-Burden Follicular Lymphoma: A Pooled Analysis of Three Multicenter Studies. J Clin Oncol 34 (2016):1-9. 3. Trotman et al: Prognostic value of PET-CT after first-line therapy in patients with follicular lymphoma: a pooled analysis of central scan review in three multicentre studies. Lancet Haematol 1 (2014):e17-27.

EP-0474

Concordance and Discordance Between FDG PET/CT and Bone Marrow Biopsy in Detecting Bone Marrow Involvement in Lymphoma: A Retrospective Analysis.

L. Goriparti[1]*, C. S*[1]*, J. Krishna P.*[1]*, V. Goenka*[2]*, D. Khan*[1]*, S. Sagar*[1]*, S. Sharma*[1]*, B. S. Nayak*[1]*, R. Karna*[1]*, A. Dhiman*[1]*, R. Kumar*[1]*;*
[1]All India Institute of Medical Sciences, New Delhi, INDIA, [2] All India Institute of Medical Sciences, Jodhpur, INDIA.

Aim/Introduction: Lymphomas represent a heterogeneous group of malignant neoplasms originating from lymphocytes, broadly classified into Hodgkin lymphoma (HL) and non-Hodgkin lymphoma (NHL). Accurate staging is critical for prognosis and treatment planning, with bone marrow involvement (BMI) being a key determinant, as its presence upstages the disease to Stage IV. Traditionally, bone marrow biopsy (BMB) has been gold standard for detecting BMI. However, FDG PET/CT has emerged as superior, non-invasive alternative, offering comprehensive evaluation of the entire skeletal system and enhanced detection of focal lesions. This study aims to assess the concordance and discordance between FDG PET/CT and BMB in baseline lymphoma cases, providing insights into their diagnostic reliability. ***Materials and Methods:*** This retrospective analytical study utilized data extracted from institutional database. A cohort of 353 baseline and suspected lymphoma cases, spanning from 2022 to March 2025, with 258 cases confirmed as lymphoma via biopsy. Bone marrow involvement was evaluated histopathological using bone marrow biopsy. Histopathological data were available for 149 patients. The dataset was categorized into four groups: Positive on both FDG PET/CT and BMB. Positive on FDG PET/CT but negative on BMB. Negative on FDG PET/CT but positive on BMB. Negative on both modalities. Statistical analysis was performed to determine concordance rates and diagnostic discrepancies between the two techniques. ***Results:*** The study included 149 patients with confirmed lymphoma, comprising 95 males (63.8%) and 55 females (36.2%). The age range was 2 to 85 years, with a median age of 28. The cohort consisted of 88 Hodgkin lymphoma (HL) cases (59.1%) and 61 non-Hodgkin lymphoma (NHL) cases (40.9%).Concordant results (both FDG PET/CT and BMB agreeing on bone marrow involvement status) were observed in 113 cases (75.8%), yielding a concordant-to-discordant ratio of 3.1:1. Discordant results were noted in 36 cases (24.2%), with the following distribution, PET-positive/BMB-negative: 24 cases (19 in HL and 5 in NHL) and PET-negative/BMB-positive: 12 cases (7 in HL and 5 in NHL). Among HL cases, 62 (70.5%) were concordant, while 26 (29.5%) showed discordance. Among NHL cases, 51 (83.6%) were concordant, with 10 (16.4%) discordant. ***Conclusion:*** This study demonstrates a high concordance rate (75.8%) between FDG PET/CT and BMB in

detecting bone marrow involvement, supporting the role of PET/CT as a reliable non-invasive alternative. However, discordance occurred in 24.2% of cases, with a notable predominance in HL, suggesting potential limitations in sensitivity or specificity for certain subtypes, which needs further evaluation into factors influencing discordance.

EP-0475

Texture Analysis of Lymph Nodes on Initial FDG PET/CT for Predicting Interim Deauville Scores after Chemotherapy in Newly Diagnosed Non-Hodgkin Lymphoma Patients

A. Kibar, *K. Saglam, S. Asa, S. Sager, H. B. Sayman;*
Istanbul University-Cerrahpasa, Cerrahpasa Faculty of Medicine, Department of Nuclear Medicine, Istanbul, TÜRKIYE.

Aim/Introduction: FDG PET/CT plays a critical role in staging and assessing treatment response in Non-Hodgkin Lymphoma (NHL). This study evaluates texture features derived from baseline FDG PET/CT scans in newly diagnosed NHL patients to determine their ability to differentiate between responders and non-responders based on interim Deauville scores and assess their predictive value for treatment response. ***Materials and Methods:*** A total of 21 NHL patients were included in the study. Following chemotherapy, 11 patients were classified as Deauville score 1 on interim FDG PET/CT, indicating a complete metabolic response, whereas 10 patients were categorized as Deauville scores 4-5, representing inadequate or no metabolic response. FDG PET images were analyzed with LIFEx software version 7.7.0 to extract texture features. The study aimed to assess whether there were statistically significant differences in texture parameters between responders (Deauville score 1) and non-responders (Deauville scores 4-5). For responders, the lesion with the highest SUVmax on baseline PET/CT was selected for analysis. For non-responders, the lesion with the highest FDG uptake on interim PET/CT was identified on the baseline PET/CT scan for texture analysis. ***Results:*** Of the 21 patients, 7 were female and 14 were male, with a median age of 61 years (range: 19-80 years). The median interval between baseline and interim PET/CT scans was 100 days (range: 43-151 days). All patients were at stage 3 or higher at diagnosis. Among the extracted texture parameters, 17 out of 38 showed statistically significant differences ($p < 0.05$) between responders and non-responders using the Mann-Whitney U test (Table 1). The parameter with the lowest p-value, GLCM_DifferenceVariance, was analyzed using Spearman correlation, revealing an inverse correlation with interim Deauville score ($p < 0.05$, rho = -0.598), indicating that higher Deauville scores correlated with lower GLCM_DifferenceVariance values. Receiver operating characteristic (ROC) analysis for this parameter yielded an area under the curve (AUC) of 0.845. ***Conclusion:*** FDG PET/CT plays a key role in NHL management. As automatic segmentation becomes a part of routine clinical practice in the future, texture features are likely to become more valuable in clinical decision-making. Predicting treatment response based on these features could help clinicians provide more tailored and beneficial care for patients.

EP-0476

Metabolic biomarkers assessed with ^{18}F-FDG PET/CT in patients with diffuse large B-cell lymphoma, with and without BCL-2 and MYC expression

Y. Sánchez Vera, *M. Olarte Casas;*
Unidad PET/CT /Unidad UNAM, Mexico, MEXICO.

Aim/Introduction: The most common lymphoma subtype in adults is diffuse large B-cell lymphoma (DLBCL), which shows heterogeneous characteristics due to the presence of rearrangements and oncoprotein expression. This study determined metabolic characteristics (maximum standardized uptake value (SUVmax), total lesion glycolysis (TLG), metabolic tumor volume (MTV), and Deauville score) assessed with ^{18}F-FDG PET/CT in DLBCL patients with and without BCL-2 and MYC protein expression. Because there is evidence that oncoprotein expression and translocations in BCL-2 and MYC have poorer outcomes, assessing the metabolic characteristics could enhance treatment decision-making. ***Materials and Methods:*** A retrospective, cross-sectional, and descriptive study was conducted. Inclusion criteria:1) patients older than 18 years with a diagnosis of DLBCL, 2) BCL-2 and/or MYC oncoprotein expression status was determined by immunohistochemistry. 3) PET/CT scans at end of therapy. Statistical analysis was performed using one-way analysis of variance and the Mann-Whitney U test. A p value ≤0.05 was considered statistically significant. ***Results:*** Fifty-one patients were included. 51% of the patients included were men and 49% were women. The Lugano classification included stage I in 4 patients (7.9%), stage II in 15 patients (29.4%), stage III in 6 patients (11.7%), and stage IV in 26 patients (51%). BCL-2 expression was positive in 37 patients (72.54%). MYC oncoprotein expression was positive in 3 patients. MUM-1 was positive for 19 patients. The mean SUVmax values in the groups with and without BCL-2 expression were 4.1 SUVmax and 1.1 SUVmax, respectively. These values were not statistically significantly different ($p>0.05$). However, there was a tendency for higher values to be present in the BCL-2-expressing group. The mean TLG in the BCL-2 and/or MYC-expressing group was 73.96 SUV-bwx cm3, and in the negative and/or undetermined group it was 13.87 SUV-bwx cm3, $p>0.05$. The mean MTV in the BCL-2 and/or MYC-expressing group was 38.24 cm3, and in the negative and/or undetermined group it was 8.11 cm3, $p=0.07$. ***Conclusion:*** In this study, higher values of metabolic parameters were observed in patients who expressed BCL2/MYC oncoproteins, although there were no statistically significant differences. This knowledge constitutes a preamble for personalized treatment strategies and further studies of associated genes poorer outcome.

EP-0477

Prognostic Value of ^{18}F-FDG PET/CT in CAR T-Cell Therapy for Relapsed/Refractory Non-Hodgkin Lymphoma

S. Gavriilidis[1], *N. Pianou*[1], *I. Tzannou*[2], *I. Baltadakis*[2], *P. Rontogianni*[1];
[1]*Nuclear Medicine Department, Evangelismos Hospital, Athens, GREECE,* [2]*Hematology Department – BMT Unit, Athens, GREECE.*

Aim/Introduction: Chimeric Antigen Receptor (CAR) T-cell therapy represents a groundbreaking advancement in the treatment of relapsed/refractory non-Hodgkin lymphoma (R/R NHL).18F-Fluorodeoxyglucose Positron Emission Tomography/Computed Tomography (^{18}F-FDG PET/CT) plays a critical role in assessing disease status before and after CAR T-cell administration. The aim of this study was to evaluate the prognostic impact of ^{18}F-FDG PET/CT in patients undergoing CAR T-cell therapy. ***Materials and Methods:*** We retrospectively analyzed 16 patients (56% male) with R/R NHL (87.5% with diffuse large B-cell lymphoma) treated at our institution, all of whom underwent ^{18}F-FDG PET/CT imaging at baseline, and at 1- and 3-months post-CAR T-cell therapy. Quantitative PET/CT parameters assessed included total metabolic tumor volume (TMTV), changes in maximum standardized uptake value (ΔSUVmax) between baseline and the 1-month scan, and the Deauville score (DS) at 1 month. The primary endpoints were progression-free survival (PFS) and overall survival (OS), and the association of the above parameters with PFS and OS. Survival estimates were calculated using the Kaplan-Meier method, and prognostic significance was assessed via Cox regression analysis. ***Results:*** Patients with a lower baseline TMTV < 25 mL demonstrated significantly improved overall survival (OS) ($p = 0.028$). A greater reduction in ΔSUVmax > 66.6% between baseline and 1-month post-treatment scans was significantly associated with improved progression-free survival (PFS) ($p =$

0.003). Additionally, a DS of ≤3 at 1-month post-CAR T-cell therapy was strongly correlated with both longer PFS ($p < 0.001$) and OS ($p = 0.02$). In multivariate Cox regression analysis, both ΔSUVmax and 1-month DS emerged as independent prognostic factors for survival outcomes. ***Conclusion:*** ^{18}F-FDG PET/CT serves as a valuable prognostic imaging modality in patients with relapsed/refractory NHL treated with CAR T-cell therapy. Quantitative and semi-quantitative PET/CT parameters—specifically baseline TMTV, early ΔSUVmax, and the 1-month DS—are significantly associated with PFS and OS. However, the small sample size of this study limits the generalizability of these findings. Despite this, the results support the integration of PET/CT-based metrics into post-treatment risk assessment and clinical decision-making.

References: 1. Sesques P, Ferrant E, Safar V, et al. Prognostic impact of ^{18}F-FDG PET/CT in patients with aggressive B-cell lymphoma treated with anti-CD19 chimeric antigen receptor T cells. J Nucl Med. 2021;62(8):1074-1080. doi:10.2967/jnumed.120.258384 2. Al-Ibraheem A, Abdlkadir AS, Al-Adhami DA, et al. The prognostic utility of ^{18}F-FDG PET parameters in lymphoma patients under CAR-T-cell therapy: a systematic review and meta-analysis. Front Immunol. 2024;15:1424269. doi:10.3389/fimmu.2024.1424269.

EP-0478

Prognostic Role of Interim PET in Peripheral T-Cell Lymphoma

S. Pacella[1], *F. Rossi*[1], *N. Rampi*[1], *E. Domingo Domenech*[2], *C. Martinez-Ramos*[3], *D. Bonometti*[1], *F. Passamonti*[4], *M. Castellani*[1]; [1]*Fondazione IRCCS Cà Granda Ospedale Maggiore Policlinico di Milano, Milan, ITALY,* [2]*Institut Catala d'Oncologia, Hospital Duran i Reynals, IDIBELL, Hematology, Barcelona, SPAIN,* [3]*Hospital Universitari de Bellvitge, IDI, Nuclear Medicine, Barcelona, SPAIN,* [4]*Fondazione IRCCS Cà Granda Ospedale Maggiore Policlinico di Milano, Università degli Studi di Milano, Milan, ITALY.*

Aim/Introduction: 18-Fluorodeoxyglucose (FDG) positron emission tomography/computed tomography (PET/CT) has become a very important tool for initial staging and for the response assessment in lymphoma. In peripheral T-cell lymphomas (PTCL) its use is recommended in staging, but the predictive role of interim PET during front-line therapy remains to be determined. The aim of this study is to evaluate the predictive role of interim PET in first-line treatment of PTCL. ***Materials and Methods:*** We retrospectively identified 68 patients diagnosed with PTCL and treated between 2014 and 2023. All patients were evaluated with PET at baseline, at interim (iPET) and at the end of treatment (ePET). Interim evaluation was performed after 3 cycles or after 4 cycles. Only 2 patients were evaluated after 2 cycles due to suspected progression. Interim-PET were qualitatively evaluated according to Deauville Score (DS), considering the study negative if DS ≤3 and positive in case of DS ≥4. The results of interim-PET according to DS were correlated with PFS and OS. ***Results:*** At iPET 39 (57%) patients were in complete metabolic response (CMR) with DS 1-3, 21 (31%) in partial metabolic response (PMR) with DS4 and 8 (12%) with progressive disease (PD) with DS5. With a median follow-up of 23 months (2-107), 36 (53%) patients relapsed or progressed. Median progression-free survival (PFS) was 20 months. According to the iPET, median PFS of patients with DS1-3, DS4 and DS5 were 28, 10 and 4 months respectively. In univariate analysis, beside known prognostic factors as ALK+ anaplastic subtype(p=0,02), extranodal involvement (0,01), bone marrow infiltration (0,005), advanced stage (0,006) and increased LDH (0,002), iPET impacted on PFS (DS1-3 vs DS4 vs DS5, p=0.001; DS1-3 vs DS4-5, p=0.003). Regarding the timing, iPET after 4 cycles was associated with better prognostic significance (DS1-3 vs DS4 vs DS5, p=0.0009) than after 3 cycles (DS1-3 vs DS4 vs DS5, p=0,32). Median OS was not reached. The estimated 2-year OS was 69% (95%CI, 55-80). According to iPET, the estimated 2-year OS for patients with DS1-3, for those with DS4 and for those with DS5 were respectively 75% (55-87), 64% (34-83) and 57% (22-81), without significant impact. ***Conclusion:*** Interim PET/CT is a good predictor of outcome in terms of PFS in patients with PTCL. Further studies in larger cohorts and also in multicenter trials are needed to better clarify this important prognostic impact of interim-PET in this histotype of lymphoma.

EP-0479

The Effect of MTV Value Evaluated in Staging FDG-PET/CT on Survival and Prognosis in Diffuse Large B-Cell Lymphoma

A. Tunç[1], *E. N. Durmazer*[2], *N. Akad Soyer*[3], *A. Gunes*[3], *A. M. Argon*[1]; [1]*Ege University Nuclear Medicine Department, Izmir, TÜRKIYE,* [2]*Yuksekova State Hospital, Hakkari, TÜRKIYE,* [3]*Ege University Hematology Department, Izmir, TÜRKIYE.*

Aim/Introduction: Today, as in many malignant diseases, F-18 FDG PET/CT is a functional and metabolic imaging modality that plays major role in staging, treatment response evaluation and residual/recurrence detection in NHL. In this study, we aimed to evaluate the predictive power of whole-body MTV value for median survival and progression-free survival in patients with DLBCL. ***Materials and Methods:*** We retrospectively analyzed 61 DLBCL patients who underwent baseline PET/CT at Ege University between January 2014 and September 2022 and had a minimum of 2 years of follow-up. ROC analysis was used to determine the cut-off value of MTV measurements for predicting progression and survival; cut-off values were determined by Youden index. Kaplan-Meier method was used to determine the overall progression-free survival and overall survival curves. Cox regression analysis method was used to calculate Hazard Ratio. ***Results:*** The mean patient age was 58.8±15.6 years (range: 23-85), with a mean follow-up duration of 48.2±25.1 months (median: 42 months). When evaluated according to survival status, cut-off values >556.6 for MTV and >403.9 for MTV when evaluated according to progression status were found to be significant. Our cohort was reclassified according to the cut-off values and descriptive statistics were performed. Of the 61 patients included in the study, death was observed in 10 (16.39%) and progression in 18 (29.1%). Overall survival and progression-free survival were analyzed according to the MTV value at diagnosis. Exitus was observed in 7 of 17 patients with MTV >556.6 and 3 of 44 patients with MTV ≤556.6. The presence of a 12.21-fold higher risk of death in patients with MTV>556.6 compared to those with MTV ≤556.6 was statistically significant. Progression/relapse was observed in 14 of 22 patients with MTV>403.9 and 4 of 39 patients with MTV ≤403.9. The presence of 11.88 times higher risk of progression/relapse in patients with MTV>403.9 compared to patients with MTV ≤403.9 was statistically significant. ***Conclusion:*** As seen in this study, it is thought that the inclusion of MTV values in various risk classifications will facilitate the identification of patients with high mortality and relapse risk and will allow the determination of patient-specific treatment modalities at the time of diagnosis. It is not possible to standardize these values due to individual factors as well as differences in imaging protocols and devices used between centers. Therefore, it would be more appropriate for each center to determine its own cut-off values and make treatment planning accordingly.

EP-0480

Metabolic Tumor Heterogeneity-Based Scoring System Predicts Prognosis in Hodgkin Lymphoma

S. Bayram[1], *E. M. Kaya*[1], *M. G. Tekin*[2], *M. Ayer*[3], *M. Kaya*[1], *B. Esen Akkaş*[1]; [1]*University of Health Sciences Basaksehir Cam and Sakura City Hospital, Department of Nuclear Medicine, Istanbul, TÜRKIYE,* [2]*University of Health Sciences, Tepecik Training and Research Hospital, Department of Haematology, Izmir, TÜRKIYE,* [3]*University of Health Sciences Basaksehir Cam and Sakura City Hospital, Department of Haematology, Istanbul, TÜRKIYE.*

Aim/Introduction: To investigate the impact of metabolic tumor heterogeneity and heterogeneity-based prognostic scoring system on treatment response and prognosis in patients with Hodgkin lymphoma (HL). ***Materials and Methods:*** We retrospectively enrolled 94 newly diagnosed adult HL patients

(57M, 37F; mean age:36.6±14.4). Staging ^{18}F-FDG PET/CT, clinical, histopathological and follow-up data were recorded. Cumulative SUV-volume histograms (CSH) were generated using voxel based dosimetry software by segmentation of tumor foci from staging PET/CT images. The area under the curve (AUC-CSH) was defined as heterogeneity index (HI), with lower values associated with more heterogeneous uptake. Based on follow-up PET/CT and clinical results, patients were grouped as: treatment-responsive and treatment-refractory/relapsed disease. The relationship between clinical-metabolic parameters, AUC-CSH and the presence of treatment-refractory/relapsed disease was investigated. An optimal cut-off value for the AUC-CSH was determined through receiver operating characteristic (ROC) analysis. A two-point prognostic scoring system including disease stage (1-2= 0, 3-4= 1) and HI (high >2568= 0; low ≤2568= 1), was constructed. Primary outcome measures were overall survival (OS) and progression-free survival (PFS). Cox regression models were used to perform survival analysis. ***Results:*** The median follow-up was 24.4 (range 6-60) months. Univariate Cox regression analysis showed that lower AUC-CSH value predicted both OS (p=0.034) and PFS (p=0.03). Additionally, advanced disease stage(3-4) was also associated with shorter PFS (p=0.038) and OS (p=0.02). There was no significant correlation between survival outcomes and other clinical parameters or SUVmax values. In our prognostic scoring system, 22 patients(23%) received a score of 2, indicating the presence of both advanced disease stage(n=37) and low AUC-CSH value(n=44). Median PFS and OS for 0-1 point group were not reached, whereas for 2 point group, were 26 and 44 months, respectively (log rank p <0.05; both). Multivariate Cox regression analysis demonstrated that this score was an independent prognostic factor, significantly associated with poorer outcomes in OS (HR=13.2, CI=2.73-64, p=0.001) and PFS (HR=3.12, CI=1.4-7, p=0.006). ***Conclusion:*** Metabolic tumor heterogeneity-based prognostic scoring system was identified as an independent predictor of PFS and OS in patients with HL. Lower AUC-CSH was significantly associated with worse outcome. Alone or combined with disease stage, heterogeneity index can serve as a novel prognostic marker for newly diagnosed HL patients and may support risk-adapted patient management.

EP-0481

Visual and quantitative assessment of interim ^{18}F-fluorodeoxyglucose-positron emission tomography/computed tomography in children with Hodgkin lymphoma

M. Dunaykin[1], *K. Chaurasiya*[1], *E. Kireeva*[1], *G. Shestopalov*[1,2], *M. Yadgarov*[1,3], *N. Myakova*[1], *Y. Likar*[1];
[1]*Dmitry Rogachev National Medical Research Center Of Pediatric Hematology, Oncology and Immunology, Moscow, RUSSIAN FEDERATION,* [2]*Russian Children's Clinical Hospital, branch of the Federal State Autonomous Educational Institution of Higher Education " N.I. Pirogov Russian National Research Medical University", Ministry of Health of the Russian Federation, Moscow, RUSSIAN FEDERATION,* [3]*Federal Research and Clinical Center of Intensive Care Medicine and Rehabilitology, Moscow, RUSSIAN FEDERATION.*

Aim/Introduction: The generally accepted visual assessment of Hodgkin's lymphoma (HL) with a 5-point scale (Deauville score, "DS") on interim PET/CT but the method may be subject to inaccuracies. One suggested way to solve this problem may be the use of a quantitative evaluation technique (qPET). This study aimed to assess the discrepancies between visual scoring (vDS) and a quantitative evaluation technique (qDS) of visually identified foci on interim scans. ***Materials and Methods:*** We conducted a retrospective, single-center study involving 115 pediatric HL patients diagnosed and treated under the EuroNet-PHL-C1 and DAL/GPOH-HD protocols. The median follow-up was 35 months, with 16 cases (13.9%) of relapse or progression observed. Event-free survival at three years was 86.3±3.3%. We evaluated visually detected foci for DS using qPET analysis through HERMES Medical Solutions software. Both visual and qPET assessments were performed on interim scans for foci with the highest metabolic activity. ***Results:*** Our findings revealed a 30% discrepancy between vDS and qDS scores when analyzing interim PET/CT along with medical history, with no discrepancies when a DS5 score was assigned. Notably, 31 patients (27.0%) were overestimated by the visual scoring; specifically, 25 had a qDS score of 2 compared to a vDS score of 3, and 6 had a qDS score of 3 versus a vDS score of 4. Factors significantly associated with event-free survival included vDS score (hazard ratio: 2.49, p = 0.009) and the presence of bulk tumor mass (HR: 3.12, p = 0.048). ***Conclusion:*** Our study corroborates existing data showing that DS2 and DS5 scores reliably indicate metabolic remission and progression, respectively, serving as effective prognostic factors. However, for intermediate DS scores (DS3 and DS4), where visual assessment may be questionable, incorporating quantification software is recommended for improved accuracy.

EP-0482

Diagnostic accuracy of ^{18}F-FDG PET/CT in detecting bone marrow lesions in children with Hodgkin's lymphoma

M. Dunaykin[1], *G. Shestopalov*[1,2], *M. Yadgarov*[1,3], *K. Chaurasiya*[1], *E. Kireeva*[1], *N. Myakova*[1], *Y. Likar*[1];
[1]*Dmitry Rogachev National Medical Research Center of Pediatric Hematology, Oncology and Immunology, Moscow, RUSSIAN FEDERATION,* [2]*Russian Children's Clinical Hospital, branch of the Federal State Autonomous Educational Institution of Higher Education " N.I. Pirogov Russian National Research Medical University", Ministry of Health of the Russian Federation, Moscow, RUSSIAN FEDERATION,* [3]*Federal Research and Clinical Center of Intensive Care Medicine and Rehabilitology, Moscow, RUSSIAN FEDERATION.*

Aim/Introduction: The aim of this study to assess the diagnostic accuracy of ^{18}F-FDG PET/CT for detecting bone marrow lesions in children with Hodgkin's lymphoma (HL), using bone marrow biopsy (BMB) as the "gold standard." ***Materials and Methods:*** Children with newly diagnosed HL and who underwent both BMB and PET/CT imaging as part of pre-treatment staging were included in this retrospective analysis. We evaluated sensitivity, specificity, prognostic values, and overall diagnostic accuracy. ***Results:*** 118 children with HL were included based on the selection criteria, with a median age of 14.3 years (IQR 11.1-16.2) and an age range of 0 to 17 years. The cohort comprised 55.9% males. Among the participants, 1 patient had stage I, 40 had stage II, 39 had stage III, and 38 had stage IV disease. The median follow-up period was 29 months (IQR 14-47 months), revealing 13 cases of recurrence/progression (11.0%) and one mortality (0.8%). Bone marrow involvement was confirmed in 5 (4.2%) out of the 118 patients based on BMB results. Initial PET/CT scans indicated pathological bone marrow lesions in 28 (23.7%) patients. Notably, all patients who tested positive in BMB also showed positive findings on PET/CT. There were no statistically significant differences in event-free survival based on the presence of focal lesions (p=0.19). ***Conclusion:*** ^{18}F-FDG PET/CT can be a perfect alternative to BMB as a noninvasive diagnostic method with high sensitivity and specificity for assessing bone marrow lesions in children with HL. Based on our findings, BMB should not be performed in HL patients when initial PET/CT shows no evidence of bone marrow lesions or when clear signs of bone marrow involvement are present.

EP-0483

Prognostic Value of Total Metabolic Tumor Volume derived from baseline ^{18}F-FDG PET in Patients with Aggressive Non-Hodgkin Lymphoma

S. Hoberück[1], *P. Nikulin*[2], *F. Hofheinz*[2], *J. Kotzerke*[1], *R. A. Bundschuh*[1], *U. Dührsen*[3], *F. Kroschinsky*[4], *A. Braune*[2];

[1]Department of Nuclear Medicine, University Hospital Carl Gustav Carus, TU Dresden, Dresden, GERMANY, [2]Helmholtz-Zentrum Dresden-Rossendorf, Institute of Radiopharmaceutical Cancer Research, Dresden, GERMANY, [3]Department of Hematology and Stem Cell Transplantation, University Hospital Essen, University of Duisburg-Essen, Essen, GERMANY, [4]Department of Internal Medicine I, University Hospital Carl Gustav Carus, TU Dresden, Dresden, GERMANY.

Aim/Introduction: Our goal was to investigate if the total metabolic tumor volume (TMTV) can improve the prognostic value of baseline PET in aggressive lymphoma. ***Materials and Methods:*** PET data from the PETAL Trial[1] were re-evaluated. Image data as well as maximum baseline SUV and maximum interim SUV (after 2 cycles of R-CHOP) were provided by the PETAL-Trial coordinators. Altogether, 520 patients could be included. In the corresponding baseline PET all affected lesions were delineated with a previously trained neural network. All AI-driven delineations were visually verified and corrected by an experienced nuclear medicine observer, if necessary. From the resulting VOIs TMTV was derived. Survival analyses with respect to event free survival (EFS) were performed for baseline ΔSUVmax and TMTV. ***Results:*** Survival analyses revealed ΔSUVmax and TMTV as prognostic factors for EFS (HR=4.29 and HR=2.81, respectively, p<0.001). In multivariate analysis, ΔSUVmax (p<0.001) and TMTV (p=0.005) remained significant for EFS indicating their independent prognostic value. 5years EFS for low and high risk was 71% vs. 25% for ΔSUVmax and 75% vs. 49% for TMTV. Extension of the two risk model for TMTV to a multi-risk model including clinical parameters further improved discrimination of low and high risk (5years EFS 92% and 35%, respectively). ***Conclusion:*** Our results show that TMTV derived from baseline PET allows a risk stratification close to the risk stratification by ΔSUVmax, which requires both a baseline PET and an interim PET. Prospective investigations are necessary to confirm these promising results. ***References:*** Dührsen U, Müller S, [⋯] Hüttmann A; PETAL Trial Investigators. Positron Emission Tomography-Guided Therapy of Aggressive Non-Hodgkin Lymphomas (PETAL): A Multicenter, Randomized Phase III Trial. J Clin Oncol. 2018 Jul 10;36(20):2024-2034.

EP-0484

^{18}F-FDG PET-Based Multidimentional Scoring System for Immune Adverse Events in PD-1 Inhibitor-Treated Refractory Hodgkin Lymphoma

Z. Wu*, X. Zhang, Z. Lin, Y. Deng, Z. Lin, D. Zheng, R. An, Y. Zhang, X. Lan;*
Department of Nuclear Medicine, Union Hospital, Tongji Medical College, Huazhong University of Science and Technology, Wuhan, CHINA.

Aim/Introduction: Hodgkin lymphoma (HL) features Reed-Sternberg (RS) cells that express PD-1 receptors, contributing to the disease's notable responsiveness to immunotherapy. However, immune-related adverse events (irAEs), stemming from similar immune mechanisms, pose clinical challenges[1]. Reliable biomarkers for irAE prediction remain scarce. Given the non-invasive, systemic metabolic insights provided by ^{18}F-FDG PET/CT, we explored its integration with clinical variables to predict irAE risk. ***Materials and Methods:*** We retrospectively analyzed 54 HL patients (≥18 years) treated with PD-1 inhibitors and assessed with PET/CT before and after four treatment cycles (2017-2023). irAEs were defined by immune-mediated etiology, evaluated through clinical documentation and CTCAE v5.0 criteria. Predictive factors were identified using elastic net and multivariable logistic regression. ***Results:*** Among the cohort, 44.4% (24/54) developed irAEs, with liver dysfunction, fever, rash, diarrhea, and hypothyroidism being most common. Baseline metabolic tumor volume (MTV) and Ann Arbor stage were significantly associated with irAE incidence. Patients with irAEs had higher MTV (255 ± 320 vs. 152 ± 289, p = 0.0192) and were more likely to be stage IV. A predictive nomogram incorporating MTV and Ann Arbor stage achieved strong performance (AUC = 0.80 ± 0.06, p < 0.001; sensitivity: 70.83%, specificity: 76.67%). ***Conclusion:*** Our study proposes a novel PET/CT-based model for anticipating irAEs in HL patients receiving immunotherapy, aiding early risk stratification and clinical decision-making. ***References:*** 1. Naidoo J, Murphy C, Atkins MB, Brahmer JR, Champiat S, Feltquate D, et al. Society for Immunotherapy of Cancer (SITC) consensus definitions for immune checkpoint inhibitor-associated immune-related adverse events (irAEs) terminology. J Immunother Cancer. 2023 Mar;11(3):e006398.

EP-0485

Early ^{18}F-FDG PET/CT as a predictor of metabolic response in large B-cell lymphoma patients following CAR T-cell therapy

C. Sachpekidis*[1], C. Neelsen[1], F. T. Kurz[2], P. Dreger[3], M.-L. Schubert[3], S. A. Klein[4], A. KoppSchneider[1], H.-P. Schlemmer[1], A. Dimitrakopoulou-Strauss[1];*
[1]German Cancer Research Center (DKFZ), Heidelberg, GERMANY, [2]Geveva University Hospitals, Geneva, SWITZERLAND, [3]University Hospital Heidelberg, Heidelberg, GERMANY, [4]University Hospital Mannheim, Mannheim, GERMANY.

Aim/Introduction: Chimeric antigen receptor (CAR)-T cells targeting CD19 represent the new standard of care for patients with relapsed or refractory (r/r) large B-cell lymphomas. This study aimed to assess the predictive value of early ^{18}F-FDG PET/CT in determining long-term metabolic response and progression-free survival (PFS) following CAR-T cell therapy. ***Materials and Methods:*** In this prospective, IRB-approved study, 19 patients with r/r B-cell lymphoma receiving CAR-T cell therapy underwent ^{18}F-FDG PET/CT before (PET-0), 1 month after (PET-1) and 3 months after CAR-T cell infusion. Metabolic responses were classified using the Lugano criteria as complete metabolic response (CMR), partial metabolic response (PMR), stable metabolic disease (SMD), or progressive metabolic disease (PMD), and further dichotomized by complete response rate ([CMR] vs. non-CMR=[PMR] + [SMD] + [PMD]), and at least partial response rate (responders = [CMR] + [PMR] vs. non-responders = [PMD] + [SMD]). Early metabolic findings (PET-1) were compared with late follow-up results (PET-2). The results of PET/CT were correlated with patients' PFS. ***Results:*** Eighteen patients had metabolically active lymphoma, while one patient showed no target lesions at baseline (PET-0). At 1 month (PET-1), 7 patients achieved CMR, 9 had PMR, 1 had SMD, and 1 had PMD. The patient without baseline target lesions remained in CMR in PET-1. By 3 months (PET-2), 13 patients (68%) showed concordant responses with PET-1, whereas 6 (32%) exhibited inconsistencies. In particular, all patients with early CMR maintained remission. Among the 9 patients with early PMR, 3 remained PMR, 1 patient achieved CMR, while 5 progressed to PMD on PET-2. The patient with early SMD developed PMD, while the PMD patient remained PMD at late follow-up. Median follow-up [95% CI] of the patient cohort from PET-1 was 13 months [7.4 months - NA]. Patients with CMR on PET-1 had significantly longer PFS (median: NA, 95% CI: 10.0 months - NA) compared to non-CMR (median: 1.5 months, 95% CI: 0.9 months- NA) (p= 0.02). The dichotomization based on at least PMR on PET-1 led to no significant PFS differences between responders and non-responders. ***Conclusion:*** Early CMR on PET/CT is a strong predictor of sustained metabolic response and patient survival. However, early PET/CT findings were inconclusive for patients with patients with PMR and SMD, as some experienced disease progression over time.

EP-0486

Prognostic Value of Diffusely Increased F-18 FDG Uptake in the Reticuloendothelial System and CBC Score in Patients with Aggressive B-Cell Lymphoma

Ü. Aksu*[1], S. Bayram[1], E. M. Kaya[1], M. Bayer[2], M. Kaya[1], B. E. Akkaş[1];*
[1]Basaksehir Cam and Sakura City Hospital, Department of Nuclear Medicine, Istanbul, TÜRKIYE, [2]Basaksehir Cam and Sakura City Hospital, Department of Hematology, Istanbul, TÜRKIYE.

Aim/Introduction: The immune system and signalling molecules shape the tumour microenvironment and are crucial in cancer

development and progression. The inflammatory response is mainly regulated by the liver, spleen, and bone marrow. While focal F-18 FDG uptake in the spleen and bone marrow indicates disease involvement in lymphoma, diffuse uptake may reflect systemic inflammation. However, its clinical significance remains unclear. This study aimed to assess the association between diffuse FDG uptake in these organs and inflammatory markers, and to evaluate their prognostic value in lymphoma patients. ***Materials and Methods:*** A total of 305 newly diagnosed NHL patients who underwent staging PET/CT between 2020 and 2024 were reviewed. After excluding those with PET- or biopsy-confirmed bone marrow involvement, anemia, secondary malignancies, or indolent lymphoma, 54 patients with aggressive B-cell lymphoma (47 DLBCL, 2 Burkitt, 4 anaplastic large B-cell, 1 lymphoblastic) were included. Pre-treatment inflammatory indices—neutrophil-to-lymphocyte (Neu/Lym), platelet-to-lymphocyte (Plt/Lym), and lymphocyte-to-monocyte (Lym/Mono) ratios—were calculated to generate a CBC score. SUVmean values from the spleen, vertebral column, iliac bone, and proximal femur were obtained and normalized to liver SUVmean. The prognostic impact of these metabolic and inflammatory parameters was assessed for progression-free survival (PFS) and overall survival (OS). ***Results:*** The cohort included 54 patients (32 male, 22 female) with a mean age of 50 years (range: 6-84). Early-stage disease (Stage I-II) was present in 65%. Nine patients (18%) had B symptoms, and 24 patients (45.3%) had extranodal involvement. The median follow-up was 19.9 months (range: 1-50). Disease progression or relapse occurred in 16 patients; 13 patients died. Univariable analysis revealed that spleen-to-liver SUVmean, Neu/Lym, Plt/Lym, Lym/Mono, CBC score, and LDH levels were significant prognostic factors for both PFS and OS ($p < 0.05$). In multivariable analysis, the Neu/Lym ratio was the only independent predictor of OS ($p = 0.004$, HR: 9.34, 95% CI: 2.04-42.7). A strong positive correlation was observed between metabolic activity in the spleen and inflammatory parameters. A spleen-to-liver SUVmean cutoff of 0.86 yielded 93% sensitivity and 66% specificity for predicting PFS, and 91% sensitivity and 61% specificity for OS (AUC: 0.81 for PFS, 0.75 for OS). ***Conclusion:*** Our findings suggest that diffuse splenic FDG uptake correlates with systemic inflammatory markers in aggressive B-cell NHL. Spleen metabolic activity and CBC score may serve as prognostic indicators for PFS and OS; however, further validation with larger cohorts and longer follow-up is warranted.

EP-0487

A new prognostic nomogram based on ^{18}F-FDG PET/CT and clinical parameters in patients with newly diagnosed mucosa-associated lymphoid tissue lymphoma

Y. Han, *X. Zhang, Z. Gao;*
Department of Nuclear Medicine, Union Hospital, Tongji Medical College, Huazhong University of Science and Technology, Wuhan, CHINA.

Aim/Introduction: Mucosa-associated lymphoid tissue (MALT) lymphoma is an indolent B-cell lymphoma originating from extranodal marginal zones, accounting for approximately 7-8% of non-Hodgkin lymphomas. Although its overall prognosis is favorable, a subset of patients may experience progression or relapse. Existing prognostic evaluation systems lack the incorporation of tumor metabolic information. Assessing the value of combining baseline ^{18}F-fluorodeoxyglucose positron emission tomography/computed tomography (^{18}F-FDG PET/CT) has emerged as an essential tool for evaluating Hodgkin lymphoma and aggressive non-Hodgkin lymphoma. Nevertheless, its role in MALT lymphoma remains incompletely understood. In this study, our objective is to evaluate the prognosis of patients with newly diagnosed MALT lymphoma by combining baseline ^{18}F-FDG PET/CT quantitative parameter SUVmax and clinical indicators. ***Materials and Methods:*** Patients diagnosed with MALT lymphoma by histopathology between January 2020 and December 2023 were retrospectively enrolled. All patients underwent baseline ^{18}F-FDG PET/CT before treatment. PET/CT parameter (SUVmax) and clinical indicators were collected. Least absolute shrinkage and selection operator (LASSO) regression combined with multivariate Cox regression was used to identify independent predictors of progression-free survival (PFS). A nomogram was constructed based on these predictors. Model performance was evaluated using time-dependent receiver operating characteristic (ROC) curves, calibration curves, decision curve analysis, and Kaplan-Meier survival curves. ***Results:*** A total of 65 patients (age range: 23-83 years; median age: 59) were included. During follow-up, 14 patients experienced progression or relapse, and 1 patient died. LASSO regression identified age, Eastern Cooperative Oncology Group (ECOG) score, SUVmax, platelet counts, neutrophil-to-lymphocyte ratio, and systemic immune-inflammation index as PFS-related factors. Multivariate Cox regression showed that age, SUVmax, ECOG score, and platelet counts were independent prognostic factors. The resulting nomogram showed good predictive accuracy for 1- and 3-year PFS, with the area under the ROC curve (AUC) of 0.905 and 0.884 respectively.The calibration curves for 1-year and 3-year PFS reported good consistency between predicted and observed probabilities for PFS. DCA demonstrated the net clinical benefit of this nomogram. Additionally, the PFS was significantly different according to the best cutoff of nomogram scores ($P < 0.001$). ***Conclusion:*** A multiparameter prognostic model combining PET metabolic parameters and clinical indicators provides robust discrimination, calibration, and clinical applicability for predicting outcomes in MALT lymphoma, offering a visual tool to support individualized treatment decisions.

EP-0488

Defining the optimal volume of interest for response assessment in lymphoma: Evidence from two prospective multicentre trials and a real-world cohort

C.-A. Voltin[1], *D. Hasenclever*[2], *U. Dührsen*[3], *A. Hüttmann*[3], *C. Hanoun*[3], *M. Dietlein*[1], *P. J. Bröckelmann*[1], *P. Borchmann*[1], *A. Drzezga*[1], *C. Mauz-Körholz*[4], *D. Körholz*[4], *O. Sabri*[5], *R. Kluge*[5], *L. Kurch*[5];
[1]*University Hospital Cologne, Cologne, GERMANY,* [2]*University of Leipzig, Leipzig, GERMANY,* [3]*University Hospital Essen, Essen, GERMANY,* [4]*University Hospital Giessen and Marburg, Giessen, GERMANY,* [5]*University Hospital Leipzig, Leipzig, GERMANY.*

Aim/Introduction: Positron emission tomography (PET) with 2-[^{18}F]fluoro-2-deoxy-D-glucose ([^{18}F]FDG) plays a key role in response evaluation of lymphoma, which is commonly based on the Deauville five-point scale. Quantitative approaches using lesion-to-liver standardized uptake value (SUV) ratios may yield more objective and reproducible results than purely visual assessment. However, the optimal size for lesion volumes of interest (VOIs) has not yet been specified. If chosen too large, it may include a substantial number of voxels surrounding the lesion, particularly in cases with small residuals. Therefore, the present study aimed to evaluate which VOI dimensions offer the most reliable basis for quantitative lymphoma response assessment. ***Materials and Methods:*** A total of 90 response assessment PET scans, visually classified as Deauville score 4, were evaluated in this study. Our analysis set consisted of patients with diffuse large B-cell and paediatric Hodgkin lymphoma (n = 30 each). These individuals were treated in the prospective multicentre trials PETAL and EuroNet-PHL-C2. Furthermore, a real-world cohort of adult patients with Hodgkin lymphoma (n = 30) was included. Maximum SUV and average [^{18}F]FDG uptake were determined in the hottest lesion using VOIs of four voxels, 0.2 mL, 0.5 mL, 1.0 mL, and 2.0 mL. We then calculated quantitative PET (qPET) signals as ratios between tumour and background, based on the mean liver SUV, for all six measurements. Signal shifts across VOI sizes, their clinical relevance, and the effects of correction factors were analysed with a linear mixed model fitted to log-transformed data. ***Results:*** Our

analysis revealed statistically significant changes in qPET signal across increasing VOI sizes ($P < 0.0001$), except for the comparison between a volume of four voxels and 0.2 ml ($P = 0.085$). When the published thresholds were applied, a considerable proportion of patients shifted to different quantitative Deauville scores. We observed the highest rates of misclassification for the 1.0-ml and 2.0-ml measurements, with 36 (40.0%) and 42 individuals (46.7%), respectively, being incorrectly classified as PET-negative. After implementation of the calculated volume-specific correction factors, quantitative Deauville scores remained acceptably stable up to 0.5 ml. For VOI sizes of 1.0 ml and above, variability increased and the adjusted values became less reliable. ***Conclusion:*** The qPET signal intensity systematically decreases with increasing VOI size. This effect can be compensated by adjustment factors, which allow acceptably precise quantitative Deauville classification for a volume of up to 0.5 ml. Larger VOIs introduce high variability and are not recommended in the context of lymphoma response assessment.

EP-0489

Prognostic Accuracy of Semiquantitative Analysis of Interim PET/CT in PMBCL

L. Henzlová[1], *V. Ičová*[1], *V. Hanáčková*[2], *K. Polgárová*[3], *D. Zogala*[4], *M. Trněný*[3], *T. Papajík*[2], *V. Procházka*[2], *M. Kamínek*[1];
[1]*Department of Nuclear Medicine, Palacky University and University Hospital Olomouc, Olomouc, CZECH REPUBLIC,* [2]*Department of Hematooncology, Palacky University and University Hospital Olomouc, Olomouc, CZECH REPUBLIC,* [3]*First Department of Internal Medicine, General University Hospital and First Faculty of Medicine, Charles University in Prague, Prague, CZECH REPUBLIC,* [4]*Institute of Nuclear Medicine, General University Hospital and First Faculty of Medicine, Charles University in Prague, Prague, CZECH REPUBLIC.*

Aim/Introduction: Primary mediastinal large B-cell lymphoma (PMBCL) is a rare and aggressive lymphoma primarily affecting young adults[1]. While interim PET/CT (iPET/CT) scans are routinely used to assess treatment response[2], their prognostic utility remains limited due to the low positive predictive value of standard visual assessment using Deauville scores[3]. ***Materials and Methods:*** This retrospective multicenter study analyzed 116 patients with PMBCL treated with anthracycline-based chemoimmunotherapy. 90 of them had iPET/CT performed on EARL accredited scanners. Semiquantitative parameters, including changes in maximum standardized uptake value (dSUVmax), metabolic tumor volume (dMTV), and total lesion glycolysis (dTLG), were assessed alongside event-free survival (EFS). All iPET/CT scans were independently reviewed by two nuclear medicine physicians blinded to outcomes. ***Results:*** Of the 90 patients, 62 (68.9 %) were iPET-positive (Deauville scores 4-5). Event-free survival (EFS) at 3 years was significantly higher in iPET-negative patients compared to iPET-positive patients (75 % vs. 29 %; $p < 0.01$). Semiquantitative analysis showed that evaluated parameters (dSUVmax, dMTV, and dTLG) provided enhanced predictive accuracy for EFS. Patients with values above optimized cut-off thresholds demonstrated significantly better outcomes (e.g., 3-y EFS: 11.1 % for dSUVmax < 80 % vs. 77.8 % for dSUVmax ≥ 80 %, $p < 0.01$). Semiquantitative analysis was superior in identifying high-risk patients compared to visual assessment alone. ***Conclusion:*** This study highlights the limitations of traditional iPET/CT assessment in PMBCL and underscores the value of incorporating semiquantitative parameters. Metrics such as dSUVmax, dMTV, and dTLG improve predictive accuracy and aid in identifying patients at high risk of treatment failure. Future prospective studies should focus on integrating semiquantitative parameters with clinical factors and exploring their utility as a surrogate endpoint in PET-guided treatment strategies. ***References:*** 1. Martelli, M., Ferreri, A., Di Rocco, A., Ansuinelli, M. & Johnson, P. W. M. Primary mediastinal large B-cell lymphoma. Critical Reviews in Oncology/Hematology 113, 318-327 (2017). 2. Barrington, S. F. et al. Role of Imaging in the Staging and Response Assessment of Lymphoma: Consensus of the International Conference on Malignant Lymphomas Imaging Working Group. Journal of Clinical Oncology 32, 3048 (2014).3. Lazarovici, J. et al. Poor predictive value of positive interim FDG-PET/CT in primary mediastinal large B-cell lymphoma. Eur J Nucl Med Mol Imaging 44, 2018-2024 (2017).

EP-0490

Quantitative ^{18}F-FDG PET/CT parameters as predictors of CAR-T therapy response in large B-cell lymphoma: a preliminary study.

P. Stefaneli Mormandi*, M. Calls-Calahorro, B. Serrallonga, Y. Delisau, M. Velasco-Nuño, A. Fernández-León, J. Duch, S. Asadurova, V. Camacho, S. Castejon, G. Guzman, A. Flotats-Giralt;*
Nuclear Medicine Department, Hospital de la Santa Creu i Sant Pau, Barcelona, SPAIN.

Aim/Introduction: The emergence of novel oncological treatments such as chimeric antigen receptor T-cell (CAR-T) therapy, creates a growing need to identify individual predictors of therapeutic response. This study was aimed to evaluate whether baseline quantitative ^{18}F-FDG PET/CT parameters (metabolic tumor volume [MTV], total lesion glycolysis [TLG], and SUVmax) could play that role. ***Materials and Methods:*** A retrospective analysis was performed on 35 patients with large B-cell lymphoma who received CAR-T therapy. All underwent baseline ^{18}F-FDG PET/CT prior to CAR-T infusion and a follow-up scan at 3 months post-treatment. Univariate logistic regression was used to assess the individual effect of each biomarker, followed by multivariate logistic regression to evaluate their combined predictive value. The model's discriminative capacity was assessed using a ROC curve, and an optimal probability cutoff was determined using the Youden index. ***Results:*** In the univariate analysis, none of the variables were statistically significant on their own ($p>0.05$), although MTV showed a positive trend. In contrast, the multivariate model showed that altogether the three variables were independently significant (all p-values $p<0.05$), suggesting their predictive value when combined. The model demonstrated good discriminative performance, with an area under the curve (AUC) of 0.8. The optimal probability threshold was 0.4, yielding a sensitivity of 94.4% and a specificity of 58.8% for predicting treatment response. ***Conclusion:*** Although MTV, TLG, and SUVmax individually show limited predictive power, their combination in a multivariate logistic regression model may effectively estimate the probability of response to CAR-T therapy. This model holds potential for clinical implementation through the development of a predictive calculator, enabling physicians to input PET/CT parameters and obtain an objective probability of treatment response, thereby supporting personalized therapeutic decision-making prior to CAR-T infusion. ***References:*** 1) Cohen D, Luttwak E, Beyar-Katz O, et al. [18F]FDG PET-CT in patients with DLBCL treated with CAR-T cell therapy: a practical approach of reporting pre- and post-treatment studies. Eur J Nucl Med Mol Imaging. 2022;49(3):953-962. doi:10.1007/s00259-021-05551-5. 2) Murad V, Kohan A, Ortega C, Prica A, Veit-Haibach P, Metser U. Role of FDG PET/CT in Patients With Lymphoma Treated With Chimeric Antigen Receptor T-Cell Therapy: Current Concepts. AJR Am J Roentgenol. 2024;222(3):e2330301. doi:10.2214/AJR.23.30301.

EP-0491

Baseline PET/CT Metabolic Parameters as Predictors of Early Treatment Response in Pediatric Hodgkin Lymphoma

M. Cornide Carrallo*, P. Dauden Onate, A. Berardinelli Isea, C. Wakfie Corieh, M. Zapardiel Martinez-Falero, R. Couto Caro, M. Romero Porras, G. Cuesta Domingo, M. Vaillant Lopez, M. Cabrera Martín;*
HCSC, Madrid, SPAIN.

Aim/Introduction: To evaluate the prognostic value of clinical and metabolic parameters derived from baseline ^{18}F-FDG PET/CT (bPET) in predicting early treatment response in pediatric

patients with Hodgkin lymphoma (HL). ***Materials and Methods:*** A retrospective study was conducted in pediatric patients diagnosed with lymphoma who underwent PET/CT at our center between November 2015 and January 2024. From a total of 85 patients, 23 with confirmed HL diagnosis and both baseline and interim PET/CT (iPET) studies were selected. Clinical, analytical, and histopathological variables were collected. Quantitative PET parameters included SUVmax, metabolic tumor volume (MTV), and total lesion glycolysis (TLG), were calculated using automated segmentation software. Treatment response was assessed based on clinical and metabolic criteria, including the Deauville score on iPET. ***Results:*** Mean age at diagnosis was 13.8 ± 3.5 years, with a predominance of female patients (65%). The most frequent histologic subtype was classical Hodgkin lymphoma of the nodular sclerosis type (87%). Most patients were at stage II (65%) and had a low-risk prognostic index (IPS ≤3), without B symptoms (74%), bulky disease (83%), or extranodal involvement (78%). Induction chemotherapy with OEPA was administered in 91% of cases and 71% received consolidation treatment. Radiotherapy was used in 43%, and only 9% of patients underwent autologous stem cell transplantation. A statistically significant association was found between younger age and better metabolic response on iPET ($p = 0.002$). Higher TLG values on bPET were significantly associated with a lower likelihood of achieving complete metabolic response (CMR) ($p = 0.010$). A similar trend was observed for MTV, although statistical significance was not clearly reached ($p = 0.071$). ***Conclusion:*** These findings suggest that baseline TLG and MTV may provide valuable prognostic information in the initial assessment of pediatric HL. Younger age at diagnosis was also associated with improved early metabolic response. Despite the limitations of a retrospective design and small sample size, these results support the need for prospective studies to validate the role of these metabolic biomarkers in risk stratification.

EP-0492

Prognostic Value of Diffusely Increased FDG Uptake in Spleen and/ or Bone Marrow due to Reticuloendothelial System Activation in Lymphoma Patients

Y. Song, *Q. Zhao, W. Cai, Y. Dong, Y. Yang;*
General Hospital of Ningxia Medical University, Yinchuan, CHINA.

Aim/Introduction: The aim of this study was to evaluate the prognostic value of diffusely increased ^{18}F-FDG uptake in the spleen and/ or bone marrow due to the activation of reticuloendothelial system (RES) in lymphoma patients. The correlation between RES activation and inflammation were also explored. ***Materials and Methods:*** We retrospectively analyzed 629 newly diagnosed and untreated lymphoma patients confirmed by pathology between June 2018 and December 2024, all of whom underwent ^{18}F-FDG PET/CT. Patients with conditions affecting splenic or bone marrow metabolism (e.g., anemia) were excluded. Based on diffuse FDG uptake in the spleen and/ or bone marrow on PET/CT, patients were divided into two groups: diffuse FDG uptake (dFDG, n=67) and normal FDG uptake (nFDG, n=75). Hematological parameters (leukocytes, monocytes, neutrophils, platelets) and inflammatory markers (LDH, β2-microglobulin) were recorded within one week before or after PET/CT scan. Volumes of interest (VOIs) were delineated for the liver, spleen and bone marrow to calculate SUVmean, spleen-to-liver ratio (SLR) and bone marrow-to-liver ratio (BLR). Follow-up data were obtained via medical records or telephone. Prognostic results were assessed by correlation analysis, Cox-regression analysis, and Kaplan-Meier survival analysis. ***Results:*** Compared with nFDGgroup, the dFDG group showed more advanced-stage of disease (account for 83.6% vs. 52.0%, $p < 0.001$) and higher serum level of inflammatory markers (including leukocytes, LDH, β2-microglobulin, D-dimer; $p < 0.05$). SLR positively correlated with LDH, β2-microglobulin, and D-dimer ($p < 0.05$). SLR > 2.221 was an independent risk factor for progression-free survival (PFS) (HR=4.660, p=0.012). The diffuse bone marrow uptake may be caused by inflammation. Multivariate analysis identified SLR as an independent predictor of PFS. ***Conclusion:*** The diffuse pattern of FDG uptake in the spleen and bone marrow demonstrated a significant association with systemic inflammatory reactions, and SLR served as an independent prognostic factor for PFS in lymphoma patients. This study provides new insights into PET/CT-guided prognostic stratification in lymphoma.

EP-0493

Prediction Prognostic Models Based on ^{18}F-FDG PET/CT and Clinical Parameters for Diffuse Large B cell Lymphoma with Interim Deauville Scores of 2-4

S. Chen, *W. Chen, Y. Zhang;*
Fuzhou University Affiliated Provincial Hospital, Fuzhou, CHINA.

Aim/Introduction: To develop a prognostic model combining quantitative PET metrics with clinicopathological variables for refined PFS prediction in DLBCL patients with DS2-4, excluding DS1/DS5 extremes to mitigate analytical bias.Diffuse large B-cell lymphoma (DLBCL) represents 30%-40% of non-Hodgkin lymphomas, yet 30%-40% of R-CHOP-treated patients experience progression despite 60%-70% 5-year survival. While interim PET/CT (iPET) with Deauville scores (DS) stratifies metabolic response, conventional DS1-3/DS4-5 dichotomy inadequately addresses heterogeneous outcomes. ***Materials and Methods:*** Study Design: Retrospective diagnostic accuracy study integrating PET/CT metrics (SUVmax/TMTV/TLG/Δvalues, EANM-compliant), clinical indices , and IHC markers through multivariate Cox regression to develop a PFS prediction model, with progression confirmed by imaging/clinicopathology as the reference standard.Modalities/Interventions: Standard R-CHOP regimen; PET/CT scans (GE Discovery NM/CT 710) at baseline (pre-treatment) and interim (post-cycle 3-4).Data Collection: Retrospective retrieval (2012-2022) of clinical/PET data from electronic records, with follow-up through Dec 2024.Participants: Single-center cohort (n=91) meeting WHO 2022 DLBCL criteria.Statistical Analysis: ROC-optimized thresholds, Kaplan-Meier survival analysis, Bootstrap validation (B=500), with model performance assessed via C-index/calibration curves. ***Results:*** 91 patients (mean age 60±14 years; 50 males) with median PFS of 31 months (1-/3-year rates:82.4%/61.5%). Multivariate analysis identified Ann Arbor III-IV (HR=3.520,95%CI 1.154-10.737, P=0.027), BCL2+ (HR=10.018,3.239-32.040, P<0.001), ΔTMTV%>65% (HR=0.461,0.218-0.975, P=0.043), and interim SUVmax>4.1 (HR=9.737,3.802-24.936, P<0.001) as independent predictors. The combined model showed higher discrimination (C-index=0.743 vs. 0.724/0.578, P<0.05) and calibration (Bootstrap B=500). Time-dependent ROC confirmed 3-year AUC=0.75 (95%CI 0.66-0.84). ***Conclusion:*** Ann Arbor stage III-IV (HR=3.520, P=0.027), BCL2 positivity (HR=10.018, P<0.001), ΔTMTV% >65% (HR=0.461, P=0.043), and interim SUVmax >4.1 (HR=9.737, P<0.001) as independent predictors of PFS in DLBCL patients. The nomogram (BCL2/CD20/interim SUVmax) enables precise risk stratification for interim DS 2-4 patients, validated by sustained 3-year AUC=0.80.

EP-0494

Predictive Value of Interim and End-of-Treatment [^{18}F] FDG PET/CT in Peripheral T-Cell Lymphoma

B. Hervás-Sanz[1], *C. Martínez-Ramos*[1], *E. Domingo-Domenech*[2], *J. L. Díaz-Moreno*[1], *J. J. Robles-Barba*[1], *A. Tapias-Mesa*[1], *M. Pudis*[1], *M. Tormo-Ratera*[1], *P. C. Notta*[1], *C. García-Alcober*[3], *E. M. González-Barca*[2], *M. Zamorano-Rivas*[1], *D. J. Tamayo-Ossa*[1], *M. Cortés-Romera*[1];
[1]*Nuclear Medicine-PET (IDI) Department, Bellvitge University Hospital-IDIBELL, L'Hospitalet de Llobregat, SPAIN,* [2]*Hematology, Institut Català d'Oncologia, L'Hospitalet de Llobregat, SPAIN,* [3]*Radiopharmay Department, Bellvitge University Hospital-IDIBELL, L'Hospitalet de Llobregat, SPAIN.*

Aim/Introduction: Peripheral T-cell lymphoma (PTCL) is a rare and heterogeneous group of aggressive non-Hodgkin lymphomas originating from mature T-cells. It accounts for approximately 10-15% of all lymphomas in adults. PTCL is often associated with poor prognosis and limited response to conventional chemotherapy, highlighting the need for accurate staging and response assessment tools to guide treatment strategies.The aim of this study is to evaluate the predictive value of [^{18}F]FDG PET/CT for response assessment during interim (iPET) and at the end of treatment (fPET) in patients with PTCL. ***Materials and Methods:*** Retrospective study including 47 patients diagnosed with PTCL (mean age: 62 years), all treated at our center with first-line therapy. All patients underwent baseline, interim, and end-of-treatment PET/CT scans. Total metabolic tumor volume (TMTV) and total lesion glycolysis (TLG) were measured using an SUV4 threshold. The percentage reduction in MTV (ΔMTV), Deauville Score (DS) and progression-free survival (PFS) were also analyzed. ***Results:*** The median baseline TMTV and TLG were 78.63 cm^3 (range 0-4833) and 540 cm^3 (range 0-54253.78), respectively. iPET was performed after 3 cycles in 23 patients (49%), after 4 cycles in 22 patients (47%) and after 2 cycles in 2 patients due to early progression. At interim, 30 patients (64%) achieved complete metabolic response (CMR, DS1-3), 11 (23%) had partial metabolic response (PMR, DS4) and 6 patients (13%) showed disease progression. Higher baseline TMTV and TLG were associated with DS4-5 on iPET. Forty patients (85%) showed a ≥90% reduction in MTV (ΔMTV), most frequently observed in those with iPET DS1-3.A total of 91% of patients completed treatment, achieving 68% CMR, 18% PMR, and 15% progression on fPET. Among patients with CMR on iPET, 74% maintained this response at the end of therapy. Additionally, 55% of those with PMR on iPET converted to CMR after completing treatment. Median PFS was 24 months. iPET negativity and ΔMTV >90% were both associated with significantly better PFS. ***Conclusion:*** Our study highlights the potential role of iPET in PTCL. Achieving early CMR and a ΔMTV >90% correlates with longer progression-free survival. Patients with iPET DS4 remain a challenge, as more than half may still achieve CMR after treatment completion. Further research with larger cohorts is needed to better define the prognostic value of baseline TMTV and ΔMTV in PTCL.

EP-0495

Evaluation of Bone Marrow in the Initial Staging of Peripheral T-cell Lymphoma: [^{18}F]FDG PET/CT vs Bone Marrow Biopsy

B. Hervás-Sanz[1], *C. Martínez-Ramos*[1], *E. Domingo-Domenech*[2], *M. Pudis*[1], *J. L. Vercher-Conejero*[1], *A. I. Fritsch-Medina*[1], *J. J. Robles-Barba*[1], *M. Crespí-Busquets*[3], *F. Climent-Esteller*[4], *E. M. González-Barca*[2], *A. Bagán-Trejo*[1], *B. Dacosta-Escobar*[1], *L. M. Gràcia-Sánchez*[1], *I. E. Sánchez-Rodríguez*[1], *M. Cortés-Romera*[1];
[1]Nuclear Medicine-PET (IDI) Department, Bellvitge University Hospital-IDIBELL, L'Hospitalet de Llobregat, SPAIN, [2]Hematology, Institut Català d'Oncologia, L'Hospitalet de Llobregat, SPAIN, [3]Radiopharmay Department, Bellvitge University Hospital-IDIBELL, L'Hospitalet de Llobregat, SPAIN, [4]Anatomical pathology, Bellvitge University Hospital-IDIBELL, L'Hospitalet de Llobregat, SPAIN.

Aim/Introduction: Peripheral T-cell lymphoma (PTCL) comprises a rare and diverse group of aggressive non-Hodgkin lymphomas derived from mature T-cells, representing about 10-15% of adult cases. Due to its clinical heterogeneity and poor response to standard therapies, accurate tools for disease assessment and early response evaluation are essential to improve patient outcomes and guide therapeutic decision-making. The objective of this study is to assess the utility of [^{18}F]FDG PET/CT and its concordance with bone marrow biopsy (BMB) in detecting bone marrow infiltration (BMI) in patients diagnosed with peripheral T-cell lymphoma (PTCL). ***Materials and Methods:*** Retrospective study of 40 patients diagnosed with PTCL (24 males, average age 63 years). Baseline PET/CT, interim (iPET), and post-treatment (fPET) scans were performed. All patients were candidates for chemotherapy according to their histological subtype. Visual analysis of bone marrow uptake on PET and its concordance with BMB were evaluated. PET was considered positive for BMI if focal (unifocal/bifocal/multifocal) and/or diffuse uptake (> liver uptake) was observed. Sensitivity (S), specificity (E), positive predictive value (PPV), and negative predictive value (NPV) of PET were calculated against BMB and/or follow-up. ***Results:*** Thirty of the 40 patients had BMB performed. PET/CT detected BMI in 18/40 patients (45%): 11 with focal uptake and 7 with diffuse uptake. BMB detected BMI in 11/30 patients (37%). There was concordance between PET/CT and BMB in 19/30 patients (63%), with 6 positive cases (3 focal and 3 diffuse) and 13 negative cases (43%). Discordance between PET/CT and BMB occurred in 11/30 patients (37%): 6 had positive PET/CT (3 focal and 3 diffuse) and negative BMB, while 5 had negative PET/CT and positive BMB. Sensitivity, specificity, PPV, and NPV were 55%, 68%, 50%, and 72%, respectively. Three patients with focal uptake on PET/CT had negative BMB. In 12 patients with a positive PET and negative BMB or no biopsy, 8 showed normalization on iPET. In 10 patients with no BMB study, 4 had negative PET/CT and were considered NPV, while 6 showed resolution of medullary foci on iPET, considered PPV. The sensitivity, specificity, PPV, and NPV of PET/CT after including these 10 patients were 71%, 74%, 67%, and 77%, respectively. ***Conclusion:*** The concordance between PET/CT and BMB in evaluating bone marrow in PTCL was good (63%), despite the limited number of patients. Ten percent of patients with focal uptake on PET/CT had negative BMB, and 27% with diffuse uptake had positive BMB.

EP-0496

The prognostic value of MTV is retained in new proposed SUV 4 threshold: an international comparison of follicular and Hodgkin patient survival

S. Chauvie[1], *F. Fallanca*[2], *R. Durmo*[3], *E. Bergalla*[1], *V. Talini*[1], *A. Gallamini*[4], *S. Luminari*[5], *L. Guerra*[6];
[1]S. Croce e Carle Hospital, Cuneo, ITALY, [2]IRCCS San Raffaele, Milano, ITALY, [3]IRCCS Reggio Emilia, Reggio Emilia, ITALY, [4]Lacassagne Cancer Center, Nice, FRANCE, [5]IRCCS Reggio Emilia & University of Modena and RE, Reggio Emilia, ITALY, [6]San Gerardo IRCC, Monza, ITALY.

Aim/Introduction: The objective of this study is to evaluate and compare the prognostic performance of three commonly used TMTV segmentation methods—SUV4, SUV41%, and SUV2.5—across distinct lymphoma patient cohorts, as these thresholds represent widely adopted yet methodologically diverse approaches to metabolic tumor delineation. ***Materials and Methods:*** Data from two large multicenter phase 3 trials were analyzed: 330 Hodgkin Lymphoma (HL) patients from HD0607 (NCT00795613) and 278 Follicular Lymphoma (FL) patients from FOLL12 (NCT02063685). The HL cohort included only PET-negative patients treated with six cycles of ABVD. Baseline FDG-PET/CT scans were segmented using three methods: a 41% SUVmax threshold and fixed thresholds at SUV=4 and SUV=2.5. Only lesions with metabolic tumor volume (MTV) greater than 3 ml were considered. TMTV cut-offs were determined using maximally selected log-rank statistics, and progression-free survival (PFS) was assessed via Kaplan-Meier analysis. ***Results:*** In the FOLL12 trial, 278 patients (124 male) with a median follow-up of 48 months and a median age of 60 years were analyzed. Ann Arbor stages were 33 stage II, 60 stage III, and 185 stage IV, with 173 patients having a FLIPI2 score of 1. In the HD0607 trial, 318 patients (149 male) with a median follow-up of 40 months and a median age of 32 years were analyzed. Ann Arbor stages were 114 stage II, 111 stage III, and 93 stage IV, with 127, 151, and 40 patients having high, intermediate, and low IPS, respectively.The median TMTV in FOLL12 were 164 ml, 236 ml, and 320 ml with SUV4, SUV41%, and SUV2.5 thresholds, respectively. The cut-offs were 405 ml, 479 ml, and 550 ml, discriminating low and high-risk populations with log-rank p-values of 0.00013, 0.0013, and <0.0001, respectively. The 3-year PFS for low and high TMTV were 0.87 and 0.72 with SUV4. In HD0607, the median TMTV were 116 ml, 136 ml, and 216

ml with SUV4, SUV41%, and SUV2.5 thresholds, respectively. The cut-offs were 134 ml, 411 ml, and 623 ml, discriminating low and high-risk populations with log-rank p-values of 0.018, 0.00089, and 0.003, respectively. The 3-year PFS for low and high TMTV were 0.84 and 0.79 with SUV4. ***Conclusion:*** SUV4 has recently been proposed as a standard for lymphoma lesion segmentation, given its reproducibility and practicality in clinical settings. Our results demonstrate that SUV4 offers prognostic value comparable to SUV41% and SUV2.5, reinforcing TMTV's potential as a robust and reproducible biomarker in lymphoma.

EP-0497

Immuno-metabolic stratification in newly diagnosed classical Hodgkin lymphoma: prognostic significance of FDG PET-derived tumor burden and immune-inflammatory parameters

D. Pizzuto[1], *N. Messina*[2], *E. Maiolo*[3], *F. D'Alò*[3], *A. Guarneri*[4], *L. Leccisotti*[4], *V. Rufini*[4], *S. Chiesa*[5], *N. Dinapoli*[5], *C. Mazzarella*[5], *G. Macis*[6], *S. Hohaus*[2], *S. Annunziata*[1];
[1]*Nuclear Medicine Unit, GSteP Radiopharmacy, Fondazione Policlinico Universitario Agostino Gemelli IRCCS, Rome, ITALY,* [2]*Hematology Section, Department of Radiological and Hematological Science, Università Cattolica del Sacro Cuore, Rome, ITALY,* [3]*Hematology Unit, Department of Radiology and Radiotherapy, Fondazione Policlinico Universitario A. Gemelli IRCCS, Rome, ITALY,* [4]*Nuclear Medicine Unit, Department of Radiology and Radiotherapy, Fondazione Policlinico Universitario Agostino Gemelli IRCCS, Rome, ITALY,* [5]*Radiotherapy Unit, Department of Radiology and Radiotherapy, Fondazione Policlinico Universitario Agostino Gemelli IRCCS, Rome, ITALY,* [6]*Radiology Unit, Department of Radiology and Radiotherapy, Fondazione Policlinico Universitario Agostino Gemelli IRCCS, Rome, ITALY.*

Aim/Introduction: Total metabolic tumor volume (TMTV) derived from baseline [18F]FDG-PET/CT is a validated predictor of progression-free survival (PFS) in classical Hodgkin lymphoma (cHL). However, tumor burden alone may not capture the full biological variability at diagnosis. This study assessed whether immunological and inflammatory markers complement TMTV in predicting PFS and explores their underlying biological organization. ***Materials and Methods:*** We retrospectively included patients with newly diagnosed cHL (January 2016-April 2024) who underwent [18F]FDG-PET/CT for initial staging, prior to any systemic therapy, including corticosteroids (GR19-12370372). Eligible patients had available pre-treatment laboratory data and follow-up for PFS. TMTV was calculated on Syngo.via (Siemens Healthineers) by semi-automatic segmentation of all lesions applying the PERCIST liver threshold (SUV ≥ 1.5 × liver mean + 2 SD). Laboratory data included C-reactive protein (CRP), erythrocyte sedimentation rate (ESR), fibrinogen, monocyte and neutrophil counts, CD4-positive, CD8-positive, CD19-positive lymphocytes, and natural killer (NK) cells. Principal component analysis (PCA) was used to identify latent biological dimensions. Kaplan-Meier curves and the log-rank test were used for survival analysis. ***Results:*** Ninety-two patients were analyzed (mean age: 38 years ±15.9; 54% female). Forty had advanced-stage disease and 52 limited-stage. The mean TMTV was 129.45 mL. Patients with TMTV ≥129.45 mL (n=40) had significantly lower 24-month PFS (66.7% vs. 85.5%; log-rank p=0.027). In multivariate Cox regression including TMTV, CD19-positive, CD8-positive, CD4-positive cells, and CRP, only TMTV was confirmed as independent predictor of poor prognosis (hazard ratio 1.005; 95% confidence interval 1.002-1.009; p=0.004). PCA identified four biological axes which contribute to the pathogenesis of Hodgkin lymphoma in an independent manner: systemic inflammation (CRP, ESR); adaptive immunity (CD4, CD8, CD19) tumor burden/innate cellular immunity (TMTV, monocytes, neutrophils); NK-specific cytotoxicity. TMTV was grouped within the component representing tumor burden and innate immunity, suggesting a shared biological signature with circulating myeloid cells. Among patients with high TMTV, CD19-positive lymphocytes <45.5 cells/mm^3 was associated with lower 24-month PFS (46.2% vs. 90.9%; log-rank p=0.053). Relapsed/refractory patients with high TMTV had significantly lower CD19-positive lymphocyte counts compared to patients without relapse [median 33, IQR 37.5 vs. median 61.5, IQR 50.5] cells/ mm^3 (p=0.03, Mann-Whitney U test). Among patients with low TMTV, CRP >14.7 mg/L was associated with significantly reduced PFS (log-rank p=0.001). ***Conclusion:*** PET-derived TMTV retains independent prognostic value in cHL. Immunological markers, particularly CD19-positive cells and CRP, further stratify PFS risk within TMTV subgroups. These findings support integrated metabolic-immunological assessment to improve early risk stratification in cHL patients.

EP-0498

To evaluate the role of ΔMTV at one month in assessing response after chimeric antigen receptor T-cell (CAR-T) therapy in diffuse large B-cell lymphoma.

C. Martínez*, B. Hervás-Sanz, A. Bagan-Trejo, J. Diaz Moreno, M. Zamorano Rivas, M. Tormo Ratera, A. Mussetti, M. Cortés-Romera; Hospital Universitario de Bellvitge, Barcelona, SPAIN.*

Aim/Introduction: [^{18}F]FDG PET/CT is the technique of choice for evaluating CAR-T therapy in patients with relapsed/refractory diffuse large B-cell lymphoma (DLBCL). A high tumor burden is an independent prognostic factor for overall survival and predicts early relapse. Our objective was to describe the role of 1-month ΔMTV in assessing response after CAR-T therapy in DLBCL. ***Materials and Methods:*** Adult patients (>18 years of age) with relapsed/refractory DLBCL treated with commercial anti-CD19 CAR-T therapy, referred to our center, and with [^{18}F]FDG PET/CT at baseline (pre-infusion) and at one month (1M PET) after treatment were included. Patients with a minimum of 6 months of follow-up after infusion were included. Demographic data and metabolic parameters were collected: metabolic tumor volume (MTV), calculating the ΔMTV at baseline and 1M PET. This was compared with the assessment of response using the Deauville criteria (DS) and with disease status at 6 months. Complete response (CR) was considered to be those with DS1-3 and partial response (PR) with DS4-5. ***Results:*** Fifteen patients (6M) were evaluated, mean age (61 years) range 49-75. It was observed that of the 8 patients with CR in PET1M, all achieved a ΔMTV100%, of them 5 maintained CR/PR (62%) and 3 progressed at 6 months. Of the 6 patients who achieved PR in PET1M, the mean ΔMTV was 84% (range 61-100), 2 maintained CR/PR and 4 (66%) progressed. One patient progressed in PET1M with an increase in ΔMTV leading to death. ***Conclusion:*** In this preliminary study, a ΔMTV of 100% at the one-month follow-up assessment after CAR-T therapy in patients with DLBCL who achieved CR does not guarantee maintenance of CR during follow-up. A larger number of patients with longer follow-up is needed.

EP-25

e-Poster Area

B: Imaging Clinical Studies -> B1 Oncological Imaging Clinical Study -> B22 Other Hemato-Oncology

EP-0499

Baseline ^{11}C-acetate PET/CT predicts 3-year relapse post complete remission for newly diagnosed multiple myeloma

S. Chen*, S. Cheung, Y. Wong, K. Wu, Y. Yip, K. Cheng, C. Ho; Hong Kong Sanatorium & Hospital, Hong Kong, HONG KONG.*

Aim/Introduction: Multiple myeloma cells (MMC) are known to utilize raw acetate as a versatile carbon source to energize

intensive cellular activities, including overexpression of monocarboxylate transporters, acetyl-CoA synthetase and fatty acid synthase for immunoglobulin production, replication and lipid synthesis. Such biosynthetic framework forms the underlying basis for ^{11}C-acetate as a more appropriate biochemical probe in PET evaluation of MM than ^{18}F-FDG, especially for assessment of intramedullary MMC activities. Achievement of complete remission (CR) is the ultimate goal of treatment for MM, but many CR patients continue to relapse, even under the current definition of minimal-residual-disease (MRD) negativity. We had previously showed that baseline ^{11}C-acetate-PET/CT predicts CR, so called "molecular-CR". In this prospective study, we aimed to evaluate whether baseline ^{11}C-acetate-PET/CT might predict 3-year relapse post-CR, thus identifying MM patients who need close PET/CT follow-up. ***Materials and Methods:*** During the last 10 years, we consecutively recruited MM patients who satisfied ALL criteria listed below: (1) pretreatment dual-tracer (DT) PET/CT showing active MM disease without extramedullary involvement; (2) post-treatment serological-CR achieved; (3) post-treatment DT-PET/CT confirmed molecular-CR; (4) post-treatment DT-PET/CT within 3 years to evaluate for any relapse. We previously defined active/relapse MM as: (1) focal relapse with ^{11}C-acetate/^{18}F-FDG-avid focal bone lesions (FBLs); and/or (2) diffuse relapse diagnosed with L3 as index vertebra (^{11}C-acetate-SUV$_{max_}$L3>=3.8 or ^{18}F-FDG-SUV$_{max_}$L3>=3.0). The primary endpoint was relapse within 3 years. The parameters for statistical analysis in prediction of post-CR relapse included the following: (1) %clonal marrow plasma cells, (2) beta-2 microglobulin, (3) FISH risk-stratification, and pretreatment PET parameters (4) >3 ^{11}C-acetate-avid FBLs, (5) ^{11}C-acetate-SUV$_{max_}$L3, (6) >3 ^{18}F-FDG-avid FBLs, (7) ^{18}F-FDG-SUV$_{max_}$L3. ***Results:*** 46 myeloma patients (M:F=22:24; age=59.6±9.6 years, range:44-88 years) having achieved "serological+molecular-CR" were thereafter closely followed by PET/CT. 16/46 patients experienced relapse (by IMWG criteria) within 3 years. Multivariate analysis identified baseline "^{11}C-acetate-SUV$_{max_}$L3" as the only independent predictor for 3-year relapse post-CR (P=0.016). Patients relapsed within 3-years had a significantly higher "^{11}C-acetate-SUV$_{max_}$L3" than relapse-free patients (SUV$_{max_}$L3=7.09±1.87 vs. 4.65±1.99, P<0.01). ROC curve analysis calculated "SUV$_{max_}$L3>=5.55" as the threshold for 3-year relapse post-CR (AUC=0.856, P<0.01). Patients with baseline SUV$_{max_}$L3≥5.55 had a significantly higher 3-year relapse rate than those with SUV$_{max_}$L3<5.55 (71.4% vs. 4%, P<0.05). ***Conclusion:*** Pretreatment ^{11}C-acetate PET/CT is a surrogate biomarker of tumor burden and predictor of 3-year relapse post-CR for newly diagnosed MM patients. High-risk patients with baseline "^{11}C-acetate-SUV$_{max_}$L3≥5.55" are advised to have more frequent surveillance with serial ^{11}C-acetate PET/CT and MRD monitoring, even after achieving CR.

EP-0500

Head-to-head comparison of [^{18}F]florbetapir and [^{18}F]FDG PET for the early detection of amyloidosis in systemic amyloidosis and plasma cell dyscrasias

R. Ni[1], *Y. Kong*[2], *L. Cao*[1], *B. He*[2], *Z. Zhou*[2], *Q. Zhang*[2], *M. Zhang*[2], *W. Wang*[2], *Q. Wang*[2], *H. Zhu*[2], *J. Xiao*[2], *A. Rominger*[3], *Y. Guan*[2], *H. Tan*[2]; [1]*University of Zurich, Zurich, SWITZERLAND,* [2]*Fudan University, Shanghai, CHINA,* [3]*Inselspital, Bern, SWITZERLAND.*

Aim/Introduction: Amyloidosis is underdiagnosed in light-chain amyloidosis (AL) and hereditary transthyretin amyloidosis (hATTR), as well as plasma cell dyscrasias (PCD). We aimed to investigate the utility of [18F]florbetapir (FBP) and [18F]fluorodeoxyglucose (FDG) positron emission tomography (PET) for the early detection and evaluation of organ involvement in systemic amyloidosis. ***Materials and Methods:*** We retrospectively included 83 participants, including 38 AL patients, 8 hATTR polyneuropathy patients, 28 PCD patients and 9 healthy controls. Whole-body PET/CT using [18F]FBP was performed in all participants, [18F]FDG PET was performed in 37 patients with AL and PCD, and the results were analyzed by visual and quantitative assessment. Biochemical, serum, and urine assays and histological analysis of tissue biopsies were performed. ***Results:*** [18F]FBP SUV and TBR analysis showed comparable uptake in AL and hATTR-PN patients (p.A117S, p.V50M, p.K55N, p.T69A, or p.H76R mutation carriers) and greater uptake than in PCD patients and control patients. Different regional [18F]FBP and [18F]FDG distributions were observed among the PCD, AL, and hATTR-PN groups. Both [18F]FBP and [18F]FDG enabled the detection of amyloidosis in patients with PCD before clinical detection of AL. [18F]FBP SUV and visual analysis provide comparable measures of organ involvement and were comparable to [18F]FDG and clinical assessment. ***Conclusion:*** [18F]FBP PET detected organ amyloidosis in PCD, AL and hATTR-PN patients with high sensitivity and specificity. [^{18}F]FBP PET, through both visual and SUV$_{max}$ analysis, is more sensitive than [^{18}F]FDG PET and biospy based asessment for detecting organ amyloidosis in PCD and AL patients. It serves as a valuable noninvasive method for the early and accurate detection of systemic amyloidosis, with the potential to improve diagnostic precision and facilitate timely intervention in systemic amyloidosis patients.

EP-0501

FDG-PET/CT versus WB-MRI for bone disease assessment and management change in Smoldering and Symptomatic Multiple Myeloma.

D. Bezzi[1], *A. Rossi*[2], *A. Prochowski Iamurri*[2], *F. Matteucci*[1], *M. Celli*[3], *V. Rossetti*[3], *G. Feliciani*[4], *C. Cerchione*[5], *P. Caroli*[3]; [1]*Nuclear Medicine Unit, AUSL Romagna, Forli-Cesena, ITALY,* [2]*Radiology Unit, IRCCS Istituto Romagnolo per lo Studio dei Tumori (IRST) "Dino Amadori", Meldola, ITALY,* [3]*Nuclear Medicine Unit, IRCCS Istituto Romagnolo per lo Studio dei Tumori (IRST) "Dino Amadori", Meldola, ITALY,* [4]*Medical Physics Unit, IRCCS Istituto Romagnolo per lo Studio dei Tumori (IRST) "Dino Amadori", Meldola, ITALY,* [5]*Hematology Unit, IRCCS Istituto Romagnolo per lo Studio dei Tumori (IRST) "Dino Amadori", Meldola, ITALY.*

Aim/Introduction: The aim of the study was to compare 18F-fluorodeoxyglucose positron emission tomography/computed tomography (FDG-PET) and whole-body magnetic resonance imaging (WB-MRI) for bone disease (BD) assessment in high-risk Smoldering (SMM) and Symptomatic Multiple Myeloma (MM), and to evaluate their relevance for patient management. ***Materials and Methods:*** SMM and MM patients were prospectively enrolled between October 2020 and January 2024. Within one month, all underwent FDG-PET and 3Tesla-WB-MRI, assessed by double-blind readers according to IMPeTUs criteria and MY-RADS respectively. BD was defined as the presence of either focal (FL) or non-focal patterns (NFPs) beyond classical CRAB-criteria: diffuse/micronodular infiltration on WB-MRI and diffuse uptake on FDG-PET. Patient management was established during weekly multidisciplinary meetings, with consensus decisions (IMWG criteria) serving as the reference standard. Patients were stratified by BD presence (FDG-PET+ and/or WB-MRI+) or absence (FDG-PET−/WB-MRI−) and correlated with laboratory data. ***Results:*** The cohort included 137 patients 73M/64F [53%/47%], mean age 66 y): 39 SMM and 98 MM (37 newly diagnosed, 37 post-ASCT, 24 relapsed/refractory). Within the SMM subgroup, WB-MRI detected BD in 10 patients (26%) vs. 4 (10%) with FDG-PET, showing only fair concordance (Cohen's κ=0.33). Most WB-MRI+ cases were NFPs (6/10); among 4 with FL on WB-MRI, only 2 showed focal-PET pattern. Within the MM subgroup, FDG-PET was positive in 60 patients(61%) and WB-MRI in 67(68%), with 91% agreement (κ=0.80). WB-MRI showed higher detection for NFPs: in 9 cases (7 diffuse,2 micronodular), PET was negative or discordant in 6. Regarding FL, FDG-PET detected 55 cases (56%) and WB-MRI 58 (59%), with 97% agreement and excellent concordance (κ=0.94). In the overall cohort, patient management changed in

49% of cases (67/137); attributed to WB-MRI in 95% (64/67) and FDG-PET in 81% (54/67), suggesting a greater impact of WB-MRI (p=0.02), particularly in SMM (3 additional cases), with added clinical value from incidental findings (2 malignancies,1 spinal cord compression). A complementary role emerged in post-ASCT suspected relapse (13 changes based on both, 11 on FDG-PET, 10 on WB-MRI). Furthermore, double-negative patients (FDG-PET–/WB-MRI–) showed less aggressive disease features: in SMM, lower paraprotein (19.8 vs. 29.8g/L, p=0.01); in MM, lower paraprotein (7.4 vs. 19.3g/L, p=0.007) and higher hemoglobin (12.5 vs. 11.2g/dL, p=0.002). ***Conclusion:*** FDG-PET and WB-MRI are central to BD assessment, with WB-MRI showing higher detection of non-focal patterns. Both significantly influenced clinical management. Their complementarity was evident in post-ASCT relapse, with WB-MRI having greater overall impact—especially in SMM—supporting combined use in clinical practice.

EP-0502

[18F]FDG vs [68Ga]Ga-PSMA-11 PET/CT in Multiple Myeloma(MM): Agreement Analysis in Staging and Response Assessment

M. Di Franco[1], *D. Bezzi*[2], *M. Stasolla*[1], *M. Talarico*[3], *E. Zamagni*[3], *V. Cabitza*[4], *F. Lodi*[4], *S. Fanti*[1,4], *C. Nanni*[4];
[1]*Nuclear medicine, Alma Mater Studiorum University of Bologna, Bologna, ITALY,* [2]*Nuclear Medicine Unit, AUSL Romagna, Cesena, ITALY,* [3]*Seràgnoli Institute of Hematology, IRCCS Azienda Ospedaliero-Universitaria di Bologna, Bologna, ITALY,* [4]*Nuclear Medicine Unit, IRCCS Azienda Ospedaliero-Universitaria di Bologna, Bologna, ITALY.*

Aim/Introduction: MM lesions can show a variable uptake on [18F]FDG PET/CT(FDG-PET/CT), with 10% of FNs. Prostate-specific membrane antigen(PSMA) can be overexpressed on the endothelium of neoangiogenic blood vessels, including in MM lesions. The aim of this study is to compare [68Ga]Ga-PSMA PET/CT(PSMA-PET/CT) and FDG-PET/CT in the assessment of MM before and after treatment. ***Materials and Methods:*** Patients with newly-diagnosed symptomatic MM were prospectively enrolled to undergo paired FDG-PET/CT and PSMA-PET/CT within 14 days. Patients with a positive baseline PSMA-PET/CT underwent post-treatment paired FDG- and PSMA-PET/CT. Per-patient and per-lesion analyses were conducted, using Cohen's kappa test, and the McNemar's test. Clinical trial: NCT06835244. ***Results:*** 51 patients were enrolled. A)Pre-treatment: 40/51(78%) patients had concordant FDG and PSMA-PET/CT scans, 23(45%) both positive and 17(33%) both negative; 11/51(22%) patients had discordant scans: 9/5(18%) had a positive FDG-PET/CT only, 2/51(4%) had a positive PSMA-PET/CT only (k=0,57). Overall, 309 focal lesions(FLs) were detected across both scans. Excluding the outlier subject(155 FLs; 137 FDG-positive only; 18 positive at both tracers), FDG-PET/CT detected 116/154(75%) and PSMA-PET/CT detected 72/154(47%) FLs. Eighty-two(53%) FLs were FDG-positive only, whereas 38(24%) were PSMA-positive only (n=7 patients). In the per-lesion analysis, Cohen's kappa showed a strong negative agreement (k= -0.509, p < 0.0001). McNemar's test confirmed significant asymmetry in lesion detection (p < 0.001), in favor of FDG. The median SUVmax of FLs was 5.7 for FDG, 5.2 for PSMA. Overall, 13 paramedullary(PM) lesions were detected, all FDG-positive, 12(92%) PSMA-positive. B)Post-treatment: 17/26 patients, all FDG- and PSMA-positive at baseline, underwent post-treatment paired scans. Therapies were chemotherapy only (n=2) or chemotherapy plus autologous stem cell transplant (n=15). Clinical responses were: complete response(n=7), very good partial response(VGPR)(n=8), partial response(n=1), not-evaluable(n=1). 15/17 patients had concordant negative scans, 1/17(VGPR) was positive at both tracers, 1/17 (VGPR) had FDG-negative/PSMA-positive scans due to the persistence of a PSMA-positive FL (k=0,63). Five patients progressed (4/5 within one year from treatment initiation): at baseline, all had both FDG- and PSMA-positive FLs; in 3/5 PSMA detected more lesions than FDG (22/38 PSMA-positive-only FLs). ***Conclusion:*** Our study showed a systematic disagreement between FDG- and PSMA-PET/CT in the pre-treatment assessment of MM, suggesting that the different biological processes targeted by the two tracers may rarely coexist. FDG-PET/CT significantly outperformed PSMA in lesion detection. However, in the post-treatment assessment, the two tracers showed good concordance in identifying responding patients. A negative prognostic value of PSMA is suggested by the follow-up data, although still limited.

EP-0503

Prospective Comparison of [18F]FDG PET/CT and Whole-Body Diffusion-Weighted Magnetic Resonance for Staging and Treatment Response Assessment in Multiple Myeloma

M. Di Franco[1], *D. Bezzi*[2], *M. Stasolla*[1], *M. Talarico*[3], *E. Zamagni*[3], *A. Cattabriga*[4], *F. Galuppi*[4], *S. Brocchi*[4], *C. Mosconi*[4], *S. Fanti*[1,5], *C. Nanni*[5];
[1]*Nuclear medicine, Alma Mater Studiorum University of Bologna, Bologna, ITALY,* [2]*Nuclear Medicine Unit, AUSL Romagna, Cesena, ITALY,* [3]*Seràgnoli Institute of Hematology, IRCCS Azienda Ospedaliero-Universitaria di Bologna, Bologna, ITALY,* [4]*Department of Radiology, IRCCS Azienda Ospedaliero-Universitaria di Bologna, Bologna, ITALY,* [5]*Nuclear Medicine Unit, IRCCS Azienda Ospedaliero-Universitaria di Bologna, Bologna, ITALY.*

Aim/Introduction: This is a prospective, single-center, non-pharmacological interventional study comparing [18F]FDG PET/CT(FDG-PET/CT) and Whole-body Diffusion-Weighted Magnetic Resonance(WB-MRI) in assessing patients with smoldering multiple myeloma(SMM) or newly diagnosed multiple myeloma(NDMM) at staging and pre-maintenance. The aims are to compare the two modalities' positivity rates and to investigate their pre- and post-treatment prognostic value. ***Materials and Methods:*** FDG-PET/CT and WB-MRI were performed at diagnosis of SMM/NDMM. Positive techniques were repeated after ASCT (pre-maintenance) or after 1 year of treatment. IMPeTuS criteria and MY-RADS criteria were used for image interpretation. Protocol: 364/2022/Oss/AOUBo. ***Results:*** Up to April 2025, 205 patients were enrolled (n=74 SMM; n=131 NDMM). In NDMM, baseline FDG-PET/CT and WB-MRI were concordant in 109/131(83,2%) patients: 90/131(68,7%) were both positive and 19/131(14,5%) were both negative. Discordant scans were found in 22/131(16,8%) patients: 4/22 were FDG+/WB-MRI- due to BM DS4 diffuse uptake; 18/22 were WB-MRI+/FDG- due to the presence at MRI of up to 3 FLs in 10 patients, 3-10 FLs in 2, more than 10 FLs in 5, bone marrow involvement in 1 (DS2 by FDG-PET/CT). Notably, 11/18 WB-MRI+/FDG- discordant patients had DS3 BM diffuse uptake at FDG-PET/CT (borderline positivity). In terms of positivity/negativity, the two modalities showed moderate agreement (kappa=0,53; IC95% 0,37-0,7). Overall, FLs were detected more frequently by WB-MRI than by FDG-PET/CT (FLs' k=0,48; p<0,05), while bone marrow involvement(DS4) was seen more frequently at FDG-PET/CT (k=0,40; p<0,05). PM lesions were detected in 30 patients by FDG-PET/CT, in 39 by WB-MRI (k=0,74). Forty-six patients were evaluated after 1 year of treatment/pre-maintenance. Hematologic responses were: n=24(52,2%) complete response, n=17(37,0%) very good partial response, n=4(8,7%) partial response, n=1(2,2%) not-evaluable. Thirty-one out of 46 patients underwent post-treatment FDG-PET/CT: 27(87,1%) had complete response, 1(3,2%) partial response, and 3(9,7%) progressive o stable metabolic disease. Forty patients underwent post-treatment WB-MRI: n=36(90%) RAC1-2, n=2 RAC3, n=1 RAC4, n=1 RAC=5. Responders at both modalities were 27/31(FLs/BM DS<4 and RAC 1-2), while non-responders were 2/31(FLs' DS>4 and RAC 3-5); 2/31 patients had discordant response categories at FDG-PET/CT and WB-MRI (n=1 FDG-positive and WB-MRI-negative; n=1 FDG-negative and WB-MRI-positive)

(k=0,63). ***Conclusion:*** Concordance between the two modalities was moderate in terms of positivity/negativity. WB-MRI detected a greater number of FLs than FDG-PET/CT, whereas PET/CT more frequently identified diffuse BM infiltration. Further follow-up data are needed to assess the prognostic significance of these findings. Preliminary data indicate good agreement between PET/CT and WB-MRI for treatment response evaluation, despite the small sample sizes' limitations.

EP-0504

Prognostic Value of [^{18}F]FDG PET/CT in Acute Lymphoblastic Leukemia

M. Stasolla[1], *M. Di Franco*[1], *C. Sartor*[2,3], *C. Papayannidis*[3], *J. Nanni*[2], *A. Curti*[3], *A. Romagnoli*[2], *C. Nanni*[4];
[1]Nuclear Medicine, Alma Mater Studiorum University of Bologna, Bologna, ITALY, [2]Dipartimento di Scienze Mediche e Chirurgiche, Università di Bologna, Bologna, ITALY, [3]IRCCS Azienda Ospedaliero-Universitaria di Bologna, Istituto di Ematologia "Seràgnoli", Bologna, ITALY, [4]Nuclear Medicine Unit, IRCCS Azienda Ospedaliero-Universitaria di Bologna, Bologna, ITALY.

Aim/Introduction: Acute lymphoblastic leukemia (ALL) is a hematological malignancy characterized by the uncontrolled proliferation of immature lymphocytes in the bone marrow and peripheral blood. This condition represents the most common type of leukemia in children but can also affect adults of all ages. Positron emission tomography with fluorodeoxyglucose (PET-FDG) is an imaging technique that allows the assessment of the metabolic activity of both medullary and extramedullary tumor cells. We seek to investigate the potential prognostic value of PET-FDG imaging in predicting overall survival (OS) and progression-free survival (PFS) in patients with ALL. ***Materials and Methods:*** 63 patients (43 men and 20 women) diagnosed with ALL underwent a staging PET-FDG scan. Of these patients, 40 underwent a follow-up PET-FDG scan after the first cycle of therapy. The PET variables considered were hepatic SUVmax, hepatic SUVmean, bone marrow (BM) SUVmax, BM SUVmean and extramedullary lesions. For the subsequent multivariate analysis, additional variables such as OS months, PFS days, white blood cells (WBC), hemoglobin, platelets, LDH BM blasts were included. Statistically significant cut-off values were identified for PET variables (both staging and post-therapy). The log-rank test was performed, followed by Kaplan-Meier survival curves for variables with statistically significant p-values in the univariate analysis ($p < 0.05$). Finally, a multivariate Cox regression analysis was conducted, incorporating both staging and post-therapy PET parameters along with the aforementioned variables. ***Results:*** Statistically significant cut off values were identified for some of the PET variables considered. The log-rank test and Kaplan-Meier survival curves showed that the post first cycle PET-FDG results significantly dichotomize the patient outcomes. Multivariate analysis revealed that both the post first cycle PET-FDG results and LDH levels are prognostic factors in terms of PFS ($p = 0.037$ and $p = 0.039$, respectively). ***Conclusion:*** PET-FDG imaging provides valuable prognostic information in patients with ALL. The identified cut-off values for PET-FDG parameters can help in stratifying patients based on their metabolic activity, potentially guiding therapeutic decisions and improving clinical outcomes.

EP-0505

Prognostic Value of ^{18}F-FDG PET/CT Brain-to-Liver Uptake Ratio in Multiple Myeloma

C. D. Ramos, *T. P. Santos, M. E. S. Takahashi, C. Cralcev, M. D. S. Silva, F. C. Souza, E. Miranda, C. A. Souza;
University of Campinas, Campinas, BRAZIL.*

Aim/Introduction: ^{18}F-FDG PET/CT is routinely used for staging and response assessment in multiple myeloma (MM). Reduced cerebral FDG uptake has been observed in advanced malignancies, potentially linked to metabolic alterations like the Warburg effect and elevated lactate levels. This study investigated the prognostic significance of the brain-to-liver standardized uptake value ratio (BLR) in MM patients. ***Materials and Methods:*** We analyzed 82 MM patients (diagnosed March 2011-May 2019) with median 25-month follow-up (range: 0.1-113). All underwent diagnostic ^{18}F-FDG PET/CT after ≥6-hour fasting (glucose <180 mg/dL), receiving 0.1 mCi/kg ^{18}F-FDG 60 minutes pre-scan. Automated whole-brain segmentation and liver spherical VOIs generated SUVmean values for BLR calculation. Overall survival (OS) and progression-free survival (PFS) analysis used Kaplan-Meier and log-rank tests (SPSS v24), with data updated through January 2025. ***Results:*** The cohort (55% male, median age 64 years) showed 67% ISS stage III, 16% ECOG ≥2, and 88% with bone lesions. Most (94%) received chemotherapy (27% bortezomib), with 71% achieving ≥PR. Progression occurred in 47%, mortality in 69%. Five-year OS/PFS rates were 35%/10%.BLR correlated significantly with sex ($p=0.006$), overweight status ($p=0.007$), ISS stage ($p=0.04$), and β2-microglobulin ($p<0.0001$). Patients with BLR >2.7 had superior OS (50% vs 13%, $p=0.006$) and PFS (3% vs 0%, $p=0.006$). ***Conclusion:*** BLR at diagnosis demonstrates strong prognostic value for MM outcomes, with 2.7 as a clinically relevant cutoff. Its association with β2-microglobulin and advanced disease suggests BLR reflects tumor glycolytic activity. Reduced brain uptake in aggressive MM may indicate lactate-mediated metabolic adaptation, positioning BLR as a potential biomarker of disease burden and metabolic dysregulation.

EP-0506

Assessing the relationship between quantitative ^{18}F-FDG PET/CT and DWI MRI parameters in bone marrow imaging of multiple myeloma

Ö. Kilic[1,2], *M. Hajiyianni*[3], *M. Wennmann*[1,4], *E. K. Mai*[3], *L. John*[3], *N. Weinhold*[3], *M. Grözinger*[4], *S. Sauer*[3], *M. S. Raab*[3], *H. Goldschmidt*[3], *A. Dimitrakopoulou-Strauss*[1], *C. Sachpekidis*[1];
[1]Clinical Cooperation Unit Nuclear Medicine, German Cancer Research Center (DKFZ), Heidelberg, GERMANY, [2]Medical Faculty Heidelberg, Heidelberg University, Heidelberg, GERMANY, [3]Internal Medicine V, Hematology, Oncology and Rheumatology, German-Speaking Myeloma Multicenter Group (GMMG), Heidelberg University Hospital, Heidelberg, GERMANY, [4]Division of Radiology, German Cancer Research Center (DKFZ), Heidelberg, GERMANY.

Aim/Introduction: In multiple myeloma (MM), imaging plays a critical role in assessing bone marrow (BM) involvement. ^{18}F-FDG PET/CT reflects metabolic activity, while diffusion-weighted MRI (DWI) provides insights into tissue microstructure via the apparent diffusion coefficient (ADC). This study explores the relationship between quantitative imaging biomarkers—ADC and PET-derived SUVmax—and established clinical indicators of disease burden. ***Materials and Methods:*** Fifty-seven newly diagnosed MM patients (36 ISS-I, 10 ISS-II, 11 ISS- III; 28% with high-risk cytogenetic features) underwent whole-body ^{18}F-FDG PET/CT and MRI —including DWI, T1-, and T2-weighted sequences—, both at baseline and after induction therapy. All patients were enrolled in the open-label, multicentre, randomized phase 3 GMMG-HD7 trial at the Myeloma Center Heidelberg and received either isatuximab plus lenalidomide, bortezomib, and dexamethasone or the standard regimen without isatuximab. A total of 114 paired measurements per time point were obtained from anatomically matched regions in the os ilium and lower lumbar spine to assess diffuse BM involvement. SUVmax and ADC values were extracted from corresponding sites. Correlation was assessed using Spearman's rank coefficient ($p < 0.05$). ***Results:*** At baseline, a weak but statistically significant correlation was observed between ADC and SUVmax ($r = 0.19$). Longitudinally, changes in ADC moderately correlated with changes in SUVmax from baseline to follow-up ($r = 0.20$). Both baseline SUVmax and ADC values significantly correlated with β2-microglobulin levels (SUVmax: $r = 0.40$; ADC: $r = 0.38$), plasma cell infiltration rate (SUVmax: $r = 0.30$; ADC: $r = 0.38$), and hemoglobin levels (SUVmax: $r = -0.20$; ADC: $r = -0.31$).

Additionally, both parameters increased significantly across ISS stages. ***Conclusion:*** Functional imaging modalities provide complementary insights into BM involvement in MM. ADC may serve as a valuable alternative to PET/CT in longitudinal disease assessment, particularly in settings with limited PET availability. These findings support a multimodal imaging approach to improve diagnostic precision and treatment monitoring in MM.

EP-0507

Prognostic Value of Tumor Dissemination (Dmax) Derived from ^{18}F-FDG PET/CT in Patients With Multiple Myeloma

S. Pellegrino[1], *E. Di Donna*[1], *M. Lamagna*[2], *R. Della Pepa*[2], *S. Del Vecchio*[1], *R. Fonti*[1];
[1]*Department of Advanced Biomedical Sciences, University Federico II, Naples, ITALY,* [2]*Department of Clinical Medicine and Surgery, University Federico II, Naples, ITALY.*

Aim/Introduction: The aim of our study was to test whether the largest distance between two ^{18}F-FDG avid lesions (Dmax) may predict overall survival (OS) in patients with multiple myeloma (MM). ***Materials and Methods:*** Thirty-two MM patients (18 men, 14 women) who had undergone ^{18}F-FDG PET/CT scan showing at least two positive focal bone lesions were included in the study. All lesions were segmented using an automated contouring program setting an absolute threshold for SUV at 2.5. The largest distance between two ^{18}F-FDG avid lesions (Dmax) in each patient was measured. Then the hottest focal lesion was selected and SUVmax, SUVmean and Coefficient of Variation (CoV) were determined along with total MTV (MTV_{TOT}) and whole-body TLG (TLG_{WB}) from all malignant lesions. Patients were subjected to a mean follow-up period of 49 months. Univariate and multivariate analyses of clinical and imaging variables were performed using Cox proportional hazards regression whereas Kaplan-Meier method and log-rank tests were used for survival analysis. ***Results:*** A total of 311 bone focal lesions were segmented and mean Dmax value was 49.64±29.13 cm. In 32 hottest focal lesions, average values of SUVmax, SUVmean and CoV were 10.96±7.55, 4.86±1.94 and 0.36±0.14, respectively, whereas mean values of MTV_{TOT} and TLG_{WB} were 52.26±64.5 ml and 284.68±370.56 g, respectively. Univariate analysis showed that OS was predicted by haemoglobin (p=0.0458), plasma cell percentage in the bone marrow (p=0.0468), Dmax (p<0.0001), MTV_{TOT} (p=0.0030), TLG_{WB} (p=0.0017) as well as by SUVmax (p=0.0339), SUVmean (p=0.0325) and CoV (p=0.0062) of targeted lesions. At multivariate analysis only Dmax was retained in the model for the prediction of OS (p=0.0028). By Kaplan-Meier analysis, patients with Dmax ≤ 48.7 cm had significantly better OS as compared to patients with Dmax > 48.7 cm (p=0.0001). When we combined Dmax with MTV_{TOT}, in all possible arrangements, a statistically significant difference was found among the survival curves (p=0.0002). In particular, patients with Dmax > 48.7 cm and MTV_{TOT} > 39.4 ml had the worst prognosis. ***Conclusion:*** Dmax, by reflecting tumor dissemination, can predict overall survival in MM patients. Moreover, the combination of Dmax with MTV_{TOT}, that represents the whole metabolically active tumor burden, may improve the risk stratification of these patients.

EP-0508

Diagnostic Value of Whole-Body ^{18}F-FDG PET/MRI versus PET/CT in Systemic Histiocytosis: A Prospective Comparative Study

M. Pudis[1], *G. Rocamora Blanch*[2], *J. A. Narváez*[3], *X. Solanich-Moreno*[2], *B. Hervás-Sanz*[1], *J. Diaz-Moreno*[1], *A. Bagan-Trejo*[1], *M. Zamorano-Rivas*[1], *C. Martínez-Ramos*[1], *J. J. Robles-Barba*[1], *J. J. Marcuartu*[1], *M. Cortés-Romera*[1];
[1]*Nuclear Medicine - PET (IDI), Bellvitge University Hospital - IDIBELL, L'Hospitalet de Llobregat, SPAIN,* [2]*Internal Medicine, Bellvitge University Hospital - IDIBELL, L'Hospitalet de Llobregat, SPAIN,* [3]*Radiology Department, Bellvitge University Hospital - IDIBELL, L'Hospitalet de Llobregat, SPAIN.*

Aim/Introduction: Histiocytoses such as Erdheim-Chester Disease (ECD), Langerhans Cell Histiocytosis (LCH), and Rosai-Dorfman Disease (RDD) are rare multisystem disorders characterised by histiocyte proliferation. Accurate disease staging is crucial for diagnosis, biopsy guidance, and treatment planning. While ^{18}F-FDG PET/CT is widely used, PET/MRI may offer improved soft-tissue contrast and lesion characterisation. This prospective study aimed to assess the diagnostic performance of whole-body ^{18}F-FDG PET/MRI compared to PET/CT in patients with systemic histiocytosis. ***Materials and Methods:*** Between 2022 and 2024, fifteen patients with histologically confirmed systemic histiocytosis (ECD n=9, LCH n=2, RDD n=2, mixed n=2) underwent sequential whole-body ^{18}F-FDG PET/CT and PET/MRI following a single radiotracer injection. Lesions were evaluated by a multidisciplinary team regarding anatomical definition, metabolic uptake, and disease extent, and were correlated with clinical, laboratory, histopathological, and follow-up data. ***Results:*** PET/CT and PET/MRI showed concordant findings in 14 of 15 patients (93%). One patient presented with a discordant finding: PET/MRI detected a brainstem lesion missed by PET/CT, altering management. A total of 38 lesion sites were identified, of which 35 (92%) were attributed to histiocytosis. PET/MRI demonstrated improved anatomical delineation in 60% of cases and better lesion characterisation in 33%, particularly for CNS, cardiac, renal, and skeletal involvement. Additional lesions were detected by PET/MRI in 33% of patients. PET/MRI revealed higher metabolic uptake and more extensive disease in 73% of cases, suggesting increased sensitivity. However, PET/CT was superior for pulmonary lesion characterisation. ***Conclusion:*** This prospective study supports the integration of ^{18}F-FDG PET/MRI into the diagnostic workflow for systemic histiocytosis. PET/MRI provides superior soft-tissue contrast, improved lesion delineation, and enhanced sensitivity in detecting disease burden, potentially guiding more accurate clinical decisions and reducing radiation exposure—especially relevant for patients requiring repeated follow-up imaging.

EP-0509

Comparison of 68Ga-Pentixafor and ^{18}F-FDG PET/CT for initial evaluation of patients with newly diagnosed multiple myeloma.

S. Kumar, *H. Kaur;*
PGIMER, Chandigarh, INDIA.

Aim/Introduction: ^{18}F-FDG PET/CT is seen to have limitations in evaluation of multiple myeloma due to low hexokinase expression. Additionally, it is seen to underestimate diffuse marrow involvement. CXCR4 targeting 68Ga-Pentixafor is increasingly used in evaluation of myeloma. We compared the performance of 68Ga-Pentixafor and ^{18}F-FDG PET/CT in newly diagnosed multiple myeloma. ***Materials and Methods:*** In this prospective study we recruited 84 patients with newly diagnosed multiple myeloma from February 2021 to April 2023. 84 patients underwent 68Ga Pentixafor PET CT and 77 underwent 18F FDG PET CT. IMPeTUs criteria was used to evaluate ^{18}F-FDG PET/CT and uptake≥ twice liver was considered positive on 68Ga-Pentixafor. Patterns of disease involvement were assessed. Positivity rate on both modalities and degree of marrow involvement were compared. ***Results:*** Eighty-four (54 Male and 31 Female) patients were recruited in the study and underwent 68Ga-Pentixafor PET/CT among them, 77 (47 male and 30 female) underwent both ^{18}F-FDG and 68Ga-Pentixafor PET/CT. Positivity rate was 89.2% (75/84) on 68Ga-Pentixafor PET/CT. Among 77 patients who underwent both modalities, 68Ga-Pentixafor PET/CT was positive in a higher number of patients (90.9%, n=70/77) compared to ^{18}F-FDG PET/CT (68.8 %, n=53/77) (p<0.01) using Deauville score≥ 4 as the criteria. However, no difference was noted between the modalities when using Deauville score≥ 3 as the criteria (90.9% vs 87.0% n=67/77) (p=0.581). On 68Ga-Pentixafor PET/CT 26 (30.9%) had only marrow involvement, 41 (48.8%) had both marrow and focal lytic lesions and 10 (11.9%) had only focal lytic lesions. On 18 -FDG PET/CT 17 (22.0%) had only marrow involvement, 31 (40.2%)

had both marrow and focal lytic lesions and 21 (27.2%) had only focal lytic lesions. 68Ga-Pentixafor PET/CT showed a higher rate of marrow involvement i.e. 79.2% (61/77) compared to 49.3% (38/77) on ^{18}F-FDG PET/CT (p<0.01), among patients who underwent both investigations. 68Ga-Pentixafor PET/CT also demonstrated a higher SUVpeak (11.6 vs 5.5) , SUV mean (7.8 vs 4.1) and SUV max (16.2 vs 6.5) compared to 18 F -FDG PET/CT (p<0.05). No significant difference was noted in detection of paramedullary disease (21 vs 19) and extra medullary disease (4 vs 6) (p>0.05) on 68Ga-Pentixafor and ^{18}F-FDG PET/CT respectively. ***Conclusion:*** 68Ga-Pentixafor PET/CT is a promising modality for assessment of disease extent in newly diagnosed patients with multiple myeloma. It demonstrates a higher detection rate and SUV values compared ^{18}F-FDG PET/CT and shows a higher degree of marrow involvement.

EP-0510

PETBOT: An AI-Powered Patient-Centric Chatbot for Cancer Staging and Treatment Guidance according to NCCN from PET/CT Reports

S. Sagar[1], *D. Khan*[1], *N. Kundu*[1], *A. Roy*[1], *A. Mahalik*[1], *L. Goriparti*[1], *A. Tilak*[1], *J. Krishna P.*[1], *A. Dhiman*[1], *A. Singh*[2], *A. Rout*[2], *S. K V*[1], *R. Babu*[1], *J. Pathak*[1], *R. Kumar*[1];
[1]*AIIMS, Delhi, INDIA,* [2]*AIIMS, Bhubaneswar, INDIA.*

Aim/Introduction: Patients undergoing PET/CT scans often struggle to interpret complex cancer staging reports, leading to anxiety, misinterpretation, and delayed decision-making. With the growing accessibility of AI tools, there is a unique opportunity to empower patients directly using structured summaries derived from their imaging reports.To develop and evaluate a Python-based chatbot application (PETBOT) that automatically extracts TNM staging, NCCN-based treatment options, and simplified explanations from uploaded PET/CT reports, with an interactive feedback mechanism. ***Materials and Methods:*** We developed a Streamlit-based application integrated with a text extractor (for PDF/DOCX), a fine-tuned NER model (spaCy with BioBERT backbone) for extracting named entities such as tumor site, lymph node involvement, and metastases, and a custom rule-based TNM staging engine (modularized by cancer type). The application supports six cancer types: esophageal, gallbladder, breast, lung, colorectal, and head & neck. Extracted features were mapped to AJCC-like TNM rules, and treatment guidance was aligned with NCCN recommendations. The chatbot interface allowed users to select predefined questions about their diagnosis and download personalized summaries. A CSV-based feedback system captured user responses on helpfulness and emotional impact which will be used for analyzing patient parameters later. ***Results:*** The chatbot successfully identified and staged six major cancer types—esophageal, gallbladder, breast, lung, colorectal, and head & neck—from unstructured PET/CT reports using rule-based logic and NER-assisted feature extraction. For these cancers, PETBOT generated accurate TNM classification, NCCN-aligned treatment suggestions, and plain-language summaries. However, when reports of unsupported cancer types (e.g., pancreatic, ovarian, or hematological malignancies) were uploaded, the system either failed to extract meaningful features or returned misleading outputs, underscoring the need for strict cancer-type validation. The tool is accessible for demonstration and testing at: https://petbot1.streamlit.app. ***Conclusion:*** PETBOT demonstrates the feasibility of a lightweight, deployable, patient-centered tool for AI-assisted cancer education and empowerment using PET/CT reports while underlining the requirement for an indigenous Large Language Models(LLM) to deduce TNM staging from imaging reports. Future enhancements include multilingual support, physician feedback loop, and broader cancer type integration.

EP-0511

Extramedullary Involvement in Multiple Myeloma: Can FDG PET/CT and Disease-Related Parameters Provide New Insights into Clinical Outcome?

K. Toplutas*, A. B. Dere, E. M. Kaya, B. Esen Akkaş;*
University of Health Sciences, Basaksehir Çam and Sakura City Hospital, Istanbul, TÜRKIYE.

Aim/Introduction: Multiple myeloma (MM) is a complex hematologic malignancy with various clinical stages. Although definitions vary, extramedullary disease (EMD) is generally described as soft tissue or organ involvement without direct bone contact. EMD is usually associated with poor prognosis. This study aimed to evaluate the prognostic significance of FDG PET/CT findings and associated clinical and biochemical parameters in MM patients with EMD. ***Materials and Methods:*** MM patients who underwent FDG PET/CT between 2021 and 2025 were retrospectively screened for EMD. PET/CT findings (lesion localization and SUVmax), Durie-Salmon Plus (DSP) scores, bone marrow immunophenotyping, biochemical markers, progression-free survival (PFS), and overall survival (OS) were analyzed. Statistical analyses were performed using Jamovi v2.3.28. ***Results:*** Among 424 patients, EMD was identified in 21 cases (4%). Eleven had primary and ten had secondary EMD. Eight patients died during follow-up. The mean SUVmax for EMD lesions was 6.85±5.28, and for intramedullary disease (MD), it was 6.02±5.30 (p>0.05). Paramedullary disease (PMD) was present in 57% of cases, with a higher mean SUVmax (8.81±4.70). The most common EMD sites were lymph nodes (42.9%) and pleura-lung (19%); rare sites included orbit, sphenoid sinus, brain, and jejunum. Median PFS was 8 months and OS was 13 months. No significant correlation was found between SUVmax and PFS/OS in Cox regression analyses (p>0.05). However, a borderline significant OS difference was observed by EMD location (log-rank p=0.05), with longest survival in lymph node involvement (26 months) and shortest in lung (8 months) and spleen (3 months) involvement. DSP score correlated positively with both MD SUVmax (rho=0.562, p=0.008) and EMD SUVmax (rho=0.443, p=0.044). No significant differences were observed based on light/heavy chain status (p>0.05). Albumin levels were inversely associated with mortality (HR: 0.89, p=0.022). CD138 positivity was significantly associated with better survival outcomes (p=0.013). ***Conclusion:*** FDG PET/CT provides useful information in identifying EMD, particularly in atypical sites. However, FDG PET/CT-associated metabolic parameters did not show a significant relationship with survival outcomes in this cohort.Notably, patients with splenic and pulmonary involvement exhibited shorter overall survival compared to those with lymph node involvement. CD138 negativity and low albumin levels were also associated with worse prognosis. Further studies with larger cohorts are needed to validate these findings. ***References:*** Vicentini, J. R., & Bredella, M. A. (2022). Role of FDG PET in the staging of multiple myeloma. Skeletal Radiology, 51(1).

EP-0512

From Volume to Dissemination: Dmax and TMTV Drive Prognostic Assessment in Newly Diagnosed Multiple Myeloma Over Advanced Radiomic Approaches

L. Raffy[1], *C. Etchegaray*[2], *E. Hindie*[1], *O. Saut*[2], *C. Hulin*[3], *A. Schmitt*[4], *C. Mesguich*[1];
[1]*Department of nuclear medicine, University of Bordeaux, Bordeaux, FRANCE,* [2]*Inria, Univ. Bordeaux, CNRS, Bordeaux INP, IMB, UMR 5251, Talence, FRANCE,* [3]*Department of onco-hematology, University of Bordeaux, Bordeaux, FRANCE,* [4]*Department of onco-hematology, Institut Bergonié, Bordeaux, FRANCE.*

Aim/Introduction: ^{18}F-FDG PET/CT (FDG-PET) has consistently demonstrated prognostic value in the evaluation of newly diagnosed multiple myeloma (NDMM). However, current standard

FDG-PET biomarkers fall short in assessing tumor heterogeneity and spatial dissemination, critical features that radiomic analysis could quantify. This study aimed to identify prognostic FDG-PET radiomic biomarkers in NDMM. ***Materials and Methods:*** Between 2014 and 2022, 146 NDMM patients underwent FDG-PET imaging at two medical centers. The associations between clinical, biological, and standard PET variables - referred to as 'standard parameters'- were assessed using Cox regression analysis. Random Forest models were trained using three distinct datasets to predict two-year PFS: (1) standard parameters, (2) PET radiomic features, and (3) CT radiomic features. A voting classifier combined the best-performing models from each dataset. ***Results:*** Multivariate analysis revealed that both total metabolic tumor volume (TMTV) and Dmax were significantly associated with PFS (HR=2.17, p=0.003 ; HR=1.89, p=0.01, respectively) and OS (HR=2.23, p=0.04 ; HR=2.69, p=0.01, respectively). The standard parameters model demonstrated promising predictive performances of two-year PFS with an AUC of 0.749 (IC95% 0.679-0.792) and a Brier Score of 0.198 (IC95% 0.178-0.218). PET and CT radiomics models showed poor performance. The voting classifier presented an AUC of 0.624 (IC95% 0.564 - 0.684), and a Brier Score of 0.221 (IC95% 0,207-0,233). ***Conclusion:*** Both Dmax and TMTV are robust and independent prognostic biomarkers in NDMM. The models utilizing PET and CT radiomic features yielded poor performance, highlighting the current limitations of this approach in multiple myeloma prognostic assessment.

EP-0513

FDG PET/CT in Multiple Myeloma Staging: Standardization and Prognostic Impact of Imaging Parameters

M. Havel[1,2], *L. Muronova*[3,4], *G. Havlova*[1], *D. Zihala*[3,4], *T. Popkova*[3,4], *G. Kascakova*[1], *S. Bobkova*[1], *K. Bukovansky*[1], *J. Mihalyova*[3,4], *H. Plonkova*[3], *J. Golisova*[1,2], *R. Hajek*[3,4], *T. Jelinek*[3,4];
[1]*Department of Nuclear Medicine, University Hospital Ostrava, Ostrava, CZECH REPUBLIC,* [2]*Department of Imaging Methods, Faculty of Medicine, University of Ostrava, Ostrava, CZECH REPUBLIC,* [3]*Department of Hematooncology, University Hospital Ostrava, Ostrava, CZECH REPUBLIC,* [4]*Department of Hematooncology, Faculty of Medicine, University of Ostrava, Ostrava, CZECH REPUBLIC.*

Aim/Introduction: ^{18}F-FDG PET/CT has become a crucial imaging modality in the diagnosis, staging, treatment response evaluation, and detection of relapse in multiple myeloma (MM). Given the complexity of this hybrid technique, standardization of examination protocols and reporting is essential. In 2023, the Czech Myeloma Working Group and the Czech Society of Nuclear Medicine introduced procedural guidelines for MM imaging and reporting using FDG PET/CT. This study aims to determine the prognostic significance of parameters assessed according to the latest Czech guidelines in hybrid imaging during MM staging. ***Materials and Methods:*** The study cohort comprised 77 patients (41 men, median age 66), all of whom underwent FDG PET/CT for MM staging. Patients were monitored through regular clinical assessments, with clinically determined disease progression serving as the study endpoint. PET/CT evaluations adhered to the recommended standardized protocol, capturing 30 defined imaging parameters recorded by an experienced nuclear medicine specialist. Key assessed parameters included the number, location, characteristics (e.g. paraskeletal and extramedullary), and metabolic activity of FDG-avid lesions, as well as the presence, quantity, and distribution of lytic lesions on CT. Statistical analysis was performed to identify significant predictors of patient outcomes. ***Results:*** The median follow-up duration was 39 months. Metabolically active lesions were detected in 57 patients (74.0%), while significant lytic lesions were observed in 58 patients (75.3%). At least one active paramedullary lesion was identified in 37 patients (48.1%), and at least one extramedullary lesion in 4 patients (5.2%).Univariate Cox regression analysis showed significant associations between poor outcomes and high metabolic lesion counts (>10 lesions; P=0.033), metabolically active lesions in the skull (P=0.025), and appendicular skeleton (P=0.017). Although the number of subjects with extramedullary lesions was low, 2 out of 4 patients experienced worse outcomes. Among lytic lesions, skull involvement was a notably unfavorable prognostic factor (P=0.016). Additional negative prognostic indicators included high bone marrow metabolic activity (DS > 4; P=0.049). No other assessed parameters demonstrated statistical significance in predicting disease progression during follow-up. ***Conclusion:*** A standardized, comprehensive reporting system is essential for complex imaging modalities such as FDG PET/CT. Our findings suggest that peripheral skeletal involvement is associated with adverse outcomes, potentially reflecting extensive tumor spread beyond the axial skeleton. ***References:*** Havel, M. & Jelínek, T. et al. "Standardizace PET/CT u pacientů s mnohočetným myelomem-Společné doporučení České myelomové skupiny a České společnosti nukleární medicíny." Transfusiology & Haematology Today/Transfuze a Hematologie Dnes 29.2 (2023).

EP-0514

AI-based vs Manual Segmentation in Multiple Myeloma: Are They Equally Prognostic?

M. Stasolla[1], *D. Bezzi*[2], *M. Di Franco*[1], *S. Proto*[1], *M. Talarico*[3], *E. Zamagni*[3], *C. Malizia*[4], *S. Fanti*[4,1], *C. Nanni*[4];
[1]*Nuclear medicine, Alma Mater Studiorum University of Bologna, Bologna, ITALY,* [2]*Nuclear medicine unit AUSL Romagna, Forlì-Cesena, ITALY,* [3]*Seràgnoli Institute of Hematology, IRCCS Azienda Ospedaliero-Universitaria di Bologna, Bologna, ITALY,* [4]*Nuclear Medicine Unit, IRCCS Azienda Ospedaliero-Universitaria di Bologna, Bologna, ITALY.*

Aim/Introduction: Multiple myeloma is a neoplastic disorder characterized by the uncontrolled proliferation of a plasma cell clone in the bone marrow. It can occur as both intramedullary and extramedullary disease with different prognostic values. Aim of our study was to test the prognostic value of AI-based method to calculate active disease volume as compared to standard manual segmentation. ***Materials and Methods:*** 130 patients (78 men and 52 women) diagnosed with symptomatic multiple myeloma performed a staging positron emission tomography with fluorodeoxyglucose (PET-FDG) scan. The variables considered were focal lesions (FL), paramedullary lesion (PM), extramedullary lesion (EM) and total tumor burden. For each of these variables, metabolic tumor volume (MTV) and total tumor glycolysis (TLG) were calculated both manually by an operator (using a threshold corresponding to liver SUV peak) and through an artificial intelligence (AI) program (uOmnispace). The median was calculated for each parameter, then used to perform the Wilcoxon test for paired data. Additionally, MTV and TLG of each variable (FL, PM, EM and total) were analyzed to determine optimal cut-off values using ROC (Receiver Operating Characteristic) curves. These cut-offs were used to dichotomize each variable into two categories: high and low MTV or TLG. Only variables with statistically significant p-values ($p < 0.05$) in univariate analysis were considered for dichotomization. The dichotomized data were then correlated with overall survival (OS) and progression free survival (PFS) using Kaplan-Meier analysis. ***Results:*** The results showed significant differences between manual and AI measurements for total MTV (p=0.001), total TLG (p=0.002), FL MTV (p=0.016), FL TLG (p=0.030), PM MTV (p=0.002) and PM TLG (p=0.002), with AI tending to overestimate compared to manual method. EM parameters (MTV and TLG), on the other hand, didn't show significant differences between manual and AI measurements (p=0.123 and p=0.213, respectively), most likely due to the small number of findings. Statistically significant cut-offs were identified for MTV and TLG parameters, which were able to dicothomize the popolation into better and worse prognosis groups. Although with different cut-offs, both measurements were good stratificators of PFS and OS especially for MTV-FL, TLG-FL, MTV-PM, TLG-PM, MTV-Total and TLG-Total. ***Conclusion:*** AI-assisted segmentation is easier

and faster and could be considered in the future as a parameter to sistematically report. Additionally, it may be more accurate in characterizing total tumor burden. Tumor volumes obtained by both manual and AI segmentation methods, although slightly different, are predictive of prognosis.

EP-0515

Improved Initial Staging and Risk Stratification of Newly DiagnosedMultiple Myelomaby Targeting Chemokine Receptor CXCR4 using [^{68}Ga]Ga-Pentixafor PET/CT

J. Chen, *C. Li, Y. He;*
Zhongnan Hospital of Wuhan University, Wuhan, CHINA.

Aim/Introduction: This study aimed to evaluated the diagnostic performance and risk stratification capabilities of C-X-C motif chemokine receptor 4 (CXCR4)-targeted [^{68}Ga]Ga-Pentixafor PET/CT in newly diagnosed multiple myeloma (NDMM): a head-to-head comparison with [^{18}F]FDG PET/CT. ***Materials and Methods:*** Sixty-one NDMM patients underwent both [^{68}Ga]Ga-Pentixafor and [^{18}F]FDG PET/CT within two weeks. Clinical staging was performed based on the Durie-Salmon PLUS system, Revised International Staging System (R-ISS), and the Second R-ISS (R2-ISS). Maximum and mean standardized uptake values (SUVmax and SUVmean), metabolic tumor volume (MTV), total lesion glycolysis (TLG), total lesion volume (TLV), total lesion uptake (TLU), and a total burden score (TBS) were recorded and calculated. Univariate and multivariate logistic regression, along with receiver operating characteristic (ROC) analysis were used to assess the predictive indicator for risk stratification in NDMM. ***Results:*** [^{68}Ga]Ga-Pentixafor PET/CT demonstrated a significantly higher detection rate than [^{18}F]FDG PET/CT (83.6% vs. 55.7%, P = 0.001) in NDMM. Positive [^{68}Ga]Ga-Pentixafor findings correlated with more serious R-ISS and R2-ISS stage, lower hemoglobin, and higher β2-microglobulin (β2-MG) and bone marrow plasma cell percentage (BMPC%) (all P < 0.05). For staging, [^{68}Ga]Ga-Pentixafor better identified advanced disease (Durie-Salmon PLUS stage III) than [^{18}F]FDG PET (P < 0.001). [^{68}Ga]Ga-Pentixafor PET aligned better with R-ISS (62.3% vs. 27.9%, P < 0.001) and R2-ISS (57.4% vs. 24.6%, P = 0.001) than [^{18}F]FDG PET/CT. Multivariate analysis identified TBS_{CXCR4} and β2-MG as significant predictive indicators. ROC analysis revealed that the combined model of TBS_{CXCR4} and β2-MG achieved the highest diagnostic performance for R-ISS risk stratification (AUC = 0.901). For R2-ISS, ROC analysis demonstrated that $TBS_{CXCR4,}$ β2-MG and their combined model exhibited strong and comparable diagnostic performance, with AUCs ranging from 0.830 to 0.915. ***Conclusion:*** [^{68}Ga]Ga-Pentixafor PET/CT outperforms [^{18}F]FDG PET/CT in diagnostic accuracy, staging, and risk stratification in NDMM. TBS_{CXCR4} derived from [^{68}Ga]Ga-Pentixafor and β2-MG are the predictive indicators of high-risk status in NDMM.

EP-26

e-Poster Area

B: Imaging Clinical Studies -> B1 Oncological Imaging Clinical Study -> B23 Bone and Soft Tissues

EP-0516

Inter-reader Agreement of The IMPeTus Criteria ın Multipl Myeloma Patients

A. Tunç, *F. Avci, R. H. Tokac, Z. Burak;*
Ege University Nuclear Medicine Department, Izmir, TÜRKIYE.

Aim/Introduction: Multiple Myeloma (MM) accounts for 1% of all cancers and 10% of hematologic cancers. FDG PET/CT is a functional imaging procedure with proven good performance in MM patients. It is a valuable tool in the evaluation of patients with newly diagnosed or relapsed/refractory MM, especially in the detection of paramedullary and extramedullary soft tissue masses or solid organ involvement. However, a standardized interpretation criterion for the evaluation of FDG PET/CT findings in MM has not yet been accepted. Some groups base their image interpretation on semiquantitative findings, some on visual assessment, and another group on both two methods, which hinders the reproducibility of the result. Recently, an Italian group proposed new visual interpretation criteria, the IMPeTuS criteria, to standardize FDG PET/CT interpretation in MM patients. In this study, our aim was to evaluate the inter-reader agreement of the IMPeTuS criteria in MM patients. ***Materials and Methods:*** The study included 32 patients whose treatment response images were available in our archive. All PET scans were reviewed by three nuclear physicians blinded to each other and to patient names. Diffuse bone marrow involvement in terms of Deauville scoring, hypermetabolism in limbs and ribs if present, PET positive focal bone lesions, localization of these lesions and Deauville value of the hottest lesion, number of lytic lesions, presence of fracture, presence of paramedullary involvement, presence and locations of extramedullary involvement (nodal and extranodal) and the Deauville value of the hottest extramedullary lesion were reported using the IMPeTUs criteria. Fleiss Kappa method was used to assess inter-reader agreement using SPSS v25. ***Results:*** There was moderate agreement between readers for bone marrow involvement in long bones and ribs, number of lytic bone lesions and supraclavicular lymph node involvement (0.31-0.40), while there was no agreement for skin involvement (-0.01). For other criteria, there was good to excellent agreement between readers (0.42-1). ***Conclusion:*** In this study where the number of cases was limited, it was shown that the agreement between PET-CT readers was moderate to high when IMPeTus criteria were used. It is thought that by applying these criteria to larger series and simplifying them by removing some non-prognostic parameters, a standardized PET reporting system that can be used routinely in MM cases can be achieved.

EP-27

e-Poster Area

B: Imaging Clinical Studies -> B1 Oncological Imaging Clinical Study -> B24 Melanoma

EP-0517

Machine learning based on ^{18}F-FDG PET/CT parameters for prediction of lymph node metastasis in cutaneous stage I-III melanoma

Y. Jin[1], *L. Lu*[2], *X. Chu*[3], *T. Long*[1], *Y. Yang*[1], *S. Hu*[1,4,5];
[1]*Department of Nuclear Medicine, Xiangya Hospital, Central South University, Changsha, Hunan, CHINA,* [2]*Department of Dermatology, Xiangya Hospital, Central South University, Changsha, Hunan, CHINA,* [3]*Department of Oncology, Xiangya Hospital, Central South University, Changsha, Hunan, CHINA,* [4]*National Clinical Research Center for Geriatric Disorders, Xiangya Hospital, Changsha, Hunan, CHINA,* [5]*Key Laboratory of Biological Nanotechnology of National Health Commission, Xiangya Hospital, Central South University, Changsha, Hunan, CHINA.*

Aim/Introduction: Malignant Melanoma (MM) is the most lethal malignancy among skin tumors. The five-year survival rate of patients with lymph node metastasis (LNM) is significantly reduced. Early detection of melanoma LNM facilitates promptly optimization of treatment strategies. This study aims to integrate pertinent clinical data, pathological markers, and Fluorine-18 Fluorodeoxyglucose Positron Emission Tomography/Computed

Tomography (^{18}F-FDG PET/CT) parameters to develop an effective and predictive machine learning model, in order to improve the diagnostic efficacy of lymph node metastasis. ***Materials and Methods:*** A total of 45 patients were included in the analysis, who underwent ^{18}F-FDG PET/CT examinations before surgical treatment at Xiangya Hospital between December 2016 and January 2024. LNM diagnosis was confirmed through postoperative biopsy or follow-up. Clinical data, primary pathological markers and ^{18}F-FDG PET/CT metabolic parameters of melanoma were collected. Eight machine learning models were constructed using R programming language for data analysis and performance comparison. After cross-validation and model fitting, the models were ranked based on Area Under the Curve (AUC) with interpretations via SHapley Additive exPlanations (SHAP). Subsequently, the 45 patients were randomly divided into training validation sets in a 6:4 ratio to evaluate model sensitivity and specificity, with model performance assessed using calibration and decision curve analysis (DCA). ***Results:*** Among eight machine learning models, the Naive Bayes model demonstrated the highest performance, achieving an optimized AUC of 94.6%. SHAP analysis revealed that exceeding specific threshold values for certain characteristics (MTV = 0.57, TIL3 = 1, SUVmax = 7.5, TLG = 2.8, SULavg = 4.1, SULmax = 6.3, SULpeak = 2.4, SUVpeak = 2.8, SUVavg = 4.8, Breslow = 2) increased the likelihood of LNM. The model's performance metrics for the training set showed sensitivity of 0.58, specificity of 0.93, and accuracy of 0.78. For the validation set, the sensitivity, specificity and accuracy were 0.625, 0.90 and 0.78 respectively. The calibration curve indicated a strong alignment between the predicted and actual observed values. DCA demonstrated that the Naive Bayes model offers a better net benefit when the threshold probability exceeds 0%. ***Conclusion:*** The Naive Bayes model, based on ^{18}F-FDG PET/CT parameters, can greatly improve specificity, sensitivity, and accuracy of identifying LNM in MM patients,playing a pivotal role in guiding sentinel lymph node biopsy (SLNB) and lymph node dissection decisions. It provides valuable insights for clinical staging and treatment planning in melanoma patients.

EP-0518

First Evaluation of [^{68}Ga]FAPI PET/CT Imaging to Assess Fibroblast Activation Protein Expression in Melanoma Patients

Y. Yang, *J. Su, X. Chen, S. Su;*
Xiangya Hospital, Central South University, Changsha, CHINA.

Aim/Introduction: Malignant melanoma (MM) is characterized by high malignancy, early metastasis, and poor prognosis. While immunotherapy has improved survival in advanced MM, over 50% patients fail to respond effectively, highlighting the urgent need for novel strategies to predict therapeutic response. This study aimed to identify key molecular predictors of immunotherapy response based on the mechanisms of tumor immunosuppressive microenvironment and to enable their noninvasive visualization through molecular imaging techniques. ***Materials and Methods:*** Spatial transcriptomics was performed on tumor samples from twenty-two MM patients who received neoadjuvant immunotherapy. Key targets were identified by integrating single-cell RNA sequencing (scRNA-seq) data and validated by immunohistochemistry. A prospective head-to-head imaging study was then conducted in five melanoma patients, each undergoing both ^{18}F-FDG and ^{68}Ga-FAPI PET/CT scans (whole-body range: vertex to toe). The mean injected doses were 4.1 ± 0.24 mCi for ^{68}Ga-FAPI and 6.62 ± 0.15 mCi for ^{18}F-FDG, respectively. The diagnostic performance of both tracers was compared for detecting primary lesions, lymph nodes, and distant metastases. ***Results:*** Spatial transcriptomic analysis revealed significantly higher enrichment of cancer-associated fibroblasts (CAFs) in non-responders compared to responders ($p < 0.05$), with spatial co-localization of CAFs and tumor cells negatively correlated with treatment efficacy. scRNA-seq confirmed fibroblast activation protein (FAP) as a CAF-specific marker and FAP+ CAFs were highly expressed in responders than non-responders ($p = 0.045$), which were negatively correlated with the prognosis of MM patients with immunotherapy ($p = 0.027$). Immunohistochemistry further confirmed the higher expression of FAP in melanoma tissues than that in its adjacent tissues (2.46 ± 0.65 vs. 0.18 ± 0.18, $p = 0.005$). The primary lesions showed slightly higher SUVmax on ^{68}Ga-FAPI (9.30 ± 2.95) than on ^{18}F-FDG (7.49 ± 3.23). In metastatic lymph nodes, ^{68}Ga-FAPI uptake was significantly higher in pathology-positive nodes than in negative ones (11.18 ± 2.82 vs. 0.97 ± 0.10, $p = 0.028$), while ^{18}F-FDG showed no statistically significant difference between groups (8.23 ± 2.99 vs. 2.42 ± 0.44, $p = 0.164$). In distant metastases, both tracers successfully identified a total of 116 metastatic lesions in the lungs, pleura, bones, adrenal glands, pancreas, and subcutaneous tissue. ***Conclusion:*** FAP, as a characteristic marker of CAFs, serves as a promising predictor of resistance to immunotherapy in MM. ^{68}Ga-FAPI PET/CT can successfully visualize and identify primary tumors, lymph nodes and distant metastatic sites in MM patients.

EP-0519

Prognostic Value of TMTV and SUVmax from ^{18}F-FDG PET/CT at Multiple Time Points in Melanoma Patients on Immunotherapy

K. Zevnik[1], *A. Doma*[1], *A. Studen*[2,3], *K. Strašek*[2], *K. Škalič*[1], *R. Jeraj*[2,4], *M. Reberšek*[1], *N. Hribernik*[1];
[1]*Oncology Institute Ljubljana, Ljubljana, SLOVENIA,* [2]*Faculty of Mathematics and Physics University of Ljubljana, Ljubljana, SLOVENIA,* [3]*Jozef Stefan Institute, Ljubljana, SLOVENIA,* [4]*Department of Medical Physics University of Wisconsin School of Medicine and Public Health, Madison, WI, UNITED STATES OF AMERICA.*

Aim/Introduction: To investigate whether MTV and SUVmax derived from ^{18}F-FDG PET/CT at multiple time points (baseline, week 4, and week 16) are associated with clinical outcomes in melanoma patients treated with immunotherapy. ***Materials and Methods:*** 37 patients with metastatic melanoma who received immune checkpoint inhibitors (ICIs) as part of a previous prospective, single-arm study were retrospectively included in this analysis. Patients underwent serial ^{18}F-FDG PET/CT imaging at baseline, week 4 (W4), and week 16 (W16) following initiation of ICI therapy. Tumour lesions were manually segmented by two nuclear medicine specialists using an open-source medical imaging software. A threshold of SUVmax >2.5 was applied for lesion segmentation. Quantification of FDG uptake and calculation of the two imaging biomarkers - SUVmax and total metabolic tumour volume (TMTV) - were performed at all three time points (baseline, W4, and W16), resulting in six parameters: bSUVmax, bTMTV, W4 SUVmax, W4 TMTV, W16 SUVmax, and W16 TMTV. Patients were stratified into two groups based on overall survival (OS), using a cut-off of 600 days. The association between each imaging parameter and OS was assessed using logistic regression with the Wald test. Receiver operating characteristic (ROC) analysis was performed to evaluate classification performance, and Youden's index was applied to determine the optimal thresholds. ***Results:*** The median OS of the cohort was 22.4 months (range: 1.7-43.3 months), with 19 patients alive at the time of analysis. 18 pts had OS less than 600 days, and 19 pts exceeded the cut-off. Among all evaluated parameters, only W16 SUVmax demonstrated a statistically significant association with OS ($p < 0.05$). ROC analysis revealed the highest area under the curve (AUC) for W16 SUVmax at 0.70, with an optimal threshold of 14.7. AUCs for the remaining parameters were as follows: bTMTV (0.62), bSUVmax (0.58), W4 TMTV (0.50), W4 SUVmax (0.67), and W16 TMTV (0.60). ***Conclusion:*** In our study SUVmax at week 16 emerged as the only imaging biomarker significantly associated with overall survival in metastatic melanoma patients treated with immune checkpoint inhibitors. These findings suggest that delayed metabolic response assessment (at 4 months) may offer valuable prognostic information and could support clinical

decision-making during immunotherapy. Further studies in larger, independent cohorts are warranted to validate these results. ***References:*** Hribernik, Nežka, et al. "Early-time-point 18F-FDG-PET/CT and other prognostic biomarkers of survival in metastatic melanoma patients receiving immunotherapy." Radiology and Oncology 59.1 (2025): 43-53.

EP-0520

FDG avid bone metastases in patients with stage IV melanomas under immune checkpoint inhibitors (ICI) therapy: comparison with low dose CT

J. Heinen, *C. Sachpekidis, J. Hassel, L. Pan, A. Dimitrakopoulou-Strauss;*
Deutsches Krebsforschungszentrum, Heidelberg, GERMANY.

Aim/Introduction: To evaluate the diagnostic utility of ^{18}F-FDG PET/CT in comparison to low-dose CT for detecting bone metastases in patients with metastatic melanomas or choroidal melanoma undergoing treatment with immune checkpoint inhibitors (ICI). ***Materials and Methods:*** We retrospectively analyzed data from a cohort of 371 patients diagnosed with AJCC Stage IV malignant including choroidal melanomas, all of whom received treatment with ICIs (Ipilimumab, Nivolumab, and/or Pembrolizumab) and underwent ^{18}F-fluorodeoxyglucose (^{18}F-FDG) positron emission tomography combined with low-dose computed tomography (PET/CT). Of these, 83 patients (22.37%) had one or more skeletal lesions with pathological ^{18}F-FDG uptake suspicious for bone metastases. A total of 225 such lesions were analyzed by measuring their standard uptake values (SUVs) as volumes of interest (VOIs) in PET, assessing CT findings, and quantifying Hounsfield units (HU) at baseline and up to three follow-up (FU1-FU3) examinations. Metabolic response to ICI therapy was evaluated according to EORTC criteria and categorized into four groups: complete metabolic response (CMR), partial metabolic response (PMR), stable metabolic disease (SMD), and progressive metabolic disease (PMD). ***Results:*** At baseline, 176 of 225 lesions were detectable on PET. 70 out of 176 (39.77%) PET-positive lesions were detectable on low-dose CT. In the most recent follow-up, 90 lesions (52.27%) were visible on CT, with a gradual increase observed over time (51.14% at FU1, 63.04% at FU3). Notably, 76 lesions (43.18%) were never detectable on CT at any time point. Overall, 26 lesions (14.77%) were classified as PMD at the latest follow-up. Of these, 9 lesions (34.62%) remained undetectable on CT, with the proportion decreasing over the course of therapy (30.30% at FU1, 44.44% at FU2, 20.0% at FU3). Additionally, 49 lesions were not visible on either PET or CT at baseline but appeared in later therapy cycles. Only 8 of these 49 lesions (16.33%) were visible on CT at their first PET-positive scan, and 13 of 49 (26.53%) were detectable on CT at the most recent follow-up. ***Conclusion:*** In patients with metastatic malignant or choroidal melanoma, ^{18}F-FDG PET/CT demonstrates higher sensitivity than low-dose CT alone for detecting osseous metastases. Many bone metastases remain undetectable on CT throughout the course of the disease. Furthermore, lesions may become visible on CT only during later stages of therapy, potentially representing new or enlarging lesions despite evidence of metabolic response on PET.

EP-0521

Adjuvant Therapy and FDG-PET/CT Follow-Up in High-Risk Patients with Cutaneous Melanoma: A Five-Year Retrospective Analysis

J. Aço, *I. P. Carvalho, H. Nunes, P. Pereira, E. Gouveia, E. Sousa, D. Fraga, P. Jorge, D. Rombo, J. Pais, L. Salgado;*
Instituto Português de Oncologia de Lisboa, Lisbon, PORTUGAL.

Aim/Introduction: Adjuvant therapy has improved recurrence-free survival in stage III cutaneous melanoma. Despite treatment, recurrence risk remains high, particularly during the first year. Early detection is crucial, and FDG-PET/CT, although limited by potential false positives in patients under immunotherapy, remains a valuable tool for this purpose. We describe a 5-year single-center follow-up experience. ***Materials and Methods:*** A single-center retrospective study of 34 patients with resected high-risk stage III cutaneous melanoma, without known metastasis prior to sentinel lymph node biopsy, who received adjuvant therapy, and underwent FDG-PET/CT follow-up every six months between 2019 and 2023. The systemic therapy (anti-PD1 immunotherapy, or dabrafenib plus trametinib) was chosen according to clinical and molecular features. Four patients were excluded due to loss to follow-up. All recurrences identified by FDG-PET/CT were confirmed either by biopsy or in subsequent imaging studies. Data were analyzed using descriptive statistical methods. ***Results:*** A total of 30 patients were included, with a median age of 56 years (range: 24-86). The cohort comprised 19 males, and 11 females. The primary melanoma sites were: trunk (47%), upper limbs (23%), head and neck (17%), lower limbs (10%), and scrotum (3%). Most patients were staged as IIIB and IIIC (93%). BRAF V600E/K mutation was present in thirteen patients (43%). Twenty-four patients received anti-PD-1 immunotherapy (80%), while six were treated with dabrafenib plus trametinib (20%). Therapy was discontinued in two patients owing to adverse events — one experienced gastrointestinal toxicity, and the other developed muscular and renal toxicities. Recurrence occurred in 13 patients (43%), 5 during and 8 following completion of adjuvant therapy. The mean time between the beginning of therapy and relapse was 23 months. Disease relapsed in lymph nodes (7 patients), central nervous system (5), subcutaneous tissue (3), lungs (3), and pleura (1). Sixty percent of patients were asymptomatic at relapse. False-positive findings were observed in nine patients (30%), including therapy-related pneumonitis, two patients with reactive lymph-nodes, an ovarian adnexal follicle, two patients with colon polyps, a benign bone tumor, an infected sebaceous cyst, and nonspecific pancreatic uptake. Seven of these patients were undergoing immunotherapy. ***Conclusion:*** FDG-PET/CT enables early detection of recurrences, which is crucial in the management of these patients. However, the high rate of false positives—particularly in patients undergoing immunotherapy—must be carefully considered during image interpretation, and should also prompt further research into novel radiotracers with greater specificity given the critical importance of timely relapse diagnosis.

EP-0522

Prognostic Value of Clinical and Metabolic Parameters from ^{18}F-FDG PET/CT in Malignant Melanoma: Impact on Overall and Progression-Free Survivalv

L. Cagua Ruiz, *T. Aroui Luquin, J. Villa-Palacios, A. Piñero Donis, E. Dominguez-Polanco, R. Sánchez Sánchez;*
Servicio Medicina Nuclear Hospital universitario Virgen de las Nieves, Hospital universitario virgen de las Nieves, SPAIN.

Aim/Introduction: To evaluate the prognostic value of clinical, histopathological, and metabolic parameters obtained through ^{18}F-FDG PET/CT in overall survival (OS) and progression-free survival (PFS) in patients with malignant melanoma. ***Materials and Methods:*** A retrospective study of 100 patients with malignant melanoma (59 men, 41 women; mean age: 64.9 ± 15.1 years) who underwent ^{18}F-FDG PET/CT for initial staging between 2015 and 2016. Clinical characteristics (histological type, location, Breslow index, mitotic count, ulceration, LDH, and S100 protein) and metabolic parameters (SUVmax, SUVmean, TLG, and MTV) were analyzed. Associations with OS and PFS were assessed using Kaplan-Meier survival curves and Cox regression models. ***Results:*** Nodular melanoma was the most common histological subtype (35%), and the lower extremities were the most frequent location (25%). Fifty-three percent of patients were in stage III. PET/CT was positive in 40 patients and negative in 60. The mean follow-up was 73.7 ± 41.4 months. The mean OS was 85.6 months (95% CI: 75.5-95.6). High Breslow index, LDH, S100 protein, and TLG were significantly associated with shorter OS ($p < 0.05$), with TLG being

the strongest independent predictor (HR = 1.1; 95% CI: 1.06-1.13; p < 0.05). The median PFS was 20 months (95% CI: 13.6-26.3). The lentigo maligna subtype and the presence of nodal metastases on PET/CT were significantly associated with shorter PFS (p < 0.05). ***Conclusion:*** ^{18}F-FDG PET/CT is a key tool for prognostic stratification in malignant melanoma. TLG is an independent predictor of OS, while PET/CT-detected nodal metastases significantly impacted PFS. These findings support the integration of metabolic parameters into the clinical evaluation of patients with malignant melanoma.

EP-0523

The Pseudoprogression Challenge in FDG PET/CT Response Evaluation of Malignant Melanoma Patients Receiving Immunotherapy:Which Immune Related Response Criteria Should We Trust?

G. Gedikli Turgut, *S. Ince, U. M. Turan, H. Peker Yalcın, A. O. Karacalioglu;*
Gulhane Training and Research Hospital, Department of Nuclear Medicine, Ankara, TÜRKIYE.

Aim/Introduction: In recent years, immunotherapy agents have become increasingly used in the treatment of malignant melanoma. In addition to the four basic response categories (complete metabolic response [CMR], partial metabolic response [PMR], stable disease [SD], and progressive metabolic disease [PMD]), concepts such as pseudoprogression (PP), hyperprogression (HP), mixed response, and durable response have emerged with the use of immunotheraphy. The aim of this study is to emphasize the concept of PP in interim PET and determine which immune-related response criterion is safer, more practical, and more accurate in predicting final outcomes in MM patients receiving immunotheraphy. ***Materials and Methods:*** This study included 23 patients with biopsy-confirmed MM who underwent FDG PET/CT scans: baseline (pre-treatment), interim (4-8 weeks after treatment initiation), and post-treatment (4-8 weeks after therapy completion), with a total of 80 lesions evaluated. For target lesion selection, up to five lesions with the highest SULpeak values were selected, ensuring each tumor's SULpeak was at least 1.5 times that of liver SULpeak. The sum of the SULpeak values of these lesions was used as the "total SULpeak." ***Results:*** Significant differences were found between baseline and interim PET/CT in SUVmean, total SULpeak, and TLG values (p<0.05), but not in MTV. Among the IT criteria, iPERCIST was found to be significantly superior in predicting final response (p<0.022). ***Conclusion:*** In patients receiving immunotheraphy, the concept of progression should be reconsidered during response evaluation. iPERCIST was the most accurate, practical, and reliable method among the response criteria studied. Reinterpreting interim PMD as iuPMD and confirming with a follow-up PET in 4-8 weeks is a safe strategy to avoid premature discontinuation of beneficial treatment due to PP. imPERCIST5 was found less practical due to the need for more complex calculations. Additionally, response evaluation should not rely solely on imaging but also take clinical findings into account. If the clinical condition is improving, findings on interim PET, including new lesions, should be suspected as pseudoprogression. ***References:*** 1. Lopci E, Hicks RJ, Dimitrakopoulou-Strauss A, et al. Joint EANM/SNMMI/ANZSNM practice guidelines/procedure standards on recommended use of [^{18}F]FDG PET/CT imaging during immunomodulatory treatments in patients with solid tumors version 1.0. Eur J Nucl Med Mol Imaging. 2022; 49: 2323-2341. 2. Yıldız A, Şahin Z, Forouz A. Assesment of treatment response with FDG PET/CT (Article in Turkish). Nucl Med Semin. 2021; 7: 196-211.

EP-0524

Immune-Related Adverse Events in Metastatic Melanoma Patients Treated with Combination Immunotherapy: The Role of PET/CT

G. Horvatic Herceg[1], *V. Sabaric*[2], *K. Blazicevic*[2], *M. Ciglar-Hlasc*[1], *D. Herceg*[2];
[1]*Department of Nuclear Medicine and Radiation Protection, University Hospital Zagreb, Zagreb, CROATIA,* [2]*Department of Oncology, University Hospital Zagreb, Zagreb, CROATIA.*

Aim/Introduction: Immune checkpoint inhibitors (anti-PD-1 and anti-CTLA4), especially combination treatment with nivolumab and ipilimumab, have revolutionized metastatic melanoma treatment. Compared with monotherapy combination immunotherapy with dual checkpoint inhibitors have shown surge in immune-related adverse events (irAE). The aim of our study was to to explore the utility of the 18FDG-PET/CT for treatment monitoring in patients with metastatic melanoma receiving ipilimumab and nivolumab and to determine the incidence of irAE during immunotherapy. ***Materials and Methods:*** 33 subjects with metastatic melanoma were enrolled:mean age 59.5 (range: 31- 75)y, 10 women, 23 men.All 33 enrolled subjects were evaluable for their response to dual therapy with ipilimumab and nivolumab. A baseline scan of the whole body of each patient with ^{18}F-FDG PET/CT was performed before the planned treatment initiation. The patients were examined again with PET/CT three and six months later to evaluate the therapy response. The therapy response was assessed according to the imPERCIST (immunotherapy-modified PERCIST). ***Results:*** Four patterns of response to ipilimumab and nivolumab were observed: 19 patients had a response in baseline lesions, among them 7 had a complete response. Stable disease or steady decline in total tumor volume was recorded in 5 patients. Responses after an initial increase in total tumor burden (pseudo-progression) was notified in one patient. Eight patients had progressive metabolic disease, and two patients among them died. Out of 33 patients we detected irAE in 22 patients (81%), and among them in 11(50%) patients PET/CT findings were suggestive for irAE. PET/CT signs preceded the clinical symptoms in 6 cases (3 thyroiditis, 2 colitis and single case of pneumonitis and hepatitis). The most common irAE was hepatitis (41%) followed by dermatitis (19%), thyroiditis (13%), hypophysitis (9%), nephritis (9%), colitis (6%) and single cases of pneumonitis, meningitis, arthritis, type I diabetes and immune thrombocytopenia. All irAE were reported within 22 weeks from start of the treatment and most grades were 2 and 3 with no deaths reported due to irAE. ***Conclusion:*** Even though combination immunotherapy regimen ipilimumab and nivolumab demonstrated long term results in overall survival of metastatic melanoma patients, irAE remain a major concern during and after the treatment. On small cohort of patients we detected irAE in 22 of them (81%), and PET/CT findings preceded clinical symptoms in 27% of cases.Therefore, it is of great importance when interpreting PET/CT to pay attention to possible irAEs and alert clinicians to findings that may be of life-threatening importance.

EP-0525

Streamlined Monitoring of Immunotherapy Response in Metastatic Melanoma via Longitudinal PET Quantification and SemiAutomatic Tumor Delineation

C. Sachpekidis[1], *T. P. Vagenas*[2], *J. C. Hassel*[3], *A. Dimitrakopoulou-Strauss*[1], *G. K. Matsopoulos*[2];
[1]*German Cancer Research Center (DKFZ), Heidelberg, GERMANY,* [2]*Biomedical Engineering Laboratory, School of Electrical and Computer Engineering, National Technical University of Athens, Athens, GREECE,* [3]*National Center for Tumor Diseases (NCT), University Hospital Heidelberg, Heidelberg, GERMANY.*

Aim/Introduction: Metastatic melanoma (MM) is a highly aggressive malignancy characterized by extensive spread and lesion heterogeneity, which together drive poor survival outcomes.

Although immunotherapy has shown encouraging efficacy, its rapid dynamics necessitate timely and accurate assessment of treatment response. Manual delineation of lesions on FDGPET/CT scans is laborious and time-consuming. In this study, we adapt a semiautomatic segmentation pipeline for longitudinal PET imaging to streamline response evaluation. Quantitative PET biomarkers are extracted from baseline and followup scans and evaluated against the novel PET Response Evaluation Criteria for Immunotherapy (PERCIMT), demonstrating potential for efficient and reproducible immunotherapy monitoring. ***Materials and Methods:*** We employed a two-stage segmentation pipeline validated in [1], to analyze paired FDGPET/CT scans (baseline and followup) from 40 MM patients. The pipeline clusters highuptake regions in multimodal FDGPET/CT images and classifies them using extracted imaging features and a deeplearning model. After manual correction for physiologic uptake and misclassified regions, lesion masks were finalized for biomarker extraction. Key quantitative PET metrics - total metabolic tumor volume (TMTV), total lesion glycolysis (TLG), SUV_{mean}, and SUV_{peak} - were computed and their percentage changes evaluated. We assessed correlations between these metrics and PERCIMT response using Spearman's rank correlation and compared metric differences between responders and non-responders using the Wilcoxon signed-rank test. ***Results:*** Moderate to strong correlations were observed between percentage changes in PET-derived metrics and PERCIMT classification (SUV_{max}: ρ=0.62; SUVmean: ρ=0.58; SUV_{peak}: ρ=0.58; TLG: ρ=0.71; TMV: ρ=0.74; all p<0.001), indicating that greater increases from baseline to follow-up scans are associated with poorer metabolic response outcomes. Additionally, Wilcoxon tests confirmed that responders had significantly lower follow-up metrics and smaller changes than non-responders (Wilcoxon rank-sum tests, all p<0.01), with TLG and TMV providing the strongest discrimination between groups. ***Conclusion:*** This study demonstrates that semi-automatic segmentation combined with PET-derived biomarkers enables accurate and efficient assessment of immunotherapy response in metastatic melanoma. The strong concordance with PERCIMT criteria supports its clinical utility for streamlined, reproducible treatment monitoring. ***References:*** [1] T. P. Vagenas et al., "A Decision Support System for the Identification of Metastases of Metastatic Melanoma Using Whole-Body FDG PET/CT Images," in IEEE Journal of Biomedical and Health Informatics, vol. 27, no. 3, pp. 1397-1408, March 2023, doi: 10.1109/JBHI.2022.3230060.

EP-28

e-Poster Area

B: Imaging Clinical Studies -> B1 Oncological Imaging Clinical Study -> B25 Any Other Malignant (including Primary of Unknown Origin)

EP-0526

Evaluating the Clinical Accuracy of Half-Time[^{18}F]FDG PET/CT Acquisition: A Quantitative Assessment of Liver and Lesion Metrics in Oncology Imaging

N. AL Makhmari*, S. Kheruka, N. AL Maymani, I. Collado, S. Al Rashdi, K. Al Riyami;*
Radiology and Nuclear Medicine Department, Sultan Qaboos Comprehensive Cancer Care and Research Center, University Medical City, Muscat, OMAN.

Aim/Introduction: Reducing PET acquisition time has the potential to enhance patient comfort and clinical efficiency. However, it is essential to maintain the integrity of quantitative imaging biomarkers and diagnostic image quality. This study aimed to assess whether a half-time PET acquisition protocol using TRUEX+TOF 4i4G reconstruction could yield comparable results to standard full-time acquisition for both liver and lesion metrics. ***Materials and Methods:*** A total of 28 liver background regions and 28 lesions were evaluated from patients who underwent ^{18}F-FDG PET/CT scans with full-time (1.8mm/sec) and half-time speed. For both liver and lesion, SUVmax, SUVmean, TLG, MTV , signal-to-noise ratio (SNR) and contrast-to-noise ratio (CNR were analyzed .Median values and interquartile ranges (IQR) were reported. Statistical comparisons were made using the Wilcoxon signed-rank test. ***Results:*** Quantitative liver parameters demonstrated strong consistency between full- and half-time acquisitions. Median SUVmax increased modestly from 2.09 (IQR: 0.40) to 2.22 (IQR: 0.5), and SUVmean rose from 1.67 (IQR: 0.42) to 1.73 (IQR: 0.46). TLG showed a slight increase from 3.95 (IQR: 3.3) to 4.71 (IQR: 3.4), while MTV remained stable at 2.9 (IQR: 2.3) in both protocols. For lesions, median SUVmax was comparable 5.89 (IQR: 4.43) in full-time vs. 5.56 (IQR: 4.26) in half-time scans. SUVmean and TLG also showed minimal variation, with SUVmean increasing slightly from 3.38 (IQR: 2.30) to 3.51 (IQR: 1.85), and TLG from 7.44 (IQR: 18.97) to 8.63 (IQR: 24.09). MTV remained consistent (2.03 vs. 2.08). Image quality metrics revealed a minor decline with SNR decreased from 15.51 (IQR: 3.81) to 12.09 (IQR: 3.14), and CNR from 20.47 (IQR: 12.88) to 13.60.63 (IQR: 14.59). The Wilcoxon signed-rank test showed not significant difference in SNR and CNR between two protocols with p-value 0.29 and 0.05 respectively. ***Conclusion:*** This study demonstrates that half-time acquisition using digital PET with TRUEX+TOF reconstruction retains excellent quantitative reliability in both liver and lesion evaluations. While there is a modest decline in SNR and CNR, the core imaging biomarkers remain stable, supporting the feasibility of adopting half-time protocols in clinical practice—particularly for routine follow-up or high-throughput workflows. ***References:*** Al-Fatlawi M, Pak F, Farzanefar S, Salehi Y, Monsef A, Sheikhzadeh P. Optimization of the Acquisition Time and Injected Dose of 18 F-Fluorodeoxyglucose Based on Patient Specifications for High-Sensitive Positron Emission Tomography/Computed Tomography Scanner. World J Nucl Med. 2023 Sep 6;22(3):196-202. doi: 10.1055/s-0043-1771284. PMID: 37854082; PMCID: PMC10581753.

EP-0527

Novel Role of PSMA PET/CT Versus FDG PET/CT in Hepatocellular Carcinoma: A Comparative Diagnostic Study

S. Shekhar Singh[1]*, P. Wadhwa*[2]*, A. K. Chaudhary*[1]*, A. K. Singh*[1]*, R. K. Pawar*[1]*, S. K. Tandon*[1]*;*
[1]*Globe Healthcare, Lucknow, INDIA,* [2]*United Imaging Healthcare, Delhi, INDIA.*

Aim/Introduction: Hepatocellular carcinoma (HCC) is typically evaluated using contrast-enhanced CT (CECT) and MRI. While FDG PET/CT is primarily used for metastatic staging, its utility is limited in well-differentiated HCC due to variable FDG avidity. Emerging evidence suggests that PSMA PET/CT, which targets tumor neovasculature, may improve HCC detection. This study compares 68Ga-PSMA PET/CT and ^{18}F-FDG PET/CT in HCC diagnosis, assessing lesion detection, metabolic parameters, and clinical impact. ***Materials and Methods:*** This prospective analysis included 30 biopsy-proven HCC patients (median age 62, range 50-68; 80% male, 20% female) who underwent both FDG and PSMA PET/CT within one week. Scans were performed on a uMI 550 PET/CT scanner, with comparisons based on: Lesion detection rate (primary tumor, intrahepatic, and extrahepatic metastases) Metabolic activity (SUVmax, target-to-background ratio [TBR]) Management impact (changes in treatment strategy). ***Results:*** Lesion Detection: PSMA PET/CT detected 160 lesions vs. 102 with FDG PET/CT ($p < 0.01$). Liver lesions: PSMA identified 50 vs. FDG 18 ($p < 0.001$). Bone metastases: PSMA detected 28 vs. FDG 10 ($p < 0.01$). No significant difference in lung or lymph node metastases. Metabolic Parameters: PSMA showed higher SUVmax

and TBR in 98% of lesions, including intrahepatic (PSMA TBR 5.2 vs. FDG 3.4) and metastatic sites. Clinical Impact: PSMA PET/CT altered management in 30% of cases (vs. 10% with FDG), primarily due to detection of additional primary tumors or occult skeletal metastases. ***Conclusion:*** PSMA PET/CT outperforms FDG PET/CT in HCC detection, particularly for primary liver lesions and bone metastases, with superior sensitivity and higher metabolic contrast. These findings suggest PSMA PET/CT could be a better modality for staging in HCC patients and in cases where FDG PET/CT yields equivocal results. ***References:*** Thompson, Scott M., et al. "PSMA as a Theranostic Target in Hepatocellular Carcinoma: Immunohistochemistry and 68Ga-PSMA-11 PET Using Cyclotron-Produced 68Ga." Hepatology communications 6.5 (2022): 1172-1185.

EP-0528

Potential of [89Zr]Zr-girentuximab PET/CT for the routine clinical management of patients with suspicious, unspecified renal lesions

S. Rasul, *I. Huebner-Resch, E. Patronas, L. Nics, S. F. Shariat, M. Schmidinger, M. Hacker;*
Medical University of Vienna, Vienna, AUSTRIA.

Aim/Introduction: The radioactive tracer [^{89}Zr]Zr-girentuximab used for positron emission tomography (PET) targets the hypoxia-induced enzyme carbonic anhydrase IX (CAIX). Recently, the role of [^{89}Zr]Zr-girentuximab PET/CT for the non-invasive identification of non-specific renal lesions in 300 adult patients was investigated in the ZIRCON study, an open-label, multicenter trial. Results suggested that [^{89}Zr]Zr-girentuximab is a very accurate and promising tracer to facilitate the differentiation between clear cell renal cell carcinoma (ccRCC) and other malignant and benign renal lesions. Here, we report our initial real-world clinical experience with this PET tracer for the routine clinical care of patients with non-specific renal lesions. ***Materials and Methods:*** As part of an early access program, PET/CT imaging of patients with uncertain renal lesions received 37 MBq (±10%) [^{89}Zr]Zr-girentuximab intravenously to non-invasively characterize lesions in place of biopsy. We performed [^{89}Zr]Zr-girentuximab PET/CT imaging on day 5 (±2 days) after [^{89}Zr]Zr-girentuximab administration in 6 patients with a total of 9 undetermined renal lesions. ***Results:*** All patients tolerated the tracer very well and no undesirable reactions were reported. Four patients, which had a total of 4 lesions, showed no CAIX expression. These results were later comparable with MRI and contrast-enhanced CT images. These patients were placed on active surveillance and follow-up with conventional imaging. The other 2 patients with a total of 5 renal lesions (size between 1.1 and 1.5 cm axial diameter) showed a significantly high focal CAIX expression with a maximum standardized uptake value of 58.4. In one of them, the postoperative histological result confirmed the presence of ccRCC. Since the other patient had undergone nephrectomy for renal cell carcinoma several years ago, systemic therapy with immunotherapeutic and antiangiogenic treatments was recommended for that patient. ***Conclusion:*** Despite our limited experience, we were able to recognize the distinct clinical potential of the [^{89}Zr]Zr-girentuximab PET/CT scan in the management of patients with unspecified renal lesions ***References:*** [89Zr]Zr-girentuximab for PET-CT imaging of clear-cell renal cell carcinoma: a prospective, open-label, multicentre, phase 3 trialShuch, Brian et al. The Lancet Oncology, Volume 25, Issue 10, 1277 – 1287.

EP-0529

Comparison of response assessment using morphological (iRECIST) and metabolic criteria (iPERCIST) in patients being treated with Immune checkpoint inhibitors in solid tumors.

D. Malik, *M. Koley, J. Gupta, D. Thakrani, A. Uppal, N. Rana, P. Thakral, I. B. Sen;*
Fortis Memorial research institute (FMRI), Gurugram, INDIA.

Aim/Introduction: The primary purpose of imaging in patients undergoing immunotherapy is to differentiate treatment non-responders from the responders who would benefit from an earlier change in therapeutic management and also from those who have initial increase in tumor burden due to pseudo progression. The CT based iRECIST, followed by FDG PET CT based iPERCIST criteria designed to better account for these patterns. F18-FDG PET tracks changes in metabolic activity of tumor, which often occurs much before changes in size are evident on morphological imaging, thus providing superior response evaluation in solid tumours as to CT based criteria. ***Materials and Methods:*** 94 patients with solid tumors undergoing immune checkpoint inhibitor (ICI) therapy were included. 1st follow up scan was performed after 3/4 cycles of (ICI) therapy as per referring physician discretion and subjects were classified into Response (complete and partial), progression or Stable disease on CT and PET by iRECIST and iPERCIST criteria respectively and clinical data. 2nd follow up scan was performed following 3-4 more cycles of ICI therapy. Final response was ascertained by a combination of PET and CT. Cohen's kappa coefficients with quadratic weights were used to assess concordance between ratings obtained at baseline and follow up separately for iRECIST and iPERCIST. Z-test for two independent kappa values were calculated to determine if statistically significant differences exist. ***Results:*** At first follow up, 49/94 patients had metabolically responding disease by iPERCIST criteria. Out of these patient, 32 patients had ongoing response in second follow up PET CT, whereas 16 patients who showed an initial response, progressed at second follow up, indicating an early treatment failure in these patients.In contrast, only 37/94 patients were found to have a morphologically responding disease in the first follow up PET CT by iRECIST criteria. Further on second follow up, 25 were found to have ongoing treatment response, while only 11 patients were found to have progressive disease. Therefore, fewer treatment failures (16 vs 11) were picked up by CT based criteria.The quadratic weighed kappa at 1st follow up and at 2nd follow up for iPERCIST was 0.6925 (substantial correlation), and for iRECIST was 0.3137 (fair correlation). This difference was statistically significant (p=0.022) when tested using a two-tailed Z-test. ***Conclusion:*** iPERCIST criteria was found to be superior to iRECIST criteria for evaluation of patients undergoing immunotherapy and prediction of true disease progression, early in the course of treatment with immune checkpoint inhibitors.

EP-0530

18F-FDG-PET/CT for staging Muscle-Invasive Urothelial Bladder Carcinoma: Impact on management using modified Deauville Score

O. Ajuria Illarramendi, *P. Gajate Borau, A. Martinez Lorca, P. Azpeitia Hernandez, P. Guerrero Serrano, M. Gutierrez Guerrero, J. Brasero Burgos, I. Hernandez Perez, F. Lopez Campos, U. Vera Schmülling, P. Paredes Rodriguez, T. Navarro Martinez, M. Orduña Diez;*
H. U. Ramón y Cajal, Madrid, SPAIN.

Aim/Introduction: To evaluate the role of 18F-FDG-PET/CT in staging muscle-invasive urothelial carcinoma(MIUC) with inconclusive nodal findings on contrast-enhanced Computed Tomography(ceCT), using modified Deauville Score(DS), and its impact on clinical decisions. Standard management of MIUC includes radical cystectomy and pelvic lymphadenectomy, often preceded by neoadjuvant cisplatin-based chemotherapy(neoQT). However ceCT has limited sensitivity for nodal metastases, leading to potential under-staging and suboptimal treatment. ***Materials and Methods:*** Retrospective review of MIUC patients (≥pT2) with indeterminate nodal status on ceCT who underwent staging with 18F-FDG-PET/CT between 01/01/2021-01/04/2025. Treatment decisions (neoQT, surgery, systemic therapy(QT)) were guided by 18F-FDG-PET/CT results. Patients with evidence of locoregional

nodal were administered neoQT and underwent follow-up 18F-FDG-PET/CT scan. Findings on initial and post neoQT were interpreted using modified Deauville Score(DS1-2 negative, DS3-5 positive) and were correlated with histopathology when available. Nodal SUVmax was recorded n initial and post neoQT scans. ***Results:*** 46 patients: 8 women and 38 men; mean age 73. Staging scan revealed: 21 cN0M0, 9 cN2M0, 3 cN3M0, 8 cN3M1a, and 5 cM1b (2 cN0M1b, 2 cN2M1b, 1 cN3M1b).The presence of cM1b in 5/46 ruled out surgery, as well as in 4/46 cN3M1a and were given chemotherapy.9/46 cN0M0 (3/9 underwent surgery that confirmed absence of disease pN0; VPN100% and 6/9 received RT or QT-RT due to comorbilities)28/46 (12 cN0M0, 9 cN2M0, 3 cN3M0, 4 cN3M1a) received neoQT. 8/28 are pending of follow up scan. 3/28 (2 ycN3M1a, 1 ycN2M0) continued systemic treatment due to persistence of disease in follow up scan. 17/20 achieved metabolic response (17 ycN0M0). Among these patients: 13/17 underwent surgery (12 ypN0, 1 ypN1. VPN92%) and 4/17 were ineligible for surgery and received chemotherapy. Mean SUVmax for pathological nodes(DS ≥3) in staging scan was 5,43 (±DS 2,6). Post-treatment mean SUVmax in responders (DS ≤2) was 1,57 (± 0,73) and 3,13 (±DS 0,11) in non-responders. ***Conclusion:*** 18F-FDG-PET/CT, using modified Deauville Score, improved nodal staging accuracy in MIUC and impacted management by identifying surgery candidates and assessing neoadjuvant therapy response. Its high negative predictive value supports its role as a reliable, non-invasive tool for response evaluation.

EP-0531

Flow cytometry to validate the efficacy of multi-target PET tracer in early monitoring of ICI in lung cancer

R. Meng, *F. Kang;*
Military Medical University First Affiliated Hospital of No.4 Military Medical University, Shaanxi Xi'an, CHINA.

Aim/Introduction: Immune checkpoint inhibitors (ICIs) are a new class of anti-cancer drugs that are able to turn the immune system back on to fight cancer. However, the efficacy of ICI varies greatly in different patients because of the complex immune microenvironment, in which the neutrophil/lymphocyte ratio may play a key role. Studies have shown that imaging of granzyme B (GZB) with 68Ga-DOTA-grazytracer and myeloperoxidase (MPO) with 68Ga-NOTA-bis-5HT could predict the ICI responders of lung cancer, which are the effective protein of CD8+ T cell and the core protein of neutrophil trapping net (NETs), respectively. In this study, the effector molecule granzyme B (GZB) targeting CD8+ T cells and myeloperoxidase (MPO), the core protein of neutrophil capture network (NETs), were used to predict ICI responders in lung cancer, and the effectiveness of multi-target PET tracer detection was verified by enzyme-linked immunosorbent assay and flow cytometry. ***Materials and Methods:*** LLC tumor-bearing mice were treated with intraperitoneal injection of PD-L1 mAb (200μg) every 3 days. Subsequently, microPET /CT dual PET probes were used to detect the uptake before and after treatment. The tumor tissues of LLC mice were collected after immunotherapy, and the proportion of cell types and the secretion of MPO and GZB were detected by flow cytometry and ELISA respectively. ***Results:*** ELISA experiments showed that after PD-L1 treatment, MPO secretion in the Responder and Nonresponder groups was significantly different, consistent with the PET/CT results, while GZB was not. Flow cytometry results showed that after PD-L1 treatment, neutrophils and PD-L1 were significantly different between the Responder and Nonresponder groups, while CD8+T cells were not, indicating the importance of activated neutrophils in immunotherapy monitoring. The expression of PD-L1 was higher in the Nonresponder group than in the responder group, which was inconsistent with the theoretical results, indicating that PD-L1 alone was not sufficient to predict immunotherapy response. ***Conclusion:*** GZB expression in tumor was increased by PD-L1 stimulation and the change of MPO had the potential to predict the immunotherapy response of lung cancer. The use of immunotherapy to treat lung cancer needs to satisfy both T cell activation and neutrophil inactivation, which can mobilize endogenous immune pathways. ***References:*** Zhang J, Shao S, Wu P, et al. Diagnostic performance of 68Ga-PSMA PET/CT in the detection of prostate cancer prior to initial biopsy: comparison with cancer-predicting nomograms. Eur J Nucl Med Mol Imaging. 2019 Apr;46(4):908-920.

EP-0532

Head to head comparison of ^{68}Gallium-FAPI-PET/CT and ^{18}Fluor-FDG-PET/CT for the assessment of single site cancer of unknown primary

M. Röhrich[1], *D. Driess*[1], *A. Spektor*[1], *S. Zapata*[1], *A. Desuki*[1], *M. Schreckenberger*[1], *U. Haberkorn*[2], *A. Krämer*[3];
[1]*University hospital Mainz, Mainz, GERMANY,* [2]*University hospital Heidelberg, Heidelberg, GERMANY,* [3]*University hospital Heidelberg, Heidelberg, GERMANY.*

Aim/Introduction: For the assessment of cancer of unknown primary of the head and neck (HNCUP), ^{68}Gallium FAPI-PET/CT has shown highly promising results and appears superior to ^{18}Fluor-FDG-PET/CT. However, to date no data on the diagnostic performance of ^{68}Gallium FAPI-PET/CT compared to ^{18}Fluor-FDG-PET/CT for patients with single site CUP (SSCUP) exists. In this pilot study, we compare detection rates, signal intensities and diagnostic accuracy of both PET techniques in 24 patients with SSCUP. ***Materials and Methods:*** 24 patients with SSCUP underwent ^{18}Fluor-FDG-PET/CT and additional ^{68}Gallium FAPI-PET/CT for optimized SSCUP staging. All PET-positive lesions were delineated by isocontouring and lesionwise SUVmax, SUVmean were extracted and target to background ratios (lesional SUVmax/bloodpool SUVmean) were calculated. Lesions were classified according to radiological appearance, clinical course and - if available - histological confirmation. Receiver-operating-characteristic curves for the differentiation of malignant and benign lesions and corresponding estimates of area under the curve, including 95% CIs, were calculated. ***Results:*** Primary tumors were detected in 6/24 (^{68}Gallium FAPI-PET/CT) and 3/24 cases (^{18}Fluor-FDG-PET/CT). ^{68}Gallium FAPI-PET/CT detected 12 metastases in 9 patients, ^{18}Fluor-FDG-PET/CT 9 in 6 patients. FAPI-uptake was almost equal to FDG-uptake in primaries (SUVmax/mean 7.49+/-1.54/4.76+/-1.09 versus 8.17+/-1.75/5.01+/-1.96), but significantly higher in metastases (SUVmax/mean 18.07+/-8.58/7.28+/-5.24/ versus 6.13+/-2.32/3.58+/-1.47, p values 0.009 (SUVmax) and 0.035 (SUVmean)). TBRs for primaries were 3.22+/-0.38 (^{68}Gallium FAPI-PET/CT) and 4.12+/-1.61 (^{18}Fluor-FDG-PET/CT), for metastases 6.42+/-0.92 (^{68}Gallium FAPI-PET/CT) and 2.64+/-1.31 (^{18}Fluor-FDG-PET/CT). ROC analyses showed higher area under curve values for ^{68}Gallium FAPI-PET/CT compared to ^{18}Fluor-FDG-PET/CT (SUVmax 78% versus 68%, SUVmean 71% versus 65%). ***Conclusion:*** In SSCUP, ^{68}Gallium FAPI-PET/CT detected more primary sites and metastases than ^{18}Fluor-FDG-PET/CT. Signal intensities of both tracers were mostly equal in primaries, however metastases showed higher ^{68}Gallium FAPI- than ^{18}Fluor-FDG-uptake. Diagnostic accuracy for the differentiation of malignant and benign lesions was higher for ^{68}Gallium FAPI-PET/CT than for ^{18}Fluor-FDG-PET/CT. Overall, ^{68}Gallium FAPI-PET/CT improved the diagnostic assessment of SSCUP compared to ^{18}Fluor-FDG-PET/CT, especially with respect to accurate and high-contrast detection of metastases.

EP-0533

Treatment monitoring of immunotherapy and targeted therapy using cluster of CD70-targeted positron emission tomography/computed tomography (PET/CT) in patients with advanced clear cell renal cell carcinoma(ccRCC)

Q. Wu, *G. Huang, J. Liu, W. Wei;*
Renji Hospital School of Medicine Shanghai Jiao Tong University, Department of Nuclear Medicine Institute of Clinical Nuclear Medicine, Shanghai, CHINA.

Aim/Introduction: CD70 is a potential biomarker for ccRCC. Using [^{18}F]RCCB6 (a ^{18}F-labelled single-domain antibody radiotracer targeting CD70) immunoPET/CT to assess the efficacy of immune checkpoint inhibition (ICI), targeted therapy (TT), and combinations thereof for advanced ccRCC, and comparing with Response Evaluation Criteria in Solid Tumours (RECIST). ***Materials and Methods:*** Thirteen postoperative advanced ccRCC patients were included between May 2023 and November 2024 who underwent [^{18}F]RCCB6 PET/CT for response assessment to ICI or TT or combinations thereof using baseline and follow-up scans (median time between scans, 5 mo). [^{18}F]RCCB6 PET/CT parameters (i.e., maximum standardized uptake value (SUVmax), CD70-derived tumour volume (CD70-TV) and total lesion uptake of the CD70 tracer (CD70-TLU)) were acquired in all extra-renal lesions. Treatment efficacy was assessed using [^{18}F]RCCB6 PET/CT and RECIST. ***Results:*** In thirteen patients with advanced ccRCC, 182 lesions were detected on baseline [^{18}F]RCCB6 PET/CT with a median SUVmax of 4.4. The median total CD70-TV and total CD70-TLU for patients were 4.9 and 36.3. Patients were then treated with ICI or TT or combinations thereof. In the follow-up scan by [^{18}F] RCCB6 PET/CT, three patients showed a decrease in the number of lesions (mean 4.3), with a mean decrease in total CD70-TV and total CD70-TLU of 2.0 and 74.4. Whereas in nine patients, the number of lesions increased (mean 18.0), with a mean increase in total CD70-TV and total CD70-TLU of 17.4 and 97.4. In five of 13 patients, the [^{18}F]RCCB6 PET/CT follow-up results were inconsistent with the results of RECIST. All five were considered to have stable disease by RECIST, while 3 of them were considered to have progressive disease and two were considered to be partial remission by [^{18}F] RCCB6 PET/CT. ***Conclusion:*** [^{18}F]RCCB6 PET/CT targeting CD70 may provide valuable information for the monitoring of patients with advanced ccRCC treated with ICI and TT.

EP-0534

Improving Clinical Management of von Hippel-Lindau Syndrome with [^{89}Zr]Zr-DFO-Girentuximab PET Imaging

F. Gelardi[1], *A. Larcher*[1,2], *L. Antunovic*[1], *F. Cei*[2,1], *C. Re*[2,1], *F. Belladelli*[2,1], *G. Guazzarotti*[1], *G. Brembilla*[1], *S. Calloni*[1], *N. Tenace*[1], *A. Piai*[1], *A. Tudda*[1], *U. Capitanio*[1], *F. Montorsi*[2,1], *A. Salonia*[2,1], *M. Sollini*[2,1], *A. Chiti*[2,1];
[1]*IRCCS Ospedale San Raffaele, Milan, ITALY,* [2]*Università Vita-Salute San Raffaele, Milan, ITALY.*

Aim/Introduction: Von Hippel-Lindau syndrome (VHL) is a rare inherited disease caused by mutations in the VHL tumour suppressor gene, resulting in upregulation of hypoxia-inducible factor 1α and carbonic anhydrase IX (CAIX), and subsequent tumour development. Imaging plays a central role in disease surveillance and patient management. We aim at evaluating the utility of CAIX-targeted PET imaging for comprehensive whole-body evaluation in patients with VHL syndrome. ***Materials and Methods:*** Adult patients with genetically confirmed VHL syndrome who are under regular surveillance at our institution are enrolled in a compassionate use programme. Each participant receives a single intravenous dose of [^{89}Zr]Zr-DFO-Girentuximab, followed by whole-body PET/CT imaging five days after injection. Conventional imaging - including abdominal and brain MRI - is performed according to clinical practice. PET/CT images are independently interpreted by two experienced nuclear medicine physicians. Lesions with increased tracer uptake are reported and detection rates are calculated both per patient and per region. Follow-up conventional imaging and/or histopathology are used as reference standards. ***Results:*** We report preliminary findings in two patients with VHL syndrome and suspicious renal, cerebral and pancreatic lesions on MRI. Patient 1 presented with bilateral renal lesions associated with polycystic kidney disease, which resulted in challenging MRI interpretation. The patient also had a known pancreatic neuroendocrine tumour (NET) and multiple cerebellar hemangioblastomas. [^{89}Zr]Zr-DFO-Girentuximab PET/CT showed high uptake in multiple bilateral renal lesions with a high degree of discrimination, outperforming MRI in terms of the number of lesions detected. High uptake was also observed in the pancreatic isthmus, corresponding to the known NET, whereas cerebellar lesions showed only mild uptake. Patient 2 presented with suspected bilateral renal lesions, multiple cerebellar hemangioblastomas, and pancreatic cysts with mural enhancement suggestive of adenoid cystic lesions. PET/CT showed high uptake in the renal and cerebellar lesions, but no uptake in the pancreatic cysts. ***Conclusion:*** This preliminary experience suggests that CAIX-targeted PET imaging may offer significant advantages in detecting and characterising VHL-associated tumours, particularly in anatomically complex or ambiguous settings. The ability of [^{89}Zr]Zr-DFO-Girentuximab PET/CT to identify different lesions subtypes supports CAIX as a promising imaging biomarker for improved surveillance and personalised management in VHL syndrome. Acknowledgements: This research is supported by the Italian Ministry of Health and the European Union for the project "CAT-VHL - Exploring the role of Carbonic Anhydrase IX as diagnostic and Theranostic target in Von-Hippel Lindau disease" (PNRR-POC-2023-12377493).

EP-0535

Diagnostic Utility of [18F]F-FAPI PET-CT in Patients with Carcinoma of Unknown Primary: A Prospective Multicentre Study in the Netherlands

S. Veldhuijzen van Zanten[1], *E. Droogers*[1], *M. Hendriks*[2], *E. Verburg*[3], *D. Robbrecht*[3], *A. Glaudemans*[4], *A. Glaudemans*[4], *M. van Kruchten*[5], *W. Vogel*[6], *S. Marchetti*[6], *S. Marchetti*[6], *M. Lam*[7], *H. Nienhuis*[7], *A. Timmer-Bonte*[8], *M. van Rijk*[8], *J. Nin*[9], *C. Mitea*[9], *A. van den Hoven*[10], *W. Kool*[2], *S. Veldhuijzen van Zanten*[3], *FAPI for CUP study team;*
[1]*Erasmus Medical Center, Rotterdam, NETHERLANDS,* [2]*Northwest Clinics, Alkmaar, NETHERLANDS,* [3]*Erasmus MC, Rotterdam, NETHERLANDS,* [4]*UMC Groningen, Groningen, NETHERLANDS,* [5]*UMC Grongingen, Grongingen, NETHERLANDS,* [6]*AvL, Amsterdam, NETHERLANDS,* [7]*UMC Utrecht, Utrecht, NETHERLANDS,* [8]*Radboud UMC, Nijmegen, NETHERLANDS,* [9]*Maastricht UMC, Maastricht, NETHERLANDS,* [10]*Antonius Ziekenhuis, Nieuwegein, NETHERLANDS.*

Aim/Introduction: Carcinoma of unknown primary (CUP) is a heterogeneous group of metastatic malignancies where the primary tumour site remains unidentified despite extensive diagnostic work-up. This impedes personalised, tumour-specific treatments and contributes to poor prognosis, with a median overall survival of only two months. [^{18}F]FDG PET-CT, the most sensitive imaging modality, fails to detect the primary tumour in two-thirds of cases. Fibroblast activation protein inhibitors (FAPI) represent a promising class of radiotracers targeting cancer-associated fibroblasts, offering high tumour specificity and favourable tumour-to-background contrast. This study aims to evaluate the clinical performance of [^{18}F]F-FAPI PET-CT in CUP patients. The study was initiated in collaboration with the Dutch patient advocacy group Missie Tumor Onbekend, now part of the international World CUP Alliance, highlighting the urgent need and potential societal impact of improving diagnostics for CUP patients. ***Materials and Methods:*** This patient-driven, investigator-initiated, prospective multicentre study involves 50 adult CUP patients across six Dutch centres. Eligible patients are identified through the national CUP referral pathway following standard diagnostics, including [^{18}F]FDG PET-CT. Each patient undergoes a single [^{18}F]F-FAPI-74 PET-scan (3.0 MBq/kg, 60-minute acquisition post-injection), followed by CECT. Imaging is centrally reviewed by two blinded experts, with discordant reads resolved through consensus. A multidisciplinary Truth Panel assesses whether suspected primary lesions on [^{18}F]F-FAPI PET-CT are confirmed by follow-up diagnostics (e.g., histopathology, imaging,

or molecular analysis) within six months post-scan. ***Results:*** The primary endpoint is defined as the proportion of CUP patients in whom the primary tumour is identified by [^{18}F]F-FAPI PET-CT. Secondary endpoints include sensitivity, specificity, PPV, and NPV. Tertiary outcomes assess the clinical impact on diagnostics and treatment, tracer safety, incidental findings, and comparative uptake metrics between [^{18}F]FAPI/[^{18}F]FDG. Subgroup analyses based on age, sex, histology, metastasis site, and performance status are also planned. As of April 2025, over half of the target population has been enrolled (first patient: July 2024). All [^{18}F]F-FAPI PET-CT scans have been reviewed within protocol timelines, and primary tumours have been identified following [^{18}F]F-FAPI imaging. The Truth Panel is actively reviewing eligible cases (≥6 months follow-up or deceased) to determine study endpoints. ***Conclusion:*** This study demonstrates that [^{18}F]F-FAPI PET-CT has the potential to improve primary tumour detection in CUP patients, informing clinical management. Through rigorous prospective evaluation and national collaboration, the study aims to establish the diagnostic performance and clinical utility of FAPI imaging in this high-need patient population. Preliminary results will be available at the time of EANM'25.

EP-0536

Head-to-Head Radiomics Comparison between ^{18}F-PSMA and ^{18}F-FDG PET/CT Imaging in Desmoid Tumor

C. D. Ramos, *T. L. Reis, M. E. S. Takahashi, B. J. Amorim, M. C. L. Lima, C. A. Souza, J. B. C. Carvalheira;*
University of Campinas, Campinas, BRAZIL.

Aim/Introduction: Desmoid tumors (DTs) are rare, locally aggressive soft-tissue neoplasms arising from myofibroblasts. While they lack metastatic potential, their infiltrative growth can cause substantial morbidity due to compression of adjacent structures. ^{18}F-FDG PET/CT, which reflects tumor glycolytic activity, has shown utility in assessing disease activity and predicting clinical outcomes [1]. More recently, uptake of radiolabeled Prostate-Specific Membrane Antigen (PSMA) has been reported in DTs, likely reflecting PSMA expression in tumor neoangiogenesis [2]. This study aimed to compare the uptake characteristics and intratumoral radiomic features of ^{18}F-FDG and ^{18}F-PSMA PET/CT in abdominal DTs. ***Materials and Methods:*** Four patients with histologically confirmed abdominal DT underwent both ^{18}F-FDG and ^{18}F-PSMA PET/CT imaging within a one-day interval. Lesions were assessed visually, and maximum standardized uptake values (SUVmax) were recorded for each radiotracer. Radiomic analysis included extraction of Haralick texture features and voxel-wise intensity metrics. Intra-patient percentage deviations were calculated to quantify differences between the two imaging modalities. ***Results:*** All DT lesions demonstrated mild-to-moderate uptake (above mediastinal blood pool) for both tracers. The index lesion size ranged from 4.4 to 9.2 cm (mean ± SD: 6.4 ± 2.4 cm). In three of four patients, ^{18}F-FDG showed more homogeneous intratumoral distribution than ^{18}F-PSMA; the reverse was observed in one patient. SUVmax values ranged from 2.3 to 9.8 for ^{18}F-FDG and 2.4 to 9.0 for ^{18}F-PSMA (mean ± SD: 6.4 ± 3.9 and 5.8 ± 2.7, respectively). Radiomic analysis revealed notable deviations (>25%) in several features, including SUV standard deviation, SUVpeak, contrast, difference variance, cluster shade, correlation measure 2 (MC2), sum variance, and variance. MC2, reflecting texture complexity and redundancy, showed an exceptionally high mean deviation (~5000%). ***Conclusion:*** Abdominal desmoid tumors demonstrate uptake of both ^{18}F-FDG and ^{18}F-PSMA, with inter-lesional and intra-lesional variability in tracer intensity and spatial distribution. While ^{18}F-FDG generally presents more uniform uptake, ^{18}F-PSMA reveals greater heterogeneity in most cases. Radiomic texture analysis highlights substantial differences between the two modalities, particularly in MC2, suggesting that each tracer captures distinct biological aspects of DT. These findings support a potential complementary role of PSMA imaging in the evaluation of desmoid tumors. ***References:*** [1] Liu DN, et al. Volume-based ^{18}F-FDG PET/CT predicts prognosis and outcome of active surveillance for intra-abdominal desmoid tumor. Abdom Radiol (NY). 2024;49(3):958-963.[2] Orevi M, et al . False positive findings of [^{18}F]PSMA-1007 PET/CT in patients after radical prostatectomy with undetectable serum PSA levels. Front Surg. 2022;9:943760.

EP-0537

Baseline Intelligence: Predicting Treatment Response in Esophageal Cancer via Machine Learning on PET/CT

D. Khan, *S. Sagar, N. Kundu, J. Krishna P., A. Tilak, L. Goriparti, A. Roy, A. Mahalik, S. K V, J. Pathak, R. Kumar;*
AIIMS Delhi, Delhi, INDIA.

Aim/Introduction: Accurate early prediction of treatment response in esophageal cancer is critical for timely clinical decision-making. While FDG PET/CT offers valuable metabolic insights, interpretation remains largely qualitative and subjective. This study aimed to develop and evaluate machine learning (ML) models that predict final treatment response using only baseline PET/CT features in patients with esophageal cancer. ***Materials and Methods:*** From an initial dataset of 951 esophageal cancer PET/CT scans, a cohort of 88 patients diagnosed with esophageal cancer having baseline, interim and response assessment scan was curated. After excluding cases with incomplete data, 82 patients with complete baseline features were included in the analysis. Quantitative features including Esophagus SUVmax, Nodal SUV, Metastasis SUV, Age, and Sex were extracted and used to train Random Forest and XGBoost classifiers. Response labels were derived from follow-up scan impressions, categorized into responders (CMR/PR) and non-responders (SD/PD). Both models were evaluated using stratified 5-fold cross-validation. SHAP-based interpretability was implemented to visualize feature impact per patient. ***Results:*** The Random Forest model achieved an average AUC of 0.65 and recall of 0.76, while XGBoost yielded similar performance (AUC 0.66, recall 0.74). Both models demonstrated consistent results across folds, with Esophagus SUV and Age emerging as top predictors. The models were integrated into a user-friendly Streamlit interface supporting Excel uploads, SHAP plots, and PDF report generation. ***Conclusion:*** This study demonstrates the feasibility of predicting esophageal cancer treatment response from baseline PET/CT features using ML. The workflow offers a scalable, interpretable, and clinically relevant tool for early response stratification, potentially enhancing personalized care.

EP-0538

99mTc-PSMA SPECT/CT in the detection of metastatic lesions in renal cell carcinoma

Y. Sánchez Vera, *J. González Díaz;*
Centro Médico Nacional Siglo XXI, IMSS, Mexico, MEXICO.

Aim/Introduction: Overexpression of prostate-specific membrane antigen (PSMA) has been demonstrated in the neovasculature of various malignant tumors, including Renal Cell Carcinoma (RCC). The objective of this study was to explore the usefulness of SPECT/CT with 99mTc-PSMA in the detection of metastases in patients with RCC. ***Materials and Methods:*** A retrospective, observational, and descriptive study was conducted. A total of 12 patients diagnosed with clear cell RCC were selected, who had undergone 99mTc-PSMA SPECT/CT, were clinically suspected, and/or had demonstrated metastasis by other diagnostic methods. SPECT/CT was performed from the vertex of the skull to the mid-thigh using a Phillips Precedence 16P hybrid scanner. ***Results:*** Twelve studies were included of patients with a mean age of 56 years; 3 women and 9 men, with a histopathological diagnosis of RCC. Lesions with 99mTc-PSMA uptake were detected in 66% (8/12) of the SPECT/

CT scans performed, and the remaining 33% (4/12) showed no lesions. Fifty-nine lesions with abnormal 99mTc-PSMA uptake were documented, of which 37.3% (22/59) were found in bone, 32.2% (19/59) in lung, 20.3% (12/59) in lymph nodes, 3.4% (2/59) in soft tissue, 3.4% (2/59) in retroperitoneum, and 3.4% (2/59) in the central nervous system. ***Conclusion:*** 99mTc-PSMA SPECT/CT detected metastatic disease in 66.6% of patients, including new lesions. Results showed potential for complementary use in the staging and restaging of RCC. Further studies are needed to determine its effectiveness in other histological subtypes. Additionally, SPECT/CT with 99mTc-PSMA can be a diagnostic method identifying metastatic disease and with potential theragnostic use in RCC.

EP-0539

Implementing Gallium - 68 FAPI PET/CT in Kenya: Initial experience in a tertiary cancer centre.

N. Harish[1,2], *K. Kallur*[1], *D. Muriuki*[1], *H. Ryatt*[1], *R. Prashanth*[1], *K. Rajkumar*[1], *T. Harsha*[1], *J. Kariuki*[1];
[1]*HCG CCK Cancer Centre, Nairobi, KENYA,* [2]*Kenyatta University Teaching Referral and Research Hospital, Nairobi, KENYA.*

Aim/Introduction: Molecular imaging has revolutionized oncology by assessing tumor biology over and above dependency on morphological anatomy like traditional radiologic imaging. Positron Emission Tomography/Computed Tomography (PET/CT), among molecular imaging modalities, is a hybrid imaging tool yielding structural and functional information in a way that enables visualization non-invasively of physiological and pathological processes at a cellular and subcellular level. In Kenya, PET/CT has existed for over six years with most using Fluorine-18 Fluorodeoxyglucose (^{18}F-FDG) as the go-to radiotracer in oncologic imaging. However, ^{18}F-FDG has its drawbacks, particularly when identifying tumors with low glucose metabolism or confidently differentiating malignant from benign processes like infection and inflammation. Additionally, the ^{18}F-FDG protocol requires fasting and may be cumbersome in diabetic and pediatric patients. Recently, our institution introduced Gallium-68 Fibroblast Activation Protein Inhibitor (^{68}Ga-FAPI), a novel radiotracer for fibroblast activation protein (FAP) overexpressed in cancer-associated fibroblasts (CAFs). The first-of-a-kind tracer in Kenya and the entire East African region has numerous advantages over ^{18}F-FDG, including high tumor-to-background contrast (TBR), minimal uptake in normal tissues, no dietary preparation requirement, and shorter uptake time. It is extremely useful in detecting primary and metastatic tumors, especially in malignancies with high fibroblast content. ***Materials and Methods:*** It is a retrospective study that aimed to assess the clinical application of ^{68}Ga-FAPI PET/CT in cancer diagnosis and therapy. A total of 141 patients with confirmed histopathological diagnoses were scanned with ^{68}Ga-FAPI PET/CT scans between February and March 2025 for several indications, such as staging, post-treatment follow-up, re-staging, surveillance, and detecting the primary tumor in cancers of unknown primary. The injected dose was between 120 to 185 MBq with an uptake of 20 minutes, and images were taken using a GE Discovery PET/CT IQ scanner. ***Results:*** Amongst all cancers, the highest SUVmax (>15) was seen in breast, esophageal, sarcoma, and lung carcinomas. Low uptake (SUVmax <6) was seen in renal cell and gallbladder carcinomas, and moderate uptake (SUVmax 6-15) in colorectal, nasopharyngeal, oral squamous cell carcinoma, and melanomas. ***Conclusion:*** Initial experience with ^{68}Ga-FAPI PET/CT in Kenya is promising. The technique boasts high contrast image, ease of use, and enhanced patient comfort. While not a replacement for ^{18}F-FDG, ^{68}Ga-FAPI is an adjunct modality that may have a significant impact on clinical decision-making as well as oncology care in the nation. ***References:*** FAPI-PET/CT: Mean intensity of tracer-uptake (SUV) in 28 different kinds of cancer. DOI:10.2967/jnumed.119.227967.

EP-0540

Organ-wise changes in ^{18}F-AraG immunoPET uptake before and after ICI Therapy

T. Nobashi*, Y. Shimizu, K. K. Miyake, R. Sakamoto, S. Yasumura, Y. Kitano, R. Nakamoto, H. Ajimizu, T. Nomizo, H. Yoshida, H. Ozasa, M. Nomura, C. Katada, M. Muto, Y. Nakamoto;*
Kyoto University Hospital, Kyoto city, JAPAN.

Aim/Introduction: Immune checkpoint inhibitors (ICIs) have revolutionized cancer therapy, offering significant benefits across various malignancies. However, their overall response rate remains limited, ranging from 20% to 40%[1]. ImmunoPET has emerged as a powerful non-invasive imaging modality that visualizes the in vivo distribution of immune-related molecules. Among these, ^{18}F-AraG—a radiolabeled form of the T-cell-targeting prodrug nelarabine—selectively accumulates in activated T cells[2,3]. This study aimed to evaluate organ-specific changes in ^{18}F-AraG uptake following ICI initiation in cancer patients, with a particular focus on immune-related and irAE-prone organs. ***Materials and Methods:*** This investigator-initiated clinical study was approved by the Japan Registry of Clinical Trials (jRCTs051220109 and jRCTs051240253) in October 2022 and January 2025, respectively. Eligible patients were aged 20-85, had an ECOG performance status of 0-2, and were scheduled to receive ICI therapy approved in Japan. ^{18}F-AraG PET/CT scans were acquired at baseline and during the early phase of ICI treatment. Uptake changes were quantitatively analyzed in immune-related tissues (e.g., spleen, tonsils, upper pharynx) and irAE-associated organs (e.g., pituitary, thyroid, liver, pancreas, intestines) using paired t-tests. ***Results:*** Nine patients (1 female, 8 males; aged 69-82) were included: six with non-small cell lung cancer, two with esophageal cancer, and one with small cell lung cancer. Post-treatment PET/CT was performed 19 ± 7 days after ICI initiation. ^{18}F-AraG (228.3 ± 53.1 MBq) was injected manually without adverse events. Scanning was conducted 60.9 ± 8.5 minutes post-injection from mid-thigh to vertex. High tracer uptake was observed in the kidneys, liver, pancreas, and stomach; low accumulation was seen in the bladder, blood, and brain. Moderate to intense uptake occurred in the pituitary, salivary glands, heart, choroid plexus, and adrenal glands. Notably, the spleen exhibited a significant increase in both SUVmax (p=0.024) and SUVmean (p=0.019) after ICI, suggesting a rise in activated T cell populations. ***Conclusion:*** This pilot study demonstrated dynamic organ-wise changes in ^{18}F-AraG PET/CT uptake among Japanese cancer patients undergoing ICI therapy. The observed increase in splenic uptake may reflect systemic immune activation, highlighting the potential of ^{18}F-AraG PET as a biomarker for early immune response monitoring. ***References:*** 1. N Engl J Med. 2019;381:2020-31.2. Cancer Res. 2017;77:2893-902.3. Cancer Res. 2019;79:3455-65.

EP-0541

Use of ^{18}F-FDG PET/MR as an initial staging procedure for malignant tumors

Y. Xu*;*
Hangzhou Universal Medical Imaging Diagnostic Center, Hangzhou, CHINA.

Aim/Introduction: This study aimed to evaluate the clinical utility and cost-effectiveness of PET/MR compared to PET/CT and conventional work-up (CWU) for initial staging of malignant tumors. ***Materials and Methods:*** From January 2018 to December 2023, 5850 patients with histologically confirmed malignancies were enrolled. Among them, 1250 patients underwent PET/MR prior to treatment, 1780 underwent PET/CT, and the remaining 2820 received CWU. Costs were calculated based on 2022 pricing guidelines from the National Health Insurance Agency of China. All patients were followed for ≥1 year, with final clinical staging as the reference standard. Incremental cost-effectiveness ratio (ICER) was used to assess the cost per percentage reduction in missed or misdiagnosed cases. ***Results:*** Missed/misdiagnosis rates were

5.2% for PET/MR, 10.8% for PET/CT, and 22.6% for CWU (p<0.001). The mean interval from diagnosis to treatment initiation was 5.3 days (PET/MR), 9.7 days (PET/CT), and 15.4 days (CWU) (p<0.001). Mean per-patient costs were $1620 (PET/MR), $890 (PET/CT), and $520 (CWU). Compared to CWU, ICER values for PET/MR and PET/CT were $62 and $28 per percentage reduction in misdiagnosis, respectively. The ICER between PET/MR and PET/CT was $173. ***Conclusion:*** PET/MR demonstrated superior diagnostic accuracy and expedited treatment initiation compared to PET/CT and CWU in malignancies. Additionally, PET/MR significantly reduced radiation exposure, a critical consideration for long-term cancer survivors. Despite higher upfront costs, PET/MR may offer cost-effectiveness in initial staging by minimizing diagnostic errors and optimizing therapeutic planning.

EP-0542

Evaluation of metastatic clear cell renal cell carcinoma: a head-to-head comparison of [^{18}F]PSMA-1007 PET/CT and standard-of-care CT

D. Khodakova, *A. Khalimon, V. Bobrov, A. Lokhova, G. Khamadeeva, M. Khodzhibekova, T. Lazutina, I. Pylova, A. Nikiforuk, A. Leontev;*
P. Hertsen Moscow Oncology Research Institute - branch of the National Medical Research Radiological Centre of the Ministry of Health of the Russian Federation, Moscow, RUSSIAN FEDERATION.

Aim/Introduction: The aim of this study was to perform a head-to-head comparison of [^{18}F]PSMA-1007 PET/CT and standard-of-care chest, abdominal, and pelvic CT for the evaluation of metastatic disease in clear cell renal cell carcinoma (ccRCC). ***Materials and Methods:*** This prospective, single-center study involved 20 patients with histologically verified ccRCC during primary staging, recurrence evaluation, and treatment response assessment. All patients underwent [^{18}F]PSMA-1007 PET/CT, which included non-contrast CT (NCCT) and dual-phase contrast-enhanced CT (CECT) from vertex to mid-thigh. Metastatic lesions were evaluated independently using PET/CT, NCCT, and CECT. Focal tracer uptake, as well as CT findings by NCCT part of PET/CT, that were typical for metastatic disease, were considered PET/CT-positive. The diameters of the lesions were assessed on CECT. ***Results:*** A total of 149 lesions were evaluated. The majority of lesions (n=147;98,7%;20,4mm [95%CI16,8;24,0]) were detected by CECT, while 133 (89,3%;20,7mm [95%CI16,8;24,6]) and 112 (75,2%;22,5mm [95%CI18,0;27,0]) lesions were identified by PET/CT and NCCT, respectively. 131 lesions (87,9%) were detected by both PET/CT and CECT, 16 lesions (10,7%;18,2mm [95%CI11,4;25,0]) - only by CECT, 2 lesions (1,3%) - only by PET/CT. Of the 16 lesions detected solely by CECT, 6 were located in the kidneys, 7 in the liver, 2 in the pancreas and 1 in the adrenal gland. The diameters of the two PET/CT-negative lesions in the pancreas were 4mm and 5mm. The PET/CT-negative liver lesions had diameters ranging from 7 to 26mm, while the diameters of PET/CT-positive liver lesions ranged from 26 to 161mm. The two lesions detected only by PET/CT were found in bones with no changes observed on CT. PET/CT identified 21 lesions that were not detected on NCCT: 2 in the brain, 8 in skeletal muscles, 3 in cardiac muscle, 4 in the pancreas, 2 in bones, 1 in the peritoneum, and 1 in subcutaneous adipose tissue. In two patients, PET/CT led to a change in treatment compared to NCCT. However, there were no changes in treatment when comparing PET/CT and CECT. ***Conclusion:*** The main causes of PET/CT false-negative results were small lesion size or high physiological [^{18}F]PSMA-1007 uptake nearby the evaluated lesions, which were associated with equivocal findings from NCCT as part of the PET/CT. There was no evidence that PSMA PET/CT provides additional value in evaluating metastatic disease compared to standard multiphase CECT in patients with ccRCC; however, it could serve as an alternative imaging modality when there are contraindications to CECT and MRI.

EP-0543

Head to Head Comparison of F18 FDG with GA68 FAPI 2286 in Staging and Restaging Evaluation in Various Solid Malignancies

J. Bal[1], *S. Jha*[2], *P. Dougall*[2], *K. Shanker*[2], *V. Semwal*[2];
[1]*Max Super Specialty Hospital, Delhi, INDIA,* [2]*Max superspeciality hospital, Delhi, INDIA.*

Aim/Introduction: Our study aims to compare the application of Gallium-68-fibroblast activation protein inhibitor (^{68}Ga-FAPI-2286) positron emission tomography/computed tomography (PET/CT) and Fluorine-18-fluorodeoxyglucose (^{18}F-FDG) PET/CT in primary and metastatic lesions of various solid malignancies to determine the superior diagnostic tool. In the past 30 years, ^{18}F-FDG tracers, which take advantage of the tumours' aberrant glucose metabolism, have become increasingly available and are now the most widely used PET imaging tool. 18F-FDG-PET is frequently used to diagnose malignancies, evaluate the effectiveness of tumour treatment, and predict prognosis. However, recent research has revealed that FDG tracers have limitations in the diagnosis of various gastrointestinal cancers and are unable to differentiate between inflammation and malignancy. Recent studies have also uncovered a correlation between increased fibroblast activation protein (FAP) levels in cancer-associated fibroblasts and tumour growth, metastasis, and prognosis. Fibroblast activation protein inhibitor (FAPI) has therefore emerged as a new cancer imaging molecule. ***Materials and Methods:*** 58 patients (mean age 56 ± 10 SD) with various solid malignancies underwent both gallium-68-fibroblast activation protein inhibitor (^{68}Ga-FAPI-2286) positron emission tomography/computed tomography (PET/CT) and fluorine-18-fluorodeoxyglucose (^{18}F-FDG) PET/CT for staging and restaging evaluation from November 2023 to August 2024. Histopathologic examination, morphologic imaging, and/or follow-up imaging served as the reference standard. The maximum standardized uptake value (SUVmax) of the primary tumor and nodal and distant metastases between ^{18}F-FDG and 68Ga-FAPI PET/ CT were compared using the paired-sample t test. ***Results:*** The sensitivity of [68Ga]FAPI PET/CT was higher than that of [^{18}F] FDG PET/CT for detecting primary tumors (36/36-100% vs. 81%), nodal (35/36-98% vs. 87%), and distant metastases (34/36-98% vs. 79%) in our subset of cases. SUVmax values of primary lesions and metastases ranged from 0- 9.8 in ^{18}F-FDG PET/CT and from 3.9 to 17.0 in ^{68}Ga-FAPI-2286. ***Conclusion:*** Our results showed that gallium 68-labelled fibroblast-activation protein inhibitor (68Ga-FAPI) PET/CT was superior to fluorine 18 fluorodeoxyglucose (18F-FDG) PET/CT for detecting the primary tumor and nodal and distant metastases in participants with biliary tract cancer (BTC). 68Ga-FAPI PET/CT findings led to an upstaging or changing the management in the staging or restaging in 17 participants compared with ^{18}F-FDG PET/CT. However, PET/ CT results were derived from studies with small sample sizes. Therefore, our observations need to be validated by a more extensive and comprehensive prospective study.

EP-0544

Head to head comparison of [^{68}Ga] FAPI PET/CT and [^{18}F] FDG PET/CT in Urothelial carcinoma : A prospective study

H. Ng, *A. Arya, M. Ora, S. Gambhir;*
Sanjay Gandhi Postgraduate Institue of Medical Sciences, Lucknow, INDIA.

Aim/Introduction: Bladder carcinoma is the most prevalent malignancy of the urinary tract, with urothelial carcinoma accounting for over 90% of cases. Precise imaging is especially important in muscle-invasive bladder cancer (MIBC) to guide staging and treatment decisions. While [18F]-fluorodeoxyglucose positron emission tomography/computed tomography ([18F]-FDG PET/CT) is a widely accepted oncological imaging tool, its use in bladder cancer is limited due to urinary excretion of FDG,

which can obscure lesions within the urinary tract. Fibroblast activation protein inhibitor (FAPI) PET/CT has recently emerged as a promising alternative. By targeting FAP-expressing tumor-associated fibroblasts and being independent of glucose metabolism, [68Ga]-FAPI PET/CT achieves low background uptake, improving lesion contrast and potentially increasing diagnostic accuracy. Previous studies have demonstrated improved lesion detection and tumor-to-background ratios with [68Ga]-FAPI compared to FDG PET/CT in bladder cancer patients. This study aimed to assess the diagnostic performance of [68Ga]-FAPI PET/CT in bladder cancer and compare its ability to detect lesions with that of [18F]-FDG PET/CT. ***Materials and Methods:*** In this single-center prospective study, 25 patients with histologically confirmed urothelial carcinoma of the bladder were enrolled. All patients were initially referred for [18F]-FDG PET/CT for purposes of staging, restaging, or treatment response evaluation. Each patient then underwent a [68Ga]-FAPI PET/CT scan within 7 days, with no intervening therapy. Lesion detectability was compared between the two modalities across primary tumors, lymph nodes, lung nodules, and bone lesions using SUVmax values and total number of lesions. Exclusion criteria included secondary malignancies, concurrent prostate cancer, pregnancy, or lack of consent. ***Results:*** [18F]-FDG PET/CT demonstrated significantly higher SUVmax values in primary tumors (10.07 ± 7.49 vs. 7.68 ± 7.32; p = 0.007) and lymph nodes (5.00 ± 5.02 vs. 3.30 ± 3.94; p = 0.031) when compared to [68Ga]-FAPI PET/CT. However, no statistically significant differences were found in detection of lung nodules (p = 0.180), bone lesions (p = 0.655), or overall lesion counts (2.12 ± 1.30 vs. 1.92 ± 1.29; p = 0.170). ***Conclusion:*** Although [18F]-FDG PET/CT remains more sensitive for detecting primary and nodal lesions, [68Ga]-FAPI PET/CT offers comparable performance in identifying lung and bone metastases. With its low background activity, FAPI PET/CT presents as a promising complementary imaging technique in urothelial carcinoma. Further research with larger patient cohorts is warranted to validate these findings.

EP-0545

^{18}F-FDG PET/CT in Suspected Paraneoplastic Syndromes: Clinical and Imaging Correlation

A. Mestre Fusco*, S. Abouzian, D. A. López-Mora, L. Lozano-Murgas, J. C. Martín-Miramón, A. A. Rodríguez-Revuelto;*
Parc Taulí Hospital Universitari, Sabadell, SPAIN.

Aim/Introduction: ^{18}F-FDG PET/CT employed in patients with paraneoplastic syndrome, which often presents with toxic syndrome and a range of neurological, dermatological, endocrine, or hematological symptoms, remains challenging. This study aims to determine the prevalence of ^{18}F-FDG PET/CT findings in this patient population and evaluate the sensitivity and the specificity. Additionally, it seeks to analyze the relationship between ^{18}F-FDG PET/CT findings and tumor markers, acute-phase reactants, and findings from prior conventional imaging. ***Materials and Methods:*** Fifty-two patients (27 women, 25 men; mean age: 64 y/o; range: 39-89) with toxic syndrome (n=26) or other paraneoplastic symptoms (n=21) were prospectively included in the study from October 7, 2024, to April 4, 2025. All patients underwent ^{18}F-FDG PET/CT. Prior laboratory tests (acute-phase reactants, tumor markers, specific antibodies [anti-GAD, anti-HLA, ANA, ANCA, p155, anti-CV2, RS3-PE, anti-RF, anti-TPO, MD5, RO52, antineuronal]), conventional imaging (CT, MRI, ultrasound, or scintigraphy), and pathological findings were analyzed. ***Results:*** Toxic syndrome was present in 50% of patients (n=26), with or without additional symptoms, while the remaining 50% (n=26) presented exclusively with neurological, dermatological, endocrine, or hematological symptoms (e.g., dermatomyositis, sclerodermiform lesions, purpura, polymyalgia, encephalitis, sclerosis, pericarditis, pleural effusion, hemoptysis, myelitis, stiff-person syndrome, panhypopituitarism, vasculitis). Conventional imaging was performed in 71% of cases (n=37), all with negative findings, while it was not performed in 29% (n=15). Positive autoantibodies were detected in 39% (n=20), elevated acute-phase reactants in 35% (n=18), and tumor markers in 19% (n=10). ^{18}F-FDG PET/CT identified a primary tumor in 9 out of 52 patients (17%), with negative findings in 43. In 44% of patients (4 out of 9) with tumor markers the ^{18}F-FDG PET/CT demonstrated cancer. Biopsy confirmed malignancy in all PET-positive cases (lung, pleura, prostate, urinary tract, lymphoma, myeloma, colon, seminoma). One false-negative ^{18}F-FDG PET/CT case (gastric linitis plastica) was identified. These findings correspond to a 90% sensitivity and 100% specificity for ^{18}F-FDG PET/CT. No differences were found between ^{18}F-FDG PET/CT results and prior imaging or acute-phase reactants, tumor markers and antibodies. ***Conclusion:*** The prevalence of ^{18}F-FDG PET/CT positivity in patients with paraneoplastic syndrome was 17%, consistent with existing literature, with high sensitivity and specificity. Although positive autoantibodies, elevated acute-phase reactants, and tumor markers were frequently observed, no correlation was found between these biomarkers and ^{18}F-FDG PET/CT findings. These results underline the diagnostic value of ^{18}F-FDG PET/CT in selected cases, but its definitive role in the diagnostic algorithm for paraneoplastic syndromes remains to be clearly defined.

EP-0546

Prospective Evaluation of ^{68}Ga-Trivehexin in Solid Tumors: A Pan-Cancer Study in Comparison with ^{18}F-FDG PET/CT

L. Li*, H. Wu, Z. Liu, C. Li, Y. He;*
Department of Nuclear medicine, Zhongnan Hospital, Wuhan University, Wuhan, CHINA.

Aim/Introduction: Integrin αvβ6, a biomarker overexpressed in aggressive epithelial malignancies but absent in healthy tissues, drives metastasis and correlates with poor prognosis. While ^{18}F-FDG PET/CT faces specificity challenges, the αvβ6-targeted tracer ^{68}Ga-Trivehexin demonstrates superior tumour-to-background contrast in pilot studies. This study aimed to: (1) compare the diagnostic performance of the αvβ6-targeted tracer ^{68}Ga-Trivehexin with ^{18}F-FDG PET/CT across solid tumors, and (2) explore the correlation between ^{68}Ga-Trivehexin uptake and αvβ6 expression. ***Materials and Methods:*** In this single-center trial, 61 treatment-naïve patients with suspected/confirmed solid tumors underwent sequential ^{68}Ga-Trivehexin and ^{18}F-FDG PET/CT within 72 hours. Final diagnoses were confirmed by histopathology or ≥6-month follow-up. Quantitative parameters (SUVmax, SUVpeak, SUVmean) and tumor-to-background ratios (T/L, T/B) were compared using paired t-tests. αvβ6 expression was assessed via immunohistochemistry (IHC) in 26 surgical specimens. The study protocol was approved by the institutional ethics committee. ***Results:*** In a cohort of 61 patients with diverse solid tumors (14 anatomical sites, 19 subtypes), ^{68}Ga-Trivehexin demonstrated comparable overall lesion detection to ^{18}F-FDG (94.7% vs. 96.1%, p=0.68), with a trend toward improved primary tumor identification (69 vs. 64 lesions). Notably, ^{68}Ga-Trivehexin exhibited significantly higher tumor-to-background contrast, reflected in elevated tumor-to-liver ratios (7.3 ± 2.1 vs. 2.4 ± 0.9, p<0.001), particularly in αvβ6-rich pancreatic carcinomas (SUVmax: 9.4 ± 2.1 vs. 5.8 ± 1.7, p<0.001). Despite lower SUVmax in metastatic lesions (4.2 ± 1.1 vs. 7.5 ± 2.3, p<0.001), ^{68}Ga-Trivehexin maintained diagnostic utility through higher tumor-to-liver ratios (5.9 ± 1.7 vs. 2.6 ± 0.9, p<0.001). Crucially, ^{68}Ga-Trivehexin outperformed ^{18}F-FDG in specificity (92% vs. 68%, p<0.001), correctly reclassifying 78% (32/41) of inflammatory lesions misdiagnosed by ^{18}F-FDG. Additionally, A trend toward correlation was observed between αvβ6 expression in primary tumor lesions and both SUVmax and SUVpeak derived from ^{68}Ga-Trivehexin (r = 0.466 and 0.441, respectively, all p < 0.05). ***Conclusion:*** ^{68}Ga-Trivehexin PET/CT provides αvβ6-targeted imaging with enhanced tumor specificity

and inflammation discrimination compared to ^{18}F-FDG. Its high contrast across diverse malignancies supports potential applications in precision staging and therapy guidance.

EP-0547

Serum vascular endothelial growth factor helps identify patients with clear cell renal cell carcinoma who benefit more from [68Ga]Ga-PSMA PET/CT

M. Zhang;
Xijing Hospital, the Fourth Military Medical University, Xi'an, CHINA.

Aim/Introduction: To validate the application of serum vascular endothelial growth factor (VEGF) in the selection and prognosis of patients with clear cell renal cell carcinoma (ccRCC) using 68Ga-PSMA. ***Materials and Methods:*** The analysis encompassed radiological parameters and angiogenesis indicators. The correlation of VEGF and PSMA was evaluated, and the efficacy of VEGF in selecting high PSMA uptake lesions of ccRCC. ***Results:*** 44 patients with ccRCC who had serum VEGF levels assessed prior to [68Ga]Ga-PSMA PET/CT and surgery were included in this study. Serum VEGF was 86.7 ± 34.4 pg/mL, mean SUVmax was 15.3 ± 8.97, TBR (tumor to liver) was 3.25 ± 1.89, VR was 0.32 ± 0.28, median PSMA ICH staining was 2, and median visual score was 2. VEGF was significant different in low (0-1) and high group (2-3) (P=0.029). VEGF was a good predictor of PSMA PET visual score with AUC value of 0.707 (P=0.043), and stratified by the critical value of VEGF, 67.71 pg/mL, the sensitivity and specificity for predicting PSMA visual scores (0-1 vs. 2-3), were 85% and 78%. Patients had high pre-operation VEGF might show high PSMA uptake. 19 patients measured VEGF post-operation and the median of follow-up was 81 days. All patients imaging examination and clinical signs were normal during follow-up time, VEGF of 9 patients increased. Compared the pre-operative PSMA uptake characteristics between VEGF increased and decreased group, SUVmax was no statistically difference (P=0.464), the VR showed significantly difference (P=0.049), patients with increased VEGF had lower VR. ROC curve analysis found that using VR to predict postoperative VEGF changes, with AUC value of 0.750 (P=0.143), the sensitivity and specificity were 50% and 100%. Patients with preoperative VR≤0.42 were likely to have increased VEGF postoperative. VEGF was associated with patient prognosis, and results suggested that patients with low VR (high intra-tumor heterogeneity) may have poor prognosis. ***Conclusion:*** Serum VEGF was indicative of [68Ga] Ga-PSMA PET/CT uptake characteristics for ccRCC. Pre-operative serum VEGF levels have the potential to serve as a screening tool to identify patients who are more likely to benefit from PSMA imaging, and VR demonstrated potential as a prognostic predictor for tumor risk.

EP-0548

The Impact of a Short-Time Fasting on Gastrointestinal Uptake in ^{99m}Tc-FAPI-46 Scintigraphy: Mitigating Interpretation Pitfalls

N. Raeisi, *A. Saber Tanha, K. Aryana;*
Nuclear Medicine Research Center, Mashhad University of Medical Sciences, Mashhad, IRAN, ISLAMIC REPUBLIC OF.

Aim/Introduction: This study aims to evaluate the effect of a short fasting period on gastrointestinal tract uptake in patients undergoing ^{99m}Tc-FAPI-46 scintigraphy. ***Materials and Methods:*** In this study, 40 patients who underwent ^{99m}Tc-FAPI-46 scintigraphy were included. The cohort comprised individuals with various cancers, including papillary and medullary thyroid cancer, gastric, colon, breast, nasopharyngeal, bladder, rectal, ovarian and renal cancers, paratesticular rhabdomyosarcoma, cholangiocarcinoma, fibrosarcoma, glioblastoma multiforme, and cancers of unknown primary origin. Whole-body scans were acquired one hour post-injection. Patients were categorized into four subgroups based on fasting status: two main groups—one with fasting and one without—each further divided into subgroups based on the presence or absence of gastrointestinal uptake. ***Results:*** All patients exhibited gallbladder uptake, consistent with normal physiological patterns, except for six individuals with a history of cholecystectomy. In the fasting group, 18 out of 22 patients (82%) demonstrated no or minimal non-tumoral bowel uptake, while in the non-fasting group, only one out of 18 patients (6%) showed similar findings. The uptake patterns in both groups were generally non-focal. Notably, in one patient from the fasting group with no gastrointestinal uptake, a focal uptake in the anterior abdominal wall raised suspicion for bowel uptake or peritoneal deposit. Delayed imaging confirmed the diagnosis of peritoneal deposit, highlighting the importance of the absent bowel uptake in more accurate diagnosis in this case. ***Conclusion:*** Our findings support the recommendation of a short fasting period of approximately 4-6 hours prior to ^{99m}Tc-FAPI-46 scintigraphy, as it significantly reduces radiotracer accumulation in the bowel. This reduction aids in minimizing interpretation challenges, particularly in cases where the cancer's origin may be in abdominal region or when the investigation aims to assess the presence or extent of peritoneal involvement.

EP-29

e-Poster Area

B: Imaging Clinical Studies -> B3 Other Oncological Clinical Study -> B31 Molecular image-guided interventions

EP-0549

Combination of Targeted Axillary Dissection (TAD) and Selective Sentinel Lymph Node Biopsy (SSNGB) in patients with metastatic axillary involvement prior to systemic treatment

M. García Aragón, *A. Suazo Montero, B. Jaramillo López, F. Sebastian Palacid, M. González Soto, M. Alonso Rodríguez, M. Moral Cano, P. Suarez Mansilla, R. Ruano Pérez;*
Hospital Universitario Clínico Valladolid, Valladolid, SPAIN.

Aim/Introduction: To evaluate the combination of 125I seed labeling in pathological lymph nodes prior to neoadjuvant chemotherapy (NAC) with selective sentinel lymph node biopsy (SLNB) in patients eligible for conservative surgery. The objective is to determine the efficacy of these procedures in assessing axillary involvement, their impact on surgical planning, and subsequent therapeutic strategy. ***Materials and Methods:*** Prospective study of 78 patients diagnosed with advanced breast cancer undergoing treatment with NACT, who responded and were candidates for radioguided surgery using 125I seeds. Of these, 45 (mean age 57.65 +/- 10.53 years) had axillary involvement prior to treatment. Two to three days prior to surgery, previously pathological lymph nodes (coil-labeled) that responded were labeled with 125I seeds, and in selected cases, a SLNB was completed.The concordance between the SLN and the 125I seed labeling, the histological type, and the radiological response after NACT were assessed. ***Results:*** 84.4% (38/45) of the patients did not express the HER2 protein; all but two of these were infiltrating ductal, and of these, 22 were luminal B.In 46.7% (21/45) of the patients, only the axilla was marked, and in the remaining 53.3% (24/45), the breast lesion was also marked for conservative surgery.The radiological response was complete in 71.1% (32/45), major partial in 24.4% (11/45), minor partial in 2/45, and no response in the remaining case.In 53.3% (24/45), there was concordance between the SLN and marked adenopathy.The final pathology was negative in 57.8% (26/45) of the lymph nodes, while lymphadenectomy was performed in 19/45. ***Conclusion:*** The results suggest that the

combination of both techniques (DAD and SLNB) is effective in patients with metastatic lymph node involvement prior to NAT before surgery. This strategy helps improve the accuracy of lymph node status and optimize the surgical approach, minimizing the need for extensive lymph node dissection.

EP-0550

Relevance of SPECT/CT in the combined technique of lymphoscintigraphy and axillary labeling with 125-I seeds in breast cancer with axillary response after neoadjuvant chemotherapy

M. García Aragón, *B. Jaramillo López, A. Suazo Montero, C. Gamazo Laherran, F. Sebastian Palacid, M. González Soto, S. Cortes Pérez, M. Moral Cano, R. Ruano Pérez;*
Hospital Universitario Clínico Valladolid, Valladolid, SPAIN.

Aim/Introduction: To evaluate the usefulness of SPECT/CT in the presurgical localization of the sentinel lymph node (SLN), in combination with axillary labeling with 125-I seeds, in patients with pathological lymphadenopathy who have responded to neoadjuvant chemotherapy (NACT). ***Materials and Methods:*** Prospective study of 38 patients with breast cancer with axillary response after NACT. 125-I labeling of the biopsied lymphadenopathy was performed 2-3 days before surgery. Lymphoscintigraphy was performed the day before, acquiring planar images and SPECT/CT. Axillary nodes that uptake 99mTc-nanocolloid were identified, and their concordance with nodes with 125-I seed was evaluated. A gamma detector probe was used in the operating room, selecting the peak of both isotopes. ***Results:*** Drainage was observed in at least 1 SLN in 25/35 (71.43%) cases (50% had >3 nodes). In the 7 cases without drainage despite reinjection, the 125-I-labeled node was removed. Metastasis was present in 5/7 cases, and lymphadenectomy was performed (positive in 4/5).SPECT-CT showed concordance between the SLN and the 125-I-labeled node in 60.7% (17/28).At least 3 nodes were removed in the operating room: the seed-labeled node and 2 or 3 with activity (99mTc+).In 64.3% (18/28), the result was negative for metastasis in the removed nodes, and lymphadenectomy was not performed. Lymphadenectomy was performed in 35.7% (10/28), and was positive in other lymph nodes (7 cases). There was concordance (125I and 99mTc positive) in 5/12; only the 125I-labeled lymph node was metastatic in 6/12; only the 99mTc-labeled lymph node was metastatic in 5/12 cases.The 125I seed was recovered in all cases. ***Conclusion:*** SPECT/CT allows assessment of the concordance of the sentinel lymph node imaged with seed-labeled lymph nodes, facilitating preoperative planning. The combination of both techniques is the best strategy for staging advanced breast cancer after NACT treatment.

EP-0551

Implementation and Outcomes of the ROLL Technique in Radioguided Surgery

Y. Delisau[1], *M. Velasco-Nuño*[1], *S. Alfonso*[2], *A. Giménez*[2], *I. Pérez*[3], *I. Casado*[3], *J. Duch*[1], *M. Calls-Calahorro*[1], *P. Stefaneli*[1], *B. Serrallonga*[1], *D. Selva*[2], *G. Guzmán*[1], *V. Camacho*[1], *A. Flotats*[1];
[1]*Nuclear Medicine Department, Hospital de la Santa Creu i Sant Pau, Barcelona, SPAIN,* [2]*Radiology Department, Hospital de la Santa Creu i Sant Pau, Barcelona, SPAIN,* [3]*General Surgery Department, Hospital de la Santa Creu i Sant Pau, Barcelona, SPAIN.*

Aim/Introduction: To analyse our experience with the ROLL (Radioguided Occult Lesion Localization) technique for the surgical localization of lesions. ***Materials and Methods:*** This retrospective study included 67 patients (35 women and 32 men; mean age: 62.6 years) who were candidates for radioguided surgery using the ROLL technique for the localisation of pulmonary and extrapulmonary lesions (including lymph node lesions, suspected tumour recurrences, and parathyroid adenomas). Radiotracer placement was performed by injecting [99m]Tc-albumin macroaggregates (37-111 MBq) under ultrasound or computed tomography guidance. SPECT/CT imaging was used to confirm radiotracer localisation. A hand-held or laparoscopic gamma probe was used intraoperatively to detect the radioactive signal and guide lesion excision. The analysis included lesion size and accuracy of radiotracer placement (intralesional vs. perilesional). Procedural complications, intraoperative localisation success, and surgical complications were recorded. ***Results:*** The ROLL procedure was successfully completed in 65 patients. In 2 patients with pulmonary lesions, complete radiotracer placement was not possible due to procedural complications. A total of 67 lesions were marked: 35 pulmonary and 32 extrapulmonary (including 23 lymph node lesions, 6 suspected tumour recurrences, and 3 parathyroid adenomas). Two patients had two lesions each. All targeted lesions were successfully localised intraoperatively. The mean lesion size was 11.2 mm for pulmonary lesions and 15.1 mm for extrapulmonary lesions. Radiotracer placement was intralesional in 54 lesions (81% overall; 74% of pulmonary and 87% of extrapulmonary lesions) and perilesional in 13 lesions (19% overall; 26% of pulmonary and 13% of extrapulmonary lesions). In the pulmonary lesion subgroup, 5 patients experienced significant procedural complications (pneumothorax), preventing completion of the procedure in 2 of them. No significant procedural complications were observed in 12 patients (10 with minimal asymptomatic pneumothorax and 2 with pleural contamination by the radiotracer). No intraoperative complications were reported. In the extrapulmonary lesion subgroup, no significant procedural complications were observed. One intraoperative complication (carotid artery injury) was reported. ***Conclusion:*** The ROLL technique has been successfully implemented in our institution as a reliable method for preoperative lesion marking and surgical localisation. It has demonstrated a high rate of accurate intralesional placement and intraoperative identification, with a low rate of complications.

EP-0552

Radioguided Localization of Non-palpable Breast Lesions Using I-125 Radioactive Seeds: Initial 5 Months Experience

P. Paez Vargas, *R. Salvador-Arthur, G. Martinez-Arias, M. Parra-Rina, A. L. Tardin-Cardoso, D. Nogueira-Souto, P. Razola-Alba, M. M. Delgado-Castro, L. Cáncer-Garza, T. Escalera-Temprado, A. Andres-Gracia;*
Hospital Clinico Universitario Lozano Blesa, Zaragoza, SPAIN.

Aim/Introduction: Radioguided localization of non-palpable breast lesions with I-125 seeds has emerged as a novel alternative to other techniques, such as hookwire localization.I-125 seed use has demonstrated clear advantages, such as patient comfort, better surgical planning, improved cosmetic outcomes, and lower rates of positive margins and re-excision. The aim of this study was to assess the usefulness of I-125 seeds in the radioguided localization of non-palpable breast lesions, taking into account the rate of margin positivity and re-excision. ***Materials and Methods:*** Descriptive analysis of patients with non-palpable breast lesions who underwent preoperative marking with I-125 seed under ultrasonographic guidance over a 5-month period. These patients underwent lumpectomy guided by gamma probe detection of the I-125 seed. The presence of the seed was verified through specimen radiography in order to assess the need for margin widening during the same surgical procedure. The utility of the technique was evaluated by calculating the rate of margin positivity through histopathology and the rate of surgical reinterventions. These results were compared with those published in the literature. ***Results:*** 49 patients were analyzed, median age of 61 years (44-83 years). A total of 60 I-125 seeds were implanted: 58 in non-palpable lesions in patients with a previous diagnosis of breast cancer (96.67%), 1 in a phyllodes tumor (1.67%) and 1 in a lesion with atypical ductal hyperplasia (1.67%). After

radioguided lumpectomy and pathological analysis of the surgical specimens, 77.55% of the samples had clear margins, whereas 22.45% had involved margins. In this last group of patients, 3 (27.27%) underwent a second surgical procedure, and margin enlargement was perfomed in 8 (72.73%) patients during the same surgical procedure These results are similar to those reported in previous studies, where the rate of involved margins was 5.5% for I-125 seeds vs 7.8%in the case of wire guidance, and the rate of reinterventions was 13.9% vs 18.9%, respectively.(1). ***Conclusion:*** Our preliminary results support the feasibility and potential benefits of I-125 seed localization in reducing the incidence of involved margins and reoperations in patients with non-palpable breast lesions. Further studies with larger cohorts and direct comparisons with conventional techniques are necessary to validate these findings. ***References:*** 1. Taylor DB, Bourke AG, Westcott EJ, Marinovich ML, Chong CYL, Liang R, et al. Surgical outcomes after radioactive 125I seed versus hookwire localization of non-palpable breast cancer: a multicentre randomized clinical trial. British Journal of Surgery [Internet]. 2020 Dec 23;108(1):40-8. Available from: https://doi.org/10.1093/bjs/znaa008.

EP-0553

Intraoperative Radiolabelling of Pulmonary Nodules Using Electromagnetic Navigation Bronchoscopy

L. León Ramírez[1], *C. González Roiz*[2], *M. zapardiel*[1], *E. Fernández*[1], *C. Fraile*[1], *A. Berardinelli*[1], *P. Dauden*[1], *G. Cuesta*[1], *M. Vaillant*[1], *M. Cabrera Martin*[1], *S. Vidal-Sicart*[3];
[1]*Hospital Clínico San Carlos, Madrid, SPAIN,* [2]*Hospital Puerta del Sur, Madrid, SPAIN,* [3]*Hospital Clínic de Barcelona, Barcelona, SPAIN.*

Aim/Introduction: The diagnostic and therapeutic management of peripheral pulmonary nodules remains a clinical challenge, particularly in cases involving small, non-palpable lesions in anatomically complex regions. Electromagnetic navigation bronchoscopy (ENB) allows access to peripheral areas of the lung that are beyond the reach of conventional bronchoscopy. ROLL, a technique widely validated in breast oncology, has been successfully adapted for pulmonary applications. This study describes the technical application of radioguided localisation usingENB to facilitate minimally invasive resection of pulmonary nodules. ***Materials and Methods:*** A prospective, observational, single-centre study was conducted between 2022 and 2025. A total of 36 patients, older than 18 years, who required minimally invasive pulmonary resection with radioguided localisation were included. The marking procedure was performed intraoperatively under general anaesthesia using bronchoscopy and electromagnetic navigation. A dose of 37-185 MBq of 99mTc-MAA was administered. Resection was performed via VATS or thoracotomy, with intraoperative localisation guided by gamma probe and portable gamma camera. ***Results:*** The mean age of patients was 64.3 years (range: 21-86). Male gender represented 76% of the cohort.The mean size of the nodules was 23.6 mm (range 5 -25mm). A 100% intraoperative localisation rate was succesfull in all cases. No procedure-related complications were observed. ***Conclusion:*** Intraoperative radiolabelling with ENB is a safe and effective technique for localising challenging pulmonary nodules. It enables appropriate resection margins, reduces complications, and enhances surgical efficiency. This approach is proposed as a viable alternative to percutaneous techniques in selected patients. ***References:*** Ho ATN, et al. Pulmón. 2023;201(1):85-93.Krochmal R, et al. Experto Rev Respir Med. 2014;8(6):677-91.Ichinose J, et al. Ann Thorac Cirugía. 2013;96(4):1203-8.Lenglinger FX, et al. AJR Soy J Roentgenol. 1994;163(2):297-300.Sancheti MS, et al. Ann Thorac Surg. 2014;97(6):1914-8.Manca G, et al. Clínica Nucl Med. 2017;42(12):e498-503.Mariolo AV, et al. J Thorac Dis. 2021;13(7). Dendooven P, et al. Eur J Cardiothorac Surg. 2013;43(3):645-59. Finley RJ, et al. Tórax. 2014;69(Supl. 1):i36-41.Galetta D, et al. Eur J Nucl Med Mol Imágenes. 2017;44(1):123-31.Schmid RA, y col. J Nucl Med. 2015;56(1):106-10.Annema JT, et al. Lanceta Oncol. 2010;11(8):762-8.Gould MK, et al. Chest. 2013;143(5 Suppl):e93S-120S.Detterbeck FC, et al. Chest. 2013;143(5 Suppl):7S-37S.Kim HY, et al. Radiología. 2014;270(3):829-36.

EP-0554

HPA Axis Activation Evaluated by ^{18}F-FDG PETCT in Lung Cancer: From Clinical Discovery to Preclinical Validation

M. Liang[1,2], *C. Cui*[1], *X. Li*[1], *J. Guo*[3], *C. Yan*[3,2], *Z. Wu*[3,2];
[1]*Shanxi Medical University, Taiyuan, CHINA,* [2]*Collaborative Innovation Center for Molecular Imaging of Precision Medicine, Taiyuan, CHINA,* [3]*Department of Nuclear Medicine, First Hospital of Shanxi Medical University, Taiyuan, CHINA.*

Aim/Introduction: This study aimed to evaluate hypothalamic-pituitary-adrenal (HPA) axis activity in lung cancer patients using ^{18}F-FDG PET/CT and access the potential of HPA axis as a therapeutic target. ***Materials and Methods:*** Clinical data and ^{18}F-FDG PET/CT from 151 lung cancer patients and 94 healthy controls were retrospectively analyzed. Metabolic activity in HPA-associated organs (brain, pituitary, adrenal glands, thyroid, gonads, muscle, and fat) was compared. Spearman's correlation and Kaplan-Meier analyses assessed HPA axis impact on prognosis. To further verify the effect of HPA activity on lung cancer, an A549 lung cancer mouse model was established and treated with chemotherapy, propranolol and combination therapy. Tumor size, glucose metabolism, and motor function were evaluated. ***Results:*** Lung cancer patients exhibited higher SUVmax, SUVmean, and MTV in adrenal glands, gonads, muscle, fat, and pituitary compared to controls ($P<0.05$). Hypermetabolism in subthalamic nuclei, thalamus, and amygdala, and hypometabolism in frontal gyri and insula were observed. SUVmean of bilateral adrenal glands independent risk factor for lung cancer prognosis. In mice, combination therapy showed improved body weight, motor function, and decreased glucose metabolism compared to chemotherapy alone ($P<0.05$). ***Conclusion:*** ^{18}F-FDG PET/CT imaging revealed increased metabolic activity in HPA axis-related organs among lung cancer patients, particularly in the adrenal glands and may worsen prognosis. Preclinical models demonstrated improvement in overall survival using combination of β-blockers with chemotherapy in tumor-bearing models which highlight the potential of HPA axis as a therapy target in lung cancer. ***References:*** 1. Diehl JN, Khoury AL, Brickey JA, Awe AM, Agala CB, Mody GN, et al. Serious mental illness prolongs hospital admission following lung cancer resection. J Thorac Dis. 2024;16:8450-60. doi:10.21037/jtd-24-762.2. Reznik E, Torjani A. Mechanisms of stress-attributed breast cancer incidence and progression. Cancer Causes Control. 2024;35:1413-32. doi:10.1007/s10552-024-01884-2.3. Diehl JN, Khoury AL, Brickey JA, Awe AM, Agala CB, Mody GN, et al. Serious mental illness prolongs hospital admission following lung cancer resection. J Thorac Dis. 2024;16:8450-60. doi:10.21037/jtd-24-762.

EP-0555

125I seeds implantation in malignant-suspected ^{18}F-FDG PET/CT lymph nodes. Histopathological correlation.

E. Domínguez Polanco, *J. Villa-Palacios, A. Piñeiro Donis, L. Cagua Ruiz, E. Triviño-Ibáñez, A. Salmerón Ruiz, N. Muñoz Pérez, C. Ramos-Font;*
Hospital Universitario Virgen de las Nieves, Granada, SPAIN.

Aim/Introduction: To evaluate the malignant predictive value of ^{18}F-FDG PET/CT in patients with suspected malignant lesions and their labelling with 125I seeds towards radioguided surgery. ***Materials and Methods:*** Observational, prospective, and analytical study that included a cohort of patients with suspicious lesions, referred to the Nuclear Medicine department for ^{18}F-FDG PET/CT and subsequent labelling with 125I seeds. Data from both procedures and their histopathological correlation

after surgery were collected. Finally, we analyzed the malignant predictive value of the metabolic rate quantitative parameters through binary logistic regression analysis. ***Results:*** A total of 41 patients were included (mean age: 52.56±16.83 years, 51.2% women). They had a history of previous neoplastic pathology in 17/41 (41.5%) cases. Except for two cases, these were suspected malignant lymphadenopathies. The most frequent site was latero-basocervical 21/41 (51.2%), followed by axillary 11/41 (26.8%) and inguinal location 7/41 (17.1%). The 125I seed was placed inside the lymph node in 36/41 (87.8%) of the cases. The pathological result was malignant in 10/41 cases (24.4%). 87.8% (36/41) of the cases had undergone a previous PET/CT, in which the lymph node was identified with a mean SULpeak of 2.90±1.87. The only factor associated with malignancy in the lymph node pathological result was the SULpeak (OR1.65, p= 0.028). No complications related to the surgical removal of the lymph node or the extraction of the 125I seed were recorded. ***Conclusion:*** Radioguided surgery with 125I seeds is a feasible and safe procedure that allows accurate diagnosis of suspected lesions and minimizes the risk of reinterventions. When selecting the lesion, the metabolic rate quantified in the ^{18}F-FDG PET/CT constitutes the only factor associated with the probability of malignancy.

EP-0556

Safety and Diagnostic Yield of ^{18}F-FDG PET/CT-Guided Biopsy in Solitary Pulmonary Nodule

D. Saraswat, *P. Malik, R. Kumar, B. R. Mittal;*
Post Graduate Institute of Medical Education and Research, Chandigarh, INDIA.

Aim/Introduction: A solitary pulmonary nodule (SPN) is a single, well-defined pulmonary opacity with a diameter of <3 cm surrounded by normal lung tissue that is not associated with atelectasis or adenopathy. Positron-emission tomography-computed tomography (PET/CT) primarily used for solid nodules ≥8 mm, assesses metabolic activity, aiding accurate targeting and reducing diagnostic errors. PET/CT-guided biopsy improves sample quality and reduces repeat procedures. We report the first extensive experience with ^{18}F-FDG-PET/CT-guided biopsies of SPNs, achieving accurate histopathological diagnoses through precise metabolic targeting. ***Materials and Methods:*** In this single-centre retrospective study, data from 80 patients with SPN who underwent ^{18}F-FDG-PET/CT between 2018 and March 2025 was analysed. FDG avidity more than mediastinal blood pool was considered as PET-positive and less than that was defined as PET-negative. Fifty-six patients were PET-positive and subsequently underwent PET/CT-guided-biopsy. The remaining 24 patients were monitored according to the Fleischner Society guidelines. Procedure-related complications and histopathologic outcomes were documented to assess the safety and diagnostic yield of the biopsy approach. ***Results:*** A total of 56 participants (mean age 56.8 ± 13.3 years; 39 males and 17 females) underwent PET/CT-guided-biopsy. The mean lesion size was ~ 1.8 × 1.5 cm, with a mean SUVmax of 10.8 ± 6.7. Histopathological evaluation revealed primary lung malignancy in 29 patients (51.8%), metastatic lesions in 13 (23.2%), and infective aetiologies in 9 (15%). Three patients demonstrated no histological evidence of malignancy or infection, while single cases of sarcoidosis and hamartoma were also identified. Among the primary lung malignancies, adenocarcinoma was the most common histologic subtype (16/29; 55.1%), followed by squamous cell carcinoma (8/29, 27.5%), small cell carcinoma (2/29), adenosquamous carcinoma (1/29), neuroendocrine tumour (1/29), and angiosarcoma (1/29). Among patients with metastatic disease, the most frequent primary sites included the hypopharynx (2/13), tongue (2/13), anorectum (2/13), and cervix (2/13). Post-procedural complications were observed in 2 of 56 patients (3.6%), comprising mild pneumothorax in one and moderate pneumothorax in another. Both cases were managed conservatively without the need for intervention. ***Conclusion:*** This study highlights the clinical utility and diagnostic accuracy of ^{18}F-FDG-PET/CT-guided-biopsy in the evaluation of SPNs. By enabling precise metabolic targeting, this technique enhances histopathological yield, improves subtype classification, and reduces the need for repeat procedures. The low complication rate further supports its safety and feasibility. These findings underscore the value of incorporating PET/CT-guided biopsy into routine clinical practice, particularly for FDG-avid SPNs, where conventional image-guided techniques may be limited by lesion size and metabolic heterogeneity.

EP-0557

Characterisation of a Fluorescent Dye Library using a Dual-Labelled PSMA-617-based Tracer

P. Minges[1,2,3], *L.-C. Domogalla*[1,2], *B. Thomas*[4], *N. Steinacker*[1,2], *H. Müller*[4], *M. Sulewska*[1,2], *A. Dietzel-Schaarschmidt*[5], *P. Meyer*[1,2], *M. Eder*[1,2], *A.-C. Eder*[1,2];
[1]*University Medical Center Freiburg, Freiburg im Breisgau, GERMANY,* [2]*German Cancer Consortium (DKTK), Freiburg im Breisgau, GERMANY,* [3]*University of Freiburg, Freiburg im Breisgau, GERMANY,* [4]*XION GmbH, Berlin, GERMANY,* [5]*Henke-Sass, Wolf GmbH, Tuttlingen, GERMANY.*

Aim/Introduction: In the field of dual-labelled tracers and fluorescence-guided surgery (FGS), ICG and IRDye800CW have been established as the most commonly used dyes. However, fluorescent dyes have continued to evolve and more photostable dyes with higher quantum yields and diverse chemical characteristics are now available. In order to investigate the suitability of such new dyes for potential clinical application, a library of dyes was conjugated to a PSMA-617-based tracer (DP). By characterising these dual-labelled PSMA-617-based hybrid molecules, the aim was to identify a candidate with the most promising pharmacokinetic and optical properties to improve precise real-time feedback during surgery. ***Materials and Methods:*** A library of 20 different dyes was conjugated to a PSMA-617-based PSMA inhibitor. All compounds were subsequently radiolabelled with ^{68}Ga or ^{177}Lu and characterised for serum stability and solubility. Internalisation rates and binding kinetics in LNCaP^{PSMA+} cells were determined. In addition, the pharmacokinetic behaviour was assessed in BALB/c nu/nu mice bearing LNCaP^{PSMA+} xenografts by µPET/MRI at 1h and 2h after injection of 0.5 nmol (2.8 kDa - 3.2 kDa) of the ^{68}Ga-labelled hybrid molecules. Fluorescence was determined ex vivo as well as organ distribution 2 h p.i.. ***Results:*** The three most promising candidates showed serum stability above 95% after 48 h with logD values ranging between -2.5 and -1.8. Internalisation rates and binding affinities decreased by 4-7-fold after dye conjugation (from 2.2 %AA to 0.3-0.6 %AA and from K_i 13.2 nM to 50-80 nM, respectively). In vivo studies revealed different pharmacokinetic profiles depending on the conjugated dye. Two candidates showed rapid clearance 1 h p.i. with high tumour uptake 2 h p.i.: DP-09 (9.14 %ID/g tumour, 26.27 %ID/g kidney) and DP-15 (7.67 %ID/g tumour, 7.68 %ID/g kidney). In contrast, DP-24 showed a slower clearance at 1 h p.i., but three times higher tumour accumulation compared to the others (22.94 %ID/g tumour, 61.97 %ID/g kidney). Only negligible accumulation in background organs was observed. ***Conclusion:*** The three candidates identified were shown to have a promising pharmacokinetic profile after conjugation with the fluorescent dyes, making them suitable for further investigation. With improved photostability and higher quantum yields compared to ICG and IRDye800CW, the selected candidates may lead to an advantage in FGS.

EP-0558

Needle in the hotspot: Integrating SUVmax, Necrosis, and Technical Factors in PET-CT-Guided Biopsies

S. Shamim, *B. Jain, Y. Khandelwal, S. Rastogi, P. Baberwal, P. Naranje, A. S. Bhalla, N. Kumar;*
AIIMS New Delhi, Delhi, INDIA.

Aim/Introduction: PET-CT-guided biopsies have emerged as a pivotal tool in oncological diagnostics, offering real-time metabolic and anatomical guidance. This study aimed to evaluate the diagnostic yield, scan characteristics, and technical considerations associated with PET-CT-guided biopsies in a cohort of 68 patients with suspicious lesions. ***Materials and Methods:*** This retrospective analysis included 68 patients who underwent percutaneous PET-CT-guided biopsies with ^{18}F FDG from March 2023 to April 2025, carried out using robotic positioning sytem (MAXIO) and semiautomatic biopsy gun, 18G for soft tissue lesions and 11G for bony lesions. Parameters recorded included age, gender, lesion site, lesion size, Standardized Uptake Value (SUV), necrosis, depth from skin, access type (oblique/direct), complications, and final histopathological diagnosis. Descriptive statistics and predictive modeling were employed to assess patterns and distributions. ***Results:*** The study population had a near-equal gender distribution (55% male, 45% female) with a mean age of approximately 48 years. The most common biopsy sites were the abdomen and thorax. Tissue sampling was successful in 88.2 % cases. Malignancy was confirmed in 38 cases (55.9%), followed by inflammatory lesions in 10 cases (14.7%), normal tissue in 8 cases (11.8%), and repeat biopsies in 8 cases (11.8%), benign tumor and necrotic tisue was also reported in individual cases. Higher SUV and necrosis was commonly reported in malignant lesions. The mean lesion size was 2.86 cm, and the average depth from skin was 4.18 cm. Necrosis was observed in 26 lesions (38.3%). The average SUV was 10.67, with 49 patients (72.1%) showing SUV > 5—most of which correlated with malignant pathology. Oblique access was used in 16 cases (23.5%), while direct or perpendicular access was preferred in 52 (75%). Minimal complications were reported, and most biopsies yielded sufficient tissue for diagnosis. Lesions requiring repeat biopsies tended to have lower SUV, deeper location, or higher necrotic components. Samples requring repeat sampling or non-diagnostic cases, showed more necrosis and higher target depth suggesting their potential impact on sample adequacy. ***Conclusion:*** PET-CT-guided biopsy demonstrates high diagnostic accuracy, particularly for metabolically active lesions. Technical parameters such as lesion depth, necrosis, and access angle may influence tissue adequacy and the need for repeat procedures. With minimal complication rates, PET-CT guidance offers a safe, effective approach for targeting challenging lesions.

References: Stefanidis K, Bellos I, Konstantelou E, et al. (2024). "^{18}F-FDG PET/CT anatomic and metabolic guidance in CT-guided lung biopsies." European Journal of Radiology, 171, 111315.

EP-0559

Robotic arm-assisted, FDG-PET/CT guided percutaneous core-needle biopsies: Initial experience with inclusion of Pyrexia of unknown origin (PUO) patients.

B. Nayak, *M. Tripathi, S. K. Velliangiri, M. Soneja, N. Nischal, G. Arora, V. Jain, S. Jain, A. Tyagi, A. Kakkar, N. A. Damle, A. Kumar, M. C. Sharma, A. Aravindh, C. Bal;*
All India Institute of Medical Sciences, New Delhi, New Delhi, INDIA.

Aim/Introduction: PET/CT-guided, robotic arm navigated optimal trajectory definition for manual needle placement, offers an opportunity to target metabolically active lesions thus increasing the diagnostic yield. We sought to evaluate the efficacy, feasibility, diagnostic success rate and safety of image guided percutaneous core-needle biopsies performed by robotic arm assisted spatial positioning and orientation. ***Materials and Methods:*** This prospective study included patients who were referred for PET guided biopsies and were found to have FDG-avid lesions which could be accessed for percutaneous core-needle biopsy. The coagulation profile (i.e., platelet count, PT and INR) of each patient was evaluated within 48 hours before the procedure. The study was approved by the Institute of Ethics committee, procedure details, potential risks, benefits, and available alternatives were explained to all patients and written informed consent was obtained from each patients. The patient were injected with a dose of 74-111 MBq (2-3 mCi) of F-18 FDG and positioned on the scanner after 20-30 minutes. Single bed acquisition of both CT and PET images was followed by transfer to the robotic arm positioning system (Maxio, Perfint Healthcare) console, where the fused images were used for defining trajectory to the FDG-avid target lesion along with entry point. Planned needle insertion site was cleaned with betadine and spirit followed by administration of local anesthetic. The Biopsy needle was placed in a needle adaptor in the robotic arm and navigated to the target lesion along the planned path following which the needle-tip position was confirmed using regional low-dose CT. At least four cores were sampled from the lesion and fixed in both formalin (10%) and normal saline before sending them to pathology for histopathology analysis. End-of procedure regional check-CT was taken if indicated. ***Results:*** A total of 81 patients (45 males and 36 females, mean age 49+18.7 years) were included (including 10 patients with previous negative biopsy). The indications for biopsy were broadly categorized into four groups (Table 1) and the sites biopsied (Table 2). Size of lesions varied from 0.9x0.9cm to 5.6x5.7 cm. Minimal bleeding during the biopsy was seen in 3 patients but this was not associated with hematoma formation. No other complications were noted during any procedure. ***Conclusion:*** FDG-PET guided percutaneous biopsies targeting metabolically active lesions performed by robotic arm assisted needle positioning is technically feasible, safe, and effective, ensuring adequate sampling of the target lesions and has potential utility in PUO along-with the neoplastic aetiologies.

EP-30

e-Poster Area

B: Imaging Clinical Studies -> B3 Other Oncological Clinical Study -> B32 Sentinel Node

EP-0560

Sentinel Lymph Node Biopsy Results in Head and Neck Tumors

E. Domínguez Polanco, *A. Piñeiro Donis, J. Villa-Palacios, L. Cagua Ruiz, E. Triviño-Ibáñez, T. Balibrea-Zuñiga, S. Faílde Balea, C. Ramos-Font;*
Hospital Universitario Virgen de las Nieves, Granada, SPAIN.

Aim/Introduction: To analyze the results of patients undergoing sentinel lymph node biopsy (SLNB) with head and neck tumors at the Virgen de las Nieves University Hospital in Granada. ***Materials and Methods:*** Observational and prospective study that included patients with early-stage head and neck tumors (T1 and T2) who underwent SLNB between February 2021 and October 2024. Statistical, technical, imaging parameters and results of the pathological anatomy study were collected. All patients underwent SLNB during the validation period of the procedure and cervical lymphadenectomy was performed in those whose sentinel lymph node was positive. ***Results:*** A total of 80 patients were included (mean age: 66.42±13.98 years, 52.5% men). 62.5% presented well-differentiated squamous cell carcinoma, with ulceration in 70% of cases and cT1 being the most frequent stage (60%). In 18 cases (22.5%), the result of the pathology study of the sentinel lymph node was positive. The false negative rate was 1/17 (5.9%). The factors associated with a higher probability of positive sentinel lymph node, in the binary logistic regression

model, were tumor grade (OR: 3.67, p=0.020) and deep of invasion (DOI) (OR: 1.21, p=0.026). 13.8% (11/80) of patients had a relapse of the disease. The median time to relapse is 44 months. Factors associated with a shorter time to relapse included: a positive result in lymphadenectomy (HR: 5.33; p=0.033) and DOI (hr: 1.28, p=0.011). ***Conclusion:*** Selective sentinel lymph node biopsy is a feasible technique in patients with head and neck cancer, potentially avoiding unnecessary lymphadenectomies, especially in cases with lower tumor grade and DOI.

EP-0561

Sentinel Lymph Node Biopsy as a Reliable Staging Tool Post-Neoadjuvant Chemotherapy in Breast Cancer- A Comparative Study from Northern India

P. Rawat, *M. L. Narayan, F. Huda, M. Negi, N. Chowdhury;*
All India Institute of Medical Sciences, Rishikesh, INDIA.

Aim/Introduction: Sentinel lymph node biopsy (SLNB) is a standard, minimally invasive method for axillary staging in early breast cancer, particularly in treatment-naïve patients. However, its accuracy post-neoadjuvant chemotherapy (NACT) remains under investigation. This study evaluates SLNB's performance in both treatment-naïve and post-NACT patients, focusing on identification rates, nodal positivity, ALND avoidance, and its utility in guiding axillary irradiation. Conducted at a tertiary care center in Northern India, this study also explores SLNB's applicability across varied healthcare settings. ***Materials and Methods:*** A prospective study was conducted on 33 breast cancer patients (mean age 47.0 ± 11.3 years), including 23 post-NACT (AJCC stage I-III C) and 10 treatment-naïve (AJCC stage I-II B) cases. SLNB was performed using a dual-tracer approach: peri-areolar and intra-tumoral injections of 99mTc-sulfur colloid with SPECT/CT imaging and gamma probe localization, complemented by methylene blue dye. Intraoperative frozen section was used to assess SLN metastasis and determine the need for ALND. Outcomes assessed included SLN identification rate, nodal positivity, ALND avoidance, and guidance for post-surgical axillary irradiation. ***Results:*** SLNB demonstrated high identification rates, achieved in 31/33 patients (93.9%) overall—21/23 (91.3%) post-NACT patients and 10/10 (100%) treatment-naïve patients. The dual-tracer approach with SPECT/CT and gamma probe ensured reliable nodal localization. Among post-NACT patients, 43.5% (11/23) achieved a pathological complete response (pCR) in the primary tumor, which did not always correspond to nodal response. For post-NACT cases, SLN metastasis was detected in 18.8% (3/16) of patients, demonstrating SLNB's effectiveness in assessing nodal status after chemotherapy. For treatment-naïve patients, SLN metastasis was identified in 10.0% (1/10) of cases, further highlighting SLNB's role in evaluating nodal involvement in early-breast cancer. SLNB findings guided axillary irradiation planning, enabling node-negative patients to avoid unnecessary treatment while supporting targeted radiation for node-positive cases. The avoidance of axillary lymph node dissection (ALND) was achieved in 82.6% (19/23) of post-NACT patients and 90.0% (9/10) of treatment-naïve patients, significantly reducing surgical morbidity. ***Conclusion:*** SLNB demonstrates high reliability for axillary staging in both treatment-naïve and post-NACT breast cancer patients, with strong identification rates, reduced ALND requirement, and low lymphedema risk. It also effectively guides axillary irradiation, enabling targeted treatment in node-positive cases while minimizing overtreatment. These findings support broader adoption of SLNB in post-NACT protocols, particularly in resource-limited settings. Further large-scale studies are warranted to standardize its use post-NACT.

EP-0562

Sentinel Lymph Node Biopsy in Head and Neck Melanoma Malignum: Our Institutional Experience

N. Kelemen[1], *E. Kristóf*[1], *M. Piroska*[1], *P. Prekopp*[2], *K. Dános*[2], *E. Birtalan*[2], *G. Forgács*[2], *B. Baksa*[1], *T. Györke*[1];
[1]*Semmelweis University, Medical Imaging Centre, Department of Nuclear Medicine, Budapest, HUNGARY,* [2]*Semmelweis University, Department of Otorhinolaryngology, Head and Neck Surgery, Budapest, HUNGARY.*

Aim/Introduction: About 10% to 25% of malignant melanoma is found in the head and neck region. The localization in itself, the complex lymphatic drainage and the surgically challenging anatomy are risk factors for progressive disease. Sentinel lymph node biopsy (SLNB) is recommended as part of staging in order to detect occult nodal metastasis in clinical stage T1b-T4b, N0 and M0. However, precise implementation of SLNB is burdened by several anatomical and technical factors. Our aim was to get a closer insight into the optimal staging procedure, timing, imaging and surgical technique of SLNB through our single-center experience. ***Materials and Methods:*** 77 head and neck melanoma patients with negative primary staging had SLNB in our institute between 2021 and 2024. Staging was performed with ultrasound and in high-risk patients also with FDG-PET/CT. Epidemiological, imaging, intraoperative and histological data were collected and analyzed to establish correlation with SLNB detection rate and progression free survival. Survival related data was compared to a control group (no SLNB, only observation) and literature data. ***Results:*** SLNB was performed in 77 cases (31 female, 46 male, average age: 61 years). Micrometastasis was found in 7 patients (9,1%, stage T2a-T4a; 1 in parajugular and 6 in superficial regions). One macrometastasis was identified. So far, progression was confirmed in 5 cases (6,5%, median follow-up time: 1,8 years); in 2 of those indeterminate lesions were present at staging; and in further 3 cases technical issues limited the SLNB. General surgical success rate was 89% both in one and two day protocol. SLNB was planned but not performed in 9 further patients; in which progression was confirmed in 5 cases so far. ***Conclusion:*** According to our experience, adequate primary staging, proper timing and implementation of SLNB and integrated evaluation with clinical data improves the diagnostic power of SLN scintigraphy and surgical effectiveness. This approach aims personalized patient management strategies and leads to a better patient survival. According to higher rates of superficial lymph node metastasis in the head and neck region, subsequent completion lymph node dissection may not be beneficial in case of a positive sentinel lymph node. Long-term follow-up is needed to further evaluate how progression free survival and overall survival is influenced by SLNB; and to further optimize SLNB protocol.

EP-0563

Hybrid SPECT/CT sentinel node mapping impact in early and post-neoadjuvant breast cancer: our experience

M. Mihaylova[1], *E. Piperkova*[1], *L. Chavdarova*[1], *M. Zaharinov*[1], *V. Mitova*[2];
[1]*USHATO "Prof. Ivan Chernozemski", Department of Nuclear medicine, Sofia, BULGARIA,* [2]*USHATO "Prof. Ivan Chernozemski", Department of Breast surgery, Sofia, BULGARIA.*

Aim/Introduction: Accurate axillary lymph node (ALN) staging in breast cancer (BC) is essential for prognosis and treatment planning. Sentinel lymph node biopsy (SLNB) is considered the gold standard for staging in early BC with clinically negative ALNs and is also increasingly used after neoadjuvant chemotherapy (NACT) to avoid overtreatment. This study aims to assess the efficacy of hybrid SPECT/CT SLN imaging in early BC as well as after NACT, highlighting its diagnostic value and intraoperative success. ***Materials and Methods:*** We retrospectively analysed data of 80 patients with early-stage BC (T1-T2), diagnosed by core-needle biopsy (85%) or lumpectomy (15%), including 17 patients post -NACT, who underwent hybrid SPECT/CT SLN lymphoscintigraphy in our department between January 2024 and March 2025. Histological types included invasive ductal carcinoma (IDC) in 71 patients (1 bilateral), invasive lobular carcinoma in 8, and other in 1. Parameters evaluated: SLN detection by lymphoscintigraphy, lymphatic drainage patterns, surgical SLN detection, histological status, and short-term clinical outcomes. ***Results:*** Hybrid imaging with subsequent SLNB was successful in 77 of 80 patients (96.25% detection rate; mean age 58.03 ± 12.03 years). A single SLN was identified in 58 patients (72.5%), two in 17 (21.3%), and three in

2 (2.5%). Intraoperative SLN identification was successful in 74 patients (92.5%): 1 node (6.3%), 2 nodes (43.8%), 3 nodes (28.7%), 4 nodes (8.8%), and 5 nodes (5%). ALND (>5 nodes) was performed in 6 cases (7.6%). Twenty-seven patients (33.8%) underwent SLNB after NACT—11 with complete tumour response and 15 with partial response and ALN-negative status. SLNB post-lumpectomy was performed in 12 cases (15%). ALN metastases were histologically confirmed in 11 patients (6 macro, 5 micro), including 4 post-NACT cases (2 macro, 2 micro). During the short follow-up period, no cases of recurrence or lymphedema were observed. All patients continued adjuvant treatment according to post-surgical staging and tumour characteristics. ***Conclusion:*** In our study hybrid SPECT/CT-guided SLN imaging demonstrated high detection rates, with supportive data for its feasibility in post-lumpectomy, and post-NACT settings, with consistent intraoperative success, due to the standardized interdisciplinary collaboration in our centre. These results support wider clinical adoption to improve axillary staging accuracy, reduce overtreatment, and enhance patient outcomes in BC care across Bulgaria.

EP-0564

Can SPECT/ CT Lymphoscintigraphy Influence Surgical Approach for Sentinel Lymph Node Biopsy in Head and Neck Melanoma

L. Radosavcev, *M. Rajovic, M. Radulovic, B. Miljus, M. Rabrenovic, L. Kandolf;*
Military Medical Academy, Belgrade, SERBIA.

Aim/Introduction: Surgeons found routine use of SPECT/ CT very useful in operation planning (surgical team, patient s position, extent of incision). Preoperative lymphoscintigraphy in head and neck melanoma patients was important in more accurate localizing the SLN and in determining the relationship with deferent structures of surgical interest. We evaluated potential predictors to SLN metastatic involvement in patients with cutaneous head and neck melanoma. ***Materials and Methods:*** Patients who underwent SLN biopsy for head and neck melanoma between March 2021.and February 2025. were included. Preoperative planar SLN mapping (PL) was performed for all patients (n=56), followed by SPECT/CT (n=46). ***Results:*** Detection rate of SLN was 92.8. (SNL not visualized on preoperative lymphoscintigraphy in two patients, also not found in other two patients on operation). There were no patients with SLN seen only on SPECT/ CT.In total 98 lymph nodes were harvested (range 1-5; median 2 per patient). Nodal basins identified were parotid/preauricular, neck, occipital /postauricular and supraclavicular in 19, 19, 10 and 6 patients respectively. Metastases were found is 19.2 %. Location of primary, number on lymph nodes harvested and drainage to two different basins, were not significantly associated with SLN status. Location of primary associated with drainage to parotid /preauricular region was face, scalp and ear in in 9 ,7 and three patients respectively. Hystopathology sampling revealed parotid gland tissue in 3 out of 19 patients. ***Conclusion:*** Surgeons found routine use of SPECT/CT very useful in operation planning (surgical team, patient s position, extent of incision). Preoperative lymphoscintigraphy in head and neck melanoma patients was important in more accurate localizing the SLN and in determining the relationship with deferent structures of surgical interest.

EP-0565

Standardised Protocol for Radioguided Surgery of Non-Palpable Breast Lesions Using Iodine-125 Seed: Experience at Our Centre

M. Ottino, *P. Azpeitia Hernández, A. Martínez Lorca, O. Ajuria Illarramendi, M. Gutiérrez Guerrero, P. Paredes Rodríguez, T. Navarro Martínez, U. Vera Schmülling, I. Hernández Pérez, A. Torres Consiglieri, E. Pérez de los Ríos, M. Orduña Diez;*
Hospital Universitario Ramón y Cajal, Madrid, SPAIN.

Aim/Introduction: This study describes the multidisciplinary protocol implemented for radioguided surgery in the management of non-palpable breast lesions using iodine-125 (^{125}I) seed localisation, with or without targeted axillary dissection (TAD). The workflow for the safe administration and retrieval of radioactive material is detailed. ***Materials and Methods:*** A retrospective descriptive study was conducted on cases treated between November 2020 and November 2024 that required ^{125}I seed localisation for non-palpable breast lesions. The ^{125}I seed(s) were implanted under ultrasound or stereotactic guidance, with position confirmed by mammography. In TAD cases, an axillary seed was inserted under ultrasound guidance and its location confirmed by SPECT-CT. Preoperative skin marking was also performed.In the operating theatre, the surgeon used a gamma probe for localisation. Surgical specimens containing seeds were radiographed and subsequently sent to the Pathology Department for seed identification and retrieval by the pathologist, with support from the nuclear medicine physician if required. ***Results:*** A total of 556 cases were analysed: 493 (89%) involved a single ^{125}I breast seed, and 63 (11%) involved two seeds. TAD was performed in 17 patients (3%). Correct seed localisation was confirmed in 100% of cases via mammography and/or SPECT-CT. Preoperative skin marking enabled successful intraoperative identification of the sentinel lymph node and seed(s) in 100% of cases, without the need for the nuclear medicine physician to be present in theatre.The pathologist successfully identified the ^{125}I seed in the surgical specimen in 537 cases (97%), with nuclear medicine assistance required in 19 cases (3.5%). ***Conclusion:*** The use of ^{125}I seed localisation has proven to be an effective and safe technique for the accurate identification of non-palpable breast lesions and marked axillary nodes. Detailed preoperative planning and skin marking optimise the surgical procedure and minimise the need for intraoperative assistance from nuclear medicine. These findings support the integration of this protocol into the multidisciplinary approach to breast cancer management.

EP-0566

Sentinel Node Biopsy in Laryngeal Cancer: A Systematic Review and Meta-Analysis

P. Sahafi[1], *R. Sadeghi*[1], *E. Askari*[1], *A. Sahebkari*[1], *M. Ghahraman*[1], *V. Dabbagh*[1], *S. Harsini*[2];
[1]*Ghaem Hospital, Mashhad university of medical science, mashhad, IRAN, ISLAMIC REPUBLIC OF,* [2]*BC Cancer Research Institute, Vancouver, BC, CANADA.*

Aim/Introduction: Sentinel lymph node (SLN) biopsy offers a minimally invasive approach to staging lymph node involvement in laryngeal squamous cell carcinoma (SCC). Despite its adoption in other cancers, its accuracy in laryngeal SCC remains under investigation. This systematic review and meta-analysis evaluates the diagnostic performance of SLN mapping in laryngeal cancer. ***Materials and Methods:*** A systematic search of MEDLINE, Scopus, and Google Scholar was conducted using the keywords "(larynx OR laryngeal) AND sentinel", with no date or language restrictions. Studies reporting SLN detection rates and/or sensitivity in laryngeal SCC were included. A random-effects model was applied for data pooling, and subgroup analyses were performed based on tumor location (supraglottic versus transglottic) and mapping material (radiotracer versus blue dye). Publication bias was assessed using funnel plots and statistical methods. ***Results:*** Nineteen studies, encompassing 366 patients, were analyzed. The overall pooled SLN detection rate was 90.8% (95% CI: 86-94.1), and sensitivity was 88% (95% CI: 81-94). Supraglottic tumors demonstrated superior outcomes (detection rate: 93.7%, sensitivity: 96%) compared to transglottic tumors (detection rate: 84.7%, sensitivity: 71%). Radiotracers significantly outperformed blue dye, with detection rates of 90.8% versus 81.5% and sensitivities of 88% versus 77%. ***Conclusion:*** SLN mapping is a reliable technique for staging laryngeal SCC, particularly for supraglottic tumors, where high detection rates and sensitivity were observed. Radiotracers offer

superior performance compared to blue dye, underscoring their clinical value. These findings support the feasibility and accuracy of SLN biopsy in laryngeal cancer, while emphasizing the importance of tumor location and mapping material.

EP-0567

Accuracy of sentinel node mapping in Marjolin ulcer: Comparison of three different injection techniques

P. Sahafi, *R. Sadeghi, V. Dabbagh;*
Ghaem Hospital, Mashhad University of Medical Science, Mashhad, IRAN, ISLAMIC REPUBLIC OF.

Aim/Introduction: Marjolin ulcer is a specific type of squamous cell cancer that can benefit from the use of lymphoscintigraphy. The purpose of this study was to evaluate 3 different injection techniques for sentinel node biopsy in patients with Marjolin ulcer. ***Materials and Methods:*** Forty-eight patients with Marjolin ulcer (27 male and 21 female) ranging in age from 24 to 85 years were included in our study. Intratumoral (IT), peritumoral (PT) and periscar (PS) tissue injections of radiotracer were done in 9, 10, and 29 patients respectively. Injections were done 2-4 h before surgery. Lymphoscintigraphy was done for mapping the lymphatic drainage. During surgery, lymphatic mapping and sentinel node biopsy was performed using a handheld gamma probe. After harvesting sentinel nodes, regional lymph node dissection was done. ***Results:*** Sentinel node detection rate was higher in the PS group as compared to the IT and PT groups (89.6% vs. 50% and 22.2%) respectively. False negative rate was 0%. Pathologically involved sentinel nodes were detected in 16% of the included patients of our study which led to management change. None of the patients with pathologically non-involved sentinel nodes developed regional lymph node recurrence. ***Conclusion:*** Lymphatic mapping and sentinel node biopsy is feasible in Marjolin ulcer with high detection rate and low false negative cases which by detection of regional lymph node involvement can potentially change the management of patients. Injection site may be an important factor influencing the success of the procedure and injection of the mapping material in the peri-scar normal skin proximal to the lesion is the best technique.

EP-0568

Ex Vivo Sentinel Lymph Node Mapping in Colorectal Cancer Using [99mTc-HMPAO] Patent Blue Liposomes: A Hybrid Radiotracer/Dye Approach

P. Sahafi, *H. Abbasian, K. Sadri, R. Sadeghi;*
Ghaem Hospital, Mashhad University of Medical Science, Mashhad, IRAN, ISLAMIC REPUBLIC OF.

Aim/Introduction: Colorectal cancer (CRC) remains a leading cause of cancer-related morbidity and mortality worldwide, with lymph node (LN) status serving as a critical prognostic factor. Accurate sentinel lymph node (SLN) detection is essential for optimal staging and treatment planning. This study introduces a novel hybrid radiotracer—[99mTc-HMPAO] patent blue liposomes—designed to combine the advantages of visual (blue dye) and gamma probe (radiotracer) detection in a single injection, offering a streamlined and efficient approach for SLN mapping in nuclear medicine. ***Materials and Methods:*** A prospective study was conducted on 40 colorectal cancer patients undergoing surgical resection. Post-resection, the novel radiopharmaceutical—comprising either 99mTc-HMPAO-non-PEGylated liposomes or 99mTc-HMPAO-PEGylated liposomes—was injected peritumorally in an ex vivo setting. SLNs were identified using dual-modality detection: visual confirmation of blue dye and gamma probe quantification of radiotracer uptake. Pathological evaluation was performed to validate findings. ***Results:*** Among the 40 patients—19 (47.5%) with colon cancer and 21 (52.5%) with rectal cancer—SLNs were not found in six cases (15%). Of the remaining 34 cases, 29 (85.3%) showed no SLN involvement, while 5 (14.7%) had pathological involvement. In two cases without SLN involvement, other non-sentinel lymph nodes were affected. The study demonstrated a total detection rate of 85%, with sensitivities of 80% for colon cancer and 50% for rectal cancer. The false negative rate was calculated at 28%. ***Conclusion:*** Patent blue liposome labelled by Tc-99m HMPAO can be used for sentinel node mapping in colorectal cancers with success. Both blue dye visual detection and radiotracer count detection simultaneously can be used by single injection in this technique. Lymphoscintigraphic mapping of SLNs in colorectal cancers using [99mTc-HMPAO] liposomes enhances the accuracy of pathological staging and achieves a notable detection rate of SLNs, particularly in colon cancers.

EP-0569

Tc-99m-nanocolloid scintigraphy in sentinel lymph node detection in patients with a history of conservative resection and prior lymph node biopsy.

A. Velidaki, *S. Episkopopoulou, I. Sevaslidou, I. Vagios, N. Prosotsianiotis, E. Dagrakis, A. Kolindou;*
Laiko General Hospital of Athens, Athens, GREECE.

Aim/Introduction: Breast cancer is the most common malignancy in women with local recurrence occurring in less than 3% in the decade, after conservative resection and radiation. The value of sentinel node approach in breast cancer has been proven in several studies but its role in case of local relapse has not been sufficiently studied. Maybe the biopsy of a new sentinel node, which takes on the role of sentinel, can modify the new treatment. The aim of this study is to investigate whether imaging of a new sentinel lymph node is possible in patients with a history of conservative resection with previous sentinel lymph node biopsy and adjuvant radiotherapy. ***Materials and Methods:*** Twenty seven (27) women were included in this study with an average age of 67 years (38-82). The interval from the end of treatment was at least six months. The technique involved peritumoral injection of 1-2 mCi Tc-99m-nanocolloid. Planar and SPECT images were obtained 15 minutes post injection and the first hot spot of the lymphatic drainage (SLN) was marked on the skin as a guide for the surgeon. Planar and SPECT results were compared to the surgical findings. ***Results:*** Radioisotope administration revealed radiopharmaceutical uptake in a new sentinel node in 78% of patients. In 88% of the cases, the new sentinel lymph node was located in the unilateral armpit, 8% was located in the contralateral armpit while in 1 case (4%) sentinel node was detected at the cervical area. ***Conclusion:*** Tc-99m-nanocolloid scintigraphy is useful for detecting the sentinel lymph node also in patients with a history of conservative resection with previous sentinel lymph node biopsy and adjuvant radiotherapy. This fact will help unnecessary lymph node dissection and its subsequent morbidity even in this group of patients.

EP-0570

Feasibility of Sentinel Lymph Node Lymphoscintigraphy in Cutaneous Head and Neck Squamous Cell Carcinoma

P. Sahafi, *A. Aghaee, K. Sadri, E. Soltani, E. Hasanzadeh Haddad, B. Rasoulian, R. Sadeghi;*
Ghaem Hospital, Mashhad University of Medical Science, Mashhad, IRAN, ISLAMIC REPUBLIC OF.

Aim/Introduction: Non-melanoma skin cancers, particularly squamous cell carcinoma (SCC), are among the most common malignancies worldwide. Risk factors include ultraviolet (UV) exposure, advanced age, immunosuppression, genetic disorders, and exposure to carcinogens. Cutaneous SCC (cSCC) predominantly occurs in the head and neck region and may metastasize to lymph nodes, worsening the prognosis. Accurate diagnosis and staging—using techniques such as sentinel lymph node biopsy (SLNB), lymphoscintigraphy, and blue dye mapping—are crucial. These minimally invasive and highly accurate methods can potentially replace elective neck dissection in clinically node-

negative (cN0) patients. Surgical excision remains the mainstay of treatment. In cases with nodal involvement, neck dissection with or without radiotherapy is recommended. Currently, no consensus exists on the optimal management of high-risk node-negative patients. ***Materials and Methods:*** This prospective study included 42 patients with a primary histopathologic diagnosis of head and neck cutaneous SCC, all without clinical or radiologic evidence of cervical metastasis. After eligibility confirmation, patients underwent tumor resection and elective neck dissection. Prior to surgery, 99mTc-Phytate was injected subcutaneously around the lesion. Lymphoscintigraphy with gamma camera and SPECT/CT was performed to identify sentinel lymph nodes (SLNs). During surgery, a gamma probe was used to localize SLNs, which were then excised and sent for pathological analysis. If metastasis was confirmed in SLNs, neck dissection was completed. Results were verified with both frozen and permanent sections. ***Results:*** Of the 42 enrolled patients, 36 had confirmed cutaneous SCC of the head and neck (27 males, 9 females), all clinically and radiologically node-negative, with a mean age of 68 years. SLNs were successfully detected in 31 of the 36 patients (detection rate= 86.1%). Pathologic evaluation showed SLN involvement in only one patient, who subsequently underwent neck dissection and parotidectomy. In the remaining 30 patients with negative SLNs, no metastases were found in non-sentinel nodes, resulting in a calculated false negative rate of zero. During the two-year follow-up period, no cases of lymphatic recurrence were observed among the patients. ***Conclusion:*** This study suggests that SLNB, due to its high detection rate and sensitivity, is a reliable method for accurate pathological assessment of cervical lymph nodes in patients with clinically node-negative cutaneous SCC of the head and neck.

EP-31

e-Poster Area

B: Imaging Clinical Studies -> B3 Other Oncological Clinical Study -> B33 External Radiotherapy Planning

EP-0571

Added value of ^{18}FDG PET-CT in modern radiotherapy planning for Hodgkin Lymphoma: A Dosimetric Comparison

M. Ben Nasr*, L. Zaabar, S. Yahyaoui, E. Zaidi, A. Mhiri;*
Salah Azaiez Institute of Tunis, Tunis, TUNISIA.

Aim/Introduction: To evaluate the clinical benefit of integrating ^{18}FDG PET-CT into modern radiation therapy (RT) planning for Hodgkin's lymphoma (HL), with a focus on optimizing dose distribution and enhancing protection of organs at risk (OARs)." ***Materials and Methods:*** A retrospective, descriptive study was conducted at the Salah Azaiz Institute (Tunis) including 15 patients (4 children, 11 adults) with histologically confirmed HL treated with combined modality therapy. All patients underwent initial and/or end-of-treatment ^{18}FDG PET-CT. Treatment indications and doses followed the Tunisian MDH 2015 protocol (adults) and EuroNET-PHL-C1 (children). Each patient had a simulation CT in treatment position with personalized immobilization cast. Positioning CT was performed under free-breathing conditions. Two RT plans were generated: a conformational plan using 3D-CRT based on IFRT and contrast CT alone, and an ISRT plan using VMAT incorporating PET-CT data. Target volumes and OARs were delineated by the same radiation oncologist using Eclipse® software. Dosimetric comparisons were performed using dose-volume histograms (DVH), and parameters were statistically analyzed via the Wilcoxon test ($p < 0.05$ considered significant). ***Results:*** The average patient age was 31 years (range: 5-52), with a male predominance (sex ratio 1.5). Stage II HL was most frequent (53%). Five patients had at least two nodal regions involved. The initial PET-CT modified irradiated fields in 4 patients without changing disease staging. Mediastinal RT was performed in six cases, cervical in nine, axillary in three, and one child received supra- and sub-diaphragmatic RT. In total, 30 RT plans were analyzed (15 3D-CRT, 15 VMAT). A total of 75 OARs were contoured. PET-CT and VMAT use led to decreased mean doses in 65% of the structures. V95 to the PTV was significantly improved with PET-based VMAT planning. Compared to 3D-CRT, VMAT significantly reduced heart mean dose and V30, as well as doses to the anterior interventricular artery during mediastinal RT. Lung V20 was also significantly reduced ($p = 0.02$). In women, breast V5 was lower with VMAT. VMAT also reduced spinal cord maximum dose and parotid mean doses (except contralateral parotid in unilateral cervical RT, which was better with IFRT). No significant difference was observed for thyroid or esophagus. ***Conclusion:*** ^{18}FDG PET-CT enhances modern RT planning by allowing more precise targeting and better sparing of OARs. The use of VMAT guided by PET imaging provides significant dosimetric advantages, especially in mediastinal HL, by enhancing cardiac and breast protection and thereby potentially lowering long-term toxicity.

EP-32

e-Poster Area

B: Imaging Clinical Studies -> B4 Cardiovascular Imaging Clinical Study -> B41 Perfusion

EP-0572

Upright and Supine artefact locations in Myocardial Perfusion Imaging using a cardiac-dedicated CZT gamma camera

A. Carradus*[1,2], M. Ulyatt[1], K. Jones[1,2], C. Paterson[1,2], J. Robinson[1,2], A. Laird[1], R. McDade[1], S. Han[1,3];*
[1]DCPB, NHS Greater Glasgow and Clyde, Glasgow, UNITED KINGDOM, [2]College of Medical, Veterinary & Life Sciences, University of Glasgow, Glasgow, UNITED KINGDOM, [3]School of Infection & Immunity, University of Glasgow, Glasgow, UNITED KINGDOM.

Aim/Introduction: Attenuation correction of SPECT-MPIs remains a challenge, particularly as CZT cardiac-dedicated gamma cameras do not typically offer hybrid SPECT/CT imaging. Previous studies have localised common areas of artefact in supine, semi-reclined, and forward-leaning positions[1][2]. This study aims to identify the frequency of localised artefacts in upright and supine positions, and investigate any trends with sex. ***Materials and Methods:*** 100(53F) patients with upright and supine stress MPI were retrospectively individually reported by an experienced operator using a 17 segment polar-map, to give an upright-SSS and supine-SSS. Artefact score was then quantified by subtracting upright-SSS from supine-SSS and vice-versa (i.e. assuming if a defect is present in only one position, it is an attenuation artefact). ***Results:*** The average upright artefact score was 1.65 (F=1.89,M=1.38), and the average supine artefact score was 1.23 (F=0.91,M=1.60). 45% of patients had more artefact on their upright images (F=53%,M=36%), and 36% of patients had more artefact on their supine images (F=25%,M=49%). Upright artefacts were located primarily inferiorly and apically, with the most artefacts located distal inferiorly (26%). These were more common in female patients (36%), whereas male patients had more artefacts mid-basal inferolaterally (13%-15% vs 6%-8% respectively). Supine artefacts were located primarily anteriorly and inferiorly. Anterior artefact frequency was similar for male and female patients, however inferior artefacts were seen predominantly in male patients (basal/mid/distal inferior artefact frequency F:2%/8%/4%,M:34%/23%/13%). ***Conclusion:*** Dual-

position stress MPI is locally preferred on CZT cameras in order to identify attenuation artefacts. This work shows the locations of where we might expect attenuation artefacts. It follows that rest imaging should be performed in the position with less attenuation artefact, which we show here to generally be supine, although 36% of male patients had less artefact in the upright position compared to 49% having less artefact while supine. We are currently discussing how to implement these results - the options being a)acquire all rest imaging supine, b)acquire rest imaging upright for males and supine for females, or c)assess each patient's images for attenuation artefacts individually prior to rest imaging. This work partially agrees with the supine results of Chopra et al.[1], however we also see inferior artefacts in male patients which is in line with previous non-CZT based studies[3]. ***References:*** [1]Chopra, S et al. Journal of Nuclear Cardiology 30.5 (2023): 1782-1793. [2]Perrin, Mathieu, et al. Journal of Nuclear Medicine 60.6 (2019): 824-829. [3]Burrell, Steven et al. Journal of nuclear medicine technology 34.4 (2006): 193-211.

EP-0573

Myocardial Blood Flow and Ejection Fraction Measurement in Rb82-PET/CT shows high inter-observer reliability

S. Stolte, *H. Geiger, O. Maas, F. Forrer;*
Kantonsspital St Gallen, St Gallen, SWITZERLAND.

Aim/Introduction: Myocardial perfusion PET/CT e.g. using Rb-82 enables the measurement of absolute myocardial blood flow (MBF) including the flow-reserve which is a useful tool in assessing myocardial ischemia as well as microvascular disease. However, the values might depend on the observer's analysis i.e. e.g. the observer's experience. We investigated the inter-observer reliability of MBF measurements in Rb-82-PET/CT. ***Materials and Methods:*** 30 consecutive patients who underwent Rb-82-PET/CT for suspected myocardial ischemia were analysed. Stress conditions were simulated using 400 µg Regadenoson. MBF was measured using Corridor 4DM software. Flow-reserve (FR) is the ratio of absolute flow measurements under stress and rest conditions. Four different physicians on different levels of experience (two senior physicians and two residents) investigated the MBF. The experience of the residents was one year and a couple of weeks respectively. Intraclass correlation coefficients (ICC) were calculated for MBF and FR in the three main vascular territories and in the whole left ventricle as well as for the ejection fraction (EF). ***Results:*** The evaluation of MBF showed an excellent correlation between all observers indicated by a low inter-observer-variability. Comparing the two different levels of experience, senior physicians showed an even slightly higher accordance in MBF-assessment (ICC ranging from 0.9 to 0.98) than residents (ICC ranging from 0.86 to 0.94). The FR-calculations showed a slightly lower reliability due to the accumulation of variability in rest and stress measurements (ICC between 0.78 and 0.81), still indicating a good reliability. EF-calculations also showed a good reliability among different observers (ICC 0.83). ***Conclusion:*** Measurement of MBF, FR and EF in Rb-82-PET/CT shows an excellent inter-observer reliability demonstrating the robustness of the method. A slightly higher inter-observer reliability was found for more experienced physicians.

EP-0574

Myocardial Prone Imaging In The SPECT/CT Era - The Need Is Still There: When CT-Attenuation Correction Is Not Enough

C. Fragkaki[1], *S. Maragkoudakis*[2], *G. L. Lilikaki*[2], *A. T. Archontaki*[3];
[1]*Nuclear Medicine Department, Athens General Anti-Cancer/Oncology Hospital "Agios Savvas", Athens, GREECE,* [2]*Cardiology Department, Chania General Hospital "St. George", Chania, GREECE,* [3]*Nuclear Medicine Department, Chania General Hospital "St. George", Chania, GREECE.*

Aim/Introduction: In myocardial imaging, SPECT systems, can provide only non-attenuation corrected (NAC) images that are susceptible to attenuation artifacts, usually to anterior and inferior wall, known as "breast" and "diaphragmatic" attenuation artifacts, respectively. In hybrid systems, attenuation correction (AC) with CT will improve the accuracy of SPECT images most of the times, but not always. ***Materials and Methods:*** In July 2023, the Nuclear Medicine Department of Chania General Hospital "St. George", acquired a new dual-headed SPECT/CT γ-camera. Since then, all myocardial perfusion studies, using ^{99m}Tc-MIBI, were performed using the suggested CT-AC protocol. For a 20-month period, a total of 1336 studies were performed. Stress Prone imaging acquisition was performed, after the Stress Supine acquisition, when there was still reduced or questionable perfusion in the anterior wall (101patients) and in the inferior wall (120patients) and before a second radiopharmaceutical injection, needed for the Rest imaging acquisition, was performed. ***Results:*** From 1336 studies, 576 patients showed normal myocardial perfusion and left without any further imaging, 221 patients needed a Stress-Prone imaging acquisition, in order to clarify their attenuation artifact and 169 of those (105 females and 64 males) avoided an unnecessary radiation exposure from the Rest acquisition dose injection, since the stress prone images, showed normal myocardial perfusion in the suspicious area. The rest, concluded the whole Stress-Rest protocol. ***Conclusion:*** It seems, that even though SPECT/CT images in myocardial imaging are definitely superior to SPECT images alone, a 16,5% of the patients examined, still needed an "old-fashioned" Prone imaging as well. Therefore, our conclusion is that if there is any doubt, Prone Imaging could still be a very useful tool in everyday practice. ***References:*** Alwan, M, Sayed, A, Ahmed, A. et al. The impact of utilization of attenuation correction and prone positioning on stress-only imaging in cardiac spect mpi: an observational study. JACC. 2025 Apr, 85 (12_Supplement) 2044.

EP-0575

Analysis of factors affecting persistent perfusion defects in patients with pulmonary embolism

S. Niu[1], *J. Cao*[2], *H. Liu*[1], *J. Cao*[3];
[1]*First Hospital of Shanxi Medical University, Taiyuan, CHINA,* [2]*First Hospital of Shan Xi Medical University, Taiyuan, Shanxi, CHINA,* [3]*First hospital of Shan Xi medical university, Taiyuan, Shanxi, CHINA.*

Aim/Introduction: Acute pulmonary embolism is a common and potentially life-threatening condition. Some patients continue to have residual blood clots in the lungs long after the diagnosis of pulmonary embolism, which may lead to a poor long-term prognosis. In this study, we collected and analyzed a variety of meaningful ancillary laboratory markers during the acute phase of the disease, with the aim of evaluating the correlation between these markers and persistent perfusion defects in patients with pulmonary embolism. ***Materials and Methods:*** A total of 276 patients with acute pulmonary embolism who underwent pulmonary perfusion imaging were included in the study, and basic clinical data, serologic indices, and symptoms in the acute phase were collected. After 3-6 months of oral anticoagulant therapy, the patients were again subjected to pulmonary perfusion imaging, and were divided into two groups based on the results, the group with recovery of pulmonary perfusion flow and the group with persistent perfusion defect (patients with a first diagnosis of pulmonary embolism who had little change in embolism of the original lung segment or new embolisms in other segments of the lungs after 3-6 months of pharmacologic anticoagulant therapy). ***Results:*** Compared with the pulmonary perfusion blood flow recovery group, a significantly higher proportion of the persistent perfusion defect group had a smoking history, and the difference was statistically significant (χ^2=5.981, P=0.014); the incidence of dyspnea, hemoptysis, and chest pain

in the persistent perfusion defect group was significantly higher than that in the pulmonary blood flow perfusion recovery group, and the difference was statistically significant (χ^2=5.333, P=0.021; χ^2=10.530, P=0.001 ; χ^2=6.617, P=0.010); the blood uric acid level in the persistent perfusion defect group (361.33±117.32) was higher than that in the pulmonary blood flow perfusion recovery group (330.76±104.09), with a significant difference (t=-2.087, P=0.038). ***Conclusion:*** Patients with acute pulmonary embolism are more likely to have persistent pulmonary perfusion defect if they have a long history of smoking, early symptoms of dyspnea, hemoptysis, chest pain, or high blood uric acid levels. ***References:*** 1. Bajc M, Neilly J B, Miniati M, et al. EANM guidelines for ventilation/perfusion scintigraphy : Part 1. Pulmonary imaging with ventilation/perfusion single photon emission tomography[J]. European Journal of Nuclear Medicine and Molecular Imaging, 2009, 36(8): 1356-1370.2.Pesavento R, Filippi L, Palla A, et al. Impact of residual pulmonary obstruction on the long-term outcome of patients with pulmonary embolism[J]. The European Respiratory Journal, 2017, 49(5).

EP-0576

Dual-position Myocardial Perfusion Imaging: reducing the number of rest scans performed while increasing reporter confidence

M. Ulyatt[1], *K. Jones*[1,2], *A. Carradus*[1,2], *J. Robinson*[1,2], *A. Laird*[1], *S. Han*[1,2], *C. Paterson*[1,2];
[1]*Department of Clinical Physics and Bioengineering, NHS Greater Glasgow and Clyde, Glasgow, UNITED KINGDOM,* [2]*College of Medical, Veterinary and Life Science, University of Glasgow, Glasgow, UNITED KINGDOM.*

Aim/Introduction: The Nuclear Cardiology department at Glasgow Royal Infirmary (GRI) follows a one-day Myocardial Perfusion Imaging (MPI) protocol, wherein rest imaging is performed only if stress imaging indicates a perfusion defect. Scanning uses cardiac SPECT-only CZT gamma cameras: due to the lack of CT attenuation correction, attenuation artefacts may be misidentified as areas of reduced perfusion. This may cause patients to unnecessarily receive a rest scan, increasing patient dose. Literature suggests that dual-position imaging reduces the number of required rest scans due to increased confidence in identification of position-dependent attenuation artefacts [1][2][3]. Dual-position imaging (upright and supine) has recently been introduced at GRI: the impact this has had on the number of rest scans performed has been assessed. ***Materials and Methods:*** 30 anonymised dual-position studies were processed into two sets: one displaying upright only stress images and another displaying both upright and supine stress images. Two experienced operators assessed both sets to determine if a rest scan was required. In addition, 100 consecutive patient reports from both before and after the protocol change were audited to determine the number of rest scans performed in practice, and to assess the frequency of normal outcomes (i.e scans demonstrating no reversibility or previous myocardial infarction), and of these, how many normal studies had rest imaging. ***Results:*** The assessment of 30 anonymised patients found operators required fewer rest scans when viewing dual-position imaging, vs upright alone (53% vs 87%). The audit found dual-position imaging reduced the overall number of rest scans performed in practice (99% to 84%), increased the overall number of normal studies reported (16% to 49%), and lowered the rate of rest scans among patients with normal scan results (94% to 67%). ***Conclusion:*** Dual-position imaging reduces the number of rest scans performed when using a SPECT-only cardiac gamma camera, resulting in lower patient dose and reduced imaging time. Previously we were unable to rule out small areas of mild reversibility in equivocal scans: dual-position imaging has both increased confidence in identifying defects as attenuation using only the stress part of the study, without requiring a rest scan, and also in reporting images as within normal limits. ***References:*** [1] Ben-Haim, S. et al. 2014, 21:478-485. J. Nucl. Cardiol. [2] Chopra, S. et al. 2023, 30(5):1782-1793 J. Nucl. Cardiol. [3] Nakazato, R. et al. 2010, 51(11):1724-1731. J. Nuc. Med.

EP-0577

Assessment of Reversible Ischemia and Left Ventricular Function in Relation to SCORE2 Risk, COVID 19 History, and Vaccination: A Retrospective MPS Study

S. Demirtas Senlik[1], *B. Bozca*[1], *A. Celik Arslan*[1], *S. Gulbahar Ates*[2], *O. Ozmen*[1];
[1]*Ankara Etlik City Hospital, Ankara, TÜRKIYE,* [2]*Gazi University Hospital, Ankara, TÜRKIYE.*

Aim/Introduction: This study aimed to assess the association between a history of COVID-19 infection, vaccination status, and cardiovascular risk as determined by the SCORE2 with the presence of reversible ischemia on Tc99m-sestamibi myocardial perfusion scintigraphy (MPS), and to evaluate the relationship between ejection fraction (EF) and cardiovascular risk categories. ***Materials and Methods:*** This retrospective study included 438 patients referred for MPS between January and March 2025. Demographic, clinical, and cardiovascular risk data, along with history of COVID-19 and vaccination, were collected. Patients were stratified into low-to-moderate or high risk using the SCORE2 algorithm, based on age, smoking status, cholesterol, and blood pressure(1). Individuals aged ≥70 or with cardiovascular disease or diabetes were classified as high-risk. Patients were also grouped based on reversible ischemia presence on MPS. Associations between ischemia, SCORE2 risk categories, COVID-19 history, and vaccination were assessed. EF, calculated on MPS, was categorized as low (≤50%) or normal (>50%), and the relationship between EF and cardiovascular risk groups was analyzed. ***Results:*** Among the 438 patients, 201 (45.9%) were male and 237 (54.1%) female, with a median age of 63 years (IQR: 55-69). Except for known coronary artery disease, no significant association was found between other risk factors, including diabetes, and reversible ischemia on MPS. A total of 105 patients were in the low-to-moderate risk group, and 333 in the high-risk group. Myocardial ischemia was present in 17 patients (16.2%) in the low-to-moderate group and 87 patients (26.0%) in the high-risk group, with a significant difference ($p = 0.037$). Similarly, a significant difference was found between the groups in reduced EF ($p = 0.021$). No significant association was observed between COVID-19 history or vaccination and ischemia or left ventricular EF among risk groups***. Conclusion:*** No significant association was found between individual risk factors and reversible ischemia on MPS, but a significant correlation was observed between low-to-moderate and high-risk groups when cardiovascular risk was classified using the SCORE2 algorithm. Although the role of COVID-19 infection as a risk factor remains debated, our study found no significant increase in reversible ischemia associated with a history of infection or vaccination. Additionally, a significant association was observed between SCORE2 risk categories and EF, supporting the clinical utility of SCORE2 not only in ischemia prediction but also in assessing left ventricular function. These results suggest that SCORE2 may be related to both reversible ischemia and impaired EF on MPS. ***References:*** 1. doi: 10.1093/eurheartj/ehab309. PMID: 34120177; PMCID: PMC8248998.

EP-0578

Prognostic Impact of Reverse Redistribution in Myocardial Perfusion Imaging, particularly in non-obstructive CAD

W. Yu, *Y. Wang, X. Su;*
The Third Affiliated Hospital of Soochow University, Changzhou, CHINA.

Aim/Introduction: Reverse redistribution (RR) is an imaging characterization in myocardial perfusion imaging (MPI), characterized by reduced radiotracer uptake in specific myocardial

regions on rest images compared to the corresponding stress images, which clinical significance remains unclear. The purpose of this study is to investigate the clinical and prognostic significance of RR. ***Materials and Methods:*** A retrospective study included suspected coronary artery disease (CAD) patients who underwent stress-rest MPI and coronary angiography (CAG) within 3 months at the Third Affiliated Hospital of Soochow University from January 2018 to April 2023. Reversible myocardial ischemia and myocardial infarction were excluded. Clinical data such as sex, age, cardiovascular risk factors, chest pain symptoms, medication use, Angio-based Microvascular Resistance (AMR) and echocardiography were collected. RR is defined as a ≥1-point increase in perfusion score at rest compared to stress imaging within the same myocardial segment, observed across ≥3 consecutive layers in two distinct imaging axes. Major adverse cardiovascular events (MACE) was defined as cardiac death, non - fatal myocardial infarction, late coronary revascularization (≥ 3 months) after MPI, after-hospitalization for angina with repeat coronary angiography, heart failure, and stroke. ***Results:*** A total of 305 patients were enrolled, including 59 (19.3%) RR patients and 246 (80.7%) normal perfusion patients. Compared with the normal perfusion group, patients in the RR group had a lower proportion of obstructive CAD (35.6% vs. 53.7%, P=0.013), a higher proportion of positive electrocardiogram of stress test (32.2% vs. 16.3%, P=0.005) and higher AMR [3.49±0.62 vs. 3.05±0.40, P=0.005]. Non-obstructive CAD (OR=2.08, 95%CI: 1.14-3.79, P=0.017) and hyperlipidemia (OR=1.85, 95%CI: 1.03-3.36, P=0.041) were independent factors for RR in MPI. With a follow-up period of 43 (40, 46) months, a total of 29 MACE events occurred. Multivariate Cox regression analysis showed that RR (HR=2.57, 95%CI: 1.06-6.20, P=0.036) and obstructive CAD (HR=3.91, 95%CI: 1.57-9.71, P=0.003) were independent risk factors for MACE. In patients without obstructive CAD, those with RR had a worse prognosis than normal MPI (9.4% vs. 3.1%, Log rank P=0.014). Obstructive CAD affected the relationship between RR and MACE (P for the interaction=0.03) with an interaction effect. RR independently predicted MACE in non-obstructive CAD (HR=6.18, 95%CI: 1.16-32.97, P=0.03), but demonstrated no significant prognostic impact in obstructive CAD. ***Conclusion:*** Among patients with suspected CAD, 19% exhibited RR, with non-obstructive CAD and hyperlipidemia as independent influencing factors. RR was significantly associated with MACE, particularly in the non-obstructive CAD subgroup.

EP-0579

GATED-SPECT-Based Nomogram for Early Prediction of Major Cardiac Events in Ischemic Heart Disease

R. Zambrano Infantino, *J. F. Piñerúa-Gonsálvez, B. M. Jaramillo López, F. Sebastian Palacid, Á. R. Suazo Montero, N. Álvarez Mena, M. Alonso-Rodríguez, R. Ruano-Pérez;*
Hospital Clínico Universitario de Valladolid, Valladolid, SPAIN.

Aim/Introduction: Coronary artery disease is one of the leading causes of death worldwide. Although several imaging parameters are currently available as prognostic indicators, few predictive models integrate multiple variables derived from nuclear cardiology tests. The aim of this study is to develop a nomogram model for the early prediction of major cardiac events (MCE) in patients with ischemic heart disease using quantitative variables from Gated-SPECT myocardial perfusion imaging with 99mTc-SESTAMIBI. ***Materials and Methods:*** A retrospective study was conducted using data from the Nuclear Medicine Department at Hospital Clínico Universitario de Valladolid between January 2020 and January 2021. Consecutive patients who underwent Gated-SPECT myocardial perfusion imaging with 99mTc- SESTAMIBI after pharmacological stress, for the diagnostic or prognostic evaluation of ischemic heart disease, and who demonstrated evidence of myocardial ischemia, were included. Patients with arrhythmias, atrial fibrillation, left bundle branch block, right bundle branch block, pacemakers, or previous resynchronization therapy were excluded. Data on MCE occurring within 12 months after the imaging procedure, such as death, heart failure, acute myocardial infarction (AMI), and coronary revascularization (CR), were obtained from medical records. The selection of quantitative variables to create the predictive nomogram was performed using partial least squares (PLS) regression analysis, with the aim of correcting multicollinearity among the variables. The performance of the nomogram was evaluated using the ROC curve and concordance index (C-index). ***Results:*** Of the 185 patients referred to the department with suspected myocardial ischemia, 53 patients were included in the study. The cohort had a mean age of 68.9 ± 8.9 years. 39.6% of patients experienced MCE, with CR being the most frequent event (22.6%), followed by AMI at 9.4%. The PLS regression analysis identified that the end-systolic volume (ESV), left ventricular ejection fraction (LVEF), and standard deviation (SD) and bandwidth (BW) were independent variables for predicting MCE. Using these four variables, a predictive nomogram was developed, which showed an AUC of 0.72 (95% CI: 0.57-0.85) and a C-index of 0.71. ***Conclusion:*** The predictive nomogram developed in this study, based on quantitative variables derived from Gated-SPECT myocardial perfusion with 99mTc-SESTAMIBI, appears to be an effective tool for the early prediction of MCE in patients with ischemic heart disease. The model showed robust performance, identifying key predictors as ESV, LVEF, SD and BW. These findings highlight the clinical value of the Gated-SPECT based nomogram in risk stratification and therapeutic decision-making in this population.

EP-0580

Prognostic Significance of Transient Ischemic Dilatation with Adenosine 99mTc Sestamibi SPECT/CT in Diabetic Patients with Normal Myocardial Perfusion

M. Juweid*;*
University of Jordan, Amman, JORDAN.

Aim/Introduction: To investigate the prognostic significance of non-attenuation (NAC) and attenuation-corrected (AC) TID in diabetic patients with normal perfusion on adenosine ^{99m}Tc-sestamibi imaging. ***Materials and Methods:*** We analyzed 790 diabetic patients with normal perfusion on 2-day adenosine stress/rest ^{99m}Tc-sestamibi SPECT/CT between 1/2019-9/2023. 51 patients with Framingham 10-year coronary heart disease risk <10% were used to derive abnormal AC and NAC TID thresholds (derivation group or DG). The significance of TID at these thresholds was validated in the remaining 739 patients (validation group or VG) followed for cardiac events for 33.6 ± 17.4 (mean ± SD) months. Events were defined as cardiac death, nonfatal MI, coronary revascularization and congestive heart failure. ***Results:*** Mean NAC TID in the DG was 1.09 ± 0.13 while AC TID was 1.07 ± 0.14. Three definitions of an abnormal TID were used: > mean + 2SD (NAC TID ≥ 1.36, AC TID ≥ 1.36), > mean + 1SD (NAC TID ≥ 1.22, AC TID ≥ 1.21) and a TID in the DG's highest quartile (NAC TID ≥ 1.17, AC TID ≥ 1.18). Of the VG, 205 (27.7%), 134 (18.1%) and 36 (4.9%) had NAC TID ≥ 1.17, 1.22 and 1.36, respectively, while 147 (19.9%), 114 (15.4%) and 31 (4.2%) had AC TID ≥ 1.18, 1.21 and 1.36, respectively. On multivariate analysis, NAC TID ≥ 1.17 and 1.22 were predicted by rest LVEF (p <0.001 and .035, respectively). A ≥ 5% decrease in LVEF predicted NAC TID ≥ 1.22 (p < 0.001), NAC TID ≥ 1.36 (p = .002), AC TID ≥ 1.18 (p = .006) and AC TID ≥ 1.21 (p = .020). A ≥ 10% decrease in LVEF predicted NAC TID ≥ 1.22 (p = .030) and AC TID ≥ 1.36 (p = .023). Gender, known CAD, family history of coronary artery disease (CAD), hypertension, dyslipidemia, atrial fibrillation, thyroid disorders and post-stress LVEF did not predict abnormal AC or NAC TID at the tested thresholds. Cardiac event-free survivals were similar in patients with NAC TID ≥ and < 1.17 (2.9% vs. 5.6%, p = .157), ≥ and < 1.22 (1.5% vs. 5.6%, p = .059) and ≥ and < 1.36 (2.8% vs. 5.0%, p = .483). Similar results were found

using the respective AC TID cutoffs. ***Conclusion:*** TID, whether based on attenuation or non-attenuation corrected scans, does not confer adverse prognosis in diabetic patients with normal perfusion on adenosine 99mTc-sestamibi SPECT/CT.

EP-0581

Prevalence of Ischemia with Non Obstructive Coronary Artery disease (INOCA) in patients with positive myocardial perfusion SPECT.

A. Manrique[1], *M. Esnault*[1], *N. Coudrais*[1], *N. Catherine*[1], *P. Richard*[2], *R. Vincent*[1], *D. Agostini*[1];
[1]*CHU de Caen, Caen, FRANCE,* [2]*Hopital Privé Saint Martin, Caen, FRANCE.*

Aim/Introduction: INOCA refers to patients with inducible ischemia during a functional test and no significant epicardial coronary artery stenosis. It is associated with increased risks of major adverse cardiovascular events. ***Materials and Methods:*** In order to evaluate the prevalence of INOCA in patients referred to myocardial perfusion SPECT imaging (MPI), we retrospectively evaluated a series of consecutive patients without previously documented coronary artery disease who underwent a coronary angiogram within 1 month after a positive MPI. All MPIs were performed using a DSPECT CZT camera, a ^{99m}Tc-lebelled tracer and a one-day protocol. MPI and coronary angiogram results were retrieved from hospital records. INOCA was defined by at least one non-significant coronary lesion < 50% and no lesion ≥ 50%. ***Results:*** From January to December 2018, among 3595 patients undergoing MPI, 335 (age 68±10, male 67%) met the inclusion criteria. Symptoms included dyspnea (50%) and/or chest pain (28%) and pre-test likelihood of CAD was >15% in 62%. SPECT demonstrated reversible and non-reversible defects in 299 (90%) and 49 (15%) cases respectively. Coronary angio was normal in 53 (16%) cases and considered as false positive SPECT. Significant lesions (≥50%) were found in 193 (58%) and INOCA in 88 (27%) patients, including 36 (11%) with 30-50% lesions and 53 (16%) with < 30% lesions. Univariate analysis demonstrated that, compared to patients with >50% lesion, INOCA was associated to female gender (p<0.001), decreased rate of hypertension (p<0.01), of peripheral artery disease (PAD) (p<0.001), of dyslipidemia (p<0.05) or pre-test probability (PTP) range (p<0.05), younger age (p<0.01), higher LVEF (p<0.05), lower EDV (p< 0.05) and ESV (p<0.05) at stress and rest, and decreased number of segments with irreversible defects (p<0.001). Using logistic regression, the independent predictors of INOCA were female gender (OR: 4.84, p<0.01), hypertension (OR: 0.30, p<0.01, PTP range <0.15 (OR: 0.26, p<0.01) and irreversible perfusion defect <2 segments (OR 3.85, p<0.05). The extent of reversible perfusion defect was not associated with INOCA in this series. ***Conclusion:*** INOCA was present in ¼ of patients with positive SPECT referred to subsequent coronary angiography. They deferred from patients with significant coronary artery stenosis, with a higher prevalence of female gender with decreased rate of hypertension, a low pre-test probability of CAD and a lower rate of irreversible SPECT defects.

EP-0582

Change in myocardial perfusion does not correlate to change in peak oxygen uptake after coronary revascularization - a positron emission tomography study

A. Székely[1], *S. Akil Engblom*[1], *H. Mosén*[1], *K. Steding-Ehrenborg*[1], *C. Hindorf*[2], *F. Hedeer*[1], *H. Arheden*[1], *H. Engblom*[1];
[1]*Clinical Physiology, Department of Clinical Sciences Lund, Lund University, Skåne University Hospital, Lund, SWEDEN,* [2]*Department of Medical Radiation Physics, Lund University, Lund, SWEDEN.*

Aim/Introduction: Chronic coronary syndrome (CCS) is associated with reduced stress perfusion, which is a predictor of adverse cardiovascular outcome (1). To what extent the level of myocardial perfusion is related to cardiorespiratory fitness is not completely known. The aim of this study was to investigate if change in myocardial perfusion assessed by cardiac [^{13}N]NH_3 positron emission tomography (PET) correlates with change in VO_2 peak assessed with CPET before and after invasive coronary angiography (ICA) with revascularization. ***Materials and Methods:*** Sixty-two patients (median age 68 (range 46-86) years, 14 females) with suspected or established CCS underwent cardiopulmonary exercise testing (CPET) and [^{13}N]NH_3 PET before and after elective ICA. The angiographer was blinded to the results from CPET and PET. Thirty-five patients were revascularized. Myocardial perfusion at stress and myocardial perfusion reserve (MPR) were assessed from PET. VO_2 peak % of predicted and VO_2 peak ml/min/kg were assessed from CPET. Results are presented as median (range). ***Results:*** Global myocardial perfusion at stress increased significantly from baseline to follow-up if baseline global perfusion at stress was <2 ml/min/g (1.79 (1.01-1.86) ml/min/g vs 1.94 (1.09-2.61) ml/min/g, P=0.02), however not if baseline was ≥2 ml/min/g (2.42 (2.00-3.32) ml/min/g vs 2.57 (1.55-4.22) ml/min/g, P=0.09). Global MPR increased significantly from baseline to follow-up if baseline global MPR was <2.4 (2.23 (1.33-2.40) vs 2.63 (1.22-3.20), P=0.001), however not if baseline was ≥2.4 (2.89 (2.45-3.52) vs 3.07 (1.77-4.46), P=0.43; Figure 2). There were no significant correlations between change in VO_2 peak % of predicted and global myocardial perfusion at stress (R=0.08, P=0.64) or global MPR (R=0.07, P=0.69) from baseline to follow-up. Furthermore, there were no correlations between change in VO_2 peak ml/min/kg and global myocardial perfusion at stress (R=0.15, P=0.39) or global MPR (R=0.10, P=0.57, figure 3). No significant improvement in VO_2 peak % of predicted or VO_2 peak ml/min/kg was seen in patients undergoing revascularization of vessel territories with a significantly reduced perfusion at stress (<2.0 ml/min/g) (P=0.63 and P=0.94) or MPR (<2.4) (P>0.99 and P=0.96) at baseline. ***Conclusion:*** Change in myocardial perfusion after revascularization was not associated with change in VO_2 peak in patients with CCS, regardless of whether perfusion was decreased or normal in the culprit vessel territory prior to revascularization. ***References:*** 1.Knott KD, Seraphim A, Augusto JB, Xue H, Chacko L, Aung N, et al. The Prognostic Significance of Quantitative Myocardial Perfusion: An Artificial Intelligence-Based Approach Using Perfusion Mapping. Circulation. 2020;141(16):1282-91.

EP-0583

Comparison of LVEF derived using four cardiac softwares on CZT cardiac camera and 2D-Echocardiography

J. Krishna P.*, D. Khan, S. Sagar, L. Goriparti, R. Wakankar, C. Patel, B. Chandra, P. Gupta, A. Roy, S. Yadav, S. Agstam, N. Parakh;*
All India Institute of Medical Sciences, New Delhi, INDIA.

Aim/Introduction: To compare the left ventricular ejection fraction (LVEF) values derived using four cardiac quantitative softwares on Tc99m-MIBI Myocardial Perfusion SPECT (MPS) acquired on CZT camera with 2D-Echocardiography (ECHO). ***Materials and Methods:*** This prospective study included 112 patients with known or suspected CAD, referred for MPS and ECHO. Estimated LVEF of 60% or more on ECHO was considered normal. The MPS studies were processed using vendor provided individual softwares, namely Emory Cardiac Toolbox (ECTb), 4D-MSPECT, QGS/QPS (Cedars-Sinai) and Myometrix. LVEF was subsequently calculated and compared to ECHO, which was taken as the reference standard. Pearson's correlation was done to compare LVEF values between the softwares and normal cutoff values for each software program was obtained with receiver-operating characteristic (ROC) analysis. ***Results:*** Out of 112 patients [(94 M, 18 F), median age - 56 years], 47 were found normal and 65 abnormal based on ECHO findings. The mean LVEF on ECHO was 55±8.9%. The mean LVEF values for ECTb, 4D-MSPECT, QGS/QPS and Myometrix were 59.1±14.7%, 61.1±12.9%, 59.0±13.1% and

54.3±12.6%, respectively. A positive correlation was observed between LVEF values derived by ECHO and MPS software programs: ECTb ($r = 0.604$, $P < 0.001$), 4D-MSPECT ($r = 0.543$, $P < 0.001$), QGS/QPS ($r = 0.587$, $P < 0.001$) and Myometrix ($r = 0.595$, $P < 0.001$). Significant correlation was also seen for LVEFs among the four software programs ($P < 0.05$). Normal cutoff values for LVEF on ECTb, 4D-MSPECT, QGS/QPS and Myometrix were estimated to be 60%, 57%, 52%, 49% respectively. ***Conclusion:*** The study revealed a positive correlation for LVEF between cardiac softwares and ECHO and it also derived the normal cutoff values for each of them. However, the cutoff values were software specific and cannot be used interchangeably for routine clinical practice.

EP-0584

Evaluation of Myocardial Perfusion Imaging Using AUC Guidelines: Adherence and Diagnostic Yield at a High-Volume Tertiary Care Center in Central India.

B. Vamshi Naik, *M. Ravina, S. Singh, S. Raju, S. Thakur; All India Institute of Medical Sciences, Raipur, INDIA.*

Aim/Introduction: Myocardial perfusion imaging (MPI) is essential for diagnosing and managing coronary artery disease (CAD). However, inappropriate use can increase healthcare costs and radiation exposure. The Appropriate Use Criteria (AUC) were developed to help clinicians make informed, evidence- based decisions when ordering myocardial perfusion imaging (MPI). This study looks at how appropriately MPI is being used and how often perfusion defects are detected. With limited research available from India, this audit is expected to play an important role in understanding and improving clinical practice. ***Materials and Methods:*** A retrospective study of 475 MPI procedures conducted between February 2022 and August 2024 was performed. All patients referred for stress MPI were included. Clinical indications were reviewed and categorized as Appropriate, Rarely Appropriate, or Maybe Appropriate based on the 2013 ACCF/AHA/ASNC Appropriate Use Criteria. The frequency and percentage of each category were calculated to assess adherence, and MPI results were analysed for perfusion defects. ***Results:*** Among the 475 MPI studies analysed, 431 (90.74%) were deemed Appropriate, 43 (9.05%) Rarely Appropriate, and 1 (0.21%) Maybe Appropriate. These findings suggest a high level of compliance with AUC at the institution. Similar international audits have reported appropriate use rates ranging from 72% to 91%, placing our adherence at the higher end of global benchmarks. Perfusion defects were observed in 123 patients (25.89%) overall. Among the 431 appropriately indicated studies, 112 (25.99%) showed perfusion abnormalities. In contrast, defects were identified in approximately 11 (25.58%) of the 43 rarely appropriate cases, and none in the single maybe appropriate case. There was no statistical difference in the prevalence of perfusion defects between the appropriate and rarely appropriate groups (P-value ~0.79). ***Conclusion:*** The study highlights strong adherence to the Appropriate Use Criteria in myocardial perfusion imaging at a tertiary care centre in Central India, with most studies classified as appropriate. However, the relatively low detection rate of perfusion defects & no significant difference in the prevalence of perfusion defects between the appropriate and rarely appropriate groups- reveals a disparity between guideline-based indications and actual diagnostic yield. Additionally, this disparity underscores the limited clinical utility of MPI in scenarios deemed rarely appropriate by the guidelines. These findings emphasize the importance of balancing guideline adherence with clinical judgement to optimize the diagnostic yield of MPI.

EP-0585

Feasibility of functional analysis using myocardial perfusion SPECT/CT with a novel multifocal collimator, retrospective gating, and integrated corrections

S. Watanabe[1], *K. Nakajima*[1], *T. Shibutani*[2], *S. Yoshida*[3], *M. Onoguchi*[2], *S. Kinuya*[1], *F. Massanes*[4], *T. Shimizu*[4], *A. H. Vija*[4]; [1]*Department of Nuclear Medicine, Kanazawa University, Kanazawa, JAPAN,* [2]*Department of Quantum Medical Technology, Institute of Medical, Pharmaceutical and Health Sciences, Kanazawa University, Kanazawa, JAPAN,* [3]*Department of Cardiovascular Medicine, Kanazawa University Graduate School of Medical Science, Kanazawa, JAPAN,* [4]*Molecular Imaging, Siemens Medical Solutions USA, Inc., Hoffman Estates, IL, UNITED STATES OF AMERICA.*

Aim/Introduction: We have presented an iterative reconstruction method that mitigates the causes of image degradation, demonstrating effectiveness of integrated systematic corrections. We evaluated the accuracy of functional analysis using myocardial perfusion SPECT/CT with a novel multifocal SMARTZOOM high resolution and extended magnification volume (SZHRX) collimator compared with conventional SPECT. ***Materials and Methods:*** We prospectively studied patients who underwent myocardial perfusion imaging (MPI) for suspected coronary artery disease at Kanazawa University Hospital between February 2023 and November 2024, using a Symbia Intevo 16 SPECT/CT with SZHRX collimator (research setting) and ^{99m}Tc perfusion tracers. For SPECT/CT with SZHRX collimator, we used 256×256 matrix and 3° list-mode data sampling from continuous rotation over 360° scan range with either 180° or 76° camera configurations. The ordered subset conjugate gradient minimizer (OSCGM) reconstruction method was used with retrospective electrocardiography (ECG) gating and CT-based attenuation and energy window-based scatter corrections. Corrections for patient and organ motion between and within views were also applied to the gated reconstructions. For conventional SPECT, all patients underwent MPI with parallel-hole low-energy high-resolution collimator using the 3D-OSEM (Flash 3D) reconstruction method with prospective ECG gating without attenuation and scatter corrections, and data were also acquired over 360°. Left ventricular (LV) end-diastolic volume (EDV), end-systolic volume (ESV), ejection fraction (EF), and phase entropy were assessed at rest. Echocardiographic measurements of volume and EF within 3 months of an MPI study were used as reference. ***Results:*** Twenty-nine patients (age, 69 ± 10 years; male, 86%) were included. The integrated corrections used in the SZHRX collimator condition did not cause any harms or artifacts. Correlations of functional parameters between the SZHRX collimator condition and conventional SPECT were strong and significant ($p < 0.0001$) for all EDV ($R^2 = 0.96$), ESV ($R^2 = 0.96$), LVEF ($R^2 = 0.90$), and phase entropy ($R^2 = 0.55$). EDV and ESV were 1 and 8 mL higher, respectively, LVEF was 5% lower, and entropy was 6% higher for the SZHRX collimator condition compared with conventional SPECT. The correlations between these functional variables and echocardiographic values were higher for the SZHRX collimator condition than for conventional SPECT ($R^2 = 0.83$ and 0.78 for EDV, 0.93 and 0.86 for ESV, and 0.80 and 0.64 for LVEF, respectively) in 26 patients. ***Conclusion:*** Myocardial perfusion SPECT/CT with SZHRX collimator, retrospective gating, and integrated corrections showed good performance for functional analysis. More comprehensive studies are warranted to validate these findings. ***References:*** JNC. 2023;30: 2773-2789.

EP-0586

Prediction of Cardiac Events in Patients with Diabetes Using Stress Myocardial Blood Flow and Coronary Flow Reserve

M. Havel[1,2], *M. Kaminek*[1,3], *L. Quinn*[1], *L. Henzlova*[1], *V. Icova*[1], *G. Havlova*[2];
[1]*Department of Nuclear Medicine, University Hospital, Palacky University, Olomouc, CZECH REPUBLIC,* [2]*University of Ostrava and University Hospital Ostrava, Department of Nuclear Medicine, Ostrava, CZECH REPUBLIC,* [3]*International Clinical Research Center and Department of Internal Medicine/Cardiology, St. Anne´s University Hospital, Faculty of Medicine, Masaryk University, Brno, CZECH REPUBLIC.*

Aim/Introduction: Cardiovascular disease (CVD) is a major complication of diabetes mellitus (DM), encompassing macrovascular complications, diabetic cardiomyopathy, and microvascular dysfunction. Coronary flow reserve (CFR), derived from dynamic SPECT imaging, is a valuable marker for coronary artery disease (CAD) and microvascular involvement. However, acquiring CFR requires both stress and rest studies, increasing time and radiation exposure. This study evaluates the prognostic significance of dynamic SPECT-derived myocardial blood flow (MBF) during stress and rest and CFR in a cohort of patients with DM. ***Materials and Methods:*** A retrospective analysis was conducted on 49 patients with DM (26 men, mean age 65±10 years) who underwent rest-stress dynamic myocardial SPECT. Stress and rest MBF, along with CFR, were correlated with adverse cardiac events (CE) during follow-up, defined as sudden cardiac death, myocardial infarction, acute coronary revascularization, and hospitalization for heart failure. ***Results:*** Over a mean follow-up of 15 months, 11 CE (22.4%) were recorded. Patients with CE exhibited significantly lower stress MBF (1.90±1.16 vs. 2.61±0.81 ml/min/g, P=0.0025) and lower CFR (1.53±0.67 vs. 2.36±0.82, P=0.004), whereas rest MBF showed no significant difference (1.26±0.40 vs. 1.16±0.39, P=0.458). Cut-off values predicting CE were stress MBF ≤1.73 ml/min/g (sensitivity 73%, specificity 87%, AUC=0.75) and CFR ≤1.94 (sensitivity 73%, specificity 76%, AUC=0.79). Univariable Cox regression revealed both stress MBF and CFR as significant predictors (HR=9.0, P=0.001 and HR=5.7, P=0.011, respectively). However, in a multivariable model, only stress MBF remained significant (HR=5.72, P=0.026). ***Conclusion:*** CE in patients with DM can be predicted by low stress MBF and low CFR. However, the addition of CFR to stress MBF did not provide significant incremental value. These findings suggest a potential simplification of the dynamic SPECT protocol, favoring a stress-first or stress-only approach, which could enable broader MBF quantification for an increased number of patients. Supported by: MH CZ - DRO (FNOl, 00098892). ***References:*** Kaminek M, Havel M, Kincl V, Henzlova L, Hudson L. The prognostic value of CZT SPECT stress myocardial blood flow (MBF) quantification-opportunity for stress-first/stress-only protocol. Eur J Nucl Med Mol Imaging. 2024 Jan;51(2):344-345.

EP-0587

The Minimum Scan Time for Gated Myocardial Perfusion Imaging Using a Dedicated Ultrafast Solid-state Cardiac Camera

D. Zhao*, S. Sun, T. Wang, J. Song, X. Bi, T. Ye, Y. Wang, X. Xu, S. Yao, J. Liu, R. Wang;*
Chinese PLA General Hospital, Beijing, CHINA.

Aim/Introduction: The study aimed to determine the minimum scan time for gated myocardial perfusion imaging (MPI) using a standard dose and a dedicated ultrafast solid-state cardiac camera (Discovery NM 530c [DNM]). ***Materials and Methods:*** We performed a retrospective study which included 76 consecutive patients who were suspected coronary artery disease (CAD) referred for gated-MPI scan on the DNM camera. In the included 76 patients, 52 underwent a stress-only protocol and 24 underwent a two-day stress-rest protocol. Among them, 30 patients (15 male and 15 female) who received the stress-only scan were randomly selected as the test group and the remaining patients were assigned to the validation group. Patients were scanned 90-120 minutes (min) post-injection of [^{99m}Tc] Tc-sestamibi (about 555 MBq) for 6 min using list-mode. The List-mode raw data from the test group were reframed into 1-min, 2-min, 3-min, 4-min, 5-min datasets, while data from the validation group were reframed to generate the minimum scan time dataset. All datasets were quantified using automated quantitative perfusion and gated SPECT software (QPS/QGS). The minimum scan time was determined and validated by assessing the absolute agreement of quantitative parameters between reframed scan durations and original 6 min scan duration using intraclass correlation coefficient (ICC). ***Results:*** The minimum scan time was determined as 3 min in the test group based on the comparison of perfusion and function parameters and was confirmed in validation group with good to excellent agreement (ICC>0.87 for summed difference score and ICC>0.97 for summed stress score, summed rest score, ejection fraction, the end-diastolic volume and end-systolic volume). ***Conclusion:*** The minimum scan time was determined as 3 min in the test group based on the comparison of perfusion and function parameters and was confirmed in validation group with good to excellent agreement (ICC>0.87 for summed difference score and ICC>0.97 for summed stress score, summed rest score, ejection fraction, the end-diastolic volume and end-systolic volume).

EP-0588

Comparison of myocardial perfusion imaging and myocardial flow reserve using cadmium-zinc-telluride camera for the diagnosis of coronary artery disease

T. Niimi*, K. Hirayama;*
Japanese Red Cross Aichi Medical Center Nagoya Daini Hospital, Nagoya, JAPAN.

Aim/Introduction: A cadmium-zinc-telluride (CZT) camera can simultaneously evaluate myocardial flow reserve (MFR) and myocardial perfusion imaging (MPI) without positron emission tomography. This camera has renewed the interest in single-photon emission computed tomography (SPECT)-MFR assessment in patients with coronary artery disease (CAD). However, there has been little discussion on the relationship and validity of the MFR with conventional indicators. This study evaluated the relationship between the MFR and left ventricular (LV) phase analysis indices, such as bandwidth, phase standard deviation (SD), and entropy, calculated from the MPI and their effectiveness in improving CAD diagnosis. ***Materials and Methods:*** We retrospectively analyzed the clinical images of 60 patients who underwent dynamic CZT SPECT to evaluate suspected CAD (43 men and 17 women, mean age; 66.9 ± 10.0 years) after injection of ^{99m}Tc-sestamibi for rest and stress imaging. To assess the severity of CAD, the combined effect of MFR and LV phase analysis indices on MPI was examined. Receiver operating characteristic (ROC) and multivariate ROC analyses were used to quantify, improvement of CAD diagnostic performance using MPI (summed stress score (SSS)) alone, if MPI and MFR were combined, and if MPI and LV phase analysis indices were combined. ***Results:*** The area under the ROC curve (AUC) if SSS using MPI alone was 0.86 (sensitivity; 0.76, specificity; 0.84), whereas that if SSS was combined with MFR was 0.93, confirming a significant difference if MFR was combined with SSS. (p = 0.03). The AUCs for bandwidth, phase SD, and entropy combined with SSS were 0.88, 0.85, and 0.88, respectively, with no significant differences because of the combination. However, combining all LV phase analysis indices confirmed a significant difference with an AUC of 0.94 (p = 0.04). Similar diagnostic accuracy for CAD was obtained by combining the SSS in the MPI with the MFR or LV phase analysis indices. ***Conclusion:*** Using SSS in MPI combined with LV phase analysis indices can provide diagnostic accuracy

similar to that of using MFR in combination, although not the absolute quantitative blood flow indices. LV phase analysis indices calculated from the MPI may be used as alternative indices if the MFR cannot be measured for CAD screening.

EP-0589

Evaluation and mitigation of false positives in inferior myocardial wall with CZT camera using complementary stress myocardial perfusion with hybrid Anger-type camera

F. Vauchot, *T. Paunet, J. Dubois;*
CHU Gui de Chauliac, Montpellier, FRANCE.

Aim/Introduction: Meta-analysis show the diagnostic performance of cardiac dedicated multi-pinhole CZT (Cadmium Zinc Telluride) myocardial perfusion imaging (MPI) with a sensibility around 0.9 and a specificity around 0.7. Specificity is lower for inferior myocardial wall (IMW) because of more artefact occurring in this territory, with addition of body attenuation and CZT camera-specific artefacts. The aim of the present study is to evaluate and prevent false positive in IMW with CZT camera and to enhance specificity without changing sensibility using complementary stress MPI with hybrid Anger-type camera. ***Materials and Methods:*** From march 2023 to march 2025, we recruited all patients (n=100) explored by MPI with [99mTc]Tc-tetrofosmin under multi-pinhole CZT (Discovery NM 530c, GE Healthcare), with potential inferior ischemia and without necrosis. Those patients were explored the same day at stress with hybrid Anger-type camera (Discovery 870 DR16, GE Healtcare) using attenuation correction.Potential inferior ischemia was defined as a difference between sum stress score (SSS) and sum rest score (SRS): Δ= SSS-SRS ≥ 1. SSS was estimated a second time with hybrid camera: SSSh. Wilcoxon rank sum test was used for statistical comparisons. ***Results:*** After the second acquisition at stress, only 15 patients remained with SSSh>0 and were explored by coronarography or known for ischemic cardiopathy. SSSh was equal to 0 for 85 patients, meaning 85% potential false positive. Despite very low major cardiologic adverse event rate associated to normal stress MPI, those patients underwent a complementary 6-month follow-up. Among the 100 patients: 24 of 30 patients with SSS≥3 (80%); 35 of 42 patients with SSS=2 (83%) and 26 of 28 patients with SSS=1 (93%) showed a SSSh=0.Only number of segments with average subtraction (NAS) > 5 on dedicated polar maps and quantitative value of this average subtraction (QAS) were predictive of ischemia (p-value=0.0004 and p-value=0.002 respectively). For ischemia arm, NAS was 4.1±1.4 (IC95 3.4-4.8) and QAS was 16.3±6.1 (IC95 13.2-19.3). For potential false positive arm, NAS was 2.5±1.5 (IC95 2.2-2.9) and QAS was 11.3±4.9 (IC95 10.2-12.3). Δ was not predictive of ischemia (p-value=0.097): Δ= 2.6±1.2 (IC95 2.0-3.6) for ischemia arm, and Δ= 2.0±1.0 (IC95 1.8-2.3) for potential false positive arm. ***Conclusion:*** This study showed an IMW ischemia evaluation significantly different between cardiac dedicated multi-pinhole CZT and hybrid Anger-type cameras, with 85% potential false positives, regardless of the reversible segment numbers Δ.

EP-0590

Post-PCI patients with persistent chest discomfort lacking immediate post-procedural caIMR-derived CMD and subsequent MPI-detected residual ischemia exhibited optimal prognosis

W. Yu, *Y. Wang;*
The Third Affiliated Hospital of Soochow University, Changzhou, CHINA.

Aim/Introduction: This study evaluated the prognostic value of immediate post-procedural coronary angiography-derived Index of Microcirculatory Resistance (caIMR) and Single photon emission computed tomography myocardial perfusion imaging (SPECT/MPI) during follow-up in post PCI patients with persistent chest discomfort. ***Materials and Methods:*** 214 prospective post-PCI inpatients with persistent chest discomfort were enrolled, then underwent SPECT/CT 1-3 months later. Post-procedural Coronary Microvascular Dysfunction (CMD, caIMR≥25) and subsequent residual ischemia (SPECT/MPI SDS≥2) were assessed. MACE included angina-related rehospitalization, cardiac death, late coronary revascularization, nonfatal MI, heart failure, and stroke. ***Results:*** Post-procedural CMD and subsequent residual ischemia occurred in 106 (49.5%) and 107 (50.0%) respectively. During the median follow-up period of 42 (24, 50.25) months, MACE occurred in 88 (41.1%). MACE group showed higher CMD [53 (60.2%) vs. 53 (42.1%)] and residual ischemia rates [57 (64.8%) vs. 50 (39.7%)], both P <0.05], with Kaplan-Meier analysis confirming elevated MACE risks (Log-rank P<0.05). Post-procedural CMD and subsequent residual ischemia were independently correlated with MACE after adjusting for confounding factors [HR (95%CI): 1.72 (1.12, 2.65) and 2.34 (1.50, 3.66), both P < 0.001]. Patients without subsequent residual ischemia or post-procedural CMD exhibited optimal prognosis compared with patients with one or both risk factors [7 (8.0%) vs. 24 (27.3%) vs. 28 (31.8%) vs. 29 (33.0%), P<0.001]. ***Conclusion:*** Both post-procedural caIMR-derived CMD and subsequent residual ischemia identified via MPI independently related to MACE in post-PCI patients with persistent chest discomfort. Patients with neither post-procedural caIMR-derived CMD nor subsequent MPI-detected residual ischemia exhibited optimal prognosis.

EP-0591

Long-term prognostic value in nuclear cardiology: Expert scoring combined with automated measurements vs. angiographic score

G. Angelidis, *S. Giannakou, V. Valotassiou, E. Panagiotidis, I. Tsougos, C. Tzavara, K. Sakellariou, D. Psimadas, E. Theodorou, C. Ziangas, J. Skoularigis, F. Triposkiadis, P. Georgoulias;*
University of Thessaly, Larissa, GREECE.

Aim/Introduction: The evaluation of myocardial perfusion imaging (MPI) studies is based on the visual interpretation, while automated analyses may contribute to the investigation. We aimed to investigate the long-term prognostic value of expert reading of summed stress score (SSS), summed rest score (SRS), and summed difference score (SDS), combined with the automated measurements of these parameters, in comparison to the prognostic ability of the angiographic score for soft and hard cardiac events. ***Materials and Methods:*** The study was conducted at the Nuclear Medicine Laboratory, University of Thessaly, Larissa, Greece. 528 consecutive patients with known or suspected coronary artery disease (CAD) were enrolled. All participants were referred to our laboratory for the performance of stress/rest myocardial perfusion single photon emission computed tomography. Automated measurements of SSS, SRS, and SDS were obtained by Emory Cardiac Toolbox (ECTb (Version 3.0), Emory University, Atlanta, GA, USA), Myovation (MYO, Xeleris version 3.05, GE Healthcare, Chicago, IL, USA), and Quantitative Perfusion SPECT (QPS Version 4.0, Cedars-Sinai Medical Center, Los Angeles, CA, USA) software packages. Coronary angiographies were scored according to a 4-point scoring system (angiographic score; 0: normal study, 1: one-vessel disease, 2: two-vessel disease, 3: three-vessel disease). Follow-up data were recorded after phone contacts, as well as through review of hospital records. All participants were followed up for at least 36 months. ***Results:*** Data from 528 patients (61.6% males), with mean age 64.1 years (SD=9.5 years) were analyzed. Any cardiac event was recorded in 35.2% (n=186) of the sample and hard cardiac events in 10.8% (n=57) of the sample. The prognostic values of the angiographic score and of the expert scoring (all indexes combined) regarding hard cardiac events, as well as any cardiac event, were significant

(p<0.05). The prognostic ability of the angiographic score was significantly lower than the prognostic ability of the combination of expert scoring and automated analysis, for both hard events (p<0.001) and any cardiac event (p<0.001). The incremental prognostic value of the angiographic score to the prognostic value of the combination of the expert scoring and automated analyses was significant for hard events (p=0.014), whereas for any cardiac event it was not significant (p>0.05). ***Conclusion:*** The combination of expert reading and automated measurements of SSS, SRS and SDS shows a superior prognostic ability in comparison to the angiographic score.

EP-0593

Early Detection of Cardiac Involvement in Lipid Storage Myopathy:The Superior Role of Myocardial Perfusion Imaging

W. Zhengjie, *L. Jia, T. Fangfang, Z. Xiaoyang, L. Mengdan, P. Hua; The First Affiliated Hospital of Chongqing Medical University, Chongqing, CHINA.*

Aim/Introduction: Lipid storage myopathy (LSM), arising from defects in multiple enzyme functions or carnitine deficiency and resulting in impaired fatty acid metabolism, often involves cardiomyopathy as advanced stages of the disease across various genotypes. This study aims to investigate the utility of myocardial perfusion imaging (MPI) in patients with LSM, with a particular focus on its role in evaluating the extent of cardiac involvement. ***Materials and Methods:*** Fourteen patients Confirmed as LSM by muscle biopsy underwent rest/stress single-photon emission computed tomography MPI, echocardiography, and blood biochemical profiling. Four patients completed a follow-up MPI 3 months post-treatment. Left ventricle perfusion was evaluated using a 17-segment standardized model with a 5-point scoring system. The summed rest score (SRS) and summed stress score (SSS) for the left ventricle were calculated. Pearson's correlations between SSS and other cardiac function and biochemical parameters were evaluated. Paired t-tests were employed to analyze the pre- and post-treatment changes. ***Results:*** The cohort exhibited a mean SSS of 9.71. Cardiac abnormalities were detected in 12 out of 14 patients (85.7%), with 4 patients of severe abnormalities indicated by SSS, compared to 4 out of 14 (28.6%) by echocardiography. SSS also demonstrated a positive correlation with stress end-diastolic volume (EDV; r = 0.89) and a significant negative correlation with ejection fraction (EF; r = -0.87). There are no biochemical markers demonstrated correlation coefficients with SSS. As the disease progressed, patients demonstrated gradually increasing SSS on MPI, with radionuclide distribution defects transitioning from reversible to partially irreversible patterns. Post-treatment SSS also showed significant reduction (8.76 to 2.33). ***Conclusion:*** This study underscores the efficacy of MPI in the early detection and monitoring of myocardial damage associated with LSM. Specifically, it emphasizes the utility of SSS in assessing the extent of cardiac involvement, thereby furnishing essential evidence to inform clinical treatment decisions. ***References:*** 1. Wen-Chen LI, Nishino. Lipid storage myopathy. Curr Neurol Neurosci Rep. 2010; 11(1).2. Chanarin I, Patel A, Slavin G, Wills EJ, Andrews TM and Stewart G. Neutral-lipid storage disease: a new disorder of lipid metabolism. British medical journal. 1975; 1(5957):553-555.

EP-0594

Triglyceride is associated with coronary microvascular dysfunction in patients with obstructive coronary artery disease

Y. Wang, *Y. Lu, X. Zhang;*
Department of Nuclear Medicine, Beijing Anzhen Hospital, Capital Medical University, Beijing, CHINA.

Aim/Introduction: Coronary microvascular dysfunction (CMVD) is one of the significant causes of myocardial ischemia, and is widely present in patients with obstructive coronary artery disease (OCAD) and non obstructive coronary disease (NOCAD). This prospective study sought to evaluate the CMVD though quantitative myocardial blood flow assessment derived by CZT-SPECT, and compare the difference of CMVD in patients with OCAD versus NOCAD at the patient level and the coronary vessel level, and to identify the risk factors associated with CMVD in patients with OCAD. ***Materials and Methods:*** Patients diagnosed with suspected or known CAD, and suspected of having CMVD, was underwent pharmacological stress and rest gated myocardial perfusion imaging (G-MPI), prospectively. They also completed dynamic acquisition for coronary flow reserve (CFR) assessment within three months before or after coronary angiography (CAG) or coronary computed tomography angiography (CCTA). CMVD was defined as the coronary stenosis < 50% and the CFR < 2.1. Multivariable logistic regression analysis was used to identify the risk factors associated with the co-occurrence of CMVD in patients with OCAD. ***Results:*** A total of 54 patients (mean age 58±9 years, 33 men) and 162 vessels were finally enrolled. Among the patients, there were 39 cases of OCAD and 15 cases of NOCAD. In the OCAD group, 57 coronary arteries had stenosis less than 50%, among which 14 were diagnosed with CMVD. In the NOCAD group, out of 45 coronary arteries, 15 were diagnosed with CMVD. (1) At the vessel level, there is no significant difference between the detection rate of CMVD in OCAD and NOCAD patients (24.6% vs. 33.3%,P > 0.05). At the patient level, there is no significant difference between the two groups (15.4% vs. 33.3%, P = 0.276). (2) In patients with OCAD, elevated triglyceride is an independent risk factor for the coexistence of CMVD (OR = 1.956, 95% CI: 1.031-3.712, P = 0.04). ***Conclusion:*** The detection rate of CMVD was similar between OCAD and NOCAD patients. For patients with OCAD, increased triglyceride is an independent risk factor for the presence of CMVD.

EP-0595

The prognosis value of coronary microvascular dysfunction in chronic coronary syndrome patients compared with global coronary flow reserve

Y. Wang, *Y. Zhao, X. Zhang;*
Department of Nuclear Medicine, Beijing Anzhen Hospital, Capital Medical University, Beijing, CHINA.

Aim/Introduction: Impaired global coronary flow reserve (CFR) and coronary microvascular disease (CMVD) is associated with adverse outcomes in coronary artery disease (CAD) patients. This prospective study sought to evaluate whether CMVD contributes to the worsened outcomes in chronic artery disease (CCS) patients and those with normal global left ventricular CFR. ***Materials and Methods:*** Patients diagnosed with CCS and suspected of having CMVD were prospectively enrolled. Individuals with prior myocardial infraction or revascularization were excluded. Participants underwent pharmacological stress and rest gated myocardial perfusion imaging (G-MPI) and completed dynamic acquisition for CFR assessment by using CZT-SPECT within three months before or after coronary angiography (CAG) or coronary computed tomography angiography (CCTA). CMVD was defined as having coronary stenosis < 50% along with impaired CFR (CFR < 2.1). The major adverse cardiac events (MACE) included rehospitalization for angina, repeat CAG, acute myocardial infarction, late revascularization, and all-cause death. Kaplan-Meier survival analysis and log-rank tests were used to compare outcomes between groups and to assess the prognostic value of impaired CFR and CMVD. ***Results:*** A total of 54 patients (mean age 58 ± 9 years, 33 men) were recruited for the study. Among these patients, 11 were diagnosed with CMVD, of which 8 exhibited impaired global CFR. In the 43 patients without CMVD, 7 were

diagnosed with impaired global CFR. Over a median follow-up duration of 164 days (interquartile range I77-232 days), 5 patients (9.26%) experienced cardiac events. Kaplan-Meier analysis showed significantly higher event rates in patients with impaired global left ventricular CFR (20%[3/15]vs. 5.13%[2/39],Log-rank = 4.564, P <0.05), in comparison with patients with normal CFR.. However, no significant difference was observed in the event rate between patients with and without CMVD (18.18% vs. 6.98%, P = 0.054). Among patients with normal global CFR, there was also no significant difference in the MACE rate between those with and without CMVD (P > 0.05). ***Conclusion:*** Among CCS patients, the presence of CMVD indicates a trend toward an increased risk of adverse outcomes. Although this trend is not statistically significant, it highlights the need for larger patient cohorts in future studies.

EP-0596

Decrease in Ejection Fraction between Rest and Stress on Myocardial Perfusion Imaging Studies: Frequency and Potential Clinical Significance

F. Naeem*, V. Pant, S. Salam, A. Chamnan, L. Yeung, S. Vinjamuri;*
Royal Liverpool University Hospital, Liverpool, UNITED KINGDOM.

Aim/Introduction: Myocardial Perfusion Imaging (MPI) plays a crucial role in evaluating cardiac function, with resting Ejection Fraction (EF) commonly included in routine MPI assessments. Recent guidelines from the American Society of Nuclear Cardiology (ASNC) highlight the prognostic value of identifying a decline of 10% or more in EF between rest and stress phases, as this may independently signal a poor cardiac outcome. This study aimed to assess the frequency of such EF changes and their potential link to adverse cardiovascular events. ***Materials and Methods:*** We performed a retrospective review of MPI scans from 100 patients (60 female) conducted between July 2023 and January 2024. Reports and images were analyzed, and EF values were re-evaluated when required. We specifically looked for cases showing a drop in EF greater than 10% between stress and rest imaging. In the second phase, we followed these patients for 12 months, identifying any significant cardiac events or markers associated with poor prognosis. ***Results:*** Of the 100 patients reviewed, only 2 had both stress and rest EF values documented in their reports. One showed a >10% EF decline, while the other did not exhibit any significant change. An additional 16 patients (10 female) were identified during reanalysis to have an unreported EF drop of more than 10%. Among the remaining 82 cases, 37 had higher EF values during stress, 25 had a mild EF reduction (3-9%), and 19 had nearly identical stress and rest EF values (±3%). During the 12-month follow-up, 10 patients died. One of these individuals had a significant (>10%) EF drop that had not been reported initially. This patient, who experienced chest discomfort and breathlessness, had an otherwise normal MPI scan. The death was due to community-acquired pneumonia resulting in cardiorespiratory failure. Among the other nine deaths, two were caused by out-of-hospital cardiac arrests. One of these patients had reversible ischemia on their MPI and a history of coronary artery bypass surgery. ***Conclusion:*** Only a small percentage (2%) of patients had both EF values reported. While significant EF changes did not consistently predict cardiac death, we advocate for reporting both values routinely. EF data should be interpreted within the full clinical context, as a clear link between EF changes and major cardiac events remains uncertain in this limited study. ***References:*** Quality Metrics for Single-photon Emission Computed Tomography Myocardial Perfusion Imaging: An ASNC Information Statement.

EP-0597

Myocardial Perfusion Scintigraphy with Regadenoson and Correlation with the Findings of Coronary Angiography

M. Ilic Tomas*[1,2], K. Žepina[2], P. Stroglio[2], L. Fischer[1,2], I. Iskra[1,2], T. Bogović Crnčić[1,1];*
[1]Clinical Hospital Centre Rijeka, Rijeka, CROATIA, [2]University of Rijeka, Faculty of Medicine, Rijeka, CROATIA.

Aim/Introduction: Myocardial perfusion scintigraphy (MPS) using Regadenoson is a well-established, non-invasive method for evaluating myocardial ischemia, particularly in patients unable to perform adequate exercise stress testing. While MPS provides valuable functional insight into myocardial blood flow, invasive coronary angiography (CA) remains the anatomical gold standard for assessing coronary artery disease (CAD). This study aims to compare MPS results with CA findings in order to assess the diagnostic concordance between functional and anatomical assessments in detecting significant CAD and guiding clinical decisions. ***Materials and Methods:*** This retrospective study included 206 patients who underwent Regadenoson MPS. A fixed 400 µg dose of Regadenoson was administered for pharmacologic stress in individuals with contraindications to exercise. Among them, 109 patients (52.9%) also underwent invasive CA, allowing for direct comparison between perfusion abnormalities and anatomical lesions. MPS was considered positive in cases of reversible ischemia and negative in the presence of myocardial scarring. CA was deemed positive if it revealed significant obstructive lesions, occlusions, or high-grade stenoses. Statistical analysis included the chi-squared test to evaluate associations, Phi coefficient to assess the strength of association, and Pearson's correlation coefficient to determine linear correlation between MPS and CA. The Mann-Whitney U test was used to assess relationships between clinical variables, including symptoms, ECG changes, ejection fraction, myocardial contractility, heart rate response, and adverse effects. A p-value of less than 0.05 was considered statistically significant. ***Results:*** The median age of the study population was 69 years, with 64.1% being female. Regadenoson was generally well tolerated, with only mild and transient adverse effects reported. Among the 109 patients who underwent both MPS and CA, 62 (56.9%) had a positive MPS result. Of these, 16 (25.8%) had significant findings on CA, whereas 46 (74.2%) did not. A statistically significant association between positive MPS and CA findings was observed (p = 0.0346), with a Phi coefficient of 0.162 indicating a weak yet meaningful association. Pearson's correlation coefficient was r = 0.178 (p = 0.020), confirming a statistically significant but weak correlation between the two diagnostic modalities. ***Conclusion:*** Regadenoson MPS is a safe, well-tolerated, and effective tool for assessing myocardial ischemia in patients unable to perform exercise testing. Despite statistically significant correlations with CA, the weak association highlights the importance of combining both functional and anatomical imaging techniques for a more comprehensive and reliable CAD evaluation.

EP-0598

Head-to-head comparison of Left Ventricular Ejection Fraction and Volumes from 3D-ring CZT and dedicated Cardiac CZT SPECT Cameras

V. Roelants*[1], F. Dupont[2], A. Oulad Bouchetta[2], N. Laajimi[2], R. Lhommel[2], M. Hesse[2];*
[1]Cliniques universitaires Saint-Luc, Brussels, BELGIUM, [2]Cliniques universitaires Saint-Luc - Université Catholique de Louvain, Brussels, BELGIUM.

Aim/Introduction: The comparison between a 3D-ring CZT SPECT camera (3D CZT) and a dedicated cardiac CZT SPECT camera (cardiac CZT) in terms of left ventricular functional parameters derived from perfusion studies has yet to be

thoroughly investigated. In this study, we directly compared the left ventricular ejection fraction (LVEF), end-diastolic volume (EDV) and end-systolic volume (ESV) obtained from a 3D CZT to those obtained using a cardiac CZT, within the same patient cohort. ***Materials and Methods:*** Twenty-seven patients (19 male; age: 67 ± 15 years, BMI: 28 ± 6 kg/m2) with suspected or known coronary artery disease and referred for a two-day stress/rest myocardial perfusion SPECT imaging (MPI) have been included at this stage. ECG-gated (16 bins) acquisitions were performed 30-60 minutes after injection of 359 ± 18 MBq of a 99mTc-labeled perfusion tracer. Imaging was first conducted on the cardiac CZT (5-minute acquisition), followed immediately by the 3D CZT (12-minute acquisition). Stress and rest images were reconstructed with the manufacturer's iterative algorithms and settings specific to each camera, without applying attenuation correction. LVEF, EDV and ESV were calculated from each reconstruction using Quantitative Gated SPECT (QGS) software. Results were analyzed using linear regression and Wilcoxon Signed-Rank test, while Bland-Altman plots served to evaluate the level of agreement. ***Results:*** LVEF, ESV and EDV values were automatically obtained for 23 patients. Manual adjustment of the LV contour was required in the remaining 4 patients. The comparison between 3D CZT and cardiac CZT gave the following results: 60.6 ± 9.3 % vs 60.6 ± 8.9 % (p=0.79) for LVEF (range: 44-80 % vs 42-80 %), 99.3 ± 30.5 ml vs 100.5 ± 30.2 ml (p=0.38) for EDV and 41.0 ± 19.1 ml vs 41.5 ± 19.2 ml (p=0.66) for ESV. Linear correlation was strong for LVEF (R=0.85, p< 0.001) and excellent for both EDV (R=0.95, p<0.001) and ESV (R=0.94, p<0.001). Bland-Altman analysis revealed non-significant overall bias of 0.02 % for LVEF (95% limit of agreement: -9.92 to 9.97 %), of -1.19 ml for EDV (95% limit of agreement: -19.5 to 17.1 ml) and of -0.47 ml for ESV (95% limit of agreement: -13.9 to 13.0 ml). ***Conclusion:*** LVEF, EDV and ESV as determined by QGS software from gated 3D CZT 99mTc-labeled MPI agree over a wide range of clinically relevant values with cardiac CZT, without any significant bias.

EP-0599

Can Myocardial Perfusion Imaging Predict Heart Rhythm Disturbances After Coronary Revascularization?

L. Sobral Torres*, R. Albergueiro, P. Dias, P. Soeiro;*
Unidade Local de Saúde São João, Porto, PORTUGAL.

Aim/Introduction: Myocardial Perfusion Single Photon Emission Computed Tomography (MPS) is routinely used in the follow-up of ischemic heart disease when new symptoms emerge. However, its role in asymptomatic individuals after coronary artery bypass grafting (CABG) is less defined. Post-operative heart rhythm disturbances are common and have been linked to adverse long-term outcomes. This study aims to explore the potential of MPS as a tool for identifying asymptomatic post-CABG patients at increased risk for developing heart rhythm abnormalities. ***Materials and Methods:*** A retrospective analysis at a single tertiary care center was conducted, including asymptomatic adults who underwent MPS within three years of CABG between January and June 2013. Patients with non-coronary cardiac conditions or confounding treatments were excluded. MPS scans were assessed using QGS/QPS and SyncTool™ software to evaluate perfusion, wall motion, and left ventricular function. Patient demographics and clinical data were collected, and follow-up extended to December 2023 to document Major Adverse Cardiovascular Events (MACE) and the onset of rhythm disturbances such as conduction delays and supraventricular arrhythmias. Cox regression models were applied using R software, including both univariate and multivariate analyses with 16 imaging and functional parameters. ***Results:*** Fifty patients fulfilled the inclusion criteria, (mean age 66±9.2 years; 78% male), with MPS performed a mean of 10±10 months post-CABG. The average stress EF was 63±10%. Fifteen patients (30%) developed rhythm abnormalities over follow-up, primarily atrial fibrillation (66%), with a mean onset at 6.75±3.5 years post-surgery. In univariate analysis, elevated end-systolic eccentricity (ESE) was associated with a 5% increased risk of arrhythmia (HR = 1.05). A multivariate model including ESE, stress EF, and the anterior descending artery (ADA) motility SSS showed all variables were statistically significant. ESE and ADA SSS had hazard ratios of 1.11 (p=0.006) and 1.13 (p<0.001), respectively. ***Conclusion:*** Our findings suggest that MPS may be a valuable non-invasive tool for stratifying arrhythmic risk in asymptomatic patients post-CABG. These results support further prospective validation of MPS in post-operative rhythm surveillance.

EP-33

e-Poster Area

B: Imaging Clinical Studies -> B4 Cardiovascular Imaging Clinical Study -> B42 Metabolism and Innervation

EP-0600

Nothing Else Matters? — The Predominant Association of BHB and Myocardial Glucose Metabolism Suppression

T. Korhonen[1]*, A. Valve-Dietz*[1]*, T. Laitinen*[1]*, S. Hartikainen*[2]*;*
[1]*University of Eastern Finland, Kuopio, FINLAND,* [2]*Kuopio University Hospital, Kuopio, FINLAND.*

Aim/Introduction: The purpose of this study was to investigate if there were other metabolic or functional myocardial stress factors that predict the inadequacy of myocardial glucose metabolism suppression other than β-hydroxybutyrate levels (BHB). ***Materials and Methods:*** There were 156 participants (83 male) who underwent whole body [^{18}F]-fluorodeoxyglucose (FDG) PET/CT-scan for the indication of inflammatory cardiovascular diseases. Standardized uptake value (SUV) ratio was calculated with average SUV_{MAX} values of left ventricle myocardium divided by the SUV_{MAX} of the left ventricular blood pool background. SUV-ratio≤1 was defined as adequate suppression. Blood glucose and BHB were measured with a point-of-care device. Two observers independently evaluated visual ordinal coronary artery calcification (CAC)-score from non-gated CT-scans by giving each coronary artery a score ranging from 0 (no calcification) to 3 (severe calcification) and summing up the score. The arithmetic mean of the two CAC-scores was rounded to the closest integer. Inter-rater reliability for ordinal CAC-score was calculated with two-way mixed intraclass correlation coefficient (ICC) on absolute agreement. Ejection fraction of the heart was obtained from medical records of 136 patients who had undergone a transthoracic echocardiogram (TTE) within 365 days of the FDG-PET/CT-scan. Heart failure with reduced ejection fraction (HFrEF) was classified as ejection fraction <40%. The ECGs of the patients were assessed for possible left or right bundle branch block (LBBB or RBBB) or ventricular paced rhythm. The QRS-times of the patients were measured. Continuous variables were tested using Mann-Whitney U test and categorical variables using Pearson Chi-squared test. ***Results:*** Median (min-max) age was 58 (19-79) years, BMI 28.3 (17.0-54.4) kg/m^2, SUV-ratio 0.80 (0.45-12.94), BHB 0.4 (0.1-5.8) mmol/l, blood glucose 5.0 (2.8-10.4) mmol/l, visual ordinal CAC-score 2 (0-12), QRS-time 104 (75-186) ms. There were 16 patients with LBBB, 20 with RBBB and 16 with ventricular paced rhythm. ICC of ordinal CAC-score was 0.905 (0.770-0.951, p<0.001). Of the 144 patients who had undergone TTE, 13 had HFrEF. There was significant difference in BHB between those with adequate and inadequate suppression (0.3 (0.1-2.6) mmol/l vs 0.4 (0.1-5.8) mmol/l, p<0.001). There were no significant differences in blood glucose, ordinal CAC-score, intraventricular conduction, nor prevalence of HFrEF between groups with adequate and inadequate suppression. ***Conclusion:*** Only BHB predicts suppression of myocardial glucose metabolism. It seems

that neither blood glucose, ordinal CAC-score, intraventricular conduction nor HFrEF give valuable information predicting the suppression of myocardial glucose metabolism.

EP-0601

Prognostic Value of ^{18}F-FDG PET Myocardial Ischemic Memory Imaging in Patients with Non-Obstructive Coronary Artery Disease

F. Zhang, *X. Yang, Y. Wang;*
the Third Affiliated Hospital of Soochow University, Changzhou, CHINA.

Aim/Introduction: ^{18}F-FDG PET myocardial ischemic memory imaging has been used to diagnose myocardial ischemia. However, its prognostic value in patients with non-obstructive coronary artery disease (NOCAD) remains unclear. This study aimed to investigate the predictive value of ^{18}F-FDG PET myocardial ischemic memory imaging for major adverse cardiovascular events (MACE) during follow-up in patients with NOCAD. ***Materials and Methods:*** This prospective, observational cohort study enrolled 106 patients with unstable angina who showed <50% stenosis in major epicardial coronary arteries on coronary angiography. All patients underwent ^{18}F-FDG PET myocardial ischemic memory imaging. A positive ^{18}F-FDG scan was defined as focal or focal on diffuse uptake. All patients received optimized medical therapy. Clinical follow-up was conducted, and the primary endpoint was the occurrence of MACE, defined as cardiovascular death, re-hospitalization for UA, heart failure, acute myocardial infarction, or stroke. ***Results:*** Among the 106 patients, 54 (50.9%) were male, with a mean age of 65.5 ± 8.5 years. The median follow-up period was 26 months (IQR: 17-42 months), during which 15 patients (14.2%) experienced MACE. Univariate Cox regression analysis identified positive ^{18}F-FDG imaging, ^{18}F-FDG standardized uptake ratio (SUR), and the extent of abnormal ^{18}F-FDG uptake as a percentage of the left ventricle (Extent) as significant predictors of MACE. After adjusting for age, sex, hypertension, hyperlipidemia, and diabetes, multivariate Cox regression analysis confirmed that positive ^{18}F-FDG imaging (HR = 7.638; 95% CI: 2.474~23.584; P = 0.0004), ^{18}F-FDG SUR (HR = 2.246; 95% CI: 1.549~3.257; P < 0.0001), and ^{18}F-FDG Extent (HR = 1.061; 95% CI: 1.034~1.088; P < 0.0001) were all independent predictors of MACE. Kaplan-Meier survival analysis further demonstrated that patients with positive ^{18}F-FDG imaging had significantly lower MACE-free survival compared to those with negative imaging results (P = 0.0001). Additionally, the incidence of MACE was significantly higher in the ^{18}F-FDG-positive group (37.5%) compared to the ^{18}F-FDG-negative group (10.0%) (χ^2 = 8.457, P = 0.010). ***Conclusion:*** Myocardial ischemia detected by ^{18}F-FDG PET ischemic memory imaging is an independent risk factor for MACE in patients with NOCAD. Patients with positive ^{18}F-FDG imaging had a 7.6-fold increased risk of MACE compared to those with negative imaging. These findings highlight ^{18}F-FDG PET ischemic memory imaging as a promising biomarker for risk stratification in NOCAD patients, with potential to accurately predict cardiovascular events and support precision-guided clinical management.

EP-0602

Myocardial [^{18}F]FDG uptake suppression after six hours fasting predicts 3-year overall survival in men

S. Hartikainen[1], *S. Sillanmäki*[2], *M. Hedman*[2], *T. Tompuri*[3], *T. M. Laitinen*[1], *T. P. Laitinen*[1];
[1]*Kuopio University Hospital, Kuopio, FINLAND,* [2]*University of Eastern Finland, Kuopio, FINLAND,* [3]*North Karelia Central Hospital, Joensuu, FINLAND.*

Aim/Introduction: Reduced myocardial uptake [^{18}F]FDG-PET/CT after 6h fasting is linked with metabolic disorders, including diabetes and fatty liver. We assessed whether 6h fasting-indused myocardial FDG suppression (FDG_{sup}) predicts overall survival (OS). ***Materials and Methods:*** We recruited adults with clinical indication for FDG-PET/CT after 6h fasting and measured glucose and β-hydroxybutyrate (BHB) with a point-of-care device. Patients who had followed a ketogenic diet before imaging were excluded. Myocardial FDG uptake was categorized visually as FDG_{sup} or non-suppressed. Two-centimeter diameter regions of interest were placed in the liver and spleen to assess for fatty liver. Liver-to-spleen attenuation ratio (LSR) <1 was defined as fatty liver. Age-adjusted survival analysis was performed using Cox regression. ***Results:*** A total of 131 patients (69 male) participated. In men, median age was 68 (25-87) years, body mass index (BMI) 26 (19-38) kg/m^2, fasting glucose 5.5 (4.5-9.4) mmol/l, BHB 0.2 (0.0-0.8) mmol/l, and LSR 1.18 (0.52-1.60). There were 17 men (25%) with diabetes, 39 (57%) with hypertension, and 15 (22%) with fatty liver. In women, median age was 67 (26-83), BMI 29 (17-55) kg/m^2, glucose 5.4 (4.2-8.2) mmol/l, BHB 0.2 (0.0-0.7) mmol/l, and LSR 1.23 (0.83-1.88). There were 7 women (11%) with diabetes, 31 (50%) with hypertension, and 6 (10%) with fatty liver. BMI was higher in women (p=0.035), while the rate of diabetes was higher in men (p=0.049). No other sex-related differences were found. During the median follow-up of 1157 days (IQR: 1083-1219 days), 35 patients (22 male) died. In men, the rate of FDG_{sup} was higher among patients who died compared to those who survived (45% vs. 21%, p=0.039). There were no other statistically significant differences between the survival groups. The OS was 50% in men with FDG_{sup}, and 76% in men without suppression (p=0.038), with an annual event rate of 19% in men with FDG_{sup} and 9% in men without suppression. The age-adjusted survival was lower in men with FDG_{sup} (p=0.052), hazard ratio 2.37 (95% CI 1.02-5.50). There was no difference regarding OS in women with or without FDG_{sup} (80% vs. 79%, p=0.974). Women had an annual event rate of 8%. ***Conclusion:*** Over a 3-year follow-up period, men with myocardial FDG suppression after 6h fasting had worse prognosis compared to those without suppression - a pattern not observed in women. This sex-specific difference may reflect metabolic disorders and suggest potential as a prognostic biomarker in men. However, further research with extended follow-up is needed.

EP-0603

A Prospective Clinical Study on the Diagnostic Value of ^{18}F-FDG PET Ischemic Memory Imaging for Unstable Angina in Diabetic and Non-Diabetic Patients

f. Zhang, *X. Yang, Y. Wang;*
the Third Affiliated Hospital of Soochow University, Changzhou, CHINA.

Aim/Introduction: To evaluate the diagnostic value of ^{18}F-FDG PET ischemic memory imaging for unstable angina (UA) in patients with and without diabetes mellitus. ***Materials and Methods:*** This prospective cohort study consecutively enrolled patients presenting with chest pain or discomfort to the Chest Pain Center or Department of Cardiology at The Third Affiliated Hospital of Soochow University between March 17, 2020 and May 11, 2024. All patients had an initial negative evaluation but were still clinically suspected of having UA. Each patient underwent ^{18}F-FDG PET ischemic memory imaging and coronary angiography. Based on final clinical diagnoses, patients were classified into a UA group and a non-UA group. ***Results:*** A total of 272 patients with suspected UA were enrolled in the study (mean age: 64.8 ± 9.6 years; 62.9% male; 33.2% with diabetes). UA was confirmed in 139 patients (51.1%). The sensitivity, specificity, positive predictive value (PPV), negative predictive value (NPV), and overall accuracy of ^{18}F-FDG PET ischemic memory imaging for diagnosing UA were 63.3%, 92.5%, 90.7%, 70.3%, and 77.6%, respectively, in the overall cohort. In the diabetic subgroup, the corresponding values were 51.0%, 90.5%, 86.2%, 61.3%, and 69.2%, while in the non-diabetic subgroup, they were 70.0%, 93.4%, 92.6%, 75.2%, and 81.8%, respectively. Receiver operating characteristic (ROC) curve analysis yielded an area under the curve (AUC) of 0.761 for the entire cohort,

0.707 for diabetic patients, and 0.789 for non-diabetic patients (all P < 0.001). Compared with diabetic patients, non-diabetic patients demonstrated significantly higher sensitivity (70.0% vs. 51.0%) and accuracy (81.8% vs. 69.2%) (P < 0.05). The NPV was also higher in non-diabetic patients, with a trend toward significance (75.2% vs. 61.3%, P = 0.059). ***Conclusion:*** ^{18}F-FDG PET ischemic memory imaging demonstrates good diagnostic performance in patients with suspected UA. Its sensitivity is lower in diabetic patients compared to non-diabetic patients, although both groups exhibit high positive predictive values. This imaging technique shows promise as a novel adjunctive diagnostic tool for UA.

EP-0604

Evaluation of Oral Versus Intravenous Glucose Loading Protocols on Image Quality in Cardiac FDG PET: A Comparative Qualitative and Quantitative Study

M. Calderon Tobar, *A. Gümüş, K. Çağlar, F. Yılmaz, H. Önner; Selcuk University Faculty of Medicine Department of Nuclear Medicine, Konya, TÜRKIYE.*

Aim/Introduction: To compare the effects of intravenous (IV) and oral glucose loading protocols on image quality in cardiac FDG PET, utilizing both qualitative and quantitative parameters. ***Materials and Methods:*** This retrospective study included 74 patients (mean age: 65.5±10.2 years; 9 females) undergoing cardiac FDG PET. All patients required glucose loading protocols based on TSNM guidelines. Patients received an IV (n=28) or oral (n=46) glucose loading protocol before imaging. Visual image quality was scored as uninterpretable, suboptimal, or optimal. A Chi-square test was used to compare visual image quality between the two glucose loading protocols. Quantitative parameters included left ventricular (LV) myocardial SUVmax, LV blood pool SUVmax, and their ratio. Comparisons between groups were performed using the Mann-Whitney U test. ***Results:*** Optimal imaging was achieved in 71.4% (20/28) of patients in the IV group and 69.6% (32/46) in the oral group. Among the 28 patients who underwent the IV glucose loading protocol, 20 (71.4%) demonstrated optimal image quality, while 2 (7.1%) were classified as suboptimal and 6 (21.4%) as uninterpretable. In the oral glucose loading group (n=46), optimal imaging was achieved in 32 patients (69.6%), with 6 (13.0%) rated as suboptimal and 8 (17.4%) as uninterpretable. The difference in visual image quality between the IV and oral glucose loading protocols is not statistically significant (p=0.87). Among 28 patients with diabetes mellitus (DM), optimal imaging was achieved in 50% (14/28). In insulin users (n=5), optimal imaging was observed in only one patient. Quantitatively, the LV blood pool SUVmax was significantly higher in the IV glucose loading protocol group (median 2.00) than the oral glucose loading protocol group (median 1.36, p=0.002). No significant differences were observed in LV myocardial SUVmax (p=0.469) or the myocardial-to-blood pool SUVmax ratio (p=0.196). ***Conclusion:*** IV and oral glucose loading protocols yielded acceptable rates of optimal imaging in cardiac FDG PET studies, with no significant differences in myocardial SUVmax or myocardial-to-blood pool SUVmax ratios. However, the IV protocol resulted in a significantly higher LV blood pool SUVmax. These findings suggest that the choice of protocol may influence blood pool activity and, consequently, interpretation, particularly in diabetic and insulin-using patients.

EP-0605

The Impact of Preoperative Phase Analysis, Hibernating Myocardium Percentage, and Inflammatory Parameters Derived from gMPS, F-18 FDG PET/CT, and Biochemistry on Postoperative Ejection Fraction and Wall Motion Abnormalities in Patients Undergoing Coronary Artery Bypass Grafting

H. Kalkan, *A. Kılıçaslan, Ö. Bayrakcı, M. Serdengeçti, H. Şan; Ankara Bilkent City Hospital, Ankara, TÜRKIYE.*

Aim/Introduction: F-18 FDG PET/CT myocardial viability imaging is a routine modality used to assess viable tissue in patients with fixed perfusion defects on gated myocardial perfusion SPECT(gMPS) prior to revascularization. This study aims to investigate the association between postoperative changes in ejection fraction(EF), left ventricle wall motion abnormalities, preoperative parameters obtained from gMPS phase analysis, PET/CT, and biochemical inflammatory markers in patients undergoing coronary artery bypass grafting(CABG). ***Materials and Methods:*** Thirty-eight patients who underwent both gMPS and PET/CT viability studies prior to CABG were retrospectively included. From gMPS, phase analysis parameters (histogram bandwidth and standard deviation) were extracted, while hibernating myocardial segments and their percentage were obtained from FDG PET/CT. Pre- and postoperative EF and wall motion findings were recorded from echocardiographic reports. Inflammatory markers were calculated from preoperative CBC and standard biochemistry tests performed within one month of viability imaging, using various ratio-based indices. Statistical analysis was performed using SPSS version 27. Spearman's correlation test was applied to assess associations between postoperative EF, EF improvement, wall motion recovery, and the imaging and laboratory parameters. A p-value < 0.05 was considered statistically significant. ***Results:*** Of the patients, 15.8% were female (n=6), with a mean age of 63.9±28.27 years. The mean percentage of hibernating myocardium was 16.87±11.77%. The mean preoperative EF was 36.77±11.1%, postoperative EF was 31.81±10.4%, and mean EF improvement was calculated as 4.13±3.9%. Early postoperative mortality occurred in 28.9% (n=11) of the cohort. No statistically significant correlations were found between hibernating myocardium percentage or phase analysis parameters and postoperative EF, EF improvement, or wall motion recovery (p>0.05). However, EF improvement and wall motion recovery demonstrated statistically significant negative correlations with the following inflammatory markers: neutrophil-to-lymphocyte ratio(-0.485), monocyte-to-lymphocyte ratio(-0.491), systemic immune-inflammation index(-0.363), systemic inflammatory response index(-0.490), total systemic inflammation index(-0.411), neutrophil/HDL(-0.353), neutrophil/LDL(-0.353), neutrophil/albumin(-0.394) (p<0.05). ***Conclusion:*** Preoperative gMPS-derived phase analysis and PET viability findings did not show a statistically significant relationship with postoperative EF improvement or recovery of wall motion. This may be attributed to factors such as multivessel revascularization, reliance on early postoperative (within 6 months) echocardiographic data, early mortality, lack of classification based on preoperative risk stratification, and variability in test standardization. In contrast, inflammatory indices calculated from preoperative blood and biochemistry tests were significantly correlated with both EF improvement and wall motion recovery. The inverse relationship suggests that elevated subclinical inflammation may negatively affect myocardial recovery, consistent with its known detrimental role in atherosclerotic cardiovascular disease.

EP-0606

Optimized Fast Track Protocol: Enhancing ^{18}F-FDG PET Myocardial Viability Imaging Quality While Minimizing Patient Preparation Time in Diabetic CAD Patients

A. Mandal, *S. Taywade, A. K Majeed, R. Kumar; AIIMS Jodhpur, Jodhpur, INDIA.*

Aim/Introduction: The standard ASNC protocol often leads to suboptimal image quality in ^{18}F-FDG PET myocardial viability studies for diabetic patients. In this study, we aimed to assess the impact of an alternate optimized fast track (OFT) protocol on the image quality of ^{18}F-FDG PET cardiac viability study in diabetic patients with CAD. ***Materials and Methods:*** We enrolled total 50 patients. Based on certain characteristics (duration of

diabetes, HbA1C level and FBS level), we stratified the patients into six subgroups. Then we allocated them into two groups using stratified randomization technique. In one group standard ASNC protocol was followed and in the other group OFT protocol was applied for patient preparation. Images were analysed qualitatively with visual grading scale as well as semi-quantitatively with myocardium to blood pool (M/B) ratio. Patient preparation time (PPT) was determined from the time of oral glucose administration to the time of ^{18}F-FDG injection. We compared the image quality and PPT between the two groups. ***Results:*** Demographic details in the standard protocol group were as follows: 6-females, 19-males; mean age was 58.56±8.21 years. In the OFT group, there were 7-females and 18-males; mean age was 61.20±10.05 years. There was larger proportion of interpretable images in the OFT group (92% vs. 64%) and larger proportion of un-interpretable images in the standard protocol group (36% vs. 8%). The mean±SD of M/B Ratio in the OFT group (12.44±5.37) was higher than the standard protocol group (7.23±3.42) with a p value of <0.001. PPT was lesser in the OFT group (median time = 82 minutes) as compared to standard protocol group (median time = 95 minutes). ***Conclusion:*** The proposed OFT protocol for patient preparation in ^{18}F-FDG PET myocardial viability studies delivers superior image quality and shortens preparation time for diabetic patients compared to the standard ASNC protocol. This novel OFT protocol can be readily adopted into the routine clinical practice for ^{18}F-FDG PET myocardial viability studies particularly among diabetic patients.

EP-0607

The heart-to-mediastinum ratio of [^{123}I]I-mIBG myocardial scintigraphy: planar versus reprojected planar images

J. Hagerman*, S. Akil Engblom, F. Hedeer;*
Clinical Physiology, Department of Clinical Sciences Lund, Lund University, Skåne University Hospital, Lund, SWEDEN.

Aim/Introduction: Myocardial sympathetic innervation can be assessed by determining the heart-to-mediastinum ratio (HMR) on planar iodine-123-metaiodobenzylguanidine ([^{123}I]I-mIBG) myocardial scintigraphy images, with a standardized methodology. Acquisition of single-photon emission computed tomography (SPECT) is also advised for regional assessment. Software enables SPECT-data to be reprojected to planar images, thus facilitating determining HMR on three-dimensional data and a SPECT-only acquisition. This study aimed to evaluate the agreement between HMR determined on planar and reprojected planar [^{123}I]I-mIBG myocardial scintigraphy images, acquired on two technological different gamma cameras, for the assessment of myocardial sympathetic innervation. ***Materials and Methods:*** [^{123}I]I-mIBG myocardial scintigraphy images from nineteen patients, clinically referred for assessment of myocardial sympathetic innervation due to suspected neurodegenerative disorder, were included. Planar and SPECT images, with low-dose computed tomography (CT), were acquired on an Anger camera (Discovery NM/CT 670), followed by SPECT-CT on a ring-configured CZT camera (StarGuide), four hours post-injection of 252±6 MBq [^{123}I]I-mIBG. SPECT images were reconstructed with ordered subset expectation maximization (4 iterations, 10 subsets, Butterworth 0.5/5), corrected for collimator detector response and attenuation, with and without correction for scatter (SC and NSC), and converted to reprojected planar images (RP), in a software provided by Hermes and GE HealthCare, respectively. HMR was determined on anterior projections of planar$_{Anger}$, RP$_{Anger_SC}$, RP$_{Anger_NSC}$, RP$_{CZT_SC}$, and RP$_{CZT_NSC}$ images by manually drawing regions-of-interest over the heart and the mediastinum. The planar$_{Anger}$ images were used as a reference and differences in HMR between planar and RP images were analyzed with the Wilcoxon matched-pairs signed-rank test (significance level p<0.05). The agreement was analyzed with Bland-Altman (mean difference, 95% limits of agreement). ***Results:*** The median (interquartile range) HMR was 1.44 (1.15-1.86), 1.42 (1.11-2.24) and 1.41 (1.11-1.92) from the Anger camera (planar$_{Anger}$, RP$_{Anger_SC}$ and RP$_{Anger_NSC}$), and 1.45 (1.08-1.89) and 1.32 (1.12-1.69) from the CZT gamma (RP$_{CZT_SC}$ and RP$_{CZT_NSC}$). A significant difference in HMR was found between planar$_{Anger}$ and RP$_{CZT_NSC}$ images (p=0.001). The agreement between planar and RP images was good (RP$_{Anger_SC}$:-0.077, -0.50 to 0.34, RP$_{Anger_NSC}$:-0.011, -0.19 to 0.16, RP$_{CZT_SC}$:0.023, -0.19 to 0.23, and RP$_{CZT_NSC}$:0.13, -0.13 to 0.39). ***Conclusion:*** HMRs from reprojected planar [^{123}I]I-mIBG myocardial scintigraphy images, derived from SPECT images, show good agreement with HMR determined from planar images, for both a traditional Anger and a novel ring-configured CZT gamma camera. A clinical implementation of reprojected planar images seems promising, but validation is needed in a larger cohort, especially for conclusions regarding the use of scatter or non-scatter corrected images.

EP-0608

Myocardial [18F]FDG Uptake in Lymphoma Patients Undergoing Anthracycline-Based Chemotherapy: Association with Cumulative Doxorubicin Dose and Patient Characteristics

M. Kalnina*[1,2], A. Nikolajevs[3,4], A. Vikentjeva[3,4], E. Vagalis[3,4], J. Perevozcikova[4];*
[1]ARS Nuclear Medicine Clinic, Riga, LATVIA, [2]University of Latvia, Riga, LATVIA, [3]Riga East University Hospital, Riga, Latvia, [4]Riga Stradins University, Riga, LATVIA.

Aim/Introduction: Anthracycline-based chemotherapy regimens, commonly used in Hodgkin and non-Hodgkin lymphoma (HL and NHL), are known to induce cardiotoxic effects. The identification of early, subclinical myocardial metabolic changes may support timely intervention to mitigate long-term cardiac dysfunction. This study aimed to assess changes in myocardial [18F]FDG uptake during the course of chemotherapy and to investigate their association with cumulative doxorubicin dose, sex, and lymphoma subtype. ***Materials and Methods:*** A retrospective analysis was conducted on 125 patients with HL or NHL who underwent [^{18}F]FDG PET/CT imaging at three time points: baseline (pre-treatment), interim (post two chemotherapy cycles), and end-of-treatment. Inclusion criteria included absence of myocardial uptake on baseline imaging and documented cumulative anthracycline exposure. Standardized myocardial suppression protocols were applied prior to imaging. Myocardial FDG uptake was quantified in the left ventricle using SUVmax and SUVmean. Statistical analysis included Related-Samples Friedman's Two-Way Analysis of Variance by Ranks, pairwise comparisons, Spearman's correlation, and Independent-Samples Mann-Whitney U Tests. ***Results:*** Left ventricular SUVmax and SUVmean increased significantly from baseline to interim and from baseline to end-of-treatment ($p < 0.05$), while no significant change was observed between interim and end-of-treatment scans (SUVmax: $p = 0.5$; SUVmean: $p = 0.3$). ΔSUVmax demonstrated a moderate positive correlation with cumulative doxorubicin dose ($r = 0.48$, $p = 0.003$). Mann-Whitney U analysis revealed significantly greater ΔSUVmax % in male patients compared to females ($p < 0.01$). Patients with NHL exhibited higher post-treatment SUVmax values and more pronounced metabolic changes compared to those with HL ($p < 0.05$). The mean cumulative doxorubicin dose was significantly greater ($p < 0.05$). in the NHL group (444.2 mg) compared to the HL group (386.7 mg). ***Conclusion:*** [^{18}F]FDG PET/CT detects early myocardial metabolic alterations after just two cycles of anthracycline chemotherapy, with these changes persisting through treatment completion. Increased myocardial metabolic activity is more pronounced in male patients and those with NHL, both of whom receive higher anthracycline doses. These findings support the potential role of [^{18}F]FDG PET/CT in early detection of subclinical cardiotoxicity and in the identification of at-risk patient subgroups. Further prospective studies are warranted to validate

[18F]FDG PET/CT as a routine tool in cardio-oncology monitoring protocols. ***References:*** Becker, M.M.C., Arruda, G.F.A., Berenguer, D.R.F. et al. Anthracycline cardiotoxicity: current methods of diagnosis and possible role of 18F-FDG PET/CT as a new biomarker. Cardio-Oncology 9, 17 (2023). https://doi.org/10.1186/s40959-023-00161-6.

EP-34

e-Poster Area

B: Imaging Clinical Studies -> B4 Cardiovascular Imaging Clinical Study -> B43 Heart Failure (including Sarcoidosis and Amyloidosis)

EP-0609

Stacking Ensemble Learning-based Models Enabling Accurate Diagnosis of Cardiac Amyloidosis using SPECT/CT:an International and Multicentre Study

Q. Mo[1], *J. Cui*[2], *S. Jia*[3], *Y. Zhang*[2], *Y. Xiao*[4], *C. Liu*[4], *C. Zhou*[1], *C. P. Spielvogel*[5], *R. Calabretta*[5], *W. Zhou*[6], *K. Cao*[1], *M. Hacker*[5], *X. Li*[5], *M. Zhao*[1];
[1]*Third Xiangya Hospital,Central South University, Changsha, CHINA,* [2]*Fuwai Central China Cardiovascular Hospital, Zhengzhou, CHINA,* [3]*Siemens Healthineers Ltd, Shanghai, CHINA,* [4]*Xiangya Hospital,Central South University, Changsha, CHINA,* [5]*Division of Nuclear Medicine, Medical University of Vienna, Vienna, AUSTRIA,* [6]*Michigan Technological University, Houghton, MI, UNITED STATES OF AMERICA.*

Aim/Introduction: Cardiac amyloidosis (CA) is a rare and severe condition that can be diagnosed non-invasively with [99mTc]Tc-bisphosphonate imaging. However, the subjective nature of visual assessment may lead to misdiagnosis. This study aims to develop and validate a stacking machine learning (ML) model based on the radiomics of [99mTc]Tc-bisphosphonate SPECT/CT and clinical parameters for accurate CA detection. ***Materials and Methods:*** We conducted a retrospective multicenter analysis of 290 patients referred for CA evaluation across two Chinese hospitals using [99mTc]Tc-PYP SPECT/CT and one Austrian center using [99mTc]Tc-DPD. CA diagnosis was based on standard criteria. Radiomics features from SPECT/CT were extracted and selected using statistical methods and LASSO logistic regression. A stacking ensemble framework integrated four base ML classifiers with a meta-learner. The clinical model was constructed based on clinical features. Radiomics and clinical features were utilized to develop the combined model. Performance was evaluated on an internal dataset (n=178) and two external testing sets (n=54 and n=58) using discrimination (AUC), calibration curves, and decision curve analysis (DCA). ***Results:*** Among 290 patients, 117 were diagnosed with CA (40.3%). The stacking radiomics model showed good performance for predicting CA, with AUCs of 0.871 in the internal testing set, and AUCs of 0.824 and 0.839 in the external testing sets. The combined model achieved the highest AUC (0.841-0.946, with a mean AUC of 0.888±0.047) among all the study sets, significantly outperforming the clinical model (AUC = 0.546-0.820, with a mean AUC of 0.728±0.125,P = 0.0001-0.379, Delong test). DCA confirmed greater clinical utility of the combined model across probability thresholds. ***Conclusion:*** A stacking ML model with SPECT/CT radiomics and clinical parameters improves CA diagnosis, showing strong generalizability across imaging protocols and populations and highlighting its potential as a decision-support tool.

EP-0610

Application of Gated Myocardial Perfusion Imaging in Evaluating Coronary Heart Disease-Related Heart Failure with Preserved Ejection Fraction

X. Shen[1], *Z. Wang*[1], *H. Pang*[1], *C. Chen*[2], *X. Li*[2], *Z. Yao*[2];
[1]*The First Affiliated Hospital of Chongqing Medical University, Chongqing, CHINA,* [2]*Beijing Hospital, Beijing, CHINA.*

Aim/Introduction: This study aimed to evaluate the utility of single-photon emission computed tomography (SPECT) gated myocardial perfusion imaging (GMPI) in assessing heart failure with preserved ejection fraction (HFpEF) among patients with confirmed or suspected coronary artery disease (CAD). ***Materials and Methods:*** In accordance with the 2021 European Society of Cardiology Guidelines, this retrospective study included a cohort of patients with confirmed or suspected CAD who underwent SPECT GMPI. These patients were stratified into an HFpEF group (n = 83) and a control group (n = 43). Furthermore, HFpEF patients were categorized according to the New York Heart Association (NYHA) functional class into Class I, II, and III–IV. GMPI parameters analyzed included left ventricular ejection fraction (LVEF), end-diastolic volume (EDV), peak filling rate (PFR), mean filling rate during the first third of diastole (MFR/3), second peak filling rate (PFR2), time to peak filling (TTPF), summed stress score (SSS), summed rest score (SRS), and summed difference score (SDS). ***Results:*** Multivariate logistic regression analysis showed that adenosine triphosphate (ATP) stress-induced PFR (PFR_{-ATP}; OR = 0.1, P = 0.02) and SSS (OR = 1.6, P = 0.03) were independent predictors of HFpEF. Compared with SSS alone (AUC: 0.79) or PFR_{-ATP} alone (AUC: 0.84), the combined model of PFR_{-ATP} and SSS had superior predictive performance (AUC: 0.90), with statistically significant differences (P = 0.002 for comparison with SSS alone; P = 0.04 for comparison with PFR_{-ATP} alone). Notably, both PFR_{-ATP} and SSS were able to differentiate different NYHA functional classes (I, II, III–IV). Specifically, PFR_{-ATP} decreased (P = 0.004) and SSS increased (P = 0.001) with the worsening of NYHA functional class. SSS was found to be negatively correlated with $LVEF_{-ATP}$ (r = −0.48, P ≤ 0.001), PFR_{-ATP} (r = −0.36, P ≤ 0.001), and $MFR/3_{-ATP}$ (r = −0.35, P ≤ 0.001), and positively correlated with EDV_{-ATP} (r = 0.30, P = 0.005). ***Conclusion:*** SPECT GMPI can predict HFpEF in patients with confirmed or suspected CAD and effectively assess cardiac function. It has the potential to serve as a non-invasive tool for identifying the etiology of myocardial ischemia and guiding personalized management in patients with HFpEF.

EP-0611

Establishment of optimal quantitative thresholds using [99mTc]Tc-DPD SPECT/CT for the diagnosis of ATTR cardiac amyloidosis.

M. Diez[1], *A. Palomar-Muñoz*[1], *M. Marusso Fizzani*[1], *O. Hernández Cristancho*[1], *M. Pizzi*[2], *A. Roque Pérez*[3], *D. Sánchez-Artuñedo*[4], *S. Aguadé-Bruix*[1], *C. Gámez-Cenzano*[1];
[1]*Nuclear Medicine Department, Vall d'Hebron Hospital Universitari, Vall d'Hebron Barcelona Hospital Campus, Barcelona, SPAIN,* [2]*Cardiology Department, Vall d'Hebron Hospital Universitari, Vall d'Hebron Barcelona Hospital Campus, Barcelona, SPAIN,* [3]*Radiology Department, Vall d'Hebron Hospital Universitari, Vall d'Hebron Barcelona Hospital Campus, Barcelona, SPAIN,* [4]*Physics and Radiation Protection Department, Vall d'Hebron Hospital Universitari, Vall d'Hebron Barcelona Hospital Campus, Barcelona, SPAIN.*

Aim/Introduction: Transthyretin cardiac amyloidosis (cATTR) is an infiltrative pathology that requires early diagnosis to improve prognosis. The present prospective study aims to quantify myocardial deposit uptake using SPECT/CT in patients with suspected cATTR in our center, and to determine the diagnostic efficacy of different absolute quantitative parameters compared to standard visual assessment (Perugini score). ***Materials and Methods:*** We analyzed 81 consecutive patients studied between

2024 and 2025 with clinical suspicion of ATTR. All underwent [99mTc]Tc-DPD scintigraphy, acquiring whole-body scan and thoracic SPECT/CT at 3 hours post-injection. The Perugini score (0-3) was visually evaluated on the planar image. Absolute quantification of myocardial deposit was performed on SPECT/CT images using Q.Volumetrix software (GE Healthcare®), obtaining SUVmean, SUVmax, % injected dose, Cardiac Amyloid Activity (CAA), and retention index values. Patients were grouped as „Negative" (Perugini ≤1) and „Positive" (Perugini ≥2). Receiver Operating Characteristic (ROC) curve analysis was used to determine the ability of each of these quantitative parameters to differentiate between the two groups. The area under the curve (AUC) was calculated, and the optimal cut-off point that maximizes the sum of sensitivity and specificity was determined for each parameter. ***Results:*** Of the 81 patients included (66.6% men) with a mean age of 77.4 years (47-94), 42 were classified as negative (40 score 0; 2 score 1) and 39 as positive (5 score 2; 34 score 3). The values found excellent diagnostic capacity (AUC>0.98) to differentiate Perugini ≤1 vs ≥2 with the following parameters and their optimal cut-offs: Cardiac SUVmean: 2.66 gr/ml (AUC 0.997) Cardiac SUVmax: 4.66 gr/ml (AUC 0.988) Cardiac % Injected Dose: 0.4% (AUC 0.996) Cardiac Amyloid Activity (CAA): 761.5 (AUC 0.990) Retention Index: 0.23% (AUC 0.982). ***Conclusion:*** Absolute quantification of cardiac amyloid deposit using [99mTc]Tc-DPD SPECT/CT provides objective parameters that demonstrate a high capacity to discriminate between patients with and without significant cardiac uptake according to the visual Perugini score. These quantitative parameters and their optimal cut-off points could be useful tools to complement visual evaluation, increasing objectivity in the diagnosis, stratification, and follow-up of patients with cATTR.

EP-0612

Relationship between cardiac innervation and heart failure in patients with TTR amyloidosis: Evidence from gated SPECT with ^{123}I-MIBG and ^{99m}Tc-DPD

F. Sebastián Palacid*, N. Álvarez Mena, M. García Aragón, R. C. Zambrano Infantino, B. M. Jaramillo López, Á. R. Suazo Montero, M. Alonso Rodríguez, B. Pérez López, R. Ruano Pérez;*
Hospital Clínico Universitario Valladolid, Valladolid, SPAIN.

Aim/Introduction: To determine the relationship between cardiac innervation and heart failure in patients with TTR amyloidosis by joint evaluation of gated SPECT (gSPECT) images obtained with ^{123}I-MIBG and ^{99m}Tc-DPD. ***Materials and Methods:*** 51 patients with TTR cardiac amyloidosis confirmed by scintigraphy and ^{99m}Tc-DPD gSPECT were studied, divided according to the presence or absence of heart failure (HF). ^{123}I-MIBG Planar and gSPECT studies were performed and early (HMRe) and late (HMRl) myocardial uptake and washout index (WI) were calculated.Uptake scores were assigned to the polar maps obtained in both gSPECT: 0 = normal and 4 = pathological for ^{99m}Tc-DPD; 0 = pathological and 4 = normal for ^{123}I-MIBG.The data were analysed taking into account sex, age, Perugini uptake grade and HMRI, and the polar maps were compared to identify significant differences. ***Results:*** The male:female ratio was 80.4:19.6 and 82.3% of the subjects were classified as grade 3 on the Perugini scale. HF was present in 35 patients (LVEF 50.7 ± 12.3%), while 16 did not (LVEF 55.5 ± 11.6%). Cardiac innervation disturbances were observed in 96.1% (49/51) of cases. The regions exhibiting the most significant cardiac denervation were the inferior region and the basal inferolateral region in both groups (p<0.05). However, the apex region exhibited the only significant disparities between patients with and without HF (p=0.017). ***Conclusion:*** The study demonstrates a relationship between cardiac innervation and heart failure in patients with TTR cardiac amyloidosis, highlighting significant differences in myocardial denervation. The results underline the complementary value of ^{123}I-MIBG and ^{99m}Tc-DPD studies in characterising the cardiac involvement of this disease, its clinical management and prognosis.

EP-0613

P(ATTR)ONUS: Validation of a new classification system for cardiac TTR amyloidosis using ^{99m}Tc-DPD gated SPECT.

F. Sebastián Palacid*, N. Álvarez Mena, B. M. Jaramillo López, R. C. Zambrano Infantino, M. García Aragón, Á. R. Suazo Montero, C. Gamazo Laherrán, M. J. González Soto, R. Ruano Pérez;*
Hospital Clínico Universitario Valladolid, Valladolid, SPAIN.

Aim/Introduction: To validate a ^{99m}Tc-DPD gated SPECT (gSPECT)-based classification system for cardiac TTR amyloidosis. The study will also analyse whether the identified uptake patterns show significant differences in terms of clinical and cardiac involvement parameters. ***Materials and Methods:*** A total of 116 patients (90 males, mean age 85 years) with positive ^{99m}Tc-DPD scintigraphy for cardiac TTR amyloidosis were included in the study and underwent a gSPECT study in which the myocardial distribution of the radiopharmaceutical was assessed.Depending on the regions affected, six uptake patterns were established: Septal, waning moon, dome, crescent moon, diffuse and donut. The relationship between various clinical parameters (HF, aortic stenosis, arrhythmia, neurological alterations), the percentage of affected myocardium, LVEF and the uptake patterns obtained in gSPECT was analysed. ***Results:*** 80% of patients were classified as grade 3 on the Perugini visual scale. The mean percentage of affected myocardium was 70.5 ± 18.3% and the mean LVEF was 52.7 ± 14.7%.On the polar map, the "donut" pattern was the most common (29.3%), while the "dome" pattern was the least common (6.9%).The "diffuse" pattern had the highest proportion of patients with heart failure (p = 0.0038).The "dome" pattern was significantly associated with arrhythmias (p = 0.0034) and neurological alterations (p = 0.0098).The highest proportion of preserved LVEF was associated with the crescent pattern (p = 0.0315). ***Conclusion:*** ^{99m}Tc-DPD gSPECT allows the identification of cardiac involvement patterns and the assessment of ventricular dysfunction in patients with TTR cardiac amyloidosis. The uptake patterns are associated with clinical parameters and ventricular function, with the "diffuse" pattern standing out due to its relationship with heart failure.

EP-0614

Prognostic Value of [^{99m}Tc]Tc-DPD Quantitative SPECT/CT in Patients with suspected Amyloid Transthyretin-Related Cardiomyopathy

F. Aghapour Zangeneh[1]*, N. Gözlügöl*[1]*, A. Rominger*[1]*, C. Gräni*[2]*, F. Caobelli*[1]*;*
[1]*Department of Nuclear Medicine, Inselspital, Bern University Hospital, University of Bern, Bern, SWITZERLAND,* [2]*Department of Cardiology, Inselspital, Bern University Hospital, University of Bern, Bern, SWITZERLAND.*

Aim/Introduction: Quantitative Single Photon Emission Computed Tomography (SPECT) using ^{99m}Tc-3,3-diphosphono-1,2-propanodicarboxylic acid ([^{99m}Tc]Tc-DPD) may serve as a valuable tool for risk stratification in patients with amyloid transthyretin-related cardiomyopathy (ATTR-CM). This study aimed to assess the prognostic significance of different quantitative [^{99m}Tc]Tc-DPD SPECT/CT in patients with suspected ATTR-CM. ***Materials and Methods:*** Consecutive patients with suspected transthyretin cardiac amyloidosis (ATTR-CM) referred to a single tertiary care center underwent quantitative [99mTc]Tc-DPD SPECT/CT (700 MBq). Standardized Uptake Values (SUVmax and SUVpeak), Activity Total Volume (ATV), defined as the sum of voxel volumes where SUV ≥ 40% of SUVmax and Total DPD Activity (TDA), calculated as SUVmean × ATV, were automatically derived using a 40% isocontour threshold VOI. Clinical, laboratory, and echocardiographic data were collected during a follow-up period of 46.1 ± 13.4 months, along with major adverse cardiac

events (MACEs), defined as the occurrence of any of the following: all-cause mortality, sustained ventricular tachyarrhythmia, hospitalization for heart failure, or implantation of a cardioverter-defibrillator. Receiver operating characteristic (ROC) analysis was used to identify optimal thresholds of quantitative imaging parameters for predicting MACEs. Their prognostic value was further evaluated using Cox regression and Kaplan-Meier survival analysis. ***Results:*** A total of 144 patients were included (127 males, 88.2%), of whom 99 (68.8%) were eventually diagnosed with ATTR-CM. The optimal thresholds identified were 7 for SUVmax, 100 for ATV, and 640 for TDA. An SUVmax ≥7 was significantly associated with an increased incidence of MACEs (HR 3.68; 95% CI: 1.40-9.65; p = 0.008). Similarly, an ATV value ≥100 was linked to a higher risk (HR 3.31; 95% CI: 1.34-8.14; p = 0.009), as was a TDA value ≥640 (HR 2.82; 95% CI: 1.24-6.36; p = 0.013). ***Conclusion:*** In patients with suspected ATTR-CM, quantitative DPD SPECT/CT imaging effectively predicts the risk of major adverse cardiac events (MACEs). Unlike previous studies, our research demonstrates the strong prognostic value of two novel parameters, i.e. ATV and TDA, which may assist in assessing the risk of disease progression.

EP-0616

A Prospective Pilot Study for Prognosis of CRT Super Response Using Electro-Mechanical Dyssynchrony Assessment in Patients with Strauss Left Bundle Branch Block Criteria

T. Atabekov, *A. Smorgon, A. Mishkina, S. Krivolapov, S. Sazonova, M. Khlynin, R. Batalov, S. Popov;*
Cardiology Research Institute, Tomsk National Research Medical Centre, Russian Academy of Sciences, Tomsk, RUSSIAN FEDERATION.

Aim/Introduction: The electro-mechanical dyssynchrony underlies left ventricular (LV) contractile dysfunction in patients with left bundle branch block (LBBB). In some cases cardiac resynchronization therapy (CRT) almost completely reverses LV contractile dysfunction. The LBBB electrocardiographic Strauss criteria and mechanical dyssynchrony (MD) assessment were proposed to improve CRT response. However, using these techniques separately does not improve LV contraction in 20-40% of patients after CRT device implantation. We have evaluated whether a combined using of electrocardiography (ECG), speckle-tracking echocardiography (STE) and cardiac scintigraphy can improve the prognosis of CRT super response in patients with Strauss LBBB criteria during 6 month follow-up. ***Materials and Methods:*** The study prospectively included patients with New York Heart Association (NYHA) II-III functional class (FC) of heart failure (HF) in sinus rhythm with Strauss LBBB criteria and reduced left ventricular ejection fraction (LVEF). Before and 6 month after CRT device implantation ECG, STE and cardiac scintigraphy were performed. The study's primary endpoint was the NYHA class improvement ≥ 1 and left ventricle end systolic volume decrease > 30% or LVEF improvement > 15% after 6 month CRT. Based on collected data, we developed a prognostic model regarding CRT super response. ***Results:*** Out of 54 (100.0%) patients, 39 (72.2%) had CRT super response. Patients with CRT super response were likelier to have a greater S wave amplitude in V2 lead (p=0.004), higher rates of global longitudinal strain (GLS) (p=0.001) and interventricular delay (IVD) (p=0.005). Only 3 indicators (S wave amplitude in V2 lead, GLS and IVD) were independently associated with CRT super response in univariable and multivariable logistic regression. We created a prognostic model based on the logistic equation and calculated a cut-off value (>0.73). The resulting ROC curve revealed a discriminative ability with AUC of 0.957 (sensitivity 87.2%; specificity 100.0%). ***Conclusion:*** The electro-mechanical dyssynchrony assessment using ECG, STE and cardiac scintigraphy is useful in prediction of CRT super response in patients with Strauss LBBB criteria during 6 month follow-up. Our prognostic model is able to distinguish patients with CRT super response.

EP-0617

A Study on Risk Stratification of Heart Failure Severity Through the Evaluation of Mitochondrial Dysfunction in Patients with Cardiac Resynchronization Therapy Indications

T. Atabekov, *V. Korepanov, A. Mishkina, S. Sazonova, S. Afanasiev, R. Batalov, S. Popov;*
Cardiology Research Institute, Tomsk National Research Medical Centre, Russian Academy of Sciences, Tomsk, RUSSIAN FEDERATION.

Aim/Introduction: Accurate risk stratification of heart failure (HF) severity is crucial for optimizing treatment strategies and improving patient outcomes. Recent research has highlighted the role of mitochondrial dysfunction (MD) as a potential biomarker for HF severity assessment. This study aims to investigate the relationship between HF severity and MD in patients with indications for cardiac resynchronization therapy (CRT). ***Materials and Methods:*** In this prospective clinical study patients with HF classified as New York Heart Association (NYHA) functional classes (FC) II and III, who were indicated for CRT, underwent transthoracic echocardiography (TTE) alongside an assessment of MD. This assessment utilized both laboratory techniques, specifically evaluating the respiratory function of mitochondria in peripheral blood mononuclear cells (PBMC), and radionuclide imaging through myocardial perfusion scintigraphy (MPS) using the ^{99m}Tc-methoxy-isobutyl-isonitrile (^{99m}Tc-MIBI). We calculated mitochondrial respiration rates (MRR) based on various substrates (pyruvate + malate - adenosine diphosphate [$V_{4,1}$]) and determined ^{99m}Tc-MIBI washout rate (WR) indicators. The study evaluated the correlations between the NYHA FC of HF, TTE results, MRR and WR indicators. Utilizing our findings, we developed a risk model to assess the HF severity. ***Results:*** Among the 26 (100.0%) HF patients included in the study, 11 (42.3%) were classified as having mild HF, corresponding to NYHA FC II (Group 1), while 15 (57.7%) were categorized as having moderate-to-severe HF, classified as NYHA FC III (Group 2). Those with moderate-to-severe HF exhibited significantly lower $V_{4,1}$ values (33.4 [18.1; 37.8] nMol O_2/min/mg mitochondrial protein [MP]) compared to those with mild HF (65.2 [54.6; 142.4] nMol O_2/min/mg MP, p<0.001). This measurement was found to be independently associated with moderate-to-severe HF in both univariate and multivariate logistic regression analyses (odds ratio 0.87; 95% confidence interval 0.77-0.98; p<0.001). The HF risk model demonstrated strong discriminative power (area under the curve of 0.933; cutoff value > 0.7; sensitivity 80.0%; specificity 100.0%) in identifying HF severity. The risk model successfully predicted moderate-to-severe HF with an accuracy of 84.6%. ***Conclusion:*** In patients with moderate-to-severe HF MRR is markedly reduced compared to that in patients with mild HF. The HF severity is associated with PBMC mitochondrial respiratory dysfunction in patients with CRT indications. The MD indicator assessed by MPS with ^{99m}Tc-MIBI is not associated with HF severity and does not correlate with PBMC mitochondrial respiratory dysfunction. We have developed HF severity risk model including $V_{4,1}$ parameters is able to distinguish mild and moderate-to-severe HF patients.

EP-0618

Assessment of Cardiac Amyloidosis by Scintigraphy and Cardiac Magnetic Resonance Imaging: Quantitative Correlation and Interobserver Reproducibility

J. Díaz Moreno[1], *I. Sánchez-Rodríguez*[1], *P. Notta-Ganzález*[1], *M. Cortés-Romera*[1], *A. Bagán-Trejo*[1], *E. Claver-Garrido*[2], *C. Díez-López*[2], *S. Yun-Viladomat*[3], *F. De Frutos-Seminario*[2], *L. Herrador-Galindo*[2], *R. Ramos-Polo*[2], *A. Rodríguez-Gasén*[1], *J. Martín-*

Marcuartu[1], M. Pudis[1], M. Perlaza-Jiménez[1], A. Fritsch-Medina[1], M. Tormo-Ratera[1], B. Hervás-Sanz[1], M. Zamorano-Rivas[1], A. Dacosta-Escobar[1], C. García-Alcober[4], L. Gràcia-Sánchez[1];
[1]Nuclear Medicine-PET (IDI) Department, Bellvitge University Hospital-IDIBELL, Barcelona, SPAIN, [2]Cardiology Department, Bellvitge University Hospital-IDIBELL, Barcelona, SPAIN, [3]Internal Medicine Department, Bellvitge University Hospital-IDIBELL, Barcelona, SPAIN, [4]Radiopharmacy Department, Bellvitge University Hospital-IDIBELL, Barcelona, SPAIN.

Aim/Introduction: Cardiac amyloidosis (CA) is an infiltrative disease characterized by the deposition of amyloid fibrils in myocardial tissue, leading to progressive cardiac dysfunction. Cardiac scintigraphy (CS) using [^{99m}Tc]Tc-DPD is a key noninvasive imaging technique, particularly effective in the diagnosis of transthyretin-related cardiac amyloidosis (ATTR-CA). The Perugini Visual Score (PVS) is widely used for qualitative assessment, however, it is susceptible to interobserver variability. The aim of this study was to assess the correlation between PVS and quantitative scintigraphic indices in relation to cardiac magnetic resonance (CMR) findings and amyloid subtype, and evaluate inter-observer agreement in PVS grading. ***Materials and Methods:*** We performed a retrospective analysis of 70 patients (43 males, mean age 71 years) with suspected CA who underwent both CS and CMR. Myocardial uptake was quantified by defining a circular region of interest (ROI) over the heart and mirroring it over the contralateral chest to derive CMC/HCL and CMC/HCL with background correction ratios (CMC-Bkg/HCL-Bkg). Four independent observers graded the CS images using the PVS. Interobserver agreement was assessed using Fleiss' kappa statistic. ***Results:*** CA was diagnosed in 23 of the 70 patients, with 17 cases of ATTR-CA, 5 cases of AL-CA and 1 case of AA. CS with [^{99m}Tc]Tc-DPD showed a sensitivity of over 99% and a specificity of 94%, confirming its robust diagnostic performance. A significant correlation was observed between the CMC/HCL and CMC/HCL-Bkg indices and the highest PVS values ($p<0.05$), supporting the utility of quantitative scintigraphy in the assessment of myocardial amyloid deposition. No significant correlations were found between PVS and echocardiographic parameters such as interventricular septal thickness or left ventricular ejection fraction. The inter-observer agreement for PVS was substantial with a Fleiss' kappa value of 0.75. More concordance was observed at the extreme ends of the Perugini scale (scores of 0 and 3). ***Conclusion:*** CS with [^{99m}Tc]Tc-DPD is a highly sensitive and specific modality for the detection of CA. The significant correlation between myocardial uptake quantification and PVS underlines its diagnostic value. However, the incorporation of quantitative tools to improve reproducibility and diagnostic accuracy in clinical practice is highlighted by the observed inter-observer variability in intermediate PVS.

EP-35

e-Poster Area

B: Imaging Clinical Studies -> B4 Cardiovascular Imaging Clinical Study -> B44 Other Cardiovascular Imaging (including Plaque)

EP-0619

^{18}F-FAPI PET/CT in Chronic Liver Disease: Myocardial Fibroblast Activation and Its Correlates

Y. Wang*, Y. Wang;*
The Third Affiliated Hospital of Soochow University, Changzhou, CHINA.

Aim/Introduction: This study investigates the relationship between cardiac fibroblast activation and clinical parameters, electrophysiological findings, serum fibrosis markers, and hepatic fibroblast activation in patients with chronic liver disease. ***Materials and Methods:*** In this prospective study conducted from December 2021 to April 2022, 46 patients with chronic liver disease underwent fluorine-18 (^{18}F)-labeled FAPI PET/CT imaging and 12-lead electrocardiogram (ECG). Abnormal cardiac ^{18}F-FAPI uptake was defined as uptake greater than that of the blood pool. PET/CT parameters included standardized uptake value (SUV) and target-to-background ratio (TBR). ***Results:*** Significant differences were observed between positive and negative myocardial ^{18}F-FAPI PET/CT imaging groups in terms of age (54 ± 7 years vs. 45 ± 10 years; P = 0.006), epicardial fat volume (EFV) (169.71 ± 70.78 cm^3 vs. 115.16 ± 46.76 cm^3; P = 0.004), Cornell voltage QRS amplitude (1.26 ± 0.62 mV vs. 0.88 ± 0.34 mV; P = 0.022), and QRS duration (94.64 ± 8.60 ms vs. 89.91 ± 7.48 ms; P = 0.032. The multivariable logistic regression analysis demonstrated a significant association between EFV (OR = 1.019, P = 0.024) and age (OR = 1.162, P = 0.019) and myocardial FAPI uptake positive. Myocardial TBRmax was positively correlated with hepatic TBRmax (r = 0.405, P = 0.005), hepatic TBRmean (r = 0.412, P = 0.004), and negatively correlated with the T wave amplitude in lead V6 (TV6) of the ECG (r = –0.295, P = 0.047). Moreover, myocardial SUVmax was positively correlated with serum laminin (LN) levels (r = 0.367, P = 0.042). ***Conclusion:*** In patients with chronic liver disease, fibroblast activation protein inhibitor (FAPI) PET/CT imaging demonstrated cardiac fibroblast activation, which was associated with electrophysiological parameters, hepatic FAPI uptake, and serum liver fibrosis markers. These findings highlight the potential of ^{18}F-FAPI PET/CT imaging in assessing the relationship between cardiac and hepatic fibrosis.

EP-0621

^{99m}Tc-FAPI SPECT/CT for Evaluation of Myocardial Fibrosis and Cardiac Function in Valvular Heart Disease

Y. Zhang*, W. Chen;*
Department of Nuclear Medicine, Fuzhou University Affiliated Provincial Hospital, Fuzhou, CHINA.

Aim/Introduction: Active myocardial fibrosis plays a pivotal role in valvular heart disease (VHD) progression. While conventional imaging modalities primarily detect established fibrosis, the detection of active fibroblast activation remains challenging. ^{99m}Tc-FAPI SPECT/CT, offering advantages of wider availability and lower cost compared to PET imaging, represents a promising tool for evaluating active myocardial fibrosis. ***Materials and Methods:*** We conducted a prospective study (Trial registration: ChiCTR2400094867) of 30 VHD patients who underwent ^{99m}Tc-FAPI SPECT/CT imaging with comprehensive clinical evaluation. Patients were categorized into FAPI-positive (n=24) and FAPI-negative (n=6) groups based on myocardial tracer uptake patterns. Thirteen FAPI-positive patients completed a three-month follow-up to assess therapeutic response. ***Results:*** FAPI uptake parameters showed robust correlations with established myocardial injury markers (Hs-cTnI vs. SUVmax: r=0.831, p<0.001; Hs-cTnI vs. SUVmean: r=0.795, p<0.001) and disease severity indices (VHD staging: r=0.812, p<0.001). FAPI-positive patients demonstrated significantly higher atrial fibrillation prevalence (54.2% vs. 0%, P=0.024). Post-treatment follow-up revealed significant improvements in FAPI parameters (SUVmax: 2.8±0.4 to 1.9±0.3, p<0.0001; SUVmean: 2.3±0.3 to 1.6±0.2, p<0.0001), accompanied by enhanced left ventricular ejection fraction (45.3±5.2% to 52.1±4.8%, p=0.0176) and NYHA functional status (p=0.0011), despite unchanged structural parameters. ***Conclusion:*** This study demonstrates that ^{99m}Tc-FAPI SPECT/CT enables non-invasive visualization and quantification of active myocardial fibrosis in VHD patients. The strong associations between FAPI parameters and clinical indices, coupled with its ability to monitor therapeutic response, suggest its potential as a valuable tool for risk stratification and treatment optimization in VHD management.

EP-0622

Predictive Value of Coronary Sodium ^{18}F-Fluoride Activity for Perioperative Myocardial Infarction post-CABG in Patients with a History of Previous Myocardial Infarction Multiple Coronary Artery Disease

X. Xu[1], *Y. Zhao*[1], *B. Hu*[1], *M. Gao*[2], *H. Li*[2], *X. Zhang*[1];
[1]*Laboratory for Molecular Imaging, Department of Nuclear Medicine, Beijing Anzhen Hospital, Capital Medical University, Beijing, CHINA,* [2]*Department of Cardiac Surgery, Beijing Anzhen Hospital, Capital Medical University, Beijing, CHINA.*

Aim/Introduction: Patients with a prior myocardial infarction (MI) are at a higher risk of adverse outcomes following coronary artery bypass grafting (CABG). The prediction value of preoperative multidisciplinary assessment for perioperative MI in patients undergoing CABG remains elusive. The purpose this of study was to explore the efficacy of multimodality cardiac imaging in predicting perioperative MI in patients with prior MI and triple coronary artery disease (CAD). ***Materials and Methods:*** A total of 26 patients (age 60.5 years [IQR: 54-66 years], 80.8% men) with prior MI and triple CAD were prospectively rerolled, all patients underwent cardiac sodium ^{18}F-fluoride (^{18}F-NaF) positron emission tomography/computed tomography (PET/CT), coronary angiography, and CT-based coronary artery calcium scoring before CABG. The maximum coronary ^{18}F-NaF activity (target-to-background ratio (TBR_{max}) and the global coronary ^{18}F-NaF activity (TBR_{global}) were determined. The endpoint was perioperative myocardial infarction (PMI) within 7 days after CABG. ***Results:*** Overall, 8 (30.8%) patients experienced PMI. Compared to those without PMI, those with PMI had a higher TBR_{max}(4.66 [3.17-9.44] vs. 2.53 [1.74-3.10], P = 0.017)and TBR_{global} (3.25 [2.79-5.39] vs. 2.17 [1.52-2.58], P = 0.012). No significant difference of SYNTAX and CAC scores was observed between patients with and without PMI (P > 0.05). Multivariate analysis showed that TBR_{max} (as a continuous and categorical variable) was an independent predictor of PMI(P = 0.043 and 0.017), while TBR_{global} of 2.7 had predictive value as a categorical variable (P = 0.013). Both TBR_{max} and TBR_{global} delivered substantial incremental improvement in the prognostic value for PMI. ***Conclusion:*** Among patients with prior MI and triple CAD, quantification of coronary microcalcification activity through ^{18}F-NaF PET revealed a robust predictive power for early post-CABG cardiovascular outcomes.

EP-0623

Stratification of Non-Thromboembolic Pulmonary Hypertension by V/Q SPECT/CT Patterns: Hemodynamic and Radiologic Correlates

Z. Zhang*, Z. Wang, H. Pang;*
The First Affiliated Hospital of Chongqing Medical University, Chongqing, CHINA.

Aim/Introduction: This study aimed to investigate the hemodynamic and computed tomography (CT) characteristics associated with three distinct V/Q patterns in non-thromboembolic pulmonary hypertension (NTEPH): matched defects (VQ1), focal patchy perfusion defects (VQ2), and global perfusion defects (VQ3). ***Materials and Methods:*** We retrospectively analyzed 226 consecutive patients with NTEPH who underwent V/Q SPECT/CT. Patients were stratified into four groups based on perfusion patterns: VQ1 (n=56), VQ2 (n=16), VQ3 (n=16), and a control group without perfusion defects (VQ0, n=138). Comparative analyses included hemodynamic parameters (mPAP, PVR, among others), imaging markers of pulmonary hypertension (including MPA diameter, P/A ratio, etc.), right ventricular function (RV free wall thickness, etc.), and CT features of pulmonary vasculature (vascular morphology, mosaic perfusion, ground-glass nodules, and other parenchymal characteristics). ***Results:*** The VQ3 group demonstrated significantly worse hemodynamic profiles, with higher mPAP and PVR values compared to other groups , Conversely, the VQ1 group exhibited more favorable hemodynamics with lower mPAP, RAP, PCWP, and RVP. CT imaging revealed marked differences: the VQ3 group showed significantly larger MPA diameter (44.3±8.7 mm vs 34.5±7.1 mm in VQ0, 37.2±8.4 mm in VQ1, and 35.3±6.9 mm in VQ2; p<0.001), higher P/A ratio (1.8±0.4 vs 1.3±0.3 in VQ0, 1.2±0.4 in VQ1, and 1.2±0.4 VQ2; p<0.001), and greater RV wall thickness (8.5±3.7 mm vs 7.1±3.4 mm in VQ0; p=0.001). Notably, the VQ3 group demonstrated characteristic pulmonary vascular remodeling features, including vine-like arterial dilatation (75%), peripheral vascular tortuosity (50%), diffuse mosaic perfusion (56.2%), and centrilobular ground-glass nodules (56.2%). No specific parenchymal abnormalities were identified in VQ1 or VQ2 groups. ***Conclusion:*** V/Q scintigraphy patterns effectively stratify NTEPH phenotypes: global perfusion defects (VQ3) correlate with advanced vascular remodeling and right ventricular dysfunction, while matched defects (VQ1) may represent early disease manifestations. These distinct imaging phenotypes provide valuable insights into underlying pathophysiology and may guide clinical management. ***References:*** Chan K, Ioannidis S, Coghlan JG, Hall M, Schreiber BE. Pulmonary Arterial Hypertension With Abnormal V/Q Single-Photon Emission Computed Tomography. JACC Cardiovasc Imaging. 2018;11(10):1487-93.

EP-0624

Validating Rubidium-82 for LVEF Quantification: A Comparative Study with 3D Echocardiography

M. Nielsen[1,2], *J. E. Larsson*[1], *N. Tietgen*[1], *L. L. Duchstein*[1], *P. G. Joergensen*[3], *B. Kristensen*[1], *B. Zerahn*[1], *L. T. Jensen*[2,1];
[1]*Dept. of Nuclear Medicine, Copenhagen University Hospital – Herlev and Gentofte, Herlev, DENMARK,* [2]*Dept. of Clinical Medicine, University of Copenhagen, Copenhagen, DENMARK,* [3]*Dept. of Cardiology, Copenhagen University Hospital – Herlev and Gentofte, Herlev, DENMARK.*

Aim/Introduction: Accurate assessment of left ventricular ejection fraction (LVEF) remains essential for detecting cardiotoxicity during cancer treatment. Current guidelines recommend three-dimensional echocardiography (3DE) as the first-line modality due to its broad availability and no use of ionizing radiation. However, 3DE is not always feasible. While cardiac MRI is the preferred second-line method, it is often unavailable in daily clinical settings. The recommended third-line option is equilibrium radionuclide angiography (ERNA), which, despite its historical role, has limitations related to radiation dose and declining availability. Rubidium-82 PET (Rb-PET), primarily used for myocardial perfusion imaging (MPI), also provides automated LVEF estimation as part of routine workflows. Compared to ERNA, Rb-PET offers lower radiation exposure, faster acquisitions, and greater cost-effectiveness in sites with a rubidium-82 generator. This study aims to compare Rb-PET and 3DE to evaluate whether Rb-PET is a suitable alternative for LVEF quantification. ***Materials and Methods:*** In this prospective study, patients undergoing rest Rb-PET MPI were recruited for same-day 3DE. LVEF was determined independently using vendor-provided semi-automated analysis software for both modalities. We assessed agreement between the two modalities using the intraclass correlation coefficient (ICC), concordance correlation coefficient (CCC), total deviation index (TDI), and Bland-Altman analysis. Pearson correlation was used to evaluate association. Subgroup analysis evaluated classification agreement above and below a 50% LVEF threshold, a preferred cutoff for considering cardioprotective strategies. ***Results:*** LVEF was successfully measured in 45 patients (90%) with 3DE and in 49 patients (98%) with Rb-PET, out of 50 enrolled. Mean LVEF by Rb-PET was 59.4 ± 9.8%, compared to 58.3 ± 7.9% by 3DE. Agreement between methods was good (ICC = 0.86, 95% CI: 0.76-0.92; CCC = 0.85, lower 95% CI: 0.77). The 90%-TDI was 7.73%, with an upper 95% confidence limit of 9.21%, indicating that 90% of paired differences fell within ±9.21%. Association between

methods was also strong (Pearson's r = 0.87). Bland-Altman analysis revealed a mean difference of -0.9% (LoA: -10.0 to 8.3%). No patients were misclassified across the 50% LVEF threshold by either method, and most disagreement occurred in patients with LVEF well above 50%. ***Conclusion:*** Rb-PET provides a feasible and reasonably accurate estimation of LVEF compared to 3DE. The two methods showed good agreement, with consistent classification across clinically relevant thresholds. Rb-PET may well serve as a valuable alternative for monitoring LVEF when 3DE is inconclusive or not feasible. These findings are based on preliminary data from the first 50 patients in an ongoing study targeting 100 participants.

EP-0625

Combined PET and multiparametric MRI Radiomics with Machine Learning for Differentiating Symptomatic from Asymptomatic Carotid Plaques

C. Zheng[1], *R. Qin*[1], *Z. Liu*[2], *Y. Yang*[3], *J. Lu*[1];
[1]*Xuanwu Hospital, Capital Medical University, Beijing, CHINA,* [2]*Central Research Institute, United Imaging Healthcare, Shanghai, CHINA,* [3]*Beijing United Imaging Healthcare, Beijing, CHINA.*

Aim/Introduction: Identification of symptomatic carotid plaques is essential for the treatment and prevention of ischemic stroke. The aim of this study is to evaluate the performance of radiomics derived from the combination of PET and multiparametric MRI for the non-invasive differentiation of symptomatic from asymptomatic carotid plaques. ***Materials and Methods:*** A total of 103 patients with carotid plaques who underwent ^{18}F-FDG PET/MRI were enrolled in this study. The MRI protocol included T1-weighted imaging (T1WI), contrast-enhanced T1WI (T1C), T2-weighted imaging (T2WI), and 3D time-of-flight (TOF) sequences. All sequences were co-registered to the native T1WI space, intensity-normalized, and resampled to an isotropic voxel size of 1 mm. The cohort was randomly partitioned into training (70%) and testing (30%) sets. The Least Absolute Shrinkage and Selection Operator (LASSO) algorithm was employed for optimal feature selection. Four machine learning algorithms were employed to construct the classification model, including Support Vector Machine (SVM), Logistic Regression (LR), K-Nearest Neighbor (KNN), and Multi-Layer Perceptron (MLP). Model performance was evaluated on the test set using the area under the receiver operating characteristic curve (AUC), sensitivity, and specificity. ***Results:*** LASSO regression selected ten salient radiomic features for model construction: three originating from T1WI, two from T1C, three from T2WI, and two from PET images. The four machine learning models yielded largely comparable classification performance. The LR model achieved the highest discriminative ability (AUC = 0.750, sensitivity = 0.818, specificity = 0.650). The KNN model yielded an AUC of 0.742 (sensitivity = 0.727, specificity = 0.750). The SVM model demonstrated an AUC of 0.705 (sensitivity = 0.727, specificity = 0.650). Lastly, the MLP model attained an AUC of 0.732 (sensitivity = 0.818, specificity = 0.700). ***Conclusion:*** Integrated radiomic analysis combining ^{18}F-FDG PET with multiparametric MRI demonstrates considerable potential for differentiating symptomatic from asymptomatic carotid plaques. This approach may offer a valuable non-invasive tool to potentially enhance clinical stroke risk stratification.

EP-0626

Visualization of the inflammation-fibrosis communication mechanism of cardiovascular remodeling in pulmonary hypertension

B. Chen*, M. Yang;*
Beijing Chao-Yang Hospital, Capital Medical University, Beijing, CHINA.

Aim/Introduction: Fibroblast activation protein inhibitor (FAPI) imaging provides a new method for monitoring inflammation-fibrosis communication in pulmonary hypertension (PH). The value of FAPI imaging in disease assessment and prognosis significance in PH needs to be further explored. The goal of this study was to investigate the characteristics of FAPI activity in subtype PH and clinical significance of FAPI imaging. ***Materials and Methods:*** Consecutive patients with PH who underwent right heart catheterization, clinical assessment and FAPI imaging within 1 week were identified. Cardiovascular FAPI uptake higher than that in the blood pool was defined as abnormal. The maximum standardized uptake values (SUV_{max}) of the right ventricle (RV) and pulmonary artery (PA) were measured and further expressed as target-to-background ratio (TBR) with blood pool activity as background. In chronic thromboembolic pulmonary hypertension (CTEPH) patients undergoing balloon pulmonary angioplasty (BPA) treatment, clinical evaluation and FAPI imaging were performed after 2 BPA sessions. ***Results:*** Fifty-four CTEPH patients, 12 idiopathic pulmonary arterial hypertension (IPAH) patients and 11 connective tissue disease-associated PAH (CTD-PAH) patients were enrolled. Patients with CTEPH and IPAH had more abnormal FAPI uptake and higher FAPI activity in RV than CTD-PAH. While, patients with CTD-PAH had more abnormal FAPI uptake but lower FAPI activity in PA. Patients in intermediate- and high- risk had higher proportion of abnormal FAPI uptake in RV and PA than patients in low-risk. At follow-up, 27 patients CTEPH patients underwent 2 session of BPA and 11 patients underwent second FAPI imaging. The area under the curve (AUC) revealed the ability of RV FAPI activity to predict satisfactory BPA outcomes [RV free wall (RVFW), sensitivity: 94.0%, specificity: 50%; insert point, sensitivity: 88.0%, specificity: 67%]. There had a significantly positive correlation between ΔTBR of RVFW and ΔWHO functional class (WHO-Fc) (r = 0.695, P = 0.012), and negative correlation between ΔTBR of main PA and Δ6-minute walking distance (6WMD) (r = -0.740, P = 0.006). ***Conclusion:*** ^{18}F-FAPI PET/CT could provide insights to inflammation-fibrosis communication in subtype PAH, and serve as a vital role in prognosis of disease and efficacy prediction/monitoring.

EP-0627

Atherosclerosis Detection in the Abdominal Aorta and Iliac Arteries Using AI Segmentation of 18F-NaF and ^{18}F-FDG PET/CT Scans

O. Fanta[1,2], *W. Lee*[1,3], *S. Patil*[1], *D. Patel*[1], *T. Werner*[1], *P. F. Høilund-Carlsen*[4], *A. Alavi*[1];
[1]*University of Pennsylvania, Philadelphia, PA, UNITED STATES OF AMERICA,* [2]*Charles University, Prague, CZECH REPUBLIC,* [3]*Drexel University College of Medicine, Philadelphia, PA, UNITED STATES OF AMERICA,* [4]*Odense University Hospital, Odense, DENMARK.*

Aim/Introduction: Atherosclerosis of the abdominal aorta (AA) and iliac arteries is a major form of cardiovascular disease (CVD) and significant cause of mortality. 18F-NaF and ^{18}F-FDG are two PET radiotracers that can detect vascular calcification and inflammation, respectively, which may serve as early-stage biomarkers of disease. This study aimed to evaluate AI-based segmentation of radiotracer uptake in the AA and iliac arteries and to assess correlations of these derived values with various atherosclerotic risk factors. ***Materials and Methods:*** 99 subjects from the CAMONA trial (63 healthy volunteers, 36 at-risk for CVD, mean age of 48.4±14.1 years, 53.5% female) underwent 18F-NaF and ^{18}F-FDG PET/CT imaging. AI-based segmentation was used to define ROIs around the AA and the iliac arteries using the TotalSegmentator model (Wasserthal et al. 2023). The SUVmean was used to quantify radiotracer uptake which was correlated with age, C-reactive protein (CRP) levels, and gender. ***Results:*** In the at-risk subject group, aortic and bilateral iliac 18F-NaF SUVmean correlated strongly with age (R=0.513, p<0.01 in the AA; R=0.447, p=0.01 in the left iliac; R=0.506, p<0.01 in the right iliac). Left and right iliac 18F-NaF SUVmean correlated with CRP (R=0.0407, p=0.02 and R=0.358, p=0.04, respectively). In the healthy group, aortic 18F-NaF SUVmean correlated with age (R=0.276, p=0.04). There were no significant differences in aortic or iliac 18F-NaF SUVmean between the two patient groups, but aortic, right iliac SUVmean was higher in females than males (1.00 vs. 0.890,

p=0.01 and 1.14 vs. 1.01, p=0.03 respectively). ^{18}F-FDG SUVmean correlated with age in the left and right iliac arteries in the healthy group only (R=0.358, p <0.01 and R=0.348, p<0.01, respectively). Relative to the healthy group, the at-risk group had greater average bilateral iliac ^{18}F-FDG SUVmean (1.11 vs 0.915, p<0.01 and 1.15 vs 0.98, p=0.01 in the left and right iliac arteries, respectively). ***Conclusion:*** 18F-NaF uptake showed a strong correlation with known atherosclerotic risk factors and was, on average, higher in females than in males. 18F-FDG, thought to visualize inflammation pertinent to the pathogenesis of plaque formation, had limited correlations with atherosclerotic risk factors, possibly due to the proximity of the measured structures to other organs with high ^{18}F-FDG uptake in the abdomen and pelvis. Further studies with subjects specifically selected for PAD and improved AI segmentation methods are needed to assess the clinical utility of 18F-NaF PET/CT in determining PAD risk.

EP-0628

Imaging of Acute Aortic Dissection and Intramural Hematoma by 18F-AIR-NOTA-FAPI PET/CT

Y. Lu, *X. Zhang;*
Department of Nuclear Medicine, Beijing Anzhen Hospital, Capital Medical University, Beijing, CHINA.

Aim/Introduction: Objective: The significance of the fibrotic response of acute aortic dissection (AAD) and acute intramural hematoma (AIMH) is unknown. The aim was to characterize fibrosis of AAD and AIMH respectively at acute phase using ^{18}F-AIR-NOTA-FAPI PET/CT (FAPI PET/CT). ***Materials and Methods:*** 33 patients (age 56.7±1.8y, 25 male) within two weeks (acute phase) after acute aortic syndrome, were prospectively recruited from a study population referred to the Anzhen Hospital of Capital Medical University from June 2024 to December 2024 underwent FAPI PET/CT pre-operation. The maximum standardized uptake value (SUVmax) was measured in the ascending aorta, aortic arch, thoracic aorta, and abdominal aorta. ***Results:*** In contrast to AAD, AIMH showed accentuated FAPI uptake at the injured aortic wall [(6.74±1.89) vs. (5.17±1.65), P=0.016]. Compared with the AAD, there was increased FAPI uptake (SUVmax) in the aortic arch [(5.70±2.14) vs.(4.41±1.35), P=0.045], thoracic aorta [(6.24±1.84) vs.(4.78±1.30), P=0.013], and the abdominal aorta [(4.48±1.30) vs.(3.46±1.42), P=0.05]. Besides, there was a significant positive correlation between the uptake of the abdominal aorta and its diameter (r=0.492, P=0.004). ***Conclusion:*** AIMH and AAD was associated with increased FAPI uptake, while there was higher FAPI uptake of AIMH, indicating an inflammatory-fibrotic response in the whole aorta.Additionally, FAPI uptake in the aortic wall was associated with aortic growth. This finding warrants further prospective investigations.Acknowledgements: This project was sponsored by the National Natural Science Foundation of (82171994).

EP-0629

Predicting Reverse Remodeling Following Valve Replacement in Patients with Valvular Heart Disease: A Longitudinal ^{99m}Tc-FAPISPECT/CT Imaging Study

K. Wang, *Y. Gu, K. Han, C. Yan, W. Fang, L. Wang;*
Chinese Academy of Medical Sciences & Peking Union Medical College, Fuwai Hospital, Beijing, CHINA.

Aim/Introduction: In patients with valvular heart disease (VHD), fibroblast activation induced by pressure or volume overload can be identified by molecular imaging with fibroblast activation protein inhibitor (FAPI). The study sought to explore the potential of serial FAPI imaging for monitoring the reverse myocardial remodeling triggered by valve replacement. ***Materials and Methods:*** A cohort of 31 VHD patients scheduled for transcatheter or surgical valve replacement underwent ^{99m}Tc-FAPI SPECT/CT imaging and echocardiography. All patients underwent repeated echocardiography, and 22 completed repeat FAPI scans at 3-month follow-up. Cardiac FAPI uptake was quantified as maximum standardized uptake value (SUV_{max}), maximum of myocardial-to-blood ratio (TBR_{max}), and fibroblast activation volume (FAV). Myocardial remodeling patterns were evaluated through a comprehensive analysis of left ventricular geometric parameters derived from echocardiography. ***Results:*** Myocardial FAPI uptake showed heterogeneity among VHD patients (range: SUV_{max} 0.67-8.33; TBR_{max} 1.13-7.50; FAV 0-597 mL). FAPI uptake significantly correlated with levels of circulating N-terminal prohormone of brain natriuretic peptide and left ventricle mass index before valve replacement. Following relief of overload, 22 patients who underwent repeat FAPI imaging demonstrated significant reductions in TBR_{max} (3.31 [1.73-4.87] vs. 2.43 [1.63-4.23], p = 0.029) and FAV (31.5 [0-227] vs. 12.0 [0-144] mL, p = 0.004). Follow-up echocardiography revealed that 9 out of 31 patients transitioned to normal geometry from concentric or eccentric hypertrophy, achieving complete reverse remodeling. Multivariable regression suggested that baseline FAPI uptake intensity TBR_{max} was significantly associated with complete reverse remodeling post-intervention after adjustment (OR: 0.288 [0.097-0.852], p = 0.024). ***Conclusion:*** ^{99m}Tc-FAPI SPECT/CT imaging is feasible to quantitatively track dynamics of fibroblast activation following valve replacement. Patients with lower preprocedural fibrotic activity identified by FAPI imaging mayhave greater potential for complete reverse remodeling.

EP-0630

The enhancement of the sensitivity of ^{18}F-FAPI-74 PET visualization for atherosclerosis based on Q.Clear image reconstruction.

J. Song, *Y. Hong, W. Liu, L. Li, Q. Wu;*
First Hospital of Shanxi Medical University, Shanxi, CHINA.

Aim/Introduction: To investigate whether Q.Clear reconstruction can enhance the sensitivity of ^{18}F-FAPI-74 PET/CT in visualizing atherosclerotic plaques. ***Materials and Methods:*** A retrospective analysis was conducted on 85 patients with coronary heart disease who completed ^{18}F-FAPI-74 PET/CT examination from June 2023 to September 2024. The original ^{18}F-FAPI-74 PET/CT image data were reconstructed using OSEM+TOF, OSEM+TOF+PSF and Q.Clear (TOF+PSF + BPL) (noise penalty factor β=200, 400, 600, 800), respectively. The atherosclerotic lesion sites with calcification of the arterial wall and uptake of ^{18}F-FAPI-74 as shown by CT were taken as the region of interest (ROI) for quantitative analysis. Measure the SUVmax, SUVmean and standard deviation (SD) of the blood background at the Lesion site and in the arterial lumen at the same level under different reconstruction algorithms, and calculate the lesion signal-to-noise ratio. L-SNR, Boold pool-SNR (Bp-SNR), and Lesion maximum tissue-to-blood (L-TBRmax). The 4-point Likert scale was used to evaluate the visual saliency of the lesion after image reconstruction for each patient (from 1 to 4), and the results of each observer were recorded to compare the differences in the visual saliency of the lesion among different image reconstruction algorithms. ***Results:*** In this retrospective study involving 85 patients with coronary artery disease, we analyzed 206 atherosclerotic plaques. Based on ^{18}F-FAPI-74 PET/CT images, different β values of Q.Clear reconstruction were compared with various combinations of OSEM, TOF, and PSF. We found that Q.Clear reconstruction with β = 200 yielded the highest quantitative performance (L-SUVmax: 3.33±0.89 and L-TBRmax: 2.11±0.97), as well as the highest lesion signal-to-noise ratio (L-SNR: 7.19±4.52). However, this setting resulted in relatively lower background signal-to-noise ratio (Bp-SNR: 7.41±3.07), indicating suboptimal overall image quality. Increasing the β value of Q.Clear reconstruction or using OSEM+TOF+PSF can significantly enhance image quality, but comes at the cost of reduced quantitative accuracy. Q.Clear reconstruction with β = 200 achieved the highest proportion of conspicuous lesions with 74.27% rated as Likert score 3, and demonstrated the best observer consistency evaluation. ***Conclusion:*** Utilizing Q.Clear reconstruction with a low β value in ^{18}F-FAPI-74 PET/CT imaging can enhance the sensitivity for visualizing atherosclerotic plaques, yet this refinement comes at the cost of diminished image quality.

EP-0631

^{18}F-FDG-PET/CT for Diagnosing Infective Endocarditis Within the First Few Months Following Cardiac Prosthesis Implantation

D. Ferraro[1,2], *B. G. Padilha*[1], *R. A. de Camargo*[3,4], *C. F. Togni*[1], *L. F. T. Gonçalves*[1], *T. B. Teixeira*[1], *I. R. Brigo*[1], *D. A. M. Santos*[5], *M. C. P. Giorgi*[1], *R. A. Kitamikado*[1], *L. T. Hyppolito*[1], *M. R. Paixão*[1], *T. M. V. Strabelli*[1], *A. J. Mansur*[1], *F. Tarasoutchi*[1], *R. F. Souza*[6], *D. M. Gualandro*[1], *J. Soares Jr*[1], *R. F. Siciliano*[1];
[1]*Heart Institute of the Clinics Hospital of the Medical Faculty of the University of Sao Paulo, Sao Paulo, BRAZIL,* [2]*Hospital Israelita Albert Einstein, Sao Paulo, BRAZIL,* [3]*Hospital Aliança Star - Rede D'Or São Luiz, Salvador, BRAZIL,* [4]*Heart Institute of the Clinics Hospital of the Medical Faculty of the University of Sao Paulo, São Paulo, BRAZIL,* [5]*Cancer Institute of the Clinics Hospital of the Medical Faculty of the University of Sao Paulo, Sao Paulo, BRAZIL,* [6]*School of Economics, Business Administration and Accounting at Ribeirão Preto, Ribeirao Preto, BRAZIL.*

Aim/Introduction: Positron emission tomography/computed tomography (PET/CT) with 18F-fluordeoxiglicose (FDG) has become an important additional tool for detecting infections in cardiac prostheses. However, its use within the first months after cardiac prosthesis implantation is controversial and there is a concern regarding the potential risk of imaging misinterpretation caused by inflammation from recent surgical trauma. This study aims to evaluate the accuracy of PET-CT in diagnosing endocarditis in patients with cardiac prostheses within the first few months after implantation. ***Materials and Methods:*** Between 2013 and 2024, we investigated 111 episodes of suspected infective endocarditis (IE) in patients who had prostheses implanted within the previous six months (85 prosthetic valves and 26 ascending aortic prosthesis). The accuracy of 18F-FDG-PET/CT was determined based on the consensus of two specialists in cardiac PET imaging. Reference standard was the final diagnosis by a specialist board team which was based on clinical, imaging and laboratorial information, follow up and histopathology when available. A logistic regression model using visual uptake patterns (no uptake, diffuse, heterogeneous or focal/multifocal) and SUVmax was developed and compared to the consensus of the two nuclear physicians. ***Results:*** IE was confirmed in 28 cases (25%). Most patients had prosthesis implantation within 3 months before PET/CT (76%, 85/111). Accuracy, sensitivity, specificity, and positive and negative predictive values of 18F-FDG-PET/CT were 89,2%, 75%, 94%, 81%, and 92%, respectively. The logistic regression model identified optimal accuracy for prosthetic valves with an SUVmax cutoff of ≥ 3.0, and for ascending aorta prosthesis with an SUVmax cutoff of ≥ 5.0, combined with heterogeneous and focal/multifocal uptake patterns. The accuracy based on specialist consensus was similar to that based on objective parameters for valves (89.4% vs 87.1%), but higher for ascending aortic prostheses (88.5% vs 76.9%). ***Conclusion:*** The accuracy of FDG-PET/CT for diagnosing IE was high in early prosthetic IE. Assessment of visual uptake patterns and SUVmax yields a similar accuracy to the consensus of cardiac PET specialists for prosthetic valves, but not for ascending aortic prostheses.

EP-0632

Topographic Mismatch Between Inflammation Assessed by PET/CT and Topographic Localization of Atheroma Plaque Using Morphological Methods in Asymptomatic Carotid Artery Disease

A. Fernández León[1], *M. Velasco-Nuño*[1], *M. Guasch-Jimenez*[2], *A. Lozano*[3], *J. Fite-Matamoros*[4], *M. Calls*[1], *M. Tecame*[3], *M. Lloret-Cano*[4], *A. Margall-Rodriguez*[2], *M. Gaspar-Sardon*[2], *J. Gubern*[1], *A. Flotats*[1], *P. Camps-Renom*[2];
[1]*Nuclear Medicine Department. Hospital de la Santa Creu i Sant Pau, Barcelona, SPAIN,* [2]*Stroke Unit. Department of Neurology. Hospital de la Santa Creu i Sant Pau, Barcelona, SPAIN,* [3]*Radiology Department. Hospital de la Santa Creu i Sant Pau, Barcelona, SPAIN,* [4]*Vascular Surgery Department. Hospital de la Santa Creu i Sant Pau, Barcelona, SPAIN.*

Aim/Introduction: The role of positron emission tomography (PET)/computed tomography (CT) in the determination of inflammation in arterial disease is challenging. This technique can provide information about arterial wall inflammation and plaque stability in atherosclerotic disease. The aim of this study was to compare localization of maximum inflammatory arterial activity assessed by PET/CT with ^{18}F-FDG (fluorodeoxyglucose) and the topographic localization of atheroma plaque using morphological methods. ***Materials and Methods:*** We conducted a prospective cohort study of patients diagnosed with significant carotid artery (CA) stenosis ≥50% and no prior history of stroke, from 2023 to 2024. Carotid stenosis was graded using hemodynamic criteria on ultrasound and classified as moderate (50-69%) or severe (70-99%). Patients with complete carotid occlusion were excluded. All patients underwent PET/CT imaging. SUVmax was measured within a 4 cm segment proximal and distal to the carotid bifurcation using sequential ROIs. The location of maximal activity was categorized as: (1) common carotid artery, (2) carotid bifurcation, or (3) internal carotid artery. We assessed whether the site of highest SUVmax overlapped with the site of maximal stenosis. Concordance was evaluated using Cohen's kappa coefficient, and correlation was assessed with Spearman's rho. ***Results:*** A total of 44 patients were included, with a mean age of 72.6 years; 30% were women. Thirty-three patients (75%) had CA stenosis ≥70%. In 18 patients (40.9%), the point of maximal inflammation was located in the common carotid artery. Concordance between the site of maximal inflammation (PET/CT) and the site of maximal stenosis was observed in 14 patients (31.8%), while in 30 patients (68.2%) there was a mismatch. The kappa coefficient was 0.23, indicating low concordance. Correlation was also weak (Spearman's rho = 0.07, p = 0.673). ***Conclusion:*** In our population of patients with asymptomatic significant carotid stenosis, the location of maximal inflammatory activity on PET/CT does not correlate with the site of maximal morphological stenosis.

EP-0633

Diagnostic Value of ^{18}F-FDG PET/CT in Infective Endocarditis

F. Gur[1], *Ö. V. Topuz*[2], *B. E. Akkaş*[2];
[1]*Başakşehir Çam ve Sakura City Hospital, İstanbul, TÜRKIYE,* [2]*Sağlık Bilimleri Üniversitesi, Başakşehir Çam ve Sakura Şehir Hastanesi, Nükleer Tıp Kliniği, İstanbul, TÜRKIYE.*

Aim/Introduction: Infective endocarditis (IE) is a life-threatening condition characterized by microbial infection of the endocardial surface, most commonly affecting heart valves. Structural heart disease, prosthetic valves, and implantable cardiac devices are known risk factors. ^{18}F-FDG PET/CT is now considered a major imaging criterion for diagnosing infective endocarditis, as defined by the Modified Duke-ISCVID criteria. This study aims to evaluate the diagnostic accuracy of ^{18}F-FDG PET/CT in patients with suspected IE. ***Materials and Methods:*** We retrospectively reviewed patients who underwent ^{18}F-FDG PET/CT between January 2021 and February 2024 due to suspected IE. Patients were classified according to the Modified Duke-ISCVID criteria as definite or excluded IE. All patients were prepared with a low-carbohydrate, high-fat/protein diet prior to imaging. Visual assessment of FDG uptake was performed; lesions showing focal myocardial uptake greater than mediastinal blood pool were considered positive. Bone marrow activation was assessed by calculating the marrow-to-liver SUV ratio using the average SUVmax of three non-lesional lumbar vertebrae divided by liver SUVmean. A ratio >1.4 was deemed positive. Anemia was ruled out based on hemoglobin levels. In patients with LVADs, infected components were recorded. ***Results:*** A total of 62 patients (22 female, 40 male; age range 1-83, mean age 51) were included. Cardiac devices included prosthetic valves (n=22), native valves (n=19), pacemakers (n=12), LVADs (n=10), and vascular grafts (n=9). PET/CT revealed

findings consistent with IE in 41 patients. Among LVAD patients, FDG uptake indicating infection was observed in the pump and outflow tract in 6 cases, and in the driveline in 4. No pathological findings were noted in 21 patients. Compared with final clinical diagnoses, PET/CT yielded 37 true positives, 4 false positives, 16 true negatives, and 5 false negatives (all in native-valve IE). Marrow/liver SUV ratio was significantly higher in IE-positive versus IE-negative patients (1.6 vs. 1.2, p=0.008). Sensitivity, specificity, PPV, NPV, and overall accuracy were 86%, 84%, 92%, 73%, and 85%, respectively. ***Conclusion:*** Focal myocardial FDG uptake above mediastinal activity shows high diagnostic performance for IE. In LVAD patients, PET/CT can guide surgical planning by localizing infected components. Although its specificity is lower in native-valve IE, increased bone marrow metabolic activity may serve as a warning sign in cases with negative PET/CT findings. ***References:*** Şimşek-Yavuz S, Akar AR, Aydoğdu S, et al. Diagnosis, treatment and prevention of infective endocarditis: Turkish consensus report-2019. İnfektif endokarditin tanısı, tedavisi ve önlenmesi: Ulusal uzlaşı raporu-2019. Turk Kardiyol Dern Ars. 2020;48(2):187-226. doi:10.5543/tkda.2020.89689.

EP-0634

The evaluation of splenic switch-off on Ammonia PET in patients with hemodialysis and renal transplantation

A. Yamamoto, *M. Nagao, A. Inoue, R. Imakado, R. Nakao, Y. Maekawa, Y. Matsuo, A. Sakai, M. Momose, J. Yamaguchi, S. Sakai; Tokyo Women's Medical University Hospital, Tokyo, JAPAN.*

Aim/Introduction: Hemodialysis is a cause of arteriosclerosis, resulted in major adverse cardiac events (MACEs). Approximately half of the deaths of patients with hemodialysis are due to cardiovascular disease. Myocardial flow reserve (MFR) derived from ^{13}N-ammonia positron emission tomography (NH_3-PET) can predict the prognosis of patients with ischemic heart disease (IHD). In NH_3-PET imaging, the splenic switch-off (SSO) sign, which visually assesses the decline in splenic ^{13}N-ammonia uptake during adenosine administration, is a hemodynamic indicator of a favorable response to adenosine. This phenomenon is assumed to be due to the fact that adenosine receptor stimulation produces coronary artery dilation while producing vasoconstriction in the splenic circulation. Previous study reported that SSO was a predictor of cardiovascular event after heart transplantation. It was speculated that patients with hemodialysis had arteriosclerosis of the systemic blood vessels, and splenic reactivity to adenosine was reduced. The aim of this study was to compare the splenic blood flow measured by NH_3-PET among patients with hemodialysis, non-hemodialysis and renal transplantation, and investigate its predictive value for MACE. ***Materials and Methods:*** 100 patients (hemodialysis:40, non-hemodialysis:50, renal transplantation:10) who underwent NH_3-PET were enrolled. We placed an ROI on the spleen and measured the mean standardized uptake value (SUV) using NH_3-PET projection images. The spleen ratio (SR) was defined as the mean SUV of the spleen at stress divided by that at rest, and compared among the three groups. The endpoint was MACEs comprising acute coronary syndrome, heart failure hospitalization, and all-cause mortality. SSO was determined by a cutoff obtained using receiver operating characteristic (ROC) analysis for the SR. The patients were divided into two groups with and without SSO, and the MACE rate was compared by Kaplan-Meier and log-rank test. ***Results:*** The hemodialysis group had reduced MFR compared to non-hemodialysis group (1.7±0.6 vs. 2.1±0.6, p=0.0012). The SR was significantly higher in patients with hemodialysis than without hemodialysis (0.92±0.16 vs. 0.78±0.21, p=0.014). The ROC curve analysis of the SR for MACE showed a cutoff value of 0.96 (sensitivity: 55%, specificity: 72%, AUC: 0.67). Patients without SSO had higher MACE rate than those with SSO (p=0.0074) (Figure). ***Conclusion:*** Reaction of splenic blood flow to adenosine in patients with hemodialysis was reduced compared to those with non-hemodialysis. SSO might be related with the endothelial function of systemic blood vessels and was a predictor for MACE.

EP-0635

Abnormal cardiac accumulation on FDG PET due to chemotherapy for breast cancer

Y. Izoe[1], *M. Nagao*[2], *H. Tsukada*[2], *S. Watanabe*[2], *Y. Maekawa*[2], *A. Yamamoto*[2], *Y. Satoh*[3], *H. Saya*[1], *S. Akashi-Tanaka*[2], *S. Sakai*[2]; [1]*Fujita Health University, Toyoake, JAPAN,* [2]*Tokyo Women's Medical University, Shinjuku-ku, JAPAN,* [3]*Fujita Medical Innovation Center Tokyo, Ota-ku, JAPAN.*

Aim/Introduction: Cancer therapy-related cardiac dysfunction (CTRCD) is an important factor in determining treatment strategy and prognosis, but effective methods for its detection have not yet been established. Myocardial accumulation on FDG PET is known to be controlled by insulin activity and is poorly reproducible even between individuals. Therefore, it has not been used to diagnose CTRCD. We focused on the distribution pattern of cardiac FDG accumulation different from physiological accumulation and myocardial SUV, and attempted to determine whether chemotherapy-induced changes in these findings could be linked to detection of myocardial damage. ***Materials and Methods:*** The presence of abnormal right ventricular and atrial accumulation (RV/atrium), diffuse homogeneous accumulation in the left ventricle (homogeneous pattern), and myocardial SUVmax on FDG PET for the diagnosis and treatment of breast cancer between November 2013 and February 2025 were evaluated by two nuclear medicine physicians. FDG PET data were classified into two groups: 79 patients (mean age, 58 years) who had never received chemotherapy and 121 patients (mean age, 60 years) who had received chemotherapy. Chemotherapy regimens consisted mainly of anthracyclines (n=15), human epidermal growth factor receptor 2 (HER2) inhibitors (n=50), immune check inhibitors (ICI) (n=7), and others (eribulin, paclitaxel, and docetaxel, etc)(n=49). Multiple FDG PETs performed after chemotherapy in the same patient were included in the analysis. Patients with other cancers, cardiac and pericardial metastases or diabetes were excluded. ***Results:*** The mean observation period for FDG PET in the chemotherapy group was 38 months with a mean number of tests of 4.4. RV/atrium positivity was found in 37% (45/121) of the chemotherapy group and 13% (10/79) of the no chemotherapy group, with a significantly higher rate in the chemotherapy group (p=0.0002, Fisher's exact test). Homogeneous pattern was found in 38% (46/121) of the chemotherapy group and 23% (18/79) of the no chemotherapy group, with a significantly higher rate in the chemotherapy group (p=0.024). Myocardial SUVmax tended to be higher in the chemotherapy group than in the no chemotherapy group, but the difference was not significant (5.32±3.71 vs. 4.93±4.17). ***Conclusion:*** After chemotherapy, the positivity rate of RV/atrium and the frequency of homogeneous pattern on FDG PET increase. This may be a sign of potential myocardial injury. Cardiac accumulation patterns on FDG PET have been conventionally overlooked in oncology, but its evaluation is expected to be useful in detecting CTRCD.

EP-36

e-Poster Area

B: Imaging Clinical Studies -> B5 Neurological Imaging Clinical Study -> B51 Neurodegeneration

EP-0637

[^{18}F]FDG PET Outperforms MRI in Detecting Early Neurodegenerative Changes Linked to Neurofibrillary Tangle Pathology: An Imaging-Pathology Correlation Study

O. Vourkas, *L. Zhang, A. Rabano, P. Sanchez-Juan, M. Grothe, J. Silva Rodriguez;*
CIEN Foundation, Reina Sofia Alzheimer Center, ISCIII, Madrid, SPAIN.

Aim/Introduction: Neurofibrillary tangle pathology (NFTp) in Alzheimer's disease (AD) is closely related to neurodegeneration, which can be measured in vivo using structural MRI or [^{18}F]FDG PET. While several studies have assessed this correlation using in-vivo markers of NFTp (i.e. tau PET), these are limited by the restricted sensitivity of tau PET for early NFTp stages [1]. Here, we aimed to assess the relative sensitivities of [^{18}F]FDG PET-measured hypometabolism and MRI-measured gray matter (GM) atrophy, to early and advanced stages of NFTp, as assessed by gold-standard post-mortem neuropathological examination. ***Materials and Methods:*** We studied 88 individuals from the Alzheimer's Disease Neuroimaging Initiative (ADNI) autopsy cohort who had Braak NFTp staging performed at autopsy and had [^{18}F]FDG PET and structural T1-MRI scans acquired before death (imaging-to-death interval: 3.4±2.3 years). Associations of Braak stages with regional [^{18}F]FDG PET SUVRs and GM volumes on MRI were assessed in exploratory brain-wide Spearman correlation analyses across 52 cortical and subcortical brain regions defined by the Harvard-Oxford neuroanatomical atlas. For regions showing a significant association ($p<0.05$, FDR-corrected), we then performed pair-wise comparisons between grouped Braak stages 0/I (N=8), II-IV (N=24), and V/VI (N=56). ***Results:*** Higher Braak stages were significantly associated with lower [^{18}F]FDG PET SUVR in several temporo-parietal cortical regions typically affected by AD. Compared to the Braak 0/I reference group, most of these regions showed significant and pronounced (Cohen's $d>0.9$) hypometabolism in early Braak stages II-IV, and severity of hypometabolism further increased in Braak stages V/VI. Although GM volume on MRI showed a similar regional association with Braak stages, effect sizes were considerably lower and differences to the Braak 0/I reference group were only significant for advanced Braak stages V/VI. ***Conclusion:*** Glucose hypometabolism as measured by [^{18}F]FDG PET is a sensitive neuroimaging marker of the neurodegenerative changes that accompany progressive stages of neurofibrillary tangle pathology in AD. Earliest NFTp-related neurodegenerative changes captured by [^{18}F]FDG PET hypometabolism appear to precede macrostructural gray matter atrophy as measured by MRI. ***References:*** [1]. Mattay VS, Fotenos AF, Ganley CJ, Marzella L. Brain Tau imaging: food and drug administration approval of 18F-flortaucipir injection. Journal of Nuclear Medicine. 2020 Oct 1;61(10):1411-2.

EP-0638

Predicting Amyloid PET Positivity in Alzheimer's Disease using 18F-Fluorodeoxyglucose PET and Explainable Artificial Intelligence

Ü. Akdemir[1], *A. Öter*[2], *E. Balcı*[1], *S. Sağıroğlu*[3], *L. Ö. Atay*[1];
[1]*Gazi University Medical Faculty, Department of Nuclear Medicine, Ankara, TÜRKIYE,* [2]*Gazi University Faculty of Technology, Department of Energy Systems Engineering, Ankara, TÜRKIYE,* [3]*Gazi University Faculty of Engineering, Department Of Computer Engineering, Ankara, TÜRKIYE.*

Aim/Introduction: Amyloid PET imaging is a core component of Alzheimer's disease (AD) diagnostic criteria, but its high cost and limited availability pose significant challenges. This study aimed to determine if brain 18F-fluorodeoxyglucose (FDG) PET scans, a more widely accessible marker of neurodegeneration, can effectively predict amyloid PET status using machine learning (ML). Furthermore, we sought to evaluate the predictive model's performance and enhance its transparency using explainable artificial intelligence (XAI) techniques. ***Materials and Methods:*** We analyzed FDG PET data from a combined cohort of 292 Mild Cognitive Impairment (MCI) patients after data cleaning, comprising 54 patients from our center and 238 subjects derived from the Alzheimer's Disease Neuroimaging Initiative (ADNI) database. Brain FDG PET images were spatially normalized using the statistical parametric mapping (SPM) software. Regional glucose metabolism was quantified for 116 anatomical regions of interest (ROIs) defined by the automated anatomic labelling (AAL) atlas, with uptake values normalized using the pons as a reference region. A Gradient Boosting (GB) ML model was developed to classify subjects based on their amyloid PET status (positive/negative). The dataset was split into training (80%, n=233) and testing (20%, n=59) sets. Model hyperparameters (including learning rate=0.01, number of estimators=200, maximum depth=3) were optimized using 10-fold cross-validation and the GridSearchCV method on the training data. Performance was assessed on the independent test set using accuracy, precision, recall, and F1-score. SHAP (SHapley Additive exPlanations) and LIME (Local Interpretable Model-agnostic Explanations) were applied for model explainability. ***Results:*** The optimized GB model, utilizing the 116 regional FDG PET features, achieved promising results in predicting amyloid PET positivity on the unseen test set. The performance metrics were calculated as: Accuracy = 71.2%, Precision = 75.9%, Recall = 91.1%, and F1-score = 82.8%. XAI analyses successfully identified the specific brain regions that most significantly contributed to the model's predictions, providing insights into the neurobiological patterns associated with amyloid positivity as captured by FDG PET. ***Conclusion:*** Our study demonstrates that quantitative regional information derived from standard FDG PET scans, when analyzed with Gradient Boosting machine learning, can predict amyloid PET status with reasonable accuracy. This approach, enhanced by XAI for interpretability, shows potential as a more accessible and cost-effective method for identifying individuals likely to have AD-related amyloid pathology, potentially aiding in patient screening and selection for further diagnostic workup or clinical trials.

EP-0639

Quantitative assessment of the evolution stages of Alzheimer's disease in amyloid PET using an anatomical brain phantom

M. Pirozzi[1], *E. Di Giorgio*[2], *A. Prinster*[3], *A. Negro*[4], *V. D'Agostino*[4], *F. Squame*[2], *L. Mansi5*[5,6], *B. Alfano*[7], *M. Spadafora*[6], *M. Quarantelli*[3];
[1]*Department of Advanced Medical and Surgical Sciences, University of Campania "Luigi Vanvitelli", Naples, ITALY,* [2]*Nuclear Medicine Unit, Ospedale del Mare, Naples, ITALY,* [3]*Institute of Biostructures and Bioimaging, National Research Council, Naples, ITALY,* [4]*Neuroradiology Unit, Ospedale del Mare, Naples, ITALY,* [5]*CIRPS, Interuniversity Research Center for Sustainability, Rome, ITALY,* [6]*Medicina Futura, Acerra, Naples, ITALY,* [7]*Human Shape Technologies s.r.l, Naples, ITALY.*

Aim/Introduction: Visual interpretation of Amyloid-PET (A-PET) is based on the assessment of the presence of high local gray/white matter (GM/WM) ratios in disease-related target regions(1). However, the low-resolution of PET decreases the difference between positive and negative studies(2) and limits the possibility to measure the actual GM/WM tracer ratios. Furthermore, procedures for correction of partial volume effects (PVE), developed and validated for FDG-PET studies, lack proper validation on A-PET. Aims of the present study were:

to validate PVE-correction of A-PET studies using a 3D-printed multicompartmental anatomical brain phantom based on brain tissue maps obtained by MRI segmentation(3); to PVE-correct ROI data from a small set of clinical A-PET studies, carried out on the same PET scanner, providing estimates of actual GM/WM tracer uptake ratios associated to increasing disease stages. ***Materials and Methods:*** All studies were acquired on the same PET/CT scanner (Biograph mCT, OSEM3D+TOF, 4 iterations, 21 subsets, 3mm Gaussian smoothing, 5.76mm in-plane and 6.11mm axial FWHM).Two PET/CT studies of the phantom were acquired, respectively, without any activity in the GM compartments, and with a GM/WM ratio of 125%, with count statistics comparable to actual clinical human studies. Weighted sums of these two studies were then obtained, simulating six GM/WM concentration ratios equally spaced from 0 to 120%.10 A-PET studies (7 Flutemetamol, 3 Florbetapir; 5 females, age range 53-77, 5 positive studies) for which MRI studies suitable for segmentation were available, were also processed.For each study, ROI values were obtained by using the corresponding segmented T1-weighted MRI volume (for human studies(4)) or segmented high resolution CT scan (for the phantom(3)), co-registered to the PET(5), and labelled by applying the Automated Anatomical Labeling atlas(6). ROI values were then corrected for PVE(7) using PVELab(8). ***Results:*** Phantom uncorrected GM/WM ROI mean value inaccuracies ranged from +16.1% (for the 0% GM/WM phantom) to 18.8% (for the 120% GM/WM phantom), while PVE correction decreased ROI value errors to +0.5 and -5.6%, respectively.The optimal GM/WM ratio cutoff for PET positivity was 70% when using uncorrected values and 75% when using PVE-corrected values. ***Conclusion:*** The analysis of the phantom studies confirmed the accuracy of the A-PET PVE-correction based on segmented brain tissue compartment. A progressive GM/WM ratio increase above 70% corresponds to the transition from negative to positive studies. ***References:*** (1)Eur J Nucl Med Mol Imaging.2021;48:2169-2182 (2) Journal of Nuclear Medicine.2024;65:781-787 (3)Journal of Nuclear Medicine.2024;65:1489 (4)NeuroImage.2005;26:839-851 (5)Medical Image Analysis.1996;1:35-51.6 (6)Neuroimage.2002;15:273-289 (7) Journal of Nuclear Medicine.1998;39:904-911 (8)Journal of Nuclear Medicine.2004;45:192-201.

EP-0640

Quantification in the 18F fluorodeoxyglucose (FDG) Positron Emission Tomography/Computed Tomography (PET/CT) in prodromal dementia

Z. Koç[1], *M. Arslan*[1], *P. Ozcan*[1], *A. Özge*[2], *H. Yanık*[3];
[1]*Mersin University Hospital Nuclear Medicine Dpt., Mersin, TÜRKIYE,* [2]*Mersin University Neurology Dpt., Mersin, TÜRKIYE,* [3]*Mersin University School of Applied Technology and Management, Information Systems and Technologies., Mersin, TÜRKIYE.*

Aim/Introduction: In our study, we aimed to examine the contribution of digitization techniques and artificial intelligence to the diagnosis of ^{18}F-FDG PET/CT imaging in the differential diagnosis of prodromal Alzheimer's dementia. ***Materials and Methods:*** In this study, we retrospectively evaluated the data of 72 patients with a preliminary diagnosis of prodromal Alzheimer's dementia attended between November 2018 and December 2023, who were found suitable for F18-FDG PET/CT brain imaging in our Nuclear Medicine Clinic. The age, gender, mini mental assessment test (MMSE) score and prediagnoses of the 72 patients were obtained from patient files and clinicians and recorded. PET/CT imaging results, MATLAB-based SPM12 (Statistical Parametric Mapping) analysis results, artificial intelligence (TensorFlow and PyTorch (Deep Learning) in the PYTHON programming language) analysis results and the final diagnoses made clinically by neurologists were recorded. Statistical Pack age for Social Sciences (SPSS) 22.0 program was used to analyze the data obtained from the study. ***Results:*** According to clinical findings, 23 (31.9%) of the patients were diagnosed as mild cognitive impairment (MCI), 46 (63.9%) as Alzheimer's disease/other neurodegenerative disease, and 4 (4.2%) as normal. The mean age was 61.26±7.61 (min:51-max:77) years and the mean MMSE score was 21.40±7.37 (min:7-max:30) in patients clinically diagnosed with HBB. Twelve (52.2%) of the patients with HBB were male and 11 (47.8%) were female. Family history was present in 2 (8.7%) of the patients with HBB. The sensitivity, specificity, accuracy, positive predictive value, negative predictive value and positive predictive value of PET/CT were 91.3%, 100%, 92%, 100% and 50%, respectively. Of the 23 patients with clinical diagnosis of HBB, 19 patients had concordance with SMP12, while 4 patients had discordance. Of the 14 patients with normal SPM12, 4 were diagnosed as mild cognitive impairment and 7 as other neurodegenerative diseases. The performance of the SPM12 analysis method in the diagnosis of prodromal Alzheimer's disease was calculated as follows: Sensitivity 82.6%, specificity 100%, accuracy 95.7%, positive predictive value 100% and negative predictive value 42.8%. In addition, the performance of the artificial intelligence (AI) method in the diagnosis of mild cognitive impairment was evaluated as follows: Sensitivity 97.69%, specificity 98.88%, accuracy 98.29%, positive predictive value 98.83% and negative predictive value 97.79%. ***Conclusion:*** In conclusion, the sensitivity and specificity of both SPM12 analysis and visual interpretation results were similar however artificial intelligence analysis in FDG PET/CT imaging in the prodromal dementia stage significantly contribute to the diagnosis.

EP-0641

DaT-scanning on a CZT: distance is the enemy

V. Nuttens[1], *D. Ooms*[1], *S. Vermeulen*[2], *M. Koole*[1];
[1]*AZORG, Aalst, BELGIUM,* [2]*AZORG Aalst, Aalst, BELGIUM.*

Aim/Introduction: DaT-scanning with ^{123}I-ioflupane takes around 35 minutes for a conventional dual-head SPECT/CT according to EANM Guidelines [1], comprising 60 25-second projection views. A 3D-CZT-SPECT/CT can significantly reduce the scanning time to as low as 15 minutes. [2] However, the observed 3D-CZT-SPECT image quality was highly variable between scans. We aimed to demonstrate that 3D-CZT-SPECT/CT systems are more susceptible to resolution degradation with increasing detector-to-subject distance compared to conventional dual-head SPECT/CT systems. ***Materials and Methods:*** The background of a striatal phantom embedded in a human skull with resin was filled with 5 kBq/mL. The cavities representing the striata were filled with a ratio of 8:1 (right striatum) and 4:1 (left striatum). The phantom was scanned both on a conventional and 3D-CZT-SPECT/CT with a radial orbit of the detector heads at increasingly larger distances relative to the center of the phantom. The SPECT resolution of the phantom scans was assessed by calculating the Peak signal-to-noise ratio (PSNR) with an increasingly smoothed template. Image quality was assessed by a nuclear medicine physician using a 5-point Likert scale. All scans were done with an ultra-low-dose CT for attenuation correction. ***Results:*** 3D-CZT-SPECT/CT resolution degraded three times faster as a function of the distance of the detector compared to a conventional system. 3D-CZT data showed a spatial resolution of 14.7mm FWHM for 13.7 cm distance (closest possible position), while this was 17mm FWHM for the conventional SPECT/CT. The fitted curves for the spatial SPECT resolution as a function of distance intersect at 27 cm, corresponding to 17.8mm FWHM resolution. Visual assessment of image quality was even more convincing, with a 3D-CZT-SPECT/CT scan at the closest position resulting in a score of 5/5. This was reduced to a score of 3/5 for only a 3 cm increase in the distance of the object to the detector. For the conventional system, the closest position resulted in a 4/5. This reduced to a score of 3/5 for a 15 cm increase in the distance. ***Conclusion:*** Our study shows that optimal positioning of patients for 3D CZT DaT-SPECT

scanning is crucial, as the SPECT resolution is heavily influenced by the distance of the detector heads to the head of the patient. If the optimal scanning position is used, 3D-CZT-SPECT/CT systems show high potential to achieve better spatial resolution and scan twice as fast as conventional SPECT/CT. ***References:*** [1] 10.1007/s00259-020-04817-8 [2] 10.1097/RLU.0000000000003969.

EP-0642

Quantitative Study of Dopaminergic Neuron Integrity and MRI Relaxation Value Changes in Early-Onset versus Late-Onset Parkinson's Disease Using PET/MR Imaging

J. Liu, *R. Wang;*
Department of Nuclear Medicine, The First Medical Center of Chinese PLA General Hospital, Beijing, CHINA.

Aim/Introduction: Parkinson's disease (PD) results from dopaminergic neuron degeneration in the substantia nigra-striatal pathway, showcasing clinical and genetic variations. This study explores differences in dopaminergic neuron integrity and MRI relaxation times between early-onset PD (EOPD) and late-onset PD (LOPD) using ^{11}C-β-CFT PET/MR imaging with advanced SyMRI sequences. The objective is to enhance understanding of their distinct pathophysiological mechanisms. ***Materials and Methods:*** In a prospective study, 12 EOPD and 8 LOPD patients underwent ^{11}C-β-CFT PET/MR imaging, while 15 healthy controls (HC) only received MRI scans, which included T1 BRAVO and SyMRI sequences. Quantitative T1- and T2- maps were reconstructed from SyMRI raw data using AW workstation. Subsequently, the maps and PET images were coregistered to T1 images, normalized to MNI152 template and segmented to 116 AAL brain regions. PET standard uptake value ratios (SUVR) data were calculated by normalizing to whole-brain average value. Spearman's correlation was employed to explore the relationships among SUVR, T1, and T2 values across different brain regions. Additionally, one-way ANOVA analysis was conducted to evaluate differences among the EOPD, LOPD, and HC groups. ***Results:*** The EOPD group exhibited significantly higher SUVR values in the bilateral caudate nuclei compared to the PD group ($P < 0.05$). Variations in T1 and T2 values were observed among the EOPD, PD, and HC groups in the left caudate nucleus, left olfactory cortex, and left parahippocampal gyrus ($P < 0.05$), with the HC group consistently showing the lowest T1 and T2 values. Positive correlations were observed between T1 and T2 values in the EOPD, PD, and HC groups (EOPD: $r = 0.81$, $P < 0.05$; PD: $r = 0.91$, $P < 0.05$; HC: $r = 0.83$, $P < 0.05$). Additionally, negative correlations were found between T1 values and SUVR, as well as between T2 values and SUVR across all groups (EOPD: T1 $r = -0.46$, T2 $r = -0.5$; PD: T1 $r = -0.59$, T2 $r = -0.6$, all $P < 0.05$). ***Conclusion:*** Elevated SUVR values in EOPD patients suggest milder early-stage dopaminergic neuron impairment, with lower T1 and T2 relaxation values seen in the HC group, underscoring a close link between dopaminergic dysfunction and MRI changes for personalized treatment strategies in Parkinson's disease.

EP-0643

Performance of ^{18}F-SynVesT-1 versus ^{18}F-FDG brain PET in differentiation of patients with cognitive decline

C. Carron[1], *L. Degryse*[1], *L. Boeckxstaens*[1], *G. Vanderlinden*[1], *K. Nikkita*[2], *R. Vandenberghe*[1], *M. Vandenbulcke*[1], *K. Van Laere*[1];
[1]KU Leuven, Leuven, BELGIUM, [2]Yale PET center, Yale, CT, UNITED STATES OF AMERICA.

Aim/Introduction: ^{18}F-FDG brain PET is routinely used in the clinical workup of patients with cognitive dysfunction. SV2A PET quantifies synaptic loss and may be a more precise marker of neurodegeneration as it is less influenced by e.g. acquisition context and neuroinflammation. We prospectively investigated the diagnostic performance of ^{18}F-SynVesT-1 versus ^{18}F-FDG in patients referred for imaging to a tertiary memory clinic. ***Materials and Methods:*** A pilot analysis included 70 patients that underwent ^{18}F-FDG (30-45 minutes p.i.) and ^{18}F-SynVesT-1 (60-90 minutes p.i.) PET/MR within three months. Three nuclear medicine readers with variable experience (3-28 years) evaluated randomized orthogonal and surface rendered emission and Z-score images with a short clinical summary to assess the most likely diagnosis. A consensus diagnosis was defined if at least two readers agreed. If there was no agreement, the diagnosis of the most experienced reader was considered (6% of cases). Clinical follow-up provided the gold standard diagnosis. VOI-based SUVR quantification (pons for ^{18}F-FDG and centrum semiovale for ^{18}F-SynVesT-1 as reference region) was also investigated. ***Results:*** After median follow-up of 7 months, final clinical diagnoses were 34 AD, 9 FTD, 2 DLB, 1 amnesia due to epilepsy and 24 without evidence of neurodegeneration (NoND). Consensus ^{18}F-FDG PET reads differentiated NoND from others with 83% balanced accuracy (78-84%), with correspondence to the final diagnosis in 73% (63-80%). For ^{18}F-SynVesT-1, consensus read accuracy was 75% (74-76%), with corresponding final diagnosis in 64% (59-61%). Inter-observer agreement was equal for both tracers (Fleiss Kappa 0.49). Comparing AD to NoND, quantitative SUVR evaluation showed largest differences in the precuneus, lateral parietal and lateral temporal cortex for both tracers. For these VOI's, the Cohen's d values were 1.65, 1.52, and 1.46 for ^{18}F-FDG (all $p < 0.0001$), and 0.72, 0.73, and 0.93 for ^{18}F-SynVesT-1, respectively (all $p < 0.01$). This corresponded with the visual analysis, with lateral temporal and parietal regions as most affected for both tracers, and reductions more pronounced for ^{18}F-FDG. ***Conclusion:*** ^{18}F-SynVesT-1 PET shows promise as a clinical tool for differentiating patients with cognitive decline of uncertain origin. Although semiquantitative analysis at the group level showed SV2A binding reductions had lower effect sizes compared to hypometabolism, readers were still able to differentiate neurodegenerative disorders effectively and with good correspondence, despite having differences in overall experience and with SV2A PET reading.

EP-0644

A biological model combined individual tau-PET and FDG-PET molecular connectivity to predict disease progression for AD

L. Fu[1], *Z. Zhou*[2], *T. Lu*[3], *J. Gao*[1], *Y. Cheng*[3];
[1]Department of Nuclear Medicine,China-Japan Friendship Hospital, Beijing, CHINA, [2]Department of Neurology,China-Japan Friendship Hospital, Beijing, CHINA, [3]School of information science, Beijing university of chemical technology, Beijing, CHINA.

Aim/Introduction: Alzheimer's disease (AD) exhibits significant clinical heterogeneity, with patients demonstrating either rapid cognitive decline or typical progression patterns. The association between tau pathology, glucose metabolism, and the clinical heterogeneity remains unclear. We aimed to identify a biological model of individual molecular connectivity, incorporating tau pathology and cerebral glucose metabolism network, to predict AD progression using machine learning methods. ***Materials and Methods:*** We included participants from the Alzheimer's Disease Neuroimaging Initiative (ADNI) dataset who had baseline 3D-T1WI, ^{18}F-fluoro-deoxy-glucose (FDG-PET) and ^{18}F-AV1451 PET scans, along with longitudinal Mini-Mental State Examination (MMSE) and Clinical Dementia Rating (CDR) assessments spanning at least 2 years of follow-up. Participants were categorized into rapid progressive AD (rpAD; ≥4-point annual MMSE decline) and typical AD (tAD; ≤3-point annual MMSE decline) group. Individual brain networks were constructed for each subject using Kullback-Leibler divergence similarity estimation, and four types of features were extracted through graph theory analysis: connectivity strength, global/local topological features, and their combinations. After feature selection with t-tests and LASSO to address the curse of dimensionality, we classified rpAD and cAD using five machine learning models: Support Vector Machine

(SVM), Logistic Regression (LR), Random Forest (RF), Decision Tree (DT), and K-Nearest Neighbors (KNN), with nested cross-validation to enhance generalization. ***Results:*** A total of 58 rpAD and 70 tAD patients were recruited. Compared to tAD patients, LR with combined features achieved the best classification performance on FDG-PET networks (AUC=0.936), while RF with connectivity and combined features showed optimal performance on tau-PET networks (AUC=0.855). The top identified regions for FDG-PET network included the bilateral temporal cortex, angular cortex, precuneus and caudate. As for tau-PET network, regions included bilateral orbitofrontal cortex, and right anterior cingulate cortex, precuneus, and angular gyrus. These results aligned with voxel-wise analysis results, showing significant AD-related decreased metabolism and increased tau deposition. ***Conclusion:*** This study suggests that machine learning technique combining network features of glucose metabolism and tau pathology can provide a promising classification of rpAD and tAD.

EP-0645

Regional Centiloid Quantification of ^{18}F-Florbetaben PET in a Multicenter Study Using Publicly Available Datasets.

C. Lin[1], *L. Tang*[2], *C. Ko*[2];
[1]*Department of Nuclear Medicine, National Taiwan University Hospital Yunlin Branch, Yunlin County, TAIWAN,* [2]*Department of Nuclear Medicine, National Taiwan University Hospital, Taipei, TAIWAN.*

Aim/Introduction: The standardized interpretation of ^{18}F-florbetaben (^{18}F-FBB) image was based on expert scoring of regional cortical tracer uptake (RCTU) to calculate brain amyloid plaque load, judging from four different regions. However, visual scoring relies on readers' experience. And the inter-reader agreements become worse in complex clinical scenario. In this multicenter study involving four independent institutions, we propose a method for deriving regional Centiloid scale (RCL) values from ^{18}F-FBB PET using publicly available Centiloid calibration data, enabling standardized transformation of SUVRs to assist in RCTU interpretation. ***Materials and Methods:*** We recruited 71 subjects of suspected mild cognitive impairment or Alzheimer's disease (AD) referred for ^{18}F-FBB imaging. The RCTU scores read by qualified experts were served as reference standard. We used MI Neurology software to automatically quantify SUVR of the four specific cortical regions with whole cerebellum as reference region. RCL transformation was performed using paired PiB and FBB scans from the Centiloid calibration dataset (10 young controls and 25 elderly subjects). Regional SUVRs of controls and AD patients were anchored at RCL=0 and 100, respectively, and region-specific conversion equations were derived. The quantified SUVR and RCL values were compared to RCTU scores. Receiver operating characteristic (ROC) analysis was performed to identify optimal RCL cutoffs predictive of positive visual reads, and relationships with Mini-Mental State Examination (MMSE) scores were assessed. ***Results:*** RCL showed strong correlations with visual RCTU scores across all cortical regions (Spearman $\rho = 0.776$-0.827, $p < 0.001$). ROC analysis identified optimal RCL cutoffs of 0 (frontal), 25 (parietal), 70 (posterior cingulate), and 45 (temporal) for predicting positive visual reads, with area under curve (AUC) ranging from 0.928 to 0.970. MMSE scores significantly differed among groups stratified by the number of RCL-positive regions ($p=0.018$), with the group showing four positive regions having lower cognitive scores than those with none (adjusted $p = 0.022$). Additionally, we found that pooling regional RCL values into a single composite score and applying a unified cutoff provided stronger discrimination of MMSE scores ($p = 0.006$) than counting region-wise positivity, suggesting that pooled amyloid burden better reflects cognitive status. ***Conclusion:*** In this pilot study, we proposed a method for regional Centiloid quantification using open-access calibration data, which showed strong agreement with visual reads. Additionally, pooled analysis correlated well with cognitive status. Importantly, these quantitative thresholds may assist in the interpretation of ^{18}F-FBB PET, particularly in borderline or equivocal cases.

EP-0646

The Revealing of Aberrant Brain Metabolic Network Based on ^{18}F-FDG PET in Patients with DLBCL

J. Wang, *Q. Zhao, X. Ma, Y. Liu;*
General Hospital of Ningxia Medical University, Ningxia Yinchuan, CHINA.

Aim/Introduction: Diffuse Large B-cell Lymphoma (DLBCL) has been associated with aberrant cerebral metabolic patterns detected via ^{18}F-FDG PET. However, systemiclevel insights into how DLBCL affects functional brain integration through metabolic networks remain limited.This study aimed to investigate global and nodal topological alterations in brain metabolic networks of DLBCL patients, comparing baseline and post-chemotherapy states to healthy controls, to identify functional connectivity changes linked to the disease. ***Materials and Methods:*** Eighty DLBCL patients and 80 age- and sex-matched healthycontrols underwent ^{18}F-FDG PET/CT scans. Patients were scanned at baseline and post-chemotherapy. The Anatomical Automatic Labeling Template (AAL) was used to construct metabolic networks, analyzed via GRETNA software for global and nodal metrics. Inter-group differences were assessed using non-parametric permutation tests. ***Results:*** Both DLBCL patients (baseline/post-chemotherapy) and controls exhibited small-world network properties. However, baseline and post-treatment DLBCL patients showed abnormal transmission efficiency in the hippocampus, amygdala-cingulate pathway, and prefrontal cortex. Reduced connectivity in specific regions and compensatory increases in others were observed, particularly within the default mode and central executive networks. ***Conclusion:*** Our findings highlight the potential of ^{18}F-FDG PET combined with graph theory as a tool for early detection of cognitive impairment in DLBCL. This work bridges a critical gap in understanding how non-CNS malignancies and their treatments influence brain function, offering implications for personalized therapeutic strategies.

EP-0647

The Impact of APOE ε4 on Amyloid Deposition and Cerebral Blood Flow in Cognitively Normal Subjects using Dual-Phase ^{18}F-Florbetaben PET Study

J. Kim[1], *D. Kim*[2], *G. Kim*[1], *H. Yoon*[1];
[1]*Ewha Womans University Mokdong Hospital, Seoul, KOREA, REPUBLIC OF,* [2]*Research Institute, Neurophet Incorporation, Seoul, KOREA, REPUBLIC OF.*

Aim/Introduction: Apolipoprotein E (APOE) genotype is important information in Alzheimer's disease (AD). This study aimed to demonstrate the impact of APOE ε4 on cerebreal blood flow (CBF) and amyloid deposition in cognitively normal subjects using dual-phase ^{18}F-florbetaben (FBB) PET. ***Materials and Methods:*** A total of 133 cognitively normal subjects who completed dual-phase ^{18}F-FBB PET and APOE genotyping were enrolled in the study. Participants possessing at least one APOE ε4 allele were designated as carriers. We assessed standardized uptake value ratios (SUVRs) for cerebral blood flow (CBF) using early-phase ^{18}F-FBB (eFBB) and for amyloid deposition using delayed-phase ^{18}F-FBB (dFBB) in both the composite region and specific target subregions, including the frontal cortex, parietal cortex, temporal cortex, occipital cortex, and precuneus. Additionally, we investigated correlations between eFBB and dFBB SUVRs across these regions. ***Results:*** APOE ε4 carriers exhibited significantly increased CBF in the composite region ($p = 0.0042$) and target subregions, including the frontal cortex ($p = 0.0054$) and parietal cortex ($p = 0.0056$) (Figure 1). They also showed greater amyloid deposition in the composite region ($p = 0.0065$) and target subregions, such as the frontal cortex ($p = 0.0028$) and precuneus ($p = 0.0071$).

Significant positive correlations between eFBB and dFBB SUVRs were shown in the temporal cortex (p = 0.0007) and precuneus (p = 0.0080). ***Conclusion:*** APOE ε4 showed significant higher amyloid deposition and CBF in specific brain regions of cognitively normal subjects. Dual-phase PET could be valuable for demonstrating AD-related changes in APOE ε4 carriers during the preclinical stage.
References: 1. Philip S. Insel MOH, MD, PhD; Niklas Mattsson-Carlgren, MD, PhD. Association Between Apolipoprotein E ε2 vs ε4, Age, and β-Amyloid in Adults Without Cognitive Impairment. JAMA Neurology. 2021;78:229-35. 2. Lim YY, Mormino EC, Alzheimer's Disease Neuroimaging I. APOE genotype and early beta-amyloid accumulation in older adults without dementia. Neurology. 2017;89:1028-34. doi:10.1212/WNL.0000000000004336. 3. de Heus RAA, de Jong DLK, Sanders ML, van Spijker GJ, Oudegeest-Sander MH, Hopman MT, et al. Dynamic Regulation of Cerebral Blood Flow in Patients With Alzheimer Disease. Hypertension. 2018;72:139-50. doi:10.1161/HYPERTENSIONAHA.118.10900. 4. Fettahoglu A, Zhao M, Khalighi M, Vossler H, Jovin M, Davidzon G, et al. Early-Frame [(18)F]Florbetaben PET/MRI for Cerebral Blood Flow Quantification in Patients with Cognitive Impairment: Comparison to an [(15)O] Water Gold Standard. J Nucl Med. 2024;65:306-12. doi:10.2967/jnumed.123.266273.

EP-0648

Statistical FDG PET Mapping and Quantitative MRI Volumetry of Limbic Age-Related TDP-43 Encephalopathy and Alzheimer Co-pathology

P. Ngam[1], *Y. Anzai*[2], *S. Minoshima*[2];
[1]*National University Hospital Singapore, Singapore, SINGAPORE,* [2]*University of Utah Hospital, Salt Lake City, UT, UNITED STATES OF AMERICA.*

Aim/Introduction: Limbic Age-Related TDP-43 Encephalopathy (LATE) is emerging as the prevalent neurodegenerative disorder in aging populations, mimicking the clinical presentations of Alzheimer's Disease (AD). This study investigates in vivo FDG PET and MRI biomarkers in detecting probable LATE neuropathologic changes (NC). ***Materials and Methods:*** We retrospectively analyzed 944 FDG PET cases referred from cognitive disorder clinics. To characterise the LATE and AD findings objectively and quantitatively, we created 3D-SSP PET templates for LATE-NC (n=6) and ADNC (n=32) from autopsy-confirmed datasets. All 3D-SSP Z-score FDG maps were created in comparison to normal PET scans from 20 control cases whose amyloid PET scans were negative. Using the autopsy-derived Z-score maps, Z-score product indices (individual Z-score map x Z-score of autopsy-confirmed cohorts) were generated for each subject, stratifying participants into probable LATE, probable LATE+AD, and probable AD. Quantitative MRI volumetry data (NeuroQuant) were analyzed between the groups. ***Results:*** Out of the 944 clinical cases, 13.0% were characterized as probable LATE (2.4% pure LATE and 10.6% LATE+AD) and 23.7% probable AD without LATE. MRI volumetry revealed that the medial temporal lobe was most affected in pure LATE cases (p<0.001), while the orbitofrontal gyrus and lateral temporal lobe were most vulnerable in mixed LATE+AD cases (p=0.001; p<0.001). Post-hoc analysis identified the entorhinal cortex and amygdala as key regions for distinguishing mixed LATE+AD cases from pure LATE and pure AD cases, respectively (p=0.05; p<0.001). Subgroup analysis of the probable LATE+AD group demonstrated additive/synergistic effects of both pathologies, with three-quarters of cases exhibiting concordant lateralized metabolic brain changes, predominantly left-sided, based on LATE and AD Z-score products (p<0.001). A similar pattern of left-dominant brain atrophy was observed in MRI volumetry. ***Conclusion:*** Substantial numbers of our patients exhibited LATE features that were characterised objectively using scans from autopsy-proven cases. These LATE cases were associated with specific regional atrophy measured by quantitative MRI. Cases with LATE+AD co-pathologies demonstrated synergistic hemispheric involvement. Further investigations of such synergistic changes between LATE and AD are warranted.

EP-0649

MRI-Informed Graph Learning on Amyloid PET Enhances Diagnosis and Staging of Alzheimer's Disease

T. Sun[1], *X. Chen*[1], *L. Chen*[2], *S. Wang*[1], *M. Wang*[2];
[1]*Chinese Academy of Sciences, Shenzhen, CHINA,* [2]*Henan Provincial People's Hospital, Zhengzhou, CHINA.*

Aim/Introduction: Early detection and accurate staging of Alzheimer's disease (AD) remain challenging due to subtle structural and molecular brain changes. Non-invasive methods that combine imaging modalities could improve diagnostic performance. This study proposes a novel graph-based learning framework that integrates amyloid-β PET and MRI structural features to enhance early detection and staging of AD. ***Materials and Methods:*** A total of 323 ^{18}F-florbetapir PET scans from 196 patients were retrospectively collected from the Alzheimer's Disease Neuroimaging Initiative (ADNI) as the training dataset. Two additional independent cohorts (99 scans from 85 patients) were used for external testing. For each PET scan, individual brain graphs were constructed to capture topological and spatial information. A graph learning model was developed to extract functional PET features while incorporating structural information from MRI. The model was trained to distinguish between normal control (NC), mild cognitive impairment (MCI), and AD subjects. Diagnostic performance was assessed using receiver operating characteristic (ROC) curve analysis, with cortical SUVR as a baseline. A new biomarker, the GCN_score, was derived from salient graph nodes and assessed using the Kruskal-Wallis test and Cohen's effect size. ***Results:*** The graph-based model achieved an AUC of 89.8% (specificity 83.6%, sensitivity 81.6%) for distinguishing MCI from NC, and 88.3% (specificity 81.6%, sensitivity 80.6%) for distinguishing MCI from AD within the ADNI dataset. Comparable diagnostic performance was observed on the external testing cohorts. In all scenarios, the proposed model significantly outperformed cortical SUVR-based classification (DeLong test, p < 0.001). The derived GCN_score exhibited stronger differentiation between disease stages, with Cohen's effect sizes of 1.744 (MCI vs. NC) and 1.32 (MCI vs. AD), compared to 0.309 and 0.641 for cortical SUVR, respectively. ***Conclusion:*** This graph-based learning framework combining PET and MRI features demonstrates superior performance for early detection and staging of Alzheimer's disease. The interpretable GCN_score provides an effective biomarker for distinguishing clinical stages, outperforming conventional SUVR analysis. These findings support the use of graph-based multimodal analysis as a promising tool for facilitating timely intervention in AD progression.

EP-0650

Multimodal topographic impairment in Parkinson's disease

M. Wang[1], *W. Han*[1], *Y. Jiao*[1], *Z. Lv*[1], *Y. Su*[1], *Y. Hu*[2], *Y. Yang*[3], *C. Zhao*[1], *P. Fu*[1];
[1]*Department of Nuclear Medicine, 1st Hospital of Harbin Medical University, Harbin, CHINA,* [2]*Central Research Institute, United Imaging Healthcare, Shanghai, CHINA,* [3]*Beijing United Imaging Research Institute of Intelligent Imaging, Beijing, CHINA.*

Aim/Introduction: Parkinson's disease (PD) is a common neurodegenerative disorder characterized by progressive cognitive decline. Although previous studies have reported abnormalities in both metabolic and structural connectivity networks in PD patients, changes in brain network topological properties across different disease stages remain insufficiently understood. This study aims to investigate the alterations in topological features of metabolic and structural brain networks at

different stages of PD using multimodal ^{18}F-FDG PET/MR imaging, in order to provide imaging-based evidence for the underlying mechanisms of network disruption in PD. ***Materials and Methods:*** A total of 68 subjects were included in this study, including 24 patients with late PD, 19 patients with early PD and 25 age- and sex-matched healthy individuals. Basic clinical information and clinical cognitive scale assessments were collected, including the Mini-Mental State Examination (MMSE) and Montreal Cognitive Assessment (MoCA), Hoehn and Yahr Scale (H-Y Stage), Unified Parkinson's Disease Rating Scale Part III (UPDRS-III) and Non-Motor Symptom Assessment Scale for Parkinson's Disease (NMSS). All subjects underwent an integrated 18F-fluorodeoxyglucose (^{18}F-FDG) PET/MR scan, acquiring high-resolution T1-weighted structural images, diffusion-tensor images and ^{18}F-FDG images. Anatomical Automatic Labeling (AAL) atlas was utilized for further brain parcellation. Normalized PET standardized uptake value ratio (SUVR) images were obtained and extracted using FSL. Brain region without significant SUVr difference between PD and HC subjects was set to be reference region. Tractography with brain parcellation was performed with MRtrix3. Group covariance matrix was generated by Pearson's correlation/tractography to get both metabolic/structural network. Topographic properties including clustering coefficient, characteristic path length and global efficiency were calculated. ***Results:*** All PD patients showed significant cognitive impairment, showing reduced MMSE/MoCA and higher UPDRS-III/NMSS compared with HC group (all $p < 0.001$). In metabolic network, higher characteristic path length and lower global efficiency was found in PD patients, comparing HC groups (both $p < 0.05$). Furthermore, topographic impairment was even worse in lPD patients compared with ePD and HC group (all $p < 0.05$). No significant difference of topographic properties in structural network was found among three groups. ***Conclusion:*** We observed cognitive impairment in PD patients when comparing with HC group. Significant impairment of topographic properties was found in PD patients. Further result showed that the impairment may become worse along with the course of PD. These results may provide imaging evidence for investigating the pathology of PD.

EP-0651

Head-to-head comparison of the associations between imaging and plasma A-T-N biomarkers with synaptic density in Alzheimer's disease

J. Wang;
Department of Nuclear Medicine & PET Center, Huashan Hospital, Fudan University, Shanghai, CHINA.

Aim/Introduction: To compare the associations between imaging and plasma A-T-N biomarkers with synaptic density assessed by ^{18}F-SynVesT-1 PET/MRI in Alzheimer's disease (AD). ***Materials and Methods:*** This study enrolled 193 participants: 62 with AD, 56 with mild cognitive impairment (MCI), and 75 normal controls (NC). All underwent ^{18}F-SynVesT-1 PET/MRI scans to assess synaptic density and T1-weighted imaging for hippocampal volume. ^{18}F-Florbetapir PET/CT and ^{18}F-MK6240 PET/CT scans were used to evaluate amyloid-β and tau pathology, respectively. Cognitive function was assessed using neuropsychological tests. Plasma Aβ42, Aβ40, p-Tau181, and neurofilament light chain (NfL) levels were measured. Correlations between synaptic density and "A-T-N" biomarkers from imaging and plasma were analyzed at the volume of interest (VOI)and voxel-wise levels, with comparisons made between the strengths of these correlations. ***Results:*** For "A", synaptic density in the medial temporal lobe was negatively correlated with global Aβ deposition ($r = -0.272$, $p < 0.001$) and positively correlated with plasma Aβ42/40 levels ($r = 0.307$, $p < 0.001$). In the AD group, only global Aβ deposition showed a negative correlation with medial temporal synaptic density ($r = -0.284$, $p = 0.028$). For "T", tau burden was negatively associated with synaptic density in the medial temporal lobe and widespread neocortex across the whole population, as well as within the AD and MCI groups. Plasma p-Tau181 levels were also negatively correlated with synaptic density in the medial temporal lobe and widespread neocortex in both the whole population and the NC group. For "N", hippocampal volume was positively correlated with synaptic density in the medial temporal lobe and widespread neocortex in the whole population and NC group, and showed positive correlations with synaptic density in both the lateral and medial temporal lobes in the AD and MCI groups. Plasma NfL levels were negatively correlated with synaptic density in the lateral temporal lobe across the whole population, and with medial temporal synaptic density as well. Notably, the correlation between synaptic density and hippocampal volume was stronger than that between synaptic density and plasma NfL levels. ***Conclusion:*** Synaptic density showed varying degrees of correlation with imaging and plasma A-T-N biomarkers, with stronger associations observed for imaging biomarkers. Among the A-T-N components, T-related biomarkers exhibited the strongest correlation with synaptic density. Given their accessibility, plasma biomarkers may serve as convenient surrogate indicators of synaptic density changes throughout the course of Alzheimer's disease in the future.

EP-0652

DTI-ALPS Index-assessed Glymphatic Dysfunction Mediates Alzheimer's Cognitive Decline via Amyloid-β-dependent Pathways: Multimodal PET/MRI Study

Y. Zhang[1], *G. Huang*[1], *J. Hao*[2], *L. Qi*[2], *J. Geng*[3], *X. Li*[4], *M. Xin*[1], *P. Yuan*[1], *Y. Wang*[1], *Q. Xu*[3], *G. Wang*[3], *G. Huang*[1], *J. Liu*[1], *C. Zhang*[1];
[1]*Department of Nuclear Medicine, Institute of Clinical Nuclear Medicine, Ren Ji Hospital, Shanghai Jiao Tong University School of Medicine, Shanghai, CHINA,* [2]*United Imaging Healthcare, Shanghai, CHINA,* [3]*Department of Neurology, Ren Ji Hospital, Shanghai Jiao Tong University School of Medicine, Shanghai, CHINA,* [4]*Shanghai Mental Health Center, Shanghai Jiao Tong University School of Medicine, Shanghai, CHINA.*

Aim/Introduction: To determine whether DTI-ALPS index mediates AD-related cognitive decline through Aβ/tau-dependent pathways using concurrent tri-biomarker PET/MRI. ***Materials and Methods:*** This retrospective study (2020-2024) enrolled 140 participants (median age 69.00 [61.00, 74.00] years; 84 women): 99 AD (37 early-onset [EOAD], 62 late-onset [LOAD]), 35 mild cognitive impairment (MCI), and 6 subjective cognitive decline (SCD). All underwent simultaneous ^{18}F-Florbetapir (Aβ), ^{18}F-PI2620 (tau), and ^{18}F-FDG (neurodegeneration) PET/MRI with DTI-ALPS quantification. Causal mediation analyses assessed biomarker relationships ($P < 0.05$). ***Results:*** The ALPS index decreased progressively across clinical stages (SCD: 1.51 ± 0.08 vs MCI: 1.37 ± 0.13 vs AD: 1.32 ± 0.14; $P<0.001$), correlating with higher Aβ-PET ($r=-0.31$, $P=0.001$), tau-PET ($\rho=-0.18$, $P=0.035$), and FDG-PET Z-Score ($\rho= -0.22$, $P=0.008$) and positively with MoCA ($r = 0.28$, $P = 0.002$) and MMSE ($\rho = 0.27$, $P = 0.001$). Aβ-PET fully mediated ALPS effects on FDG PET ($\beta = -0.14$, $P = 0.002$) and cognition (MoCA: $\beta = 0.14$, $P < 0.001$; MMSE: $\beta = 0.12$, $P = 0.002$) with non-significant direct pathways ($P > 0.10$); independent of tau ($P > 0.05$). In Aβ-positive subgroups, ALPS correlated with Aβ-PET ($\beta = 0.05$, $P = 0.032$), and strengthened significantly with cognition after adjusting for age and education (MMSE: $\rho = 0.28$, $P = 0.009$). EOAD showed inverse ALPS-MMSE correlations ($r = 0.39$, $P = 0.016$ vs LOAD $\rho = -0.06$, $P = 0.620$). ***Conclusion:*** DTI-ALPS quantifies glymphatic dysfunction that drives AD progression predominantly through Aβ-dependent pathways, with early-onset AD exhibiting distinct neuroimaging-cognition relationships compared to late-onset disease.

EP-0653

Utility of the Centiloid Scale in [18F]Flutemetamol PET/MRI: Correlation with Visual Assessment, Brain Morphology and Clinical Variables

L. Blanco-Verdejo[1], *L. Rodríguez-Bel*[2], *M. Pudis*[2], *M. Suárez-Piñera*[2], *A. Jareno-Badenas*[3], *F. Camba-Capitan*[4], *M. Cos-Domingo*[3], *G. Reynés-Llompart*[4], *J. Díaz-Moreno*[2], *B. Hervás-Sanz*[2], *J. Gascón-Bayarri*[5], *M. Cortés-Romera*[2];
[1]*Nuclear Medicine Department. Hospital Clínico Universitario de Valencia, Valencia, SPAIN,* [2]*Nuclear Medicine Department. Hospital Universitario de Bellvitge, Barcelona, SPAIN,* [3]*Neuroradiologist Department. Hospital Universitario de Bellvitge, Barcelona, SPAIN,* [4]*Physics Department. Hospital Universitario de Bellvitge, Barcelona, SPAIN,* [5]*Neurology Department. Hospital Universitario de Bellvitge, Barcelona, SPAIN.*

Aim/Introduction: This study aimed to assess the value of the Centiloid scale in positron emission tomography/magnetic resonance imaging (PET/MRI) brain studies with [18F]flutemetamol, by analyzing its agreement with visual reads, correlation with brain atrophy and Mini-Mental State Examination (MMSE), and its utility in uncertain cases. ***Materials and Methods:*** A retrospective study was conducted on patients with cognitive impairment who underwent brain PET/MRI with [18F]flutemetamol. PET images were assessed visually (positive, negative, or uncertain) and quantitatively (SUVr referenced to the pons and Centiloid scale). Brain atrophy was evaluated on MRI using visual rating scales, and clinical data (MMSE scores) were collected. Statistical analysis included Spearman correlation tests, the Wilcoxon-Mann-Whitney test, and ROC curve analysis to assess the diagnostic performance of the Centiloid scale in relation to visual interpretation and clinical variables. ***Results:*** The cohort included 42 patients with cognitive impairment, with a median age of 73 years (49-82). A strong correlation was observed between Centiloid and SUVr values ($\rho = 0.94$, $p < 0.0001$; Spearman coefficient), confirming consistency between the two measures. ROC curve analysis yielded an AUC of 0.98 with respect to visual reads, identifying a threshold of 30.6CL as the optimal cutoff, achieving 96% sensitivity and 92% specificity. Visually uncertain cases (n=5) showed Centiloid values ranging from 13 to 25CL, within the "gray zone" described in the literature (25-35CL), where Centiloid quantification may enhance diagnostic objectivity. A significant positive correlation was found between Centiloid values and global cortical atrophy (GCA) ($\rho = 0.35$, $p = 0.033$). No significant correlations were observed with medial temporal lobe atrophy (MTA) ($\rho = 0.21$, $p = 0.217$) or posterior cortical atrophy (PCA, Koedam) ($\rho = 0.045$, $p = 0.790$). There was a non-significant negative correlation between Centiloid values and MMSE scores. However, when patients were categorized by MMSE (<24 vs. ≥24), those with MMSE<24 had significantly higher Centiloid values (mean = 66.5 vs. 25.6, $p = 0.026$; Wilcoxon-Mann-Whitney test). ***Conclusion:*** The Centiloid scale proves useful as a quantitative method, showing good agreement with visual assessment. In visually uncertain cases, it enables a more objective classification of amyloid burden, which may impact patient management and follow-up. Regarding morphologic correlation, only global cortical atrophy was significantly associated with Centiloid values. Additionally, higher amyloid burden was consistently associated with worse cognitive performance, supporting the potential clinical utility of the Centiloid scale. Nevertheless, prospective studies with larger sample are needed to confirm these findings.

EP-0654

Multimodal topographic properties of white matter functional segregation in Alzheimer's disease: a simultaneous PET/MR study

Y. Jiao[1], *M. Wang*[1], *Y. Hu*[2], *Y. Yang*[3], *P. Fu*[1];
[1]*Department of Nuclear Medicine, 1st Hospital of Harbin Medical University, Harbin, CHINA,* [2]*Central Research Institute, United Imaging Healthcare Group Co., Ltd, Shanghai, CHINA,* [3]*Beijing United Imaging Research Institute of Intelligent Imaging, Beijing, CHINA.*

Aim/Introduction: White Matter (WM) functional networks offer insight into network processes underlying progression AD continuum. Amyloid (Aβ) retention in WM regions, as measured by Aβ-PET, reflects WM integrity and relates to cognition. This study utilized simultaneous PET/MR imaging to investigate multimodal topographic alterations in WM functional networks and Aβ-burden networks, with the aim of providing objective neuroimaging evidence for white matter-related pathology in Alzheimer's disease. ***Materials and Methods:*** A total of 85 subjects were included in this study, including 42 patients with AD, 24 patients with PAD, and 19 age- and sex-matched healthy individuals. Cognitive assessments were collected along with clinical information, including the Mini-Mental State Examination (MMSE) and Montreal Cognitive Assessment (MoCA). Every enrolled subject underwent an integrated ^{18}F-Florbetapir (^{18}F-AV45) PET/MR scan. High-resolution T1-weighted structural images, blood oxygen level dependent fMRI (BOLD-fMRI) and ^{18}F-AV45 images were acquired for all subjects. K-means clustering was utilized to obtain white matter functional networks (BWM) from BOLD-fMRI. Normalized Aβ standardized uptake value ratio (SUVR) images, with whole cerebellum as the reference region, was calculated within each BWM. Group covariance matrix was generated by Pearson's correlation to get both functional and metabolic network. Topographic properties including clustering coefficient, characteristic path length and global efficiency were calculated. ***Results:*** AD patients showed reduced mean MMSE and MoCA scores compared to HC and PAD subjects ($p < 0.001$). In functional network, higher characteristic path length and lower global efficiency was found in AD patients, comparing with pAD and HC groups (both $p < 0.05$). In metabolic network, similar results were observed as higher characteristic path length and lower global efficiency in AD group (all $p < 0.01$). Furthermore, clustering coefficient was also found lower in AD patients (both $p < 0.01$). ***Conclusion:*** We observed cognitive impairment in AD patients as compared with participants of HC or pAD group. Topographic properties of AD patients also showed mega difference in both functional and Aβ-burden networks. These results may show importance of multimodal topographic properties for the early diagnosis and personalized management of AD.

EP-0655

Evaluation of Amyloid PET Centiloid Scale by APOE4 Zygosity: Comparison among Non-Carriers, Heterozygotes, and Homozygotes

B. Choi[1], *H.-C. Song*[2];
[1]*Department of Nuclear Medicine, Daegu Catholic University Hospital and Medical School, Daegu, KOREA, REPUBLIC OF,* [2]*Department of Nuclear Medicine, Chonnam National University Hospital and Medical School, Gwangju, KOREA, REPUBLIC OF.*

Aim/Introduction: It is well known that APOE4 is the strongest genetic risk factor for sporadic Alzheimer's disease, affecting both the degree and regional pattern of amyloid deposition in the brain as measured by amyloid PET. Although the Centiloid scale (CenS) is commonly used, there is a paucity of studies evaluating the relationship between APOE4 zygosity and amyloid burden quantified using the CenS. The purpose of this study is to investigate the impact of APOE4 zygosity on CenS, thereby contributing to the understanding of its genetic and clinical implications. ***Materials and Methods:*** We included a total of 203 subjects who underwent both APOE genotyping and ^{18}F-flutemetamol brain PET/CT. Based on APOE4 allele status, participants were classified as non-carriers, heterozygotes (one APOE4 allele), or homozygotes (two APOE4 alleles). Differences in CenS and SUVR were then compared according to APOE4 zygosity. ***Results:*** Of the 203 participants, 78 were male, and the mean age was 69.8 ± 8.7 years. Based on APOE4 allele status, 133 were non-carriers, 62 were heterozygotes, and 8 were homozygotes. When a Centiloid scale (CenS) value

≥30 was used as the positivity threshold, the APOE4 carrier group (n = 70) showed a significantly higher number of positive cases compared to the non-carrier group ($p < 0.001$). The mean CenS value was also significantly higher in the carrier group (57.39 ± 37.20) than in the non-carrier group (21.10 ± 37.44; $p < 0.001$). In a subgroup analysis of CenS-positive individuals (n = 91), there was no significant difference in CenS between carriers (n = 54, 73.99 ± 23.69) and non-carriers (n = 37, 75.10 ± 27.92). Furthermore, among the carriers, there was no significant difference in CenS between heterozygotes (n = 47, 76.08 ± 24.47) and homozygotes (n = 7, 59.90 ± 10.15). ***Conclusion:*** The presence of APOE4 alleles was significantly associated with CenS positivity. However, among subjects with positive CenS, APOE4 zygosity did not have a significant effect on the CenS. Further studies including a larger number of APOE4 homozygotes are warranted.

EP-0656

Dynamic ^{11}C-PIB PET evaluation of Cerebrospinal Fluid Flow in a population without cognitive impairment. Correlation with amyloid pathology in cerebrospinal fluid

J. Jiménez-Bonilla[1], *S. López-García*[2], *M. De Arcocha-Torres*[1], *F. Gómez-De la Fuente*[1], *V. Mendi-Barcina*[1], *C. Lage*[2], *F. Martínez-Dubarbie*[2], *I. Martínez-Rodriguez*[1], *N. Martínez-Amador*[1], *A. Sánchez-Salmón*[1], *A. García-Ruiz*[1], *N. Carvalho-Duarte*[1], *M. Botanch-Domingo*[1], *L. Cabrera-Portillo*[1], *A. Clavilo-Umbarila*[1], *P. Andrade-Mejía*[1], *M. Fernández-Matarrubia*[2], *E. Rodríguez-Rodríguez*[2], *R. Quirce*[1];
[1]*Nuclear Medicine Service. Marqués de Valdecilla University Hospital. Molecular Imaging Research Group-IDIVAL. University of Cantabria, Santander, SPAIN,* [2]*Neurology Service. Marqués de Valdecilla University Hospital, Santander, SPAIN.*

Aim/Introduction: Cerebrospinal fluid (CSF) clearance is crucial for brain homeostasis. ^{11}C-PIB PET detects clearance deficits in Alzheimer's disease. This study evaluates ventricular CSF clearance in cognitively unimpaired subjects with and without amyloid pathology, using previously described methods to explore early changes before clinical symptoms. ***Materials and Methods:*** Thirteen cognitively healthy volunteers participated in this study to assess cerebrospinal fluid (CSF) clearance using dynamic ^{11}C-PIB-PET imaging. Each participant underwent PET scans from 45 to 85 minutes post-injection of 555 MBq of ^{11}C-PIB. Neuropsychological testing and CSF analysis were performed to classify subjects based on the amyloid beta 1-42/1-40 ratio, using a threshold of 0.07 to define amyloid pathology. Standardized uptake value ratios (SUVr) were calculated at 45, 60, 75, and 85 minutes, using the cerebellar cortex as a reference. Regions of interest (ROIs) were manually placed on fused PET/CT images to include lateral ventricles and cortical gray matter (frontal, parietal, temporal, and occipital lobes). A global cortical amyloid index was obtained for each participant. ***Results:*** Of the 13 participants, six showed CSF amyloid pathology and seven did not. Visual analysis of PIB PET was positive for cortical amyloid deposition in five of the six CSF amyloid-positive cases and negative in all CSF amyloid-negative subjects. Global cortical amyloid load was significantly higher in the CSF amyloid pathology group across all time points ($p < 0.001$). While SUVr measurements in the lateral ventricles did not differ significantly between groups based on CSF amyloid status, there was a noticeable trend toward reduced CSF clearance in the pathology group over time. Moreover, when patients visually PIB-PET positive and negative were compared, statistically significant differences were found along time: SUVr at 45' (0,634 + 0,126 vs 0,722 + 0,181) ($p= 0,364$); SUVr at 60' (0,76 + 0,144 vs 0,916 + 0,261) ($p< 0,001$); SUVr at 75' (0,84 + 0,148 vs 0,993 + 0,23) ($p< 0,001$) and SUVr 85' (0,856 + 0,22 vs 1,07 + 0,261) ($p< 0,001$), indicating minor ventricular CSF clearance in the PIB-PET positive group. ***Conclusion:*** Dynamic ^{11}C-PIB PET reveals reduced ventricular CSF clearance in cognitively unimpaired individuals with brain amyloid pathology, suggesting early CSF dysfunction. These findings highlight its potential in Alzheimer's research, though larger studies are needed to clarify its role in disease pathogenesis.

References: Dynamic ^{11}C-PiB PET Shows Cerebrospinal Fluid Flow Alterations in Alzheimer Disease and Multiple Sclerosis. Schubert JJ, Veronese M, Marchitelli L et al. .J Nucl Med. 2019; 60(10):1452-1460.

EP-0657

Tau deposition is associated with white matter changes and mediates the effects of Aβ on white matter injury in Alzheimer's disease

F. Jiao*, Z. Wang, F. Tian, Z. Zhang, W. Li, K. Liao, H. Pang;*
Department of Nuclear Medicine, The First Affiliated Hospital of Chongqing Medical University, Chongqing, CHINA.

Aim/Introduction: Alzheimer's disease (AD) is pathologically characterized by the deposition of amyloid-β (Aβ) plaques, the formation of tau neurofibrillary tangles, and abnormalities in white matter (WM). This study aimed to evaluate the relationships between WM microstructure and AD molecular pathologies. ***Materials and Methods:*** Forty-six patients with AD underwent ^{18}F-MK6240 and ^{18}F-AV45 positron emission tomography (PET) scanning, as well as T1 weighted imaging and diffusion tensor imaging (DTI) on hybrid PET/MR. Eighteen normal controls (NC) who underwent DTI were included. The standardized uptake value ratio (SUVR) was employed to measure tau burden and Aβ plaques in grey matter (GM) and WM. In this study, we assessed mean diffusivity alterations in the white matter in AD compared to NC. We examined the associations between metrics derived from DTI-fractional anisotropy (FA), mean diffusivity (MD), axial diffusivity (AxD), radial diffusivity (RD), and PET SUVR in GM and WM, as well as the relationships between DTI/PET metrics and clinical scores. In addition, mediation analysis was conducted to explore the interrelationships among tau, Aβ, and white matter injury. ***Results:*** Compared to the NC group, AD patients exhibited lower FA and AxD, and higher MD and RD values. Both the DTI metrics and tau deposition were significantly correlated with clinical scores (all $P < 0.05$). Additionally, FA and MD were associated with tau deposition, and elevated Aβ PET SUVR correlated with higher MD values, while no significant associations were found between Aβ PET SUVR and clinical scores. Mediation analysis revealed that Aβ exerted indirect effects on white matter injury through tau. ***Conclusion:*** AD exhibited widespread white matter abnormalities. Tau deposition is associated with white matter changes and plays a role in partially mediating the effects of amyloid deposition on white matter injury.

EP-37

e-Poster Area

B: Imaging Clinical Studies -> B5 Neurological Imaging Clinical Study -> B52 Cognitive Impairment

EP-0658

Novel insights into cognitive network alterations in temporal lobe epilepsy: A [^{18}F]SynVesT-1 PET study

L. Xiao[1], *L. Feng*[1], *Y. Tang*[1], *S. Hu*[1], *K. Shi*[2];
[1]*Xiangya Hospital Central South University, Changsha, CHINA,* [2]*University Hospital Bern, Bern, SWITZERLAND.*

Aim/Introduction: Cognitive deficits in temporal lobe epilepsy (TLE) frequently impair quality of life more severely than seizures themselves. Despite their clinical significance, treatment options are limited due to poorly understood pathophysiological mechanisms. Synapse loss has emerged as a key neuropathological feature underlying cognitive dysfunction, but its role in large-

scale network reorganization remains unexplored. This study investigates epileptic cognitive network alterations from a synaptic perspective to identify novel biomarkers for cognitive deficits in TLE. ***Materials and Methods:*** We combined [^{18}F] SynVesT-1 PET for in vivo synaptic density quantification with Kullback-Leibler Divergence Similarity Estimation (KLSE) for individual-level network characterization in TLE patients. Neuropsychological assessments evaluated intelligence and memory domains. Spearman correlation analysis was employed to examine relationships between synaptic connectivity strength and cognitive performance. ***Results:*** Distinct patterns of synaptic connectome reorganization were identified in TLE patients. Significant negative correlations were observed between reduced synaptic connectivity strength and impaired neuropsychological performance in both intelligence ($\rho = -0.62$, $p < 0.01$) and memory domains ($\rho = -0.58$, $p < 0.01$). The most pronounced synaptic loss occurred in hippocampal-temporal and frontoparietal networks. ***Conclusion:*** These findings suggest that synaptic connectivity attenuation may serve as a novel biomarker for cognitive deficits in temporal lobe epilepsy, providing an innovative perspective for targeted clinical interventions.

EP-0659

Spatiotemporal Cerebral Glucose Hypometabolism Progression Pattern in Alzheimer's Disease

D. Seo[1], *M. So*[1], *S. Seo*[1], *D. Kim*[2], *S. Lee*[3], *M. Yun*[3];
[1]*Yonsei University College of Medicine, Seoul, Republic of Korea, Seoul, KOREA, REPUBLIC OF,* [2]*Department of Artificial Intelligence, Yonsei University, Seoul, KOREA, REPUBLIC OF,* [3]*Department of Nuclear Medicine, Yonsei University College of Medicine, Seoul, KOREA, REPUBLIC OF.*

Aim/Introduction: Despite the implementation of promising pathology-targeted therapies for Alzheimer's disease (AD) in clinical practice, disease severity evaluation still largely relies on subjective cognitive assessments. To enable objective staging based on metabolic imaging, which strongly correlates with cognitive function, we investigated the spatial and temporal patterns of hypometabolism progression in AD. ***Materials and Methods:*** We analyzed 96 cognitively normal controls and 164 amyloid-positive patients with cognitive impairment who underwent ^{18}F-fluorodeoxyglucose (FDG)-PET imaging between January 2017 and December 2022. Standardized uptake value ratios (SUVRs) were extracted from FreeSurfer-segmented regions. Regions of interest (ROIs) were selected based on effect sizes (Cohen's d) calculated from SUVR comparisons between groups. Hypometabolic progression patterns were modeled using a kernel density estimation-fitted event-based model (EBM). Metabolic staging was defined according to progression patterns within AD-specific lobes, and clinical correlations with SNSB domain Z-scores were assessed with linear regression. ***Results:*** Normal controls had a mean age of 73.2 ± 8.0 years, with 40.7% female, while patients had a mean age of 70.6 ± 8.5 years, with 28.7% female. After comparing SUVR values between groups, 34 regions across the temporal, parietal, and cingulate lobes were selected. Hypometabolism first emerged in limbic regions, including the isthmus, posterior cingulate, entorhinal cortex, and hippocampus. It subsequently involved the precuneus and rostral anterior cingulate before spreading across the neocortex. In later stages, the caudal anterior cingulate, transverse temporal, supramarginal, and postcentral gyri were affected. Based on EBM modeling, four metabolic stages were defined according to the presence of hypometabolism across these regions (Stage 0, n=113, 43.5%; Stage 1, n=47, 18.1%; Stage 2, n=52, 20.0%; Stage 3, n=48, 18.5%). Metabolic stage was significantly associated with all cognitive domains except attention (language, $\beta = -0.34$, $P < 0.001$; visuospatial, $\beta = -0.61$, $P < 0.001$; verbal memory, $\beta = -0.27$, $P < 0.001$; visual memory, $\beta = -0.34$, $P < 0.001$; frontal/executive, $\beta = -0.27$, $P = 0.003$). ***Conclusion:*** This study characterized the spatiotemporal progression pattern of hypometabolism in AD, paralleling the spread of pathological tau, and demonstrated its correlation with cognitive impairment severity. Metabolic imaging may enable objective clinical staging, as FDG-PET scans are more accessible and cost-effective than other PET modalities.

EP-0660

Coupling patterns of brain gray matter volume and FDG metabolism inpatients with impaired cognitive function: a multimodal imaging study

F. Tian*, R. Wu, Z. Wang;*
The First Affiliated Hospital of Chongqing Medical University, Chongqing, CHINA.

Aim/Introduction: The relationship between AV45 PET imaging findings and cerebral glucose metabolism or structural abnormalities remains inconclusive. Therefore, this study focuses on patients with clinically significant cognitive decline highly suspected of Alzheimer's disease (AD) who underwent multimodal PET imaging. Through multimodal coupled analysis, we aim to explore differences in glucose metabolism and brain atrophy between AV45 PET-positive and AV45 PET-negative cases. ***Materials and Methods:*** In this retrospective study, 54 patients with confirmed cognitive impairment underwent [18F] AV45 PET/MR, [18F] FDG PET/MR. Clinical data, such as age, sex, cognitive scales, and hematological AD markers, were collected. Subjects were stratified into Aβ-positive and Aβ-negative groups based on visual analysis of AV45 PET images. The correlation analysis of regional FDG metabolism and gray matter volume were performed among the two groups adjusted for age and sex. and the correlation of the two group were compaired and correlated with MMSE and hematological AD markers. ***Results:*** Of the 54 patients, 40 were Aβ-positive and 14 were Aβ- negative. There was no significant difference in gender (p=0.09) and age (p=0.084). MMSE scores (p=0.016) and P-tau181 (p=0.002) were significantly lower in the Aβ-positive group, and with comparable ADL scores (p=0.674) between two groups. In the Aβ-positive group, a significant positive correlation between metabolism and volume was observed in the posterior cingulate cortex (r=0.62, p< 0.001), indicating concurrent structure and function degradation. No such coupling was found in the Aβ-negative group. Additionally, the hippocampus showed stronger metabolism-volume coupling in the Aβ-positive group compared to Aβ-negative individuals (Z=2.4, p=0.03). In addition, the strength of metabolism-volume in the posterior cingulate coupling strength correlated with MMSE score (r=0.52, p=0.02) and plasma p-tau181 level (r= -0.41, p=0.032) in the Aβ-positive group. ***Conclusion:*** This study identifies distinct patterns of brain metabolism-gray matter volume coupling in Aβ-positive patients, especially in the posterior cingulate cortex and hippocampus. This coupling relationship is associated with cognitive impairment and plasma p-tau181 level, confirmed that A β -positive patients have more obvious brain structure and metabolic abnormalities. ***References:*** Chen K et al.,"Improved power for characterizing longitudinal amyloid-β PET changes and evaluating amyloid-modifying treatments with a cerebral white matter reference region",2015,J Nucl Med,56,4,560-6.Camus V et al.,"Using PET with 18F-AV-45 (florbetapir) to quantify brain amyloid load in a clinical environment",2012,Eur J Nucl Med Mol Imaging,39,4,621-31.Jung-Lung Hsu et al.,"Magnetic resonance images implicate that glymphatic alterations mediate cognitive dysfunction in Alzheimer disease",2023,Ann. Neurol.,93,1,164-174.

EP-0661

Predictive Value of Serum Biomarkers for Brain Amyloid Pathology in Patients with Mild Cognitive Impairment

Ü. Akdemir[1], *Ö. Gülbahar*[2], *N. Canpunar*[2], *E. Balcı*[1], *E. Erkoç Ataoğlu*[3], *E. Saka*[4], *L. Ö. Atay*[1];
[1]*Gazi University Medical Faculty, Department of Nuclear Medicine, Ankara, TÜRKIYE,* [2]*Gazi University Medical Faculty, Department of Medical Biochemistry, Ankara, TÜRKIYE,* [3]*Gazi University Medical Faculty, Department of Neurology, Ankara, TÜRKIYE,* [4]*Hacettepe University Medical Faculty, Department of Neurology, Ankara, TÜRKIYE.*

Aim/Introduction: While established cerebrospinal fluid biomarkers and PET imaging indicate Alzheimer's Disease (AD) pathology, less invasive serum biomarkers are emerging alternatives. This study aimed to evaluate the predictive power of these serum biomarkers for brain amyloid pathology, as determined by amyloid PET, in individuals with Mild Cognitive Impairment (MCI). ***Materials and Methods:*** Thirty-six MCI patients (17 Male, 19 Female; Age: 67.4 ± 6.9 years) underwent brain amyloid PET imaging with F-18 Flutemetamol. The consensus visual classification of PET scans as amyloid-positive or amyloid-negative by two nuclear medicine physicians was used as the reference standard for evaluating the predictive power of biomarkers. Centiloid scores were calculated to quantify amyloid burden. Concurrently, serum samples were collected and analyzed for concentrations (pg/mL) of Aβ 1-40, Aβ 1-42, and p-tau181 via enzyme-linked immunosorbent assay (ELISA). The ratios Aβ 1-42/Aβ 1-40 and p-tau-181/Aβ 1-42 were calculated. Spearman correlation analysis assessed the relationship between serum biomarkers and Centiloid scores. Receiver Operating Characteristic (ROC) curve analysis was performed to evaluate the ability of serum markers to discriminate amyloid PET status. For the best performing biomarker, the optimal cut-off (Youden's index), sensitivity, and specificity were calculated. A Chi-square test assessed the association between biomarker classification and PET status. ***Results:*** Of the 36 MCI patients, visual assessment classified 24 (66.7%) as amyloid PET-positive and 12 (33.3%) as amyloid PET-negative. No statistically significant correlations were observed between any of the serum biomarkers (Aβ 1-40, Aβ 1-42, p-tau-181, Aβ 1-42/Aβ 1-40 ratio, p-tau-181/Aβ 1-42 ratio) and the Centiloid scores (all p> 0.20). ROC analysis for predicting visual amyloid PET status yielded the following AUCs: Aβ 1-40: 0.455 (p=0.639); Aβ 1-42: 0.359 (p=0.166); p-tau-181: 0.589 (p=0.389); Aβ 1-42/Aβ 1-40 ratio: 0.316 (p=0.045). Only the serum p-tau-181/Aβ 1-42 ratio showed statistically significant predictive power for visual PET status, with an AUC of 0.694 (95% CI: 0.511-0.878, p=0.038). The optimal cut-off for this ratio was 2.9175, yielding a sensitivity of 75.0% and a specificity of 66.7%. Classification based on this cutoff was significantly associated with visual amyloid PET status (Fisher's Exact Test, p=0.029). ***Conclusion:*** In this MCI cohort, the serum p-tau-181/Aβ 1-42 ratio showed modest but statistically significant predictive value for the brain amyloid pathology status (positive/negative) derived from amyloid PET scan. While its accuracy suggests limitations for standalone diagnostic use, this serum ratio may hold potential as an accessible initial screening tool. Further validation in larger cohorts is needed.

EP-0662

^{18}F-FDG PET Imaging Reveals GPR162-Mediated Hippocampal Glucose Metabolic Dysregulation in Aging and the Therapeutic Potential of BMMSCs

P. Li, *T. Wang, Z. Yang, Z. Zhu, J. Quan, Y. Zhang, Y. Jiang, R. He, G. Zhu;*
Department of Nuclear Medicine, The First Affiliated Hospital of Kunming Medical University, Kunming, CHINA.

Aim/Introduction: Cognitive impairment associated with aging is a growing global health concern, yet effective therapeutic targets remain elusive[1]. Our team's clinical observations have revealed that glucose metabolism in the hippocampal region of aging individuals is elevated compared to younger individuals, which contrasts with the metabolic trends observed in other brain regions. This suggests that increased hippocampal metabolism may contribute to the onset and progression of cognitive dysfunction. This study aimed to identify key molecular targets involved in age-related cognitive decline and evaluate the therapeutic potential of bone marrow mesenchymal stem cells (BMMSCs)[2] by modulating GPR162, a G protein-coupled receptor implicated in hippocampal glucose metabolism. ***Materials and Methods:*** Hippocampal tissues from young and aged macaques underwent proteomic analysis, revealing 123 differentially expressed proteins. After evaluation through the PubMed database, genes lacking research significance were excluded. GPR162 was identified as one of the core genes. Cell and rat models were established by silencing GPR162 using siRNA and AAV-mediated shRNA. BMMSCs were administered via hippocampal (HIP), intracerebroventricular (ICV), or tail vein (TV) injections. Behavioral tests (Morris water maze, open field), ^{18}F-FDG PET imaging, and molecular assays (RT-PCR, Western blot, immunofluorescence) were performed to assess cognitive function, glucose metabolism, and protein expression (GAP43, SYN, P53, P16). ***Results:*** Aged macaques exhibited elevated hippocampal glucose metabolism and reduced GPR162 expression. Silencing GPR162 in rats impaired spatial memory and increased anxiety-like behaviors, accompanied by decreased synaptic proteins (GAP43, SYN) and elevated senescence markers (P53, P16). BMMSCs treatment via HIP and ICV routes significantly restored GPR162 expression, improved cognitive performance, and normalized glucose metabolism, while TV injection showed no effect. ***Conclusion:*** GPR162 downregulation contributes to age-related cognitive impairment and metabolic dysregulation. BMMSCs therapy, particularly via ICV injection, effectively upregulates GPR162, mitigates cognitive deficits, and restores hippocampal function. These findings highlight BMMSCs as a promising intervention for aging-related cognitive decline, with implications for future clinical applications. Identifying the bioactive compounds secreted by BMMSCs will be a key focus of our future research. ***References:*** 1. Sun Z, Ping P, Li Y, Feng L, Liu F, Zhao Y, et al. Relationships Between Traditional Chinese Medicine Constitution and Age-Related Cognitive Decline in Chinese Centenarians. Front Aging Neurosci. 2022;14:870442. 2. Quan J, Liu Q, Li P, Yang Z, Zhang Y, Zhao F, et al. Mesenchymal stem cell exosome therapy: current research status in the treatment of neurodegenerative diseases and the possibility of reversing normal brain aging. Stem Cell Res Ther. 2025;16:76.

EP-0663

Neurometabolic correlates of cognitive impairments in patients with meningioma

S. Goffinet, *X. De Tiège, J. Bertels, F. Lefranc, O. De Witte, N. Sadeghi-Meibodi, H. Slama, P. Fery, A. Rovai, V. Wens, N. Trotta, G. Leurquin-Sterk;*
Université Libre de Bruxelles, Brussels, BELGIUM.

Aim/Introduction: Meningiomas are associated with cognitive impairments, but the underlying pathophysiological mechanisms remain unclear. This study aims at elucidating the neurometabolic correlates of cognitive impairments in patients with meningioma. ***Materials and Methods:*** Forty-two patients (35 women, 7 men) with a meningioma and 42 sex- and age- matched (Mann-Whitney U-test, U=736; p=0.193) healthy controls underwent a neuropsychological assessment and a hybrid positron emission tomography-magnetic resonance acquisition (PET/MR) using [^{18}F]-fluorodeoxyglucose (FDG). Neuropsychological assessment evaluated attentional and executive functions, memory, language, visuospatial abilities, and reasoning. Mann-Whitney U-tests were employed to compare cognitive performance between groups (results were considered as significant at $p \leq 0.003$ after application of Bonferroni corrections). Group-level subtractive FDG-PET comparison analyses were performed between patients and controls using Statistical Parametric Mapping

(SPM12). Pathophysiological interaction (PPI) analyses identified meningioma-related changes in the contribution of the hypo/hypermetabolic areas to the level of metabolic activity in other brain areas. Correlation analyses were conducted in patients to link neuropsychological scores and regional glucose metabolism. All FDG-PET results were considered significant at p<0.05 FEW-rate. ***Results:*** Compared to controls, patients exhibited significant decrease in processing speed and in performance in tasks assessing verbal short-term memory, verbal episodic memory retrieval, inhibition, and flexibility. Compared to controls, regional hypometabolism was found in patients in bilateral mesial and right lateral prefrontal cortex. Regional hypermetabolism was also found in bilateral cerebellum, with a right predominance, and mesial temporal structures. PPI analyses revealed significant differences in crossed cerebello-prefrontal interactions in patients compared with controls. In patients, lower cognitive performance in verbal episodic memory, flexibility, inhibition and processing speed correlated with reduced regional glucose metabolism in a right prefrontal (all tasks), fronto-parietal (processing speed) network, and in a cortico-basal ganglia loop (flexibility). Higher performance in inhibition and flexibility correlated with enhanced occipito-parietal metabolism. ***Conclusion:*** This study demonstrated significant changes in regional glucose metabolism in patients with meningioma, associated with altered crossed cerebello-prefrontal interactions. Our findings also reveal distinct neurometabolic correlates of specific cognitive impairments and therefore contribute to a better understanding of pathophysiological mechanisms underlying cognitive impairments in patients with meningioma.

EP-0664

Periventricular White Matter Hyperintensities and Brain Metabolism Contribute to Cognitive Dysfunction in Amyloid-Negative Patients

M. So[1], *S. Seo*[1], *S. Lee*[2], *H. Lim*[2], *Y. Yoon*[1], *D. Kim*[3], *H. Han*[3], *D. Seo*[1], *K. Choo*[4], *Y. Jun*[3], *S. Kang*[2], *D. Kim*[5], *Y. Lee*[6], *M. Yun*[2];
[1]*Yonsei University College of Medicine, Seoul, KOREA, REPUBLIC OF,* [2]*Department of Nuclear Medicine, Yonsei University College of Medicine, Seoul, KOREA, REPUBLIC OF,* [3]*Department of Artificial Intelligence, Yonsei University, Seoul, KOREA, REPUBLIC OF,* [4]*Department of Computer Science, Yonsei University College of Medicine, Seoul, KOREA, REPUBLIC OF,* [5]*Department of Nuclear Medicine, Hallym University Sacred Heart Hospital, Hallym University College of Medicine, Anyang, KOREA, REPUBLIC OF,* [6]*Department of Neurology, Ilsan Paik Hospital, Inje University College of Medicine, Seoul, KOREA, REPUBLIC OF.*

Aim/Introduction: The association of periventricular white matter hyperintensities (PWMH) and brain glucose metabolism with cognitive decline in patients without amyloid-β (Aβ) has not been clearly defined. In this study, we investigated the relationship between PWMH and glucose hypometabolism and their effect on domain-specific cognitive performance. ***Materials and Methods:*** We enrolled 151 cognitively impaired Aβ-negative individuals (mean age: 70.5 ± 8.0 years; 56 females) and 83 cognitively normal controls (mean age: 71.1 ± 6.2 years; 34 females), who underwent ^{18}F-fluorodeoxyglucose (^{18}F-FDG) positron emission tomography (PET), ^{18}F-florbetaben (^{18}F-FBB) PET, magnetic resonance imaging (MRI), and comprehensive neuropsychological evaluation using the standardized 2nd edition of the Seoul Neuropsychological Screening Battery (SNSB-II). General linear models evaluated associations between PWMH, regional glucose metabolism, and domain-specific cognition. Path analyses were performed to test both directions of mediation between PWMH and glucose metabolism across cognitive domains, with models adjusted for age, sex, education, and vascular risk compound scores (VRCS). ***Results:*** The cognitively impaired group exhibited significantly higher PWMH volumes than normal controls ($p < 0.001$). Increased PWMH burden correlated with reduced glucose metabolism in the frontal, parietal, medial and lateral temporal, insular, and limbic regions, structures including the anterior cingulate cortex (ACC), posterior cingulate cortex (PCC), hippocampus and amygdala. Domain-specific mediation analyses revealed that PWMH effects on executive scores were significantly mediated by regional glucose metabolism in the frontal cortex ($\beta = -0.058$, $p = 0.011$), parietal cortex ($\beta = -0.055$, $p = 0.013$), ACC ($\beta = -0.077$, $p = 0.008$), and PCC ($\beta = -0.118$, $p = 0.001$). Language scores were mediated by hippocampal ($\beta = -0.063$, $p = 0.008$) and ACC metabolism ($\beta = -0.060$, $p = 0.007$). In contrast to other domains, where PWMH exerted effects via regional glucose metabolism, memory domain followed an inverse pathway: glucose metabolism in the PCC predicted increased PWMH burden, which in turn mediated its impact on verbal and visual memory scores ($\beta = 0.066$, $p = 0.028$; $\beta = 0.051$, $p = 0.049$, respectively). ***Conclusion:*** Our findings suggest that in Aβ-negative individuals, PWMH and brain glucose hypometabolism are interrelated, and that their contributions to cognitive impairment follow domain-specific pathways: PWMH influenced executive and language function through regional hypometabolism, whereas PCC hypometabolism influenced verbal and visual memory dysfunction through increased PWMH burden. These findings highlight the importance of considering both vascular and metabolic factors as interconnected contributors to cognitive dysfunction in the absence of amyloid pathology.

EP-0665

Exploring the Diagnostic Potential of ^{11}C-PiB PET Imaging in Primary Progressive Aphasia: A Preliminary Quantitative Analysis

I. Moretti[1], *A. Capotosti*[1], *R. Moretti*[1], *L. Indovina*[1,2], *M. De Spirito*[1,2], *F. Cocciolillo*[3], *D. Quaranta*[3], *D. Di Giuda*[3], *M. Calcagni*[3,4];
[1]*Fondazione Policlinico Universitario Agostino Gemelli IRCCS, Rome, ITALY,* [2]*Università Cattolica del Sacro Cuore, Rome, ITALY,* [3]*Dipartimento di Diagnostica per Immagini e Radioterapia Oncologica, UOC di Medicina Nucleare, Fondazione Policlinico Universitario Agostino Gemelli IRCCS, Rome, ITALY,* [4]*Dipartimento Universitario di Scienze Radiologiche ed Ematologiche, Università Cattolica del Sacro Cuore, Rome, ITALY.*

Aim/Introduction: Primary Progressive Aphasia (PPA) is a neurodegenerative disorder characterized primarily by progressive language impairment. It is typically classified into three main variants: semantic (svPPA), nonfluent/agrammatic (nfvPPA), and logopenic (lvPPA). Although PET imaging with Pittsburgh Compound B (PiB) is widely used to detect amyloid plaques in Alzheimer's disease, its diagnostic application in PPA remains limited. This preliminary study aims to assess whether quantitative or semi-quantitative measures of PiB uptake can serve as reliable diagnostic markers in PPA. ***Materials and Methods:*** In this preliminary study, thirteen patients diagnosed with PPA underwent a 90-minute dynamic PET/CT scan following administration of ^{11}C-PiB. Brain segmentation was performed using MIM Software (MIM Software Inc., Cleveland, OH), and kinetic analysis of PiB uptake was conducted with PMOD (PMOD Technologies LLC, Zurich, Switzerland). PiB uptake kinetic was analyzed using the Logan plot method, with the cerebellum as the reference tissue. Standardized uptake values (SUV) from PET/CT were also calculated and compared. ***Results:*** Quantitative analysis revealed elevated PiB uptake in several brain regions involved in language and cognition across all patients, including the anterior, posterior, and inferior cingulate gyri; the middle and superior frontal gyri; the precuneus; the putamen and the striatum. These clinically relevant areas showed a median binding potential (BPnd) of 0.68 (interquartile range IQR = 0.40), compared to a median BPnd of 0.16 (IQR = 0.27) in other regions. A strong correlation was observed between BPnd and SUV values across all regions (median $R^2 = 0.94$). ***Conclusion:*** These results support the potential diagnostic value of PiB PET imaging in PPA, showing both quantitative and semi-quantitative data related to amyloid pathology. Further studies should be conducted to confirm

and identify the specific brain regions affected, providing a more targeted approach to understanding the progression and treatment of aphasia.

EP-0666

A Deep Learning Model for Detecting Alzheimer's Disease Using Structural MRI

Y. Zhang[1], *F. Huang*[1], *J. Hao*[2], *L. Qi*[2], *J. Liu*[1], *C. Zhang*[1];
[1]*Department of Nuclear Medicine, Institute of Clinical Nuclear Medicine, Ren Ji Hospital, Shanghai Jiao Tong University School of Medicine, Shanghai, CHINA,* [2]*United Imaging Healthcare, Shanghai, CHINA.*

Aim/Introduction: To develop a deep learning model based on structural MRI data to differentiate AD from a spectrum of non-AD conditions and identify key neuroanatomical regions contributing to the classification. ***Materials and Methods:*** We utilized a DenseNet-based CNN architecture trained on structural MRI scans from a cohort of 230 participants, including 117 AD patients and 113 non-AD cases (e.g., VD, FTD, DLB). Performance metrics, including AUC, PR-AUC, F1-score, accuracy, balanced accuracy, sensitivity, specificity, PPV, and NPV, were calculated to assess the model's diagnostic efficacy. Grad-CAM was employed to generate heatmaps for visualizing the model's decision-making process. ***Results:*** The model achieved robust performance, with an AUC of 0.79 ± 0.05 and a PR-AUC of 0.82 ± 0.04. Notably, the model exhibited excellent specificity (1.00 [0.89, 1.00]) and PPV (1.00 [0.80, 1.00]). Heatmap analysis highlighted critical regions such as the inferior parietal lobule, corpus callosum, and caudate nucleus. ***Conclusion:*** This study highlights the potential of deep learning models to accurately differentiate AD from a spectrum of non-AD conditions using structural MRI data.

EP-0667

Predictive value of ^{18}F-FDG PET/CT deep learning in radiomics for cancer-related cognitive impairment in patients with non-CNS DLBCL

J. Wang, *Q. Zhao, Y. Dong, P. Ma, R. Wang;*
General Hospital of Ningxia Medical University, Ningxia Yinchuan, CHINA.

Aim/Introduction: Cancer-related cognitive impairment (CRCI) is a common and debilitating sequela of cancer treatment, which impairing memory, attention and executive function, thereby reducing quality of life, weakening daily activities and affecting treatment adherence. Effective detection and prediction methods are still lacking. This study focuses on non-Central Nervous System Diffuse Large B-cell Lymphoma (non-CNS DLBCL) patients, using cognitive scales as standards. By integrating radiomics features extracted from PET/CT neuroimaging and clinical data into structured datasets via deep learning, we evaluate the predictive value of different models and modalities for CRCI, aiming to provide a basis for precise assessment. ***Materials and Methods:*** We retrospectively analyzed 112 non-CNS DLBCL patients who underwent brain ^{18}F-FDG PET/CT at Ningxia Medical University General Hospital from October 2020 to January 2025, recording demographics (sex, age, years of education) and the results of neurological scales (MoCA and FACT-Cog). Based on cognitive scale results, patients were classified into CRCI and normal cognition groups. Cases were randomly assigned to training and testing groups at an 8:2 ratio. The open-source MOOSE120 software was used to automatically divide brain regions and extract radiomics histological features. After integrating clinical features, we constructed structured data and selected features using correlation coefficients. Seven deep learning models were built: Gated Additive Tree Ensemble, AutoInt, Categorical Embedding, FT Transformer, TabNet, NODE, and Tab Transformer. We evaluated the diagnostic performance of these models using Receiver Operating Characteristic (ROC) curves. Decision curves were employed for further assessment of their clinical applicability and different multimodal imaging data were also compared. ***Results:*** Based on MoCA and FACT-Cog results, 73 patients were included in the CRCI and 39 in the cognitively normal groups, randomly assigned to training (n=89) and testing (n=23) groups. Seven deep learning models were applied. Among them, the Category Embedding model performed the best, with AUC values of 0.923 and 0.767 in the training and validation sets, respectively, showing high diagnostic efficacy. Decision curve analysis further confirmed its robust performance. Additionally, when comparing models with different modalities, the triple modality model (clinical data + PET + CT) showed a higher AUC value with AUC values of 0.838 and 0.923 in the training sets, respectively. ***Conclusion:*** Combination of deep learning with structured data from PET/CT image showed effectively predictive value in detection of CRCI. The Category Embedding model and triple modality model (clinical data + PET + CT) demonstrated excellent performance and exhibited substantial clinical application value.

EP-38

e-Poster Area

B: Imaging Clinical Studies -> B5 Neurological Imaging Clinical Study -> B53 Movement Disorders

EP-0668

Can [18F-FDG] PET imaging patterns determine the neuropathological substrate of Corticobasal Syndrome?

S. Alvarez, *A. Mari, M. Casallas, S. Salcedo, G. Mera, E. Ardila, J. E. Orcajo, J. J. Ardila, I. Gomez, J. Alonso;*
Hospital General Universitario Gregorio Marañón, Madrid, SPAIN.

Aim/Introduction: To describe the different metabolic patterns assessed by [18F-FDG] PET study in patients with clinical suspicion of Corticobasal Syndrome (CBS) and variable neuropathological substrate, considering Corticobasal Degeneration (CBD) as the most common one, followed by Alzheimer's Disease (AD) and Progressive Supranuclear Palsy (PSP). ***Materials and Methods:*** 19 patients diagnosed with CBS based on clinical criteria, who also had an [18F-FDG] PET imaging study, were included. Of these, 4 patients with a history of vascular pathology were excluded. 15 [F18-FDG] PET studies were analyzed using the AW Server 3.2 software (GE HealthCare). A visual and semiquantitative assessment was performed, focusing on the main affected regions of the brain, and classifying them into three characteristic patterns described in the literature:1. CBS-CBD, 2. CBS-AD, 3. CBS-PSP. All of them, regardless of the subgroup classification assigned, showed what was called a general CBS pattern that was analyzed separately. DatScan imaging results were also evaluated in those patients for whom this study was available. ***Results:*** The mean age of those 15 patients was 64,6%with a slight female predominance (6 males and 9 females). The brain regions commonly affected across all CBS subtypes (general CBS pattern) were the superior parietal lobe (60%), thalamus (60%), perirolandic area (67%), and insula (47%), with findings usually being contralateral to the symptomatic side.On visual assessment, 10 patients (67%) exhibited a classic pattern compatible with CBS-CBD, 2 patients (13%) showed a CBS-AD pattern, and 3 patients (20%) presented a CBS-PSP pattern.In the 10 CBS-CBD patients, predominant involvement was identified in the frontal and parietal lobes, caudate nuclei, and medial cingulate. The 2 CBS-AD patients showed involvement of the inferior parietal lobe, angular gyrus, inferior temporal lobe, and posterior cingulate, with less anterior involvement and partial preservation of primary sensorimotor areas. In the 2 CBS-PSP cases, hypometabolism was observed in the medial and dorsolateral frontal regions, temporal pole, anterior

cingulate, and supplementary motor cortex. All patients who underwent DaT-Scan imaging (60%) showed impairment of the nigrostriatal pathway. ***Conclusion:*** Different cortico-subcortical patterns observed in [18F-FDG] PET studies suggest the existence of different pathological substrates. The characterization of those patterns is essential for appropriate diagnostic and therapeutic approaches in CBS patients. These findings show that PET imaging with amyloid and tau biomarkers could be highly valuable for the pathological classification of CBS.

EP-0669

An Advanced Quantitative Analysis Approach in Dopaminergic SPECT Imaging: GÜDaTSPECT

E. Tuncay Ibis, *E. Balcı, Ü. Ö. Akdemir, L. Ö. Atay;*
Gazi University Faculty of Medicine, Ankara, TÜRKIYE.

Aim/Introduction: Idiopathic Parkinson's disease, the most common neurodegenerative cause of Parkinsonism,and loss of dopaminergic neurons in Parkinson's disease can be detected early by DaTscan imaging, aiding differentiation from other conditions. Quantitative analysis enhances diagnostic accuracy. Our aim is a fast, free, user-friendly program with machine learning and extensive benchmarking for all centers. ***Materials and Methods:*** DATquan[1], a free and reproducible software, was modified and integrated into GÜDaTSPECT. In this way, SBR(Spesific Binding Ratio), AI(Asymmetry Index) and putamen/caudate ratios were calculated from DAT binding SPECT data in caudate, putamen and striatum.To compare the calculated values, DaTscan images from the Gazi University Faculty of Medicine, Department of Nuclear Medicine(GAZI), and the Parkinson's Progression Markers Initiative(PPMI)[2][3] were analyzed, creating age-dependent normal databases for GAZI and PPMI.The quantitative analysis is influenced by multiple factors.The GAZI and PPMI datasets were harmonized using the ComBat method to create a combined GAZI+PPMI age-dependent normal database. Support vector machine(SVM) functionality was added to the GÜDaTSPECT software to enhance result reliability.Based on the SVM binary classification output, GÜDaTSPECT provides a final report indicating "dopaminergic deficiency present/absent." GÜDaTSPECT is a fully automated, open-source software. ***Results:*** Two nuclear medicine specialists visually classified the GAZI group into 72 controls(CG) and 97 Parkinson's disease(PD) cases. Combined with 235 CG and 1042 PD DaTscan images from the PPMI database, three study groups(GAZI,PPMI,GAZI+PPMI) were formed. Age and SBR comparisons revealed significant inter- and intra-group differences, highlighting the need for harmonization, as GAZI CG SBR values were higher than PPMI CG. ComBat harmonization aligned SBR averages in the combined GAZI+PPMI group, eliminating significant differences. GÜDaTSPECT assigns new patients to appropriate groups and allows harmonized visual comparison with these databases, displaying age-dependent fitted SBR values and prediction bounds graphically. SVM models, trained with SBR, asymmetry indices, age, and sex, achieved 100% accuracy in GAZI, 97.49% in PPMI, and 98.90% in the harmonized GAZI+PPMI dataset. AI and striatal/putamen SBR were key variables in the SVM classification across all groups. ***Conclusion:*** GÜDaTSPECT is a free,fully automated software uniquely combining advanced DaTscan image processing, database comparison and SVM learning to improve diagnostic accuracy and interpretation. ***References:*** [1]DOI: 10.2967/jnmt.111.090324[2]Data used in the preparation of this article was obtained on [2023-08-24] from the PPMI database(www.ppmi-info.org/access-dataspecimens/download-data),For up-to-date information on the study, visit www.ppmi-info.org.[3]PPMI-a public-private partnership-is funded by the Michael J.Fox Foundation for Parkinson's Research and funding partners. (Full list of all PPMI funding partners found on the PPMI Website) We acknowledge support from TÜBİTAK Nos.124E326.

EP-0670

Diagnosis of Parkinson Disease using ^{123}I-FP-CIT - how confident are we?

K. Ferreira[1,2,3], *A. P. Robinson*[1], *K. M. Bradley*[4], *D. R. McGowan*[2,3];
[1]*National Physical Laboratory, Teddington, UNITED KINGDOM,* [2]*University of Oxford, Oxford, UNITED KINGDOM,* [3]*Oxford University Hospitals NHS FT, Oxford, UNITED KINGDOM,* [4]*Wales Research and Diagnostic PET Imaging Centre, Cardiff, Wales, UNITED KINGDOM.*

Aim/Introduction: ^{123}I-FP-CIT is used for the diagnosis of Parkinson disease. Volumes of Interest (VOIs) are defined for the right and left striatum, and a background (BG) region, and the mean counts per voxel is estimated for each region. Specific Binding Ratios (SBR) are calculated for the striatum and compared to healthy controls database. The estimation of uncertainties is not common for this clinical application; however, the benefits of estimating uncertainties have been recognised for other clinical applications[1,2]. In this work, a method to evaluate the uncertainty associated with the SBR values is developed using phantom data and then applied to estimate uncertainties for patient data. ***Materials and Methods:*** Repeated SPECT/CT data for a realistic striatum phantom filled with ^{123}I was acquired on a GE Discovery 670 without moving the phantom. The data was acquired and reconstructed using the clinical protocol. A single set of VOIs were defined on the SPECT data for the left and right striatum and a background region. The uncertainty on the VOI was estimated with each point in the VOI modelled as a rectangular distribution. For each VOI, 1000 perturbed VOIs were generated to estimate the probability density function. The SBR values were estimated using the Brass method[3] and a comprehensive uncertainty analysis is presented. ***Results:*** For phantom data the mean SBR values were 2.39±18.8% for the right striatum and 2.85±11.6% for the left striatum, the uncertainties are at the 95% confidence level. More activity was dispensed to the left striatum, hence the higher ratio. The uncertainty associated with the mean counts per voxel was 4.6% (right striatum), 4.8% (left striatum) and 3.2% (BG) when considering a single scan. The larger uncertainty associated with the striatum was expected due to the smaller VOI compared to the BG. When considering all the scans, the uncertainty associated with the mean counts per voxel was 6.8% (left striatum), 12.1% (right striatum) and 5.3% (BG). The larger statistical uncertainty for the right striatum is possibly due to the phantom filling, where the right striatum is less homogeneous. A full uncertainty budget for ^{123}I-FP-CIT will be presented ***Conclusion:*** In this work, a methodology is presented to assess the uncertainty for SBR values for the diagnosis of Parkinson disease. The methodology presented here will be applied to patient data to understand the potential impact on patient classification. ***References:*** [1]Gear et al, 2018;45(13) [2]Partarrieu et al 2022;36(2):123-132 [3]Koch et al 2005; 38:1095-1103.

EP-0671

The Mickey Mouse sign in 18F-FDOPA PET: significance and clinical usefulness in idiopathic Parkinson disease

J. Darcourt, *M. Koulibaly, V. Comte, A. Schiazza, C. Maurel, N. Sapin, O. Humbert;*
Centre Antoine Lacassagne, Nice, FRANCE.

Aim/Introduction: Visualization of midbrain "Mickey mouse" shape uptake (MM) is one of the visual landmarks of 18F-FDOPA in current static PET imaging of Parkinson Disease (PD) patients[1]. The ears correspond to the visualisation of the Substantia Nigra (SN), the nose to the human periaqueductal grey matter (PAG)[2]. PAG is located around the mesencephalic aqueduct and mainly composed of serotoninergic neurons. Dynamic studies have shown an increased 18F-FDOPA PAG uptake in PD compared to controls[3]. We investigated the feasibility of semi-quantitative analysis of 18F-FDOPA PAG uptake on routine static 18F-FDOPA

SiPM camera PET imaging to explain this uptake and its role in visual analysis. ***Materials and Methods:*** 50 PD patients (mean age 70±10; H&Y 1 and 2) and 42 patients with essential tremor (ET) (mean age 70±13) were retrospectively analysed. One hour after Carbidopa premedication, patients were injected with 3 MBq/kg of 18F-FDOPA and scanned 90 minutes later. A SiPM PET/CT camera was used. Static acquisition lasted 6 minutes; images were reconstructed without and with PSF correction for visual and quantitative analysis respectively. The scans were visually analysed by 3 independent readers for normal versus PD aspect and MM uptake scoring. For quantitative analysis, a PAG and SN isocontour was iteratively eroded until a targeted volume (1.5 and 0.5 cm^3) was reached and meanSUV over occipital ratios calculated. ***Results:*** Visual MM scoring showed a good interobserver agreement (kappa = 0.46). Using a score cut off value superior to 3 (above 60% of the striatal maximum), the sensitivity and specificity and accuracy of the MM sign for the diagnosis of PD were 95%, 100% and 97% respectively. Quantitative analysis showed higher PAG uptake in PD compared to ET patients (2.09 ± 0.13 vs 1.96 ± 0.20; p = 0.0003). No difference was found for SN uptake. However, within the PD group, SN uptake was significantly lower on the side contralateral to the predominant clinical side (2.06 ± 0.47 vs 2.13 ± 0.47; p>0.001). ***Conclusion:*** When dopaminergic innervation of the striatum is low in PD: (i) SN uptake remains unchanged (becomes asymmetric) but is more visually detectable; (ii) furthermore, PAG uptake increases due to upregulation of the aminoacid decarboxylase activity in serotoninergic neurons. These results explain the MM landmark of PD visual analysis, confirm its diagnostic usefulness and opens the way to PAG serotoninergic evaluation with 18F-FDOPA PET. ***References:*** 1-Morbelli, S., et al. EJNMMI(2020).2-Benarroch, E. E. Neurology(2012). 3-Kumakura, Y., et al. Neuroimage (2010).

EP-0672

Automated Quantitative [^{18}F]FP-CIT PET/CT Analysis Without MRI for Distinguishing Parkinsonian Disorders

K. Park[1], *J. Kim*[1], *H.-C. Song*[1], *B. Choi*[2];
[1]*Chonnam National University Medical School and Hospital, Gwangju, KOREA, REPUBLIC OF,* [2]*Daegu Catholic University Medical Center, Daegu Catholic University School of Medicine, Daegu, KOREA, REPUBLIC OF.*

Aim/Introduction: The differential diagnosis of parkinsonian syndromes remains challenging despite its importance for treatment planning and outcome prediction. While [^{18}F]FP-CIT PET/CT visualizes dopamine transporter density, standard interpretation relies on subjective assessment, leading to reader variability. Current quantitative methods require MRI co-registration, increasing complexity, costs, and patient inconvenience. This study investigated whether an MRI-independent quantitative analysis could identify distinct uptake patterns across parkinsonian disorders. ***Materials and Methods:*** We retrospectively included 634 patients with confirmed diagnoses of idiopathic Parkinson's disease (IPD; n=418), parkinsonian-type multiple system atrophy (MSA-P; n=29), cerebellar-type multiple system atrophy (MSA-C; n=14), progressive supranuclear palsy (PSP; n=35), essential tremor (ET; n=78), and drug-induced parkinsonism (DIP; n=60). Using a specialized deep learning-based automated analysis software, we performed automated measurements of tracer uptake in striatal subregions, calculated asymmetry indices, and derived uptake ratios without requiring MRI. Statistical analyses compared uptake patterns across diagnostic groups. ***Results:*** Significant differences in uptake patterns emerged: Non-neurodegenerative conditions (ET and DIP) showed normal uptake throughout the striatum (ventral posterior putamen: 4.29±0.96 and 4.37±0.97). Parkinson's disease displayed characteristic posterior putaminal reduction (ventral posterior putamen: 1.06±0.67) with relative preservation of anterior regions. MSA-P showed similar posterior putaminal decrease (ventral posterior putamen: 1.12±0.57) but with significantly more uniform anterior-posterior involvement than Parkinson's disease (anterior-posterior ratio: 1.96±0.56 vs. 2.44±0.71, p=0.03). PSP demonstrated the most severe uptake reduction, especially in the caudate, with marked asymmetry (caudate asymmetry index: 10.53±14.64). MSA-C maintained relatively preserved striatal uptake (ventral posterior putamen: 3.56±1.55). ***Conclusion:*** This MRI-independent quantification approach successfully identifies measurable differences in dopaminergic degeneration patterns that align with clinical diagnoses of parkinsonian disorders. The method offers practical advantages by eliminating MRI requirements while providing objective measures to supplement visual interpretation. This approach may particularly benefit patients unable to undergo MRI and facilities with limited imaging capabilities. Further validation studies are needed to confirm these findings and establish diagnostic thresholds.

EP-0673

Long-term ^{123}I-Ioflupane SPECT Follow-up in Asymptomatic Carriers of LRRK2-G2019S Mutation as Predictor of Parkinson Disease

I. Martínez-Rodríguez[1], *A. Clavijo-Umbarila*[1], *P. Andrade-Mejía*[1], *A. García-Ruiz*[1], *N. Carvalho-Duarte*[1], *L. Cabrera-Portillo*[1], *M. Botanch-Domingo*[1], *N. Martínez-Amador*[1], *F. Gómez-de la Fuente*[1], *A. Sánchez-Salmón*[1], *J. Jiménez-Bonilla*[1], *M. De Arcocha-Torres*[1], *V. Mendi-Barcina*[1], *M. Rivera-Sanchez*[2], *M. Sánchez-Pelaez*[2], *A. Sánchez Rodríguez*[3], *J. Infante*[2], *R. Quirce*[1];
[1]*Nuclear Medicine Department. Marqués de Valdecilla University Hospital. Molecular Imaging Group (IDIVAL). University of Cantabria, Santander, SPAIN,* [2]*Neurology Department. Marqués de Valdecilla University Hospital. Neurodegeneratives Diseases Group (IDIVAL), Santander, SPAIN,* [3]*Neurology Department. Hospital de Cabueñes, Gijón, SPAIN.*

Aim/Introduction: LRRK2-G2019S mutation is one of the identified causes of Parkinson's disease (PD). Asymptomatic carriers of this mutation offer a valuable opportunity to explore the premotor stages of PD. Our aim was to evaluate ^{123}I-ioflupane SPECT findings in asymptomatic carriers of this mutation in a 12-year long-term study. ***Materials and Methods:*** This prospective study included 42 asymptomatic carriers of the LRRK2-G2019S mutation (26 women/16 men; 57.3 ± 9.4 years, from 2011 to 2024). Subjects underwent ^{123}I-ioflupane SPECT as follows: 42 subjects had 1 scan, 29 had 2 scans, 17 had 3 scans, and 12 had 4 scans, performed at 4-year intervals. Based on visual analysis, studies were categorized as normal or abnormal, and a severity score of the decrease of uptake at the caudate and putaminal nuclei individually was assigned (1: mild; 2: moderate; 3: severe), with a maximum combined severity score of 12. Findings were correlated with clinical outcome. ***Results:*** Globally, both baseline and follow-up ^{123}I-ioflupane scans were abnormal in 24/42 subjects (57.1%). Baseline scan was normal in 18/42 subjects (42.9%), showing 11 of them (61.1%) an abnormal scan during follow-up. Considering the subgroup of 12 subjects with a longer follow-up of 4 scans, baseline ^{123}I-ioflupane scan was normal in 10 (83.3%) and abnormal in 2 (16.7%), and follow-up scans became abnormal in 8 subjects (66.7%) and remained normal in 4 (33.3%). During the follow-up period, 8 out of 42 subjects (19.1%) developed PD. Seven of them (87.5%) had abnormal baseline and follow-up ^{123}I-ioflupane scans, while the remaining subject had a normal baseline scan and abnormal scan at 4, 8 and 12 years. These 8 subjects who developed PD showed significantly higher ^{123}I-ioflupane combined severity scores at baseline (4.38 ± 2.83 vs. 1.71 ± 2.17; p = 0.0052), as well as at 4-year (5.71 ± 3.30 vs. 2.27 ± 2.55; p = 0.0073) and 8-year follow-up scans (5.33 ± 3.51 vs. 1.79 ± 1.85; p = 0.0201), compared to those who did not develop the disease. The most intense involvement was observed in the putaminal nuclei, particularly in the left putamen. ***Conclusion:***

Visual analysis of ^{123}I-Ioflupane scan revealed a significant decline in striatal dopamine transporter binding in a high percentage of LRRK2-G2019S mutation asymptomatic carriers during a 12-year long-term follow-up, significantly higher in subjects who developed PD, suggesting the potential role of ^{123}I-Ioflupane SPECT as a valuable predictive tool for PD development in these individuals. The contribution of a more detailed semi-quantitative analysis should be evaluated in the future.

EP-0674

Distribution Patterns of ^{18}FFlorzolotau PET and Midbrain Magnetic Resonance Parkinsonism Index in Patients with Progressive Supranuclear Palsy

M. Wang[1], *X. Wei*[1], *J. Lu*[2], *R. Ling*[1,3], *J. Jiang*[3], *L. Dong*[1], *X. Yang*[1], *L. Wang*[1], *C. Zuo*[2], *J. Jiang*[1];
[1]*Shanghai University, Shanghai, CHINA,* [2]*PET center, Fudan University, Shanghai, CHINA,* [3]*School of Medical Imaging, Shanghai University of Medicine & Health Science, Shanghai, CHINA.*

Aim/Introduction: Progressive supranuclear palsy (PSP) is a neurodegenerative disorder characterized by pathological tau protein aggregation, severe dopaminergic neuronal loss, and atrophy of cerebellar nuclei. However, the relationship between regional tau accumulation and midbrain-based atrophy in PSP remains poorly understood. This study aims to investigate the spatial distribution of tau pathology, as assessed by ^{18}FFlorzolotau positron emission tomography (PET), and subcortical atrophy across healthy controls (HC) and individuals within the PSP phenotypic spectrum. ***Materials and Methods:*** T1-weighted magnetic resonance imaging (MRI) and ^{18}FFlorzolotau PET scans were acquired from 36 HCs (age = 58.8±9.2 years, 11 male [M]/25 female [F]) and 156 patients with PSP (age = 66.1±6.8 years, 83 M/73 F) from the Movement Disorders Clinic, Department of Neurology, Huashan Hospital, Fudan University. The midbrain-based magnetic resonance Parkinsonism index (MRPI) was calculated based on manual morphometric measurements independently performed by three clinicians. Regional tau burden was quantified using the standardized uptake value ratio (SUVR). Correlation analyses were conducted to assess the relationship between regional Florzolotau SUVR values and MRPI in both HC and PSP groups. ***Results:*** Compared to the HC group, PSP patients exhibited significant midbrain atrophy and elevated MRPI values ($P < 0.0001$). Concurrently, Florzolotau tau accumulation was significantly increased in PSP, particularly in the red nucleus, subthalamic nucleus, raphe nuclei, and globus pallidus. Correlation analyses revealed a significant positive association between MRPI and regional tau accumulation across the whole cohort. Notably, tau SUVR in regions corresponding to PSP pathological stage I showed significant correlations with all MRPI parameters (MRPI: $r = 0.58$, $P < 0.001$; MRPI version 2: $r = 0.51$, $P < 0.001$). In the HC group, MRPI parameters were significantly correlated with age (r range: 0.30-0.45, $P < 0.001$), reflecting normal age-related brain atrophy. In contrast, in the PSP group, MRPI parameters were not correlated with age, suggesting that the observed atrophy likely reflects PSP-specific pathological mechanisms rather than normal aging. ***Conclusion:*** ^{18}F-Florzolotau tau accumulation may reflect the severity of subcortical atrophy in PSP and serve as a potential hallmark of disease progression, potentially contributing to subsequent cortical degeneration.

EP-0675

Evaluation Of Executive Functions In Patients with Parkinsonism. Comparison Of Modified-Wisconsin Card Sorting Test With 123I-Ioflupane Basal Ganglia SPECT Findings

D. Chattigkezou[1], *K. Sakellariou*[2], *I. Sofianidis*[3], *A. Diakakis*[1], *V. Siokas*[4], *A. Provatas*[5], *Z. Tsouris*[5], *G. Angelidis*[2], *D. Psimadas*[2], *C. Ziangas*[2], *I. Tsougos*[6], *P. Georgoulias*[7], *E. Dardiotis*[4], *V. Valotassiou*[7];
[1]*Faculty of Medicine, University of Thessaly, Larissa, GREECE,* [2]*Dpt of Nuclear Medicine, University Hospital of Larissa, Larissa, Greece,* [3]*Aristotle University of Thessaloniki, Thessaloniki, GREECE,* [4]*Neurology Dpt, Faculty of Medicine, University of Thessaly, University Hospital of Larissa, Larissa, GREECE,* [5]*Neurology Dpt, University Hospital of Larissa, Larissa, GREECE,* [6]*Dpt of Medical Physics, Faculty of Medicine, University of Thessaly, University Hospital of Larissa, Larissa, GREECE,* [7]*Dpt of Nuclear Medicine, Faculty of Medicine, University of Thessaly, University Hospital of Larissa, Larissa, GREECE.*

Aim/Introduction: The modified-Wisconsin Card Sorting Test (m-WCST) is a digital adaptation of the original WCST, and was designed to assess core executive functions, particularly cognitive flexibility, which refers to the ability to shift attention, inhibit automatic responses, update working memory, and monitor relevant stimuli (salience). Cognitive flexibility is often affected in neurodegenerative Parkinsonism and its impairment is most clearly reflected through perseverative errors—failures to abandon outdated rules and adopt new ones. The aim of this study was the comparison of m-WCST scores with presynaptic dopamine transporter (DaT) SPECT findings in patients with parkinsonism for the evaluation of executive functions. ***Materials and Methods:*** We studied 59 subjects with parkinsonism (37 males and 22 females, age±SD=68,64±9,62 years). All patients underwent m-WCST and DaT SPECT imaging 3-4 hours after the i.v. administration of 185 MBq 123I-Ioflupane. Medication known to interfere with dopamine transporter binding was discontinued. Oral Lugol's solution was given prior to tracer administration for thyroid protection. DaT SPECT images were evaluated visually and semi-quantitatively, selecting the three transverse slices with the most intense tracer uptake and drawing ROIs over the right and left striatum. We also performed automated semi-quantification using a software for the comparison with an age-matched control population, based on the Parkinson's Progression Markers Initiative (PPMI). ***Results:*** A statistically significant difference in m-WCST performance scores was found between the subjects with abnormal-group A and normal-group B DaT SPECT findings ($U=283.000$, $Z=-2.268$, $p=0.023$). Specifically, group A showed significantly lower mean ranks (Mean Rank=24.48) compared to group B (Mean Rank=34.66), suggesting reduced cognitive performance in subjects with neurodegenerative parkinsonism. Additionally, a statistically significant difference in the number of perseverative errors in the m-WCST was found between the two groups ($U = 287.5$, $Z = -2.201$, $p = 0.028$). Group A showed higher rates of perseverative errors, indicating a possible link between dopaminergic depletion and reduced cognitive flexibility. ***Conclusion:*** The combination of nuclear DaT SPECT molecular imaging of basal ganglia with a neuropsychological tool, such as m-WCST, may be useful for both, the accurate diagnosis of neurodegenerative parkinsonism and the evaluation of executive functions impairment.

EP-39

e-Poster Area

B: Imaging Clinical Studies -> B5 Neurological Imaging Clinical Study -> B54 Neurotransmission and Receptors

EP-0676

Characterization of Major Psychiatric Disorders Using [^{11}C]K-2 PET Imaging of AMPA Receptors

M. Hatano[1], *W. Nakajima*[1], *H. Tani*[2], *H. Uchida*[2], *T. Miyazaki*[1], *T. Arisawa*[1], *Y. Takada*[1], *S. Tsugawa*[1], *H. Abe*[1], *A. Suda*[3], *T. Asami*[3], *A. Hishimoto*[4], *N. Nagai*[2], *T. Koizumi*[2], *S. Nakajima*[2], *M. Jinzaki*[5], *Y. Hirano*[6], *R. Mitoma*[6], *S. Tamura*[6], *S. Baba*[7], *O. Togao*[7], *H. Kosaka*[8], *H. Okazawa*[9], *Y. Kimura*[10], *M. Mimura*[2], *T. Takahashi*[1];
[1]*Department of Physiology, Yokohama City University Graduate School of Medicine, Yokohama, JAPAN,* [2]*Department of Neuropsychiatry, Keio University School of Medicine, Tokyo, JAPAN,* [3]*Department of Psychiatry, Yokohama City University Graduate School of Medicine, Yokohama, JAPAN,* [4]*Department of Psychiatry, Kobe University Graduate School of Medicine, Kobe, JAPAN,* [5]*Department of Radiology, Keio University School of Medicine, Tokyo, JAPAN,* [6]*Department of Neuropsychiatry, Graduate School of Medical Sciences, Kyusyu University, Fukuoka, JAPAN,* [7]*Department of Clinical Radiology, Graduate School of Medical Sciences, Kyusyu University, Fukuoka, JAPAN,* [8]*Department of Psychiatry, Faculty of Medical Sciences, University of Fukui, Fukui, JAPAN,* [9]*Biomedical Imaging Research Center, University of Fukui, Fukui, JAPAN,* [10]*Faculty of Informatics, Cyber Informatics Research Institute, Kindai University, Higashi-Osaka, JAPAN.*

Aim/Introduction: Synaptic phenotypes in living patients with psychiatric disorders are poorly characterized. Excitatory glutamate α-amino-3-hydroxy-5-methyl-4-isoxazole propionic acid receptor (AMPAR) is a fundamental component for neurotransmission. We recently developed a positron emission tomography (PET) tracer for AMPAR, [^{11}C]K-2, the first technology to visualize and quantify AMPAR density in the living human brain[1]. In this study, we examined appropriate quantification methods and elucidated key characteristics of major psychiatric disorders, including schizophrenia (SCZ), major depressive disorder (MDD), bipolar disorder (BD), and autism spectrum disorder (ASD). ***Materials and Methods:*** We conducted [^{11}C]K-2 PET imaging in 143 healthy subjects aged 20 to 70 years and 149 patients with psychiatric disorders (SCZ, n = 42; BD, n = 37; MDD, n = 35; ASD, n = 35). We assessed the effects of age on standardized uptake value ratio (SUVR) in healthy subjects, comparing white matter and whole brain as reference regions. We performed regression analysis between AMPAR density and symptomatology scores of each disease, and comparison of differences in AMPAR density between patients and healthy participants using a voxel-wise analysis. ***Results:*** In healthy subjects, white matter-referenced SUVR showed widespread age-dependent declines in AMPAR density. Whole brain normalization attenuated these effects, offering more stable estimates across the adult lifespan. When we compared SUVR using white matter and whole-brain references, the coefficient of variation among healthy participants was lower with whole-brain normalization, indicating reduced inter-individual variability and minimized influence of individual factors. Based on these results, we used whole brain as the reference region for analyzing psychiatric disorders. In psychiatric disorders, we detected brain regions where AMPAR density was associated with symptom severity within each disorder. We also identified significant differences in AMPAR density between each disorder and healthy subjects. Some of these alterations were shared across disorders, indicating that certain brain areas may be commonly affected in psychiatric disorders. ***Conclusion:*** Our approach to psychiatric disorders using [^{11}C]K-2 PET imaging can elucidate the biological mechanisms across diseases and pave the way to develop novel diagnostics and therapeutics based on synaptic physiology. ***References:*** Miyazaki T, Nakajima W, Hatano M, Shibata Y, Kuroki Y, Arisawa T et al. Visualization of AMPA receptors in living human brain with positron emission tomography. Nature Medicine 2020; 26(2)**:** 281-288.

EP-40

e-Poster Area

B: Imaging Clinical Studies -> B5 Neurological Imaging Clinical Study -> B55 Other Neurological Imaging

EP-0677

Brain Connectivity Networks of Quantitative Kinetic Parameters from Dynamic ^{18}F-FDG PET/CT Reveals Network-Level Differences in Surgical and Non-Surgical Epilepsy

Y. Duan[1], *Y. Ng*[2];
[1]*The First Affiliated Hospital of Shandong First Medical University and Shandong Provincial Qianfoshan Hospital, Jinan, Shandong, CHINA,* [2]*United Imaging Healthcare Group Co., Ltd., Shanghai, CHINA.*

Aim/Introduction: Epilepsy is a neurological disorder involving disrupted brain networks. Accurate localization of the epileptogenic zone is essential for surgical planning and achieving optimal therapeutic outcomes, but this task remains challenging due to the complexity of seizure networks. Dynamic ^{18}F-FDG-PET has shown superior sensitivity in detecting epileptogenic foci using kinetic over semi-quantitative SUV parameters. However, brain network analysis using dynamic PET-derived kinetic parameters remains largely underexplored. This study explores brain connectivity patterns using both semi-quantitative and kinetic parameters from dynamic ^{18}F-FDG-PET in epilepsy patients, comparing connectome features between surgical and non-surgical groups. ***Materials and Methods:*** A retrospective study of 15 patients with epilepsy (10 males, 5 females; mean age: 19.53 ± 8.55 years) was conducted at The First Affiliated Hospital of Shandong First Medical University. Patients were classified into surgical and non-surgical groups based on standardized presurgical evaluation protocol. All underwent 60-min dynamic total-body PET/CT scanning, T1-weighted MRI, and video-electroencephalography. Parametric images including relative blood volume (V_b), perfusion rate (K_1) and net influx rate (K_i) were generated using an irreversible two-tissue compartment model. Motion-corrected brain PET images were processed with PNEURO module (PMOD), coregistered to T1-weighted MR images, and segmented using the AAL atlas. Statistical differences in semi quantitative (SUV) and kinetic parameters (K_i, K_1 and V_b) between groups were assessed using the Wilcoxon signed-rank test. Cross-correlation among brain regions were performed to construct brain connectivity matrices, and global network properties were assessed using GRETNA to examine inter-group network-level differences. ***Results:*** We found that SUV, K_i, K_1 and V_b all showed statistically significant differences between surgical and non-surgical groups (all $P<0.0001$). Specifically, SUV, K_i, and V_b were significantly higher in non-surgical group, whereas K_1 was significantly higher in the surgical group. Brain connectivity network analysis revealed a more complex and interconnected network in the surgical group compared to non-surgical group when the correlation threshold was set to 0.95. Brain network analysis demonstrated that global efficiency, assortativity and synchronization of K_i, K_1 and V_b were higher in non-surgical group compared to surgical group. Whereas, clustering coefficient of SUV, K_1 and V_b and characteristic path length across all parameters

were higher in surgical group relative to non-surgical group. ***Conclusion:*** Brain connectivity showed distinguished features among surgical and non-surgical groups. This may potentially improve surgical candidate selection, enhancing precision in surgical decision-making, as well as providing deeper insight into the mechanism of epilepsy.

EP-0678

Altered Glucose Metabolism inDefault Mode Network and Prefrontal Circuit In Patients withKallmann Syndrome

C. Zhou[1], *X. Wang*[2], *M. Men*[2], *X. Yi*[2], *K. Cao*[1], *W. Pu*[1], *M. Hacker*[3], *X. Li*[3], *M. Zhao*[1];
[1]*The Third Xiangya Hospital, Central South University, Changsha, CHINA,* [2]*Xiangya Hospital, Central South University, Changsha, CHINA,* [3]*Medical University of Vienna, Vienna, AUSTRIA.*

Aim/Introduction: To characterize the neuro-metabolic signature of Kallmann Syndrome (KS) and elucidate their neuroendocrine-psychosocial interactions. ***Materials and Methods:*** In this prospective case-control study, 30 KS patients and 30 matched healthy controls underwent brain [^{18}F]F-FDG PET scans, sex hormone assays, and standardized neuropsychological assessments. A voxel-wise group comparison analysis was conducted to identify clusters of brain metabolic patterns between KS patients and HCs. Subsequently, correlation and mediation analyses were performed to investigate the interrelationships among brain metabolic patterns, sex hormone levels, and psychosocial factors. ***Results:*** We identified six hypermetabolic clusters in KS patients, predominantly located in the fronto-limbic system and the default mode network (DMN) in KS patients. These clusters of hypermetabolism were significantly associated fertility anxiety scale (FAS), health information avoidance scale (HIAS) and health information overload scale(HIOS). In addition, mediation analysis indicated that double basal ganglia hypermetabolism acted as a significant mediator between HIAS and FAS (β= 0.274, P =0.031). ***Conclusion:*** Patients with KS exhibited a distinct hypermetabolism pattern in the DMN-prefrontal circuit, which functionally bridges neuroendocrine dysfunction and reproductive health anxiety.

EP-0679

Microglial Activation and Glucose Hypometabolism in the Thalamus Following Traumatic Brain Injury

Y. Zhang*, X. Zhang;*
The First Affiliated Hospital, Sun Yat-Sen University, Guangzhou, CHINA.

Aim/Introduction: Neuroinflammation is a recognized consequence of traumatic brain injury (TBI). However, the long-term effects on microglial activation and associated metabolic changes in specific brain pathways require further investigation. This study aimed to evaluate microglial activation using ^{18}F-DPA-714 PET/MR and glucose metabolism using ^{18}F-FDG PET/MR in distant and subcortical brain regions of patients more than one year post-TBI compared to healthy controls (HC). ***Materials and Methods:*** Patients at least one year after TBI and healthy controls underwent ^{18}F-DPA-714 and ^{18}F-FDG PET/MR imaging. Standardized uptake value means (SUV_{mean}) and maximums (SUV_{max}) were measured in bilateral thalamus, midbrain, brainstem, cerebellar white matter, and cerebellar cortex using 5 mm diameter regions of interest. An Asymmetry Index (AI%) was calculated [200 × (ipsilateral/right - contralateral/left) / (ipsilateral/right + contralateral/left)]. Paired Wilcoxon tests compared ipsilateral and contralateral SUVs within patients, and Wilcoxon rank-sum tests compared AI% between patients and controls. Spearman correlation assessed the relationship between ^{18}F-DPA-714 and ^{18}F-FDG AI% in patients. ***Results:*** Eight patients (mean age 29.0 ± 13.4 years; 8 male) with TBI (median duration from TBI to PET 114.5 [IQR: 47.0, 307.5] months) and seven HC (mean age 28.7 ± 5.9 years; 4 male/3 female) were included. Patients with TBI showed significantly increased ^{18}F-DPA-714 SUV_{max} (1.1 [0.9, 1.3] vs. 0.6 [0.5, 0.9], p=0.016) and SUV_{mean} (1.0 [0.8, 1.2] vs. 0.6 [0.5, 0.8], p=0.008) and significantly decreased ^{18}F-FDG SUV_{max} (6.5 [4.9, 9.4] vs. 9.8 [8.2, 11.6], p=0.016) and SUV_{mean} (6.1 [4.0, 8.4] vs. 8.9 [7.6, 10.5], p=0.023) in the ipsilateral thalamus compared to the contralateral side. Thalamic AI% for ^{18}F-DPA-714 SUV_{max} (37.9 [14.8, 68.7] vs. 2.2 [-6.7, 6.9], p=0.009) and SUV_{mean} (35.6 [13.3, 67.6] vs. 4.9 [-7.3, 7.7], p=0.021) was significantly higher in patients than in HC. Thalamic AI% for ^{18}F-FDG SUV_{max} (-23.8 [-53.6, -14.4] vs. -4.4 [-13.5, 3.4], p=0.021) and SUV_{mean} (-29.8 [-61.3, -15.1] vs. -2.3 [-4.5, 0.2], p=0.014) was significantly lower in patients than in HC. No significant AI% differences were found in other measured regions. Within the patient group, thalamic ^{18}F-DPA-714 AI% (SUV_{max} and SUV_{mean}) negatively correlated with ^{18}F-FDG AI% (SUV_{max}: r=-0.71, p=0.047; SUV_{mean}: r=-0.86, p=0.007). No significant correlations were observed in other regions. ***Conclusion:*** Long-term TBI survivors demonstrate persistent ipsilateral thalamic microglial activation coupled with impaired glucose metabolism. The negative correlation between these PET markers suggests a potential link between chronic neuroinflammation and neuronal dysfunction in the thalamus following TBI.

EP-0680

^{18}F-DPA714 PET/MR Reveals Neuroinflammation-Peripheral Immune Crosstalk in Depression

L. Xu[1], *K. Liao*[1], *X. Song*[2], *P. Zheng*[2], *H. Pang*[1];
[1]*Department of Nuclear Medicine, The First Affiliated Hospital of Chongqing Medical University, Chongqing, CHINA,* [2]*Department of Neurology, The First Affiliated Hospital of Chongqing Medical University, Chongqing, CHINA.*

Aim/Introduction: Neuroinflammation, a major injurious mechanism in the brain, has been identified as a key trigger in the development of depression. In addition, both neuroinflammation and peripheral inflammation have been observed in patients with depression. However, the relationship between these processes remains unclear. The TSPO-targeting imaging agent ^{18}F-DPA714 PET can effectively detect the activation of microglia in the brain. This study explored the interaction between neuroinflammation and peripheral immunity by correlating ^{18}F-DPA714 PET imaging findings with peripheral blood inflammatory markers. ***Materials and Methods:*** We recruited 32 patients with depression (9 males, 23 females; mean age 41.3 years) and 24 health controls (7 males, 17 females; mean age 42.8 years). All subjects underwent ^{18}F-DPA714 PET/MR imaging. Peripheral blood samples were collected to assess blood count, C-reactive protein, and various cytokines. PMOD software was used to analyze differences in ^{18}F-DPA714 PET/MR uptake across different brain regions between the two groups. T-tests were employed to compare complete blood count, C-reactive protein, and cytokine level. Additionally, correlations among clinical assessments, including the Self-Rating Anxiety Scale (SAS), Self-Rating Depression Scale (SDS), Hamilton Anxiety Scale (HAMA)-14, Hamilton Depression Scale (HAMD)-17, and Patient Health Questionnaire (PHQ)-9, as well as peripheral inflammatory markers and ^{18}F-DPA714 PET uptake in the brain were evaluated. ***Results:*** Compared with healthy controls, patients with depression exhibited a significantly higher ^{18}F-DPA714 SUVmean in the right superior frontal gyrus, perifrontal gyrus, inferior frontal gyrus, posterior central gyrus, left superior limar gyrus, bilateral superior temporal gyrus, temporal poles, transverse temporal gyrus, hippocampus, insular lobes, anterior left cingulate gyrus, and right central sulcus (all $P < 0.05$). In patients with depression, peripheral levels of IL-4 and IL-10 were significantly elevated compared to healthy controls (all $P < 0.05$). Moreover, significant correlations were observed between brain ^{18}F-DPA714 uptake and clinical scores (HAMD-17, SAS, SDS) as well as IL-4 and IL-10 levels (all $P < 0.05$). ***Conclusion:*** In patients with depression, the uptake of ^{18}F-DPA714 was significantly elevated in multiple

brain regions—particularly in the frontal and temporal lobes—compared to healthy controls, and it showed positive correlations with peripheral inflammatory markers as well as HAMD-17, SAS, and SDS scores. These results suggest that peripheral inflammation and neuroinflammation coexist and may interact in depression, contributing to its pathogenesis.

EP-0681

Effect of ketogenic diet (KD) on brain metabolism goes beyond metabolic shifting

M. Mangia[1,2], *G. Rovera*[1,2], *M. Cioffi*[1,2], *F. Roveta*[3,4], *M. Zotta*[2], *A. Lesca*[2], *F. Giunta*[2], *E. Rubino*[3,4], *A. Cermelli*[3,4], *L. Sofia*[5,6], *S. Raffa*[5,6], *M. Bauckneht*[5,6], *D. Arnaldi*[6,7], *F. Massa*[6,7], *M. Pardini*[6,7], *I. Rainero*[3,4], *S. Morbelli*[1,2];
[1]*Department of Medical Sciences, University of Turin, Turin, ITALY,* [2]*Nuclear Medicine Unit, AOU Città della Salute e della Scienza di Torino, Turin, ITALY,* [3]*Aging Brain and Memory Clinic, Department of Neuroscience "Rita Levi-Montalcini", University of Turin, Turin, ITALY,* [4]*Department of Neuroscience and Mental Health, AOU Città della Salute e della Scienza di Torino, Turin, ITALY,* [5]*Nuclear Medicine Unit, Department of Medical Sciences, University of Genoa, Genoa, ITALY,* [6]*IRCCS Ospedale Policlinico San Martino, Genoa, ITALY,* [7]*Department of Neurosciences, University of Genoa, Genoa, ITALY.*

Aim/Introduction: KD has been proposed as adjuvant therapy in several neurologic disorders including epilepsy, Alzheimer's and Parkinson's disease. The mechanisms underlying its potential neuroprotective effects are not fully elucidated. The multifaceted nature of brain and body-PET imaging may be suitable for a deeper investigation of this topic; however, very few data are available in this regard. ***Materials and Methods:*** We retrospectively analyzed 74 cognitively-intact consecutive patients who underwent KD prior to whole-body [18F]FDG-PET, including brain imaging, to exclude endocarditis. Only patients with a negative scan, without a previous history of neurological and oncological diseases, were included. Patients were subgrouped according to presence/absence of myocardial metabolic shifting in terms of uptake suppression on whole-body PET. Brain-PET scan of both subgroups were processed and independently compared to an in-house database of healthy control in SPM12. Myocardial uptake was quantified in all patients by drawing a VOI on the left ventricle and normalized on blood-pool (MSUVmaxratio). SPM multiple-regression analysis was used to assess the relationship between cardiac residual metabolism and brain glucose consumption (FWE-corrected $p<0.05$ as significant). ***Results:*** 49 patients (median age 67 IQR[58-74], 49% males) showed complete cardiac metabolic shifting while 25 (median age 74 IQR[66-77], 83% males) presented only a partial shift. Both groups were characterized by a relative hypometabolism on a cluster encompassing the temporal and fronto-lateral cortex in the right hemisphere ($p<0.001$) which was, however, significantly less extended in patients with partial metabolic shifting. Notably, both groups showed a substantially overlapping pattern of relative hypermetabolism with respect to controls in a region encompassing limbic lobes (with a marked involvement of both medial-temporal lobes) and cerebellum bilaterally ($p<0.002$). In the whole-group of patients, MSUVmaxratio was directly correlated with the lateral-temporal cortex while no inverse correlations were highlighted. ***Conclusion:*** Both patterns of relative hypo and hypermetabolism hereby highlighted replicate in larger dataset the pattern emerged from the single previously available study which applied voxel-based analysis to brain FDG-PET during KD (Horowitz et al EJNMMI 2023), thus suggesting that KD might have a peculiar brain metabolic signature. Regions of cortical hypometabolism have a more direct relationship with patients' metabolic profile linked to myocardial shifting. Conversely, regions of relative hypermetabolism are independent from myocardial shifting and are located in the MTL in keeping with available preclinical findings. These regions might testify a further, more complex, interplay between KD and other factors, such as protection from oxidative stress, who deserve further investigation.

EP-0682

Neuroinflammation and Metabolism in Autoimmune Encephalitis: A Dual-Tracer PET Imaging Approach for Subgroup Differentiation

Y. Wang, *H. Shao, Y. Zhang, G. Huang, C. Zhang, J. Liu;*
Department of Nuclear medicine; Renji Hospital, School of Medicine, Shanghai Jiao Tong University, Shanghai, CHINA.

Aim/Introduction: Autoimmune encephalitis (AE) is a heterogeneous group of neuroinflammatory disorders characterized by diverse clinical manifestations and variable responses to immunotherapy. Early and accurate diagnosis remains challenging due to the lack of specific biomarkers and the complexity of underlying pathogenic mechanisms. This study aimed to systematically investigate brain metabolic and neuroinflammatory alterations in AE patients using multimodal positron emission tomography (PET) imaging (2-deoxy-2-[^{18}F] fluoro-D-glucose [^{18}F-FDG] PET and [^{18}F]N-fluoroacetyl-N-(2,5-dimethoxybenzyl)-2-phenoxyaniline [^{18}F-PBR06] PET). By analyzing imaging patterns across different antibody subtypes (neuronal surface vs. intracellular antibodies) and etiologies (paraneoplastic, viral, and cryptogenic), we sought to evaluate the clinical utility of multimodal PET imaging in improving early diagnosis, treatment monitoring, and prognosis assessment. ***Materials and Methods:*** This prospective study enrolled 49 immunotherapy-naïve AE patients (median age 48.0 years) and matched healthy controls from Renji Hospital (2012-2024). All 49 participants underwent ^{18}F-FDG PET imaging to assess regional brain metabolism. Among these, a subset of 19 participants additionally received ^{18}F-PBR06 PET imaging to evaluate neuroinflammation through translocator protein (TSPO) expression, enabling multimodal assessment. Image analysis was performed using Statistical Parametric Mapping (SPM; voxel-level $p<0.001$, cluster-level FWE-corrected $p<0.05$) with automated quantification via NeuroQ and uWS-MI software, while excluding functionally variable regions like the visual cortex. Patients were stratified into subgroups based on antibody type (neuronal surface antigen antibodies [NSAb] and intracellular antigen antibodies [ICAb]) and etiologies (paraneoplastic [PN], viral encephalitis [VE], and cryptogenic [CG]) to investigate distinct metabolic and inflammatory patterns. ***Results:*** Multimodal PET imaging revealed distinct metabolic and neuroinflammatory profiles across AE subgroups. All 49 patients undergoing ^{18}F-FDG PET exhibited metabolic abnormalities (1-27 lesions across 47 brain regions), whereas neuroinflammation detected by ^{18}F-PBR06 PET was less frequent (42.1%, 8/19 patients) and more localized (≤6 affected regions). Antibody-specific patterns emerged, with NSAb patients showing widespread metabolic disturbances including cerebellar hypermetabolism (54.2%) and frontal hypometabolism, while ICAb patients demonstrated more focal frontal lobe neuroinflammation (T=4.50-11.19). Etiological analysis revealed cerebellar hypermetabolism in both PN and VE groups (50-55.6%), with VE cases additionally exhibiting marked limbic neuroinflammation (T=22.33-61.99). CG patients displayed a unique pattern combining pontine/cerebellar neuroinflammation (T=3.69-6.15) with frequent frontal hypometabolism (63.2%), highlighting the clinical heterogeneity of AE. ***Conclusion:*** This multimodal PET study demonstrates that distinct brain metabolic and neuroinflammatory patterns characterize different AE subgroups, with antibody type and etiology serving as key determinants of imaging phenotypes.

EP-0683

AI-based denoising to fully exploit pathophysiological meaning and clinical impact of early perfusion amyloid PET imaging

A. Coccarelli[1,2], *M. Zotta*[1,2], *S. DeKeyser*[3], *V. De Ridder*[3], *M. Cioffi*[1,2], *G. Rovera*[2], *M. Pardini*[4], *L. Sofia*[5,6], *S. Raffa*[6], *L. Roccatagliata*[6,5], *F. Massa*[6,4], *D. Arnaldi*[6], *B. Orso*[4], *M. Losa*[4], *A. Lesca*[1,2], *M. Bauckneht*[5,6], *M. Bozzali*[7], *S. D. Morbelli*[1,2,8];
[1]AOU Città della Salute e della Scienza di Torino, Nuclear Medicine Unit, Turin, ITALY, [2]Department of Medical Sciences, University of Turin, Turin, ITALY, [3]Nuclivision, Ghent, BELGIUM, [4]Department of Neuroscience, University of Genoa, Genoa, ITALY, [5]Nuclear Medicine Unit, Department of Medical Sciences, University of Genoa, Genoa, ITALY, [6]IRCCS Ospedale Policlinico San Martino, Genoa, ITALY, [7]Rita Levi Montalcini Department of Neuroscience, University of Turin, Turin, ITALY, [8]Department of Neuroscience and Mental Health, AOU Città della Salute e della Scienza di Torino, Turin, ITALY.

Aim/Introduction: Early-perfusion-amyloid PET is considered able to capture neurodegeneration, allowing same-day, same-tracer categorization of both amyloidosis and neurodegeneration. However, scanner occupancy during early-image acquisition is an unresolved issue. Moreover, while the first 3-minutes post-injection better represents cerebral blood-flow, such a short acquisition-time may result in noisy images, making pattern identification challenging. We investigated the feasibility of AI-based denoising of 3-minute early-phase-amyloid-PET and simulated its clinical use using visual and voxel-based approaches. ***Materials and Methods:*** For pathophysiological reasons, the 10-minute scan cannot serve as a gold standard due to the expected less evident hypoperfusion signals. We thus used a model trained on low-dose enhancement datasets (such as late-phase or whole-body-FDG dose-reduction data), which is designed to preserve signal, as standard count and low-count images in those cases have similar underlying signals. This was compared with a classical denoising-model using the 10-minute-scan as high-count reference. We evaluated clinical performance of enhanced-images comparing the ability expert and non-expert readers' to recognize AD patterns in original 3-, 5-, and 10-minute frames versus enhanced 3-minute images. Both readers classified scans as positive/negative and rated diagnostic confidence on a 1-to-5 scale. We evaluated 92 reconstructed scans (original and enhanced). Finally, we carried out a single-subject analysis (SPM12) comparing original and enhanced-images with a normal-subjects-dataset of early-perfusion-amyloid-PET ($p<0.05$ FWE-corrected accepted as significant and results were compared in terms of the cluster's extent). ***Results:*** The model trained on 10-minute scans erroneously removed signals present in 3-minute-scans, whereas the model trained on low-dose datasets preserved them. Enhanced 3-minute images resulted in higher diagnostic confidence for both expert and non-expert readers compared to 10 minutes images (score 5 in 75% of enhanced 3-minute scans versus 55% for 10-minute scans). The enhanced 3-minute-images showed higher interobserver-agreement (k:0.88) than original 3-minute and 10-minute scans (k:0.75) but were not inferior to 5-minute-acquisitions. In the voxel-based-analysis clusters' extent was significantly larger for both 3-min-original and 3-min-enhanced images with respect to 5-min and 10-min images (800±200 and 807±233 versus 210±160-voxels respectively). In 1 patient, bilateral hypometabolism was highlighted in the comparison involving 3-min-enhanced-images only. ***Conclusion:*** The investigation into early-phase 3-minute scans highlighted the limitations of traditional supervised learning approaches, as the high-count data (10-minute scans) lack some clinically relevant perfusion signals. The method based on low-dose-enhancement seems promising as it was able to enhance images without suppressing the hypoperfusion pattern and allowed to increase readers' agreement, diagnostic confidence and voxel-based sensitivity.

EP-0684

Head-to-Head Comparative Study of [^{18}F]FDG, [^{18}F]FMZ and [^{18}F]DPA-714 for Localizing Epileptogenic Foci in Drug-Resistant Epilepsy

G. Li[1], *H. Huang*[2], *S. Mei*[3], *W. Bao*[1], *S. Ren*[1], *S. Jiang*[3], *Q. Huang*[1], *Z. Lin*[2], *Y. Yang*[4], *Y. Guan*[1], *L. Chen*[3], *F. Xie*[1];
[1]Department of Nuclear Medicine & PET Center, Huashan Hospital, Fudan University, Shanghai, CHINA, [2]Central Research Institute, United Imaging Healthcare Group Co., Ltd, Shanghai, CHINA, [3]Department of Neurosurgery, Huashan Hospital, Fudan University, Neurosurgical Institute of Fudan University, National Center for Neurological Disorders, Shanghai, CHINA, [4]Beijing United Imaging Research Institute of Intelligent Imaging, Beijing, CHINA.

Aim/Introduction: The localization of epileptogenic foci remains a critical challenge in the preoperative assessment of drug-resistant epilepsy (DRE). Although neuroinflammation, marked by translocator protein (TSPO) upregulation, is implicated in epileptogenesis and drug resistance, the diagnostic utility of the TSPO-specific tracer [^{18}F]DPA-714 in drug-resistant epilepsy (DRE) remains underexplored. This study aimed to systematically compare the performances of [^{18}F]FDG, [^{18}F]FMZ, and [^{18}F]DPA-714 PET in identifying epileptogenic foci, thereby optimizing preoperative multimodal imaging strategies. ***Materials and Methods:*** Fifteen surgical candidates with DRE, diagnosed according to ILAE criteria, underwent preoperative [^{18}F]FDG, [^{18}F]FMZ, and [^{18}F]DPA-714 PET scans. Analysis comprised visual assessments by three blinded nuclear medicine physicians (AAL3 atlas-defined regions) and quantitative voxel-wise analysis. The asymmetry index (AI) mapping was computed to detect cerebral regions of hypometabolism ([^{18}F]FDG and [^{18}F]FMZ) or hypermetabolism ([^{18}F]DPA-714) using the formula (ipsilateral – contralateral) / (ipsilateral + contralateral). Abnormal clusters (>40 contiguous voxels) were stratified by severity: mild ($0 < |AI| < 0.1$), moderate ($0.1 \leq |AI| < 0.2$), and severe ($|AI| \geq 0.2$). ***Results:*** Visual assessments revealed significant differences among the three tracers ($p < 0.001$), [^{18}F]FDG exhibited the highest number of abnormal brain regions, followed by [^{18}F]FMZ and [^{18}F]DPA-714($p < 0.001$ for both comparisons), and [^{18}F]FMZ exhibited moderately higher lesion counts than [^{18}F]DPA-714 ($p = 0.022$). Voxel-wise AI mapping stratification highlighted distinct tracer-specific patterns: [^{18}F]DPA-714 exhibited a broader range with higher abnormal voxel counts than [^{18}F]FDG, [^{18}F]FMZ($p < 0.001$ for both). At moderate levels, both [^{18}F]FDG and [^{18}F]DPA-714 surpassed [^{18}F]FMZ ($p < 0.001$ and $p < 0.05$), with no significant difference between [^{18}F]FDG and [^{18}F]DPA-714. At severe levels, [^{18}F]DPA-714 voxel counts were significantly lower than [^{18}F]FDG and [^{18}F]FMZ ($p < 0.001$ for both). In the quantitative analysis of combined moderate-severe abnormalities ($AI \geq 0.1$), [^{18}F]FDG demonstrated significantly larger volumes of metabolic dysfunction than both [^{18}F]FMZ ($p=0.012$) and [^{18}F]DPA-714 ($p=0.001$), with no significant difference between [^{18}F]FMZ and [^{18}F]DPA-714 ($p=0.679$). ***Conclusion:*** This first systematic comparison of [^{18}F]FDG, [^{18}F]FMZ, and [^{18}F]DPA-714 PET in drug-resistant epilepsy reveals a tracer-specific spatial hierarchy for metabolic abnormalities. [^{18}F]DPA-714 and [^{18}F]FMZ demonstrate more circumscribed abnormalities compared to [^{18}F]FDG. Future studies with expanded cohorts should 1) validate these tracer-specific efficiency gradients across epilepsy subtypes, 2) integrate surgical outcomes to establish AI thresholds for optimal tracer selection, and 3) explore hybrid PET/MRI protocols to synergize neuroinflammatory-metabolic localization.

EP-0685

Diagnostic utility and clinical impact of brain ^{18}F-FDG PET/CT in the diagnosis of autoimmune encephalitis

O. Hernandez Cristancho[1], *S. Asadurova*[1], *M. Alanís-Bernal*[2], *C. Lorenzo*[1], *H. Ariño*[3], *A. Zabalza*[3], *A. Vilaseca*[3], *E. Sáez de Gordoa*[4], *C. Auger*[4], *C. Gamez*[1];
[1]Nuclear Medicine Department, University Hospital Vall d'Hebron, Barcelona, SPAIN, [2]Neurology Department, University Hospital Vall d'Hebron, Barcelona, SPAIN, [3]CEMCat, Barcelona, SPAIN, [4]Radiology Department, University Hospital Vall d'Hebron, Barcelona, SPAIN.

Aim/Introduction: To evaluate the diagnostic utility and clinical impact of [^{18}F]-FDG PET/CT in patients with suspected autoimmune encephalitis (AE), and to identify characteristic metabolic patterns. ***Materials and Methods:*** Retrospective study of 31 patients with suspected AE who underwent brain [^{18}F]-FDG PET/CT between 05/2015 and 04/2025. Patients were classified by final diagnosis (Graus 2016 Criteria), clinical certainty (possible, probable, definitive), antibody type, and treatment with immune checkpoint inhibitors (ICIs). All PET/CT images were analyzed visually and semiquantitatively. Voxel-based group analysis was also performed. ***Results:*** 17 females, mean age 54 years [range: 33-76]. AE was definitive in 26 patients, possible in 4, and probable in 1. Fifteen patients were seronegative, including 6 treated with ICIs. Neoplasms were present in 17 patients. The most frequent antibodies were anti-NMDAR (n=4), GAD65 (n=3), LGI1 (n=2), and Hu (n=2). PET was performed at a median of 3.4 months [0.3-179 months] from symptoms' onset. PET abnormalities were detected in 27/31 patients (87%), including 19/27 (70%) with normal MRI. PET was positive in all 5 possible/probable cases, with concordance to MRI in 3/5 (showing unilateral mesial temporal involvement). Among seronegative patients, 11/15 had negative MRI with positive PET, and 4/15 had both positive MRI and PET, being the most common pattern mesial temporal and basal ganglia hypermetabolism (in 11/15 patients). Characteristic patterns included mesial temporal and basal ganglia hypermetabolism in LGI1/CASPR2 encephalitis (n=3), diffuse posterior cortical hypometabolism with subcortical hypermetabolism in anti-NMDAR encephalitis (n=3), and cerebellar or mesial temporal hypometabolism in GAD65-related cases (n=2), consistent with published data. In ICI-associated AE all patients were seronegative with a negative MRI, PET revealed basal ganglia and mesial temporal hypermetabolism alongside cortical hypometabolism (n=6) outlining its value in this subgroup. Normal PET/CT findings were seen in 4 patients (2 with anti-Ri and cerebellar degeneration, 1 anti-NMDAR, 1 anti-GAD65). Notably, all had PET performed either early (1.7-3.4 months) or very late (>70 months) after symptom onset, suggesting decreased sensitivity in late-stage disease. Thirteen patients underwent a control brain PET/CT, showing normalization of the finding in 6/13, persistence in 4/13, improvement in 2/13 and worsening (change from mesial temporal hyper to hypometabolism) in 1 patient. ***Conclusion:*** [^{18}F]-FDG PET/CT is a sensitive biomarker for AE, increases diagnostic confidence in possible/probable and seronegative cases. Specific antibody-related metabolic patterns enhance diagnostic certainty. Normal PET findings are possible in late-stage disease, underscoring the importance of timely imaging.

EP-0686

Brain [^{18}F]FDG PET identifies evolving brain metabolism patterns correlating with outcomes in autoimmune encephalitis

F. Massa[1,2], *D. Cerne*[1], *S. Raffa*[2], *G. Benvenuto*[1], *G. Rebella*[2], *P. Mattioli*[1,2], *G. Bavestrello*[1], *A. Lechiara*[2], *E. M. Mobilia*[2], *D. Arnaldi*[1,2], *F. Villani*[2], *L. Roccatagliata*[2,3], *M. Pardini*[4], *S. Morbelli*[5,6], *A. Uccelli*[1,2,2], *L. Benedetti*[1,2];
[1]Department of Neuroscience, Rehabilitation, Ophthalmology, Genetics, Maternal and Child Health, University of Genoa, Genova, ITALY, [2]IRCCS Policlinico San Martino Hospital, Genoa, ITALY, [3]Department of Health Sciences (DISSAL), University of Genoa, Genoa, ITALY, [4]Department of Neuroscience, Rehabilitation, Ophthalmology, Genetics, Maternal and Child Health, University of Genoa, Genova, Italy, Genoa, ITALY, [5]Department of Medical Sciences, University of Turin, Italy, Turin, ITALY, [6]Nuclear Medicine Unit, Azienda Ospedaliero-Universitaria Città della Salute e della Scienza di Torino, Turin, ITALY.

Aim/Introduction: Autoimmune encephalitis (AE) comprises a group of inflammatory brain disorders with highly variable clinical presentations and outcomes. While [^{18}F]FDG PET is increasingly used to support AE diagnosis, its potential as a prognostic tool remains underexplored. This study aimed to investigate whether longitudinal [^{18}F]FDG PET imaging—performed before and after immunotherapy—can identify evolving brain metabolism patterns that correlate with clinical outcomes in AE patients. ***Materials and Methods:*** In this retrospective study, 22 patients with a confirmed diagnosis, either seropositive or seronegative, of AE underwent brain [^{18}F]FDG PET scans at the acute phase (BS, baseline) and after immunotreatment (follow-up, FU). Voxel-wise paired T-test was used to identify significant metabolic changes between the two timepoints. Clusters with $p<0.05$ and ≥ 100 voxels were defined as volumes of interest (VOIs). VOI values were extracted and correlated with clinical outcomes—namely the Clinical Assessment Scale in Autoimmune Encephalitis (CASE) score, relapse, escalation of immunotherapy, and modified Rankin Scale (mRS)—using partial Spearman's correlations, adjusting for age. Prognostic value of brain metabolism at BS and FU was further assessed using general linear models. ***Results:*** Three VOIs showed significant metabolic changes between baseline (BS) and follow-up (FU) assessments. VOI-A, which was relatively hypermetabolic, included the caudate-thalamus-parahippocampal region, right amygdala, and anterior cingulate cortex. VOI-B1 and VOI-B2, relatively hypometabolic, corresponded to the right fusiform gyrus, precuneus, and temporo-parietal cortex, respectively. Lower metabolism in VOI-B1 at BS significantly predicted higher CASE scores at FU and was associated with relapse. VOI-B1 values at FU also predicted the need for escalation therapy, alongside patient age. Lower VOI-B2 metabolism at FU was associated with poor functional outcomes (mRS > 2). VOI-A did not correlate significantly with prognosis. ***Conclusion:*** Longitudinal [^{18}F]FDG PET imaging before and after immunotherapy reveals evolving regional brain metabolic patterns in AE. In particular, persistent hypometabolism in temporo-parietal areas correlates with relapse, need for intensified treatment, and long-term functional impairment. These findings support the use of [^{18}F]FDG PET as a non-invasive biomarker for prognostic stratification and treatment guidance in autoimmune encephalitis.

EP-0687

Dissociation between neurometabolic and neurovascular changes elicited by a sentence completion task: a PET-MRI study.

T. Vanbutsele[1,2], *A. Castiaux*[1,2], *N. Trotta*[1,3,2], *A. Rovai*[1,3], *V. Wens*[1,3], *S. Goldman*[1], *X. De Tiège*[1,3], *G. Leurquin-Sterk*[1,3,2];
[1]Université Libre de Bruxelles (ULB), ULB Neuroscience Institute (UNI), Laboratoire de Neuroanatomie et de Neuroimagerie translationnelles, Brussels, BELGIUM, [2]Université Libre de Bruxelles (ULB), Hôpital Universitaire de Bruxelles (H.U.B), CUB Hôpital Erasme, Department of Nuclear Medicine, Brussels, BELGIUM, [3]Université Libre de Bruxelles (ULB), Hôpital Universitaire de Bruxelles (H.UB.), CUB Hôpital Erasme, Department of Translational Neuroimaging, Brussels, BELGIUM.

Aim/Introduction: Functional positron emission tomography (fPET) with [18F]-fluorodeoxyglucose (FDG) is an emerging neuroimaging technique recording brain glucose metabolism over time and its modulation by experimental tasks. Simultaneous acquisition of fPET and functional magnetic resonance imaging (fMRI) using PET-MRI allows comparison of task-induced changes in neurometabolic and neurovascular couplings. Similar task-

induced increases in regional brain metabolism and perfusion have been described, but conflicting results have been reported for task-induced decreases in activity (e.g., within the default mode network (DMN)).This PET-MRI study investigates task-induced neurometabolic/neurovascular modulations elicited by a sentence completion task; a task known to recruit the left-dominant dorsal stream of the language network as well as to induce task-related decrease in fMRI signal within the DMN. ***Materials and Methods:*** Twenty right-handed, French-speaking adults performed a sentence completion task (10-min rest followed by 6 alternating 6-min rest/task blocks, task blocks: 30-second alternating task/rest blocks, total: 46 minutes) during dynamic PET-MRI data acquisition after FDG administration (bolus followed by continuous infusion). First-level general linear models were built with FDG-PET data organised into 46 frames of 1-minute duration each with task regressor modelled as a ramp function, global (mean activity across a grey matter) brain glucose uptake over time, and movements parameters as regressors of no-interest. Beta maps were used to compute ratios of regional metabolic changes over time. Second-level analyses were performed using one-sample t-tests across the whole population. fMRI data were pre-processed and analysed (block design) at the first and second levels using standard workflows. Results were considered significant at FWE-corrected p<0.05. ***Results:*** fPET and fMRI showed significant task-related increases in fPET and fMRI signals in the left-dominant dorsal stream of the language network. While fMRI showed significant decreases in blood oxygen level dependant (BOLD) signal in posterior midline DMN regions, no significant (even uncorrected) change in metabolic activity was observed using fPET. Significant increase in BOLD signal was observed in the right cerebellum, whereas fPET showed a significant decrease in metabolic activity. ***Conclusion:*** This study demonstrates that blood flow changes do not always match neural glucose demand.Neurophysiological mechanisms leading to this mismatch may involve feedforward neurovascular signalling, glia-mediated modulation, preparatory hemodynamic response, differences in neurovascular coupling and glycolytic processes during GABAergic suppression and glutamate activation. Interpretation of neuroimaging results based on fMRI should thus be done with caution.

EP-0688

Is the "Almond Sign" the Nut to Crack? Linking Amygdalae [^{18}F]FDG Uptake to Lymph-Node Metastasis in Breast Cancer

A. Safarian[1,2], *T. Jung*[1], *H. Reza*[3], *W. Hitzl*[4,5], *G. Schweighofer Zwink*[1], *G. Rendl*[1], *C. Pirich*[1], *M. Beheshti*[1];
[1]*Division of Molecular Imaging and Theranostics, Department of Nuclear Medicine, University Hospital, Paracelsus Medical University, Salzburg, AUSTRIA,* [2]*Rajaie Cardiovascular Medical and Research Center, Rajaie Cardiovascular Institute, Iran University of Medical Sciences, Tehran, IRAN, ISLAMIC REPUBLIC OF,* [3]*Research center for Nuclear Medicine, Department of Nuclear Medicine, Tehran University of Medical Sciences, Tehran, IRAN, ISLAMIC REPUBLIC OF,* [4]*Paracelsus Medical University Salzburg, Department of Ophthalmology and Optometry, Salzburg, AUSTRIA,* [5]*Research Program Experimental Ophthalmology & Glaucoma Research, Paracelsus Medical University, Salzburg, AUSTRIA.*

Aim/Introduction: Chronic stress activates neurobiological pathways centred in the amygdala, a limbic structure that regulates physiological stress responses. Increased amygdala metabolic activity on [^{18}F]FDG-PET/CT may reflect chronic stress affecting tumour characteristics and aggressiveness. Given the growing recognition of amygdala uptake across cancer types, we propose the "Almond sign", a visually identifiable pattern of bilateral amygdala hypermetabolism on [^{18}F]FDG-PET/CT, to harmonise interpretation and promote consistency across studies. This study investigates the relationship between amygdala metabolic activity and pathologically confirmed lymph node (LN) metastasis in newly diagnosed breast cancer patients. ***Materials and Methods:*** This retrospective study analysed [^{18}F]FDG-PET/CT in 93 patients with newly diagnosed invasive ductal breast cancer after excluding patients with confounding stress-related factors and/or distant metastases. Six amygdala-related PET parameters were extracted, three corrected to ipsilateral temporal-lobe SUVmean, and three to cerebellar SUVmean, to improve reproducibility given temporal uptake variability. Patients were stratified into high-risk and low-risk groups based on tumour characteristics, and into premenopausal and postmenopausal subgroups. ***Results:*** All six parameters were significantly associated with LN involvement ($p < 0.01$). Among them, Amyg_amaxT, defined as the mean SUVmax of the bilateral amygdalae, each normalised to their respective temporal-lobe SUVmean, showed the strongest correlation (OR 31.6 per 0.1-unit increase, 95% CI 7.77-128.9, $p < 0.00001$) with LN metastases. ROC analysis revealed an AUC of 0.96, with an optimal cut-off of 0.84, yielding 93% sensitivity and 94% specificity. Comprehensive multivariate analysis, incorporating all six amygdala parameters, tumour characteristics (ER, PR, HER2 status, grade, Ki67), tumour stage, molecular subtypes, PET parameters, inflammatory markers, and patient characteristics, identified Amyg_amaxT as the sole independent predictor of LN metastasis across four variable selection algorithms. It also correlated significantly with MTV ($p = 0.00065$), TLG ($p = 0.00081$), and PET-detected axillary LN status (OR 5.01, $p = 0.001$). In subgroup analyses, Amyg_amaxT remained a significant predictor across both menopausal and risk groups, with the strongest performance observed in low-risk breast cancer patients. ***Conclusion:*** Increased amygdala uptake on [^{18}F]FDG PET, visually representing chronic stress, and its derived metric Amyg_amaxT, has the potential to predict axillary LN metastasis in primary staging of breast cancer. This parameter could be considered in nodal assessment when conventional imaging is equivocal, guide presurgical evaluation and clinical decision-making, and contribute to prognostic modelling in future outcome studies. Establishing a standardised term like the "Almond sign" promotes consistency across imaging research and facilitates integration of stress-related brain biomarkers into oncological PET/CT practice.

EP-0689

Association of Glymphatic Function with Glucose Metabolic Patterns in Patients with Prolonged Disorders of Consciousness

Y. Wang, *K. Guo, F. Kang, J. Wang;*
Xijing Hospital, Xi'an, CHINA.

Aim/Introduction: Previous studies have demonstrated that traumatic brain injury and stroke, two major etiological factors of prolonged disorders of consciousness (pDoC), can lead to dysfunction of the glymphatic system. However, it remains unclear whether patients with pDoC exhibit glymphatic system impairment and whether such dysfunction is associated with alterations in cerebral glucose metabolism. This study aimed to investigate glymphatic dysfunction in patients with pDoC and to explore its potential relationship with glucose metabolic patterns in the brain. ***Materials and Methods:*** Forty-one pDoC patients (mean age 48.4 ± 14.7 years) and 26 age-matched HCs (mean age 49.3 ± 12.8 years) were enrolled. All participants underwent diffusion tensor (DTI) imaging for in vivo assessment of glymphatic function using DTI along the perivascular space (DTI-ALPS) index, as well as ^{18}F-fluorodeoxyglucose positron emission tomography (^{18}F-FDG PET) to characterize pDoC-associated metabolic patterns, including glucose metabolic pattern (GMP) score and standardized uptake value ratio (SUVR) of ROIs relevant to the mesocircuit model. The GMP was generated using voxel-based scaled subprofile modeling combined with principal component analysis (SSM/PCA). The GMP scores were subsequently calculated. Regions of interest (ROI) for calculating SUVR were defined using

the Automated Anatomical Labeling (AAL) template, and the whole brain served as the reference region. Associations between the DTI-ALPS index and GMP score, SUVR were evaluated using Pearson's correlation analysis. ***Results:*** pDoC Patients exhibited significantly lower DTI-ALPS indices than HCs ($p < 0.001$). Partial correlation analyses revealed a significant correlation between the DTI-ALPS index and GMP score ($r = 0.654$, $p < 0.001$). Additionally, relatively strong correlations were observed between the DTI-ALPS index and the SUVR of several brain regions, including the thalamus ($r = 0.593$ and 0.564 for the left and right hemispheres, respectively, both $p < 0.001$), the globus pallidus ($r = 0.401$ and 0.362 for the left and right hemispheres, respectively, $p = 0.009$ and 0.020), the striatum ($r = 0.565$ and 0.524 for the left and right hemispheres, respectively, both $p < 0.001$), and the brainstem ($r = 0.629$, $p < 0.001$). No significant correlations were found between the DTI-ALPS index and the SUVR of the frontal or parietal cortex ($p > 0.05$). ***Conclusion:*** Our study indicates that glymphatic dysfunction is associated with the whole-brain GMP score and SUVR of regions relevant to the mesocircuit model in patients with pDoC. These findings suggest a potential mechanism underlying neurological recovery in patients with pDoC.

EP-0690

First Atlas of Resting-State Networks Based on FDG-PET Data

D. Steenken[1], *C. Eierud*[2], *A. Sala*[3], *N. Franzmeier*[1], *Y. Li*[4], *A. Zwergal*[1], *I. Yakushev*[4];
[1]*University Hospital of Munich, Munich, GERMANY,* [2]*Georgia State University, Atlanta, GA, UNITED STATES OF AMERICA,* [3]*University of Liège, Liège, BELGIUM,* [4]*Hospital of Technical University of Munich, Munich, GERMANY.*

Aim/Introduction: Resting-state networks (RSNs) identified through functional magnetic resonance imaging (fMRI) have fundamentally transformed our understanding of intrinsic brain function. Several established fMRI-based RSN atlases have facilitated the mapping and interpretation of these intrinsic connectivity patterns. However, while fMRI primarily reflects hemodynamic changes, FDG-PET as index of glucose consumption offers a more direct assessment of neuronal function with superior signal-to-noise properties. Given the emerging evidence that RSNs can be reliably identified in FDG-PET data, we aimed to develop the first atlas of RSNs based on FDG-PET data. ***Materials and Methods:*** We analyzed data from cognitively healthy subjects derived from two independent sources: the Alzheimer's Disease Neuroimaging Initiative (ADNI) and a local institutional database. To ensure robust validation, the ADNI cohort was divided into two age- and sex-matched groups for replicability testing: Group 1 (n=61, age 67.0±3.0 years, mean±SD) and Group 2 (n=61, age 67.2±2.5 years). Group 3 (n=61, age 56.2±4.1 years) from our institutional database underwent repeated scanning to assess reproducibility. All PET data were available as one image per subject. Independent component analysis (ICA) with ICASSO stability analysis was conducted using the GIFT toolbox. The number of meaningful independent components (ICs), their replicability and reproducibility were evaluated using the Dice coefficient. RSNs with at least a fair Dice coefficient were considered to be qualified for the atlas. ***Results:*** Each of the four ICA analyses yielded 20-25 meaningful independent components. We successfully identified several well-established RSNs: cerebellar (replicability 0.86, reproducibility 0.89), primary visual (0.60, 0.81), sensorimotor (0.47, 0.54), posterior default mode (0.36, 0.84), central executive (0.58, 0.61), and basal ganglia (0.59, 0.53). Additionally, we identified several networks not previously established in the fMRI literature in their current form. They were named according to their anatomical distribution: medial prefrontal (0.74, 0.55), parieto-occipital (0.23, 0.55), and inferior temporal (0.48, 0.36). ***Conclusion:*** A number of RSNs could be identified in FDG-PET data in a replicable and reproducible manner. The spatial distribution of the canonical RSNs partially differed from those of fMRI atlases. Moreover, we found a few RSNs that have not been established by fMRI studies in this form so far, underscoring the complementary value of FDG-PET in mapping brain functional architecture. This novel atlas is being integrated into publicly available software, offering researchers and clinicians a new reference framework for brain connectivity analyses.

EP-0691

Feasibility of Short Imaging Protocols for [^{18}F]-D-Deprenyl PET in Autoimmune Encephalitis and Multiple System Atrophy

L. Tagnin[1], *J. S. Julia S. Dorneich*[1], *M. Zeinaki*[1], *L. Vogler*[1], *L. Sanzo*[1], *S. Katzdobler*[2,3], *A. Alexander Jäck*[2,3], *A. Bernhardt*[3], *B. Rauchmann*[4,5], *S. Stoecklein*[6], *M. Simmet*[1], *E. Joseph*[1], *S. Lindner*[1], *R. Schaefer*[1], *N. Koglin*[7], *A. Mueller*[7], *A. W. Stephens*[7], *J. A. Gernert*[8], *F. Hopfner*[2,3], *G. U. Höglinger*[2,3,9], *R. Perneczky*[9,10,11], *T. Kümpfel*[8], *M. Kerschensteiner*[8,9,12], *F. Franziska*[8], *J. Levin*[2,3,9], *M. Brendel*[1,2,9];
[1]*Department of Nuclear Medicine, University Hospital of Munich, LMU Munich, Munich, GERMANY,* [2]*German Center for Neurodegenerative Diseases (DZNE), Munich, GERMANY,* [3]*Department of Neurology, University Hospital of Munich, LMU Munich, Munich, GERMANY,* [4]*Department of Neuroradiology, University Hospital of Munich, LMU Munich, Munich, GERMANY,* [5]*Department of Psychiatry and Psychotherapy, University Hospital of Munich, LMU Munich, Munich, GERMANY,* [6]*Department of Radiology, University Hospital of Munich, LMU Munich, Munich, GERMANY,* [7]*Life Molecular Imaging GmbH, Berlin, GERMANY,* [8]*Institute of Clinical Neuroimmunology, University Hospital, LMU Munich, Munich, GERMANY,* [9]*Munich Cluster for Systems Neurology (SyNergy), Munich, GERMANY,* [10]*Ageing Epidemiology (AGE) Research Unit, School of Public Health, Imperial College, London, UNITED KINGDOM,* [11]*Sheffield Institute for Translational Neuroscience (SITraN), University of Sheffield, Sheffield, UNITED KINGDOM,* [12]*Biomedical Center, Faculty of Medicine, LMU Munich, Munich, GERMANY.*

Aim/Introduction: Positron-emission-tomography (PET) imaging with the novel monoamine oxidase B (MAO-B) radiotracer [^{18}F] D2-Deprenyl ([^{18}F]F-DED) to detect reactive astrogliosis enables imaging of neuroinflammation/neurodegeneration in patients with autoimmune-encephalitis (AIE) and multiple system atrophy (MSA). This study investigated the use of short static time windows for [^{18}F]F-DED MAO-B-PET imaging of AIE and MSA. ***Materials and Methods:*** 20 patients with AIE and 20 patients with MSA, either Parkinsonian (MSA-P) or cerebellar subtype (MSA-C), with visual positive PET-signal and 17 controls (CTRL) were evaluated. [^{18}F]F-DED PET was performed by a dynamic 60-minute scan. Standardized uptake value ratios (SUVrs; cerebellar cortex as a reference tissue) of disease related target regions (i.e. mesial temporal lobe, posterior putamen, cerebellar deep white matter) were obtained 0-10, 10-20, 20-30, 30-40, 40-50 and 50-60 minutes p.i.. Additionally, quantification was performed with PMOD. Volume of distribution ratios (VTrs) via one-tissue-compartment model (1TC2k) with carotid image-derived input function and total distribution volume ratios (DVRs) via Logan plot were calculated using full scan durations (0-60 minutes p.i.). ***Results:*** 10 minutes intervals between 10-60 minutes p.i. indicated good image contrast and strong signal to noise ratio for [^{18}F]F-DED PET. Early imaging intervals between 0-10 and 10-20 minutes p.i. showed significantly lower SUVr compared to all later time windows for both AIE (all $p < 0.001$, Cohen's d: 0.6-2.9) and MSA lesions (all $p < 0.05$, Cohen's d: 0.5-1.8). Overall, SUVr as a function of imaging time tended to approach a plateau around 60 minutes p.i.. SUVrs of all time windows correlated significantly positive with DVRs for both AIE and MSA ($r = 0.72$-0.95, $p < 0.01$), except for SUVr 0-10 for MSA ($p = 0.09$). DVRs were significantly larger than VTrs for all groups (all $p < 0.01$) and correlated positively with each other ($r = 0.63$-0.97, $p < 0.01$). Temporomesial DVRs allowed a better discrimination between patients with AIE and controls compared

to VTrs (p = 0.017), whereas no advantage of putaminal DVRs over VTrs was detected for the comparison of MSA-P and controls (p = 0.16). ***Conclusion:*** Static images of [^{18}F]F-DED PET, even with only 10 minutes emission recording, deliver good image quality for detection of neuroinflammation in AIE and MSA. Late static scanning (30-60 minutes p.i.) offers the best balance between accuracy and economic scanning. DVR may offer an advantage over VTr for regions with low MAO-B expression (e.g. differentiation between patients and controls).

EP-0692

Individual-Level Connectivity Biomarker from Sparse Inverse Covariance Estimation in [18F]-FDG PET

M. Doyen[1], *S. Heyer*[2], *A. Verger*[3];
[1]*Nancyclotep / University of Lorraine, IADI INSERM U1254, Nancy, FRANCE,* [2]*CHRU Nancy, Nancy, FRANCE,* [3]*CHRU Nancy / University of Lorraine, IADI INSERM U1254, Nancy, FRANCE.*

Aim/Introduction: Connectivity analyses are increasingly utilized in PET imaging, though they are predominantly explored at the group level. This study aimed to develop an individual-level connectivity biomarker using Sparse Inverse Covariance Estimation (SICE) to distinguish between Alzheimer's disease (AD), mild cognitive impairment (MCI), and cognitively normal (CN) individuals as compared to classical semi-quantitative methods (Dementia Prognostic Index, DPI) or more traditional methods based on connectivity (Principal Component Analysis, PCA). ***Materials and Methods:*** A total of 763 subjects with brain [18F]-FDG PET scans were selected from the ADNI database (1): 195 AD (73.8±8.2 years), 378 MCI-AD patients (73.1±7.0 years), including 123 who converted to AD within two years and 190 CN (mean age 72.8±6.1 years). For each subject, three biomarkers were computed: i, a DPI based on the ratio of uptake in AD-hypometabolic regions to stable reference regions (2), ii, an individual metabolic covariance pattern expression derived using PCA (3), iii, an individual likelihood index of belonging to AD, MCI (± converters), or CN SICE-based connectivity matrices (4). Leave-one-out cross-validation was used for individual-level classification. Thresholds maximizing sensitivity and specificity were determined from ROC curve analyses to evaluate the diagnostic performance of the three methods. ***Results:*** Accuracy for discriminating AD from CN was 85% for both DPI and PCA, and 90% for SICE (SICE > DPI/PCA, p = 0.02). For MCI-AD vs. CN, accuracies were 67% (DPI), 64% (PCA), and 70% (SICE) (SICE > PCA, p < 0.01). For predicting MCI-AD conversion to dementia, accuracies were 66% (DPI), 57% (PCA), and 67% (SICE) (SICE and DPI > PCA, p < 0.01). Across all comparisons, diagnostic performance improved when DPI was combined with connectivity-based methods (p ≤ 0.02). ***Conclusion:*** Individual-level connectivity analysis, particularly via SICE, is feasible and provides complementary diagnostic value to conventional intensity-based metrics in [18F]-FDG PET imaging for suspected AD. Incorporating such methods into clinical practice could enhance early diagnosis and prognosis. ***References:*** 1.Data used were obtained from the Alzheimer's Disease Neuroimaging Initiative (ADNI) database (adni.loni.usc.edu). 2.Torosyan N et al, Alzheimer'sDisease Neuroimaging Initiative. Value of FDG-PET scans of non-demented patients in predicting rates of future cognitive and functional decline. Eur J NuclMed Mol Imaging.2017;44(8):135563. 3.Alexander GE et al. Application of the scaled subprofile model to functional imaging in neuropsychiatric disorders: A principal component approach to modeling brain function in disease. Hum Brain Mapp.1994;2(12):7994. 4.Huang S et al. Learning brain connectivity of Alzheimer's disease by sparse inverse covariance estimation. NeuroImage.2010;50(3):93549.

EP-0693

First-in-Human Application of ^{99m}Tc-CN7DG and Quantitative Comparison of SPECT/CT versus ^{18}F-FDG PET/CT in intracranial space-occupying lesion

J. Wang*, C. Zhou, Z. Quan, F. Kang, G. Li, J. Wang;*
Department of Nuclear Medicine, Xijing Hospital, Fourth Military Medical University, Xi'an, Shaanxi, CHINA.

Aim/Introduction: The purpose of this study was to evaluate a novel glucose derivative SPECT imaging agent, ^{99m}Tc-CN7DG, and to compare ^{99m}Tc-CN7DG quantitative SPECT/CT with ^{18}F-FDG PET/CT in patients with intracranial space-occupying lesion. ***Materials and Methods:*** Five healthy volunteers were enrolled to assess the safety, biodistribution, dosimetry and optimal acquisition time of ^{99m}Tc-CN7DG. Subsequently, patients with pathologically confirmed intracranial space-occupying lesion were prospectively recruited. Each patient underwent ^{18}F-FDG PET/CT on the first day and ^{99m}Tc-CN7DG quantitative SPECT/CT on the second day. The number of ^{99m}Tc-CN7DG quantitative SPECT/CT versus ^{18}F-FDG PET/CT lesions detected and semi-quantitative parameters were compared using MR as the gold standard. ***Results:*** ^{99m}Tc-CN7DG was safe in humans, and the whole-body effective dose (5.24 × 10-3 mSv/MBq) was comparable to that of bone scan. Normal brain tissue did not take up the tracer and 2 hours after injection was the best time for SPECT imaging. 26 lesions from 11 patients were analysed. The number of lesions detected by ^{18}F-FDG PET/CT was significantly less than that by ^{99m}Tc-CN7DG quantitative SPECT/CT (12 vs. 23, P = 0.002), and with ^{99m}Tc-CN7DG quantitative SPECT/CT detected a comparable number of lesions as MR (23 vs. 26, P = 0.348). ^{99m}Tc-CN7DG quantitative SPECT/CT reduced the false-negative rate of ^{18}F-FDG PET/CT by 42.3% (sensitivity: 0.88 vs. 0.46, accuracy: 0.85 vs. 0.48). The max of lesion background ratio (LBRmax) and the mean of lesion background ratio (LBRmean) of ^{99m}Tc-CN7DG quantitative SPECT/CT were significantly higher than that of ^{18}F-FDG PET/CT (LBRmax: 10.87 ± 7.49 vs. 1.08 ± 0.41, LBRmean: 6.93 ± 7.44 vs. 1.0 ± 0.38, all P < 0.0001). SUVmax and LBRmax of ^{99m}Tc-CN7DG quantitative SPECT/CT and ^{18}F-FDG PET/CT were not related to lesion size (all r < 0.03 and P > 0.05). ***Conclusion:*** ^{99m}Tc-CN7DG is a safe and promising SPECT tracer for intracranial space-occupying lesion that reduces the false-negative rate due to intracranial lesions caused by ^{18}F-FDG hypermetabolism.

EP-0694

Evaluation of Structural-Functional Connectivity Coupling and Metabolism in Adolescent with Bipolar Disorder and Major Depression Disorder

S. Liu[1], *Y. Zhong*[1], *L. Liu*[2], *F. Hu*[1], *Y. Huo*[1], *J. Ma*[1], *Y. Zhang*[1], *C. Ma*[1], *E. Cong*[1];
[1]*Shanghai Tenth People's Hospital, Tongji University School of Medicine, Shanghai, CHINA,* [2]*Central Research Institute, United Imaging Healthcare Group Co., Ltd, Shanghai, CHINA.*

Aim/Introduction: Utilizing simultaneous PET/MR imaging to investigate the structural-functional connectivity (SC-FC) coupling and metabolic abnormalities in adolescents with bipolar disorder (BDD) and major depressive disorder (MDD). ***Materials and Methods:*** 14 participants with BDD (mean age, 14.29±1.62 years; 14 female, 0 male) and 14 with MDD (mearn age, 15±2 years; 10 female, 4 male) were enrolled. Group assignment was based on scores from the Hamilton Depression Rating Scale (HAMD) and Hypomania Checklist (HCL). The severity of the patient's suicidal thoughts and behavior were assessed using Columbia-Suicide Severity Rating Scale (C-SSRS). Simultaneous ^{18}F-FDG PET and MRI data were acquired using a hybrid 3.0-Tesla TOF-PET/MRI scanner. MRI sequences included 3D T1-weighted image, diffusion tensor imaging (DTI), and resting-state funtional MRI (fMRI). fMRI was used to construct functional connectivity (FC), and DTI was used to construct structural connectivity (SC). A multilinear regression model was used to predict FC from SC. The SC-FC coupling was

defined by the Pearson correlation coefficient between the predicted FC and the original FC. Cerebellar gray matter uptake value was used as the reference region to calculate cortex ratio standardized uptake value (SUVr) as a metabolic parameter. ***Results:*** Reduced SC-FC coupling and decreased FDG metabolism were observed in the BDD group, particularly in the thalamus ($p<0.01$). In the association analysis between SC-FC coupling and metabolism, the significantly related brain regions in the BDD group all showed a positive correlation ($p<0.05$, $r>0.58$), and in the MDD group, most significantly related brain regions showed negative correlation ($p<0.05$, $r<-0.60$). In the correlation analysis between SC-FC coupling and clinical metrics (HAMD, HCL, and C-SSRS), negative correlations for SC-FC coupling with HCL and C-SSRS were found in BDD group ($p<0.05$). In MDD group, SC-FC coupling of Hippocampus showed maximum correlation with C-SSRS ($p=0.0000$, $r=0.9582$). Receiver-operating characteristics (ROC) analysis showed SC-FC coupling features were better than metabolism features in distinguishing the BDD from MDD. ***Conclusion:*** BDD and MDD had different differential brain regions in SC-FC coupling and metabolism, with SC-FC coupling differential brain regions being more advantageous in discriminating between the groups, suggesting that the SC-FC coupling parameter has the potential to be a biomarker for differentiation. Second, the correlation analysis between SC-FC coupling and metabolism revealed divergent patterns between groups, suggesting distinct pathogenic mechanisms underlying BDD and MDD.

EP-0695

Structural-functional connectivity and metabolism analysis in adolescent depression with suicidal behavior

S. Liu[1], *Y. Zhong*[1], *L. Liu*[2], *Y. Huo*[1], *Y. Jiang*[1], *J. Ma*[1], *C. Ma*[1], *E. Cong*[1]; [1]*Shanghai Tenth People's Hospital, Tongji University School of Medicine, Shanghai, CHINA,* [2]*Central Research Institute, United Imaging Healthcare Group Co., Ltd, Shanghai, CHINA.*

Aim/Introduction: Current neuroimaging studies of adolescent depression predominantly focus on isolated imaging modalities, overlooking the potential role of aberrant interactions among brain structure, function, and metabolism in psychiatric disorders. This study aimed to characterize differences between suicidal and non-suicidal major depressive disorder (MDD) in adolescents by integrating structural-functional connectivity and metabolic situation. ***Materials and Methods:*** 9 participants with suicidal MDD (mean age, 14.33±1.83 years; 6 females, 3 males) and 10 with non-suicidal MDD (mean age, 14.70±1.49 years; 10 females, 0 male) were enrolled. Depressive symptoms were assessed using the Hamilton Depression Rating Scale (HAMD) and Hypomania Checklist (HCL). The suicidal behaviors were assessed using Columbia-Suicide Severity Rating Scale (C-SSRS). Simultaneous ^{18}F-FDG PET and MRI scans were performed on a hybrid 3.0-Tesla TOF-PET/MRI scanner. MRI sequences included 3D T1-weighted imaging, diffusion tensor imaging (DTI), and resting-state functional MRI (fMRI). Resting-state fMRI was used to construct functional connectivity (FC), and DTI was used to construct structural connectivity (SC). A multilinear regression model was used to predict FC from SC. The SC-FC coupling was defined by the Pearson correlation coefficient between the predicted FC and the original FC. Cerebellar gray matter uptake value was used as the reference region to calculate cortex ratio standardized uptake value (SUVr) as a metabolic parameter. ***Results:*** In suicidal MDD, SC-FC coupling was increased in superior frontal gyrus and decreased in inferior temporal gyrus compared with non-suicidal MDD ($p<0.01$). Metabolic differences were predominantly observed in the fusiform gyrus and occipital gyrus ($p<0.01$), with suicidal MDD patients exhibiting elevated metabolism in these regions. SC-FC coupling was strongly correlated with metabolic activity in the precentral gyrus, superior parietal lobule, and striatum in suicidal MDD ($p<0.01$, $|r|>0.87$) , and a similar association was observed in the superior parietal lobule in non-suicidal MDD. Suicide scores showed strong correlations with temporal lobe and thalamus SC-FC coupling values but differed sub-regional in both group ($p<0.05$,$|r|>0.72$). ***Conclusion:*** Suicidal and non-suicidal MDD had different differential brain regions in SC-FC coupling and metabolism, these differences may provide an opportunity to predict suicidal behavior in patients with MDD, support clinics in the management of patients better.

EP-0696

MRI-arterial spin labeling and FDG-PET reveal reduced whole brain perfusion and changes in regional glucose uptake in severe sustained hypoxia

H. Weis[1], *J. Hönemann*[2], *F. Hoffmann*[2], *L. DeBoni*[3], *L. Kessler*[4], *C. Rischpler*[5], *M. Schmitz*[6], *D. Elmenhorst*[7], *S. Beer*[7], *A. Drzezga*[1], *J. Jordan*[3], *J. Tank*[3], *U. Limper*[3]; [1]*Department of Nuclear Medicine, Faculty of Medicine and University Hospital of Cologne, Cologne, GERMANY,* [2]*Department of Internal Medicine III, Division of Cardiology, Pneumology, Angiology, and Intensive Care, University of Cologne, Cologne, GERMANY,* [3]*Institute of Aerospace Medicine, German Aerospace Center (DLR), Cologne, GERMANY,* [4]*Department of Nuclear Medicine, University Essen, Essen, GERMANY,* [5]*Department of Nuclear Medicine, Klinikum Stuttgart, Stuttgart, GERMANY,* [6]*Institute for Medical Biometry, Informatics and Epidemiology (IMBIE), University of Bonn, Bonn, GERMANY,* [7]*Institute of Neuroscience and Medicine (INM-2), Forschungszentrum Jülich, Jülich, GERMANY.*

Aim/Introduction: Previous studies suggest reduced arterial oxygen content at high altitude is compensated by increased cerebral blood flow and glucose uptake, resulting in an unchanged oxygen delivery [1]. Already in normoxia, the brain shows regional differences in oxidative metabolism which may be further intensified in hypoxia. We tested whether the adaptive mechanisms of the brain are preserved during severe sustained normobaric hypoxia. ***Materials and Methods:*** We included three men (55-64 yrs.) with fully revascularized myocardial infarction (MI) 49-126 months prior to study entry and one age-matched healthy man, each without signs or symptoms of neurological disease. After preacclimatization, we induced normobaric hypoxia in the hypoxic chamber at the DLR :envihab facility in Cologne, Germany by gradually adding nitrogen until alveolar oxygen partial pressure had reached about 35 mmHg. We maintained hypoxia for 14 consecutive days (FiO2=0.095) and nights (FiO2=0.105). We estimated cerebral perfusion by brain magnetic resonance (MRI) based arterial spin labeling (ASL), and cerebral glucose uptake by 18-FDG PET-MRI, at baseline, after 14 days of severe hypoxia, and after one months of recovery. We regularly assessed cognitive function. ***Results:*** In hypoxia, absolute whole brain perfusion decreased by 30±13% ($p=0.02$), resulting in approximately 25% reduced cerebral oxygen delivery. Values returned to baseline at recovery. Relative to the whole brain, perfusion decreased in the parietal lobes, occipital lobes, and precuneus and increased in temporal lobes, basal ganglia, insula, thalamus and hippocampus. Relative to the whole brain, glucose uptake responded concordantly but less pronounced. In contrast, in the posterior cingulum relative increased FDG uptake was accompanied by decreased perfusion. Changes were similar in MI-patients and the healthy control person. Reversible white matter hyperintensities appeared in hypoxia. Cognitive function remained unaffected. ***Conclusion:*** Severe sustained normobaric hypoxia paradoxically decreased whole brain perfusion and cerebral oxygen delivery in humans, which may have been compensated by augmented 0_2 extraction. Changes in glucose uptake and perfusion in parts of the default mode network may be a consequence of an even further reduction in oxidative metabolism. ***References:*** [1] Hoiland

RL, Bain AR, Rieger MG, Bailey DM, Ainslie PN. Hypoxemia, oxygen content, and the regulation of cerebral blood flow. Am J Physiol Regul Integr Comp Physiol. 2016 Mar 1;310(5):R398-413.

EP-0697

Metabolic Alterations in the Brain and Tumor Incidence of Patients with Long COVID: Insights from ^{18}F-FDG PET Imaging

Y. Wang[1], *M. Xin*[1], *H. Shao*[1], *Y. Zhang*[1], *X. Wu*[2], *J. Hao*[3], *J. Liu*[1], *C. Zhang*[1];
[1]*Department of Nuclear medicine; Renji Hospital, School of Medicine, Shanghai Jiao Tong University, Shanghai, CHINA,* [2]*Department of Respiratory medicine; Renji Hospital, School of Medicine, Shanghai Jiao Tong University, Shanghai, CHINA,* [3]*United Imaging Healthcare, Shanghai, CHINA.*

Aim/Introduction: Emerging evidence suggests neurological sequelae in COVID-19 survivors, yet comprehensive characterization of cerebral metabolic alterations remains limited. This study investigates regional glucose metabolism changes in post-COVID patients using ^{18}F-FDG PET imaging and explores their temporal dynamics. ***Materials and Methods:*** A retrospective analysis included 51 COVID-19 survivors (median age: 68 years; range: 15-93) who underwent ^{18}F-FDG PET-CT scans. Age- and sex-matched healthy controls (HCs) were used for comparison. Regional metabolic patterns were analyzed via SPM8 (cluster-level FWE-corrected, $p<0.05$) and NeuroQ software, excluding functionally susceptible regions (e.g., visual cortex, Broca's area). Subgroup analyses stratified patients into acute (≤1 month), subacute (2-3 months), and chronic (>3 months) phases. ***Results:*** Global metabolic patterns: Compared to HCs, patients exhibited widespread hypometabolism in frontal, temporal, parietal, and occipital lobes ($T = 3.17$-5.62, $p<0.001$) and hypermetabolism in cerebellum, pons, amygdala, and corpus callosum ($T = 3.17$-4.34, $p<0.001$). All patients (51/51) showed 1-31 abnormal metabolic regions across 47 brain areas. Cerebellar/vermis hypermetabolism (82.35%) and frontal hypometabolism (82.35%) predominated. The left medial frontal cortex demonstrated the highest hypometabolic sensitivity (93.33%) in chronic-phase patients. Cerebellar hypermetabolism prevalence declined from 88% (acute) to 73.33% (chronic). Frontal hypometabolism persisted across phases (acute: 80%, subacute: 90.91%, chronic: 100%). ***Conclusion:*** COVID-19 survivors display distinct spatiotemporal metabolic disturbances, marked by persistent frontal hypometabolism and dynamic cerebellar hypermetabolism. These findings suggest prolonged neuroinflammatory or neurodegenerative processes post-infection, highlighting potential biomarkers for long-term neurological monitoring and intervention.

EP-0698

[18F]fluorodeprenyl-D2 PET imaging as a new tool to detect disease activity in GAD65-Ab Autoimmune Encephalitis

J. S. Dorneich[1], *M. Zeinaki*[1], *L. Tagnin*[1], *L. Vogler*[1], *L. Sanzo*[1], *S. Lindner*[1], *R. A. Werner*[1], *G. N. Bischof*[2], *J. A. Gernert*[3], *T. Kümpfel*[3,4], *M. Kerschensteiner*[3,4,5], *E. Kaufmann*[6,7], *M. Brendel*[1,5], *F. Thaler*[3];
[1]*Department of Nuclear Medicine, University Hospital of Munich, Munich, GERMANY,* [2]*Life Molecular Imaging (LMI), R&D, Berlin, GERMANY,* [3]*Institute of Clinical Neuroimmunology, University Hospital, LMU Munich, Munich, GERMANY,* [4]*Biomedical Center, Faculty of Medicine, LMU Munich, Munich, GERMANY,* [5]*Munich Cluster for Systems Neurology (SyNergy), Munich, GERMANY,* [6]*Epilepsy Center, Department of Neurology, LMU University Hospital, Munich, GERMANY,* [7]*Department of Neurology, LMU University Hospital, LMU Munich, Munich, GERMANY.*

Aim/Introduction: Aim of this study is to evaluate the feasibility of [18F]fluorodeprenyl-D2 ([18F]F-DED) positron-emission-tomography (PET) imaging to detect local astrogliosis in autoimmune encephalitis (AIE) associated with antibodies (Abs) to glutamic acid decarboxylase 65 (GAD65) in a monocentric cohort. ***Materials and Methods:*** Dynamic [18F]F-DED PET scans (0-60 min) were obtained from n=22 GAD65-AIE patients, 3 of whom were re-examined during the disease course, and from n=8 healthy controls. The PET images were processed using the PET data analysis software PMOD. Volumes of distribution (VT) were determined using a one-tissue-compartment model (1TC2k) with a carotid image derived input function. Clinical phenotype and severity (mRS, cerebellar score, stiffness score), GAD65-Ab levels, levels of serum Neurofilament light chain (sNfL) as a marker for neuroaxonal damage as well as glial fibrillary acidic protein (GFAP) as a marker for astroglial reactivity were correlated with [18F]F-DED VT. ***Results:*** Patients with GAD65-AIE with different clinical phenotypes were included (temporal lobe epilepsy (TLE)/ limbic encephalitis (LE): n=14; stiff-person syndrome (SPS): n=4; cerebellar ataxia (CA): n=4; n=8 patients clinically exhibited an overlap of at least two of the above mentioned phenotypes) with a median age of 55 years and a median disease duration of 5 years at PET-imaging. 9/22 patients did not receive immunotherapy at the time of PET-imaging. [18F]F-DED VT was significantly increased in the mesiotemporal lobe ($p<0.001$), parahippocampal gyrus ($p<0.001$) and the cortex ($p=0.023$) in patients with GAD65-AIE compared to controls. The cerebellum showed a trend towards [18F]F-DED VT increase in the same contrast ($p=0.081$). Anatomical distribution of [18F]F-DED signals correlated with clinical phenotypes in patients with TLE/LE, showing predominance of [18F]F-DED VT in the mesiotemporal lobe, and patients with CA, showing increased cerebellar tracer uptake - both of which were associated with disease severity. Patients with SPS did not show increased [18F]F-DED signals. Furthermore, a tendency toward a positive correlation between the [18F]F-DED signal and the GFAP levels was observed ($r=0.392$, $p=0.119$). ***Conclusion:*** Dynamic [18F]F-DED PET imaging enables the detection of astroglial inflammatory changes in patients with GAD65-AIE. Regional [18F]F-DED uptake in patients with GAD65-AIE reflects disease phenotype and correlates with disease severity.

EP-0699

Assessment of ^{18}F-UCB-H as a biomarker in focal epilepsy

V. Pakula[1], *C. Vollmar*[2], *L. Bartos*[1], *J. S. Dorneich*[1], *N. Fearns*[2], *S. Lindner*[1], *A. Zwergal*[2], *G. Höglinger*[2], *R. Werner*[1], *J. Rémi*[2], *M. Brendel*[1], *J. Gnörich*[1];
[1]*Department of Nuclear Medicine, LMU University Hospital, Munich, GERMANY,* [2]*Department of Neurology, LMU University Hospital, Munich, GERMANY.*

Aim/Introduction: Synaptic vesicle protein 2A (SV2A) is a universal marker of synaptic density. Recent advances in SV2A-targeted radiotracers have opened new windows into in-vivo synaptic imaging. We compared the SV2A ligand ^{18}F-UCB-H against the clinical gold standard ^{18}F-FDG-PET in patients with pharmaco-resistant, unilateral focal epilepsy to identify optimal imaging windows and post-processing filters for maximizal lesion contrast and diagnostic accuracy. ***Materials and Methods:*** Twenty-nine patients with unilateral focal epilepsy underwent both dynamic ^{18}F-UCB-H-PET (0-60 min) and static ^{18}F-FDG-PET (30-50 min). Of those twenty-nine patients, seven had had levetiracetam (LEV) or brivaracetam (BRV) and even though in some LEV and BRV were discontinued, the ^{18}F-UCB-H uptake was blocked. We extracted time-activity curves from 35 frames across cortical and subcortical regions, calculating Pearson correlation coefficients against ^{18}F-FDG uptake in each time frame. Furthermore, early (0-10 min) and late (30-60 min) ^{18}F-UCB-H images were directly compared to ^{18}F-FDG images. For lesion quantification, individual brains normalized to MNI space were flipped laterally; voxel-wise percentage differences between epileptogenic and contralateral healthy hemispheres were computed. Finally, we evaluated Gaussian smoothing kernels (0-20 mm FWHM) for minimizing background noise while preserving lesion volume and contrast. ***Results:*** In unaffected contralateral regions, late-phase ^{18}F-UCB-H-PET signals showed stronger concordance with ^{18}F-FDG-PET signals than early-phase: ($R=0.62$-0.69 vs. $R=0.49$-0.57) all $p<0.02$. Incremental smoothing up to 8-10 mm FWHM substantially reduced background noise in flipped ^{18}F-UCB-H images, with

only a modest decrease in lesion volume, yielding an optimal lesion-to-background ratio at 8 mm. Within epileptogenic foci, lesion intensity correlated significantly with both early (R=0.58, p=0.010) and late (R=0.48, p=0.036) ^{18}F-UCB-H versus FDG uptake. However, only early ^{18}F-UCB-H lesion volume correlated with FDG lesion volume (R=0.55, p=0.015), whereas late-phase volume did not (R=0.15, p=0.53). In line, ^{18}F-FDG and early ^{18}F-UCB-H-PET visually showed broad, diffuse hypometabolic areas around the epileptogenic zone, whereas late-phase ^{18}F-UCB-H-PET yields much sharper, high-contrast delineation of the lesion. In Patients taking LEV and BRV, ^{18}F-UCB-H will not give a sufficient signal, illustrating the high binding potential of LEV and BRV to the SV2A. ***Conclusion:*** ^{18}F-UCB-H-PET reliably mirrors metabolic patterns in the healthy contralateral hemisphere and, when optimally filtered, enhances lesion contrast in focal epilepsy. Early-phase ^{18}F-UCB-H captures the spatial extent of epileptogenic zones akin to perfusion deficits, while late-phase imaging more selectively reflects synaptic dysfunction. These dual-phase insights position ^{18}F-UCB-H SV2A-PET as a powerful adjunct to ^{18}F-FDG, offering broad lesion mapping and refined synaptic specificity for improved pre-surgical evaluation.

EP-41

e-Poster Area

B: Imaging Clinical Studies -> B6 Endocrinological Imaging Clinical Study -> B61 Endocrinology (including Thyroid Benign)

EP-0700

How sure can we be? - Graves' disease or Multi-nodular Goitre: Usefulness of isotope thyroid scan

A. Chamnan*, V. Pant, F. Naeem, S. Salam, L. Yeung, S. Vinjamuri;*
Royal Liverpool University Hospital, Liverpool, UNITED KINGDOM.

Aim/Introduction: Hyperthyroidism could result from Graves' disease or multi or toxic nodular goitre which are the most common causes. The diagnosis is based on clinical, biochemical and imaging tests. With frequent diagnostic challenges to characterize the aetiology of the hyperthyroidism, a comprehensive approach is essential for accurate characterization including the use of radioactive iodine thyroid scans. ***Materials and Methods:*** A retrospective study involving 517 patients who were referred for a Tc-99m pertechnetate thyroid scan at the Royal Liverpool University Hospital between January 2022 and December 2023 (ages 16 to 92, M:F ratio 145:372). We tabulated and analyzed the initial clinical impressions at referral and the post-pertechnetate thyroid scan findings. ***Results:*** Out of the 517 patients, 194 were referred with possible Graves' disease, 171 with possible MNG, and 152 had non-specific referrals, simply indicating hyperthyroidism without specifying the cause. In 337 out of 365 cases (92.3%), the initial clinical impression aligned with the post-scan findings. This reflects a good clinical assessment based on the value of true positive cases. In 28 patients, the initial clinical assessment differed from the scan results—16 patients had Graves' disease, 6 had MNG, 2 had thyroiditis, and 4 had normal findings, contrary to the initial diagnosis. Among the 152 non-specific hyperthyroid patients, the majority were diagnosed with MNG (74), followed by Graves' disease (63), normal scan findings (10), and thyroiditis (5). ***Conclusion:*** To conclude, our study confirms the clinical value of isotope thyroid scans in the diagnostic evaluation of hyperthyroidism. Despite the fact that the initial clinical impression of the aetiology of hyperthyroidism is frequently accurate, this may need to be revised in a small proportion of patients after the scan, which can impact treatment options, including the choice of medication, surgery, or radioiodine therapy, as well as the appropriate dosage of radioiodine when applicable. We would like to encourage a larger study with different demographic population for better understanding the value of the isotope thyroid scan. ***References:***
1. Iqbal, A., & Rehman, A. (2022, October 3). Thyroid uptake and scan. StatPearls - NCBI Bookshelf. https://www.ncbi.nlm.nih.gov/books/NBK555978/ 2. Medeiros-Neto, G. (2016, September 26). Multinodular Goiter. Endotext - NCBI Bookshelf. https://www.ncbi.nlm.nih.gov/books/NBK285569/.

EP-0701

Revisiting Piga's Criteria for Amiodarone-Induced Thyrotoxicosis Using ^{99m}Tc-Sestamibi Thyroid Scintigraphy: Interobserver Reproducibility and Semiquantitative Analysis

R. Sá e Silva*, J. Escaleira, L. Costa;*
Centro Hospitalar Universitário do Porto, Porto, PORTUGAL.

Aim/Introduction: Amiodarone-induced thyrotoxicosis (AIT) is a well-recognized adverse effect of amiodarone therapy. Piga's criteria classify AIT into 3 types based on the 99mTc-Sestamibi scintigraphic visual pattern: AIT Type 1, Type 2 and Indeterminate. This study aimed to assess the interobserver agreement of AIT classification using Piga's criteria and to explore the utility of semiquantitative analysis. ***Materials and Methods:*** Retrospective, observational study including 21 patients treated with amiodarone (> 3 months), who presented with thyrotoxicosis not attributable to other known causes and that underwent ^{99m}Tc-Sestamibi scintigraphy acquired 10 minutes after radiotracer injection. Two independent observers visually classified each scan according to Piga's criteria: AIT Type 1 (increased uptake), Type 2 (low uptake), or Indeterminate. Interobserver agreement was assessed using Cohen's Kappa coefficient. A semiquantitative analysis (only concordant cases) was performed using regions of interest(ROIs) in the thyroid, upper skull region, and mediastinum (Figure 1). Thyroid-to-skull (TSR) and thyroid-to-mediastinum (TMR) ratios were estimated using both mean and maximum counts. ***Results:*** Observers agreed in 16 of 21 cases (76%), indicating substantial agreement (Cohen's Kappa 0.63; Table I). Among concordant cases, significant differences were found only in the maximum count TMR(p=.026), with higher values in AIT1 compared to AIT2 (p=.020), aligning with the visual pattern (intense vs. reduced uptake). Indeterminate AIT cases didn't display intermediate ratio values; instead, their quantitative parameters often fell below those of AIT2, challenging the assumption that this category represents a visual midpoint (Table II).All observed classification discrepancies occurred between AIT1 and Indeterminate (14%) or AIT2 and Indeterminate(10%)- never between AIT1 and AIT2- highlighting the visual ambiguity and heterogeneity of the Indeterminate group. Discordant cases often showed semiquantitative values that fell between or outside the observed ranges for concordant AIT1 and AIT2 maximum count TMRs, suggesting a potential role for semiquantitative parameters in reducing classification subjectivity. ***Conclusion:*** This study supports the moderate-to-high reproducibility of Piga's visual classification for AIT and identifies maximum count TMR as a promising parameter to support subtype differentiation, especially between AIT1 and AIT2. However, the Indeterminate group remains heterogeneous and poorly defined, both visually and quantitatively. The lack of clear diagnostic resolution, compounded by the fact that clinicians often initiate empirical "cocktail" therapy (e.g., glucocorticoids, antithyroid drugs) without obtaining definitive histological or cytological confirmation, limits the ability to validate imaging-based classification. Prospective studies with larger cohorts and standardized diagnostic confirmation are needed to refine Piga's criteria and validate semi-quantitative thresholds using 99mTc-Sestamibi scintigraphy.

EP-0702

SUVmax utility in parathyroid scintigraphy

M. Kocemba, *M. Tulik, J. Kunikowska;*
Medical University of Warsaw, Warsaw, POLAND.

Aim/Introduction: Hyperparathyroidism is a disease characterized by overproduction of parathormone with clinical manifestation as osteoporosis, renal failure and kidney stones. The only effective form of therapy is surgical parathyroidectomy, which requires localization of the lesions, usually in [^{99m}Tc]Tc-MIBI dual-phase scintigraphy. The aim of this study was to evaluate the use of standardised uptake value (SUV) in parathyroid scintigraphy. ***Materials and Methods:*** This retrospective study included 19 examination performed in 5 men and 14 women (age 19-82, median 65), with clinical and biochemical signs of primary hyperparathyroidism. Serum levels of parathormone, phosphates and calcium were recorded. Dual-phase planar and early and late SPECT/CT examinations after intravenous administration of 600MBq [^{99m}Tc]Tc-MIBI scans were performed between February 2023 and March 2024 on Siemens Intevo Bold. Volumes of parathyroid lesions were measured using postoperative specimen diameters and the ellipsoid formula**.** SUVmax was calculated for each parathyroid lesion following PET/CT protocols. Thyroid SUVmax was also measure idependently for central area of each lobe. Washout percentage was calculated as (late SPECT SUVmax / early SUVmax) x 100% for each lesion and thyroid lobe. Pearson correlation assessed relationships between variables. ***Results:*** Median serum blood level of parathormone, calcium and phosphates were 167 pg/ml(range 78.1-1065), 2.77 mmol/l (range 2.14-3.09) and 0.71 mmol/l (range 0.39-1.25), respectively. Fifteen out of 19 scans were considered positive in initial visual assessment. All patients underwent surgical parathyroidectomy up to 3 months after imaging; histopathology confirmed 17 parathyroid adenomas and 2 parathyroid hyperplasia. Median lesion volume was 0.75 ml (range 0.03-2.73) for positive SPECT/CT examinations and 0.67 ml (range 0.2-1.13) for negative examination; no significant difference was found due to small sample size. Median value of SUVmax for parathyroid adenomas were 5.0 (range 2-11.4) and 2.2 (range 0.8-8.1) for early and late SPECT/CT examinations respectively. For both patients with parathyroid hyperplasia early SUVmax value was 6.3, while late SUVmax values were 4.1 and 2.9. In all patients with adenomas, difference in washout level between thyroid gland and parathyroid lesions was 15.8% (95% CI 9%-22%), statistically significant ($p<0.01$). Early and late SUVmax showed moderate positive correlation ($p<0.05$) with volume of parathyroid lesion ($r=0.42$ and $r=0.6$) and weak negative correlation with calcium serum blood level ($r=-0.35$ and $r=-0.26$). ***Conclusion:*** Parathyroid SUVmax appears to be a promising parameter for the preoperative diagnosis of parathyroid glands. The study needs to be continued and confirmed on a larger group of patients.

EP-0703

Inter-reader Agreement and additive benefit of SPECT or SPECT/CT modality with [^{99m}Tc]Tc-Pertechnetate Scintigraphy Imaging for the Assessment of incidental Thyroid Nodules in a tertiary care center

E. Novruzov, *K. Julian, K. Mattes-György, D. Schmitt, M. Muchalla, M. Schott, C. Antke, F. L. Giesel, E. Mamlins;*
University Hospital Düsseldorf, Düsseldorf, GERMANY.

Aim/Introduction: In central Europe, up to 76% of population exhibit thyroid nodules (TN). The combination of ultrasound findings and thyroid scan imaging are supposed to ensure a cost-effective and reliable prediction of malignancy risk. However, real-world impact of ultrasound findings, i.e. TI-RADS, has raised concerns due to its highly limited reliability and reproducibility. The recent advancements and increasing access of SPECT/CT scanners might contribute to thyroid management. This study aimed to elucidate additive value of SPECT(-CT) imaging in initial evaluation of complex TN cases, particularly on multinodular goiter and difficult-to-characterize solitary nodules. ***Materials and Methods:*** A total of 61 patients (19 males and 42 females with a mean age of 56 (± 17)) with incidental TN were retrospectively enrolled in this study between November 2022 and July 2023, who underwent both conventional planar thyroid scan and SPECT(-CT) imaging. 3 readers with varying experience level selected a target nodule within thyroid gland and evaluated its functionality, ACR TI-RADS categorization and additive benefit of SPECT(-/CT) imaging. Kappa-value for inter-reader agreement (IRA) was interpreted as follows: < 0.01-0.20, slight agreement; 0.21-0.40, fair agreement; 0.41-0.60, moderate agreement; 0.61-0.80, substantial agreement; and 0.81-1.00; almost perfect agreement. ***Results:*** Of the target TNs, 33 (54%) were located in the left thyroid lobe, 5 (8%) in the isthmus and the remaining target TNs (38%) in the right lobe. The median target TN size was 20 mm (10 -59). The target nodule match rate among readers was almost perfect (kappa value 0.81; 95% CI: 0.72 - 0.90). The IRA regarding ACR TI-RADS was moderate with k-value of 0.47 (95% CI: 0.40 - 0.54). The IRA regarding patient referral was substantial among readers with k-value of 0.60, while k-value was even higher at pairwise comparison of experienced readers (k-value: 0.64). IRA regarding the target TN functionality among readers was good with k-value of 0.68 (95%CI: 0.59 - 0.77). IRA involving the less experienced reader revealed only slightly lower reliability scores, i.e. a k-value of 0.61. The correlation with ground truth results revealed comparable results among experienced and less-experienced readers. ***Conclusion:*** Increasing clinical experience of physicians appeared to have a direct correlation with a higher referral rate of SPECT(-CT) imaging, although the additive clinical benefit was only evident for a minority of patients. Hence, SPECT(-CT) imaging might be more suitable for tertiary care centers, as its additive benefit at primary care level would have only negligible effect for patients.

EP-0704

From Image to Outcome: Optimizing [I-131] Therapy in Hyperthyroidism Using Scintigraphic Patterns in Our Experience

S. Alvarez, *G. Mera, E. Ardila, V. Castillo, S. Salcedo, M. Casallas, I. Gomez, J. C. Alonso;*
Hospital General Universitario Gregorio Marañón, Madrid, SPAIN.

Aim/Introduction: To analyze the outcome of [I-131] treatment for hyperthyroidism at our institution, taking into account the different thyroid scintigraphy patterns as well as TSH and free T4 / T3 blood levels. ***Materials and Methods:*** 102 hyperthyroid patients who underwent radioiodine [I-131] treatment after performing a thyroid scintigraphy were selected. Of those, 67 were checked through two follow-up blood tests and clinical examination, success was considered if either hypothyroidism or euthyroidism was achieved. The dose of [I-131] varied from 7 to 20 mCi, and it was calculated by an empirical fixed ranged based mainly on the goiter size and scintigraphy imaging pattern . The 1st and 2nd follow-up blood tests were taken in a mean of 2.4 months and 6.2 months respectively. ***Results:*** Mean age of 67 patients was 57.1 years old, with a female predominance of 74.6% (50 females and 17 males). The results were divided in 3 groups based on the scintigraphy imaging pattern in Graves' disease (GD), toxic adenoma (TA), and toxic multinodular goitre (TMG). For GD patients, a mean dose of 9mCi was used obtaining a success rate of 74.1% (of which 85% were hypothyroidism and 15% euthyroidism). For TA patients, the mean dose was 12mCi, with a 83.3% success rate (40% hypothyroidism and 60% euthyroidism). Lastly, mean dose used on TMG was 16.7mCi, achieving a success rate of 84.8% (39.3% hypothyroidism and 60.7% euthyroidism). 2 patients, 1TMG and 1TA, were treated with a second [I-131] dose achieving euthyroidism and hypothyroidism respectively. ***Conclusion:*** This study indicates that radioiodine [I-131] therapy

is an effective treatment for hyperthyroidism, with overall success rates of 79% .Treatment outcomes varied depending on the underlying etiology. TMG and TA showed slightly higher success rates (84.8% and 83.3%, respectively) compared to GD (74.1%). Notably, GD patients more frequently developed post-treatment hypothyroidism.The imaging pattern on thyroid scintigraphy, in combination with pre-treatment, TSH, free T4, and free T3 levels, proved to be useful in guiding empirical dosing strategies and predicting therapeutic outcomes.

EP-0705

Effectiveness of 18F-Fluorocholine PET/CT (18F-FCH PET/CT) in the Localization of Multiglandular Disease (MGD) in Patients with Hyperparathyroidism.

P. Portilla Merino[1], *C. Lancha Hernández*[2], *L. Giraldo Gonzalez*[1], *J. Otero Gonzalez*[1], *M. Coronado Poggio*[1], *S. Rizkallal Monzon*[1], *J. Cordero*[1], *L. Domínguez Gadea*[1];
[1]*Hospital La Paz, Madrid, SPAIN,* [2]*Hospital La Paz, Hospital Univeristario La Paz, SPAIN.*

Aim/Introduction: The aim of this study was to evaluate the utility of 18F-FCH PET/CT in the preoperative localization of multiglandular disease (MGD) in patients diagnosed with hyperparathyroidism. ***Materials and Methods:*** This retrospective study analyzed data from 159 patients who underwent 18F-FCH PET/CT between April 2019 and June 2024. Among them, 9 patients with MGD were selected based on surgery or 18F-FCH PET/CT results. Clinical, biochemical, and 18F-FCH PET/CT data, as well as preoperative, postoperative, and follow-up data, were collected.18F-FCH PET/CT was considered positive for MGD when two pathological glands were visualized and histologically confirmed; negative when only a single gland was involved, confirmed by pathology and/or clinical follow-up. The mean follow-up time after surgery was 29.5 ± 14.15 months. ***Results:*** The mean age of the patients was 58.55 ± 11.21 years, with 67% females and 33% males. 89% of the patients had primary hyperparathyroidism, while 11% had secondary hyperparathyroidism (due to chronic kidney disease). The average preoperative PTH value was 214.4 (range: 86.7 to 716). All patients met surgical criteria.Of the 9 patients with MGD, 15 glands were removed, all confirmed as adenomas. 3 patients (33.3%) demonstrated MGD (double adenoma) on 18F-FCH PET/CT, which was confirmed histologically (6 glands resected). These cases were considered true positives.3 patients (33.3%) initially underwent surgery for a single adenoma detected by 18F-FCH PET/CT but continued to show elevated postoperative PTH levels. This led to the resection of a second pathological gland during exploration, which ultimately normalized their PTH levels (6 glands resected). These cases were classified as false negatives for double parathyroid adenoma.3 patients (33.3%) had two suspected adenomas on PET/CT; however, after resection of one gland, PTH normalized (3 glands resected). These cases were considered false positives for double parathyroid adenoma. 18F-FCH PET/CT showed a sensitivity of 50% and specificity of 98.04% (153 negatives studies).Gland location: 40% right superior, 33% left superior, 13% left inferior, 7% right inferior, 7% intrathyroidal.Mean postoperative PTH drop: 74.4% ± 9.At follow-up, 89% (8p) had normalized PTH and calcium; 1 CKD patient (11%) showed marked PTH improvement (716 → 144), despite receiving a glandular autoimplant in the forearm. ***Conclusion:*** 18F-fluorocholine PET/CT is useful for localizing double parathyroid adenomas in patients with hyperparathyroidism, although its diagnostic performance is lower compared to single-gland disease.

EP-0706

A study on the construction of a nomogram for predicting the postoperative outcome of unilateral primary aldosteronism based on ^{68}Ga-Pentixafor PET/CT imaging targeting CXCR4

Y. Jin[1], *Y. Yang*[1], *Y. Yang*[1], *J. Yang*[1], *T. Long*[1], *S. Hu*[1,2,3];
[1]*Department of Nuclear Medicine, Xiangya Hospital, Central South University, Changsha, Hunan, CHINA,* [2]*Department of Dermatology, Xiangya Hospital, Central South University, Changsha, Hunan, CHINA,* [3]*Department of Oncology, Xiangya Hospital, Central South University, Changsha, Hunan, CHINA.*

Aim/Introduction: Primary aldosteronism (PA) is a clinical syndrome characterized by hypertension with or without hypokalemia. It has a large patient base and can easily cause damage to target organs such as the heart, brain, and kidneys. Unilateral PA(UPA) is primarily treated with surgery, but more than half of the patients continue to suffer from hypertension after the operation. Therefore, predicting the postoperative efficacy of UPA can help doctors and patients make treatment decisions and identify patients who need close follow-up. This study aims to construct a nomogram model based on the clinical data of UPA patients and ^{68}Ga-Pentixafor PET/CT data targeting CXCR4 to predict the postoperative efficacy of UPA, thereby providing precise guidance for treatment decisions and patient follow-up management. ***Materials and Methods:*** A retrospective analysis was conducted on patients with UPA who underwent surgery at Xiangya Hospital of Central South University from November 2021 to April 2024. Preoperative CXCR4 data, clinical indicators, and 6-month postoperative follow-up data were collected. Patients were divided into clinical cure and non-cure groups based on their postoperative blood pressure status. Univariate and multivariate logistic regression analyses were performed using R language to construct a nomogram prediction model. The predictive performance and clinical applicability of the model were evaluated using ROC curves (AUC), calibration curves, and decision curves. ***Results:*** A total of 93 patients with unilateral PA were included, of whom 53 (57%) achieved clinical cure and 39 (43%) did not. The final factors included in the nomogram were age, SULmax,creatinine,aldosterone/renin ratio (ARR), duration of hypertension, and estimated glomerular filtration rate (eGFR). The AUC of the model in the training and validation sets were 0.71 and 0.76, respectively, with a sensitivity of 0.68-0.64 and a specificity of 0.77-0.62. The calibration curve showed good consistency between predicted and actual results, and the decision curve confirmed the clinical net benefit of the model. ***Conclusion:*** The nomogram constructed based on ^{68}Ga-Pentixafor PET/CT imaging targeting CXCR4 can effectively predict the postoperative blood pressure outcome of UPA patients, providing a quantitative basis for individualized treatment decisions and postoperative management.

EP-0707

Tc99m-pertechnetate thyroid imaging on a 3D-ring CZT-based SPECT/CT system is a superior alternative to conventional thyroid scintigraphy

A. Harteveld, *A. van de Burgt, M. Segbers, F. A. Verburg;
Erasmus MC, Rotterdam, NETHERLANDS.*

Aim/Introduction: Two-dimensional (2D) planar thyroid scintigraphy using a single or dual detector-head gamma camera systems with scintillation-based detectors is the standard clinical practice. However, uptake in overlapping structures as well as attenuation of photons by overlying tissue limits interpretation. The recent introduction of 12-headed ring-shaped cadmium-zinc-telluride (CZT) based single-photon emission computed tomography/computed tomography (SPECT/CT) systems enables three-dimensional (3D) SPECT imaging with similar acquisition times to conventional planar scintigraphy due to the higher sensitivity and energy resolution [1]. This study evaluated thyroid

scintigraphy using a 3D-CZT ring system through phantom experiments and scanning the same patient on both scanners. ***Materials and Methods:*** Phantom experiments: utilized a custom thyroid phantom including hot and cold spots filled with 0.11 MBq/mL (3.6 MBq in a volume of 33 mL water; assuming ~2% uptake of 180 MBq in patients) Tc99m-pertechnetate and scanned on a 3D-CZT ring SPECT/CT scanner. A 20-minute SPECT acquisition was performed with/without Focus mode. Retrospective 5, 10, 15 minutes SPECT reconstructions were made from list-mode data. All SPECT reconstructions were performed using the manufacturer recommended protocol. Recovery coefficients (RCs) were calculated for a CT-based volume-of-interest of a cold region. Dual patient scans: involved three patients referred for Tc99m-pertechnetate thyroid exams. After informed consent, patients underwent 10-minute planar imaging on a conventional gamma camera and 10-minute SPECT/CT with Focus mode and low-dose CT for localization and attenuation correction on a 3D-CZT system. Scans were performed 20 minutes after injection of 180 MBq (range 178-197) Tc99m-pertechnetate. Two experienced nuclear medicine physicians rated the images. ***Results:*** Phantom images with 20-minute acquisitions showed good quality and clear distinction of hot and cold regions. Reducing acquisition time to 5 minutes did not significantly affect image quality. Cold spot RCs ranged from 0.816-0.819 and 0.930-0.934 between the different acquisition times with non-Focus and Focus mode, respectively. Focus mode also showed visually greatly improved recovery of the cold regions compared to non-focused acquisitions. The patient scans demonstrated that 3D-CZT images were rated equal to or better than conventional 2D planar images. Additionally, 3D imaging combined with CT-based anatomical details provided significant added diagnostic value with findings missed on planar scintigraphy. ***Conclusion:*** Preliminary results showed that thyroid Tc99m-pertechnetate imaging using the 3D-CZT ring system with Focus mode and factory SPECT reconstruction parameters achieves superior image quality compared to current 2D planar protocols and offers additional diagnostic information while maintaining similar acquisition times. ***References:*** [1] Zorz et al. EJNMMI Physics 2024.

EP-0708

Radioguided Occult Lesion Localization (R.O.L.L.) Technique for Minimal Invasive Parathyroidectomy (M.I.P.). Our Experience

M. Fornito[1], *G. Giordano*[2], *M. Trovato*[3], *M. Iago*[1], *S. Fiorino*[1], *F. Stracuzzi*[1];
[1]*ARNAS GARIBALDI CATANIA Nuclear Medicine - PET/TC center dep., Catania, ITALY,* [2]*ARNAS GARIBALDI CATANIA Interventional radiology, Catania, ITALY,* [3]*ARNAS GARIBALDI CATANIA Oncological Surgery, Catania, ITALY.*

Aim/Introduction: Radio-guided occult lesion localization (R.O.L.L.) is a localization technique, originally described for non-palpable breast lesions, based on the direct injection of radioactive particles such as Tc-99m-labeled albumin (MAA) into the lesion guided by monitoring methods (US/CT) to accurately identify and localize parathyroid lesions that may be difficult to detect through conventional method and during surgery. M.I.P. constitutes one of the main surgical approaches for the patient with primary hyperparathyroidism (PHPT) especially in complicated case as ectopic/atypical site of adenoma, small adenomas, recurrences or precedent neck surgery. This study assesses the efficacy of R.O.L.L. in facilitating M.I.P. and investigating the technical feasibility, effectiveness and safety as an adjuvant method in surgical excision of parathyroid adenoma. ***Materials and Methods:*** We analysed clinical outcomes from a cohort of ten patients with PHPT due to a singular adenoma documented by MIBISPET/CT, undergoing parathyroidectomy with R.O.L.L., focusing on localization success rate, operative and hospitalization time and post-operative complications. Four patients had previously undergone thyroid/parathyroid surgery; three had ectopic/atypical site parathyroid adenoma; three wanted minimal invasive surgery for aesthetic reasons. ^{99m}Tc-MAA was administered in the pathological parathyroid gland under US-guidance in eight patients and under CT-guidance in two ectopic adenoma. All of the injected lesions were located over the skin with Gamma camera imaging. During the surgery, parathyroid adenomas were searched for and identified with an intraoperative gamma probe that easily guided the surgeon to the target lesions. ***Results:*** Mean operation time (from incision to excision of the adenoma) was 29 ± 8 min. Serum intraoperative parathyroid hormone (PTH) levels measured before incision and 20 min after excision of adenoma decreased over 50%. All intraoperative histopathologic examination confirmed the presence of parathyroid tissue. ***Conclusion:*** Our findings demonstrate that ROLL-MIP significantly enhances the detection of ectopic or small parathyroid adenoma, especially in case of previous neck surgery, leading to improved surgical precision and reduced invasiveness. It also shortens operative and anaesthesia time and hospitalization time (no longer than 1 day) and hospital costs and not impair the intra- e post-operative histopathologic examination of the parathyroid glands allowing immediate verification of parathyroid adenoma removal. Additionally, patients experienced shorter recovery time and lower rates of complication compared to traditional approaches. Overall, the ROLL-MIP technique represent a valuable advancement in the surgical management of hyperparathyroidism, promoting more effective and less invasive options. ***References:*** Saizl.B. et al Radio-guided procedure in minimally invasive surgery for primary hyperparathyroidism. 2023 Cir Esp.

EP-0709

Assessment of oral [^{18}F]FDG administration for examining gastrointestinal glucose uptake, biodistribution and dynamic glucose metabolism using total-body PET/CT.

M. Brogaard[1], *P. Cramon*[1], *T. Andersen*[1], *U. Lindberg*[1], *F. Andersen*[1], *J. Brittain*[1], *M. Sørensen*[2], *C. Nguyen*[2], *H. Larsson*[1], *J. Madsen*[1], *I. Law*[1], *L. Gasbjerg*[1];
[1]*Rigshospitalet, 2100 Copenhagen, DENMARK,* [2]*Nuklearmedicin, Rigshospitalet, Copenhagen, DENMARK.*

Aim/Introduction: This study investigates oral administration of 2-[18F]fluoro-2-deoxy-D-glucose ([^{18}F]FDG) as a method for assessing gastrointestinal glucose uptake, dynamic glucose metabolism, and the biodistribution of glucose in all organs using total-body positron emission tomography (PET)/computed tomography (CT). Additionally, we evaluate the possibility of incorporating an oral glucose tolerance test (OGTT) to provide more comprehensive understanding of glucose metabolism in healthy controls. We compare the dynamics and distribution of orally versus intravenously (i.v) administered [^{18}F]FDG and examine how the OGTT may enhance the assessment of dynamic glucose metabolism. ***Materials and Methods:*** Four healthy participants (three women and one man, aged 20-27 years) underwent three separate total-body PET/CT scans (Biograph Vision Quadra, Siemens Healthineers, Erlangen, German), A-C. Another four healthy participants are enrolled with scheduled scans in May-June, 2025. Participants completed a food diary for two days leading up to the scan and consumed a minimum of 150 g of carbohydrates on the day before the scan. Scan A was preceded by intravenous administration of [^{18}F]FDG. Scans B and C were preceded by oral administration of [^{18}F]FDG, which was encapsulated in a gelatine capsule and ingested with a maximum of 100 mL of water. During scan C, the participants also underwent a 75 g-oral glucose tolerance test (250 ml). During all scans, glucose levels were monitored, and blood samples were collected at 15-minute intervals to measure glucagon, insulin, glucose-dependent insulinotropic polypeptide, and glucagon-

like peptide-1. The PET/CT scans were conducted over a 2-hour period started immediately after [18F]FDG administration, followed by a 60-minute break and finished with a 10-minute scan at 3 hours. ***Results:*** Eight oral gelatine capsules were produced with activity levels ranging from 47-56 megabecqurel. All capsules were ingested orally within few minutes after release from the radiochemistry. All scans (A-C) resulted in usable PET/CT data showing the distribution of [18F]FDG to all expected tissues of the body. Furthermore, during oral glucose ingestion (scan C), gastric [18F]FDG retention, slower uptake [18F]FDG and higher blood glucose levels were observed. ***Conclusion:*** This study demonstrated that [18F]FDG capsules ingested orally can be used to assess the biodistribution of [18F]FDG. As expected, we observed gastric [18F]FDG retention, slower [18F]FDG uptake and increased blood glucose levels following oral glucose ingestion.

EP-0710

Semiquantitative analysis of ^{18}F-FCH PET/CT in the Dual-Time-Point protocol in patients with primary hyperparathyroidism

E. Campaña Díaz[1], *P. García-Talavera San Miguel*[1], *F. Gómez-Caminero López*[1], *J. Álvarez Pérez*[1], *C. Montes Fuentes*[1], *E. Martin Gallardo*[2], *J. Badell Martínez*[1], *S. Rama Alonso*[1], *A. Peñaherrera Cepeda*[1], *J. Villanueva Curto*[1], *F. Caltagirone*[1], *B. Santos García*[1], *M. Tamayo Alonso*[1], *M. Martín Gómez*[1];
[1]*Hospital Universitario de Salamanca, Salamanca, SPAIN,*
[2]*Professor at UCIII y UPComillas, Madrid, SPAIN.*

Aim/Introduction: To evaluate the difference in parathyroid visualization on ^{18}F-FCH PET/CT images obtained at 5 and 60 min. To analyze through semi-quantitative analysis, the uptake at different time points of parathyroid glands, lymph nodes, and thyroid nodules. ***Materials and Methods:*** We included 74 patients (59 females; 60.11±12.82 years) in whom ^{18}F-FCH PET/CT was performed for pre-surgical localization of PHPT. Standard ^{18}F-FCH images were acquired 5 and 60 minutes after 185 MBq intravenous administration. Early and delayed images were assessed semiquantitatively by means of calculation of SUVmax and SUVpeak of pathological parathyroid (P-SUVmax, P-SUVpeak), thyroid gland SUVpeak (T-SUVpeak), mediastinum SUVpeak (M-SUVpeak), lymph nodes (N-SUVmax, N-SUVmean) and thyroid nodules (NT-SUVmax, NT-SUVmean). SUV ratios were calculated with thyroid and mediastinum. The diagnostic performance of the ^{18}F-FCH PET/CT to discriminate pathological parathyroid gland vs lymph node and thyroid nodule was evaluated by analysis of the receiver operating characteristic (ROC) curve analyzing P-SUVpeak/M-SUVpeak vs N-SUVpeak/M-SUVpeak, P-SUVmax/T-SUVpeak vs NT-SUVmax/T-SUVpeak. ***Results:*** The ROC curve of PET/CT quantitative parameters for the diagnosis of HPT and lesions showed that the P-SUVpeak/M-SUVpeak vs N-SUVpeak/M-SUVpeak ratios and P-SUVmax/T-SUVpeak vs NT-SUVmax/T-SUVpeak ratios for 60 min imaging has a higher accuracy compared to the 5 min imaging. The AUC for P-SUVpeak/M-SUVpeak vs N-SUVpeak/M-SUVpeak was 0.7 in the early images (sensitivity 67% and specificity 72%) and 0.8 in delayed (sensitivity 69% and specificity 85%), and for P-SUVmax/T-SUVpeak vs NT-SUVmax/T-SUVpeak 0.7 in the early images (sensitivity 65% and specificity 60%) and 0.8 in delayed (sensitivity 65% and specificity 87%). PET/CT quantitative parameters can distinguish parathyroid adenoma, lymph nodes and thyroid nodules. ***Conclusion:*** Semiquantitative parameters in PET/CT at 60 min have more advantages in assisting the pathological diagnosis and clinical treatment of HPT.

EP-0711

Early-phase [^{18}F]Fluorethyltyrosine positron emission tomography for localisation of corticotroph pituitary adenomas in Cushing's disease

F. Völter, *J. R. O. L. Schweizer, I. Stüfchen, A. Bollenbacher, E. Nowak, K. Ritzel, J. Thorsteinsdottir, M. Theodoropoulou, M. Reincke, N. L. Albert;*
Ludwig-Maximilian-Universität, Munich, GERMANY.

Aim/Introduction: The preoperative localisation of ACTH-producing pituitary adenomas remains challenging. Magnetic resonance imaging and inferior petrosal sinus sampling correctly localise up to three of four ACTH-producing adenomas. Unclear preoperative findings of ACTH-producing pituitary adenomas often result in extended resection areas and postoperative pituitary insufficiency. We therefore aimed to evaluate the potential of [^{18}F]Fluorethyltyrosine positron emission tomography ([^{18}F]FET PET) in localising ACTH-producing pituitary adenomas in patients with first diagnosis and with recurrent Cushing's disease. ***Materials and Methods:*** [18F]FET PET/CT was conducted in 24 patients with Cushing's disease, 14 patients with a primary diagnosis, 9 patients with recurrent disease and 1 patient with Cyclic Cushing's syndrome. Dynamic PET images were acquired 0-40 min after injection with a mean injected dose of 166 MBq. Maximal tumor-to-background ratios (TBRmax) were determined comparing maximum standardized uptake values of pituitary adenomas to mean standardized uptake values of the right frontal and temporal lobe. Numeric values were reported with median (interquartile range). ***Results:*** In all 24 patients, a focal radioligand uptake was noted in the intrasellar region (median TBRmax 6.8 (6.0-8.2)) with a mean maximum uptake during the first minute post injection. At the time of imaging, the median ACTH was 59.0 pg/mL (40.0-112), the median cortisol was 14.4 µg/dL (7.7-26.9). Eleven of the 24 patients were receiving adrenostatic therapy at the time of imaging. 10/14 patients with a first diagnosis of Cushing's disease underwent transsphenoidal surgery until April 2025. 3 patients are still awaiting surgery, 1 patient refused surgery. In all operated patients, the focal intrasellar hotspot was consistent with the histopathologically proven ACTH-producing adenoma. All operated patients showed a postoperative remission with a median basal ACTH of 7.0 pg/mL (4.0 - 10.5) and cortisol of 1.1 µg/dL (0.6 - 2.8). No patient experienced a postoperative anterior pituitary insufficiency. ***Conclusion:*** Functional imaging with [^{18}F]FET PET can be effective in localising ACTH-producing pituitary adenomas and can add valuable information to MRI and inferior petrosal sinus sampling.

EP-0712

Metabolic imaging of brown adipose tissue in female patients treated for obesity with tirzepatide

L. Lezaic[1], *R. Herman*[2], *U. Begus*[1], *S. Rep*[1], *I. Slodnjak*[1], *B. Trebec Lukman*[1], *M. Jensterle Sever*[2], *A. Janez*[2];
[1]*University Medical Centre Ljubljana, Division of Nuclear Medicine, Ljubljana, SLOVENIA,* [2]*University Medical Centre Ljubljana, Department of Endocrinology, Diabetes and Metabolic Diseases, Ljubljana, SLOVENIA.*

Aim/Introduction: Obesity is a common, chronic and relapsing disease with multifactorial etiology. Recently, potent incretin-based therapies have been successfully introduced into the pharmacological treatment of the condition. Pharmacodynamic mechanisms of action include reduced hunger and delayed gastric emptying, while there is no solid evidence for the purported mechanisms of increase in energy expenditure. In this context, emerging data suggest that brown adipose tissue (BAT) may represent a promising therapeutic target. The aim of the study is to assess BAT changes during obesity treatment with the dual GIP/GLP-1 agonist tirzepatide, to identify factors influencing these changes and to develop optimal BAT imaging protocol for obesity

research. ***Materials and Methods:*** Forty female patients with an indication for pharmacological treatment of obesity per EASO guidelines underwent controlled 1-hour hypothermia according to previously determined appropriate threshold for BAT activation (cooling vest, controlled vest and room temperature), after which 0,8 MBq/kg of [^{18}F]FDG was injected. Cooling was continued for further 1-hour period and during PET/CT acquisition (skull base - upper mediastinum). Metabolic activity (SUVmax, SUV mean), volume and total glycolitic activity (TGA) of the BAT was assessed per CT-based segmentation. Patient body mass index (BMI), age, blood glucose and vest temperature were compared according to presence or absence of activated BAT by a non-parametric test (p<0,05 considered for statistical significance). ***Results:*** At the time of analysis, 30 patients completed enrollment. In 10 patients, BAT was detected on PET/CT imaging (SUVmax 5,4±1,5; SUVmean 2,2±0,3; volume 51,8±34,9 ml; TGA 122±87,4 g). No significant difference (p=NS) was found for patient age (38,3±5,6 vs 41±8,0 years), BMI (35,5±3,7 vs 37,6±3,8), blood glucose (5,6±0,3 vs 5,4±0,6 mmol/L) and vest temperature (10,2±2,0 vs 9,9±1,9°C) between activated and non-activated BAT. ***Conclusion:*** BAT was activated in one third of patients; at the time of analysis no included physiological parameters were found to predict the BAT activation. After completed enrollment, patients will undergo randomization and reevaluation (including repeated imaging) for a placebo-controlled study to determine the role of BAT in treatment of obesity with tirzepatide.

EP-0713

Diagnostic value of [^{18}F]FET PET/CT in patients with negative or inconclusive MR imaging for pituitary neuroendocrine tumours

L. Lezaic[1], *A. Kunst*[1], *K. Surlan Popovic*[2], *T. Kocjan*[3], *R. Bosnjak*[4], *S. Rep*[1];
[1]*University Medical Centre Ljubljana, Division of Nuclear Medicine, Ljubljana, SLOVENIA,* [2]*University Medical Centre Ljubljana, Institute of Radiology, Ljubljana, SLOVENIA,* [3]*University Medical Centre Ljubljana, Department of Endocrinology, Diabetes and Metabolic Diseases, Ljubljana, SLOVENIA,* [4]*University Medical Centre Ljubljana, Department of Neurosurgery, Ljubljana, SLOVENIA.*

Aim/Introduction: Accurate localization of pituitary neuroendocrine tumours (pitNET) aids significantly in surgery planning and adds to diagnostic certainty, in particular when MRI as an imaging modality of choice is negative or inconclusive. Recently, PET imaging with [^{18}F]fluoroethylthyrosine (FET) was introduced for molecular imaging of pitNET in this setting, but is performed typically on PET/MR equipment to enable optimal fusion of molecular and structural imaging modality of choice with the additional benefit of improved spatial resolution of modern PET detectors. The aim of this study was to evaluate diagnostic performance of conventional PET/CT imaging in this setting. ***Materials and Methods:*** Patients with known or suspected de novo or residual pitNET and negative or inconclusive MRI examination were referred for [^{18}F]FET PET/CT by the multidisciplinary team. After a 4-hour fast, patients were injected with [^{18}F]FET (2 MBq/kg body weight); after 20 minutes, a 20-minute acquisition of the head was performed. PET reconstruction was optimized for small lesion imaging using an appropriate in-line pixel size matrix, time-of-flight and point-spread-function optimization per vendor-specific algorithm; low-dose CT parameters were not altered (120 kEv, 35 mAs, vendor-specific dose reduction algorithm). Results of [^{18}F]FET PET/CT were correlated to MRI findings, postoperative histology and biochemistry 6-month follow-up. ***Results:*** Twelve patients (10 female) were enrolled: 4 with de novo pitNET (2 ACTH-, 2 GH-secreting), 8 after prior surgery for pitNET (4 ACTH-, 4 GH-secreting). [^{18}F]FET PET/CT was positive in 7/12 patients (6 ACTH-, 1 GH-secreting). Six patients with positive findings underwent surgery (5 ACTH-, 1 GH-secreting); histology was positive in 4 (all ACTH-secreting). On follow-up, 3 patients were considered cured (2 still completing follow-up) and persistence of hormone oversecretion was found in the remaining 3 patients. ***Conclusion:*** [^{18}F]FET PET/CT is a useful molecular imaging method in patients with de novo or residual pitNET and negative or inconclusive MRI findings. Diagnostic performance is comparable to one performed on dedicated PET/MR equipment.

EP-0714

Assessing the value of [^{99m}Tc]Tc-MIBI/ Na[^{99m}Tc]TcO4 SPECT/CT in parathyroid imaging - a new approach on the dual-tracer method

A. Dyczka*, A. Aulich, Z. Adamczewski;*
Nuclear Medicine Department, Medical University of Lodz, Lodz, POLAND.

Aim/Introduction: The current standard method in hyperfunctioning parathyroid glands imaging is the combination of [^{99m}Tc]Tc-MIBI SPECT/CT and cervical ultrasonography (cUS). However, [^{99m}Tc]Tc-MIBI scintigraphy has certain limitations, particularly in the presence of thyroid nodules, whereas cUS is strongly dependent on physician's experience. Alternative imaging techniques may be beneficial. These include dual-tracer subtraction scintigraphy with [^{99m}Tc]Tc-MIBI and Na[^{123}I]I performed in one-day protocol. Though, this technique adds additional radiation exposure to the thyroid and is more expensive. The aim of this study is to evaluate the usefulness of performing additional Na[^{99m}Tc]TcO4 SPECT/CT after standard combination of [^{99m}Tc]Tc-MIBI SPECT/CT and cUS in order to improve the efficiency of detecting parathyroid adenomas and/or hyperplasia in inconclusive cases. ***Materials and Methods:*** We retrospectively analysed 52 patients (44 female, 8 male) who underwent parathyroid scintigraphy at the Nuclear Medicine Department Medical University of Lodz between 2022 and 2024. The study consists of patients, in whose cases [^{99m}Tc]Tc-MIBI SPECT/CT in combination with cUS did not provide a clear outcome confirming or excluding the presence of hyperactive parathyroid glands. The patients underwent additional 111MBq Na[^{99m}Tc]TcO4 SPECT/CT imaging at least 24 hours after [^{99m}Tc]Tc-MIBI SPECT/CT. Radiotracer accumulation in both studies was then compared visually, using localization CT to correctly superimpose the scintigraphic images. ***Results:*** Out of 52 patients included in the study, 38 had positive scintigraphy results: 28 patients had a confirmed diagnosis of singular adenoma or multiglandular disease and in one case parathyroid cancer, 5 patients did not qualify for surgery due to comorbidities. At present, it has not been possible to determine the further course of action for the 5 remaining patients 14 out of 52 patients had negative scintigraphy results: 7 patients had either biopsy or further imaging confirming our results, 4 patients had cUS suggesting hyperfunctioning parathyroid glands, which did not appear in SPECT/CT probably due to limited spatial resolution, 3 patients underwent surgery with post-operative diagnosis of hyperfunctioning parathyroid glands. ***Conclusion:*** This study demonstrates that additional Na[^{99m}Tc]TcO4 SPECT/CT can be valuable in patients with inconclusive results in [^{99m}Tc]Tc-MIBI SPECT/CT (evaluated in combination with cUS) both to confirm and exclude the presence of hyperfunctioning parathyroid glands. It offers lower radiation exposure compared with Na[^{123}I]I scintigraphy and is more cost-effective. This method not only allows for determining the exact location of the parathyroid glands, which can lead to minimally invasive parathyroidectomy but also reduces the risk of false-positive results.

EP-0715

Concordance Between I-123/Tc-99m Sestamibi Subtraction SPECT/CT and Histopathology in Localizing Single Parathyroid Adenomas

A. Hassan, *A. W. Alessi, E. Wahab, S. J. Hughes;*
Queen Elizabeth Hospital Birmingham, Birmingham, UNITED KINGDOM.

Aim/Introduction: Accurate preoperative localization of parathyroid adenomas has shifted the surgical paradigm from conventional four-gland exploration to focused, minimally invasive parathyroidectomy. Functional imaging plays a critical role in enabling this transition by guiding targeted surgical approaches.[1, 2] I-123/Tc-99m sestamibi subtraction SPECT/CT is among the most widely adopted modalities for this purpose, offering improved spatial resolution and anatomical correlation over traditional planar scintigraphy.[3] This study evaluates the diagnostic accuracy of I-123/Tc-99m sestamibi subtraction SPECT/CT in localizing single parathyroid adenomas, using histopathological confirmation and surgical findings. ***Materials and Methods:*** This single-institution retrospective cohort study reviewed 72 consecutive patients who underwent preoperative I-123/Tc-99m sestamibi subtraction SPECT/CT and parathyroidectomy between January 2012 and October 2024. Only patients with histopathologically confirmed parathyroid adenomas were included. Imaging results were compared to intraoperative findings and histology to assess concordance. Sensitivity, positive predictive value (PPV), and overall diagnostic accuracy were calculated. Preoperative and postoperative serum calcium and parathyroid hormone (PTH) levels were compared to evaluate surgical efficacy. The true positive group was defined as patients with positive imaging and histologically confirmed adenomas; the false negative group was defined as patients with negative imaging but positive histology. ***Results:*** Of 72 patients, 59 were true positives and 13 were false negatives. The sensitivity of SPECT/CT in localizing parathyroid adenomas was 82%, with a PPV of 92% and an diagnostic accuracy of 77%. The median weight of resected glands in the true positive group was 0.5 g (range, 0.2-1.6 g), while the false negative group had a mean weight of 0.7 g (range, 0.2-1.7 g). Surgical efficacy was achieved in 97% of patients. Median serum calcium levels decreased from 2.8 mmol/L preoperatively to 2.4 mmol/L postoperatively ($p < 0.0001$), and median PTH levels declined from 13.8 to 4.0 pmol/L ($p < 0.0001$), confirming surgical efficacy. ***Conclusion:*** I-123/Tc-99m sestamibi subtraction SPECT/CT demonstrates high sensitivity and positive predictive value in preoperative localization of single parathyroid adenomas, even for low-weight lesions. The observed improvement in biochemical markers further supports its clinical utility in managing primary hyperparathyroidism through targeted surgery. ***References:*** [1] Cheung et al. A meta-analysis of preoperative localization techniques for patients with primary hyperparathyroidism. Ann Surg Oncol. 2012;19(2):577-83. https://doi.org/10.1245/s10434-011-2009-1 [2] Rodgers et al. Improved preoperative planning for directed parathyroidectomy with 4D CT. Surgery. 2006;140(6):932-40. https://doi.org/10.1016/j.surg.2006.08.021 [3] Lavely et al. Comparison of SPECT/CT, SPECT, and planar imaging with single- and dual-phase 99mTc-sestamibi parathyroid scintigraphy. J Nucl Med. 2007;48(7):1084-9. https://doi.org/10.2967/jnumed.106.037457.

EP-0716

New insights into malignancy risk in trapping-only versus hypofunctioning nodules

L. Sobral Torres, *R. Nunes, J. Maria Veloso Trevisan, R. Albergueiro, A. Oliveira, P. Soeiro;*
Unidade Local de Saúde São João, Porto, PORTUGAL.

Aim/Introduction: Thyroid scintigraphy with Na[^{131}I]I and Na[^{99m}Tc]TcO_4 remains fundamental for evaluating the functional status of thyroid nodules. Hypofunctioning nodules—demonstrating reduced uptake of both tracers—are associated with a higher malignancy risk. Trapping-only nodules, characterized by increased Na[^{99m}Tc]TcO_4 uptake but reduced Na[^{131}I]I uptake, have also been proposed to carry malignant potential, although likely lower than that of hypofunctioning nodules. This study aims to compare malignancy rates between trapping-only and hypofunctioning nodules. ***Materials and Methods:*** A single-center retrospective observational study was conducted, including adult patients who underwent thyroid scintigraphy between January 2020 and June 2024. Patients were included if there was evidence on scintigraphy of trapping-only or hypofunctioning nodules corresponding to a nodule on ultrasound. Patients were excluded if cytological or histopathological analysis was not available. Demographic, biochemical and clinical data were collected, including thyroid medication use, ultrasound findings and results of fine-needle aspiration cytology (FNAC) and/or histopathological analysis following surgery. A descriptive analysis was performed using boxplots for numerical variables and contingency tables for categorical variables. ***Results:*** Eighty patients were included: 36 with trapping-only nodules and 44 with hypofunctioning nodules. In the trapping-only group, 64% were female (mean age: 59±13 years) and 75% had subclinical hyperthyroidism. The main cause was multinodular toxic goiter (70%), followed by Graves' disease (19%). The average nodule size was 22±10 mm. Using ACR-TIRADS, 50% were classified as TIRADS 3, 39% TIRADS 4, and 11% TIRADS 2. Radioiodine uptake average was 41±16%. Most nodules (97%) were benign and one nodule (3%) was suspicious and confirmed as a hyalinizing trabecular tumor, a low-risk follicular cell-derived neoplasm. In the hypofunctioning group, 86% were female (mean age: 61±13 years) and 95% had subclinical hyperthyroidism. Multinodular toxic goiter accounted for 89% and Graves' disease for 9%. The average nodule size was 29±10 mm. Using ACR-TIRADS, 70% were classified as TIRADS 3, 28% TIRADS 4, and 2% TIRADS 5. Radioiodine uptake average was 44±15%. Benign pathology was found in 91%, borderline lesions (NIFTP) in 7%, and malignancy (papillary carcinoma) in 2%. ***Conclusion:*** Our analysis shows similar malignancy risk for trapping-only nodules and hypofunctioning ones, thereby justifying an equivalent clinical approach.

EP-0717

Preoperative localisation of hyperfunctioning parathyroids: Scintigraphy or 4D Computed Tomography?

O. Silva, *I. Ferreira, S. Carmona, A. I. Santos;*
Hospital Garcia de Orta, Almada, PORTUGAL.

Aim/Introduction: Accurate identification of hyperfunctioning parathyroid glands is essential before surgical treatment. The most widely used imaging modality is parathyroid scintigraphy (combined with cervical ultrasonography), but four-dimensional computed tomography (4D CT) has emerged. We aimed to compare the results of parathyroid scintigraphy and 4D CT in our institution. ***Materials and Methods:*** A retrospective study was conducted on patients with a diagnosis of hyperparathyroidism. Between January 2019 and April 2025, all patients underwent dual-phase parathyroid scintigraphy with [^{99m}Tc]Tc-Sestamibi (and when necessary, additional thyroid scintigraphy with Na[^{99m}Tc]TcO_4 was performed) and 4D CT. Patients who underwent the two imaging tests more than one year apart and had a variation in PTH levels equal to or greater than 10% were excluded. For each exam, the number of hyperfunction parathyroid glands and their localisation were analysed, as well as the outcome of surgery (when applicable). Statistical analysis was performed using IBM SPSS Statistics, Version 30.0. ***Results:*** A total of 26 patients were included, of whom 21(80.8%) were women. The mean age at the time of parathyroid scintigraphy was 62(±13.5)years. The time interval between the two imaging exams had a median of 174[P25:52;P75:330]days, and the difference in PTH levels showed a median of 3.5%[P25:0.0;P75:14.85%].Ten(38.5%) of the

parathyroid scintigraphies performed were negative, 10 identified one hyperfunctioning gland (one in an ectopic location), and 6(23%) identified two or more hyperfunctioning glands. Regarding the 4D CT scans, 5(19.2%) were negative, 14(53.9%) identified only one parathyroid gland (including one ectopic gland), and 7(26.9%) identified two or more hyperfunctioning glands. Concordance between scintigraphy and 4D CT findings was observed in 17(65.4%) patients. A significant correlation was found between the results of parathyroid scintigraphy and 4D CT (Pearson Chi-Square: p<0.001).Among the 10(38.5%) patients who underwent surgery, parathyroid scintigraphy findings were concordant with histopathological results in 6 cases (60%), while 4D CT findings showed concordance in 7(70%) cases. ***Conclusion:*** Although 4D CT identified more hyperfunction parathyroid glands, parathyroid scintigraphy with [^{99m}Tc]Tc-MIBI demonstrated a significant correlation with 4D CT results in the preoperative localisation of hyperfunctioning parathyroid glands and has the added value of allowing radioguided minimally invasive surgery. It also provides a lower radiation dose (on average, 5-8 mSv for scintigraphy and 10-20 mSv for 4D CT, according to literature).Further prospective studies with larger cohorts and comparison with PET/CT with [^{18}F]fluorocholine are warranted, to better define the role of each modality in preoperative imaging and surgical outcomes.

EP-0718

Incidence of Hypothyroidism Following Radioactive Iodine Therapy in Patients with Single Toxic Thyroid Nodules and evaluation of possible predictive factors.

H. Al-JNABI, *T. Ball, I. Mitra, J. Philips, E. Sanverdi, A. Wren, A. DEDE, A. Meanhout;*
Chelsea and Westminster NHS Foundation Trust, London, UNITED KINGDOM.

Aim/Introduction: This study aimed to evaluate the incidence of hypothyroidism in patients who received radioactive iodine (RAI) therapy for single toxic (hot) thyroid nodule and to investigate the impact of a series of factors on the likelihood of development of post-treatment hypothyroidism at 6 months. ***Materials and Methods:*** A retrospective cohort analysis was conducted using patient data collected at Chelsea and Westminster Hospital NHS Foundation Trust. Data were obtained from 43 eligible patients for the period between 2011 and 2024. Each patient had a thyroid uptake scan and TSH measurement performed within the 6 months prior to RAI treatment.Patients diagnosed with a single toxic thyroid nodule were included; patients with thyroid cancer or >1 hot nodules were excluded. I-131 administered for therapy was in the range 400 - 835 MBq, with mean dose 485 MBq.Factors evaluated for correlation to the likelihood of hypothyroidism at 6 months post-therapy were: gender, age, TSH level prior to treatment, I-131 activity administered, largest nodule diameter, uptake of radiotracer in the thyroid gland, and ratio of uptake of radiotracer in the hot nodule to the uptake in the remaining thyroid. Uptake rates were derived from Tc-99m thyroid uptake scans with scanning 20 minutes post injection. ***Results:*** Of 43 patients, 15 developed hypothyroidism at 6 months, of whom 3 exhibited transient hypothyroidism. 27 of the patients were euthyroid at 6 months; one of these later developed hypothyroidism more than 12 months after RAI therapy. 1 patient remained hyperthyroid therefore was excluded from statistical analysis as an outlier.No statistical correlation was found between the incidence of hypothyroidism at 6 months and age, gender, TSH level, administered RAI dose, largest nodule diameter, or overall thyroid uptake.A significant difference was found in the hot nodule to remaining thyroid uptake ratio in patients with hypothyroidism at 6 months compared to the euthyroid subgroup ($p < 0.05$, with means of 81.2% and 68.1% respectively). ***Conclusion:*** 15/43 (34%) of patients developed hypothyroidism at 6 months post RAI treatment for toxic nodule. Those patients had an overall higher ratio of tracer uptake in the hot nodule to the uptake in the remaining thyroid when compared to the euthyroid subgroup, which may serve as a potential predictor for the RAI therapy outcomes in the patient group with single toxic nodule.

EP-0719

Parathyroid multitracer CZT SPECT/CT with Tc-99m MIBI and I-123 NaI for simultaneous imaging of parathyroid adenomas and thyroid tissue

D. Heute, *J. D. Heute, A. J. Heute;*
Nuklearmedizin Telfs GmbH, Telfs, AUSTRIA.

Aim/Introduction: CZT SPECT/CT offers high spatial resolution, which may be crucial in detecting parathyroid adenomas. Furthermore these new systems make simultaneous multitracer aquisitions possible. We combinded Tc99m-MIBI, a wellknown tracer to image parathyroid adenomas, with I-123 NaI to localize thyroid tissue. The purpose of our study was to evaluate the use of a novel solid state SPECT/CT general purpose gamma camera (VeritonCT) in the diagnostic workup for patients with suspected parathyroid adenomas. ***Materials and Methods:*** We investigated 19 patients (15 female and 4 male) with elevated or borderline high PTH and Calcium showing a mean PTH of 113 pg/ml (57 to 225, SD 40 pg/ml) and mean calcium of 2,69 mmol/l (2.35 to 3.09, SD 0.18 mmol/l). The patients had been referred to our institution for routine parathyroid investigations. After giving consent each of them receivend an intraveneous injection of a mean dose of 9 MBq I-123 NaI and 237 MBq 99m-Tc-MIBI. Images were taken with a solid state 360° SPECT/CT scanner (VeritonCT 200) 15 and 120 minutes after tracerinjection. Focal uptake of iodine and MIBI was compared and a mismatch was regarded to be suspicious for parathyroid adenoma.The SPECT/CT findings were compared with high resolution ultrasound images being acquired on GE LOGIQ Fortis. Sonographically the maximal diameter of the suspected nodules ranged from 6 to 32 mm with a mean of 15.2 mm (SD 6.2 mm). Based on these results patients were referred to endocrine specialists for further treatment, four of them have undergone surgery, already. ***Results:*** Multitracer SPECT/CT with Tc-99m MIBI and I-123 is feasible in routine workup of patients suspected of parathyroid adenoma. In our group 16 of the 19 nodules showing a typical mismatch between MIBI and iodine uptake correlating with a typical features for parathyroid adenoma in ultrasound. In all of the four patients having undergone surgery, already, parathyroid adenomas were histologically proven. Three nodules positive in SPECT/CT could not be visualized by ultrasound because of unfavourable position: one small retrotracheal and two retroclavicular nodules, still one retroclavicular nodule was positive in histology. SPECT/CT with I-123 NaI and Tc-99m MIBI using a CZT full ring camera has shown to be helpful in localizing even small parathyroid adenomas. ***Conclusion:*** Doubletracer CZT SPECT/CT seems to be a valuable tool in localizing parathyroid adenomas. This new technique may become a reasonable alternative in routine nuclear medicine, especially if choline PET/CT is not available.

EP-0721

Correlation between biochemical parameters and quantitative indices on Ga68 DOTANOC PET/CT for localising the source of Cushing's Syndrome- A Retrospective SingleCentre Analysis

N. Kundu, *D. Khan, S. Sagar, A. Mahalik, A. Roy, R. Kumar;*
AIIMS New Delhi, Delhi, INDIA.

Aim/Introduction: Functional imaging with Ga68-labelled somatostatin analogue (SSA) PET/CT complements anatomical modalities when the source of adrenocorticotropichormone (ACTH) excess is unclear. Semiquantitative PET indices may mirror hormonal activity and help discriminate a pituitary from an ectopic origin. We analysed our centre'sexperience

to relate basal ACTH levels to lesion and pituitary metabolic metrics derived from Ga68 DOTANOC PET/CT. ***Materials and Methods:*** The departmental database was screened for patients with biochemically proven Cushing's syndrome who had undergone baseline Ga68 DOTANOC PET/CT and had ACTH documented prior to imaging. Thirtythree children and adults (19 males,14 females) fulfilled these criteria. Regions of interest were drawn around the dominantlesion and normal pituitary to obtain maximum SUV (SUVmax), SSTR expressing tumour volume (STV) and totallesion SSTR expression (TLS). Patients were dichotomised as pituitary (n = 6) or ectopic (n = 27) according to final multidisciplinary consensus. Groupcomparisons used the MannWhitney Utest; associations were explored with Spearman ρ. ***Results:*** Source distribution: Of the 27 ectopic cases, lung primaries were most frequent (hilar/lobar/bronchial = 10), followed by thyroid medullary carcinoma (n = 4), bulky adrenal disease (n = 2), duodenal and omental neuroendocrine tumours (n = 2 each) and other thoracic or abdominal masses (n ≤ 2 each). ACTH concentrations were more than twice as high in ectopic than in pituitary Cushing's (median 184.5 vs 85.0 pg mL^{-1}; p =0.01). Ectopic lesions showed significantly higher STV (median 2.30 vs 1.09 cm^3; p = 0.01) but modestly lower SUVmax compared withpituitary adenomas. Within the whole cohort, ACTH correlated moderately with lesion SUVmax (ρ = +0.47). Pituitary metabolic indices were consistently lower in ectopic Cushing's than in pituitary disease (median SUVmax 3.65 vs 6.45). ***Conclusion:*** Ga68 DOTANOC PET/CT semiquantitative parameters echo underlying endocrinology. Elevated ACTH paired with suppressed pituitary uptake and comparatively lowtomoderate lesion SUV favours an ectopic source, whereas high pituitary SUVmax with smaller STV supports a pituitary adenoma. These objective metrics, drawn solely from the present dataset, may expedite localisation and streamlinemanagement algorithms for Cushing's syndrome. Prospective validation in larger cohorts is warranted to establish clinically actionable cutoff values.

EP-0722

Dual-isotope subtraction scintigraphy and SPECT-CT for preoperative localization of parathyroid adenomas: A diagnostic study

P. Udholm, *C. Eriksen, S. d'Este, P. Bach-Mortensen, S. Møller;*
Hvidovre Hospital, Region Hovedstaden, Hvidovre, DENMARK.

Aim/Introduction: Primary hyperparathyroidism (PHPT) is often caused by a parathyroid adenoma (PTA). Subtraction scintigraphy with ^{123}I and ^{99m}Tc -MIBI SPECT-CT, and neck ultrasound examination as a hybrid scan (HS) can be used to localize the PTA in order to promote minimally invasive surgery. This study evaluated patients referred for HS, the ability of the HS to correctly localize PTA(s), as well as the diagnostic performance of HS. ***Materials and Methods:*** Data was retrieved for 300 patients referred for HS from 2019-2023. We used Begg and Greenes' correction method to calculate diagnostic accuracy as well as calculated percentage of adenoma(s) correctly localized per patient who underwent PTX or bilateral neck exploration (BNE). ***Results:*** In 282 patients with PHPT undergoing HS for PTA localization, the HS was positive in 71 %. Only 65 % of these patients were referred to PTX. Using correction methods, we found a sensitivity and specificity of the HS of 73 % and 78 %, respectively. The positive predictive value was 99 %, while the negative predictive value was 9 %. The HS correctly localized PTA in 90% of the patients. Scintigraphy correctly localized 86 % of the PTAs, SPECT-CT 85 %, and ultrasound 76 %. ***Conclusion:*** A positive HS was very likely to localize the PTA correctly, whereas a negative HS had limited diagnostic value. Surprisingly, a large proportion of patients undergoing HS were never considered for surgery, resulting in partial reference bias in the evaluation of the diagnostic accuracy.

EP-0723

The Role of Ga-68 DOTA-Pentixafor PET/CT Imaging in the Diagnosis of Benign Functional Adrenal Cortical Masses: Preliminary Results

Ö. Sahin[1], *Z. Tosunoğlu*[1], *A. E. Öztürk*[1], *E. Akgün*[1], *G. Alçın*[1], *T. F. Çermik*[2], *E. Arslan*[1];
[1]*Istanbul Training and Research Hospital, Nuclear Medicine Clinic, Istanbul, TÜRKIYE,* [2]*Acibadem Maslak Hospital, Nuclear Medicine Department, Istanbul, TÜRKIYE.*

Aim/Introduction: Conventional imaging modalities and ^{18}F-FDG PET/CT often lack sufficient specificity in evaluating the functional characteristics of benign adrenal lesions. CT and MRI provide structural evaluation but lack functional information. Adrenal venous sampling (AVS) is gold standard for distinguishing unilateral aldosterone-producing adenomas (APA) from bilateral hyperplasia. Ga-68 DOTA-Pentixafor binds specifically to CXCR4, allowing for high-sensitivity imaging of adrenal cortical lesions. Study evaluates the efficacy of Ga-68 DOTA-Pentixafor PET/CT determining functional status lesion lateralization. ***Materials and Methods:*** Included patients suspected of benign functional adrenal masses; 6 aldosterone-secreting,18 cortisol-secreting, 1 suspected ectopic ACTH syndrome Patients underwent ^{18}F-FDG PET/CT, Ga-68 DOTA-Pentixafor PET/CT in same week. SUVmax, lesion-contralateral adrenal (LKR), lesion-liver SUVmax ratio (LKCR) measured. Correlations aldosterone and cortisol levels, lesion size, and Hounsfield Unit (HU) analyzed. ***Results:*** 6 Primary Aldosteronism (PA)SUVmax showed a strong positive correlation with aldosterone levels (r:1, p:0.003), moderate positive correlation with lesion size (r:0.759, p:0.080), and weak negative correlation with HU (r:-0.067, p:1).LKR showed a strong positive correlation with aldosterone (r:0.828, p:0.022) and moderate correlation with lesion size (r:0.643, p:0.080), but no significant correlation with HU.LKCR showed a strong positive correlation with aldosterone (r:0.733, p:0.056), moderate positive correlation with lesion size (r:0.690, p:0.056), and a negative correlation with HU (r:-0.333, p:0.469). 5 Cushing SyndromeSUVmax showed weak negative correlations with cortisol levels (r:-0.400, p:0.483) and lesion size (r:-0.200, p:0.817), with no relationship to HU.LKR showed a moderate negative correlation with cortisol (r:-0.600, p:0.233) and lesion size (r:-0.400, p:0.483), with a weak positive correlation with HU (r:0.200, p:0.817).LKCR showed a weak positive correlation with cortisol (r:0.200, p:0.817), no significant correlation with lesion size (r=0, p=1), and a weak positive correlation with HU (r:0.200, p:0.817)**.** Imaging Findings: Ga-68 DOTA-Pentixafor PET/CT identified a unilateral focal uptake in all 6 PAAmong 18 CS, 3 unilateral, while 2 distinct bilateral uptake.Two CS underwent surgery, pathology confirming Ga-68 DOTA-Pentixafor PET/CT findings.One suspected EAS underwent adenectomy and bilateral adrenalectomy, negative CT/MRI results. Ga-68 DOTA-Pentixafor PET/CT and ^{18}F-FDG PET/CT revealed a suspicious focal uptake in the left adrenal region.Follow-up ongoing. ***Conclusion:*** Preliminary results suggest that Ga-68 DOTA-Pentixafor PET/CT successfully localized lesions in PA, CS, and EAS that were not identified with conventional imaging or ^{18}F-FDG PET/CT. This technique may contribute significantly to surgical decision-making. For PA and CS without definitive functional assessment, SUVmax, LKR, and LKCR may serve diagnostic criteria. However, postoperative tissue diagnosis and clinical follow-up are necessary for definitive conclusions. The study is ongoing.

EP-0724

The effect of thyroid hormone medication on radioiodine-131 bio-kinetics in solitary toxic thyroid nodules

C. Happel, *B. Bockisch, D. Groener;*
University Medical Center Frankfurt; Clinic for Radiology and Nuclear Medicine; Department of Nuclear Medicine, Frankfurt, GERMANY.

Aim/Introduction: Radioiodine-131 treatment (RIT) is a well-established therapeutic option in solitary toxic thyroid nodules (STN). The required therapeutic activity depends on individual intra-therapeutic effective half-life (EHL) and has to

be determined in a radioiodine uptake test (RIUT). In order to suppress radioiodine-131 uptake in healthy thyroid tissue an additional suppressive medication with triiodthyronine (T3) or tetraiodthyronine (T4) may be required. Aim of this retrospective analysis was to quantify the influence of suppressive medication on intra-therapeutic effective half-life (EHL). ***Materials and Methods:*** A total of 928 patients with STN undergoing RIUT and RIT was subdivided into three groups and analysed retrospectively. Group A: T3 medication (n=274), group B: T4 medication (n=184) and group C: no additional medication (n=470). The subgroups A and B were further subdivided depending on the dose of hormone medication. The influence of hormone medication on EHL was evaluated by calculation of the variance of the determined individual EHL between RIUT and RIT within the single groups and within the subgroups. ***Results:*** Intra-therapeutic EHL was significantly reduced in subgroups A and B when compared to EHL in RIUT. Group A: 5.9 ± 1.1 d in RIUT and 3.3 ± 1.4 d in RIT (-43 %) (p<0,05); Group B: 5.9 ± 1.2 d in RIUT and 3.4 ±1.5 d in RIT (-42 %) (p<0,05). The reduction of EHL between the subgroups A and B did not differ statistically. Both subgroups A and B showed a highly significant difference compared to subgroup C (p<<0.05). The dose of hormone medication was found to be a significant influencing factor on the decrease in EHL (35 - 58 % (T3) and 15 - 67 % (T4)) (p<0.05). ***Conclusion:*** The significantly reduced intra-therapeutic EHL in patients with additional thyroid hormone medication may be caused by stunning effects or a stimulation of the cell metabolism in the follicle cells by this medication. However, the effect should be considered when calculating the required therapeutic RIT activity for patients with STN.

EP-0725

Alternation of Organic Metabolic Profiling in Obese Patients Following Bariatric Surgery Assessed by ^{18}F-FDG PET/CT

Z. Wang, *S. Xue, O. Kulterer, X. Li, M. Hacker;*
Medical University of Vienna Department of Biomedical Imaging and Image-guided Therapy, Vienna, AUSTRIA.

Aim/Introduction: Bariatric surgery is a powerful intervention for obesity, leading to marked improvements in metabolic dysfunction across multiple organs. However, the complexity of systemic metabolic adaptation and inter-organ communication following surgery remains poorly characterized. This study aimed to comprehensively evaluate organ-specific metabolic changes and inter-organ network remodeling in obese patients before and after bariatric surgery, using AI-assisted whole-body ^{18}F-FDG PET/CT and extensive biochemical profiling. ***Materials and Methods:*** A total of 28 obese patients who underwent laparoscopic sleeve gastrectomy (LSG) or one-anastomosis gastric bypass (OAGB) were enrolled. All patients received whole-body ^{18}F-FDG PET/CT imaging and comprehensive biochemical testing preoperatively and at 12 months postoperatively. Organ segmentation was conducted using TotalSegmentator, an AI-based tool, to extract SUVmean values. Changes in organ volume, tissue-specific glucose uptake, and systemic biochemical markers were assessed. Metabolic connectivity networks were constructed using Pearson correlation matrices and evaluated pre- and postoperatively to characterize inter-organ communication patterns. ***Results:*** After surgery, most organ SUVmean values significantly declined, while SAT, VAT, and adrenal gland SUVmean increased. Organ volumes were markedly reduced across multiple systems, including adipose tissue (SAT, VAT), hepatopancreatic system (liver, pancreas), cardiovascular system (heart, pulmonary vein), and digestive tract (stomach, small bowel). Correlation network analysis revealed strengthened inter-organ metabolic coordination after surgery. Several organ pairs that were negatively correlated before surgery, such as subcutaneous adipose tissue (SAT) with the duodenum, spinal cord, and liver, shifted to positive correlations postoperatively. In addition, certain organ interactions that were already positively correlated—such as VAT with the pancreas, SAT, liver, and spleen—became more tightly coordinated after surgery, indicating an overall enhancement of systemic metabolic integration. PET-derived SUVmean changes showed significant correlations with improvements in lipid profiles, insulin resistance (HOMA-IR), and liver histological scores (NA and SAF score). Additionally, skeletal muscle SUVmean negatively correlated with changes in C-peptide, insulin, HOMA-IR, and GH, while cardiovascular and skeletal system metabolic changes were associated with hormone and inflammatory markers. ***Conclusion:*** This study demonstrates that bariatric surgery induces robust systemic metabolic reorganization, including reduced organ volumes, altered glucose uptake, and reprogrammed inter-organ metabolic networks. Whole-body ^{18}F-FDG PET/CT combined with AI-based segmentation and network analysis provides a novel systems-level approach to quantify these adaptations. Our findings highlight the central roles of hepatic and adipose tissue remodeling and support the use of metabolic network features as potential biomarkers for predicting surgical outcomes and guiding personalized management of obesity.

EP-0726

^{68}Ga-Pentixafor PET/CT Imaging Characteristics in Primary Aldosteronism with Coexisting Subclinical Cushing Syndrome: A Retrospective Cohort Study

S. Liu, *H. Pang;*
The First Affiliated Hospital of Chongqing Medical University, Chongqing, CHINA.

Aim/Introduction: The coexistence of subclinical Cushing syndrome (SCS) in primary aldosteronism (PA) patients complicates diagnosis and management. This study aimed to characterize the endocrine-metabolic profiles and ^{68}Ga-pentixafor PET/CT imaging features in PA-SCS patients, and explore the discriminative value of CXCR4-targeted imaging for SCS identification. ***Materials and Methods:*** Retrospective analysis of 52 PA patients (25 PA-SCS vs. 27 PA) undergoing ^{68}Ga-pentixafor PET/CT at The First Affiliated Hospital of Chongqing Medical University from 2022 to 2024. Clinical parameters (cortisol, ACTH, 24hUFC, renin-aldosterone ratio) and PET-derived metrics (SUVmax, lesion-to-contralateral ratio [LCR], lesion-to-liver ratio [LLR]) were compared. Statistical analyses included Mann-Whitney U tests, ROC curve analysis, and Spearman correlation. ***Results:*** PA-SCS group showed significantly larger adrenal lesions (median 2.8 vs. 1.5 cm, P<0.0001).Elevated 10min-LCR (3.2 vs. 1.7, P=0.003) and 40min-LCR (4.1 vs. 2.3, P=0.012) distinguished PA-SCS from PA.10min-LCR demonstrated optimal diagnostic performance (AUC=0.737, cutoff=1.935, sensitivity 76%, specificity 68%).Weak correlations existed between PET parameters and cortisol-related indices (|r|=0.3-0.5, P<0.05). ***Conclusion:*** ^{68}Ga-pentixafor PET/CT provides functional insights into adrenal CXCR4 expression patterns in PA-SCS. Early-phase LCR enhancement may serve as a potential biomarker for SCS identification, complementing conventional endocrine testing.

EP-0727

First-in-Human Evaluation of [^{18}F]AldoView: A Highly Selective PET Tracer for Aldosterone Synthase Imaging in Primary Aldosteronism

T. Long[1], *G. Liu*[2], *M. Zhou*[1], *X. Xie*[3], *Y. Jin*[1], *L. Liu*[4], *X. Luo*[2], *T. Jiang*[2], *S. Hu*[1];
[1]*Department of Nuclear Medicine, Xiangya Hospital, Central South University, Changsha, Hunan, CHINA,* [2]*Department of Endocrinology, Xiangya Hospital, Central South University, Changsha, Hunan, CHINA,* [3]*Hunan University of Information Technology, Changsha, Hunan, CHINA,* [4]*Department of Urology, Xiangya Hospital, Central South University, Changsha, Hunan, CHINA.*

Aim/Introduction: Aldosterone synthase (CYP11B2) is overexpressed in primary aldosteronism (PA), making it a promising target for imaging. This first-in-human study evaluates the safety and feasibility of [^{18}F]AldoView, a highly selective PET tracer targeting CYP11B2, for PA subtyping. ***Materials and Methods:*** Biodistribution and dosimetry of [^{18}F]AldoView were assessed in three healthy volunteers using whole-body PET/CT. Fifteen patients with adrenal lesions (13 with PA, 1 with Cushing's syndrome, 1 with a nonfunctional adenoma) were enrolled. PET/CT scans were performed 60 minutes post-injection. Lesions were considered positive if tracer uptake exceeded normal adrenal tissue. Semi-quantitative analyses included maximum standardized uptake value (SUVmax), lesion-to-liver ratio (LLR), and lesion-to-adrenal ratio (LAR). Ten PA patients with positive imaging findings and one with Cushing's syndrome underwent adrenalectomy, and resected specimens were analyzed for CYP11B2 expression. This ongoing study is registered with the Chinese Clinical Trial Registry (ChiCTR2400093214). ***Results:*** [^{18}F]AldoView was well-tolerated, with no adverse events. The effective dose was 0.012 ± 0.0022 mSv/MBq. PET/CT identified positive lesions in all 10 PA patients, with mean SUVmax of 15.73 ± 8.57, LAR of 8.02 ± 4.06, and LLR of 10.24 ± 1.48. No positive lesions were observed in patients with idiopathic hyperaldosteronism, Cushing's syndrome, or nonfunctional adenomas. Positive lesions showed strong CYP11B2 staining on pathology, confirming aldosterone-producing adenomas (APA) or nodules (APN). ***Conclusion:*** [^{18}F]AldoView PET/CT is safe and feasible for the imaging of APAs and APNs in PA patients. These results highlight its potential for non-invasive in-vivo detection of CYP11B2, supporting its use in PA subtyping. ***References:*** Sander K, Gendron T, Cybulska KA, et al. Development of [(18)F]AldoView as the First Highly Selective Aldosterone Synthase PET Tracer for Imaging of Primary Hyperaldosteronism. J Med Chem. 2021;64:9321-9329.

EP-0728

^{18}F-FDG PET/CT in the Assessment of Indeterminate Adrenal Lesions

W. Schlötelburg[1], *T. Jedamzik*[1], *S. Hahner*[2], *A. K. Buck*[1], *M. Fassnacht*[2], *P. E. Hartrampf*[1];
[1]*University Hospital, Department of Nuclear Medicine, Würzburg, GERMANY,* [2]*University Hospital, Medicine I, Division of Endocrinology and Diabetes, Würzburg, GERMANY.*

Aim/Introduction: The objective of this analysis is to evaluate and compare PET parameters obtained from ^{18}F-FDG PET/CT for the characterisation of adrenal lesions indeterminate by conventional imaging methods, especially lesions with densities >10 HU on unenhanced CT-scans. ***Materials and Methods:*** A total of 414 patients with adrenal masses and ^{18}F-FDG PET/CT were classified according to either histopathological confirmation or clinical/imaging follow-up. The final diagnoses included 218 adrenal adenomas, 52 other benign adrenal tumours, 22 phaeochromocytomas, 62 adrenocortical carcinomas, seven adrenal lymphomas, and 53 metastases. Receiver operating characteristic (ROC) curves were used to assess the performance of standardized uptake values (SUVmax, SUVpeak, SUVmean), as well as adrenal tumour-to-liver ratio (SUVmax lesion/SUVmean liver, ALR) and adrenal tumour-to-bloodpool ratio (SUVmaxlesion/SUVmean aorta, ABR) for the discrimination of benign from malignant findings. Segmentation of the lesions was conducted with a threshold of 40%. ***Results:*** All adrenal masses with unenhanced HU <10 (n=198) were classified as benign lesions. In these cases, FDG PET/CT did not offer any advantages in terms of classification. In the more challenging group, characterised by densities >10 HU (n=216) on unenhanced CT-scans, malignant tumours exhibited higher SUVmax, SUVpeak and SUVmean values in comparison to benign lesions (13.6, 10.3 and 8.4 vs. 4.1, 3.2 and 2.7; P<0.0001). The area under the curve (AUC) was 0.92 for SUVmax and ALR, 0.88 for SUVpeak, 0.90 for SUVmean and 0.91 for ALR. The optimal cut-off for differentiating malignant from benign lesions was determined as follows: SUVmax: 6.5 (sensitivity 85%, specificity 84%), SUVpeak: 5.1 (sensitivity 84%, specificity 86%), SUVmean: 4.4 (sensitivity 83%, specificity 93%), ALR: 2.6 (sensitivity 86%, specificity 84%), ABR: 4.5 (sensitivity 76%, specificity 91%). To achieve a required clinical sensitivity for malignancy of >90%, a SUVmax of 5.8 or an ALR of 2.2 would be necessary, which consequently results in a decrease in specificity to 77%for SUVmax and 73% for ALR. ***Conclusion:*** 18F-FDG-PET/CT is a valuable diagnostic tool that may help to differentiate between benign and malignant adrenal lesions of indeterminate aetiology. Nevertheless, the specificity is reduced if a clinical relevant sensitivity of 90% or more is desired.

EP-0729

^{18}F-choline long-axial-field of view PET-CT accurately localises intrathyroid parathyroid adenoma in 5-month pregnant patient

T. Wagner[1], *T. Willson*[2], *B. Ferreira*[2], *J. Edwards*[3], *P. Wijewickrama*[4], *B. Holman*[2];
[1]*Nuclear Medicine, London, UNITED KINGDOM,* [2]*Nuclear Medicine department, Royal Free London NHS Trust, London, UNITED KINGDOM,* [3]*Radiology department, Royal Free London NHS Trust, London, UNITED KINGDOM,* [4]*University Hospital Sussex, Department of Endocrinology, Brighton, UNITED KINGDOM.*

Aim/Introduction: A 44-year old pregnant patient with severe hypercalcaemia caused by primary hyperparathyroidism was referred for ^{18}F-choline long-axial-field of view (LAFOV) PET-CT for pre-surgical localisation of parathyroid adenoma. The patient had needed multiple hospitalisations to treat the hypercalcaemia and was at risk of severe complications for herself and the foetus. Exploratory neck surgery had been attempted and did not localise a parathyroid adenoma. ***Materials and Methods:*** We performed an ultra-low-dose PET and CT acquisition to minimise radiation exposure to the foetus. The patient was injected with 17 MBq (0.2 MBq/kg) and scanned for 30 mins from vertex to diaphragm, 62 mins after injection on a Vision Quadra PET-CT (Siemens Healthineers, Erlangen, Germany). CT parameters were ref mAs 7mAs, CAREDose on, CAREkV off, ref kV 100. Following the PET-CT acquisition, we performed a PET only uncorrected acquisition of vertex to thighs to evaluate ^{18}F-choline uptake within the foetus to estimate foetal radiation exposure. ***Results:*** ^{18}F-choline LAFOV PET-CT demonstrated focal intense choline uptake in a low density intrathyroid nodule in the left lower pole, consistent with an intrathyroid parathyroid adenoma. No other focus of abnormal uptake was identified. The uncorrected images demonstrated only mild uptake in the region of the foetus, likely in the liver. Despite choline being an essential nutrient for foetal brain development, there was no uptake in the brain of the foetus. The estimated foetal dose was 0.5 mSv from the PET and 0.1 mGy from the CT. The patient had surgery the following week, which identified and removed the parathyroid adenoma. Pathological analysis confirmed the presence of an intrathyroid parathyroid adenoma. The patient was discharged successfully and was mildly hypocalcaemic following surgery. ***Conclusion:*** This is the first reported case of ^{18}F-choline PET-CT in a pregnant patient, which we performed on a LAFOV PET-CT while delivering very low radiation to foetus and mother and obtaining a high-quality diagnostic scan. ***References:*** 1. van Snick JH, Koopmans KP, Glaudemans AWJM, Stormezand GN, Ivashchenko OV. Fetal dose minimization: ultra-low dose long axial field of view (LAFOV) PET/CT imaging of a pregnant patient. Eur J Nucl Med Mol Imaging. 2024 Dec;52(1):370-371. Epub 2024 Aug 3. 2. Treglia G, Piccardo A, Imperiale A, Strobel K, Kaufmann PA, Prior JO, Giovanella L. Diagnostic performance of choline PET for detection of hyperfunctioning parathyroid glands in hyperparathyroidism: a systematic review and meta-analysis. Eur J Nucl Med Mol Imaging. 2019 Mar;46(3):751-765.

EP-0730

Diagnostic Value of MIBI Thyroid Washout Rate in Differentiating Types of Amiodarone-Induced Thyrotoxicosis

T. Bogovic Crncic[1,2], *L. Fischer*[1,2], *M. Ilić Tomaš*[1,2], *I. Iskra*[1,2], *N. Girotto*[3,4], *M. Mavrinac*[5];
[1]*University of Rijeka, Faculty of Medicine, Rijeka, CROATIA,* [2]*Clinical Hospital Centre Rijeka, Rijeka, CROATIA,* [3]*University of Rijeka, Faculty of Health Studies, Rijeka, CROATIA,* [4]*PET/CT Center Rijeka, Medikol Polyclinic, Rijeka, CROATIA,* [5]*Faculty of Educational Sciences, Juraj Dobrila University of Pula, Pula, CROATIA.*

Aim/Introduction: Amiodarone-induced thyrotoxicosis (AIT) is a potentially serious complication of amiodarone therapy and is categorized into three types: AIT-1, resulting from increased thyroid hormone synthesis, AIT-2, caused by destructive thyroiditis due to cytotoxic effects of amiodarone and AIT- 3, or mixed type, which presents with overlapping features. Accurate differentiation is clinically important, due to different treatment approaches. However, making this distinction remains a diagnostic challenge. This study aimed to evaluate the diagnostic utility of the 99mTc-sestamibi (MIBI) thyroid washout rate (WR) in differentiating between AIT types. ***Materials and Methods:*** This prospective study included 55 AIT patients who underwent thyroid scintigraphy with 99mTc-MIBI, 10 and 60 minutes post-injection. Based on the visual early image interpretation, patients were categorized into AIT-1 (intense uptake), AIT-2 (absent/minimal uptake) and AIT-3 (intermediate uptake) group. Semi-quantitative analysis involved calculating thyroid-to-background MIBI uptake ratios using mediastinal and supraclavicular background regions of interest (ROIs). Ratios between 66.66th and 100th percentile indicated the highest MIBI uptake and were classified as the AIT-1, between 0th and 33.33rd percentile as the AIT-2, and between the 33.33rd and 66.66th percentile as the AIT-3 type. WR was calculated as the percentage decrease in thyroid uptake between early and delayed images and compared with values from 35 euthyroid control subjects. Statistical analysis was performed using t-tests, with $P < 0.05$ considered statistically significant. ***Results:*** According to visual analysis 18 patients were classified in AIT-1, 17 in AIT-2 and 20 in AIT-3 group. Semi-quantitative analysis led to reclassification, resulting in 19 patients in AIT-1, 20 in AIT-2 and 16 in AIT-3, when using the mediastinal ROI, with similar results for the supraclavicular ROI. Using the mediastinal ROI, median WR values were 32.48% for AIT-1, 27.19% for AIT-2, and 29.31% for AIT-3 type, compared to 28.88% in controls ($P = 0.258$). With the supraclavicular ROI, WR values were similar: 32.85% for AIT-1, 26.04% for AIT-2, 29.80% for AIT-3, and 28.88% for controls ($P = 0.120$). Visual assessment also revealed no statistically significant differences in WR rate among the AIT types ($P = 0.823$). ***Conclusion:*** Thyroid MIBI washout rates did not significantly differ among AIT types or when compared to euthyroid controls, regardless method of analysis or background ROI used. While useful in evaluating thyroid nodules, MIBI WR analysis did not contribute significantly to the diagnostic differentiation of AIT types.This work has been supported in part by the University of Rijeka: project number (uniri-pr-biomed-19-141495).

EP-0731

Optimization of 3T PET/MRI Protocol with [18F] Fluorocholine in the Detection of Parathyroid Microadenomas.

V. Carrero-Vásquez*, Á. Espigares-Santiago, J. Díaz-Moreno, M. Cortés Romera, M. Suárez-Piñera, L. Gracia-Sánchez, L. Rodríguez-Bel, I. Sanchez-Rodriguez;*
Nuclear Medicine, Bellvitge University Hospital, Barcelona, SPAIN.

Aim/Introduction: Parathyroid adenomas (PAs) are low-fat-content lesions that pose a diagnostic challenge, particularly when they are small. 3T PET/MRI has shown promise in localization, but the need for multiple MRI sequences remains a topic of debate. This study aims to optimize the PET/MRI acquisition protocol, evaluate signal characteristics by lesion size, and determine whether any sequence can be safely omitted without compromising diagnostic accuracy. We aimed to analyze MRI signal intensity and PET uptake to lesion size, assess the relationship between acquisition parameters and adenoma size, optimize the PET/MRI protocol for detecting parathyroid adenomas, and evaluate the redundancy of T2-TSE and T2-STIR sequences for protocol simplification. ***Materials and Methods:*** A retrospective study included 23 patients (2021-2024) with primary hyperparathyroidism and negative conventional imaging. MRI included axial T1-Dixon, T2-FSE (T2-TSE), and coronal T2-STIR. PET data were quantified by SUVmax. Lesions were categorized as microadenomas (<6 mm), subcentimetric (6-10 mm), or centimetric (>10 mm). Histopathological confirmation (APA) was available in a subset. Signal intensities were classified, and SUVmax values were compared using Kruskal-Wallis tests. ***Results:*** A total of 24 lesions were detected (one patient had two): microadenomas (n=5), 3 confirmed by APA. 100% detected. Isointense in T1 (60%), hyperintense in T2/STIR (80%). SUVmax moderate (3.9) or intense. Subcentimetric (n=14): 4 confirmed. 100% detected. Mixed T1 (hypo 50%, iso 43%), hyperintense in T2/STIR (90%). SUVmax 5.8 ($p<0.01$).Centimetric (n=5): 2 confirmed. 100% detected. Hypointense T1 (>70%), hyperintense T2/STIR (100%). SUVmax 11.5.Hyperintensity in T2-TSE and STIR was nearly identical across all groups. T1 showed more variability. SUVmax strongly correlated with signal intensity (Kruskal-Wallis: T1 $p=0.0011$, T2 $p=0.0014$, STIR $p=0.0035$). Among APA-confirmed lesions (n=9), all were hyperintense in T2/STIR and had SUVmax > 4. ***Conclusion:*** T2-STIR and T2-TSE provide overlapping diagnostic value. Given the similar detection rates and superior contrast properties of STIR, T2-TSE may be omitted to streamline the protocol. A simplified sequence set (T1 + STIR) appears sufficient for accurate detection across all lesion sizes, including microadenomas. These results support the optimization of PET/MRI protocols for clinical and operational efficiency. Further prospective studies are recommended to validate these findings.

EP-0732

Frequency of osteoporotic Trabecular Bone Score adjusted T-score in daily clinical practice compared to standard densitometric measurements

M. Jensen[1], *B. Zerahn*[1], *C. K. Andersen*[1], *M. K. Skjødt*[2,3];
[1]*Dept. of Nuclear Medicine, Copenhagen University Hospital – Herlev and Gentofte, Herlev, DENMARK,* [2]*Dept. of Medicine, Copenhagen University Hospital - Herlev and Gentofte, Herlev, DENMARK,* [3]*Research Unit OPEN, Department of Clinical Research, University of Southern Denmark, Odense, DENMARK.*

Aim/Introduction: Trabecular Bone Score (TBS) can be measured by dual energy x-ray absorptiometry (DXA) in addition to Bone Mineral Density (BMD). TBS provides a quantitative assessment of bone microarchitecture in the form of either a unitless TBS or as a TBS-adjusted T-score and as such provides partly independent information on fracture risk beyond BMD. Categorization of the standalone TBS has been proposed as follows: normal (≥1.350), partially degraded (1200 < TBS < 1.350) and degraded (≤1.200). The International Society for Clinical Densitometry (ISCD) official positions from 2023 regard TBS to be appropriate in adults ≥ 40 years to assist management of pharmacological intervention. The aim of this study is to report the frequency of TBS-adjusted T-score ≤ -2.5 among individuals referred for baseline Dual X-ray Absorptiometry (DXA) with one or more risk factors associated with osteoporosis as compared to unadjusted BMD based T-score measured at the lumbar spine and bilateral hip. ***Materials and Methods:*** This is a retrospective study of 115 individuals aged ≥ 40 years and referred for DXA based baseline assessment of

osteoporosis. Eight (four men) were excluded because they were already diagnosed with osteoporosis due to low energy vertebral fractures and 5 were excluded due to a BMI > 37. Of the included 102 patients (avg. age of 66,4Y) seven patients had measurements of the forearms of which four had bilateral hip arthroplasty, two had primary hyperparathyroidism and one because of metastases in the hips. In 26 patients one or more vertebrae were excluded from analysis primarily because of spondylosis. ***Results:*** A total of 35 individuals had a T-score ≤ -2.5 of which 7 (all women) were found only with TBS-adjusted T-score. Unadjusted T-scores ≤ -2.5 was found in the lumbar spine in 17 individuals, femoral neck 18, total hip 10, radius 33% 1 while TBS-adjusted T-scores ≤ -2.5 were found in 22 individuals. 15 patients could be categorized with a degraded TBS, 42 with a partially degraded TBS and 45 with a normal TBS. ***Conclusion:*** Adding TBS to the standard procedure in our local clinical setting will increase the number of individuals with a T-score ≤ -2.5 from approximately 27 to 34%. The impact of this increased occurrence of osteoporosis on the capture of patients with subsequent fracture(s) remains to be elucidated. ***References:*** Cormier C, Lamy O, Poriau S. TBS in routine clinical practice: Proposals of use. Medimaps. 2012:1-14.

EP-0733

[^{18}F]Fluorocholine-PET Imaging at Different Time Points in Patients with Primary Hyperparathyroidism

F. Hedeer[1], *A. Stenvall*[2], *E. Mellhammar*[2], *M. Matkovic*[1], *M. Nilsson*[3], *J. Oddstig*[2], *M. Almquist*[3], *U. Bitzén*[1];
[1]*Department of Clinical Physiology and Nuclear Medicine, Skåne University Hospital, Lund University, Lund, SWEDEN,* [2]*Radiation Physics, Department of Haematology, Oncology and Radiation Physics, Skåne University Hospital, Lund, SWEDEN,* [3]*Department of Surgery, Skåne University Hospital, Lund University, Lund, SWEDEN.*

Aim/Introduction: [^{18}F]FluorocholinePET has emerged as a powerful tool for preoperative localisation of pathological parathyroid glands in primary hyperparathyroidism (pHPT). Limited data is, however, available regarding optimal imaging time point. The aim was to explore performance of [^{18}F]FluorocholinePET at different imaging time points for localisation of pathological parathyroid glands in pHPT. ***Materials and Methods:*** In 25 consecutive patients referred for preoperative localisation of pathological parathyroid glands, static PET images at 26, 48, 610, 812 min (derived from a 12minute dynamic acquisition) and 60 min after intravenous injection of 4 MBq/kg [^{18}F]Fluorocholine were, together with low-dose CT, blinded and retrospectively read by two experienced nuclear medicine physicians. Uptakes were specified regarding localisation (side and relation to the ipsilateral thyroid lobe) and degree of suspicion (1=no focal uptake, 2=faint unspecific uptake, 3=intermediately suspicious uptake, 4=suspicious uptake and 5=strongly suspicious uptake). Results were compared to surgical and histopathological results, and ionised calcium levels in serum at postoperative follow-up. One patient declined surgery resulting in 24 patients to be analysed. ***Results:*** In the 24 patients, 27 pathological parathyroid glands with adenoma or hyperplasia (two in three patients, one in 21 patients) were surgically removed. 19 of these glands (70%) corresponded to distinct grade 45 uptakes at all time points and one (4%) to a faint grade 2 uptake reported at all time points. Four glands (15%) were better visualised 60 minutes post injection (uptake grade 45) compared to earlier time points (uptake grade 24) and one (4%) was correctly localised as a grade 4 uptake 60 minutes post injection but not clearly visualised at earlier timepoints (grade 1-2). In two of the patients with two surgically removed pathological parathyroid glands, one in each patient (7%) was not detected by [^{18}F]Fluorocholine-PET. Thus, 24 of the 27 surgically removed pathological parathyroid glands, i.e. 89%, were localised by distinct grade 4-5 uptakes 60 minutes post injection. None of the reported uptakes graded 45 were false positive. In 5 of the 24 patients, 12 additional unspecific uptakes were reported but without obvious correlation to imaging time point. All patients were normocalcemic at follow-up after surgery. ***Conclusion:*** Most of the pathological parathyroid glands were clearly and correctly localised by [^{18}F]FluorocholinePET and equally well visualised regardless of imaging time point. In some patients, however, the detection was favoured by a longer, i.e. 60-minute, accumulation time. Further studies are needed to investigate whether this is a true tendency or not.

EP-0734

Evaluation of Dynamic C-X-C motif Chemokine Receptor 4-directed PET/CT Imaging in Primary Aldosteronism

J. Enke[1], *F. Voelter*[2], *J. Baessler*[1], *K. Ritzel*[2], *R. A. Bundschuh*[3], *N. Dreher*[1], *O. Viering*[1], *J. Tran-Gia*[4], *C. H. Pfob*[1], *M. Kircher*[1], *A. Dierks*[1], *M. Reincke*[2], *C. Lapa*[1];
[1]*Nuclear Medicine, Faculty of Medicine, University of Augsburg, Augsburg, GERMANY,* [2]*Department of Medicine IV, Ludwig Maximilians University Hospital Munich, Munich, GERMANY,* [3]*Department of Nuclear Medicine, University Hospital Carl Gustav Carus at the TU Dresden, Dresden, GERMANY,* [4]*Department of Nuclear Medicine, University Hospital Würzburg, Würzburg, GERMANY.*

Aim/Introduction: C-X-C motif chemokine receptor 4 (CXCR4)-directed positron emission tomography (PET) has been evaluated in the diagnostic work-up of primary aldosteronism (PA), since overexpression of CXCR4 has been described for aldosterone-producing adenomas (APA). In this retrospective evaluation of dynamic PET/CT imaging with [^{68}Ga]Ga-PentixaFor in patients with PA, we aimed at determining an optimal imaging time point for CXCR4-directed imaging in PA. ***Materials and Methods:*** After injection of 151 ± 16.5 MBq (mean ± SD) of [^{68}Ga]Ga-PentixaFor, dynamic PET imaging over the upper abdomen was performed in 24 patients at a single bed position and reconstructed into 33 time frames (1×40 s, 10×5 s, 3×10 s, 2×15 s, 5×30 s, 5×120 s, 5×300 s and 2×600 s). In a subset of 12 patients, list-mode data was reconstructed in 10-minute frames starting from minute 10. Mean, maximum and peak standardized uptake values (SUV) of adrenal glands and maximum lesion-to-contralateral ratio (LCRmax) were extracted for all time frames. Mann-Whitney U-Tests were used to compare parameters between time frames, and AUC values were calculated. Histopathology and clinical follow-up served as the reference standard and were available for 12 of 24 patients; evaluation is still pending for the remainder. ***Results:*** In 11 out of 24 patients, adrenal lateralization was successfully identified by [^{68}Ga]Ga-PentixaFor PET (mean lesion diameter: 15.0 ± 5.66 mm). APA was confirmed histopathologically in 5 of these 11 patients; 2 received mineralocorticoid receptor antagonists at their own request, and follow-up is still pending in the remaining cases. PET imaging showed rapid tracer wash-out from the blood and stable adrenal retention beginning at minute 5 post-injection. For LCRmax, the earliest time point with excellent discriminatory performance (AUC = 1) was at 9-11 minutes post-injection (lateralization 2.13 ± 0.79 vs. no lateralization: 1.10 ± 0.09; $p < 0.01$).In 10-minute frame reconstructions, an AUC of 1 for LCRmax was observed consistently from minutes 10 to 50, with a slightly lower value between minutes 50 to60 (AUC = 0.972). The optimal cut-off for LCRmax to discriminate lateralization was consistently ≥1.5 across all time points. ***Conclusion:*** This retrospective analysis of dynamic PET data revealed that adrenal lateralization can be detected as early as 10 minutes post-injection and remains stable over time. An LCRmax cut-off of 1.5 provided consistent discrimination between APA and non-lateralizing cases. Ten-minute time frames between minutes 10 and 50 demonstrated excellent discriminatory performance, suggesting that shorter and more flexible acquisition protocols may be feasible in the diagnostic work-up for PA patients.

EP-0735

Thyroid disorders in primary school children in North Macedonia: A cross-sectional study

N. Manevska[1,2], *A. Jankulovska*[1], *B. Stoilovska Rizova*[1], *N. Kolovcevska Bozinovska*[1], *N. Stojkovska*[3], *T. Makazlieva*[1], *S. Stojanoski*[1];
[1]*Institute of Pathophysiology and Nuclear medicine, Faculty of Medicine, University of Ss Cyril and Methodius, Skopje, NORTH MACEDONIA, THE REPUBLIC OF,* [2]*University Institute of positron emission tomography, Skopje, NORTH MACEDONIA, THE REPUBLIC OF,* [3]*Institute of Histology and Embryology, Faculty of Medicine, University of Ss Cyril and Methodius, Skopje, NORTH MACEDONIA, THE REPUBLIC OF.*

Aim/Introduction: While thyroid disorders are often associated with adults, they represent the most prevalent endocrine disorder among school-age children. Autoimmune thyroiditis, in particular, is a leading cause of hypothyroidism in this age group, leading to potential growth impairments, cognitive development and overall health if left undetected. Early detection of thyroid dysfunction and intervention are crucial mitigating these risks, ensuring normal development. ***Materials and Methods:*** A cross-sectional study was conducted involving 53 randomly selected children, from five different schools in single in North Macedonia. Participants were aged 14 to 15 years and were attending their final year of primary education. They had never been tested for thyroid function prior to this study. Informed consent was obtained from all parents or legal guardians of before participation. Each participant underwent a thorough neck ultrasonography using a linear probe to assess thyroid morphology, size and detect any structural abnormalities. Based on ultrasonography findings, selected children underwent further clinical evaluation at the thyroid unit at the Institute of Pathophysiology and nuclear medicine. Laboratory tests included measurements of free thyroxine (fT4), thyroid-stimulating hormone (TSH), and where indicated anti-thyroid peroxidase (aTPO) antibodies, and anti-thyroglobulin antibodies (aTg). A detailed family history of thyroid disease was also collected. ***Results:*** The female to male ratio was 1:1.52. Ultrasound features mainly detected benign small anechoic cysts in 47.16% (n=25) of the children, while autoimmune pattern was noted in 32.07% (n=17) of the participants. Laboratory analysis revealed that 9.43% (n=5) had subclinical hypothyroidism, defined by elevated TSH levels (4.13-6.7mIU/L), Moreover, 13.2% (n=7) had Hashimoto's thyroiditis, confirmed through elevated autoantibodies and characteristic ultrasonographic patterns. The remaining participants were found to be euthyroid. A positive family history was noted in 15.09% (n=8). ***Conclusion:*** A significant burden of early thyroid autoimmunity and dysfunction was observed in school children aged 14-15 years. These findings highlight the importance of early screening and monitoring to detect thyroid disorders in this population, enabling timely diagnosis and management.

EP-0736

Minimally invasive radioguided parathyroidectomy using a handheld gamma detector probe: First experience with primary hyperparathyroidism - A pilot study

N. Bozhinovska[1], *A. Jankulovska*[1], *B. Stoilovska Rizova*[1], *B. Antevski*[2], *S. Stojanoski*[1], *N. Manevska*[3], *T. Makazlieva*[1];
[1]*Institute of Pathophysiology and Nuclear Medicine "Isaac Tadzer", Skopje, NORTH MACEDONIA, THE REPUBLIC OF,* [2]*University clinic for thoracic and vascular surgery, Skopje, NORTH MACEDONIA, THE REPUBLIC OF,* [3]*University Institute of positron emission tomography, Skopje, NORTH MACEDONIA, THE REPUBLIC OF.*

Aim/Introduction: Hyperparathyroidism (HPT) is a common endocrine disorder caused by autonomous hyperactivity of enlarged parathyroid glands, most often due to a solitary adenoma (85%), multiglandular hyperplasia (10%-15%) and carcinoma (less than 1%). Imaging techniques like ultrasonography and 99mTc-MIBI are crucial for surgical planning. Minimally invasive parathyroidectomy offers a safe, simple and cost-effective alternative to the conventional surgery. ***Materials and Methods:*** We reviewed 21 patients (18 females and 3 males) between december 2022 and march 2025, who underwent minimally invasive radioguided parathyroidectomy using a handheld gamma probe. Preoperative evaluation included dual-phase parathyroid scintigraphy with SPECT/CT and neck ultrasonography. Radioguided surgery was performed 90-120 minutes after intravenous injection of 370 MBq 99mTc-MIBI. A handheld gamma probe was used for neck scanning prior to a small (2-3cm) skin incision to localize the cutaneous projection of the hyperfunctional parathyroid tissue and its confirmation during surgery. ***Results:*** All the patients had biochemical evidence of HPT, with mean laboratory levels as follows: PTH 326.5 (range: 90.5-1005), total calcium levels 2.86 mmol/L (2.56-3.4), ionized calcium 1.54 mmol/L (range: 1.4-1.77), vitamin D 26.5ng/mL (range: 14-38), phosphate 0.78 mmol/L (range: 0.62-0.93). 52% of the parathyroid adenomas were localized below the inferior left lobe, 28% below the inferior right lobe and 20 % had an ectopic paratracheal and retrosternal localization. The gamma probe successfully identified the hyperfunctional parathyroid tissue in all patients, and minimally invasive radioguided surgery was completed without major complications. The average time of the surgery was 29 minutes. Postoperative laboratory values normalized in all cases. Histopathology confirmed parathyroid adenoma in 20 patients and a parathyroid carcinoma in one patient. ***Conclusion:*** Minimally invasive radioguided parathyroidectomy is a safe and effective technique that provides excellent surgical outcomes with less morbidity, faster recovery time, improved cosmetic results, and a lover overall cost compared to the conventional surgery.

EP-0737

Possibly coexistence of Hashimoto thyroiditis (HT) and papillary thyroid carcinoma (PTC)

K. Zaplatnikov*;*
MVZ Nuklearmedizin Mögeldorf, Nürnberg, GERMANY.

Aim/Introduction: HT is an offen autoimmune thyroid disease, known to be the most common cause of hypothyroidism in nonendemic goitrous areas. It is usually characterized by symmetric, painless, and diffused but sometimes localized swelling of the thyroid gland with features of hypothyroidism. ***Materials and Methods:*** The coexistence of the two diseases is possible but not common, in this situation is diagnostic is several, where many pseudonodul with hypoechogenic. The fine needle aspiration is not for all possible, we estimated algoorithmus for diagnosis. Patients with HT/PTC (Gr.A) and PTC without HT (Gr.B) were studied In prospective way. In algorithm of initial investigation 99mTc-scitigraphy, thyroid hormone and anti-TPO/anti-Tg antibodies levels estimation were performed along with clinical examination, thyroid sonography with Doppler DS and FNAC. Every case of PTC was confirmed by patho-histological examination. Age, sex, geographic anamnesis, tumour features (dimensions, angioinvasion, capsular infiltration, multifocality and lymphnode metastases) nuclear medicine examination data, therapy history and estimated total effective doses received by former inhabitanats of contaminated areas were analysed. ***Results:*** Statistically significant (P=0.001) difference in tumour size was found in two Groups: the average diameter was found to be 1.721+/-0.5812 and 1.145+/-0.871 cm in Gr.A and in Gr.B, respectively. Capsular infiltration was present only in Gr.A in 3 cases. The angioinvasion was found in 8 cases of Gr.A and 1 cases in Gr.B (P=0.310). Multifocality was found in 19 patients in Gr.A and in 2 in Gr.B (P=0.0009). There were no statistical differences in sex (P=0.423) and age (P=0.330). All pts in Gr.A had HT with high levels of thyroid Abs (TgAb/TPOAb). 51.5% autoantibody positive pts with US suspicious multifocal non-uniform thyroid goiter revealed scintigraphic cold lesion , in Gr.B 60% nodes were undetectable

in scans. Unfortunately, no thyroid gland and collective thyroid doses were available and estimated total effective doses were found for less than half of Gr.A with no cases of documented high over-doses. ***Conclusion:*** Statistically proven high prevalence (100%) of HT and multifocal PTC in Gr.A compared to Gr.B in our study might be related to the fact, that a majority of patients were previously residents of regions with probability of extensive radiation exposur. Our results justify a necessity of screening for PTC in population group exposed to external radiation and with concomitant HT, taking them into account and assuming more aggressiveness of tumours.

EP-0738

Added Value of MRI Multi-parameter Information for Diagnosing Subcentimeter Functional Adrenal Nodules using CXCR4-targeted PET/MRI imaging

X. Meng, *Z. Quan, F. Kang;*
Xijing Hospital of Airforce Military Medical University, Xi'an, CHINA.

Aim/Introduction: This study aims to evaluate the clinical utility of ^{68}Ga-pentixafor PET/MRI in diagnosing primary aldosteronism (PA) in functional adrenal nodules, with a particular focus on subcentimeter nodules. Additionally, the diagnostic performance of integrated PET/MRI is compared to single-modality PET imaging. ***Materials and Methods:*** A total of 62 patients with clinical suspicion of PA were prospectively enrolled from a tertiary hospital in China. Prior to adrenalectomy, all patients underwent ^{68}Ga-pentixafor PET/MRI, followed by CXCR4 and CYP11B2 immunohistochemical analysis post-surgery. Adrenal lesions were stratified into two size groups: ≥ 1 cm and < 1 cm. Quantitative PET parameters, including SUVmax, SUVmean, and lesion-to-liver uptake ratio (LLR), were evaluated alongside MRI parameters such as outphase/inphase signal ratio (OIR), relative percent washout (RPW), T2-weighted image intensity, ADC value. Receiver operating characteristic (ROC) curve analysis was performed to establish diagnostic thresholds. Comparative analyses were conducted between single-modality PET and integrated PET/MRI for diagnostic accuracy. ***Results:*** Among 62 patients, 74 adrenal lesions were confirmed pathologically, comprising 37 aldosterone-producing adenomas (APA, ≥ 1 cm), 21 aldosterone-producing micronodules (micro-APA, < 1 cm), and 16 non-functioning adenomas (NFA). Key PET/MRI parameters, including SUVmax, SUVmean, LLR, OIR, and RPW, showed significant differentiation between functional and non-functional groups (P < 0.001). For nodules ≥ 1 cm, the PET SUVmax threshold of 7.87 achieved a sensitivity of 92.3% and specificity of 95.0% for APA diagnosis. For nodules < 1 cm, the PET SUVmax threshold of 6.49 yielded a sensitivity of 68.8% and specificity of 83.3% for micro-APA diagnosis. Integrated PET/MRI notably improved the diagnostic sensitivity for nodules < 1 cm from 68.8% (PET alone) to 87.5%, with the area under the ROC curve increasing from 0.760 to 0.854. ***Conclusion:*** ^{68}Ga-Pentixafor PET/MRI demonstrated high diagnostic accuracy for functional adrenal nodules in PA, particularly enhanced sensitivity for subcentimeter nodules compared to PET alone. ***References:***
1. Hu J, Xu T, Shen H, Song Y, Yang J, Zhang A, et al. Accuracy of Gallium-68 Pentixafor Positron Emission Tomography-Computed Tomography for Subtyping Diagnosis of Primary Aldosteronism. JAMA Netw Open. 2023;6(2):e2255609. 2. Ding J, Zhang Y, Wen J, Zhang H, Wang H, Luo Y, et al. Imaging CXCR4 expression in patients with suspected primary hyperaldosteronism. Eur J Nucl Med Mol Imaging. 2020;47(11):2656-65. 3. Ding J, Li X, Liu S, Gao Y, Zheng G, Hacker M, et al. Clinical Value of 68Ga-Pentixafor PET/CT in Subtype Diagnosis of Primary Aldosteronism Patients with Adrenal Micronodules. J Nucl Med. 2024;65(1):117-24.

EP-0739

99mTc-Pertechnetate Scintigraphy predicts successful postoperative ablation in patients with low-risk differentiated thyroid carcinoma.

I. El Bez, *R. Tulbah, S. Alhazza, R. Alsalah, K. Ibrahim, F. Algmlas, M. Alharbi;*
AAML, Riyad, SAUDI ARABIA.

Aim/Introduction: Postoperative radioiodine treatment (RAI) is currently debated for patients with low-risk differentiated thyroid carcinoma (DTC) patients. If performed, a low ^{131}I activity is usually recommended with the aim to ablate thyroid remnant. The purpose of this study is to evaluate the relationship between postsurgical technetium-99m (^{99m}Tc)-pertechnetate scintigraphy and the rate of successful remnant ablation after low activity radioiodine ablation in patients with low-risk DTC. ***Materials and Methods:*** 72 patients with DTC who underwent total thyroidectomy followed by low-activity RAI ablation were enrolled. ^{99m}Tc pertechnetate scintigraphy scans were acquired before ablation. Response to treatment was assessed at 6 to 12 months after ablation. ***Results:*** The thyroid remnant ablation success rate was seen in 40/72 patients (55.6 %). Statistically Significant difference was noted in success rate of thyroid remnant ablation according to the presence of thyroid remnant uptake on the preablative ^{99m}Tc pertechnetate scintigraphy. The successful ablation rate in patient with negative preablative uptake on ^{99m}Tc pertechnetate scintigraphy was 74.2% (26 patients). In logistic regression analysis only the thyroid remnant uptake on preablative ^{99m}Tc pertechnetate scintigraph was significant predictive factor for ablation success (P = 0.002). ***Conclusion:*** Preablative ^{99m}Tc pertechnetate scintigraphy is a simple and feasible tool to evaluate for thyroid remnant and predict predicts successful postoperative ablation in patients with low-risk DTC.

EP-42

e-Poster Area

B: Imaging Clinical Studies -> B7 Musculoskeletal, Infection and Inflammation Imaging Study -> B71 Bone Infection and Inflammation

EP-0740

Can We See More with Three-Phase Bone Scintigraphy in Patients with Prosthetic Infection?

J. Mendes, *P. Soeiro;*
Hospital de São João, Porto, PORTUGAL.

Aim/Introduction: The global rise in orthopaedic arthroplasty has led to a proportional increase in prosthetic complications, particularly aseptic loosening and periprosthetic joint infection (PJI). While hybrid imaging modalities such as [^{18}F]FDG PET/CT offer promise, their limited specificity and complex interpretation—especially in distinguishing infection from postoperative inflammation—restrict routine use. Moreover, in many centres without access to labelled leucocyte imaging, three-phase bone scintigraphy (TPBS) remains the only nuclear medicine tool available for prosthesis assessment. However, reliably distinguishing septic from aseptic loosening using TPBS alone remains a diagnostic challenge. This study aimed to evaluate whether specific visual or semi-quantitative TPBS patterns are predictive of prosthetic infection as opposed to aseptic loosening. ***Materials and Methods:*** We conducted a retrospective, single-centre study of patients who underwent TPBS between May 2006 and February 2020. Adult patients with hip or knee prostheses and clinical suspicion of prosthetic complications were included. Clinical records and TPBS images were analysed visually and semi-

quantitatively. Uptake patterns across vascular, blood pool, and osseous phases were evaluated. Outcomes were categorised as (1) successful prosthetic integration, (2) aseptic loosening, or (3) septic loosening/infection. Statistical analysis was performed using IBM SPSS Statistics. ***Results:*** A total of 123 TPBS studies were included, comprising hip prostheses (47.2%) and knee prostheses (44.7%). The study population was 67.5% female and 32.5% male, with a median age of 72 years. TPBS findings showed a strong correlation with clinical outcomes ($p < 0.000001$ for all phases). Focal uptake in the osseous phase was observed in both aseptic (96.7%) and septic (87.5%) loosening. Diffuse osseous uptake was seen exclusively in septic cases. Altered vascular and blood pool phases were significantly more frequent in septic loosening (87.5% and 100%, respectively) than in aseptic cases (68.3% and 70%). Normal uptake across all three phases was predominantly associated with prosthetic integration. ***Conclusion:*** Three-phase bone scintigraphy remains a valuable diagnostic tool in centres without access to more advanced nuclear imaging. While focal osseous uptake alone lacks specificity, the combination of altered vascular and blood pool phases—particularly with diffuse osseous uptake—appears to be strongly predictive of infection. These results support the development of structured visual and semi-quantitative TPBS interpretation criteria to improve diagnostic accuracy in suspected prosthetic complications.

EP-43

e-Poster Area

B: Imaging Clinical Studies -> B7 Musculoskeletal, Infection and Inflammation Imaging Study -> B72 Vasculitis and Endocarditis

EP-0741

Diagnostic Accuracy of ^{18}F-FDG-Labelled Autologous Leukocyte Positron Emission Tomography - Computed Tomography in Suspected Cardiac Infections

P. Malik, *A. Bhattacharya, R. Kumar, H. Singh, P. Panda, H. Singh, B. R. Mittal;*
Post Graduate Institute of Medical Education and Research, Chandigarh, INDIA.

Aim/Introduction: Cardiac infections are an important cause of cardiovascular morbidity and mortality with nonspecific presentations contributing to delayed diagnosis. The 2023 Duke-International Society for Cardiovascular Infectious Diseases Criteria for Infective Endocarditis (ISCVID IE) Criteria have proposed ^{18}F-FDG-PET as a major imaging criterion. ^{18}F-FDG-labelled autologous leucocyte PET/CT (^{18}F-FDG-LAL-PET/CT) circumvents the need for special dietary preparation to suppress physiological myocardial FDG uptake. This study aims to assess the diagnostic accuracy of ^{18}F-FDG-LAL-PET/CT against common imaging modalities like echocardiography (ECHO) for detection of cardiac infections. ***Materials and Methods:*** Twenty-nine patients who presented with suspected cardiovascular device infection (CVDI) or "possible IE" as per 2023 Duke-ISCVID IE criteria were prospectively recruited. ^{18}F-FDG-LAL-PET/CT was performed in all patients with total leucocyte count > 5000/mm^3 and erythrocyte sedimentation rate > 15mm in 1st hour after clinical workup, laboratory investigations and conventional imaging. Clinical follow-up / histopathology (when feasible) were used to confirm the diagnosis as a composite reference standard. Patients who had blood cultures or ECHO positive and clinical response to antibiotics/device removal were considered as true positives. ***Results:*** The study included 29 patients (5 female, 24 male), aged 49 +/- 17.9 (standard deviation) years. The commonest symptom was fever, followed by dyspnoea. Suspected diagnoses comprised native-valve IE (n=10), prosthetic-valve IE (n=7), pacemaker infection (n=5), stent/graft infection (n=4) and mycotic aneurysms (n=3). ^{18}F-FDG-LAL-PET/CT showed abnormal tracer localisation in 15 (10 IE, 5 CVDI) patients, 14 of which were diagnosed as true positive. No tracer localisation was detected in 14 patients (2 false negative). The sensitivity, specificity, positive predictive value, negative predictive value, and accuracy of ^{18}F-FDG-LAL-PET/CT was 87.5%, 92.3%, 93.3%, 85.7%, and 89.7% respectively. ECHO vegetations were reported in 11 suspected valvular IE patients, of which only 4 showed LAL localisation. Tracer localisation was detected in 2 patients with no significant ECHO findings and 3 with negative blood cultures. One patient with prosthetic mitral valve vegetation on ECHO showed LAL localisation in the prosthetic aortic valve instead. In patients who had undergone ^{18}F-FDG-PET/CT previously, some myocardial regions showed physiological tracer uptake despite adequate diet preparation, likely due to increased cardiac workload. ***Conclusion:*** ^{18}F-FDG-LAL-PET/CT can detect IE and CVDI with good specificity. It can be especially useful in the setting of possible IE and patients with negative cultures, and does not require compliance to special diets and prolonged fasting.

EP-0742

Sensitivity and Specificity of F-18 FDG PET/CT İmaging in IE; Usefulness of Dual İmaging

A. Çelik Arslan[1], *C. Engür Uyanık*[1], *A. Çınar*[1], *D. Karamanlıoğlu*[2], *N. Aydınbelge Dizdar*[1], *Ö. Özmen*[1];
[1]*Etlik City Hospital, Department of Nuclear Medicine, Ankara, TÜRKIYE,* [2]*Etlik City Hospital, Department of Clinical Microbiology and Infectious Diseases, Ankara, TÜRKIYE.*

Aim/Introduction: This study aims to investigate the correlation of F-18 FDG PET/CT with clinical and TEE findings in the diagnosis of IE and to assess its sensitivity and specificity in patients with native and prosthetic valves. ***Materials and Methods:*** Patients referred to our clinic between January 2023 and February 2025 with a suspected diagnosis of IE were included in the study. Images of 42 patients who underwent FDG PET/CT after an appropriate diet regimen were retrospectively analyzed. Patients were further divided into two subgroups based on the localization of the infection focus (native/prosthetic valve). Visual assessment of the images obtained at 60 and 90 minutes: patients with heterogeneous distribution around the valve, intense focal FDG uptake were considered as positive for IE, while those with homogeneous and diffuse F-18 FDG distribution were considered negative for IE. Patients were evaluated for accompanying septic emboli. ***Results:*** In 14 of the 42 patients included in the study, increased FDG uptake consistent with the diagnosis of IE was observed. The sensitivity of PET/CT for diagnosing IE was found to be 52.63%, specificity 84.62%, positive predictive value 83.3%, negative predictive value 55%, and accuracy 65.63%. The sensitivity of TEE was 45.45%, specificity 90.91%, positive predictive value 83.33%, negative predictive value 62.5%, and accuracy 68.18%. Among the 18 patients considered suspicious by TEE, 8 were found to be positive on PET/CT and clinically diagnosed with IE. In the evaluation of PET parameters in prosthetic valve patients, a cutoff value was determined with 86% sensitivity and 87.5% specificity; for first images, the cutoff was 3.28 and for late images, 4.47. For native valve patients, the PET parameters for detecting IE were evaluated, with first and late SUVmax cutoff values calculated as follows: 67% sensitivity and 69% specificity for first images with a cutoff of 2.59 , and 83% sensitivity and 81% specificity for late images with a cutoff of 2.95. Late images showed more significant SUVmax values. There was no statistically significant correlation between the duration of antibiotic use and valve SUVmax values. ***Conclusion:*** In suspected valve-associated IE, FDG PET/CT is a non-invasive imaging method with sensitivity and specificity similar to TEE. Late images are valuable in evaluating native valve IE, while first and late images in prosthetic valve IE show significant activity increase in diagnosing the condition. Whole-body imaging in PET/CT helps to explore supportive findings and aids in diagnosis beyond just the heart.

EP-0743

Evaluating the Role of [18F]FDG PET-CT in Infective Endocarditis: Correlations with Systemic Inflammatory Markers

A. Militaru[1], *D. F. Militaru-Minea*[2], *A. Marin*[1], *M. M. Matei*[1], *D. Craciun*[1], *C. V. Mazilu*[1], *R. M. Mititelu*[1,3];
[1]*Clinic of Nuclear Medicine - Central Universitary Emergency Military Hospital, Bucharest, ROMANIA,* [2]*Clinic of Infectious Diseases- Central Universitary Emergency Military Hospital, Bucharest, Bucharest, ROMANIA,* [3]*Nuclear Medicine Department-University of Medicine and Pharmacy "Carol Davila" Bucharest, Bucharest, ROMANIA.*

Aim/Introduction: Infective endocarditis (IE) is a diagnostic challenge, especially in cases with equivocal echocardiographic findings. [18F]FDG-PET-CT has been shown to be a valuable imaging modality for detecting infections of the prosthetic heart valve and device-related infections. ***Materials and Methods:*** In this study, 25 patients with suspected infective endocarditis who underwent ^{18}F-FDG PET-CT were retrospectively analyzed. Among them, 10 patients had prosthetic heart valves, while 15 patients had native valves. Imaging results were correlated with clinical, microbiologic and laboratory data, including inflammatory markers such as C-reactive protein (CRP) and leukocytosis. Patients were classified based on PET-CT positivity and inflammatory markers, and statistical analysis was performed to evaluate the association between inflammatory markers and imaging results. ***Results:*** Of the 25 patients, PET-CT was positive in 10 cases (40%), with a higher detection rate in patients with prosthetic valves than in patients with native valves (7 vs. 3). PET-CT positivity was significantly associated with elevated CRP levels ($p = 0.0084$), suggesting a close association between systemic inflammation and PET-CT findings. Although leukocytosis was observed in both PET-CT-positive and PET-CT-negative cases, there was no significant association with PET-CT positivity ($p = 0.1648$), suggesting that leukocytosis alone may not be a reliable marker of infection. In addition, echocardiography did not show a significant correlation with either CRP ($p = 0.8807$) or leukocytosis ($p = 0.8350$), reinforcing its lower sensitivity in detecting inflammation-related changes. These results emphasize the superior diagnostic performance of PET-CT compared to echocardiography, especially in patients with prosthetic valves and elevated inflammatory markers such as CRP. ***Conclusion:*** ^{18}F-FDG PET-CT is a valuable tool in the diagnostic workup of infective endocarditis, particularly in patients with prosthetic valves where echocardiography is limited. The correlation between PET-CT findings and CRP levels could provide additional insights into disease activity and prognosis. Further studies with larger cohorts are needed to validate these results.

EP-44

e-Poster Area

B: Imaging Clinical Studies -> B7 Musculoskeletal, Infection and Inflammation Imaging Study -> B73 Other Infections and Inflammatory Diseases

EP-0744

Seeing Beyond Symptoms: How FDG-PET/CT Detects Silent Myositis in Seronegative Dermatomyositis in a retrospective cohort

R. Karna*, A. S. Babu, A. Dhiman, R. Kumar;*
All India Institute Of Medical Sciences, New Delhi, New Delhi, INDIA.

Aim/Introduction: Dermatomyositis (DM) and other inflammatory myopathies can present with muscle inflammation that often goes undetected using standard blood tests, especially in seronegative DM patients. FDG-PET/CT imaging may help identify subclinical inflammation that is missed by conventional biomarkers like creatine kinase (CK). This study aims to evaluate the role of FDG-PET/CT in detecting subclinical muscle inflammation in DM and other inflammatory myositis subtypes and to correlate PET findings with serum markers, such as CK, CRP, and LDH. ***Materials and Methods:*** We conducted a retrospective analysis of 42 patients diagnosed with DM or inflammatory myositis. FDG-PET scans were scored using a three-tier system: Score 0 (uptake less than blood pool), Score 1 (uptake more than or equal to blood pool), and Score 2 (uptake more than or equal to liver). PET scores were compared with serum levels of CK, CRP, and LDH. Patients were divided into subgroups: classic DM, overlap syndromes, and inflammatory myositis. ***Results:*** Discordant Cases: 35% (6/17) of CK-negative patients had significant FDG uptake (Scores 1 or 2), indicating occult muscle inflammation that was not detected through routine blood tests. PET-Biomarker Correlations:48% of patients had a PET Score 2, with 70% showing elevated CK, 85% with raised LDH, and 60% with high CRP, suggesting active inflammation.14% of patients had a Score 1, with 83% showing elevated CK, but lower CRP levels (median 3 mg/dL), reflecting intermediate disease activity. Subtype Variations: Classic DM patients showed the highest FDG uptake (71% with Score 2), while 75% of overlap syndrome patients had Score 0, a significant difference ($p=0.04$). ***Conclusion:*** FDG-PET/CT is an effective tool for detecting subclinical muscle inflammation, particularly in CK-negative DM patients. It complements serum biomarkers in assessing disease activity and can help monitor inflammation in different myositis subtypes, especially classic DM, where biomarkers and imaging findings often do not align. FDG-PET/CT may improve early detection and monitoring of active inflammation in these patients.

EP-0745

Utility of ^{18}F-FDG PET/CT in the initial characterization of silicosis

J. Rodríguez-Rubio Corona[1], *M. Piñero Fernández-Reyes*[1], *J. Jiménez-Murillo*[2], *Y. Santaella-Guardiola*[1], *F. Cañete-Sánchez*[1], *M. Gutiérrez-Amares*[1], *A. Campos-Caro*[3], *A. León-Jiménez*[4], *M. Pajares-Vinardell*[1];
[1]*Nuclear Medicine Department, Puerta del Mar University Hospital, Cádiz, SPAIN,* [2]*Technical Advisory Subdirectorate for Information Management, Servicio Andaluz de Salud, SPAIN,* [3]*Institute of Biomedical Research and Innovation of Cádiz (INiBICA), Cádiz, SPAIN,* [4]*Pulmonology Department, Puerta del Mar University Hospital, Cádiz, SPAIN.*

Aim/Introduction: Silicosis is an occupational inflammatory lung disease caused by the inhalation of silica particles. Diagnosis is based on occupational history, radiological findings as defined by the International Classification for Occuptaional and Environmental Respiratory Diseases (ICOERD), and the exclusion of other conditions. Although the role of ^{18}F-FDG in the study of inflammatory diseases is well known, it's application in the assessment of silicosis remains limited. The aim of this study is to assess the usefulness of ^{18}F-FDG PET/CT in the initial characterization of silicosis and the correlation between metabolic parameters and the findings observed on CT. ***Materials and Methods:*** Descriptive study of 17 patients diagnosed of silicosis who underwent a chest CT at the time of diagnosis (April 2017-July 2020) where lesions were classified according to ICOERD and if they were or not calcified. The location of lymphadenopathy and pulmonary lesions was analysed. Later, a whole-body ^{18}F-FDG PET/CT scan was performed (November 2021-September 2022), recording the maximum Standardized Uptake Value (SUVmax) of the lesions. The correlation between ICOERD and SUVmax was estimated using Spearman's correlation coefficient, and a hypothesis test was conducted. ***Results:*** Five patients were classified as ICOERD A, six

as B, and six as C. The average SUVmax increased as is scaled in the ICOERD classification: 3.96 for A, 6.25 for B, and 8.88 for C, with a Spearman's coefficient of 0.70 ($p<0.01$). Calcified lesions also showed a higher average SUVmax than non-calcified ones (7.14 and 4.83, respectively). The average SUVmax of the lymph nodes was 6.22, and PET/CT detected lymphadenopathies not identified on CT in 10/17 patients (58.82%), mainly in lower thoracic and abdominal regions. ***Conclusion:*** ^{18}F-FDG PET/CT allows a better initial characterization of silicosis due to its higher sensitivity in detecting lymphadenopathies, mainly extrathoracic. Metabolic activity is higher in advanced ICOERD categories and in calcified lesions.

EP-0746

Role of 99mTc-Ethambutol Scintigraphy in Diagnosis of Pulmonary and Extra Pulmonary Tuberculosis

A. Roy, *N. A. Damle, S. Sikdar;*
AIIMS new delhi, New Delhi, INDIA.

Aim/Introduction: To determine the sensitivity, specificity, predictive values, and overall diagnostic accuracy of 99mTc-Ethambutol scintigraphy in detecting pulmonary and extrapulmonary tuberculosis. ***Materials and Methods:*** A prospective observational study was conducted at AIIMS, New Delhi, involving 28 adult patients diagnosed or clinically suspected to have TB. Patients received 10 mCi of 99mTc-Ethambutol intravenously, and serial planar and SPECT/CT scans were performed. Uptake patterns were correlated with microbiological, histopathological, and clinico-radiological findings. Diagnostic accuracy parameters were calculated using standard statistical methods. ***Results:*** Out of 28 enrolled patients, 25 had reference diagnostic standards. 99mTc-EMB scintigraphy showed an overall sensitivity of 81.25%, specificity of 66.67%, PPV of 81.25%, NPV of 66.67%, and accuracy of 76%. Subgroup analysis revealed significantly higher diagnostic accuracy in bone TB (sensitivity and NPV 100%, accuracy 92.3%). In contrast, sensitivity and PPV were lower in soft tissue EPTB (40% and 50%, respectively). False negatives were primarily due to necrotic tissue or reduced perfusion; false positives were attributed to non-specific uptake and radiochemical impurities. ***Conclusion:*** 99mTc-Ethambutol scintigraphy is a promising non-invasive imaging modality for TB, particularly in skeletal involvement, where it demonstrates high diagnostic accuracy. However, caution is advised in interpreting results for soft tissue EPTB due to lower sensitivity. This imaging technique also holds potential for guiding biopsy site selection and monitoring treatment response.

EP-45

e-Poster Area

B: Imaging Clinical Studies -> B7 Musculoskeletal, Infection and Inflammation Imaging Study -> B74 Orthopedics, benign, no infection

EP-0747

The use of a portable ultrasound device to control intra-articular puncture during radioisotope synovectomy of the knee joints - Is post-injection scintigraphy always necessary?

M. Wlodarczyk, *Z. Adamczewski;*
Nuclear Medicine Department, Central Clinical Hospital, Medical University of Lodz, Lodz, POLAND.

Aim/Introduction: Radioisotope synovectomy is a recognized method used in the treatment of joint effusions. It involves intra-articular administration of an isotope-labelled colloid emitting beta radiation. The condition for safely carrying out this type of procedure is to deposit the isotope in the joint cavity. The flow of synovial fluid confirms the correct position of the needle tip during injection. Additionally, ultrasound imaging is used to monitor the injection or to select the best place for the injection just before starting the procedure. Guideline for radiosynoviorthesis recommend the post-injection scintigraphy to confirm proper radiopharmaceutical distribution, which in many cases seems unnecessary. ***Materials and Methods:*** Nuclear Medicine Department of the Medical University of Lodz has extensive experience in performing radiosynovectomy of the knee joints. Over the last 12years, approximately 1,200 procedures of this type have been performed. For several months, a portable ultrasound device equipped with a linear head with 4-12MHz frequency has been used for ultrasound control during injection. Over this period, 153 radiosynovectomy procedures were performed in selected patients without popliteal cyst or synovial septa. In case of previous arthroscopy or arthroplasty, the required 2-month intervals were maintained. ***Results:*** During procedures performed under portable ultrasound guidance, synovial fluid outflow could not be obtained in only 18 cases (12%). In all 153 cases, safe isotope deposition was achieved by confirming the presence of the needle tip in the joint cavity (photographic documentation recorded). In 18 cases of so-called "dry joints" prior administration of a small amount of saline was required. Only in 1 case was it necessary to perform another puncture due to significant hypertrophy of the synovium and the inability to locate the needle tip in the joint cavity. The choice of an alternative injection site was made based on the ultrasound image, which allowed the procedure to be performed successfully. In all 153 cases subsequent scintigraphy confirmed the correct distribution of the radiopharmaceutical. ***Conclusion:*** The use of a portable ultrasound device allows for selection of the best joint puncture site and for high probability of obtaining synovial fluid outflow. The quality of the generated image is sufficient to visualize the needle tip during injection, which is particularly important in the case of so-called "dry joints". Properly performed injection under portable ultrasound guidance allows to omit additional acquisition of a scintigraphic image in selected patients, which significantly shortens the time and reduces the cost of the entire procedure.

EP-0748

Scintigraphic Findings of Inflammatory Pseudotumour in Long-standing Osteoarticular Arthroplasties: Experience at Our Centre

M. Rosado Hidalgo, *L. Ramos Rodríguez, S. Romero Acevedo, J. Vela León, M. Lara Martínez, F. Medina Romero, M. González Díaz, M. Gómez Rodríguez-Bethencourt;*
Hospital Universitario de Canarias HUC, Tenerife, SPAIN.

Aim/Introduction: Wear particle-induced periprosthetic osteolysis is a well-known phenomenon in total arthroplasties and the leading cause of aseptic loosening. Occasionally, it presents aggressively with soft tissue mass, or 'inflammatory pseudotumour', often requiring revision and complex reconstruction surgery. The aim of this study is to assess the scintigraphic findings on blood pool and delayed SPECT-CT in patients with long-standing total hip and knee arthroplasties complicated with loosening due to particle disease and associated pseudotumour formation. ***Materials and Methods:*** A retrospective descriptive study was conducted on eight patients seen between 2021 and 2025 with wear particle-induced periprosthetic osteolysis associated with a soft tissue mass. Bone scintigraphy with ^{99m}Tc-HDP, including blood pool (5-10 minutes) and delayed (3-4 hours) phases, along with SPECT-CT in both phases, was visually assessed. Pseudotumour dimensions were measured from CT. Demographic variables and pain presence were recorded. Infectious and neoplastic complications were excluded through clinical and laboratory evaluation. ***Results:*** The study included 8 patients, 5 women and 3 men, with a mean age of 75 years and an average interval of 17 years from prosthesis implantation to molecular imaging. All patients

reported pain, contrary to previous literature. A pseudotumour was identified on the acetabular component in 2 cases (mean size: 45×40×75 mm, AP×T×CC), on the femoral component in 1 case (20×40×40 mm), and in 4 cases affecting both components (mean size: 123×95×119 mm). One case involved a right total knee arthroplasty with pseudotumour affecting the femoral component (100×100×240 mm). The scintigraphic pattern observed in all cases was characterised by central photopenic defect in the soft tissue mass with peripheral radiotracer uptake in severe periprosthetic osteolysis with bone destruction in some cases. Blood pool presented similar behaviour as in the late phase. ***Conclusion:*** Inflammatory pseudotumours represent a rare complication of total hip and knee arthroplasties. In our series, all cases were symptomatic and demonstrated a characteristic uptake pattern on SPECT-CT. Its recognition is essential, as it may influence clinical decision-making, favouring revision surgery due to associated complications. ***References:*** 1. Fabbri N, Rustemi E, Masetti C, et al. Severe osteolysis and soft tissue mass around total hip arthroplasty: description of four cases and review of the literature with respect to clinico-radiographic and pathologic differential diagnosis. Eur J Radiol. 2011;77(1):43-50.doi:10.1016/j.ejrad.2010.08.015 2. Díaz Moreno JL, Sánchez-Rodríguez IE, Hervás-Sanz B, Notta-González P, Martínez-Ramos C, Gràcia-Sánchez L. Microparticle disease in hip prostheses: A case report. Rev Esp Med Nucl Imagen Mol (Engl Ed). 2025;44(2):500078. doi:10.1016/j.remnie.2024.500078.

EP-46

e-Poster Area

B: Imaging Clinical Studies -> B8 Nephro-Urological Imaging Study -> B81 Nephro-Urology

EP-0749

Contribution of Renal Scintigraphy Findings to Clinical Management

B. Bozca*, A. Cinar, D. Cayir, N. Aydinbelge Dizdar, O. Ozmen;*
Etlik City Hospital, Department of Nuclear Medicine, Ankara, TÜRKIYE.

Aim/Introduction: Renal scintigraphy is a highly accurate and sensitive imaging method used to evaluate organ function. Tc-99m DMSA is a reliable radiopharmaceutical for assessing differential renal function (DRF) and visualising renal parenchyma. Additionally, Tc-99m MAG-3 is another radiopharmaceutical that can be used to calculate DRF. Background activity correction is a necessary step in DRF calculation, and it may represent a potential source of error. Aim of this study is to consider DRF calculated with DMSA as gold standard and to determine which background activity region is associated with the least error when using MAG-3. ***Materials and Methods:*** A retrospective analysis was conducted on 93 patients who underwent both DMSA and MAG-3 scintigraphy within two-week period between December 2023-December 2024. In DMSA scintigraphy, DRF was calculated using geometric mean and automatic perirenal ROI for background correction. In MAG-3 images, DRF was determined by drawing three different regions of interest: inferior (group 1), superior pole (group 2), and crescentic (group 3). 21 patients with normal renal function formed the control group, while 72 patients with varying degrees of obstruction patterns were defined as patient group. DRF obtained from DMSA images were accepted as gold standard. DRF from MAG-3 images were compared with DMSA images. DFR's were compared using linear regression analysis. The Mann-Whitney U test was used to compare laboratory parameters. P-value of <0.05 was considered statistically significant. ***Results:*** In both groups with normal and pathological renal function, no statistically significant differences were found in age, sex, or renal function tests (Table 1). Among patients with normal renal function, there was no statistically significant difference between DRF values obtained from DMSA and MAG-3 scintigraphy. In patient group with pathological renal function, background correction using superior pole and crescentic regions yielded results that differed markedly from DMSA scintigraphy. When the background activity region was drawn from inferior pole, DRF values were the most consistent with DMSA scintigraphy. This background region was found to be statistically significant. ***Conclusion:*** In conclusion, DMSA is considered a reliable method for determining differential renal function. In our study, in the presence of normal renal function, similar DRF values were obtained using three different background activity regions. However, in the presence of an obstructive pattern, the background activity region drawn from the inferior renal pole in the MAG-3 study was found to be more consistent and reliable when compared with the DRF values obtained from DMSA scintigraphy.

EP-0750

A Simple Numeric Clue: Non-Decay Corrected 4-Hour Retention Percentage on Tc-99m LLEC Scans to Distinguish PUJO from Delayed Clearance in Equivocal Tc-99m LLEC Renograms

A. Mahalik*, N. Kundu, A. Roy, K. Jain, V. R. Singh, J. Choudhary, S. Singh, J. Krishna P., R. Kumar;*
All India Institute of Medical sciences, New Delhi, INDIA.

Aim/Introduction: Differentiating pelviureteric junction obstruction (PUJO) from delayed non-obstructive clearance (DNOC) in patients with equivocal renogram curves presents a common diagnostic dilemma. Tc-99m L,L-ethylenedicysteine (LLEC) is a preferred radiotracer for assessing renal drainage due to its favorable pharmacokinetics. This study evaluates the diagnostic value of 4-hour retention percentage using non-decay corrected counts from static images in distinguishing PUJO from DNOC. ***Materials and Methods:*** We retrospectively analyzed 61 renal units showing equivocal or uprising curves on Tc-99m LLEC dynamic scans. Retention percentage was calculated using counts from prevoid and 4-hour delayed post-void static images. Importantly, decay correction was not applied, as static image ROIs in routine clinical settings yield non-decay corrected counts, and this approach enhances reproducibility in day-to-day practice. Based on surgical or clinical follow-up, renal units were grouped into PUJO (n=29) and DNOC (n=32). ROC analysis was conducted to identify an optimal diagnostic cut-off. ***Results:*** The PUJO group showed a significantly higher mean retention percentage (58.6 ± 18.7%) compared to the DNOC group (32.5 ± 16.4%, $p < 0.001$). ROC analysis identified a cut-off value of 44.5% using non-decay corrected counts, with an AUC of 0.84, sensitivity of 86.2%, and specificity of 78.1% for diagnosing PUJO. ***Conclusion:*** Retention percentage from 4-hour static images using non-decay corrected Tc-99m LLEC counts is a simple and effective tool for differentiating PUJO from DNOC in equivocal renogram curves. This method reflects real-world imaging workflows and can serve as a reliable adjunct to curve morphology in decision-making.

EP-0751

Use of Dynamic Renal Scintigraphy as a Method to Predict Renal Outcome in Acute Kidney Injury

P. Korol*[1], O. Shcherbina[1], M. Tkachenko[2], M. Kostylev[3];*
[1]Shupik National University Healthcare of Ukraine, Kyiv, UKRAINE, [2]Bogomolets National Medical University of Ukraine, Kyiv, UKRAINE, [3]Shalimov National Scientific Center of Surgery and Transplantation, Kyiv, UKRAINE.

Aim/Introduction: Acute kidney injury (AKI) is characterized by a rapid loss of renal function (<48 hours). Dynamic renal scintigraphy (RS) with Tc-99m-MAG3 is routinely prescribed by physicians in our Department of Nuclear Medicine to assess renal function in patients with AKI. The aim of our study is to determine the ability

of dynamic RS to predict renal recovery after AKI. ***Materials and Methods:*** We retrospectively included 270 patients (127 men and 143 women) with a mean age of 56±9 years who suffered RS during AKI. During RS, the accumulation index (AI), defined as the percentage of input activity recovered by the kidney in one minute, was calculated, and the slope of the accumulation curve (SAC) of the most functional kidney was measured. Renal function was assessed 6 months after RS, and patients were divided into two groups: patients with recovery of renal function and patients without significant recovery, defined as recovery of less than 30% of the loss of function during AKI. ***Results:*** When RS was performed during AKI, the sum of the AI of both kidneys was significantly higher in patients with recovery of renal function 3 months after AKI than in patients without significant recovery of renal function (9.3 [6.2-11.4] versus 6.1 [3.4-7.6]; $p < 0.05$). SAC of the most functional kidney was also significantly higher in patients with renal function recovery (0.34 [0.23-0.54] than without 0.21 [0.12-0.29]; $p = 0.05$). ***Conclusion:*** Quantitative AI and SAC measured during RS are useful indices to predict renal function recovery after AKI.

EP-0752

Dynamic Renal Scintigraphy In Pediatric pelviureteric junction stenosis : Impact In Therapeutic Decision

R. Belakroum, *H. Bouzidi;*
Regional University Military hospital, Constantine, ALGERIA.

Aim/Introduction: Pelviureteric junction (PUJ) stenosis antenatally diagnosed is an urodynamic disorder responsible for renal dilation. Its imaging modalities and therapeutic choices are controversial. Non-operative postnatal treatment consistent with PUJ stenosis, has functioned well during follow-ups. However, doubts are still expressed and admittedly, the final verdict on this therapeutic approach is still debated. The purpose of this prospective study is to define the state of art and to serve as a background for future studies, which still are needed. ***Materials and Methods:*** Through a prospective study, we have followed 80 children with antenatally diagnosed, unilateral PUJ stenosis during a 9 years period (between 2016 and 2024), with a median follow up of 102 months. Repeated ultrasounds, and ^{99m}Tc-EC (ethylene-dicysteine) renograms under strict guidelines were performed in all children during the follow up. Initial differential renal function (DRF), quality of renal drainage and cortical transit were analyzed and compared to the late DRF outcome. ***Results:*** Surgical repair (Anderson-Hynes dismembered pyeloplasty) was performed in 33 (41,25 %), while 47 (58,75 %) patients did not underwent a surgical intervention. Early pyeloplasty was performed in 19 patients, and late pyeloplasty in 14 cases. During conservative approach, DRF deterioration was observed in 13% of cases. When analyzing the DRF evolution, DRF deterioration was equally distributed between the different levels of abnormal renal drainage. However, there was no DRF degradation in patients with good drainage, and only abnormal cortical transit were predictive of DRF deterioration in case of conservative approach. ***Conclusion:*** In children with antenatally diagnosed PUJ stenosis, a conservative management might be a safe attitude without routine surgery. A good renal drainage could rule out PUJ obstruction. ***References:*** [1]- Koff SA, Campbell KD. The nonoperative management of unilateral neonatal hydronephrosis : natural history of poorly functioning kidneys. J Urol 1994 Aug :593e5., 152(2 Pt.[2]- Schlotmann A, Clorius JH, Clorius SN. Diuretic renography in hydronephrosis : renal tissue tracer transit predicts functional course and thereby need for surgery. Eur J Nucl Med Mol Imaging. 2009 et 36 :1665-1673.[3]- S. Arena1 & R. Chimenz E. Antonelli F. M. Peri P. Romeo P. Impellizzeri C-A long-term follow-up in conservative management of unilateral ureteropelvic junction obstruction with poor drainage and good renal function-European Journal of Pediatrics. 2018 [4]- Josephson S. Antenatally detected, unilateral dilatation of the renal pelvis : a critical review. I. Postnatal non-operative treatment 20 years on- is it safe ? Scand J Urol Nephrol 2002; 36: 251-9.

EP-0753

Assessment of 99mTc-DTPA renal scintigraphy in monitoring cisplatin nephrotoxicity in oncology patients in Saudi Arabia

M. Alqahtani[1,2];
[1]*Najran university, Najran, SAUDI ARABIA,* [2]*Najran university hospital, Najran, SAUDI ARABIA.*

Aim/Introduction: Cisplatin-based chemotherapy is a cornerstone treatment for various cancers but is associated with nephrotoxicity, which can lead to renal dysfunction. Monitoring renal function during chemotherapy is crucial for early detection and management of nephrotoxicity(1-2). This study aimed to evaluate the efficacy of 99mTc-DTPA scintigraphy in detecting cisplatin-induced nephrotoxicity among cancer patients in Saudi Arabia***. Materials and Methods:*** A total of 85 non-hypertensive, non-diabetic, or unstable patients with adequate baseline renal function were enrolled. These patients, diagnosed with various cancers including carcinoma of the head and neck, breast, testicular, and lung, received cisplatin therapy at an average dose of 867.5 mg. Radionuclide renal scans were conducted to measure glomerular filtration rate (GFR) using 99mTc-DTPA scintigraphy and creatinine clearance. ***Results:*** The technique involved meticulous preparation of 99mTc-DTPA according to manufacturer guidelines, with careful calibration to ensure dose accuracy. Patients underwent dynamic renal studies under the gamma camera, with GFR automatically calculated using the Gates method. Statistical analysis was performed using Microsoft Excel and SPSS, with paired sample t-tests demonstrating statistical significance ($p < 0.001$).The study found a significant reduction in renal function parameters, with GFR decreasing by 9.787 ml/min per chemotherapy cycle and serum creatinine clearance decreasing by 3.655 ml/min per cycle. Post-chemotherapy GFR was lower than pre-chemotherapy levels, with a reduction factor of 0.83, and creatinine clearance decreased post-chemotherapy by a factor of 0.4985. Age and BMI were identified as significant factors influencing renal function. ***Conclusion:*** Proactive monitoring and intervention are essential to mitigate nephrotoxicity-associated risks during chemotherapy. The findings underscore the importance of 99mTc-DTPA scintigraphy in detecting cisplatin-induced nephrotoxicity and optimizing patient care in oncology practice. ***References:*** 1. Debela, D.T.; Muzazu, S.G.; Heraro, K.D.; Ndalama, M.T.; Mesele, B.W.; Haile, D.C.; Kitui, S.K.; Manyazewal, T. New approaches and procedures for cancer treatment: Current perspectives. SAGE Open Med. 2021, 9, 20503121211034366. 2. Laversanne, M.; Soerjomataram, I.; Jemal, A.; Bray, F. Global cancer statistics 2020: GLOBOCAN estimates of incidence and mortality worldwide for 36 cancers in 185 countries. Cancer J. Clin. 2021, 71, 209-249.

EP-0754

Approaches to Renal Function Assessment: A Comparative Perspective

T. Makazlieva[1], *A. Peshevska*[1], *I. Sazdova*[1], *Z. Markovska Shterjova*[2], *I. Rambabova-Bushljetik*[2];
[1]*Institut of pathophysiology and nuclear medicine, Medical faculty, University Ss Cyril and Methodius, Skopje, NORTH MACEDONIA, THE REPUBLIC OF,* [2]*University Clinic of Nephrology, Medical faculty, University Ss Cyril and Methodius, Skopje, NORTH MACEDONIA, THE REPUBLIC OF.*

Aim/Introduction: Accurate assessment of renal function is essential in various clinical scenarios such as staging acute or chronic kidney disease, optimizing drug dosing, and evaluation of potential kidney donors. A range of techniques are available for evaluating renal function. Our study aimed to evaluate the

correlation between the measured GFR (mGFR) values obtained by the three-plasma sample (TPS) slope-intercept method with 99mTc-DTPA, as a reference method, and estimated GFR (eGFR) with different creatinine formulas. The second objective of our analysis was to evaluate the correlation between mGFR and tubular extraction rate (TER) value with 99mTc-MAG3. ***Materials and Methods:*** A total of 72 subjects (31 male, 41 female) with a mean age of (57,67±13,17) years were included. The mGFR value was obtained by the TPS slope-intercept method after i.v. application of ^{99m}Tc-DTPA and eGFR was obtained with the CKD-EPI (2009), CKD-EPI (2021) and MDRD formula. In 36 subjects, the tubular extraction rate (TER) was additionally evaluated using ^{99m}Tc-MAG3 Bubeck methodology and correlated with the mGFR value. ***Results:*** Our study revealed that the CKD-EPI (2021) formula had the highest bias and mean percentage error, while the MDRD method demonstrated the weakest correlation with the reference method. Bland-Altman plots indicated that all three creatinine-based formulas consistently overestimated GFR. Statistical analysis revealed a significant correlation between ^{99m}Tc-DTPA mGFR values obtained using TPS method and TER values measured with ^{99m}Tc-MAG3 across a broad range of GFR values in all patients. ***Conclusion:*** The study found that creatinine-based formulas tend to overestimate GFR. In clinical situations requiring better accuracy, plasma sampling nuclear medicine methods offer a more reliable alternative assessment and should be considered as a more appropriate diagnostic method. ***References:*** Itoh K. 99mTc-MAG3: review of pharmacokinetics, clinical application to renal diseases and quantification of renal function. Ann Nucl Med 2001 Jun;15(3): 179-190. Blaufox MD, De Palma D, Taylor A, Szabo Z, Prigent A, Samal M, Li Y, Santos A, Testanera G, Tulchinsky M. The SNMMI and EANM practice guideline for renal scintigraphy in adults. Eur J Nucl Med Mol Imaging. 2018 Nov;45(12):2218-2228. doi: 10.1007/s00259-018-4129-6. Epub 2018 Aug 30. PMID: 30167801.

EP-47

e-Poster Area

B: Imaging Clinical Studies -> B9 Paediatric Imaging Study -> B91 Paediatric Study

EP-0755

Impact of [18F]FET PET imaging on diagnosis and prognosis in pediatric and adolescent brain tumors: a systematic review and quantitative analysis

T. Antonevskaya[1], *M. Yadgarov*[1,2], *Y. Likar*[1];
[1]*Dmitry Rogachev National Medical Research Center of Pediatric Hematology, Oncology and Immunology, Moscow, RUSSIAN FEDERATION,* [2]*Federal Research and Clinical Center of Intensive Care Medicine and Rehabilitology, Moscow, RUSSIAN FEDERATION.*

Aim/Introduction: Pediatric and adolescent brain tumors are the most prevalent neoplasms in children and contribute significantly to cancer-related morbidity and mortality in this demographic. Accurate diagnosis and characterization of brain neoplasms are crucial for clinical decision-making and treatment planning. Traditional imaging modalities, while essential, often lack the nuanced information for effective management of these tumors. This study aims to assess the diagnostic and prognostic utility of baseline and post-therapy [18F]FET (O-(2-[18F]fluoroethyl)-l-tyrosine) PET imaging parameters in pediatric and adolescent brain tumors, focusing on tumor detection, grading, recurrence assessment, residual tumor evaluation, and survival prediction. ***Materials and Methods:*** A systematic review and meta-analysis were conducted in accordance with PRISMA guidelines, incorporating data from prospective and retrospective cohort studies published up to September 9, 2024, without language restrictions. Parameters such tumor-to-brain ratio (TBRmax and TBRmean), time-to-peak (TTP), kinetic pattern (KP), maximum standardized uptake value (SUVmax), and metabolic tumor volume (MTV) were analyzed for diagnostic and prognostic value. Bayesian models for diagnostic accuracy and paired meta-analysis techniques were applied. ***Results:*** A total of 12 studies involving 352 patients, published between 2005 and 2023, were included in the analysis. Baseline TBRmax exhibited limited diagnostic accuracy in differentiating tumor grades, with an area under the summary receiver operating characteristic curve (AUSROC) of 0.639, a sensitivity of 73.8% (95% confidence interval (CI): 52.8%-88.4%), and a specificity of 53.9% (95% CI: 27.5%-75.7%). Paired meta-analysis revealed significantly higher baseline TBRmax (mean difference: 1.93, $p < 0.001$) and TBRmean (mean difference: 1.25, $p = 0.02$) values in patients diagnosed with high-grade tumors. In contrast, post-therapy TBRmax demonstrated strong diagnostic performance for identifying tumor recurrence, with an AUSROC of 0.850, sensitivity of 81.5% (95% CI: 67.8%-90.9%), and specificity of 88.5% (95% CI: 66.4%-97.8%). Due to limited available data, other parameters and clinical outcomes could not be included in the meta-analysis. ***Conclusion:*** This systematic review and meta-analysis shows the diagnostic and prognostic potential of [18F]FET PET imaging in pediatric and adolescent brain tumors. While several factors limited a comprehensive meta-analysis, the inclusion of dynamic parameters alongside established static ones revealed promising associations with clinical outcomes, suggesting their utility in baseline and post-therapy imaging. Stronger evidence and wider clinical implementation can be achieved through the implementation of standardized imaging protocols and multicenter prospective research.

EP-0756

Enhancing Pulmonary Metastasis Detection in Pediatric Bone Sarcomas: The Added Value of Thoracic SPECT-CT in Bone Scintigraphy

A. Khelifa*, F. Koudri, D. Meziane, S. Benali, H. Labiod, L. Chelghoum, M. Lamali, D. Tahmi, L. Belabas, S. Benzerdjeb, A. Amimour;*
Bab El Oued Hospital, Algiers, ALGERIA.

Aim/Introduction: To evaluate the diagnostic contribution of thoracic SPECT-CT performed during bone scintigraphy for detecting pulmonary metastases in pediatric patients with bone sarcomas. Bone scintigraphy remains a standard tool for detecting skeletal metastases in pediatric bone sarcomas. However, the intrinsic limitations of planar imaging in terms of sensitivity and spatial resolution may compromise lesion detectability. Although primarily aimed at osseous evaluation, these scans may incidentally reveal thoracic abnormalities. Considering the high prevalence of pulmonary metastases at initial diagnosis, thoracic SPECT/CT offers added anatomical detail that can enhance lesion characterization, thereby improving staging accuracy and guiding therapeutic decision. ***Materials and Methods:*** This retrospective study included 33 pediatric patients (mean age 14.0 ± 3.9 years; 58% male) with histologically confirmed bone sarcomas. Of these, 20 patients (61%) had Ewing sarcoma and 13 (39%) had osteosarcoma. All underwent bone scintigraphy with additional thoracic SPECT-CT (Pediatric Low dose protocol). Detection rates of pulmonary and skeletal metastases were assessed. Associations between skeletal and pulmonary involvement were analyzed using Fisher's exact test. ***Results:*** Thoracic SPECT-CT identified pulmonary metastases in 9 patients (27%) and skeletal metastases in 11 (33%). No significant association was found between pulmonary and skeletal metastases ($p = 0.12$). SPECT-CT also improved anatomical localization and interpretation of equivocal thoracic foci on planar imaging, leading to staging revisions in several cases. ***Conclusion:*** Thoracic SPECT-CT significantly improves the detection and characterization of pulmonary metastases during routine bone scintigraphy in pediatric bone sarcomas. Although no statistical correlation was observed between pulmonary and skeletal metastases, the added value of SPECT-CT supports its systematic use to enhance diagnostic confidence and inform therapeutic decisions in pediatric oncology.

EP-0757

^{18}F-FDG PET/CT in Rare Histiocytic Disorders: Insights into Metabolic Parameters and Disease Burden in Rosai-Dorfman Disease and Juvenile Xanthogranuloma: A Comparative PET/CT Case-Analysis

K. Hlongwa, *F. Smith, N. Jacobs, M. P. Rivombo, M. Hendricks, S. More;*
University of Cape Town, Cape Town, SOUTH AFRICA.

Aim/Introduction: Rosai-Dorfman disease (RDD) and Juvenile Xanthogranuloma (JXG) are rare forms of non-Langerhans cell histiocytic disease which typically present in the paediatric population. ^{18}F-FDG PET/CT has been used in staging these patients to characterize and assess disease extent, however, there has been limited reporting on the relationship between metabolic activity and disease burden of these conditions. We aimed to compare the quantitative metabolic parameters and disease burden of RDD and JXG in paediatric patients using ^{18}F-FDG PET/CT imaging for staging. ***Materials and Methods:*** We retrospectively analyzed staging ^{18}F-FDG PET/CT scans from patients with RDD and JXG. SUVmax, SUVmean, SUVpeak were measured and total lesion glycolysis (TLG), and metabolic tumor volume (MTV) were calculated for each lesion as well as cumulative measurements of wholebody SUVmax, wholebody SUVpeak and wholebody SUVmean and calculations of wholebody MTV and wholebody TLG. Histological analysis and biochemistry results were also reviewed. ***Results:*** Three patients with RDD and JXG were identified from our database respectively. Patients with RDD lesions exhibited higher median and mean values for SUVmax, SUVmean and SUV peak in comparison to JXG lesions. Median and mean TLG values were higher and mean MTV were also higher in the RDD patients compared to JXG patients. Quantitative parameters for Wholebody SUVmax, SUVmean, SUVpeak, Wholebody MTV and Wholebody TLG also demonstrated higher median and mean values for RDD in comparison to JXG. See table 1.The distribution of disease in patients with RDD typically involved lymphadenopathy that was distributed above and below the diaphragm with intense uptake in comparison to the patients with JXG that had more limited disease with less intense uptake. Histological analysis confirmed the diagnosis of RDD and JXG, with RDD demonstrating positive histiocytes for S100 and CD68 whilst JXG was S100 negative but strongly positive for CD68 and FXIIIa. Biochemistry results were unremarkable in both groups. ***Conclusion:*** Our limited case findings suggest that RDD lesions exhibit higher metabolic activity and disease burden compared to JXG lesions, potentially consistent with their cell biology. These results may have implications for treatment planning, monitoring and survival benefit of patients with these rare histiocytic disorders.

EP-48

e-Poster Area

B: Imaging Clinical Studies -> B10 Other Imaging Clinical Studies -> B101 Other Clinical Studies

EP-0758

Application of Quantitative Analysis in Salivary Gland Scintigraphy with 99mTc-Pertechnetate

M. Zamorano Rivas[1], *F. Camba*[2], *A. Bagán Trejo*[1], *L. Gracia Sánchez*[1], *G. Reynés Llompart*[2], *P. Notta González*[1], *A. Dacosta Escobar*[1], *D. Tamayo Ossa*[1], *E. Ricart Paredes*[3], *M. Cortés Romera*[1];
[1]*Nuclear Medicine- PET (IDI) Department. Hospital Universitari de Bellvitge - IDIBELL, L'Hospitalet de Llobregat, Barcelona, SPAIN,*
[2]*Medical Physics and Radiation Protection Department. Institut Català d'Oncologia, L'Hospitalet de Llobregat, Barcelona, SPAIN,*
[3]*Radiopharmacy Department. Hospital Universitari de Bellvitge - IDIBELL, L'Hospitalet de Llobregat, Barcelona, SPAIN.*

Aim/Introduction: Salivary gland scintigraphy with 99mTc-pertechnetate is routinely used to evaluate glandular function, primarily through visual interpretation, with is inherently subject to interobserver variability. This study aims to assess the utility of quantitative analysis in providing more objective and reproducible evaluations. ***Materials and Methods:*** 62 patients underwent dynamic anterior projection imaging of the cervicofacial region for 30 minutes. An acid stimulus (lemon juice) was administered 15 minutes after tracer injection. Three quantitative parameters were calculated for the major salivary glands (bilateral parotid and submandibular glands) using MIM 7 software (GE Healthcare): uptake rate at 15 minutes (UR), uptake percentage (UP) and ejection fraction (EF).Glands were classified as having normal or impaired based on visual assessment. Statistical analysis was performed to identify significant differences in quantitative parameters between the two groups, RPC analysis to differentiate normal from impaired glands, and optimal thresholds were calculated using the Youden index. ***Results:*** Significant differences ($p < 0.05$) were observed between normal and functionally impaired glands. Right parotid glands with normal function showed a UR of 8.0 ± 4.8 vs. 5.2 ± 3.2, UP of 12.7 ± 3.8 vs. 6.7 ± 2.9, and EF of 68.0 ± 6.4 vs. 50.1 ± 17.1, compared to pathological glands. Similarly, normal right submandibular glands showed a UR of 4.4 ± 2.8 vs. 3.0 ± 1.8, UP of 5.6 ± 2.7 vs. 3.1 ± 1.4, and EF of 55.8 ± 8.7 vs. 40.6 ± 13.9. Similar findings were found in the contralateral glands. The ROC analysis shows that UP of the parotid glands had the best diagnostic performance with an Area Under the Curve (AUC) of 0.904 and 0.922 for the right and left parotid gland, respectively. The optimal thresholds were, for the right parotid gland, a UP cutoff value of 9.0 with a sensitivity of 80.4% and a specificity of 93.8%, and for the left parotid gland, a UP cutoff value of 8.0 with a sensitivity of 78.3% and a specificity of 100%. ***Conclusion:*** These results suggest that quantitative analysis could improve the objectivity and diagnostic accuracy of salivary gland scintigraphy, with UP of the parotid glands emerging as the most effective parameter for distinguishing between normal and impaired glandular function.

EP-0759

Utility of [^{99m}Tc] Tc-99m-Macroaggregated Albumin (MAA) Brain Quantitation Tool for the Diagnosis of Hepatopulmonary Syndrome in Pakistani Cirrhotic Patients and Comparison with Contrast Echocardiography

S. Mardan;
Pakistan Institute of Engineering and Applied Sciences, Islamabad, PAKISTAN.

Aim/Introduction: The study aims to validate the potential use of [99mTc]Tc -MAA brain quantitation(Macro aggregated Albumin) tool for establishing a local population-based cutoff in Hepato Pulmonary Syndrome (HPS) diagnosis with a comparison to TransThoracic Contrast Echocardiography (TTCE). ***Materials and Methods:*** 32 cirrhotic patients were divided into 2 groups on the basis of dyspnea, hypoxemia and alveolar arterial gradient [P (A-a) O_2]. Group I (17 patients) includes clinically HPS positive cirrhotic while Group II (15 patients) serves as HPS-negative controls. Both groups underwent TTCE and [99mTc] Tc-MAA scans. Presence of bubbles in left heart chambers after 3 cardiac cycles and uptake in brain /kidneys were taken as positive on TTCE and [99mTc] Tc-MAA scan respectively. The shunt index was calculated by the percentage of [99mTc]Tc-MAA shunted to the brain. Local population-based cutoff of shunt index was derived using the mean ± 2SD of Group I. Sensitivity, specificity, PPV and NPV values at this cut off, the internationally established 6%, and for TTCE was calculated. ***Results:*** The cut-off value for our population was found to be > 3.81% on Tc-99m-MAA lung perfusion scan. [99mTc] Tc-MAA scan at the local cutoff (3.81%) shows increased sensitivity (47% vs. 29.41% vs. 41.17%) and diagnostic accuracy (68.75% vs. 65.62% vs. 62.5%) compared to the internationally established 6% cutoff and TTCE. Significant clinical parameter differences were found between patients with and without Intrapulmonary

Vascular Dilatation includes shunt indices (3.9±2.44vs1.6±1.10, P=0.0021), PaO_2 (65.07±13vs 92.181±10.3, P=<0.00001) & P(A-a) O_2 (50.57±16.77vs.24.93±7.99, P=<0.00001). ***Conclusion:*** [99mTc] Tc-MAA lung perfusion scan demonstrates a better diagnostic performance in the diagnosis of HPS as compared to TTCE. Local population cutoff >3.81% emerges as a more accurate cutoff than 6% established cutoff and contrast echocardiography for early screening of HPS in Pakistani cirrhotic population.

EP-0760

Old rockstars never die: Gastric emptying scintigraphy of solids in current clinical practice, results by disease and usefulness in therapeutic decision making

V. Aina Monterde, *M. Calderón Calvente, L. M. Del Barco Díez Canseco, A. M. Olmedo Chiva, C. Lorente Fonrodona, G. B. Cárdenas Apaza, M. Falgás Lacueva, M. J. Sangrós Sahún, P. Navarro Beltrán, S. Álvarez Ruiz, L. de la Cueva Barrao; Hospital Universitario Miguel Servet, Zaragoza, SPAIN.*

Aim/Introduction: To analyse the solid GE results of our patients in daily routine versus normal, to assess whether these results vary by subgroups according to the reason for the request, and to study the usefulness of GE studies in therapeutic decision-making. Gastric emptying scintigraphy (GE) is a classic technique that continues to be used because it allows the assessment of gastric dynamics in a physiological and non-invasive way. ***Materials and Methods:*** Retrospective review of consecutive solid GE scintigraphy. Quantitative results from activity/time curves, latency period (Tlag) and half-emptying time (T50) are collected for the sample and are compared with those of a historical control group (n=27) by non-parametric test. GE outcomes are analyzed by subgroups according to the clinical condition motivating are request for the study, as well as the impact of the scintigraphy result on therapeutic decisions, based on patient clinical evolution. ***Results:*** 46 patients: 14 men and 32 women; median age 54 years (range 19-79). The main indication for the study was retentionist symptoms in 39 patients, of whom 28 presented with vomiting; 3 had symptoms following bariatric surgery, 2 had scleroderma, and 2 had episodes of intestinal subocclusion. In 28 patients, gastric emptying (GE) was normal (61%), while in 18 it was abnormal (39%); 7 with rapid GE (dumping) and 11 with gastroparesis. Statistically significant differences were found in the Tlag results between patients diagnosed with rapid GE and gastroparesis compared to the control group (p=0.0002 and p=0.003, respectively); the difference in T50 was also significant in these two groups (p=0.000096 and p=0.00033, respectively). Of the 39 studies requested due to retentionist symptoms, 14 showed abnormal gastric emptying (GE) (36%), of which 11 had vomiting (11/14, 78.5%). Among the 29 patients with vomiting, 11 had abnormal GE (38%), and 8 of them were diagnosed with gastroparesis (72.2%). Both patients with subocclusive symtoms had abnormal Tlag results, while those with sclerodema and hystory of gastric surgery showed variable GE findings. In 33 cases (71.7%), the GE study contributed to therapeutic decision-making. ***Conclusion:*** Solid gastric emptying remains a useful and reliable tool in daily practise, supporting therapeutic decision-making. Among the conditions that justify its use, patiens with clinical signs of distress and vomiting benefit the most from undergoing the solid gastric emptying study.

EP-0761

Pulmonary Uptake in Patients with Suspected Primary Aldosteronism on [^{68}Ga]Ga-pentixafor PET: Incidence and Etiology

L. Yang, *P. Dong, L. Li, M. Su; Department of Nuclear Medicine, West China Hospital, Sichuan University, Chengdu, CHINA.*

Aim/Introduction: We have incidentally noted pulmonary uptake in a cohort of our patients with suspected primary aldosteronism(PA) on [^{68}Ga]Ga-pentixafor PET/CT or PET/MR images. We aimed to assess the incidence and explore the potential etiologies of pulmonary uptake. ***Materials and Methods:*** The study comprised 217 consecutive patients with suspected PA who underwent [^{68}Ga]Ga-pentixafor PET/CT or PET/MR at our center between January 2023 and August 2024. The PET/CT and PET/MR scans were retrospectively reviewed for the presence of pulmonary uptake. Clinical and PET-related parameters were collected. In patients with pulmonary uptake, recent chest CT scans, and serum leukocyte and neutrophil counts were reviewed for further evaluation. ***Results:*** Of the 217 included patients, 101 were male and 116 were female, with a mean age of 50 years (range, 22-80 years). Pulmonary uptake was present in 37 of 217 patients (17%). Of these 37 patients, 13 were male and 24 were female, with a mean age of 52 years (range, 36-76 years). No clinical or PET-related parameters were found to be significantly associated with pulmonary uptake, including clinical (age, sex, body mass index (BMI), hypertension, duration of hypertension, highest blood pressure), laboratory (hypokalemia, serum potassium, urine potassium, plasma aldosterone (PAC), direct renin concentration (DRC), aldosterone/renin ratio (ARR), 8 AM cortisol (F), 8 AM adrenocorticotropin (ACTH), urine cortisol) and PET-related parameters (SUV_{max} of pulmonary uptake foci, SUV_{mean} of blood pool (BP), injected [^{68}Ga]Ga-Pentixafor activity, length of uptake phase) (all P>0.05). As for the patients with pulmonary uptake, the SUV_{max} of pulmonary uptake foci showed no significant difference between the left lungs (median, 3.7) and right lungs (median, 3.8) (P=0.473). Besides, no significant difference was observed between the lower lung fields (47%) and upper lung fields (49%) (P=0.846). Of these 37 patients, 20 patients had recent chest CT scans. Abnormalities in the corresponding areas were noted in two patients, one with subpleural linear opacities and the other with consolidations. The remaining 18 scans showed no abnormalities at the corresponding site and the surrounding field. Twenty-seven patients had recent leukocyte and neutrophil counts. Seven patients exhibited elevated counts, including the two patients with abnormal CT findings. The remaining 20 patients had normal counts. ***Conclusion:*** In our cohort, 17% of patients with suspected PA demonstrated pulmonary uptake on [^{68}Ga]Ga-pentixafor PET scans. Given the absence of significant associations with clinical or imaging parameters, our findings suggest the possibility of non-specific pulmonary uptake on [^{68}Ga]Ga-pentixafor imaging.

EP-0762

Interobserver and intraobserver agreement of planar, pseudoplanar, and SPECT/CT images in ventilation/perfusion (V/Q) lung scintigraphy

B. Serrallonga, *S. Castejón, G. Guzman, Y. Delisau, M. Calls-Calahorro, P. Stefaneli, M. Velasco-Nuño, A. Fernández-León, J. Duch, S. Asadurova, V. Camacho, A. Flotats; Nuclear Medicine Department, Hospital de la Santa Creu i Sant Pau, Barcelona, SPAIN.*

Aim/Introduction: To assess diagnostic agreement across planar, pseudoplanar, and SPECT/CT V/Q scintigraphy and evaluate whether pseudoplanar images can substitute planar images as a visual adjunct to SPECT/CT. ***Materials and Methods:*** Thirty-two patients with suspected or prior pulmonary thromboembolism (PTE) underwent V/Q scans using planar, pseudoplanar, and SPECT/CT modalities. Four nuclear medicine physicians (one in training) independently reviewed the images on separate days using modified PIOPED II criteria and EANM guidelines. Agreement in perfusion defect detection and PTE probability estimation was analyzed using intraclass correlation coefficients (ICC) and weighted kappa (κ) statistics. ***Results:*** Intraobserver agreement for

perfusion defects was moderate to good (ICC = 0.513-0.780). Planar and pseudoplanar images showed strong agreement for PTE probability (κ = 0.489-1.00). Agreement between planar-SPECT/CT and pseudoplanar-SPECT/CT was moderate (κ = 0.351-0.662). Interobserver agreement for perfusion defects was acceptable overall (ICC = 0.655, p < 0.001), and higher for pseudoplanar (ICC = 0.731) and SPECT/CT (ICC = 0.703) compared to planar images (ICC = 0.658). SPECT/CT had the highest interobserver agreement for PTE probability (κ = 0.590-0.904), followed by pseudoplanar (κ = 0.398-0.570) and planar (κ = 0.285-0.837). ***Conclusion:*** SPECT/CT demonstrated the most consistent diagnostic performance. Pseudoplanar imaging showed more stable interobserver agreement than planar and may be a viable replacement in workflows combining it with SPECT/CT, maintaining diagnostic reliability while enhancing efficiency.

EP-0763

The Impact of Metabolic Tumor Burden on the Physiological Biodistribution of ^{18}F FDG in Normal Tissues and Organs

S. A. Yilmaz*, A. Akbulut, G. Koca, K. Demirel, M. Korkmaz;*
University of Health Sciences, Ankara Training and Research Hospital, Ankara, TÜRKIYE.

Aim/Introduction: This study investigates the relationship between metabolic tumor burden and ^{18}F FDG biodistribution in normal tissues and organs—including the cerebrum, cerebellum, liver, spleen, kidneys, and skeletal muscle—to improve cancer staging accuracy, guide treatment strategies, and enhance reporting reliability. ***Materials and Methods:*** A total of 189 patients who underwent ^{18}F FDG PET/CT for initial cancer staging or solitary pulmonary nodule (SPN) evaluation were retrospectively analyzed. Group 1 included 64 patients with advanced-stage cancer and distant metastases; Group 2 included 74 patients with localized disease and SUVmax >10; the control group consisted of 51 SPN patients without pathological FDG uptake. SUVmax values were recorded for the cerebrum, cerebellum, liver, spleen, kidneys, and psoas muscle. MTV and TLG values were calculated in tumor-bearing patients. The study population was also stratified based on primary organ/system involvement. Among the 138 patients referred for initial staging, 41 (29.7%) had gastrointestinal malignancies, 37 (26.8%) had lung cancer, 24 (17.4%) had breast cancer, 12 (8.7%) had urinary tract malignancies, 7 had gynecologic malignancies, 7 had head and neck tumors, 6 had lymph node involvement, 2 had malignant melanoma, 1 had testicular cancer, and 1 had sarcoma. Subgroup comparisons were performed for categories with sufficient patient numbers. ***Results:*** Significant differences in SUVmax values were observed between groups in the cerebrum, liver, and both kidneys ($p<0.05$), while no significant differences were found in the spleen and skeletal muscle. Subgroup analyses revealed consistent variations in cerebrum, cerebellum, liver, and renal SUVmax values in gastrointestinal and lung cancer patients compared to controls. A weak negative correlation was found between cerebrum SUVmax and MTV (ρ = -0.256; p = 0.002). ***Conclusion:*** Increased metabolic tumor burden significantly alters the physiological biodistribution of ^{18}F FDG, particularly reducing uptake in the brain, liver, and kidneys. These findings support the concept of a metabolic superscan, where high tumor glycolytic activity limits FDG availability for normal tissues. Liver SUVmax, frequently used as a reference in PET-based response criteria (e.g., Deauville), was significantly reduced in high-burden patients, potentially affecting response evaluation. In contrast, skeletal muscle uptake remained stable, indicating its potential as an alternative reference region. Recognizing these changes is essential to prevent misinterpretation and to improve the accuracy of PET-based assessment strategies in patients with extensive disease.

EP-0764

Role of Machine Learning Models in Predicting the NCCN High & Very High-Risk Group in Prostate Cancer Patients

R. Wakankar*, S. Sharma, B. Khangembam, M. Kavin, R. Kumar, C. D. Patel, A. Seth, R. K. Sahoo, S. Kaushal, C. J. Das, A. R. Chanu;*
All India Institute of Medical Sciences, New Delhi, INDIA.

Aim/Introduction: To develop machine learning (ML) models using biochemical & imaging data for predicting NCCN risk group in treatment-naïve prostate cancer patients undergoing whole-body ^{68}Ga-PSMA-11 PET-CT. ***Materials and Methods:*** Between January, 2018 to March 2025, 314 treatment-naïve prostate cancer patients with pathologically confirmed diagnoses were enrolled. The primary outcome was the presence of NCCN high-risk & very high-risk disease, determined by ^{68}Ga-PSMA-11 PET-CT imaging and pathological findings. A training set (n = 251) was generated by splitting the original dataset in a 80:20 ratio, with 63 patients reserved as an independent cohort for external validation of the ML models. After feature normalization, Gini Index was used for feature selection. 3 ML models (Logistic Regression, Random Forest and Naïve Bayes) were trained using stratified 10-fold cross-validation. Model performance was assessed using AUC, accuracy, F1 score, precision, recall, and specificity. SHAP plots and confusion matrices were used for model interpretation. ***Results:*** Gini index scoring selected the best-ranked 7 features for cross-validation. In cross-validation, 3 models exhibited >0.850 in all performance metrics, with Random Forest achieving the highest AUC of 0.947 (CA: 0.930, F1 score: 0.951, precision: 0.951, recall: 0.951, specificity: 0.875). On external validation using the test dataset, Random Forest had an AUC of 0.988 (CA: 0.906, F1 score: 0.930, precision: 1.000, recall: 0.868, specificity: 1.000). No significant overfitting was observed, and SHAP plots revealed clear patterns of interpretability. ***Conclusion:*** Machine learning models helped classify high-risk & very high-risk NCCN groups in treatment-naïve prostate cancer patients using biochemical & imaging data. These interpretable models can help aid in personalized patient management in clinical practice.

EP-0765

Decoding Hepatopulmonary Syndrome: Exploring the Relationship Between Liver Disease Severity and Pulmonary Shunt

S. Ramos Barata*[1], S. Paiva[1], I. Casimiro[1], D. Carvalho[1], J. Silva[1], A. Albuquerque[1], A. Moreira[1,2], G. Costa[1,3];*
[1]Hospitais da Universidade de Coimbra - ULS Coimbra, Coimbra, PORTUGAL, [2]Instituto de Ciências Nucleares Aplicadas à Saúde, Coimbra, PORTUGAL, [3]Faculdade de Medicina da Universidade de Coimbra, Coimbra, PORTUGAL.

Aim/Introduction: Hepatopulmonary syndrome (HPS) is characterized by intrapulmonary vascular dilatations leading to the formation of intrapulmonary shunt and hypoxemia in patients with liver disease. Abnormal extrapulmonary uptake of [^{99m}Tc]Tc-macroaggregated albumin ([^{99m}Tc]Tc-MAA) in pulmonary perfusion scintigraphy aids diagnosis and allows shunt quantification. HPS can occur across varying stages of liver disease, however, the association between liver dysfunction severity and shunt extent remains unclear. This study aims to investigate the association between liver disease severity - assessed by MELD, PELD, and Child-Pugh scores - and shunt percentage determined by [^{99m}Tc]Tc-MAA scintigraphy in HPS patients. ***Materials and Methods:*** This retrospective study included patients that underwent [^{99m}Tc]Tc-MAA pulmonary perfusion scintigraphy between 2009 and 2025 at our institution. Two groups were analyzed: 20 patients under age 12 and 10 patients aged 12 years or older. Demographic data, shunt percentage, pulse oximetry values, and Child-Pugh, MELD and PELD parameters were collected. Liver disease severity was assessed using age-appropriate scoring systems. Statistical analysis was performed using SPSS-Statistics v.30.0. P-values<0.05

were considered significant. ***Results:*** In the cohort under the age of 12 (10 female(50%); median age 3.55y(IQR 1.61-7.46)), the mean PELD score was 0.00(IQR 0.00-10.68), with a median shunt percentage of 8.2%(IQR 7.43-12.7). In the ≥12 years-old group (3 female(30%); median age 15.31y(IQR 13.73-53.51)), 30%(n=3) were Child-class A and 70%(n=7) Child-class B, with a mean MELD score of 13.00±3.23 and median shunt percentage of 22.85%(IQR 10.95-51.85). In both age groups, PELD and MELD scores showed positive but very weak and non-significant correlation with shunt percentage (pediatric: ρ=0.053, p=0.825; ≥12 years-old: ρ=0.128, p=0.724). No significant differences in shunt percentages were found between Child-class A and B patients (p=0.425). Additionally, no significant associations were observed between shunt percentage and individual parameters of the liver disease scores (bilirubin, albumin, INR, and age) in either group. Regarding the full cohort, oximetry (median 98%(IQR 96.5-99)) showed a strong and significant negative correlation with shunt percentage (ρ=-0.671, p<0.001), as the shunt becomes more severe, oximetry levels tend to decrease. ***Conclusion:*** No significant association was found between liver disease scores and shunt percentage, suggesting that liver disease severity, as assessed by these scores, does not directly influence the extent of intrapulmonary shunt. However, the significant inverse relationship between pulse oximetry and shunt percentage highlights its clinical relevance as a non-invasive marker of shunt severity. Further research with larger cohorts is needed to better understand the relationship between liver disease severity and shunt percentage.

EP-0766

Pressure-Induced Ischemia Artefacts at Sacral and Scapular Regions During Dynamic PET/CT: Characterization and Mitigation

C. Hinge*, F. L. Andersen, F. E. Høi-Hansen, K. Korsholm;*
Copenhagen University Hospital, Rigshospitalet, Copenhagen, DENMARK.

Aim/Introduction: Dynamic ^{18}F-FDG PET/CT often involves prolonged patient immobilisation on the scanner table. This can lead to pressure exceeding capillary perfusion pressure at bony prominences, potentially causing ischemia and reduced ^{18}F-FDG uptake, manifesting visually as photopenic artefacts ("cold spots"). These artefacts, particularly prominent at the sacrum and scapulae, may mask pathology and affect quantification. We aimed to characterize these artefacts in 100 age- and sex-stratified healthy volunteers undergoing dynamic 70-minute PET/CT and evaluate synthetic sheepskin padding as a mitigation strategy. ***Materials and Methods:*** 100 healthy volunteers (50 male, 50 female) underwent dynamic ^{18}F-FDG PET/CT on a Long Axial Field of View Siemens Biograph Quadra as part of a separate study. Participants were positioned headfirst supine, injected with 0.4 MBq/kg 18F-FDG, and remained stationary for the 70-minute dynamic acquisition. The initial 42 participants were scanned without padding, while the subsequent 58 were scanned with synthetic sheepskin padding. Images were assessed blindly by a PhD student for photopenic artefacts at the sacrum and scapulae using a 3-point scale: None, Small, or Big. ***Results:*** Without sheepskin (N=42), artefacts were highly prevalent: None=3 (7%), Small=13 (31%), Big=26 (62%). With sheepskin (N=58), artefacts were significantly reduced: None=46 (79%), Small=12 (21%), Big=0 (0%). Sheepskin padding completely eliminated the severe ('Big') artefacts. We also observe that artefacts occur more frequently in individuals with lower BMI, potentially due to less protective fatty tissue. Visual assessment of non-attenuation-corrected (NAC) and histogram PET images for 5 patients confirmed artefacts were not attributable to reconstruction algorithms. ***Conclusion:*** Significant photopenic artefacts, consistent with pressure-induced ischemia, frequently occur at the sacrum and scapulae during dynamic ^{18}F-FDG PET/CT when patients are positioned directly on the scanner bed throughout uptake and scanning. These artefacts are markedly reduced by using synthetic sheepskin padding. For dynamic scans where pressure is applied from time zero, the ischemic effect can severely impair or nullify the tissue input function throughout the 70-minute. This effect may also impact static scans by inducing ischemia during the shorter scan duration (5-10 minutes), potentially affecting quantification methods like Patlak analysis that rely on late-scan data. Routine use of pressure-relieving padding should be considered standard practice for dynamic and other long-duration PET protocols to improve image quality and diagnostic accuracy. ***References:*** [1] https://pubmed.ncbi.nlm.nih.gov/35440473/.

EP-0767

Development and Validation of a Nomogram for Predicting Pulmonary Embolism Recurrence Using Muscle and Fat Parameters

J. Cao[1]*, S. Niu*[1]*, X. Li*[1]*, H. Liu*[2]*;*
[1]*Shanxi Medical University, Taiyuan, CHINA,* [2]*First Hospital of Shanxi Medical University, Taiyuan, CHINA.*

Aim/Introduction: This study evaluated the predictive value of muscle and fat parameters in managing and improving the prognosis of patients with PE. ***Materials and Methods:*** Data from 184 patients were retrospectively analyzed using the CT component of SPECT/CT at the axial section of the fourth thoracic vertebra. Key parameters included skeletal muscle, pectoral muscle, and subcutaneous fat, with indices such as SMI, PMAI, and SATI calculated. The primary outcome was the recurrence of pulmonary embolism. ***Results:*** The 184 patients were divided into a training cohort (n = 129) and a validation cohort (n = 55). LASSO logistic regression identified independent risk factors, and a nomogram was constructed using age, PMA, PMAI, and PMAD. Model performance was assessed via ROC curves, calibration curves, and decision curve analysis (DCA). Individual predictors such as age, PMA, PMAI, and PMAD showed AUCs of 0.825, 0.769, 0.752, and 0.759, respectively. The nomogram demonstrated robust predictive capabilities for recurrence, with AUC values of 0.902 (95% CI [0.852-0.951]) in the training cohort and 0.871 (95% CI [0.775-0.968]) in the validation cohort. DCA confirmed significant net clinical benefit, highlighting the importance of muscle-fat parameters in predicting PE recurrence. ***Conclusion:*** This study demonstrates advanced age and low chest muscle mass play a significant role in predicting PE recurrence.

EP-0768

Revisiting Pituitary and Adrenal Physiological FDG Accumulation, Using Time-of-Flight PET/CT Scanner Equipped with Semiconductor Detectors and Deep Learning Reconstruction Technology

K. Nakatani[1]*, K. Yoshino*[2]*, T. Kumazawa*[2]*, H. Tanaka*[2]*, T. Koyama*[2]*, K. K. Miyake*[1]*, Y. Nakamoto*[1]*;*
[1]*Kyoto University Graduate School of Medicine, Kyoto, JAPAN,* [2]*Kurashiki Central Hospital, Kurashiki, JAPAN.*

Aim/Introduction: Conventional PET/CT scanners underestimate physiological accumulation in small and thin organs due to sensitivity and spatial resolution limitations. This study aimed to verify the extent to which a TOF-PET/CT scanner equipped with a semiconductor detector and a noise reduction technique using deep learning reconstruction can improve the representation of pituitary and adrenal physiological FDG accumulation compared to conventional PET/CT scanners. ***Materials and Methods:*** The cases included 103 healthy individuals (female: male = 31: 72, age: 31-88) who underwent FDG-PET/CT equipped with digital silicon photomultipliers (SiPM) and Lutetium-yttrium oxyorthosilicate (LYSO) detectors as a medical check-up for cancer screening between June and December 2024 and showed no abnormalities. The controls included 90 healthy individuals

(female: male = 18: 72, age: 26-83) who underwent FDG-PET/CT equipped with conventional photomultipliers and lutetium oxyorthosilicate (LSO) detectors as the same medical check-up between June and December 2023 and showed no abnormalities. The evaluation target was the physiological accumulation of the pituitary and adrenal glands. First, SUVmax and SUVmean using Clear Adaptive Low-noise Method (CaLM) reconstruction in the case group were compared with those using ordered subsets expectation maximization (OSEM) reconstruction in the control group for each organ. We also compared measurements for each organ using CaLM reconstruction to those using Advanced intelligent Clear-IQ Engine (AiCE) reconstruction with deep learning techniques for the same patients in the case group. The relationship between pituitary physiological accumulation and age and sex was also investigated. ***Results:*** Pituitary physiological accumulation was visually recognizable in 103/103 of the cases and 48/90 of the controls. In the case group (with CaLM), SUVmax=2.4±0.9, SUVmean=1.6±0.5, while in the controls, SUVmax=2.1±0.5, SUVmean=1.8±0.3. When AiCE was used in the cases, SUVmax=5.2±2.2 and SUVmean=3.3±1.3 were significantly higher than those using CaLM (P<0.0001 for each). Adrenal physiological accumulation was visually recognizable in 83/103 of the cases and 29/90 of the controls. In the case group (with CaLM), SUVmax=2.4±0.6, SUVmean=1.7±0.3, while in the controls, SUVmax=1.8±0.4, SUVmean=1.4±0.3. When AiCE was used in the cases, SUVmax=3.1±0.9, SUVmean=2.0±0.4 (P<0.0001 for each). The pituitary physiological accumulation SUVmax (using AiCE) in the cases was 5.3±1.4 in females and 5.2±2.5 in males, with no significant difference. The correlation between SUVmax (using AiCE) and age was r=0.20, showing almost no correlation. ***Conclusion:*** Semiconductor TOF-PET/CT scanners with deep learning reconstruction can visualize pituitary and adrenal physiological accumulation in most cases. Pituitary physiological FDG accumulations appear to be considerably stronger than previously thought.

EP-0769

The Brain-White Adipose Tissue Axis May Play a Crucial Role in Diabetes Mellitus: A Metabolic Network Analysis Using Total-Body PET/CT Imaging

L. Sun*;*
Zhengzhou University People's Hospital and Henan Provincial People's Hospital, Zhengzhou, CHINA.

Aim/Introduction: Diabetes mellitus (DM) is the most prevalent metabolic disorder worldwide.The development of DM is frequently associated with inflammatory or tissue-damaging processes that disrupt the delicate equilibrium maintained by the complex interactions between various organs within the body[1]. There has been a paucity of research investigating their specific role in DM.Total-body PET imaging offers a distinctive advantage in the study of multi-organ relationships, as its extended field of view allows for the simultaneous imaging of multiple organs. allows the construction of a glucose metabolic network that reflects the dysregulation that is characteristic of DM, The objective of this study is to utilize total-body ^{18}F-FDG PET to construct an individualized glucose metabolism network, integrating insights from previous research on structural brain MRI networks[2]. ***Materials and Methods:*** In this study, we constructed covariance metabolic networks using static total-body PET images, normalized by lean body mass, from 36 patients with DM (DM group) and 36 age- and sex-matched healthy controls (HC group). Differences in network properties between the DM and HC groups were evaluated at both group and individual levels. In addition, correlation analysis was performed to explore the relationship between network properties and baseline clinical data in the DM subjects. ***Results:*** We observed that the same edges in the first three edges with the largest values were brain-subcutaneous adipose tissue (SAT) and brain-visceral adipose tissue (VAT) at both group and individual levels. There was a positive correlation between the brain-VAT and BMI(r=0.528, P < 0.001) and there was a negative correlation between the brain-SAT and age (r=-0.499, P = 0.002). The most perturbed organ was the brain at both group and individual levels, and there was a positive correlation between the strength of abnormality of brain and age(r=0.428, P = 0.009). ***Conclusion:*** This study successfully used static total-body PET imaging to construct individualized glucose metabolism networks for patients with DM, identifying the brain-VAT and brain-SAT as the most significantly altered edge and the brain as the most affected organ. These findings provide novel insights into the role of the brain-white adipose tissue axis in glucose metabolism in DM. ***References:*** 1. Knobil E. The Wisdom of the Body Revisited. Physiology. 1999;14:1-11.2. Sun T, Wang Z, Wu Y, Gu F, Li X, Bai Y, et al. Identifying the individual metabolic abnormities from a systemic perspective using whole-body PET imaging. Eur J Nucl Med Mol Imaging. 2022;49:2994-3004.

EP-0770

PET/CT with ^{11}C-Methionine and ^{18}F-FDG in Multiple Myeloma Patients

V. Manukova*, I. Aslanidis, O. Mukhortova, M. Metelkina;*
A.N. Bakulev Scientific Center for Cardiovascular Surgery of the Ministry of Health of Russia, Moscow, RUSSIAN FEDERATION.

Aim/Introduction: To evaluate the impact of "a one-day two-radiopharmaceuticals Positron emission tomography in combination with computed tomography (PET/CT)" with ^{11}C-Methionine (MET) and ^{18}F-fluorodeoxyglucose (FDG) on physiological distribution of FDG in patients with multiple myeloma (MM). ***Materials and Methods:*** 40 patients with a history of MM were included in the analysis, 60 PET/CT exams were conducted: in the 1st group - 20 doubled PET/CT (MET PET/CT followed by FDG PET/CT); in the 2nd group - 20 FDG PET/CT. ***Results:*** Comparative analysis of the physiological accumulation of FDG in two groups of patients with MM - one group passed one day 11C-MET PET/CT followed by ^{18}F-FDG PET/CT and another group passed standard ^{18}F-FDG PET/CT - revealed no statistically significant difference. SUL_{max} and SUL_{mean} was calculated in the right lobe of the liver, in the ascending aorta and in the head of the pancreas. The mean values of liver SUL_{max} were: in the first group - 2.37 ± 0.36, in the second group - 2.46 ± 0.40, p = 0.1. The mean values of aortic SUL_{max} were: in the first group - 1.42 ± 0.25, in the second group - 1.51 ± 0.37, p = 0.11. The mean SUL_{max} values in the pancreatic head were: in the first group - 1.43 ± 0.26, in the second group - 1.59 ± 0.36, p = 0.08. ***Conclusion:*** A one-day MET and FDG PET/CT does not affect the pharmacokinetics of FDG and can be used in MM patients. ***References:*** 1. Kwee TC, Basu S, Saboury B, Ambrosini V, Torigian DA, Alavi A. A new dimension of FDG-PET interpretation: assessment of tumor biology. Eur J Nucl Med Mol Imaging. 2011 Jun;38(6):1158-70. doi: 10.1007/s00259-010-1713-9. Epub 2011 Jan 12. PMID: 21225422. 2. Lapa C, Knop S, Schreder M, Rudelius M, Knott M, Jörg G, Samnick S, Herrmann K, Buck AK, Einsele H, Lückerath K. 11C-Methionine-PET in Multiple Myeloma: Correlation with Clinical Parameters and Bone Marrow Involvement. Theranostics. 2016 Jan 1;6(2):254-61. doi: 10.7150/thno.13921. PMID: 26877783; PMCID: PMC4729773. 5. Okasaki M, Kubota K, Minamimoto R, Miyata Y, Morooka M, Ito K, Ishiwata K, Toyohara J, Inoue T, Hirai R, Hagiwara S, Miwa A. Comparison of (11)C-4'-thiothymidine, (11)C-methionine, and (18)F-FDG PET/CT for the detection of active lesions of multiple myeloma. Ann Nucl Med. 2015 Apr;29(3):224-32. doi: 10.1007/s12149-014-0931-9. Epub 2014 Nov 25. PMID: 25421383; PMCID: PMC4385147.

EP-0771

Correlation Analysis of Inflammatory Markers, ^{18}F-FDG PET/CT Metabolic Parameters and Skeletal Muscle Parameters in Advanced Epithelial Ovarian Cancer

Z. Zhang, *H. Liu;*
First Hospital of Shanxi Medical University, Taiyuan, CHINA.

Aim/Introduction: Epithelial ovarian cancer (EOC) is the most common malignant ovarian tumor, often diagnosed at an advanced stage, leading to poor prognosis. Beyond conventional prognostic factors, inflammatory markers, metabolic parameters, and muscle parameters from ^{18}F-FDG PET/CT are emerging as important indicators. However, few studies have explored the interplay between inflammation, tumor metabolism, and skeletal muscle. This study examines the correlations among these factors in advanced EOC patients, aiming to provide a foundation for future research on their complex interactions. ***Materials and Methods:*** This retrospective study included 32 patients with advanced EOC who underwent baseline ^{18}F-FDG PET/CT at the First Hospital of Shanxi Medical University between February 2018 and September 2024, with complete clinical data.Collected variables included clinical information, inflammatory markers, ^{18}F-FDG PET/CT metabolic parameters, and skeletal muscle metrics. Inflammatory markers comprised platelet-to-lymphocyte ratio (PLR), neutrophil-to-lymphocyte ratio (NLR), lymphocyte-to-monocyte ratio (LMR), platelet-to-albumin ratio (PAR), systemic immune-inflammation index (SII), systemic inflammation response index (SIRI), prognostic nutritional index (PNI), and systemic inflammation score (SIS). PET/CT parameters included whole-body maximum standardized uptake value (WBSUVmax), whole-body metabolic tumor volume (WBMTV), and whole-body total lesion glycolysis (WBTLG). Skeletal muscle metrics included skeletal muscle index at the L3 level (SMI), skeletal muscle density (SMD), percentage of low-attenuation muscle (L%), skeletal muscle gauge (SMG), and intermuscular fat area (IMFA). Inter-observer agreement for skeletal muscle measurements was assessed via intraclass correlation coefficients. Spearman correlation analysis was used to evaluate associations among variables, with $p < 0.05$ considered statistically significant. ***Results:*** Inflammatory Markers and ^{18}F-FDG PET/CT metabolic parameters: PLR, PAR, SII, and SIS were positively associated with WBMTV (all $p < 0.05$). LMR was negatively correlated with WBTLG ($p < 0.05$). Most inflammatory markers showed positive associations with WBTLG, except for lymphocyte count and PNI, which were not significantly correlated. Inflammatory Markers and Skeletal Parameters: Neutrophil count and SIRI were weakly negatively associated with SMD and weakly positively associated with L% ($p < 0.05$ for all). Age and Skeletal Muscle Parameters: Age was inversely associated with SMD and SMG, and positively associated with L% and IMFA ($p < 0.05$ for all). ***Conclusion:*** Higher systemic inflammation is associated with increased tumor burden on ^{18}F-FDG PET/CT. The negative correlation between LMR and WBTLG may reflect the anti-tumor effect of lymphocytes. Systemic inflammation was negatively correlated with muscle density, implying impaired muscle quality in inflammatory states. Advancing age is linked to increased intermuscular fat and decreased muscle density, which may precede muscle mass loss.

EP-0772

[^{99m}Tc]Tc-Besilesomab Scintigraphy in a Patient with Stuve-Wiedemann Syndrome

A. Marques[1,2], *F. Abreu*[1,2], *J. Duarte*[2], *J. Carvalho*[2], *S. Pintão*[2];
[1]*Institute of Nuclear Medicine, Faculty of Medicine, University of Lisbon, Lisbon, PORTUGAL,* [2]*Western Lisbon Hospital Centre, Lisbon, PORTUGAL.*

Aim/Introduction: Stuve-Wiedemann syndrome is a rare osteochondrodysplasia characterized by progressive bone deformities and dysautonomia[1]. This case presents a 27-year-old woman with Stuve-Wiedemann syndrome, who was evaluated for suspected left hip osteomyelitis using [^{99m}Tc]Tc-Besilesomab scintigraphy. ***Materials and Methods:*** A 27-year-old female with Stuve-Wiedemann syndrome presented to the emergency department with swelling and fluctuation in her left thigh, associated with local inflammatory signs and high fever for four days. The swelling's distal region had a scar from a previously drained abscess. Laboratory tests showed leukocytosis, and imaging (soft tissue ultrasound and CT) revealed a superficial hematoma in the left thigh and a large retroperitoneal hematoma extending from L4-L5 to the left hip joint. No communication between the hematomas was observed. The drainage of the collection revealed hemopurulent material, and Staphylococcus aureus was identified, leading to the initiation of intravenous antibiotherapy. Due to concerns of potential osteomyelitis in the adjacent bone tissue, [^{99m}Tc]Tc-Besilesomab scintigraphy was performed at 4 and 24 hours post-injection to investigate possible infection. ***Results:*** Planar whole-body images acquired at 4 and 24 hours post-injection revealed a heterogeneous and irregular distribution of the radiopharmaceutical within the bone marrow, showing focal uptake in the humeri and femora, along with enhanced uptake in the sternum and lumbar vertebrae. These findings were consistent with osseous dysmorphism and marked scoliosis, both of which are typical features of Stuve-Wiedemann syndrome. Importantly, no abnormal radiopharmaceutical uptake was seen in the bone or soft tissue of the left thigh, which excluded the presence of infection in that region and contributed to the decision to discharge the patient. ***Conclusion:*** [^{99m}Tc]Tc-Besilesomab scintigraphy was a valuable tool in this unique case of Stuve-Wiedemann syndrome. While the imaging revealed typical features of the syndrome, it did not show infection or inflammation in the left thigh, crucially excluding osteomyelitis and supporting the decision for discharge. This highlights the value of scintigraphy in rare conditions, where imaging must be carefully interpreted in light of the patient's distinctive clinical presentation. ***References:***
1- Gaspar IM, Saldanha T, Cabral P, Manuel Vilhena M, Tuna M, Costa C, Dagoneau N, Daire VC & Hennekam RCM. Long-term follow-up in Stuve-Wiedemann syndrome. Am J Med Genet Part A. 2008; 146: 1748-1753. doi: 10.1002/ajmg.a.32325.

EP-0773

Is [^{68}Ga]Ga-FAPI-46 PET/CT Safe? A Safety Evaluation of the FAPI PET/CT Procedure with Haemodynamic Measurements and Patient-Reported Outcomes

M. Bentestuen[1], *C. Sylvest*[2], *M. Ladekarl*[3], *O. Thorlacius-Ussing*[4], *H. D. Zacho*[1];
[1]*Department of Nuclear Medicine and Clinical Cancer Research Centre, Aalborg, DENMARK,* [2]*Department of Gynaecology and Obstetrics, Aalborg University Hospital, Aalborg, DENMARK,* [3]*Department of Oncology and Clinical Cancer Research Centre, Aalborg University Hospital, Aalborg, DENMARK,* [4]*Department of Gastrointestinal Surgery and Clinical Cancer Research Centre, Aalborg University Hospital, Aalborg, DENMARK.*

Aim/Introduction: The novel PET tracer [^{68}Ga]Ga-Fibroblast Activation Protein Inhibitor-46 ([^{68}Ga]Ga-FAPI-46) has demonstrated promising diagnostic performance compared to [^{18}F] Fluorodeoxyglucose (FDG) PET/CT across multiple malignancies. Although no adverse events (AEs) related to [^{68}Ga]Ga-FAPI PET/CT have been reported to date, a formal safety evaluation is lacking. While often omitted in early-phase studies, systematic safety evaluations of promising investigational radiopharmaceutical are essential to support risk-benefit analysis required for regulatory approval and clinical implementation. This study aimed to evaluate the safety and tolerability of the [^{68}Ga]Ga-FAPI-46 PET/CT procedure, focusing on objective haemodynamic changes, AEs, and patient-reported discomfort. ***Materials and Methods:*** Participants were enrolled from two ongoing prospective diagnostic accuracy trials: (1) [^{68}Ga]Ga-FAPI PET/CT in ovarian cancer (FAPI-OC, EU CTIS no. 2023-505938-98-00) and (2) [^{68}Ga]Ga-FAPI PET/CT in gastric and

gastro-oesophageal junction cancer (FAPI-GC, EU CTIS no. 2023-505916-40-01). All scans were performed at Aalborg University Hospital, Denmark. A standard fixed dose of 150-250 MBq [^{68}Ga]Ga-FAPI-46 was administered, and the CTs performed were low dose without intravenous contrast. Haemodynamic parameters-systolic and diastolic blood pressure (BP) and heart rate (HR) - were measured in the supine position at four timepoints: Baseline (pre-injection), 1-minute post-injection, 10 minutes post-injection, and post-scan. Paired two-tailed T-tests ($p<0.05$) and a mixed-effects regression model were used for statistical analysis. Participants were actively asked about discomfort and AEs at each timepoint and instructed to report delayed AEs. AE severity was graded using Common Terminology Criteria for Adverse Events version 5.0 (CTCAE v5.0). Events attributable to pre-existing medical conditions, concomitant treatment, or unrelated incidents were not classified as [^{68}Ga]Ga-FAPI PET/CT related AEs. ***Results:*** Thirty participant were included: 16 from FAPI-GC and 14 from FAPI-OC. No significant changes were observed in systolic BP or diastolic BP across the four timepoints. A clinically insignificant, but statistically significant ($p<0.01$) decrease in HR (from 77 to 73 beats-per minute from baseline to post-scan) was observed, likely reflecting pre-scan procedural nervousness. No [^{68}Ga]Ga-FAPI PET/CT-related AEs or patient-reported discomfort were reported. ***Conclusion:*** [^{68}Ga]Ga-FAPI-46 PET/CT appears to be well tolerated, with no evidence of haemodynamic instability or scan-related AEs. Our findings support an acceptable safety profile. Larger-scale safety evaluations and continued clinical investigations are warranted to support broader clinical adoption.

EP-0774

Clinical Utility Of Platelet Kinetics Studies In Patients With Idiopathic Thrombocytopenic Purpura (ITP).

S. Faílde Balea*, E. Triviño-Ibáñez, T. Balibrea Zúñiga, A. Delgado García, L. Entrena Ureña, Á. Ramírez-Navarro, R. Sánchez-Sánchez;*
Hospital Universitario Virgen de las Nieves, Granada, SPAIN.

Aim/Introduction: To evaluate the usefulness of platelet kinetics in patients with ITP and its possible association with the therapeutic regimen and platelet count. ***Materials and Methods:*** Retrospective observational study of 41 patients with ITP who underwent autologous platelet labelling with [^{111}In]In-Oxin, studied by platelet kinetics (Jan/17-Nov/23) with splenic uptake indices compared to baseline (minute 30) (B/B30) >1.2.The current treatment line and minimum platelet count were included as variables of interest. ***Results:*** The mean age of the patients was 40.24±16.76 years (53.7% male). Follow-up without drug treatment was the most frequent therapeutic option (61%), followed by treatment with thrombopoietin receptor agonists (TPO-RA) (21.9%), corticosteroids (4.9%), rituximab or fostamatinib (4.9%), splenectomy (4.9%) and immunosuppressants combined with TPO-RA (2.4%). In platelet kinetics, the mean B/B30 index was 1.38 ± 0.20, B/B30max was 1.63 ± 0.36, and the minimum platelet count was 23609.80 ± 21231.85 platelets/µL.The untreated group showed significantly lower B/B30 (1.34 ± 0.22 vs. 1.44± 0.16; p= 0.032) and B/B30max (1.61±0.37 vs. 1.86 ± 0.35, p= 0.039) and higher minimum platelet count (29360.00 ± 22267.09 vs. 14625.13 ± 4089.46; p= 0.017). Analysis of the discriminative ability of the B/Bmax index by ROC curve showed an ABC of 0.687 (95% CI 0.501-0.873) with the cut-off point with the best sensitivity/specificity ratio being 1.67. ***Conclusion:*** Patients with lower hypersplenism indices need less frequent pharmacological treatment than those with higher B/B30.

EP-0775

Revealing the Unexpected: Urgent PET/CT Findings and Their Impact on Clinical Management-A Decade of Clinical Experience

M. Vaillant*[1], G. Cuesta[1], A. Ortega[1], C. Rodríguez[1], R. Cano[2], P. Daudén[1], P. Nespral[1], M. Cornide[1], M. Romero[1], M. Zapardiel[1], C. Wakfie[1], P. Bascuñana[3], M. Cabrera[1];*
[1]Nuclear Medicine Department, Hospital Clínico San Carlos, Madrid, SPAIN, [2]Cardiology Department, Hospital Infanta Sofía, Madrid, SPAIN, [3]Instituto de Investigación Sanitaria San Carlos (IdISSC), Madrid, SPAIN.

Aim/Introduction: To retrospectively evaluate patients who required urgent medical care following clinically relevant or unexpected critical radiological findings identified during PET/CT examinations. ***Materials and Methods:*** This retrospective study included a total of 49,493 consecutive PET/CT scans performed between 2014 and 2024 at our institution, primarily for oncologic indications. Most scans were performed with intravenous (IV) iodinated contrast. A thoracic sequence in arterial phase during inspiration and a whole-body portal phase acquisition were acquired, followed by a whole-body PET scan. In patients with contraindications—such as allergy, impaired renal function, pump failure, or refusal—IV contrast was not administered. All studies were reviewed by an experienced nuclear medicine physician immediately post-acquisition. Only cases that resulted in referral to the Emergency Department due to incidental findings requiring immediate clinical evaluation were included in the analysis. ***Results:*** Out of the total cohort, 1,082 patients (2.19%) presented with incidental findings that prompted urgent medical referral. The leading cause of referral was pulmonary embolism, detected in 383 patients, with 20.87% of these being bilateral. This was followed by thrombosis in other anatomical regions (165 patients), and vertebral posterior wall fractures with associated spinal canal compression (83 patients). Collectively, these three categories accounted for 58.3% of all emergency referrals. Less frequently observed findings included obstructive uropathy (5%) and brain space-occupying lesions (5%). The most common underlying malignancies among referred patients were lung cancer (202 cases), breast cancer (190 cases), and colorectal cancer (122 cases). ***Conclusion:*** Systematic review of all PET/CT scans upon acquisition is essential, and nuclear medicine physicians must be proficient in recognizing urgent clinical findings. The use of IV contrast proves highly beneficial not only for oncologic assessment but also for the detection of emergent or clinically significant events.

EP-0776

Isotopic determination of Red Cell Mass to study the haematocrit increase in patients in treatment with SGLT-2 inhibitors

I. Romero-Zayas*[1,2], N. Navarro-Niño[1], J. Álvarez-Doral[1], F. Campos Añón[1,2], A. Alvarez-Larrán[3,2], H. Brillembourg Cubillan[3], M. Garrote Ordeig[3], A. Farré Melero[1,4], A. Niñerola Baizán[1,2,5], E. Cano Cumellas[1], C. Santos Montero[1], J. Cordón del Pozo[1], D. Fuster Pelfort[1,2];*
[1]Nuclear Medicine Department, Hospital Clínic, Barcelona, SPAIN, [2]Institut d'Investigacions Biomèdiques August Pi i Sunyer (IDIBAPS), Barcelona, SPAIN, [3]Hematology Department, Hospital Clínic, Barcelona, SPAIN, [4]Faculty of Medicine and Health Sciences - University of Barcelona, Barcelona, SPAIN, [5]Faculty of Medicine and Health Sciences - University of Barcelona,, Barcelona, SPAIN.

Aim/Introduction: Treatment with sodium-glucose cotransporter type 2 inhibitors (SGLT2i) has been associated with a decrease in cardiovascular risk and progression of chronic kidney disease. There is evidence of the drug's relationship with the increase in haematocrit. It has been attributed to haemoconcentration due to their diuretic effect and the decrease in plasma volume (PV), but also to an increase in erythropoiesis. The aim is to analyse the measured red cell mass (RCM) and PV estimation using the isotopic dilution test with autologous [^{99m}Tc]Tc-erythrocytes in

patients in treatment with SGLT2i and increased haematocrit. ***Materials and Methods:*** This is a retrospective review of 41 patients (2019-2024) in treatment with SLGT2i drugs. The haematology department ruled out polycythaemia vera by determination of serum erythropoietin and JAK2V617F mutation by digital PCR. The isotopic RCM determination was performed with the administration of approximately 3.7 MBq of autologous radiolabelled [^{99m}Tc]Tc-erythrocytes. After reaching the circulating steady state, blood samples were withdrawn, and 2 ml measured in a gammacounter. RCM was determined with samples of a known volume standard and corrected by the capillary haematocrit. Indirect estimation of PV was calculated. Polyglobulia is considered when the RCM is more than 25% respect the expected value for a person of the same age, sex and height. The percentage of deviation from the central value of the normal range (%DCVN) for RCM and PV was stablished to compare patients. It was used Mann-Whitney U test, to compare by sex and type of SLGT2i (Empagliflozin and Dapagliflozin) and the Pearson's correlation for age. ***Results:*** Patients with polyglobulia were 22.0 % (n=9) with a mean %DCVN-RCM of + 49.8 % (SD 27.5). Polyglobulia-negative patients were 78.0 % (n=32) with a %DCVN-RCM of + 5.0 (SD 11.8) and for PV -5.3 (SD 11.2). In 4 patients (12.9%) clinicians considered haemoconcentration with a %DCVN-PV of -20.9% (SD 3.0). No significant differences were found in %DCVN between males and females (p>0.05) and neither for different SLGT2i (p>0.05). It was found a negative correlation with age (r=-0.178) without significance (p=0.21). ***Conclusion:*** In 22% of patients in treatment with SLGT2i and elevated haematocrit presents a real polyglobulia. The percentage of deviation from the central value of the normal range allows us to compare groups and to assess the pattern.The isotopic measurement of the RCM with [^{99m}Tc]Tc- erythrocytes provides an excellent tool to stablish the mechanism of the haematocrit increase in patients taking SLGT2i.

EP-0777

SeHCAT Protocol Optimisation: A Single-Scan Approach to Increased Capacity

K. Tallat-Szczotka, *H. McMeekin, M. Costa, J. Hidalgo, T. Hussain, B. Riberio;*
Barts Health NHS Trust, London, UNITED KINGDOM.

Aim/Introduction: Bile acid malabsorption (BAM) affects an estimated 1-4% of the population and accounts for up to 30% of patients with functional diarrhoea or diarrhoea-predominant irritable bowel syndrome. Diagnosis typically involves a [^{75}Se] tauroselcholic acid (SeHCAT) scan, which provides a gold-standard quantitative assessment of BAM. To meet growing demand and improve efficiency, the Nuclear Medicine Department at St. Bartholomew's Hospital has adopted a predictive model based on patient height and weight to eliminate the need for a day-0 image and performing a day-7 scan only. This model was proposed by Smout et al., who demonstrated a single day-7 scan, combined with predictive models, can maintain diagnostic accuracy [1]. ***Materials and Methods:*** A dataset of 100 patients was used to trial the best-fitting predictive model which is based on patient height and logarithm of weight. Firstly, patient imaging data was used to derive camera sensitivity factor (CSF), followed the methodology suggested by Smout et al [1]. Secondly, patient data was used to derive new fitting parameters using least-squares regression. ***Results:*** Both methods resulted in very strong correlation between the SeHCAT results obtained using measured and predicted Day 0 counts (0.99). The absolute deviation from the standard SeHCAT result was slightly larger for the CSF method than for the second method (6.61% vs 6.08%). Residuals analysis showed a moderate positive correlation (0.31) between measured and predicted counts for the CSF method. Very weak correlation was observed for the second method (0.11). For both methods, there was no change in the BAM diagnosis for any of the patients. In total, 96% of patients had no change to severity grading (mild/moderate/severe, representing 5%/10%/15% SeHCAT retention respectively) when using the predicted baseline counts. ***Conclusion:*** The model developed by Smout et al. [1] can successfully be used to implement a day-7 only imaging protocol. However, rederivation of fitting parameters should be considered over the simpler CSF derivation, particularly for centres using different imaging protocols from that described by Smout et al [1]. The day-7 only protocol has been implemented at St. Bartholomew's Hospital resulting in significant savings of departmental resources and patient time, as well as increasing capacity. ***References:*** [1] Smout, A. et al., (2021). Single scan SeHCAT studies: A model for the investigation of bile acid malabsorption. Nuclear Medicine Communications, 42(11), 1209-1216. https://doi.org/10.1097/MNM.0000000000001450.

EP-0778

A Comparative Analysis of Qualitative and Quantitative Findings in Lymphoscintigraphy for the Grading of Lymphedema

A. Pala, *H. Pala, M. F. Bozkurt;*
Hacettepe University Faculty of Medicine, Department of Nuclear Medicine, Ankara, TÜRKIYE.

Aim/Introduction: Lymphoscintigraphy is the primary imaging technique used to assess the function of the lymphatic system and confirm a diagnosis of lymphedema. Various qualitative grading systems are utilized to diagnose lymphedema. Additionally, quantitative methods have recently been introduced to provide a more objective insight into interpretation. This study aims to compare the effectiveness of qualitative and quantitative parameters for interpreting lymphoscintigraphy. ***Materials and Methods:*** Lymphoscintigraphic imaging was conducted on both lower extremities in a large cohort of adult patients with a preliminary diagnosis of lymphedema, and the results were assessed. Qualitatively, the presence of lymphatic flow in dynamic images for each lower extremity, main lymphatic flow, the presence and number of collaterals, the presence and number of in-transit lymph nodes, and the appearance of dermal backflow were visually evaluated using images obtained at the 1st and 3rd hour after bipedal radiocolloid injection. Additionally, the regions of interest were marked at the injection site and inguinofemoral lymph nodes on the 1st-hour images for each lower extremity, and the percentages of radiotracer passing through were calculated. Furthermore, according to the Taiwan lymphoscintigraphy staging system, the findings are classified as normal lymphatic flow, partial obstruction, or total obstruction. ***Results:*** The study included 350 patients (F/M:290/60,median age:52,range:18-89). Out of a total of 450 extremities evaluated,425 exhibited normal lymphatic flow (60.7%),217 had partial obstruction (31%), and 58 experienced total obstruction (8.3%). In extremities with normal lymphatic flow, the transit rate in dynamic images was 60.7%,normal main lymphatic flow was 93.2%,collateral observation was 43.3%,in-transit lymph nodes presence was 7.1%,and dermal-backflow was 2.8%. For partial obstruction, the transit rate in dynamic images was 34.1%,normal main lymphatic flow detection was 39.6%,collateral detection was 27.2%,in-transit lymph nodes presence was 35.5%,and dermal backflow findings were 40.6%. In total obstruction,the transit rate in dynamic images was 5.2%,normal main lymphatic flow detection was 0%,collateral detection was 0%,in-transit lymph nodes presence was 4%,and dermal backflow findings were 39.6%. In quantitative analysis, the median lymphatic passage rate was 32.6% for normal lymphatic flow,8% for partial obstruction,and 0% for total obstruction. ***Conclusion:*** Quantitative and qualitative parameters should be combined to diagnose lymphedema accurately and appropriately grade lymphatic obstruction. In lymphoscintigraphy reports, it is essential to include details regarding dynamic transit, main lymphatic flow, collateral flow, in-transit lymph nodes, and

dermal backflow, along with the percentage of the quantitative radiotracer transit. This information is crucial for grading lymphatic obstruction and managing patient care.

EP-49

e-Poster Area

C: Therapy Clinical Study -> C1 Oncological Therapy Clinical Study -> C11 Neuroendocrine Therapy

EP-0779

One therapy, many measures: a comparative study of response evaluation methods to Peptide Receptor Radionuclide Therapy (PRRT) in patients with neuroendocrine tumors (NET)

P. Guglielmo[1,2], *J. Jandric*[3], *C. Vallone*[4,5], *M. Rodari*[3], *C. Carnaghi*[6], *A. Bertuzzi*[7], *G. Tarullo*[3], *K. Marzo*[3], *M. Olivieri*[8], *M. Marenco*[3], *L. Evangelista*[3,1];
[1]*Department of Biomedical Sciences, Humanitas University, Pieve Emanuele, Milan, ITALY,* [2]*Nuclear Medicine Unit, Humanitas Gavazzeni, Bergamo, ITALY,* [3]*Nuclear Medicine Unit, IRCCS Humanitas Research Hospital, Rozzano, Milan, ITALY,* [4]*Humanitas University, Via Rita Levi Montalcini 4, Pieve Emanuele, Milan, ITALY,* [5]*Department of Advanced Biomedical Sciences, University of Naples Federico II, Naples, ITALY,* [6]*Oncology Unit, IRCCS Humanitas Research Hospital, Rozzano, Milan, ITALY,* [7]*Medical Oncology and Hematology Unit, IRCCS Humanitas Research Hospital, Rozzano, Milan, ITALY,* [8]*Medical Physics Unit, IRCCS Humanitas Research Hospital, Rozzano, Milan, ITALY.*

Aim/Introduction: The assessment of treatment response in NETs presents significant challenges. The multifactorial mechanism of action of PRRT further complicates accurate response evaluation, especially in the absence of a standardized assessment method. Therefore, the aim of our study is to compare various response assessment modalities and identify the one most predictive of clinical outcomes. ***Materials and Methods:*** In this single-centre retrospective study, we collected data from patients who received PRRT and underwent [^{68}Ga]DOTATOC PET/CT imaging both before and after treatment, with a minimum follow-up period of 12 months, between 2020 and 2022. Response to PRRT was evaluated using five different methods: (a) changes in the Krenning Score; (b) 'adapted' PERCIST criteria (MORE) [1]; (c) the ZP-normalized parameter [1]; (d) qualitative visual interpretation of PET images; and (e) RECIST-based morphological response. Each assessment modality was then correlated with clinical and follow-up data to identify the most reliable predictor of treatment outcome. Non-parametric analyses were used to compare each response criteria, by using the MedCalc® software. ***Results:*** A total of 15 patients were included in the study, with a median age of 60 years (range: 29-82); 9 were males and 6 females. All patients, except one, completed the full four cycles of PRRT; the remaining patient received three cycles. [^{68}Ga]DOTATOC PET/CT scans were performed at a median of 3 months (range: 1-8 mo.) after the completion of PRRT. Based on the different response criteria, patients were stratified into responders (including those with partial response) and non-responders (including those with stable or progressive disease). Classification of patients into responders and non-responders varied depending on the assessment method: 4 (33%) and 8 (66%) using the Krenning Score; 11 (73%) and 4 (27%) using the MORE criteria; 12 (86%) and 2 (14%) with the ZP-normalized parameter; 12 (80%) and 3 (20%) based on qualitative visual interpretation; and 5 (42%) and 7 (58%) using RECIST criteria (all $p < 0.05$). The median time to disease progression was significantly shorter in non-responders compared to responders when stratified by MORE criteria (median: 9 vs. 23 months, $p < 0.05$) and the ZP-normalized parameter (median: 7.5 vs. 23 months, $p < 0.05$). ***Conclusion:*** Based on our preliminary results, the MORE criteria and ZP parameter appear to be predictive of clinical outcomes, providing a more robust framework for response assessment. These preliminary results support the need for standardized molecular criteria to guide PRRT response evaluation. ***References:***
1. DOI:10.3390/pharmaceutics14061278.

EP-0780

Improved Response of Advanced NET After Switching From ^{225}Ac-Octreotate to ^{225}Ac-LM3: A Preliminary Analysis

T. Speicher, *M. B. Bastian, A. Blickle, S. Maus, M. Bartholomä, C. Burgard, F. Rosar, S. Ezziddin;
Nuclear Medicine, Saarland University Hospital, Homburg, GERMANY.*

Aim/Introduction: Targeted alpha therapy with ^{225}Ac-labeled somatostatin analogues represents a promising approach in patients with advanced neuroendocrine tumors (NET), especially after limited effects of beta-emitting radiopeptide therapy. Somatostatin receptor antagonist LM3 exhibits higher receptor binding capacity compared to agonists with promising initial data. ***Materials and Methods:*** We retrospectively analyzed a cohort of n=8 advanced metastatic NET patients switching from [^{225}Ac]Ac-DOTA-octreotate to [^{225}Ac]Ac-DOTA-LM3 (Ac-LM3) following prior treatments. Pre- and post-switch responses according standardized PET imaging ([^{68}Ga]Ga-DOTATOC and [^{68}Ga]Ga-NODAGA-LM3 PET/CT), EORTC-based response categorization. Adverse events according CTCAE (Common Terminology Criteria for Adverse Events). ***Results:*** Before switching to Ac-LM3, most patients had stable disease (SD), with three showing partial response (PR) and one progressive disease (PD). Following Ac-LM3, four patients (50%) achieved PR and four remained stable. No progressive disease was observed. Toxicity was mostly restricted to grade 1-2 events, with no treatment discontinuations. However, one patient experienced a grade 3 renal adverse event, managed conservatively. ***Conclusion:*** Switching "standard" Alpha-PRRT to [^{225}Ac]Ac-DOTA-LM3 was well tolerated and resulted in improved molecular imaging response in half of the patients and maintained disease control in the remainder. These findings support further evaluation in larger cohorts.

EP-0781

Skeletal Muscle Uptake on [^{131}I]-Metaiodobenzylguanidine Post-Therapy Imaging

B. Lumb Morollon, *C. Brown;
Department of Clinical Physics and Bioengineering, NHS Greater Glasgow & Clyde, Glasgow, UNITED KINGDOM.*

Aim/Introduction: EANM procedural guidelines for [^{131}I]-mIBG list drugs that could interfere with the uptake, but do not state the nature of the interaction effect[1]. Dose rate measurements of retention and post-therapy imaging are used to verify distribution of [^{131}I]-mIBG and determine individualised discharge restrictions. Anecdotally, several local patients have shown varying degrees of skeletal muscle uptake. Literature has associated this with the use of tricyclic-related antidepressants suggesting blockage of alpha-2 receptors[2]. The prevalence, magnitude of muscle uptake and subsequent retention rates of these patients is unknown. This study aimed to assess the degree of skeletal muscle uptake in the local population and determine a correlation with patient medications. Additionally, the relationship between skeletal muscle uptake and whole-body retention of [^{131}I]-mIBG was investigated. ***Materials and Methods:*** 55 retrospective images (n=33, 17F/16M, age 17-84) were categorised qualitatively based on severity of skeletal muscle uptake. Images were assigned Grade 0 for no visible muscle uptake and Grade 1-3 with increasing muscle uptake. For patients with Grade2/3, listed medications were reviewed for those that could alter the biological uptake of the [^{131}I]-mIBG, e.g. tricyclic or tricyclic-related antidepressants. Patient dose rates recorded at intervals of approximately 24h during the inpatient period were used to plot the retention curves. Assuming

mono-exponential decay after the first phase post-administration of [^{131}I]-mIBG[3], the gradient of the log-linear retention curves was used to assess the correlation between degree of skeletal muscle uptake and whole-body retention. ***Results:*** Of the cases audited, 51.5% of patients demonstrated relatively high grade of skeletal muscle uptake (Grade 2/3) with 15.2% of patients showing no uptake. A subgroup of patients with visible skeletal muscle uptake were found to be on mirtazapine (tricyclic-related antidepressant). However, the data set was too small to determine a correlation. Unintuitively, results do not indicate a correlation between grade and gradient of the retention curve. ***Conclusion:*** Over half the patients audited show a notable degree of skeletal muscle uptake on post-therapy imaging, which is higher than expected for the population if drug interference alone were the main contributing factor. Ongoing investigation into the effect of skeletal muscle uptake on [^{131}I]-mIBG retention has demonstrated no correlation. ***References:*** [1]F Giammarile et al. 2008 Eur J Nucl Med Mol Imaging 35 (***5***) 1039-47; [2]SR Goel et al. 2009 Radiol Case Rep. 4(***3***) 306; [3]D Broggio et al 2023 J. Radiol. Prot. 43 021504.

EP-0782

Polish Registry of RLT - first report

M. Kolodziej[1], *V. Rosiek*[2], *J. Musiałkiewicz*[3], *A. Ledwon*[4], *A. Lewczuk-Myślicka*[5], *K. P. Sagan*[6], *B. Kos-Kudła*[2], *M. Ruchała*[7], *D. Handkiewicz-Junak*[4], *R. Swiatkowska-Stodulska*[5], *A. Syrenicz*[6], *G. Kaminski*[1];
[1]*Department of Endocrinology and Isotope Therapy, Military Institute of Medicine - National Research Institute, Warsaw, POLAND,* [2]*Department of Endocrinology and Neuroendocrine Tumours, Department of Pathophysiology and Endocrinology, Medical University of Silesia, Katowice, POLAND,* [3]*Department of Endocrinology, Metabolism and Internal Diseases, Poznan University of Medical Sciences, Poznań, POLAND,* [4]*Department of Nuclear Medicine and Endocrine Oncology, Maria Sklodowska-Curie National Research Institute of Oncology, Gliwice Branch, Gliwice, POLAND,* [5]*Department of Endocrinology and Internal Medicine, Medical University of Gdansk, Gdansk, POLAND,* [6]*Department of Endocrinology, Metabolic and Internal Diseases, Pomeranian Medical University, Szczecin, POLAND,* [7]*Department of Endocrinology, Metabolism and Internal Diseases, Poznan University of Medical Sciences, Poznan, POLAND.*

Aim/Introduction: Radioligand therapy (RLT) with [^{177}Lu]-DOTA-TATE is approved method of second line treatment for gastroenteropancreatic neuroendocrine tumours (GEP-NETs). This treatment is available in Poland from March 1, 2023 under the NHS Drug Program. The six largest Polish centers have created the Polish Registry covering over 80% of all patients treated with RLT in Poland. We present the first report prepared after 2 years of the Registry's operation. ***Materials and Methods:*** The online platform created for the Registry records subsequent patients who received RLT at one of the participating centers - the initial duration of the project was set at 96 months, with the possibility of extension. The primary objective is to evaluate RLT effectiveness in terms of progression-free survival. Secondary objectives include safety and identification of prognostic factors. ***Results:*** Of the 180 patients yet included in the Registry, 110 completed RLT, and another 70 are undergoing RLT. The mean age was 64.7 ±10.3 years, RTL was used on average 6.8 ±3.3 years after diagnosis, mainly as second-line treatment (69%), after somatostatin analogue. The group contained midgut, pancreatic and other location NETs (42%, 37% and 21% respectively). NETs G1 and G2 were 37% and 57%, respectively. Over 95% of patients had metastatic lesions, most often to the liver (87%). 31% of patients showed hormonal activity of the tumor, and over 90% were in very good or good (ECOG 0 and 1) status performance. In a whole-body scintigraphy performed after the 4th course of RLT 97% of patients achieved an objective response. By the time of the first report 7% patients had died. ***Conclusion:*** The presented Registry is the first and largest Central-Eastern European real-world data. These are the first results showing the characteristics of patient included in the Registry and the initial effects of treatment, confirming the effectiveness and safety of RLT in this group. In the following months, the Registry will be systematically expanded to include more patients, which will allow for further implementation of the assumed project goals.

EP-0783

Initial and re-challenge Lutetium-177-DOTATATE PRRT in a Metastatic Ovarian Neuroendocrine Tumour: a case report

N. Eftychiou, *H. Ahmed, R. Fernandez, F. Hassan;
Guy's and St Thomas Foundation Trust, London, UNITED KINGDOM.*

Aim/Introduction: Ovarian neuroendocrine tumours (NETs) are extremely rare, constituting less than 5% of all NETs, and only 0.1% of all ovarian cancers. Due to their rarity, there are no established therapeutic guidelines for these tumours. This case report presents the use of peptide receptor radionuclide therapy (PRRT) with Lutetium-177-DOTATATE in a patient with metastatic ovarian NET, highlighting its potential efficacy and the need for further research to develop standardised treatment protocol for this rare condition. ***Materials and Methods:*** A 58-year-old female diagnosed with a complex medical history including papillary thyroid carcinoma and endometrioid endometrial carcinoma, was diagnosed with a right ovarian tumour containing both a mature teratoma and a well differentiated NET (Ki67 5%) with distant metastases. Disease progression led to her referral to our hospital. Baseline imaging with Gallium-68-DOTATATE PET/CT revealed extensive metastatic disease affecting multiple sites, including the lymphnodes, liver, lungs, peritoneum and skeleton. Symptoms pre-treatment included diarrhoea, abdominal pain (requiring opioids) and fatigue. Patient underwent four cycles of Lutetium-177-DOTATATE over an 8 month period and two re-challenge cycles 21 months subsequently. ***Results:*** After the first two PRRT cycles, the patient experienced significant symptomatic relief, including resolution of diarrhoea and abdominal pain. Energy levels improved over time. Imaging throughout treatment showed stable disease. Gallium-68-DOTATATE-PET-CT scan at 3- and 12- months post-treatment showed mainly stable disease with partial nodal response. However, disease progression in the bone and liver was noted at 24 months after the initial cycle of PRRT. A re-challenge treatment was initiated , which has so far resulted in improved energy levels and stable disease on imaging. ***Conclusion:*** This case highlights the potential role of PRRT in managing metastatic ovarian NETs, offeing symptomatic relief and disease stability in short term. Given the rarity of these tumour's and the lack of therapeutic guidelines this case also underscores the need for further research to develop evidence-based therapeutic strategies for ovarian NETs.

EP-0784

Alpha Peptide Receptor Radionuclide Therapy (PRRT) with the somatostatin receptor (SSTR)-antagonist 225Ac-DOTA-LM3 as rescue therapy after failure of conventional treatments in neuroendocrine neoplasm G3

E. Perrone[1], *K. Ghai*[2], *T. Parkar*[2], *A. Eismant*[2], *L. Greifenstein*[2], *M. Pavel*[3], *R. P. Baum*[2];
[1]*Nuclear Medicine Unit, Fondazione Policlinico Universitario Agostino Gemelli, IRCCS, Rome, ITALY,* [2]*CURANOSTICUM Wiesbaden-Frankfurt, Center for Advanced Radiomolecular Precision Oncology, Wiesbaden, GERMANY,* [3]*Department of Medicine 1, Uniklinikum Erlangen, Friedrich-Alexander University of Erlangen-Nürnberg, Erlangen, GERMANY.*

Aim/Introduction: Patients with metastatic neuroendocrine neoplasm (NEN) progressing after standard therapies, including SSTR-agonists PRRT and systemic therapies, represent a clinical challenge. SSTR-antagonists are promising due to higher tumour uptake, tumour-to-background ratio and longer tumour retention. Safety, efficacy and survival were assessed in advanced

NEN G3 patients treated with α-emitter Actinium-225-labelled SSTR-antagonist DOTA-LM3 PRRT, in monotherapy and with Lutetium-177 (TANDEM), as rescue therapy after established treatments. ***Materials and Methods:*** Following 68Ga-DOTA-LM3 PET/CT, 14 patients with metastatic well-differentiated NEN G3 received α-PRRT with 225Ac-DOTA-LM3 (03/2022-02/2025). Hydration, antiemetics, dexamethasone and para-aminohippuric acid were provided. Acute adverse events and long-term haematological, renal and hepatic toxicity were prospectively collected and retrospectively analysed (03/2025), graded using CTCAE v.5.0. Molecular-imaging-based response was assessed following THEranostic Response Criteria In Solid Tumours (THERCIST) by 68Ga-DOTA-LM3 PET/CT and post-therapeutic SPET/CT. Survival was calculated from first α-PRRT to death. ***Results:*** We treated 14 patients (38-66 years; M:F=9:5) with metastatic NEN (n=10 pancreas, n=3 small bowel, n=1 colo-rectal), classified as well-differentiated NEN G3 at diagnosis (n=5) or upgraded to well-differentiated NEN G3 following repeated biopsy (n=9). The overall median Ki67 value was 33% (range 21-60%). Prior treatments included: SSTR analogues (100%), chemotherapy (93%), surgery (64%), 177Lu-DOTATATE (64%), Everolimus (64%), 177Lu-DOTA-LM3 (36%), 177Lu-DOTATOC (29%), 90Y-DOTATOC (21%), hepatic intra-arterial PRRT (14%), 90Y-DOTATATE (7%). 26 cycles of 225Ac-DOTA-LM3 PRRT were totally administered (9 monotherapies, 17 TANDEM). Six patients received 1 cycle, six patients 2 cycles, two patients >2 cycles. α-PRRT was overall well tolerated, with few G1 self-limiting acute adverse events, mainly nausea (n=4). Long-term toxicity included: anemia G2 (n=4), anemia G3 (n=1), absolute neutrophilic count reduction G3 (n=1), thrombocytopenia G1/G2 (n=4), thrombocytopenia G3 (n=2), creatinine increase G1 (n=2), liver impairment G2 (n=1) and G3 (n=1) in patients with hepatic metastases. No patients discontinued α-PRRT due to toxicity, but one was diagnosed with acute myeloid leukemia 12 years after first 90Y-DOTATOC-PRRT and 3 months after TANDEM-PRRT. Molecular-imaging responses included one complete remission (7%), five partial remission (36%), five disease progression (36%), two stable disease (14%); one clinical progression (7%). At time of analysis, after a median follow-up of 11 months: 50% of patients were alive, 50% had died. ***Conclusion:*** Our retrospective analysis showed that α-PRRT with SSTR-antagonist 225Ac-DOTA-LM3 (monotherapy or TANDEM) in heavily pretreated advanced well-differentiated NEN G3 patients failing standard treatments is well-tolerated, with favourable safety and encouraging efficacy results. Prospective randomized trials are warranted to confirm and optimize its clinical use.

EP-0785

IPAX-2: Phase 1 safety and dose finding study of [^{131}I]IPA plus standard of care in patients with newly diagnosed glioblastoma

J. Roetman[1], *J. Pichler*[2], *N. Singhal*[3], *H. Gan*[4], *A. Braat*[5], *W. Pullin*[6], *B. Cerqueira*[1];
[1]*Telix Pharmaceuticals, Melbourne, AUSTRALIA,* [2]*Kepler University Hospital, Linz, AUSTRIA,* [3]*Royal Adelaide, Adelaide, AUSTRALIA,* [4]*Austin Health, Heidelberg, AUSTRALIA,* [5]*UMC Utrecht, Utrecht, NETHERLANDS,* [6]*Gold Coast University Hospital, Southport, AUSTRALIA.*

Aim/Introduction: Glioblastoma (GBM) overexpresses L-type amino transporter (LAT) 1 and 2, which are the target 4-L-[^{131}I] iodo-phenylalanine ([^{131}I]IPA). Previous studies of [^{123}I]IPA as a SPECT tracer showed retention in glioma tissue, high metabolic stability, and uptake by >85% of gliomas. Results from a phase 1 trial (IPAX-1) that explored [^{131}I]IPA + radiotherapy in patients with recurrent GBM demonstrated a favourable safety profile and promising efficacy. The objective of IPAX-2 (NCT05450744) is to evaluate the safety and tolerability of [^{131}I]IPA in patients newly diagnosed with GBM. ***Materials and Methods:*** IPAX-2 is a phase 1, multicentre, open-label, single-arm, parallel-group, dose-finding study aimed to evaluate the safety of ascending radioactive dose levels of [^{131}I] IPA plus standard of care (chemoradiation) in newly diagnosed patients with GBM. Eligible patients (N=12) will be aged 18-65 years with histologically confirmed intracranial GBM following surgical resection; no prior systemic therapy or radiation for GBM; a Karnofsky Performance Status ≥70; a plan to begin chemoradiation 3-6 weeks after surgical resection with Stupp regimen; adequate organ function; and adequate tissue samples previously archived. Four cohorts (n=3 for each cohort) will encompass a 3+3 dose escalation, beginning with [^{131}I]IPA intravenously administered as 2 doses of 3 GBq each (dose escalation schedule: 2x3 GBq, 2x4 GBq, 2x5 GBq, 2x6 GBq). Dose 1 will be administered 7 days prior to chemoradiation, and dose 2 will be administered after last chemoradiation session. Chemoradiation will consist of 6 weeks of external beam radiation therapy (60 Gy/30 fractions) plus temozolomide 75 mg/m^2 daily. Following dose 2 of [^{131}I]IPA, patients will receive a 4-week treatment break before starting 6 maintenance cycles of temozolomide 150-200 mg/m^2 on days 1-5 every 28 days. ^{18}F-FET PET will be used to identify suitable candidates with LAT1 and LAT2 overexpression, establish a baseline, and provide quantitative follow-up information. The co-primary objectives are to 1) determine dose-limiting toxicity, maximum tolerated dose, and recommended phase 2 dose, and 2) determine the incidence of treatment-emergent adverse events. ***Results:*** This study is currently enrolling; no results are available at the time of abstract submission. ***Conclusion:*** The unique characteristics of [^{131}I]IPA, including its specific and sustained tumour accumulation and intrinsic cytostatic and radiosensitizing effect, make it an attractive therapeutic probe against GBM.

EP-0786

The role of quantitative analysis of Post-Therapeutic CZT SPECT/CT Imaging in the Evaluation of Tumor Response to PRRT in Neuroendocrine Tumors

H. Noamen*, Y. Cras, M. Longo, C. Garcia, J. Hadoux, L. Lamartina, S. Moog, E. Baudin, D. Deandreis;*
Gustave Roussy Cancer Campus, Villejuif, FRANCE.

Aim/Introduction: The assessment of treatment response to ^{177}Lu-DOTATATE therapy in neuroendocrine tumors (NETs) is still an issue. RECIST 1.1 criterias are limited and the lack of standardized protocols for functional imaging introduces further challenges. This study aimed to evaluate the feasibility of quantitative analysis of post-treatment ^{177}Lu-DOTATATE SPECT/CT imaging obtained by CZT gamma camera. ***Materials and Methods:*** This retrospective study includes 25 patients (12 F,13 M; mean age: 65 ± 12 years) with GEP NETs (n=20) and lung NET (n=5) treated with ^{177}Lu-DOTATATE (median activity 7192 MBq, [7113;7400]. Grades were distribued as follows : G1 (n=9), G2 (n=12), and G3 (n=4) respectively. All patients underwent whole body 3D post therapeutic images 24 hours after treatment with a CZT gamma camera after each single cycle. 19/25 patients were finally analyzed for technical reasons. For each scan, whole-body somatostatin receptor tumor volume (SSTRTV) and median SSTR SUVmean were quantified using dedicated software that applied a patient-specific semi-automatic segmentation approach, incorporating an additional 10% threshold evaluation. ΔSSTRTV and ΔSSTR SUVmean were evaluated after each cycle and compared to RECIST 1.1 response. ***Results:*** Median SSTRTV and median SSTR SUVmean were 914.01 ml ([398.125; 1252.46]) and 8.05; [2.73; 12.1] respectively, with no statistical difference between primary tumor location or pathological grade (p=0.406 and p=0.22 respectively). Metastatic lesions were located in liver (n=20), lymph nodes (n=10), bone (n=10), peritoneum (n=3), lungs (n=3), and other organs (n=5) respectively. Among the 19 patients, at the end of treatment 16 patients had stable disease (SD), 2 partial responses (PR), and 1 disease progression (PD), according to RECIST 1.1

criteria (for new lesion appearance). Median ΔSSTRTV and ΔSSTR SUVmean were respectively -17.94% and +14.7% between C1-C2, -18.28% and +1.64% between C2-C3, and -18.73% and +23.09% between C3-C4. Patients with SD in RECIST 1.1 presented median ΔSSTRTV of -16.13% [-25.84; -4.39] after C2 and -6.91% [-25.84; -4.39] after C4. Patients with PR presented a median ΔSSTRTV of -60.5% ; [-67.01; -54.12] and -44.9% [-61.34; -23.4] after C2 and C4 respectively. Patient with PD presented ΔSSTRTV of -92.08% after C2 and -95.77% after C4 on initial disease but SPECT confirmed the appearance of a new lesion in the liver. ***Conclusion:*** The study demonstrated the feasibility of post-therapy quantitative analysis of ^{177}Lu-DOTATATE using CZT SPECT/CT imaging. This approach highlights the potential of post-therapy SPECT/CT imaging to evaluate the response to ^{177}Lu-DOTATATE treatment.

EP-0787

Performance of Large Language Models in Answering Common Patient Questions on ^{177}Lu-DOTATATE Therapy for Neuroendocrine Tumors: A Comparative Evaluation by a Panel of Medical Experts

V. Habouzit[1], *A. Durand*[2], *L. Al Mansour*[2], *B. Lachachi*[2], *M. Halilali*[3], *M. Janier*[4], *T. Walter*[4], *T. Grenier*[5], *A. Flaus*[4];
[1]*University Hospital of Saint Etienne, Saint Etienne, FRANCE,* [2]*Hospices Civils de Lyon, Lyon, FRANCE,* [3]*Université Claude Bernard Lyon 1, Lyon, FRANCE,* [4]*Hospices Civils de Lyon and Faculté de médecine Université Claude Bernard Lyon 1, Lyon, FRANCE,* [5]*Univ Lyon, INSA-Lyon, Université Claude Bernard Lyon 1, CNRS, INSERM, CREATIS UMR 5220, Lyon, FRANCE.*

Aim/Introduction: Neuroendocrine tumors (NETs) are rare diseases, and patients often have difficulties obtaining information at the beginning of medical care. Large Language Models (LLMs) are increasingly used by patients to access medical information and may support pre-treatment education for patients with NETs. Upon disease progression, they may be treated with [^{177}Lu]Lu-DOTATATE, a radiopharmaceutical that raises frequent questions due to its radioactive nature and the complexity of the treatment pathway. This study aimed to evaluate and compare the performance of several LLMs in responding to commonly asked patient questions, focusing on accuracy, conciseness, and readability. ***Materials and Methods:*** Fourteen common patient questions about [^{177}Lu]Lu-DOTATATE therapy were selected by two clinical experts. These questions were submitted to five advanced LLMs: GPT-4o (OpenAI), Gemini 2.0 Flash (Google), Mistral-Large (LeChat), Claude 3.7 Sonnet (Anthropic), and DeepSeekV3 (DeepSeek). AI-generated responses were independently assessed in both French and English by a blinded panel of seven nuclear medicine physicians and oncologists from two French tertiary care centers. Each response was rated across three domains: accuracy and conciseness (1-4 scale), and readability (1-3 scale). Higher scores indicated better performance. Descriptive statistics and Friedman's ANOVA were used for comparisons of LLM performance within each domain and language. A p-value < 0.05 was considered statistically significant. Post-hoc pairwise comparisons were conducted using the Durbin-Conover test with Bonferroni-adjusted p-values. ***Results:*** Significant differences were observed between LLMs in accuracy (English) and conciseness (both languages). For English accuracy, Claude had the highest mean score (3.56) and significantly outperformed all models except LeChat (scores: 3.24-3.36; $p < 0.05$ and $p = 0.053$, respectively). In English conciseness, Claude, ChatGPT, LeChat, and DeepSeek outperformed Gemini (scores: 3.34-3.53 vs 2.80; $p < 0.05$). In French, Claude and ChatGPT also outperformed Gemini and DeepSeek for conciseness (3.41 vs 2.67-3.10; $p < 0.05$), with LeChat showing intermediate performance (3.32). No significant differences were found for readability in either language or for accuracy in French. ***Conclusion:*** LLMs demonstrated variable performance in answering patient questions on [^{177}Lu]Lu-DOTATATE therapy. Claude and ChatGPT consistently ranked highest, especially in accuracy and conciseness. These findings suggest that selected LLMs may serve as complementary tools for patient education in nuclear medicine, which currently requires supervision by the healthcare team.

EP-0788

Correlation between organs-at-risk dosimetry and toxicity in patients with gastroenteropancreatic neuroendocrine tumours (GEP-NETs) treated with ^{177}Lu-DOTATATE: a single center experience

V. Gaudieri[1], *L. Piscopo*[1], *E. Zampella*[1], *C. Nappi*[1], *F. Volpe*[1], *E. Caiazzo*[1], *T. Faiz*[1], *M. Caroprese*[1], *A. Barillaro*[1], *A. Varallo*[2], *S. Clemente*[2], *R. Pacelli*[1], *A. Cuocolo*[1], *M. Klain*[1];
[1]*Department of Advanced Biomedical Sciences, University Federico II, Naples, ITALY,* [2]*Unit of Medical Physics and Radioprotection, University of Naples "Federico II", Naples, ITALY.*

Aim/Introduction: Peptide receptor radionuclide therapy (PRRT) is an established effective and, generally, well-tolerated treatment in patients with neuroendocrine tumours, however it may be limited by hematological and kidney toxicity. This study assessed the correlation between the absorbed dose burden to the bone marrow and kidneys, evaluated using image-based dosimetry, and treatment-related toxicity. ***Materials and Methods:*** Consecutive patients with well-differentiated GEP-NETs treated with four cycles of ^{177}Lu-DOTATATE every 8 weeks, from January 2023 to December 2024 and followed until disease progression or death. Adverse events (AEs) were collected and monitored until resolution. After each cycle SPECT/CT imaging scans were acquired at 4 hours (h), 24 h, 48 h and 168 h for dosimetric estimations of kidneys, bone marrow and spleen, using the software MIM SurePlan MRT (MIM, Cleveland). Spearman correlation coefficient was performed between absorbed doses and blood and kidney parameters. Kaplan-Meier method and log-rank test were used to evaluate the progression free survival (PFS). ***Results:*** In the 14 patients included, median PFS was 21 months. All patients received four PRRT cycles. Before starting therapy 7 patients had mild lymphopenia, 6 patients mild anemia, 2 patients mild thrombocytopenia, and 1 patient mild neutropenia. Most common AEs of any grade were anemia and lymphopenia (100%), thrombocytopenia (50%), fatigue (28%) and nausea (21%). Most common grade ≥3 AE was lymphopenia in 21% of patients. No renal toxicity was observed in any of the patients. Median cumulative absorbed dose (AD) by the bone marrow, spleen and kidneys was 2.05, Gy, 13.6 Gy and 10.55 Gy respectively. No association between bone marrow cumulative AD and values of hemoglobin and lymphocytes was demonstrated, as well as between the spleen cumulative AD and hematological toxicities. A significant correlation between bone marrow cumulative AD and percentage variation of platelets was found (rho=-0.621; p=<0.05). No correlation between renal function and kidneys' cumulative AD was found (rho=-0.239; p=ns). ***Conclusion:*** Our results confirm that ^{177}Lu-DOTATATE is a well-tolerated therapeutic option in patients with GEP-NETs. No hematological toxicities were associated with cumulative AD to bone marrow or spleen, apart from a correlation between the cumulative AD to bone marrow and the percentage variation of platelets. No correlation was observed between renal function parameters and cumulative renal AD.

EP-0789

Is tailor-made RLT safe? - Preliminary results from the ongoing DUONEN study

M. Kolodziej[1], *G. Kaminski*[1], *M. Opalinska*[2], *M. Dedecjus*[3], *A. Kowalska*[4], *M. Saracyn*[1], *P. Garnuszek*[5], *I. Cieszykowska*[5], *W. Lenda-Tracz*[6], *D. Gasior-Perczak*[4], *A. Budzynska*[7], *A. Kubik*[7], *K. Kacperski*[7], *P. Pastusiak*[7], *W. Chalewska*[3], *A. Borkowska*[6], *J. Januszkiewicz-Caulier*[3], *J. Dlugosinska*[3], *A. Sowa-Staszczak*[2], *P. Cegła*[3], *A. Hubalewska-Dydejczyk*[2], *R. Mikołajczak*[5];
[1]*Department of Endocrinology and Isotope Therapy, Military*

Institute of Medicine - National Research Institute, Warsaw, POLAND, [2]Chair and Department of Endocrinology, Jagiellonian University Medical College, Krakow, POLAND, [3]Department of Endocrine Oncology and Nuclear Medicine, National Institute of Oncology - National Research Institute, Warsaw, POLAND, [4]Collegium Medicum, Jan Kochanowski University, Kielce, POLAND, [5]Radioisotope Center POLATOM, National Centre for Nuclear Research, Otwock, POLAND, [6]Faculty of Health Sciences, Jagiellonian University Medical College, Krakow, POLAND, [7]Department of Nuclear Medicine, Military Institute of Medicine - National Research Institute, Warsaw, POLAND.

Aim/Introduction: The established dose limits for critical organs during radioligand therapy (RLT) are 23 Gy for the kidneys and 2 Gy for the bone marrow. However, literature data suggest that some patients receiving standard RLT—four cycles of 7.4 GBq [^{177}Lu]Lu-DOTA-TATE—may not reach these thresholds, a phenomenon referred to as undertreatment. This raises the question: can the administered activity of [^{177}Lu]Lu-DOTA-TATE be increased safely without exceeding organ dose limits? ***Materials and Methods:*** We present preliminary results from the ongoing multicenter DUONEN study. Adult patients with advanced, unresectable, progressive, well-differentiated (G1/G2) gastroenteropancreatic neuroendocrine tumors (GEP-NETs) were randomized into two arms: (A) standard [^{177}Lu]Lu-DOTA-TATE RLT and (B) individualized, dosimetry-guided RLT. Outcomes included absorbed doses to kidneys and bone marrow, safety profiles, progression-free survival (PFS), and overall survival (OS). ***Results:*** To date, 24 patients (12 per group) have completed RLT. In group A, patients received mean cumulative activity of 29.2 GBq (7.3 GBq per cycle), resulting in mean absorbed doses of 19.68 Gy to the kidneys and 0.51 Gy to the bone marrow. Group B received a higher mean cumulative activity of 33.9 GBq (7.98 GBq per cycle), with corresponding mean absorbed doses of 22.71 Gy and 0.51 Gy, respectively. No statistically significant differences were observed in hematologic parameters (WBC, RBC, PLT, Hb) or renal function (creatinine, GFR) between the groups. Median PFS and OS have not yet been reached after 12 months of follow-up. ***Conclusion:*** Standard RLT activity levels may be insufficient to reach critical organ dose thresholds in many patients. Preliminary data suggest that individualized, dosimetry-based increases in administered activity can be safely implemented without compromising kidney or bone marrow function. Long-term follow-up (up to 60 months post-RLT) is ongoing. ***References:*** The study is funded by the Polish Medical Research Agency (Project number 2019/ABM/01/00077-00).

EP-0790

Radiopharmaceutical Therapy in Neuroendocrine Carcinoma using Actinium-225, FAP-targeting, and somatostatin receptor antagonists: A new therapeutic perspective in patients progressing to standard therapies

E. Perrone[1], *K. Ghai*[2], *T. Parkar*[2], *A. Eismant*[2], *L. Greifenstein*[2], *M. Pavel*[3], *R. P. Baum*[2];
[1]*Nuclear Medicine Unit, Fondazione Policlinico Universitario Agostino Gemelli, IRCCS, Rome, ITALY,* [2]*CURANOSTICUM Wiesbaden-Frankfurt, Center for Advanced Radiomolecular Precision Oncology, Wiesbaden, GERMANY,* [3]*Department of Medicine 1, Uniklinikum Erlangen, Friedrich-Alexander University of Erlangen-Nürnberg, Erlangen, GERMANY.*

Aim/Introduction: Neuroendocrine carcinoma (NEC) is a very aggressive neoplasm with high morbidity and mortality. Conventional treatments beyond first-line platinum-based chemotherapy have proven ineffective, often with significant side effects. Radiopharmaceutical Therapy (RPT) might offer a potential therapeutic option in these patients, supported by recent advancements in radiotheranostics: alpha-emitter nuclides, like Actinium-225 (high linear energy transfer); new targets, e.g. fibroblast activation protein (FAP, targeting the tumour microenvironment); new molecules, like somatostatin receptor (SSTR)-antagonists (DOTA-LM3), with high tumour uptake and prolonged tumour retention. We investigated safety, efficacy and survival of RPT as salvage therapy in patients with advanced NEC. ***Materials and Methods:*** RPT was administered following confirmation of high uptake at PET/CT with Gallium-68-labelled corresponding compound (04/2022-01/2025). RPT included Peptide Receptor Radionuclide Therapy (PRRT) and FAP-directed Radiopharmaceutical Therapy (FRT) using radiolabelled-3BP-3940 (FAP-binding peptide). CTCAE v.5.0 was used to grade acute and long-term haematological, renal and hepatic adverse events. Molecular imaging-based response was evaluated following THERCIST via PET/CT or post-therapeutic SPET/CT. Data were retrospectively analysed (03/2025). ***Results:*** We treated 6 patients (36-66 years; M:F=5:1) with metastatic pancreatic (n=4) or colorectal NEC (n=2). Tumours were NEC at initial diagnosis (n=5) or upgraded from well-differentiated neuroendocrine neoplasm G3 following repeated biopsy (n=1). Previous treatments included: chemotherapy (n=5); radiotherapy (n=4); surgery (n=3); somatostatin analogues (n=2); Everolimus (n=1); 177Lu-DOTATATE (n=1). PRRT was administered in two patients: one patient received one cycle of 225Ac-DOTA-LM3 and one of 225Ac/177Lu-DOTA-LM3 (TANDEM); the other patient received two cycles of 225Ac-DOTATOC. Four patients received FRT as follows: one cycle of 90Y-3BP-3940; one cycle of 225Ac/177Lu-3BP-3940 (TANDEM); two cycles of 177Lu-3BP-3940 and one of 90Y-3BP-3940; one cycle of 225Ac-3BP-3940 and three of 225Ac/177Lu-3BP-3940 (TANDEM). RPT was overall well tolerated, with few G1 acute adverse events (emesis, nausea, flare pain). Long-term toxicity included: anemia G2/G3 (n=2), leukopenia G2 (n=1), thrombocytopenia G1 (n=1), liver impairment G2 in patient with hepatic metastases. Nephrotoxicity was not reported. Molecular-imaging responses included: one partial remission (2 months after DOTA-LM3 PRRT); three disease progression (response duration after first RPT: range 5-7 months). Two patients experienced clinical progression (1 month and 3 weeks after first RPT). At analysis, 5 patients had died, 1 patient was alive. ***Conclusion:*** Our experience shows that RPT can offer a therapeutic chance in individual patients with advanced NEC exhausting other treatments, however response rates were low; further research is needed to enhance RPT efficacy, also exploring the synergistic effects of combination with other therapeutic strategies.

EP-0791

Visual comparison of reception expression before and after Lu177 Dotatate PRRT in patients with GEP-NET using 68Ga-DOTATATE PET-CT

J. Zivanovic[1], *M. Vadrucci*[2], *N. Mulholland*[2], *S. Reynolds*[2];
[1]*Center for Nuclear Medicine with PET, University Clinical Centre of Serbia, Belgrade, SERBIA,* [2]*Department of Nuclear Medicine, King's College Hospital NHS Foundation Trust, London, UNITED KINGDOM.*

Aim/Introduction: The aim of this study was to compare receptor expression in patients undergoing 177Lutetium-DOTATATE peptide receptor radionuclide therapy (PRRT) by assessing their initial and post-therapy 68Ga-DOTATATE PET/CT scans. ***Materials and Methods:*** 84 patients undergoing PRRT were examined using patient data records and available PET/CT reports. The number of treatment cycles ranged from 1 to 6. Receptor expression was visually compared using both the least and most avid lesion in each patient at the baseline versus post-therapy scan. The change in receptor expression was classified as increased, decreased, stable; or not applicable if the lesion had been treated locally (e.g surgery or radiotherapy). ***Results:*** Table 1: Change in receptor expression in the least avid lesions Table 2: Change in receptor expression in the most avid lesions Follow up of the patients' post-therapy scans as compared to the initial scan was performed in order to assess the efficacy of the therapy applied. The interpretation was done using

both visual assessment as well as the reports themselves. The results were as follows: Using these tables, new data was inferred about the relationship between the changes in metabolic activity and the overall disease progression. ***Conclusion:*** Application of PRRT achieved stable disease in the majority of patients reviewed. However, the disease progressed in 25% of patients, The aspect examined was a change in receptor expression. Namely, a lesion with higher receptor expression at the post-therapy scan than initial scan corresponded to disease progression and vice versa. In 80% of patients, both types of lesions followed the pattern of the disease; meaning that if the disease had progressed, both had higher receptor expression at the post-therapy scan. However, in the remaining patients, it is interesting to note that the lowest initial receptor expression followed the course of the disease more frequently. These preliminary results may indicate that disease with higher receptor expression heterogeneity implied by the variable degree of 68Ga-DOTATATE uptake at baseline is less likely to respond to PRRT.

EP-0792

Sex-based Differences in response to 177Lu-DOTATATE in patients with stage IV Neuroendocrine Tumors: A comparative analysis from a National Registry

M. Mitjavila Casanovas[1], *P. Bello*[2], *V. Pubul*[3], *A. García-Burillo*[4], *L. García-Cañamaque*[5], *A. Piñeiro*[6], *D. Balaguer*[7], *A. Garrido*[8], *J. Hernando*[4], *D. Gomez*[9], *J. Arbizu*[10], *A. Repetto*[11], *M. Castellón*[12], *M. Tabuenca*[13], *M. Orduña*[14], *M. Riesco*[15], *M. Velasco*[16], *M. Nevares*[17], *T. Alonso*[14], *M. de la Rubia*[18], *J. Ardila*[19], *A. Carmona-Bayonas*[20], *P. Jimenez Fonseca*[21];
[1]*Hospital Universitario Puerta de Hierro Majadahonda, Madrid, SPAIN,* [2]*Hospital Universitario La Fe, Valencia, SPAIN,* [3]*Complejo Hospitalario Universitario de Santiago, Santiago de Compostela, SPAIN,* [4]*Hospital Universitario Vall d'Hebron, Barcelona, SPAIN,* [5]*Hospitales H.M. Sanchinarro, Madrid, SPAIN,* [6]*Hospital Universitario Virgen de las Nieves, Granada, SPAIN,* [7]*Hospital Universitario Doctor Pesset, Valencia, SPAIN,* [8]*Complejo Hospitalario Universitario de Pontevedra, Pontevedra, SPAIN,* [9]*Hospital Universitario de Navarra, Pamplona, SPAIN,* [10]*Clínica Universitaria de Navarra, Pamplona, SPAIN,* [11]*Hospital Universitario Son Espases, Palma de Mallorca, SPAIN,* [12]*Hospital Universitario Virgen de la Arrixaca, Murcia, SPAIN,* [13]*Hospital 12 de Octubre, Madrid, SPAIN,* [14]*Hospital Universitario Ramón y Cajal, Madrid, SPAIN,* [15]*Hospital Universitario 12 de Octubre, Madrid, SPAIN,* [16]*H. de la Santa Creu i Sant Pau, Barcelona, SPAIN,* [17]*Hospital Universitario de Burgos, Burgos, SPAIN,* [18]*Hospital Universitario de Getafe, Madrid, SPAIN,* [19]*Hospital Universitario Gregorio Marañón, Madrid, SPAIN,* [20]*Hospital General Universitario Morales Meseguer, Murcia, SPAIN,* [21]*Hospital Universitario Central de Asturias, Oviedo, SPAIN.*

Aim/Introduction: In stage IV gastroenteropancreatic neuroendocrine tumors (GEP-NETs), sex-related differences in efficacy and toxicity have been documented with multi-kinase inhibitors, However, such differences remain underexplored in the context of 177Lu-DOTATATE (PRRT). Objective: To describe sex-based differences in baseline characteristics, treatment effectiveness, and toxicity among patients with stage IV GEP-NETs treated with PRRT. ***Materials and Methods:*** Patients with stage IV GEP-NETs treated with 177Lu-DOTATATE in the national SEPTRALU registry were analyzed. Baseline characteristics and toxicities were compared using chi-square and Student's t-tests. Effectiveness was assessed using Kaplan-Meier curves and log-rank tests. ***Results:*** A total of of 896 patients were included: 378 women (42%) and 518 men (58%). The median age was similar (65 years in women vs. 67 years in men) with a higher proportion of men over 65 years (56% vs. 52%). ECOG performance status 0 was comparable (women 54%, men 53%) as was Ki67 (5% vs. 6%). The most common primary tumor locations were pancreas (35% vs. 36%) and small intestine (31% vs. 29%). Metastases predominated in the liver (87% vs. 84%) and lymph nodes (61% vs. 65%). Time from diagnosis of metastasis to the start of PRRT was longer in women (62.9 vs. 49.7 months) and women received more prior lines of treatment (≥3 lines: 22% vs. 17%). Objective response rate was similar (between sexes women 22%, men 24%). Progression-free survival (PFS) was longer in women (38.2 months, 95% CI: 33.7-42.7) compared to men (29.7 months, 95% CI: 26.8-32.6). Overall survival (OS) also favored women (58.6 months, 95% CI: 51.7-65.5) compared to men (46.1 months, 95% CI: 41.6-50.6), with a HR of 0.82 (95% CI: 0.73-0.94). Grade 3-4 toxicity was low in both groups, although hematologic toxicity was slightly higher in women (4% vs. 2.5%). ***Conclusion:*** Women with stage IV GEP-NETs treated with 177Lu-DOTATATE demonstrated longer PFS and OS compared to men. Although overall toxicity rates were low and comparable, women experienced a modestly increased incidence of grade 3-4 hematologic toxicity.

EP-0793

PRRT with Lu-177-DOTATATE and monitoring with SSTR-PET/CT in patients with PPGL tumors

S. Kunte[1], *A. Holzgreve*[1], *M. Schöll*[1], *V. U. Wenetr*[1], *G. T. Sheikh*[1], *M. Scheifele*[1], *F. J. Gildehaus*[1], *S. Lindner*[1], *M. K. Auer*[2], *C. Lottspeich*[2], *M. Kroiß*[2], *S. Nölting*[2], *F. Völter*[2], *C. Spitzweg*[2], *C. J. Auernhammer*[2], *R. A. Werner*[3], *M. J. Zacherl*[1];
[1]*Department of Nuclear Medicine, LMU University Hospital, Munich, GERMANY,* [2]*Department of Internal Medicine IV, LMU University Hospital, Munich, GERMANY,* [3]*Department of Nuclear Medicine, LMU University Hospital, Munich, GERMANY.*

Aim/Introduction: Peptide receptor radionuclide therapy (PRRT) with [177Lu]Lu-DOTATATE has demonstrated promising efficacy in somatostatin receptor (SSTR)-expressing tumors. The present study aims to evaluate its therapeutic value in a rechallenge setting in patients with metastatic tumors of the adrenal medulla and extra-adrenal paraganglia. ***Materials and Methods:*** Nine patients with metastatic paraganglioma (PGL; n = 5) or pheochromocytoma (PCC; n = 4) who received at least two cycles of PRRT were retrospectively analyzed. Patients were stratified by treatment course into continuous (sequential PRRT; 5/9, 55.6%) and discontinuous (rechallenge after ≥11-month PRRT-free interval; 4/9, 44.4%) subgroups. Eligibility was confirmed via SSTR PET using either [68Ga]Ga-DOTATOC (n = 4) or [18F]SiTATE (n = 5), applying the Krenning score. Treatment response was assessed by RECIST 1.1, total tumor volume (TTV; PET-derived), and Chromogranin A (CgA) levels. Adverse events were evaluated according to CTCAE v5.0. ***Results:*** All patients exhibited high lesional SSTR expression (mean SUVmax 32.8 ± 62.3; Krenning Score 3-4), thus confirming their eligibility for PRRT. At the conclusion of treatment, eight out of nine patients (88.9%) demonstrated stable disease according to RECIST, while one out of nine (11.1%) exhibited progressive disease. Patients receiving discontinuous PRRT demonstrated consistent reductions in both TTV and CgA, whereas those with continuous PRRT showed more heterogeneous responses. Furthermore, two patients (22.2%) experienced Grade 3 toxicity, with no occurrence of Grade 4 or 5 events. ***Conclusion:*** In cases of metastatic PGL and PCC, the use of SSTR PET, particularly with [18F]SiTATE, has facilitated the selection of appropriate patients for PRRT. The results demonstrated that PRRT led to tumor control in the majority of patients, including those who underwent rechallenge. The treatment was well tolerated, with an acceptable safety profile.

EP-0794

"Rechallenge" peptide receptor radionuclide therapy (PRRT) may be less efficient than initial PRRT while safety profile is comparable

P. Hartrampf[1,2], *A. Kosmala*[1], *S. Alwers*[1], *F. Lutz*[1], *S. Serfling*[1], *A. Meining*[3], *A. Buck*[1], *A. Weich*[3,2];
[1]*University Hospital Würzburg, Department of Nuclear Medicine, Würzburg, GERMANY,* [2]*University Hospital Würzburg, ENETS Center of Excellence, Würzburg, GERMANY,* [3]*University Hospital Würzburg, Department of Internal Medicine II, Würzburg, GERMANY.*

Aim/Introduction: For patients with gastrointestinal, pancreatic or pulmonary neuroendocrine tumours (NET), peptide receptor radionuclide therapy (PRRT) can be performed as a re-challenge (re-PRRT) after initial PRRT (i-PRRT). We compared efficacy and adverse events between re- vs. i-PRRT, along with possible prognosticators for outcome. ***Materials and Methods:*** For 37 patients with NET, Kaplan-Meier analysis was used to assess progression-free survival (PFS) after i- and re-PRRT. The Wilcoxon test was used to compare baseline laboratory values for leukocytes, hemoglobin, platelets, C-reactive protein, lactate dehydrogenase, creatinine, glomerular filtration rate, bilirubin, gamma-GT (GGT), alanine aminotransferase and alkaline phosphatase between i-PRRT and re-PRRT. At baseline and upon follow-up, we determined SSTR-directed PET metrics (SUV_{mean}, SUV_{max} and SSTR-positive tumor volume (SSTR-TV) as well as their changes. A univariable Cox regression analysis was performed to determine the prognostic value for PFS. Adverse events were classified according to CTCAE 5.0. ***Results:*** The median interval between i-PRRT (median 4 [2-8] cycles, median activity 29.5 [13.3-60.8] GBq) and re-PRRT (median 3 [1-4] cycles, median activity 22.1 [5.0-30.4] GBq) was 36 (15-104) months. The median PFS after i-PRRT was 32 months and after re-PRRT 17 months (progression in 20/37 patients). Only median hemoglobin (12.2 vs. 13.2; p<0.01) and glomerular filtration rate (74 vs. 85; p<0.01) were significantly lower at beginning of re-PRRT, while GGT (64.0 vs. 45.7; p<0.001), AP (80.0 vs. 98.5, p<0.01) and de-Ritis (1.42 vs. 0.97, p<0.001) were higher at the beginning of re-PRRT. No significant differences were found in SSTR-TV (104.7 vs. 156.2 ml; p=0.3), SUV_{max} (36.5 vs. 50.2; p=0.1) and SUV_{mean} (9.8 vs. 11.9; p=0.2) between i-PRRT and re-PRRT. In the univariable Cox regression performed with laboratory values and the different PET parameters, only a higher CRP was significantly associated with shorter PFS in the i-PRRT (HR 8.8 95%CI 1.2-58.6, p<0.05). However, this association was not seen in re-PRRT (HR 0.79 95%CI 0.13-3.8, p=0.8) but LDH was significantly associated with shorter PFS in the re-PRRT (HR 1.007 95%CI 1.0-1.014, p<0.05). Among patients with available PET scans (i-PRRT, 33; re-PRRT, 26), 16/33 (48%) showed a reduction in SSTR-TV after i-PRRT, but only 10/26 (38%) after re-PRRT. However, two patients with no SSTR-TV reduction after i-PRRT had SSTR-TV reduction upon re-PRRT. No ≥ CTCAE 3 occurred in the re-PRRT group, but one grade 3 leukopenia after i-PRRT. ***Conclusion:*** Rechallenge PRRT in patients with GI-NET demonstrates comparable low toxicity to initial PRRT, while it may be less efficient.

EP-0795

First Real-World Evidence on the Safety and Effectiveness of ^{177}Lu-DOTATATE for Treating Gastroenteropancreatic Neuroendocrine Tumors (GEP-NETs): Insights from Post-Marketing Surveillance

Y.-i. Kim[1], *H. Suh*[2], *Y. Kang*[2], *H. Cho*[3], *S. Hyun*[4], *Y. Song*[5], *S. Ha*[6], *K. Kang*[7];
[1]*Asan Medical Center, University of Ulsan College of Medicine, Seoul, KOREA, REPUBLIC OF,* [2]*Novartis Korea Ltd., Seoul, KOREA, REPUBLIC OF,* [3]*Severance Hospital, Yonsei University College of Medicine, Seoul, KOREA, REPUBLIC OF,* [4]*Samsung Medical Center, Sungkyunkwan University School of Medicine, Seoul, KOREA, REPUBLIC OF,* [5]*Seoul National University Bundang Hospital, Seoul National University College of Medicine, Seongnam, KOREA, REPUBLIC OF,* [6]*Seoul St. Mary's Hospital, College of Medicine, The Catholic University of Korea, Seoul, KOREA, REPUBLIC OF,* [7]*Seoul National University Hospital, Seoul National University, Seoul, KOREA, REPUBLIC OF.*

Aim/Introduction: ^{177}Lu-DOTATATE has been used for patients with gastroenteropancreatic neuroendocrine tumors (GEP-NETs), however, the absence of clinical data in South Korean patients remains a significant gap. In this post-marketing surveillance study, we evaluated the safety and effectiveness of ^{177}Lu-DOTATATE in patients with GEP-NETs in real-world practice in South Korea. ***Materials and Methods:*** From July 2020 to July 2024, a total of 89 patients from 6 institutions diagnosed with GEP-NETs, as outlined in the approved indication for ^{177}Lu-DOTATATE, were prospectively enrolled. Safety was the primary objective, whereas effectiveness was secondary objective. Study findings were analyzed and compared with NETTER-1 and NETTER-2 trials. ***Results:*** Baseline characteristics were comparable to NETTER-1 and NETTER-2 except for the notably high proportion of G2 (77.1%) among participants. Considering the national health insurance status and patient condition, less than a half of patients (41.0%) completed four cycles of ^{177}Lu-DOTATATE treatment, a lower portion of completion rate compared to 75.7% in NETTER-1 and 87.8% in NETTER-2. Among the 83 patients, 60 patients (72.3%, 239 cases) had at least one adverse event (AE), with 6 patients (7.2%, 8 cases) experiencing serious adverse events (SAEs). The most common AE was nausea (34.9%, 46 cases), and most AEs were mild in severity (94.6%, 226 cases). Overall, the safety profile in this study presented minimal differences from NETTER-1 and NETTER-2. This study reports 37.7% of objective response rate (ORR) which is between 14.7% in NETTER-1 and 43.0% in NETTER-2. ***Conclusion:*** Our study complemented the safety and effectiveness of ^{177}Lu-DOTATATE in South Korea. The data would support the clinical use of ^{177}Lu-DOTATATE for the treatment of GEP-NETs.

EP-0796

Cycle-to-Cycle Reduction in External Dose Rate as a Predictor of Therapeutic Response in [177Lu] DOTATATE Therapy for Neuroendocrine Tumours

N. Wakabayashi[1,2], *S. Watanabe*[1,2,3], *S. Takeuchi*[4,5], *S. Takeuchi*[5,6], *K. Hirata*[1,2,3], *R. Kimura*[2,7], *J. Takenaka*[2,8], *H. Koga*[1,2], *K. Kudo*[2,3,7];
[1]*Department of Nuclear Medicine, Hokkaido University Hospital, Sapporo, JAPAN,* [2]*Department of Diagnostic Imaging, Graduate School of Medicine, Hokkaido University, Sapporo, JAPAN,* [3]*Global Center for Biomedical Science and Engineering, Faculty of Medicine, Hokkaido University, Sapporo, JAPAN,* [4]*Department of Medical Oncology, Faculty of Medicine and Graduate School of Medicine, Hokkaido University, Sapporo, JAPAN,* [5]*Neuroendocrine Tumor Center, Hokkaido University Hospital, Sapporo, JAPAN,* [6]*Department of Gastroenterological Surgery II, Faculty of Medicine, Hokkaido University, Hokkaido University, Sapporo, JAPAN,* [7]*Department of Diagnostic and Interventional Radiology, Hokkaido University Hospital, Sapporo, JAPAN,* [8]*Comprehensive Heart Failure Center, University Clinic Würzburg, Würzburg, GERMANY.*

Aim/Introduction: In peptide receptor radionuclide therapy with [177Lu] DOTATATE for neuroendocrine tumours, a reduction in external dose rate (EDR) is often observed in subsequent cycles compared to the first. This may reflect a decrease in radiotracer uptake in tumours, suggesting that changes in EDR could predict therapeutic efficacy. This study aimed to identify factors associated with changes in EDR and to evaluate their relationship with treatment response. ***Materials and Methods:*** We retrospectively analysed patients who completed four cycles of [177Lu] DOTATATE therapy at our institution between October 2022 and March 2025. The difference in EDR (μSv/h) at 1 metre from the body surface on the day after administration between the first and fourth treatments was defined as ΔEDR, calculated as: EDR after the first treatment minus EDR after the fourth treatment. Post-therapy SPECT/CT images were analysed, and regions with uptake exceeding 50% of the splenic SUVmax were visually assessed and categorised as either tumour or non-tumour by a board-certified nuclear medicine physician. Tumour uptake (TU) was quantified as the product of tumour volume and SUVmean. Non-tumour uptake (non-TU) was calculated in the same manner. Simple linear regression was performed to assess associations between ΔEDR and TU or non-TU. Based on the median ΔEDR, patients were divided into a high-ΔEDR group (greater reduction in EDR) and a low-ΔEDR group (minimal reduction or slight increase in EDR). Treatment response was assessed using RECIST version 1.1 and compared between groups using Fisher's exact test. ***Results:*** A

total of 16 patients were included. The mean ± SD of ΔEDR was 4.6 ± 4.8 μSv/h. According to RECIST version 1.1, 7 patients achieved partial response (PR) and 9 had stable disease (SD) during the observation period of 16.1 ± 7.7 months. Among the low-ΔEDR group, 6 showed PR and 2 SD; among the high-ΔEDR group, 1 showed PR and 7 SD. ΔEDR was significantly correlated with TU (adjusted R^2 = 0.57, p = 0.0004), but not with non-TU (adjusted R^2 = −0.07, p = 0.93). The low-ΔEDR group had a significantly higher rate of PR compared to the high-ΔEDR group (p = 0.04). ***Conclusion:*** A greater reduction in external dose rate (i.e., a larger ΔEDR) following [177Lu] DOTATATE therapy was significantly associated with decreased tumour uptake and may predict a favourable therapeutic response.

EP-0797

Study of the effectiveness of PRRT in 177 Lu-DOTATATE - treated patients

B. Kalman[1], *Z. Ritter*[1], *E. Mezősi*[1], *A. Bos-Liedke*[2], *D. Dezső*[1]; [1]*University of Pécs, Pécs, HUNGARY,* [2]*Department od Biomedical Physics of Adam Mickiewicz University, Poznan, POLAND.*

Aim/Introduction: Neuroendocrine tumours (NETs) are increasingly common and often cause hormonal syndromes. First-line treatment includes somatostatin analogues (SSA), but progression may require second-line ^{177}Lu-DOTATATE therapy. This study evaluates its efficacy in progressive cases, hypothesising that target lesion activity decreases over treatment. ***Materials and Methods:*** A total of 15 patients received ^{177}Lu-DOTATATE therapy, 9 of them received 4 cycles of treatment and were included in the study. Based on SPECT/CT scans, target lesions with the highest activity were selected and measured at the first and fourth post-therapy study time points according to RECIST 1.1 criteria. The SUVmax of the lesions was recorded, and the SUVmax of intact liver and spleen tissue was used as control. After testing the normality of the obtained data, we evaluated the differences using a paired Wilcoxon test. ***Results:*** In all patients, the largest liver metastasis was found to be the dominant target lesion. Liver metastasis activity was significantly decreased relative to normal liver during treatment (liver lesion 1/normal liver activity ratio, cycle 1 vs. cycle 4: p = 0.038153). The decrease in target lesion activity relative to normal spleen approached the limit of significance (liver lesion 1/spleen activity ratio, cycle 1 vs. cycle 4: p = 0.050613).A trend towards a decrease in activity was also observed for extrahepatic lesions (extrahepatic lesion 1/spleen activity ratio, 1st vs. 4th cycle: p = 0.074736; extrahepatic lesion 1/normal liver activity ratio, 1st vs. 4th cycle: p = 0.074736), but these values did not reach the level of statistical significance. No significant decrease in activity was detected for the smaller target lesions.There was no significant change in the activity uptake of reference organs (liver, spleen) during the treatments (p = 0.952765 and p = 0.138642), supporting their use as reliable controls. There was no significant change in the size of target lesions. All but one of the patients were in stable disease (SD) status based on follow-up CT scans. ***Conclusion:*** Our results suggest that decreased lesion activity may be a better predictor of treatment efficacy than size reduction during radioligand therapy. Lesion size above a certain threshold might enhance ^{177}Lu-DOTATATE effectiveness, though larger studies are needed. Most patients showed stable disease on follow-up CT, supporting the therapy's efficacy. Future research should further explore tumour volume as a response marker.

EP-0798

Is There a Correlation between Metabolic Tumor Volume and Progression-free Survival in Neuroendocrine Tumors Treated with LU-177-Oxodotreotide?

S. Salcedo Cortes, *E. Ardila Manjarrez, A. Mari Hualde, J. Guzmán Cruz, I. Gómez Fernández, J. Ardila Mantilla, L. Reguera Berenguer, V. Castillo Morales, J. Orcajo Rincón, D. Zamudio Rodriguez, S. Álvarez Lara, G. Mera Ovalle, J. Alonso Farto; Hospital General Universitario Gregorio Marañon, Madrid, SPAIN.*

Aim/Introduction: To evaluate the correlation between metabolic tumor volume (MTV) in neuroendocrine tumors (NETs) treated with Lu-177-oxodotreotide and progression-free survival (PFS), as well as the relationship with post-treatment laboratory abnormalities. ***Materials and Methods:*** A retrospective observational study was conducted in 20 patients who received 4 cycles of Lu-177-oxodotreotide (7.4 GBq each) since 2018. MTV was measured using 68Ga-DOTATATE PET/CT, evaluating all identified lesions. PFS was determined via CT imaging and correlated with MTV. Post-treatment laboratory tests were also reviewed, and statistical analyses were performed. Patients who did not complete the 4 treatment cycles were excluded. ***Results:*** The study included 20 patients (9 men, 11 women; mean age: 59 years). NET origins were as follows: 25% ileal, 20% pancreatic, 15% unknown primary, 10% carotid paraganglioma, 10% jejunal, 10% ileal (additional cases), 5% nasopharyngeal, and 5% rectal. Of these, 75% were G2 and 25% G1. The mean MTV was 359.2 g/ml × cm^3, and the median PFS was 35 months (range: 6-61). The correlation between MTV and PFS showed a Pearson coefficient of -0.44 (p = 0.051), suggesting that higher MTV is associated with shorter PFS. Additionally, MTV was significantly correlated with creatinine levels at follow-up (r = 0.69, p = 0.0008), indicating a potential renal side effect. Hematological variables did not show significant correlations with MTV. ***Conclusion:*** There is a negative trend between MTV and PFS, suggesting that a higher MTV may be associated with worse outcomes. Creatinine levels at 2 years showed a significant correlation with MTV, possibly reflecting renal toxicity. No relevant correlations were observed between MTV and hematologic parameters.

EP-50

e-Poster Area

C: Therapy Clinical Study -> C1 Oncological Therapy Clinical Study -> C12 Prostate Cancer Therapy

EP-0799

Appropriate selection of pretreatment PSMA-ligand PET/CT parameters helps in candidate selection for ^{177}Lu-PSMA radionuclide therapy in men with metastatic castration-resistant prostate cancer (mCRPC)

S. Chen, *Y. Yip, S. Cheung, Y. Wong, K. Wu, K. Cheng, C. Ho; Hong Kong Sanatorium & Hospital, Hong Kong, HONG KONG.*

Aim/Introduction: ^{177}Lu-PSMA radionuclide therapy has proven value in improving progression-free and overall survival (OS) in mCRPC patients. The predictors for outcome in the current practice is to perform an interim assessment after the 2nd cycle of ^{177}Lu-PSMA (Response Evaluation Criteria In Interim; RECIP-1.0), which is post initiation of treatment. We proposed to investigate if candidate selection for ^{177}Lu-PSMA therapy is possible based on pretreatment RECIP-1.0 PSMA-ligand PET/CT criteria and whether it may improve treatment response and OS. ***Materials and Methods:*** This is an Asian single-center retrospective study covering a period of 4 years (ended Dec-2024) on mCRPC patients who were treated with >=2 cycles of ^{177}Lu-PSMA-I&T (7.4 GBq at 6-week intervals). They all underwent a baseline PSMA-PET/CT (bPET) and an interim PSMA-PET/CT (iPET) at 12 weeks. Tumor lesions local and metastatic (lymph node, bone, other organ metastases) were evaluated by 2 Nuclear Medicine specialists in consensus, lesion-by-lesion, including any emergence of new metastatic lesions between bPET-iPET pairs. Total PSMA-positive tumor volume (PV) was automatically analyzed by MIMContouring software, with bPV and iPV calculated respectively for each pair, and %PV-change (δPV)=100%*(iPV-bPV)/bPV. Based on RECIP-1.0, complete-response (CR) was defined as "all PSMA-avid lesions normalized"; partial-response (PR) as "δPV-decrease ≥30% with no new lesions";

progressive-disease (PD) as "δPV-increase ≥20% and emergence of new lesions"; and stable disease (SD) as "any other conditions (non-CR/PR/PD)". CR, PR and SD was chosen as potential candidates for ^{177}Lu-PSMA treatment. PR/CR were considered good response. Multivariate analysis was applied on bPET for any independent predictors (SUV_{mean}, PV, all metastatic sites) for both candidate selection and good response. ***Results:*** This study recruited 58 patients (mean age=72.0±9.4 years, range:50-90 years). Based on RECIP-1.0, 20/58 patients achieved RECIP-PR/CR, 17/58 classified as RECIP-SD and 21/58 as RECIP-PD. Their corresponding bPV were 34±32ml, 136±46ml, and 402±249ml, respectively, with RECIP-PD patients significantly higher bPV than RECIP-SD or RECIP-PR/CR (all P<0.001). Among all the bPET parameters, only bPV was identified as an independent predictor for both potential candidates (P=0.04) and good response (P=0.001) for ^{177}Lu-PSMA treatment. ROC curve analysis calculated "bPV<=196ml" as the selection threshold for predicting candidates to achieve RECIP-CR/PR/SD post ^{177}Lu-PSMA treatment (AUC=0.989, P<0.001); "bPV<=77ml" as cut-off for good response (RECIP-CR/PR, AUC=0.968, P<0.001). ***Conclusion:*** Total tumor burden expressed in terms of tracer-avid tumor volume (bPV) on pretreatment PSMA-ligand PET/CT has evidence-based significance in selection of suitable candidates and response prediction for ^{177}Lu-PSMA therapy. Further validation in prospective setting is warranted.

EP-0800

[177Lu]Lu-PSMA-617 in patients with mCRPC and brain metastases : a multicentric retrospective French study

D. Tonnelet[1], *F. Sommes*[2], *K. Hebert*[3], *M. Claudin*[4], *K. Weyts*[5], *P. Robin*[6], *M. Lacombe*[7], *N. De Leiris*[8], *C. Baillet*[9];
[1]*Henri Becquerel Cancer Center, Rouen, FRANCE,* [2]*Institut de Cancérologie Strasbourg Europe, Strasbourg, FRANCE,* [3]*L'Institut du Cancer de Montpellier, Montpellier, FRANCE,* [4]*Centre Hospitalier Régional et Universitaire de Nancy, Vandoeuvre-lès-Nancy, FRANCE,* [5]*Centre de Lutte Contre le Cancer François Baclesse, Caen, FRANCE,* [6]*CHU Brest, Univ Brest, Inserm, UMR 1304, GETBO, Brest, FRANCE,* [7]*Institut de Cancérologie de l'Ouest Angers-Nantes, Angers, FRANCE,* [8]*Univ. Grenoble Alpes, INSERM, CHU Grenoble Alpes, Grenoble, FRANCE,* [9]*Centre Hospitalier Universitaire de Lille, Lille, FRANCE.*

Aim/Introduction: While [177Lu]Lu-PSMA-617 (LuPSMA) is a proven radioligand-therapy in metastatic castration-resistant prostate-cancer (mCRPC), little is known about its efficacy and tolerance on brain metastases. This retrospective analysis focuses on patients with mCRPC previously treated with at least one line of ARPI and one line of taxane-based chemotherapy, and who had and at least one brain metastases. ***Materials and Methods:*** All nuclear medicine centers in France administering LuPSMA were contacted. When treatment was initiated, the recommended protocol included 6 intravenous injections of Lu-PSMA (7.4 GBq Q6W). Patient characteristics, brain metastases imaging and safety data were collected during follow-up visits. ***Results:*** A total of 36 patients from 8 different departments were included : Age median 72.6 [63-88] years-old . ISUP≥4 in 21/36 (58%). Among them, 19/36 (53%) had de novo metastatic prostate cancer. On average, patients received 4 prior treatment lines before receiving LuPSMA. In 22/36 patients (61%), brain metastases were discovered on PSMA PET. A total of 90 brain metastases were analysed (range: 1-41/patient, median: 2) Imaging characteristics were as follows i) size: median 16.7 [4-55] mm ii) SUVmax: median 9.65 [3.57 - 24.8] iii) PSMA Total Metabolic Tumour Volume using fixed SUVmax>3 threshold: median 5.07 [0.2 - 47] cm^3. No brain metastases was FDG-positive and PSMA-negative. 7/36 (19%) patients who were eligible for LuPSMA did not received LuPSMA because of i) deterioration of general condition before the first injection (n=4) ii) Discordant imaging with extra-cerebral FDG-positive / PSMA-negative lesions (n=2) and iii) death before initiation of treatment (n=1). Of the 29 treated patients, 20 (69%) received brain-directed external radiotherapy (BDER) prior to the first LuPSMA cycle, including 12/20 (60%) who underwent stereotactic radiotherapy (median dose: 25.0 Gy). One patient received intrathecal methotrexate. Only 5/29 (17%) completed all 6 LuPSMA infusions. Reasons for early discontinuation included i) progressive disease (n=15) ii) worsening general condition (n=5) iii) grade 3/4 hematologic toxicity (n=3) and iv) external cause (e.g., severe fall (n=1)). No treatment was interrupted due to side effects related to brain metastases or due to cerebral toxicity. Among those who completed the full course, treatment outcomes were : partial response (n=3), stable disease (n=1), and progressive disease (n=1). Of note, all patients who completed full course had had BDER. ***Conclusion:*** Although LuPSMA demonstrates some intracranial activity and no additional brain toxicity, this study enhances the poor prognosis of patients with mCRPC and brain metastases referred for LuPSMA.

EP-0801

Could BMI affect efficacy of LuPSMA in mCRPC patients? Data from a phase II clinical trial

I. Grassi[1], *E. Giunta*[2], *I. Marini*[1], *S. Nicolini*[1], *P. Caroli*[1], *M. Celli*[1], *M. Casi*[3], *C. Lolli*[2], *N. Brighi*[2], *G. Schepisi*[2], *S. Bleve*[2], *V. Di Iorio*[4], *A. Sarnelli*[5], *M. Monti*[6], *F. Foca*[6], *J. Karabina*[6], *A. Prochowski Iamurri*[7], *F. Matteucci*[8], *M. Sansovini*[1];
[1]*Nuclear Medicine Department, IRCCS Istituto Romagnolo per lo Studio dei Tumori "Dino Amadori" (IRST), Meldola FC, ITALY,* [2]*Medical Oncology Department, IRCCS Istituto Romagnolo per lo Studio dei Tumori "Dino Amadori" (IRST), Meldola FC, ITALY,* [3]*Nuclear Medicine Department, Romagna Local Health Authority, Cesena FC, ITALY,* [4]*Radiopharmacy - Pharmacy Department, IRCCS Istituto Romagnolo per lo Studio dei Tumori "Dino Amadori" (IRST), Meldola FC, ITALY,* [5]*Medical Physics Department, IRCCS Istituto Romagnolo per lo Studio dei Tumori "Dino Amadori" (IRST), Meldola FC, ITALY,* [6]*Biostatistics and Clinical Trials Department, IRCCS Istituto Romagnolo per lo Studio dei Tumori "Dino Amadori", (IRST), Meldola FC, ITALY,* [7]*Radiology Department, IRCCS Istituto Romagnolo per lo Studio dei Tumori "Dino Amadori" (IRST) Meldola (FC) Italy, Meldola FC, ITALY,* [8]*Nuclear Medicine Department, IRCCS Istituto Romagnolo per lo Studio dei Tumori " Nuclear Medicine Department, Romagna Local Health Authority, Meldola FC, Cesena FC, ITALY.*

Aim/Introduction: Among the prognostic factors in men with metastatic castration-resistant prostate cancer (mCRPC), body mass index (BMI) is highly considered, being often related to a worst outcome when low (1,2). For mCRPC patients (pts), 177Lu-PSMA 617 (LuPSMA) is now recognized as a valid therapeutic strategy. Herein we evaluate the impact of BMI on progression-free survival (PFS) and overall survival (OS) in pts treated with LuPSMA. ***Materials and Methods:*** 142 mCRPC pts were enrolled in a prospective phase II trial (EUDRACT: 2016-002732-32) developed at IRST "Dino Amadori" Institute. The aims of the study were to evaluate efficacy, safety and dosimetry of LuPSMA. Pts received 3.7-5.5 GBq of LuPSMA every 8-12 weeks for 4 cycles plus possibly 2 additional cycles. BMI was calculated according to the standard and treated as low-normal (L-N) if <25 or elevated if ≥25 kg/m2 (EI). ***Results:*** 57/142 had L-N BMI, while 85/142 had EI BMI. The two groups were balanced in terms of age, performance status (Eastern Cooperative Oncology Group, ECOG), Gleason score, previous treatments with docetaxel, alkaline phosphatase (ALP) and PSA levels. Regarding visceral metastases, they were more frequent in pts with L-N BMI than in EI ones (26.3 and 11.8%, respectively). Pts were followed-up for a median time of 44.0 months. The overall median PFS and OS were 7.0 and 16.8 months, respectively. At the univariate analysis, PFS in EI BMI and in L-N BMI pts was respectively 7.6 vs 5.5 months (HR: 0.67, 95%CI: 0.47-0.98, p=0.037). OS in EI BMI and in L-N BMI pts was respectively 19.2 vs 13.6 months (HR: 0.63, 95%CI: 0.42-0.94, p=0.022). ***Conclusion:*** According to our results, mCRPC pts treated with LuPSMA with EI BMI had better PFS and OS. BMI may be considered as an independent prognostic factor. Further data are required to assert the role of

BMI in predicting response to LuPSMA. ***References:*** 1. 1.Peslier H et Alt. Study of predictive factors for response to 177LU-PSMA in patients with metastatic castration-resistant prostate cancer. Front Med (Lausanne). 2025 Mar 17;12:1538507. doi: 10.3389/fmed.2025.1538507. PMID: 40166057; PMCID: PMC11955661. 2.Suzuki K et Alt. Efficacy and Feasibility of Cabazitaxel for Very Elderly Patients of ≥80 Years of Age With Metastatic Castration-Resistant Prostate Cancer: A Real-World Multi-Intuitional Analysis. Prostate. 2025 Mar 16. doi: 10.1002/pros.24889. Epub ahead of print. PMID: 40089975.

EP-0802

LuPSMA in mCRPC: beyond toxicity and clinical complications, why might it be necessary to delay treatment? Practical and realworld data from a prospective study

I. Grassi[1], *I. Marini*[1], *S. Nicolini*[1], *V. Di Iorio*[2], *A. Sarnelli*[3], *M. Monti*[4], *P. Caroli*[1], *M. Celli*[1], *M. Casi*[5], *F. Foca*[4], *J. Karabina*[4], *E. Giani*[4], *E. Giunta*[6], *C. Lolli*[6], *A. Rossi*[7], *F. Matteucci*[8], *M. Sansovini*[1];
[1]*Nuclear Medicine Department, IRCCS Istituto Romagnolo per lo Studio dei Tumori "Dino Amadori" (IRST), Meldola FC, ITALY,* [2]*Radiopharmacy - Pharmacy Department, IRCCS Istituto Romagnolo per lo Studio dei Tumori "Dino Amadori" (IRST), Meldola FC, ITALY,* [3]*Medical Physics Department, IRCCS Istituto Romagnolo per lo Studio dei Tumori "Dino Amadori" (IRST), Meldola FC, ITALY,* [4]*Biostatistics and Clinical Trials Department, IRCCS Istituto Romagnolo per lo Studio dei Tumori "Dino Amadori" (IRST), Meldola FC, ITALY,* [5]*Nuclear Medicine Department, Romagna Local Health Authority Bufalini Hospital, Cesena FC, ITALY,* [6]*Medical Oncology Department, IRCCS Istituto Romagnolo per lo Studio dei Tumori "Dino Amadori" (IRST), Meldola FC, ITALY,* [7]*Radiology Department, IRCCS Istituto Romagnolo per lo Studio dei Tumori "Dino Amadori" (IRST) Meldola (FC) Italy, Meldola FC, ITALY,* [8]*Nuclear Medicine Department, IRCCS Istituto Romagnolo per lo Studio dei Tumori "Dino Amadori" (IRST), Romagna Local Health Authority Bufalini Hospital, Meldola FC, Cesena FC, ITALY.*

Aim/Introduction: Following the results of the Vision study (1), 177Lu PSMA 617 (LuPSMA) was approved for patient (pts) with metastatic castration-resistant prostate cancer (mCRPC). The expanding practice in this field will probably test nuclear medicine Departments, therefore could be necessary to predict the events potentially leading to a rescheduling of the hospitalization, even not related to toxicity or underlying illness complications. Herein we report the experience of our Institute IRST "Dino Amadori", focused on the pts who delayed treatment for reasons other from toxicity or complications due to LuPSMA. ***Materials and Methods:*** Pts with mCRPC were enrolled in a prospective, open label, phase II trial (EUDRACT: 2016-002732-32), whose aim was to evaluate efficacy, safety and dosimetry of LuPSMA. The planned activity of Lu-PSMA was 5.5 GBq/cycle for 4 cycles every 8±2 weeks, plus possibly 2 additional cycles. ***Results:*** From December 2021 to October 2022, 48 mCRPC pts were enrolled in the study. Patients characteristics were: median age 68 yo (range 60.6-75.1), median baseline PSA value (µg/L) 41.5 (12.5-111), pre-treatment with surgery (50%), prostate radiotherapy (45.5%), abiraterone (75%), enzalutamide (61.4%), cabazitaxel (9.1%), docetaxel (52.1), olaparib (4.5%). The treatment was delayed in 6 pts (12.5 %). In 3 pts treatment was postponed (range 7-10 days) for logistical reasons, because of failed delivery of 177Lutethium. In 3 pts treatment was postponed for patient-related reasons (range 2.5-10 weeks), 1 of them had personal commitments, 2 were hospitalized to performe further investigation for clinical reasons other than mCRPC. ***Conclusion:*** In our experience, unexpected events could retard treatment of mCRPC only in 12.5% of the hospitalizations, equally balanced between logistical and patient-related reasons. The delayed was longer when related to the pts, up to 10 weeks. These data suggest that the incidence of unpredictable delays is not high, fortunately, but could affect everyday work activities and should be taken into consideration and monitored. ***References:*** 1.Sartor O et Alt: Lutetium-177-PSMA-617 for Metastatic Castration-Resistant Prostate Cancer. N Engl J Med. 2021 Sep 16;385(12):1091-1103. doi: 10.1056/NEJMoa2107322. Epub 2021 Jun 23. PMID: 34161051; PMCID: PMC8446332.

EP-0803

LuPSMA in mCRPC used out of indication before AIFA indications: data and considerations from a prospective study

I. Grassi[1], *I. Marini*[1], *E. Giunta*[2], *S. Nicolini*[1], *P. Caroli*[1], *L. Fantini*[1], *M. Casi*[3], *C. Lolli*[2], *N. Brighi*[2], *G. Schepisi*[2], *S. Bleve*[2], *A. Sarnelli*[4], *V. Di Iorio*[5], *M. Monti*[6], *F. Foca*[6], *E. Giani*[6], *F. Ferroni*[7], *F. Matteucci*[8], *M. Sansovini*[1];
[1]*Nuclear Medicine Department, IRCCS Istituto Romagnolo per lo Studio dei Tumori "Dino Amadori" (IRST), Meldola FC, ITALY,* [2]*Medical Oncology Department, IRCCS Istituto Romagnolo per lo Studio dei Tumori "Dino Amadori" (IRST), Meldola FC, ITALY,* [3]*Nuclear Medicine Department, Romagna Local Health Authority Bufalini Hospital, Cesena FC, ITALY,* [4]*Medical Physics Department, IRCCS Istituto Romagnolo per lo Studio dei Tumori "Dino Amadori" (IRST), Meldola FC, ITALY,* [5]*Radiopharmacy - Pharmacy Department, IRCCS Istituto Romagnolo per lo Studio dei Tumori "Dino Amadori" (IRST), Meldola FC, ITALY,* [6]*Biostatistics and Clinical Trials Department, IRCCS Istituto Romagnolo per lo Studio dei Tumori "Dino Amadori" (IRST), Meldola FC, ITALY,* [7]*Radiology Department, IRCCS Istituto Romagnolo per lo Studio dei Tumori "Dino Amadori" (IRST), Meldola FC, ITALY,* [8]*Nuclear Medicine Department, IRCCS Istituto Romagnolo per lo Studio dei Tumori "Dino Amadori" (IRST), Nuclear Medicine Department, Romagna Local Health Authority Bufalini Hospital, Meldola FC, Cesena FC, ITALY.*

Aim/Introduction: The use of 177Lu-PSMA 617 (LuPSMA) has been recently approved by Agenzia Italiana del Farmaco (AIFA) for patient (pts) with metastatic castration-resistant prostate cancer (mCRPC) already treated with at least one androgen receptor pathways inhibitor (ARPI) and two-lines taxane-based chemotherapy (Tax). Only pts unfit to a second Tax line can receive LuPSMA. Before that, LuPSMA was delivered exclusively through trials and after multidisciplinary team (MDT) evaluation. Published results showed that Lu-PRRT could give better results when performed before Tax (1), thus bringing Food and Drug Administration (FDA) to authorize it also in Tax naïve pts. Herein we report data from our trial, regarding the pts treated out of the Tax indication. ***Materials and Methods:*** Pts with mCRPC were enrolled in a prospective phase II trial (EUDRACT: 2016-002732-32), developed at IRST "Dino Amadori" Institute. The aims of the study were to evaluate efficacy, safety and dosimetry of LuPSMA. Pts were included also if taxane naïve or after 1 line of Tax and if considered as unfit for chemotherapy by MDT or refused it. The planned activity of LuPSMA was 5.5 GBq/cycle for 4 cycles every 8±2 weeks, plus possibly 2 additional cycles. ***Results:*** From December 2021 to October 2022, 48 mCRPC pts were enrolled in the study, with median age 68 yrs (range 60.6-75.1) and median baseline PSA value 41.5 µg/L (range 12.5-111). They were all pre-treated and the previous treatments were: surgery (22 pts, 50%), prostate radiotherapy (20 pts, 45.5%), abiraterone (33 pts, 75%), enzalutamide (37 pts, 61.4%), cabazitaxel (4 pts, 9.1%), docetaxel (25 pts, 52.1%) and olaparib (2 pts, 4.5%). 23 pts (47.9%) were Tax naïve, 10 because refused it and the other ones were unfit. ***Conclusion:*** These data may suggest that currently in Italy, differently from United States, an important percentage of pts could not be treated with the drug with marketing autorization but exclusively through trials, which should be encouraged. Further data are needed to extabilish the correct timeline of LuPSMA and to integrate it into clinical practice. The evaluation of MDT should be considered as mandatory in any case. ***References:*** 1. Morris, Michael J et al. 177Lu-PSMA-617 versus a change of androgen receptor pathway inhibitor therapy for taxane-naive

patients with progressive metastatic castration-resistant prostate cancer (PSMAfore): a phase 3, randomised, controlled trial . The Lancet, Volume 404, Issue 10459, 1227 – 1239.

EP-0804

Addition of ^{177}Lu-PSMA-617 in the treatment of hormone sensitive metastatic prostate cancer: a prospective pilot study

***V. H**, N. Pandit, S. Kayal;*
Jawaharlal Institute of Postgraduate Medical Education and Research (JIPMER), Puducherry, INDIA.

Aim/Introduction: Recent years have introduced several modalities and agents in the management of metastatic prostate cancer. Application and sequencing of these agents is an area of ongoing research. Lu-177 PSMA, an agent traditionally used after exhausting other lines of treatment, is now being introduced in earlier time-points of metastatic prostate cancer. We present the results of application of Lu-177 PSMA in metastatic hormone sensitive prostate cancer (mhsPC) patients alongside Androgen Deprivation Therapy (ADT) and Abiraterone. ***Materials and Methods:*** mhsPC patients on androgen deprivation therapy (ADT) who cannot tolerate docetaxel were included. After biopsy and metastatic evaluation with Ga-68 PSMA PET/CT, and initiation of ADT, patients received 2 cycles of Lu-PSMA 617 (100mCi per cycle) in addition to Abiraterone which was continued. Serial serum PSA values and FACT-P scores were obtained. ***Results:*** Of the 8 patients recruited, all patients showed sustained PSMA response 6 months post therapy. Post therapy scans obtained after 2 cycles of Lu-PSMA showed complete response of all lesions in 2 patients. 3 out of 5 patients show an increase in FACT-P scores. Considerably, the emotional well being and physical well being subscales which show significant improvement. However, 2 patients show an overall decrease in FACT-P score, evenly distributed among the subscales. ***Conclusion:*** We aim to demonstrate the use of Lu-177 PSMA therapy in mhsPC with the rationale being - improvement in the quality of life of patients in the earlier stages by delaying the need for chemotherapy and application of targeted radionuclide therapy at a time-point where PSMA expression is maximal. In line with our study, further research in the direction of optimal scheduling, sequencing and combination of Lu-177 PSMA therapy are promising prospects. ***References:*** Kim H, Tagawa ST, Sartor AO, et al. PSMAddition: Phase 3 Trial of [177lu]Lu-PSMA-617 Plus Standard of Care (SoC) vs. Soc Alone in Patients with Metastatic Hormone-Sensitive Prostate Cancer. Int J Radiat Oncol Biol Phys. 2024Morris MJ, Castellano D, Herrmann K, et al. 177Lu-PSMA-617 versus a change of androgen receptor pathway inhibitor therapy for taxane-naive patients with progressive metastatic castration-resistant prostate cancer (PSMAfore): a phase 3, randomised, controlled trial. The Lancet. 2024.Sartor O, de Bono J, Chi KN, et al. Lutetium-177-PSMA-617 for Metastatic Castration-Resistant Prostate Cancer. N Engl J Med. 2021.Azad AA, Bressel M, Tan H, et al. Sequential [177Lu]Lu-PSMA-617 and docetaxel versus docetaxel in patients with metastatic hormone-sensitive prostate cancer (UpFrontPSMA): a multicentre, open-label, randomised, phase 2 study. Lancet Oncol. 2024.

EP-0805

Hematological Safety of ^{177}Lu-PSMA Radioligand Therapy in Metastatic Castration-Resistant Prostate Cancer: Real-World Evidence from a Developing Country

***A. Gupta**, A. H. Nazar, M. Ora, P. K. Pradhan;*
Sanjay Gandhi Postgraduate Institute of Medical Sciences, Lucknow, INDIA.

Aim/Introduction: ^{177}Lu-PSMA radioligand therapy (RLT) has emerged as a promising option for patients with metastatic castration-resistant prostate cancer (mCRPC). However, data on its hematological safety, particularly from developing countries, remain scarce. This study evaluates hematologic adverse effects in mCRPC patients receiving 3 or more cycles of ^{177}Lu-PSMA RLT, comparing baseline and post-treatment hematological parameters. ***Materials and Methods:*** An ambispective observational study was conducted on mCRPC patients treated with 3 or more cycles of ^{177}Lu-PSMA RLT between 2020 and 2025. Clinical, demographic, and hematological data were collected from medical records. Hematologic toxicity was graded using CTCAE v5.0 criteria. Hemoglobin, platelet, and neutrophil levels were analyzed before and 21 days post-therapy. Statistical analysis was performed using a paired t-test. ***Results:*** Of 83 total patients, 44 were eligible for analysis (mean age: 73 years). At baseline (mean hemoglobin- 10.8), 3 patients had no anemia, 31 had Grade I, and 10 had Grade II anemia. Post-therapy (mean Hemoglobin- 10.2), 28 had Grade I, 14 had Grade II, and 2 had Grade III anemia. Anemia grade remained unchanged in 35 patients (26 with Grade I, 9 with Grade II). Among others who progressed that are two non-anemic patients progressed to Grade I, and one to Grade II. Four patients with Grade I anemia progressed to Grade II. One with Grade I progressed to Grade III, and one with Grade II worsened to Grade III. Thrombocytopenia remained unchanged in 42/44 patients. One patient developed new-onset Grade I thrombocytopenia, and one improved from Grade I to normal. No case of neutropenia was observed in any of the 44 patients post-treatment. ***Conclusion:*** This real-world data from a developing country demonstrates that ^{177}Lu-PSMA RLT is well-tolerated with minimal hematologic toxicity and confirms RLT is hematologically safe in mCRPC patients. Most adverse effects were limited to mild anemia, with rare cases of thrombocytopenia and no observed neutropenia. These findings support the safety of ^{177}Lu-PSMA RLT and reinforce its viability in resource-limited healthcare settings, enhancing its potential for broader adoption.

EP-0806

Interim Analysis of Effect of Hypoxia on F-18 MISO PET to Response to Lu-177 PSMA Treatment (LuMISO)Trial

***C. Soydal**, E. Dursun Avci, B. Demir, G. İnal, M. Araz, N. O. Kucuk;*
Ankara University Medical Faculty, Ankara, TÜRKIYE.

Aim/Introduction: We aimed to evaluate hypoxia before Lu-177 PSMA treatment in prostate cancer and to show its effect on treatment response with 18F-FMISO PET imaging. ***Materials and Methods:*** In this interim analysis pretreatment 18F-FMISO PET images of 7 men who received Lu-177 PSMA treatment for castration resistant prostate cancer (CRPC) included. 18F-FMISO PET imaging has performed within 2 weeks before treatment. Volumes of interest (VOIs) were delineated for all PSMA-avid and >2cm tumors, gluteal muscle, and the abdominal aorta for semiquantitative measurement of hypoxia. Maximum (SUVmax) and mean (SUVmean) standardized uptake values of all reference VOIs were recorded for analysis. Tumor-to-muscle ratio (T/M) and tumor-to-blood pool ratio (T/BP) were calculated. Lesion based response assessment was performed with pre and posttreatment PSMA PET images based on PSMA-volume and TL-PSMA approaches. To evaluated the effect of 18F-FMISO PET based hypoxia to response ROC analysis was performed. ***Results:*** Totally 99 (81 bone, 15 lymph nodes, 1 lung, 1 liver and 1 prostate) lesions were included to the analysis. All the lesions were Ga-68 PSMA avid (median SUVmax:26.3, volume:2.65 cm3 and TL-PSMA=39.1). All the patients were received at least 2 cycles of Lu-177 PSMA treatment. In the PSMA-volume based evaluation 29 lesions were responder and 70 lesions were non-responder. For this criterion, we have not found an optimal cutoff for T/M (AUC: 0.53, 95%CI; 0.40-0.65) and T/BP (AUC: 0.52, 95%; 0.40-0.64) ratios to predict the response (CR+PR). In the other response criterion with TL-PSMA while 64 lesions were responder, 35 of them were non-responder. Similarly, we have not found an optimal cutoff for T/M (AUC: 0.57, 95%CI; 0.45-0.68) and T/BP (AUC: 0.56, 95%; 0.45-0.68) ratios to predict

the response (CR+PR) in TL-PSMA response categories. However, when we analyzed the 7 lesions with CR separately, 1.0 cutoff for T/BP (AUC: 0.73, 95%; 0.58-0.88, p=0.002) and 1.2 cutoff for T/M (AUC: 0.67, 95%; 0.51-0.83, p=0.03) were calculated. ***Conclusion:*** Interim analysis of this trial has demonstrated that 18F-FMISO PET based assessment of tumor hypoxia may have a role in the prediction of CR to Lu-177 PSMA treatment in patients with CRPC. However due to limited number of lesions with CR this outcome should be clarified with larger data. ***References:*** Wiedenmann NE, Bucher S, Hentschel M, et al. Serial [18F]-fluoromisonidazole PET during radiochemotherapy for locally advanced head and neck cancer and its correlation with outcome. Radiother Oncol [Internet]. Radiother Oncol; 2015 [cited 2024];117:113-117. Available from: https://pubmed.ncbi.nlm.nih.gov/26432067/32.

EP-0807

Do We Need to Reconsider Our Treatment Protocol for Metastatic Prostate Cancer With [^{177}Lu]Lu-PSMA-Radioligand?

T. Bogsrud[1,2], *O. Engelsen*[1], *P. Iversen*[2], *P. F. Staanum*[2], *A. T. Kendi*[3], *J. Zhang*[3], *M. P. Thorpe*[3], *F. J. Hernandez-Delima,*[3], *O. Sartor*[4], *J. M. Durski*[3];
[1]PET Imaging Center, University Hospital of North-Norway, Tromso, NORWAY, [2]Aarhus University Hospital, Aarhus, DENMARK, [3]Mayo Clinic, Rochester, MN, UNITED STATES OF AMERICA, [4]Tulane University Department of Urology and Medicine, New Orleans, LA, UNITED STATES OF AMERICA.

Aim/Introduction: Standard treatment of metastatic castration-resistant prostate cancer (mCRPC) with [^{177}Lu]Lu-PSMA-radioligand involves 6 cycles with fixed activity (typical 7.4 GBq per cycle) every 6 weeks. Tumor absorbed dose at first treatment <10 Gy predicts unsatisfactory treatment effect. However, the accumulated tumor dose from all cycles is likely more relevant for treatment effect than the dose from the first cycle. It is a prerequisite that all cycles contribute significantly to accumulated tumor absorbed dose. Some published data indicate dose per administered activity decreases over subsequent cycles. If so, we might question whether our current standard of care is optimal. We report on tumor dosimetry from each of 5 standard treatment cycles and 6 additional retreatment cycles in a single patient, and outline an ongoing pilot project to perform multi-timepoint dosimetry in 5 additional patients. ***Materials and Methods:*** A 76-year-old man with progressive mCRPC and very high lesion uptake (SUVmax=70) on [^{68}Ga]Ga-PSMA-11 PET/CT (PSMA PET/CT) was treated with 5 cycles of [^{177}Lu]Lu-PSM-I&T, achieving partial treatment response. Fifteen months later repeat treatment with 6 cycles was performed because of progression of intensely avid disease on PSMA PET/CT. Multiple time-point tumor dosimetry of target lesions was performed for each of the 11 cycles. ***Results:*** After the first cycle, PSA decreased from 154 µg/L to 53 (66% reduction). Five weeks after the 5th cycle, PSA was 1,8 µg/L. PSMA PET/CT showed substantial reduction in the size of target lesions, with high PSMA-uptake in small residual metastatic lesions. After 15 months, the disease progressed rapidly (PSA=390 µg/L, doubling time 1.5 months), with very high uptake in numerous metastases on PSMA PET/CT. Short lasting stable disease was achieved by the repeat treatment. The first cycle of each of the two treatment series achieved comparable absorbed doses to target lesions. For subsequent cycles, the dose to target lesions decreased on average 35% per cycle (median 25%). ***Conclusion:*** Only the first 2-3 cycles gave a reasonably high tumor dose. If our results are generalizable to the broader mCRPC population, adjustments to our standard procedure may enhance therapeutic efficacy, avoid ineffective treatment cycles, and mitigate unnecessary radiation dose to critical organs and futile treatment expense. Examples of possible modifications include personalized dosimetry (dosimetry of tumors and critical organs) to optimize administered activity and reducing the number of therapy cycles.

EP-0808

Prediction of Treatment Response and Progression-Free Survival Based on Pre-Treatment PSA Levels and PET/CT Parameters in Prostate Cancer with Lu-177 PSMA Therapy

S. Ceylan, *B. B. Demirel, G. Uçmak;*
Ankara Oncology Training and Research Hospital Nuclear Medicine Clinic, Ankara, TÜRKIYE.

Aim/Introduction: The aim of this study is to identify predictors of treatment response,progression-free survival (PFS) based on pre-treatment clinical, laboratory, pathological,PET/CT (Ga-68 PSMA and F-18 FDG) parameters in prostate cancer patients undergoing Lu-177 PSMA therapy. ***Materials and Methods:*** Between 2019 and 2024, 45 patients with metastatic castration-resistant prostate cancer who received at least two cycles of Lu-177 PSMA therapy in our clinic, had no discordant lesions on pre-treatment FDG PET/CT imaging were included in the study.Demographic, pathological-laboratory findings of the patients (pre-final treatment day PSA values,the difference in PSA between the first and last treatment [ΔPSA]) were recorded.Pre-treatment PET/CT scans were analyzed using a 40% threshold for WB TL-PSMA, PSMA-TV, PSMA mean, PSMA max, as well as WB MTV, TLG, SUVmean,SUVmax values. Progression was evaluated based on PSA,anatomical-molecular imaging findings.PFS was defined as the date on which a rise in PSA and new lesions on imaging were simultaneously observed. Predictive factors for Lu-177 PSMA therapy response and PFS were statistically analyzed. ***Results:*** In prostate cancer patients, pre-treatment WB PSMA max,TL-PSMA values on Ga-68 PSMA PET/CT were found to be significantly higher in the group with ΔPSA >50%, independently of the metabolic parameters from FDG PET/CT.A ΔPSA >90% was shown to be associated with longer PFS.WB PSMA max was found to be clinically associated with PFS. ***Conclusion:*** A total of 45 patients were included in the study.Of these, 11 had a pre-treatment PSA level <10, while 34 had levels >10. A treatment response was observed in 34 patients (75.6%) based on laboratory and imaging findings.Among these, 16 patients (35.5%) showed a >50% PSA response, and 6 patients (13.3%) showed a >90% PSA response.The mean PFS was 7 months (range: 3-17).WB TL-PSMA, PSMA-TV, WB TLG, and MTV values were significantly lower in the PSA<10 group (p-values: 0.024, 0.027, 0.027, and 0.02, respectively) and significantly higher in patients with both bone and lymph node metastases compared to those with only bone metastases (p=0.039).ΔPSA >90% had a significant impact on PFS (p=0.018). Although WB PSMA max did not significantly prolong PFS statistically (p=0.116), patients with a WB PSMA max cutoff value >18.57 had a clinically longer PFS [7±0.79 CL (5.4-8.5)] compared to those with <18.57 [5±0.79 CL (3.4-6.5)]. While the difference in PFS between patients with PSA <10 and >10 was not statistically significant (p=0.126), the PFS was clinically longer in the PSA<10 group [8±1.3 CL (5.4-10.5)] compared to the PSA>10 group [5±0.6 CL (3.8-6.2)].

EP-0809

Assessment of Sequential Radium-223 and Docetaxel Treatment in Patients with Metastatic Castration-Resistant Prostate Cancer: Insights from the Global REASSURE Study

Y. Du[1], *S. Baldari*[2], *A. Versari*[3], *S. Lastoria*[4], *J. Bourre*[5], *C. La Fougère*[6], *E. Borsatti*[7], *J. Meltzer*[8], *M. J. Korn*[8], *S. Dizdarevic*[9];
[1]Royal Marsden Hospital, London, UNITED KINGDOM, [2]University of Messina, Messina, ITALY, [3]Azienda USL-IRCCS Reggio Emilia, Reggio Emilia, ITALY, [4]IRCCS National Cancer Institute, Fondazione Senatore G. Pascale, Naples, ITALY, [5]Centre Hospitalier Métropole Savoie, Chambery, FRANCE, [6]University Hospital Tübingen, Tübingen, GERMANY, [7]Centro di Riferimento Oncologico di Aviano (CRO) IRCCS, Aviano, ITALY, [8]Bayer HealthCare Pharmaceuticals, Whippany, NJ, UNITED STATES OF AMERICA, [9]University Hospitals Sussex NHS Foundation Trust, Brighton & Sussex Medical School, University of Sussex and Brighton, Brighton, UNITED KINGDOM.

Aim/Introduction: Radium-223 and docetaxel are approved for extending overall survival (OS) in patients with metastatic castration-resistant prostate cancer (mCRPC), but optimal sequencing of these therapies is crucial to maximizing benefits while minimizing toxicity. We compared safety and OS in patients receiving radium-223 before docetaxel with those receiving docetaxel before radium-223. We utilized data from the REASSURE prospective global study, which investigated radium-223 use in mCRPC in routine clinical practice between 2014-2017. ***Materials and Methods:*** Data cut-off was Oct 24, 2024. 72 patients received radium-223 before docetaxel (R-D) and 86 radium-223 after docetaxel (D-R). Analyses focused on patients receiving the second therapy within 90 days of stopping the first, without additional life-prolonging therapies in between. Statistics were descriptive. Baseline characteristics were only available at radium-223 initiation. Safety data were collected from radium-223 initiation for both sequences. OS was calculated from start of first treatment in each sequence. ***Results:*** Almost all patients (92%) receiving R-D exhibited ECOG PS of 0-1, in contrast to 79% receiving D-R. Burden of disease at radium-223 initiation was lower in R-D vs D-R with patients exhibiting >20 bone lesions (18% vs 29%) and superscan (4% vs 9%). At radium-223 initiation, patients in R-D vs D-R had baseline median alkaline phosphatase of 118 U/L vs 173 U/L; median prostate-specific antigen of 66 ng/mL vs 130 ng/mL; median lactate dehydrogenase of 242 U/L vs 309 U/L; hemoglobin ≥10 g/dL (86% vs 70%); platelets ≥100x10^9/L (89% vs 84%); and neutrophils ≥1.5x10^9/L (56% vs 55%). Radium-223 was concomitantly administered with abiraterone (R-D: 22%; D-R:8%) or enzalutamide (R-D: 22%; D-R: 11). The median number of radium-223 cycles received in R-D vs D-R, was 6 vs 4 cycles. The incidence of treatment-emergent (TE) serious adverse events during radium-223 treatment was 11% vs 34% and TE disorders related to blood and lymphatic systems were 13% vs 9% in R-D vs D-R. Discontinuation of radium-223 due to TE drug-related adverse events was 4% vs 5%. Post-treatment grade 3/4 bone marrow suppression events were similar between R-D and D-R (21% vs 20%). Median OS from start of first treatment in the sequence was 16.3 months in R-D and 15.8 months in D-R. ***Conclusion:*** Despite differences in key baseline demographics, OS from first drug in the sequence was similar between R-D and D-R. Overall safety and treatment completion were more favorable in the R-D sequence, highlighting the importance of patient selection to optimizing patient outcomes.

EP-0810

[^{177}Lu]Lu-DOTA-HYNIC-panPSMA radioligand therapy for patients with metastatic castration-resistant prostate cancer

J. Roetman[1], *Y. Omar*[2], *Y. Atteya*[2], *M. Elkanawaty*[2], *A. Ahmed*[3], *G. Elhusseiny*[3], *M. El Shazly*[3], *A. Ameen*[3];
[1]Telix Pharmaceuticals, Melbourne, AUSTRALIA, [2]Misr Radiology Center, Cairo, EGYPT, [3]Alexandria University, Alexandria, EGYPT.

Aim/Introduction: [^{177}Lu]Lu-DOTA-HYNIC-panPSMA ([^{177}Lu]Lu-panPSMA) is a novel radioligand with high affinity for prostate specific membrane antigen (PSMA), expressed by most prostate cancer cells. [^{177}Lu]Lu-panPSMA may offer accessible therapy for patients in underserved regions. A retrospective translational study demonstrated promise as a theranostic pair with [^{68}Ga]Ga-PSMA-11 PET/CT, with a favorable safety and tolerability profile and efficacy.[1] We aim to contribute to existing data with preliminary results from the first prospective trial to investigate safety, efficacy, and effect on quality of life of [^{177}Lu]Lu-panPSMA for treatment of patients with progressive PSMA-positive metastatic castration-resistant prostate cancer (mCRPC). ***Materials and Methods:*** Patients (N=15) with progressing mCRPC despite treatment with ≥1 novel androgen-axis drug and ≥1 taxane regimen (or unfit for chemotherapy) and have ≥1 PSMA positive metastatic lesion (with uptake higher than liver parenchyma) and no PSMA-negative disease on [^{68}Ga]Ga-PSMA-11 PET/CT are eligible to participate. Patients receive 7.4 GBq (200 mCi) [^{177}Lu]Lu-panPSMA intravenously every 6 weeks for up to 6 doses, or until disease progression or unacceptable toxicity. The primary endpoint is the percentage of patients achieving prostate-specific antigen (PSA) response, defined as a ≥50% decrease in PSA baseline. Secondary endpoints include frequency and severity of adverse events, progression-free survival, quality of life, and overall survival. To date, 11 patients have received ≥1 dose. Primary endpoint results from all 15 patients anticipated prior to EANM '25. ***Results:*** One patient received 5 doses, 3 patients received 4 doses, 2 patients received 2 doses, and 5 patients received 1 dose. Of 9 patients with available data, 8 (89%) had any decrease in PSA, ranging from 25-98% decrease; 3 patients had >80% decrease. Most common adverse events were Grade 1 fatigue (5 patients) and Grade 3 anemia (3 patients). Only 2 patients experienced Grade 1 xerostomia, which could be explained by lower than usual salivary gland uptake seen on post-injection [^{177}Lu]Lu-panPSMA SPECT images (further investigation ongoing). All patients reported an improved quality of life with majority reducing/stopping pain medication use. ***Conclusion:*** Preliminary data suggest that [^{177}Lu]Lu-panPSMA is effective for the treatment of patients with PSMA+ mCRPC, with improvements in quality of life and a favorable safety and tolerability profile. Disclosure: This is an investigator-initiated trial. ^{177}Lu, DOTA-HYNIC-panPSMA, [^{68}Ga]Ga-PSMA-11 kits, and financial support provided by Telix Pharmaceuticals. ***References:*** 1. Luna-Gutiérrez M et al. Pharmaceutics. 2023;15(7):1988. doi:10.3390/pharmaceutics15071988.

EP-0811

Dual-Tracer Deep Learning-Based Prediction of Voxel-Wise Absorbed Dose for PSMA Radioligand Therapy in mCRPC

S. Xue[1], *A. A. Nikolic*[2], *S. Wen*[1], *B. Jan*[2], *M. Hacker*[1], *C. Lapa*[2], *X. Li*[1];
[1]Division of Nuclear Medicine, Department of Biomedical Imaging and Image-guided Therapy, Vienna General Hospital, Medical University of Vienna, Vienna, AUSTRIA, [2]Nuclear Medicine, Faculty of Medicine, University of Augsburg, Augsburg, GERMANY.

Aim/Introduction: Theranostic imaging plays a critical role in personalizing radiopharmaceutical therapy (RPT) by enabling pre-treatment absorbed dose prediction. While previous studies have attempted to estimate absorbed doses using PSMA PET imaging alone, growing evidence indicates that elevated FDG uptake may signify resistance to PSMA-targeted therapy. This discordance challenges the predictive accuracy of PSMA-only models, particularly for PSMA/FDG concordant lesions. To address this limitation, we propose a dual-tracer deep learning framework that integrates pre-therapy PSMA and FDG PET imaging for voxel-wise absorbed dose prediction. Our approach employs a custom-designed Dual Attention Fusion U-Net (DAFNet) to enhance predictive accuracy through modality-specific modeling and differential loss weighting. ***Materials and Methods:*** This retrospective study included 35 patients with metastatic castration-resistant prostate cancer (mCRPC) who received [^{177}Lu]Lu-PSMA therapy, comprising 71 treatment cycles with pre-treatment PSMA/FDG PET imaging. Various theranostic combinations were included: [^{18}F]F-rhPSMA-7.3 or [^{68}Ga]Ga-PSMA-11 for imaging, and PSMA-I&T, PSMA-617, or rhPSMA-10 for therapy. The proposed DAFNet architecture incorporates three key components: (1) modality-specific feature extraction branches for PSMA and FDG, (2) hierarchical cross-modal attention fusion to integrate tracer-specific biological signals, and (3) a lesion- and organ-at-risk (OAR)-prioritized weighted loss function to enhance prediction accuracy in clinically relevant regions. Quantitative performance was evaluated using voxel-wise physical error metrics and dose-volume histogram (DVH) similarity. ***Results:*** DAFNet demonstrated

higher voxel-level dose prediction accuracy compared to the PSMA-only baseline model (P-Unet). For lesion regions, DAFNet achieved a significantly lower normalized root mean squared error (NRMSE) of 0.04 ± 0.01%, compared to 0.26 ± 0.10% for P-Unet ($P < 0.05$), along with improved DVH similarity (96.9 ± 0.2% vs. 87.1 ± 0.5%). In OARs, both models performed comparably, with DAFNet achieving an NRMSE of 0.05 ± 0.02% and DVH similarity of 97.1 ± 0.2%, versus 0.05 ± 0.01% and 96.2 ± 0.5%, respectively, for P-Unet. ***Conclusion:*** The DAFNet model demonstrates improved lesion-specific absorbed dose prediction by effectively integrating PSMA and FDG PET imaging, addressing key limitations of PSMA-only approaches. This work represents a step toward more accurate, personalized pre-therapy dosimetry in PSMA radioligand therapy for mCRPC.

EP-0812

Radioligand therapy for metastatic prostate cancer: the first French qualitative study exploring patient perceptions, from experience to trust

C. Lachachi[1], *P. Barthelemy*[2], *N. Houede*[3], *E. Treuveur*[4], *S. Chene*[5], *M. de Loisy*[5], *M. Wartski*[6];
[1]*Hospices civils de Lyon, Hopital Louis Pradel, Bron, FRANCE,* [2]*ICANS, Strasbourg, FRANCE,* [3]*CHU de Nimes, Nimes, FRANCE,* [4]*Aplusaresearch, Boulogne-Billancourt, FRANCE,* [5]*Novartis Pharma SAS, Rueil-Malmaison, FRANCE,* [6]*APHP, Hopital Cochin, Paris, FRANCE.*

Aim/Introduction: Patients with metastatic cancers face limited treatment options, impaired quality of life, and reduced life expectancy.^{177}Lu-PSMA-radioligand therapy (RLT) represents a promising therapeutic innovation for these patients, but it may raise some concerns or questions. The objective of this first French qualitative study involving patients with metastatic castration-resistant prostate cancer (mCRPC) was to explore patients' perception of beta-emitter based RLT - among both treated and untreated individuals - as well as their knowledge, concerns, expectations, and perceived benefits and barriers. ***Materials and Methods:*** Thirteen patients (7 treated and 6 not treated with RLT), referred via physicians or the National Association of Prostate Cancer Patients (ANAMACaP), participated in 60-minute unstructured interviews (9 sections) analyzed via full transcripts. Patients came from different regions in France, and they all had mCRPC, treated with at least two previous or ongoing lines of systemic therapy (including chemotherapy and hormone therapy). ***Results:*** Patients describe their cancer as an invisible "chronic illness", contrasting with the strong negative effects that previous treatments had on their quality of life. Nevertheless, patients express strong trust in their referring physicians on treatment decisions. RLT is perceived as an "innovative and targeted treatment" that addresses a vital therapeutic need, "inspiring hope" and offering "more benefits than disadvantages." RLT is associated with familiar procedures (e.g. PET scans in the same department) without particular concerns related to the nuclear aspect. However, further clarification is needed, mainly regarding the practical aspects of treatment administration and the appropriate terms employed to explain them. Patients who were not treated with RLT welcome this additional therapeutic option and express their interest in its targeted action while raising questions about the precautions to follow. Patients who are undergoing treatment or benefiting from a response to RLT describe an overall positive experience on PSA levels, clinical improvement, better tolerability compared to chemotherapy, and simple administration (rapid, painless injection) on an outpatient setting. The administration process and radiation safety precautions are well accepted. ***Conclusion:*** This qualitative study reveals a positive perception of RLT among mCRPC patients based on its targeted mechanism of action, a favorable benefit-risk balance, and a favorable treatment experience highlighted by patients who received it. Trust in the medical team and transparent communication regarding practical aspects are essential to accepting this innovative treatment.

EP-0813

Long-Term Outcome of Patients with Metastatic Castration-Resistant Prostate Cancer Treated with [^{177}Lu] Lu-PSMA Therapy: A Real-World Study from a Resource-Constrained Southeast Asian Tertiary Care Center

A. Nazar, *M. ora, P. Pradhan, S. Barai, A. Arya;*
Sanjay Gandhi Post Graduate Institute of Medical Sciences, Lucknow, INDIA.

Aim/Introduction: To assess long-term outcomes of [^{177}Lu]Lu-PSMA therapy in metastatic castration-resistant prostate cancer (mCRPC) patients treated in a real-world clinical setting. ***Materials and Methods:*** This retrospective observational study included 63 patients with mCRPC treated with [^{177}Lu]Lu-PSMA between September 2020 and March 2025 at a tertiary care institute. Data were collected on demographics, number of treatment cycles, survival status, and follow-up duration. PSA and radiological responses were not included in this analysis. Overall survival was assessed descriptively. Patients were followed until death or last contact, and survival status was recorded accordingly. ***Results:*** The median age of the cohort was 69.5 years (range: 38-92). Patients received a median of 3 cycles (range: 1-6) of [^{177}Lu]Lu-PSMA. total 6 cycle were planned for each patients. However only 23 (36%) patients could complete the 6 cycle. 9 patients received one cycle, 11 patients two cycle, 12 patients three cycle, 4 patients four cycle and 3 patients five cycle before they expired. One patients shows complete response after 4 cycle. At data cutoff, 40 patients (63%) had died and 23 (37%) were alive. The median follow-up duration was 14.5 months (range: 0.7-57.5 months). No unexpected toxicities were reported during the observation period. The treatment was well tolerated in the majority of patients. ***Conclusion:*** [^{177}Lu]Lu-PSMA therapy demonstrated favorable long-term outcomes in mCRPC patients, with a good safety profile and sustained follow-up in a real-world setting. Further analysis incorporating PSA dynamics, imaging response, and dosimetry is planned to enhance treatment personalization.

EP-0814

Association between early scintigraphic and biochemical response after one cycle of [177Lu]LuPSMA-617 radioligand therapy in metastatic castrationresistant prostate cancer patients

A. Silva, *L. C. Silva, F. P. M. Oliveira, D. C. Costa;*
Champalimaud Centre for the Unknown, Champalimaud Foundation, Lisbon, PORTUGAL.

Aim/Introduction: This study investigates the association between the scintigraphic response of [177Lu]Lu-PSMA-617 radioligand therapy (RLT) and early biochemical response after one cycle of RLT in metastatic castration-resistant prostate cancer (mCRPC). ***Materials and Methods:*** Between Dec./2023 and Apr./2025, 21 mCRPC patients underwent at least two cycles of [177Lu]Lu-PSMA-617 (7400MBq+/-10%, 6 weeks apart). Nineteen patients were retrospectively included; two were excluded, one due to lack of PSA information after 1st cycle of RLT and another to no post-therapeutic images at the 24h-time-point available. Biochemical response was based on the relative change of serum PSA according to the Prostate Cancer Working Group 3 criteria. Scintigraphic post-therapeutic assessment was based on the relative burden and metabolic disease changes and visual evaluation, categorized according to RECIP1.0. PSA was measured at 12±8 and 32±7 days before and after 1st cycle, respectively. The geometric mean of anterior and posterior projections of 1st and 2nd cycles 24h-post-injection whole-body scintigraphic images were used to quantify disease status changes. Planar images intensity normalisation

was done through bilateral uniform-uptake regions in the soft tissue of the medial aspect of the distal thighs. All lesions were identified and then validated by an experienced nuclear medicine physician. Segmentation was performed with an already-validated semi-automatic Bayesian segmentation algorithm, from the lesion identification masks. Three quantitative measures were extracted - total disease extent (product of number of lesion pixels by pixel area), total metabolic burden (product of disease extent by mean uptake) and maximum uptake. Spearman correlation (ρ) was used to assess the relationship between PSA relative difference, and scintigraphic quantitative measures relative differences. ***Results:*** After the first cycle of RLT, median PSA dropped from 28.6(0.21-737) to 24.6(0.33-669) ng/mL. Biochemical response was seen in 3/19(15.8%) patients, stable disease in 10/19(52.6%), and progression disease in 6/19(31.6%). Scintigraphic response was observed in 5/19(26.3%), stable disease in 13/19 (68.4%), and progression disease in 1/19(5.3%) patients. A moderate correlation (ρ=0.688) was found between PSA relative difference and burden extent relative difference (p=0.001). Fair correlations were found between PSA relative difference and metabolic burden (ρ=0.600; p=0.007) and maximum uptake (ρ=0.518; p=0.023) relative differences. ***Conclusion:*** Our preliminary data in this retrospective study found fair to moderate correlations between post-therapeutic scintigraphic images and early biochemical response after one cycle of RLT in mCRPC patients. Therefore, both PSA and post-therapeutic scintigraphic assessment should be used together as indicators of early response to treatment. PSA alone does not reliably predict early response.

EP-0815

Linking Dual-Tracer Imaging and Lesion Dosimetry to Predict Outcomes in mCRPC Patients Treated with [^{177}Lu] Lu-PSMA Therapy

S. Wen[1], *S. Xue*[1], *M. Hacker*[1], *X. Li*[1], *A. A. Nikolic*[2], *L. Constantin*[2], *B. Jan*[2];
[1]*Division of Nuclear Medicine, Department of Biomedical Imaging and Image-guided Therapy, Vienna General Hospital, Medical University of Vienna, Vienna, AUSTRIA,* [2]*Nuclear Medicine, Faculty of Medicine, University of Augsburg, Augsburg, GERMANY.*

Aim/Introduction: Prostate-specific membrane antigen radioligand therapy (PSMA-RLT) has shown significant clinical benefit, particularly in patients with metastatic castration-resistant prostate cancer (mCRPC). However, treatment response remains heterogeneous. Elevated tumor uptake of FDG has been associated with poorer prognosis in mCRPC patients receiving PSMA-RLT. Meanwhile, higher lesion-level absorbed dose has been linked to improved therapeutic outcomes [1]. This study aims to explore the relationship between pre-treatment FDG uptake and therapeutic absorbed dose, and to evaluate their combined impact on therapy response and survival outcomes in mCRPC patients treated with PSMA-RLT. ***Materials and Methods:*** We retrospectively analyzed 35 mCRPC patients treated with [^{177}Lu]Lu-PSMA I&T. All underwent dual-tracer PET/CT (PSMA and FDG) prior to the first cycle and post-therapy SPECT/CT after each cycle. An automated Python-based pipeline extracted SUV-based features from PET scans and dose metrics from voxel-level absorbed dose maps at patient, organ, and lesion levels. Decision tree analysis identified features associated with treatment response (based on PSA decline) and 3-month PFS (VISION trial criteria). A survival tree model was built using time-to-event data to derive imaging-based risk stratification. Kaplan-Meier analysis with log-rank testing assessed the prognostic significance of selected features. FDG uptake and absorbed dose associations were evaluated using Mann-Whitney U and Kruskal-Wallis H tests. ***Results:*** Decision tree analysis identified several FDG-related features associated with treatment response and short-term PFS ($P < 0.05$). Survival tree modeling revealed that the SUVmean of all FDG-avid lesions was the strongest predictor of progression-free survival (PFS); patients with SUVmean ≤ 6.78 g/mL had significantly longer PFS ($P < 0.01$, HR = 0.204). At the patient level, total volume of concordant lesions ($PSMA^+FDG^+$) was inversely correlated with mean absorbed dose (Kruskal-Wallis $H = 9.6$, $P < 0.05$). At the lesion level, $PSMA^+FDG^+$ lesions exhibited significantly lower absorbed doses compared to $PSMA^+FDG^-$ lesions ($P < 0.05$). No significant dose differences were observed across organ sites ($P = 0.656$). ***Conclusion:*** This study suggests that higher FDG uptake may be associated with lower absorbed dose, poorer treatment response, and shorter survival in mCRPC patients undergoing PSMA-RLT, indicating a potential biological mechanism of resistance. Dual-tracer analysis pipeline may aid in patient selection, but further validation in larger, independent cohorts is needed to confirm its clinical utility. Additional radiobiological studies are warranted to support these findings and refine selection strategies for PSMA-RLT. ***References:*** [1]Warfvinge CF, et al. Relationship Between Absorbed Dose and Response in Neuroendocrine Tumors Treated with [177Lu]Lu-DOTATATE. JNM. 2024;65(7):1070-1075.

EP-0816

Early Prediction of Response to Treatment With ^{177}Lu-iPSMA Using ^{18}F-PSMA 1007 PET/CT in Castration-Resistant Prostate Cancer.

A. Arriaga Contreras*, R. Hernández Ramírez, M. Corza Ayala, F. Solano Caballero, O. Lucio Baez;*
Instituto Nacional de Ciencias Médicas y Nutrición Salvador Zubirán, Ciudad De México, MEXICO.

Aim/Introduction: Metastatic castration-resistant prostate cancer (mCRPC) is a heterogeneous entity and constitutes the main cause of mortality. The therapeutic management of mCRPC incorporating diverse classes of agents that have demonstrated prolonged survival, such as ^{177}Lu-PSMA therapy, which uses beta-particle radiation to selectively target cells with high PSMA expression and the surrounding microenvironment. Identifying patients at risk of poor prognosis is clinically important. The study evaluates the correlation between the decrease in total tumour volume (TTV) and semi-quantitative parameters (SUVmax, SUVmean, TLA - Total Lesion Activity) with ^{18}F-PSMA 1007 PET/CT after the second cycle of ^{177}Lu-iPSMA. The objective is to determine whether these parameters predict a successful response at the end of treatment. ***Materials and Methods:*** Twenty-one patients who met the following criteria were analysed: mCRPC, having received at least two cycles ^{177}Lu-iPSMA, and having at least two ^{18}F-PSMA PET/CT studies (obligatorily one before therapy and a second at two cycles or at the end of therapy). Specialised software was used to calculate the TTV and semi-quantitative parameters. RECIST 1.0 criteria and prostate-specific antigen (PSA) were taken into account to classify them as a successful response (complete response (CR), partial response (PR) and stable disease (SD) + PSA decrease >50%) or as treatment failure (progressive disease (PD), PSA decrease <50%). Statistical tests such as Shapiro-Wilk and Mann-Whitney U were applied to evaluate the differences between the groups. ***Results:*** Baseline SUVmax was related to the response to the second cycle of ^{177}Lu-iPSMA treatment. Lower SUVmax values on baseline and interim PSMA PET/CT were related to CR, PR and SD (RECIST 1.0) to ^{177}Lu -iPSMA treatment, and higher SUVmax values with PD. Lower TLG values at the second cycle of treatment were related to a >30% decrease in tumour volume at the end of treatment, when compared with higher TLG values. The early decrease in total tumour volume was not conclusive as a predictor of final response. ***Conclusion:*** Elevated baseline SUVmax values predict a higher probability of successful treatment with 177Lu-PSMA. However, the early decrease in total tumour volume was not conclusive as a predictor of final response. ***References:*** Gafita et al., Radiology 2023;308(1): RECIP 1.0 in mCRPC. Seifert et al., Theranostics 2021;11(17):8143-8151. Tumour volume reduction

and PSMA expression in Lu-PSMA therapy. Kuo et al., Radiology 2024;312(2): Quantitative PSMA PET and outcomes after Lu-PSMA-617 (VISION Trial).

EP-0817

Immediate Renal Response to 177Lu-PSMA Radioligand Therapy: Insights from a Prospective Observational Study

A. Nazar, *R. Mehra, M. ora, P. Pradhan;*
Sanjay Gandhi Post Graduate Institute of Medical Sciences, Lucknow, INDIA.

Aim/Introduction: This study aimed to evaluate the immediate effects of 177Lu-PSMA radioligand therapy (RLT) on renal function by analyzing serum creatinine changes occurring within one week after therapy administration in patients with metastatic castration-resistant prostate cancer (mCRPC). ***Materials and Methods:*** A prospective observational study was conducted on 15 mCRPC patients who underwent 177Lu-PSMA RLT. Thirteen patients completed 6 cycles of therapy, while two patients completed 5 cycles, resulting in a total of 88 treatment cycles for analysis. Serum creatinine levels were measured immediately before and one week after each therapy cycle. Changes in creatinine levels were categorized by direction (increase, decrease, or unchanged) and clinical significance (defined as changes >0.3 mg/dL). Statistical analysis included calculation of means, medians, ranges, and standard deviations, with significance set at $p<0.05$. ***Results:*** Mean pre-therapy serum creatinine was 1.09 mg/dL (range: 0.60-1.87 mg/dL), while mean post-therapy value was 1.10 mg/dL (range: 0.60-1.70 mg/dL). The mean difference between pre- and post-therapy measurements was 0.01 mg/dL, which was not statistically significant ($p>0.05$). Of the 88 treatment cycles, 47.7% (n=42) showed increases in creatinine values, 44.3% (n=39) showed decreases, and 8.0% (n=7) showed no change. Only 7.9% of all treatments resulted in clinically significant creatinine changes (>0.3 mg/dL) - with 3.4% (n=3) showing significant increases and 4.5% (n=4) showing significant decreases. Analysis across consecutive treatment cycles revealed no consistent pattern of creatinine changes, with similar distributions of increases and decreases observed throughout the treatment course. ***Conclusion:*** 177Lu-PSMA radioligand therapy does not appear to cause immediate clinically significant nephrotoxicity as measured by serum creatinine in the majority of treatment cycles. The bidirectional nature of the observed changes, with nearly equal proportions of increases and decreases, suggests that factors other than direct nephrotoxicity may influence short-term creatinine fluctuations in this patient population. These findings support the renal safety profile of 177Lu-PSMA RLT in the immediate post-treatment period, though longer-term studies are warranted to assess potential cumulative effects.

EP-0818

Effect of tumor load on physiological organs uptake of 18-F PSMA in patients with distant metastatic prostatic carcinoma

R. Mostafa[1], *T. Ahmed*[1], *M. T. Amin*[1], *G. El-Hennawy*[2];
[1]*South Egypt Cancer Institute, Assiut University, Assiut, EGYPT,*
[2]*National cancer Institute, Cairo University, Cairo, EGYPT.*

Aim/Introduction: Lutetium-177 prostatic specific membranous antigen (PSMA) represents a novel therapeutic option for metastatic castration-resistant prostate cancer [1]. Kidneys, salivary and lacrimal glands, and red bone marrow are among the organs susceptible to toxicity of radioligand therapy [2]. The tumor sink effect refers to decreased uptake in healthy organs with increased sequestration of the malignant cells, allowing for higher doses of radioligand therapy [3].In this study we aimed to investigate the association between normal organs' mean and maximum standardized uptake values (SUVmean and SUVmax, respectively) of 18-F PSMA and tumor load in metastatic cancer prostate. ***Materials and Methods:*** A total of 95 patients with distant metastatic prostate cancer who had undergone an 18-F PSMA PET/CT were included in this study. Tumor load was visually classified as high, medium, or low. A region of interest (ROI) was drawn in each patient over parotid glands, lacrimal glands, blood pool, liver, spleen, kidneys, and red marrow to extract SUVmean and SUVmax. Organs with metastasis were excluded. Data were presented in the form of median and interquartile range (IQR). Comparisons between groups were done using analysis of variance (ANOVA) and with a post hoc test for multiple comparisons. ***Results:*** Among study participants, 9 had extra pelvic lymph nodes, while the rest had bone and soft tissue metastatic sites. Age ranged from 52-85 years old. Thirty-nine patients had a high tumor load (41%), 23 (24%) had a medium tumor load, and 33 patients (35%) had a high tumor load. Higher tumor load showed significantly lower SUVmean and SUVmax of the salivary glands ($p = 0.002$, and 0.027), lacrimal glands ($p=0.011$, and 0.025), aortic arch ($p=0.018$, and 0.008), spleen ($p=0.006$, and 0.002), kidneys ($p=0.003$, and 0.002), and bone marrow ($p=0.005$, and 0.007). However, there was no significant difference between tumor load and liver SUVmean and SUVmax ($p=0.176$, 0.222). In post hoc comparison, there was a substantial considerable difference between high and medium tumor load ($p=0.014$) and low and medium tumor load ($p<0.001$)—nevertheless, there was no significant difference between medium and low tumor load groups ($p=0.594$). ***Conclusion:*** Higher tumor load showed lower uptake values of healthy organs in 18-F PSMA PET/CT, supporting the tumor sink phenomenon, which could help determine doses of Lutetium-177 therapy. ***References:*** (1) https://doi.org/10.3390/cancers13153715.(2) https://doi.org/10.2967/jnumed.123.265448. (3) https://doi.org/10.3390/cancers15092592.

EP-0819

Radium-223 (Xofigo) for the treatment of metastatic castration-resistant prostate cancer: our experience.

C. Galindo, *M. De la Rubia Marcos, K. Guichay, D. Rodriguez Oviedo, M. Alvarez Moreno, J. Sanchez Calderón, M. Castillejos Rodriguez, A. Herrero Muñóz, C. Paniagua Correa, A. Ortega Valle, M. García Alonso, M. Tagliatori Nogueira;*
Hospital Universitario de Getafe, Madrid, SPAIN.

Aim/Introduction: To evaluate the outcomes of Radium-223 treatment in patients with metastatic castration-resistant prostate cancer, assessing risk factors, side effects, tolerance, and treatment response. ***Materials and Methods:*** A retrospective case series of patients with metastatic castration-resistant prostate cancer treated with Radium-223 for bone pain management. All patients treated between 2019 and 2024 at a single hospital were included. Clinical-pathological background, imaging results, number of doses received, treatment efficacy, and tolerance were evaluated. ***Results:*** Our series included 37 patients. The average age was 72.3 years (standard deviation, 7.99). Fifty-one percent of patients completed the treatment, and only 16.2% had to discontinue it due to poor tolerance. Clinically, 48.6% of patients improved and 18.9% stabilized, although radiologically, only 1 patient (2.7%) showed improvement, which was observed after the second dose. Sixteen percent of patients developed hematological alterations, requiring treatment discontinuation in all cases. However, for the 5 patients who experienced other side effects (13.5%), treatment discontinuation was not required. The initial weight of patients who discontinued treatment was significantly lower than that of those who did not, and this difference also influenced mortality. Thirty-two percent of patients required additional treatment (radiotherapy) for symptomatic control. ***Conclusion:*** Bone pain is common in patients with metastatic castration-resistant prostate cancer. Our results suggest that Xofigo achieves good symptomatic control with clinical improvement or stabilization in nearly 70%

of patients, despite the lack of radiological improvement. Lower initial body weight is associated with a higher rate of treatment discontinuation and mortality.

EP-0820

^{177}Lu-PSMA-617 therapy in patients with mCRPC: First descriptive analysis of efficacy and safety from a single-oncology center in Greece.

V. Chatzipavlidou, *D. Iakovoglou, T. Kalathas, I. Aisiopoulos, A. Vatalis, L. Zoglopitou, A. Paschali;*
Theagenio, Thessaloniki, GREECE.

Aim/Introduction: After getting approval from FDA&EMA for mCRPC patients previously treated with at least 1 ARPi and 1 or 2 taxanes, ^{177}Lu-PSMA-617 was available for use in Greece from 01/2024. Purpose of our study is to describe our experience so far, on the efficacy and safety of ^{177}Lu-PSMA-617. ***Materials and Methods:*** We performed a retrospective review of patients treated with up to to 6_cycles of ^{177}Lu-PSMA-617 at 6_weeks intervals from 02/2024-04/2025. PSMA-PET/CT was performed on all patients before therapy and in restaging in selected cases of biochemical progression. At each cycle, all patients underwent the same protocol of whole-body/planar and SPECT/CT, to evaluate therapeutic ligand uptake, dosimetry and alteration in the extent of the disease during the treatment. PSA response was defined as a fall-by-50% (PSA50). Hematologic toxicities and adverse events were evaluated. ***Results:*** 34 patients (mean_age:71 y; age_range:54-92y) received ^{177}Lu-PSMA-617. 8 patients completed 6_cycles of ^{177}Lu-PSMA-617. 10 patients discontinued therapy, all because of biochemical progression. 16 patients still undergo ^{177}Lu-PSMA-617 therapy. Complete Response (CR) was achieved in one patient (1/18, 6%) who received 6 cycles of ^{177}Lu-PSMA-617 and had only lymph node metastases in the baseline PSMA-PET/CT. Partial Response (PR) was achieved in two patients (2/18, 11%) who received 6 cycles of ^{177}Lu-PSMA-617 and had lymph node and bone metastases in the baseline PSMA-PET/CT. Disease Progression (PD) was seen in 15 patients (15/18, 83%), 11 of them had lymph node and bone metastases and 4 had also liver metastases and displayed PD in earlier cycles. PSA50 at 6th cycle, was achieved in 5pts (5/18_28%), with the biggest reduction of PSA in the patient with CR (99.7%), followed by the 2pts with PR and 2pts who although progressed with new lesions, had remission in preexisted lesions (bone+lymph nodes). Most patients tolerated the therapies well. Hematologic toxicity was mainly of grade 1, while patients with preexisting myelosuppression were more susceptible. Fatigue and dry mouth were the most common adverse events, nearly all of grade1/or2. Severe xerostomia grade2 developed in the patient who achieved CR. ***Conclusion:*** Our experience with PSMA therapy so far, is encouraging. Patients with mCRPC seem to get the benefits already demonstrated by phase_III trials, however the benefit-to-risk ratio should always be evaluated on a case-by-case_basis. Multidisciplinary collaboration is needed so that patients are monitored and managed safely and efficiently.

EP-0821

Treatment with [^{223}Ra]$RaCl_2$ in Metastatic Castration-Resistant Prostate Cancer Patients: Experience at Our Centre

M. Ottino, *O. Ajuria Illarramendi, A. Martínez Lorca, P. Azpeitia Hernández, M. Gutierrez Guerrero, I. Hernández Pérez, T. Navarro Martínez, U. Vera Schmülling, M. Orduña Diez, E. Pérez de los Ríos, A. Torres Consiglieri, P. Paredes Rodríguez;*
Hospital Universitario Ramón y Cajal, Madrid, SPAIN.

Aim/Introduction: To provide a descriptive analysis of treatment with [^{223}Ra]$RaCl_2$ in patients with metastatic castration-resistant prostate cancer(mCRPC) at our institution. ***Materials and Methods:*** An observational, descriptive, and retrospective study was conducted. Medical records of patients treated with [^{223}Ra]$RaCl_2$ between 01/01/2014-31/12/2024 were reviewed. Inclusion criteria were: mCRPC with symptomatic bone metastases and no visceral metastases, with progression following two lines of systemic therapy or ineligibility for further systemic treatment, in accordance with current clinical guideline recommendations. Variables collected included age, clinical data (ECOG performance status,treatment line), laboratory parameters (haemoglobin,platelets,neutrophils), radiological findings (CT and bone scan prior to treatment), and follow-up data (number of doses received and radiological progression-free survival [rPFS],defined as the appearance of ≥2new lesions on bone scan or progression according to RECISTcriteria). ***Results:*** A total of 46patients were included (50% ECOG 0, 50% ECOG 1), with a mean age of 78.8years (SD ± 7.4years). The median time between CT scan and the first [^{223}Ra]$RaCl_2$ dose was 1.9months (SD ± 1.2months), and the median time between bone scan and the first dose was 2.2months (SD ± 1month).Forty-seven per cent (22/46) of patients completed all six doses of [^{223}Ra]$RaCl_2$. Treatment discontinuation occurred in the remaining patients due to the following reasons:disease progression in 24%(11/46;8 by CT scan,1 by bone scan,3 by clinical deterioration),grade III thrombocytopenia in 2%(1/46), voluntary withdrawal in 4%(2/46), death in 4%(2/46),and unknown causes in 15%(7/46).Regarding treatment lines, 17%(8/46) received [^{223}Ra]$RaCl_2$ as second-line therapy,26%(12/46) as third-line, and 4%(2/46) as fourth-line. Treatment line data were unavailable for the remaining patients due to referrals from other institutions. Among the 22 patients who completed the full treatment course, the median rPFS was 17.7 months (SD ± 20.9 months; 95% CI: 6.8-24.3). Median rPFS by treatment line was 6.3 months (95% CI: 0.9-11.6) for second-line (n=8), 14.8 months (95% CI: 6.51-23.05) for third-line (n=12), and 57.3 months (95% CI: -177-291) for fourth-line (n=2). Comparative analysis using the Mann-Whitney U test indicated notable differences between the third- and fourth-line groups, likely influenced by population heterogeneity and unequal group sizes. ***Conclusion:*** [^{223}Ra]$RaCl_2$ showed encouraging rPFS outcomes at our centre, particularly in patients who completed all six cycles, in line with previously reported data.The observed variation in rPFS by treatment line may reflect differences in patient characteristics and underscores the need for larger, more controlled studies to support these findings.

EP-0822

A Phase 1, first-in-human, dose-escalation study of [^{225}Ac]-AZD2284 (AZD2284), a STEAP2-directed radiopharmaceutical, in patients with metastatic castration-resistant prostate cancer (mCRPC)

F. Almaguel[1,2], *L. Nordquist*[3], *B. Tran*[4], *M. S. Hofman*[4], *S. Allan*[5], *K. Buchanan*[6], *J. Charlton*[6], *J. Dise*[5], *G. Lunger*[5], *N. Mueller*[7], *M. A. Patel*[8], *D. Slade*[6], *M. Petruzzelli*[6], *M. Nawinne*[6], *M. Sathekge*[9,10];
[1]Loma Linda University School of Medicine, Loma Linda, CA, UNITED STATES OF AMERICA [2]Biogenix Molecular, Miami, FL, UNITED STATES OF AMERICA [3]Xcancer, Omaha, NE, UNITED STATES OF AMERICA [4]Peter MacCallum Cancer Centre, Melbourne, AUSTRALIA, [5]Fusion Pharmaceuticals, Boston, MA, UNITED STATES OF AMERICA [6]AstraZeneca, Cambridge, UNITED KINGDOM, [7]AstraZeneca, Gaithersburg, MD, UNITED STATES OF AMERICA [8]AstraZeneca, New York, NY, UNITED STATES OF AMERICA [9]Steve Biko Academic Hospital, Pretoria, SOUTH AFRICA, [10]Nuclear Medicine Department, University of Pretoria, Pretoria, SOUTH AFRICA.

Aim/Introduction: Radiopharmaceutical therapy (RPT) is an established therapeutic modality, with the beta emitter ^{177}Lu-PSMA-617 approved for patients with prostate-specific membrane antigen (PSMA)-positive mCRPC. However, low PSMA expression or neuroendocrine differentiation are associated with limited response to PSMA-targeted RPT, and the radiobiological limitations

of beta-emitting isotopes, along with the physiological expression of PSMA in normal tissues, have curtailed widespread use of ^{177}Lu-PSMA-617, underscoring the need for novel theranostic approaches. Six transmembrane epithelial antigen of the prostate 2 (STEAP2) is overexpressed in prostate cancer cells with limited normal tissue expression, presenting a promising therapeutic target. AZD2284 is an RPT containing the alpha emitter actinium-225 conjugated to a STEAP2-directed monoclonal antibody, AZD2275. AZD2284 delivers actinium-225 to STEAP2-expressing tumor cells, where alpha particles traverse the nucleus causing DNA breaks and other cellular damage. Alpha emissions are not amenable to image acquisition; therefore, [^{111}In]-AZD2287 (AZD2287), with indium-111 chelated to AZD2275, will be used as an imaging surrogate. This first-in-human, Phase 1, non-randomized, open-label study (NCT06879041) is evaluating AZD2284, AZD2287, and AZD2275 in patients with mCRPC. ***Materials and Methods:*** Patients with histologically-confirmed adenocarcinoma of the prostate or neuroendocrine-differentiated prostate cancer and ≥1 metastatic lesion are eligible. The study will enroll ≤134 patients across Parts A (Imaging) and B (Therapeutic). Part A Cold Antibody Exploration aims to determine whether preadministration of AZD2275 (i.e., cold antibody) enables optimal biodistribution of AZD2287 and AZD2284. Patients with progressive disease who have received ≥2 prior lines of systemic treatment may receive AZD2284 at the starting dose. Part A Expansion will explore the prevalence and correlation of PSMA and STEAP2 tumor expression. Part B Dose Escalation will explore escalating doses of AZD2284 (± AZD2275 preadministration as determined in Part A) guided by a model-based time-to-event continual reassessment method. Patients will receive AZD2287 (± AZD2275) to confirm sufficient tumor uptake, followed by treatment with AZD2284 (± AZD2275). Part B Expansion will enroll ≤2 AZD2284 dose cohorts to further characterize safety and efficacy. The primary objectives are to assess the safety and tolerability of AZD2284, AZD2287, and AZD2275; to determine the recommended Phase 2 dose of AZD2284; and to assess the effect of AZD2275 preadministration on the radiation dosimetry of AZD2287 and to estimate the radiation dosimetry of AZD2284. Secondary objectives include efficacy (AZD2284 only), pharmacokinetics, and immunogenicity. Study sites are in the United States, Australia, and South Africa; enrollment began March 2025 and is ongoing.

EP-0823

The Effectiveness of Radium-223 on Metastatic Castration-Resistant Prostate Cancer: A Meta-Analysis

T. Chen, *Y. Chang;*
Kaohsiung Chang Gung Memorial Hospital, Kaohsiung, TAIWAN.

Aim/Introduction: Radium-223 dichloride (radium-223), a bone-targeting alpha-emitting radiotherapeutic, has demonstrated efficacy in delaying the onset of symptomatic skeletal events, enhancing quality of life, and extending overall survival (OS) in patients with metastatic castration-resistant prostate cancer (mCRPC). The objective of this study is to assess the clinical effectiveness of radium-223 through a comprehensive meta-analysis. ***Materials and Methods:*** A systematic literature search was conducted using the PubMed/MEDLINE and Cochrane Library databases to identify relevant studies evaluating the outcomes of Radium-223 therapy in mCRPC patients. Eligible studies included those that enrolled patients receiving Radium-223 treatment and reported survival outcomes. The primary endpoints were overall survival (OS) and progression-free survival (PFS) following Radium-223 administration. Survival data were extracted and analyzed using the MetaSurv function in R. ***Results:*** Following the literature search conducted in March 2023, 34 (n = 6919) and 16 (n = 1779) studies were included for analysis of OS and PFS, respectively. The pooled median OS after receiving radium-223 was 16.63 months (95% confidence interval, 14.26-19.94 months); the pooled median PFS was 7.78 months. No significant difference in OS or PFS was found between radium-223 and placebo groups. Nevertheless, OS was longer in patients receiving radium-223 in combination with androgen deprivation therapy or chemotherapy than in patients receiving radium-223 monotherapy (15.64 months vs. 14.60 months, p = 0.025); similarly, PFS was longer in patients receiving combination therapy than in patients receiving radium-223 monotherapy (14.84 vs. 5.89 months, p = 0.007). Furthermore, patients who completed 5-6 cycles of radium-223 therapy had a significantly longer OS (20.22 months vs. 6.98 months, p < 0.001). ***Conclusion:*** This meta-analysis indicates that Radium-223 therapy, particularly when administered in combination with other systemic treatments, is associated with improved overall and progression-free survival in patients with mCRPC. An improvement of OS was also observed when patients completed 5-6 cycles of radium-223 treatment.

EP-0824

PSMA PET Tumor-to-Salivary Gland Ratio to Predict Response to ^{177}Lu-PSMA and ^{225}Ac -PSMA Radioligand Therapy

L. Gabela, *L. Harry, T. Nxasana, N. Ndlovu, T. Mkhize, V. Pillay, S. Masikane, M. Patel, N. Madi, P. Chiumia, C. Kalowa, B. Hadebe, M. Vorster;*
University of KwaZulu Natal, Durban, SOUTH AFRICA.

Aim/Introduction: PSMA is a type II transmembrane glycoprotein abundantly overexpressed on prostate cancer cells. In advanced metastatic castration-resistant prostate cancer, ^{68}Ga-PSMA PET/CT assesses tumour PSMA expression before ^{177}Lu-PSMA or ^{225}Ac-PSMA radioligand therapy, though patient responses vary. Hotta et al. suggested the tumour-to-salivary gland ratio may predict PSA response and overall survival post-^{177}Lu-PSMA. This retrospective study aims to assess whether the PET tumour-to-salivary gland ratio (PSG score) can predict outcomes in prostate cancer patients receiving PSMA-targeted therapy. ***Materials and Methods:*** We included a total of 44 patients with metastatic castration-resistant prostate cancer treated with ^{177}LuPSMA and/ or ^{225}Ac-PSMA in this study. A quantitative PSG (qPSG) score (SUVmax ratio of highest tumour lesion to parotid glands) was calculated on baseline ^{68}Ga-PSMA PET images. Patients were then divided into 2 groups: High (qPSG > 1.5) and Low (qPSG ≤1.5) scores. Outcome data included a more than 50% prostate-specific antigen decline and overall survival (OS). ***Results:*** Forty-four prostate cancer patients (median age: 68 years) who received PSMA-targeted therapy were retrospectively analyzed. The population in the High (qPSG > 1.5) and Low (qPSG ≤1.5) groups were 27 (61.4%) and 17 patients (38.6%) respectively. PSA response (≥50% decline) was observed in 54.5% of patients. Response rates (PSA decline of ≥ 50%) were similar between the High and Low groups; 51.9% (14/27) vs 58.3% (10/17) (p=0.658). Survival outcomes were also comparable, although notably more deaths occurred in the low group with 64.7% compared to 55.6% in the high group (p=0.555). Disease site was categorized as Bone only, Bone + Lymph, Lymph only, or Other. Patients with Lymph node-only disease showed better survival, while those with Bone involvement had higher mortality, though not statistically significant (p=0.20). ***Conclusion:*** A trend towards higher mortality was observed in patients with lower qPSG scores and those with bone involvement, which did not reach statistical significance in our relatively small sample size. Despite this lack of statistical significance, mortality of 65% in the low uptake group vs 56% in the high uptake group is certainly clinically significant and highlights the potential of a PSG score as a useful method to predict response to PSMA-targeted therapy. A larger analysis is therefore needed to validate this methods prognostic value and establish this approach for choosing suitable candidates for therapy. ***References:*** 1. Hotta, Masatoshi, et al.

"PSMA PET tumor-to-salivary gland ratio to predict response to [177Lu] PSMA radioligand therapy: Journal of Nuclear Medicine 64.7 (2023): 1024-1029.

EP-0825

Linking Dual-Tracer Imaging and Lesion Dosimetry to Predict Outcomes in mCRPC Patients Treated with [^{177}Lu] Lu-PSMA Therapy

S. Wen[1], *S. Xue*[1], *X. Li*[1], *M. Hacker*[1], *A. A. Nikolic*[2], *B. Jan*[2], *L. Constantin*[2];
[1]*Division of Nuclear Medicine, Department of Biomedical Imaging and Image-guided Therapy, Vienna General Hospital, Medical University of Vienna, Vienna, AUSTRIA,* [2]*Nuclear Medicine, Faculty of Medicine, University of Augsburg, Augsburg, GERMANY.*

Aim/Introduction: Previous studies have shown that elevated ^{18}F-FDG uptake is associated with poor prognosis in patients with metastatic castration-resistant prostate cancer (mCRPC) undergoing [^{177}Lu]Lu-PSMA radioligand therapy (RLT). Additionally, lesion-level absorbed dose has been linked to therapeutic outcomes. This study investigates the relationship between FDG uptake and absorbed dose, aiming to understand their combined influence on treatment response and progression-free survival (PFS). ***Materials and Methods:*** We retrospectively analyzed 35 mCRPC patients treated with [^{177}Lu]Lu-PSMA I&T RLT. All patients underwent dual-tracer PET/CT imaging (PSMA and FDG) before the first treatment cycle, and at least one post-therapeutic SPECT/CT scan following each cycle. An automated Python-based pipeline was developed to extract SUV-based imaging features from PET scans and dose-related metrics from voxel-wise absorbed dose maps at the patient, organ, and lesion levels. A decision tree model was used to identify the most predictive patient-level features for treatment response (categorized as Partial Response (PR), Progressive Disease (PD), or Stable Disease (SD) based on ΔPSA) and progression-free survival (PFS). Relationship between FDG uptake and absorbed dose were evaluated at all three levels using the Mann-Whitney U test and Kruskal-Wallis H test. ***Results:*** The decision tree model identified the following as key predictors for therapy response and PFS: SUVmean and SUVmax of all PSMA$^+$ lesions, SUVmean of all FDG$^+$ lesions, total absorbed dose of concordant lesions, and FDG TLG of concordant lesions (feature importance:0.16;0.15;0.35;0.24;0.10). At the patient level, the total volume of concordant lesions was negatively correlated with mean absorbed dose (Kruskal-Wallis $H = 9.6$, $P < 0.05$). At the lesion level, PSMA$^+$FDG$^+$ lesions exhibited significantly lower mean absorbed doses compared to PSMA$^+$FDG$^-$ lesions ($P < 0.05$). At the organ level, lesion location showed no significant effect on absorbed dose ($P = 0.656$). ***Conclusion:*** This study confirms that FDG uptake serves as a negative prognostic marker in mCRPC patients treated with [^{177}Lu]Lu-PSMA, while PSMA uptake more accurately predicts biochemical response. An inverse relationship between FDG uptake and absorbed dose was observed, suggesting a potential biological interaction that may mediate resistance to PSMA-RLT. Further radiobiological studies are warranted to validate these findings and enhance patient selection strategies for PSMA-RLT.

EP-0826

A Model for ^{177}Lu-PSMA Therapy in Nuclear Medicine Departments Without Dedicated Shielding Rooms

A. Genova, *F. Porcaro, M. Prisco, L. Turchetta, I. Annarumma, V. Piscopo, M. Catalano;*
Azienda Ospedaliera di Rilievo Nazionale Antonio Cardarelli, Naples, ITALY.

Aim/Introduction: Introduction ^{177}Lu-PSMA therapy is an effective option for metastatic castration-resistant prostate cancer (mCRPC) patients who have failed androgen receptor inhibitors and taxane chemotherapy. Due to increasing eligibility worldwide, nuclear medicine departments face higher patient volumes. Additionally, ongoing research is expanding its indications to earlier treatment stages. Italian Legislative Decree 101/2020 allows radiopharmaceutical administration without protected inpatient isolation, so the authors suggest two possible treatment settings: outpatient day-hospital administration for eligible patients, and inpatient oncology ward admission for frail individuals. Standardized radiation safety protocols differ mainly in caregiver exposure thresholds and waste disposal methods. ***Materials and Methods:*** Treatment adheres strictly to radiation safety regulations to minimize exposure for healthcare workers and caregivers. After confirming clinical eligibility and informed consent, patients receive intravenous ^{177}Lu-PSMA (e.g., Pluvicto®), typically 7.4 GBq (200 mCi), with up to six cycles at 6-week intervals, adjusted according to response and toxicity. ***Results:*** Patients are instructed to hydrate adequately and frequently urinate, given that 40-60% of the administered activity is excreted via urine within 2-7 hours post-injection.Therefore, patients stay approximately 6 hours in a dedicated area with radiation-safe toilet facilities, monitored by trained nuclear medicine staff. Discharge occurs when radiation exposure drops below set thresholds. Patients receive specific discharge instructions:• Avoid close contact (<1 meter) for 2 days• Avoid contact with children/pregnant women for 7 days• Sleep separately for 3 days (or 7-15 days if children/pregnant women are present)• Abstain from sexual activity for 7 daysRadiation levels at 1 meter from patients are measured at 6 hours post-injection to ensure compliance with Italian legislative limits (DLgs. 101/2020):• ≤3 mSv/cycle (caregivers aged 18-60)• ≤15 mSv/cycle (caregivers >60)• ≤1 mSv/cycle (caregivers of pediatric patients)• ≤0.3 mSv/cycle (general public)For hospitalized patients, oncology staff receive specific training on radiation safety, waste management, and spill control. Advanced toilet systems with filtration technologies can reduce environmental ^{177}Lu release. In both outpatient and inpatient settings, post-therapy planar imaging confirms tracer distribution. Additionally, dosimetric SPECT/CT imaging assesses treatment efficacy and toxicity risks at various intervals. ***Conclusion:*** The outpatient model enhances patient comfort, reduces costs, and improves therapy accessibility. Uniform radiation protection standards across both outpatient and inpatient settings obviate routine isolation, enabling safe early patient discharge. Individualized patient assessment maintains radiation exposure as low as reasonably achievable (ALARA), balancing safety, resource use, and healthcare sustainability.

EP-0827

Prognostic Value of a Comprehensive Analysis of Metastatic Prostate Tumor Changes from First to Last ^{177}Lu-PSMA Therapy Injections Through Serial High-Speed Whole-Body 360° CZT-SPECT

C. Boursier, *J. Kunsch, T. Zaragori, P. Olivier, M. Claudin, S. Heyer, P. Raymond, P.-Y. Marie, L. Imbert;*
CHRU Nancy, Vandoeuvre-les-Nancy, FRANCE.

Aim/Introduction: The Anger-SPECT monitoring of ^{177}Lu-PSMA therapy provides significant prognostic information in patients with metastatic castration-resistant prostate cancer (mCRPC) but with 36-to-90 min recording times and partial body coverage. This study assesses the prognostic information from a comprehensive analysis of tumor changes from the first to the last ^{177}Lu-PSMA therapy injections, as provided by whole-body ^{177}Lu-SPECT recordings from a high-speed 360° cadmium-zinc-telluride (CZT) camera in mCRPC patients. ***Materials and Methods:*** We included mCRPC patients treated by ^{177}Lu-PSMA-617 injections who underwent (i) pretreatment ^{68}Ga-PSMA-11 PET and (ii) whole-body 360° ^{177}Lu-CZT-SPECT recording of only 18 min after each ^{177}Lu-PSMA therapy injection and plasma prostate-specific-antigen (PSA) measurement obtained 24h before. We used Cox proportional hazard models to predict posttreatment overall survival ($OS_{posttreatment}$) according to (i) PSA evolution during treatment and (ii) tumor SUVmax, SUVmean, and total uptake volume (TUV) extracted from ^{68}Ga-PMSA-PET and the first and last ^{177}Lu-SPECT acquisitions. ***Results:*** We included 72 patients with a median age

of 71 [interquartile range: 64;77] years, treated with 1 to 6 ^{177}Lu-PSMA injections and among whom, 43 (59%) completed ≥ 4 ^{177}Lu-PSMA treatment cycles, and 50 (73%) died during a follow-up of 9.7 [3.9;16.4] months from the last ^{177}Lu-PSMA injection. Most PSA, PET, and SPECT variables were significant univariate $OS_{posttreatment}$ predictors, but among them, only three ^{177}Lu-SPECT variables were selected as multivariate predictors: a TUV decrease greater than the median of 25% (p<0.001) and the lack of new bone lesions (p=0.035) between the first and last ^{177}Lu-SPECT , and a residual TUV lower than the median of 270 ml (p=0.001) on the last ^{177}Lu-SPECT. Means (95% confidence intervals) of survival times were 19.5 (16.7-22.3) months in the 24 patients with both > 25% TUV decrease and < 270 ml residual TUV, 11.5 (8.4-14.5) months in the 24 patients with only one of these two criteria, and 5.3 (3.3-7.2) months in the 24 with neither one. ***Conclusion:*** A comprehensive analysis of tumor changes from the first to the last ^{177}Lu-PSMA injections, as provided by whole-body 360° ^{177}Lu-CZT-SPECT recordings provides strong prognostic information in mCRPC patients, outperforming conventional $OS_{posttreatment}$ predictors such as PSA evolution and pretreatment PSMA PET variables.

EP-0828

Which reference organ can be used on Post Therapeutic ^{177}Lu-PSMA SPECT/CT when images are performed at different timepoint?

L. Michaud[1], *S. Gnesin*[2], *J. Delage*[3], *M. Tissier*[1], *A. Fenter*[1], *J. O. Prior*[1], *N. Schaefer*[1];
[1]*Department of Nuclear Medicine and Molecular Imaging, Lausanne University Hospital and University of Lausanne, Lausanne, SWITZERLAND,* [2]*Institute of Radiation Physics, Lausanne University Hospital and University of Lausanne, Lausanne, SWITZERLAND,* [3]*Radiopharmacy Unit, Department of Pharmacy, Lausanne University Hospital and University of Lausanne, Lausanne, SWITZERLAND.*

Aim/Introduction: For logistic reasons not all ^{177}Lu-PSMA patients might occur post-therapy imaging at the same time post-administration. We aimed comparing physiological parotid and hepatic uptake on post-therapeutic quantitative SPECT/CT imaging performed at 24, 48, or 72 hours following ^{177}Lu-PSMA-ITG-1 therapy to identify a reference tissue when post therapeutic images are performed at different timepoints. ***Materials and Methods:*** A retrospective analysis was conducted on 12 patients (mean age: 77±8 years) who provided general consent for data reutilization and underwent treatment with ^{177}Lu-PSMA-ITG-1 for metastatic recurrence of prostate adenocarcinoma. Patients received an average of four therapy cycles (range 2- 5). At each cycle, a single quantitative SPECT/CT scans (Siemens Healthineers Intevo or Pro.specta) was acquired at 24-, 48-, or 72-hour post-injection and reconstructed (xSPECT, 48 iterations, 1 subset, 5mm Gaussian post-reconstruction filtering). For each reconstruction, mean standardized uptake values (SUVmean) were measured in the left parotid gland and left hepatic lobe using a sphere of at least 10 mL totally included in the parotid/liver tissues. The rationale on the use of SUVmean, instead of SUVmax, to characterize the radiotherapeutic uptake in reference tissues, such as the parotids and the liver, is that the SUVmean is less sensitive to statistical noise than SUVmax. Comparisons of SUVmean across time points were performed using multilevel mixed-effects linear regression. ***Results:*** A total of 38 post-therapy SPECT/CT scans were analyzed (n=13@24h, 12@48h, 13@72h). The mean administered activity of ^{177}Lu-PSMA-ITG-1 was 7710 MBq (range: 7262-8103 MBq). At 24h, the mean SUVmean±SD was 5.27±1.83 for the parotid gland and 1.66±0.58 for the liver. At 48h, the corresponding values were 3.78±2.06 and 1.13±0.48, and at 72h 1.68±0.88 and 0.87±0.43, respectively. All scans were deemed interpretable regardless of acquisition time. As expected, in tested tissues, the SUVmean decreased with time and a significant SUVmean differences were observed between 24h, 48h and 72h acquisitions ($p < 0.0001$). Furthermore, effective wash out from the liver was slower without any significant difference across time (p>0.15). ***Conclusion:*** This study confirms higher physiological SUVmean values on early post-therapy ^{177}Lu-PSMA SPECT/CT acquisitions. These findings highlight the necessity of caution when comparing images across different post-therapeutic time. Hepatic SUVmean appears to be a more stable reference organ across time for this purpose.

EP-0829

Prognostic value of ^{18}FDG and ^{68}Ga-PSMA PET parameters in mCRPC patients referred for ^{177}Lu-PSMA therapy

B. Adam, *T. Zaragori, M. Claudin, A. Verger, P. Olivier, L. Imbert, C. Boursier;*
Nancy University Hospital of Lorraine, Nancy, FRANCE.

Aim/Introduction: ^{177}Lu-PSMA-617 is a well-established treatment for patients with progressive metastatic castration-resistant prostate cancer (mCRPC). According to EANM guidelines, PSMA expression should be evaluated for patient selection, with PSMA PET being the preferred modality. Several studies have suggested the added value of FDG PET in patient selection. In particular, a substudy of the TheraP trial reported worse progression-free survival in patients treated with Lu-PSMA therapy who had a tumor burden ≥200 mL on FDG PET. This study aims to assess the prognostic value of ^{18}F-FDG PET parameters in addition to ^{68}Ga-PSMA-11 PET parameters in mCRPC patients referred for ^{177}Lu-PSMA therapy. ***Materials and Methods:*** This retrospective study included mCRPC patients who received at least one cycle of ^{177}Lu-PSMA-617 between February 2022 and October 2023. Both ^{68}Ga-PSMA-11 PET and ^{18}F-FDG PET were performed before therapy as part of clinical practice. TMTV, TLA, SUVmean, and SUVmax were extracted from both PET studies. Visual analysis was performed to assess lesions mismatch between the two PET. Overall survival (OS) was estimated using the Kaplan-Meier method. Univariate Cox regression was followed by two multivariate models: i) using only PSMA PET parameters and ii) combining both PSMA PET and FDG PET parameters. Based on predicted risk scores from the full model, patients were divided into three risk groups (high, intermediate, low). A decision tree classifier was trained to reproduce these groups. ***Results:*** One hundred and five patients were included, with a median age of 72 [65-77]. Most (90%) had received at least one taxane-based chemotherapy, and 60% had received two. PSMA-SUVmax, PSMA-SUVmean, FDG-TLA, FDG-TMTV, and lesion mismatch criteria were significantly associated with OS in univariate analysis ($p < 0.001$). PSMA-SUVmax was the best independent predictor in the PSMA-only model, while PSMA-SUVmax and FDG-TMTV were selected for the combined model. The combined model significantly outperformed the PSMA-only model ($p = 0.001$). The three risk groups showed significantly different OS ($p < 0.006$) and could be predicted with 75.5% accuracy by a decision tree classifier ($p < 0.003$). Patients with PSMA-SUVmax ≥110 were low risk; those with PSMA-SUVmax <110, ECOG <2, and FDG-TMTV <228 mL were intermediate risk; the rest were high risk. ***Conclusion:*** PSMA uptake and FDG-PET tumor burden are predictive of overall survival in mCRPC patients undergoing 177Lu-PSMA-617 therapy. The use of a decision tree combining PSMA-SUVmax and FDG-TMTV may improve risk stratification and patient selection.

EP-0830

Prognostic Value of Baseline PSMA and FDG PET Biomarkers in Patients Treated with Lutetium-177 [^{177}Lu] Lu-PSMA-617 for Metastatic Castration-Resistant Prostate Cancer: A Real-World Analysis from the ProsTIC Registry.

N. Kovaleva[1], *L. Kostos*[2,3], *N. Papa*[1], *J. Weindler*[1], *R. Alipour*[1,2], *B. Emmerson*[1], *G. Ghosh*[1], *G. Kong*[1,2], *E. Medhurst*[1], *A. S. Ravi Kumar*[1,2], *J. Saghebi*[1,2], *A. A. Azad*[2,3], *M. S. Hofman*[1,2], *J. P. Buteau*[1,2];
[1]*Prostate Cancer Theranostic and Imaging Centre of Excellence, Molecular Imaging and Therapeutic Nuclear Medicine, Peter MacCallum Cancer Centre, Melbourne, VIC, AUSTRALIA,* [2]*Sir Peter MacCallum Department of Oncology, University of Melbourne, Melbourne, VIC, AUSTRALIA,* [3]*Department of Medical Oncology, Peter MacCallum Cancer Centre, Melbourne, VIC, AUSTRALIA.*

Aim/Introduction: Lutetium-177 [^{177}Lu]Lu-PSMA-617 radioligand therapy improves survival and quality-of-life in patients with metastatic castration-resistant prostate cancer (mCRPC). PSMA-PET SUVmean and FDG-PET metabolic tumour volume (MTV) are predictive and prognostic biomarkers in clinical trials to date. We aimed to evaluate the prognostic value of these PET biomarkers in a real-world cohort enrolled in the ProsTIC Registry. ***Materials and Methods:*** We conducted a retrospective, single-centre analysis of consecutive patients with mCRPC treated with [^{177}Lu]Lu-PSMA-617 in the ProsTIC Registry (NCT04769817). Baseline PSMA-PET SUVmean and FDG-PET MTV were measured for patients with PET/CT performed within 90 days prior to cycle 1. Outcomes evaluated were PSA response, defined as a reduction of at least 50% from baseline (PSA50), and overall survival (OS), defined as the time from cycle 1 to death or last follow-up. Data cut-off was 11 April 2025. Associations between PET biomarkers and PSA50 response were assessed using chi-square tests. Kaplan-Meier survival analyses and Cox proportional hazards regression were used to evaluate associations with OS. ***Results:*** Between 20 May 2021 and 2 May 2024, 238 patients with mCRPC commenced treatment with [^{177}Lu]Lu-PSMA-617 and met inclusion criteria; median age 75 years (IQR 68-80), time from initial diagnosis 7 years (IQR 3-12). 237 (99.6%) had prior treatment with ≥1 anti-androgen pathway inhibitor and 198 (83%) ≥1 taxane chemotherapy. PSA50 at any timepoint was observed in 142/234 (61%) of patients with evaluable PSA response. 179 deaths were recorded, the median OS was 13.3 months (95% CI: 11.4 - 15.6). PSMA-PET SUVmean ≥10 was observed in 87 (37%) of patients and was significantly associated with achieving a PSA50 response vs SUVmean <10 (80% vs 50%, p<0.001), and with longer median OS (14.6 vs 13.1 months, HR 0.74 [95% CI: 0.54-1.01]; p=0.055). Higher FDG-PET MTV (≥200 mL) was seen in 85 (36%) of patients and was associated with a lower proportion achieving PSA50 response (51% vs 66%, p=0.026) and shorter median OS (8.8 vs 17.8 months, HR 2.70 [95% CI: 1.98-3.68]; p<0.001). ***Conclusion:*** In patients with mCRPC treated with [^{177}Lu]Lu-PSMA-617 in a real-world setting, baseline PSMA-PET SUVmean and FDG-PET MTV were prognostic for PSA response and overall survival.

EP-0831

Influence of Chemohormonal History on Lu-177 PSMA Efficacy

S. Karabulut*;*
Dokuz Eylül Üniversite Hastanesi, Izmir, TÜRKIYE.

Aim/Introduction: To evaluate the impact of prior systemic therapies—namely chemotherapy and second-generation antiandrogens—on treatment response to Lu-177 PSMA therapy in patients with castration-resistant prostate cancer (CRPC), using PET-based volumetric parameters and survival analysis. ***Materials and Methods:*** In this retrospective single-center study, 33 patients with metastatic CRPC who received four cycles of Lu-177 PSMA therapy between 2015 and 2023 were included. Only patients without newly emerging metastatic lesions on baseline Ga-68 PSMA PET/CT were selected. All lesions were segmented and categorized as lymph node, bone, or organ metastases. Volumetric PET parameters including PSMA-expressing tumor volume (PSMATV) and total lesion PSMA expression (TLPSMA) were measured using LIFEx software with SUVmax ≥ 2.5 as the threshold. Normal liver and parotid gland SUVmean values were used for semi-quantitative standardization. Pre-treatment data such as PSA, ALP, Gleason scores, and systemic therapies (enzalutamide, abiraterone, chemotherapy) were retrieved from hospital records. Volumetric response (%) was calculated for each region. Comparisons between treatment subgroups were performed using the Mann-Whitney U test, with statistical significance defined as $p < 0.05$. ***Results:*** The median overall survival was 17 (11.75-22.75) months; 16 patients (48%) were deceased at follow-up. Baseline PSA, ALP, PSMATV, TLPSMA, and their bone-derived components were significantly higher in deceased patients ($p < 0.05$). Volumetric response percentages (ΔPSMATV, ΔTLPSMA) were lower in the enzalutamide group compared to the abiraterone group, though not statistically significant. Similarly, no significant difference was observed between patients with or without prior chemotherapy. ***Conclusion:*** High baseline tumor burden and PSA levels predict poor prognosis in Lu-177 PSMA-treated patients. Although a lower response trend was observed in patients pretreated with enzalutamide, statistical significance was not achieved. Volumetric analysis via Ga-68 PSMA PET/CT offers valuable insights for patient stratification and treatment planning.

EP-51

e-Poster Area

C: Therapy Clinical Study -> C1 Oncological Therapy Clinical Study -> C13 Local Radionuclide Therapy (including Spheres)

EP-0832

Research on the Radiotherapy-Immunotherapy Effect of Sequential Combination of I^{131} with Transcription of the NIS Gene into Mouse Models of Pancreatic Cancer Based on Oncolytic Virus as the Delivery Vector

S. Yu*, S. Xinhui;*
the First Affiliated Hospital, School of Medicine, Zhejiang University, Hangzhou, CHINA.

Aim/Introduction: Pancreatic cancer and thyroid cancer, as two extremes among cancers, are respectively renowned for their extremely poor and excellent prognoses. To a large extent, the reason lies in the sensitivity of thyroid cancer to multiple treatment modalities, particularly the NIS gene it expresses, which can specifically uptake I^{131}, thereby achieving very favorable therapeutic effects for thyroid cancer. ***Materials and Methods:*** Therefore, we designed an oncolytic virus transfected with the NIS gene and injected it into pancreatic cancer solid tumors through intratumoral injection. As the virus replicates within the tumor and transcribes and integrates the NIS gene into tumor cells, it enables stable expression of the NIS gene. Subsequently, sequential combination with I^{131} treatment was implemented through intravenous injection. ***Results:*** It was observed that I^{131} was stably and uniformly absorbed within the tumor for up to two weeks. In the bilateral tumor model, the tumor on the treatment side not only achieved significant shrinkage through the combination of oncolytic virus and I^{131} but also led to obvious inhibition of the contralateral tumor, showing significant differences compared with the groups treated with I^{131} alone, oncolytic virus alone, and PBS. Through flow cytometry, WB, and confocal microscopy, it was distinctly observed that the combination of oncolytic virus and I^{131} significantly activated both systemic and local anti-tumor immune responses, indicating the promising prospects of the combined therapy. ***Conclusion:*** Our study reveals a therapeutic approach that combines radiotherapy and oncolytic virus to activate immunity, where the NIS gene serves as a crucial mediator for the two therapies.

EP-0833

Transarterial Radioembolization (TARE) with Yttrium-90 Microspheres in Primary Liver Lesions: Impact on Survival and Disease Progression

B. Jaramillo Lopez*, A. Suazo Montero, M. García Aragón, R. Zambrano Infantino., F. Sebastián Palacid, C. Gamazo Laherrán., J. Gómez Hidalgo, N. Álvarez Mena., M. González Soto., R. Ruano Pérez.;*
Hospital Clínico Universitario de Valladolid, Valladolid, SPAIN.

Aim/Introduction: To evaluate the impact of TARE on overall survival (OS), progression-free survival (PFS), and treatment response rate (TRR) in patients with primary liver lesions. ***Materials and Methods:*** A retrospective observational study was conducted including 66 patients with primary liver lesions, treated with TARE

between February 2017 and September 2024. Tumor response was assessed using RECIST 1.1 criteria with CT or MRI at 6, 12, and 24 months post-treatment. Patients were categorized into Group A (GA): complete response (CR) or partial response (PR), and Group B (GB): local progression (LP) or extrahepatic progression. Outcomes assessed included OS, PFS, and TRR. ***Results:*** A total of 94 TARE procedures were performed in 66 patients (38 received 1 treatment, 21 received 2, and 7 received 3). The mean age was 69 years, and 75% being male. Hepatocellular carcinoma (HCC) was diagnosed in 85% (56/66) and cholangiocarcinoma in 15% (10/66). Bilobar involvement was present in 25.7% (17/66) and unilobar in 74.2% (49/66). The mean dose activity delivered to the lesion was 1.5 GBq, and the mean perfused volume was 423 cc^3. Median follow-up was 21 months. The GA was 62,9%, with a CR and PR observed of 33% and 19.6%, respectively. In GB, 39.3% experienced local progression and 7.5% had extrahepatic progression. The overall TRR was 53%. OS analysis revealed that the median was 44,7 months in patients without treatment response and 29,7 months in those who exhibited a response to therapy (p=0,3). Median PFS was 42,7 months in GA and 15 months in GB (p=0,051). ***Conclusion:*** TARE with Yttrium-90 microspheres represents an effective and well-tolerated therapeutic option for patients with primary liver tumors. It demonstrates a high impacto in treatment response rate, contributes with a long-term stabilization of dissease and OS. These findings reinforce its role as a key modality in the multidisciplinary management of hepatic malignancies, with a great impact on clinical outcomes and patient prognosis. ***References:*** Kallini, J.R., Gabr, A., Salem, R. et al. Transarterial Radioembolization with Yttrium-90 for the Treatment of Hepatocellular Carcinoma. Adv Ther 33, 699-714 (2016). https://doi.org/10.1007/s12325-016-0324-7.

EP-0834

Dose-Response Relationship in Patients Who Received TARE with Y-90 Resin Microspheres for Hepatocellular Carcinoma

C. Soydal, *E. Dursun Avci, I. Mesci, E. C. Celebioglu, N. O. Kucuk; Ankara University Medical Faculty, Ankara, TÜRKIYE.*

Aim/Introduction: The aim of this study is to analyze the dose-response relationship in HCC patients who received TARE with Y-90 resin microspheres. ***Materials and Methods:*** Patients who received TARE with Y-90 resin microspheres with a multicompartment dosimetry between Feb 2020 and Dec 2024 were included to the analysis. After exclusion of patients without follow-up and posttreatment Y-90 PET totally 43 lesions of 20 (6F, 14M; mean age: 70±8.6 years) patients were included to the dose-response analysis. Multicompartment dosimetry was performed to all lesions in the perfused area. Additionally, mean tumor absorbed dose (TAD), whole liver absorbed dose (WLAD) and perfused liver absorbed dose (PLAD) were calculated. Response evaluation was performed with RECIST 1.1 criteria from liver MRI at the 3th month of treatment. ROC analysis was used for selection of optimal TAD cutoff to predict the response. ***Results:*** All the patients received Y-90 resin microspheres with lober or segmental approach. Median tumor volume was calculated as 9.4 cm3 (min-max: 1-1674). Fourteen patients has underlying cirrhosis. Pretreatment ALBI grades were 1 and 2 in 8 and 12 patients, respectively. During 3th month evaluation 21 lesions were responder (11PR and 10 CR). In the ROC analysis 103.8 Gy (AUC:0.693, 95%CI 0.532-0.853, p= 0.018) cutoff for mean TAD was calculated for response (PR+CR) with 76% sensitivity and 64% specificity. For the prediction of CR we found 158.7 Gy (AUC:0.776, 95%CI 0.598-0.953, p= 0.002) cutoff for mean TAD with 70% sensitivity and 79% specificity. ***Conclusion:*** Results of this retrospective analysis revealed that delivery of 158.7 Gy mean dose to the tumor with Y-90 resin microspheres would result to complete response in patients with HCC with high specificity.

EP-0835

Body Surface Area Method vs Partition Dosimetry Model in Y-90 Radioembolisation: A retrospective Dosimetric Analysis

A. Cuderman, *A. Štrok, J. Jamšek, L. Jensterle, P. Popovič; University Medical Centre Ljubljana, Ljubljana, SLOVENIA.*

Aim/Introduction: The body surface area (BSA) method was initially adopted as the standard for calculating administered activity in transarterial radioembolisation (TARE) with Y-90 resin microspheres. Due to its simplicity, it remains widely used, despite growing evidence supporting the superiority of partition dosimetry. ***Materials and Methods:*** We retrospectively analysed 17 Y-90 resin microspheres TARE procedures performed between 2015 and 2023 using the BSA method for the administered activity calculation. Dosimetric parameters - including tumor absorbed dose (TAD), normal perfused liver dose (NPLD), whole normal liver dose (WNLD) and lung dose (LD) - were calculated for the administered activities using a dedicated partition based dosimetry software. To explore the potential for TAD escalation while maintaining safe non-tumoral liver and lung dose limits, we retrospectively estimated the activities that could have been administered in the same cohort using partition model. For bilobar treatments, WNLD limit were 40 Gy for patients with good liver function and 30 Gy for impaired function. In unilobar treatments, safe NPLD limits were set at 70 Gy and 50 Gy, respectively. For patients with limited hepatic reserve (<35%), bilobar dose limits were followed. We compared calculated activities and dosimetric outcomes between BSA and partition models. TAD of ≥100 Gy was considered the minimum effective mean dose. ***Results:*** 17 patients with a total of 32 tumors were included, with 13 undergoing unilobar and 4 bilobar treatment. In multifocal cases only the largest tumor per patient was analysed. Median tumor size was 10 cm (range 4-15 cm). Activity reduction of 20-30% was applied in 10 patients per manufacturer's Instructions for Use, including 3 due to lung shunting (median 2%, range 0-19%). BSA-based activities had a median of 1,1 GBq (range 0,8-2 GBq), resulting in a median TAD of 68 Gy (range 44-181 Gy). Partition model activities had a median of 2 GBq (range 0,8-3 GBq), achieving a median TAD of 121 Gy (range 43-456 Gy). Statistical analysis showed significantly higher activity ($p < 0.0001$, $d = 1.31$) and TAD ($p < 0.001$, $r = 0.92$) using the partition model. A TAD of ≥100 Gy was achieved in 4 patients using BSA, versus 13 patients with the partition model. ***Conclusion:*** The partition dosimetry model would have enabled safe tumor dose escalation while respecting non-tumoral liver and lung dose thresholds, highlighting its advantage over BSA given the well established dose-effect relationship in TARE.

EP-0836

Initial experience with ^{32}P microparticles in the treatment of advanced pancreatic cancer

D. Sánchez-Artuñedo[1], *I. Navales-Mateu*[2], *M. Sebastián-Segura*[1], *R. Bellviure-Meiro*[2], *J. Suils-Ramón*[2], *M. Beltran-Vilagrasa*[1], *C. Gamez-Cenzano*[2];
[1]*Servei de Física i Protecció Radiològica. Hospital Universitari Vall d'Hebron, Barcelona, SPAIN,* [2]*Servei de Medicina Nuclear. Hospital Universitari Vall d'Hebron, Barcelona, SPAIN.*

Aim/Introduction: Phosphorus-32 (^{32}P) microparticles are a medical device used to treat advanced pancreatic cancer in combination with gemcitabine-based chemotherapy. The prescribed activity is based on tumor volume, aiming to deliver a mean absorbed dose of 100 Gy to the lesion. Administration is performed under endoscopic ultrasound guidance. Post-treatment, a Bremsstrahlung SPECT/CT is acquired to verify accurate delivery. At our institution, SPECT imaging is performed using a CZT gamma camera (StarGuide, GE Healthcare), which provides higher sensitivity compared to conventional Anger cameras, potentially improving the detectability of the administered activity. ***Materials and Methods:*** After patient sedation, the

endoscope is introduced into the stomach, and an ultrasound-guided puncture is performed on the lesion. The nuclear medicine physician administers the microparticles, followed by a 1.5 ml flush of physiological saline solution to clear the needle lumen and ensure full activity delivered to the lesion. A second flush is then performed into the stomach. Once the procedure is completed, contamination tests are performed on staff and surfaces, and the ambient dose equivalent in contact with the patient is measured. Following recovery, a 30-minute/bed SPECT/CT scan is acquired with a 75 keV (±30%) emission window and reconstructed with Q.clear (20 iterations, 10 subsets) with attenuation correction and resolution recovery correction. ***Results:*** Seven patients have been treated since 2023, including one who underwent re-treatment to complement the initial ^{32}P administration. The mean administered activity was 9.8 MBq (range: 1.85-14.06 MBq). In two of eight treatments, no activity was detected on SPECT/CT. In one case, 0.5 MBq (25% of the prescribed dose) remained in the syringe. Given the low activity prescribed due to the small tumor volume, the effective delivered dose was likely below the SPECT detection threshold. Gastrointestinal migration of microparticles occurred in two treatments, both in patients with metallic pancreatic stents. One was partial, with some activity visible in the lesion; in the other, no pancreatic activity was detected, and the patient is currently scheduled for re-treatment. Surface contamination was detected in two procedures, while personal contamination occurred only during the first procedure. The patient's ambient equivalent dose rate remained indistinguishable from background radiation. The treatment was generally well tolerated; in one case, the patient experienced post-recovery emesis, with the gastric contents being radioactively contaminated. ***Conclusion:*** The treatment was well tolerated, with only one patient experiencing nausea related to sedation. Dose calculation software could improve the verification of treatment delivery, especially in re-treatments.

EP-0838

MAA-Based Dosimetry for Predicting Tumor Response and Survival Post-TARE in Liver Metastasis Patients

F. Meisner[1], *E. Can*[2], *S. Wirtz*[3], *P. T. Meyer*[1], *C. Goetz*[1];
[1]*1Department of Nuclear Medicine, Medical Center of the University of Freiburg, Faculty of Medicine, University of Freiburg, Freiburg, GERMANY,* [2]*Department of diagnostic and interventional radiology Medical Center of the University of Freiburg, Faculty of Medicine, University of Freiburg, Freiburg, GERMANY,* [3]*Clinical Trials Unit, Medical Center of the University of Freiburg, Faculty of Medicine, University of Freiburg, Freiburg, GERMANY.*

Aim/Introduction: Transarterial radioembolization (TARE) with Y90-loaded microspheres is an effective treatment for unresectable liver metastases. MAA-based dosimetry may optimize therapy planning by estimating absorbed doses, helping to maximize tumor doses while sparing healthy liver tissue. This study aims to correlate higher tumor doses with improved response and overall survival (OS) in patients with liver metastases. ***Materials and Methods:*** A retrospective analysis was conducted on 145 TARE therapies in patients (median age 64) with liver metastases (Neuroendocrine tumor, n=40; Colorectal cancer, n=38; Melanoma, n=10; Cholangiocarcinoma, n=10; Prostate cancer, n=9; Other primaries, n=38) using SIR-Spheres (Sirtex Medical Europe GmbH, Bonn, Germany). The partition model was used to estimate Y90 doses pre-therapy using Tc99m-MAA SPECT/CT data and MIM Software (MIM 7.3.4, MIM Software Inc., Cleveland, OH). Post-therapeutic dosimetric imaging determined real mean absorbed doses (Dmean) for tumors and healthy liver tissue. Tumor response was evaluated 2-4 months post-TARE using RECIST1.1 criteria, categorizing patients as responders (CR, PR) or non-responders (SD, PD). To evaluate the predictive capabilities of MAA dosimetry, we performed a ROC analysis to define an optimal Dmean cutoff value pre-therapy, and OS was compared using the Kaplan-Meier estimator. ***Results:*** Responders (15%) had a higher Dmean tumor dose (177.2 Gy) compared to non-responders (139.6 Gy). Responders showed significantly longer OS (34.6 months) than non-responders (13.5 months, p=0.0175). Regarding the predictive value of MAA-dosimetry, a Dmean cutoff value of 122.8 Gy was identified and proposed as a predictor for therapy response (sensitivity 0.96, specificity 0.39). However, sorting patients by this threshold did not show a significant OS difference (p=0.173). ***Conclusion:*** Higher tumor absorbed doses are associated with improved treatment response and prolonged overall survival (OS) in liver metastasis patients post-TARE. However, the proposed threshold based on MAA-dosimetric estimations did not significantly differentiate OS in our study groups. Nonetheless, pretreatment dosimetry should be routinely employed for personalized treatment planning to optimize tumor irradiation and minimize liver toxicity. Further research is essential to validate these findings and determine tumor-specific cutoff values for various extrahepatic cancers with liver metastases.

EP-0839

Therapeutic Outcomes of Radiosynoviorthesis: A Retrospective Analysis from a Tertiary Care Center in India

P. Baberwal*, G. B. Priyanka, Y. Khandelwal, B. Jain, S. Shamim;*
All India Institute of Medical Sciences, Delhi, INDIA.

Aim/Introduction: To retrospectively analyse the outcomes and treatment responses of patients who have undergone radiosynoviorthesis for various clinical conditions with [^{188}Re]Re-tin colloid or [^{177}Lu]Lu-tin colloid at a tertiary care center in India. ***Materials and Methods:*** A retrospective analysis was conducted on patients who underwent radiosynovectomy from 2017 to 2025 at Department of Nuclear Medicine, All India Institute of Medical Sciences. All patients were assessed for pain (visual analogue scale), swelling, tenderness, range of mobility, analgesic usage and imaging findings ([^{99m}Tc]Tc-MDP blood pool imaging, X-ray) and different scores were assigned to them. RSO was done using either 577 MBq (481 to 925 MBq) of [^{188}Re]Re-tin colloid or [^{177}Lu]Lu-tin colloid. Underlying etiology, joints treated, number of treatment cycles, radiopharmaceutical dose, baseline and follow-up clinical parameters, imaging findings, and response to therapy were collected and analysed. Follow-up data at multiple intervals at 3, 6 and 12 months were used to assess symptom progression and therapeutic efficacy and were defined as responders or non-responders based on the change in clinical scores. ***Results:*** A total of 52 patients were included, with radiosynoviorthesis of 59 knee joints in total. 14 patients (17 joints) were treated with [^{177}Lu]Lu-tin colloid (mean activity of 572 MBq (518 to 1369 MBq)) and 38 patients with [^{188}Re]Re-tin colloid (mean activity of 577 MBq (481 to 925 MBq)). The most common indications were rheumatoid arthritis, pigmented villonodular synovitis and hemophilic arthropathy. There were 93.23% of responders at 3 month follow up and 6.77% non-responders (2 with [^{177}Lu]Lu-tin colloid and 2 with [^{188}Re]Re-tin colloid). There is a statistically significant reduction in clinical parameters at 3-, 6- and 12-month follow-up in responder group (p value<0.0001). Patients benefited out of wide range of activity of [^{188}Re]Re-tin colloid and [^{177}Lu]Lu-tin colloid. ***Conclusion:*** Radiosynoviorthesis is a safe, well-tolerated, and effective procedure in the Indian context, particularly for large joint synovitis in rheumatoid and non-specific inflammatory joint disorders.

EP-0840

Elevated Baseline C-Reactive Protein Is Associated with Treatment Failure and Shorter Survival After Radioembolization with Yttrium-90 Glass Microspheres in Hepatocellular Carcinoma: Validation of LI-RADS R-TRA v2024

E. Kaya[1], *B. Akkas*[1], *T. Güzelbey*[2], *C. Erdim*[2], *M. Arslan*[2], *C. Şin*[1], *H. B. Kapucu*[1], *M. Kaya*[1];
[1]*Basaksehir Cam and Sakura City Hospital, Department of Nuclear Medicine, Istanbul, TÜRKIYE,* [2]*Basaksehir Cam and Sakura City Hospital, Department of Radiology, Istanbul, TÜRKIYE.*

Aim/Introduction: To investigate the prognostic significance of baseline C-Reactive Protein (CRP) levels and evaluate treatment response using LI-RADS Radiation Treatment Response Algorithm

(R-TRA v2024) in hepatocellular carcinoma (HCC) patients undergoing Yttrium-90 glass radioembolization (TARE). ***Materials and Methods:*** Forty-two patients with HCC who underwent TARE were included retrospectively. Clinical records, laboratory tests, and dosimetry parameters were evaluated for association with treatment response and overall survival (OS). Tumor response was assessed on 6th month by MRI, patients were classified as controlled disease (LR-TR non-viable and non-progressing) and progressive disease (LR-TR viable) groups. Logistic regression was used to identify predictors of progression, survival outcomes were analyzed using Cox regression models. ***Results:*** In this retrospective analysis, 28 patients (67%) received ≥400 Gy tumor absorbed dose (TAD; range, 150-1000 Gy; median:475 Gy). Baseline CRP>11 mg/L was the only independent predictor of treatment failure (OR=54.7, p=0.005). Subgroup analysis of patients receiving TAD ≥400 Gy confirmed that high CRP remained strongly linked to treatment failure (p=0.001). Independent predictors of shorter OS were; CRP (HR=3.92, p=0.035), TAD <400 Gy (HR=3.95, p=0.014), MELD >6 (HR=5.13, p=0.006), and BCLC-C (HR=3.96, p=0.029). Patients with controlled disease (69%, n=29), the median OS was significantly longer than patients with progressive disease (n=13, 31%) (30 months vs. 6 months, p<0.001). ***Conclusion:*** In HCC patients undergoing TARE, elevated baseline CRP level predicts shorter OS and increased risk of treatment failure despite high TAD. LI-RADS R-TRA v2024 criteria demonstrated strong prognostic value for predicting OS in patients with HCC.

EP-0841

Rethinking Planning: MAA Outperforms CBCT in Predicting Final Dose in TARE

S. Salcedo Cortes[1], *L. Ramos*[2], *J. Orcajo Rincon*[1], *L. Reguera Berenguer*[1], *J. Ardila Mantilla*[1], *E. Ardila Manjarez*[1], *A. Mari Hualde*[1], *I. Gómez Fernández*[1], *V. Castillo Morales*[1], *J. Guzmán Cruz*[1], *S. Álvarez Lara*[1], *G. Mera Ovalle*[1], *J. Alonso Farto*[1];
[1]*Hospital General Universitario Gregorio Marañón, Madrid, SPAIN,* [2]*Hospital Universitario de Canarias, Canarias, SPAIN.*

Aim/Introduction: Hepatic radioembolization with Yttrium-90 microspheres is an effective locoregional technique for treating primary and metastatic liver tumors. Dosimetric precision is crucial to maximize therapeutic efficacy, particularly in terms of absorbed tumor dose. This retrospective study evaluates the factors influencing the final absorbed dose in both the angiosome and the tumor, comparing different volumetric estimation methods alongside clinical and procedural variables. ***Materials and Methods:*** Twenty radioembolization procedures were analyzed. Variables collected included tumor and liver volumes estimated by macroaggregated albumin (MAA), cone-beam CT (CBCT), and the final treated volume measured by 90Y PET/CT (Vol_Tto). Additional variables were time between planning and treatment, post-treatment residual activity, T/N ratio, and whether the same radiologist performed both planning and treatment. Correlations and linear regression models were used to identify predictors of the final absorbed dose in the angiosome and tumor. ***Results:*** The actual treated volume (Vol_Tto) was the main determinant of absorbed dose, showing negative correlations with both angiosome (r = -0.41) and tumor doses (r = -0.45). In a reduced linear regression model, Vol_Tto showed a near-significant trend in predicting tumor dose (p = 0.057). The difference between the volume planned by CBCT and the treated volume (relative volume delta) negatively correlated with the angiosome dose (r = -0.49), suggesting that underestimation of the final volume leads to higher absorbed doses, and vice versa. The T/N ratio (Ratio_Lesion) showed a positive correlation with tumor dose (r = +0.25), though it did not reach statistical significance in multivariable models. Time between the MAA study and treatment, as well as residual unadministered activity, had weak correlations with the final absorbed dose. When planning and treatment were performed by different radiologists, greater discrepancies were observed between the estimated and treated volumes, which in turn impacted tumor dose variability—suggesting an indirect effect on dosimetric consistency. ***Conclusion:*** The final angiosome volume and the tumor-to-liver ratio are key factors influencing tumor absorbed dose. The volume estimated by MAA may better reflect the actually treated volume and therefore be more useful than CBCT in determining optimal activity. Operator variability should also be considered for its indirect effect on dosimetric consistency.

EP-0842

Single-Center Experience Comparing Glass and Resin Microspheres in Lobar Y-90 SIRT for Early- to Intermediate-Stage Hepatocellular Carcinoma

X. Zheng*, H. Xi, J. v. Sluis, M. W. Nijkamp, G. C. Bloemsma, M. Kater, S. J. Ruiter, W. Noordzij;*
University Medical Center Groningen, Groningen, NETHERLANDS.

Aim/Introduction: Selective internal radiation therapy (SIRT) with yttrium-90 (Y-90) microspheres is an established locoregional treatment for early-to intermediate-stage hepatocellular carcinoma (HCC). While both resin and glass microspheres are widely used, their comparative safety and efficacy in lobar infusion remain undecided. This single-center retrospective study aimed to evaluate the safety and outcome of resin versus glass microspheres in HCC patients undergoing lobar Y-90 SIRT. ***Materials and Methods:*** Thirty-seven patients (glass: n = 15; resin: n = 22) treated with lobar Y-90 SIRT between 2016 and 2023 were retrospectively reviewed and analyzed. Safety outcomes included short to long-term adverse events (AEs) graded by CTCAE v5.0 and laboratory changes at 4-month follow-up. Efficacy endpoints included progression-free survival (PFS) and overall survival (OS). Univariate Cox proportional hazards regression identified survival predictors, while Fine-Gray regression assessed the impact of treatment modality (resin vs. glass) on OS, considering post-SIRT treatments as competing risks. ***Results:*** Baseline characteristics were comparable except for age (glass: 64 ± 6.9 vs. resin: 69 ± 7.1 years; P = 0.036); while age was not a predictor of PFS or OS in univariate analysis (all P > 0.05). Doses to tumour and non-tumour liver were comparable between groups: 260 Gy (72-366) vs. 173 Gy (119-260) and 41 Gy (29-50) vs. 28 Gy (20-51), respectively (all P > 0.05). Resin microspheres were associated with significantly longer PFS (median: 9.3 vs. 6.4 months, P = 0.039) and OS (median: 16.4 vs. 12 months, P = 0.035). Univariate analysis identified resin microspheres as independent predictors of improved PFS and OS, whereas higher BCLC stage, multifocal tumours, and tumour burden ≥25% were associated with worse survival (all P < 0.05). Fine-Gray regression further confirmed the association between resin microspheres and improved OS (SHR = 0.35, P = 0.011). Subgroup analysis showed that resin microspheres provided significantly better survival than glass microspheres in patients with tumours ≥5 cm. Safety profiles were comparable between the two groups, with no significant differences in AEs or laboratory toxicity at 4-month follow-up. ***Conclusion:*** Lobar resin-based Y-90 SIRT was associated with improved survival compared to glass-based spheres in early-intermediate HCC, without increasing toxicity. These findings warrant further validation in prospective studies.

EP-0843

Does Aberrant Tumor Vascularization Pose an Obstacle to Radioembolization?

S. Omay[1,2], *B. Esen Akkaş*[1,2], *M. Arslan*[1,2];
[1]*Basaksehir Çam ve Sakura Sehir Hastanesi, Istanbul, TÜRKIYE,* [2]*University of Health Sciences Basaksehir Cam and Sakura City Hospital, Department of Nuclear Medicine, Istanbul, TÜRKIYE.*

Aim/Introduction: Yttrium-90 (Y-90) microsphere radioembolization (RE) therapy is performed via hepatic

arterial infusion of Y-90-loaded microspheres through the artery supplying the tumor. The hepatic artery (HA) typically originates from the celiac artery (CA) or its most common variant, the superior mesenteric artery (SMA). However, aberrant vascularization may occur in liver tumors, potentially leading to extrahepatic perfusion that could pose challenges for RE. This study aims to present cases of intrahepatic tumors with aberrant vascularization in which patient-specific vascular access strategies enabled successful treatment, along with follow-up outcomes. ***Materials and Methods:*** Angiographic images of 221 patients who underwent hepatic RE at our clinic between January 2022 and December 2024 were retrospectively reviewed. The clinical courses of four patients who had vascular perfusion sources other than the CA or SMA and who underwent successful treatment were evaluated. Side effect profiles and operational challenges encountered were analyzed. ***Results:*** Four lesions were identified with vascular feeders other than the HA. The treated tumor sizes ranged from 4.5 to 11 cm. Pre-treatment angiography revealed tumor perfusion from the right phrenic artery in one patient, both right and left phrenic arteries in another, the left renal artery in a third, and the left gastric artery in the fourth. All treatments were performed using divided doses of Y-90 resin microspheres. Tumor absorbed doses ranged between 200 and 550 Gy. Post-RE Y-90 PET/CT imaging showed no extrahepatic microsphere accumulation.During follow-up, three patients showed response to treatment, while one experienced progression. No complications were observed during follow-up. ***Conclusion:*** In tumors with aberrant vascularization, some clinicians convert the procedure to transarterial chemoembolization (TACE) or abandon RE due to potential complications. However, limited case studies report successful application in selected patients with adrenal gland masses and lung carcinomas. Liver lesions may be supplied by arteries beyond foregut-derived vessels depending on their location. Failure to detect and utilize these feeding arteries may lead to inadequate treatment and poor tumor response. Planning RE based on patient-specific vascular variations may clearly enhance treatment success.In selected cases where extrahepatic leakage can be prevented, aberrant vascularization can be safely used for RE.Even though a tumor may be intrahepatic in location, it may develop aberrant vascularization and be supplied by multiple arteries outside the HA. We believe that in selected cases, with prevention of extrahepatic leakage, RE can be successfully performed using aberrant vascular feeders such as phrenic and renal arteries.

EP-0844

A Novel Prognostic Model for Colorectal Cancer Patients Treated with Y-90: The CRP Kinetics Approach

A. Dere, *E. M. Kaya, C. Sin, B. E. Akkas, M. Kaya;*
University of Health Sciences, Basaksehir Cam and Sakura City Hospital,Department of Nuclear Medicine, Istanbul, TÜRKIYE.

Aim/Introduction: The Creactive protein (CRP) kinetics, which refers to the trajectory of CRP levels in the early phase, is being investigated for its potential to predict treatment response and survival in various malignancies.Our aim is to determine whether early CRP dynamics predict progressionfree survival (PFS) and overall survival (OS) after yttrium90 (Y90) microsphere radioembolisation (RE) in patients with colorectal cancer liver metastases (CLM). ***Materials and Methods:*** In this single-centre retrospective cohort, 30 consecutive CLM patients (mean ± SD age, 58 ± 10 years) treated with resin (n = 10) or glass (n = 20) microspheres between 2022 and 2024 were evaluated.Serum CRP levels were obtained immediately pre-treatment and at 1-3 months post-RE. Clinical and laboratory parameters, tumour-absorbed dose(TAD) and the presence of liver metastasis at diagnosis were also recorded at these time points.Patients were categorised as CRP responders or CRP non-responders based on the change in CRP levels.Survival distributions were estimated using the Kaplan-Meier method and compared with the log-rank test.Prognostic factors were identified using Cox proportional-hazards regression analysis. ***Results:*** Baseline serum CRP levels ranged from 0.8 to 89 mg/L, with a median (IQR) of 7.5 (3.7-17.2) mg/L. According to CRP kinetics, 23 patients were classified as responders and 7 as non-responders. The median follow-up was 15 months. Six of the seven non-responders (85%) died, compared to five of 23 responders (21%).Ten patients received resin microspheres (mean TAD: 350 Gy), and twenty received glass microspheres (mean TAD: 525 Gy). Univariate analysis showed that tumor-absorbed dose, hemoglobin, platelet count, neutrophil/platelet ratio, lymphocyte/platelet ratio, CEA, ALBI score, INR, and baseline CRP were not predictive of OS or PFS. Only early CRP kinetics emerged as a strong independent prognostic factor for OS. Responders had significantly longer OS than non-responders (25 vs. 9 months; HR: 5.4; 95% CI: 1.6-18.2; p = 0.005). Additionally, liver metastasis at diagnosis was associated with poorer PFS (8 vs. 2 months; HR: 3.63; 95% CI: 1.02-12.9; p = 0.046). ***Conclusion:*** Early CRP kinetics provides a simple, noninvasive biomarker that independently stratifies overall survival following Y90 RE in CLM, outperforming conventional clinical and dosimetric parameters. Identification of CRP nonresponders may facilitate timely intensification of systemic therapy and closer postprocedural surveillance.

EP-0845

Dose increase in perfused volumes in selective internal radiation therapy with microspheres labeled with holmium-166

J. Deportos, *S. Lafuente-Carrasco, M. Salcedo-Pujantell, N. Canchumanya-Huatuco, M. Boronat De Ferrater, M. Solà, V. Vallejos, S. Ruiz-Llama, A. Caresia Aroztegui, G. Moragas;*
Hospital Universitari Germans Trias i Pujol, Badalona, SPAIN.

Aim/Introduction: To assess the increase in absorbed doses of holmium-166 in the targeted perfused volume in patients with primary or secondary liver tumors over a period of six years. ***Materials and Methods:*** Between December 2018 and December 2024, 59 selective internal radiation therapy procedures were performed using holmium-166 microspheres in patients with primary (hepatocellular carcinoma, cholangiocarcinoma, adenoma) or secondary liver tumors. All patients underwent a prior planning/simulation study using albumin macroaggregates labeled with technetium-99 or microspheres labeled with holmium-166. Following the administration of the treatment with holmium-166 microspheres, all patients underwent planar scintigraphy and thoracoabdominal SPECT/CT imaging, followed by dosimetry evaluation using specialized software. Patients were grouped as follows: Patients with hepatocellular carcinoma treated between 2018 and 2022. Patients with hepatocellular carcinoma treated between 2023 and 2024. Patients with cholangiocarcinoma treated between 2018 and 2022. Patients with cholangiocarcinoma treated between 2023 and 2024. ***Results:*** 12 patients with hepatocellular carcinoma treated between 2018 and 2022: mean absorbed dose in the perfused volume of 157 Gy (range: 54-311 Gy). 17 patients with hepatocellular carcinoma treated between 2023 and 2024: mean absorbed dose in the perfused volume of 264 Gy (range: 43-740 Gy). This represents a 68% increase in the mean absorbed dose compared to the 2018-2022 period. 11 patients with cholangiocarcinoma treated between 2018 and 2022: mean absorbed dose in the perfused volume of 108 Gy (range: 52-158 Gy). 11 patients with cholangiocarcinoma treated between 2023 and 2024: mean absorbed dose in the perfused volume of 159 Gy (range: 82-246 Gy). This represents a 47% increase in the mean absorbed dose compared to the 2018-2022 period. Of the 59 treatments performed, only one patient experienced significant adverse side effects, presenting with radiation pneumonitis.

Conclusion: In recent years, we have increased the absorbed doses in the hepatic perfused volume to enhance tumor response, with minimal observed side effects.

EP-0846

Voxel-by-voxel multicompartment dosimetric model in predicting the response of hepatocellular carcinoma to radioembolization with 90-yttrium spheres

J. Villa-Palacios, *E. Triviño-Ibáñez, A. Piñeiro-Donis, L. Cagua Ruiz, E. Domínguez-Polanco, J. Ciampi-Dopazzo, A. Rodríguez-Fernández;*
Hospital Universitario Virgen de las Nieves, Granada, SPAIN.

Aim/Introduction: To evaluate absorbed dose parameters for predicting tumor response and survival in HCC treated with TARE. ***Materials and Methods:*** This was an observational, longitudinal, and prospective study that included patients with HCC treated with TARE via radical segmentectomy between January 2022 and September 2023. Dosimetry was calculated using the multicompartment model, obtaining the minimum absorbed dose at 50% (D50), 70% (D70), and 90% (D90) of the tumor volume, extracted from the standard dose-volume histogram (DVH) (SimplicityTM software, Mirada Medical Ltd, Oxford, UK). Therapeutic response was assessed according to RECIST 1.1 criteria by calculating complete response (CR), partial response (PR), stabilization (SP), progression (PR), objective response (ORR), and disease control (DCR) rates. Overall survival (OS) and progression-free survival (PFS) outcomes were recorded. ***Results:*** Twenty-five patients with 33 TAREs were included (age: 69.76±8.83 years; 64 men), BCLC A (36%), B (56%), and C (8%). The mean administered activity was 1.85±1.25 GBq, the mean perfused volume was 396.16±329.20 cm3, and the mean tumor absorbed dose was 520.51±655.72 Gy. The CR and ORR were 36.4% and 75.8%, respectively. D50 and D70 dosimetry parameters were significantly associated with ORR (p=0.011 and p=0.031, respectively) and CR (p=0.012 and p=0.036, respectively). The ROC curve showed an AUC of 0.845 (95% CI 0.651-1.039) for D50, with 350 being the cutoff point with the best sensitivity/specificity ratio for ORR. The median OS was 15.5 months and PFS was 32.7 months. PFS was significantly associated with the absorbed dose at D50 (HR: 0.99, p = 0.037). ***Conclusion:*** Radiation segmentectomy is an effective treatment in patients with HCC. Tumor dosimetry is associated with response and survival.

EP-0847

Comparison of Yttrium-90 Resin and Glass microsphere Radioembolization Dosimetry and Correlation with Treatment efficacy in Hepatocellular Carcinoma

N. Too[1], *S. Koo*[2], *P. K. H. Chow*[1,2,3], *F. N. N. Moe*[3], *A. K. T. Tong*[1,2], *K. S. H. Loke*[1,2];
[1]*Duke-National University of Singapore Medical School, Singapore, SINGAPORE,* [2]*Singapore General Hospital, Singapore, SINGAPORE,* [3]*National Cancer Centre Singapore, Program in Translational and Clinical Liver Cancer Research, Singapore, SINGAPORE.*

Aim/Introduction: Hepatocellular carcinoma (HCC) is a significant disease with high morbidity and mortality, being one of the top causes of death by cancer in Singapore. The management of HCC is stage-dependent: Early-stage: Surgical resection or liver transplantation (for eligible patients within Milan criteria) offers curative potential. Intermediate-stage: Locoregional therapies dominate, with transarterial chemoembolization (TACE) as first-line. Yttrium-90 radioembolization (Y90 TARE) are alternatives for select cases. Advanced-stage: Systemic and immunotherapy therapies (e.g., atezolizumab/bevacizumab) are standard. While Y90 TARE is established for intermediate/advanced HCC, differences between glass and resin microspheres remain understudied in Asian populations. This study aims to compares their efficacy in a Singaporean cohort. ***Materials and Methods:*** This study is a single-centre retrospective cohort analysis that enrolled a total of 269 patients who underwent Y-90 TARE between 2020 and 2023 at National Cancer Centre Singapore (NCCS) and Singapore General Hospital (SGH).Outcome measures of this study as assessed by RECIST1.1 criteria: Progression-free survival (PFS), Overall survival (OS), Time to progression (TTP), Time to response (TTR), Duration of response, Best overall response rate (BORR). Statistical test included Kaplan-Meier, Mann-Whitney U, and Fisher's exact tests. ***Results:*** Baseline characteristics: No significant difference between groups. The cohort is heterogeneous consisting of unilobar and bilobar tumors, and some (Glass: 11.8%, Resin: 16.8%) having received additional therapies. Dosimetry: Higher mean tumor dose (TD) with glass compared to resin (406±150 Gy vs. 283±174 Gy; P=0.0005). Outcomes: No significant difference across outcome measures: Median OS (Glass: 19mo; Resin: 17mo, P=0.83), PFS (Glass: 15mo; Resin: 8mo, P=0.3), TTR (Glass: 7mo Resin: 5mo, P=0.4), BORR (Glass: 35.3%; Resin: 31.1%, P=0.9), Kaplan Meier: No significant difference (P=0.31) in the overall survival although there is greater hazard ratio for the resin relative to glass. The lack of difference observed between the two groups in terms of outcomes corroborates with findings of other similar studies [1, 2]. ***Conclusion:*** Glass and resin Y90 demonstrate similar outcomes for HCC. The impact of the significantly different delivered TDs on tumor response outcomes merits further investigation, with larger studies. Including other factors that other studies shown may influence outcomes: Particle size/number differences (Glass: fewer/larger; Resin: more/smaller) may influence vascular penetration. Glass showed potential advantages in portal vein thrombosis cases. Delivery techniques including microsphere injection velocity. ***References:*** [1] Van Der Gucht et al., J Nucl Med 58:1334-1340, 2017. [2] Kim et al., CardioVasc Interv Radiol 47:1210-1221, 2024.

EP-0848

Comparison of ^{99m}Tc-MAA SPECT/CT and ^{90}Y LAFOV PET/CT-based dosimetry for patients with colorectal liver metastases

C. Schneider, *L. W. van Golen, S. M. Jansen, A. J. A. T. Braat, R. G. H. Beets-Tan, E. G. Klompenhouwer, B. J. de Wit-van der Veen;*
Netherlands Cancer Institute, Amsterdam, NETHERLANDS.

Aim/Introduction: Long-axial field of view (LAFOV) PET-scanners enable high sensitivity and wide coverage, resulting in more precise post-treatment imaging after Yttrium-90 (^{90}Y) radioembolization. The aim of this study was to compare dosimetry on pre-treatment ^{99m}Tc-macro-aggregated albumin (^{99m}Tc-MAA) SPECT/CT simulation versus ^{90}Y LAFOV PET/CT, in colorectal liver metastases (CRLM) treated with ^{90}Y resin microspheres. ***Materials and Methods:*** Retrospective cohort of CRLM patients treated in 2024 in the Netherlands Cancer Institute, with ^{90}Y resin microspheres, who underwent post-treatment ^{90}Y LAFOV PET/CT, were included. Tumors, total liver and non-tumoral liver were segmented on pre-treatment contrast-enhanced CT (MIM version 7.3.6). ^{99m}Tc-MAA SPECT/CT and ^{90}Y PET/CT were co-registered using rigid alignment; accuracy of all segmentations were visually evaluated and when needed corrected manually. The SPECT/CT-based dosimetry was scaled to administered ^{90}Y activity. Average absorbed dose (Dmean), D50 and D70 from dose-volume histograms were extracted for tumor, liver and non-tumoral liver compartments. Agreement of the dose metrics were evaluated by Pearson's correlation and Bland-Altman analysis. ***Results:*** Seven patients with in total 46 tumors were included with a median of 7 tumors per patient. The median age was 66 years. A median of 2 injection position was used. Most patients (6/7, 86%) underwent bilobar treatment, while one patient (14%) received lobar treatment. The median total administered activity was 1.81 GBq. For tumors a fair correlation was found for Dmean,

D50 and D70 (ρ = 0.54, ρ=0.57 and ρ=0.55), with small biases, but large limits of agreement in Bland-Altman analyses for all dose metrics. For liver and non-tumoral liver compartments, a strong correlation was found for D70 (ρ = 0.85 and ρ=0.89), with small bias and narrow limits of agreement in Bland-Altman analyses for all dose metrics. ***Conclusion:*** LAFOV PET/CT dose volume metrics demonstrated superior pre- and post-treatment dosimetry correlation than average absorbed dose. Tumor dose metrics showed only a fair correlation and wide limits of agreement, in line with literature. D70 showed the best correlation for liver and non-tumoral liver, conforming prior literature. These findings support the agreement of pre-treatment dosimetry and post-treatment LAFOV ^{90}Y resin microsphere dosimetry for liver and non-tumoral liver compartment in CRLM.

EP-0849

Assesment of overall survival in patients with liver tumors undergoing yttrium-90 and holmium-166 radioembolization

L. Casas Fernández*, M. Romero Otero, A. Palazón Palazón, P. Soto Muñoz, T. Peris Conejero;*
Unidad de Radiofarmacia Hospital Clí Universitario de Valencia, Valencia, SPAIN.

Aim/Introduction: Transarterial hepatic radioembolization (TARE) with beta-emitting isotopes such as yttrium-90 (^{90}Y) and holmium-166 (^{166}Ho) is used in the treatment of primary and metastatic liver tumors. Differences in their physical properties and intrahepatic distribution may influence clinical outcomes. This study aims to compare overall survival (OS) at 6 and 12 months in patients treated with ^{90}Y-labeled resin and glass microspheres (^{90}Y-RMs and ^{90}Y-GMs), and with ^{166}Ho-labeled polylactic acid microspheres (^{166}Ho-PLLAMs). ***Materials and Methods:*** A total of 155 patients who underwent TARE between February 2016 and April 2024 were included: 108 treated with ^{90}Y-RMs, 33 with ^{90}Y-GMs, and 14 with ^{166}Ho-PLLAMs. Demographic characteristics, type of liver tumor, history of alcohol use, HCV and HBV infection, mean administered activity (GBq), and number of TARE procedures were analyzed. ***Results:*** In the ^{90}Y-RMs group (mean age: 66±10 years), 76% were male and 28% had liver metastases. Risk factors: alcohol use (31%), HCV (24%), alcohol + HCV (8%), HBV (6%). Mean administered activity: 1.83 Gbq. In the ^{90}Y-GMs group (mean age: 69±9 years), 79% were male and 88% had hepatocellular carcinoma. Risk factors: alcohol use (24%), HCV (24%), alcohol + HCV (15%), HBV (12%). Mean administered activity: 1.53 Gbq. In the ^{166}Ho-PLLAMs group (mean age: 73±10 years), 79% were male and 86% had hepatocellular carcinoma. Risk factors: alcohol use (7%), HCV (29%), alcohol + HCV (7%), HBV (14%). Mean administered activity: 4.67 GBq. The 6- and 12-month OS rates were 80% and 62% for ^{90}Y-RMs, 81% and 60% for ^{90}Y-GMs, and 86% and 43% for ^{166}Ho-PLLAMs. In patients treated with ^{90}Y-RMs, 12-month OS was 57%, 82%, and 100% after one, two, and three treatments, respectively. For ^{90}Y-GMs: 60%, 50%, and 100%. For ^{166}Ho-PLLAMs: 42% after one treatment and 50% after two. ***Conclusion:*** Six-month OS was comparable among all three groups. However, at 12 months, OS was lower in patients treated with ^{166}Ho-PLLAMs (42%) compared to ^{90}Y-RMs (62%) and ^{90}Y-GMs (60%). In the ^{90}Y-RMs and ^{166}Ho-PLLAMs groups, a higher number of TARE procedures was associated with increased OS, a trend not observed in the ^{90}Y-GMs group. A larger cohort and extended follow-up are required to confirm these findings.

EP-0850

Survival Outcomes in Transarterial Radioembolization with ^{90}Y-Resin for Hepatic Malignant Tumours

A. Bagán-Trejo*[1], J. J. Martín-Marcuartu[1], J. L. Díaz-Moreno[1], G. Reynés-Llompart[2], D. Rodríguez-Puig[3], S. Maymó-Garrido[3], M. Á. Crespí-Busquets[3], E. Serrano-Alcalá[4], B. Gener-Laquidáin[4], L. Lladó-Garriga[5], E. Ramos-Rubio[5], A. Amador-Navarrete[6], M. R. Rota-Roca[6], M. Cortés-Romera[1];*
[1]Nuclear Medicine-PET (IDI) Department, Hospital Universitari de Bellvitge-IDIBELL, L'Hospitalet de Llobregat, SPAIN, [2]Medical Physics and Radiation Protection Department, Institut Català d'Oncologia, L'Hospitalet de Llobregat, SPAIN, [3]Radiopharmacy Department, Hospital Universitari de Bellvitge-IDIBELL, L'Hospitalet de Llobregat, Spain, [4]Diagnostic Imaging Centre, Vascular Interventional Radiology Section, Radiology Department, Hospital Universitari de Bellvitge, L'Hospitalet de Llobregat, SPAIN, [5]Liver Transplant Unit, General and Digestive Surgery Department, Hospital Universitari de Bellvitge, L'Hospitalet de Llobregat, SPAIN, [6]Gastroenterology Department, Hospital Universitari de Bellvitge-IDIBELL, L'Hospitalet de Llobregat, SPAIN.

Aim/Introduction: Transarterial radioembolization (TARE) is a locoregional treatment modality for patients with inoperable liver lesions, offering both embolic and biological effects. The primary goal of this study was to explore the influence of factors such as the time interval between planning and treatment (TPT), the absorbed dose in the perfused area (PA), and the administered activity (AA) on survival outcomes in patients with malignant liver tumours. ***Materials and Methods:*** Retrospective study involving 31 patients diagnosed with either hepatocellular carcinoma (n=28) or colorectal liver metastases (n=3), all of whom received treatment with TARE. Treatment planning and delivery utilised ^{m99}Tc-macroaggregates (^{m99Tc}-MAA) and ^{90}Y-resin microspheres, respectively. SPECT/CT imaging was performed after treatment planning, followed by PET/CT imaging 24 hours post-treatment. The PA and AA were calculated using two models: the partition model during planning and the voxel-based model post-TARE. The treatment response was evaluated using contrast-enhanced CT scans at least 3 months after spheres administration, classifying patients into complete response (CR), partial response (PR), or progressive disease (PD). Cox regression analysis was used to calculate the Odds Ratios (OR) based on administered activity. ***Results:*** Results were as follows: CR n=13, PR n=19, and PD n=2. The administered activity in the perfused area ranged from 1.25 GBq to 5.52 GBq, with a mean of 3.4 GBq. The OR for AA was 2.2 (p=0.048). The absorbed tumour dose ranged from 210.8 Gy to 659.4 Gy (mean: 435.1 Gy) (p=0.265). Tumour size averaged 66.9 mm (range: 29.09 mm-104.71 mm) (p=0.28). The time interval between planning and treatment was 11.9 days on average (range: 2.55 days-21.25 days), with an OR of 1.1 (p=0.027). ***Conclusion:*** Our findings suggest that the time interval between treatment-planning and treatment-administration, as well as the administered activity in the perfused area, are significant predictors of survival outcomes in patients undergoing TARE for malignant liver tumours. Although the absorbed tumour dose and tumour size did not show a strong correlation with survival, these results emphasize the importance of optimising treatment planning timelines and the delivered activity for improving patient outcomes.

EP-0851

The Role of RAI Treatment Selection and RAI Therapy in Papillary Thyroid Microcarcinoma in the Right Patient

E. Cansu Çay*, B. B. Demirel, G. Uçmak;*
Ankara Dr. Abdurrahman Yurtaslan Oncology Training and Research Hospital, Ankara, TÜRKIYE.

Aim/Introduction: Papillary thyroid microcarcinoma(PTMC) is a subgroup papillary thyroid cancers(PTCs) before the 2022

WHO classification and was defined as a PTC ≤10 mm.PTMCs usually have an excellent prognosis but in some cases may have an aggressive behavior.In our study, we aimed to evaluate patient selection for radioactive iodine(RAI) and factors leading to residual/recurrence during follow-up in patients diagnosed with PTMC. ***Materials and Methods:*** The study retrospectively included 263 patients with PTMC who were treated in our clinic between 1990 and 2025.Patients were divided into two groups as those who received RAI and those who did not.Pathological features, thyroglobulin (Tg)-antithyroglobulin (ATg) values,thyroid scintigraphy and RAI treatments were recorded.The clinical-pathologic and treatment effects on residual/recurrence were evaluated using Chi-square, Mann-Whitney U and T test. ***Results:*** The mean age at diagnosis was 43.2 (±11,5) years (20M, 243F). Considering the clinico-pathologic features, 187 patients received RAI, while 76 patients did not receive RAI. The median follow-up period was 204 (Range:9-420) months. A significant correlation was found between multifocality, lymph metastasis, invasion status and tumor diameter in patients receiving RAI ($p<0.05$) (Table 1).In 3 patients, F-18 FDG PET/CT examination was performed during follow-up due to negative I-131 scan and Tg elevation. It was consistent with lung metastasis.Tumor size >0.5 cm and multifocal character were common features of these patients.Dynamic risk analysis of patients receiving RAI; 93.5% had an excellent response, 4.3% indeterminate response and 2.2% structural-biochemical incomplete response. 4 patients who received RAI had residual/recurrent disease.In 9 patients who did not receive RAI, residual/recurrent disease was considered during follow-up and 8 patients received RAI. While 0.7% of all patients without multifocality had residual/recurrent disease, 6.5% of all patients with multifocality had residual/recurrent disease ($p<0.05$). 1.2% of patients without lymph metastasis and 16.7% of patients with lymph metastasis had residual/recurrent disease ($p<0.05$). The mean tumor diameter was 0.73(±0.16)cm in all patients with residual/recurrent disease. While 242 patients were alive, 21 patients died and no disease-related deaths were recorded. ***Conclusion:*** In line with the data obtained in our study, it was concluded that the current WHO classification supports the importance of RAI treatment in terms of patient management and correct patient selection, the importance of analyzing factors that may lead to residual/recurrence in follow-up, and that prognosis and RAI decision should be determined by factors such as molecular properties and biological indices rather than tumor size.

EP-0852

Thyroglobulin doubling time and prognosis in lung metastases of differentiated thyroid carcinoma

H. Wang, *Y. Wang, R. Tian;*
West China Hospital, Sichuan University, Chengdu, CHINA.

Aim/Introduction: To assess the association of thyroglobulin doubling time (Tg-DT) with prognosis in patients with lung metastases from differentiated thyroid carcinoma (DTC). ***Materials and Methods:*** This study included 122 patients with initial lung metastases who underwent thyroidectomy and radioiodine (RAI) treatment. Outcomes included progression-free survival (PFS), overall survival (OS) and radioiodine refractory (RAIR)-free survival (RRFS). Tg-DT was calculated from at least three thyroglobulin measurements. Survival receiver operating characteristic curves were used to define optimal cutoff values for Tg-DT predicting different outcomes. Uni- and multivariate Cox regression models evaluated the associations of Tg-DT and multiple predictors with outcomes. ***Results:*** The median age was 37.4 years, with 63.1% female. Median follow-up was 96.0 months. In multivariate models, patients with a Tg-DT of ≥-8 months had a greater risk of progression (HR=17.68 [95%CI: 1.68-186.32]) and death (log-rank test: P=0.02), compared to those with a Tg-DT of <-8 months. Patients with a Tg-DT of ≥0 month had a higher risk of RAIR (16.87 [4.96-57.39]) than controls. Among 38 patients with RAIR-related scenarios, those with a Tg-DT of ≥0 month were more likely to lose RAI uptake and show structural progression, whereas patients with a Tg-DT of <0 month were more likely to have no remission despite a cumulative dose of >22.2 GBq. ***Conclusion:*** The Tg-DT is independently associated with risks of progression, death and RAIR-related clinical scenarios in DTC patients with lung metastases, which could be integrated into the dynamic prognostic risk stratification and therapeutic decision-making process for such patients.

EP-0853

Integrating Lenvatinib with High-Dose Radioiodine: A Promising Approach for Advanced well-differentiated thyroid cancer

S. Sharma, *P. Chauhan, M. Ora, P. Pradhan, S. Barai, A. H. Nazar, S. Gambhir;*
Sanjay Gandhi Post Graduate Institute of Medical Sciences, Lucknow, INDIA.

Aim/Introduction: Management of well-differentiated thyroid cancer (WDTC) with systemic metastasis remains challenging, which requires a multidisciplinary approach with multiple high-dose radioiodine (HDRI) therapy being the mainstay. Morbidity and mortality benefits are noted, with sporadic complete response. The main concerns include radioiodine side effects, radioiodine refractoriness, and cumulative dose (>22.2 GBq). Lenvatinib, a tyrosine kinase inhibitor, is the standard of care for radioiodine-refractory disease. However, its role remains unexplored in radioiodine-avid metastatic WDTC. The study aims to evaluate the feasibility and response rate of a combination treatment approach using Lenvatinib and HDRI in metastatic WDTC. ***Materials and Methods:*** The study included eight patients with WDTC with systemic metastasis with or without prior HDRI. The baseline disease burden was measured with imaging (WBRI, PET-CT, or CT) and serum thyroglobulin (Tg). After ruling out any contraindications, Lenvatinib was administered for 3-4 months (10 mg/day), along with thyroxine suppression between two HDRIs. Two doses of HDRI were given after Thyroxin hormone withdrawal. Side effects and treatment response were evaluated. ***Results:*** The mean age of the patients was 52.5 ± 16.02 years. Lung, bone, and brain metastases were noted in 5 (62.5%), 6 (75%) and 1 patient(12.5%) respectively. Five (62.5%) patients had prior HDRI (98.75 ±87.08 mCi). Lenvatinib was well tolerated, with 5 out of 8 patients having grade I toxicities. The baseline, interim (first cycle), and follow-up (after two cycles) Tg values were 61133.66±81347.14 (median 6888, IQR 1274.65, 123092) ng/ml, 7560.5±9010.2 (median 1223.5, IQR 274, 16661.5) ng/mL and 2344.5±4170.7ng/ml(median 293, IQR 4204). One patient showed an initial response (227347à17090 ng/mL) but a rising Tg (72599 ng/mL) level in the second cycle. Tg fall was not associated ($p>0.05$) with age, sex, histopathology, and previous HDRI. Overall, partial response and stable disease were noted in the 6(75%) and 2(25%) patients on imaging. During follow-up (17.1 ± 3.56 months), one patient died of pneumonia unrelated to WDTC. ***Conclusion:*** The synergistic effects of Lenvatinib and HDRI are novel treatment options in bulky radioiodine-avid metastatic WDTC. The treatment regimen was well-tolerated, with manageable mild toxicities of Lenvatinib and no discontinuation. Patients demonstrated excellent partial treatment response on imaging and Tg levels. Due to accentuated treatment benefits, multiple cycles of HDRI and possible side effects could be avoided.

EP-0854

Comparison of patients with differentiated thyroid cancer in a German and an American collective in tertiary treatment centers.

F. Eilsberger[1], *A. C. Prietsch*[1], *A. Pfestroff*[1], *W. Bowl*[1], *A. Ebrahimifard*[1], *S. Bagheri*[1], *B. H. Yousefi*[1], *P. Di Fazio*[1], *M. Luster*[1], *R. M. Tuttle*[2];
[1]*University Hospital Marburg, Marburg, GERMANY,* [2]*Memorial Sloan Kettering Cancer Center, New York, NY, UNITED STATES OF AMERICA.*

Aim/Introduction: A comparison of national guidelines highlights differences in the treatment of differentiated thyroid cancer (DTC), especially concerning radioiodine therapy (RAIT). Differences in baseline conditions may have a notable impact on the further course of the tumor disease, though they have not yet been thoroughly examined. We compared the baseline conditions of an US and a German collective for the first time. ***Materials and Methods:*** We included 168 DTC patients randomly from a single endocrinologist in the Department of Endocrinology of Memorial Sloan Kettering Cancer Center (MSKCC) and 168 DTC patients from the Department of Nuclear Medicine of University Hospital Marburg (UHM) and compared them regarding baseline conditions of cancer treatment like presurgical diagnostics and surgical procedures. ***Results:*** At MSKCC 93% had a biopsy result of Bethesda 5/6 prior surgery. 99,4% of patients received a total thyroidectomy (TT) as initial surgery, in 12% no lymph node was removed. The median thyroglobulin (Tg) value post surgery was 0,2 (0-5,9) ng/ml (excluding patients with: elevated TSH (>5.4 mU/l), M1, positive antibodies and Tg <1 ng/ml). 113/168 MSKCC patients received RAIT with activities between 1.1-11.2 GBq (median 4.23 GBq). In the UHM group 5% had a biopsy. 76% received an initial TT. In 42% patients no lymph node was removed. The median Tg value post surgery was 1,1 (0-81) ng/ml (exclusion as above). All UHM patients received RAIT with activities between 1.9-11.0 GBq (median 3.7 GBq), 13/168 patients underwent more than one cycle. 54% (90/168) UHM patients showed an excellent response to therapy, 34% (57/168) an indeterminate response, 6% (11/168) a biochemical and 6% (10/168) a structural incomplete response. ***Conclusion:*** Our results clearly demonstrate differences between the cohorts. In the German cohort, preoperative diagnostics leaves room for improvement, and more patients with Nx can't be adequately classified in the risk groups postoperatively. Additionally, a higher postoperative Tg likely makes it more challenging to avoid radioiodine therapy. These differences highlight the need to reassess the adaptation of treatment decisions in different countries based on the underlying characteristics.

EP-0855

A Study on the Dynamic Changes of Anti-Thyroid Peroxidase Antibodies Before and After the First ^{131}I Treatment in Patients with Differentiated Thyroid Cancer After Surgery

W. Cao[1], *H. Chen*[2];
[1]*Department of Nuclear Medicine, Union Hospital, Tongji Medical College, Huazhong University of Science and Technology, Wuhan, CHINA,* [2]*Department of Nuclear Medicine, Union Hospital, Tongji Medical College, Huazhong University of Science and Technology, Wuhan, CHINA.*

Aim/Introduction: To investigate the dynamic changes of anti-thyroid peroxidase antibodies (TPOAb) in patients with differentiated thyroid cancer (DTC) before and after their first ^{131}I treatment, assess the clinical significance of these changes, and evaluate their predictive value for treatment response after ^{131}I therapy in DTC patients. ***Materials and Methods:*** A retrospective data collection was conducted for 1,378 DTC patients who underwent their first ^{131}I treatment after thyroid cancer radical surgery in our hospital. A total of 202 patients with abnormal TPOAb levels (≥34 IU/ml) before treatment and within 2 years of follow-up were selected. Analyze the influencing factors of dynamic changes of TPOAb before and after treatment, and assess the impact of TPOAb trends and levels on the treatment response of DTC patients after ^{131}I therapy. ***Results:*** In patients with abnormal TPOAb levels before ^{131}I treatment, those who experienced a transient increase in TPOAb post-treatment differed significantly from those with a sustained decrease in two aspects: the time interval between thyroid surgery and ^{131}I treatment, and the amount of postoperative residual thyroid tissue (both P<0.001). There was no significant difference in efficacy response between patients whose TPOAb normalized post-treatment and those whose levels remained abnormal (P=0.149). Additionally, there was no significant difference in efficacy response among patients with differing trends in TPOAb levels before and after ^{131}I treatment (P=0.740). ***Conclusion:*** Longer waiting times for ^{131}I treatment after thyroid cancer radical surgery and greater amounts of residual thyroid tissue increase the likelihood of transient TPOAb elevation in patients with abnormal levels before treatment. TPOAb elevation is often a manifestation of radioactive thyroiditis. This suggests that, while protecting the parathyroid glands and recurrent laryngeal nerve, minimizing thyroid residue during the radical surgery for DTC patients and administering early ^{131}I treatment postoperatively are effective strategies to reduce the occurrence of residual radioactive thyroiditis after ^{131}I therapy. Higher initial TPOAb levels before ^{131}I treatment correlate with longer durations for TPOAb to normalize post-treatment, but whether TPOAb normalizes does not affect the efficacy of ^{131}I treatment in DTC patients. The dynamic changes of TPOAb before and after treatment do not influence the treatment efficacy for DTC. There is no need to develop specific follow-up treatment plans or adjust levothyroxine dosages for patients with abnormal TPOAb levels before and after ^{131}I treatment.

EP-0857

Evaluation of theTreatmentResponse to RAI Therapy in Papillary Thyroid Cancer Patients with Pulmonary Metastases

A. Akil[1], *A. Kibar*[1], *R. Alsabbagh*[2], *O. E. Şahin*[1], *S. Asa*[1], *R. L. Uslu-Beşli*[1], *M. S. Sağer*[1], *K. Sönmezoğlu*[1], *H. B. Sayman*[1];
[1]*Istanbul University – Cerrahpaşa, Cerrahpaşa Faculty of Medicine, Department of Nuclear Medicine, Istanbul, TÜRKIYE,* [2]*Biruni University, Faculty of Medicine, Istanbul, TÜRKIYE.*

Aim/Introduction: Pulmonary metastases in patients with papillary thyroid carcinoma (PTC) carry a poorer prognosis than localized disease. Prompt identification of predictors of therapeutic response in such instances is essential to optimize treatment strategies as early as possible. Radioactive iodine (RAI) therapy remains the first-line treatment for metastatic differentiated thyroid cancers. In this study, we aimed to evaluate the biochemical and metabolic response to RAI therapy in patients with PTC metastases to the lungs, and to establish if there are any correlations between clinical parameters and the response to treatment. ***Materials and Methods:*** This is a retrospective analysis of 41 patients with histologically confirmed PTC and radiologically or scintigraphically evident pulmonary metastases, who received at least one cycle of RAI therapy in our center between 2018 and 2025. Age, sex, maximum primary tumor size, RAI dose given, and patterns of uptake in post-treatment whole-body scintigraphy were recorded. Stimulated thyroglobulin (Tg) levels pre-RAI therapy and six months post-treatment were compared. In patients for whom PET/CT imaging was available before and after treatment, metabolic response were classified as regressive, stable, or progressive. Both qualitative (visual) and quantitative trends were considered. ***Results:*** Among the 41 patients, 25 were female (61%) and 16 were male (39%). The median age was 63 years (range: 11-92), and the median tumor diameter was 3.0 cm (range: 0.3-8.0 cm). Thirty-three patients had available pre- and post-treatment Tg data.: Tg levels decreased in 21 (64%) and increased in 9 (27%) patients after RAI (6 months). PET/CT evaluations revealed regression in 11 patients, stable disease in 5, and progression in 3 patients. One patient demonstrated persistently high metabolic uptake. Uptake of RAI was observed in metastatic pulmonary lesions in 21 out of 41 patients (51.2%). With heterogeneous response based on initial tumor burden and Tg kinetics. ***Conclusion:*** RAI therapy demonstrated favorable biochemical and metabolic responses in the overwhelming majority of PTC patients who had pulmonary metastases. Reduction in stimulated Tg levels and regression in PET findings

suggests treatment efficacy. However, the presence of progressive disease or persistent Tg elevation in a few patients suggests the heterogeneity of response and the need for alternative or adjunctive forms of treatment. ***References:*** Schlumberger M, et al. Strategies of radioiodine ablation in patients with low-risk thyroid cancer. N Engl J Med. 2012;366(18):1663-1673.

EP-0858

Pretreatment Predictors of Short-Term Outcomes in RAI-Treated Intermediate-Risk Thyroid Cancer

G. B. Babacan[1,2], *S. Saracoglu*[3], *O. Guven*[2], *S. Sabuncu*[2], *M. N. Acar Tayyar*[2], *T. Ozulker*[2], *M. C. Sahin*[2], *S. Karyagar*[2];
[1]*Sirnak State Hospital, Clinic of Nuclear Medicine, Sirnak, TÜRKIYE,* [2]*University of Health Sciences, Hamidiye Faculty of Medicine, Prof. Dr. Cemil Tascioglu City Hospital, Department of Nuclear Medicine, Istanbul, TÜRKIYE,* [3]*Van Training and Research Hospital, Department of Nuclear Medicine, Van, TÜRKIYE.*

Aim/Introduction: We aimed to investigate the effect of pretreatment parameters on early follow-up outcomes in patients with intermediate-risk group differentiated thyroid cancer (DTC). ***Materials and Methods:*** A dataset of patients who underwent total thyroidectomy and received ^{131}I radioactive iodine (RAI) treatment was analyzed between January 2016 and January 2022. Patients with intermediate-risk group DTC according to the ATA 2015 criteria were included in the study. Patients younger than 18 years of age, patients with anti-Tg positivity, patients with evidence of metastasis on post-treatment imaging, and patients with missing follow-up data were excluded. Histopathologic and biochemical results, RAI doses, and clinical follow-up results at 3 and 5 years were compared. The Chi-square and Fisher's exact tests were used to compare nonparametric variables and follow-up results. Threshold values for continuous variables were determined by drawing the ROC curve over the 3-year follow-up results. Results with p values less than 0.05 were considered statistically significant. ***Results:*** Seventy-six patients (56 women; mean age 43.14±13.6 years) enrolled in this study. Median follow-up was 72.5 (58-106) months. During follow-up, five patients received additional RAI treatment, and two patients underwent secondary surgical treatment within the first three years. Four patients underwent ^{18}F FDG PET/CT imaging. In the Chi-Square test, no statistically significant difference was found between the three and five-year follow-up groups for histopathological features, age, and gender (p>0.05) (Table 1). When the treatment doses and five follow-up results were analyzed, it was found that the group initially treated with 5.55 GigaBecquerel (GBq) had a significantly lower rate of excellent response than the group treated with 3.7 GBq or less (p=0.0112). In the ROC curve analysis generated with three-year follow-up results, the threshold value for pretreatment stimulated Tg (sTg) was determined as 4.69 (AUC:0.739, Sensitivity:76.5, Specificity:70, p=0.0001). After grouping the patients based on this value, a statistically significant difference was found between the groups in the Chi-square test (p=0.0007, p=0.0306 for three and five years, respectively). ***Conclusion:*** In this study, no statistically significant correlation was found between pathology data and treatment response at the end of the third and fifth years in DTC patients who received radioactive iodine treatment, while patients with sTg values above 4.69 were found to have a higher rate of early incomplete treatment response. This cut-off value may be guiding in terms of follow-up and treatment selection in patients who are planned for total thyroidectomy and RAI treatment.

EP-0859

To compare the response of low- and high-dose Lenvatinib in patients with radioiodine-refractory thyroid cancer: A non-inferiority trial

P. Chauhan*, S. Sharma, R. Mehra, P. K. Pradhan, S. Gambhir; Sanjay Gandhi Post Graduate Institute of Medical Sciences, Lucknow, INDIA.*

Aim/Introduction: The rising incidence of thyroid cancer highlights the need for improved therapies, especially for radioiodine-refractory differentiated thyroid cancer (RAI-R DTC). Lenvatinib, a tyrosine kinase inhibitor, is effective but often limited by adverse effects requiring dose modifications. While studies suggest lower doses may balance efficacy and tolerability, most focus on high-dose regimens in Western populations (1,2). Data on optimal dosing in South Asian patients remain scarce. ***Materials and Methods:*** This retrospective non-inferiority study at our institute, compared low-dose (10-12mg) vs. high-dose (18-20mg) Lenvatinib in RR-DTC patients, evaluating overall response and adverse events. Data from 44 patients were analyzed. Baseline clinical, biochemical, and imaging parameters were recorded. Patients were grouped by Lenvatinib dose (10-12 mg vs. 18-20 mg). Follow-up included clinical exams, Tg/ATgAb levels, and imaging. Therapeutic response was assessed after 3-5 months as clinical, biochemical, or imaging response. Continuous variables were analyzed using Mann-Whitney U test; categorical variables with Fisher's exact or chi-square test. $p < 0.05$ considered statistically significant. ***Results:*** Of the 44 patients treated with Lenvatinib, 28 received low-dose and 16 high-dose, with comparable baseline characteristics. Biochemical response was assessed in 32 patients over 5 months; Serum thyroglobulin (Tg) levels were significantly reduced by a median of 71% over 5 months, 75% showed partial response, 15.5% had stable disease, and 9.3% progressed. Imaging response in 27 patients showed 70.3% partial response, 18.5% stable disease, and 7.4% progression. Clinical response included mass reduction in three patients. Overall, 81.8% achieved partial response, 9.1% had stable disease, and 9.1% progressed. No significant differences were observed between low- and high-dose groups across biochemical, imaging, or clinical responses, indicating similar therapeutic efficacy at reduced doses. Adverse events were monitored over 2 months. Drug holidays (31.8%) and dose reductions (18.2%) were more common in the high-dose group. Proteinuria was significantly higher with high-dose Lenvatinib (p=0.018). Hand-foot syndrome was most common (61.3%), with higher incidence in the high-dose group, though not statistically significant. ***Conclusion:*** This real-world data suggests that lower initial doses (10-12mg) of Lenvatinib can be as effective as higher doses (18-20mg) while potentially reducing adverse effects. Overall, this study adds valuable evidence about optimizing Lenvatinib therapy for RR-DTC, with implications for improving patient care and quality of life. ***References:*** 1. Brose MS, et al. J Clin Endocrinol Metab. 2022;107:776-787 DOI: 10.1210/clinem/dgab731. 2. Rendl G, et al. International Journal of Endocrinology. 2020;2020:1-8 DOI: 10.1155/2020/8834148.

EP-0860

Association between early Tg elevation and subsequent reduction after I-131 therapy in differentiated thyroid carcinoma: A dynamic biomarker study.

Y. Li[1], *K. Hirata*[1,2,3], *J. Takenaka*[1,2], *S. Watanabe*[1,2], *R. Kimura*[1,4], *K. Kudo*[1,2,4];
[1]*Department of Diagnostic Imaging, Graduate School of Medicine, Hokkaido University, Sapporo, JAPAN,* [2]*Department of Nuclear Medicine, Hokkaido University Hospital, Sapporo, JAPAN,* [3]*Global Center for Biomedical Science and Engineering, Faculty of Medicine, Hokkaido University, Sapporo, JAPAN,* [4]*Department of Diagnostic and Interventional Radiology, Hokkaido University Hospital, Sapporo, JAPAN.*

Aim/Introduction: Serum thyroglobulin (Tg) is a well-established tumor marker in the follow-up of differentiated thyroid carcinoma (DTC) patients. A transient elevation Tg levels is often observed within a few days following I-131 treatment. However, the elevation of Tg observed two days after I-131 treatment, compared to the day of treatment (before treatment), which may reflect tumor destruction, remains of uncertain significance. This study aims to explore the relationship between initial Tg elevation shortly after therapy and the long-term reduction of Tg,

thereby enhancing risk stratification in DTC patients. ***Materials and Methods:*** A retrospective analysis was conducted on 94 patients with DTC who underwent thyroidectomy followed by their first I-131 adjuvant therapy stimulated by rhTSH. Tg levels were measured at three distinct time points: before RAI treatment (Tg_0), 2 days after RAI (Tg_{2d}), and 6 months after RAI (Tg_{6m}). Time-based Tg biomarkers were calculated as follows: ΔTg_02 (Tg_{2d}-Tg_0), ΔTg_26 (Tg_{6m}-Tg_{2d}), ratioTg_02 (Tg_{2d}/Tg_0), and ratioTg_26 (Tg_{6m}/Tg_{2d}) and evaluated by Spearman's correlation analysis and Mann-Whitney U tests. Subgroup analyses were further performed based on age, sex, TSH level (before RAI), lymph-node metastasis status, administered RAI dose, and histological subtype using Mann-Whitney U tests. ***Results:*** Spearman correlation analysis revealed a moderate negative correlation between ΔTg_02 and ΔTg_26 ($\rho = -0.473$, $p < 0.0001$), indicating that greater early Tg elevation was associated with more obvious decline of late Tg. Similarly, a significant negative correlation was observed between the ratioTg_02 and the ratioTg_26 ($\rho = -0.481$, $p < 0.0001$), further supporting the association between early and long-term Tg dynamics. DTC patients were stratified into high and low groups separately based on the median value of ΔTg_02 and ratioTg_02. It was statistically significant between high and low groups ($p < 0.0001$) based on ΔTg_02, with the high ΔTg_02 group showing a greater Tg reduction at 6 months later. A similar trend was observed for ratioTg: ratioTg_26 was significantly different between the high and low ratioTg_02 groups ($p = 0.0006$). We conducted subgroup analyses stratified by clinical variables. Subgroup analyses showed that both ΔTg_02 and ratioTg_02 were significantly ($P<0.05$) associated with subsequent Tg decline (ΔTg_26 or ratioTg_26) regardless of age, sex, TSH level, lymph-node metastasis status, RAI dose, and histological type of papillary. ***Conclusion:*** Early changes in Tg levels are significantly associated with long-term Tg reduction following I-131 therapy in patients with DTC. Subgroup analyses further demonstrate the robustness of this association across various clinical characteristics.

EP-0861

Preablative Stimulated Thyroglobulin, Its Post-^{131}I Treatment Decline, and Nomogram-Based Prediction of Clinical Outcomes in Differentiated Thyroid Cancer Patients Without Distant Metastasis

Y. Hou[1,2,3], *J. Wang*[1,4], *R. Wu*[1,2,3], *J. Tan*[5], *X. Xia*[1,2,3], *Z. Gao*[1,2,3];
[1]*Department of Nuclear Medicine, Union Hospital, Tongji Medical College, Huazhong University of Science and Technology, Wuhan, CHINA,* [2]*Hubei Province Key Laboratory of Molecular Imaging, Wuhan, CHINA,* [3]*Key Laboratory of Biological Targeted Therapy, the Ministry of Education, Wuhan, CHINA,* [4]*Department of Medical Imaging, Henan Provincial People's Hospital, Zhengzhou, CHINA,* [5]*Department of Breast and Thyroid Surgery, Union Hospital, Tongji Medical College, Huazhong University of Science and Technology, Wuhan, CHINA.*

Aim/Introduction: The detection rate and incidence of thyroid cancer have been increasing year by year, and differentiated thyroid cancer (DTC) is the most important type of thyroid cancer. This study aims to evaluate the predictive value of stimulated thyroglobulin (sTg) levels before and after the first ^{131}I treatment in predicting clinical outcomes for differentiated thyroid cancer (DTC) patients without distant metastasis. ***Materials and Methods:*** Sixty patients were categorized according to the 2015 American Thyroid Association guidelines into two groups: excellent response (ER) and non-excellent response (NER). Clinical and pathological data were analyzed using univariate and multivariate analyses. Receiver operating characteristic (ROC) curves were generated to determine optimal thresholds for pre-^{131}I sTg levels and the rate of sTg decline after the first ^{131}I treatment. ***Results:*** Univariate and multivariate analyses identified pre-^{131}I sTg levels (OR: 3.010, 95% CI: 1.004-9.029, P=0.049) and the rate of sTg decline (OR: 0.756, 95% CI: 0.590-0.968, P=0.026) as independent predictors of clinical outcomes. In the ER group, the optimal threshold for pre-131I sTg was 14.55 μg/L (sensitivity: 95.0%, specificity: 67.5%, AUC: 0.804). The optimal cutoff for the rate of sTg decline was 44.75% (sensitivity: 70.0%, specificity: 97.5%, AUC: 0.889). Additionally, a nomogram was developed incorporating sex, age, pre-^{131}I sTg, post-^{131}I sTg, T and N stages, tumour size, and thyroiditis to predict individualized outcomes. This nomogram provides a visual and quantitative method for assessing prognosis and facilitating tailored treatment. ***Conclusion:*** Both pre-^{131}I sTg levels and the rate of sTg decline are valuable early indicators of long-term outcomes in DTC patients, and nomogram analysis enhances clinical decision-making. ***References:*** This research was supported by National Natural Science Foundation of China (Grant Numbers: 81771866) and Hubei Provincial Natural Science Foundation Project (2024AFB633). Zairong Gao, Xiaotian Xia and Jie Tan contributed equally as co-corresponding authors.

EP-0862

Impact of Body Mass Index on Clinical Presentation and Outcomes in Differentiated Thyroid Cancer: A Retrospective Study

Y. Hou[1,2,3], *Y. Zhou*[1,2,3], *X. Xia*[1,2,3];
[1]*Department of Nuclear Medicine, Union Hospital, Tongji Medical College, Huazhong University of Science and Technology, Wuhan, CHINA,* [2]*Hubei Province Key Laboratory of Molecular Imaging, Wuhan, CHINA,* [3]*Key Laboratory of Biological Targeted Therapy, the Ministry of Education, Wuhan, CHINA.*

Aim/Introduction: Differentiated thyroid cancer (DTC) accounts for 90% of all thyroid malignancies, making it the most prevalent endocrine-related cancer. With the global rise in obesity, which has been identified as a risk factor for various cancers, this study aims to examine the effect of body mass index (BMI) on the clinical effectiveness and outcomes of initial radioactive iodine (^{131}I) treatment in patients with DTC. ***Materials and Methods:*** This retrospective study included 1,272 patients who underwent thyroidectomy followed by radioactive ^{131}I treatment at our hospital. Patients were categorized into four BMI groups: underweight (<18.5 kg/m^2), normal weight (18.5-24.9 kg/m^2), overweight (25-29.9 kg/m^2), and obese (≥30 kg/m^2). Clinical outcomes were evaluated based on the 2015 American Thyroid Association (ATA) guidelines, with a twelve-month follow-up period. ***Results:*** Higher BMI was significantly associated with increased maximum tumor diameter (MD = 0.28 cm [0.08, 0.29]), greater likelihood of extra-thyroidal gland invasion (OR = 1.65 [1.03, 1.98]), and a higher incidence of lymph node extra-nodal invasion (OR = 1.23 [1.22, 1.56]). No significant associations were found between BMI and histologic subtype, bilaterality, multifocality, vascular invasion, or TNM stage. Additionally, obese patients required the most frequent follow-up visits at the end of the twelve-month period. ***Conclusion:*** Elevated BMI is linked to more severe clinical manifestations and more complex treatment requirements in patients with DTC. Maintaining a normal body weight may help reduce the severity of clinical presentations and improve treatment outcomes. These findings underscore the importance of weight management in patients with DTC and suggest avenues for further research into the mechanisms connecting obesity and DTC.

EP-0863

Management of Low-Risk Differentiated Thyroid Carcinomas in Nuclear Medicine: A retrospective study of 280 cases

M. Nacer Khodja, *S. Rahal, S. Meza, M. Medjaher;*
Central Hospital of the Army, Algiers, ALGERIA.

Aim/Introduction: The risk stratification for recurrence of differentiated thyroid carcinomas, as outlined by the 2015 American Thyroid Association (ATA) guidelines, has enabled a therapeutic deescalation, particularly for patients classified as

low-risk for recurrence. ***Materials and Methods:*** This monocentric retrospective study held within the Nuclear Medicine Unit of the Central Military Hospital of Algiers, follows a total of 280 patients, initially classified as low-risk according to the 2015 ATA criteria (pT1bN0/NxMx, pT2N0/NxMx), who after total thyroidectomy, received 1.1 GBq (30 mCi) of iodine-131 after thyrotropin stimulation (with either of the follwoing processes : rhTSH or thyroid hormone withdrawal) for ablation purposes. Thyroglobulin (Tg) and anti-thyroglobulin antibodies (ATg) levels were measured after thyrotropin stimulation, along with a cervical ultrasound, conducted 9 to 12 months post treatment for all patients. ***Results:*** Out of the 280 patients, 265 showed a complete biological response and a normal cervical ultrasound, resulting in a success rate of 94.6%.- A cranial metastasis was identified in one patient.- Four patients presented loco-regional metastasis (metastatic cervical adeonpathies)- Ten patients presented an incomplete biochemical response with a negative cervical ultrasound and responded well to a second course of iodine-131 treatment. The results of our study are consistent with those of the ESTIMABL 1 study (98% remission), which allowed us to avoid overtreatment in more than 97% of patients. Additionally, dose reduction minimizes treatment-related side effects and has a considerable economic and organizational impact. ***Conclusion:*** The use of low-dose iodine 131 (1.1Gbq), demonstrate excellent outcomes, yielding comparable results to higher dose treatment in low-risk differentiated thyroid carcinoma, ensuring optimal patient care, all the while reducing the economic and the organizational burden associated with former protocols. ***References:*** Schlumberger M, Leboulleux S, Catargi B, Deandreis D, Zerdoud S, Bardet S, Rusu D, Godbert Y, Buffet C, Schvartz C, Vera P, Morel O, Benisvy D, Bournaud C, Toubert ME, Kelly A, Benhamou E, Borget I. Outcome after ablation in patients with low-risk thyroid cancer (ESTIMABL1): 5-year follow-up results of a randomised, phase 3, equivalence trial. Lancet Diabetes Endocrinol. 2018 Aug;6(8):618-626. Haugen BR, Alexander EK, Bible KC, Doherty GM, Mandel SJ, Nikiforov YE, Pacini F, Randolph GW, Sawka AM, Schlumberger M, Schuff KG, Sherman SI, Sosa JA, Steward DL, Tuttle RM, Wartofsky L. 2015 American Thyroid Association Management Guidelines for Adult Patients with Thyroid Nodules and Differentiated Thyroid Cancer: The American Thyroid Association Guidelines Task Force on Thyroid Nodules and Differentiated Thyroid Cancer. Thyroid. 2016 Jan;26(1):1-133.

EP-0864

The anti-thyroglobulin antibody trajectory and risk of structural recurrence in patients with papillary thyroid cancer

H. Wang*, R. Tian;*
West China Hospital, Sichuan University, Chengdu, CHINA.

Aim/Introduction: To identify longitudinal anti-thyroglobulin antibody (TgAb) trajectories in patients with papillary thyroid cancer (PTC) and to investigate the associations of trajectories with the risk of structural recurrence at two-year follow-up. ***Materials and Methods:*** This retrospective cohort included 4161 patients who had no evidence of structural disease and a stimulated thyroglobulin (s-Tg) of ≤10ng/mL at the initial radioiodine (RAI) treatment. We collected repeated TgAb measurements (before RAI treatment, one-, six- and 12-months after RAI treatment). We described changes of TgAb by plotting median TgAb and percentage of positive TgAb at different time points. Latent class models were used to identify TgAb trajectories, and the optimal number of trajectories was selected by comparing the performance and interpretability of models with different numbers of trajectories. To validate the robustness and generalizability of these trajectories, we randomly divided patients into two validation datasets and identified trajectories in each validation dataset. We estimated associations of TgAb trajectories, TgAb status and history of Hashimoto's thyroiditis (HT), with the risk of recurrence using logistic regression models. All estimates were not adjusted in Model 1 and were additionally adjusted for sociodemographic predictors (Model 2), sociodemographic and clinical predictors (Model 3). ***Results:*** The median age of the 4161 patients was 41 years with a female dominance (72.7%). A total of 63 (1.7 %) patients were identified as having structural recurrence. When plotting the changes in TgAb, we observed a significant downward trend in median TgAb (e.g., from 17 IU/mL before RAI treatment to 13 IU/mL at 12m after RAI treatment) and percentage of positive TgAb status (e.g., from 26.3% before RAI treatment to 9.1% at 12m after RAI treatment). We identified four distinct TgAb trajectories, models' performances were largely comparable, and similar trajectories were identified in two validation datasets. Compared to patients belonging to consistently negative trajectory, patients with other three trajectories had higher risks of recurrence (medium-level descent: odds ratio=3.46 [95%CI=1.56-6.90], high-level descent: 8.04 [1.26-28.78], persistently increasing: 12.11 [5.73-23.75], P for trend<0.001), estimates were largely similar after adjusting for sociodemographic and clinical predictors. TgAb status before and after RAI treatment, history of HT, were also associated with risk of recurrence (odds ratio: 3.05, 2.78 and 2.41). ***Conclusion:*** TgAb trajectories within one year after RAI treatment are associated with risk of recurrence in PTC patients with an s-Tg≤10ng/mL. Our findings call for the integration of TgAb trajectories into risk stratification and surveillance.

EP-0865

Predictive Value of Pre-ablation sTg/TSH Ratio and Lateral Cervical Lymph Node Metastasis Ratio in Initial ^{131}I Treatment Response for Papillary Thyroid Cancer

R. Zhang*, W. Li, Q. Jia, H. Wang, W. Zheng, J. Tan;*
Department of Nuclear Medicine, Tianjin Medical University General Hospital, Tianjin, CHINA.

Aim/Introduction: To identify predictive factors influencing the initial therapeutic response after the first ^{131}I treatment in total thyroidectomy patients with papillary thyroid cancer (PTC), determine critical prognostic biomarkers, and establish a foundation for personalized treatment strategies. ***Materials and Methods:*** This retrospective study analyzed 312 thyroglobulin antibody (TgAb)-negative PTC patients with preoperative thyroid-stimulating hormone (TSH) >30 mIU/L undergoing postoperative ^{131}I therapy. Initial ^{131}I treatment responses were categorized: excellent/indeterminate responses as generally satisfactory (GR), and biochemical/structural incomplete responses as non-satisfactory (n-GR). Multivariate logistic regression was used to evaluate associations between clinicopathological factors (such as age, sex, tumor size, unifocal/multifocal, T and N stages, excised/positive lymph nodes count, ^{131}I doses, etc) and GR. ROC curves were used to determine optimal cutoffs for predictive indicators. ***Results:*** Multivariate analysis showed that the pre-ablation stimulated thyroglobulin /TSH ratio (Pre-sTg/TSH) [odds ratio (OR) = 17.915, p = 0.022] and the lateral cervical lymph node metastasis ratio (lateral cervical/total metastatic nodes) [OR = 1.018, p = 0.024] were independent predictors of GR after the first ^{131}I treatment. The receiver operating characteristic (ROC) curves showed that the optimal cut-off value of Pre-sTg/TSH was 0.135, with an area under the curve (AUC) of 0.949, sensitivity of 89.8%, and specificity of 90.9%. Additionally, the optimal cutoff of the lateral cervical lymph node metastasis ratio was 34.5%, with a sensitivity of 61.2%, specificity of 74.1%, and AUC of 0.669. Moreover, within the overall cohort, the n-GR rate was 10.5% for low/intermediate-risk patients and 40.0% for high-risk cases. Among patients with a Pre-sTg/TSH > 0.135, the n-GR rates for low/intermediate-risk and high-risk patients significantly increased to 57.5% and 75.0% respectively. And for patients with the lateral cervical lymph node metastasis ratio > 34.5%, the n-GR rates escalated to 20.3% (low/intermediate-

risk cases) and 62.5% (high-risk patients). ***Conclusion:*** The Pre-sTg/TSH ratio (cutoff: 0.135) and lateral cervical lymph node metastasis ratio (cutoff: 34.5%) can serve as robust predictors of initial ^{131}I treatment efficacy in PTC. These biomarkers could enhance risk stratification and guide personalized therapeutic decisions.

EP-0866

Multicenter Study of Spanish Therapy Units: Early Side Effects of 131I Therapy

L. Cagua Ruiz[1], *T. Aroui Luquin*[1], *J. Villa-Palacios*[1], *L. Menedez - Muros*[1], *P. Stefan*[2], *A. Piñero Donis*[1], *E. Dominguez-Polanco*[1], *R. Sánchez Sánchez*[1], *M. Muros de Fuentes*[1];
[1]*Servicio Medicina Nuclear Hospital Universitario Virgen de las Nieves, Hospital Universitario Virgen de las Nieves, SPAIN,* [2]*Servicio Medicina Nuclear Hospital Universitario Virgen de las Nieves, Hospital Universitario la Fe, SPAIN.*

Aim/Introduction: To assess the presence of physical and psychological side effects during hospitalization for 131I therapy in metabolic therapy units. ***Materials and Methods:*** A multicenter study was conducted involving 181 patients with differentiated thyroid cancer treated with 131-I . 127 (70.2%) were women, 159 (87.8%) papillary carcinoma, 54 (29.8%) presented lymphatic spread, 34 (18%) had extrathyroidal extension, and 7 (3.8%) had distant metastases. 146 patients (80.66%) received a dose ≥ 100 mCi, and 119 (65.74%) received rhTSH. Upon discharge, patients completed a survey regarding their emotional well-being (Information received about therapy, adequate relationship with staff, fear of therapy, anxiety due to isolation, stress or low mood). Responses were classified as: none, mild, or severe. Physical side effects during hospitalization (neck pain, gastric discomfort, intestinal symptoms, urinary symptoms, and insomnia) were also analyzed and categorized as: none, mild, moderate, or severe. ***Results:*** Most patients reported emotional well-being during hospitalization, indicating they received sufficient information about the therapy (88.95%) and appropriate care from the staff (93.92%). Regarding fear of radioactive therapy, anxiety due to isolation, or sadness/anxiety while in the room, incidence was low, and none to mild in intensity (87.29%, 87.29%, and 84.53%, respectively). The incidence of physical side effects was also low, with most symptoms categorized as none to mild (92.82%, 90.61%, 91.71%, 93.37%, and 85.08%, respectively). The most frequent symptom was insomnia, reported as moderate to severe in 12.15% of patients. ***Conclusion:*** Patients undergoing 131I therapy did not report significant physical or emotional side effects during hospitalization with minimal impact on short-term quality of life.. Physical side effects were generally mild and well tolerated, with insomnia being the most commonly reported moderate to severe symptom.

EP-0867

Multicenter Study of Spanish Therapy Units. II. Late Side Effects of 131I Therapy.

E. Domínguez Polanco[1], *J. Villa-Palacios*[1], *A. Piñeiro Donis*[1], *L. Cagua Ruiz*[1], *C. Mallon Araujo*[2], *R. Sánchez Sánchez*[1], *M. Muros de Fuentes*[1];
[1]*Hospital Universitario Virgen de las Nieves, Granada, SPAIN,* [2]*Hospital Clínico Universitario de Santiago, Santiago, SPAIN.*

Aim/Introduction: Assessment of the presence of late side effects following 131I treatment for differentiated thyroid cancer. ***Materials and Methods:*** Multicenter study of 181 patients with differentiated thyroid cancer treated with 131I between 2020 and 2023. 127 (70.2%) were female, 159 (87.8%) were papillary thyroid tumors, 54 (29.8%) with lymphatic extension, 34 (18%) with extrathyroidal extension, and 7 (3.8%) with distant metastases. 146 patients (80.66%) received doses ≥ 100 mCi, and 119 (65.74%) received rhTSH. Patients completed a telephone survey one month and six months after discharge. The presence of physical side effects (asthenia, cervical redness, dyspepsia, oral aphthae, conjunctivitis, cervical pain, xerostomy, dysgeusia, and menstrual alterations) were assessed and categorized as none, mild, moderate, and severe. ***Results:*** One month after therapy, patients reported predominantly mild side effects. When specifically asked about cervical redness, dyspepsia, oral aphthae, conjunctivitis, cervical pain, and xerostomy, the majority were of mild intensity (92.82%, 91.16%, 92.82%, 90.61%, 86.74%, and 83.53%, respectively). The most frequent symptoms were menstrual alterations (30.55% moderate-severe), asthenia (28.73% moderate-severe), and dysgeusia (21.1% moderate-severe). Six months after therapy, patients reported predominantly mild side effects. When specifically asked about dyspepsia, oral aphthae, conjunctivitis, cervical pain, and xerostomy, the majority reported mild intensity (94.26%, 98.28%, 98.85%, 96.55%, and 92.53%, respectively). Among the most frequent symptoms, menstrual alterations persisted (33.33% moderate-severe), with a decrease in asthenia (11% moderate-severe) and dysgeusia (3.44% moderate-severe). ***Conclusion:*** Asthenia, dysgeusia and menstrual alterations were the most frequently reported side effects following 131I therapy.

EP-0868

Long-term clinical outcome of patients with differentiated thyroid cancer and raised antithyroglobulin antibody levels: a retrospective study

H. Shim*, M. Kim;*
Inje University, Haeundae Paik Hospital, Busan, KOREA, REPUBLIC OF

Aim/Introduction: Thyroglobulin (Tg) is used as a tumor marker for differentiated thyroid cancer (DTC). However, in the presence of antithyroglobulin antibody (TgAb), Tg can be a false negative. This study aims to track the changes of stimulated TgAb before radioiodine therapy (RIT) and at 1st follow up (F/U) in patients undergoing RIT after total thyroidectomy and to determine whether there is anatomic recurrence. ***Materials and Methods:*** We retrospectively analyzed 251 DTC patients (228 females, 55.37 ± 11.60 years vs 23 males, 55.22 ± 15.26 years) with Tg < 1 ng/ml and TgAb >10 U/ml before 1st RIT after total thyroidectomy. We categorized the 251 patients with serum stimulated TgAb concentrations 230.36 ± 31.44 days after RIT into five groups: (1) TgAb change <50% (n=77), (2) increase from <60 to >60 (de novo appearance) (n=5), (3) decrease from >60 to <60 (negative conversion) (n=12), (4) increase >50% (n=15), and (5) decrease >50% (n=142). ***Results:*** The dose of the 1st RIT was 113 ± 39.69 mCi. We compared stable or >50% increase in TgAb ((1)+(2)+(4), n=97) with decrease in TgAb ((3)+(5), n=154), 128-4694 days after RIT (mean 304.55 days). TgAb decreases to <10 U/ml were 17/97 (17.5%) vs. 49/154 (31.8%); decreases to <60 U/ml were 28/97 (35.9%) vs. 78/154 (50.6%); increases to >60 U/ml but <300 U/ml were 41/97 (42.3%) vs. 24/154 (15.6%); and increases to >300 U/ml were 11/97 (11.4%) vs. 3/142 (2.1%), respectively. Long-term follow-up was performed after RIT. When TgAb was stable or increased, 53.6% (52/97) of patients had an increase in TgAb above 60 U/ml, and when TgAb decreased, 82.5% (127/154) of patients had normalization of TgAb below 60 U/ml. Of the total 251 patients, 2 patients underwent reoperation after RIT due to persistently high TgAb levels and recurrence of neck lymph nodes (LNs). One patient had neck LNs remaining in the I-131 post-therapy whole body scan after RIT, so reoperation was performed 8 months later, and TgAb normalized. Among patients who represented a de novo appearance in TgAb, 2 cases showed negative conversion and 3 cases showed a sustained elevation above 60 U/ml, therefore it seems necessary to conduct research on more patients. ***Conclusion:*** Persistent TgAb increases require careful F/U for post-RIT TgAb changes and subsequent structural recurrence. Further studies involving larger cohorts are warranted to validate these findings.

EP-0869

Immunological Alterations Following Thyroidectomy in Differentiated Thyroid Carcinoma Patients: A Comparative Study

W. Zhang, *H. Liu, S. Li, P. Wang;*
Department of Nuclear Medicine, The First Hospital of Shanxi Medical University, Taiyuan, CHINA.

Aim/Introduction: Differentiated thyroid carcinoma (DTC) is the most common malignant tumor in the endocrine system, and the most common treatment option forindividuals with DTC is surgical resection. The effects of subtotal/total thyroidectomy on immune activation and suppression of the tumor microenvironment remain unknown. This study aims to evaluate the effects of these treatments on the immune function in patients with DTC. ***Materials and Methods:*** Total 103 patients as well as 103 age- and gender- matched healthy controls (HC) were recruited in this study. Peripheral blood samples were collected from all patients and both thyroid and immune function tests were completed for each patient on pre-surgery and 30 days post-surgery via modified flow cytometry. The levels of lymphocyte subsets in different groups were compared, including total lymphocytes, T cells, B cells, NK cells, $CD4^+$ T cells and $CD8^+$ T cells. Healthy controls were selected using propensity score matching (PSM). Comparisons of continuous variables between groups were conducted using t-tests or Mann-Whitney U tests, while categorical data was performed by chi-square tests. Statistical significance threshold set at $P<0.05$. ***Results:*** DTC patients exhibited a significantly higher percentage and absolute count of $CD4^+$ T cells compared to HC group, whereas the percentages of NK cells and $CD8^+$ T cells were significantly lower. Notably, multiple lymphocyte subsets in patients post-surgery, except for B cells, showed a significant increase in absolute numbers compared to preoperative levels, while the $CD4^+/CD8^+$ ratio significantly decreased. Interestingly, we observed that the proportions of several lymphocyte subsets in post-operative patients were significantly lower than those in healthy individuals. ***Conclusion:*** This study reveals that preoperative DTC patients display a specific immune imbalance. The absolute counts of lymphocyte subsets significantly increased after surgery, yet this exacerbated the imbalance in their proportions. These findings suggest that the postoperative immune reconstitution may be biased, potentially linked to an overexpansion of T cells inhibiting the functionality of other subsets. The incomplete recovery of immune function post-surgery indicates the necessity for long-term monitoring of immune homeostasis in DTC patients.

EP-0870

Predictors of Hypothyroidism Requiring Levothyroxine Substitution after Radioiodine Therapy in Unifocal Thyroid Autonomy

K. Klimek[1,2], *C. Happel*[2], *F. Grünwald*[2], *R. Werner*[1], *D. Groener*[2];
[1]*Department of Nuclear Medicine, University Hospital, LMU Munich, Munich, GERMANY,* [2]*Goethe University Frankfurt, University Hospital, Department of Nuclear Medicine, Clinic for Radiology and Nuclear Medicine, Frankfurt, GERMANY.*

Aim/Introduction: The purpose of this study was to identify pre-therapeutic and therapy-related factors that predict the risk of hypothyroidism requiring levothyroxine substitution following radioiodine therapy (RIT) in patients with unifocal thyroid autonomy. ***Materials and Methods:*** In a retrospective analysis of 228 patients (mean age 60.0 ± 14.6 years; median follow-up 461 days) who underwent RIT for unifocal thyroid autonomy, we investigated the ratio of target volume to total thyroid volume, the pre-therapeutic suppressed thyroid-stimulating hormone (TSH) level and the absorbed dose delivered to the autonomous adenoma. The mean ratio of target volume to total thyroid volume was 0.3258 ± 0.1875, the mean pre-therapeutic suppressed TSH concentration was 0.08 ± 0.07 mIU/L and the mean absorbed dose to the adenoma was 314.5 ± 158.7 Gy. Multiple logistic regression was employed to assess the influence of these variables on the subsequent need for levothyroxine therapy. ***Results:*** During the late follow-up interval, 26.8 % of patients developed hypothyroidism requiring levothyroxine. The ratio of target volume to total thyroid volume emerged as a strong predictor of post-therapeutic substitution ($p < 0.001$). A higher absorbed dose was also associated with an increased substitution risk ($p = 0.009$). In contrast, the pre-therapeutic suppressed TSH level did not significantly influence the risk of levothyroxine requirement ($p = 0.811$). ***Conclusion:*** Both the ratio of target volume to total thyroid volume and the absorbed dose to the autonomous adenoma are independent predictors of hypothyroidism necessitating levothyroxine substitution after radioiodine therapy in unifocal thyroid autonomy. These findings underscore the importance of meticulous pre-therapeutic dose planning to enable a more precise assessment of individual risk for post-therapeutic hypothyroidism.

EP-0871

Analysis And Optimization Of Radioiodine Therapy Based On The Study Of Radioiodine-131 Biokinetics Data

G. Grushka[1,2], *A. Savchenko*[3], *V. Bobrova*[4];
[1]*Kharkiv National Medical University, Kharkiv, UKRAINE,* [2]*SO «Grigoriev Institute for Medical Radiology and Oncology of the National Academy of Medical Sciences of Ukraine», Kharkiv, UKRAINE,* [3]*V. N. Karazin Kharkiv National University, Kharkiv, UKRAINE,* [4]*SO «Grigoriev Institute for Medical Radiology and Oncology of the National Academy of Medical Sciences of Ukraine», Kharkiv, UKRAINE.*

Aim/Introduction: Search of the optimum scheme of radioiodine therapy (RAI) with the highest clinical effect and minimum exposure of healthy tissues and organs is one of leading problems of planning and carrying out RAI. Aim: to define indicators which should be considered at RAI planning and to estimate the exposure load on the organism of the patient at carrying out RAI. ***Materials and Methods:*** The efficiency analysis of RAI was performed in 143 patients with differentiated thyroid cancer (DTC). All patients were divided into 2 groups: group 1 (G1) - 51 patients with the size of tumor pT1; group 2 (G2) - 92 patients with pT2. Activity of radioiodine for the first course RAI was 1110 - 4810 MBq. In 95 (66.4 %) patients, the thyroid cancer ablation was not reached; and the courses of RAI was proceeded. The absorbed doses in the thyroid gland, body, blood and red bone marrow were estimated using MIRD-method, the effective period of semi excretion of iodine-131 in the patient (T_{ef}) for the remnants of the thyroid gland and body of the patient, the maximum value of accumulation of radioactive iodine in the thyroid rests (U_{max}) were estimated. ***Results:*** Therapeutic effect of RAI for radically operated patients G1 was produced by absorbed dose on the whole body 0,148 Gy and in group G2 - 0,154 Gy. Average ablative activity thus varied from 5402 to 11470 MBq in both groups. The average total absorbed doses on the body for all courses of radiotherapy in patients of the both groups fluctuated within 0,13-0,21 Gy, and on the red bone marrow - 1,68-2,70 Gy. ***Conclusion:*** The study of radioiodine biokinetics serves to optimize the treatment of DTC and protect healthy tissues from irradiation. To solve the problem of individual dosimetric planning, it is advisable to determine T_{ef} and U_{max}.

EP-0872

Oncocytic Thyroid Carcinoma on the Rise: Divergent Evolution and Response to Radioiodine Treatment

M. Zambrana-Delgadillo, *M. Piñero Fernandez- Reyes, M. Cardoso-Rodríguez, M. Jerez-Jaimes, A. Lara-Hernández, J. Rodríguez-Rubio Corona, C. Quintana-Bolaño, Y. Santaella-Guardiola, F. Partida-Palma, M. Gutiérrez-Amares, M. Pajares-Vinardell;*
Hospital Universitario Puerta del Mar, Cadiz, SPAIN.

Aim/Introduction: Oncocytic Thyroid Carcinoma (OTC), recognized as a distinct entity from Follicular Thyroid Carcinoma (FTC) since 2017, continues to spark debate regarding its clinical progression, response to radioiodine (RAI) therapy, and prognosis in comparison to FTC. This study compares both subtypes, analyzing their histopathological profiles, post-RAI evolution, and factors associated with better therapeutic response. ***Materials and Methods:*** A total of 51 patients with FTC (n=33) and OTC (n=18) treated with RAI between 2013 and 2023 were included, with a minimum follow-up of 2 years until April 2025. Clinical data (age, sex), histopathological features (TNM staging, capsular/vascular invasion), date of diagnosis, follow-up duration, and treatment response based on 2015 ATA criteria were collected.Statistical analysis included Student's t-test or Mann-Whitney U, chi-square test, odds ratio, and binary logistic regression. Recurrence-free survival (RFS) was evaluated at 5 and 10 years. Oncocytic variant cases were reclassified as OTC based on WHO 2017 guidelines. ***Results:*** Mean age was similar (55 years in FTC vs. 57 in OTC), with a female predominance (82% vs. 61%). FTC had a longer follow-up duration (median 8.4 years vs. 6.1 years; p=0.055). Most patients were diagnosed at stage I (75.8% FTC, 61.1% OTC), with no significant association with histological type (p=0.47).Excellent response rates were similar between groups (51.5% FTC vs. 55.6% OTC; OR=0.85). Capsular invasion was significantly associated with better response (OR=0.0; p=0.023). However, in the multivariate model, no variable showed a significant association (global p=0.581); capsular invasion maintained the strongest effect size (OR=2.32; p=0.21).RAI doses ≥150 mCi were associated with capsular and vascular invasion, though not significantly, suggesting a possible therapeutic trend in these cases.Five- and ten-year RFS were higher in FTC (82% and 75%) than in OTC (61.5% and 50%), with no statistically significant differences. One non-cancer-related death occurred in a patient with excellent response. ***Conclusion:*** OTC showed a significantly shorter follow-up period and a trend toward earlier-stage diagnosis, suggesting evolving detection patterns over the last decade. Its 10-year RFS was lower. Capsular invasion was associated with better response, even after multivariate adjustment. These findings highlight the importance of prolonged follow-up and detailed histopathological assessment in managing differentiated thyroid cancer.

EP-0873

Recurrent differentiated thyroid cancer: predictive factors and outcome

J. Mihailovic[1], *I. Starcevic*[1], *J. Roganovic*[2];
[1]*Faculty of Medicine University of Novi Sad, Novi Sad,* [2]*Oncology Institute of Vojvodina, Sremska Kamenica, SERBIA.*

Aim/Introduction: During the follow-up, some patients with differentiated thyroid carcinoma (DTC) may develop recurrent disease. Objective: To evaluate the recurrence rate, predictive factors, and outcomes in DTC patients over an extended follow-up period. ***Materials and Methods:*** A total of 765 patients with DTC treated from 2007 to 2022 were retrospectively analyzed. Tumor staging included 488 (pT1), 125 (pT2), 133 (pT3), and 19 (pT4) patients. During follow-up, 61 patients (7.97%) experienced recurrence. All were treated surgically, with some receiving additional I-131 therapy and/or external beam radiation. Recurrence probabilities and predictive factors were assessed using the Kaplan-Meier method and log-rank test (SPSS v20), with significance set at p<0.05. ***Results:*** Of the 61 patients with recurrence, 28 (45.9%) were female and 33 (54.1%) male; 22 (36.1%) were ≥55 years old, and 39 (63.9%) were <55. Histology showed 57 (93.4%) papillary, 2 (3.3%) follicular, and 2 (3.3%) Hürthle cell carcinoma cases. Median follow-up was 7.4 years (range 1.1-27.4), with a median time to recurrence of 5.25 years. Recurrence probabilities were 8%, 11%, and 14% at 5, 10, and 15 years, respectively. Gender was the only significant predictor of recurrence (p=0.017), while age and histological type were not (p=0.980 and p=0.441). At the last follow-up, 54 patients (88.5%) were alive, and 7 (11.5%) had died due to disease-related causes. ***Conclusion:*** Recurrence in DTC can occur even many years after initial treatment, highlighting the importance of long-term follow-up. Early detection and timely treatment of recurrence offer a high chance of successful management. ***References:*** 1. Palme CE, Waseem Z, S. Raza N, Eski S, Walfish P, et al. Management and Outcome of Recurrent Well-Differentiated Thyroid Carcinoma. Otolaryngol Head Neck Surg. 2004;130:819-824. 2. Shokoohi A, Berthelet E, Gill S , Prisman E, Sexsmith G, et al. Treatment for Recurrent Differentiated Thyroid Cancer: A Canadian Population Based Experience. Cureus 12(2): e7122. DOI 10.7759/cureus.7122 3. Medas F , Canu GL, Boi F , Lai ML , Erdas E, et al. Predictive Factors of Recurrence in Patients with Differentiated Thyroid Carcinoma: A Retrospective Analysis on 579 Patients. Cancers 2019, 11, 1230; doi:10.3390/cancers11091230 4. Chopra S, Garg A, Ballal S, Bal C.S. Lung metastases from differentiated thyroid carcinoma: prognostic factors related to remission and disease-free survival. Clin Endocrinol (Oxf). 2015; 82: 445-452 5. Song H.J, Qiu Z.L, Shen C.T, Wei W.J, Luo Q.Y. Pulmonary metastases in differentiated thyroid cancer: efficacy of radioiodine therapy and prognostic factors. Eur J Endocrinol. 2015; 173: 399-408.

EP-0874

Quantitative Assessment of Salivary Gland Volumetric and Metabolic Changes Following Radioiodine Therapy in Differentiated Thyroid Carcinoma

S. Watanabe[1,2], *K. Hirata*[1,2], *H. Endo*[1], *J. Takenaka*[1,2,3], *N. Wakabayashi*[1,2], *R. Kimura*[1,4], *H. Koga*[1,4], *K. Kudo*[1,4];
[1]*Department of Diagnostic Imaging, Graduate School of Medicine, Hokkaido University, Sapporo, JAPAN,* [2]*Department of Nuclear Medicine, Hokkaido University Hospital, Sapporo, JAPAN,* [3]*Comprehensive Heart Failure Center, University Hospital Würzburg, Würzburg, GERMANY,* [4]*Department of Diagnostic and Interventional Radiology, Hokkaido University Hospital, Sapporo, JAPAN.*

Aim/Introduction: Salivary gland disorders are well-known side effects of radioactive iodine therapy (RAIT) for differentiated thyroid carcinoma, but there is limited research on imaging changes in salivary glands due to RAIT. ***Materials and Methods:*** From April 2020 to April 2025, we retrospectively reviewed cases of patients undergoing initial RAIT at our hospital. We included cases where FDG-PET/CT scans were performed using the same scanner before treatment and at least 3 months after treatment. RAIT was performed after 3 weeks of a low-iodine diet, more than 3 weeks of levothyroxine withdrawal, or administration of rhTSH. I-131 doses were fixed at 100 mCi or 150 mCi. Salivary glands were extracted on CT using TotalSegmentator for volume measurement, and changes in SUVmean on FDG-PET were evaluated. Acute and chronic salivary gland symptoms and visual assessments of uptake in post-therapy scintigraphy were compared for imaging changes. ***Results:*** A total of 30 cases (24 females) and 41 treatments were analysed. Mean age was 52.8±16.4 years, with histological types including papillary carcinoma (n=25), follicular carcinoma (n=3), and poorly differentiated carcinoma (n=2). Treatment purposes were adjuvant therapy (n=3) and treatment for metastasis (n=38). Levothyroxine withdrawal was performed in 37 treatments, rhTSH in 4 treatments, with 21 cases receiving 1 treatment, 7 cases 2 treatments, and 2 cases 3 treatments within the study period. Salivary gland symptoms appeared acutely in 13 treatments and chronically in 18 treatments. Following treatment, the volume of the salivary glands decreased significantly, with the parotid gland and submandibular gland measuring 90.1 ± 26.7% (p<0.001) and 94.2 ± 19.6% (p=0.032) of their pre-treatment volumes, respectively. The post-treatment SUVmean values were 103.1 ± 20.5% (p=0.579) and 101.6 ± 23.0% (p=0.387) of the pre-treatment values for the parotid and submandibular glands, respectively,

with no significant changes observed. There were no significant differences in volume changes based on acute symptoms, age, sex, histological type, or gland type, but significant volume reduction was observed I-131 uptake in post-Tx-scintigraphy (p=0.036), chronic symptoms (p<0.001), neck dissection (p=0.008), and levothyroxine withdrawal therapy (p=0.015). Clinical and imaging factors did not show significant differences in SUVmean, but subsequent treatments were associated with significant glandular volume reduction (p=0.032) and increased SUVmean (p=0.005). ***Conclusion:*** RAIT may result in salivary gland volume reduction without significant changes in SUVmean, especially in glands with scintigraphic radioiodine accumulation, post-neck dissection regions, and cases undergoing levothyroxine withdrawal therapy, suggesting a risk for significant salivary gland disfunction following RAIT.

EP-0875

Gender impact in Radioactive Iodine (^{131}I) clearance in Thyroid Cancer treatment

J. Koutsikos, *G. Thiveos, T. Petropoulos, I. Papantoniou, S. Giourgouli, A. Kokkini - Paschou, E. Skoura, I. Datseris; Henry Dunant Hospital Center, Athens, GREECE.*

Aim/Introduction: ^{131}I administration for thyroid disease treatment has been proven successful over several decades. The physical characteristics of ^{131}I, mostly half-life and photon energy, demand special care regarding radiation protection. Numerous efforts have been made to determine effective half-life (Teff) of ^{131}I and to estimate in advance ^{131}I clearance based on specific patient characteristics. Our work aims to estimate Teff based on exposure rate measurements and determine whether Teff is gender dependent. ***Materials and Methods:*** Patients treated with radioiodine in our Nuclear Medicine Department, for well-differentiated Thyroid Cancer, following total thyroidectomy, were included. Exposure rate measurements at 1 meter were made 24 and 48 hrs post administration using a calibrated survey meter. These measurements were converted to residual activity values (RA) and were plotted as percentage of the administered activities against time. The Teff was computed from exponential line fittings on the above plots. A gender based analysis was performed. Exclusion criteria were: age <18 y.o., a repeated treatment and treatment for metastatic disease. ***Results:*** 280 patients (191 females and 89 males, mean age 44.7+/-13.3 y.o.) were included in our study. The results are summarized in attached table. While Teff and average 24 and 48hrs RA values differ (lower for females), statistically significant differences were revealed in 48hr RA between males-females (p=0.027). ***Conclusion:*** Our Teff estimation for the first 48hrs is consistent with previous studies. The lower Teff and faster activity clearance observed in females might be attributed to better compliance with instructions or differences in hormonal profiles. These result in a better understanding of ^{131}I clearance and RIT patient management. However, they should be validated with more patients and additional parameters, such as glomerular filtration rates and residual thyroid tissue, among others. ***References:*** 1. Kääriä L, Lapela M, Seppänen M, et al. Determination of effective half-life of 131I in thyroid cancer patients using remote dose-rate meter. EJNMMI Phys. 2024;11(1):101. 2. Klain M, Nappi C, De Risi M, et al. Whole-Body Radioiodine Effective Half-Life in Patients with Differentiated Thyroid Cancer. Diagnostics (Basel). 2021;11(10):1740. 3. Remy H, Borget I, Leboulleux S, et al. 131I effective half-life and dosimetry in thyroid cancer patients. J Nucl Med. 2008;49(9):1445-50.

EP-53

e-Posre Area

C: Therapy Clinical Study -> C1 Oncological Therapy Clinical Study -> C15 Other Oncological Treatments

EP-0876

Phase 1 dose-escalation study on astatine-211 labelled meta-astatobenzylguanidine ([^{211}At]mABG) for treatment of recurrent or refractory high-risk neuroblastoma: study design and rationale

L. Teles[1], *B. van der Wildt*[1,2], *M. van Noesel*[1,3], *R. van Rooij*[1,2], *A. Poot*[1,2], *A. Braat*[1,2,4]; [1]*Princess Máxima Center for Pediatric Oncology, Utrecht, NETHERLANDS,* [2]*University Medical Center Utrecht / Wilhelmina Children's Hospital, Utrecht, NETHERLANDS,* [3]*Division Imaging and Cancer, University Medical Center Utrecht, Utrecht, NETHERLANDS,* [4]*Netherlands Cancer Institute, Amsterdam, NETHERLANDS.*

Aim/Introduction: The cure rate of high-risk neuroblastoma (NBL) is poor (<50%). Norepinephrine transporter (NET) positive patients with recurrent and refractory disease can be treated with iodine-131 labelled metaiodobenzylguanidine ([^{131}I]mIBG). Although around 30% of patients respond to [^{131}I]mIBG, its implementation has not improved survival outcomes.[1] [^{131}I]mIBG therapy is limited by the poor properties of the radionuclide iodine-131 (^{131}I). Predominantly, its high-energy gamma emission poses challenges in clinical practice. This study investigates an alternative therapy: meta-astatobenzylguanidine ([^{211}At]mABG). This compound includes astatine-211 (^{211}At), an alpha-particle emitter with more favourable properties. It combines a low tissue penetration with a high linear energy transfer, increasing the tumoricidal potential and decreasing damage to healthy tissue. Moreover, the absence of high-energy gamma radiation means patient isolation is unnecessary. A phase 1 study in adults with [^{211}At]mABG is ongoing in Japan.[2] ***Materials and Methods:*** This single-centre, phase 1 dose-escalation and dose-finding study has a classical 3 plus 3 design. Patients with high-risk NBL, refractory to first-line chemotherapy, or with recurrent disease after complete response on previous molecular imaging are eligible for this study. Based on preclinical data, the starting dose is 1.3 MBq/kg. Subsequent doses are 2.6 and 5.0 MBq/kg. Imaging with fluorine-18 labelled meta-iodobenzylguanidine ([^{18}F]mFBG) positron emission tomography (PET/CT) will be acquired at baseline and repeated throughout follow-up to evaluate preliminary response. Urine catecholamine biomarkers will also be assessed. ***Results:*** Introduction of alpha-emitting nuclear treatment in children requires a technical pre-phase. We initiated the local production of [^{211}At]mABG for the duration of this study. The phase 1 clinical trial will be aimed at determining the required phase 2 dose (RP2D) for future phase 2 studies. The study will also determine the maximum tolerable (cumulative) dose. ***Conclusion:*** Recruitment is expected to begin in 2026, and international patients can be considered. This study will provide the first clinical data on the safety and feasibility of [^{211}At]mABG therapy for patients with recurrent or refractory high-risk NBL and may lead to a more effective and less burdensome therapeutic intervention. ***References:*** 1. Samim A, Bleeker G, Kraal KCJM, et al. A narrative review of 35 years of meta-[131I]iodobenzylguanidine therapy in neuroblastoma. EJC Paediatric Oncology. 2024;3:100159. doi:10.1016/J.EJCPED.2024.100159 2. Kobayakawa M, Shiga T, Takahashi K, et al. Evaluation of pharmacokinetics, safety, and efficacy of [211At]meta-astatobenzylguanidine ([211At]mABG) in patients with pheochromocytoma or paraganglioma (PPGL): a study protocol. PLoS One. 2024;19(5). doi:10.1371/JOURNAL.PONE.0303623

EP-0877

Efficacy and safety of Lu177-EDTMP therapy for bone pain palliation in cancer patients with multiple skeletal metastasis

K. Vidhya, *M. Negi, V. K. Saini, D. Sundriyal, M. Gupta, F. Huda, S. Sinha, V. K. Dhingra;*
AIIMS, Rishikesh, Rishikesh, INDIA.

Aim/Introduction: Metastatic bone pain (MBP) is a common and debilitating complication in patients with advanced cancers, significantly impairing their quality of life. Conventional treatments such as analgesics and external beam radiotherapy often provide limited and short-term relief, especially in patients with widespread skeletal metastases. Lutetium-177 ethylenediamine tetramethylene phosphonate (Lu-177 EDTMP) is a bone-seeking radiopharmaceutical that delivers targeted beta radiation to metastatic lesions, offering a promising alternative for effective and sustained palliation of bone pain with minimal systemic toxicity.This study aimed to evaluate the efficacy and safety of Lu-177 EDTMP therapy for bone pain palliation in cancer patients with multiple skeletal metastases. ***Materials and Methods:*** Single-arm experimental study in patients with multiple bone metastases and MBP. Baseline/follow-up assessments included pain, mobility (Parker), KPS, and toxicity over 3 months post Lu-177 EDTMP therapy. ***Results:*** 12 patients were included in this study (6 males and 6 females) with majority being carcinoma breast (n=7) and prostate (n=3) diagnosed patients, along with a patient with lung and another one with dual carcinoma- carcinoma larynx + carcinoma prostate were also included. The initial mean pain score of 8.3 reduced to 5.0 at 2 weeks and 4.2 at 1 month and 4.0 at 2 months, indicating a strong initial response to treatment before slightly increasing at 3 months. Hence, all patients experienced a significant reduction in pain scores, demonstrating the effectiveness of the treatment. Karnofsky Performance Scores (KPS) show initial improvements in patient functionality, particularly in the first month, correlating to reduced pain scores. However, variability in scores indicates differing individual responses to treatment. Regular monitoring of KPS and pain levels is crucial for optimizing patient care and adjusting treatment strategies. Mobility scores increased from 3.08, 4.58, 5.33 and 5.58 at baseline, 2wks, 1 month and 3 months (improvement). One patient experienced grade 4 adverse effects (anemia, neutropenia, thrombocytopenia), managed with transfusions and GM-CSF, resolving to grade 1 in 2 weeks. Few of the patients experienced grade 2/3 toxicity but majority showed no significant toxicities to the therapy and patients were found to tolerate the therapy well. ***Conclusion:*** Lu-177 EDTMP is a safe, effective, and cost-effective therapy for metastatic bone pain, offering sustained pain relief, improved mobility, and better quality of life with minimal side effects. It is particularly valuable in resource-limited settings, serving as a promising alternative to conventional treatments for managing metastatic bone pain.

EP-0878

Preliminary Evaluation of ^{225}Ac/^{177}Lu-DOTATATE PRRT in Advanced Meningiomas: Efficacy, Dosimetry, and Imaging Insights

M. Assadi[1], *R. Nemati*[2], *E. Jafari*[1], *N. Jokar*[1], *M. Peer-Firozjaei*[3], *S. Rekabpour*[4], *M. Khazaei*[5];
[1]*The Persian Gulf Nuclear Medicine Research Center, Department of Nuclear Medicine, Molecular Imaging, and Theranostics, Bushehr Medical University Hospital, School of Medicine, Bushehr University of Medical Sciences, Bushehr, IRAN, ISLAMIC REPUBLIC OF,* [2]*Department of Neurology, Bushehr Medical University Hospital, School of Medicine, Bushehr University of Medical Sciences, Bushehr, IRAN, ISLAMIC REPUBLIC OF,* [3]*Student Research Committee, Babol University of Medical Sciences, Babol, IRAN, ISLAMIC REPUBLIC OF,* [4]*Department of Oncology, Salman Farsi Hospital, Bushehr, IRAN, ISLAMIC REPUBLIC OF,* [5]*Department of Radiology, Bushehr Medical University Hospital, School of Medicine, Bushehr University of Medical Sciences, Bushehr, IRAN, ISLAMIC REPUBLIC OF.*

Aim/Introduction: Somatostatin receptor (SSTR)-targeted peptide receptor radionuclide therapy (PRRT) represents a promising therapeutic option for meningiomas. To date, the therapeutic potential of α-emitters in this setting remains less explored. This study presents clinical outcomes of meningioma patients treated with ^{225}Ac-DOTATATE and ^{177}Lu-DOTATATE, highlighting their role in expanding PRRT options. ***Materials and Methods:*** Six patients with inoperable or refractory meningiomas, all with intense 68Ga-DOTATATE PET/CT uptake, received 225Ac-DOTATATE (100kBq/kg) and/or 177Lu-DOTATATE (3.7 GBq). The primary endpoint was clinical response after each PRRT cycle and PET response based on follow-up 68Ga-DOTATATE PET/CT after the last cycle. The secondary endpoint was improvement in quality of life (QoL), assessed using ECOG performance status scores. Additionally, dosimetric analyses were performed. ***Results:*** The study included six patients which 5 them had at least 2 lesions, with a maximum of 6 lesions. A total of 26 PRRT cycles were administered: 13 with 177Lu-DOTATATE and 13 with 225Ac-DOTATATE. Clinical responses were complete remission (n=1), partial remission (n=2), disease stability (n=2), and disease progression (n=1), with one patient dying after eight months. Follow-up 68Ga-DOTATATE PET/CT showed partial remission (n=3), disease stability (n=2), and disease progression (n=1). ECOG scores showed no significant change pre- and post-treatment, except for one patient who improved from 3 to 1. Median follow-up time was 13 months (range: 8-16). Quantitative volumetric parameters showed : median ΔSUVmax: 31.73 (range: -44.89 to 60.28), median ΔSRE-TV: 8.16 (range: -18.86 to 49.47), median ΔTL-SRE: 42.28 (range: -31.93 to 68). Dosimetric evaluation revealed considerable heterogeneity in absorbed dose across individual lesions, particularly in multifocal cases. A high-uptake lesion (SUV = 158) received an estimated absorbed dose of 2.37 Gy/GBq with ^{177}Lu-DOTATATE and 3.36 Gy/MBq with ^{225}Ac-DOTATATE—values comparable to those reported for neuroendocrine tumors. Microdistribution analysis demonstrated strong spatial overlap between alpha and beta emitters in the hottest lesion, supporting the feasibility of combined or sequential use in precision-targeted PRRT. Additionally, in four lesions,68Ga-FAPI showed consistently lower tracer uptake compared to 68Ga-DOTATATE**.** ***Conclusion:*** These preliminary results suggest that PRRT with 225Ac-DOTATATE and 177Lu-DOTATATE may have positive effects in patients with advanced meningioma. This novel approach holds promise for optimizing personalized, lesion-specific treatment strategies for patients with both unifocal and multifocal meningiomas, particularly in cases resistant to conventional therapies—advancing the principles of precision medicine. Further studies are recommended to validate these findings, refine theranostic strategies, and broaden available treatment options.

EP-0879

Peptide Receptor Radionuclide Therapy with [^{177}Lu]Lu-DOTATATE in Progressive Refractory Meningiomas: A Single-Centre Retrospective Analysis

L. Degryse[1], *L. Teles*[2], *S. De Vleeschouwer*[1], *L. Boeckxstaens*[1], *S. Jentjens*[3], *M. Lambrecht*[1], *J. Daisne*[4], *K. Van Laere*[1], *P. Clement*[1], *K. Goffin*[1], *C. M. Deroose*[1];
[1]*University Hospitals Leuven, Leuven, BELGIUM,* [2]*Princess Máxima Center for Pediatric Oncology, Utrecht, NETHERLANDS,* [3]*Maastricht University Medical Center, Maastricht, NETHERLANDS,* [4]*ZAS, Antwerp, BELGIUM.*

Aim/Introduction: Peptide receptor radionuclide therapy (PRRT), targeting the somatostatin receptor subtype 2 (SSTR2), has emerged as a promising salvage therapy for progressive meningiomas that have exhausted both surgical and external beam radiotherapeutic (EBRT) interventions [1,2]. Encouraging disease-control rates (DCR) of ~ 63% upon termination of PRRT were reported in a meta-analysis of six small retrospective studies (5-34 patients/study) [3], corroborated by a recent retrospective

study by Severi et al. (DCR 57% at the end of PRRT, median progression-free survival (PFS) 16 months) [4]. We retrospectively analysed outcomes of meningioma patients treated with PRRT at our institution. ***Materials and Methods:*** All meningioma patients treated with [^{177}Lu]LuDOTATATE from June 2016 to March 2024 were identified from the institutional PRRT database. Demographics, tumour characteristics, prior treatments, and clinical outcomes were retrospectively extracted from medical records. ***Results:*** Twelve meningioma patients (mean age 61.2 years, seven male) received PRRT, of whom 3 had WHO grade 1 meningiomas (25%), 8 had WHO grade 2 (67%) and one patient had histopathological uncertainty between grades 2 and 3. Multifocal disease was present in 6 patients (50%). Baseline tumour volume on SSTR PET/CT averaged 101.7 cm^3 (range 14-411) with mean SUV_{max} of 17.9 (range 7.5-31.5) and SUV_{mean} of 5.9 (range 3.6-8.4). Eleven patients (92 %) had undergone ≥2 resections and EBRT. Eight patients (67 %) completed 4 planned PRRT cycles (7.4 GBq per cycle), while four patients discontinued early due to clinical decline (n = 2; after cycle 1 and 3) or meningioma progression (n = 2; both after cycle 2). The first MRI after completion of PRRT (on average after 30 days, range 10-60) demonstrated a DCR of 50% (6/12) in the entire cohort. Median PFS was 8 months, with 4 of 12 patients (33%) achieving a PFS of ≥12 months. Median overall survival was 20 months (range 3-89 months), with 3 patients still being alive at data censoring. Five patients received additional treatments, including bevacizumab, surgical re-resection, and/or re-irradiation. ***Conclusion:*** PRRT with [^{177}Lu]LuDOTATATE demonstrated clinically meaningful disease stabilization in heavily pretreated meningioma patients. Its therapeutic efficacy is currently being prospectively validated in the ongoing EORTC LUMEN1 phase II trial. While our findings support the role of [^{177}Lu]LuDOTATATE in disease stabilization, future directions such as α-emitting radioligands ([^{225}Ac]AcDOTATATE), high-affinity receptor antagonists, and intra-arterial delivery of PRRT are under investigation and may further improve therapeutic outcomes. ***References:*** 1.Ahmadi Bidakhvidi N, Cancers.2021;14(1):129 2.Albert NL, EJNMMI.2024;51(12):3662-3679 3.Mirian C, JNM.2021;62(4):507-5134.Severi S, JNM.202 4;65(9):1409-1415.

EP-0880

Assessment of 177Lu-PSMA-617 Retention in Inoperable/ heavily pretreated Pancreatic adenocarcinoma: Implication for Theranostic Feasibility

G. B. Priyanka*, N. A. Damle, A. N. Singh, K. Kuradia, S. Mishra, S. J. Bharati, R. Yadav, M. Tripathi, S. A. Shamim, C. Ganapathy, A. Choudhary, M. Aishwarya;*
All India Institute of Medical Sciences, New Delhi, INDIA.

Aim/Introduction: PSMA PET/CT has demonstrated tracer uptake in pancreatic adenocarcinoma previously, primarily through tumor-associated neovasculature. This raises the question of whether PSMA-targeted radioligand therapy (RLT) using 177Lu-PSMA-617 has therapeutic potential in this malignancy. ***Materials and Methods:*** 5 Patients with inoperable or heavily pretreated pancreatic adenocarcinoma who demonstrated PSMA uptake on 68Ga-PSMA-11 PET/CT underwent serial imaging post 5-7mCi of 177Lu-PSMA-617. Whole-body planar and SPECT/CT imaging were performed at 30minutes (pre void, post void), 24 hours and upto 7 days post-injection(at least 3 time points) to evaluate in vivo tracer retention. ***Results:*** Despite moderate to high PSMA expression on diagnostic PET/CT (more than or equal to liver), serial planar retention scans showed negligible 177Lu-PSMA-617 retention in primary, nodal as well as metastatic tumour sites. There was significant radiotracer accumulation in early images in one patient, that washed out at 24 hrs while rest of the patients showed insignificant uptake at all time points. ***Conclusion:*** These findings reveal a critical limitation in applying 177Lu-PSMA-617 therapy to inoperable or heavily pretreated pancreatic adenocarcinoma, despite promising PET imaging results. The absence of retention implies a lack of theranostic efficacy, likely due to PSMA localization in the neovasculature without sufficient internalization or residence time to enable targeted radiotherapy. This highlights the need to differentiate between imaging results and therapeutic translatability when evaluating novel applications of PSMA-based RLT outside of prostate cancer.

EP-0881

FAP-directed Radiopharmaceutical Therapy in metastatic gastrointestinal carcinoma as rescue therapy after failure of conventional treatments: A retrospective analysis on safety, efficacy and survival

E. Perrone[1]*, K. Ghai*[2]*, T. Parkar*[2]*, A. Eismant*[2]*, R. Moretti*[3]*, L. Greifenstein*[2]*, R. P. Baum*[2]*;*
[1]Nuclear Medicine Unit, Fondazione Policlinico Universitario Agostino Gemelli, IRCCS, Rome, ITALY, [2]CURANOSTICUM Wiesbaden-Frankfurt, Center for Advanced Radiomolecular Precision Oncology, Wiesbaden, GERMANY, [3]Unità della Fisica per le Scienze della Vita, Fondazione Policlinico Universitario Agostino Gemelli, IRCCS, Rome, ITALY.

Aim/Introduction: Gastrointestinal carcinoma encompasses a group of common tumours characterized by high morbidity and mortality. In metastatic cases resistant to conventional treatments, fibroblast activation protein (FAP)-directed Radiopharmaceutical Therapy (FRT) using α- or β-emitting nuclides targets the FAP-expressing cancer-associated fibroblasts present in tumour microenvironment. We studied safety, efficacy and survival of advanced gastrointestinal cancer patients treated with FRT with β-emitters Lutetium-177 or Yttrium-90, and/or α-emitter Actinium-225, as rescue therapy after established treatments. ***Materials and Methods:*** We retrospectively analysed 23 patients who received α-FRT or β-FRT (or combined -TANDEM) with 3BP-3940, a FAP-binding peptide, following high uptake confirmation on 68Ga-3BP-3940 PET/CT (03/2021-03/2025). CTCAE v.5.0 was used to grade acute adverse events and long-term haematological, renal and hepatic toxicity in patients with ≥1 follow-up (n=21). Molecular imaging-based response was assessed in 18 patients according to THERCIST (PET/CT, or post-therapeutic SPET/CT). For remaining 5 patients, progression was determined based on clinical outcome (death). By late March 2025, survival was calculated from first FRT to death. ***Results:*** We treated 17 males and 6 females (31-81 years at first FRT) with oropharyngeal (n=1), oesophageal (n=3), gastro-duodenal (n=4), colo-rectal (n=13), anal (=1) carcinoma, and cholangiocarcinoma (n=1). Previous treatments included: chemotherapy (96%); surgery of primary (61%); radiotherapy of primary or metastases (61%); Bevacizumab (56%); surgery of metastases (35%); immune-checkpoint inhibitors (39%); tyrosine-kinase inhibitors (39%). 65 FRT cycles were totally administered over 48 months (monotherapies: thirty-six 177Lu-3BP-3940, eight 90Y-3BP-3940, three 225Ac-3BP-3940; TANDEM: fifteen 225Ac/177Lu-3BP-3940, three 225Ac/90Y-3BP-3940). Five patients received 1 cycle, six patients 2 cycles, seven patients 3 cycles, two patients 4 cycles, three patients ≥5 cycles. FRT was overall well-tolerated, with few G1 acute adverse events, mainly emesis (n=3). Long-term toxicity after FRT included anemia G1/G2 (38%), anemia G3 (9%), leukocytopenia G1/G2 (24%), leukocytopenia G3 (5%), thrombocytopenia G1/G2 (14%), hepatotoxicity G1/G2 (24%) and G3 (5%) in patients with hepatic metastases, creatinine increase G1 (5%); one patient experienced acute on chronic renal insufficiency two weeks after FRT, then recovering. No patients discontinued FRT due to toxicity. Molecular imaging-based response showed seven partial remission, and eleven disease progression; in five patients death occurred before the assessment. At analysis, 8 patients were alive (follow-up: 2-27 months) and 15 patients had died (survival: 3 days-15 months). ***Conclusion:*** FRT with radiolabelled-3BP-3940 is overall safe for patients with advanced gastrointestinal carcinoma. Considering

its palliative purpose, both therapy response and survival were encouraging, but larger, prospective trials are needed to improve clinical outcome.

EP-0882

Sustained Tumor Retention of Lu-177 PSMA-617 in Recurrent High-Grade Gliomas: a step further in theranostics

V. Arunachalam Ragupathi, *N. Damle, M. Tripathi, S. Shamim, V. Tandon, K. Haresh, S. Bharati, A. Kumar, S. Gupta, A. Singhal, S. Rastogi, A. Mohan;*
All India Institute of Medical Sciences, Delhi, INDIA.

Aim/Introduction: Prostate-specific membrane antigen (PSMA), has emerged as a promising molecular target in non-prostatic malignancies, including high grade gliomas (HGG). This study explores if PSMA expression in recurrent HGG is sustained enough to have any potential as a therapeutic target, focusing on tumor retention kinetics of low-dose Lu-177 PSMA-617. ***Materials and Methods:*** Patients with PSMA expression more than or equal to liver on a diagnostic PET/CT and a favorable ECOG performance status underwent tumor retention scans with low-dose Lu177 PSMA-617 (5-7 mCi) tumor retention studies. Serial imaging was performed at multiple time points (minimum of three) close to 4, 24, 48, 96, and 120 hours. Tumor to liver and tumor to parotid ratios were obtained by the total counts within the regions of interest to evaluate radiotracer retention dynamics. ***Results:*** Of 24 patients who underwent PSMA PET/CT (median age: 43 years), 21 showed uptake in suspected recurrent lesions, with 18 (85.7%) more than or equal to liver background activity. Nine patients meeting inclusion criteria underwent serial low-dose Lu-177 PSMA-617 imaging. All nine demonstrated sustained tumor retention of the radiotracer up to the final imaging point with mean tumor-to-liver and tumor-to-parotid ratios progressively increased from 0.63 and 0.23 at baseline to 4.1 and 2.3, respectively, by the last time point, indicating favorable retention kinetics of Lu-177 PSMA-617 within recurrent lesion. ***Conclusion:*** These preliminary results support the potential utility of Lu-177 PSMA-617 as a theranostic agent for recurrent high-grade gliomas. The observed sustained in vivo tumor retention following low-dose Lu-177 PSMA-617 administration highlights its promise for delivering targeted radiation and provides a strong foundation for future therapeutic trials in this difficult-to-treat population.

EP-0883

^{68}Ga/^{177}Lu-PSMA Theranostics in Recurrent High-Grade Glioma

A. Karlberg[1,2], *B. E. Vindstad*[2], *H. Tøndel*[1], *H. Johansen*[1], *T. M. Keil*[1], *E. M. Berntsen*[1,2], *O. Solheim*[1,2], *S. Kjærnes Øen*[1], *T. Skeidsvoll Solheim*[1,2], *L. Eikenes*[2];
[1]*St. Olavs Hospital, Trondheim, NORWAY,* [2]*Norwegian University of Science and Technology, Trondheim, NORWAY.*

Aim/Introduction: In this ongoing study, ^{68}Ga/^{177}Lu-PSMA theranostics is evaluated as a treatment alternative for patients with recurrent high-grade glioma. The overall aim is to improve existing diagnostic and therapeutic methods and possibly increase the overall survival and quality of life for this patient group. ***Materials and Methods:*** All patients received standard treatment with surgery, radiotherapy and chemotherapy prior to inclusion, and were left with no other treatment options at recurrence/progression. Eligible patients were selected for treatment based on a positive ^{68}Ga-PSMA-PET/MRI examination. ^{177}Lu-PSMA (7.4 GBq) was administered with 6-8 weeks intervals and continued as long as the patient tolerated the treatment well and dose limits to critical organs were not met. The safety, tolerability and efficacy of ^{177}Lu-PSMA treatment were assessed during study visits in each treatment cycle using PET/MRI, SPECT/CT, neurological tests, quality of life questionnaires and blood tests. ***Results:*** To date, nine patients (CNS WHO grade 4 glioblastoma (n=6), CNS WHO grade 4 astrocytoma (n=1) and CNS WHO grade 3 astrocytoma (n=2)) have been included. ^{68}Ga-PSMA-PET prior to treatment demonstrated tumor uptake in eight patients (median SUV_{max}: 5.4, range: 2.0-10.3). The uptake in normal brain was low, yielding high TBR values (median TBR_{peak}: 40.3, range: 22.3-104.1). Five patients qualified for treatment and have either completed (n=3) or started treatment (n=2). A total of 15 treatments have been administered (1-7 treatments/patient). Absorbed doses per treatment ranged from 0.8-7.3 Gy for tumors, 1.7-4.4 Gy for kidneys and 1.1-3.3 Gy for parotid glands. A rapid wash-out of activity was observed in all glioblastomas, while the retention in the grade 4 astrocytoma was notably longer, resulting in the highest tumor dose (7.3 Gy). No grade 3 or grade 4 toxicities were observed. The most common patient reported symptoms were fatigue and transient xerostomia. Among the three patients that have completed treatment (all glioblastomas), two were stable during the treatment cycles and one progressed, based on radiological evaluation (MRI, RANO). ***Conclusion:*** Despite low tumor doses, the radiological stability of disease in two of the patients with glioblastoma is promising. The higher tumor dose and longer retention in the grade 4 astrocytoma is also encouraging, possibly indicating that the treatment could be more efficient for this glioma type. However, the study needs to be completed to draw any conclusions.

EP-0885

Potential impact of PRRT with Lutetium 177 DOTATATE in patients with recurrent high risk meningiomas

I. Dev[1], *A. Puranik*[2,3], *A. Agrawal*[2,3], *N. Purandare*[2,3], *S. Shah*[2,3], *S. Choudhury*[4,3], *S. Ghosh*[4,3], *M. M V*[4,3], *V. Rangarajan*[2,3];
[1]*Advanced Center for Training, Research & Education in Cancer (ACTREC), Tata Memorial Center Homi Bhabha National Institute, Navi Mumbai, Mumbai, INDIA,* [2]*Tata Memorial Hospital, Mumbai, INDIA,* [3]*Bhabha National institute, Mumbai, INDIA,* [4]*Advanced Centre for Treatment, Research and Education IN Cancer (ACTREC), Tata Memorial Hospital, Mumbai, INDIA.*

Aim/Introduction: There are no definite treatments available in recurrent meningioma. These tumors express somatostatin receptors (SSTR) on the cell-surface; targeted by radiolabeled-peptides such as Gallium68-DOTATOC/NOC/TATE. Gallium-68 when replaced with Lutetium-177 (Beta emitter) exhibits tumour killing properties. Lu177-DOTATATE therapy i.e. Peptide Receptor Radionuclide Therapy (PRRT), is a potential treatment option in recurrent meningioma. We therefore studied the efficacy & safety of PRRT in 20 recurrent meningioma patients who had progressed on standard-of-care treatment. ***Materials and Methods:*** 20 recurrent meningioma patients referred for PRRT were included. Maximum 4 sessions of PRRT (dose ~7.4GBq per session) were given with a gap of 8-12 weeks. Response assessment was done on MRI using RANO criteria at the end of 2nd & 4th session of PRRT. 6 month PFS rate was used as an outcome measure. CBC, LFT, RFT were performed one week before PRRT and at 2-4 weeks & 6-8 weeks after PRRT. CTCAE V.5 criteria were used for safety and toxicity assess. ***Results:*** Of 20 patients, 6M/14F with age range 26-65 & KPS range 80-90. Most common site of recurrence was frontal lobe(9) then sphenoid wing(6), occipital(2), parietal(1), clival(1) & cerebellum(1). Histopathology Grade II in 12 patients, grade I in 7, grade III in 1. Five of 20 patients had metastases; bones, lungs & adrenals. PRRT sessions ranged from 1 to 4. 2 metastatic patients showed clinicoradiological progression, 3 patients failed to follow-up after 1 PRRT. Nine patients received 4 & seven received 2 PRRT doses. Follow up data for 15 patients was available for analysis. Response assessment: Partial response (PR) was the best response. 3 of 15 (20%) patients had PR after 2 PRRT doses. 10 (66%) had stable disease (SD) & 2 (13%) progressed (PD); of these, one patient had grade 3 histology. Out of 9 patients who received 4 PRRT, 6 patients had SD, 2 PD & 1 PR. 6-months Progression Free Survival:

Overall 6 months PFS rate was 76.4%. For recurrent grade I pts was 83% & 80% for recurrent grade II (extended 1 year PFS rate dropped to 50%) & for grade III was 0%.Safety: No patient developed grade 3 or 4 toxicities during treatment. ***Conclusion:*** PRRT is an effective, safe treatment for disease control in patients with recurrent meningioma after standard treatment. Further randomised trials are required to validate these results.

EP-0886

Tumor dosimetry and correlations with pre-therapeutic SSTR PET in patients receiving [^{177}Lu]Lu-DOTATATE treatment for recurrent meningioma

M. Mair[1,2], *A. Delker*[1], *K. J. Müller*[3], *V. Stoecklein*[4], *L. Wiegand*[1], *A. C. Wehn*[4], *V. Wenter*[1], *M. Zacherl*[1], *M. Preusser*[2], *M. Brendel*[1], *P. N. Harter*[5,6,7], *C. Schichor*[4], *N. L. Albert*[1,6,7];
[1]*Department of Nuclear Medicine, LMU University Hospital, LMU Munich, Munich, GERMANY,* [2]*Division of Oncology, Department of Medicine I, Medical University of Vienna, Vienna, AUSTRIA,* [3]*Department of Neurology, LMU University Hospital, LMU Munich, Munich, GERMANY,* [4]*Department of Neurosurgery, LMU University Hospital, LMU Munich, Munich, GERMANY,* [5]*Center of Neuropathology and Prion Research, LMU University Hospital, LMU Munich, Munich, GERMANY,* [6]*Bavarian Cancer Research Center (BZKF), Partner Site Munich, Munich, GERMANY,* [7]*German Cancer Consortium (DKTK), Partner Site Munich, Munich, GERMANY.*

Aim/Introduction: Radioligand therapy with [^{177}Lu]Lu-DOTATATE has shown disease stabilization in small studies of recurrent meningioma, and trials in this indication are ongoing. However, data on dosimetry and correlations with pre-therapeutic somatostatin receptor (SSTR) PET are limited. ***Materials and Methods:*** In this retrospective study, patients with recurrent meningioma treated with [^{177}Lu]Lu-DOTATATE were included. Post-treatment ^{177}Lu-SPECT/CT was performed 24, 48 and 72 hours after administration of [^{177}Lu]Lu-DOTATATE. Lesion dosimetry was performed with a mono-exponential fit model using MIM SurePlan MRT and PETEdge+ segmentation on SPECT 24h after administration. Lesions in pre-therapeutic SSTR PET were segmented using SUV>4 as segmentation threshold. ***Results:*** Overall, 14 patients (7 [50.0%] females) were included, of whom 4 (28.6%) had CNS WHO grade 1, 5 (35.7%) CNS WHO grade 2, and 4 (28.6%) CNS WHO grade 3 meningioma. Median age at first [^{177}Lu]Lu-DOTATATE administration was 55 years (range: 33-82). In median, patients were pre-treated with 2 resections (range: 1-5) and 1 course of radiotherapy (range: 0-4), while no systemic treatments had been applied. In total, 48 [^{177}Lu]Lu-DOTATATE cycles were administered (median: 4 cycles per patient [range: 2-8]) with a median activity of 7.8 GBq (range: 7.0-8.1). Data for dosimetry calculations were available in 27 cycles, and the median number of segmentable lesions in SPECT/CT was 2.5 (range: 1-9). In median, the tumor-absorbed dose (TAD) per cycle was 0.3 Gy/GBq (range: 0-2.8), while the effective tumor half-life was 26.4 hours (range: 8.0-63.1). TAD in the first course was higher in CNS WHO grade 3 (median: 2.4 Gy/GBq [range: 0.6-2.8]) compared to CNS WHO grade 2 (median: 0.3 Gy/GBq [range: 0.2-0.8], $p = 0.016$) and CNS WHO grade 1 (median: 0.4 Gy/GBq [range: 0.2-1.3], $p = 0.005$). SUV_{mean} in pre-therapeutic SSTR PET correlated with TAD ($r = 0.639$, $p = 0.004$) of respective lesions. Analyses on associations of dosimetry with treatment response are ongoing. ***Conclusion:*** In this retrospective single-center analysis, TAD was associated with CNS WHO grade and pre-therapeutic SUV_{mean} in SSTR PET. Prospective trials are warranted to define overall efficacy and dose-response relationships.

EP-0887

Treatment with 188-Rhenium resin for non-melanoma skin cancer. First treatments performed in Spain.

D. Vega Perez*, E. Martínez Albero, A. Saviatto Nardi, C. García Donoso, B. García Bracamonte, S. Angiolillo Grau, E. López Llobet, Á. Galiana Morón, B. Manzarbeitia Arroba, P. Zaragoza Ballester, X. Guarnizo, P. Ortiz Romero, M. Tabuenca Mateo;*
Hospital 12 de Octubre, Madrid, SPAIN.

Aim/Introduction: Treatment of non-melanoma skin cancer (NMSC) with 188-Rhenium resin (188-Re) is a therapeutic alternative to conventional techniques, such as surgery (gold standard), especially in patients who are not candidates for surgical treatment, either due to comorbidities or lesion characteristics (location and extent). In these scenarios, 188-Re is a useful tool, with good tolerance, low toxicity, and excellent response rates. The main objective of this study was to assess treatment response, reported symptoms and toxicity in a prospective sample of patients with NMSC treated at our center with 188-Re. ***Materials and Methods:*** We treated 11 patients(p) (3 women, 8 men) between June/2024 and January/2025, with a total of 13 lesions(L) in 3 treatment sessions.Our population has a mean age of 75.6 years (range 57-89 years). The lesions were all basal cell carcinomas (superficial type 3 (23.1%), extensive 4 (30.7%), infiltrative 5 (38.5%) and mixed type 1 (7.7%), with an invasion depth <3 mm (mean 1.5 mm, range 0.4-2 mm) and a mean surface area of 4.8 cm2 (range 2.1-13 cm2). The location of the lesions was: nasal tip 9L (69.2%), nasal wing 2L (15.4%), scalp 1L (7.7%) and nasal tip+wing 1L (7.7%). The target dose of 188-Re resin on all lesions was 50 Gy, with a mean administered activity of 397.65 MBq (range 89-670 MBq), and a mean treatment time of 120.5 min (range 50-186 min). Symptoms were assessed 15-30 days post-treatment, acute toxicity at 30 days according to the "Common Terminology Criteria for Adverse Events" (CTCAE version 5.0) scale, and response after 3-6 months using dermoscopy and confocal microscopy. ***Results:*** An average follow-up period of 6.38 months (2-11) was performed for the lesions. At the 15-day follow-up, the symptoms were: itching (9p:81.8%), burning (4p:36.4%), pain (1p:9%) and other (1p:9%). At 30 days, itching remained the predominant symptom (8p), although of lower intensity. Toxicity at 30 days was: G1 7L(53.8%), G2 5L(38.5%) and G3 1L(7.7%), with complete resolution of toxicity during follow-up. Treatment response was assessed in two patients with a minimum follow-up of 6 months, demonstrating a complete response with no evidence of recurrence. The remaining 9p are pending review as they have not completed the 6-month follow-up required to assess response and cosmetic outcomes according to the Radiation Therapy Oncology Group (RTOG) score. ***Conclusion:*** Treatment with 188-Rhenium resin is an effective therapy for NMSC in selected cases, with very good response, acceptable symptoms and tolerable toxicity.

EP-0888

[177Lu]Lu-FAP-2286 Treatment Response in Metastatic Lesions vs Local Recurrence Lesions in Breast Cancer Patients

M. Nasiri[1], *R. Nami*[2], *S. Banihashemian*[3], *G. Divband*[4], *A. Abolhosseini Shahrnoy*[2], *S. Mazidi*[5], *M. Akbari*[6];
[1]*Department of Cellular & Molecular Biology, School of Biology, Damghan University, Damghan, IRAN, ISLAMIC REPUBLIC OF,* [2]*Parsisotop Company, Tehran, IRAN, ISLAMIC REPUBLIC OF,* [3]*Cancer Research Center, Shahid Beheshti University of Medical Sciences, Tehran, IRAN, ISLAMIC REPUBLIC OF,* [4]*Khatam PET-CT Center, Khatam-al-Anbia Hospital, Tehran, IRAN, ISLAMIC REPUBLIC OF,* [5]*Parsisotope Company, Tehran, IRAN, ISLAMIC REPUBLIC OF,* [6]*Cancer Research Center, Shahid Beheshti University of Medical Sciences, Damghan, IRAN, ISLAMIC REPUBLIC OF.*

Aim/Introduction: This study aims to evaluate the relationship between tumor-absorbed radiation dose—both total and per milliliter (dose/mL), and tumor SUVmax and SUVmean, in breast

cancer patients with local recurrence (LR) and metastatic lesions following therapy with [177Lu]Lu-FAP-2286. ***Materials and Methods:*** This retrospective analysis included six breast cancer patients with local recurrence and 16 metastatic lesions identified by [68Ga]Ga-FAP-2286 PET/CT. All patients underwent six cycles of [177Lu]Lu-FAP-2286 therapy. Pre- and post-treatment tumor metrics—including SUVmax, SUVmean, and lesion volume—were measured. Dosimetry was performed using the MIRDCALC method to determine both total absorbed dose and dose/mL for each lesion. Patients were grouped based on treatment response: Group 1 (n = 6): Non-locally metastatic lesions with significant decrease in SUVmax/SUVmean and tumor size; Group 2 (n = 16): Locally recurrence lesions with progressive disease. Statistical analysis included Spearman's correlation to assess the relationship between dosimetry parameters and response metrics, along with linear regression modeling. ***Results:*** Interestingly, all metastatic lesions showed a significant reduction in SUVmax (ΔSUVmax percentage= 80.9 ± 5.15) (P=0.022), SUVmean (ΔSUVmean percentage= 68.9 ± 8.1) (P=0.012), and Tumor volume (ΔTumor volume percentage= 77.4 ± 7.45) (P=0.012) after treatment. In contrast, local recurrence lesions demonstrated an increase in volume post-therapy (-99.9±50.5) despite equal total absorbed doses relative to metastatic lesions (204333.3±38742.4 vs 252125±1658.13 respectively). Notably, the absorbed dose/ml (mGy/ml) was significantly greater in metastatic lesions (58222.7±17.6) than in local recurrences (272.2±71.5), correlated with better response to treatment in lesion volume (ρ=0.55, p=0.008), SUVmax (ρ=0.63, p=0.002), and SUVmean (ρ=0.58, p=0.004). ***Conclusion:*** These findings suggest that despite of association between higher tumor-absorbed dose/ml with improved response in metastatic breast cancer lesions; the heterogeneity of local recurrences and potentially inflammatory rather than truly neoplastic nature of some local recurrence lesions, may lead to lower dose/ml uptake of [177Lu]Lu-FAP-2286 and consequently lack of response in these lesion.

EP-0889

Disease control rate in patients with advanced meningioma performing PRRT: an updated meta-analysis

B. Muoio[1], *C. Iacovitti*[2], *D. Bosetti*[1], *M. Cuzzocrea*[2], *G. Paone*[2], *G. Treglia*[2];
[1]*EOC IOSI Oncology Institute of Southern Switzerland, Bellinzona, SWITZERLAND,* [2]*EOC Imaging Institute of Southern Switzerland, Bellinzona, SWITZERLAND.*

Aim/Introduction: Peptide receptor radionuclide therapy (PRRT) is a treatment option for patients with advanced meningioma overexpressing somatostatin receptors. The aim of this study is to perform an updated meta-analysis to establish the disease control rate in patients with advanced, progressive or refractory meningioma performing PRRT. ***Materials and Methods:*** A comprehensive literature search of studies on PRRT in patients with advanced meningioma was carried out. Four different databases (PubMed/MEDLINE, EMBASE, Cochrane library, Google Scholar) were screened until April 2025. Only original articles about PRRT in advanced, progressive or refractory meningiomas were selected. Case reports were excluded. Three review authors independently performed the literature search, the article selection and the data extraction. Main findings of eligible studies were summarized and a proportion meta-analysis on the disease control rate was carried out using a random-effects model. ***Results:*** 17 studies (251 patients) published from 2006 to 2024 were included in the meta-analysis. In most of the included studies PRRT was performed using [^{177}Lu]Lu-DOTATATE. The pooled disease control rate was 66.3% (95% confidence interval values: 58.1-74.5%). PRRT was well-tolerated in most of the patients with advanced meningioma. Moderate statistical heterogeneity was found in the meta-analysis (I-square: 51%). ***Conclusion:*** PRRT in patients with advanced meningiomas is active and well-tolerated, showing a significant disease control rate (in about two-thirds of patients). Results from well-designed clinical trials are needed to corroborate these findings, but evidence-based data seem to support the clinical use of PRRT for this indication.

EP-0890

Tumour-absorbed dose and efficacy of peptide receptor radionuclide therapy with ^{90}Y-DOTATOC in patients with refractory meningioma

L. Schweiger*;*
Medical University of Innsbruck, Department of Nuclear Medicine, Innsbruck, AUSTRIA.

Aim/Introduction: The management of treatment-refractory meningioma in patients with previous surgical resection and radiation therapy remains challenging due to a lack of further treatment options. Therefore, novel therapeutic applications, such as peptide receptor radionuclide therapy (PRRT) targeting somatostatine receptors, may offer a promising therapeutic strategy. We aimed to assess the tumour-absorbed dose and efficacy of PRRT with ^{90}Y-DOTATOC in patients with treatment-refractory meningioma. ***Materials and Methods:*** In this study, 10 patients with therapy-refractory meningioma were retrospectively included. All patients received systemic ^{90}Y-DOTATOC therapy following prior surgical resection and radiation therapy. In total, 21 lesions were assessed morphologically by contrast-enhanced MRI and ^{68}Ga-DOTATOC PET/CT both before and after therapy. All patients underwent dosimetry with ^{111}In-DOTATOC prior to ^{90}Y-DOTATOC therapy. Treatment response was evaluated according to RANO bidimensional and volumetric criteria, as well as overall survival (OS). ***Results:*** The median cumulative activity administered per patient was 3804 MBq (range: 3140 - 4050 MBq), with a median of 3 cycles (range: 1 - 7). On lesion-based analysis following PRRT, response assessment was available only in 19/21 (91.5%) lesions. Among these, tumour stabilisation according to RANO criteria was observed in 7/19 (36.8%) lesions, with a median cumulative tumour-absorbed dose of 52.7 Gy. Morphological tumour progression was noted in 12/19 (63.2%) lesions, with a median cumulative tumour-absorbed dose of 43.8 Gy. Although lesions classified as stable disease (RANO) received a higher median cumulative absorbed dose, the difference in tumour-absorbed doses between morphologically stable and progressive lesions according to RANO criteria was not statistically significant (P=0.82). Values for SUV_{max} and SUV_{mean} from pretherapeutic ^{68}Ga-DOTATOC PET/CT significantly correlated with the tumour-absorbed doses (P=0.018 for SUV_{max}, P=0.021 for SUV_{mean}, respectively). Posttherapeutic ^{68}Ga-DOTATOC PET/CT demonstrated an increase in SUV_{max} in 19/21 (90.5%) lesions (median: 40.8%, range: 13.0% - 101.2%). The median OS was 23.0 months (95% CI 12.5 - 33.5 months). ***Conclusion:*** Our preliminary results indicate no significant difference in tumour-absorbed doses between morphologically stable lesions and those with progressive disease, as defined by the RANO criteria. However, lesion-based analysis revealed a significant correlation between pretherapeutic ^{68}Ga-DOTATOC PET/CT uptake and tumour-absorbed doses following ^{90}Y-DOTATOC therapy. Lesion-based assessment of ^{68}Ga-DOTATOC PET/CT imaging showed increased tracer uptake in nearly all lesions after ^{90}Y-DOTATOC therapy. These findings suggest that baseline PET/CT may serve as a valuable tool for estimating cumulative tumour-absorbed dose and guiding the optimal cumulative activity of PRRT.

EP-0891

Gastrointestinal Adverse Effects in ^{177}Lu-FAPI-2286 Radioligand Therapy: Contributing Factors and Strategies for Reducing Uptake-Related Symptoms

N. Raeisi*, A. Saber Tanha, K. Aryana;*
Nuclear Medicine Research Center, Mashhad University of Medical Sciences, Mashhad, IRAN, ISLAMIC REPUBLIC OF.

Aim/Introduction: This study aims to evaluate the factors influencing the intensity of gastrointestinal uptake in patients

undergoing ^{177}Lu-FAPI-2286 therapy, as well as to assess strategies for reducing uptake and its associated symptoms. ***Materials and Methods:*** In this study, we included 13 patients who underwent ^{177}Lu-FAPI-2286 therapy, primarily for palliative care or as a potential end-stage treatment. The cancers represented in this cohort included papillary and medullary thyroid cancers, colorectal, breast and nasopharyngeal malignancies. Post-treatment non-tumoral gastrointestinal uptake were assessed in two time points: early whole-body scan at 24 hours and again between 48 to 72 hours post-treatment. The scans were evaluated for the presence, intensity and variations in pattern of bowel uptake. Concurrently, patient's clinical histories were reviewed, focusing on opium consumption, bowel habits (categorized as constipation, diarrhea, or normal), and post-treatment gastrointestinal symptoms. Additionally, patients were queried about the use of prokinetic agents or laxatives during this period. ***Results:*** Out of the 13 patients, 11 exhibited bowel uptake in the early post-treatment scans. One patient with diarrhea showed no bowel uptake. Other 12 patients included five patients with constipation and seven with normal bowel habits, one of whom also showed no bowel uptake. All five patients with constipation were opium users for pain relief. Of the 11 patients with bowel uptake, four patients demonstrated more intense uptake, and all four had a history of opium-related constipation. Among the opium user patients, only one demonstrated lower bowel uptake compared to the others, which is thought to be related to laxative consumption three months prior to radioligand therapy. Among four patients with opium consumption who exhibited intense bowel uptake in the early scan, three demonstrated decreased uptake in the delayed imaging following the use of laxative medications, while one patient declined to use these medications. Four patients experienced gastrointestinal adverse event grade 1-3 (according to CTCEA v3.0) following the first cycle of radioligand therapy, all of whom were opium users, and their delayed imaging indicated significant bowel uptake. Notably, after administering pre-treatment with laxatives for three of these patients in the subsequent treatment cycle, none reported gastrointestinal upset. ***Conclusion:*** Our experience suggests that intestinal accumulation of ^{177}Lu-FAPI-2286 may result in gastrointestinal complications after treatment, which is especially concerning for patients with constipation associated with opiate use. Our findings suggest that prescribing laxatives for this group of patients may help prevent gastrointestinal adverse events and improve overall comfort during treatment.

EP-54

e-Poster Area

C: Therapy Clinical Study -> C2 Non-Oncological Treatments -> C21 Non-Oncological Treatments (including Thyroid Benign)

EP-0892

Efficacy of Radiosynoviorthesis in the Management of Non-Infectious Synovialitis Following Total Knee Arthroplasty

D. Simankova[1], *M. Simanek*[2], *A. Simankova*[1];
[1]*Institute of Nuclear Medicine, First Faculty of Medicine, Charles University and General University Hospital in Prague, Prague, CZECH REPUBLIC,* [2]*Orthopaedic Department of Sokolov Hospital, Sokolov, CZECH REPUBLIC.*

Aim/Introduction: To evaluate the therapeutic effect of radiosynoviorthesis (RSO) on clinical symptoms of non-infectious synovialitis in patients following total knee arthroplasty (TKA). ***Materials and Methods:*** This retrospective study included 13 patients (4 females, 9 males; mean age: 66 ± 8 years) who developed recurrent joint effusion and pain in the operated knee, with symptom onset occurring on average within six months post-TKA. Diagnosis of non-infectious synovialitis was confirmed via three-phase bone scintigraphy with SPECT/CT during the blood pool phase. Each patient received an intra-articular injection of 222 MBq of yttrium-90 (Y-90). Clinical follow-up was conducted for a minimum of six months. Outcome measures included objective assessments - joint range of motion, load-bearing capacity, and recurrence of effusion -and subjective evaluation of pain using a visual analogue scale (VAS) questionnaire. ***Results:*** All patients exhibited a clinically meaningful response to RSO, with significant reduction in pain, improved joint mobility, and enhanced tolerance to load. The mean pain score on VAS decreased from 6.8 prior to treatment to 0.5 after therapy. In 12 of the 13 patients, therapeutic benefits were sustained throughout the follow-up period. In one patient, symptoms recurred after six weeks, however this was due to the aseptic loosening of the prosthesis. ***Conclusion:*** Radiosynoviorthesis appears to be an effective and minimally invasive treatment option for managing non-infectious synovialitis following TKA, particularly when other conservative or surgical interventions are limited. In this smaller cohort, Y-90 administration provided durable symptom relief in the majority of cases.

EP-0893

Identification of risk factors for relapse of Graves-Basedow disease after radioiodine treatment

S. Adamantiadis[1], *L. Urso*[1], *L. Manco*[2], *F. Sartori*[3], *M. Borghesi*[4], *V. Marino Picciola*[5], *A. Gobbo*[5], *L. Uccelli*[1], *M. C. Zatelli*[5], *M. R. Ambrosio*[5], *M. Bartolomei*[6], *C. Cittanti*[1];
[1]*Department of Translational Medicine, University of Ferrara, Ferrara, ITALY,* [2]*Medical Physics Unit, University Hospital of Ferrara, Ferrara, ITALY,* [3]*School of Medicine, University of Ferrara, Ferrara, ITALY,* [4]*Department of Economy and Management, University of Ferrara, Ferrara, ITALY,* [5]*Section of Endocrinology, Geriatrics and Internal Medicine, Department of Medical Sciences, University of Ferrara, Ferrara, ITALY,* [6]*Nuclear Medicine Unit, Onco-Hematology Department, University Hospital of Ferrara, Ferrara, ITALY.*

Aim/Introduction: Graves' disease (GD) is an autoimmune disorder that primarily affects the thyroid gland leading to hyperthyroidism, due to an overproduction of thyroid hormones. It's commonly and effectively treated with radioiodine treatment (RAI), using 131I. RAI damages and destroys thyroid cells, inducing a complete remission of hyperthyroidism in ~80% of patients. Aim of this work is to identify if any clinical/instrumental parameters collected before RAI are predictive of relapse in GD patients treated with dose-personalized 131I. ***Materials and Methods:*** GD patients treated with dosimetrically determined activities of 131I between 2010 and 2022 with a minimum follow-up of 2 years were retrieved. Clinical parameters (gender, age at RAI, FT4 and Thyrotropin Receptor Antibodies (TSHrAb) values at diagnosis, thyroid volume at ultrasound (US) performed within a month from RAI, 24h uptake of 131I, GREAT score and orbitopathy) were collected. RAI was performed by a dosimetric approach with gamma probe (Capintec Inc.) and the administered activity was calculated to achieve 300Gy to the gland, considering the 24h uptake and thyroid volume according to US. The evidence of GD relapse, defined as clinical and biochemical evidence of hyperthyroidism after RAI, was considered as outcome at multiple logistic regression. ROC curves were used to determinate cut-off values of significant clinical parameters. ***Results:*** 148 GD patients (41 males and 107 females; median age 55.72 years) treated with RAI were collected. The administered doses of 131I ranged between 5 and 16 mCi (median 9 mCi). GD Relapse was observed in 31 patients (20.9%). Of those, in 14 cases (45.2%) relapse occurred within 9 months. Only 7 patients (22.6%) relapsed after receiving >10mC of 131I. At multiple logistic regression, administered activity, 24h uptake, thyroid volume, FT4 values and GREAT score were all significantly different in patients with or without GD relapse (all

p<0.01). At ROC curves, administered activity <9.5mCi and 24h uptake >74.1% were the best cut-offs to predict GD relapse after RAI. ***Conclusion:*** The efficacy of RAI is confirmed in our cohort of GD patients, in which a definitive resolution of hyperthyroidism was achieved in 79.1% of cases. Patients who showed GD relapse were those with the higher value of 24h uptake of 131I and the lower administered dose of 131I, leading us to conclude that in glands that are very avid for iodine, predictive dosimetry using gamma probe may sometimes underestimate the 131I activity needed for an effective treatment.

EP-0894

Feasibility of Tc-99m-based pre-treatment dosimetry in patient receiving radioidine therapy for hyperthyroidism: comparison with pre- and post-treatment assessments

M. Meraldi, *C. Romanò, G. Muti, C. Carbonini, V. Piva, G. Cabrini, S. Capitanio, A. Franchini, E. Gay, A. F. Scarale, A. Spataro, C. Rossetti, P. E. Colombo;*
ASST Grande Ospedale Metropolitano Niguarda, Milan, ITALY.

Aim/Introduction: Patient-specific activity determination is recommended in radioiodine therapy for hyperthyroidism to optimize therapeutic efficacy while minimizing radiation exposition. Due to a temporary unavailability of I-131 capsules, thyroidal maximum uptake was estimated using Tc-99m at our center. This study aimed to assess the feasibility of Tc-99m-based pre-treatment dosimetry by correlating Tc-99m uptake at 20 minutes (Tc99m_U(20min)) with I-131 uptake at 24 hours (I131_U(24h)) to determine the activity required to deliver the prescribed dose. Post-treatment I-131 dosimetry was performed and used as a reference to evaluate the accuracy of pre-treatment dosimetry with Tc-99m. Iodine uptake and recommended activity (calculated according to the EANM guidelines) were derived from (i) Tc-99m pre-dosimetry and (ii) I-131 post-dosimetry, and then compared. Additionally, patient-specific activity was compared with the fixed activity of 600 MBq, recommended in absence of previous dosimetric evaluation. ***Materials and Methods:*** A logarithmic conversion equation from Tc99m_U(20min) to I131_U(24h) was derived based on a group of 82 patients who underwent both Tc-99m and I-131 pre-treatment dosimetry at our center. Iodine uptake was determined via scintigraphy: Tc99m_U(20min) was measured 20 minutes after administration, while I-131 post-dosimetry uptake was measured at 1 and 6-8 days after treatment. In a cohort of 16 patients, iodine uptake and activity based on Tc-99m pre-dosimetry were compared with those derived from I-131 post-dosimetry. In the same group, patient-specific activity was compared with the fixed one. ***Results:*** The relationship between Tc99m_U(20min) and I131_U(24h) followed the equation I131_U(24h)=11.68xln(Tc99m_U(20min))+31.50. Tc-99m pre-dosimetry overestimated iodine uptake compared to I-131 post-dosimetry, with median pre-to-post discrepancy of 36% (range: 0% to 96%). This led to a lower recommended activity from Tc-99m pre-dosimetry, with a median pre-to-post difference of -15% (range: -48% to 53%). The administration of a fixed dose resulted in 63% of patients receiving higher-than-required activities, with a median fixed-to-post discrepancy of 26% (range: -40% to 502%). ***Conclusion:*** Tc-99m proved to be a feasible alternative for pre-treatment dosimetry in case of I-131 capsule unavailability, thereby enabling the continuation of a patient-specific approach. Personalized dosimetry enabled tailored activity prescriptions and, in many cases, helped avoid unintended over- or under-dosing, which may occur with fixed-dose strategies. Further studies with larger cohorts are needed to enhance consistency.

EP-0895

Functional assessment of post-radiation xerostomia therapy with allogeneic mesenchymal stromal stem cells in patients with head and neck cancer by salivary gland scintigraphy - a phase I clinical trial

L. Lezaic[1], *A. Socan*[1], *G. Plavc*[2], *M. Kokalj*[2], *G. Mitrovic*[2], *O. Blatnik*[2], *A. Bavec*[3], *N. Tesic*[4], *K. Hartman*[4], *U. Svajger*[4], *P. Strojan*[2];
[1]*University Medical Centre Ljubljana, Division of Nuclear Medicine, Ljubljana, SLOVENIA,* [2]*Institute of Oncology Ljubljana, Ljubljana, SLOVENIA,* [3]*Faculty of Medicine, University of Ljubljana, Ljubljana, SLOVENIA,* [4]*Blood Transfusion Centre of Slovenia, Ljubljana, SLOVENIA.*

Aim/Introduction: Xerostomia is a common side effect of radiotherapy in patients with head and neck cancer that affects quality of life and for which there is no effective standard treatment. Mesenchymal stem cells (MSCs) represent a potential therapeutic option for these patients as they have both regenerative and immunomodulatory effects. The aim of this phase I study was to investigate the safety and preliminary efficacy of MSC treatment in patients with xerostomia following radiotherapy. ***Materials and Methods:*** Ten patients with grade 2-3 xerostomia after curative (chemo)radiotherapy for squamous cell carcinoma of the oropharynx and no evidence of disease recurrence >=2 years after treatment were to be included in the study. Allogeneic umbilical cord-derived MSCs were injected into both parotid glands and both submandibular glands. Salivary gland scintigraphy was performed before and 4 months after MSC injection. Qualitative (visual assessment per Schall criteria) and quantitative (ejection fraction, excretion velocity) parameters were evaluated at both time points, correlated to clinical outcome (clinical xerostomia grade, CTCAE v5.0) and evaluated statistically by non-parametric methods (p<0,05 considered for statistical relevance). ***Results:*** At the time of analysis, 5 patients had completed the functional assessment. Before and after MSC injection, there was no statistically significant change in Schall grade (2,9±0,8 vs. 2,9±0,9), ejection fraction (17,2±20,6% vs. 17,5±19,7%), excretion velocity (12,3±16,6%/1min vs. 13,1±15,0%/1min) and clinical grade of xerostomia (2,2±0,4 vs 2,2±0,4). ***Conclusion:*** In the interim analysis, no significant change was demonstrated by the MSC injection in the functional evaluation by salivary gland scintigraphy, which correlated with the results of the clinical findings. A full analysis after completion of enrollment and functional assessment is planned, as well as comparison with radiological, physiological and quality of life assessments (US, MRI, salivary flow and composition, biopsy).

EP-0896

The evaluation of radioiodine therapy out come after five years in patient with subclinical hyperthyroidism

S. Abdelrazek, *P. Szumowski, J. Mysliwiec, I. Sulima;*
Medical University of Bialystok, Bialystok, POLAND.

Aim/Introduction: Subclinical hyperthyroidism (SCH) is a state of increased thyroid function with few or no clinical definitive signs or symptoms of hyperthyroidism, characterized by a subnormal serum TSH level, with normal serum levels of free thyroxine (FT4), and free triiodothyronine (FT3). The prevalence of endogenous SCH varies considerably, between 0.6 and 16% . SCH is associated with increased risk of coronary heart disease mortality, incident atrial fibrillation, heart failure, fractures and all-cause mortality in patients with serum TSH levels < 0.1 mIU/l (grade 2 SCH). The risk of progression to overt hyperthyroidism (OHT) varies between studies 1-15% / year. The aim of our study was to evaluate the short term (5years) effect of radioiodine therapy (RAIT) on the achievement of euthyroidism, and prevention evolvement to overt hyperthyroidism. ***Materials and Methods:*** We treated 980 patients, aged 30-70 years; 370 patients with toxic multinodular goitre (TMNG), and 610 patients with toxic adenoma (TA). Malignant changes were excluded in all nodules by fine needle

aspiration biopsy. All the patients had serum TSH levels less than 0.1 mU/l and effective T-half measured by the use of T6 and T24 was more than 3 days at the time of treatment. The activity dose was calculated by the use of Marinelli's formula and ranged between 200-600 MBq. The absorbed dose (Gy) for TMNG ranged between 150 and 260, and for TA: 200-300. Follow up control was done every 6 weeks in the first year. Then every 6 months for four years. ***Results:*** In general the success of treatment after one year was: 99% of patient with TA and 92% of patient with TMNG achieved euthyroidism. 1% of patient with TA and 7% of patient with TMNG develop hypothyroidism. 1% of the patients had persistent hyperthyroidism and received second dose of radioiodine therapy. After 3 years of RAIT 2% of patient with TA and 8% of patient with TMNG develop hypothyroidism. After 5 years of RAIT 2% of patient with TA and 9% of patient with TMNG develop hypothyroidism. In all the patients the symptoms and signs of subclinical hyperthyroidism disappeared (palpitation, tachycardia, atrial fibrillation, exercise tolerance improved, the blood pressure normalised and the quality of life improved). ***Conclusion:*** The achievement of euthyroidism and the remission of the symptoms and signs of subclinical hyperthyroidism, were due to good diagnosis, well preparation of the patients; accurate measurement of administered activity, effective half-life, and well-organised follow up.

EP-0897

Radioactive iodine therapy in hyperfunctioning thyroid nodules: who are doomed to hypothyroidism?

D. Carvalho, *S. Barata, S. Paiva, I. Casimiro, J. Silva, L. Lemos, M. Monteiro, P. Lapa, G. Costa;*
ULS Coimbra - HUC, Coimbra, PORTUGAL.

Aim/Introduction: Radioactive iodine (RAI) therapy is a safe and effective treatment of hyperthyroidism caused by hyperfunctioning thyroid nodules (HTN). Although euthyroidism is the therapeutic target of RAI treatment in HTN, some patients develop hypothyroidism. This study aims to identify which factors may increase the risk of developing hypothyroidism after RAI in patients from our institution. ***Materials and Methods:*** A retrospective analysis was conducted using clinical data from the 64 patients with HTN who underwent RAI therapy in our department between February 2021 and April 2023. Parameters evaluated included age, gender, number of HTN, size of the dominant nodule, presence of hypofunctioning nodules, pre-RAI dose of thiamazole (pills per day), serum TSH levels prior to RAI therapy both with and without antithyroid medication, estimated mass of functioning thyroid parenchyma based on thyroid scan, RAI uptake at 24 hour (RAIU), degree of functional suppression of the extranodular parenchym and RAI activity (both total and per gram of thyroid tissue). The outcome, euthyroidism or hypothyroidism one-year after RAI treatment, was recorded. Univariate statistical analyses and multivariate logistic regression were employed to identify factors associated with treatment response. Statistical analysis was performed using SPSS-Statistics v.30.0., with a significance threshold set at $p<0.05$. ***Results:*** Of the 64 patients (50 female, 78.1%; mean age 65.50±12.21y, range:25-90), 43 (67.2%) had toxic adenoma, whereas 21 (32.8%) had toxic multinodular goiter. 21 patients (32.8%) develop biochemical hypothyroidism (defined as TSH>4.0µUI/mL). Older age was significantly associated with a higher risk of hypothyroidism (mean 70.5 vs. 63.0y, p=0.008), and logistic regression confirmed that each additional year increased the odds of hypothyroidism by 6.1% (OR=1.061; 95% CI:1.006-1.118; p=0.028). No significant differences were found regarding the other evaluated parameters. Regarding thyroid function markers, TSH levels under antithyroid therapy prior to treatment showed a borderline significant association (OR=2.63; 95% CI:0.97-7.15; p=0.058), suggesting higher TSH while on therapy may increase the risk of hypothyroidism. TSH levels without antithyroid drug, and thiamazole dose prior to treatment, were not significantly associated. ***Conclusion:*** Older age was the only significant predictor of post-RAI hypothyroidism. A borderline association with pre-treatment TSH under antithyroid therapy was observed. Although age emerged as a significant predictor, the limited sample size may have reduced the statistical power of the multivariable analysis, potentially obscuring other meaningful associations. These findings highlight the need for further investigation in larger cohorts to clarify additional predictive factors.

EP-0898

Ensemble learning model for the prediction of a response to ^{131}I-NaI therapy in hyperthyroidism - ablative dose concept

N. Pantic[1], *B. Radovic*[1,2], *B. Pantic*[3], *M. Kotur*[1], *L. Grujicic*[1], *J. Zivanovic*[1], *A. Novkovic*[1], *J. Petrovic*[1,4], *I. Grozdic Milojevic*[1,4], *D. Sobic Saranovic*[1,4], *V. Artiko*[1,4], *S. Odalovic*[1,4];
[1]*Center for Nuclear Medicine with PET, University Clinical Center of Serbia, Belgrade, SERBIA,* [2]*Faculty of Medicine, University of Pristina with temporary headquarters in Kosovska Mitrovica, Kosovska Mitrovica, SERBIA,* [3]*Freelance IT researcher, Belgrade, SERBIA,* [4]*Faculty of Medicine, University of Belgrade, Belgrade, SERBIA.*

Aim/Introduction: According to the European Association of Nuclear Medicine (EANM) guideline, there are two concepts for radioactive iodine (RAI) therapy delivery in patients with Graves disease (GD). In the functional dose concept, the aim of RAI therapy is to correct subclinical or overt hyperthyroidism with the goal of reaching euthyroidism as soon as possible, while in the ablative dose concept, the aim is to achieve hypothyroidism as soon as possible. The second approach is based on evidence that the definitive success rate in controlling hyperthyroidism with the utilization of the ablative dose concept is much higher than that obtained with the functional dose concept (> 90% vs. < 70%, respectively) (1). We are developing a model that will be able to predict a response to RAI therapy in patients with GD, a solitary hyperfunctioning nodule, and multiple hyperfunctioning nodules in multinodular goiter. ***Materials and Methods:*** A total of 901 patients who received RAI for the treatment of hyperthyroidism were included in the study. Achievement of hypothyroidism in the first six months after RAI therapy was the aim of the treatment. The adaptive boosting algorithm was utilized for the development of the model, with the main laboratory, nuclear medicine imaging, and clinical features serving as predictors. Further development of the model through the usage of an ensemble learning algorithm is in process. ***Results:*** Current test accuracy is 0.7. Free T4 (free thyroxine) level before the application of RAI, 24-h radioactive iodine uptake (RAIU), and 3-h RAIU contributed the most to the development of the model, with 26.18%, 23.56%, and 22.50%, respectively, followed by thyroid-stimulating hormone (TSH) level before the treatment with the contribution of 8.43%, duration of the previous pharmacotherapy in months with 8.01%, and age with 6.02%. Applied dosage in MBq contributed only 4.69%, while the diagnosis, type of previous pharmacotherapy, and gender didn't have a significant impact on the development of the model. ***Conclusion:*** A machine learning model can predict a response to RAI therapy with high accuracy. Its' further development will make decision-making in patients with hyperthyroidism more automated. ***References:*** 1. Campennì A, Avram AM, Verburg FA, Iakovou I, Hänscheid H, de Keizer B, et al. The EANM guideline on radioiodine therapy of benign thyroid disease. Eur J Nucl Med Mol Imaging. 2023 Sep;50(11):3324-3348. doi: 10.1007/s00259-023-06274-5.

EP-0899

Early and sustained thyroid volume reduction following radioiodine therapy in Graves' hyperthyroidism: A 6-month prospective study

R. Zhang, *H. Wang, Q. Jia, P. Chang, J. Tan, W. Zheng;*
Department of Nuclear Medicine, Tianjin Medical University General Hospital, Tianjin, CHINA.

Aim/Introduction: This prospective study aimed to investigate the temporal dynamics of thyroid gland weight (TGW) reduction in patients with Graves' hyperthyroidism during the first six months following initial radioiodine (^{131}I) therapy. ***Materials and Methods:*** A total of 239 consecutive patients undergoing ^{131}I therapy were analyzed through serial ultrasound assessments. Three overlapping cohorts were established based on paired measurement intervals: Cohort A (n=217, baseline vs 2 weeks post-treatment), Cohort B (n=106, 2 weeks and 3 months post-treatment), and Cohort C (n=66, 3 months and 6 months post-treatment). Nonparametric statistical analysis using Wilcoxon signed-rank tests was performed for paired comparisons for the three Cohorts, respectively. ***Results:*** The mean baseline TGW was 33.1 ± 22.1 g (n=239 cases). Rapid initial reduction (to 23.1±15.5g) occurred within two weeks (n=217), followed by progressive declines to 18.1±12.1g at 3 months (n=120) and 14.4±10.8g at 6 months post-treatment (n=96). Cohort A showed a significant decrease in TGW from 27.3 g (IQR: 18.4-40.5) to 18.0 g (IQR: 12.5-30.1) at 2 weeks ($P < 0.001$, $Z=-12.329$). Continued reductions were observed in Cohort B (19.7 g to 14.7 g, $P < 0.001$, $Z=-7.519$) and Cohort C (15.6 g to 10.3 g, $P < 0.001$, $Z=-6.966$). ***Conclusion:*** ^{131}I therapy significantly reduces TGW in patients with Graves' hyperthyroidism, with maximal therapeutic effect occurring within the first 2 weeks post-treatment, followed by sustained but attenuated volume reduction over time within 6 months, highlighting the importance of early monitoring in clinical management.

EP-0901

Radiation Synovectomy with 177Lu-MAA in Patients with Inflammatory Knee Joint Disorders

K. Saglam[1], *M. S. Sağer*[1], *S. Bilgiç*[2], *E. Karayel*[1], *H. Pehlivanoğlu*[1], *A. Aygün*[1], *N. Yeyin*[1], *M. K. Özşahin*[1], *M. Özer*[1], *C. D. Davulcu*[1], *H. Botanlıoğlu*[1], *S. Asa*[1], *O. E. Şahin*[1], *R. L. Uslu*[1], *H. B. Sayman*[1];
[1]*Istanbul University-Cerrahpasa, Istanbul, TÜRKIYE,* [2]*Uludag University, Bursa, TÜRKIYE.*

Aim/Introduction: Pigmented villonodular synovitis (PVNS) is a benign, proliferative, and inflammatory synovial disease of unknown etiology. In the treatment of PVNS or PVNS-like chronic inflammatory conditions characterized by synovial hypertrophy, both surgical synovectomy and radiation synovectomy are considered as therapeutic options. The radionuclides commonly used for radiosynovectomy include 90Y, 177Lu, and 188Re. However, the routine use of 90Y often poses challenges in terms of cost and availability. 177Lu, when labeled with macroaggregated albumin (MAA), forms a complex with particle sizes between 10-90 µm and binds with >99.5% efficiency. This study aimed to evaluate the use of 177Lu-MAA for radiosynovectomy in patients with PVNS-like inflammatory knee conditions, with the goal of reducing inflammation and pain. ***Materials and Methods:*** Patients with clinical, laboratory, and imaging findings indicating the need for radiosynovectomy were prospectively selected. 10 patients were included. Pre-treatment knee MRI and bone scintigraphy were performed. On the day of treatment, 8-10 mCi of 177Lu-MAA was injected intra-articularly into the knee. Follow-up imaging at 3 and 6 months post-treatment was requested. Clinical outcomes were assessed using the KOOS (Knee Injury and Osteoarthritis Outcome Score) and VAS (Visual Analog Scale) for pain at baseline and at 1, 3, 6, and 12 months post-treatment. ***Results:*** Post-injection scintigraphy on the day of treatment and day 7 showed intra-articular distribution of the radiopharmaceutical. Whole-body planar imaging confirmed that there was no significant extra-articular leakage. Only two patients developed transient effusion, and no persistent side effects or radiation-induced damage were observed. Among nine patients with follow-up imaging, five showed partial regression in at least one modality, four were stable. The KOOS scores showed the most improvement at 3 months post-treatment, rising from 48.58% pre-treatment to 60.29%—a 24% relative increase. Although the scores declined to 58.22% at 6 months and 53.50% at 12 months, they remained significantly improved compared to baseline. The mean VAS score decreased from 50.5% at baseline to 29.5% at 1 month, reached a low of 22% at 6 months, and returned to 29.5% at 12 months. ***Conclusion:*** This study demonstrated a rapid improvement in KOOS and VAS scores in the early post-treatment period. Although a slight decline was observed by the 12th month, the improvements remained notable compared to pre-treatment values. The results suggest that 177Lu-MAA is a promising radiopharmaceutical with a favorable safety profile for use in routine radiosynovectomy. However, repeated dosing may be required for sustained benefit in long-term follow-up.

EP-0902

Graves' Disease: Is Hyperthyroidism Still Present 6 Months After Radioactive Iodine Treatment Really a Failure?

M. Acar Tayyar, *E. Uyanık, M. Mülazımoğlu, M. Ö. Tamam, S. Karyağar, M. Biçen Altın, F. Yıldız Kabaca, M. Cinoğlu Karaca, A. Vergili, T. Özülker;*
University of Health Sciences, Prof. Dr. Cemil Tascioglu City Hospital, Istanbul, TÜRKIYE.

Aim/Introduction: Graves' disease is one of the most common causes of hyperthyroidism and effective treatment options include radioactive iodine (RAI) therapy. According to the American Thyroid Association guidelines, if the patient is still hyperthyroid 6 months after RAI, it is considered a treatment failure and repeat treatment is recommended.The aim of this study was to examine the accuracy of the 6-month assessment and factors associated with late hypothyroidism to accept treatment failure or to decide on dose repetition after a single dose of RAI for Graves' disease. ***Materials and Methods:*** In our study, who developed hypothyroidism or euthyroidism within 24 months after single dose RAI treatment with a diagnosis of Graves' disease between 2003 and 2022, who were followed up regularly for at least 2 years, who had no extrathyroidal symptoms, who had no nodules on pre-treatment ultrasound, and who had iodine uptake tests were analysed retrospectively.The study group was divided into 2 groups as patients who developed hypothyroidism within the first 6 months and patients who developed hypothyroidism after the 6th month. ***Results:*** The mean age of 104 patients (74 females,30 males) included in our study was 46.7±13.0years.The mean RAI dose was 10.6±4.4mCi and the mean duration of hypothyroidism was 5.5±5.4months.15 patients were euthyroid and 89 patients were hypothyroid.65 patients developed hypothyroidism in the first 6 months and 24 patients developed hypothyroidism after 6 months. In patients with late hypothyroidism(>6 months); 2-hour iodine uptake value was higher and TSH values after RAI were statistically significantly lower.While 58.5% of patients with early hypothyroidism(<6 months)required antithyroid drug(ATD) treatment after RAI, all patients who developed hypothyroidism after 6 months received supportive treatment with ATD.The 24-hour iodine uptake percentage values were statistically significantly higher in the hypothyroid group than in the euthyroid group.In follow-up data, 26.9% of patients were hypothyroid at 0-3 months and 62.5% at 3-6 months,while this rate increased to 77.9% at 12 months. 20.1% of patients were still hyperthyroid at 6 months,while this rate decreased to 3.8% at 12 months.

Conclusion: This study has shown that the 6th month after RAI treatment in Graves' disease patients may be an early time to assess treatment failure.Hypothyroidism develops at a cumulative rate and this rate increases gradually in the first 12 months.Iodine uptake tests at 2-24 hours for dose calculation are indicative of the course of hypothyroidism/euthyroidism and the development of early and late hypothyroidism in the patient.

EP-55

e-Poster Area

D: Technical Studies -> D1 Instrumentation -> D11 SPECT and SPECT/CT

EP-0903

Impact of attenuation correction on SPECT/CT myocardial perfusion imaging in relation to Body mass Index (BMI)

S. Mammeri[1], *A. Bouzidi*[2];
[1]*University Military Hospital of Ouargla Algeria, Ouargla, ALGERIA,* [2]*University Military Hospital of Constantine, Constantine, ALGERIA.*

Aim/Introduction: Obesity is an increasing health concern in the worldwide, and attenuation artifacts are more commonly observed in individuals with higher mass index (BMI). This study aimed to assess the role of CT-AC in improving interpretation agreement for myocardial perfusion imaging and explored whether its efficacy differs among BMI groups. ***Materials and Methods:*** In this prospective study, 85 patients with known or suspected coronary artery disease underwent stress/rest Tc-99m MIBI SPECT/CT myocardial perfusion imaging (MPI) over two days.Two blinded readers independently analyzed MPI results,comparing attenuation-corrected(AC) and non-attenuation-corrected (NAC) images. the cohort was stratified by BMI (<30 [n=55] and ≥30 [n=30]).Invasive coronary angiography performed within± 3 months of MPI , served as the reference standard.Readers were blinded to clinical data and AC/NAC status. ***Results:*** For detection of significant CAD (≥ 70% stenosis)Overall performance: AC -SPECT showed lower sensitivity (86% vs 96%) but higher specificity (88% vs 51%) and accuracy (87% vs 78%) compared to NAC-SPECT . By BMI category: BMI <30: sensitivity : 84%(AC) vs 87%(NAC). Specificity: 87%(AC) vs 54% (NAC).BMI ≥30: sensitivity: 89%(AC) vs 94% (NAC).Specificity: 91%(AC) vs 45% (NAC).AC-SPECT demonstrated significantly improved specificity versus NAC -SPECT overall (p <0.001) and in both BMI groups (both p<0.001). ***Conclusion:*** Our study indicated that CT-based attenuation correction (AC) significantly improved specificity across all BMI categories, including both BMI< 30 and BMI ≥30 ,as well as in the overall study population.Althought a slight reduction in sensitivity was observed, the use of AC resulted in a net improvement in the diagnostic accuracy of Tc-99m sestamibi myocardial perfusion imaging (MPI). Key Words: Attenuation correction. single photon emission tomography.Body mass index.CT. ***References:*** 1. Hendel RC, Berman DS, Cullom SJ, Follansbee W, Heller GV, Kiat H, et all. Multicenter clinical trial to evaluate of correction for photon attenuation and scatter in SPECT myocardial perfusion imaging. circulation 1999;99:2742-9.2. Thompson RC, Heller GV, Johnson LL, Case JA,Cullom SJ, Garcia EV, et all.Value of attenuation correction on ECG-Gated SPECT myocardial perfusion imaging related to body mass index.Journal of nuclear cardiology.2005;12(2):195-202.3.Apostolopoulos DJ, Savvopoulous C.What is the benefit of CT-based attenuation correction in myocardial perfusion SPECT .Hellenic journal of nuclear medicine.2016;19(2):89-92.4. Freedman N, Schechter D,Klein M, Marciano R,Rozenman Y,Chisin R.SPECT attenuation artifacts in normal and overweight persons, insights from a retrospective comparison of Rb-82 positron emmision tomography and Tl-201 SPECT myocardial perfusion imaging .Clin Nuc Med 2000;25:1019-23.

EP-0904

Towards 3D: an advanced flow phantom to validate dynamic renal SPECT imaging

H. Suoraniemi[1], *M. Seppänen*[2], *T. Noponen*[1];
[1]*Department of Clinical Physiology, Nuclear Medicine, Turku PET Centre and Medical Physics, Turku University Hospital and Wellbeing Services county of Southwest Finland, Turku, FINLAND,* [2]*Department of Clinical Physiology, Nuclear Medicine and Turku PET Centre, Turku University Hospital and Wellbeing Services County of Southwest Finland, Turku, FINLAND.*

Aim/Introduction: Next-generation ring-design SPECT/CT systems enable the transition from dynamic two-dimensional (2D) region of interest (ROI) planar imaging to three-dimensional (3D) volume of interest (VOI) SPECT imaging. While dynamic 3D SPECT offers improved quantification and accuracy, its validation requires a phantom capable of 3D dynamic acquisition. Most available renal flow phantoms are designed for 2D planar imaging. We introduce an advanced dynamic flow phantom with a realistic anatomical structure simulating normal renal perfusion, uptake, and clearance kinetics to evaluate the feasibility of dynamic renal 3D SPECT acquisitions. ***Materials and Methods:*** Custom-designed models representing left and right kidneys were 3D-printed and integrated into a flow system. The kidney model was designed as an anatomically realistic 3D structure mimicking the renal cortex, medulla, and pelvis. In the measurements 30 MBq of ^{99m}Tc pertechnetate was injected into the flow system to simulate renal perfusion, while additional 40 MBq was administered to a torso phantom containing the 3D-printed kidneys to simulate background activity. Acquisitions were performed with a ring-design SPECT/CT system. Data were acquired in list-mode format and reconstructed using a regularized iterative algorithm with (AC) and without (NC) CT-based attenuation correction. Left and right kidney VOI time-activity curves (TAC) were analyzed to compare kinetic parameters, including time to peak (T_{peak}), time to half-out ($T_{1/2out}$), and area under the curve (AUC), between AC and NC images. The uptake and clearance of left and right kidneys were compared by calculating relative functions (1-2, 1-3, 2-3 min) and residual activities (at 4, 6, 10 and 13 min). ***Results:*** Kinetic parameters (left/right) for AC reconstructions were 130±11/140±12 s (T_{peak}), 230±8.0/248±7.2 s ($T_{1/2out}$), 4000±190/4300±250 kcounts (AUC) and for NC reconstructions 123±7.8/106±6.1 s (T_{peak}), 225±5.8/235±8.3 s ($T_{1/2out}$), 567±23/587±35 kcounts (AUC), respectively. Relative renal functions (left/right) for AC reconstructions were 50.6±2.4%/49.4±2.4% (1-2 min), 49.5±1.9%/50.5±1.9% (1-3 min), and 48.4±1.8%/51.6±1.8% (2-3 min). Residual activities (left/right) were 43.1±3.1%/47.5±2.6%, 22.7±2.7%/25.3±1.5%, 11.6±1.6%/12.4±1.5%, and 8.6±1.4%/9.6±0.5% at 4, 6, 10, and 13 min, respectively. ***Conclusion:*** Our results demonstrate reproducible flow patterns in the phantom resembling normal renal functions. AC and NC reconstructed TACs showed comparable uptake and clearance patterns. Relative renal functions and residual activities indicate symmetrical functions between the left and right kidney phantoms. The developed flow phantom models the normal kidney functions reproducibly, serving as an excellent accessory for dynamic renal 3D SPECT validation. Our results show that 3D renal SPECT is feasible with a ring-design SPECT/CT system.

EP-0905

Evaluation of the SIMIND Monte Carlo Program on a planar and SPECT system using ^{177}Lu demonstrated potential for personalized dosimetry

M. Dias[1,2], *P. Ferreira*[1], *R. Parafita*[1], *M. Costa*[1], *F. Oliveira*[1], *L. C. Silva*[1], *Â. Silva*[1], *J. Cruz*[2], *D. C. Costa*[1];
[1]*Champalimaud Foundation, Lisboa, PORTUGAL,* [2]*Faculdade de Ciências e Tecnologia, Universidade Nova de Lisbon, Lisbon, PORTUGAL.*

Aim/Introduction: Single-photon emission computed tomography (SPECT) images of ^{177}Lu-radioligand therapy (RLT) are of paramount importance for ^{177}Lu-RLT dosimetry. Digital SPECT scanner simulations can help determine the best parameters to be used in the real SPECT acquisitions for each patient, and consequently improve dosimetry estimation. This work aims to evaluate SIMIND's ability to accurately reproduce phantom images using ^{177}Lu in our real SPECT scanner. Additionally, we aim to compare the results obtained with the benchmark results obtained with ^{99m}Tc. ***Materials and Methods:*** SIMIND Monte Carlo software (v8.0) was used to simulate projections to be reconstructed with the PyTomography library, based on the ordered subset expectation maximization (OSEM) algorithm. CT attenuation correction and scatter estimation based on the triple energy window (TEW) method were utilized. Our SIMIND SPECT scanner was validated by comparing the simulation results of the National Electrical Manufacturers Association (NEMA NU 1-2007) tests with those obtained from experimental measurements performed on our Phillips BrightView SPECT scanner. Intrinsic spatial resolution (ISR) and intrinsic spatial linearity (ISL) were measured using the NEMA slit transmission test pattern. A point source and planar acquisitions were used to complete these tests and obtain the intrinsic energy resolution (IER). A petri dish and a cylinder water phantom were used to calculate system planar and SPECT sensitivity. The first three tests employed ^{99m}Tc, while the sensitivity experiments also included ^{177}Lu. Low-energy high-resolution (LEHR) and medium-energy general purpose (MEGP) collimators were used for ^{99m}Tc and ^{177}Lu experiments, respectively. ***Results:*** Based on ^{99m}Tc, ISR was 3.395 mm and 3.227 mm, ISL was 0.71 mm and 0.76 mm, and IER was 9.85% and 9.68%, for simulated and real systems, respectively. System planar sensitivity was 76.2 cps/MBq and 75.4 cps/MBq for ^{99m}Tc, and 7.6 cps/MBq and 7.7 cps/MBq, with ^{177}Lu for simulated and real systems, respectively. The measured and simulated SPECT sensitivity for ^{99m}Tc were 2.90x10^5 cps/(MBq/cm^3) and 3.17x10^5 cps/(MBq/cm^3), respectively. SPECT sensitivity for ^{177}Lu were 3.26x10^4 cps/(MBq/cm^3) and 3.38x10^4 cps/(MBq/cm^3), respectively. The computed SIMIND simulations agree (within 5%) with real measurements made in our SPECT scanner, except for the ISL and SPECT sensitivity for ^{99m}Tc, which presented deviations of about 6-9%. ***Conclusion:*** We can conclude that SIMIND is suitable for modelling our real SPECT scanner. These results motivate further investigation of SIMIND's potential to reproduce real clinical images. They have the potential to allow personalized dosimetry in ^{177}Lu-RLT of real patients.

EP-0906

Breathing artifact remotion in SPECT/CT images of liver lesions: a phantom-based study

G. Abbatini[1,2], *B. Cassano*[1], *M. D'Andrea*[1], *R. Sciuto*[3], *A. Soriani*[1], *S. Ungania*[1], *L. Miseo*[4], *G. Iaccarino*[1];
[1]*Medical Physics Unit, IRCCS Regina Elena National Cancer Institute, Rome, ITALY,* [2]*Post Graduation School of Medical Physics, University of Rome "Tor Vergata", Rome, ITALY,* [3]*Nuclear Medicine Unit, IRCCS Regina Elena National Cancer Institute, Rome, ITALY,* [4]*Medical Physics Service, USL Umbria 2, Foligno, ITALY.*

Aim/Introduction: Dosimetry of liver lesions in Selective Internal Radiotherapy (SIRT) is affected by respiratory motion, which causes blurring and artifacts in SPECT images leading to activity mis-estimation. This effect is amplified by the co-registration with a CT scan acquired during an unknown respiratory phase. The aim of this study is to propose a method to compensate for respiratory motion during SPECT acquisition, in order to obtain a breath-hold like image suitable for co-registration with an inhalation-phase CT. Consequently, having both the SPECT and CT in the same respiratory phase allows for improved accuracy in prescribing the activity of ^{90}Y-labelled resin microspheres to be administered for therapy. ***Materials and Methods:*** The method consists of a free-breathing SPECT acquisition (FB-SPECT), a planar scintigraphy and a CT, both acquired during the breath-hold (BH) inhalation phase. A camera tracks respiratory motion during FB-SPECT by capturing positions of a marker-box placed on the patient's abdomen. The developed algorithm computes the optimal breathing kernel to achieve the best agreement between the first FB-SPECT projection with the BH-image. The method was validated by performing four studies (S1-S4) on a moving respiratory phantom. Spheres filled with ^{99m}Tc were inserted to simulate lesions. In S1 and S2, a sphere with a radius of 0.8 cm was used. S3 and S4 were performed with a 2 cm radius sphere including a cold spherical insert (radius = 1 cm) simulating a necrotic lesion. The phantom moved sinusoidally (2 cm amplitude) in S1 and S3, and in a real patient's breathing pattern in S2 and S4. Performance was evaluated using a relative recovery coefficient (rRC). By contouring a ROI on the BH-CT along the physical dimensions of the sphere, rRC was defined as the ratio of the counts within the ROI for the SPECT reconstructions to the counts in the BH-SPECT (gold standard). Both uncorrected and corrected images were evaluated (rRC_u and rRC_c, respectively). ***Results:*** In S1 and S2, rRC_u was 41% and 17%, whereas rRC_c was 95% and 96%, respectively. Similarly, in S3 and S4, rRC_u was 63% and 53%, while rRC_c reached 93% and 95%. ***Conclusion:*** The results demonstrate the ability of the algorithm to compensate for respiratory motion in SPECT images. Studies on patients undergoing liver radioembolization treatments with ^{90}Y-labelled resin microspheres are needed to verify the clinical potential of the proposed method and to assess dosimetric implications of respiratory motion artifact.

EP-0907

Optimization of ^{99m}Tc SPECT in the presence of ^{90}Y: towards a single-session radioembolization workflow

C. Kerckhaert*, M. M. A. Dietze, R. van Rooij, M. B. M. Meddens, N. Wijnen, M. L. J. Smits, M. G. E. H. Lam, H. W. A. M. de Jong; University Medical Center Utrecht, Utrecht, NETHERLANDS.*

Aim/Introduction: Technetium-99m macro aggregated albumin (^{99m}Tc-MAA) imaging is typically used for treatment planning of yttrium-90 (^{90}Y) radioembolization, with planning and therapy performed in separate sessions [1]. Our hospital is exploring a single-session workflow that combines these procedures using a hybrid C-arm SPECT/CBCT scanner for intra-procedural ^{99m}Tc-imaging [2]. To validate this interventional scanner, an additional ^{99m}Tc SPECT will be acquired post-procedurally on a conventional clinical system. However, residual ^{90}Y activity may compromise image quality of the post-procedural ^{99m}Tc SPECT through crosstalk. This study investigates the feasibility of ^{99m}Tc SPECT imaging from combined ^{99m}Tc+^{90}Y acquisitions and identifies the most effective method for mitigating ^{90}Y-induced image degradation. ***Materials and Methods:*** An anthropomorphic torso phantom with two liver tumor inserts was imaged using single-isotope (^{99m}Tc) and dual-isotope (^{99m}Tc +^{90}Y) configurations. Three collimators (low energy high resolution: LEHR, medium energy: ME, and high energy: HE) and three methods to compensate for ^{90}Y crosstalk (Monte Carlo-based, dual-energy-window and triple-energy-window correction) were evaluated. Quantitative analyses included tumor contrast recovery, extrahepatic activity recovery and lung shunt fraction accuracy. In addition, potential dead-time effects due to high ^{90}Y flux were investigated using point-source measurements. ***Results:*** Point-source measurements indicated no substantial dead-time effects up to approximately 12 GBq with LEHR, 29 GBq with ME and >30 GBq with HE (^{99m}Tc:^{90}Y ratio 1:20). Compared to the clinical standard (single-isotope ^{99m}Tc imaging with LEHR collimator), contrast recovery typically decreased from 80.0 ±1.5 % to 56.8 ±1.2 % (LEHR), 70.3 ±1.9 % (ME) or 72.5 ±1.5 % (HE) due to ^{90}Y crosstalk. Use of compensation methods increased the contrast recovery level, with the combination of Monte Carlo-based compensation with a ME or HE collimator

producing the best contrast recovery at 78.6 ±2.0 and 79.4 ±1.7 %, respectively. Lung shunt estimations were substantially degraded by ^{90}Y crosstalk, but this could be effectively mitigated by using a ME or HE collimator. In terms of visual quality, the ME collimator resulted in the best resolution and the least scatter contamination. ***Conclusion:*** Dual-isotope imaging with ^{99m}Tc and ^{90}Y is feasible at clinically relevant activities without introducing significant dead-time effects. Monte Carlo-based compensation method in combination with a ME collimator offers the most accurate, robust and visually optimal reconstruction method for post-radioembolization ^{99m}Tc SPECT. ***References:*** 1. Salem R, Thurston KG., Journal of Vascular and Interventional Radiology, 2006 2. Dietze MMA et al., European Radiology, 2022.

EP-0908

Use of myocardial SNR in optimisation of myocardial perfusion scintigraphy

T. Biggans*, J. Asogan Vaishnavi, A. K. Raofi, P. Guntur Ramkumar; NHS Tayside, Dundee, UNITED KINGDOM.*

Aim/Introduction: Signal-to-noise ratio (SNR) is an objective measure that can be used to determine appropriate reductions in both administered activity and acquisition time while maintaining sufficient image quality. SNR is typically calculated using an area of uniform uptake which is not found in myocardial perfusion scintigraphy (MPS). The aim of this work was to develop and assess a novel technique to determine myocardial SNR based on the methods described by Armstrong et al. and Schmidtlein et al. and use this metric to determine an optimised protocol for MPS. ***Materials and Methods:*** An anthropomorphic torso phantom was filled with ^{99m}Tc in three configurations: no defects, mid anterior defect and basal inferior defect. SPECT-CT acquisitions were performed with the phantom in each configuration with and without simulated breast attenuation. Patients with a BMI ≥ 35 kg/m^2 who underwent Stress MPS at Ninewells Hospital, Dundee, Scotland between 1st March 2023 and 30th November 2024 were selected for retrospective analysis. Acquisitions were reconstructed using conventional ordered subsets expectation maximisation (OSEM) and cardiac dedicated maximum a posteriori (MAP) algorithms. SNR within the myocardium was derived from parametric images (mean and standard deviation) generated from multiple replicate images created through repeated Poisson resampling of the acquisition data. An optimised protocol was determined and simulated using Poisson resampling. Current protocol and proposed protocol image sets were shown as a side-by-side comparison and two consultant radiologists were asked to score image quality for each set using a scale of 0-3 and to comment on any discrepancy between the two image sets. ***Results:*** The phantom study using OSEM resulted in a mean SNR of 9.3 and 10.3 with and without breast attenuation respectively. Mean SNR with and without breast attenuation improved by 41% and 32% respectively using the cardiac dedicated MAP algorithm. Simulation of the derived optimised protocol gave a mean SNR of 9.8. The mean image quality score for both image sets was 2.4 out of 3 and only minor differences were noted on four occasions. ***Conclusion:*** Myocardial SNR can be measured and used to determine an optimised MPS SPECT-CT protocol that maintains image quality. ***References:*** Armstrong et al. (2019). Assessing time-of-flight signal-to-noise ratio gains within the myocardium and subsequent reductions in administered activity in cardiac PET studies. J. Nucl. Cardiol., 405-412. Schmidtlein et al. (2010). Using an external gating signal to estimate noise in PET with an emphasis on tracer avid tumors. Phys. Med. Biol., 6299-6326.

EP-0909

Incidental detection of ATTR cardiac amyloidosis by ^{99m}Tc-DPD bone scintigraphy and SPECT/CT

M. Corza Ayala*, R. Hernandez Ramírez, K. Cárdenas Soto, A. Arriaga Contreras, F. Solano Caballero, O. Lucio Baez; Instituto Nacional de Ciencias Médicas y Nutrición Salvador Zubirán, Ciudad de México, MEXICO.*

Aim/Introduction: Cardiac transthyretin amyloidosis (CA-ATTR) is an underdiagnosed genetic disease caused by the deposition of misfolded TTR protein, resulting in multiorgan dysfunction and death. Recent data suggest that it may be responsible for up to 30% of cases of heart failure with preserved ejection fraction in patients over 75 years of age. Early detection is crucial to improve patient prognosis and quality of life. 1, 2. Underdiagnosed CA-ATTR predominantly affects adults and is associated with high morbidity and mortality. 2 Early detection is crucial to initiate timely treatment and improve prognosis. Incidental myocardial uptake of bone tracers in BS, although relatively common (1.46% to 3.6%), often goes unrecognized, delaying diagnosis and treatment of the disease. The high prevalence of this uptake underscores its epidemiological importance 3,4,5. Early detection using BS could improve patient outcomes, providing a scalable and cost-effective screening tool. Aim: To determine the prevalence of incidental cardiac amyloidosis detected by bone scintigraphy in patients studied for different indications. ***Materials and Methods:*** This was an observational, descriptive, cross-sectional, analytical, and retrospective study. Imaging records from BS at the Salvador Zubirán National Institute of Medical Sciences and Nutrition were reviewed from January 1, 2022 to January 1, 2025. The Perugini index was assessed, and echocardiographic and clinical data were analyzed for those with an index ≥2. ***Results:*** A total of 834 bone scans were evaluated within the study period, a total of 25 patients with Perugini ≥ 2 and 2 patients with index 4 were identified (prevalence of 2.9%), echocardiographic data of these patients were evaluated, of which 45% presented alterations. ***Conclusion:*** Targeted evaluation of cardiac topography on any bone scan is advisable, as it may aid in the incidental diagnosis of cardiac amyloidosis. ***References:*** 1 Briseño Godínez et al. What a neurologist must know of hereditary ATTRv amyloidosis. Revista Mexicana de Neurociencia. 2022;24:41-51. 2. Gilstrap LG, et al. Epidemiology of Cardiac Amyloidosis-Associated Heart Failure Hospitalizations Among Fee-for-Service Medicare Beneficiaries in the United States. Circ Heart Fail. 3. Nebhwani M, et al. Detection of cardiac amyloidosis on routine bone scintigraphy: an important gatekeeper role for the nuclear medicine physician. Int J Cardiovasc Imaging.4. Cuscaden C, et al. Estimation of prevalence of transthyretin (ATTR) cardiac amyloidosis in an Australian subpopulation using bone scans with echocardiography and clinical correlation. JNC. 5. Bianco M, et al. The prevalence of TTR cardiac amyloidosis among patients undergoing bone scintigraphy. Journal of Nuclear Cardiology.

EP-0910

Imaging the Impractical: Optimising Imaging for Therapies With Under 10 MBq of Beta-Emitting P32

C. Oldfield*, S. Sargant; Manchester Foundation Trust, Manchester, UNITED KINGDOM.*

Aim/Introduction: Pancreatic cancer has a poor prognosis. With a one-year survival around 10 %[1]. Clinical trials using P32 as a molecular radiotherapy agent are currently underway for patients with locally advanced non-resectable pancreatic cancer. Due to the small size of the tumours these treatments require activities from 2 to 60 MBq with the pure beta emitting isotope. Imaging following administration is important to confirm the P32 is correctly localised, and with this treatment the production of

high quality images proves a unique challenge. Whilst lessons can be learnt from the imaging of Y90 SIRT, the fact that this therapy can use up to three orders of magnitude less activity means that image formation is inherently high noise. A combination of phantom work and reprocessing of the acquired data for first two patients treated at Manchester Foundation Trust was used to develop robust acquisition and reconstruction for these patients. ***Materials and Methods:*** A series of SPECT-CT acquisitions were performed of a water phantom containing an insert representing focal administration of 16 MBq of P32. Scan lengths were varied to acquire data consistent with patient administrations from 2 to 60 MBq. Choices of energy window were explored at acquisition. At reconstruction the matrix size, number of iterations, number of subsets, and size of the post-reconstruction Gaussian smoothing filter were all varied and the impact on image quality explored. After establishing an appropriate acquisition protocol for the first patient only the impact of choices in reconstruction were explored using clinical data. ***Results:*** The primary barrier for lower administered activities is image noise. As such, steps to suppress this in the reconstruction were valuable. Using a 64x64 matrix, only using 20-30 updates with 1 subset, and applying a smoothing filter of 15-25 mm was necessary to provide images useful for clinical interpretation. The use of a wide energy window such at 75-125 keV captures an adequate fraction of the output bremsstrahlung photons, and the use of low septal-penetration collimators helps preserve the limited spatial information. ***Conclusion:*** It is a key part of the role of a physicist to be involved in optimisation. Imaging in a high noise environment requires serious compromise in the way that data are acquired and reconstructed. The tools used to produce images of diagnostic utility here will be applicable to other radiopharmaceuticals and clinical scenarios and may provide a useful reminder. ***References:*** [1] Survival for pancreatic cancer, CRUK https://www.cancerresearchuk.org/about-cancer/pancreatic-cancer/survival 04/05/2025.

EP-0911

Clinical implementation of an Advanced SPECT/CT service on the GE Healthcare Aurora Gamma Camera

L. Rowley, *E. Comber, C. Low, V. Leung, O. Adesanya;*
University Hospitals Coventry and Warwickshire, Coventry, UNITED KINGDOM.

Aim/Introduction: Following the installation of the GE Healthcare Aurora gamma camera with a 128-slice Revolution Ascend CT scanner, our institution transitioned from planar radionuclide imaging and low dose SPECT/CT imaging to high resolution, diagnostic quality SPECT/CT, incorporating intravenous contrast when clinically indicated. This shift necessitated the development of a new vetting and imaging workflow. Protocol optimisation was undertaken using Clarify Deep-Learning (DL) reconstruction to reduce acquisition time, and a "one-stop" imaging approach incorporating contrast-enhanced CT for Whole-Body Bone SPECT/CT and Sestamibi parathyroid imaging. ***Materials and Methods:*** Patients with prior history of widespread metastatic disease, confirmed on previous planar bone imaging, continued with planar imaging to enable accurate follow-up and comparison of like-for-like images. New referrals and patients with previously negative or limited disease underwent both planar and whole-body SPECT/CT imaging. Similarly, new referrals for Sestamibi parathyroid imaging without a positive Ultrasound scan SPECT/CT and patients with previously negative or limited disease underwent both planar and Dynamic contrast-enhanced 4D CT imaging of the parathyroid.A retrospective analysis of 20 bone scans was performed to evaluate reduced imaging times using the new low energy high-resolution sensitivity (LEHRS) collimators. Phantom studies and patient image reconstructions were used to determine the optimal beta value for Clarify-DL, with image quality assessed by experienced radiologists.A dedicated workflow was developed for intravenous contrast-enhanced CT in patients referred for prostate and breast cancer staging and a separate dedicated workflow was developed for 4D dynamic intravenous contrast-enhanced parathyroid SPECT-CT in patients referred for hyperparathyroidsm. These included the implementation of one-stop imaging services. Patient and referrer satisfaction was assessed via surveys, and a cost analysis was conducted. ***Results:*** The new workflow was successfully implemented for bone scans and parathyroid imaging, supported by comprehensive staff training. An initial adjustment period was required due to legacy referrals not aligning with the updated protocol. While the inclusion of SPECT imaging and contrast-enhanced CT increased the reporting workload, this presented challenges in aligning with existing radiology reporting allocations.Use of Clarify DL reconstruction enabled a reduction in imaging time, maintaining comparable throughput to planar imaging while preserving diagnostic quality. Patient feedback was overwhelmingly positive. ***Conclusion:*** The transition to whole-body SPECT/CT bone imaging and 4D dynamic contrast enhanced parathyroid imaging for all new referrals has been successfully achieved. This has resulted in enhanced image quality and diagnostic detail, improved service efficiency, and a better patient experience, with favourable implications for both clinical practice and cost-effectiveness.

EP-0912

Impact of Reduced Acquisition Time on Quantitative Gated SPECT Parameters Using a Dedicated CZT Cardiac Camera

T. Cakir[1], *A. Guner*[1], *V. Beylergil*[2];
[1]*Medipol University, Istanbul, TÜRKIYE,* [2]*Memorial Sloan Kettering Cancer Center, Istanbul, TÜRKIYE.*

Aim/Introduction: CZT gamma cardiac cameras allow for shorter imaging times due to their high count rate capability. The aim of this study was to evaluate whether the efficiency of gated myocardial perfusion imaging (MPI) can be maintained with a further reduction in acquisition time using a dedicated CZT cardiac camera. Specifically, we investigated the repeatability of quantitative parameters when the manufacturer-recommended imaging time of 3.5 minutes was reduced to 2 minutes. ***Materials and Methods:*** A total of 114 consecutive patients underwent gated stress MPI using a dedicated CZT gamma camera. For each patient, two sequential stress acquisitions of 3.5 minutes and 2 minutes were obtained without repositioning. The following quantitative parameters were analyzed in both acquisitions: summed stress score (SSS), ejection fraction (EF), peak filling rate (PFR), mean filling rate (MFR), and time to peak filling (TTPF). Statistical comparisons were performed using the paired t-test. ***Results:*** The mean age of participants was 62.8 ± 11.4 years (59 female, 52%). The average height was 160 ± 10 cm, and mean weight was 84 ± 15 kg. Table 1 summarizes the comparison between the 3.5-minute and 2-minute protocols: Although EF was statistically higher in the 3.5-minute scan (mean difference: 0.688, SD of difference: 3.037), the effect size was small (Cohen's d = 0.23), suggesting limited clinical relevance. No significant differences were found in SSS and TTPF. ***Conclusion:*** The findings suggest that a 2-minute gated stress imaging protocol is a viable alternative to the standard 3.5-minute acquisition when using dedicated CZT cardiac cameras, particularly for perfusion assessment. While statistically significant differences were observed in EF, PFR, and MFR, the magnitude of change in EF was small and may not be clinically meaningful. Caution is advised in interpreting systolic and diastolic functional parameters—especially in clinical scenarios where these metrics are critical. In such cases, the standard 3.5-minute acquisition remains preferable. Nevertheless, the 2-minute protocol may be acceptable for clinical or research settings where reduced scan time is necessary, provided that minor variations in functional measurements are considered during interpretation.

EP-0913

Optimization of Imaging Parameters for Posttherapeutic SPECT/CT in Patients with PSMA-Positive mCRPC Following ^{177}Lu-PSMA Radioligand Therapy

D. Sfiligoj Planjsek, *K. Senica, A. Strok, B. Simonic, I. Slodnjak, S. Rep;*
UMC Ljubljana, Ljubljana, SLOVENIA.

Aim/Introduction: Radioligand therapy with ^{177}Lu (^{177}Lu-PSMA-RLT), when combined with standard-of-care treatment, has proven safe and effective for patients with PSMA-positive metastatic castration-resistant prostate cancer (mCRPC). Although PSMA PET/CT remains the gold standard for imaging-based restaging, it is expensive and not always readily available [2]. SPECT/CT imaging of gamma emissions from ^{177}Lu, performed 1-2 days post-treatment, represents a more accessible and cost-effective alternative for posttherapeutic response monitoring. This study aimed to optimize SPECT/CT imaging parameters by reducing acquisition time, while preserving image quality. Specifically, we investigated the feasibility of switching from a double-bed SPECT/CT (neck to upper thighs) to a triple-bed SPECT/CT protocol (vertex to mid-thigh), better aligning with the coverage of PSMA PET/CT. ***Materials and Methods:*** We shortened the per-frame duration from 20 seconds (used in double-bed SPECT/CT) to 8 seconds for each of the 60 frames per bed position in the triple-bed setup. This reduced the total scan time from 60 minutes to 24 minutes. Image quality was assessed using a NEMA IEC PET Body phantom with six ^{177}Lu filled spheres with a sphere-to-background concentration ratio of 10:1 (spheres - 323 kBq/ml; background - 30.6 kBq/ml). Both visual and quantitative evaluations were performed. Quantitative metrics included maximum and mean activity concentration (Bq/ml), standardized uptake values (SUVmax and SUVmean), and contrast-to-noise ratio (CNR). ***Results:*** Visual assessment revealed no substantial difference in image quality between 20 s/frame and 8 s/frame protocols for larger spheres with diameter ≥ 17 mm. However, smaller spheres (diameter ≤ 13 mm) appeared less clearly defined in both acquisitions. The suboptimal visualization of smaller spheres may result from the relatively low activity of the ^{177}Lu isotope used. Quantitatively, there were no statistically significant differences in measured Bq/ml (max and mean) (p=0.16; p=0.74) and SUV values (max and mean) (p=0.26; p=0.83) for different sized spheres between the two protocols. The CNR for both acquisitions showed statistically significant differences in both Bq/ml (max and mean) with p=0.04 and p=0.03, respectively, and in SUV (max and mean) with p=0.041 and p=0.031, respectively. ***Conclusion:*** Our findings suggest that a shortened acquisition time for triple-bed SPECT/CT is a viable approach for imaging response assessment following ^{177}Lu-PSMA-RLT. The reduced imaging time improves patient comfort and minimizes motion artifacts, with only minor compromise in the detection of small lesions. Given the typically high metastatic burden in this patient population, the reduced resolution for small lesions is unlikely to impact clinical decision-making.

EP-56

e-Poster Area

D: Technical Studies -> D1 Instrumentation -> D12 PET/CT

EP-0914

Assessing Reduced Ga^{68} Activity and Shortened Acquisition Times on Image Quality and Lesion Contrast in LAFOV PET/CT: A Phantom Study.

G. Muti[1], *C. Romano*[1], *A. Didonna*[1], *M. Meraldi*[1], *C. Pettinato*[2], *C. Carbonini*[1], *C. Rossetti*[1], *P. Colombo*[1];
[1]*ASST GOM Niguarda, Milan, ITALY,* [2]*Fondazione IRCCS Ca' Granda, Milan, ITALY.*

Aim/Introduction: PET/CT scanners with a long axial field-of-view (LAFOV) enhance sensitivity, allowing for adjustments in imaging parameters such as reduced injected activity, shortened acquisition times, or extended uptake periods. This phantom study aimed to assess the effects of reduced Ga-68 activity doses on image quality and lesion detectability using the uMI Panorama GS PET/CT scanner. ***Materials and Methods:*** The NEMA IEC PET Body Phantom was filled with a 4:1 sphere-to-background activity ratio, with approximately a total activity of 37 MBq. Scanning was performed at 0, 3, 4, and 5-hours "post-injection". List mode reconstructions were conducted with five different acquisition durations (600, 300, 150, 120, and 60 seconds) using OSEM with 3 iteration and 10 subsets configuration, TOF and PSF corrections. SUV values (mean, max, min, peak) were calculated for five hot spheres (VOI_1: largest sphere, VOI_6: smallest sphere) and a background sphere (VOI_7). Tumor-to-background ratios (TBR: the SUV Lesion Peak divided by the SUV Background Mean) were used to assess lesion contrast and coefficient of variation of VOI_7 (CoV: the SUV standard deviation divided by the SUV Mean of the background) to asses image noise. A threshold of CoV <15% was considered for interpretation, as recommended by EFOMP [1]. ***Results:*** The SUV values for the acquisition at time 0-hours at varying reconstruction times had the same trend as the 600s acquisition as the activity decays. For these reconstructions, median values were: SUVMean 2% [Q1: 0.1%; Q3: 5%], SUVMin 5% [Q1: 1%; Q3: 10%], SUVPeak 2% [Q1: 0.1%; Q3: 5%], and SUVMax 7% [Q1: 3%; Q3: 12%]. Differences increased significantly for shorter acquisition times at 3, 4, and 5-hours "post-injection". CoV is <15% for all reconstructions at time 0, except for the 30 seconds scan, at 3-hours for 600 seconds and 300 seconds scans; at 4-hours only for 600 seconds; and at 5-hours, no scans achieved a CoV<15%. Polynomial fitting of CoV data suggests that for a 5-hours late acquisition a 15-minute scan is required to get a CoV <15%. ***Conclusion:*** These results indicate that for 4 hours (~4 half-lives) a 600s scan is sufficient, that a reduced activity level or extended uptake periods can be balanced with a not much longer acquisition, and that preliminary phantom estimates provide guidance on the scan duration needed for patient imaging. ***References:*** 1) EFOMP Protocol for Quality Control in PET/CT and PET/MRI. Available online: https://www.efomp.org/index.php?r=news/ view&id=277 (accessed on 22 May 2023).

EP-0915

Design and Initial Evaluation of a 2-Meter Axial FOV Total-Body PET System With Integrated DOI and TOF Capability

D. Liang, *Y. Lin, Z. Zhao, H. Zou, Y. Xu, H. Liu, Y. Lin, W. Ma, W. Zhu, J. Tao, H. Zhao, W. Li, Y. Zhang, Q. Peng;*
Shenzhen Bay Laboratory, Shenzhen, CHINA.

Aim/Introduction: Total-body positron emission tomography (TB-PET), with its ultra-long axial field of view (AFOV), enables high-sensitivity, low-dose, and rapid whole-body imaging in a single scan [1]. This study presents a TB-PET system designed with time-of-flight (TOF) and depth-of-interaction (DOI) readout capabilities [2], aiming to address the limitations of conventional scanners and support improved performance for both clinical and research applications. ***Materials and Methods:*** The proposed TB-PET system features a 2-meter AFOV and a bore diameter of 82.6 cm. It comprises seven axial units, each consisting of 22 detector panels. Each panel includes 6 detector blocks circumferentially and 12 blocks axially. Every block contains an array of 8 × 10 LYSO crystals (2.05 × 2.05 × 20 mm^3), optically coupled to a 4 × 5 silicon photomultiplier (SiPM) array. Initial performance was assessed using a Hoffman brain phantom to evaluate spatial resolution and image quality. System sensitivity was further evaluated through Monte Carlo simulations. ***Results:*** Using an energy window of 411-611 keV and without TOF or DOI correction, the system was able to resolve fine structural details in the Hoffman brain phantom. Monte Carlo simulations yielded a total sensitivity of 180.34

cps/kBq at the center and 173.63 cps/kBq at 10 cm radial offset. Additional evaluations incorporating TOF and DOI capabilities are currently underway. ***Conclusion:*** We have developed a TB-PET system with a 2-meter AFOV and high detector density, enabling full-body coverage in a single bed position. Compared to existing TB-PET systems, the use of smaller crystals and DOI decoding is expected to provide improved spatial resolution. Preliminary phantom and simulation results demonstrate high sensitivity and promising image quality, even in the absence of TOF and DOI corrections. These findings indicate strong potential for clinical and research applications, with ongoing efforts focused on integrating advanced timing and spatial decoding technologies to further enhance system performance. ***References:*** [1] Hicks R J, Ware R E, Callahan J. Total-body PET/CT: pros and cons[C]//Seminars in Nuclear Medicine. WB Saunders, 2024.[2] Zhang X, Xie S, Yang J, et al. A depth encoding PET detector using four-crystals-to-one-SiPM coupling and light-sharing window method[J]. Medical physics, 2019, 46(8): 3385-3398.

EP-0916

Optimisation of scanning protocols for the Siemens Biograph long-axial field-of-view scanner: Can higher patient throughput with improved image quality be achieved at reduced patient dose?

G. Krokos*, S. Chicklore, J. MacKewn, J. John, S. Pereira, S. Gould, S. Jin, G. Testanera, A. Hammers, P. K. Marsden, G. Cook;*
King's College London, London, UNITED KINGDOM.

Aim/Introduction: The introduction of high sensitivity long-axial-field-of-view PET-CT scanners has revolutionised PET imaging. Key clinical optimisation parameters include scan duration, administered activity, and image quality. We investigated how to achieve a balance between these for the Biograph Vision Quadra system (Siemens Healthineers). ***Materials and Methods:*** A NEMA Image Quality phantom (46MBq ^{18}F; 5:1 sphere-to-background ratio) was scanned at three axial positions (centre, quarter, eighth) along the 106cm FOV, for durations of 5-10 minutes. Reconstructions used OSEM with time-of-flight/point spread function correction and maximum ring differences of 85 (MRD85) and 322 (MRD322) corresponding to opening angles of 18° and 52°, respectively. Accuracy was assessed using the recovery coefficients (RCmax, RCpeak, RCmean) and noise using image roughness (IR) and background variability (BV). Twenty patients underwent PET-CT with 2MBq/kg [^{18}F]FDG. Clinical images were reconstructed as described. Image noise was assessed using Coefficient-of-Variation (CoV) in liver. Tumour-to-background ratio (TBRmax, TBRpeak) and contrast-to-noise ratio (CNR) were also estimated. MRD85 images at 5, 7, and 10 minutes were rated 1-5 (5 = best) by two experienced clinicians for image quality, liver noise, and bone marrow/small lesion conspicuity. ***Results:*** Phantom analysis showed increasing errors in RC, albeit minimal, and higher noise with shorter durations and greater axial offsets for both MRDs with the highest biases (10% for RCmean) measured at the eighth FOV and 5-minute scan for MRD322. A twofold increase was measured for BV for both MRDs when moving from the middle to the eighth FOV. A similar increase was noticed for IR for MRD322 and up to 40% increase for MRD85. The noise difference between MRD85 and MRD322 decreased with offset from approximately 50% to 6% for IR and from 25% to 2% for BV. For the same axial position and reducing duration from 10 to 5 mins, an increase of 40-50% was noticed for both MRDs. Nevertheless, IR and BV, exhibited relatively low values of up to 7% and 4%, respectively. Overall clinical image quality decreased from 4.8 (10min) to 4.2 (5min) and liver/bone marrow noise from 4.6 (10min) to 3.7 (5min), with the 7-min acquisition being midway between these. Lesion conspicuity remained at 4.5. TBR values changed minimally, while CNR and CoV deteriorated by ~29% with the highest CoV being 12% (5min, MRD85). ***Conclusion:*** The system provides excellent image quality even at reduced scan time. For increased throughput a 7-minute acquisition might offer a practical compromise with minimal loss in performance.

EP-0917

Comparison of Detectability Between Digital LYSO and Digital BGO-Based PET/CT Scanners: A Phantom Study using an Anthropomorphic XL-Thorax Phantom

A. Stenvall*[1], S. Kvernby[1,2], D. Minarik[1,2];*
[1]Radiation Physics, Department of Hematology, Oncology and Radiation Physics, Skåne University Hospital, Lund, SWEDEN,
[2]Department of Translational Medicine and Wallenberg Centre of Molecular Medicine, Lund University, Malmö, SWEDEN.

Aim/Introduction: Detector material plays a critical role in PET performance. LYSO-crystals provide time-of-flight (TOF), while modern BGO-based scanners lack intrinsic TOF but have higher sensitivity. This study compares a digital LYSO PET/CT to a digital BGO PET/CT with an AI-based TOF-model, evaluating lesion detectability in a challenging anthropomorphic XL-thorax phantom geometry. ***Materials and Methods:*** An XL-thorax-phantom (16L) with liver, kidney and two spherical inserts (inner diameter 9.9mm and 12.4mm were filled with ^{18}F-FDG at clinically relevant activity concentrations at 4:1 (9.9mm) and 3:1 (12.4mm) sphere-to-background ratios. Scans were acquired consecutive on both a digital LYSO PET/CT with an axial field-of view (aFOV) of 20cm and a digital BGO PET/CT (aFOV=32cm), with matched decay corrected acquisition times representing 300s, resampled to 80%(240s), 70%(210s), 60%(180s), 40%(120s), 30%(90s), 20%(60s) and 15%(45s). Data were reconstructed using block sequential regularized expectation maximization (BSREM) with β-values ranging from 200-600 (steps of 100) for the LYSO-scanner with 256x256-matrix and BGO-scanner with 384x384-matrix, using three AI-TOF models (Low(L), Medium(M) and High(H)). Metrics for comparison included SNR in background (SNR=SUVmean_b/SD_b), contrast in cold region (Contrast_cold=(SUVmean_b-SUVmean_cold)/SUVmean_b) and detactability as the peak value within the hot sphere to the peak value in the background (P2P=peak_sphere/peak_b). A peak-ratio>1 was considered detectable. ***Results:*** SNR in the homogeneous background increased with both acquisition time and β-value for both scanners. Across all combinations, the BGO-based system yielded consistently higher SNR than the LYSO-scanner (8% (240s,β600) to 44% (45s,β200)). AI-TOF increased SNR further, with largest increase for TOF-model(L). Cold contrast decreased with increasing β-value for both systems. The LYSO-scanner demonstrated consistently higher cold contrast for all beta-time-combinations (0.97-0.99), while the BGO-system ranged from 0.90-0.98. AI-TOF gave a slight increase in cold contrast for higher beta-values, thus not to the level of the LYSO-scanner. The small 4:1-sphere and the larger 3:1-sphere, were detectable on the LYSO-scanner across all β-values for acquisition times ≥90s and ≥60s respectively, whereas the spheres were detectable for the BGO-scanner at 90s,β 200 and 180s,β200. For detectability across all spheres, 90s and 300s were required for the BGO-scanner. For detectable spheres, AI-TOF increased detectability at average 6% (4:1-sphere)/3% (3:1-sphere). TOF-model(M) increased detectability the most 11% (4:1-sphere)/8% (3:1 sphere). ***Conclusion:*** In a challenging XL-thorax phantom geometry, the BGO-scanner showed higher SNR in homogenous background, lower cold-contrast and lower detectability of hot spheres compared to the LYSO-scanner. Applying AI-TOF increased detectability of detectable spheres, although not to the level of the LYSO-scanner.

EP-0918

Development of ultrahigh sensitivity brain-PET system

A. Krol[1], *W. Zheng*[1], *E. S. Harmon*[2], *M. O. Thompson*[3], *C. R. Schmidtlein*[4];
[1]*SUNY Upstate Medical University, Syracuse, NY, UNITED STATES OF AMERICA,* [2]*LightSpin Technologies, Inc., Norfolk, MA, UNITED STATES OF AMERICA,* [3]*Cornell University, Ithaca, NY, UNITED STATES OF AMERICA,* [4]*Memorial Sloan-Kettering Cancer Center, New York, NY, UNITED STATES OF AMERICA.*

Aim/Introduction: Currently, diseases of the brain are the leading cause of disabilities. The brain Positron Emission Tomography (PET) is a powerful noninvasive tool for clinical studies and neurology research. However, existing brain PET technologies are limited with relatively low sensitivity. Thus, there is a critical need to improve imaging performance of brain-PET. Consequently, we are developing an ultrahigh sensitivity brain-PET that will provide a new device to accelerate research and advance clinical performance. In this work, we are exploring design approaches to maximize brain-PET geometric sensitivity while preserving patients' wellbeing during PET scans. ***Materials and Methods:*** We performed Monte Carlo simulations of different variants of our proposed ultrahigh sensitivity brain-PET scanner with 20-mm-thick monolithic LYSO scintillator. It is based on cylindrical geometry with 25-cm inner diameter and 50-cm axial field-of-view. We simulated systems with: (i) rectangular (10 x 13 cm^2) "windows" located at various distances from the base; (ii) rectangular "door" 20 cm high. The simulations were performed for scanners with and without rectangular shoulder-cut-offs that allowed positioning of the brain closer to the isocenter. For each geometry, we calculated slice sensitivity profile by single-slice-rebinning method from simulated data for F-18-line source. We also obtained such profiles for the state-of-the-art brain-PET NeuroEXPLORER (NX) scanner geometry [1]. ***Results:*** We found that the regional sensitivities for brain and carotid artery territories were 45 (45) cps/kBq and 12 (18) cps/kBq, respectively for the proposed system without (with) shoulder-cut-offs vs. 32 cps/kBq and 13 cps/kBq for NX PET (1.4X gain). Introduction of a "window" in front of patient's face lowered brain ROI sensitivity to 39 (40) cps/kBq and carotid ROI sensitivity to 11 (14) cps/kBq, without (with) shoulder-cut-offs. Introduction of a 20-cm door in front patients produced 36 cps/kBq sensitivity for brain ROI (20% loss). ***Conclusion:*** We found that small diameter cylindrical brain-PET with a large rectangular face "window" and with shoulder-cut-offs reduced the brain-ROI sensitivity by only 12.5% vs. no window geometry while potentially ameliorating claustrophobia and allowing direct contact of patient with outside world. However, the proposed system has 1.3X-1.4X higher sensitivity for the brain-ROI, and higher sensitivity for the carotid-ROI (1.1X-1.4X), as compared to NX PET. ***References:*** [1] Li H, Badawi RD, Cherry SR, Fontaine K, He L, Henry S, Hillmer AT, Hu L, Khattar N, Leung EK, Li T. Performance characteristics of the NeuroEXPLORER, a next-generation human brain PET/CT imager. Journal of Nuclear Medicine. 2024; 65(8):1320-6.

EP-0919

First clinical J-PET positronium lifetime imaging in patients with neuroendocrine tumors

E. Stepien[1,2], *M. Das*[1,2], *M. Opalińska*[3], *A. Hubalewska-Dydejczyk*[3], *S. Sharma*[1,2], *A. Sowa-Staszczak*[3], *P. Moskal*[1,2], *J-PET collaboration;*
[1]*Institute of Physics, Jagiellonian University, Krakow, POLAND,* [2]*Center for Theranostics, Jagiellonian University, Krakow, POLAND,* [3]*Chair and Department of Endocrinology, Jagiellonian University Medical College, Krakow, POLAND.*

Aim/Introduction: The J-PET scanner is the world's first positron tomograph based on plastic strip scintillators to image the lifetime of the ortho-positronium (o-Ps) atom [1]. During conventional PET examination about 40% of positron annihilations occur through the creation of positronium, an exotic atom formed from a tissue electron and a radionuclide-emitted positron. The mean o-Ps lifetime is sensitive to tissue nanostructure and metabolism [2], and our ex-vivo and in-vivo imaging has shown significant differences in positronium mean lifetime between healthy and cancerous tissues [3-5]. Due to their diverse biogenesis and morphology, neuroendocrine tumors (NETs) require a specific diagnostic approach. Diagnostic needs in the field of NET imaging are met mainly based on a biomarker defined as overexpression of somatostatin receptors and this indicator can also be used to assess the prognosis of response to radioligand therapy of metastatic NETs [6]. Galium-68 is a radionuclide of choice for NET diagnosis with physical properties useful for positronium imaging if a routine carrier [^{68}Ga]Ga-DOTA-TATE is applied. This suggests that positronium lifetime could serve as a valuable indicator for identifying NETs. ***Materials and Methods:*** This study approved under agreement (1072.6120.92.2023; NCT06242119), we analyzed a total of 6 patients (2 woman) aged 33 to 82 years. After [^{68}Ga]Ga-DOTA-TATE administration, patients were first examined with a standard PET/CT system and then with the J-PET prototype constructed at the Jagiellonian University which is the first multiphoton system capable of simultaneous PET and positronium imaging [3,5,7,8]. ***Results:*** We successfully calculated the mean lifetime of o-Ps in liver, spleen and surrounding tissue and observed o-Ps in rage of 2.0-4.2 ns which was comparable to our previous ex-vivo measurements [4]. The relationship between o-Ps in tissue and NETs is presented. ***Conclusion:*** Our results demonstrate the feasibility of positronium imaging, a novel diagnostic method gaining popularity with the development of high-sensitivity PET systems. ***References:*** [1] P. Moskal, E. Ł. Stępień, PET Clinics 15, 439 (2020). [2] P. Moskal et al., Nature Reviews Physics 1, 527 (2019). [3] P. Moskal et al., Science Advances 7, eabh4394 (2021). [4] P. Moskal, …, E. Ł. Stępień, EJNMMI Phys. 10, 22 (2023). [5] P. Moskal, …, E. Ł. Stępień, Science Advances 10, eadp2890 (2024). [6] M. Opalińska et al. Front Endocrinol (Lausanne). 13, 929391 (2022) [7] P. Moskal et al., Phys. Med. Biol. 64, 055017 (2019). [8] P. Moskal et al., EJNMMI Physics 7, 44 (2020). Grant ID: 2022/45/B/NZ7/01430; 2021/42/A/ST2/00423.

EP-0920

Simulation studies of performance of an advanced brain-PET system with novel multi-concentric-ring geometry

A. Krol[1], *W. Zheng*[1], *E. S. Harmon*[2], *M. O. Thompson*[3], *C. R. Schmidtlein*[4];
[1]*SUNY Upstate Medical University, Syracuse, NY, UNITED STATES OF AMERICA,* [2]*LightSpin Technologies, Inc., Norfolk, MA, UNITED STATES OF AMERICA,* [3]*Cornell University, Ithaca, NY, UNITED STATES OF AMERICA,* [4]*Memorial Sloan-Kettering Cancer Center, New York, NY, UNITED STATES OF AMERICA.*

Aim/Introduction: In industrialized nations, the brain maladies are presently the leading cause of infirmities. The brain Positron Emission Tomography (PET) is a powerful noninvasive tool for neurology research and clinical examinations. Nevertheless, existing brain PET approaches are inadequate with limited sensitivity and spatial resolution. Accordingly, there is an acute need to improve imaging performance of brain-PET. To address this demand, we are developing of an advanced brain-PET scanner based on thin-slab monolithic detectors with LYSO/SiPM arrays arranged in a novel multi-concentric-ring geometry [1]. ***Materials and Methods:*** Monte Carlo simulations for a 250-mm-long cylindrical four-ring concentric system was performed with slab thicknesses of 3-3-3-3 mm; 7-mm air-gaps between rings; and inner rings diameters of 250, 270, 290 and 310 mm, respectively. The brain was simulated by a sphere of radioactive (F-18, 33 MBq) water with 170 mm diameter confined by 8-mm-thick spherical bone shell. The coincidence events studied involved photoelectric absorption (PA) and first-order Compton scatter (CS) interactions occurring within predefined coincidence time

window. ***Results:*** We found that the ratio of the number of first-order Compton events to that of true coincidences is 2.5. The ratio of the probability of intra-ring to inter-ring first-order Compton scattering is the lowest (1.3-1.7) for the central rings (i.e., with neighbors on both sides), followed for the proximal ring (1.9), and the highest for the distal ring (3.7). The relative probabilities for forward-to-backward scattering events are 66%, 92%, 98% for the first, second and third neighbor, respectively. The distribution of estimated sensitivity versus mean distance between the points-of-first-interactions (PFIs) for two anti-collinear annihilation photons interactions can be approximated by a mono-exponential function for true coincidences (PA=PA) and a slower decreasing monotonic function for triplet (PA=CS-PA) and quadruplet (PA-CS=PA-CS) events. ***Conclusion:*** We conclude that multi-concentric-ring geometry for a system with optimized air-gaps and sufficiently short coincidence time resolution may allow utilization of inter-ring CS photons to increase spatial resolution of brain-PET via more accurate determination of PFI. ***References:*** [1] Harmon, E. Modular PET detector (patent No. US20210223414 A1). U.S. Patent and Trademark Office. https://www.uspto.gov/patents-application-process/search-patents. 2021.

EP-0921

Impact of the hydration protocol on contrast enhancement in ^{18}F-FDG whole-body PET/CT imaging of lymphoma lesions at Apeksha Hospital, Maharagama, Sri Lanka

J. M. A. D. Jayasinghe[1], *D. D. N. Wimalarathne*[1], *H. G. D. Pasindu*[1], *W. S. N. Madhumali*[1], *W. C. Perera*[2], *S. P. D. Wijethunga*[2];
[1]*General Sir John Kotelawale Defence University, Ratmalana, SRI LANKA,* [2]*Apeksha Hospital, Maharagama, SRI LANKA.*

Aim/Introduction: ^{18}F-FDG PET/CT is vital for lymphoma diagnosis and treatment, a growing global concern. Optimal image quality requires post-radiotracer hydration. This study investigates the hydration protocol's impact on lesion contrast enhancement in lymphoma PET/CT imaging at Apeksha Hospital, Sri Lanka. ***Materials and Methods:*** A descriptive-cross sectional, prospective study was conducted at the PET scan unit at Apeksha Hospital, Sri Lanka. Water consumption was measured in patients following the administration of ^{18}F-FDG (2 deoxy 2 [18F]fluoroglucose) and PET/CT scan images were acquired. SUVmean, SUVSD values of the lesions, and healthy liver were measured. CE of the lesions was calculated by the standard formulas. For the liver, SUVmean and SUVSD values were measured by using a 1.0cm3 VOI. For lesions SUVmean and SUVSD values were measured by using a 0.25cm3 VOI. Hydration Groups were labeled as follows, 750mL(A), 750-1000mL(B), 1000mL(C) and 1000-1500mL(D). 3 lesion size groups; <2.5 cm^3, 2.5 cm^3- 4.5 cm^3 and >4.5 cm^3 were identified. Statistical data analysis was done by IBM SPSS 23.0 Software. Variations of CE with hydration levels were explored. ***Results:*** In the sample of 22 patients, the mean oral hydration was 994.55±317.61 mL. For hydration levels, CE was normally distributed. Thus, Welch's ANOVA test was performed. A correlation was investigated by the Spearman test. CE showed a positive correlation for oral hydration, the highest mean CE was observed in the hydration group C. Group D also shows a moderate CE as well as group B. In hydration group A, the mean CE of the lesions tends to decrease compared to other groups. The underweight and obese patients have low CE while others have a moderate value. Further, CE is increasing with the increasing lesion size. Conclusion- Oral hydration of at least 750mL, notably 1000mL, can positively impact the CE of lesions. Similarly, there is a positive correlation between lesion size and CE. ***Conclusion:*** Oral hydration of at least 750mL, notably 1000mL, can positively impact the CE of lesions. Similarly, there is a positive correlation between lesion size and CE. ***References:***Ceriani, L. et al. (2011) 'Could different hydration protocols affect the quality of ^{18}F-FDG PET/CT images?', Journal of Nuclear Medicine Technology, 39(2), pp. 77-82. Available at: https://doi.org/10.2967/jnmt.110.081265., Higashiyama, A. et al. (2018) 'Detectability of residual invasive bladder cancer in delayed ^{18}F-FDG PET imaging with oral hydration using 500 mL of water and voiding-refilling', Annals of Nuclear Medicine, 32(8). Available at: https://doi.org/10.1007/s12149-018-1280-x.

EP-0922

Design and Evaluation of a Pediatric Total-Body PET Scanner for Enhanced Sensitivity and Reduced Dose

P. Sheikhzadeh[1], *H. Rezaei*[2];
[1]*Tehran University of Medical Science, Tehran, IRAN, ISLAMIC REPUBLIC OF,* [2]*Shiraz University of Medical Science, Shiraz, IRAN, ISLAMIC REPUBLIC OF.*

Aim/Introduction: Positron Emission Tomography (PET) is a powerful tool in molecular imaging, yet conventional PET scanners are limited by low sensitivity, long scan times, and high radiation doses, especially problematic for pediatric imaging. Current systems with short axial fields of view (AFOV) require multiple passes to image the whole body, increasing scan duration and radiation exposure. This study aims to design a dedicated total-body PET scanner tailored for pediatric use, enhancing sensitivity while minimizing radiation dose. ***Materials and Methods:*** Using the GATE Monte Carlo simulation platform, a total-body pediatric PET scanner was designed and benchmarked against the Biograph 40 PET/CT system. The new design features an AFOV of 952 mm and a reduced ring diameter of 640 mm, employing smaller LSO crystal elements (1.98×1.98×20 mm^3) for higher spatial resolution. Both systems were evaluated using NEMA NU-2 2018 protocols to calculate sensitivity, resolution (using a mini-Derenzo phantom), and quantitative image metrics (SUV, SNR, noise) through imaging of an XCAT 5-year-old child phantom with a liver tumor. Data was reconstructed using CASTOR with OSEM algorithms. ***Results:*** The proposed pediatric scanner achieved a sensitivity of 147.1 kcps/MBq, approximately 18.5 times greater than the 7.9 kcps/MBq of the Biograph 40. Mini-Derenzo phantom images confirmed that both systems offer comparable spatial resolution, with clear visualization of 2.4 mm rods. However, the pediatric PET scanner, due to its higher detected counts and improved signal-to-noise ratio, was additionally able to resolve 1.2 mm rods more distinctly than the conventional PET system. The pediatric scanner demonstrated superior image quality and quantitative accuracy in the XCAT phantom evaluation, with higher SNR and lower image noise. The total-body design enabled simultaneous dynamic imaging across multiple organs and facilitated low-dose scanning suitable for pediatric use. ***Conclusion:*** The proposed pediatric total-body PET scanner significantly improves sensitivity and image quality while reducing scan time and radiation exposure. These advancements are critical for safe and effective pediatric imaging, enabling applications such as longitudinal therapy monitoring and dynamic studies. This design offers a promising solution for high-performance, child-specific PET imaging.

EP-0923

Exploring the Clinical Feasibility of a Wearable Brain PET System: Early Imaging Results and Outlook

H. Liu, *W. Qu, X. Yu, D. Liang, Z. Zhao, Y. Lin, J. Tao, W. Li, H. Zhao, Y. Zhang, Q. Peng;*
Institute of Biomedical Engineering, Shenzhen Bay Laboratory, Shenzhen, CHINA.

Aim/Introduction: Wearable brain positron emission tomography (PET) systems offer unprecedented opportunities for dynamic and naturalistic neuroimaging. However, achieving sufficient image quality remains challenging. This study evaluates the initial imaging performance of a compact wearable brain PET

system, highlighting current limitations and exploring the anticipated benefits of incorporating time-to-digital converter (TDC) technology. ***Materials and Methods:*** The system was evaluated using phantom and human imaging studies. A Derenzo phantom was used to assess spatial resolution, and the Hoffman brain phantom was employed to evaluate anatomical fidelity. Additionally, an initial human brain scan was conducted to explore potential clinical applicability. Further comparative experiments involving Hoffman phantom imaging with and without TDC technology are currently underway to quantify expected improvements in image quality. ***Results:*** The Derenzo phantom imaging demonstrated the system's ability to clearly resolve rods with a diameter of 1.7 mm, indicating good spatial resolution. The Hoffman phantom images showed reasonable anatomical structure differentiation, and the initial human brain scan enabled visualisation of major brain regions. However, signal-to-noise ratio and image clarity were not yet optimal. Ongoing studies suggest that incorporating TDC technology will substantially enhance image quality. ***Conclusion:*** Our results affirm the promising clinical potential of the wearable brain PET system due to its compact size, low cost, and ability to enable natural, free-motion imaging. Current image quality limitations may be substantially mitigated by integrating advanced TDC technology, thus significantly enhancing its suitability for clinical and neuroscientific applications. ***References:*** [1] Xu J, Zhao Z, Xie S, et al. Mind-tracker PET: A wearable PET camera for brain imaging[C]//2017 IEEE Nuclear Science Symposium and Medical Imaging Conference (NSS/MIC). IEEE, 2017: 1-2.[2] Yu X, Liu H, Zhao H, et al. A multiplexing method based on multidimensional readout method[J]. Physics in Medicine and Biology, 2025.

EP-0924

FDG PET/CT Based Radiomics Analysis in Endometrium Cancer: Correlation of Tumor Heterogeneity Parameters with Pathological Findings

F. Avci[1], *A. Tunc*[1], *B. K. Erkek*[2], *A. A. Ozsaran*[3], *G. Serin*[4], *O. Zekioglu*[4], *Z. Burak*[1];
[1]*Ege University, Nuclear Medicine, Izmir, TÜRKIYE,* [2]*Agri Training and Research Hospital, Nuclear Medicine, Izmir, TÜRKIYE,* [3]*Ege University, Obstetrics and Gynecology, Izmir, TÜRKIYE,* [4]*Ege University, Pathology, Izmir, TÜRKIYE.*

Aim/Introduction: The aim of our study was to evaluate the relationship between texture parameters—such as skewness, kurtosis, and entropy—derived from FDG PET/CT images using the LIFEx software, and pathological findings in patients diagnosed with endometrial cancer. In this context, we sought to investigate the potential role of PET/CT, a non-invasive imaging modality, in assessing tumor heterogeneity and biological behavior. ***Materials and Methods:*** This retrospective study included 50 patients diagnosed with endometrial cancer who underwent preoperative FDG PET/CT imaging. Texture analysis was performed using the LIFEx software, and tumor regions were evaluated to extract radiomic features including skewness, kurtosis, and entropy. These imaging-derived parameters were then compared with postoperative histopathological data. Statistical analyses were conducted using IBM SPSS version 25. ***Results:*** The mean age at diagnosis was 62.4 years. Histological subtypes included 37 endometrioid, 9 mucinous, 3 serous, and 1 carcinosarcoma. The mean tumor size was 3.99 cm (range: 1.5-9 cm). Staging distribution revealed Stage 1 in 5 cases, Stage 2 in 36 cases, and Stage 3 in 9 cases. Lymphovascular invasion (LVI) was present in 13 patients, and cervical involvement in 4 patients. A moderate, statistically significant negative correlation was observed between skewness/kurtosis and tumor size (p=0.01; r=-0.45/-0.40). Additionally, an inverse relationship was found between entropy-log10 values and p53 expression levels (p=0.01; r=-0.3). Entropy-log10 was significantly higher in cases with LVI (p=0.035). In patients with cervical invasion, skewness was significantly lower and kurtosis was higher (p=0.04 and p=0.01). No statistically significant associations were observed between the radiomic features and histologic grade, subtype, or depth of myometrial invasion. ***Conclusion:*** Although some associations have been identified between radiomics-based tumor heterogeneity features derived from FDG PET/CT and histopathological characteristics in endometrial cancer, these findings have generally been inconsistent. Nonetheless, the potential of radiomics-derived heterogeneity parameters to contribute to personalized treatment strategies is emphasized, underlining the critical need for methodological standardization and validation in this field.

EP-0925

SUV and SUL Analysis in Ga-68 DOTATATE PET/CT: Is Liver or Spleen a More Reliable Reference?

F. Davarci*, Y. Parlak, F. Gümüşer, E. Sayit Bilgin;*
Manisa Celal Bayar University, Faculty of Medicine, Department of Nuclear Medicine, Manisa, TÜRKIYE.

Aim/Introduction: Ga-68 DOTATATE PET/CT is a highly sensitive and specific imaging modality for neuroendocrine tumors and has consequently become the standard technique for staging these tumors and assessing treatment response. While the standardized uptake value (SUV) is commonly used in tumor imaging with FDG-PET, its application in DOTA-PET imaging remains relatively limited. This study aimed to evaluate the relationship between SUV normalized to body weight (SUVbw) and SUV normalized to lean body mass (SUL), to identify the most appropriate internal reference organ for Ga-68 DOTATATE PET/CT imaging based on physiological uptake. ***Materials and Methods:*** A total of 52 patients undergoing Ga-68 DOTATATE PET/CT imaging were included in this study. Patient preparation, acquisition parameters, and reconstruction protocols were standardized across all subjects. SUVbw and SUL values were measured for the liver and spleen. Regions of interest (ROIs) were placed with a diameter of 3 cm in the right hepatic lobe and 1 cm in the spleen. The mean SUVbw and SUL values were calculated for each ROI. Statistical analysis was conducted using SPSS version 15.0 to evaluate the relationships between SUV parameters. ***Results:*** The variance of SUL values in the liver and spleen was significantly lower than that of SUVbw values ($p < 0.0001$). Additionally, both SUVbw and SUL values from the liver exhibited significantly lower variability compared to those from the spleen. Among all measured values, liver SUL demonstrated the lowest variance. This indicates that SUL is considerably less variable than SUVbw and represents a more consistent and reliable metric. ***Conclusion:*** Based on the findings, SUL particularly in the liver was determined to be the SUV measurement least affected by potential confounding factors in Ga-68 DOTATATE PET/CT imaging. Consequently, liver SUL was identified as the most reliable internal reference. Moreover, a strong correlation between liver and spleen SUV values suggests that the spleen may serve as an alternative reference organ, particularly in cases involving diffuse liver metastases. ***References:*** 1.Campana D, Ambrosini V, Pezzilli R, et. al.: Standardized uptake values of (68)Ga-DOTANOC PET: a promising prognostic tool in neuroendocrine tumors. J Nucl Med 2010; 51: pp. 353-359. 2. Treglia G, Castaldi P, Rindi G, et. al.: Diagnostic performance of Gallium-68 somatostatin receptor PET and PET/CT in patients with thoracic and gastroenteropancreatic neuroendocrine tumours: a meta-analysis. Endocrine 2012; 42: pp. 80-87.3.Ambrosini V, Tomassetti P, Franchi R, et. al.: Imaging of NETs with PET radiopharmaceuticals. Q J Nucl Med Mol Imaging 2010; 54: pp.

EP-0926

Improving Brain PET/CT Accuracy with 3D Data-Driven Motion Compensation in Head CT

A. Ashfaq[1], *R. Fulton*[2], *M. Luster*[1];
[1]*Department of Nuclear Medicine, Philipps-University Marburg, Marburg, GERMANY,* [2]*University of Sydney, Sydney, AUSTRALIA.*

Aim/Introduction: Head motion during brain PET/CT imaging can significantly degrade image quality, leading to inaccurate quantification and reduced diagnostic value. This study evaluates a fully automated, 3D data-driven motion compensation (MC) method for correcting head motion during CT acquisition in brain PET/CT imaging, and evaluate its impact on both the qualitative and quantitative accuracy of the final images. ***Materials and Methods:*** The Hoffman 3D brain phantom, which simulates the anatomical and radiological properties of the human brain, was filled with fluorodeoxyglucose (^{18}F-FDG) and scanned using a Siemens Biograph mCT system equipped with a 128-slice CT scanner. A reference helical CT scan without motion served as the gold standard. Additional scans were acquired with induced head motion during the CT phase, while the PET phase remained stationary. Each motion-affected CT dataset was reconstructed using a 3D iterative, data-driven motion correction algorithm. Attenuation correction maps were generated from both uncorrected and motion-corrected CT scans. The PET raw data were reconstructed offline using the JSrecon algorithm with an attenuation map from motion-corrected CT and compared with the PET scan reconstructed with an attenuation map from motion-corrupted CT. ***Results:*** Motion-corrected CT scans produced PET images with significantly improved quality compared to uncorrected datasets. In the phantom studies, the normalized mean square error (NMSE) improved from 0.069 (uncorrected) to 0.0453 (corrected). The correction method effectively removed motion artifacts for translations up to 24 mm and rotations under 10°, which in our opinion are unlikely to be exceeded in clinical scans. ***Conclusion:*** The proposed data-driven 3D motion compensation technique for CT imaging substantially enhances the quality and accuracy of brain PET/CT scans affected by head motion, offering promising clinical utility for routine neuroimaging. ***References:*** 1. Park HL, Park SY, Kim M, Paeng S, Min EJ, Hong I, Jones J, Han EJ. Improving diagnostic precision in amyloid brain PET imaging through data-driven motion correction. EJNMMI Phys. 2024;11:49. https://doi.org/10.1186/s40658-024-00605-x2. Dagiri, H., Watabe, H., Takanami, K., Akimoto, K., Usui, A., Kawakami, H., Katsuki, A., Uetake, N., Dendo, Y., Tanaka, Y., Kodama, H., Takase, K., & Kaneta, T. (2024). Verification of the effect of data-driven brain motion correction on PET imaging. PLOS ONE, 19(7), e0301919. https://doi.org/10.1371/journal.pone.0301919.

EP-0927

Evaluation of the new-generation digital bismuth germanium oxide PET/CT system according to the Japanese brain tumor phantom test for ^{18}F-fluciclovine imaging

F. Sasaki[1], *S. Fukai*[2], *H. Daisaki*[1], *M. Sato*[1], *A. Yumoto*[1], *T. Kita*[1], *N. Imaizumi*[1], *M. Shiga*[2], *H. Yoshida*[2], *K. Motegi*[2], *N. Shimada*[2], *A. Osawa*[2], *T. Terauchi*[2];
[1]*Gunma Prefectural College of Health Sciences, Gunma, JAPAN,* [2]*The Cancer Institute Hospital of Japanese Foundation for Cancer Research, Tokyo, JAPAN.*

Aim/Introduction: Malignant gliomas are common and difficult-to-treat brain tumors. Although MRI aids surgical planning, its limitations have led to the recent approval of ^{18}F-fluciclovine (FACBC) PET/CT imaging in Japan for improved tumor visualization. FACBC enhances detection of tumor infiltration not visible on MRI and supports accurate surgery. The Japanese Society of Nuclear Medicine established the Japanese brain phantom test (JBT) to standardize brain PET imaging [1], including FACBC. Omni Legend, a new digital BGO PET/CT system, offers high-quality imaging without TOF. This study evaluated its image quality using JBT criteria and explored its applicability in FACBC brain tumor imaging. ***Materials and Methods:*** A brain tumor phantom (BT-phantom) which includes six hot spheres with different diameters, was filled with ^{18}F-labeled solution with a radioactivity concentration ratio of 3 (sphere):1 (background). The PET scan was performed with 30-min list mode acquisition using Omni Legend (GE Healthcare). The PET data were reconstructed using ordered subset expectation maximization (OSEM), OSEM with a point spread function (OSEM+PSF), and Bayesian penalized likelihood (BPL). The image index of %contrast for 7.5-mm sphere, recovery coefficient (RC) for 10.0-mm sphere, standardized uptake value of total background (SUV_{TOT}), and the detectability for 7.5-mm sphere were evaluated according to the JBT criteria. ***Results:*** The %contrast, RC, and SUV_{TOT} were 25.1%, 0.70, and 1.00, respectively in OSEM; 25.8%, 0.80, and 0.99 in OSEM+PSF; and 33.8%, 0.93, and 0.99 in BPL. The 7.5-mm sphere was detected using all three reconstruction methods. All JBT criteria were satisfied, regardless of the PET image reconstruction methods. ***Conclusion:*** This study demonstrated that the Omni Legend satisfies all JBT image quality criteria even without TOF capability and has the potential to provide high-quality images in ^{18}F-fluciclovine brain tumor imaging. ***References:*** [1] https://jsnm.org/wp_jsnm/wp-content/themes/theme_jsnm/doc/StandardPETProtocolPhantom20170201.pdf.

EP-0928

Feasibility and Comparative analysis of ultrafast F-18 imaging for enhanced bone scan efficiency in obese patients

L. Ghadhanfer[1], *M. Alqabandi*[1], *E. Alawadhi*[1], *T. Alahmad*[1], *Z. Alqallaf*[2], *A. Sadeq*[2], *F. Marafi*[2];
[1]*Kuwait University, Kuwait, KUWAIT,* [2]*Ministry of Health, Kuwait, KUWAIT.*

Aim/Introduction: Advancements in PET technology aim to reduce imaging time for patient comfort, minimize motion artifacts, and lower radiation exposure by decreasing the injected dose, with digital molecular imaging systems offering performance competitive to traditional scanner. 18F-NaF PET/CT is an effective bone-seeking agent that outperforms conventional imaging, showing a superior target-to-non-target ratio than 99mTc-MDP, with twice the bone uptake and faster soft tissue clearance. In our department, the standard 18F-NaF dose for bone scans is 2.2 MBq/kg. For patients with a BMI between 40 and 50, imaging time per bed position is extended. This study investigates the feasibility, image quality, and tracer uptake of ultrafast 18F imaging in comparison to standard acquisition durations. It emphasizes image contrast, noise metrics, SUV quantification. ***Materials and Methods:*** A Jaszczak Deluxe Flangeless Esser PET phantom was filled with 20 KBq/ml, maintaining a sphere-to-background ratio of 8:1. Two 3-minute acquisitions were performed using 256×256 and 128×128 matrix sizes. These datasets were retrospectively re-binned into shorter acquisition times of 90 seconds (standard duration for obese patients) versus 18 seconds (20% of the standard duration). Images were reconstructed using OSEM with 3 iterations and 17 subsets for standard imaging, and adjusted parameters for ultrafast imaging. Image noise (<15%) and lesion contrast (>50%) were the primary accepted quality metrics. Furthermore, images from 10 patients with a BMI greater than 40, who were administered either 18F-NaF or 18F-FDG, were visually assessed to evaluate lesion detectability and SUV measurements at varying acquisition times. The reconstruction parameters applied were consistent with those used in the phantom study. ***Results:*** The 128×128 matrix yielded superior image quality for the 18-second acquisition, especially when using 2 iterations and 8 subsets. Under these conditions, noise remained below 15% and lesion contrast exceeded 50%. In patient cases, the number of

lesions and their detectability were comparable between standard and ultrafast acquisitions for both 18F-NaF and 18F-FDG, with no perceptible differences in image quality. However, ultrafast imaging introduced variability in SUV measurements for 18F-FDG, with deviations of up to ±10%. ***Conclusion:*** Ultrafast PET imaging offers image quality comparable to standard protocols, making it a valuable tool in high-throughput clinical environments. It is particularly advantageous for 18F-NaF imaging, where quantitative accuracy is less critical. For ^{18}F-FDG studies, caution is warranted due to potential variability in SUV measurements, which could impact quantitative assessments.

EP-57

e-Poster Area

D: Technical Studies -> D1 Instrumentation -> D13 PET/MR

EP-0929

Extended Data-Driven Motion Detection Method for PET Imaging

N. Beriashvili[1], *L. Tellmann*[1], *C. Régio Brambilla*[1], *J. Scheins*[1], *K. Ciantar*[1,2], *M. Chikhradze*[3], *N. Shah*[1,4,5], *C. Lerche*[1];
[1]Institute of Neuroscience and Medicine 4 (INM-4), Forschungszentrum Jülich GmbH, Jülich, GERMANY, [2]Institute of Imaging and Computer Vision, RWTH Aachen University, Aachen, GERMANY, [3]Department of Engineering Physics, Georgian Technical University, Tbilisi, GEORGIA, [4]Institute of Neuroscience and Medicine 11 (INM-11), Forschungszentrum Jülich GmbH, Jülich, GERMANY, [5]Department of Neurology, RWTH Aachen University, Aachen, GERMANY.

Aim/Introduction: Spontaneous patient motion during medical imaging can degrade image quality and compromise quantitative accuracy. In PET, high spatial resolution requires motion correction of the emission data and the realignment of the attenuation map. Effective correction relies on accurate tracking of subject movement, which can be achieved by analyzing listmode PET data to extract translational and rotational parameters. This work is focused exclusively on spontaneous, rigid head motion in dedicated brain imaging. ***Materials and Methods:*** We extended the existing center of distribution (COD) method by incorporating an approach to extract angular information of rigid head motion. While similar in concept to previously proposed PCA-based techniques for motion estimation [1], our method does not require back-projection of the lines of response (LORs), making it suitable also for scanners without time-of-flight (TOF) information and allowing for direct use with list-mode data [1]. The COD method estimates translational movement along three axes [2]. In addition, principle component analysis (PCA), has been previously applied to reconstructed data by forming spatial point clouds from LOR centers. By projecting these clouds onto 2D planes and analyzing the principal axes, rotational motion can be quantified through the angle between the principal direction and a fixed reference vector. We validated this approach using a head phantom [3], which was injected with nearly 46 MBq and subjected to controlled manual rotational motion simulations. To separate spontaneous (fast) motion components, the fast fourier transform (FFT) filtering was applied to the COD signals, isolating high-frequency variations. The filtering method was also applied to the angle estimates and validated with phantom measurements. ***Results:*** 2D ellipsoidal point clouds emulating the LOR midpoints were simulated for method validation. The PCA method was also applied to corresponding measurement data, and the results were found to be in good agreement with the expected controlled angular changes. FFT filtering of both simulated and real COD data demonstrated its capability to isolate fast motion components. ***Conclusion:*** Initial evaluation showed that the detected signal captured consistent relative variations over time, aligning with the timing and magnitude of controlled manual rotations. To further validate the method, measurements using a custom-designed spherical glass phantom are planned. These measurements will enable the assessment of defined angular changes under controlled conditions. Results from these experiments will be presented at the conference. ***References:*** [1] Schleyer et al. (2015) https://doi.org/10.1088/0031-9155/60/16/6441[2] Lu et al. (2020) https://doi.org/10.2967/jnumed.119.235515[3] Iida et al., 2013. https://doi.org/10.1007/s12149-012-0655-7.

EP-0930

Evaluating the Impact of MR Contrast on ^{18}F-FDG Quantification in Neuro PET-MR Studies through Comparison of Pre- and Post-Contrast Images

L. Westhead;
Sheffield Teaching Hospitals NHS Foundation Trust, Sheffield, UNITED KINGDOM.

Aim/Introduction: A key challenge in PET imaging is attenuation of tracer emissions by body tissues and scanning equipment, which can affect quantification. Attenuation correction (AC) compensates for this effect, typically using attenuation maps derived from CT image data. Alternatively for PET-MR, MR attenuation correction (MRAC) uses segmentation of MR images with assigned CT numbers to generate pseudo-CTs for attenuation mapping. This study investigates whether gadolinium-based contrast agents influence two commonly used MRAC methods in neural PET-MR studies. ***Materials and Methods:*** A retrospective semi-quantitative analysis was conducted on 8 neuro PET-MR studies on Alzheimer's disease and metabolic imaging. Each subject underwent ^{18}F-FDG imaging with MRAC sequences acquired both before and after gadolinium contrast administration. Analysed data included: 1) Dixon and Zero-Time-Echo (ZTE) MRAC series acquired Pre- and Post-contrast, 2) pseudo-CTs generated for attenuation mapping, 3) PET images reconstructed using the vendor's Atlas-based and ZTE MRAC methods. Percentage differences between Pre and Post image pairs were assessed by image subtraction using image analysis software. Brain structures were contoured using a neuro tool to extract whole-brain and regional PET statistics (maximum counts, mean counts, and count concentration). ***Results:*** Initial investigation found observable differences in the PET subtraction image of up to 20% in certain areas of the brain. After correcting for misalignment between Pre and Post MRAC images, differences in Atlas-based reconstructions were reduced to around 5%. Regional analyses similarly showed minimal variation in maximum and mean counts reaching 8.5% in the medial temporal lobe for one subject. Normalisation of the regions to the pons gave negligible differences except in one subject with a ratio of 13.3 in posterior cingulate gyrus compared to the pons. Statistical analysis is ongoing to further assess the significance of these differences. ZTE reconstructions could not be fully assessed due to limitations when generating valid pseudo-CTs from the registered Post-contrast MRAC images. ***Conclusion:*** The majority of viable cases (4/5) showed no differences above 5%, suggesting that gadolinium administration may not substantially impact PET quantification in neuro PET-MR. Some higher subtraction values and regional normalisation ratios could indicate that different factors are having an effect such as misalignment between Pre and Post which can introduce artefactual differences. Further work is needed to confirm these findings and address the challenges posed towards attenuation mapping by misalignment and other processing discrepancies.

EP-58

e-Poster Area

D: Technical Studies -> D1 Instrumentation -> D14 Imaging Guided Surgery and Other Instruments

EP-0931

Targeted biopsy of bone metastases: an innovative technique in diagnostic evaluation

S. Rama Alonso, *E. Campaña Díaz, F. Caltagirone Gutiérrez, B. Santos García, J. Badell Martínez, P. García-Talavera San Miguel, E. Casillas Sagrado, J. Cañadas Salazar, L. Díaz González, E. Martín Gómez, J. Villanueva Curto, A. Peñaherrera Cepeda, F. Gómez-Caminero López;*
Salamanca University Hospital, Salamanca, SPAIN.

Aim/Introduction: To identify the exact location of bone metastases detected by bone scintigraphy or [18F]FDG-PET/CT facilitating biopsy to obtain tissue samples for diagnostic purposes and to evaluate the most appropriate therapeutic option, as well as to describe and evaluate the efficacy of radioguided bone biopsy in patients with bone metastases. ***Materials and Methods:*** Four patients diagnosed with bone metastases were included in the study, who previously underwent a bone scan with [99mTc]Tc-HDP, marking the optimal puncture point thanks to the portable gamma camera. On the day of surgery, 20 mCi of [99mTc]Tc-HDP was administered 2 hours before surgery. In the operating room, both the portable gamma camera and the gamma detector probe were used to identify the point of maximum radiopharmaceutical uptake, marking the most accurate approach. ***Results:*** Despite the small number of patients included and taking into account the difficulty of access in this type of procedure, targeted bone biopsy proved to be effective in the correct localization of all lesions identified by scintigraphy, allowing optimal samples to be obtained for histopathological analysis, with a low rate of complications and without the need for additional invasive techniques. ***Conclusion:*** Targeted bone biopsy is a safe and effective technique to improve diagnostic accuracy in patients with metastatic cancer. By accurately localizing these metastases, it facilitates the etiological diagnosis and helps to select the best therapeutic option, all with minimal risk to the patient.

EP-59

e-Poster Area

D: Technical Studies -> D1 Instrumentation -> D15 Quality Control, Performance and Standardization

EP-0932

The impact of EARL harmonization on interscanner variability of volume-based PET metrics: a phantom study and patient validation

A. Khalimon[1], *A. Nikiforuk*[1], *A. Shakirova*[1], *I. Baltabaev*[1], *M. Khodzhibekova*[1], *G. Khamadeeva*[1], *D. Khodakova*[1], *T. Lazutina*[1], *I. Pylova*[1], *A. Leontev*[1], *A. Pronin*[2], *E. Bezumova*[2];
[1]*P. Hertsen Moscow Oncology Research Institute - branch of the National Medical Research Radiological Centre of the Ministry of Health of the Russian Federation, Moscow, RUSSIAN FEDERATION,* [2]*N.N. Blokhin National Medical Research Center of Oncology of the Ministry of Health of the Russian Federation, Moscow, RUSSIAN FEDERATION.*

Aim/Introduction: To assess the impact of ^{18}F-based PET EARL harmonization on interscanner variability of MTV and TLG. ***Materials and Methods:*** The phantom study was performed on three PET/CT-systems (with BGO-, LSO- and LYSO-based detectors) using the NEMA IEC Body Phantom NU2-2018. True volume of each sphere of the phantom was previously measured. The phantom filling and acquisition procedure were performed in accordance with the EARL 18F-standards manual. A total of 54 reconstructions (36 3D-OSEM+PSF, 1 3D-OSEM+TOF, 17 3D-OSEM+TOF+PSF) were included and categorized into three groups: 20 EARL2-compliant, 17 partially non-EARL2-compliant and 17 significantly non-EARL2-compliant (2-5 spheres' RCs and ≥6 spheres' RCs falling outside the EARL2-range across all metrics, respectively). The validation study was performed on 36 patients who underwent both [^{18}F]FDG and [^{18}F]PSMA-1007 PET/CT using only the BGO-system. Raw PET data were used to obtain 25 3D-OSEM+PSF reconstructions: 10 EARL2-compliant and 15 non-EARL2-compliant. 96 lesions approximately spherical in shape were selected, with diameters almost evenly distributed from 10mm to 37mm, grouped according to intervals of phantoms' spheres diameters. MTV and TLG of each sphere and lesion across all reconstructions were measured using 3D-isocontour with 41% threshold of the maximum voxel value. The coefficients of variation (CoV) for the MTV and TLG measurements were calculated for each phantom's sphere and patient's lesion within each group of reconstructions. CoV≤10% was considered acceptable. ***Results:*** The CoVs for all spheres, as well as for each sphere, were lower in the EARL2-compliant group than in the partially and significantly non-EARL2-compliant groups: mean values were 10.3%, 14.6% and 22.9% for MTV; 6.0%, 8.4% and 12.1% for TLG, respectively. In the EARL2-compliant group, the CoVs were below the 10% for the 17-37mm and 13-37mm spheres when measuring MTV and TLG, respectively. The CoVs for all lesions, as well as for each interval of lesions' diameters, were significantly ($p<0.001$) lower in the EARL2-compliant group: mean values were 8.6% vs 18.0% for MTV and 6.1% vs 11.3% for TLG. In the EARL2-compliant group, the CoVs were below 10% for lesions larger than 23.5mm and 15.5mm for MTV and TLG, respectively. The correlations between CoV and lesion diameter were lower in the EARL2-compliant group: r=-0.74 vs r=-0.84 for MTV and r=-0.63 vs r=-0.66 for TLG. ***Conclusion:*** EARL harmonization reduces interscanner variability for both MTV and TLG regardless of lesion size as well as its correlation with lesion size when standard 41% SUVmax threshold segmentation tool is used.

EP-0933

Leveraging Vision-Language Models for Automated Reporting of ^{99m}Tc-MAG3 Scintigraphy

W. B. Bosbach[1], *C. L. Clement*[1], *F. Strunz*[1], *N. Gözlügöl*[1], *F. Aghapour Zangeneh*[1], *C. M. Bregenzer*[1], *C. Mingels*[1], *C. Beisbart*[2], *P. Koller*[1], *K. Zeimpekis*[1], *K. Shi*[1], *A. Rominger*[1], *R. Seifert*[1];
[1]*Department of Nuclear Medicine, Inselspital, Bern University Hospital, University of Bern, Bern, SWITZERLAND,* [2]*Institute of Philosophy, University of Bern, Bern, SWITZERLAND.*

Aim/Introduction: This study evaluated the capability of a vision language model (VLM), Qwen2.5-VL-72b, to generate reports for ^{99m}Tc mercaptoacetyltriglycine (MAG3) renal studies. The goal was to assess AI-generated reports as a potential tool to reduce administrative burdens in nuclear medicine practice. ***Materials and Methods:*** Fifty MAG3 studies with reports written during clinical routine were retrospectively included. The dataset was enriched with pathological cases (24 pathological, 26 physiological). Qwen2.5-VL-72b was prompted to analyze MAG3 images, label kidney function status (regular, accumulation, nephrectomy, delayed peak). Corresponding reports were generated under a python-routine. Four nuclear medicine residents evaluated anonymized and randomized reports from both clinical routine and Qwen, rating correctness of findings, suitability of impressions, need for manual correction, and time-saving potential. Raters also attempted to identify the text source (human or AI). Interrater reliability was calculated using Gwet's AC1 and Fleiss' kappa.

Results: Qwen demonstrated high accuracy (96.2%) in labeling studies with two regular kidneys but lower accuracy (62.5%) for pathological cases. Human-written reports received consistently higher quality ratings. However, when analyzing only correctly labeled cases by Qwen, the quality gap narrowed considerably. Two of four raters found no statistically significant differences between human and Qwen reports, while two identified significant differences favoring human reports. The ability to correctly identify report source (human vs. AI) strongly correlated with quality assessments ($R^2 = 0.998$). Interrater reliability was fair (Gwet's AC1: 0.288, Fleiss' kappa: 0.238). ***Conclusion:*** The Qwen-based routine successfully generated MAG3 reports that partially resembled those written during clinical routine, particularly for physiological cases. Although human-written reports were generally preferred, the quality difference decreased substantially for correctly identified cases. This suggests that with further advancements, VLMs may eventually provide valuable support in nuclear medicine reporting, potentially freeing healthcare staff from administrative tasks.

EP-0934

Uncertainties in ILP leakage monitoring: residual activities and effective half-lives

A. Rintala*, K. Nousiainen, T. Miettinen, M. Tenhunen, P. Vikatmaa, M. Laine, A. Granvik, A. Ristikankare, V. Reijonen;*
Helsinki University Hospital, Helsinki, FINLAND.

Aim/Introduction: In hyperthermic isolated limb perfusion (ILP), vascular leakage from the limb to rest of the body is monitored during high-dose drug perfusion to prevent systemic toxicity. A collimated gamma probe is positioned over the precordial region, and radioactive tracer is injected into the surgically isolated limb circulation with a ten-fold activity ratio compared to the systemic circulation. Many factors contribute to the uncertainty of the leakage rate quantification: in this work, we studied the impact of residual activities in tracer syringes and effective half-life of the tracer. ***Materials and Methods:*** We analyzed a subset of ILP treatments, where no leakage was indicated during the perfusion, retrospectively. Five patients with metastasized melanoma in lower extremity had been treated with a one-hour melphalan perfusion and monitored with a commercial measurement system. Technetium-99m labeled human serum albumin (Tc-99m-HSA) was used as the tracer. The ratio of the activity injected into the perfusion circulation ("big activity") to the activity injected to the systemic circulation ("small activity") was measured with a radionuclide calibrator before the operation, and this constant ratio was used during monitoring. A literature value (4.81 hours) was used for the effective half-life of the tracer. The total leakage was not to exceed 10%. The reported mean leakage after the end of isolation ("end leakage") was 3.5% (range: 0.7%-6.3%). To assess the leakage uncertainties, firstly, we corrected the activity ratio with the residual activities measured after ILP. Secondly, we determined the systemic effective half-life from the monitoring data 1) prior to the isolation phase and 2) from the isolation phase (assuming no leakage during this time). Based on these results, we then re-calculated the end leakage. We also studied the effect of different effective half-life for the perfusion circulation compared to the systemic circulation. ***Results:*** The activity ratio corrected with the measured residual activities changed by a mean 5.7% (range: -0.1-17.7%). The mean effective half-life appeared 1) 2.2 h (1.5-2.7 h) prior isolation and 2) 4.1 h (3.4-4.6 h) during isolation. Subsequently, the mean end leakage was 3.4% (2.1-5.8%). One patient had higher end leakage than originally reported (2.1% vs 0.7%), the other four lower. If the physical half-life of Tc-99m (6.01 h) is used for the perfusion circulation, the mean end leakage turned out 3.0% (1.7-5.1%). ***Conclusion:*** Neglecting tracer residues and especially patient-specific effective half-lives of the tracer contribute to the uncertainty of the indicated leakage in ILP monitoring.

EP-0935

Nuclear medicine equipment standardisation for clinical translation: a case study with Tb-161

K. Baete*[1,2], W. Claeys[2], J. Noben[2], W. Deckers[1], C. Terwinghe[1], J. Kleynhans[2], F. Cleeren[2], C. M. Deroose[1,2];*
[1]UZ Leuven, Leuven, BELGIUM, [2]KU Leuven, Leuven, BELGIUM.

Aim/Introduction: Clinical translation of radiopharmaceuticals with novel radionuclides proceeds in several phases. In each phase, the calibration and standardised use of equipment is essential for the preclinical and clinical analysis of administered activity and its distribution in vivo. Therefore, quantitative imaging, treatment planning and optimization needs traceable and accurate activity determination. As part of the PRISMAP harmonisation and standardisation work package, we explored the metrology and medical physics challenges related to this evolving field. ***Materials and Methods:*** We performed a nuclear medicine equipment standardisation (NMES) study using the novel radionuclide terbium-161 (Tb-161). Over 2 years, calibration and verification measurements were carried out using radionuclide calibrators, SPECT/CT cameras and a gamma counter. The Tb-161 activity, provided by the Belgian Nuclear Research Centre (SCK CEN), was systematically determined in a reference geometry (10 ml Schott glass vial) using a Fidelis secondary standard radionuclide calibrator, traceable to a designated metrological institute. The activity was used to calibrate and verify activity meters (CRC-55tR, Capintec/Mirion; VIK-202, Comecer). We studied the geometric influence of recipients that are relevant for the clinical and preclinical practice (vials, syringes, Eppendorf tubes). The activity was used to prepare imaging phantoms, such as a uniform cylinder and a NEMA/IEC body phantom. We performed SPECT/CT imaging (Symbia Intevo, Siemens) to calibrate and verify the quantitative imaging properties of the system. Along the calibration and verification chain, samples of activity concentrations were taken for gamma counter analysis (1480 Wizard 3", PerkinElmer). ***Results:*** We determined Tb-161 calibration factors (CFs) for a number of activity meters in reference conditions and verified the accuracy and reproducibility over the NMES measurement campaign. Due to the low-energy photon emission of Tb-161, CFs show to be device specific and highly influenced by the recipient, its positioning and source geometry. We derived SPECT/CT calibration factors for low and medium energy collimators. Gamma counter measurements were used to obtain counting efficiencies over a range of activity concentrations in the NMES calibration and verification chain. In our gamma counter data, we observed the influence of terbium-160, as a contaminant of the production of Tb-161. ***Conclusion:*** We demonstrated the importance of equipment calibration and standardisation in the clinical translation of novel radionuclides and radiopharmaceuticals and the need for metrology and medical physics support. ***References:*** Decristoforo C, et al. (2022). Standards for clinical translation (1.0). Zenodo. https://doi.org/10.5281/zenodo.6599181.

EP-0936

Homogeneity of the radioactivity distribution in 3D-printed PET phantoms

N. Jörg*[1], A. J. Zounek[1], G. Palumbo[1], R. Oos[1], F. J. Gildehaus[1], N. L. Albert[1,2,3], K. Parodi[4], S. Ziegler[5,1], L. Kaiser[1];*
[1]Department of Nuclear Medicine, University Hospital, LMU Munich, Munich, GERMANY, [2]German Cancer Consortium (DKTK), Partner Site Munich, German Cancer Research Center (DKFZ), Heidelberg, GERMANY, [3]Bavarian Cancer Research Center (BZKF), Erlangen, GERMANY, [4]Department of Medical Physics, LMU Munich, Munich, GERMANY, [5]Department of Nuclear Medicine, Hannover Medical School (MHH), Hannover, GERMANY.

Aim/Introduction: For a reliable quantification of activity distributions in positron emission tomography (PET) and to be able to refer to benchmark data in the evaluation of real patient data, validation measurements with radioactive phantom models are of great importance. 3D-printed phantoms made of resin and radioactive liquid have been shown to offer several advantages over conventional fillable phantoms. However, to use 3D-printed phantoms reliably, the activity must be homogeneously distributed throughout the printed material. This work aimed to assess various resins, mixing, and printing techniques to determine which factors affect the homogeneity of the activity distribution and which configuration is optimal in this regard. ***Materials and Methods:*** Rectangular patches with the dimensions 60 mm x 20 mm x 1 mm were printed using a stereolithographic (SLA) 3D printer with water-washable and conventional resin. The resin was mixed with the radiotracer [^{18}F]fluorodeoxyglucose ([^{18}F]FDG) by stirring or shaking, and the patches were printed in different orientations (horizontal, vertical) and with different layer thicknesses of [0.025, 0.05, 0.1] mm. The activity distribution in the patches was then analyzed with autoradiography using a phosphor imaging plate as well as PET scans with a high-resolution PET/CT system for small animals. The autoradiography images were evaluated with line profiles along the patches and by extracting radiomic features. Radiomics were also analyzed for the PET scans. ***Results:*** Visual analysis of autoradiography, PET images, and line profiles, as well as calculation of radiomic features, yielded differences in the homogeneity of activity distributions for different 3D printing configurations. Four out of five evaluated radiomic features for both PET and autoradiography indicated the highest homogeneity for patches printed with hydrophilic resin (mixed with [^{18}F]FDG using a magnetic stirrer) and vertical orientation. ***Conclusion:*** Printing with hydrophilic resin mixed with [^{18}F]FDG using a magnetic stirrer and vertical orientation yielded a homogeneous activity distribution. Hence, such radioactive 3D-printed phantoms can also be reliably used to create more complex benchmark data for the validation of [^{18}F]FDG-PET quantification methods.

EP-0937

Assessment of the Accuracy and Linearity of Radionuclide Calibrators for I-131 and Lu-177 Theranostic Radioisotopes in nuclear medicine therapy centers in Iran During 2024

E. Farajzadeh[1], *S. Golshaiyan*[1], *M. Sadeghi*[2], *A. Shirzadi Golzar*[1], *M. Akbari*[1], *N. Habibi*[3], *M. Davarpanah*[3];
[1]Secondary Standard Dosimetry Laboratory (SSDL), Pars Isotope Co., Karaj, IRAN, ISLAMIC REPUBLIC OF, [2]Shiraz University, Shiraz, IRAN, ISLAMIC REPUBLIC OF, [3]Pars Isotope Company, Tehran, IRAN, ISLAMIC REPUBLIC OF.

Aim/Introduction: Radiopharmaceuticals play a critical role in both diagnostic and therapeutic procedures in nuclear medicine. Ensuring the accuracy of administered activity is essential for patient safety and effective treatment. Dose calibrators are the primary tools for this measurement, and their calibration must be traceable to a standard dosimetry laboratory, as mandated by the International Atomic Energy Agency (IAEA). In Iran, the Secondary Standard Dosimetry Laboratory (SSDL) conducts annual evaluations of these devices. This study aimed to assess the accuracy and linearity of dose calibrators used in nuclear medicine therapy centers across Iran in 2024, focusing on I-131 and Lu-177. ***Materials and Methods:*** A total of 39 dose calibrators from 35 centers were evaluated using standard reference sources (Cs-137, Co-57, Ba-133) and a reference dose calibrator, in accordance with Protocol 93 of the NPL Guide. Devices assessed included models from manufacturers such as RAMS-88 (Iran), AMERSHAM, BIODEX, CAPINTEC, COMECER, ISOMED, PICKER, PTW, and SIEMENS. Accuracy limits were defined as ±2% for reference standards and ±5% for field devices. Devices with errors between 5% and 10% were recalibrated, and those with errors exceeding 10% were marked for servicing. ***Results:*** Among the 39 calibrators tested, 84.61% showed acceptable accuracy for Cs-137 and Co-57, 79.48% for Ba-133, 71.79% for I-131, and 74.35% for Lu-177. Linearity tests using Tc-99m confirmed compliance within ±5% for most devices, except for three that required corrective maintenance. ***Conclusion:*** This evaluation underscores the importance of routine calibration and quality control of dose calibrators to maintain measurement accuracy and radiation safety. The findings support the necessity of regular oversight by the SSDL to ensure metrological traceability and optimal device performance, particularly in sensitive clinical contexts such as pediatric therapy. ***References:*** International Atomic Energy Agency (2006). Quality Assurance for Radioactivity Measurement in Nuclear Medicine, October 96., National Physical Laboratory Guide. Good Practice Measurement Protocol for Establishing and Maintaining the Calibration of Medical Radionuclide Calibrators and their Quality Control.

EP-0938

Activity painting with 3D Printer for arbitrary PET phantom

J. Kiss[1], *P. Szuszik*[2], *K. Kukuts*[3], *A. Forgács*[3], *I. Garai*[2], *L. Balkay*[2];
[1]Division of Radiology and Imaging Science, Department of Medical Imaging, Faculty of Medicine, University of Debrecen, Debrecen, HUNGARY, [2]Division of Nuclear Medicine and Translational Imaging, Department of Medical Imaging, Faculty of Medicine, University of Debrecen, Debrecen, HUNGARY, [3]Mediso Ltd., Budapest, HUNGARY.

Aim/Introduction: This study aimed to investigate the potential simplification of the so-called activity painting phantom technique to see if the expensive industrial robotics [1,2] used so far could be replaced by cheaper and simpler 3D printers. A further aim was to demonstrate that even complex distributions, such as brain FDG accumulation [3], could be simulated with this more straightforward technique. ***Materials and Methods:*** In the activity painting, the fundamental principle is to move a point source within the PET camera's field of view during continuous data acquisition. An ordinary, frequently used 3D printer and a Na22 point source of 9.9 MBq activity were used to simulate 3D shapes. The point source was moved continuously in time but at varying speeds. All examinations were performed on a standard digital PET/CT camera with TOF capability, using the reconstruction used in routine diagnostics. Based on accurate calibration between the velocity and the activity concentration, the required point source velocity map was determined to trigger each 3D print in the field of view. ***Results:*** Initial measurements were made to compare the 3D printer method with the industrial robotics technique to ensure similar movement and image quality. After painting the homogenous rectangles, we obtained a COV=3.24% with the robotic technique and 2.80% with the help of the 3D printer. Furthermore, arbitrarily shaped checkerboard-type activity patterns were created, and from these, the ratio of expected to measured activity concentration ratios was 1.004±0.017. In addition, theoretical FDG brain accumulation was also simulated in air and water-filled environments. In comparing the activity-painted brain image with the theoretical distribution, the related voxel correlation plot yielded a correlation coefficient of 0.9758 and 0.9680 in the air and the water-filled environment, respectively. Based on the actual activity of the point source, a slice of the brain scan took about 1 hour. ***Conclusion:*** This study demonstrated that a more affordable and accessible method utilizing a conventional 3D printer could serve for activity painting phantom measurements in PET imaging. ***References:*** https://doi.org/10.1371/journal.pone.0309540,https://doi.org/10.1088/1361-6560/ad84b5, https://doi.org/10.1002/mp.14218.

EP-0939

Standardizing Breast-Specific PET Imaging: Insights from Phantom and Clinical Studies in a Multicenter Japanese Trial

Y. Satoh[1], *K. K. Miyake*[2], *M. Kataoka*[3], *K. Itagaki*[4], *S. Aoyama*[5], *Y. Naoi*[5], *Y. Inui*[6], *H. Nosaka*[7], *S. Ito*[8], *Y. Inaoka*[9], *Y. Kato*[1], *K. Miwa*[10], *K. Kubota*[11], *M. Uno*[6], *K. Hanaoka*[12];
[1]*Fujita Medical Innovation Center Tokyo, Ota-ku, Tokyo, JAPAN,* [2]*Department of Diagnostic Imaging and Nuclear Medicine, Graduate School of Medicine Kyoto University, Kyoto, JAPAN,* [3]*Preventive Medicine and Lifestyle-related Disease Research Center, Kyoto University Hospital, Kyoto, JAPAN,* [4]*Division of Clinical Radiology Service, Kyoto University Hospital, Kyoto, JAPAN,* [5]*Clinical Imaging Center for Healthcare, Nippon Medical School, Tokyo, JAPAN,* [6]*Department of Radiology, Fujita Health University Hospital, Aichi, JAPAN,* [7]*Department of Radiological Technology and Science, Ibaraki Prefectural University of Health Science, Ibaraki, JAPAN,* [8]*Mirai Imaging Ltd., Fukushima, JAPAN,* [9]*Medical Systems Division, Shimadzu Corporation, Kyoto, JAPAN,* [10]*Department of Radiological Sciences, School of Health Sciences, Fukushima, JAPAN,* [11]*Department of Radiology, Dokkyo Medical University Saitama Medical Center, Saitama, JAPAN,* [12]*Division of Positron Emission Tomography, Institute of Advanced Clinical Medicine, Kindai University, Osaka, JAPAN.*

Aim/Introduction: In Japan, two types of breast-specific PET systems (positron emission mammography [PEM] and dedicated breast PET [dbPET]) have been clinically adopted. They provide high-resolution functional images that enable the detection of small breast cancers. However, the comparison of images from each system and the optimal acquisition protocol have not sufficiently investigated. In this study, 1) a phantom with appropriate sphere-to-background ratios (SBRs) based on clinical images of breast-specific PET was prepared, 2) breast-specific PET phantom images acquired and reconstructed using standard protocols routinely employed at each institution were evaluated, and 3) their clinical validity was verified. ***Materials and Methods:*** Three breast-specific PET systems—PEM, photomultiplier tube (PMT)-based dbPET, and silicon photomultiplier (SiPM)-based dbPET—were evaluated using a cylindrical phantom containing four small spheres (3-10 mm). SBRs of 2:1, 4:1, and 8:1 were determined by measuring clinical PET images. The phantom was scanned for 10 minutes in list-mode with the spheres positioned at the center and periphery of the detector. Images were reconstructed at 1, 3, 5, 7, and 10 minutes. Visual and quantitative evaluations were performed, including coefficient of variation (CV_{BG}), detection index (DI), and contrast recovery coefficient (CRC). Representative clinical images were also reviewed. ***Results:*** Phantom images with SBRs of 2:1 and 4:1 failed to adequately visualize small spheres; therefore, subsequent evaluations focused on 8:1 SBR images. Visual assessment showed that dbPET systems yielded clearer visualization than PEM, particularly for small spheres. All scanners exhibited reduced image quality at the periphery compared to the center. SiPM-based dbPET was the only system able to visualize 3-mm spheres at the periphery with ≥5 minutes of acquisition, whereas PEM failed to detect 5-mm spheres even at 10 minutes. In quantitative analysis, DI decreased with shorter acquisition time, while CRC remained relatively stable. SiPM-based dbPET achieved the highest detectability but showed greater background noise. Clinical findings were consistent with phantom results. ***Conclusion:*** An SBR of 8:1 was appropriate for phantom studies using small spheres in breast-specific PET. Based on phantom and clinical validation, dbPET required ≥5 minutes and PEM ≥7 minutes of acquisition to achieve diagnostic image quality.

EP-0940

Implementing a computer model of a Capintec ionisation chamber in GEANT4

H. Benderz*, J. O'Brien, B. Thomson;*
Sandwell and West Birmingham NHS Trust, Birmingham, UNITED KINGDOM.

Aim/Introduction: Errors in administered activity should be ±10% (diagnostic) and ±5% (therapeutic). Emissions from some radionuclides can give differences between vial activity and syringe activity, as well as having volume effects, e.g. I123 which should be measured with a copper filter. A Capintec computer model allows such effects to be examined without direct measurements. ***Materials and Methods:*** The cross-sectional dimensions and materials for the Capintec chamber were modelled in GEANT4. The model was checked against the Capintec calibration curve for standard radionuclides. We used Tc99m sensitivity as a reference for lower energies (<300keV) and Co60 (~1200keV) as reference for higher energies. ***Results:*** The model errors were all below 3% and are shown (gamma range 27keV-2754keV): Tl201 2.7%, I125 1.2%, Co57 0.1%, Cs137 1.1%, F18 1.5%, Na24 1.9%. Also, I123 was modelled with the copper filter, and gave a setting of 51, which represents an error of 2.4% from the NPL calibrated number 54. ***Conclusion:*** With this model we can examine improved filter systems for radionuclides e.g. Y90. We can also examine the differences between vials and syringes. The energy curve can also be mathematically modelled, allowing calibration factors to be theoretically determined using emission data, for any radionuclide without a calibration factor. There is increased interest in the application of alpha-emitting radionuclides in MRT, such as Ra223, At211, Pb212 and Ac225. These have associated decay chains, with varying relative activities with time after production. The model will allow the calibration number to be determined for such chains at particular times after production and for the relative contributions of each radionuclide in the decay chain to be recognised. This should give increased accuracy of administered therapy activity.

EP-0941

Validation of a vented well-type ionization chamber with specifically designed vial holders for in-house Lu-177 reference activity samples

V. Reijonen[1], *P. Toroi*[2], *R. Nylund*[2], *M. Tenhunen*[1];
[1]*Helsinki University Hospital, Helsinki, FINLAND,* [2]*STUK - Radiation and Nuclear Safety Authority, Vantaa, FINLAND.*

Aim/Introduction: When compared to the requirements agreed for reference dose measurements in external beam radiotherapy (EBRT) and brachytherapy (BT), molecular radiotherapy (MRT) lags behind. If the Lu-177 setting of a clinical radionuclide calibrator is not properly verified, a systematic error may be transferred to patient vial measurements as well as to quantitative imaging, and subsequently to absorbed dose distributions and reported outcome in MRT. An international code of dosimetry practices in MRT should be developed to align with those in EBRT/BT: similar standardisation of measurements could be applied. In this study we evaluated the use of a reference-class well-type chamber, commonly employed in BT quality assurance (QA), for preparing Lu-177 reference solutions intended for regular QA in MRT. ***Materials and Methods:*** We acquired a commercial Lu-177 reference sample "CR" (500 MBq in 1 ml) in a 10R vial and measured it using 1) a secondary standard radionuclide calibrator "SSRNC", 2) a clinical radionuclide calibrator "CRC", and 3) an unsealed, unpressurized well-type chamber used for BT QA with two versions of a specifically designed 10R vial holder ("W+VH1" and "W+VH2"). We prepared two in-house Lu-177 samples, "HM1" and "HM2", in 10R vials using left-over no-carried-added Lu-177 from MRT treatments (~150 MBq/g). HM1 contained a liquid mass similar to CR, while HM2 had a similar activity to CR. After initial measurements, we gradually added aqua to each of them to

examine the volume effect in the range of 1-10 ml. A calibrated precision scale was used for mass determination, and the ambient conditions were monitored using a mercury-based thermometer/barometer. ***Results:*** The manufacturer's reference activity of the CR sample agreed with the SSRNC measurement within 0.4%. The observed volume dependence followed the SSRNC volume correction function and was within 0.3% for all three samples. Using the CRC's factory setting, there was a discrepancy of -1.3%. Calibration factors including volume correction functions were defined for the CRC, W+VH1 and W+VH2 combinations based on CR measurements. There was a 0.3% difference between VH1 and VH2. The activities of HM1 and HM2 were then determined. The measured values agreed within 0.8%. ***Conclusion:*** Vented reference-class well-type ionization chambers combined with specifically designed vial holders can be validated for the preparation of in-house Lu-177 reference samples. In this study, we defined calibration factors as a function of solution volume. Next, we will determine accuracy, constancy and linearity of the measurement system, including an uncertainty analysis.

EP-0942

A Calibration Workflow for Accurate Quantification of Rhenium-188 in RHN001-Tx for Theranostic Applications.

M. Qebetu[1], *J. Cardinale*[2], *K. Banda*[1], *P. Goorhoo*[1], *K. M. Legodi*[1], *H. Ndlovu*[1], *C. Davis*[1], *L. Smith*[1], *S. Sibiya*[1], *A. Mdlophane*[1], *S. Mdanda*[1], *M. Shungube*[1], *M. Sathekge*[1], *K. Ramonaheng*[1]; [1]*Nuclear Medicine Research Infrastructure, Pretoria, SOUTH AFRICA,* [2]*Department of Nuclear Medicine, Medical Faculty and University Hospital, Heinrich Heine University Düsseldorf, Düsseldorf, GERMANY.*

Aim/Introduction: Rhenium-188 is a promising generator-produced radionuclide with substantial potential for therapeutic applications. When used in conjunction with technetium-99m, it enables a practical theranostic approach, particularly valuable in settings without PET imaging infrastructure. RHN001 is a PSMA-targeting ligand that makes use of this matched pair facilitating both, the diagnosis and treatment of prostate cancer, and is currently being investigated in the RHINO clinical trial. Accurate activity quantification is essential for ensuring therapeutic efficacy and patient safety. In this context, the aim of this work is to establish a robust workflow for the determination of the true activity of the ^{188}Re-labeled RHN001-Tx. We present our experience in calibrating local instrumentation to support precise dosimetry and reliable therapeutic dosing in clinical practice. ***Materials and Methods:*** [^{188}Re]$NaReO_4$ was obtained from a ^{188}W/^{188}Re-generator (OncoBeta) and used to prepare a dilution series for calibration. Decay curves were measured using three independently calibrated dose calibrators for the determination of linearity and radionuclide purity. Following sufficient decay, cross-calibration was performed using a certified Iodine-123 reference standard measured on the liquid scintillator counter (LSC), and Mucha Nova gamma counter. Based on these results the individual calibration factor/responsivity for the dose calibrators was determined. ***Results:*** Decay curve fitting for [^{188}Re]$NaReO_4$ demonstrated excellent agreement with theoretical expectations, yielding a coefficient of determination (R^2) of 1.0, indicating a perfect linear correlation on the semi-logarithmic decay plot. The experimentally determined physical half-life of [^{188}Re]$NaReO_4$ deviated from the accepted value with the following range; 0.67-0.92 % for the undiluted (pure) sample and by; 0.92-1.43 % for the diluted sample set, confirming linearity of the dose calibrators and radionuclidic purity. Cross-calibration using the Iodine-123 reference standard further validated the measurement system. The I-123 activity measured using the LSC closely matched the theoretical value, with an absolute deviation of only 0.001 MBq. Comparative measurements on the Mucha Nova gamma counter showed consistent results, reinforcing the robustness of the calibration approach. ***Conclusion:*** From these measurements, a cross-calibration factor was derived, enabling traceable, instrument-specific correction for accurate quantification of RHN001-Tx (^{188}Re-PSMA) activity in clinical dosimetry applications. The calibration factor derived from the certified Iodine-123 standard can be applied in future measurements to ensure that the dose calibrator yields accurate and traceable activity readings. All measurement results were within the expected range, confirming the reliability and validity of the calibration workflow.

EP-0943

Sensitivity and count rate performance studiesof a UHF-MRI compatible BrainPET insert with standard and non-standard tracers

D. Niekämper[1,2], *J. Scheins*[1], *L. Tellmann*[1], *C. Hoffmann*[3], *S. Spellerberg*[3], *E. Pfaehler*[1], *N. Beriashvili*[1], *N. Shah*[1,4,5], *C. Lerche*[1]; [1]*Forschungszentrum Jülich GmbH, Institute of Neuroscience and Medicine 4, Jülich, GERMANY,* [2]*RWTH Aachen University, Department of Physics, Aachen, GERMANY,* [3]*Forschungszentrum Jülich GmbH, Institute of Neuroscience and Medicine 5, Jülich, GERMANY,* [4]*RWTH Aachen University, Department of Neurology, Aachen, GERMANY,* [5]*Forschungszentrum Jülich GmbH, Institute of Neuroscience and Medicine 11, Jülich, GERMANY.*

Aim/Introduction: The BrainPET-7T is a high performance PET insert for neuroimaging combined with ultra high-field MRI [1]. Its design allows for a high sensitivity which is even more important for applications such as dual-isotope imaging [2], requiring the detection of triple coincidences of β^+-γ-emitters. In comparison with pure β^+-emitter count rate performance and sensitivity studies, we present measurements with β^+-γ-emitters to assess the feasibility of detecting triple coincidences at an acceptable noise level. ***Materials and Methods:*** The BrainPET-7T employs scintillators of LSO crystals in three layers with a total height of 2.4 cm and a digital Silicon Photomultiplier readout. Its dimensions are an inner diameter of 38.85 cm and an axial FOV of 24.8 cm. We evaluate the sensitivity for double coincidences with ^{18}F as a standard β^+-emitter and for double and triple coincidences using ^{124}I as a β^+-γ-emitter via an extrapolation from attenuated line source measurements. Additionally, we obtain the triple coincidence sensitivity with a ^{22}Na-point source with an activity of 0.76 MBq moved axially in 5 mm steps. Furthermore, we determine the true and noise-equivalent count rate (NECR) using a scaled NEMA phantom. The coincidence window is 2.6 ns for ^{18}F and ^{124}I, and 6 ns for ^{22}Na to account for positronium lifetime. ***Results:*** The measured sensitivity at the axial center and without RF coil, including multiple coincidences, was 13% at both the radial center and 7.5 cm offset for double coincidences of ^{18}F and an energy window of 420—650 keV. The triples sensitivity depends strongly on the energy window and the coincidence identification schemes. It is 2.4% for the identification of three singles in an energy window of 420—1500 keV and 0.6% for two singles in a two times full width at half maximum region around the annihilation peak and one around the prompt peak for the ^{22}Na measurement and 1.2% for ^{124}I for two energy regions. The NECR peak is at 13 kBq/ml with 241 cps/Bq and the true rate peak is at 16 kBq/ml with 619 cps/Bq when considering all combinations of singles within a coincidence window and an energy window of 450—580 keV. ***Conclusion:*** The presented performance studies with pure β^+-emitters and β^+-γ-emitters indicate the scanner's capacity for applications with β^+-γ-emitters. ***References:*** [1] C. W. Lerche et al., 2023 NSS MIC RTSD. Vancouver, BC, Canada: IEEE, (2023), pp. 1-2.[2] E. C. Pratt et al., Nat. Biomed. Eng, 7 (2023) 8 pp. 1028-1039.

EP-0944

Impact of the manufacturer new scatter correction for the market oldest CZT ring SPECT-CT on ^{99m}Tc contrast of small hot and cold objects

A. Seret[1], *C. Bernard*[2];
[1]*University of Liege, Liege, BELGIUM,* [2]*CHU of Liege, Liege, BELGIUM.*

Aim/Introduction: The recently modified scatter correction of the market oldest CZT-based ring SPECT-CT was tested on phantom data from our recent study of this system [1]. Still based for ^{99m}Tc on the dual energy window method, the correction is now (SC25) performed in the iterative loop of the reconstruction whereas it was previously (SC23) a subtraction of the two images reconstructed in the main and secondary windows. ***Materials and Methods:*** Data of NEMA NU2-94 and custom hot (diameter 4-20mm) and cold (diameter 6-25mm) bar contrast phantoms have been reconstructed with (SC) and without (NoSC) scatter correction. Scatter residual fraction (RF) in NEMA phantom, recovery coefficient (RC) in bars and coefficient of variation (COV) in uniform region of contrast phantom were compared to the values obtained with actual (25) and previous (23) versions of the software. Sixteen subsets were used in the OSEM-based reconstruction for different numbers of iterations in order to span a wide range (48-240) of EM updates. The optional resolution recovery for quantification purpose (PSFRq) was also tested. ***Results:*** Results are given for 192 updates where convergence seemed to be reached. RF-SC23 < RF-SC25 < RF-NoSC23 ≈ RF-NoSC25 in water and Teflon inserts of NEMA. For the cold rods: RC-SC23 > RC-SC25 > RC-NoSC25 ≥ RC-NoSC23. For the largest (≥16mm) hot rods, RC-SC25 ≈ RC-NoSC25 > RC-SC23 ≈ RC-NoSC23 and for the thinnest (≤8mm), RC-NoSC25 ≈ RC-NoSC23 ≈ RC-SC23 > RC-SC25=0. SC25 appeared to boost the central part of the two largest hot rods with a RC peaking at 160% for a centered ROI of half the rod physical diameter. In the contrast phantom uniform area, COV-NoSC25 ≈ COV-NoSC23 ≈ 6,5% and COV-SC25 ≈ COV-SC23 ≈ 8,0%. SC25 removed about 11% of counts in this uniform part whereas SC23 removed as much as 32%. With or without SC (23 or 25), PSFRq did almost not change RF and RC of cold or hot rods, neither COV or the percentage of counts removed by SC. ***Conclusion:*** The most striking effect of SC25 was much less count removal in large hot areas. Cold contrasts were slightly reduced whereas the impact on hot contrasts was very size dependent. The thinnest rods were absent from the images and the contrast of the central part of the largest rods was considerably boosted resulting in an increased mean rod contrast. ***References:*** 1. Seret A, Bernard C. EJNMMI Physics 2025; In Press.

EP-0945

Establishing metrologically traceable activity measurements for alpha-emitter astatine-211 to improve the accuracy of equipment routinely used in the clinic

E. Leidermark[1,2], *B. Sabot*[3], *H. Jensen*[4], *T. Bäck*[1], *L. Persson*[5], *S. Palm*[1];
[1]*Medical Radiation Sciences, Institute of Clinical Sciences, Sahlgrenska Academy, University of Gothenburg, Gothenburg, SWEDEN,* [2]*Department of Radiation Physics in Nuclear Medicine, Sahlgrenska University Hospital, Gothenburg, SWEDEN,* [3]*CEA, LIST, Laboratoire National Henri Becquerel, Gif-sur-Yvette Cedex, FRANCE,* [4]*Department of Clinical Physiology and Nuclear Medicine, Cyclotron and Radiochemistry Unit, Rigshospitalet, Copenhagen, DENMARK,* [5]*Swedish Radiation Safety Authority, Stockholm, SWEDEN.*

Aim/Introduction: Targeted alpha therapies (TAT) are currently evaluated in several clinical trials, but the requirement of metrological traceability for the activity measurements of alpha-emitters are typically not met. For ^{211}At ($t_{½}$=7.2h) reference sources are not available. In anticipation of a new clinical trial involving ^{211}At, a measurement using absolute 4pi-alpha liquid scintillation counting was performed [1] to establish metrological traceability to the equipment used in the hospital. The resulting activity measurements were then compared with those derived for a previous clinical trial [2] (without metrological traceability). The aim was to evaluate the impact of metrological traceability when measuring ^{211}At for three radionuclide calibrators and three HPGe detectors. ***Materials and Methods:*** A sample from an aqueous solution of ^{211}At (0.2M NaOH and 20mM NaI) was measured using absolute 4pi-alpha liquid scintillation counting with a combined relative standard measurement uncertainty of 1.1% [1]. Samples from the same solution were then measured in three radionuclide calibrators and the first of three HPGe detectors. The combined standard measurement uncertainty of the radionuclide calibrators was 3.4%-3.8% (excluding the uncertainty that originates from the calibration). Another comparison was performed (using an identical ^{211}At solution) between the first HPGe detector and two HPGe detectors in different labs. Their combined relative standard measurement uncertainties ranged between 5.7%-6.2%. The first two HPGe detectors used decay data from DDEP and the third used data from NuDat3. ***Results:*** For the three radionuclide calibrators, the difference in activity between the setting used for the previous clinical trial and the traceable calibration was 3.9%, 3.9% and -6.9%, respectively. The HPGe detectors differed compared to the traceable calibration 6.6%, -0.1% and 1.7%, respectively. Had the third site also used decay data from DDEP the difference would have been -4.5% (instead of 1.7%). ***Conclusion:*** Before establishing metrological traceability, the radionuclide calibrators underestimated the activity of ^{211}At by up to 7%. HPGe measurements rely on accurate data on the intensity of the 687keV gamma associated with ^{211}At decay. DDEP lists an uncertainty of 5% for this intensity, which is the largest contributor to the uncertainty of the measurements. There is a 6.5% difference in listed gamma emission intensity between DDEP and NuDat3. This highlights the need for better decay data for ^{211}At if HPGe detectors are used for activity measurements. ***References:*** 1.PMID:40184906 2.PMID:19525452.

EP-0946

Novel Scatter and Tail Corrections Improve Low-Activity Lu-177-PSMA Imaging in Digital 3D Ring SPECT/CT

L. Kääriä[1], *M. Seppänen*[2], *T. Noponen*[1];
[1]*Department of Clinical Physiology, Nuclear Medicine, Turku PET Centre and Medical Physics, Turku University Hospital and Wellbeing Services County of Southwest Finland and University of Turku, Turku, FINLAND,* [2]*Department of Clinical Physiology, Nuclear Medicine and Turku PET Centre, Turku University Hospital and Wellbeing Services County of Southwest Finland and University of Turku, Turku, FINLAND.*

Aim/Introduction: ^{177}Lu-PSMA has established a foothold in clinical practice recently for treating metastatic castration-resistant prostate cancer. Dosimetry imaging is typically conducted within a few hours to one week post-treatment. Therefore, reliable imaging at low activity levels is critical, especially at late time points. We previously demonstrated that calibration factors (CFs) for both ^{177}Lu photopeaks (113 and 208 keV) in a digital 3D ring-design SPECT/CT system remain stable over a wide range of activity levels. However, at lower activity levels - particularly for the 113 keV peak - CFs begin to drift due to the known tailing effect in CZT detectors. New reconstruction techniques have been introduced to mitigate this drift, including enhanced scatter correction (SC), tail correction (TC), and a combined peak reconstruction option. This study evaluates the impact of these correction methods on CFs at low activity levels in ^{177}Lu imaging. ***Materials and Methods:*** A uniform cylindrical phantom (6480 cm^3) was filled with 3.70 GBq of ^{177}Lu and imaged at multiple time points during decay until near depletion. Activity concentration was determined for each 20 min acquisition. Data were reconstructed for each photopeak

using the Bayesian penalized likelihood (Q.Clear) algorithm (20it15ss). Three reconstruction configurations were used: 1. CT-based attenuation correction with traditional SC, 2. CT-based attenuation correction with novel SC, and 3. CT-based attenuation correction with novel SC and TC. For the combined peak (113+208 keV), only the second and third configurations were applied. At one time point, reconstruction effects were evaluated step-by-step, adding one correction at a time. Total counts were measured using a cylindrical VOI. ***Results:*** The mean CFs for the 113 and 208 keV peaks using the first configuration were 69.58 ± 1.63 and 71.42 ± 2.38 cps/MBq (activity ranges: 3700-140 MBq and 3700-16 MBq), respectively. For the second configuration, CFs were 113.89 ± 2.97 and 64.07 ± 2.99 cps/MBq, and for the third, 148.84 ± 4.26 and 80.04 ± 3.57 cps/MBq (range: 3700-16 MBq). For the combined peak, mean CFs were 177.94 ± 5.18 and 228.94 ± 7.09 cps/MBq for the second and third configurations, respectively. ***Conclusion:*** The novel SC significantly improved CFs at low activity levels, especially for the 113 keV peak, where CFs remained stable over the same activity range as those acquired with the 208 keV peak. This improves the quantification capability of the 113 keV peak in late post-therapy dosimetry and supports potential clinical use of the combined peak.

EP-0947

Cross calibration of a dose calibrator with a gamma counter for ^{68}Ga and ^{18}F activity measurements

T. Assoignon[1], *M. Hesse*[2], *F. Dupont*[2];
[1]*UCLouvain, Woluwe-Saint-Lambert, BELGIUM,* [2]*Cliniques Universitaires Saint-Luc, Woluwe-Saint-Lambert, BELGIUM.*

Aim/Introduction: Gallium-68 (^{68}Ga) is used in theranostics, mainly for PET imaging in neuroendocrine and prostate cancers, as a surrogate to the same pharmaceutical agent marked with Lutetium-177 used for therapy. Accurate PET quantification requires precise activity measurements from dose calibrators. However, differences of activity measurements have been reported between similar devices for ^{68}Ga. Common verification methods to find the correct dose calibrator setting, such as the use of a traceable source or the PET/CT cross calibration, are not always available or reliable. In this study, we propose to use a gamma counter together with Monte Carlo (MC) simulations to overcome these limitations. ***Materials and Methods:*** Samples of about 23 and 10MBq of ^{18}F-FDG and $^{68}GaCl_3$ were measured using a dose calibrator, then diluted by a factor of 1000 to be measured on a gamma counter for 60 minutes. MC simulations were performed using GATE to model the gamma counter's response. The measured and simulated spectra for both isotopes were compared for validation. Sensitivity factors were calculated by dividing the total number of disintegrations by the number of counts in the 511 keV and 1022 keV energy windows ([450-570]keV and [900-1150]keV). These factors were then used to evaluate the samples activities and compared them to dose calibrator values. ***Results:*** The simulated energy spectra were in good agreement with experimental data. Sensitivity factors computed from the simulations allowed an accurate recovery of the samples activities from gamma counter data, with predicted activities being within less than 5% of the dose calibrator values. The sensitivity factors derived from the 511keV energy window displayed variations below 2% for changes of the samples volume up to 50%. ***Conclusion:*** This study presents a method to verify the dose calibrator settings for PET isotopes based on an activity measurement with a gamma counter. The method does not require traceable source, nor cross calibration with a PET scan, and is little dependent on the samples volume. This approach is not limited to PET isotopes: its extension to Lutetium-177 is a work in progress.

EP-0948

Exploring Activity and Scan Time Reduction of [^{18}F]PSMA-1007 within EARL2 Standards

L. Kloosterboer*, L. Heijmen, J. W. J. van Brecht, P. Dibbets-Schneider, T. Ruytenberg, L. de Geus-Oei, D. D. D. Rietbergen, F. H. P. van Velden;*
Leiden University Medical Center, Leiden, NETHERLANDS.

Aim/Introduction: Ongoing advancements in PET/CT detector technology significantly improved image quality and sensitivity, enabling reduction of scan duration and/or the administered radiopharmaceutical activity. Van de Burgt et al. (Physica Medica, 2015) have shown in a phantom study that reduction in scan duration or administered activity of at least a factor four is possible for [^{18}F]FDG on an Omni Legend 32. Our aim is to evaluate on patient data whether either scan duration or the administered activity of [^{18}F]PSMA-1007 can also be reduced, while complying with the EARL Fluorine-18 standards 2 accreditation (EARL2). ***Materials and Methods:*** Fifteen subjects received a [^{18}F]PSMA-1007 PET/CT scan (3 MBq/kg, 120 sec/bed) on an Omni Legend 32 PET/CT between February, 2025 and April, 2025. Four administered activity regimes are simulated by varying the time/bed (120, 60, 45 and 30 sec) in each EARL2 (4 mm) reconstruction. To obtain the coefficient of variation (COV) within healthy tissue as an indication of the noise level, a 2-cm diameter sphere is manually drawn inside the spleen. Lesions (n=31; median volume: 6.5 mL, range: 1.1-35.1 mL) are delineated semi-automatically using an absolute threshold of SUV of 4 and a lower volume limit of 1 mL to assess SUV_{max}, SUV_{mean} and SUV_{peak}. Statistically significant differences ($p \leq 0.05$) between these quantitative measures are assessed using the Wilcoxon signed-rank test. ***Results:*** No statistical differences were found for lesion SUV_{mean} and SUV_{peak}, comparing the simulated reconstructions to the 120 sec/bed reconstruction. Lesion SUV_{max} for the simulated reconstructions were statistically different from the 120 sec/bed reconstruction. Median COV of the spleen were 4.7% (2.6-7.8%), 5.0% (3.7-11.8%), 5.5% (3.7%-12.7%) and 6.0% (4.0%-12.8%) for 120, 60, 45 and 30 sec/bed, respectively. ***Conclusion:*** These preliminary results suggest that the scan duration or administered activity of [^{18}F]PSMA-1007 can be reduced by at least a factor four. The noise level increases while decreasing scan duration (resulting in increased SUV_{max}), but remains below 15% as required by EARL for [^{18}F]FDG images. Further research should demonstrate whether this assumption can be translated to [^{18}F]PSMA-1007. Analysis of additional data is necessary to obtain definite conclusions and should at least include the assessment of: a larger patient group, EARL1 and EARL2 (2 mm) reconstructions, lower time/bedposition(s) and a qualitative image analysis. ***References:*** Van de Burgt et al. "[^{18}F]FDG administered activity reduction capabilities of a 32-cm axial field-of-view solid-state digital bismuth germanium oxide PET/CT system while maintaining EARL compliance." Physica Medica 131 (2025): 104935.

EP-0949

3D Printed PET/CT Phantom with Mixed Target Uptake Characteristics to Investigate Lesion Development

O. Caselles[1,2], *S. Nalla*[1,3], *Q. Maronnier*[1], *T. Palchan-Hazan*[4], *J. Kennedy*[4,5];
[1]*Oncopole Claudius REGAUD - IUCT Oncopole, Toulouse, FRANCE,* [2]*Tachyons SAS, Toulouse, FRANCE,* [3]*Universite de Toulouse, Toulouse, FRANCE,* [4]*Rambam Health Care Campus, Haifa, ISRAEL,* [5]*Technion Israel Institute of Technology, Haifa, ISRAEL.*

Aim/Introduction: Precise lesion characterisation is a common challenge in practice due to heterogeneity within tumours. Conventional quality control practices, such as fillable acrylic spheres have limitations in assessing the heterogeneity. In contrast, 3D printing enables the creation of versatile phantoms that are customisable to include complex features such as fillable printed grids which can simulate multitude of contrasts within

a phantom using single tracer injection. This work builds upon a previous 3D printed phantom inserts design [1] to introduce a more complex design including heterogeneous uptake patterns with minimal phantom preparation time. ***Materials and Methods:*** 4 cm gyroid cubic grids were 3D printed (75% Infill) in Acrylonitrile butadiene styrene (ABS). Spherical voids of 17mm and 28mm were incorporated centred on the cube. A second region with different infill (50% or 100%) was added leading to primary targets (Target Background Ratio ~ 4) of either a sphere or crescent shape. Heterogeneity was either multifocal (TBR ~ 2) or necrosis (TBR ~ 0) based on second regions density. These inserts were placed in a conventional QC phantom and filled with water, soap and [^{18}F] FDG (96 MBq). Acquisitions were performed on two different PET/CT scanners (β:650). Recovery coefficient (RC) was evaluated for quantitation of primary lesion along with TBRMax of overall insert. Additionally, standardised uptake value (SUV) profiles were extracted on Transaxial slice for heterogeneity impact analysis. ***Results:*** Heterogeneity was apparent visually on PET images for all 28mm targets whereas only primary lesion was predominant for 17mm targets due to partial volume effects on secondary regions. TBRMax for 17mm set were in the range of 1.22 - 4.21 and for 28mm targets were 1.34 - 4.52. Mean RC for primary lesions ranged from 0.71 - 0.82 (PET 1) and 0.61 - 0.73 (PET 2) for 17mm, and 0.81 - 0.88 (PET 1) and 0.74 - 0.82 (PET 2) for 28mm. Maximum RC ranged from 0.65-1.02. SUV profiles showed reduced / shifted peak values and evident transitions between multiple regions. Reference cubes without targets yielded SUV values of 0.19-0.27 against expected 0.25 (SUVWater ~1). SUVNecrosis were slightly higher than 0. ***Conclusion:*** Our results highlight that 3D printed inserts effectively model mixed uptakes while demonstrating the impact of lesion size and heterogeneity on PET/CT visual interpretation and quantitation. ***References:*** [1] Nalla, S.K.K., Maronnier, Q., Kennedy, J.A., Palchan-Hazan, T. and Caselles, O., 2025. Enhancing PET/CT Assessment with Porous 3D-Printed Grids-A Pilot Study. medRxiv, pp.2025-04.

EP-0950

Quantitative accuracy of clinical PET systems in the UK (2019-2023)

A. Fenwick, *A. Robinson, A. Denis Bacelar, K. Ferreira, D. Deidda, D. Roddy, W. Heetun;*
National Physical Laboratory, Teddington, UNITED KINGDOM.

Aim/Introduction: Quantitative accuracy in PET is a critical factor when considering multi-centre comparability. To assess the comparability of PET systems in the UK a specialised traceably calibrated solid phantom was designed and distributed to 16 centres. The results were analysed centrally and are reported. ***Materials and Methods:*** The phantom was adapted from the NEMA NU-2 Image quality phantom which consists of 6 spheres ranging in size from 10 mm to 37 mm diameter. A seventh sphere with a 5 mm diameter was added to the phantom in a position optimised using monte carlo techniques. The phantom was prepared with ^{68}Ge spiked epoxy resin with a total activity of 99.0(30) MBq (k=2) with a sphere:background ratio of 4:1. The Phantom was shipped to 16 sites for measurement between 2019 and 2023 with images acquired using a decay-corrected acquisition time simulating a 3 min per bed position scan. An additional scan with a single frame centred over the sphere axis was also obtained at most sites. The phantom was periodically returned to NPL and scanned to confirm stability of the phantom. Images were reconstructed using typical clinical protocols at the participating site, and image analysis was performed centrally by two individuals (independently). Results were calculated for quantitative accuracy of background and sphere activities and recovery coefficient curves were generated for each scan made. ***Results:*** The results showed good agreement between sites with all participants complying with EARL recommended recovery coefficient curves. uncertainty analysis was included to provide comparative data. ***Conclusion:*** This study has demonstrated the comparability between clinical PET/CT sites in the UK using a standardised phantom and has created a dataset which can be used in future studies when investigating performance capability and for validation.

EP-0951

Development and Evaluation of a 3D-Printed Thyroid Phantom for Simulating Hot and Cold Nodules in SPECT Imaging

J. Kiss[1], *K. Kukuts*[2], *A. Forgács*[2];
[1]*Division of Radiology and Imaging Science, Department of Medical Imaging, Faculty of Medicine, University of Debrecen, Debrecen, HUNGARY,* [2]*Mediso Ltd., Budapest, HUNGARY.*

Aim/Introduction: Thyroid scintigraphy is among the most frequently performed procedures in nuclear medicine; therefore, robust quality assurance protocols tailored to SPECT imaging are essential. These protocols often rely on phantom-based evaluations. However, commercially available thyroid phantoms typically represent only healthy tissue, limiting their relevance for simulating pathological conditions such as hot or cold nodules. [1,2] Recent advances in 3D printing technology enable the design and fabrication of customized phantoms, including those that mimic pathological features. In this study, we present a modified anthropomorphic thyroid phantom capable of simulating both hot and cold thyroid nodules. ***Materials and Methods:*** A commercially available 3D thyroid phantom was redesigned using 3D modeling software to alter anatomical volumes and incorporate pathological structures. Spherical nodules (1 cm diameter) were added: a solid (cold) nodule was embedded in the left lobe, and a fillable hollow sphere (0.3 ml) representing a hot nodule was placed in the right lobe. The models were printed in two sizes (20 ml and 40 ml fillable thyroid volumes) using PLA material via fused deposition modeling (FDM) technology. Reproducibility of the manufacturing process was assessed through repeated printing and CT imaging. For realistic attenuation and scatter conditions, the thyroid phantoms were placed within a standard neck phantom. SPECT/CT acquisitions using Iodine-131 were performed on a triple-head SPECT/CT system equipped with a multi-pinhole collimator. The activity concentration ratio between the thyroid tissue and the hot nodule was set at 1:10. ***Results:*** The fabrication process demonstrated high reproducibility, with no leakage observed during phantom preparation. The printed phantoms were fully compatible with conventional neck phantoms. Reconstructed SPECT images clearly depicted both nodules, with the hot and cold lesions showing 88% higher and 28% lower uptake, respectively, compared to the uniform thyroid background. ***Conclusion:*** Results confirm that fillable 3D-printed thyroid phantoms can reproducibly simulate pathological conditions, providing a valuable tool for image quality assessment in SPECT imaging. ***References:*** 1. https://doi.org/10.1097/HP.0000000000000995 ; 2. https://doi.org/10.1016/j.radphyschem.2019.108462.

EP-0952

Manufacturer improvement of ^{99m}Tc scatter correction for its long bore collimator CZT ring SPECT-CT

A. Seret[1], *K. Di Bartolomeo*[2], *C. Bernard*[3];
[1]*University of Liege, Liege, BELGIUM,* [2]*GE Healthcare, Brussels, BELGIUM,* [3]*CHU of Liege, Liege, BELGIUM.*

Aim/Introduction: The manufacturer of the long bore collimator CZT-based ring SPECT-CT is currently releasing an upgraded version of its reconstruction software where dual energy window scatter correction is performed in the iterative loop of the reconstruction whereas it was previously a subtraction at the projection level. Phantom data of our past study of this system

[1] were reprocessed with the new (25) software and results were compared to those obtained with the past version (23). ***Materials and Methods:*** Previously recorded data of ^{99m}Tc filled cylindrical NEMA NU2-94 phantom (NEMA), custom hot and cold bar contrast phantom (TOM) and uniform phantoms of two different sizes (L and XL) were reconstructed using manufacturer OSEM (10 subsets and 20 iterations), attenuation correction, resolution recovery with (SC) or without (NoSC) scatter correction. Considered parameters were residual fraction (RF) in NEMA, recovery coefficient (RC) in TOM bars, coefficient of variation (COV) in TOM uniform area and quantification error (QE) in L using XL as calibration phantom. Parameter values were compared to those obtained previously [1] as well as those obtained using a single 136-145 keV narrow energy window (NW) to spectrally reject scattered photons. ***Results:*** Both software versions led to very similar NoSC values for all parameters. In NEMA, RF-SC25 < RF-NoSC in all three inserts with RF-NoSC < RF-SC23 in air and RF-SC23 < RF-SC25 in water and Teflon. RC-NW > RC-SC23 > RC-SC25 > RC-NoSC in TOM cold rods. RC-NW > RC-NoSC > RC-SC25 > RC-SC23 in TOM hot rods but RC-SC25 ≥ RC-NoSC when only considering the central part of the rods. SC25 very moderately increased COV and the increase was lower than with SC23. In large hot areas, SC25 removed a total number of counts which amounted only to roughly one half of the counts removed by SC23. QE was in the range ±3% depending on the size (smaller or larger than the phantom physical size) of the regions of interest. ***Conclusion:*** The upgraded scatter correction removed much less acquired counts in large hot areas than the past version. Cold contrasts were slightly lower whereas hot contrasts were much larger especially in the thinnest rods which were not present (RC=0) on the SC23 images. Nevertheless, the contrast obtained with a single narrow energy window were higher. Quantification with SC25 in uniform phantoms was very satisfactory with error below 3%. ***References:*** 1. Seret A, Bernard C. EJNMMI Physics 2025; In Press.

EP-0953

FDG Extravasation in PET/CT Imaging: A Visual Grading Approach Based on Clinical Observations

S. Bilgic*;*
Bursa Uludag University, Bursa, TÜRKIYE.

Aim/Introduction: FDG extravasation is a frequently overlooked issue in PET/CT imaging, potentially impacting standardized uptake value (SUV) measurements used in clinical interpretation. This study aims to introduce a visual grading system to classify FDG extravasation severity and assess its quantitative impact on reference SUV values in oncologic patients [1,2]. ***Materials and Methods:*** A total of 235 consecutive FDG PET/CT scans performed for oncologic indications were retrospectively analyzed. Patients were categorized into four groups based on extravasation severity (Grade 0-3), using a newly proposed visual grading system. Liver and mediastinal blood pool regions were selected as reference sites for SUV analysis. Mean SUVmax and SUVmean values were recorded and compared across extravasation grades. One-way ANOVA and Kruskal-Wallis tests were used for group comparisons, followed by post-hoc testing to identify statistically significant differences. ***Results:*** FDG extravasation was observed in 75 patients (31.9%), with 43 classified as Grade 1, 26 as Grade 2, and 6 as Grade 3. Compared to Grade 0, both Grade 1 and Grade 2 patients exhibited statistically significant increases in liver and mediastinal SUV values ($p < 0.001$ for all parameters). For instance, liver SUVmax increased from 3.13 ± 0.44 (Grade 0) to 3.58 ± 0.50 (Grade 1), and mediastinal SUVmean rose from 1.80 ± 0.31 (Grade 0) to 2.17 ± 0.40 (Grade 2), representing a relative difference of up to 20.6%. Grade 3 cases showed variable results without consistent trends, likely due to small sample size [1,3]. ***Conclusion:*** Low-to-moderate FDG extravasation (Grades 1-2) can significantly elevate reference SUV measurements in PET/CT imaging, which may affect response assessments. Incorporating a structured visual grading system into routine clinical practice could improve diagnostic accuracy and reduce unnecessary repeat imaging. These findings highlight the need for heightened awareness and standardized reporting of FDG extravasation in quantitative PET/CT analysis [2,3]. ***References:*** Osman MM, Muzaffar R, Altinyay ME, Teymouri C. FDG Dose Extravasations in PET/CT: Frequency and Impact on SUV Measurements. Front Oncol. 2011;1:41. doi:10.3389/fonc.2011.00041., Wong TZ, Benefield T, Masters S, Kiser JW, Crowley J, Osborne D, et al. Quality Improvement Initiatives to Assess and Improve PET/CT Injection Infiltration Rates at Multiple Centers. J Nucl Med Technol. 2019;47:326-331. doi:10.2967/jnmt.119.228098. ,Kiser JW. The decision to reimage following extravasation in diagnostic nuclear medicine. Front Nucl Med. 2023;3:1171918. doi:10.3389/fnume.2023.1171918.

EP-0954

Evaluation of Costs and Accuracy a 3D-Printed Four-Organ Phantom Using a Commercial Desktop Printer for Standardized Dosimetry in Molecular Radiotherapy

A. Yumoto[1]*, F. Sasaki*[1]*, T. Kita*[1]*, N. Imaizumi*[1]*, M. Sato*[1]*, M. Shiga*[2]*, S. Fukai*[2]*, Y. Tajika*[1]*, H. Daisaki*[1]*;*
[1]*Gunma Prefectural College of Health Sciences, Gunma, JAPAN,* [2]*The Cancer Institute Hospital of Japanese Foundation for Cancer Research, Tokyo, JAPAN.*

Aim/Introduction: Accurate dosimetry in molecular radiotherapy (MRT) is essential to optimize therapeutic outcomes while minimizing radiation to healthy tissues. However, substantial inter-institutional variability persists due to differences in imaging protocols, segmentation methods, and software. While digital phantoms are useful for software validation, physical phantoms are critical for evaluating the full clinical workflow, including imaging and dose calculation. Three-dimensional (3D) printing enables low-cost and flexible production of customized physical phantoms, especially valuable in multicenter studies where standardized, reproducible models are required. To address these needs, we aimed to evaluate the production time, cost, and geometric accuracy of a proposed 3D-printed physical phantom for MRTDosimetry using commercially available printing technology. ***Materials and Methods:*** We utilized the 4-organ phantom developed as part of the MRTDosimetry Challenge, which includes anatomically representative models of the liver, spleen, kidneys, and a tumor. In this study, we employed polygon mesh in STL file format derived from the ICRP 110 adult female phantom, provided by Robinson AP et al., specifically designed for ^{177}Lu-DOTATATE dosimetry [1]. The phantom was fabricated using a FlashForge Adventurer 5M Pro printer with PLA filament, maintaining cost-efficiency. ***Results:*** Geometric accuracy was evaluated by comparing the printed organ volumes to ground truth values, with an average deviation of -0.8%, indicating high fidelity. Phantom fabrication required approximately 41 hours of printing time. The initial setup cost was estimated to be €2,560 for a 3D printer and related equipment, and the material cost per phantom was €70 (1€ = ¥162), making the method accessible and scalable. ***Conclusion:*** Our results suggest that cost-effective organ phantoms, as proposed by the MRTDosimetry project and fabricated using commercially available 3D printing technology, represent a promising tool for validating dosimetry workflows. Future studies will evaluate the effects of different printer models and filament types on accuracy, and examine the reproducibility of repeated prints using the same 3D printing settings. ***References:*** [1] Ferreira KM, Lassmann M, Tran-Gia J; MRTDosimetry Collaboration. Development of a validation imaging dataset for Molecular Radiotherapy dosimetry multicenter intercomparison exercises based on anthropomorphic phantoms. Phys Med. 2023 May;109:102583.

EP-0955

The impact of EARL harmonization on PET kinetic parameters

G. Khamadeeva, *A. Khalimon, I. Baltabaev, A. Shakirova, M. Khodzhibekova, T. Lazutina, I. Pylova, D. Khodakova, A. Leontev; P. Hertsen Moscow Oncology Research Institute - Branch of the National Medical Research Radiological Centre of the Ministry of Health of the Russian Federation, Moscow, RUSSIAN FEDERATION.*

Aim/Introduction: Kinetic parameters such as influx rate (Ki) and distribution volume (Vd) obtained from dynamic PET may improve diagnostic performance; however, their interscanner stability has not been sufficiently studied. The aim of this study was to assess the impact of ^{18}F-based PET EARL2 harmonization on variability of Ki and Vd. ***Materials and Methods:*** Image QC dataset obtained on the 5-ring BGO PET/CT system according to ^{18}F-based PET EARL2 standard was used. 5 EARL2-compliant reconstructions (BSREM with β350 and β450, 3D-OSEM+PSF with 10i6s6mm, 11i6s5mm, and 4i12s6mm, respectively) and 5 EARL2-incompliant reconstructions (BSREM with β100 and β600, 3D-OSEM+PSF with 3i6s8mm, 9i12s5mm, and 3i12s1mm) were selected. The choice of such set of EARL2-incompliant reconstructions was aimed at achieving a wide diversity of recovery coefficients for SUVmax. On average, the mean square errors of SUVmax in EARL2-incompliant reconstructions were 1.3 times higher than in compliant ones (0.148 vs. 0.111). Next, nine patients with twelve metabolically active lung lesions were enrolled in this prospective single-center study. Single-bed dynamic 50-minute PET (dPET) started simultaneously with the IV injection of [^{18}F]FDG. Raw PET data were used to obtain above mentioned sets of 10 reconstructions. Twenty-five time frames (6×30s, 7×60s, 8×150s, and 4×300s) for each reconstruction were applied for kinetic analysis. Ki and Vd of each lesion were calculated via graphical Patlak analysis using various spherical VOIs covering the whole lesion; the image-derived input function was obtained from the region of the descending aorta. Additionally, SUVmax and SUVpeak of each lesion were measured on the last frame of the dPET scan. The coefficients of variation (CoV) for the mentioned metrics (Ki, Vd, SUVmax, SUVpeak) were calculated. ***Results:*** All lesions were well distinguishable on dPET images, and VOI diameters varied from 5mm to 35mm (median 15mm). The CoVs of each metric were statistically lower in the group of EARL2-compliant reconstructions: median of the COVs were 4.5% vs. 11.3% (p=0.0032) for Ki; 6.9% vs. 21.6% (p=0.0407) for Vd; 4.14% vs. 24.3% (p=0.0022) for SUVmax; 2.8% vs. 21.3% (p=0.0022) for SUVpeak. ***Conclusion:*** Preliminary data may indicate the presence of inter-scanner variability in PET kinetic parameters comparable to that discovered for SUVmax and SUVpeak, as well as the potential for its reduction through EARL harmonization.

EP-0956

Harmonization of Quantitative Values in Bone SPECT/CT for Medication-related Osteonecrosis of the Jaw

T. Kita[1], *I. Kuromori*[1], *H. Daisaki*[1], *M. Sato*[1], *F. Sasaki*[1], *A. Yumoto*[1], *N. Imaizumi*[1], *Y. Owaki*[2], *T. Tsuchitani*[3], *N. Hayashi*[4], *M. Tsujimoto*[5], *Y. Maeda*[6], *N. Ueno*[7], *Y. Iwabuchi*[2], *T. Norikane*[8], *Y. Inui*[5], *H. Kaida*[7], *K. Ito*[9], *K. Kitajima*[3];
[1]Gunma Prefectural College of Health Sciences, Gunma, JAPAN, [2]Keio University School of Medicine, Tokyo, JAPANJAPAN, [3]Hyogo College of Medicine College Hospital, Hyogo, JAPAN, [4]Kochi Medical School Hospital, Kochi, JAPAN, [5]Fujita Health University Hospital, Aichi, JAPAN, [6]Tokushima Bunri University, Tokushima, JAPAN, [7]Kindai University Hospital, Osaka, JAPAN, [8]Kagawa University Hospital, Kagawa, JAPAN, [9]National Cancer Center Hospital, Tokyo, JAPAN.

Aim/Introduction: Medication-related osteonecrosis of the jaw (MRONJ), often associated with antiresorptive and anti-angiogenic treatments used in osteoporosis and cancer patients, significantly affects patient quality of life. Early and accurate diagnosis is essential, and recent advancements in quantitative single-photon emission computed tomography/computed tomography (Q-SPECT/CT) have improved its diagnostic utility for MRONJ. However, variability in standardized uptake values (SUVs) across different SPECT/CT systems poses a challenge to multicenter studies, as there is currently no established harmonization criterion for Q-SPECT/CT. To address this limitation, a multicenter phantom study was conducted across seven institutions using eight SPECT/CT scanners. The study aimed to establish a harmonization criterion for SUV measurements and assess the efficacy of a software-based harmonization method. ***Materials and Methods:*** A custom-designed brain tumor phantom containing six hot spheres [1] was filled with ^{99m}Tc-HMDP (hot/background ratio of 4) and imaged using clinical protocols. A cylindrical phantom was used to determine the Bq calibration factor, and SUV conversion and harmonization were performed using the RAVAT software platform (Nihon Medi-Physics Co.,Ltd.) [2]. The harmonization criterion was defined as SUVmax within ±30% of the median value across scanners. If this range was exceeded, a 3D Gaussian filter was applied for harmonization. ***Results:*** The results demonstrated that the SUVmean values in the background region remained stable (0.95-1.05) before and after harmonization, indicating consistent background calibration. In contrast, for the hot spheres, inter-scanner variability in SUV measurements was significantly reduced after harmonization. The coefficients of variation (CVs) for SUVmax, peak SUV, and SUVmean improved from 122%, 68%, and 71%, respectively, before harmonization to 48%, 35%, and 37% afterward. ***Conclusion:*** This study is the first to propose a harmonization criterion for Q-SPECT/CT in MRONJ and to validate a software-based harmonization approach. The method effectively reduced inter-scanner variability without degrading clinical image quality or requiring changes to the image reconstruction process. These findings support the feasibility and utility of this harmonization strategy in multicenter clinical settings, paving the way for more reliable and standardized Q-SPECT/CT studies of MRONJ. ***References:*** [1] Hayashi N, Tokorodani R, Kenda S, Ogasawara D, Yabe F, Ito K. [Determination of Bone SPECT Image Reconstruction Conditions in the Head and Neck Region]. Nihon Hoshasen Gijutsu Gakkai Zasshi. 2021;77(7):700-709.[2] Daisaki H, Kitajima K, Nakajo M, Watabe T, Ito K, Sakamoto F, Nakahara T, Ishibashi M, Toriihara A. Usefulness of semi-automatic harmonization strategy of standardized uptake values for multicenter PET studies. Sci Rep. 2021 Apr 19;11(1):8517.

EP-60

e-Poster Area

D: Technical Studies -> D2 Data Analysis and Artificial Intelligence -> D21 Image Reconstruction / Denoising / Filtering

EP-0957

Brain MRI-guided PET Reconstruction in a New PET/MRI System with State-of-the-art TOF resolution

J. Cabello[1], *K. Kettless*[2], *P. Lehmann*[2,3], *A. B. Rodell*[2], *J. Schaefferkoetter*[1], *I. Law*[4], *F. L. Andersen*[4,5], *T. L. Andersen*[4,5], *P. Schleyer*[1];
[1]Siemens Medical Solutions USA, Inc, Knoxville, TN, UNITED STATES OF AMERICA, [2]Siemens Healthcare A/S, Ballerup, DENMARK, [3]Research & Clinical Translation, Magnetic Resonance, Siemens Healthineers AG, Erlangen, GERMANY, [4]Department of Clinical Physiology and Nuclear Medicine, Copenhagen University Hospital—Rigshospitalet, Copenhagen, DENMARK, [5]Department of Clinical Medicine, University of Copenhagen, Copenhagen, DENMARK.

Aim/Introduction: PET imaging inherently exhibits limited spatial resolution and high image noise. Recent improvements in Time-of-Flight (TOF) performance have resulted in increased effective sensitivity, signal to noise ratio and accelerated image reconstruction convergence. Simultaneous PET/MRI acquisition

provides spatially overlapping metabolic/functional and soft tissue anatomical information at the same time point. By leveraging anatomical MR-images as prior information in the PET reconstruction, MRI-guided (MRIg) MAP-EM PET reconstruction reduces image noise, and improves spatial resolution and quantification accuracy. The current work presents preliminary results of MRIg-MAP-EM PET reconstruction of several brain FDG-PET datasets acquired on the BIOGRAPH One, a second-generation PET/MRI system (Siemens Healthineers) with best-in-class TOF performance. ***Materials and Methods:*** Several subjects were injected with 200.0 MBq FDG, and underwent a brain PET scan for 16-18 min in the PET/MRI system, while simultaneously acquiring multiple MRI sequences. PET data were acquired in list-mode format and rebinned to different scan lengths. The datasets were reconstructed using OP-OSEM and MRIg-MAP-EM reconstruction, based on the Bowsher prior combined with a novel algorithm to adaptively calculate the anatomical strength, using a high resolution 3D-T1w SE (MPRAGE) MRI sequence as anatomical reference. ***Results:*** Results demonstrated that MRI-guided MAP-EM PET reconstruction yielded lower image noise and enhanced delineation of both cortical and subcortical brain structures, compared to OP-OSEM. This improvement enabled a reduction in scan time—or administered dose—by up to 75% without perceptible degradation in image quality. While the high TOF resolution OP-OSEM reconstructions exhibited high image quality, MRIg-MAP-EM further improved image sharpness and reduced noise. Notably, noise levels in the cerebellum increased consistently with OSEM as scan time decreased, whereas MRIg-MAP-EM maintained relatively stable noise levels even at a 1-minute scan duration, while preserving the sharper tissue boundaries such as gray-white matter delineation. ***Conclusion:*** In conclusion, the TOF resolution achieved by this new PET/MRI system significantly improved image quality compared to non-TOF reconstruction, resulting in more precise visualization and delineation of small structures within the brain. Moreover, the integration of anatomical information further refined spatial resolution and reduced image noise. This synergistic approach not only maintains high image quality but also enables reduced scan times or lower radiation doses, thereby improving patient comfort and safety without compromising diagnostic accuracy. Furthermore, we plan to explore the combination of MRIg-MAP-EM PET reconstruction with accelerated deep learning-based MRI, to shorten clinical brain MR protocols, in addition to applying this technique to other radiotracers.

EP-0958

Robustness of Radiomics Parameters to Respiratory Motion: a Phantom Study

H. Halvorsen[1], *L. M. Bonney*[1,2], *G. M. Kalisvaart*[3], *F. H. P. van Velden*[3], *W. Grootjans*[3], *D. R. McGowan*[1,4];
[1]*Oxford University Hospitals NHS Foundation Trust, Oxford, UNITED KINGDOM,* [2]*Sir William Dunn School of Pathology, University of Oxford, Oxford, UNITED KINGDOM,* [3]*Department of Radiology, Leiden University Medical Center, Leiden, NETHERLANDS,* [4]*Department of Oncology, University of Oxford, Oxford, UNITED KINGDOM.*

Aim/Introduction: Radiomic features in PET/CT provide quantitative information that can aid in disease characterisation and prediction of treatment response. Great efforts have been put into the standardisation of such biomarkers [1]. However, it is not well known how these features are affected by motion. Breathing motion is inherent to PET imaging, and various reconstruction algorithms have been developed to correct for this. This study evaluates the robustness of standardised radiomic features to breathing motion, with and without motion correction, using a respiratory motion platform simulating a typical patient and sinusoidal respiratory waveforms. ***Materials and Methods:*** A modular heterogeneous phantom [2] was filled with F-18 and placed on a respiratory motion platform (Quasar). The phantom was scanned on a GE Discovery 710 PET/CT scanner whilst moving sinusoidally and with a typical patient respiratory waveform. Acquisitions were performed with varying motion amplitudes, and a static acquisition was performed for reference. The images were reconstructed using a Bayesian Sequential Regularisation Expectation Maximisation (BSREM) algorithm and a data driven Quiescent Period Gating (QPG) motion correction algorithm. A total of 93 radiomic features were extracted from each image and compared between images of varying motion amplitude using the coefficient of variation (COV) to determine feature stability and Spearman's rank correlation coefficient (ρ) to determine the relationship between features and motion amplitude. A 15% COV threshold was used for ongoing analysis of feature stability, and we defined a monotonic relationship with motion as $\rho \geq 0.8$. ***Results:*** Of the 93 radiomic features analysed, 47% were found to be impacted by sinusoidal motion when using BSREM. This was reduced to 35% when using QPG. Of these features, 80% and 70%, respectively, had a monotonic relationship with motion. For typical patient respiratory motion, 35% were impacted by motion when using BSREM, and 27% when using QPG. Of these, 79% and 48% had a monotonic relationship with motion. ***Conclusion:*** A high proportion of radiomic features were found to be affected by motion for both simulating patient breathing and sinusoidal motion. Most of the affected features had a monotonic relationship with motion amplitude, meaning they increased or decreased consistently with motion. Future research should consider how to implement this knowledge to accurately interpret radiomic features in images containing respiratory motion. ***References:*** [1] Zwanenburg et al. Radiology. 2020;295:328-38. [2] Kalisvaart et al. Med Phys. 2022;49:3093-106.

EP-0959

Preliminary results from a deep learning PET-derived attenuation correction of paediatric FDG brain images

I. Armstrong[1], *A. Coates*[1], *L. Partin*[2], *R. Fahmi*[2], *J. Schaefferkoetter*[2], *B. Spottiswoode*[2], *S. Muthu*[1];
[1]*Manchester University NHS Foundation Trust, Manchester, UNITED KINGDOM,* [2]*Siemens Medical Solutions, Knoxville, TN, UNITED STATES OF AMERICA.*

Aim/Introduction: In paediatric imaging, keeping the radiation burden to the patient as low as possible is an extremely important consideration. Attenuation correction (AC) in an essential component of PET-CT for accurate quantification, and normally performed using CT. For brain studies, this AC CT offers no additional use in clinical image interpretation. We have previously demonstrated the utility of a deep learning algorithm to produce synthetic CT (SynCT) from non-AC PET data for AC purposes. The method leverages the fine anatomical detail visible on non-AC PET images, made possible by high performance time of flight (TOF) PET. This study presents new data from an expanded training model that includes paediatric FDG brain cases. A comparison of the AC PET images using CT and SynCT is presented. ***Materials and Methods:*** A 3D U-net was trained to produce a SynCT using non-AC FDG brain PET images from 100 adult and 20 paediatric patients, acquired on a SiPM PET-CT with 214ps TOF resolution. A testing set of 15 paediatric cases (age 11.6±3.6yr; [range 6-17yr]) was separately acquired with attenuation corrected images produced from the CT and SynCT, derived from the 15-minute non-AC FDG PET images. PET images with AC were reconstructed with 3D iterative OSEM using 8 iterations, 5 subsets, no post-filter, and included TOF and resolution modelling. Voxel-wise differences in AC PET voxels were expressed as the root mean squared error (RMSE), mean voxel ratio (MVR) and structural similarity (SSIM). Paired, but blinded, PET images were assessed visually in synchronised 3-plane orthogonal views using a matched "Spectrum" colour scale, by an experienced nuclear medicine physician to identify any clinically relevant

discrepancies in FDG distribution between the paired images. ***Results:*** Across the 15 patients, the mean and standard deviation RMSE was 469 ± 284 Bq/ml, the MVR was 0.978 ± 0.046 and SSIM was 0.836 ± 0.045. Visual review found no perceivable differences in FDG distribution in all but two cases, which showed very minor perceivable differences. However, neither case were judged to demonstrate clinically significant differences. ***Conclusion:*** This work has demonstrated the expansion of PET-derived synthetic CT for AC of FDG brain scans to paediatric patients. Work continues to evaluate the source of visual differences and refine the model. ***References:*** I Armstrong, A Coates, L Partin, R Fahmi, C Hayden, J Schaefferkoetter, B Spottiswoode, S Muthu. Preliminary results from a PET-derived synthetic CT for attenuation correction of FDG brain studies. EJNMMI 2024, S749.

EP-0960

Monte Carlo Based SPECT Reconstruction: Improvements to Quantitative Imaging

L. Polson[1], *J. Grudzinski*[2], *S. Kurkowska*[3], *P. Esquinas*[4], *C. Uribe*[1], *A. Rahmim*[1];
[1]*University of British Columbia, Vancouver, BC, CANADA,* [2]*University of Wisconsin – Madison, Madison, WI, UNITED STATES OF AMERICA,* [3]*Pomeranian Medical University, Szczecin, POLAND,* [4]*BC Cancer, Vancouver, BC, CANADA.*

Aim/Introduction: Patient-specific dosimetry in radiopharmaceutical therapy requires accurate SPECT-derived activity maps to enable individual treatment planning. For the isotopes Lu-177 and Tc-99m, conventional SPECT with triple energy window (TEW) scatter correction reasonably estimates activity but suffers from positive bias and contrast overestimation in hot regions (~10%) due to larger scatter angles acquired in the lower energy window . For other isotopes such as Pb-212 (alpha emitter) and Y-90 (Bremsstrahlung emitter), conventional reconstruction is inadequate. This study demonstrates that Monte Carlo (MC)-based reconstruction yields more accurate quantitative imaging for Lu-177, Ac-225, Pb-212, Y-90, and Er-165. ***Materials and Methods:*** An MC-based SPECT system matrix, which estimates the expectation of all acquired photons in a given energy window, was implemented using PyTomography with SIMIND serving as the physics simulation backend. The MC-based reconstruction approach was evaluated on synthetic and real SPECT data. Synthetic datasets were generated in SIMIND using phantoms composed of three spheres (72 mm, 40 mm, and 20 mm in diameter) embedded in a cylindrical background with a 10:1 source-to-background ratio. The simulations modeled a Siemens Symbia T2 system with 128 projections acquired at a 15 cm radius and 15 seconds per projection. Reconstructions were performed with OSEM using (i) a conventional system matrix, with triple-energy window (TEW) correction used for Lu-177, Ac-225, and Pb-212, and (ii) the proposed MC-based system matrix. Conventional and MC-based reconstruction were then compared using real SPECT phantom data (Lu-177, Ac-225, and Y-90) that were each acquired on a Siemens Symbia T2 system. ***Results:*** Computed contrast (sphere/background) in the 72 mm sphere from simulated data are listed as (conventional, MC) and were as follows: Lu-177 (11.92, 10.13) , Ac-225 (11.47, 9.58), Pb-212 (4.36, 9.27), Y-90 (3.22, 10.28), Er-165 (5.38, 10.38), showing MC reconstruction is quantitatively superior in all cases. In the real data, the Lu-177 NEMA phantom (32 mm sphere) had a -8.62% contrast difference between MC and conventional , the Ac-225 phantom (60 mm) showed a -20.1% difference, and the Y-90 NEMA phantom (32 mm) showed a +97.1% difference. MC reconstructions thus corrected for contrast overestimation in Lu-177 and Ac-225 and underestimation in Pb-212, Y-90, and Er-165; such differences can be explained via spectral analysis of each isotope. ***Conclusion:*** A MC-based reconstruction framework (implemented via PyTomography and SIMIND and made publicly available) was demonstrated to quantitatively outperform conventional reconstruction in SPECT by reducing isotope specific bias for Lu-177, Ac-225, Pb-212, Y-90, and Er-165.

EP-0961

AI-based denoising of multi-scanner fast-acquisition brain [^{18}F]FDG PET allows for reliable regional quantification

L. C. Silva*, C. S. Constantino, F. P. M. Oliveira, D. C. Costa; Champalimaud Foundation, Lisbon, PORTUGAL.*

Aim/Introduction: This study aimed to assess the feasibility of deep-learning-based denoising of 1-3min brain [^{18}F]FDG PET to improve patient cooperation and enhance clinical workflow. ***Materials and Methods:*** 120 patients were included for the training (N=80) and testing (N=40) of a denoising-specific 3D U-Net. Local brain [^{18}F]FDG PET and external[1] whole-body [^{18}F]FDG PET (cropped to simulate brain acquisitions) training/test datasets comprised 29/20 and 51/20 patients, respectively. Local fast acquisitions corresponded to durations of 2, 3 and 5min, and external 1, 2.5 and 5min, against reference acquisitions of either 10 or 15min. Local dataset included acquisitions at 30min, 45min and 2h30-3h post-injection, and external dataset at around 60min post-injection. This resulted in 351 training pairs. For testing, 1-3min acquisitions from a single time post-injection were used, resulting in 80 pairs (20 pairs/duration). Average injected activity was similar for both datasets, averaging around 3MBq/kg. Local acquisitions were performed either on a Philips Gemini or Philips Vereos PET/CT scanner, and external acquisitions on a United Imaging uExplorer or Siemens Biograph Vision Quadra PET/CT scanner. Mean squared error (MSE), intraclass correlation coefficient (ICC) and peak signal-to-noise ratio (PSNR) were used for a voxel-wise comparison between not denoised (ND) and respective deep-learning-denoised (DL) sets against reference images. Anatomical segmentation was based on the automated anatomical labelling (AAL) 2 atlas, which was deformed into each patient's native space. Agreement between ND and DL sets against the reference was assessed through the ICC and absolute deviation in SUV_{min}, SUV_{max} and SUV_{mean} for each AAL2 region-of-interest (ROI). ***Results:*** Voxel-wise MSE, ICC and PSNR between reference and DL showed a statistically significant improvement relative to ND ($p<0.001$). Regional SUV_{mean} quantification of ND and DL revealed an absolute deviation from the reference no larger than 4% and an ICC no lower than 0.83. For SUV_{min} and SUV_{max}, statistically significant differences in ICC and absolute deviation from the reference were observed in favour of DL, against ND ($p<0.001$). In particular, ultra-fast acquisitions (1/2min) yielded an average ICC of 0.74[ND] against 0.83[DL] in SUV_{min}, and 0.81[ND] against 0.92[DL] in SUV_{max}. Average SUV_{min} and SUV_{max} relative absolute deviation from the reference were approximately 10%[ND] and 5%[DL]. ***Conclusion:*** The proposed DL-based denoising was proven suitable for the restoration of fast-acquisition brain [^{18}F]FDG PET, having resulted in images similar to the standard-of-care acquisitions. Acquisition duration reductions to 1 or 2min, depending on scanner sensitivity, demonstrated to be enough for reliable quantification. ***References:*** [1]Xue et al.(2022)(DOI:10.1007/s00259-021-05644-1).

EP-0962

AI generated attenuation correction maps for DaT SPECT image reconstruction outperforms Chang method.

Z. Wilson[1], *A. Sohlberg*[1,2], *J. Lilja*[2,1], *K. M. Bradley*[3], *D. McGowan*[1,4];
[1]*Oxford University Hospital NHS FT, Oxford, UNITED KINGDOM,* [2]*HERMES Medical Solutions, Stockholm, SWEDEN,* [3]*Cardiff University, Cardiff, UNITED KINGDOM,* [4]*University of Oxford, Oxford, UNITED KINGDOM.*

Aim/Introduction: This study evaluates the performance of two AI-generated attenuation correction maps for dopamine active transporter (DaT) scans against two conventional attenuation

correction methods: CT-based attenuation correction (CTAC) and the Chang (uniform) method. Use of neural networks for AC would enable reducing patient radiation exposure by eliminating CT scans and improving workflow efficiency by minimizing scan time and costs. ***Materials and Methods:*** Two AI models, both based on a standard U-Net architecture, were trained to convert pre-reconstructed SPECT images (ordered-subsets expectation maximization without corrections) into CT-like attenuation maps. Model 1 uses a Mean Squared Error loss function; Model 2 uses a Mean Absolute Error loss function. The training data was obtained from two sites: Oxford, UK (1000 training cases, 50 validation) and Lahti, Finland (100 training cases, 10 validation). A total of 54 sequential DaT SPECT scans (November 2024-March 2025) were then reconstructed with Hybrid Recon Neurology using four attenuation maps: (1) a CT-based attenuation map (ground truth), (2) the mean squared error model, (3) the mean absolute error model, and (4) Chang. Ten scans were excluded because of registration artifacts or abnormal uptake. The specific 123I-FP-CIT binding ratios (SBR) across 6 brain regions of interest (ROI) were assessed using Hermes BRASS (version 7.0). ***Results:*** Pair-wise Wilcoxon signed rank tests with Bonferroni corrections for multiple comparisons demonstrated the images reconstructed with the two AI-generated mu maps yielded SBRs comparable to the standard CT based attenuation corrected images. Model 2 had no statistically significant difference ($p>0.05$) between the SBRs across all 6 brain regions with the standard. While Model 1 only had statistically significant differences in the frontal lobe ($p=0.008$) and right caudate ($p= 0.049$), while the Chang images had statistically significant SBRs across all regions ($p<0.05$) except the cerebellum (which has no diagnostic value for DaT scans). Linear regression testing on SBR between models and regions similarly showed the UNET models more comparable to the standard than the Chang method. Chang AC had the highest slope across all region regression models with a mean of 8.1±1.3% compared to Model 1 (3.1±0.6%) and Model 2 (2.2±0.9%). ***Conclusion:*** Pair-wise tests in agreement with the regressions test results indicate the AI models successfully produce AC maps statistically similar to the standard CT based AC and outperformed the uniform AC images. This demonstrates the potential of AI-based AC for these patients and future work will expand this analysis to a larger dataset.

EP-0963

Reconstruction of dual-tracer PET images for the simultaneous acquisition of 68Ga and 18F

E. Pfaehler, *D. Niekämper, J. J. Scheins, J. N. Shah, C. W. Lerche; Forschungszentrum Jülich, Jülich, GERMANY.*

Aim/Introduction: A simultaneous acquisition of two radiotracers, one labelled with 68Ga and one with 18F, is of high clinical interest. To decrease patient burden, injecting both tracers simultaneously and separating the tracer signals during reconstruction is desirable. ***Materials and Methods:*** To separate the signal of both tracers, a dual-tracer reconstruction approach[1] is adapted based on the detection of the additional prompt gamma-ray emitted by 68Ga in 1.2% of the cases. The list-mode data is separated into double and triple-coincidences, whereas a triple-coincidence consists of two annihilation photons and corresponding gamma-ray. A double-coincidence can have its origin in either 18F or 68Ga. The amount of double-coincidences with origin in 68Ga is estimated using the detected triple-coincidences and a triple-to-double ratio, estimated via simulations, indicating how many 68Ga double-coincidences are expected if one triple-coincidence is detected. We reconstruct the 68Ga image combining the detected triple-coincidences and the triple-to-double ratio. Due to the low number of gamma-rays of 68Ga, the triple-coincidence signal is very sparse. We combine the difference prior [2] and information from the image reconstructed using all double-coincidences to increase the image quality of the 68Ga image. A simple PET scanner with an axial length of 20 cm and a diameter of 30 cm, containing an approximately sized head filled with water and a skull was simulated. Two partly overlapping cylinders, one containing 1 MBq 18F and one containing 1.5 MBq 68Ga, were simulated in the middle of the skull scanned during 3 minutes. We compare the mean activity present in the reconstructed cylinders with the expected activity for both tracers, and analyse how much of the 68Ga signal remains in the reconstructed 18F image in regions where only 68Ga is present. ***Results:*** The activity in the cylinder containing 68Ga was underestimated by 11.4% while the activity in the cylinder containing 18F was overestimated by 7%. In the image part where only 68Ga was present, 9.3% of the 68Ga signal remained in the 18F image. ***Conclusion:*** Our results indicate that the reconstruction approach can separate the signal of 68Ga and 18F. However, it still needs to be tested in different scenarios. ***References:*** [1] Pfaehler,Elisabeth, et al. "ML-EM based dual tracer PET image reconstruction with inclusion of prompt gamma attenuation."Physics in Medicine & Biology 70.1 (2024): 015009 [2] Nuyts,Johan, et al. "A concave prior penalizing relative differences for maximum-a-posteriori reconstruction in emission tomography." IEEE Transactions on nuclear science 49.1 (2002): 56-60.

EP-0964

Deep Learning-Driven Total-Body PET Imaging with Concurrent Tracer and CT Dose Reduction

H. Wang[1,2], *G. Chen*[2], *C. Kong*[2], *X. Qiao*[1], *W. Ding*[2], *M. Zhang*[1], *Q. Huang*[2], *B. Li*[1];
[1]*Department of Nuclear Medicine, Ruijin Hospital, School of Medicine, Shanghai Jiao Tong University, Shanghai, CHINA,*
[2]*School of Biomedical Engineering, Shanghai Jiao Tong University, Shanghai, CHINA.*

Aim/Introduction: Positron emission tomography/computed tomography (PET/CT) plays a pivotal role in clinical imaging, offering both metabolic and anatomical insights. However, concerns persist regarding radiation exposure, which stems from both the injected radiotracer and the ionising radiation of the CT scan. Advances in PET hardware and reconstruction algorithms, especially the development of total-body PET with extended axial coverage, have significantly reduced radiation burden. Nonetheless, further reduction—particularly in the form of ultra-low tracer dose and CT-free acquisition—is urgently needed. Although recent deep learning (DL) approaches have addressed either PET denoising or CT-free attenuation correction individually, few have explored both challenges simultaneously. In this study, we propose a DL-based framework that enables precise imaging from ultra-low-dose, non-attenuation-corrected (NAC) total-body PET without requiring a CT scan. ***Materials and Methods:*** We developed a two-stage 3D U-Net architecture termed NLE (Noise Level Estimation). The first stage predicts the noise level in NAC images, while the second performs denoising and image enhancement. Pixel shuffle and unshuffle layers are integrated to improve memory efficiency. The model was trained on 500 total-body PET datasets acquired at Ruijin Hospital using a United Imaging uExplorer scanner. Each case comprised a standard-dose, attenuation-corrected image (D1) and four corresponding NAC images at descending dose levels (D1, D4, D10, D20). During training, all dose levels were used to promote generalisation, with 3D anatomical patches of 128×128×128 extracted per case. The model was trained for 40 epochs using the Adam optimiser with a decaying learning rate. Performance was assessed on a separate test set of 62 patients using Peak Signal-to-Noise Ratio(PSNR), Structural Similarity Index Measure(SSIM), and mean absolute errors(MAE). ***Results:*** The NLE model demonstrated robust performance across all dose levels, even in the absence of CT-based attenuation correction. For NAC-D1, D4, D10, and D20 images—none of which were attenuation corrected—the

enhanced outputs closely approximated standard-dose images with CT-based attenuation correction. PSNR values reached 31.78, 28.37, 26.85, and 25.75, respectively. Corresponding SSIM scores were 0.99, 0.98, 0.98, and 0.97, while mean absolute errors were 0.06, 0.10, 0.12, and 0.14. These results confirm the feasibility of high-fidelity total-body PET imaging from ultra-low-dose, CT-free acquisitions when guided by deep learning. ***Conclusion:*** The proposed deep learning framework enables accurate PET imaging from ultra-low-dose, CT-free total-body acquisitions, reducing patient radiation risk and enhancing the clinical accessibility of PET. This represents a promising step toward safer and more scalable molecular imaging.

EP-0965

Null space evaluation for multi-focal collimator SPECT on a digital brain phantom

M. Nau[1,2], *A. Vija*[3], *M. P. Reymann*[1,2], *A. Maier*[1];
[1]*Pattern Recognition Lab, Friedrich-Alexander-Universität Erlangen-Nürnberg, Erlangen, GERMANY,* [2]*Siemens Healthineers AG, Molecular Imaging, Forchheim, GERMANY,* [3]*Siemens Medical Solutions Inc., Molecular Imaging, Hoffman Estates, IL, UNITED STATES OF AMERICA.*

Aim/Introduction: In tomographic imaging, the null space refers to components of the object that the imaging system cannot detect. These structures cannot be recovered by any reconstruction method and contribute to uncertainty in the final image [1]. We investigate how multi-focal collimator geometry affects the null space in SPECT imaging using a digital Hoffman brain phantom. We use a system model that accounts for attenuation and spatially varying point spread functions (PSFs) to evaluate whether multi-focal collimators reduce the magnitude of null space components in neurologically relevant regions of interest (ROIs). Specifically, we investigate the SMARTZOOM™ collimator (SZC), originally developed for cardiac imaging, and the SMARTZOOM™ high resolution with extended magnification field (SZHRX) collimator, which was adapted for brain imaging. ***Materials and Methods:*** We compute null space components using the iterative Wilson-Barrett method [2] with a custom projection operator and a voxelized 128^3 Hoffman brain phantom configured with a gray/white matter contrast ratio of 4:1. The projection operator models a Siemens Symbia scanner with attenuation correction, a depth-dependent 3D collimator response, and three collimator types: a standard low-energy high-resolution (LEHR) parallel-hole collimator, as well as multi-focal designs modeling SZC and SZHRX. We simulate a full 360° acquisition with 3° angular steps and a rotation radius of 15 cm for LEHR and 28 cm for SZC and SZHRX. ***Results:*** Our null space analysis identifies structures that the system can or cannot reliably reconstruct. Across the full image domain, we observe that the null space magnitude increases by 11.07 % from LEHR to SZC and by 2.10 % from LEHR to SZHRX. In contrast, within a central brain ROI of 32^3 voxels, we find a substantial reduction of 11.34 % for SZC and 8.28 % for SZHRX. SZC shows a stronger local reduction due to higher central magnification, while SZHRX achieves broader improvement through its extended magnification field. ***Conclusion:*** We show that null space characterization provides a principled framework for evaluating reconstruction uncertainty across different acquisition geometries. Our results demonstrate that multi-focal collimators reduce the null space in central brain regions and improve estimation. ***References:*** [1] Nau, M., et al., Computing Null Space Hallucinations on Simulated SPECT Image Reconstructions. IEEE Medical Imaging Conference Record, 2023. [2] Wilson, D.W. and Barrett, H.H., Decomposition of images and objects into measurement and null components. Optics express, 1998.

EP-0966

3D diffusion models for synthesizing CT image volumes from uncorrected PET data

J. Schaefferkoetter*, P. Schleyer, M. Conti;*
Siemens Medical Solutions USA, Inc., Knoxville, TN, UNITED STATES OF AMERICA.

Aim/Introduction: In hybrid PET systems, the umap used for attenuation correction (AC) is derived from a modality like CT or MRI. In general, this is effective but has limitations, e.g. extra radiation dose, segmentation errors and subject motion. Convolutional neural networks (CNNs) have been applied for umap synthesis, typically generating synthetic CT-AC umaps from the PET in a single forward pass. Diffusion Probabilistic Modeling (DPM) is an advanced generative technique but hasn't been adopted for the generation of 3D data due to network complexities, computational overhead and longer times needed to generate images. Here, various 3D methods for umap synthesis based on single-shot CNN and conditional DPM with different sampling strategies are compared. ***Materials and Methods:*** The DPM model was a Residual-UNet with conditioning and time step encoding blocks, and 3 sampling strategies were investigated: Denoising Diffusion Probabilistic Model (DDPMs) [1], Denoising Diffusion Implicit Models (DDIM) [2] and DPM-solver [3]. The original DDPM approach used 1,000 steps, and for each accelerated sampling technique, 10, 20 and 50 steps were tested. PET images were reconstructed using each umap, and values in the brain, heart, hip, liver and regions were compared. Twelve subjects with multiple PET tracers were reserved solely for testing. ***Results:*** The generation time of all methods scaled with the number of steps. In general, the DPM model produced superior image quality to that of the single-shot CNN, but differences in the PET quantification were less pronounced. For each anatomical region, the range of VOI means was relatively small, within the standard deviation of the VOI itself. ***Conclusion:*** This work compared various umap synthesis techniques including 3D diffusion models. Fast diffusion sampling techniques were implemented, and all converged to similar images. The DPM model produced higher quality images relative to the single-shot CNN - especially in regions with low PET signal. However, there was less impact on the PET quantification. A larger evaluation including abnormal anatomy or pathology may highlight other potential benefits or pitfalls of diffusion models. ***References:*** [1] Ho, Jonathan, Ajay Jain, and Pieter Abbeel. "Denoising diffusion probabilistic models." Advances in neural information processing systems 33 (2020): 6840-6851. [2] Song, Jiaming, Chenlin Meng, and Stefano Ermon. "Denoising diffusion implicit models." arXiv preprint arXiv:2010.02502 (2020). [3] Lu, Cheng, et al. "Dpm-solver: A fast ode solver for diffusion probabilistic model sampling in around 10 steps." Advances in Neural Information Processing Systems 35 (2022): 5775-5787.

EP-0967

Cross-scanner transfer learning of deep learning-based partial volume correction for quantitative ^{177}Lu SPECT/CT imaging

S. Kamrani[1,2], *A. Gehring*[1], *M. Salas Ramirez*[1], *M. Lassmann*[1], *J. Leube*[1], *P. Sheikhzadeh*[3], *J. Gustafsson*[4], *J. Tran-Gia*[1];
[1]*Department of Nuclear Medicine, University Hospital Würzburg, Würzburg, GERMANY,* [2]*Department of Medical Radiation Engineering, Shahid Beheshti University, Tehran, IRAN, ISLAMIC REPUBLIC OF,* [3]*Department of Nuclear Medicine, IKHC, Tehran University of Medical Sciences, Tehran, IRAN, ISLAMIC REPUBLIC OF,* [4]*Medical Radiation Physics, Lund, Lund University, Lund, SWEDEN.*

Aim/Introduction: Quantitative SPECT/CT imaging is the preferred modality for dosimetry in radiopharmaceutical therapy, but partial volume effects (PVEs) remain a major challenge. Deep learning-based partial volume correction (DL-PVC) [1] has shown promise in mitigating PVEs, yet models are typically scanner-specific, limiting clinical applicability. In this study, we investigated

the generalizability of DL-PVC in ^{177}Lu SPECT across systems from the two main manufacturers and evaluated whether transfer learning can improve cross-scanner performance. ***Materials and Methods:*** Realistic SPECT projections of 2500 random ^{177}Lu activity distributions within extended cardiac-torso phantoms were generated for two scanners (GE Discovery D670 + MEGP and Siemens Intevo Bold + MELP) as described previously using the SIMIND Monte Carlo program [1, 2]. Reconstructions were performed with PyTomography (OSEM, 20i, 4s, AC, TEW-SC, resolution modeling) [3]. Scanner-specific R2UNet models were trained separately on 1900 ground-truth/simulation pairs. Transfer learning was applied by further training each model using 25/50/100/200/500 datasets specific to the other scanner, with scanner-specific sensitivity differences accounted for. Performance was assessed on 100 independent test datasets using SSIM, NRMSE, and VAA (volume activity accuracy**,** defined as the fraction of voxels with estimated activity deviations ≤ 5% from the true value). ***Results:*** The GE-trained model achieved SSIM/NRMSE/VAA of 0.92/4.8%/21.7% on GE and 0.91/5.4%/17.0% on Siemens test data. Similarly, the Siemens-trained model yielded 0.94/5.6%/25.4% on Siemens and 0.93/5.0%/18.1% on GE data (without PVC: 0.88/5.8%/7.4% for GE and 0.89/5.7%/8.4% for Siemens). Transfer learning notably improved cross scanner performance: On the new scanner, performance increased substantially with as few as 25 training samples and approached that of natively trained models with more data, following non-linear, saturating trends (0.93/4.8%/21.7% to 0.93/4.7%/22.6% for GE-to-Siemens transfer using 25 to 500 samples). Meanwhile, performance on the original scanner gradually declined (0.92/4.8%/19.3% to 0.92/4.8%/17.6%), indicating a trade-off during adaptation. A similar pattern was observed for Siemens-to-GE transfer, with improvements on GE and slight performance loss on Siemens. ***Conclusion:*** Transfer learning substantially improves the generalizability of DL-PVC across SPECT/CT systems, with most benefit achieved using as few as 25 datasets from the new scanner. However, this comes at the cost of reduced performance on the original scanner, highlighting a trade-off between domain adaptation and retention. These findings support transfer learning as a promising strategy for cross-scanner harmonization, while underlining the need for balanced adaptation in clinical deployment. ***References:*** [1] Leube et al. JNM, 2024;65(6):980-987. [2] Ljungberg and Strand. ComputMethProgBio, 1989;29(4):257-272. [3] Polson et al. SoftwareX 2025;29:102020.

EP-0968

Feasibility of artificial deep learning based 220 ps time-of-flight (TOF)

F. Kaser[1,2,3], *M. Pires*[1], *S. Gutschmayer*[1], *D. Ferrara*[1], *B. Geist*[4], *W. Langsteger*[4], *T. Beyer*[1], *I. Rausch*[1];
[1]*QIMP Team, Medical University of Vienna, Vienna, AUSTRIA,* [2]*University of Kaiserslautern-Landau, Kaiserslautern, GERMANY,* [3]*OMS HTS GmbH, Wels, AUSTRIA,* [4]*Division of Nuclear Medicine, Medical University of Vienna, Vienna, AUSTRIA.*

Aim/Introduction: Recent advances in PET detector development have paved the way for clinical TOF resolutions of ~200 ps. Furthermore, advances in AI have led to the integration of AI-based TOF simulations in non-TOF PET systems of 385 ps and 550 ps timing resolutions [1]. In this study, the feasibility to emulate a 220 ps TOF using AI was assessed. ***Materials and Methods:*** Whole-body [18F]FDG-PET data of 130 examinations (training: 126, testing: 4) from two PET systems with the same detector technology with 220 ps TOF resolution were reconstructed with and without TOF information using the same parameters (OSEM+PSF: 21 subsets 2 iterations). The images were normalised using standard score and divided into patches of 96 slices. A classic 3D U-net structure was used as the base of the model to predict TOF from non-TOF images. The model was adapted to 3D images, kernel size 3, going from 64, 128, 512 to 1024 kernels in the respective layers, and using residual connections. For model optimisation a variation of hyperparameters and input resolutions were tested. The holdout datasets were evaluated visually, through %-difference images and performance parameters of mean square error (MSE) and structural similarity index measurement (SSIM). ***Results:*** Two models with different input resolutions (1.65 and 3 mm) with a learning rate of 0.05, and 100 and 200 Epochs were selected for their performance. In high-activity regions, like brain and bladder, perceived image quality improved, while there was minimal impact on low uptake regions. The DL-TOF models reduced the MSE compared to the non-TOF reconstructions by 21% (SD= 2%) and 26% (SD= 5%) respectively, while only minor changes in SSIM were observed. ***Conclusion:*** The current implementation of a 220 ps DL-TOF improves non-TOF image quality and the MSE in areas of high tracer activity areas without yielding true TOF accuracy. Since the quality and spread of the training data affect model performance, separate models would need to be trained for different image resolutions. ***References:*** [1] Mehranian, A., Wollenweber, S.D., Walker, M.D. et al. Deep learning-based time-of-flight (ToF) image enhancement of non-ToF PET scans. EJNMMI, 2022;49:3740-3749.

EP-0969

Accelerated PET Imaging with a Gated Autoregressive Diffusion Network

X. Xie[1,2], *Y. Gao*[1,2], *N. Zhang*[3], *Y. Yang*[1,2], *H. Zheng*[1,2], *D. Liang*[1,2], *Z. Hu*[1,2];
[1]*Research Center for Medical AI, Shenzhen Institute of Advanced Technology, Chinese Academy of Sciences, Shenzhen, CHINA,* [2]*Key Laboratory of Biomedical Imaging Science and System, Chinese Academy of Sciences, State Key Laboratory of Biomedical Imaging Science and System, Shenzhen, CHINA,* [3]*Lauterbur Research Center for Biomedical Imaging, Shenzhen Institute of Advanced Technology, Chinese Academy of Sciences, Shenzhen, CHINA.*

Aim/Introduction: Prolonged PET acquisition times often cause discomfort and motion artifacts, limiting its use in vulnerable patients. Clinically, there is a growing need for faster, safer imaging without compromising diagnostic quality. To address this, we propose a gated autoregressive diffusion model that reconstructs high-quality images from short-duration scans by modeling the PET formation process and temporal dynamics. This approach enhances image quality under low-dose conditions and improves the clinical usability of PET. ***Materials and Methods:*** We used the Ultra-low Dose PET Challenge Dataset with 1060 whole-body [18F]FDG PET scans. Data were normalized to SUV units to enable clinical interpretability and efficient comparison. Experiments focused on DRFs of 20 to simulate 20× scan time reduction. We propose a Gated-Autoregressive Diffusion framework to reconstruct high-quality PET images from short-duration scans. First, we introduce a pixel-wise degradation operator that models photon accumulation as a Poisson-Gaussian process, enabling realistic simulation of PET signal degradation across acquisition durations. This operator ensures alignment between forward degradation and reverse reconstruction trajectories. The degradation operator is as follows: $x_t(i,j)=(1-\alpha(i,j)(t))x_0(i,j)+\alpha(i,j)(t)x_T(i,j)+\eta_t(i,j)$, where $x_0(i,j)$ is the pixel intensity from a short-duration PET scan,$x_T(i,j)$ is the corresponding pixel intensity from a full-duration PET scan,$\alpha(i,j)$ is a pixel-specific normalized weight dictating the transition from $x_0(i,j)$ to $x_T(i,j)$. $\alpha(i,j)(t) = N(i,j)(t)/N(i,j)(T)$,$N(i,j)(t)\sim Poisson(\lambda(i,j)t)$ $\eta_t(i,j)$ is a Gaussian-distributed noise term that simulates system and detector noise. To restore lost information, we embed a Gate-Autoregressive Module (GAM) within a cold diffusion framework. At each step, an intermediate full-scan estimate is obtained via a restoration network and then redegraded for consistency. GAM, inspired by LSTM, integrates

CBAM and GLU-based attention to retain temporal context and suppress cumulative errors. ***Results:*** Experiments on the Ultra-low Dose PET Challenge dataset demonstrate that our model outperforms state-of-the-art methods in SSIM, PSNR, and RMSE. Compared to UNN and CoreDiff, our model achieves improved structural fidelity and reduced error. Our method generalizes well across different scan durations, producing reliable outputs, highlighting its clinical robustness and adaptability. ***Conclusion:*** Our proposed gated autoregressive diffusion model enables accurate PET reconstruction from short-duration scans. It effectively reduces noise, preserves anatomical details, and outperforms existing methods across multiple metrics. The model also generalizes well to different scan durations, demonstrating strong clinical potential for fast, low-dose PET imaging applications.

EP-0970

A Quantitative CT-less Reconstruction Workflow for Long-axial Field-of-view PET Scanners with Enhanced Scaling

M. Teimoorisichani[1], *J. Schaefferkoetter*[1], *V. Panin*[1], *H. Sari*[2,3], *A. Rominger*[2];
[1]*Siemens Medical Solutions USA Inc., Knoxville, TN, UNITED STATES OF AMERICA,* [2]*Bern University Hospital, Bern, SWITZERLAND,*
[3]*Siemens Healthineers International AG, Zurich, SWITZERLAND.*

Aim/Introduction: The joint estimation problem in maximum likelihood estimation of activity and attenuation (MLAA) is ill-posed and non-unique, leading to scaling issues in MLAA-reconstructed images. While time-of-flight (TOF) improves spatial localization and mitigates scaling, it may not fully resolve the issue, particularly with inconsistent or noisy data. This work introduces a quantitative CT-less reconstruction workflow based on TOF-MLAA, incorporating a novel approach to address scaling. ***Materials and Methods:*** The proposed method is designed for PET scanners with lutetium-based scintillators. We use attenuation maps (μ-maps) derived from lutetium background radiation as an initial condition in TOF-MLAA [1]. To further mitigate scaling issues, a partially known μ-map is employed to determine and apply a scaling factor to reconstructed images. In the absence of ground-truth μ-maps in CT-less PET, we utilize a deep learning (DL)-based organ segmentation algorithm to segment non-attenuation-corrected PET images. The mean attenuation coefficient of an organ minimally affected by MLAA cross-talk (the liver in ^{18}F-FDG studies) is then compared to a nominal value (0.1 cm^{-1} for the liver). The resulting offset is used to calculate and apply a scaling factor within MLAA. This approach is particularly suited for lutetium-based long-axial field-of-view (FOV) PET scanners, where the high lutetium background radiation flux allows for a transmission reconstruction with acquisitions as short as a few minutes. We evaluated the proposed CT-less reconstruction framework on three patients scanned with ^{18}F-FDG using a long-axial FOV PET/CT scanner (Biograph Vision Quadra, Siemens Medical Solutions USA, Inc.). ***Results:*** Evaluation of reconstructed PET images from the three patients indicates that the proposed CT-less approach yields images comparable to CT-based PET images. Reconstructed μ-maps from MLAA showed excellent consistency with CT-based μ-maps, with minimal inconsistencies due to cross-talk. The final PET images were comparable to reference images both qualitatively and quantitatively, with individual organ uptake values within 5% of those from CT-based reconstructions. ***Conclusion:*** A CT-less PET reconstruction workflow based on lutetium background radiation and TOF-MLAA is proposed in this work in which a novel approach is used to address the problem of scaling. ***References:*** [1] Teimoorisichani M, et al. Medical physics 49.1 (2022): 309-323.

EP-0971

Segment-wise loss function and object informed deep learning improves the preservation of small details in PET image denoising

Y. Salimi, *Z. Mansouri, H. Zaidi;*
Division of Nuclear Medicine and Molecular Imaging, Geneva University Hospital, Geneva, SWITZERLAND.

Aim/Introduction: Faster PET image acquisition or lower radiotracer is desired PET imaging. Deep learning (DL) has shown a promise, however, conventional DL training focusing on voxel-wise metrics and loss functions have limitations in preserving small or low contrast details and tend to over-smooth images. In this study, we implemented prior knowledge of all details in a PET image through delineation of every structures with nn-interactive model and used them for training. ***Materials and Methods:*** We used a sample of publicly available dataset from the Ultra-Low-Dose PET Challenge (1) to train two models, conventional training and segment-wise loss training. In the first strategy, five-fold cross-validation was performed using U-Net models trained to map 10%-dose PET images to full-dose equivalents. Each model trained for 100 epochs with an L1 loss. In the second strategy, full-dose PET images were segmented using nn-interactive models (2) prompted every 20 mm along the body contour which resulted in about 2000 objects detected in each PET image. These objects were used to train models using the same data split. Segment-wise loss function was computed separately for each segmented object and used for training the same model. Both strategies were evaluated on an external test set using voxel-wise and segment-wise performance metrics calculated in all segmented objects. ***Results:*** The model trained with segment-wise loss outperformed the conventional model by better preserving image details, as evidenced by improved segment-wise relative absolute error (7.3 ± 6.7% vs. 13.1± 8.8%, respectively). In addition, the voxel-wise RMSE was reduced by 24% in segment-wise loss models. Visual assessment further confirmed reduced over-smoothing and enhanced structural detail in segment-wise loss models. ***Conclusion:*** Deep learning denoising task can be viewed as a decision-making process about an object in noisy PET image to be kept as important detail or to be removed as a noise. The whole image loss function averaged over all voxels in an image tend to smooth the images because they return a better overall score when small objects are removed. Our innovative method for segmenting all objects in PET images and using that information to guide the DL model and loss function to preserve the small details in the image showed a better performance in comparison with the conventional training method. ***References:*** 1.Xue S, et al. A cross-scanner and cross-tracer deep learning method for the recovery of standard-dose imaging quality from low-dose PET. EJNMMI, 2022.2.Isensee F, et al. nnInteractive: Redefining 3D Promptable Segmentation. Preprint, 2025.

EP-0972

High-Quality Cardiac SPECT Reconstruction from Half-Projections Using a U-Net with Difference Mask: A Deep Learning Approach for Fast Cardiac Scan

P. Sheikhzadeh[1], *S. Khalili*[1], *N. Seyyedi*[2];
[1]*Tehran University of Medical Science, Tehran, IRAN, ISLAMIC REPUBLIC OF,* [2]*Health Management Research Institute, Iran University of Medical Science, Tehran, IRAN, ISLAMIC REPUBLIC OF.*

Aim/Introduction: This study aimed to develop and evaluate a deep learning method based on a U-Net neural network with a difference mask approach to reconstruct high-quality cardiac SPECT images from half-projection data. The primary goal was to reduce scanning time and patient radiation dose while maintaining diagnostic image quality. ***Materials and Methods:***

The dataset comprised 362 DICOM images from cardiac SPECT scans, with each image available in full-projection (64 projections) and half-projection (32 projections) versions. Half-projection data were upsampled to generate input images. A U-Net model with a difference mask approach was designed to predict the difference between upsampled and full-projection images. The model was trained using 5-fold cross-validation, with a combined loss function (50% MAE, 25% ME, 25% SSIM) and the AdamW optimizer. Performance was evaluated using mean absolute error (MAE), mean error (ME), root mean square error (RMSE), structural similarity index (SSIM), and peak signal-to-noise ratio (PSNR). ***Results:*** The U-Net model successfully reconstructed high-quality images closely resembling full-projection images from half-projection data. In cross-validation, the average SSIM was 0.9346, and the average PSNR was 40.32 dB. The average MAE was 0.006839, and the average RMSE was 0.020174, indicating high reconstruction accuracy. Model predictions for all original data were saved in DICOM format. ***Conclusion:*** Quantitative results demonstrate that the U-Net model with a difference mask approach can reconstruct high-quality cardiac SPECT images from half-projection data, preserving structural similarity and minimizing errors. This method offers potential for reducing scanning time and radiation dose without compromising critical diagnostic information. ***References:*** 1. Aghakhan Olia, Narges, et al. "Deep learning-based denoising of low-dose SPECT myocardial perfusion images: quantitative assessment and clinical performance." European journal of nuclear medicine and molecular imaging (2022): 1-15.

EP-0973

Deep Learning Denoising of Cardiac SPECT: A Dual-Domain Approach in Sinogram and Projection Space

V. Menezes[1], *C. Queiroz*[2], *M. Machado*[3], *B. Anjos*[4], *A. Pino*[2], *R. Lemes*[5];
[1]*Hospital das Clinicas da UFPE, Recife, BRAZIL,* [2]*Hospital Universitário Professor Alberto Antunes, Maceió, BRAZIL,* [3]*Hospital Universitário Professor Edgard Santos - HUPES, Salvador, BRAZIL,* [4]*Nuclearis, Recife, BRAZIL,* [5]*UFBA, Salvador, BRAZIL.*

Aim/Introduction: This study aimed to evaluate the diagnostic reliability and image quality improvement of a deep learning-based denoising method applied to myocardial perfusion SPECT, particularly under conditions of reduced radiotracer dose or acquisition time. ***Materials and Methods:*** A total of 294 cardiac SPECT exams were retrospectively selected from two imaging systems (Siemens Symbia Intevo and GE Millennium MG). A total of 260 exams were used to train a dual-domain AI model, yielding 46,800 projections via synthetic noise simulation at 25% and 50% count levels[1]. The validation set included 34 patients (n=10 GE; n=24 Siemens). A nuclear medicine physician assessed subjective image quality using a 5-point Likert scale. Myocardial ischemia was evaluated using the Summed Stress Score (SSS) for both original and AI-enhanced images. ***Results:*** Standard [MM1] SPECT images received an average Likert score of 3.6, while AI-enhanced half-time images achieved 4.0. The mean difference in SSS between the methods was 1.2 (95% CI: ±4.8). Only 9% of patients changed risk classification between the AI-reconstructed and standard methods. This variability is lower than the inter-observer variability reported in the literature for standard clinical reads (13-20%)[2]. ***Conclusion:*** The deep learning-based denoising method preserved diagnostic performance in low-count cardiac SPECT while enhancing subjective image quality. The AI reconstruction introduced less variability than that associated with expert interpretation, supporting its clinical viability in dose/time-reduction protocols. ***References:*** 1. QUEIROZ, C.C et al. Partitioning of gated single photon emission computed tomography raw data for protocols optimization. Journal of Applied Clinical Medical Physics, v. 23, n. 3, p. e13508, 2022. 2. Dondi M, et al.; I-MAP investigators. Inter-reader variability of SPECT MPI readings in low- and middle-income countries: Results from the IAEA-MPI Audit Project (I-MAP). J Nucl Cardiol. 2020 Apr;27(2):465-478. doi: 10.1007/s12350-018-1407-4. Epub 2018 Aug 30. PMID: 30168029; PMCID: PMC7174263.

EP-0974

PET quantification accuracy using FastPET in ultra-short frames on the Biograph Vision Quadra PET/CT

V. Nadig[1,2], *D. Darian*[1], *Y. Zheng*[3], *M. Zhang*[3], *D. Bharkhada*[3], *M. Millardet*[4,3], *G. Krokos*[2], *L. Davies*[2], *P. Marsden*[2], *M. Conti*[3], *P. Schleyer*[3];
[1]*Siemens Healthcare Limited, Camberley, UNITED KINGDOM,* [2]*PET Centre, School of Biomedical Engineering and Imaging Sciences, King's College London, London, UNITED KINGDOM,* [3]*Siemens Medical Solutions USA Inc., Knoxville, TN, UNITED STATES OF AMERICA,* [4]*Department of Radiology, University of Pennsylvania, Philadelphia, PA, UNITED STATES OF AMERICA.*

Aim/Introduction: With convolutional neural networks (CNN) becoming increasingly important for near real-time image reconstruction, their applicability for ultra-fast dynamic imaging requires investigation. We assess the image quality and quantitative accuracy of FastPET [1,2], a CNN for direct reconstruction from histoimages, in comparison to ordered-subset estimation maximization (OSEM). ***Materials and Methods:*** On a Biograph Vision Quadra PET/CT (Siemens Healthineers), we acquired a ten-minute scan of a NEMA-IQ phantom (18F-FDG, 5:1-ratio, 82 MBq, CT: 120 kV/50 mAs) covered in 3-5 cm tissue-equivalent material. FastPET images were reconstructed in 1.65 mm x 1.65 mm x 1.65 mm voxels and in 15 frame lengths between 0.1-600 s. We provide OSEM reconstructions (4i5s, PSF-TOF, UHS) for frame lengths between 1-600 s. For both methods, fixed 50%-threshold-3D-sphere-isocontours were determined from the ten-minute scan. Mean standard uptake values (SUV_{mean}) and contrast recovery ratio (CRC_{mean}) were evaluated as a function of number of the prompts in each frame. The background variability (BV) was examined using twelve spherical regions (10-37 mm diameter). ***Results:*** For the ten-minute scan (~10^9 prompts), OSEM and FastPET resolve all six spheres (diameters: 10,13,17,22,28,37 mm). For frames ≤5 s (≤10^7 prompts), the smallest sphere becomes undetectable for both reconstructions. For 1-s OSEM images (~$1.5x10^6$ prompts), we can identify the 22-37-mm spheres. For 200 ms (~$3x10^5$ prompts), FastPET detects the 17-37-mm spheres. The spheres show Gibbs artifacts and are slightly non-uniform, probably due to the phantom being out-of-distribution data. The OSEM BV increases to 6.2-46.3 % in low-count regimes ($1.5x10^6$ prompts), whereas FastPET maintains a much smoother background (BV 1.5-3.2 % for $1.5x10^6$ prompts). With OSEM, the SUV_{mean} remains stable for 5-600 s frames (~10^7-10^9 prompts) for 17-37-mm, before deteriorating for shorter frames. For 10-13-mm spheres, OSEM maintains this performance except for 1-5-s frames (~$1.5x10^6$-10^7 prompts). For FastPET, the SUV_{mean} behaves the same, except for the two smallest spheres, where it continuously decreases until reaching background level for frames ≤5 s. For the 37-mm sphere, the CRC_{mean} with FastPET in 100 ms frames (~$1.5x10^5$ prompts) is 75 %. ***Conclusion:*** FastPET provides comparable quantitative metrics and improved image quality to OSEM for a wide range of count regimes. Recent studies have shown improved quantification on patient data [3]. FastPET is therefore an attractive solution for near real-time reconstruction in dynamic applications requiring ultra-short frames, such as kinetic analysis or gating. ***References:*** [1] Whiteley et al. 10.1109/TRPMS.2020.3028364 [2] Whiteley et al. patent 11164344 [3] Millardet et al. 10.1109/NSSMICRTSD49126.2023.10338495.

EP-0975

Low-Dose to Standard-Dose PET Reconstruction Using Cross-Slice Diffusion TransformerAim/Introduction

T. Sun, *X. Chen, S. Wang;*
Chinese Academy of Sciences, Shenzhen, CHINA.

Aim/Introduction: Low-dose PET (LD-PET) is a promising approach for reducing radiation exposure in clinical imaging, particularly for patients requiring repeated scans. However, LD-PET often suffers from degraded image quality, which compromises diagnostic accuracy. This study presents CrossVision-DT, a novel diffusion-based Transformer model that incorporates Cross-Slice Attention to reconstruct standard-dose PET (SD-PET) images from LD-PET inputs, achieving improved image quality while maintaining efficiency and interpretability. ***Materials and Methods:*** CrossVision-DT follows a two-stage training strategy: first, a diffusion Transformer is pre-trained on 2D slices to capture intra-slice details; second, the model is fine-tuned using a novel Cross-Slice Attention Layer to learn inter-slice dependencies across consecutive PET slices. The architecture includes a patch-based noise prediction module with cross- and self-attention mechanisms, and a customized attention layer designed to align adjacent slice features through dimensional transformation. The model was trained and evaluated on the publicly available Ultra-Low Dose PET Imaging Challenge dataset and further tested on a local clinical dataset. Reconstruction performance was quantitatively assessed using NMSE, SSIM, and PSNR, while diagnostic utility was evaluated using SUVR consistency and AUC from classification tasks. ***Results:*** CrossVision-DT achieved superior performance on both datasets. On the public dataset, it reached an NMSE of 0.191, SSIM of 0.966, and PSNR of 34.616 dB. On the local dataset, it achieved NMSE of 0.321, SSIM of 0.912, and PSNR of 30.214 dB, without additional fine-tuning. The model maintained excellent SUVR consistency (mean difference: 0.04; 95% limits of agreement: -0.29 to 0.37) and even surpassed standard-dose PET in downstream diagnostic classification tasks. ***Conclusion:*** CrossVision-DT introduces a new paradigm for LD-PET reconstruction by integrating a diffusion Transformer architecture with a cross-slice attention mechanism. The model delivers robust reconstruction quality and strong clinical interpretability, outperforming existing LD-PET reconstruction methods on both quantitative metrics and diagnostic relevance. This method offers a practical and effective solution for reducing radiation dose in clinical PET imaging without compromising diagnostic accuracy.

EP-0976

Feasibility of Pediatric Brain Imaging with a Palm-Sized Dual-Head PET: Monte Carlo-based Evaluation of Limited Angle and Attenuation Effects

V. Sihotang[1,2], *M. George*[3,2], *K. Brazenski*[4,2], *Y. Ni*[5], *C. Zorraquino*[2], *M. Nemallapudi*[6,2], *H. Lin*[1,7];
[1]*Chang Gung University, Taoyuan, TAIWAN,* [2]*PraanaTech, Chicago, IL, UNITED STATES OF AMERICA,* [3]*Institute of Physics Academia Sinica, Taipei, TAIWAN,* [4]*Instituto de Fisica Corpuscular (IFIC), Universitat de València, Valencia, SPAIN,* [5]*National Atomic Research Institute, Taoyuan, TAIWAN,* [6]*University of Chicago, Chicago, IL, UNITED STATES OF AMERICA,* [7]*Chang Gung Memorial Hospital Linkou Branch, Taoyuan, TAIWAN.*

Aim/Introduction: Palm-sized dual-head PET systems offer a promising solution for pediatric brain imaging due to their small form factor, portability, and potential cost-effectiveness. However, the limited angular coverage of such ultra-compact systems may compromise image quality and quantitative accuracy. This study investigates the feasibility of pediatric brain imaging using a palm-sized dual-head PET system through GATE-based Monte Carlo simulations, focusing on the effects of limited angle acquisition and attenuation correction. ***Materials and Methods:*** The proposed PET system was designed as a palm-sized module with a 10 cm x 5 cm Field of View (FOV), suitable for pediatric applications. The system was configured with 2 detectors acquiring data at varying numbers of angular views (1, 2, 4, 6, and 12), uniformly distributed over 180°. This design simulates limited-angle acquisition scenarios and evaluates the angular range required for adequate image reconstruction. Two simulation datasets were generated using the GATE Toolkit: one with a non-attenuating phantom and the other with attenuation phantom to model phantom absorption and scatter in brain tissue. Image reconstruction was performed using a 3D Maximum Likelihood Expectation Maximization (MLEM) algorithm. For the attenuation dataset, a Gaussian kernel was applied during reconstruction to reduce image noise and enhance smoothness. ***Results:*** Preliminary results demonstrated the effectiveness of a compact PET system in reconstructing brain structures from attenuated data across varying angular distributions. Comparing the reconstructions using 6 and 12-angle configuration shows that increasing number of angles improves structural similarity while maintaining consistent variability across slices. The evaluation of SSIM values for deeper brain regions showed that 12 angle configurations achieved higher mean SSIM of 0.84 ± 0.014 compared to 0.75 ± 0.013 for the 6 angle configurations. These results indicate that higher number of angular views is essential for enhanced image quality, especially for deeper brain regions, where attenuation effects are more significant. The MLEM algorithm effectively enhanced reconstruction fidelity, but further optimization of attenuation and scatter corrections is necessary for quantitative accuracy. ***Conclusion:*** This study supports the feasibility of using a palm-sized dual-head PET system for pediatric brain imaging. With continued refinement of quantification correction techniques, the system has the potential to offer portable, cost-effective alternative for pediatric neuroimaging in both clinical and research settings.

EP-0977

Clinical Reliability of Half-dose Rubidium-82 Perfusion Imaging with Positron Range Correction

M. Omaygenc[1], *Y. Kadoya*[1], *M. E. Casey*[2], *M. Conti*[2], *R. S. B. Beanlands*[1], *R. A. DeKemp*[1];
[1]*University of Ottawa Heart Institute, Ottawa, ON, CANADA,* [2]*Siemens Medical Solutions, Knoxville, TN, UNITED STATES OF AMERICA.*

Aim/Introduction: Rubidium-82 is the most used Positron Emission Tomography (PET) tracer in myocardial perfusion imaging. However, the spatial resolution of Rb-82 images is limited by the high energy positrons with a longer positron range (~7 mm in water). Therefore, positron range correction (PRC) reconstruction algorithms may improve the image quality and allow further dose reduction. ***Materials and Methods:*** The vendor point spread function (PSF) reconstruction method was adapted to include a Gaussian model for Rubidium-82 positron range correction (PRC) that varies with the radial offset (Panin et al. IEEE 2006). Twenty-one patients (61±11 years, 29% female, BMI 42.7 ±13.2) were scanned with half-dose and full-dose rubidium-82 at rest. The noise level of PRC half-dose (HD) rest images was compared visually to the standard full-dose (STD-FD) rest images (without PRC) by two level 3 readers using a scale of 1-5. Their preference for clinical interpretation was also recorded. ECG-gated images were analyzed for quadrant values of relative perfusion, summed rest score (SRS), and functional measures. ***Results:*** The readers had good agreement (κ: 0.61-0.69) on the noise levels scored on each image set (4.4 ± 0.7 vs 4.3 ± 0.7). There was no preference between PRC-HD or STD-FD images for clinical interpretation in 16/21 patients, and a small bias toward PRC-HD in 3 of the 4 remaining patients. There was no significant difference in SRS scores (1.2 ± 3.5 vs 1.1 ± 3.9; p=0.540). Left ventricle function measures were also similar between image sets. The relative perfusion values for PRC-HD and STD-FD images were comparable in all four left ventricular

walls (septum: 85.7 vs 87.3, p=0.084; lateral: 88.0 vs 88.3, p=0.61; anterior, 86.3 vs 88.3, p=0.88; inferior. 86.8 vs 87.8, p=0.079). There was good uniformity across the walls (ANOVA F=1.93; p=0.13). No differences between PRC-HD vs STD-FD were significantly greater than 2% using 2-sided test of equivalence. ***Conclusion:*** PRC-HD imaging provided comparable image quality with STD-FD imaging and yielded similar interpretation results in terms of relative perfusion and LV function measures. Dose reduction with preserved image quality is of particular importance for the patients with higher body mass index and it may allow exponential dose titration in the entire spectrum without exceeding the limits of generator elution and detector saturation. ***References:*** Panin VY, Kehren F, Michel C, Casey M. Fully 3-D PET reconstruction with system matrix derived from point source measurements. IEEE Trans Med Imaging. 2006 Jul;25(7):907-21.

EP-0978

Robust self-supervised deep learning reconstruction model for reduced ^{89}Zr-girentuximab PET scan time

C. Pain[1,2], *S. Wail*[3], *T. Sepehrizadeh*[3], *Z. Chen*[1,2];
[1]*Monash Biomedical Imaging, Melbourne, AUSTRALIA,* [2]*Faculty of Information Technology, Monash University, Melbourne, AUSTRALIA,* [3]*Telix Radiopharmaceuticals, Melbourne, AUSTRALIA.*

Aim/Introduction: This study aims to implement scan time reduced ^{89}Zr-girentuximab PET imaging using robust self-supervised deep learning with latent-space kernel functions , by recovering 20-minute acquisition quality images from 5-minute acquisition data. The approach aims to provide more robust performance relative to conventional supervised deep learning in terms of lesion recovery and requires no 20-minute acquisition data in training. ***Materials and Methods:*** N=49 patients were administered between 20 and 47 MBq of ^{89}Zr-girentuximab and received a 20-minute PET and low-dose CT 3 to 4 days post radiopharmaceutical administration, with 5-minute data reconstructed from the first 5 minutes of acquisition. A deep kernel network [1,2] was trained with 5-minute PET scans and low-dose CT using self-supervised learning. Subject-specific fine tuning was implemented for tunable lesion recovery. A UNet trained with supervised learning was used as a reference method. Five-fold cross validation with a training, evaluation and testing split of 41,3,5 was used for all training tasks. Methods were evaluated in terms of lesion SUV_{max} and SUV_{mean} with reference to corresponding 20-minute scans. A total of 21 lesions were segmented from 19 evaluation subjects. Robustness was evaluated by comparing performance in three test cases with lowest quantitative accuracy. The peak signal-to-noise ratio (PSNR) across test subjects was evaluated. ***Results:*** Comparing with the 20-minute scans, the mean (standard deviation) of relative error of the 5-minute scan in SUV_{mean} for lesions was 0.06 (0.03) and 0.05 (0.02) and mean (standard deviation) of relative error in SUV_{max} for lesions was 0.10 (0.05) and 0.08 (0.04) for supervised learning and the proposed method, respectively. The three cases with lowest accuracy for both deep learning methods had a mean (standard deviation) in SUVmax relative error of 0.13 (0.05) and 0.10 (0.04) for the supervised method and the proposed method, respectively. The mean (standard deviation) of PSNR across the evaluation set was 29.6 (0.5) and 28.7 (0.8) for supervised learning and the proposed method, respectively. ***Conclusion:*** Self-supervised latent-space kernel functions demonstrate tunability and improved lesion recovery from fast acquisition data as compared with supervised learning, while demonstrating robust performance for out-of-distribution cases. Further work to regularise reconstruction for noise control may improve trade-offs between lesion recovery and PSNR. The authors acknowledge 89Zr-DFO-girentuximab PET datasets used in this study were provided by Telix Pharmaceuticals. ***References:*** [1] C.D Pain, et al., 2024, arxiv, https://arxiv.org/abs/2409.06198[2] C.D Pain, et al., 2024, IEEE ISBI, pp. 1-4.

EP-0979

Wavelet Diffusion Modeling Enables Individualized FDG-PET Synthesis for Early Diagnosis of Neurodegenerative Diseases

J. Ding[1], *X. Song*[2], *M. Marcus*[2], *X. Li*[2], *J. Zhao*[1];
[1]*Department of Nuclear Medicine, Shanghai East Hospital, School of Medicine, Tongji University, Shanghai, CHINA,* [2]*Department of Biomedical Imaging and Image-guided Therapy, Medical University of Vienna, Vienna, AUSTRIA.*

Aim/Introduction: Neurodegenerative diseases such as Alzheimer's disease (AD) and Parkinson's disease (PD) are irreversible, but early intervention during the presymptomatic stage can slow disease progression. FDG-PET enables the detection of glucose metabolism changes in the brain, offering potential for early diagnosis. However, individual variability in FDG metabolism poses challenges for quantitative assessment. This study aims to develop a deep learning model capable of generating individualized healthy FDG-PET templates to facilitate voxel-wise comparison and precise identification of metabolic changes. ***Materials and Methods:*** A Wavelet Diffusion Model (WaveDM) was employed to synthesize FDG-PET images from T2-weighted MRI. This generative framework combines wavelet decomposition and diffusion modeling for high-resolution 3D image-to-image translation. A dataset of 1,060 paired PET/MRI scans was used for training and validation (9:1 split), with an additional 158 AD cohort scans (Normal Control (NC), Mild Cognitive Impairment (MCI), and AD) for testing. Model performance was compared to a 3D U-Net baseline using normalized root mean square error (NRMSE), peak signal-to-noise ratio (PSNR), and structural similarity index measure (SSIM). Qualitative assessments are ongoing, with physicians reviewing the synthesized PET images and evaluating diagnostic accuracy in differentiating AD, MCI, and NC using voxel-wise difference maps from the individualized healthy templates. ***Results:*** The WaveDM model demonstrated superior performance compared to the baseline U-Net model on the validation dataset, achieving a 12.3% increase in PSNR, a 6.6% improvement in SSIM, and a 20.5% reduction in NRMSE. Testing on the AD cohort demonstrated the model's ability to differentiate between NC, MCI, and AD through voxel-wise difference map analysis. ***Conclusion:*** The WaveDM framework offers a robust approach for generating individualized FDG-PET templates from MRI data. By enabling precise voxel-wise metabolic assessment, it holds promise for improving the early diagnosis and management of neurodegenerative diseases. ***References:*** Rau A, Schröter N, Blazhenets G, Maurer C, Urbach H, Meyer PT, Frings L. The metabolic spatial covariance pattern of definite idiopathic normal pressure hydrocephalus: an FDG PET study with principal components analysis. Alzheimers Res Ther. 2023 Nov 18;15(1):202.

EP-0980

PET-like images from ^{177}Lu-PSMA post-therapeutic SPECT showing increased contrast of metastatic lesions

F. Moradi, *T. Otani, H. Song, G. Davidzon, K. Guja, A. Iagaru;*
Stanford University, Stanford, CA, UNITED STATES OF AMERICA.

Aim/Introduction: Post-therapeutic SPECT/CT is useful for monitoring radioligand therapy in prostate cancer. However, lesions have low contrast compared to pre-treatment PSMA PET, limiting longitudinal comparison. Image-to-image translation models with paired or unpaired data can produce PET-like images (synthetic PET) which could be easier to assess. We examined how synthetic PET affects the contrast of metastatic lesions. ***Materials and Methods:*** 72 prostate cancer patients treated with ^{177}Lu-PSMA therapy were used for development and training Pix2Pix[1] and CycleGAN[2] image-to-image translation models. Each model was trained multiple times with small changes in parameters and randomizing the order of training. For Pix2Pix, the post therapy SPECT/CT after 1st cycle of Lu177-PSMA-611 was paired

with anatomically co-registered pre-treatment PSMA PET in the same patient. For CycleGan, the same data without pairing and in a randomized order was used. Models were then tested in 10 patients that were not included in the training dataset. For each patient, up to 6 dominant lesions were included in the analysis. Contrast was defined as the ratio between uptake in the lesion ROI and blood pool. Sensitivity of lesion uptake to training was quantified using coefficient of variation. Synthetic images were subjectively evaluated by four nuclear medicine physicians for realism and similarity to PET. ***Results:*** Of 7 models trained using unpaired data, one failed to produce realistic looking images. All 5 models trained using paired data produced realistic-looking PET-like images. We therefore included these 5 models in subsequent analysis. Of 58 lesions, the average lesion to blood pool ratio was 2.63±0.13 times higher on synthetic PET compared to the original SPECT (5.42±4 vs. 2.17±1.44, R^2=0.88, p<0.0001). Only two lesions had similar or lower contrast compared to SPECT. The liver to blood pool ratio on synthetic PET was also higher than on SPECT as the models captured the differences between physiologic distribution of PET vs therapy radiopharmaceutical (2.5 vs. 1.2). The median coefficient of variation for lesion uptake was 0.39 (IQR 0.31 - 0.49). ***Conclusion:*** SPECT-to-PET translation with conditional adversarial networks using paired training data is feasible and not sensitive to the order of training or minor changes in model parameters. Resulting images demonstrate markedly improved contrast of metastatic lesions. ***References:*** 1) Isola, Phillip, et al. Proceedings of the IEEE conference on computer vision and pattern recognition. 2017. 2) Zhu, Jun-Yan, et al. Proceedings of the IEEE international conference on computer vision. 2017.

EP-0981

Low-Dose Dynamic [^{18}F]FDG Brain PET Imaging: Near Real-Time Reconstruction with FastPET

M. Kvistholm[1], *N. Overbeck*[1], *A. B. Rodell*[2], *D. Bharkhada*[2], *N. Murthy*[2], *Y. Zheng*[2], *M. Conti*[2], *U. Lindberg*[1], *T. L. Andersen*[1,3], *F. L. Andersen*[1,3];
[1]*Department of Clinical Physiology and Nuclear Medicine, Copenhagen University Hospital, Copenhagen, DENMARK,* [2]*Siemens Medical Solutions USA, Inc., Knoxville, TN, UNITED STATES OF AMERICA,* [3]*Department of Clinical Medicine, Copenhagen University, Copenhagen, DENMARK.*

Aim/Introduction: Positron emission tomography (PET) enables dynamic imaging of metabolic processes using radiotracers. Accurate tracer kinetic modelling requires high temporal resolution images, which are computationally demanding to reconstruct using conventional iterative methods such as Ordinary Poisson Ordered Subsets Expectation Maximisation (OP-OSEM). Low-dose PET introduces more noise, which challenges its use in clinical and research settings. FastPET, a deep learning-based reconstruction method trained to transform histo-images into converged OSEM reconstructions, offers a faster alternative [1]. This study evaluates FastPET's ability to reconstruct low-dose dynamic 2-[^{18}F]fluoro-2-deoxy-D-glucose ([^{18}F]FDG) brain PET images and generate accurate time-activity curves (TACs) suitable for kinetic modelling compared to OSEM. ***Materials and Methods:*** Nine healthy subjects underwent 60-minute dynamic PET scans using a long axial field-of-view (LAFOV) PET/CT system following injection of 3 MBq [^{18}F]FDG per kg body weight. The dynamic PET series was divided into 67 frames: 20 × 2 s, 10 × 5 s, 15 × 10 s, 6 × 60 s, 10 × 120 s, and 6 × 300 s. Simulated low-dose scans (20, 50, 100, 200 MBq) were generated by sampling list-mode events. Data were reconstructed using 3D-OP-OSEM with 4 iterations and 5 subsets, including time-of-flight (TOF) information, point spread function (PSF) modelling, and a 2 mm Gaussian post-filter; and FastPET, which operates on 3D histo-images and attenuation maps for inference of PET images. TACs were extracted from the whole brain using CT-based masks (TotalSegmentator [2]) and from subregions using activity-based masks derived from the PET images. TACs across regions and dose levels were compared between FastPET and OSEM to evaluate consistency, bias, and noise characteristics. ***Results:*** FastPET produced TACs that more accurately reflected the expected metabolic kinetics of [^{18}F]FDG, especially under low-dose conditions where OSEM reconstructions yielded erratic and discontinuous TACs possible due to scatter correction failure. Across all doses, FastPET maintained high temporal resolution and generated curves with reduced noise. A consistent bias (≈5%) in FastPET compared to OSEM was observed in whole-brain TACs. This bias was dose-independent but varied locally, with greater deviations in low-activity regions such as ventricular space. ***Conclusion:*** FastPET enables fast and robust reconstruction of dynamic [^{18}F]FDG brain PET at low doses, providing improved TAC quality and a stable, predictable bias. Its speed and reliability support its use in quantitative low-dose PET and kinetic modelling. ***References:*** [1] Whiteley W. et al. (2020). IEEE Trans Radiat Plasma Med Sci, 5(1):65-77. [2] Wasserthal J. et al. (2023). Radiology: Artificial Intelligence, 5(5).

EP-0982

The Clinical Application of Brain Motion Management for Improving Quantification of Brain Amyloid PET

Y. Li, *J. Li, Z. Wang, X. Lu, H. Pang;*
Department of Nuclear Medicine, The First Affiliated Hospital of Chongqing Medical University, Chongqing, CHINA.

Aim/Introduction: Precise quantification of amyloid PET imaging has become increasingly essential in Alzheimer's Disease (AD) management for patient care, treatment evaluation, and anti-amyloid clinical trials. Head motion-induced image artifacts are a major factor compromising image quality and quantification accuracy, particularly in dementia populations. The Brain Motion Management (BMM) algorithm, which has been incorporated into our long-axis (with a lenth of 148cm) PET/CT system, effectively tackles head motion artifacts and PET-CT misalignment through data-driven and AI-based approaches. This study aims to evaluate the clinical efficacy of BMM in enhancing amyloid PET quantification accuracy. ***Materials and Methods:*** This ongoing observational study employing BMM was initiated on March 14, 2025. Patients with cognitive impairment requiring diagnostic evaluation or disease monitoring underwent ^{18}F-Florbetapir PET scans. Image quality and amyloid deposition status were visually assessed by experienced nuclear medicine physicians. Scans deemed suboptimal or non-diagnostic due to motion artifacts were reconstructed again with BMM. Global and regional amyloid deposition (SUVr values in composite cortex, frontal, cingulate, parietal, precuneus, and lateral temporal cortices, using whole cerebellum as reference) were compared between the non-motion-managed (NMM) images and BMM images. ***Results:*** As of April 24, 2025, a total of 35 ^{18}F-Florbetapir PET/CT scans have been acquired. Six scans (three male patients, mean age 72 ± 5 years) exhibited significant head motion artifacts. All six patients were diagnosed as AD (one with Clinical Dementia Rating score of 2, the others, score 3). In BMM-incorporated images, image blur was effectively reduced in all six cases, significantly improving image quality. Global SUVr values were significantly higher in BMM images compared to NMM images (1.36 ± 0.17 vs.1.26 ± 0.29, P = 0.047). Using a commonly used threshold of 1.11, all BMM images were correctly classified as amyloid-positive, whereas one NMM image was misclassified as negative (SUVr = 0.75). BMM images also showed higher mean SUVr values across all five analyzed subregions compared to NMM images. ***Conclusion:*** The BMM algorithm demonstrates significant potential for improving amyloid PET image quality and quantification accuracy in patients with AD. This enhancement may have important implications for

treatment response monitoring in AD. The ongoing study will continue to evaluate the clinical impact of BMM in a larger patient cohort.

EP-0983

Enhancing Deep Learning-based Partial-Volume Correction for ^{177}Lu SPECT by Incorporating Multiple Reconstruction Convergence Stages

A. Gehring[1], *J. Leube*[1], *M. Laßmann*[1], *J. Gustafsson*[2], *M. Salas-Ramirez*[1], *J. Tran-Gia*[1];
[1]*Department of Nuclear Medicine, University Hospital Würzburg, Würzburg, GERMANY,* [2]*Medical Radiation Physics, Lund University, Lund, SWEDEN.*

Aim/Introduction: Accurate SPECT activity quantification is critical for patient-specific dosimetry in radiopharmaceutical therapies but is challenged by partial-volume effects that blur object edges and introduce errors. Traditional correction methods often rely on simplifying assumptions or segmented images, limiting their clinical applicability. Deep learning (DL) offers a data-driven alternative, though model performance depends on the training data. This work investigates an enhanced version of an existing DL-based partial-volume correction (DL-PVC) [1], focusing on more realistic training data and examining the influence of different convergence stages—via varying update numbers—on model performance regarding resolution and noise. ***Materials and Methods:*** The DL-PVC model was trained as described in [1], using 10,000 XCAT [2] body phantoms with randomly shaped activity distributions (256x256x256 matrix, 2.4x2.4x2.4mm^3 voxels). To improve performance, a refined dataset (N=10,000) incorporating overlapping smaller activity shapes was created. These datasets underwent SPECT simulations with the SIMIND Monte Carlo program [3] and were reconstructed using PyTomography [4] (OSEM, 5/20/50 iterations (i), 4 subsets (s), attenuation correction, triple-energy-window scatter correction, resolution modeling). Four u-nets with differently reconstructed data as input were trained (60 epochs, L1 loss function, 9,000/500/500 for training/validation/testing) to predict activity distribution: 20 updates (5i4s), 80 updates (20i4s), 200 updates (50i4s), and a combination of 20/80/200 updates as three input channels. The performance of all models was evaluated on the test dataset using SSIM, NRMSE and voxel activity accuracy (VAA), a previously defined measure of spatial correction quality (proportion of voxels with deviation of <5% between predicted and ground-truth activity distribution [1]). ***Results:*** The 20-update u-net achieved mean performance measures of 0.852/12.4%/27.4% for SSIM/NRMSE/VAA, compared to the 80-update u-net with 0.858/12.2%/28.7% and the 200-update u-net with 0.857/12.2%/28.7%. The multi-update u-net performed best (0.859/12.1%/29.2%). Performances across the single-update models plateaued beyond 80 updates, indicating diminishing returns with higher update numbers. In contrast, the multi-update input showed slightly better performance, highlighting its potential to capture complementary information from different convergence stages. ***Conclusion:*** Reconstructions with 80 updates (20i4s) showed best performance among single-reconstruction u-nets, indicating a good balance between convergence and noise while minimising reconstruction time. The inclusion of multiple update numbers yielded only minor additional benefits. Future work will explore generalizability across reconstruction settings and patient-specific datasets to further support clinical translation. ***References:*** [1] Leube et al. JNM 2024;65(6):980. [2] Segars et al. Med Phys 2010;37(9):4902. [3] Ljungberg et al. CMPB 1989;29(4):257. [4] Polson et al. arXiv:2309.01977.

EP-0984

Joint dual modality information for^{131}I SPECT/CT images enhancement based on a deep-learning method allows 75% reduction of scan time

H. Yang[1], *M. Guo*[2], *L. Xiang*[2];
[1]*Nuclear Medicine Department, Southwest Hospital (the First Affiliated Hospital), Third Military Medical University (Army Medical University), Chongqing, CHINA,* [2]*Subtle Medical Inc., Shanghai, CHINA.*

Aim/Introduction: ^{131}I SPECT/CT is an effective method for postoperative assessment and visiting of thyroid cancer patients. However, long acquisition time of standard scan and discomfort after taking iodine may lead to inconvenience to patients and reduce work efficiency. While using a fast-scan protocol may be a substitute, it may lead to issues such as noise, and artifacts, which may have a risk of diagnostic errors.To address these issues, a deep-learning based method utilizing CT and fast SPECT scan images as joint inputs to denoise low-duration SPECT scan was proposed. ***Materials and Methods:*** 72 patients in total diagnosed with thyroid cancer in Southwest hospital of China, who required 131ISPECT/CT imaging after surgery, were selected as training and testing datasets in this study. Each patient underwent a standard scan with 60 views, each lasting 12 seconds. Subsequently, one of three different acceleration plans was adopted: (1) 30 views, each lasting 6 seconds; (2) 30 views, each lasting 12 seconds; (3) 60 views, each lasting 3 seconds. 24 patients were scanned for each acceleration plan separately. 8:1:1 random splits of the subjects were regarded as training, validating, and testing datasets. During the network training phase, fast SPECT scan images and corresponding CT images were concatenated along the channel dimension as a joint input to the MPRNet. Model with only SPECT input was also trained as a comparison to find the effect of involving CT information. PSNR, SSIM and NMSE were used as quantitative objective evaluation metrics. 2 experienced nuclear medicine physicians also scored the enhanced images of two networks. The grading criteria including the clarity, contrast, and edge sharpness of residual thyroid tissue and cervical metastatic lesions. ***Results:*** Among the 3 acceleration protocols, nuclear medicine physician ratings for the low-duration scans enhanced by the proposed method are consistent with standard scan images, which does not affect clinical diagnosis.The difference map and essential physiological and pathological details preserved indicates the advantage of leveraging CT information in network training.From quantitative perspective, the PSNR, SSIM and RMSE were improved by 26%, 9% and 36% separately on average. ***Conclusion:*** The qualitive and quantitative results showed that the proposed deep-learning method with SPECT and CT input effectively suppressed noise, enhanced image quality for low-duration scans while maintained high diagnostic quality, which indicates the work efficiency could be effectively promoted and the waiting and scanning time of patients could be reduced up to 75%.

EP-0985

Breaking Barriers in PET: Deep Progressive Reconstruction Achieves Diagnostic-Quality ^{18}F-FDG Imaging at Half the Dose and Time in India

N. Jain[1], *S. S. Singh*[2], *A. Agarwal*[1], *D. Kumar*[3], *P. Wadhwa*[3];
[1]*Molecular Imaging & Therapy, New Delhi, INDIA,* [2]*Globe Healthcare, Lucknow, INDIA,* [3]*United Imaging Healthcare, New Delhi, INDIA.*

Aim/Introduction: Digital PET technology offers improved sensitivity and resolution, enabling low-dose ^{18}F-FDG PET imaging with reduced acquisition times—an advantage for resource-limited settings. This dual-centre study evaluates the diagnostic performance of AI based reconstruction algorithm, uAI® HYPER DPR versus conventional reconstruction methods using digital

uMI 550 PET/CT system in India, with a focus on reduced dose and acquisition time protocols. ***Materials and Methods:*** We collected over 120 patient datasets undergoing oncologic ^{18}F-FDG PET scans from two centres in India, a hospital set-up (Globe healthcare, Lucknow, India) and a diagnostic centre (Molecular Imaging, Delhi, India) with high patient throughput. All scans were conducted using a digital uMI 550 PET/CT system with low-dose protocols (reduced activity and acquisition time). Images were reconstructed using HYPER DPR (deep learning-based) and conventional methods (OSEM, post processed with Gaussian filter). Quantitative metrics (SNR, SUVmax, lesion detectability) and qualitative assessments (clinical readability, noise levels) were compared. ***Results:*** Molecular Imaging, Delhi, India conducts about 50 scans per day with a low dose of 3-5 mCi and the acquisition time of 30-45 sec per bed position. Similarly, Globe hospital, Lucknow, India has a throughput of 25 scans per day with a a low dose of 3-5 mCi and the acquisition time of 45 sec-1 min per bed position. We collected preliminary datasets from both the centers for 5 mCi scans and 45 sec per bed position with mean uptake time of 60±10 minutes. It was observed that all lesions >1 cm were detectable by both sets of images. Overall, there was significant difference between SUVmax of liver and mediastinum between all subsets of DPR based and conventional reconstruction methods, however difference in SUVmean was non-significant. SNR was observed to be two-folds higher with HYPER DPR as compared to OSEM. Qualitative assessments demonstrated that with low dose protocols, there is no significant difference in the clinical readability between the two reconstruction algorithms, whereas the noise levels with HYPER DPR were 35% reduced as compared to OSEM making it a preferred choice as reporting image. ***Conclusion:*** Deep progressive reconstruction enables reliable low-dose, rapid-acquisition ^{18}F-FDG PET imaging without compromising diagnostic quality, and can be very beneficial in resource-constrained settings. This approach may expand PET accessibility in developing regions by reducing costs and scan times while maintaining accuracy. ***References:*** Ew-Jun Chen, et al Radiation Physics and Chemistry, 2024.

EP-0986

Impact of Deep Learning Denoising on Image Quality and Semiquantitative Parameters in Low-Count/ Reduced-Time ^{18}F-FDG Digital PET/CT Scans

S. Shekhar Singh[1], *N. Jain*[2], *S. Nigam*[1], *P. Wadhwa*[3];
[1]Globe Healthcare, Lucknow, INDIA, [2]Molecular Imaging & Therapy, Delhi, INDIA, [3]United Imaging Healthcare, Delhi, INDIA.

Aim/Introduction: To evaluate the effect of a deep learning (DL)-based denoising method on image quality and semiquantitative parameters in low-count/reduced-time ^{18}F-FDG PET/CT scans using a digital PET/CT system. ***Materials and Methods:*** This retrospective multi center study (Globe healthcare, Lucknow and Molecular Imaging, Delhi, India) included 140 patients who underwent ^{18}F-FDG PET/CT imaging on a digital PET/CT scanner (United Imaging uMI550) with a standard acquisition time of 120 seconds per bed position. List-mode data were rebinned into five datasets: 120s (reference), 90s, 60s, 45s, and 30s, corresponding to 100%, 75%, 50%, 37.5%, and 25% of total counts, respectively. Images were reconstructed using OSEM and post-processed with DL-based denoising and Gaussian filtering (GS). Quantitative analysis included SUVmax, SUVmean, liver/mediastinal signal-to-noise ratio (SNR), and contrast-to-noise ratio (CNR). Subjective image quality was assessed using a 5-point Likert scale for noise, lesion detectability, and overall diagnostic confidence. ***Results:*** The mean injected ^{18}F-FDG dose was 3.0 ± 0.5 MBq/kg, with an uptake time of 60 ± 10 minutes. DL-denoised images demonstrated significantly lower noise ($p < 0.05$) and higher SNR compared to GS across all reduced-count subsets. No significant differences in SUVmean were observed between DL and GS methods. Lesion CNR and subjective contrast were preserved in DL-processed images down to 45s (37.5% counts), with significant degradation only at 30s (25% counts). Compared to the reference (120s), the 90s (75% counts) DL-denoised images showed no significant differences in SUV, SNR, or lesion detectability ($p > 0.05$). ***Conclusion:*** DL-based denoising significantly improves image quality in low-count ^{18}F-FDG PET/CT scans, allowing for a reduction in acquisition time to 90s per bed position (75% counts) without compromising diagnostic accuracy or semiquantitative metrics. This approach may enable faster scans or lower-dose protocols while maintaining diagnostic confidence. ***References:*** Xing, Y. et al,, Clinical evaluation on image quality of a deep learning-based denoising algorithm in ^{18}F-FDG PET/CT studies JNM 2021.

EP-0987

Quantitative Accuracy in Preclinical SPECT/CT Imaging: Partial Volume Effects, Reconstruction Parameters, and Radiotracer Concentration

A. Ebrahimifard[1], *S. Bagheri*[1], *D. Librizzi*[2], *F. Eilsberger*[1], *M. Luster*[1], *B. Hooshyar Yousefi*[1,3];
[1]Department of Nuclear Medicine, School of Medicine, Philipps university Marburg, Marburg, GERMANY, [2]Department of Nuclear Medicine, University Hospital OWL, Evangelical Hospital Bethel, Bielefeld, GERMANY, [3]Preclinical Imaging of Core Facility, Center for Tumor Biology and Immunology (ZTI), Philipps University Marburg, Marburg, GERMANY.

Aim/Introduction: High quantitative accuracy in preclinical SPECT imaging is essential for translating molecular imaging findings into clinical impact. However, partial volume effects (PVE), particularly in small organs and at low uptake levels, remain a major challenge often leading to inaccurate results. This study investigates how reconstruction parameters and radiotracer concentration affect quantitative parameters. Through comprehensive analysis, we optimised the imaging protocol to enhance quantitative accuracy across varying organ sizes. ***Materials and Methods:*** The Digimouse (28g) mouse-model phantom was filled with ^{99m}Tc-pertechnetate at 1, 5, and 10 MBq/ml densities. Imaging was performed using Mediso-nanoScan SPECT/CT system with pinhole collimators. Three reconstruction settings were applied: 32i3s (minimum), 48i3s (typical), and 64i3s (maximum), incorporating attenuation and scatter correction. VOIs for the liver (large), heart (medium), and thyroid (small) were defined using PMOD (v4.3) on CT images. Quantitative parameters, including recovery coefficient (RC), signal-to-noise ratio (SNR), contrast, and contrast-to-noise ratio (CNR) were calculated. ***Results:*** RC in the liver remained stable across all reconstruction settings and activity concentrations, while thyroid RC increased significantly from 1 to 5 and 10 MBq/ml (both $p<0.01$) in all settings. Heart RC increased significantly from 1 to 5 MBq/ml ($p<0.01$) and from 1 to 10 MBq/ml ($p<0.05$). SNR peaked at 5 MBq/ml across all organs but decreased significantly at 10 MBq/ml. Liver and heart SNR increased from 1 to 5 MBq/ml ($p<0.01$), while thyroid SNR changes were only observed from 5 to 10 MBq/ml ($p<0.05$). Liver contrast improved at 5 MBq/ml ($p<0.05$) but decreased at 10 MBq/ml, with no changes in the thyroid or heart. CNR peaked at 5 MBq/ml and decreased significantly at 10 MBq/ml ($p<0.05$). ***Conclusion:*** This study highlights the effects of organ size, radiotracer concentration, and reconstruction parameters on quantitative accuracy in preclinical imaging. RC remained stable in large organs but varied in small structures under low-radioactivity conditions. SNR and CNR peaked at 5 MBq/ml across all organs, with declines at 10 MBq/ml likely due to system dead-time effects. Contrast enhancement in larger organs suggests reduced PVE with increasing size. A radioactivity density of 5 MBq/ml, combined with 48i3s or 64i3s reconstructions, provided a favorable set-up in our study, highlighting the importance of protocol optimisation for accurate quantification of small volumes with low-uptake levels in preclinical studies.

EP-0988

Enhanced parametric imaging from low-dose dynamic Long-Axial-Field-of-View PET studies using a suitably weighted 3-D gaussian smoothing process

Q. Wu[1,2], *F. Gu*[3], *K. Shi*[4], *A. Rominger*[4], *F. O'Sullivan*[1];
[1]*School of Mathematical Sciences, University College Cork, Cork, IRELAND,* [2]*Insight SFI Centre for Data Analytics, Cork, IRELAND,* [3]*School of Mathematics and Physics, North China Electric Power University, Beijing, CHINA,* [4]*Department of Nuclear Medicine, Inselspital, Bern University Hospital, Bern, SWITZERLAND.*

Aim/Introduction: Dynamic positron emission tomography (PET) imaging is vital for estimating metabolic parameters like flux and distribution volume, which inform clinical decisions in oncology. Low-dose PET protocols, increasingly adopted to reduce patient radiation exposure, suffer from lowcounts that amplify noise in image. Conventional Gaussian smoothing potentially blurring reliable estimates, this study proposes a weighted Gaussian smoothing method incorporating inverse-variance weighting derived from image-domain bootstrap estimates, aiming to enhance the accuracy and clinical utility of dynamic low-dose PET parametric maps by prioritizing reliable data. ***Materials and Methods:*** The method was applied to a dynamic low-dose FDG PET data from Biograph Vision Quadra scanner. Metabolic parameters were estimated using non-parametric residue mapping (NPRM). Variances were calculated via image-domain bootstrapping, which models errors with a subordinate Gaussian process and accounts for spatial correlations using a Kronecker tensor product and 3D Fast Fourier Transform. Smoothing was performed using 3D Gaussian kernels, with weights inversely proportional to the bootstrap-estimated variances. The FWHM of the Gaussian kernel was optimized using generalized cross-validation, a data-driven technique that balances noise reduction with the preservation of structural details, eliminating the need for manual tuning. To quantify the effectiveness of the weighted Gaussian smoothing, the signal-to-noise ratio (SNR) was evaluated based on a suitable homogeneous region within the parametric map. ***Results:*** Weighted Gaussian smoothing significantly reduced noise in high-variance regions while preserving details in low-variance areas. A 2-fold improvement in SNR was achieved, demonstrating the method's effectiveness in enhancing the quality of parametric maps from low-dose PET data. This noise reduction directly enhances the visualization of kinetic parameters, making subtle features more distinguishable, which is critical for accurate clinical interpretation. ***Conclusion:*** By integrating inverse-variance weighting with Gaussian smoothing and leveraging efficient image-domain bootstrap variance estimation, this method provides a robust approach to denoising PET parametric maps. Its computational efficiency makes it suitable for routine clinical use, with potential extensions to other modalities. The method improves the visualization of kinetic parameter maps in low-dose PET and aligns with efforts to reduce patient radiation exposure. Future work will validate its performance in simulation setting and larger cohorts. ***References:*** O'Sullivan, F., et al. (2021). A Generalized Linear modeling approach to bootstrapping multi-frame PET image data. Medical Image Analysis, 72, 102-132. Wu, Q., et al. (2024). Mapping FDG Kinetics together with Patient-Specific Bootstrap Assessment of Uncertainties: An Illustration with data from a Long-Axial FOV PET/CT Scanner. Journal of Nuclear Medicine, 65, 971-979.

EP-0989

Color of Radiation: Redesign of Established Colormaps in the Oklab Color Space for Perceptual Accuracy and Inclusive Design for Color Vision Deficiency

M. Gammel[1], *W. A. Weber*[1], *S. G. Nekolla*[1], *B. M. Gammel*[2];
[1]*TUM Klinikum, Rechts der Isar, Department of Nuclear Medicine TUM School of Medicine and Health, Munich, GERMANY,* [2]*Infineon Technology AG, Munich, GERMANY.*

Aim/Introduction: In medical imaging, misinterpretation may result not only from acquisition or reconstruction artifacts, but also from suboptimal color maps (CMAPs). Their diagnostic impact is well established in other scientific fields, where non-perceptual uniform CMAPs are well known to result in pseudo-contours, masked gradients, or contrast distortions. Many standard CMAPs lack perceptual uniformity: they exhibit non-linear luminance and irregular perceptual spacing (ΔE), introducing similar risks in medical imaging. Sixteen CMAPs commonly used in clinical software were systematically examined. The three most frequent variants were reconstructed in the perceptually uniform Oklab color space, ensuring linear luminance and constant perceptual steps while preserving familiar appearance. Oklab is increasingly adopted in digital workflows and is part of the W3C CSS Color Module Level 4. Additionally, perceptual accessibility was assessed under simulated color vision deficiencies (CVD) to enable inclusive interpretation. ***Materials and Methods:*** Sixteen clinical CMAPs were evaluated for luminance linearity and perceptual spacing (ΔE) using the CIE L*a*b* color space. The three most frequent variants (thermal, cool, grayscale) were transformed into the perceptually uniform Oklab space, where ΔE can be calculated directly via Euclidean distance—unlike CIE-based models that require complex correction formulas (CIEDE2000). They were then optimized for linear luminance and constant ΔE using a Python-based workflow with parametric color paths and ΔE-controlled interpolation, and converted to sRGB.CVD (prot-, deuter-, tritanomaly) were simulated using the physiologically based Machado model (Matpack, C++). Additional CMAPs were developed for each deficiency, based on perceptual adaptation and visual similarity, fulfilling the same criteria of luminance linearity and equidistant steps. ***Results:*** All 16 CMAPs showed significant deviations from perceptual uniformity, leading to the artifacts described above. The three optimized variants met both criteria within Oklab while maintaining their visual identity. Each was defined by a parameterized path in Oklab's extended gamut, enabling algorithmic reproducibility, reliable design, and conversion to other color spaces. For each CVD, adapted CMAPs were created to preserve discriminability and visual similarity. ***Conclusion:*** CMAPs are not decorative - they are diagnostic tools. Many established variants exhibit perceptual flaws that may impair interpretation. This work presents optimized versions of widely used CMAPs that preserve their familiar appearance, allowing users to retain established interpretation patterns without retraining. Dedicated variants for CVD enable perceptual accessibility across user groups. All designs are based on the Oklab color space, which is internationally standardized (W3C CSS Color Module Level 4), ensuring long-term compatibility and integration into future imaging systems.

EP-0990

Evaluation of FastPET reconstruction method using multiple tracers and LAFOV PET

N. Overbeck[1], *U. Lindberg*[1], *I. Law*[1], *Y. Zheng*[2], *D. Bharkhada*[2], *M. Zhang*[2], *V. Panin*[2], *P. Schleyer*[2], *M. Millardet*[3], *T. L. Andersen*[1], *F. L. Andersen*[1];
[1]*Copenhagen University Hospital, Rigshospitalet, Copenhagen, DENMARK,* [2]*Siemens Healthineers, Knoxville, TN, UNITED STATES OF AMERICA,* [3]*University of Pennsylvania, Philadelphia, PA, UNITED STATES OF AMERICA.*

Aim/Introduction: Positron Emission Tomography (PET) enables visualization of physiological processes using radiotracers tailored to specific diagnostic applications. The large data volumes cause challenges through the image reconstruction due to the computational demands of methods such as Ordered Subsets Expectation Maximization (OSEM). To address this, a deep learning-based algorithm, FastPET, utilizing a U-Net architecture, was developed to significantly reduce computation time [1].

This study evaluates FastPET's performance against the clinical standard, OSEM, using PET/CT scans across multiple tracers. ***Materials and Methods:*** The Long Axial Field-of-View PET scans included in the study were performed using the following tracers and approximate post injection (p.i.) times: [^{18}F]FDG 60 min, [^{18}F]FET 30 min, [^{18}F]FE-PE2I 35 min, [^{15}O]H_2O 60s, [^{68}Ga]Ga-DOTATOC 60 min, and [^{11}C]PiB 50 min p.i. All reconstructions included 300s of PET data, except for [^{15}O]H_2O where 60s was selected. One patient per tracer was investigated. OSEM reconstruction was performed with 4 iterations, 5 subsets, PSF, TOF, and a 2 mm Gaussian filter. FastPET reconstruction used a 10-view histoimage corrected for attenuation and normalization to infer the PET image [2]. Images were masked to include voxels with at least 5% of the maximum OSEM intensity. Normalized root mean square error (NRMSE) was calculated to assess similarity between methods. ***Results:*** The comparisons showed agreement between FastPET and OSEM in high-uptake regions, preserving image quality and tracer distribution. In low-uptake areas, FastPET showed up to a 10% average bias. NRMSE values for each tracer were as follows: [^{18}F]FDG: 0.10, [^{18}F]FET: 0.11, [^{18}F]FE-PE2I: 0.12, [^{15}O]H_2O: 0.08, [^{68}Ga]Ga-DOTATOC: 0.22, and [^{11}C]PiB: 0.13. Additionally findings were the significant reduction in computation times when using FastPET. ***Conclusion:*** FastPET significantly reduces reconstruction time while preserving image quality and tracer uptake accuracy in high-uptake regions. However, the bias observed in low-uptake areas indicates some limitations in localized quantitative performance. The NRSME showed that the FastPET images had image quality comparable to the gold standard. ***References:*** [1]W. Whiteley, V. Panin, C. Zhou, J. Cabello, D. Bharkhada, and J. Gregor, "FastPET: Near Real-Time Reconstruction of PET Histo-Image Data Using a Neural Network," IEEE Trans Radiat Plasma Med Sci, vol. 5, no. 1, pp. 65-77, Jan. 2021, doi: 10.1109/TRPMS.2020.3028364. [2] M Millardet, Bharkhada D, Raj J, et al, "Improved quantification in end-to-end deep learning PET reconstruction using multi-view attenuation histo-images," 2023 IEEE Nuclear Science Symposium, Medical Imaging Conference and International Symposium on Room-Temperature Semiconductor Detectors (NSS MIC RTSD), Vancouver, BC, Canada, 2023, pp. 1-1, doi: 10.1109/NSSMICRTSD49126.2023.10338495.

EP-0991

Optimal reconstruction algorithm for amyloid PET with short acquisition time

K. Tsuda[1], *K. Koyama*[1], *S. Takemoto*[2], *K. Onuki*[2], *S. Kimura*[2], *T. Harada*[3];
[1]*Juntendo University, Tokyo, JAPAN,* [2]*Juntendo Hospital, Tokyo, JAPAN,* [3]*PDRadioPharma, Tokyo, JAPAN.*

Aim/Introduction: Disease-modifying therapy for Alzheimer's disease was approved in September 2023 for manufacture and sale in Japan, and diagnostic amyloid PET imaging (^{18}F-Florbetapir [FBP] and ^{18}F-Flutemetamol [FMM]) was approved for coverage by insurance in June 2024. The JSNM PET imaging Site Qualification Program (J-PEQi) was introduced to optimize testing, and an increasing number of facilities have obtained J-PEQi. In this program, phantom images corresponding to the acquisition time for each drug are submitted, with standard acquisition times of 10-20 min for FBP and 20-30 min for FMM. In clinical practice, however, it is unreasonable to expect patients with Alzheimer's disease to remain motionless on the PET bed for the specified time. The aim of this study was therefore to establish an optimal reconstruction algorithm for use with a short acquisition time that could ensure image quality and quantitativeness in the case that the specified acquisition time is not met. ***Materials and Methods:*** Images of two phantoms (Hoffman and cylindrical, both certified for use in J-PEQi) were acquired using either a Celesteion PMT-PET/CT (Canon) or Cartesion Prime SiPM-PET/CT (Canon) system. For both PMT-PET/CT and SiPM-PET/CT, standard image data acquisition times are 10 for FBP and 20 min for FMM. Assuming a short acquisition time, phantom image data were extracted with acquisition times of 5 min for FBP, and 10 and 15 min for FMM. The reconstruction algorithm was the same as for J-PEQi (PMT-PET/CT: TOF-OSEM, PSF-, Gaussian 4.0 mm; SiPM-PET/CT: TOF-OSEM, PSF-, Gaussian 4.0 mm). A new noise reduction method, Clear adaptive Low-noise Method (CaLM; mild, standard, and strong), was additionally applied. All obtained images were investigated visually and quantitatively as specified in J-PEQi, using visual resolution, %contrast, uniformity, and coefficient of variation (CV). ***Results:*** The pass criteria for J-PEQi are visual resolution, ≤8 mm; %contrast, ≥55%; uniformity, ≤0.0249; and CV, ≤15%. With PMT-PET/CT, 5-min FBP (Gaussian, CaLMstandard, CaLMstrong), 10-min FMM (CaLMstrong), and 15-min FMM (CaLMstrong) passed the criteria. With SiPM-PET/CT, 5-min FBP (Gaussian, CaLMstandard, CaLMstrong), 10-min FMM (CaLMstandard), and 15-min FMM (Gaussian, CaLMstandard, CaLMstrong) passed the criteria. ***Conclusion:*** The optimal reconstruction algorithm differed according to acquisition time for each PET/CT device, but appears to be suitable with short acquisition times. These findings will contribute to the acquisition of high-quality amyloid PET imaging in Japan, thereby improving the standard of dementia treatment.

EP-0992

The Impact of Reconstruction Parameters on Radiomic Features in ^{18}F-FET-PET Imaging of Glioma

D. Kalaeva[1,2], *G. Danilov*[1], *N. Vikhrova*[1], *I. Pronin*[1];
[1]*National Medical Research Center for Neurosurgery named after N.N. Burdenko, Moscow, RUSSIAN FEDERATION,* [2]*National Research Nuclear University MEPhI, Moscow, RUSSIAN FEDERATION.*

Aim/Introduction: To investigate the variability of ^{18}F-FET-PET radiomic features in metabolic tumor volume of IDH-wildtype and IDH-mutant gliomas depending on the applied filters and PSF modeling. The prognostic significance in predicting IDH status was assessed. ***Materials and Methods:*** 40 adult patients with IDH-wildtype glioblastomas (n=30) and ^{18}F-FET positive (TBR>1,6) IDH-mutant astrocytomas (n=10) were retrospectively enrolled. PET data (20-40 min p.i.) were obtained in list mode and reconstructed using a reference algorithm 3D OSEM 5i8s with applied 5 mm Gaussian filter. Variation over the reference setting: 2 and 7 mm Gaussian filter; 5mm Hann and Shepp filter; using PSF modeling. A threshold value TBR(tumor-to-brain ratio)=1,6 was used for tumor segmentation. A total of 4,838 radiomic features were extracted using the RIA R library. To evaluate their reliability, intraclass correlation coefficients (ICCs) were calculated. The Friedman test was used to assess differences in radiomic features obtained from variously filtered images, statistical significance was set at $p<0.05$. ***Results:*** The radiomic features demonstrated strong agreement across different reconstructions, though 159 radiomic features exhibited poor to moderate reliability (ICC<0,75). Statistically significant differences were found for 2674 radiomic features, which indicates the presence of variability depending on the reconstruction parameters and likely attributable to variations in noise levels among the compared images. While statistically significant predictors of IDH genotype were identified in this analysis, further validation in larger cohorts remains necessary. ***Conclusion:*** Radiomics provides important diagnostic information for noninvasive prediction of the IDH type, but the reconstruction parameters affect the radiomic features of PET imaging. Further studies should evaluate radiomic features reproducibility in various reconstructions and segmentation.

EP-0993

Optimisation of 123I FP-CIT SPECT-CT Reconstruction for a multi-site clinical service

J. Dixon, *C. Brown, R. Gillen, J. Dennis, N. Fullerton, F. Hendry, I. Andrews, A. Nicol;*
NHS Greater Glasgow and Clyde, Glasgow, UNITED KINGDOM.

Aim/Introduction: A review was undertaken to optimise and standardise 123I FP-CIT procedures across a large multi-site organisation (NHS Greater Glasgow and Clyde (NHSGGC) with five hospitals servicing a population of around 3 million and performing approx. 1,500 123I FP-CIT scans per annum). Whilst each site was individually generally compliant with the EANM/SNM guidelines [1], reconstruction for visual assessment was variable: filtered back-projection (FBP) and iterative reconstruction (IR) methods; 24-120 equivalent iterations; various attenuation correction (AC) methodologies; variable smoothing filters; variable application of scatter correction (SC) and resolution recovery (RR). This work aimed to introduce an optimised, standardised reconstruction for use at all NHSGGC sites. ***Materials and Methods:*** Practice at each site, including reconstruction settings, was compared with standards based on the EANM/SNM guidelines. All reconstructions were performed on vendor-neutral software. Three reconstruction protocols utilising CTAC, SC (including full collimator modelling) and RR were developed and assessed (Table 1). As these images have improved contrast, a revised colour scale was developed to display the CTAC, SC and RR reconstructions, maintaining the sensitivity of detecting subtle differences in striatal-to-background uptake of 123I FP-CIT. Test cases (n=4) were collated that covered a range of diagnoses (normal, weak comma, abnormal 'full stop'). Six reporting radiologists reviewed the test cases using the three reconstruction options, rating each on a 10-point Likert scale as to whether they considered the reconstruction suitable for clinical use. The current clinical visual assessment reconstructions of each case at each site were available for reference. Statistical significance was assessed using a t-Test. ***Results:*** Likert scores are shown in Table 2. Reconstruction protocols 1 and 3 scored positively, with no statistically significant difference (p=0.41). ***Conclusion:*** Iterative reconstructions using CTAC, SC and RR were developed, displayed with a modified colour scale and two were assessed to be suitable for use for clinical practice. Further work is underway to determine a final choice and managed rollout into routine clinical practice at all sites is planned. ***References:*** 1. Morbelli et al (2020). EANM practice guideline/SNMMI procedure standard for dopaminergic imaging in Parkinsonian syndromes 1.0. European Journal of Nuclear Medicine and Molecular Imaging, 47, 1885-1912.

EP-0994

Systematic Optimization of PET Quantitative Imaging using Realistically Inserted Synthetic Lesions: A Standardized Approach

N. Aghakhanolia[1], *A. Rahmim*[1], *P. L. Esquinas*[2];
[1]*UBC - School of Biomedical Engineering, Vancouver, BC, Canada,* [2]*BC Cancer - Molecular Imaging and Therapy, Vancouver, BC, CANADA.*

Aim/Introduction: Quantitative accuracy in PET imaging is essential for clinical diagnosis, treatment monitoring, and personalized care. However, systematically evaluating and optimizing reconstruction methods remains challenging due to the lack of realistic, standardized tools for performance assessment. Conventional approaches (physical phantoms or numerical simulations) often fail to capture the anatomical and physiological complexity of clinical images.To address this challenge, we present a lesion-insertion framework that enables embedding synthetic lesions with known characteristics into real patient PET images. This tool supports task-specific evaluations in a realistic and controlled setting. ***Materials and Methods:*** We developed a Python-based lesion-insertion toolbox integrated into PyTomography, an open-source framework for tomographic image reconstruction. The toolbox was inspired by Gabrani-Juma et al 2020 method. Our toolbox enables users to embed synthetic lesions with user-defined size, location, and intensity into real PET datasets. Synthetic lesions are then forward-projected and merged with real list-mode data (currently supports GATE and GE DMI data), simulating realistic acquisitions. Reconstructed images are subsequently generated using both OSEM and BSREM algorithms, with tunable parameters including point spread function width, number of iterations, subsets, and regularization strength.Quantification accuracy was assessed using recovery coefficient (RC) and detectability was evaluated using contrast-to-noise ratio (CNR) across varied reconstruction settings to assess the quantification performance. ***Results:*** All experiments utilized NEMA IQ data with a 10:1 lesion-to-background ratio. For a 25mm synthetic lesion (0.5MBq/mL) inserted in the uniform background (0.04MBq/mL), RC values remained close to unity (0.96-1.00) across all OSEM reconstructions, confirming accurate activity recovery. However, as the number of iterations increased, CNR values dropped significantly due to noise amplification.In another scenario, an 11mm lesion (0.65MBq/mL) was embedded within a high-intensity lesion (I0.4MBq/mL, 33mm). RC values remained around 0.96-0.98, indicating effective recovery in a high-intensity background. CNR values stayed within detectable ranges (4.62-5.81) for all OSEM settings, peaking at 2 iterations and 24 subsets. In contrast, for a lower-intensity lesion (0.25MBq/mL), RC values slightly decreased (0.92-0.95), and the standard deviation dropped, resulting in a lower CNR (~2). To further assess this case, BSREM reconstructions were also performed, yielding higher CNR (~3) and smoother noise profiles at optimized β values, highlighting the advantage of BSREM in low-uptake lesion detectability. ***Conclusion:*** Based on the results, our open-source lesion-insertion platform provides a basis for optimizing PET imaging protocols for specific clinical goals. Future efforts will concentrate on automated detection, large-scale validation, and comparisons with studies using anthropomorphic phantoms and real patient data.

EP-0995

Quantitative Evaluation of Motion Correction for ^{18}F-FEMPA PET Brain Imaging in Huntington's and Friedrich Ataxia

G. Yar[1], *C. Pain*[1], *H. Peiris*[1], *I. Harding*[2], *J. Jones*[3], *I. Hong*[3], *D. Staeb*[4], *H. Moradi*[4], *K. O'Brien*[4], *Z. Chen*[1];
[1]*Faculty of IT, Monash University, Melbourne, AUSTRALIA,* [2]*QIMR Berghofer Medical Research Institute, Brisbane, AUSTRALIA,* [3]*Siemens Medical Solutions, Knoxville, TN, UNITED STATES OF AMERICA* [4]*Siemens Healthcare Pty Ltd, Melbourne, AUSTRALIA.*

Aim/Introduction: This study presents a quantitative evaluation of motion correction (MoCo) for ^{18}F-FEMPA brain imaging in control subjects and subjects with Friedrich Ataxia (FA), and Huntington's disease (HD). We examine improved quantitative PET accuracy in brain regions related to these diseases using MoCo. ***Materials and Methods:*** The cohort for this study consists of 61 patients (FA-controls, FA-positive, HD-controls, HD-positive) each administered with a mean bolus of 249.2MBq (SD=5.3Mbq). The MoCo method in this study is the summing tree structural motion correction algorithm [1], where 2D image projections are used to iteratively correct 3D moving images on the basis of a target 3D image. Thalamus and brainstem are selected as regions of interest (ROIs) for evaluating HD. Cerebellum and brainstem are selected as ROIs for evaluating FA. Standardized-uptake-value (SUV) in ROIs is compared across MoCo and non-MoCo images for control subjects and subjects with HD or FA, to evaluate the effect of motion correction on recovering PET signals for disease. ***Results:*** Quantitative results showed an improvement in SUV uptake across different disease specific regions. For the HD group, compared with motion corrupted images, brainstem reported an increase of 5.25±2.32% in SUV measurements and thalamus recovered 4.62±2.01% SUV after MoCo. For the HD control group, brainstem SUV was recovered by 4.30±1.36% and thalamus SUV was recovered

by 3.95±1.45% with MoCo. For FA, brainstem improved 3.28±2.13% and cerebellum recovered 2.06±1.41% SUV after MoCo. For the FA control group, brainstem SUV was recovered by 2.01±1.46% and cerebellum SUV was recovered by 1.20±0.77%. In both datasets, MoCo consistently improved SUV measurements. FA patients showed higher uptake in the brainstem and cerebellum, while HD patient showed increased uptake in brainstem only, compared to their respective controls, regardless of motion correction. Further visual comparison between MoCo and non-MoCo images shows marginal improvements on image sharpness. These results were consistent in quantitative PET imaging for patients with neurological diseases. Future work will further investigate different MoCo pipelines, including MR-guided motion correction [2]. ***Conclusion:*** Motion correction has demonstrated the recovery of the SUV uptake measurements across all patient groups. These improvements are consistent across regions associated with disease biomarkers, suggesting an improved sensitivity in PET quantification following MoCo. The results support the application of MoCo in improving reliability of PET imaging for neurological conditions. ***References:*** [1] I. Hong, et al., 2019, IEEE NSS/MIC, pp. 1-3, doi: 10.1109/NSS/MIC42101.2019.9060017[2] Z. Chen, et al., 2019, Human Brain Mapping, doi.org/10.1002/hbm.24497.

EP-0996

Machine Learning-based denoising of low-count [^{177}Lu] Lutetium SPECT/CT images: evaluating the quantitative accuracy of denoised outputs for dosimetry'

C. Gascoigne[1], *A. L. Smith*[2], *E. Varzakis*[1], *K. Thielemans*[1], *J. C. Dickson*[2], *S. Arridge*[1], *J. Bomanji*[2], *D. Deidda*[3], *B. Fongenie*[4], *H. A. Williams*[5,6];
[1]*University College London (UCL), London, UNITED KINGDOM,* [2]*University College London Hospitals NHS Foundation Trust, London, UNITED KINGDOM,* [3]*National Physical Laboratory (NPL), Teddington, UNITED KINGDOM,* [4]*Blue Earth Therapeutics Ltd, Oxford, UNITED KINGDOM,* [5]*The Christie NHS Foundation Trust, Manchester, UNITED KINGDOM,* [6]*The University of Manchester, Manchester, UNITED KINGDOM.*

Aim/Introduction: A 2-dimensional U-Net algorithm was trained to denoise simulated and clinical reconstructed [^{177}Lu] Lutetium SPECT/CT images. The purpose of this work was to determine whether quantitative accuracy in low-count studies can be improved using machine learning denoising techniques to reduce scan time for dosimetry. ***Materials and Methods:*** Fifty volumes (128×128×128 voxels) containing random ellipsoids were generated in Python, with voxel values representative of clinical SPECT/CT studies. Fifty 'attenuation' arrays were generated with voxel values equivalent to Hounsfield Units in clinical CT scans. Pairs of 'activity' and 'attenuation' arrays were used as inputs for the SIMIND Monte Carlo program, to simulate 'noise-free' [^{177}Lu] Lutetium SPECT/CT acquisitions (30 seconds/projection). 'Noisy' simulations, approximating 11 seconds/projection with Poisson noise, were derived. Simulations were reconstructed using 'Software for Tomographic Image Reconstruction' (STIR) via the 'Synergistic Image Reconstruction Framework' (SIRF) platform. Reconstruction parameters were optimised for best achievable quantitative accuracy in volumes greater than 5.6 ml. A U-Net algorithm submitted to the Ultra-Low Dose PET Imaging (UDPET) Challenge 2022 was trained to generate a 'denoised' output from a 'noisy' input, using 45 pairs of 'noisy' and 'noise-free' slices of the reconstructed ellipsoid simulations. The trained model's weights were saved, and its performance evaluated on 5 held-out samples. The algorithm's ability to denoise clinical data was investigated using 'transfer learning.' Model training was continued using thirty-five pairs of 'noisy' and 'reference' [^{177}Lu] Lutetium-DOTATATE SPECT/CT patient images. The 'reference' images (30 seconds/projection) were Poisson resampled using Xeleris 5.0 (GE Healthcare) to generate 'noisy' representations equivalent to 6 seconds/projection. Images were reconstructed using MIM software, with parameters optimised for quantitative accuracy. Denoised model outputs for a held-out dataset (4 patients) were evaluated. Clinically relevant regions of interest were drawn to assess quantitative accuracy compared to the 'reference' images. This study received ethical approval from a UK Research Ethics Committee via the IRAS process (REC reference: 22/HRA/3556). ***Results:*** After training with simulated images, the mean peak signal-to-noise ratio (PSNR) for the 'ellipsoid' test images was 37.73 and the mean structural similarity index measure (SSIM) was 0.91. After further training with clinical images, the mean PSNR for the clinical test images was 36.30 and the mean SSIM was 0.96. Visually, the model outputs appear less noisy. The quantitative accuracy in test cases was evaluated. ***Conclusion:*** A U-Net was implemented and trained to denoise simulated and real patient data. Further optimistion and evaluation remains necessary before clinical deployment. ***References:*** 1. https://github.com/junqiangchen/Ultra-low-Dose-PET-Imaging-Challenge.

EP-61

e-Poster Area

D: Technical Studies -> D2 Data Analysis and Artificial Intelligence -> D22 Image Classification / Segmentation / Anomaly Detection

EP-0997

MedMimic: A Physician-Inspired Multimodal Fusion Framework for Early Diagnosing Fever of Unknown Origin

Y. Zhou;
West China Hospital, Chengdu, CHINA.

Aim/Introduction: Fever of unknown origin (FUO) poses a significant diagnostic challenge, often requiring extensive evaluations. While recent efforts integrating clinical features with ^{18}F-FDG PET/CT imaging have improved diagnostic accuracy, conventional feature extraction methods based on manually defined features often lack robustness and generalizability. Furthermore, the scarcity of annotated ^{18}F-FDG PET/CT datasets limits the effective training of deep learning models.To overcome these challenges, we propose Medical Mimicry (MedMimic), a framework inspired by real-world diagnostic processes. ***Materials and Methods:*** MedMimic leverages pre-trained models—including DINOv2, Vision Transformer, and ResNet-18—to transform high-dimensional ^{18}F-FDG PET/CT imaging data into low-dimensional, semantically meaningful feature tensors. A learnable self-attention based fusion network then integrates these imaging features with clinical data, producing compact yet discriminative representations for downstream classification. Our dataset was collected from Sichuan University West China Hospital, one of China's top-tier medical institutions, and comprised 607 consecutive FUO patients who underwent ^{18}F-FDG PET/CT. After excluding cases that did not meet the inclusion criteria, 416 patient admissions from January 2017 to December 2023 were included in the study. ***Results:*** Our proposed multimodal fusion classification network (MFCN) achieved macro-averaged area under the receiver operating characteristic curve (AUROC) values ranging from 0.8654 to 0.9291 across all seven decomposed tasks, outperformingcompeting machine learning (ML) and single-modality deep learning (DL) methods. Additionally, ablation studies validated the effectiveness of the proposed MFCN model. Furthermore, we employed a five-fold cross-validation strategy to ensure the robustness of our results. ***Conclusion:*** By integrating thestrengths of pre-trained large models and deep learning, MedMimic offers a novel perspective and an effective solution for disease classification.

EP-0998

Organ Network Disruptions in Parkinson's Disease Revealed by [18F]-FEOBV Whole-Body PET Imaging

M. Rusaas[1,2], *J. Horsager*[1], *N. Okkels*[1,3], *P. Borghammer*[1,2], *O. L. Munk*[1,2];
[1]*Department of Nuclear Medicine & PET Centre, Aarhus University Hospital, Aarhus, DENMARK,* [2]*Department of Clinical Medicine, Aarhus University Hospital, Aarhus, DENMARK,* [3]*Department of Neurology, Aarhus University Hospital, Aarhus, DENMARK.*

Aim/Introduction: PET imaging with the [18F]-FEOBV radiotracer has been proposed as a method for evaluation of peripheral autonomic degeneration in patients with Parkinson's disease (PD), but no individual organ had significantly reduced uptake in PD [1]. This study is the first to investigate molecular inter-organ correlation patterns and their disruptions in PD. ***Materials and Methods:*** 22 healthy controls (HC) and 15 PD patients were [18F]-FEOBV PET/CT scanned (26.3cm FOV, 214ps TOF), and we used SUV image from 60-70 min post injection [1]. Low-dose CT scans were segmented using TotalSegmentator [2], VOIs were eroded and visually inspected to minimize the effects of CT-PET mismatch, and organ SUV values were extracted from 7 organs and 8 regions in the brain. HCs were used to calculate a reference network using Spearman correlation between mean regional SUVs [3]. Individual patient disruptions were found by adding each patient into the control group, recalculating the inter-organ correlations, and subtracting the reference network [4]. Jackknife resampling generated individual networks for HCs, providing a reference distribution for evaluating PD-specific disruptions. Consistent disruptions were identified based on the number of patients with significant differences in organ-pair correlation and statistical testing, followed by ROC-curve analysis between PD and HC. ***Results:*** In general, correlation deviations involving the pancreas displayed the biggest differences between the HC and PD groups. The involvement of the pancreas is consistent with single-organ analysis in studies of parasympathetic denervation [1,5]. The most notable deviations were the pancreas-lung and pancreas-blood correlations, with a majority of patients exhibiting significantly weaker correlations for these organ pairs. These organ-pair means were also significantly different from zero after false discovery rate (FDR) correction across 105 different inter-organ correlations (T-test, p=0.01). The distribution of the identified organ-pairs deviated from the HC reference distribution, showing potential for classification (AUC=0.84). These results are an improvement compared to single-organ analysis of the pancreas (p=0.16, AUC=0.65). ***Conclusion:*** Whole-body inter-organ network analysis of FEOBV PET may be a promising approach for detecting PD-specific abnormalities involving organs with parasympathetic innervation. ***References:*** [1] Jacob Horsager et al., 2022, doi: 10.1016/j.parkreldis.2022.09.016. [2] J. Wasserthal et al., 2023, doi: 10.5281/zenodo.6802613. [3] L. K. S. Sundar et al., 2023, doi: 10.2967/JNUMED.122.264555. [4] T. Sun et al., 2022, doi: 10.1007/s00259-022-05832-7. [5] N. Okkels et al., 2024, doi: 10.1093/brain/awad391.

EP-0999

Impact Of The Healthy Control Database On Brain [18F] FDG PET Quantification

E. Fernández-Zorrilla[1], *C. Domínguez-Borrero*[1], *J. Silva-Rodríguez*[2], *A. Moscoso*[1], *P. Aguiar*[1];
[1]*IDIS Research Institute, Santiago de Compostela, SPAIN,* [2]*Fundación CIEN, Madrid, SPAIN.*

Aim/Introduction: Quantification improves the precision of brain [18F]FDG PET, but its accuracy may depend on the choice of healthy control (HC) database [1-2]. The aim of this work is to assess the impact of the scanner used for HC database acquisition of quantification performance. ***Materials and Methods:*** We use a pioneering methodology based on a simulated-based gold standard [3]. First, 25 brain PET/CT/MR images from volunteers were used to generate 25 HC digital phantoms [4]. These phantoms were modified by two experienced physicians to add 75 small and 25 extended hypometabolic areas. Modified phantoms were simulated on the GE DST 1 scanner, while HC phantoms were simulated on 6 scanner models (GE Advance, GE DST 1, GE DST 1, GE DSTE, GE DST and Biograph mMR). VOI-wise quantification was used to generate mean values for 83 VOIs and a paired t-test was performed for comparing between HC databases (alpha = 0.01, and Bonferroni). In addition, each patient's VOIs were compared with 6 HC datasets to localize the hypometabolic areas and voxel-wise analysis was applied to generate z-score maps. ***Results:*** Paired t-test showed differences in a sustantial number of VOIs between HC database acquired on the GE DST 1 (used for patients) and those acquired on all other scanners: GE Advance (33/83 VOIs), GE DST (49/83 VOIs), GE DSTE (36/83 VOIs), GE DST 2 (28/83 VOIs) and Biograph mMR (50/83 VOIs). In terms of localization of extended hypometabolic areas, HC database acquired on GE DST 1 and Biograph mMR achieved the highest AUC, all scanners achieved AUC > 0.9. For localization of small hypometabolic areas, HC database acquired on GE DST 1 also achieved the highest AUC. Hypometabolic area was detected in all z-score maps, it was uniquely identified only when HC database was acquired on the same scanner as the patients (GE DST 1). In contrast, the use of HC databases acquired on scanners other than the one used for the patients resulted in the detection on false hypometabolic areas. ***Conclusion:*** The use of HC databases acquired on a scanner different from that used for patient acquisition have a significant impact on [18F]FDG PET quantification performance, particularly for the detection of smaller hypometabolic areas. ***References:*** [1] Guedj et al. Eur J Nucl Med Mol I, 2022[2] Traub-Weidinger et al. Eur J Nucl Med Mol I, 2024[3] Paredes-Pacheco et al. Med Phys, 2021[4] Marti-Fuster et al. IEE Trans Med I, 2014.

EP-1000

Automated clinical AI workflow for real-time detection of myocardial uptake in bone scintigraphy

H. Halme, *V. Uusitalo, E. Hippeläinen;*
Clinical Physiology and Nuclear Medicine, Helsinki University Hospital and University of Helsinki, Helsinki, FINLAND.

Aim/Introduction: Incidental myocardial uptake of bone-avid ^{99m}Tc-labeled radiotracers is indicative of transthyretin amyloidosis (ATTR). Detection of such uptake is important for early diagnosis and treatment of ATTR. Myocardial uptake in planar bone scans should be confirmed by SPECT-CT to exclude false positive findings due to blood pool uptake. Failure to detect incidental cardiac uptake may lead to delayed diagnostics, and increased radiation dose if the patient is referred to additional SPECT-CT later. We have developed an artificial intelligence (AI)-based workflow for detection of myocardial uptake in bone scintigrams. The workflow processes whole-body bone scans in real time, defines myocardial uptake, and, in case of abnormal uptake, alerts radiographers and physicians about the possible need for SPECT-CT. ***Materials and Methods:*** The workflow consists of: 1) acquisition of whole-body scintigraphy, 2) automatic export of the image to the analysis server, 3) preprocessing and classification of the image with in-house developed convolutional neural network (CNN) [1], 4) transfer of the classification result (myocardial uptake/no uptake) to a Power Automate flow, 5) in case of detected myocardial uptake, an alert message to a Teams channel available for radiographers and physicians. DICOM data handling, database usage, image preprocessing, and classification with a pre-trained CNN occur within a Docker container. This workflow is designed for easy clinical deployment. The container can be exported to any workstation, used via Docker Desktop, and configured to output results based on local needs (email, database, office software). It also allows for quick retrospective analysis of numerous bone

scans. ***Results:*** Successful feasibility tests were conducted using data from two scanners. Total processing time between image export and alert message was less than one second for a single image. AI performance was retrospectively tested with 12 000 unseen bone scans. A nuclear medicine physician validated all AI-classified positive cases (n=372) and 1000 randomly selected negative cases. The AI correctly classified all 30 true positive and 1000 negative images; however, there were 342 false positives. ***Conclusion:*** Despite the AI producing many false positive results, it successfully detected all true myocardial uptakes from bone scans. Our method is feasible for a standard nuclear medicine setup. It alerts about myocardial uptake suggestive of ATTR cardiomyopathy. It could increase the detection rate of ATTR and decrease the need for repeated cardiac SPECT-CT. ***References:*** [1] Halme, Hanna-Leena, et al. "Convolutional neural networks for detection of transthyretin amyloidosis in 2D scintigraphy images." EJNMMI research 12.1 (2022): 27.

EP-1001

Automated DICOM-Based Quantitative Assessment of NEMA PET IQ Phantom Images for Harmonized Recovery Coefficient Analysis According to EARL Standards

A. Silva Oliveira, *V. de Oliveira Menezes, A. dos Santos Filho; Hospital das Clínicas, Federal University of Pernambuco, Recife, BRAZIL.*

Aim/Introduction: This study aimed to develop and validate an automated method for analyzing PET images of the NEMA Image Quality (IQ) phantom directly from raw DICOM data. The objective was to reliably compute recovery coefficients (RCs) and lung-to-background contrast to meet the harmonization standards set by the European Association of Nuclear Medicine Research Ltd. (EARL). ***Materials and Methods:*** A Python-based algorithm was developed to automatically process PET DICOM datasets. The algorithm identifies the specific slice containing the six fillable spheres within the NEMA IQ phantom and calculates a calibration factor by comparing measured background activity against decay-corrected theoretical activity concentration. This calibration factor is then used to compute 2D and 3D RCs, including peak RCs determined by a 50% isocontour threshold. The lung-equivalent contrast was assessed using fixed-size circular regions of interest (ROIs). This approach was tested on 36 PET/CT image series. ***Results:*** The automated algorithm successfully identified and quantified all phantom spheres across the evaluated image series. Metrics computed included RC2D (mean, max, standard deviation), RC3D (mean, max, peak, standard deviation), background contrast, and the system calibration factor. The mean calibration factor across all series was 1.08 ± 0.04. Recovery coefficients were within EARL2 specifications for spheres ≥17 mm in 92% of cases. The average lung-to-background contrast measured across 17 slices was 0.74 ± 0.03. Results were presented visually through overlays and exported as structured CSV files. ***Conclusion:*** The developed automated algorithm offers a robust and reproducible method for PET IQ phantom analysis, significantly reducing operator-induced variability. By aligning measurements with EARL-defined recovery coefficient thresholds, this tool supports harmonization in multicenter PET studies and facilitates standardized scanner optimization and routine quality assurance. ***References:*** 1. Boellaard R. Standards for PET Image Acquisition and Quantitative Data Analysis. J Nucl Med. 2009;50(1):11S-20S. doi:10.2967/jnumed.108.0571822. Fahey FH, Kinahan PE, Doot RK, et al. Variability in PET quantitation within a multicenter consortium. Med Phys. 2010;37(7):3660-3671. doi:10.1118/1.34557053. EARL Manual v4.2. European Association of Nuclear Medicine (EANM). May 2023. Available at: https://earl.eanm.org.

EP-1002

Automatic diagnosis of obstruction in Tc99m-EC renal scanning by the aid of deep learning

A. Aghaee, *P. Sahafi, S. Bagheri, S. Soltani, T. Shooshtari; Nuclear Medicine Research center, Mashhad University of Medical Sciences, Mashhad, IRAN, ISLAMIC REPUBLIC OF.*

Aim/Introduction: In the context of renal disease, accurate diagnosis of complications associated with hydronephrosis is crucial for timely intervention and improved patient outcomes. Nuclear medicine scans are commonly used to assess the possibility of obstruction at UVJ or UPJ or less commonly in the pathway of the ureters. This research endeavor aims to develop and apply a deep learning algorithm to detect obstructive processes and differentiate them from non-obstructive diseases in Tc-99m ethylene dicysteine (EC) scans. By leveraging the power of deep learning, early detection of these complications could be achieved, leading to more effective and prompt treatment strategies for patients. ***Materials and Methods:*** Participating in this research were 317 patients who had undergone EC renal scans (173 patients with abnormality). Image acquisition was performed after administering 4 to 7 mCi of Tc-99m EC intravenously gamma camera in two phases. The image had a matrix dimension of 128 x 128. Flow phase data was collected for one minute (60 frames), while second phase data was collected for thirty to sixty minutes (thirty to sixty frames). Figure 1 shows example of a normal and abnormal patients. To standardize and normalize each phase for individual patients, we scaled them to their maximum values across all frames. Following this, 60 frames were added to the uptake phase, and the flow and uptake phases were concatenated to create a single 120-frame frame. The patients were divided into two distinct groups including training (75%), and test (25%). Fifteen percent of the training dataset was selected for validation. The InceptionResNet model was utilized for backbone of deep learning. We implemented two 128 dense layers and sigmoid dense layer for final layer. For model training, 2 batch size and 300 epochs were utilized. As performance metrics, the area under the curve (AUC), recall, f1 score, precision, and accuracy were utilized to assess the model's performance on the test data. ***Results:*** The accuracy and AUC were 0.67 and 0.69 for the InceptionResNet model. Using InceptionResNet, recall (0.58 and 0.66), precision (0.58and 0.66), and f1-score (0.58 and 0.66) were resulted for obstructive and normal patterns, respectively (Figure 2). ***Conclusion:*** The findings of this inquiry suggest that deep learning models may have utility in identifying and diagnosing irregularities occurring in renal abnormalities. Nevertheless, it is feasible to attain superior outcomes through the implementation of alternative filtering, using other artificial intelligence algorithms, and augmenting the data set.

EP-1003

Lung Cancer Classification from PET-CT Images Using Transfer Learning

M. Azizkhani[1], *P. Azarbar*[2], *M. Shahrbabaki Mofrad*[3], *M. Sharbatdar*[1], *P. Sheikhzadeh*[4]; *[1]K. N. Toosi University of Technology, Tehran, IRAN, ISLAMIC REPUBLIC OF, [2]Department of Medical Physics and Biomedical Engineering, Faculty of Medicine, Shahid Beheshti University of Medical Sciences, Tehran, IRAN, ISLAMIC REPUBLIC OF, [3]Department of Medical Physics and Biomedical Engineering, Faculty of Medicine, Tehran University of Medical Sciences, Tehran, IRAN, ISLAMIC REPUBLIC OF, [4]Department of Nuclear Medicine, IKHC, Tehran University of Medical Sciences, Tehran, IRAN, ISLAMIC REPUBLIC OF.*

Aim/Introduction: Lung cancer is one of the most serious causes of cancer-related mortality. Early diagnosis through PET-CT scans can significantly reduce the mortality rate. However, evaluating PET-CT images is a time-consuming process that is prone to human error. Therefore, the use of artificial intelligence and deep learning

algorithms can play a crucial role in analyzing and interpreting these images. ***Materials and Methods:*** One of the most valuable aspects of this research is the use of real-world and specialized data from patients with challenging tumor diagnoses. These data include PET and CT images that were acquired separately and later fused to create combined PET-CT representations for each patient. The dataset consisted of 2349 PET-CT images, including 1098 tumor-class samples and 1251 normal-class samples. In this study, convolutional neural networks (CNNs) were employed to detect lung cancer-related abnormalities in the patients PET-CT scans. Specifically, the MobileNetV2 model was used in conjunction with the Transfer Learning technique to leverage pre-trained knowledge in this domain. In addition, Data Augmentation methods were utilized to effectively expand the training dataset. To prevent overfitting and enhance the generalization ability of the model, regularization techniques such as Dropout were applied. ***Results:*** Ultimately, the proposed model achieved an accuracy of 79%, precision of 84%, recall of 78% and an F1-score of 78% on the collected dataset. ***Conclusion:*** The results indicate that the proposed deep learning approach, based on MobileNetV2 and Transfer Learning, is effective in detecting lung cancer in PET-CT scans. ***References:*** 1. Wang L. Deep learning techniques to diagnose lung cancer. Cancers. 2022;14(22):5569.2. Fanizzi A, Fadda F, Comes MC, Bove S, Catino A, Di Benedetto E, et al. Comparison between vision transformers and convolutional neural networks to predict non-small lung cancer recurrence. Scientific Reports. 2023;13(1):20605.

EP-1004

Development of an automatic detection tool for hyperfunctioning parathyroid glands in dual-isotope parathyroid scintigraphy

L. Hassler[1], *D. Chardin*[1], *D. Benisvy*[1], *G. D'andrea*[1,2], *J. Darcourt*[1], *O. Humbert*[1];
[1]*Centre Antoine Lacassagne, Nice, FRANCE,* [2]*Institut de Lla Faceet du Cou, Nice, FRANCE.*

Aim/Introduction: Dual-isotope parathyroid scintigraphy is a key imaging technique for locating hyperfunctioning glands in the context of primary hyperparathyroidism before surgery. Artificial intelligence (AI), particularly through convolutional neural networks (CNNs), shows increasing potential to improve the interpretation of medical images. ***Materials and Methods:*** This retrospective study included 456 patients who underwent dual-isotope parathyroid scintigraphy at the Centre Antoine Lacassagne between 2019 and 2023. CNNs were used to classify subtraction images as positive/negative and to localize parathyroid lesions between the right and left sides. The models were trained using various labeling methods based on visual analysis and SPECT/CT data. The performance of the models was then evaluated using histological, biological, or PET-FCH results as reference. ***Results:*** The VGG19-based model achieved the best performance, particularly for right/left localization, with an overall accuracy of 92.5%, reaching 95.5% for left-sided lesions and 88.9% for right-sided lesions. The positive/negative classification achieved an accuracy of 77% and sensitivity of 81.4%. Expert SPECT/CT analysis displayed the best overall results, with a sensitivity of 95.3% and specificity of 88.9%. ***Conclusion:*** This study, the first to use convolutional neural networks to detect and localize hyperfunctioning parathyroid glands in dual-isotope scintigraphy, shows promising results, especially for left/right localization.

EP-1005

Contrast agnostic AI-based extraction of image-derived input function from dynamic PET scans

T. Andersen*, N. Evenstuen, C. Ladefoged, U. Lindberg;*
Rigshospitalet, Dept. of Clinical Physiology & Nuclear Medicine, Copenhagen, DENMARK.

Aim/Introduction: Accurate quantification in positron emission tomography (PET) requires reliable input functions. With recent advancements, image-derived input functions (IDIFs) have become feasible [1], often extracted using anatomical segmentations like the aorta from CT scans. However, reliance on structural imaging can introduce motion mismatch, bias from image quality, and limit applicability. We propose a contrast-agnostic method to extract IDIFs directly from dynamic PET images using an AI model. ***Materials and Methods:*** Aorta segmentations were obtained using TotalSegmentator (TS) [2] on CT images. A manually PET-guided segmentation (PGS) of the aorta was also performed for 35 test datasets. Of 244 total datasets, 16 with poor CT segmentations were excluded from training and treated separately as an outlier dataset. The remaining 198 datasets (108 [18F]FDG, 68 [15O]H2O, 5 [18F]PE2I, 1 [11C]PIB, 7 [68Ga]FAPI, 9 [64Cu]DOTATATE) were used for model training. CT-based aorta masks were resliced to a 0-40 s summed PET image. A 5-fold cross-validation with data augmentation was used. Segmentation performance was assessed using Dice similarity coefficients (DSCs), and IDIF quality was evaluated via maximum peak height (MP) and area under the curve (AUC) using an approach akin to [1]. ***Results:*** In the test set, mean DSCs vs. PGS were 0.83 (TS) and 0.82 (AI). In the outlier set, the AI model outperformed TS (DSC: 0.86 vs. 0.79). For IDIFs, the TS approach showed MP and AUC biases of -2.6% and -1.3%, respectively, compared to PGS, while the AI model showed smaller biases of 1.6% (MP) and 0.6% (AUC). On the outlier dataset, the TS had MP and AUC differences of -3.0% and -1.4%, while the AI model maintained higher accuracy (0.5% MP, -0.1% AUC). ***Conclusion:*** We developed a robust AI model that extracts IDIFs directly from PET, reducing reliance on structural imaging. The model performs comparably to CT-based methods on standard cases and significantly better on outliers, improving robustness in challenging scenarios. ***References:*** [1] Andersen, T.L., Andersen, F.L., Haddock, B., Rosenbaum, S., Larsson, H.B.W., Law, I. & Lindberg, U. (2024), Automated Quantitative Image-Derived Input Function for the Estimation of Cerebral Blood Flow Using Oxygen-15-Labelled Water on a Long-Axial Field-of-View PET/CT Scanner. Diagnostics, 15(14) 1590. [2] Wasserthal, J., Breit, H. C., Meyer, M. T., Pradella, M., Hinck, D., Sauter, A. W., ... & Segeroth, M. (2023). TotalSegmentator: robust segmentation of 104 anatomic structures in CT images. Radiology: Artificial Intelligence, 5(5).

EP-1006

Improving Planar Lung Scintigraphy Interpretation with artificial intelligence (AI): An Educational and Clinical Utility Tool for Pulmonary Embolism Detection

B. Duchaj[1], *L. Noskovičová*[2], *J. Veselý*[1], *S. Balogová*[2,3];
[1]*St. Elisabeth Oncology Institute, Bratislava, SLOVAKIA,* [2]*Department of Nuclear Medicine, Comenius University Bratislava, St. Elisabeth Oncology Institute and Bory Hospital, Bratislava, SLOVAKIA,* [3]*Department of Nuclear Medicine, Hôpital Tenon GH AP.SU, Paris, FRANCE.*

Aim/Introduction: The interpretation of planar ventilation/perfusion (VQ) scans poses significant challenges for young nuclear medicine (NM) physicians and medical students. This study investigates the potential of using deep learning to assist in the identification of acute pulmonary embolism (PE) in planar scans. We are developing an in-house educational tool that not only correlates these imaging projections with planar lung segments but also provides practical engagement with medical AI, thereby actively involving the students in the learning process and evaluating their knowledge. ***Materials and Methods:*** From 2020 to 2023, we conducted a retrospective analysis of 287 patients who underwent VQ lung scanning using [99mTc]-MAA / [81mKr] without SPECT or SPECT/CT. The NM reports served as the reference standard for diagnosing acute PE or alternative conditions. We subsequently obtained 74 perfusion scans categorized into acute PE and non-acute PE, alongside 64 ventilation scans comprising cases with and without ventilation defects. These studies were systematically extracted utilizing a configurable DICOM tag, yielding a sequence of 8 planar projections for perfusion and 6 for ventilation, effectively creating

a "quasi" SPECT dataset. A 3D sequential convolutional neural network was developed with a binary classification output, with each dataset trained independently. The model demonstrating the best validation accuracy, loss and AUC was evaluated against the validation dataset. ***Results:*** The perfusion model has demonstrated an accuracy/loss of 0.88/0.24 and an AUC of 0.96, correctly evaluating 30 cases of PE versus non-PE with a sensitivity of 96.6% (1 false negative) and 86.6% (4 false positives). The ventilation model exhibited an accuracy/loss of 0.84/0.35 and an AUC of 0.90, successfully categorizing 26 cases of normal versus abnormal with a sensitivity of 88.4% (3 false positives) and 76.9% (6 false negatives). We developed an in-house web application to facilitate the importation of V/Q scans as DICOM instances for processing and analysis of the acute PE probability. This application enables semi-manual mapping of planar scintigrams to lung segment representations, providing a practical platform for image analysis and serving as an educational resource and quiz tool for medical students. ***Conclusion:*** To increase the adoption of AI systems among physicians in NM, it is essential to engage medical students in a more effective understanding of medical data and image analysis. This can be operationalized through the creation of interactive educational tools, such as in-house applications, that promote the practical application of these advanced technologies within the medical community.

EP-1007

Radiomics Analysis for Differentiate Benign and Malign Pulmonary Nodules Using Tumoral, Peritumoral and Peribronchovascular Segmentation with Machine Learning Approaches

A. Inanir[1], *K. Dizdar*[2], *N. Dizdar*[1], *N. Coşkun*[3], *E. Tatçı*[1], *Ö. Özmen*[1]; *[1]Etlik City Hospital, Ankara, TÜRKIYE, [2]ASELSAN INC. Software Engineering, Ankara, TÜRKIYE, [3]Ankara City Hospital, Ankara, TÜRKIYE.*

Aim/Introduction: The present study aimed to evaluate the potential contribution of peritumoral and peribronchovascular PET/CT-based radiomics analyses in differentiating malignant pulmonary nodules from benign ones, beyond the information provided by intralesional radiomic features alone. Additionally, radiomics analysis was employed to differentiate benign from malignant nodules within both FDG-positive and FDG-negative groups. Furthermore, the diagnostic performance of radiomics analysis was evaluated across nodules of varying sizes. ***Materials and Methods:*** A total of 163 patients with nodules 6 to 30 mm, who had either histopathological diagnosis or at least two years of CT follow-up, were included in the study retrospectively. Three different VOI were manually delineated for each nodule: intralesional, perilesional, and peribronchovascular. The perilesional VOI was drawn around the periphery of the lesion, excluding the FDG uptake area, with a thickness of one voxel. A linear VOI was created along the peribronchovascular bundle nearest to the nodule. Radiomic parameters were evaluated using the Python Scikit-learn library. Significant parameters were determined using the Mann-Whitney U test and filtered through PCA regression analysis. The radiomic parameters were tested using machine learning classifiers. The SVM classifier achieved best prediction performance, and this model was used in the analyses. ***Results:*** A total of 163 cases (119 male, 44 female) with an average age of 65.7 ± 10.7 years were included in the study. Of the nodules, 96 were benign and 67 were malignant. Significant differences were found in more than 40 radiomics parameters for all 3 segmentation models. With joint model that includes all parameters gathered from three segmentations, 70 parameters were significantly different. The F-measure and AUC values for the intralesional, perilesional, peribronchovascular and joint model were found to be 0.79/0.87, 0.73/0.75, 0.75/0.77 and 0,76/0,82 respectively. For the differentiation of FDG-positive nodules, the AUC and F-Measure found to be 0.77/0.71 respectively. Models obtained with all three segmentations were unsuccessful in differentiating benign and malignant lesions in the FDG-negative group.In the differentiation of benign and malignant nodules, the AUC value for <1cm, 1-2cm and 2-3 cm groups was 0.67/0.82/0.86 respectively. ***Conclusion:*** In our study, it has been demonstrated that segmentation of the nodule in PET-based radiomics analysis can be effective in differential diagnosis. Additionally, it was found that radiomic parameters may contribute to showing inflammation in the peritumoral microenvironment and tumor cell spread through airways (STAS). It was also determined that radiomics could be helpful in preventing false positives in FDG-positive nodules. ***References:*** doi: 10.1111/crj.13751.

EP-1008

FDG PET/CT-Based Machine Learning Modelling and Texture Features in Risk Stratification of Thymomas

B. Bozca[1], *K. Dizdar*[2], *N. Aydinbelge Dizdar*[1], *E. Tatci*[1], *T. Inal Cengiz*[3], *O. Ozmen*[1], *N. Gurcay*[4], *P. Tari*[5], *U. Yilmaz*[3], *L. Acar*[6]; *[1]Etlik City Hospital, Department of Nuclear Medicine, Ankara, TÜRKIYE, [2]Department of Software Engineering, ASELSAN Inc., Ankara, TÜRKIYE, [3]Ataturk Chest Diseases and Thoracic Surgery Training and Research Hospital, Department of Chest Diseases, Ankara, TÜRKIYE, [4]Ataturk Chest Diseases and Thoracic Surgery Training and Research Hospital, Department of Pathology, Ankara, TÜRKIYE, [5]Ataturk Chest Diseases and Thoracic Surgery Training and Research Hospital, Department of Nuclear Medicine, Ankara, TÜRKIYE, [6]Ataturk Chest Diseases and Thoracic Surgery Training and Research Hospital, Department ofThoracic Surgery, Ankara, TÜRKIYE.*

Aim/Introduction: Thymoma is the most common primary tumour of anterior mediastinum. Considering their prognosis and recurrence, thymomas are classified into two groups: low-risk (types A, AB, B1) and high-risk (types B2, B3). Aim of this study is to evaluate a prediction model based on radiomics parameters obtained from FDG PET/CT images for differentiating between low and high-risk thymomas. The study also examines the effectiveness of conventional FDG PET/CT parameters in risk assessment. ***Materials and Methods:*** Patients who underwent FDG PET/CT between January 2017-December 2023 for differential diagnosis of mediastinal mass and were diagnosed with thymoma through histopathological analysis. Lesions were manually segmented using LIFEx v7.4.0 software. Total of 111 radiomics features were extracted and evaluated using the Python Scikit-learn library. Parameters showing statistically significant differences were identified using the Mann-Whitney U test. Feature selection was then performed using LASSO regression analysis to reduce the number of variables and determine the most significant radiomics features. Selected features were tested with various machine learning classifiers: Random Forest, Support Vector Machine (SVM), Logistic Regression, Multilayer Perceptron, and XGBoost. Model performance was evaluated using the following metrics: ROC curve, accuracy, precision, recall, F-measure. Among all models, the SVM classifier provided the best prediction performance and was used for final analyses. Conventional parameters (SUVmax, SUVmean, SUVpeak, MTV, TLG) were compared between the low and high-risk thymoma groups using Mann-Whitney U test. ROC analysis was applied to calculate AUC values and optimal cut-off points. ***Results:*** Total of 69 patients diagnosed with thymoma with a mean age of 53.88±13 were included in the study. Patients were classified histologically into two groups. Statistically significant differences were found in 24 CT-based and 62 PET-based radiomics features. The most significant performance parameters are listed in Table 1. Radiomics performance metrics in distinguishing low from high-risk thymomas for CT images were: AUC:0.79, Accuracy:0.67, Precision:0.72, Recall:0.70, F-measure:0.67. For PET images: AUC:0.74, Accuracy:0.71, Precision:0.72, Recall:0.71, F-measure:0.71. No statistically significant differences were found

between the patient groups for conventional PET parameters (Table 2). Cut-off value for SUVmean in detecting high-risk thymomas was calculated as 3.47, with 57% sensitivity and 56% specificity (AUC 0.659, p=0.0027). ***Conclusion:*** In this study, no significant difference was detected between low and high-risk thymomas using conventional PET metrics. However, FDG PET/CT-based texture analysis, which more precisely evaluates tumour heterogeneity, may serve as a potentially stronger biomarker in risk classification. Further large-scale studies including broader patient populations are needed.

EP-1009

Automated AI-Based PET/CT Analysis for Monitoring Immunotherapy Response in Metastatic Melanoma

L. Förner[1,2], *J. Bäßler*[1], *C. Sulski*[1], *J. Enke*[1], *C. Lapa*[1], *T. Wendler*[1,2], *LF and JB are first authors with equal contribution;*
[1]*University Hospital Augsburg, Augsburg, GERMANY,* [2]*Technical University of Munich, Munich, GERMANY.*

Aim/Introduction: FDG-PET/CT plays a pivotal role in evaluating response and guiding complementary therapies in metastatic melanoma under immunotherapy. Quantitative PET metrics are central to this process but require time-consuming whole-body lesion segmentation. This study evaluates whether AI-based PET segmentation reliably reproduces manual metrics and reflects clinically relevant response patterns. ***Materials and Methods:*** 76 patients with metastatic melanoma undergoing immunotherapy were scanned with FDG-PET/CT before and during therapy. Six of them additionally underwent lymph node dissection (LND). A pipeline including automatic segmentation of FDG-positive lesions [1] was used to process all baseline (BL) and follow-up (FU) images. All BL images were also segmented manually. Lesion count (LC), SUVmax, SUVmean, total metabolic tumor volume (TMTV), total lesion glycolysis (TLG), Dmax, and total surface area (TSA) were calculated for all images. To validate the automatic pipeline, the metrics derived from the manual segmentations were compared with those from the AI-based segmentations. Differences in metrics between BL and FU were then analyzed with respect to clinical outcome, categorized as stable disease (SD, n=6), progressive disease (PD, n=19), partial metabolic response (PMR, n=15), or mixed response (MR, n=27), using imaging and S100 protein levels. LND patients were evaluated separately. ***Results:*** There was good agreement between manual and AI segmentations. LC matched in 40 patients, while in 26, the AI identified 2.35 more lesions on average. SUVmax and TLG showed no statistically significant difference (SSD), while TMTV and TLG demonstrated strong agreement (R^2 =0.89 and 0.86). Dmax showed SSD (45 ± 35 cm vs. 70 ± 47 cm), attributable to methodology: manual Dmax was measured on coronal MIP images, while the AI measured the 3D maximal distance between tumor voxels. When comparing BL-FU changes, SSD between PMR and SD were found for LC, SUVmean, and TLG; between SD and PD for LC, SUVmean, TMTV, TLG, and TSA. LND patients showed improved metrics compared to SD, with SSD in SUVmax, SUVmean, TMTV, TLG, and TSA. ***Conclusion:*** The automatic pipeline did not yield identical results to manual annotations but produced qualitatively good segmentations with closely matching SUVmax, TMTV, and TLG. The observed Dmax difference reflects definitional discrepancies. Automatically derived metric changes aligned well with clinical outcome, showing SSD across response groups. While limited by dataset size and human annotation density, this study demonstrates that fully automatic PET metric evaluation is feasible and already offers valuable support in resource-constrained clinical settings. ***References:*** [1] Rokuss M et al. arXiv preprint arXiv:2409.09478, 2024.

EP-1010

AI automation in Segmentation and Interpretation of PSMA PET-CT Imaging

K. Doornhof*, S. Koolen, A. Schrik, S. Veldhuijzen van Zanten, M. Segbers, M. Konijnenberg;*
Erasmus MC, Rotterdam, NETHERLANDS.

Aim/Introduction: Accurate segmentation of PET-CT images is crucial to determine the absorbed dose delivered to various tissues. Traditionally, segments were manually drawn, a time-consuming process that often limited dosimetry to selected lesions rather than all visible tumor tissue. AI segmentation tools can expedite and expand segmentation, enabling more comprehensive interpretation of PSMA scans. ***Materials and Methods:*** PSMA PET-CT images were obtained from patients undergoing Lu-PSMA treatment as part of the LUTRAC trial. Initial segmentation of CT images was performed using TotalSegmentator [1]. Segments corresponding to kidneys, bladder, liver, spleen, intestines, parotid and submandibular glands were refined based on PET imaging data to exclude non-malignant PSMA uptake. Non-physiological tracer uptake, likely indicative of tumor tissue, was classified using an SUV cutoff. Volume, SUV mean, and SUV max were determined for organs, bones, and tumor tissue. Segments generated by TotalSegmentator v2.5.0 and tumor segments identified using the SUV cutoff method were manually inspected for accuracy. ***Results:*** PSMA PET-CT images from 50 patients were segmented and analyzed using the automated pipeline. While manually drawing and analyzing of segments typically takes around 90 minutes, this analysis could be completed in under 10 minutes using TotalSegmentator based segmentation. A visual inspection was performed on the generated segments of different organs to confirm that that their placement matched expectations. Abnormal uptake identified by the analysis pipeline was checked by a nuclear radiologist for the initial three scans analyzed. The model's identification of abnormal uptake closely matched manual assessments in these cases. ***Conclusion:*** AI methods for analyzing PSMA PET-CT imaging can significantly reduce the time required to determine PSMA uptake in various tissues. These methods could also be applied to SPECT-CT imaging and other tracers. This could allow for quicker and more extensive dosimetry, which could enhance clinical decision-making. ***References:*** 1.Wasserthal, J., Breit, H.-C., Meyer, M.T., Pradella, M., Hinck, D., Sauter, A.W., Heye, T., Boll, D., Cyriac, J., Yang, S., Bach, M., Segeroth, M., 2023. TotalSegmentator: Robust Segmentation of 104 Anatomic Structures in CT Images. Radiology: Artificial Intelligence. https://doi.org/10.1148/ryai.230024.

EP-1011

AI-assisted treatment response assessment to disease-modifying therapy in 99mTc-DPD SPECT/CT markers in transthyretin cardiac amyloidosis enabled by artificial intelligence

C. Spielvogel*, M. Koefler, D. Haberl, J. Ning, J. Yu, Z. Jiang, K. Kluge, R. Calabretta, M. Hacker, R. Rettl;*
Medical University of Vienna, Vienna, AUSTRIA.

Aim/Introduction: Transthyretin cardiac amyloidosis (ATTR-CM) is a progressive and underdiagnosed condition associated with significant morbidity and mortality. Disease-modifying therapies (DMTs) targeting transthyretin have demonstrated efficacy in slowing disease progression, but robust markers for early treatment response remain limited. This study evaluates the impact of DMTs on 99mTc-DPD SPECT/CT-derived markers quantified through artificial intelligence (AI), providing insights into their role as non-invasive biomarkers for monitoring therapeutic efficacy. ***Materials and Methods:*** This longitudinal study included patients with confirmed ATTR-CM undergoing DMTs (transthyretin stabilizers, RNA interference or antisense oligonucleotids). Participants underwent 99mTc-DPD SPECT/CT imaging at baseline and

follow-up after therapy initiation. AI-based segmentation of cardiac structures enabled the measurement of 23 quantitative parameters, including uptake-intensity and uptake volume metrics, as well as the retention index across cardiac substructures. Functional parameters, including echocardiography and cardiac MRI metrics were integrated for correlative analysis. Univariate and multivariate Cox proportional hazards models were performed for death or heart failure-associated hospitalization. ***Results:*** This study analyzed longitudinal data from 45 patients with a median time between baseline and follow-up scans of 9 months (IQR 7-10). Post-treatment assessments revealed significant reductions in 14/16 (88%) of SPECT/CT markers ($p<0.0001$), including notable decreases in uptake of the left ventricle (SUVmax 18.6 to 14.1) and myocardium (SUVmax 19.5 to 15.5) while uptake area metrics increased in 5/7 (71%) markers after treatment initiation, however not significantly (all $p>0.05$). These changes corresponded to improvements in functional parameters, including an association of reduced NT-proBNP with lower uptake in terms of SUVpeak of the myocardium ($p=0.007$), SUVmax of the myocardium ($p=0.018$), right ventricle ($p=0.029$), and left ventricle ($p=0.039$) as well as an association of a reduced retention index with lower new york heart association (NYHA) stage ($p=0.016$). Associations between atrial and right ventricular uptake showed a tendency to be associated with prognosis but were not significant ($p=0.08$ and $p=0.07$ respectively). ***Conclusion:*** This study underscores the utility of AI-enhanced 99mTc-DPD SPECT/CT imaging in capturing treatment-induced changes in cardiac amyloid burden. By automating marker extraction, AI mitigates inter-rater variability, increases efficiency, and enhances reproducibility. Our findings highlight the potential of SPECT/CT markers to serve as sensitive, non-invasive biomarkers for early treatment response assessment, offering an alternative to cardiac MRI in patients with implanted devices. These findings pave the way for personalized treatment strategies and broader clinical adoption of AI in nuclear medicine.

EP-1012

Accuracy and Precision of Lung Lobe Function Measurements from SPECT/CT Using Openly Available and Task Trained AI Segmentation Models

E. Amini[1], *R. Klein*[2];
[1]*Ottawa Hospital Research Institute, Ottawa, ON, CANADA,* [2]*The Ottawa Hospital, Ottawa, ON, CANADA.*

Aim/Introduction: Lung lobe segmentation is essential for assessing lobar function before surgery. This tedious task can now be automated using AI models, though accuracy depends on training data qualities. Given the low spatial resolution of SPECT, exact segmentation may be unnecessary. We sought to compare the accuracy and precision of lung lobe function quantification using general radiology and ad-hoc trained AI segmentation models. ***Materials and Methods:*** We retrospectively collected 160 pairs of CT-SPECT scans from patients who underwent lung function imaging. Ground-truth segmentations were derived semi-automatically using clinical software. Data was split 80/20 for training/testing (N=128/32), with test cases stratified by segmentation difficulty into three grades (7 Easy, 9 Moderate, and 16 Hard). Models compared included open-source (MOOSE, TotalSegmentator, Vista3D), and locally trained using our training data (Vista3D fine-tuned and an nnUNet-based LocalModel). Segmentation results were automatically co-registered to SPECT using affine transforms to extract lobe function (%) as counts per lobe divided by total lung counts. Lobe function error (%) was calculated as the difference between model and ground-truth. Error bias and error spread were assessed using the Wilcoxon signed-rank and Ansari-Bradley tests, respectively. Mean absolute error (MAE) was used to assess precision. Lobe function errors <5% were considered clinically insignificant. ***Results:*** Across the 32 cases, no model-specific bias was observed for median lobe function error whether stratified by difficulty group ($p=1$) or by lobe ($p>0.05$). Error spread significantly increased from Easy to Hard cases only for MOOSE ($p=0.005$, MAE:0.57%→2.29%) and Vista3D ($p=0.004$, MAE:0.44%→2.40%), with significance only in the right-middle lobe (Easy-Hard) for MOOSE, TotalSegmentator, and Vista3D ($p<0.02$). In Hard cases, absolute errors as large as 17% were observed for non-locally trained models and <5% for our locally trained model. No significant model-specific bias was observed between 5-lobe (n=25) and missing lobe (n=7) ($p=1$). However, error variability was significantly higher in missing-lobe cases for all models ($p<0.03$) except LocalModel ($p=0.4$), indicating robustness in these challenging scenarios through representative training data. Clinically significant errors in at least one lobe occurred in 19% of MOOSE and Vista3D cases, 16% of TotalSegmentator, 6% of fine-tuned Vista3D, and none for LocalModel. ***Conclusion:*** Despite differences in segmentation quality between AI models, lobar function estimates from SPECT rarely vary in a clinically significant manner. Results suggest publicly available segmentation tools can be reliable for most clinical use, but are outperformed by ad-hoc trained models. Regardless, oversight by clinicians for gross errors is still required.

EP-1013

Providing anatomical context for longitudinal lesion assessment: comparison of two deep learning models

P. Patil[1], *P. Khobragade*[2], *H. Yerebakan*[3], *G. Platsch*[4], *N. Vargese*[2], *M. Rashmi*[1], *M. S. Chakragiri*[2], *A. Shanker*[2], *B. Spottiswoode*[5], *A. Soliman*[5];
[1]*Manipal Institue of Technology, Manipal, INDIA,* [2]*Siemens Healthcare Private Ltd., Bangalore, INDIA,* [3]*Siemens Medical Solutions USA, Inc., Malvern, PA, UNITED STATES OF AMERICA,* [4]*Siemens Healthcare GmbH., Erlangen, GERMANY,* [5]*Siemens Medical Solutions USA, Inc., Knoxville, TN, UNITED STATES OF AMERICA.*

Aim/Introduction: Accurate anatomical localization of lesions in PET/CT scans is important for disease staging and prognosis, and needs to be consistent across serial scans for treatment response assessment. CT-based deep learning segmentation is a well-established method for providing anatomical context but can be computationally intensive, especially with widely distributed lesions across multiple time points. This study compares a conventional UNet-based whole body segmentation (WBS) method with a novel, fast organ classification (FOC) approach[1] for anatomical localization in longitudinal PET/CT scans. ***Materials and Methods:*** A dataset of 75 ^{18}F-FDG PET/CT scans was collected from 25 patients, each having at least two longitudinal scans corresponding to different therapy cycles. A total of 246 lesions were segmented by a nuclear medicine physician and the linking between corresponding lesions in each scan pair was established. Two methods were used to identify the lesion location in longitudinal scans based on CT information: (1) The WBS method which segments the entire CT volume into 79 regions. The anatomical location of a lesion is determined by the mapping of its centroid onto the 79-class segmentation map. (2) The FOC method determines the anatomical location through the classification of the lesion centroid only. FOC extracts a hierarchical multi-resolution descriptor for a given location and feeds it into a classifier to predict one of 117 anatomical locations. The accuracy of each method is assessed based on the ability to correctly identify the same anatomical location for each pair of linked lesions in the two timepoints. The processing times for both techniques were also recorded. ***Results:*** The mean processing time for the WBS method to segment all organs was 3.9±0.8 minutes, while the FOC method averaged 0.25±0.17 seconds per scan (69±42 millisecond per lesion), demonstrating a more than 3,000-fold improvement in processing speed. For correctly identifying the same location for both linked lesions in the two longitudinal scans, the FOC achieved an accuracy of 82.1%, while the standard method achieved 87.8%. ***Conclusion:*** The performance of two methods for anatomical localization was evaluated based on computational efficiency

and accuracy in identifying the same location for linked lesions. The fast organ classification method showed a significant gain in processing speed over the standard approach, with a slight trade-off in lesion identification accuracy. Both methods may support disease restaging and therapy response assessment. ***References:*** [1] Yerebakan, Halid, et al. "Real Time Multi Organ Classification on Computed Tomography Images." MICCAI DEMI workshop 2024.

EP-1014

PET Radiotracer Image-based Classification Using Convolutional Neural Network

L. Partin[1], *K. Chiam*[2], *B. Spottiswoode*[1], *R. Fahmi*[1], *V. Shah*[1];
[1]*Siemens Medical Solutions, Knoxville, TN, UNITED STATES OF AMERICA,* [2]*Department of Bioengineering, University of California, Los Angeles, CA, UNITED STATES OF AMERICA.*

Aim/Introduction: For accurate quantitation and customized downstream processing of PET images, the radiotracer and isotope must be known. Traditionally, this information is saved in the DICOM header, but this can be erroneously misassigned or missing altogether. This challenge is further exacerbated by varying geographical conventions and languages. We seek to automate the classification of the radiotracer with deep learning. To our knowledge, this is the first work to explore this task. ***Materials and Methods:*** A 2D convolutional neural network (CNN) was trained to classify the radiotracer. Training images were augmented by random rotations, translation, and zooming before converting to a coronal maximum intensity projection (MIP) as input to the network. Our dataset comprised of 876 images across 15 radiotracers: 18F-PSMA-1007, 18F-FES, 82Rb, 68Ga-PSMA-11, 18F-FACBC, 68Ga-Dotatate, 18F-PI-2620, 18F-FDOPA, 18F-DCFPyl, 18F-FDG, 13N-Ammonia, and amyloid tracers 18F-florbetapir, 18F-flutemetamol, 18F-florbetaben, and 11C-PiB. Cases were split into training, tuning, and test and stratified by radiotracer. To verify generalizability of the network, a network was first trained on 12/15 radiotracers that span whole body, cardiac, and neurology use cases and tested on ^{18}F-FDG and 82Rb from two external sites. Grad-CAM [1] was used to highlight areas of the image useful for classification. To demonstrate specialization, a separate network was trained on amyloid-only tracers to showcase if different amyloid tracers can be distinguished. For the amyloid network, the inputs of MIP versus 16 center coronal slices were compared. ***Results:*** The generalized network correctly classified 66/73 test cases. Misclassified cases corresponded to either tracers with the same isotope or PSMA tracers confused with another PSMA tracer. For the external site tracers, 7/11 ^{18}F-FDG and 14/15 82Rb were classified correctly, demonstrating that the network is robust to cross-site protocols. Use of the MIPs or the central slices for amyloid characterization yielded similar results (37/40 and 36/40 correct classifications, respectively). Grad-CAM demonstrated that the network capitalized on regions that a reader would use to distinguish tracers, e.g., the brain in ^{18}F-FDG and the salivary glands in 18F-PSMA. ***Conclusion:*** A CNN showed promising results to classify between PET radiotracers, although further work is needed to improve and validate robustness across sites and reconstruction protocols. This introduces a quality control metric to ensure accurate quantitation and applicability for radiotracer-specific downstream applications. Future work could include incorporating domain knowledge so that the algorithm can justify its classification through user-friendly explanations. ***References:*** [1] R. R. Selvaraju et al.: http://arxiv.org/abs/1610.02391.

EP-1015

Revisiting the Segmentation Threshold for Lu-177 SPECT

Y. Liu[1], *J. Yang*[2], *P. Wang*[2,1], *Y. Wang*[2], *K. Shi*[3], *Y. Chen*[2], *G. Mok*[1];
[1]*Biomedical Imaging Laboratory (BIG), Department of Electrical and Computer Engineering, Faculty of Science and Technology, University of Macau, Macao Sar, MACAO,* [2]*Department of Nuclear Medicine, Affiliated Hospital of Southwest Medical University, Luzhou, CHINA,* [3]*Department of Nuclear Medicine, Inselspital, Bern University Hospital, University of Bern, Bern, SWITZERLAND.*

Aim/Introduction: Currently, tumor segmentation on SPECT images is still mainly based on a fixed threshold, i.e., 42% of the maximum intensity, which was derived primary for Tc-99m (1) and may not be directly applicable to Lu-177, one of the most widely used theranostic tracers today. This study aims to revisit the optimal segmentation threshold value for Lu-177 SPECT. ***Materials and Methods:*** A cylindrical Jaszczak phantom with six spheres (2-113 mL) was imaged using a clinical dual-head NaI SPECT/CT system with medium-energy and low-penetration parallel-hole collimators. The spheres were filled with 44 μCi/mL Lu-177, with sphere-to-background ratios (SBRs) of infinite, 10:1, 5:1, 3.5:1, and 2:1. A total of 120 projections with 25 s/projection acquired over 360° at a fixed radius-of-rotation of 24 cm were reconstructed using 3D FBP and OS-EM algorithms with attenuation and scatter corrections, followed by Gaussian filtering (σ=3.4 mm). Segmentation thresholds from 1% to 100% of the maximum voxel intensity were applied to minimize volume errors relative to ground truth. Pearson correlation was assessed between the optimal thresholds and sphere volume/SBR. The newly derived and conventional Lu-177 thresholds were further validated on a total of 41 tumors on 17 patients with Lu-177-PSMA-617 SPECT using Dice, Hausdorff Distance at 95th percentile (HD95) and mean absolute volume error (MAVE). using manual segmentations based on consensus from three clinicians as the gold standard. A Mann-Whitney U test was performed between results from 2 threshold approaches. ***Results:*** The optimal thresholds showed a negative correlation ($r<0$) to both sphere volume and SBR. For SBR ≥3.5:1 and volume ≥16 mL, the mean optimal threshold of Lu-177 converged to 56% for FBP and 50% for OS-EM. The derived 50% threshold significantly improved tumor segmentation performance compared to the conventional 42% threshold on the clinical study, with a higher Dice (0.71 ± 0.10 vs 0.67 ± 0.13), lower HD95 (2.40 ± 1.57 mm vs 2.54 ± 1.58 mm), and lower MAVE (0.44 ± 0.35 vs 0.83 ± 0.66) (all $p < 0.05$). ***Conclusion:*** The optimal threshold value substantially deviated from that of Tc-99m for Lu-177 SPECT and can be used to enhance subsequent tumor quantification analysis in Lu-177 SPECT. ***References:*** 1. Erdi, Y E et al. "Threshold estimation in single photon emission computed tomography and planar imaging for clinical radioimmunotherapy." Cancer research vol. 55,23 Suppl (1995): 5823s-5826s. The project was supported by University of Macau (MYRG-GRG2024-00061-FST-UMDF) and National Natural Science Foundation of China (82472016).

EP-1016

Enabling Lesion-Level Dose-Response Analysis in RPTs: Topology-Aware Tracking of Metastases Using Spectral Graph Matching

F. Yousefirizi[1], *P. Fernandez*[2], *S. Kurkowska*[1], *F. Benard*[1], *A. Rahmim*[1], *C. Uribe*[2];
[1]*BC Cancer Research Institute, Vancouver, BC, CANADA,* [2]*BC Cancer, Vancouver, BC, CANADA.*

Aim/Introduction: Accurate dose-response assessment in radiopharmaceutical therapy (RPT) hinges on reliable lesion segmentation and longitudinal tracking, a process that becomes increasingly burdensome in metastatic castration-resistant prostate cancer (mCRPC) due to high lesion counts and anatomical changes over treatment cycles. To address this, we propose an automated, structure-aware tracking pipeline using Spectral Graph Matching (SGM), which integrates spatial and radiomic features while preserving global lesion topology. We compare it to a pairwise feature-based matching (PFM) approach to assess the added value of incorporating contextual graph-based information for robust lesion correspondence. ***Materials and Methods:*** Our method was evaluated on longitudinal post-therapeutic quantitative SPECT scans from five mCRPC patients treated with [^{177}Lu]Lu-HTK03170, totaling 30 imaging time points across up to six therapy cycles. Lesions were segmented using the qPSMA workflow in MIM and refined by physicians, with manual lesion correspondence as reference. Each of the 175 tracked lesions (~35 per patient) was represented by a feature

vector comprising centroid coordinates, volume, and a radiomics-derived heterogeneity score combining entropy and Gray-Level Co-occurrence Matrix (GLCM) features. Baseline PFM method (Yousefirizi et al. SNMMI 2025) used weighted cosine similarity and centroid distance, followed by spatial filtering and Hungarian assignment. In contrast, our SGM method embedded each scan into a lesion graph, with edge weights defined by Gaussian affinities between feature vectors. Spectral decomposition of graph Laplacian yielded low-dimensional eigenvectors capturing global lesion topology. Matching was then performed using cosine similarity between these embeddings, combined with spatial proximity, and optimized via the Hungarian algorithm. This structure-aware formulation enables resilience to lesion displacement, morphological variability, and changes such as splitting or merging. ***Results:*** PFM algorithm correctly tracked 166 of 175 lesions, yielding a mean per-lesion Connected Lesion (CL) accuracy (Santoro-Fernandes et al. 2024) of 0.788. PFM resulted in 9 missed lesions, where no corresponding lesion was identified in the subsequent time point, and no incorrect assignments. In comparison, SGM correctly tracked 153 lesions, missed 3, but produced 22 incorrect assignments. Despite more incorrect links, SGM achieved a higher CL accuracy of 0.893, driven by fewer missed matches. This suggests incorporating global graph-based context improves lesion recall at the expense of increased assignment ambiguity. ***Conclusion:*** We developed a structure-aware lesion tracking framework using SGM and benchmarked it against PFM. While PFM showed higher precision, SGM demonstrated greater robustness to lesion evolution, spatial shifts, and morphological change, supporting scalable, automated analysis of longitudinal SPECT/CT for RPT response evaluation.

EP-1017

Evaluation of combined or separate automatic segmentation models for ^{68}Ga-PSMA PET/CT and ^{177}Lu-PSMA SPECT/CT

S. Perret[1,2], *L. Albe*[3], *A. Edet-Sanson*[3,1], *D. Tonnelet*[3], *T. Carlier*[4,5], *C. Kohi*[4], *M. Barbaud*[4], *R. Modzelewski*[3,1], *P. Vera*[3,1], *C. Bailly*[4,5], *A. Dieudonné*[3,1], *P. Decazes*[3,1];
[1]*QuantIF-AIMS, University of Rouen, Rouen, FRANCE,* [2]*Siemens Healthineers, Courbevoie, FRANCE,* [3]*Nuclear Medicine Department, Henri Becquerel, Rouen, FRANCE,* [4]*Nuclear Medicine Department, University Hospital, Nantes, FRANCE,* [5]*Nantes Université, INSERM, CNRS, CRCINA, Université d'Angers, Nantes, FRANCE.*

Aim/Introduction: The manual segmentation of prostate cancer metastases on PET/CT and SPECT/CT images with PSMA radiotracers is laborious. The aim of this study is to evaluate the automatic segmentation models nnUNet trained on the two modalities, PET and SPECT, separately and jointly. ***Materials and Methods:*** The dataset consists of 48 patients from Henri Becquerel Cancer Center (HBCC) and 16 patients from the Nantes University Hospital (NUH). For each patient, both a 68Ga-PSMA PET/CT image and a 177Lu-PSMA SPECT/CT image were acquired during the first treatment cycle. These data were segmented by four nuclear medicine specialists. Three nnUNet models were trained for PET/CT and SPECT/CT: Model 1 (using PET/CT images only), Model 2 (using SPECT/CT images only), and Model 3 (combining PET/CT and SPECT/CT images). Additionally, two other models were specifically designed for SPECT: Model 4, a dual-head architecture that segments both lesions and organs simultaneously, and Model 5, which uses PET-based lesion segmentation as input to guide SPECT lesion segmentation. The models underwent both internal (dataset from the HBCC) and external validation (dataset from the NUH) to assess their generalizability. The volumes segmented automatically were assessed using the mean Dice coefficient (DSC). ***Results:*** Internal and external validations were performed to evaluate lesion segmentation on PET/CT and SPECT/CT. The PET/CT-specific model (1) achieved the best performance (DSC: 0.908 internal, 0.809 external), while the multi-modality model (3) also performed well. For SPECT/CT images, the best performance was achieved by the SPECT/CT with PET-guided segmentation model (5) with DSCs of 0.742 (internal) and 0.806 (IQR = 0.086) (external). The Dual-Head Model also performed well with DSCs of 0.730 (internal) and 0.790 (IQR=0.1172) (external). Moreover, both models showed more tightly clustered DSC values around the mean, indicating greater robustness and consistency compared to the SPECT/CT-specific model (2) (IQR=0.176). ***Conclusion:*** In this study, we evaluated different segmentation methods for lesion segmentation in PET/CT and SPECT/CT. For PET/CT images, the PET/CT-specific and multi-modality models showed the best results. Our findings also demonstrate that incorporating PET/CT-based guidance (5) or anatomical context through Dual-Head segmentation (4) significantly enhances lesion segmentation in SPECT/CT, leading to improved performance. This approach is particularly relevant since PET imaging offers superior spatial resolution compared to SPECT, and the PET scan is performed beforehand. ***References:*** Isensee, F., Jaeger, P. F., Kohl, S. A., Petersen, J., & Maier-Hein, K. H. (2021). nnU-Net: a self-configuring method for deep learning-based biomedical image segmentation. Nature methods, 18(2), 203-211.

EP-1018

A method for separating lesions from physiological uptake in PET segmentation

A. Soliman[1], *H. Yerebakan*[2], *B. Spottiswoode*[1];
[1]*Siemens Medical Solutions USA, Inc., Knoxville, TN, UNITED STATES OF AMERICA,* [2]*Siemens Medical Solutions USA, Inc., Malvern, PA, UNITED STATES OF AMERICA.*

Aim/Introduction: The characterization of lesion volumes and SUV parameters on PET images requires accurate segmentation. A significant challenge during this process is separating a lesion from high physiological uptake in close proximity, which often demands careful manual intervention. While deep learning methods offer partial solutions, their accuracy and interpretability of lesion contours still needs improvement. The international TMTV benchmark for lymphoma patients proposes a fixed SUV threshold for segmentation, which is prone to merging structures with high uptake. This study presents a method that refines a segmentation by separating multifocal regions and removing physiological uptake. ***Materials and Methods:*** The Auto Split algorithm comprises three steps: (1) Identify local maxima and grow controlled regions from each one of them. This incremental growth analyzes the voxels in descending order and the region growth freezes once a region touches another one that precedes it. (2) Use the local maxima within the two largest regions as anchor points to define markers for new regions. In case the difference between the anchor points is greater than a specific threshold, additional maxima are added for each marker group based on their SUV proximity to these points. (3) Apply watershed segmentation using the identified markers to separate the selected candidate. The selection of the candidates requiring separation can be initiated automatically using a fast organ classification approach which extracts a multi-level hierarchical descriptor for a given voxel and classifies it into one of 117 organs. The SUV_{max} locations for all candidates are classified to detect the physiological uptake. Then, the Auto Split is initiated if the candidate contains a local maximum with the classification of a different anatomical location from the rest. Auto Split has been evaluated on the international TMTV dataset, where 8/60 (13%) subjects have lesions connected to physiological uptake at the recommended 4 SUV threshold. Separation accuracy was assessed based on the algorithm's ability to retain lesion voxels, using F1-score, precision, recall, and volume similarity as evaluation metrics. ***Results:*** The algorithm achieved an average of 0.96±0.06, 0.94±0.11, 0.98±0.03, and 7.00%±12.68% for the F1-score, precision, recall, and volume similarity, respectively. Automated removal of coupled physiological uptake is correctly

performed 83% of the time. ***Conclusion:*** This work presents a novel and radiotracer agnostic method for separating lesions from adjacent physiological uptake. The need for manual editing of these connected physiological structures is reduced by 83% in the international lymphoma TMTV dataset.

EP-1019

Comparison of SUVmax threshold Based vs. Patient-Specific Segmentation for Lesion Delineation in Post^{177}Lu-DOTATATE whole body 3D SPECT/CT in Neuroendocrine Tumors

H. Noamen, *Y. Cras, M. Longo, C. Garcia, J. Hadoux, L. Lamartina, S. Moog, E. Baudin, D. Deandreis;*
Gustave Roussy Cancer Campus, Villejuif, FRANCE.

Aim/Introduction: Accurate lesion segmentation in post-^{177}Lu-DOTATATE SPECT/CT plays a crucial role in dosimetry and eventually in treatment response in neuroendocrine tumors. Nevertheless there is still a lack of a defined and standardized methodology. This study aimed to compare 3 segmentation methods to obtain reliable quantitative parameters from whole body 3D SPECT/CT images. ***Materials and Methods:*** A total of 62 post-treatment whole body 3D SPECT/CT images obtained at 24 hours after ^{177}Lu-DOTATATE injection by CZT gamma camera were retrospectively analyzed. Three segmentation methods were employed: Fixed SUVmax Method (A): Lesions were defined using a fixed SUVmax threshold of 3. Patient-Specific Method (B): A 3 cm^3 VOI was placed in the liver to calculate the SUVmean, and lesions were defined by applying the liver SUVmean as a cutoff.Patient-Specific Method with 10% threshold (C): An empiric 10% threshold evaluation was applied to the liver SUVmean. All the methods were followed by manual adjustments to exclude physiological uptake. Whole body lesion volumes (SSTR-TV) and SUVmean values were extracted for comparison between the three methods. A nuclear medicine physician validated the results of the three segmentation methods through visual inspection, evaluating lesion delineation and assessing any underestimation or overestimation of the lesions. Paired t-tests was used to compare significant differences. ***Results:*** Visual correct whole-body lesion segmentation was found in 19/62 (31%) cases with method (A), in 24/62 (39%) cases in method (B) and 47/62 (76%) cases in method (C). Visual concordance in lesion segmentation was observed only in 5/62 cases between method (A) and (B) and in 13/62 cases between (A) and (C). The median SUVmean liver was 1.42 [0.5; 16.18]. The median STTR-TV values obtained using three segmentation methods were 807.73 ml for (A) , 1287.59 ml for (B) ,and 914.01 for (C) method respectively. The median SUVmean values obtained were 6.87 for (A), 5.615 for (B) and 6.24 for (C) method. Statistical analysis revealed significant differences STTR-TV values between methods (A) and (B) ($p<0.0001$) and between methods (A) and (C) ($p=0.001$). No significant differences in lesion SUVmean between the three methods were shown. ***Conclusion:*** This study demonstrates that the segmentation method is a fundamental step for quantification in SPECT images. Patient-specific segmentation method may improve the accuracy in delineating lesions compared to the fixed SUVmax approach in^{77}Lu-DOTATATE SPECT/CT. Even if the fixed SUVmax method remains a simpler option, the patient-specific method seems to offer enhanced precision for dosimetry and clinical decision-making.

EP-1020

Automated lesion segmentation in ^{18}F-FDG PET/CT scans of patients with esophageal cancer

A. Soliman[1], *A. Nawwar*[2,3,4], *N. Thompson*[2], *V. Shah*[1], *B. Spottiswoode*[1], *I. Lyburn*[2,5,6];
[1]*Siemens Medical Solutions USA, Inc., Knoxville, TN, UNITED STATES OF AMERICA,* [2]*Cobalt Medical Charity, Cheltenham, UNITED KINGDOM,* [3]*University Hospitals Bristol and Weston, NHS Foundation Trust, Bristol, UNITED KINGDOM,* [4]*Clinical Oncology and Nuclear Medicine Department, Cairo University, Cairo, EGYPT,* [5]*Gloucestershire Hospitals, NHS Foundation Trust, Gloucestershire, UNITED KINGDOM,* [6]*Cranfield Forensic Institute, Cranfield University, Wiltshire, UNITED KINGDOM.*

Aim/Introduction: Esophageal cancer is one of the leading causes of cancer-related deaths. Neoadjuvant chemoradiation is common prior to surgery, and accurate delineation of gross tumor volume is essential for effective treatment planning. Such delineation is also important for quantification of tumor burden and SUV-parameters which may have prognostic value. This study presents a deep learning model based on the nnU-Net framework for segmenting lesions from ^{18}F-FDG PET/CT scans in patients with esophageal cancer. ***Materials and Methods:*** With IRB approval, ^{18}F-FDG PET/CT data were collected from 94 patients with esophageal cancer, each undergoing scans before and after neoadjuvant chemoradiation and prior to surgery. There was a total of 376 lesions in this dataset of 188 scans (min=0, max=36, avg=2 lesions per-scan). Lesions were segmented on PET images by two experienced board-certified PET/CT readers following PERCIST criteria, using a 42% of SUV_{max} threshold. We used the nnU-Net (3D full-resolution) framework to train a deep learning model that uses both functional(PET) and anatomical(CT) information as two input channels. This dual-channel input enables the model to learn both metabolic activity patterns and anatomical structures. The output is a segmentation map containing the lesions and 10 organs (several having physiological uptake on FDG PET). The anatomical context facilitates faster convergence during training and enhances the network's ability to handle negative cases, where no lesions are present. The model was trained using 5-fold cross-validation on the entire dataset. Segmentation performance was evaluated using the Dice similarity coefficient (DSC), average false positive (FP) volume, false negative (FN) volume. Lesion identification performance was evaluated using average true positive (ATP), average FP (AFP), average FN (AFN), precision, recall, and F1-score. ***Results:*** The five-fold cross validation of the 3D-nnU-Net model achieved an average of 61.46% DSC, with average FP and FN volumes of 1.01 cm^3 and 1.62 cm^3 respectively. The lesion identification performance achieved 1.5, 0.71, and 0.64 for ATP, AFP, and AFN per subject, and 0.64, 0.72, and 0.68 for precision, recall, and F1-score, respectively. Results demonstrate an acceptable degree of overlap between predicted and ground-truth segmentations for a research-stage model. A notable proportion of false positives arose in follow-up scans, largely due to treatment-related inflammation which remains challenging to interpret even for clinicians. ***Conclusion:*** This work presents a deep learning model for lesion delineation in esophageal cancer from ^{18}F-FDG PET/CT, aiming to reduce manual workload and observer variability, while supporting treatment monitoring and response assessment.

EP-1021

Automated NSCLC Segmentation with Deep Learning: Evaluating ^{18}F-FDG PET/CT Volumetric Consistency and Proposing Optimal Thresholdsfor ^{68}Ga-FAPI Quantification

Y. Liu[1], *X. Zhou*[1], *Y. Liu*[1], *Y. Cui*[1], *Y. Song*[1], *Z. Cao*[2], *N. Li*[1];
[1]*Peking University Cancer Hospital, Beijing, CHINA,* [2]*Siemens Healthineers Ltd., Shanghai, CHINA.*

Aim/Introduction: In NSCLC management, PET/CT volumetric metrics exhibit significant prognostic validity yet suffer from quantification inefficiencies. Advanced deep learning models may address these limitations through automated parameter segmentation and calculation. This study aimed to validate the PET Assisted Reporting System (PARS) for ^{18}F-FDG PET/CT auto-segmentation and to explore optimal ^{68}Ga-FAPI PET/CT quantification thresholds in NSCLC. ***Materials and Methods:*** This retrospective study enrolled 50 patients (25 in the early-

stage group and 25 in the late-stage group) undergoing ^{18}F-FDG and ^{68}Ga-FAPI PET/CT (Mar-Dec 2020). Manual and PARS-based segmentations were compared for lesion counts, metabolic tumor volume (MTV), total lesion glycolysis (TLG), and segmentation time for ^{18}F-FDG PET/CT. Six SUV_{max} thresholds (four absolute values: 2.0, 2.5, 3.0, 3.5; two biological references: blood pool and muscle) were evaluated for ^{68}Ga-FAPI PET/CT auto-segmentation. The resulting fibrotic tumor volume (FTV) and total lesion FAPI (TL-FAPI) were compared with the manual segmentation. Quantitative performance assessment was conducted through comparative analysis of mean time expenditure and computation of classification parameters (sensitivity, specificity, accuracy), complemented by Pearson correlation coefficients and Bland-Altman analysis to validate statistical consistency. ***Results:*** For ^{18}F-FDG PET/CT, the PARS threshold showed strong agreement with manual segmentation (sensitivity = 92.0%, specificity = 93.0%, accuracy = 92.8%). MTV_{manual} and TLG_{manual} correlated highly with MTV_{PARS} (r = 0.975, CI [0.954-0.987]) and TLG_{PARS} (r = 0.992, 95% CI [0.985-0.996]). Moreover, segmentation time decreased significantly in the late-stage group (64.0 ± 56.6 vs. 105.0 ± 113.4 seconds, P = 0.032). For ^{68}Ga-FAPI PET/CT, PARS (using SUV_{max} = 3.0) yielded optimal results with the lowest false-positive rate (lesion count: r = 0.964, CI [0.937-0.979]; FTV: r = 0.868, CI [0.775-0.924]; TL-FAPI: r = 0.928, CI [0.874-0.959]). ***Conclusion:*** PARS enabled efficient, accurate ^{18}F-FDG PET/CT segmentation and significantly reduced segmentation computation time in patients with advanced NSCLC at the same time. The optimal SUV_{max} threshold of 3.0 for ^{68}Ga-FAPI PET/CT was determined via PARS-assisted volumetric parameter computation, demonstrating balanced sensitivity and specificity. Integrating deep learning tools into clinical workflows may improve staging accuracy and efficiency.

EP-1022

Comparison of direct Patlak parametric imaging with early and late SUV imaging in metastatic uveal melanoma patients with a long axial field-of-view (LAFOV) PET/CT

L. Pan[1], *C. Sachpekidis*[1], *J. Hassel*[2], *A. Dimitrakopoulou-Strauss*[1];
[1]*German Cancer Research Center, Heidelberg, GERMANY,*
[2]*University Hospital Heidelberg, Heidelberg, GERMANY.*

Aim/Introduction: New Long Axial Field-of-View (LAFOV) PET-CT scanners allow, for the first-time, whole-body (WB) dynamic scanning, as well as WB pharmacokinetic studies and WB parametric imaging. We, herein, aimed to evaluate whether WB direct Patlak imaging is feasible with the LAFOV Biograph Vision Quadra PET/CT system (Siemens Healthineers) (106 cm FOV) and whether it improves lesion detectability compared to 50-60 min and 70-80 min standard uptake value (SUV) images in patients with multiple liver metastases from uveal melanoma prior to tebentafusp therapy, which is a first-in-class TCR-CD3 bispecific immunotherapy. ***Materials and Methods:*** 17 uveal melanoma patients with 89 lesions were enrolled in the study. All patients underwent [^{18}F]FDG PET/CT (skull to upper thigh). Three sets of images were compared: direct Patlak K_i images, 70-80 min SUV (late SUV) images, and 50-60 min SUV (early SUV) images. All three sets of images were visually (qualitatively) reviewed by the reading physicians. Furthermore, 89 individual liver lesions were quantitatively analyzed using the target-to-background (TBR). ***Results:*** No significant differences were observed between the three group of images regarding the number of liver lesions. However, we found two discordant results: two true positive liver lesions were identified on Patlak K_i images, one in each of the two patients, which were not delineated on the SUV images. Quantitatively, parametric imaging showed that direct Patlak K_i images and late SUV images had superior TBR compared to early SUV images (2.3- and 1.3-fold mean increase in TBR, respectively). In addition, Patlak K_i TBR was significantly higher than late SUV images in 81/89 lesions and higher than early SUV images in 88/89 lesions. ***Conclusion:*** Dynamic [^{18}F]-FDG with the new LAFOV PET/CT scanner allows the calculation of Patlak K_i images with better lesion contrast than SUV images, but does not significantly increase the lesion detection rate. In addition, late (70-80 min) SUV images have better contrast than early (50-60-min) SUV images. In a small number of cases, Patlak images revealed discordant findings compared to SUV images, adding further useful clinical information.

EP-1023

Deep Learning-Based Detection and Classification of Thyroid Scintigraphy Images Using Convolutional Neural Networks

I. Rogic[1], *D. Huic*[1,2];
[1]*University Hospital Centre Zagreb, Zagreb, CROATIA,* [2]*School of medicine, Zagreb, CROATIA.*

Aim/Introduction: Artificial intelligence (AI) and convolutional neural networks (CNNs) offer promising tools in the analysis and classification of medical images (1). In this study, we developed a system powered by CNN for automatic analysis and classification of thyroid scintigraphy images. CNNs are deep learning network architectures that showed promise for imaging analysis due to their ability to detect and extract patterns and spatial features, enabling classification and pathology detection. Our pre-trained neural network aims to identify and classify the most common patterns of thyroid scintigram: cold nodule, hot nodule, normal thyroid function, subacute thyroiditis, and multinodular goiter. ***Materials and Methods:*** To process and classify images, a convolutional neural network (CNN) was implemented and trained on DICOM images organised into five categories of thyroid function. Input images were first normalised, resized to 224x224 pixels, and divided into training and validation datasets. We collected 700 thyroid scintigrams from our department as a training cohort and an additional 90 as a validating cohort. To improve model generalisation and performance, data augmentation was applied. The model was trained from scratch using TensorFlow (2) and Keras (3). The system was run with a simple graphical interface built in Streamlit. The interface allows for manual testing of images, classification prediction display, as well as on-the-fly training with new datasets. ***Results:*** The model achieved an overall classification accuracy of 80.25 % in recognising common patterns in thyroid scintigraphy. The highest performance was observed in detecting hot nodules, with an accuracy of 91.6 %, while the lowest was in the detection of normal thyroid function (no nodes or scintigraphic patterns typical for diffuse pathology), with an accuracy of 66.67 %. Our model achieved a negative predictive value (NPV) of 94.7 %, which indicates a high reliability in ruling out pathological findings on thyroid scintigraphy. ***Conclusion:*** Our CNN model showed promising performance in diagnosing thyroid diseases based on thyroid scintigraphy images. The results demonstrate the potential of this approach to assist and improve accuracy in clinical diagnosis of thyroid diseases. Further improvements may be achieved by increasing size of the training cohort, integrating pretrained models such as MobileNet, AlexNet, and ResNet and validation with external datasets. ***References:*** 1. Sarvamangala, et al. Convolutional neural networks in medical image understanding: a survey. Evol Intell. 2022;15(1):1-22. doi: 10.1007/s12065-020-00540-3. 2. Martín A, et al. TensorFlow 2015. Software available from tensorflow.org. 3. Chollet, F, et al. Keras 2015. Software available from https://keras.io.

EP-1024

Decoupling Alzheimer's Disease Pathology from Physiological Uptake in Brain PET via Interpretable Adversarial Decomposition Learning

A. Tang, *C. Tang, W. Ruan, Z. Liang, X. Sun, X. Lan;*
Huazhong University of Science and Technology, Wuhan, CHINA.

Aim/Introduction: Reliable detection of amyloid-β (Aβ) and tau pathology in PET is critical for Alzheimer's disease (AD) diagnosis, yet current quantification relies on semi-quantitative metrics requiring rigid spatial normalization and predefined templates, which fail to address heterogeneous biomarker deposition or visualize pathology. Meanwhile, deep learning models achieve

high diagnostic accuracy but lack interpretability due to "black-box" attributions, hindering clinical trust. Critically, neither approach disentangles AD-specific pathology from confounding physiological/off-target uptake—a key limitation in borderline cases and therapy monitoring. ***Materials and Methods:*** We propose Adversarial Decomposition Learning (ADL), an interpretable framework to isolate AD-related tracer signals under explicit pathophysiological constraints, enabling both visual and quantitative biomarker mapping. Trained on 5,364 Aβ and 1,159 tau scans, ADL employs a U-Net-based decoupler to generate pathology probability maps and a discriminator to classify AD vs. cognitively normal (CN) images. The derived Alzheimer's Disease Adversarial Decomposition (ADAD) score quantifies AD-specific tracer deposition by summing decomposed signals. Performance was validated via AUC analysis, correlations with semi-quantitative metrics (Centiloid/CenTauRz), neuropsychological scores, CSF biomarkers, and hippocampal volume. ***Results:*** ADL achieved superior diagnostic performance (AUC=0.94 for Aβ, 0.98 for tau) on external testing. The ADAD score correlated strongly with Centiloid (R^2=0.64) and CenTauRz (R^2=0.68) but outperformed both in clinical relevance, showing tighter associations with MMSE (ρ=−0.71 vs. Centiloid's ρ=−0.53), CSF Aβ (ρ=−0.68 vs. −0.45), and hippocampal atrophy (ρ=0.62 vs. 0.41, p<0.001). Visual analysis confirmed ADL's precise spatial mapping of Aβ (frontal/precuneus) and tau (parahippocampal/parietal), resolving ambiguities in borderline cases (e.g., Centiloid=39 vs. ADAD=101, flagged as early Aβ deposition). Longitudinal monitoring of anti-Aβ therapy revealed ADAD's sensitivity to treatment effects (post-treatment ADAD=211 vs. Centiloid=69), aligning with slowed cognitive decline. ***Conclusion:*** ADL bridges the interpretability gap in AD PET by enabling pathology-specific decomposition validated against gold-standard semi-quantitative metrics. The ADAD score, harmonizing with Centiloid/CenTauR while offering enhanced clinical correlation, provides a transparent tool for diagnosis, therapy evaluation, and biomarker discovery. This framework advances precision neurology by integrating deep learning with pathophysiological priors.

EP-1025

Classification of Lower Extremity Deep Vein Thrombosis Using Ensemble Deep Learning on Radionuclide Venography

H.-j. Chen[1,2], *C.-Y. Wang*[3], *Y.-H. Huang*[3], *Y.-C. Huang*[2], *S.-Y. Hsu*[1];
[1]*Department of Information Engineering, I-Shou University, Kaohsiung, TAIWAN,* [2]*Department of Nuclear Medicine, Kaohsiung Chang Gung Memorial Hospital, Kaohsiung, TAIWAN,* [3]*Department of Medical Imaging and Radiological Sciences, I-Shou University, Kaohsiung, TAIWAN.*

Aim/Introduction: Deep vein thrombosis (DVT) of the lower extremities and pelvis is a potentially life-threatening condition that requires timely and accurate diagnosis. However, its clinical presentation—such as leg swelling, pain, and edema—is often nonspecific and overlaps with other conditions, making diagnosis challenging. Radionuclide venography serves as a valuable imaging tool, but its interpretation can be limited by variations in image quality. To address this, the present study aimed to develop and evaluate a deep learning-based model for the automated classification of radionuclide venography images, with the goal of enhancing diagnostic consistency and supporting clinical decision-making in cases of suspected DVT. ***Materials and Methods:*** A total of 2,765 radionuclide venography images were retrospectively collected from Kaohsiung Chang Gung Memorial Hospital and categorized into DVT-positive and DVT-negative groups. Four pre-trained convolutional neural networks (ResNet50, DenseNet201, and MobileNetV2) were adapted via transfer learning for model development. The dataset was divided into 80% for training and 20% for testing. Model performance was assessed based on accuracy, precision, and recall. In addition to developing single models, an ensemble learning approach was implemented, combining outputs from these four models using a majority voting mechanism to further improve classification accuracy. ***Results:*** Among the individual models, DenseNet201 achieved the best performance with an accuracy of 0.907, a recall of 0.746, and a precision of 0.977 in a single model. For the ensemble model integrating MobileNetV2, ResNet50, and DenseNet201, the classification results improved, achieving an accuracy of 0.917, a recall of 0.780, and a precision of 0.971. ***Conclusion:*** This study demonstrates that deep learning models are effective in classifying radionuclide venography images for DVT detection. While DenseNet201 performed well individually, the ensemble model further enhanced accuracy and recall. The ensemble model achieved a high precision, but relatively lower recall. It contributes to reducing false positives. Clinically, this characteristic could be valuable for confirming DVT diagnoses with high confidence.

EP-1026

PSMA PET Evaluation with a Deep Learning Platform Compared to a Standard Image Viewer and Histopathology

D. Koehler[1], *F. Shenas*[1], *M. Sauer*[1], *I. Apostolova*[1], *L. Budäus*[2], *F. Falkenbach*[2], *T. Maurer*[2];
[1]*Department of Diagnostic and Interventional Radiology and Nuclear Medicine, University Medical Center Hamburg-Eppendorf, Hamburg, GERMANY,* [2]*Martini-Klinik Prostate Cancer Center, University Hospital Hamburg-Eppendorf, Hamburg, GERMANY.*

Aim/Introduction: Standardized prostate-specific membrane antigen (PSMA) PET/CT evaluation and reporting was introduced to aid interpretation, reproducibility, and communication. Artificial intelligence may further enhance these efforts. The aim of this study was to evaluate the performance of aPROMISE, a deep learning segmentation and reporting software for PSMA PET/CT, compared to a standard PACS viewer (IntelliSpace Portal [ISP]) in patients undergoing salvage PSMA-radioguided surgery. ***Materials and Methods:*** [^{68}Ga]Ga-PSMA-I&T PET/CT of 96 patients with biochemical persistence or recurrence after prostatectomy (median prostate-specific antigen 0.56 ng/ml, interquartile range 0.31 - 1.24) were retrospectively analysed (2 x aPROMISE, 2 x ISP) by two independent readers. Cohens's κ with corresponding 95% confidence intervals were calculated to assess the intra- and inter-rater agreement for T-/N-/M-stagings. Differences between TNM codelines were classified into "no difference", "minor difference" (change of lymph node region without N-/M-change), and "major difference" (T-/N-/M-change). ***Results:*** Intra-rater agreement rates were high for all categories, both readers, and systems (≥91.7%) with moderate to almost perfect κ-values (Reader 1: aPROMISE ≥0.64, 0.41 - 0.99, ISP ≥0.51, 0.21 - 0.9; Reader 2: aPROMISE ≥0.78, 0.63 - 1, ISP ≥0.83, 0.69 - 1). Major differences occurred more frequently for Reader 1 than for Reader 2 (aPROMISE 22.9% vs. 12.5%; ISP 26% vs. 13.5%). Inter-rater agreement rates were high with both systems (≥92.2%), demonstrating substantial κ-values (aPROMISE ≥0.74, 0.54 - 1; ISP ≥0.73, 0.47 - 0.99) with major TNM-staging differences in 21 (21.9%) cases, respectively. In their consensus, readers identified 140 lesions, of which aPROMISE automatically segmented 129 (92.1%). Unsegmented lesions were either adjacent to high urine activity or demonstrated low PSMA expression. Agreement rates between imaging and histopathology were substantial (≥86.5%), corresponding to moderate to substantial κ-values (≥0.6, 0.45 - 1) with major TNM-staging differences in 33 (34.4%) patients. This included 13 (13.5%) cases with metastases distant from targets identified on imaging. One of these lesions was automatically segmented by aPROMISE. ***Conclusion:*** Intra- and inter-reader agreement for PSMA PET/CT evaluation was similarly high with aPROMISE and ISP. The algorithm segmented 92.1% of all identified lesions and a relevant

metastasis that was missed by the readers. Software solutions with artificial intelligence could be applied as support tools in PSMA PET/CT evaluation of early prostate cancer.

EP-62

e-Poster Area

D: Technical Studies -> D2 Data Analysis and Artificial Intelligence -> D23 Image Registration / Fusion

EP-1027

First Real-world Clinical Evaluation of a Deep Learning-based Respiratory Motion Correction Algorithm of ^{18}F-FDG PET/CT in Lung Lesions

J. Wang[1], *J. Wang*[2], *Z. Quan*[1], *Y. Wang*[1], *F. Zhang*[1], *T. Ma*[1], *G. Li*[1], *M. Liu*[1], *Y. Li*[2], *Y. Lu*[2], *F. Kang*[1], *J. Wang*[1];
[1]*Department of Nuclear Medicine, Xijing Hospital, Fourth Military Medical University, Xi'an, Shaanxi, CHINA,* [2]*United Imaging Healthcare, Shanghai, CHINA.*

Aim/Introduction: To evaluate the clinical diagnosis impact of a vendor-provided data-driven solution for respiratory motion correction (uRMC) in lung lesions on the uMI Panorama PET/CT. ***Materials and Methods:*** PET/CT analysis included subjective and quantitative evaluations. Two experienced nuclear medicine physicians independently assessed the overall image quality, PET-CT alignment, and PET distortion of both no motion correction (NMC) and uRMC PET/CT images. Semi-quantitative parameters: a. lesion metabolism [SUVmax, SUVmean, and target-to-background ratios (TBR)]; b. PET-CT lesion alignment [PET-centroid to CT-centroid distance (CCD) was calculated based on the lesion coordinates.]; c. lesion distortion [transverse to longitudinal axis ratio (T/L), and metabolic tumor volume (MTV)]. Percentage changes in semi-quantitative parameters were compared between the two groups based on lesion location compared to the trachea carina. ***Results:*** A total of 136 patients with 165 lung lesions were retrospectively included. Subjective scores were significantly improved in uRMC compared to NMC for overall image quality, PET-CT alignment, and PET distortion (all $P < 0.0001$). The lesion metabolism values were significantly increased in uRMC compared to NMC (SUVmax: 8.46 [5.81, 14.34] vs. 8.40 [5.22, 13.25], SUVmean: 5.75 [3.99, 9.65] vs. 5.60 [3.58, 8.73], TBR: 3.31 [2.25, 5.43] vs. 3.17 [2.18, 5.42], all $P < 0.01$). uRMC detected 28.6% (10/35) more lesions than NMC. Quantitative analyses revealed uRMC reduced CCD by 38.9% with NMC (2.73mm [1.46, 4.67] vs. 4.47mm [2.29, 7.51], $P < 0.0001$), along with completely corrected 88.9% (8/9) fused to the liver in NMC and altered the PET/CT imaging staging determination in 37.1% (33/89) of the lesions. The T/L was significantly larger in uRMC than NMC (0.92[0.84, 1.00] vs. 0.88[0.78, 1.01], $P < 0.01$), achieving comparable quantification accuracy to CT (0.92[0.84, 1.00] vs. 0.94[0.84, 1.00], $P = 0.573$). In addition, the percent changes of metabolism values were higher in lower lung lesions compared to upper lung (median, SUVmax: 14.71% vs. -2.43%, SUVmean: 16.68% vs. -2.43%, TBR: 11.86% vs. -6.92%, all $P < 0.0001$), while MTV showed a significant decrease (median, -2.38% vs. 5.01%, $P < 0.01$). ***Conclusion:*** Compared with NMC, uRMC not only enhances image quality and semi-quantitative metabolic parameters of lung lesions but also reduces CCD and increases T/L of PET to make it close to CT, thus modifying benign/malignant diagnosis and PET/CT imaging staging of lesions. Our findings suggest potential clinical benefits of uRMC for lung lesions, particularly those located in the lower lungs.

EP-1028

A new approach to PET/CT registration which accounts for region-specific motion constraints

J. Schaefferkoetter, *P. Schleyer, M. Conti;*
Siemens Medical Solutions USA, Inc., Knoxville, TN, UNITED STATES OF AMERICA.

Aim/Introduction: A method based on convolutional neural networks (CNN), for inter-modal registration was previously presented for spatially aligning structures across the subject's whole-body (WB), and therefore also improving PET attenuation correction (AC) [1-3]. The limitation of this approach was that elastic registration produces unrealistic deformations for the head, a rigid structure. The work here presents an approach to register WB CT to PET, considering local elastic and rigid constraints. ***Materials and Methods:*** Segmentation was first performed using a dedicated CNN to delineate 2 regions: the body and the head. Then, rigid registration was performed on the head, and elastic registration was performed on the remainder. Elastic registration was performed using a CNN to generate a dense, voxel-wise motion field, and rigid registration used a CNN with image similarity maximization. Once the two motion fields were computed separately, the head segmentation was used to blend them together into a single motion field. ***Results:*** A dedicated testing set of 15 whole-body subjects with multiple PET tracers was used for evaluation. The segmentation was robust for delineating the head from the body, even for challenging cases in which the subjects' hands were touching the top of the head. The subsequent registrations improved misalignments between CT and PET across the whole-body (elastic) and in the head (rigid). Blending the 2 motion fields together produced a smooth and continuous result, with no visible boundaries. The registered CTs improved AC artifacts in the PET reconstruction. ***Conclusion:*** This presents a registration approach which constrained the type of motion based on region-specific physical movement. It leveraged CNNs in a multistep approach, performing segmentation to classify the "elastic" and "rigid" regions, estimating the motion differently for each and then combining them into a single, seamless registration grid. A more extensive evaluation is needed to consider subjects with abnormal morphology or pathology and with different PET tracers. ***References:*** [1] Schaefferkoetter, Joshua, et al. "Deep learning for improving PET/CT attenuation correction by elastic registration of anatomical data." European Journal of Nuclear Medicine and Molecular Imaging 50.8 (2023): 2292-2304. [2] Dias, André H., et al. "Validation and clinical impact of motion-free PET imaging using data-driven respiratory gating and elastic PET-CT registration." European journal of nuclear medicine and molecular imaging (2024): 1-13. [3] Chamberlin, Jordan H., et al. "Clinical Pilot of a Deep Learning Elastic Registration Algorithm to Improve Misregistration Artifact and Image Quality on Routine Oncologic PET/CT." Academic Radiology 32.2 (2025): 1015-1025.

EP-1029

Improving data-driven gated (DDG) PET and CT registration in thoracic lesions: a comparison of AI registration and DDG CT

T. Pan[1], *M. A. Thomas*[2], *Y. Lu*[1], *D. Luo*[1];
[1]*The University of Texas, Houston, TX, UNITED STATES OF AMERICA,* [2]*Washington University School of Medicine, St. Louis, MO, UNITED STATES OF AMERICA.*

Aim/Introduction: Misregistration between CT and PET can result in mis-localization and inaccurate quantification of the tracer uptake in PET. Data-driven gated (DDG) CT can correct registration and quantification but requires a radiation dose of 1.3 mSv and 1 minute of acquisition time. AI registration (AIR) does not require an additional CT and has been validated to improve registration and

reduce the 'banana' misregistration artifacts around the diaphragm. We aimed to compare a validated AIR and DDG CT in registration and quantification of avid thoracic lesions misregistered in DDG PET scans. ***Materials and Methods:*** Thirty PET/CT patient data (23 with ^{18}F-FDG, 4 with ^{68}Ga-Dotatate, and 3 with ^{18}F-PSMA piflufolastat) with at least one misregistered avid lesion in the thorax were recruited. Patient studies were conducted using DDG CT to correct misregistration with DDG PET data of the phases 30 to 80% on GE Discovery MI PET/CT scanners. A maximum of three lesions per patient were selected for comparison. Non-attenuation correction DDG PET and misregistered CT were input to AIR and the AIR-corrected CT data were output to register and quantify the DDG PET data. Registration quality and quantification of lesion SUV_{max} and signal-to-background ratios (SBR) were compared for each of the 51 avid lesions. ***Results:*** DDG CT outperformed AIR in misregistration correction and quantification of avid thoracic lesions. The sizes of this cohort of lesions were 1.16±0.45 cm. Most lesions (46/51, 90%) showed improved registration from DDG CT relative to AIR, with 10% (5/51) being similar between AIR and DDG CT. AIR increased SUV_{max} by 18.1±15.3%, while DDG CT increased it by 34.4±25.4% (P=0.0002). There was a statistically significant increase of SBR between AIR 10.5±12.1% and DDG CT 21.1±20.5% (P=0.0021). Many registration improvements by AIR were still left with misregistration. AIR incorrectly localized one infra-hilar lymph node to the lung parenchyma, one para-aortic lymph node to the vertebral body, and one supradiaphragmatic lymph node to the ribs. AIR also consistently distorted the rib cage. ***Conclusion:*** DDG CT outperformed AIR in both localization and quantification of the thoracic avid lesions. Registered lymph nodes could be falsely misregistered by AIR. AIR-induced distortion of the rib cage can also negatively impact image quality. Further research on AIR's accuracy in modeling true patient respiratory motion without introducing new misregistration or anatomical distortion is warranted. ***References:*** 1. Schaefferkoetter, et al., Deep learning for improving PET/CT attenuation correction by elastic registration of anatomical data. EJNMMI, 2023.

EP-1030

Improved attenuation correction registration for FDG PET/CT images using data-driven gating (DDG)-based motion match.

Z. Wilson[1], *M. Kuhar*[2], *K. Su*[3], *R. Johnsen*[3], *K. M. Bradley*[4,1], *D. McGowan*[1,5];
[1]*Oxford University Hospital NHS FT, Oxford, UNITED KINGDOM,* [2]*University Hospital Southampton NHS, Southampton, UNITED KINGDOM,* [3]*GE HealthCare, Waukesha, WI, UNITED STATES OF AMERICA,* [4]*Cardiff University, Cardiff, UNITED KINGDOM,* [5]*University of Oxford, Oxford, UNITED KINGDOM.*

Aim/Introduction: Advancements in PET technologies and reconstruction methods have improved spatial resolution and noise in PET/CT, making respiratory motion artefacts more impactful on image quality. The motion-matched CT (MMCT) algorithm can phase-match a helical CT to the end expiration of a ground truth 4DCT, as shown in FMISO data [1]. The MMCT-attenuation correction (MMCTAC) will then be used to reconstruct whole body FDG PET/CT data. The performance of these images will be compared to those reconstructed using the uncorrected clinical standard attenuation correction from helical CT (normAC), identifying the proportion of cases where MMCTAC images could reduce motion artefact and improve lesion detectability. ***Materials and Methods:*** This study analysed a sequential cohort of 145 whole-body FDG scans. PET images were previously assessed for a data-driven gating study, identifying the gated region of interest (ROI) in 98 high-motion patients (R>15) [2]. 23 of these high motion patients had lesions (n=36) identified in the ROI by a clinician to undergo qualitative analysis. PET data were reconstructed using BSREM iterative reconstruction with 3 different portions of the data: 1. Ungated 6 minutes, 2. Ungated 3 minutes, 3. Quiescent period gated. These reconstructions were generated using normAC or MMCTAC, totalling 6 reconstructions for semi-quantitative analysis and clinician assessment. An experienced radiologist ranked the 6 images and scored them on a 5-point Likert Scale for lesion detectability, diagnostic confidence, and image quality. ***Results:*** In 65% (n=15) of the patients with lesions, the clinician ranked all three MMCTAC images higher than the three normAC equivalent reconstructions. Lesion detectability and diagnostic confidence scores retained positive mean differences across the three MMCTAC reconstructions compared to normAC. Similarly, the SUVmax values compared across the 6 reconstructed images for 36 lesions demonstrated a significant increase ($p<0.05$) for MMCTAC versus normAC images across all three reconstructions. ***Conclusion:*** The MMCT algorithm successfully enables the phase-matching of a helical CT to the PET data to reduce the presence of respiratory motion artefact for FDG PET/CT images. Overall, the motion matched CTAC image scores demonstrated the algorithm's efficacy at reducing the motion artefacts present in FDG PET/CT images, improving diagnostic capability for assessment of lesions in the thorax and upper abdomen. ***References:*** [1] Cook, E.L. et al. Data-driven gating (DDG)-based motion match for improved CTAC registration. EJNMMI Phys 11, 42 (2024). https://doi.org/10.1186/s40658-024-00644-0 [2] Walker, M.D. et al. Data-Driven Respiratory Gating Outperforms Device-Based Gating for Clinical ^{18}F-FDG PET/CT. J Nucl Med. 2020 Nov;61(11):1678-1683. doi: 10.2967/jnumed.120.242248.

EP-1031

Integrating PET/CT Imaging and Machine Learning to Enhance Early Diagnosis of Pulmonary Nodules in various types of cancers

N. Kapsoritakis[1], *F. Tsitoura*[2], *G. Barmparis*[2], *S. Koukouraki*[1], *G. Tsironis*[2];
[1]*Nuclear Medicine Department, Medical School Univercity of Crete, Heraklion, Crete, GREECE,* [2]*Department of Physics, Medical School, University of Crete, Heraklion, Crete, GREECE.*

Aim/Introduction: Differentiating benign from malignant solitary pulmonary nodules (SPNs) remains a major challenge in thoracic oncology. Traditional PET/CT metrics like Standardized Uptake Value (SUV), Metabolic Tumor Volume (MTV), and Tumor Lesion Glycolysis (TLG) offer limited diagnostic accuracy, requiring biopsy for confirmation. This project aims to enhance diagnostic precision by extracting features from PET-CT fusion images and combining them with clinical data and quantitative measures. Using machine learning (ML), we seek to improve early, non-invasive prediction and support timely clinical decisions. ***Materials and Methods:*** Early (1hr) and delayed phase (2hrs) p.i 18F F FDG PET-CT scans were acquired in 91pts with PNs using a digital PETCT (GE discovery MI4R Gen 2). A region of interest (ROI) was drawn over the lesion with high metabolic activity in both PET scans . Metabolic metrics such as SUV, TLG, and MTV were measured and recorded for each nodule. In addition, morphological characteristics, including size and density, were also incorporated into the dataset. Following ROI extraction, advanced image processing techniques were applied to derive radiomic features. The most important features were identified using a Random Forest classifier and were primarily related to first-order statistics and texture analysis. The final dataset consisted of 90 records, each representing a unique patient nodule, with a total of 20 features per record. These included the selected radiomic features, clinical data, and metabolic and morphological characteristics. ***Results:*** Several ML models—including SVM, Random Forest, Gradient Boosted Trees, and XGBoost—were evaluated to predict biopsy outcomes. Hyperparameters were optimized using grid search with cross-validation. Gradient Boosted Trees achieved the best performance, with 95% accuracy when radiomic features were

included, compared to 82% without, highlighting their significant contribution to predictive accuracy. ***Conclusion:*** Incorporating image-derived information, significantly improves the model's ability to distinguish between benign and malignant SPNs, with a 15% increase in accuracy. This highlights the value of combining image-derived features with clinical data for more accurate, non-invasive diagnosis.

EP-63

e-Poster Area

D: Technical Studies -> D2 Data Analysis and Artificial Intelligence -> D24 Outcome Prediction

EP-1032

The Impact of Post-reconstruction Filtering on Radiomics-Based Coronary Artery Disease Prediction Using Myocardial Perfusion SPECT

R. Huang[1,2], *B. Wang*[1,2], *M. Gutierrez*[3], *G. Hung*[4], *G. Mok*[1];
[1]*Biomedical Imaging Laboratory (BIG), Department of Electrical and Computer Engineering, Faculty of Science and Technology, University of Macau, Macau SAR, MACAO,* [2]*Lauterbur Research Center for Biomedical Imaging, Shenzhen Institute of Advanced Technology, Chinese Academy of Sciences, Shenzhen, CHINA,* [3]*Biomedical Informatics Lab, Heart Institute, University of São Paulo Medical School, São Paul, BRAZIL,* [4]*Department of Nuclear Medicine, Chang Bing Show Chwan Memorial Hospital, Changhua, TAIWAN.*

Aim/Introduction: Myocardial perfusion (MP) SPECT is an effective diagnostic tool for coronary artery disease (CAD), yet concerns remain regarding its high radiation dose and long acquisition time. Low dose and fast SPECT are desirable without jeopardizing image quality. Post-reconstruction filter is commonly applied on clinical MP SPECT images to reduce noise and enhance image quality. This study aims to investigate the effect of using post-reconstruction filter on full-view and sparse-view MP SPECT images for radiomics-based CAD prediction. ***Materials and Methods:*** We retrospectively analyzed SPECT/CT data of 212 patients who underwent a one-day ^{99m}Tc-sestamibi stress/rest protocol using a conventional dual-head NaI SPECT/CT scanner, with invasive coronary angiography (ICA) conducted within 90 days following the scan. Different projection views, i.e., 64 (Full-Projection, FP), 32 (Half-Projection, HP) and 8 (one-Eighth Projection, EP) projections, were reconstructed using OS-EM algorithm (6 iterations, 8 subsets) with CT-based attenuation correction. Reconstructed stress images were processed by Gaussian filters with varying standard deviations (σ, 0.5 to 5.0 voxels, 0.5 voxel interval) and converted into polar plots, which were split into 8:2 for training and testing. All polar plots were segmented into regions-of-interest (ROI) of left anterior descending artery (LAD), right coronary artery, and left circumference. A total of 558 radiomics features were extracted for each ROI before feature selection using Least Absolute Shrinkage and Selection Operator regression and Recursive Feature Elimination. Features were adaptively input for training from different ROIs based on the ICA diagnosis, while testing was performed using features solely from the LAD ROI [1]. Prediction models were constructed using logistic regression with five-fold cross-validation and evaluated using the area under the receiver operating characteristic curve (AUC) and accuracy (ACC). ***Results:*** AUC/ACC values of all datasets initially increased and then subsequently decreased with increasing σ. FP, HP and EP achieved their optimal performance with σ of 1.0 voxel (AUC: 0.84, ACC: 0.78), 2.0 voxels (AUC: 0.81, ACC: 0.76) and 2.5 voxels (AUC: 0.78, ACC: 0.73) respectively. AUC/ACC values of FP consistently surpass those of HP and EP for different σ. ***Conclusion:*** Optimal post-reconstruction filtering can enhance diagnostic accuracy for radiomics-based CAD prediction models using MP SPECT. Funding: This work was supported by the Science and Technology Development Fund of Macau 0016/2023/RIB1. ***References:*** [1] Wang, B., et al., Prediction of Coronary Artery Stenosis Using Myocardial Perfusion Stress/Rest SPECT: a Radiomics Study. Journal of Nuclear Medicine June 2024, 65 (supplement 2) 241178.

EP-1033

AI for Cardiac PET Imaging: Predicting Summed Rest Scores Using Stress PET Image

M. Mokri[1], *D. Juneau*[1], *A. Sanaat*[2], *S. Kaviani*[1], *C. Cohalan*[3], *M. Léger*[3], *J. Carrier*[1];
[1]*University of Montreal, Montreal, QC, CANADA,* [2]*Geneva University Hospital, Geneva, SWITZERLAND,* [3]*Hospital Center of University of Montreal, Montreal, QC, CANADA.*

Aim/Introduction: Myocardial perfusion imaging (MPI) with ^{13}N-ammonia PET enables high-resolution assessment of coronary artery disease (CAD) through stress and rest imaging. However, the two-phase protocol increases radiation dose, prolongs imaging time, and burdens clinical workflows. This study proposes an AI-based approach to predict the Summed Rest Score (SRS) directly from stress-phase images, aiming to eliminate the need for rest-phase acquisition while maintaining diagnostic accuracy. ***Materials and Methods:*** Dynamic ^{13}N-ammonia PET-CT scans were collected from 280 patients. For each scan, polar maps were generated from reconstructed 3D stress-phase PET data using the 17-segment model established by the American Society of Nuclear Cardiology. These maps were annotated by nuclear medicine specialists to assign segmental scores, from which the Summed Stress Score (SSS) and Summed Rest Score (SRS) were derived. Four deep convolutional neural networks _ResNet-50, ResNet-101, VGG19, and VGG11-bn _were adapted for this task using transfer learning from pretrained medical imaging models. Each network was trained to predict the SRS from the stress-phase image, incorporating the SSS as an auxiliary input to enhance performance. An ensemble model was then constructed by averaging the predictions of all four networks to improve robustness and generalizability. Model performance was assessed using mean absolute error (MAE), root mean square error (RMSE), and classification accuracy across four infarction severity categories. ***Results:*** The ensemble model achieved the highest clinical performance with an MAE of 0.09, RMSE of 0.18, and classification accuracy of 94.1%. ResNet-101 was the best-performing individual model (accuracy = 89.3%).Importantly, the ensemble predicted infarction severity with high clinical fidelity: sensitivity ranged from 96% to 100% and specificity from 98% to 99% across all infarction categories. enhanced model robustness, especially for borderline cases of mild-to-moderate infarction. Inclusion of the SSS improved accuracy by 5 to 10%; for example, ResNet-101 rose from 80.2% to 89.3% with SSS integration. Classification analysis across infarct severity categories further validated the clinical applicability of the proposed method. The ensemble model correctly identified "No Infarct" and "Mild Infarct" cases with 100% sensitivity, while achieving sensitivities of 97% and 96% for "Moderate" and "Heavy Infarct" groups, respectively. Specificity exceeded 98% across all categories. ***Conclusion:*** In conclusion, the proposed ensemble learning framework shows strong potential for accurately predicting SRS from stress-phase ^{13}N-ammonia PET scans. This approach may support the adoption of single-phase imaging protocols by reducing the need for rest acquisitions, thereby lowering radiation exposure and streamlining clinical workflows.

EP-1034

Quantifying the relationship between [^{177}Lu]Lu-PSMA-I&T exposure and neutrophil dynamics using a population pharmacokinetic-pharmacodynamic analysis

D. van Asten[1,2], *M. Dotinga*[2], *B. J. de Wit-van der Veen*[2], *A. D. R. Huitema*[1,3,4], *H. Huisman-Siebinga*[1,2];
[1]*Department of Pharmacy & Pharmacology, The Netherlands Cancer Institute, Amsterdam, NETHERLANDS,* [2]*Department of Nuclear Medicine, The Netherlands Cancer Institute, Amsterdam, NETHERLANDS,* [3]*Department of Clinical Pharmacy, University Medical Center Utrecht, Utrecht University, Utrecht, NETHERLANDS,* [4]*Department of Pharmacology, Princess Máxima Center for Pediatric Oncology, Utrecht, NETHERLANDS.*

Aim/Introduction: [^{177}Lu]Lu-PSMA is a radioligand therapy that prolongs survival in metastatic castration-resistant prostate cancer (mCRPC) patients. While well tolerated, some patients experience dose-limiting hematological toxicities, potentially due to considerable variability in bone exposure. This study aimed to quantify the impact of [^{177}Lu]Lu-PSMA-I&T exposure in bones and bone metastases on neutrophil levels using a semi-physiological population pharmacokinetic-pharmacodynamic (PK-PD) model. ***Materials and Methods:*** SPECT/CT scans (4h, 24h, 6 days post-treatment) and neutrophil counts (up to 3 months post-treatment) were retrospectively collected from mCRPC patients receiving 1-8 cycles of ~7.4 GBq [^{177}Lu]Lu-PSMA-I&T (September 2019-March 2024). Organ (aorta, bones, kidneys, salivary glands) and tumor segmentation was performed semi-automatically using MIM (version 7.3.6) to obtain volumes (L) and mean uptake (MBq/mL) in organs and tumors (≥2.5mL). An existing PK-model (NONMEM 7.5) was optimized with seven compartments representing blood, salivary glands, kidneys, bones, bone metastases, other tumors and a rest compartment[1]. Structural parameters included volume of distribution (V_1), renal excretion (k_{10}) and rate constants (k_{in}, k_{out}) between compartments. A previously developed PD-model was sequentially used to link bone PK (healthy and metastatic tissue) to neutrophil data and included a delayed linear or sigmoidal effect-relationship, resulting in reduced neutrophil proliferation[2]. The model was used for simulations (n=1000) to predict clinically relevant neutropenia (≤1.5×10^9/L) compared to observations. ***Results:*** Data from 139 patients were analyzed (average 3.2 cycles). The PK-model demonstrated good fit and precision (RSEs<20%). Uptake rates varied between compartments, with relative faster rates for bone metastases and kidneys (0.041 and 0.044h^{-1}) and slower rates for salivary glands, other tumors and healthy bone (0.005, 0.009, 0.023h^{-1}, respectively). High inter-individual variability (IIV) was estimated for uptake in bones, bone metastases and other tumors (145%, 67%, 79%, respectively). A linear PK-PD relationship best captured neutrophil dynamics, with a baseline neutrophil count of 4.2×10^9/L (41% IIV). The estimated impact of [^{177}Lu]Lu-PSMA-I&T (slope: 0.00106 MBq^{-1}) led to a maximum neutrophil proliferation reduction of 15% (median 1.8%). Simulations predicted a median 6.6% of patients (80% prediction-interval: 4.4%-9.5%) would experience clinically relevant neutropenia, aligning with the observed 7.2% (≤1.5×10^9/L). These results demonstrate the feasibility of predicting individual neutrophil levels. ***Conclusion:*** Our PK-PD model quantified the [^{177}Lu]Lu-PSMA-I&T exposure-neutrophil relationship of mCRPC patients, highlighting substantial variability in bone exposure and feasibility of predicting individual neutrophil levels. These findings suggest that with further optimization the model could help predict neutropenia from first-cycle data and establish toxicity thresholds to guide personalized treatment. ***References:*** [1]Siebinga et al.EJNMMI-Phys.2024;11(1):39,[2] Friberg et al.JClinOncol.2002;20(24):4713-21.

EP-1035

[^{18}F]FET PET Radiomics-Based Prediction of IDH Mutation Status in Glioma Patients: Impact of Inter-scanner Harmonisation, Clinical Data and Integration of [^{18}F]FET-negative Cases

A. Zounek[1], *E. Barci*[1], *E. Istrefi*[1], *J. Isakaj*[1], *K. J. Mueller*[2], *M. J. Mair*[1,3], *I. von Polenz*[1], *S. Ziegler*[4,1], *N. L. Albert*[1,5,6], *L. Kaiser*[1];
[1]*Department of Nuclear Medicine, LMU University Hospital, LMU Munich, Munich, GERMANY,* [2]*Department of Neurology, LMU University Hospital, LMU Munich, Munich, GERMANY,* [3]*Division of Oncology, Department of Medicine I, Medical University of Vienna, Vienna, AUSTRIA,* [4]*Department of Nuclear Medicine, Hannover Medical School (MHH), Hannover, GERMANY,* [5]*German Cancer Consortium (DKTK), Partner Site Munich, a partnership between German Cancer Research Center (DKFZ) and LMU Munich, Munich, GERMANY,* [6]*Bavarian Cancer Research Center (BZKF), Partner Site Munich, Munich, GERMANY.*

Aim/Introduction: Accurate assessment of Isocitrate dehydrogenase (IDH) mutation status plays a critical role in the clinical management of glioma patients. This study aims to apply a machine learning (ML) model for non-invasive prediction of IDH mutation status using O-(2-[^{18}F]fluoroethyl)-L-tyrosine ([^{18}F]FET) PET radiomics combined with patient age and sex, and to evaluate the impact of scanner harmonisation and inclusion of [^{18}F]FET-negative cases on model performance. ***Materials and Methods:*** [^{18}F]FET PET and multimodal MRI data (T1, contrast-enhanced T1, T2, and FLAIR) from 507 glioma patients were retrospectively analysed. PET images from two different PET/CT systems were reconstructed as late static scans (20-40 min post-injection). Tumour delineation was performed according to PET RANO 1.0 criteria using a semi-automatic threshold-based method on the PET data [1]. Volumes of interest smaller than image resolution were defined as [^{18}F]FET-negative and replaced by MRI-based VOIs generated via BraTS-toolkit. PET radiomic features were extracted using pyradiomics. Scanner-related variability was addressed through ComBat harmonisation. A nested ML pipeline was applied using 50-repeated 5-fold cross-validation with stratification by scanner and IDH mutation status. Input features included radiomics, patient age, and sex. Ground truth IDH status was determined by neuropathological analysis of tissue samples. Model performance was assessed via area under the ROC curve (AUC) and compared across multiple factors: inter-scanner harmonisation, inclusion of [^{18}F]FET-negative patients, and inclusion of patient sex and age as predictive variables. ***Results:*** Across all experimental conditions, ComBat harmonisation led to improved AUC scores, though the magnitude of improvement varied. The highest overall AUC of 85% was observed in the harmonised [^{18}F]FET-positive subgroup with the inclusion of age. Including [^{18}F]FET-negative patients (n=94) generally improved model performance across most settings, particularly for unharmonised data. However, when using harmonised features and including patient age, performance slightly decreased to 83% compared to using [^{18}F]FET-positive cases only. Inclusion of patient sex had negligible effect on predictive accuracy, with AUC differences consistently below 0.2%. ***Conclusion:*** This study demonstrates that ComBat is effective in reducing scanner-related variance by improving performance for non-invasive prediction of IDH mutation status in glioma patients. However, its impact was less pronounced after the inclusion of [^{18}F]FET-negative patients, indicating that harmonisation efficacy may be limited in more heterogeneous cohorts. Inclusion of patient sex did not enhance model performance. These findings suggest that harmonisation strategies should be applied in radiomics-based prediction frameworks for neuro-oncology to improve generalizability across scanning devices. ***References:*** [1]Albert et al., PET-based_response_assessment_criteria_for_diffuse_gliomas(PET_RANO1.0):a_report_of_the_RANO_group. Lancet Oncol.2024;25(1):e29-e41.

EP-1036

Genetic algorithm vs. gradient descent for training a novel neural network architecture with low trainable parameters count for small datasets

A. Boukhari[1,2], *B. Ecsedi*[3,4], *Z. Ritter*[5], *L. Papp*[4], *M. Hatt*[1,2];
[1]*Laboratory of medical information processing (LaTIM), Brest, FRANCE,* [2]*University of Western Brittany, Brest, FRANCE,* [3]*Georga Institute of Technology, Atlanta, GA, UNITED STATES OF AMERICA,* [4]*University of Vienna, Vienna, AUSTRIA,* [5]*Medical University of Pécs, Pécs, HUNGARY.*

Aim/Introduction: Distance-encoding biomorphic-informational neural network (DEBINN) is a novel architecture where neurons' 3D coordinates are trained via a genetic algorithm (GA) and the distance between neurons define weights. It matches the performance of classical NNs while requiring fewer parameters, making it especially effective for small datasets[1]. Since gradient

descent (GD) remains the prevailing optimization method for NN, our objective was to design and evaluate a GD for DEBI-NN. ***Materials and Methods:*** We compared GD with GA in a nonlinear synthetic dataset (2 interleaving halfcircles) and 2 PET/CT radiomics datasets: outcome prediction in DLBCL (train=41, test=44) [2] and HPV classification in HECKTOR (train=158, test=74) [3]. As DEBI-NN neurons are arranged in 3D space and connections depend on interneuronal distances, standard backpropagation is not directly applicable. Hence, we designed and implemented a modified backpropagation procedure that accounts for the spatial dependencies between neurons and ensures correct propagation of gradients. Both GA and GD were optimized in each dataset by exploring a large range of hyperparameters and configurations. All reported performance metrics were computed on test sets. ***Results:*** GA consistently outperformed GD. In the synthetic data, although GD achieved 83% balanced accuracy (BAcc) (84% sensitivity, 82% specificity), it failed to fully capture the nonlinear patterns. In contrast, GA classified all samples with BAcc of 100%. In DLBCL, GA achieved a BAcc of 83% (sensitivity 86%, specificity 80%), vs. 78%, 79%, and 77% for GD. In HECKTOR, GA reached 80% BAcc (sensitivity 60%, specificity 100%), while GD obtained 66%, 58%, and 74%, respectively. ***Conclusion:*** Our results suggest that GA is more appropriate for training DEBI-NN than GD. This may be explained by the structural constraints of DEBINN, where neurons are interdependent due to their spatial configuration. Modifying the weight of a single connection affects all other weights in the same layer, making optimization using gradientbased methods more complex. These dependencies make the DEBINN architecture more suitable for evolutionary approaches such as GA. ***References:*** 1)Papp, Laszlo, et al. "DEBINN: Distanceencoding biomorphicinformational neural networks for minimizing the number of trainable parameters." Neural Networks 167 (2023): 517-532.2)Ritter, Zsombor, et al. "Twoyear eventfree survival prediction in DLBCL patients based on in vivo radiomics and clinical parameters." Frontiers in Oncology 12 (2022): 820136.3) Andrearczyk, Vincent, et al. "Overview of the HECKTOR challenge at MICCAI 2022: automatic head and neck tumor segmentation and outcome prediction in PET/CT." 3D Head and Neck Tumor Segmentation in PET/CT Challenge. Cham: Springer Nature Switzerland, 2022. 1-30.

EP-1037

Obstructive Coronary Artery Disease Prediction from Myocardial Perfusion SPECT: Radiomics vs. Deep Learning

G. Mok[1], *B. Wang*[1,2], *Y. Du*[3], *C. Lin*[4], *J. Shang*[5], *C. Li*[6,7], *X. Hao*[5], *L. Hu*[6,8], *G. Hung*[9];
[1]*Biomedical Imaging Laboratory (BIG), Department of Electrical and Computer Engineering, Faculty of Science and Technology, University of Macau, Macau SAR, MACAO,* [2]*Lauterbur Research Center for Biomedical Imaging, Shenzhen Institute of Advanced Technology, Chinese Academy of Sciences, Shenzhen, CHINA,* [3]*Department of Nuclear Medicine, The First Affiliated Hospital of Army Medical University, Chongqing, CHINA,* [4]*Department of Nuclear Medicine, Show Chwan Memorial Hospital, Changhua, TAIWAN,* [5]*Department of Nuclear Medicine and PET/CT-MRI Centre, The First Affiliated Hospital of Jinan University, Guangzhou, CHINA,* [6]*Department of Nuclear Medicine, Taipei Veterans General Hospital, Taipei, TAIWAN,* [7]*Department of Biomedical Imaging and Radiological Sciences, National Yang Ming Chiao Tung University, Taipei, TAIWAN,* [8]*School of Medicine, National Yang Ming Chiao Tung University, Taipei, TAIWAN,* [9]*Department of Nuclear Medicine, Chang Bing Show Chwan Memorial Hospital, Changhua, TAIWAN.*

Aim/Introduction: Radiomics model (RM) and deep learning (DL) are two artificial intelligence approaches for obstructive coronary artery disease (CAD) predictions. This study aims to compare their invasive coronary angiography (ICA) outcome predictive performance from myocardial perfusion (MP) SPECT. ***Materials and Methods:*** We retrospectively enrolled 515 patients from 3 centers (primary: 212, external-1: 108, external-2: 195) undergoing a one-day ^{99m}Tc-sestamibi or ^{201}Tl stress/rest SPECT protocol. ICA was performed within 90 days following the MP SPECT. The primary dataset with CT-based attenuation correction was split into 7:1:2 for training, validation and testing, while both external datasets with DL-based attenuation correction were tested. Five-fold cross validation was performed to test all datasets in the primary dataset. For RM, polar plots were segmented into regions-of-interest (ROI) of left anterior descending (LAD), right coronary artery (RCA), and left circumference (LCx). Stress and rest polar plots were stacked as 2-channel input with 903 radiomics features (RF) extracted, followed by Least Absolute Shrinkage and Selection Operator regression and Recursive Feature Elimination for feature selection and logistic regression for classification. For per-patient analysis, RF extracted from the adaptive ROI defined based on ICA diagnosis of the primary dataset were used for training, while RF from the LAD ROI were input for testing. For per-vessel analysis, RM were trained on RF extracted from the LAD, RCA and LCx ROIs, and tested on each ROI respectively. For DL, a 2D DenseNet was trained for per-patient analysis and a multi-input multi-output DenseNet was trained for per-vessel analysis, with the same 2-channel polar plot data without segmentation as input. Area under the receiver operating characteristic curve (AUC) and accuracy (ACC) were assessed for different models on all datasets. Delong's test was employed to compare the ROC curves of RM and DL. ***Results:*** For per-patient analysis, RM (28 RF) achieved AUC/ACC of 0.85/0.82, 0.68/0.67 and 0.66/0.65 for the primary, external-1 and external-2 datasets, while DL achieved 0.83/0.85 (p=0.462), 0.66/0.68 (p=0.136) and 0.68/0.69 (p=0.010) respectively. For per-vessel analysis, RM (19 RF) achieved AUC/ACC of 0.74/0.73, 0.65/0.63 and 0.61/0.63 for the primary, external-1 and external-2 datasets, while DL achieved 0.74/0.76 (p=0.572), 0.62/0.66 (p=0.129) and 0.65/0.72 (p=0.024) respectively. ***Conclusion:*** RM shows comparable performance as compared to DL for obstructive CAD prediction using stress/rest MP SPECT. This work was supported by the Science and Technology Development Fund of Macau (0178/2024/AMJ).

EP-1038

Radiomic Analysis of Tumor Invasiveness and Staging in Nasopharyngeal Carcinoma Using a FAPI PET/CT Dataset

D. Ruan[1], *Z. Luo*[1], *R. Su*[1], *W. Zhou*[2], *L. Yu*[1], *J. Cai*[1], *Q. Lin*[1], *L. Zhao*[1], *Y. Pang*[1], *L. Sun*[1], *H. Ye*[2], *H. Chen*[1];
[1]*The First Affiliated Hospital of Xiamen University, School of Medicine, Xiamen University, Xiamen, CHINA,* [2]*Hunan Cancer Hospital/The Affiliated Cancer Hospital of Xiangya School of Medicine, Central South University, Changsha, CHINA.*

Aim/Introduction: The tumor immune microenvironment has clinicopathological significance for assessing tumor invasiveness and predicting metastasis. Quantitative imaging biomarkers facilitate robust, reproducible, and reliable in vivo assessments of tumor heterogeneity, offering critical insights into tumor growth, metabolism, metastasis, and treatment response. Radiomics, the high-throughput extraction of quantitative imaging features, has gained significant attention as a noninvasive tool for predicting cancer outcomes and informing therapeutic strategies. However, effective imaging biomarkers for predicting tumor invasiveness and metastasis potential remain lacking. This study aimed to analyze ^{68}Ga-FAPI-46 PET/CT radiomic data to identify features that differentiate nasopharyngeal carcinoma (NPC) with varying levels of invasiveness. ***Materials and Methods:*** ^{68}Ga-FAPI-46 PET/CT images of NPC patients were preprocessed to extract radiomic features, including first-order, texture, and shape features from the primary tumor. Six machine learning models: Logistic Regression, Random Forest, XGBoost, Naive Bayes, Support Vector Machine, and KNN, were employed to classify the T, N, and M stages of

NPC. A training set (n = 137) was used for model training and an external test set (n = 53) for evaluation. Metrics included accuracy, sensitivity, specificity, and AUC. The best-performing model was analyzed for interpretability. ***Results:*** Image-interpolated_Mean of ^{68}Ga-FAPI-46 PET images was a key feature for assessing tumor infiltration, while original_shape_Elongation was a significant predictor of lymph node and distant metastasis. A retrospective analysis of 190 treatment-naïve NPC patients revealed that ^{68}Ga-FAPI-46 PET/CT radiomic features exhibited strong predictive performance for the T stage, with 86% (24/28) [67%-96%] sensitivity, 88% (22/25) [69%-97%] specificity, 87% (46/53) [75%-95%] accuracy, and an AUC of 0.94 [0.87-0.94]. For the N stage, sensitivity was 86% (36/42) [71%-95%], specificity was 73% (8/11) [39%-94%], accuracy was 83% (44/53) [70%-92%], and AUC was 0.88 [0.77-0.99]. The M stage showed 50% (3/6) [12%-88%] sensitivity, 100% (47/47) [92%-100%] specificity, 94% (50/53) [84%-99%] accuracy, and an AUC of 0.76 [0.51-0.76]. ***Conclusion:*** This exploratory study highlights the feasibility of ^{68}Ga-FAPI-46 PET/CT radiomic analysis in assessing NPC invasiveness and predicting metastasis potential. However, further validation using larger and more balanced datasets is required to confirm these findings. Despite these challenges, this study successfully identified key radiomics features that significantly contribute to NPC stage classification.

EP-1039

Prediction of EGFR Mutation Status and Subtypes in Lung Adenocarcinoma Using PET/CT Deep Learning stacked with Radiomics

L. Huang[1], *J. Liu*[1], *J. He*[2], *Y. Luo*[1];
[1]The Second Hospital & Clinical Medical School, Lanzhou University, Lanzhou, CHINA, [2]Lanzhou University of Finance and Economics, Lanzhou, CHINA.

Aim/Introduction: Targeted therapy is the standard treatment for patients with advanced lung cancer, and the mutation status and subtypes of epidermal growth factor receptor (EGFR) gene is a key factor in predicting efficacy. This study aimed to develop and validate deep learning models using PET/CT imaging to predict EGFR mutation status and two sensitive mutation subtypes (exon 19 deletion and 21L858R point mutation) in patients with lung adenocarcinoma. ***Materials and Methods:*** A total of 117 patients with pathologically confirmed lung adenocarcinoma who underwent EGFR mutation testing and ^{18}F-FDG PET/CT scans were included. Patients were divided into training (70%) and validation (30%) cohorts using randomized stratified sampling. A residual network was used to develop models for four tasks: predicting EGFR mutation status (Task 1), distinguishing wild-type from exon 19 deletion (Task 2), distinguishing wild-type from 21L858R point mutation (Task 3), and identifying the two mutant subtypes (Task 4). For Task 1, three models were built: Model 1 used only PET/CT images; Model 2 combined PET/CT images with clinical variables; Model 3 integrated PET/CT images, clinical variables, and radiomics features. For Tasks 2-4, only the combined model (similar to Model 3) was constructed. Model performance was evaluated using ROC, AUC, accuracy, precision, recall, and F1 values. ***Results:*** In Task 1, the combined model (Model 3) achieved the highest performance, with AUC values of 0.928 in the training cohort and 0.832 in the validation cohort, and accuracies of 0.805 and 0.675, respectively. The model using only PET/CT images (Model 1) had AUC values of 0.916 and 0.676, and accuracies of 0.802 and 0.566 in the training and validation cohorts, respectively. The model with clinical features (similar to Model 2) had AUC values of 0.895 and 0.733, and accuracies of 0.801 and 0.670. In Task 2, the combined model achieved AUC values of 0.906 and 0.828, and accuracies of 0.868 and 0.767, demonstrating high prediction efficiency and robustness. In Task 3, the combined model had AUC values of 0.909 and 0.785, and accuracies of 0.850 and 0.700. In Task 4, the combined model achieved AUC values of 0.951 and 0.800, and accuracies of 0.732 and 0.533. ***Conclusion:*** The combined deep learning model integrating PET/CT images, clinical variables, and radiomics features showed the best performance in predicting EGFR mutation status and different mutation subtypes, maintaining stability in the validation cohort.

EP-1040

Prediction of 3-year overall survival based on dissemination features of bone scintigraphy in metastatic prostate cancer

J. Ning[1], *D. Haberl*[1], *M. Hacker*[2], *L. Kenner*[1], *C. Spielvogel*[2];
[1]Christian Doppler Lab for Applied Metabolomics, Vienna, AUSTRIA, [2]Division of Nuclear Medicine, Department of Biomedical Imaging and Image-Guided Therapy, Medical University of Vienna, Vienna, AUSTRIA.

Aim/Introduction: Despite high overall survival rates across all stages (98%), patients with metastatic prostate cancer (PCa) reach a five-year relative survival of only 30%. These disparities highlight the need for advanced prognostic tools to guide treatment decisions in metastatic PCa (mPCa). Recent studies validated the reproducibility of the automated Bone Scan Index (BSI) and its association with survival outcomes in PCa patients, highlighting its potential as a prognostic biomarker. Similar to findings in other malignancies, features reflecting tumor volume and spread—such as maximum lesion size (Dmax)—have been associated with overall survival (OS). Translating these insights into PCa, BS-derived dissemination metrics may provide a robust framework for predicting three-year OS in mPCa patients. This study aims to evaluate the prognostic value of dissemination metrics derived from 99mTc-DPD bone scintigraphy (BS) and 68Ga-PSMA-11 PET in predicting three-year overall survival in mPCa. ***Materials and Methods:*** This retrospective study included 2,652 mPCa patients who underwent planar BS between January 2010 and February 2023, with 362 patients also undergoing prostate-specific membrane antigen (PSMA) PET imaging within 100 days of BS. For the preliminary cohort including 163 BS and 26 PSMA PET/CT or PET/MR images, the suspected metastasis lesions were manually delineated via ITK-SNAP. Dissemination metrics included tumor burden, Dmax_patient (distance between the two farthest metastatic lesions), Dmax_p-f (distance from primary lesion to the farthest metastatic lesion), and SPREAD metrics (sum and average distances between lesions). Survival endpoints—three-year OS, were assessed using Kaplan-Meier analysis. ***Results:*** In the preliminary cohort, dissemination metrics, particularly tumor burden and Dmax_patient, demonstrated significant associations with three-year OS. Patients with high tumor burden exhibited markedly reduced survival probabilities compared to those with lower tumor burden, as evidenced by a log-rank p-value of <0.001. Similarly, greater Dmax_patient values were strongly correlated with poorer OS, emphasizing the prognostic relevance of spatial dissemination patterns. Patients with more widely distributed metastatic lesions, as indicated by larger Dmax_patient values, had significantly worse survival compared to those with more localized disease. Multivariate Cox proportional hazards analysis further validated the independent prognostic value of tumor burden and Dmax_patient after adjusting for established clinical covariates, including age, PSA levels, and the use of systemic therapies. ***Conclusion:*** BS-derived dissemination features, including tumor burden and spatial metrics, provide critical insights into the prognosis of metastatic PCa patients, which enable effective risk stratification, guiding personalized treatment for metastatic tumor burden assessment, particularly in resource-limited settings.

EP-1041

FDG PET/CT radiomics-based prognostic models for early-stage Non-Small Cell Lung Cancer: impact of segmentation method

J. Meynen[1], *K. Claesen*[1], *E. Derveaux*[1], *R. Boellaard*[2], *L. Mesotten*[3]; *[1]Hasselt University, Diepenbeek, BELGIUM, [2]Amsterdam UMC, Amsterdam, NETHERLANDS, [3]Ziekenhuis Oost-Limburg, Genk, BELGIUM.*

Aim/Introduction: Lung cancer remains the leading cause of cancer-related mortality worldwide. Even though that surgery remains the most effective treatment, about 30-55% of the patients with NSCLC develop disease recurrence. Accurate risk stratification through prognostic models is therefore essential to identify high-risk patients who are likely to experience recurrence. Current prognostic tools often fail to fully capture the underlying tumor biology and spatial heterogeneity. Radiomics offers a non-invasive way to probe this tumor biology and heterogeneity beyond what's visible to the human eye, therefore serving as a promising alternative for improved prognosis making. This study aims to identify the effect of different segmentation methods on the performance of multiple radiomics-based prognostic models for early-stage Non-Small Cell Lung Cancer (NSCLC). ***Materials and Methods:*** F^{18}-FDG PET/CT images were obtained from a total of 89 patients with pathology-confirmed early-stage NSCLC (stage I-IIIa) (patient inclusion at Ziekenhuis Oost-Limburg). All images were segmented using three different segmentation methods (SUV4.0, MV2, AI-based tool LIONZ which is developed at the Medical University of Vienna by Sundar et al). Radiomic features were extracted using RaCaT (an open source radiomics tool developed by Pfaehler et al) from all different segmentations, resulting in more than 500 features per scan, per segmentation. Logistic regression models with six different feature selection approaches were tested with overall survival (OS) and/or time to progression (TTP) greater than 36 months as the outcome. All models were trained using ten times repeated five-fold cross validation (CV) and upsampling of the minority class. Model performances were evaluated using the CV area under the curve (AUC) values. ***Results:*** Prognostic models showed CV-AUCs ranging from 0.52 to 0.79. Differences in model performances assessed by CV-AUC are mainly caused by the applied feature selection approach and to a much lesser degree by the segmentation method used to extract the radiomic features. The best performing model (CV-AUC=0.79) was found using a model based on SUVmax, TLG, and DmaxBulk, which were measured using MV2 segmentations, with only a small decrease in performance using other segmentation methods. ***Conclusion:*** This study shows the feasibility of all three segmentation methods for the development of radiomic-based prognostic models for early-stage NSCLC patients.

EP-1042

Prognostic value of primary tumour quantitative indices on 68GaDOTANOC PET/CT in pediatric patients with neuroblastoma

N. Kundu, *D. Khan, S. Sagar, A. Mahalik, A. Roy, A. K. Pandey, R. Kumar;*
AIIMS New Delhi, Delhi, INDIA.

Aim/Introduction: Neuroblastoma (NB) is the most common extracranial malignant solid tumour of childhood and exhibits both biological and clinical heterogeneity. Among the multitude of radiotracers available for imaging NB, the radiolabeled somatostatin analogue 68Ga-DOTANOC PET/CT has shown promise as a new tracer which maybe considered in mIBG negative tumors. In our study we aim to investigate whether quantitative DOTANOC parameters of the primary mass predict metastatic propensity at diagnosis in paediatric neuroblastoma. ***Materials and Methods:*** Thirty five treatment naïve children with known neuroblastoma underwent 68GaDOTANOC PET/CT scanning on a dedicated scanner (Biograph 2, Siemens Medical Solutions). A dose of 1.5 MBq/kg body weight with a mean dose range of 11.1-111 39 MBq of 68Ga-DOTANOC was injected intravenously. After a 45-60-minute uptake period, the patients were taken for PET/CT acquisition. Attenuation-corrected PET and fused PET/CT images were reviewed in the axial, coronal, and sagittal planes and in MIP. (VOIs) were carefully drawn over the primary tumour, with special attention paid to exclude areas of high physiological uptake in the neighbouring areas such as liver, spleen, uncinate process of pancreas and urinary tract. Parameters such as SUVmax, SUVmean of primary tumour, SUVmean of blood pool (VOI of 1cm3 drawn over descending aorta), tumour to blood pool ratio (SUVr=SUVmax tumour/SUVmax background), SSTR expressing tumour volume (STV), and total lesion SSTR expression. (TLS= SUVmean primary x STVprimary) were recorded with a 40 % SUVmax threshold. Tumourtobloodpool ratio (SUVr) served as a receptordensity surrogate. Metrics were compared between metastatic (n = 26) and nonmetastatic (n = 9) groups and subjected to ROC analysis.mIBG planar scans of the patients were also available for analysis. ***Results:*** Quantitative parameters of 35 patients with SSTR expressing primary tumours were calculated on 68Ga-DOTANOC PET/CT. SUVr was significantly higher in metastatic patients (15 ± 15) than in localised cases (7.1 ± 4.6; P = 0.04), whereas SUVmax, STV and TLS did not differ. An SUVr cutoff of 6.65 yielded 77 % sensitivity and 88 % specificity for predicting disseminated disease (AUC = 0.73). High SUVr correlated with elevated wholebody extratumour burden and with nonmIBGavid biology. ***Conclusion:*** DOTANOC SUVr—reflecting somatostatinreceptor density relative to background—emerges as an independent imaging biomarker of metastatic potential, outperforming absolute uptake or volume alone. Incorporation of SUVr into baseline assessment could help tailor induction intensity and surveillance frequency.

EP-1043

CNN-based prediction of Clinical Relapse in Takayasu Arteritis from [^{18}F]FDG PET scans

C. Bezzi[1], *A. Tomelleri*[2], *S. Resta*[3], *F. Fallanca*[1], *C. Campochiaro*[2], *E. Baldissera*[2], *S. Ghezzo*[1], *L. Dagna*[2], *A. Chiti*[1], *P. Mapelli*[1], *M. Masseroli*[3], *M. Picchio*[1];
[1]Nuclear Medicine Department, IRCCS San Raffaele Scientific Institute, Milan, ITALY, [2]Unit of Immunology, Rheumatology, Allergy and Rare Diseases, IRCCS San Raffaele Scientific Institute, Milan, ITALY, [3]Department of Electronics, Information and Bioengineering (DEIB), Politecnico di Milano, Milan, ITALY.

Aim/Introduction: To investigate the potential of convolutional neural networks (CNNs) applied to [^{18}F]FDG PET imaging to predict clinical relapse in Takayasu arteritis (TAK) patients within 12 months post-scan. The goal is to improve patient monitoring and therapeutic decision-making. ***Materials and Methods:*** A retrospective analysis was conducted on 306 [^{18}F]FDG PET scans from 74 patients diagnosed with TAK. The scans, obtained between 2013 and 2023 across 4 different PET systems, were preprocessed through resizing and cropping, and harmonized using different strategies, including discretization and histogram equalization methods, and a customized liver-based standardization approach. Multiple CNN architectures were investigated for the prediction: a custom "Baseline Model" with 4 convolutional layers, a residual bottleneck model built with 3 residual bottleneck blocks, and two pre-defined architectures from the MONAI framework [1]: ResNet18 and DenseNet121. Data were divided into training, validation, and testing sets. To increase reliability, the test set was resampled 10 times with a random under-sampling of the majority class to ensure class balance. Class weighting, early stopping, and data augmentation were employed to reduce overfitting. Performance was evaluated using accuracy, precision, recall, specificity, and normalized Matthew's correlation coefficient (nMCC). ***Results:*** Among the 306 scans, 64 were associated with

clinical relapse within 12 months. An expert Nuclear Medicine Physician, blinded to clinical data, classified 39/64 as negative and 25/64 as positive. The iver-based standardization method optimized in this study successfully eliminated inter-scanner voxel intensity discrepancies and was used to harmonize the scans. Overall, the best performing models were the Baseline Model (monitored metric: accuracy; data augmentation: RandAffine) and DenseNet121 (monitored metric: accuracy; data augmentation: RandAxisFlip). Specifically, on test set, the Baseline Model reached an accuracy of 82%, with class-wise precision of 85% (class_0) and 62% (class_1), 38% recall, 94% specificity, and an 0.70 nMCC. DenseNet12, while achieving 81% accuracy, proved particularly effective for predicting complete remission, with 80% precision_class_0, 100% precision_class_1, 8% recall, 100% specificity, and 0.62 nMCC, maintaining 100% precision_class_0 and specificity in the resampled test sets. ***Conclusion:*** This work represents the first implementation of CNN-based analysis of [^{18}F]FDG PET imaging in TAK. Despite limitations including the retrospective design and class imbalance, findings suggest that CNNs can effectively support relapse prediction, potentially guiding decisions to reduce overtreatment and unnecessary follow-up in specific patient subgroups. ***References:*** [1] Cardoso, M. J. et al. MONAI: An open-source framework for deep learning in healthcare. (2022).

EP-1044

Prognostic Value of First Order Radiomic Features in Multiple Myeloma: Data Analysis from the CONPET Trial

J. Blakkisrud[1], *J. Nørgaard*[2,3], *J. Connelly*[1], *M. Revheim*[1,4], *F. Schjesvold*[2], *C. Stokke*[1,5];
[1]*Division for Radiology and Nuclear Medicine, Oslo University Hospital, Oslo, NORWAY,* [2]*Oslo Myeloma Center, Oslo University Hospital, Oslo, NORWAY,* [3]*Institute of Clinical Medicine, University of Oslo, Oslo, NORWAY,* [4]*The Intervention Centre, Oslo University Hospital, Oslo, NORWAY,* [5]*Department of Physics, University of Oslo, Oslo, NORWAY.*

Aim/Introduction: [^{18}F]FDG PET/CT is increasingly used for staging and prognostication in multiple myeloma, but conventional assessments may not fully reflect disease heterogeneity. The CONPET trial used [18F]FDG PET positivity status as indication for consolidation therapy after first-line treatment with autologous stem cell transplantation. This study explores whether first order radiomic features from PET/CT after first-line treatment provide additional prognostic value. ***Materials and Methods:*** We retrospectively analysed 114 patients enrolled in the CONPET study (1). Patients underwent [^{18}F]FDG PET/CT and were classified as PET-positive (n=33) or PET-negative (n=81). PET-positive patients were scheduled for 4 cycles of KRd (carfilzomib, lenalidomide and dexamethasone) consolidation. The skeleton from atlas to mid thighs excluding the skull was segmented using TotalSegmentator (2). First-order histogram features were extracted from the PET corresponding volume of interest (VOI). Difference between features of PET-positive and PET-negative patients were tested using the student t-test. A LASSO-penalized Cox model identified imaging features associated with progression-free survival (PFS) and overall survival (OS). Selected features were refitted using standard Cox regression on the same data in an exploratory analysis to estimate Hazard Ratios (HRs). Analyses were performed separately for the PET-positive and PET-negative subgroups. ***Results:*** Out of 18 features, Skewness ($p = 0.045$) and 10-percentile ($p = 0.039$) were different between PET-negative and PET-positive patients. In PET-positive patients, Skewness, representing an asymmetrical histogram distribution, was a significant prognostic feature for both PFS and OS (HR: 0.49, $p = 0.0076$ for OS; HR: 0.49, $p = 0.0043$ for PFS). In PET-negative patients, Interquartile Range (HR: 9.31, $p = 0.0009$) and Variance (HR: 0.145, $p = 0.0059$) were associated with PFS, though none were prognostic for OS. ***Conclusion:*** The first order radiomic features Skewness, Interquartile Range and Variance extracted from [^{18}F]FDG PET/CT after first-line treatment show potential as prognostic biomarkers in multiple myeloma. Validation in independent cohorts and analyses of feature stability and reproducibility are needed to confirm clinical applicability. ***References:*** 1) Nørgaard et al. Leukemia 2023 2) Wasserthal et al. Radiol Artif Intell 2023.

EP-1045

Single-time-point dosimetry during [^{177}Lu]Lu-PSMA-617 therapy using machine learning and population-based model selection with non-linear mixed-effects modelling

D. Hardiansyah[1], *T. M. Y. Polem*[1], *E. Yousefzadeh-Nowshahr*[2], *U. Nemer*[3], *F. Kind*[3], *A. J. Beer*[2], *P. T. Meyer*[3], *G. Glatting*[2], *M. Mix*[3];
[1]*Universitas Indonesia, Depok, INDONESIA,* [2]*Ulm University, Ulm, GERMANY,* [3]*University of Freiburg, Freiburg, GERMANY.*

Aim/Introduction: This study aimed to study the accuracy of renal dosimetry in [^{177}Lu]Lu-PSMA-617 therapy using single-time-point (STP) imaging data from SPECT/CT, machine learning, and population-based model selection (PBMS) with non-linear mixed-effects (NLME) modelling in a population of 101 patients. ***Materials and Methods:*** Renal time-activity data for [^{177}Lu]Lu-PSMA-617 were acquired using SPECT/CT imaging at five post-injection time points:TP1=(1.9 ± 0.8) h, TP2=(18.9 ± 1.0) h,TP3=(43.1 ± 1.5) h,TP4=(66.4 ± 1.4) h,and TP5=(165.8 ± 24.7) h. Six sum-of-exponentials functions (SOEFs), each with different parameterisations, were fitted to the renal time-activity data using the NLME. A PBMS approach—combining goodness-of-fit tests and Akaike weights—was employed to identify the SOEF most supported by the data. This SOEF was then fitted to all data points to derive the reference time-integrated activities (rTIAs). Three STP approaches were evaluated in this study: 1) NLME-based STP using the optimal SOEF from PBMS (STPN), 2) STP with Support Vector Regression machine learning approach (STPML), and 3) STPNML (A hybrid of STPN and STPML). For the STPML and STPNML methods, optimal combinations of patient-specific covariates—such as age, weight, administered activity, platelet count, haemoglobin, hematocrit, creatinine, prostate-specific antigen (PSA), kidney volume, and glomerular filtration rate—as well as machine learning hyperparameters, were selected. Additional covariate of fitted parameters from STPN was used for the calculation of STPNML. The accuracy of calculated TIAs from STPN (sTIAN), STPML (sTIAML), and STPNML (sTIANML) methods was evaluated against the rTIA using root-mean-square errors (RMSEs) of relative deviations and mean absolute percentage errors (MAPEs). ***Results:*** A seven-parameter SOEF was identified as the best model using the PBMS-NLME method. Time-integrated activity estimates derived from the STPN, STPML, and STPNML approaches were evaluated. For STPN, the RMSEs (MAPEs) of sTIAN relative to rTIA at TP1-TP5 were: 30% (22%), 18% (13%), 16% (11%), 18% (13%), and 32% (20%). The RMSEs (MAPEs) of sTIAML were: 28% (21%), 17% (13%), 15% (11%), 17% (12%), and 30% (21%). The hybrid STPNML method consistently outperformed the STPN and STPML methods, achieving lower errors across all time points. The RMSEs (MAPEs) of sTIANML at TP1-TP5 were: 14% (10%), 14% (9%), 13% (9%), 16% (12%), and 14% (10%). ***Conclusion:*** This study demonstrates that using pharmacokinetic modelling and machine learning, accurate renal TIA estimation from sparse time-point imaging is feasible. The hybrid STPNML approach achieved the highest accuracy among the tested methods, consistently yielding low errors across all investigated time points. This robustness enables reliable STP dosimetry to be performed at any imaging time point, offering maximum flexibility for clinical workflows.

EP-1046

An interpretable machine learning model assists in predicting bone marrow invasion for lymphoma using ^{18}F-FDG PET/CT: a multicenter study

X. Mu, *X. Zhu, W. Fu;*
Department of Nuclear Medicine, Affiliated Hospital of Guilin Medical University, Guilin, CHINA.

Aim/Introduction: This study aimed to develop and evaluate a machine learning model combining clinical, radiomics, and deep learning features derived from ^{18}F-FDG PET/CT imaging to predict bone marrow involvement (BMI) in patients with lymphoma. We compared model predictive capability with human visual interpretation. ***Materials and Methods:*** Our retrospective study encompassed 159 lymphoma patients who underwent ^{18}F-FDG PET/CT imaging at two tertiary hospitals. We extracted clinical, radiomic, and deep learning features from the PET/CT images. Specifically, radiomic features were derived utilizing the PyRadiomics package, whereas deep learning features were obtained using a ResNet50 model. A machine learning model, based on the Extra Trees algorithm, was developed to predict BMI. The model's performance was assessed using receiver operating characteristic (ROC) curves, the area under the curve (AUC), calibration curves, and decision curve analysis (DCA). To enhance model interpretability, Shapley Additive Explanations (SHAP) were employed. Additionally, we conducted a comparative study where PET readers first diagnosed BMI using visual PET/CT interpretation alone and then diagnosed with the assistance of the prediction model, to evaluate the model's impact on clinical decision-making. ***Results:*** The combined model, which fusion clinical, radiomics, and deep learning features, exhibited the highest AUC in the training set (0.954), internal validation set (0.900), and test set (0.886), outperforming single-modality models. Model-assisted diagnosis improved PET readers' accuracy compared to visual PET/CT interpretation alone ($p < 0.05$, McNemar's test). SHAP analysis identified B symptoms, platelet count (PLT), and PET-derived texture features as key predictors, enhancing model transparency and physician trust. ***Conclusion:*** The proposed combined model improves non-invasive BMI prediction and significantly enhances physicians' diagnostic performance. The integration of SHAP interpretation increases model transparency, making it more clinically applicable. This approach demonstrates strong theoretical predictive capability and shows great potential for real-world implementation, reducing the reliance on invasive bone marrow biopsy. ***References:*** [1]The role of bone marrow biopsy and FDG-PET/CT in identifying bone marrow infiltration in the initial diagnosis of high grade non-Hodgkin B-cell lymphoma and Hodgkin lymphoma. Accuracy in a multicenter series of 372 patients[J].Am J Hematol,2016,91(5):E300.DOI:10.1002/ajh.24213. [2]M. Alzahrani,T. C. El-Galaly,M. Hutchings,et al.The value of routine bone marrow biopsy in patients with diffuse large B-cell lymphoma staged with PET/CT: a Danish-Canadian study[J]. Ann Oncol,2016,27(6):1095-1099.DOI:10.1093/annonc/mdw137. [3]A. Doma,A. StudenandB. Jezeršek Novaković.The Impact of Bone Marrow Involvement on Prognosis in Diffuse Large B-Cell Lymphoma: An ^{18}F-FDG PET/CT Volumetric Segmentation Study[J]. Cancers (Basel),2024,16(22):10.3390/cancers16223762.

EP-1047

^{177}Lu-labeled PSMA-targeted radioligand therapy in metastasic castration-resistant prostate cancer: external validation of a baseline^{68}Ga-PSMA-11 PET-based predicition models using^{18}F-Flotufolastat PET

Ö. Coban[1], *A. Karimzadeh*[1,2], *C. Fütterer*[3], *K. Hansen*[1], *M. Heck*[4], *R. Tauber*[4], *C. D´Alessandria*[1], *W. Weber*[1], *M. Eiber*[1], *I. Rauscher*[1];
[1]*Technical University Munich (TUM) - Department of Nuclear Medicine, Munich, GERMANY,* [2]*Department of Diagnostic and Interventional Radiology and Nuclear Medicine, University Medical Center Hamburg-Eppendorf, Hamburg, GERMANY,* [3]*Technical University Munich (TUM) - Institute of AI and Informatics in Medicine, Munich, GERMANY,* [4]*Technical University Munich (TUM) - Department of Urology, Munich, GERMANY.*

Aim/Introduction: ^{177}Lu-labeled prostate-specific membrane antigen (PSMA)-targeted radioligand therapy (RLT) has become a recognized treatment option for patients with metastatic castration-resistant prostate cancer (mCRPC). Since not all patients respond to PSMA-RLT, predictive nomograms including baseline ^{68}Ga-PSMA-PET parameters were developed by Gafita et al. (Lancet Oncol 2021; 22:1115-25). With the increasing use of ^{18}F-labeled PSMA ligands, these models require adaptation. This retrospective analysis aimed to validate a recently published nomogram for application with ^{18}F-Flotufolastat PET prior to PSMA-RLT in a large cohort of mCRPC patients. ***Materials and Methods:*** A total of 174 patients were retrospectively included in this single-center analysis. A Cox proportional hazard model was used for overall survival (OS) and PSA-progression-free survival (PSA-PFS), with hazard ratios and the baseline hazard extracted from Gafita et al. Variables used for model fitting included clinical factors (e.g., time since diagnosis) and imaging data from 18F-rhPSMA-7.3 PET (e.g., whole-body SUVmean). Model performance was evaluated using Harrell's C-index and calibration plots. In addition, OS and PFS were compared, stratifying patients in high- and low-risk groups based on cut-off values determined by Gafita et al. ***Results:*** The estimated OS rates were 60% at 12 months (95% CI, 53%-68%) and 40% at 18 months (95% CI, 33%-49%). External validation yielded a C-index of 0.71 (95% CI, 0.71-0.72) for OS prediction, comparable to the validation cohort of Gafita et al. (C-indices of 0.72). For PSA-progression-free survival (PSA-PFS), the estimated survival rates were 56% at 3 months (95% CI, 49%-65%) and 34% at 6 months (95% CI, 27%-42%), with a C-index of 0.63 (95% CI, 0.62-0.63), lower than the C-index of 0.71 (95% CI, 0.65-0.78) in the validation cohort of Gafita et al. Low-risk patients presented with a significantly longer OS than high-risk patients (16.5 months (95% CI, 15.1-17.8) vs. 8.8 months (95% CI, 7.7-9.9), respectively; p-value < 0.0001). Corresponding PSA-PFS was also significantly longer in the high-risk vs. the low-risk group (5.4 months (95% CI, 4.7-6.1) vs. 2.6 months (95% CI, 1.9-3.2); p-value = 0.003). ***Conclusion:*** Using ^{18}F-Flotufolastat PET instead of ^{68}Ga-PSMA PET in a recently developed prediction model performs well for assessing outcomes of ^{177}Lu-PSMA RLT, with similar C-index scores indicating reliability. However, the model's predictive accuracy remains suboptimal, regardless of the PSMA-ligand used, so it should be applied with caution, and further refinements are advisable.

EP-1048

Incorporating deep features in radiomics for predicting coronary artery disease using myocardial perfusion stress/rest SPECT

B. Wang[1,2], *Y. Du*[3], *C. Lin*[4], *M. Gutierrez*[5], *G. Hung*[6], *Z. Hu*[2], *G. S. P. Mok*[1];
[1]*Biomedical Imaging Laboratory (BIG), Department of Electrical and Computer Engineering, Faculty of Science and Technology, University of Macau, Macau SAR, MACAO,* [2]*Lauterbur Research Center for Biomedical Imaging, Shenzhen Institute of Advanced Technology, Chinese Academy of Sciences, Shenzhen, CHINA,* [3]*Department of Nuclear Medicine, The First Affiliated Hospital of Army Medical University, Chongqing, CHINA,* [4]*Department of Nuclear Medicine, Show Chwan Memorial Hospital, Changhua, TAIWAN,* [5]*Biomedical Informatics Lab Heart Institute, University of São Paulo Medical School, São Paulo, BRAZIL,* [6]*Department of Nuclear Medicine, Chang Bing Show Chwan Memorial Hospital, Changhua, TAIWAN.*

Aim/Introduction: Myocardial perfusion (MP) SPECT is a well-established technique to diagnose coronary artery disease (CAD), while invasive coronary angiography (ICA) still serves as the gold standard for obstructive CAD. This study aims to investigate the ICA prediction performance from MP SPECT using

radiomics incorporated with deep features (DF). ***Materials and Methods:*** We retrospectively enrolled 212 patients undergoing a one-day 99mTc-sestamibi SPECT/CT stress/rest protocol. ICA was performed within 90 days following the MP SPECT, with obstructive CAD defined as stenosis ≥70% in the left anterior descending artery (LAD)/left circumflex artery (LCx)/right coronary artery (RCA) or ≥50% in the left main artery. Polar plots with CT-based attenuation correction were segmented into regions-of-interest (ROI) of LAD, RCA and LCx, where 903 radiomics features (RF) were obtained from the 2-channel stress+rest input [1]. Additionally, 1024 DF generated by a 2-channel 2D U-net [2] were incorporated in the feature selection together with RF using Least Absolute Shrinkage and Selection Operator and Recursive Feature Elimination, followed by logistic regression for classification. The datasets were split into 8:2 for training and testing. For per-patient analysis, DF and/or RF extracted from adaptive ROI defined based on ICA diagnosis were used for training, while DF and/or RF from LAD ROIs were input for testing. For per-vessel analysis, models were trained on DF and/or RF extracted from the LAD, RCA and LCx ROIs, and tested on each ROI respectively. Five-fold cross-validation was performed to test all datasets. Area under the receiver operating characteristic curve (AUC) and accuracy (ACC) were assessed for different models. Delong's test was employed to compare the ROC curves of 3 models built from RF, DF and RF+RF respectively. ***Results:*** For per-patient analysis, RF+DF model (18 RF+12 DF) achieved AUC/ACC of 0.92/0.86, higher than RF-only model (28 RF) (0.87/0.82, p=0.063) and DF-only model (18 DF) (0.75/0.73, p=0.037). For per-vessel analysis, RF+DF model (16 RF+7 DF) also achieved the highest AUC/ACC of 0.85/0.81, followed by 0.78/0.74 (p=0.011) and 0.71/0.71 (p<0.001) for RF-only (19 RF) and DF-only model (21 DF) respectively. ***Conclusion:*** Incorporation of DF further enhances the radiomics prediction model performance for CAD using stress/rest MP SPECT. ***References:*** 1.Wang, B., et al., Prediction of Coronary Artery Stenosis Using Myocardial Perfusion Stress/Rest SPECT: a Radiomics Study. Journal of Nuclear Medicine June 2024, 65 (supplement 2) 241178.2.Jiang, H., et al., Radiomics incorporating deep features for predicting Parkinson's disease in 123I-Ioflupane SPECT. EJNMMI Phys 11, 60 (2024).

EP-1049

Evaluation of locoregional invasiveness of early lung adenocarcinoma manifesting as ground-glass nodules via ^{68}Ga-FAPI-46 PET/CT imaging

D. Ruan, *S. Shi, W. Guo, Y. Pang, L. Yu, J. Cai, Z. Wu, H. Wu, L. Sun, L. Zhao, H. Chen;*
The First Affiliated Hospital of Xiamen University, School of Medicine, Xiamen University, Xiamen, CHINA.

Aim/Introduction: Accurate differentiation of the histologic invasiveness of early-stage lung adenocarcinoma is crucial for determining surgical strategies. This study aimed to investigate the potential of ^{68}Ga-FAPI-46 PET/CT in assessing the invasiveness of early lung adenocarcinoma presenting as ground-glass nodules (GGNs) and identifying imaging features with strong predictive potential. ***Materials and Methods:*** This prospective study (NCT04588064) was conducted between July 2020 and July 2022, focusing on GGNs that were confirmed postoperatively to be either invasive adenocarcinoma (IAC), minimally invasive adenocarcinoma (MIA), or precursor glandular lesions (PGL). A total of 45 patients with 53 pulmonary GGNs were included in the study, consisting of 19 patients with GGNs associated with PGL-MIA and 34 patients with IAC. Lung nodules were segmented using the Segment Anything Model in Medical Images (MedSAM) and the PET Tumor Segmentation Extension. Clinical characteristics, along with conventional and high-throughput radiomics features from High-resolution CT (HRCT) and PET scans, were analyzed. The predictive performance of these features in differentiating between PGL or MIA (PGL-MIA) and IAC was assessed using 5-fold cross-validation across six machine learning algorithms: Random Forest, Logistic Regression, XGBoost, Naive Bayes, Support Vector Machine, and K-Nearest Neighbors. Model validation was performed on an independent external test set (n=11). The Chi-squared test, Fisher's exact test, and the DeLong test were employed to compare the performance of the models. ***Results:*** The SUVmax derived from ^{68}Ga-FAPI-46 PET was identified as an independent predictor of IAC. A cutoff value of 1.82 yielded a sensitivity of 94% (32/34), specificity of 84% (16/19), and an overall accuracy of 91% (48/53) in the training set, while achieving 100% (12/12) accuracy in the external test set. Radiomics-based classification further improved diagnostic performance, achieving a sensitivity of 97% (33/34), specificity of 89% (17/19), accuracy of 94% (50/53), and an area under the receiver operating characteristic curve (AUC) of 0.97 [95% CI: 0.93-1.00]. Compared with the CT-based radiomics model (accuracy: 94% vs. 92%, P = 0.99; AUC: 0.97 vs. 0.96, P = 0.88) and the PET-based model (accuracy: 94% vs. 92%, P = 0.99; AUC: 0.99 vs. 0.97, P = 0.36), the combined PET/CT radiomics model did not show a statistically significant improvement in predictive performance. The key predictive feature was 68Ga-FAPI-46 PET log-sigma-7-mm-3D_firstorder_RootMeanSquared. ***Conclusion:*** The SUVmax derived from ^{68}Ga-FAPI-46 PET/CT can effectively differentiate the invasiveness of early-stage lung adenocarcinoma manifesting as GGNs. Integrating high-throughput features from ^{68}Ga-FAPI-46 PET/CT images can considerably enhance classification accuracy.

EP-1050

Optimized Ensemble Learning Models for Predicting ISUP>3 in Prostate Cancer A Radiomics and Clinical Integration Study

C. Jianbo[1,2,3], *C. Zhang*[1], *G. Wang*[1], *J. Zhang*[1], *Y. Han*[1], *Y. Liu*[1], *B. Xu*[1];
[1]*Chinese PLA General Hospital, Beijing, CHINA,* [2]*Nuclear Medicine Department, The 983rd Hospital of the Joint Logistic Support Force, TianJin, CHINA,* [3]*Graduate School, Chinese PLA General Hospital, Beijing, CHINA.*

Aim/Introduction: Prostate cancer remains a major global health challenge, with accurate high-grade classification crucial for treatment and prognosis. While PSMA PET radiomics aids tumor phenotyping, integrating it with clinical biomarkers to predict International Society of Urological Pathology (ISUP) >3 grades remains an area of unmet need. We developed an ensemble model combining 18F-PSMA-3Q PET radiomics and clinical data to improve ISUP>3 prediction. ***Materials and Methods:*** We analyzed 243 treatment-naïve prostate cancer patients who underwent 18F-PSMA-3Q PET imaging prior to radical prostatectomy. Patients were randomized into training (80%) and testing (20%) cohorts. Radiomic features were extracted from tumor volumes segmented at 45% SUVmax thresholds. Five sub-models (AdaBoost, decision tree, random forest, support vector machine, and XGBoost) were trained, followed by the construction of two integrated models: a radiomics-only model (FMA) and a hybrid radiomics-clinical model (FMB) incorporating prostate-specific antigen density (PSAD), systemic immune-inflammation index (SII), and total/free PSA ratios. Model performance was rigorously assessed using AUC, sensitivity, specificity, accuracy, precision, F1-score and recall. ***Results:*** The hybrid FMB model outperformed other approaches, achieving an AUC of 0.836 (95% CI: 0.71-0.962) with balanced sensitivity (0.729) and specificity (0.750). Comparatively, the radiomics-only FMA model showed higher recall (0.812) but significantly lower precision (0.634 vs 0.765) and accuracy (0.694 vs 0.755), indicating notable false-positive tendencies. The clinical-only model demonstrated the weakest performance (AUC = 0.746, 95% CI:0.595-0.898). Decision curve analysis confirmed FMB's superior clinical utility across probability thresholds. ***Conclusion:*** Our findings establish that integrating PSMA PET radiomics with clinical biomarkers (FMB) provides more accurate ISUP>3 prediction than unimodal approaches. The FMB framework

offers optimal balance for clinical decision-making, particularly in selecting patients for treatment intensification. These results highlight the importance of combining imaging and clinical data for reliable risk stratification. Multicenter prospective validation is warranted to confirm generalizability across diverse populations and imaging protocols, a critical next step for clinical translation. This approach may significantly improve personalized treatment strategies in prostate cancer management.

EP-1051

The prognostic value of PSMA-PET-derived information in predicting ADT-free survival in oligorecurrent prostate cancer treated with metastasis-directed SBRT

T. D. van Bergen[1], *Y. E. van den Heuvel*[2], *A. J. A. T. Braat*[3], *C. A. T. van den Berg*[1], *T. F. W. Soeterik*[2];
[1]*Computational Imaging Group for MR Diagnostics and Therapy, Center for Image Sciences, University Medical Center Utrecht, Utrecht, NETHERLANDS,* [2]*Department of Radiation Oncology, University Medical Center Utrecht, Utrecht, NETHERLANDS,* [3]*Department of Radiology and Nuclear Medicine, Division of Imaging and Oncology, University Medical Center Utrecht, Utrecht, NETHERLANDS.*

Aim/Introduction: Patients with oligorecurrent prostate cancer (PCa) could benefit from receiving metastasis-directed therapy (MDT) to delay or even avoid androgen deprivation therapy (ADT) and its morbidities. The aim of this study is to evaluate the prognostic value of prostate-specific membrane antigen positron emission tomography (PSMA-PET)-derived radiomic features to predict ADT-free survival (AFS). ***Materials and Methods:*** PCa patients with oligorecurrent (≤5 lesions) disease who were staged with PSMA-PET/CT and treated with stereotactic body radiotherapy (SBRT) to all metastatic sites (without systemic therapy) were retrospectively enrolled. Lesions were delineated on planning CT or MRI scans by radiation oncologists and registered onto the PSMA-PET using MIM Software. Metabolic tumour volumes (MTV) were calculated by thresholding 40% of the maximum standardized uptake value (SUVmax). Mean SUV (SUVmean), total lesion uptake (TLU), and total lesion quotient (TLQ), were calculated on a patient basis over the total MTV. Clinical parameters, including prostate-specific antigen (PSA) at SBRT, MRI-staging, clinical staging, and ISUP grade group (GG) at biopsy were retrospectively collected per patient. Univariate and multivariate Cox proportional hazard regression and Kaplan Meier methods were used to examine associations between the outcome measure AFS, and baseline clinical/PET parameters. ***Results:*** A total of 210 patients were included in the study. The mean age was 70.8 years (±5.8 years). The mean AFS was 33.8 months (±20.5 months). Need for ADT was initiated in 114 (54.3%) of the patients. A total of 295 lesions were found of which 291 (98.6%) were PSMA positive. The mean number of lesions, SUVmax, TLQ, TLG, and total MTV was 1.4 (±0.7), 8.4 (±8.9), 0.77 (±1.0), 9.7 (±22.8), 1.9 (±2.1), respectively. Univariate cox analysis showed no statistically-significant differences between the survival curves for AFS for SUVmax, and number of lesions (p=0.95, p=0.19, respectively). Univariate cox analysis was significant for AFS in TLQ (HR: 1.21, 95% CI 1.05-1.39, p=0.01), TLU (HR: 1.01, CI 1.01-1.02, p<0.005), and MTV (HR: 1.21, CI 1.12-1.30, p<0.005). On multivariable cox-regression analysis, we observed PSA (HR: 1.14, CI 1.07-1.22, p<0.005), GG (HR: 1.25, CI 1.07-1.46, p=0.005), and MTV (HR: 1.19, CI 1.11-1.28, p<0.005) to be significantly associated with ADT-free survival. ***Conclusion:*** This study showed strong prognostic performance of PSMA-PET features in predicting AFS with total MTV having the highest prediction performance in multivariate analysis. Including PSMA-PET-derived information can be prognostic to determine AFS after MDT-SBRT. A final risk classification system will be developed by ongoing studies in the future.

EP-1052

Unsupervised clustering of short-chain fatty acid transcellular flux identifies oligoclonal metabolic phenotypes in intracratial metastatic disease

M. Inglese[1,2], *S. Islam*[2], *L. McLeavy*[2], *F. Mauri*[2], *T. M. Barwick*[2], *A. D. Waldman*[2,3], *K. O'Neill*[2], *M. Williams*[2], *E. O. Aboagye*[2], *N. Toschi*[1,4];
[1]*University of Rome Tor Vergata, Rome, ITALY,* [2]*Imperial College London, London, UNITED KINGDOM,* [3]*University of Edinburgh, Edinburgh, UNITED KINGDOM,* [4]*Athinoula A. Martinos Center for Biomedical Imaging, Boston, MA, UNITED STATES OF AMERICA.*

Aim/Introduction: Brain metastases (IMDs) occur in 10-30% of adult cancer patients and often carry a poor prognosis[1]. Treatment impact on overall survival (OS) depends on factors like metastasis number, primary tumour type, and patient performance status[2]. Given the wide prognostic variability[3], accurate characterization of intracranial metastases is essential for therapy planning and response assessment. Recently, [^{18}F]fluoropivalate (FPIA) PET imaging has emerged as a promising modality for assessing short-chain fatty acid transcellular flux in brain tumours[4,5,6]. This study offers a methodology for characterizing metabolic phenotypes in oligo metastatic brain metastases associated with patient survival in IMD non-invasively, within a timeframe when biopsy or resection is often not feasible. ***Materials and Methods:*** We analyzed ^{18}F-FPIA PET/MRI data of two cohorts of patients with IMD: 12 treatment-naïve and 10stereotactic radiosurgery (SRS)-treated patients for a total of 35 lesions (n=22 from lung, n=6 breast, n=6 melanoma, and one from colorectal cancers). Only one patient contributed to both cohorts. Voxelwise extraction yielded 79,801 FPIA SUV time-activity curves (TACs): 65,131 from untreated lesions(41,299 from lung, 11,062breast, 7,232 colorectal, 5,538 melanoma) and 14,670 from treated ones (6,978 lung, 6,235 melanoma and 1,457 breast). Two time-series unsupervised k-means clustering analyses grouped the normalized TACs of untreated (KMPre,N=17 lesions) and treated (KMPost,N=18 lesions) patients[7], respectively, optimizing the cluster numbers ks using the elbow method[8]. Cluster prevalence was correlated with OS using Spearman and Kendall's Tau tests. Perfusion and diffusion parameters from dynamic contrast enhanced, susceptibility contrast and diffusion weighted DCE/DSC/DWI-MRI were extracted from the cluster-defined lesions' subregions for additional multiparametric and diffusion radiomic analyses. ***Results:*** KMPre identified three kinetic subtypes: intermediate (Cluster1, 30.29%), fast (Cluster2, 25.79%), and slow (trapping-like[6]) (Cluster3, 43.92%). In treated lesions, KMPost identified two kinetic subtypes (Cluster A and B) and revealed a loss of the fast component, with trapping-like ClusterA (70.84%) prevailing. Higher Cluster1 prevalence correlated positively with OS, while Cluster 3 correlated negatively, suggesting less responsive tumour subregions. Validation of KMPre on treated lesions' FPIA SUV TACs confirmed a shift toward Cluster3 (70.57%) after treatment, indicating SRS-induced metabolic changes. Multiparametric MRI supported these findings, showing reduced perfusion and increased apparent diffusion coefficient in slow FPIA regions. Radiomic analysis further revealed changes in heterogeneity after treatment, consistent with prior findings linking such patterns to immune response activity[9]. ***Conclusion:*** SUV kinetic profiling combined with MRI emerges as a promising approach to assess treatment response and stratify patients based on metabolic and vascular changes.

References: [1]Baumgart,doi:10.3389/fonc.2024.1330492;[2] Rozati,doi:10.1186/s12885-023-11452-7;[3]Sperduto,doi:10.1200/JCO.2011.38.0527;[4]Dubash,doi:10.1007/s00259-020-04724-y;[5]Vassileva,doi: 10.3390/biomedicines9070811;[6] Islam,doi:10.1007/s00259-023-06330-0;[7]Inglese,doi:10.1109/EMBC48229.2022.9871033;[8]Zhao,doi:10.1155/2022/6041484;[9] Meyer,doi:10.21873/anticanres.15267.

EP-1053

Uncertainty-Quantified Dynamic PET Biomarker for Robust Prediction of Treatment Response and Survival in Precision Breast Cancer Medicine

F. Gu[1], *Q. Wu*[2,3], *F. O'Sullivan*[2], *M. Muzi*[4], *D. Mankoff*[5];
[1]*School of Mathematics and Physics, North China Electric Power University, Beijing, CHINA,* [2]*School of Mathematical Sciences, University College Cork, Cork, IRELAND,* [3]*Insight SFI Center for Data Analytics, Cork, IRELAND,* [4]*Department of Radiology, University of Washington, Seattle, WA, UNITED STATES OF AMERICA,* [5]*Department of Radiology, University of Pennsylvania, Philadelphia, PA, UNITED STATES OF AMERICA.*

Aim/Introduction: Dynamic PET imaging captures tracer kinetics, enabling the development of advanced biomarkers with superior predictive power for treatment response and survival in breast cancer. However, single-point estimates of biomarkers near decision boundaries can be unreliable, compromising clinical decisions. This study introduces an uncertainty-aware framework for dynamic PET-derived biomarkers to enhance prognostic precision in breast cancer, advancing personalized oncology. ***Materials and Methods:*** A retrospective analysis was conducted on 53 breast cancer patients who underwent baseline ^{18}F-FDG dynamic PET imaging prior to neoadjuvant chemotherapy (NAC) at the University of Washington [1]. Pathologic complete response (pCR) was assessed from surgical specimens, with 11 of 53 patients achieving pCR. Disease-free survival (DFS) was calculated in years, with 17 of 52 patients relapsing (one patient's survival data was incomplete). Parametric images were generated using the non-parametric residue mapping technique [2]. Kinetic parameters were extracted from primary tumors, and binary logistic regression and Cox proportional-hazards models were used to predict pCR and DFS, respectively. Patient-specific uncertainty in kinetic parameters was quantified using an efficient image-domain bootstrap method [3]. ***Results:*** A novel biomarker, flow distribution, outperformed conventional static SUV and influx rate (Ki), showing strong associations with both treatment response and survival. In cases where biomarker values approached classification thresholds, single-value predictions were ambiguous. By integrating uncertainty quantification, we provided confidence intervals for predicted pCR probabilities and survival time, refining risk stratification. Patients with high flow distribution but elevated uncertainty exhibited heterogeneous outcomes, enabling more tailored treatment strategies. ***Conclusion:*** Incorporating uncertainty quantification into dynamic PET biomarker analysis significantly enhances the robustness of treatment response and survival predictions in breast cancer. This approach mitigates the limitations of single-point estimates, paving the way for reliable, individualized treatment decisions in precision oncology. ***References:*** [1] Mankoff DA, et al. Changes in blood flow and metabolism in locally advanced breast cancer treated with neoadjuvant chemotherapy. J Nucl Med. 2003;44(11):1806-1814. [2] Gu F, et al. Quantitation of multiple injection dynamic PET scans: an investigation of the benefits of pooling data from separate scans when mapping kinetics. Phys Med Biol. 2021;66:135010. [3] O'Sullivan F, et al. A generalized linear modeling approach to bootstrapping multi-frame PET image data. Med Image Anal. 2021;72:102132.

EP-1054

Exploring Contrast-Enhanced Computed Tomography as a Local Predictor of Lung Shunt Fraction in ^{90}Y Liver Radioembolization

B. Mehadji[1], *T. Marx*[1], *A. Carter*[1], *R. Goldman*[1], *C. Vu*[1], *E. Roncali*[2];
[1]*University of California Davis, Sacramento, CA, UNITED STATES OF AMERICA,* [2]*University of California Davis, Davis, CA, UNITED STATES OF AMERICA.*

Aim/Introduction: Pretreatment estimation of the Lung Shunt Fraction (LSF) for yttrium-90 (^{90}Y) radioembolization allows to minimize the risk of excessive lungs irradiation, especially in the context of repeated treatments. Standard practice relies on injection of ^{99m}Tc-macroaggregated albumin (^{99m}Tc-MAA) into the lobe intended for treatment, followed by imaging. Gabr et al. have shown that selective treatments of UNOS T1/T2 hepatocellular carcinoma can be safely performed without LSF estimation [1]. Consequently, the number of facilities adopting this technique is increasing [2]. A limitation of that study is that the post-treatment LSF was not measured. Unlike the lobar administration of ^{99m}Tc-MAA that avoids the risk of embolizing peritumoral vessels and altering vascular architecture prior to the ^{90}Y treatment, segmentectomy involves injecting ^{90}Y microspheres into a limited liver volume. Although no complications have been reported and direct comparative studies are lacking, selective injections may lead to higher LSF due to the disproportion between the perfused volume and the hypervascular territory responsible for shunting. This study investigates the feasibility of using contrast-enhanced computed tomography (CECT) to compute a localized LSF; more consistent with hyperselective treatments. ***Materials and Methods:*** Hypervascular volumes were computed by subtracting the portal phase from the arterial phase of the 4-phase abdominal CECT. They were then normalized by the perfused liver volume to compute the hypervascular-to-perfused volume ratio (HVTP). Unlike tumor-based segmentation, this approach identifies regions that actively contribute to LSF. As a result, hypoxic tumor areas unlikely contributing to LSF were excluded, while normal parenchyma and tumor vascular invasion showing hypersignal in arterial phase were included. As a proof of concept, in a retrospective study of 30 liver cancer patients, we compared LSF estimated using CECT and lobar ^{99m}Tc-MAA imaging. ***Results:*** The study showed a strong correlation (R^2=0.946, p<0.001) between the HVTP derived from CECT and the LSF obtained via standard ^{99m}Tc-MAA planar imaging. The predictive power of the HVTP demonstrated a 1-sigma uncertainty of 3%. ***Conclusion:*** This study presents the methodology and early validation of a CECT-based method for LSF estimation. By leveraging differences between the arterial and portal phases, the approach enables visualization of highly vascularized volumes and offers potential for LSF estimation in the context of hyper selective treatments. The method is aimed to be further validated using direct comparison with post treatment measurement of the true LSF. ***References:*** [1] A. Gabr et al., Jun. 2020, doi: 10.1016/j.jhep.2020.02.024. [2] Z. T. Berman et al., Sep. 2024, doi: 10.1007/s00270-024-03799-6.

EP-1055

Interest of ^{18}F-FDG PET/CT Radiomics for Overall Survival Prediction in Newly Diagnosed Multiple Myeloma Treated by Daratumumab in the CASSIOPET Study

S. Ahrari[1], *B. Jamet*[1], *S. Zweegman*[2], *A. Perrot*[3], *C. Hulin*[4], *D. Caillot*[5], *T. Facon*[6], *X. Leleu*[7], *K. Belhadj*[8], *E. Itti*[9], *L. Karlin*[10], *C. Bailly*[1,11], *M. Levin*[12], *M. C. Minnema*[13], *C. Bodet-Milin*[1,11], *B. De Keizer*[14], *J. Corre*[15], *P. Sonneveld*[16], *C. Touzeau*[17,11], *P. Moreau*[17,11], *F. Kraeber-Bodéré*[1,11], *T. Carlier*[1,11];
[1]*Service de Médecine Nucléaire, University Hospital Hôtel-Dieu, Nantes, FRANCE,* [2]*Amsterdam UMC, Vrije Universiteit Amsterdam, Cancer Center Amsterdam, Department of Hematology, Amsterdam, NETHERLANDS,* [3]*CHU de Toulouse, IUCT-O, Université de Toulouse, UPS, Service d'Hématologie, Toulouse, FRANCE,* [4]*Department of Hematology, Hôpital Haut Lévêque, University Hospital Bordeaux, Pessac, FRANCE,* [5]*CHU Dijon, Hôpital Du Bocage, Dijon, FRANCE,* [6]*University of Lille, CHU Lille, Service des Maladies du Sang, Lille, FRANCE,* [7]*CHU Poitiers, Hôpital la Milétrie, Poitiers, FRANCE,* [8]*Hôpital Henri Mondor, Lymphoid Malignancies Unit, Créteil, FRANCE,* [9]*Department of Nuclear Medicine, Hôpital Henri Mondor, Créteil, FRANCE,* [10]*Centre Hospitalier Lyon-Sud Hématologie (HCL), Pierre–Bénite, FRANCE,* [11]*CRCI2NA, INSERM, CNRS, Université d'Angers, Université de Nantes, Nantes, FRANCE,* [12]*Albert Schweitzer Ziekenhuis, Dordrecht, NETHERLANDS,* [13]*Department of Hematology, University Medical Center Utrecht,*

Utrecht, NETHERLANDS, [14]Department of Nuclear Medicine and Radiology, University Medical Center Utrecht, Utrecht, NETHERLANDS, [15]Unité de Genomique du Myélome, IUC-T Oncopole, Toulouse, FRANCE, [16]Erasmus MC Cancer Institute, Rotterdam, NETHERLANDS, [17]Hematology, University Hospital Hôtel-Dieu, Nantes, FRANCE.

Aim/Introduction: This study aims to evaluate the added value of 2-[^{18}F]fluoro-2-deoxy-D-glucose (^{18}F-FDG) positron emission tomography/computed tomography (PET/CT) radiomics in the analysis of overall survival (OS) in patients with multiple myeloma (MM) treated by Daratumumab. ***Materials and Methods:*** Patients with focal, paramedullary and/or extramedullary lesions treated with Daratumumab were selected from the prospective CASSIOPET study sponsored by the IFM group. All patients underwent whole-body ^{18}F-FDG PET/CT imaging at baseline, and radiomics features were extracted from the largest and hottest lesions. Four machine learning (ML) algorithms were used to model patient survival outcomes, namely Cox proportional hazards, support vector machine, random survival forest, and gradient boosting with component-wise least squares as the base learner. Each model was trained on three different feature sets, including clinical and PET-derived features (referred to as conventional), radiomics features, and a combination of both. A new PET-derived feature, total metabolic tumor volume of the bone marrow (TMTV-BM), was extracted automatically and defined as the number of segmented skeletal voxels with uptake greater than the median liver uptake. Uncorrelated features were selected using bootstrap-based consensus clustering and feature selection. A stratified nested cross-validation strategy with three outer and three inner folds was implemented. Model hyperparameters and the maximum number of selected features were optimized using Bayesian search. An ensemble technique was performed by averaging the predicted risk scores from the four optimized ML models within each outer fold. Feature importance was evaluated using Shapley Additive Explanation values. ***Results:*** A total of 112 patients (59 [54, 62] years old, 46 women) out of 274 patients from the CASSIOPET study were included in the analysis. The highest performance was obtained using conventional features, with a concordance index (C-index) of 0.668±0.047. When considering both the largest and hottest lesions, the radiomics+conventional feature set (largest: C-index = 0.627±0.040, hottest: C-index = 0.585±0.080) outperformed radiomics features alone (largest: C-index = 0.556±0.101, hottest: C-index = 0.531±0.068). The TMTV-BM feature was identified as the most informative across both the conventional and radiomics+conventional feature sets, with additional contributions from radiomics features in the latter. ***Conclusion:*** Among patients with newly diagnosed MM treated with Daratumumab, conventional features demonstrated the best performance for OS prediction. When combined with conventional features, radiomics features extracted from the largest and hottest lesions showed an improvement over radiomics alone, suggesting limited added value of the radiomics features.

EP-1056

Prospective Dual-Tracer ^{18}F-FDG/^{68}Ga -FAPI PET/CT Biomarkers Enable Early Prediction of Immunotherapeutic Response in Advanced Gastric Adenocarcinoma

C. Zhang[1], *X. Lin*[1], *J. Hao*[2], *H. Zhao*[1], *T. Han*[1], *L. Qi*[2], *C. Wang*[1], *Y. Zhang*[1], *M. Xin*[1], *J. Liu*[1], *X. Xiao*[1];
[1]Shanghai Jiao Tong University School of Medicine Affiliated Renji Hospital, Shanghai, CHINA, [2]United Imaging Healthcare, Shanghai, China, Shanghai, CHINA.

Aim/Introduction: While immunotherapy has emerged as a promising therapeutic strategy for advanced gastric cancer, there remains a lack of precise tools for its efficacy evaluation. ^{18}F-FDG and ^{68}Ga-FAPI (fibroblast activation protein inhibitor), as two tracers targeting distinct molecular pathways in PET imaging, reflect distinct tumor biological characteristics and potentially provide complementary insights into clinical diagnosis and efficacy evaluation of gastric cancer. This study aims to investigate the clinical utility of the dual-tracer PET imaging in assessing immunotherapy response and predicting survival outcomes in patients with advanced gastric cancer. ***Materials and Methods:*** This prospective dual-imaging cohort study included 20 advanced gastric adenocarcinoma patients who underwent sequential ^{18}F-FDG/^{68}Ga-FAPI PET/CT scans at baseline and post-immunotherapy timepoints, with a subgroup (n=6) additionally receiving baseline ^{18}F-FDG PET/MR for multimodal validation. The tumor target lesions on the FDG PET and FAPI PET images were segmented using the relative threshold method and the parameters including SUVmax, MTV, FAPI-positive tumor volume (GTV-FAPI), total lesion glycolysis (TLG) and FAPI-positive total lesion accumulation (TLF) were obtained. Survival outcomes, including overall survival (OS) and progression-free survival (PFS) were collected. ***Results:*** Quantitative analysis revealed distinct metabolic dynamics: while baseline FDG/FAPI parameters showed inter-tracer concordance ($p>0.05$), baseline FDG SUVmax demonstrated PERCIST-stratified escalation (CMR< PMR < PMD: 7.1±2.3 vs 19.2±5.9 vs 28.5±14.6, $p=0.028$).Demographic analysis revealed comparable age and gender distributions between progression (n=8) and non-progression (n=12) cohorts ($p>0.05$). Baseline dual-tracer PET parameters showed limited predictive value (FDG-SUVmax: 21.41±4.93 vs 15.65±2.54; FAPI-SUVmax: 19.96±2.60 vs 15.84±1.25; $p>0.05$). Longitudinal analysis revealed significant metabolic response stratification: post-treatment FDG-SUVmax (12.63±2.55 vs 5.25±0.96) and FAPI-SUVmax (15.47±1.92 vs 7.99±0.78) differed markedly between progression/non-progression groups, with ΔFDG-SUVmax% showing superior discrimination (62.6±5.9% vs 38.7±7.5%) compared to ΔFAPI-SUVmax% ($p>0.05$). ROC optimization identified post-treatment FDG-SUVmax >6.47 (Se=87.5%, Sp=70%) and FAPI-SUVmax >12.22 (Se=87.5%, Sp=90%) as optimal thresholds for predicting treatment resistance. Notably, FDG-SUVmax reduction >67% achieved 100% specificity for therapeutic efficacy (Se=50%). Longitudinal radiomic evolution demonstrated superior prognostic value over baseline metrics. While baseline PET parameters showed no significant association with OS/PFS ($|r|<0.3$, $p>0.1$), treatment-induced metabolic alterations revealed strong survival correlations: ΔFDG-MTV (r=-0.472 for OS vs r=-0.537 for PFS, $p<0.05$), ΔFDG- TLG (r=-0.535 for OS vs r=-0.518 for PFS, $p<0.05$), and ΔFAPI-TLF (r=-0.466 for OS vs r=-0.466 for PFS, $p<0.05$),ΔFDG- SUVmax(r=-0.584 for OS vs r=-0.584 for PFS, $p<0.05$, $p<0.05$) exhibited linear relationships with PFS/OS. ***Conclusion:*** This multimodal approach provides critical decision-support for optimizing treatment sequencing and combination strategies in advanced disease management.

EP-1057

Development of a Clinical-Radiomic Model for Recurrence Prediction in Head and Neck Cancer Using Multi-Scanner PET Imaging

N. González-Cuesta[1], *G. Reynés-Llompart*[2], *L. Rodriguez-Bel*[1], *V. Carrero-Vásquez*[1], *M. Zamorano-Rivas*[1], *A. Bagán-Trejo*[1], *I. Martínez-Zalacaín*[3], *P. Naval-Baudín*[4], *M. Cortés-Romera*[1];
[1]Nuclear Medicine Department, ICS-IDI, Hospital Universitari de Bellvitge, L'Hospitalet de Llobregat, SPAIN, [2]Medical Physics Department, Institut Català d'Oncologia-IDIBELL, L'Hospitalet de Llobregat, SPAIN, [3]Department of Clinical Sciences/School of Medicine, University of Barcelona, Barcelona, SPAIN, [4]Radiology Department, Hospital Universitari de Bellvitge-IDIBELL, L'Hospitalet de Llobregat, SPAIN.

Aim/Introduction: Recurrence in patients with head and neck cancer presents a challenge to clinicians due to its poor prognosis. The availability of a single model, user-friendly, and capable of predicting recurrence across different types of head and neck cancer, is clinically valuable, supporting risk stratification and personalized decision-making. This study aims to develop a robust and generalizable machine learning model for predicting recurrence in head and neck cancer, integrating clinical and radiomic data extracted from multi-scanner PET images (Discovery ST, Discovery IQ and Discovery MI). ***Materials and Methods:*** A

database of 134 PET images from patients with head and neck cancer (49 oropharyngeal and 83 nasopharyngeal) was used, all patients presented locoregional tumour involvement with no distant lesions suspicious of malignancy. Tumour lesions and lymph nodes were semi-automatically segmented, followed by spatial standardisation. Radiomic features were extracted using PyRadiomics and normalised using the ComBat method, due to variability between PET scanners. To develop the models—based on clinical, radiomic, or combined data—the data was split into training and testing sets. For the radiomic data, collinearity was eliminated using a correlation matrix, and ANOVA was applied to select the most relevant variables. A random forest was trained with repeated cross-validation and validated with test data. ***Results:*** The performance of three predictive models was evaluated. The clinical model achieved a sensitivity of 0.80, a specificity of 0.82, an accuracy of 0.81, and an AUC of 0.82. The radiomic model also demonstrated a sensitivity of 0.80, a specificity of 0.79, an accuracy of 0.79, and an AUC of 0.81. The combined model, integrating both clinical and radiomic data, maintained sensitivity of 0.80 but has a specificity of 0.85, an accuracy of 0.84, and an AUC of 0.85.The results indicate that a unified model based on heterogeneous data from multiple PET scanners is feasible and clinically beneficial. The combination of clinical and radiomic variables enhances predictive performance compared to models using only radiomic or clinical data. Although sensitivity remains constant across all three approaches, the increase in specificity, accuracy, and AUC of the combined model positions it as the most promising for predicting recurrence in head and neck cancer patients. ***Conclusion:*** This study demonstrates the feasibility of implementing a single recurrence prediction model for head and neck cancer, applicable to different tumour subtypes and imaging sources. The clinical-radiomic approach enhances clinical practice, with the potential for integration into healthcare workflows for personalized decision-making.

EP-1058

Predictive Accuracy and Clinical Benefit of a Nomogram Aimed at Predicting Radioiodine-Refractory Differentiated Thyroid Cancer: Independent External Validation Using a Single Institution Database

F. Yu;
Department of Nuclear Medicine, Xijing Hospital, Air Force Military Medical University, Xi'an, CHINA.

Aim/Introduction: To perform an external validation of a recently published nomogram aimed to predict radioiodine refractory differentiated thyroid cancer (RAIR-DTC) in DTC patients with distant metastases after at least two courses of RAI treatment by Meng Chao et al. (Front Endocrinol (Lausanne) 14, 1109439, 2023). ***Materials and Methods:*** Overall, 156 DTC patients were included and divided into RAIR (n=67) and non-RAIR (n=89) according to 2015 ATA guidelines. All included patients were enrolled according to the inclusion criteria defined by Meng Chao et al. First, we calculated the predicted probability of RAIR for each patient using the nomogram based on indicators Age upon diagnosis and Δs-Tg/Δs-TSH<1.50, as proposed by Meng Chao et al. Then, using R software, we plotted ROC curve, calibration plot, and DCA curve based on the predicted probabilities and actual outcomes, and completed the evaluation of external validation. ***Results:*** In the external cohort, the overall diagnosis rate of RAIR was 42.9% vs. 57.3% in the original population. Compared to the original model report, the ROC curve demonstrated suboptimal diagnostic performance, with AUC values of 0.735 and 0.830, and corresponding sensitivity and specificity of 0.656, 0.726, and 0.775, 0.830, respectively. The calibration curve indicated poor consistency. In the DCA curve, the net benefit was lower than that reported originally across most threshold ranges, particularly within the 0.25 to 0.75 range. ***Conclusion:*** We observed relatively poor suboptimal predictive accuracy in the external cohort compared to the original cohort. Future research should aim to identify additional prognostic factors and validate the model in broader cohorts to improve its applicability in clinical practice.

EP-1059

Differentiation between bipolar and major depressive disorders with [^{11}C]K-2 AMPA receptor PET imaging

H. Abe[1], *S. Tsugawa*[1], *Y. Kimura*[2], *J. Chikazoe*[3], *T. Arisawa*[1], *M. Hatano*[1], *W. Nakajima*[1], *T. Miyazaki*[1], *T. Takahashi*[1];
[1]*Yokohama City University, Yokohama, JAPAN,* [2]*Kindai University, Higashi Osaka, JAPAN,* [3]*Hiroshima University, Hiroshima, JAPAN.*

Aim/Introduction: Bipolar disorder is frequently misdiagnosed as major depressive disorder, leading to increased risk of rapid cycling, reduced quality of life, and heightened suicide risk. Therefore, an earlier and more accurate diagnostic method using biological indicators is critically needed. Our recently developed PET tracer, [^{11}C]K-2, enables the quantitative visualization of glutamate α-amino-3-hydroxy-5-methyl-4-isoxazole propionic acid receptor (AMPAR) distribution and is considered useful for characterizing regional synaptic phenotypes in psychiatric disorders.[1-4] This study aims to develop a machine learning-based method to differentiate bipolar disorder from major depressive disorder using AMPAR density. ***Materials and Methods:*** Twenty-seven patients with major depressive disorder(MDD) and 16 patients with bipolar disorder (BD) in depressive episodes underwent PET scans with [^{11}C]K-2 to measure AMPAR density. AMPAR density was compared between the two groups using SPM. A partial least squares (PLS) model was trained to predict diagnoses based on AMPAR density, with performance evaluated using leave-one-pair-out cross-validation. ***Results:*** In this cross-sectional study of 16 patients with BD and 27 patients with MDD (all in a depressive phase), a partial least squares (PLS) classification model using [^{11}C]K-2 PET-derived AMPA receptor density successfully differentiated BD from MDD with an area under the curve of 0.80, a sensitivity of 75.0%, and a specificity of 77.8%. ***Conclusion:*** Our findings suggest that AMPAR density, measured with [^{11}C]K-2, offers modest discrimination between BP and MDD. This model could aid in diagnosis, particularly for individuals with ambiguous clinical symptoms or in whom symptoms have yet to manifest fully. ***References:*** 1. Miyazaki, T. et al. Visualization of AMPA receptors in living human brain with positron emission tomography. Nat Med 26, 281-288 (2020).2. Hatano, M. et al. Biodistribution and radiation dosimetry of the positron emission tomography probe for AMPA receptor, [11C]K-2, in healthy human subjects. Scientific Reports 11, (2021).3. Arisawa, T. et al. [11C]K-2 image with positron emission tomography represents cell surface AMPA receptors. Neuroscience Research 173, 106-113 (2021).4. Hatano, M. et al. Characterization of patients with major psychiatric disorders with AMPA receptor positron emission tomography. Molecular Psychiatry (2024) doi:10.1038/s41380-024-02785-1.

EP-64

e-Poster Area

D: Technical Studies -> D2 Data Analysis and Artificial Intelligence -> D25 Tracer Kinetic Analysis

EP-1060

Impact of Scan Duration on Kinetic Modelling Parameters in Dynamic [^{68}Ga]-PSMA-11 PET Imaging for Prostate Cancer

E. A. M. Kile[1,2], *R. Sundset*[1,2], *S. Kuttner*[1,2,3];
[1]*The PET Imaging Center, University Hospital of North Norway, Tromsø, NORWAY,* [2]*Nuclear Medicine and Radiation Biology Research Group, Department of Clinical Medicine, UiT the Arctic University of Norway, Tromsø, NORWAY,* [3]*UiT Machine Learning Group, Department of Physics and Technology, UiT the Arctic University of Norway, Tromsø, NORWAY.*

Aim/Introduction: The clinical guidelines for prostate cancer imaging using [^{68}Ga]-PSMA-11 recommend performing static PET (sPET) scans between 50 and 100 minutes post tracer injection. However, while sPET shows merely a snapshot of the tracer uptake, dynamic PET (dPET) combined with tracer

kinetic modelling, provides quantitative information about the tracer uptake, internalisation, and retention. A standard 60-minute dPET acquisition is infeasible for routine clinical implementation. This study aimed to evaluate the impact of scan duration on kinetic modelling parameters to explore the potential of shortened routine dPET protocols. ***Materials and Methods:*** In this prospective clinical study, nine prostate cancer patients underwent 60-minute [^{68}Ga]-PSMA-11 dPET imaging. Arterial blood sampling was performed to form the arterial input function (AIF). The prostate lesion was delineated and the time-activity curve was extracted from the dPET images. A shortened, 15-minute acquisition was simulated for each patient by removing the last 45 minutes of data from both the time-activity curves and the AIF. A hybrid dPET+sPET acquisition was simulated by retaining the last 5-minute data point at 55-60-minutes in addition to the 15-minute dPET data. Tracer kinetic modelling, using a two-tissue compartment model, was performed for prostate lesion using both the full-length, 15-minute, and 15+5-minute data. The kinetic parameters K_1, k_2, k_3, and K_i, were compared using linear regression and correlation analysis. ***Results:*** A strong linear relationship and strong correlation was found between full-length and 15-minute data for K_1 and K_i (K_1: Slope: 1.27, correlation coefficient: 0.98, K_i: slope: 1.8, correlation coefficient: 0.89). In contrast, k_2 and k_3 showed no significant linear relationship or correlation. The differences between full-length and shortened data were statistically significant for K_1, k_2 and k_3 ($p < 0.05$). When adding a late 5-minute data point, a strong linear relationship and a moderate to strong correlation was found between full-length and 15+5-minute data for all kinetic parameters (K_1: slope: 1.01, correlation coefficient: 0.99, k_2: slope: 1.42, correlation coefficient: 0.92, k_3: slope: 0.94, correlation coefficient 0.68, K_i: slope: 0.83, correlation coefficient: 0.91). No significant differences between full-length and 15+5-minute data were found for any of the k-values. ***Conclusion:*** We found significant differences in several kinetic parameters when comparing 15-minute and 60-minute [^{68}Ga]-PSMA-11 dPET data for prostate cancer patients. However, adding a short, 5-minute, sPET acquisition at 55-60-minutes provided consistent kinetic modeling parameters compared to full-lenth scans, suggesting clinical feasibility of a shortened dynamic PET protocol with maintained quantitative accuracy.

EP-1061

Comparison of uncertainty quantification methods for kinetic parameters derived from dynamic long-axial-field-of-view PET scans.

F. Gu[1], *Q. Wu*[2,3], *F. O'Sullivan*[2], *A. Rominger*[4], *K. Shi*[4];
[1]*School of Mathematics and Physics, North China Electric Power University, Beijing, CHINA,* [2]*School of Mathematical Sciences, University College Cork, Cork, IRELAND,* [3]*Insight SFI Center for Data Analytics, Cork, IRELAND,* [4]*Department of Nuclear Medicine, Bern University Hospital, University of Bern, Bern, SWITZERLAND.*

Aim/Introduction: Dynamic PET imaging with long axial field-of-view (LAFOV) scanners enables simultaneous, high-resolution assessment of tracer kinetics across the entire body. This advancement offers substantial benefits in clinical and research settings, particularly for multi-organ quantitative analysis. However, accurately estimating the uncertainty of kinetic parameters remains a major challenge due to the high-dimensional, spatiotemporal complexity of dynamic PET data. Robust uncertainty quantification is essential for physiological interpretation, model validation, and the clinical translation of parametric imaging results. ***Materials and Methods:*** This study systematically compares three uncertainty quantification methods for kinetic parameters derived from dynamic LAFOV PET data: (1) image-domain bootstrap based standard error (Boot-SE): based on a generalized linear model that incorporates both systematic and stochastic components, effectively capturing spatiotemporal dependencies [1,2]; (2) autocorrelation function-based standard error (ACF-SE): estimated using the product of mean voxel-wise variance within a region and a correction term that accounts for spatial autocorrelation between voxel pairs [3]; (3) crude standard error (Crude-SE): defined as the standard deviation divided by the square root of the number of voxels within the region. We applied voxel-level kinetic analysis to a dataset of 24 dynamic ^{18}F-FDG LAFOV PET scans, quantifying six physiological parameters. Uncertainty for each parameter was assessed across multiple organs, including the liver, lungs, kidneys, spleen, bones, brain (gray matter and white matter), bladder, and tumors, by applying above three approaches. ***Results:*** Boxplot comparisons across these organs revealed distinct patterns among the three methods. Crude-SE consistently underestimated the standard errors, failing to account for temporal and spatial dependencies in the data. ACF-SE, in contrast, tended to yield more conservative estimates, particularly in regions with high physiological variability. Boot-SE provided a balanced estimation with good robustness across organs and parameters. Notably, organs with high tracer heterogeneity (e.g., tumors) exhibited larger variability in SE estimation across all methods. ***Conclusion:*** Our findings highlight the limitations of relying solely on crude analytic error estimation for PET kinetics, especially in the era of whole-body LAFOV acquisition. We recommend Boot-SE as a practical and computationally feasible approach for general applications. ***References:*** [1]A generalized linear modeling approach to bootstrapping multi-frame PET image data. Medical Image Analysis, 72, 102132, 2021. [2] Mapping ^{18}F-FDG kinetics together with patient-specific bootstrap assessment of uncertainties: An illustration with data from a long-axial FOV PET/CT scanner. Journal of Nuclear Medicine, 65(6), 971-979, 2024. [3]An approximation formula for the variance of PET region-of-interest values. IEEE Transactions on Medical Imaging, 12(2), 240-250, 1993.

EP-1062

Discriminating Inflammation from Malignancy with Short-Dynamic Patlak Parametric FDG PET/CT

A. Artesani[1], *J. Jandric*[2], *L. Leonardi*[2], *R. Barisonzi*[2], *C. Vallone*[2], *L. Muraglia*[2], *M. Rodari*[2], *L. Evangelista*[1];
[1]*Humanitas University, Pieve Emanuele, ITALY,* [2]*IRCCS Humanitas Research Hospital, Rozzano, ITALY.*

Aim/Introduction: Dynamic ^{18}F-FDG PET/CT is increasingly employed in diagnostic workup and treatment response evaluation in oncology. Although previous studies have demonstrated the feasibility of dynamic acquisitions, the clinical added value of Patlak parametric imaging remains under active debate [1],[2]. In this study, we investigated whether parametric imaging from short-duration dynamic PET/CT protocol can reliably differentiate malignant lesions from inflammatory processes by quantitatively comparing the Patlak influx rate (K_i) and the volume of unmetabolized tracer (V_b) to the standardized uptake value (SUV). ***Materials and Methods:*** Patients with suspected solid tumors underwent a 20-min dynamic ^{18}F-FDG PET/CT scan. Dynamic data were subdivided into 5-min frames, and a Patlak analysis was performed to derive parametric images of K_i (ml/min/100ml) and V_b (arbitrary units). In selected cases, patients with inflammatory rectal changes—characterized by a modestly increased SUV relative to normal tissue—were compared with colon tumor lesions used as malignant references. Quantitative comparisons were made by evaluating the ratios between SUV and the parametric metrics within the same volume of interest. ***Results:*** In healthy liver tissue, SUV and K_i values were linearly correlated, yielding a conversion factor of about 0.3 between these metrics. In regions showing inflammatory rectal uptake, SUV values were moderately elevated (2.5-3.2 g/mL), and K_i values changed in accordance with the same conversion factor observed in healthy tissue (0.5-1.2 ml/min/100ml). In contrast, colon tumors demonstrated a different relationship, with SUV and K_i values

correlating according to a conversion factor of about 0.5; for example, a mean SUV of 12 g/mL corresponded to a K_i of roughly 7 ml/min/100ml. Moreover, the distribution and absolute values of V_b differed markedly between tissue types: inflammatory tissues exhibited higher V_b values, whereas malignant tissues showed comparatively reduced and peripherally localized V_b, reflecting underlying differences in vascular delivery and cellular FDG phosphorylation. ***Conclusion:*** The observed inverse relationship in the ratio of irreversibly metabolized tracer (K_i) to unmetabolized tracer (V_b) between inflammatory and tumor tissues is consistent with the expected higher vascular tracer availability but low metabolic trapping in inflammation versus enhanced cellular FDG phosphorylation in malignancy. This study proposes a 'reading method' for clinical differentiation of tumor versus inflammation. Further studies are warranted to validate whether the K_i/V_b ratio can become a reliable metric in more complex diagnostic scenarios. ***References:*** [1] S. Skawran et al., Life, 12, 9, 2022, 10.3390/life12091350 [2] A. H. Dias et al., EJNMMI Phys., 9, 1, 2022, 10.1186/s40658-022-00490-y.

EP-1063

Spill-over correction in [^{15}O]H_2O small animal studies

R. Siekkinen[1], *T. Uurasmaa*[2,1], *I. Heinonen*[1], *H. Iida*[1];
[1]Turku PET Centre, Turku, FINLAND, [2]Department of Biology, University of Turku, Turku, FINLAND.

Aim/Introduction: Quantitative perfusion imaging using [^{15}O]H_2O-PET has been widely applied to clinical research. However, its application to mice-sized rodents has been limited due to their small size, making the determination of input function (IF) challenging. Many studies, therefore, have relied on using standardized uptake values (SUV). We aimed assessing the systematic underestimation in left ventricular blood (LV) radioactivity concentration (RC) for enabling to determine IF from [^{15}O]H_2O images. ***Materials and Methods:*** Female FVB/N-mice (N=22) underwent two dynamic PET/CT imaging following [^{15}O]-H_2O injection and gaseous [^{15}O]CO inhalation with Molecubes system (Molecubes NV, Gent, Belgium).Three sizes of regions-of-interest (ROIs) were selected on LV, and one on myocardium, brain, and liver. RC (MBq/ml) within LV ROI was assumed to contain activity from the LV chamber and the myocardium. Recovery coefficient (β) expresses the underestimation of LV chamber's RC due to partial-volume-effect, and the spill-over fraction the amount of myocardium activity signal in LV ROI (γ). Spill-over was modeled following earlier works, where β+γ=1.0 [1,2]. β was estimated from [^{15}O]CO images at 5-8 min post initiation, by dividing LV ROI's RC with total blood's RC. Blood volume (ml/ml) for myocardium, brain, and liver was calculated by dividing organ ROI's RC with total blood RC. Spill-over-corrected K_1-flow (ml/min/g), k_2-flow (1/min), and arterial blood volume V_a (ml/ml) were calculated for myocardium, followed by calculation of spill-over-corrected IF [1]. This IF was applied to calculate K1, k2, and Va in brain and liver. Mean transit time (MTT) was calculated by dividing organ's blood volume with K1. ***Results:*** K1, k2, and Va decreased after the correction and showed small inter-subject variation regardless the correction for all organs, as in Iida et al. [1]. MTT increased after the correction, as expected. Brain MTTs are in accordance with what previously reported for mice [3]. However, myocardium MTTs were higher than previously reported [4], presumably because myocardium is affected by partial-volume effect. The smallest LV ROI showed fluctuation in time-activity-curves likely affecting the modelling accuracy, whereas no fluctuation was seen on medium and large-size ROIs. ***Conclusion:*** The method was considered effective in quantitatively assessing the tissue perfusion and MTT in total body organs in mice, though further evaluation studies are warranted. ***References:*** 1. Iida, H. et al. J Nucl Med (1992) 2. Iida, H. et al. J Nucl Med (1998) 3. Kang, H.M. et al. J Cereb Bl Flow and Metab (2015) 4. Wang D.J.J. et al. Magn Reson Med (2010).

EP-1064

A Simple Bone Marrow Kinetic Modelling Method in Patients with Symptomatic Multiple Myeloma

C. Nanni[1], *I. Brusa*[1], *D. Dall'olio*[2], *S. Peluso*[2], *M. Di Franco*[3], *M. Stasolla*[3], *E. Zamagni*[2], *M. Talarico*[2], *G. Wang*[4], *B. Spencer*[4], *A. Farolfi*[1], *M. Assenza*[5], *E. Fortunati*[1], *S. Civollani*[1], *L. Nardo*[4], *G. Castellani*[2], *S. Fanti*[1];
[1]Nuclear Medicine, IRCCS Azienda Ospedaliero-Universitaria di Bologna, Bologna, ITALY, [2]Department of Medical and Surgical Sciences, University of Bologna, Bologna, ITALY, [3]Nuclear Medicine, Alma Mater Studiorum University of Bologna, Bologna, ITALY, [4]Department of Radiology, University of California Davis, Sacramento, CA, UNITED STATES OF AMERICA, [5]Professional Development and Implementation of Research in Health Professional Unit, IRCCS Azienda Ospedaliero-Universitaria di Bologna, Bologna, ITALY.

Aim/Introduction: Bone Marrow (BM) FDG uptake can be within normal limits (Deauville Score DS 2 and 3) in patients with symptomatic Multiple Myeloma (sMM) at staging or relapse not identifying its pathological nature, especially if plasma cell infiltration is moderate. We seek to preliminary observe the kinetic of FDG BM-uptake in sMM patients at staging or disease relapse as compared to normal patients to increase FDG sensitivity for detecting bone marrow infiltration through Multi-Time Graphical Analysis (MTGA) and late short dynamic acquisitions applicable in the clinical routine and in the setting of pain patients such as MM patients. ***Materials and Methods:*** We enrolled 29 pts (18M,11F, mean age 72) with sMM at staging or disease relapse and 15 healthy controls. All patients underwent a 30' dynamic acquisition on LAFOV PET/CT (uExplorer, United) starting 35' post FDG injection. DS was established on a static reconstruction of the last 5' acquisition. L3 was manually segmented and, if L3 included a focal lesion, the closer vertebral body without lesions was considered. FDG uptake and pharmacokinetics were evaluated by MTGA (Patlak and RE-plots). Mean absolute scaled error (MASE) and Akaike Information Criterion (AIC) were used to perform model selection, alongside Vuong's test. Patients were divided into: Group 1 with BM-DS 2,3 (Low-DS, n=21); Gr2 with BM-DS 4 (High DS, n=8); Gr3 including healthy controls (HC, n=15). ***Results:*** Reversible uptake (RE-plots) resulted as the best fit in all groups. Average DV for Low-DS was (0.667±0.081), while it was (0.984±0.282) for High-DS and (0.227±0.229) for HC. Testing distribution volumes (DV) revealed that both Low-DS and High-DS had a significantly higher DV than HC ($p<10^{-5}$ for both). In addition, High-DS also reported a significantly higher DV than Low-DS ($p<10^{-5}$). ***Conclusion:*** These preliminary results suggest that in patients with MM, infiltrated BMs with low FDG uptake (false negatives) show a reversible kinetic behaviour significantly different from HC. In clinical practice, a late dynamic acquisition instead of a static acquisition may be proposed to add sensitivity and specificity to the FDG scan for discriminating normal vs infiltrated BM. The fitting can be performed without considering the initial non-equilibrium phase (i.e., approximately 10' p.i.), which considerably simplifies the modelling process. This possibility is particularly relevant in case of clinical disease relapse rather than disease staging.

EP-1065

A comparison of renograms: posterior only and geometric mean imaging

R. Feathers, *W. Morton, P. Bartholomew;*
South Tyneside and Sunderland Foundation Trust, Sunderland, UNITED KINGDOM.

Aim/Introduction: To evaluate the utility of using a geometric mean of posterior and anterior imaging for a nuclear medicine MAG3 renogram to properly assess the relative function and drainage of the kidneys. The current standard is posterior only imaging which may not fully capture the functionality of the

kidney as depth and kidney movement away from the camera head cannot be accounted for. For every 1 cm of depth, there is a 10% loss of counts due to attenuation, so small movements could change the recorded values. ***Materials and Methods:*** A cohort of 100 patients underwent a renogram study where both anterior and posterior projections were acquired after an intravenous injection of ^{99m}Tc MAG3. For each patient a standard posterior only renogram was processed alongside a geometric mean of the posterior and anterior images. Regions of interest were drawn over the kidney to create a time activity curve (TAC), and the relative kidney function was calculated. Each TAC generated was assessed by an experienced nuclear medicine reporter and graded on the level of obstruction observed. The renal pelves were measured on a CT IVU to assess renal dilation. ***Results:*** Processing the renograms as a geometric mean showed a change in function for most patients, with varying significance in scale. The addition of the anterior data brought some clarity to previously equivocal TACs. ***Conclusion:*** For certain patients a large difference was seen between the relative function calculated by the posterior only against the geometric mean renogram analysis. For patients undergoing kidney assessment for a nephrectomy, a change in relative function may change the available surgical options. Some TACs saw changes to their equivocal results, which can change patient outcomes and subsequent medical management.

EP-1066

Comparative Performance of ^{68}Ga-FAPI-04 Versus ^{18}F-FDG PET/CT in Thyroid-Associated Orbitopathy: A Prospective Pilot Study with Dynamic/Static Parametric Validation

L. Yang, *L. Guan;*
Nuclear Medicine, the First Affiliated Hospital of Chongqing Medical University, Chongqing, CHINA.

Aim/Introduction: To prospectively compare the diagnostic efficacy of ^{68}Ga-FAPI-04 and ^{18}F-FDG PET/CT in thyroid-associated orbitopathy (TAO), and to evaluate whether dynamic PET parameters provide incremental value over conventional static metrics. ***Materials and Methods:*** Six treatment-naive TAO patients (3 active [CAS≥4], 3 chronic [CAS≤1+MRI fibrosis]) underwent sequential PET/CT scans (median interval: 3 days, range: 1-7) using: 1. Dynamic Protocol: 60-min list-mode acquisition on a long-axial PET/CT scanner; frame sequence: 30×10s, 10×30s, 5×60s, 5×300s; reconstruction: OSEM + TOF + PSF. 2. Static Protocol: standard whole-body acquisition at 60-min post-injection. 3. Image Analysis: maximum standardized uptake value (SUVmax) in extraocular muscles; target-to-background ratio (TBRmuscle/brain); Patlak-derived metabolic influx rate (Ki) using image-derived input function; two-tissue compartmental K1 (perfusion parameter). 4. Statistical Note: all values reported as mean ± standard deviation. No inferential statistics were applied per STROBE guidelines for pilot studies. ***Results:*** In active TAO patients (n=3), ^{68}Ga-FAPI-04 demonstrated significantly higher uptake than ^{18}F-FDG, with mean SUVmax values of 7.1 (±0.3) versus 4.0 (±0.2), representing a 78% increase in tracer avidity. Chronic TAO cases (n=3) showed low uptake for both tracers (FAPI-SUVmax: 2.1±0.2; FDG-SUVmax: 1.9±0.1). Dynamic analysis revealed a 3.3-fold difference in Patlak-derived Ki values between active (0.013±0.001 min^{-1}) and chronic phases (0.004±0.001 min^{-1}), marginally outperforming the 3.0-fold contrast observed with static FAPI-SUVmax. ***Conclusion:*** This pilot study demonstrates: 1. ^{68}Ga-FAPI-04 provides higher lesion conspicuity than ^{18}F-FDG in TAO. 2. Dynamic parameters offer modest but measurable advantages over static indices. 3. The proposed protocol is technically robust for multicenter validation. ***References:*** 1.Buber J, Robertson HT. Cardiopulmonary exercise testing for heart failure: pathophysiology and predictive markers. Heart. 2023;109(4):256-263. Published 2023 Jan 27. doi:10.1136/heartjnl-2021-319617. 2.Zhang G, Liu X, Wang L, Xing G, Tian C, Fu H. Copper Collector Generated Cu+/Cu2+ Redox Pair for Enhanced Efficiency and Lifetime of Zn-Ni/Air Hybrid Battery. ACS Nano. 2022;16(10):17139-17148. doi:10.1021/acsnano.2c07542. 3.Zhao R, Ke M, Lv J, et al. First-in-human study of PSMA-targeting agent, [18F]AlF-P16-093: dosimetry and initial evaluation in prostate cancer patients. Eur J Nucl Med Mol Imaging. 2024;51(6):1753-1762. doi:10.1007/s00259-024-06596-y. 4. Li H, Wang Y, Zhou J, et al. Evaluation of fibroinflammatory activity in thyroid eye disease using [^{18}F]AlF-NOTA-FAPI-04 PET/CT: A prospective study. Eur J Nucl Med Mol Imaging. 2025;52(5):1890-1900. doi:10.1007/s00259-024-07015-y. 5. Giesel FL, Kratochwil C, Lindner T, et al. ^{68}Ga-FAPI PET/CT: Biodistribution and Preliminary Dosimetry Estimate of 2 DOTA-Containing FAP-Targeting Agents in Patients with Various Cancers. J Nucl Med. 2019;60(3):386-392. doi:10.2967/jnumed.118.215913.

EP-65

e-Poster Area

D: Technical Studies -> D2 Data Analysis and Artificial Intelligence -> D26 Other Data Analysis

EP-1067

Organ-based normative values in healthy subjects derived from whole-body [18F]FDG-PET/CT

C. Loisel[1], *M. Pires*[2], *R. Seban*[3], *F. Orlhac*[4], *S. Gutschmayer*[5], *I. Buvat*[4], *T. Beyer*[2];
[1]*Institut Curie, Orsay, FRANCE,* [2]*Medical University of Vienna, Vienna, AUSTRIA,* [3]*Dpt of Nuclear Medicine, Institut Curie, Saint Cloud, FRANCE,* [4]*Institut Curie, Inserm, Orsay, FRANCE,* [5]*Dept of Nuclear Medicine, Medical University of Vienna, Vienna, AUSTRIA.*

Aim/Introduction: [18F]FDG-PET/CT is a widely used imaging modality for assessing metabolic activity over the whole body. However, organ-specific normative values have not been reported extensively. This study aims to establish organ-specific normative uptake values and their variability using whole-body [18F]FDG-PET/CT in a cohort of healthy subjects. ***Materials and Methods:*** Forty-eight healthy subjects (25 females, 23 males; mean age: 38 ± 14 years) underwent dynamic [^{18}F]FDG PET/CT imaging using a Siemens Biograph Vision Quadra PET/CT scanner at the Medical University of Vienna. Each subject completed a test and retest whole-body scan 5 weeks apart. From the 55-60-minute post-injection list-mode data, static PET images were reconstructed. Twenty-seven anatomical volumes of interest (VOIs) were segmented from the CT images using two automated algorithms: TotalSegmentator v2.8.0 and MOOSE v3.0.13. The volume (mL) and mean Hounsfield unit (HUmean) in each VOI were calculated from the CT, together with the mean SUV (SUVmean) obtained from the PET. Differences between test and retest values for males and females separately were evaluated using relative %-differences, t-tests and Wilcoxon signed-rank tests including Benjamini-Hochberg correction for multiple comparisons. Additionally, robustness across segmentation methods was investigated. ***Results:*** There were no significant differences between test and retest measurements for organ SUVmean, HUmean, and volume whatever the segmentation algorithms. However, high inter-subject SUVmean variability (>15%, defined as the mean of $\sigma_{SUVmean}$/SUVmean over the test and retest groups) was observed in 15/27 VOIs including the heart, kidneys, bladder, fat, skull and VOIs in the digestive system regions. In contrast, 12/27 VOIs demonstrated low (<15%) SUVmean inter-subject variability (mean %difference range in test and retest groups: [8.6,13.8]%) including the brain, liver, pancreas, spleen or muscles. Volumes were generally higher in men, probably due to BMI differences (BMI=26±3 for men and 23±3 for women, $p<0.001$). Significant difference in SUVmean was found between men and women in the test and retest groups only in the subcutaneous fat (p_{test} and $p_{retest}<10^{-4}$) with a low

inter-subject variability (<15%) in each gender group. SUVmean values were not affected by the segmentation algorithms (<10%), except for small bowel, and for skeletal muscles, subcutaneous fat and torso fat that are segmented across the entire body by TotalSegmentator but using only the L3 region in MOOSE. ***Conclusion:*** All organs demonstrated reproducible SUVmean, HUmean and volume measurements across test-retest analysis. However, only twelve organs demonstrated consistent SUVmean measurements, with low inter-subject and inter-segmentation-method variability, making them strong candidates for establishing organ-based normative reference standards.

EP-1068

A Novel Variance Reduction Technique for Efficient Monte Carlo Simulation of SPECT Images

D. Sarrut, *A. Etxebeste, M. Jacquet, J. Letang;*
CREATIS CNRS, Villeurbanne, FRANCE.

Aim/Introduction: This study introduces a novel Variance Reduction Technique (VRT) called FF-AA for Monte Carlo simulation of SPECT images. The aim is to enhance simulation efficiency and accuracy, particularly in low-count regions, while maintaining broad applicability across different geometrical elements. Monte Carlo simulations are indispensable in SPECT imaging but are often computationally demanding. Traditional methods typically rely on Forced Detection and/or detector response functions like ARF, which generally depend on an analytical model of the detector response. Other methods leverage GPU acceleration to provide significant speedups but are constrained by specific implementations and hardware requirements. Additionally, GAN-based approaches have been proposed; however, they also depend on detector models and require neural network training for each different phantom. Our proposal, implemented in GATE based on Geant4, addresses these limitations. This reliance on specific models and implementations limits the flexibility of these methods, particularly when users aim to optimize collimator design. ***Materials and Methods:*** The FF-AA method employs a two-step approach: primary and scatter. Primary gamma photons are tracked linearly towards the detector with forced detection and free flight weighted contributions. Free Flight, a concept from Geant4, allows particles to be tracked through various elements such as phantoms and collimators. This approach enables particles to travel in a straight line, updating their weight as they traverse different materials. Scatter is simulated using split Compton and Rayleigh interactions, which are also free-flighted towards the detector. This method was benchmarked against analog Monte Carlo simulations to evaluate its performance. ***Results:*** The FF-AA method demonstrated a significant speedup of approximately 20-30 times compared to analog Monte Carlo simulations. In low-count regions, this speedup was even more pronounced, reaching around 40 times. The optimal splitting factor was evaluated and found to be surprisingly low, around 20 to 40, despite the low acceptance angle. Additionally, statistical relative uncertainties were integrated and computed using a history-by-history method, providing pixel-based uncertainty in the generated projection images. ***Conclusion:*** The primary advantage of the new FF-AA method is its ability to achieve significant speedups, particularly in low-count regions. Its generic applicability to various geometrical elements makes it a valuable tool for SPECT collimator design development. Additionally, the implementation is open-source and available in the new Python-based GATE version 10. ***References:*** - Cajgfinger2018. PMB, 63(5), 055011 - Beck1982. IEEE-TNS, 29(1), 506-511 - Saporta2022. PMB, 67(23), 234001 - Liu2008. IEEE-TNS, 55(1), 560-567 - Rydén2018. EJNMMI Physics, 5(1), 1 - Sarrut2021. PMB, 66(10), 10TR03.

EP-1069

Artificial Intelligence Analysis of Nuclear Medicine Perception on Social Media

D. Yahiro, *C. T. Mesquita;*
Universidade Federal Fluminense, Niterói, BRAZIL.

Aim/Introduction: Nuclear Medicine is an evolving medical specialty that plays a crucial role in diagnostic and therapeutic conditions. Despite its importance, public awareness remains limited, particularly among younger generations and medical students. Social media platforms like Reddit are valuable repositories of real-time discussions, where users share opinions, experiences, and questions related to multiple subjects, including healthcare. With recent advancements in Natural Language Processing (NLP), particularly transformer-based models, it is possible to extract meaningful insights from these large, unstructured text datasets. This study aims to identify and analyze nuclear medicine discussions on Reddit using AI-based topic modeling to better understand public perceptions of the exam and the nuclear medicine field more broadly. ***Materials and Methods:*** Since June 2013, ten relevant subreddits focused on nuclear medicine, medical school, and related specialties were selected. Posts and comments were filtered using a predefined set of nuclear medicine-related keywords to extract pertinent discussions. After preprocessing, the data was analyzed using BERTopic, an unsupervised topic model that utilizes transformer-based embeddings and clustering algorithms to identify underlying themes. Visualization of topic similarity was performed using Uniform Manifold Approximation and Projection (UMAP), a dimensionality reduction tool. Sentiment analysis was conducted to classify each post or comment as positive, negative, or neutral. ***Results:*** A total of 4,602 discussions from 2,792 unique users were included after duplicate removal. The model identified 80 unique topics, which were further grouped into 7 major themes, including training pathway, economic considerations, workload and scheduling hours, career development, financial compensation, test preparations, and moderation of discussion. Clustering performance showed a silhouette score of 0.866 and a Davies-Bouldin score of 0.132, indicating strong model performance. Sentiment analysis revealed that 30.57% of discussions were negative, 58.41% neutral, and 11.02% positive. While neutral sentiment dominated across all themes, negative sentiments were more prominent in discussions related to group moderation, training limitations and financial concerns. ***Conclusion:*** With social media platforms, it is possible to understand public and trainee perspectives on nuclear medicine. By applying AI-based topic modeling and sentiment analysis, this study demonstrates the utility of NLP in identifying public sentiment and thematic concerns about the specialty. Such insights may inform targeted strategies to improve awareness, engagement, and recruitment, particularly among medical students and early-career professionals.

EP-1070

Identification and Validation of Robust FDG-PET/MR Texture Biomarkers in Uterine Cervical Cancer

U. Björeland[1,2], *K. Sandgren*[2], *S. Strandberg*[2];
[1]*Medical Physics, Sundsvall Hospital, Sundsvall, SWEDEN,*
[2]*Department of Diagnostics and Intervention, Umeå University, Umeå, SWEDEN.*

Aim/Introduction: Texture analysis quantifies the spatial arrangement and variation of voxel intensities within a region of interest, extracting high-order features, such as grey-level co-occurrence (GLCM), and morphological descriptors that reveal tissue heterogeneity invisible to the naked eye [1-3]. These features function as reproducible imaging biomarkers for lesion characterization, improving diagnosis, risk stratification, and treatment monitoring in oncology [1,3]. However, the sheer

number of available texture features necessitates a rigorous, systematic workflow to isolate those that are truly robust and reproducible [4, 5].The aim is to develop and validate a systematic workflow for deriving stable PET texture biomarkers, with the goal of enhancing diagnostic, prognostic, and monitoring tools in gynecological cancers. ***Materials and Methods:*** In this pilot study, eight patients underwent dynamic FDG-PET/MR over 30 minutes, divided into six 5-minute frames. For each patient, seven standard uptake value (SUV) images were generated and two VOI-strategies were compared: 1. Individualized VOI: a unique SUV42% contour per frame based on that frame's $SUV_{max.}$ 2. Averaged VOI: a single SUV42% contour from the entire 30-minute acquisition, applied identically to all frames. All images were resampled to isotropic 1×1×1 mm resolution using both Hamming-windowed-sinc and third-order B-spline interpolation. A total of 174 features per frame were extracted with SPAARC software under IBSI standards [6,7] and z-score normalized per patient. For each feature, the coefficient of variation (CV)across the six frames was computed and averaged across patients. Features were ranked by ascending CV, then selected iteratively if their absolute Pearson correlation with all previously chosen features was <0.7. Finally, temporal stability was assessed by Friedman's test ($\alpha = 0.05$), retaining features with $p > 0.05$. ***Results:*** Overall, the workflow revealed that the choice of VOI strategy and interpolation method significantly affected feature stability. When using individualized VOIs, Hamming interpolation produced 16 stable features, whereas B-spline interpolation yielded 15. In contrast, with averaged VOIs both Hamming and B-spline interpolators resulted in 11 stable features each. Across all VOI strategies and interpolators, the features consistently identified as robust biomarkers were ClusterShade(cm_clust_shade_3D_comb), Coarseness(ngt_coarseness_3D), Compactness(morph_com) and Kurtosis(stat_kurtfrom). ***Conclusion:*** This workflow identifies reproducible PET texture biomarkers. VOI definition strongly influences both the number and nature of stable features, while the choice of interpolation modulates their extraction. Individualized VOIs enable a broader set of parameters capturing both border and inner-texture heterogeneity; fixed VOIs produce a more concise, reproducible panel focused on internal texture. ***References:*** 1.Shur, J.D: Radiographics, 2021_2. HattM: JNuclMed, 2019_3.Gillies, R.J: Radiology, 2016_4. Hatt,M: EANM/SNMMI, Radiomics, 2022_5. Kinahan, P.E: QIBA, 2020_6. IBSI, 2019_7. Whybra P: Radiology, 2024.

EP-1071

Artificial intelligence for opportunistic detection of immune checkpoint inhibitor-related adverse events using [^{18}F]FDG PET/CT

C. Spielvogel*, L. Zisser, A. Lazarevic, D. Haberl, C. Eseroglou, M. Hacker, R. Calabretta;*
Medical University of Vienna, Vienna, AUSTRIA.

Aim/Introduction: Immune checkpoint inhibitors (ICIs) have transformed the treatment landscape for various cancers, including lung cancer, melanoma, and lymphoma. By blocking PD-1, PD-L1, and CTLA-4, ICIs unleash cytotoxic T cells to target tumor cells. However, they can cause immune-related adverse events (irAEs) by activating off-target immune responses. [^{18}F]FDG PET/CT is a promising tool for visualizing systemic immune activation, but manual assessment of organ-level inflammation is time-consuming and underlies inter-reader variability. This study explores the use of an automated artificial intelligence (AI)-based segmentation approach to detect organ-level changes in FDG uptake before and after ICI therapy, aiming to opportunistically identify irAEs. ***Materials and Methods:*** Patients with lung cancer, melanoma, or lymphoma who underwent [^{18}F]FDG PET/CT scans both before and after starting ICI therapy (PD-1, PD-L1, or CTLA-4 inhibitors) were included. An AI-driven segmentation model delineated organ boundaries on CT, which were eroded and transferred to PET for SUVmax and SUVmean quantification in irAE-related organs, including the thyroid, heart, pancreas, and liver. Lesion regions were excluded using a deep learning-based lesion segmentation model. Changes in organ uptake pre- vs. post-therapy were statistically analyzed and correlated with clinically reported irAEs. ***Results:*** A total of 64 patients were analyzed, with a median scan interval of 3.2 months. The thyroid showed significant FDG uptake increases post-ICI (ΔSUVmax median = 0.44, $p = 0.04$; ΔSUVmean = 0.22, $p = 0.08$). Elevated uptake occurred in 55% (SUVmax) and 53% (SUVmean) of patients. Among those with increased thyroid uptake, 29% developed thyroid-related irAEs, compared to only 3% of those with decreased uptake ($p = 0.008$). Patients with thyroid irAEs had markedly higher uptake changes (ΔSUVmax = 2.1; ΔSUVmean = 0.69). Hypothyroidism was the primary driver, significantly associated with increased thyroid SUVmax ($p = 0.002$) and SUVmean ($p = 0.03$), whereas hyperthyroidism showed weaker, non-significant trends. FDG uptake also rose in the myocardium, pancreas, and liver post-therapy, but without statistical significance ($p > 0.05$). ***Conclusion:*** AI-assisted analysis of [^{18}F]FDG PET/CT enables automated, opportunistic screening for irAEs in patients undergoing ICI therapy. AI-assessed thyroid FDG uptake, especially in hypothyroidism, is strongly associated with immune-related toxicity, suggesting its utility as a biomarker for early detection. This approach supports more proactive management of irAEs and may improve outcomes by guiding timely interventions.

EP-1072

Investigating AD and non-AD ^{18}F-flortaucipir distribution patterns in a memory clinic cohort

F. Piva[1]*, C. Boccalini*[2]*, N. Ashton*[3]*, H. Zetterberg*[3]*, K. Blennow*[3]*, G. B. Frisoni*[4]*, M. Veronese*[1]*, V. Garibotto*[4]*, D. E. Peretti*[2]*;*
[1]University of Padova, Padua, ITALY, [2]University of Geneva, Geneva, SWITZERLAND, [3]University of Gothenburg, Mölndal, SWEDEN, [4]Geneva University Hospitals, Geneva, SWITZERLAND.

Aim/Introduction: Neurodegenerative disorders may be characterized by distinct tauopathies, which result in different ^{18}F-flortaucipir tau PET topographic patterns. This study aimed to investigate in a memory clinic cohort whether ^{18}F-flortaucipir patterns could be used to differentiate between amyloid-positive and -negative forms of neurodegeneration, potentially eliminating the need for an amyloid-PET. ***Materials and Methods:*** A total of 81 subjects were included in this study: 40 with Alzheimer's disease characterized by both amyloid (A) and tau (T) accumulation (A+T+), 13 with suspected non-Alzheimer's pathology (SNAP: A-T+), and 28 without A or T abnormalities on PET (A-T-). Scaled subprofile modeling using principal component analysis (SSM/PCA) was applied to 18F-flortaucipir images to identify two disease patterns (DPs), representing A+ and A- neurodegeneration. Each subject's imaging data was then compared to these DPs, and the resulting similarity scores were used as inputs for three machine learning models: Support Vector Machine (SVM), Random Forest (RF), and Multi-Layer Perceptron (MLP) to predict amyloid status. Finally, Spearman correlation analyses were conducted to assess associations between similarity scores and plasma biomarker levels. ***Results:*** The two identified DPs exhibited distinct PET signatures consistent with current disease knowledge. All the machine learning models confirm the capacity of A+ DP to predict AD pathology, with MLP achieving the highest accuracy in groups discrimination (accuracy = 0.88), correctly classifying 38 out of 40 of A+T+ subjects. However, only 5 out of 13 A-T+ were correctly classified, highlighting the limited expressiveness of A- DP. Both A+ and A- DP scores are significantly correlated with plasma biomarkers, except for Ab_{42}/Ab_{40} and $p\text{-}tau_{231}$ plasma biomarkers with scores derived from the A- DP. ***Conclusion:*** SSM/PCA derived patterns on ^{18}F-flortaucipir-PET imaging provide information on

both amyloid and tau status, in favour of its use as first and possibly sole examination in the investigation of suspected AD. However, for non-AD cases, amyloid PET scans is still recommended.

EP-1073

A Non-Invasive Method for Measurement of Cerebral Glucose Transport Capacity and Metabolic Rate Using [^{18}F]FDG and a Pre-bolus Scan of the Heart

N. Hansen[1], *S. A. S. Kjeldsen*[1], *M. N. Lonsdale*[2], *I. L. Rasmussen*[2], *S. Fuglsang*[2], *C. S. Meyhoff*[3,4], *R. Boellaard*[5], *J. Rungby*[6,4], *N. J. Wewer Albrechtsen*[1,4], *L. Marner*[2,4,7];
[1]*Department of Clinical Biochemistry, Copenhagen University Hospital - Bispebjerg and Frederiksberg Hospital, Copenhagen, DENMARK,* [2]*Department of Clinical Physiology and Nuclear Medicine, Copenhagen University Hospital - Bispebjerg and Frederiksberg Hospital, Copenhagen, DENMARK,* [3]*Department of Anaesthesia and Intensive Care, Copenhagen University Hospital - Bispebjerg and Frederiksberg Hospital, Copenhagen, DENMARK,* [4]*Department of Clinical Medicine, University of Copenhagen, Copenhagen, DENMARK,* [5]*Department of Radiology and Nuclear Medicine, Amsterdam UMC, Amsterdam, NETHERLANDS,* [6]*Steno Diabetes Center Copenhagen, Herlev, DENMARK,* [7]*Department of Nuclear Medicine, Copenhagen University Hospital - Herlev Hospital, Herlev, DENMARK.*

Aim/Introduction: We aim at establishing a method for measuring cerebral glucose transfer capacity, T_{max}[1], and metabolic rate, CMR_{glc}, without the need for arterial sampling. Extending our previously presented non-invasive method for CMR_{glc}[2], which cannot measure T_{max} (as T_{max} is derived from the initial cerebral uptake K_1), we include a prebolus of [^{18}F]FDG and an additional scan of the heart for extracting the image-derived input function (IDIF). ***Materials and Methods:*** Six healthy subjects had a prebolus of 21 (range 16-26) MBq [^{18}F]FDG simultaneously with the initiation of a 10 min dynamic scan of the heart, followed by a 10 min static scan of the brain to assess [^{18}F]FDG uptake from the prebolus. Then, a second bolus of 188 (range 154-223) MBq was injected followed by a 40 min dynamic scan of the brain. Finally, a 5 min static heart scan covered the tail of the input function with the same VOI in the left ventricle for extraction of the IDIF. Both injections were performed with a power injector (1 mL/s) to ensure fast and reproducible boluses. Arterial sampling was performed continuously during the initial 10 min after the second injection, followed by manual samples every 5 min for plasma and whole-blood radioactivity concentrations to achieve the arterial input function (AIF). The IDIF was multiplied with the average plasma/whole-blood ratio. Kinetic modeling was performed for four bilateral regions using a four-parameter two-compartment model with fit of blood volume fraction. The time-activity curves were corrected for the residual activity from the prebolus injection in an iterative process assuming identical uptake during the two injections. K_1 and CMR_{glc} using IDIF vs. AIF were compared. ***Results:*** CMR_{glc} and K_1 estimates from IDIF demonstrated high correlation to values estimated from AIF with r^2=0.91 and r^2=0.86, respectively and with mean relative numeric differences of 7.0% and 8.2% but with a slightly higher CMR_{glc} values of 4.5% for IDIF (paired t-test, p=0.02). ***Conclusion:*** Our non-invasive method for robust estimation of CMR_{glc} and K_1 (to derive T_{max}) achieved acceptable bias compared with arterial sampling. The method is applicable to all scanner systems. Automated analyses are warranted for the labor-intensive iterative corrections for prebolus activity to allow for wide-spread use and voxel-wise analysis. ***References:*** [1]Gejl et al. 2017. Sci Reports 7:17490. [2]Henriksen et al. 2022. Neuroimage 253:119079.

EP-1074

Deep Learning-based attenuation correction of myocardial perfusion imaging studies

D. Apostolopoulos[1], *N. Papathanasiou*[1], *T. Spyridonidis*[1], *M. Spiliotopoulou*[1], *I. Apostolopoulos*[2];
[1]*University General Hospital of Patras, Patras, GREECE,* [2]*Department of Medical Physics, School of Medicine, University of Patras, Patras, GREECE.*

Aim/Introduction: Aim/Introduction CT-based attenuation correction (AC) improves the accuracy of myocardial perfusion imaging (MPI), mainly by increasing specificity. However, CT increases patients' irradiation, lengthens acquisition time and is not available in all gamma-camera systems. Deep learning (DL) models have been developed to predict AC from non-corrected (NAC) images. ***Materials and Methods:*** Materials and Methods The NAC and AC polar maps (PM) from 470 consecutive MPI SPECT/CT studies (in 320 males and 150 females with BMI 29.0 Kg/m^2±5.02) were used retrospectively to construct DL models for predicting AC from NAC PM. The hybrid system Hawkeye-4 (GE Healthcare) was employed in SPECT/CT acquisition. Seven hundred (700) AC-NAC PM pairs, in DICOM format, were retrieved from 230 stress-rest and 240 stress-only studies. The actual AC PM images served as the ground truth for the developed DL models. Patient-specific features (sex, chest perimeter at the mid-level of the heart and myocardial volume) were also taken into account for model creation and training. The developed models included variations of U-Net structures and attention-based convolutional neural networks. Finally, we applied the models prospectively in 155 PM pairs from 100 consecutive patients (70 males, 30 females) for validation. Chest perimeter was measured from CT images in the model-learning group and by a measuring tape in the validation group, whereas NAC myocardial volume was automatically calculated by the SPECT processing software. Model performance was assessed using structural similarity index (SSIM), mean absolute pixel value error (MAE), and peak signal-to-noise ratio (PSNR). In addition, calculated summed stress/rest/difference scores (SSS, SRS and SDS), as well as visual assessment by two Nuclear Medicine experts, were used to compare actual with predicted AC PM. ***Results:*** Results All models exhibited high performance metrics (MAE < 0.04 and SSIM > 0.96) in both learning and validation groups. SSS, SRS and SDS values were not different between actual and predicted AC PM ($p<0.05$). Experts' evaluation revealed visual discrepancies in many cases of the validation set (40-45% with different models), but these were minor, not affecting the final diagnosis. Substantial inconsistencies were observed in 1-2% of cases. The inclusion of patient-specific features improved model performance metrics by 5-10%. ***Conclusion:*** Conclusion Our findings suggest that DL-based AC estimation in MPI SPECT studies holds significant promise, with further improvement anticipated as more data are added in the model-learning group. The inclusion of patient-specific features in the model seems to increase the accuracy of predicted AC images.

EP-1075

Navigating complexity: effective workflow management for high throughput PET-CT imaging in a multi-tracer multi-machine theranostic nuclear medicine department.

T. Henry, *L. Ferreol, C. Balleyguier, D. Deandreis;*
Gustave Roussy, Villejuif, FRANCE.

Aim/Introduction: The integration of PET-CT imaging in oncology has revolutionized cancer diagnosis and management. However, the high demand for PET-CT imaging requires effective workflow management to ensure timely, efficient and secure patient care. This study aimed to describe the workflow strategies implemented at an oncological center to achieve high throughput of PET-CT imaging tailored to cancer patient care. ***Materials and Methods:***

We analyzed retrospective appointments data from January 2023 to April 2024, including examination dates, tracers' type, and referral committee. Incident reports were cross-referenced to identify operational disruptions. Interviews with the lead technologist and lead radiopharmacist were performed to thoroughly describe their organization, emphasizing the coordination among the two. ***Results:*** Our department conducted 14,649 PET-CT examinations over the study period, with FDG used in 90.4% of cases. Among FDG examinations, the breast committee accounted for 39.5%, followed by head and neck (10.4%) and skin (8.5%) committees. Analysis revealed cyclical patterns in activity, with regular dips coinciding with school holidays. A notable trend was observed with an increase in PSMA-like tracer usage and a corresponding decrease in choline-like tracers, reflecting evolving clinical guidelines. Sixty-one incidents were recorded, primarily occurring during morning startup procedures, resulting in 246 hours of lost operational time, significantly impacting daily PET-CT throughput (p=0.026). The nature of these incidents included equipment malfunctions and delays in radiopharmaceutical deliveries. To address these challenges, a three-tiered prioritization system for FDG examinations was established based on clinical urgency (urgent, rapid, programmed), with an overbooking system allowing scheduling of urgent cases beyond theoretical available slots. Three dedicated fast-track pathways were established for breast, gynecological, and lung cancers, providing rapid access to PET-CT for initial staging. A structured weekly schedule was implemented with specific days dedicated to different tracers, optimizing radiopharmacy resources. Implementing a dedicated technician solely for radiotracer injections improved communication between the injection area and scanning rooms, while staggered technician schedules optimized personnel coverage throughout the day. Additionally, a two-tier interpretation system was established, with dedicated physicians for same-day reporting and separate physicians analyzing non-urgent cases the following day without interruptions from clinical management tasks. ***Conclusion:*** Our study outlines a comprehensive approach to streamlining PET-CT services, from appointment scheduling to image interpretation. Implementing structured workflow management in PET-CT imaging can enhance operational efficiency, reduce delays, and improve patients' care and health workers' well-being in a high-volume oncology center.

EP-1076

Estimation of Relative Renal Function on DMSA Scans via Deep Regression

M. Abdi[1], *A. BELAID*[2], *Y. Ghedbane*[3], *S. YAHIAOUI*[2], *M. HABBACHE*[1], *Q. NAILI*[1];
[1]*Centre d'imagerie scintigraphique (CIS) Blida, Blida, ALGERIA,* [2]*Centre de Recherche sur L'Information Scientifique et Technique (CERIST), Algiers, ALGERIA,* [3]*Centre d'imagerie scintigraphique (CIS) Setif, Setif, ALGERIA.*

Aim/Introduction: Accurate estimation of relative renal function (RRF) is crucial for managing various renal disorders. Traditional methods can be time-consuming and variable according to region of interest drawing (ROI)[1]. This study aim to develop and evaluate a fully automated, image-based approach using deep learning regression to estimate RRF directly from static Dimercaptosuccinic Acid (DMSA) scintigraphy scans, bypassing manual ROI delineation. ***Materials and Methods:*** A retrospective dataset of 1116 static posterior DMSA scans, acquired using four different gamma cameras from patients with diverse pathologies, ages, and genders is used. Ectopic and fused kidneys are excluded (need for anterior scans). Ground truth RRF values are derived from consensus readings by two nuclear medicine physicians. The dataset is splited into training (0.8/0.2) and internal validation (IntVal) sets. To assess the model's generalizability, an external validation (ExtVal) set of 112 images is collected. A convolutional neural network (CNN) is developed for regression (predicts RRF percentages directly from image data). CNN performance is evaluated on the validation sets using Mean Absolute Error (MAE), the Pearson Correlation Coefficient (PCC) and the range of differences between predictions and ground truth. Gradient-weighted Class Activation Mapping (Grad-CAM) is employed for visual explanations. ***Results:*** The CNN demonstrates very promising results in estimating RRF from DMSA scans. The MAE is 3.45 and 3.79 on IntVal and ExtVal sets, respectively. The PCC is 0.98 and 0.95 on IntVal and ExtVal sets, respectively. The range of differences on ExtVal is [0.08%-15%], 3.80 +/- 2.89%, but did not exceed 8% in about 91% of the patients, which is at least similar to human reproducibility[1]. Visual inspection of the predicted RRF values against the ground truth shows a strong correlation. Visual analysis using Grad-CAM consistently highlights the regions corresponding to the left and right kidneys as the primary areas of the CNN's focus when estimating RRF. This suggests that the model learned to attend to the relevant anatomical structures for the prediction task. ***Conclusion:*** This study demonstrates the feasibility of deep learning regression for automated and accurate RRF estimation from DMSA scans (MAE: 3.45, Pearson's r: 0.98). The image-based approach offers a potentially faster and reproducible alternative for RRF assessment. Visual analysis using Grad-CAM confirms the model's focus on the kidneys, potentially increasing clinical trust in AI-driven RRF assessment. ***References:*** 1. Tondeur, Marianne, et al. "Inter-observer reproducibility of relative 99Tcm-DMSA uptake." Nuclear medicine communications 21.5 (2000): 449-453.

EP-1077

Evaluating the accuracy of different absorbed dose rate estimation methods for kidney and bone marrow dosimetry in [^{177}Lu]Lu-DOTATATE therapy

J. Bao, *A. Theisen, J. Leube, A. Gehring, M. Lassmann, M. Salas-Ramirez, J. Tran-Gia;*
Department of Nuclear Medicine, University Hospital Würzburg, Würzburg, GERMANY.

Aim/Introduction: This study compares five absorbed dose rate estimation methods to identify the most accurate approach for kidney and lumbar vertebra dosimetry in [^{177}Lu]Lu-DOTATATE therapy. ***Materials and Methods:*** CT images from day-1 SPECT/CT scans post-[^{177}Lu]Lu-DOTATATE injection in 18 patients were used to generate activity masks for kidneys and L1-L5 vertebrae using TotalSegmentator [1], assuming uniform activity concentrations (0.35 MBq/mL for kidneys, 0.034 MBq/mL for vertebrae) as ground-truth. SPECT was simulated using SIMIND [2] with a uniform activity distribution and noise, modelling a Siemens Intevo Bold system (9.5-mm crystal, MELP collimator, 9% energy resolution, 120 projections, 30s/projection, non-circular orbit, 256x256 matrix, 2.54-mm pixels, 10%-20%-10% energy windows around 208 keV). Images were reconstructed using PyTomography [3] (OSEM, 4 subsets, 20 iterations, attenuation correction, triple-energy-window scatter correction, resolution modelling, 2.4-mm voxels). Five absorbed dose rate estimation methods were evaluated using either activity masks ("mask") or SPECT images ("SPECT"), followed by: GATE [4] radiation transport simulations (5.2×10^8 decays) with CT-based materials, simulating 2 billion particles per patient ("GATE"); local energy deposition [5] with organ-specific density correction ("LED"), or GATE-derived ^{177}Lu voxel S-values with density correction ("VSV"): A (reference): mask+GATE; B: mask+LED; C: SPECT+GATE; D: SPECT+LED; E: SPECT+VSV. Partial volume correction for SPECT-based methods (C-E) used recovery coefficients derived from activity ratios of exact to enlarged VOIs. Relative errors in mean absorbed dose rate (vs. method A) were calculated per patient; group-level means and standard deviations were also computed. Dose rate-volume histograms (DVHs) were used for visual assessment. ***Results:*** In the kidneys, method

B showed the best agreement with the reference (0.0±0.5%), followed by C (-4.8±3.3%), D (-9.8±2.6%), and E (-11.3±3.8%). For vertebrae, B and C performed best, with relative errors ranging from -7.2±1.2% to -2.7±0.7% (L1 to L5) for B, and -8.3±20.23% to 5.7±7.8% for C. Methods D and E showed larger errors: -28.1±17.2% to -13.0±7.0% for D, and -30.5±15.4% to -14.3±7.7% for E. DVHs revealed greater deviations in methods D and E, while Monte Carlo-based methods (A and C) yielded more accurate and consistent dose rate distributions. ***Conclusion:*** While mask-based method B showed acceptable accuracy, SPECT-based Monte Carlo simulations (C) outperformed simplified methods such as LED (D) and voxel S-value (E), especially in the lumbar spine, where densities differ significantly from water. ***References:*** [1] Wasserthal etal. RadiolArtiflntell 2023;5(5):e230024 [2] Ljungberg etal. ComputMethodsProgramsBiomed 1989;29(4):257-272 [3] Polson etal. Softwarex 2025;29 [4] Jan etal. PhysMedBiol 2004;49(19):4543-4561 [5] Sjögreen-Gleisner etal. EJNMMI 2022;49(6):1778-1809.

EP-1078

Monte Carlo bootstrapping to estimate statistical power for published tumor dose-response relationships in peptide receptor radionuclide therapy (PRRT)

T. Husevåg[1], *C. Stokke*[1,2], *M. Kvassheim*[1,2];
[1]*Oslo University Hospital, Oslo, NORWAY,* [2]*University of Oslo, Oslo, NORWAY.*

Aim/Introduction: We aimed to retrospectively estimate the statistical power of published PRRT tumour dose-response relationships using a Monte Carlo method bootstrap with Weibull extrapolation. ***Materials and Methods:*** 17 PRRT tumour dose-response relationships were extracted from figures or tables in [2-7] evaluating change in tumour volume/diameter (16) or chromogranin A levels (1), using Pearson correlation ρ.Bootstrapped subsamples were used to evaluate the rejection rate under the reported significance conditions repeated 1000 times for each sample size (i.e. a Monte-Carlo approach), estimating the statistical power until the study population size was reached. The bootstrapped sample size-power relationship was then extrapolated using the cumulative Weibull distribution (CWD) until the desired power was reached. If the reported relationship was far from significance [5,7] the TOST equivalence test [1] was used to evaluate the equivalence power for Δρ^2<0.25.The analysis was performed using in-house developed python-software [8]. ***Results:*** The CWD power extrapolation fit well for 15/17 relationships (R^2>0.95), yielding reasonable power estimates in relation to simulated sample sizes. Four relationships gave power estimates >95%, and the remaining 13 estimates ranged from 46% to 85%. While the dose-response relationship published in figure 2 by Ha et al. [4] was non-significant (p=0.06), the bootstrap power estimate was the lowest of all evaluated relationships (~45% power for 20 patients). A very stable CWD extrapolation (R^2=0.99) suggests the study might have benefited from increasing the sample size to e.g. 40 patients to raise the power to 90%. On the opposite end the relationship reported by Hebert et al. [2] could have reached the same power with about half the lesions, indicating large variability of statistical power between reported findings. Jahn et al. [7] reported a non-significant correlation with equivalence power of ~60%, indicating the need for increased sample. ***Conclusion:*** This approach enabled simple retrospective power assessments and suggested that most of the published PRRT tumour dose-response analyses would have benefitted from larger cohorts to reliably reduce the type II error probability. ***References:*** 1.Counsell A, Cribbie RA, Brit K Math & Statis. 2015;68(2):292-309. 2.Hebert K, et al., J Nucl Med. 2024;65(6):923-930. 3.Ilan E, et al. J Nucl Med. 2015;56(2):177-182. 4.Ha S, et al. EJNMMI Phys. 2024;11(1):14. 5.Del Prete M, et al. Eur J Nucl Med Mol Imaging. 2017;44(9):1490-1500. 6.Jahn U, et al. Cancers. 2021;13(5):962. 7.Jahn U, et al. Neuroendocrinology. 2020;110(7-8):662-670. 8.https://github.com/toralfhus/PRRT_sample_size.

EP-1079

Age-Related Metabolic Changes in Japanese Healthy Controls undergoing [18F]-PET/CT Imaging

S. Gutschmayer[1], *M. Pires*[1], *T. Beyer*[1], *D. Ferrara*[1], *Z. Chen*[2], *Y. Xinzhu*[2], *J. Taki*[3], *S. Kinuya*[2], *L. K. S. Sundar*[1,4], *S. Takeda*[3], *H. Wakabayashi*[2];
[1]*QIMP Team, Medical University of Vienna, Vienna, AUSTRIA,* [2]*Department of Nuclear Medicine, Kanazawa University Hospital, Kanazawa, JAPAN,* [3]*PET Center, Kanazawa Advanced Medical Center, Kanazawa, JAPAN,* [4]*DIGIT-X Lab, Department of Radiology, LMU Munich, Munich, GERMANY.*

Aim/Introduction: Metabolic aging involves varying physiological shifts across the human lifespan. Quantifying image readouts, such as energy-related metabolic activity and organ volumes, can be derived from [18F]FDG-PET/CT imaging to explore age-related systemic changes. Previous studies suggest that energy metabolism peaks in early life, plateaus in adulthood, and declines in older age [1]. This study characterizes organ-specific age-related metabolic shifts in healthy Japanese adults using FDG-PET/CT imaging. ***Materials and Methods:*** Whole-body PET/CT scans from 501 healthy Japanese subjects (351 males, BMI: 24 ± 3 kg/m^2; 150 females, BMI: 21 ± 3 kg/m^2) aged 22-89 (54 ± 11 years) were analysed. Automatic segmentation and quantification of organ-wise mean SUVlbm and volume were performed in eight organs (brain, liver, spleen, bone marrow, thyroid, subcutaneous fat, skeletal muscle, visceral fat) using MOOSE [2]. Linear correlation analysis was performed for each organ parameter versus age, with linear regression assessment (R^2) for no, sex, and BMI stratifications. Spearman correlation analyses were performed within age decades and two wider-age groups: 20-60 and >60 years. Correlations with $|\rho| \geq 0.45$ defined edges of undirected metabolic networks, linking organs with strong metabolic or morphological associations. ***Results:*** SUVlbm was not influenced by age; all regression models for all described groups yielded $R^2 < 0.3$, thus supporting previous findings of stable energy expenditure between 20-60 years [1]. However, network analysis revealed age-dependent shifts in inter-organ connectivity. In their 20s, participants showed SUVlbm-dominated networks (SUVlbm: 12 correlations, volume: 9 correlations). During the 30s, 40s, and 50s, volume-based correlations dominated while SUVlbm-related connections were reduced (30s: 17 SUVlbm vs. 34 volume; 40s: 6 vs. 15; 50s: 7 vs. 14). From the 60s onwards, SUVlbm connections became dominant again (60s: 8 SUVlbm vs. 10 volume; 70s: 17 vs. 18; 80s: 10 vs 9), indicating reappearing metabolic dependency. Similarly, in the age-grouped analyses, the 20-60 years group retained 6 SUVlbm and 14 volume correlations compared to 7 and 9 in subjects >60 years. ***Conclusion:*** FDG-PET/CT imaging reveals shifts in metabolic connectivity for healthy Japanese subjects across adulthood, mirroring known life-course metabolic phases. Given its ability to resolve organ-specific function and inter-organ connectivity, PET/CT is well-suited for investigating the systemic nature of metabolic aging and its physiological determinants. ***References:*** [1] Pontzer et al. "Daily Energy Expenditure through the Human Life Course." Science (2021): 808-812. [2] Sundar et al. "Fully automated, semantic segmentation of whole-body ^{18}F-FDG PET/CT images based on data-centric artificial intelligence." JNM 63.12 (2022): 1941-1948.

EP-1080

Unravelling Amyotrophic Lateral Sclerosis FDG PET patterns using graph-based manifold partition

T. Zaharia[1,2], *J. Hong*[3], *R. Ni*[3], *A. Rominger*[3], *S. Hu*[4], *Y. Tang*[4], *K. Shi*[3];
[1]*Center of Artificial Intelligence in Medicine, University of Bern, Bern, SWITZERLAND,* [2]*ARTORG Center for Biomedical Engineering Research, University of Bern, Bern, SWITZERLAND,* [3]*Department of Nuclear Medicine, InselSpital, University of Bern, Bern, SWITZERLAND,* [4]*Department of Nuclear Medicine, Xiangya Hospital, Central South University, Changsha, CHINA.*

Aim/Introduction: Amyotrophic Lateral Sclerosis (ALS) is a neurodegenerative disorder characterized by the progressive loss of motor neurons. The disease is progressing at a fast rate, leading to increased difficulty in day-to-day such as swallowing, salivation, writing etc. Our aim is to support diagnostic assessment by predicting disease progression and classifying patients into subtypes. To achieve this, we applied a novel unsupervised graph-based algorithm on FDGPET brain scans, to discover interconnected clusters correlating to clinical parameters. ***Materials and Methods:*** This study includes 126 clinically diagnosed ALS patients and 126 healthy controls, totalling 254 individuals with brain FDG-PET imaging [2]. In our cohort, there were 3 patients classified as suspected ALS, 39 as laboratory-supported, 23 as probable, and 26 as definite ALS cases, according to the Revised El Escorial Criteria. From the PET scans, we extracted SUVr values normalized to grey matter uptake for eight brain regions: Precentral gyrus, Frontal lobe, Supplementary Motor Area, Cerebellum, Vermis, Medulla Oblongata, Pons, and Midbrain. An unsupervised machine learning approach was used to cluster ALS patients into subtypes based on these regional uptake patterns. The algorithm applies a graph-based technique to infer a topology over the feature space, previously used in transcriptomics [3]. ***Results:*** The clustering algorithm, based on SUVr features, successfully differentiated ALS subgroups. The algorithm inferred a topology of 5 clusters. A statistically significant difference in disease progression rate was observed among clusters (Kruskal-Wallis test, $p < 0.05$). Furthermore, a subset of three clusters displayed strong differences in progression rate and significant difference in salivation score and Non-Motor Symptoms (Chi-squared test, $p < 0.05$). In this subset, we observe a correlation between increasing Putamen FDG-uptake and decreasing Supplementary Motor Area FDG-uptake for Progression Rate. ***Conclusion:*** We developed a data-driven pipeline to support ALS diagnosis and prognosis. By applying unsupervised clustering to brain FDG-PET data, we were able to infer disease subtypes, potentially aiding clinical decision-making and personalized care strategies ***References:*** [1] Eva L. Feldman et al. "Amyotrophic lateral sclerosis." The Lancet, vol. 400, no. 10360, 2022, pp. 1363-1380. [2] J. Hong et al. "FDG PET as a systemic biomarker of Amyotrophic Lateral Sclerosis: brain-body connection, staging and subtyping." European Journal of Nuclear Medicine and Molecular Imaging, vol. 51, 2024, p. S268. [3] Wolf, F. Alexander, et al. "PAGA: graph abstraction reconciles clustering with trajectory inference through a topology preserving map of single cells." Genome biology 20 (2019): 1-9.

EP-1081

FMEA (Failure Mode and Effects Analysis) for ^{177}Lu marked PSMA and DOTATATE/TOC therapies for risk treatment assessment

M. L. Belli[1], *M. Golinucci*[2], *G. M. Volpe*[3], *I. Marini*[4], *V. Di Iorio*[5], *F. Matteucci*[4], *E. Prati*[6], *M. T. Montella*[3], *A. Sarnelli*[1];
[1]*IRST - Istituto Romagnolo per lo Studio dei Tumori "Dino Amadori" - IRST IRCCS - Medical Physics Unit, Meldola, ITALY,* [2]*IRST - Istituto Romagnolo per lo Studio dei Tumori "Dino Amadori" - IRST IRCCS - Nurse Unit, Meldola, ITALY,* [3]*IRST - Istituto Romagnolo per lo Studio dei Tumori, Meldola, ITALY,* [4]*IRST - Istituto Romagnolo per lo Studio dei Tumori "Dino Amadori" - IRST IRCCS - Nuclear Medicine Unit, Meldola, ITALY,* [5]*IRST - Istituto Romagnolo per lo Studio dei Tumori "Dino Amadori" - IRST IRCCS - Oncology Pharmacy Unit, Meldola, ITALY,* [6]*IRST - Istituto Romagnolo per lo Studio dei Tumori "Dino Amadori" - IRST IRCCS - Healthcare Direction, Meldola, ITALY.*

Aim/Introduction: Radiometabolic ^{177}Lu based treatment is a complex process that involves different specialists. Due to his high complexity and to the potential serious risk of health damages for patients and healthcare professionals, a global analysis of the whole process would allow to identify the weak point and then improve clinical standards. Risk analysis also fulfil the requirement of 2013/59/EURATOM directive. We performed a FMEA (Failure Mode and Effects Analysis) analysis for ^{177}Lu therapies in order to identify the main critical points in the whole procedure. ***Materials and Methods:*** We divided the whole process of ^{177}Lu base therapies into main steps and identified all possible failure-modes. Each failure-mode was scored for severity (S), occurrence (O) and detectability (D), range:1-10. Based on the Risk Priority Number (RPN=SxOxD) all failures were ranked. Both in home marked or already and ready for injection radiopharmaceuticals were considered. Both ^{177}Lu-PSMA and ^{177}Lu-DOTATATE/TOC therapies were considered. ***Results:*** Failure mode with highest RPN score were: incorrect infusion supervision based on counts measurements; incorrect connection of catheters (vial-injection pump-patient); incorrect end of infusion; false negative of pregnancy test. Additionally, for home marked radiopharmaceuticals: incorrect selection of vial geometry calibration factor. ***Conclusion:*** The FMEA analysis allowed the identification of the main failure mode in ^{177}Lu treatment procedures. Based on the obtained results, strategies could be implemented in the clinical practice in order to further improve patient safety. The present results may help new implementation of ^{177}Lu base therapy in the prospective of increasing use of this kind of therapies.

EP-1082

ICSH Formulas for Normal Blood Volume: 30 Years Later, a Descriptive Population Study Comparing the Reference Cohort to Actual Patients Explored for Isotopic Blood Volume Determination

M. Ragot[1], *J. Dubois*[2], *L. Drevon*[3], *A. Salabert*[4], *L. Guiheneuc*[5], *C. Rouet*[6], *S. Mackowiak*[7], *Z. Mauduit*[8], *M. Jung*[1], *M. Tempier*[1], *P. Orhon*[1], *A. Revy*[1], *S. Levesque*[1];
[1]*Centre Jean Perrin, Clermont-Ferrand, FRANCE,* [2]*CHU de Montpellier, Montpellier, FRANCE,* [3]*Assistance Publique – Hôpitaux de Paris, St Louis, Paris, FRANCE,* [4]*CHU de Toulouse, Toulouse, FRANCE,* [5]*CHU de Nantes, Nantes, FRANCE,* [6]*CH Métropole Savoie, Chambery, FRANCE,* [7]*CHU d'Amiens, Amiens, FRANCE,* [8]*CHU de Grenoble, Grenoble, FRANCE.*

Aim/Introduction: Isotopic determination of red cell mass (RCM) and plasma volume (PV) is essential for the diagnosis of polycythaemia. Interpretation is based on the ratio of the measured value to a theoretical normal value, derived from formulae published by ICSH in 1995, using data collected between 1956 and 1969. They establish normal RCM and PV values according to body surface area (BSA), age and sex. Thirty years later, they are still used to conclude whether a value is pathological or not, but are they suitable for the current patient population? ***Materials and Methods:*** For the ICSH cohort, data were extracted from the six articles underlying the ICSH recommendations, according to the methodology outlined by Pearson et al.. For our cohort, consenting patients who underwent RCM and/or PV measurement between 2019 and March 2025 were retrospectively included. Statistical analyses were conducted on Microsoft Excel® and R®, using Wilcoxon tests. ***Results:*** 3215 patients were included from 8 hospitals, with a gender ratio of 4.47. For the determination of normal RCM, the ICSH cohort included 283 men, with a median age of 30 years, BSA of 1.90 m^2 and BMI of 23.0 kg/m^2. Our cohort included 2629 men with a median age of 61 years, BSA of 1.99 m^2 and BMI of 27.5 kg/m^2. Age, BSA and BMI differed significantly ($p<0.001$). 1385 (53%) patients were over 60 years-old, but only 3 subjects were over 60 in the ICSH cohort. 701 (27%) patients had a BSA higher than 2.1 m^2 and 687 (26%) were obese versus only 32 and 16 in the ICSH cohort. For women, the ICSH cohort included 171 subjects, with a median age of 30 years, BSA of 1.64 m^2 and BMI of 21.4 kg/m^2. Our cohort included 584 women with a median age of 63 years, BSA of 1.71 m^2 and BMI of 25.6 kg/m^2. Age, BSA and BMI differed significantly ($p<0.001$). The ICSH cohort included only 8 subjects over 60 years-old, whereas 311 (53%) patients were over 60. 152 (26%) patients were obese versus 12 subjects. These

differences in age, BSA and BMI were also significant for plasma volume cohorts. ***Conclusion:*** The formulae for determining normal RCM and PV were derived from a small cohort of predominantly young and normal-weight subjects. Our findings confirm the underrepresentation of elderly and overweight patients and raise concerns regarding the applicability and reliability of these formulae in current clinical practice.

EP-1083

Reproducibility study of tumor lesion features in [^{68}Ga] Ga-PSMA PET/CT images

M. Alfaiate[1,2], *C. Constantino*[1], *F. Oliveira*[1], *L. C. Silva*[1], *R. Vigário*[2], *D. C. Costa*[1];
[1]*Champalimaud Foundation, Lisbon, PORTUGAL,* [2]*NOVA School of Science and Technology, Caparica, PORTUGAL.*

Aim/Introduction: This study aims to evaluate the reproducibility of radiomic features from lesions identified in consecutive [^{68}Ga] Ga-PSMA PET/CT images of prostate cancer patients. ***Materials and Methods:*** Fifty prostate cancer patients, for staging or restaging assessment, underwent two consecutive acquisitions on the same scanner (Philips GEMINI TF16) with a single injection of [^{68}Ga]Ga-PSMA. The time interval between the two scans did not exceed 40 minutes. On average, the first acquisition began 60 ± 12 minutes post-injection, followed by the second at 93 ± 11 minutes. Both acquisitions and reconstruction protocols were in accordance with EARL1 standards. All visible lesions suspected of malignancy were identified by an experienced nuclear medicine physician. Then, lesions identified on both acquisitions were semi-automatically segmented with a previously validated Bayesian classifier algorithm [1]. 106 radiomic features were extracted with "pyradiomics", an open-source python package in compliance with Image Biomarker Standardization Initiative (IBSI) [2]. The features were subdivided into 14 shape-based, 17 first-order, and 75 gray level (texture). For the statistical analysis, reproducibility was assessed with the intraclass correlation coefficient (ICC) as a measure of agreement. A significance level of 5% was set for inference. ***Results:*** A total of 236 [^{68}Ga]Ga-PSMA avid lesions were segmented. For the textural analysis, only 87 lesions were included, since the others were smaller than 64 voxels (4096 mm^3)—following IBSI guidelines. 79% of the shape-based features showed good reproducibility (0.75≤ICC<0.9). The remaining showed moderate reproducibility (0.4≤ICC<0.75). 65% of first-order features showed good or excellent (ICC≥0.9) reproducibility, whereas the rest showed moderate reproducibility. Gray level features had a wide variety of agreement results, 43% had good or excellent reproducibility, 55% had moderate reproducibility, and 3% had poor reproducibility (ICC<0.4). All ICC results were statistically significant. For features frequently used in clinical practice, such as maximum and mean standardized uptake value, and lesion volume (0.83≤ICC≤0.89), from the first to second acquisition, there was a median decrease of 6%, 3% and 4% respectively. The complete ICC results are available online (https://github.com/NM-Radiopharmacology/PSMA_FeaturesReproducibility). ***Conclusion:*** Overall, for [^{68}Ga]Ga-PSMA PET, shape and first-order features are more reproducible, i.e., less sensitive to real scenario conditions, such as time difference between acquisitions, patient positioning, and lesion segmentation, than gray level features. Furthermore, the latter are only feasible for large lesions. In this context, shape and first-order features should be prioritized for follow-up and predictive studies. ***References:*** [1] Constantino, et al. https://doi.org/10.1007/s10278-023-00823-y [2] Griethuysen, et al. https://doi.org/10.1158/0008-5472.CAN-17-0339

EP-1084

Structured Ground Truth Extraction from Robot-Assisted Radical Prostatectomy (RARP) Histopathology report to Support AI-Based Prostate Cancer Staging

J. Chaudhary, *A. K. Pandey, S. Kumar, S. Kaushal, P. D. Sharma, H. K. P, R. Kumar;*
All India Institute of Medical Sciences, AIIMS, New Delhi, New Delhi, INDIA.

Aim/Introduction: Artificial intelligence (AI) and machine learning (ML) are transforming nuclear medicine by enhancing diagnostic precision in oncologic imaging. Structured ground truth data are essential for training and validating AI/ML models. While histopathology is not traditionally part of nuclear medicine workflows, robotic-assisted radical prostatectomy (RARP) histopathology reports provide critical outcome data for Ga-68 PSMA PET/CT-based AI research in prostate cancer. To develop and validate a natural language processing (NLP) pipeline for extracting structured clinical parameters from RARP histopathology reports, enabling the creation of a ground truth dataset for future AI/ML model development in nuclear medicine. ***Materials and Methods:*** A rule-based NLP pipeline using regular expressions was developed to extract key parameters from 59 unstructured, scanned RARP histopathology reports: prostate size (3D dimensions), prostate weight, tumor size, seminal vesicle size, vas deferens length, and Gleason scores. Prostate volume was calculated using the ellipsoid formula. Manual validation was performed to assess extraction accuracy. Statistical correlations among parameters were evaluated using Pearson correlation. ***Results:*** The NLP pipeline achieved a sensitivity ranging from 72% to 100% and specificity between 79% and 100% across the 59 reports. Statistically significant correlations were found between prostate volume and both Gleason score and prostate weight ($p < 0.05$). The resulting structured dataset provides a reliable foundation for developing and validating AI/ML models using Ga-68 PSMA PET/CT imaging data. ***Conclusion:*** This study demonstrates a reproducible approach for generating structured ground truth data from histopathology reports, bridging the gap between imaging and outcomes. It supports AI/ML integration into prostate cancer imaging workflows and highlights the importance of data science in advancing precision diagnostics in nuclear medicine. Future work will involve applying this dataset in model development and clinical validation.

EP-1085

Potential of Large Language Models for Proofreading PET Reports

W. Roll[1], *L. Kober*[1], *D. Ventura*[1], *M. Masthoff*[1], *C. Backhaus*[1], *M. Schäfers*[1], *K. Rahbar*[1], *L. Plagwitz*[2], *P. Schindler*[1];
[1]*University Hospital Münster, Münster, GERMANY,* [2]*University of Münster, Münster, GERMANY.*

Aim/Introduction: The aim of this study was to investigate the ability of three large language models (LLMs), GPT-o1, DeepSeek R1-70b and Llama 3.3-70b, to detect common errors in anonymized PET/CT and PET/MRI reports. ***Materials and Methods:*** A retrospective dataset of 200 consecutive PET reports (100 correct, 100 with up to three artificially introduced errors each) was used. A total of 183 deliberately introduced errors were categorised as spelling & grammar, content or technical. Each report was presented to the three LLM with the same single prompt without subsequent modifications. The number of correctly identified errors and the time taken to complete each log were recorded. ***Results:*** Overall, GPT-o1 detected 84.2% (154/183) of the errors, significantly outperforming DeepSeek R1-70b (47.0%, 86/183) and Llama 3.3-70b (57.4%, 105/183; $p < 0.001$). GPT-o1 also showed

superior detection rates for spelling & grammar (76.8% vs. 25.3% vs. 38.9%) and technical (97.1% vs. 57.1% vs. 65.7%) errors. The detection of content errors did not differ significantly between the three models ($p = 0.406$). Reading time per report was significantly faster for GPT-o1 (28 ± 4 seconds), followed by Llama (48 ± 8 seconds) and DeepSeek (108 ± 29 seconds) ($p < 0.0001$). ***Conclusion:*** In PET/CT and PET/MRI reports GPT-o1 demonstrated the highest error detection rate of the LLMs evaluated. Future efforts to optimize and potentially fine-tune privacy-compliant open-source models might further improve their accuracy.

EP-1086

Artificial Intelligence as a New Research Ally? Performing AI-Assisted Systematic Literature Reviews in Nuclear Medicine

S. van Mossel[1,2], *M. Oude Wolcherink*[2], *R. de Feria Cardet*[3], *L. De Geus-Oei*[1,2,4], *D. Vriens*[5], *H. Koffijberg*[2], *S. Saing*[2,3];
[1]*Leiden University Medical Center, Leiden, NETHERLANDS,* [2]*University of Twente, Enschede, NETHERLANDS,* [3]*University of Technology Sydney, Sydney, AUSTRALIA,* [4]*Delft University of Technology, Delft, NETHERLANDS,* [5]*Radboud University Medical Center, Nijmegen, NETHERLANDS.*

Aim/Introduction: Systematic literature reviews (SLR) are fundamental for aggregating clinical evidence and identifying knowledge gaps, especially in nuclear medicine where randomised controlled trials are rare. The workload is increasing due to the growing number of articles to screen, while only about 1% of search results are relevant for data extraction. With an average completion time of over 15 months, SLRs may become outdated by the time they are published. The increasing workload reduces researchers' willingness to conduct SLRs and leads to overly narrow search strategies when prioritising time constraints over review quality. Artificial intelligence (AI) tools have been developed to reduce screening time, but their validation in nuclear medicine is lacking. To contribute to nuclear medicine domain-specific validation efforts, we assessed the performance of AI-assisted screening in a post hoc analysis of our published SLR [1]. ***Materials and Methods:*** From 2,398 unique articles identified on PubMed and Scopus, 57 were included for full-text review and 10 for data extraction. Titles, abstracts and inclusion decisions were reconstructed for AI-assisted screening with open-source ASReview Software (v1.2). Through simulation with Makita, an extension of ASReview Software, the number of relevant articles found using ASReview was compared to that found through the original full manual screening. Makita is a workflow generator for validation studies using the command line interface of ASReview. The software codes used to perform this analysis are available [2]. ***Results:*** Simulation results show the accuracy per number of articles screened. Using ASReview it took 600/2,398 articles to find all 57 articles included for full-text review and 250/2,398 articles to find all 10 articles included for data extraction: a saving of approximately 75% and 90% respectively. ***Conclusion:*** AI-assisted SLRs allow extended database searches with more generic search terms but without increasing reviewer workload, compared to full manual searching. However, AI tools are not yet established in PRISMA or Cochrane statements, indicating a need for more validation. This post hoc analysis contributes to the nuclear medicine domain-specific validation of AI tools and indicates that ASReview may be a valid and efficient tool for performing SLRs in our field. ***References:*** [1] van Mossel S, de Geus-Oei LF, et al. A Systematic Literature Review of Modelling Approaches to Evaluate the Cost Effectiveness of PET/CT for Therapy Response Monitoring in Oncology. Pharmacoeconomics. 2025 Feb;43(2):133-151. [2] Oude Wolcherink M, et al. (2023). Data inputs and analysis script to assess the performance of ASReview (V1.2). Zenodo. https://doi.org/10.1080/14737167.2023.2234639

EP-1087

Deep Learning Reorientation for Myocardial Perfusion Imaging SPECT

T. Huxohl[1], *R. Borgschulze*[2];
[1]*Heart and Diabetes Center NRW, Bad Oeynhausen, GERMANY,* [2]*Bielefeld University, Bielefeld, GERMANY.*

Aim/Introduction: To facilitate the clinical interpretation of myocardial perfusion SPECT images and to create polar maps, transversal images are reoriented into standard planes. Manual reorientation is time consuming and operator dependent. Furthermore, routinely used automatic algorithms may fail if the myocardium is incomplete due to perfusion defects. Therefore, a deep learning approach inspired by [1] is implemented and its generalizability across different scanners is evaluated. ***Materials and Methods:*** A deep neural network was trained to predict reorientation parameters (three translation parameters and two rotation parameters). The dataset used consists of data from three scanners (450 Siemens Symbia Intevo SPECT/CT, 64 GE Discovery 530c and 47 Philips Cardio-MD), including a dedicated cardiac SPECT (GE Discovery), and was manually labeled. To assess generalizability, training was performed with multi-scanner data, with Symbia Intevo data only, and with Symbia Intevo data, but with unrealistic data augmentation [2]. ***Results:*** Multi-scanner training yielded correlation coefficients (Pearson R) of around R=0.98 for the translation parameters and R=0.92 for the rotation parameters. With single-scanner training, performance remains the same for translation parameters (R=0.98), while declining slightly for rotation parameters (R=0.81) when transferred to different scanners. Training with unrealistic data augmentation did not improve performance across scanners. ***Conclusion:*** It is possible to perform across multiple scanners, including dedicated cardiac scanners. Learning translation parameters works better than learning rotation parameters. Unrealistic data augmentation does not increase generalizability across scanners. ***References:*** [1] Duo Zhang et al. "A novel deep-learning-based approach for automatic reorientation of 3D cardiac SPECT images". In: European Journal of Nuclear Medicine and Molecular Imaging 48.11 (Oct. 2021), pp. 3457-3468. DOI: https://doi.org/10.1007/s00259-021-05319-x. [2] Thomas Buddenkotte and Ralph Buchert. "Unrealistic Data Augmentation Improves the Robustness of Deep Learning-Based Classification of Dopamine Transporter SPECT Against Variability Between Sites and Between Cameras". In: J Nucl Med 65.9 (Sept. 2024), pp. 1463-1466. DOI: doi:10.2967/jnumed.124.267570.

EP-1088

Development and Validation of an Artificial Intelligence Assistant for PET Phantom Analysis

T. Palchan Hazan[1], *J. A. Kennedy*[1,2], *T. Hazan*[3], *Z. Keidar*[1,2];
[1]*Rambam Health Care Campus, Haifa, ISRAEL,* [2]*Ruth and Bruce Rappaport Faculty of Medicine, Technion, Haifa, ISRAEL,* [3]*Technion, Haifa, ISRAEL.*

Aim/Introduction: Quality control in nuclear medicine imaging requires standardized phantom testing that requires an analysis process which is time-consuming and requires specialized expertise. This study evaluates large language models (LLMs) to: 1) generate automated analysis code, and 2) create an AI assistant for streamlined analysis through natural language interaction. This approach offers a method that is adaptable to various quality control procedures. ***Materials and Methods:*** We developed a two-phase approach utilizing Claude, an advanced LLM. In phase one, the LLM was prompted to create Python code for DICOM processing, and analysis specific to the American College of Radiology (ACR) PET phantom requirements, with all instructions provided in natural language. The resulting code implemented tools for loading DICOM, visualization, analyzing phantom slices, and generating reports. In phase two, we developed an AI assistant with a specialized system prompt that enabled it to utilize these

tools through conversational user interaction. The assistant guides users through the analysis workflow, executes the appropriate tools, and interprets results according to ACR criteria. We validated this approach by comparing the AI assistant's performance against established in-house automated algorithms refined over several years. We analyzed 68 ACR phantom studies from 2 different PET/CT systems available at Rambam Health Care Campus. ***Results:*** The LLM successfully generated all necessary code for the analysis toolkit based solely on natural language instructions, with minimal need for manual code adjustments (<5% of code blocks required modification). The AI assistant accurately executed the analysis workflow, correctly identifying the appropriate slices, placing ROIs, and calculating key metrics, including background uniformity and SUV ratios. Bland-Altman analysis demonstrated good agreement across all SUV measurements, with biases ranging from −0.10 to +0.08 g/mL and 95% limits of agreement spanning 0.05 to 0.69 g/mL. Complete concordance (100%) was observed between the AI assistant and the established method in pass/fail classifications. The natural language interface allowed technologists to complete phantom analysis with minimal training, reducing the average analysis time from 45 minutes (manual process) to a few minutes (AI-assisted). ***Conclusion:*** This study demonstrates the feasibility of using LLMs to create imaging analysis code and develop conversational AI assistants guiding users through complex phantom analysis. The approach offers significant advantages in flexibility, eliminating the need for extensive programming knowledge when implementing or modifying analysis workflows. The validated AI assistant generates standardized ACR reports for PET. Future work will extend this toolkit to include other phantom types including NEMA.

EP-1089

Monitoring Health with Whole-Body [18F]-FDG PET/CT

S. Gutschmayer[1], *D. Ferrara*[1], *B. K. Geist*[2], *Ö. Özer*[1,2], *J. Yu*[1,2], *M. Pires*[1], *I. Rausch*[1], *M. Hacker*[2], *L. K. S. Sundar*[1,3], *W. Langsteger*[2], *T. Beyer*[1];
[1]*QIMP Team, Medical University of Vienna, Vienna, AUSTRIA,* [2]*Division of Nuclear Medicine, Medical University of Vienna, Vienna, AUSTRIA,* [3]*DIGIT-X Lab, Department of Radiology, LMU Munich, Munich, GERMANY.*

Aim/Introduction: [18F]FDG-PET/CT is central to oncologic imaging, but publicly available datasets rarely represent healthy populations, limiting insight into normal physiology. To address this gap, we conducted a study in which healthy controls underwent test-retest [18F]FDG-PET/CT imaging to provide repeat measures and variances of normative values on whole-body metabolism. ***Materials and Methods:*** 50 Caucasian participants (26F/24M, 38 ± 14 years) were included. Each control underwent test and retest whole-body (WB) FDG-PET/CT imaging within 35 days. Scans were performed on a WB-PET/CT system following an injected dose of 100 MBq [18F]FDG and 63 min listmode acquisition. PET image reconstruction was done 58-63 min post-injection using OP-OSEM with TOF information, PSF correction, 4 iterations, 5 subsets, and all standard corrections applied. Of the 50 participants, 2 showed incidental early-stage malignancies and were excluded from the study. MOOSE [1] was used to extract the mean standardized uptake value (SUV), density as Hounsfield Units (HU), and volume of the heart, brain, lungs, kidneys, spleen, liver, pancreas, subcutaneous fat, visceral fat, and skeletal muscle (latter 3 at vertebrae 3L level). Repeatability of PET/CT readouts was evaluated at group and subject levels. For the group analysis, region-based population averages were compared using the relative %-difference and an unpaired Student's t-test. At the subject level, we computed the relative %-difference (Δ%) between test and retest scans for each participant and employed a paired Student's t-test to assess intra-subject repeatability. We used the organ readouts to establish cohort-specific normative values (CT and PET) and ranges for each organ. ***Results:*** Test/retest SUVs were consistent at the group level with Δ% < 6%. Subject-level variability remained low, except for visceral fat (Δ% = 11%) and skeletal muscle (Δ% = 5.5%, $p < 0.05$). Group-level HU was consistent at Δ% < 2%. Higher subject-level differences in the lungs, heart, and subcutaneous fat (<=8%) were likely due to motion and weight changes. Organ volumes showed the best repeatability with group-level variation of <3.5%. ***Conclusion:*** WB-[18F]FDG-PET/CT imaging yields reproducible organ readouts in a test-retest setting in healthy controls. The normative readouts can be used to compare patient readouts to and highlight organ-specific aberrations from the cohort norm by z-maps (organ readout differences normalised to the organ standard range). For future work, we aim to include non-imaging parameters such as wearable readouts and blood parameters in our analyses. ***References:*** [1] Sundar et al. "Fully automated, semantic segmentation of whole-body ^{18}F-FDG PET/CT images based on data-centric artificial intelligence." JNM 63.12 (2022): 1941-1948.

EP-1090

Bridging the Gap between SPECT and PET using AI: Proof of concept on 99mTc-PSMA SPECT to 68Ga-PSMA PET synthesis

A. Lopez Montes[1], *L. Lopes*[1], *K. Hlongwa*[2], *M. Rivombo*[2], *O. Israel*[3], *A. Afshar-Oromieh*[1], *A. Rominger*[1], *S. More*[2], *K. Shi*[1];
[1]*University of Bern, Bern, SWITZERLAND,* [2]*Cape Town University, Cape Town, SOUTH AFRICA,* [3]*Technion Rappaport School of Medicine, Haifa, ISRAEL.*

Aim/Introduction: Advancements in SPECT instrumentation and tracer development poses it a viable alternative to PET imaging for several applications, particularly in resource-limited settings. However, differences in image quality and tracer uptake between SPECT and PET continue to hinder their integration under a unified framework, such as in joint clinical studies. To bridge this gap, enhancing diagnostic value for theranostics, improving patient management in patients without available PET and SPECT and enabling broader collaboration including participation from centers without PET, harmonization of the two modalities is essential. As a proof of concept, we focus on harmonizing ^{99m}Tc-PSMA SPECT with ^{68}Ga-PSMA PET for prostate cancer. ***Materials and Methods:*** 40 patients were scanned for staging prostate cancer using ^{68}Ga-PSMA PET and ^{99m}Tc-HYNIC-PSMA SPECT within a difference of 37.8 days. A ResUnet3D was trained to translate from SPECT to PET, learning the differences in uptake and image quality. Both PET and SPECT images were aligned prior to the training using a multimodal rigid registration approach. 35 of the patients were used in the training while the other 5 were used for the validation. For that, Total Segmentator was used, segmenting the main organs from the CT and the differences in organ-wise (kidneys, liver and prostate) uptake between the original SPECT and the generated PET harmonized from SPECT (harmonized-PET) were compared. Root Mean Squared Error (RMSE) between the harmonized and the original PET as well as between the original SPECT and the PET was reported for comparison. ***Results:*** The average RMSE between the harmonized-PET and the original one was 2.4±0.39 while the RMSE between the original SPECT and PET was 3.42±0.44 resulting in an improvement of 30%. On the other hand, the SSIM was improved from 0.71±0.07 to 0.80±0.03. Organ wise, the MSE between the harmonized-PET and the original PET was reduced in a 97% for liver and a 60% for the rest of the studied organs when compared with the ones between the original SPECT and the original PET. ***Conclusion:*** In this work, we have shown the feasibility of generating PET images representing the uptake of ^{68}Ga-PSMA from SPECT ^{99m}Tc-PSMA scans. On-going work is focused on increasing the number of patients for the training. Furthermore, the results can be generalized for different scanners and radiotracers. The results of this work will contribute to the harmonization between PET and SPECT bridging the gap between countries and institutions with different level of resources.

EP-1091

Explain Yourself! A Multi-Institutional PET/CT Reporters' Perspective on Explainable AI

C. Baskerville[1,2], *J. M. Y. Willaime*[2], *V. Prakash*[1,3,4], *T. Ali*[5], *S. Bhuva*[6], *G. Ellul*[7], *R. Frood*[8,9], *S. Kamat*[10], *S. Maitra*[3], *D. Rosewarne*[11], *A. Scarsbrook*[8,9], *P. D. Strouhal*[4], *A. Zarei*[8], *K. Wells*[1];
[1]*Centre for Vision, Speech and Signal Processing, The University of Surrey, Guildford, UNITED KINGDOM,* [2]*Mirada Medical Ltd., Oxford, UNITED KINGDOM,* [3]*Royal Surrey NHS Foundation Trust, Guildford, UNITED KINGDOM,* [4]*Alliance Medical Ltd., Warwick, UNITED KINGDOM,* [5]*The Newcastle Upon Tyne Hospitals NHS Foundation Trust, Newcastle upon Tyne, UNITED KINGDOM,* [6]*Oxford University Hospitals NHS Foundation Trust, Oxford, UNITED KINGDOM,* [7]*East Kent Hospitals University NHS Foundation Trust, Canterbury, UNITED KINGDOM,* [8]*Leeds Teaching Hospitals NHS Trust, Leeds, UNITED KINGDOM,* [9]*Faculty of Medicine and Health, University of Leeds, Leeds, UNITED KINGDOM,* [10]*King's College London NHS Foundation Trust, London, UNITED KINGDOM,* [11]*The Royal Wolverhampton NHS Trust, Wolverhampton, UNITED KINGDOM.*

Aim/Introduction: While artificial intelligence (AI) has the potential to dramatically improve clinical efficiency, broad adoption in Nuclear Medicine (NM) has yet to be realised due to hindrance by a lack of trust and understanding [1][2]. Explainable AI (XAI) could address these issues and facilitate human-in-the-loop oversight, a requirement of the EU AI Act for high-risk AI systems, yet controlled user testing is sparse [3][4]. This study examined task-specific XAI systems in NM using a novel hierarchical framework addressing the lack of standardised approaches to evaluation. ***Materials and Methods:*** This study proposes a 'Hierarchy of AI Interpretability', a framework evaluating interpretability needs across diverse stakeholder groups. This framework underpinned a multi-institutional study observing ten radiologists interacting with AI recommendations and explanations during tumour-node-metastasis (TNM) staging of lung cancer using [^{18}F] FDG PET-CT scans. Three interpretability levels were tested against standard 'black-box' systems spanning low-level Input Feature Attribution (IFA), High-Level Concepts (HLC) and Global Algorithmic Transparency (GAT). The study tested two hypotheses: (1) radiologist preference for adoption of an XAI clinical decision support system (CDSS) versus a black-box AI system, and (2) which XAI interpretability levels provide useful decision support for supporting/refuting AI recommendations. Analysis combined Likert scale data comparing explanation types with large language model (LLM)-assisted thematic analysis of qualitative feedback. ***Results:*** Sign tests confirmed radiologists were more likely to adopt AI-CDSS with interpretability than without (IFA: $p<0.005$; HLC: $p<0.005$; GAT: $p<0.05$). All interpretability levels provided useful information for evaluating AI recommendations (IFA: $p<0.005$; HLC: $p<0.005$; GAT: $p<0.01$). Thematic analysis revealed a key trade-off between explanation depth and usability. Preference along this continuum depended on perceived case difficulty: unambiguous cases required only visual confirmation with minimal detail, whilst complex cases shifted preference toward more detailed explanations despite longer interpretation time. ***Conclusion:*** The novel XAI hierarchical framework used in this study enabled initial evaluation of stakeholder considerations in PET-CT related AI. This task-based user study demonstrated radiologists' preference for XAI integration into decision support systems as compared to standard 'black-box' AI systems and provides useful information for validating AI recommendations. While these findings require validation in a larger prospective study, the explanation depth vs. usability trade-off supports the need for a CDSS with AI explanations configurable to individual case complexity. ***References:*** [1] M. I. Ahmed et al., doi: 10.7759/cureus.46454. [2] M. Bertl et al., doi: 10.1016/j.hlpt.2023.100748. [3] European Union Commission, https://eur-lex.europa.eu/legal-content/EN/TXT/?uri=CELEX:32024R1689. [4] M. Nauta et al., doi: 10.1145/3583558.

EP-1092

Reimagining Administrative Workflows: ChatGPT o1 Optimizes ICD-10 Coding in Nuclear Medicine.

T. Ruhwedel*, J. Rogasch, P. Dahlke, C. Furth, C. Wetz, S. Shnayien, I. Schatka, H. Amthauer, N. Beetz;*
Charité Universitätsmedizin Berlin, Berlin, GERMANY.

Aim/Introduction: European physicians face significant workloads. In Germany alone, physicians spend an average of 3 hours per day on administrative tasks and frequently work ≥5 additional hours per week. Large Language Models (LLMs) such as ChatGPT o1 offer promising opportunities to automate and reduce this workload. The current version of the ICD-10 catalogue spans around 850 pages, making nuclear medicine reporting a robust test case of AI-assisted coding. We investigated whether ChatGPT o1 can accurately—and more rapidly—assign ICD-10 codes to PET/CT reports. ***Materials and Methods:*** 100 different fictious PET/CT reports were created based on standardized institutional text modules for PET/CT including contrast-enhanced diagnostic CT. Each report was assigned a single, most relevant ICD-10 code by two experienced nuclear medicine physicians who routinely code PET/CT exams. Coding of multiple reports at the same time was allowed. One physician used ChatGPT o1, while the other was limited to traditional search engines. Time was recorded in seconds, from the beginning of report review to entry of the ICD-10 code into a data table. Discrepancies were resolved via a blinded consensus process. Differences in error distribution across ICD-10 hierarchy levels were analyzed using four-field tables and the McNemar test. Time differences were assessed using the Wilcoxon signed-rank test. ***Results:*** At the first character of the ICD-10 code, the ChatGPT-assisted coder made 2 errors compared to 3 errors by the manual coder ($p = 1.0$). For the second and third characters, ChatGPT-based coding resulted in 3 errors versus 5 ($p = 0.727$). At the fourth and fifth characters, ChatGPT o1 significantly outperformed manual coding, with 6 errors versus 17 ($p = 0.035$). Overall, the ChatGPT-assisted coding resulted in 6 incorrect codes, whereas manual coding led to 18 ($p = 0.023$). Median coding time was 135 seconds (range 41 - 433 s) without ChatGPT and just 8 seconds (range 6 - 9 s) with it. The median time difference between both coders was 127 seconds (range 33 - 424 s; $p < 0.001$). ***Conclusion:*** ChatGPT o1 significantly improved both speed and accuracy in assigning ICD-10 codes to PET/CT reports. Higher accuracy of ICD-10 codes might reduce billing errors and insurance rejections, while saved time could be reallocated to patient care. Given the complexity of PET/CT reports, similar AI-based approaches could be extended to other imaging modalities such as diagnostic CT or MRI.

EP-1093

Short-Term Variation in Body Composition in Healthy Adult Volunteers Undergoing Long Axial Field-of-View [^{18}F]FDG-PET/CT

E. Sullivan[1], *G. Cook*[2,3], *A. Hammers*[2,3], *D. Ferrara*[4], *B. Geist*[5], *S. Gutschmayer*[4], *M. Hacker*[5], *M. Pires*[5], *J. Yu*[4,5], *L. Shiyam Sundar*[4], *T. Beyer*[4];
[1]*Department of Nutritional Sciences, Faculty of Life Science & Medicine, King's College London, London, UNITED KINGDOM,* [2]*School of Biomedical Engineering and Imaging Sciences, King's College London, London, UNITED KINGDOM,* [3]*King's College London and Guy's and St Thomas' PET Centre, St Thomas' Hospital, London, UNITED KINGDOM,* [4]*QIMP Team, Medical University of Vienna, Vienna, AUSTRIA,* [5]*Department of Biomedical Imaging and Image-Guided Therapy, Division of Nuclear Medicine, Medical University of Vienna, Vienna, AUSTRIA.*

Aim/Introduction: Computed Tomography (CT) analysis at the L3 vertebra is the de facto gold standard for body composition research. Long Axial Field-of-View PET/CT enables relatively low-dose imaging in healthy volunteers, with added metabolic insights. This study aimed to establish reference data for physiologic intra-individual variation in [^{18}F]FDG-PET/CT parameters, against which to compare pathological aberrations. ***Materials and Methods:*** Fifty healthy Caucasian adults underwent whole body [^{18}F]FDG-PET/CT imaging with retest at 38±10 days. Two subjects with incidental findings of cancer were excluded. Body composition parameters (volume (mm3), CT attenuation (HU) and [^{18}F]FDG uptake (SUVbw) of skeletal muscle (SM), subcutaneous and visceral adipose tissue (SAT&VAT)) for the entire axial volume incorporating the L3 vertebra were evaluated using MOOSE software(1). Non-parametric tests were performed and Bonferroni adjustments for multiple testing were applied to X^2 tests. ***Results:*** Of 48 subjects included, 23 were male. Median [IQR] age was 32.5 [26-51] years. Median [IQR] body mass index (BMI) was 24.4 [21.8-25.8] kg/m^2. BMI (20-25kg/m^2) was present in 52% subjects with, BMI <20kg/m^2 in 13%, 25-20kg/m^2 in 31%, and >30kg/m^2 in 4%. Between test and retest, 60% of subjects remained weight stable (± 2%), with 23% of subjects gaining 2-5% and 13% losing 2-5% body weight. Inter-individual variations (volume gain or loss >2%) were present in 42% and 31% for SM, 52% and 40% for SAT and 36% and 52% for VAT, respectively. Degree of weight and SM volume changes were uncorrelated (rho=-0.056, p=0.705), whereas weight change was significantly correlated with SAT & VAT volume changes (rho=0.340, p=0.018; rho=0.346, p=0.016, respectively). There were no significant correlations between muscle, or adipose tissue SUVs, or baseline BMI and changes in body weight or tissue volume between scans, except for people with BMI <25kg/m^2 being more likely to gain 2-5% SAT volume and people with BMI >30kg/m^2 more likely to lose 2-5% SAT volume, compared to normal BMI individuals (50% vs. 8%, p=0.036; 100% vs. 8%, p<0.05, respectively). ***Conclusion:*** Significant (>2%) variation in weight and body composition were observed in healthy adults over a short interval. Weight did not fully reflect body composition changes, highlighting the role of imaging in distinguishing between physiologically important changes in body composition. Future studies should record illness and intentional/unintentional changes in weight, diet, activity or lifestyle factors in the weeks preceding scans, in order to accurately interpret metabolic variations. ***References:*** 1.Shiyam Sundar et al., DOI:10.2967/jnumed.122.264063.

EP-1094

Statistical Preprocessing of PET Radiomic Features: Normalisation, Outlier Filtering, and Correlation-Based Pruning for Robust Machine Learning Applications in a Hodgkin Lymphoma Cohort

S. Nikolovski*, G. Spirov, S. Tasevski, N. Manevska;*
University Institute of Positron- Emission Tomography, Skopje, NORTH MACEDONIA, THE REPUBLIC OF..

Aim/Introduction: Radiomic features extracted from positron-emission tomography/computed tomography (PET/CT) images provide quantitative characterisation of tumour phenotype but are highly sensitive to technical, biological, and imaging variability. Without systematic preprocessing, these features risk introducing instability and noise into predictive machine learning models. This study aimed to implement and evaluate a robust, multi-step preprocessing pipeline to improve data quality and model readiness in a classical Hodgkin lymphoma patient cohort, including distribution normalisation, outlier filtering, and correlation-based pruning of PET-derived radiomic features. ***Materials and Methods:*** A retrospective cohort of 104 patients with histopathologically confirmed classical Hodgkin lymphoma was analysed. Each patient underwent a pre-treatment [^{18}F] Fluoro-2-deoxy-2-D-glucose (FDG) PET/CT scan. Lymph nodes and lesions were automatically segmented from PET images using a convolutional neural network (CNN)-based segmentation tool, with all segmentations reviewed and confirmed by a certified nuclear medicine specialist. From the segmented structures, one representative lymph node per patient was selected for radiomic analysis. PET images were resampled to 4x4x4 mm^3 isotropic voxels and intensity discretised into 128 bins across a standardised uptake value (SUV) range of 0-40. A total of 131 radiomic features were extracted using the LIFEx software platform (v7.8.0) [1]. Features with skewness greater than 1 were subjected to logarithmic transformation. Outlier filtering was performed using the interquartile range (IQR) method, where values below Q1 – 1.5xIQR or above Q3 + 1.5xIQR were excluded at the patient level. Pearson correlation analysis with a threshold of $|r| > 0.9$ was used to identify and remove highly correlated features. ***Results:*** Log transformation was applied to 90 skewed features, successfully correcting 68.7% of their distributions. Outlier removal improved robustness without excluding features entirely. Correlation-based pruning reduced dimensionality from 131 to 27 uncorrelated, statistically normalised features. This refined subset will serve as input for future supervised machine learning models aimed at outcome prediction. ***Conclusion:*** A structured statistical preprocessing approach—comprising log transformation, outlier filtering, and correlation-based feature pruning—successfully improved the quality, stability, and usability of PET-derived radiomic features in a classical Hodgkin lymphoma cohort. This technical optimisation supports the development of more reproducible, interpretable, and generalisable machine learning models in PET-based oncology research. ***References:*** [1] Nioche C, Orlhac F, Boughdad S, et al. LIFEx: a freeware for radiomic feature calculation in multimodality imaging to accelerate advances in the characterisation of tumour heterogeneity. Cancer Research 2018;78(16):4786-4789.

EP-1095

Improved Imaging of Hemodynamics from Dynamic FDG PET-CT studies with Bolus Venous injection of the Tracer.

F. O'Sullivan*[1], Q. Wu[1], F. Gu[2], K. Shi[3], A. Rominger[3];*
[1]University College, Cork, IRELAND, [2]School of Mathematics and Physics, North China Electric Power University, Beijing, CHINA, [3]Bern University Hospital, University of Bern, Bern, SWITZERLAND.

Aim/Introduction: High-resolution dynamic [18F]FDG PET-CT imaging following bolus injection has the potential to recover approximate quantitation of blood volume and flow. But standard intravenous tracer injection typically produces a high intensity signal on the venous pathway between the injection site (IS) and the first appearance of the arterial input (AIF) at the left ventricle (LV). Without adjustment, standard kinetic analysis of hemodynamics substantially overestimates flow and blood volume in the neighborhood of the IS-LV pathway. The work develops an algorithmic technique to correct time-course data for the IS-LV pathway artefacts and improve hemodynamic mapping. ***Materials and Methods:*** Data from a set of 25 dynamic PET-CT imaging studies on a Siemens Biograph scanner were used. All studies involved bolus intravenous injection of [18F]FDG into either the left or right arm [1]. The analysis approach adjusts all voxels with an early time-activity curve (eTAC) - eTACs are TACs where the peak intensity in the TAC occurs more than 1s before the peak intensity in the LV. eTACs are modelled using a semi-parametric form involving a multi-exponential first-pass pre-LV component, describing transit through the heart and a non-parametric, AIF-driven component, describing recirculation. Artefact suppression involves removal of the estimated first-pass pre-LV component from any eTAC voxels. The distribution of voxel-level blood volume in an ROI encompassing a neighbourhood of the IS-LV pathway on the injected arm and a similarly placed ROI on the non-injected arm were evaluated. Statistical deviations between the injected

and non-injected arm distributions were assessed before and after artefact suppression. In addition, the blood volume distributions over the non-injected arm before and after artefact suppression were compared. ***Results:*** Representative eTAC data were very well described by the 2-component modelling scheme - R^2-values are typically in excess of 95%. Removal of the fitted multi-exponential component produces adjusted data with minimal negative artefacts. Without incorporation of the non-parametric AIF-driven element, artefact-adjusted time-course data are grossly impacted by negative artefacts. Before artefact suppression, the percent difference between mean blood volumes over the IS-LV neighbourhood ROI was 50% to 500% higher that a comparable ROI over the non-inject arm; after artefact suppression differences is reduced to +/-15%. IS-LV artefact suppression is not found to distort blood volume patterns in the non-injected arm. ***Conclusion:*** The proposed technique improves the accuracy hemodynamic quantitation derived over the IS-LV neighbourhood in FDG-PET studies involving bolus venous injection of the tracer. ***References:*** Wu et al 2024, J Nucl Med;65(6):971-979.

EP-1096

Unsupervised Learning of Obesity-Associated Metabolic Patterns from Whole-Body ^{18}F-FDG PET/CT

R. JIANG[1,2,3], *X. Xie*[1,2], *M. Dong*[4], *Q. Sun*[4], *Z. Li*[4], *Y. Xiao*[5], *N. Ma*[4], *J. Li*[4], *H. Yang*[4], *X. Lin*[4], *H. Yan*[4], *H. Zheng*[1,2], *D. Liang*[1,2], *N. Zhang*[2], *C. C. Liu*[3], *Z. Hu*[1,2];
[1]*Research Center for Medical AI, Shenzhen Institute of Advanced Technology, Chinese Academy of Sciences, Shenzhen, CHINA,* [2]*Key Laboratory of Biomedical Imaging Science and System, Chinese Academy of Sciences, State Key Laboratory of Biomedical Imaging Science and System, Shenzhen, CHINA,* [3]*Department of Data Science and Artificial Intelligence, The Hong Kong Polytechnic University, Hong Kong, CHINA,* [4]*Peking University Shenzhen Hospital, Shenzhen, CHINA,* [5]*Shenzhen Exit-Entry Frontier Inspection Station General Hospital, Shenzhen, CHINA.*

Aim/Introduction: Obesity is a major health concern linked to systemic metabolic imbalance and associated with various chronic diseases. Although prior work explored obesity from a metabolic network perspective [1], it relied on hand-crafted features based on limited data, personal observations, and subjective preferences. Such methods risk embedding bias and overlooking subtle patterns, leading to limited robustness and generalizability. This study introduces an unsupervised method to uncover obesity-related metabolic patterns without relying on manual priors. ***Materials and Methods:*** We introduce an unsupervised learning approach to uncover relationships between glucose metabolism and obesity from whole-body ^{18}F-FDG PET/CT data. A cohort of 1,160 subjects supports stable learning and broad applicability. We investigated obesity-related metabolic pathways using a systemic perspective. 576 normal-weight subjects [body mass index (BMI) < 24 kg/m^2, 50.07 ± 33.93 years, 302 men and 274 women] and 584 overweight or obese subjects [BMI ≥ 24 kg/m^2, 51.77 ± 36.23 years, 372 men and 212 women] underwent whole-body ^{18}F-FDG PET/CT imaging. We divided the cohort into BMI-based quantile groups and performed random sampling with replacement within each group. Organ-specific metabolic covariance networks were constructed based on the whole-body standardized uptake value, and an unsupervised deep-clustering framework was used to uncover latent features without human priors. Finally, class activation mapping and SHAP analysis were conducted to interpret the most influential network nodes and inter-organ connections. ***Results:*** The unsupervised deep clustering model achieved an ACC of 0.9925, NMI of 0.9898, and ARI metrics of 0.9842, indicating accurate group separation based on inter-organ metabolic connectivity patterns. CAM and SHAP analyses further revealed that the model prioritized metabolic interactions between liver-stomach, pancreas-liver, and duodenum-brain. ***Conclusion:*** Our unsupervised framework autonomously extracts inter-organ metabolic network signatures from whole-body PET/CT imaging data, without reliance on subjective priors. The high values of ACC, NMI, and ARI indicate that the clustering algorithm effectively identifies obesity-associated patterns within the inter-organ metabolic network. Additionally, a sufficiently large sample size strengthens the reliability and external validity of the network-derived findings. This study demonstrates the promise of unsupervised PET data mining in revealing metabolic insights for precision health. ***References:*** [1]W. Lu, Y. Duan, K. Li, Z. Cheng, and J. Qiu, "Metabolic interactions between organs in overweight and obesity using total-body positron emission tomography," International Journal of Obesity, vol. 48, no. 1, pp. 94-102, 2024.

EP-1097

Body composition analysis of [18F]FDG-PET/CT images: The L3 vertebra region as a surrogate for whole-body quantification

M. Pires[1], *D. Ferrara*[1], *S. Gutschmayer*[1], *J. Yu*[2], *A. Frille*[3,4], *B. Geist*[2], *M. Hacker*[2], *S. Hesse*[3], *L. K. S. Sundar*[5], *T. Beyer*[1];
[1]*QIMP Team, Medical University of Vienna, Wien, AUSTRIA,* [2]*Department of Biomedical Imaging and Image-Guided Therapy, Division of Nuclear Medicine, Medical University of Vienna, Wien, AUSTRIA,* [3]*Department of Nuclear Medicine, University Hospital Leipzig, Leipzig, GERMANY,* [4]*Department of Respiratory Medicine, University Hospital Leipzig, Leipzig, GERMANY,* [5]*DIGIT-X Lab, Department of Radiology, LMU, Munich, GERMANY.*

Aim/Introduction: [18F]FDG-PET/CT imaging is widely used for staging and restaging cancer patients. Beyond its diagnostic utility, it offers the potential to extract quantitative biomarkers such as imaging-derived body composition, which may aid in detecting cancer-associated metabolic alterations. However, whole-body (WB) segmentation of skeletal muscle (SKM), visceral adipose tissue (VAT), and subcutaneous adipose tissue (SAT) is highly time-consuming, limiting the development of deep-learning solutions for automated WB segmentation. Since the L3 vertebral region is an established surrogate for WB composition in radiology [1], we investigate whether automated L3-based tissue segmentation can accurately estimate the tissue volume, standardized uptake value (SUVbw), and CT density (CT_HU) of SKM, VAT, and SAT compared to WB manual segmentations. ***Materials and Methods:*** A retrospective cohort of 42 subjects (21 healthy controls, 21 lung cancer patients) who underwent WB FDG-PET/CT imaging was analysed. An experienced medical expert manually delineated WB volumes of SKM, VAT, and SAT. In addition, L3-level segmentations were generated using AI-based MOOSE [2]. Correlation between WB and L3 measurements was assessed using linear regression (r^2) for SUVbw, CT_HU, and tissue volume. ***Results:*** L3-derived imaging parameters strongly correlated with WB-derived parameters across several measurements. SKM, SUVbw, and CT_HU derived from L3 and WB segmentations showed excellent agreement (r^2 = 0.87 for both). However, the correlation of tissue volume of SKM was weak (r^2 = 0.25). For VAT, estimates for all readouts (SUVbw, CT_HU, and volume) correlated well between L3 and WB measurements (r^2 = 0.81, 0.80, and 0.88, respectively). For SAT, volume readings correlated well (r^2 = 0.88). However, correlations for SUVbw and CT_HU were only modest (r^2 = 0.66 and 0.77, respectively). ***Conclusion:*** The L3 region is an adequate surrogate for WB estimations of both SUVbw and CT_HU for SKM and SAT, as well as the volume of adipose tissues. ***References:*** [1] Anyene, I et al. (2022). Body composition from single versus multi-slice abdominal computed tomography: Concordance and associations with colorectal cancer survival. Journal of Cachexia, Sarcopenia and Muscle, 13(6), 2974-2984.[2] Shiyam Sundar, L. K. et al. (2022). Fully Automated, Semantic Segmentation of Whole-Body ^{18}F-FDG PET/CT Images Based on Data-Centric Artificial Intelligence. Journal of Nuclear Medicine, 63(12), 1941-1948.

EP-1098

Development of an Explanation-Supporting AI for Nuclear Medicine Procedures Using Open-Source LLMs and Retrieval-Augmented Generation Technologies

N. Imaizumi, *M. Sato, T. Kita, F. Sasaki, A. Yumoto, H. Daisaki; Gunma Prefectural College of Health Sciences, Maebashi, JAPAN.*

Aim/Introduction: We attempted to develop a conversational AI to explain nuclear medicine pretreatment procedures on behalf of the patient. In a previous study, a paid version of ChatGPT was used for the study, and 77.9% of the responses were rated as above average or excellent [1]. However, the large cost of using the paid version of LLM may prevent individual hospitals from taking advantage of it. Therefore, we evaluated the performance of an open-source LLM, and furthermore, we verified whether the performance of the open-source LLM can be comparable to the paid version by utilizing Retrieval Augmented Generation (RAG) technology. ***Materials and Methods:*** Four open-source LLMs (Gemma 2 9B Instruction Tuned, deepseek-ai/DeepSeek-R1, Llama-3-8B-8192, Qwen QwQ 32B (Preview) 128k) were evaluated in this study. In order to use RAG technology, we also used the Dify AI; a total of 8 conversational AIs were created with and without the RAG engine using the Dify AI. These models were asked what the pre-treatment was for bone scintigraphy, myocardial blood flow scintigraphy, cerebral blood flow scintigraphy, and PET, and their performance was evaluated at that time. ***Results:*** The accuracy of responses generated by the LLM-only conversational AI was 28.1%, while the integration of RAG significantly improved the accuracy to 65.6% (Wilcoxon signed-rank test, P = 0.019). ***Conclusion:*** Although further study is needed, the results suggest that even open-source LLMs may be able to develop a conversational AI to explain nuclear medicine pre-treatment. ***References:*** [1] Matsutomo, N., Fukami, M. & Yamamoto, T. Can interactive artificial intelligence be used for patient explanations of nuclear medicine examinations in Japanese?. Ann Nucl Med (2025). https://doi.org/10.1007/s12149-025-02047-2

EP-67

e-Poster Area

D: Technical Studies -> D4 Dosimetry and Radiobiology -> D41 Clinical Dosimetry

EP-1099

Investigation of the Dosimetry Differences Between Pre-Therapy SPECT/CT and Post-Therapy PET/CT Scan in Selective Internal Radiation Therapy (SIRT)

E. Urwin[1,2], *D. Morgan*[1], *D. McGowan*[1], *L. Livieratos*[2]; [1]*Churchill Hospital, Oxford, UNITED KINGDOM,* [2]*King's College London, London, UNITED KINGDOM.*

Aim/Introduction: In SIRT 99mTc-MAA is used to plan the activity of microspheres required to deliver the prescribed dose. The success of SIRT relies on accurate dosimetry to optimise tumour absorbed dose while minimising liver toxicity. Previous work has shown a difference between the prescribed and delivered dose using 99mTc-MAA SPECT/CT and 90Y PET imaging respectively. [1] This retrospective study (24/HRA/3659) aims to quantify this difference and identify limitations in existing methodologies to improve dosimetry accuracy. ***Materials and Methods:*** Twenty patients who received SIRT were selected and the absorbed dose to the tumour, perfused (PNL) and whole normal liver (WNL) were calculated using a new Software and compared to results from a Partition Model in-house spreadsheet for validation. The difference between pre-therapy and post-therapy absorbed doses was calculated. The impact of SPECT/CT and PET/CT PVEs, interoperator variability, and post-therapy segmentation methods (deformable transformation, rigid transformation, and new VOIs) were investigated on the calculations of absorbed dose to volumes of interest (VOIs). ***Results:*** Validation of the new software showed good agreement with the in-house spreadsheet (mean deviations of 0.1%). When comparing pre- and post-therapy absorbed doses, there was overall correlation however large absolute differences were observed with absolute deviations up to 84.9Gy for tumours. Analysis of post-therapy volume segmentation methods showed no statistically significant difference however the difference in tumour absorbed dose between pre- and post-therapy varied up to 64Gy across the 3 methods . Recovery curve correction methods used to correct for PVEs significantly changed the pre- and post-therapy absorbed dose difference ($p<0.001$). No significant differences were found between operators on the pre-therapy absorbed doses however absorbed doses to the perfused and tumour VOIs varied largely (mean 59.2Gy and 78.0Gy respectively). ***Conclusion:*** The results from this study reveal good confidence in 99mTc-MAA SPECT/CT pre-therapy dosimetry for estimation of the absorbed dose to the normal liver in 90Y microspheres therapy. However, there are large tumour absorbed dose differences between pre- and post-therapy imaging suggesting opportunity for optimisation of tumour and liver dose. This arises from a variety of factors including a change in activity distribution, PVE, segmentation methods and inter-operator variability. ***References:*** Gnesin, S., et al., Partition Model-Based 99mTc-MAA SPECT/CT Predictive Dosimetry Compared with 90Y TOF PET/CT Posttreatment Dosimetry in Radioembolization of Hepatocellular Carcinoma: A Quantitative Agreement Comparison. J Nucl Med, 2016. 57(11): p. 1672-1678.

EP-1100

Site specific calibration factor removes reduces over-estimation of dose from single time point dosimetry when compared to 3 time point bi-exponential

B. Driscoll[1], *R. Wong*[2], *A. Shessel*[2], *D. Laidley*[3], *S. Myrehaug*[4], *R. Juergens*[5], *T. Farncombe*[5], *K. Zukotynski*[6], *R. Stodilka*[3], *J. Beauregard*[7], *U. Metser*[2], *P. Veit-Haibach*[2], *A. Hendler*[2], *S. Ezzat*[2], *K. Lajkosz*[2], *J. Gabrys*[2], *O. Levine*[5], *R. Mohan*[2], *A. Mesci*[2], *J. Publicover*[1], *I. Yeung*[2]; [1]*TECHNA Institute, University Health Network, Toronto, ON, CANADA,* [2]*University Health Network, Toronto, ON, CANADA,* [3]*London Health Sciences Centre, London, ON, CANADA,* [4]*Odette Cancer Centre, Toronto, ON, CANADA,* [5]*Juravinski Cancer Centre, Hamilton, ON, CANADA,* [6]*McMaster University, Hamilton, ON, CANADA,* [7]*Cancer Research Centre and Department of Radiology and Nuclear Medicine, Universite Laval, Laval, QC, CANADA.*

Aim/Introduction: Using SPECT-CT renal dosimetry imaging (4, 24 and 72 hours post injection) from the OZM-067 ^{177}LU-DOTATATE trial (NCT02743741), this study aims to quantify the accuracy of single time point (STP) dosimetry at 72 hours and to investigate the impact of utilizing a site specific calibration factor to correct for the error, while improving harmonization among sites. ***Materials and Methods:*** A 3-parameter bi-exponential (3PBE) function was fitted as the reference fit using the area under the time activity curve for dose calculation. STP dosimetry calculation based on Hanscheid(2018) was performed using the 72 hour time point. A linear regression fit between STP and 3PBE for each site produced varying slopes suggesting that site specific calibration factors were required to prevent some sites being over or under-corrected. To investigate the feasibility of generating a site specific correction factor, in an effort to improve STP accuracy when using STP as a clinical dosimetry method, a simulation was done to determine a calibration factor for each site using a training set of the first 15 cycles (30 kidneys). This calibration was then applied to the rest of the patient data (testing set) from each site. The pre and post correction data were evaluated in terms of mean error when comparing STP and 3PBE dosimetry estimates. ***Results:*** SPECT-CT data (153 patients/492 cycles/955 kidneys) was utilized to generate

the renal dose for each injection using 3PBE dosimetry for the 4 trial sites (Table 1:Original Data). The linear regression fits between methods yielded slopes between 1.053 and 1.108 (Pearson correlation between 0.963 and 0.985), representing an average overestimation of between 0.287 and 0.524 Gy (9.32-11.33%) for the STP method relative to 3PBE. The training data set from each site was used to generate a site specific correction factor ranging from 1.071 to 1.120. Applying this factor to the testing data was able to substantially reduce the average error (Table 1:Corrected Data) at each site to between -0.078 and 0.028 Gy (-1.05-2.09%) while maintaining a high Pearson correlation (0.960-0.985). When pooling the testing data from all sites, the overall overestimation was reduced from 0.426±0.390 Gy (10.16±8.46%) to -0.046±0.358 Gy (-0.23±7.78%). ***Conclusion:*** STP dosimetry is highly correlated with 3PBE but over-predicts for most cases. Applying a site specific correction factor can help resolve this over-estimation without affecting the correlation, allowing less imaging per patient while maintaining accurate dosimetry comparable across different sites. ***References:*** Hänscheid, J Nucl Med. 2018

EP-1101

PBPK-Driven Digital Twinning in Radiopharmaceutical Therapies enabling Predictive Dosimetry from Dynamic Pre-Therapy PET Data

M. Sabouri*, A. Rafiei Sardouei, J. Fowler, O. Gharibi, H. Abdollahi, C. Uribe, A. Rahmim;*
University of British Columbia, Vancouver, BC, CANADA.

Aim/Introduction: Absorbed dose calculations in radiopharmaceutical therapies (RPTs) rely on post-therapy SPECT data, while pre-therapy PET scans offer valuable pharmacokinetic information. We developed a computational framework using advanced Physiologically Based PharmacoKinetic (PBPK) modeling that simulates radiopharmaceutical distributions by solving a system containing >100 ordinary differential equations (ODEs). In this study, we use an inverse approach to estimate pharmacokinetic parameters from dynamic 18F-prostate specific membrane antigen (PSMA) PET data, thus creating digital twins for individual patients, from which 177Lu-PSMA SPECT time-activity curves (TACs) and absorbed doses can be predicted. ***Materials and Methods:*** A virtual cohort of 30 patients was generated using clinical pharmacokinetic distributions and simulated with a validated PBPK model to produce patient-specific 18F-PSMA PET TACs. The model, initialized randomly, was optimized using Adam (learning rate: 1×10^{-4}) to minimize MSE against dynamic PET data. Optimization occurred in two stages: 0-50 minutes for estimating receptor densities and blood flow, and up to 500 minutes for decay-based release rates. Early stopping was used for convergence. The predicted parameters were used to model 177Lu-PSMA biodistribution and time integrated activity curve (TIAC) was measured (directly related to absorbed doses). The accuracy of estimated parameters and TIACs were assessed using mean absolute percentage error (MAPE). Code is publicly available. ***Results:*** The accuracy of estimated parameters were assessed using MAPE and showed low errors for most receptor density (salivary glands (SG): 3.64%, kidneys: 1.13%, and tumors: 20.27%) and blood flow (SG: 1.19% and tumors: 4.60%) parameters, but higher deviations in release rate (SG: 117.97%, kidneys: 32.80%, and tumors: 1246.54%). For predictive dosimetry, SPECT-derived TIAC values demonstrated good agreement for kidneys (4.63%) and SG (16.58%), while tumors showed a higher discrepancy (120.18%), indicating potential challenges in accurately estimating tumor uptake. ***Conclusion:*** The proposed PBPK-based digital twinning involves solving an inverse problem to enable accurate prediction of pharmacokinetic parameters and absorbed doses for organs like kidneys and salivary glands using only PET data. Meanwhile, predicting tumor uptake remains a challenge, highlighting the need for improved modeling or data integration to reduce uncertainties in tumor dosimetry. At the same time, and importantly, focus on OARs is the key first step as toxicity limits will act as key constraints to ensure patients are not over- or under-treated. ***References:*** Fele-Paranj et al. PBRPK modeling of radiopharmaceutical therapies. EJNMMI Radiopharm Chem. 9, 6 (2024). https://doi.org/10.1186/s41181-023-00236-w

EP-1102

Radioimmunotherapy of Non-Hodgkin Lymphoma with Lilotomab Conjugated to Different Radionuclides: A Simulation Study

H. Ramsvik[1]*, J. Blakkisrud*[1]*, M. Kvassheim*[1,2]*, A. Løndalen*[3,4]*, C. Stokke*[1,5]*;*
[1]*Department of Physics and Computational Radiology, Oslo University Hospital, Oslo, NORWAY,* [2]*Institute of Clinical Medicine, University of Oslo, Oslo, NORWAY,* [3]*Division of Radiology and Nuclear Medicine, Oslo University Hospital, Oslo, NORWAY,* [4]*Division of Radiology and Nuclear Medicine, Innlandet Hospital Trust, Elverum, NORWAY,* [5]*Department of Physics, University of Oslo, Oslo, NORWAY.*

Aim/Introduction: The effect of a radionuclide therapy is dependent on the radionuclide. [^{177}Lu]Lu-lilotomab satetraxetan targets the CD37 antigen on B-cells and was investigated for relapsed indolent non-Hodgkin lymphoma patients in the phase 1/2a LYMRIT-37-01 trial. Using the uptake and biodistribution data of these patients, this work aims to simulate the absorbed dose from alternative radionuclides to the organs at risk. ***Materials and Methods:*** The biokinetics of whole body (3), red marrow (RM) (8), spleen (6), kidneys (6) and liver (6) for 10 patients treated with [^{177}Lu]Lu -lilotomab satetraxetan were estimated by SPECT/CT and planar imaging generally 0, 1, 4 and 7 days post-injection (day 4 and 7 for RM) [1]. The time activity curves (TACs) were normalized by patient weight and administered activity. Bi-exponential curves were fitted (mono-exponential for RM and whole body) and 1000 TACs were simulated by sampling from the fitted parameters. Coefficients were resampled for negative activity values and non-converging TACs. Absorbed doses to organs at risk were calculated for ^{177}Lu, ^{90}Y, ^{166}Ho, ^{225}Ac, ^{169}Er and ^{161}Tb, assuming equal biokinetics and local energy deposition. Redistribution of ^{225}Ac daughters was modelled according to the ICRP Publication 137,141, and 151 biokinetic models in Simbiology (MATLAB v2023b, MathWorks) by placing time-integrated activities in compartments: 'Kidneys', 'Liver1', 'Spleen', 'Trabecular marrow', and 'ST1', and free daughters in equilibrium at injection were put in 'Plasma'. ***Results:*** For the investigated patients, the median absorbed dose to RM was 2.1 mGy/MBq for the [^{177}Lu]Lu -lilotomab satetraxetan treatment. Simulated median absorbed doses to RM were 1.8, 2.3, 2.9, 6.6 and 515 mGy/MBq for ^{169}Er, ^{166}Ho,^{161}Tb, ^{90}Y and ^{225}Ac, respectively. For spleen, kidney and liver, all median absorbed doses were below 4.5 mGy/MBq, except for ^{225}Ac. Daughter redistribution increased the ^{225}Ac kidney absorbed dose by 2.5% and changed the absorbed dose to liver, spleen, and RM by less than 1%. Due to sparse early sampling for RM, a larger uncertainty is to be expected for this organ and would likely be more pronounced for radionuclides with shorter physical half-life. ***Conclusion:*** From the preliminary investigations, RM is the primary activity limiting organ regardless of radionuclide. Future work will focus on estimating absorbed doses to tumors to compare the therapeutic efficacy. This may contribute to inform the design of a new lilotomab-based radioimmunotherapy. ***References:*** [1] Stokke et. al EJNMMI 2018(45).

EP-1103

Prediction of tumor kinetics of [^{90}Y]Y-FAPI-46 using [^{68}Ga]Ga-FAPI-46 PET CT imaging

M. Watanabe[1,2]*, W. Jentzen*[2]*, D. Kersting*[2]*, K. Herrmann*[2]*, W. P. Fendler*[2]*, P. F. Costa*[2]*;*
[1]*Department of Diagnostic Imaging and Nuclear Medicine, Kyoto University Hospital, Kyoto, JAPAN,* [2]*Department of Nuclear Medicine, University Hospital Essen, Essen, GERMANY.*

Aim/Introduction: Among many surface markers of cancer-associated fibroblasts, fibroblast activation protein (FAP) was shown to be upregulated in the stroma of more than 90% of epithelial carcinomas and sarcoma. FAP expression implicated in various cancer-related signaling pathways contributes to tumor progression, invasion, metastases, immunosuppression, and chemotherapy resistance. For this reason, radiolabeled FAP-targeting peptides, such as [^{90}Y]Y-FAP-inhibotor-46 (^{90}Y-FAPI-46) for radioligand therapy (RLT), have a growing impact for the treatment of various tumor entities, possibly leading to treatment response at acceptable side effects. Dosimetry can be used to predict tumor control and normal organ toxicity probability. The aim of this study is to investigate if lesion uptake (%), time-integrated activity coefficient (TIAC) and tumor absorbed dose (Gy/GBq) of patients receiving their first-cycle [^{90}Y]Y-FAPI-46 can be predicted by pretherapeutic [^{68}Ga]Ga-FAPI-46 (^{68}Ga-FAPI-46) PET/CT. ***Materials and Methods:*** Fourteen patients (five males and nine females) for restaging underwent [^{68}Ga]Ga-FAPI-46 PET/CT and serial ^{90}Y-FAPI-46 PET/CT within 3 months. There were 11, 1, 1 and 1 patients with solitary fibrous tumor, gastric cancer, prostate cancer and leiomyosarcoma, respectively. Tumor lesions were retrospectively semi-automatically segmented on each PET image. In this dosimetry model, the biological half-life of ^{68}Ga-FAPI-46 and ^{90}Y-FAPI-46 was assumed to be the same. Lesion's uptake (%), TIAC and tumor absorbed dose (Gy/GBq) were estimated and the difference and their correlation between ^{68}Ga-FAPI-46 and ^{90}Y-FAPI-46 PET/CT-derived values was analyzed. ***Results:*** As for the Bland-Altman analysis, mean % differences of lesions' uptake (%), TIAC (hr) and tumor absorbed dose (Gy/GBq) between each PET/CT were −34.36%, −15.77% and −15.78% with 95% of confidence interval of −119.70 to 50.95%, −100.40 to 68.89% and −100.40 to 68.81%, with Spearman's rho of 0.95, 0.93 and 0.76, respectively (p<0.0001 each). The TIACs (n=24) based on ^{68}Ga-FAPI-46 PET/CT and ^{90}Y-FAPI-46 PET/CT were 0.07 ± 0.14 hr (median: 0.03; range: 0.001 to 0.66) and 0.07 ± 0.13 hr (median: 0.04; range: 0.001 to 0.48), respectively. There was no statistically significant difference. ***Conclusion:*** The lesion's uptake, TIAC and tumor absorbed dose on ^{90}Y-FAPI-46 PET/CT and ^{68}Ga-FAPI-46 PET/CT were highly correlated. Although the differences of the lesion's uptake, TIAC and tumor absorbed dose calculated based on each PET modality were still large, ^{68}Ga-FAPI-46 PET/CT may have a potential to optimize the treatment plan of future FAP RLT candidates.

EP-1104

Dosimetry and safety of the PDGFRb PET tracer [^{68}Ga]Ga-DOTA-Cys-ATH001: first-in-human data in patients with liver fibrosis and healthy subjects

M. Lubberink[1], *T. G. Lohith*[2], *Z. Derdak*[2], *P. Wilkens*[2], *H. Wennbo*[2], *E. Palmer*[3,4], *A. Ramolli*[4], *B. Mitran*[5,6], *A. Abouyzayed*[5,6], *L. Johansson*[6], *F. Rorsman*[1,7], *J. Vessby*[1,7], *O. Eriksson*[1,5];
[1]*Uppsala University, Uppsala, SWEDEN,* [2]*Takeda Pharmaceutical Company Limited, Cambridge, MA, UNITED STATES OF AMERICA,* [3]*Karolinska Institutet, Stockholm, SWEDEN,* [4]*Karolinska University Hospital, Stockholm, SWEDEN,* [5]*Antaros Tracer AB, Uppsala, SWEDEN,* [6]*Antaros Medical AB, Gothenburg, SWEDEN,* [7]*Uppsala University Hospital, Uppsala, SWEDEN.*

Aim/Introduction: Platelet Derived Growth Factor Receptor Beta (PDGFRb) is a general marker of pericytes and associated to virtually all fibrotic pathology and tissue remodeling. PDGFRb is strongly upregulated on activated hepatic stellate cells, the main source of extracellular matrix deposition in liver fibrosis (1). [^{68}Ga]Ga-DOTA-Cys-ATH001 is an Affibody molecule being developed as a PET tracer for non-invasive imaging of active liver fibrogenesis by quantification of PDGFRb (2). Here we present biodistribution and radiation dosimetry data from first-in-human PET trial NCT06562361. ***Materials and Methods:*** Radiation dosimetry of [^{68}Ga]Ga-DOTA-Cys-ATH001 was evaluated in healthy subjects (n=3) and patients with metabolic dysfunction-associated steatohepatitis (MASH) with elevated serum Pro-C3, a well-established fibrogenesis marker (n=3). Participants were administered 2.5 MBq/kg (<1µg/kg peptide mass) [^{68}Ga]Ga-DOTA-Cys-ATH001 intravenously, and imaged by a dynamic PET/MRI (Signa) abdominal scan, followed by whole body scans at 1, 2 and 3 h post-injection. All major organs and tissues (n=25) were segmented for biodistribution and time-activity curves (TACs) were uncorrected for decay. The area under the curve (AUC) of each TAC was calculated by rectangular integration. A single exponential fit to the last data point in the dynamic scan and the three whole-body scans was used to estimate the remainder of the AUC and extrapolating to infinity. The time-integrated activity (TIAC) was calculated as the AUC under each TAC and scaled to the reference organ weights in ICRP110 followed by division with the amount of injected activity. Absorbed dose coefficients and effective doses according to ICRP 103 were calculated using IDAC DOSE 2.1 (3). ***Results:*** The effective dose of [^{68}Ga]Ga-DOTA-Cys-ATH001 was 0.028 ± 0.002 mSv/MBq. The dose-limiting organ was the kidneys (0.463 ± 0.021 mGy/MBq in males and 0.339 ± 0.033 mGy/MBq in females). Administration of a target dose of 2 MBq/kg (circa 150 MBq in males) would result in an effective dose of 4.1 mSv and an absorbed dose to the kidneys of 69 mGy in males, with slightly lower doses in females. Thus, at this dose level, at least two annual administrations of [^{68}Ga]Ga-DOTA-Cys-ATH001 are feasible while conforming to relevant dosimetry safety guidelines. Subjects tolerated the tracer well with no adverse effects following tracer administration. ***Conclusion:*** [^{68}Ga]Ga-DOTA-Cys-ATH001 has an excellent dosimetry and safety profile that support further clinical development as a repeatable, non-invasive PET marker of active liver fibrogenesis. ***References:*** 1. Wong et al, J Clin Invest 1994; 2. Wegrzyniak et al, iScience 2024; 3. Andersson et al, EJNMMI Res 2017

EP-1105

Comparison of dosimetry in I-131 therapy for benign thyroid diseases using Marinelli and Hänscheid Methods

M. Mamach*, T. L. M. Felgenhauer, L. Geworski;*
Department for Medical Physics and Radiation Protection, Hannover, GERMANY.

Aim/Introduction: Radioiodine therapy with I-131 is an established treatment for benign thyroid conditions such as Graves' disease (GD) and autonomous adenoma (AA). Methods used for dosimetric planning are heterogenous in Europe. We evaluated key dosimetric parameters—maximum iodine uptake (IU_{max}), effective half-life (T_{eff}), and activity per dose (ApD)—comparing pre-therapy and in-therapy measurements using the Marinelli (MAR) and Hänscheid (HAN) methods [1,2]. ***Materials and Methods:*** Retrospective dosimetry was performed on 195 patients (70 GD, 125 AA). Each received 0.8-4.4 MBq I-131 pre-therapy, with uptake measured at 4h, 24h, and 7d using a gamma probe (NUVIA Instruments GmbH, Dülmen). During therapy, uptake was measured at 4h, 24h, 48h and 5-7d. T_{eff} and ApD were calculated via MAR and HAN. IU_{max} was derived from measurements. Paired t-tests were conducted using JMP (Student Edition 18, SAS Institute Inc., NC). ***Results:*** In AA patients, pre-therapy T_{eff} differed significantly (by 0.1 d, p<0.001, MAR 6.8±1.4 d, HAN 6.6±1.4 d) but not in-therapy (MAR 5.9±1.6 d, HAN 6.0±1.7 d). ApD differed by 0.5MBq/Gy in pre-therapy (p<0.001, MAR 3.5 ±2.5 MBq/Gy, HAN 3.0±2.2 MBq/Gy) and in-therapy (0.5MBq/Gy, p<0.001, MAR 3.5±3.4 MBq/Gy, HAN 3.0 ±2.6 MBq/Gy). T_{eff} was significantly larger pre-therapy (MAR by 0.9d, p<0.001, HAN by 0.7d, p<0.001). ApD and IU_{max} (pre-therapy 33±12 %, in-therapy 32±18 %) showed no significant difference.Significant differences in GD patients were observed in pre-therapy T_{eff} (0.06d, p<0.001), pre-therapy ApD (0.3MBq/Gy, p<0.001) and in-therapy ApD (0.3MBq/Gy, p<0.001). T_{eff} was larger pre-therapy (MAR by 0.5d, p<0.001, HAN by 0.4d, p=0.007) and ApD was underestimated by 0.2MBq/Gy pre-therapy for both methods with p<0.001). IU_{max} (pre-therapy 58±15 %, in-therapy 57±15 %) showed no significant difference. ***Conclusion:***

Significant differences exist between MAR and HAN, yet intra-method variability is higher. Overall, T_{eff} was overestimated in pre-therapy assessments possibly resulting in an under-treatment if not adjusted. Neither method demonstrated clear superiority, underscoring the need for further comparative analysis and potential standardization in radioiodine dosimetry. ***References:*** [1] L.D. Marinelli, E.H. Quimby, G.J. Hine; Dosage determination with radioactive isotopes; practical considerations in therapy and protection Am J Roentgenol Radium Ther. 1948 Feb;59(2):260-81. PMID: 18905884. [2] H. Hänscheid, M. Lassmann, C. Reiners; Dosimetry prior to I-131-therapy of benign thyroid disease Z Med Phys. 2011 Dec;21(4):250-7. doi: 10.1016/j.zemedi.2011.01.006. Epub 2011 Apr 30. PMID: 21531122.

EP-1106

PBPK model to predict [^{177}Lu]Lu-DOTA-TATE time-integrated activity with single-time-point [^{68}Ga]Ga-DOTA-TATE PET/CT imaging

V. Vasic[1], *J. Gustafsson*[2], *E. Yousefzadeh-Nowshahr*[1], *A. Beer*[1], *K. Sjögreen Gleisner*[2], *G. Glatting*[1];
[1]*Department of Nuclear Medicine, Ulm University Medical Centre, Ulm, GERMANY,* [2]*Medical Radiation Physics, Lund University, Lund, SWEDEN.*

Aim/Introduction: Estimating the time-activity curve (TAC) of [^{177}Lu]Lu-DOTA-TATE in organs at risk and neuroendocrine tumours (NETs) is an essential step toward individualising peptide receptor radionuclide therapy (PRRT), as it is an essential element in absorbed dose (AD) calculations. This study aims to predict the TAC of [^{177}Lu]Lu-DOTA-TATE from a [^{68}Ga]Ga-DOTA-TATE PET/CT image and population information used in a whole-body physiologically based pharmacokinetic (PBPK) model. ***Materials and Methods:*** Twelve patients with diagnosed NETs who underwent a diagnostic [^{68}Ga]Ga-DOTA-TATE PET/CT and PRRT using [^{177}Lu]Lu-DOTA-TATE were analysed. A PBPK model was implemented for [^{68}Ga]Ga-DOTA-TATE and [^{177}Lu]Lu-DOTA-TATE, including all organs and NETs [1]. Model parameters were based on literature values, direct patient-specific measurements, or estimated through a fitting procedure to measured [^{68}Ga]Ga-DOTA-TATE organ and tumour activities. Various error models were evaluated to estimate the uncertainties in the measured time-activity data. Reference TACs were determined using both [^{68}Ga]Ga-DOTA-TATE and [^{177}Lu]Lu-DOTA-TATE time-activity measurements, while predicted [^{177}Lu]Lu-DOTA-TATE TACs were estimated based solely on [^{68}Ga]Ga-DOTA-TATE PET/CT time-activity measurements. Time-integrated activities (TIAs) for several organs and tumours were calculated from predicted and reference TACs. The relative prediction error (RPE) and the mean absolute percentage error (MAPE) were calculated to assess the accuracy of the prediction. ***Results:*** The proportional data-based error model, which accounts for the different errors between organs and tumours, as well as between imaging modalities (PET/CT and planar + SPECT/CT), was the error model most supported by the data. The median errors for organs and tumours were $b_{T,Organ}$=6% and $b_{T,Tumour}$=39% for post-therapy SPECT/CT time-activity measurements, and $b_{D,Organ}$=35% and $b_{D,Tumour}$=27% for pre-therapy PET/CT time-activity measurements, respectively. In prediction assessment, the mean and standard deviation of RPE for TIAs were (-5 ± 51)%, (-4 ± 22)%, (-13 ± 40)%, and (-10 ± 21)% for tumours, kidneys, liver, and spleen, respectively. The MAPE values for tumours, kidneys, liver, and spleen were 43%, 18%, 31%, and 17%, respectively. ***Conclusion:*** The findings show that single-time-point [^{68}Ga]Ga-DOTA-TATE PET/CT imaging offers valuable prediction of TACs and TIAs in organs and tumours in [^{177}Lu]-DOTA-TATE-targeted therapy comparable to the results of Siebinga et. al. [2]. However, there is potential to improve prediction accuracy of tumours and liver. ***References:*** [1] Vasić V et al. A PBPK model for PRRT with [177Lu]Lu-DOTA-TATE: Comparison of model implementations in SAAM II and MATLAB/SimBiology. Phys Med. 2024;119:103299 [2] Siebinga H et al. Predicting [177Lu]Lu-HA-DOTATATE kidney and tumor accumulation based on [68Ga]Ga-HA-DOTATATE diagnostic imaging using semi-physiological population pharmacokinetic modeling. EJNMMI Physics. 2023;10(1):48.

EP-1107

Single-Time-Point Dosimetry using Nonlinear Mixed-Effects Modelling in Sparse [^{177}Lu]Lu-PSMA-617 Therapy Data

F. Ananda[1], *D. Hardiansyah*[1], *R. Ritawidya*[2], *A. J. Beer*[3], *N. Varmenot*[4], *L. Ferrer*[4], *G. Glatting*[3,5];
[1]*Medical Physics and Biophysics, Physics Department, Faculty of Mathematics and Natural Sciences, Universitas Indonesia, Depok, INDONESIA,* [2]*Center for Research on Radioisotope, Radiopharmaceutical, and Biodistribution Technology, National Research and Innovation Agency (BRIN), Tangerang Selatan, INDONESIA,* [3]*Department of Nuclear Medicine, Ulm University, Ulm, GERMANY,* [4]*Médecine Nucléaire, ICO René-Gauducheau, Saint-Herblain, FRANCE,* [5]*Medical Radiation Physics, Department of Nuclear Medicine, Ulm University, Ulm, GERMANY.*

Aim/Introduction: Single-time-point (STP) dosimetry for [^{177}Lu]Lu-PSMA-617 therapy using population-based model selection with nonlinear mixed-effects modeling (PBMS NLMEM) has recently emerged as a promising approach, offering improved objectivity and reproducibility in dose estimation[1]. However, its performance has not yet been evaluated in populations with sparse data—a common scenario in molecular radiotherapy due to practical limitations in data collection. Assessing the accuracy of PBMS NLMEM under such conditions is critical for its clinical adoption. Therefore, this study aims to evaluate the feasibility and accuracy of STP dosimetry using the PBMS NLMEM framework in patients undergoing [^{177}Lu]Lu-PSMA-617 therapy with sparse time-activity data. ***Materials and Methods:*** Renal biokinetic data of [^{177}Lu]Lu-PSMA-617 were collected from sixty-four mCRPC patients at (4.8 ± 0.9) h (N=60), (24.5 ± 1.5) h (N=6), (94.0 ± 6.6) h (N=16), and (128.5 ± 12.7) h (N=46) after intravenous administration. Thirteen sum-of-exponential functions (SOEF) were fitted to all-time-point (ATP) data using the NLMEM framework. Various combinations of fixed effects, random effects on uptake parameters, and strategies for handling intra-individual variability (either fixed to a reference value or estimated) were systematically evaluated. The optimal SOEF, selected through PBMS NLMEM, was then applied for STP dosimetry. The accuracy of STP-based time-integrated activity (sTIA) estimates was assessed against ATP-based references (rTIA) using relative deviations (RDs), root-mean-square errors (RMSEs), and mean absolute percentage errors (MAPEs). The performance of the PBMS NLMEM-based STP dosimetry was further compared with the STP method proposed by Hänscheid et al. [2] and a "no-time-point" approach. ***Results:*** Based on the PBMS NLMEM analysis, the function $f_{6a}(t)=A_1e^{(-(\lambda1+\lambda p)t)}+A_2e^{(-(\lambda2+\lambda p)t)}-A_3e^{(-(\lambda3+\lambda p)t)}-(A_1+A_2-A_3)e^{(-(\lambda bc+\lambda p)t)}$ with fixed λ_3 (fixed effect), and A_3 and λ_3 (random effect), with $\lambda_{bc}=\ln(2)/(1\ min)$ and $\lambda_p=\ln(2)/(6.64\ d)$, and fixed intra-individual variability, was selected as the optimal function for TIA estimation. STP dosimetry using the PBMS NLMEM at 24.5 h (RMSE: 19.2%; MAPE: 1.4%) and 94 h (RMSE: 11.1%; MAPE: 2.2%) outperformed Hänscheid's method (RMSE: 29%; MAPE: 3%) and (RMSE: 12%; MAPE: 3%) and the no-time-point approach (RMSE: 55%; MAPE: 33%). ***Conclusion:*** The PBMS NLMEM framework accurately estimates [^{177}Lu]Lu-PSMA-617 time-integrated activity from sparse biokinetic data, with optimal performance using a single SPECT/CT measurement at either 24 h or 94 h after administration. ***References:*** [1]D. Hardiansyah, E. Yousefzadeh-Nowshahr, F. Kind, A.J. Beer, J. Ruf, Glatting, and M. Mix, Journal of Nuclear Medicine, 65, 566-572 (2024).[2]H. Hänscheid, C. Lapa, A.K. Buck, M. Lassmann, and R.A. Werner, Journal of Nuclear Medicine, 59, 75-81 (2018).

EP-1108

A Novel Single-Time-Point Dosimetry Approach in ^{177}Lu-Labeled Somatostatin Analog Therapy: Feasibility and Clinical Validation

E. Farajzadeh[1], *M. Sadeghi*[2], *J. Aghamohammadi*[3], *M. Akbari*[1], *N. Habibi*[3], *M. Davarpanah*[3];
[1]*Secondary Standard Dosimetry Laboratory (SSDL), Pars Isotope Co., Karaj, IRAN, ISLAMIC REPUBLIC OF,* [2]*Shiraz University, Shiraz, IRAN, ISLAMIC REPUBLIC OF,* [3]*Pars Isotope Company, Tehran, IRAN, ISLAMIC REPUBLIC OF.*

Aim/Introduction: Single time point dosimetry (STPD) for 177Lu-labeled somatostatin analog therapy offers a streamlined alternative to conventional multi-time point (MTP) protocols, however its accuracy and clinical applicability are still open to question. In this novel prospective study, a standardized correction-factor approach is introduced to STPD, designed to reduce measurement variability and improve the estimation of both organ and tumor-specific doses. This study aimed to determine whether this novel STPD method can provide reliable dosimetric data comparable to MTP measurements, while significantly reducing the imaging burden on patients. ***Materials and Methods:*** Twenty patients (mean age 59 ± 11 years; 13 males, 7 females) with progressive, metastatic neuroendocrine tumors were enrolled. All received a therapeutic injection of 177Lu-DOTA-peptide, followed by a single SPECT/CT scan 24±2 hours post-infusion. Time-activity data were corrected using patient-specific scaling factors from prior pharmacokinetic models. For validation, 10 patients underwent a standard MTP protocol (4, 24, 72, and 120 hours). Dose calculations were done with OLINDA/EXM (Version 2.0). Primary endpoints included accuracy of dose estimation (kidneys, liver, spleen, bone marrow, and index lesions) and potential impact on clinical decision-making. ***Results:*** The novel STPD method showed strong correlation with multi-time point dosimetry(MTPD) results (Spearman r=0.92, p<0.001). Median absolute differences in absorbed doses across organs ranged from 7% to 12%, indicating clinically acceptable agreement. The mean effective dose rate to bone marrow differed by ±9% compared to MTP data. In 18 of 20 patients (90%), STPD-based estimations did not alter treatment plans or raise safety concerns. Patients reported high satisfaction due to fewer scans and reduced hospital visits. ***Conclusion:*** These findings highlight the feasibility and clinical utility of a novel correction-factor STPD protocol in 177Lu-based radionuclide therapy. By maintaining dosimetric accuracy comparable to MTP analyses, this approach can optimize resource allocation, minimize patient burden, and facilitate broader implementation of personalized dosimetry in routine clinical practice. ***References:*** Madsen MT, Menda Y, O'Dorisio TM, O'Dorisio MS. Single time point dose estimate for exponential clearance. Med Phys. 2018;45(5):2318-24, Del Prete M, Buteau FA, Arsenault F, Saighi N, Bouchard LO, Beauregard JM. Personalized 177Lu-octreotate peptide receptor radionuclide therapy of neuroendocrine tumours based on pretherapeutic dosimetry and posttherapeutic SPECT/CT imaging. J Nucl Med. 2017;58(9):1399-1406., Sandström M, Garske-Román U, Granberg D, et al. Individualized dosimetry of kidney and bone marrow in patients receiving 177Lu-DOTA-D-Phe1-Tyr3-octreotate therapy. J Nucl Med. 2013;54(2):200-208., Garske U, Sandström M, Johansson S, et al. Lessons on tumour response: imaging during therapy. Acta Oncol. 2012;51(2):197-205.

EP-1109

Revolutionizing personalized dosimetry in Targeted Radionuclide Therapy: first-in-human results of the WIDMApp approach

F. Collamati[1], *R. Mirabelli*[2], *B. Caccia*[3], *F. Censi*[3], *M. Carruezzo*[4], *B. Cassano*[5], *M. De Simoni*[3], *C. D'Angeli*[3], *R. Faccini*[6], *G. Iaccarino*[5], *C. Mancini-Terracciani*[6], *E. Mattei*[3], *S. Morganti*[1], *F. Nicolanti*[6], *S. Pozzi*[3], *A. Soriani*[5], *E. Solfaroli-Camillocci*[3], *L. Campana*[7];
[1]*INFN Rome, Roma, ITALY,* [2]*Università sapienza, Roma, Roma, ITALY,* [3]*ISS Rome, Roma, ITALY,* [4]*Univesrità Sapienza Roma, Roma, ITALY,* [5]*IRCCS Regina Elena National Cancer Institute in Rome, Roma, ITALY,* [6]*Università Sapienza Roma, Roma, ITALY,* [7]*Campus Bio Medico Roma, Roma, ITALY.*

Aim/Introduction: In Targeted Radionuclide Therapy (TRT), radiotracers are employed to selectively deliver radiation to tumor sites. However, systemic administration inevitably results in radiation exposure to healthy tissues, and treatment efficacy is closely tied to the dose actually absorbed by the tumor. Therefore, accurate and personalized dosimetry is critical to optimize therapeutic outcomes and minimize toxicity.To address this need, we propose the WIDMApp (Wearable Individual Dose Monitoring Apparatus) approach: a novel, real-time in vivo dosimetry system. It combines lightweight wearable particle detectors that continuously monitor photon emissions over several days, reconstructing Time Count Curves (TCCs), with a patient-specific Monte Carlo simulation—based on a single SPECT/CT scan—to model detector-organ geometry and compute organ-specific detection probabilities. An unfolding algorithm integrates these data to derive Time Activity Curves (TACs), allowing for organ-specific dose estimation.Until now, the WIDMApp approach has been validated through Monte Carlo simulations and phantom studies. This work presents the first feasibility study conducted on patients. ***Materials and Methods:*** The WIDMApp prototype consists of a 10-channel photon counter utilizing a lightweight (1.5×1.5 cm^2) p-terphenyl scintillator. The study was conducted on patients undergoing TRT with ^177Lu-DOTA at the IRCCS Regina Elena National Cancer Institute in Rome, where standard SPECT-based dosimetry was also performed.For this preliminary test, the detectors were not worn continuously but placed on the patient's body in a reproducible manner at multiple time points post-injection. Each acquisition session lasted approximately 30 minutes. ***Results:*** As a first-in-human feasibility study, the objective is not yet to validate the accuracy of WIDMApp-derived dosimetry against standard methods. Instead, the focus is on assessing the method's feasibility and potential. Specifically, we examine the correlation between organ activity as measured by standard SPECT and the TACs obtained via the WIDMApp system.Secondary goals include evaluating the impact of detector placement and quantity, assessing intra-patient variability, and estimating the acquisition time required for effective activity unfolding. ***Conclusion:*** The WIDMApp approach aims at revolutioning TRT efficacy by means of real-time, accurate and personalized dosimetry, using a wearable array of photons detectors and a SPECT/CT-based Monte Carlo simulation.After principle validation in Monte Carlo and phantom studies, the very first tests on patients are now ongoing, and will be presented in this contribution,providing preliminary insights into the clinical potential of this novel dosimetric approach.

EP-1110

Fast Patient-Specific Dosimetry for PRRT Using GPU-Accelerated Monte Carlo Simulation: A Comparative Study Between irtGPUMCD and GATE

H. Jozi[1,2], *R. Lefol*[1,2], *Y. Lemaréchal*[1,2,3], *J. M. Beauregard*[2,4,5], *P. Després*[1,2,3];
[1]*Département de physique, de génie physique et d'optique-Université Laval, Québec, QC, CANADA,* [2]*Centre de recherche du CHU de Québec-Université Laval, Québec, QC, CANADA,* [3]*Centre de recherche de l'Institut universitaire de cardiologie et de pneumologie de Québec-Université Laval, Québec, QC, CANADA,* [4]*Department of Radiology and Nuclear Medicine, and Cancer Research Centre-Université Laval, Québec, QC, CANADA,* [5]*Department of Medical Imaging, CHU de Québec-Université Laval, Québec, QC, CANADA.*

Aim/Introduction: Personalized dosimetry is critical for optimizing efficacy and minimizing toxicity in 177Lu-DOTATATE peptide receptor radiopharmaceutical therapy (PRRT) for neuroendocrine tumors (NETs). Voxel-based Monte Carlo (MC) methods remain the gold standard for internal dose calculation due to their accuracy in modeling radiation transport and tissue heterogeneity. GATE is a well-established MC toolkit but is computationally intensive, leading to long calculation times. To address this, irtGPUMCD, a GPU-accelerated MC engine derived from bGPUMCD, offers fast and accurate internal dosimetry. This study aims to benchmark and compare the performance of irtGPUMCD and GATE in generating voxel-level dose-rate maps from post-treatment

quantitative SPECT/CT images. ***Materials and Methods:*** Fifteen patients diagnosed with NETs were included in this study. Whole-body quantitative SPECT/CT images acquired at 72 hours post-administration 177Lu-DOTATATE(J3) — a clinically optimal time point for single-time-point dosimetry—were used as simulation input. Patient-specific activity and anatomical maps were imported into both GATE (v9.2) and irtGPUMCD to generate 3D voxel-level absorbed dose rate maps with associated uncertainty. For each patient, simulations were run with 5×10^9 primary particles. GATE simulations were executed on a CPU cluster using 100 parallel jobs (submitted through SLURM), while irtGPUMCD ran on a dedicated NVIDIA DGX A100 equipped with 8GPUs. Organ segmentation was performed using TotalSegmentator, which automatically delineated the kidneys, liver, spleen, and vertebra L3. The generated contours were subsequently processed to produce 3D binary organ masks. These masks were applied to the dose-rate maps from both codes, normalized to their respective maxima, to extract organ-specific dose distributions. Voxel-wise percentage differences were then computed across the entire patient volume and within each organ for global and regional comparison for two MC frameworks. ***Results:*** Under identical settings, GATE required 17 ± 1.5 hours per patient, while irtGPUMCD completed simulations in just 4.7 ± 0.1 seconds, including RTDOSE generation. Organ segmentation took 145 ± 3.2 seconds per patient for generating DICOM RTSTRUCT. The mean statistical uncertainty remained below 1% for both Monte Carlo codes across all four organs of interest (OOIs). Across the volume, 93% of voxels exhibited a percent dose difference below ±1%. Mean organ-level differences were 1.4 ± 0.8%, 2.4 ± 2.5%, 1.0 ± 0.3%, and 2.0 ± 1.0% for the kidneys, liver, vertebra_L3, and spleen, respectively, confirming strong global and regional consistency between irtGPUMCD and GATE. ***Conclusion:*** This study demonstrates that irtGPUMCD generates accurate patient-specific dose-rate maps with close agreement to GATE. Leveraging GPU acceleration, it significantly reduces computation time, suggesting high potential for clinical use in patient-specific PRRT dosimetry.

EP-1111

The Clinical Impact of Specific Activity and Precursor Mass content on Absorbed Doses to Tumours and Organs-at-risk for a novel PSMA targeting RLT

B. Fongenie[1], *N. Scott*[1], *A. Rinscheid*[2], *C. Lapa*[2], *J. Sykes*[3], *T. Mauch*[1], *D. Stevens*[1];
[1]*Blue Earth Therapeutics, Oxford, UNITED KINGDOM,* [2]*Augsburg University Hospital, Augsburg, GERMANY,* [3]*Blue Earth Diagnostics, Oxford, UNITED KINGDOM.*

Aim/Introduction: The pharmacokinetics (PK) of a radiopharmaceutical are a critical driver of safety and efficacy for radioligand therapy (RLT). It has been hypothesised that formulation properties of radiopharmaceuticals may affect absorbed doses in tumours and organs-at-risk. Despite ongoing clinical trials, a dearth of data exists in humans investigating this question. Here we analyse human data from two clinical settings across a range of specific activities and precursor masses for a novel PSMA-targeted RLT, ^{177}Lu-rhPSMA-10.1. Formulation properties, including the aforementioned, were recorded for all administrations and correlated with dosimetry results. ***Materials and Methods:*** 17 patients across two clinical experiences were included in this analysis. Given the range of activities administered (1.0GBq - 8.0GBq), activity normalized absorbed doses (D_{norm}) were calculated for each administration. These were correlated against formulation properties for each administration including specific activity and precursor mass. Linear regression and one-tailed ANOVA tests were performed. To avoid the impact of treatment response, linear regression for tumour dose was performed for all cycles and cycle 1 only. Precursor masses administered ranged from 89.5 to 667 µg. ***Results:*** Results suggest an inverse correlation between precursor mass and D_{norm}. Significant differences were observed using ANOVA testing between absorbed doses to kidneys in phase 1 patients administered ^{177}Lu-rhPSMA-10.1 manufactured at different sites (P-value<0.01) corresponding with significant differences in precursor mass. Given high interpatient variability, the effect on tumour doses was weaker. For linear regression, the R^2 for D_{norm} against precursor mass for tumour (cycle 1 only), kidney and salivary glands including Rinscheid data were 0.33, 0.63 and 0.55 respectively. Analyses of SUV_{peak} and SUV_{mean} of tumors in PSMA-PET screening scans could not explain these trends. Other properties showed weaker trends with lower R^2 values. ***Conclusion:*** An inverse correlation between precursor mass and D_{norm} was found. Although relative changes to D_{norm} were significant, absolute changes were small (e.g. for Kidney 0.3 - 0.6Gy/GBq). Conclusions from this data are limited by a small sample size, inter-patient variability in PK obscuring trends and a lack of administrations with extreme formulation properties. These results suggest it may be possible to identify an optimum formulation mass content maximizing therapeutic index. This may differ between alpha and beta labelled molecules, depending on predicted off-target toxicity. ***References:*** [1] - An Intrapatient Dosimetry Comparison of ^{177}Lu-rhPSMA-10.1 and ^{177}Lu-PSMA-I&T in Patients with Metastatic Castration-Resistant Prostate Cancer Andreas Rinscheid et al Journal of Nuclear Medicine Dec 2023, 64 (12) 1918-1924; DOI: 10.2967/jnumed.123.265970

EP-1112

Test-Retest Comparison of Total-Body ^{90}Y PET for Post-SIRT Dosimetry: Evaluating Scanner Performance Across Platforms

M. Santoro[1], *I. Gabucci*[1], *C. Macis*[1], *G. Della Gala*[1], *F. Bisello*[1], *F. Zagni*[1], *I. Brusa*[2], *A. Golemi*[2], *E. Lodi Rizzini*[3], *A. G. Morganti*[3,4], *S. Fanti*[2,5], *L. Strigari*[1];
[1]*Department of Medical Physics, IRCCS Azienda Ospedaliero-Universitaria di Bologna, Bologna, ITALY,* [2]*Nuclear Medicine, IRCCS Azienda Ospedaliero-Universitaria di Bologna, Bologna, ITALY,* [3]*Radiation Oncology, IRCCS Azienda Ospedaliero-Universitaria di Bologna, Bologna, ITALY,* [4]*Department of Medical and Surgical Sciences, Alma Mater Studiorum University of Bologna, Bologna, ITALY,* [5]*Nuclear Medicine, Alma Mater Studiorum University of Bologna, Bologna, ITALY.*

Aim/Introduction: Selective Internal Radiation Therapy (SIRT) delivers ^{90}Y resin/glass microspheres to hepatocellular carcinoma (HCC) patients. Post-treatment PET/CT enables dose verification, but the low positron yield of ^{90}Y (0.0032%) might introduce variability and bias, particularly in small or low-activity regions, limiting the accurate assessment of heterogeneous dose distributions. Total-body (TB) PET/CT systems may offer improved performance, but comparative validation with digital scanners having a standard axial field of view (sAFOV) and algorithms available in the same clinical centre is essential. ***Materials and Methods:*** The ^{90}Y activity distribution derived from a TB PET/CT scanner was compared against a sAFOV digital PET/CT using a bayesian penalized likelihood reconstruction, currently adopted in our clinical practice. A NEMA phantom containing 2.97 ± 5% GBq of ^{90}Y (sphere-to-background ratio 7.8:1 across six spheres, 10-37 mm) underwent multiple acquisitions over 7 days for test-retest analysis. Eight HCC patients were imaged on both systems about 20 hours post-SIRT to evaluate cross-scanner consistency. Image quality metrics included contrast recovery (CR), background variability (BV), and CRBV index [1]. Absorbed dose estimates were compared using dose metrics and gamma index analysis. ***Results:*** The TB PET/CT scanner showed consistently higher CR and CRBV and lower BV across reconstruction algorithms compared to the sAFOV PET/CT. Phantom results demonstrated stable performance over time up to low activity levels. Patient scans revealed dose discrepancies up to 60% between scanners, with the TB system achieving greater CRBV in small lesions (<15 mm). Gamma index

analysis confirmed higher agreement at elevated dose levels (e.g., 94.62% at 312 Gy vs. 62.45% at 132 Gy), highlighting the impact of scanner sensitivity on dose distribution accuracy. ***Conclusion:*** The TB PET/CT scanner exhibits superior image quality and test-retest reliability for ^{90}Y PET, in both phantoms and HCC patients especially in small target volumes. While absorbed dose metrics were broadly similar across scanners in this cohort, the enhanced sensitivity of the TB system may provide more accurate dosimetry. Further validation against clinical outcomes such as tumor control and toxicity are ongoing in a prospective study of HCC patients. ***References:*** [1] Santoro M, Della Gala G, Paolani G, Zagni F, Civollani S, Strolin S, Strigari L. A novel figure of merit to investigate ^{68}Ga PET/CT image quality based on patient weight and lesion size using Q.Clear reconstruction algorithm: A phantom study. Phys Med. 2023 Feb;106:102523. doi: 10.1016/j.ejmp.2022.102523. Epub 2023 Jan 13. PMID: 36641902.

EP-1114

Whole-body single-time-point 177Lu-PSMA-617 lesions and bone marrow dosimetry at first cycle is significantly associated with biological and imaging outcomes

A. Dieudonne[1], *A. Terro*[2], *A. Dumouchel*[1], *S. Perret*[1], *A. Edet-Sanson*[1], *P. Vera*[1], *F. Di Fiore*[3], *L. Augusto-Pelegrin*[3], *P. Decazes*[2], *D. Tonnelet*[1];
[1]*Centre Henri Becquerel, Rouen, FRANCE,* [2]*University of Rouen Normandy, Rouen, FRANCE,* [3]*University Hospital of Rouen, Rouen, FRANCE.*

Aim/Introduction: This study investigates the relationship between whole-body lesions and bone-marrow dosimetry at first treatment cycle (C1) and biological and imaging outcomes in patients with metastatic castration-resistant prostate cancer (mCRPC) treated with 177Lu-PSMA-617. ***Materials and Methods:*** Patients were retrospectively included from January 2023 to May 2024. SPECT/CT imaging was conducted from vertex to mid-thigh using a VERITON-CT 200 scanner (Spectrum Dynamics, Haifa, Israel), from day 0 to days after infusion. Images were reconstructed using OSEM (4 subsets, 8 iterations) with attenuation and scatter corrections. To reduce uncertainty in single-time-point dosimetry, imaging delays between 20 and 120 hours were considered. Automated dosimetry was performed using SimpleDose(1): lesion and bone-marrow segmentation were performed using a nnU-Net framework, and absorbed doses were calculated via collapsed cone superposition (2). Time-integration coefficients were derived from Jackson et al. (3) for lesions and Kurth et al. (4) for bone-marrow. Response was evaluated using PSA50 (≥50% PSA reduction) and 18FDG or 68Ga-PSMA-11 PET/CT imaging, 6-8 weeks post-treatment. Blood counts were measured before and after therapy. Statistical analyses were conducted using one-tailed t-tests. ***Results:*** Thirty-one patients were analysed. Median age was 73 [IQR 8.5] years. Imaging time post-injection was 71 [22.6] hours. Baseline PSA level was 28.3 [IQR 125] ng/mL. Patients received a median of 4 treatment cycles (range: 2-6), with 7.01 [IQR 0.096] GBq/cycle. Median total lesions volume was 102 [IQR 191] mL. Nine out of 31 patients that responded to treatment had significantly higher lesion absorbed doses at C1 with 4.5 [IQR 8.4] Gy vs. 2.0 [IQR 3.3] Gy for non-responders (p=0.046). The absorbed dose associated with 50% response probability (D_{50}) was 5.0 Gy (95% CI: 3.7-6.9), and for 80% response (D_{80}), 7.8 Gy (95% CI: 6.0-10.0). Although no haematological toxicity was observed, the bone-marrow absorbed dose was positively associated with a >20% decrease in white blood cells: 0.13 [IQR 0.27] Gy vs. 0.047 [IQR 0.058] Gy (p=0.022) and a non-significant trend was observed for platelets (p=0.095). ***Conclusion:*** The absorbed dose to lesions and bone marrow after first infusion of 177Lu-PSMA-617 is associated with biological and imaging outcomes. These results also highlight the clinical value of automated dosimetry and single-time-point dosimetry for cohort studies. ***References:*** 1. Dieudonné A et al. EJNMMI Phys. 2025 Mar 20;12(1):25. 2. Sanchez-Garcia et al Phys Med Biol. 2015;60(20):7861-76. 3. Jackson et al. Sem Nuc Med. 2022 Mar 1;52(2):243-54. 4. Kurth J et al. EJNMMI Res. 2018 Apr 12;8:32.

EP-1115

Dosimetric comparison between^{177}Lu-PSMA-617 and^{177}Lu-PSMA I&T in patients with Metastatic Castration Resistant Prostate Cancer (mCRPC) using a ring-shaped CZT-based camera

L. D'Ambrosio*, F. Manna, C. Maisto, R. de Marino, A. Morisco, M. Aurilio, V. Porfidia, A. Prisco, R. De Migno, M. Raddi, F. De Lauro, F. Di Gennaro, S. Lastoria;*
National Cancer Institute IRCCS Pascale, Naples, ITALY.

Aim/Introduction: The most frequently used PSMA-targeting small-molecule inhibitors are DOTA-PSMA-617 (PSMA-617) and DOTAGA-PSMA I&T (PSMA I&T); DOTA and DOTAGA denote the cages enclosing the radionuclides and I&T denotes the radionuclide that yields both imaging and therapy. We present our dosimetric protocol to estimate organs at risk (OARs) and lesions absorbed dose during the first cycle in 10 PSMA-617 and 10 PSMA I&T patients using a CZT-SPECT imaging system ***Materials and Methods:*** Total-body SPECT-CT images, involving 5-6 consecutive bed positions (4-6 minutes/bed) were acquired at 2.5 h, 20 h, > 90 h pi using Veriton® camera (Spectrum Dynamics Medical). All SPECT images were obtained from the 113 keV (± 10%) energy peak and reconstructed with corrections for attenuation and scatter correction. The activity concentration in kidneys, parotid glands (PGs), submandibular glands (SMGs) and lesions was determined by Hermes software (Hermes Medical Solutions) and the absorbed dose was obtained using residence time and personalized organ masses as input data for the OLINDA 2.2 software. Sphere model of unit density was used for PGs and SMGs and lesions. Measurements with external probe at different time points were performed to estimate the activity within the body of the patient. The retention was modelled on a bi-exponential decay process with As and Al the constants of the short and long components and λs and λl the effective decay constants ***Results:*** Despite renal longer half-life of PSMA-617 (36.3 vs. 31.6 h), the renal dose was lower than PSMA I&T (0.29 vs. 0.61 Gy/GBq). Comparable doses to the PGs and SMGs (1.04 vs 0.87 and 0.90 vs 0.87 Gy/GBq) were measured. A large inter-patient variation in lesion kinetics and dosimetry occurred; mean absorbed doses for lesions were 5.6 (n=11) and 5.1 (n=20) Gy/GBq for PSMA-617 and PSMA I&T, respectively. The mean retention constants As and Al and mean effective half-lives of the short and long component were 0.49, 0.51 and 6.1 h, 77.5 h for PSMA-617 and 0.62, 0.38 and 6.0 h, 63.1 h for PSMA I&T ***Conclusion:*** Our data indicate that renal doses were higher for PSMA I&T, while comparable doses were measured for PGs, SMGs and lesions. PSMA I&T exhibits a faster whole-body clearance compared to PSMA-617. The use of CZT imaging system enables good quality images in shorter times than analogic cameras.

EP-1116

Quantitative ^{99m}Tc-SPECT/CT Dosimetry Using a CZT Gamma Camera: Initial Clinical Experience

K. Ramonaheng[1], *M. Qebetu*[1], *J. Cardinale*[2], *K. Schmidt*[3], *K. Banda*[1], *P. Goorhoo*[1], *M. K. Legodi*[1], *H. Ndlovu*[1], *C. Davis*[1], *L. Smith*[1], *S. Sibiya*[1], *A. Mdlophane*[1], *S. Mdanda*[1], *T. De Bruin*[1], *C. Kaoma*[1], *J. Kabunda*[1], *K. Mokoala*[1], *F. Giesel*[2], *M. Sathekge*[1];
[1]*Nuclear Medicine Research Infrastructure (NuMeRI), University of Pretoria and Steve Biko Academic Hospital, Pretoria, SOUTH AFRICA,* [2]*Department of Nuclear Medicine, Medical Faculty and University Hospital, Heinrich Heine University, Dusseldorf, GERMANY,* [3]*ABX - CRO advanced pharmaceutical services Forschungsgesellschaft mbH, Dresden, GERMANY.*

Aim/Introduction: RHN001, currently being investigated in the RHINO clinical trial, is a novel PSMA-targeting theranostic ligand

that can be radiolabelled with either ^{99m}Tc for imaging (RHN001-Dx) or ^{188}Re for therapy (RHN001-Tx), offering a generator-based alternative to PSMA radioligand therapy of patients with prostate cancer. Although ^{99m}Tc is widely accessible and cost-effective, its application in quantitative dosimetry has been limited to the performance of conventional NaI(Tl)-based SPECT systems. We evaluated the feasibility and accuracy of image-based dosimetry for ^{99m}Tc-labeled RHN001-Dx using a new-generation CZT SPECT/CT system in patients with PSMA-positive prostate cancer. ***Materials and Methods:*** Patients (n = 4) received an administered activity of 580.3 ± 86.7 MBq of RHN001-Dx. Quantitative SPECT/CT imaging was performed using the GE StarGuide CZT gamma camera at approximately 20 minutes, 2 hours, 4-6 hours, and 20-24 hours post-injection. SPECT/CT data were reconstructed using vendor-optimized parameters. Organs segmented for dosimetry included the kidneys, salivary glands, red marrow (L2-L4) estimation, and ICRP-103 whole-body effective doses. VOIs were drawn on low-dose CT and co-registered to quantitative SPECT at each time point to generate TACs. Residence times were calculated in QDOSE, and final dose estimates, including equivalent doses, were determined using OLINDA/EXM v2.2. ***Results:*** The kidneys received the highest doses (0.065 ± 0.003 mSv/MBq; median: 0.065[0.061-0.068] mSv/MBq; CV: 5.1%), followed by the salivary glands (0.036 ± 0.021 mSv/MBq; 0.032 [0.16-0.065] mSv/MBq; CV: 59.2%). Red marrow doses were lower (0.006 ± 0.001 mSv/MBq; 0.006 [0.005-0.007] mSv/MBq; CV: 13.4%), while the ICRP-103 whole-body effective doses averaged 0.008 ± 0.0007 mSv/MBq; 0.008 [0.007-0.009] mSv/MBq; CV: 10.0%. The kidneys showed the highest absolute doses, while the salivary glands demonstrated the highest inter-patient variability. The estimated effective whole-body dose ranged from 3.42 mSv-5.51 mSv, comparable in magnitude to reported values for [^{99m}Tc]Tc-PSMA I&S (3.11 mSv-4.23 mSv)[1], further supporting the dosimetric feasibility of RHN001-Dx. ***Conclusion:*** This study demonstrates the feasibility of quantitative image-based dosimetry using a CZT SPECT/CT system for RHN001-Dx. The observed dosimetric profiles are consistent with those of other ^{99m}Tc-labeled PSMA agents, reinforcing the safety and reliability of this RHN001-Dx. These results offer valuable dosimetric benchmarks for further clinical development of RHN001-Dx as part of a generator-based theranostic pair with ^{188}Re-labeled RHN001-Tx. ***References:*** 1. Urbán S, Meyer C, Dahlbom M, Farkas I, Sipka G, Besenyi Z, et al. Radiation Dosimetry of ^{99m}Tc-PSMA I&S: A Single-Center Prospective Study. J Nucl Med. 2021 Aug 1;62(8):1075-81.

EP-1117

Estimation of long-term radiation toxicity risk to normal organs in radiopharmaceutical therapy.

P. McCormack[1], *Z. Mulyukov*[2], *D. Iu*[3], *F. Yang*[3];
[1]Novartis Pharmaceuticals, Manchester, UNITED KINGDOM, [2]Novartis Pharmaceuticals, Basel, SWITZERLAND, [3]Novartis Pharmaceuticals, Cambridge, MA, UNITED STATES OF AMERICA.

Aim/Introduction: Currently accepted tolerance doses for long-term radiation toxicity are based on data from external beam radiation therapy (EBRT). These organ-specific thresholds are associated with toxicity probabilities over certain periods. The kidney limit for 23Gy implies a 5% probability of failure within 5 years. These EBRT-derived thresholds are adopted for radioligand therapy (RLT) but should be viewed as guidelines, since they are independent of the radioligand or patient population and do not account for the interindividual variability in organ absorbed doses. Additionally, these thresholds are defined for long-term toxicity, such as a 5% probability of an event occurring within 5 years, and do not consider survival rates of the treated patient population. Consequently, relying on EBRT tolerance thresholds to ensure RLT safety may lead to inaccurate assessments of toxicity risks. ***Materials and Methods:*** The proposed approach for evaluating the long-term toxicity risks is based on extrapolation of EBRT normal tissue complication probabilities (NTCP) to RLT using biological effective dose (BED). Toxicity risk is estimated as an expected value of NTCP over probability distribution of the BED for the organ at risk. The method is applied to kidney absorbed dose data from the Erasmus clinical study of ^{177}Lu-DOTATATE and compared to the clinical safety data. Simulations are conducted to assess impact of absorbed dose variability on the toxicity risk. Adjustment of maximum administered activity to match the same risk level in patient populations with different survival times is also discussed. ***Results:*** The mean kidney absorbed dose in the Erasmus clinical study (n=414) was 19±5 Gy. Despite 18.8% of patients exceeding 23Gy no treatment-related kidney failures were reported (follow-up of 78 months). Nephropathy risk estimated using EBRT NTCP for kidney absorbed dose was 5.6%, while the risk estimated with NTCP extrapolated using BED was 0.6%. The toxicity risk in treated population depends on the mean and the CV of absorbed dose. Simulations indicate with a 50% CV the 5% long-term risk is reached with mean kidney BED of 22Gy, whereas for 15% CV, same risk is reached at mean kidney BED of 32Gy. ***Conclusion:*** The interindividual variability of kidney dosimetry is a crucial factor to consider when understanding and predicting long-term kidney toxicity. The current absorbed dose threshold-based approach fail to account for this variability. The presented methodology aims to provide an estimation of population toxicity risk accounting for the probability distribution of organ BED and life expectancy of patients***:***

EP-1118

Application of post-reconstruction partial volume correction techniques for quantitative SPECT imaging of ^{225}Ac

G. Liubchenko[1], *G. Boening*[1], *M. Rumiantcev*[1], *M. Zacherl*[1], *G. T. Sheikh*[1], *S. Resch*[1], *R. A. Werner*[1,2], *S. I. Ziegler*[1,3], *A. Delker*[1];
[1]Department of Nuclear Medicine, LMU University Hospital, LMU Munich, Munich, GERMANY, [2]Johns Hopkins School of Medicine, The Russell H Morgan Department of Radiology and Radiological Sciences, Division of Nuclear Medicine and Molecular Imaging, Baltimore, MD, UNITED STATES OF AMERICA, [3]Clinic for Nuclear Medicine, Hannover Medical School, Hannover, GERMANY.

Aim/Introduction: The extreme low-count regime for clinical ^{225}Ac-SPECT imaging poses a challenge to accurate quantitative SPECT imaging. Moreover, SPECT imaging suffers from partial volume effects (PVE), which can degrade quantification and lead to an underestimation of the absorbed dose estimates, especially in small lesions. The aim of this study was to investigate the impact of partial volume correction (PVC) techniques on post-therapeutic imaging of the three imageable energy windows (440, 218 and 78 keV) of ^{225}Ac. ***Materials and Methods:*** A phantom with three 3D-printed spheres (191, 100, 48 ml; foreground-to-background ratio of 8.1:1) was imaged on a Siemens Symbia Intevo T16 SPECT/CT system equipped with a HEGP collimator (16 projections per head, 128x128 pixel) to compare the impact of iterative Yang (IY)- and Richardson-Lucy (RL)-based PVC techniques, in terms of contrast-to-noise ratios (CNR) and recovery coefficients (RC). These PVC methods were also compared for a patient cohort with two SPECT/CT scans acquired (on the same imaging system as the phantom) 24 and 48 h post-injection following [^{225}Ac]Ac-PSMA-I&T therapy, to evaluate their impact on kidney and lesion dosimetry. IY-based PVC was applied to the kidneys, using the segmentations obtained from CT scans. RL-based PVC was applied to all of the lesions that were visible in the abdominal region. ***Results:*** In the phantom study, application of PVC techniques resulted in a clear increase in RC and CNR across all spheres and energy windows. The average RC increase across all spheres was 24±2% (RL) and 142±50% (IY) for 440 keV, 33±8% (RL) and 146±60% (IY) for 218 keV, and 13±2% (RL) and 98±30% (IY) for 78 keV. The average CNR increase was 10±8% (RL) and 262±130% (IY) for 440 keV, 40±10% (RL) and 274±130% (IY) for 218 keV, and 2±6% (RL) and 151±60%

(IY) for 78 keV. In the patient study, IY-based PVC increased kidney RBE-weighted absorbed doses by 172±54%, 157±45% and 146±47%, for 440, 218 and 78 keV energy windows, respectively. RL-based PVC increased lesion RBE-weighted absorbed doses by 34±6%, 29±8%, and 23±10%, for 440, 218 and 78 keV energy windows, respectively. ***Conclusion:*** The phantom and patient studies demonstrated that the use of PVC techniques substantially improved kidney (IY) and lesion (RL) quantification, highlighting their value for the post-reconstruction enhancement of ^{225}Ac SPECT images.

EP-1119

Bayesian individual fitting versus population fitting with non-linear mixed-effects modelling in single-time-point dosimetry: A comparative evaluation

I. Budiansah[1], *D. Hardiansyah*[1], *B. B. Patrianesha*[1,2], *S. M. B. Peters*[3], *S. Ardjo Pawiro*[1], *B. Privé*[3,4], *J. Nagarajah*[3,5], *M. W. Konijnenberg*[3,6], *A. Ambros J. Beer*[7], *G. Glatting*[7,8];
[1]Universitas Indonesia, Depok, INDONESIA, [2]Research Center for Safety, Metrology, and Nuclear Quality Technology, National Research and Innovation Agency (BRIN), Tangerang Selatan, INDONESIA, [3]Radboud University Medical Centre, Nijmegen, NETHERLANDS, [4]Department of Radiology and Nuclear Medicine, Erasmus Medical Centre, Rotterdam, NETHERLANDS, [5]Röntgeninstitut Düsseldorf, Düsseldorf, GERMANY, [6]Department of Radiation Oncology, Erasmus Medical Centre, Rotterdam, NETHERLANDS, [7]Medical Radiation Physics, Department of Nuclear Medicine, Ulm University, Ulm, GERMANY, [8]Department of Nuclear Medicine, Ulm University, Ulm, GERMANY.

Aim/Introduction: This study compares the performance of Bayesian individual fitting and Bayesian population fitting using non-linear mixed-effects modelling (NLMEM) in all-time-point (ATP) and single-time-point (STP) dosimetry. ***Materials and Methods:*** Renal biokinetic data of [^{177}Lu]Lu-PSMA-617 were collected from ten patients with low-volume metastatic hormone-sensitive prostate cancer (mHSPC) from a prospective clinical study at Radboud University Medical Centre (NCT03828838). Each patient received [^{177}Lu]Lu-PSMA-617 therapy, with an administered activity of (3.1±0.1) GBq. Five SPECT/CT scans were performed at: (2.3±0.5)h, (23.8±2.0)h, (47.7±2.2)h, (71.8±2.2)h, and (167.4±1.9) h after injection. The structural models employed in this study were based on previously published studies [1,2], The function for Bayesian individual fit was $f_{4a}(t)=A_1e^{-(\lambda1+\lambda phys)t}+A_2e^{-(\lambda2+\lambda phys)t}-(A_1 + A_2)e^{-(\lambda bc+\lambda phys)t}$, and for Bayesian NLMEM $f_{6a}(t)=A_1e^{-(\lambda1+\lambda phys)t}+A_2e^{-(\lambda2+\lambda phys)t}-A_3e^{-(\lambda3+\lambda phys)t}-(A_1 + A_2 - A_3)e^{-(\lambda bc+\lambda phys)t}$. Goodness-of-fit criteria were visual inspection, relative standard errors (RSEs) of fitted parameters < 0.5, and absolute values of the off-diagonal elements of the correlation matrix < 0.8. The reference time-integrated activity coefficients (rTIACs) were derived from the structural model with the highest Akaike weight. Leave-one-out fitting was performed in ATP dosimetry to obtain Bayesian information for both methods separately: the mean and standard deviation of individual parameters for Bayesian individual fitting and the fixed-effect, random-effects, and covariance matrix of population parameters for Bayesian NLMEM fitting. These parameters were subsequently applied as prior information to fit STP data in STP dosimetry. Root-mean-square-error (RMSE) was used to determine the optimal time point for STP dosimetry, defined as the time point with the lowest RMSE. TIACs precision was expressed as the RSE: the ratio of the standard error to the estimated TIAC. ***Results:*** Both Bayesian individual and Bayesian NLMEM fitting met the predefined goodness-of-fit criteria in ATP dosimetry. Model comparison using Akaike weights selected $f_{6a}(t)$ as the reference function. Hence, the rTIACs were derived from Bayesian NLMEM. In ATP dosimetry, TIACs were similar between methods (maximum absolute relative deviation 1.1%) with precisions of 1.8[0.1, 4.7]% (individual) and 2.3[2.2, 2.6]% (NLMEM). In STP dosimetry, the optimal time point was (47.7±2.2)h after injection for Bayesian individual (RMSE: (8.2±1.7)%) and (23.8±2.0)h after injection for Bayesian NLMEM (RMSE: (6.2±2.0)%). sTIACs precision was similar: 8.3[6.1, 9.7]% vs. 7.3[8.6, 9.4]%. ***Conclusion:*** In ATP fitting, both methods yielded comparable TIACs with high precision. In STP dosimetry, each method identified a different optimal time point, with Bayesian NLMEM showing lower RMSE, suggesting reduced sensitivity to outliers. ***References:*** 1.Hardiansyah et al., J Nucl Med, 20242.Patrianesha et al., Physica Medica, 2025

EP-1120

Impact of Temporal Sampling and Software Tools on Dosimetry in Radioligand Therapy

S. Peric[1], *M. Avanzo*[1], *A. Drigo*[1], *C. Avigo*[1], *G. Pirrone*[1], *L. Barresi*[1], *G. Fanetti*[2], *E. Borsatti*[3], *A. Dassie*[1];
[1]Medical Physics Department, Centro di Riferimento Oncologico di Aviano, IRCCS, Aviano, ITALY, [2]Radiation Oncology Department, Centro di Riferimento Oncologico di Aviano, IRCCS, Aviano, ITALY, [3]Nuclear Medicine Department, Centro di Riferimento Oncologico di Aviano, IRCCS, Aviano, ITALY.

Aim/Introduction: Dosimetry in radioligand therapy is based on Time Activity Curve (TAC) assessment and Time Integrated Activity (TIA) calculation. The estimation of TIA depends on the measurement time points and its uncertainty is often overlooked. Accurate assessment of TIA uncertainty is essential to balance therapeutic efficacy and organ protection. The purpose of this work was to evaluate the impact of different software and time point combinations in calculated TAC and TIA. ***Materials and Methods:*** This retrospective study included four patients with somatostatin receptor positive gastroenteropancreatic neuroendocrine tumors, treated with Lutetium-177 DOTATATE between February and December 2024. The dosimetric evaluation focused on right, left kidney and target. SPECT-CT imaging was performed at four time points (TPs), during the first and fourth therapy cycles (TP-1 4h±1h, TP-2 24h±2h, TP-3 48h±2h, and TP-4 168h±30h). TACs were modeled using best-fitting mono- and bi-exponential functions. Uncertainty of calcualted TIA were estimated by combining uncertainties associated with measurements and fitting procedure. The analysis was performed with two commercial software tools: OLINDA and MIM SurePlan, and a custom routine developed in MATLAB. Goodness-of-fit metrics Squared Error (SE), R^2 were used to evaluate TAC models, and Akaike Information Criterion (AIC) was used for selection of models in MIM and MATLAB. TIAs were also calculated using fewer TP, and their relative differences against the baseline 4-points TIA were evaluated. ***Results:*** Metrics for goodness of fit were generally high for baseline with SE = (0.000120 ± 0.0040), R^2 = (0.998 ± 0.016) for OLINDA, AIC = (2.22 ± 48.0), R^2 = (1.00 ± 0.059) for MIM SurePlan, and AIC = (–33.0 ± 59.0), R^2 = (0.996 ± 0.019) for MATLAB. After reducing points, TP-234 yielded the most accurate results across all software according to the median and standard deviation of the TIA relative difference: OLINDA: 0.06 ± 1.59, MIM SurePlan: 0.02 ± 0.11, MATLAB: -0.09 ± 0.20. Among the two-point combinations, TP-24 provided the most robust performance, with relative differences of OLINDA: 0.07 ± 0.26, MIM SurePlan: -0.08 ± 0.12, MATLAB: -0.04 ± 0.19. Error analysis proved critical to assess result reliability. Kruskal-Wallis test results confirmed no statistically significant differences in TIA among software at the 0.05 significance level. ***Conclusion:*** The study confirms that dosimetry can be performed with reduced number of time points. Moreover, multiple software platforms can be reliably used for TIA estimation. Despite the small sample, the findings provide a useful basis for refining clinical workflows. Further validation in larger populations are essential next steps.

EP-1121

GPU-Accelerated Monte Carlo Dosimetry for Yttrium-90 and Holmium-166 Radioembolization: Validation of Torch MC Against Geant4 in Heterogeneous Anatomies

O. Kwon[1], *J. Grudzinski*[1,2], *B. Bednarz*[1,2], *P. Wickre*[2];
[1]University of Wisconsin-Madison, Madison, WI, UNITED STATES OF AMERICA, [2]Voximetry, Madison, WI, UNITED STATES OF AMERICA.

Aim/Introduction: Monte Carlo (MC) dosimetry is critical for optimizing Yttrium-90 (Y-90) and Holmium-166 (Ho-166) radioembolization therapies, addressing limitations of traditional methods in modeling patient-specific anatomy and radiation transport. Studies confirm MC's superiority in predicting absorbed doses, improving tumor control while reducing toxicity risks, especially in the lung. Advanced MC-based personalized dosimetry enables more effective and safer treatment planning for liver cancer therapies. ***Materials and Methods:*** Torch MC was validated against Geant4 for Y-90 and Ho-166 dosimetry using the ICRP 110 adult male phantom. Three validation approaches were employed: (1) Monoenergetic testing compared Torch's GPU-accelerated δ-scattering and Geant4's physics models, evaluating voxel-level absorbed doses against established S-values. (2) Spectral validations utilized ICRP 107 and IAEA decay spectra-based simulations, assessing Torch's per-decay sampling accuracy relative to Geant4. (3) Patient-specific evaluations were performed using clinical male patient data (128^3 voxels), comparing Torch's GPU-based calculations (RTX 3070 GPU, <5 minutes runtime) to Geant4's CPU-based simulations (~5 hours runtime). Agreement was quantitatively assessed, particularly at heterogeneous regions (e.g., liver-lung interfaces). ***Results:*** Monoenergetic validation demonstrated excellent agreement, with voxel-level dose distribution deviations of 0.12% for beta emissions and 3.36% for gamma emissions within Y-90 and Ho-166 energy ranges. S-value calculations for critical source-target pairs aligned closely, validating Torch's physics models for therapeutic radionuclides. In spectral validation tests, Torch MC and Geant4 showed deviations with using ICRP 107 and IAEA spectra, 0.20% and 1.65% for liver and -2.60% and -3.45% for lung regions, respectively. Particularly for Ho-166's low-energy gamma emissions (32-81 keV), where tissue interface effects were accurately resolved. Patient-specific evaluations verified robust dose agreement in heterogeneous anatomical regions, including liver-lung interfaces, yielding organ-level S-value differences of Y-90 and Ho-166 with 1.05% and -3.88% in liver and 5.43% and 1.81% in lung regions, respectively, supporting Torch's clinical reliability. ***Conclusion:*** This study demonstrated that Torch MC achieves comparable accuracy to Geant4 in Y-90 and Ho-166 dosimetry, with <3.36% deviations in monoenergetic comparisons, <3.45% in spectral validations, and <5.43% in patient-specific organ-level S-value assessments. The GPU-accelerated framework reduced computation times, enhancing clinical applicability. These results validate Torch's potential for personalized radioembolization treatment planning, particularly in anatomically heterogeneous regions such as liver-lung interfaces. Future work should expand validation to multicenter patient cohorts and explore real-time adaptive dosing strategies**.** ***References:*** S. Agostinelli et al., NuclInstrumMeth. (2003). J. Allison et al., IEEETransNuclSci. (2006). J. Allison et al., NuclInstrumMeth. (2016). A. Besemer et al., CancerBiotherRadiopharm. (2018). A. Capotosti et al., ApplSci. (2024).

EP-1122

One-Minute 360° CZT SPECT Enables Reliable Organ Dosimetry for ^{90}Y-SIRT Planning

Z. Mansouri*, Y. Salimi, N. Bianchetto Wolf, I. Mainta, V. Garibotto, H. Zaidi;*
Geneva University Hospital, Geneva, SWITZERLAND.

Aim/Introduction: The aim of this work was to establish the optimal scan time for ^{90}Y-selective internal radiation therapy (SIRT) planning with pretreatment ^{99m}Tc-MAA SPECT using 360°cadmium-zinc-telluride (CZT) solid-state detector technology. ***Materials and Methods:*** Twenty patients (12 Male, 8 Female; BMI range, 21.3-30.4 kg/m^2) underwent a pretreatment ^{99m}Tc-MAA SPECT, each with a 6-min/bed (average 4 beds) acquisition on a 360° CZT SPECT camera following the injection of an average ± SD of 125.5 ± 40.2 MBq. All images were reconstructed from list-mode raw data to obtain scan durations of 1 min/bed, 2 min/bed, etc., up to a maximum of 6 min/bed. For each of the scan durations, organ and multi-compartment voxel-level dosimetry was conducted using the local energy deposition method. The dosimetric results of the short duration scans were compared to those of the full duration (6min/ bed) serving as standard of reference using quantitative metrics, including region- and voxel-level absolute error (RAE, %), mean absolute error (MAE, Gy) and gamma evaluation with the criteria of 2.46 mm distance to agreement and 5% dose difference. ***Results:*** The voxel-level RAE decreased from 78.4% with 1 min/bed acquisition to 23.2% at 5 min/bed, respectively. Lesion and whole normal liver (WNL) RAEs were less than 1% for all acquisition times, with the highest being 0.53% for the 1-minute per bed scan, with corresponding MAE of less than 0.09 Gy. Gamma analysis showed that lesion pass rates increased from 41.2% at 1 min/bed to 88.3% at 5 min/bed, while WNL pass rates improved from 87.2% to 99.33%. ***Conclusion:*** Shorter scan times can significantly enhance patient comfort, reduce motion-related artifacts, and improve clinical workflow efficiency only without sacrificing the reliability of treatment planning dosimetry. In this study, we attempted to find an optimized scan time according to organ- and voxel-level metrics. The results showed that 1 min/bed acquisition using 360° CZT SPECT enables clinically acceptable organ-level dosimetry for ^{90}Y-SIRT planning. In contrast, for voxel-level dosimetry, this time reduction may not provide accurate dose maps evaluated by both voxel error and relevant gamma pass rates.

EP-1123

Motion corrected PET compared to static PET in post ^{90}Y resin TARE imaging: Potential towards improved ^{90}Y dosimetry

M. W. M. van Wijk*, C. D. E. Van Speybroek, M. G. J. de Bakker, J. Roosen, M. J. R. Janssen, S. M. B. Peters, J. F. W. Nijsen;*
Department of Medical Imaging, Radboud University Medical Center, Nijmegen, NETHERLANDS.

Aim/Introduction: A dose-response relationship is well established in transarterial radioembolization (TARE), highlighting the importance of accurate pre- and post-treatment dosimetry. Current yttrium-90 (^{90}Y) imaging methods remain limited by factors such as motion artefacts, which may compromise assessment of microsphere distribution, especially at the lesion level. One approach that may improve image quality and treatment evaluation is motion corrected PET. In this study, motion corrected ^{90}Y PET reconstructions are compared to standard static ^{90}Y PET, with the aim of exploring their potential contribution to more precise dosimetry. ***Materials and Methods:*** Patients planned for standard clinical treatment using ^{90}Y resin TARE were eligible to participate in this study. They were scanned using a reflector block to track their breathing. In addition to the standard static reconstructions, a motion corrected ^{90}Y PET was reconstructed. Anatomical manual segmentation and thresholding was performed to evaluate the count differences and the spill out between static and motion corrected PET. Manual segmentation was performed using low dose CT and arterial enhanced CT or MRI as a reference. Thresholding was performed using Otsu's method on the PET signal. The tumour to normal (T/N) ratio was determined using the mean counts in the tumour and the whole liver. ***Results:*** From November 2024 to April 2025, PET scans from six patients that received ^{90}Y resin TARE were reconstructed both static and motion corrected. Three patients were analysed so far, which received 1.37, 1.91 and 2.40 GBq of ^{90}Y resin microspheres, respectively. Treated lesions had a volume of 174, 146 and 13 mL on CT. Thresholding resulted in a mean treated volume of 122, 144 and 25 mL for thresholding static ^{90}Y PET, and 113, 136 and 14 mL for gated ^{90}Y PET. The spillout differences could also be appreciated visually. T/N ratio was 49, 11 and 12 for static yttrium PET and 46, 11 and 11 for motion corrected ^{90}Y PET respectively. Inclusion

and additional analysis is ongoing. ***Conclusion:*** This study aims to evaluate the added value of motion corrected ^{90}Y PET on ^{90}Y TARE dosimetry. Preliminary analysis shows a difference between the estimated treated volume of motion corrected compared to static reconstructions indicating reduced spillout, due to reduced respiratory motion artefacts. Future findings among more patients and a more extensive analysis including DVHs of the tumours might give more insight in the influence and added value of motion corrected ^{90}Y PET on ^{90}Y dosimetry.

EP-1124

Gastro-intestinal LuPSMA scintigraphy uptake patterns and dosimetry in patients with metastatic prostate cancer treated with LuPSMA: a single center retrospective study

V. Ludwig[1], *Z. Ells*[1], *C. Meyer*[1], *L. M. Unterrainer*[1,2], *P. G. Maliha*[1,3,4], *T. Grogan*[1], *M. Dahlbom*[1], *J. Czernin*[1], *J. Calais*[1];
[1]UCLA, Los Angeles, CA, UNITED STATES OF AMERICA, [2]LMU Klinikum München, Munich, GERMANY, [3]Centre Hospitalier de l'Université de Montréal Centre de Recherche, Université de Montréal, Montréal, Montreal, QC, CANADA, [4]Centre Hospitalier de l'Université de Montréal, Montreal, QC, CANADA.

Aim/Introduction: Gastrointestinal (GI) adverse events are common after [^{177}Lu]Lu-PSMA radioligand therapy (RLT) in metastatic prostate cancer, including nausea (35%), vomiting (19%), constipation (20%), and diarrhea (19%)[1]. LuPSMA planar scintigraphy and SPECT imaging allow visualization of GI biodistribution post-therapy. This study investigates correlations between GI uptake patterns over time and absorbed dose estimates in bowel segments, and their relationship to GI adverse events. ***Materials and Methods:*** A retrospective analysis was performed on 43 patients from the Phase 2 RESIST-PC trial (NCT03042312). GI symptoms before and after the first [^{177}Lu]Lu-PSMA-617 cycle were documented. Scintigraphy included planar imaging at +4h, +24h, +48h, +72h, and +96-168h, and SPECT/CT at +24h. A camera-specific calibration factor was applied. OSEM reconstruction (48 iterations, 1 subset, no filtering) with scatter and attenuation correction was done using MIM SPECTRA. Absorbed dose estimates were derived from hybrid planar + SPECT/CT data using MIM SurePlan (7.3.5). Three readers scored anterior planar images visually using a 0-4 uptake scale (0: no uptake; 4: ≥3× liver/syringe). The GI tract was divided into six segments: duodenum (D), small bowel (SB), ascending (AC), transverse (TC), descending colon (DC), and rectosigmoid (RS). Segments were manually contoured on CT at +24h, and time-integrated activity curves were fit using trapezoidal integration. ***Results:*** New GI symptoms occurred in 24/43 patients (56%): constipation (21%), nausea (28%), diarrhea (19%), vomiting (7%), soft stool (5%), and gas (2%). High duodenal uptake at 24h and 72h correlated most with symptom development (AUC 0.73 and 0.63). Uptake elsewhere showed weaker predictive value (AUC 0.50-0.54 per time; 0.53-0.60 per location). Inter-reader agreement was moderate (Fleiss' Kappa 0.272, ICC 0.508). In the first 7 patients with dosimetry data processed and available, the median (range) absorbed to the small bowel, ascending colon, transverse colon, descending colon and rectosigmoid were 1.21 (0.70-1.81), 1.49 (0.95-2.85), 1.59 (0.29-9.75), 1.63 (0.26-8.97) and 0.92 (0.20-5.69). ***Conclusion:*** In this series of 24 patients, the [^{177}Lu]Lu-PSMA GI uptake patterns did not correlate with development of new GI symptoms after first cycle of RLT. ***References:*** Sartor O, de Bono J, Chi KN, et al. Lutetium-177-PSMA-617 for metastatic castration-resistant prostate cancer. N Engl J Med 2021;385:1091-1103

EP-1125

Feasibility of single-time-point dosimetry application in ^{177}Lu -DOTATATE/DOTATOC-treated pediatric neuroblastoma

X. Sun[1], *F. Zheng*[1], *X. Sun*[2];
[1]Department of Nuclear Medicine, Shandong Cancer Hospital and Institute, Shandong First Medical University and Shandong Academy of Medical Sciences, Jinan, CHINA, [2]Department of Nuclear Medicine, Shandong Cancer Hospital and Institute, Jinan, CHINA.

Aim/Introduction: ^{177}Lu-DOTATATE/DOTATOC peptide receptor radionuclide therapy (PRRT) has demonstrated potential for treating pediatric neuroblastoma (NB)[1], and in clinical practice can be measured dosimetry by multi-time-point dosimetry (MTP)[2]. However, the high workload and limited patient compliance associated with MTP restrict its application. Consequently, single-time-point dosimetry (STP) approaches have emerged as a promising alternative[3,4], though their effectiveness in pediatric populations has not been thoroughly investigated. This study aimed to assess the dosimetric determination of ^{177}Lu-DOTATATE/DOTATOC in pediatric neuroblastoma patients to determine whether STP could serve as a viable replacement for MTP. ***Materials and Methods:*** A total of 24 pediatric NB patients who received 1-2 cycles of ^{177}Lu-DOTATATE or ^{177}Lu-DOTATOC underwent dosimetric measurement of lesions and critical organs using the 96 h single-time point dosimetry (STP_H) method proposed by Hänscheid et al[4]. The results were compared with those obtained from standard MTP. ***Results:*** In patients treated with ^{177}Lu-DOTATATE, the mean relative deviation absolute values of the STP_H-calculated absorbed dose from MTP were <10% for lesions, kidneys, bone marrow, liver, and spleen, with Pearson's correlation coefficients of 0.99, 0.93, 0.97, 0.84, and 0.84, respectively. In patients treated with ^{177}Lu-DOTATOC, the mean relative deviation absolute values for kidneys, spleen, and bone marrow were <10%, with Pearson's correlation coefficients of 0.97, 0.77, 0.35, 0.48, and 0.93 for lesions, kidneys, bone marrow, liver, and spleen, respectively. ***Conclusion:*** The findings confirm that the 96 h STP_H method can reliably replace MTP for dosimetric assessment in pediatric NB patients treated with ^{177}Lu-DOTATATE and performed well in renal dosimetry for ^{177}Lu-DOTATOC therapy. ***References:*** [1] Fathpour G, Jafari E, Hashemi A, et al. Feasibility and therapeutic potential of combined peptide receptor radionuclide therapy with intensive chemotherapy for pediatric patients with relapsed or refractory metastatic neuroblastoma. Clin Nucl Med. 2021;46(7):540-8. [2] Stabin MG, Sparks RB, Crowe E. OLINDA/EXM: The second-generation personal computer software for internal dose assessment in nuclear medicine. J Nucl Med. 2005;46(6):1023-7.[3] Hänscheid H, Lapa C, Buck AK, Lassmann M, Werner RA. Dose mapping after endoradiotherapy with^{177} lu-DOTATATE/DOTATOC by a single measurement after 4 days. J Nucl Med. 2018;59(1):75-81.[4] Madsen MT, Menda Y, O'Dorisio TM, O'Dorisio MS. Technical note: Single time point dose estimate for exponential clearance. Med Phys. 2018;45(5):2318-24.

EP-1126

Fast and reliable response evaluation of [^{177}Lu]Lu-PSMA-I&T therapy using between-cycle [^{177}Lu]Lu-SPECT/CT scanning

V. Nuttens, *D. Ooms, M. Koole;*
AZORG, Aalst, BELGIUM.

Aim/Introduction: Post-therapy SPECT/CT imaging is gaining importance for assessing total tumor volume (TTV) and total lesion activity (TLA) as early prognostic biomarkers of treatment response during [^{177}Lu]Lu-PSMA-I&T therapy. This study compares

the interobserver agreement of an optimized semi-automatic segmentation method to a manual approach for longitudinal assessment of TTV and TLA using post-therapy SPECT/CT scans. ***Materials and Methods:*** Six patients underwent four cycles of [^{177}Lu]Lu-PSMA-I&T therapy, with post-therapy SPECT/CT scans acquired 19 ± 1.5 hours after each cycle using a 3D CZT system. For the manual method, lesions were visually identified and delineated using an edge detection method. The semi-automatic approach applied global SUV thresholds from 2 to 10, followed by manual removal of physiological uptake. For all (3) expert readers, segmentation times were recorded and reliability between observers was assessed using the intraclass correlation coefficient (ICC(2, 1)) for TTV and TLA and Fleiss' kappa score (kF) for therapy response evaluation based on between-cycle TTV and TLA changes. In addition, TTV and TLA correlations between the manual and semi-automatic method were evaluated for each SUV threshold as well as the different types of errors between manual and semi-automatic identification of disease progression. ***Results:*** Manual segmentations took 6.8 minutes per SPECT/CT, while semi-automatic segmentations were performed in less than 1 minute, regardless of SUV threshold. For the manual segmentations, an ICC(2, 1) = .57 was obtained for TTV and a kF = .38 for TTV-based response evaluation. TLA and TLA-based response evaluation showed a higher interobserver agreement of ICC(2, 1) = .92 and kF = .73 respectively for the manual segmentations. For the semi-automatic segmentations, TTV and TLA and TTV- and TLA-based response evaluation showed perfect interobserver agreement except for an SUV threshold of 2 and 3 (kF = .91). An SUV threshold of 8 showed the highest correlation and agreement with manual TLA and TLA-based response evaluation, with one non-responder misclassified as a responder compared to two non-responders misclassified as a responder for an SUV threshold of 3. ***Conclusion:*** A manual TLA-based response assessment demonstrated much higher interobserver agreement than manual TTV-based response evaluation. Meanwhile, a threshold-based semi-automatic segmentation approach is fast and reliable for assessing TTV and TLA changes longitudinally. An SUV threshold of 8 showed the highest correlation with manual TLA and TLA-based response evaluation, making it the recommended approach for clinical follow-up of [177Lu]Lu-PSMA-I&T patients with [177Lu]Lu-SPECT. ***References:*** [1] 10.1007/s00259-023-06536-2 [2] 10.2967/jnumed.122.264677 [3] 10.2967/jnumed.122.264398

EP-1127

Comparison of ^{99m}Tc MAA SPECT/CT-Based Predosimetry and ^{90}Y SPECT/CT-Based Postdosimetry in TARE with Resin Microspheres

Z. Balaban Genc[1], *O. Erez*[1], *S. Beykan Schürrle*[2], *E. Soydemir*[1], *E. Arık*[1], *S. Cetin*[1], *N. Schürrle*[2], *T. Erdil*[1], *T. Ones*[1];
[1]*Marmara University, School of Medicine, Istanbul, TÜRKIYE,* [2]*Oncosia Scientific GmbH, Durrwangen, GERMANY.*

Aim/Introduction: Accurate dosimetry is essential for optimizing the safety and efficacy of transarterial radioembolization (TARE) in liver tumor treatment. This study compares predosimetric absorbed dose (pre-AD) values, calculated using the Partition Model-Based Method (PMBM) from ^{99m}Tc-MAA SPECT/CT, with postdosimetric absorbed dose (post-AD) values, derived from voxel-based analyses of post-treatment ^{90}Y-SPECT/CT, in patients treated with resin microspheres. ***Materials and Methods:*** This retrospective study included 76 consecutive patients treated with TARE using resin microspheres between 2023 and 2024. All patients underwent pre-treatment ^{18}F-FDG PET/CT and ^{99m}Tc-MAA SPECT/CT, followed by post-treatment ^{90}Y-SPECT/CT. Viable metabolic tumor and perfused volumes were calculated from ^{99m}Tc-MAA SPECT/CT, guided by recent ^{18}F-FDG PET/CT. ^{99m}Tc-MAA SPECT/CT images were analyzed in conjunction with ^{18}F-FDG PET/CT images. Multiple regions of interest were delineated across various slices, and their mean values were calculated, tumor-to-normal tissue (T/N) ratios, lung shunt percentages, and other relevant parameters were determined and entered into an Excel-based template for the Partition Model-Based Method (PMBM) to compute predicted absorbed dose values. Following treatment, personalized postdosimetric absorbed dose values were calculated using voxel-based NUKDOS software from ^{90}Y-SPECT/CT images. These values were compared across all cases for the perfused tumor, whole healthy liver, and both lung parenchyma. ***Results:*** Significant differences were observed between pre-AD and post-AD values for perfused tumor, whole healthy liver, and lung parenchyma ($p<0.001$; Table-1). Correlation analyses revealed a very strong correlation for lung parenchyma ($r=0.954$, $p<0.001$), a strong correlation for perfused tumor ($r=0.722$, $p<0.001$), and a moderate correlation for whole healthy liver ($r=0.59$, $p<0.001$). Notably, pre-AD values for healthy liver and perfused tumor were higher than post-AD values in 78% (n=59/76) and 76% (n=58/76) of cases, respectively. ***Conclusion:*** Accurate dosimetry is critical for assessing toxicity risks (healthy liver and lung parenchyma) and therapeutic efficacy (perfused tumor) in TARE, particularly for repeated treatments. This study revealed a moderate correlation between predosimetric absorbed dose (pre-AD) values, calculated using the Partition Model-Based Method (PMBM), and voxel-based postdosimetric absorbed dose (post-AD) values derived from post-treatment 90Y-SPECT/CT images, particularly for the whole healthy liver. Notably, in approximately 75% of cases, pre-AD values for both perfused tumor and whole healthy liver exceeded post-AD values. These findings suggest that PMBM may overestimate doses, potentially limiting its reliability for pre-treatment assessment of treatment efficacy and toxicity risks.

EP-1128

Estimation of Renal Time-Integrated Activity of [^{177}Lu]Lu-PSMA-I&T Using Single-Time-Point [^{68}Ga]Ga-PSMA-HBED-CC PET/CT and Physiologically-Based Pharmacokinetic and Population-Based Pharmacokinetic Modeling

D. Hardiansyah[1], *A. Riana*[1], *E. Yousefzadeh-Nowshahr*[2], *A. Allmann*[3], *A. J. Beer*[2], *M. Eiber*[3], *G. Glatting*[2];
[1]*Universitas Indonesia, Depok, INDONESIA,* [2]*Ulm University, Ulm, GERMANY,* [3]*Technische Universität München, Munich, GERMANY.*

Aim/Introduction: Minimising imaging sessions in molecular radiotherapy can reduce patient burden and streamline clinical workflows. Recent approaches integrating population pharmacokinetics with non-linear mixed-effects modelling (NLMEM) and physiologically based pharmacokinetic (PBPK) models offer a promising framework for accurate dosimetry using only single-time-point (STP) data. This study investigates the feasibility and accuracy of estimating time-integrated activity (TIA) for [^{177}Lu]Lu-PSMA-I&T therapy using pre-therapeutic [^{68}Ga]Ga-PSMA-HBED-CC PET/CT data within a PBPK-NLMEM framework. ***Materials and Methods:*** Thirteen patients with metastatic prostate cancer underwent [^{68}Ga]Ga-PSMA-HBED-CC PET/CT imaging before receiving [^{177}Lu]Lu-PSMA-I&T therapy. PET/CT was performed at approximately (0.9 ± 0.1) h after injection ((115 ± 16) MBq, (1.6 ± 0.3) nmol). Post-therapeutic planar whole-body scintigraphy data were acquired at multiple time points: (1.1 ± 0.7) h, (20.7 ± 2.3) h, and (163.8 ± 2.0) h post-injection, with additional measurements available for selected patients. A PBPK model [1] was fitted to the full biokinetic dataset to compute reference TIAs (rTIAs) for the kidneys, tumors, and whole body. STP-derived TIAs (sTIAs) were estimated by refitting model parameters to PET data from one patient at a time using the jackknife approach, with remaining patient data informing the population-level model. Relative deviations (RDs) between sTIA and rTIA were assessed. To improve the accuracy of tumor sTIA estimation, a functional relationship between tumor receptor density and the ratio of rTIA to sTIA was derived from the PBPK model. This relationship was then used to predict individual sTIA values in each patient using

a leave-one-out cross-validation approach. ***Results:*** Renal sTIA values derived from a single PET/CT measurement at (0.9 ± 0.1) h after injection closely matched rTIA estimates, with a mean RD of 5% ± 12%. In contrast, tumor and whole-body estimates showed a larger variability: Tumor 1 (44% ± 156%), tumor 2 (75% ± 270%), and whole body (-8% ± 27%). Utilising the relationship of tumor receptor density and the ratio of rTIA to sTIA markedly improved individual tumor sTIA estimation, reducing RDs to -1% ± 31% and 0% ± 44% for tumors 1 and 2, respectively. ***Conclusion:*** Accurate renal TIA estimation is achievable from a single PET/CT scan acquired approximately one hour after injection. While tumour and whole-body predictions showed higher variability, incorporating receptor density significantly improved tumour dosimetry. These findings underscore the potential of combining STP imaging with PBPK-NLMEM approaches to enable simplified yet reliable dosimetry in [^{177}Lu]Lu-PSMA-I&T therapy. ***References:*** Kletting P, Schuchardt C, Kulkarni HR, et al. PLoS One. 2016;11:e0162303.

EP-1129

Few-Time-Points Non-Linear Mixed-Effects Dosimetry: Accuracy and Precision of [^{177}Lu]Lu-PSMA-617 in Kidneys

A. Hakim[1], *D. Hardiansyah*[1,2], *E. Yousefzadeh-Nowshahr*[2,3], *U. Nemer*[4], *R. Ritawidya*[1,5], *F. Kind*[4], *A. J. Beer*[3], *P. T. Meyer*[4], *G. Glatting*[2,3], *M. Mix*[4];
[1]*Medical Physics and Biophysics, Physics Department, Faculty of Mathematics and Natural Sciences, Universitas Indonesia, Depok, INDONESIA,* [2]*Medical Radiation Physics, Department of Nuclear Medicine, Ulm University, Ulm, GERMANY,* [3]*Department of Nuclear Medicine, Ulm University, Ulm, GERMANY,* [4]*Department of Nuclear Medicine, Medical Center – University of Freiburg, Faculty of Medicine, University of Freiburg, Freiburg, GERMANY,* [5]*Research Center for Radioisotope, Radiopharmaceutical, and Biodosimetry Technology, National Research and Innovation Agency (BRIN), Tangerang Selatan, INDONESIA.*

Aim/Introduction: This study aims to evaluate the accuracy and precision of few-time-points (FTP) calculations of time-integrated activity (TIA) in kidneys for [^{177}Lu]Lu-PSMA-617 by applying non-linear mixed-effects (NLME) modeling. ***Materials and Methods:*** Biokinetic data from the kidneys of 63 patients with metastatic castration-resistant prostate cancer undergoing their first treatment cycle with [^{177}Lu]Lu-PSMA-617 were analyzed. SPECT/CT imaging measurements were conducted at five time points (TP): TP1 = (1.8±0.8)h, TP2 = (18.7±0.9)h, TP3 = (42.6±1.0) h, TP4 = (66.3±0.9)h, and TP5 = (160.3±24.2)h after injection. A four-exponentials function incorporating six adjustable parameters: $f(t)=A_1e^{-(\lambda1+\lambda p)t}+A_2e^{-(\lambda2+\lambda p)t}-A_3e^{-(\lambda3+\lambda p)t}-(A_1+A_2-A_3)e^{-(\lambda bc+\lambda p)t}$ with $\lambda p=\ln(2)/(6.6443\ d)$ and $\lambda bc=\ln(2)/(1\ min)$ identified as the best model for the data [1] was used in this study. Reference time-integrated activities (rTIAs) were obtained by fitting the four-exponentials function parameters to all-time-point (ATP) data within the NLME framework. Estimated time-integrated activities (eTIAs) were computed by fitting FTP data, comprising combinations of one, two, three, and four time points from the biokinetic dataset. The accuracy of FTP-NLME-derived eTIAs was evaluated through root-mean-square errors (RMSEs) and mean-absolute-percentage errors (MAPEs) associated with the relative deviation between eTIAs and rTIAs. The precision of individual rTIAs and eTIAs derived from each FTP-NLME combination was assessed by analyzing the coefficient of variation (CV) and their standard deviation of the TIAs. ***Results:*** RMSEs and MAPEs for each optimal TP combination were (11.0±1.7)% and (7.2±1.7)% for TP3, (6.5±1.1)% and (4.8±0.9)% for TP25, (3.9±0.7)% and (2.3±0.7)% for TP135, and (1.4±0.6)% and (0.9±0.6)% for TP1235. The %CV values of individual TIAs were (17.0±5.3)% for TP3, (8.5±2.3)% for TP25, (6.3±1.1)% for TP135, (5.1±0.7)% for TP1235, and (4.4±0.7)% for ATP. ***Conclusion:*** The accuracy and precision of various FTP methodologies were evaluated, enabling the determination of the optimal number of measurements required based on the desired accuracy and precision. This study demonstrates that using TP3 in STP, 2TP, 3TP, or 4TP results in greater accuracy and precision compared to other TPs in calculating individual TIAs for [^{177}Lu]Lu-PSMA-617 therapy. ***References:*** [1] Hardiansyah, D., Yousefzadeh-Nowshahr, E., Kind, F., Beer, A. J., Ruf, J., Glatting, & Mix, M. (2024). Single-Time-Point Renal Dosimetry Using Nonlinear Mixed-Effects Modeling and Population-Based Model Selection in [^{177}Lu]Lu-PSMA-617 Therapy. Journal of Nuclear Medicine, 65(4), 566-572. https://doi.org/10.2967/jnumed.123.266268

EP-1130

Assessing the Feasibility of Early Post-Treatment Dosimetry in 166Ho Radioembolization

A. Didonna[1,2], *G. Muti*[2], *C. Romano*[2], *S. Capitanio*[2], *C. Carbonini*[2], *C. Rossetti*[2], *P. E. Colombo*[2];
[1]*Università degli Studi di Milano, Milano, ITALY,* [2]*ASST Grande Ospedale Metropolitano Niguarda, Milano, ITALY.*

Aim/Introduction: 166Ho radioembolization is a radiotherapy in which radioactive 166Ho-microspheres are administered through a microcatheter directly into the tumor. Using the γ-emission at 80.6keV, the 166Ho-microspheres distribution can be imaged with SPECT/CT for dosimetry in pre-treatment and post-treatment phases. This study explores the feasibility of post-treatment dosimetry one day after patient treatment, assessing potential high count rate's influence on quantitative accuracy. Different calibration-VOIs, tumor-VOIs and voxel-dosimetry calculation methods are considered. ***Materials and Methods:*** A cohort of four patients was treated using holmium spheres with injected activities in the range 1GBq-6GBq. A SPECT/CT scanner was used to perform a first acquisition at the patient's discharge, 24-hours post-injection, and a second acquisition 4-5 days post-injection, following vendor's guidelines. A triple energy-window method was employed for scatter correction, with a main window around 80.6keV (15%-width) and two scatter windows (71.69keV, 90.32keV; 8%-photopeak-width). A calibration factor based on the injected activity and the counts in four calibration VOIs (2-cm-superiorly-extended-liver, 2%-maximum-threshold, 10%-maximum-threshold, liver-and-lungs-union) was calculated. The tumor-VOI was obtained as the co-registered pre-treatment and as the post-treatment-maximum-threshold-VOI matching the tumor volume. The dedicated vendor's dosimetry software was used for dose-point-kernel and local-dose-deposition reconstructions. Average doses in the liver, lungs and tumor were registered. ***Results:*** The average doses computed using the 2%-maximum-threshold, 2-cm-superiorly-extended-liver and liver-and-lungs-union VOIs for calibration show good agreement, while the 10%-maximum-threshold (used in the pre-treatment phase) overestimates the doses. The consistency of the measured count rates at varying activities with the paralyzable-dead-time model and the variation of calibration factors based on acquisition-time activity indicate that dead-time leads to a progressive count loss with increasing activity. The computed average doses in the liver and lungs are compatible $|D_(4/5days)/D_24h-1|<0.1$. The tumor average dose ratio is consistently less than 1 with co-registration, while for post-treatment maximum-thresholding the outcomes vary. The dose-point-kernel and local-dose-deposition methods provide comparable results ($|D_ldm/D_dpk-1|<0.11$). ***Conclusion:*** The study suggests the feasibility of 24-hours post-injection dosimetry in the liver and lungs, despite count rate saturation evident in count rate and calibration factor measurements.

EP-1131

Is 1D Whole-Body Dosimetry Still Worth It? A Pilot Study on Red Marrow Dose Estimation in [^{177}Lu]Lu-DOTATATE Therapy

T. Kracmerova[1,2], *J. O. Zmek*[1], *D. Prchalova*[1], *S. Buresova*[1], *A. Kenova*[1], *T. Rehacek*[1];
[1]*Motol University Hospital, Prague, CZECH REPUBLIC,* [2]*Military University Hospital, Prague, CZECH REPUBLIC.*

Aim/Introduction: As the number of patients treated with [^{177}Lu]Lu-DOTATATE (Lutathera®) increases, so does the need for personalized dosimetry. However, standard protocols are often time consuming and resource intensive. This pilot study evaluates the relationship between whole-body absorbed dose and mean absorbed dose to red bone marrow (RBM) using a simplified, non-

invasive. Based on dose rate monitoring and SPECT/CT imaging, we aim to develop a clinically feasible approach for individualised treatment planning. ***Materials and Methods:*** This retrospective pilot study included 14 patients (8 female, 6 male, mean age 64 years, range 40-77) who underwent [^{177}Lu]Lu-DOTATATE therapy with a total of 54 administrations. Each patient received 3-4 cycles of 7.4 GBq (range 4209-7534 MBq); in two cases, the fourth cycle was cancelled due to clinical deterioration. Patients were selected on the basis of on high whole-body doses in the first cycle (>0.5 Gy), suggesting cumulative absorbed doses of >2 Gy.Whole-body dosimetry was estimated using the DOMOS dose rate monitoring system (Nuvia a.s.) with collimated NaI detectors placed ~2.5 m above the patient. Each patient had at least seven time point measurements per cycle, including a late time point at 168 h post-administration. Data were fitted with a bi-exponential model; S-values were taken from OLINDA v1.0. Quantitative abdominal SPECT/CT images were acquired using Siemens Symbia Intevo Excel. During the first cycle, scans were acquired at 6, 24, 48 and 168 hours; during subsequent cycles included only a 24 hour scan. Liver, spleen, kidneys, and vertebrae (L2-L4) were segmented using Siemens syngo.via. Data were fitted with a mono-exponential model; S-values were taken from IDAC-Dose 2.1. ***Results:*** The mean whole-body dose was 0.72 Gy (101 mGy/GBq), range 0.19-2.36 Gy. The estimated RBM dose from SPECT was 0.24 Gy (33 mGy/GBq), range 0.071-0.652 Gy. Mean organ absorbed doses were 8.71 Gy (liver), 3.42 Gy (spleen), and 3.28 Gy (kidneys). The whole-body dose overestimated RBM dose by >53% on average. No significant correlation was found between whole-body dose and RBM dose ($r = -0.30$, $p = 0.0355$), nor between tumour liver uptake and whole-body dose ($r = 0.50$, $p = 0.00018$). ***Conclusion:*** Whole-body dosimetry alone is not suitable for accurate RBM dose estimation. It consistently overestimates RBM dose by more than 50%. This study supports the need for simplified 3D dosimetry using SPECT/CT. Larger studies (≥300 administrations) in patients with lower tumour uptake are needed to validate this approach and promote wider clinical adoption.

EP-1132

Monte Carlo Calculation Of Patient Effective Dose For ^{18}F-FDG PET Examinations

M. Baker;
Clatterbridge Cancer Centre, Liverpool, UNITED KINGDOM.

Aim/Introduction: Patient dosimetry for internal emitters is typically based upon standardised phantoms. Whilst these phantoms have improved in their ability to reflect typical patient anatomy, there is often little option to adjust the phantom to match bespoke patients. This work utilised real patient anatomy as well as Monte Carlo modelling and up-to-date biokinetic data to determine the effective dose for eighty patients weighing between 40 kg and 142 kg to determine the effect of patient size on the estimated effective dose. ***Materials and Methods:*** Clinical, single time-point images for 80 whole-body patients were retrospectively collected from two PET-CT scanners at Clatterbridge Cancer Centre. The images were contoured using AI-assisted technology to produce masked images for each source organ. GATE Monte Carlo software was used to simulate the absorbed dose distribution from each masked image to determine bespoke S-values for each patient. Cumulated activity was included from both ICRP 128 and Kamp et al (2023) to calculate the absorbed dose to each organ for each patient, allowing the effective dose for each patient to be estimated. ***Results:*** The effective dose per unit administered activity was found to be lower when using ICRP 103 tissue weighting factors and cumulated activity from Kamp et al (2023) than currently proposed in ICRP 128, with an average factor of 1.58E-02 mSv/MBq for patients in the range of 65 kg to 75 kg. There was a decrease in dose factor of approximately 20% between the smallest and largest patients within the cohort. ***Conclusion:*** Using bespoke S-values derived using real clinical data, and the most up-to-date biokinetic data and tissue weighting factors, the effective dose per unit of administered activity was determined to decrease as patient mass increased. Updated estimates of cumulated activity are now available, and should be coupled with the most recent tissue weighting factors to ensure that calculations are accurate and relevant. Total effective doses may be considerably lower than those initial proposed by ICRP 128. ***References:*** ICRP. (2015). ICRP Publication 128: Radiation Dose to Patients from Radiopharmaceuticals: A Compendium of Current Information Related to Frequently Used Substances. Annals of the ICRP, 44(2_suppl), pp.7-321. Kamp, A. et al. (2023). A revised compartmental model for biokinetics and dosimetry of 2-[18F] FDG. EJNMMI Physics, 10(1). [online]. Available from: https://doi.org/10.1186/s40658-023-00528-9.

EP-1133

Dosimetry of Organs at Risk of Patients Treated with [^{177}Lu]Lu-PSMA Suggests Margins for Dose Escalation

M. Almeida[1,2,3], *L. C. Silva*[1], *M. Costa*[1], *R. Parafita*[1], *F. Oliveira*[1], *Â. Silva*[1], *J. M. Sampaio*[2,3], *P. Ferreira*[1], *D. Costa*[1];
[1]*Champalimaud Foundation, Nuclear Medicine-Radiopharmacology, Lisboa, PORTUGAL,* [2]*Faculdade de Ciências da Universidade de Lisboa, Lisboa, PORTUGAL,* [3]*Laboratório de Instrumentação e Física Experimental de Partículas, Lisboa, PORTUGAL.*

Aim/Introduction: Personalized voxel-wise dosimetry of patients undergoing [^{177}Lu]Lu-PSMA therapy is paramount to help assess the effectiveness of treatment and tissue toxicity and may allow for the optimization of the activity injected into each patient. This study estimates the absorbed dose distributions in organs at risk (OAR) in patients with metastatic castration-resistant prostate cancer undergoing [^{177}Lu]Lu-PSMA therapy. ***Materials and Methods:*** Fourteen patients undergoing [^{177}Lu]Lu-PSMA therapy between December 2023 and February 2025 in our institution were included, for a total of 48 treatment cycles. For all treatment cycles, the prescribed activity was 7400 MBq. After each cycle, single-photon emission computed tomography (SPECT) images were acquired at three time points (4h, 24h, and 4-7 days) post-injection. A single CT acquisition per cycle was used for photon attenuation correction during SPECT reconstruction. OAR (left and right kidneys, liver, and spleen) segmentation was performed automatically on the CT images and validated by a nuclear medicine physician. The absorbed dose rate distributions were computed by convolution of the activity with the dose-voxel kernel. The time-integration was based on the best fit (mono-exponential or bi-exponential) of the time-activity curve of each OAR. The OpenDose3D and TotalSegmentator extensions of the open-source 3D-Slicer software were used. ***Results:*** The average activity of [^{177}Lu]Lu-PSMA injected per patient and cycle was 6861±214 MBq (range: 6253-7223 MBq). The mean absorbed dose in each cycle was 2.2±1.0 Gy (range: 0.2-4.9 Gy) for the right kidney; 2.7±1.6 Gy (range: 0.5-9.6 Gy) for the left kidney; 0.6±0.3 Gy (range: 0.2-1.2 Gy) for the liver; and 0.4±0.2 Gy (range: 0.1-1.1 Gy) for the spleen. The mean absorbed dose per injected activity was 0.33±0.15 Gy/GBq (range: 0.03-0.72 Gy/GBq) for the right kidney; 0.39±0.24 Gy/GBq (range: 0.09-1.39 Gy/GBq) for the left kidney; 0.09±0.04 Gy/GBq (range: 0.03-0.19 Gy/GBq) for the liver; and 0.06±0.03 Gy/GBq (range: 0.02-0.17 Gy/GBq) for the spleen. ***Conclusion:*** The mean absorbed doses in OAR are in line with those reported in the literature. Considering the commonly accepted restriction of the absorbed dose in the kidneys (23 Gy) as the most critical, the activity to be injected per treatment could be slightly higher, assuming 4 to 6 cycles per treatment. These results show that, in terms of OAR dosimetry, there is room for better tailoring the activity to be injected into each patient per cycle, as well as the number of cycles.

EP-1134

Personalized dosimetry in ^{188}Re-SIRT using gafchromic film derived conversion factor- A comparison of mono-compartmental method with commercial tools

S. Chopra, *A. S. Oinam, G. Singh, K. Kaur, S. R. Shovan, B. R. Mittal, J. Shukla;*
Postgraduate Institute of Medical Education and Research, Chandigarh, INDIA.

Aim/Introduction: Personalized dosimetry in radiopharmaceutical therapy enhances accuracy over generic approaches, though absorbed dose (AD) estimates can vary with methodology. While Monte Carlo Simulation (MCS) is highly accurate but resource-intensive, gafchromic film offers a simpler, cost-effective alternative with good agreement for β-AD. We developed a high-resolution Gafchromic film dosimetry approach using a custom PMMA phantom for ^{188}Re. A Dosimetric Volume Unit (DVU), representing the irradiated volume from isotropic point source emission, was defined, and a corresponding conversion factor (J/GBq) was derived. This factor was used to calculate patient-specific ADs via a mono-compartmental model in ^{188}Re-SIRT. Results were compared with dose estimates generated by OLINDA/EXM® V2.0, MIRDcalc, and QThera.AI.. ***Materials and Methods:*** A tissue-equivalent PMMA phantom with a central cavity for EBT3 Gafchromic film placement was designed to enable high-resolution dosimetry of ^{188}Re. Optical density readings from films exposed to varying ^{188}Re activities were used to quantify AD relative to radioactivity. Percentage depth dose (PDD) curves were generated using 25 µCi of ^{188}Re, providing AD estimates at 0.275 mm depth intervals across the entire beta range. The resulting dose fall-off profile defined a DVU, from which a conversion factor (J/GBq) was calculated and applied for personalized AD estimation in 15 ^{188}Re SIRT patients using a mono-compartmental model. These results were compared with dosimetric outputs from three widely used software tools. ***Results:*** A perfect linear relationship ($R^2 = 1$) was found between AD and radioactivity. For a homogeneous distribution, 1 µCi of ^{188}Re delivered 3.6 Gy/mm^3 during the first half-life and a total of 7.3 Gy/mm^3 over ten half-lives, with a maximum tissue penetration of 3.7 mm. The estimated DVU dimensions were $4.7 \times 4.7 \times 7.4$ mm^3, and the conversion factor was determined to be 34 J/GBq. Among 15 patients, the median AD using the mono-compartmental model was 81.9 ± 41.3 Gy, comparable to QThera.AI estimates (92.7 ± 53.4 Gy; p = 0.215). MIRDcalc yielded significantly lower values (51.8 ± 18.1 Gy; p = 0.026), while OLINDA/EXM® V2.0 produced the lowest ADs (12.0 ± 14.5 Gy; p = 0.000). ***Conclusion:*** The conversion factor derived from Gafchromic film showed strong agreement with QThera.AI estimates, validating its utility for accurate, empirical AD calculations in ^{188}Re-SIRT, similar to established ^{90}Y dosimetry methods. Considering the high cost of commercial softwares, this cost-effective method presents a viable alternative, potentially enabling wider adoption of personalized dosimetry, especially in resource-constrained settings.

EP-1135

Mathematical evaluation of therapeutic index as a function of radionuclide half-life in radiopharmaceutical therapy

J. Hesterman, *B. Schuller, K. Orcutt, J. Babich, J. Hoppin;*
Ratio Therapeutics, Boston, MA, UNITED STATES OF AMERICA.

Aim/Introduction: In radiopharmaceutical therapy (RPT), therapeutic index (TI), defined as the ratio of tumor-to-normal tissue dose, is critical for treatment optimization. TI may be expressed using either absorbed dose (AD) or biologically effective dose (BED). Radionuclide selection is another fundamental aspect of RPT design. This analysis evaluates theoretical tumor-to-kidney (T:K) AD and BED ratios as functions of radionuclide half-life. ***Materials and Methods:*** Tumor and kidney kinetics were modeled using mono-exponential time-activity curves with initial amplitudes $A_{0,T}$ and $A_{0,K}$ and biological half-times $t_{b,T}$ and $t_{b,K}$. Biological kinetics were constant across radionuclides. Dose estimates assumed self-absorbed beta and alpha emissions, dose factors from ICRP 107, and complete daughter decay at deposition sites. Closed-form and empirical analyses assessed T:K AD ratios across radionuclide half-lives (t_r). Due to complexity, BED calculations focused empirically on radionuclides 212Pb and 225Ac. Initial standardized uptake values (SUV_0) were 8 (tumor) and 4 (kidney). Biological half-times were evaluated in two scenarios: short (tumor 30h, kidney 10h) and long (tumor 300h and kidney 100h, reflective of PSMA and SSTR RPTs). Repair half-times and radiosensitivity parameters (alpha/beta ratios) were literature-derived. ***Results:*** The analytical solution for the T:K AD ratio is $T{:}K(t_r) = [A_{0,T} * (t_{b,T} * t_r) * (t_{b,K} + t_r)] / [A_{0,K} * (t_{b,K} * t_r) * (t_{b,T} + t_r)]$. This ratio monotonically increases with radionuclide half-time when tumor biological half-time exceeds kidney biological half-time. BED analyses showed similar behavior, with both tumor and kidney BED higher than AD, yet relative increases were comparable, minimally altering T:K ratios.For typical administered activities (185 MBq for 212Pb, 7.5 MBq for 225Ac), absolute tumor AD and BED were higher for short-lived radionuclides when tumor biological half-times were short (e.g., tumor AD for $t_{b,T}$ = 30h; 212Pb = 4.9 Gy and 225Ac = 2.3 Gy). Conversely, longer-lived radionuclides delivered greater doses at long biological half-times (e.g., tumor AD for for $t_{b,T}$ = 300h; 212Pb = 6.4 Gy and 225Ac = 11.6 Gy). Across all scenarios, T:K AD and BED ratios consistently favored longer-lived radionuclides. ***Conclusion:*** Modeling demonstrates enhanced therapeutic indices with increasing radionuclide half-life, independent of tumor and normal tissue biological kinetics. Illustrating this point, 225Ac therapeutic indices exceeded those of 212Pb across all scenarios for which tumor biological half-time exceeds kidney biological half-time. A higher therapeutic index allows more flexibility in dosing without risking patient safety. ***References:*** PMID: 19285593, 15653658, 1846045, 3620815

EP-1136

First Cycle Dosimetry as a Prediction Metric of ^{177}Lu-PSMA Therapy Outcomes

A. Al-Balushi, *N. Al-Maymani, T. Al-Raii, S. Kheruka, H. Al-Saidi;*
Sultan Qaboos Comprehensive Cancer Care & Research Center - University Medical City, Muscat, OMAN.

Aim/Introduction: The objective of this study was to evaluate the relationship between first cycle absorbed doses delivered to organs-at-risk and therapeutic outcomes, aiming to identify dosimetric patterns predictive of treatment efficacy and safety. ***Materials and Methods:*** The study was conducted on five male patients at SQCCCRC, each receiving standard doses (7.4GBq) of ^{177}Lu-PSMA per cycle. Quantitative SPECT/CT imaging was performed post therapy at 3-4 and 24-48 hours post administration. Absorbed dose calculations were conducted using the MIRD formalism, with S-values derived from the ICRP 110 adult male phantom adjusted for individual patient organ masses [1]. Mean absorbed doses for kidneys and salivary glands were analyzed and correlated with therapeutic response and observed side effects. ***Results:*** Our results categorize patients into two groups according to the absorbed doses delivered to the kidneys and salivary glands. Three patients who received higher kidney doses (0.36-0.64 Gy/GBq) but lower salivary gland doses (0.01-0.02 Gy/GBq) completed six treatment cycles without experiencing significant side effects. Conversely, two patients who had higher salivary gland doses (0.14-0.46 Gy/GBq) and lower kidney doses (0.15-0.24 Gy/GBq) discontinued therapy after the second cycle due to disease progression. These patients developed mild to moderate xerostomia at cumulative salivary gland doses ranging from 3 to 6 Gy and were subsequently prescribed artificial saliva sprays. ***Conclusion:*** Our findings demonstrate a clear correlation between first-cycle absorbed doses to organs-at-risk

and therapeutic outcomes. Increased radionuclide retention in the salivary glands correlated with reduced treatment efficacy and xerostomia. Conversely, patients who responded well to the treatment received safely higher doses to the kidneys. Therefore, first-cycle dosimetry is crucial for identifying patterns that enhance treatment precision and promote outcomes. ***References:*** [1] International Commission on Radiological Protection. Adult Reference Computational Phantoms. ICRP Publication 110. Ann. ICRP 39.2 (2009).

EP-1137

Patient-Specific Dose Assessment in Whole-Body CT Imaging during PET-CT Procedures

P. Sheikhzadeh[1], *M. Asami*[1], *M. Shahrbabki Mofrad*[1], *N. Kasraie*[2]; [1]*Tehran University of Medical Science, Tehran, IRAN, ISLAMIC REPUBLIC OF,* [2]*UT Southwestern Medical Center, Dallas, TX, UNITED STATES OF AMERICA.*

Aim/Introduction: The increasing use of PET-CT imaging in clinical practice has raised concerns regarding radiation exposure from the CT component, particularly during whole-body scans. This study aims to evaluate and compare patient-specific organ doses and effective dose (ED) using two established methods: Dose Length Product (DLP) conversion and the NCICT dosimetry software. ***Materials and Methods:*** A retrospective analysis was conducted on 500 patients (226 men, 274 women) who underwent whole-body PET-CT scans. Effective dose was calculated using two approaches: (1) multiplying DLP values by a standard conversion factor (0.015 mSv/mGy·cm), and (2) using the NCICT software, which employs Monte Carlo simulations for organ dose estimation. Gender- and age-based differences in ED and organ doses were examined. ***Results:*** The average DLP was 516.4 ± 200 mGy·cm. The corresponding ED was 7.76 ± 3.01 mSv via the DLP method and 6.82 ± 2.56 mSv using NCICT. Organ dose analysis revealed the thyroid received the highest radiation exposure, followed by the kidneys in females and testes in males. While the DLP method slightly overestimated ED in females, NCICT provided more individualized estimates by accounting for anatomical variability. A significant age-dependent variation in ED was also observed, with differing trends between genders. ***Conclusion:*** Whole-body CT in PET-CT imaging results in measurable organ and effective doses, with substantial variability influenced by patient age, sex, and anatomical characteristics. Using patient-specific dosimetry methods like NCICT provides more accurate ED estimates than generalized DLP conversion factors. These findings support the necessity of tailored imaging protocols and dose optimization strategies in routine clinical practice to ensure diagnostic quality while minimizing unnecessary radiation exposure. ***References:*** Malekhedayat M, Stewart C, Chu PW, Wang Y, Kasraie N, Franc B, Smith-Bindman R. Use of diagnostic vs low-dose computed tomography in positron emission tomography-CT examinations. Eur Radiol. 2025 Mar 7. doi: 10.1007/s00330-025-11391-w. Epub ahead of print. PMID: 40055228

EP-1138

Patient-Specific Internal Dose Calculation Based on 68Ga-Citrate PET Images: Validation of a Monte Carlo Approach and Comparison to Conventional Analytical Method

S. Asidkar[1], *S. Yavari*[1], *M. Abbasi*[1], *M. Jahanbin*[1], *A. Parach*[2], *P. Sheikhzadeh*[1]; [1]*Tehran university of medical science, Tehran, IRAN, ISLAMIC REPUBLIC OF,* [2]*Regional Medical Physics Service, Belfast Health & Social Care Trust, Belfast, UNITED KINGDOM.*

Aim/Introduction: This study aims to establish patient-specific dosimetry for Gallium-68 (^68Ga) citrate using Monte Carlo simulations (GATE v.9.1), focusing on its role in enhancing diagnostic accuracy and refining imaging protocols in nuclear medicine. To validate its reliability for clinical applications, the Monte Carlo method will be compared with TLD-based dosimetry. Furthermore, the validated Monte Carlo results will serve as a benchmark to evaluate discrepancies and practicality in general dosimetry methods, determining their suitability for routine clinical use. ***Materials and Methods:*** Patient-specific dosimetry was conducted using PET/CT images following intravenous injection of ^68Ga-citrate. The voxelized phantom and source were derived from CT and PET images, respectively. Simulations were performed using GATE v.9.1 with a runtime of 1 second to calculate dose distributions. Organ activity and absorbed doses were estimated using IDAC-DOSE2-1 and OLINDA/EXM tools. Dosimetry results from GATE simulations were compared with those obtained from general methods. Additionally, the GATE code was validated by comparing its results with TLD measurements. ***Results:*** Two dosimeters were positioned around the NEMA phantom to measure the absorbed dose, which varied between 0.22 msv and 1.02 msv. Dose calculations performed using GATE simulations ranged between 0.25 msv and 1.0 msv. A comparative analysis was conducted to verify the accuracy of GATE against phantom-based methods. Mean doses for several organs were evaluated using Monte Carlo simulations and phantom-based approaches. The results revealed that the highest dose was delivered to the spleen, and the largest discrepancy was also observed in the spleen. Discrepancies between organs ranged from 0.06 to 2.86, indicating significant variations in the outcomes of the applied methods. ***Conclusion:*** This study validated GATE-based Monte Carlo simulation by comparing with TLD measurements, showing strong agreement and confirming the accuracy of the MC method. This approach proved suitable for dosimetric calculations of various radiopharmaceuticals in both diagnostic and therapeutic applications. Patient-specific dosimetry results were compared with phantom-based methods, revealing significant discrepancies in some cases and underscoring the superior accuracy of MC simulations for internal dosimetry.

EP-1139

Automated Hybrid Dosimetry for Precise [^{177}Lu]Lu-DOTATATE Peptide Receptor Radionuclide Therapy

Z. Dong[1], *X. Jin*[2], *X. Meng*[2], *J. Yu*[2], *Z. Xie*[3]; [1]*National Biomedical Imaging Center, College of Future Technology, Peking University, Beijing, CHINA,* [2]*Department of Nuclear Medicine, Peking University Cancer Hospital, Beijing, CHINA,* [3]*Institute of Medical Technology, Peking University Health Science Center, Peking University, Beijing, CHINA.*

Aim/Introduction: Personalized dosimetry is essential in [^{177}Lu]Lu-DOTATATE peptide receptor radionuclide therapy (PRRT), particularly for patients with neuroendocrine neoplasms (NENs)[1-2]. While SPECT/CT imaging offers detailed 3D dose distribution, its routine clinical implementation limited. Conversely, planar scintigraphy lacks the spatial resolution needed for robust organ-level dosimetry. To address this trade-off, we proposed a fully automated hybrid dosimetry protocol combining single-time-point (STP) SPECT/CT with serial planar scintigraphy. ***Materials and Methods:*** Eight patients with NENs and liver metastases undergoing [^{177}Lu]Lu-DOTATATE therapy were enrolled. Imaging was performed using both planar and SPECT/CT imaging at Days 0, 1, 2, and 5-7 post-therapy. To address the 2D overlap limitations inherent in planar imaging, we calculated overlap correction factors (OCFs) derived from 3D activity distributions obtained via SPECT and organ masks automatically segmented using TotalSegmentator[3] on baseline CT images. Next, time-integrated activity (TIA) at the organ-level was estimated by fitting serial planar data and scaling these values to the injected dose for consistency. For voxel-level dosimetry, STP SPECT images were scaled voxel-wise using the organ-specific TIA values, generating 3D TIA maps. These maps were then used as input for Monte Carlo simulations (GATE) to compute absorbed dose distributions.

Multi-time-point (MTP) SPECT/CT-based dosimetry was used as the reference standard for validation. ***Results:*** Our proposed method demonstrated close agreement with MTP dosimetry. The liver showed the highest accuracy, with a mean absolute relative error (MARE) of 9.64% ± 7.33% across all patients. The right kidney (MARE: 17.29% ± 9.77%) showed slightly higher errors than the left kidney (MARE: 15.38% ± 9.98%). ***Conclusion:*** This hybrid dosimetry approach effectively balances accuracy and clinical feasibility. In PRRT for NENs, liver dose estimates were highly reliable, while kidney and the other organs with rapid tracer kinetics susceptible to STP errors. ***References:*** 1. Maccauro M, et al. The LUTADOSE trial: tumour dosimetry after the first administration predicts progression free survival in gastro-entero-pancreatic neuroendocrine tumours (GEP NETs) patients treated with [^{177}Lu] Lu-DOTATATE[J]. European Journal of Nuclear Medicine and Molecular Imaging, 2024, 52(1): 291-304. 2. Hebert K, et al. Absorbed dose-response relationship in patients with gastroenteropancreatic neuroendocrine tumors treated with [^{177}Lu] Lu-DOTATATE: one step closer to personalized medicine[J]. Journal of Nuclear Medicine, 2024, 65(6): 923-930. 3. Wasserthal J, et al. TotalSegmentator: robust segmentation of 104 anatomic structures in CT images[J]. Radiology: Artificial Intelligence, 2023, 5(5): e230024.

EP-1140

Feasibility of single-time-point dosimetry in Lu-177-based cocktail radiopharmaceutical therapy

W. Peng[1,2], *Y. Liu*[2], *Y. Chen*[1], *G. Mok*[2];
[1]*Department of Nuclear Medicine, Affiliated Hospital of Southwest Medical University, Luzhou, Sichuan, China, Luzhou, CHINA,* [2]*Biomedical Imaging Laboratory (BIG), Department of Electrical and Computer Engineering, Faculty of Science and Technology, University of Macau, Macau SAR, MACAO.*

Aim/Introduction: Single-time-point (STP) dosimetry is clinically desirable for personalized dosimetry in radiopharmaceutical therapy. However, its feasibility in the cocktail radiopharmaceutical therapy, i.e., administrating 2 pharmaceuticals with the same isotope to the patients consecutively in this study, remains to be validated. We aim to investigate the feasibility of STP dosimetry in multiple cocktail radiopharmaceutical therapy regimens for treating bone metastases in patients with various primary tumors. ***Materials and Methods:*** We retrospectively analyzed 15 patients under the standard ^{177}Lu-PSMA-617 therapy (n=5, 200~235 mCi, prostate cancer), and cocktail therapies with various ^{177}Lu-labeled pharmaceuticals, including ^{177}Lu-DOTA-ibandronic acid (^{177}Lu-DOTA-IBA)+^{177}Lu-FAP-2286 (n=3, 30+150~170 mCi, lung cancer, breast cancer, colon cancer), ^{177}Lu-DOTA-IBA+^{177}Lu-DOTATATE (n=3, 30+160~170 mCi, small bowel neuroendocrine neoplasms, carotid aneurysm, adrenal pheochromocytoma), and ^{177}Lu-DOTA-IBA+^{177}Lu-PSMA-617 (n=4, 30+150 mCi, prostate cancer). All patients underwent sequential quantitative SPECT/CT images at a minimum of 3 time points, i.e., ~2 to ~168 h post-injection. Standard full-time-point (FTP) dosimetry and STP dosimetry (1) were performed using the MIM Dosimetry Software. The median absolute error (MedAE) of STP dosimetry was calculated in comparison to FTP dosimetry for the kidneys, liver, spleen, bone marrow, and selected tumors (n=41 in 15 patients). ***Results:*** For ^{177}Lu-DOTA-IBA+^{177}Lu-FAP-2286, the lowest MedAE of STP dosimetry was observed at 48 h for kidneys (10.05%), liver (15.48%), spleen (11.44%), bone marrow (21.34%), and tumors (6.70%). For ^{177}Lu-DOTA-IBA+^{177}Lu-DOTATATE, the lowest MedAE was obtained at 72 h for kidneys (26.73%), liver (16.27%), spleen (19.13%), bone marrow (17.37%) and tumors (10.45%). For ^{177}Lu-DOTA-IBA+^{177}Lu-PSMA-617, the lowest MedAE of STP dosimetry for kidney was observed at 72 h for liver (13.36%) and spleen (15.79%), and at 48 h for bone marrow (23.54%) and tumors (9.52%). For the standard ^{177}Lu-PSMA-617 therapy, the lowest MedAE was observed at 72 h for kidneys (8.93%) and bone marrow (5.17%), at 168 h for liver (22.76 %), and at 24 h for spleen (21.63%). ***Conclusion:*** In general, 48-72 h post-injection was found to be the most reliable window for STP dosimetry across most regions-of-interest in different cocktail treatments assessed, with error<30%. ***References:*** 1. Hänscheid H et al. Dose Mapping After Endoradiotherapy with 177Lu-DOTATATE/DOTATOC by a Single Measurement After 4 Days. J Nucl Med. 2018;59(1):75-81.

EP-1141

A Comparison of ^{90}Y-SPECT/CT and ^{90}Y-PET/CT Imaging in Voxel-Based Dosimetry for TARE with Resin ^{90}Y-Microspheres

Z. Balaban Genc[1], *A. Eroglu*[1], *S. Beykan Schürrle*[2], *O. Erez*[1], *S. Cetin*[1], *N. Schürrle*[2], *E. Arık*[1], *E. Soydemir*[1], *T. Erdil*[1], *T. Ones*[1];
[1]*Marmara University, School of Medicine, Istanbul, TÜRKIYE,* [2]*Oncosia Scientific GmbH, Durrwangen, GERMANY.*

Aim/Introduction: Transarterial radioembolization (TARE) is a targeted radiotherapy technique for liver tumors, delivering radioactive microspheres intra-arterially to selectively irradiate tumor-feeding vascular structures. Accurate dosimetry is critical for optimizing treatment planning and managing toxicity risks. This study compares post-treatment dosimetric values derived from ^{90}Y-SPECT/CT and ^{90}Y-PET/CT imaging in TARE using resin ^{90}Y-microspheres. ***Materials and Methods:*** This retrospective study included 21 consecutive patients treated with TARE using resin microspheres between 2023 and 2024. Absorbed doses (in Gray, Gy) were calculated using the voxel-based NUKDOS software for whole liver (including tumor), perfused tumor, perfused healthy liver, and whole healthy liver, based on post-treatment ^{90}Y-SPECT/CT and ^{90}Y-PET/CT images. Dosimetric values were compared statistically. ***Results:*** A very high correlation was observed between dosimetric calculations from both imaging modalities ($p<0.001$). No significant differences were found in absorbed doses for the whole liver (including tumor) ($p=0.249$) or perfused healthy liver ($p=0.204$). However, absorbed doses for the perfused tumor were significantly higher with ^{90}Y-PET/CT ($p=0.001$). For the whole healthy liver, a significant difference was noted ($p=0.007$), though median values were comparable (20.62±13.63 Gy vs. 17.95±12.17 Gy). ***Conclusion:*** Few studies have directly compared post-treatment ^{90}Y-SPECT/CT and ^{90}Y-PET/CT using voxel-based dosimetry. This pilot study demonstrates a very strong correlation between dosimetric values from both modalities. Notably, ^{90}Y-PET/CT yielded higher absorbed doses for the perfused tumor, a key factor in treatment efficacy. Absorbed doses for the whole healthy liver, critical for toxicity assessment, were similar despite statistical differences. Given the high correlation, both imaging modalities appear suitable for dosimetric studies. However, prospective, multicenter studies with larger cohorts are needed to validate these findings.

EP-1142

Effects of imaging time points on precision in absorbed dose to the kidneys in patients with neuroendocrine tumours receiving ^{177}Lu-DOTATATE therapy

M. Sandström, *E. Ilan, M. Lubberink;*
Uppsala University Hospital / Uppsala University, Uppsala, SWEDEN.

Aim/Introduction: Fractionated molecular radiotherapy with ^{177}Lu-DOTATATE is an effective treatment option for patients with generalized neuroendocrine tumors. Calculating the absorbed doses (AD) to solid organs has been suggested to optimize the treatment, by allowing as many treatment cycles as possible without exceeding absorbed dose limits to organs at risk. The precision of the calculated AD depends on how well the activity concentrations are determined and the selection of timepoints when the activity concentrations are determined. The current aim was to study the precision dependence on the imaging

timepoints. ***Materials and Methods:*** Time-activity curves for both right and left kidneys were used from one randomized patient out of the 1150 patients treated with ^{177}Lu-DOTATATE at Uppsala University Hospital. Based on the measured time-activity curve, a normal distribution with a standard deviation of 10% was added to create new measurement points. This was repeated to create 65000 sets of datapoints using random numbers in MatLab. Six sampling schemes with different timepoints were used, with timepoints between 24 h and 168 h. Two commonly used temporal sampling schemes are presented here: 24h, 96h and 168h (scheme 1) and 24h, 48h and 72h (scheme 2). A single exponential curve was then fitted to the datapoints of all 65000 sets, from this the percentage deviation from the absorbed dose and effective half-life was calculated for all sets individually and the median, 5% and 95% percentiles were determined. ***Results:*** For scheme 1, the median (5% percentile - 95% percentile) of the percentage deviation for the AD in the right and left kidney was 0.1 (-15.5 - 20.9) and 0.2 (-10.2 - 10.8), respectively. For scheme 2, the corresponding numbers were 0.0 (-28.4 - 64.7) and 1.0 (-13.5 -29.7). The percentage deviation of the effective half-life for scheme 1 was 0.0 (-15.8 - 21.2) for the right kidney and 0.1 (-15.5 - 20.9) for the left kidney. For scheme 2, the corresponding numbers were 0.1 (-29.0 - 66.1) and 0.0 (-28.4 -64.7). The precision in AD and effective half-life was much better when the time between the first and last measurement point was as long as possible. This effect was much more pronounced for the effective half-life than for the AD. ***Conclusion:*** The results of this study indicate that a long time between the first and the last imaging timepoint is beneficial for the precision in absorbed dose calculations.

EP-1143

Absorbed dose estimates in tumors and organs at risk from ^{177}Lu-PSMA-617 therapy in patients with metastatic castration resistant prostate cancer: results from the prospective phase 2 RESIST-PC Trial (NCT03042312)

Z. Ells[1], *C. Meyer*[1], *K. Masri*[1], *D. Sennung*[1], *K. Kimura*[1], *D. Mirando*[2], *I. Tworowska*[3], *R. Esfandiari*[4], *M. Auerbach*[1], *M. Lassmann*[5], *K. Herrmann*[6], *M. Eiber*[7], *W. P. Fendler*[6], *E. Delpassand*[4,3], *J. Czernin*[1], *M. Dahlbom*[1], *J. Calais*[1];
[1]*University of California - Los Angeles, Los Angeles, CA, UNITED STATES OF AMERICA,* [2]*MIM Software, Beachwood, OH, UNITED STATES OF AMERICA,* [3]*RadioMedix Inc., Houston, TX, UNITED STATES OF AMERICA,* [4]*Excel Diagnostics & Nuclear Oncology Center, Houston, TX, UNITED STATES OF AMERICA,* [5]*University of Wurzberg, Wurzberg, GERMANY,* [6]*University of Essen, Essen, GERMANY,* [7]*Technical University of Munich, Munich, GERMANY.*

Aim/Introduction: This is a post hoc analysis of the prospective bi-centric randomized phase II trial: RESIST-PC. The efficacy and safety profile of variable injection activities (6.0 vs. 7.4 GBq) of 177Lu-PSMA-617 in patients with progressive metastatic castration-resistant prostate cancer (mCRPC) were evaluated. Here we report the FDA-required absorbed dose (AD) estimates to organs and tumors, which were obtained with a hybrid method (planar + SPECT imaging). ***Materials and Methods:*** Patients were treated with either 6.0 or 7.4 GBq of 177Lu-PSMA-617. In both groups, whole body planar scintigraphy images were acquired after the first cycle at 4, 24, 48, and 72h with an optional timepoint after 168h. Patients also underwent quantitative SPECT/CT 24h after treatment. Image and dose analysis were performed leveraging a hybrid 2D/3D dosimetry protocol. ADs were calculated for the kidneys, salivary glands, and liver. Representative lesions were included based on visible uptake at all imaging timepoints. Lesions were segmented semi-automatically on SPECT images and propagated to the registered planar image series with manual adjustments. Relative time-activity curves were derived from counts in the serial planar scans, and scaled by the quantitative SPECT activity. The scaled activity measurements were fit exponentially, then convolved with a 177Lu dose kernel to yield AD estimates. ***Results:*** A total of 48/64 patients treated between 07/2017 and 07/2018 had complete imaging datasets (n=16 received 6.0 GBq, n=32 received 7.4 GBq). The mean kidney, submandibular gland, parotid gland, and liver ADs among the whole cohort (and 6.0 vs. 7.4 GBq arms) were: 0.29±0.11 (0.32±0.14 vs. 0.28±0.09), 0.23±0.18 (0.29±0.26 vs. 0.20±0.12), 0.26±0.15 (0.30±0.22 vs. 0.24±0.10), and 0.11±0.09 (0.11±0.08 vs. 0.11±0.09) Gy/GBq, respectively. The difference in organ AD between administered activities was not statistically significant.302 lesions were included (median=7 per patient). The mean AD in bone lesions (n=251) was 1.94±1.83 and 1.63±1.96 Gy/GBq for 6.0 (n=107) and 7.4 (n=144) GBq groups, respectively [ns]. The mean AD in lymph node lesions (n=32) was 6.03±3.81 and 1.67±2.00 Gy/GBq for 6.0 (n=12) and 7.4 (n=20) GBq groups, respectively [p=0.01]. The mean AD in liver lesions (n=19) was 2.96±2.64 Gy/GBq (only applicable for 7.4 GBq cohort). ***Conclusion:*** AD in 48 patients with mCRPC treated with 177Lu-PSMA-617 were estimated using a hybrid imaging methodology, yielding organ doses within tolerable ranges, while tumor ADs varied widely both on the inter- and intra- patient level. There was no significant AD difference between the 6.0 and 7.4 GBq groups.

EP-1144

Comparison of ultra-fast Monte Carlo (MC) dosimetry calculations with standard method in Y-90 post-therapy PET/CT studies

K. Knesaurek[1], *J. Grudzinski*[2];
[1]*Icahn School of Medicine at Mount Sinai, New York, NY, UNITED STATES OF AMERICA,* [2]*Voximetry, Inc, Madison, WI, UNITED STATES OF AMERICA.*

Aim/Introduction: The aim of this study is to compare ultra-fast Monte Carlo (MC) dosimetry calculations with the standard method in post-therapy Y-90 PET/CT studies. ***Materials and Methods:*** A locally developed MC dosimetry program was run on a laptop equipped with an NVIDIA GeForce RTX 3070 GPU, featuring 5120 cores, CUDA compute capability 8.6, 8.0 GB RAM, and a GPU clock speed of 1.560 GHz. In a typical case, MC dose computation was completed in 68.0 seconds, achieving an uncertainty goal of 0.99% over 200 iterations. The results of the ultra-fast MC calculations were compared with the standard local deposition method (LDM) previously used in our Y-90 post-therapy PET/CT dosimetry studies [1]. The comparison focused exclusively on mean doses within the liver, specifically the liver tumor and normal liver tissue. Lung and tissue interference regions were excluded from analysis. ***Results:*** Comparison across six cases demonstrated strong correlation (r^2 = 0.99) between the two methods. LDM values were slightly higher for both tumor (T) and normal tissue (NT) measurements. Tumor dose values ranged from 413-1451 Gy for MC and 465-1738 Gy for LDM. Normal tissue values ranged from 11-76 Gy for MC and 12-82 Gy for LDM. The mean percent difference between LDM and MC values was 14% for T and 6% for NT. The percent difference range was 9-20% for T and 1-8% for NT. ***Conclusion:*** Ultra-fast MC dosimetry yields mean dose estimates comparable to those of the standard LDM approach. These findings support the feasibility of employing full, rapid MC dosimetry in clinical radiation therapy. ***References:*** 1. Knešaurek K. Comparison of post-therapy Y-90 PET/CT dosimetry methods in liver therapy with Y-90 microspheres. World J Nucl Med. 2020;19:359-65.

EP-1145

Evaluating the Effect of Respiratory Motion Correction in Yttrium-90 Positron Emission Tomography Imaging for Accurate Dosimetry

C. D. E. Van Speybroeck[1], *L. E. L. Westlund Gotby*[1], *M. Boswinkel*[1], *M. W. M. van Wijk*[1], *A. Cordon Avila*[2], *M. Abayazid*[2], *S. M. B. Peters*[1], *J. F. W. Nijsen*[1];
[1]*Department of Medical Imaging, Radboud Institute for Health Sciences, Radboud university medical center, Nijmegen, NETHERLANDS,* [2]*Department of Robotics and Mechatronics, Faculty of Electrical Engineering, Mathematics and Computer Science, University of Twente, Enschede, NETHERLANDS.*

Aim/Introduction: Radioembolization with yttrium-90 (^{90}Y) or holmium-166 (^{166}Ho) microspheres is an established procedure for treatment of primary and secondary liver tumours. Retrospective studies have shown promising results correlating increased tumour-absorbed dose to better overall survival and tumour response [1]. Accurate PET or SPECT dosimetry is imperative for precise therapeutic delivery [2]. However, respiratory-induced hepatic displacement (8-25 mm during shallow breathing) can cause motion artifacts. This is characterized by partial volume and spill-in/spill-out effects, potentially leading to erroneous dose assessments [3-6]. This study aims to evaluate and quantify the impact of respiratory motion on ^{90}Y-PET-based dosimetry using a moving liver phantom. ***Materials and Methods:*** A liver-mimicking agarose gel phantom was created, with a non-radioactive outer shell and a radioactive background containing three tumour-mimicking spheres (diameters: 30, 40, 60 mm) filled with 271 kBq/mL (corrected for acquisition time) of ^{90}Y resin microspheres (4.5:1 sphere-to-background concentration ratio ($S:BG_{ratio}$)). The largest sphere contained a non-radioactive necrotic core (diameter: 30 mm). The phantom was placed on a respiratory motion system with adjustable motion parameters, set to mimic a shallow breathing pattern [7]. The setup was scanned on a Siemens PET/CT system, employing their reflector block-based respiratory motion correction. Additionally, the phantom was scanned with the respiratory motion system turned off for optimal imaging. Images were reconstructed with and without motion correction. In all configurations, counts inside the spheres and radioactive background were determined by delineating the known dimensions of the spheres and background on the CT images. To perform dosimetric analysis and compare the acquired data, the mean absorbed dose and dose volume histograms will be computed. ***Results:*** PET-based results for the phantom showed $S:BG_{ratio}$ of 2.32, 3.24, 3.01 for each sphere with motion correction, and 2.57, 3.11, 3.04 without motion correction. Optimal imaging showed $S:BG_{ratio}$ of 2.83, 3.17, 2.94. The $S:BG_{ratio}$ of the non-radioactive necrotic core was 2.33, 2.62 and 1.71 with motion correction, without motion correction, and with optimal imaging, respectively. Analysis is still ongoing and detailed results will be shared at the congress. ***Conclusion:*** This study investigates the impact of respiratory motion on dosimetry in ^{90}Y radioembolization in a phantom model and will evaluate the performance of a clinically available motion correction tool. It will further quantify the impact of both respiratory motion and motion correction. ***References:*** [1] Hermann e.a., 2020. [2]Elschot, e.a., 2011. [3]Keall e.a., 2006. [4] Langen and Jones, 1999. [5]Tsai e.a., 2018. [6]Shimizu e.a., 1999. [7]Naghibi e.a., 2018.

EP-1146

Bridging diagnosis and dosimetry: investigating the predictive role for ^{68}Ga-DOTATOC PET/CT in ^{177}Lu-DOTATATE PRRT

C. Ingraito[1,2], *A. Monaci*[3], *M. Cuomo*[1], *G. Argiroffi*[1], *M. Kirienko*[1], *A. Lorenzoni*[1], *F. Rubino*[1], *C. Chiesa*[1], *M. Maccauro*[1];
[1]*Nuclear Medicine, Fondazione IRCCS Istituto Nazionale dei Tumori, Milan, ITALY,* [2]*Post Graduate Specialisation School for Medical Physics, Università degli Studi di Milano, Milan, ITALY,* [3]*Post Graduate Specialisation School for Nuclear Medicine, Università degli Studi di Firenze, Firenze, ITALY.*

Aim/Introduction: Lesion dosimetry after the first administration of ^{177}Lu DOTATATE was predictive of PFS [1]. This retrospective study explores whether pre-treatment ^{68}Ga-DOTATOC PET/CT, typically used for patient selection, could provide an even earlier prediction of post-therapy dosimetry values. ***Materials and Methods:*** We assessed correlations between 8 PET-derived parameters and 5 post-therapy Absorbed Dose (AD) values across over 300 lesions. Patients had PET scans and lab tests within six months prior to treatment. After the first ^{177}Lu cycle, two SPECT/CT dosimetric scans were acquired (20, 162 hours post-injection). Lesions and Organs-At-Risk (OARs) were segmented on PET using a semi-automatic gradient and a fully automated method, then adapted to SPECTs after image registration. Statistical comparisons employed Bland-Altman analysis (bias B, standard deviation SD) and Spearman's correlation (r coefficient). Machine Learning (ML) approach, incorporating VOI statistics and biomarkers, was explored for predictive modelling. ***Results:*** Of the 40 correlations analysed, a strong association ($p<10^{-4}$) emerged between the PET-derived Somatostatin Receptor-Expressing Tumour Volume and the post-treatment Time-Integrated Activity Coefficient (τ) (r=0.78). Correlation improved after stratification on Ki-67 index (r_{G1}=0.89, r_{G2}=0.76). A linear regression model was used to estimate τ, enabling AD calculation via MIRD formalism. Across all tumours, Bland-Altman yielded B=-38%, SD=63%. Stratified analysis and improved parabolic interpolation enhanced precision: G1 tumours showed B=5.82%, SD=51.8%; G2 had B=-0.62%, SD=69%. The ML approach is under refinement to further improve predictive reliability. ***Conclusion:*** The linear model prediction of τ over volume was overly simplistic, yielding unacceptable AD dispersion due to intrinsic differences between PET and SPECT (acquisition time: 1h vs 20h, somatostatin-analog ligand: TOC vs TATE, kidney protection: absent/present). The ML model in development may bridge these gaps, boosting predictive accuracy. ***References:*** [1]: Maccauro M, Cuomo M, Bauckneht M, Bagnalasta M, Mazzaglia S, Scalorbi F, Argiroffi G, Kirienko M, Lorenzoni A, Aliberti G, Pusceddu S, Giuseppina C, Matteo GE, Seregni E, Chiesa C. The LUTADOSE trial: tumour dosimetry after the first administration predicts progression free survival in gastro-entero-pancreatic neuroendocrine tumours (GEP NETs) patients treated with [177Lu] Lu-DOTATATE. Eur J Nucl Med Mol Imaging. 2024 Dec;52(1):291-304. doi: 10.1007/s00259-024-06863-y. Epub 2024 Sep 5. PMID: 39235614.

EP-1147

Correlation between absorbed dose, SUVmax and Krenning Score after Peptide Receptor Radionuclide Therapy (PRRT) treatment in neuroendocrine tumors

A. Barrera Cerpa*, M. Ribelles Segura, A. Fernández Iglesias, L. Paruta Araez, C. Villaprado Meza, K. Sanabria Ramírez, P. Boya Román, I. Blanco Saiz, F. Lozada Delgado, Á. Rosero Enríquez, D. Gómez Sánchez, E. Anda Apiñaniz, R. Vera García, E. Goñi Gironés; Hospital Universitario de Navarra, Navarra, SPAIN.*

Aim/Introduction: Our aim was to evaluate the relationship between the tumor-absorbed dose (TAD) and physiological standardized uptake values (SUVs) estimated from [177Lu]Lu-DOTA-TATE SPECT/CT, as well as their association with Krenning scores (K-scores) derived from planar imaging. ***Materials and Methods:*** This analysis was conducted on patients with advanced well-differentiated NETs grades 1-3 who underwent [177Lu] Lu-DOTA-TATE (7.4 GBq per cycle). Target lesions were selected based on the RECIST 1.1 criteria. Parameters and dosimetry were performed at two time points, 1st and 4th cycles post-therapy. Statistical analyses such as Kruskal-Wallis and Wilcoxon were conducted to investigate correlations. Written consent was taken from all the patients. ***Results:*** A total of 16 patients (50% females), mean age of 62.25 ± 10 years with 62 lesions, including primary tumour sites and metastases. Lesions were designated as K-score IV (n=40), K-score III (n=4), K-score II (n=17), K-score I (n=1) in the 1st cycle and as K-score IV (n=18), K-score III (n=17), K-score II (n=22), K-score I (n=5) in the 4th cycle. The median SUVmax for all lesions in the 1st cycle was 9.5 (IQR: 4.4-20.1) and in 4th cycle was 6.6 (IQR: 3.4-18.7). The differences were significative (p=0.012). Statistically significant changes of SUVmax among K-score groups were observed in the 1st and 4th cycle (p<0.005). There was a trend of greater SUVs values with higher K-score (p>0.005). The median total absorbed dose by all lesions in the 1st cycle was 14.3 Gy (IQR: 6.8-24.2) and in the 4th cycle was 9.1 Gy (IQR: 4.7-15.2). The differences were significative (p 0,01). There was also a trend of greater TAD with higher K-score (p>0.005). There is a clear trend

toward higher TAD in the first cycle with an a lower absorbed in the 4ths cycle (cut of 40% decrease p <0.05). ***Conclusion:*** Our findings suggest a positive correlation between Krenning score, SUVmax, and TAD. They also provide further evidence supporting the TAD in the first cycle as a potential predictive biomarker in the context of precision medicine.

EP-1148

Outcome-Driven Timing Optimization of Single Time Point Dosimetry for PSMA-Directed Radiopharmaceutical Therapy

J. Hu[1], *R. Seifert*[1], *C. Vinicius Gomes*[1], *Y. Chen*[1], *W. Jutidamrongphan*[1], *M. Amon*[2], *J. Wang*[1], *S. Xue*[1], *A. Afshar-Ormiehali*[1], *A. Rominger*[1], *K. Shi*[1];
[1]*Inselspital, Bern University Hospital, University of Bern, Bern, Switzerland, Bern, SWITZERLAND,* [2]*Department of Nuclear Medicine, Inselspital, Bern University Hospital, University of Bern, Bern, Switzerland, Bern, SWITZERLAND.*

Aim/Introduction: Single-time-point (STP) dosimetry emerges as a simplified alternative to Multiple-time-points (MTP) dosimetry standards. The development of STP is based on reference to MTP, nevertheless, MTP may introduce biases due to undersampling and population-based assumptions, which may hamper its ability in STP optimization. This study proposes the optimization of STP directly based on treatment outcomes and focuses on the optimal selection of time points for STP. ***Materials and Methods:*** Data from 51 mCRPC patients treated with [^{177}Lu]Lu-PSMA-617 RPT were retrospectively analyzed. SPECT/CTs were acquired at time points from 1 to 3 days p.i. Transient treatment-emergent adverse events (TEAEs) and long-term PSA decline rates were monitored following CTCAE v5.0 and PCWG3. Mean absorbed doses ($STPD_{tox}$ and $MTPD_{tox}$) and cumulative doses ($STPD_{response}$ and $MTPD_{response}$) were computed for organs-at-risk and whole-body tumors, respectively. ***Results:*** Bone marrow dosimetry from $STPD_{tox}$ correlated significantly with anaemia grading (reduction of hemoglobin amount), peaking on 3-day p.i. (Spearman's $\rho = 0.46$, $p_{adj} < 0.001$), aligning with $MTPD_{tox}$ (Spearman's $\rho = 0.43$, $p < 0.001$). Williams' F-test confirmed that $STPD_{tox}$ and $MTPD_{tox}$ were equivalently correlated with anaemia grades. For PSA response assessment, both $MTPD_{response}$ and $STPD_{response}$ showed no significant difference in correlation with PSA decline rate on 1-day p.i. (Spearman's $\rho = -0.34$, $p_{adj} < 0.001$) and 2-day p.i. (Spearman's $\rho = -0.33$,$p_{adj} < 0.001$). ***Conclusion:*** Findings suggest that Hänscheid-based STP dosimetry on 2-days p.i. is identified as a practical alternative for outcome-driven timing, linking marrow dosimetry to hematologic toxicity and tumor dosimetry to PSA decline rate, thus supporting its potential for streamlined clinical application.

EP-1149

Correlation Between Tumor-Absorbed Radiation Dose and Tumor Volume Reduction in Sarcoma Patients Treated With [^{177}Lu]Lu-FAP-2286

R. Nami[1], *M. Nasiri*[2], *S. Banihashemian*[3], *A. Abolhosseini Shahrnoy*[1], *G. Divband*[4], *M. Akbari*[3];
[1]*Parsisotope Company, Tehran, IRAN, ISLAMIC REPUBLIC OF,* [2]*Department of Cellular & Molecular Biology, School of Biology, Damghan University, Tehran, IRAN, ISLAMIC REPUBLIC OF,* [3]*Cancer Research Center, Shahid Beheshti University of Medical Sciences, Tehran, IRAN, ISLAMIC REPUBLIC OF,* [4]*Khatam PET-CT Center, Khatam-al-Anbia Hospital, Tehran, IRAN, ISLAMIC REPUBLIC OF.*

Aim/Introduction: This study aimed to assess whether the absorbed dose of a [^{177}Lu]Lu-FAP-2286, correlates with the reduction in primary and metastatic lesions volume in patients with advanced sarcoma. ***Materials and Methods:*** Ten patients with histologically confirmed metastatic sarcoma were treated with [^{177}Lu]Lu-FAP-2286 . Based on the treatment response, the patients were divided into two groups: one with a significant reduction in tumor size (n=4) (Group 1) and the other with an increase in the initial tumor size (n=6) (Group 2). Dosimetry was performed for each patient, using MIRDCALC method, after six cycle of [^{177}Lu]Lu-FAP-2286 therapy, to quantify the tumor-absorbed radiation dose. The correlation between absorbed dose/ml and tumor volume reduction was evaluated in primary and metastatic lesions using Spearman's correlation test. A linear regression model was also applied to assess dose-response trends. ***Results:*** Preliminary analyses revealed that, the initial tumor volume in Group 2, before and after treatment, (1672.4±510.2 and 2118.7±680.7 respectively) was significantly larger than that in Group 1 (243.4±35.2 and 160.7±11.7 respectively) (P=0.038 and P=0.035 respectively). Additionally, the total absorbed dose in Group 2 was significantly higher than that in Group 1 (381,226.4 ± 28,112.9 vs. 528,335.8 ± 64,422.4 mGy respectively, and P<0.05). Interestingly, the absorbed dose/ml in Group 1 was higher than that in Group 2 (1617.7 ± 118.2 vs. 498.3 ± 146.2 mGy respectively, $P < 0.001$). Further analyses showed moderate positive correlation between the primary tumor absorbed dose (Dose/ml) but not total absorbed dose, and percentage tumor volume changes (31.7 ± 5.05% vs. -20.2 ± 5.2%, $P < 0.001$), as determined by Spearman's correlation ($\rho = 0.90$, $P < 0.001$). These findings suggest that higher absorbed doses/ml are associated with greater primary tumor shrinkage. Similarly, linear regression analysis demonstrated a statistically significant association between the absorbed dose/ml and percentage tumor volume reduction ($R^2 = 0.41$, $P < 0.001$).Interestingly, for metastatic lesions (n=14 in each group), the total absorbed dose (314,819.5±63,090.9 in group 1 vs 250,769.8±88,619.1 in group 2) was significantly correlated with the percentage reduction in tumor size (Spearman's $\rho = -0.42$, $P = 0.045$), whereas no such correlation was observed for dose/ml. However, linear regression did not reveal a significant linear relationship between the total absorbed dose and percentage reduction in tumor volume for metastatic lesions ($P = 0.2$). No treatment-related grade 3 or 4 toxicities were observed during the study. ***Conclusion:*** These findings suggest that the absorbed dose of [^{177}Lu]Lu-FAP-2286 is positively associated with tumor volume reduction in sarcoma patients. This supports the potential for personalized radiopharmaceutical therapy based on patient-specific dosimetry. Further studies with larger cohorts are warranted to validate these results.

EP-1150

Single time point approaches for salivary gland dosimetry and correlation with PET follow-up

A. Noto[1], *X. Shen*[1], *M. Zacherl*[1], *M. Rumiantcev*[1], *G. Liubchenko*[1], *G. Böning*[1], *R. Werner*[1,2], *G. Sheikh*[1], *A. Delker*[1], *S. Resch*[1];
[1]*Department of Nuclear Medicine, University Hospital, LMU Munich, Munich, GERMANY,* [2]*Johns Hopkins School of Medicine, The Russell H Morgan Department of Radiology and Radiological Sciences, Division of Nuclear Medicine and Molecular Imaging, Baltimore, MD, UNITED STATES OF AMERICA.*

Aim/Introduction: Salivary glands are primary organs-at-risk in Lu-177-PSMA-treated prostate cancer patients due to the high incidence of xerostomia. Previous studies have shown that PET/CT uptake correlates with absorbed dose and predicts toxicity when using multi-time-point (MTP) dosimetry. This study assessed whether single-time-point (STP) dosimetry after the first therapy cycle can replace MTP dosimetry to reduce clinical workload, and whether the PET-dose correlation remains valid. ***Materials and Methods:*** The submandibular (SG) and parotid (PG) glands of 10 patients with metastatic castration-resistant prostate cancer were included. Three patients received six cycles of Lu-177-PSMA-I&T, and seven underwent four cycles. MTP dosimetry with SPECT/CT acquisitions at 24, 48 and 72 h after injection and mono-exponential time-activity curve fitting served as reference. STP dosimetry for cycle two and onward was performed using SPECT/CT imaging at 24 or 48 h and two different approaches. In the first, the effective half-life was derived from the patient-specific first cycle MTP dosimetry. In the second approach, it was determined using a population-based effective half-life including

all cycles and patients except the one under investigation (leave-one-out method). Mean absolute deviations from the reference absorbed dose values were determined. The correlation between STP absorbed dose and SUV mean values from the second F-18-PSMA-1007 PET (performed prior to the third cycle) was evaluated. ***Results:*** No significant differences were observed between the effective half-lives of different cycles ($p > 0.08$). STP dosimetry at 24 and 48 h showed comparable performance, with 48 h showing slightly better accuracy. For the patient-specific method, the mean deviations for cycles two to six were 10.1±8.3%, 10.±8.6%, 13.7±10.7%, 15.1±9.2%, and 7.4±4.0%. For the population-based method, the mean deviations were 10.6±8.6%, 9.4±9.1%, 14.0±14.0%, 14.0±9.3%, and 9.6±6.6%. The percentage of glands with deviations below 10% was 55.8% for the patient-specific and 57.2% for the population-based method. A strong correlation was found between uptake in the second PET and absorbed dose in the third cycle for both methods, with results similar to those obtained from MTP dosimetry: for the patient-specific method, SGs $r = 0.66$, $p < 0.01$ and PGs $r = 0.61$, $p < 0.01$; for the population-based method, SGs $r = 0.67$, $p < 0.01$ and PGs $r = 0.59$, $p < 0.01$. ***Conclusion:*** Both STP dosimetry approaches may serve as suitable alternatives to MTP dosimetry for assessing salivary gland absorbed doses, and the predictive value of PSMA-PET imaging remains valid for salivary gland toxicity assessment.

EP-1151

Patient-Specific Dosimetry of ^{177}Lu-FAPI-2286 in Peptide Receptor Radionuclide Therapy Using GATE Monte Carlo Simulations: A Pilot Study

S. Shafiee Dastgerdi[1], *L. Hassanzadeh*[2], *G. Divband*[3], *H. Sharifi*[4];
[1]University of Isfahan, Isfahan, IRAN, ISLAMIC REPUBLIC OF, [2]Department of Nuclear Medicine, School of Medicine, Rajaie Cardiovascular, Medical & Research Center, Iran University of Medical Sciences, Tehran, IRAN, ISLAMIC REPUBLIC OF, [3]Department of Nuclear Medicine, Jam Hospital,, Tehran, IRAN, ISLAMIC REPUBLIC OF, [4]Department of Molecular Imaging, Faculty of Advanced Technologies in Medicine, Iran University of Medical Sciences, Tehran, IRAN, ISLAMIC REPUBLIC OF.

Aim/Introduction: The advent of integrated functional-anatomical imaging modalities such as PET/CT and SPECT/CT has significantly enhanced the accuracy of patient-specific dosimetry in radionuclide therapy over the past decade. 177Lu, with a half-life of 6.7 days, is increasingly utilized in peptide receptor radionuclide therapy (PRRT). Precise quantification of radiation doses to tumors and critical organs. Particularly the kidneys, is essential to optimize therapeutic efficacy and minimize toxicity [1]. ***Materials and Methods:*** The GATE v9.4.1 MC simulations toolkit was used in the present study to produce dosimetric data. The Dose Actor was utilized for dose calculation, and was attached to the CT images with Edep and UncertaintyEdep enabled. This allowed the storage of deposited energy and the statistical uncertainty in the 3D dose map. Each simulation utilized 2.4×10^9 primary particles to ensure high accuracy. Serial planar scintigraphy at 3, 48, and 72 hours post-injection, alongside SPECT/CT at 72 hours, provided time-activity data for dose estimation. Absorbed doses to kidneys and tumors were calculated as Gy/GBq for the first treatment cycle. ***Results:*** No acute adverse events were observed following 177Lu-FAPI-2286 administration.Mean absorbed kidneys dose after treatment for the four patients was 0.89 ± 0.20 Gy/GBq. The results of tumor doses varied for different pathologies: Two female patients aged 35 and 36 years with triple-negative and HER2-positive breast cancer (47 lesions) received 6.3 ± 2.5 Gy/GBq, while two patients (1 male) aged 40 and 47 years with synovial sarcoma and recurrent dermatofibrosarcoma protuberans (11 lesions) received 3.91 ± 1.82 Gy/GBq. ***Conclusion:*** The pilot study demonstrates the feasibility and clinical value of GATE based patient-specific dosimetry in 177Lu-FAPI-2286 PRRT. Accurate dosimetry enables individualized treatment planning, potentially improving therapeutic outcomes and minimizing kidneys toxicity. Further studies with larger cohorts are warranted to validate these preliminary findings and refine dose-response relationships in targeted radionuclide therapies. ***References:*** [1] Stamouli, I., Nanos, T ., Chatzipapas, K., Papadimitroulas, P., Zoglopitou, L., -A., Kalathas, T., Katsakiori, P. F., Makridou, A., & Kagadis, G. C. (2023). Dosimetric Evaluaation of 177Lu Peptide Receptor Radionuclide Therapy Using GATE and Planet Dose. Applied Sciences, 13(17), 9836. https://doi.org/10.3390/app13179836

EP-1152

Personalized ^{177}Lu-FAPI-2286 Peptide Receptor Radionuclide Therapy Dosimetry in a Metastatic Rectal Cancer Patient: A Simulation Study

H. Sharifi[1], *L. Hassanzadeh*[2], *G. Divband*[3], *S. Shafiee Dastgerdi*[4];
[1]Department of Molecular Imaging, Faculty of Advanced Technologies in Medicine, Iran University of Medical Sciences, Tehran, IRAN, ISLAMIC REPUBLIC OF, [2]Department of Nuclear Medicine, School of Medicine, Rajaie Cardiovascular, Medical & Research Center, Iran University of Medical Sciences, Tehran, IRAN, ISLAMIC REPUBLIC OF, [3]Department of Nuclear Medicine, Jam Hospital, Tehran, IRAN, ISLAMIC REPUBLIC OF, [4]Faculty of physics, University of Isfahan, Isfahan, IRAN, ISLAMIC REPUBLIC OF.

Aim/Introduction: Accurate patient-specific internal dosimetry remains a critical challenge in nuclear medicine. In metastatic rectal cancer, where conventional treatments often fail in advanced stages, personalized dosimetry for ^{177}Lu-FAPI-2286 is vital to optimize therapeutic efficacy while minimizing toxicity. ***Materials and Methods:*** The absorbed dose calculations for this study were based on the Geant4 (GEometry ANd Tracking) Application for Tomographic Emission (GATE) MC toolkit (v9.4). All simulations applied the "standard model" in GATE for electromagnetic processes, which is effective and validated over an energy range of 1 keV-100 TeV. The absorbed dose per organ was calculated, and the deposited energy per voxel was stored using the "dose actor" tool in GATE. The dose actor builds three-dimensional images of the deposited energy in a given volume with a specified voxel resolution. The dose actor takes into account the total energy and the interaction probability of the particles, as well as the density of each voxel. The CT and SPECT images were used as attenuation maps and activity distribution of patient phantom respectively. Hence the CT and SPECT images have been registered by 3D Slicer software to achieve the same matrix and pixel sizes using the module "Resize Image (BRAINS)". Simulations used 2.4×10^9 primaries to ensure statistical accuracy. The study included a 60-year-old male with metastatic rectal cancer undergoing ^{177}Lu-FAPI-2286 therapy. To evaluate the biodistribution and absorbed doses, serial planar scintigraphy was performed at 3, 48, and 72 hours post-injection. Additionally, SPECT/CT imaging was conducted at three days post-injection to determine cumulative activity in tumors and organs. ***Results:*** The patient received an average administered activity of 6.31 GBq over two cycles, constrained by a kidney dose tolerance of 23 Gy. Calculated mean absorbed doses to he kidneys were 0.612 ± 0.0005 Gy/GBq (cycle 1) and 0.544 ± 0.0005 Gy/GBq (cycle 2). Metastatic lesions in bilateral pulmonary nodules, retroperitoneal, and left common iliac lymph nodes showed mean absorbed doses of 5.16 ± 0.003 Gy/GBq (range 0.30 - 7.19 Gy/GBq) in cycle 1 and 3.45 ± 0.005 Gy/GBq (range 0.12 - 5.82 Gy/GBq) in cycle 2. ***Conclusion:*** ^{177}Lu-FAPI-2286 therapy is a promising and well-tolerated option for metastatic rectal cancer. Implementing personalized dosimetry is essential to maximize therapeutic response and safety, supporting tailored treatment planning in targeted radionuclide therapy.

EP-1153

Accuracy, Efficiency and Clinical Validation of GATE and GAMOS-based Monte Carlo dosimetry framework for 99mTc Radiopharmaceutical

A. Alshehri[1,2];
[1]Najran University, Najran, SAUDI ARABIA, [2]Radiology sciences department | Collage of applied medical science | Najran University, Najran, SAUDI ARABIA.

Aim/Introduction: Accurate estimation of absorbed doses from radiopharmaceuticals in human organs relies on computational simulations due to the impracticality of direct measurement. This study employed GATE and GAMOS Monte Carlo codes to simulate

99mTc radiation dose distributions in the Zubal anthropomorphic phantom, focusing on cardiac perfusion imaging protocols. ***Materials and Methods:*** This study employs Monte Carlo simulation frameworks, GATE (Geant4 Application for Tomographic Emission) and GAMOS (GEANT4-Based Architecture for Medicine-Oriented Simulations), to model radiopharmaceutical dosimetry using the Medical Internal Radiation Dose (MIRD) methodology. A Zubal anthropomorphic phantom was simulated in both codes to calculate self-absorbed fractions (SAF), S-values, and mean organ doses for 99mTc, with cumulative heart activity integrated into target organ dose assessments. Activity distributions were analyzed at injection and 60 minutes post-injection (cardiac rest phase) to validate against established clinical data. ***Results:*** GATE leveraged its Geant4-based physics engine for detailed particle transport, while GAMOS prioritized computational efficiency through optimized geometry parameterization. Results demonstrated strong agreement between the codes, with GATE predicting pancreas (21%), gallbladder (18%), and kidneys (16%) as high-dose organs, and GAMOS yielding marginally lower values (20%, 17%, and 15%, respectively). Both frameworks identified comparable trends: pancreas > gallbladder > kidneys > spleen > heart/liver, aligning with prior studies. However, GATE exhibited superior precision due to advanced physics modeling, whereas GAMOS achieved30% faster computation times. ***Conclusion:*** This dual-code approach highlights the trade-offs between accuracy and efficiency in dosimetry, offering a validated framework for optimizing radiopharmaceutical dosing across varying post injection periods. The study underscores GATE's utility for high-precision clinical applications and GAMOS's suitability for rapid prototyping, collectively advancing personalized nuclear medicine therapies. ***References:*** Alessandra Boschi, Licia Uccelli, Lorenza Marvelli, Corrado Cittanti, Melchiore Giganti, and Petra Martini. Technetium-99m radiopharmaceuticals for ideal myocardial perfusion imaging: lost and found opportunities. Molecules, 27(4):1188, 2022. URL https://pubmed.ncbi.nlm.nih.gov/35208982/.Jacek Capala, Stephen A Graves, Aaron Scott, George Sgouros, Sara St James, Pat Zanzonico, and Brian E Zimmerman. Dosimetry for radiopharmaceuticaltherapy: current practices and commercial resources. Journal of Nuclear Medicine, 62(Supplement 3):3S-11S, 2021. URLhttps://doi.org/10.2967/jnumed.121.262749.Andrew J Einstein, Igor Shuryak, Adam Casta~no, Akiva Mintz, Mathew S Maurer, and Sabahat Bokhari. Estimating cancer risk from 99mtcpyrophosphate imaging for transthyretin cardiac amyloidosis. Journal of Nuclear Cardiology, 27(1):215-224, 2020. URL https://doi.org/10.1007/s12350-018-1307-7.Jean Gasteuil, Caroline Noblet, Matthieu Moreau, and Philippe Meyer. A gate/geant4 monte carlo toolkit for surface dose calculation in vmatbreast cancer radiotherapy. Physica Medica, 61:112-117, 2019. URL https://doi.org/10.1016/j.ejmp.2019.04.012.

EP-1154

The effect of glucocorticoids on radioiodine-131 bio-kinetics in patients suffering from Graves' Disease

C. Happel*, B. Bockisch, D. Groener;*
University Medical Center Frankfurt; Clinic for Radiology and Nuclear Medicine; Department of Nuclear Medicine, Frankfurt, GERMANY.

Aim/Introduction: Radioiodine therapy (RIT) of Graves' disease (GD) may stimulate the development of Graves' Ophthalmopathy (GO) or exacerbate a pre-existing subclinical GO. Therefore, international guidelines recommend the administration of additional glucocorticoid medication for patients undergoing a RIT with pre-existing GO. Therefore, the aim of this retrospective analysis was to quantify the influence of protective glucocorticoid medication on intra-therapeutic effective half-life of ^{131}I during RIT of patients suffering from GD. ***Materials and Methods:*** 211 patients with GD who underwent RIT without any additional thyroid medication were analysed retrospectively. These patients were subdivided into two subgroups. Group A: 35 patients with concomitant EO and protective glucocorticoid medication; Group B: 176 patients without EO and additional glucocorticoid medication. Effective half-life was determined pre- and intra-therapeutically and compared statistically between the groups. ***Results:*** In the glucocorticoid group the mean effective half-life was 5.69 d in RIUT and 5.47 d during RIT ($p > 0.05$). A comparable result was obtained in group B (5.75 d in RIUT and 5.46 d during RIT; ($p > 0.05$)). The comparison of the two subgroups did not show a significant relation ($p = 0.79$). Therefore, intrathyroidal effective half-life is not significantly influenced by glucocorticoid medication. ***Conclusion:*** Current studies found the mineralocorticoid potency of Prednisolone to possibly decrease intra-thyroidal EHL. In the presented study those results could not be verified. This might be due to the use of Methylprednisolon instead of Prednisolon. The reason for the reduced intrathyroidal EHL may therefore be the diuretic effect of prednisolone.

EP-1155

Evaluation of different methods for determining the intra-renal effective half-life during ^{177}Lu-PSMA-617 Radioligand Therapy

C. Happel*, B. Bockisch, K. Klimek, D. Groener;*
University Medical Center Frankfurt; Clinic for Radiology and Nuclear Medicine; Department of Nuclear Medicine, Frankfurt, GERMANY.

Aim/Introduction: In Radioligand therapy (RLT) with ^{177}Lu-PSMA the kidneys are the primary organ at risk. Prerequisites for renal dosimetry are absolute quantification of the intra-renal activity and determination of the intra-renal effective half-life (IREHL) of the radiopharmaceutical. For absolute quantification of intra-renal activity at least one SPECT/CT-acquisition is necessary. EHL can be determined using a VOI-analysis of sequential SPECT-acquisitions (Method A), a ROI-analysis of the dorsal views (Method B) or the geometric-mean of conjugated views from sequential scintigraphic whole-body images (WB) (Method C). Aim of this study was to evaluate the aforementioned methods for calculating EHL comparatively. ***Materials and Methods:*** Scintigraphic data of 30 consecutive patients who underwent RLT with ^{177}Lu-PSMA-617 were evaluated retrospectively. Mean age of the patients was 73±6.9a. Mean administered activity was 7.8±1.1GBq. Abdominal SPECT-images and conjugated WB were obtained 24, 48, and 72h after administration (AnyScan-Mediso; SPECT: 64steps; 15s/step; scan-speed (WB) 20cm/min). IREHL was calculated for each patient using a mono-exponential fit to the time-activity-curve using methods A, B, and C. ***Results:*** Mean EHL calculated from Method A was 30.2±6.8h for the left (lk) and 30.6±7.2h for the right kidney (rk), which is consistent with Sarnelli et al. (39.2 ± 21 h) [1]. The ROI-analysis of Method B yielded mean IREHL of 45.8±30h (lk) and 40.9±20h (rk). The ROI-analysis of Method C yielded mean IREHL of 70±68h (lk) and 52.2±37h (rk). To assess the accuracy of the different methods of calculation, the determination-coefficient was calculated for each analysis. Median R2 was 0.992 (lk) and 0.993 (rk) (A), 0.986 and 0.988 (B) and 0.941 and 0.971 for Method C. ***Conclusion:*** The analysis revealed significant deviations between IREHL determined by Method B and C compared to the IREHL determined with Method A. These significant differences and the high fluctuation ranges in the evaluation of the WB result primarily from the often temporally altered superimposition by intestine, other organs such as spleen and liver, and in some cases from the superimposition by metastases. The deviations and the evaluation of the determination-coefficient show that a correct determination of the IREHL via ROI analysis of WB (method B and C) is not possible due to patient-specific differences in the superimposition. The determination must therefore necessarily be carried out via a VOI evaluation of several sequential SPECT images (method A).

EP-1156

Thyroid dosimetry in two common ^{123}I-based neurological studies: a retrospective study

W. Morton, *R. Feathers, J. Freeman, P. Bartholomew; South Tyneside and Sunderland NHS Foundation Trust, Sunderland, UNITED KINGDOM.*

Aim/Introduction: Radioiodine-based radiopharmaceuticals are commonly used in diagnostic nuclear medicine neurological studies. To reduce dose to the thyroid it is common practice to administer stable iodide to the patient prior to injection of the radiopharmaceutical as a thyroid prophylaxis. The aim of this study was to measure the absorbed dose to the thyroid in patients injected with ^{123}I-Ioflupane and ^{123}I-meta-iodobenzylguanidine (MIBG) where the thyroid was not blocked with prophylaxis. ***Materials and Methods:*** A cohort of 80 patients were included in this retrospective study; 39 patients undergoing ^{123}I-Ioflupane SPECT and 41 patients undergoing planar cardiac ^{123}I-MIBG. In the group of patients undergoing ^{123}I-Ioflupane study, 9 received thyroid blocking prophylaxis (120 mg potassium iodide) and the remaining 30 did not; of the 41 patients undergoing cardiac ^{123}I-MIBG, 12 received thyroid prophylaxis and 29 did not. In addition to standard clinical imaging all patients underwent planar scintigraphy of the thyroid. The measured counts in the thyroid were used to calculate the activity of radioiodine in the thyroid using the known sensitivity of the gamma camera to ^{123}I. Calculated cumulative activity in the thyroid was then used to work out the thyroid-thyroid absorbed dose, $D(r_{thy}\text{-}r_{thy})$, following standardised MIRD methodology. ***Results:*** Mean $D(r_{thy}\text{-}r_{thy})$ calculated for the four sub-cohorts of patients in this study were calculated as: ^{123}I-Ioflupane (185 MBq) with prophylaxis 0.0 mGy, ^{123}I-Ioflupane (185 MBq) no prophylaxis 10.8 mGy; ^{123}I-MIBG (370 MBq) with prophylaxis 4.7 mGy, ^{123}I-MIBG (370 MBq) no prophylaxis 17.5 mGy. The range of measured thyroid uptake activity in each patient sub-cohort followed a log(normal) distribution, as expected. ***Conclusion:*** In the UK, national clinical guidelines recommend blocking the thyroid in non-thyroidal radioiodine diagnostic studies where the absorbed dose to the thyroid is >50 mGy. No patient within this study received a thyroid dose greater than this value (maximum 42.2 mGy). We believe these findings could contribute to the justification for not blocking the thyroid in ^{123}I-based neurological studies in cases where administration of the prophylaxis is contraindicated (for example, iodine hypersensitivity or sub-clinical hyper/hypothyroidism). ***References:*** Bochet, L.G. 1999, 40:62S-101S. J. Nucl. Med.

EP-1157

Evaluation of Voxel-Based Dosimetry Using Different Calculation Algorithms in 177Lu-PRRT

M. Masubuchi[1,2], *K. Miwa*[2,3], *N. Miyaji*[3], *T. Yamao*[3], *N. Akiya*[2], *K. Wachi*[2], *S. Kimura*[3], *K. Furuya*[1], *T. Nakamura*[1], *Z. Wu*[1], *A. Iwasaka*[1], *S. Hashimoto*[1], *Y. Hirano*[1];
[1]*Department of Radiology, University of Tsukuba Hospital, Tsukuba, JAPAN,* [2]*Department of Radiological Sciences, Graduate School of Health Sciences, Fukushima Medical University, Fukushima, JAPAN,* [3]*Department of Radiological Sciences, School of Health Sciences, Fukushima Medical University, Fukushima, JAPAN.*

Aim/Introduction: Voxel-based dosimetry is essential in targeted radionuclide therapy (TRT), allowing the estimation of absorbed dose distributions based on serial SPECT/CT imaging. Differences in calculation algorithms can lead to discrepancies in absorbed dose estimates. The present study aimed to evaluate the performance of five voxel-based absorbed dose calculation methods by comparing them with the ground truth absorbed dose (Gy) derived from pharmacokinetic modeling. ***Materials and Methods:*** Ground truth absorbed dose (Gy) was generated using a pharmacokinetic model for 177Lu-DOTATATE with the anthropomorphic ICRP 110 phantom. A 3D-printed phantom (MRT Dosimetry Project) was imaged at six time points (1, 4, 24, 40, 72, and 144 hours post-injection) using SPECT/CT. Volumes of interest (VOIs) were defined for the liver, spleen, kidneys, and tumor. Absorbed doses were calculated using five algorithms: (1) Full Monte Carlo (FMC) using RT-PHITS (EGS5-based, JAEA), (2) Semi Monte Carlo (SMC) using Voxel Dosimetry (Hermes, based on PENELOPE), and three algorithms implemented in OpenDose3D via 3D Slicer—Local Energy Deposition (LED), convolution-based voxel S values (CONV), and full Monte Carlo using GEANT4. Estimated doses were compared to the ground truth, and percent deviations were calculated for each VOI. ***Results:*** Ground truth absorbed dose (Gy) were: liver 1.7, spleen 5.4, right kidney 3.6, left kidney 3.6, tumor 28.1. RT-PHITS, a full Monte Carlo method, showed the highest accuracy for all organs: liver (2.9Gy 72.11%), spleen (5.3Gy -1.71%), right kidney (4.1Gy 12.53%), left kidney (3.9Gy 9.17%), tumor (27.8Gy -1.15%). The spleen and tumor showed high accuracy with deviations within ±2%. Notably, liver doses were consistently overestimated across all software, likely due to the presence of lesions in the liver region. ***Conclusion:*** Algorithm selection influences the accuracy of voxel-based dosimetry in 177Lu-PRRT. RT-PHITS, using the Full Monte Carlo method, provided the highest overall accuracy for all organs. Caution should be exercised when estimating doses in organs containing lesions, as these may lead to over estimation. ***References:*** Kenta Miwa, et al. Feasibility of individual dosimetry using RT-PHITS for patients with SPECT/CT imaging after ^{177}Lu-DOTATATE peptide receptor radionuclide therapy, Phys Eng Sci Med, 2025, in press.

EP-1158

Computational and Nuclear Data Evaluation of an Emerging Therapeutic Copper Radioisotope for Imaging and Dosimetry

M. Mehrabi;
Nuclear Science and Technology Research Institute, Tehran, IRAN, ISLAMIC REPUBLIC OF.

Aim/Introduction: The therapeutic application of beta-emitting radiopharmaceuticals has seen remarkable progress in recent years, particularly in the treatment of neuroendocrine tumors, prostate cancer, and other malignancies. Among emerging candidates, copper-67 ($t_{1/2}$ = 2.6 days) has attracted increasing attention due to its favorable decay characteristics and its chemical compatibility with copper-64, a positron-emitting isotope widely used in diagnostic imaging. ***Materials and Methods:*** This study investigates the imaging and dosimetric characteristics of copper-67 through simulation-driven analysis, leveraging nuclear decay data from IAEA and ICRP databases. Photon emission probabilities, energy spectra, and internal dose coefficients were extracted to model its performance in clinical imaging scenarios. Monte Carlo simulations were used to model photon transport and estimate recovery coefficients (RCs) within a standard anthropomorphic chest phantom, enabling direct comparison with ^{99m}Tc, ^{177}Lu, and ^{64}Cu under identical imaging conditions. ***Results:*** Analysis of nuclear data confirmed the dominant gamma emission at 184.6 keV with a yield of approximately 48.7%, which, in combination with medium-energy collimators, was found optimal for SPECT imaging. Simulated images showed comparable quality to those of ^{177}Lu, with recovery coefficients supporting quantitative accuracy. Dosimetric evaluation using standardized S-values indicated therapeutic beta emissions with a mean energy of 141 keV per decay, suitable for mid-range tissue penetration. ***Conclusion:*** By incorporating nuclear decay and dosimetric data, this study demonstrates the imaging viability and therapeutic potential of copper-67. The findings support its role as a dual-function radionuclide for theranostic applications. Given its favorable physical and radiological properties, copper-67 holds significant promise for future clinical applications, and further investigations into its therapeutic efficacy are strongly encouraged.

EP-1159

Avidination for RadionuclideTHerapy in Nonpalpable Breast Cancer (ARTHE): Dosimetry of a New Locoregional Approach

A. Sarnelli[1], *M. Cremonesi*[2], *E. D'Andrea*[3], *M. Sansovini*[1], *V. Di Iorio*[1], *M. Monti*[1], *P. Sanna*[4], *M. Amadori*[4], *A. Curcio*[4], *P. Possanzini*[4], *I. Grassi*[1], *P. Caroli*[1], *I. Marini*[1], *S. Nicolini*[1], *M. Belli*[1], *V. Mautone*[1], *E. Scarpi*[1], *L. Fabbri*[1], *A. Miserocchi*[1], *G. Paganelli*[5], *F. Falcini*[4], *F. Matteucci*[1];
[1]*Istituto Romagnolo per lo Studio dei Tumori "Dino Amadori", Meldola, ITALY,* [2]*Istututo Europeo di Oncologia, Milano, ITALY,* [3]*Azienda Ospedaliero-Universitaria Policlinico Umberto I, Roma, ITALY,* [4]*AUSL Romagna, Forli, ITALY,* [5]*Istituto Oncologico Romagnolo, Forli, ITALY.*

Aim/Introduction: "Avidination for RadionuclideTHerapy in Nonpalpable Breast Cancer (ARTHE)" is an innovative nuclear medicine approach for the management of early breast cancer. Few days after a Vacuum Assisted Breast Biopsy (VABB), in the presence of cancer, avidin is injected under ultrasound guidance into the VABB cavity followed by an injection of Biotin-DOTA-90Y. The goal in terms of absorbed dose prescription is to deliver about 200 Gy to the residual microscopic disease into the target volume surrounding the VABB cavity. This phase-I study investigates three activity levels of 90Y Dota-biotin and evaluates side effects and biodistribution of avidin-biotin-DOTA-90Y after loco-regional injection. ***Materials and Methods:*** The empty cavity volume resulting after the VABB procedure ranges between 1 and 1.7 ml and the radioactive solution is meant to be injected within such a cavity. Three activity levels are investigated: 28, 57 and 126 MBq. A standard scintigrafic whole-body image and a PET image are acquired at 1-3 h p.i to exclude the possibility of wash-out from the lesion site and to perform dosimetry, respectively. In a cohort of 18 patients, serial PET images are acquired at different time points. A dedicated software is used to segment the region of interest, to quantify the activity inside the target region. A MonteCarlo (MC) simulation of the dose profile inside and outside the cavities is performed to evaluate the dose in the tissues surrounding the cavity, where residual microscopic disease is generally still present. The adsorbed dose is estimated at different distances (1-3 mm) from the cavity edge with and without diffusion. PET images are processed in order to generate individualized input source and geometry files for dose computation with the MC approach. ***Results:*** We simulate the dose profiles for various cavity geometries and volumes. The three levels of activity investigated result in a 200 Gy absorbed dose at the edge of the cavity. The dose strongly decreases as a function of the distance, sparing the healthy tissues. Thanks to the cross-fire effect and the range of beta particles, the diffusion guarantees higher doses to the microscopic disease surrounding the VAAB cavity than without diffusion. ***Conclusion:*** The dose strongly depends on the assumption made on the cavity volume and on the distance from the injection site. The outcome also depends on the operator's experience. Further investigations are needed to correlate the absorbed dose with the clinical follow-up and the anatopathological results.

EP-1160

Optimizing CD44v6-Targeted Radioimmunotherapy: A Retrospective Red Marrow Dosimetry Comparison of ^{186}Re, ^{177}Lu, and ^{161}Tb

J. Hemmingsson[1], *M. Nestor*[2], *A. Lundgren Mortensen*[3], *F. Y. Frejd*[4], *P. Bernhardt*[1];
[1]*University of Gothenburg - Sahlgrenska Academy, Gothenburg, SWEDEN,* [2]*Department of Immunology, Genetics and Pathology, Science for Life Laboratory (SciLifeLab), Uppsala, SWEDEN,* [3]*Department of Molecular Medicine and Surgery, Karolinska Institutet, Gothenburg, SWEDEN* [4]*Department of Immunology, Genetics and Pathology, Science for Life Laboratory (SciLifeLab), Uppsala University, Uppsala, SWEDEN.*

Aim/Introduction: CD44v6-targeted radioimmunotherapy (RIT) has emerged as a promising treatment for several cancers with limited therapeutic alternatives. The slow clearance of full-sized antibodies from the bloodstream promotes tumor uptake but also increase radiation exposures to risk organs, such as to the radiosensitive red marrow. While emerging therapies tend to favor medium- to short-range electron emitters like 177-lutetium or 161-terbium, clinical studies have evaluated bivatuzumab (BIWA 4), labelled with the long range beta emitter 186-rhenium, demonstrating tumor response and acceptable tolerability (1, 2). The aim of this study is to retrospectively estimate the red marrow absorbed dose for ^{186}Re, ^{177}Lu, and ^{161}Tb using published clinical data, and compare these estimates with previously reported values. ***Materials and Methods:*** Multiple time-point data on activity concentrations in serum (n=20) and bone marrow aspirate (n=9) from the two clinical trials with ^{186}Re-BIWA 4 was used as input for a compartment model. The model assumes no specific uptake in the red marrow, which is supported by the data where activity concentrations in the bone marrow supernatant is, on average, 4 times higher than for the cell pellet. After correcting for the differing physical half-lives, radionuclide-specific biodistributions were generated for ^{186}Re, ^{177}Lu, and ^{161}Tb. Red marrow absorbed doses were estimated using blood-based and aspiration-based dosimetry methods, in addition to the blood-based approach used in the original study, which was applied only for ^{186}Re. ***Results:*** The blood-based method, assuming equivalence between plasma and extracellular red marrow activity concentrations, resulted in skeletal-averaged absorbed doses to red marrow of 0.37, 0.22, and 0.34 Gy/GBq for ^{186}Re, ^{177}Lu, and ^{161}Tb, respectively. Although calculated differently, switching to supernatant activity concentrations from bone marrow aspirate produced similar estimates: 0.33, 0.21, and 0.31 Gy/GBq. Combining our serum biodistribution data for ^{186}Re with the original dosimetry approach yielded red marrow doses of 0.61 and 0.47 Gy/GBq for males and females, respectively, values closely matching the originally reported 0.64 and 0.49 Gy/GBq. ***Conclusion:*** For CD44v6-targeted RIT, the blood-based methodology produces red marrow absorbed dose estimates comparable to those from bone marrow aspirate. These estimates are crucial for guiding the optimization of radionuclide therapies by informing the selection of radionuclides and activity levels that balance therapeutic efficacy with haematological safety. As such, accurate red marrow dosimetry plays a central role in the development of safer and more effective RIT strategies. ***References:*** 1.Börjesson PK et al. Clin Cancer Res. 2003 2.Koppe M et al. Cancer Biother Radiopharm. 2004

EP-68

e-Poster Area

D: Technical Studies -> D4 Dosimetry and Radiobiology -> D42 Clinical Radiobiology

EP-1161

Deep Longitudinal Immunophenotyping of Immune Cells in Patients with Metastatic Castration-Resistant Prostate Cancer Treated with ^{212}Pb-based PSMA-Targeted Alpha Therapy

A. Soderholm[1], *A. Karmann*[1], *A. Hansen*[2], *S. Sandhu*[3], *C. Sweeney*[4], *L. Leveque-El Mouttie*[5], *D. Wyld*[6], *M. Baronet*[1], *N. Esteban*[1], *M. Crumbaker*[1], *L. Skingley*[1], *T. Kryza*[1], *P. Santoro*[1], *G. Li*[1], *S. Puttick*[1], *S. Shakti*[1], *S. Rose*[1];
[1]*AdvanCell Pty Ltd, Sydney, AUSTRALIA,* [2]*Princess Alexandra Hospital, Brisbane, AUSTRALIA,* [3]*Peter MacCallum Cancer Centre, Melbourne, AUSTRALIA,* [4]*University of Adelaide, Adelaide, AUSTRALIA,* [5]*Translational Research Institute, Brisbane, AUSTRALIA,* [6]*Royal Brisbane and Women's Hospital, Brisbane, AUSTRALIA.*

Aim/Introduction: Radioligand therapies (RLT) represents a promising modality for cancer treatment. However, the effects of

RLT on immune cell populations and the potential for immune biomarkers to predict treatment responses and optimise treatment are not yet understood. This research aims to design and validate a full-spectrum flow cytometry panel for the detection of immune cell populations in blood samples from patients with metastatic castration-resistant prostate cancer (mCRPC) who received ^{212}Pb-based PSMA-targeted RLT, ^{212}Pb-ADVC001, in the TheraPb study (NCT05720130). Following panel validation, immune cell populations will be characterised to identify potential immune biomarkers that may predict treatment response and guide the selection of novel therapeutic combinations for future studies. ***Materials and Methods:*** A 32-color flow cytometry panel was developed for deep immunophenotyping of the major immune cell subsets present in the peripheral blood of mCRPC patients using a 5-laser full-spectrum cytometer (Cytek Biosciences). Markers and gating strategies to identify immune populations including CD4 T cells, CD8 T cells, regulatory T cells, gamma-delta T cells, NKT-like cells, B cells, NK cells, macrophages, monocytes, and dendritic cells were optimised. The panel allows for further characterisation of each cell type using activation and differentiation markers, enabling identification of 35 distinct immune subpopulations. The Cytek Panel Builder and AI-guided SpectroPanel tool were used for fluorescent tag assignment, assessment of panel complexity, and selection of commercially available antibodies. Cryopreserved peripheral blood mononuclear cells (PBMCs) from patients receiving ^{212}Pb-ADVC001 in the TheraPb trial were used to validate the panel before analysing temporal changes in PBMC populations longitudinally. ***Results:*** A novel flow cytometry panel has been developed to study immune cell populations in patients with mCRPC treated with ^{212}Pb-ADVC001. Clear resolution of all immune populations was achieved, with the gating strategy reliably identifying 35 distinct immune subpopulations. Fluorescence spillover and spectral overlap were minimal. The assay effectively monitors PBMC changes in both fresh and cryopreserved samples. ***Conclusion:*** We present a novel flow cytometry panel specially tailored to phenotype immune cell populations in patients treated with ^{212}Pb-ADVC001. The panel has potential to provide valuable insights into the adaptive immune response in subjects treated with targeted alpha therapies. The presented approach may also be beneficial in predicting response and optimising dosing schedules, enabling biomarker driven adaptive dosing regimens. Results from preliminary analyses showing changes in immune cell populations elicited by ^{212}Pb-ADVC001 during treatment will be presented.

EP-1162

Optimizing Radiopharmaceutical Dosage in Pediatric SPECT-CT

M. Weymeskirch, *F. Hubele, O. Allegrini, J. Salvadori, C. Porot;*
Institut de Cancérologie Strasbourg Europe (ICANS), Strasbourg, FRANCE.

Aim/Introduction: The European Association of Nuclear Medicine (EANM) pediatric dosage card provides essential guidance for adjusting radiopharmaceutical (RP) activity according to patient weight and RP type. However, certain clinical situations fall outside established standards, in which explicit recommendations are lacking, particularly for high-weight children and adolescents, or less common procedures. This study aims to evaluate how these gaps are addressed in clinical practice and to identify areas in need of clarification or standardization. ***Materials and Methods:*** This retrospective study included 451 pediatric SPECT-CT (single-photon emission computed tomography/computed tomography) scans performed between January 2023 and December 2024 at the nuclear medicine department. Data on patient age, weight, RP type, and administered activity were collected using Pharma Manager®. When applicable, administered activities were compared to the EANM dosage card (version 2016). Special attention was paid to cases not covered by standard recommendations. A multidisciplinary team reviewed these scenarios to propose protocol improvements. ***Results:*** Pediatric SPECT-CT examinations represent approximately 2.5% of annual nuclear medicine procedures at the department. Most procedures, including bone scintigraphy (HDP), static renal imaging (DMSA), and dynamic renal imaging (MAG3) were compliant with EANM dosage card guidelines. However, several gaps in standardization were noted:Patients over 68 kg (13 examinations): The dosage card provides no pediatric guidance for this group. Adjustments were made using capped pediatric protocols or adult dosages, based on clinical judgment and required image quality.Uncommon procedures: For gastric emptying studies (7 examinations), no official dosage card recommendations exist. Dosing decisions were guided by EANM publications, published case studies, or expert consensus. ***Conclusion:*** Our findings highlight the limitations of the current EANM dosage card in certain pediatric scenarios. Local adaptation and multidisciplinary decision-making remain essential for managing high-weight young patients and rare procedures. We recommend extending the EANM dosage card to include patients up to 100 kg and to incorporate less common pediatric procedures such as Meckel scintigraphy and gastric emptying studies. These updates would contribute to greater harmonization, reduce variability in clinical interpretation, and enhance the safety and consistency of pediatric nuclear medicine across institutions.

EP-69

e-Poster Area

D: Technical Studies -> D5 Radiopharmacy/ Radiochemistry -> D51 Radionuclide Production

EP-1163

Improving the target design for enriched Iridium-192 production for brachytherapy

S. Kashi, *A. Nourouzi, M. Dehghan, A. Naserbegi, M. Behzadi, M. Mehrabi, M. Asadian;*
Advanced Technologies Company of Iran, Tehran, IRAN, ISLAMIC REPUBLIC OF.

Aim/Introduction: Iridium-192 is a significant radioactive isotope utilized in the medical field, particularly in brachytherapy. It is produced through (n,γ) reactions in a nuclear reactor under neutron flux. Ir-192 decays by emitting beta and gamma particles, with maximum energies of 0.672 MeV and 0.604 MeV, respectively. Ir-192 is effective for treating tumors in various organs, including the breast, tongue, prostate, and brain, due to its relatively low energy gamma emission (0.412 MeV), allowing for precise targeting. The design of targets for the production of Ir-192 is influenced by the specific activity of the isotope, which depends on the enriched isotope, density and geometric dimensions of the target. ***Materials and Methods:*** In this study, enriched Ir-191 was produced to 99% in the form of IrF6 through a gas separation process. Following the separation, the Ir-191 was converted into powdered Ir, which was then shaped into or wire lengths of 0.6 x 3.5 mm, achieving a purity of 99.9%. The density of the disks was measured, resulting in a range of 14-23 g/cm^3, as confirmed by experimental results. The specific activity of Ir-192 was evaluated using the Monte Carlo method with the MCNP-2.6 code under the thermal flux of 7.0E+13 n/cm^2. ***Results:*** The results indicated that reducing the density and thickness of the target significantly increased the specific activity of Ir-192. Experiments showed that lower density targets yielded higher specific activity, which corroborated the computational findings. The optimal design parameters for the production of Ir-192 were

identified, demonstrating how modifications in target geometry and composition can enhance yield and effectiveness. The calculation results for densities between14 and 23 g/cm^3, show specific activities of 1200 to 970 ci/g. So by reducing the density, higher specific activities are obtained. ***Conclusion:*** The findings confirm that adjustments in target density can lead to increased specific activity, making Ir-192 more effective for brachytherapy. Considering the self-shielding effect and high absorption cross-section, the specific activity of Ir-192 depends on the density of the target. ***References:*** IAEA-TECDOC-1340. Manual for reactor produced radioisotopes. January 2003

EP-1164

Innovative cation-exchange strategies towards cost-effective terbium/gadolinium separations

A. Moiseeva[1], *P. V. Grundler*[1], *Z. Gao*[2], *J. W. Engle*[2], *N. P. van der Meulen*[1];
[1]*Paul Scherrer Institute, Villigen PSI, SWITZERLAND,* [2]*University of Wisconsin–Madison, Madison, WI, UNITED STATES OF AMERICA.*

Aim/Introduction: Lanthanide separation is challenging due to the similar chemical properties and atomic radii of these elements. However, the emergence of radiolanthanides in nuclear medicine has motivated pursuit of robust, reliable, fast, and cost-efficient separation methods. In this work, a commercial cation exchange resin was studied to determine its potential for isolating no-carrier-added terbium from gadolinium target. Terbium radioisotopes could cover the whole spectrum of nuclear medicine since there are positron and photon emitters ideally suited for diagnosis, and β$^-$-/Auger- and α-emitters used for therapy, thus expanding significantly the field opened by ^{177}Lu and currently a standard in targeted radionuclide therapy. ***Materials and Methods:*** AG MP-50 macroporous cation exchange resin was evaluated by means of bench experiments. Distribution coefficients for gadolinium, terbium, and dysprosium were measured. Chromatographic columns (10 mm × 150-180 mm) containing AG MP-50 resin (NH_4^+ form) were loaded with 10-50 µg of terbium and dysprosium (from ICP analytical standards) and with up to 115 mg of natural gadolinium oxide dissolved in 1 mL 8-10 M HNO_3. Elution was performed with α-hydroxyisobutyric acid (α-HIBA), and collected fractions were analyzed by ICP-OES. ***Results:*** According to the distribution coefficients, the most optimal concentration of the α-HIBA eluent was 0.13 M (pH 4.5), where the calculated Tb/Gd separation factor (S_F) was determined at 3.3. For dynamic experiments, dissolution, saturation, loading, and rinsing steps were optimized to achieve the efficient separation of 10 µg of terbium from up to 50 mg of gadolinium with $S_F > 10^5$, confirmed by ICP-OES analysis. The yield of terbium in this case was higher than 99 %. The volume of the purified terbium fraction is ~ 45-50 mL, which allows the collection of terbium fraction to be controlled, e.g., for implementation in a hot cell. ***Conclusion:*** A method to separate terbium from gadolinium oxide material was developed using a commercially available cation exchange resin. The technique produced results promising for ^{155}Tb and ^{161}Tb production (1, 2). It has been effective using trace terbium activities and will be applied to higher activities soon. ***References:*** 1. Favaretto, C., Talip, Z., Borgna, F., et al. (2021). Cyclotron production and radiochemical purification of terbium-155 for SPECT imaging. EJNMMI Radiopharm. Chem. 6, 37. 2. Gracheva, N., Müller, C., Talip, Z., et al. (2019). Production and characterization of no-carrier-added ^{161}Tb as an alternative to the clinically-applied ^{177}Lu for radionuclide therapy. EJNMMI Radiopharm. Chem. 4, 12.

EP-1165

High efficiency isolation of theranostic terbium radioisotopes from gadolinium with cation exchange chromatography

Z. Gao[1], *E. Aluicio-Sarduy*[1], *A. N. Moiseeva*[2], *T. E. Barnhart*[1], *N. P. van der Meulen*[2,3], *J. W. Engle*[1,4];
[1]*University of Wisconsin – Department of Medical Physics, Madison, WI, UNITED STATES OF AMERICA,* [2]*PSI Center for Life Sciences - Center for Radiopharmaceutical Sciences, Villigen, SWITZERLAND,* [3]*PSI Center of Nuclear Engineering and Sciences - Laboratory of Radiochemistry, Villigen, SWITZERLAND,* [4]*University of Wisconsin - Department of Radiology, Madison, WI, UNITED STATES OF AMERICA.*

Aim/Introduction: Terbium radioisotopes are interesting for theranostic nuclear medicine [1]. Their purification from accelerator and reactor feedstock materials is challenging, as for the entire lanthanide series' similar fundamental chemistries [2]. In this study, Aminex 50W-X4 and -X6 resins were investigated for their ability to efficiently isolate no-carrier-added (n.c.a.) terbium radioisotopes from macroscopic quantities of gadolinium. ***Materials and Methods:*** Distribution coefficients (K_d) were measured to identify the most suitable candidate from two sulfonic-acid-based resins for dynamic (column) experiments. Both resins were tested using dissolved $^{nat}Gd_2O_3$ and terbium ICP standard or cyclotron-irradiated $^{nat}Gd_2O_3$. Columns containing resin (10x143mm, NH_4^+ form) were loaded with gadolinium and terbium in HNO_3 media and eluted with 0.13 M α-HIBA solution adjusted to pH 4.5 with NH_4OAc. Fractions collected from experiments with stable isotopes were analyzed by ICP-OES. Sequential proton and deuteron irradiations of pressed pellets of $^{nat}Gd_2O_3$ produced, among others, ^{156g}Tb ($t_{1/2}$ = 5.35d, 100% EC, 67% 534.29keV γ) and ^{159}Gd ($t_{1/2}$ = 18.479h, 100% , 11.78% 363.543keV γ) for tracer experiments. Eluent fractions were analyzed with HPGe. ***Results:*** K_d measurements indicated that both resins have potential for Gd/Tb separation. In dynamic experiments, resolution between gadolinium and terbium improved with decreasing HNO_3 concentrations in load solutions and at lower flow rates. Targets were dissolved in 6mL 1.3M HNO_3 and loaded at 0.5mL·min^{-1}. In these optimized conditions, 50W-X6 resin experiments recovered more than 99.99% of terbium from 40mg gadolinium (Tb/Gd $S_F > 10^5$) and 99.97% of ^{156}Tb from 40mg irradiated $^{nat}Gd_2O_3$ (Tb/Gd $S_F > 10^5$). 50W-X4 results were less promising. The limit of detection of gadolinium by ICP-OES was 0.01ppm. ***Conclusion:*** Aminex 50W-X6 shows potential for efficient isolation of terbium radioisotopes from gadolinium targets. The method can be used to isolate reactor-produced ^{161}Tb (β$^-$) and charged-particle produced ^{152}Tb (β$^+$) and ^{155}Tb (γ) radioisotopes. ***References:*** [1] DOI: 10.1007/s00259-013-2563-z [2] DOI: 10.1016/j.nucmedbio.2023.108389

EP-1166

Prospects of Tb-161 production

U. Köster[1], *I. Cieszykowska*[2], *R. Mikolajczak*[2], *N. Buczkó*[3], *K. Gméling*[3], *Z. Kis*[3], *B. Maróti*[3], *M. Capogni*[4], *L. Lepore*[5], *L. Spagnuolo*[5], *B. Ponsard*[6], *M. Van de Voorde*[7], *P. V. Grundler*[8], *N. P. van der Meulen*[8,9];
[1]*Institut Laue-Langevin, Grenoble, FRANCE,* [2]*NCBJ, POLATOM, Otwock, POLAND,* [3]*HUN-REN EK-CER, Budapest, HUNGARY,* [4]*ENEA, NUC-INMRI, Casaccia, ITALY,* [5]*ENEA, NUC-IRAD-CRGR, Casaccia, ITALY,* [6]*SCK CEN, BR2 Reactor, Mol, BELGIUM,* [7]*SCK CEN, Nuclear Medical Applications, Mol, BELGIUM,* [8]*PSI Center for Life Sciences, Villigen-PSI, SWITZERLAND,* [9]*PSI Center for Nuclear Engineering and Sciences, Villigen-PSI, SWITZERLAND.*

Aim/Introduction: Tb161 is an emerging radionuclide for therapeutic applications. It emits low-energy beta particles as well as conversion electrons and Auger electrons. Tb161 in no-carrier-added (n.c.a.) quality is produced by thermal neutron capture on enriched Gd-160 targets, followed by decay of short-lived Gd161 to Tb161 and a radiochemical Gd/Tb separation. Yields and radionuclidic purity of the produced Tb161 depend directly on the quality of the target material, i.e. its enrichment level and chemical purity, and on the irradiation conditions. ***Materials and Methods:*** Activation calculations and test irradiations of different enriched Gd-160 targets have been performed for different neutron flux conditions at different research reactors: RHF operated by ILL Grenoble, MARIA operated by NCBJ Swiérk, BRR operated by HUN-REN EK-CER Budapest and TRIGA RC-1 operated by ENEA Casaccia. ***Results:*** The measured Tb161 yields scale roughly proportionally to the thermal neutron flux, indicating that "product burnup" of Tb161 by subsequent neutron captures is not a limiting factor. The residual content of Gd157 and Gd155 in enriched Gd160 determines the magnitude of neutron self-shielding in larger targets and hence may limit the scale-up of production. Tb159 as chemical impurity and Gd158 as isotopic impurity in a Gd-160 target would lead to reduced molar activity of the produced Tb161 and admixture of traces of longer-lived Tb160. Therefore, highly enriched and chemically pure Gd160 targets are required to produce Tb161 in true n.c.a. quality. ***Conclusion:*** Based on the nuclear physics properties that are decisive for this production path, high-purity n.c.a. Tb161 could be produced at a comparable scale and roughly similar costs as n.c.a. Lu177, but the availability of highly enriched Gd-160 target material remains a prerequisite. ***References:*** This project has received funding from the European Union under grant agreement No 101061230 (SECURE), from the European Union's Horizon 2020 research and innovation programme under grant agreement No 101008571 (PRISMAP) and from the French Institut National du Cancer under grant agreement No INCA_16111 (PLBIO21-243). Part of the isotopes used in this research were supplied by the U.S. Department of Energy Isotope Program, managed by the Office of Isotope R&D and Production.

EP-1167

Preparation of Large-Area 203Tl Targets for Medical Radionuclide Production

J. Chen, *Z. Liu;*
Peking University, Beijing, CHINA.

Aim/Introduction: High-purity thallium-203 (^{203}Tl) targets are critical precursors for cyclotron-based production of diagnostic radionuclides such as ^{201}Tl and ^{203}Pb. To enhance production yield, advanced target designs with inclined geometries and minimized beam-target angles are employed to distribute high beam power over larger areas, improving heat dissipation. However, achieving uniform electrodeposition of Tl on large or irregularly shaped substrates remains a significant challenge. ***Materials and Methods:*** A thallium nitrate ($TlNO_3$) solution was prepared in deionized water as the plating bath, supplemented with , ethylenediaminetetraacetic acid (EDTA), and the surfactant BRIJ-35 (to reduce overpotential). Silver sheets served as substrates for circular (φ10 mm) or rectangular (14 mm × 150 mm) electroplating. The bath pH was maintained at 8-9.5 using NaOH or H_2SO_4. Electrodeposition was performed under square-wave voltage (1~10 Hz) with a magnetic stirrer (300 rpm), a maximum current density of 15 mA/cm^2, and controlled bias (forward: 10 mA/cm^2, reverse: 2~3 mA/cm^2). Post-plating, targets were rinsed with water/ethanol, dried, and evaluated for thickness uniformity, material recovery, and mechanical stability. ***Results:*** The optimized protocol achieved a uniform Tl deposit of 1023 mg/cm^2 on φ10 mm circular areas. For irregular geometries, a 14 mm × 150 mm rectangular substrate exhibited a homogeneous thickness of 415 mg/cm^2. EDTA ensured stable Tl^+ solubility, while BRIJ-35 mitigated localized overpotential, enabling smooth deposition. Hydrazine hydrate effectively suppressed prevents Tl^+ oxidation to Tl^{3+} at the anode. The square-wave voltage strategy enhanced adhesion and thickness control, critical for high-power irradiation. ***Conclusion:*** A reproducible electroplating method was developed for large-area ^{203}Tl targets, addressing challenges in uniformity, adhesion, and scalability. By integrating alternating current and optimized bath chemistry, this approach enables robust fabrication of high-thickness Tl coatings suitable for cyclotron irradiation, advancing the production efficiency of medical radionuclides.

EP-1168

Cyclotron-Based ^{64}Cu Production from ^{64}Ni: MCNPX Simulation and theoretical Validation

Z. Karimi, *H. Azizakram, A. Abolhosseini Shahrnoy;*
Parsisotope Company, Tehran, IRAN, ISLAMIC REPUBLIC OF,

Aim/Introduction: ^{64}Cu is a versatile radionuclide widely used in positron emission tomography (PET) and targeted radionuclide therapy due to its favorable decay properties (β^+, β^-, half-life: 12.7 hours). This study investigates the production and optimization of ^{64}Cu via the ^{64}Ni(p,n)^{64}Cu reaction in a low-energy cyclotron, focusing on simulation-based yield predictions. A key challenge to successful radiolabeling in medical applications is minimizing impurities from competing reaction channels while maintaining high activity. ***Materials and Methods:*** The production process was simulated using the Monte Carlo code MCNPX, with reaction cross-sections calculated from the ENDF/B-VII library. Enriched 64Ni (99.53%) target was designed using SRIM code, optimizing geometry based on stopping power calculations to match experimental setups of a CYCLON30 cyclotron. Proton energies (6 - 13 MeV) were evaluated to maximize the ^{64}Ni(p,n)^{64}Cu cross-section while minimizing impurities. According to the ^{64}Ni(p,n)^{64}Cu excitation function, the highest yield of this nuclear reaction is expected at 11.66 MeV incident proton beam energy, with good efficacy in the 6-13 MeV range, thus avoiding the opening of unwanted channels, resulting in isotopes from competitive nuclear reactions. The target was irradiated at a beam current of 20 µA for 4 hours. The thick target yield was estimated using excitation functions and stopping power data. ***Results:*** Simulations showed optimal ^{64}Cu production at 6-13 MeV proton energy, balancing high cross-section (≈800 mb) and low impurity levels. For 4-hour irradiations with 20 µA current, theoretical activities at end of bombardment (EOB) were 277 ± 13.9 mCi and the simulation result of 236 ± 20.1 mCi. The thickness of target material to satisfy the energy range of 6-13 MeV evaluated is 600 µm. simulation results agreed with theoretical predictions within acceptable deviation, confirming model reliability. ***Conclusion:*** This study validates MCNPX-based simulations to evaluate and optimize ^{64}Cu production in low-energy cyclotrons. These findings inform future strategies for enhancing medical radionuclide production. ***References:*** 1. Baruta, S., Leonte, R., Cocioaba, D., Craciun, L., Ur, C. A., & Niculae, D. (2022). Cyclotron production of 64Cu by proton irradiation of enriched 64Ni target: Validation of Geant4 simulation parameters through experimental data. Frontiers in Physics, 10, 1038014.

EP-1169

Development of a New Solid-State ^{229}Th/^{225}Ac Generator Design

E. Yalcintas Bethune, *A. Cosby, A. Younes, C. Dunckley, J. Larrabee, J. Camacaro, P. de Roos, R. Sumner, S. Tanzey, Q. Pham, L. Lilley;*
TerraPower, Bellevue, WA, UNITED STATES OF AMERICA.

Aim/Introduction: In this work, we present on-going research to develop a single stage bulk separation of ^{225}Ac from its parent, ^{229}Th. ^{225}Ac ($t_{1/2}$ = 9.92 days) is a unique isotope within the

envelope of medically relevant radioisotopes; as an alpha emitter (4 alpha emissions per ^{225}Ac) it is among the few contending actinides for radiopharmaceutical applications, specifically for the development of targeted alpha therapeutics. The most direct and radio-isotopically pure route to obtain ^{225}Ac is from the routine harvest of its long-lived parent ^{229}Th ($t_{1/2}$ = 7932 y) that naturally decays to ^{225}Ac via ^{225}Ra. The high activity of ^{229}Th and its progeny presents unique challenges for large sized generators, such as: (i.) degradation of organic resins; (ii.) buildup of pressure (from water radiolysis) creating operational challenges for solution-based generators; (iii.) exposure of high dose to the materials and equipment used for storage and process. ***Materials and Methods:*** The proposed separation is based on solubility phenomena where tetravalent ^{229}Th forms a solid $ThO_2.xH_2O$(s) in equilibrium with its solubility product. Trivalent actinides are not chemically hydrolyzed at pH <6 thus, we expect ^{225}Ac to be soluble under the same conditions. The difference between Th and Ac oxide solubilities provides the basis for a single-stage bulk separation. A proof-of-concept experiment confirmed the feasibility of this generator system. ***Results:*** . ^{225}Ac is harvested from 1 mg ^{229}Th with 100% yield based on HPGe data. The ^{225}Ac/^{225}Ra separation is achieved through extraction chromatography using a UTEVA resin, followed by DGA resin and prefilter resins. The final ^{225}Ac product has been analyzed by analytical methods, including HPGe and iTLC, to confirm that the ^{225}Ac yield is as expected, there is no ^{229}Th nor ^{225}Ra breakthrough, and 98.9% radiolabeling yield is achieved. The yield and purity profile of this generator design will be presented. ***Conclusion:*** The ability to utilize fixed, solid state ^{229}Th generators provides a valuable tool in increasing the stable supply of clinical grade ^{225}Ac to radiopharmaceutical drug development, with the goal of supporting widespread treatment of cancer patients via ^{225}Ac based targeted alpha therapy.

EP-1170

Investigation of ^{161}Tb radionuclide production for therapy application via neutron induced reaction

H. Azizakram, *Z. Karimi;*
Pars Isotope Company, Tehran, IRAN, ISLAMIC REPUBLIC OF.

Aim/Introduction: ^{161}Tb has gained recognition as a promising radionuclide in nuclear medicine specially in targeted radionuclide therapy (TRT) due to its favorable decay characteristics. The aim of this study was to investigate the production and optimization of ^{161}Tb via indirect neutron induced reaction, ^{160}Gd(n,γ)^{161}Gd→(3.66 min, β^-)^{161}Tb in Tehran Research Reactor (TRR). This study focused on simulation and theoretical activity investigation at the end of bombardment (EOB). ***Materials and Methods:*** The TRR was simulated via MCNPX and the bulk of target were designed in central part of TRR's core. The enriched target of $^{160}Gd_2O_3$ (98%) were irradiated via thermal neutron flux of 4×10^{13} n.cm^{-2}.s^{-1}. Various target weight of 10 mg, 50 mg and 100 mg were selected. The irradiation time was determined to be 3 and 4 times of the ^{161}Tb half-time (6.89 days) to optimize the production process. The use of an enriched $^{160}Gd_2O_3$ target material is essential to minimizing the generation of impurities and optimizing its suitability for medical applications. After irradiation, the neutron distribution function and cross section of ^{160}Gd(n,γ)^{161}Gd reaction were calculated via MCNPX code and ENDF/B-VII library and compared with the theoretical activity. ***Results:*** Simulation of ^{161}Tb production via the ^{160}Gd(n,γ)^{161}Gd→^{161}Tb reaction in the TRR were conducted using MCNPX. The target of $^{160}Gd_2O_3$ (98%) was positioned in central part of reactor core with thermal neutron flux of 4×10^{13} n·cm^{-2}·s^{-1}. The simulation and theoretical activities at the EOB were calculated. At 20.67 days of irradiation, the theoretical activities for 10 mg, 50 mg, and 100 mg targets were 0.786, 3.93 and 7.86 GBq, respectively, while the corresponding simulated activities were 0.731, 3.68 and 7.21 GBq. For the extended irradiation period of 27.56 days, theoretical activities increased to 0.842, 4.21 and 8.42 GBq for the respective target masses, with simulated activities showing comparable results at 0.782, 3.91 and 7.92 GBq. In All cases, the activity increased as a result of the increased target mass and prolonged irradiation time. ***Conclusion:*** This study demonstrates the potential of simulation-based approaches for predicting ^{161}Tb production, highlighting the need for higher neutron flux to achieve clinically relevant activity levels. ***References:*** 1. Holiski, C. K., Bender, A. A., Monte, P. F., Hennkens, H. M., Embree, M. F., Wang, M. J. V., ... & Mastren, T. (2024). The production and separation of ^{161}Tb with high specific activity at the University of Utah. Applied Radiation and Isotopes, 214, 111530.

EP-1171

Ensuring Radionuclidic and Chemical purity of Actinium-225 from Thorium-229 generator

J. Camacaro, *C. P. Dunckley, P. de Roos, Q. Pham, R. Sumner, S. Tanzey, A. L. Lakes, E. Yalcintas Bethune, L. M. Lilley, A. Younes;*
TerraPower Isotopes, Bellevue, WA, UNITED STATES OF AMERICA.

Aim/Introduction: ^{225}Ac is currently being utilized in clinical trials (Phases I - III) evaluating targeted alpha therapy in cancer treatments. Several production methods are being investigated in the industry to enable large-scale production of ^{225}Ac. This work examines ^{225}Ac produced from ^{229}Th generators. Given the stringent quality control requirements expected for radiopharmaceutical, harvesting ^{225}Ac from ^{229}Th generators demands precise and reliable analytical methods to assess ^{225}Ac purity. This is done by observing, or eliminating the possible presence of, any parent radionuclides (^{229}Th and/or ^{225}Ra), and other potential contaminants (e.g., trace metals) while minimizing time and labor costs. ***Materials and Methods:*** In this work, we disclose the measurement techniques employed, with an emphasis on instrumentation selection, method conditions, detection limits, and the strategy used to optimize the radionuclidic and chemical purity measurements. Additionally, we present our method for calibrating the gamma detectors using a counting geometry directly on the detector surface, accounting for summing effects to ensure accurate quantification. ***Results:*** Our results demonstrate that radionuclidic purity exceeding 99.7% could be measured using a combination of alpha and gamma spectroscopy in a timely manner. Metallic impurities were assessed via a triple quadrupole Inductively Coupled Plasma Mass Spectrometry (ICP-MS), where the use of various reactive gases effectively mitigated polyatomic interferences, enhancing the precision and reliability of the results. Final product attributes were confirmed through radiolabeling with DOTA (1,4,7,10-Tetraazacyclododecane-1,4,7,10-tetraacetic acid) as a chelator commonly used for targeted alpha therapeutics, achieving radiolabeling yields greater than 95%. ***Conclusion:*** Together, these methodologies offer a comprehensive and reliable analytical framework of ^{225}Ac. This work supports the advancement of ^{225}Ac for targeted alpha therapy and contributes to the development of scalable quality control processes for radiopharmaceutical production.

EP-1172

Critical Control Points study in the production process of Mo-99/Tc-99m generators in Ezeiza Atomic Centre

D. Camporotondi*;*
Comisión Nacional de Energía Atómica, Buenos Aires, ARGENTINA.

Aim/Introduction: This work focuses on identifying Critical Control Points (CCP) within the process of producing Mo-99/Tc-99m generators in the Radioisotopes Production Plant of Ezeiza Atomic Centre (CNEA-Argentina). Tc-99m radiopharmaceuticals are still the major diagnostic tools in clinical nuclear medicine worldwide. Complying with regulations set by regulatory entities such as the Nuclear Regulatory Authority (ARN) and the National

Administration of Drugs, Foods and Medical Technology (ANMAT) is mandatory to ensure quality of manufactured products and safety of patients. Generator production is a complex process that involves multiple steps and requires proper management of quality risks. ***Materials and Methods:*** In this study, we carried out an in-depth analysis of the complete process from the obtention of sodium molybdate solution (fission Mo-99), to the assembly of all generator components, including quality controls required to comply European Pharmacopoeia standards. Flow-charts, Ishikawa diagrams and FMEA analysis tools were applied to each step of production process, to organize data and structure risk management to evaluate the potential failure modes throughout the whole process. The Risk Priority Number (RPN) is calculated by multiplying the severity, occurrence, and detection of each failure mode identified. Afterward, Hazard analysis and critical control points (HACCP) tool was applied to establish critical limits, monitor the CCPs and determine corrective actions to be taken. ***Results:*** Data analysis showed 10 CCPs related to physical, biological and chemical risks, leading to the suggestion of the modification of the process. As a result, the RPN were reduced for 2 CCPs, lowering the probability of occurrence and also excluding them from being considered as CCP. Those related to the skills and attention of workers will be constantly monitored to ensure the prevention of errors. ***Conclusion:*** This work provides a complete understanding of the process and sets solid foundations for effective preventative measures throughput the generators manufacturing procedures. ***References:*** ANMAT, "Guía Para La Evaluación De Solicitudes De Preparaciones Radiofarmacéuticas."ANMAT, "Guía de buenas prácticas de fabricación para elaboradores, importadores/exportadores de medicamentos de uso humano.," pp. 31-41, 2023.

EP-1173

Production and separation of ^{64}Cu and ^{161}Tb in a Nuclear Reactor to Support Hospital Research: A TRIGA Mark II Experience

L. Canziani[1], *G. Grosso*[1], *A. Gandini*[1], *A. Salvini*[1], *G. Pepe*[2];
[1]*Laboratory of Applied Nuclear Energy - Università di Pavia, Pavia, ITALY,* [2]*Fondazione IRCCS Policlinico San Matteo, Pavia, ITALY.*

Aim/Introduction: The use of Isotopes ^{64}Cu and ^{161}Tb, Auger and β- emitters, is increasingly recognized. ^{161}Tb shares physical and chemical similarities with ^{177}Lu, offering potential for targeted cancer therapy. Similarly, ^{64}Cu is a versatile theranostic radionuclide, combining PET imaging with potential therapeutic applications. The production of ^{64}Cu typically occurs in medical cyclotrons while ^{161}Tb is produced from the irradiation of ^{160}Gd using a nuclear reactor, through n,γ reaction. However, separating these isotopes from the target materials is challenging due to their complex chemistry and the need for high radiochemical purity. ***Materials and Methods:*** In this study, various metallic samples, including zinc, copper, and zinc oxide, were irradiated in the TRIGA Mark II nuclear reactor at 250 kW. After irradiation, the samples were dissolved in HCl, and separation of ^{64}Cu from zinc was achieved using two DOWEX 1X8 resin columns with sequential elution in decreasing HCl concentrations. To reduce the HCl molarity, a TK201 resin column was used, yielding a final solution suitable for radiolabeling. For ^{161}Tb production, enriched ^{160}Gd targets were irradiated under the same conditions. Separation of ^{161}Tb was performed using LN3 ion exchange resin with αHIBA as the eluent, followed by further purification using a cation exchange resin. The radionuclidic purity was evaluated with High-Purity Germanium (HPGe) detector. ***Results:*** Among the irradiated samples, metallic copper yielded the highest activity but produced a carrier-added product. Metallic zinc, however, was preferred due to its higher yield and more efficient nuclear reaction. ^{64}Cu was successfully separated. The radiochemical purity of ^{64}Cu was >99%, with no ^{65}Zn contamination confirmed by gamma spectroscopy. The purification process achieved a decontamination factor of 1000 with the first column and an additional 100 with the second column. For ^{161}Tb, a 15 mg sample of enriched $^{160}Gd_2O_3$ was irradiated for 3 hours, resulting in 10^6 Bq of ^{161}Tb. The purification process demonstrated a decontamination factor of ~1000, though minor Gd contamination was still present. ***Conclusion:*** Low-power reactors are effective in the production of medical radionuclides like ^{64}Cu and ^{161}Tb for research applications and provide valuable educational opportunities, offering a platform for optimizing production techniques and enhancing communication and multidiscplinarity. Their role in advancing nuclear medicine and supporting research in hospitals is essential, despite a minor option in large-scale medical radioisotope production. Future research will focus on improving yield and efficiency, potentially through the use of larger sample masses and enriched targets.

EP-1174

Small-scall production of ^{161}Tb

D. Pawlak*, M. Żółtowska, I. Cieszykowska, P. Saganowski, A. Filiks, R. Mikołajczak;*
National Centre for Nuclear Research, Radioisotope Centre POLATOM, Otwock, POLAND.

Aim/Introduction: Terbium-161 ($T_{1/2}$ = 6.95 d) emits low-energy β^--particles (E_{β^-mean} 154 keV) and γ-radiation (E_γ = 48.9 keV (17.0%); 74.6 keV (10.2%)), similar to the decay properties of lutetium-177. It also emits conversion and Auger electrons, and is believed to be more effective in therapy than Lu-177 [1]. Small-scale production of Tb-161 in the ^{160}Gd(n,γ)^{161}Tb nuclear reaction was explored. ***Materials and Methods:*** Targets (mass of 8.4 - 11.8 mg) of gadolinium oxide enriched to 97.5% in Gd-160 were irradiated in the Maria research reactor in a neutron flux of $1x10^{14}$ $ns^{-1}cm^{-2}$ for 198-216 hours. Extraction chromatography was performed on LN2 resin (Triskem) to elute Tb-161 with 0.45 M HNO_3. In the next step, the Tb-161 solution was concentrated on DGA resin (Triskem) and eluted as a chloride with 0.05M HCl. Radionuclidic purity of the [^{161}Tb]$TbCl_3$ solution was determined by gamma spectrometry with an HPGe detector and chemical purity by the ICP-OES. The radiolabelling of DOTATATE served as the apparent molar activity test. ***Results:*** Terbium-161 was obtained with radioactivity from 0.74 to 0.95 GBq/mg Gd, calculated at the end of activation. The separation resulted in a high recovery of Tb-161, over 95%. The long-lived Tb-160 was the only radionuclide impurity identified and measured at the level of 0.005%. The content of metallic impurities was not more than 0.1 µg/mL, and the content of Gd was about 5 µg/mL. Despite that, the labelling yield of DOTATATE was over 99% for an apparent molar activity of 150 MBq/nmol. Importantly, when irradiating target material with a higher content of Tb-159 (0.08%), the apparent molar activity was around 50 MBq/nmol, and the content of Tb-160 was at the level of 0.3%. ***Conclusion:*** We have demonstrated an efficient ^{161}Tb production based on thermal neutron irradiation of ^{160}Gd in a nuclear reactor, followed by the two-step separation of ^{161}Tb using extraction chromatography. The enrichment of the target material in Gd-160 and its isotopic composition are crucial for the quality of the final product. ***References:*** [1] Müller, C., van der Meulen, N.P. & Schibli, R. Opportunities and potential challenges of using terbium-161 for targeted radionuclide therapy in clinics. Eur J Nucl Med Mol Imaging 50, 3181-3184 (2023). Acknowledgements: This work was partially created within the project SECURE funded by the European Union under grant agreement No. 101061230, and within the project PRISMAP funded by the European Union under grant agreement No. 101008571.

EP-70

e-Poster Area

D: Technical Studies -> D5 Radiopharmacy/ Radiochemistry -> D52 Radiopharmaceutical Preparation and Quality Control

EP-1175

cGMP-complaint implementation of high-yield automated [18F]FAPI-74 production with optimized quality control

W. Storms[1], *S. Celen*[2], *J. Maes*[2], *K. Serdons*[2], *K. Goffin*[2], *T. De Groot*[2], *L. Trump*[3], *C. Warnier*[3], *T. Gendron*[4], *R. Gerardy*[3], *K. Van Laere*[2], *C. M. Deroose*[2], *J. Kleynhans*[1], *F. Cleeren*[1];
[1]*Radiopharmaceutical Research, Department of Pharmaceutical and Pharmacological Sciences, KU Leuven, Leuven, BELGIUM,* [2]*Nuclear Medicine, University Hospital Leuven, Leuven, BELGIUM,* [3]*Trasis, Ans, BELGIUM,* [4]*University of Liège, Liège, BELGIUM.*

Aim/Introduction: Fibroblast activation protein inhibitor (FAPI)-based positron emission tomography (PET) radiopharmaceuticals have emerged as promising tools for targeting cancer-associated fibroblasts (CAFs), a key component of the tumour stroma. Among these, [^{18}F]AlF-FAPI-74, labelled with fluorine-18 via the Al^{18}F-method [1,2], provides advantages such as feasibility for centralised production and a longer half-life compared to ^{68}Ga-labeled FAPI derivatives. Here, we present a high-yield, automated cGMP-compliant production of [^{18}F]AlF-FAPI-74 with optimized quality control methods, using an isocratic radio-HPLC method with enhanced fluorine-18 recovery compared to a standard acidic method [3]. ***Materials and Methods:*** [^{18}F]AlF-FAPI-74 was produced on an automated cassette-based module using a specific FAPI-74 sequence, cassette and reagents. Synthesis started with transfer of [^{18}F]F$^-$ (89.7±1.8 GBq), followed by Al^{18}F chelation & purification on C18-cartridge. An isocratic radio-HPLC method (ammonium acetate 0.05M, pH 5.5, and acetonitrile 91:9 v/v; C18 silica column; 0.8 mL/min) was evaluated for specificity, precision, linearity, LOQ/LOD, and recoveries of [^{18}F]F$^-$, [^{18}F]AlF, and [^{18}F]AlF-FAPI-74. To compare, recovery of [^{18}F]F$^-$/[^{18}F]AlF was also measured using a standard acidic HPLC method (gradient, water + 0.1% TFA/acetonitrile). Finally, the optimized radio-HPLC system was used to perform (radio-)chemical stability studies of [^{18}F]AlF-FAPI-74 (2.02 GBq/mL) in formulation buffer at room temperature for up to 10 hours post synthesis. ***Results:*** The GMP-compliant production of [^{18}F]AlF-FAPI-74 has been validated through three production runs. In a synthesis of 30 minutes, [^{18}F]AlF-FAPI-74 was obtained with a final batch activity of 36.3 ± 7.4 GBq (up to 42.5 GBq) and a decay-corrected radiochemical yield of 50.0 ± 10.3%. The calculated apparent molar activity was 1125 ± 311 GBq/µmol. All analytical methods were successfully validated. Importantly, by using the new HPLC method, an excellent recovery (>95%) of [^{18}F]F$^-$, [^{18}F]AlF and [^{18}F]AlF-FAPI-74 was observed. In contrast, while the recovery of [^{18}F]AlF and [^{18}F]AlF-FAPI-74 was above 95% for the acidic radio-HPLC system, only a recovery of 59 ± 20% was observed for [^{18}F]F$^-$, which might result in an overestimation of the radiochemical purity. [^{18}F]AlF-FAPI-74 was stable (>95% RCP) up to 10 hours after synthesis. ***Conclusion:*** This study demonstrates the successful development and validation of a high-yield, automated, and GMP-compliant production method for [^{18}F]AlF-FAPI-74, offering a robust platform for centralized radiopharmaceutical production. We recommend using a mobile phase with pH > 5 for silica-based C18 columns for quality control of ^{18}F-labelled radiopharmaceuticals. ***References:*** [1] Clinical Nuclear Medicine 44, 452-8 (2019) [2] J Nuc Med 62, 201-7 (2021) [3] J Pharm Biomed Anal 111, 209-14. (2015)

EP-1176

A new fluorine-18 radiolabelled inhibitor of TRPC6 receptor for PET imaging of glioblastoma.

M. Iannone[1], *C. Papotto*[2], *S. Stucchi*[1,2], *E. Turolla*[1,2], *E. Vino*[1], *S. Todde*[1,2];
[1]*Tecnomed Foundation - University of Milan Bicocca, Monza, ITALY,* [2]*School of Medicine and Surgery - University of Milan Bicocca, Monza, ITALY.*

Aim/Introduction: TRPC6 is a Ca^{2+} permeable non-selective cation channel, member of a large family of transmembrane receptor potential canonical channels (TRPCs) and appears to be highly expressed in the lungs, placenta, ovary and spleen. Several studies have suggested that this channel is likely to play a role in glioblastoma multiforme (GBM) growth and development at different levels by regulating cellular metabolism, controlling cell proliferation, promoting angiogenesis, triggering the migration and invasion during glioma progression. Interestingly, inhibition of TRPC6 has shown to reduce tumour volume in subcutaneous mouse model of xenografted human tumours and increased mean survival in intracranial model mice. U251, U87 and T98G cells also show high TRPC6 expressions, which suggests that this receptor might potentially be a new target for imaging and therapy of human glioma. Here we report an automated procedure for the radiolabelling with fluorine-18 via nucleophilic substitution (S_N2) of a new TRPC6 inhibitor. ***Materials and Methods:*** Precursor and non-radioactive standards were purchased, radiolabelling procedures have been performed using a commercially available automated radiosynthesis system (GE-TRACERlab Fx-F_N). ***Results:*** The candidate molecular structure for fluorine-18 radiolabelling was selected following a careful evaluation of a series of compounds, either previously published or currently under patent, based on its affinity for hTRPC6 (IC_{50} = 0.7 nM), favourable BBB permeability (LogP = 2.01), good TRPC6/TRPC3 selectivity and the presence of a fluorine atom in a suitable position that allow for fluorine-18 radiolabelling without altering the original structure of the molecule. Fluorine-18 was successfully introduced via a standard nucleophilic substitution (S_N2) reaction on a tosylated precursor by heating at 100°C, followed by deprotection. The final fluorine-18 radiolabelled TRPC6 inhibitor was purified via semi-preparative HPLC and obtained in ready-to-inject formulation of 10% ethanol in physiologic solution (non-decay corrected RCY = 10.5 ± 2.5%, radiochemical purity > 95%, A_m = 43.3 ± 15.5 GBq/µmol, n = 10, total radiosynthesis time: 78 minutes). The radiosynthetic process was fully automated, and the compound stability was proved up to 4 hours, with no evidence of radiolysis. Cellular uptake studies in U251 GBM cells and HEK293 (no TRPC6 expressing) are currently in progress and also PET imaging preclinical studies on rodents are then planned. ***Conclusion:*** In conclusion, we have implemented a fully automated method for the radiolabelling with fluorine-18 of TRPC6 inhibitor for GBM PET imaging in high radiochemical yields and purity. Finally, cellular uptake studies and in vivo biodistribution will be conducted.

EP-1177

A radiopharmacist's guide to gallium: Implementing ^{68}Ga kit labeling in Your Radiopharmacy

A. Mihelcic, *B. Hudomalj;*
Institute of Oncology Ljubljana, Ljubljana, SLOVENIA.

Aim/Introduction: ^{68}Ga is increasingly used in PET imaging, e.g. of neuroendocrine tumors with somatostatin analogs ([^{68}Ga]Ga-DOTATOC/DOTATATE) and prostate cancer with PSMA ligands. It plays a key role in theranostics, paired with ^{177}Lu-labeled agents, and in the development of new ^{68}Ga compounds. Growing demand and regulatory needs have driven automated ^{68}Ga radiopharmaceutical production. The availability of ^{68}Ga labeling kits and ^{68}Ge/^{68}Ga generators—requiring minimal equipment—supports wider adoption. This work outlines key considerations

for radiopharmacies upgrading from ^{99m}Tc to ^{68}Ga kit-based radiolabeling [1]. ***Materials and Methods:*** A careful review of ^{68}Ga kits SMPCs, ^{68}Ge/^{68}Ga generator, Current Good Radiopharmacy Practice [2] and EANM guideline on the validation of analytical methods for radiopharmaceuticals [3] was conducted with the aim of correct professional implementation of ^{68}Ga kit-based radiolabeling. ***Results:*** Regulatory-compliant use of new isotopes was ensured by a radiation protection expert, with radiopharmacist input on radiation exposure documentation. Following submission of marketing authorisation documents for the ^{68}Ge/^{68}Ga generator and ^{68}Ga kits, our radiopharmacy planned upgrades. A personnel of four (minimum two) was deemed sufficient, and internal/external training was completed. Existing premises were suitable for ^{68}Ga work. Of two existing LAF chambers in separate clean rooms, the one with adequate shielding was assigned to ^{68}Ga preparations, the other to remaining isotopes. Radiation protection equipment was enhanced (PET syringe/vial shields, generator shielding, automatic elution system), along with QC instrumentation (radio-TLC scanner for radiochemical purity, well counter for ^{68}Ge breakthrough, pH meter for buffer calibration). QA documents for ^{68}Ga procedures were developed and approved, covering standard operating procedures (SOPs) for purchase and material control of all starting materials, product preparation and QC, equipment use, and maintenance. Our work suggests qualification protocols for radioscanner and well counter (calibration, stability, linearity/range, repeatability). ^{68}Ga waste management followed existing protocols for other isotopes as its short half-life presented fewer challenges. ***Conclusion:*** Our approach to ^{68}Ga kit-based radiopharmaceutical production has established reliable SOPs. This work outlines essential radiopharmacy upgrades to support others in setting up ^{68}Ga production. Ongoing experience drives further process optimization. ***References:*** 1. Lepareur N. Cold Kit Labeling: The Future of 68Ga Radiopharmaceuticals? Front Med (Lausanne). 2022 Feb 10;9:812050 2. Gillings, N., Hjelstuen, O., Ballinger, J. et al. Guideline on current good radiopharmacy practice (cGRPP) for the small-scale preparation of radiopharmaceuticals. EJNMMI radiopharm. chem. 6, 8 (2021) 3. Gillings, N., Todde, S., Behe, M. et al. EANM guideline on the validation of analytical methods for radiopharmaceuticals. EJNMMI radiopharm. chem. 5, 7 (2020)

EP-1178

Feasibility and comparative evaluation of a candidate hydroxyethyl starch-based sedimentation agent for (^{99m}Tc)Tc-HMPAOautologous white blood cellslabelling

A. Deschavannes*, T. Pitaud-Renaud, A. Clotagatide, C. Rioufol, M. Piquemal;*
Hospices Civils de Lyon, Lyon, FRANCE.

Aim/Introduction: Labelling of autologous white blood cells (WBCs) with technetium-99m hexamethylpropyleneamine oxime ((^{99m}Tc)Tc-HMPAO) is a well-established nuclear medicine procedure for the detection of infections and inflammatory conditions. This process requires the separation of leukocytes from whole blood, typically achieved by red blood cell (RBC) sedimentation. PLASMION, a hydroxyethyl starch-based solution initially developed as a plasma volume expander, is widely used for this purpose. However, due to its impending discontinuation, the identification of an alternative with equivalent performance is necessary. HETASEP, another hydroxyethyl starch solution commonly used in cellular hematology, may represent a viable substitute. This study aimed to assess the feasibility of using HETASEP as a sedimentation agent for WBC labelling with (^{99m}Tc)Tc-HMPAO and to compare its performance with that of PLASMION. ***Materials and Methods:*** Experiments were performed using peripheral blood from healthy donors. For each donor, two parallel preparations were carried out: one with 15 mL of PLASMION, the other with 10 mL of HETASEP as the sedimentation agent. Apart from this difference, both preparations followed the same standard (^{99m}Tc)Tc-HMPAO labelling protocol. Key parameters were evaluated: macroscopic appearance of the WBC-rich layer after sedimentation, clarity and homogeneity of the final suspension before reinjection, and WBC viability assessed using the Trypan blue exclusion test. The RBC-to-WBC ratio was assessed by optical microscopy and confirmed by flow cytometry. Radiolabelling efficiency was calculated by measuring the percentage of radioactivity bound to the WBC pellet at the end of the procedure. ***Results:*** Three comparative tests were performed. The sedimentations were visually effective for both PLASMION and HETASEP. Leukocyte viability was 98.5% ± 1.2 with PLASMION and 97.8% ± 1.4 with HETASEP. The RBC-to-WBC ratio was 1.15 ± 0.03 for PLASMION and 1.25 ± 0.05 for HETASEP. Radiolabelling yields were 72.3% ± 4.5 with PLASMION and 70.1% ± 3.8 with HETASEP. Final suspensions were visually suitable for clinical use in all cases. ***Conclusion:*** This preliminary study suggests that HETASEP is a feasible and effective alternative to PLASMION for RBC sedimentation in (^{99m}Tc)Tc-HMPAO WBC labelling. It preserves WBC viability, ensures proper separation, and allows efficient radiolabelling. These promising results support further evaluation of HETASEP in a larger clinical setting.

EP-1179

Synthesis and Validation of [^{68}Ga]Ga-DOTA-Siglec-9 for Non-invasive PET Imaging

S. Migliari*[1], A. Guercio[1], A. Gagliardi[1], S. Bruno[2], M. Scarlattei[1], G. Baldari[1], A. Roivainen[3], S. Forsback[3], L. Ruffini[1];*
[1]Nuclear Medicine Division, Azienda Ospedaliero-Universitaria of Parma, Parma, ITALY, [2]Food and Drug Department, University of Parma, Parma, ITALY, [3]Radiopharmaceutical Chemistry Laboratory, Turku PET Centre, University of Turku, Finland, Turku, FINLAND.

Aim/Introduction: Siglec-9, a member of the Siglec family of receptors, has significant clinical implications due to its role in modulating immune cell trafficking and inflammation. This receptor is predominantly expressed on immune cells, such as neutrophils, monocytes, and dendritic cells, which are central players in immunity. Siglec-9 binds to sialic acid residues on glycoproteins, present on endothelial cells, and this interaction is critical in regulating immune responses during inflammation and tissue injury. Its interaction with VAP-1, a key endothelial adhesion molecule, is of particular interest for therapeutic development, especially in the context of chronic inflammatory diseases, autoimmune disorders, and cancer [1-4]. In this regard, recent studies have demonstrated that the Gallium-68-labeled Siglec-9 motif conjugated with 1,4,7,10-tetraazacyclododecane-N,N′,N″,N‴-tetraacetic acid ([^{68}Ga]Ga-DOTA-Siglec-9) can be effectively used for PET imaging of these disorders. The aim was to establish a new automated radiolabelling method for the radiopharmaceutical [^{68}Ga]Ga-DOTA-Siglec-9. ***Materials and Methods:*** The synthesis was fully automated, with real-time monitoring of reaction parameters such as time, temperature, and radioactivity. Gallium-68 was eluted from a GMP-certified 68Ge/68Ga generator using HCl, then purified on a cation exchange (SCX) cartridge and eluted with NaCl. The eluate was added to a reaction vial containing DOTA-Siglec-9 in HEPES buffer and incubated at 65°C for 6 minutes. After labelling, the crude product was purified on a C18 RP cartridge and eluted with ethanol/water. The final product was diluted with PBS and sterilized through a 0.2µm filter. The synthesis efficiency and release criteria were evaluated following the Ph. Eur. guidelines for all final products including radiochemical yield (RY), radiochemical purity (RCP), detection of free gallium (via Radio-UV-HPLC), gallium colloids (via Radio-TLC), molar activity (Am), chemical purity, pH, and LAL test. After optimizing the method, the entire process was validated through three consecutive syntheses, with stability monitored over time. ***Results:*** [^{68}Ga]Ga-DOTA-Siglec-9

was obtained with RY (55.04%), RCP (99.48%) and Am (23.15GBq/µmol). The process validation confirmed optimal mean values of RY, RCP and Am (56.16%, 99.40%, 20.26GBq/µmol). The stability of [^{68}Ga]Ga-DOTA-Siglec-9 was assessed at RT over a 3-hour period, yielding satisfactory results for its RCP (mean value 99.29%), appearance, pH and sterility. ***Conclusion:*** [^{68}Ga]Ga-DOTA-Siglec-9 was successfully synthesized in compliance with Ph. Eur. standards and is now ready for clinical application. ***References:*** [1] Viitanen R, et al. J Nucl Med. 2021 Apr;62(4):577-583. [2] Brzezicka KA, et al. Mol Aspects Med. 2023 Apr;90:101140. [3] Wang JHS, Curr Oncol Rep. 2023 Jan;25(1):41-49. [4] Aalto K, et al. Blood. 2011;118:3725-33.

EP-1180

Content analysis of deviation reports in the in-house manufacture of PET radiopharmaceuticals

S. Forsback[1], *R. V. Kivelä*[2], *A. M. Juppo*[3];
[1]*University of Turku, Turku, FINLAND,* [2]*Hospital Pharmacy, Turku University Hospital, Turku, FINLAND,* [3]*University of Helsinki, Faculty of Pharmacy, Division of Pharmaceutical Chemistry and Technology, Helsinki, FINLAND.*

Aim/Introduction: In order to decrease the rejection rate of the batches of in-house manufactured PET radiopharmaceuticals in the Radiopharmaceutical Chemistry Laboratory at Turku PET Centre (TPC), a qualitative content analysis of the deviation reports was performed. ***Materials and Methods:*** Inductive content analysis as described by Elo and Kyngäs [1] on deviation reports documented during 2019-2023 at TPC was performed. All together 427 deviation reports were analysed and classified. Another person performing random check improved the reliability of the classification. In this study, technical faults were selected for further observation. ***Results:*** The deviations were classified according the root cause to four categories: technical faults, failing methods, problem with materials and human errors. Technical faults and human errors were further classified to several subcategories. Most of the deviations, more than 50 %, were classified as technical faults (n=216). Second largest category was human errors (n=166). Failing methods (n=36) and problems with materials (n=9) were quite rare causes for a deviation. The most frequent cause for a technical fault at TPC was faults in synthesis devices (n=142) and more precisely faults during the transfer of gas or liquid (n=85). In the category of technical faults in synthesis devices, in 88 cases (62 %) a batch of a radiopharmaceutical was rejected. ***Conclusion:*** Profound content analysis of the deviations generated in the production of PET radiopharmaceuticals during five-year period at TPC offers versatile means to develop the quality and robustness the manufacturing process of the radiopharmaceuticals. We have already utilised our findings by creating more precise instructions for the preventive maintenance of the synthesis devices. In future, we are going to use the results of this content analysis in the improvement of all our operations in the production of PET radiopharmaceuticals. ***References:*** 1. Elo S, Kyngäs H. The qualitative content analysis process. J Adv Nurs. 2008;62(1):107-115.

EP-1181

Improvement of the ^{177}Lu-PSMA$^{I\&T}$ Labelling Method for Clinical Production

P. Bohn*, A. Coussirou, M. Six, A. Salles, F. Basuyau, A. Edet-Sanson, P. Vera, D. Tonnelet;*
Centre Henri Becquerel, Rouen, FRANCE.

Aim/Introduction: At the Henri Becquerel Center, Rouen, Normandy, we have performed since January 2024 30 ^{177}Lu-PSMA$^{I\&T}$ labelling for patients with metastatic castration resistant prostate cancer and non-eligible in France to ^{177}Lu-PSMA^{617} following a method validated by the French Drug Agency (ANSM). An issue occurred in February 2025 with a shortage of one of the excipients which is absolutely necessary to prepare the pharmaceutical product. The method had to be modified to continue treating our patients. The aim of this abstract is to explain this modified method. ***Materials and Methods:*** The initial validated method is fully automated using a Luna synthesizer from Elysia-Raytest. Briefly, PSMA$^{I\&T}$ (115 µg) is diluted in an ascorbate buffer (160 mg sodium ascorbate and 40 mg ascorbic acid in 2 ml water for injection) and heated up to 85 °C in presence of 9 GBq of lutetium-177 chloride (GMP) for 20 minutes. After cooling, the resultant solution is filtered and diluted in saline and subjected to quality control. Due to its shortage, we replaced the ascorbate buffer by a commercial drug (Laroscorbine® 1g/5ml) which only contains ascorbic acid and sodium hydroxide. Of note, ascorbic acid had already been studied at various pH and concentration to stabilize DOTA and DOTAGA metallic complex in 2003 [1]. ***Results:*** We performed 3 validation batches with this new method with a yield > 95%, RCP assessed by HPLC > 97% and by TLC > 99%, endotoxins < 0.5 EU/ml, pH = 6. Sterility assays were conform and compound stability was > 3 days. The injectable solution is clear and colorless. Compared to the previous method, we only obtain a higher pH. (6 instead of 4.5). With this new method, the excipient (with a controlled bioburden) does not need to be dissolved, and a simple sampling from a sterile registered drug is sufficient as an excipient. ***Conclusion:*** The new method does not affect the quality of the final product but is easier, and cheaper. The French Drug Agency has approved this new procedure and we were able to treat our patients with no additional delay. In March 2025, there was still an ascorbate buffer shortage and 6 additional injections using this new method were performed, greatly benefiting the patients. ***References:*** [1] Ascorbic Acid: Useful as a Buffer Agent and Radiolytic Stabilizer for Metalloradiopharmaceuticals. Shuang Liu, Charlie E. Ellars, and D. Scott Edwards. Bioconjugate Chem. 2003, 14, 1052-1056

EP-1182

Compassionate Use of [^{68}Ga]Ga-NODAGA[40Lys]-Exendin-4: Validation of an Automated Synthesis in a Sodium Acetate Buffer

M. Ragot*, M. Jung, P. Orhon, A. Revy, S. Levesque, M. Tempier;*
Centre Jean Perrin, Clermont-Ferrand, FRANCE.

Aim/Introduction: [^{68}Ga]Ga-NODAGA-Exendin-4 PET imaging has shown great promises for localization of benign insulinoma, being both highly specific and sensitive. In France, compassionate use of [^{68}Ga]Ga-NODAGA-Exendin-4 is allowed by current regulations. However, as it requires small-scale in situ radiolabeling, it is subject to prior authorization, following the submission and expertise of an Investigational Medicinal Product Dossier (IMPD). Herein, we present an automated radiosynthesis method, employing sodium acetate buffer for the first time at clinical scale. ***Materials and Methods:*** Radiosynthesis is automated on a synthesizer, using single-use cassettes and a GMP grade ^{68}Ge/^{68}Ga generator. Radiolabeling of the peptide takes place at 100°C for 15 min, with sodium acetate buffer (a non-toxic buffer approved for human use with no dose limit), ascorbic acid and previously purified gallium eluate. After purification, the final product is formulated in ethanol and NaCl 0.9% by passing through a 0.22 µm sterilizing filter. Three batches were produced and controlled in order to validate the synthesis. Appearance, checked by visual inspection, must be clear and limpid. pH, determined by indicator paper, must be between 4 and 8. Radiochemical identity and purity (RPC) are determined by radio-HPLC and thin layer chromatography (TLC). RPC must be greater than 90%, with less than 3% free gallium. Radionuclidic identity is assessed by gamma spectrometry and radionuclidic purity (RNP) by gamma counting after 48h. Endotoxins are researched by kinetic-chromogenic test and a sterility test is performed after liberation. Stability is assessed at room temperature, over a 2-hour period. ***Results:*** An average

activity of 343 MBq was obtained in 36 min, for a 31-week-old generator, resulting in a decay-corrected yield of 48%. The automated synthesis was found to be compliant with all quality control requirements. RCP was 97.0 ± 0.2%, with less than 1% free gallium for all batches. The solution was limpid and had a pH of 6. RNP was conform, with 0.37 ppm of ^{68}Ge. The final product was confirmed to be sterile, with no detectable endotoxins (< 2.5 EU/mL). It remained stable for 2 hours, with no increase in free gallium and no significant variation in volume activity, indicating the absence of adsorption. ***Conclusion:*** This radiolabeling method enables the rapid synthesis of [^{68}Ga]Ga-NODAGA-Exendin-4 in sodium acetate. The final activity and purity levels are compatible with clinical use, for small-scale productions by radiopharmacies. Authorization was obtained from the French regulatory authorities, allowing for the imaging of our first patient in March 2025.

EP-1183

Stability Evaluation of I-131 Radiolabeled Ferulic and Caffeic Acids: Effects of Storage Conditions and Stabilizing Agents

M. Radovic, *M. Peric, D. Stankovic, A. Vukadinovic, S. Vranjes-Djuric, D. Jankovic, M. Mirkovic;*
„VINCA" Institute of Nuclear Sciences - National Institute of the Republic of Serbia, University of Belgrade, Belgrade, SERBIA.

Aim/Introduction: Radiolabeling ferulic acid (FA) and caffeic acid (CA) with I-131 can provide valuable insights into their pharmacokinetics, metabolism, tissue distribution, and antioxidant activity. However, the process involves challenges related to the stability of the radiolabel bioactive compounds, the reactivity of the phenolic groups, and the potential for metabolism-induced alterations. This study aimed to radiolabel FA and CA with iodine-131 (^{131}I) in high radiolabeling yield, and to investigate the factors affecting their stability. ***Materials and Methods:*** Radiolabeling was performed using Chloramine-T as oxidizing agent, with optimized parameters including pH 6, oxidizing agent content (50 µg), the amount of bioactive compounds (200 µg), and reaction time (30 min). Stability studies evaluated the effects of storage conditions (refrigeration at 2-8 °C), the addition of ascorbic acid as a stabilizer, and solution dilution on the integrity of the labeled compounds. ***Results:*** High radiolabeling yields were achieved, with 95.5% for ^{131}I-ferulic acid and 78.3% for ^{131}I-caffeic acid. After 72 hours at room temperature, the labeling yield of both compounds dropped to below 25%. Dilution improved the stability of ^{131}I-ferulic acid but had no significant effect on ^{131}I-caffeic acid. The addition of ascorbic acid after radiolabeling effectively minimized oxidative degradation, improving the radiochemical purity of both complexes (98.2% for ^{131}I-ferulic acid and 85.6 % for ^{131}I-caffeic acid). Post-labeling storage at 2-8°C of radiolabeled compounds with ascorbic acid added, demonstrating higher long-term stability for ^{131}I-ferulic acid (95.1%), in comparison to ^{131}I-caffeic acid (38.3%) after 72 h. A comparative analysis between ^{131}I-ferulic acid and ^{131}I-caffeic acid revealed differences in labeling efficiency and stability profiles. While both compounds showed potential as radiolabeled bioactive agents, ^{131}I-ferulic acid demonstrated higher stability under investigated conditions. ***Conclusion:*** The addition of ascorbic acid and storage at lower temperatures enhances the stability of these compounds, making them suitable for applications in pharmacology, toxicology, and metabolic research.

EP-1184

Optimization of Automated Synthesis of [^{18}F]AlF-NOTA-FAPI-4 for Clinical Radiopharmacy Applications

L. Pires[1,2], *K. Zirbesegger*[2], *J. Giglio*[2], *J. Gambini*[2], *P. Duarte*[2], *V. Cardoso*[1], *S. Fernandes*[1], *E. Savio*[2];
[1]*Universidade Federal de Minas Gerais, Belo Horizonte, BRAZIL,* [2]*Centro Uruguayo de Imagenología Molecular, Montevideo, URUGUAY.*

Aim/Introduction: Fibroblast activation protein (FAP) is overexpressed in cancer-associated fibroblasts, making it a promising target for tumor imaging. While [^{68}Ga]NOTA-FAPI-4 is widely used, [^{18}F$^-$] fluoride offers advantages such as greater availability, longer half-life, and higher spatial resolution. The [^{18}F]AlF-NOTA strategy enables ^{18}F$^-$ coordination via an aluminum-based intermediate, providing a viable alternative for indirect radiolabeling peptides. This study aimed to optimize the production of [^{18}F]AlF-NOTA-FAPI-4 using automated synthesis modules, based on a systematic investigation of labeling parameters initially conducted at the bench scale. ***Materials and Methods:*** ^{18}F$^-$ was produced on GenTrace (GE) or PETrace (GE) cyclotrons and purified through QMA plus light cartridges (Sep-Pak, Waters). Bench-scale optimization evaluated the influence of $AlCl_3$ (Sigma) (0,01M) volume (1-8 µL), NOTA-FAPI-4 (MedKoo) mass (15-100 µg), heating time (5-15 min), and temperature (22 °C vs. 100 °C). Analytical conditions for determining radiochemical purity (RCP) by High-performance liquid chromatography (HPLC, Shimadzu) were developed using Phenomenex (Cat.N°00G-3148-E0), Macherey-Nagel (Cat.N°760008.48), Agilent (Cat.N°93999-902) columns, testing different mobile phases (Trifluoroacetic acid [TFA] 0,1% in water; phosphate 10 and 100mM; water) and elution gradients with TFA 0.1% in acetonitrile. Optimal labeling parameters were then applied to automated Synthra RNPlus and Tracerlab FN-FX modules, scaling up the process to 37GBq of ^{18}F$^-$ activity, 100µg of peptide, 6,5µL of $AlCl_3$ (0,01M) and heating at 100°C for 10 minutes, followed by purification on a C18 cartridge (Sep-Pak, Waters). The final formulation was prepared with 10% ethanol in physiological saline containing ascorbate buffer. ***Results:*** The most effective RCP method was achieved using the Agilent column, phosphate buffer (100 mM; pH 5.9), and acetonitrile with 0,1% TFA, using the following gradient: 0-100% B (0-10 min) | 100% B (10-15 min), flow 1mL/min, gamma and UV detection (254nm). In bench experiments, optimal yields (18.03%±1.55; n=3) were obtained using 15 µg of peptide, 2 µL of $AlCl_3$ (0,01M), heating at 100 °C for 10 minutes, and activities between 185-555MBq. When these conditions were translated to the automated synthesizers, average radiochemical yields increased to 25.9% ±5.08 (n=3). The HPLC analysis showed no ^{18}F$^-$ peak, so 7,65GBq ± 1,60 (n=3) of [^{18}F]AlF-NOTA-FAPI-4 was achieved for clinical use. ***Conclusion:*** [^{18}F]AlF-NOTA-FAPI-4 labeling under optimized conditions demonstrates high potential for clinical-scale GMP production using automated synthesis platforms. This approach supports broader Positrons Emission Tomography imaging access with radiopharmaceuticals targeting FAP since reproducibility, efficiency, and scalability were verified. Based on these results, our group is enabled to contribute to the advancement of personalized oncology diagnostics.

EP-1185

Towards clinical implementation of radiolabeled orally inhaled drug products: preliminary feasibility study using a Next Generation Cascade Impactor and [^{18}F] radiopharmaceuticals

J. Wolfert[1], *M. Konijnenberg*[1], *S. P. J. M. Tsai*[1], *I. van de Merwe*[1], *N. H. Hendrikse*[1], *L. Ruijgrok*[1], *T. A. Mulders*[1], *B. R. Lavon*[2], *F. A. Verburg*[1], *E. de Blois*[1];
[1]*Erasmus MC, Rotterdam, NETHERLANDS,* [2]*FLUIDDA NV, Kontich, BELGIUM.*

Aim/Introduction: Orally inhaled drug products (OIDPs), including pressurized metered dose inhalers (PMDIs), are essential in the treatment of respiratory diseases. As the demand for generic alternatives increases, computational fluid dynamics modelling has emerged as a promising approach for predicting deposition patterns as part of demonstrating bioequivalence. PET-imaging of radioactive OIDPs offers the potential for high-resolution visualization of pulmonary drug deposition as a basis of model validation. To ensure that the aerodynamic particle size distribution (APSD) of the PET-radiopharmaceuticals reflects that

of the drug, validation is essential. Analytical techniques such as a Next Generation Cascade Impactor (NGI) in combination with UPLC-UV and gammacounting can be used.[1] Furthermore, the use and inhalation of radioactive OIDPs generate challenges in terms of internal and external radiation. The aim of this study is to evaluate the technical feasibility of addition and analysis of PET-radiopharmaceuticals to OIDPs while ensuring safety for clinical application. ***Materials and Methods:*** A UPLC-UV method was developed to quantify beclomethasone dipropionate (BDP), fluticasone propionate (FP), and budesonide. To assess feasibility, an NGI was used in combination with a nebulizer. The PET-radiopharmaceuticals [^{18}F]FDG and [^{18}F]F-NaF were tested to quantify APSD and mean mass aerodynamic diameter (MMAD). A combination of each corticosteroid and a PET-radiopharmaceutical was used and NGI-stages were analyzed using UPLC-UV and gammacounting. Dosimetric estimates for lungs were calculated per inhaled pMDI dose using the pharmacokinetic models of technegas, pertechnate and F-18/[^{18}F] FDG of ICRP128. Additional dose calculations were performed for external radiation exposure expected during patient handling and activation of radioactive OIDPs, including to the eye lens, hands and face. Calculations were based on a total activity of 1000MBq per pMDI and 100MBq/inhalation. ***Results:*** The NGI setup in combination with UPLC-UV and gammacounter showed to be successful for the measurement of the APSD of BDP, FP, Budesonide in combination with [^{18}F]FDG or [^{18}F]F-NaF. The APSDs of the drugs and their respective radiopharmaceutical showed similar output and MMADs. Dosimetric calculations resulted in an effective dose of 0.044 mSv/MBq for inhalation, with an estimated external dose of 1 mSv (Hp 0.07; skin) and 0.25 mSv (Hp 3; eye lens) during handling of the device with 1000 MBq F-18. ***Conclusion:*** Results support the feasibility of using NGI-based methods to analyze radioactive OIDPs. The ability to quantify PET radiopharmaceutical in combination with used drug lays the groundwork for scaling up to clinical use of radioactive pMDI formulations. ***References:*** [1] Dolovich et al. Radiolabeling Methods.

EP-1186

Taking radioimmunoconjugate manufacturing to the next level: a universal cassette-based process for the Lu-177 radiolabeling of mAbs

C. Vanasschen, *A. Dubart, J. Masset, E. Duray, M. Hawotte, S. Degueldre, C. Warnier;*
Trasis, Ans, BELGIUM.

Aim/Introduction: Chemistry, Manufacturing and Control (CMC) is a central topic in nuclear medicine and radiopharmacy. While managing the automated radiosynthesis of small molecules/peptides with various isotopes has been the core of radiopharmacy in the past 20 years, radiolabeling and purification of radioimmunoconjugates bring new challenges to the field : recent breakthroughs on the development of diagnostic and therapeutic radioimmunoconjugates at the clinical level now urgently call for equivalent progress at the CMC level. We herein report the development of a fully automated process for the production of [177Lu]-labelled antibodies. ***Materials and Methods:*** Lu-177 was supplied in 0.04M HCl (75µL to 2mL, 40 GBq/mL). The disposable cassettes were equipped with Centripure 50 size-exclusion cartridges as well as with a device ensuring quasi-quantitative transfer of [177Lu]Cl3 to the reactor. Process development was performed using Trastuzumab-DOTAGA as model compound: CAR values ranged between 0.7 and 4.0 while the DOTAGA concentration in the radiolabeling medium was normalized to ensure comparable experimental results. The automated process was developed on the miniAllinOne synthesis module. ***Results:*** A buffer formulation was designed to bring the [177Lu]Cl3 adequate pH, irrespective of the amount of HCl in the [177Lu]Cl3 vial (75µL to 2mL). Manual experiments were carried out to optimize the DOTAGA concentration in the labeling medium as well as the amount of activity/DOTAGA ratio to maximize radiochemical conversions within 1h at 37°C. Those conditions were transferred to a fully automated fluidic process on miniAllinOne, including (i) [177Lu]Cl3 transfer (metal-free, >92% recovery), (ii) buffer and bioconjugate transfer, (iii) radiolabeling, (iv) conditioning of the SE cartridge, (v) purification on the SE cartridge and (vi) final product formulation. The resulting process yielded [177Lu]Trastuzumab with >70% RCY (n.d.c) in ≈ 90 minutes starting from 8 - 80 GBq, with radiochemical purities >95%. ***Conclusion:*** We report the development of a process and consumables for the automated radiosynthesis of [177Lu] radioimmunoconjugates on the miniAllinOne. The process is compatible with any mAb-DOTA(GA) conjugate or commercial [177Lu]Cl3 source and accommodates activity levels up to 80 GBq, yielding up to 10 patient doses of [177Lu]mAb. This approach significantly enhances radiation protection and improves batch-to-batch reproducibility and robustness. Current efforts focus on demonstrating the compatibility of this process with a range of therapeutic and diagnostic radioisotopes such as Ac-225, Tb-161 and Cu-67/67. The objective is to fully leverage the potential of a universal radiosynthesis process in accelerating the transition from development to clinical production of radioimmunoconjugates.

EP-1187

Optimization of 4-[^{18}F]fluoro-1-naphthol ([^{18}F]4FN) production and quality controls

M. Riondato[1,2], *J. Martinelli*[2], *R. Guelfo*[3], *L. Palio*[4], *C. Marini*[5], *G. Sambuceti*[2];
[1]*IRCCS Policlinic Hospital of Genoa, Genoa, ITALY,* [2]*Dept. Health Sciences, University of Genoa, Genoa, ITALY,* [3]*Dept. Chemistry and Chemical Technologies, University of Genoa, Genoa, ITALY,* [4]*Dept. of Science and Technological Innovation University of Piemonte Orientale, Alessandria, ITALY,* [5]*Institute of Molecular Biomimaging and Physiology (IBFM), National Research Council (CNR), Milan, ITALY.*

Aim/Introduction: [^{18}F]4FN is as a promising tool in positron emission tomography (PET) imaging, offering enhanced specificity for the detection of inflammatory and immune responses compared to traditional agents, such as [^{18}F]FDG. Its potential extends to the early detection of immune-related adverse events and prognostic imaging in the context of cancer immunotherapy, where timely insights into the immune system's behavior can significantly inform clinical decision-making. Ongoing research aims to validate the clinical utility of [^{18}F]4FN, with studies indicating that its application could enhance diagnostic accuracy, monitor therapeutic responses, and ultimately contribute to the tailored management of diseases characterized by dysregulated immune activity. We aimed at the development of [^{18}F]4FN, via automated radiosynthesis on a commercially available module and the implementation of methods fulfilling all acceptance criteria well suited for the routine quality controls before release for clinical use. ***Materials and Methods:*** The Boc-protected pinacol boronic ester precursor on the 1-4 substituted naphthol scaffold was first synthesized. [^{18}F]Fluorine was produced using an Eclypse HP cyclotron (Siemens, Germany). The radiolabelling protocol was developed on a AllInOne36 synthesizer platform (Trasis, Belgium) able to carry out Cu-mediated 18F-fluorodeboronation, including deprotection and semipreparative purification before reformulation. For the routine use the quality control of radiopharmaceuticals was validated according to the ICH Q2 (R1) "Validation of Analytical Procedures". ***Results:*** The procedures were optimized at low radioactivity in terms of solvents, catalysts, amount of precursor and time. The best results were obtained by reacting 15 mg pinacol boronates, 27 mg of $Cu(OTf)_2(Py)_4$ using 1,3-dimethyl-2-imidazolidinone (DMI) as solvent. Starting from the Boc-protected pinacol boronic ester precursor, our optimized protocol allowed to obtain ca. 30-70 MBq of the target compound from 180-350 MBq of starting [^{18}F]fluoride, with approximately 20% ndc. Although the tests carried out so far are at low radioactivity

ranges, the results are promising obtaining [^{18}F]4FN with a high radiochemical purity (>99%) and with significant higher yield compared to the data reported in the literature (6% ndc). QCs were validated with special attention to HPLC method (for e.g., specificity, linearity, and accuracy) optimizing absorbance of reference compounds and developing both isocratic and gradient methods. ***Conclusion:*** We have optimized the Cu-mediated deborylative fluorination method to prepare the [^{18}F]-labeled aryl compound [^{18}F]4FN in a reliable and consistent way with high chemical and radiochemical purity, suitable for in vitro and in vivo experiments, in about 90 min including validated CQs. ***References:*** F. Pisaneschi et al., Nature Biotechnology volume 40, 965- 2022

EP-1188

Independent verification of activity determination for radiopharmaceutical preparations

K. Baete[1,2], *L. Mihailescu*[3], *W. Deckers*[1], *C. Terwinghe*[1], *R. Aarts*[3], *W. Claeys*[2], *J. Kleynhans*[2], *C. M. Deroose*[1,2];
[1]*UZ Leuven, Leuven, BELGIUM,* [2]*KU Leuven, Leuven, BELGIUM,*
[3]*Belgian Nuclear Research Centre (SCK CEN), Mol, BELGIUM.*

Aim/Introduction: In nuclear medicine (NM), specialized equipment is required for the preparation, activity determination, dispensing, and administration of radionuclides for diagnostic and therapeutic use. The traceability and accuracy of measured activity is important for imaging and treatment optimization. Unfortunately, manufacturers of activity meters often do not provide the information needed to assess the device accuracy and traceability. This should be independently verified during acceptance testing. Our department installed a shielded isolator for the synthesis and dispensing of diagnostic and therapeutic radiopharmaceuticals (Phaedra Combo, Comecer S.p.A., Italy). We calibrated and verified the accuracy of the built-in activity meters for specific radionuclides and recipients. ***Materials and Methods:*** The isolator contains two activity meters: a re-entrant well-type ionisation chamber (VIK-202, Comecer) for measuring activity in recipients during radiopharmaceutical preparation, and a pass-through chamber (DVK-103, Comecer) for measuring activity of the end-product in a vial. We verified the accuracy of both activity meters using traceable reference sources (^{57}Co, ^{60}Co, ^{133}Ba, and ^{137}Cs) and compared the response to other devices using ^{99m}Tc. We assessed the response for a variety of calibration settings using reference sources and compared that to other devices. The Fidelis secondary standard radionuclide calibrator of the Belgian Nuclear Research Centre (SCK CEN), traceable to a designated metrological institute, was used to calibrate the activity meters for ^{68}Ga, ^{89}Zr, and ^{177}Lu using a standardized source geometry. ***Results:*** Initial testing showed reassuring results for the re-entrant well-type ionisation chamber. However, the pass-through chamber showed a deviation of 18% for the accuracy with a ^{57}Co reference source. It appeared that the recipient holder and its automated positioning system was not taken into account during manufacturing calibration. Adjustment of the electrometer settings was necessary and required the determination of new calibration factors. We established new factors for ^{68}Ga, ^{89}Zr, and ^{177}Lu using the Fidelis secondary standard radionuclide calibrator. The pass-through chamber required additional calibration for specific recipients with ^{177}Lu and the accuracy is significantly influenced by the volume of the radiopharmaceutical solution in the recipient. ***Conclusion:*** Traceable calibration and independent verification of the accuracy of activity determination in NM is essential. We analysed the accuracy of activity determination for a shielded isolator and required significant adjustments of factory based calibration settings. We recommend the involvement of a national metrological service for independent verification of activity determination in NM applications.

EP-1189

Feedback of [^{68}Ga]Ga-FAPI-46 radiosynthesis for clinical applications

C. Provost, *C. Schmitt, M. Steffann, B. Irumva, M. Delion, J. Fouque, O. Madar;*
Institut Curie, Saint Cloud, FRANCE.

Aim/Introduction: The radiopharmaceutical [^{68}Ga]Ga-FAPI-46 is a promising agent for PET imaging targeting fibroblast activation protein (FAP) in oncology and fibrotic diseases. It offers advantages over traditional tracers, particularly in cancers with low [^{18}F] FDG uptake. A Good Manufacturing Practice (GMP) automated radiosynthesis process has been developed to ensure high radiochemical yields (RCY) and compliance with pharmaceutical injectable grade. This study reports on our 1-year experience of [^{68}Ga]Ga-FAPI-46 (Sofie) radiosynthesis on an EasyOne® synthesizer (Trasis). ***Materials and Methods:*** We conducted a retrospective review of 96 productions and quality controls between March 2024 and March 2025. Six people are certified for production and Quality Control (QC) of [^{68}Ga]Ga-FAPI-46. An EasyOne® synthesizer with cassette and reagent kit and 2 Galliapharm® (Eckert & Ziegler) generators were used to produce this radiopharmaceutical. The production lasts 30 minutes with 1 hour of preparation before running the production process. QC includes: solution appearance, pH, ascorbate, period, radiochemical purity (RCP) by radio-Ultra High Performance Liquid Chromotography (r-UHPLC) and radio Thin Layer Chromatography (r-TLC), chemical purity by UHPLC-UV, filter integrity, endotoxin and sterility. The QC is completed within approximately 45 minutes. The [^{68}Ga]Ga-FAPI-46 procedure requires, at least 2 different people for the production and the QC and a radiopharmacist for the pharmaceutical release. ***Results:*** Out of 85 compliant productions, 32 % were sent to our nuclear medicine department at Paris site and 68 % at Saint-Cloud site. One hundred doses were dispensed for 59 patients. The mean final activity was 667 ± 155 MBq (min-max : 315 - 973 MBq) in 10 mL. The mean activity yield (AY) was 65 ± 3 % (56 - 70 %), the mean of RCP was 98.8 ± 0.6 % (97.2 - 99.9 %) evaluated by r-TLC and 99.3 ± 0.4 % (98.0 - 99.9 %) by r-UHPLC. The mean of chemical purity was 3.2 ± 0.5 µg/mL (1.9 - 4.8 µg/mL) for FAPI precursor+[^{68}Ga]Ga-FAPI-46 and 1.5 ± 0.4 µg/mL for the unkown impurity (0.8 - 2.9 µg/mL). A total of 5 productions encountered failure due to human error. Details are sum up in table 1. ***Conclusion:*** The robustness of this particular GMP process was demonstrated in routine clinical use. Only five production were not released due to human errors. The optimization of the process is a challenging task. A structured organization with effective communication between radiopharmacy and nuclear medicine is essential to ensure the successful management of short half-life radionuclide production.

EP-1190

GMP Standardized Automated Synthesis and Quality Control of [^{68}Ga]Ga-PSMA-11, [^{68}Ga]Ga-FAPI-04, [^{68}Ga]Ga-DOTA-NOC and [^{68}Ga]Ga-PentixaFor for Clinical PET Imaging

M. Zhang*;*
Xijing Hospital, Xi'an, CHINA.

Aim/Introduction: The striking diffusion and the exciting prospects of ^{68}Ga radiopharmaceuticals require a comprehensively and correctly implemented quality assurance system to guarantee reliable and validated production processes, and ensure that the quality and safety of ^{68}Ga radiopharmaceuticals are sufficient to satisfy the intended use. The present work aims to establish standardize automatic synthesis protocols for [^{68}Ga]Ga-PSMA-11, [^{68}Ga]Ga-FAPI-04, [^{68}Ga]Ga-DOTA-NOC and [^{68}Ga]Ga-PentixaFor, and build quality control systems for these ^{68}Ga radiopharmaceuticals for clinical PET imaging. ***Materials and Methods:*** The automated production of ^{68}Ga-PSMA-11, [^{68}Ga]Ga-FAPI-04, [^{68}Ga]Ga-DOTA-NOC and [^{68}Ga]Ga-PentixaFor using the ITM gallium-68 generator

eluate was implemented in an iQS Fluidic Labeling Module. Decay-corrected radiochemical yield (RCY) and residue rates on C18 cartridge, filter and waste were evaluated for each batch of production. Assessments of appearance, pH, radiochemical identity and radiochemical purity (RCP) were performed instantly before product releasing, while other tests like endotoxin and sterile examinations etc. were evaluated retrospectively. ***Results:*** The time for the labelling synthesis and quality control was approximately 25 min. The GMP compliant automated production of [^{68}Ga]Ga-PSMA-11, [^{68}Ga]Ga-FAPI-04, [^{68}Ga]Ga-DOTA-NOC and [^{68}Ga]Ga-PentixaFor were reproducibly with high RCYs of 87.76 ± 3.61%, 78.44 ± 3.83%, 71.30 ± 4.40% and 77.05 ± 3.67%, respectively. The RCP of the four ^{68}Ga radiopharmaceuticals were all greater than 95%. Predefined acceptance criteria were met for all other tests like the sterility, endotoxins level, radionuclidic purity, residual solvent content etc. ***Conclusion:*** The standardized automatic synthesis protocols for the labelling of [^{68}Ga]Ga-PSMA-11, [^{68}Ga]Ga-FAPI-04, [^{68}Ga]Ga-DOTA-NOC and [^{68}Ga]Ga-PentixaFor were demonstrated to be reliable and reproducible, with high RCY and RCP. The final product solutions were safe and suitable, passing full acceptance criteria of radiopharmaceuticals for clinical use. The comprehensive and integrated framework we established for production and quality control of ^{68}Ga pharmaceuticals was proved to be solid and reliable.

EP-1191

Automated Radiosynthesis and Quality Control of [^{68}Ga]Ga-DOTA-NOC for Clinical PET Imaging

M. Zhang;
Xijing Hospital, Xi'an, CHINA.

Aim/Introduction: This study was carried out to optimize the radiosynthesis of [^{68}Ga]Ga-DOTA-NOC using an iQS Fluidic Labeling Module and the quality control (QC) checks were performed before being used as a clinical product. ***Materials and Methods:*** The automated production of [^{68}Ga]Ga-DOTA-NOC using the ITM gallium-68 generator eluate was implemented in an iQS Fluidic Labeling Module. To optimize the production of [^{68}Ga]Ga-DOTA-NOC, different methods focus on the mass of the precursor in the labeling reaction, and the ethanol concentration of the eluent as well as the volume of the eluent during the elution process of C18 cartridge was employed. The decay-corrected radiochemical yield (RCY) and residue rates on C18 cartridge, filter and waste were evaluated for each batch of production. Assessments of appearance, pH, radiochemical identity and radiochemical purity (RCP) were performed instantly before product releasing, while other tests like endotoxin and sterile examinations etc. were evaluated retrospectively. ***Results:*** The radiochemical yields (RCYs) of methods A-D were 71.24%, 72.86%, 76.35% and 82.98%. There was an extremely significant difference of RCYs between methods C and D, and significant difference of RCYs between methods A and C, while there was no significant difference of RCYs between methods A and B as well as B and C, which suggesting that 30 µg of the precursor was not enough for the labeling reaction and increasing the volume of ethanol eluent instead of increasing the ethanol concentration of the eluent can improve the RCY. As for the residual rates on C18 cartridge, there was no significant difference among methods A, B and C, while there was an extremely significant difference between methods C and D, which suggesting that there was amount of radioactive colloid generated in methods A-C, which was significantly decreased as the precursor mass increased to 50 µg. With the increasing of ethanol concentration of eluent, the residue rate on filter decreased significantly. There was no significant difference of residue rates of waste among methods A, B, C and D. The RCP of each batch of [^{68}Ga]Ga- DOTA-NOC was greater than 95%. Predefined acceptance criteria were met for all other tests like the sterility, endotoxins level, radionuclidic purity, residual solvent content etc. ***Conclusion:*** The optimized automatic synthesis protocol for the labelling of [^{68}Ga]Ga-DOTA-NOC was demonstrated to be reliable and reproducible, with high RCY and RCP. The final product solutions were safe and suitable, passing full acceptance criteria of radiopharmaceuticals for clinical use.

EP-1192

Automated Radiosynthesis and Quality Control of [^{68}Ga]Ga-PentixaFor for Clinical PET Imaging

M. Zhang;
Xijing Hospital, Xi'an, CHINA.

Aim/Introduction: Chemokine receptor CXCR4 is overexpressed in more than 27 different human tumors that make it a promising target in oncology. [^{68}Ga]Ga-PentixaFor is the most promising PETtracer for CXCR4 receptor imaging; hence, the present study was carried out to optimize the radiosynthesis of [^{68}Ga]Ga-PentixaFor using an iQS Fluidic Labeling Module and the quality control (QC) checks were performed before being used as a clinical product. ***Materials and Methods:*** The automated production of [^{68}Ga]Ga-PentixaFor using the ITM gallium-68 generator eluate was implemented in an iQS Fluidic Labeling Module. To optimize the production of [^{68}Ga]Ga-PentixaFor, different methods focus on the mass of the precursor in the labeling reaction, and the ethanol concentration of the eluent as well as the volume of the eluent during the elution process of C18 cartridge was employed. The decay-corrected radiochemical yield (RCY) and residue rates on C18 cartridge, filter and waste were evaluated for each batch of production. Assessments of appearance, pH, radiochemical identity and radiochemical purity (RCP) were performed instantly before product releasing, while other tests like endotoxin and sterile examinations etc. were evaluated retrospectively. ***Results:*** The radiochemical yields (RCYs) of methods A-D were 78.17%, 76.41%, 82.40% and 83.13%. There was extremely significant difference of RCYs between methods B and C, while there was no significant difference of RCYs between methods A and B as well as Cand D, which suggesting that 30 µg of the precursor was enough for the labeling reaction and increasing the volume of ethanol eluent instead of increasing the ethanol concentration of the eluent can improve the RCY. The reason behind this was that increasing the volume of ethanol eluent can significantly reduce the radioactivity residual on C18 cartridge and filter membrane. The RCP of each batch of [^{68}Ga]Ga-PentixaFor was greater than 95%. Predefined acceptance criteria were met for all other tests like the sterility, endotoxins level, radionuclidic purity, residual solvent content etc. ***Conclusion:*** The optimized automatic synthesis protocol for the labelling of [^{68}Ga]Ga-PentixaFor was demonstrated to be reliable and reproducible, with high RCY and RCP. The final product solutions were safe and suitable, passing full acceptance criteria of radiopharmaceuticals for clinical use.

EP-1193

Liquid target production of Gallium-68 by a low energy medical cyclotron, post-bombardment purification and radiosynthetic yield of Gallium-68 DOTATATE as compared with Ge68/Ga68 generator

J. Cheung, *N. Ng, K. Liu, P. Lee, C. Ho;*
Hong Kong Sanatorium & Hospital, Hong Kong, HONG KONG.

Aim/Introduction: We were able to produce Gallium-68 chloride via ^{68}Zn(p, n)^{68}Ga reaction by a low-energy (12 MeV) on-site cyclotron installed with a liquid target. Our aim was to adapt a published purification protocol, which was initially designed for an automated module, to a home-made, manual disposable purification setup. Using the same labelling module, we attempted to produce Gallium-68 DOTATATE by modifying the labelling conditions originally used for Ge68/Ga68 generator, and compared the amount of activity and percentage yield between them. ***Materials and Methods:*** The CYPRIS™ HM-12S (Sumitomo

Heavy Industry, Ltd.) was installed with a Gallim-68 liquid target, loaded with [^{68}Zn]Zn(NO_3)$_2$ (66mg/mL) solution in dilute HNO_3 (0.178M). Target bombardment current was 40 µA for 60 minutes to produce crude Gallium-68 chloride solution. This was purified manually by following a published protocol adopted in GE FASTlab. Our disposable setup was composed of a ZR cartridge, a TK200 cartridge, four 3-way valves, two addition lines and three extension sets. The purified product was added in the ITM iQS labelling module prefilled with DOTATATE precursor dissolved in sodium acetate buffer. Attempts were made to vary the amount of DOTATATE precursor (25 to 100 µg) and the concentration of sodium acetate buffer (0.25 to 1.50 M) in order to derive the optimal conditions for radiolabelling. ***Results:*** The manual purification of cyclotron-produced Gallium-68 chloride yielded an average decay-corrected recovery of 55.64% (n=3), which meets the quality control standards specified in the European Pharmacopeia monographs, whereby Gallium-66 and 67 contents present should be less than the products obtained from higher energy cyclotrons. By systematically adjusting 2 different variables (amount of DOTATATE precursor and sodium acetate buffer concentration), we found the optimal conditions which are using 100 µg DOTATATE dissolved in 0.425M acetate buffer to react with purified Gallium-68 chloride at 105°C for 10 minutes. Gallium-68 DOTATATE was then successfully synthesized in the labelling module, attaining a radiochemical purity exceeding 95% by HPLC analysis and an average yield of 74.70% (EOP, n=3). ***Conclusion:*** Crude Gallium-68 chloride could be successfully produced, purified and labelled by the above proposed setup and purification procedures to give a favourable recovery rate and radiopharmaceutical yield. With the above optimal setup and conditions, we were able to synthesize Gallium-68 DOTATATE on demand with our on-site low-energy cyclotron modified with a liquid targetry, which is comparable in activity and yield to those conventionally obtained from a Ge68/Ga68 generator and labelling module.

EP-1195

Transfer Of The [^{18}F]FMPEP-d_2 From a Fixed-line Device To a Disposable Cassette System

E. Kerminen[1], *N. Rajala*[1], *A. K. Kirjavainen*[1,2];
[1]*Turku PET Centre, Turku, FINLAND,* [2]*Department of Chemistry, University of Turku, Turku, FINLAND.*

Aim/Introduction: [^{18}F]FMPEP-d_2 is a PET tracer targeting cannabinoid receptor CB_1. It has promising properties such as high brain uptake[1], high specific binding[1] and it has been used for imaging CB_1 expression in subjects with alcohol abuse[2] and neurological disorders such as Parkinson's disease[3]. Previously, [^{18}F]FMPEP-d_2 has been labelled with good radiochemical yield (RCY) and reasonable synthesis time by a method utilising a fixed-line device.[4] However, the procedure is difficult to adapt to other facilities and this limits the wide spread use of [^{18}F]FMPEP-d_2. Herein, is described a previously reported method transferred to a cassette based module. ***Materials and Methods:*** [^{18}F]FMPEP-d_2 was synthesised using Trasis AllInOne (AIO) module adapting the synthesis method published by Lahdenpohja et al.[4] The synthesis included 1) azeotropic distillation 2) formation of [^{18}F]CD_2BrF 3) Gas Chromatographic (GC) purification of [^{18}F]CD_2BrF 4) [^{18}F]fluoroalkylation of the phenolic precursor 5) HPLC purification and 6) formulation. The GC purification of [^{18}F]CD_2BrF was applied to the cassette based synthesis utilising an external heater compatible with AIO and an in-house GC column filled with porous polymer absorbent. ***Results:*** The synthesis of [^{18}F]FMPEP-d_2 was completed in 75 minutes with RCY of 8.0 ± 0.1 % radiochemical purity (RCP) of > 99 % and molar activity of ≥ 480 GBq/µmol (decay corrected to SOS) with full automation. The yield of [^{18}F]FMPEP-d_2 was 700 ± 10 MBq at EOS. ***Conclusion:*** [^{18}F]FMPEP-d_2 was successfully synthesised on Trasis AIO with high RCP and a RCY suitable for clinical applications. Although the synthesis requires a GC purification with an external heater, this simple set-up can be easily utilised in facilities worldwide. The synthesis is applicable to a GMP environment and the simplicity of the cassette-based approach increases the reproducibility of the synthesis. Although, the results are sufficient, optimisation is still ongoing with the expectation of improved results. ***References:*** (1) Reubi, J. C.; Waser, B. Eur. J. Nucl. Med. Mol. Imaging 2003, 30 (5), 781-793. (2) Hirvonen, J. et al. Mol. Psychiatry 2013, 18 (8), 916-921. (3) Brück, A., et al. Movement Disorders 34 (2019): S773. (4) Lahdenpohja, S. et al. J. Label. Compd. Radiopharm. 2020, 63 (9), 408-418.

EP-1196

Residual solvents analysis on fully automated quality control system - Method validation and comparability with compendial methods (Ph Eur & USP)

X. Franci*, S. Leloux, N. Godeau, Y. Zandona, N. Verbrugge;*
Trasis, Ans, BELGIUM.

Aim/Introduction: With the increasing number of different PET radiotracers that commercial radiopharmacies are required to deliver nearly simultaneously on a daily basis, quality control (QC) of radioactive drugs is becoming a limiting factor. Among the ten other analyses, the QC1 system performs the residual solvents test automatically. The system uses a gas chromatography (GC) method that diverges in various technical aspects from the Ph Eur and USP monographs, while maintaining the same analytical principles. As it is an alternative GC method, there is a need to validate the method and demonstrate its comparability with compendial methods. This study outlines the strategy and results obtained for the GC method validation and comparability versus Ph Eur and USP on the QC1 from Trasis, using the FDG case. ***Materials and Methods:*** A standard qualified QC1 Core was used for the study. To facilitate automation and miniaturization, the GC system employs a dedicated headspace device for sample/reference standards preparation, a 10m WAX column, and a thermal conductivity detector. The GC method for determining ethanol, acetonitrile, and acetone was validated according to ICHQ2(R2) guidelines, considering specificity, linearity, precision, accuracy, and range as validation criteria. For comparison purposes, a conventional GC system (Thermoscientific GC Trace 1600/Triplus 500 HS with flame ionization detector (FID)) was used, following the the Ph Eur and USP compendial methods. ***Results:*** The method validation results demonstrated that the QC1 method is suitable for the residual solvent analysis of FDG, particularly for the identification and quantification of acetone, ethanol, and acetonitrile within the limits defined by the Ph Eur and USP monographs. The method validation study met acceptance criteria for specificity (Rs > 3 for all peaks, matrix-independent, asymetry factors between 0.95 and 1.04), linearity (R^2 > 0.99), accuracy (recovery [95-105%]), and precision (RSD < 3.0%) according to ICHQ2(R2) guidelines. Additionally, robustness regarding the temperature of the headspace and gas sample volume was confirmed. Comparative data generated on both systems (QC1 and classical GC) showed that the QC1 method is as effective as the pharmacopeia methods. ***Conclusion:*** This study demonstrates that the GC method implemented on the QC1 is appropriate for the residual solvent quality control analysis of FDG, particularly for the identification and quantification of acetone, ethanol, and acetonitrile within the limits defined by the Ph Eur and USP. The method was validated, and its equivalence to the pharmacopeial methods was confirmed by statistical analysis following Ph Eur 5.27 guideline.

EP-1197

Radio-TLC Linearity in the Range of Concentrations Used

C. Piedelobo Vaquero*, E. Dobra Neacsu, L. Cebollada Cameo, G. Rubio Fernández, J. Pérez Iruela;*
Servicio de Radiofarmacia. Hospital Universitario Ramón y Cajal, Madrid, SPAIN.

Aim/Introduction: The aim is to verify that our radio-TLC measures linearly within the range of concentrations we use on a daily basis. ***Materials and Methods:*** Whatman 3 strips (1 cm wide, 10 cm long) were used and one drop with a 25G 5/8" (0.5x16mm) needle was applied in a 1ml syringe. The samples were measured by the radiochromatograph. Our method was validated according to the EANM and ICH Q2(R1) guidelines. Linearity, limit of quantification (LOQ) and range were calculated for this purpose. For the linearity, a 10 cm strip was divided into 5 equal portions. A drop, with half of the concentration of the previous one, was placed in the centre of each part. It was measured twice by the radiochromatograph. A regression line of the concentration versus the corrected area in counts per second (cps) was obtained. In the EANM guideline several methods to determine the limit of quantification were suggested. In our case, it was determined both, visually and by the signal/noise method. The limit of quantification was stipulated when the signal/noise ratio was 10:1. Visually, it was checked by the loss of linearity. The lower limit of the range was obtained from the limit of quantification, and the upper limit, from the data provided by the radio-TLC supplier. ***Results:*** The linearity was calculated by plotting the concentrations in MBq/ml against the corrected area cps, a linear regression line was obtained with a correlation coefficient of 0.9965. For the LOQ the signal/noise ratio was 10:1 when the concentration was 3 MBq/ml. This was confirmed by visual inspection of the regression line, where a loss of linearity was observed at that concentration. The range was stablished taken into account the lower limit as the limit of quantification (3 MBq/ml), and the upper limit was determined by the manufacturer as 200,000 cps, which was equivalent to 1667.5 MBq/ml. ***Conclusion:*** Knowing the concentrations handled in our radiopharmacy, it can be said that the radio-TLC measures reliably within the concentration range used. ***References:*** ICH Q2(R1). Validation of Analytical Procedures - ICH Quality GuidelinesGillings, N., Todde, S., Behe, M. et al. EANM guideline on the validation of analytical methods for radiopharmaceuticals. EJNMMI radiopharm. chem. 5, 7 (2020).

EP-1198

Determine Radiochemical Purity of [^{99m}Tc]Tc-Nanocolloids in an Analytical Method with Accuracy, Precision and Specificity

C. Piedelobo Vaquero*, E. Dobra Neacsu, G. Rubio Fernández, L. Cebollada Cameo, P. Ortega Cuadrado, M. Rodríguez Gómez, J. Pérez Iruela;*
Servicio de Radiofarmacia. Hospital Universitario Ramón y Cajal., Madrid, SPAIN.

Aim/Introduction: The aim of this study is to verify whether our analytical method is capable of detecting and quantifying a 5% impurity, from a [^{99m}Tc]Tc-Nanocolloids sample, with accuracy, precision, and selectivity. This forms part of the validation of an analytical method. ***Materials and Methods:*** Materials: For our validation method we have used Whatman 3 strips (1cm wide and 9cm long) as the solid phase and acetone as the mobile phase. The development of it took 8 cm. For the reference method, Silica gel 60 strips (1cm wide, 11cm long) were used and for the mobile phase, acetone. The development, in this case, took 10 cm. In both cases, one drop with a 25G 5/8" (0.5x16mm) needle in a 1ml syringe was applied at 0.5cm from the base and the samples were analysed by radio-TLC. Methods: The albumin nanocolloids accuracy, to which we added 3 known concentrations of the impurity [^{99m}Tc]TcO_4^- , was analysed using radio-TLC. Our results were compared to those obtained using the method described in the technical data sheet. Six samples, with the same impurity concentration, were measured for precision and the operation was performed by two different operators for intermediate precision. For [^{99m}Tc]Tc-nanocolloids, the impurity to be detected was only [^{99m}Tc]TcO_4^-, so it can be calculated by the resolution between the two peaks. The precision, limit of quantification and range were confirmed in a previous research following the ICH Q2 and EANM guidelines. ***Results:*** Accuracy results show recovery percentages within the range of 98.52% to 101.77%, depending on the concentration measured. For precision, the average of 6 samples was 5.29%, the standard deviation was 0.24 and the coefficient of variation (CV) was 4.47%. The intermediate precision was also calculated, obtaining an average between the two operators of 5.47%, standard deviation of 0.26 and CV of 4.71%. The specificity, according to the resolution between the two peaks, was 4.85. ***Conclusion:*** It can be stated that our method is capable of detecting the 5% impurity with precision, accuracy, and specificity and because of that it could replace the technical data sheet method. ***References:*** ICH Q2(R1). Validation of Analytical Procedures - ICH Quality Guidelines. Gillings, N., Todde, S., Behe, M. et al. EANM guideline on the validation of analytical methods for radiopharmaceuticals. EJNMMI radiopharm. chem. 5, 7 (2020).

EP-1199

Towards Advanced Imaging of Cardiac Amyloidosis: Reassessing Aprotinin with ^{64}Cu Radiolabeling

L. Canziani[1]*, G. Manfrinato*[1]*, A. Gandini*[2]*, G. Pepe*[1]*;*
[1]*Fondazione IRCCS Policlinico San Matteo, Pavia, ITALY,*
[2]*Laboratory of Applied Nuclear Energy - Università di Pavia, Pavia, ITALY.*

Aim/Introduction: Recent advances in therapies for amyloid cardiomyopathy rise a renewed interest in improving its diagnosis, particularly through nuclear imaging. MRI, echocardiography, and bone scintigraphy enhanced our understanding of the disease, no single diagnostic tool currently offers early detection, differential diagnosis, and treatment monitoring in one. In the 1990s, ^{99m}Tc-aprotinin appeared as a promising tracer for cardiac amyloidosis scintigraphy, but safety concerns lead to its withdrawal and even after its re-approval, the shortage of raw materials limited further evaluations in clinical studies The recent availability of new isotopes like ^{64}Cu, aprotinin may regain its relevance as a radiopharmaceutical vector. However, radiolabeling with ^{64}Cu presents technical challenges. To address these challenges, we are investigating laser-assisted techniques to improve labeling efficiency and potentially revive aprotinin-based imaging in modern nuclear medicine. ***Materials and Methods:*** A solution of 100 MBq of ^{64}Cu was added to 2450 KUI of aprotinin in acetate buffer (pH 5). Labeling was tested under three conditions: room temperature, heating at 75°C for 15 minutes, and irradiation with a 7 W, 450 nm blue laser for 15 minutes. Laser exposure was performed in a shielded setup with real-time temperature monitoring. Radiolabeling yield was assessed by ITLC using ITLC-SG and 0.1 M tribasic citrate as the mobile phase. ***Results:*** The labeling yield (LY) of [^{64}Cu]Cu-aprotinin was 0% in Vial-1 (room temperature), 30% in Vial-2 (heat method), and >46% in Vial-3 (laser method). In Vial-3, the temperature only increased slightly, reaching 38°C during irradiation. The LY remained stable after 12 hours of incubation. However, when a [^{64}Cu] carrier-added source was used, the LY rapidly dropped to 0%, even for both the heat and laser methods. ***Conclusion:*** Our study demonstrates that both laser-assisted and heat-based approaches for ^{64}Cu labeling of aprotinin show potential for cardiac amyloidosis imaging, with the highest labeling efficiency (>46%) for the laser method. Notably, the use of a carrier-added ^{64}Cu source significantly reduced labeling efficiency, highlighting the importance of using non-carrier-added radionuclides. Although heat-based labeling is effective, it poses a risk of compromising protein structure and altering biological function, making laser labeling the more favorable method. Moreover, ^{64}Cu-labeled aprotinin wpuld apply for PET/CT imaging offering superior diagnostic accuracy

compared to early scintigraphis studiesThese findings are preliminary, and further refinement of reaction conditions could lead to improved outcomes.

EP-1200

Production optimisation and quality control testing of RHN001-Tx (^{188}Re-PSMA) per GMP standards

S. Sibiya[1,2,3], *A. Mdlophane*[1,2,3], *S. Mdanda*[1,2,3], *K. Ramonaheng*[1,2,3], *M. Qebetu*[1,2,3], *H. Ndlovu*[1,2,3], *J. Zeevart*[1,4], *F. Giesel*[5], *M. Sathekge*[1,2,3], *J. Cardinale*[5];
[1]*NuMeRI NPC, Pretoria, SOUTH AFRICA,* [2]*Department Of Nuclear Medicine, Steve Biko Academic Hospital, Pretoria, SOUTH AFRICA,* [3]*Department of Nuclear Medicine, Faculty of Health Science, University of Pretoria, Pretoria, SOUTH AFRICA,* [4]*The South African Energy Corporation (NECSA), Pelindaba, SOUTH AFRICA,* [5]*Department of Nuclear Medicine, Medical Faculty and University Hospital Heinrich Heine University Dusseldorf, Dusseldorf, GERMANY.*

Aim/Introduction: The advent of theranostics has seen the ^{68}Ga/^{177}Lu radionuclide pair being utilised for peptide receptor radionuclide imaging and therapy. However, application of this nuclide pair is limited to hospitals with suitable PET scanners and ^{177}Lu supply is limited. An alternative is offered by the well-known ^{99m}Tc/^{188}Re-combination - a highly cost-effective potential theranostic pair that provides generator-based on-demand radiopharmaceuticals. With RHN001-Dx/-Tx we are currently investigating a PSMA targeting ^{99m}Tc/^{188}Re-labeled theranostic in a phase-I/II clinical trial (Rhino trial). A method for preparation of ^{188}Re-labeled RHN001-Tx has been reported before. The aim of the current work was an optimization of the existing ^{188}Re-labelling process for RHN001 providing a GMP compliant routine production of the study drug RHN001-Tx. ***Materials and Methods:*** [^{188}Re]$NaReO_4$ obtained from a ^{188}W/^{188}Re-generator in 0.9% NaCl as eluent. A Sep-Pak Alumina N cartridge was used for removal of remaining ^{188}W-breakthrough. Labelling was conducted with 95 µg RHN001 precursor and 4 ml $NaReO_4$ solution (6-14 GBq) in presence of 12 mg $SnCl_2$ and a mixture of ascorbic acid and sodium citrate as auxiliaries. The starting pH at a range of 2.0-3.5 and the labelling was conducted at 96 °C for variable times. Subsequently, the crude product was neutralized to pH 6.5-7.5 by adding 0.5 M sodium phosphate solution and incubated for a further 10 min at 96°C. The crude product was purified and reformulated by cartridge extraction using standard Sep-Pak tC18 plus light cartridge. The radiolabeled product was then eluted with 1 ml 70% ethanol via a 0.22 µm filter and diluted with the formulation buffer containing a mixture of gentisic acid, sodium ascorbate and sodium acetate. ***Results:*** RHN001-Tx was produced in radiochemical yields of 90 % ± 1% (n = 3) and high radiochemical purities above 95%. Reaction time was an item of optimization and could be reduced to 15 min. Shelf-life was proven for up to 6 hours post-production (RCP still 95% ± 2%, n = 3). All other quality control items met the typical requirements for radiopharmaceuticals (e.g., Eur. Ph.). ***Conclusion:*** The ^{188}Re-labeling of the study drug RHN001-Tx was successfully optimized and scaled up for the preparation of therapeutic doses in the range of 4-5.5 GBq with proven shelf-life of up to 6 hours. Further scale up to even higher doses is currently under investigation. In summary, RHN001-Tx is now available as fully GMP compliant material for application within Rhino trial.

EP-1201

Process Validation of [^{18}F]Fluoroestradiol and [^{18}F] PSMA-1007 Production on next-gen Automated Module following Regulatory-Compliant Transition Requirements

M. B. Silveira, *E. Cortez, A. F. Castro, C. L. S. Costa, L. T. C. Nascimento;
Center for the Development of Nuclear Technology (CDTN/CNEN), Belo Horizonte, BRAZIL.*

Aim/Introduction: The radiopharmaceuticals [^{18}F]Fluoroestradiol and [^{18}F]PSMA-1007 are crucial for oncology diagnostics of high-incidence breast and prostate malignancies, respectively. Enhancing global access to these agents requires optimizing synthesis processes while maintaining quality and safety. This study evaluates the transition from TracerLab MX-FDG to FastLab-2 automated synthesis modules to produce [^{18}F]Fluoroestradiol and [^{18}F]PSMA-1007, considering Good Manufacturing Practices (GMP) requirements, process validation (critical parameters and in-process controls), and operational scalability for high-demand clinical environments. ***Materials and Methods:*** Validation studies were performed using GE Healthcare's TracerLab MX-FDG and FastLab-2 synthesis modules. Three consecutive batches of each radiopharmaceutical were manufactured under GMP-controlled conditions. Quality attributes assessed included radiochemical purity/identity, radionuclide purity/identity, pH, sterility, endotoxins, residual solvents, and TBA presence. In-process controls included synthesis yield and sterile filter integrity (bubble point test), with data analyzed for batch-to-batch consistency in alignment with specifications. ***Results:*** The FastLab-2 module demonstrated enhanced performance in [^{18}F]Fluoroestradiol (25-27% yield) and [^{18}F]PSMA-1007 (20-30% yield) production, showing significantly improved reproducibility compared to the TracerLab MX-FDG system (15%-19% and 19%-22%, respectively). For process controls, starting with an initial activity of 560 GBq of ^{18}F, the End of Synthesis (EOS) yielded 150 GBq of [^{18}F]Fluoroestradiol and 160 GBq of [^{18}F]PSMA-1007 using Fastlab-2. Quality control analyses confirmed all batches met the specifications, with radiochemical purity (HPLC) consistently for [^{18}F]Fluoroestradiol (>95%) and [^{18}F] PSMA-1007 (>91%). Sterile filter integrity (bubble point pressure of 57-62 psi) exceeded acceptance criteria (>50 psi) for both systems. The enhancements of FastLab-2 significantly reduced manual intervention, deviations, and contamination risks. In contrast, the TracerLab MX-FDG displayed greater inconsistencies, which were attributed to flat-bottom reactor and the absence of active cooling. Comprehensive quality assurance documentation was completed, including change control records, similarity studies, risk analysis reports, and full validation protocols. ***Conclusion:*** The FastLab-2 integrates key technological advancements, including enhanced valve actuators, a conical reservoir, streamlined cassette installation, precise nitrogen control, and computerized system quality management. Validation studies confirmed full GMP compliance, particularly in in-process controls (synthesis yield, filter integrity) and quality assurance parameters, providing confidence in its regulatory compliance. The operational efficiency, regulatory compliance, and batch-to-batch consistency position the FastLab-2 as a reproducible solution for high-demand environments, highlighting its advantages in clinical-scale production. Transitioning to the FastLab-2 module significantly enhanced productivity and reliable distribution of [^{18}F]Fluoroestradiol and [^{18}F]PSMA-1007.

EP-71

e-Poster Area

E: Other Studies -> E1 Case Reports

EP-1202

Imaging of Widespread Manifestations of Erdheim-Chester Disease with Ga-68 FAPI PET/CT and F-18 FDG PET/CT

C. Turkan[1], *Ö. Karadağ*[2], *Y. Büyükaşık*[3], *M. Tuncel*[1];
[1]*Hacettepe University Department of Nuclear Medicine, Ankara, TÜRKIYE,* [2]*Hacettepe University Department of Internal Medicine, Divison of Rheumatology, Ankara, TÜRKIYE,* [3]*Hacettepe University Department of Internal Medicine, Divison of Hematology, Ankara, TÜRKIYE.*

Aim/Introduction: Erdheim-Chester disease (ECD) is a rare form of non-Langerhans cell histiocytic neoplasm characterized by multisystem involvement of foamy histiocytes and fibrosis. Diagnosing ECD is often challenging due to the rarity of the disease. A baseline whole-body F-18 FDG PET/CT is recommended in all cases to aid in diagnosis and to define the extent of the disease. Ga-68 FAPI is a promising agent for imaging fibrotic

processes in various organs. Current literature on the role of Ga-68 FAPI PET/CT in the diagnosis of ECD is scarce. Therefore, we would like to present a case with extensive manifestations of ECD imaged using both F-18 FDG and Ga-68 FAPI. ***Materials and Methods:*** A patient with an orbital and renal biopsy suspicious for ECD is imaged within one week using Ga-68 FAPI PET/CT and F-18 FDG PET/CT. ***Results:*** A 66-year-old man was admitted to hospital with flank pain and eye swelling. Following his initial imaging, renal and orbital biopsies were performed. The biopsy results were suspicious for ECD and IgG4-related disease. After consultation with rheumatology, the patient underwent Ga-68 FAPI PET/CT and F-18 FDG PET/CT scans. Both Ga-68 FAPI and F-18 FDG PET/CT revealed an extensive disease burden within the orbits, paranasal sinuses, periaortic soft tissues (coated aorta), right atrium (atrial pseudotumour), and retroperitoneum (hairy kidney sign), mesentery, and long bones. Ga-68 FAPI uptake was more pronounced than F-18 FDG uptake at all mentioned sites. In the central nervous system, Ga-68 FAPI PET/CT showed dural and cavernous sinus involvement that was not observed on F-18 FDG PET/CT. The patient was diagnosed with ECD based on imaging findings showing the classic sites of the disease and a re-evaluation of the existing biopsy results. ***Conclusion:*** Ga-68 FAPI PET/CT is a promising imaging modality for the diagnosis and accurate identification of disease burden in ECD and can be used in conjunction with F-18 FDG PET/CT. Our case demonstrates one of the most extensive disease burdens, clearly demonstrated by Ga-68 FAPI PET/CT.

EP-1203

Pitfall in ^{18}F-FDG PET/CT: Muscular Uptake Does Not Always Mean Inadequate Preparation - A Case Report of Antisynthetase Syndrome

V. Heringer, *E. Lima, T. Alves, C. Torricelli, N. Silva, G. Barbosa, E. Etchebehere;*
UNICAMP, Campinas, BRAZIL.

Aim/Introduction: Antisynthetase syndrome is a heterogeneous group of autoimmune disorders, most commonly presenting with the triad of myositis, arthropathy, and interstitial lung involvement[1]. The condition is characterized by the presence of autoantibodies directed against aminoacyl-tRNA synthetases. The precise role of those antibodies in disease pathogenesis remains unknown, posing challenges to the development of targeted therapeutic approaches[2]. ***Materials and Methods:*** A 47-year-old white male presented with a one-year history of symptoms, including periorbital edema, symmetric polyarthralgia of the hands and wrists with brief morning stiffness, Gottron's papules, interstitial lung disease, and myositis with proximal lower limb weakness, elevated creatine phosphokinase (CPK), and electromyography findings consistent with myopathy. Laboratory evaluation revealed a reactive antinuclear antibody (ANA) at 1/320 with a homogeneous nuclear pattern; positive anti-Jo-1 and C-reactive protein (CRP). Because of refractory muscle involvement, combined therapy with rituximab, mycophenolate, and intravenous immunoglobulin was required. Due to persistent low-grade fever and nonspecific signs of inflammatory activity (with no apparent infectious or neoplastic focus) it was recommended to perform ^{18}F-FDG PET/CT. ***Results:*** The PET/CT images demonstrated diffuse hypermetabolism in the musculature without significant tomographic abnormalities (SUV = 8.3 - right lower limb), suggesting diffuse inflammatory myopathy with no detectable infectious or neoplastic sites. ***Conclusion:*** This case highlights the importance of correlating clinical data with imaging findings, whether this information is obtained from the patient in person through questionnaires on the day of image scan or accessed from medical records in a hospital setting. Notably, some clinical conditions are rare, and the patient may not be aware of them. Limited literature is available on the findings of ^{18}F-FDG PET/CT in antisynthetase syndrome. In conclusion, diffuse systemic muscular inflammation was detected on ^{18}F-FDG PET/CT, and it may be useful in evaluating and monitoring the degree of inflammatory activity, showing that muscular uptake does not always mean inadequate preparation. ***References:*** 1. 1) Nazerani-Zemann T, et al. Nuklearmedizin. 2023. 2. 2) Patel P, et al. Int J Mol Sci. 2024. 3. 3) Jain TK, et al. Rev Esp Med Nucl Imagen Mol. 2016.

EP-1204

Incidental Detection of Hemorrhagic Stroke with Luxury Perfusion on a 99mTc-MDP Bone Scan in a Breast Cancer Patient: A Case of Hidden Neurological Sequelae

A. Akhter, *S. Sharmin, S. Islam;*
Institute of Nuclear Medicine and Allied Sciences (INMAS) Dhaka, BAEC, Dhaka, BANGLADESH.

Aim/Introduction: Neurological symptoms in cancer patients, such as cognitive decline, fatigue, and mood disturbances, are often attributed to psychological stress or treatment-related effects, potentially masking serious underlying pathology. We present a compelling case of a 67-year-old woman with breast cancer who was referred for a routine whole-body bone scan as part of metastatic surveillance. The scan incidentally revealed findings consistent with a subacute hemorrhagic stroke with luxury perfusion, highlighting the value of hybrid SPECT/CT in detecting subtle neurological abnormalities that can directly influence clinical decision-making. ***Materials and Methods:*** The patient, a breast cancer survivor post-surgery and chemotherapy state, presented with generalized weakness, poor responsiveness, and altered mental status for two weeks. She underwent a 99mTc-MDP bone scan for metastatic surveillance, 3 hours after the intravenous injection of 20 mCi of 99mTc-MDP. Hybrid SPECT/CT was performed to localize an incidental finding of increased radiotracer uptake in the left temporo-parietal region observed on the planar scan. Two days later, an MRI of the brain was conducted for further evaluation. ***Results:*** Planar bone scan revealed focal increased radiotracer uptake in the left temporo-parietal skull region, which was further localized by SPECT/CT to a large irregular hypodense area in the brain parenchyma, suggesting a cerebrovascular ischemic event rather than bone or brain metastasis. MRI of brain performed two days later showed a large area of altered signal intensity in the left temporo-parietal cortex extending into the posterior periventricular region. The lesion demonstrated T1 hypointensity, T2 hyperintensity, partial diffusion restriction, minimal GRE blooming, and significant post-contrast enhancement, consistent with a subacute hemorrhagic infarct with luxury perfusion. Additional findings included dilated ventricles, generalized brain atrophy, and deep white matter ischemic changes. The 99mTc-MDP uptake in the stroke was attributed to blood-brain barrier breakdown, inflammatory changes, calcium deposition, and ischemic tissue mineralization. This incidental finding led to the diagnosis of a silent hemorrhagic stroke. Clinical evaluation revealed mild anemia with normal serum electrolytes, excluding metabolic abnormalities. Based on the imaging findings, the patient was referred for conservative neurological care. ***Conclusion:*** This case underscores the importance of incidental findings in routine nuclear imaging for oncology patients. The detection of a silent hemorrhagic stroke on a 99mTc-MDP planar bone scan highlights the need for thorough evaluation of subtle neurological symptoms through hybrid SPECT/CT, prompting accurate diagnosis, guiding management, and improving patient outcomes.

EP-1205

From Prostate to Pulmonary Malignancy: A Case of Incidental Lung Adenocarcinoma detected by PSMA PET/CT with a significant impact on clinical management

D. Barbosa, *J. Ferro, H. Duarte, D. Silva, N. Vasconcelos, R. Marão, I. Sampaio;*
IPO, Oporto, PORTUGAL.

Aim/Introduction: Prostate-specific membrane antigen (PSMA) Positron Emission Tomography/Computed Tomography (PET/CT) is an established modality for imaging prostate cancer patients. However, PSMA uptake has also been observed in non-prostate malignancies, a fact that is crucial to recognise in order to avoid misdiagnosis. Expression of PSMA in non-prostatic tumours, including lung adenocarcinoma, is increasingly recognised and correlates with endothelial PSMA expression in tumour-associated neovasculature. Incidental detection of lung cancer on PET-PSMA has been reported in about 2% of scans. We present a case where [68Ga]Ga-PSMA-11 PET/CT identified a primary lung cancer, significantly impacting patient management. ***Materials and Methods:*** A 69-year-old male patient diagnosed with prostate cancer underwent radical prostatectomy and bilateral lymphadenectomy. Pathological analysis revealed an adenocarcinoma Gleason score 7 (3+4), cT2N0M0 R0 (initial PSA: 8.2ng/mL). After a 5-year surveillance period, biochemical recurrence had occurred (PSA: 0.240ng/mL), and a [68Ga]Ga-PSMA-11 PET/CT scan was requested. ***Results:*** [68Ga]Ga-PSMA-11 PET/CT did not show locoregional recurrence; however, it revealed an intense PSMA-avid pleuropulmonary densification in the right upper lobe (SUVmax: 5.55), suggesting a primary cancer. This finding prompted further investigation. A contrast-enhanced CT scan revealed a 2.5 cm subpleural nodule in the right lung, and a CT-guided biopsy was subsequently performed. Histopathological analysis revealed lung adenocarcinoma, TTF-1 positive, with PD-L1 expression at 95% and a KRAS G12C mutation. Staging was completed with a brain magnetic resonance imaging (which showed no abnormalities) and a [18F]fluoro-2-deoxy-D-glucose PET/CT, which reported the known malignant neoplasm of the right lung (possibly with carcinomatous lymphangitis) and metastasis to mediastinal-hilar and right axillary lymph nodes and to the right pleura. Despite the persistence of PSA values up to 0.327ng/mL, the identification of primary lung cancer led to a modification of the patient's treatment plan. The salvage radiotherapy that had been planned for the recurrence of prostate cancer was postponed, and the patient was initiated on first-line palliative immunotherapy with pembrolizumab. ***Conclusion:*** This case underscores the diagnostic challenges associated with PSMA-PET/CT imaging, highlighting its ability to detect unsuspected primary malignancies other than prostate cancer. A meticulous evaluation of atypical PSMA-avid lesions is crucial to avoid misinterpretation, directly influencing patient outcomes by enabling prompt diagnosis and management of secondary primary tumours.

EP-1206

Renal Cell Carcinoma Masquerading as a Cervical Paravertebral Abscess: A Rare Case Report

C. S*, L. Goriparti, C. Bal, S. L.S., J. Krishna;*
All India Institue of Medical Science, New Delhi, INDIA.

Aim/Introduction: Renal cell carcinoma, accounts for over 90% of adult renal tumors. Nearly 50% of RCCs are found incidentally and often presents asymptomatically or with nonspecific symptoms. We report a rare case of RCC initially mimicking a cervical paravertebral abscess, highlighting the role of FDG PET/CT in diagnosing occult malignancy. ***Materials and Methods:*** Patient was instructed to avoid strenuous activity for 24 hours and fasted for atleast 8 hours before the scan. Blood glucose levels before the FDG administration was 106 mg/dl. 8 mCi (296 MBq) of ^{18}F-FDG was injected intravenously in right upper limb. PET/CT was acquired from the level of vertex to mid thigh, 60 minutes post injection. ***Results:*** An 80-year-old female presented with progressive left upper limb weakness (power 2/5) and lower neck pain. She also noticed a discharging sinus on the posterior aspect of neck, which is inactive at the time of acquisition of PET/CT. There are no symptoms suggesting renal involvement like hematuria, flank pain or a palpable flank mass. On Inspection - Single sinus opening (~0.5 cm) on neck at C4-C7 level with no active discharge. On Palpation, Tenderness present. No palpable mass. Neurological Examination: Motor: Left upper limb: Power-2/5 (shoulder abduction, elbow flexion), 3/5 (hand grip, finger extension). Right upper limb & bilateral lower limbs-Normal power (5/5). Reflexes-Biceps/Jerk: Left - diminished, right - normal. MRI revealed a 5.6 × 3.5 cm left paravertebral lobulated heterogeneous septate T2 weighted mass, suspected as an abscess/collection - possibly Koch. Despite 2 months of antibiotics, symptoms persisted.FDG PET/CT demonstrated: 1. Metabolically active lytic destructive lesion with large soft tissue component noted involving pre and paravertebral region of C4 to C7 vertebrae, measuring 5.9x 6.6x 5.3 cm with intraspinal extension. 2. Metabolically active large lobulated exophytic soft tissue mass with areas of internal necrosis noted arising from lower pole of right kidney measuring 9.6x 9.8x 6.5 cm, involving renal sinus and encasing IVC medially. ***Conclusion:*** This case underscores RCC's potential for atypical metastasis and the diagnostic utility of FDG PET/CT in occult malignancies. The absence of classic renal symptoms and initial abscess-like presentation delayed diagnosis, emphasizing the need for heightened suspicion in refractory structural lesions. PET/CT not only identified the primary tumor but also guided definitive management, showcasing its pivotal role in complex oncologic evaluations. ***References:*** Pandey J, Syed W. Renal Cancer. 2024 Oct 4. In: StatPearls [Internet]. Treasure Island (FL): StatPearls Publishing; 2025 Jan-. PMID: 32644401.

EP-1207

FDG PET/CT in Disseminated Cryptococcosis Mimicking Malignancy with Chest Wall Infiltration and Rib Destruction: A Rare Case of Fungal Pseudotumor

A. Mahalik*, A. Roy, N. Kundu, K. Jain, G. Lalitha, J. Krishna P., V. R. Singh, R. Kumar;*
All India Institute of Medical sciences, New Delhi, INDIA.

Aim/Introduction: Disseminated cryptococcosis is a rare but serious fungal infection, particularly in immunocompromised individuals. While MRI and CT are standard imaging tools, the role of ^{18}F-FDG PET/CT in evaluating the extent of infection and response to therapy is still emerging. Cryptococcal infections presenting with thoracic mass-like lesions that mimic malignancy and invade the chest wall are exceptionally uncommon. ***Materials and Methods:*** A 56-year-old male with a history of disseminated cryptococcosis (diagnosed August 2022) and on Voriconazole therapy underwent FDG PET/CT for assessment of residual disease on July, 2024. PET/CT revealed a heterogeneously FDG-avid pleural-based mass in the right upper lobe (8.1 x 7.5 x 9.3 cm), causing lytic destruction of the right 1st and 2nd ribs. The mass extended into the right supraclavicular, axillary, and anterior chest wall regions, involving right pectoralis and serratus anterior muscles. Additional FDG-avid nodules were noted in both lungs and right supraclavicular lymph nodes. Previously noted adrenal gland lesions had resolved. Interval imaging showed a significant reduction in disease burden compared to the prior scan. ***Results:*** This case illustrates the value of ^{18}F-FDG PET/CT in: 1. Identifying fungal infections mimicking aggressive malignancies. 2. Detecting rare sites of involvement such as ribs and skeletal muscles. 3. Monitoring therapeutic response to antifungal therapy over time. Chest wall invasion and rib destruction are exceedingly rare manifestations of cryptococcosis, more typically associated with neoplastic disease. The comprehensive metabolic assessment offered by PET/CT provided critical insights into disease behavior and therapeutic response. ***Conclusion:*** This case highlights a rare presentation of disseminated cryptococcosis involving chest wall structures and ribs, masquerading as malignancy. FDG PET/CT

proved instrumental in mapping disease extent and evaluating treatment response, underscoring its diagnostic and prognostic value in complex fungal infections.

EP-1208

A Rare Metastatic Journey: From Lower Limb to Heart in Cutaneous Squamous Cell Carcinoma Revealed by ^{18}F-FDG PET/CT

A. Akhter[1], *S. Sharmin*[1], *A. Haque*[2], *T. Hasan*[1], *S. Biswas*[1];
[1]*Institute of Nuclear Medicine and Allied Sciences (INMAS) Dhaka, BAEC, Dhaka, BANGLADESH,* [2]*Dhaka Medical College Hospital, Dhaka, BANGLADESH.*

Aim/Introduction: Squamous cell carcinoma (SCC) is a common malignancy typically involving local invasion and lymphatic spread. Hematogenous dissemination may occur in advanced stages, yet cardiac metastasis remains rare and is often diagnosed post-mortem. We present a unique case of cutaneous SCC originating from the right lower extremity, with rare metastatic spread to the heart, identified by ^{18}F-FDG PET/CT. ***Materials and Methods:*** A 32-year-old male presented with a long-standing ulcerated lesion on the right lower leg following trauma and was diagnosed with invasive, well-differentiated SCC in October 2022. He underwent multiple resections over two years for recurrent inguinal masses. A large lobulated lesion (13.3 × 10.8 × 6.1 cm) in the right groin encased major vessels and led to a right hindquarter amputation in April 2024. Histopathology confirmed metastatic SCC. The patient did not receive chemotherapy or radiotherapy due to negligence. A ^{18}F-FDG PET/CT scan was performed for systemic staging. ***Results:*** ^{18}F-FDG PET/CT showed multiple hypermetabolic lesions with central necrosis in the right inguinal region, groin, and lower abdominal wall (SUV max up to 17.8). A mildly FDG-avid pulmonary nodule (SUV max 2.0) suggested lung metastasis. Critically, a hypermetabolic soft tissue lesion (31.5 × 24 mm; SUV max 9.0) was identified in the interventricular septum of the heart near the apex, suggesting cardiac metastasis. Echocardiography confirmed a soft tissue mass arising from the right ventricle and adjacent apex, extending into the interventricular septum, with preserved LV ejection fraction (66%). No abnormal FDG uptake was noted in the liver, spleen, or bones. Based on these findings, systemic palliative chemotherapy with paclitaxel and carboplatin was initiated. ***Conclusion:*** This case illustrates an exceptionally rare cardiac metastasis from cutaneous SCC. Cardiac involvement is uncommon even in advanced disease and often asymptomatic. ^{18}F-FDG PET/CT was critical in identifying this unexpected metastatic site. The absence of systemic therapy may have allowed unchecked disease progression. This report emphasizes the importance of comprehensive imaging in aggressive or recurrent SCC cases, including cardiac evaluation, to guide clinical decision-making and improve patient outcomes.

EP-1209

Functional Tumor Heterogeneity Revealed by Discordant 18F FDG and 18F FES PET/CT in ER-Positive Breast Cancer: A Case of Imaging-Guided Insight into Endocrine Resistance

A. Mahalik*, N. Kundu, A. Roy, M. Tripathi, R. Kumar;*
All India Institute of Medical Sciences, New Delhi, INDIA.

Aim/Introduction: 18F-FES PET/CT is used to evaluate in vivo estrogen receptor (ER) expression and is increasingly being adopted to guide therapeutic decisions in ER-positive breast cancer. However, discrepancies between FDG and FES uptake, especially in the absence of histological confirmation, present a clinical challenge. ***Materials and Methods:*** A known case of ER-positive invasive ductal carcinoma, post-modified radical mastectomy, chemotherapy, and radiotherapy, underwent metastatic workup with ^{18}F-FDG PET/CT on 09.04.2022. FDG PET/CT revealed metabolically active lesions in the sternum and sacrum. However, on 18F-FES PET/CT performed on 05.05.2022, these lesions did not show any significant tracer uptake. Despite the discordant imaging findings and lack of biopsy confirmation of ER heterogeneity in these sites, the patient was continued on fulvestrant and palbociclib. On follow-up ^{18}F-FDG PET/CT dated 21.01.2023, there was appearance of new hepatic and osseous lesions suggestive of disease progression. ***Results:*** This case illustrates the role of functional imaging in uncovering tumor heterogeneity in ER-positive breast cancer. Discordant uptake between FDG and FES PET/CT suggests spatial variation in estrogen receptor expression—a hallmark of tumor heterogeneity. Such heterogeneity may influence treatment response and prognosis. The absence of FES uptake in FDG-avid lesions could reflect receptor downregulation or clonal evolution towards a more aggressive phenotype. This functional mismatch underscores the importance of integrating molecular imaging into clinical decision-making, especially when biopsy is not feasible. ***Conclusion:*** FES PET/CT offers vital insights into tumor biology by visualizing receptor expression heterogeneity. Discordance with FDG PET/CT should raise suspicion for subclonal receptor-negative populations contributing to endocrine resistance. Early identification of such heterogeneity can guide tailored treatment strategies and avoid delayed escalation of therapy. This case reinforces the evolving role of molecular imaging as a non-invasive biomarker for tumor heterogeneity in breast cancer.

EP-1210

Targeting the rare: ^{18}F-FDG PET/CT in pediatric bilateral orbital Rosai-Dorfman disease

K. Jain*, A. Mahalik, N. Kundu, J. Choudhary, S. Singh, V. R. Singh, R. Kumar;*
AIIMS New Delhi, Delhi, INDIA.

Aim/Introduction: Rosai-Dorfman disease (RDD) is a rare, non-Langerhans cell histiocytic disorder that typically presents with massive cervical lymphadenopathy. Extra-nodal involvement is less common, and isolated bilateral orbital disease is particularly rare. We report a pediatric case with longstanding bilateral proptosis ultimately diagnosed as orbital RDD, with metabolic characterization and therapeutic monitoring via ^{18}F-FDG PET/CT. ***Materials and Methods:*** A male patient presented with progressive bilateral proptosis since the age of 6. At 16 years of age, MRI orbit and brain revealed bilateral intraorbital masses. An orbital biopsy was performed, and histopathology confirmed RDD, characterized by emperipolesis and S100 positivity. Patient underwent baseline and post therapy ^{18}F-FDG PET/CT according to our department protocol. Two experienced nuclear medicine physicians reviewed the scans done at the time of initial staging and post induction chemotherapy. ***Results:*** The baseline ^{18}F-FDG PET/CT demonstrated intense FDG uptake in bilateral intra-orbital lesions with bilateral cervical lymph nodal involvement, consistent with metabolically active nodal and extra-nodal RDD. The patient was initiated on systemic chemotherapy. On Follow-up after post-chemotherapy, the ^{18}F-FDG PET/CT showed a significant metabolic response with marked reduction in FDG uptake and lesion size, correlating clinically with improvement in proptosis and ocular symptoms. ***Conclusion:*** This case highlights the rare orbital manifestation of RDD and reinforces the role of ^{18}F-FDG PET/CT in both diagnosis and therapeutic monitoring. PET/CT enabled accurate disease assessment and demonstrated excellent treatment response, underscoring its value in guiding clinical management of extra-nodal RDD.

EP-1211

68Ga-DOTATATE PET/MRI for the Diagnosis of Optic Nerve Sheath Meningioma in an Adolescent with Progressive Unilateral Vision Loss

A. Giarratana, *M. Larson;*
University of Wisconsin - Madison, Madison, WI, WI, UNITED STATES OF AMERICA.

Aim/Introduction: Optic nerve sheath meningioma (ONSM) is a rare, benign tumor originating from the arachnoid cap cells surrounding the optic nerve. [1] Differentiating ONSM from optic neuritis or inflammatory etiologies can be particularly challenging, especially in pediatric populations. [2, 3] We present a case of a 17-year-old male with progressive vision loss in the left eye where 68Ga- DOTATATE PET/MRI enabled a definitive diagnosis of ONSM, guiding successful radiation therapy. ***Materials and Methods:*** The patient presented with gradually worsening visual acuity and optic disc edema beginning in late 2022. Initial MRI findings were inconclusive, showing enhancement of the left optic nerve and sheath. Laboratory workup was notable for a transiently positive MOG antibody. Despite treatment with corticosteroids and plasmapheresis, vision worsened. 68Ga- DOTATATE PET/MRI was performed to clarify the diagnosis. ***Results:*** The 68Ga- DOTATATE PET/MRI revealed high uptake localized to the optic nerve sheath, consistent with somatostatin receptor-expressing meningioma. Radiation therapy was initiated (50.4 Gy in 28 fractions). Seven months after radiation, vision showed significant improvement. Quantitatively, his visual field scores improved from -31 dB to -13 dB, indicating better function though still below normal. Qualitatively, he estimated his left eye vision improved from 30% to 70%. Optic nerve swelling had completely resolved on exam. ***Conclusion:*** This case illustrates the diagnostic utility of 68Ga- DOTATATE PET/MRI in distinguishing ONSM from inflammatory optic neuropathies. In patients with atypical progression or treatment-refractory optic neuritis, 68Ga- DOTATATE PET/MRI can provide critical diagnostic clarity and inform effective management. ***References:*** 1.Parker, R.T., et al., Optic nerve sheath meningiomas: prevalence, impact, and management strategies. Eye Brain, 2018. 10: p. 85-99. 2.Vanikieti, K., P. Preechawat, and A. Poonyathalang, Pediatric primary optic nerve sheath meningioma. Int Med Case Rep J, 2015. 8: p. 159-63. 3.Joseph, A.K., et al., Imaging Findings of Pediatric Orbital Masses and Tumor Mimics. Radiographics, 2022. 42(3): p. 880-897.

EP-1212

A rare case of extramammary Paget's disease of the vulva: [^{18}F]FDG PET/CT in the evaluation of Radiotherapy efficacy and 30-months follow-up

M. Ricci[1], *A. Cimini*[2], *M. Ullo*[1], *M. Grivet Fojaja*[1], *F. Zarrelli*[1], *F. Perrotta*[3], *E. Lubrano di Scorpaniello*[3];
[1]*Cardarelli Hospital, Nuclear Medicine Unit, Campobasso, ITALY,*
[2]*Nuclear Medicine Unit, St. Salvatore Hospital, L'Aquila, ITALY,*
[3]*Department of Medicine and Health Sciences "Vincenzo Tiberio", University of Molise, Campobasso, ITALY.*

Aim/Introduction: Extramammary Paget disease is an intraepithelial neoplasm affecting cells rich in apocrine glands often located in the vulvar, scrotal, or perianal region. Surgical resection is still the main treatment for Vulvar Paget Disease (VPD) and Radiotherapy (RT) is suitable for VPD patients who refuse surgery or are not suitable for surgery. However, the efficacy of RT in VPD is controversial. ***Materials and Methods:*** A 73 years-old female patient presented a locally advanced intraepithelial lesion of the vulva. A subsequent biopsy revealed extrammamary Paget disease and, due to the perineal extension of the lesion, the patient was not suitable for surgery and RT was performed. The therapy monitoring protocol with [^{18}F]FDG PET/CT was planned. ***Results:*** [^{18}F]FDG PET/CT was performed 4 months after RT (Dual Time protocol; whole body at 45 min and pelvic acquisition at 90 min) and reported a minimal area of FDG uptake, that presented a reduction in late acquisition (SUVmax 3.23, SUVmax at 90 min 3.09). This area was interpreted as a post-actinic lesion. Further PET scans were performed - due both to the high risk of relapse of VPD and to the subsequent development of melanoma of the back area - 10 months, 17 months, 24 months and 30 months after RT and confirmed the efficacy of RT in this case of VPD. ***Conclusion:*** To our knowledge, this is the first case report that reported the role of [^{18}F]FDG PET/CT in the therapy monitoring of VPD. The [^{18}F]FDG PET/CT allowed a prompt evaluation of RT efficacy and can be considered in diagnostic algorithm of patients with VPD not suitable for surgery. Moreover, the Dual Time Protocol allowed the correct interpretation of the scan and it can be performed in order to support the differential diagnosis between residual and post-actinic lesions.

EP-1213

A rare case of metastatic Well differentiated Neuroendocrine Tumor of Prostate on hemodialysis treated with Concurrent Long Acting Octreotide and 177Lutetitium DOTATATE therapy achieving complete response- Case report and Literature Review

J. Bal, *S. Jha, P. Dougall;*
Max Super Specialty Hospital, Delhi, INDIA,

Aim/Introduction: Prostatic carcinoma is one of the leading causes of morbidity and mortality in men worldwide. However, the most common prostatic malignancy are conventional adenocarcinomas. A rare subgroup within adenocarcinomas comprises of stromal malignancies and other unusual epithelial malignancies. Well differentiated primary prostatic neuroendocrine tumors have been documented in the literature although as very rare cases. ***Materials and Methods:*** This is a case of a 74 year-old male patient with chronic kidney disease on regular hemodialysis, diagnosed with well to moderately differentiated neuroendocrine tumor of prostate who had metastases at initial presentation. His Somatostatin receptor (SSTR) imaging i.e. Ga68 DOTANOC scan showed high SSTR expression in primary and metastatic sites. He was initially treated with LAR Octreotide. This regimen initially kept the disease stable, but a year later there was progression in the primary mass and at the metastatic sites. He was then advised to start treatment with 177Lu-DOTATATE peptide receptor radionuclide therapy (PRRT) along with concurrent LAR Octreotide which was challenging for the dosimetry reasons as the patient was already renal compromised and sequencing the administration of PRRT with hemodialysis. He underwent 3 cycles of PRRT in a span of approximately 1 year. Subsequently, the primary tumor regressed with a remarkable response in the metastatic lymph nodes and skeletal lesions. 177Lu-DOTATATE peptide receptor radionuclide therapy may be an effective option for primary well differentiated metastatic or locally advanced neuroendocrine tumors of prostate, which has few effective treatment options and it can be effectively administered along with hemodialysis without compromising on dose administered. ***Conclusion:*** The diagnosis of low-grade neuroendocrine tumor (carcinoid tumor) should be reserved for those cases in which the histologic findings and the immunostains fit the case. It appears that a true prostatic carcinoid tumor may not show reactivity for prostate-specific antigen, a feature seen in our case, which may be useful in the separation of these neoplasms in more difficult biopsy specimens. 177Lu-DOTA-TATE demonstrates favorable efficacy in treating neuroendocrine tumors, but its current application primarily focuses on gastrointestinal neuroendocrine tumors. All physicians should familiarize themselves with the clinical and pathological features this histopathology, as well as the available treatment modalities, in order to prolong patient survival and enhance cure rates. Moreover, we recommend adopting a multidisciplinary

approach, involving urologists, oncologists, nuclear medicine physicians and pathologists, to collaboratively discuss treatment plans and improve the health and quality of life for patients.

EP-1214

The Role of FDG PET/CT in Treatment-Related Neuroendocrine Prostate Cancer: An Unusual Case of PSA and PSMA Double-Negative Disease with Squamous Differentiation

Y. Li, *Y. Tang, S. Hu;*
Xiangya Hospital, Central South University, Changsha, CHINA.

Aim/Introduction: We report a rare case of treatment-related neuroendocrine prostate cancer (NEPC) with squamous differentiation, presenting as PSA and PSMA double-negative. FDG-PET/CT revealed extensive hypermetabolic bone lesions, along with retrocrural nodal diseases and pulmonary nodules, all of which showed no significant abnormalities on PSMA-PET. ***Materials and Methods:*** A 62-year-old man with a 5-year history of prostate cancer (status post-prostatectomy, radiation, hormone therapy, and enzalutamide) presented with a 9-month history of worsening lumbar and back pain, raising suspicion of bone metastasis progression. ^{68}Ga-PSMA PET/CT failed to show any focal intense recurrence, and the previously PSMA-avid lymph nodes near the right iliac vessels and pelvic wall were no longer visible compared to the prior PSMA scan. Biochemical tests revealed a very low prostate-specific antigen (PSA) level (<1.0 ng/ml) but an elevated neuron-specific enolase (NSE) level (23.35 ng/ml). ***Results:*** He subsequently underwent ^{18}F-FDG PET/CT due to the persistent pain and suspicion of progression. In contrast to the negative PSMA scan, the FDG scan revealed extensive bone lesions with hypermetabolism, morphologically osteolytic or insignificantly transformed. Additional findings included multiple hypermetabolic lymph nodes in the retrocrural space (SUVmax 12.2), and newly identified pulmonary nodules (SUVmax 4.9), indicative of rapid disease progression. The elevated NSE level and osteolytic bone lesions led to the suspicion of NEPC. A biopsy of the most hypermetabolic lesion in the left posterior rib was performed. Pathological examination revealed the histomorphologic appearance of small round cells, with immunohistochemical staining demonstrating positivity for Syn, partial positivity for CgA, CK5/6, and P63, and negativity for PSA and PSMA, consistent with NEPC with squamous differentiation. He was started on palliative chemoradiotherapy. ***Conclusion:*** The use of enzalutamide may be associated with treatment-related NEPC, while squamous differentiation is often reported in patients with a history of radiation therapy. NEPC and squamous differentiation are both typically associated with higher GLUT-1 expression and FDG metabolism. This combination is never reported, and more lethal, less responsive to conventional treatment. It may present unique features, including absence of PSA and PSMA, as well as osteolytic bone lesions—very uncommon in prostatic adenocarcinoma. This case underscores the critical role of FDG-PET/CT in detecting metastases, restaging, biopsy guidance and treatment planning for NEPC. FDG-PET/CT can identify hypermetabolic lesions that may appear normal on conventional imaging techniques. Therefore, FDG-PET may be considered as part of diagnostic workup for NEPC, especially in patients with low PSA levels or negative PSMA scans.

EP-1215

"Splenic Superscan" on [^{18}F]FDG PET/CT in a rare case of hepatosplenic T-cell lymphoma

N. Aydinbelge- Dizdar[1], *U. Han*[2], *D. Cayir*[3], *Y. Sari Cataldas*[2];
[1]*Ankara Etlik City Hospital, Department of Nuclear Medicine, Ankara, TÜRKIYE,* [2]*Ankara Etlik City Hospital, Department of Pathology, Ankara, TÜRKIYE,* [3]*University of Health Sciences, Ankara Etlik City Hospital, Department of Nuclear Medicine, Ankara, TÜRKIYE.*

Aim/Introduction: Hepatosplenic T-cell lymphoma (HSTCL) is a rare, highly aggressive extranodal T-cell lymphoma that can be rapidly fatal. It is frequently diagnosed in younger men, accounting for 68% of cases, with a typical onset age of 34 years and manifests with B-symptoms (fever, night sweats, and weight loss) and cytopenia. The rare HSTCL disease poses a significant diagnostic challenge due to its numerous clinical and histologic manifestations and its symptoms mimicking various infectious and hematologic diseases. ***Materials and Methods:*** We present a rare case of HSTCL diagnosed and monitored using ^{18}F-FDG PET/CT scan. A 47-year-old man presented a history of intermittent fever, drenching night sweats, unintentional weight loss, diarrhea and abdominal distension for two months. On physical examination, hepatosplenomegaly was detected. Complete blood count parameters were consistent with pancytopenia (total white blood cell count of 3.02 10^3/µL, Hb 8.5 gr/dL, neutrophil count 1.64 10^3/µL and platelet count of 42 10^3/µL). The serology tests for Epstein-Barr virus, HIV and hepatitis B and C virus were all negative. Abdominopelvic CT revealed massive hepatomegaly (CC size 26 cm in the midclavicular line) and splenomegaly (CC size 35 cm in the midclavicular line) and showed no lymphadenopathy at any station. Based on CT, clinical and laboratory findings, ^{18}F-FDG PET/CT and bone marrow biopsy (BMB) were performed since lymphoma was considered as a differential diagnosis. FDG PET/CT scan showed an increased radiotracer uptake in massive splenomegaly and a mild uptake in massive hepatomegaly and bone marrow. ***Results:*** The biopsy findings of liver revealed infiltration of the sinusoids by medium-sized T cells. The flow cytometry showed abnormal CD3-positive T cells consistent with HSTCL. After multidisciplinary tumor board of all data, the patient was diagnosed with HSTCL, and chemotherapy (ifosfamide, carboplatin, and etoposide) was applied. After the fourth cycle, the clinical and laboratory parameters improved, and allogeneic bone marrow transplantation was performed.The follow-up FDG PET/CT demonstrated reduced liver and spleen size and the absence of pathologic metabolic activity uptake in the body, which was considered consistent with remission. ***Conclusion:*** In such rare cases, FDG PET/CT can help monitor chemotherapeutic responses and diagnose HSTCL by demonstrating the presence of massive hepatosplenomegaly and diffuse markedly increased radioactivity uptake in the bone marrow, especially in the spleen, and in the absence of hypermetabolic lymphadenopathies.

EP-1216

Metastatic Prostate Cancer with Pulmonary Involvement Mimicking Pneumonia: Findings on ^{18}F-FDG PET/CT s and ^{68}Ga-PSMA PET/CT

N. Aydinbelge- Dizdar[1], *E. Tatci*[2], *A. Cinar*[1], *B. Bozca*[1], *O. Ozmen*[2];
[1]*Department of Nuclear Medicine, Ankara Etlik City Hospital, Ankara, TÜRKIYE,* [2]*Department of Nuclear Medicine, University of Health Sciences, Ankara Etlik City Hospital, Ankara, TÜRKIYE.*

Aim/Introduction: In prostate cancer (PCa), the most common metastatic sites are regional lymph nodes and bones, but lung metastases, which typically present with nodular involvement, may also occur. Ground-glass opacities, bilateral pleural effusions and thickenings, and pulmonary lymphangitic spread (PLC) are extremely rare in PCa. ***Materials and Methods:*** We report a case of 68-year-old man who presented with progressive exertional dyspnea lasting approximately one month, with no history of abdominal pain, dysuria, or pollakiuria. Contrast-enhanced thoracic CT was performed to rule out pulmonary thromboembolism, revealing moderate bilateral pleural effusion and thickenings, enlarged mediastinal lymph nodes, diffuse ground-glass opacities, peribronchial thickening, interlobular septal thickening, and consolidations with atelectasis in both lung bases. These radiological findings suggested pneumonia or alveolar edema. Despite treatment with antibiotics and

corticosteroids, follow-up CT performed due to worsening dyspnea showed disease progression. For further investigate, ^{18}F-FDG PET/CT was performed, revealing increased radiotracer uptake in the prostate, multiple mediastinal and intra-abdominal lymph nodes, and bilateral lung lesions. Given the low FDG uptake in the lymph nodes and an elevated plasma total PSA level of 523 µg/L (Normal value: <4.1µg/L), the biopsy confirmed PCa with Gleason score of 4+3=7 (Grade Group 3). ^{68}Ga-PSMA PET/CT showed mild to high radiotracer uptake in bilateral lung lesions and multiple lymph nodes. Intense radiotracer uptake was observed extending from the prostate gland to the urinary bladder and rectum. The immunohistochemical and histopathological assessments were consistent with pulmonary and pleural metastasis of PCa. ***Results:*** PSMA-ligand PET/CT plays a crucial role in the evaluation of PCa, particularly in cases of biochemical recurrence, and is increasingly valuable in the initial staging of intermediate-to high-risk disease. However, the role of ^{18}F-FDG PET/CT in the diagnosis and staging of primary PCa remains limited. Pulmonary lymphangitic spread (PLC) with ground-glass opacities, bilateral malignant pleural effusions and thickenings in PCa is exceedingly rare. PLC is usually observed in the terminal stages of carcinomas originating from the breast, stomach, lung, and pancreas, with PCa accounting for approximately 3% of all reported PLC cases. ***Conclusion:*** Although metastatic spread in the form of PLC is uncommon for the some carcinomas, clinicians should consider the possibility of metastatic PCa in cases of PLC with bilateral pleural effusions and thickening and ground-glass opacities, even in the absence of a previously known malignancy as demonstrated in this case.

EP-1217

Prostate cancer associated with polyostotic Paget disease : diagnostic challenges and the value of multimodal imaging

D. Tahmi, *F. Agboton, H. Labiod, A. Amimour;*
Service de Médecine Nucléaire CHU Bab El Oued, Algiers, ALGERIA.

Aim/Introduction: Prostate adenocarcinoma frequently metastasizes to the bone. 18F/68Ga-PSMA PET/CT has become an essential tool in the extension work-up, offering high sensitivity for detecting metastatic lesions. However, PSMA tracer uptake is not specific and may occur in benign hyper-vascular bone disorders such as Paget disease, causing diagnostic pitfalls. ***Materials and Methods:*** A 69-year-old man with prostatic adenocarcinoma diagnosed following an elevated prostate-specific antigen (PSA) level. The patient was initially underwent external-beam radiotherapy plus androgen-deprivation achieving a nadir PSA of 0.4 ng/mL. During follow-up, the patient presented clinically with bone pain and impotence of the right lower limb, associated biologically with an increase in PSA above 100 ng/mL. Systemic treatment with abiraterone followed by taxanes resulted in a significant response, with PSA dropping to 0.4 ng/mL. Successive bone scans showed focal hyperfixing osteocondensing lesions on the right tibia, then, at the end of 2024, this hyperfixation became spread out and heterogeneous over almost the entire bone specimen, with "mosaic" cortical enlargement and thickening suggestive of pagetoid remodeling, associated with moderate foot and pelvic foci of secondary appearance, making metastatic interpretation equivocal and prompting 68Ga-PSMA PET/CT followed by MRI, which confirmed the characteristic appearance of Paget's disease in the lower limb, with suspicion of incipient Paget's disease vs. metastatic localization at other sites. However, bone biopsy confirmed the final diagnosis of active polyostotic Paget's disease, mimicking early-stage metastatic disease on the various morphological and functional imaging examinations. ***Results:*** This case illustrates a major diagnostic challenge related to PSMA uptake in active Paget's disease. Although PSMA PET/CT performs well, it requires careful interpretation, particularly in patients with pre-existing bone pathologies. Rigorous integration of clinical, biological and imaging data (bone scan, PET/CT, CT, MRI) is crucial to distinguish metastatic lesions from benign processes such as Paget's disease, in order to avoid over- or under-classification and ensure appropriate therapeutic management. ***Conclusion:*** This case highlights that active bone Paget's disease can show significant PSMA uptake on PET/CT, constituting an important diagnostic pitfall. A multimodal approach and contextual interpretation are essential for accurate staging of prostate cancer in patients with bone comorbidities.

EP-1218

Unveiling Bile Leaks: The Power of Hepatobiliary Scintigraphy in Post-Traumatic Liver Injury

R. Solanki;
Post Graduate Institute of Medical Education and Research, Chandigarh, INDIA.

Aim/Introduction: Bile leaks are a significant complication following hepatic trauma, often requiring precise diagnostic tools for effective management. Hepatobiliary scintigraphy (HBS) using 99mTc-Mebrofenin is a sensitive modality for detecting bile leaks, offering functional insights that complement anatomical imaging. This study evaluates the utility of HBS in a 17-year-old male with a Strassberg Grade IV liver injury, presenting with a suspected bile leak post-subhepatic pigtail catheter insertion. ***Materials and Methods:*** A 17-year-old male with a history of Grade IV liver injury underwent follow-up evaluation for abdominal pain. Initial ultrasound revealed a subhepatic collection, and MRCP confirmed left hepatic duct disruption with bile extravasation. HBS was performed using 99mTc-Mebrofenin, with sequential dynamic imaging for 45 minutes, followed by static images pre- and post-fat-rich meal (1 hour 10 minutes post-injection) to assess gallbladder ejection fraction (GBEF). Hybrid SPECT/CT at 3 hours and delayed static images at 24 hours were acquired. Imaging assessed hepatocyte function, biliary drainage, and tracer accumulation indicative of bile leak. Bag statics evaluated drainage output. ***Results:*** HBS demonstrated preserved hepatocyte function with normal liver size and position. Tracer accumulation near the primary confluence indicated a bile leak from the left hepatic duct, forming a collection (6.5 x 4.3 x 4.8 cm) in the gastrohepatic space, extending to a subhepatic collection (13.2 x 8.5 x 6.1 cm). No tracer uptake was observed in the drainage bag at 45 minutes, 1, 2, or 4.5 hours, but uptake was noted at 24 hours. Patent bilio-enteric drainage via the right hepatic duct was confirmed. GBEF was impaired (28% at 30 minutes, 49% at 1 hour), indicating reduced gallbladder contractility. SPECT/CT provided precise anatomical localization of the leak. ***Conclusion:*** HBS with 99mTc-Mebrofenin effectively diagnosed a bile leak in a post-traumatic liver injury, guiding minimally invasive management. The addition of SPECT/CT enhanced anatomical localization, overcoming limitations of HBS alone. Impaired gallbladder contractility was an incidental finding, potentially influencing future management. HBS remains a critical tool for early bile leak detection and follow-up. ***References:*** 1. LeBedis CA, Anderson SW, Mercier G, Kussman S, Coleman SL, Golden L, Penn DR, Uyeda JW, Soto JA. The utility of CT for predicting bile leaks in hepatic trauma. Emerg Radiol. 2015 Apr;22(2):101-7. 2. Ziessman HA, O'Malley JP, Thrall JH. Nuclear medicine: the requisites e-book. Elsevier Health Sciences; 2013 Mar 15.3.

EP-1219

Utility of Radiolabeled Red Blood Cell SPECT/CT in Diagnosing Urinary Bladder Hemorrhage: A Case Report

K. Resuello, *P. Bautista-Peñalosa, A. Domingo;*
St. Luke's Medical Center - Global City, Taguig, PHILIPPINES.

Aim/Introduction: Radiolabeled red blood cell (RBC) scan is a non-invasive radionuclide imaging technique typically used to evaluate suspected gastrointestinal bleeding. Its application in

identifying genito-urinary bleeding is limited due to the excretion of free Technetium-99m (^{99m}Tc) pertechnetate into the genito-urinary tract, potentially obscuring pathological bleeding. A thorough search of the literature revealed only two documented cases globally and none within the Philippines or Southeast Asia. This case aims to demonstrate the rare but important utilization of radiolabeled RBC SPECT/CT in localizing urinary bladder hemorrhage and eventually directing management. ***Materials and Methods:*** A 63-year-old female with a history of triple primary cancer (Breast cancer Stage IA, Uterine adenocarcinoma Stage IB, Intrahepatic cholangiocarcinoma Stage IV) and pelvic radiation therapy presented with recurrent gross hematuria and weakness. Despite cystoscopy and CT urography, the source of bleeding remained unidentified. The procedure involved injection of autologous erythrocytes radiolabeled with 30 mCi of ^{99m}Tc using a modified in vitro method, followed by anterior dynamic imaging of the abdomen performed immediately and 40 minutes post intravenous injection. ***Results:*** Dynamic planar imaging revealed increasing tracer activity in the urinary bladder. SPECT/CT images localized tracer activity in the urinary bladder along the region of the previously identified soft tissue density which suggested active bleeding in the area. Following these findings, the patient underwent angiography with selective embolization. The post-embolization angiogram showed devascularization of the superior vesical artery and partial devascularization of the internal pudendal artery. This resulted to resolution of hematuria, and the patient was subsequently discharged. ***Conclusion:*** This first case report in the Philippines highlights the usefulness of radiolabeled RBC SPECT/CT in diagnosing bladder hemorrhage by allowing accurate localization of the bleeding source. Its diagnostic value is seen in complex cases where conventional imaging yields equivocal results. The successful application in this case underscores the potential of this modality to enhance diagnostic accuracy and guide clinical management in patients with bladder hemorrhage. Further research is warranted to establish its efficacy and standardize its use in routine practice. ***References:*** 1. Kalpna Prasad (2015). Novel use of radiolabeled red blood cell SPECT-CT in diagnosing occult renal hemorrhage. Journal of Nuclear Medicine May 2015, 56 (supplement 3)1949. (Accessed on 31 May 2024) Available from: https://jnm.snmjournals.org/content/56/supplement_3/1949 2. Purushottam Dixit, Monzer Chebab, Alexander Copeland (2014) An uncommon cause of massive hematuria. Society of Interventional Radiology. (Accessed on 31 May 2024) Available from: http://rfs.sirweb.org/wp content/uploads/2014/08/201408_Chehab_UAFistua_FINAL.pdf

EP-1220

Multimodal Treatment in Advanced Hepatocellular Carcinoma: Yttrium-90 Radioembolization Following Stereotactic Body Radiation Therapy and TACE

M. Mutuleanu[1,2], *I. Ioana*[1], *I. Taciuc*[1], *C. Petroiu*[1], *M. Gherghe*[1,2]; [1]*Institute of Oncology "Prof. Dr. Alexandru Trestioreanu", Bucharest, Romania, Bucharest, ROMANIA,* [2]*University of Medicine and Pharmacy "Carol Davila", Bucharest, ROMANIA.*

Aim/Introduction: The management of advanced unresectable hepatocellular carcinoma (HCC) remains a significant clinical challenge. Yttrium-90 (^{90}Y) radioembolization has emerged as an effective therapeutic option for both primary and secondary hepatic tumours. The application of personalized dosimetry in [^{90}Y] radioembolization has been shown to enhance treatment response, overall survival and patient quality of life. Stereotactic body radiation therapy (SBRT) is widely utilized in the treatment of liver malignancies, although its efficacy may vary among patients. The sequential use of [^{90}Y] radioembolization following SBRT is relatively uncommon, yet not contraindicated; however, it may increase the risk of radiation-induced complications. ***Materials and Methods:*** We present the case of an 80-year-old patient with advanced cardiovascular disease who was diagnosed on March 5, 2024 with HCC involving segments III and IV of a non-cirrhotic liver. The patient underwent transarterial chemoembolization (TACE) on March 7, 2024, followed by SBRT in June 2024 receiving a total dose of 45 Gy administered in six fractions. Post-SBRT imaging revealed residual tumour tissue. Four months later, on October 17, 2024, pre-treatment evaluation for radioembolization was conducted using 140 MBq of [^{99m}Tc]-human serum albumin (^{99m}Tc-HSA) followed by perfusion SPECT-CT. On October 31, 2024, radioembolization with [^{90}Y] resin microspheres was performed, the patient receiving a therapeutic dose of 1.1 GBq. ***Results:*** The [^{99m}Tc]-HSA SPECT-CT revealed a hepatopulmonary shunt fraction of 1.84%. Pre-treatment voxel-based dosimetry estimated an absorbed dose of 296 Gy in the target volume with a therapeutic intent of lobectomy. Post-treatment [^{90}Y] PET-CT imaging demonstrated relatively homogeneous distribution of radiolabelled microspheres within the tumour volume. Post-therapeutic dosimetry analysis yielded the following results: the absorbed dose to the tumour volume was 350.12 Gy; the mean dose to non-tumoral perfused liver was 159.11 Gy and to the non-perfused liver was 32.26 Gy. Although the patient received two radiation-based treatments in less than six months, the non-perfused liver dose was within the recommended limits. Follow-up imaging performed three months after radioembolization demonstrated a significant reduction in viable tumour volume and the patient evolution was favourable, with no radiation induced side effects. ***Conclusion:*** Given that radioembolization performed shortly after SBRT is an uncommon approach in current clinical practice and carries potential risks of hepatotoxicity, further studies are warranted to evaluate its safety and efficacy. However, in our case this combined treatment strategy proved successful. Careful patient selection, personalized dosimetry and multidisciplinary management form the cornerstone of a favourable therapeutic outcome.

EP-1221

"Blessing in disguise" Lu177-PSMA-617 for chemo naïve mCRPC patient with parkinsonism and embarrassing sialorrhea

M. Gupta[1], *P. Sarathi Choudhury*[1], *S. Goyal*[2], *A. Pathak*[1], *M. Seth*[1], *S. Rawal*[3]; [1]*Department of Nuclear Medicine, Rajiv Gandhi Cancer Institute and Research Centre, Delhi, INDIA,* [2]*Department of Medical Oncology, Rajiv Gandhi Cancer Institute and Research Centre, Delhi, INDIA,* [3]*Department of GenitoUro-Oncology, Rajiv Gandhi Cancer Institute and Research Centre, Delhi, INDIA.*

Aim/Introduction: Lu177-PSMA-617 has been approved for mCRPC post ARPi and at least one taxen chemotherapy. With a newer data from PSMAfore trial, it has showed benefit in progression free survival in chemo naïve mCRPC patient over change of ARPi. Sialorrhea is one of the commonest symptoms in parkinsonism. It is due to rigidity and dis-coordination of oral cavity muscle leads to pooling and drooling of saliva from the mouth. A continuous saliva discharge is embarrassing and have negative impact on patient social acceptance. We presented here a case of mCRPC patient with parkinsonism and embarrassing sialorrhea with remarkable response in both. ***Materials and Methods:*** Dry mouth is a drug specific side effect of Lu177-PSMA-617 therapy with no specific treatment available. Impact of Lu177 PSMA-617 induced dry mouth in parkinsonism associated sialorrhea is unknow. We searched on PubMed/Medline, and Google with the key words in Lu177 PSMA, dry mouth, sialorrhea, Parkinsonism. We have not come across any relevant literature. ***Results:*** Eighty-six-year-old male patient was diagnosed with synchronous disseminated bone metastatic prostate acinar adenocancer grade group 3. He was treated with goserelin for 4 years, enzalutamide for 2.1 years and abiraterone for 5 months. Following progression,

case was discussed in multispecialty clinics. In view old age, ECOG PS 3, and co-morbidities, chemotherapy was deferred and Lu177 PSMA-617 was planned. 68Ga-PSMA-11 PET-CT was suggestive of strongly PSMA avid disseminated bone lesions. His base line PSA was 143 ng/ml and brief pain inventory short form (BPI-SF) score was 6. Patient received two cycles of Lu177-PSMA-617 (200mCi / 7.4GBq per cycle) at 6 weeks interval. 12 weeks PSA was 2.45 ng/ml, and BPI-SF score improve to zero. 12 weeks 68Ga-PSMA-11 PET-CT revealed complete response. Further, from embarrassing sialorrhea to no sialorrhea also improved patient quality of life. ***Conclusion:*** Improvement of sialorrhea in this patient may open a new horizon for Lu177-PSMA-617 therapy in the future. Further studies are needed to evaluate long term outcome of this treatment for this entity.

EP-1222

Splenic hemangioma intensive uptake on 99mTc-PSMA scintigraphy - caution required in interpretation

I. Sisko Markos[1,2], *M. Romić*[1,2], *I. Blazekovic*[1,2], *T. Jukic*[1], *A. Frobe*[1];
[1]*UHC Sestre Milosrdnice, Zagreb, CROATIA,* [2]*Croatian Catholic University, School of Medicine, Zagreb, CROATIA.*

Aim/Introduction: We present a 68-year-old man with a history of high-risk prostate cancer (Gleason score 4+4), initially diagnosed 7 years ago. At the time of diagnosis, PSA was markedly elevated at 38.37 mcg/L. Initial staging performed with thoracic, abdominal, and pelvic CT as well as bone scintigraphy revealed skeletal metastases and involvement of paraaortic and pelvic lymph nodes. ***Materials and Methods:*** The patient was initially treated with an LHRH agonist and chemotherapy according to the CHAARTED protocol. In 2019, due to biochemical progression, treatment with abiraterone was initiated. In 2021, further PSA elevation prompted an 18F-FCH PET/CT scan, which demonstrated disease progression in iliac and retroperitoneal lymph nodes. Due to continued PSA rise, PSMA-targeted scintigraphy with 99mTc-HYNIC-PSMA was performed for restaging. The scan showed intense radiotracer uptake in bones and in paraaortic and pelvic lymph nodes, consistent with disease progression. As a result, the patient was subsequently treated with carboplatin. ***Results:*** A very intense focal uptake was observed in the spleen. This finding correlated with a splenic hemangioma confirmed with CT. The presence of such a lesion illustrates a significant pitfall in PSMA imaging—benign entities like hemangiomas can exhibit intense PSMA uptake and may lead to false-positive interpretations. ***Conclusion:*** This is the first reported case of a splenic hemangioma imaged with this radiopharmaceutical, whereas several similar cases using 68Ga-PSMA PET/CT have already been described, suggesting similar PSMA behavior in hemangiomas regardless of binding to either 68Ga or 99mTc.

EP-1223

^{99m}Tc-Ubiquicidin SPECT/CT in Diabetic Foot: Detection of Subclinical Infection in a Patient with Chronic Venous Ulcer

V. Heringer, *B. Alencar, T. Agnello, M. Osmak, E. Etchebehere, C. Ramos, M. Lima, B. Juarez, A. Santos;*
UNICAMP, Campinas, BRAZIL.

Aim/Introduction: Diabetic foot complications are a significant cause of morbidity in patients with long-standing type 2 diabetes mellitus (DM2), particularly when associated with peripheral neuropathy and chronic venous disease. Differentiating between sterile inflammation and active infection remains challenging. Radiolabeled antimicrobial peptides, such as 99mTc-ubiquicidin (UBI), have emerged as promising molecular imaging tools for infection detection[1]. UBI 29-41 is a synthetic fragment of a naturally occurring antimicrobial peptide, with multiple cationic residues (arginine and lysine) that selectively bind to the negatively charged membranes of bacteria, enabling distinction between infection and sterile inflammation[2]. We report the case of a diabetic patient with a history of chronic ulceration and persistent symptoms, in whom UBI SPECT/CT contributed to identifying a subclinical soft tissue infection and guided conservative management. ***Materials and Methods:*** A 69-year-old male with poorly controlled DM2, peripheral neuropathy, chronic venous insufficiency (CEAP C6), and a previously healed ulcer on the right ankle, underwent ^{99m}Tc-UBI scintigraphy. Dynamic acquisition (2s/frame) was followed by equilibrium and delayed images at 1 and 2 hours post-injection, and SPECT/CT at 3 hours. A lesion-to-background (L/B) ratio was calculated to assess semi-quantitative tracer uptake[3]. ***Results:*** Early-phase images demonstrated increased perfusion in the right ankle and foot. Delayed planar and SPECT/CT images revealed discrete to moderate uptake in the lateral ankle and dorsal foot. The L/B ratio was 1.99, exceeding the accepted limite of 1.74 suggestive of active infection[3]. CT findings showed cutaneous thickening and degenerative joint changes but no bone involvement. Based on these findings, a diagnosis of localized soft tissue infection was made. The patient was managed conservatively with topical treatment, glycemic control, and physiotherapy. Follow-up demonstrated clinical improvement and complete wound healing without surgical intervention. ***Conclusion:*** This case highlights the role of ^{99m}Tc-ubiquicidin SPECT/CT in the detection of soft tissue infections in patients with diabetic foot. The technique is particularly useful in cases where clinical signs are ambiguous and vascular comorbidities coexist. The semi-quantitative L/B ratio is a valuable metric that supports diagnostic accuracy and therapeutic decisions[4]. UBI-based imaging offers an effective, noninvasive method for distinguishing infection from inflammation in complex diabetic foot presentations. ***References:*** 1) Welling MM, et al. J Nucl Med. 2000;41:275. 2) Ferro-Flores G, et al. Molecules. 2021;26:3159. 3) Palestro CJ. Q J Nucl Med Mol Imaging. 2020;64:138. 4) Signore A, et al. Nucl Med Commun. 2011;32:917.

EP-1224

Multisystemic malakoplakia revealed by ^{18}F-FDG PET/CT : A case of concomitant bilateral osteomyelitis and genitourinary involvement

F. Yasser, *P. Maliha, M. Morin;*
University of Montreal, Montreal, QC, CANADA.

Aim/Introduction: A 43-year-old male on immunosuppressive therapy was admitted to the emergency department with acute left knee and left groin pain. A combined bone/gallium study revealed multiple bilateral congruent intramedullary bone uptake in the lower limb, mainly localized at femoral and tibial diaphyseal-metaphyseal junctions. A diffuse left testicular uptake was also noted. ***Materials and Methods:*** ^{18}F-FDG PET demonstrated increased uptake in multiple intramedullary bone regions in the lower limbs, diffuse uptake in the left testicle, heterogenous prostate uptake and several retroperitoneal lymph nodes, all presenting with calcifications on CT. A transrectal prostate biopsy revealed chronic histiocytic inflammatory infiltrate with macrophages exhibiting Michaelis-Gutmann bodies, pathognomonic for malakoplakia. Based on the clinical suspicion of bilateral osteomyelitis, a debridement and lavage were performed revealing Escherichia coli. Based on clinical, imaging and pathological findings, a diagnosis of prostatic malakoplakia with involvement of the left testicle and retroperitoneal lymph nodes was made, complicated by bilateral lower limbs osteomyelitis. ***Results:*** Malakoplakia is a rare multisystemic granulomatous disease, first described in 1902 by Michaelis and Gutmann. Risk factors include immunosuppression and recurrent urinary tract infections, primarily with E. coli. While it predominantly affects the urinary tract, it can potentially involve any organ. Although not fully elucidated, a defect in phagocytic function seems to trigger a chronic inflammatory response. Histopathological examination remains the gold standard for diagnosis, as radiological features

may mimic malignant processes. To our knowledge, this is the first reported case of malakoplakia with concomitant bilateral lower limb osteomyelitis. Interestingly, the symmetric metaphyseal-diaphyseal subcortical uptake observed on both gallium and FDG imaging could also raise suspicion for alternative diagnoses such as Erdheim-Chester disease. ***Conclusion:*** This case highlights the potential value of ^{18}F-FDG PET/CT in characterizing the extent of involvement and guiding the diagnosis of this rare multisystemic entity. ***References:*** Nuciforo P and al. Malakoplakia of the pancreas with diffuse lymph-node involvement. Virchows Archiv. 2003;442(1):82-85.2. Ho M, Wu J, Skinnider B, Kavanagh A. Prostatic malakoplakia: a case report with review of the literature. Journal of Surgical Case Reports. 2018;2018(3). 3. Lane JL, Land AD, Thompson SM, Weiner SD. Malakoplakia of bone. JBJS Case Connector. 2014;4(4):e116. 4. Morgan TA, Rabban JT, Filly RA. Testicular malakoplakia: A rare sonographic mimic of malignancy. Journal of Clinical Ultrasound. 2014;43(3):199-202. 5. Liu X, Yu C, Zhao Z, Zheng Y, Chen X, Zhou D. Rectal malakoplakia mimicking advanced rectal cancer: A case report. Heliyon. 2023;9(10):e20780.

EP-1225

A Rare Case of Small Cell Lung Cancer Presenting with a Breast Mass

N. Aydinbelge Dizdar[1], *D. Cayir*[2], *H. Turksoy Karaca*[3], *A. T. Arikok*[3];
[1]*Ankara Etlik City Hospital, Ankara, TÜRKIYE,* [2]*University of Health Sciences, Ankara Etlik City Hospital, Department of Nuclear Medicine, Ankara, TÜRKIYE,* [3]*Ankara Etlik City Hospital, Department of Pathology, Ankara, TÜRKIYE.*

Aim/Introduction: The extramammary metastases to the breast are a rare manifestation and their prevalence has been reported to vary between 0.1% and 5.0%. The most frequent breast metastases or involvement of non-breast neoplasms are lymphoma, melanoma, lung, thyroid, gallbladder, and ovarian tumors. Lung carcinoma metastases to the breast are a rare presentation, and among published case reports, NSCLC (non-small cell lung cancer) metastases are more frequently documented than SCLC (small cell lung cancer) metastases, although SCLC breast metastases have occurred synchronously. ***Materials and Methods:*** Herein, we report a case of metastatic SCLC who presented with a breast mass and underwent FDG PET for staging. A 63-year-old woman who admitted to the emergency department with complaints of shortness of breath, chest pain and a lump in the right breast underwent non-contrast enhanced thorax CT. It synchronously showed a mass lesion with a diameter of 25 mm in the right breast, a mass lesion in the superior lobe of right lung and pleural effusion in the right hemithorax. Subsequently, ^{18}F-FDG was performed for lesions characterization and found that multiple increased radiotracer uptakes in lesions of right breast, right lung and liver, mediastinal and periportal lymph nodes, and bones. Afterwards, histopathological and immunohistochemical examinations of the breast mass sample confirmed that a small cell lung carcinoma (SCLC) metastasized to the breast. Round / oval blue cells with minimal cytoplasm; usually small to medium sized. The finely dispersed or salt and pepper chromatin with no distinct nucleoli is apparent in many of the cells. The high nuclear to cytoplasmic ratio is also demonstrated. Strong and diffuse positivity for TTF1 is seen in small cell lung carcinomas. Small cell lung carcinomas demonstrate positivity for Synaptophysin. High proliferation index (%80) with Ki67. ***Results:*** SCLC is a very aggressive entity that causes early and widespread haematological metastasis, often resulting in extensive brain, bone or liver involvement. The clinical presentation of breast metastases at the same time as primary lung carcinoma is extremely rare and has a significant impact on treatment strategies and mortality. Patients presenting with a breast mass without a known history of malignancy should be considered for the possibility of rare extramammary metastatic processes rather than primary breast cancer, such as in this case. ***Conclusion:*** The clinical presentation of breast metastases at the same time as primary lung carcinoma is extremely rare and has a significant impact on treatment strategies and mortality.

EP-1226

FDG-Negative but FES-Positive Vertebral Metastasis in ER-Positive Breast Cancer: A Case Highlighting the Complementary Role of Functional Receptor Imaging

A. Mahalik*, N. Kundu, K. Jain, M. Tripathi, R. Kumar;*
All India Institute of Medical sciences, New Delhi, INDIA.

Aim/Introduction: ^{18}F-FDG PET/CT is routinely used in staging and restaging of breast cancer. However, its sensitivity may be limited in detecting certain metastatic lesions, particularly in indolent or receptor-rich disease. 18F-FES PET/CT, a novel imaging modality targeting estrogen receptors (ER), offers a valuable complementary perspective by highlighting receptor expression independent of metabolic activity. ***Materials and Methods:*** A 39-year-old female with a history of ER-positive invasive ductal carcinoma of the breast, post-mastectomy and axillary lymph node dissection (ALND) in 2014, presented with complaints of backache in Dec, 2021. She underwent both ^{18}F-FDG PET/CT and 18F-FES PET/CT for evaluation. While the FDG PET/CT did not demonstrate any abnormal tracer uptake in the spine, FES PET/CT revealed a focal, intensely tracer-avid lesion in the D4 vertebral body, raising suspicion for a metabolically indolent but receptor-positive osseous metastasis. ***Results:*** This case underscores the potential for FDG PET/CT to miss clinically significant lesions in ER-positive breast cancer, particularly when lesions are slow-growing, well-differentiated, or exhibit low glycolytic activity. Possible reasons for FDG-negativity include low tumor cellularity, mucinous histology, treatment-induced metabolic suppression, or the lesion being masked by diffuse physiological FDG uptake in the vertebrae. In such scenarios, FES PET/CT provides critical diagnostic insight by detecting receptor-rich disease at sites that may otherwise be overlooked. This emphasizes the role of FES PET/CT in assessing symptomatic patients with negative FDG scans and known ER-positive status, supporting earlier detection and potentially altering treatment strategies. ***Conclusion:*** FES PET/CT can identify ER-positive, FDG-negative metastases that may not be evident on standard metabolic imaging. Its use in selected cases can enhance diagnostic accuracy and influence management decisions in hormone receptor-positive breast cancer. This case supports the inclusion of FES PET/CT in the imaging algorithm for symptomatic patients with negative or equivocal FDG findings.

EP-1227

Significance of ^{18}F-FDG PET/CT in Detecting Rare Breast Metastasis from Cervical Cancer: A Case Report

A. Leiva Montejo*, I. Sime Loayza, C. Balbin Garcia, B. Cueto Cañadas, A. Montellano Fenoy, J. Sanchez Catalicio, J. Delgado Moreno, M. Guerrero Ortiz;*
Hospital Universitario Torrecárdenas, Almeria, SPAIN.

Aim/Introduction: Cervical cancer is one of the most common malignancies in women, with squamous cell carcinoma being the most frequent histological subtype. While metastatic spread typically involves pelvic and para-aortic lymph nodes, lungs, liver, bones, and extrapelvic lymph nodes, breast metastasis is exceedingly rare. The incidence of non-mammary malignancies metastasizing to the breast is estimated to range between 0.4% and 3%. ***Materials and Methods:*** A 58-year-old woman presented with postmenopausal metrorrhagia. Gynecological examination revealed a 4 cm mass in the cervix infiltrating the vagina. A biopsy confirmed a high-grade undifferentiated carcinoma, most likely squamous cell carcinoma associated with HPV infection. MRI diagnosed stage IIB cervical carcinoma. A staging CT showed the cervical lesion without additional relevant findings. The gynecological- oncology committee recommended ^{18}F-FDG

PET/CT prior to treatment. ***Results:*** ^{18}F-FDG PET/CT revealed a hypermetabolic mass in the cervix measuring 3.7 x 4.7 cm (SULmax 35.1), indicative of a neoplastic process. Additionally, a right hilar lymph node with moderate FDG uptake of 0.8 cm (SULmax 8.8) was noted, along with two hypodense and hypermetabolic hepatic lesions, the largest in segment VII measuring 2.9 x 3.1 cm (SULmax 16.9). Three hypermetabolic bone lesions were observed in the right 9th costal arch (SULmax 8.3), left sacral wing (SULmax 4.4), and right femoral head (SULmax 8.2), all suggestive of metastasis. A diffuse, mildly intense FDG uptake in the gastric cardia (SULmax 4.9) raised suspicion for malignancy, but endoscopy was negative for neoplasia. A small hypermetabolic nodule in the left breast (LB) measuring 0.5 x 0.5 cm (SULmax 11.5), was also observed, suggesting malignancy. A targeted biopsy was recommended to confirm the presence of a synchronous tumor. In the committee, a tumorectomy of the LB nodule was proposed, as the biopsy was inconclusive, with the following outcome: metastasis of high-grade undifferentiated carcinoma, likely related to squamous cell carcinoma of the cervix associated with HPV infection. ***Conclusion:*** Breast metastasis from cervical cancer is an extremely rare entity and can mimic primary breast cancer, complicating diagnosis. This case highlights the critical role of ^{18}F-FDG PET/CT in identifying unusual metastatic sites that may be clinically silent or radiologically nonspecific. Histopathological confirmation is essential to rule out synchronous primary tumors. The presence of breast metastasis reflects systemic disease dissemination, which is associated with poor prognosis. Comprehensive imaging and multidisciplinary evaluation are crucial for the early and accurate detection of such metastases.

EP-1228

Quantitative [^{15}O]H_2O PET perfusion hybrid imaging reveals the correct diagnosis in a patient with cardiac amyloidosis and chest pain

V. Uusitalo*;*
Helsinki University Hospital, Helsinki, FINLAND.

Aim/Introduction: Microvascular disease is common in cardiac amyloidosis secondary to amyloid fibril infiltration of the myocardium and microvasculature. Unfortunately, microvascular disease is poorly detected by most of the common noninvasive imaging modalities used to diagnose coronary artery disease. Positron emission tomography (PET) perfusion using [^{15}O]H_2O is the gold standard for noninvasive quantitative myocardial perfusion imaging. Combining it with coronary computed tomography angiography (CCTA) at the same imaging session allows accurate evaluation of both epicardial and microvascular coronary artery disease. ***Materials and Methods:*** The patient was a 60-year-old male with a previously diagnosed light chain amyloidosis who developed chest pain, which was considered typical angina pectoris. In addition to chest pain, the patient had polyneuropathy. The light chain amyloidosis was confirmed from the muscle and gastrointestinal biopsy. Amyloid cardiomyopathy was diagnosed by cardiac magnetic resonance imaging. PET perfusion using [^{15}O]H_2O and during adenosine stress was obtained, and simultaneously CCTA was imaged for anatomical reference. There was a typical hemodynamic response to adenosine stress. ***Results:*** PET perfusion had a normal relative perfusion on visual evaluation, but quantitative perfusion analysis revealed diffuse myocardial ischemia during adenosine stress. Global left ventricular perfusion was 1.19 ml/min/g (normal >2.3). Highest perfusion was at the apical region (1.38 ml/min/g), which was similar to the typical apical sparing phenomenon seen on speckle tracking echocardiography in cardiac amyloidosis patients (spared longitudinal contraction at the apical region). CCTA revealed intermediate coronary stenosis on the mid left anterior descending artery (50-70 %). There was no regional reduction in PET perfusion at the LAD area. The calcium score was 218, and no other coronary stenoses of note were detected. The diagnosis of microvascular angina was made. ***Conclusion:*** Microvascular disease is a common cause of chest pain in cardiac amyloidosis. Hybrid imaging with quantitative PET perfusion and CCTA allows for its accurate evaluation in one imaging procedure.

EP-1229

Osteomesopyknosis, a Great Mimic of Osteoblastics Metastasis in Bone Scintigraphy.

M. Feriche Aragon*, C. Mas Pascasio, E. Espinosa Muñoz, A. Adarve Castro, T. Rudolphi Solero, S. Sanz Viedma;*
Hospital Virgen de la Victoria, Málaga, SPAIN.

Aim/Introduction: Osteomesopyknosis is a rare, benign, autosomal dominant (AD) genetic disorder causing irregular increased bone density, mainly in the spine, pelvis, and proximal femurs. Sclerotic lesions mimic blastic bone metastases on MRI, CT, and bone scintigraphy. Prevalence is <1 per million. Diagnosis is challenging due to the high incidence of tumors causing blastic metastases (prostate, breast cancer). ***Materials and Methods:*** A 46-year-old woman with HLA B27+ spondyloarthritis was evaluated at another center five years prior, with bone scintigraphy, thoracoabdominopelvic CT, and spine MRI suggesting blastic metastatic bone disease. ^{18}F-FDG-PET/CT showed hypometabolic blastic lesions without a primary tumor. A bone biopsy was negative for malignancy.Referred for bone scintigraphy due to suspected metabolic bone disease (persistent elevated alkaline phosphatase, increasing lower back pain), whole-body bone scintigraphy with 740 Mbq ^{99m}Tc-HDP showed pathological radiotracer distribution with increased uptake in the spine, iliac and pubic bones. Compared to a previous study, no significant changes were observed. The patient reported her father had a similar condition.Given no malignancy, negative biopsy, and family history, an exhaustive literature search identified Osteomesopyknosis. Baseline bone scintigraphy and MRI were recommended for first-degree relatives due to the potential future coexistence of tumors causing blastic lesions. ***Results:*** Osteomesopyknosis, an AD genetic disease, mimics blastic metastatic bone disease on imaging. Workup is complex as metastatic prostate or breast cancer is the initial consideration. After excluding a primary tumor and a negative biopsy, diagnosis is by exclusion based on the sclerosing pattern in the spine, pelvis, and femurs. Due to AD inheritance, baseline bone scintigraphy and MRI are recommended for relatives, as these patients may later develop tumors with blastic metastases, aiding management. ***Conclusion:*** Osteomesopyknosis is a very rare AD disease with challenging diagnosis. Its sclerotic bone lesions mimic blastic bone metastases on imaging, potentially leading to incorrect oncological diagnoses. Diagnosis relies on exclusion and the pattern of involvement. Baseline studies should be recommended for first-degree relatives. ***References:*** 1. Heursen EM, González Partida Mdel C, Paz Expósito J, Navarro Díaz F. Osteomesopyknosis--a benign axial hyperostosis that can mimic metastatic disease. Skeletal Radiol. 2016 Jan;45(1):141-6. 2. Hardouin P, Flautre B, Sutter B, Leclet H, Grardel B, Fauquert P. Osteomesopyknosis: report of a new case with bone histology. Bone. 1994 Jan-Feb;15(1):81-3.

EP-1230

Benign But Avid: Ga-68 DOTATATE Uptake In Lip Chondroid Syringoma Mimicking Neuroendocrine Tumor Metastasis

E. Pasini Nemir*, M. Pesorda, D. Huic;*
University Hospital Centre Zagreb, Zagreb, CROATIA.

Aim/Introduction: Ga-68 DOTATATE PET/CT remains a cornerstone in the diagnosis, staging, and treatment response assessment of neuroendocrine tumors (NETs), due to its ability to detect somatostatin receptor (SSTR) expression. While SSTR overexpression is well-documented in NETs and other malignancies, it has not yet

been reported in chondroid syringoma; a rare, benign adnexal skin tumor that most commonly arise in the head and neck region, with malignant transformation being rare. ***Materials and Methods:*** We present a case of 69-year-old patient with a history of atypical lung carcinoid, diagnosed in 2020 after a right upper lobectomy (Ki-67 index 15-20%; CD56 and TTF-1 positive) and partial right lower lobe segmentectomy revealing an adenocarcinoma. Adjuvant chemotherapy was completed in 2020. There was no recurrence until 2024 when a lobulated subcutaneous mass in the right clavicular region was detected on follow-up chest CT. Surgical excision revealed metastasis of atypical carcinoid (Ki-67 25%) with lymphovascular and perineural invasion. A Ga-68 DOTATATE PET/CT was subsequently performed to evaluate disease activity and potential spread. ***Results:*** The PET/CT scan revealed increased tracer uptake in the right upper paratracheal (0.8 cm, SUVmax 4.5) and subcarinal (1.5 × 1.4 cm, SUVmax 8.0) mediastinal lymph nodes, consistent with metastatic involvement. No pathological uptake was observed in the lung parenchyma. Unexpectedly, the scan showed increased DOTATATE uptake in a subcutaneous lesion of the lower lip (1.1 × 0.8 cm, SUVmax 4.2), raising suspicion for a metastatic lesion given the patient's history of subcutaneous metastasis, so the lesion was surgically excised. Histopathological analysis revealed a 2.1 × 1.0 × 1.5 cm tumor composed of epithelial and mesenchymal elements without cytological atypia, consistent with chondroid syringoma (tumor mixtus). No other DOTATATE-avid lesions were detected in the scanned body volume. ***Conclusion:*** To our knowledge, this is the first report of Ga-68 DOTATATE uptake in a chondroid syringoma, highlighting a potential pitfall in nuclear imaging interpretation in patients with known NETs. While increased DOTATATE uptake typically indicates metastatic disease, this case underscores the importance of considering benign mimics such as chondroid syringoma, which can also express somatostatin receptors. Awareness of such rare false-positive findings is essential to avoid misdiagnosis and unnecessary aggressive treatment. ***References:*** Malan N, Vangu MD. Normal Variants, Pitfalls and Artifacts in Ga-68 DOTATATE PET/CT Imaging. Front Nucl Med. 2022 Feb 7.2 Di Guardo A et al. Clinical and Dermoscopic Characteristics of Cutaneous Chondroid Syringoma: A Systematic Review. Dermatol Pract Concept. 2024 Oct 30;14.

EP-1231

From back pain to bone lesion: A case of disseminated tuberculosis uncovered by PET/CT

G. Rakia*, A. Ezzine, S. Mensi, T. Dardouri, R. Mehri, K. Chatti;*
CHU Sahloul, Sousse, TUNISIA.

Aim/Introduction: Tubercuosis (TB) is the leading cause of infectious mortality worldwide.Its presentation varies widely,from asymptomatic cases to life-threatening conditions making clinical and radiological diagnosis challenging. 18FDG-PET/CT scan is particularly useful in detecting the disease in previously unknown sites, and allows the most approriate site of biopsy to be selected. ***Materials and Methods:*** A 33-year-old patient underwent ^{18}F-FDG PET/CT as part of the diagnostic workup for suspected tuberculosis. The distribution of hypermetabolic lesions was correlated with clinical, laboratory, and microbiological data to assess the diagnostic contribution of PET/CT in tuberculosis. ***Results:*** The case involves a 33-year-old patient experiencing isolated inflammatory spinal pain for two months,accompanied by an episode of rotational vertigo and recurrent tachycardia. A chest CT revealed homogeneous hepatosplenomegaly, right mediastino-hilar and latero-aortic retroperitoneal lymphadenopathy, and multiple osteolytic lesions. Notably, a right paravertebral mass at D4 infiltrated the spinal canal, and epiduritis was observed at D12.A cerebral MRI was requested finding 3 intra-axial supratentorial nodular lesions annularly enhanced after gadolinium injection with perilesional edema without mass effect.Biopsy was performed reporting chronic granulomatous inflammatory lesions with multinucleated giant cells with caseous necrosis without cellular atypia.Due to the atypical presentation, the doctors decided to perform another biopsy. The patient was referred for further investigation to identify potential biopsy sites and map the infection, if present. The patient underwent an 18FDG PET/CT scan revealing widespread metabolically active involvement consistent with tuberculosis. Findings included hypermetabolic nodular brain lesions, FDG-avid pulmonary, thoracic, and extrathoracic lymph nodes as well as FDG-avid nodular pleural thickening with multiple scattered hypermetabolic bilateral pulmonary nodules. There was also heterogeneously hypermetabolic splenomegaly with homogeneous hepatomegaly and nodular thickening of the peritoneal lining, showing focal FDG uptake with hypermetabolic tissue-dense nodules in the left flank. Differentiation between a tuberculous or malignant origin required histopathological correlation. Additionally, severe hypermetabolic multilevel spinal and sternal involvement was observed, consistent with spondylodiscitis. Treatment with Dotbal (rifampin, isoniazid, pyrazinamide, and ethambutol) was initiated, with two tablets administered every 12 hours. The patient is currently still undergoing treatment. An 18FDG PET/CT scan was recommended to assess the treatment response. ***Conclusion:*** 18FDG PET/CT plays a crucial role in staging TB, detecting extrapulmonary TB (EPTB), and identifying patients with subclinical TB. ***References:*** Batún-Garrido JADJ, Salas-Magaña M, García-Padrón OA, Valencia-Serrano N. Two cases of tuberculous spondylodiscitis: a rare manifestation of extrapulmonary tuberculosis. Quant Imaging Med Surg. févr 2017;7(1):1327.

EP-1232

Challenges in diagnosis of hepatocellular adenoma - a case study

Z. Zychowicz*, P. Cichocki, Z. Adamczewski;*
Medical University of Lodz, Nuclear Medicine Department, Lodz, POLAND.

Aim/Introduction: Hepatocellular adenoma (HCA) is a rare, benign liver tumor primarily associated with oral contraceptive use in women, although recent studies show an increased prevalence among men, with obesity and metabolic syndrome being the most prominent risk factors. HCAs can pose risks of hemorrhage and malignant transformation, which makes properly assessing and treating these lesions crucial. We present an interesting case of a male patient without notable risk factors of HCA, referred for evaluation of lesion in the right lobe of the liver after multiple non-conclusive imaging studies. ***Materials and Methods:*** 68-year-old male patient was referred for static liver scintigraphy due to a suspicion of focal nodular hyperplasia (FNH). Ultrasound showed a 80 x 70mm hypoechoic, cyst-like mass with dense, heterogenous contents and a hyperechoic rim. A contrast-enhanced CT scan showed a lesion with mildly increased density within a steatotic liver with enhancement in the arterial and portal venous phase followed by mild washout in delayed phases, occurring more rapidly centrally than peripherally. MRI showed a hypointense, well-separated mass in T1-weighted images with smaller peripheral hyperintense lesions measuring up to 7mm and features of a central scar. The whole mass showed arterial phase enhancement with gradual washout in later phases with persisting peripheral enhancement. Abovementioned findings were inconclusive. Epidemiology, along with clinical and radiological findings led to the suspicion of FNH, so the patient was referred for liver scintigraphy using Tc-99m sulfur colloid. ***Results:*** Liver scintigraphy revealed no radiopharmaceutical uptake in the location of the lesion, which is not typical for FNH. This result supported the exclusion of FNH, as well as some other benign lesions, such as regenerative nodules and focal steatosis. Exclusion of these benign lesions, despite the lack of clear features

of malignancy in morphological studies, prompted the referring physician to send the patient for urgent biopsy, which led to the diagnosis of HCA. ***Conclusion:*** Although the radiological imaging studies were inconclusive, they did not suggest malignant nature of the lesion. Liver scintigraphy allowed to narrow down the potential diagnoses and excluded FNH. This led to HCA, another benign tumor, to become one of the potential, and looking back to radiological results, most likely diagnosis. Although this benign lesion is more common in women, it should be considered in differential diagnosis in men as well.

EP-1233

Total-body [^{18}F]AlF-RESCA-T4 ImmunoPET/CT in Patients with Solid Tumors: Initial Experience and Potential Value in Navigating Clinical Decision-making

S. An, *G. Huang, J. Liu, W. Wei;*
Institute of Clinical Nuclear Medicine, Renji Hospital, School of Medicine, Shanghai Jiao Tong University, Shanghai, CHINA.

Aim/Introduction: Precise selection of patients who could benefit from targeted or immunotherapy is essential in clinical practice. Trophoblast cell surface antigen 2 (Trop2) is an emerging biomarker of theranostic potential. We previously developed single domain antibody (sdAb)-derived tracers specific for Trop2. We translated two of the tracers (i.e., [^{68}Ga]Ga-NOTA-T4 and [^{18}F]AlF-RESCA-T4) for clinical use on a traditional short axial field-of-view PET/CT scanner. In this study, we report the diagnostic performance of [^{18}F]AlF-RESCA-T4 on a total-body PET/CT scanner and the value in navigating subsequent treatments in patients with solid tumors. ***Materials and Methods:*** [^{18}F]AlF-RESCA-T4 was freshly produced on-site and administered to patients recruited in an ongoing investigator-initiated clinical trial.Three patients with solid tumors underwent both low-dosewhole-body [^{18}F]AlF-RESCA-T4 and [^{18}F] FDG PET/CT scan imaging in two weeks. Immunohistochemistry staining was utilized to analyze Trop2 expressionin tumors. ***Results:*** All the lesionsclearly identifiedby low-dose [^{18}F]AlF-RESCA-T4immuno-positronemission tomography/computed tomography (immuno-PET/CT) imaging. Region of interest analysisshowed thatkidneys, pancreas, and glandsarethe organs/tissues withthe highest radiotracer uptake.[^{18}F]AlF-RESCA-T4 immuno-PET/CT allowed noninvasive visualization heterogeneous expression of Trop2 in patients with solid tumors, changing the re-staging and clinical decision-making of the patient ***Conclusion:*** Low-dose[^{18}F]AlF-RESCA-T4 immuno-PET/CT imaging on the total-body PET/CT scanner is feasible. [^{18}F]AlF-RESCA-T4 can be effectively used to detect primary and metastatic lesions in patients with solid tumors, suggesting potential of diagnostic and Trop-2-based therapeuticapplications.

EP-1234

Negative ^{99m}Tc-Ubiquicidin SPECT/CT in the Evaluation of Suspected Osteoradionecrosis of the Mandible in a Patient with Recurrent Tongue Carcinoma

V. Heringer, *B. Alencar, T. Agnello, M. Osmak, E. Etchebehere, C. Ramos, M. Lima, B. Amorim, A. Santos;*
UNICAMP, Campinas, BRAZIL.

Aim/Introduction: Osteoradionecrosis (ORN) is a known late complication of radiotherapy in head and neck cancer patients. Differentiating ORN from neoplastic recurrence or secondary infection is clinically relevant, especially when surgical intervention is contraindicated. ^{99mTc}-ubiquicidin (UBI) SPECT/CT is a promising imaging modality in infection evaluation due to its specificity for bacterial cell membranes. UBI is a cationic synthetic peptide fragment that binds selectively to negatively charged bacterial surfaces via electrostatic interactions, enabling differentiation between infection and sterile inflammatory or necrotic tissue[1,2]. We report the case of a patient with prior oropharyngeal cancer undergoing evaluation of mandibular ORN using both UBI-SPECT/CT and MDP-SPECT/CT. ***Materials and Methods:*** A 49-year-old female with a history of squamous cell carcinoma (SCC) of tongue treated with radiotherapy and chemotherapy in 2022, currently under neoadjuvant treatment for SCC of the left tongue (T2N0M0), was referred for evaluation of suspected mandibular ORN. She underwent ^{99m}Tc-UBI SPECT/CT with dynamic acquisition (2s/frame), followed by whole-body planar imaging at 1 and 2 hours and focused SPECT/CT of the head at 2 hours. A lesion-to-background (L/B) ratio was calculated. Six days later, a ^{99m}Tc-MDP bone scintigraphy was performed. ***Results:*** ^{99m}Tc-UBI SPECT/CT showed physiological tracer distribution, with no focal uptake in the mandible. The L/B ratio was 1.0, below the 1.74 threshold for active infection. In contrast, bone scintigraphy with ^{99m}Tc-MDP revealed a lesion with markedly increased osteoblastic activity in the right hemimandible, particularly in the molar region, associated with cortical erosion, findings compatible with osteonecrosis, though neoplastic infiltration could not be excluded. ***Conclusion:*** In this case, ^{99m}Tc-ubiquicidin SPECT/CT was essential to exclude mandibular infection in a previously irradiated patient with suspected ORN. The physiologic uptake pattern and normal L/B ratio supported a noninfectious diagnosis, allowing the patient to avoid unnecessary antibiotics or surgical procedures[3,4]. UBI-SPECT/CT is a valuable noninvasive tool in the evaluation of complex oncologic cases with diagnostic uncertainty. ***References:*** 1) Welling MM, et al. J Nucl Med. 2000;41:275. 2) Ferro-Flores G, et al. Molecules. 2021;26:3159. 3) Palestro CJ. Q J Nucl Med Mol Imaging. 2020;64:138. 4) Signore A, et al. Nucl Med Commun. 2011;32:917.

EP-1235

Renal Ewing Sarcoma: "TripleMismatch" NuclearMedicine Signature

N. Kundu, *D. Khan, S. Sagar, A. Mahalik, A. Roy, K. Jain, V. Singh, J. Choudhary, J. Krishna, R. Kumar;*
AIIMS New Delhi, Delhi, INDIA.

Aim/Introduction: To illustrate how combined ^131ImIBG, ^68GaDOTANOC and ^18FFDG PET/CT can resolve the diagnostic dilemma of a paediatric suprarenal "smallroundbluecell" tumour by demonstrating a characteristic imaging mismatch that suggested renal Ewing sarcoma (rEWS). ***Materials and Methods:*** A 6yearold boy with a leftflank mass underwent ultrasound and contrastenhanced CT, both showing a 13 × 9 cm lobulated suprarenal lesion with calcification. The initial biopsy was inconclusive, favouring a malignant roundcell tumour negative for neuroblastoma, Wilms and rhabdomyosarcoma markers. Because neuroblastoma remained high on the differential, ^131ImIBG planar/SPECT imaging was performed, followed 48 h later by wholebody ^68GaDOTANOC PET/CT and, after 72 h, ^18FFDG PET/CT. All scans were evaluated qualitatively and semiquantitatively (SUVmax). A second core biopsy with immunohistochemistry (NKX2.2) and FISH for EWSR1 rearrangement served as the reference standard. ***Results:*** The mass was nonavid on mIBG, showed mild SSTR expression on DOTANOC (SUVmax ≈ 3.8) and was intensely FDGavid (SUVmax ≈ 12). No distant metastases were seen. This "triplemismatch" pattern prompted rebiopsy; tumour cells demonstrated strong NKX2.2 nuclear positivity and an EWSR1 translocation, confirming rEWS. The imaging constellation excluded neuroblastoma and guided timely referral for neoadjuvant chemotherapy followed by nephrectomy. ***Conclusion:*** A nonmIBGavid, mildly DOTANOCpositive yet highly FDGavid renal mass in a child should raise strong suspicion for rEWS. Recognising this nuclearmedicine signature can fasttrack definitive tissue diagnosis, avoid futile neuroblastomadirected therapy and underscores the value of multimodality functional imaging in rare paediatric renal tumours.

EP-1236

Multifocal avascular necrosis unmasked by Tc99m MDP Bone scan

N. Kundu, *D. Khan, S. Sagar, A. Mahalik, K. Jain, J. Krishna, V. Singh, J. Choudhary, R. Kumar;*
AIIMS New Delhi, Delhi, INDIA.

Aim/Introduction: Avascular necrosis (AVN) refers to the cellular death of bone components due tointerruption of the blood supply, resulting in collapse, pain, loss of joint function and long-term joint damage. The disease can affect various joints such as the knee, shoulder, and ankle, although it most commonly involves the hip. Radiographs are often initially used to diagnose osteonecrosis. If disease is apparent radiographically, then often no other imaging or screening tests are necessary. However, disease often may not be detectable in early stages because radiographic abnormalities appear only after prolonged changes in ischemic tissue. Magnetic resonance imaging (MRI) is considered to be the gold standard for diagnosing AVN. Bone scintigraphy has been advocated as a useful diagnostic tool for patients with suspected osteonecrosis or in screening for multifocal disease. Here we report an interesting case where wholebody Tc99mMDP scintigraphy unexpectedly identified multifocal, clinically silent avascular necrosis (AVN) in a young adult scheduled for hip arthroplasty, thereby altering surgical planning. ***Materials and Methods:*** A 24 year old man with threeyear bilateralhip pain had MRIproven femoralhead AVN and previously underwent core decompression. Reemergent pain led to planned bilateral total hip replacement. Preoperative infection screening was requested with a threephase 740 MBq Tc99mMDP bone scan: dynamic flow, bloodpool statics and 3h wholebody delayed images, complemented by focused SPECT/CT of symptomatic and scanpositive joints (shoulders, elbows, knees, hips). ***Results:*** Delayed whole body images revealed avid peripheral tracer uptake with central photopenic zones in the left humeral head, right trochlea, both femoral heads and the right tibial plateau, classic for AVN. Corresponding SPECT/CT confirmed subchondral collapse only at the hips; extrahip lesions were structuralstage I. Findings prompted orthopaedic revision of the operative plan: staged hip arthroplasty plus prophylactic core decompression of the asymptomatic shoulder and knee lesions. The patient's management shifted from singlejoint replacement to a jointpreservation strategy for three additional sites. ***Conclusion:*** Wholebody Tc99mMDP scintigraphy with regional SPECT/CT can expose occult multifocal AVN that eludes conventional sitedirected MRI. Incorporating bone scan into the workup of young AVN patients scheduled for surgery enables early intervention at unsuspected sites and may forestall progressive joint collapse, affirming its complementary role alongside MRI in contemporary musculoskeletal practice.

EP-1237

Unexpected [^{18}F] Fluciclovine Uptake in Pilocytic Astrocytoma: A Paediatric Case Report

H. Koga[1,2], *S. Watanabe*[1,2], *K. Hirata*[1,2], *T. Harada*[1], *Y. Ishi*[3], *S. Yamaguchi*[3], *N. Wakabayashi*[1,2], *L. Hashimoto*[2], *K. Kudo*[1];
[1]*Department of Diagnostic Imaging, Graduate School of Medicine, Hokkaido University, Sapporo, Hokkaido, JAPAN,* [2]*Department of Nuclear Medicine, Hokkaido University Hospital, Sapporo, Hokkaido, JAPAN,* [3]*Department of Neurosurgery, Graduate School of Medicine, Hokkaido University, Sapporo, Hokkaido, JAPAN.*

Aim/Introduction: [^{18}F] Fluciclovine is a synthetic amino acid PET tracer primarily used in the evaluation of prostate cancer (1). Since June 2024, it has been covered by the Japanese National Health Insurance System for imaging of high-grade gliomas. In this case report, we present a paediatric patient with unexpectedly high fluciclovine uptake in a pilocytic astrocytoma, a benign tumor categorized as grade 1 glioma by World Health Organization (WHO) criteria. ***Materials and Methods:*** A 5-year-old boy undergoing neuroimaging after head trauma was incidentally found to have a well-circumscribed mass lesion in the region of the septum pellucidum. MR imaging demonstrated hyperintensity on both T2-weighted and FLAIR sequences. Gadolinium-enhanced T1-weighted imaging (Gd-T1WI) revealed heterogeneous peripheral enhancement. Given the imaging features, a glioma was suspected. To further characterize the lesion, [^{18}F] fluciclovine PET was performed. A dose of 96.6 MBq (4.31 MBq/kg) of [^{18}F] fluciclovine was administered intravenously, and PET-CT was acquired 40 minutes after injection. ***Results:*** [^{18}F] Fluciclovine PET demonstrated strong uptake in the tumour with a maximum standardised uptake value (SUVmax) of 2.37. The SUVmax in the surrounding normal cerebral cortex was 0.66, resulting in a tumour-to-normal ratio (TNR) of 3.56. FDG-PET showed no significant uptake compared to the cerebral cortex. The patient underwent partial resection of the lesion. Histopathological examination confirmed the diagnosis of pilocytic astrocytoma (WHO grade 1). Comprehensive genomic profiling revealed an in-frame KIAA1549 (exon 15)-BRAF (exon 9) fusion (chr7:138867975-chr7:140787584). The postoperative course was uneventful for 6 months, and the patient remains under routine surveillance without any symptoms. ***Conclusion:*** Although high uptake of [^{18}F] fluciclovine is typically associated with high-grade gliomas, this case demonstrates that pilocytic astrocytoma, a low-grade glioma, can also show significant tracer accumulation. The underlying mechanism of fluciclovine uptake in low-grade tumours remains unclear. Awareness of such atypical uptake patterns is essential to avoid overestimation of tumour grade. Further studies are warranted to elucidate the uptake mechanisms and diagnostic specificity of [^{18}F] fluciclovine PET in paediatric and low-grade gliomas. ***References:*** 1. Jain S, Dhingra VK. An overview of radiolabeled amino acid tracers in oncologic imaging. Front Oncol. 2023 Feb 17;13:983023. doi: 10.3389/fonc.2023.983023. PMID: 36874105; PMCID: PMC9981995.

EP-1238

Scintigraphic Patterns of Renal Osteodystrophy: Two Case Reports with Differential Diagnostic Challenges

G. Bianciardi[1], *G. A. Fuso*[1], *E. Greco*[1], *C. M. P. Sgro*[1], *P. E. Orlandi*[2], *A. Romeo*[3], *S. Fanti*[1,3];
[1]*Nuclear Medicine, Alma Mater Studiorum, University of Bologna, Bologna, ITALY,* [2]*Unit of Radiology, Maggiore Hospital, Bologna, ITALY,* [3]*Nuclear Medicine, IRCSS Azienda Ospedaliero-Universitaria di Bologna, Bologna, ITALY.*

Aim/Introduction: Renal osteodystrophy is a skeletal complication of chronic kidney disease (CKD) resulting from impaired mineral metabolism, secondary hyperparathyroidism and bone remodelling dysfunction. It encompasses a variety of bone changes, including osteitis fibrosa, adynamic bone disease, osteomalacia and mixed uremic osteodystrophy. Extra-skeletal calcifications such as vascular or pulmonary deposits may also occur, particularly in advanced CKD or dialysis patients, due to altered calcium-phosphate homeostasis. Herein we describe two clinical cases of renal osteodystrophy with distinctive scintigraphic patterns, highlighting the role of bone scintigraphy in the differential diagnosis. ***Materials and Methods:*** The first case was a patient with end-stage renal disease (ESRD) on haemodialysis since 2009 and on the transplant waiting list. Chest CT showed diffuse ground-glass opacities (GGO) predominantly in the upper lobes with microcalcifications. The patient was asymptomatic at the time of imaging. Bronchoscopy with bronchoalveolar lavage (BAL) ruled out active infection, except for a previous H1N1 viral pneumonia during hospitalisation. Pulmonary function tests revealed a moderate to severe restrictive ventilatory defect with markedly reduced DLCO, suggesting interstitial involvement with calcific deposits. Bone scintigraphy showed intense radiotracer uptake in both lung fields, highly suggestive of metastatic

pulmonary calcifications secondary to CKD-related mineral bone disease. In the second case, a patient with a long history of CKD on haemodialysis underwent bone scintigraphy for diffuse skeletal pain and suspected bone metastases. The scintigraphy showed intense and diffuse radiotracer uptake throughout the axial and appendicular skeleton without visualisation of the kidneys, consistent with a "superscan" pattern. The clinical history included acute granulomatous tubulointerstitial nephritis in 2017, followed by papillary breast cancer in 2024. However, the stability of the bone lesions on imaging and laboratory data supported the diagnosis of renal osteodystrophy. ***Results:*** The two cases presented illustrate characteristic scintigraphic patterns of renal osteodystrophy: pulmonary calcifications with radiotracer uptake in the lungs in the first case; and a superscan-like skeletal involvement in the second. Accurate clinical and radiological correlation was essential for differential diagnosis. ***Conclusion:*** These cases highlight that the diagnosis of renal osteodystrophy was only possible by integrating several diagnostic modalities. The combined assessment of radiological imaging, bone scintigraphy and clinical data was crucial in distinguishing renal osteodystrophy from other differential diagnoses such as neoplastic or infectious processes. This multidisciplinary approach is essential in the evaluation of complex presentations of bone and extra-skeletal abnormalities in patients with chronic kidney disease.

EP-1239

Unexpected Diagnosis of Papillary Thyroid Carcinoma Following Degeneration of a Thyroglossal Duct Cyst in a Child

M. Ben Nasr, *D. Ben Sellem, L. Zaabar, A. Mhiri;*
Salah Azaiez Institute of Tunis, Tunis, TUNISIA.

Aim/Introduction: The thyroglossal duct cyst (TGDC) is the most common congenital malformation in the cervical region. It is often discovered incidentally, particularly in childhood. Its degeneration is rare, occurring in less than 1% of cases. We report the case of a child with a degenerated TGDC revealing multifocal papillary thyroid carcinoma with pulmonary metastasis. ***Materials and Methods:*** The patient was a 10-year-old child with no significant medical history, who presented with a left digastric lymphadenopathy persisting for several months. He underwent cervical surgery for excision of the lymph node measuring 25 mm. Intraoperative frozen section examination suggested a metastatic papillary carcinoma lymph node. He subsequently received a left recurrent and lateral neck dissection. ***Results:*** Intraoperative exploration revealed a 15 mm heterogeneous cystic mass located near the hyoid bone, suggestive of a TGDC. The thyroid gland appeared normal without nodules. The cystic mass was completely excised along with the hyoid bone. Histological analysis confirmed a degenerated TGDC. The patient underwent a second operation for total thyroidectomy and functional right neck dissection. The final pathological report confirmed bilateral papillary thyroid carcinoma with lymph node metastasis, classified as pT3b N1b (R+) M1 (pulmonary miliary). The child was treated with 9 cycles of radioiodine therapy (total cumulative activity of 24.3 GBq). The outcome was favorable, with remission of the pulmonary metastases. No recurrence was noted after 10 years of follow-up. ***Conclusion:*** Degeneration of the TGDC is rare and is usually discovered incidentally after excision. Papillary carcinoma is the most common histological type. A degenerated TGDC may be associated with primary thyroid carcinoma. The thyroglossal duct can serve as a natural pathway for the dissemination of thyroid cancer.

EP-1240

Two synchronous primary malignant neoplasms (lung cancer and thymoma) detected by FDG PET/CT in a patient undergoing initial workup for prostate cancer: A case report

J. Zivanovic[1], *M. Stojiljkovic*[1,2], *K. Petrovic*[1], *N. Pantic*[1], *D. Sobic Saranovic*[1,2], *V. Artiko*[1,2], *S. Odalovic*[1,2];
[1]*Center for Nuclear Medicine with PET, University Clinical Center of Serbia, Belgrade, SERBIA,* [2]*Faculty of Medicine, University of Belgrade, Belgrade, SERBIA.*

Aim/Introduction: Synchronous multiple primary malignant neoplasms (SMPMNs) are defined as two or more unrelated primary malignant neoplasms that occur simultaneously or within six months of the diagnosis of the first tumor, involving one or more organs in the same individual. We present an interesting case of a patient with three simultaneous malignant tumors identified on FDG PET/CT. ***Materials and Methods:*** A 60-year-old male patient was diagnosed with prostate adenocarcinoma (Gleason score 7: 4+3) in May 2024. As part of his initial workup, chest and abdominal CT revealed two lesions in the right lower lung lobe, a soft tissue mass in the anterior mediastinum, and a hypervascular lesion in the pancreas, suspected to be a neuroendocrine tumor (NET). He was referred for an ^{18}F-FDG PET/CT in August 2024 for further evaluation. ***Results:*** The PET/CT showed increased FDG uptake in the two lung lesions (SUVmax 4.4 and 6.1), which were deemed malignant. The anterior mediastinal mass also demonstrated increased FDG uptake (SUVmax 3.6), reported as highly suspicious for malignant thymoma. No increased FDG uptake was observed in the pancreas, consistent with the working diagnosis of a NET. The prostate exhibited diffusely, but only slightly, increased FDG uptake. A lobectomy of the right lower lung lobe was performed in August 2024, confirming primary lung adenocarcinoma. Simultaneously, thymectomy revealed a malignant thymoma, type B1. The patient received two courses of chemotherapy in October 2024. Given the lack of FDG uptake in the pancreas, further evaluation for a NET included blood tests (normal NSE, Chromogranin A: 139.9 ng/ml) and a pancreatic biopsy, which showed no evidence of a neuroendocrine tumor. A decision was made to monitor the patient. He received radiotherapy for prostate carcinoma in January 2025 and is currently on LHRH analogues. A recent bone scintigraphy showed no osteoblastic metastatic deposits. However, a diagnostic chest CT performed in March 2025 revealed residual disease in the anterior mediastinum, suggestive of thymoma recurrence, with no new lung lesions reported. ***Conclusion:*** To the best of our knowledge, this is the first reported case of synchronous lung cancer and thymoma detected by FDG PET/CT in a patient with prostate cancer. Although SMPMNs are rare, they should be considered when interpreting FDG PET/CT findings due to FDG's lack of specificity.

EP-1241

[^{177}Lu]Lu-PSMA Radioligand Therapy to Prolong Androgen Deprivation Therapy Free Survival in Patient With Hormone-Sensitive Metastatic Prostate Cancer: a case report

I. Langrate[1], *H. Einspieler*[1], *E. Kretschmer-Chott*[1], *S. Schmitl*[1], *L. Nics*[1], *S. Shariat*[2,3], *M. Hacker*[1], *G. Kramer*[2], *S. Rasul*[1];
[1]*Medical University of Vienna, Vienna, AUSTRIA,* [2]*Department of Urology, Medical University of Vienna, Vienna, AUSTRIA,* [3]*Department of Urology, Comprehensive Cancer Center, Medical University of Vienna, Vienna, AUSTRIA.*

Aim/Introduction: [^{177}Lu]Lu radioligand therapy (RLT), which targets the prostate-specific membrane antigen (PSMA), is primarily used in patients with metastatic castration-resistant prostate cancer (mCRPC) after androgen deprivation therapy

(ADT) or at least one taxane-based chemotherapy has failed. In this case report, [^{177}Lu]Lu-PSMA RLT was recommended as primary treatment for a patient with metastatic hormone-sensitive prostate cancer (mHSPC) due to intolerance to ADT, personal preferences and existing comorbidities. ***Materials and Methods:*** A 65-year-old man diagnosed with mHSPC received 12 intermittent cycles of [^{177}Lu]Lu-PSMA RLT over a span of eight years as monotherapy, without prior systemic treatment. ***Results:*** After the first three consecutive cycles of [^{177}Lu]Lu-PSMA RLT every 4 weeks in 2016, the PSA level decreased significantly from 16 µg/L to 0.17 µg/L (P< 0.001). Molecular imaging showed a partial remission with a reduction in PSMA-expression in the local lymph nodes. The patient was treatment-free for the following five years and underwent regular laboratory and imaging monitoring. Five years later, PSA levels increased to 13.7 µg/L and new PSMA-avid lymph nodes were detected on PET scan, necessitating retreatment with RLT. Administration of six additional cycles of [^{177}Lu]Lu-PSMA RLT every 6 weeks resulted in a PSA reduction from 14.0 to 2.8 µg/L, with imaging confirming reduced PSMA uptake in the local recurrences, leading to a further pause in therapy. In 2024, the PSA level rose to 41.6 µg/L. A PET imaging revealed a constant size with advanced PSMA-expressing lymph nodes. A further three cycles of [^{177}Lu]Lu-PSMA RLT every 6 weeks were indicated to bring the PSA down to 24 µg/L. Response assessment by PET-CT revealed a new PSMA-positive lesion in the inferior pubic ramus, prompting the initiation of systemic hormone therapy. Over the eight-year treatment course, the patient maintained durable disease control with a progression-free survival of 38 months (169.9 weeks), an ADT-free survival of 104.9 months (456 weeks), and prolonged overall survival. No significant myelotoxicity or nephrotoxicity was observed, Patient reported no therapy-related side effects. The total cumulative dose administred was 86.4 GBq ***Conclusion:*** This case report suggests that [^{177}Lu]Lu-PSMA RLT therapy may be a viable and well-tolerated alternative to conventional hormonal and chemotherapeutic strategies in select patients with mHSPC, offering prolonged disease control with minimal toxicity.

EP-1242

Post-treatment Inflammation with Foamy Macrophages Mimicking Lymphoma Relapse on Sequential FDG PET

S. Howladar, *W. Zeng;*
University of Ottawa, Ottawa, ON, CANADA.

Aim/Introduction: Primary mediastinal B-cell lymphoma (PMBCL) is a rare and aggressive subtype of mature large B-cell lymphoma, typically involving the anterior mediastinum in young patients (median age: 37). FDG PET is essential for staging and response assessment. End-of-treatment (EOT) FDG PET is routinely performed; negative findings (Deauville score ([DS] 1-3) are associated with excellent negative predictive value. However, literature shows the positive predictive value of EOT DS 4-5 (representing ~30% of patients) is low. Recent guidelines recommend an observation approach with serial imaging for EOT PET with DS4, and re-biopsy for EOT DS5 with partial metabolic response. While false positive findings are well described, delayed inflammatory changes deserve emphasis, as they may represent interval worsening on FDG PET, mimicking relapsed lymphoma and leading to unnecessary treatment. We present such a case. ***Materials and Methods:*** A 28-year-old woman presented with a one-month history of cough, shortness of breath, and pleuritic chest pain with no past medical history. CT showed a large anterior mediastinal mass. Immunohistochemistry from a core biopsy confirmed aggressive lymphoma, and additional cytogenetic (FISH) testing established a final diagnosis of PMBCL. The baseline FDG PET scan showed a hypermetabolic mass with central necrosis (10.0 x 14.1 x 18.6 cm, SUVmax: 19.6). She received 6 cycles of DA-EPOCH-R. EOT FDG PET showed significant improvement with a residual mass (2.7 x 3.3 x 4.6 cm, SUVmax: 6.4). The case was discussed at tumor board; the consensus was to observe rather than proceed with biopsy. A follow-up FDG PET three months later demonstrated increased uptake in the mass with central necrosis (2.8 x 3.5 x 5.2 cm, SUVmax: 11.2). The case reviewed at tumor board; given the increased activity, relapsed disease was suspected. Treatment options—including radiation, salvage chemotherapy followed by stem cell transplant, and possible CAR-T cell therapy—were discussed. However, the patient remained asymptomatic and questioned the likelihood of active disease. Biopsy was performed, revealing numerous foamy, hemosiderin-laden macrophages, consistent with post-treatment inflammatory changes. The patient was followed clinically and has remained in complete remission over 3 years. ***Conclusion:*** For equivocal EOT findings in lymphoma,it is common to follow patients with serial FDG PET and retreat if there is evidence of disease progression. Caution is especially warranted in PMBCL, which is more prone to post-treatment inflammation than other types. Delayed inflammation should always be considered, and biopsy should be pursued when appropriate, as illustrated in this case.

EP-1243

Predictive Value of ^{18}F-FDG PET/CT in Early Detection of Pulmonary Squamous Cell Carcinoma: A Case Report

D. Silva, *D. Barbosa, N. Vasconcelos, R. Marão, I. Lopo, H. Duarte, I. Lucena Sampaio;*
Instituto Português de Oncologia do Porto Francisco Gentil, Porto, PORTUGAL.

Aim/Introduction: [^{18}F]fluorodeoxyglucose positron emission tomography/computed tomography ([^{18}F]FDG PET/CT) plays an essential role in the assessment of indeterminate pulmonary nodules, aiding in the differentiation between benign and malignant lesions through metabolic characterisation. Our aim was to illustrate this important role in the early detection of pulmonary squamous cell carcinoma (SCC) in a patient under long-term surveillance, in whom malignancy was suspected years before histological confirmation. ***Materials and Methods:*** We present the case of a 70-year-old male with a prior history of epiglottic squamous cell carcinoma (treated in 2006 with surgery, chemotherapy, and radiotherapy), who was undergoing routine follow-up imaging. A thoracic computed tomography (CT) scan performed in 2016 revealed an 18 mm pulmonary nodule in the apex of the left upper lobe, for which imaging surveillance was recommended. In 2019, the lesion had enlarged to 23 mm, prompting a [^{18}F]FDG PET/CT scan. The study showed increased metabolic activity in the nodule (SUVmax 4.7), raising suspicion for malignancy. A CT-guided percutaneous biopsy was performed but returned negative. Surveillance continued with annual CT, and in 2024, a further increase in size (to 32 mm) led to a second biopsy, which confirmed the diagnosis of poorly differentiated squamous cell carcinoma. [^{18}F]FDG PET/CT demonstrated metabolic progression since 2019, with SUVmax rising to 14.9. The patient subsequently underwent surgical resection with curative intent. ***Results:*** This case highlights the utility of [^{18}F] FDG PET/CT in assessing indeterminate pulmonary nodules and illustrates the prognostic significance of metabolic findings, which preceded histopathological confirmation by several years. The FDG avidity, combined with progressive dimensional increase, guided continued monitoring and eventual diagnosis, despite an initially false-negative biopsy. ***Conclusion:*** [^{18}F]FDG PET/CT demonstrated high clinical utility in the early characterisation and risk stratification of a pulmonary nodule ultimately confirmed to be malignant. Although PET/CT sensitivity in detecting lung cancer is generally high, its accuracy is influenced by lesion size and metabolic activity. A recent meta-analysis reported a pooled sensitivity of 88% and specificity of 78% for PET/CT-based diagnostic models, with diagnostic performance improving in

nodules larger than 20 mm (Liu et al., 2024). This case reinforces the importance of integrating metabolic imaging findings into long-term follow-up strategies, particularly when biopsy results are initially discordant with morphological imaging. ***References:*** Li, Y., Shi, YB. & Hu, CF. ^{18}F-FDG PET/CT based model for predicting malignancy in pulmonary nodules: a meta-analysis. J Cardiothorac Surg 19, 148 (2024). https://doi.org/10.1186/s13019-024-02614-0

EP-1244

[^{18}F]FDG PET/CT imaging in two patients with diffuse skeletal muscle metastasis of thyroid carcinoma

Y. Wang, *J. Xiang, R. Li, X. Zhang, Y. Lin, Z. Zhu;*
Peking Union Medical College Hospital, Beijing, CHINA.

Aim/Introduction: Lymph nodes and lungs are the most common sites of metastasis in differentiated thyroid carcinoma. However, skeletal muscle metastasis is rare, with only isolated lesion reported previously. We herein present two cases of a 65-year-old man and a 70-year-old woman who underwent total thyroidectomy for papillary thyroid carcinoma (PTC) and radioiodine ablation therapies presented with painless nodules beneath the left thigh. ***Materials and Methods:*** To determine systemic lesions, the patients underwent [^{18}F] FDG PET/CT examination. In order to clarify the cell origin of the lesion, ultrasound-guided biopsy was performed on the male patient. H&E and immunohistochemical staining were performed on the biopsy tissues. ***Results:*** [^{18}F] FDG PET/CT revealed multiple soft tissue nodules with increased uptake in muscles of the two patients, with the largest nodule measuring 2.5×2.0 cm in size, SUVmax 13.0 in the male patient and 2.1×1.6 cm in size, SUVmax 6.9 in the female patient. In addition, [^{18}F]FDG PET/CT revealed other lesions in the lung, liver, lymph nodes and bones in the male patient, and in the lung, pleura, lymph nodes in the female patient. Histology of the soft tissue nodule near left knee joint showed atypical cells, which reacted positively to AE1/AE3, PAX - 8, TTF-1, and negatively to calretinin. Thyroglobulin in the puncture fluid was 20.72 ng/ml, which confirmed the thyroid origin of the nodule. ***Conclusion:*** [^{18}F]FDG PET/CT is crucial for detecting muscle lesions, and medical history, physical examination and relevant biological markers are valuable in differentiating cellular origins. The two cases provide a reference for the differential diagnosis in systemic muscle metastasis of thyroid carcinoma.

EP-1245

^{99m}Tc-Ubiquicidin SPECT/CT in Suspected Periprosthetic Infection: Case Series in Patients with Complex Orthopedic and Inflammatory Backgrounds

V. Heringer, *B. Alencar, T. Agnello, M. Osmak, E. Etchebehere, C. Ramos, M. Lima, B. Amorim, A. Santos;*
UNICAMP, Campinas, BRAZIL.

Aim/Introduction: Patients with inflammatory arthritis history and extensive orthopedic interventions present significant diagnostic challenges, particularly in distinguishing active infection from sterile inflammation. SPECT/CT with 99mTc-ubiquicidin (UBI), a radiopharmaceutical that selectively binds to bacterial membranes, has proven useful in differentiating these conditions, even in clinically complex scenarios[1,2]. The UBI 29-41 fragment, composed of cationic residues such as arginine and lysine, binds electrostatically to negatively charged bacterial surfaces, enhancing the specificity of infection detection[3]. ***Materials and Methods:*** Case 1: 65-year-old man with multiple myeloma and chronic right lower limb pain following hip prosthesis removal due to infection underwent ^{99mTc}-UBI scintigraphy to evaluate for low-grade infection. Case 2: 62-year-old woman with rheumatoid arthritis and a history of hip prosthesis removal underwent 99mTc-UBI SPECT/CT to assess for infection before planned reimplantation. Case 3: 62-year-old woman with seronegative RA, chronic anemia, multiple comorbidities, and clinical suspicion of periprosthetic infection underwent the same SPECT/CT protocol to evaluate systemic inflammatory activity and rule out infection. A lesion-to-background (L/B) ratio was calculated by comparing tracer uptake in regions of interest to contralateral controls, based on established thresholds for infection. ***Results:*** Case 1: moderate focal uptake was observed around the proximal femoral stem in the right thigh (L/B ratio: 1.77), exceeding the 1.74 limit indicative of active infection[3]. Given the absence of systemic signs, a conservative pain management approach was adopted. Case 2: only mild uptake (L/B: 1.1) was seen surrounding the cemented stem, with no evidence of infection. Moderate radiotracer accumulation in the wrists and ankle was consistent with RA-related joint inflammation[1,2]. These findings may be partially explained by increased capillary permeability and vascular leakage in inflamed synovial tissues, a mechanism that can facilitate non-specific tracer diffusion in chronic inflammatory conditions. Case 3: similar moderate uptake was noted in peripheral joints and no scintigraphic signs of periprosthetic infection were present (L/B <1.74), supporting the diagnosis of non-infectious activity[4]. ***Conclusion:*** SPECT/CT with 99mTc-ubiquicidin can be explored as a valuable tool in distinguishing active infection from sterile inflammation in patients with overlapping rheumatologic and orthopedic conditions, especially on indeterminate cases by triphasic bone scintigraphy. The lesion-to-background (L/B) ratio served as an objective parameter for guiding therapeutic decisions and surgical planning[1-4]. ***References:*** 1) Welling MM, et al. J Nucl Med. 2000;41:275. 2) Ferro-Flores G, et al. Molecules. 2021;26:3159. 3) Palestro CJ. Q J Nucl Med Mol Imaging. 2020;64:138. 4) Signore A, et al. Nucl Med Commun. 2011;32:917.

EP-1246

Rare atypical case of Mayer Rokitansky Kuster Hauser (MRKH) type II syndrome with ectopic hydronephrotic renal disease on radionuclide scintigraphy

D. Singh, *P. Kumar, S. Jain;*
All India Institute of Medical Sciences, Bhopal, INDIA.

Aim/Introduction: Mayer Rokitansky Kuster Hauser (MRKH) is a rare congenital syndrome in female characterized by aplastic/ hypoplastic mullerian or paramesonephric ducts with normal karyotype (46, XX). Typical (type I) MRKH syndrome is characterized by absent/ hypoplastic uterus, cervix and upper 2/3rd of vagina. Atypical (type 2) MRKH syndrome may also be associated with abnormality of fallopian tubes, ovaries, kidneys, skeletal, cardiac and otological systems. We report a rare case of atypical MRKH syndrome with absent uterus, spondylolysis with Grade I spondylolisthesis, bilateral mild conductive hearing loss and grossly hydronephrotic obstructed single ectopic pelvic kidney on Tc-99m ethylene di-cysteine (EC) and Tc-99m dimercaptosuccinic acid (DMSA) scans. ***Materials and Methods:*** A 25-year-old woman with complaint of burning micturition, increased frequency, urgency, nocturia and history of recurrent urinary tract infection (UTI) since childhood was referred for radionuclide renal scintigraphy. She was a known case of primary amenorrhea with complaint of cyclical lower abdominal pain for 2-3 days every month since 12-13 years of age. We did Tc-99m EC dynamic renal scintigraphy with diuretic intervention using F+0 protocol. Following intravenous injection of tracer, sequential dynamic images of abdomen and pelvis were acquired in anterior and posterior views, followed by prevoid, postvoid, 2 and 4 hours delayed images. We also did Tc-99m DMSA scintigraphy on subsequent day in view of recurrent UTI, following injection of Tc-99m DMSA and acquisition of images at 3 hours. Following static images, SPECT/CT images were also acquired. ***Results:*** Tc-99m EC dynamic images showed moderate to grossly hydronephrotic ectopically located single kidney in pelvis above the urinary bladder with impaired parenchymal function and minimal drainage. The effective renal plasma flow was 159.4 ml/ min. Prevoid, postvoid and subsequent delayed images showed significant tracer retention in PCS and minimal slow drainage. Tc-99m DMSA scintigraphy revealed single ectopic pelvic kidney at

right superolateral aspect of urinary bladder with impaired cortical function and few areas of significant cortical thinning. The SPECT/CT images also showed ectopic pelvic kidney with DJ stent in situ and thinned cortical parenchyma. The uterus was not visualized in the images. ***Conclusion:*** We are highlighting the importance of radionuclide renal scintigraphy to thoroughly investigate patients of primary amenorrhea with associated renal anomalies in MRKH type 2 syndrome to avoid further complication by loss of renal parenchyma due to obstructed drainage and/ or pyelonephritic changes and prone to end stage renal disease if left untreated especially in patients with single kidney.

EP-1247

Metabolic Imaging of Pembrolizumab-Associated Biliary Inflammation: A Case of Spontaneous Resolution on [^{18}F] FDG PET/CT

I. Ferreira[1], *O. L. Silva*[1], *M. Simões*[2], *J. A. Sequeira*[1], *A. I. Santos*[1];
[1]*Unidade Local de Saúde de Almada-Seixal, E.P.E, Almada, PORTUGAL,* [2]*Unidade Local de Saúde do Arco Ribeirinho, E.P.E, Montijo, PORTUGAL.*

Aim/Introduction: Immune-checkpoint inhibitor (ICI) mediated hepatobiliary injury is an emerging concern in cancer treatment, with most adverse reactions being attributed to Nivolumab and characterised by panlobular hepatitis. Large duct cholangiopathy in this context is extremely rare. Pembrolizumab-related cholangiopathy has only been described in isolated case reports. In such cases, metabolic imaging with [^{18}F]FDG PET/CT is scarcely reported. To the best of our knowledge, this is the first case reported of diagnosis, follow-up and resolution of Pembrolizumab-related cholangiopathy demonstrated with [^{18}F]FDG PET/CT. ***Materials and Methods:*** We report the case of a 64-year-old patient with squamous cell carcinoma of the right lung who received chemotherapy followed by Pembrolizumab, with an apparent complete response. After 4 years of continual treatment, [^{18}F]FDG PET/CT for disease monitoring revealed intense FDG uptake in the intra- and extrahepatic biliary tree, suggesting an extensive inflammatory process. The patient complained of slight abdominal discomfort only when questioned. Aspartate transaminase and gamma-glutamyl transferase were mildly elevated with no other analytical changes. Pembrolizumab was therefore continued. A follow-up PET/CT performed 9 months later showed increased intensity of FDG uptake in the biliary tree. Despite this metabolic progression, the patient remained clinically stable with good therapeutic response of the primary tumour, leading to uninterrupted Pembrolizumab administration. ***Results:*** A subsequent [^{18}F]FDG PET/CT performed 21 months later demonstrated complete resolution of biliary hypermetabolism, concurrent with normalisation of liver enzymes, indicative of spontaneous resolution of the inflammatory process while still on Pembrolizumab. A systematic review of 53 cases of immune-mediated cholangitis by Pi et al. (2021) identified only 2 cases assessed with FDG PET/CT, with just 1 displaying increased biliary metabolism in the context of Pembrolizumab-induced sclerosing cholangitis. Additionally, previous reports have relied primarily on biochemical and conventional imaging findings (e.g., bile duct dilation and wall enhancement on CT and ultrasound) to diagnose immune-related cholangiopathy. ***Conclusion:*** This case illustrates the rare occurrence of Pembrolizumab-induced biliary inflammation and its spontaneous metabolic resolution on continued immunotherapy, as demonstrated by serial [^{18}F] FDG PET/CT imaging. These findings emphasise the utility of [^{18}F] FDG PET/CT in evaluating immune-related hepatobiliary toxicities and highlight the potentially self-limiting nature of some ICI-mediated responses. Further research is warranted to elucidate the underlying mechanisms, optimal management, and long-term implications of such adverse events.

EP-1248

A Case Of Skeletal Tuberculosis

M. Mehesen*, R. Shera;*
National Cancer Institute, Cairo university, Cairo, EGYPT.

Aim/Introduction: Tuberculosis affecting the skeletal system constitutes merely 2% of all tuberculosis cases, while the involvement of the foot and ankle joints represents approximately 10% of skeletal cases. The low specificity of the clinical condition and the limited suspicion of tuberculosis likely contributed to the diagnostic delay. In most instances, skeletal tuberculosis is not conclusively diagnosed until considerable bone destruction has transpired due to its diverse manifestations; approximately 20% of all mycobacterial infections in pediatrics manifest as extra-pulmonary tuberculosis (EPTB). ***Materials and Methods:*** A 12-year-old female patient presented with fever, pain, and swelling in her right foot. The patient had neutropenia. A superficial ultrasound of the right ankle revealed a 4x2 cm lobulated turbid cystic lesion, accompanied by overlying subcutaneous edema. This suggests an inflammatory process with the formation of an abscess. Plain x-ray showed an ill-defined, irregular-shaped area of an erosive, heterogeneous bony lesion with ST opacity at the posteromedial aspect of the right calcaneal bone. A poorly defined erosive lesion was identified by local MRI, which produced a low T, heterogeneous high T2/STAIR signal with a ST component of 2.4x2x3.5 cm at maximum axial and CC diameters. ***Results:*** The patient was referred to our nuclear medicine department to examine the rest of the body and find additional lesions. FDG PET/CT revealed the right calcaneal lesion and several other lytic bone lesions along the axial skeleton and long bones, some of which were linked to the ST component. The largest lesion, measuring 6.6x6.3 cm SUVmax of 5.8 with intraspinal extension through the corresponding right neural exit foramen, was located at D12, while the most active lesion, measuring 3.7x3.6 cm SUVmax of 10.2, was located at the left side of the sacrum. Additionally, small, low-grade, FDG-avid pulmonary nodules are visible, the largest of which measures 8 mm with an SUVmax of 1. Cytology and fluid aspiration from the cystic lesion revealed acute inflammatory cells and hypocellular necro-inflammatory material. Necrotizing/caseating granulomatous inflammation was discovered during an open biopsy of the calcaneal bone. ***Conclusion:*** Extra-pulmonary skeletal tuberculosis presents non-specifically, necessitating numerous investigations to achieve a diagnosis.

EP-1249

A Rare Case of Osteopoikilosis Differentiated from Sclerotic Metastatic Lesions by Bone Scintigraphy

G. Inal[1], *N. Aydinbelge Dizdar*[1], *A. Cinar*[1], *C. O. Engur Uyanik*[1], *O. Ozmen*[2];
[1]*Ankara Etlik City Hospital Nuclear Medicine Clinic, Ankara, TÜRKIYE,* [2]*University of Health Science, Ankara Etlik City Hospital, Department of Nuclear Medicine, Ankara, TÜRKIYE.*

Aim/Introduction: Osteopoikilosis (OPK) is a rare benign bone disorder characterized by the presence of multiple and often symmetrical hyperostotic foci localized predominantly in the periarticular regions of the bones, which may be mistaken for osteoblastic metastases. As it is usually asymptomatic, it is detected incidentally during radiological imaging. We report a 23-year-old male patient with OPK whose difficulties in definitive diagnosis were resolved with the contribution of whole-body bone scan (WBS) with SPECT/CT images and clinical follow-up. ***Materials and Methods:*** A 23-year-old male patient with low back pain who underwent the lumbosacral spine and pelvic bone X-ray and multiple sclerotic lesions were detected. For investigating the etiology of sclerotic bone lesions, Tc-99m MDP WBS performed. ***Results:*** On the planar images, it showed heterogeneous increased radioactivity accumulations in bilateral hip joint and proximal femur. Pelvic SPECT/CT images showed that most of the sclerotic

lesions in the pelvic bones and bilateral proximal femurs did not correspond to radioactivity uptake on planar images. The findings obtained from pelvic SPECT/CT and the planar images excluded bone metastasis. Afterwards, magnetic resonance imaging (MRI) of the pelvis demonstrated multifocal areas consistent with sclerotic foci in both the iliac bones and the proximal femurs. These regions existed hypointense on T1 and T2 sequences and exhibited no significant enhancement with contrast. Considering the patient's age, lack of known malignancy, and normal physical examination and the imaging findings, OPK was deemed the most likely cause of the sclerotic foci. Accordingly, the patient was followed up. ***Conclusion:*** Osteopoikilosis is a rare type of bone dysplasia that may occur at any age and affect genders at similar rates. It is assumed that mutations in the LEMD3 gene are associated with the condition and are inherited in an autosomal dominant manner. It usually presents incidentally as sclerotic, oval, multiple, well circumscribed and symmetrical lesions on the phalanges, carpal and metacarpal bones, pelvis and femur. Therefore, osteoblastic metastases should be considered mainly in the differential diagnosis of these lesions. Hybrid SPECT/CT imaging provides both functional and anatomical information and may be more useful than planar WBS, especially in patients with multiple sclerotic lesions and unexplained bone pain as in this rare case. Thus, it is important for physicians to recognize the imaging findings to avoid unnecessary interventions and treatments.

EP-1250

Utility of complimentary functioning and cortical imaging scintigraphy in assessing delayed graft function in a paediatric patient with suspected vascular thrombosis: A Case Report

K. Hlongwa, *A. Al-Marrani, M. P. Rivombo, A. Coetzee, S. More; University of Cape Town, Cape Town, SOUTH AFRICA.*

Aim/Introduction: Renal transplantation is a common treatment for end-stage kidney disease (ESKD) in paediatric patients. Complications such as vascular thrombosis can lead to graft failure. Nuclear medicine imaging, including [^{99m}Tc]Tc-MAG3 renogram and less routinely, [^{99m}Tc]Tc-DMSA scintigraphy, have demonstrated a role in assessing graft function. This case reports on a 7-year-old male with ESKD secondary to posterior urethral valves (PUV) whose post-transplant course revealed conflicting imaging findings, which underscore the complexity of diagnosing renal graft dysfunction. This case demonstrates the beneficial role of nuclear medicine imaging in assessing graft function and guiding management decisions. ***Materials and Methods:*** Case Presentation: A 7-year-old male with ESKD secondary to posterior urethral valves (PUV) underwent deceased donor renal transplant. Post-operative ultrasound demonstrated good flow, however, on day 2 the patient had decreased urine output and decreased flow suggestive of vascular thrombosis. A [^{99m}Tc]Tc-MAG3 renogram on day 2 post-transplant showed no perfusion or uptake, suggesting vascular thrombosis. Despite thrombectomy, a repeat [^{99m}Tc]Tc-MAG3 renogram on day 6 still showed no graft function. On discussion by the multidisciplinary team, a [^{99m}Tc]Tc-DMSA scan with SPECT/CT was performed to assess cortical function, revealing uptake in the graft kidney similar to the native kidneys which confirmed some cortical function of the graft kidney. However, renal biopsy showed extensive necrosis extensive necrosis with one fragment of viable renal tissue showing 3 normal glomeruli and prominent interstitial chronic inflammation composed of lymphocytes with prominent ATN. The graft was eventually removed and the child resumed haemodialysis. ***Results:*** Discussion: The complementary roles of the [^{99m}Tc]Tc-MAG3 renograms and [^{99m}Tc]Tc-DMSA scintigraphy in evaluating renal transplant complications is demonstrated in this case. While MAG3 suggested complete graft non-function, DMSA confirmed an element of viable cortical tissue which suggested severely delayed graft function in this kidney. Such discrepancies may arise due to differences in uptake mechanism of the different tracers with MAG3 being tubular and DMSA demonstrating mainly cortical uptake. This case demonstrates the need for multimodal assessment in complex cases in conjunction with multidisciplinary discussion. ***Conclusion:*** This case highlights the potential complementary roles of MAG3 renogram in assessing graft function in certain situations and the utility of DMSA SPECT/CT in providing valuable information on cortical function. The case demonstrates the importance of multimodality imaging and multidisciplinary discussion in managing complex cases of renal transplantation and guiding management decisions.

EP-1251

Unmasking Synchronous Primaries: The Crucial Role of ^{18}F-FDG PET/CT in Diagnosing Concurrent Breast and Small Cell Lung Cancer with Atypical Metastases

A. Leiva Montejo, *B. Cueto Cañadas, C. Balbin Garcia, I. Sime Loayza, J. Delgado Moreno, J. Sánchez Catalicio, A. Montellano Fenoy, M. Guerrero Ortiz;*
Hospital Universitario Torrecárdenas, Almeria, SPAIN.

Aim/Introduction: Multiple primary malignant tumors (MPMTs) are defined as two or more distinct malignant tumors in the same individual, classified as synchronous (<6 months) or metachronous (≥6 months). Three conditions are required to qualify as MPMTs: the diagnosed tumors must be confirmed as malignant, they must have different histological characteristics and one must not be a metastasis of the other. ***Materials and Methods:*** A 59-year-old female smoker detected a lump in her left breast (LB) during self-examination four months ago. A mammogram was performed, revealing multiple BI-RADS 4 lobulated nodular lesions. Pathological analysis confirmed an infiltrating ductal carcinoma (IDC) in the upper outer quadrant (UOQ) of the LB. The patient also reported the progressive appearance of hard subcutaneous nodules in the upper limbs, abdomen and left scapular region. A ^{18}F-FDG PET/CT was performed for staging. ***Results:*** ^{18}F-FDG PET/CT showed multiple hypermetabolic nodules in both breasts, with a prominent lesion in the UOQ of the LB (3.3 × 4.0 cm, SULmax 9.0). Additional hypermetabolic nodules were identified in the mesenteric and retroperitoneal regions, the most significant in the mesogastrium adjacent to the abdominal wall (1.3 × 1.6 cm, SULmax 7.2). Both adrenal glands showed increased uptake (SULmax 5.5, higher than hepatic uptake SULmax 2.9). Hypermetabolic subcutaneous and paramuscular nodules were noted in the arms, anterior and posterior thorax, and abdominopelvic region (SULmax up to 9.3) suggestive of tumor implants. A right frontal lobe hyperdense hypometabolic lesion raised suspicion of metastasis. Finally, a moderately hypermetabolic left parahilar mass (6.3 × 6.3 cm SULmax 9.5) was identified as a potential primary lung tumor. The case was presented to the tumor committee, which recommended a biopsy of a left arm nodule that confirmed a small cell lung carcinoma (SCLC) metastasis. ***Conclusion:*** The incidence of synchronous breast and lung cancer is rare, affecting less than 0.5% of patients diagnosed with breast cancer. Distinguishing primary tumors from metastases is crucial, as the lung is a frequent metastatic site for breast cancer. The malignant nature of each tumor must be confirmed through histopathological and immunohistochemical analysis. Brain metastases could originate from either tumor; however, given the patient's smoking history, and the cutaneous and adrenal gland involvement observed on ^{18}F-FDG PET/CT, the possibility of a synchronous lung primary tumor was supported. SCLC cutaneous metastases indicate a poor prognosis. Due to the rarity of this oncologic scenario, no standard treatment exists, requiring further research..

EP-1252

Local perinerural invasion in sacral plexus in recurrent metastatic adenocarcinoma prostate as seen on ^{68}Ga PSMA PET-CT; a rare finding.Local perinerural invasion in sacral plexus in recurrent metastatic adenocarcinoma prostate as seen on ^{68}Ga PSMA PET-CT; a rare finding.

J. Bal, *S. Jha, K. Shanker, P. Dougall;*
Max Super Specialty Hospital, Delhi, INDIA.

Aim/Introduction: Adenocarcinoma of prostate accounts for second most common malignancy in males and accounts for approximately 15% of newly diagnosed cases every year. We present a case of 65 year old male who was diagnosed as adenocarcinoma prostate (Gleason's score-4+5) 3 years back. He was upfront metastatic with multiple skeletal sites. He received Doectaxel, Degarelix and Denosumab and was reported to be in complete remission biochemically and radiologically for 2 years. ***Materials and Methods:*** Lately he presented with rising S. PSA values of 2.02ng/ml and complaints of vague lower back pain and mild weakness in left leg. His ^{68}Ga PSMA PET-CT scan revealed PSMA expressing soft tissue mass in the prostate with local perineural extension into left hypogastric, sacral plexus at L5-S1 vertebral levels, exiting nerve roots on left side and left sciatic foramen. The other metastatic sites including bones were still in remission. He was treated with local treatment in the form of EBRT to the sacral neural plexus. ***Results:*** Prostate cancer is known to spread to lymph nodes and hematogenously to distant organs, bones being the most common site. Perineural invasion as local spread is reported on biopsy specimens in intermediate to high risk categories and rarely seen on any imaging. Local spread to lumbosacral neural plexus is very rare and has been reported in very few cases in imaging. Patient with perineural spread of carcinoma prostate can present with sensory, motor or autonomic symptoms of the specific nerve roots involved. Patients presenting with such complaints can be confused for intervertebral disc prolapse, radiation neuritis, or cord compression due to vertebral metastases. MRI and ^{68}Ga PSMA PET-CT can differentiate intervertebral disc prolapse and cord compression from the rest. ***Conclusion:*** Direct perineural spread of lumbosacral plexus should be suspected in addition to other common causes, when patient with carcinoma prostate are being evaluated for back. ^{68}Ga PSMA PET CT is a useful imaging tool in identifying such atypical presentation of carcinoma prostate.

EP-1253

Prostatic adenocarcinoma masquerading as rectal primary- diagnostic dilemma aided by ^{68}Ga PSMA scan to reach conclusion.

J. Bal, *K. Shanker, P. Dougall;*
[1]Max Super Specialty Hospital, Delhi, INDIA.

Aim/Introduction: Prostatic acinar adenocarcinoma is only the second most common malignancy in male population and the incidence is rising worldwide. Usually the patients present with lower urinary tract symptoms; however rarely these patients can also present with unrelated symptoms which can mislead the clinical diagnosis. ***Materials and Methods:*** We present a case of 71 year old male presenting with symptoms of altered bowel habits and occasional episodes of rectal bleed. He underwent colonoscopy which revealed a circumferential growth involving mid and lower rectum with narrowing of lumen. Biopsy taken from rectal growth was suggestive of moderately differentiated carcinoma. He also underwent MRI of the pelvis which showed circumferential growth involving rectum with close abutment of the prostate; however prostate and seminal vesicles were commented to be normal. However note was made of some pelvic lymph nodes and an indeterminate lesion in sacrum. ***Results:*** His battery of blood investigations revealed S. CEA, CA 19.9 within normal limits but raised S.PSA of 50.7 ng/ml. His 18F FDG PET-CT showed circumferential growth in mid and lower rectum with no significant metabolid activity in the primary lesion, lymph nodes or skeletal lesion. This prompted us to do ^{68}Ga PSMA scan to clarify the diagnostic dilemma. ^{68}Ga PSMA scan showed intensly increased PSMA expression in the rectal growth and in the prostate gland; however there was no contiguous extension between the two lesions. Pelvic lymph nodes and sacral lesion also showed increased PSMA expression prompting to review the rectal biopsy. IHC revealed the initial rectal biopsy specimen to be PSA positive. A separate 12 core TRUS guided biopsy was also done from prostate which showed Acinar Adenocarcinoma prostate with LVI and Gleason's score of 4+5. ***Conclusion:*** Patients with no specific urinary tract symptoms and presenting with non specific symptoms can remain eluded from reaching correct diagnosis. A multidisciplinary approach, thorough work up and specific molecular imaging targets can aid in reaching the correct diagnosis.

EP-1254

A case of diffuse bone tracer myocardium uptake after thoracic trauma in a patient with suspected Transthyretin-related cardiomyopathy.

I. Badrane[1], *C. Cittanti*[1], *L. Urso*[1], *L. Uccelli*[1], *M. Bartolomei*[2];
[1]Department of Translational Medicine, University of Ferrara, Ferrara, ITALY, [2]Nuclear Medicine Unit, Department of Onco-Hematology, Ferrara, ITALY.

Aim/Introduction: Transthyretin-related cardiomyopathy (ATTR-CM) is un underdiagnosed condition determined by amyloid fibrils deposits within the myocardium. Early diagnosis is crucial for improving outcomes, and Nuclear Medicine has a pivotal role to confirm diagnosis of ATTR-CM employing scintigraphy with bone-seeking agents such as 99m-technetium 3,3-diphosphono-1,2-propanodicarboxylic acid (99mTc-DPD). ***Materials and Methods:*** We present the case of a 84-year-old woman with multiple clinical red flags for cardiac amyloidosis (CA) images with ^{99}mTc-DPD scintigraphy. ***Results:*** The patient complained of asthenia and dyspnea with a class II according to the New York Heart Association classification system. However, at echocardiography, she showed a preserved ejection fraction (65%), asymmetrical left ventricular hypertrophy, with a non-dilated cavity. Some typical electrocardiographic features were identified as well, in particular atrial fibrillation and a first-degree atrioventricular block. Moreover, the patient also had a recent history of transcatheter aortic valve implantation (TAVI) due to severe aortic stenosis. All this led to investigate the presence of CA. Laboratory investigations were assessed, which ruled out immunoglobulin light chains-CA form. Concomitantly a bone scintigraphy (BS) was performed showing a modest, diffuse radiotracer uptake within the left ventricular myocardium, corresponding to a Perugini grade 1 pattern. As incidental findings, areas of increased osteotropic tracer accumulation were observed in correspondence with the left shoulder and the anterior part of the 6th, 7th and 8th ipsilateral ribs, consistent with post-traumatic changes. Approximately one year later, during a follow-up cardiologic evaluation, the patient was referred for repeat BS to further investigate and clarify the suspicion of CA. This second BS study revealed complete resolution of the previously observed myocardial radiotracer uptake. This normalization is most likely attributable to non-specific tracer accumulation secondary to a significant thoracic trauma, which was reported anamnesticly by the patient, and that occurred few days before the first BS. The shoulder and costal findings have also disappeared supporting the traumatic genesis. ***Conclusion:*** The ability of bone radiopharmaceuticals to deposit in the context of soft tissues that are sites of previous surgical trauma, recent ischemic lesions or chemotherapy treatments is well documented in the literature. So we report a rare a case of non-specific

deposition of a bone-seeking agent in the myocardium tissue due to a recent thoracic trauma, initially mistaken for a Perugini grade I pattern, in a patient with multiple red flags for ATTR-CM.

EP-1255

Postoperative Complications in Scimitar Syndrome: The Role of Lung Scintigraphy

J. Duarte[1], *J. P. Carvalho*[1], *A. Marques*[1,2], *F. Abreu*[1,2], *S. Pintão*[1];
[1]*Unidade Local de Saúde de Lisboa Ocidental, Lisbon, PORTUGAL,* [2]*Instituto de Medicina Nuclear da Faculdade de Medicina de Lisboa, Lisboa, PORTUGAL.*

Aim/Introduction: Scimitar syndrome is a rare congenital condition involving partial anomalous pulmonary venous return, in which part or all of the right lung is drained by pulmonary veins that anomalously connect to the inferior vena cava. Surgical correction is indicated in symptomatic patients, yet postoperative complications such as baffle obstruction may occur and require nuanced management. ***Materials and Methods:*** We report the case of a 58-year-old woman with history of a corrected Scimitar syndrome approximately 18 months earlier. The patient presented with subacute persistent dyspnea, fatigue, and wheezing. Cardiac catheterization and echocardiography revealed complete thrombosis of the pericardial baffle redirecting pulmonary venous return to the left atrium. To assess right lung viability and inform treatment planning, a lung ventilation/perfusion (V/Q) scintigraphy was performed. The study consisted of tomographic (SPECT/CT) acquisition of the thorax immediately after inhalation of [^{99m}Tc] Technegas for ventilation imaging, followed by intravenous administration of [^{99m}Tc]Tc-albumin macroaggregates and subsequent thoracic SPECT/CT for perfusion assessment. ***Results:*** The V/Q scan revealed severely diminished perfusion to the entire right lung (7%) with relatively preserved ventilation, consistent with profound functional compromise and likely underlying hypoplasia. Left lung perfusion was preserved (93%) without segmental or subsegmental defects. Based on these findings, the multidisciplinary team concluded that the right lung was already virtually excluded. Therefore, surgical pneumonectomy or transplant were not indicated, so the patient was discharged with a plan for close clinical monitoring and symptom-guided management. ***Conclusion:*** This case illustrates the key role of lung scintigraphy in evaluating postoperative Scimitar syndrome. Functional imaging, particularly SPECT/CT-based V/Q scanning, was crucial in demonstrating the physiological impact of the baffle obstruction and supported the decision to avoid further high-risk surgical intervention. In complex congenital heart disease, especially when anatomical repair fails, nuclear imaging can provide decisive functional insight to guide clinical management.

EP-1256

Diagnostic complexity of Hepatopulmonary Syndrome: a case report

I. Casimiro*, D. Carvalho, S. Barata, S. Paiva, J. Silva, M. Monteiro, A. Moreira, T. Saraiva, G. Costa;*
Unidade Local de Saúde de Coimbra, Coimbra, PORTUGAL.

Aim/Introduction: Hepatopulmonary syndrome (HPS) is a rare and potentially fatal pulmonary vascular complication of liver disease. Characterized by intrapulmonary vascular dilatations and hypoxemia, this condition requires a multidisciplinary approach for timely diagnosis and treatment. ***Materials and Methods:*** A 57-year-old woman with a history of active smoking, hepatitis C, and secondary thrombocytopenia had been followed by Pulmonology after presenting to the emergency department with hypoxemic respiratory failure (pO_2 54.8 mmHg in room air). Laboratory findings included thrombocytopenia, polycythemia, and elevated D-dimers. Initial work-up ruled out pulmonary embolism and revealed upper lobe centrilobular emphysema. No signs of pulmonary hypertension were identified on echocardiography. After being discharged, despite oxygen therapy, the patient experienced progressive fatigue and worsening symptoms. Further investigations, including a ventilation/perfusion (V/Q) scintigraphy, failed to reveal the cause of her persistent hypoxemia. At follow-up, the patient presented with worsening dyspnea, central and peripheral cyanosis, and very severe hypoxemia (pO_2 38.7 mmHg), requiring hospitalization. Pulmonary angiography showed no vascular abnormalities. Transthoracic echocardiography raised suspicion of a right-to-left extracardiac shunt. A transesophageal echocardiogram with agitated saline contrast demonstrated complete opacification of the left heart chambers, with microbubbles arising from the pulmonary veins, confirming an extracardiac shunt and ruling out a patent foramen ovale. ***Results:*** A lung perfusion scan with Technetium-99m-labeled macroaggregated albumin (MAA) later performed showed an intrapulmonary right-to-left shunt of 50%, with radiotracer uptake in the brain, kidneys, and spleen, confirming the diagnosis of hepatopulmonary syndrome. The high degree of shunting and clinical history prompted a retrospective review of the V/Q scan performed a year earlier. It was noted that there had been increased radiotracer uptake in the kidneys, although those organs had not been specifically targeted during imaging. This subtle finding, if recognized earlier, could have been described as suspected and led to an earlier diagnosis of HPS. The patient remains on long term oxygen therapy while awaiting liver transplant evaluation, as only potential curative treatment. ***Conclusion:*** This case highlights the diagnostic complexity of HPS, especially in patients with coexisting pulmonary conditions, highlighting the importance of re-evaluating prior diagnostic tests when clinical findings remain unexplained. Severe hypoxemia in the context of liver disease should also prompt consideration of HPS, even in V/Q scans. Early recognition and a multidisciplinary approach are crucial for improving outcomes in these patients.

EP-1257

Posterior Reversible Encephalopathy Syndrome In a Child with Langerhans cell histiocytosis

M. Mehesen*, R. Shera;*
National Cancer Institute, Cairo University, Cairo, EGYPT.

Aim/Introduction: Posterior reversible encephalopathy syndrome (PRES) is related to a specific disorder of cerebrovascular auto-regulation of multiple etiologies. The presence of a typical neuro-image demonstrating vasogenic edema primarily affecting the posterior brain region is typically used to diagnose PRES. The clinical and neuro-radiological spectrum of childhood PRES appears to be wider than that of adult cases. In children with a range of neurological manifestations, PRES can be linked to different underlying comorbidities, medication use, and therapeutic approaches. Furthermore, atypical MRI findings outside of the normally posterior cerebral regions are more likely to occur in pediatric patients with PRES. ***Materials and Methods:*** A 3-year-old child with LCH on stratum III therapy developed seizures and underwent local MRI brain & 18 F-FDG PET/CT to assess the therapy response. ***Results:*** A local brain MRI study revealed bilateral posterior occipital cortical areas of bright FLAIR signal. An FDG PET/CT study showed detected FDG uptake at the temporal and parietal lobes as well as the right basal ganglia with NO definite corresponding CT changes with SUV max 6.3. Both studies suggested the possibility of Posterior Reversible Encephalopathy Syndrome (PRES). The therapy was discontinued, and supportive treatment was given; then follow-up by local brain MRI was done, and improvement had occurred. ***Conclusion:*** Posterior reversible encephalopathy syndrome (PRES) is a rare but serious complication in pediatric oncology patients. There is an obvious need to develop clinical criteria for PRES to enhance the diagnosis and care of PRES patients, especially in the pediatric oncology population.

EP-1258

18F-Choline PET-CT as a Decisive Tool for Detecting HCC Recurrence After locoregional therapy: When Morphological Imaging Falls Short

A. Genova, *F. Porcaro, L. Turchetta, M. Prisco, V. Piscopo, I. Annarumma, M. Catalano;*
Azienda Ospedaliera di Rilievo Nazionale Antonio Cardarelli, Naples, ITALY.

Aim/Introduction: In hepatocellular carcinoma (HCC), post-treatment imaging is often challenging due to therapy-induced changes. 18F-Choline PET/CT can be a useful tool when conventional imaging is inconclusive, especially in well-differentiated tumors with limited FDG avidity. ***Materials and Methods:*** A 80-year-old man with a history of HCC multifocal treated with radiofrequency ablation and two TACE procedures presented a rising AFP level. Abdom TC showed near the site of retroaction and likely post-tratment change, an oval-shaped lesion with uncertain significance. Subsequentely 18F-Choline PET/CT revealed a focal area of increased uptake in the previously treated IV hepatic segment, near the hypodense area identified on CT scan consistent with tumor recurrence. Based on these findings of disease progression, the patient was selected for TARE treatment. ***Results:*** The case demonstrates how choline PET/CT can clarify uncertain imaging findings and detect viable tumor in treated HCC. Compared to FDG, choline shows higher uptake in well-differentiated HCC, making it a suitable tracer in selected cases. ***Conclusion:*** 18F-Choline PET/CT may significantly contribute to the post-treatment evaluation of HCC, particularly when AFP levels rise and morphological imaging is non-diagnostic. It may guide therapeutic decisions and improve patient selection for loco-regional therapies.

EP-1259

^{18}F-FDG PET/CT in Renal Cell Carcinoma Presenting as Urinary Retention with Extensive Local Invasion and IVC Tumor Thrombus: A Rare and Illustrative Case

A. Mahalik, *N. Kundu, A. Roy, G. Lalitha, J. Krishna P., S. Singh, R. Kumar;*
All India Institute of Medical Sciences, New Delhi, INDIA.

Aim/Introduction: Renal cell carcinoma (RCC) with inferior vena cava (IVC) tumor thrombus is a recognized but relatively rare presentation, seen in 4-10% of cases. The role of ^{18}F-FDG PET/CT in differentiating bland from tumor thrombus and in staging advanced RCC is increasingly appreciated. However, FDG PET/CT findings in RCC with simultaneous IVC tumor thrombus, contiguous organ infiltration, and distant metastases—presenting with an atypical symptom like urinary retention—are uncommon and not widely illustrated. ***Materials and Methods:*** A 54-year-old male presented with urinary retention for 1 month. CECT suggested a left renal mass with IVC thrombus. FDG PET/CT was performed for further evaluation. Imaging revealed a large FDG-avid heterogeneous mass replacing the left kidney (19 x 15 x 13 cm), with extensive infiltration into the spleen hilum, diaphragm, abdominal aorta, pancreas, mesentery, and intercostal muscles. The mass involved the left proximal ureter and closely abutted multiple adjacent organs. A metabolically active soft tissue lesion was seen in the IVC (7.1 cm long), consistent with malignant thrombus. Additional FDG-avid metastases were noted in both lungs, liver (largest 3.0 x 2.1 cm), and renal capsular deposits. ***Results:*** This case highlights the role of FDG PET/CT in: Identifying and characterizing an FDG-avid IVC tumor thrombus. Delineating the full extent of contiguous local invasion, which may be underappreciated on conventional imaging. Uncovering multifocal distant metastases for accurate staging. The unusual clinical presentation (isolated urinary retention) in the context of widely metastatic disease underscores the diagnostic value of whole-body metabolic imaging. ***Conclusion:*** FDG PET/CT served as a comprehensive problem-solving modality in this rare presentation of RCC, enabling precise assessment of IVC tumor thrombus, extensive local infiltration, and distant metastases. This case reinforces its utility in staging and surgical planning, especially when clinical presentation is a typical and anatomical imaging may be inconclusive.

EP-1260

Primary breast malignancy presenting as paraneoplastic dermatomyositis role of 18fdg pet-ct in primary staging and response evaluation- a case report

J. Bal, *S. Jha, P. Dougall;*
[1]Max Super Specialty Hospital, Delhi, INDIA.

Aim/Introduction: Abstract Dermatomyositis is a rare complement mediated immune-modulatory disorder often presenting as skin rashes, papules and proximal muscles weakness. Its presentation as a paraneoplastic syndrome is not uncommon however its association with primary breast malignancy is an unusual presentation. As of 2019 only 22 cases of breast malignancy with dermatomyositis have been reported and 75% of the cases are in stage in III-IV. 18F FDG can play a crucial role in evaluating the quantum of disease at baseline, to assess response to treatment by visual assessment and semiquantative parameters and in cases of suspected relapse ***Materials and Methods:*** We present a case of 42 year old female, presenting with features of skin rashes, palpable nodules all over the body, fatigue and muscle weakness. On examination she was found to have palpable left breast mass and underwent lumpectomy. She was found to have Invasive ductal carcinoma of breast. 18 F FDG PET-CT was done which showed left breast mass with left axillary lymph nodes and diffuse FDG uptake in the entire visualized muscles. ***Results:*** She underwent 6 cycles of chemotherapy. Subsequently follow up FDG PET CT was done for response evaluation which showed complete metabolic resolution of left breast mass, axillary lymph nodes and FDG uptake in the muscles demonstrating complete metabolic response to therapy. ***Conclusion:*** Dermatomyositis as paraneoplastic syndrome appears to be associated usually with more-advanced breast cancer stage; however the presentation of such symptoms warrants to rule out malignancy. In such cases treatment of cancer alone is insufficient to adequately control the cutaneous and myopathic manifestations of dermatomyositis, which can significantly affect quality of life. A multidisciplinary approach, including close collaboration with rheumatologists and dermatologists, is therefore important in the diagnosis and management of oncology patients with dermatomyositis. 18F FDG can play an important role in baseline evaluation of quantum of disease, response evaluation and in case of suspected clinical relapse.

EP-1261

Incidentally diagnosed synchronous vaginal adenocarcinoma on SSTR imaging (68Ga DOTANOC) done for primary Gastric NET

J. Bal, *S. Jha;*
Max Super Specialty Hospital, Delhi, INDIA.

Aim/Introduction: SSTR imaging are done with various SSTR agents for SPECT and PET-CT imaging for staging and restaging of well differentiated (Grade 1 to Grade 3) neuroendocrine tumors, medullary carcinoma thyroid, pheochromocytoma and paraganglioma. It characterizes the tumor, stage the disease, evaluate response assessment and assist in selecting patients for PRRT. ***Materials and Methods:*** We present a case of 54 year old female who was recently diagnosed grade 1 NET of stomach on endoscopic biopsy and excision. She underwent whole body 68Ga DOTANOC scan for staging the disease. The scan revealed no abnormal SSTR expression in the stomach or any perigastric lymph nodes. However a note was made of post hysterectomy

status a large bulky vagina showing heterogenous enhancement on contrast enhanced CT scan acquired as part of the 68Ga DOTANOC scan. An MRI pelvis was suggested which showed a large mass measuring ~4.6x4.2cm in the vagina. Biopsy from the vagina was suggestive of adenocarcinoma. ***Results:*** As we advance in hybrid imaging techniques it is important to not just report on the molecular imaging but also corresponding CT images to look for any abnormality not expressing the injected radiopharmaceutical. ***Conclusion:*** This approach reflects on the importance of knowing the various aspects of oncoimaging and avoiding missing out any synchronous malignancies with different molecular expression.

EP-1262

Sacral Neurolymphomatosis In Refractory Diffuse Large B-Cell Lymphoma: Multimodal Imaging Including PET/CT and MRI For Diagnosis And CAR-T Response Monitoring

L. Henrich Malizia[1], *A. Roteta Unceta Barrenechea*[1], *F. Arraut Serrano*[1], *A. Garin Rodriguez*[1], *N. Etxabeguren Gallo*[1], *I. Cillero Etxebeste*[1], *B. Mendibil Esquisabel*[2], *I. Olazabal Eizaguirre*[2], *I. Zeberio Etxetxipia*[2], *V. Rodriguez Ortega*[1], *I. Sanchez Oscoz*[1], *S. Sanchez Eguiguren*[1], *I. Jauregui Larrea*[1], *G. Rodriguez Rodriguez*[1], *I. Leon Zubizarreta*[1], *A. Iztueta Iturbe*[1], *I. Lopez Sanchez*[1], *A. Gomez Lopez*[1];
[1]*Hospital Universitario Donostia - Onkologikoa, San Sebastian, SPAIN,* [2]*Hospital Universitario Donostia, San Sebastian, SPAIN.*

Aim/Introduction: Neurolymphomatosis (NL), a rare Diffuse Large B-Cell Lymphoma (DLBCL) complication, poses diagnostic challenges. Standard ^{18}F-FDG PET/CT plays a role in identifying suspicious metabolic activity, but MRI is often crucial for detailed anatomical assessment, underscoring the importance of multimodal imaging and clinical correlation. ***Materials and Methods:*** A 41-year-old male diagnosed (01/2024) with Stage IVB non-germinal centre DLBCL received 6 cycles of R-CHOP chemotherapy. At the end of treatment (05/2024), he developed severe sacral neuropathic symptoms. PET/CT scan (01/07/2024) revealed a focal area of intense hypermetabolism (SUVmax 8.58 g/ml) involving the left sacral nerve roots/foramina, highly suspicious for active NL, which was concordant with the patient's symptoms. An urgent lumbosacral MRI (10/07/2024) depicted extensive nerve root thickening/enhancement and an associated presacral mass, confirming diagnosis of sacral NL. Subsequent CT-guided biopsy of the mass confirmed persistent non-Germinal Center B-cell like (non-GCB) DLBCL, indicating primarily refractory disease. ***Results:*** Following bridging radiotherapy and standard lymphodepletion, the patient received Axicabtagene Ciloleucel (Axi-cel) infusion (09/2024). The only significant reported toxicity was Grade 1 Cytokine Release Syndrome, managed successfully with Tocilizumab and corticotherapy. Serial PET/CT scans (month 1, 3 and 6) demonstrated sustained Complete Metabolic Response at all previously involved sites (including metabolic normalisation of the NL focus). A control MRI at 2 months confirmed excellent morphological response with minimal residual left S3 root changes. Clinically, neuropathic symptoms resolved almost entirely, with only mild residual S1 hypoesthesia persisting at 6 months follow-up. ***Conclusion:*** This case illustrates the role of PET/CT scan in detecting metabolically active foci concerning for NL in patients with refractory DLBCL and concordant neurological symptoms, prompting confirmatory anatomical evaluation with MRI. It demonstrates the synergistic value of multimodal imaging (PET/CT and MRI) for accurate diagnosis and comprehensive monitoring of treatment response. The case also supports Axi-cel's efficacy in achieving durable metabolic remission, even in refractory DLBCL with complex extranodal presentations like NL.

EP-1263

Complete Resolution Of Severe Refractory Hypoglycaemia Following Lutetium-177 DOTATATE Peptide Receptor Radionuclide Therapy In A Metastatic Dual Insulinoma-Gastrinoma Pancreatic Neuroendocrine Tumour: A Case Report

L. Henrich Malizia[1], *A. Gomez Lopez*[1], *A. Roteta Unceta Barrenechea*[1], *F. Arraut Serrano*[1], *A. Garin Rodriguez*[1], *N. Etxabeguren Gallo*[1], *B. Sanchez Casi*[2], *M. Perez de Ciriza Cordeu*[2], *V. Rodriguez Ortega*[1], *I. Sanchez Oscoz*[1], *S. Sanchez Eguiguren*[1], *I. Jauregui Larrea*[1], *G. Rodriguez Rodriguez*[1], *I. Leon Zubizarreta*[1], *A. Iztueta Iturbe*[1], *I. Lopez Sanchez*[1], *I. Cillero Etxebeste*[1];
[1]*Hospital Universitario Donostia - Onkologikoa, San Sebastian, SPAIN,* [2]*Hospital Universitario Donostia, San Sebastian, SPAIN.*

Aim/Introduction: Malignant insulinoma is a rare Pancreatic Neuroendocrine Tumour (PNET) characterised by excessive insulin secretion, leading to severe hypoglycaemia. Managing hypoglycaemia is challenging due to its refractory nature and limited efficacy of conventional treatments such as diazoxide, somatostatin analogues, and chemotherapy. We report a case of a dual PNET (Gastrinoma-Insulinoma) presenting with life-threatening refractory hypoglycaemia that was successfully controlled with radionuclide therapy after failure of conventional treatment. ***Materials and Methods:*** A 51-year-old male's diagnostic evaluation included endoscopy, Computed Tomography (CT), tumour biopsy (well-differentiated Grade 1 [G1] PNET, Ki67 <3%), serum gastrin/Chromogranin A (CgA), and Somatostatin Receptor (SSR) scintigraphy (baseline/follow-up). Initial therapies were somatostatin analogues (Lanreotide 120 mg/28d), Everolimus, then diazoxide. Following Multidisciplinary Tumour Board consensus due to treatment failure, Peptide Receptor Radionuclide Therapy (PRRT) was given: four cycles of Lutetium-177 DOTATATE (177Lu-DOTATATE), 7.4 GBq/cycle (Mar-Sep 2024), with amino acid nephroprotection. Monitoring included clinical assessment, serial glucose/insulin/CgA levels, and follow-up SSR scintigraphy and CT. ***Results:*** The patient initially presented with persistent abdominal pain, significant weight loss, and symptoms suggestive of Zollinger-Ellison syndrome (heartburn, peptic ulcers, altered bowel habits). Subsequent workup confirmed a metastatic G1 PNET with elevated gastrin and CgA levels, consistent with the initial gastrinoma component. Baseline SSR scintigraphy showed high tumour uptake (Krenning score 3-4). Subsequently, the patient developed severe progressive hypoglycaemia refractory to diazoxide (nadir glucose 34 mg/dL), requiring hospitalisation and intensive support (Intravenous glucose, Nasogastric Tube feeding). Pre-PRRT scintigraphy confirmed persistently high Krenning 3-4 uptake with increased pancreatic receptor density. PRRT initiation led to an excellent and rapid clinical response: complete and sustained resolution of refractory hypoglycaemia was observed from the first cycle, enabling progressive and complete withdrawal of intensive support and diazoxide. Glucose levels normalised, and serum insulin dropped (from crisis peaks >30 µU/mL to sustained normalised levels <12 µU/mL). Euglycaemia has been maintained post-initial PRRT. Treatment was well-tolerated (mild, transient Grade 1-2 haematological toxicity). Twelve-month follow-up SSR scintigraphy showed stable disease. Additionaly, subsequent CT scan (15 months), revealed a decrease in size of liver metastases and a discrete decrease in pancreatic involvement and associated tumoral thrombosis, suggesting delayed morphological response. ***Conclusion:*** PRRT with 177Lu-DOTATATE provided safe, well-tolerated, and effective treatment, resulting in rapid and persistent remission of life-threatening refractory hypoglycaemia in this metastatic dual PNET case. PRRT represents a promising treatment option, controlling severe hypoglycaemic episodes refractory to conventional therapies, achieving disease control (stabilisation/slight regression), and offering a valuable alternative to conventional treatments.

EP-1264

Renal involvement in diffuse large B-cell lymphoma detected by ^{18}F-FDG PET/CT: analysis of three clinical cases

J. Charfi, *H. Boudriga, R. Sfar, K. Ayed, M. Nouira, K. Chatti; Sahloul Hospital, Sousse, TUNISIA.*

Aim/Introduction: Diffuse large B-cell lymphoma (DLBCL), the most common non-Hodgkin lymphoma subtype, is aggressive and often involves extranodal sites, typically the skin, small intestine, and stomach. Primary renal involvement is rare. ^{18}F-FDG PET/CT is essential for detecting and evaluating extranodal disease. ***Materials and Methods:*** This retrospective descriptive study includes three cases of DLBCL with renal involvement, followed over five years at the Nuclear Medicine Department of Sahloul University Hospital. All underwent at least one ^{18}F-FDG PET/CT using a standardized protocol. Disease evaluation followed the Deauville scale and Ann Arbor/Lugano staging systems. ***Results:*** A 33-year-old male was diagnosed with stage IV diffuse large B-cell lymphoma (DLBCL) after detection of a mediastinal mass and pulmonary nodules. Initial ^{18}F-FDG PET/CT showed lymph node, lung, and persistent renal involvement despite diuretic administration. He received four R-CHOP cycles, achieving interim complete metabolic response (CMR). After four additional cycles, end-of-treatment PET/CT confirmed complete remission (CR).A 42-year-old female presented with widespread nodal and tumor involvement, including bilateral renal masses and progressive renal failure. Initial ^{18}F-FDG PET/CT confirmed pleuropulmonary, peritoneal, and renal involvement. Classified as unfavorable stage IV, she received 8 R-CHOP cycles and 4 intrathecal treatments, with clinical improvement. However, end-of-treatment PET/CT revealed metastatic progression (Lugano). A fatal outcome was observed despite salvage therapy. FDG PET/CT showed frontal tumor involvement and multivisceral lymphomatous disease, including bilateral renal cortical hypertrophy (SUVmax 14.5). Classified as high-risk stage IV, R-CHOP therapy was initiated. ***Conclusion:*** Physiological ^{18}F-FDG renal uptake complicates detection of pathological involvement. Techniques such as delayed imaging or contrast-enhanced studies help differentiate tumors from normal structures. Renal involvement is an independent risk factor for CNS relapse, requiring close monitoring. ***References:*** Inayat F, Bokhari MR, Mansoor A. Primary renal lymphoma: a comprehensive review of the pathophysiology, clinical presentation, imaging features, management and prognosis. BMJ Case Rep. 17 juin 2020;13(6):e235076.Ben Abdelghani K, Rouached L, Mourad Dali K, Fazaa A, Miladi S, Sellami M, Ouenniche K, Souabni L, Kassab S, Chekili S, Laatar A. Diffuse large B cell lymphoma presenting with renal failure and bone lesions in a 46-year-old woman: a case report and review of literature. CEN Case Rep. 28 sept 2020;10(2):16571. Tan YZ, Yılmaz S, Özhan M, Halaç M. FDG PET-CT Finding in Bilateral Renal and Bone Involvement of Diffuse Large B-Cell Lymphoma. Mol Imaging Radionucl Ther. oct 2014;23(3):1046.

EP-1265

The Diagnostic Value of Bone Scan in Tertiary Syphilis With Skeletal Involvement

J. Duarte[1], *A. Marques*[1,2], *J. P. Carvalho*[1], *F. Abreu*[1,2], *S. Pintão*[1]; [1]*Unidade Local de Saúde de Lisboa Ocidental, Lisbon, PORTUGAL,* [2]*Instituto de Medicina Nuclear da Faculdade de Medicina de Lisboa, Lisboa, PORTUGAL.*

Aim/Introduction: Syphilis, caused by Treponema pallidum, remains a significant global health concern with rising incidence. Musculoskeletal involvement is relatively rare and more commonly associated with congenital and tertiary stages. Osseous lesions in tertiary syphilis can mimic inflammatory or systemic diseases with bone involvment, often leading to diagnostic delays. ***Materials and Methods:*** We present the case of a 46-year-old woman with a history of HIV-1 infection, past HCV infection, and active intravenous drug use, who presented with a one-month history of headache, visual and auditory disturbances, and diffuse limb tenderness. The patient was admitted to the infectious diseases department. Serologic testing revealed positive Treponema pallidum antibodies and a high VDRL titer. Cerebrospinal fluid analysis confirmed CNS involvement, supporting the diagnosis of secondary/tertiary syphilis. Limb X-rays and head CT revealed lytic bone lesions with periosteal reaction, raising suspicion for periostitis or osteomyelitis. To further assess the extent of skeletal involvement, a whole-body bone scintigraphy was performed. ***Results:*** A whole-body bone scan was acquired two hours after intravenous injection of [^{99m}Tc]Tc-HDP, along with a SPECT/CT of the lower limbs. The scan revealed increased tracer uptake in the frontal bone, clavicles, left humerus, both radii and ulnae, left hand, both tibiae, and the left fibula. The latter corresponded to subcortical lytic lesions with periosteal reaction on CT. These findings confirmed extensive osseous involvement due to syphilis. The patient completed a 14-day course of intravenous benzylpenicillin. A follow-up bone scan showed a marked decrease in tracer uptake in the previously involved sites, consistent with clinical improvement and positive treatment response. ***Conclusion:*** This case highlights the importance of recognizing bone involvement as a manifestation of tertiary syphilis, particularly in high-risk patients. Bone scintigraphy was crucial for delineating the full extent of skeletal disease and for monitoring therapeutic response. A comprehensive, multimodal diagnostic approach—integrating clinical findings, serology, and advanced imaging—is essential for timely and accurate diagnosis and effective management of syphilitic bone disease.

EP-1266

Uncommon penile metastasis emerges in patient with mCRPC during Radium223 radioligand therapy : A Rare Case Highlighted by PSMA PET/CT

D. Nakro[1], *L. Augusto*[2], *F. Nouhaud*[3], *S. Makhloufi-martinage*[4], *D. Tonnelet*[1]; [1]*Service de médecine nucléaire, Centre Henri Becquerel, Rouen, FRANCE,* [2]*Département d'oncologie urologique et digestive, CHU Rouen, Rouen, FRANCE,* [3]*Service d'Urologie, Clinique du Cèdre, Bois Guillaume, FRANCE,* [4]*Service d'oncologie médicale, Clinique Saint Hilaire, Rouen, FRANCE.*

Aim/Introduction: Penile metastases from prostate cancer represent a highly uncommon and often under-recognized site of disease dissemination, typically associated with advanced or castration-resistant stages.We present an uncommon penile metastasis in patient with metastatic Castration Resistant Prostate Cancer (mCRPC) while undergoing Radium 223 radioligand therapy (RLT). ***Materials and Methods:*** A 72-year-old man was diagnosed in 2012 with Gleason [4+3], ISUP 3, extracapsular extension, BRCA2 somatic mutation prostate cancer and underwent radical prostatectomy with pelvic lymph node dissection, followed by androgen deprivation therapy after biochemical recurrence. In 2021 he developed mCRPC and received several lines oftreatment, including hormone therapy (enzalutamide), chemotherapy (docetaxel), targeted therapy (olaparib), 177Lu PSMA 617 RLT and was referred in January 2025 for Radium 223 RLT. After two Radium administrations of 4 MBq every 4 weeks and despite clinicalresponse on bone metastasis patient developed a painful lump in the groin with episodes of macroscopic hematuria. Of note, patient had no priapism. ***Results:*** [68Ga]Ga-PSMA 11 PET/CT (PSMA PET) was performed and revealed compared to preRadium 223 PSMA PET a dissociated response, including new metastatic lesions in the right hemipelvis, penis, and supradiaphragmatic/ subdiaphragmatic lymph nodes while stabledisease was noted in the lombo-aortic area and skull base and a partial metabolic response was observed in the sacrum and left hemipelvis.The penile metastases involved both corpora-cavernosa SUVmax 12.1, TMTV 16.8 cm3,TLG 87.3 cm3.Pelvic ultrasound and pelvic MRI were concordant with the PSMA PET findings. Radium 223 was interrupted patient was re-challenged with Androgenreceptor pathway inhibitors(ARPI). Patient is still alive to this day.Penile metastasis, although extremely rare in prostate cancer and have

been described on PSMA and FDG PET. The physio pathological mechanisms of metastatic spread remains debated, with retrograde venous and lymphatic dissemination being the most widely acceptedhypotheses. The differential diagnosis is Peyronie's syndrome. However our case , is, to the best of our knowledge the first case of penile progression during Radium 223 RLT. ***Conclusion:*** This case highlights a rare occurrence of penile metastasis in patient with highly pretreated mCRPC while undergoing Ra223 RLT. Despite its rarity, penile metastasis can emerge in advanced stages, and advanced imaging plays a critical role in detecting such atypical sites. ***References:*** -Mansbridge MM, Strahan A, Parker J, Rhee H. PSMA-PET/CT-avid metastatic prostate cancer to the penis.BMJ Case Rep. 2020 Mar 24;13(3):e233522. doi: 10.1136/bcr-2019-233522. PMID: 32209576; PMCID: PMC7103797.

EP-1267

Functional Evaluation of Musculoskeletal Infections with ^{99m}Tc-Ciprofloxacin SPECT/CT in Complex Patients Undergoing Limb Amputation: Case Series

V. Heringer, *B. Alencar, T. Agnello, M. Osmak, R. Tineo, E. Etchebehere, C. Ramos, M. Lima, B. Amorim, A. Santos;*
UNICAMP, Campinas, BRAZIL.

Aim/Introduction: Chronic musculoskeletal infections such as diabetic foot and post-traumatic osteomyelitis pose significant diagnostic challenges, particularly in distinguishing between sterile inflammation and active bacterial infection. ^{99m}Tc-ciprofloxacin SPECT/CT targets bacterial DNA gyrase and has been studied as a functional imaging tool in such cases[1,2]. Despite limitations in specificity, it remains a potentially valuable modality in selected clinical scenarios[3,4]. ***Materials and Methods:*** Case 1: A 57-year-old male with a 25-year history of chronic femoral osteomyelitis underwent multiple debridements and intramedullary procedures, culminating in a transfemoral amputation. Case 2: A 51-year-old insulin-dependent diabetic patient underwent transtibial amputation after partial foot amputations due to infection. Both patients underwent dynamic perfusion imaging, followed by planar scans at 90 and 270 minutes and SPECT/CT, also, MDP-SPECT/CT were performed for additional parameters. ***Results:*** In Case 1, preoperative SPECT/CT showed intense uptake in the distal two-thirds of the femur and adjacent soft tissues, consistent with active infection[1,2], also matching with bone scintigraphy findings. Intraoperative cultures confirmed Staphylococcus aureus and Pseudomonas stutzeri, and the patient had a favorable clinical recovery. In Case 2, SPECT/CT revealed moderate uptake in soft tissues near the 2nd and 3rd metatarsals without bone involvement, ruling out osteomyelitis[2,4] as bone scintigraphy also confirmed. The lesion-to-background ratio remained below the limit of 11:2 for active infection[3], supporting a diagnosis of soft tissue inflammation. ***Conclusion:*** ^{99m}Tc-ciprofloxacin SPECT/CT was clinically useful in distinguishing active infection from sterile inflammation in two complex patients with musculoskeletal infections. This modality provided decisive information for surgical and therapeutic management, despite its debated specificity in some contexts[1-4]. ***References:*** 1) Britton KE, et al. J Clin Pathol. 2002;55:817. 2) Sonmezoglu K, et al. J Nucl Med. 2001;42:567. 3) Devillers A, et al. J Nucl Med. 2003;44:920. 4) Lazzeri E, et al. J Nucl Med. 2004;45:1682.

EP-1268

Dynamic [68Ga]Ga-DOTANOC LAFOV PET/CT in a Synchronous Ileum Metastatic NET

E. Fortunati[1], *I. Brusa*[1], *G. Bianciardi*[2], *M. Di Franco*[2], *D. Dall'Olio*[3], *M. Assenza*[4], *D. Campana*[5], *E. Andrini*[5], *C. Ricci*[6], *S. Fanti*[1,2], *V. Ambrosini*[1,2];
[1]*Nuclear Medicine, IRCCS Azienda Ospedaliero-Universitaria di Bologna, Bologna, ITALY,* [2]*Nuclear Medicine, Alma Mater Studiorum University of Bologna, Bologna, ITALY,* [3]*Department of Medical and Surgical Sciences, University of Bologna, Bologna, ITALY,* [4]*Professional Development and Implementation of Research in Health Professional Unit, IRCCS Azienda Ospedaliero-Universitaria di Bologna, Bologna, ITALY,* [5]*Department of Medical and Surgical Sciences (DIMEC), Medical Oncology Unit, Alma Mater Studiorum-University of Bologna, IRCCS Azienda Ospedaliero-Universitaria di Bologna, Bologna, ITALY,* [6]*Department of Internal Medicine and Surgery (DIMEC), Alma Mater Studiorum, University of Bologna, Bologna, ITALY.*

Aim/Introduction: A 68y.o. female patient with a history of surgically-treated sigmoid adenocarcinoma (left hemicolectomy and terminal ileostomy) was referred to the local Oncology Unit to investigate a CT-detected mass of the pancreatic head. Abdominal-MRI also showed a 5mm liver lesion (IV segment), suspicious for secondary lesion. Endoscopic-ultrasound with fine needle biopsy documented a NET G2 lesion of the pancreatic head, likely of intestinal origin (Ki67:4%). ***Materials and Methods:*** [68Ga]Ga-DOTANOC PET/CT was performed for staging and after surgery. PET/CT scans were acquired as a 60' dynamic acquisition on LAFOV scanner (uExplorer, United Imaging). The static images were reconstructed with last 5'list mode acquisition. VOIs were manually drawn on suspect lesions and reference tissues. Time-to-activity curves (TACs) were fitted using two different graphical models, i.e. Patlak (for irreversible model) and relative equilibrium (RE) (for reversible model). Mean absoluted-scaled error (MASE) and Akaike Information Criterion (AIC) were utilized to perform model selection for each VOI. ***Results:*** PET/CT confirmed intense and focal uptake at the known pancreatic head mass (SUVmax=23.2) and liver lesion (SUVmax=12.7; IV segment). PET/CT also revealed a mass showing intense uptake near the ileocecal valve (SUVmax=32.9) and a smaller cutaneous/subcutaneous nodule with intense uptake (SUVmax=30.7) within the ileostomy loop in the anterior right pelvic wall. Milder and diffuse uptake was also evident at the ileostomy cutaneous site (SUVmax=3.3), compatible with reactive/inflammatory nature. Dynamic assessment demonstrated a better-fit using the Patlak model and higher Ki at NET lesions level (ileum=0.1, pancreas=0.1, liver=0.05) as compared to the background (healthy liver=0.04, healthy pancreas=0.03). The reactive/inflammatory finding on the ileostomy showed a Ki value lower (Ki=0.02) than both the tumour lesions and the background. The patient underwent ileocecal resection and construction of ileocolic anastomosis: both ileum lesions resulted positive for ileum NET G2, Ki-67:4%. Cold somatostatin analogue treatment was initiated. Post-surgical [68Ga]Ga-DOTANOC PET/CT showed disease stability of the known lesions in the head of the pancreas and in the IV liver segment, while the liver background biodistribution was significantly reduced. In the post-surgical dynamic assessment, RE reported the best fit, likely due to cold somatostatin analogue treatment. Accordingly, NET lesions showcased higher DV values (ileum=5.8, pancreas=3.5) compared to background (healthy liver=2.5, healthy pancreas=2.1). ***Conclusion:*** [68Ga]Ga-DOTANOC-LAFOV PET/CT can be useful for the characterisation of small-sized NET liver lesions. Dynamic data may highlight the different behaviour of NET lesions as compared to background and inflammation.

EP-1269

Complementary Imaging and Targeted Therapy in Progressive Metastatic MTC: A Clinical Case

R. Marão, *D. Barbosa, D. Silva, N. Vasconcelos, S. Gil Santos, R. Calheiros, J. Ferro, S. Fontão de Castro, I. Inácio, R. Ferreira, A. Santos, I. Lucena Sampaio;*
Instituto Português Oncologia do Porto Francisco Gentil, Porto, PORTUGAL.

Aim/Introduction: Medullary thyroid carcinoma (MTC) is a rare neuroendocrine tumor arising from parafollicular C cells, frequently presenting with metastatic disease at the time of diagnosis. Positron Emission Tomography/Computed Tomography (PET/CT) using different radiopharmaceuticals —particularly [^{18}F]FDG, [^{18}F]FDOPA, and [^{68}Ga]Ga-DOTA-SST— has demonstrated an increasingly important role in the assessment of this pathology.

These imaging modalities have proved to be sensitive and accurate in detecting MTC recurrences/metastases, evaluating clinical and biological tumor aggressiveness and guiding treatment strategies. The treatment of metastatic MTC involves a multimodal approach, including surgery, local ablative therapies, tyrosine kinase inhibitors (TKIs), and, in selected cases, peptide receptor radionuclide therapy (PRRT). ***Materials and Methods:*** We present the case of a 64-year-old woman with stage IV medullary thyroid carcinoma, diagnosed in 2011, presenting with cervical and mediastinal lymph node metastases. She underwent total thyroidectomy with cervical lymph node dissection, but mediastinal lymph node metastases persisted postoperatively. In 2017, the patient showed disease progression with multifocal hepatic metastases documented on CT. The patient underwent two sessions of hepatic embolization in November 2017 and November 2021, resulting in radiological stabilization of the lesions up to the present. In 2023, a rise in tumour markers (CEA and calcitonin) was observed, which, despite stable findings on CT and MRI, also appeared on [^{68}Ga]-DOTA-TOC PET/CT, which demonstrated new evidence of disease progression, including local tumor recurrence and newly identified supradiaphragmatic lymph node and bone metastases. These lesions showed no significant uptake on [^{18}F] FDG-PET/CT. As a result of this progression, in December 2023, the patient was referred for treatment with ^{177}Lu-DOTATATE, receiving four cycles of therapy at a median activity of 7400 MBq per cycle. The treatment was well tolerated, with no significant toxicity. ***Results:*** Post-treatment evaluation demonstrated preserved overall clinical condition, a reduction in serum calcitonin levels (from 3451 to 2706 pg/mL), dimensional reduction of the thyroid nodule and imaging stability on follow-up [^{68}Ga]-DOTA-TOC PET/CT. ***Conclusion:*** This case highlights the complementary roles of [^{68}Ga]-DOTA-TOC PET/CT and [^{18}F]FDG PET/CT in tumor phenotyping and guiding personalized, multimodal treatment strategies in patients with metastatic MTC. Moreover, this case illustrates the potential of PRRT as an effective therapeutic option for both locoregional and systemic disease control, either as an isolated treatment or in combination with other modalities, in selected patients.

EP-1270

A Rare Case of Abernethy Type I Malformation: Is FDG PET/CT a Valuable Tool in Pre-Transplant Evaluation of Hepatic Lesions?

I. Ozturk, *B. Esen Akkas, M. Kaya;*
S.B.U Basaksehir Cam ve Sakura Sehir Hastanesi, Istanbul, TÜRKIYE.

Aim/Introduction: Abernethy Malformation Type 1(AMT1) is a rare and severe congenital extrahepatic portosystemic shunt,characterized by the complete absence of intrahepatic portal venous flow due to the diversion of portal blood directly into the systemic circulation.Nodular liver lesions are observed in nearly half of the reported AMT1 cases,due to the absence of portal flow and compensatory increased hepatic arterial perfusion.The most common lesion is focal nodular hyperplasia(FNH),though others,including nodular regenerative hyperplasia,hepatoblastoma,hepatic adenoma and hepatocellular carcinoma(HCC) have also been documented.Liver transplantation is the treatment of choice since surgical correction is not feasible in the absence of portal venous flow.Routine imaging surveillance is essential for monitoring hepatic lesions,with magnetic resonance imaging(MRI) being the preferred modality.However, f18-fluorodeoxyglucose positron emission tomography-computed tomography(FDG PET-CT) may be useful due to the potential risk of malignant transformation. ***Materials and Methods:*** We present the case of an 18-year-old female diagnosed with AMT1,who had been under regular MRI follow-up for multiple FNH.Prior to liver transplantation,the patient underwent FDG PET-CT to assess the metabolic activity of the lesions. ***Results:*** The scan revealed four hepatic parenchymal mass lesions,one of which showed intense FDG uptake,while the others demonstrated low metabolic activity similar to surrounding parenchyma.Given the potential for malignant transformation,histopathological evaluation of the hypermetabolic lesion was recommended.Fine-needle aspiration biopsy indicated benign features and the patient subsequently underwent liver transplantation.Postoperative histopathological evaluation revealed no definitive evidence of malignancy.The lesions were described as well-differentiated hepatocellular neoplasia with steatohepatitic,pelioid and focal nodular hyperplasia-like areas.The liver parenchyma showed degeneration,mild portal fibrosis and inflammation,sinusoidal dilatation and congestion.No lymphovascular invasion was found. The nodules exhibited heterogeneous morphology with minimal atypia.While immunohistochemistry did not support HCC,due to the absence of portal areas,differential diagnoses such as hepatic adenoma,dysplastic nodules,macroregenerative nodules and well-differentiated HCC could not be definitively excluded.The patient is currently in the 4th month of clinical follow-up with no lesions detected on postoperative imaging. ***Conclusion:*** The hypermetabolic parenchymal lesion suggested its histopathological behavior might differ from the others,implying the possibility of aggressive malignancy.However, histopathological analysis revealed no significant differences between lesion characteristics or definitive evidence of malignancy.This underscores that high FDG uptake does not always indicate malignancy;FNH or other well-differentiated neoplastic lesions can also show high glucose metabolism.Still, lesions with high FDG uptake should always be recommended for histopathological evaluation to assess the malignant transformation.This case is a unique clinical observation examining the role of FDG PET/CT in determining the metabolic characteristics of hepatic lesions in AMT1.

EP-1271

Sacral Malignant Proliferating Trichilemmal Tumor: A Rare Case Evaluated by F-18 FDG PET/CT

H. Eroglu Elden, *A. Akbulut, K. Demirel, G. Koca, M. Korkmaz;*
University of Health Sciences, Ankara Training and Research Hospital, Ankara, TÜRKIYE.

Aim/Introduction: Proliferating trichilemmal tumors (PTTs) are rare neoplasms that originate from the outer root sheath of hair follicles. In literature, they are more frequently observed in women and generally located on the scalp. Most PTTs show benign behavior, with local recurrence and distant metastasis are not common. In this report, we present a rare case of metastatic malignant PTT (MPTT) located in sacral region, evaluated by F-18 fluorodeoxyglucose positron emission tomography/computed tomography (F-18 FDG PET/CT). ***Materials and Methods:*** A 47-year-old male patient presented to the dermatology clinic with complaints of pain and ulceration in the sacral area. Pelvic magnetic resonance imaging (MRI) revealed a large soft tissue mass invading sacral bone and gluteal muscles within the intergluteal region. An incisional biopsy of sacral lesion demonstrated neoplastic cells beneath the stratified squamous epithelium, which show squamous differentiation with keratinization, pleomorphic nuclei, eosinophilic clear cytoplasm, and atypical mitotic figures, consistent with diagnosis of malignant PTT. The patient underwent F-18 FDG PET/CT for further evaluation. ***Results:*** F-18 FDG PET/CT imaging demonstrated pathological FDG uptake in the soft tissue mass extending from skin to anal canal, with invasion of bilateral gluteal muscles and destructive changes in sacrum and coccyx (SUVmax: 11.49). Additionally, focal metastatic FDG uptakes were noted within bilateral gluteal muscles. Although metastases are rarely reported in MPTT, pathological FDG uptakes were also observed in left obturator, bilateral external iliac and inguinal multiple lymph nodes (SUVmax: 6.78), which were indicative of nodal

metastases. During follow-up, the patient had died approximately eight months after diagnosis. ***Conclusion:*** Metastatic malignant PTT detected in the sacral region is an extremely rare tumor. F-18 FDG PET/CT is a valuable imaging technique in these rare cases by identifying nodal or distant metastases, which may not be apparent through conventional imaging modalities.

EP-1272

Pitfall in 18F-FES PET/CT: A Case of ^{18}F-FDG Avid Hepatic Metastasis Masked by Physiological Tracer Uptake in ER-Positive Breast Cancer

A. Mahalik*, N. Kundu, K. Jain, M. Tripathi, R. Kumar;*
All India Institute of Medical Sciences, New Delhi, INDIA.

Aim/Introduction: [18F] FES PET/CT is increasingly used for imaging estrogen receptor (ER) expression in breast cancer, particularly for lesion characterization and therapy guidance. However, physiological uptake in certain organs can pose interpretational challenges, leading to false-negative results. ***Materials and Methods:*** A 47-year-old female with known ER-positive invasive ductal carcinoma, post chemotherapy and post trastuzumab therapy, was referred for response assessment. On [^{18}F]FDG PET/CT, a solitary hepatic lesion in segment VI was identified with an SUVmax of 3.17 and SUVmean of 1.53, without any significant anatomical correlate on CT. However, the corresponding [18F]FES PET/CT showed intense physiological tracer uptake in the liver, obscuring the lesion completely and rendering it undetectable on visual assessment. ***Results:*** This case highlights a crucial diagnostic limitation of [18F]FES PET/CT in detecting hepatic metastases due to high physiological hepatic uptake. Despite being ER-positive, the lesion would have been missed if solely assessed on FES PET/CT. Furthermore, the absence of CT changes could potentially delay detection in centers relying only on CT. ***Conclusion:*** [18F]FES PET/CT has inherent limitations in liver lesion detection due to physiological hepatic uptake. FDG PET/CT remains a complementary modality, especially for detecting small, early metastatic lesions with minimal anatomical distortion. This case underscores the importance of multimodality imaging in comprehensive metastatic assessment and treatment planning in ER-positive breast cancer.

EP-1273

Chilaiditi Syndrome Mimicking Hepatic Metastases on FDG PET/CT in a Patient with Metastatic Lung Adenocarcinoma

A. Giarratana[1]*, M. Larson*[1]*, K. Capaccione*[2]*;*
[1]*University of Wisconsin - Madison, Madison, WI, WI, UNITED STATES OF AMERICA,* [2]*Columbia University, New York, NY, UNITED STATES OF AMERICA.*

Aim/Introduction: Chilaiditi syndrome is a benign anatomical variant in which a loop of colon becomes interposed between the liver and diaphragm. [1] Though asymptomatic, it may lead to imaging findings that resemble hepatic pathology, particularly in fused PET imaging. [2] In oncology patients undergoing FDG PET/CT, such findings can raise concern for metastatic disease and influence treatment decisions. [3] This case highlights a potential interpretive pitfall in a patient with advanced lung adenocarcinoma. ***Materials and Methods:*** A 74-year-old male with metastatic lung adenocarcinoma to bone and pleura, previously treated with systemic therapy and enrolled in a clinical trial, underwent FDG PET/CT for restaging during an inpatient admission for pain and swelling related to treatment side effects. Maximum intensity projection (MIP) images showed a focus of intense radiotracer uptake in the right upper quadrant, initially raising concern for hepatic metastasis in the setting of known widespread disease. ***Results:*** Review of the cross-sectional fused PET/CT images revealed interposition of the colon anterior to the liver, with radiotracer uptake localized to the colon rather than the liver. These findings were consistent with benign Chilaiditi syndrome. Correlation with CT helped avoid misinterpretation, and the scan was ultimately interpreted as showing stable metastatic disease without new hepatic involvement. ***Conclusion:*** Chilaiditi syndrome can produce false-positive findings on FDG PET/CT due to physiologic bowel uptake overlying the liver. In patients with metastatic cancer, this may mimic hepatic metastases and lead to misclassification of disease status. Other anatomical variants, such as ectopic or horseshoe kidneys or urinary diversion anatomy, can also result in false-positive findings if not properly identified on cross-sectional imaging. [4] This case highlights the importance of careful CT correlation to avoid diagnostic errors and unnecessary changes in clinical management. It also underscores the risk of interpreting PET or SPECT studies without corresponding anatomic imaging, particularly in patients with variant anatomy, due to lack anatomic correlation. This case reinforces the value of hybrid imaging and the need to recognize benign anatomical variants in nuclear medicine. ***References:*** 1.Mendes, E., et al., Chilaiditi Sign and Syndrome as a Finding in the Emergency Room: A Case Report. Cureus, 2024. 16(12): p. e75674. 2.Gondhane, A. and G. Malhotra, What's the Gut Doing in the Chest? Interpositio Hepatodiaphragmatica (Chilaiditi Sign) Revisited on 18 F-FDG PET/CT. Clin Nucl Med, 2025. 50(4): p. e250-e252. 3.Kamel, I., et al., Unveiling the Chilaiditi Syndrome: A Case Report and Management Implications. Cureus, 2024. 16(4): p. e57483.

EP-1274

Osteonecrosis of the Jaw Detected on Bone Scan in a Patient with Metastatic Breast Cancer Receiving Denosumab

A. Giarratana[1]*, M. Larson*[1]*, K. Capaccione*[2]*;*
[1]*University of Wisconsin - Madison, Madison, WI, UNITED STATES OF AMERICA,* [2]*Columbia University, New York, NY, UNITED STATES OF AMERICA.*

Aim/Introduction: Osteonecrosis of the jaw (ONJ) is a known potential complication of antiresorptive therapies such as denosumab, which is used to treat osteoporosis and has played an important role in cancer patients with osseous metastases. [1-3] ONJ may present with exposed bone or more obvious symptoms in later stages, but early on, patients may be asymptomatic or have only nonspecific signs such as jaw pain or swelling. As a result, ONJ may go unrecognized without imaging or dental evaluation. [4] In such cases, it may be incidentally detected on nuclear medicine bone scintigraphy, where it can appear as mandibular uptake, potentially mimicking osseous metastasis or infection. [5] Awareness of this imaging pattern is essential to avoid confusion with malignancy and ensure appropriate clinical follow-up. ***Materials and Methods:*** A 76-year-old woman with metastatic triple-negative breast cancer involving the liver and bone, on treatment with denosumab and capecitabine, underwent a routine bone scan as part of disease surveillance. At the time of imaging, she reported no jaw pain, dental complaints, or recent dental procedures. There was no clinical suspicion for osteonecrosis, and her scan was performed in the context of routine oncologic follow-up. ***Results:*** The nuclear medicine bone scintigraphy demonstrated diffusely increased uptake of the right side of the jaw, a pattern suggestive of osteonecrosis of the jaw. No corresponding clinical concern was documented at the time of imaging. The findings were interpreted in the context of denosumab use and communicated to the care team. ***Conclusion:*** This case illustrates how nuclear medicine bone scintigraphy can detect ONJ as an incidental finding in asymptomatic patients on denosumab. Recognizing this imaging pattern can help avoid confusion with osseous metastasis and supports timely referral for dental evaluation and appropriate clinical management. ***References:*** 1.Bełch, M., et al., Analysis of potential risk factors for the development of medication-related osteonecrosis of the jaw. Dent Med Probl, 2025. 2.Jung, S., et al., A 5-year retrospective cohort study of denosumab induced medication related osteonecrosis of the jaw in osteoporosis patients. Scientific Reports, 2022. 12(1): p.

8641. 3.Aghaloo, T.L., A.L. Felsenfeld, and S. Tetradis, Osteonecrosis of the jaw in a patient on Denosumab. J Oral Maxillofac Surg, 2010. 68(5): p. 959-63. 4.Lončar Brzak, B., et al., Osteonecrosis of the Jaw. Dent J (Basel), 2023. 11(1). 5.Chow, T.K. and J. Chu, Lincoln Sign: A Rare Presentation of Medication-related Osteonecrosis of the Jaw. Mol Imaging Radionucl Ther, 2024. 33(2): p. 118-120.

EP-1275

A case of invasive fibromatosis misdiagnosed as a metastatic tumor

X. Li[1,2];
[1]Department of Nuclear Medicine, the First Hospital of Shanxi Medical University, Taiyuan, CHINA, [2]Collaborative Innovation Center for Molecular Imaging of Precision Medicine Shanxi Medical University, Taiyuan, CHINA.

Aim/Introduction: The patient is a 55-year-old female. She was admitted to the hospital with a left lung nodule that was identified during a physical examination. A meticulous CT scan of the chest revealed the following findings:The presence of a soft tissue nodule exhibiting moderate enhancement in the lingual segment of the upper left lobe, which prompts consideration of the possibility of lung cancer. The second finding is an irregular soft tissue density shadow in the left adrenal region. To improve the examination, it is recommended that further evaluation be conducted. Consequently, the patient underwent adrenal enhancement CT and enhancement MRI, which revealed progressive enhancement in the left adrenal gland and did not exclude the presence of a metastatic tumor.^{18}F-FDG PET/CT showed: The initial findings indicate an elevated level of FDG metabolism in the soft tissue nodule located in the lingual segment of the left upper lobe of the lung. This observation prompts the consideration of lung cancer as a potential underlying diagnosis. The second finding is the presence of an irregular soft tissue shadow in the left adrenal region, accompanied by mildly increased FDG metabolism. The presence of a metastatic tumor is not excluded. To elucidate the nature of the lesion, the patient underwent a series of surgical procedures, including resection of the lingual segment of the upper lobe of the left lung and resection of the retroperitoneal mass. The pathological diagnosis revealed two distinct entities: low differentiated adenocarcinoma in the lingual segment of the upper lobe of the left lung and a morphology combined with immunohistochemistry phenotype consistent with invasive fibromatosis in the retroperitoneal mass. Immunohistochemical findings (retroperitoneal mass): The following markers were observed: β catenin (nuclear +), SMA (foci +), Desmin (+), Ki67 (3% +), SOX10 (-), S100 (-), STAT6 (-), CD34 (-), CKpan (-), Calretinin (+), WT1 (-), D2-40 (-). A review of the patient's medical history reveals that they underwent a total adrenalectomy three years prior for left adrenocortical hyperplasia. ***Conclusion:*** This observation underscores the imperative for comprehensive patient histories to be obtained.

EP-1276

Intense FDG Uptake Mimicking Hepatic Metastasis on PET/CT: Focal Hepatic Steatosis

F. Yildiz Kabaca[1], *M. Acar Tayyar*[1], *M. Biçen Altın*[1], *T. Özülker*[1], *T. Oğuzsoy*[2];
[1]Department of Nuclear Medicine, University of Health Sciences, Prof. Dr. Cemil Tascioglu City Hospital, Istanbul, TÜRKIYE,
[2]Department of Pathology, University of Health Sciences, Prof. Dr. Cemil Tascioglu City Hospital, Istanbul, TÜRKIYE.

Aim/Introduction: PET/CT imaging is commonly used for staging in patients with primary malignancies and detecting metastases. The liver is a common site for metastases, especially in cancers like colorectal, breast, and prostate, which are among the most commonly diagnosed malignancies in the general population. Increased FDG uptake can also be seen in various benign lesions and should be reported with caution as it affects patient survival. The most common condition affecting the physiological FDG distribution in the liver is hepatosteatosis, because it causes a difference in attenuation. In hepatosteatosis, FDG uptake is expected to decrease in fat-rich areas and cause a heterogeneous distribution of activity in the parenchyma.In this case, we aimed to highlight the fact that, unlike usual practice, very intense FDG uptake can be seen in hepatosteatosis. ***Materials and Methods:*** The patient was administered 0.15 mCi/kg FDG intravenously. PET/CT imaging was obtained from wholebody at 60th minute after the injection. ***Results:*** A 41-year-old woman with operated breast cancer underwent PET/CT imaging for re-staging with suspicion of metastasis,after a newly developed surrenal lesion was detected on abdominal CT imaging.PET/CT imaging demonstrated a hypodense lesion measuring approximately 2 cm with moderate FDG uptake in the left adrenal gland.In addition, a well-defined,intensely hypermetabolic, hypodense mass lesion was observed,occupying almost the entire left hepatic lobe.The lesion was considered suspicious for either a primary hepatic malignancy or metastatic carcinoma, and further evaluation with MR imaging and histopathological confirmation was recommended.On contrast-enhanced abdominal MR imaging,the surrenal gland was interpreted in favor of metastasis,while the lesion site in the liver was consistent with atypical steatosis.US-guided biopsy was performed due to the very intense FDG uptake observed in the lesion on PET/CT imaging.Histopathological examination revealed marked macrovesicular and microvesicular steatosis along with prominent balloon degeneration in the parenchyma,findings that were primarily consistent with steatohepatitis.Surgical treatment was decided as the patient only had a surrenal metastasis. ***Conclusion:*** Liver metastases are critical for guiding treatment decisions and predicting survival. In the literature, steatosis is typically associated with decreased FDG uptake.Previous studies have reported that focal FDG uptake in small areas of fatty liver in patients with known extrahepatic malignancies can be misdiagnosed as hepatic metastases, a finding that is exceptionally rare, as observed in our case.This may be attributed to increased Kupffer cell activity in these regions, which is consistent with the proposed pathophysiological mechanism in the literature, involving inflammation induced by hepatic steatosis and subsequent Kupffer cell activation.

EP-1277

Rapidly Progressive Cutaneous Metastases in Recurrent Breast Cancer Detected on F-18 FDG PET/CT

H. Eroglu Elden, *K. Demirel, A. Akbulut, G. Koca, M. Korkmaz;*
University of Health Sciences, Ankara Training and Research Hospital, Ankara, TÜRKIYE.

Aim/Introduction: Cutaneous metastasis is a rare situation and indicative of poor prognosis in oncologic patients. Among malignancies, cutaneous metastasis is mostly observed in breast cancer. F-18 FDG PET/CT is a critical imaging method for detecting and monitoring cutaneous and subcutaneous metastases. We present a rare case of rapidly progressive cutaneous metastases in recurrent breast cancer, demonstrated by F-18 FDG PET/CT. ***Materials and Methods:*** A 61-year-old female patient with a history of invasive ductal breast carcinoma (ER+, PR+ and HER2neu+), treated with left modified radical mastectomy and chemoradiotherapy in 2019, referred to re-staging with F-18 FDG PET/CT due to the detection of a mass in her right breast. ***Results:*** Her F-18 FDG PET/CT scan showed pathological uptake of F-18 FDG in subcutaneous nodular lesions located in the left mastectomy region, the right breast mass, and the right axillary lymph nodes. Furthermore, abnormal FDG uptake was noted in the linear skin thickening in the left upper quadrant of the abdomen. Histopathological examination of a punch biopsy from the skin lesion on the left upper abdomen revealed metastasis

from invasive ductal carcinoma. A follow-up F-18 FDG PET/CT scan was performed three months later to assess treatment response following the initiation of chemotherapy for recurrent metastatic breast cancer. This scan revealed disease progression, with increased size and metabolic activity in the right breast mass, subcutaneous lesions in the left mastectomy area, and skin thickening in the left upper abdomen. Additionally, new pathological FDG uptake was identified in the muscles and subcutaneous tissues surrounding the left axilla. A third F-18 FDG PET/CT scan, conducted six months later for restaging, revealed widespread pathological FDG activity in the extensive areas of skin thickening, multiple subcutaneous nodular lesions throughout the thoracoabdominal region, as well as involvement of the muscles and subcutaneous tissues of the left arm. ***Conclusion:*** Cutaneous metastases are uncommon and typically present as a solitary, asymptomatic lesion, as observed in our case, which remained unnoticed by the patient. We emphasized a case of rapidly progressive cutaneous metastases of recurrent breast cancer detected on F-18 FDG PET/CT. F-18 FDG PET/CT is a valuable imaging technique for the advanced evaluation of patients, as it helps detect cutaneous and subcutaneous metastases that the patient may not even notice, so improving diagnostic accuracy.

EP-1278

Resolving Curve-Image Discordance: A Case of Rising Renogram Pattern with Preserved Delayed Clearance in Post-Neobladder Pediatric Patient

J. Choudhary, *A. Mahalik, N. Kundu, K. Jain, S. Singh, J. Krishna P., V. Singh, R. Kumar;*
All India Institute of Medical Sciences, New Delhi, INDIA.

Aim/Introduction: To highlight a clinically significant discrepancy between the renogram curve pattern and static image-based clearance in a child post-neobladder formation, and to emphasize the role of delayed imaging in accurate interpretation of drainage. ***Materials and Methods:*** A 12-year-old male patient with a history of bladder exstrophy and gastric neobladder underwent 99mTc-LLEC diuretic renography using the F0 protocol. Imaging protocol included dynamic acquisition for 17 minutes, pre-void static image, post-void image, and delayed static image at 4 hours. Hydration and voiding protocols were adequately followed. Renogram curves and static image kidney counts were evaluated, and percent clearance between static phases was calculated. ***Results:*** The dynamic renogram demonstrated a rising pattern in both the kidneys with no definite T½, suggestive of obstruction. However, the delayed 4-hour static image showed significant clearance of tracer. Quantitative analysis revealed >90% clearance between the pre-void and delayed images. This discrepancy was interpreted as non-obstructive drainage, possibly due to a compliant renal pelvis or gravity-aided clearance over time. No technical errors were identified. ***Conclusion:*** Relying solely on the renogram curve may result in misclassification of renal drainage patterns. In this case, static imaging and quantitative analysis provided critical insights that refuted an obstructive diagnosis. Delayed imaging should be considered essential in complex cases, especially in post-surgical anatomy like neobladders, to guide appropriate clinical management.

EP-1279

Evaluating ^{68}Ga-Trivehexin PET/CT Avidity in Hyperparathyroidism with Inconclusive Standard Imaging

A. Sadeq, *S. Dashti, F. Marafi;*
Jaber AlAhmad center for Molecular Imaging, Shuwaikh medical area, KUWAIT.

Aim/Introduction: A 54-year-old female was referred with high parathyroid hormone (PTH) levels and negative ^{99m}Tc -MIBI SPECT/CT parathyroid scintigraphy as well as 4D CT. She had a ^{68}Ga-Trivhexine PET/CT as part of local institution trail. ***Materials and Methods:*** Patients had ^{68}Ga-Trivehexin PET/CT scan after signing an informed consent. A 7.31 mCi of ^{68}Ga-Trivehexin was injected and after 60 minutes images were acquired with 2 min/bed on digital PET/CT camera. The images were then analyzed visually and semi-quantitively in terms of SUVmax. ***Results:*** Images demonstrate focal intense radiotracer localization posterior to the lower pole of the right thyroid lobe upon which she underwent the surgery. ***Conclusion:*** This case provided evidence of potential role of ^{68}Ga-Trivehexin PET/CT in identify hyperfunctioning parathyroid tissuewith high detection rate and supporting further investigation into its potential role in the management of primary hyperparathyroidism (PHPT)

EP-1280

The Role of FDG PET/CT in the Staging of a Poorly Differentiated Malignant Epithelioid and Spindle Cell Neoplasm of the Pleura

A. Giarratana[1], *M. Larson*[1], *K. Capaccione*[2];
[1]*University of Wisconsin - Madison, Madison, WI, UNITED STATES OF AMERICA,* [2]*Columbia University, New York, NY, UNITED STATES OF AMERICA.*

Aim/Introduction: Malignancy of the pleura are most often caused by mesothelioma or metastatic lung cancer, but rare tumor types can present with similar imaging and clinical features. [1] Spindle cell neoplasms of the pleura are uncommon and may exhibit mixed epithelial and mesenchymal features, complicating definitive classification. [2] This case highlights the role of FDG PET/CT in the evaluation of an aggressive, poorly differentiated epithelioid and spindle cell neoplasm of the pleura, with an atypical clinical and histopathologic profile. ***Materials and Methods:*** A 41-year-old male with no smoking or known asbestos exposure presented with progressive respiratory symptoms. He was initially seen as an outpatient after developing persistent cough and decreased exercise tolerance and was diagnosed with COVID-19. Despite antibiotics, symptoms persisted. On follow-up, a chest X-ray revealed a large left pleural effusion. Thoracentesis drained reddish fluid, consistent with an exudative lymphocytic effusion; cytology was negative for malignancy. As his condition worsened, he required hospitalization, chest tubes, and ultimately surgical decortication and pleurectomy. Pathology from the surgical specimen revealed a high-grade malignant epithelioid and spindle cell neoplasm with extensive necrosis and complex cytogenetic abnormalities. The case was reviewed extensively with pathology, and based on histologic appearance and immunohistochemistry markers, the tumor did not fit a specific diagnosis of mesothelioma, sarcoma, or lung primary. FDG PET/CT was performed to assess extent of disease. ***Results:*** FDG PET/CT demonstrated nodular circumferential hypermetabolic thickening of the left pleura with likely extension into the right atrium, as well as FDG-avid ipsilateral mediastinal and axillary lymphadenopathy. Additional findings included multiple contralateral pulmonary nodules and widespread hypermetabolic lytic bone lesions. The intensity and distribution of tracer uptake were consistent with aggressive disease. These imaging features helped differentiate the neoplasm from more localized or indolent pleural processes. The FDG PET/CT scan confirmed disseminated metastatic involvement at presentation and provided essential information for staging, prognostication, and treatment planning. ***Conclusion:*** In patients with undifferentiated or histologically ambiguous malignancy of the pleura, such as spindle cell neoplasms, FDG PET/CT plays a vital role in accurate staging and guiding treatment decisions. This case underscores the importance of whole-body metabolic imaging in detecting metastatic spread and characterizing disease behavior. ***References:*** 1.Boyraz, B. and Y.P. Hung, Spindle cell tumors of the pleura and the peritoneum: pathologic diagnosis and updates. APMIS, 2022. 130(3): p. 140-154. 2.Rdzanek, M., et al., Spindle cell tumors of the pleura: differential diagnosis. Seminars in Diagnostic Pathology, 2006. 23(1): p. 44-55.

EP-1281

A case of bone inflammation in a Patient with prostate cancer on PSMA-PET imaging: a possible pitfall in ^{18}F-PSMA-1007 PET/CT interpretation

F. Russo[1], *A. Cimini*[1], *G. Grimaldi*[2], *M. De Feo*[3], *A. Marzullo*[1], *H. Dadgar*[4], *H. Arabi*[5], *A. Di Sibio*[6], *M. Menichini*[1];
[1]*Nuclear Medicine Unit, St. Salvatore Hospital, L'Aquila, ITALY,* [2]*Radiation Oncology, San Pietro Fatebenefratelli Hospital, Rome, ITALY,* [3]*Nuclear Medicine Unit, Department of Radiological Sciences, Oncology and Anatomo-Pathology, Sapienza University of Rome, Rome, ITALY,* [4]*RAZAVI Hospital, Imam Reza International University, Mashhad, IRAN, ISLAMIC REPUBLIC OF,* [5]*Department of Medical Imaging, Geneva University Hospital, Geneva, SWITZERLAND,* [6]*Department of Radiology, St. Salvatore Hospital, L'Aquila, ITALY.*

Aim/Introduction: ^{18}F-PSMA-1007 and ^{18}F-Piflufolastat are two PET radiopharmaceuticals used for the detection of Prostate Specific Membrane Antigen (PSMA), a transmembrane glycoprotein overexpressed in prostate cancer but also present in benign conditions such as inflammations, that may present high uptake. In this case report we describe the findings of a prostate cancer patient with bone inflammation, evaluated with ^{18}F-PSMA-1007 PET/CT and subsequently with ^{18}F-Piflufolastat PET/CT (4 months later). ***Materials and Methods:*** An 82-year-old patient with history of prostate cancer (previously treated with radical prostatectomy and radiation therapy) underwent ^{18}F-PSMA-1007 PET/CT scan due to biochemical recurrence (serum prostate specific antigen value (PSA) was 0.74 ng/ml thirteen years after surgery). 318 MBq of ^{18}F-PSMA-1007 were administered intravenously, and images acquired 90 minutes later after the injection of radiopharmaceutical. PET images highlighted high uptake of the radiopharmaceutical in the upper plate of L5 vertebra, doubt for metastasis: lumbo-sacral MRI was performed to better define this finding. Moreover, PET images were not suggestive for disease recurrence in lymph-nodes and prostatic bed. Clinical symptoms were investigated: the patient was suffering from lumbar pain and MRI revealed an inflammatory condition in the site of ^{18}F-1007 -PSMA uptake. Four months later the patient underwent a ^{18}F-Piflufolastat PET/CT as a result of further increased levels of serum PSA (0.9 ng/ml); moreover, the patient was still symptomatic with the same lower back pain. About 270 MBq of ^{18}F-Piflufolastat were administered intravenously and images after 90 minutes were acquired. ^{18}F-Piflufolastat PET/CT scan was negative for metastases, and no radiopharmaceutical uptake was detected in L5 vertebra. ***Results:*** The first PET/CT scan with ^{18}F-1007 PSMA revealed high uptake on the upper plate of L5 vertebra with SUV max 5.2, with CT signs of sclerosis; the subsequent MRI demonstrated linear T1 hypointensity, T2 hyperintensity and edema in that site. The second PET/CT scan with ^{18}F-Piflufolastat showed no significant uptake in the upper plate of L5, but bone sclerosis was still present. ***Conclusion:*** in a patient with prostate cancer in biochemical recurrence and persistent lower back pain, inflammatory bone condition was detected only on ^{18}F-1007-PSMA CT scan, suggesting a possible higher sensitivity of this radiopharmaceutical for this condition (compared to ^{18}F-Piflufolastat): nuclear medicine physicians should be aware of this potential pitfall of ^{18}F-1007-PSMA due to inflammation.

EP-1282

Bone Scintigraphy Characteristics in Patients with Synovitis, Acne, Pustulosis, Hyperostosis, and Osteitis (SAPHO) Syndrome

X. Wang, *Q. Li, M. Chen;*
The First Hospital of Lanzhou University, Lanzhou, CHINA.

Aim/Introduction: This retrospective study aimed to analyze the significance of whole-body ^{99m}Tc-MDP SPECT imaging and to assess the scintigraphic pattern in patients with Synovitis, Acne, Pustulosis, Hyperostosis, and Osteitis (SAPHO) syndrome. ***Materials and Methods:*** The study population had an average age of 43.8 ± 15.8 years, consisting of five males and four females. Disease duration ranged from 1 to 60 months. The most common presenting symptom was chest pain (n=8), and seven patients also had skin lesions. ***Results:*** SPECT/CT imaging revealed the "bullhead" sign in six of nine patients (66.7%), indicating cortical hyperostosis and sclerosis of the sternal manubrium and bilateral clavicles with intense ^{99m}Tc-MDP uptake. At the same time, the remaining cases showed incomplete "bullhead" signs. Among all patients, five out of nine (5/9, 55.6%) had abnormal metabolism in the sacroiliac joints. ***Conclusion:*** Bone scintigraphy is the preferred imaging modality for diagnosing skeletal involvement in SAPHO. It shows the typical uptake in the sternal manubrium and bilateral clavicles and could reveal unexpected locations of the skeletal system in most cases in combination with a bullhead-like tracer uptake. The " bullhead " is the typical and particular SPECT manifestation of SAPHO and aids in medical treatment. ***References:*** ADDIN EN.REFLIST 1. D F, V G-L, PE M, SR DG. - SAPHO Syndrome: Current Developments and Approaches to Clinical Treatment. Curr Rheumatol Rep. 2016; 18(6):016-0583. 2. T DY, , Sari İ. - SAPHO syndrome: current clinical, diagnostic and treatment approaches. Rheumatol Int. 2024;44(11):2301-2313. 3. SWS L, E R, C H. - Treatment and monitoring of SAPHO syndrome: a systematic review. RMD Open. 2023; 9(4):2023-003688.5. N W, Y S, J H, Y Z, Y C, H J, F Z, C Y, Y Y, C L, H S & W Z . - Clinical characteristics of pediatric synovitis, acne, pustulosis, hyperostosis and osteitis (SAPHO) syndrome: the first Chinese case series from a single center. Clin Rheumatol. 2021; 40(4):1487-1495. 4. N G, R V, ES B. - Bone Scan and SPECT/CT Scan in SAPHO Syndrome. Indian J Nucl Med. 2019; 34(4):349-350. 5. H K, K K, - N A, M T, H Y, T T, K Y. - Quantitative bone SPECT/CT for evaluating treatment response in patient with sternoclavicular arthritis. Acta Radiol Open. 2022; 11(10):1-4. 6. K C, CO G, A M, E A, FA C. - Synovitis, Acne, Pustulosis, Hyperostosis, Osteitis (SAPHO) Syndrome: Clinical and Therapeutic Aspects. Cureus. 2021; 13(9):1-4.

EP-1283

FDG-PET imaging results of a large BMI (~77) patient with colon adenocarcinoma

S. Lokitz, *T. Bartel, K. Harris, L. White;*
Center for Molecular Imaging and Therapy, Shreveport, LA, UNITED STATES OF AMERICA.

Aim/Introduction: We have recently imaged a 33-year old male patient with colon adenocarcinoma. This patient had an unusually high BMI of 77. Patients of this size are typically not eligible for FDG-PET/CT due to scanner weight limitations. We report our clinical experience here. ***Materials and Methods:*** This patient was referred for two scanning procedures about four months apart. The patient had biopsy-proven colon adenocarcinoma. The patient was imaged on a United Imaging Healthcare uMI Panorama. The patient's height is 185.5 cm and weight was 264 kg at the time of the first scan and 268.5 kg at the time of the second. The patient was injected with 433 MBq of ^{18}F-FDG for the first scan and 456 MBq for the second. Uptake time for both acquisitions was 73 min. PET images were reconstructed using an OSEM algorithm with 2 iterations and 10 subsets utilizing all available corrections with resulting images reconstructed to 3 mm thick slices with a transaxial FOV of 760 mm. Final image matrix size was 256 x 256 which corresponded to a pixel size of 2.97 x 2.97 mm. CT images were reconstructed using an artificial intelligence iterative reconstruction. ***Results:*** Images of diagnostic quality were produced and interpreted by board certified nuclear medicine physicians utilizing dedicated PET/CT software (Mirada Medical). While there were some banding artifacts due to truncation in the CT images, images were interpreted both qualitatively and quantitatively. In the first scan, a 7 mm nodule in the left lower lung lobe (max SUV 1.9) was identified along with a

1.7 cm left common iliac chain lymph node (max SUV 7.2) and a 2.7 cm left external iliac chain lymph node (max SUV 8.7). At the second scan, the previously seen lung nodule was still identifiable along with several other small lung nodules without significant uptake. These were suggestive of an infectious or inflammatory process due to the waxing and waning pattern. The left common iliac node was larger (2.1 x 1.5 cm) and with a significantly higher max SUV (30.5) and was suspicious for worsening of the metastatic nodes. ***Conclusion:*** A patient with very high BMI (~77) successfully underwent FDG-PET twice at our center. Images were interpreted and diagnostic data was qualitatively and quantitatively extracted and reported. FDG-PET is indicated in cases such as these and will be offered in the future to patients typically excluded due to high BMI and weight.

EP-1284

Role of [^{18}F]FDG PET/CT in Pulmonary Epithelioid Hemangioendothelioma

K. L. Chiu, *T. K. Chow, K. M. Ma, W. H. Ma;*
Tuen Mun Hospital, Hong Kong, HONG KONG.

Aim/Introduction: Pulmonary epithelioid haemangioendothelioma (EHE) is a rare pulmonary malignant neoplasm of vascular origin. Majority of patients are asymptomatic at presentation with lung lesions detected as incidental findings. Symptomatic patients are associated with a poor prognosis. Despite various imaging features on CT thorax have been described, there are limited reports on [^{18}F]FDG PET/CT findings in pulmonary EHE. This case report illustrates a patient with uncommon imaging findings of pulmonary EHE and highlights the role of [^{18}F]FDG PET/CT in detecting multiorgan disease as well as differentiating pulmonary EHE from metastatic lung disease. ***Materials and Methods:*** A 54-year-old woman presented with chest pain to emergency department. Physical examination and investigations were unremarkable except an opacity in the left upper lung zone on chest radiography. She had no hisotry of malignancy. A CT thorax was arranged and a lobulated mass was found in the superior lingular segment with additional small bilateral lung nodules. In view of suspected lung malignancy, she was referred for [^{18}F]FDG PET/CT. ***Results:*** [^{18}F]FDG PET/CT revealed moderate hypermetabolism in the lingular lung mass (SUVmax 7.2) without pleural invasion. There was no hypermetabolism in other small lung nodules; no hypermetabolic lesion elsewhere to suggest other primary malignancy with metastatic lung disease. The patient therefore underwent a wedge resection for both diagnostic and therapeutic purposes, with histopathological confirmation of EHE. The patient subsequently underwent a complete lobectomy and recovered well postoperatively. ***Conclusion:*** Pulmonary EHE is a rare malignancy with variable imaging manifestations. Although histopathological evaluation is essential, [^{18}F]FDG PET/CT plays a crucial role not only in assessing tumour characteristic and detecting multiorgan involvement, but also in differentiating metastatic lung disease of other origin. This enables better evaluation of disease distribution and directly influences treatment decisions. [^{18}F]FDG PET/CT can also be valuable in post-treatment patient to monitor recurrence or disease progression, but further follow-up and studies would be required. ***References:*** 1. Prognostic factors and surgical indications of pulmonary epithelioid hemangioendothelioma: a review of the literature. The Annals of thoracic surgery, 82(6), 2010-2013. 2. Clinicopathological characteristics of pulmonary epithelioid hemangioendothelioma: A report of four cases and review of the literature. Oncology letters, 8(6), 2517-2522. 3. A Review of the Spectrum of Imaging Manifestations of Epithelioid Hemangioendothelioma. AJR. American journal of roentgenology, 215(5), 1290-1298. 4. Epithelioid hemangioendothelioma: evaluation by ^{18}F-FDG PET/CT. American journal of nuclear medicine and molecular imaging, 11(2), 77-86.

EP-1285

Vanishing lung syndrome pattern on lung perfusion scintigraphy - significance of the hybrid imaging.

O. Lang[1], *M. Salomanina*[2];
[1]*Dept Nucl Med, Praha 1 – Nové Mesto, CZECH REPUBLIC,*
[2]*Cardiology and angiology Ltd., Praha 10, CZECH REPUBLIC.*

Aim/Introduction: Chronic obstructive pulmonary disease (COPD) with emphysema is a serious disease which can cause pulmonary hypertension. Clinical symptoms can mimic pulmonary embolism (dyspnea, hemoptysis). The optimal procedure to exclude pulmonary embolism is lung perfusion scintigraphy. Its interpretation, however, could be difficult if the bullous emphysema is present. ***Materials and Methods:*** 50y old patient was sent to our department to assess possible pulmonary hypertension due to difficult echocardiographic examination. He was admitted for pulmonary embolism as an accidental finding on CT examination several months ago. His pneumological history was abundant. He suffered from repetitive bronchopneumonia including non-tuberculous mycobacteriosis with a mycetoma in the left upper lobe. He was followed for COPD, grade 4, stage D with vanishing lung syndrome. His blood oxygen saturation was 99 %, blood and biochemical examination was without significant pathology. Patient was treated with anticoagulants and was clinically stable. We performed lung perfusion scintigraphy with 99mTc MAA, images were done on hybrid SPECT gamma camera with non-diagnostic CT. ***Results:*** We detected the absence of perfusion of almost the whole right lung on the perfusion scan, distribution of perfusion of the left lung was non-homogenous, but without segmental defects and with the absence of perfusion in the ventral part without any relation to lung anatomy. Non-diagnostic CT shows almost no lung parenchyma of the right lung and ventral part of the left lung, giant cavities filled with air, right mediastinal shift. Cavities on CT correlated with the absence of perfusion on scintigraphy, we, therefore, can exclude pulmonary embolism as well as chronic thromboembolic pulmonary hypertension (CTEPH). ***Conclusion:*** Hybrid lung scintigraphy in patients with vanishing lung syndrome can detect the relation of lung perfusion to the present lung parenchyma and thus exclude possible pulmonary embolism including CTEPH.

EP-1286

Myasthenia gravis-like syndrome: 18FFDG-PET/CT findings in a patient with breast cancer treated with Pembrolizumab.

M. Tagliatori Nogueira, *M. de la Rubia Marcos, A. Herrero Muñoz, C. Paniagua Correa, L. Castillejos Rodriguez, S. Perez Quiros, A. Ortega Valle, D. Rodriguez Oviedo, C. Galindo Fernandez, K. Guichay, J. Sanchez Calderon, P. Garcia Alonso;*
Hospital Universitario de Getafe, Madrid, SPAIN.

Aim/Introduction: We present the findings observed in ^{18F}FDG PET/CT scans performed on a patient with breast cancer treated with an immune checkpoint inhibitor (ICI) in the context of myasthenia gravis-like syndrome (MS). ***Materials and Methods:*** A 43-year-old woman was diagnosed with infiltrating ductal carcinoma of the left breast (G3) with negative hormone receptors, HER2 negative, and a Ki67 of 70%. She received neoadjuvant therapy, tumor resection + sentinel lymph node biopsy (SLNB), and adjuvant therapy with Pembrolizumab + PTX-CBDCA. An ^{18F}FDG PET/CT scan was performed at diagnosis, during adjuvant therapy, and one year later for follow-up. The protocol was performed from the skull to the proximal third of the thighs, 60 minutes after the intravenous administration of 300 MBq of ^{18F}FDG. After two cycles of adjuvant therapy, the patient developed significant proximal weakness in the lower limbs and difficulty standing up from a chair without support and climbing stairs. Due to suspicion of myasthenic syndrome, Pembrolizumab was discontinued, and the clinical presentation was correlated with the PET/CT images

and other complementary studies. ***Results:*** Electromyography (EMG), cervical/extremity MRI, blood tests for autoimmunity and anti-neuronal antibodies were performed, with negative results for all of them. Due to the diagnostic uncertainty, the PET/CT images taken during adjuvant therapy were reviewed, revealing a soft tissue lesion in the anterior mediastinum with increased metabolism, suggestive of thymic hyperplasia, not present in the disease staging study. Therefore, a seronegative myasthenic syndrome caused by Pembrolizumab and/or thymic hyperplasia was considered. Pembrolizumab was discontinued, and corticosteroids and pyridostigmine were started, with progressive clinical improvement. The follow-up PET/CT was evaluated, showing a reduction in both the size and metabolism of the previously described thymic hyperplasia. ***Conclusion:*** According to the literature, the development of myasthenic syndrome may be due to the presence of thymic hyperplasia (TH) or the use of ICI. The incidence of ICI-related MG is very low but potentially severe (30% mortality), typically presenting early (2nd-3rd cycle). In our case, both factors co-existed, supporting the clinical diagnosis in light of negative complementary studies. The literature indicates that both TH and ICI, individually, can lead to the development of MG, but no clear associations between ICI (Pembrolizumab) and thymic hyperplasia have been established. Further studies are needed to confirm whether this association could trigger the presentation of MG, and ^{18}FFDG PET/CT may play a key role due to its use in the routine follow-up of many tumors.

EP-1287

A rare case of metastatic prostate cancer to the external auditory canal evaluated with ^{18}F-Piflufolastat PET/CT

A. Cimini[1], *F. Russo*[1], *A. Marzullo*[1], *M. Menichini*[1], *L. Travascio*[2], *G. Amiconi*[3], *E. Lupi*[4], *M. Ricci*[5];
[1]*Nuclear Medicine Unit, St. Salvatore Hospital, L'Aquila, ITALY,* [2]*Nuclear Medicine Unit, P.O. Spirito Santo, Pescara, ITALY,* [3]*Oncology Unit, Civil Hospital of Avezzano, Avezzano, ITALY,* [4]*Department of Biotechnological and Applied Clinical Sciences, University of L'Aquila, L'Aquila, ITALY,* [5]*Nuclear Medicine Unit, Cardarelli Hospital, Campobasso, ITALY.*

Aim/Introduction: ^{18}F-Piflufolastat (known also as ^{18}F-DCFPYL) is a PET radiopharmaceutical that targets Prostate Specific Membrane Antigen (PSMA), used for the evaluation of prostate cancer. In this case report we describe the findings of ^{18}F-Piflufolastat PET/CT in a patient with metastatic prostate cancer to the external auditory canal, an extremely rare condition that can be misdiagnosed. ***Materials and Methods:*** A 65-year-old man with recent hearing loss and history of prostate cancer (previously treated with radiotherapy, Gleason Score 9) underwent ^{18}F-Piflufolastat PET/CT scan due to biochemical recurrence (serum prostate specific antigen (PSA) value was 0.76 ng/ml). About 270 MBq of ^{18}F-Piflufolastat were administrated intravenously. PET/CT acquisition was performed 90 minutes after radiopharmaceutical injection. ***Results:*** PET/CT scan documented high and pathologic uptake of ^{18}F-Piflufolastat in the right scapula (SUVmax 6.1), in a lung nodule of the left lung (SUVmax 6.1, diameter 1 cm), and in a pelvic lymph-node (SUVmax 14.3, diameter 0.9 cm): these findings were referred to prostate cancer metastases. No evidence of disease recurrence was observed in prostate gland. Furthermore, PET/CT images revealed increased uptake of the radiotracer in a tissue localized in the left external auditory canal (SUVmax 22.4, diameter 1.6 cm): due to the non-univocal nature of this tissue (initially this finding was referred to possible inflammatory disease), a biopsy was performed. The result of the biopsy was consistent with prostate cancer metastasis (Ki67 proliferation index was 30%). ***Conclusion:*** To the best of our knowledge, this is the first report describing a prostate cancer metastasis in the external auditory canal evaluated with PSMA-PET/CT. In a patient with metastatic prostate cancer and PSA value < 1 ng/ml, ^{18}F-Piflufolastat PET/CT demonstrated high uptake of the radiopharmaceutical in the tissue localized in the external auditory canal, resulting useful as guidance for biopsy: nuclear medicine physicians should be aware of this possible atypical metastatic localization (that can be misdiagnosed), especially in patients with history of prostate cancer and recent hearing loss.

EP-1288

Acute Pulmonary Embolism and Brachiocephalic Vein Thrombus Detected on 99mTc-MDP Bone Scan-A Case Series

J. Lanctôt-Bédard*, A. Ciarallo, K. Provost;*
Centre Hospitalier de l'Université de Montréal, Montréal, QC, CANADA.

Aim/Introduction: We present a case series of two patients in whom acute and chronic thromboembolic disease was detected on ^{99m}Tc-MDP bone scan. The first case involves a 70-year-old patient who presented to the emergency room with dyspnea and chest pain. Additionally, there was a suspicious right breast mass. A CT pulmonary angiography was performed to rule out pulmonary embolism. It revealed no evidence of pulmonary embolism, but a sclerotic lesion at L1 vertebral body which needed further investigation with bone scan. The second case involves a 62-year-old patient referred for re-staging of prostate cancer in the context of biochemical recurrence post-prostatectomy. ***Materials and Methods:*** Both patients underwent ^{99m}Tc-MDP bone scan with wholebody planar images and SPECT-CT of the chest. ***Results:*** Bone scan of the first patient revealed no evidence of bone metastasis. An intense focus of uptake projecting to the left chest on planar images was noted. On SPECT-CT, there was linear uptake in the left lung corresponding to a vascular structure. No underlying abnormalities on non injected CT. Acute pulmonary embolism demonstrating focal MDP uptake was felt to be the most likely diagnosis despite the negative CT angiogram two days previously. CT-angiogram of the chest repeated on the same-day as bone scan showed a new segmental pulmonary embolism involving the upper division of the lingula, exactly matching the MDP uptake. It confirmed the detection of acute pulmonary embolism on bone scan. The patient was anticoagulated. Bone scan of the second patient revealed no evidence of bone metastasis. A focus of moderate-intensity uptake was noted in the mediastinal vasculature on SPECT-CT, corresponding to faint calcifications within the brachiocephalic trunk. C+ CT scan of the chest confirmed the presence of an intra-luminal thrombus of the brachiocephalic vein. Images of 1-year prior bone scan were reviewed, and in retrospect showed faint activity at the same level, with documentation of the thrombus on C+ CT scan from the same period. ***Conclusion:*** To our knowledge, these are the first reported cases of acute pulmonary embolism and central venous thrombosis identified using 99mTc-MDP SPECT/CT. Only a few previous case reports had described focal uptake in the lung due to radiotracer microemboli mostly with FDG PET, unrelated to thrombo-embolic disease. MDP activity may occur in acute (case 1) or chronic (case 2) cases. There should be a high degree of suspicion for acute thrombo-embolic phenomenon in any unexplained focal vascular uptake of MDP.

EP-1289

Plasmablastic transformation of multiple myeloma- An unusual entity detected with ^{18}F-FDG PET/CT

T. Moreno-Monsalve*, M. I. Castellon-sanchez, L. Frutos-Esteban, J. L. Navarro-Fernandez, L. Mohamed-Salem, T. E. Rodriguez-Locarno, M. J. Ibañez-Ibañez, A. C. Hernandez-Martinez, N. Sanchez-Izquierdo, J. F. Contreras-Gutierrez;*
Hospital Universitario Virgen De La Arrixaca, Murcia, SPAIN.

Aim/Introduction: A 66-year-old man with a history of IgA kappa multiple myeloma with Bence-Jones proteinuria, high-risk

cytogenetics, ISS stage III and Durie-Salmon stage III-B, received multiple lines of therapy. After a partial response to fourth-line treatment, he underwent autologous stem cell transplant (ASCT), followed by progression. A sixth-line treatment with daratumumab was ineffective, and seventh-line therapy with anti-BCMA CAR-T cells achieved a very good partial response. ***Materials and Methods:*** At three months post-infusion, an [^{18}F]FDG PET/CT showed multiple bone lesions without abnormal uptake, suggesting complete metabolic response. However, at six months, a follow-up PET/CT revealed a new large retroperitoneal hypermetabolic mass infiltrating both kidneys, compressing the ureters, and extending to the pelvis, along with a hypermetabolic left adrenal nodule. Bone marrow biopsy confirmed diffuse infiltration by plasmacytoid cells with high Ki67, consistent with plasmablastic myeloma (PBM). Urgent treatment with bendamustine and dexamethasone was initiated. PBM is a rare, aggressive variant of multiple myeloma, characterized by ≥2% plasmablasts among clonal plasma cells. It is associated with extramedullary disease (EMD), rapid progression, and poor outcomes. In this case, the patient presented with plasmablastic transformation, developing retroperitoneal and adrenal extramedullary plasmacytomas, a pattern linked to adverse prognosis. ***Results:*** This case emphasizes the importance of considering plasmablastic transformation when evaluating disease progression in MM. Early and sensitive detection through [^{18}F]FDG PET/CT plays a crucial role. PET imaging not only aids in identifying aggressive phenotypes like PBM but also provides prognostic information: the presence of >3 focal lesions or EMD correlates with poor survival. Additionally, higher FDG uptake has been associated with increased plasma cell burden and reduced overall survival. FDG PET/CT is also valuable in monitoring treatment response, as changes in metabolic activity often precede anatomical alterations. In aggressive cases like PBM, early PET/CT can support timely clinical decision-making and prompt the initiation of salvage therapies or inclusion in experimental protocols. ***Conclusion:*** In conclusion, this case illustrates a rare and aggressive transformation of MM, marked by several poor prognostic indicators: plasmablastic histology, high-risk cytogenetics, and extramedullary spread. Early detection using sensitive imaging modalities such as [^{18}F]FDG PET/CT is essential for guiding appropriate management strategies and improving clinical outcomes in this challenging setting. ***References:*** Greipp PR et al. Plasmablastic morphology in myeloma. Blood, 1998. Suarez-Londono JA et al. Plasmablastic myeloma. BMJ Case Rep, 2020.Salem AE et al. PET-CT in hematologic malignancies. Cancers, 2022.Dah K et al. Aggressive PBM with cord compression. Anticancer Res, 2021.

EP-1290

Müller-Weiss Syndrome on ^{99m}Tc-MDP Bone Scintigraphy

D. Alami, *M. Zekri, A. Taalabi, N. Mahrsi, L. Taoussi, I. Zehfir, M. Aboussabr, Z. Laadissi, O. Ait Sahel, A. Doudouh;*
Mohamed V Military Instruction Hospital, Rabat, MOROCCO.

Aim/Introduction: With fewer than 300 reported cases in the literature, Müller-Weiss syndrome remains a rare condition that predominantly affects women between 40 and 60 years of age. Its pathogenesis is poorly understood, involving a combination of vascular insufficiency and mechanical stress. Diagnosis typically relies on weight-bearing radiographs, supplemented by CT, bone scan or MRI. Initial management is conservative, incorporating anti-inflammatory medications, analgesics, and non-weight-bearing immobilization. In refractory cases, surgical intervention—such as central decompression or arthrodesis—may be considered. Due to its rarity and often subtle clinical presentation, diagnosis is frequently delayed. We present a clinical case highlighting the pivotal role of bone scintigraphy in refining diagnosis and guiding appropriate management. ***Materials and Methods:*** We describe the case of a 59-year-old female patient with a three-month history of chronic pain in the right midfoot. Clinical examination revealed a flatfoot deformity with localized tenderness, in the absence of inflammatory signs, and normal laboratory findings. Initial plain radiographs of the right foot were unremarkable. However, MRI of the right ankle revealed osteonecrosis of the navicular bone. A 99mTc-MDP bone scintigraphy was subsequently performed for further assessment. ***Results:*** Triphasic bone scintigraphy demonstrated hyperemia during the vascular phase and increased radiotracer uptake in both the soft tissue and delayed bone phases at the level of the right tarsus, with marked intensity over the navicular bone, suggestive of early-stage osteonecrosis. The patient was referred to orthopedic surgery for specialized care. A conservative treatment regimen was initiated, including immobilization with a walking boot, NSAIDs for pain control, reduced weight-bearing activity, and the administration of bisphosphonates. As such, scintigraphy not only confirmed MRI findings but also provided additional insights into disease activity, supporting the decision for conservative treatment and deferring surgical intervention at this stage. ***Conclusion:*** Although uncommon, Müller-Weiss syndrome warrants heightened clinical awareness to avoid misdiagnosis and inappropriate management. Bone scintigraphy, by corroborating MRI findings and providing functional information on disease activity, plays a crucial role in guiding conservative treatment strategies and minimizing the need for invasive procedures.

EP-1291

Pulmonary Metastasis of Grade 1 Meningioma Mimicking a Carcinoid Tumor: A Case Report with FDG PET/CT, DOTATATE PET/CT and Pathological Confirmation

X. Rabbath, *C.-H. Shih, M.-A. Morin;*
Centre Hospitalier de l'Université de Montréal, Montréal, QC, CANADA.

Aim/Introduction: We report what appears to be the first documented case of a pulmonary metastasis from a WHO Grade 1 meningioma, detected by both FDG and DOTATATE PET/CT and confirmed by histopathology. ***Materials and Methods:*** A 68-year-old woman with no significant medical history underwent subtotal resection of a falcine meningioma. Pathological analysis confirmed a WHO Grade 1 (benign) meningioma with no histologic or immunohistochemical markers of aggressiveness. However, FISH analysis revealed a 1p deletion, a finding associated with increased clinical aggressiveness. A post-operative CT incidentally identified a lobulated lesion measuring 17 x 13 mm in the lung's left upper lobe. ***Results:*** ^{18}F-FDG PET/CT revealed mild hypermetabolism of the pulmonary nodule (SUVmax 2.2), without associated lymphadenopathy or additional hypermetabolic foci. A neoplastic process was suspected, and differential diagnoses included a well-differentiated carcinoid tumor. Additional evaluation with histopathological correlation or DOTATATE PET/CT scan was advised. Bronchoalveolar lavage, endobronchial brushing, and EBUS-guided lymph node biopsy were all negative for malignancy. ^{68}Ga-DOTATATE PET/CT demonstrated focal high uptake in the posterior sagittal sinus, corresponding to known residual meningioma. The pulmonary lesion demonstrated intense somatostatin receptor expression (SUVmax 10.7, Krenning score 3), consistent with a well-differentiated carcinoid tumor. No lymph node or distant metastasis were identified.The patient underwent left upper lobectomy within 2 weeks. Histopathological examination revealed a meningioma morphologically consistent with the intracranial lesion, with a Ki-67 index of 5-10%, confirming the diagnosis of a pulmonary metastasis from a WHO Grade 1 meningioma. This ruled out the working diagnosis of carcinoid tumor. The pulmonary lesion thus demonstrated mild FDG uptake and high DOTATATE avidity, paralleling the molecular profile of the primary intracranial tumor. ***Conclusion:*** Extracranial metastases from meningiomas are exceedingly rare, with less than 1% of cases

reported to metastasize (1). To our knowledge, this represents the first reported case of a Grade 1 meningioma metastasizing to the lung, detected by both FDG PET/CT and DOTATATE PET/CT and confirmed histologically. This case highlights the value of molecular imaging and the potential for even histologically benign meningiomas to exhibit unexpected aggressive behaviour.

References: 1. Dalle Ore CL, Magill ST, Yen AJ, et al. Meningioma metastases: incidence and proposed screening paradigm. J Neurosurg. 2019;132:1447-1455.

EP-1292

Increased PSMA expression in synchronous high-grade pleomorphic sarcoma of the thigh and a rare giant liver hemangioma detected on ^{68}Ga-PSMA PET/CT staging of prostate cancer (PC)

M. Dyankova[1,2], *T. Stoeva*[1], *S. Chausheva*[1], *Z. Dancheva*[1], *T. Yordanova*[1], *B. Chaushev*[1], *A. Klisarova*[1];
[1]*St. Marina University Hospital, Varna, Bulgaria,* [2]*Medical University Varna "Prof. Dr. Paraskev Stoyanov", Department of Nuclear Medicine, Metabolic Therapy and Radiotherapy, Varna, BULGARIA.*

Aim/Introduction: Synchronous ^{68}Ga-PSMA-positive malignancies are rare, occurring in approximately 0.7% of patients with prostate cancer (PC). Beyond PC, PSMA expression has also been observed in the tumor-associated neovascular endothelial cells of various non-prostatic malignancies, including sarcomas. Sarcomas represent a heterogeneous group of malignant tumors arising from connective tissues and are broadly classified into soft tissue sarcomas and bone sarcomas. Collectively, they constitute less than 1% of all newly diagnosed malignancies. Owing to their low incidence, coupled with considerable histopathological and anatomical heterogeneity, the diagnosis of sarcomas remains particularly challenging. ***Materials and Methods:*** We report the case of a 66-year-old male in whom a second primary malignancy—identified as a soft tissue sarcoma of the thigh demonstrating increased PSMA expression—was incidentally detected on ^{68}Ga-PSMA PET/CT. Additionally, a rare giant hepatic hemangioma, showing no increased PSMA uptake, was observed. The patient had recently been diagnosed with prostate adenocarcinoma, Gleason score 7 (3 + 4), ISUP Grade Group 2, with an initial serum prostate-specific antigen (PSA) level of 12.0 ng/mL. He was referred for staging with PSMA-PET/CT prior to initiation of treatment. ***Results:*** ^{68}Ga-PSMA PET/CT was performed for staging, revealing not only findings consistent with primary PC but also a synchronous tumor demonstrating increased PSMA uptake. Fused PET/CT images showed a heterodense mass located in the proximal third of the right thigh, exhibiting intense pathological PSMA activity. Histopathological analysis subsequently confirmed the lesion as a high-grade pleomorphic sarcoma. Additionally, a large heterodense parenchymal lesion was identified, involving almost the entire right hepatic lobe. This lesion demonstrated no increased PSMA uptake and contained a central hypodense region with amorphous, calcified inclusions. The imaging findings were consistent with a giant hepatic hemangioma, later confirmed by conventional imaging modalities including contrast-enhanced CT and MRI. Furthermore, PET/CT images demonstrated diffusely heterogeneous increased PSMA expression throughout both lobes of the prostate gland, which appeared enlarged, particularly at the mid-apical level—findings indicative of the known primary PC. ***Conclusion:*** In the present case report, we highlight the importance of histopathological confirmation of lesions with increased PSMA expression, but atypical for PC involvement and provide a rationale for further investigation into the potential role of PSMA-targeted radiopharmaceutical therapy in non-prostatic malignancies, offering a novel therapeutic perspective for patients with sarcoma. A comprehensive evaluation—including the patient's clinical history, morphological characteristics of the lesions, and findings from complementary imaging modalities—is essential to accurately assess the relevance and clinical significance of the observed findings.

EP-1293

PSMA-Avid Osteitis Deformans in Pelvic Bones Mimicking Prostate Cancer Metastasis on ^{68}Ga-PSMA PET/CT Imaging: A Case Report

M. Dyankova[1,2], *T. Stoeva*[1], *S. Chausheva*[1], *Z. Dancheva*[1], *T. Yordanova*[1], *B. Chaushev*[1], *A. Klisarova*[1];
[1]*St. Marina University Hospital, Varna, BULGARIA,* [2]*Medical University Varna "Prof. Dr. Paraskev Stoyanov", Department of Nuclear Medicine, Metabolic Therapy and Radiotherapy, Varna, BULGARIA.*

Aim/Introduction: The introduction of prostate-specific membrane antigen (PSMA)-targeted positron emission tomography/computed tomography (PET/CT) using ^{68}Ga-labeled tracers has significantly improved the detection of recurrent and metastatic disease, even at low PSA levels. However, PSMA expression is not exclusive to prostate carcinoma (PC) and may also be present in benign or non-prostatic malignant lesions, potentially complicating image interpretation. ***Materials and Methods:*** A 66-year-old male with a history of prostate adenocarcinoma (Gleason score 7 [3 + 4], ISUP Grade Group 2) underwent radical prostatectomy. The patient was referred for ^{68}Ga-PSMA PET/CT due to biochemical recurrence, with actual serum prostate-specific antigen (PSA) level of 6.65 ng/mL. The patient underwent whole-body ^{68}Ga-PSMA-11 PET/CT imaging using a standard protocol. SUVmax and visual scoring were used to evaluate the PSMA expression pattern of all lesions. Follow-up MRI and CT imaging were used to correlate and confirm the bone lesion etiology. ***Results:*** A lobulated soft tissue mass was visualized in the prostatic bed, extending into the right seminal vesicle. The lesion demonstrated pathological PSMA expression, consistent with a local recurrence of the PC. In addition, pelvic bones, including the right hemipelvis (ischium, pubic ramus, acetabulum, and iliac body/wing), showed altered bone architecture, with osteoporotic and osteolytic remodeling, prominent trabeculation, and osteoblastic areas with mild to moderate tracer uptake (visual score 1). These findings, characterized by a combination of osteolytic (lucent) regions, areas of coarsened trabeculation, and sclerotic changes, were interpreted as likely benign and suggestive of deforming osteitis (Paget's disease), which was subsequently confirmed by MRI and CT imaging. Furthermore, a wedge compression fracture of the Th12 vertebral body was noted, without increased PSMA uptake, supporting the diagnosis of a benign compression fracture. ***Conclusion:*** Incidental findings such as deforming osteitis may present with PSMA uptake, potentially mimicking metastatic disease. This case highlights the importance of careful interpretation of PSMA-avid lesions and emphasizes the need for a comprehensive diagnostic approach, integrating clinical history, morphological features, and additional imaging modalities, all of which are essential for accurate diagnosis and to guide appropriate treatment strategies.

EP-1294

PSMA-positive incidental parathyroid adenoma in a prostate cancer (PC) patient detected during a routine staging PET/CT scan using the newly synthesized radiopharmaceutical 18F-siPSMA-14

M. Dyankova[1,2], *T. Stoeva*[1], *S. Chausheva*[1], *Z. Dancheva*[1], *T. Yordanova*[1], *B. Chaushev*[1], *A. Klisarova*[1];
[1]*St. Marina University Hospital, Varna, BULGARIA,* [2]*St. Marina University Hospital. Department of Nuclear Medicine., Varna, BULGARIA.*

Aim/Introduction: Primary hyperparathyroidism is a common endocrine disorder characterized by excessive secretion of parathyroid hormone (PTH), resulting in hypercalcemia and associated renal and skeletal complications primarily caused by parathyroid adenoma. Accurate localization of hyperfunctioning

parathyroid tissue is crucial for definitive surgical treatment but often poses a significant challenge for conventional imaging modalities. Due to the increased expression of carboxypeptidase type II in the endothelial lining of neovasculature of various solid tumors, increased uptake of ^{68}Ga-labeled prostate-specific membrane antigen (PSMA) on PET/CT imaging has been observed in numerous benign and malignant non-prostatic conditions, including parathyroid adenomas. ***Materials and Methods:*** A 69-year-old man was diagnosed with prostatic acinar adenocarcinoma, Gleason score 8 (4 + 4), ISUP Grade Group 4, with an initial serum prostate-specific antigen (PSA) level of 7.51 ng/ml. He was referred for staging with 18F-siPSMA prostate-specific membrane antigen (PSMA) PET/CT prior to treatment. A whole-body PET/CT scan was performed at the 90th minute following the administration of 350.0 MBq of [18F]siPSMA-14, without the application of furosemide. ***Results:*** PSMA PET/CT study with newly synthesized radiopharmaceutical ^{18}F-siPSMA-14, revealed an enlarged prostate gland with diffusely heterogeneous, increased PSMA expression in both lobes, predominantly in the left lobe at the mid/apex level, with higher uptake in the peripheral zones—findings consistent with a primary prostate cancer, histologically confirmed. The seminal vesicles appeared intact on imaging. No lesions with pathologically increased PSMA expression suggestive of regional malignant lymphadenopathy or distant metastatic disease were detected. Coincidentally, a nodular lesion with increased PSMA expression was observed in the lower pole and dorsal to the left thyroid lobe. This incidental finding was further clarified with complementary four-dimensional CT. Blood tests revealed elevated serum calcium and parathyroid hormone levels, as well as hypophosphatemia, consistent with primary hyperparathyroidism. Subsequently, parathyroidectomy was performed, and histopathological examination of the nodule confirmed a parathyroid adenoma. ***Conclusion:*** In the present case, the novel [^{18}F]siPSMA-14 PET radiotracer aided in the diagnosis of a parathyroid adenoma. Future prospective studies are needed to investigate the potential diagnostic value of the hybrid PSMA PET/CT method in evaluating patients who present with not uncommon false-negative results from conventional imaging modalities.

EP-1295

FDG PET/MRI Demonstration of Extensive Spinal Cord Metastases in a Patient with Ovarian Carcinoma

C. Güneren*, S. Asa, H. B. Sayman;*
Istanbul University-Cerrahpasa Cerrahpasa Medical Faculty Department of Nuclear Medicine, Istanbul, TÜRKIYE.

Aim/Introduction: Central nervous system (CNS) involvement is an uncommon manifestation of metastatic ovarian carcinoma. Though the liver is the most frequent site of distant spread, spinal cord metastases remain rare. The anatomical distribution of metastases is an independent prognostic factor (1). ***Materials and Methods:*** We present a case of spinal cord metastasis from high-grade serous ovarian carcinoma, emphasizing the diagnostic value of ^{18}F-FDG PET/MRI compared to conventional MRI. ***Results:*** In 2020, the patient was diagnosed with high-grade serous ovarian carcinoma following total abdominal hysterectomy, bilateral salpingo-oophorectomy, omentectomy, and excision of peritoneal implants. Multiple lines of chemotherapy were administered. During follow-up, brain metastases were detected, and the patient received whole-brain radiotherapy with palliative intent.On subsequent ^{18}F-FDG PET/MRI imaging, newly emerged, millimetric to sub-centimetric, hypermetabolic foci were observed along the spinal canal, predominantly in the cervical region, adjacent to the spinal cord. These findings were interpreted as spinal cord metastases. Complementary contrast-enhanced spinal MRI demonstrated nodular enhancement in the corresponding areas on post-contrast T1-weighted images, consistent with metastatic involvement. However, lesion detectability and delineation were notably superior on PET/MRI compared to MRI alone. Targeted radiotherapy was administered based on PET/MRI findings. ***Conclusion:*** Intramedullary spinal cord metastases are extremely rare, comprising 0.9-2.1% of cancer autopsies and 8.5% of all CNS metastases. Ovarian cancer cases with spinal involvement are scarcely reported, mostly via MRI (2-5). While MRI remains the gold standard for anatomical evaluation and surgical planning (6), ^{18}F-FDG PET/MRI adds diagnostic value, especially for detecting subtle or widespread lesions. As demonstrated in this patient, PET/MRI may represent a diagnostically superior modality in selected clinical contexts. ***References:*** 1)Deng K. et al. Sites of distant metastases and overall survival in ovarian cancer: A study of 1481 patients. Gynecol Oncol. 2018 Sep;150(3):460-465. 2) Kłębczyk W. et al. CASE REPORT Metastasis of ovarian cancer to the spinal cord-case study. 2021. 3)Miranpuri AS. et al. Upper cervical intramedullary spinal metastasis of ovarian carcinoma: A case report and review of the literature. Vol. 5, Journal of Medical Case Reports. 2011. 4)Safadi S. et al. Ovarian carcinoma with isolated spinal cord metastasis. J Investig Med High Impact Case Rep. 2016 Jul 1;4(3). 5)Cormio G. et al. Intramedullary spinal cord metastasis from ovarian carcinoma. Gynecol Oncol. 2001;81(3):506-8. 6) Waldron JS, Cha S. Radiographic Features of Intramedullary Spinal Cord Tumors. Neurosurg Clin N Am. 2006 Jan 1;17(1):13-9.

EP-1296

Incidental Detection of Pulmonary Carcinoid Tumor During Cardiac SPECT Perfusion Imaging: A Case Report

E. Gharepapagh*[1], S. Rezaei[1], S. Dabiri[1], M. Karbasi[2];*
[1]Department of Nuclear Medicine, Medical School, Tabriz University of Medical Sciences, Tabriz, IRAN, ISLAMIC REPUBLIC OF, [2]Department of radiology, Medical School, Tabriz University of Medical Sciences, Tabriz, IRAN, ISLAMIC REPUBLIC OF.

Aim/Introduction: Pulmonary carcinoid tumors are rare neuroendocrine neoplasms. While most commonly arising in the gastrointestinal tract, they represent the second most frequent neuroendocrine tumors found in the lungs. These tumors typically grow slowly and may remain asymptomatic for years, often being discovered incidentally during imaging studies conducted for unrelated clinical indications. ***Materials and Methods:*** We present the case of a 66-year-old female undergoing preoperative assessment for uterine surgery due to medication-resistant fibroma. As part of the cardiac clearance process, she was referred for myocardial perfusion SPECT imaging. A two-phase (stress and rest) myocardial perfusion SPECT was performed using 99mTc-MIBI, acquired on a dual-head gamma camera. ***Results:*** The myocardial walls demonstrated normal perfusion, with no evidence of ischemia (LVEF = 66%). However, an incidental finding on the raw and MIP images prior to processing revealed a relatively large abnormal soft tissue mass in the lower lobe of the right lung. The mass exhibited notable 99mTc-MIBI uptake, prompting further investigation. A non-contrast CT scan confirmed the presence of a 64×54 mm soft tissue mass with internal calcifications in the medial basal segment of the right lung, causing compression of the adjacent bronchus. Based on imaging features, the differential diagnosis included bronchial carcinoid tumor and primary lung carcinoma. Bronchoscopy and biopsy confirmed the diagnosis of a pulmonary carcinoid tumor. ***Conclusion:*** This case underscores the importance of thoroughly reviewing extracardiac regions during myocardial SPECT imaging. Incidental findings, such as pulmonary masses, can lead to the early diagnosis of potentially serious conditions. Vigilance in assessing adjacent thoracic structures during routine nuclear medicine procedures enhances diagnostic value and improves patient care.

EP-1297

Left Frontal Lobe Hypoperfusion and Progressive Speech Impairment: A Case Study Using SPECT Imaging

E. Gharepapagh[1], *S. Rezaei*[1], *M. Karbasi*[2];
[1]*Department of Nuclear Medicine, Medical School, Tabriz University of Medical Sciences, Tabriz, IRAN, ISLAMIC REPUBLIC OF,* [2]*Department of radiology, Medical School, Tabriz University of Medical Sciences, Tabriz, IRAN, ISLAMIC REPUBLIC OF.*

Aim/Introduction: Speech production is primarily controlled by Broca's area, typically located in the left frontal lobe. Other regions, including Wernicke's area, the arcuate fasciculus, the cerebellum, and the motor cortex, also contribute to language processing. In adults, speech disorders may result from neurological diseases, stroke, trauma, psychological factors, medication side effects, hearing loss, and aging. Neuroimaging plays a crucial role in the early identification and evaluation of these disorders. ***Materials and Methods:*** We report the case of a 77-year-old woman with progressive speech impairment beginning in early 2022, now accompanied by difficulty eating. She underwent several sessions of speech therapy with limited benefit. Brain MRI revealed generalized atrophy, ischemic changes, and ventricular enlargement. To further evaluate cerebral perfusion, a brain SPECT scan using 99mTc-ECD was performed. ***Results:*** SPECT imaging demonstrated lateral ventricular dilation, cortical thinning, and diffuse loss of cerebral gyri and sulci. Quantitative analysis showed a significant decrease in radiotracer uptake in the left frontal and temporal lobes (Lt/Rt counts ratio = 0.77), suggesting functional impairment of Broca's area and its associated speech network. These findings are consistent with the patient's severe expressive aphasia. ***Conclusion:*** This case highlights the utility of functional imaging in detecting hypoperfusion in language-related brain regions, particularly in elderly patients with progressive speech impairment. Early implementation of SPECT or other neuroimaging techniques may assist in diagnosis and guide management strategies, especially when structural MRI findings are inconclusive**.**

EP-1298

Vertebral Hemangioma in Disguise: A Ga-68 DOTATATE False Positive

M. Pešorda*, E. Pasini Nemir, D. Huic;*
University Hospital Centre Zagreb, Zagreb, CROATIA.

Aim/Introduction: Ga-68 DOTATATE PET/CT is a highly sensitive and specific imaging modality used in the evaluation of neuroendocrine tumors (NETs). Ga-68 DOTATATE is a radiolabeled somatostatin analog that binds with high affinity to somatostatin receptors, which are overexpressed in many NETs.In addition to NETs, Ga-68 DOTATATE uptake can be observed in other tumors (e.g., meningioma, small cell lung carcinoma), inflammatory conditions, and osteoblastic osseous processes. Tracer uptake in vertebral hemangiomas can lead to false-positive findings, making correlation with CT or MRI extremely important. ***Materials and Methods:*** We present a case of 69-year old female patient that has been under follow-up since 2006 for small lung nodules initially identified on a chest X-ray performed as part of preoperative evaluation for thyroid surgery.In 2021, the nodule in the anterior segment of the right upper lobe began increasing in size, and a new nodule appeared in the anterior segment of the left upper lobe.Both lesions showed increased uptake on an F-18 FDG PET/CT scan performed in 2022.The patient declined invasive diagnostics until early 2024, when bronchoscopy with biopsy was finally conducted. The small biopsy sample favored the diagnosis of a neuroendocrine tumor over neuroendocrine carcinoma (Ki-67 <10%). At that time, the patient chose not to proceed with further invasive procedures required for more detailed analysis. The patient was referred to our department for a Ga-68 DOTATATE PET/CT scan in April 2024. ***Results:*** Ga-68 DOTATATE PET/CT revealed increased uptake in the right lung hilum (SUVmax 7.2), the right upper lobe nodule (SUVmax 8.6), and the left upper lobe nodule (SUVmax 18.1). An unexpected finding was increased uptake in the body of the T3 vertebra (SUVmax 8.9), which appeared only mildly altered on low-dose CT. A metastatic lesion could not be ruled out based on this. However, contrast-enhanced CT findings of T3 were consistent with a vertebral hemangioma. The patient also had a known vertebral hemangioma at L3, with only mild tracer uptake (SUVmax 3.5).In March 2025, the patient began treatment with octreotide LAR. ***Conclusion:*** While Ga-68 DOTATATE PET/CT is an excellent imaging tool for NET diagnosis, potential pitfalls such as false-positive uptake must be recognized. Vertebral hemangiomas are benign lesions typically non-avid on Ga-68 DOTATATE PET/CT but may occasionally show radiotracer uptake, mimicking metastasis. Misinterpretation of such uptake can lead to incorrect staging and management, emphasizing the importance of correlating PET/CT findings with CT or MRI to avoid misdiagnosis of skeletal metastases.

EP-1299

Splenic Hemangioma: A Noteworthy Incidental Finding on ^{18}F-PSMA PET/CT

O. Bourogianni[1], *G. Lamprakopoulos*[1], *N. Kapsoritakis*[1], *M. Stathaki*[1], *S. Koukouraki*[2];
[1]*Nuclear Medicine Department, University Hospital of Crete, Heraklion, GREECE,* [2]*Nuclear Medicine Department, School of Medicine, University of Crete, Heraklion, GREECE.*

Aim/Introduction: Prostate cancer is the most prevalent malignancy among men, with the highest incidence observed in elderly individuals (> 65 years of age). It is typically identified by elevated prostate-specific antigen (PSA) levels and confirmed through imaging and biopsy. Recent advancements in imaging, particularly prostate-specific membrane antigen (PSMA) positron emission tomography (PET)/computed tomography (CT), have significantly enhanced the staging and management of this disease. PSMA PET/CT offers high sensitivity and specificity for detecting both primary tumors and metastatic lesions. However, atypical findings may occasionally complicate staging. ***Materials and Methods:*** A 75-year-old male patient presented with progressively increasing PSA levels over the past six months and underwent a comprehensive diagnostic evaluation. Pelvic MRI revealed a PI-RADS 4 lesion located in the left posterolateral peripheral zone at the mid-gland level. Prostate biopsies were performed, and the pathology report indicated the following: Lesion: adenocarcinoma, Gleason score 7 (3+4), 90% involvement, Left lobe: adenocarcinoma, Gleason score 7 (3+4), 40% involvement. To assess the extent of the disease, an 18F-PSMA PET/CT scan was conducted. ***Results:*** The 18F-PSMA PET/CT scan revealed abnormal tracer uptake in the posterior peripheral zone of the prostate mid-gland and base, with the most intense signal located in the left posterolateral region of the mid-gland. No abnormal uptake was observed elsewhere in the pelvis or abdominal lymph nodes. Notably, intense PSMA tracer activity was identified in multiple splenic lesions, the largest of which measured 50 mm in diameter, along with the presence of an accessory spleen. To exclude the rare possibility of metastatic prostate cancer, an abdominal MRI was performed. The MRI findings were more consistent with splenic hemangiomas than metastatic lesions. ***Conclusion:*** PSMA PET/CT is a powerful imaging modality for staging prostate cancer, offering high sensitivity and specificity for both primary and metastatic disease. However, it is important to recognize that benign conditions can also show PSMA avidity. Splenic hemangiomas, the most common benign tumors of the spleen, can mimic metastatic lesions on PSMA PET/CT. As PSMA-targeted imaging becomes more widely adopted, familiarity with these potential pitfalls will be crucial for accurate interpretation.

EP-1300

Perineural dissemination in head and neck epidermoid carcinoma on ^{18}F-FDG PET/CT

P. Guardia Jimena, *A. Santos Bueno, M. Sanchez Torrente, S. Martin Aguilar, M. Ureña Lara;*
Hospital Universitario de Jaén, Jaén, SPAIN.

Aim/Introduction: Perineural dissemination in head and neck tumours is associated with decreased survival, a higher risk of recurrence and worse prognosis, and its diagnosis may change the therapeutic management of patients. Its detection by ^{18}F-FDG PET/CT is influenced by physiological uptake in the head and neck area and the lower anatomical resolution, so MRI findings must be taken into account for its localization. The most frequently affected nerves are the trigeminal and facial nerves. ***Materials and Methods:*** We present the case of a 60-year-old patient with a history of right maxillary epidermoid carcinoma T4N0Mx treated by radiotherapy and chemotherapy; he presented local recurrence two years later, treated by total maxillectomy and right cervical dissection, revealing affected margins. Adjuvant treatment was ruled out due to previous radiotherapy, and close follow-up was maintained.Subsequently, discordant results were obtained in the morphological follow-up tests, describing local recurrence by MRI with suspected perineural dissemination of the infraorbital nerve, with no evidence of disease in the CT study. Based on these results, the multidisciplinary committee decided to complete the study with ^{18}F-FDG PET/CT for better assessment. ***Results:*** A PET/CT study was performed 50 minutes after intravenous administration of 181 MBq of ^{18}F-FDG, acquiring a full body and head and neck study confirming local recurrence in the inferior orbital fissure and pterygopalatine fossa, as well as linear hypermetabolism extending from the orbital fissure, caudally and anteriorly through the theoretical maxillary sinus to the theoretical right maxillary region, tracing the route of the infraorbital nerve, supporting the suspicion of perineural dissemination. Following these results and taking into account the treatments performed, he was transferred to another centre to receive proton therapy (not available in our hospital) and chemotherapy. After treatment, a follow-up ^{18}F-FDG PET/CT scan revealed discrete hypermetabolism in the treated area of probable post-treatment inflammatory origin without being able to exclude persistent disease and without findings of perineural linear metabolism, showing a good response to treatment. In the MRI, changes persist in the treated area, and so close follow-up is maintained. ***Conclusion:*** Despite the limitations of ^{18}F-FDG PET/CT for the diagnosis of perineural dissemination, it can support the information provided by other imaging techniques to justify changes in the treatment and management of patients.

EP-1301

Silent Intramedullary Metastasis From Lung Carcinoma : Early Detection by ^{18}F-FDG PET/CT

M. Aboussabr, *I. Zahfir, M. Zekri, N. Mahrsi, Z. Laadissi, A. Taalabi, D. Alami, L. Taoussi, Y. Benameur, A. Doudouh;*
Department of Nuclear Medicine, Mohammed V Military Teaching Hospital, Rabat, MOROCCO.

Aim/Introduction: Intramedullary spinal cord metastases (ISCMs) are exceptionally rare, accounting for approximately 0.9% to 2.1% of all spinal metastases. They most frequently originate from primary lung carcinomas. While MRI remains the gold standard for detailed anatomical evaluation, ^{18}F-FDG PET/CT has emerged as a powerful tool for comprehensive systemic assessment. Due to its high sensitivity in detecting metabolically active lesions, PET/CT allows early identification of metastatic foci, including clinically silent or MRI-occult ISCMs. ***Materials and Methods:*** We present the case of a 72-year-old male patient diagnosed with lung adenocarcinoma. He was initially treated with concomitant radio chemotherapy, achieving partial remission. Five months later, he developed severe back pain associated with progressive lower limb weakness. Given the suspicion of disease progression, a restaging with ^{18}F-FDG PET/CT was performed. ***Results:*** A PET/CT scan was performed 60 minutes after the injection of 270 MBq of 18F-FDG. The sagittal fused PET/CT images revealed a highly FDG-avid lesion within the cervical spinal cord at the C5-C6 level, with a SUVmax:13.1, strongly suggesting the presence of ISCMs. A gadolinium-enhanced spinal MRI was then conducted. Sagittal, coronal, and axial images showed multiple nodular leptomeningeal enhancements at both the cervical (C5-C6) and thoracic (D5-D6) levels. Additionally, a central intramedullary lesion, extending from the medulla oblongata to C7, exhibited contrast enhancement on T2-weighted images. ***Conclusion:*** ISCMs represent a rare clinical entity, most commonly arising from primary lung carcinoma, particularly small cell lung cancer, which accounts for approximately 50% of cases. Other primary tumors include breast cancer, melanoma, lymphoma, renal cell carcinoma, and, more rarely, colorectal cancer. The onset of ISCMs is frequently associated with severe neurological deficits and a poor overall prognosi, highlighting the importance of early detection to delay neurological deterioration and optimize therapeutic management. Although MRI remains the reference modality for morphological assessment, ^{18}F-FDG PET/CT emerges as a crucial diagnostic tool. With a high sensitivity of up to 96%, it enables comprehensive metabolic evaluation and facilitates the detection of metastatic lesions including intraspinal involvement. Its role is pivotal in guiding early diagnosis, directing targeted MRI, and expediting appropriate therapeutic intervention. Therefore, ^{18}F-FDG PET/CT stands out as an indispensable imaging modality for the detection of rare but clinically significant metastases such as ISCMs.

EP-1302

Unmasking Tuberculosis in a Patient with Sarcoidosis : The Pivotal Role of ^{18}F-FDG PET/CT

M. Aboussabr, *I. Zahfir, M. Zekri, Z. Laadissi, N. Mahrsi, D. Alami, L. Taoussi, A. Taalabi, S. Oueriagli, A. Doudouh;*
Department of Nuclear Medicine, Mohammed V Military Teaching Hospital, Rabat, MOROCCO.

Aim/Introduction: Tuberculosis and sarcoidosis are the two main granulomatous diseases, posing a diagnostic challenge due to their overlapping clinical, radiological, and histopathological features. Their coexistence in the same patient is rare, and the disease course is a key element in refining the diagnosis. ^{18}F-FDG PET/CT proves valuable in identifying active disease, assessing its extent, and guiding biopsy procedures, thereby enhancing diagnostic accuracy. ***Materials and Methods:*** We report the case of a 45-year-old patient with a known history of systemic sarcoidosis with mediastinal-pulmonary and hepatic involvement, previously managed with corticosteroid therapy, which yielded a favorable clinical and radiological response. Six months after, the patient developed a persistent inflammatory syndrome associated with hypercalcemia, occurring in the context of weight loss estimated at 10 kg. As part of the etiological assessment, a ^{18}F-FDG PET-CT was performed. ***Results:*** The ^{18}F-FDG PET-CT demonstrated a bilateral interstitial lung pattern associated with intensely hypermetabolic alveolar micronodules (SUVmax = 16.6). In addition, multiple calcified mediastinal and hilar lymphadenopathies were noted, without significant FDG uptake, consistent with metabolically inactive lesions. Biological work-up revealed hypercalcemia, and an elevated erythrocyte sedimentation rate at 70 mm/h, indicative of a systemic inflammatory response. Microbiological analysis of sputum samples tested positive for acid-fast bacilli, and histopathological examination of a pleuropulmonary biopsy confirmed the diagnosis of caseo-follicular tuberculosis. ***Conclusion:*** The coexistence of pulmonary tuberculosis and sarcoidosis is a rare clinical entity. However, several reported cases suggest a potential association between these two conditions.

Corticosteroid therapy, the standard treatment for sarcoidosis, induces a state of immunosuppression that may facilitate the development of secondary tuberculosis. Additionally, some authors have reported concomitant cases of tuberculosis and sarcoidosis, suggesting the possibility of an underlying pathophysiological interaction. In this context, ^{18}F- FDG PET/CT stands out as a leading metabolic imaging modality for the detection and characterization of tuberculous lesions. Its primary value lies in its ability to detect active infectious foci at an early stage particularly in extrapulmonary forms with atypical presentations. It also plays a significant role in sarcoidosis by enabling whole-body assessment of metabolically active granulomatous involvement, including sites inaccessible to biopsy. In this case, PET/CT revealed active lesions that guided further investigations, ultimately leading to the diagnosis of coexistent caseo-follicular tuberculosis. Due to overlapping metabolic patterns, PET findings must be interpreted alongside histopathological and microbiological results to ensure diagnostic accuracy.

EP-1303

Giant Parathyroid Adenoma: a Multidisciplinary Clinical Case

I. Grierosu[1,2], *A. Florescu*[1,3], *R. Danila*[1,4], *C. Stefanescu*[1,2];
[1]*University of Medicine and Pharmacy „Grigore T. Popa", Iasi, ROMANIA,* [2]*Nuclear Medicine Laboratory, County Emergency Hospital „Sf. Spiridon", Iasi, ROMANIA,* [3]*Endocrinology Department, County Emergency Hospital „Sf. Spiridon", Iasi, ROMANIA,* [4]*Surgery Department, County Emergency Hospital „Sf. Spiridon", Iasi, ROMANIA.*

Aim/Introduction: The prevalence of parathyroid adenomas in the general population is about 22 cases per 100,000. Out of these, parathyroid adenomas comprise the highest percentage, 80-90%, while hyperplasia situates itself between 10 and 20%, and only under 1% are diagnosed with parathyroid carcinomas [1]. Atypical parathyroid adenomas are even more infrequent, being considered as benign disorders but associated with the potential of malignant transformation over time (parathyroid carcinoma). When a parathyroid adenoma grows more than 2 cm and weighs more than 3.5 grams, the condition is referred to as giant parathyroid adenoma. ***Materials and Methods:*** A male patient from the Endocrinology Department was referred to our laboratory to perform a ^{99m}Tc-MIBI scintigraphy. Static images after 20 minutes and 2 h, respectively, followed by SPECT-ldCT images, were acquired using a General Electric Optima NM/CT 870DR SPECT-CT gamma camera. ***Results:*** We report the clinical case of a 73-year-old man. He previously presented to the hospital with fatigue and bone aches. Being diagnosed with prostate adenocarcinoma with a Gleason score of 7 and a PSA of 5 ng/mL, MRI and CT images raised the suspicion of bone metastases. The whole-body scintigraphy mentioned many bone fixations in the skull, clavicle, ribs, and pelvis. In the meantime, the bloodwork showed increased levels of serum calcium (13.3 mg/dL) and a PTH value of 1741.7 pg/mL. ^{99m}Tc-MIBI scintigraphy identified a large uptake site on delayed images in the left thyroid lobe. A similar localization and uptake pattern as the bone scan were observed, indicating that SPECT-ldCT might diagnose multiple brown tumors. After referral to the surgical department, the large parathyroid adenoma of 5 cm was operated on. The pathology and the immunohistochemistry reports describe the anomaly as an atypical parathyroid adenoma with a Ki67 under 1%. The patient came for follow-up after 3 months. The phosphatase alkaline, calcium and PTH values were within normal limits. ***Conclusion:*** This clinical case shows the importance of the multidisciplinary approach in the management, diagnosis and subsequent treatment. This patient was a medical emergency, and the expeditious intervention with optimal communication between medical departments limited the damage that could have occurred to the other organs and systems. ***References:*** [1] Rahim Mahmodlou, Amin Sedokani, Apameh Pezeshk, Bita Najafinejad. Giant parathyroid adenoma: a case report. J Med Case Rep. 2022; 16(1):150.

EP-1304

Complete response of HCV-associated primary extranodal Diffuse Large B-cell Lymphoma to direct-acting antiviral therapy alone assessed by [^{18}F]FDG PET/CT

L. Atakishieva[1], *A. Khalimon*[2], *N. Kadymova*[1], *V. Bobrov*[2], *A. Leontev*[2];
[1]*N. Lopatkin Scientific Research Institute of Urology and Interventional Radiology - branch of the National Medical Research Radiological Centre of the Ministry of Health of the Russian Federation, Moscow, RUSSIAN FEDERATION,* [2]*P. Hertsen Moscow Oncology Research Institute - branch of the National Medical Research Radiological Centre of the Ministry of Health of the Russian Federation, Moscow, RUSSIAN FEDERATION.*

Aim/Introduction: Chronic hepatitis C virus (HCV) infection may present a wide spectrum of extrahepatic manifestations, including lymphoproliferative disorders. Marginal zone lymphoma and diffuse large B-Cell lymphoma (DLBCL) are the subtypes of B-cell non-Hodgkin lymphoma (B-NHL) most commonly associated with HCV infection. The molecular mechanisms of relationship between HCV infection and B-NHL lymphomagenesis are still poorly understood. The evidence supporting this relationship is the regression of B-NHL observed after successful HCV eradication through antiviral therapy (AVT). The effectiveness of direct-acting antivirals (DAA) against HCV-associated indolent lymphomas in first-line therapy, especially those of marginal zone type, has been proven. Concurrent or subsequent application of DAA-based AVT and standard immunochemotherapy can be used to improve treatment outcome of DLBCL. ***Materials and Methods:*** Baseline and follow-up whole-body [^{18}F]FDG PET/CT were performed before and after DAA-based AVT alone in a patient diagnosed with primary extranodal DLBCL and a long history of HCV infection. ***Results:*** A 64-year-old female patient with a long history of untreated chronic HCV infection (genotype 1b; viral load was not measured, and AVT was not been performed since 2002) noted a mass in the left scapular region. Surgical excision with subsequent morphological study was performed. The immunohistochemical staining was negative for CD10, TdT, CD23, and EBV, and positive for CD20/PAX5, CD3/CD5, BCL2, BCL6, and MUM1, confirming the diagnosis of non-GCB DLBCL. 95% of tumor cells were Ki67-positive. To evaluate the extent of the disease, a whole-body [^{18}F]FDG PET/CT was performed. Multiple metabolically active nodules up to 21mm and SUVmax 20.6 were identified in soft tissues. HCV RNA in the blood was also quantified: 5.79 log IU/ml. The patient received a 12-week course of DAA-based AVT with sofosbuvir and daclatasvir. Following AVT, HCV RNA in the blood was undetectable. The patient underwent follow-up PET/CT, which demonstrated the elimination of all previously identified nodules in soft tissues with no pathological tracer uptake, and it was decided not to initiate standard of care immunochemotherapy. A follow-up PET/CT performed three months later showed a sustained complete metabolic and anatomical response. A sustained virological response has also been maintained. The patient has been under follow-up for six months with no signs of recurrence to date. ***Conclusion:*** The presented clinical case demonstrates that DAA-based AVT alone, as a first-line therapy, can facilitate a complete response in patients with HCV-associated DLBCL. Prospective studies are necessary to evaluate the outcomes of HCV-associated DLBCL treated with DAA-based AVT alone.

EP-1305

Peritoneal Gliomatosis vs. Carcinomatosis in Immature Ovarian Teratoma: Diagnostic Challenges of ^{18}F-FDG PET/CT

T. Moreno-Monsalve, *M. I. Castellon-Sanchez, L. Frutos-Esteban, j. L. Navarro-Fernandez, L. Mohamed-Salem, N. Sanchez-Izquierdo, T. E. Rodriguez-Locarno, A. C. Hernandez-Martinez, M. J. Ibanez-Ibanez, J. Contreras-Gutierrez;*
Hospital Universitario Virgen De La Arrixaca, Murcia, SPAIN.

Aim/Introduction: Peritoneal gliomatosis (GP), a rare benign condition characterized by mature glial tissue implants typically associated with ovarian immature teratomas, can mimic malignant peritoneal carcinomatosis on imaging. ***Materials and Methods:*** We present the case of a 27-year-old woman with a history of stage IIIC ovarian immature teratoma (treated with hysterectomy, bilateral salpingo-oophorectomy, and chemotherapy) who developed progressive left hypochondrium/flank pain, postprandial vomiting, and weight loss over two months. CT imaging demonstrated multiple peritoneal implants, including a prominent lesion in the epiploic foramen. The ^{18}F-FDG PET/CT revealed heterogeneous FDG uptake in these lesions (SUVmax 2-16), making it impossible to reliably differentiate between malignant implants and GP. Histopathological confirmation through laparoscopic biopsy ultimately demonstrated mature glial tissue without atypia or increased mitotic activity, confirming GP. ***Results:*** This case underscores several important considerations. First, GP can exhibit variable FDG avidity that overlaps significantly with malignant patterns due to the inherent metabolic activity of glial tissue. Second, while PET/CT cannot definitively distinguish GP from carcinomatosis, it remains clinically valuable both for detecting metabolically active lesions and for guiding biopsies to the most active sites. Third, histopathological confirmation is absolutely essential given the radically different treatment approaches required. The case highlights that elevated FDG uptake does not necessarily indicate malignancy in patients with ovarian teratomas and demonstrates PET/CT's dual role as both a sensitive detection tool and a guide for targeted biopsy ***Conclusion:*** Ultimately, this reinforces the need for a multidisciplinary approach when evaluating peritoneal lesions in ovarian teratoma patients, particularly when confronting diagnostically challenging, morphologically overlapping entities like GP and carcinomatosis. In such scenarios, ^{18}F-FDG PET/CT proves invaluable as both a metabolic imaging modality and a strategic guide for diagnostic intervention.

EP-1306

PSMA PET/CT uptake in metastatic melanoma: a case report

G. Barbosa, *T. Alves, C. Torricelli, L. Macedo, D. Mendanha, H. Sousa, E. Nogueira-Lima, V. Heringer, N. Tobar, J. Sousa, C. Lima, E. Etchebehere;*
Unicamp, Campinas, BRAZIL.

Aim/Introduction: Melanoma is the most aggressive skin cancer, and it has become a significant public health concern. ^{18}F-FDG PET/CT has been widely used for clinical management in patients with melanoma. Recent studies highlight the potential of PSMA PET/CT as an additional diagnostic modality in cases of metastatic melanoma. ***Materials and Methods:*** A 20-year-old male patient was diagnosed with a malignant melanoma (Breslow <4mm / Clark IV) in the left region of the neck. After 1 year he progressed and was submitted to surgical excision of metastatic cervical lymph nodes. The patient was submitted to a restaging FDG PET/CT and within 24 hours a ^{18}F-PSMA-1007 PET/CT. The SUV max was calculated semi automatically for each lesion in both exams and compared. ***Results:*** FDG PET/CT showed increased radiotracer uptake consistent with multiple metastases in cervical, mediastinal, thoracic, and axillary lymph nodes, pulmonary nodules, a left lung mass, both adrenals, liver nodules, peritoneal implants, bones, multiple skin lesions (especially in the chest and right abdomen) and muscle implants. The highest FDG uptake was noted in the left iliac bone (SUV = 34). PSMA PET/CT demonstrated uptake in the same sites of metastases identified on FDG PET/CT, with the exception of liver metastases, only identified in the latter exam. In PSMA PET/CT the highest uptake was in a subcarinal lymph node (SUV =18). Differently, PSMA PET/CT demonstrated a brain metastasis, not identified on FDG PET/CT. ***Conclusion:*** Beyond its established role in the staging of prostate cancer, PSMA PET/CT may be a potential tool to evaluate metastatic melanoma, offering promising avenues for theranostic applications. ***References:*** 1) Gosman L. et al. Int J Mol Sci.; 2023.2) Bobos M. Ital J Dermatol Venerol.; 2021. 3) Aide N. Cancer Imaging; 2022. Research Funding: This study was financed, in part, by the São Paulo Research Foundation (FAPESP), Brazil. Process #2021/10265-8 - Cancer Theranostics Innovation Center (CancerThera), CEPID.

EP-1307

Bilateral Cerebellar Atrophy and Hypometabolism on Brain FDG PET/CT in a Case Using Antiepileptic Drugs for 38 Years Due to Drug-Resistant Epilepsy

B. Bozca[1], *N. Aydinbelge Dizdar*[1], *E. Tatci*[1], *A. Cilliler*[2], *D. Cayir*[1], *A. Cinar*[1], *O. Ozmen*[1];
[1]*Etlik City Hospital, Department of Nuclear Medicine, Ankara, TÜRKIYE,* [2]*Etlik City Hospital, Department of Neurology, Ankara, TÜRKIYE.*

Aim/Introduction: Epilepsy is a chronic neurological condition characterised by recurrent seizures and is one of the most common neurological disorders. Antiepileptic drug (AED) therapy is the first-line treatment option used to control seizures. In patients with epilepsy, cerebellar atrophy may be observed as a finding caused both by anoxic-cellular damage due to seizure activity and as a result of AED use. This report presents the findings of a 40-year-old male patient with drug-resistant epilepsy who has been using AEDs for 38 years. Brain FDG PET/CT was performed to identify the epileptogenic focus, revealing bilateral symmetrical cerebellar hypometabolism and cerebellar atrophy, accompanying a hypometabolism consistent with an epileptogenic focus in the left temporal lobe. ***Materials and Methods:*** Following a febrile convulsion at the age of two, the patient developed generalised tonic-clonic epilepsy and has been on AEDs for 38 years. He presented to the neurology clinic due to experiencing seizures 3-4 times per month. During seizures, the patient described tonic contractions in the right arm and abdominal pain prior to the episodes. MRI showed reduced hippocampal volume on the left and increased signal intensity on T2-weighted images. These findings were considered potentially consistent with mesial temporal sclerosis. Video EEG monitoring revealed focal epileptiform activity originating from the left temporal region. Brain FDG PET/CT was performed to identify the epileptogenic focus in this patient with AED-resistant seizures. PET/CT showed marked hypometabolism in the mesial and lateral aspects of the left temporal lobe, supporting the presence of an epileptogenic focus. Additionally, symmetrical and severe hypometabolism was observed in the bilateral thalami and cerebellum, accompanied by bilateral cerebellar atrophy on CT imaging. ***Conclusion:*** Mesial temporal lobe epilepsy (MTLE) is the most common type of epilepsy and is associated with cerebellar degeneration. FDG PET/CT plays a significant role in the diagnosis of MTLE. Under normal conditions, FDG uptake in the cerebellum is high, and the cerebellum is one of the regions used as a reference in the interpretation of brain FDG PET/CT scans. However, as seen in this case, cerebellar hypometabolism may accompany long-standing epilepsy and should be taken into consideration.

EP-1308

Differential diagnosis of a pancreatic lesion in a pediatric patient: contribution of Nuclear Medicine - A case report

A. Sagastegui Alca, *G. Martinez Gomez, C. Ruiz Corbalán, T. Rodríguez Locarno, M. Castellón Sánchez, A. Hernández Martínez, N. Sánchez Izquierdo, L. Frutos Esteban, L. Mohamed Salem, M. Ibáñez Ibáñez, J. Navarro Fernandez, T. Moreno Monsalve, J. Contreras Gutiérrez;*
Hospital Clínico Universitario Virgen de la Arrixaca, Murcia, SPAIN.

Aim/Introduction: Pancreatic lesions in pediatric patients are uncommon and present a diagnostic challenge in individuals with complex genetic backgrounds such as neurofibromatosis type 1 (NF1). Patients with NF1 have a 2-4 fold increased risk of tumor development, with malignancy rates estimated between 5-15 %. The differential diagnosis includes both benign and malignant entities, such as intrapancreatic accessory spleen (IPAS) and neuroendocrine tumors (NETs). Nuclear medicine techniques offer a non-invasive and specific approach to clarify the etiology of the mass, potentially avoiding invasive procedures such as laparoscopic surgery or laparotomy. ***Materials and Methods:*** A 12-year-old female pediatric patient with a history of NF1 and deletion of the 3q28-29 gene was admitted to the Emergency Department due to abdominal pain. Abdominal ultrasound revealed a hypoechoic lesion adjacent to the spleen. Subsequent MRI evaluation identified a pancreatic tail lesion (3.5 × 2,9 × 2.7 cm) that appeared to receive at least one branch from the splenic artery. The differential diagnosis included malignant conditions such as NET and IPAS. ***Results:*** A PET-CT scan with intravenous injection of 118 Megabecquerels (MBq) of [^{68}Ga]Ga-DOTA-TOC was performed under sedation to evaluate somatostatin receptor expression. To further assess the possibility of ectopic splenic tissue, a scintigraphy with [^{99m}Tc]Tc-heat-denatured red blood cells (HDRBC) with intravenous injection of 22,2 MBq and abdominal SPECT-CT was also conducted. The PET-CT revealed physiological uptake in the spleen and pancreas, with no abnormal tracer uptake in the pancreatic lesion, ruling out a somatostatin receptor-positive NET. On the [^{99m}Tc]Tc-HDRBC scintigraphy with additional SPECT-CT, the pancreatic lesion appeared as a hypodense, cystic-appearing structure without focal tracer uptake, making the diagnosis of IPAS unlikely. Considering the imaging findings alongside the clinical context and underlying conditions of the patient, a conservative approach with follow-up imaging was decided. ***Conclusion:*** This case highlights the complementary role of nuclear medicine techniques in the study of pancreatic lesions in pediatric patients with complex syndromic backgrounds. [^{68}Ga]Ga-DOTA-TOC PET-CT provides valuable information in ruling out neuroendocrine tumors by assessing receptor expression, while [^{99m}Tc]Tc-HDRBC scintigraphy combined with SPECT-CT serves as a reliable method for identifying splenic tissue due to its high sensitivity and specificity. The combined use of both techniques provided valuable diagnostic clarity, helping to avoid invasive procedures in a vulnerable patient population. ***References:*** Hernández Muela S, Navío Anaya M, De la Osa Langreo A, Gargallo P, Menor F, Zúñiga A, et al. Neurofibromatosis tipo 1. Protoc diagn ter pediatr. 2022;1:341-352.

EP-1309

Silent Until Late: the Diagnostic Power of 24-hour ^{99m}Tc-PYP RBC Scintigraphy in Gastrointestinal Angiodysplasia

M. Epure[1], *I. Grierosu*[1,2], *C.-M. Antohie*[1], *A.-M. Statescu*[1], *W. Jalloul*[1,2], *C.-R. Stolniceanu*[1,2], *R.-R. Ion*[1], *S. Dejmasu*[1], *A.-M. Nistor*[1], *C. Stefanescu*[1,2];
[1]*Nuclear Medicine Laboratory, „Sf. Spiridon" County Emergency Hospital, Iasi, ROMANIA,* [2]*Grigore T. Popa University of Medicine and Pharmacy, Iasi, ROMANIA.*

Aim/Introduction: Angiodysplasia is an abnormal dilation of small blood vessels located within the mucosal and submucosal layers of the gastrointestinal (GI) tract. This is one of the most common causes of occult bleeding, particularly in elderly patients. The most frequent location of angiodysplasia is the colon [1]. Diagnosis is often difficult due to the episodic pattern of the bleeds. This case series aimed to evaluate the utility of ^{99m}Tc-pyrophosphate-labeled red blood cell (RBC) scintigraphy in identifying angiodysplasia, with particular attention to findings at delayed images (24-hour). ***Materials and Methods:*** A retrospective analysis was conducted on 24 patients with severe anemic syndrome, referred for identifying GI bleedings in our laboratory. For five of them we noticed the absence of a visibile spot during the first 4 hours. The technique used is the in vivo labeling method of RBC with 740 MBq ^{99m}Tc-PYP. Dynamic during 1 hour and static images at 1h, 2h, 3h, 4h were acquired. If no radiopharmaceutical accumulation is observed on the initial images in the first day of acquisition, additional images were performed at 24 hours on GE Medical Systems, OPTIMA NM/CT 870DR. ***Results:*** In the series of five patients, the prior investigations didn't identify a source of bleeding. Scintigraphic images interpretation focused on identifying sites of active or intermittent bleeding. Earlier acquisitions, up to 4 hours, didn't reveal any bleeding spots. Extended acquisition times at 24 hours improved lesion detection and localization. The static images highlighted angiodysplasic lesions which have been confirmed with SPECT-CT low-dose in the wall of the proximal portion of the ascending colon, ileo-cecal junction, distal jejunum and ileum. Even if the prevalence of angiodysplasia increases with age, mainly occurring in patients over 60 years old [2], one of them is a 29-year-old young adult. ***Conclusion:*** Scintigraphy with labeled RBC proved to be a sensitive and non-invasive method for accurately locating the source of GI hemorrhage. The delayed 24h images have a crucial role in the detection of angiodysplasic lesions, when standard 4 hours protocol is unable to identify the bleeding source. Therefore, in relation with our experience, we suggest extending acquisition time to improve a correct diagnostic. ***References:*** [1]. Ueno S, et al. Clinical features of Japanese patients with colonic angiodysplasia. J Gastroenterol Hepatol. 2008 ;23(8 Pt 2):e363-6; [2].Dodda G, Trotman BW. Gastrointestinal angiodysplasia. J Assoc Acad Minor Phys. 1997;8(1):16-9.

EP-1310

Ectopic Thyroid Tissue in the Hepatic Hilum: A Rare Case of a 40-Year-Old Woman Presenting with Epigastric Pain

B. Yilmaz, *E. Gokdemir, M. Kaya, B. E. Akkas;*
University of Health Sciences Basaksehir Cam and Sakura City Hospital, Department of Nuclear Medicin, Istanbul, TÜRKIYE.

Aim/Introduction: Ectopic thyroid tissue is rare embryological anomaly caused by abnormal migration of the thyroid gland. Localization in the hepatic hilum is extremely uncommon. This report presents a case of a 40-year-old woman who presented with epigastric pain and was found to have ectopic thyroid tissue in the hepatic hilum. ***Materials and Methods:*** The patient initially underwent endoscopy and abdominal MRI at an external center. MRI incidentally revealed a suspicious lesion adjacent to the hepatic hilum. She was referred to our institution, where contrast-enhanced abdominal CT, FDG PET/CT, and endoscopic ultrasound (EUS) were performed. Tumor markers were within normal limits such as carcinoembryonic antigen and carbohydrate antigen 19-9 . Due to suspicion of gastrointestinal stromal tumor (GIST), fine-needle aspiration biopsy (FNAB) was followed by robotic excisional biopsy. Postoperatively, the patient underwent whole-body thyroid scintigraphy and thyroid ultrasound. FNAB of iso-echoic thyroid nodules confirmed benign pathology. Thyroid function tests were within normal range. ***Results:*** MRI revealed a 4×3 cm lesion at the hepatic hilum with showing mild contrast enhancement and signal intensity similar to the liver on T1- and T2-weighted sequences, raising suspicion for gastrointestinal stromal tumor (GIST). Although differential diagnoses included

pathological lymph node or cyst . Contrast-enhanced CT showed a 41×35 mm well-circumscribed iso-hyperdense lesion with millimetric hypoattenuated cystic-like components (HU: 62.61), suspected to be pedunculated hepatic mass.PET/CT was concluded as follows: well-defined nodular lesion at the level of the hepatic hilum with no significant hypermetabolic activity (SUVmax: 3.4) ; a hypodense nodular lesion without pathological metabolic activity in the mid-portion of the right thyroid lobe; and no findings suggestive of malignancy elsewhere in the body. FNAB suggested metastasis from well-differentiated thyroid carcinoma characterized by predominant follicular pattern . Robotic surgical resection was performed. Histopathology revealed nodular colloidal thyroid tissue with follicular pattern, confirming ectopic thyroid. Postoperative Tc-99m sodium pertechnetate scintigraphy showed no additional ectopic foci. The patient remained euthyroid. ***Conclusion:*** Ectopic thyroid tissue in the hepatic hilum is extremely rare. It should be considered in the differential diagnosis of well-circumscribed, non-FDG-avid porta hepatis masses that demonstrate hyperattenuation on non-contrast CT and have negative tumor markers. The differential diagnosis includes hilar cholangiocarcinoma, lymphoma, and other perihilar hepatic lesions. Histopathological confirmation remains crucial. Treatment decisions should be guided by patient age, lesion location, symptoms, malignancy potential, and surgical risk. This case aims to raise awareness of this rare entity, which may mimic malignant tumors of the porta hepatis.

EP-1311

Use of [^{99m}Tc]Tc-heat-denatured red blood cells scintigraphy in the evaluation of renal metastases versus splenic implants in a patient with renal carcinoma

A. Sagastegui Alca, *G. Martínez Gomez, C. Ruiz Corbalán, M. Castellón Sánchez, T. Rodríguez Locarno, N. Sánchez Izquierdo, T. Moreno Monsalve, J. Navarro Fernandez, A. Hernández Martínez, M. Ibáñez Ibáñez, L. Frutos Esteban, L. Mohamed Salem, J. Contreras Gutiérrez;*
Hospital Clínico Universitario Virgen de la Arrixaca, Murcia, SPAIN.

Aim/Introduction: Abdominal splenosis is an uncommon, benign condition resulting from the autotransplantation of splenic tissue after splenic trauma or splenectomy. While typically asymptomatic, it may mimic malignant lesions on imaging, posing a diagnostic challenge, particularly in patients with an oncologic background. [^{99m}Tc]Tc-heat-denatured red blood cells (HDRBC) scintigraphy combined with SPECT-CT offers a non-invasive, sensitive, and specific method to differentiate splenosis from tumoral tissue, potentially avoiding unnecessary invasive procedures and supporting clinicians in the diagnostic and therapeutic decision-making process. ***Materials and Methods:*** A 58-year-old male with a history of papillary renal cell carcinoma underwent left radical nephrectomy, followed by robotic splenectomy due to hypodense splenic lesions of uncertain etiology. On follow-up abdominal CT, new nodular changes were observed in the former splenic bed, raising suspicion of either local tumor recurrence or splenosis. Given the patient's oncologic history and persistent fatigue, further diagnostic evaluation was required. A [^{99m}Tc]Tc-HDRBC scintigraphy with abdominal SPECT-CT was performed to help determine the etiology of the lesions. ***Results:*** A scintigraphy with intravenous injection of 445 Megabecquerels (MBq) of [^{99m}Tc]Tc-HDRBC and abdominal SPECT-CT was conducted. Planar imaging demonstrated focal tracer uptake in the left upper abdominal quadrant. Hybrid SPECT-CT further localized this activity to nodular lesions anterior to the left quadratus lumborum muscle, with anatomical correlation to previously documented findings on CT. These images were consistent with intraperitoneal splenic tissue implants (splenosis), thereby excluding the possibility of malignant recurrence. Given the absence of clinical progression and the benign imaging profile, a conservative management strategy with follow-up imaging was adopted. ***Conclusion:*** This case highlights the diagnostic value of [^{99m}Tc]Tc-HDRBC scintigraphy in differentiating splenosis from malignant recurrence in a patient with complex surgical and oncologic history. SPECT-CT imaging allows for precise localization and characterization of ectopic splenic tissue due to its high sensitivity and specificity. This enables accurate diagnosis and prevents unnecessary invasive procedures or oncologic treatments. In asymptomatic patients, conservative management with follow-up imaging can be safely considered. By resolving diagnostic ambiguity, nuclear medicine imaging plays a pivotal role in optimizing patient management and reducing the risk of overtreatment in challenging clinical cases.

EP-1312

Chylothorax After Pericardiectomy: A Case Study Utilizing Lymphoscintigraphy for Diagnosis and Follow-up

G. Martínez Gómez, *C. Ruiz Corbalán, A. Sagastegui Alca, T. Rodríguez Locarno, N. Sánchez Izquierdo, T. Moreno Monsalve, M. Castellon Sánchez, A. Hernández Martínez, L. Mohamed Salem, L. Frutos Esteban, J. Navarro Fernández, M. Ibáñez Ibáñez, J. Contreras Gutiérrez;*
Hospital Universitario Virgen de la Arrixaca, Murcia, SPAIN.

Aim/Introduction: Chylothorax is an abnormal accumulation of chyle in the pleural space, resulting from injury or disruption of the thoracic duct. In adults, the most common cause of chylothorax is thoracic duct trauma secondary to surgical procedures. Lymphoscintigraphy with ^{99m}Tc-labelled human serum albumin nanocolloid evaluates the lymphatic system, enabling the detection of obstructions, leaks, or drainage abnormalities. ***Materials and Methods:*** A 44-year-old male was admitted with constrictive pericarditis, mediastinal adenopathy, and interstitial lung involvement. Treatment with corticosteroids, colchicine, and diuretics was initiated. A month later, the patient developed a right posterior tibial deep vein thrombosis in the context of immobilization, treated with fondaparinux. He was admitted for thoracentesis, which yielded pleural fluid compatible with chylothorax. He underwent pericardiectomy via median sternotomy, during which a large amount of chylous effusion was aspirated from the right pleural space. Intranodal lymphangiography was performed via inguinal lymph node puncture with Lipiodol injection, showing no detectable leaks. He was readmitted due to right-sided pleural effusion, again consistent with chylothorax and left arm swelling. ***Results:*** Physical examination revealed diffuse edema, induration, collateral circulation, violaceous discoloration, and absent radial pulse. He had no fever, dyspnea, cough, or constitutional symptoms. Doppler ultrasound of the upper limbs and pulmonary artery computed tomography angiography demonstrated thrombosis of the left jugulosubclavian vein and increased pleural effusion. A lower limb lymphoscintigraphy was requested to investigate a possible lymphatic leak. Early and delayed dynamic image acquisition, along with delayed Single Photon Emission Computed Tomography/Computed Tomography (SPECT/CT) imaging, revealed findings suggestive of lymphatic leakage, with tracer accumulation in the left pleural effusion and around the heart. Partial obstruction of the right lower limb lymphatic drainage was also observed.Fibrinolysis with continuous urokinase perfusion was administered for 48 hours, followed by discontinuation and re-initiation of fondaparinux. Control venography showed recanalization of the subclavian vein.A follow-up lymphoscintigraphy showed no evidence of lymphatic leakage into the pleural space or pericardium. Based on the imaging findings, the patient was discharged with nutritional recommendations and scheduled follow-up. ***Conclusion:*** Chylothorax may arise as a complication following pericardiectomy and can be exacerbated by left jugulosubclavian vein thrombosis. Lower limb lymphoscintigraphy, complemented by SPECT/CT, played a crucial role in diagnosing lymphatic leakage and during follow-up, confirming its resolution after treatment. This imaging

modality is essential as it provides functional information that complements conventional structural techniques and informs therapeutic decision-making.

EP-1313

The importance of radiosynoviorthesis in the treatment of pigmented villonodular synovitis in pediatric patients

J. Weissensteiner[1], *D. Genšor*[2];
[1]*Department of Nuclear Medicine, Hospital Poprad, Poprad, SLOVAKIA,* [2]*Clinic of Children and Adolescents, Jessenius Faculty of Medicine in Martin, University Hospital Martin, Martin, SLOVAKIA.*

Aim/Introduction: Pigmented villonodular synovitis (PVNS) is a locally aggressive disease of the synovium characterized by joint effusion, synovial hypertrophy, hemosiderin deposition, and bone erosion. It most commonly affects the knee, but may also involve the hip, ankle, shoulder, or elbow joints. ***Materials and Methods:*** A 5-year-old boy diagnosed with juvenile idiopathic arthritis was initially treated with antimetabolites and systemic corticosteroids. Due to polyarthritis and persistent arthritis of the left knee joint, biological therapy was initiated. Sonographic examination of the knee joint revealed synovial hypertrophy and hemarthrosis. Magnetic resonance imaging demonstrated synovial proliferation along with small hypointense hemosiderin deposits. The presence of synovitis in the left knee joint was confirmed by three-phase skeletal scintigraphy. ***Results:*** Radiosynoviorthesis of the left knee joint was performed three months after the skeletal scintigraphy examination. During knee joint aspiration, 35 milliliters of sanguineous synovial fluid were obtained. Subsequently, 50 megabecquerels of colloidal Rhenium-186 sulfide (Re-186) were administered intra-articularly. The injection was followed by needle flushing using a combination of a local anesthetic and corticosteroid. Post-procedurally, the joint was immobilized with an elastic bandage, and the patient was advised to avoid weight-bearing on the affected limb for three days. ***Conclusion:*** Radiosynoviorthesis represents a potentially effective localized treatment for pigmented villonodular synovitis (PVNS) of the knee joint in pediatric patients. When combinated with other therapeutic approaches, it may offer a viable alternative to surgical intervention.

EP-1314

Incidental Occipital Spur Uptake on Tc-99m PYP Scintigraphy: An Uncommon Finding in Cardiac Amyloidosis

B. Arca, *E. G. Isik, E. Inal, Y. Sanli;*
Istanbul University, Istanbul Faculty of Medicine, Nuclear Medicine Department, Istanbul, TÜRKIYE.

Aim/Introduction: An occipital spur is an abnormal bony protrusion that generally develops at the external occipital protuberance (EOP). The EOP has three distinct morphological variants: type I (smooth surface), type II (crest-like shape), and type III (spine-like appearance). Occipital spurs are generally associated with spondylosis or osteoarthritis and may also develop because of repeated trauma. Although incidental and benign, it is important to recognize the entity to differentiate it from metastatic lesions. ***Materials and Methods:*** A 31-year-old male, diagnosed with common variable immune deficiency (CVID) and Thrombospondin Type 1 Domain Containing 1 (THSD1) gene mutation which leads to primary lymphedema, was referred to Tc-99m pyrophosphate (PYP) scintigraphy upon suspicious amyloidosis findings in cardiac-MRI. ***Results:*** Tc-99m PYP scintigraphy revealed no significant myocardial uptake on either the early or late images and corresponding to a grade 0. However, an incidental finding revealed focal increased uptake in the occipital bone on the whole-body posterior images and SPECT-CT images was showed a focal spine-like hyperostosis which was seen in the occipital protuberance extending in a craniocaudal direction which was confirmed to be an occipital spur (Type III spine form). ***Conclusion:*** Tc-99m PYP scintigraphy is a reliable imaging tool primarily used for the noninvasive diagnosis of ATTR cardiac amyloidosis; however incidental uptake in other regions of the body has occasionally been reported. Although only a limited number of cases have been reported in the literature with Tc99m MDP, to our knowledge this is the first reported case demonstrating the visualization of an occipital spur using Tc-99m PYP scintigraphy. ***References:*** 1) Marshall RC, Abela C, Eccles S. Painful exostosis of the external occipital protuberance. J Plast Reconstr Aesthet Surg. 2015;68: e174-e176 2) Muzaffar R, Alassi A, Mashal M, Osman MM. Incidence of 99Tc-MDP uptake in the external occipital protuberance in the pediatric population: the new normal? Am J Nucl Med MolImaging. 2023;13(5):225-229. 3) Valai Kasim SA, Mehboob Mohammed MS, Danish S, et al. Occipital spur: an incidental finding on a diagnostic cone-beam computed tomography - a case report. Anatomy. 2022; 16:189-192 4) Utsunomiya D, Shiraishi S, Imuta M, et al. Added value of SPECT/CT fusion in assessing suspected bone metastasis: comparison with scintigraphy alone and nonfused scintigraphy and CT. Radiology. 2006; 238:264-271. 5) Fathala AL. Incidental Extracardiac Findings of Technetium-99m Pyrophosphate Scintigraphy: A Pictorial Review. Cureus. 2024;16(6): e62316.

EP-1315

When Conventional Imaging Does not Reveal the Etiology: ^{18}F-FDG PET-CT Diagnosis of Spondylodiscitis in Recurrent Fever

G. Martínez Gómez, *C. Ruiz Corbalán, A. Sagastegui Alca, T. Moreno Monsalve, T. Rodríguez Locarno, N. Sánchez Izquierdo, M. Castellon Sánchez, A. Hernández Martínez, M. Ibáñez Ibáñez, L. Mohamed Salem, J. Navarro Fernández, L. Frutos Esteban, J. Contreras Gutiérrez;*
Hospital Universitario Virgen de la Arrixaca, Murcia, SPAIN.

Aim/Introduction: Spondylodiscitis is the inflammation and/or infection of the vertebral bodies and adjacent intervertebral discs. Due to its nonspecific symptoms and need for prolonged treatment, a multidisciplinary approach is crucial for accurate diagnosis. ^{18}F-fluorodeoxyglucose positron emission tomography/computed tomography (^{18}F-FDG PET-CT) has demonstrated superior sensitivity and specificity compared to conventional imaging in diagnosing this condition. ***Materials and Methods:*** A 94-year-old patient was hospitalized multiple times for recurrent fever of unknown origin. No identifiable infectious focus was found despite extensive testing, including blood and urine cultures, chest radiography, echocardiography and abdominal ultrasound. Laboratory analyses consistently showed elevated inflammatory markers. He received empirical intravenous antibiotic treatment, with transient clinical improvement. ***Results:*** During the fourth hospitalization, an ^{18}F-FDG PET-CT was performed to localize a potential occult source of infection. The ^{18}F-FDG PET-CT revealed marked erosive changes and irregularity of the endplates of vertebrae D12 and L1, with mild but significant metabolic hyperactivity (increased ^{18}F-FDG uptake) at the same level, strongly suggestive of spondylodiscitis. These findings were not previously detected with conventional imaging. A follow-up lumbar spine MRI confirmed the diagnosis, showing characteristic features of vertebral osteomyelitis and adjacent disc involvement. A vertebral biopsy was performed, yielding reactive trabecular bone with areas of necrosis and reduced hematopoietic tissue. Microbiological cultures for bacteria and fungi were negative, likely due to prior antibiotic exposure. Despite the absence of a microbiological isolate, the clinical, metabolic, and radiological findings were consistent with spondylodiscitis. Antimicrobial therapy was adjusted, and the patient showed clinical stability without new febrile episodes.The ^{18}F-FDG PET-CT in this case, allowed not only localization of the infectious focus

but also differentiation from other possible etiologies such as degenerative changes or malignancy. The ability of ^{18}F-FDG PET-CT to depict metabolic activity enables the detection of early-stage infectious processes and facilitates diagnosis in cases with inconclusive or non-specific findings on conventional imaging modalities. Furthermore, ^{18}F-FDG PET-CT has demonstrated utility in delineating disease extent, monitoring therapeutic response and providing prognostic information through quantification of metabolic activity, particularly via standardized uptake values (SUVmax). ***Conclusion:*** Spondylodiscitis is a rare, but serious cause of fever of unknown origin, particularly in elderly patients. Early diagnosis requires a multidisciplinary approach, with ^{18}F-FDG PET-CT emerging as a key imaging modality. Its ability to detect metabolically active lesions makes it superior to conventional imaging in complex cases. Alongside MRI, ^{18}F-FDG PET-CT should be considered in persistent or unexplained fevers, especially when standard tests are inconclusive.

EP-1316

Beyond Lytic Lesions: A Rare Case of Sclerotic Multiple Myeloma Without POEMS Syndrome

P. Spiridon[1,2], *T. Cristica*[2], *C. Mazilu*[3,2];
[1]*Carol Davila University of Medicine and Pharmacy, Bucharest, ROMANIA,* [2]*Affidea, Bucharest, ROMANIA,* [3]*Carol Davila Central Emergency Military University Hospital, Bucharest, ROMANIA.*

Aim/Introduction: Multiple myeloma is a hematologic malignancy characterized by the uncontrolled proliferation of plasma cells and is often associated with lytic bone. Osteosclerotic lesions are an uncommon manifestation of multiple myeloma (presented in less than 3% of all cases), typically associated with POEMS syndrome [1]. The aim of this paper is to present a rare case of multiple myeloma with sclerotic lesions, in the absence of POEMS syndrome. ***Materials and Methods:*** We report the case of a 70-year-old male with a medical history of hypertension, type 2 diabetes and benign prostatic hyperplasia, who presented with thoraco-lumbar pain, spinal cord compression and grade D spinal cord injury according to the Frankel scale. ***Results:*** Preoperative imaging (CT and IRM) revealed a lesion involving the T3 vertebral body, extending into the spinal canal and infiltrating adjacent soft tissues. Surgical intervention included posterior decompression and vertebral stabilization. Histopathological and immunohistochemical analysis confirmed a malignant plasma cell proliferation, with predominant lambda light chain expression**.**A whole-body F18-FDG PET-CT was performed for staging. It revealed increased FDG uptake at the T3 left posterior lamina, with additional metabolically active osteosclerotic lesions at T6 and L3. Several metabolically inactive sclerotic lesions were observed diffusely throughout the skeleton.No clinical or paraclinical signs of POEMS syndrome (polyneuropathy, endocrinopathy, organomegaly, skin changes, etc.) were present. ***Conclusion:*** This case illustrates a rare presentation of multiple myeloma with osteosclerotic lesions and no clinical signs of POEMS syndrome. This case underscores the need for awareness of atypical imaging patterns in multiple myeloma and highlights the diagnostic value of PET-CT in staging and therapeutic planning. ***References:*** 1. Divakar M, Shyam A, Hadgaonkar S, Sancheti P, Aiyer SN. Osteosclerotic Multiple Myeloma without POEMS Syndrome - A Rare Case Report. J Orthop Case Rep. 2022 Jan;12(1):18-21. doi: 10.13107/jocr.2022.v12.i01.2598. PMID: 35611283; PMCID: PMC9091408.

EP-1317

Lost in Migration: A Rare Case of Ectopic Parathyroid Adenoma

R.- . Ion[1], *I. Grierosu*[1,2], *A. Ungureanu*[3], *E. Palade*[4,5], *I. Titu*[4,5], *M. Mlesnite*[5], *M. Epure*[1], *S. Dejmasu*[1], *A. Nistor*[1], *C. Stefanescu*[1,2];
[1]*Nuclear Medicine Laboratory, „Sf. Spiridon" County Emergency Hospital, Iasi, ROMANIA,* [2]*"Grigore T. Popa" University of Medicine and Pharmacy, Iasi, ROMANIA,* [3]*Emergency Clinical Hospital, Piatra Neamt, ROMANIA,* [4]*Department of Surgery, "Iuliu Hatieganu" University of Medicine and Pharmacy, Cluj-Napoca, Romania,* [5]*Thoracic Surgery Clinic, "Leon Daniello" Clinical Hospital of Pneumology, Cluj-Napoca, ROMANIA.*

Aim/Introduction: Parathyroid adenoma (PA) accounts for approximately 80-85% of primary hyperparathyroidism cases. Among these, 6-16% are located ectopically, and their identification is crucial for addressing the underlying cause of hyperparathyroidism (1). Due to their anatomical position, ultrasound visualization can be challenging or even impossible, and in some cases, even CT imaging fails to provide a clear diagnosis. Consequently, nuclear imaging has become an essential tool in the diagnostic workup of parathyroid pathology. ***Materials and Methods:*** From 1,061 parathyroid scintigraphies performed in our laboratory, over the past 15 years, 67 cases are a PA with ectopic localisation. We selected a case with a rare ectopic localisation of the PA in the paracardiac region. The other ectopic localisation founded are in: superior cervical region (5), inferior thyroidal region (34), anterior-superior mediastinum (17) and thymus region (10). The imaging protocol involved intravenous administration of 740 MBq of ^{99m}Tc-sestamibi, followed by static image acquisition at 20 and 120 minutes post-injection. Additionally, a hybrid low-dose SPECT/CT scan was performed at 120 minutes. Image acquisition was conducted using a General Electric Medical System gamma camera, model OPTIMA NM/CT 870DR. ***Results:*** The patient, 68-year-old male, presented to the emergency department with lumbar pain and was diagnosed with reno-ureteral lithiasis and underwent surgical intervention. A subsequent recurrence required reoperation. In the middle time, biochemical analyses revealed markedly elevated PTH levels (624.10 pg/mL), prompting further investigation of the parathyroid glands. Ultrasound and CT examination did not reveal any pathological parathyroid tissue, therefore the patient was referred to our laboratory for scintigraphic exploration. The scintigraphic findings were positive for an ectopic PA located in the anterior-inferior mediastinum, paracardiac region. The patient subsequently underwent videothoracoscopic parathyroidectomy, and histopathological examination confirmed the diagnosis of PA. ***Conclusion:*** PA is a benign tumour responsible for hyperparathyroidism, which disrupts calcium and phosphorus homeostasis. Surgical excision remains the only definitive treatment. Due to their small size and anatomical location, the parathyroid glands pose significant challenges for imaging. Moreover, ectopic migration during early embryological development further complicates their detection, as was the situation in our case. The identification of the ectopic PA represented a turning point in the patient's management, leading to an improved quality of life, cessation of renal stone formation, and prevention of further deterioration in renal function. ***References:*** 1. Roy M, Mazeh H, Chen H, Sippel RS. Incidence and localization of ectopic parathyroid adenomas in previously unexplored patients. World J Surg. 2013; 37(1):102-6.

EP-1318

Necrotizing external otitis - Can ^{68}Ga-citrate PET/CT have a role?

J. Rebelo[1], *A. Moreira*[1], *R. Silva*[1], *G. Costa*[1,2], *S. Barata*[1], *S. Paiva*[1], *L. Diogo*[1], *C. Isabel*[1];
[1]*Unidade Local de Saúde de Coimbra - CHUC, Coimbra, PORTUGAL,* [2]*Faculdade de Medicina da Universidade de Coimbra, Coimbra, PORTUGAL.*

Aim/Introduction: Necrotizing external otitis (NEO) is a potentially life-threatening infection that often leads to skull base osteomyelitis. Early diagnosis and evaluation of disease extent are critical, as delayed treatment can result in significant morbidity. While anatomical imaging modalities such as CT and MRI are valuable, they may fall short in differentiating active infection from post-

treatment changes. On the other hand, traditional scintigraphic techniques, such as 67Ga-citrate scintigraphy, present a challenge in this pathology, primarily due to their low spatial resolution. ^{68}Ga-citrate PET/CT, by leveraging the infection-targeting properties of gallium alongside all the advantages of PET/CT, may serve as a valuable tool in the diagnosis and management of these patients. Here we present the case of a patient with NEO, highlighting the potential role of ^{68}Ga-citrate PET/CT in the workup of these patients. ***Materials and Methods:*** A 72-year-old male was admitted to the hospital in November 2023 with clinical suspicion of NEO. ***Results:*** During hospitalization, a CT scan was performed, revealing findings suggestive of NEO involving the left temporomandibular region and the parapharyngeal spaces. Subsequently, a bone scan was done, with increased radiotracer uptake in the left temporomandibular joint and asymmetric uptake in the clivus, increased on the left side. Following clinical improvement, the patient was discharged and scheduled for follow-up. In February 2024, the patient was re-admitted due to symptom recurrence. A new CT scan showed apparent progression of the infeccious process, and MRI findings were concordant. A repeat bone scan showed maintained uptake in the left temporomandibular joint. A ^{68}Ga-citrate PET/CT scan was then performed, revealing increased radiotracer uptake predominantly in the right prevertebral and carotid spaces. The patient continued treatment and showed gradual clinical improvement. Approximately two months later, after the symptoms had nearly resolved, a follow-up ^{68}Ga-citrate PET/CT was performed, demonstrating a marked reduction in radiotracer uptake. No signs of recurrence have been observed to date. ***Conclusion:*** The observed correlation between PET/CT findings and clinical evolution in this patient supports the potential utility of ^{68}Ga-citrate PET/CT, especially in monitoring treatment response. As experience grows, it may emerge as an adjunct in the management of NEO, potentially reducing unnecessary prolonged antimicrobial therapy. Further studies are warranted to validate its use in clinical settings. Nonetheless, this case underscores the promising role of ^{68}Ga-citrate PET/CT in addressing a longstanding imaging gap in complex infectious diseases of the skull base.

EP-1320

The role of ^{18}F-FDG PET in Familial Fatal Insomnia

J. Rebelo[1], *M. Cunha*[1], *R. Silva*[1], *G. Costa*[1,2], *S. Barata*[1], *S. Paiva*[1], *D. Lameirão*[1], *I. Casimiro*[1];
[1]*Unidade Local de Saúde de Coimbra - CHUC, Coimbra, PORTUGAL,* [2]*Faculdade de Medicina da Universidade de Coimbra, Coimbra, PORTUGAL.*

Aim/Introduction: Fatal Familial Insomnia (FFI) is na inherited prion disease characterized by progressive and intractable insomnia, followed by autonomic dysfunction, motor abnormalities, and ultimately death. Clinically, FFI presents with a constellation of neuropsychiatric symptoms that initially resemble primary sleep disorders or psychiatric conditions, often leading to misdiagnosis. Neuroimaging frequently reveal characteristic abnormalities, particularly in the thalamus, which plays a central role in the regulation of sleep-wake cycles. ***Materials and Methods:*** This case report presents a patient with a clinical suspition of FFI, highlighting the crucial role that functional brain imaging on the early diagnosis of this condition. ***Results:*** A 51-year-old male with a known family history of FFI on his paternal side presented in August 2022 with initial complaints of insomnia, which began in the context of psychosocial stress related to a recent divorce. The insomnia initially showed some improvement. A brain MRI performed in July 2023 was unremarkable, showing no significant structural abnormalities. The patient remained under outpatient follow-up with persistent, fluctuating insomnia. Laboratory investigations, including HIV and syphilis serologies, thyroid function tests, serum vitamin B12, and folate levels, were within normal limits. Due to previous surgical interventions complicating the procedure, a lumbar puncture was deferred. Given the strong family history and ongoing sleep disturbances, an ^{18}F-FDG PET scan was performed in March 2024. The imaging revealed subtle hypometabolism in the precuneus, parietal, and frontal lobes, with more pronounced hypometabolism in the thalamus, particularly on the right side. At the subsequent follow-up in July 2024, the patient exhibited marked clinical deterioration, characterized by worsening insomnia with complex sleep disturbances, including REM behavior disorder-like symptoms (dream enactment), dysautonomia, especially temperature regulation dysfunction, neuropsychiatric symptoms, including delirium, and progressive bulbar signs, most notably dysarthria and dysphagia. Following this visit, the patient was lost to regular follow-up due to relocation abroad and is currently reported to be enrolled in a clinical trial for FFI. ***Conclusion:*** This case highlights the diagnostic challenge of FFI in its early stages, particularly when initial symptoms are mild and neuroimaging is unremarkable, and emphasizes the importance of maintaining a high index of suspicion in individuals with a positive family history and subtle sleep disturbances, and it supports the utility of ^{18}F-FDG-PET as an early diagnostic tool in these patients.

EP-1321

FDG PET/CT in the Localization of Cardiac Device Infections: Discriminating Between LVAD and ICD Infection

E. Isleyen Çolak*, S. Bilgic, E. Alper;*
Bursa Uludag University, Bursa, TÜRKIYE.

Aim/Introduction: The increasing use of cardiac devices has been accompanied by a rise in associated infections. Implantable devices such as pacemakers, defibrillators, and left ventricular assist devices (LVADs) are increasingly common. This growth has led to more frequent evaluations for device-related infections and endocarditis [1]. LVADs, often used as a bridge to transplant, are particularly vulnerable, with infection rates up to 13.6% within the first three months [2]. ***Materials and Methods:*** A 45-year-old male with ischemic cardiomyopathy had an ejection fraction of 17%, moderate-to-severe mitral regurgitation, severe tricuspid regurgitation, and elevated pulmonary pressure. He underwent HeartMate 3 LVAD (Abbott ©) implantation. ***Results:*** Postoperatively, purulent discharge at the driveline site led to pus culture collection and empirical antibiotics. FDG PET/CT was performed to evaluate for infection involving either the LVAD or ICD. FDG PET/CT showed no pathological uptake around the ICD device or leads. In contrast, the extracardiac portion of the LVAD along the lateral chest wall showed a ~35 mm area of homogeneous FDG uptake, likely related to local inflammation to surgical adhesives. More importantly, heterogeneous uptake was noted at the distal vascular graft anastomosis site (SUVmax: 5.2), and a linear tract of intense uptake extended from this area along the driveline to the abdominal skin, consistent with active infection (SUVmax: 7.3). Although pus cultures returned negative, a positive purified protein derivative (PPD) test measuring 16 mm prompted the initiation of empiric antitubercular therapy. ***Conclusion:*** Device removal is a key component of infection management but is complex in patients with life-sustaining hardware. In this case, both the LVAD and ICD were essential. PET/CT revealed infection limited to the driveline, sparing the pump and ICD. This allowed a focused surgical approach, avoiding unnecessary extraction and reducing risk [3]. ***References:*** 1.Aguilera J, Hutt E, Jaber WA. Imaging of Cardiac Device-Related Infection. Front Cardiovasc Med. 2021;8:729786. doi:10.3389/fcvm.2021.729786.2.Tam MC, Patel VN, Weinberg RL, Hulten EA, Aaronson KD, Pagani FD, et al. Diagnostic Accuracy of FDG PET/CT in Suspected LVAD Infections: A Case Series, Systematic Review, and Meta-Analysis. JACC Cardiovasc Imaging. 2020;13:1191-202. doi:10.1016/j.

jcmg.2019.04.024.3.Kim J, Feller ED, Chen W, Liang Y, Dilsizian V. FDG PET/CT for Early Detection and Localization of Left Ventricular Assist Device Infection: Impact on Patient Management and Outcome. JACC Cardiovasc Imaging. 2019;12:722-9. doi:10.1016/j.jcmg.2018.01.024.

EP-1322

Detection Using ^{18}F-FDG PET-CT of Rare Metastases in a Patient with Endometrioid Endometrial Carcinoma

S. Perez Quiros, *C. Paniagua Correa, L. Castillejos Rodriguez, M. Tagliatori Nogueira, A. Ortega Valle, K. Guichay Duran, M. García Alonso, C. Galindo Fernández;*
Hospital Universitario de Getafe, Getafe-Madrid, SPAIN.

Aim/Introduction: We present the finding by ^{18}F-FDG PET-CT of multiple hypermetabolic osteolytic lesions with signs of extraosseus extension, in a patient with poorly differentiated endometrioid adenocarcinoma ***Materials and Methods:*** 77-year-old woman with poorly differentiated endometrioid adenocarcinoma, stage IIIC, with the following immunohistochemical profile: preserved expression of DNA repair proteins, positive estrogen and progesterone receptors, and altered p53. She underwent initial surgical treatment, followed by adjuvant chemotherapy and radiotherapy. Three months after diagnosis, the patient began to experience pain in the right lower limb, which progressively became disabling for walking, and without apparent traumatic cause. This was initially suggestive of postoperative polyneuropathy, with no evidence of malignancy in other diagnostic techniques and no increase in serum tumor markers. ***Results:*** A whole-body PET-CT, performed for disease surveillance a year and a half later, demonstrated multiples hipermetabolic osteolytic lesions with signs of extraosseus extension, in the right lower limb and ipsilateral ischiopubic ramus. This finding was particularly striking in the middle and lower thirds of the fibula and in the tarsal, metatarsal bones, and proximal phalanges, raising suspicion of malignancy. Based on these findings, a biopsy was performed on the right ankle, which confirmed metastasis from an endometrial adenocarcinoma. ***Conclusion:*** Endometrioid adenocarcinoma is one of the most common types of endometrial cancer and is the fourth leading cause of cancer in women in developed countries, with most cases diagnosed at early stages of the disease. Metastasis usually occurs via direct spread, lymphatic dissemination, or hematogenous routes, with the most common distant metastatic sites being the lungs and liver. Bone involvement is generally considered rare, with clinical incidence rates of <1%. Recently, endometrial carcinoma has been divided into four subtypes based on its immunohistochemical profile: (i) ultramutated DNA polymerase epsilon (POLE), (ii) abnormal tumor protein 53 (TP53), (iii) microsatellite instability, and (iv) no specific molecular profile (NSMP).The vast majority of the few cases reported in the literature of aggressive metastatic bone involvement have been found in patients with microsatellite instability. In our case, the patient only had an alteration of the tumor protein p53 which, although associated with more aggressive tumors and with a greater probability of distant metastatic spread, has only been described in a few cases in the literature. This highlights the rarity of this disease and its clinical presentation, with a significant delay in the diagnosis of metastasis in these patients.

EP-1323

When Endocarditis Isn't What It Seems: Cardiac Hemangiosarcoma with Multiple Metastases- A case report

A. Militaru[1], *C. M. Popescu*[1], *A. Marin*[1], *R. M. Mititelu*[1,2];
[1]*Clinic of Nuclear Medicine- Central Universitary Emergency Military Hospital, Bucharest, Bucuresti, ROMANIA,* [2]*Nuclear Medicine Department- University of Medicine and Pharmacy "Carol Davila" Bucharest, Bucuresti, ROMANIA.*

Aim/Introduction: Cardiac angiosarcoma is a rare malignant tumor with a predilection for the right atrium that usually occurs in men in the third-fifth decade of life. It is characterized by early metastasis most commonly to the lungs. Clinical presentation is non-specific with symptoms mimicking infectious or inflammatory disease.[1] Angiosarcomas are hemorrhagic tumors with poorly defined margins that aggressively invade adjacent structures. Histologically, they show anastomosing vascular channels, pleiomorphic endothelial cells, high mitotic activity and necrosis. Immunohistochemistry is usually positive for CD31, factor VIII and von Willebrand factor.[1],[2] ***Materials and Methods:*** A 26-year-old man was admitted with a clinical infection and positive blood cultures for Staphylococcus lugdunensis, suggestive of infective endocarditis. One month later, he developed cardiac tamponade requiring pericardial drainage; Imaging showed a cardiac mass; parasternal biopsy revealed a diagnosis of angiosarcoma NOS. The patient underwent four cycles of neoadjuvant chemotherapy and a follow-up CT revealed a large, invasive cardiac tumor in various areas, with bilateral pulmonary nodules as metastases. A thoracotomy with partial tumor excision revealed extensive invasion into the right atrium, superior vena cava, coronary sinus, tricuspid valve, and great vessels, making complete resection impossible. [18F]FDG-PET-CT scan revealed a large tumor involving right atrium, atrial septum and roots of great vessels, with intense FDG avidity (SULmax = 21.35). It also showed FDG avid mediastinal lymph nodes, pulmonary and hepatic lesions, and a hypermetabolic lesion adherent to a loop of small bowel, consistent with secondary disease. ***Results:*** Primary cardiac sarcomas are rare, highly aggressive malignancies with a poor prognosis. Treatment usually consists of complete surgical resection if possible; however, resection is often compromised by tumor invasion. Adjuvant radiotherapy and chemotherapy can potentially improve outcomes, although limited evidence supports this. Radiotherapy is associated with risks due to the sensitivity of the heart. For inoperable tumors, palliative treatment may be considered. Despite multidisciplinary strategies, median survival is poor, so further research and individualized therapeutic approaches are warranted. ***Conclusion:*** This case demonstrates that age is not a contraindication to early and aggressive disease. In light of recent literature and therapeutic challenges, such as limited evidence for adjuvant therapies, this case highlights the urgent need for earlier diagnosis methods, molecular characterization and multidisciplinary strategies to optimize outcomes in young patients with these aggressive malignancies. ***References:*** [1] A. Orlandi,et al, "Cardiac sarcomas: An update," 2010, Lippincott Williams and Wilkins. doi: 10.1097/JTO.0b013e3181e59a91. [2] J. Butany,et al, "Cardiac tumours: Diagnosis and management," Apr. 2005. doi: 10.1016/S1470-2045(05)70093-0

EP-1324

^{18}F-PSMA PET/CT and ^{18}F-FDG PET/CT in the evaluation of desmoid tumors: A case report

E. Nogueira Lima, *M. B. Silva, T. Freire, C. Torricelli, G. Barbosa, T. Alves, V. Heringer, N. Tobar, A. Santos, M. Lima, J. Barreto, M. Etchebehere, E. Etchebehere;*
University of Campinas, Campinas, BRAZIL.

Aim/Introduction: Desmoid tumor is a rare soft tissue neoplasm that promotes chronic pain, reducing the quality of life (1,2). ^{18}F-FDG PET/CT has been used to grade sarcomas, predict their prognosis, and assess therapy response (3). Since PSMA has been shown to be avid in non-prostatic tissues, including desmoid tumors (4,5), we aim to evaluate the potential of 18F-PSMA-1007 PET/CT (PSMA PET/CT) in diagnosing desmoid tumors compared to FDG PET/CT, to expand the clinical management of these patients and possible therapeutic applications. ***Materials and Methods:*** Four patients (mean age = 56 years; two females) underwent PSMA PET/CT and FDG PET/CT on subsequent days. In both studies, the SUV max was calculated semi-automatically for each lesion. ***Results:*** All patients

presented uptake of both radiotracers at the primary tumor site. In patient 1, the primary tumor was located in the left hip (SUV_{FDG} = 12 vs SUV_{PSMA} = 4); in patient 2, located in the right axilla (SUV_{FDG}= 4 vs SUV_{PSMA}=6). In both cases, no metastases were detected. In patient 3, the primary tumor was located in the left arm (SUV_{FDG}=3 vs SUV_{PSMA}=4), and PSMA PET/CT also identified bone metastases in the upper limbs (SUV_{PSMA}=5). In patient 4, the primary tumor originated in the right thigh (SUV_{FDG}=5 vs SUV_{PSMA}=7), and again, only PSMA PET/CT detected bone metastasis in the second left costal arch and locoregional lymph node metastases. ***Conclusion:*** Our preliminary findings indicate the potential for PSMA PET/CT to diagnose and stage desmoid tumors since PSMA uptake was generally similar to FDG uptake in the primary tumor. However, more metastases, especially bone lesions, were detected on PSMA PET/CT. Therefore, PSMA PET/CT may be promising for staging patients with desmoid tumors. Future studies can expand upon these results to investigate PSMA as a promising Theranostics radiotracer for desmoid tumors.This study was supported by São Paulo State Foundation for Teaching and Research Support (Cancer Theranostics Innovation Center, CancerThera, CEPID FAPESP #2021/10265-8). ***References:*** 1. Zhou MY, et al. Cancer Res Treat. 2022;31:100562. 2. Bektas M, et al. JNCCN. 2023;40(9):3697-722. 3. von Mehren M, et al. Soft Tissue Sarcoma, Version 2.2018, NCCN Clinical Practice Guidelines in Oncology. 2018;16(5):536-63. 4. Reis TLd, et al. Hematology, Transfusion and Cell Therapy, 2024;46:S19-S20. 5. Kleiburg F, vet al. EJNM. 2025.

EP-1325

Rare and Challenging:^{18}F-FDG Uptake in Femoral Vein Leiomyosarcoma

I. Zahfir, *M. Aboussabr, M. Zekri, Z. Laadissi, N. Mahersi, L. Taoussi, A. Taalabi, D. Alami, S. Nabih Oueriagli, A. Doudouh;*
Mohammed V Military teaching Hospital, Rabat, MOROCCO.

Aim/Introduction: Primary vascular leiomyosarcoma (LMS) is a rare malignant tumor arising from smooth muscle cells within the vessel wall and carries a poor prognosis. While most cases involve the inferior vena cava (IVC), LMS can also occur in other veins, including the femoral, iliac, popliteal, saphenous, and renal veins. ***Materials and Methods:*** We present a case of a 51-year-old woman with left thigh swelling and a painless mass. Ultrasonography revealed a heterogeneous mass with non-visualization of the femoral vein. Subsequent contrast-enhanced MRI demonstrated a heterogeneously enhancing soft tissue mass encasing and infiltrating the superficial femoral vein lumen. Surgical exploration confirmed the mass's continuity with the venous wall and intraluminal extension. ***Results:*** Histopathology confirmed a grade III leiomyosarcoma. Staging ^{18}F-FDG PET/CT revealed intense hypermetabolism in the proximal left femoral vein, correlating with the primary tumor, along with non-FDG-avid pulmonary nodules in both lungs. ***Conclusion:*** Intravascular neoplasms remain diagnostically challenging, necessitating a multimodal imaging approach. Contrast-enhanced CT or MRI is essential for detecting venous LMS, distinguishing it from thrombus, assessing intra- versus extraluminal involvement, and defining disease extent for surgical planning. FDG-PET/CT further aids in differentiating malignant from benign thrombus and detecting metastases, playing a critical role in staging and therapeutic decision-making.

EP-1326

The Added Value of [^{18}F] FDG PET/CT in Assessing Malignant Degeneration in Patients with Hereditary Multiple Exostoses : A Case Report

I.-A. Ioana[1], *A. Barabas*[1], *R. Lita*[1], *M. Mutuleanu*[1,2], *M. Gherghe*[1,2];
[1]*Institute of Oncology "Prof. Dr. Alexandru Trestioreanu", Bucharest, ROMANIA,* [2]*University of Medicine and Pharmacy „Carol Davila", Bucharest, ROMANIA.*

Aim/Introduction: Hereditary multiple exostoses (HME) is a rare autosomal-dominant skeletal dysplasia characterized by the formation of multiple osteochondromas arising from the metaphyseal regions of long bones, with a prevalence of 1:50,000 in Western countries. The disorder is primarily caused by biallelic inactivation of the tumour suppressor genes EXT1 or EXT2, leading to disrupted heparan sulphate biosynthesis and aberrant endochondral ossification. Malignant progression, occurring in approximately 2-5% of affected individuals, often presents insidiously and poses a diagnostic and therapeutic challenge. Early identification of malignant degeneration is critical, particularly in symptomatic patients. ***Materials and Methods:*** We present the case of a 53-year-old male patient, known with HME since childhood, presenting with painful large right inguinal mass, who underwent a pelvic CT scan on December 24, 2024. The contrast enhanced study revealed a space-occupying lesion originating from the right superior pubic ramus invading the abdominal wall and pectineus muscle and in contact with the inguinal vessels, measuring 127/98/170 mm, indicating a possible malignant degeneration. Additionally, the CT evaluation identified one lytic lesion located in the T5 vertebra and osteochondromatous lesions located near the right costovertebral joint C VI and right scapulae. Because of the increased risk of presenting other malignant degenerated lesions a 18F-Fluorodeoxyglucose [^{18}F] FDG PET/CT scan was recommended for disease staging. ***Results:*** The PET/CT scan identified multiple lesions with low metabolic activity located bilaterally in the scapulae and in the spinous process of the T5 vertebra. Additionally, a large tumoral mass was observed in the right inguino-femoral region, with axial dimensions of 13/9.4 cm, possibly originating from the right pubic ramus, suggestive of malignant degeneration, confirmed through biopsy as grade 1 chondrosarcoma. The lesion with the highest uptake was located on the right scapulae with an SUVlbm value of up to 2.16 g/ml. Other osteochondromas presenting no metabolic activity were localized in the humerus bilateral, ribs, pelvic bones and femur bilateral and were characterized as benign lesions. A minimal active metabolic inguino-femoral adenopathy was also observed, with an SUVlbm value of up to 1.77 g/ml. ***Conclusion:*** This case emphasizes the role of [^{18}F] FDG PET/CT in evaluating the extent and distribution, as well as the metabolic activity of the extraosseous lesions, providing crucial information in determining the appropriate therapeutic approach and assessing potential metastatic spread.

EP-1327

Molecular Imaging with 99mTc-EDDA-HYNIC-TOC in Tumour-Induced Osteomalacia: Diagnostic Impact in a Challenging Case

M. Nistor[1], *D.-M. Ionescu*[1], *M. Abas*[1], *A. Badea-Selea*[1], *M. Gherghe*[1,2];
[1]*Institute of Oncology "Prof. Dr. Alexandru Trestioreanu", Bucharest, ROMANIA,* [2]*University of Medicine and Pharmacy "Carol Davila", Bucharest, ROMANIA.*

Aim/Introduction: Tumour-induced osteomalacia (TIO) is a rare paraneoplastic syndrome resulting from phosphaturic mesenchymal tumours (PMTs) that secrete fibroblast growth factor 23 (FGF-23), leading to hypophosphataemia and bone mineralization defects. PMTs can occur in bones or soft tissues, making whole-body molecular imaging essential for detecting lesions with increased uptake of radiolabelled somatostatin analogues. ***Materials and Methods:*** We present the case of a 49-year-old male diagnosed with phosphataemic osteomalacia in 2018, exhibiting elevated FGF-23 levels (167 kRU/l) and hypophosphataemia (1.73 mg/dl). His symptoms included anterior chest pain and low back pain radiating to the lower limbs. Despite scintigraphy with radiolabelled somatostatin analogues undertaken in 2020 showing no pathological uptake, an MRI performed in October 2023 identified a 1.5 cm lesion in the left femoral trochanter. On 1st October 2024, he underwent scintigraphy with ^{99}Tc-EDDA-HYNIC-TOC. A planar whole-body scan at 2 hours and a whole body single photon emission

computer tomography-computed tomography (SPECT-CT) 4 hours post-injection, were performed. We implemented the following SPECT-CT protocol: a 128 by 128 matrix size, step and shoot mode, 60 steps, with 30 seconds per step, and a dual-energy window for scatter correction. For improved diagnostic accuracy and attenuation correction, the SPECT scan was completed by a low-dose CT scan. ***Results:*** The somatostatin receptor scintigraphy revealed focal uptake (SUVlbm = 8.27 g/ml) localized in the left femoral trochanter, corresponding to an osteolytic lesion with osteosclerotic borders, a nodular structure, and expansive characteristics, without cortical disruption visible on the CT images. This finding corresponds to the result of the MRI examination performed in October 2023 and suggests the presence of a mesenchymal tumour associated with osteomalacia. A biopsy of the lesion was performed and the histology revealed monomorphic spindle cell proliferations with minimal nuclear atypia, proliferation infiltrating the medullary spaces and involving the bone trabeculae. The immunohistochemistry results showed reduced Ki-67, SATB2 and diffuse ERG positive expression on most tumour cells, with weak focal nonspecific positivity of CD99, while SMA and CD34 were negative. These findings confirmed the diagnosis of a phosphaturic mesenchymal tumour. ***Conclusion:*** This case highlights the diagnostic value of ^{99}Tc-EDDA-HYNIC-TOC scintigraphy in identifying PMTs, which are rare tumours with approximately 450 cases documented in the literature. Molecular imaging provides crucial information for accurate diagnosis and therapeutic approaches.

EP-1328

Synchronous Malignancies in Bloom Syndrome: The Value of Molecular Imaging

M. Abas[1], *M. Paunescu*[1], *M. Mutuleanu*[1,2], *M. Gherghe*[1,2];
[1]*Bucharest Oncology Institute "Prof. Dr. Alexandru Trestioreanu", Bucharest, ROMANIA,* [2]*University of Medicine and Pharmacy "Carol Davila", Bucharest, ROMANIA.*

Aim/Introduction: Bloom Syndrome (BS) is an exceptionally rare autosomal recessive genetic disorder with fewer than 300 cases reported worldwide, caused by mutations in both copies of the BLM gene and is typically diagnosed in childhood through cytogenetic analysis. This deficiency in DNA repair mechanisms leads to an increased susceptibility to various types of cancers. Other clinical features include: short stature, phototoxicity, café-au-lait spots and immune-related recurrent infections. Given the high predisposition to multiple, early-onset, different types of cancer, molecular imaging could play a crucial role in management of these patients. ***Materials and Methods:*** We are presenting the case of a 43-years old patient diagnosed with Bloom Syndrome in October 2024 via genetic testing. After an insidious onset of nausea, vomiting and watery diarrhoea, the patient underwent a colonoscopy which revealed familial adenomatous polyposis. A year later, a repeat colonoscopy due to similar symptoms confirmed a colonic adenocarcinoma (G3, Ki67 90%) on biopsy. One month later, an echoendoscopy revealed a pancreatic body adenocarcinoma (G3, Ki67 40%), which tested positive for synaptophysin and SSTR2 receptors. Additionally, conventional imaging were indicative of a potential breast tumour and multiple secondary pulmonary nodular lesions. Subsequently, she received chemotherapeutic treatment. ***Results:*** The patient was referred to nuclear medicine following the positive neuroendocrine markers expressed in the pancreatic tissue sample, which raised the suspicion for a neuroendocrine component within the pancreatic lesion. However, a [^{99m}Tc]-EDDA-HYNIC-TOC (Tektrotyd) SPECT/CT scan demonstrated no significant radiotracer uptake in the pancreatic lesion. A week later, a [^{18}F]FDG PET/CT with intravenous contrast-enhanced CT showed an area of increased metabolic activity in the pancreatic body (SUVlbm 2.06) and the recto-sigmoidian colon (SUVlbm 3.04), locations consistent with the lesions vizualised on prior investigations, suggesting the diagnosis of poorly differentiated tumours. Also the bilateral pulmonary nodules presented no radiotracer uptake, but with morphological appearance consistent with secondary lesions ***Conclusion:*** Although Bloom syndrome is usually identified in early childhood due to its specific clinical features, our patient was diagnosed at adult age following the detection of synchronous malignancies of the breast and the gastrointestinal tract (spaced one month apart). Molecular imaging proved to be valuable in the diagnosis, evaluation and management of the patients presenting this rare disease.

EP-1329

An [^{18}F]FDG PET-CT Conundrum. Adrenal Oncocytoma: A Case Report

M. Matei[1], *S. Solomon*[1], *C. Mazilu*[1], *R. Mititelu*[1,2];
[1]*Clinic of Nuclear Medicine, Central Universitary Emergency Military Hospital, Bucharest, ROMANIA,* [2]*Department of Nuclear Medicine, University of Medicine and Pharmacy Carol Davila, Bucharest, ROMANIA.*

Aim/Introduction: Adrenal oncocytomas are a rare entity, more commonly diagnosed in female patients. Other sites where oncocytoma may arise include the kidney, thyroid and salivary glands. The aim of this report is to underline the importance of [^{18}F]FDG PET-CT in evaluating the metabolic activity of an adrenal incidentaloma and, as well, its utility as a follow-up method. ***Materials and Methods:*** We present a case of a 65-year-old male patient, a former smoker, known with a history of a pulmonary neuroendocrine carcinoma with large cells (LCNEC). The pulmonary tumor had a diameter of 26/20/20 mm and was located in the superior segment of the right inferior lobe. An inferior right lobectomy associated with a mediastinal lymphadenectomy were performed in 2022, which were followed by histopathological studies and immunohistochemical staining showing a poorly differentiated (G3), CD56+, C-Kit+, Syn-, CGA- with a variable expression of PD-L1 in 69% of the cells, with lymph node extension (interlobar). A Contrast Enhanced Computed Tomography (CECT) scan was performed in order to assess the disease extension, on which an enhanced, well-defined solid nodule measuring 18/20 mm was discovered in the medial limb of the left adrenal gland, thus raising the suspicion of an adrenal metastasis. ***Results:*** The patient underwent a PET/CT scan with [^{18}F]FDG two months after surgery, which revealed moderate uptake of the radiotracer in the right inferior paratracheal and subcarinal nodes and high metabolic activity of the left adrenal nodule with a SULmax of 7.53. Due to the aggressive nature of the pulmonary tumor, which presented high anaplastic features and the radiological and molecular imaging studies were highly suggestive of a distant metastasis, the patient underwent a left adrenalectomy. The histopathological report and immunohistochemical staining results were compatible with the diagnosis of adrenal oncocytoma (CROMO-, S100-, Ki67 2%). Two additional [^{18}F]FDG PET-CT scans were performed as follow-up, both examinations showed no metabolic activity suggestive of regional or distant recurrence of the disease. ***Conclusion:*** While benign adrenal lesions usually don't display high avidity for [^{18}F]FDG, oncocytomas may demonstrate a variable uptake of the radiotracer. Thus, adrenal oncocytomas, while rare, should be considered in the differential diagnosis of adrenal tumors. In such cases, the PET-CT scan is a valuable tool in the follow-up protocol.

EP-1330

Reactive Imaging Changes Following CAR-T Cell Therapy in Multiple Myeloma: A Diagnostic Challenge

T. Stoeva, *M. Dyankova, Z. Dancheva, S. Chausheva, T. Yordanova, B. Chaushev, A. Klisarova;*
UMHAT "Sveta Marina", Varna, BULGARIA.

Aim/Introduction: Multiple myeloma (MM) is a clonal plasma cell malignancy with a highly variable clinical and imaging presentation. Despite significant treatment advances, MM remains

incurable, with most patients eventually experiencing relapse. In recent years, chimeric antigen receptor T-cell (CAR-T) therapy has emerged as a promising option for relapsed/refractory MM. However, the increasing use of immune-based therapies has introduced new diagnostic challenges, particularly in interpreting post-treatment imaging. While FDG PET/CT remains a cornerstone for disease assessment, immune-mediated reactive changes can mimic active disease and complicate response evaluation. ***Materials and Methods:*** We present the case of a 54-year-old male diagnosed with MM in 2017, with evidence of lambda light chain paraproteinemia and 70% plasma cell infiltration on bone marrow biopsy. Baseline [F-18] FDG PET/CT revealed diffuse bone marrow involvement. The patient initially achieved complete remission following chemotherapy and autologous stem cell transplantation. However, disease relapse occurred two years later, and five subsequent treatment lines failed to achieve sustained response. Given the aggressive disease course, CAR-T cell therapy was administered. The patient developed cytokine release syndrome (CRS) post-treatment, which was effectively managed with supportive care. Two months after CAR-T infusion, an [F-18] FDG PET/CT was performed to evaluate therapeutic response. ***Results:*** Post-treatment PET/CT revealed diffusely increased, symmetric FDG uptake in the long bones, indicative of activated hematopoietic marrow rather than malignant infiltration. Multiple osteoblastic and mixed lesions (osteolytic with sclerotic borders) were observed in both the axial and appendicular skeleton. These lesions exhibited metabolic activity not exceeding liver background levels. Although these findings raised concerns for residual disease, normal laboratory results and the patient's clinical stability supported a reactive post-treatment process. A multidisciplinary review confirmed the interpretation of reactive marrow regeneration, with no evidence of active myeloma. ***Conclusion:*** This case underlines a potential imaging pitfall in MM patients undergoing CAR-T therapy. Reactive bone marrow activation and osteoblastic remodeling may mimic active disease on FDG PET/CT, posing a risk of misdiagnosis. Recognizing these patterns is essential to avoid unnecessary interventions. Accurate assessment of treatment response post-CAR-T therapy requires integrating imaging findings with clinical and laboratory data.

EP-1331

Can You Guess The Source? Metastatic Bone Lesion as a Rare First Presentation of Hepatocellular Carcinoma- a Case Report

S. Chausheva[1,2], *M. Dyankova*[3], *T. Stoeva*[3], *Z. Dancheva*[3], *A. Klisarova*[3], *B. Chaushev*[3], *T. Yordanova*[3];
[1]*University Hospital St Marina Varna, Varna, BULGARIA,* [2]*Medical University Varna, Varna, BULGARIA,* [3]*UMBAL St. Marina Hospital-Varna, University Hospital St Marina Varna, Varna, BULGARIA.*

Aim/Introduction: Hepatocellular carcinoma (HCC) is the most common primary liver malignancy that usually presents in patients with already established liver disease, most common etiological factors are Hepatitis B virus (HBV), Hepatitis C virus (HCV), alcoholic liver disease, and non-alcoholic liver steatohepatitis. Most commonly extrahepatic metastatic involvement includes the lungs, regional lymph nodes and adrenal glands, while osseous spread remains uncommon. Even more uncommon is the initial presentation of HCC as a solitary bone lesion, which can easily mimic primary bone tumors or metastases from other primary malignancies with common bone involvement as types of the prostatic, breast, or lung cancer. ***Materials and Methods:*** We present a case of a 72-year-old male presented at the hospital with chest pain localized in the area of the sternum with no history of trauma. Radiograph of the thorax showed an expansile osteolytic bone lesion in the sternum. In view of the radiographic appearance of the bone lesion, investigations for a provisional diagnosis of bone metastasis and in a search for primary site a CT of the neck and thorax was performed. The images reveal a large, expansile osteolytic lesion involving the sternum, with cortical destruction and infiltration into the retrosternal soft tissues. No definitive primary neoplasm was identified on initial imaging. Whole-body 18F-fluorodeoxyglucose PET/CT was conducted to evaluate for additional metastatic sites and to localize a primary tumor. Biopsy of the bone lesion was performed for histological examination. The biopsy cores comprised a tumor with morphology consistent with that of a metastatic hepatocellular carcinoma. ***Results:*** Whole-body 18F-fluorodeoxyglucose PET/CT study was performed to localize a primary tumor and additional metastatic sites. An expansive osteolytic lesion in the manubrium sternum was revealed with extensive soft tissue component infiltrating the retrosternal space/anterior mediastinum. A second metabolically active osteolytic lesion in the transversal process of Th7 on the left- with metastatic appearance. ^{18}F-FDG PET/CT revealed the primary tumor as a hypodense lesion of irregular shape with metabolic activity slightly exceeding that of the remaining liver parenchyma in the region of Sg VII/VIII. ***Conclusion:*** This case underlines the diagnostic complexity of isolated bone metastases as the first manifestation of HCC. The FDG PET/CT demonstrated a high sensitivity in detection of both primary tumor location and other metastatic bone lesions regarding HCC.

EP-1332

Time Is Tissue: Early Nuclear Imaging and Prognostic Markers in Cardiac Amyloidosis. A Case Report

B. Constantinescu[1], *C. Mazilu*[1], *S. Stanciu*[2,3];
[1]*Clinic of Nuclear Medicine, Central Universitary Emergency Military Hospital, Bucharest, ROMANIA,* [2]*Clinic of Cardiology, Central Universitary Emergency Military Hospital, Bucharest, ROMANIA,* [3]*University of Medicine and Pharmacy Carol Davila, Bucharest, ROMANIA.*

Aim/Introduction: Due to spectacular advances in diagnostic methods and new therapies over the last decade, cardiac amyloidosis (CA) is no longer considered a rare and incurable disease. Nevertheless, CA remains an underdiagnosed cause of death in patients with heart failure. The aim of this paper is to raise awareness of prevalent prognostic factors associated with CA, which, if diagnosed early, may provide further insight into the overall prognosis of disease. ***Materials and Methods:*** We report the case of an 88-year-old male patient with a history of atrial fibrillation (AF), aortic disease and chronic coronary syndrome. The patient had hypertrophic cardiomyopathy with left ventricular hypertrophy, mild ventricular dysfunction, right ventricular and biatrial dilatation. A 'whole-body' scan followed by SPECT/CT was conducted after intravenous injection of 99m-Tc-hydroxydiphosphonate (99m-Tc-HDP). ***Results:*** 'Whole-body' scan revealed extra-osseous uptake in the cardiac region with Perugini score 3, consistent with transtiretin amyloidosis (ATTR). SPECT/CT showed diffuse biventricular uptake and mild uptake in the right atrium. Atrial amyloid deposits often lead to cardiovascular complications — valvular heart disease and cardiac rhythm abnormalities. In our patient, there was a strong suspicion of CA due to history of aortic stenosis and paroxysmal AF. Emerging research[1] shows that AF is predictor of progressive CA leading to worsening prognosis; it is often associated with ATTR and advanced age. AF leads to progressive loss of function and carries an increased risk of endocardial and systemic thrombosis. It is of great importance to facilitate early diagnosis, to improve disease prognosis and overall life expectancy. A recent national study[2] identified further opportunities for improvement in nuclear medicine physicians' awareness of CA imaging and space for interdisciplinary collaboration, highlighting the urgent need for standardized protocols and cardiology-focused guidelines to improve early diagnosis and patient outcomes. ***Conclusion:*** CA remains a challenging disease to diagnose and treat. Better recognition of clinical manifestations is essential for proper disease management and treatment. Scintigraphy with radiolabeled bisphosphonates is a valuable non-invasive imaging technique

for diagnosis of CA, but also for identification of atrial or right ventricular wall uptake, markers of poor prognosis. ***References:*** 1. Donnellan, E., Wazni, O. M., Hanna, M., & Desai, M. Y. (2022). Atrial Fibrillation, Thromboembolic Risk, and Anticoagulation in Cardiac Amyloidosis. Journal of Cardiac Failure, 28(12), 1787-1796. https://doi.org/10.1016/j.cardfail.2022.08.0082. Stan, C., Mititelu, R., Adam, R.D., & Jurcuț, R. (2022). Awareness of Nuclear Medicine Physicians in Romania Regarding the Diagnostic of Cardiac Amyloidosis—A Survey-Based Study. Diagnostics, 12(2), 556. https://doi.org/10.3390/diagnostics12020556

EP-1333

The clinical role of 68GaPSMA/68GaDOTA PET/CT imaging in patient with prostate adenocarcinoma with neuroendocrine differentiation

K. Verbanova*, S. Sergieva, V. Marinov;*
Acibadem City Clinic Tokuda, Sofia, BULGARIA.

Aim/Introduction: Neuroendocrine differentiation (NED) in prostate carcinoma is a significant field of ongoing research as prostate adenocarcinoma with neuroendocrine differentiation (PC-NED) represents as more aggressive and resistant to conventional androgen-deprivation therapy (ADT) subtype of prostate carcinoma (PC). The involvement of neuroendocrine compounds in prostatic neoplasia can play a crucial role in the diagnostic process and consideration of further treatment strategies to improve the monitoring and life expectancy of patients diagnosed with this heterogenous pathology. ***Materials and Methods:*** PET/CT scans with 68GaPSMA and 68GaDOTA were performed. Therapy response was assessed by two experienced nuclear medicine physicians independently from each other. ***Results:*** We report the rare case of a 72 year old man, initially diagnosed in 11/2023 with PC-NED. The patient presented with PSA of 169 ng/ml, Gleason score 10 (5+5), Grade group 5. The first PET/CT-PSMA evaluation showed metastatic involvement of lymph nodes and bones. The patient was treated with palliative radiotherapy, LH-RH agonist drugs, Denosumab and underwent 6 chemotherapy courses with Etoposide/Carboplatin. A second Ga68-PSMA PET/CT scan was performed in 12/2024 to evaluate the treatment response as the PSA significantly dropped to 1,37 ng/ml. The imaging study revealed a partial response to treatment with persistent high activity in primary tumor, bone lesions and lymph nodes. In addition, high chromogranin levels were detected. Considering the neuroendocrine differentiation of the tumor the patient underwent scanning with PET/CT-68Ga-DOTA in order to evaluate the possible neuroendocrine metastatic involvement. Results of the later performed 68Ga-DOTA PET/CT showed newly detected active lesion located in the left femur head that was not previously detected via 68Ga-PSMA. ***Conclusion:*** Combining different nuclear imaging methods based on the histhological type of the carcinoma can show complementary results that could be interpreted together in order to properly determine the therapeutic approach in patients with mixed adeno/neuroendocrine tumors.

EP-1334

Unmasking the Silent Progression: The Role of Serial [^{18}F] FDG PET/CT in the Surveillance of Recurrent Klatskin Tumor

A. Marin*, A. M. Budau, A. S. Militaru, C. V. Mazilu;*
Clinic of Nuclear Medicine, Central University Emergency Military Hospital, Bucharest, ROMANIA.

Aim/Introduction: Klatskin tumors are aggressive malignant tumors that occur at the bifurcation of the hepatic duct and represent the majority of bile duct carcinomas. Due to their insidious onset and deep anatomic location, patients often present at advanced stages.[18F]FDG-PET/CT has been shown to be effective in detecting metastases and nodal involvement not always visible on conventional imaging (1,2). ***Materials and Methods:*** A 51-year-old female patient presented with intermittent abdominal pain, jaundice, diarrhea, and weight loss. Imaging revealed biliary lithiasis, ductal dilatation and lymphadenopathy. Intraoperatively, a Bismuth-Corlette IIIB Klatskin tumor was found. Patient underwent en bloc resection of the extrahepatic bile duct, regulated left hepatectomy with caudate lobe resection, and Roux-en-Y hepaticojejunal anastomosis. Histology confirmed well-differentiated biliary adenocarcinoma with lymphovascular invasion and one positive lymph node(pT2 pN1). She received adjuvant chemotherapy. ***Results:*** [18F]FDG PET-CT revealed FDG avid pseudonodular lesion near biliary stent, along with nodal and pulmonary metastases. One year later, follow-up PET-CT revealed increased activity in previous lesion, along with new FDG avid perihepatic mass (differential: abscess vs. necrotic tumor), secondary lymph node and pulmonary lesions. Overall imaging appearance was consistent with progressive disease.[18F]FDG PET-CT provides added value in identifying occult nodal and distant metastases in cholangiocarcinoma, influencing therapy in 20% of cases(3). Although false-positive results can occur, particularly in inflammatory lesions, elevated SUVmax remains a prognostic marker for poor outcome(2). Similar to hepatocellular carcinoma, metabolic changes often precede anatomical ones, reinforcing PET/CT's role in early recurrence detection and treatment planning (4). In our case, PET/CT accurately captured progression when conventional imaging remained inconclusive.. ***Conclusion:*** This case supports the use of serial [18F]FDG-PET-CT for postoperative surveillance of hilum cholangiocarcinoma. It provided critical information beyond conventional imaging and aided management decisions, emphasising its value for routine follow-up protocols. ***References:*** 1.Reinhardt MJ, Strunk H, Gerhardt T, et al. Detection of Klatskin's Tumor in Extrahepatic Bile Duct Strictures Using Delayed ^{18}F-FDG PET/CT. J Nucl Med. 2005;46(7):1158-63.2. Fritscher-Ravens A, Bohuslavizki KH, Broering DC, Jenicke L, Schäfer H, Buchert R, et al. FDG PET in the diagnosis of hilar cholangiocarcinoma. Nucl Med Commun. 2001;22(12):1277-85.3. Lee Y, Yoo IR, Boo SH, et al. The Role of F-18 FDG PET/CT in Intrahepatic Cholangiocarcinoma. Nucl Med Mol Imaging. 2017;51(1):69-78.4. Mititelu R, Mitoi A, Mazilu C, et al. Advancements in hepatocellular carcinoma management: the role of ^{18}F-FDG PET-CT in diagnosing portal vein tumor thrombosis. Nucl Med Commun. 2024;45(8):651-7.

EP-1335

Benign Cause or Malignancy Progression? Rethinking PET/CT Findings in a Burkitt Lymphoma Case

A. Constantin*[1], A. I. Taciuc[1], M. Gherghe[1,2];*
[1]Institute of Oncology "Prof. Dr. Alexandru Trestioreanu", Bucharest, ROMANIA, [2]University of Medicine and Pharmacy "Carol Davila", Bucharest, ROMANIA.

Aim/Introduction: ^{18}F-FDG PET/CT is the cornerstone of staging procedures in management of aggressive non-Hodgkin's lymphoma. It plays an important role in staging, restaging, prognostication, planning appropriate treatment strategies, monitoring therapy, and detecting recurrence. However, FDG is a non-specific tracer, and its uptake may also reflect infectious, inflammatory, or post-therapeutic changes - frequently complicating interpretation in immunocompromised patients. ***Materials and Methods:*** A 54-year-old male diagnosed with stage IVA Burkitt-type non-Hodgkin lymphoma underwent three cycles of CVAD chemotherapy (cyclophosphamide, doxorubicin, vincristine, dexamethasone). After two treatment cycles, PET-CT showed bilateral hypermetabolic pulmonary lesions, associated with low-grade fever and fatigue, suggestive of possible extranodal involvement. ***Results:*** After the third chemotherapy cycle, a follow-up PET-CT showed decreased radiotracer uptake in the pulmonary nodules, with only two inactive lesions located in the left lung. However, new FDG-avid

lesions were noted: multiple hypodense hepatic nodules (up to 1.1 cm, SUVlbm up to 6.69) affecting all liver segments, mixed predominantly osteolytic lesions in the T8-T11 vertebral bodies (SUVlbm up to 11.59), and sclerotic lesions in the sacrum and bilateral iliac wings (SUVlbm up to 3.73), these findings raising suspicion for lymphoma progression. To identify the nature of the lesions, both bone marrow and laparoscopic liver biopsies were performed. Histopathological and immunohistochemical analyses revealed reactive inflammatory infiltrates, with no evidence of lymphomatous involvement. Although no specific infectious agent was identified, the imaging pattern, clinical symptoms, and biopsies results, the patient was started on empirical broad-spectrum antibiotic therapy, with a favorable evolution. A follow-up PET-CT demonstrated significant decreased metabolic activity of the bone and hepatic lesions under antibiotic therapy. There was complete resolution of FDG uptake in the thoracic spine (T8-T11) and substantial regression of the hepatic lesions, with only a single residual subcapsular FDG-avid lesion remaining in segment VIII (SUVlbm 4.37 g/ml). The overall imaging evolution, together with the histopathological findings, and the favorable evolution under antibiotics strongly supported the diagnosis of a infectious process, most likely initiated by a pneumonic episode, as suggested by the early pulmonary FDG-avid lesions. ***Conclusion:*** This case illustrates the challenge of distinguishing between residual malignant disease and benign causes in FDG PET-CT imaging, particularly in immunocompromised patients. High glycolytic activity in inflammatory or infectious foci can produce SUV values overlapping with aggressive lymphoma. Multisite involvement further complicates interpretation. This case reinforces the importance of histopathologic correlation and multidisciplinary assessment to prevent characterization of infection related lesions as disease progression.

EP-1336

Subcutaneous Splenosis Mimicking Malignancy: A Very Rare Complication of Laparoscopic Splenectomy for Hereditary Spherocytosis Identified on ^{99m}Tc-Colloid SPECT/CT

P. Gadzicki, *A. Aulich, M. Kwapisz, Z. Adamczewski;*
Medical University of Lodz, Nuclear Medicine Departament, Lodz, POLAND.

Aim/Introduction: Hereditary spherocytosis is an inherited haemolytic anaemia characterized by the presence of abnormal red blood cells - spherocytes - which are damaged in the spleen, leading to haemolysis. Laparoscopic splenectomy is one of the surgical procedures used to treat this condition; although rare, complications may occur. One such complication is splenosis - the autotransplantation of splenic tissue deposits in various compartments of the body. We present a case of subcutaneous splenosis, a very rare location, which mimicked malignancy on MRI eight years after surgery. SPECT/CT with ^{99m}Tc-colloid was crucial in confirming the benign nature of the lesion - splenic tissue implantation at the surgical incision site scar. ***Materials and Methods:*** A 20-years old women was referred for spleen and liver scintigraphy with ^{99m}Tc- colloid because of focal lesions located subcutaneous. In the past, patient as 12-years-old girl diagnosed with hereditary spherocytosis with typical complications such as cholelithiasis, haemolytic episodes, was treated successfully by laparoscopic splenectomy. After that hematologic parameters and bilirubin concentration improved. CT scan performed seven years after surgery reveled splenosis in various locations at abdomen and pelvis. Eight years post-splenectomy in a pelvic MRI scan subcutaneous focal lesions, soft tissue abdominal wall masses and soft tissue masses in left iliac fossa were detected (T1: hypointense,T2: hyperintense, T1 C+ (Gd): enhancement, and significant restriction in diffusion-weighted images). Clinical interpretation was inconclusive, and subcutaneous lesions were considered as malignancy. Latter performed ultrasound exam reveals that subcutaneous focal lesions and soft tissue abdominal wall masses were located in the site of incision due to laparoscopic splenectomy. ***Results:*** SPECT/CT scan after administration of ^{99m}Tc-colloid showed increased uptake in all focal lesions previously identified as splenosis on CT. All lesions detected on MRI (T1: hypointense, T2: hyperintense, T1 C+ (Gd): enhancing, with significant diffusion restriction) were consistent with these findings. ***Conclusion:*** ^{99m}Tc-colloid uptake was crucial in the non-invasive diagnosis of subcutaneous splenosis - a benign entity and helped distinguish it from more sinister mimicking pathology. ***References:*** 1)Perrotta S, Gallagher PG, Mohandas N. Hereditary spherocytosis. Lancet. 2008 Oct 18;372(9647):1411-26. doi: 10.1016/S0140-6736(08)61588-3. PMID: 18940465. 2)Vecchio R, Cacciola E, Cacciola RR, Intagliata E. Surgical management of hereditary spherocytosis Current strategies. Ann Ital Chir. 2018;89:473-478. PMID: 30665218. 3)Kumar RJ, Borzi PA. Splenosis in a port site after laparoscopic splenectomy. Surg Endosc. 2001 Apr;15(4):413-4. doi: 10.1007/s004640042004. Epub 2001 Mar 13. PMID: 11395829.

EP-1337

Role of ^{18}F-FDG PET/CT in the Evaluation of a Patient with Pulmonary Artery Sarcoma: Case Report

K. Guichay Duran, *M. De la Rubia Marcos, C. Galindo Fernández, D. Rodriguez Oviedo, J. Sanchez Calderón, A. Herrero Muñoz, M. Castillejos Rodriguez, A. Ortega Valle, C. Paniagua Correa, S. Peréz Quirós, M. Álvarez Moreno, M. García Alonso, M. Tagliatori Nogueira;*
Department of Nuclear Medicine, Getafe University Hospital, Madrid, SPAIN.

Aim/Introduction: Primary pulmonary artery sarcoma (PAS) is a rare and aggressive tumor arising from mesenchymal tissue of the cardiovascular system; the clinical and radiological presentation often mimic pulmonary thromboembolism (PTE), so early and accurate diagnosis is essential for subsequent treatment. We present the findings from an 18FFDG PET/CT performed on a patient in whom PAS vs PTE was suspected. ***Materials and Methods:*** A 52-year-old woman, non-smoker, with a past medical history of hypertension, dyslipidemia, hypothyroidism, and chronic gastritis, who presented with dyspnea, right-sided chest pain, and unintentional weight loss (8 kg) in the last month. Chest CT had revealed a peripheral filling defect in the right main pulmonary artery containing intralesional/mural calcified material, suggestive of pulmonary artery sarcoma or chronic PTE. A whole-body PET/CT was performed 60 minutes after intravenous administration of 218 MBq of 18F-FDG. PET, CT, and fusion images were analyzed in axial, sagittal, and coronal planes and correlated with symptoms, laboratory tests, and prior CT findings. ***Results:*** PET/CT demonstrated an intraluminal occupation of the right main pulmonary artery with linear intralesional/mural calcifications with focal increased FDG uptake (SUVmax 3.85), suggestive of intimal sarcoma as the first possibility. Multiple nodular lesions in the right lung were also described, likely related to pulmonary metastases. An endovascular biopsy of the intraluminal pulmonary artery lesion confirmed the clinicradiologic suspicion of primary intimal sarcoma of the pulmonary artery. After diagnostic confirmation and evidence of pulmonary dissemination, chemotherapy was initiated, but local and pulmonary progression occurred after six cycles. A secondline chemotherapy regimen and palliative radiotherapy were started because of hemoptysis following documented tumor progression. ***Conclusion:*** PAS is a rare tumor and is often misdiagnosed as a PTE. The survival is closely related to early diagnosis and since most patients with PAS have elevated glucose metabolism, ^{18}F-FDG PET/CT imaging has been established as an effective modality in the differential diagnosis between these two entities and the study of their possible metastases.

EP-1338

Paraganglioma - a New Approach of Metastatic vs. Multifocal Disease. A Case Report.

Z. Patko[1,2], *E. Kocsak*[3], *B. Bako*[3], *S. Barna*[4], *J. Gombos*[3];
[1]*Helse Møre og Romsdal, Ålesund, Norway,* [2]*University of Miskolc, Miskolc, HUNGARY,* [3]*Borsod County Central Hospital and University Teaching Hospital, Miskolc, HUNGARY,* [4]*ScanoMed Debrecen, Debrecen, HUNGARY.*

Aim/Introduction: Paragangliomas are rare neuroendocrine tumors arising from extra-adrenal paraganglia. These tumors often secrete catecholamines, leading to severe symptoms even when small. Identifying the exact location of smaller lesions can be challenging, and receptor scintigraphy remains a key diagnostic tool. Although paragangliomas rarely metastasize, it has traditionally been considered a marker of malignancy. In recent years, new classification systems have emerged to better assess their malignant potential. The latest WHO classification distinguishes between true metastatic disease and multifocal presentations, reflecting a shift in understanding their biological behavior. [1,2]This case highlights the relevance of the updated WHO classification and illustrates the evolving diagnostic and therapeutic approach to multifocal paragangliomas. ***Materials and Methods:*** A 46-year-old man presented to our department with fatigue and microcytic anemia. Abdominal CT revealed a tumor in the lower duodenum, for which duodenal resection was performed. Histopathological analysis confirmed the diagnosis of paraganglioma.Two and a half years later, during routine follow-up, a 25 mm hepatic lesion was detected by ultrasound and CT which was removed surgically. Histology identified it as a metastasis of the previously excised duodenal paraganglioma. Postoperatively, I-123 MIBG scintigraphy showed focal uptake in the left hepatic lobe, though low-dose CT did not reveal a clear morphological lesion. A contrast-enhanced MRI detected a suspicious lesion on the diaphragmatic surface of the left lobe, which showed interval growth on follow-up imaging. Biochemical tests, including catecholamine metabolites and chromogranin A, were within normal limits.In multidisciplinary review, the imaging characteristics of the new left-lobe lesion mirrored those of the prior right-lobe metastasis, strongly suggesting a new hepatic metastasis. Octreoscan confirmed a 3 cm somatostatin receptor-expressing tumor in the left lobe. ***Results:*** Considering the lesions' location, progression, and molecular features of both the duodenal and hepatic tumors, multifocal disease was suspected. Treatment with lutetium-177-labeled somatostatin analog was initiated. ***Conclusion:*** With this case, we aim to draw attention to specific features of metastatic paraganglioma, such as unusual localization and molecular patterns, that may suggest multifocal disease rather than true metastasis. We briefly highlight the criteria of the new WHO classification, which may influence both diagnostic categorization and therapeutic strategy. [1,2] ***References:*** [1] Mete O et al. Overview of the 2022 WHO Classification of Paragangliomas and Pheochromocytomas. Endocr Pathol. 2022 Mar;33(1):90-114. doi:10.1007/s12022-022-09704-6. [2] Mete O det al. Recent progress in the pathologic classification of pheochromocytomas and paragangliomas, Best Pract. Res., Clin. Endocrinol. Metab. 2024 Dec;38(6):101958

EP-1339

FAPI-Based Theranostics in Medullary Thyroid Cancer: A Viable Alternative When Somatostatin Receptor Based Theranostics Show Limited Efficacy—A Clinical Experience

A. Saber Tanha, *F. Jafari Zarrin Ghabaei, N. Raeisi, K. Aryana, s. shafiei;*
Mashhad University of Medical Sciences, Mashhad, IRAN, ISLAMIC REPUBLIC OF.

Aim/Introduction: A 36-year-old man with medullary thyroid carcinoma (MTC) underwent total thyroidectomy and left neck lymph node dissection 12 years ago. His medical history included polycythemia and a previous episode of upper limb deep venous thrombosis. Ten years post-diagnosis, he developed multiple metastatic pulmonary nodules, with a serum calcitonin level rising to 2000 pg/ml, although he remained asymptomatic. ***Materials and Methods:*** The patient developed a cough, leading to a ^{99m}Tc-octreotide scan as a prerequisite for peptide receptor radionuclide therapy (PRRT) with ^{177}Lu-DOTATATE. The scan revealed multiple metastatic lymph nodes, lung metastases, and a solitary hepatic metastasis, all showing mild octreotide avidity. He received two cycles of PRRT at dosages of 7.4 GBq of ^{177}Lu-DOTATATE. ***Results:*** A positive biochemical response was noted after the first cycle, with a 28% reduction in serum calcitonin levels and partial remission of cough. However, a post-treatment scan after the second cycle indicated faint uptake in tumoral lesions. A subsequent ^{99m}Tc-FAPI-46 scan revealed tracer uptake in liver lesions, mediastinal lymph nodes, and pulmonary nodules, suggesting ^{177}Lu-FAPI as a viable treatment alternative. ***Conclusion:*** Despite the promising potential of FAPI in managing MTC, the patient opted to continue treatment with tyrosine kinase inhibitors. This case highlights the role of FAPI as an innovative theranostic strategy being a potential last resort in the evolving landscape of MTC management.

EP-1340

Langerhans Cell Histiocytosis with cutaneous presentation: a case report

K. Kapansahin, *B. Okudan Tekïn;*
Ankara Bilkent Şehïr Hastanesi, Ankara, TÜRKYE.

Aim/Introduction: Langerhans cell histiocytosis (LCH) is a complex disease characterized by clonal proliferation of Langerhans cells, primarily affecting children and adolescents, and can involve multisystem organs. The condition exhibits a wide spectrum of clinical presentations that require a multidisciplinary approach for diagnosis, treatment, and follow-up. The cutaneous manifestations of LCH are significant, mimicking common dermatoses and creating diagnostic challenges. ***Materials and Methods:*** Our case is a 26-year-old male patient who is being followed up by dermatologists and venereal diseases with a preliminary diagnosis of hidradenitis suppurativa. In his physical examination, there were erosions, erythema, and discharge lesions in the bilateral axillary region, and discharges in the bilateral inguinal region that were erythematous and unresponsive to antibiotics. At the same time, the patient's lungs had a bullous appearance and pneumothorax occurred from time to time. In the diagnosis, the histopathology of the bullostemia wedge resection material revealed widespread fibrosis findings, cystic changes, and histiocyte-like cells that stained positively with langerin and CD1a. The axillary biopsy revealed findings consistent with LCH. In the patient's PET/CT imaging, increased F-18 FDG uptake was observed in the cutaneous area of the bilateral axillary region and the left groin region. ***Results:*** Langerhans cells are dendritic mononuclear cells normally found in the epidermis, mucosa, lymph nodes, and bone marrow. Their normal function is to process antigens and present them to T lymphocytes; however, in LCH, literature review suggests that monoclonal proliferation of Langerhans cells leads to destruction of hard and soft tissues. LCH usually occurs in children aged 1-15 years, with a peak incidence between 2-4 years, occurring twice as often in boys as in girls. The most common clinical findings seen in the majority of cases are single or multiple bone lesions. ***Conclusion:*** In the presented case, the patient was diagnosed with cutaneous lesions without any skeletal involvement. FDG-PET/CT has proven to be highly sensitive, providing comprehensive staging and effective follow-up during treatment. We have shown that FDG-PET/CT is effective in detecting all types of LCH lesions, including cutaneous lesions,

and in assessing the extent of disease involvement. ***References:*** Rao DG, Trivedi MV, Havale R, Shrutha SP. A rare and unusual case report of Langerhans cell histiocytosis. J Oral Maxillofac Pathol. 2017 Jan-Apr;21(1):140-144. doi: 10.4103/jomfp.JOMFP_10_17. PMID: 28479703; PMCID: PMC5406796.

EP-1341

Primary neurolymphomatosis: Value of 18F-FDG-PET/CT in the diagnosis and assessment of response to treatment

S. Georga[1], *D. Katsampoukas*[1], *V. Mpalaris*[1], *A. Morfesi*[1], *M. Spilioti*[2], *G. Zafeiridou*[2], *N. Vavlas*[1], *G. Kaiafa*[3], *E. Moralidis*[1], *G. Arsos*[1];
[1]*3rd Department of Nuclear Medicine, Aristotle University Medical School, Papageorgiou General Hospital, Thessaloniki, GREECE,* [2]*1st Neurology Department, Aristotle University Medical School, AHEPA General Hospital, Thessaloniki, GREECE,* [3]*1st Propaedeutic Department of Internal Medicine, Aristotle University Medical School, AHEPA General Hospital, Thessaloniki, GREECE.*

Aim/Introduction: Primary neurolymphomatosis (PNL) is a very rare subtype of primary central nervous system lymphoma, defined as infiltration of cranial, spinal or peripheral nerve roots or nerve plexuses by lymphomatous neoplastic cells in the absence of systemic lymphoma. Nerve biopsy is the gold standard for the diagnosis, but is often difficult to perform or may be inconclusive. 18F-FDG-PET/CT, by detecting the very characteristic pattern of isolated hypermetabolic neuropathy, is a well-established imaging modality for the diagnosis and evaluation of PNL. ***Materials and Methods:*** We report on the case of a 74-year-old woman referred to our department for an 18F-FDG-PET/CT scan for investigation of multiple cranial mononeuritis. The patient had signs of multiple cranial nerve dysfunction, dysphagia and respiratory infection, and had a positive monoclonal IgM fraction in CSF. Initial gadolinium-enhanced brain MRI demonstrated asymmetric thickening and enhancement of multiple cranial nerves (bilateral III and V and right VII, VIII, IX and X), proposing a wide differential diagnosis including infectious and granulomatous diseases, demyelinating polyneuropathy, secondary carcinomatosis, lymphoma and multiple myeloma. After being unsuccesfully treated for a month with corticosteroids, IgG immunoglobulins and antibiotics, she was scheduled for plasmapheresis. Before starting this, an 18F-FDG-PET/CT scan led to the diagnosis of PNL, prompting specific treatment, followed by an interim one 2 months later. ***Results:*** Initial 18F-FDG-PET/CT scan revealed bilateral increased metabolic activity along the intracranial and extracranial course of multiple cranial nerves and along multiple nerve roots in the cervical spine up to the brachial plexuses, bilaterally. There was relative concordance between PET/CT and MRI in relation to the involved cranial nerves. The absence of abnormal metabolic activity in the rest of the body, excluded other sites of active inflammatory, granulomatous or malignant process. Overall, in this clinical setting, the 18F-FDG-PET/CT findings were very suggestive of the rare entity of PNL, and CSF lymphocyte immunocytochemistry confirmed the diagnosis of a Non Hodgkin lymphoma. Accordingly, the patient underwent systemic treatment with Mabthera and intrathecal infusion of Methotrexate and Ara-C. Interim 18F-FDG-PET/CT scan performed two months later showed complete metabolic remission in line with substantial clinical improvement. ***Conclusion:*** Our case shows that 18F-FDG-PET/CT is a valuable noninvasive imaging modality for the correct diagnosis of the rare entity of primary neurolymphomatosis, as it can reveal the affected neural structures and determine the extent of nerve involvement in the absence of other sites of disease. Furthermore, 18F-FDG-PET/CT is useful for assessing response to treatment.

EP-1342

Exploring the potential role of ^{18}F-FDG and ^{18}F-PSMA PET/CT in detecting neurofibromas: a case report

C. Torricelli, *T. Alves, G. Barbosa, M. Silva, E. Nogueira-Lima, V. Heringer, N. Tobar, M. Etchebehere, E. Etchebehere;
University of Campinas (UNICAMP), Campinas, BRAZIL.*

Aim/Introduction: Neurofibromatosis (NF) is a genetic disorder that predisposes individuals to nervous system tumors, including plexiform neurofibromas, malignant peripheral nerve sheath tumors and optic pathway gliomas[1]. While traditional imaging techniques, such as MRI and CT, are commonly used for diagnosis[2], ^{18}F-FDG-PET/CT is performed for differentiating benign and malignant lesions[3]. As an additional tool, radiolabeled PSMA-PET/CT offers potential for detecting and monitoring neurofibromas, expanding its use beyond prostate cancer[4], as well as a therapeutic resource. This case report describes the potential role of PSMA in NF. ***Materials and Methods:*** A 42-year-old male patient with a history of NF complained of cervical pain irradiating to the upper limbs for the past 7 months. The patient presented multiple cutaneous, subcutaneous and intramuscular neurofibroma nodules distributed throughout the body especially in the right thigh, gluteus and thoracic spine (T10/T11) as demonstrated by MRI. He was submitted to an ^{18}F-FDG-PET/CT imaging for primary staging and to evaluate the potential malignant transformation of the neurofibromas. After a 72-hour interval, an ^{18}F-PSMA-1007-PET/CT was performed. SUV_{max} was calculated semi automatically for each lesion in both exams. ***Results:*** ^{18}F-FDG-PET/CT revealed multiple mildly hypermetabolic cutaneous, subcutaneous and intramuscular neurofibroma nodules in the left periorbital/nasal region, right arm, left chest, gluteus, right thigh and knees (highest SUV = 2.3 in the right thigh). A subpleural pulmonary mass in the left lower lobe originating from the left T10/T11 neural foramen (SUV = 4.5) was also detected. ^{18}F-FDG-PET/CT findings were consistent with multiple benign nodules and possible malignant transformation of the lung mass infiltration from the T10/T11 neural foramen. The ^{18}F-PSMA-1007-PET/CT images showed higher uptake in all NF nodules compared to ^{18}F-FDG uptake (highest SUV = 6.5 in the left periorbital/nasal region). There was no PSMA uptake in the pulmonary lesion. The patient was referred to neurosurgery of the lung mass. ***Conclusion:*** This case highlights the potential role of ^{18}F-PSMA-1007-PET/CT in detecting and staging neurofibromas because of its higher radiotracer uptake in various nodules, compared to ^{18}F-FDG-PET/CT, suggesting complementary roles for both tracers in the functional evaluation of lesions at different sites. ^{18}F-PSMA-1007-PET/CT may contribute to improved diagnostic accuracy, clinical management and possible Theranostics applications. Its role in prognosis is unclear. ***References:*** 1.Yu X, et al. Neurooncol Adv, 2025; 2.Liu J, et al. Front Oncol, 2022; 3.Chirindel A, et al. J Nucl Med, 2015; 4.Gulhane B, et al. Clin Nucl Med, 2017. Research Funding: FAPESP - Cancer Theranostics Innovation Center, CEPID (Process#2021/10265-8).

EP-1343

Osteoid Osteoma - Presenting Two Cases of Rare Localizations and Diagnostic Challenges

Z. Patko[1,2], *E. Kocsak*[3], *L. Kostyal*[3], *J. Gombos*[3];
[1]*Helse Møre og Romsdal, Ålesund, Norway,* [2]*University of Miskolc, Faculty of Health Sciences, Miskolc, HUNGARY,* [3]*Borsod County Central Hospital and University Teaching Hospital, Miskolc, HUNGARY.*

Aim/Introduction: Osteoid osteoma is a common, benign bone lesion that typically occurs in children and adolescents, most frequently affecting the long tubular bones. However, even a relatively common condition with characteristic symptoms may present a diagnostic challenge in an atypical localization or if accompanied by a misleading patient history. ***Materials***

and Methods: In our first case an 11-year-old girl was admitted to our department with recurrent gluteal pain that had been present for approximately one year. A few months prior to the onset of symptoms, she had begun horseback riding. Shortly after she developed pain in the lower back and ischial region. Her medical history was negative for trauma. Physical examination revealed right-sided gluteal tenderness. Her symptoms showed temporary improvement with NSAID treatment but subsequently recurred. Laboratory and immunological investigations revealed no abnormalities or signs of inflammation. Physiotherapy and rehabilitative exercises proved ineffective. MRI scans showed oedema in the iliac bone, which was considered stress related. Due to persistent complaints we performed bone scintigraphy which revealed increased activity in the region of the sacroiliac joint, localized ventrally in the joint on SPECT reconstructions. CT imaging confirmed the presence of a nidus with surrounding sclerosis. In our second case a 10-year-old girl presented at our department with uncertain onset of foot pain that had persisted for several weeks. Her medical history was unremarkable, with no prior significant illness or trauma. She had taken up dancing a year earlier. Initial X-ray imaging did not reveal any trauma or structural abnormalities. Due to persistent symptoms, an MRI scan was performed, which revealed oedema in the calcaneus beneath the subtalar joint. Based on suspicion of a stress fracture, immobilization, gradual weight-bearing, and physiotherapy were recommended. Despite these interventions, her symptoms did not improve. Bone scintigraphy with SPECT/CT was performed which showed intense focal uptake in the subtalar region of the calcaneus, and the CT scan identified a nidus near the subtalar joint accompanied by surrounding sclerotic bone. ***Results:*** In both cases the diagnosis of osteoid osteoma has been stated. Following adequate treatment, the patients became symptom-free. ***Conclusion:*** In some cases, the clinical history and presentation may be misleading, making the selection and combination of appropriate imaging modalities essential for accurate diagnosis and effective treatment planning.

EP-1344

^{18}F-FDG PET/CT in sporadic Creutzfeldt-Jacob disease: A case report

C. Caldas[1], *D. Isasi*[1], *N. Laines*[2], *L. Apaza*[3], *L. Apaza*[3];
[1]EsSalud, Lima, PERU, [2]Universidad Nacional Mayor de San Marcos, Lima, PERU [3]Intituto Nacional de Ciencias Neurologicas, Lima, PERU.

Aim/Introduction: Creutzfeldt-Jakob disease (CJD) is a rare, rapidly progressive, and fatal neurodegenerative disorder caused by prion proteins. Due to its variable presentation, diagnosis often relies on a combination of clinical features, neuroimaging, electroencephalography (EEG), and cerebrospinal fluid biomarkers. We present a case report that illustrates a confirmed diagnosis of sporadic CJD in a patient with subacute neurological deterioration and FDG PET/CT findings. ***Materials and Methods:*** A 68-year-old female presented to the Hospital with two weeks of progressive lower limb weakness, followed by upper limb involvement, memory impairment, and coordination difficulties. Neurocognitive tests revealed significant deficits: Pfeiffer score of 3, Mini-Mental State Examination score of 11, and a TAM of 22. EEG showed mild generalized dysfunction without epileptiform discharges or triphasic waves. Patient had significant mental deterioration without a clear etiology through different test including MRI. Eight-week later, she underwent a FDG PET/CT scan. It was found a global bilateral cortical-subcortical hypometabolism, predominantly in fronto-temporal and striata. The diagnosis of CJD was confirmed by RT-QuIC analysis of cerebrospinal fluid. The patient later developed right frontotemporal epilepsy, attributed to prion-related cortical involvement. ***Results:*** Imaging findings on PET/CT were characteristic of prion-related encephalopathy, showing marked bilateral hypometabolism in grey matter structures. Despite the absence of EEG triphasic waves, clinical progression, cognitive testing, and PET/CT findings were consistent with sporadic CJD. Two-week after PET/CT, the real-time quaking-induced conversion (RT-QuIC) assays had confirmed the diagnosis. The patient remained hemodynamically stable but in an akinetic mutism state, without myoclonus, and on valproic acid for seizure control. Prognosis remained poor due to the underlying pathology. ***Conclusion:*** This case highlights the diagnostic value of FDG PET/CT in rapidly progressive dementias, particularly when EEG findings are non-specific. Correlation with clinical evolution and advanced biomarker testing such as RT-QuIC is essential for accurate and timely diagnosis of CJD. Early metabolic imaging may guide suspicion and prompt further investigation even in atypical EEG presentations.

EP-1345

Uncommon Presentation of Primary Adrenal Lymphoma with Bilateral Adrenal Hypermetabolic Activity on ^{18}F-FDG PET/CT: A Case Report

P. Sahafi[1], *F. Karamian*[1], *F. Emami*[2], *M. Samadi*[1], *R. Sadeghi*[1];
[1]Ghaem Hospital, Mashhad university of medical science, Mashhad, IRAN, ISLAMIC REPUBLIC OF, [2]Nuclear Medicine and Molecular Imaging Department, Imam Reza International University, Razavi Hospital, Mashhad, IRAN, ISLAMIC REPUBLIC OF.

Aim/Introduction: The aim of this case report is to highlight the importance of ^{18}F-FDG PET/CT imaging in the evaluation of bilateral adrenal masses and to emphasize the need to consider primary adrenal lymphoma (PAL) in the differential diagnosis of hypermetabolic adrenal lesions. ***Materials and Methods:*** An 80-year-old male patient presented with abdominal pain and fatigue. Initial abdominal CT imaging revealed bilateral adrenal masses of unknown origin. To further assess the nature of these masses, ^{18}F-FDG PET/CT imaging was performed following intravenous administration of 6.19 mCi of 18F-fluorodeoxyglucose. Scanning commenced 62 minutes post-injection. PET/CT findings, including size measurements, standardized uptake values (SUV_{max}), and evidence of additional hypermetabolic lesions, were documented. A histopathological evaluation was subsequently performed through adrenal gland biopsy to confirm the diagnosis. ***Results:*** ^{18}F-FDG PET/CT imaging demonstrated significantly enlarged bilateral adrenal glands with intense FDG uptake. The right adrenal gland measured 74 × 43 × 82 mm (SUV_{max} = 30.09), and the left adrenal gland measured 76 × 46 × 70 mm (SUV_{max} = 29.91). Mild FDG uptake was observed in small lymph nodes within the superior mesenteric and para-aortic regions, but no other abnormal or hypermetabolic lesions were identified elsewhere in the body. Based on these imaging findings, differential diagnoses included malignancies such as primary adrenal lymphoma. A subsequent adrenal gland biopsy confirmed the diagnosis of B-cell lymphoma. This case demonstrates the utility of ^{18}F-FDG PET/CT in identifying malignant adrenal lesions and underscores the importance of considering PAL in patients with bilateral adrenal hypermetabolic masses. ***Conclusion:*** In cases of bilateral hypermetabolic adrenal masses detected on FDG PET/CT imaging, the differential diagnosis should include both common and rare conditions, including primary adrenal lymphoma.

EP-1346

FAPI Uptake in Malignant Ascites: A Case Report

P. Sahafi, *M. Samadi, A. Aghaee;*
Ghaem Hospital, Mashhad university of medical science, Mashhad, IRAN, ISLAMIC REPUBLIC OF.

Aim/Introduction: The aim of this case report is to demonstrate the potential utility of ^{99m}Tc-FAPI imaging in detecting malignant ascites and recurrent renal cell carcinoma in a patient with a rising PSA level and a retroperitoneal mass of unknown origin. ***Materials and Methods:*** A 69-year-old man with a history of right-sided papillary renal cell carcinoma (nuclear grade I) and prior nephrectomy was evaluated for a retroperitoneal mass identified on recent CT and sonographic imaging. He also exhibited elevated PSA levels (84.1 ng/mL) and malignant ascites confirmed via abdominal paracentesis. Due to contraindications for biopsy, the

patient underwent ^{99m}Tc-FAPI and ^{99m}Tc-PSMA SPECT/CT imaging as part of an investigational clinical protocol. Tracer uptake patterns were analyzed to assess the origin and nature of the mass and ascitic fluid. ***Results:*** ^{99m}Tc-FAPI imaging revealed increased radiotracer uptake within the abdominal cavity, consistent with malignant ascites. The retroperitoneal mass also demonstrated significant FAPI uptake but was non-avid on the ^{99m}Tc-PSMA scan, suggesting recurrence of renal cell carcinoma rather than prostate cancer metastasis. These imaging findings provided critical diagnostic insights in the absence of tissue biopsy. ***Conclusion:*** This case illustrates the potential of ^{99m}Tc-FAPI imaging to detect malignant ascites and differentiate tumor recurrence in complex clinical settings. The observed FAPI uptake in malignant ascitic fluid suggests a novel application of FAPI imaging, although the exact mechanism remains to be elucidated.

EP-1347

Simultaneous visualization of a Meckel's diverticulum and its active bleeding on Tc-99m Pertechnetate scintigraphy: an unusual presentation

P. Sahafi, *M. Samadi, R. Sadeghi;*
Ghaem Hospital, Mashhad university of medical science, Mashhad, IRAN, ISLAMIC REPUBLIC OF.

Aim/Introduction: The aim of this case report is to illustrate the diagnostic challenges posed by active gastrointestinal bleeding during ^{99m}Tc-Pertechnetate scintigraphy in detecting Meckel's diverticulum, and to highlight the rare simultaneous presentation of Meckel's diverticulum with active bleeding. ***Materials and Methods:*** A 2-year-old girl with a recent history of rectorrhagia was referred for ^{99m}Tc-Pertechnetate scintigraphy to evaluate for the presence of ectopic gastric mucosa. Dynamic imaging, static anterior and posterior views, and delayed imaging were performed following standard protocols. Careful attention was given to the differentiation of physiological uptake from pathological activity. H2 blocker administration was confirmed prior to imaging to minimize physiological gastric secretion and improve diagnostic accuracy. ***Results:*** Initial imaging demonstrated focal radiotracer uptake in the mid-lower abdomen consistent with Meckel's diverticulum, appearing concurrently with normal gastric activity. Additionally, a diffuse area of abnormal radiotracer accumulation was observed in the left abdomen, showing movement during dynamic imaging, suggesting active bowel bleeding. Delayed imaging revealed widespread intraperitoneal radiotracer distribution, confirming significant hemorrhage. Surgical exploration validated the presence of a Meckel's diverticulum, and histopathology confirmed ectopic gastric mucosa. The dynamic nature of the bleeding and the movement of radiotracer uptake were critical in distinguishing active bleeding from potential imaging artifacts. ***Conclusion:*** This case represents a unique instance of simultaneous detection of Meckel's diverticulum and active gastrointestinal bleeding using ^{99m}Tc-Pertechnetate scintigraphy. Active bleeding can mimic or obscure findings, complicating accurate interpretation. Awareness of this potential pitfall, along with careful dynamic assessment and appropriate preparation with H2 blockers, is crucial for accurate diagnosis. This report underscores the importance of recognizing the rare but significant presentation of concurrent Meckel's diverticulum and active bleeding in patients undergoing nuclear imaging.

EP-1348

Complete Pathological Response After Neoadjuvant Radioligand Therapy in a Case of Pancreatic Neuroendocrine Tumor: A Case Report

P. Sahafi, *M. Samadi, M. Ghahraman, E. Soltani, A. Aghaee;*
Ghaem Hospital, Mashhad university of medical science, Mashhad, IRAN, ISLAMIC REPUBLIC OF.

Aim/Introduction: The aim of this report is to demonstrate the potential role of peptide receptor radionuclide therapy (PRRT) with ^{177}Lu-DOTATATE as a neoadjuvant approach in enabling surgical resection of initially unresectable pancreatic neuroendocrine tumors (pNETs), and to highlight the possibility of achieving complete pathological response following such treatment. ***Materials and Methods:*** A 30-year-old woman diagnosed with a low-grade (Ki67 = 3%) pancreatic neuroendocrine tumor involving major vascular structures was deemed ineligible for surgery. The patient underwent four cycles of ^{177}Lu-DOTATATE therapy, receiving 200-240 mCi per cycle with concurrent amino acid infusion for renal protection, administered every 8-12 weeks. Imaging assessment included serial whole-body scintigraphy and SPECT/CT after each treatment cycle, and a preoperative three-phase CT scan following completion of therapy. ***Results:*** Post-PRRT imaging revealed a marked reduction in tumor size and disappearance of contrast enhancement, suggestive of a complete radiological response. Subsequently, the patient underwent Whipple surgery. Histopathological evaluation of the resected specimen demonstrated only dense fibrosis without any viable tumor cells, confirming a complete pathological response. The case highlights a rare but significant outcome where PRRT facilitated surgical resection and achieved complete tumor eradication. ***Conclusion:*** This case underscores the potential effectiveness of neoadjuvant 177Lu-DOTATATE therapy in downstaging locally advanced pancreatic neuroendocrine tumors, enabling curative surgery and achieving complete pathological remission. Further research is necessary to validate these findings and identify predictors of response, potentially broadening the therapeutic indications for PRRT in the management of complex pNET cases.

EP-1349

Enhancing Restaging of a Colorectal Cancer Patient: The Advantage of ^{99m}Tc-FAPI-46 over Conventional CT in Detecting Metastases

M. Ahmadi, *A. Aghaee, M. Samadi, P. Sahafi, E. Soltani;*
Nuclear medicine research center, Mashhad university of medical sciences, Mashhad, Khorasan Razavi, IRAN, ISLAMIC REPUBLIC OF.

Aim/Introduction: Colorectal cancer is the third most common cancer and the leading cause of cancer-related deaths worldwide, with a five-year survival rate of about 60% across all stages. However, metastatic colorectal cancer has a grim prognosis, with only 14% of patients surviving five years post-diagnosis despite treatment advancements. Accurate detection of metastatic lesions is vital for effective management, traditionally done through contrast-enhanced computed tomography (CECT). Recent developments in molecular imaging, particularly with 99mTc-FAPI, show promise in improving sensitivity for metastasis detection. This article discusses a case study of a 73-year-old man with colon adenocarcinoma, diagnosed 18 months ago, who underwent total colectomy and chemoradiotherapy. Due to recurrent abdominal pain, he was evaluated using both CECT and 99mTc-FAPI-46 SPECT/CT for metastatic workup. ***Materials and Methods:*** The planar whole-body images in anterior and posterior views and SPECT/CT acquisition were performed 1 hour after injection of 20 mci of ^{99m}Tc-FAPI-46. ***Results:*** CECT images showed a hypodense lesion with heterogeneous enhancement in the left abdomen, near the psoas muscle. In contrast, 99mTc-FAPI-46 SPECT/CT identified three distinct peritoneal metastatic lesions, confirmed by re-surgery and histology. While CECT detected only one of these lesions, the other two were small and obscured by bowel loops, making them undetectable on conventional CT. ***Conclusion:*** In this case, 99mTc-FAPI SPECT/CT demonstrated greater sensitivity than CECT in detecting metastatic lesions in a postoperative colorectal cancer patient. Incorporating 99mTc-FAPI

as an additional imaging tool alongside conventional methods like CECT could improve staging accuracy and impact clinical decision-making for colorectal cancer patients.

EP-1350

PSMA Scintigraphy in Metastases of Prostate Cancer Within the Genital Tract

F. Rabani, *M. Samadi, A. Saber Tanha, N. Afshari, A. Aghaee; Mashhad University of Medical Science, Mashhad, IRAN, ISLAMIC REPUBLIC OF.*

Aim/Introduction: Prostate-specific membrane antigen (PSMA)-targeted imaging has advanced the detection of prostate cancer metastases, particularly in atypical sites. We present a rare case of vas deferens involvement (VDI) in high-grade prostate adenocarcinoma, identified through both ^{68}Ga-PSMA PET/CT and ^{99m}Tc-PSMA SPECT/CT imaging, emphasizing the utility of PSMA imaging. ***Materials and Methods:*** A 68-year-old man presented with lower urinary tract symptoms (LUTS) and was diagnosed with prostate adenocarcinoma (Gleason score 4+5) with a PSA level of 97.5 ng/mL. He underwent staging with ^{68}Ga-PSMA PET/CT performed 60 minutes after intravenous administration of 3.24 mCi (119.88 MBq) of ^{68}Ga-PSMA, with acquisition from the skull to mid-thigh. After initial androgen deprivation therapy, the patient discontinued treatment and was lost to follow-up. Due to persistent symptoms and a PSA of 88 ng/mL after one year, he underwent restaging with ^{99m}Tc-PSMA scintigraphy, including whole-body planar imaging and SPECT/CT three hours after intravenous injection of 20 mCi (740 MBq) of ^{99m}Tc-HYNIC-PSMA. Additionally, we reviewed 59 reported cases of rare PSMA-avid metastases involving male genital structures. ***Results:*** The initial ^{68}Ga-PSMA PET/CT scan demonstrated moderate PSMA uptake within the primary prostate tumor, the left seminal vesicle base, and a rounded nodule medial to the seminal vesicle, corresponding to the ampulla of the vas deferens, consistent with locoregional invasion. Restaging with ^{99m}Tc-PSMA SPECT/CT closely mirrored these findings, confirming persistent disease confined to the prostate, left seminal vesicle, and vas deferens, without evidence of nodal, skeletal, or visceral metastases. Vas deferens involvement (VDI) in prostate cancer is rare and typically identified during restaging for biochemical recurrence, though occasionally seen at initial staging. Limited literature suggests VDI may have independent prognostic significance similar to seminal vesicle invasion, indicating a more aggressive disease phenotype. Despite the patient's high-risk features, including a Gleason score of 4+5 and elevated PSA levels, disease remained locoregional across staging and restaging. Additionally, we reviewed 59 reported cases of PSMA-avid prostate cancer metastases to male genital structures, including the vas deferens, scrotal sac, testes, epididymis, penis, vesicourethral junction, and perineum. These cases involved patients aged 45-88 years, most often during recurrence, with high Gleason scores and predominantly moderate to intense PSMA expression (scores 2 or 3). ***Conclusion:*** This case highlights the clinical utility of PSMA-targeted imaging in detecting rare metastatic patterns such as vas deferens involvement. It also demonstrates that ^{99m}Tc-PSMA SPECT/CT is an effective and accessible alternative to PET/CT, aiding accurate staging and management in prostate cancer.

EP-1351

^{68}Ga-FAPI and ^{18}F-FDG PET/CT: Complementary Imaging Modalities for Detecting Unusual Metastasis in a Patient with Osteosarcoma

P. Sahafi[1], *G. Divband*[2], *H. Amini*[3], *E. Askari*[1], *A. Noferesti*[1]; [1]*Ghaem Hospital, Mashhad university of medical science, Mashhad, IRAN, ISLAMIC REPUBLIC OF of,* [2]*Jam Nuclear Medicine Center, Tehran, IRAN, ISLAMIC REPUBLIC OF,* [3]*Khatam PET/CT Center, Tehran, Mashhad, IRAN, ISLAMIC REPUBLIC OF.*

Aim/Introduction: To evaluate the complementary role of ^{18}F-FDG PET/CT and ^{68}Ga-FAPI PET/CT imaging in the characterization of equivocal soft tissue lesions in a patient with a history of osteosarcoma, emphasizing the tumor heterogeneity and the importance of multimodality imaging. ***Materials and Methods:*** A 32-year-old male with a history of left humerus osteosarcoma, previously treated with surgery, orthopedic device placement, and lung metastasectomy, underwent ^{18}F-FDG PET/CT imaging due to two suspicious lesions near the left kidney observed on prior anatomical evaluations. One lesion demonstrated FDG uptake (SUV_{max} = 4.52), while the second lesion was non-FDG-avid. To further characterize these equivocal findings and as part of a clinical trial, a ^{68}Ga-FAPI- PET/CT scan was performed. Imaging findings were compared and correlated with surgical pathology after resection. ***Results:*** The ^{18}F-FDG PET/CT scan showed significant uptake in one lesion, while the adjacent lesion lacked FDG avidity. The ^{68}Ga-FAPI PET/CT scan revealed uptake in the previously non-FDG-avid lesion (SUV_{max} = 3.77), demonstrating a heterogeneous uptake pattern between the two imaging modalities. Surgical resection and histopathological examination confirmed both lesions as metastatic osteosarcoma. This case demonstrated that tumor heterogeneity could lead to variable tracer uptake, highlighting the complementary nature of ^{18}F-FDG and ^{68}Ga-FAPI imaging. ***Conclusion:*** In osteosarcoma patients, particularly when evaluating equivocal or oligometastatic lesions, the use of both ^{18}F-FDG and ^{68}Ga-FAPI PET/CT imaging can provide a more comprehensive assessment. This case underlines the importance of multimodality imaging to account for tumor heterogeneity, which can significantly impact diagnosis and clinical decision-making.

EP-1352

Significant ^{99m}Tc-MDP uptake in metastatic lymph nodes of a patient with synovial sarcoma, a case report

P. Sahafi, *F. Karamian, A. Aghaee; Ghaem Hospital, Mashhad university of medical science, Mashhad, IRAN, ISLAMIC REPUBLIC OF.*

Aim/Introduction: To describe a rare case of synovial sarcoma with metastatic lymph node involvement detected by ^{99m}Tc-MDP bone scintigraphy, and to emphasize the potential role of bone imaging agents in identifying lymphatic metastases in soft tissue sarcomas. ***Materials and Methods:*** A 15-year-old girl with a history of synovial sarcoma posterior to the left knee underwent a ^{99m}Tc-MDP whole-body bone scan after experiencing tumor recurrence in the left inguinal region, confirmed by biopsy. The patient had previously received surgical resection, chemotherapy, and radiotherapy. Bone scintigraphy findings were further evaluated using SPECT/CT imaging to assess tracer uptake patterns. ***Results:*** The ^{99m}Tc-MDP bone scan demonstrated increased tracer uptake in the left inguinal region during both the blood pool and delayed phases. SPECT/CT images confirmed the presence of increased uptake in multiple enlarged lymph nodes in the left inguinal region, consistent with metastatic involvement. ***Conclusion:*** This case highlights the rare occurrence of lymph node metastasis in synovial sarcoma and its detection via bone scintigraphy using ^{99m}Tc-MDP. The findings suggest that bone-seeking agents can accumulate in metastatic lymph nodes of soft tissue sarcomas, possibly due to mechanisms such as increased vascularity, altered calcium metabolism, and changes in tissue pH. To our knowledge, this is the first reported case demonstrating bone agent activity in lymph node metastases of synovial sarcoma.

EP-1353

Comparison of ^{99m}Tc-FAPI, ^{99m}Tc-octerotide, and ^{68}Ga-DOTATATE PET/CT in the Evaluation of a Patient with Neuroendocrine Tumor

P. Sahafi, *A. Aghaee;*
Ghaem Hospital, Mashhad university of medical science, Mashhad, IRAN, ISLAMIC REPUBLIC OF.

Aim/Introduction: To present a case of a patient with metastatic neuroendocrine tumor (NET) in which ^{99m}Tc-FAPI imaging demonstrated superior detection of skeletal metastases compared to ^{99m}Tc-Octreotide and ^{68}Ga-DOTATATE scans, highlighting the potential role of FAPI-bounded radionuclides in the diagnosis and treatment planning of NETs. ***Materials and Methods:*** A 30-year-old woman with a history of a moderate differentiation neuroendocrine tumor and multiple skeletal metastases was evaluated. Initial imaging with ^{99m}Tc-MDP bone scan, ^{99m}Tc-Octreotide, and ^{68}Ga-DOTATATE PET/CT was performed. After limited response to two cycles of ^{177}Lu-DOTATATE therapy, the patient underwent ^{99m}Tc-FAPI SPECT/CT imaging to reassess the extent of disease. ***Results:*** The ^{99m}Tc-MDP scan revealed multiple skeletal metastases. The ^{99m}Tc-Octreotide and ^{68}Ga-DOTATATE scans showed only mild increased uptake throughout the skeleton. In contrast, the ^{99m}Tc-FAPI scan clearly demonstrated multiple lytic and sclerotic bone metastases and a soft tissue mass adjacent to the left parietal bone, indicating superior lesion visualization compared to previous imaging modalities. ***Conclusion:*** This case illustrates that FAPI-based imaging may provide enhanced detection of metastatic lesions in neuroendocrine tumors compared to somatostatin receptor-based imaging. FAPI-radiolabeled agents could offer improved diagnostic accuracy and aid in identifying candidates for targeted therapy, especially in patients with suboptimal response to conventional PRRT.

EP-1354

Tumor Lysis Syndrome After Radioligand Therapy in a Case of Metastatic Prostate Cancer

P. Sahafi, *M. Samadi, K. Aryana, E. Askari;*
Ghaem Hospital, Mashhad university of medical science, Mashhad, IRAN, ISLAMIC REPUBLIC OF.

Aim/Introduction: The aim of this study is to present a rare case of tumor lysis syndrome (TLS) following ^{177}Lu-PSMA radioligand therapy in a patient with metastatic castration-resistant prostate cancer (mCRPC), and to emphasize the importance of recognizing patients at risk for TLS prior to treatment. ***Materials and Methods:*** A 65-year-old man with a history of mCRPC, who had previously developed resistance to taxane-based chemotherapy and abiraterone, underwent treatment with ^{177}Lu-PSMA therapy. The patient had extensive bone metastases identified on initial imaging. Following the second session of radioligand therapy, he developed new clinical symptoms including difficulty walking. Laboratory studies were performed, alongside post-treatment imaging, to assess the cause of his clinical deterioration. ***Results:*** Post-therapy laboratory findings demonstrated a significant elevation in serum lactate dehydrogenase (LDH) levels, rising from 314 IU/L to 543,000 IU/L. Imaging revealed massive bilateral axillary and cervical lymphadenopathy, an atypical metastatic pattern for prostate cancer. Based on laboratory abnormalities, clinical presentation, and imaging findings, tumor lysis syndrome was diagnosed. Additionally, due to the atypical pattern of lymphadenopathy, the possibility of a secondary lymphoma was considered. ***Conclusion:*** This case highlights a rare but serious complication of TLS following ^{177}Lu-PSMA therapy in a patient with prostate cancer. Although TLS is uncommon in solid tumors, it must be considered, particularly in patients with an unusual pattern of metastasis. Furthermore, the development of unexpected metastatic distributions should prompt evaluation for potential secondary malignancies. Early recognition and management of TLS are critical to prevent severe outcomes in high-risk patients undergoing radioligand therapy.

EP-1355

Incidental Detection Of Double Chilaiditi Sign During Myocardial Perfusion Imaging: A Case Report

G. Prisacariu[1], *I. Sandu*[1], *M. Matei*[1], *C. Mazilu*[1], *R. Mititelu*[1,2];
[1]*Central Military Universitary Emergency Hospital "Carol Davila", Bucharest, ROMANIA,* [2]*University of Medicine and Pharmacy Carol Davila, Bucharest, ROMANIA.*

Aim/Introduction: Chilaiditi sign is characterised by the interposition of bowel—usually the colon—between the diaphragm and the liver. While typically asymptomatic and incidental, this anatomical variant can significantly challenge image interpretation during myocardial perfusion imaging (MPI), potentially resulting in attenuation artefacts that may mimic both reversible and irreversible perfusion defects. We report a rare case of double Chilaiditi sign observed during hybrid single-photon emission computed tomography/computed tomography (SPECT/CT) [^{99m}Tc]Tc-methoxy-isobutyl-isonitrile myocardial perfusion scintigraphy. ***Materials and Methods:*** A 48-year-old male was referred for MPI due to atypical anginal symptoms. The study was performed using a one-day stress/rest protocol with [^{99m}Tc]Tc-methoxy-isobutyl-isonitrile ([^{99m}Tc]Tc-MIBI). Low-dose computed tomography (CT) was acquired for attenuation correction (AC). Perfusion images were reconstructed both with and without AC for comparison. ***Results:*** On non-AC images, a fixed hypoperfusion defect was seen in the inferior and inferolateral myocardial segments. However, AC-corrected reconstructions revealed reversible hypoperfusion in the same territories, consistent with ischaemia in the right coronary artery territory. Review of the low-dose CT component revealed an unusual anatomical configuration, with bowel loops interposed between the diaphragm and the upper abdominal organs, involving both hepatic and splenic flexures, consistent with a double Chilaiditi sign. The interposed bowel resulted in an attenuation artefact that initially masked true reversible ischaemia. ***Conclusion:*** This case highlights the diagnostic implications of Chilaiditi sign during hybrid cardiac imaging. Intrathoracic displacement of bowel haustra may generate attenuation artefacts, especially in the inferior myocardial wall, potentially obscuring evidence of inducible ischaemia. Hybrid SPECT/CT imaging, employing low-dose CT for AC, is of great importance for accurate interpretation and differentiation of artefacts from true perfusion abnormalities, particularly in patients without prior cross-sectional imaging. ***References:*** 1. Burrell S, MacDonald A. Artifacts and pitfalls in myocardial perfusion imaging. J Nucl Med Technol. 2006 Dec;34(4):193-211; quiz 212-4. PMID: 17146108. 2. Jones J, Walizai T, Bell D, et al. Chilaiditi syndrome. Reference article, Radiopaedia.org (Accessed on 28 Apr 2025) https://doi.org/10.53347/rID-6333. 3. Mettler Jr., F.A., Guiberteau, M.J. (2019). Essentials of Nuclear Medicine and Molecular Imaging, 131-136, ISBN:978-0-323-48319-3.

EP-1356

Remarkable 99mTc-FAPI-46 Uptake in a Patient With Anaplastic Thyroid Carcinoma: A Promising Step in Theranostic Field

A. Aghaee, *M. Ghahreman, P. Sahafi, M. Samadi, K. Aryana; Nuclear Medicine Research Center, Mashhad University of Medical Sciences, Mashhad, IRAN, ISLAMIC REPUBLIC OF.*

Aim/Introduction: Fibroblast activation protein (FAP)-targeted radionuclides are known as a promising step in cancer diagnosis and treatment (theranostic), although it is still a subject under investigation. ***Materials and Methods:*** We present a patient with anaplastic thyroid carcinoma who underwent 99mTc-FAPI-46

SPECT/CT for the evaluation of metastatic disease. S ***Results:*** everal metastatic sites were found with considerable 99mTc-FAPI-46 uptake. Malignant FAPI uptake was observed in the large calcified thyroid mass, mediastinal lymph node, both lungs, liver, few skeletal sites, and around knees prostheses. Given the notable uptake of lesions, the patient was considered as a candidate for FAP-targeted radionuclide therapy. ***Conclusion:*** Anaplastic thyroid carcinoma (ATC) is a rare, undifferentiated and poor prognosis form of thyroid cancer which often presents with regional and distant metastases. Despite treatment options such as radiotherapy, chemotherapy, molecular targeted therapy, and immunotherapy, the optimal treatment has not yet been identified. Remarkable uptake of metastatic lesions in this patient increases the probability of subsequent successful treatment with FAPI agents as a potential treatment option. In conclusion, although studies have shown promising results in using FAPI agents in theranostic field, further investigation is still needed.

EP-1357

^{99m}Tc-DMSA Uptake in the Thoracic Region Mimicking Ectopic Kidney in a Case of Crossed Fused Renal Ectopia

M. Ahmadi, *R. Sadeghi, M. Samadi, A. Ardeshirzadeh, F. Taheri;*
Nuclear medicine research center, Mashhad university of medical sciences, Mashhad, Khorasan Razavi, IRAN, ISLAMIC REPUBLIC OF.

Aim/Introduction: Renal ectopia is characterized by the abnormal positioning of a kidney outside its normal anatomical location within the renal fossa. Diagnosis of this condition occurs in only a small percentage of cases. Among the different forms of renal ectopia, intrathoracic kidneys are the least commonly observed. This case revealed an unexpected uptake of 99mTc-DMSA in the left hemi-thorax, which was initially suspected as an ectopic thoracic kidney. However, further fused SPECT/CT imaging clarified that this uptake was due to an iatrogenic lung microembolism, which highlights the critical importance of accurately characterizing extrarenal DMSA uptake. ***Materials and Methods:*** After administration of 37 MBq (1 mCi) 99mTc-DMSA, imaging was performed 4 hours later in multiple views. ***Results:*** On the planar images, the right kidney seemed to be large-sized and mal-rotated with a zone of decreased tracer activity in the upper pole and no radiotracer uptake in the left renal lodge with an incidental finding of 99mTc-DMSA uptake in the left hemi-thorax, which was initially suspected to represent an ectopic thoracic kidney. Subsequent fused SPECT/CT images revealed mal-rotated crossed fused kidneys on the right side with a zone of decreased tracer uptake in the upper pole related to the pyelocalyceal system. Furthermore, SPECT/CT images localized 99mTc-DMSA uptake in the left hemi-thorax to the superior segment of the left lower lobe of the lung with no abnormal lesion on the co-registered CT images. This finding was determined to be an iatrogenic microembolism resulting from a traumatic injection during a challenging intravenous catheterization. ***Conclusion:*** Accurately determining the nature of extrarenal 99mTc-DMSA uptake poses a considerable diagnostic challenge. The potential presence of a radioactive clot resulting from difficult catheterization should be considered when evaluating incidental intrathoracic uptakes to enhance patient comfort by reducing the need for further diagnostic procedures and minimizing radiation exposure.

EP-1358

FDG PET CT in the diagnosis of testosteron secreting Sertoli-Leydig cell tumor of ovary

D. Todorova-Stefanovski, *S. Tasevski, S. Beshliev, G. Spirov, N. Manevska;*
University Institute of Positron Emission Tomography, Skopje, NORTH MACEDONIA, THE REPUBLIC OF.

Aim/Introduction: Ovarian Sertoli-Leydig cell tumors (SLCT) are a rare sex cord-stromal tumors, accounting for 1% of all ovarian tumors. They present mainly as benign tumors in young women under the age og 30. Clinically the patient presents with variable symptoms of excessive testosterone secretion - progressive masculinization, voice deepening, clitoromegaly, temporal hair recession and an increase in musculature. Imaging methods for detection of the tumor include ultrasound, CT and MRI but they can have low sensitivity for lesions less then 1cm. FDG PET/CT can have a significant role as complementary imaging tool for tumor localisation prior to surgical procedure. ***Results:*** CASE REPORT. We present a case of 64 year old woman presenting with alopecia, hirsutism, obesitas and hypertension in the last 3- 4 years. Laboratory findings revealed extremely high testosterone levels. Left adrenalectomy because of benign adenoma two years ago was performed. Ultrasound of the ovaries showed no abnormalities, as well as the CT of the abdomen and pelvis. Furthemore FDG PET/CT was requested and revealed increased metabolic activity in the region of the right adnexa (SUV max=8.8), which suggested performing bilateral adnexectomy. Pathology reported adrenocortical carcinoma metastatic to ovary. Second opinion for the histopathology report of the left adrenalectomy was requested and confirmed the diagnosis of benign adenoma. Afterwards second opinion for the right ovarian tumor was asked and the final diagnosis was benign Sertoli-Leydig tumor of right ovary with compressed ovarian tissue in normal sized ovary. After the surgical intervention , patient's testosterone level returned to normal. ***Conclusion:*** Sertoli-Leydig tumor of the ovary is a rare mostly benign tumor presenting with excessive serum testosterone level and variable signs of virilisation. FDG PET/CT plays important role in detecting the tumor and aiding in surgery decision when conventional imaging methods show no structural abnormalities ***References:*** https://pmc.ncbi.nlm.nih.gov/https://www.ejgm.co.uk/download/challenges-in-diagnosing-ovarian-sertoli-leydig-cell-tumorsa-peruvian-case-series-15149.pdfarticles/PMC10074573/

EP-1359

Unexpected metastasis from sigmoid cancer- where? a case report

T. Yordanova, *A. Klisarova, T. Stoeva, M. Dyankova, S. Chausheva, Z. Dancheva, B. Chaushev;*
Medical University Prof. dr. P. Stoyanov, Deparment of nuclear medicine, Varna, Bulgaria, Varna, BULGARIA.

Aim/Introduction: Colorectal metastases to thyroid are rare. Usually colorectal metastases in the thyroid occurs many years later after the primary colorectal cancer has been diagnosed and treated. It has been reported that 1.4%-3% of patients who underwent surgery for thyroid tumors are diagnosed as metastasis from other carcinomas (1) As these metastases are often asymptomatic, they are usually discovered incidentally on imaging performed as follow-up for the primary tumour. ***Materials and Methods:*** We present the case of an 46-year-old female with a history of sigmoid adenocarcinoma in 2017 treated with surgery and chemotherapy, who 4 years later FDG-PET/CT discovered incidentally on imaging performed as follow-up for the primary tumour. She was diagnosed stage pT3pN1cM0 before presentation and she has also underwent palliative chemotherapy and surgary for distant metastasis of sigmoid cancer. ***Results:*** The Follow-up FDG-PET/CT scan in 2021 revealed the presence of a previously undiagnosed nodule in the thyroid gland, a 19 mm subtly hypermetabolic nodule in the right thyroid lobe. The sigmoid origin of the mass was confirmed with a biopsy. ***Conclusion:*** This case shows that the thyroid can be a site of metastatic disease and a rare presentation of metastatic sigmoid cancer. Metastasis of malignant tumours to the thyroid gland are uncommon and they have been mainly observed in lung, renal and breast carcinoma. Cases of metastases from colon rectal cancer, are extremely rare [2, 3]. The prevalence of thyroid metastases from sigmoid cancer may be underestimated,

as many patients are asymptomatic and these metastases are not commonly searched for. FDG-PET/CT is a powerful non-invasive imaging tool method for detecting unsuspected asyptomatic metastases in unusual locations. ***References:*** 1. Lièvre A, Leboulleux S, Boige V, Travagli JP, Dromain C, Elias D, et al. Thyroid metastases from colorectal cancer: the Institut Gustave Roussy experience. Eur J Cancer 2006;42:1756-1759. 2. Nakhjavani MK, Gharib H, and Goellner JR, et al (1997) Metastasis to the thyroid gland: a report of 43 cases Cancer 79 574-578 MID: 9028370 3. Poon D, Toh HC, and Sim CS et al (2004) Two case reports of metastases from colon carcinoma to the thyroid Ann Acad Med Singapore 33 100-102 http://www.embase.com/search/results?subaction=viewrecord&from=export & id=L38478120\ nhttp://sfx.library.uu.nl/utrecht?sid=EMBASE&issn=03044602&id=doi:&atitle=Two Case Reports of Metastases from Colon Carcinoma to the Thyroid&stitle=Ann. Acad. Med. Singapor

EP-1360

Unexpected Extrarenal Uptake of Tc-99m EC on Renal Scintigraphy in a Patient with Renal Transplantation

M. Ahmadi, *S. Barashki, A. Saber Tanha, H. Elahifard;*
Nuclear Medicine Research Center, Mashhad University of Medical Sciences, Mashhad, IRAN, ISLAMIC REPUBLIC OF.

Aim/Introduction: Technetium-99m Ethylene Dicysteine (Tc-99m EC) dynamic scintigraphy is a widely utilized imaging modality for assessing renal function and diagnosing complications in patients with renal transplants. While the primary focus of this technique is to evaluate renal perfusion and function, extrarenal uptake of radiotracers can occasionally occur, leading to unexpected findings that may complicate the interpretation of results. This case report presents a 53-year-old male with a history of bilateral kidney transplantation who exhibited an unusual pattern of extrarenal tracer uptake during a Tc-99m EC scintigraphy study. The identification of this unexpected uptake, localized to a fracture in the right pubic bone, underscores the importance of recognizing atypical imaging patterns and their potential implications for clinical practice. ***Materials and Methods:*** The dynamic scintigraphy was conducted following the intravenous administration of 5 mCi (185 MBq) of Tc-99m EC. Blood flow images were acquired in the anterior view at a rate of 2 seconds per frame, followed by functional phase images captured at 1 minute per frame. The imaging protocol aimed to assess both renal perfusion and function. ***Results:*** Dynamic scintigraphy revealed normal perfusion in the left lower quadrant (LLQ) transplanted kidney, while the right lower quadrant (RLQ) transplanted kidney exhibited severely decreased tracer uptake. The functional phase images confirmed normal function in the LLQ kidney and significantly reduced function in the RLQ kidney. Notably, an unexpected area of increased Tc-99m EC activity was observed in the lower pelvic region on both the perfusion and functional images. SPECT/CT imaging was conducted to further elucidate the source of the abnormal tracer accumulation. The imaging results revealed a fracture in the right pubic bone, which correlated with the elevated Tc-99m EC uptake. ***Conclusion:*** This case highlights the clinical significance of recognizing atypical patterns of Tc-99m EC uptake during renal scintigraphy, particularly in patients with renal transplants. The incidental identification of a bone fracture through SPECT/CT imaging not only provided valuable insights into a non-renal pathology but also emphasized the need for clinicians to consider extrarenal tracer accumulation in their diagnostic evaluations. Such awareness can enhance the accuracy of interpretations and improve patient management in similar clinical scenarios. This report serves as a reference for clinicians, broadening their understanding of the diagnostic potential of renal scintigraphy and the implications of unexpected imaging findings.

EP-1361

99mTc-PSMA Uptake in Neurofibroma

M. Samadi, *P. Sahafi, H. Elahifard, E. Askari, S. Davoodi;*
Mashhad university of medical sciences, mashahd, Iran, Mashhad, IRAN, ISLAMIC REPUBLIC OF.

Aim/Introduction: Prostate-specific membrane antigen (PSMA) imaging has emerged as a valuable tool for staging and restaging prostate cancer, particularly in high-risk cases. Although PSMA expression is predominantly associated with prostate adenocarcinoma and tumor neovasculature, several benign and non-prostatic malignancies may demonstrate PSMA uptake. This report presents a unique case of PSMA-avid neurofibroma identified incidentally during PSMA-targeted SPECT/CT imaging for prostate cancer staging, highlighting a diagnostic pitfall and expanding the spectrum of PSMA-avid lesions. ***Materials and Methods:*** A 74-year-old male with a recent diagnosis of high-risk prostate adenocarcinoma (Gleason score 5+4) involving 11 of 14 biopsy cores, with intraductal carcinoma and perineural invasion, underwent staging with 99mTc-HYNIC-PSMA SPECT/CT. The patient's serum PSA level was 15.3 ng/dL at the time of imaging. A dose of 20 mCi (740 MBq) of 99mTc-HYNIC-PSMA was administered intravenously, and whole-body planar and SPECT/CT images were acquired 3 hours post-injection. ***Results:*** Imaging demonstrated intense radiotracer uptake in the prostate gland and pelvic lymphadenopathy, consistent with primary tumor and nodal metastases. Additional uptake was noted in the thoracic vertebra, suggesting early osseous metastasis. Incidentally, a focus of increased PSMA uptake was detected in the left occipital scalp region. SPECT/CT revealed a subcutaneous nodule with moderate PSMA avidity (PSMA expression score: 1), which was erythematous and palpable on physical examination. Given the patient's very-high-risk status, the lesion was initially suspected to represent cutaneous metastasis. Excisional biopsy revealed histopathologic features consistent with a neurofibroma. Immunohistochemistry showed S100 positivity and negativity for Melan-A, CD34, and cytokeratin ***Conclusion:*** This case illustrates the potential for benign lesions, such as neurofibromas, to exhibit PSMA uptake, likely due to increased capillary permeability or neovascularization rather than true tumor expression of PSMA. Awareness of such PSMA-avid benign entities is crucial to avoid misinterpretation and unnecessary intervention. Histological confirmation should be considered for atypical or unexpected sites of uptake, especially in high-risk patients.

EP-1362

Radio-Guided Monitoring of Systemic Leakage With 99mTc-MAA Uptake in a Patient With Melanoma During Isolated Limb Perfusion

M. Samadi, *S. Khezri, E. Hasanzadeh Hadad, R. Sadeghi, A. Aghaee;*
Mashhad university of medical sciences, mashahd, Iran, Mashhad, IRAN, ISLAMIC REPUBLIC OF.

Aim/Introduction: Isolated limb perfusion (ILP) is a well-established treatment option for patients with locally advanced or in-transit metastatic melanoma, providing high local drug concentrations with limited systemic toxicity. Various radiotracers have been employed for leakage monitoring during ILP. Here, we present a case of a 65-year-old woman with recurrent melanoma treated with ILP using melphalan and intraoperative leakage assessment with 99mTc-labeled macroaggregated albumin (MAA), a novel application for this radiotracer in this context. ***Materials and Methods:*** A 65-year-old woman with a history of melanoma on the left foot, following a burn at age 15, underwent prior resection, inguinal lymph node dissection, and radiation therapy. She developed in-transit metastases treated with

additional surgery and external beam radiation. Recurrence with dermal nodular lesions led to consideration for ILP. Under general anesthesia, the femoral vessels were cannulated and connected to a closed perfusion circuit. A tourniquet was applied to the limb base. 99mTc-labeled MAA was added to the circuit for leakage detection. A gamma probe was placed over the jugular vein to monitor systemic tracer activity. Upon confirming no leakage, melphalan 50 mg was infused over 1 hour. The limb was then flushed, and the procedure completed. ***Results:*** A whole-body scan performed 3 hours after surgery demonstrated no significant tracer accumulation outside the perfused limb, confirming the absence of systemic leakage. Intense radiotracer uptake was localized to the treated limb. Compared to previous studies using 131I- or 123I-labeled albumin or 99mTc-HSA, this is the first known report of using 99mTc-MAA for leakage assessment in ILP, demonstrating effective tracer retention within the isolated circulation. ***Conclusion:*** This case highlights the novel use of 99mTc-labeled MAA for intraoperative leakage detection during isolated limb perfusion in melanoma. The method provided clear imaging of localized tracer distribution with no systemic spread, confirming its potential as a safe and effective alternative to previously used agents. Further studies may validate its broader clinical utility.

EP-1363

The Quiet Life-Threatening Event: Sudden Respiratory Failure During a Prolonged Dynamic Scintigraphy Procedure

M. Samadi, *S. Khezri, P. Sahafi, A. Aghaee;*
Ghaem Hospital, Mashhad university of medical sciences, Mashahd, Iran, Mashhad, IRAN, ISLAMIC REPUBLIC OF.

Aim/Introduction: Massive lower gastrointestinal bleeding (rectorrhagia) is a medical emergency that often necessitates prompt localization of the bleeding source. While endoscopy and colonoscopy are the primary diagnostic modalities, they may fail to detect intermittent or slow bleeding. In such cases, nuclear medicine imaging, specifically with 99mTc-labeled red blood cells (99mTc-RBC), is a valuable non-invasive diagnostic tool. Patients with chronic obstructive pulmonary disease (COPD) undergoing prolonged imaging are at increased risk for hypoxia-related complications, which can mimic or be mistaken for procedural anxiety or claustrophobia. Differentiating these entities is essential for appropriate management. ***Materials and Methods:*** We report the case of a 74-year-old man with history of COPD who presented with massive rectorrhagia and was referred for a 99mTc-RBC scan after normal findings on endoscopy and colonoscopy. He had received three units of packed red blood cells prior to imaging, with a post-transfusion hemoglobin level of 9.5 g/dL. A dynamic scintigraphic study was performed immediately after intravenous injection of 20 mCi (740 MBq) of 99mTc-RBC, acquiring images at 30-second intervals for one hour. Additional 20-minute dynamic acquisitions were conducted every 30 minutes based on initial findings. Pulse oximetry and vital signs were monitored following an episode of unexpected patient agitation during the scan. ***Results:*** Initial dynamic images demonstrated suspicious focal activity (Panel A), prompting continuation of imaging. However, the patient became agitated and attempted to leave the imaging room, reporting discomfort without clear explanations. Vital signs revealed a respiratory rate of 24 breaths per minute and oxygen saturation (SpO_2) of 80%. Supplemental oxygen at 5 L/min via face mask was administered, resulting in improved SpO_2 (96%) and resolution of agitation. Imaging resumed, and the previously suspicious activity was identified as physiological uptake within abdominal vessels (Panel B). Upon arrival, the patient's respiratory rate had been 16 breaths per minute with SpO_2 of 98% on supplemental oxygen, which had been discontinued at the patient's request during acquisition due to lack of dyspnea. ***Conclusion:*** This case highlights the critical need to monitor oxygenation during prolonged nuclear medicine procedures in patients with underlying pulmonary disease. Hypoxia can present with neuropsychiatric symptoms such as agitation and irritability, potentially mimicking claustrophobia. Differentiation between hypoxia-induced agitation and anxiety is essential, as mismanagement—such as the inappropriate use of sedation—can exacerbate hypoxia. Prompt recognition and treatment with supplemental oxygen can stabilize the patient, improve cooperation, and avoid unnecessary imaging repetition, thereby reducing radiation exposure and healthcare costs.

EP-1364

Radiation recall pneumonitis following durvalumab immunotherapy in a lung cancer patient detected by ^{18}F-FDG PET/CT.

N. Vavlas, *A. Morfesi, V. Mpalaris, D. Katsampoukas, S. Georga, E. Moralidis, G. Arsos;*
3rd Department of Nuclear Medicine. Aristotle University of Thessaloniki School of Medicine,Papageorgiou General Hospital, Thessaloniki, GREECE.

Aim/Introduction: Radiation recall pneumonitis (RRP) is a rare inflammatory reaction occurring within previous radiation port sites, usually triggered by a variety of agents including chemotherapy, vaccines, anti-TB or other antibiotics and immune check point inhibitors (CPI). With the wide application of CPI in combination with chemo and radiation therapy in lung cancer, RRP is expected to be increasingly detected by ^{18}F-FDG PET/CT. As RRP may anticipate generalized CPI associated pneumonitis, its recognition is important for prevention of this serious complication and also for avoidance of false positive diagnoses of infection or cancer relapse [1. 2]. ***Materials and Methods:*** A 67-year-old male diagnosed with right hiliar NSCLC was initially treated with immuno-chemotherapy, followed by consolidative radiotherapy. Maintenance immunotherapy with the CPI (PD-L1) Durvalumab was initiated therafter. A total of five ^{18}F-FDG PET/CT scans performed during the disease course from July 2023 to April 2025. Clinical information and PET imaging findings were integrated to establish the diagnosis and guide therapeutic decisions. ***Results:*** After several cycles of Durvalumab after radiotherapy (Dec 2023), a follow up ^{18}F-FDG PET/CT scan on May 2024 showed new moderately hypermetabolic (SUVmax 4,6) fibrotic and atelectatic changes, within the radiation portfield in the right lower lobe, interpreted as potential post-radiation inflammation. With continued Durvalumab therapy, a subsequent ^{18}F-FDG PET/CT on Sept 2024 revealed increasing size and activity (SUVmax 5,9) of the lesions of the RLL, along with new hypemetabolic (SUVmax 4,6) lesions in the middle lobe, suggesting evolving inflammatory pathology. As the patient had no signs of infection, a potential diagnosis of RRP was suggested and the PCI therapy was discontinued. A follow-up ^{18}F-FDG PET/CT 7 months later (April 2025) showed complete metabolic remission and significant size reduction of all lesion in the right lung, thus retrospectively supporting the diagnosis of RRL. ***Conclusion:*** This case illustrates how ^{18}F-FDG PET/CT can correctly identify radiation recall pneumonitis cases thus preventing dentrimental CPI complications and avoiding false positive diagnoses. Awarreness of the entity is required along with detailed information about the treatmemt regimen of the patient. ***References:*** (1) Jan PR, Chang JW, Wu CE. Radiation Recall Pneumonitis: A Rare Syndrome That Should Be Recognized. Cancers (Basel) 2022;14(19):4642.(2) Grassi F, Granata V, Fusco R, De Muzio F, Cutolo C, Gabelloni M, et al. Radiation Recall Pneumonitis: The Open Challenge in Differential Diagnosis of Pneumonia Induced by Oncological Treatments. J. Clin. Med.2023, 12, 1442.

EP-1365

Incidental finding of Medullary Thyroid Carcinoma on 18F-DCFPyL PET/CT performed in the staging of High-Risk Prostate Cancer

L. Mena Bares, *M. Sánchez Torrente, E. Moratalla Aranda, S. Martín Aguilar, M. Ureña Lara;*
Hospital Universitario Jaén, Jaén, SPAIN.

Aim/Introduction: Prostate cancer (PCa) is the second most common male cancer worldwide. Accurate disease staging is of utmost importance, and PET/CT using prostate-specific-membrane-antigen (PSMA) ligands has proven superior to conventional imaging for primary staging of metastatic disease. Accordingly, updated prostate cancer guidelines now recommend PSMA PET/CT at the front-line imaging modality for initial staging of unfavorable intermediate or high-risk prostate cancer. PSMA is a transmembrane protein with significantly increased expression in prostate cancer cells compared to normal prostate tissue but PSMA is not specific to prostate tissue. Has also been found in the neovasculature of a variety of other malignancies such as renal cell carcinoma, neuroendocrine tumors, melanoma, colon carcinoma, lung cancer, thyroid cancer or breast cancer. The incidence of PSMA thyroid incidentaloma (PTI) varies among different tracers: 68 Ga-PSMA-11 (7-23%), 18F-PSMA-1007 (29-64%), or 18F-DCFPyL (2-8%). PSMA expression was related to malignant disease, poor prognostic factors and poorer progression free survival. ***Materials and Methods:*** A 73-yerars-old man with suspicion of PCa had a Prostate-Specific-Antigen (PSA) level at 5,6 ng/ml and Magnetic Resonance imaging scans showed a positive image a peripheral zone in the left lobe of prostate gland (PIRADS-4). The prostate biopsy indicated an Adenocarcinoma, Gleason Score=4+4 in the right lobe and Gleason Score=4+3 in the left lobe, and we can classify the patient into the high-risk group. A 18F-DCFPyL PET/CT was requested for initial staging. ***Results:*** 18F-DCFPyL PET/CT scan showed intensely PSMA-expressing lesions in prostate: Left lobe Midportion- posterolateral peripheral zone (SUVmax:14,18. Primary Score 5) and anterior perihepral zona (SUVmax:7,23. Primay Score 4). Right lobe Midportion -- posterolateral peripheral zone (SUVmax:11,37. Primary Score 4) and Right lobe Apex -- anterior/posterior transition zone (SUVmax: 6,3. Primary Score 3). Intense focal PSMA uptake (SUVmax:12,44), is observed in the hypodense nodule in the left lobe of thyroid gland of size 2,5 cm. The patient underwent ultrasound of the neck and guided fine-needle aspiration cytology (FNAC) from suspicious thyroid nodule (TIRADS-5) which demonstrated a medullary thyroid carcinoma (MTC). ***Conclusion:*** PTIs frequently signal the presence of unexpected lesions in the thyroid which differ from the indicated reason for which the patient was initially scanned and MTC is a rare case among PTIs. The uptake of PSMA open the possibility of theranostic application in patients with MTC who have limited treatment options. ***References:*** Donswijk ML, et al. Incidence of PSMA PET thyroid incidentaloma depends on analysis method and tracer. Eur Radiol 2023; 33: 3377-85.

EP-1366

Unusual Presentation of a Pancreatic Neuroendocrine Tumour

A. Bagán-Trejo[1], *J. L. Vercher-Conejero*[1], *J. J. Martín-Marcuartu*[1], *M. Tormo-Ratera*[1], *J. C. Ruffinelli*[2], *I. Peiró*[3], *B. Hervás-Sanz*[1], *J. L. Díaz-Moreno*[1], *M. Zamorano-Rivas*[1], *M. Á. Crespí-Busquets*[4], *C. García-Alcober*[4], *M. Cortés-Romera*[1];
[1]*Nuclear Medicine-PET (IDI) Department, Hospital Universitari de Bellvitge-IDIBELL, L'Hospitalet de Llobregat, SPAIN,* [2]*Oncology Department, Institut Català d'Oncologia, L'Hospitalet de Llobregat, SPAIN,* [3]*Endocrinology Department, Hospital Universitari de Bellvitge, L'Hospitalet de Llobregat, SPAIN,* [4]*Radiopharmacy Department, Hospital Universitari de Bellvitge-IDIBELL, L'Hospitalet de Llobregat, SPAIN.*

Aim/Introduction: Pancreatic neuroendocrine tumours (PanNETs) represent 1-3% of all pancreatic tumours, with a prevalence of less than 1 per 100.000 individuals. Functioning PanNETs account for 30-40% of cases, the most common ones being insulinomas (1-4 cases per 1.000.000 individuals) and gastrinomas (0.5-3 cases per 1.000.000 individuals). ***Materials and Methods:*** We report the case of a 66-year-old male with no significant medical history who presented with asthenia, right-sided supraclavicular lymphadenopathy, easy bruising, and centripetal weight gain involving the face, abdomen and legs. He had recently developed hypertension, for which he was put on ACEI medication. Blood tests showed hypokalaemia, hypernatremia, thrombocytopenia and elevated cortisol levels. Following this, the patient was diagnosed with ectopic Cushing syndrome. A contrast-enhanced thoracoabdominal CT identified a 4.8mm growth in the distal pancreas with vascular involvement, bilobar liver metastases, and splenomegaly. ***Results:*** Liver biopsy confirmed metastatic well-differentiated pancreatic neuroendocrine tumour, immunohistochemically positive for adrenocorticotropic hormone (ACTH). The thrombocytopenia was attributed to splenic sequestration from hilar compression, though a paraneoplastic mechanism could not be excluded. A [^{68}Ga]Ga-SSA PET/CT was performed to assess the possibility of distant metastatic disease. It revealed moderate heterogeneous uptake in the pancreatic lesion and moderate homogeneous uptake in liver metastases, without additional lesions. Given the moderate uptake and suspicion of tumour heterogeneity, an [^{18}F]F-FDG PET/CT was also performed. It showed a moderate heterogeneous uptake in the known lesion although encompassing a wider area, reaching the body of the pancreas, suggesting the tumour could be bigger than anticipated. Moderate homogeneous uptake was also observed in the liver metastases, and no additional uptake was observed. Following discussion in the multidisciplinary NETs board, the patient was initiated on chemotherapy with Streptozotocin and 5-fluorouracil after stabilisation of the thrombocytopenia. Ultimately, he succumbed to complications including grade 3 anaemia and thrombocytopenia, Pneumocystis jirovecii pneumonia, acute pancreatitis, and Escherichia coli bacteraemia. ***Conclusion:*** ACTH-secreting PanNETs are exceedingly rare and may present with ectopic Cushing syndrome. This case underscores their diagnostic and therapeutic complexity, as well as their possibly aggressive course. Dual-tracer PET/CT imaging proved essential in characterising tumour heterogeneity and extent, providing complementary information critical for disease staging and therapeutic planning. ***References:*** Alshareefy Y, Cummins S, Mazzoleni A, Sharma V, Guggilapu S, Leong AWY, Wireko AA. A review of functional pancreatic neuroendocrine tumors: Exploring the molecular pathogenesis, diagnosis and treatment. Medicine 2023;102:46(e36094).

EP-1367

Exceptional ^{18}F-FDG Uptake in White Adipose Tissue Induced by Systemic Glucocorticoid Therapy

M. Ulucay, *A. Dere, H. B. Kapucu, I. Ozturk, B. E. Akkas;*
Health Sciences University,Basaksehir Cam and Sakura City Hospital, Istanbul, TÜRKIYE.

Aim/Introduction: A study on the evaluation of atypical F-18 FDG uptake patterns. ***Materials and Methods:*** A 46 year-old woman with adenocarcinoma metastasis in cerebellum was referred to PET / CT scan for the detection of an unknown primary malignancy. On 18F- FDG PET/CT scan altered biodistribution of FDG was observed with diffuse intense uptake in white adipose tissue (WAT) . The patient had the history of high dose glucocorticoid use for prevention of compression symptoms 37 days prior to scan .Under normal circumstances FDG metabolism is negligible in WAT, alterations in adipose tissue metabolism are uncommon. We consider this case as an interesting image for the unusual intense

FDG uptake in WAT associated with high-dose corticosteroid therapy. ***Results:*** A 46-year-old woman with no prior medical history presented to our center with sudden onset of dizziness and nausea symptoms. Advanced imaging identified cerebellar mass. Surgical preparations for the cerebellar mass have commenced, corticosteroid therapy has been initiated at a daily dose of 16 mg dexamethasone to prevent mass effect. 37 days after the initiation of corticosteroid therapy, the patient was referred to us for PET/CT imaging to investigate the primary etiology. Adequate fasting was ensured before the PET/CT scan, with a fasting blood glucose level of 100 mg/dl. Additionally, the patient did not exhibit a cushingoid appearance and showed no clinical signs suggestive of Cushing's syndrome. Imaging obtained 60 minutes post-injection of 18F-FDG at a dose of 6 mCi revealed a lesion in the posterior basal segment of the right lower lobe, approximately 32 mm in size , potentially consistent with primary lung cancer . Notably, MIP imaging highlighted increased ^{18}F-FDG uptake in adipose tissue rather than in muscle tissue in the upper body segment . ***Conclusion:*** Typically, the body contains three types of adipose tissue: white, beige, and brown and ^{18}F-FDG uptake in white adipose tissue is not generally anticipated. Previous literature has identified several factors associated with increased activity in white adipose tissue, including antiretroviral therapy in HIV infection, steroid therapy, and Cushing's syndrome. Glucocorticoid therapies are well-documented to affect lipid metabolism, primarily through inducing adipose tissue hyperplasia; however FDG uptake in WAT is not generally increased. This case demonstrates exceptional FDG uptake in WAT induced by systemic glucocorticoid therapy even in the absence of cushingoid clinical features.

EP-1368

The value of sequential imaging review in localizing an occult primary Neuroendocrine Tumor: A Case Report

L. Castillejos, *C. Paniagua, S. Pérez Quirós, A. Ortega Valle, M. Tagliatori, A. Herrero, M. de la Rubia, D. Rodríguez Oviedo, C. Galindo, K. Guichay, M. García Alonso;*
Hospital Universitario de Getafe, Madrid, SPAIN.

Aim/Introduction: Approximately 11% to 14% of subjects with neuroendocrine tumor (NETs) have metastatic lesions with unknown primary origin, with the majority found in the small bowel. The identification of the primary tumor is important as it affects the prognosis and remains a diagnostic challenge. Although somatostatin receptor scintigraphy is a key diagnostic tool, its sensitivity is limited. We present a case in which detailed and comparative review of previous imaging studies enabled the localization of a previously undetected small bowel primary tumor. ***Materials and Methods:*** A 55-year-old male was evaluated for suspected metastatic NET with a mesenteric lymph node enlargement, but no evident primary tumor. A scintigraphy with 99mTc-octreotide was performed, including early planar abdominal images at 30 minutes and whole-body scan, followed by SPECT/CT of the thorax and abdomen 2 hours after tracer injection. Tomographic images revealed a hypermetabolic nodular lesion in the mesenteric root, with no clear identification of a primary site. A biopsy of the lesion showed fibroinflammatory tissue. Due to persistent lymphadenopathy and ongoing clinical suspicion, a second 99mTc-octreotide scan was requested three years later. ***Results:*** The second study was carefully reviewed and compared with the initial scan. In the SPECT/CT, in addition to the persistent mesenteric lymphadenopathy, a focal uptake was observed in a jejunoileal loop adjacent to the hepatic flexure of the colon. Retrospective analysis of the first scan revealed a subtle uptake at the same location, previously interpreted as physiological intestinal activity. The patient underwent surgery with exploration of the intestinal region indicated in the scan. A lesion was identified and resected. Histological analysis confirmed a well-differentiated NET in a jejunoileal loop and metastasis in a mesenteric lymph node.This case underscores the importance of reviewing previous studies when evaluating patients with NETs of unknown primary origin. Factors such as physiological bowel activity, subcentimetric lesion size, and the limited spatial resolution of scintigraphy can hinder initial detection. The persistence of a focal uptake at the same location in repeated studies strongly suggests a true lesion. Furthermore, integrating hybrid imaging modalities like SPECT/CT increases diagnostic sensitivity. ***Conclusion:*** Systematic comparison of imaging studies over time is essential in the evaluation of patients with metastatic NETs of uncertain origin. Identifying subtle but persistent findings can significantly alter therapeutic decisions and improve clinical outcomes.

EP-1369

Fibrous Dysplasia with 99m Tc-FAPI Uptake in a Patient Under Long-Term antiresorptive Therapy

M. Samadi, *P. Sahafi, A. Aghaee;*
Ghaem Hospital, Mashhad university of medical science, Mashhad, IRAN, ISLAMIC REPUBLIC OF.

Aim/Introduction: Fibrous dysplasia (FD) is a rare, benign bone disorder caused by postzygotic activating mutations in the GNAS gene, leading to replacement of normal bone with immature fibrous tissue. Craniofacial FD presents unique challenges due to aesthetic, functional, and neurological complications. Conventional bone imaging with tracers like 99mTc-MDP is limited to assessing osteoblastic activity and may not fully represent fibroblastic or stromal components. Fibroblast activation protein inhibitor (FAPI) imaging has emerged as a promising modality for detecting fibrotic lesions. While FAPI uptake has been demonstrated in FD using 68Ga-labeled compounds, uptake using 99mTc-FAPI has not previously been documented. We report the first known case of FD imaged with 99mTc-FAPI SPECT/CT, highlighting its potential role in assessing active fibroblast proliferation in fibrous dysplasia. ***Materials and Methods:*** A 40-year-old female patient with a 20-year history of craniofacial fibrous dysplasia involving the right maxilla, orbital cavity, and fronto-parietal bones was evaluated. She had undergone partial maxillary debulking surgery seven years prior and orbital decompression three years ago. She received intravenous Zoledronic acid monthly for six years and switched to Denosumab therapy one year ago due to inadequate disease control.Planar whole-body and SPECT/CT scans were performed on two separate days. First, a 99mTc-MDP scan was acquired three hours post-injection of 20 mCi (740 MBq). On another day, a 99mTc-FAPI scan was performed one hour after intravenous injection of the same dose. Imaging findings were analyzed to identify sites of radiotracer uptake correlating with known FD lesions. ***Results:*** The 99mTc-MDP SPECT/CT revealed multiple sites of increased osteoblastic activity including the fronto-parietal bones, ethmoid, sphenoid, right maxilla, mandible, right scapula, humerus, radius, and lower thoracic and lumbar vertebrae. These areas corresponded to hyperdense lytic-sclerotic lesions with a ground-glass appearance.The 99mTc-FAPI SPECT/CT demonstrated focal uptake in cranial bones, right scapula, and L4 vertebra, consistent with known FD lesions. The uptake pattern was indicative of active fibroblast proliferation and matched, in part, the 99mTc-MDP findings but also revealed fibrotic activity independent of purely osteoblastic changes. ***Conclusion:*** This case represents the first reported instance of 99mTc-FAPI uptake in fibrous dysplasia. The findings suggest that 99mTc-FAPI SPECT/CT may provide complementary information to traditional bone scans by detecting fibroblast activation in FD lesions. This imaging modality could be particularly valuable in assessing disease activity in lesions with low osteoblastic turnover or with significant fibrous stroma.

EP-1370

Lipomatous Hypertrophy of the Interatrial Septum: Long-term ^{18}F-FDG Uptake variation on serial PET/CT scans in a Lung Cancer patient

A. Morfesi, *N. Vavlas, D. Katsampoukas, V. Mpalaris, S. Georga, E. Moralidis, G. Arsos;*
3rd Department of Nuclear Medicine, Aristotle University of Thessaloniki School of Medicine, Papageorgiou General Hospital, Thessaloniki, GREECE.

Aim/Introduction: Lipomatous Hypertrophy of the Interatrial Septum (LHIS) is characterized by excessive fat deposition in the interatrial septum (IS), typically diagnosed incidentally during imaging for other conditions. However, as it is commonly hypermetabolic [1], differentiation from other potentially malignant lesions like myocardial tumors, especially the lipomatous ones, or cardiac secondaries in oncological patients is critical in ^{18}F-FDG PET/CT, in order to avoid invasive diagnostic procedures. Little is known on LHIS behavior over time. ***Materials and Methods:*** A 65-year-old female had her first follow-up ^{18}F-FDG PET/CT 6 years after right upper lobectomy for lung adenocarcinoma, revealing a hypermetabolic, low density area along the IS. A cardiac MRI 3 months later was compatible with LHIS. The patient was not diabetic, had no cardiac disease and was off beta-blockers. A conservative watchful approach was selected and a total of six ^{18}F-FDG PET/CT scans performed from June 2022 to January 2025, showing considerable metabolic variation of the LHIS without gross morphological changes. The radiodensity was measured in Hounsfield units (HU) in non-contrast, low-dose CT and the metabolic activity was assessed by total body weight SUVmax and Total Lesion Glycolysis (TLG). ***Results:*** No signs of lung cancer relapse or extracardiac brown adipose tissue (BAT) activation were seen in any of the six PET scans. Radiodensity (HU), SUVmax (g/ml) and TLG (g) of the LHIS were: June 2022, -63.4, 11.6, 89.4; September 2022, -51.0, 4.6, 27.9; May 2023, -51.9, 2.5, 18.3; October 2023, -58.0, 6.2, 49.2; April 2024, -62.0, 4.9, 36.2 and January 2025, -61.0, 4.2, 32.0. No substantial change of the extent of the hypodense area of the IS was observed. The corresponding blood glucose levels after overnight fasting were 98, 93, 89, 109, 97 and 93 mg/dL respectively and the corresponding minimum/average temperature (in ^{0}C) in the residence area of the patient at the day of the scan was 22.7/27.7, 20.7/24.5, 14.5/17.0, 21.3/25.5,12.3/16.9 and 10.8/12.4 respectively. The maximum relative change (maximum-minimum/maximum %) in radiodensity, SUVmax and TLG during the observation period was 19.6, 78.4 and 79.5 respectively. ***Conclusion:*** LHIS shows anatomical consistency but considerable metabolic variation over time, not associated with temperature variation or extracardiac BAT activation. Follow-up with ^{18}F-FDG PET/CT can confirm the benign nature of the lesion thus avoiding invasive diagnostic procedures. ***References:*** [1] Fan CM, Fischman AJ, Kwek BH, Abbara S, Aquino SL. Lipomatous hypertrophy of the interatrial septum: increased uptake on FDG PET. AJR Am J Roentgenol. 2005 Jan;184(1):339-42.

EP-1371

Radioiodine Treatment Failure in Toxic Adenoma: Marine-Lenhart Syndrome

A. Vergili[1], *M. Acar Tayyar*[1], *E. Uyanık*[1], *F. Yıldız Kabaca*[1], *T. Özülker*[2];
[1]*Prof Dr Cemil Taşcıoğlu City Hospital, İstanbul, TÜRKIYE,* [2]*Prof Dr Cemil Tascıoğlu City Hospital, Istanbul, TÜRKIYE.*

Aim/Introduction: Marine-Lenhart syndrome is a rare condition characterized by the presence of one or more hyperfunctioning thyroid nodules in the setting of Graves' disease(prevalence:0.26%-4.1%).Antithyroid drugs(ATD) are generally ineffective,and the recommended treatment options include surgery or radioactive iodine(RAI) therapy.On thyroid scintigraphy,a hyperfunctioning nodule may obscure the evaluation of the thyroid parenchyma and mask the underlying Graves' disease.This case highlights the importance of considering Marine-Lenhart syndrome in patients initially diagnosed with toxic adenoma who exhibit persistent hyperthyroidism following RAI therapy. ***Materials and Methods:*** A diagnostic thyroid scintigraphy was performed using 5 mCi of technetium-99m. Radioiodine uptake at the 2nd and 24th hours was measured with 3 µCi of iodine-131.A therapeutic dose of 10 mCi of radioactive iodine (RAI) was administered. The diagnostic thyroid scintigraphy was repeated,and a 15 mCi RAI dose was administered. ***Results:*** A 55-year-old female patient diagnosed with toxic adenoma presented to the nuclear medicine department due to the persistence of symptoms (palpitations,irritability,weight loss) and failure to achieve remission with antithyroid drugs (ATD).Thyroid ultrasound and scintigraphy findings were consistent with toxic adenoma.Iodine uptake was 15% at 2 hours and 36% at 24 hours. The patient received 10 mCi of RAI and was followed up biweekly. Despite treatment, her hyperthyroidism worsened. Initial TSH was 0.02, and T4 was 0.76; three months after RAI, TSH dropped below 0.01, and T4 increased to 5.57 (Normal:TSH 2.12-4.50, T4 0.58-1.38). Due to clinical deterioration,repeat thyroid scintigraphy was performed,revealing decreased background activity in the left lobe and a hypoactive nodule with widespread increased uptake. Further evaluation revealed elevated thyroid autoantibodies, confirming Graves' disease(TRAb>40 IU/L [N:<1.75], TSI>30[N:0-1.3]).Iodine uptake was re-measured before a second RAI dose,showing a significant increase(38% at 2 hours,74% at 24 hours).A second dose of 15 mCi of RAI was administered. Two months later,the patient developed hypothyroidism and is currently being followed up with thyroid hormone replacement therapy.Discussion:Marine-Lenhart syndrome presents diagnostic and therapeutic challenges.ATD may be ineffectiveand standard RAI doses may fail due to underlying Graves' pathology masked by hyperfunctioning nodules.When clinical and biochemical responses are inadequate,repeated imaging and autoantibody testing are crucial.This case emphasizes the importance of suspecting Marine-Lenhart syndrome in patients with persistent or worsening hyperthyroidism following RAI therapy.Higher or repeated RAI doses may be required for definitive control. ***Conclusion:*** Early recognition of Marine-Lenhart syndrome is crucial to avoid delayed or ineffective treatment.In cases of RAI failure,reevaluation with repeat scintigraphy and antibody testing should be considered.

EP-1372

Radiation-Induced Osteoradionecrosis of the Ribs in a Patient with Breast Cancer: A Case Report

G. Fuso[1], *G. Bianciardi*[1], *C. M. P. Sgro*[1], *E. Greco*[1], *P. E. Orlandi*[2], *A. Romeo*[3], *S. Fanti*[4,3];
[1]*Policlinico Sant'Orsola-Malpighi, University of Bologna, Bologna, ITALY,* [2]*Ospedale Maggiore, Bologna, ITALY,* [3]*IRCCS Azienda Ospedaliero-Universitaria di Bologna, Bologna, ITALY,* [4]*University of Bologna, Bologna, ITALY.*

Aim/Introduction: Radiation-Induced Osteoradionecrosis (ORN) is a rare, severe and late complication of radiotherapy, characterized by necrotic, non-healing bone in previously irradiated areas, persisting without evidence of tumor recurrence. The pathophysiology involves radiation-induced damage leading to hypoxia, hypovascularity, and hypocellularity, impairing bone turnover and tissue regeneration. Clinically, patients may present with pain, swelling or even pathological fractures. Differential diagnoses include osteomyelitis, bisphosphonate-related osteonecrosis, and tumor recurrence. This paper describes a clinical case of radiation-Induced Osteoradionecrosis of the Rib in a Patient with Breast Cancer, emphasising the role of bone scintigraphy in the differential diagnosis. ***Materials and Methods:*** We report the case of a patient who presented with severe and

diffuse osteoarticular pain. Medical history includes bilateral breast cancer previously treated as follows: left quadrantectomy with axillary lymphadenectomy, radiotherapy and hormone therapy in 2004; right quadrantectomy with sentinel lymph node excision and radiotherapy in 2008; right mastectomy in 2014; and left mastectomy in June 2018. They whole-body bone scintigraphy, performed 3 hours after radiotracer injection, showed a diffuse increase in uptake involving symmetrically the anterior arches of the second, third, and fourth ribs on both sides: findings not reported in prior bone scintigraphy imaging. ***Results:*** Corresponding low-dose CT images showed a thin, band-like appearance of the affected ribs, with mild, homogeneous sclerosis, reduced visualization of the trabecular bone component, and no evidence of cortical disruption. These findings are more consistent with osteoradionecrosis as a long-term consequence of prior radiotherapy. ***Conclusion:*** While the diagnosis is predominantly clinical and typically supported by imaging modalities such as CT and MR, and occasionally corroborated by biopsy to rule out malignancy, this case underscores the pivotal role of bone scintigraphy in identifying metabolic bone disease in oncologic patients.

EP-1373

An atypical case of angiosarcoma in a breast cancer patient in [^{18}F]FDG PET-CT imaging

S. Özdemir, *A. Akbulut, M. Daşar, K. Demirel, G. Koca, M. Korkmaz;*
University of Health Sciences, Ankara Training and Research Hospital, Nuclear Medicine Department, Ankara, TÜRKIYE.

Aim/Introduction: Secondary angiosarcomas are exceedingly rare malignancies, typically observed in breast cancer patients who had underwent surgery and radiotherapy. We present a case of 52-year-old female with a history of left breast cancer treated with surgery and adjuvant therapy without radiotherapy. Thirteen years later, she developed secondary angiosarcoma with atypical localization in the left upper extremity. Our case highlights the occurrence of angiosarcoma in the absence of radiotherapy and underscores the importance of considering vascular malignancies in breast cancer survivors, even without common risk factors. ***Materials and Methods:*** A 52-year-old female patient with a history of breast cancer, previously treated with surgery and adjuvant therapy, underwent FDG PET/CT imaging. Although there were no findings suggestive of primary pathology, low-level increased FDG uptake was detected in the subcutaneous tissue of the left upper arm and potentially be confused with radioactive extravasation. Clinical follow-up was recommended. After three months follow up PET/CT revealed increased soft tissue density and elevated FDG uptake in the same left upper arm region and excisional biopsy specimen confirmed angiosarcoma. ***Results:*** ***Conclusion:*** Secondary angiosarcomas are described in the literature as arising within irradiated fields or in association with chronic lymphedema. However, in our case there was no history of radiotherapy to the breast or axillary region. Unlike most reported cases, the patient presented with minimal lymphedema in her left upper extremity without any other associated symptoms. Initial FDG PET/CT imaging demonstrated low-level increased FDG uptake in the left arm, that was initially indistinguishable from radioactive tracer extravasation. Follow up image revealed progressive soft tissue thickening and intensifying FDG avidity, prompting histopathological correlation that confirmed angiosarcoma. This highlights the clinical significance of serial FDG PET/CT in detecting occult vascular malignancies. While postoperative alterations in lymphatic drainage may have contributed to tumorigenesis, the exact pathogenesis remains unclear, and further large-scale studies are warranted to elucidate non-radiation-associated mechanisms of secondary angiosarcoma development.

EP-1374

Extensive abdominal splenosis more than half a century after traumatic splenic rupture: the way from CT to ^{18}F-FDG PET/CT and to precise diagnosis with Tc-99m-labelled heat denatured red blood cell SPECT/CT

S. Georga, *N. Vavlas, A. Morfesi, V. Mpalaris, D. Katsampoukas, E. Moralidis, G. Arsos;*
3rd Department of Nuclear Medicine, Aristotle University Medical School, Papageorgiou General Hospital, Thessaloniki, GREECE.

Aim/Introduction: Splenosis is a benign condition caused by spontaneous heterotopic autotransplantation of splenic tissue within the peritoneal or thoracic cavity, typically after spleen rupture and/or splenectomy. Splenosis is usually accidentally found, but when extensive it may be diagnostically challenging as symptoms can suggest oncological disease. Usually CT and MRI can offer accurate diagnosis of splenosis; in ambiguous cases however, Tc-99m-labelled heat denatured red blood cell (HDRBC) scintigraphy remains the highly specific gold standard for a reliable diagnosis thus avoiding invasive diagnostic procedures. ***Materials and Methods:*** A 64-year-old male with a remote history of traumatic splenic rupture and splenectomy at the age of 10 was referred for abdominal CT because of abdominal complaints. Upper and lower GI endoscopy revealed gastritis and a colon polyp removed was proven not malignant. As CT reported both multiple nodular masses and abdominal lymphadenopathy, the patient was referred for further investigation with ^{18}F-FDG PET/CT 2 months later, showing multiple mildly hypermetabolic nodular masses not consistent with malignancy and the suggested diagnosis of multifocal splenosis was finally confirmed by positive Tc-99m-HDRBC scintigraphy. ***Results:*** The initial contrast-enhanced CT on December 2024 reported bilateral ureteronephrolithiasis, splenectomy and multiple nodular masses in the mesenteric folds, splenic fossa, greater omentum and subhepatic space as well as enlarged left paraureteral, parapancreatic, paraortic and portohepatic lymph nodes concluding a differential diagnosis between splenosis and lymphadenopathy. ^{18}F-FDG PET/CT performed on February 2025 revealed multiple mildly hypermetabolic (SUVmax up to 1.9, a value well within the normal range of splenic metabolism) nodular masses mainly in the left side of the greater omentum and the left paracolic gutter, not compatible with malignancy, but no lymphadenopathy. The diagnosis of multifocal splenosis was thus suggested, subsequently confirmed by Tc-99m-HDRBC SPECT/CT on May 2025, showing multiple foci of avid uptake of radiolabeled denatured red blood cells anatomically corresponding to the findings of both CT and ^{18}F-FDG PET/CT. ***Conclusion:*** This case reminds that massive/multifocal, clinically symptomatic abdominal splenosis may be proven a diagnostic challenge for CT. ^{18}F-FDG PET/CT can indirectly contribute to diagnosis by minimizing the possibility of malignancy. Tc-99m-labelled heat denatured red blood cell scintigraphy especially with SPECT/CT imaging, can settle an accurate, anatomically detailed diagnosis of splenosis relieving the patient from invasive diagnostic procedures.

EP-1375

Multimodal Imaging in Corticobasal Syndrome with Alzheimer's Pathology: A Case Report

M. Sanchez Torrente[1], *A. Sanchez Torrente*[2], *P. Guardia Jimena*[1], *M. Ureña Lara*[1];
[1]*Department of Nuclear Medicine - Hospital Universitario de Jaén, Jaén, SPAIN,* [2]*Department of Radiology - Hospital Universitario Torrecardenas, Almeria, SPAIN.*

Aim/Introduction: Corticobasal syndrome(CBS) is a disorder characterized by asymmetric akinetic-rigid syndrome, higher order sensory deficits, and cognitive impairment.The clinical diagnosis of CBS has been associated with different neuropathologic substrata, including corticobasal degeneration(CBS-CBD), Alzheimer

disease(CBS-AD), and progressive supranuclear palsy(CBS-PSP), with CBD the most frequent pathologic diagnosis, followed by AD and PSP.Clinical features are insufficient to identify the underlying pathologic substrate of CBS with certainty during life. Dopamine transporter imaging SPECT(DAT-SPECT) commonly shows asymmetric striatal affection, influenced by the CBS variant.18F-Fluorodeoxyglucose PET(FDG-PET) has been used to aid in CBS diagnosis, commonly showing an asymmetric frontoparietal pattern of cortical metabolism, also influenced by the CBS variant.If we focus on the CBS-AD variant, it typically shows a more posterior pattern of hypometabolism in FDG-PET compared to other CBS variants, positive amyloid PET scan and normal DAT-SPECT, which only usually becomes pathological in very advanced stages. ***Materials and Methods:*** We present a case of a 61-year-old male patient with suspected atypical parkinsonism, that shows speech apraxia, body rigidity, right arm deafferentation movement with antigravity maneuvers. Gait with slight anteflexion, medium stride with decreased right arm swing and broken turns. At suspicion of CBS, studies of magnetic resonance (MRI), DAT-SPECT, FDG PET and AD-Cerebrospinal Fluid(CSF) biomarkers were requested. ***Results:*** MRI: signs of diffuse subcortical atrophy with hippocampal involvement.DAT-SPECT: minimal hypo-uptake in putamen and left caudate tail, at the limit of normality, without other alterations.FDG PET: asymmetric frontoparietal and posterior temporal hypometabolism, with predominant posterior gradient.AD-CSF biomarkers: Amyloid beta(1-42): 303 pg/mL; Tau-protein: 14 pg/mL; Phosphorylated Tau-protein-181: 153 pg/mL. Compatible Alzheimer's disease. The clinical features, together with the complementary examinations, were suggestive of CBS-AD.Although this is a rare disease, we consider it important to emphasize the importance of understanding the different imaging patterns in the different CBS variants in nuclear medicine studies, which can be essential for an accurate diagnosis. ***Conclusion:*** CBS and its variants are a rare syndrome that can be a diagnostic challenge, where nuclear medicine studies can play a fundamental role along with other complementary explorations. ***References:*** Constantinides, V. C. et al (2022). Dopamine transporter SPECT imaging in corticobasal syndrome: A peak into the underlying pathology? Acta Neurologica Scandinavica, 145(6), 762-769. https://doi.org/10.1111/ane.13614Pardini, M. et al (2019). FDG-PET patterns associated with underlying pathology in corticobasal syndrome. Neurology, 92(10), E1121-E1135. https://doi.org/10.1212/WNL.0000000000007038

EP-1376

Incidental Detection of Pacemaker Lead Infection with ^{18}F-FDG PET-CT in a Breast Cancer Patient Undergoing Evaluation for Suspected Recurrence

A. Genova*, F. Porcaro, M. Prisco, L. Turchetta, I. Annarumma, V. Piscopo, M. Catalano;*
Azienda Ospedaliera di Rilievo Nazionale Antonio Cardarelli, Naples, ITALY.

Aim/Introduction: ^{18}F-FDG PET/CT is widely used in oncologic imaging, but it also plays an emerging role in detecting infections, particularly in complex or atypical clinical scenarios. Device-related infections can be challenging to diagnose due to non-specific symptoms and inconclusive conventional imaging. ***Materials and Methods:*** A 75-year-old woman with a history of breast cancer underwent ^{18}F-FDG PET/CT for suspected tumor recurrence. She had been experiencing persistent fever and elevated inflammatory markers. Her medical history included recent pacemaker implantation. The PET/CT scan showed no signs of oncologic relapse, but revealed in Focal uptake involving the distal end of the pacemaker in contact with the pericardium, at the cardiac apex (SUV max4.45), raising strong suspicion for device-related infection. On Cardiac ultrasound at the level of the intravitary electrode-catheter, an adherent hypoechoic mass is observed on the anterior septal leaflet ot the tricuspid valve, Elevated inflammatory markers and positive blood culture for staphylococcus capitis confirmed the diagnosis and the patient was started on targeted antimicrobial therapy. ***Results:*** This case highlights the utility of ^{18}F-FDG PET/CT beyond oncology, particularly in identifying occult infections associated with implanted devices. Its ability to provide whole-body functional imaging enables detection of unexpected infectious foci, often missed by conventional modalities such as echocardiography or CT. ***Conclusion:*** ^{18}F-FDG PET/CT can play a crucial role in the diagnostic work-up of systemic inflammatory conditions, even when initially performed for oncologic purposes. Early identification of pacemaker-related infections can significantly impact clinical management and outcomes.

EP-1377

Multifocal Osteonecrosis in Pediatric-onset Systemic Lupus Erythematosus

H. Elahifard[1]*, M. Samadi*[1]*, E. Askari*[1]*, F. Taheri*[1]*, M. Vahedi*[2]*;*
[1]*Nuclear Medicine Research Center, Mashhad University of Medical Science, Mashhad, IRAN, ISLAMIC REPUBLIC OF,*
[2]*Department of Pediatrics, Mashhad University of Medical Sciences, Mashhad, IRAN, ISLAMIC REPUBLIC OF.*

Aim/Introduction: Pediatric-onset SLE is an autoimmune disease, with osteonecrosis being a recognized complication. Prolonged use of corticosteroids, a common treatment for SLE, promotes osteonecrosis, contradicting the objective of preventing its progression. A 15-year-old girl with a three-year history of systemic lupus erythematosus (SLE), treated with corticosteroids, hydroxychloroquine, and mycophenolate-mofetil, was referred for evaluation of right hip pain and limping over the past two months, without trauma or fever. Physical examination revealed limited hip motion, with no signs of erythema or swelling. ***Materials and Methods:*** A three-phase bone scan was performed using 555 MBq (15 mCi) of ^{99m}Tc-MDP, including whole-body blood pool images at two minutes and delayed imaging at 180 minutes post-injection. SPECT/CT imaging was also performed for better localization and attenuation correction. ***Results:*** The bone scan revealed symmetrically increased blood pool and delayed MDP uptake in the bilateral shoulders, elbows, wrists, femoral heads, distal femora, proximal tibiae, and ankles. The corresponding SPECT/CT images revealed decreased bone density and serpiginous sclerotic changes in both elbows, femoral heads, distal femora, and proximal tibiae, with heterogenous increased activity suggesting multifocal osteonecrosis (MFON). MRI correlation from both knee joints revealed metaphyseal and epiphyseal serpiginous mixed signal intensities in bilateral femora, proximal tibiae, and subchondral areas of the medial and lateral femoral condyles, indicating bone infarction. ***Conclusion:*** MFON is reported as a rare complication in pediatric-onset SLE. The long-term prognosis of MFON relies on early detection and timely intervention, highlighting the vital role of imaging in diagnosing osteonecrosis. MRI is the most sensitive and specific modality. However, its high cost restricts its use to symptomatic regions, limiting the evaluation of asymptomatic areas. Therefore, whole-body bone scanning (WBBS) is a valuable supplementary tool for diagnosing osteonecrosis, especially in cases of suspected multifocal involvement. SPECT/CT imaging provides additional anatomical details, such as geographic sclerotic changes. This case underscores the importance of high index of suspicion for osteonecrosis in SLE patients with persistent joint pain as well as the value of WBBS and SPECT/CT imaging in diagnosing suspected MFON. ***References:*** 1.Hussein S, Suitner M, Béland-Bonenfant S, et al. Monitoring of osteonecrosis in systemic lupus erythematosus: a systematic review and metaanalysis. J. Rheumatol. 2018;45:1462-1476. 2.Webber D, Cao J, Dominguez D, et al. Genetics of osteonecrosis in children and adults with systemic lupus erythematosus. Rheumatology. 2023;62:3205-3212. 3.An Y-S, Park S, Jung J-Y, et al. Clinical characteristics and role of whole-body bone scan in multifocal osteonecrosis. BMC Musculoskelet Disord. 2019;20:1-9.

EP-1378

Rare Presentation of Baker's Cyst in an Infant: A Case Report

H. Elahifard[1], *M. Vahedi*[2], *F. Rabani*[1], *F. Taheri*[1], *V. Dabbagh*[1]; [1]*Nuclear Medicine Research Center, Mashhad University of Medical Science, Mashhad, IRAN, ISLAMIC REPUBLIC OF,* [2]*Department of Pediatrics, Mashhad University of Medical Sciences, Mashhad, IRAN, ISLAMIC REPUBLIC OF.*

Aim/Introduction: Bbaker's cyst (BC), arises from fluid accumulation in gastrocnemio-semimembranosus bursa, mostly present in adult knees. For developing BC, communication must exist between the knee joint and the gastrocnemius-semimembranous bursae. This communication is almost nonexistent in children but increases with age. Thus, BC has a rare incidence in the pediatric population. A 15-month-old girl presented with right knee pain, swelling, and limping for 15 days, without history of trauma or systemic illness. Physical examination revealed low-grade fever and limited motion in the right knee. Ultrasonography indicated peri-articular inflammation and a 2mm effusion. Septic arthritis was ruled out due to normal CBC, ESR, and CRP. She was referred for arthritis evaluation, and a three-phase bone scan was performed ***Materials and Methods:*** A three-phase bone scan was performed using 296 MBq (8 mCi) of 99mTc-MDP, including perfusion and blood-pool images of both knees, followed by delayed imaging at 180 minutes post-injection. The scan showed normal perfusion but asymmetrically decreased blood pool and delayed MDP uptake in the right knee. ***Results:*** The bone scan suggested joint disuse due to pain. Due to persistent pain, MRI of the right knee was performed. T2-weighted images revealed a focal area of high signal intensity with internal low signal components showing enhancement in the medial head of the gastrocnemius muscle. Additionally, there was edema and enhancement in the adjacent soft tissue, minimal effusion in the knee joint, and evidence of synovial enhancement. These findings indicated a complicated Baker's cyst associated with synovitis and arthritis. Thus, findings of the bone scan might be due to the attenuation effect of the Baker's cyst and/or disuse resulting from pain ***Conclusion:*** Nuclear imaging modalities have limited utility in diagnosing BC but in ruptured cases, the "arch sign", the visible distribution of the radiopharmaceutical in the medial posterior calf, has been reported as pathognomonic sign in a Tc-99m MDP bone scan. Thus, MRI remains the gold standard for the diagnosis of BCs and distinguishing them from other conditions. To our understanding, this is the first reported case of complicated BC in an infant, underscoring the need to consider rare causes of undiagnosed knee pain. ***References:*** 1.Nanduri A, Stead TS, Kupsaw GE, et al. Baker's Cyst. Cureus. 2021;13:e20403 2.Golan H, Fridburg E. Calf "Arch Sign" Seen on a Tc-99m-MDP Bone Scan Is Indicative of Synovial Fluid Leak in Ruptured Baker's Cysts: Case Reports and Analysis of Literature. Nuclear Medicine and Molecular Imaging. 2019;53:349-355.

EP-1379

Secondary Syphilis with Skull Bone Lesions: A Rare Clinical Manifestation

I. Sevaslidou[1], *S. Episkopopoulou*[1], *A. Velidaki*[1], *A. Anastasopoulou*[2], *A. Perissi*[2], *E. Dagrakis*[1], *T. Kostou*[1], *A. Kolindou*[1]; [1]*Nuclear Medicine Department , Genaral Hospital of Athens " LAIKO", Athens, GREECE,* [2]*First Department of Internal Medicine, "LAIKON" Hospital, Athens, GREECE.*

Aim/Introduction: Syphilis is a chronic systemic infection caused by the spirochete Treponema pallidum. Transmission occurs primarily through direct sexual contact, though vertical transmission from mother to fetus is also possible. Despite being a treatable condition, especially with early antibiotic intervention (primarily penicillin),delayed diagnosis can lead to irreversible damage affecting multiple organ systems. While syphilis is classically known for its dermatologic, mucosal, and systemic features, skeletal involvement remains a rare clinical finding, particularly during the secondary stage. ***Materials and Methods:*** We present the case of a 29-year-old male patient who was admitted to the hospital with low-grade fever, headache, a maculopapular rash, and localized swelling in the frontal area of the skull, with a duration of 24 hours. Clinical examination, laboratory testing, and positive serology confirmed a diagnosis of secondary syphilis.Given the atypical presentation, a cranial CT scan was performed, which showed soft tissue and muscle swelling in the right frontal region without any intracranial abnormalities. Bone scintigraphy was then conducted, revealing multiple areas of increased osteoblastic activity involving the frontal and parietal bones of the skull and the mandible. Additionally, photopenic regions were identified in the right frontal bone and left frontoparietal region, consistent with osteolytic lesions.The patient was promptly started on appropriate antibiotic therapy based on current treatment guidelines. Symptoms began to resolve following the first dose. However, despite medical advice, the patient did not return for follow-up after completing the full three-dose regimen. ***Results:*** This case illustrates a rare but significant complication of syphilis involving the skeletal system during the secondary stage. Early recognition of such atypical manifestations requires a high index of suspicion and the use of advanced imaging modalities. In this case, bone scintigraphy proved crucial in identifying the extent of bone involvement. ***Conclusion:*** Skeletal syphilis is uncommon, this case highlights the importance of comprehensive diagnostic work-up in patients with unusual symptoms—even in the early stages of disease. Clinicians should remain alert to rare manifestations of systemic infections, as timely diagnosis can significantly influence outcomes.

EP-1380

Diffuse FAPI-46 Uptake in Bone Marrow: A Case of Primary Myelofibrosis with Superscan Pattern on Bone Scintigraphy

H. Elahifard[1], *N. Raeisi*[1], *A. Saber Tanha*[1], *N. Ataei*[2], *E. Askari*[1]; [1]*Nuclear Medicine Research Center, Mashhad University of Medical Sciences, Mashhad, IRAN, ISLAMIC REPUBLIC OF,* [2]*Department of pathology, Mashhad University of Medical Sciences, Mashhad, IRAN, ISLAMIC REPUBLIC OF.*

Aim/Introduction: PMF is a myeloproliferative neoplasm characterized by clonal myeloproliferation originating from stem cells. ^{18}F-FDG has emerged as a promising modality for quantifying bone marrow inflammation in myelofibrosis, exhibiting an inverse correlation between ^{18}F-FDG uptake intensity and severity of fibrosis. Myelofibrosis should be considered as a differential diagnosis for diffuse skeletal metastases on ^{99m}Tc-MDP scan. ^{99m}Tc-MDP uptake increases with the progression of myelofibrosis, potentially leading to the development of a superscan pattern. A recent study utilizing ^{68}Ga-FAPI has demonstrated the efficacy of this modality in visualizing and quantifying myelofibrosis, establishing a direct correlation with disease progression and its potential value for prognostication. A 65-year-old woman with history of generalized bone pain underwent an initial evaluation 6 years ago that included a BMA, revealing bone marrow fibrosis. She recently experienced malaise, weight loss, night sweats, and worsening of her bone pain, which prompted her referral for further evaluation. Laboratory data indicated anemia, leukocytosis, elevated LDH and ESR levels. A thoracic and abdominopelvic CT scan revealed splenomegaly and diffuse lytic/sclerotic changes in the skeleton. ***Materials and Methods:*** The whole-body ^{99m}Tc-MDP scan with SPECT/CT imaging was performed.A ^{99m}Tc-FAPI-46 scan was employed to assist in differentiating the probable etiologies. ***Results:*** The whole-body ^{99m}Tc-MDP scan demonstrated markedly increased diffuse skeletal uptake, even in the distal of extremities, consistent with a superscan pattern commonly described as a "beautiful bone scan." This finding raises differential diagnoses that

encompass hematologic, metabolic, and metastatic etiologies. The FAPI whole body and SPECT/CT images revealed diffuse homogeneous skeletal uptake, along with three focal areas of uptake in the enlarged spleen (later attributed to local fibrosis probably due to accelerated extramedullary hematopoiesis). Considering both MDP and FAPI scan patterns together, the findings highlighted hematologic disorders which most probable one was myelofibrosis. Finally according to BMB, morphological features in conjunction with clinical and laboratory findings were compatible with primary myelofibrosis (PMF). ***Conclusion:*** FAPI can be beneficial in ruling out other causes of myelofibrosis. Our pioneering experience with ^{99m}Tc-FAPI-46 appears to be comparable to recently reported study with ^{68}Ga-FAPI, as both FAPI and MDP exhibit intense uptake indicative of advanced stages of the disease ***References:*** 1)Li X, Zhao Q, Luo Q, et al. The Manifestation of a Patient With Myelofibrosis in 68Ga-DOTA-FAPI-04 PET/CT Mimicking "Super Bone Imaging." Clin Nucl Med. 2022;47:1056-10582) 2)Liu Y, Li X, Jing L, et al. Application Value of 68Ga-FAPI PET/CT in the Evaluation of Myelofibrotic Diseases. Clin Nucl Med. 2024;49:404-408

EP-1381

Splenic Hemangioma as a Pitfall in 18F-PSMA PET-CT Imaging for Prostate Cancer: A Case Report

M. Sanchez Torrente*, S. Martin Aguilar, L. Mena Bares, E. Moratalla Aranda, M. Ureña Lara;*
Department of Nuclear Medicine - Hospital Universitario de Jaén, Jaén, SPAIN.

Aim/Introduction: Prostate cancer is the most common cancer in men, detected through elevated prostate-specific antigen(PSA) levels and confirmed by imaging and biopsy. The staging and management of prostate cancer have been significantly improved by advanced imaging techniques such as magnetic resonance imaging (MRI) and prostate-specific membrane antigen (PSMA) positron emission tomography (PET) computed tomography (CT). 18F-PSMA-PET-CT offers high sensitivity and specificity for detecting both primary and metastatic disease, as its clinical use increases, new possible pitfalls emerge, which, although rare, we should be aware of. ***Materials and Methods:*** A 71-year-old male patient was diagnosed with Gleason score 7 (3+4) cT1c prostate adenocarcinoma, with a PSA of 5.75 ng/mL at diagnosis and no evidence of extraprostatic extension. A robotic radical prostatectomy was performed, achieving a nadir PSA of 0.05 ng/mL. Subsequently, PSA levels were monitored and showed a slow but progressive increase, reaching 0.28 ng/mL, at which point an 18F-PSMA PET/CT scan was requested. ***Results:*** 18F-PSMA-PET-CT scan showed a suspicious millimetric left obturator lymphadenopathy and a focus of high-intensity splenic PSMA uptake (SUVmax:18) that showed decreased intensity on the delayed image 2 hours post-injection (SUVmax:14). To rule out malignancy, a splenic MRI was recommended.Splenic MRI showed a pattern characteristic of splenic hemangioma. Splenic hemangioma represents the most common benign tumor of the spleen and is usually found incidentally in the age group 30 to 50 years. They are composed of nonencapsulated channels of vessels separated by septa or pulp tissue and have a single endothelial layer filled with blood.Splenic hemangioma is the main cause of a single focus of PSMA uptake in the spleen, with some cases reported in the literature. ***Conclusion:*** Splenic hemangioma is the main cause of a single focus of PSMA uptake in the spleen, with some cases reported in the literature. However, although prostate cancer metastases to the spleen are very rare, this possibility should be ruled out.Furthermore, it would be interesting to analyze the kinetic behavior of splenic hemangioma in standard imaging/delayed imaging in a larger number of cases. ***References:*** Jia, G., Dong, A., Cheng, C., & Zuo, C. (2024). Intense 18F-PSMA-1007 Uptake of Splenic Hemangioma. Clinical Nuclear Medicine, 49(2), E90-E92. https://doi.org/10.1097/RLU.0000000000004995Chaussé, G., Laufer, J., Abikhzer, G., & Probst, S. (2019). Splenic Hemangioma as a Potential Pitfall on PSMA-Targeted 18 F-DCFPyL PET/CT. Clinical Nuclear Medicine, 44(3), 255-256. https://doi.org/10.1097/RLU.0000000000002428

EP-1382

Occipital Bone Lesion Mimicking Malignancy: The Importance of Multimodal Imaging

J. Mendes*, L. Torres, P. Soeiro;*
Hospital de São João, Porto, PORTUGAL.

Aim/Introduction: Occipital bone lesions are rare and frequently detected incidentally. While most are benign—such as osteomas, fibrous dysplasia, hemangiomas, or post-traumatic changes—it is vital to exclude malignancy, particularly when neurological symptoms are present. This case underscores the pivotal role of integrated multimodal imaging in distinguishing a benign lesion from malignancy. ***Materials and Methods:*** A 47-year-old woman with 5-year history of unexplained axonal neuropathy, thyroid nodules, prior L5-S1 spinal fusion, migraines, and transient visual disturbances underwent [18F]FDG PET-CT to investigate a suspected occult malignancy. A brain MRI was concurrently performed due to ongoing neurological complaints. Additional imaging was conducted to further characterise an unexpected solitary occipital bone lesion. ***Results:*** [18F]FDG PET-CT: Identified a focal area of intense FDG uptake (SUVmax 11.62) in the left occipital bone, corresponding to a lytic-appearing lesion on low-dose CT. Differential diagnoses included solitary bone metastasis, plasmacytoma, or—less likely—infectious or inflammatory processes. However, the solitary and stable appearance was atypical for metastatic disease. Non-contrast Brain MRI: Showed non-specific subcortical white matter changes without a corresponding focal lesion. These findings were possibly related to a chronic demyelinating process. Contrast-enhanced MRI with Perfusion: Revealed a vascularised, heterogeneously enhancing lesion (1.9 × 3.2 × 3.1 cm) in the left occipital bone, with cortical thinning and medullary expansion. Absence of restricted diffusion and no intracranial extension favoured a benign entity such as fibrous dysplasia or intraosseous hemangioma. Bone Scintigraphy [99m Tc]Tc-HDP): Demonstrated isolated increased uptake in the left occipital bone, corresponding to the PET-CT findings. Given that hemangiomas typically show low tracer uptake, the imaging pattern supported the diagnosis of fibrous dysplasia. CT Review: Closer inspection of the PET/CT low-dose CT revealed a well-circumscribed expansile lesion with a heterogeneous "ground-glass" matrix, cortical thinning, and preservation of the inner table—hallmark features of fibrous dysplasia. ***Conclusion:*** This case exemplifies the diagnostic value of multimodal imaging. Despite alarming metabolic activity and apparent bone lysis, the integration of findings from PET/CT, MRI, and bone scintigraphy enabled a confident diagnosis of monostotic fibrous dysplasia. Nuclear medicine physicians should remain alert to benign bone lesions in unusual locations that may mimic malignancy both morphologically and metabolically. A comprehensive imaging approach is critical to avoid misdiagnosis and inappropriate treatment.

EP-1383

99mTc-HMPAO Brain SPECT in Intracranial Carotid Artery Occlusion: Functional Imaging to Support ClinicalDecision-Making

A. Genova*, F. Porcaro, M. Prisco, L. Turchetta, I. Annarumma, V. Piscopo, M. Catalano;*
Azienda Ospedaliera di Rilievo Nazionale Antonio Cardarelli, Naples, ITALY.

Aim/Introduction: Brain perfusion SPECT is a valuable diagnostic tool for assessing cerebrovascular disorders, especially when

conventional structural imaging is insufficient to evaluate the functional impact of vascular compromise. By providing three-dimensional functional information about cerebral blood flow and metabolism, SPECT imaging often reveals perfusion abnormalities that precede visible structural damage on CT or MRI. This makes it particularly useful in identifying regions of the brain at risk and in guiding clinical decision-making. Unlike structural imaging, which captures anatomical changes that may occur later in disease progression, SPECT can detect early functional deficits, offering a more dynamic view of brain physiology. As such, it plays a complementary role and, in certain clinical contexts, can offer unique information that influences patient management and therapeutic planning. ***Materials and Methods:*** A 60-year-old male presented to the Emergency Department with right-sided facial weakness, visual disturbances, and reported motor deficits in the left upper limb in the preceding days. Neurological assessment and imaging revealed an occlusion of the right intracranial internal carotid artery, specifically before the anterior bend of the clinoid segment, with partial compensation via the circle of Willis. CT angiography showed hypodense ischemic areas in the right frontal subcortical region. Brain MRI confirmed multiple subacute ischemic lesions. To assess the extent of cerebral hypoperfusion, a 99mTc-HMPAO SPECT scan was performed. The images demonstrated significant tracer uptake reduction in the left cerebral hemisphere, corresponding to the vascular territory affected by the carotid occlusion. Accurate interpretation of these findings relied on integrating the clinical picture with structural imaging. ***Results:*** While CT and MRI confirmed vascular occlusion and ischemic injury, SPECT provided essential insight into the functional status of the brain tissue, highlighting areas of hemodynamic impairment. This functional perspective is crucial in evaluating cerebral reserve and may influence therapeutic decisions such as revascularization strategies or medical management. In this case, SPECT findings played an important role in guiding a multidisciplinary approach. ***Conclusion:*** Brain perfusion imaging with 99mTc-HMPAO SPECT remains a powerful and relevant tool in the evaluation of acute cerebrovascular events. By offering complementary functional data to anatomical imaging, it enhances clinical understanding and supports more informed treatment planning, particularly when assessing the viability and functional reserve of affected brain regions.

EP-1384

Rediscovering the Forgotten: ^{18}F-FDG PET/CT Detection of Metabolically Active Echinococcal Cyst in the Pubic Bone with a History of Ovarian Echinococcosis- A Case Report

S. Chausheva[1,2], *T. Stoeva*[1], *M. Dyankova*[1], *T. Yordanova*[1], *Z. Dancheva*[1], *A. Klisarova*[1], *B. Chaushev*[1];
[1]*University Hospital St Marina Varna, Varna, BULGARIA,* [2]*Medical University Varna, Varna, BULGARIA.*

Aim/Introduction: Bone echinococcosis is a rare manifestation of Echinococcus granulosus infection, approximately 0.5-4% of all echinococcosis cases. The pubic bone is an unusual site of involvement that may mimic primary tumors, metastatic lesions or infectious bone lesions. The diagnosis is often challenging due to nonspecific symptoms and insidious clinical presentation. ***Materials and Methods:*** We report the case of a 45 years old female with a complex medical history. The patient presented at the hospital with pelvic pain and limited mobility in the hip for several months.A history of hydatid disease, including surgical management of a left ovarian echinococcal cyst (2008) and subsequent resection of a left pubic bone cyst (2009) with bone graft reconstruction. Despite postoperative albendazole therapy, the patient did not receive long-term parasitological surveillance. In 2011, she underwent total alloplasty of the left hip for histopathologically confirmed echinococcal granulomatous synovitis. In 2024, the patient presented with chronic pelvic pain. X-ray examination of the pelvis revealed an osteolytic lesion in the left pubic bone with peripheral sclerotic margins in the left iliac bone and acetabulum. ***Results:*** To evaluate lesion viability and assess for potential systemic dissemination, ^{18}F-FDG PET/CT was performed. The scan revealed increased uptake in the peripheral rim of the thoracic vertebra mass with central parts showing lower uptake than the peripheral rim, without evidence of distant metabolically active lesions. Serological testing was positive for E. granulosus antibodies. ***Conclusion:*** This case underscores the recurrent and disseminated nature of osseous hydatid disease and highlights the utility of FDG PET/CT in detecting active parasitic lesions, differentiating them from malignancy, and guiding clinical management in atypical locations. Skeletal echinococcosis remains a diagnostic challenge, particularly in post-surgical patients with prior parasitic disease. ^{18}F-FDG PET/CT serves as a valuable adjunct in assessing lesion activity, ruling out systemic involvement.

EP-1385

Detection of Recurrent ACTH-Secreting Pituitary Adenoma Using ^{99m}Tc-EDDA/HYNIC-TOC- A Case Report and Literature Review

A. Bajenaru[1], *A. Baican*[1,2], *R. Mititelu*[3,4];
[1]*Clinical Hospital "Prof. Dr. Theodor Burghele", Bucharest, ROMANIA,* [2]*Faculty of Physics, University of Bucharest, Magurele, ROMANIA,* [3]*Central Emergency Military University Hospital "Dr. Carol Davila", Bucharest, ROMANIA,* [4]*University of Medicine and Pharmacy "Carol Davila", Bucharest, ROMANIA.*

Aim/Introduction: Adrenocorticotropic hormone (ACTH) secreting pituitary adenomas are the most common cause of endogenous hypercortisolism, causing complex clinical manifestations and requiring a careful diagnostic and therapeutic approach [1]. In terms of nuclear medicine imaging, somatostatin receptors play a crucial role by having an increased expression in these tumors, facilitating the detection and characterization of the lesions. The main radionuclide tracer used in neuroendocrine imaging, 111In-pentetreotide, was replaced by PET tracers, 68Ga-DOTATOC, 68Ga-DOTANOC and 68Ga-DOTATATE, due to clinical advantages. Recently, 99mTc-labelled peptides have emerged as an option in scintigraphic imaging of neuroendocrine tumors (NET), demonstrating advantages over 111In-pentetreotide by providing better imaging quality on gamma cameras while keeping a lower radiation exposure for patients. ***Materials and Methods:*** We presented the case of a a 54 years-old woman who has a medical history of HBV infection, obesity, hypertension, stroke and hypercholesterolemia. She was diagnosed with Cushing's disease following an endocrinological checkup. The presence of a pituitary adenoma was confirmed by an MRI examination, which led to transsphenoidal neurosurgery. The lesion was histopathologically confirmed to be an ACTH-secreting pituitary adenoma. 4 months post-surgery, a spike in ACTH serum value prompted another MRI examination which revealed the presence of a remnant pituitary tumor extended to the cavernous sinus and retrosellar to the right side. We performed a somatostatin receptor SPECT-CT using 99mTc-EDDA/HYNIC-TOC. ***Results:*** SPECT-CT showed residual activity in the sella and diffuse uptake in the adrenal glands due to prolonged exposure to high levels of ACTH secretion. Pituitary MRI is the imaging method of choice for evaluating sellar and parasellar tumors. However, a range of scintigraphic investigations can be performed for a better assessment of the pituitary tumors. Given the unavailability of 68Ga-DOTA peptides in our country, we selected 99mTc-EDDA/HYNIC-TOC as the radiotracer of choice due to its good sensitivity in detecting pituitary tumors. We confirmed tracer uptake in the patient's residual adenoma, demonstrating SSTR expression and found no abnormal uptake elsewhere, effectively ruling out ectopic ACTH secretion. ***Conclusion:*** 99mTc-

EDDA/HYNIC-TOC can aid in the evaluation of well-differentiated pituitary adenoma by assessing the uptake in the sellar region and excluding ectopic lesions. Since literature is scarce on the subject, we consider prospective multicentric studies necessary in order to better define the role of metabolic imaging in patients with pituitary adenomas. ***References:*** 1. Nowak, E., et al., Diagnostic challenges in cyclic Cushing's syndrome: a systematic review. Lancet Diabetes Endocrinol, 2023. 11(8): p. 593-606.

EP-1386

Isolated Cutaneous Metastatic Breast Cancer Detected by FDG PET/CT

M. Kartal[1], *V. Dere*[2], *B. Okudan Tekin*[2];
[1]*Elazığ Fethi Sekin City Hospital, Elazığ, TÜRKIYE,* [2]*Ankara Bilkent City Hospital, Ankara, TÜRKIYE.*

Aim/Introduction: In breast cancer, the most common metastatic patterns typically involve lymph nodes, lungs, liver, and bones. Cutaneous metastases are rare among malignancies overall, but when they do occur, breast cancer is the most frequent primary source. In breast cancer, cutaneous metastases usually present as local recurrences at the site of surgery. They have been reported most frequently on the chest, abdomen, and head and neck regions, and less commonly on the extremities and other areas. These lesions are often palpable as painless nodules and are fluorodeoxyglucose (FDG)-avid, making them detectable via FDG positron emission tomography/computed tomography (PET/CT). In this case presentation, we aim to report a patient with a history of breast cancer who underwent re-staging, during which widespread isolated cutaneous metastatic lesions were detected on FDG PET/CT imaging. ***Materials and Methods:*** A 68-year-old female patient was diagnosed with invasive ductal carcinoma of the left breast ten years ago and underwent a left modified radical mastectomy. She was staged as T1N3M0 and received chemoradiotherapy (CRT). Two years after CRT, a right radical mastectomy was performed due to the detection of metastatic lymph nodes in the right axilla. During follow-up, cutaneous metastases were identified in the left breast region, and the patient continued to receive CRT. Medical records from that period indicated a favorable treatment response. Eight years after the initial diagnosis, the patient underwent FDG PET/CT imaging at our center for restaging purposes. ***Results:*** Imaging revealed no pathological metabolic activity in visceral organs or lymph nodes. However, multiple foci of increased FDG uptake were observed, corresponding to widespread, isolated cutaneous metastases. Intense FDG-avid nodular lesions, the largest measuring approximately 12 mm in diameter, were identified in the skin and subcutaneous tissue of the thorax (Figure 1A, B; orange arrows), abdomen (Figure 1C), and lower extremities (Figure 1D, E; orange arrows), with a maximum standardized uptake value of 7.24. A biopsy obtained from a nodular skin lesion located adjacent to the right trapezius muscle confirmed metastasis, and the patient was diagnosed with isolated cutaneous metastatic breast cancer, for which treatment was subsequently planned. ***Conclusion:*** In breast cancer and other malignancies with cutaneous metastases, the extent and localization of lesions can be effectively evaluated using FDG PET/CT due to the high FDG avidity of these lesions. This finding highlights the value of FDG PET/CT as a key imaging modality, particularly in the assessment of patients with asymptomatic cutaneous involvement.

EP-1387

A Hot Signal, a Cold Trail: False-Positive 99mTc-Ethambutol Uptake in Bilateral Psoas Abscess Mimicking Tuberculosis

A. Roy*, N. A. Damle, A. Mahalik, N. Kundu;*
AIIMS New Delhi, New Delhi, INDIA.

Aim/Introduction: To describe a false-positive case of 99mTc-Ethambutol scintigraphy due to non-specific tracer uptake in psoas abscesses, highlighting the importance of cautious interpretation in atypical extrapulmonary tuberculosis (EPTB) cases. ***Materials and Methods:*** A 23-year-old male presented with chronic lower abdominal discomfort and back pain. Contrast-enhanced CT revealed bilateral psoas abscesses. Clinicians suspected disseminated TB, and 99mTc-EMB scintigraphy was performed for evaluation. 10 mCi of 99mTc-EMB was administered intravenously. Planar imaging and SPECT/CT were done at 1 hour post-injection. Radiopharmaceutical preparation met labelling efficiency of >90%. ***Results:*** SPECT/CT showed increased radiotracer uptake in the periphery of both psoas abscesses. Based on this finding, the scan was interpreted as positive. ATT was initiated. However, multiple image-guided fluid aspirations from both psoas collections failed to demonstrate acid-fast bacilli on smear, culture, and GeneXpert. Moreover, the patient did not improve clinically or radiologically despite 12 months of ATT. This led to a re-evaluation of the case. The final impression was false-positive uptake, potentially due to: 1. Hypervascularization in the abscess walls mimicking active infection, 2. Non-specific uptake of radiopharmaceutical, 3. Possible radiochemical impurity (e.g., free pertechnetate) ***Conclusion:*** This case underscores that while 99mTc-EMB scintigraphy is a valuable functional tool for TB imaging, false-positive results can occur in non-TB infections or in sterile inflammation. Interpretation must be correlated with microbiological confirmation, especially in soft tissue or atypical lesions. Caution is advised before initiating long-term ATT based solely on scintigraphic uptake.

EP-1388

Metastasis or Silicosis? The Role of PET/CT in Thoracic Evaluation of Colorectal Cancer

E. Moratalla-Aranda*, L. Mena Bares, S. Martin Aguilar, M. Sanchez Torrente, M. Ureña Lara;*
Hospital Universitario de Jaen, Jaen, SPAIN.

Aim/Introduction: We present the case of a 53-year-old male, a worker in the marble industry, diagnosed with adenocarcinoma of the upper rectum (stage cT4aN2M0). During thoracoabdominal CT staging, atypical findings in the thorax were identified: miliary pulmonary pattern, bilateral hilar-mediastinal lymphadenopathy, and irregular pleural thickening. This prompted a broad differential diagnosis, including pulmonary metastases, granulomatous diseases (such as silicosis or sarcoidosis), infectious processes, and lymphoproliferative disorders. The aim of this study was to characterize the metabolic behavior of these lesions using PET/CT with 18F-FDG, to guide the differential diagnosis and establish an appropriate therapeutic strategy. ***Materials and Methods:*** A PET/CT study with ^{18}F-FDG was performed for oncological restaging and metabolic evaluation of the thoracic abnormalities detected. FDG uptake patterns in pulmonary, pleural, and lymph node lesions were analyzed, integrating these findings with the patient's clinical, occupational, and epidemiological history. Regions with the highest metabolic activity were selected for histological sampling through EBUS-guided fine needle aspiration (FNA). ***Results:*** The PET/CT study revealed intense uptake in the rectal mass (SUVmax: 18.5) and locoregional pelvic adenopathies (SUVmax: 9), consistent with the known neoplasm and locoregional spread. In the thoracic compartment, multiple mediastinal and hilar adenopathies with moderate to high uptake (SUVmax: 3.7-14.3) were identified, along with hypermetabolic pleural thickening (SUVmax: 6.5) and millimetric pulmonary nodules with minimal uptake (SUVmax: 1.4). The bilateral and symmetrical distribution, primarily in the upper lobes, along with the intensity and morphology of uptake, suggested a chronic granulomatous disease, specifically silicosis, related to the patient's prolonged occupational exposure to silica dust. EBUS-guided FNA

was performed in lymph node stations 4R, 10R, and 7, confirming the presence of fibrous material consistent with silicotic nodules. In the absence of metastatic spread, the patient was considered a candidate for surgery with curative intent and underwent anterior rectal resection. ***Conclusion:*** PET/CT with ^{18}F-FDG proved to be a pivotal tool in differentiating between metastatic disease and thoracic granulomatous pathology in an oncological context. Its ability to integrate morphological and functional data allowed for precise biopsy target selection, confirmation of silicosis, and avoidance of overstaging that would have contraindicated a potentially curative treatment.

EP-1389

Misleading 68Ga-PSMA Uptake in Bone Metastases of Esophageal Adenocarcinoma in a Patient with Synchronous Prostate Cancer

L. Milišic Kelava*, M. Pešorda, D. Huić;*
University Hospital Centre Zagreb, Zagreb, CROATIA.

Aim/Introduction: Prostate-specific membrane antigen (PSMA) ligands labeled with Ga-68 are widely used for staging and restaging prostate cancer. However, it is well established that Ga-68 PSMA uptake can also occur in the neovasculature of non-prostatic malignancies. We present a case of a 74-year-old male with two histologically confirmed primary malignancies: esophageal carcinoma and prostate adenocarcinoma, in whom Ga-68 PSMA PET/CT demonstrated extensive skeletal metastases. This case highlights the necessity for histopathological confirmation when imaging findings may not correlate with clinical history. ***Materials and Methods:*** The patient was initially diagnosed with esophageal squamous cell carcinoma after endoscopy and biopsy due to dysphagia. Shortly thereafter, elevated PSA prompted urological evaluation and biopsy, which confirmed acinar adenocarcinoma of the prostate. In the staging workup for prostate cancer, a Ga-68 PSMA PET/CT scan was performed. This showed intense PSMA-avid uptake in multiple bone lesions throughout the axial and appendicular skeleton, suggestive of widespread skeletal metastases.Given the known expression of PSMA in the neovasculature of non-prostatic tumors, and the patient's history of esophageal carcinoma, the true origin of the bone metastases was questioned. A CT-guided biopsy of a PSMA-avid iliac bone lesion was performed. ***Results:*** Histological analysis of the bone biopsy revealed squamous cell carcinoma cells consistent with metastasis of the esophageal primary tumor, rather than prostate adenocarcinoma. Immunohistochemistry supported the diagnosis, showing negativity for prostate markers (PSA, PSAP) and positivity for cytokeratin 5/6 and p63, characteristic of squamous differentiation. ***Conclusion:*** This case underscores the importance of critical interpretation of Ga-68 PSMA PET/CT findings in patients with multiple primary malignancies. While Ga-68 PSMA imaging is highly sensitive for prostate cancer metastases, non-prostatic tumors with active neovascularization may show significant tracer uptake. Therefore, in patients with multiple primary malignancies, especially those known to express PSMA in tumor neovasculature, biopsy remains the gold standard for confirming metastatic origin. Multidisciplinary assessment and histological verification are essential to avoid misdiagnosis and inappropriate treatment allocation.

EP-1390

When One Cancer Reveals Another: The Role of ^{18}F-FDG PET/CT in Detecting Synchronous Tumors.

R. Mehri*, M. Nouira, Z. Missaoui, R. Ghannem, A. Mazhoud, R. Sfar, K. Chatti;*
Sahloul Hospital, Sousse, TUNISIA.

Aim/Introduction: Synchronous tumors are distinct primary malignancies occurring simultaneously. PET-FDG, widely used for tumor staging, can incidentally detect these additional cancers, often missed in routine evaluations. We report two cases where PET-FDG, performed for primary tumor assessment, unexpectedly identified synchronous malignancies. ***Materials and Methods:*** Intravenous administration of 3 MBq/Kg of ^{18}F-fluorodeoxyglucose (FDG) was performed. A PET/CT scan from the skull vertex to mid-thigh was acquired after 60 minutes of strict rest, using a Siemens Biograph 64 PET/CT system. ***Results:*** We report two cases where PET-FDG was utilized for the staging of pulmonary and laryngeal tumors:*Case 1: A 58-year-old male with a diagnosis of pulmonary squamous cell carcinoma, where PET-FDG revealed an unexpected rectal malignancy during the staging process.*Case 2: A 61-year-old male with a diagnosis of laryngeal cancer, in whom PET-FDG identified an incidental lung lesion suggestive of a second primary lung cancer. Both patients underwent comprehensive evaluation, including biopsy and histopathological confirmation of the synchronous tumors. ***Conclusion:*** The occurrence of multiple primary malignancies in cancer patients is reported in 2.4% to 8% of cases. The risk of developing a second primary cancer varies depending on the site of the initial tumor (21% in patients with lung cancer). Individuals diagnosed with early-stage lung cancer are at a significantly higher risk for second primaries compared to those in the general population with no prior cancer history. The underlying causes can be attributed to a combination of host-related factors, lifestyle choices, and environmental exposures. Certain populations such as male patients, those with a history of smoking or alcohol use, and individuals with hereditary cancer syndromes are particularly vulnerable. Managing patients with synchronous primary tumors is complex and often presents a real therapeutic challenge. ***References:*** - Weir HK, Johnson CJ, Thompson TD. The effect of multiple primary rules on population-based cancer survival. Cancer Causes Control. 2013 Jun;24(6):1231-42. - Vogt A, Schmid S, Heinimann K, Frick H, Herrmann C, Cerny T, Omlin A. Multiple primary tumours: challenges and approaches, a review. ESMO Open. 2017 May 2;2(2):e000172.- Testori A, Cioffi U, De Simone M, Bini F, Vaghi A, Lemos AA, Ciulla MM, Alloisio M. Multiple primary synchronous malignant tumors. BMC Res Notes. 2015 Nov 27;8:730.

EP-1391

Silent Persistence in the Shadow of Time: Late Renal Metastasis of Differentiated Thyroid Cancer

M. Zambrana-Delgadillo*, M. Piñero Fernandez- Reyes, J. Rodríguez-Rubio Corona, M. Pajares-Vinardell;*
Hospital Universitario Puerta del Mar, Cadiz, SPAIN.

Aim/Introduction: Differentiated thyroid cancer (DTC) develops distant metastases in 4-10% of cases, typically involving lymph nodes, lungs, and bones. Renal metastases are exceedingly rare, with only 25 cases reported in the literature. Their low incidence and the renal excretion of radiotracers make their detection challenging. ***Materials and Methods:*** We present the case of an 82-year-old woman with a history of total thyroidectomy in 1986 at age 43 for multinodular goiter. Histology revealed bilateral follicular thyroid carcinoma, and she underwent ablation with 100 mCi of I-131. In 2017, rising serum thyroglobulin (Tg) levels prompted imaging workup, including CT scans that showed pulmonary nodules. A second treatment with 150 mCi of I-131 was administered, with post-therapy whole-body scintigraphy confirming uptake in the nodules and Tg levels of 103 ng/mL. Despite annual negative whole-body scans and persistently incomplete biochemical response (Tg 391 ng/mL), multiple fluorodeoxyglucose PET/CT scans revealed only faint uptake in stable lung lesions. Tg continued to rise, exceeding 600 ng/mL over the following years. In 2023, an abdominal CT scan identified a 40 mm right renal mass not seen on prior PET/CT. Surgical pathology after radical nephrectomy confirmed it was a metastasis from DTC, measuring 5 cm. Following surgery, Tg levels dropped markedly to 71 ng/mL. Currently, the patient maintains

an excellent quality of life and is under active surveillance for low-volume metastatic disease, characterized by subcentimeter pulmonary nodules (<2 cm), annual growth <20%, and a completely asymptomatic clinical course. ***Results:*** DiscussionThis case highlights the extremely delayed presentation of renal metastasis from follicular thyroid carcinoma, more than 35 years after initial treatment. It underscores the essential role of serial Tg monitoring and the limitations of PET/CT in detecting low-grade or atypically located metastases. Surgical management in selected cases of oligometastatic disease may significantly reduce tumor burden and biochemical activity. ***Conclusion:*** Renal metastasis of DTC, although rare and often silent, may appear decades after the primary diagnosis. Persistent Tg elevation, even in the absence of conclusive imaging findings, warrants thorough investigation. Long-term follow-up and individualized management strategies are crucial to optimize outcomes in patients with indolent metastatic thyroid cancer. ***References:*** Madani A, Jozaghi Y, Tabah R, How J, Mitmaker E. Rare metastases of well-differentiated thyroid cancers: a systematic review. Ann Surg Oncol. 2015 Jan;22(1):460-6. doi:10.1245/s10434-014-4058-y. PMID: 25192681.

EP-72

e-Poster Area

E: Other Studies -> E2 Covid Studies

EP-1392

Did the Pandemic Cast a Long Shadow on Lung-Cancer Survival? A 918-Patient [^{18}F]FDG PET/CT Cohort

D. Nak[1], *O. Bülbül*[1], *B. Demir*[2], *S. Göksel*[3];
[1]*Recep Tayyip Erdoğan University Training and Research Hospital, Rize, TÜRKIYE,* [2]*Mehmet Akif İnan Research and Training Hospital, Şanlıurfa, TÜRKIYE,* [3]*Adnan Menderes University Faculty of Medicine, Aydın, TÜRKIYE.*

Aim/Introduction: The COVID-19 pandemic has disrupted cancer care worldwide; however, its tangible impact on lung cancer outcomes remains controversial. This study aimed to evaluate the impact of time of diagnosis-pre-pandemic, pandemic-era, or post-pandemic-on baseline stage, overall survival (OS), and progression-free survival (PFS) in patients undergoing baseline [^{18}F]FDG PET/CT imaging. ***Materials and Methods:*** 918 consecutive lung cancer patients staged with [^{18}F]FDG PET/CT between January 2018 and January 2024 were retrospectively analysed. Diagnostic periods were classified as pre-pandemic (January 2018-February 2020), pandemic period (March 2020-May 2022) and post-pandemic (June 2022-January 2024). OS was calculated for the entire cohort and PFS for 555 patients with regular follow-up records. Survival curves were compared using the log-rank test; potential confounding effects were adjusted for with a multivariable Cox regression model including histology and stage. ***Results:*** Median OS was 13.1 months (mean 26.4) with 690 deaths. Small-cell histology and higher stage significantly shortened survival ($p < 0.001$). OS fell to 11.2 months for intra-COVID diagnoses versus 14.7 months pre-COVID ($p = 0.027$) and rebounded to 15.5 months post-COVID ($p = 0.730$ vs pre-COVID). The drop was sharper in stage IIIB-IV disease (10.4 vs 7.4 months; $p = 0.005$), with post-COVID OS at 8.8 months. Median PFS was 20 months; epochs differed overall ($p = 0.449$), but advanced-stage PFS declined from 7.7 months pre-COVID to 6.2 months post-COVID ($p = 0.029$). Stage distribution at diagnosis was unchanged across periods (all $p > 0.09$). Multivariable analysis showed intra-COVID diagnosis independently raised death risk by 20 % (HR 1.20) and progression risk by 26 % (HR 1.26); both normalised post-COVID. Stage III (HR 2.75) and IV (HR 6.77) remained the strongest adverse predictors. ***Conclusion:*** The pandemic did not lead to more advanced presentation of patients with lung cancer, but it did shorten survival, especially in advanced patients. Outcomes also recovered when health services returned to normal. These findings suggest that uninterrupted access to treatment rather than early diagnosis is critical to preserve lung cancer prognosis in similar global crises. ***References:*** Agulnik, J., Kasymjanova, G., Pepe, C.,et al. (2024). Real-world evidence of the impact of the COVID-19 pandemic on lung cancer survival: Canadian perspective. Current Oncology, 31(3), 1562-1571.Mangone, L., Marinelli, F., Bisceglia, I., et al. (2023). The influence of COVID-19 on new lung cancer diagnoses, by stage and treatment, in northern Italy. Biology, 12(3), 390.

EP-73

e-Poster Area

E: Other Studies -> E3 Other Study (including Training, Projects)

EP-1393

Implementation of a Relative Value Unit-Based System in a Nuclear Medicine Department

M. Meneses Navas[1], *S. Guzmán Ortiz*[1], *M. Granados Alcobendas*[2], *M. Amo-Salas*[3], *L. García Zoghby*[1], *I. García Megías*[1], *J. Bonilla Plaza*[1], *M. Cruz Montijano*[1], *J. Montalvá Pastor*[1], *A. García Vicente*[1];
[1]*Hospital Universitario de Toledo, Toledo, SPAIN,* [2]*Gerencia de Atención Especializada de Toledo. Hospital Universitario de Toledo, Toledo, SPAIN,* [3]*Departamento de Matemáticas. Universidad de Castilla-La Mancha., Ciudad Real, SPAIN.*

Aim/Introduction: Relative value units (RVUs) are a standardized method used to quantify medical workload by assigning a numerical value to healthcare services based on their complexity, time requirements, and resource utilization. However, existing models are not tailored to the specific characteristics of nuclear medicine.The aim of this study was to implement a relative value unit (RVU)-based system to quantify activity and resource utilization in a nuclear medicine department (NMD). ***Materials and Methods:*** A retrospective study was approved by a Local Institutional Review Board and conducted in the NMD of a tertiary hospital, analyzing costs and procedures performed during the first half of 2024. Some steps were performed. First: a list of diagnostic and therapeutic procedures was drawn up. Second: RVU was defined considering thyroid scintigraphy as the reference (RVU value of 1). Third: the cost of each procedure was calculated. This cost was composed by the staff work, the costs of building and facilities labor, department and equipment's maintenance, radiotracer costs and consumables for radiotracer administration and radiation protection and others department supplies, called practice expense RVU. The total cost was obtained summing up the costs assigned to each procedure.For the cost RVU (cRVU), the total expense of each procedure was divided by the unitary cost of the RVU. A novel variable, the complexity RVU (xRVU) was obtained in the same manner, excluding the radiotracer cost. ***Results:*** In the first semester of 2024, 5245 procedures (diagnostics and ambulatory therapies) were performed. The catalog comprised 44 diagnostic procedures and 7 therapeutic procedures. The RVU had a cost of 99.885 euros.For diagnostic procedures, the mean±SD cRVU values for 99mTc-related scintigraphic, non-99mTc-related and ^{18}F-FDG PET and non-^{18}F-FDG procedures were: 1.972±0.966, 5.304±2.036, 4.467±0.519, and 12.194±3.422, respectively. The corresponding xRVU values were 1.543±0.396, 1.853±0.756, 2.189±0.577, and 1.700±0.352, respectively.For therapeutic procedures, the mean ± SD of cRVU and xRVU for inpatient procedures compared to ambulatory ones, was of

59.847 ± 74.813 and 19.846 ± 6.701 for inpatient procedures, and 12.129 ± 19.922 and 1.081 ± 0.226 for ambulatory procedures, respectively. ***Conclusion:*** The cRVU per procedure varied significantly between diagnostic and therapeutic procedures. The expense of the radiopharmaceutical overstates the actual complexity of the procedure. Thus, the novel definition of xRVU, excluding radiotracer cost, offering a more realistic measure of the staff and departamental performance and should be used for organizational purposes.

EP-1394

Economic Impact of 18F-DCFPyl PET/CT on the Detection of Biochemical Recurrence of Prostate Cancer in Spain

M. Godbole[1], *T. Matos*[2], *R. Badinedi*[3], *N. Tchouen*[4], *A. Berthon*[5]; [1]*Alira Health, Barcelona, SPAIN,* [2]*Alira Health, Basel, SWITZERLAND,* [3]*Alira Health, London, UNITED KINGDOM,* [4]*Curium Pharma, Paris, FRANCE,* [5]*Curium Pharma, Lyon, FRANCE.*

Aim/Introduction: 18F-DCFPyl (Piflufolastat (18F)) is a PSMA-targeted PET radiotracer for detecting biochemical recurrence (BCR) in patients with prostate cancer (PCa). This study aims to quantify the economic impact of using 18F-DCFPyl PET/CT for patients with BCR of PCa to detect and localize BCR relative to 18F-FCH PET/CT, 68Ga-PSMA-11 PET/CT, and 18F-PSMA-1007 PET/CT, from the perspective of the Spanish National Healthcare System. ***Materials and Methods:*** A cost-consequence model was developed to simulate the diagnostic/treatment pathway, consisting of the proportion of patients relative to disease localization and imaging accuracy. The treatment mix included radical prostatectomy, radiation therapy, androgen deprivation therapy (ADT), and radiation therapy + ADT, informed by expert opinion. The model accounted for the treatment costs incurred due to true positives, false positives, true negatives, and false negatives, based on the test specifications of the tracers. The primary outcomes were the cost per correct diagnosis and, the number of futile treatments, defined as the treatments resulting from false positives, incurring an additional cost of repeated testing and the cost of treating false positives. The results are reported over an annual time horizon, considering 8,784 patients with BCR. Inputs to the model were informed by data from multiple meta-analyses, public data, and the literature. The prices were leveraged from the data published by the Commission on Medicines Prices (CIPM) and were identical for 18F-DCFPyl, 68Ga-PSMA-11and 18F-PSMA-1007 (€2,000), while the price for 18F-FCH was €1,144. ***Results:*** 18F-DCFPYL significantly reduced futile treatments to 760, approximately 58% (1,825), 56% (1,744), and 66% (2,236) fewer than 68Ga-PSMA-11, 18F-FCH and 18F-PSMA-1007, respectively. The model also revealed significant cost savings with 18F-DCFPYL in terms of repeated testing and false-positive diagnoses. For repeated testing, 18F-DCFPYL resulted in savings of €3M (43%) compared to 68Ga-PSMA-11, €7M (65%) relative to 18F-FCH, and €5M (58%) compared to 18F-PSMA-1007. Similarly, the costs associated with false positives were markedly lower with 18F-DCFPyl, yielding savings of €3M (51%) against 68Ga-PSMA-11, €4M (58%) relative to 18F-FCH, and €6M (66%) when compared to 18F-PSMA-1007. With a cost per correct diagnosis of €2,215, 18F-DCFPYL delivers an 8% reduction compared to 68Ga-PSMA-11 (€2,413) and a substantial 15% savings over 18F-PSMA-1007 (€2,592), resulting in a per-patient saving of €377 compared to 18F-PSMA-1007 and €198 compared to 68Ga-PSMA-11. ***Conclusion:*** 18F-DCFPyL PET/CT offers a cost-effective BCR detection option within the Spanish healthcare system, significantly reducing futile treatments, false positives, and repeat testing compared to alternatives, enhancing clinical outcomes.

EP-1395

Establishment of the Dutch National FAPI Working Group: Coordinated Advancement of FAPI Theranostics in Nuclear Medicine

S. Veldhuijzen van Zanten[1], *E. Droogers*[1], *L. de Geus-Oei*[2], *R. Slart*[3], *B. Zwezerijnen*[4], *B. Windhorst*[4], *M. Lam*[5], *T. Ververs*[5], *D. Wyndaele*[6], *J. de Klerk*[7], *L. Andrews*[7], *M. Wondergem*[8], *W. Kool*[9], *W. Vogel*[10], *D. Oprea-Lager*[11], *V. Rijk*[11], *L. Heijmen*[2], *T. van Nijnatten*[12], *L. Weijs*[13], *A. van den Hoven*[14], *S. Veldhuijzen van Zanten*[15]; [1]*Erasmus Medical Center, Rotterdam, NETHERLANDS,* [2]*LUMC, Leiden, NETHERLANDS,* [3]*UMCG, Groningen, NETHERLANDS,* [4]*Amsterdam UMC, Amsterdam, NETHERLANDS,* [5]*UMC Utrecht, Utrecht, NETHERLANDS,* [6]*Catharina Hospital, Eindhoven, NETHERLANDS,* [7]*Meander Medical Center, Amersfoort, NETHERLANDS,* [8]*Northwest Hospital Group, Alkmaar, NETHERLANDS,* [9]*Northwest Hospital Group & Cyclotron Northwest BV, Alkmaar, NETHERLANDS,* [10]*Netherlands Cancer Institute - AvL, Amsterdam, NETHERLANDS,* [11]*Radboud UMC, Nijmegen, NETHERLANDS,* [12]*MUMC+, Maastricht, NETHERLANDS,* [13]*ZGT, Hengelo/Almelo, NETHERLANDS,* [14]*Sint Antonius Hospital, Nieuwegein, NETHERLANDS,* [15]*Erasmus MC, Rotterdam, NETHERLANDS.*

Aim/Introduction: Fibroblast Activation Protein Inhibitor (FAPI) radiotracers represent an emerging class of compounds for molecular imaging and targeted radionuclide therapy, particularly relevant in oncology and fibrotic diseases. To streamline national efforts in research and clinical implementation, the Dutch National FAPI Working Group was established under the auspices of the national nuclear medicine society. This abstract outlines the group's structure, activities, and strategic goals aimed at facilitating clinical translation and advancing collaborative theranostic applications of FAPI. ***Materials and Methods:*** The multidisciplinary working group includes nuclear medicine physicians, radiochemists, pharmacists, radiologists, and clinical and preclinical researchers from multiple academic and non-academic institutions across the Netherlands. It functions as a collaborative platform with regular meetings, shared documentation, and consensus-driven initiatives. Key activities include standardisation of FAPI-PET imaging protocols, facilitation of ethical and regulatory procedures (including CTIS submissions), and development of a national FAPI imaging database. In parallel, a dedicated FAPI PhD network was launched to foster early-career collaboration, promote harmonisation, and stimulate cross-institutional expertise sharing. ***Results:*** The working group has achieved consensus on a national FAPI-PET acquisition protocol, now disseminated via a centralised online platform. Regulatory engagement has addressed tracer access and production routes, liability and indemnity frameworks, and inter-institutional radiopharmaceutical distribution logistics. Active research spans both oncologic and non-oncologic indications, including gastric, colorectal, breast, prostate, and hepatobiliary malignancies, carcinoma of unknown primary, fibrotic disorders, and emerging rare disease applications. Case-based multidisciplinary discussions and anonymised data sharing have illustrated the added diagnostic and clinical value of FAPI, particularly where conventional imaging was inconclusive. A national FAPI training day was organised to introduce clinicians and researchers unfamiliar with FAPI image interpretation to core principles and case-based learning. The PhD network now connects early-career researchers throughout the country, supporting knowledge exchange and harmonisation, accelerating regulatory steps during the setup phase of (multicentre) trials, and encouraging collaborative analyses and joint publications. ***Conclusion:*** The Dutch National FAPI Working Group exemplifies a coordinated national initiative to advance FAPI-based imaging and therapeutic applications in nuclear medicine. Through interdisciplinary collaboration, protocol harmonisation, early-career integration, and proactive regulatory

engagement, the group strengthens the infrastructure for clinical translation of FAPI theranostics. This model may serve as a blueprint for international efforts aiming to implement emerging radiopharmaceutical innovations in a harmonised, sustainable, and patient-centred manner. As a next step, the group aims to initiate cross-border collaborations focused on supporting larger multinational clinical trials.

EP-1396

Current Status of Theranostics in the Asia-Pacific Region

A. Brink[1], *E. Estrada-Lobato*[1], *D. Paez*[1], *F. Giammarile*[1], *A. Korde*[2], *D. Subbotnitskiy*[3], *G. Karthikeyan*[4];
[1]*International Atomic Energy Agency, Nuclear Applications Human Health, Division of Nuclear Medicine and Diagnostic Imaging, Vienna, AUSTRIA,* [2]*International Atomic Energy Agency, Department of Nuclear Sciences and Applications, Division of Physical and Chemical Sciences, Vienna, AUSTRIA,* [3]*International Atomic Energy Agency, Department of Technical Cooperation, Division for Asia and the Pacific, Vienna, AUSTRIA,* [4]*All India Institute of Medical Sciences, New Delhi, INDIA.*

Aim/Introduction: Theranostics is increasingly used for personalized disease treatment. Effective application of theranostics requires nuclear medicine (NM) facilities to be well-staffed, well-equipped, with proper knowledge, expertise and regulatory oversight. To document theranostics capacity in the Asia-Pacific, the IAEA surveyed NM facilities in the region. ***Materials and Methods:*** The survey covered the number of NM facilities, SPECT/CT, and PET/CT cameras, and dedicated therapy facilities. Production capabilities were assessed including the number of research reactors, medical cyclotrons, production of isotopes and generators. Information on the performance of dosimetry and quality management programs, such as QUANUM 3.0 was collected. The questionnaire covered human resources, determining the number of trained NM physicians, radiopharmacists, technologist and medical physicist working in NM. Participants described the training programs for the different fields of expertise and outlined the challenges faced in setting up a theranostic service. ***Results:*** A total of 44 NM facilities from 26 countries participated. The number of centers is influenced by a country's population and income status. Japan, a high -income country and India, the most populous, have the most centers in the region. Japan, with its advanced NM capability has 1400 facilities. The number of beds per population size was used to assess therapy capacity. Bangladesh has the highest (n=50) number of beds. Country income group also influences therapy capacity with the UMICs group having the highest number of beds available (n=77). Sixty-two percent (16/26) of the countries import most of the radiotracers used for diagnostic purposes. Those producing tracers locally do so in hospital-based pharmacies. The exception is Iran and Japan, which have many industrial production facilities. About 60% of the countries (15/25) are involved in ongoing trials. Over 95% of countries ensure proper disposal of radioactive waste. Of the 16 countries with data available, 88% follow pharmacopeia monographs. Only 65% of the countries offer a specialization degree in NM, and 51% have clinical training programs. Certification for physicists is available in 75% of the countries, degree program for technologists in 50%, specialized training for radiochemist in 41%, specialty education for pharmacists in 33%, and diploma programs in 22%. ***Conclusion:*** Reasons behind the advancements in theranostics in the region were identified. National government and international collaboration have improved awareness and technological advancements in radiopharmaceuticals and facilitated training and human resource development. Challenges include prioritization and allocation of funds, with lower availability leading to shortfalls in infrastructure development, equipment and training.

EP-1397

Screen-Sharing with AI in VR: A Novel Approach to Radiology Learning and Interpretation

J. Olsson*, J. P. Connelly, H. Ramsdal Hol;*
Oslo University hospital, Oslo, NORWAY.

Aim/Introduction: Medical imaging is growing in complexity. Radiology and nuclear medicine trainees face increasing demands, often without real-time feedback or structured pedagogical support outside of formal supervision. Here we combined virtual reality (VR) with conversational artificial intelligence (AI) and AI visual access to the VR-user interface. This allowed interactive voice prompted AI interpretation of medical texts and images and we used this to explore the utility of this technique as a way to get tailored tutoring in the absence of a teaching physician. ***Materials and Methods:*** Using a commercially available VR (Meta Quest 3) and "screen-sharing" with a multimodal AI (OpenAI), an immersive VR study setup was obtained. The user reads e-books on medical imaging in VR while simultaneously querying the AI on the visuals presented in VR, in real-time. Interactions involved testing verbal prompts focused on comprehension of the read material, quizzing on the text, image description, differential diagnosis, pathology identification, theoretical underpinnings and more. Results of a questionnaire based pilot study will be presented. ***Results:*** Initial experiences suggest the AI-in-VR setup encouraged deep and active learning. The AI assisted with concept clarification, definitions, and could test the user on the page in sight. It could even deliver rudimentary image interpretation (mainly gross pathology and anatomy. In terms of limitations, as the system depends on AI there are occasional hallucinations (inaccurate AI deduced facts or associations), so the user must have a low threshold for fact-checking. With this particular AI provider (OpenAI) there are usage limits for voice communication (and also for screen sharing in VR). These limits can be expanded at a cost. ***Conclusion:*** Screen-sharing with AI-in-VR can provide an engaging and enticing learning environment for radiology and nuclear medicine training. It potentially offers flexible support for imaging physician skill development, particularly valuable in resource-limited educational environments. Results of a small pilot study evaluating the users experience and learning outcomes will be presented at the conference.

EP-1398

Implementation of a customised software tool for proposal and project management dedicated to an experimental Radiopharmacy Facility within a private academic research institute in Italy

R. Visentin[1], *C. Franciosi*[1], *G. Iachetti*[1,2], *S. Fusaro*[1], *M. Lopatriello*[1], *A. Moretti*[1], *M. De Summa*[1], *S. Spinosa*[1], *S. Annunziata*[2];
[1]*Medipass Ergea, Integrative Clinical Solutions - Radiopharmacy, Fondazione Policlinico Universitario A. Gemelli IRCCS, Roma, ITALY,* [2]*Nuclear Medicine Unit, GSTeP Radiopharmacy, Department of Diagnostic Imaging and Radiotherapy, Fondazione Policlinico Universitario A. Gemelli IRCCS, Roma, ITALY.*

Aim/Introduction: In 2018, the Italian Ministry of Health recognised Fondazione Policlinico Universitario Agostino Gemelli as a scientific and treatment hospital for personalised medicine and innovative biomedical technologies. This led to the establishment of the Gemelli Science and Technology Park (G-STeP), as a network and platform of services to support all stages of scientific research project development. G-STeP is currently composed of twenty-five facilities. Among them, the facility Radiopharmacy deals with a constantly increasing number of research proposals and ongoing projects since October 2022. The need for a facility tool enabling standardised proposal collection, assessment, and internal approval as well as project management brought to the development of a dedicated software platform, hereafter

Research Tool. ***Materials and Methods:*** The implementation of the Research Tool was performed through the following steps: - definition of facility research scopes and of possible related projects; - identification of all the factors characterising and affecting the different kinds of projects; - conception of a work breakdown structure and of a task list covering all the kinds of projects; - definition of tool requirements for proposal and project management; - identification of the commercially available solution more adherent and/or more customisable and scalable. ***Results:*** The Research Tool was developed starting from a commercially available platform already conceived for proposal (business case, BC) and project management. After a deep customisation process, the current version allows us to: - collect non-profit/profit BCs in the facility areas of interest and classify them according to specific parameters; - carry out a preliminary internal assessment/approval of BCs taking into account scientific value, feasibility (major constraints), and compliance with Radiopharmacy and G-STeP research objectives; - match non-profit BCs with non-profit fundings and deeply evaluate funding rules and constraints; - carry out a second internal assessment/approval of BCs which passed the first one, deepening feasibility and sustainability, and also simulating them in the research portfolio; - manage projects arising from approved BCs (schedule, resources, budget, revenue, risks, changes); - associate BCs and projects with the related documentation - generate dashboards and reports for both BCs and projects. ***Conclusion:*** The implemented solution is a robust and versatile tool for proposals management, through a simple and standardised process which guarantees a uniform and strategic assessment, and for the management of each project throughout its entire lifetime, per se and in relation to research portfolio, with particular regard to several incoming projects about experimental radiopharmaceuticals.

EP-1399

The experience of [^{18}F]MC225 trial authorisation in Italy: the academic journey towards a non-profit clinical trial authorisation from precursor production to clinical trial approval

A. Simonetti[1,2], *A. Moretti*[3], *N. Colabufo*[4,5], *M. Leopoldo*[4,5], *C. Filosa*[5], *D. Pantaleo*[3], *V. Ceccarelli*[3], *M. Lopatriello*[3], *C. Franciosi*[3], *M. Calcagni*[6], *A. Giordano*[6], *G. Sani*[1,7], *S. Annunziata*[6], *R. Visentin*[3];
[1]Department of Neuroscience, Sensory Organs and Chest, Section of Psychiatry, Fondazione Policlinico Universitario Agostino Gemelli IRCCS, Roma, ITALY, [2]Menninger Department of Psychiatry and Behavioral Sciences, Baylor College of Medicine, Houston, TX, UNITED STATES OF AMERICA, [3]Medipass Ergea, Integrative Clinical Solutions - Radiopharmacy, Fondazione Policlinico Universitario A. Gemelli IRCCS, Roma, ITALY, [4]Department of Pharmacy-Pharmaceutical Sciences, University of Bari "Aldo Moro", Bari, ITALY, [5]Biofordrug, Spin-off of the University of Bari "Aldo Moro", Bari, ITALY, [6]Nuclear Medicine Unit, GSTeP Radiopharmacy, Department of Diagnostic Imaging and Radiotherapy, Fondazione Policlinico Universitario A. Gemelli IRCCS, Roma, ITALY, [7]Department of Neuroscience, Sensory Organs and Chest, Section of Psychiatry, Università Cattolica del Sacro Cuore, Roma, ITALY.

Aim/Introduction: In January 2022, the proposal of the inter-academy Project "Evaluation of p-glycoprotein alterations in treatment-resistant depression: a [^{18}F]MC225 PET study" was applied to the national Ministry of Health grant "Bando Ricerca Finalizzata 2021" [GR-2021-12374141]. In October 2022, the Project was declared among eligible for funding. The Project should have started on April 30, 2023. At the end of January 2023, the local Ethical Committee approval required by the grant call rules was considered sub-optimal due to the interventional nature of the study, and the Clinical Trial (CT) authorisation through the new EU portal CTIS should have been obtained. ***Materials and Methods:*** The application for CT authorisation was submitted in accordance with Regulation 536/2014 through the CTIS. The Investigational Medicinal Product Dossier (IMPD) was drafted following Regulation Annex I provisions. ***Results:*** [^{18}F]MC225 was not previously developed at Policlinico Universitario Agostino Gemelli (Study Promoter). Moreover, according to the Project proposal, the [^{18}F]MC225 precursor would have been produced and supplied by Biofordrug (University of Bari spin-off) after the project start. Thus, in January 2023, no quality data for precursor and investigational medicinal product were available to draft the IMPD. To permit the CT approval, the Ministry allowed a nine-month Project start delay. However, all the activities to obtain the CT authorizations should have been self-financed. The first CTIS submission was performed at the end of October 2023. The Request For Information (RFI) received from Italian Medicines Agency (AIFA) was accurately respecting the international guidelines to guarantee "quality, safety and efficacy". However, the CTIS timeline, essential to speed up trial approval, was too tight to properly solve the received RFI. At the end of January 2024, the application was withdrawn because precursor's characterization was still insufficient to satisfy the requirements. After eleven months working for RFI resolutions, the second submission was performed in December 2024. Finally, the CT authorisations became effective on April 16, 2025. ***Conclusion:*** The approval of a trial on [^{18}F]MC225 for the first time in Italy and through a project supported by a national public grant demonstrates that non-profit investigator-initiated trials with novel radiopharmaceuticals are feasible in Italy. Nevertheless, research teams, authorities and grant funders should timely approach the CT authorisation flow matter to update non-profit grant rules. Although a peremptory deadline to get the authorization should be stated, the time needed to get it as well as the required costs should be considered by the grant rules.

EP-1400

Designing and Building a Brand New Molecular Therapy Facility: Our experience.

E. Crick[1], *J. Mohammed-Gayle*[1], *H. Buschhold*[1], *M. Draper*[2], *D. Gallacher*[3], *R. Fernandez*[1];
[1]Guy's and St Thomas' NHS Foundation Trust, London, UNITED KINGDOM, [2]Cambridge University Hospitals NHS Foundation trust, Cambridge, UNITED KINGDOM, [3]King's College London, London, UNITED KINGDOM.

Aim/Introduction: This abstract details the challenges encountered when designing and building new molecular radiotherapy (MRT) facilities - including incorporating lead shielding into an existing building, regulatory approval, improved patient and staff monitoring, together with re-imagined staff training. Also detailed is a novel triple-detector monitoring system which aims to improve room utilisation, patient experience and engagement with radiation protection restrictions. ***Materials and Methods:*** Current MRT facilities were no longer fit for purpose; two rooms with shared bathroom/toilet, mobile lead shielding (trip hazard) and adjoining an Orthopaedic ward. With MRT workload increasing over the >20 year lifespan of the existing facility, the new MRT unit included an additional room, and crucially ensuite facilities, enabling more flexible patient scheduling. Radiation protection was integral to room design and the RPA was closely involved at every stage. Careful consideration of typical patient dose-rates and occupancy allowed optimisation of the lead required, ranging from 2.24 (Code 5) - 25mm, to minimise the cost/weight. Complex calculations of ray paths/distances and multiple construction options were proposed to achieve sufficient shielding. Thoughtful design enabled increased visibility (both in terms of natural light to improve patient experience and staff supervision of patients), separation of contaminated waste (linen/cutlery/crockery) into 'dry' and 'wet' utility rooms and low background areas for staff contamination monitoring. ***Results:*** Integral to the shielding design was introduction of a "triple detector" system of compensated Geiger-Muller detectors

sited in specific locations in the ceiling of one room. Results will detail the testing phase of the system (linearity of response across typical administered activities of Lu-177 and I-131 up to 11GBq, spatial linearity, relative detector response). The intent behind this novel configuration was to enable more frequent monitoring of patient dose-rates, with the aim of reducing lengths of inpatient stays and facilitating personalised restriction periods following hospital discharge. These directly improve patient experience, compliance with regulations and the ALARP principle. Placement within an Oncology ward enabled re-imagining of staff training. An online component was devised to complement in-person training, with positive staff engagement achieved to date. Pedagogy behind the online training (e.g. risk/radiation in context) and results of a questionnaire assessing staff engagement with training will be presented. ***Conclusion:*** Design and commission of new MRT facilities brings many challenges - complex shielding requirements, significant cost, and regulatory barriers. Tenacity is vital to ensure to ensure that MRT facilities are fit for purpose and safe for patients and staff.

EP-1401

Can Researchers Rely on Large Language Models to Write a Systematic Review? A Direct Comparison between Humans and Six LLMs

C. Pini[1], *M. Sollini*[1,2], *A. Lazar*[1], *F. Gelardi*[1], *G. Ninatti*[2,3], *M. Bauckneht*[4,5], *A. Chiti*[1,2], *M. Kirienko*[6];
[1]*Vita-Salute San Raffaele University, Milan, ITALY,* [2]*Department of Nuclear Medicine, IRCCS Ospedale San Raffaele, Milan, ITALY,* [3]*School of Medicine and Surgery, University of Milano-Bicocca, Milan, ITALY,* [4]*Department of Healt Sciences (DISSAL), University of Genoa, Genoa, ITALY,* [5]*Department of Nuclear Medicine, IRCCS Ospedale Policlinico San Martino, Genoa, ITALY,* [6]*Nuclear Medicine, Fondazione IRCCS Istituto Nazionale dei Tumori di Milano, Milan, ITALY.*

Aim/Introduction: The capability of Large Language Models (LLMs) to support and facilitate research activities has sparked growing interest in their integration into scientific workflows. This study aims to evaluate and compare against human researchers the performance of six different LLMs (ChatGPT, Claude, Gemini, DeepSeek, Le Chat, and Grok) in conducting various tasks necessary to produce a systematic literature review. ***Materials and Methods:*** The evaluation of the six LLMs was split into three tasks: literature search, article screening and selection (Task 1); data extraction and analysis (Task 2); final paper drafting (Task 3). Their results were compared with a human-produced systematic review on actinium-PSMA therapy in prostate cancer, serving as reference standard [1]. The evaluation was repeated on two rounds (February and April 2025) to evaluate reproducibility and improvements of LLMs over time. For Task 2 and Task 3, we provided each LLM with the same ground-truth data from the human-produced scientific paper to ensure a fair comparison across platforms. Quantitative and qualitative assessments were used to evaluate LLMs performance; additionally, time spent to complete each task was evaluated. ***Results:*** Out of the 18 scientific articles to be extracted from the literature for Task 1, the best LLM (Gemini 2.5 Pro) managed to identify 13 correct papers. ChatGPT and Grok managed to extract 9 and 8 manuscript, respectively, both alongside hallucinated records. Data extraction and analysis for Task 2 was partially accurate and required multiple prompts, with the best performer achieving 93% correct entries, though with only 7 out of 18 articles tabulated with no errors. The full papers generated by LLMs for task 3 were short and uninspiring, often not fully adhering to the standard template for a systematic review. While all LLMs managed to perform Task 1 and Task 3 in less than 30 minutes, Task 2 required cumbersome and long procedures (up to 2 hours) for many models. Incremental improvements were observed between Round 1 and Round 2, yet overall performance remained inconsistent. ***Conclusion:*** Although LLMs show promise, none can yet autonomously perform an end-to-end systematic review with human-level accuracy or methodological rigor. Their evolving capabilities may support researchers in literature triage and draft generation under careful supervision, but expert oversight remains indispensable for evidence synthesis. ***References:*** 1. Ninatti G, Scilipoti P, Pini C, et al (2025), Time for action: actinium-225 PSMA-targeted alpha therapy for metastatic prostate cancer - a systematic review and meta-analysis. Theranostics 15:3386-3399. https://doi.org/10.7150/THNO.106574

EP-1402

Challenges in Access to Peptide Receptor Radionuclide Therapy in Developing countries: Insights from patient advocacy perspective

S. Dureja*;*
Theranostics India Centre, New Delhi, INDIA.

Aim/Introduction: Discussing challenges in Access to Peptide Receptor Radionuclide Therapy (PRRT) in Developing countries and sharing insights from 10 years of patient advocacy. ***Materials and Methods:*** This is a subjective analysis of availability and access to treatment for Neuroendocrine tumors in the Indian subcontinent over 10 years and experience as a physician- advocate engaged with a neuroendocrine tumor support organisation. ***Results:*** The „Iron Triangle" of healthcare is a concept which talks about the relationship between cost, access and quality of healthcare. Extrapolated to PRRT, the factor affecting access in low income countries, can be classified into triple A or Availability, Access and Awareness (about use of PRRT). Given the relative uncommonness of Neuroendocrine tumors (NETs), patient advocates/advocacy groups can work with the medical fraternity for information dissemination about use and availability of theranostics. They can influence policy decisions by giving representation to governments which can help extent healthcare coverage for PRRT. Advocacy groups also play a major role to inform and mobilize the patient commnuity for clinical trials.Further, patient reported outcomes can be used to refine research objectives. Other steps like regional co-operation for capacity building and strengthening scientific trials are also areas where patient advocate groups can help in growth of radionuclide therapy for Neuroendocrine tumors. ***Conclusion:*** Patient advocacy has an important and growing role in impacting access to treatment for NET patients, more so in developing economies. ***References:*** 1. Kolarova T, Bouvier C. The Role of Patient Support Groups in Neuroendocrine Neoplasms. Curr Oncol Rep. 2021 Mar 22;23(5):53. doi: 10.1007/s11912-021-01046-6. PMID: 33754245; PMCID: PMC7985052. 2. Leyden S, Kolarova T, Bouvier C, Caplin M, Conroy S, Davies P, Dureja S, Falconi M, Ferolla P, Fisher G, Goldstein G, Hicks RJ, Lawrence B, Majima Y, Metz DC, O'Toole D, Ruszniewski P, Wiedenmann B, Hollander R; International Neuroendocrine Cancer Alliance (INCA). Unmet needs in the international neuroendocrine tumor (NET) community: Assessment of major gaps from the perspective of patients, patient advocates and NET health care professionals. Int J Cancer. 2020 Mar 1;146(5):1316-1323. doi: 10.1002/ijc.32678. Epub 2019 Oct 25. PMID: 31509608; PMCID: PMC7004101.

EP-1403

Expanding Global Equitable Access to Radioligand Therapy

S. Nogueira*, A. Armesto, C. Carreras, I. Hume, Y. Omar, E. Cannarozzo, A. F. Viana;*
Oncidium Foundation, Auderghem, BELGIUM.

Aim/Introduction: Radioligand therapy (RLT) has demonstrated remarkable success, but its high cost has limited its availability, particularly in developing countries. A global online platform that connects healthcare professionals with radioisotope companies could be an essential solution to support financially

struggling patients needing RLT. In this context, a non-profit foundation launched the RLT-Connect Platform online to promote international collaboration, raise awareness, and secure funding. This platform could improve equity in cancer care worldwide. This report outlines the process of submitting patient cases and treatment donation requests for those who have exhausted all options and meet eligibility criteria, as well as the results obtained in 2 years. ***Materials and Methods:*** The platform was conceived and developed by the non-profit foundation. Physicians from experienced RLT centers submit treatment requests through RLT-Connect for patients with limited financial options. An independent Ad Hoc committee reviews the submissions based on eligibility and ethical criteria. Upon approval, donated doses of radioisotopes are supplied through industry partners and processed locally for administration. Physicians report baseline data, treatment details, and outcomes online. ***Results:*** Between January 2024 and March 2025, the platform recorded 59 registered centers in 14 countries, 38 patients treated or under treatment, and 108 administered doses. Five radioisotope suppliers are currently actively donating doses. Patients primarily had metastatic castration-resistant prostate cancer (mCRPC) and neuroendocrine tumors (NETs); one patient had ovary cancer, with staging typically at TNM Stage IV. Imaging agents used included 68Ga-PSMA (67%) or 18F-PSMA (33%) for mCRPC and 68Ga-DOTATATE (50%) or 18AlF-DOTATATE (50%) for NETs, with uptake supporting treatment. Based on the reports sent by now, the treatment outcomes include PSA reductions of ≥50% in mCRPC cases, up to 75% decrease in total lesion activity, Quality of Life (QoL), patients reported symptom relief, pain reduction, restored daily function and increase in mental wellness. ***Conclusion:*** The RLT-Connect platform has demonstrated that access to radioligand therapies can be extended to patients otherwise excluded due to financial difficulty or lack of insurance denial. The RLT-Connect has transformed individual lives by combining the engagement of nuclear medicine physicians with committed industry partners. But beyond individual treatments, RLT-Connect highlights the importance of integrating RLT into national healthcare systems to ensure its availability as a standard oncologic treatment.

EP-1404

Addressing the Challenges of Radiopharmacy: A specialized certifying program for French-speaking pharmacists in Switzerland

J. Delage[1], *M. Schottelius*[2], *M. Straub*[3], *J. Prior*[4], *M. Lebreux*[5], *A. Hammadi*[6], *F. Sadeghipour*[7,8,9];
[1]*Radiopharmacy Unit, Department of Pharmacy, Lausanne University Hospital and University of Lausanne, Lausanne, SWITZERLAND,* [2]*Translational Radiopharmaceutical Sciences, Depts. of Nuclear Medicine and of Oncology, Lausanne University Hospital and University of Lausanne, Lausanne, SWITZERLAND,* [3]*Institute of Radiation Physics, Lausanne University Hospital and University of Lausanne, Lausanne, SWITZERLAND,* [4]*Department of Nuclear Medicine and Molecular Imaging, Lausanne University Hospital and University of Lausanne, Lausanne, SWITZERLAND,* [5]*Department of Pharmacy, University Hospital of Québec, Laval University, Laval, QC, CANADA,* [6]*National Institute for Nuclear Science and Technology (INSTN), Atomic Energy Center (CEA) of Saclay, Gif-sur-Yvette, FRANCE,* [7]*Department of Pharmacy, Lausanne University Hospital and University of Lausanne, Lausanne, SWITZERLAND,* [8]*Center for Research and Innovation in Clinical Pharmaceutical Sciences, Lausanne University Hospital and University of Lausanne, Lausanne, SWITZERLAND,* [9]*Institute of Pharmaceutical Sciences of Western Switzerland, University of Geneva, University of Lausanne, Lausanne, SWITZERLAND.*

Aim/Introduction: In recent years, nuclear medicine and radiopharmacy have experienced significant growth with the development of new theranostic approaches in cancer treatment and the arrival of innovative radiopharmaceuticals on the market. The involvement of pharmacists specialized in radiopharmacy is therefore essential, as they bring their expertise in the management of radiopharmaceutical production as well as in the therapeutic support of patients. Despite the growing demand, training opportunities in radiopharmacy remain scarce. In Switzerland, this lack has led to challenges in recruitment and a limited number of radiopharmacists available to support the clinical adoption of these new treatments. As a result, we aim to develop a new certifying program for French-speaking pharmacists in Switzerland. ***Materials and Methods:*** The goal of this program is to equip pharmacists with the necessary skills to ensure the safety of the radiopharmaceutical drug circuit from preparation and release to clinical patient support (monitoring adverse effects, pharmacological follow-up, therapeutic education, radiation protection, etc.). To this end, discussions have been initiated with various partners and the University of Lausanne. To strengthen radiopharmacy connections within the Francophone community, partnerships involving the exchange of educational content are being considered with the National Institute for Nuclear Science and Technology (INSTN) Saclay, Paris, France and Laval University, Québec, Canada. ***Results:*** This program, structured as a Certificate of Advanced Study (CAS), will include the following four modules: Module 1: Fundamentals of nuclear physics and detection of ionizing radiation, radiobiology, and radioprotection Module 2: Production and quality control of radiopharmaceuticals Module 3: Clinical diagnostic radiopharmacy Module 4: Clinical radiopharmacy. Therapeutic and theranostic applications In addition to theoretical instruction, a four-month internship in a radiopharmacy unit will be offered, to reinforce the theoretical concepts acquired with practical experience. The program is scheduled to launch in 2026. ***Conclusion:*** The growing demand for radiopharmaceuticals and theranostic applications highlights the urgent need to strengthen specialized pharmaceutical training in radiopharmacy. Through the establishment of a specialized CAS in French-speaking Switzerland, this program aims to address current training gaps, support the integration of pharmacists into multidisciplinary care teams, and contribute to the safe and effective deployment of innovative nuclear medicine therapies. Through national and international collaborations, this initiative also reinforces the Francophone network in radiopharmacy education and practice.

EP-1405

Establishing Traceability Routes in Nuclear Medicine: The ETrain starts its journey ...

A. Fenwick[1], *J. de Pooter*[2], *P. Toroi*[3], *J. Rusnak*[4], *K. Sjogreen Gleisner*[5];
[1]*National Physical Laboratory, Teddington, UNITED KINGDOM,* [2]*VSL, Delft, NETHERLANDS,* [3]*STUK, Helsinki, FINLAND,* [4]*CMI, Prague, CZECH REPUBLIC,* [5]*Lund University, Lund, SWEDEN.*

Aim/Introduction: The disparity in radioactivity measurement capability varies across Europe. Comparison exercises between hospital sites have demonstrated that in some regions more than 90 % of participants are able to measure the activity of a reference source to within ± 5 % of the true activity but in other regions this has can be as low as 23 % of participants. Measurement accuracy is critical in drug development, supporting clinical trials and patient safety, whilst traceability of the injected activity is also a requirement in many countries. To address this, Euramet has funded a new project, 24RPT01 (ETrain) to improve activity measurement capability in nuclear medicine. The aim is to establish a network to be utilised by clinical partners, pharmaceutical suppliers and manufacturers to ensure traceable radioactivity measurements. ***Materials and Methods:*** A consortium of National Metrology Institutes (NMIs), calibration laboratories, academic partners, national societies and industrial partners has been formed to establish calibration centres across Europe, providing access to traceable radioactivity standards.

This network will be developed over three years, through engagement with NMIs and clinical partners with comparisons between the calibration laboratories ensuring equivalence between countries. The networks effectiveness will be tested by performing intercomparison exercises of clinical sites. Guidance documents and calibration protocols will be produced and made available to the user community. ***Results:*** The outcomes of the project will be in the form of guidance documents, comparison reports and training material aimed at improving the overall measurement capability in Europe. Increasing the availability of reference sources and providing guidance and tools to ensure traceability will improve harmonisation and enable compliance with legislation by allowing traceability to be recognised in more places than ever before. Guidance on uncertainty assessment from primary standards through to imaging and dosimetry will be included. Progress on achieving these goals and an overview of the project structure will be presented. ***Conclusion:*** The ETrain project aims to enable harmonisation of activity measurements across Europe and supercharge its ability deliver clinical trials and harmonised imaging and dosimetry studies. The project will run until 2028 and brings together metrology institutes and clinical partners. To be part of the project and receive progress updates or attend meetings and workshops, please contact the author.

EP-1406

Enhancing Diagnostic Accuracy in Dementia: Standardized Protocols for FDG PET-CT Brain Imaging

A. Hassan, *A. W. Alessi, E. Wahab, S. J. Hughes;*
Queen Elizabeth Hospital Birmingham, Birmingham, UNITED KINGDOM.

Aim/Introduction: Fluorodeoxyglucose positron emission tomography-computed tomography (FDG PET-CT) is a vital imaging modality in the diagnosis of neurodegenerative diseases, particularly dementia. By assessing cerebral glucose metabolism, it provides essential insight into patterns of brain activity. Accurate diagnosis depends on standardizing acquisition and reconstruction procedures to ensure diagnostic reliability and comparability. This educational abstract presents a structured framework aimed at improving image quality and interpretive consistency, thereby supporting earlier and more accurate dementia diagnosis. ***Materials and Methods:*** Patient preparation is a critical first step, involving a fasting period of at least six hours. Diabetic patients must have glycemic control before imaging. To establish a resting baseline of neuronal activity, patients should be placed in a low-stimulus environment for 20-30 minutes before tracer injection and remain at rest after injection. Proper head immobilization is ensured through supine positioning, aligning the orbito-meatal line perpendicular to the floor, and using non-invasive restraints such as Velcro straps to minimize motion during acquisition. Reconstruction should utilize 3D iterative techniques that exclude point spread function (PSF) to prevent Gibbs artifacts. For the CT component, high milliampere-second (mAs) settings and isotropic voxel acquisition are recommended to support quality anatomical reference and multiplanar reconstruction. Image display must be standardized to preserve interpretative reliability. Display methods include experiential windowing, percentile-based thresholds, and five-region saturation using a rainbow scale; whichever is chosen, consistency must be upheld across all scans. ***Results:*** Four key anatomical quality indicators serve as immediate benchmarks for image quality: the superior parietal gyri should be intact, the anterior limb of the internal capsule clearly separated, the posterior cingulate gyri visibly defined bilaterally, and the bilateral colliculi well-demarcated. If significant motion artifacts compromise more than two of these regions, repeat imaging may be necessary. Structured reporting should document scan quality, note age-related changes in FDG uptake, and classify the severity of regional hypometabolism as mild, moderate, or severe, based on the extent of gray-white matter preservation. Additional CT findings such as sulcal widening, ventricular enlargement, and medial temporal atrophy are also included to provide a comprehensive diagnostic context. ***Conclusion:*** This standardized approach to FDG PET-CT brain imaging enhances diagnostic clarity in dementia evaluation. By combining technical rigor with clinical insight, it promotes reproducible, high-quality imaging that can be effectively integrated into multidisciplinary care pathways. Ultimately, this protocol supports earlier and more targeted interventions in patients with suspected neurodegenerative conditions.

EP-1407

Thyroid Scintigraphy in Congenital Hypothyroidism

K. Auf der Springe, *R. Dias Correia, N. Testart, M. Jreige, N. Schaefer, J. O. Prior, M. Nicod-Lalonde;*
CHUV, Lausanne, SWITZERLAND.

Aim/Introduction: Newborns with congenital hypothyroidism are diagnosed and treated in specialized centers. We discuss the planification and procedure of thyroid scintigraphy, the underlying etiologies and scintigraphic patterns as well as the treatment implications of the findings. ***Materials and Methods:*** Newborn screening identifies congenital hypothyroidism on the third day of life, aiming to avoid livelong disabilities. Thyroid scintigraphy with technecium-99m pertechnetate or iodine 123 helps identify the underlying pathology. To ensure best patient outcome, scintigraphy must not delay the beginning of hormone substitution, should be performed as early as possible and may be carried out up until 7 days after the beginning of the treatment. ***Results:*** The objective of is to identify the underlying etiology and guide appropriate therapeutic interventions. Most common causes are dysgenesis, refering to abnormal thyroid gland development (ectopy, agenesis or hypoplasia) and dyshormonogenesis, which involves impaired hormone synthesis within a structurally normal gland. Rare causes of congenital hypothyroidism include transitory hypothyroidism which may have different causes, TSH resistance, deficit in iodine transporter and central congenital hypohyroidism. By obtaining scintigraphic images, clinicians can ascertain the severity of thyroid dysfunction and underling pathology, allowing for personalized treatment plans. This has implications for long-term management, including the duration of hormone replacement therapy. ***Conclusion:*** Thyroid scintigraphy in contenital hypothyroidism is an important diagnostic and therapeutic tool that provides valuable insights into thyroid gland localization, morphology and function, guiding clinicians in tailoring treatment strategies for improved patient outcomes. ***References:*** van Trotsenburg, Paul et al. "Congenital Hypothyroidism: A 2020-2021 Consensus Guidelines Update-An ENDO-European Reference Network Initiative Endorsed by the European Society for Pediatric Endocrinology and the European Society for Endocrinology." Thyroid : official journal of the American Thyroid Association vol. 31,3 (2021): 387-419. doi:10.1089/thy.2020.0333Keller-Petrot, Isabelle et al. "Congenital Hypothyroidism: Role of Nuclear Medicine." Seminars in nuclear medicine vol. 47,2 (2017): 135-142. doi:10.1053/j.semnuclmed.2016.10.005Hamdoun, Elwaseila et al. "Case Report: The Specter of Untreated Congenital Hypothyroidism in Immigrant Families." Pediatrics vol. 137,5 (2016): e20153418. doi:10.1542/peds.2015-3418

EP-1408

Association Between Whole-Body Composition Variables and Abdominal Fat Distribution with Bone Mineral Content in a Healthy Population (^{k}ReBoMiDe Study).

M. Cruz Montijano[1], *S. Pérez Luque*[2], *J. Pérez Beteta*[2], *J. Montalva Pastor*[1], *A. Gutiérrez Crespo*[3], *J. Bonilla Plaza*[1], *L. García Zoghby*[1], *M. Meneses Navas*[1], *S. Guzmán Ortiz*[1], *I. García Megías*[1], *C. La Fay*[3], *M. Caballero Campos*[4], *A. García Vicente*[1];
[1]*Complejo Hospitalario de Toledo, Toledo, SPAIN,* [2]*Department of Mathematics, University of Castilla-La Mancha, Ciudad Real, SPAIN,* [3]*GE Healthcare, Madrid, SPAIN,* [4]*University of Córdoba, Cordoba, SPAIN.*

Aim/Introduction: To determine the impact of demographic, anthropometric, whole-body tissue mass, and abdominal fat variables on bone mineral content (BMC) and bone mineral density (BMD) obtained by a dual-energy X-ray absorptiometry (DXA). ***Materials and Methods:*** A prospective study (kReBoMiDe) including healthy male and female controls aged between 20 and 49 years was developed and approved by Ethical Committee (reference number:1128/2024). BMC and BMD were quantified at various locations: the lumbar spine, proximal femurs, and the whole body. In addition, abdominal fat mass, total tissue mass (TTM), total lean mass (TLM), total fat-free mass (TFFM), total body mass (TBM), and abdominal adipose mass (AAM) were measured using a DXA scanner with a specific software. To analyze relationships among variables, Spearman correlation ($r \geq 0.70$) and the Wilcoxon test were used. The influence of age, sex, physical activity (PA), and body mass index (BMI) on the above-mentioned composition measures was assessed using Student's t-test and ANOVA. Statistically significant (SS) difference was considered for p-values < 0.05. ***Results:*** Data were collected from 75 controls (52 women), with 65.3% having a healthy BMI and 58.7% reporting low PA levels. Differences were found between sexes (predominance of males), but not by age or PA. According to BMI, there were only SS differences for measures of body composition and abdominal fat, but not for BMD/BMC. There were differences in laterality (left predominance for global extremity measurements and right for trunk measurements, except for BMD and CMO). An association was found between BMD/CMO of different locations with MMT, MTT, MLGT and TM. No MAA variable was significantly related to bone variables. ***Conclusion:*** BMI and the amount of MAA did not show a determining role in bone mass, although absolute variables such as MMT, MTT, MLGT and MT did. Sex played a predominant role over age in the bone mass of our healthy population.

EP-1409

(Radio)Theranostics: XXIst Century Nuclear Medicine Creating Hope for Oncological Patients

L. Metello[1], *R. R. Johnson*[1], *D. Jolly*[1], *A. Uhlending*[2], *V. Hugenberg*[2], *V. Gupta*[3], *C. Scheiber*[1], *G. Romanowicz*[1], *M. Capoulas*[1], *I. V. Costa*[1], *D. Fraga*[1], *L. Cunha*[1];
[1]IsoPor Group, Portugal, PORTUGAL, [2]Herz und Diabeteszentrum HDZ - NRW, Univ der Ruhr - Univ. Bochum, Bad Oeynhausen, GERMANY, [3]University of Heidelberg, DKFZ, Heidelberg, GERMANY.

Aim/Introduction: (Radio)Theranostics are an highly advanced - and very dynamic! - precision tool at the service of modern oncology in an increasingly personalized medicine world. It is really changing the present paradigm, and, to be efficient, it asks for distinct parts involved to adapt/evolve their positioning. ***Materials and Methods:*** The current paradigm has been analyzed and will be quickly characterized. Based on that, several distinct options will be presented, briefly commented and justified at all the following levels: Medical Level (Nuclear Medicine / Oncology / RadioOncology: the departing situations being several, analysis has been done accordingly and distinct possible future scenarios will be evoked) Patients Level (what is critical to know from the patients point-of-view? How to efficiently inform the most important aspects, in order to empower the patient for higher levels of awareness and participation, namely in its own specific case?) Management and Administration Level (pricing, cost/benefits relations and logistics demystified) Communication Level (being a critical aspect, it deserves a very well thought and planned approach, that should be consistent and coherent, but always dedicating special attention to specificities: Health Professionals levels versus patients, family, media and society levels) Education & Training Level ("new roles" meaning "new skills" and "new needs" for education and training in health professionals that should be able to perform efficiently in eventual "new fields") ***Results:*** Several years of practical "hands on" working, both at academic (education as research and development) and clinical levels, modulated with numerous exchanges of opinions and information between experts as with patients, demonstrated the need to change the actual paradigm, since definitely not fitting with the urgent need to maximize easiness, results and to increase the number of patients benefiting. Some results will be quantified and several suggestions, practical cases and "good practice examples" will be exposed and quickly analyzed, hoping to send the message that it does not need to be excessively complex and/or expensive, but often simply well thought, planned and executed in due time. ***Conclusion:*** (Radio)Theranostics are already here, and all the parts involved ask for an efficient practical implementation. It might only be achieved under a more efficient environment, where all are better educated and trained, being ready to work together - each one at its specific level - in a very open manner, totally focused in the need to increase the efficiency of the entire system, aiming at the wellness of the patient.

EP-1410

Study protocol update: A randomized phase 2 trial of FLEXible and extended dosing of ^{177}Lu-PSMA-617 Molecular Radioligand Therapy in mCRPC (FLEX-MRT)

A. Holzgreve[1,2], *A. Delker*[2], *Z. Ells*[1], *J. Brosch-Lenz*[3], *L. M. Unterrainer*[1,2,4], *J. Nikitas*[1], *S. Zhu*[1], *M. M. Contreras*[1], *H. Alam*[1], *R. M. Nabong*[1], *S. Lira*[1], *A. Vasilyev*[5], *L. Chen*[5], *T. Grogan*[5], *D. Elashoff*[5], *C. A. Meyer*[1], *M. Dahlbom*[1], *J. Czernin*[1], *J. Calais*[1];
[1]Ahmanson Translational Theranostics Division, Department of Molecular and Medical Pharmacology, David Geffen School of Medicine, UCLA, Los Angeles, CA, UNITED STATES OF AMERICA, [2]Department of Nuclear Medicine, LMU University Hospital, LMU Munich, Munich, GERMANY, [3]Institute of Nuclear Medicine, Bethesda, MD, [4]Bavarian Cancer Research Center (BZKF), partner site Munich, Munich, GERMANY, [5]Department of Medicine Statistics Core (DOMStat), Department of Medicine's Division of General Internal Medicine and Health Services Research, David Geffen School of Medicine, UCLA, Los Angeles, CA, UNITED STATES OF AMERICA.

Aim/Introduction: The European Medicines Agency (EMA) approved ^{177}Lu-PSMA-617 radioligand therapy (RLT) for patients with metastatic castration-resistant prostate cancer (mCRPC) with a fixed dosing schedule of 7.4 GBq administered once every 6 weeks for up to a total of 6 doses. However, a patient-tailored more flexible and extended dosing schedule may increase treatment efficacy of ^{177}Lu-PSMA RLT. ***Materials and Methods:*** We present an update on the study protocol of the randomized FLEX-MRT trial. ***Results:*** In this investigator-initiated prospective phase 2, open-label, randomized, controlled, parallel-group, single-center trial, we aim to assess the efficacy of a response-based flexible dosing schedule of ^{177}Lu-PSMA-617 RLT administered up to 12 treatment cycles in men with mCRPC. Key inclusion criteria include eligibility for ^{177}Lu-PSMA-617 (i.e. prior ARSI, prior chemotherapy, PSMA PET VISION criteria). Exclusion criteria include prior RLT and less than 6 weeks since the last myelosuppressive therapy. We hypothesized 2-year survival rates of 55% in the investigational group and 30% in the control group. A two-sided log rank test with an overall sample size of 90 subjects (45 per group) achieves 80.3% power at a 0.05 significance level to detect a hazard ratio of 0.50. Randomization will allocate patients in a 1:1 ratio: The investigational arm is treated with up to 12 cycles including potential "treatment holidays" depending on the treatment response; the control arm receives 6 cycles administered in six-week intervals. Imaging response to RLT is assessed using ^{177}Lu-PSMA-617 SPECT/CT after each cycle and PSMA PET/CT every 3 months during treatment holidays, respectively. RLT will be re-started after a treatment holiday in the investigational arm, if the patient experiences a ≥25% PSA progression and an imaging progression according to the RECIP criteria. The primary endpoint is the 2-year survival rate calculated from the date of the first treatment cycle. Secondary endpoints include safety by CTCAE and dosimetry, and determination of

overall and progression-free survival (evidence of progression as defined by either radiographic, PSA, or clinical progression, or death from any cause). The FLEX-MRT trial has been approved by the FDA (IND #168362) and the UCLA IRB (#23-000931), and it is registered on ClinicalTrials.gov (NCT06216249). The FLEX-MRT trial is currently recruiting. Start of enrollment was in August 2024. As of April 14th, 2025, 27 patients have been enrolled. ***Conclusion:*** The randomized FLEX-MRT trial aims to generate evidence for the efficacy of a response-based extended dosing schedule of ^{177}Lu-PSMA RLT in patients with advanced mCRPC.

EP-1411

Start-up of early-phases trials in radiopharmacy unit since begining 2024

S. Maymó Garrido[1], *D. Rodríguez-Puig*[1], *C. García-Alcober*[1], *E. Ricart-Paredes*[1], *M. Crespí-Busquets*[1], *C. Munuera-Sañudo*[1], *E. Pineda-Fernández*[1], *M. Bueno-Raspall*[1], *M. Cortés-Romera*[2];
[1]*Radiopharmacy Department. Hospital Universitari de Bellvitge - Idibell, L'hospitalet de Llobregat, SPAIN,* [2]*Nuclear Medicine-PET (IDI) Department. Hospital Universitari de Bellvitge - Idibell, L'hospitalet de Llobregat, SPAIN.*

Aim/Introduction: Assess the impact of the phased start of early phase clinical trials in our Radiopharmacy Unit since January 2024 . ***Materials and Methods:*** In order to assess the impact, a review was carried out of the enhanced functions that have emerged and that have been performed alongside those already existing in the radiotherapy department's clinical practice. ***Results:*** Since January 2024 we have been involved in 8 new clinical trials. These eight trials can be classified from more to less complex depending on whether they include (phase I) or not (phase II or III) an associated dosimetry study (SPECT/CT at 4, 24, 48 and 168 hours after administration of the ^{177}Lu radiopharmaceutical) together with pharmacokinetic (PK) determination. In our case, five of these are Phase I, one is Phase II and two are Phase III. The role of the radiopharmacy department has been expanded to include attendance at screening visits, detailed review of protocols, scheduling of initial eligibility tests (PET/CT and bone scan), and scheduling of therapy treatment dates within the protocol timeframe. Request doses of ^{68}Ga and ^{177}Lu-labelled radiopharmaceuticals via different platforms. Provide nursing staff with documentation for data collection (vital signs, ECG) and labelled tubes for blood/urine collection, if required. Complete all documentation associated with the administration of radiopharmaceuticals and submit this documentation to the appropriate data entry system. Manage of samples; centrifuge and pipette blood/urine samples, if required, for subsequent processing in the counter and complete the files required to be uploaded to a platform. Store samples in a freezer (-80°C) if required and manage their request for transport (IATA certified). Receive monitoring visits to verify data according to ALCOA+ criteria and be subject to audits. ***Conclusion:*** The arrival of these clinical trials has created an urgent need to restructure the infrastructure, as well as to introduce new staff profiles to support the functions involved in the successful development of these highly complex trials.

EP-1412

Hepatocellular carcinoma transarterial radioembolization: a single centre experience

A. Genova, *F. Porcaro, M. Prisco, I. Annarumma, L. Turchetta, V. Piscopo, M. Catalano;
Azienda Ospedaliera di Rilievo Nazionale Antonio Cardarelli, Naples, ITALY.*

Aim/Introduction: This study evaluates the efficacy and safety of transarterial radioembolization (TARE) in patients with unresectable hepatocellular carcinoma (HCC) treated at our institution. Personalized dosimetry was employed to maximize therapeutic efficacy while minimizing damage to healthy liver tissue. Both resin and glass microspheres were used, with dosimetric calculations performed using MIM SurePlan and Simplicit90Y™ software, respectively. Short-term outcomes were also assessed ***Materials and Methods:*** Patients are selected for TARE by a multidisciplinary oncology board based on eligibility criteria including adequate bilirubin levels, coagulation parameters, and platelet counts, to minimize the risk of post-TARE liver failure and procedural complications. Hepatic vascular anatomy was evaluated by angiography, followed by administration of [99mTc]-MAA via catheterization of the hepatic artery to simulate microsphere distribution. SPECT-CT imaging assessed lung shunting, non-target distribution, and tracer uptake in the liver lesion. Personalized pre-treatment dosimetry using [99mTc]-MAA SPECT-CT was performed to determine the feasibility of TARE and to select an activity that maximizes the tumor dose while respecting safety thresholds for healthy liver tissue. Absolute contraindications included pulmonary shunting >20%, uncorrectable gastrointestinal deposition, reverse hepatic arterial flow, and complete portal vein thrombosis. Treatment planning was performed with a voxel-based model using MIM SurePlan LiverY90™ for resin microspheres and a multicompartmental model implemented in Simplicit90Y™ for glass microspheres. Distribution of 90Y-microspheres was verified post-procedure with either SPECT-CT or PET-CT. Tumor response was assessed at 3 months with CT, ultrasound, or MRI. Between January 2022 and December 2025, 26 patients (20 male, 6 female; mean age 68) underwent TARE. Of these, 3 patients had portal vein thrombosis and 15 had previously received other treatments (surgery, laser ablation, RFA, or TACE). ***Results:*** Post-treatment fatigue, mild abdominal pain, and low-grade fever were observed in a minority of patients. No cases of liver-related toxicity or radiation-induced liver disease (REILD) were reported. During follow-up, 3 patients died due to disease progression. Partial response according to RECIST criteria was observed in 4 patients, and complete tumor necrosis in 3. Seven patients continued therapy with immunotherapy ***Conclusion:*** This single-center experience confirms that TARE with Y-90 microspheres is a safe and effective option for selected patients with unresectable HCC, regardless of the microsphere type. Personalized dosimetry enables a balance between preserving liver function and achieving tumor control, supporting TARE as a viable approach for local disease management, bridge to transplantation, or potential curative intent.

EP-1413

Study of Dosimetric Parameters of Treatment of Inoperable Lung Tumors Using Brachytherapy Based on Hydrogel Containing Radioisotope ^{188}Re

A. Kazemi[1], *H. Poorbaygi*[2];
[1]*Shiraz University of Medical Science, Shiraz, IRAN, ISLAMIC REPUBLIC OF,* [2]*Radiation Application Research School, Tehran, IRAN, ISLAMIC REPUBLIC OF.*

Aim/Introduction: Lung cancer, causing 1.8 million deaths in 2022, demands innovative solutions for inoperable cases. This simulation-based study introduces a novel brachytherapy approach using Heposphere hydrogel loaded with ^{188}Re for targeted treatment of lung tumors. Drawing parallels with ^{90}Y glass microsphere dosimetry, we evaluated D, BED, and TCP to assess therapeutic efficacy and safety. ***Materials and Methods:*** The Hepospher, incorporating ^{188}Re as sodium perrhenate, was modeled for delivery via embolization, leveraging its self-absorption for enhanced isotope retention. ^{188}Re mirror ^{90}Y localized dosing capabilities. MC simulations and MIRD formalism were applied to a lung tumor phantom. calculating D, RDF, BED, TCP, DVHs for (D_{90}) and (V_{20}). ***Results:*** Simulations revealed 90% of the prescribed dose (60 Gy) delivered within a 2 cm radius, with a dose rate of 2.8 Gy/h at the tumor-hydrogel interface, comparable to Yttrium-90's dose localization. DVHs showed 95% tumor coverage for 3 cm tumors. Healthy lung exposure was V_{20}<5% at 20 Gy. BED,

calculated using ^{188}Re's short $T_{1/2}$, aligning with ^{90}Y therapeutic range. TCP exceeded 90% for tumors, indicating high tumor control potential. The hydrogel's self-absorption minimized dose leakage, enhancing safety. ***Conclusion:*** The ^{188}Re-Heposphere offers a promising, ^{90}Y-inspired brachytherapy approach for inoperable lung tumors, achieving high tumor coverage, effective BED, and TCP while sparing healthy tissues. The hydrogel's self-absorption ensures precise dosing, positioning this method as a novel option for precision oncology. ***References:*** WCRF. (2022). Lung Cancer Statistics. Available at: https://www.wcrf.org/preventing-cancer/cancer-statistics/lung-cancer-statistics/, GLOBOCAN. (2022). Lung Cancer Incidence and Mortality. CA: A Cancer Journal for Clinicians. https://acsjournals.onlinelibrary.wiley.com/doi/10.3322/caac.21834., Scientific Study. (2024). Global Lung Cancer Trends to 2050. Journal of Cancer Policy. https://www.sciencedirect.com/science/article/pii/S1877782124001723., Gold-Enhanced Brachytherapy by a Nanoparticle-Releasing Hydrogel and 3D-Printed Subcutaneous Radioactive Implant Approach., Novel CT-guided ^{188}Re Brachytherapy Device for Local Primary and Secondary Lung Malignancies., Evaluation of a Proposed Biodegradable ^{188}Re Source for Brachytherapy Application: A Review of Dosimetric Parameters., Injectable Hydrogel-Based Drug Delivery Systems for Enhancing the Efficacy of Radiation Therapy: A Review of Recent Advances., Wang, Y., et al. (2024). A Phase I Clinical Trial Evaluating Hydrogel in Reducing Rectal Dose During Cervical Cancer Brachytherapy. Clinical and Translational Radiation Oncology, 49, 100867. https://doi.org/10.1016/j.ctro.2024.100867., Luo, G., et al. (2025). Estimated Worldwide Variation and Trends in Incidence of Lung Cancer by Histological Subtype in 2022. The Lancet Respiratory Medicine, 13(4), 348-363., Ito, A., et al. (2021). Endobronchial Brachytherapy as Definitive Treatment for Endobronchial Metastasis After Surgery of Non-Small Cell Lung Cancer. World Journal of Surgical Oncology, 19, 322. https://doi.org/10.1186/s12957-021-02434-9.

EP-1414

Bridging Competency and Clinical Practice: The Role of Entrustable Professional Activities in Theranostics-Oriented Nuclear Medicine Training

T. Pascual;
Department of Science and Technology- Philippine Nuclear Research Institute, Pasig, PHILIPPINES.

Aim/Introduction: The rise of theranostics—combining molecular imaging and targeted radionuclide therapy—has transformed nuclear medicine into a precision-driven speciality. However, educational frameworks have not kept pace with this clinical evolution. Despite the widespread adoption of competency-based models such as those from ACGME, CanMEDS, and UEMS, Entrustable Professional Activities (EPAs) are still inconsistently integrated into many modern nuclear medicine training curricula. This gap risks inadequate preparation of trainees for the complex, multidisciplinary, and rapidly evolving demands of theranostics. ***Materials and Methods:*** Review of literature and qualitative description of relevant findings. ***Results:*** EPAs represent critical, observable tasks that define professional roles and responsibilities. In alignment with international competency frameworks, six EPAs essential to theranostics-focused nuclear medicine education are proposed: 1.Interpret and report theranostic imaging studies (CanMEDS: Medical Expert; ACGME: Patient Care, Medical Knowledge). 2.Develop and personalize radionuclide therapy plans (UEMS: Clinical Skills; ACGME: Systems-Based Practice). 3.Counsel patients on theranostic procedures and outcomes (CanMEDS: Communicator, Health Advocate). 4.Collaborate within multidisciplinary teams in theranostics (CanMEDS: Collaborator; ACGME: Interpersonal Skills). 5.Ensure compliance with radiation safety and ethical standards (CanMEDS: Professional; ACGME: Professionalism). 6.Incorporate evidence-based research into theranostic practice (CanMEDS: Scholar; ACGME: Practice-Based Learning and Improvement). These Entrustable Professional Activities (EPAs) support a structured learning progression, enhance accountability, and align with a competency-based framework that mirrors the realities of clinical practice. They are rooted in educational philosophies such as constructivism and situated learning, which emphasize experiential and reflective learning. EPAs serve as scaffolds that gradually develop a learner's autonomy and trustworthiness, bridging the gap between theoretical knowledge and independent professional practice. Recent updates in theranostic training requirements, including new radiopharmaceuticals, patient-centred care, and interdisciplinary roles, necessitate a curriculum redesign to incorporate EPA-based assessment. Without these changes, nuclear medicine physicians may graduate lacking demonstrated proficiency in critical areas of theranostics. ***Conclusion:*** Integrating EPAs into nuclear medicine curricula is essential for preparing clinically competent, ethically grounded physicians capable of delivering advanced theranostic care. EPA inclusion ensures that training keeps pace with innovation, supporting educational outcomes and healthcare excellence. ***References:*** 1.Ten Cate O. (2005). Entrustability of professional activities and competency-based training. Medical Education, 39(12), 1176-1177.2.Frank JR, et al. (2015). CanMEDS 2015 Physician Competency Framework. Royal College of Physicians and Surgeons of Canada.3.ACGME (2023). Milestones and EPAs: Advancing GME through Competency-Based Assessment.4.UEMS (2022). European Training Requirements for Nuclear Medicine.5.Dory V, et al. (2021). EPAs in medical education: A meta-narrative review. Medical Teacher, 43(5), 497-503.

EP-1415

Evaluation of the European Kidney Function Consortium (EKFC) GFR predicting equation in Chronic Kidney Disease staging using 99mTc-DTPA measured GFR as the reference standard

G. Arsos[1], *A. Morfesi*[1], *N. Vavlas*[1], *A. Kalaitzoglou*[1], *D. Katsampoukas*[1], *K. Lazaridis*[1], *E. Manou*[2], *E. Moralidis*[1];
[1]3rd Department of Nuclear Medicine, Aristotle University of Thessaloniki School of Medicine, Papageorgiou General Hospital, Thessaloniki, GREECE, [2]Nephrology Clinic, Papageorgiou General Hospital, Thessaloniki, GREECE.

Aim/Introduction: Serum/plasma Creatinine (SCr) and/or Cystatin C-based equations are useful clinical tools for GFR estimation (eGFR) and Chronic Kidney Disease (CKD) staging. During the last decades, a continuously growing number of such equation is proposed with the more recent European Kidney Function Consortium equation (EKFC, 2020) and CKD-EPI Creatinine Equation (CKD-EPI 2021) already commonly applied [1]. However, as urine/plasma clearance of exogenous tracers, remains the gold standard for GFR measurement, we aim to explore the performance of the EKCF equation in CKD staging in adult Caucasian patients, in comparison with GFR measured by 99mTc-DTPA plasma clearance (mGFR-DTPA). ***Materials and Methods:*** GFR was measured for clinical purposes in 796 adult Caucasian patients (age 18-90 years, 44.0% females, 11.9% prospective kidney donors) by 99mTc-DTPA plasma clearance (bolus i.v. injection, 3 blood samples at 2, 3 and 4 hours post-injection and monoexponential modeling according to BSNM). SCr was measured (mg/dL) with an ID-LC/MS calibrated Jaffe method. eGFR was estimated (in ml/min/1.73 m^2) by the EKFC equations (eGFR-EKCF). Patients were classified in G1, G2, G3 and G4+5 CKD stages according to mGFR-DTPA limits of ≥90, 60-89, 30-59 and <30 ml/min/1.73 m^2, respectively. The number of patients allocated in each CKD stage according to both mGFR-DTPA and eGFR-EKCF was calculated and agreement was assessed by k-statistics . ***Results:*** SCr, mGFR-DTPA and eGFR-EKCF (mean±SD) were 1.5±0.9, 57.2±26.7 and 59.8±28.2 respectively. In comparison to mGFR-DTPA CKD staging, eGFR-EKCF totally

staged correctly 582 patients (73.1%), upstaged 110 (13.8%) and downstaged 104 (13.1%), p<0.001. In a per-stage analysis, the corresponding figures were 73 (73.7%), 26 (26.3%) 0.0 (0.0%); 179 (66.5%), 27 (10.0%), 63 (23.5%); 195 (73.0%), 57 (21.3%), 15 (5.7%) and 135 (83.9%), 0 (0.0%), 26 (16.1%) for stages G1, G2, G3 and G4 respectively. ***Conclusion:*** Chronic Kidney disease staging using eGFR by EKCF equation, misclassify more than a quarter of the patients, with grossly equal up- ang downstaging contribution. As CKD staging by eGFR is common in clinical practice, supporting important decisions (nephrologic referral, drug withdrawal etc), measured GFR should be the choice when accurate CKD staging is felt to be crucial. ***References:*** 1. Pottel H, Bjork J, Courbebaisse M et al. Development and Validation of a Modified Full Age Spectrum Creatinine-Based Equation to Estimate Glomerular Filtration Rate. Ann Intern Med 2020 doi:10.7326/M20-4366

EP-1416

Awareness of Green Imaging and Sustainability Among Nuclear Medicine Professionals: A Cross-Sectional Study

E. Alawadhi[1], *A. Khalaf*[1], *L. Ghadanfer*[1], *M. Awadh*[1], *F. Busakher*[1], *A. Almutairi*[1], *A. Aldousari*[1], *M. Rawashdeh*[2];
[1]*Kuwait University, Kuwait, KUWAIT,* [2]*Gulf Medical University, Ajman, UNITED ARAB EMIRATES.*

Aim/Introduction: Medical imaging contributes significantly to healthcare's environmental footprint due to energy consumption, equipment use, and waste generation. Green imaging integrates eco-friendly principles into medical imaging practices. This concept has emerged in response to rising concerns regarding climate change, healthcare-related waste, and energy use in medical facilities. Despite global efforts, awareness and adoption of green imaging practices remain limited. This study aims to evaluate healthcare professionals' awareness, knowledge, and attitudes towards sustainable practices in nuclear medicine departments. Furthermore, our study seeks to identify the barriers and motivators influencing the adoption of environmentally sustainable practices. ***Materials and Methods:*** The study will use a cross-sectional survey distributed through Microsoft Forms to healthcare professionals working in nuclear medicine departments in Kuwait, including physicians, residents, technologists, technicians, nurses, pharmacists, and medical physicists. The survey was conducted anonymously over seven weeks. The questionnaire was based on a validated previous study (1). The survey had seven sections: demographics, sustainability awareness, climate change, nuclear medicine practices, barriers to sustainability, education and training needs, and open-ended questions. The online link and QR code were distributed via phone and social media. Data were analysed descriptively and inferentially. ***Results:*** A total of one hundred and seventy participants completed the survey. Our findings revealed a limited familiarity with green imaging practices, with only 9% reporting being very familiar, and 60% were unfamiliar with the concept of sustainability in medical imaging. The majority of the healthcare workers had not attended advanced training courses on sustainability or training courses on recycling before. Despite this knowledge gap, 78% of respondents recognised the importance of sustainability in healthcare and believed it positively impacts patient care and the healthcare system. Most participants agreed that the main obstacles to embracing this concept were inadequate training (35%), lack of support (31%), lack of leadership (24%), safety concerns (21%), lack of authority (15%), cost (15%), facility limitations (11%), staff attitudes (10%), and time constraints (8%), which were the least cited barriers. Respondents demonstrated a strong interest in receiving training and additional support for education related to green imaging initiatives. ***Conclusion:*** This study underscores the limited awareness of sustainable imaging practices among nuclear medicine professionals. Strengthening education and integrating eco-friendly protocols are key to advancing environmentally conscious healthcare delivery. Increasing awareness and promoting sustainable practices in nuclear medicine can significantly contribute to environmentally responsible healthcare. ***References:*** (1) Rawashdeh, M (2024). Radiography, 30, 62-73.

EP-1417

Tc^{99m}DPD SPECT/CT in Adults With ATTR CM: Three Years Experience in a Private Medical Diagnostic Center

P. Karampina[1], *A. Antonopoulos*[2], *D. Venetsanos*[2], *M. Triantafillou*[3], *V. Penesopoulou*[4], *S. Christodoulou*[1], *C. Vlachopoulos*[2];
[1]*KOSMOIATRIKI SA, Nuclear medicine dpt, Athens, GREECE,* [2]*Cardiogenetics Unit, 1st Cardiology Department, National and Kapodistrian University of Athens, Athens, GREECE,* [3]*KOSMOIATRIKI SA, radiology dpt, Athens, GREECE,* [4]*KOSMOIATRIKI SA, cardiology dpt, Athens, GREECE.*

Aim/Introduction: To prove the existence of cardiac amyloidosis through Tc99m DPD SPECT/CT. ***Materials and Methods:*** This is a retrospective study involving 62 adults (37 males, 25 females) aged 38-92 (mean age: 79.6 years) from August 2022 to April 2025. Whole body SPECT/CT bone scans were performed 150 min after the injection of 740MBq Tc99m DPD with adequate acquisition parameters. Additional static images and myocardial tomography were obtained. The collaboration was excellent. ***Results:*** 25 out of 62 adults had myocardial uptake: Grade I: 5 adults, Grade II: 4 adults, Grade III: 16 adults. 37 adults had a negative study. The cause of examination for 52 patients was cardiological issues (HF, AF, lower limb edema, hypertension, fatigue). Specifically, 29 of them had serious aortic valve stenosis and got preoparative TAVI assessment. From the remaining 10 patients, 8 got an examination because of prostate cancer and 2 to follow up on their hip replacement surgery. All 10 of them had myocardial uptake. ***Conclusion:*** Whole body SPECT/CT bone scans contribute to earlier diagnosis of ATTR CM. As a result, patients start earlier treatment, with improvement of their quality of life.

EP-1418

Head-to-Head Comparison of ^{18}F-PSMA-1007 and ^{18}F-FDG PET/CT in Metastatic Colorectal Cancer

R. Tineo, *A. Portilho, F. Zarpelao, J. Carvalheira, C. Ramos; University of Campinas, Campinas, BRAZIL.*

Aim/Introduction: ^{18}F-FDG PET/CT is a well-established imaging modality in the management of colorectal cancer (CRC). However, the search for a radiotracer with theranostic potential in CRC remains ongoing. Radiolabeled Prostate-Specific Membrane Antigen (PSMA), widely used in prostate cancer imaging and therapy, is also expressed in tumor-associated neovasculature and has demonstrated uptake in various non-prostatic malignancies. This study aimed to compare ^{18}F-FDG and ^{18}F-PSMA-1007 PET/CT imaging in patients with metastatic CRC. ***Materials and Methods:*** Five patients (three males; mean age: 69.4 ± 3.3 years) with histologically confirmed colorectal adenocarcinoma (four colonic, one rectal; two with resected primary tumors) underwent both ^{18}F-FDG and ^{18}F-PSMA-1007 PET/CT within a maximum interval of seven days. Image interpretation was performed by two nuclear medicine physicians and one radiologist. For each modality, the number and location of detected lesions, maximum standardized uptake value (SUVmax), and inter-modality concordance were assessed. ***Results:*** Primary tumor uptake was observed on ^{18}F-FDG PET/CT in all three patients with unresected lesions (SUVmax: 5.6, 32.2, and 8.5), whereas ^{18}F-PSMA-1007 demonstrated only faint uptake in one case (SUVmax: 2.0).Metastatic lesions were identified in lymph nodes, lungs, and liver, all of which showed significant FDG avidity (median SUVmax = 8.3; range: 5.3-13.4). ^{18}F-PSMA uptake was observed in metastatic sites in four patients (median SUVmax = 4.4; range: 4.0-24.4). Notably, in one patient, hepatic metastases showed higher uptake with ^{18}F-PSMA than ^{18}F-FDG

(SUVmax: 24.4 vs. 10.1); however, this uptake was perilesional and likely represented a false-positive finding due to biliary excretion and tumor-related biliary compression, as ^{18}F-PSMA-1007 is primarily hepatobiliary-excreted. ***Conclusion:*** ^{18}F-PSMA-1007 PET/CT demonstrated substantially lower sensitivity than ^{18}F-FDG PET/CT in detecting both primary and metastatic colorectal lesions. The findings suggest limited utility of PSMA-based imaging—and, by extension, PSMA-targeted theranostic approaches—in patients with metastatic CRC.

EP-74

e-PosterArea

Technologists e-Poster

EP-1419

Investigating the Radiobiological Response of Combinations of DNA Repair Inhibitors with AR Suppression in Advanced Prostate Cancer

A. Alshehri*;*
Radiological Sciences Department, Collage of Applied SScience, Najran University, Najran, SAUDI ARABIA.

Aim/Introduction: Current treatment options for mCRPC are primarily based around AR suppression and taxane-based chemotherapy, however, primary or acquired treatment resistance is an inevitability. This has created an urgent need for the development of novel therapies targeting alternative molecular targets apart from the AR and microtubule, which can not only be utilised as single agents but are effective as combination therapies with current AR targeting agents such as Abiraterone and Enzalutamide. In an in vitro setting, the impact of PARP inhibitors has been well categorised, including PCa settings, there are no studies investigating the biological response of combinations of Olaparib with Abiraterone and Enzalutamide or their radiobiological response with combined with the additional effects of radiation. Such studies are important for informing future clinical study designs and eventually patient treatment. The aim of this study is to investigate the radiological response of the combination of DNAs repair inhibitors with AR suppression ***Materials and Methods:*** In vitro experiments using AR-sensitive (LNCaP) and AR-insensitive (PC3) prostate cancer cell lines, alongside osteoblastic (SJSA-1) models were conducted. The cells were treated with Radium-223 and/or AR inhibitors (Abiraterone, Enzalutamide). DNA damage and protein expression related to DNA repair through Western blotting were assessed. Additionally, cell cycle distribution and apoptosis were analyzed using flow cytometry and PARP-cleavage assays. ***Results:*** The induction of synthetic lethality through the co-inhibition of AR and PARP proves an attractive treatment option for PCa. The results have demonstrated that in an in vitro setting, combinations of Olaparib with Abiraterone or Enzalutamide showed increased efficacy over their use as single agents both with and without radiation, supported by increased levels of DNA damage and cell death. Combinations of Abiraterone and Olaparib proved to be more cytotoxic than combinations of Enzalutamide and Olaparib, highlighting the continuing evidence of increased benefit with Abiraterone over Enzalutamide. ***Conclusion:*** There is a clear need for treatment intensification in advanced PCa settings and co-inhibition with combinations of AR and PARP suppression may help overcome resistance and may be beneficial in subsets of patients harbouring DNA repair mutations. ***References:*** Jones CU, Hunt D, McGowan DG, et al (2011) Radiotherapy and Short-Term Androgen Deprivation for Localized Prostate Cancer. New England Journal of Medicine 365:107-118Zelefsky MJ, Reuter VE, Fuks Z, Scardino P, Shippy A (2008) Influence of Local Tumor Control on Distant Metastases and Cancer Related Mortality After External Beam Radiotherapy for Prostate Cancer. J Urol 179:1368-1373

EP-1420

Ga-68 Fatty Acids as Myocardial Perfusion PET Agents

T. Ertay*, M. Kuzucu;*
Dokuz Eylul University, Izmir, TÜRKIYE.

Aim/Introduction: Developing suitable radiopharmaceuticals for PET imaging is very important for targeted biological processes. Due to the chemical properties of the Ga-68 radionuclide and its advantages such as obtaining it from the generator, there has been great progress in pet radiopharmaceuticals in labeling with the Ga-68 radionuclide recently. Fatty acids are important biomolecules that play important roles in biological systems and cause changes in the pathophysiology of myocardial diseases. The aim of this study is to label fatty acids with Ga-68 and evaluate the radiochemical efficiency of labeled. ***Materials and Methods:*** In this study, oleic acid and palmitic acid were used as fatty acid molecules for labeling with Ga-68. DTPA was used as a bifunctional chelating agent. For the synthesis of fatty acids, a homogeneous solution was obtained with NaOH solution. Then, labeled fatty acids were prepared by adding DTPA and sodium acetate solution. The 68Ga radionuclide was taken from the elution solution, added to the labeled fatty acids and heated. For labeling efficiency of the synthesized 68Ga DTPA-fatty acid components were evaluated by TLC method. Amonium Acetat and metanol (50:50) were used as mobile phases. ***Results:*** Labeled and free Ga-68 were analyzed by chromotograpy. The Rf values of labeled fatty acids with Ga-68 was observed as 0.7, while free 68Ga was observed as 0.2 in chromatography. Both molecules showed similar values. The results showed that the labeled compound could be used in PET imaging. This study may contribute to the development of new and effective radiopharmaceuticals in the field of myocardial PET imaging. In cardiovascular applications such as myocardial imaging, the use of fatty acids can provide valuable information in assessing the metabolic activity of cardiac muscle. ***Conclusion:*** In this study, the synthesis of fatty acids, their complexation with DTPA and their labeling with 68Ga radionuclide were examined in detail. The results show that fatty acids were successfully synthesized, complexed with DTPA and labeled with 68Ga radionuclide. These results indicate that Ga-68 labeled fatty acids can be used as a potential tool in biomedical imaging and diagnostic applications. Furthermore, rapid clearance of the DTPA complex from non-target organs is essential for radiopharmaceuticals designed for myocardial imaging. Integrating these features into the final design of the 68Ga-labeled fatty acid complex may provide the potential to achieve desired pharmacokinetics for cardiac metabolic imaging.

EP-1421

PET/CT protocol for Hepatocellular Carcinoma (HCC) evaluation: a multi-phase approach to improve diagnostic sensitivity

K. Shyli*, F. Firinu, A. Sotgiu, F. Casaburo, C. Serra, F. Oliverio, A. Lomartire, G. Paolacci, S. Fraschina, M. Mantovani, G. Cafiero, I. Papagni;*
ASST Grande Ospedale Metropolitano Niguarda, Milan, ITALY.

Aim/Introduction: The recent development of high-sensitivity systems LAFOV PET/CT enables the implementation of advanced protocols aimed at achieving a more accurate and comprehensive metabolic characterization of the hepatocellular carcinoma (HCC). This work describes an optimized clinical protocol currently in use at our Hospital Niguarda with the United Imaging Panorama GS PET/CT, combining an early dynamic acquisition, a standard scan, and a delayed scan to maximize diagnostic information and improve patient compliance. ***Materials and Methods:*** The protocol begins

with a 30-minute early dynamic acquisition immediately following ^{18}F-FDG injection (3 Mbq/kg), using a 256x256 matrix and OSEM reconstruction (3 iterations, 10 subsets, with TOF) over a 148 cm axial field of view to exploit the system's full-body sensitivity. The dynamic phase includes 25 frames: 6 × 10s, 2 × 30s, 6 × 40s, 7 × 120s, and 2 × 300s. A low-dose CT (100 kV, 30 ref. mAs) is used solely for attenuation correction, with AI-based reconstruction to enhance anatomical visualization. A 3-minute whole-body acquisition is then performed at 60 minutes post-injection using a higher-quality CT (120 kv, 60 ref. mAs). Finally, a delayed acquisition at 120 minutes is acquired with the same low-dose CT settings and AI-based reconstruction. All scans are performed with the patient's arms positioned down to minimize respiratory motion artifacts. The 30-minute dynamic scan duration is supported by literature as a balanced approach, providing sufficient metabolic data while maintaining good patient tolerability compared to longer dynamic acquisitions. Each exam produces approximately 1.5TB of data that are processed and stored after the work session. ***Results:*** This protocol was applied to 20 patients, all of whom successfully complete the exam with good tolerability. The combination of multiphase acquisitions enabled detailed temporal assessment of FDG uptake in hepatic lesions. The dynamic phase allows the analysis of tracer kinetics, particularly assessing tracer uptake in lesions. The standard acquisition provided an assessment of systemic tracer distribution, enabling the identification of potential secondary sites and comparison with the initial dynamic data. The delayed scan offered differential tracer retention analysis in suspicious lesions, useful for increasing lesion-to-background contrast and detecting low-uptake lesions early. These features allowed for a comprehensive evaluation of hepatic lesions, improving diagnostic sensitivity. ***Conclusion:*** This multiphase protocol offers a clinically sustainable and highly informative approach to HCC evaluation. The high sensitivity of the total-body PET system, combined with AI-enhanced reconstruction, supports improved diagnostic performance in clinical practice.

EP-1422

Deep Learning-Based Non-Invasive Histological Grading of Hepatocellular Carcinoma via Multi-Modal Fusion of Dual-Tracer PET/CT and Clinical Data

K. Li[1], *H. Chen*[2], *C. Ho*[1], *J. Yoo*[2], *L. Lin*[2];
[1]*Hong Kong Sanatorium and Hospital, Hong Kong, HONG KONG,*
[2]*The Hong Kong Polytechnic University, Hong Kong, HONG KONG.*

Aim/Introduction: Histological grading of hepatocellular carcinoma (HCC) critically influences patient prognosis and treatment decisions. Currently, biopsy remains the standard for grading tumors, yet it carries substantial risks including bleeding, infection, and sampling bias due to tumor heterogeneity. Multi-modal PET/CT imaging combining fluorodeoxyglucose (FDG) and acetate (ACT) tracers has demonstrated promise in reflecting tumor metabolic and proliferative activities. However, effectively integrating multi-modal imaging features with clinical data through advanced deep learning strategies to achieve automated and accurate HCC grading remains a significant challenge. ***Materials and Methods:*** This study retrospectively analyzed imaging and clinical data from a cohort of 93 patients diagnosed with HCC who underwent surgical resection or biopsy at the Hong Kong Sanatorium and Hospital. Inclusion criteria included histopathologically confirmed HCC, availability of dual-tracer PET/CT imaging (comprising [18F]FDG and [11C]ACT scans) within one month of surgery or biopsy, and histopathology reports. Histological grading served as the ground truth for model training and validation. Clinical data including demographic variables (age, sex), hepatitis status (HBV, HCV, or none), and alpha-fetoprotein (AFP) levels. To address class imbalance, focal loss was employed, and a 3-fold cross-validation strategy ensured robust performance evaluation. Dual-phase PET/CT images were processed using two parallel 3D SwinUNETR encoders: one shared PET encoder and one shared CT encoder. KL and JS divergence losses were applied between PET and CT representations to encourage inter-modality consistency. Clinical features were normalized and embedded into tokens using a multi-layer perceptron. To facilitate early fusion of imaging and clinical information, an Early Gated Cross-Attention (EGCA) mechanism was introduced to dynamically modulate modality contributions. ***Results:*** The model integrating clinical features with both ACT and FDG PET/CT imaging achieved the best performance, yielding a macro-average AUC of 0.8034 ± 0.0136 and a precision of 0.7088 ± 0.0501. Combining ACT and FDG PET/CT imaging without clinical data achieved an AUC of 0.7527 ± 0.0349 (precision: 0.6563 ± 0.0240). Integrating clinical features with ACT imaging alone resulted in an AUC of 0.6736 ± 0.0323 (precision: 0.6054 ± 0.0156), while combining FDG PET/CT with clinical features but without ACT imaging produced the lowest performance, with an AUC of 0.6381 ± 0.0248 and a precision of 0.6018 ± 0.0174. ***Conclusion:*** Our study presents a non-invasive HCC grading framework that integrates dual-tracer PET/CT and clinical data. The proposed EGCA fusion strategy enhances grading accuracy by adaptively balancing modality contributions, offering a potential alternative to biopsy and supporting more personalized clinical decisions.

EP-1423

Impact of Patient Hydration on Urinary Bladder Activity in ^{68}Ga-PSMA-11 PET/CT Imaging

R. Fendi, *A. Nasr, I. Ceric Andelius, F. Hedeer;*
Lund University Hospital, Lund, SWEDEN.

Aim/Introduction: Introduction: PSMA-PET/CT imaging is a well-established imaging modality for the detection of prostate cancer. However, varying physiological uptake patterns of different PSMA-ligands, particularly the high accumulation in the urinary bladder, can complicate the identification of tumor lesions near the bladder. Aim: The aim of this study was to determine if whether increased patient hydration before the examination reduces bladder activity, by comparing 68Ga-PSMA-11 activity concentrations in the bladder in well-hydrated patients versus those with standard hydration. ***Materials and Methods:*** Twenty-five patients scheduled for ^{68}Ga-PSMA-11-PET/CT in the afternoon were instructed to drink 1-1.5 liters of water at home in the morning of the examination day and an additional 1 liter of water on-site prior to imaging. Another twenty-five patients served as the control group; they received no specific instructions regarding water intake at home and drank 1 liter of water on-site only. Images were analyzed using HERMIA Hybrid Viewer (Hermes Medical Solutions, Stockholm, Sweden). Multiple regions of interest were drawn around the bladder and merged into a volume of interest (VOI). A Mann-Whitney U-test was performed on the extracted VOI:s for SUVmean, SUVmax and SUVpeak (1 cm3) to assess differences between the two groups, where a p-value of <0,05 was considered to indicate statistical significance. ***Results:*** No statistically significant differences were observed in SUVmean, SUVmax, or SUVpeak between the well-hydrated and control groups. The median SUVmean was 10.8 vs. 10.4 (p = 0.60), SUVmax was 20.3 vs. 14.3 (p = 0.11), and SUVpeak was 17.7 vs. 14.3 (p = 0.41), respectively. ***Conclusion:*** For patients undergoing ^{68}Ga-PSMA-11-PET/CT, consuming additional water before the examination does not significantly reduce the physiological activity in the urinary bladder.

EP-1424

Impact of different Chemotherapeutic agents on baseline SUV of Liver and Blood Pool in Hodgkin Lymphoma Patients.

R. Nawaz, *S. Nausheen, N. Ihsan, R. Kaleemi, N. Ahmed, T. Mahmood;*
Jinnah Postgraduate Medical Center, Karachi, PAKISTAN.

Aim/Introduction: Background: Standardized Uptake Value (SUV) measurements in FDG PET/CT play a pivotal role in the staging and response assessment of Hodgkin Lymphoma (HL). Baseline SUV levels in the liver and mediastinal blood pool serve as key reference points in response criteria such as Deauville scoring. However, variations in SUV due to pre-treatment with different chemotherapeutic agents may affect interpretation and clinical decision-making. Objective: This study aims to evaluate the impact of various chemotherapeutic regimens on baseline SUV measurements of the liver and mediastinal blood pool in patients diagnosed with HL. ***Materials and Methods:*** Methods: A retrospective analysis was conducted on HL patients who underwent baseline FDG PET/CT imaging after administration of different chemotherapeutic agents. Patients were grouped based on the type of induction chemotherapy received prior to imaging. SUVmean and SUVmax of the liver and blood pool were measured and compared across groups using statistical analysis to determine significant variations. ***Results:*** Preliminary findings suggest that certain chemotherapeutic agents, particularly those with hepatotoxic or metabolic effects, influence baseline liver and blood pool SUV values. Variations were observed in both SUVmean and SUVmax, with statistically significant differences in select groups. ***Conclusion:*** The type of chemotherapeutic agent administered prior to baseline FDG PET/CT imaging may alter physiological FDG uptake in reference organs, potentially impacting Deauville scoring and therapeutic assessment in HL. Standardization or adjustment for such effects may be necessary for more accurate interpretation of PET/CT results. ***References:*** 1. Gallamini A, Barrington SF, Biggi A, et al. The predictive role of interim positron emission tomography in Hodgkin lymphoma. Curr Hematol Malig Rep. 2012;7(3):193-199. doi:10.1007/s11899-012-0133-2 2. Meignan M, Gallamini A, Haioun C. Report on the First International Workshop on Interim-PET-Scan in Lymphoma. Leuk Lymphoma. 2009;50(8):1257-1260. doi:10.1080/10428190903040048 3. Boellaard R, O'Doherty MJ, Weber WA, et al. FDG PET and PET/CT: EANM procedure guidelines for tumour PET imaging: version 1.0. Eur J Nucl Med Mol Imaging. 2010;37(1):181-200. doi:10.1007/s00259-009-1297-4 4. Juweid ME, Stroobants S, Hoekstra OS, et al. Use of positron emission tomography for response assessment of lymphoma: consensus of the Imaging Subcommittee of International Harmonization Project in Lymphoma. J Clin Oncol. 2007;25(5):571-578. doi:10.1200/JCO.2006.08.2305 5. Freudenberg LS, Antoch G, Schueller J, et al. FDG-PET/CT in restaging of patients with lymphoma. Eur J Radiol. 2006;58(3):445-453. doi:10.1016/j.ejrad.2005.12.024

EP-1425

Role of FDG PET-CT in Planning Therapeutic Intervention in Hepatocellular Carcinoma (HCC).

R. Nawaz*, R. Kaleemi, S. Nausheen, N. Ihsan, N. Ahmed, T. Mahmood;*
Jinnah Postgraduate Medical Center, Karachi, PAKISTAN.

Aim/Introduction: Intorduction: Hepatocellular carcinoma (HCC) remains a leading cause of cancer-related mortality worldwide, often diagnosed at an advanced stage. While conventional imaging modalities like CT and MRI play a critical role in HCC diagnosis and staging, the integration of metabolic imaging through 18F-fluorodeoxyglucose positron emission tomography-computed tomography (FDG PET-CT) offers additional insights that can refine therapeutic planning.Objective:To evaluate the utility of FDG PET-CT in influencing therapeutic decision-making in patients with HCC by assessing metabolic activity, detecting extra-hepatic spread, and identifying aggressive tumor phenotypes. ***Materials and Methods:*** A prospective analysis was conducted on HCC patients undergoing FDG PET-CT prior to therapy. Imaging findings were correlated with locoregional therapies (TACE/RFA). Parameters such as SUVmax, tumor-to-liver ratio (TLR), and presence of distant metastases were assessed. ***Results:*** FDG PET-CT demonstrated added value in 32% of cases by altering the therapeutic approach, most notably by detecting extrahepatic metastases not identified on conventional imaging. High FDG uptake was associated with poorly differentiated HCC and unfavorable prognostic markers. PET findings led to avoidance of futile surgical or locoregional interventions in a significant subset. ***Conclusion:*** FDG PET-CT is a valuable adjunct in the therapeutic planning of HCC, offering metabolic characterization that complements anatomical imaging. It aids in refining staging, guiding personalized treatment strategies, and potentially improving clinical outcomes. ***References:*** Khan MA, Combs CS, Brunt EM, Lowe VJ, Linehan DC, Lawrence TS, et al. Positron emission tomography scanning in the evaluation of hepatocellular carcinoma. J Hepatol. 2000;32(5):792-7, Park JW, Kim JH, Kim SK, Kang KW, Park KW, Choi JI, et al. A prospective evaluation of ^{18}F-FDG and 11C-acetate PET/CT for detection of primary and metastatic hepatocellular carcinoma. J Nucl Med. 2008;49(12):1912-21, Cho Y, Lee I, Lee D, Kim YI, Choi H, Kim SH, et al. Prognostic value of ^{18}F-FDG PET/CT in hepatocellular carcinoma treated with transarterial chemoembolization. Nucl Med Mol Imaging. 2013;47:156-62, Torizuka T, Tamaki N, Inokuma T, Magata Y, Sasayama S, Yonekura Y, et al. In vivo assessment of glucose metabolism in hepatocellular carcinoma with FDG-PET. J Nucl Med. 1995;36(10):1811-7, Cieslak KP, Bennink RJ, de Graaf W, Borel Rinkes IH, van Gulik TM. ^{18}F-FDG PET-CT predicts recurrence and survival after liver transplantation for hepatocellular carcinoma. Nucl Med Commun. 2016;37(12):1277-85, Matsuo Y, Shinohara M, Yamaguchi S, Mitsuyoshi H, Kamiyama T, Todo S, et al. Prognostic value of FDG PET in patients with hepatocellular carcinoma undergoing hepatic resection. Ann Surg Oncol. 2014;21(7):2222-9.

EP-1426

Comparison of two vs one CT for attenuation correction in myocardial MPS SPECT/CT imaging on a system with Smartzoom collimators

C. Kullberg[1]*, S. Kvernby*[2]*, F. Hedeer*[1]*, H. Mosén*[1]*, S. Saran*[1]*;*
[1]Department of Clinical Physiology and Nuclear Medicine, Skåne University Hospital, Lund, SWEDEN, [2]Radiation Physics, Department of Haematology, Oncology and Radiation Physics, Skåne University Hospital, Lund, Sweden, Department of Translational Medicine and Wallenberg Centre of Molecular Medicine, Lund University, Malmö, Sweden, Lund, SWEDEN.

Aim/Introduction: In myocardial perfusion SPECT (MPS) imaging, photons attenuated within the patient may give a false imaging of the heart and also affect the clinical decision. Using low-dose CT the MPS imaging can be corrected for attenuation by a density map. Normally the CT is done consecutively with the MPS imaging in a SPECT/CT scan, both in the stress and rest. We want to see if it is possible to lower the radiation exposure to patients doing single CT for both scans.The aim was to investigate if using a single CT, acquired from the stress acquisition, for attenuation correction in both stress and rest images results in the same clinical assessment. ***Materials and Methods:*** A total of 13 patients (5 women; BMI range 19-40, mean 26) referred for a clinical stress/rest MPS due to suspected ischemic heart disease were included. Patients were scanned with one day protocol using ^{99m}Tc-Tetrofosmin on a SPECT/CT camera with Smartzoom collimators. Attenuation correction of the MPS images was applied in two different ways: 1. With attenuation maps acquired from both stress and rest low-dose CT acquision respectively, and 2. With attenuation map from low-dose CT stress-imaging applied for both the stress and rest MPS images. All images were analyzed in QGS/QPS (Cedars Sinai) and Summed Stress Score (SSS), Summed Rest Score (SRS) and Summed Difference Score (SDS) were obtained together with individual perfusion values, normalized to a database from healthy population, representing the 17-segment model were measured. Differences between the methods were evaluated using paired

t-test. Two senior physicians performed a holistic visual assessment of all images in consensus, blinded to the attenuation correction method applied. Findings were graded as none ischemic, mild ischemic, ischemic, infarction. The vessel territory (LAD, RCA, LCx) was also stated in the case of decreased perfusion. ***Results:*** There were no significant differences (p>0.05) in perfusion scores between the two attenuation correction methods in any of the 17 segments in any patient. The visual assessment was identical in 11 out of the 13 patients. However, in two patients there was a difference in the visual assessment, where both patients changed from ischemic to mild ischemic, and in one of them a suspected infarction was missed. ***Conclusion:*** Using the same low-dose CT for attenuation correction in stress and rest MPS imaging is feasible in a majority of cases, however, in some cases the interpretation of the examination may be altered.

EP-1427

Intergrated Nuclear Medicine Imaging Assessment of Amyloid Burden, Sympathetic innervation, and Microvascular function in ATTR-CM

T. Lee[1], *Y. Chen*[1], *Y. Huang*[1], *A. Yu*[2], *C. Tsai*[2], *M. Su*[3], *S. Hsieh*[4], *C. Chao*[4], *Y. Lin*[2], *K. Ko*[5], *M. Cheng*[1];
[1]*Department of Nuclear Medicine National Taiwan University Hospital and National Taiwan University College of Medicine, Taipei City, TAIWAN,* [2]*Department of Internal Medicine, Division of Cardiology National Taiwan University Hospital and National Taiwan University College of Medicine, Taipei City, TAIWAN,* [3]*Department of Medical Imaging National Taiwan University Hospital, Taipei City, TAIWAN,* [4]*Department of Neurology National Taiwan University Hospital and National Taiwan University College of Medicine, Taipei City, TAIWAN,* [5]*Department of Nuclear Medicine National Taiwan University Cancer Center, Taipei City, TAIWAN.*

Aim/Introduction: Hereditary transthyretin amyloid cardiomyopathy (ATTR-CM) is an inherited disorder characterized by the deposition of misfolded transthyretin (TTR) proteins in the myocardium. The progressive amyloid accumulation impairs myocardial tissue and autonomic nerve terminals. Technetium-99m-labeled pyrophosphate (Tc-99m PYP) scintigraphy is widely used for diagnosing ATTR-CM by both visual scoring and quantitative uptake ratios. I-123 metaiodobenzylguanidine (I-123 mIBG) scintigraphy provides information on myocardial sympathetic innervation, while dynamic myocardial perfusion imaging (MPI) enables quantitative evaluation of coronary microvascular function. Despite the clinical relevance of these modalities, few studies have integrated them to explore their interrelationships in ATTR-CM. ***Materials and Methods:*** Patients with genetically confirmed or highly suspected ATTR-CM underwent Tc-99m PYP scintigraphy, I-123 mIBG scintigraphy, dynamic MPI, echocardiography, and NT-proBNP testing. Quantitative imaging parameters included the heart-to-contralateral (H/CL) ratio, heart-to-lung (H/L) ratio, and standardized uptake value (SUV) from PYP scans; early and delayed heart-to-mediastinum ratios, as well as the washout ratio, from mIBG scans; and resting/stress myocardial blood flow (MBF) along with myocardial perfusion reserve (MPR) from MPI. Correlation analyses were performed using Spearman's rank correlation coefficient. ***Results:*** Eleven male patients (mean age 62.3 ± 12.8 years; 8 with A97S, 1 with Val30Met, 1 with E66D, and 1 wild-type) were enrolled. Eight patients had positive PYP scans (visual score ≥2). The mIBG washout ratio was significantly positively correlated with NT-proBNP ($\rho = 0.697$), interventricular septal thickness ($\rho = 0.636$), left ventricular posterior wall thickness in diastole ($\rho = 0.673$), and amyloid burden, as measured by multiple Tc-99m PYP uptake parameters: H/CL ratio ($\rho = 0.697$), H/L ratio ($\rho = 0.729$), and SUV ($\rho = 0.747$) (all $p < 0.05$). Among these patients, six completed dynamic MPI. Global post-stress MBF and MPR values showed a negative correlation with amyloid burden, although the associations did not reach statistical significance. In contrast, global resting MBF was significantly negatively correlated with H/CL ratio ($\rho = -0.886$), H/L ratio ($\rho = -1.000$), and SUV ($\rho = -0.943$) (all $p < 0.05$). A non-significant negative relationship was also observed between resting MBF and the mIBG washout ratio. ***Conclusion:*** Multimodal nuclear imaging offers comprehensive insights into ATTR-CM pathophysiology. Sympathetic denervation, as indicated by the mIBG washout ratio, is closely associated with both amyloid burden and functional markers. Furthermore, resting myocardial blood flow might be related with sympathetic innervation appears impaired in proportion to amyloid deposition. These findings highlight the potential utility of integrated imaging in ATTR-CM assessment.

EP-1428

Semi Automated fusion technique to create PET-MRI like dataset in Cardiac & Pelvic pathologies, in a limited resource setting.

R. Nawaz*, S. Nausheen, R. Kaleemi, N. Ihsan, N. Ahmed, T. Mahmood;*
Jinnah Postgraduate Medical Center, Karachi, PAKISTAN.

Aim/Introduction: PET-CT is an established yet valuable imaging tool for staging prostate cancer. Its applications are extending beyond just staging and response evaluation of cancer. Its role in infection & inflammation is well established. Major challenge for PET-CT in pelvis and Cardiac imaging is limited anatomic information, where growing demand of PET-MRI is being observed. But acquisition of PET-MRI is not a financially viable option due to its excessive capital & operational cost. Objective: To evaluate the benefits of semi-automated fusion technique to generate PET-MRI like dataset in pelvic & cardiac PET-CT. ***Materials and Methods:*** This prospective study included 25 patients who underwent both CMR and PET-CT scans for Cardiac Imaging (17), a PSMA PET-CT and routine Pelvis MRI for prostate (08).Cardiac FDG PET-CT was predominantly performed to rule out Cardiac Sarcoidosis, with an already available CMR, the delayed GAD Axial T1 dataset was manually fused with TOF-AC PET.Similarly, a PSMA PET-CT was performed for staging of Prostate cancer and an MRI performed during prior workup was utilized, and AX T2 dataset was manually fused with TOF-AC PSMA PET. ***Results:*** By manually fusing MRI dataset with ^{18}F-FDG Cardiac PET & 18F-PSMA-1007 prostate PET, significant advantage was observed at lung myocardium interface & capsular/lymphatic anatomy respectively. Which otherwise pose a major challenge to rule out on PET-CT dataset. ***Conclusion:*** In our patient pool we observed although PET-MRI has an added advantage of simultaneous acquisition as well as multiparametric MRI being a decider. But in a limited resource setting manual fusion technique can add value and PET-MRI like dataset gives a better insight of anatomy compared to a PET-CT. ***References:*** 1. Yuji Nakamoto et al. American Journal of Roentgenology Volume 188 issue 1, https://doi.org/10.2214/AJR.05.0708.2. Bar-Shalom R, Valdivia AY, Blaufox MD. PET im-aging in oncology. Semin Nucl Med 2000;30:150-185.3. Hustinx R, Benard F, Alavi A. Whole-body FDG-PET imaging in the management of patients withcancer. Semin Nucl Med 2002; 32:35-46.4. Antoch G, Saoudi N, Kuehl H, et al. Accuracy ofwhole-body dual-modality fluorine-18-2-fluoro-2-deoxy-D-glucose positron emission tomographyand computed tomography (FDG-PET/CT) for tu-mor staging in solid tumors: comparison with CTand PET. J Clin Oncol 2004; 22:4357-4368.5. Goerres GW, Burger C, Schwitter MR, et al.PET/CT of the abdomen: optimizing the patientbreathing pattern. Eur Radiol 2003; 13:734-739.

EP-1429

Comparison of Specific Binding Index of Regional DaTSCAN Imaging vs. MRI Striatal Volumetric Measurements

K. Priftis[1], *M. Paphiti*[2], *A. Zafeirakis*[3], *K. Roussopoulos*[4,1], *G. S. Limouris*[4,3];
[1]*Nucl Med Dept, Central Clinic, Athens, GREECE,* [2]*Cyclotron Section, Pharmazac SA, Athens, GREECE,* [3]*Nucl Med Dept, Army Share Fund Hospital of Athens, Athens, GREECE,* [4]*Nuclear Medicine, Medical School, National and Kapodistrian University, Athens, GREECE.*

Aim/Introduction: In vivo neuroimaging techniques in correlation with MRI imaging, offers a potential which can reliably assess early clinical and pre-clinical diagnosis in Parkinson's disease. The aim of this study was to compare striatal's volume from MRI volumetric measurements with the Specific Binding Index (SBI) from regional DaTSCANS results. ***Materials and Methods:*** In thirty five patients both dopaminergic imaging using I123-FP-CIT SPECT and MRI scanning were performed. Specific Binding Index (SBI) has been calculated from regional DaTSCAN both for left and right striatum respectively, by applying the formulas: SBI left=(Cv left/ Cb-Vv)/Vs and SBI right=(Cv right/ Cb-Vv)/ Vs where: Cv left: total counts in left striatum ROI, Cv right: total counts in right striatum ROI Cb: total counts in background region divided by volume of the background region. Vv: Volume of ROI, Vs: Volume of standard striatum (set to 11.2 ml) MRI imaging has been evaluated by employing highspatial resolution T2- weighted sequence such as T2- weighted/ Gradient-SpinEcho followed by a contiguous echo planar imaging sequence at the mid-brain striatal level in sagital projection. Multi- planar reconstruction images have been analysed and volumetric measuerements created in order to compare volume in relation to the SBI results. Statistical significance of these results was assessed using the Mann-Whitney test. ***Results:*** The overall results show a significant relation between the two imaging modalities for discriminating normal, Parkinsonian Syndromes (PS) and Essential Tremor (ET) patients . The following table represents the: average % decrease of striatum volume according to MRI, DaTSCAN Striatal SBI and Vissual Assessement. Category of Patients DaTSCAN SBI MRI volume Vissual Assessement ET -14.0 % (p=0.023) - 12.5% (p=0.05) 5-15 % PD -27.7 % ((p=0.04) -26.5% (p=0.007) >15 ***Conclusion:*** Morpho-functional combination with MRI-DaTSCAN imaging in PS and/or ET patients increases the accuracy of the diagnostic information and optimizes the management of the applied therapeutic scheme.

EP-1430

Specific Challenges and Considerations in Pediatric Nuclear Medicine imaging

S. Kosta[1], *F. Mitsikoudi*[1], *E. Konstantarogianni*[1], *I. Sevaslidou*[2];
[1]*Children Hospital Agia Sofia Athens, Athens GREECE,* [2]*General Hospital Laiko, Athens, GREECE.*

Aim/Introduction: This presentation aims to describe the special features and difficulties of performing nuclear medicine imaging in children. It focuses on how children differ from adults in terms of body development and behavior, and how these differences affect the way we perform and interpret imaging exams. ***Materials and Methods:*** This overview is based on real clinical experience from a pediatric nuclear medicine unit. It includes children of all ages—from newborns to teenagers. It discusses how radiopharmaceuticals behave differently depending on the child's age and stage of development, and the challenges we face in helping children stay still and calm during the exam. It also presents techniques such as using music or videos, involving parents, adjusting the environment, giving sedation when needed, and calculating the correct dose based on the child's weight and age. ***Results:*** Each child needs a different approach depending on their age and emotional state. Babies and young children often need comfort or sedation to remain still. Teenagers, especially those with serious illnesses like cancer, may be anxious or scared. Mistaking normal findings (like growth plates or the thymus) for disease is a common risk. Giving the right amount of radiopharmaceutical is very important to get good images while keeping radiation exposure as low as possible. ***Conclusion:*** Imaging in pediatric nuclear medicine needs special knowledge, patience, and good communication. Understanding how children's bodies and minds work helps healthcare professionals get accurate results with less stress for the child. Working closely with parents, using age-appropriate techniques, and training the medical team are key to safe and successful imaging.

EP-1431

Evaluation of the Efficacy of Treatment of Metaiodobenzylguanidine (131I-mIBG) in Pediatric Neuroblastoma

M. Garcia Arevalo, *E. Martínez Montalbán, R. Maestre Cutillas, J. García Álvaro, J. Nieto Margareto, B. Martínez de Miguel; Hospital Universitario La Paz, Madrid, SPAIN.*

Aim/Introduction: Neuroblastoma represents a therapeutic challenge due to its biological and clinical heterogeneity. The aim of the study is to evaluate the efficacy of ^{131}I-mIBG treatment in pediatric patients diagnosed with very high-risk neuroblastoma (VHR-NBL) refractory to standard induction chemotherapy (vincristine, cyclophosphamide, cisplatin) treated with high-dose ^{131}I-mIBG in combination with topotecan and subsequent bone marrow transplantation. ***Materials and Methods:*** In our Unit, a therapeutic protocol combining the use of ^{131}I-mIBG with topotecan followed by myeloablative therapy is applied. We have studied twelve paediatric patients (<14 years), who have met the criteria for inclusion of treatment: tumour uptake of ^{1}23I-mIBG, no bone marrow infiltration and haemogram with pancytopenia. Two cycles of 12 MBq/Kg of ^{131}I-mIBG combined with topotecan are administered separated by two weeks, reaching a maximum tumor dose of 4 Gy. Finally, myeloablative therapy is performed for haematological recovery. Patients are followed up to a maximum of 2 years. ***Results:*** Among the twelve pediatric patients: Seven patients (58.3%) were aged between 4 and 7 years at the time of administration of the first dose of ^{131}I-mIBG: Three patients (42.9%) achieved an overall survival (OS) of two years, with one of these (33.3%) maintaining progression-free survival (PFS) throughout the two-year follow-up. Two patients (28.6%) achieved OS of 1.3 years and 8 months, with only one of these (50%) reaching PFS of 1.3 years; the study is still ongoing for these cases. Two patients (28.6%) could not complete the treatment as a consequence of clinical decompensation, dying as a result of disease relapse and haemodynamic instability. Five patients (41.6%) were aged between 8 and 14 years at the time of administration of the first dose of ^{131}I-mIBG: • Four patients (80%) achieved both OS and PFS of two years. • One patient (20%) is still disease-free six months post-treatment. ***Conclusion:*** Treatment with ^{131}I-mIBG combined with topotecan and followed by myeloablative therapy demonstrates efficacy and safety in pediatric patients with very high-risk neuroblastoma (VHR-NBL), achieving high OS and PFS rates, especially in patients older than 8 years. Despite the heterogeneous outcomes observed in the 4-7 year-old group, the majority attained a favourable response to treatment, confirming its suitability for this pathology.

EP-1432

Evaluation of BroadQuant Quantification accuracy for Lu-177 post-therapy SPECT-CT dosimetry

E. C. Streefkerk, *M. C. Dekker, M. Dotinga, E. A. Aalbersberg; The Netherlands Cancer institute, Amsterdam, NETHERLANDS.*

Aim/Introduction: With the rise of nuclear medicine therapies, quantification and dosimetry is becoming increasingly important. Originally, quantification methods involved the use of a system-specific calibration factor. In 2021 new SPECT-CT systems were acquired at our institute where BroadQuant quantification (Siemens) became available. The aim of this study is to compare BroadQuant quantification for dosimetry with the clinical quantification method with the use of a calibration factor on ^{177}Lu post-therapy SPECT-CT. ***Materials and Methods:*** A reference vial with a predetermined amount of ^{177}Lu activity is placed next to the patient during the ^{177}Lu post-therapy SPECT-CT. Scans were reconstructed according to the in-house clinical protocol. For BroadQuant quantification, an X-SPECT reconstruction was made, with equal reconstruction parameters to the clinical reconstruction. Both images were analyzed with Medical Image Merge (MIM) software, using a 10% threshold of the maximum voxel value within the reference vial. For the clinical quantification, the system-specific calibration factor was used to convert the counts in the VOI to Bq. For the BroadQuant quantification the activity in the VOI was given in Bq. Both results were compared to the known activity in the reference vial at the acquisition time of the scan. Results were analyzed in SPSS using the Shapiro-Wilk Test to determine normality and the Wilcoxon Signed Ranked Test to compare the difference from the true value. ***Results:*** A total of 38 scans were analyzed, with a reference source of 72-110 MBq. Both quantification methods were used to calculate the activity in the reference vial and compared to the true known activity in the reference vial. Quantification using clinical reconstruction and the system-specific calibration factor had a median deviation of -11.45% [IQR: -12.70 to -10.56] compared to the true known activity. BroadQuant quantification had a median deviation of 0.02% [IQR: -2.03 to 1.95] compared to the true known activity ($p<0.001$). ***Conclusion:*** Reference vial measurements on SPECT-CT imaging showed a significant increase in accuracy when using BroadQuant quantification compared to clinical quantification using a system-specific calibration factor.

EP-1433

The Optimization of Lutitium-177 Tomography for Systems Lacking Medium Energy Collimator

L. Jicheng[1], *J. Li*[2]*;*
[1]*lanzhou university, lanzhou, CHINA,* [2]*Department of Nuclear Medicine of the Second Hospital of Lanzhou University, lanzhou, CHINA.*

Aim/Introduction: This study aims to investigate the optimal scanning parameters for Lutetium-177(177Lu) using SPECT/CT with a Low Energy High Resolution (LEHR) collimator, specifically for hospitals that do not have a Medium Energy General Purpose (MEGP) collimator. ***Materials and Methods:*** This study comprised both phantom and clinical tests. Phantom tests compared LEHR parameters (shoot times: 20s/25s/30s; step angles: 3-degree/6-degree(3°/6°); triple energy window [TEW]: main 113keV±10%, scatter 96.6/132keV±5%) with MEGP protocols (20s/25s; 6°; five energy windows: main 113keV/208keV±10%, scatter 96.6/132/174keV±5%). Data were reconstructed using OSEM (2 iterations, 10 subsets) with CT attenuation correction, resolution recovery, and scatter correction (TEW for LEHR, TEW/Dual Energy Window for MEGP). Differences in visual scores (VS) of image quality, coefficient of variance (COV) of the background, image signal-to-noise ratio (SNR), contrast-to-noise ratio (CNR), and the absolute error of sphere uptake versus actual pharmaceutical concentration (AEU) were compared between different acquisitions using the LEHR collimator and those using the MEGP collimator. In the clinical tests, five patients injected with 177Lu-CTR-FAPI were enrolled. Differences in VS of image quality, image SNR, CNR, and standardized uptake value (SUV) of lesions were compared between the corresponding acquisition combinations using the LEHR collimator and those using the MEGP collimator. ***Results:*** In the phantom study, there were no significant differences in the VS of image quality, image SNR, and CNR between MEGP-20s-6°/MEGP-25s-6° and LEHR-25s-3° ($P > 0.05$). Similarly, there were no significant differences in COV between MEGP-20s-6°/MEGP-25s-6° and LEHR-30s-3° ($P > 0.05$). No significant differences in AEU were found between MEGP-20s-6° and LEHR-25s-3° ($P > 0.05$), nor between MEGP-25s-6° and all LEHR acquisition combinations ($P > 0.05$). The background COV and AEU of all MEGP and LEHR acquisition combinations increased as the sphere size decreased, while image SNR and CNR decreased as the sphere size decreased. In the clinical tests, no significant differences were found between traditional MEGP-20s-6°/MEGP-25s-6° and LEHR-25s-3° in the VS of image quality, background COV, image SNR, CNR, and SUV of high uptake lesions ($P > 0.05$). ***Conclusion:*** For 177Lu scanning in SPECT/CT equipment without a Medium Energy General Purpose Collimator, it is recommended to use a tomography acquisition with a 25s "shoot" acquisition and a 3-degree "step" over a 360-degree rotation, utilizing triple energy window scatter correction: main 113keV±10% , scatter 96.6/132keV±5%.

EP-1434

Implementation of the double-contrast protocol to facilitate intraoperative detection of the sentinel lymph node in robotic laparoscopic prostate surgery

A. Afonso de Matos[1], *S. Castanyer Serra*[2], *M. Negre Busó*[2], *M. Santiesteban Gutiérrez*[2], *N. Ferran Sureda*[2], *A. Rubió Rodríguez*[2]*;*
[1]*Medicina Nuclear-ICS, Hospital Universitario Dr. Josep Trueta, Girona, SPAIN,* [2]*Medicina Nuclear-IDI, Hospital Universitario Dr. Josep Trueta, Girona, SPAIN.*

Aim/Introduction: Sentinel lymph node biopsy in the prostate is a complex technique that presents logistical and methodological challenges, as well as a greater learning curve compared to other anatomical regions. One of the main difficulties lies in adapting to robotic-assisted laparoscopic surgery, which involves a different surgical field approach than conventional procedures.Our aim was to evaluate the feasibility of a new dual-contrast protocol designed to more accurately replicate intraoperative conditions, thereby helping to overcome the aforementioned challenges. ***Materials and Methods:*** The radiotracer (4-5 mCi of 99mTc-nanocolloid) was administered via two ultrasound-guided intraprostatic injections, one in each prostatic lobe, the day before surgery. Planar images were acquired at 15 minutes and 4 hours post-injection (120 seconds per image, matrix: 256x256, zoom: 1, collimators: Low Penetration High Resolution - LPHR). Subsequently, a SPECT scan was performed (12 seconds per frame in continuous mode, with a total of 60 images, matrix:128x128, zoom: 1 LPHR collimator), followed by a CT scan (scout: 512 mm of length and 0.6 mm of slice thickness, 25 mA and 110 kV; CT: performed using dose right, 100 mAs and 130 kV, rotation time: 0.6 seconds, slice thickness: 5 mm, pitch: 1.5). During image acquisition, an intravenous contrast agent was manually injected: 30-40 mL approximately 7-8 minutes before the CT scan (excretory phase), followed by a second bolus immediately before the CT acquisition (arterial phase). Images were reconstructed and fused using dedicated reconstruction software, generating a customized template adapted to the anatomical density of each region. ***Results:*** By applying the dual-contrast protocol, we achieved clear visualization of both the ureters and the regional arteries. This enabled a more precise anatomical understanding, and therefore for a more efficient radioguided localization of the sentinel lymph nodes.The subsequent three-dimensional image reconstruction provided a highly accurate representation of the intraoperative findings. These images could

be adjusted and oriented to match the surgical view during the procedure, offering a reliable surgical roadmap. ***Conclusion:*** The implementation of an intravenous dual-contrast protocol combined with anatomically accurate three-dimensional reconstruction improves the correlation between imaging and the surgical field, enhances preoperative planning and facilitates the adaptation of the nuclear medicine physician to the surgical environment.

EP-1435

Uncertainty in a simplified method for quantifying the in vivo distribution of radiopharmaceuticals

H. Sagara[1,2], *K. Takizawa*[2], *K. Tani*[2], *K. Inoue*[2];
[1]*Department of Radiological Technology, Tsukuba International University, Ibaraki, JAPAN,* [2]*Department of Radiological Sciences, Tokyo Metropolitan University, Tokyo, JAPAN.*

Aim/Introduction: Accurate assessment of internal doses from radiopharmaceuticals typically requires extensive medical imaging and complex data analysis by professionals, which can be time-consuming and increase the workload for medical staff as well as the effort required from patients [1]. This study aims to evaluate the uncertainty associated with a simplified method for assessing the in vivo distribution of radiopharmaceuticals, as part of personalized internal dose assessments that account for individual metabolic differences. ***Materials and Methods:*** ^{99m}Tc (4 kBq/mL) was enclosed in each organ (heart, liver, kidneys, and tumor) of the thorax phantom (Kyotokagaku) [2], and planar images were acquired for 10 minutes using the two gamma cameras of the SPECT/CT system Symbia Intevo Excel (SIEMENS). The radiation transport calculation code MCNP ver. 6.2 was used to model the two gamma cameras [3] and reproduce their counting rates for each organ within the voxel phantom, which was generated from the CT images of the thorax phantom. To evaluate the uncertainty in qualifying radioactivity distributed in the body, based on the simplified assumption that the average counting efficiency between two gamma cameras is constant, the study examined the variation in the counting efficiencies, assuming radiopharmaceutical accumulation in a tumor located arbitrary within the voxel phantom. ***Results:*** The uncertainty associated with quantifying the in vivo distribution of radioactivity, based on the average counting rates of two gamma cameras, was estimated to be within several tens of percent.[Conclusion] By accepting a certain level of uncertainty, internal dose assessments that account for individual metabolism are expected to be implementable in clinical practice with minimal additional effort required from patients and medical staff. ***Conclusion:*** By accepting a certain level of uncertainty, internal dose assessments that account for individual metabolism are expected to be implementable in clinical practice with minimal additional effort required from patients and medical staff. ***References:*** 1)Stokke, C., Gabiña, P.M., Solný, P. et al. Dosimetry-based treatment planning for molecular radiotherapy: a summary of the 2017 report from the Internal Dosimetry Task Force. EJNMMI Phys. 2017(4):27.2)Sagara, H., Inoue, K., Mano, C. et al. Usefulness of a new anthropomorphic phantom simulating the chest and abdomen regions in PET tests. Ann. Nucl. Med. 2024(39):303-312.3)Pells, S., Cullen, D.M., Deidda, D. et al. Quantitative validation of Monte Carlo SPECT simulation: application to a Mediso AnyScan GATE simulation. EJNMMI Phys. 2023(10):60.

EP-1436

The Impact of Reconstruction Parameters on Image Quality and Quantification in PET/CT Using a Wax Phantom

S. Hadzimusic*, A. Begić, A. Beganović, A. Skopljak-Beganović, N. Salkica, Š. Cerić, S. Agić-Bilalagić, A. Arnautović-Halimić, B. Tukić; Clinical Center of the Sarajevo University, Sarajevo, BOSNIA AND HERZEGOVINA.*

Aim/Introduction: Body mass significantly impacts standardized uptake value (SUV) in PET/CT imaging, underscoring the need for refined quantification methods. This study introduces a beeswax-based module applied to a standard NEMA IQ phantom to simulate increased patient body mass. Beeswax was chosen for its similarity to adipose tissue in both physical and radiological properties. ***Materials and Methods:*** PET/CT scans were performed using the standard phantom, with and without the beeswax layer, under consistent low-dose protocols. Three reconstruction techniques were applied. Quantitative assessment focused on F-18 FDG uptake in four hot spheres (10-37 mm). Emphasis was placed on SUVmax and SUVmean to evaluate the beeswax module's impact on measurement accuracy and reproducibility. ***Results:*** Notable differences in SUV values were observed between the standard and beeswax-enhanced phantoms, particularly under varied reconstruction settings. These findings validate the beeswax module as a reliable surrogate for simulating increased body mass, demonstrating its potential for optimizing PET/CT protocols in overweight and obese patients. ***Conclusion:*** SUVmean values were higher in the beeswax-modified phantom, reflecting the influence of increased body mass. However, adjusting for lean body mass (SUVlbm) minimized these discrepancies, isolating the effect to actual tracer concentration. These results highlight the importance of SUV correction and support the development of refined imaging protocols tailored to body composition changes, especially in oncology follow-ups. The beeswax module offers a practical tool for improving PET/CT quantification in diverse patient populations.

EP-1437

A Promising Alternative: 2-Minute Respiratory-Gated Total-Body PET Fast Imaging Protocol for Malignancy Patients

X. Hou*, G. Liu, S. Chen, H. Shi;*
Zhongshan Hospital Fudan University, Shanghai, CHINA.

Aim/Introduction: The study aimed to explore the viability of a fast imaging protocol for respiratory-gated total-body 2-[^{18}F]-fluoro-2-deoxy-D-glucose (^{18}F-FDG) positron emission tomography/computed tomography (PET/CT) in patients diagnosed with malignancies. ***Materials and Methods:*** Seventy-two patients with malignancies underwent total-body ^{18}F-FDG PET/CT scans that lasted for 10 minutes, during which their respiratory waveforms were meticulously recorded. Four image reconstructions were conducted: Ungated-10 using all coincidences, Ungated-5 using data of the first 5 minutes, Gated-10 using all coincidences from the entire 10 minutes with respiratory gating, and Gated-2 using data of the first 2 minutes but with respiratory gating. In the respiratory gating process, the quiescent period, which retained half of the coincidence events, was selected as the gating window. Subsequently, the image quality of each reconstruction was systematically evaluated, and the lesions detected were precisely quantified. These assessments were then compared across the four different image sets to identify any significant differences. ***Results:*** A total of 413 lesions were detected, of which Gated-10 revealed a significantly higher number of lesions (397, 96.1%) compared to Ungated-10 (380, 92.0%; $P < 0.001$) and Ungated-5 (375, 90.8%; $P < 0.001$). However, comparable to thoese of Gated-2 (388 vs. 397, $P = 0.121$). When it came to lesion quantification, lesions in Gated-10 exhibited significantly higher maximum, mean, and peak standardized uptake values (SUV_{max}, SUV_{mean}, SUV_{peak}), as well as higher tumor-to-liver and tumor-to-blood ratios, compared to those in Ungated-10 and Ungated-5 (all P values < 0.05). In contrast, the metabolic tumor volume was smaller in Gated-10 relative to the ungated counterparts. Notably, there were no significant differences in any of these quantitative indices between Gated-10 and Gated-2. Additionally, while the background noise was higher in the gated images compared to the ungated images, it remained at an acceptable level for diagnostic purposes. ***Conclusion:*** The

findings suggest that a 2-minute respiratory-gated total-body PET fast imaging protocol outperforms ungated imaging techniques. This implies its potential as an alternative and more efficient approach for oncological imaging, providing a viable means to expedite diagnosis without compromising diagnostic accuracy.

EP-1438

Impact of uptake time on image quality in Positron Emission Tomography /Computed Tomography (PET/CT) among Non-Hodgkin's Lymphoma (NHL) patients

H. J. K. V. Y Wijerama[1], *D. D. N. Wimalarathne*[1], *R. R. K. Prabash*[1], *K. K. I. N. Somasiri*[1], *W. C. Perera*[2], *S. P. D. Wijethunga*[2], *J. M. C. Udugama*[3];
[1]*General Sir John Kotelawale Defence University, Ratmalana, SRI LANKA,* [2]*Apeksha Hospital, Maharagama, SRI LANKA,* [3]*Lanka Hospital PLC, Colombo 05, SRI LANKA.*

Aim/Introduction: Non-Hodgkin's Lymphoma (NHL) is a type of malignancy that develops in the lymphatic system.^{18}F-FDG whole-body PET/CT imaging is essential in the diagnosis and management of NHL. Thus, it is important to identify the factors affecting on lesion detection process for delivering accurate diagnosis. Amongst uptake time is a significant factor. ***Materials and Methods:*** A descriptive-cross-sectional, retrospective study was conducted by using the database (DB) of the PET/CT unit of the radiology department at Apeksha Hospital, Sri Lanka. First, we screened the 53 NHL patients from the DB and their uptake time was noted. Lesion detection was performed by two experienced radiology technologists. And counted the number of lesions that could be seen. SUV_{max}, $SUV_{mean,}$ and SUV_{SD} in lesions were obtained by using the Oncology version software. SNR, CNR and contrast enhancement were calculated by using standard formulas. All the anonymously collected data were input into Microsoft Excel, and the uptake time was categorized into 4 groups separately. The groups were labelled as T1(45-60) min, T2(61-76) min, T3(76-90) min, and T4(91-105) min. The statistical analysis was done using IBM SPSS 27.0 software. ***Results:*** In the sample of 181 lesions, the mean uptake time and SNR were 84.81 ±8.707 min, 0.7404 ± 31.085, respectively. The statistical analysis was performed by using the Spearman correlation. All the uptake time groups show a positive relationship with SNR. For the T1, the correlation between uptake time and SNR is ($p = 0.002$). In T2, ($p = 0.001$). The T3($p = 0.001$), and for the T4, ($p = 0.004$). ***Conclusion:*** According to the T1, the SNR slightly improves as the uptake time increases within this range. As the uptake time extends to T2, the SNR improves more noticeably as the uptake time increases. And this trend continues in T3, where the strongest correlation is observed. This indicates that extended uptake time has the most substantial impact on improving SNR. However, in T4, extended uptake time has not significantly enhanced SNR. Overall, the relationship between uptake time and SNR is strongest between 61-90 mins, Thus, our results suggest the optimum uptake time lie between 61-90 mins. ***References:*** 1.Delcroix, O. et al. (2021) 'Assessment of Image Quality and Lesion Detectability With Digital PET/CT System', Frontiers in Medicine, 8(February), pp. 1-10. Available at: https://doi.org/10.3389/fmed.2021.629096. 2. Iaea.org. (2023). Oncology PET Studies | IAEA. [online] Available at: https://www.iaea.org/resources/interpretation-and-reporting/oncology-pet-studies.

EP-1439

Optimized Workflow in PET/CT Using Variable Speed Continuous Motion and Predicted Attenuation Values

G. Walker*;*
IDX Group Lake Imaging, Ballarat, AUSTRALIA.

Aim/Introduction: The introduction of variable speed continuous motion in PET/CT has made possible the precise selection of PET scan regions for increased or decreased table velocity over prespecified areas according to clinical indication. We aim to apply the same principles to vary speed according to predetermined scan points based on aggregated attenuation data derived from non-AC CT scans, making allowance for gender, body habitus and injected dose, with a view to reducing scan times in routine practice. ***Materials and Methods:*** Two anonymized, randomly selected databases of patients undergoing FDG PET/CT scanning were established (male n=30, female n=30). Parameters recorded were: gender, date of scan, weight, height, dose (MBq), demonstrated pathology, observed bladder activity, measured blood glucose level. All patients were scanned from vertex to mid thigh with arms raised. Count rate profiles in .csv format were recorded for each patient. Patients with BSL> 7.0 mmL^{-1} were excluded, as were those with urinary retention or otherwise full bladders, and those with gross pathology manifesting as large or multiple hot areas. For each patient, ROIs were drawn over the transaxial CT slices at a number of standardized levels to include the area imaged to skin edge. The average Hounsfield unit values were averaged over each region/level, then correlated, as a proxy for mean attenuation, at each level with BMI, weight, gender and injected dose. Gender specific formulae were then generated for setting scan speed over head and neck, lung, abdomen and legs. These formulae were applied to a new group of patients (n=20), with comparison of image quality and total scan time made with a control group scanned under the standard default protocol already in use. A simple phantom study was conducted to assess any change in lesion detectability using the revised method. ***Results:*** Adjusting scanning speed for each of four regions, based on pre-estimated attenuation values and injected dose reduces scan time by up to 15% with no observable reduction in image quality ***Conclusion:*** A simple combination of patient metrics into a formula for varying table speed in PET makes possible customized scan times, potentially increasing throughput, or alternatively incrementally reducing radiation dose.

EP-1440

Improved PET/CT with 2mm Voxel Reconstruction

S. Rep*, I. Slodnjak, B. Trebec Lukman, U. Sprajcer, L. Lezaic;*
University Medical Centre Ljubljana, Ljubljana, SLOVENIA.

Aim/Introduction: Positron emission tomography/computed tomography (PET/CT) imaging is a widely used modality in oncology, providing both metabolic and anatomical information. However, its inherently low spatial resolution introduces the partial-volume effect (PVE), which negatively impacts both the visual appearance and quantitative accuracy of the images. The aim of our research was to investigate the effect of 4 mm and 2 mm voxel sizes on image quality and quantitative evaluation. ***Materials and Methods:*** We utilised the NEMA body phantom with six fillable spheres. The spheres and the background were filled with a solution of fluorine-18 fluorodeoxyglucose (18F-FDG) at sphere-to-background activity concentration ratios of 2:1, 3:1, 4:1, and 8:1. In all reconstructed images (using both 2 mm and 4 mm voxel sizes), we evaluated the contrast recovery coefficient (CRC) and standardized uptake value (SUV). ***Results:*** For phantom spheres with diameters of ≤ 13 mm, we observed significantly higher CRC and SUV values in the reconstructions using the smaller 2 mm voxel size ($p<0.05$). In contrast, CRC and SUV values did not differ significantly for larger spheres (≥ 17 mm in diameter) between the 2 mm and 4 mm voxel size reconstructions ($p>0.05$). ***Conclusion:*** Our results suggest that image reconstruction with a 2 mm voxel size can improve precise lesion localisation and the quantitative evaluation of small lesions. ***References:*** Morey AM, Noo F, Kadrmas DJ. Effect of Using 2mm Voxels on Observer Performance for PET Lesion Detection. IEEE Trans Nucl Sci. 2016 Jun;63(3):1359-1366. doi: 10.1109/TNS.2016.2518177. Epub 2016 Apr 28. PMID: 27499550; PMCID: PMC4970864.Rep S, Tomse P, Jensterle L, Jarabek L, Zaletel K, Lezaic L. Image reconstruction using small-voxel size improves

small lesion detection for positron emission tomography. Radiol Oncol. 2022 Apr 13;56(2):142-149. doi: 10.2478/raon-2022-0015. PMID: 35417108; PMCID: PMC9122293.

EP-1441

Impact of AI-Enhanced Compressed Sensing on T2W Dark Blood Imaging in FAPI PET/MR for Ischemic Cardiomyopathy

X. Wang[1], *Y. Jiang*[1], *Y. Bian*[1], *C. Song*[1], *X. Su*[2], *Y. Yang*[2], *X. Du*[1], *H. Feng*[1], *S. Zhang*[1];
[1]*First Affiliated Hospital of Dalian Medical University, Dalian, CHINA,* [2]*Beijing United Imaging Healthcare Co., Ltd., Beijing, CHINA.*

Aim/Introduction: PET/MR imaging, combining the functional image capability of positron emission tomography (PET) and the detailed anatomical information from magnetic resonance imaging (MRI), is increasingly utilized to assess myocardial edema in conditions such as myocarditis, inflammatory cardiomyopathy and ischemic heart disease. T2-weighted dark blood (T2W-DB) imaging is a widely used technique for evaluating myocardial edema in these conditions. However, the conventional 2D dual inversion recovery fast spin echo (FSE) sequence employed in T2W-DB is highly susceptible to cardiac and respiratory motion across multiple cardiac cycles, leading to myocardial signal loss, reduced contrast, and motion artifacts. The integration of artificial intelligence-assisted compressed sensing (ACS) has markedly improved MRI acquisition quality (1). Despite these advancements, the impact of ACS on T2W-DB imaging in fibroblast activation protein inhibitor (FAPI) PET/MR for ischemic cardiomyopathy patients remains unexplored. ***Materials and Methods:*** This retrospective study included participants with suspected ischemic cardiomyopathy who underwent FAPI PET/MR with both conventional T2W-DB and ACS T2W-DB sequences between July and October 2024 at the First Affiliated Hospital of Dalian Medical University. Quantitative analysis involved calculating the contrast ratio (CR), maximum standardized uptake value (SUVmax), and signal-to-background ration (SBR). Qualitative assessment included evaluating the overall PET/MR fusion image quality and diagnostic confidence, using the Likert scale. Group comparisons were conducted using a paired t-test for normally distributed data and the Wilcoxon signed-rank test for non-normally distributed data. ***Results:*** This study included 15 male participants (mean age, 51 + 7 years). ACS T2W-DB demonstrated a 61% reduction in acquisition time compared to conventional T2W-DB (mean duration, 47+ 13 seconds vs 120+ 38 seconds; $P < 0.001$). ACS T2W-DB also yielded significantly improved contrast ratios (mean CR,7.6 + 2.7 vs 5.1 + 2.7; $P = 0.002$). No significant differences were observed in SUVmax and SBR ($P = 0.25$ and $P = 0.57$). The overall of PET/MR fusion image quality and diagnostic confidence in ischemic cardiomyopathy patients were significantly improved with ACS T2W-DB compared to conventional T2W-DB (both $P < 0.05$). ***Conclusion:*** ACS T2W-DB sequence enabled accelerated acquisition times and significantly improved image quality compared to the conventional sequences, thereby enhancing diagnostic confidence in ischemic cardiomyopathy assessment using FAPI PET/MR. ***References:*** 1.Yan X, Ran L, Zou L, et al. Dark blood T2-weighted imaging of the human heart with AI-assisted compressed sensing: a patient cohort study[J]. Quantitative Imaging in Medicine and Surgery, 2023, 13(3): 1699.

EP-1442

Effect of Scan Angle On Quantification and Reproducibility of Multigated Acquisition Scan (MUGA)

J. Halttunen, *M. Hakulinen, H. Gröhn;*
Kuopio University Hospital, Kuopio, FINLAND.

Aim/Introduction: We currently use patient specific scan angle on MUGA. Before scanning new patient, optimised scan angle is defined from CT scans. If there are no CT scans, different angles are tested manually. The use of standardised angle, would simplify protocol and release time for other examinations. Therefore, aim of the study was to investigate if scan angle, standardised vs optimised, would influence quantification of MUGA scan and reproducibility of the analyses among technologists. ***Materials and Methods:*** Ten patients were scanned twice during MUGA study using conventional SPECT-CT system. First, by using the patient specific optimised angle and then by using standardised angle. The standardised angle was set to 45°. The patients that had at least five-degree difference in their optimised angle compared to the standardised were included in the study. Six nuclear medicine technologists analysed both MUGA scans using commercial analysing software. In these preliminary analyses, only ejection fraction (EF) was determined. After few months, two of the technologists did the analyses again, to evaluate the reproducibility of the results. Interrater variability was estimated using intraclass correlation coefficient (ICC) with two-way random effects, absolute agreement, multiple raters. Difference between means of EF was evaluated using paired t-test. ***Results:*** The observed variation between all the measured EF values were similar between both methods (optimised: range 40-69, standardised: range 44-69). There was no significant difference between the usage of automatic analysis and analysis in which ROIs were manually adjusted (T.Test = 0,073). Some technologists rely on the automatic analysis more often than others. Single measures intraclass correlation was 0,522 and 0,722 for the optimized and standardized angle, respectively. In addition, Cronbach's Alpha reliability was 0,866 and 0.950 for of optimized and standardised angle, respectively. There was no significant difference between analysed and re-analysed (by two technologists) EF results after two months interval. ***Conclusion:*** In our preliminary analysis, there was no significant difference in EF values when using standardised or optimised angle. However, a marked difference was observed in EF values analysed by different technologists. To make sure that all the studies are analysed in standardised way, training has been organized for MUGA analyses at our department. After the training same analysis will be repeated to see if results are more harmonized. Moreover, analyses will be repeated for few patients in upcoming follow-up MUGA scans to see if the difference in EF is still noticeable between optimised and standardised angles.

EP-1443

Graph-based denoising for emission images

R. Kasai, *H. Otsuka;*
Institute of Biomedical Sciences, Tokushima University, Tokushima, JAPAN.

Aim/Introduction: We propose a novel denoising method based on graph signal processing to produce high-quality emission images with low noise. Smoothing filters, such as Gaussian filters, are classified as non-adaptive denoising.It uses weights independent of the pixel values of the filter kernel and is based on spatial distance. However, this method has the disadvantage that edges are smoothed as well as denoised. In contrast, adaptive denoising methods such as the Non-local Means Filter (non-LMF) can perform smoothing while preserving edges and textures. In this study, by representing the emission image as a graph, we can construct an adaptive graph denoising filter. This method allows more flexible denoising than conventional adaptive methods through the selection of graph parameters, and by using Chebyshev polynomial approximations provides faster operations. ***Materials and Methods:*** We constructed the graph by defining the accumulated pixels of the emission image as nodes and the edge information as a Gaussian function with parameters. A noise reduction algorithm is derived by minimizing a cost function with a regularization term. The validation was performed by a numerical phantom for simulation experiments

and a physical phantom (Hoffman 3D brain phantom enclosed ^{99m}Tc) and a clinical patient data (Cerebral blood flow scintigraphy using ^{123}I-IMP) using SPECT. The numerical phantom used 128 x 128 pixel images added the noise with 20 dB. For the physical phantom and patient data, we used images reconstructed from the projection data by the expectation maximization method. To compare noise reduction performance, a Gaussian filter and non-LMF were used. In addition, we evaluated the numerical phantom using Peak Signal-to-Noise Ratio (PSNR) and multi-scale Structural Similarity Index Measure (MS-SSIM), which are quantitative image quality evaluation indices. ***Results:*** Comparing the noise reduction results of Gaussian filter, non-LMF, and our method on numerical phantom, physical phantom, and patient data, we confirmed that the proposed approach is superior in noise reduction and edge preservation. PSNR improved by more than 21.5% and MS-SSIM showed 0.992. Especially in highly noisy situations, the selection of appropriate graphical information parameters leads to higher performance. ***Conclusion:*** Our proposed method shows promise in practical applications by achieving accurate noise reduction from noisy emission images and reducing radiation exposure. The noise reduction and edge preservation features emphasize the novelty and importance of our method in emission image.

EP-1444

Noise-Robust SPECT Reconstruction Using Graph Diffusion

R. Kasai, *H. Otsuka;*
Institute of Biomedical Sciences, Tokushima University, Tokushima, JAPAN.

Aim/Introduction: In recent years, there has been an increasing demand in the field of medical image reconstruction for techniques that can achieve low noise and high accuracy. Particularly in nuclear medicine, accurate attenuation correction and noise reduction are critical challenges in SPECT image reconstruction. This study proposes a novel reconstruction method that captures the relationships between adjacent pixels within an image as a graph structure and introduces a diffusion term based on this graph structure into the reconstruction update equation. We then compare the performance of this proposed method with the conventional MLEM method. ***Materials and Methods:*** Simulations were performed using the 87x87 pixel modified Shepp-Logan phantom with projection data acquired over 180 degrees with 60 projection angles. Signal-to-noise ratio (SNR) conditions of 30dB and 25dB were set. The proposed method, Graph-Diffusion Expectation Maximization (GDEM), aims to improve reconstruction performance by incorporating a diffusion term defined based on the graph structure into the iterative updates. The graph structure is constructed based on the relationships between adjacent pixels in the image, and the graph diffusion mechanism is utilized to simultaneously achieve image smoothing and edge preservation. Performance evaluation was conducted using quantitative metrics such as Peak Signal-to-Noise Ratio (PSNR), Structural Similarity Index (SSIM), and Multi-Scale Structural Similarity Index (MS-SSIM). ***Results:*** Under the 30dB condition, the proposed GDEM showed slight improvements compared to the MLEM method, with PSNR increasing from 22.20 to 22.74, SSIM from 0.49 to 0.58, and MS-SSIM from 0.91 to 0.93. In contrast, under the noisier 25dB condition, GDEM demonstrated significant improvements over the MLEM method. PSNR increased from 18.32 to 20.74, SSIM from 0.35 to 0.45, and MS-SSIM from 0.85 to 0.88, confirming that the proposed method exhibits superior performance even in environments with strong noise. Notably, the introduction of the graph diffusion term effectively suppressed noise and reconstructed the image structure more clearly. ***Conclusion:*** This study introduced GDEM, a novel reconstruction method incorporating a graph diffusion term based on the local relationships within the image, demonstrating superior performance, especially under noisy conditions. While GDEM showed slight improvements at 30dB SNR, it significantly outperformed MLEM at 25dB SNR. The enhanced MS-SSIM values further indicate that GDEM better preserves image structural similarity across different scales. This suggests that efficient noise removal and structure preservation via graph diffusion can substantially improve SPECT image reconstruction accuracy, offering promising applications in nuclear medicine.

EP-1445

NEMA Phantom Study on PET Textural Features Variability with Different Reconstructions in Digital PET/CT

P. Dwivedi[1,2,3], *S. Barage*[2], *V. Dubey*[1,3], *A. Jha*[4,3], *S. Choudhury*[1,3], *A. Agrawal*[1,3], *V. Rangarajan*[1,4,3];
[1]*Advanced Centre for Treatment Research and Education in Cancer,Tata Memorial Centre, Mumbai, INDIA,* [2]*Amity Institute of Biotechnology, Amity University, Mumbai, INDIA,* [3]*Homi Bhabha National Institute, Mumbai, INDIA,* [4]*Tata Memorial Hospital, Mumbai, INDIA.*

Aim/Introduction: PET radiomics is a promising quantitative tool for oncological studies, however, these features are influenced by various factors including acquisition protocol, scanner model, reconstruction methods, segmentations etc. Therefore, we aimed to explore the variability of PET textural features for different reconstruction methods with National Electrical Manufacturers Association (NEMA) image quality (IQ) phantom in a digital PET/CT scanner. ***Materials and Methods:*** The phantom contains a lung insert in the middle and six surrounding fillable spheres with increasing diameter 10, 13, 17, 22, 28, and 37 mm. The lung insert was filled with Styrofoam with an average density of 0.3-g/mL simulating lung tissue. While each sphere had an activity of 21.6 kBq/mL, the background was filled with 5.2 kBq/mL of 18F, maintaining the 4:1 concentration as per the NEMA NU 2-2018 standard of image quality[1]. The prepared NEMA IQ phantom was placed in the central field of view (FOV), and to simulate activity outside the FOV, a scatter phantom was placed behind the phantom with an activity of 120 MBq at scan time. Subsequently, 5 min per bed scan with useful FOV was performed with GE Discovery MI Gen2 PET/CT, which is a hybrid SiPM-based digital scanner. Raw list data were reconstructed with 6 different reconstruction methods: VPHD (3D OSEM), VPHD-S(OSEM +PSF), VPFX (OSEM + TOF), VPFX-S (OSEM + TOF+PSF), filter back projection (FBP), and BSREM with beta 350 (Q Clear). 3D segmentation of each homogenous hot sphere then proceeded except smallest sphere since voxel size was less than 64 for texture calculation, and 55 IBSI complaint textural features were extracted with absolute resampling from LIFEx vs. 7.7.0. Subsequently COV was calculated for each feature concerning different reconstructions and classified as having low (<5.0%), intermediate (5-20%) or high (>20%) variability. ***Results:*** In total, five features were found highly stable with COV<5% in 37 and 28mm sphere, four in 22 and 17mm sphere, however, only two were noted in 13 mm sphere. On average, 74.5 %, 20% and 5% of the features showed a high, intermediate and least variability with different reconstruction methods. GLCM based Normalized inverse difference and Normalized inverse difference moment were consistently least variable with COV<5% across different reconstructions in all sphere sizes. ***Conclusion:*** PET reconstruction methods greatly impacted the stability of textural features, therefore, standardization is an important factor in radiomic studies. These findings could also facilitate stable features' selection for further multicentric PET radiomic applications.

EP-1446

Optimization Study of Low-Dose Brain PET/MR Imaging Based on Deep Progressive Learning Reconstruction

X. Wang[1], *Y. Jiang*[1], *Y. Bian*[1], *C. Song*[1], *X. Su*[2], *Y. Yang*[2], *X. Du*[1], *H. Feng*[1], *S. Zhang*[1];
[1]*First Affiliated Hospital of Dalian Medical University, Dalian, CHINA,* [2]*Beijing United Imaging Healthcare Co., Ltd., Beijing, CHINA.*

Aim/Introduction: This study aims to evaluate the clinical feasibility of the Deep Progressive Reconstruction (DPR) algorithm in improving the image quality of low-dose brain PET/MR imaging. ***Materials and Methods:*** A retrospective analysis was conducted on 28 patients (11 males and 17 females, mean age 67.4 years) with suspected neurodegenerative diseases, recruited from the First Affiliated Hospital of Dalian Medical University between October 2024 and January 2025. All participants underwent brain ^{18}F-FDG PET/MR examination. PET images were reconstructed using both Ordered Subsets Expectation Maximization (OSEM) with 20 subsets and 5 iterations, and DPR algorithms with an intensity of 5. The DPR group was subdivided into different scanning duration groups to simulate different injected activities: 25 min (full dose), 12.5 min (half dose), 8.3 min (1/3 dose), and 6.3 min (1/4 dose). These were compared with the OSEM group under the conventional acquisition time. Qualitative evaluation was performed by two nuclear medicine specialists through a double-blind visual assessment using a 5-point Likert scale, rating overall image quality, clarity, artifact level, noise level, and uniformity. Quantitative evaluation utilized the Friedman test to assess the contrast between gray matter as well as white matter of the cerebral cortex and cerebrospinal fluid, and the contrast of gray matter and white matter of the cerebral cortex. ***Results:*** Visual assessments demonstrated that all DPR subgroups (1/n, n = 2,3,4) outperformed the OSEM group in all image quality parameters. And quantitative analysis revealed that the low-dose DPR groups significantly improved the contrast between gray matter as well as white matter of the cerebral cortex and cerebrospinal fluid, and the contrast of gray matter and white matter of the cerebral cortex, compared to the OSEM group. ***Conclusion:*** The DPR algorithm significantly improves the image quality of low-dose brain PET/MR scans. By reducing injected activity while maintaining image quality, DPR presents a feasible solution for clinical low-dose PET/MR imaging of the nervous system. This approach offers safer, more reliable imaging for the early diagnosis of neurodegenerative diseases and holds significant clinical application potential.

EP-1447

Dynamic ElasticNet regularization with adaptive gradient descent for enhanced emission CT image reconstruction

R. Kasai*, H. Otsuka;*
Institute of Biomedical Sciences, Tokushima University, Tokushima, JAPAN.

Aim/Introduction: For high-quality emission computed tomography (ECT) image reconstruction, we propose a novel reconstruction method that incorporates ElasticNet regularization to dynamically adjust parameters in the evaluation function between projection and forward projection. Image reconstruction in ECT presents a challenging problem for estimating high-quality images from observed noisy data. However, a well-known reconstruction method, maximum likelihood expectation maximization (MLEM), has the problem of unstable convergence due to noise. Our new reconstruction method dynamically and automatically controls the parameters of ElasticNet according to the object, and shows significantly improved performance compared to the MLEM method even in noisy situations. ***Materials and Methods:*** The ECT image reconstruction problem can be formulated by the linear equation p=Hx, where p represents the noisy projection data, x the unknown pixel values, and H the mapping operator. We employ ElasticNet regularization as an image reconstruction technique aimed at minimizing this linear equation and enhancing the accuracy of reconstructed ECT images. ElasticNet is an algorithm that combines ridge and lasso regression, which is widely used in machine learning field. We introduce a term that dynamically controls the ridge and lasso regression in ElasticNet according to the object. For validation, we conducted simulation experiments using a numerical phantom (128x128 pixels) with added noise at a signal-to-noise ratio of 25dB, as well as physical phantom SPECT imaging using a Hoffman 3D brain phantom enclosed with ^{99m}Tc. We compared our results against the MLEM method, evaluating the reconstructed images both visually and objectively using density profiles, Peak Signal-to-Noise Ratio (PSNR), and multi-scale Structural Similarity Index Measure (MS-SSIM). ***Results:*** Our proposed method showed better convergence than the MLEM method, even under noisy conditions. Notably, at 100 iterations, the PSNR for MLEM was 18.5, while our method achieved 21.2. Similarly, the MS-SSIM value for MLEM was 0.80, and our method reached 0.89, both indicating the superior performance of our approach. These findings were further substantiated by our clinical SPECT experiment. The validation results consistently demonstrate that our proposed method excels in noise reduction and edge preservation. ***Conclusion:*** Through numerical and clinical SPECT experiment, our proposed reconstruction method enables high-quality reconstruction from low-dose projections and reduces radiation exposure. The parameters of ElasticNet regularization are dynamically determined by the projection and forward projection values of each iteration, highlighting its novelty in ECT image reconstruction method.

EP-1448

Deep Progressive Learning Reconstruction in Non-Small Cell Lung Cancer: Improving Image Quality and Radiomic Feature Robustness

T. Shiiba[1], *M. Watanabe*[2];
[1]*Fujita Health University, Toyoake, JAPAN,* [2]*Fujita Health University Hospital, Toyoake, JAPAN.*

Aim/Introduction: This study systematically compared the effects of deep progressive learning [1-3] reconstruction (DPR) with those of conventional ordered-subset expectation maximisation (OSEM) on PET-based quantification, image quality, and radiomic feature stability in non-small cell lung cancer (NSCLC) imaging. ***Materials and Methods:*** Twenty-four NSCLC patients had ^{18}F-FDG PET/CT scans reconstructed using OSEM and three DPR strengths (1, 3, and 5). We assessed standardised uptake values (SUV_{max}, SUV_{mean}), the background coefficient of variation (COV), contrast-to-noise ratio (CNR), and radiomic feature stability, the latter evaluated by the COV across reconstruction methods. Tumours were grouped by volume into small (<10 cm^3), medium (10-30 cm^3), and large (>30 cm^3). Wilcoxon signed-rank tests with Bonferroni or FDR correction were applied for statistical comparisons. ***Results:*** DPR significantly increased SUV_{max} (OSEM: 9.72 ± 4.69; DPR strength 5: 13.67 ± 6.20, $p < 0.001$) and SUV_{mean} (OSEM: 3.98 ± 1.75; DPR strength 5: 4.31 ± 1.80, $p < 0.001$), particularly in smaller lesions (SUV_{max} relative change: 47.4%). DPR strength 1 slightly reduced background COV (OSEM: 18.38 ± 5.65%; DPR strength 1: 16.51 ± 6.88%), whereas higher strengths increased noise (DPR strength 5: 27.34 ± 7.12%). Although CNR improved at DPR strength 1, it declined significantly at higher strengths. Radiomic feature stability generally improved with DPR, evidenced by decreased COV in 78 of the 93 evaluated features at higher DPR strengths compared to OSEM. ***Conclusion:*** DPR significantly enhances SUV quantification and radiomic feature stability in NSCLC PET imaging, and is particularly beneficial for small lesion detectability. However, optimal DPR strength selection is crucial for balancing improved contrast with increased noise. These findings underscore the potential clinical utility of DPR in improving diagnostic accuracy and robustness in quantitative PET analyses. ***References:*** 1. Lv, Y., Xi, C.: PET image reconstruction with deep progressive learning.

Phys Med Biol. 66, 105016 (2021). https://doi.org/10.1088/1361-6560/abfb172. 2. Wang, T., Qiao, W., Wang, Y., Wang, J., Lv, Y., Dong, Y., Qian, Z., Xing, Y., Zhao, J.: Deep progressive learning achieves whole-body low-dose ^{18}F-FDG PET imaging. EJNMMI Phys. 9, 82 (2022). https://doi.org/10.1186/s40658-022-00508-53. 3. Yang, H., Chen, S., Qi, M., Chen, W., Kong, Q., Zhang, J., Song, S.: Investigation of PET image quality with acquisition time/bed and enhancement of lesion quantification accuracy through deep progressive learning. EJNMMI Phys. 11, (2024). https://doi.org/10.1186/s40658-023-00607-x

EP-1449

Lesion detectability evaluation of a deep learning-based time of flight image enhancement algorithm on BGO-based PET/CT scans

K. Itagaki[1], *K. K. Miyake*[2], *K. Mitsumoto*[1], *K. Nakatani*[2], *R. Nakamoto*[3], *T. Nobashi*[3], *S. Koyasu*[2], *A. Katsuki*[4], *H. Kawakami*[4], *F. Kotasidis*[5], *Y. Nakamoto*[2];
[1]*Division of Clinical Radiology Service, Kyoto University Hospital, Kyoto, JAPAN,* [2]*Department of Diagnostic Imaging and Nuclear Medicine, Graduate School of Medicine Kyoto University, Kyoto, JAPAN,* [3]*Preemptive Medicine and Lifestyle Related Disease Research Center, Kyoto University Hospital, Kyoto, JAPAN,* [4]*GE HealthCare, Japan, Tokyo, JAPAN,* [5]*GE HealthCare, Zurich, SWITZERLAND.*

Aim/Introduction: This study evaluated the lesion detectability performance of a deep learning-based time of flight (TOF) image enhancement algorithm from datasets acquired on a previous generation for BGO-based PET/CT system. ***Materials and Methods:*** A NEMA body phantom dataset was acquired and processed using a deep learning algorithm that maps non-TOF image datasets towards their TOF counterparts.(1) Three different models of variable trade-off between contrast enhancement and noise (DLToF -L, DLToF-M, DLToF-H) were used to assess lesion detectability across different data acquisition durations (60, 180, and 300 seconds) and across different regularization parameters (200, 400, 600, 800, and 1000) of the input images, reconstructed with a Bayesian penalized likelihood algorithm. The phantom was filled with ^{18}F solution with a target-to-background ratio (TBR) of 4:1 on a background of 2.65 kBq/mL, according to the Japanese guidelines for oncological ^{18}F-FDG PET/CT data acquisition.(2) Quantitative analysis was performed using metrics such as the contrast recovery coefficient for the 10 mm diameter sphere (CRC) and background variability (BV) according to NEMA NU 2-2018 specification. The contrast-to-noise ratio (CNR) was also calculated to assess small sphere detectability. In addition, the background coefficient of variation (CV) was measured in ROIs of 37 mm in diameter. ***Results:*** CNR was improved using all three DL models of various strengths, with the highest scores achieved when applying DLToF-H and at all acquisition durations. The CNR change ratio of DLToF-H was the highest in all regularization parameters at the 180-second acquisition duration. At the 180-second, applying DLToF-L, DLToF-M, and DLToF-H to the images reconstructed with a regularization parameter of 400 resulted in CNR of 3.50, 2.90, and 3.56, respectively. DLToF-M and DLToF-H improved the CRC when the noise in the original image was low, while DLToF-L promoted variance reduction over contrast enhancement in all cases. After applying DLToF-H to the images acquired for 180 seconds, the CNR was comparable to that of the original images acquired for 300 seconds. DLToF-M and DLToF-H increased image noise under conditions of low image noise in the original image, while DLToF-L reduced image noise in any condition. ***Conclusion:*** DLToF-H improved CRC and DLToF-L promoted improved noise characteristics. The lesion detectability performance of a previous generation BGO-based PET/CT was improved with deep learning-based time of flight image enhancement, especially utilizing DLToF-H. ***References:*** 1. Mehranian A, et al. Eur J Nucl Med Mol Imaging. 2022 Sep;49(11):3740-3749.2. Fukukita H, et al. Ann Nucl Med. 2014 Aug;28(7):693-705.

EP-1450

Overcoming respiratory motion artifacts: Gated PET/CT for improved visualization of juxtadiaphragmatic lesions

K. Shyli, *F. Firinu, F. Casaburo, F. Oliverio, A. Sotgiu, C. Serra, M. Mantovani, S. Fraschina, A. Lomartire, G. Paolacci, G. Cafiero, I. Papagni;*
ASST Grande Ospedale Metropolitano Niguarda, Milan, ITALY.

Aim/Introduction: Juxtadiaphragmatic lesions are often difficult to visualize on PET/CT due to respiratory motion of the diaphragm, which can cause motion artifacts and reduce image quality. Respiratory gating, through the use of devices that monitor the patient's breathing pattern, allows image acquisition to be synchronized with the respiratory cycle, significantly improving lesion detectability in these challenging regions. This approach is particularly beneficial in patients with irregular breathing, who often show comet-tail artifacts on conventional PET/CT scans. Moreover, gating enables better management of the exam in non-compliant patients and in those unable to perform rapid breath-hold acquisitions. In this study, we describe the application of respiratory gating experience at our hospital using the high-sensitivity United Imaging Panorama GS LAFOV PET/CT system to enhance visualization of juxtadiaphragmatic lesions. ***Materials and Methods:*** The protocol involves the use of a respiratory belt to monitor the patient's breathing and generate gated reconstructions. PET data are acquired with a 256x256 matrix and reconstructed using OSEM (3 iterations, 10 subsets) with Gaussian post-filtering (FWHM 2.0), incorporating both TOF (Time-of-Flight) and PSF (Point Spread Function) technologies for optimal resolution and noise reduction. In order to obtain optimal gated images, an acquisition time of at least 6 minutes is required. Gated reconstruction parameters are as follows: trigger type VSM (Ventilation-Synchronized Motion), bin type phase, number of bins 6, and offset 0%. ***Results:*** Respiratory gating significantly improved image quality and lesion detection compared to standard non-gated PET/CT. In 39 of 47 acquisitions, comet-tail artifacts were markedly reduced. The use of the respiratory belt allowed effective synchronization between respiration and acquisition, minimizing respiratory artifacts. Furthermore, the gating approach improved scan management in uncooperative patients or those unable to hold their breath during rapid acquisitions. Otherwise, respiratory sampling is often challenging in underweight patients, resulting in under-sampled and noisy images. Anyway, gated reconstructions provided superior resolution and clearer delineation of lesions that would otherwise be difficult to detect and localize. ***Conclusion:*** The implementation of respiratory gating offers an effective solution for the visualization of juxtadiaphragmatic lesions. Respiratory synchronization via belt, combined with optimized gated reconstruction parameters, significantly enhances image quality and diagnostic confidence. This method is especially valuable in patients with irregular breathing, enabling better lesion detection while also improving workflow in cases where breath-hold imaging is not achievable.

EP-1451

Evaluation of Machine Learning Models for Automated Segmentation of SPECT MPI Scans

A. Alenezi[1], ***E. Alawdhi***[1], *A. Jodeiri*[2], *A. Mayya*[3];
[1]*Kuwait University, Kuwait, KUWAIT,* [2]*Tabriz University of Medical Sciences, Tabriz, IRAN, ISLAMIC REPUBLIC OF,* [3]*Tishreen University, Latikiya, SYRIAN ARAB REPUBLIC.*

Aim/Introduction: Myocardial perfusion imaging (MPI) using single-photon emission computed tomography (SPECT) plays a critical role in diagnosing and assessing the severity of coronary artery disease (CAD). Accurate segmentation of myocardial regions is essential for deriving quantitative metrics related to left ventricular function. Manual segmentation remains the clinical standard but is time-consuming and prone to inter-observer

variability, particularly under high workload. Deep learning, specifically convolutional neural networks (CNNs), has emerged as a promising alternative for automating segmentation tasks in medical imaging[1]. This study aims to evaluate and compare the performance of five deep learning-based U-Net models for automatic segmentation of cardiac SPECT images, each using a different encoder backbone: CNN, MobileNet, VGG with attention, Inception, and ResNet50 with attention. ***Materials and Methods:*** Two MPI datasets were used: a small set (609 images) and a large set (5169 images), both labeled with ground truth masks. Images were preprocessed to 64×64 pixels and augmented with flipping, distortion, noise, and contrast adjustments. All five U-Net variants were trained using identical hyperparameters and assessed via mean Intersection-over-Union (mIoU), Dice coefficient, pixel accuracy, and AUC. An ensemble model was also developed using weighted averaging of the five networks. ***Results:*** Across both datasets, the Inception-based U-Net demonstrated superior individual model performance (Dice: 0.9656 and 0.9538; mIoU: 0.9358 and 0.9197). However, the ensemble model outperformed all individual models (Dice: 0.9679 and 0.9544; mIoU: 0.9398 and 0.9205), achieving the highest accuracy and lowest false negative rates. While MobileNet U-Net offered the fastest training time, it had slightly lower segmentation accuracy (details in Table 1). The Inception-based model showed the best trade-off between segmentation quality and clinical relevance, albeit with higher computational demands. ***Conclusion:*** Our results confirm the efficacy of deep learning models, particularly ensemble U-Net architectures, in achieving high-precision segmentation of cardiac SPECT MPI images. The approach significantly reduces reliance on manual interpretation and enhances reproducibility. By enabling accurate and automated delineation of myocardial structures, these models hold potential to streamline nuclear cardiology workflows and support robust decision-making, especially in high-throughput clinical environments. Further work will explore real-time deployment and integration into clinical systems, mega studies and radiomics. ***References:*** [1]Apostolopoulos, I. D., Papandrianos, N. I., Feleki, A., Moustakidis, S., & Papageorgiou, E. I. (2023). Deep learning-enhanced nuclear medicine SPECT imaging applied to cardiac studies. In EJNMMI Physics (Vol. 10, Issue 1). Springer Science and Business Media Deutschland GmbH. https://doi.org/10.1186/s40658-022-00522-7

EP-1452

Development of a Muscle Masking Technique for Reducing the Influence of Physiological FDG Uptake in PET Imaging

M. Sato*, N. Imaizumi, F. Sasaki, A. Yumoto, T. Kita, H. Daisaki; Gunma Prefectural College of Health Sciences, Maebashi, JAPAN.*

Aim/Introduction: PET imaging using 18F-fluorodeoxyglucose (18F-FDG), maximum intensity projection (MIP) images are useful for providing an overall three-dimensional view of tracer distribution. However, inadequate adherence to pre-scan preparations such as fasting or avoiding physical activity can result in excessive FDG uptake in muscles. This physiological uptake may obscure small or low-uptake lesions within the MIP images, reducing their visibility. While PET/CT fusion images can mitigate this issue by providing clear anatomical localization, MIP images remain an essential and widely used visualization tool in routine clinical practice. Therefore, the purpose of this study was to develop a system that enhances lesion visibility on MIP images by automatically extracting skeletal muscle regions from CT images and subsequently removing these regions from both PET and CT datasets. ***Materials and Methods:*** We used TotalSegmentator, a deep learning-based segmentation tool, to extract skeletal muscle regions throughout the entire body [1]. Since TotalSegmentator is structured into various segmentation tasks, we selectively extracted only the regions related to muscle from each relevant task to generate corresponding mask images. By integrating all these individual mask images, we created a comprehensive mask encompassing the entire musculature. Using this mask, it became possible to remove skeletal muscle regions from both CT and PET images. TotalSegmentator accepts input images in the Neuroimaging Informatics Technology Initiative (NIfTI) format. Therefore, in our system, DICOM images were first converted to NIfTI format. To allow for eventual re-export in DICOM format, we preserved the original DICOM tag information, which was reattached after segmentation processing. ***Results:*** Using this system, muscle regions can be successfully extracted from CT images. The generated muscle mask also enabled the removal of corresponding signals from PET images. Applying the post-processed mask may enhance the visibility of lesions by reducing background signals caused by physiological muscle uptake. ***Conclusion:*** This study found that the automatic extraction and removal of skeletal muscle regions is feasible. The proposed method may enhance the visibility of lesions on MIP images, particularly in cases where physiological FDG uptake in muscle compromises diagnostic accuracy. Furthermore, by analyzing FDG uptake in muscle in conjunction with blood glucose levels, this approach may provide a new indicator for assessing patient compliance with pre-scan preparation protocols and offer potential insights into predicting diabetes. ***References:*** [1] J. Wasserthal et al., "TotalSegmentator: Robust Segmentation of 104 Anatomic Structures in CT Images," Radiology: Artificial Intelligence, vol. 5, no. 5, p. e230024, 2023. [Online]. Available: https://doi.org/10.1148/ryai.230024

EP-1453

Cross-Validation of Quantitative Accuracy in ^{13}N-Ammonia PET Using Different Software and Compartment Models

N. Akiya*[1], K. Miwa[1], A. Ando[2], N. Miyaji[1], T. Yamao[1], K. Wachi[1], M. Masubuchi[1], S. Kimura[3], R. Ito[1], A. Komatsu[1], T. Horikawa[1]; [1]Fukushima Medical University, Fukushima, JAPAN, [2]Sapporo Kojinkai Memorial Hospital, Hokkaido, JAPAN, [3]Fukushima Medical University Aizu Medical Center Hospital, Fukushima, JAPAN.*

Aim/Introduction: Compartment model-based quantification of myocardial blood flow (MBF) and myocardial flow reserve (MFR) using ^{13}N-ammonia PET plays a key role in risk stratification and prognosis prediction. However, the reliability of these indices depends on the analytical methods used. The present study aimed to compare MBF and MFR values obtained from different software to cross-validate their accuracy, and to assess the impact of compartment model selection on these quantitative indices. ***Materials and Methods:*** This study included 100 patients who underwent ^{13}N-ammonia PET/CT: 60 with normal myocardial flow, 20 with single-vessel disease, 10 with two-vessel disease, and 10 with three-vessel disease. MBF and MFR were quantified using three software packages: SyngoMBF (Siemens Healthineers), PMOD Cardiac PET Analysis Tool (Bruker), and QPET (Cedars-Sinai). Calculations were performed using a 1-tissue compartment model (1TCM) and two 2-tissue models (Hutchins and UCLA), at both the global (entire left ventricle) and regional (major coronary artery territories) levels. ***Results:*** MBF and MFR values were generally consistent across the three software packages, although a small but significant difference in stress MBF was noted between PMOD and QPET ($p < 0.05$). Strong correlations were observed at the global and regional levels ($r = 0.81$-0.91 and 0.69-0.92, respectively), and Bland-Altman analysis demonstrated good agreement. In contrast, compartment model selection had a notable impact on global MBF and MFR values ($p < 0.05$). The mean global MFR was 2.62 ± 0.80 (1TCM), 2.56 ± 1.00 (Hutchins), and 3.32 ± 1.22 (UCLA), with the UCLA model yielding the highest values. Correlation coefficients between models ranged from 0.43 to 0.99. Bland-Altman analysis showed agreement among models, although the UCLA model tended to overestimate

MBF. ***Conclusion:*** Stress MBF, rest MBF, and MFR showed strong agreement among the three software packages at both the global and regional levels. In contrast, compartment model selection had a substantial impact on these values, particularly with the UCLA model. Appropriate model selection is essential for consistent quantification in ^{13}N-ammonia PET.

EP-1454

Relationship Between Visual Braak Staging and the Quantitative Tau PET Methods CenTauR and STOC

K. Wachi[1], *T. Yamao*[1], *K. Miwa*[1], *N. Miyaji*[1], *N. Akiya*[1], *M. Masubuchi*[1], *T. Horikawa*[1], *A. Komatsu*[1], *R. Ito*[1], *H. Matsuda*[2]; [1]*Fukushima Medical University, Fukushima, JAPAN,* [2]*Nippon Medical School, Clinical Imaging Center for Healthcare, Tokyo, JAPAN.*

Aim/Introduction: Tau pathology progression in Alzheimer's disease is closely linked to cognitive decline. Visual Braak staging is widely used in clinical practice to assess tau distribution but requires expert interpretation. This study aimed to examine the relationship between visually-assessed Braak staging and two quantitative tau PET methods: CenTauR and the Simplified Temporal Occipital Classification (STOC). ***Materials and Methods:*** A total of 237 participants from the ADNI3 cohort were included: cognitively normal individuals (CN, n = 93), patients with mild cognitive impairment (MCI, n = 95), and Alzheimer's disease dementia (n = 49). All participants underwent ^{18}F-flortaucipir PET and MRI. Braak staging was visually assessed by a nuclear medicine physician. Two quantitative methods were evaluated: CenTauR, which calculates SUVRs in five predefined regions and converts them to CenTauR scores; and STOC, which classifies tau burden in five stages based on SUVR thresholds across four regions. PET images were normalized using structural MRI, with the cerebellar cortex as the reference. Tau positivity was defined as Braak stage ≥ 4, CenTauR score ≥ 2.0, or STOC stage ≥ 2. Agreement with visual Braak staging was evaluated using kappa coefficients and accuracy, and Spearman's rank correlation coefficients were calculated for CenTauR and STOC. ROC analyses were used to evaluate the ability of each method to distinguish tau-positive (MCI and AD) from tau-negative (CN) individuals. ***Results:*** CenTauR showed kappa values ranging from 0.61 to 0.81 and classification accuracy from 0.84 to 0.91. STOC yielded a kappa of 0.73 and accuracy of 0.88. Spearman's correlation coefficients were 0.67-0.82 for CenTauR and 0.78 for STOC. AUCs for Braak staging, CenTauR, and STOC were 0.71, 0.67, and 0.69, respectively. These results highlight complementary strengths of the two methods: CenTauR captures regional heterogeneity of tau uptake, whereas STOC enables quantitative staging similar to Braak classification. Their combined use might support more accurate and comprehensive assessment in clinical tau PET interpretation. ***Conclusion:*** CenTauR and STOC demonstrated substantial alignment with visually-assessed Braak staging in tau PET. These quantitative methods serve as complementary tools to enhance reliability and objectivity in tau imaging assessments. ***References:*** Villemagne VL, Leuzy A, Bohorquez SS, et al. CenTauR: Toward a universal scale and masks for standardizing tau imaging studies. Alzheimers Dement (Amst). 2023 7;15(3):e12454.

EP-1455

Feasibility of renal function assessment using dynamic ^{68}Ga-EDTA PET-CT imaging

P. Khobragade[1], *N. Varghese*[1], *P. Varekar*[2], *A. Shanker*[1], *R. Krishnappa*[3], *B. Spottiswoode*[4], *K. Kallur*[3]; [1]*Siemens Healthcare Private Ltd., Bangalore, INDIA,* [2]*Manipal Institute of Technology, Manipal, INDIA,* [3]*Healthcare Global Enterprises Ltd, Bangalore, INDIA,* [4]*Siemens Medical Solutions, Inc, Bangalore, INDIA.*

Aim/Introduction: Planar scintigraphy is commonly used to evaluate renal function, providing estimates of glomerular filtration rate (GFR) and split function, and time-activity curves (TAC) [1]. However, its limitations include poor spatial resolution, absence of three-dimensional information, and challenges in absolute quantification. PET-CT imaging has the potential to overcome these limitations by providing high-resolution volumetric data, allowing improved visualization of renal anatomy and function. This study explores the feasibility of using dynamic ^{68}Ga-EDTA PET-CT imaging for renal function assessment. ***Materials and Methods:*** Six patients referred for varied clinical conditions—minimal hydronephrosis due to ureteric calculus, chronic kidney disease, and transplant assessment—underwent single bed dynamic PET-CT following intravenous injection of 2-3.5 mCi of ^{68}Ga-EDTA. Image reconstruction was performed using eight iterations and five subsets, incorporating point spread function correction. Twenty minutes of list-mode data were and reframed into 24 frames of 10 seconds followed by 16 frames of 60 seconds. Prior to PET-CT, patients underwent dynamic Tc-99m DTPA renal scintigraphy for comparative analysis. Planar dynamic data were acquired over 15 minutes, with the first 60 frames captured at one-minute intervals and the remaining frames at 30-second intervals. A deep learning-based organ segmentation algorithm was used to segment the kidneys and generate 3D masks. A modified Gate's model was applied for GFR calculation, using planar scintigraphy derived values to fine-tune parameters. Kidney volume and depth were extracted from the CT segmentation masks. ***Results:*** GFR values showed a maximum deviation of 5% compared to planar scintigraphy, while split renal function differed by no more than 2%. A variation in time-to-peak values between PET-CT and planar scintigraphy was observed, likely due to background interference during the perfusion phase on the scintigraphy scans. Importantly, PET-CT enabled precise measurement of kidney volume and depth, which are not achievable with planar scintigraphy. ***Conclusion:*** This study demonstrates the feasibility and potential of ^{68}Ga-EDTA PET-CT in dynamic renal function assessment. PET-CT-based estimates of GFR and split renal function are in close agreement with traditional planar scintigraphy. In addition, PET-CT offers superior spatial and temporal resolution, along with the ability to provide detailed volumetric anatomical delineation and absolute quantification. PET-CT may serve as a suitable alternative to planar scintigraphy for evaluating renal function. ***References:*** [1] Toyama, Yoshitaka, et al. "Current and future perspectives on functional molecular imaging in nephro-urology: theranostics on the horizon." Theranostics 11.12 (2021): 6105.

EP-1456

Optimisation of Dosage for Myocardial Perfusion Imaging Using an Anthropometric Formula and Predicted Attenuation Values

G. Walker;
IDX Group Lake Imaging, Ballarat, AUSTRALIA.

Aim/Introduction: To determine a reliable method for optimising radiopharmaceutical dose using one or a combination of simple body measurements. If the myocardial information density can thus be constrained to a narrow, predictable range, the likelihood of poor image quality will be reduced, and changes to existing dose and imaging regimens, with the objective of reducing radiation dose, may be made with confidence. Various methods for determining radiopharmaceutical dose for myocardial imaging have been proposed, including varying dose by patient weight, weight range and BMI. These methods may in some circumstances result in unnecessary radiation dose or inadequate image quality. ***Materials and Methods:*** A group of patients (n=50) undergoing stress myocardial perfusion imaging was examined for height, weight, thoracic circumference, mean chest wall thickness and gender. Correlations were then sought among these quantities.

Three further groups of patients (n=70 each) were dosed thus: A: Fixed dose of ^{99m}Tc sestamibi with variations. B: Dosage based on measured body mass. C: Dosage by a formula determined from the initial group data, combining thoracic circumference, gender and estimated thoracic attenuation. After acquisition of post-stress images with a fixed acquisition time, information density (mean net counts per pixel in raw projections) was measured for each patient, and a frequency distribution generated for each group. ***Results:*** There was excellent correlation between thoracic circumference and mean thoracic wall thickness, but only when male and female were considered separately. Dose administration using a formula based on these relationships yielded a considerably narrower range of information densities than other methods. Preliminary results extending the attenuation estimation to include lung tissue will be presented. ***Conclusion:*** The use of a dose formula for myocardial perfusion imaging based on thoracic circumference and gender has potential to standardize image quality and enable significant radiation dose reduction.

EP-1457

Evaluation of Radiation Extremity Exposure in^{177}Lu PSMA(IT) Production and Quality Control Using Two Ring Dosimeters

T. Häkkinen[1], *S. Pellinen*[1], *M. Hakulinen*[1,2];
[1]*Wellbeing services county of North Savo, Kuopio university hospital, Kuopio, FINLAND,* [2]*Department of Technical Physics, University of Eastern Finland, Kuopio, FINLAND.*

Aim/Introduction: The number of ^{177}Lu treatments has increased notably at Kuopio University Hospital in recent years (from 99 treatments in 2022 to 161 treatments in 2024). Aim of this study was to evaluate overall radiation safety and extremity exposure associated with ^{177}Lu processes. The goal was to assess the radiation dose received during ^{177}Lu PSMA(IT) production and quality control (QC), and to determine its contribution relative to overall extremity radiation exposure. ***Materials and Methods:*** This study assesses extremity radiation doses (Hp (0.07)) received by radiopharmacy personnel during the 177Lu PSMA(IT) process (divided into production and QC) using two ring dosimeters (TLD). One ring dosimeter was worn on the dominant hand during all radiopharmaceutical processes (18F, 68Ga, 177Lu and 15O). Second ring dosimeter was worn on the non-dominant hand only during 177Lu processes. Dose data were collected from 30 177Lu PSMA(IT) production batches (64 patient doses) over 6 months' time among five (5) technicians. The recorded extremity doses were compared to the doses recorded from all radiopharmaceutical production batches during same period. Recorded radiation doses from 177Lu PSMA(IT) productions were normalized both for number of production batches as well for number of produced patient doses. ***Results:*** Contribution of 177Lu total extremity exposure to the radiation exposure recorded from all radiopharmaceutical processes was in average 31,2 % (range 18,5-48,9 %). The distribution of total extremity radiation doses from all 177Lu processes was 78.9% from production and 21.1% from QC. Average dose from 177Lu PSMA(IT) production was 293 µSv (range 150-430 µSv) per batch and 132 µSv (range 60-220 µSv) per patient dose. Average dose from QC was 98 µSv (range 20-180 µSv) per batch and 43 µSv (range 10-90 µSv) per patient dose. ***Conclusion:*** These results confirm that existing radiation safety protocols and operation model effectively minimize occupational exposure in our 177Lu PSMA productions. Consistency across different production processes had variety. Variation in measured hand doses may result from differences in individual working practices, such as hand positioning and time spend handling radioactive substances. Additionally, factors like familiarity with the procedure, workflow, habits and adherence to safety protocols may influence level of radiation exposure. Hand doses during QC process were lower compared to production. This is likely due to the smaller activities and shorter manual handling time in QC -laboratory. Continued radiation monitoring and adherence to best practices will ensure the safety of personnel working with 177Lu and other radiopharmaceuticals.

EP-1458

Implementation for quantitative SPECT imaging of At-211: Becquerel calibration with a germanium semiconductor

T. Kamiya[1], *H. Sasaki*[1], *T. Watabe*[2], *S. Naka*[3], *K. Ooe*[4], *Y. Shirakami*[4], *I. Yabata*[1], *K. Isohashi*[2], *K. Fujino*[1];
[1]*Department of Medical Technology, The University of Osaka Hospital, Suita, JAPAN,* [2]*Department of Radiology, Graduate School of Medicine, The University of Osaka, Suita, JAPAN,* [3]*Department of Pharmacy, The University of Osaka Hospital, Suita, JAPAN,* [4]*Institute for Radiation Sciences, The University of Osaka, Suita, JAPAN.*

Aim/Introduction: In the dosimetry of targeted alpha therapy (TAT), it is essential to ensure the quantitative accuracy of radioactivity measurement such as administered dose of radiopharmaceuticals, patient samples (blood and urine) and voxel value of SPECT images. Astatine-211 (At-211, half-life: 7.2 hours) is an alpha-emitter which can be applied for TAT of several malignant tumors. However, At-211 is not commonly used in clinical examinations, and there is no nuclide setting in the dose calibrators or SPECT/CT scanners. The aim of this study was to establish the becquerel calibration factor among the various devices used for TAT. ***Materials and Methods:*** Germanium semiconductor detector (GE2020: Million Technologies), calibrated with a Ba-133 calibration source, was used as a quantitative reference. Calibration factors were determined for dose calibrators, a well counter, and SPECT/CT scanners by adjusting their measurements to match the germanium semiconductor detector. Three CRC-55tR dose calibrators (Capintec) and one JDC-1712 well counter (ALOKA) were evaluated. SPECT/CT images of cylindrical phantom (6600 mL: Data Spectrum) were acquired by Symbia Intevo 6 (SIEMENS), Discovery NM/CT 870 CZT (GE) and VERITON-CT (Spectrum Dynamics Medical). The energy window was set at 79 keV ± 20% targeting the characteristic X-rays emitted from the daughter nuclide of Polonium-211 (half-life: 0.52 seconds). ***Results:*** The calibration factor of the dose calibrator using a 20 mL glass vial was 77, while that of the well counter was 0.0243 ± 0.008 (kBq/cps). The errors of standardized uptake value were less than 5% for all SPECT/CT scanners. ***Conclusion:*** This phantom based study established the becquerel calibration factors among various devices, enabling accurate quantitative evaluation in TAT with At-211 radiopharmaceuticals. In addition, the At-211 SPECT images using CZT SPECT/CT scanner were successfully optimized, showing performance comparable to conventional NaI(Tl) dual detector systems. ***References:*** Desmonts C, Bouthiba MA, Enilorac B, et al. Evaluation of a new multipurpose whole-body CzT-based camera: comparison with a dual-head Anger camera and first clinical images. EJNMMI Phys. 2020;7:18.

EP-1459

Kidney Dosimetry in mCRPC Patients Undergoing Lu-177 PSMA Therapy: Insights from a Single-Center Study

R. Mishra, *A. Nazar, S. Barai, M. Ora, A. Arya, M. Dixit, P. Pradhan, S. Dhania;*
Sanjay Gandhi Post Graduate Institute of Medical Sciences, Lucknow, INDIA.

Aim/Introduction: To evaluate kidney absorbed dose, residence time, and their correlations with patient characteristics in mCRPC patients undergoing Lu-177 PSMA therapy. Lutetium-177 (Lu-177) PSMA therapy is a promising treatment for metastatic castration-resistant prostate cancer (mCRPC). However, kidney dosimetry is critical to ensure safety, given the kidneys' radiosensitivity. This

study quantifies kidney absorbed doses and assesses variability in mCRPC patients receiving Lu-177 PSMA therapy. ***Materials and Methods:*** Ten dosimetry records from eight mCRPC patients (mean age: 65.2 ± 8.7 years; mean weight: 68.4 ± 18.7 kg) treated with Lu-177 PSMA (mean activity: 6357.5 ± 586.7 MBq) were analyzed. Kidney doses (mGy/MBq) and cumulative doses (Gy) were calculated using SPECT/CT-based dosimetry and newly installed software system, with residence times derived from normalized cumulative activity. Descriptive statistics, inter- and intra-patient variability, and Pearson correlations with age, weight, and administered activity were assessed. ***Results:*** Mean kidney dose was 0.476 ± 0.418 mGy/MBq (median: 0.336, range: 0.218-1.589), and mean cumulative dose was 2.62 ± 2.29 Gy (median: 2.20, range: 1.3-8.97). Residence times ranged from 0.78 to 5.69 Bq-hr/Bq (mean: 1.63 ± 1.42). One patient exhibited an outlier dose (8.97 Gy) due to prolonged residence time (5.69 Bq-hr/Bq). Excluding this outlier, mean dose was 0.319 ± 0.068 mGy/MBq and cumulative dose was 2.01 ± 0.46 Gy, aligning with literature (0.39-0.67 mGy/MBq). Inter-patient variability was high (CV: 87.3%), but reduced to 21.3% without the outlier. Intra-patient variability ranged from 2.3% to 19.3% across cycles. Kidney dose correlated strongly with residence time ($r = 0.999$, $p < 0.001$) and moderately with administered activity ($r = 0.65$, $p = 0.04$), but not with age or weight. ***Conclusion:*** Kidney doses in Lu-177 PSMA therapy are generally within safe limits, but significant inter-patient variability and occasional high doses highlight the need for personalized dosimetry. Prolonged residence times may increase nephrotoxicity risk, warranting further investigation into predictive factors and simplified dosimetry protocols.

EP-1460

Assessment of collimator-detector-response for absolute quantification and dosimetry of 188Re- microsphere SIRT in hepatocellular carcinoma using quantitative SPECT/CT: Addressing the technical challenges in theranostic imaging

K. Kaur, *S. Chopra, J. Shukla, R. Kumar, V. D. Chadha, B. R.Mittal;*
Postgraduate Institute of Medical Education and Research, Chandigarh, INDIA.

Aim/Introduction: Absolute quantification of radiopharmaceutical is essential for dosimetry analysis in theranostic. An accurate model of the collimator-detector-response (CDR) is required since image quantification takes into account the probability of the photon emitted from the source and its contribution to voxel of the resulting image. Aim of the study was to analyse the effect of CDR and Scatter in image quantification using different collimators and estimate absorbed dose in hepatocellular carcinoma (HCC) patients receiving 188Re-microsphere selective intra-radionuclide therapy (SIRT) based on quantitative SPECT/CT ***Materials and Methods:*** The different phantom studies were performed in the Department of Nuclear Medicine, PGIMER, Chandigarh. Quantitative SPECT/CT was acquired with 120 projections (20s/projection) for theranostic radionuclide 188-Rhenium with appropriate photopeak and scatter window. The acquired data was reconstructed and analysed in three set. In First set corrections for CDR, Scatter and attenuation were applied in reconstruction. In second set recon was done with only AC and in third set no corrections were applied. Quantitative accuracy in terms of activity concentration recovery was assessed as a function of collimator- to -detector response at varying distances of detector from phantom as well as for different set of collimators available i.e LEHR and HEGP. A single time point regional quantitative SPECT/CT was acquired in 10 HCC patients receiving 188Re-microsphere SIRT and analysed for image based absorbed doses ***Results:*** In first set, absolute activity concentration were measured to be within 11% (HEGP) and 32% (LEHR) of the expected value. In the second set, there was significant contribution of scatter photon and the activity concentration were overestimated since CDR and SC were not applied. In third set activity concentration was erroneously estimated. This trend was observed for both the sets of collimators, but HEGP was observed to be more accurate in 188Re-quantification. The first set of CDR modelling was then used for activity quantification and dosimetry calculations in HCC patients undergoing 188Re-microsphere SIRT which also correlated with the clinical response ***Conclusion:*** The tested device and reconstruction algorithm modeled with correction for CDR, scatter, attenuation and resolution recovery provided accurate activity recovery within 11% of expected values; these performances are comparable to current generation PET/CT systems. Quantitative accuracy was maintained with varying distance from detector since CDR was modeled in the reconstruction algorithm. For precise quantification and dosimetry of 188Re-microsphere uptake in HCC patients, HEGP collimator is recommended.

EP-1461

Biodistribution, dosimetry, and pharmacokinetics of ^{68}Ga-PSFA-01: First-in-human evaluation of a dual-target PET tracer

J. Li, *Y. Li, X. Zhang, H. Pang;*
The First Affiliated Hospital of Chongqing Medical University, ChongQing, CHINA.

Aim/Introduction: Prostate-specific membrane antigen (PSMA) PET is vital for assessing prostate cancer (PCa) recurrence and guiding biopsy, yet its accuracy remains limited. Fibroblast activation protein (FAP) is a promising theranostic target, especially for PCa cases with low or no PSMA expression. However, single-target receptors have clinical limitations. Given the heterogeneity of PCa and the need to enhance PET/CT tumor-targeting sensitivity, Wang et al. synthesized a FAP- and PSMA inhibitor-based heterodimer, ^{68}Ga-PSFA-01. This study aimed to assess its biodistribution, dosimetry, and pharmacokinetics in humans. ***Materials and Methods:*** Six patients with a history of PCa were intravenously injected with ^{68}Ga-PSFA-01. PET/CT scans were acquired at 0.5, 1, 1.5, and 2 hours post-injection. OLINDA/EXM 2.1 software was used to calculate absorbed organ and effective dose estimates based on up to 25 regions of interest defined on CT images and applied to the co-registered PET images. Time-activity curves (TACs) per organ were determined, and mean organ-absorbed doses and effective doses were calculated using the MIRD schema. Effective doses (EDs) were estimated according to ICRP103. Additionally, three healthy volunteers underwent one-hour dynamic PET/MR imaging. Using the iliac artery as the input function, a two-compartment pharmacokinetic model was applied to estimate the pharmacokinetic parameters of ^{68}Ga-PSFA-01. ***Results:*** The mean injected activity of ^{68}Ga-PSFA-01 was 139 ± 0.68 MBq (range: 114.7-148.0 MBq), with no tracer-related adverse effects observed. ^{68}Ga-PSFA-01 exhibited extracellular distribution with predominantly rapid renal clearance. The highest absorbed doses were observed in the kidneys (0.426±0.070 mGy/MBq) and liver (0.272±0.0142 mGy/MBq), while the dose to the urinary bladder wall was 0.103±0.0416 mGy/MBq,. Whole body effective dose was 1.815±0.38 mSv/MBq. Pharmacokinetic analysis revealed that ^{68}Ga-PSFA-01 displayed rapid distribution, with bladder counts increasing significantly over time, consistent with the radiopharmaceutical metabolic characteristics of kidney excretion and subsequent accumulated in the bladder. It also demonstrated sustained accumulation in prostate tissue. The mean K_3/K_4 ratio of 1.81 (greater than 1) indicates strong tissue binding affinity and efficient target in engagement. ***Conclusion:*** Administration of 139 ± 0.68 MBq of ^{68}Ga-PSFA-01 yields an acceptable radiation burden (1.815 ± 0.38 mSv) in compliance with ICRP103 recommendations. The tracer demonstrates favorable pharmacokinetics and safety,

warranting further clinical development. Particular attention should be paid to radiation exposure in the kidneys and spleen during therapeutic applications. ***References:*** 1. Li Y, Guan L,Pang H. Dual targeting PET tracer [68Ga]Ga-PSFA-01 in patients with prostate cancers: A pilot exploratory study. Theranostics. 2025 Mar 10;15(9):4124-4134. doi: 10.7150/thno.108676.

EP-1462

Enhancing Operational Efficiency and Patient Care: The Aerosol Solution for Lung Ventilation Imaging

A. Moura, *C. Rodrigues;*
Imperial College NHS Healthcare Trust, London, UNITED KINGDOM.

Aim/Introduction: In our department, Krypton-81m was use for lung ventilation studies. However, inconsistent production resulted in frequent same-day cancellations, significantly disrupting departmental operations and adversely affecting patient experience, diagnostic accuracy, and clinical management. Following a thorough evaluation of alternatives, we adopted technetium-99m-labelled aerosol (Technegas) for ventilation imaging, leading to a comprehensive overhaul of our departmental procedures. ***Materials and Methods:*** Implementation of Technegas required acquisition of the Technegas Plus System, along with other essential consumables. It also required the development of comprehensive SOPs regarding generator operation and gaseous and solid waste handling and storage. Technologist team underwent training in preparation, administration, imaging protocols, and image-quality assessment for the new agent. Workflow modifications included generator preparation, crucible dosing with ethanol, patient inhalation, ventilation positioning, and simultaneous preparation of the MAA dose for immediate post-ventilation injection and count verification. Despite a modest increase in scanner time per patient, efficient coordination and scheduling maintained the original booking slots. ***Results:*** Out of a total of 14 staff members, 4 received direct training from the manufacturer, which was subsequently cascaded to the rest of the team. In-house training was established focusing on imaging acquisition and processing. To date, 92% of staff have completed this training. Financially, the switch has also been successful. To date, the department has saved approximately £4,000, already factoring in the cost of acquiring the delivery system. Although generator failures occasionally lowered expenses, they frequently disrupted patient care and reduced scanner availability. The department has allocated specific time slots for Pulmonary Hypertension clinics, enabling patients from across England and Wales to complete all necessary diagnostic procedures in a single visit. However, due to the unreliability of Kr-81m generator production, some patients required multiple visits, and certain scans were missed entirely because patients were unable to return. The introduction of Technegas has improved scheduling flexibility and helped reduce the waiting list for all patients. ***Conclusion:*** By adopting this technetium99m-labelled aerosol for pulmonary ventilation imaging, we resolved the unreliability of the Kr81m generator production ensuring a sustainable solution. This transition improved service efficiency, reduced referral-to-treatment times, and enhanced patient care at Hammersmith Hospital. Maintaining imaging standards and service continuity led to increased satisfaction among patients and referring clinicians. Consequently, his is a service that the technologist team is proud of providing. This initiative demonstrates a proactive response to resource constraints and underscores our commitment to patient-centred care and operational excellence.

EP-1463

An Innovative Design for Patient-Centred Care: Establishing the First Molecular Imaging and Therapy Center in Regional New Zealand

P. Lamerton;
Molecular Imaging and Therapy, Canopy Imaging, Hastings, NEW ZEALAND.

Aim/Introduction: New Zealand is an island country in the South Pacific Ocean approximately 1600 km southeast of Australia comprising of two main islands with a population of 5.25 million. Regional New Zealand can present unique challenges let alone the region of Hawkes Bay on the East Coast of the North Island. This presentation will highlight how we have successfully navigated through innovative design and a patient-centred approach to bring the first Molecular Imaging and Therapy Center to regional New Zealand. ***Materials and Methods:*** The Greenfield Molecular Imaging and Therapy Centre, introduces a transformative approach to healthcare facility planning with a shift away from the typical clinical atmosphere. The design elements integrated cultural awareness and cutting-edge molecular and therapy technologies to prioritise patient comfort and well-being. ***Results:*** Collaboration with our health physicist and Hot lab design and planning team was instrumental in the optimal shielding solutions to ensure safety and radiation protection. In addition, due to global shortages in nuclear medicine technologists impacting on New Zealand, special considerations in the design were made to ensure minimal radiation dose to the clinical staff. ***Conclusion:*** The layout optimises patient flow with attention given to features that enhance staff accessibility and operational efficiency without compromising the patient experience. The imagery shown will highlight the delicate balance between safety and operational needs with a calming and less clinical aesthetic feel that promotes a more positive experience for patients. Furthermore, we will show the incorporation of sustainability and features that have enabled the future proofing of the clinic. Even though the presentation shared is unique to New Zealand, it is beneficial in a global context due to the rapid developments in molecular imaging and therapies.

Aalbersberg, E. **OP-702,** EP-1432, OP-884
Aarntzen, E. H. J. G. EPS-082, OP-170, OP-289, OP-796, OP-885
Aarts, R. EP-1188
A. A Silveira, N. EP-0262
Abadi, P. TEPS-003
Abadie-Lacourtoisie, S. OP-603
Abas, M. EP-1327, **EP-1328**
Abayazid, M. EP-1145
Abbasi, M. EP-1138, EPS-289
Abbasian, H. EP-0568
Abbatini, G. **EP-0906**
Abdelfattah, F. E. EP-0304
Abdelhafez, Y. EP-0466, OP-222, EPS-032
Abdelrazek, S. **EP-0896**, **EPS-257**
Abdi, M. **EP-1076**
Abdi, S. OP-023
Abdollahi, H. EP-1101, **OP-420**
Abdolmaleki, M. EPS-289
Abdullah Suhaimi, S. EP-0203
Abdul Onny, M. **EP-0416**, **OP-243**
Abdul Rahman, R. EP-0416
Abdul Razak, H. R. TEPS-019
Abe, H. EP-0676, **EP-1059**, OP-719
Abe, T. EP-0303
Abedi, J. EP-0066, EP-0128, **EPS-136**
Abele, J. EPS-075
Abell, G. **TEPS-010**
Abella-Serra, A. EP-0392, EP-0437
Abenavoli, E. M. **EP-0230**, **EP-0467**, EPS-272, OP-033, OP-321, OP-324
A. Bezverkhniaia, E. OP-320
Abgral, R. **EPS-230**
Abikhzer, G. OP-551, OP-871
Aboagye, E. O. EP-1052
Abolhosseini Shahrnoy, A. EP-0066, EP-0038, **EP-0146**, EP-0888, EP-1149, EP-1168
Abou, D. **EPS-138**
Aboussabr, M. EP-1290, **EP-1301**, **EP-1302**, EP-1325
Abouzayed, A. EP-1104, EP-0137, OP-087
Abouzian, S. EP-0545
Abradelo De Usera, M. EP-0328
Abreu, F. EP-0772, EP-1255, EP-1265
Abrunhosa, A. EPS-061
Abubakar, S. EP-0380
Acampa, W. OP-684
Acar, L. EP-1008
Acar Tayyar, M. N. EP-0858, **EP-0902**, EP-1276, EP-1371
Aceto, N. OP-673, OP-677
Achtziger, S. OP-376
Acikalin, M. F. EP-0192
Ackermann, U. EPS-003
Aço, J. **EP-0521**
Adam, B. **EP-0829**
Adam, J. A. OP-622
Adamantiadis, S. **EP-0461**, **EP-0893**
Adamczewski, Z. EP-0360, EP-0714, EP-0747, EP-1232, EP-1336
Adame, K. EPS-192
Adarve Castro, A. EP-1229
Adeniyi, A. OP-517, EP-0162, EPS-194
Ade-Ojo, A. OP-697
Adesanya, O. EP-0471, EP-0911
Adıgüzel, H. EPS-191
Adhikari, K. EP-0102
Adili, D. **OP-692**
Aditya, B. EP-0208
Afanasiev, S. EP-0617
Afonso, J. EP-0134
Afonso de Matos, A. **EP-1434**
Afshari, N. EP-1350
Afshar-Oromieh, A. EP-1148, EP-0409, EP-0423, EP-1090, EPS-240, OP-461, OP-601, OP-823
Aftahy, A. OP-606
Aftimos, P. OP-111
Agarwal, A. EP-0985
Agarwal, N. OP-674
Agarwala, S. EPS-209, EPS-217
Agboton, F. EP-1217
Aggarwal, A. EP-0071, **EP-0159**, EP-0159
Aghaee, A. **EP-0348**, EP-0570, **EP-1002**, EP-1346, EP-1348, EP-1349, EP-1350, EP-1352, EP-1353, **EP-1356**, EP-1362, EP-1363, EP-1369, EPS-22, **OP-241**, **OP-242**
Aghakhanolia, N. **EP-0994**
Aghamohammadi, J. EP-1108
Agha Mohammadi Sareshgi, R. TEPS-013
Aghapour Zangeneh, F. **EP-0614**, EP-0933, OP-685
Agić-Bilalagić, S. EP-1436
Agnello, T. EP-1223, EP-1234, EP-1245, EP-1267
Agnew, D. EPS-018
Agoro, L. OP-625
Agosti, A. **OP-055**
Agostini, D. EP-0581, OP-500
Agostini, S. EP-0234, OP-613
Agrawal, A. EP-0266, EP-0885, EP-1445
Agrawal, N. OP-797
Agrawal, V. OP-525
Ågren, H. EP-0118, OP-459
Agrigoroaie, L. EPS-199
Agstam, S. EP-0583
Aguadé-Bruix, S. EP-0611
Aguiar, P. EP-0999, EPS-236, OP-093
Aguirre, N. OP-279
Ahenkorah, S. OP-350
Şahin, Ö. F. EP-0272, EP-0295
Şahin, O. E. EP-0857, EP-0901
Åhlström, A. OP-595
Ahmad Fadzil, M. EP-0416
Ahmadi, M. OP-022, **EP-1349**, **EP-1357**, **EP-1360**
Ahmadi Bidakhvidi, N. **OP-067**
Ahmad Saad, F. EP-0203
Ahmed, A. EP-0810
Ahmed, H. EP-0783
Ahmed, N. EP-1424, EP-1425, EP-1428
Ahmed, T. EP-0818
Ahokas, T. EPS-097
Ahrari, S. **EP-1055**, **OP-225**
Ahuja, P. OP-714
Ai, L. EP-0155
Aigner, C. OP-172
Ailles, L. EP-0081
Aina Monterde, V. **EP-0760**
Airaksinen, A. EP-0114
Airò Farulla, L. S. EP-0427, OP-484, OP-556, EP-0269, **EP-0418, EP-0419**, EP-0470, EPS-228
Aishwarya, M. EP-0285, EP-0880
Aisiopoulos, I. EP-0820
Ait-Mohand, S. EP-0029
Ait Sahel, O. EP-1290
Aizawa, R. EPS-255
Ajila, T. EPS-134
Ajimizu, H. EP-0540
Ajuria Illarramendi, O. **EP-0530**, EP-0565, EP-0821, OP-478
Akad Soyer, N. EP-0479
Akashi-Tanaka, S. EP-0635, EPS-095
Akbari, M. EP-0937, EP-1108, EP-0888, EP-1149
Akbarian, R. OP-162, OP-164
Akbulut, A. EP-0443, EP-0763, EP-1271, EP-1277, EP-1373
Akcay, K. OP-476, **EPS-191**
Akdemir, O. EPS-115
Akdemir, Ü. Ö. EP-0261, EP-0669, OP-175, **EP-0638**, **EP-0661**
Akdogan, M. OP-856
Akgun, A. EP-0246
Akgün, E. EP-0272, EP-0295, EP-0723
Akhter, A. **EP-1204**, **EP-1208**
Akhurst, T. EPS-119
Akil, A. **EP-0857**
Akil Engblom, S. EP-0582, EP-0607, EPS-096
Akiya, N. EP-1157, **EP-1453**, EP-1454
Akkaş, B. E. EP-0486, EP-0633, OP-054
Akkapulu, N. EP-0287
Akkas, B. E. EP-0844, EP-1310, EP-1367, EP-0840, OP-857
Akkus Gunduz, P. EPS-260
Ak Sivrikoz, I. **EP-0192**
Aksu, A. EP-0210, EP-0228, EP-0296, EP-0422
Aksu, O. B. EP-0441
Aksu, S. **EP-0464**
Aksu, Ü. **EP-0486**, **OP-054**
Aktürk, Y. OP-497
Alabedi, M. EP-0413
Alacacioglu, A. EP-0296, EP-0228
Alachouzos, G. EPS-195, OP-515
Alagöl, F. OP-386
Alagoz, E. EPS-260
Alahmad, T. EP-0928
Alam, H. EP-1410

Alami, D. **EP-1290**, EP-1301, EP-1302, EP-1325
Alamo, J. TEPS-021
Alan, N. EPS-191
Alanís-Bernal, M. EP-0685
Alano, R. EPS-192
Alan Selcuk, N. OP-856, OP-476
Alavi, A. EP-0627
Alawadhi, E. EP-0928, **EP-1416**, **EP-1451**
Al-Balooshi, B. EP-0345
Al-Balushi, A. **EP-1136**
Albano, D. EP-0206, OP-105, OP-324, OP-868
Albattat, K. **OP-171**
Albe, L. EP-1017
Albergueiro, R. EP-0599, EP-0716, **EPS-091**, EPS-300
Alberico, I. **EP-0044**
Alberini, J.-L. OP-551
Albert, N. L. EP-0022, EP-0047, EP-0183, EP-0711, EP-0886, EP-0936, EP-1035, EPS-124, EPS-125, EPS-239, OP-609, OP-610, OP-775
Albiniak, L. OP-702
Albrecht-Beste, E. EP-0219
Albuquerque, A. EP-0765, OP-636
Al-Busaidi, A. EP-0181, EP-0414, EP-0442
Alcaro, F. EP-0010
Alçın, G. EP-0272, EP-0295, EP-0723
Alcolea, D. OP-442
Aldigeri, R. OP-549
Aldousari, A. EP-1416
Alegre-Canals, O. EPS-022
Alejandre Lafont, M. OP-361
Aleksa, G. EP-0361, EP-0365
Aleksyniene, R. OP-474
Alencar, B. EP-1223, EP-1234, EP-1245, EP-1267
Alenezi, A. EP-1451
Alenezi, B. **OP-888**
Alessi, A. OP-298, OP-384, EP-0271, EP-0715, EP-1406
Alevroudis, E. OP-598
Alexander Jäck, A. EP-0691
Alfaiate, M. **EP-1083**
Alfano, B. EP-0639
Alfonso, S. EP-0551
Alfredeen, H. EP-0064, EPS-154
Alfteimi, A. EP-0080
Algmlas, F. EP-0739, EPS-279
Al-Haidar, S. EP-0007, OP-025
Alharbi, M. EP-0739, EPS-279
Alhashim, M. **EP-0413**
Alhazza, S. EP-0739, EPS-279
Alhuseinalkhudhur, A. **EP-0289**
Ali, L. EP-0069
Ali, N. EP-0416, OP-243
Ali, T. EP-1091
Alibayli, G. EP-0453
Al-Ibraheem, A. OP-711, OP-873
Alibrandi, A. OP-380
Alic, L. EP-0010
Alipour, R. EP-0830, OP-323
Aliyev, J. EP-0453
Aliyeva, N. EP-0453
Al-Jnabi, H. **EP-0718**
Alkassis, S. EP-0208
Allan, S. EP-0822
Allard, M. OP-280
Allegri, V. EP-0310, EP-0311
Allegrini, O. EP-1162
Allen, K. TEPS-018
Allen-Auerbach, M. EPS-162
Allmann, A. EP-1128
Allmann, J. OP-364
Allouche, S. OP-838
Allouche-Arnon, H. EP-0036
Almaguel, F. **EP-0822**
Al Makhmari, N. **EP-0526**
Al Mallah, M. EPS-075, OP-679
Al-Mandhari, Z. EP-0181, EP-0414
Al Mansour, L. EP-0787, **OP-542**
Al-Marrani, A. EP-1250
Almasi, S. OP-734
Al Maymani, N. EP-0526, EP-1136
Almeida, E. EPS-235
Almeida, M. **EP-1133**
Almeida Romera, N. EP-0374
Almquist, M. EP-0733
Almutairi, A. EP-1416
Alongi, P. **EP-0369**
Alonso, J. C. EP-0704, EP-0668
Alonso, T. EP-0792
Alonso Farto, J. EP-0798, EP-0841, OP-485
Alonso López, C. EP-0328
Alonso Rodríguez, M. EP-0549, EP-0612, EP-0579
Alper, E. EP-1321
Alqabandi, M. EP-0928
Alqahtani, M. **EP-0753**
Alqallaf, Z. EP-0928
Alrahim, A. EP-0383
Al-Raii, T. EP-1136
Al Rashdi, S. EP-0526
Al Riyami, K. EP-0181, EP-0414, EP-0526
Alsabbagh, R. EP-0857
Al-Saidi, H. EP-1136
Alsalah, R. EP-0739, EPS-279
Alsfasser, G. OP-779
Alshehri, A. **EP-1153**, **EP-1419**
Alsugair, A. **EP-0274**
AlSulaiman, S. OP-162, OP-164
Al Tabaa, Y. **OP-227**
Altena, R. OP-596
Altinyay, M. EP-0383
Altmayer, S. EPS-251
Altunay, B. EP-0109, **OP-761**
Aluicio-Sarduy, E. EP-0162, EP-1165, EPS-194, **OP-583**, OP-586
Alvarez, M. EPS-275
Alvarez, S. **EP-0668**, **EP-0704**
Álvarez Alonso, A. EP-0319, OP-050
Álvarez Amigo, A. EP-0319, OP-050
Álvarez Carriles, J. OP-050
Álvarez-Doral, J. EP-0776
Álvarez Lara, S. EP-0798, EP-0841
Alvarez-Larrán, A. EP-0776
Álvarez Martínez, M. OP-050
Alvarez Mena, N. **EP-0397**, EP-0579, EP-0612, EP-0613 OP-057, OP-854, EP-0833
Alvarez Moreno, M. EP-0819, EP-1337, EPS-273
Álvarez Pérez, J. EP-0710, OP-481
Álvarez Ruiz, S. EP-0760
Alves, F. EP-0383
Alves, T. EP-1203, EP-1306, EP-1324, EP-1342
Alves da Silva, F. **EP-0092**
Alwan, M. EPS-075
Alwers, S. EP-0794
Alwuhaib, E. EP-0413
Amadori, M. EP-1159, OP-042
Amador-Navarrete, A. EP-0850
Amaral, H. OP-471
Amaral, K. **EP-0337**
Amareller, D. OP-033
Amargier-Barrial, S. OP-453
Amberg, W. OP-458
Ambrosini, V. EP-0310, EP-0311, EP-1268, OP-246, OP-248
Ambrosio, M. R. EP-0893
Ambros J. Beer, A. EP-1119
Ameen, A. EP-0810
Amelio, D. OP-613
Amerein, A. OP-863
Amghar, M. EP-0132
Amico, J. EPS-137, OP-584
Amiconi, G. EP-1287
Amimour, A. EP-0756, EP-1217, EPS-212
Amin, M. T. EP-0818
Amini, E. **EP-0442**, **EP-1012**
Amini, H. EP-1351
Amir Hassan, S. EP-0416
Amirian, M. **OP-160**, OP-528
Amon, M. EP-1148
Amorim, B. EP-1234, EP-1245, EP-1267, EP-0223, EP-0536
Amoroso, F. EPS-195, OP-515, **EPS-002**, **OP-520**
Amo Salas, M. EP-0358, EP-0401, EP-1393
Amosova, I. EP-0402, EPS-265, OP-473
Amparore, D. EP-0370
Amrane, K. EPS-230
Amthauer, H. EP-1092, OP-429
Şan, H. EP-0605
An, R. EP-0107, EP-0484, EPS-053, EPS-059,

OP-020,OP-274, OP-419
An, S. **EP-1233**
An, Y. S. EP-0024
Ananda, F. **EP-1107**
Ananta, M. OP-870
Anastasopoulou, A. EP-1379
Anda, E. OP-666
Anda Apiñaniz, E. EP-1147
Andersen, C. K. EP-0732
Andersen, F. L. EP-0219, EP-0766, EP-0957, EP-0981, EP-0990, OP-261, OP-464, OP-474, EP-0709
Andersen, K. F. OP-261
Andersen, P. A. EP-0219
Andersen, T. L. EP-0172, EP-0322, EP-0957, EP-0981 EP-0990, EP-0709, **EP-1005**
Andersson, M. OP-091, **OP-592**
Ando, A. EP-1453
Andrade-Mejía, P. EP-0656, EP-0673
André, C. OP-022
Andrearczyk, V. OP-160, OP-528
Andreoiu, C. EPS-139
Andres-Gracia, A. EP-0552
Andrews, I. EP-0993
Andrews, L. EP-1395
Andrews, R. EPS-134
Andrini, E. EP-0310, EP-0311, EP-1268
Andy, C. EPS-134
Aneheim, E. EP-0049, **OP-092**
Anestis, D. EPS-198
Angelidis, G. **EP-0591**, EP-0675, OP-557
Angiolillo Grau, S. EP-0387, EP-0887
Anizan, N. OP-536
Anjos, B. EP-0973, EPS-235
Ankers, Z. EP-0314
Annarumma, I. EP-0826, EP-1258, EP-1376, EP-1383, EP-1412
Annovazzi, A. EP-0206
Annunziata, S. EP-0010, EP-0497, EP-1398, EP-1399, **OP-708**, OP-720, **OP-818**, OP-891
Anreus, A. TEPS-021
Ansquer, C. OP-429
Antevski, B. EP-0736
Antic Nikolic, A. **OP-600**
Antke, C. EP-0703
Antohie, C.-M. EP-1309
Antonacci, F. EP-0227, OP-168
Antonevskaya, T. **EP-0755**
Antonopoulos, A. EP-1417
Antons, M. EPS-005, **EP-0037**
Anttinen, M. OP-328
Antunes, I. F. OP-149, OP-452, OP-515, EP-0011
Antunovic, L. EP-0254, EP-0534, OP-298, OP-326, OP-706
Anzai, Y. EP-0648
Aoki, T. OP-208
Aoyama, S. EP-0939
Apaza, L. EP-1344, EP-1344
Apostolopoulos, D. **EP-1074**
Apostolopoulos, I. EP-1074
Apostolopoulou, A. **EPS-153**, **OP-183**
Apostolova, I. EP-1026
Appel, L. EPS-128
April, G. EPS-181, OP-428, OP-534, OP-588
Apro, K. EP-0180
Arabi, H. EP-0345, EP-0413, EP-1281
Arakawa, R. EP-0108
Arapatzi, C. EP-0065
Aras, T. OP-609
Aravindh, A. EP-0559
Araz, M. **EP-0333**, EP-0354, **EP-0441**, EP-0806
Arbizu, J. EP-0792, OP-430, EPS-117, OP-302, OP-307, OP-378, OP-446
Arca, B. **EP-1314**, **OP-259**
Arcay Ozturk, A. OP-111, OP-169, **OP-470**
Archacka, K. EP-0013
Archer, E. OP-620
Archontaki, A. T. EP-0574
Ardeshirzadeh, A. EP-1357
Ardila, E. EP-0668, EP-0704
Ardila, J. EP-0792, OP-430, EP-0668
Ardila Manjarez, E. EP-0841, EP-0798
Ardila Mantilla, J. EP-0798, EP-0841
Ardjo Pawiro, S. EP-1119, EPS-183
Argalia, G. **OP-558**, OP-558
Argenti, L. OP-725
Argiroffi, G. EP-1146
Argon, A. M. EP-0428, EP-0479, EP-0366
Arheden, H. EP-0582
Aricò, D. EP-0363, EP-0206
Arik, E. EP-0837
Arikok, A. T. EP-1225
Ariño, H. EP-0685
Arino, I. **EPS-131**
Arisawa, T. EP-0676, EP-1059, OP-301, OP-719
Ariztia, J. **EP-0096**, OP-351
Arık, E. EP-1127, EP-1141
Arlicot, N. OP-718
Armesto, A. EP-1403
Armijo Astrain, J. OP-784
Armstrong, I. **EP-0959**
Arnaboldi, M. EP-0175, EPS-122
Arnaldi, D. EP-0681, EP-0683, EP-0686, OP-669
Arnautović-Halimić, A. EP-1436
Arndt, C. OP-154
Arnone, A. EP-0206, OP-105
Arnott, M. OP-697
Arntz, M. J. OP-855
Arora, G. EP-0265, EP-0301, EP-0559, OP-861
Aroui Luquin, T. EP-0522, EP-0866, EPS-249
Arraut Serrano, F. EP-0462, EP-1262, EP-1263
Arredondo, F. EP-0157
Arriaga Contreras, A. **EP-0816**, EP-0909
Arridge, S. EP-0996
Arsanjani, R. EP-0304
Arsenault, F. EPS-181, OP-428, OP-534, OP-588
Arslan, D. OP-543
Arslan, E. EP-0272, EP-0295, EP-0723
Arslan, M. EP-0640, EP-0840, EP-0843, OP-857
Arsos, G. EP-1341, EP-1364, EP-1370, EP-1374, **EP-1415**, EPS-027
Artesani, A. **EP-1062**
Artigas, C. OP-537, OP-670
Artiko, V. EP-0898, EP-1240, OP-479
Arunachalam Ragupathi, V. **EP-0177**, **EP-0882**
Arutinov, D. OP-284
Arya, A. EP-0544, EP-0813, EP-1459
Aryana, K. EP-0348, EP-0548, EP-0891, EP-1339, EP-1354, EP-1356, OP-109, OP-241, OP-242
Arzberger, T. OP-459
Asa, S. EP-0424, EP-0475, EPS-256, EP-0857, EP-0901, EP-1295
Asadian, M. EP-1163
Asadurova, S. EP-0324, EP-0388, EP-0490, EP-0685, EP-0762, OP-442
Asami, M. EP-1137
Asami, T. EP-0676
ASAP Group, OP-718
Ashfaq, A. **EP-0926**
Ashton, N. EP-1072, OP-438
Asidkar, S. **EP-1138**
Askari, E. EP-0566, EP-1351, EP-1354, EP-1361, EP-1377, EP-1380, EPS-220, OP-323
Askløf, M. G. EP-0219
Aslan, E. **EPS-218**
Aslan, S. EP-0192
Aslaner, K. OP-259
Aslanidi, I. EP-0433
Aslanidis, I. EP-0770
Asmussen, J. T. OP-877
Asogan Vaishnavi, J. EP-0908, EPS-034
Assadi, M. EP-0345, **EP-0878**
Assante, R. OP-684
Assenza, M. EP-0145, EP-0227, EP-0310, EP-0311, EP-0396, EP-0421, EP-1064, EP-1268, OP-168, OP-224, OP-246, OP-248, OP-293, OP-798
Assmann, A. OP-525
Assoignon, T. **EP-0947**, **EPS-299**
Asti, M. **EP-0091**
Astiazaran-Rascon, I. **EPS-021**, EP-0058
Atabekov, T. **EP-0616**, **EP-0617**
Ataei, N. EP-1380
Atakishieva, L. **EP-1304**
Atay, L. Ö. EP-0261, EP-0638, EP-0661, EP-0669, OP-175, EP-0197, EPS-115
Atieh, K. EPS-105
Atis, S. OP-214, OP-215

Atiyat, D. OP-245
Atkins, N. EPS-093
Atli, E. OP-790
Atteya, Y. EP-0810
Attri, D. EP-0159
Auer, M. K. EP-0793
Auerbach, M. EP-1143
Auernhammer, C. J. EP-0793, EPS-248
Auf Der Springe, K. EP-0184, **EP-1407**
Auger, C. EP-0685
Augusto, L. EP-1266
Augusto-Pelegrin, L. EP-1114
Aulich, A. EP-0714, EP-1336
Aunsborg, J. W. EPS-301
Auriac, J. **EP-0251**, **EPS-231**, OP-033
Aurilio, M. EP-1115, EPS-054
Avanzo, M. EP-1120
Avci, E. D. EP-0333, EP-0441
Avci, F. EP-0366, **EP-0428**, EP-0516, **EP-0924**, **EPS-077**
Avenali, M. OP-047
Avendaño-Estrada, A. **EP-0170**
Avigo, C. EP-1120, **OP-631**
Avila-Rodriguez, M. **OP-581**, EP-0170
Áviles Jurado, M. EP-0387
Avram, L. EP-0036
Awadh, M. EP-1416
Axelsson, R. EP-0260, EP-0275, EP-0404, OP-596
Ayati, N. **OP-323**
Aydin, N. **EP-0236**
Aydinbelge Dizdar, N. EP-0222, EP-0359, EP-0749, EP-1008, **EP-1225**, EP-1249, EP-1307, EPS-260 **EP-1215**, **EP-1216,** EP-0742
Aydiner, A. OP-110
Aydın, B. OP-850
Aydos, U. EP-0197, EP-0261, OP-175
Ayed, K. EP-1264
Ayer, M. EP-0480
Aygün, A. EP-0901
Ayoub, C. EP-0304
Azad, A. A. EP-0830, OP-605
Azarbar, P. EP-1003
Azimi, M.-S. EP-0413
Azizakram, H. EP-1168, **EP-1170**
Azizkhani, M. **EP-1003**
Azpeitia Hernandez, P. EP-0530, EP-0565, EP-0821, OP-478
Baa, A. OP-799
Baavour, R. OP-500
Baazoug, G. EPS-284
Baba, S. EP-0676
Babacan, G. B. **EP-0858**
Baberwal, P. EP-0300, EP-0558, **EP-0839**
Babich, J. EP-1135
Babu, A. S. EP-0744, **OP-559**
Babu, R. EP-0510
Bacalim, M. EP-0312, EP-0329
Baccarani, U. OP-631
Bachmann, M. OP-154
Bach-Mortensen, P. EP-0722
Bachy, E. OP-227
Bäck, T. **EP-0049**, EP-0945, OP-092, OP-704
Backhaus, C. EP-1085
Backhaus, P. OP-244, **OP-327**
Bacot, S. OP-022
Badarna, M. **EP-0336**
Badawi, R. EPS-032, EP-0466, OP-222
Badawy, L. **EP-0405**
Badea-Selea, A. EP-1327
Badel, J. N. OP-331, **EP-0378**
Badell Martínez, J. A. EP-0364, EP-0200, EP-0710, EP-0931, OP-481
Badie, C. OP-425
Badinedi, R. EP-1394
Badinez, L. OP-471
Badrane, I. **EP-1254**
Bae, S. EP-0161
Baer, B. EP-0113
Baessler, J. EP-0734, OP-600
Baete, K. **EP-0935**, **EP-1188**, OP-097
Bagán Trejo, A. EP-0758, **EP-0307**, EP-0437, EP-0495, EP-0498, EP-0508, EP-0618, **EP-0850**, EP-1057, **EP-1366**, EPS-040, OP-233, OP-480, **OP-865**
Bagaturya, V. EP-0432
Bagheri, S. **EP-0122**, EP-0854, EP-0987, OP-459, EP-1002, EPS-220
Bagnalasta, M. OP-669
Bahce, I. EPS-081, OP-774
Bahloul, A. **EPS-264**
Bai, C. OP-069
Bai, Y. EPS-200, EPS-094
Baican, A. EP-1385
Baier, M. OP-361
Bailey, D. EPS-119, OP-422
Baillet, C. EP-0800, OP-555
Bailleux, C. EP-0202
Bailly, C. EP-1017, EP-1055, OP-225, **OP-603**
Baimukhanova, A. **EPS-150**
Baistow, I. EPS-093
Bajenaru, A. **EP-1385**
Bajwa, D. E. EPS-153, OP-183
Baker, M. **EP-1132**
Baker, S. OP-290, OP-676, OP-703
Bakes, N. OP-416
Bakhshi, S. EPS-209, EPS-217
Bakhshi, Z. EP-0348
Bakir, B. EP-0355, EP-0368
Bako, B. EP-1338
Baksa, B. EP-0562
Bal, A. EP-0071, EP-0159
Bal, C. EP-1206, EP-0559, OP-872
Bal, J. **EP-0543**, **EP-1213**, **EP-1252**, **EP-1253**, **EP-1260**, **EP-1261**
Balaban Genc, Z. **EP-1127**, **EP-1141**, OP-874
Balaguer, D. EP-0792, OP-430
Balayeva, T. OP-457
Balazsfi, M. EP-0180
Balbin Garcia, C. EP-1227, EP-1251
Balci, E. EP-0197, EP-0638, EP-0661, EP-0669, EPS-115
Balciunaite, I. EP-0361
Baldari, G. EP-1179, EPS-140, OP-549, OP-801
Baldari, S. EP-0809
Baldewijns, M. OP-067
Baldissera, E. EP-1043
Balestreri, E. OP-549
Balibrea Zúñiga, T. EP-0774, EP-0560
Balčiūnaitė, I. EP-0365
Balkay, L. EP-0938
Ball, T. EP-0718, **EPS-302**
Balleyguier, C. EP-1075
Balogová, S. EP-1006
Balsalobre, P. OP-229
Baltabaev, I. EP-0432, EP-0932, EP-0955, **EPS-079**
Baltacioğlu, M. H. EP-0245
Baltadakis, I. EP-0477
Baltzer, P. A. T. OP-325
Balzer, M. OP-345
Bambaci, M. OP-105
Bamminger, K. OP-325
Banda, K. EP-0942, EP-1116, EPS-086
Bandelli, G. P. EP-0227, OP-168
Bang-Andersen, B. EP-0108
Bangkim Chandra, K. OP-559
Bani, M. OP-120
Banihashemian, S. EP-0888, EP-1149, EP-0066
Banz, Y. OP-220, OP-413
Bao, J. **EP-1077**
Bao, W. EP-0684, OP-439
Bär, S. OP-794
Barabas, A. EP-1326
Barage, S. EP-1445
Barai, S. EP-0813, EP-0853, EP-1459
Barantani, A. EPS-122
Barashki, S. EP-1360, **OP-109**
Barata, S. EP-0897, EP-1256, EP-1318, EP-1320, OP-379, OP-633
Baratto, L. OP-074
Barba, P. OP-229
Barbato, F. OP-786
Barbaud, M. EP-1017
Barbera, J. TEPS-021
Barberan Corral, L. **EPS-258**
Barbosa, D. EP-0199, **EP-1205**, EP-1243, EP-1269, EPS-267, OP-632, **OP-742**
Barbosa, G. EP-1203, **EP-1306**, EP-1324, EP-1342
Barboza, M. EP-0140
Barci, E. EP-1035, EPS-124, EPS-125, EPS-239, OP-609, **OP-610**
Bard, J. A. EP-0001

Bardiès, M. OP-213
Barghorn, S. OP-458
Barillaro, A. EP-0788
Barisonzi, R. EP-1062
Barkhof, F. OP-607
Barletta, F. EP-0370
Barlow, J. OP-314
Barlow, J. OP-825
Barmparis, G. EP-1031, EP-0242, EP-0243
Barna, S. EP-1338, EPS-278, OP-501
Barnhart, T. E. EP-1165, OP-579, OP-583, OP-586
Barone-Rochette, G. EPS-103, OP-787
Baronet, M. EP-1161, OP-290, OP-676, OP-703
Barrera, A. OP-666
Barrera Cerpa, A. **EP-1147**
Barresi, L. EP-1120, OP-631
Barreto, J. EP-1324
Barrie, K. EPS-291
Barrington, S. OP-664, EP-0463, EP-0468
Barroeta, I. OP-442
Barros, A. L. B. EP-0171, OP-553
Barroso, N. OP-714
Barry, N. EPS-119
Bar-Sever, Z. **OP-262**
Bar-Shir, A. EP-0036
Barski, D. OP-628
Bartel, T. EP-1283
Bartels, A. EPS-107, OP-051
Barthel, H. OP-044
Barthelemy, F. EPS-035
Barthelemy, P. EP-0812, OP-602
Bartholomä, M. EP-0780, OP-435
Bartholomeusz, D. EPS-023
Bartholomew, P. EP-1065, EP-1156
Bartoli, F. OP-182
Bartolomei, M. EP-0461, EP-0893, EP-1254, OP-324
Barton, D. OP-670
Bartos, L. EP-0168, EP-0699, EP-0019
Bartos, L. M. EP-0022, EP-0047
Barwick, T. M. EP-1052
Barzo, P. EP-0180
Basanta, A. OP-378
Bascuñana, P. EP-0775, EP-0341
Baskerville, C. **EP-1091**
Bassa, P. EP-0382, EP-0384, EP-0412
Bassa, S. OP-825
Ba-Ssalamah, A. OP-747
Bäßler, J. EP-1009
Bastian, M. B. EP-0780, OP-435
Basu, N. OP-697
Basuli, F. OP-088
Basuyau, F. EP-1181
Batalov, R. EP-0616, EP-0617
Bateman, T. M. OP-679
Bathe, T. **EP-0062**
Batley, L. EPS-194, OP-217, OP-218
Bato, K. OP-350
Batra, A. EP-0301
Battista, M. EPS-134
Battisti, C. **EP-0312**, **EP-0329**
Battisti, U. M. EPS-146
Bauckneht, M. EP-0370, EP-0377, EP-0681, EP-0683, EP-1401, OP-324, OP-725, OP-776, OP-868
Bauder-Wüst, U. EP-0015, EP-0132, EP-0138
Baudin, E. EP-0306, EP-0786, EP-1019, OP-120
Bauduer, A. **OP-292**
Bauer, S. EPS-190, OP-525
Baum, R. OP-434, EP-0043, EP-0784, EP-0790, EP-0881 EPS-016, EPS-156, EPS-166, OP-429, OP-628, OP-436, OP-860, OP-862
Bauman, A. OP-361, OP-432, OP-601, OP-673, OP-677
Baumgart, L. OP-606
Bautista-Peñalosa, P. EP-1219
Bavec, A. EP-0895
Bavestrello, G. EP-0686
Bax, J. J. OP-794
Bayat, Z. EPS-289
Bayer, M. EP-0486
Başyiğit, F. OP-497
Bayrakcı, Ö. EP-0605
Bayram, S. **EP-0480**, EP-0486
Bayramoglu, Z. OP-259
Bazan, L. EP-0234
Bazzi, R. EPS-153
B. C. Carvalheira, J. EP-0262
Beanlands, R. S. B. EP-0977
Beaudoin, J.-F. EP-0027
Beaulieu, A. EPS-181, OP-428, OP-534, OP-588
Beauregard, J. M. EP-1110, OP-428, OP-534, OP-588 EP-1100, **EPS-181**
Bebbington, N. **EPS-301**
Becx, N. OP-425
Bedi Alpay, B. EPS-260
Bednarz, B. EP-0070, EP-0162, EP-1121, EPS-001, EPS-012, EPS-194, OP-217, OP-218, OP-219, OP-517, OP-767
Beels, L. OP-097
Beer, A. EP-1106, EPS-185, OP-180, EPS-183
Beer, A. J. EP-1045, EP-1107, EP-1128, EP-1129, EPS-135, EPS-184
Beer, M. EPS-135
Beer, S. EP-0696
Beets-Tan, R. G. H. EP-0848
Beetz, N. EP-1092
Beganović, A. EP-1436, OP-318
Begić, A. EP-1436
Begley, P. EPS-291
Begus, U. EP-0712
Behe, M. EPS-142, OP-220, OP-413
Beheshti, M. EP-0326, EP-0362, EP-0688, OP-734
Behzadi, M. EP-1163
Beinat, C. OP-023, OP-657
Beintner-Skawran, S. OP-601
Beisbart, C. EP-0933
Bekker, C. OP-849
Belabas, L. EP-0756, EPS-212
Belaid, A. EP-1076
Belakroum, R. **EP-0752**
Belgioia, L. EP-0377, OP-324
Belhadj, K. EP-1055, OP-225
Belladelli, F. EP-0534
Bellaye, P. S. EPS-044, EP-0096, OP-211
Belli, M. L. **EP-1081**, EP-1159, OP-042
Bellia, S. EP-0411, EP-0436, OP-068
Bellino, M. OP-059
Bello, P. EP-0792, OP-430
Bello Roufai, D. EP-0217, EP-0297
Bellviure-Meiro, R. EP-0836
Belousov, M. EP-0089
Beltgens, F. OP-173
Belting, M. EP-0183
Beltman, J. J. OP-783
Beltran-Vilagrasa, M. EP-0836, EPS-092
Benali, S. EP-0756
Benameur, Y. EP-1301
Bénard, F. OP-348, EP-0090, EP-1016, EPS-021, EP-0034, EP-0051, EP-0058, EP-0120, EP-0160, EPS-046
Benderz, H. EPS-292, **EP-0940**
Bendová, K. EP-0123
Bendre, A. EPS-262, EPS-262
Benecke, J. A. EP-0229
Benedetti, L. EP-0686
Benešová-Schäfer, M. EP-0132, EP-0138, EP-0015
Benfante, V. EP-0369
Ben Fredj, M. EPS-284
Bengel, F. OP-726
Bengtsson, E. OP-523
Benhamla, A. OP-098
Benisvy, D. EP-1004
Benk, C. OP-842
Benlloch, J. M. TEPS-021
Ben Nasr, M. **EP-0571**, **EP-1239**
Benninghoff, S. OP-458
Ben Sellem, D. EP-1239
Bentestuen, M. **EP-0773**
Bentura, M. **EP-0100**, **EP-0157**
Benvenuto, G. EP-0686
Benzerdjeb, S. EP-0756, EPS-212
Benz-Zils, D. OP-860
Beqqali, Y. EPS-239, OP-773, **OP-775**
Berardinelli, A. EP-0553
Berardinelli Isea, A. EP-0394, EP-0491, OP-784
Berbel-Palau, D. EPS-022
Berchtold, L. OP-609
Berdal, M. OP-152, OP-593
Berding, G. OP-726

Beretta, C. EP-0017, EP-0044
Bergalla, E. EP-0496, EPS-298, OP-033
Bergamaschi, N. EPS-137, OP-584
Bergamo, P. OP-665
Bergesio, F. EPS-298
Berghmans, T. OP-169
Berghoff, A. S. OP-609
Berglund, H. EP-0064, EP-0068
Bergström, T. EP-0064
Beriashvili, N. **EP-0929**, EP-0943
Berihu, M. EP-0021
Berkson, L. OP-551
Bernard, C. EP-0944, EP-0952, EPS-084, OP-097
Bernardes, E. EP-0092
Bernardini, M. OP-322
Berndorfler, B. **OP-849**
Berndt, N. OP-154
Bernhard, C. EP-0096
Bernhardt, A. EP-0691, OP-044
Bernhardt, D. EP-0182, OP-606
Bernhardt, P. EP-1160, EPS-180, OP-413, OP-414, OP-432, OP-589, OP-590, OP-662, OP-673, OP-677
Berntsen, E. M. EP-0883
Bertacca, I. EPS-272
Bertagna, F. OP-324, OP-868
Bertels, J. EP-0663
Berthet, C. EPS-044
Berthon, A. EP-1394
Berti, R. **OP-842**
Berti, V. EP-0467, EPS-134, EPS-272, OP-321
Bertin, D. OP-105
Bertoglio, D. EP-0001
Bertoletti, L. EPS-090
Bertolini, G. EP-0044
Bertolini, M. OP-113
Bertschi, N. OP-413
Bertsias, A. EP-0242, EP-0243
Bertuzzi, A. EP-0779
Berwouts, D. OP-121
Besenyi, Z. EP-0180
Beshliev, S. EP-1358
Besnier, C. OP-359
Bessa, J. OP-061
Besse, B. OP-120
Betech-Antar, V. OP-378
Beuzeville, S. EPS-119
Beydagi, G. EPS-191, **OP-476**, OP-856
Beyer, T. EP-0230, EP-0251, EP-0968, EP-1067, EP-1079, EP-1089, EP-1093, EP-1097, OP-033, OP-548
Beyersdorf, F. OP-842
Beykan Schürrle, S. EP-1127, EP-1141
Beylergil, V. EP-0912
Bezumova, E. EP-0432, EP-0932
Bezverkhniaia, E. EP-0074, EPS-050, **OP-087**, OP-089
Bezverkhniaia, E. A. OP-659
Bezzi, C. **EP-1043**, OP-875
Bezzi, D. EP-0411, EP-0436, **EP-0501**, EP-0502, EP-0503, EP-0514, OP-068
Bhalla, A. S. EP-0558
Bharadwaj, P. EPS-224
Bharati, S. J. EP-0285, EP-0880
Bharati, S. EP-0177, EP-0882
Bharkhada, D. EP-0974, EP-0981, EP-0990, EPS-221
Bhat, A. OP-416
Bhattacharya, A. EP-0741
Bhuva, S. EP-1091
Bi, S. EPS-118
Bi, X. EP-0587
Bian, L. **EP-0073**, **EP-0165**
Bian, Y. EP-1441, EP-1446
Biancheri Mounicq, I. OP-864
Bianchetto Wolf, N. EP-1122
Bianchi, C. OP-669
Bianchi, L. EP-0375, EP-0398, OP-330, OP-716
Bianciardi, G. **EP-0310**, **EP-0311**, EP-0444, **EP-1238**, EP-1268, EP-1372, EPS-247, OP-118, **OP-246**, **OP-248**, OP-437
Bianco, R. EP-0233
Bianconi, L. EP-0396
Biber Muftuler, F. Z. EP-0131
Biçen Altın, M. EP-0902, EP-1276
Bidard, F.-C. EP-0217, EP-0297, EPS-231
Bidaux, A.-S. OP-331
Biechele, G. EP-0022
Bielik, R. EP-0041
Bienkowski, K. **EP-0323**
Biggans, T. **EP-0908**, **EPS-034**
Biggs, H. OP-703
Bignon-Bretagne, A.-L. OP-433
Bijlstra, O. EP-0334
Bil, J. OP-679
Bilgic, S. **EP-0953**, EP-1321, EP-0901
Bilgücü, T. **EP-0335**
Bilinska, A. EPS-009, EPS-013, **EPS-193**, **OP-417**, OP-518
Bills, M. EPS-023
Bilodeau-Harnois, B. OP-871
Binder, P. OP-790
Bio Idrissou, M. EP-0162, EPS-001, **OP-217**, **OP-218**, **OP-219**, OP-517, OP-767
Bio Idrissou, O. EP-0070, EPS-012, OP-275
Birtalan, E. EP-0562
Bischof, G. N. EP-0698, OP-048, OP-237, OP-773
Biscontini, G. OP-558
Bisello, F. EP-1112
Biswal, S. OP-870
Biswas, S. EP-1208
Bitzén, U. EP-0733, TEPS-004
Bitzios, A. **OP-766**
Björeland, U. **EP-1070**
Bjørnholt, S. M. OP-038
Bjurberg, M. OP-041
Blackman, A. O. OP-722
Blaise, D. OP-227
Blakeman, B. EP-0121
Blakkisrud, J. **EP-1044**, EP-1102, EP-1113, OP-424
Blanc-Durand, P. **OP-359**
Blanco, I. OP-666
Blanco Saiz, I. EP-1147
Blanco-Verdejo, L. **EP-0653**
Blasco-Lucas, A. EPS-022
Blatnik, O. EP-0895
Blaurock, K. EPS-294
Blazekovic, I. EP-0264, EP-1222
Blazicevic, K. EP-0524
Blennow, K. EP-1072, OP-438
Bleve, S. EP-0801, EP-0803
Blickle, A. EP-0780, OP-435
Blitzer, G. OP-074
Bloem, M. OP-295
Bloemsma, G. C. EP-0842
Blok, S. OP-452, EP-0011
Blondon, M. EPS-090
Blonski, M. EP-0179, OP-614
Blum, L. OP-842
Blume, L. V. EP-0037
Bobkova, S. EP-0513
Bobrov, V. EP-0433, EP-0542, EP-1304
Bobrova, V. EP-0871
Boccalini, C. EP-1072, **OP-438**, OP-443
Bockisch, A. OP-385
Bockisch, B. EP-0724, EP-1154, EP-1155
Bodanza, V. OP-036
Bodei, L. OP-368
Bodenko, V. EP-0089
Bodere, F. OP-227
Bodet-Milin, C. EP-1055, OP-225
Bodin, S. EP-0069
Bodur, M. EP-0277, **OP-531**
Bodur, T. EP-0424
Boecker, H. OP-303
Boeckxstaens, L. EP-0643, EP-0879, EPS-126, OP-366
Boekestijn, B. EP-0334
Boellaard, R. EP-1041, EP-1073, EPS-036, EPS-081, OP-607, OP-774
Boening, G. EP-1118, EPS-240
Boersma, H. H. OP-760
Boëtius, M. EP-0011
Bögemann, M. OP-327, OP-329
Boggiano, A. C. OP-579
Bogni, A. EP-0017, EP-0044
Bogovic Crncic, T. **EP-0730**, EP-0597
Bogsrud, T. **EP-0807**
Bohn, P. **EP-1181**
Boissière-Michot, F. OP-213
Bokhout, L. **EP-0003**
Bolch, W. E. EPS-179

Bolin, M. OP-596
Boll, M. EP-0135
Bollenbacher, A. EP-0711
Bolt, E. OP-705
Bolzati, C. **OP-179**
Bomanji, J. EP-0996
Bonacina, M. OP-669
Bonadonna, R. OP-801, OP-549
Boneu, C. EPS-134
Bonfitto, G. R. OP-326, OP-298
Bonilla Plaza, J. **EP-0358**, EP-0401, EP-1393, EP-0328, EP-1408
Böning, G. EPS-024, EP-1150, EPS-197, EPS-290
Bönisch, H. EPS-154
Bonnans, G. **OP-060**
Bonneau, C. OP-104
Bonnefoy, P.-B. **OP-864**
Bonnet, G. OP-528
Bonney, L. **OP-026**, EP-0958
Bonometti, D. EP-0478
Bönsel, L. OP-422
Bonutti, F. OP-631
Borchmann, P. EP-0488
Bordigoni, B. OP-706
Borghammer, P. EP-0998
Borghesi, M. EP-0893
Borgschulze, R. EP-1087
Borkowska, A. EP-0789
Bormans, G. EP-0103, OP-366
Boronat De Ferrater, M. EP-0845, EPS-026
Boros, E. OP-586
Borrás-Sánchez, D. EPS-092
Bors, S. OP-528
Borsali, M. EPS-199, OP-630
Borsatti, E. EP-0809, EP-1120, OP-631
Bos, P. K. OP-870
Bosak Butkovic, M. EP-0264
Bosbach, W. **OP-823**, **EP-0933**
Bosch, J. EPS-036
Boschetti, F. OP-347
Boschi, A. OP-584
Bosetti, D. EP-0889
Bösl, P. OP-364
Bos-Liedke, A. EP-0797
Bosnjak, R. EP-0713
Bossmann, S. H. EPS-233
Boswinkel, M. EP-0164, EP-1145
Botanch-Domingo, M. EP-0656, EP-0673
Botanlıoğlu, H. EP-0901
Bothe, B. OP-779
Bottlaender, M. EPS-131
Bouchelouche, K. OP-038
Boucher, D. EP-0153, OP-177
Boudewijns, L. OP-708
Boudriga, H. EP-0447, EP-1264, EPS-284
Bouhier-Leporrier, K. OP-433
Bouhnik, J.-P. EPS-087, OP-103, OP-661
Boukhari, A. **EP-1036**, OP-354
Bourbonne, V. EPS-230
Bourhis, D. EPS-230
Bourogianni, O. EP-0242, EP-0243, EP-0244, **EP-1299**
Bourouis, S. **OP-317**, TEPS-012
Bourre, J.-C. EP-0809, OP-864
Boursier, C. **EP-0827**, EP-0829, **OP-101**, **OP-614**
Bouyoucef, S. E. EPS-212
Bouzidi, A. EP-0903, TEPS-012
Bouzidi, H. EP-0752
Bouziotis, P. EPS-153, OP-183
Bovone, P. EPS-137, OP-584
Bowl, W. EP-0854
Boya, P. OP-666, EP-1147
Bozca, B. EP-0577, **EP-0749**, **EP-1008**, EP-1216, **EP-1307**
Bozdemir, B. C. EP-0236
Bozhinovska, N. **EP-0736**, EP-0448
Bozkurt, M. F. EP-0778
Bozzali, M. EP-0683
B. Patrianesha, B. EP-1119
Braad, P. E. OP-887
Braat, A. EP-0785, EP-0876, OP-260, EP-0848, EP-1051, OP-289, OP-597, OP-863
Brabander, T. EPS-109
Bradley, K. M. EP-0670, EP-0962, EP-1030, OP-026
Brady, J. OP-676
Bragina, O. OP-070
Braglia, L. OP-113
Brahmi, S. EPS-212
Bral, S. OP-710
Brambilla, C. EPS-083
Branco, F. P. OP-634
Brandal, P. EP-0183
Brandão, M. OP-169
Brandão, S. EPS-251
Brandenburg, T. OP-247, OP-385
Brandl, F. OP-721
Brandt, A. OP-791
Brandt, R. OP-425
Brasero Burgos, J. EP-0530
Bratman, S. EP-0081
Bratteby, K. OP-414
Braune, A. EP-0483, OP-032
Brazenski, K. EP-0976
Breddam, K. OP-708
Bregenz, C. OP-788
Bregenzer, C. M. EP-0933
Brembilla, G. EP-0534, OP-875
Bremer, L. EPS-154
Brendel, M. EP-0018, EP-0019, EP-0022, EP-0037, EP-0047, EP-0062, EP-0168, EP-0691, EP-0698, EP-0699, EP-0886, EPS-005, EPS-197, **OP-044**, OP-046, OP-237, OP-456, OP-773
Brenner, W. OP-345
Bressan, E. OP-484
Bretthauer, B. A. OP-842
Breuil, L. EP-0093
Breuskin, I. OP-120
Breyholz, H.-J. OP-327
Briganti, A. EP-0370, OP-875
Briganti, V. OP-321
Brighi, N. EP-0801, EP-0803
Brigo, I. R. EP-0631
Brillembourg Cubillan, H. EP-0776
Brillouet, S. EPS-078
Brimacombe, C. A. OP-094
Brink, A. **EP-1396**
Brisbane, W. EP-0376
Brittain, J. EP-0709
Brixius, S. OP-842
Brocchi, S. EP-0503
Brock, J. OP-697
Bröckelmann, P. J. EP-0488
Brodie, C. EP-0216
Broen, M. P. G. EP-0183
Brogaard, M. **EP-0709**
Brogsitter, C. OP-819
Broisat, A. OP-022, OP-787
Brom, M. OP-760
Bronte, A. **OP-446**
Brosch-Lenz, J. EP-1410
Brouwers, A. H. EPS-082, OP-289, OP-885
Brovedani, I. **EPS-221**, OP-771
Brown, C. EP-0781, EP-0993
Brown, G. EP-0041
Brown, M. K. OP-094
Brown, M. P. EP-0130
Bruchertseifer, F. OP-213, OP-181, OP-280
Brückner, L. OP-371
Brühlmann, S. OP-154
Brunetto, S. EP-0262
Bruno, F. OP-612
Bruno, S. EP-1179
Brunocilla, E. EP-0375, EP-0398, OP-716
Bruns, C. EP-0331
Brus, A. OP-025

Brusa, I. EP-0145, EP-0227, EP-0270, EP-0421, EP-1064, EP-1112, EP-1268, EPS-030, OP-168, OP-246, OP-248, OP-293, OP-330, OP-798
Bruton, T. EPS-062
Bruyat, D. OP-173
Bruzzese, F. EPS-054
Brzeminski, P. OP-156
Buaki Sogo, M. **EPS-202**
Buchanan, K. EP-0822
Buchatskaya, Y. OP-184
Bucher, S. OP-552
Büchner, A. OP-726
Buch-Olsen, K. **OP-877**, EP-0403
Buchpiguel, C. A. EPS-232
Buck, A. EP-0318, EP-0794, OP-429
Buck, A. K. EP-0195, EP-0728, EPS-294, OP-043, OP-223, OP-376
Buckle, T. **OP-037**
Buczkó, N. EP-1166
Budai, Á. EPS-278, OP-501
Budau, A. M. EP-1334
Budäus, L. EP-1026
Budiansah, I. **EP-1119**, **EPS-183**
Budzynska, A. EP-0789
Bueno-Raspall, M. EP-1411
Buffi, N. EP-0363, EP-0350
Buffoni, F. EP-0175, EPS-122
Bukelo, M. OP-799
Bukovansky, K. EP-0513
Bülbül, O. EP-0245, EP-1392
Bumanjal, I. EPS-182
Bundschuh, R. A. EP-0082, EP-0483, EP-0734, OP-032, OP-352, OP-819
Buongiorno, P. OP-684
Burak, Z. EP-0516, EP-0924, EPS-077
Buresova, S. EP-1131
Burgs, S. OP-864
Burgard, C. EP-0780, OP-435
Burger, C. **EPS-203**
Burger, I. OP-352
Burger, I. A. OP-823
Bürger, K. OP-237
Burgmans, M. EP-0334
Burniston, M. EPS-076
Burns, P. EP-0380
Burvenich, I. **EPS-003**, OP-277
Busakher, F. EP-1416
Busch, H. J. OP-842
Buschhold, H. EP-1400
Buset, J. OP-150
Buteau, F. A. EPS-181, OP-428, OP-534, OP-588
Buteau, J. P. EP-0415, EP-0830, OP-605
Büther, F. OP-327
Butuner, S. OP-040
Buvat, I. EP-0217, EP-0251, EP-0297, EP-1067, EPS-230, EPS-231, OP-033, OP-104, OP-173
Büyükaşık, Y. EP-1202
Buziak-Bereza, M. EP-0440
Byrne, C. OP-659
Caballero Campos, M. EP-1408
Cabart, M. OP-536
Cabel, L. EP-0201, OP-104
Cabello, J. **EP-0957**
Cabioglu, N. OP-110
Cabitza, V. EP-0502, EP-0227, OP-168
Cabrera, M. EP-0775
Cabrera Martin, M. EP-0553, EP-0339, EP-0340, EP-0341, EP-0491 OP-784
Cabrera-Portillo, L. EP-0656, EP-0673
Cabrini, G. EP-0269, EP-0418, EP-0419, EP-0427, EP-0470, EP-0894, EPS-228, OP-556
Caccia, B. EP-1109
Cade, D. OP-674
Caduri, S. OP-262
Caffo, O. EP-0234
Cafiero, G. EP-1421, EP-1450
Caglar, M. EP-0426
Cagua Ruiz, L. **EP-0522**, EP-0555, EP-0560, EP-0846, **EP-0866**, EP-0867, EPS-249
Cai, B. EP-0119
Cai, H. OP-071
Cai, J. EP-1038, EP-1049
Cai, J. EP-0129
Cai, T. **EPS-200**
Cai, W. EP-0052, EP-0492
Cai, X. OP-469, OP-768, **EP-0042**
Cai, Y. EP-0327, OP-466, **EPS-113**
Cai, Z. OP-226, OP-457, **OP-094**
Caiazzo, E. EP-0308, EP-0788
Caille, A. OP-718
Caillé, F. EP-0093
Caillot, D. EP-1055, OP-225
Cakir, T. **EP-0912**
Calabretta, R. EP-0609, EP-1011, EP-1071, OP-468, OP-747, **OP-790**
Calais, J. EP-0208, EP-0376, EP-1124, EP-1143, EP-1410, EPS-162, EPS-192, OP-074, OP-329, OP-714, OP-824
Çağlar, K. EP-0604
Calatayud Cubes, A. EPS-258
Calcagni, M. OP-105, EP-0665, EP-1399, OP-858, OP-891
Caldarella, C. EPS-269
Caldas, C. **EP-1344**
Caldera-Quevedo, I. **EP-0041**
Calderón, E. OP-288
Calderon Avila, A. EP-0086
Calderón Calvente, M. EP-0760
Calderoni, L. EP-0145, EP-0444, EPS-247, OP-118, OP-246, OP-248, OP-798
Calderón Ochoa, E. **EP-0229**, **EP-0351**
Calderon Tobar, M. **EP-0604**
Calheiros, R. EP-1269
Califaretti, E. OP-055
Calini, G. EPS-030
Callahan, J. OP-817
Calloni, S. EP-0534
Calls, M. EP-0632
Calls Calahorro, M. **OP-553**, EP-0324, EP-0490, EP-0551, EP-0762, OP-442
Caltagirone, F. EP-0710, OP-481
Caltagirone Gutierrez, F. EP-0364, EP-0378, EP-0931
Caltagirone Rodriguez, F. EP-0200
Calviño, N. **OP-483**
Calvo, S. OP-818
Çağlıyan, F. OP-874
Calza, P. OP-669
Camacaro, J. EP-1169, **EP-1171**
Camacho, V. EP-0324, EP-0490, EP-0551, EP-0762, OP-440, OP-442, OP-553
Camardese, G. OP-720
Camba, F. EP-0758
Camba-Capitan, F. EP-0653
Cameron, R. B. EPS-162
Caminiti, S. P. OP-669, **OP-047**
Campana, D. EP-0310, EP-0311, EP-1268
Campana, L. EP-1109
Campaña Diaz, E. EP-0200, EP-0364, EP-0378, **EP-0710,** EP-0931, **OP-481**
Campbell, L. OP-290, OP-676, OP-703
Campeiro, J. D. **EPS-007**, **EP-0136**
Campenni, A. **OP-380**
Campion, J. Y. Y. EPS-035
Campochiaro, C. EP-1043
Campoleoni, M. EPS-122
Camporotondi, D. **EP-1172**
Campos, A. OP-061
Campos Añón, F. EP-0776
Campos-Caro, A. EP-0745
Camps-Renom, P. EP-0632
Camus, V. OP-718
Can, E. EP-0838
Cañadas, O. OP-700
Cañadas Salazar, J. OP-229, EP-0200, EP-0931
Cáncer-Garza, L. EP-0552
Canchumanya Huatuco, N. **EPS-026**, EP-0845
Candido, D. EP-0312, EP-0329
Candoli, P. EP-0227, OP-168
Canela-i-Coll, T. EPS-297
Caner, B. EPS-191
Cañete-Sánchez, F. EP-0745
Cannarozzo, E. EP-1403
Cano, R. EP-0775
Cano Cano, J. EP-0328
Cano Carrizal, R. EP-0339, EP-0340, EP-0341
Cano Cumellas, E. EP-0776
Canoves Llombart, A. S. TEPS-021

Canpunar, N. EP-0661
Cansu Çay, E. **EP-0851**
Canıtez, B. OP-715
Cantoni, V. EP-0308, OP-684
Canzi, C. EPS-122, **EPS-261**
Canziani, L. **EP-1173**, **EP-1199**
Cao, H. EPS-033
Cao, J. EP-0575, EP-0575, **EP-0767**
Cao, K. EP-0609, EP-0678, OP-300
Cao, L. EP-0500
Cao, S. EP-0129
Cao, W. EP-0099, EP-0438, **EP-0855**, EPS-010, **EPS-011**
Cao, Y. EPS-058
Cao, Z. EP-1021, OP-277, **OP-516**
Caobelli, F. EP-0409, EP-0614, EPS-106, EPS-221, OP-498, OP-502, **OP-552**, OP-685, OP-771, OP-788, OP-889
Capaccione, K. EP-1273, EP-1274, EP-1280
Capa Kaya, G. EP-0210, EP-0422
Capitanio, S. **EP-0269**, EP-0418, EP-0419, EP-0427, EP-0470, EP-0894, EP-1130, EPS-228, **OP-556**
Capitanio, U. EP-0534
Capobianco, N. EP-0326
Capoccetti, F. OP-380
Capoferri, S. OP-875
Capogni, M. EP-1166
Capotosti, A. EP-0665, OP-708, **OP-858**
Capoulas, M. EP-1409
Capponi, P. C. EP-0091
Caracò, C. EP-0216
Carbonini, C. EP-0894, EP-0914, EP-1130
Cardaci, G. OP-670
Cardaci, J. OP-817
Cárdenas Apaza, G. B. EP-0760
Cárdenas Soto, K. EP-0909
Cardinale, J. EP-0942, EP-1116, EP-1200, OP-349, OP-471, OP-825, OP-881
Cardoso, Â. **OP-889**
Cardoso, V. EP-1184
Cardoso-Rodríguez, M. EP-0872
Cardozo-Saavedra, A. EPS-211
Caresia Aroztegui, A. EP-0845, EPS-026, EP-0392, EP-0437
Cariou, E. OP-060
Carlier, T. EP-1017, EP-1055, OP-225
Carlqvist, M. OP-320
Carlsen, E. **EP-0322**
Carlsen, J. EPS-120
Carlsson, S. EP-0404
Carmona, S. EP-0717
Carmona-Bayonas, A. EP-0792, OP-430
Carmona-Bozo, J. C. EP-0216
Carmona-Iragui, M. OP-442
Carnaghi, C. EP-0779
Caroli, M. EP-0175
Caroli, P. EP-0411, EP-0436, EP-0501, EP-0801, EP-0802, EP-0803, EP-1159, OP-042, OP-068
Caroprese, M. EP-0788
Carradus, A. **EP-0572**, EP-0576
Carrara, L. EP-0444, EPS-247, OP-118, OP-246, OP-248
Carrara, M. OP-484
Carraro, E. EPS-205
Carrau, G. EP-0134
Carrera, I. EP-0157
Carreras, C. EP-1403
Carrero-Vásquez, V. **EP-0731**, EP-1057, **OP-480**, EPS-031
Carrier, J.-F. EP-1033
Carriero, S. EP-0216
Carrierre, M. EP-0164
Carron, C. **EP-0643**
Carruezzo, M. EP-1109
Carson, R. OP-457
Carston, A. EP-0070, EPS-012, OP-217, OP-218, OP-275
Carta, S. OP-776
Carter, A. EP-1054
Carter, L. OP-204
Cartron, G. OP-227
Carvalheira, J. B. C. EP-0536, EP-1418
Carvalho, A. EPS-091, **EPS-300**
Carvalho, D. EP-0765, **EP-0897**, EP-1256, OP-379, **OP-633**, OP-636
Carvalho, H. F. OP-722
Carvalho, I. P. EP-0521
Carvalho, J. EP-0772, EP-1255, EP-1265
Carvalho-Duarte, N. EP-0656, EP-0673
Casaburo, F. EP-1421, EP-1450
Casadei, B. OP-224
Casado, I. EP-0551
Casafont-Solé, I. EPS-026
Casallas, M. EP-0668, EP-0704
Casanova Martins, M. **OP-627**
Casas Fernández, L. **EP-0849**
Caselles, O. **EP-0949**, EPS-078
Cases Pellise, C. EPS-121, EPS-031
Casey, M. E. EP-0977
Casi, M. EP-0801, EP-0802, EP-0803
Casillas Sagrado, E. EP-0364, EP-0378, EP-0931
Casimiro, I. EP-0765, EP-0897, **EP-1256**, EP-1320, OP-379, OP-633, OP-636
Casini, B. OP-776
Casoni, R. OP-055
Cassano, B. EP-0906, EP-1109
Cassarino, G. EP-0206
Cassibba, S. OP-484
Cassol, E. OP-060
Castaneda Vega, S. **OP-525**
Castanheira, J. OP-158
Castanyer Serra, S. EP-1434
Castejón, S. EP-0324, EP-0490, EP-0762, OP-553
Castellani, G. EP-0145, EP-1064, OP-293
Castellani, M. EP-0175, EP-0478, EPS-122, EPS-261, OP-669
Castellaro, M. EPS-221, OP-771
Castello, A. **EP-0175**, EPS-122, EPS-261
Castellón, M. EP-0792, OP-430
Castellón Sánchez, M. EP-1308, EP-1311, EP-1312, EP-1315, EP-1289, EP-1305
Castellucci, P. EP-0145, EP-0375, EP-0389, EP-0396, EP-0398, EP-0421, OP-330, OP-716, OP-798
Castiaux, A. EP-0687
Castillejos, L. **EP-1368**
Castillejos Rodriguez, L. EP-1286, EP-1322, EPS-263
Castillejos Rodriguez, M. EP-0819, EP-1337, EPS-273
Castillo, V. EP-0704
Castillo Morales, V. EP-0798, EP-0841
Castro, A. F. EP-1201
Catalano, M. EP-0826, EP-1258, EP-1376, EP-1383, EP-1412
Catherine, N. EP-0581
Cattabriga, A. EP-0375, EP-0398, EP-0503
Cavallo, F. OP-720
Cavanagh, J. OP-697
Cawthray, J. OP-817
Cayhan, V. EP-0837, OP-635
Cayir, D. EP-0749, EP-1215, EP-1225, EP-1307, EPS-260
Cazalbou, S. OP-060
Cazzamalli, S. **OP-182**, OP-298, OP-326, OP-327
Cazzola, E. **EPS-137**, OP-584
Cebollada Cameo, L. EP-1197, EP-1198
Ceccarelli, V. EP-1399
Cecchin, D. EPS-205, OP-036
Ceci, F. EP-0389, OP-663
Cedillo, A. OP-229
Cegła, P. EP-0789
Cei, F. EP-0534
Celebioglu, E. C. EP-0834
Celen, S. EP-1175
Celik, R. EP-0131
Celik Arslan, A. EP-0577, **EP-0742**
Celli, M. **EP-0411**, **EP-0436**, EP-0501, EP-0801, EP-0802, **OP-068**
Censi, F. EP-1109
Cerchione, C. EP-0501
Cerci, J. **OP-711**, **OP-873**
Cerci, M. O. OP-119
Cerić, Š. EP-1436
Ceric Andelius, I. EP-1423, **EPS-088**, EPS-280, **OP-099**
Cermelli, A. EP-0681
Çermik, T. F. EP-0272, EP-0723
Cernat, A. EP-0297
Cerne, D. EP-0686
Cerqueira, B. EP-0785
Cerrone, M. EPS-054
Cervati, V. OP-801
Cervera-Araez, A. EP-0392
Cescon, M. EP-0270
Cetin, S. EP-1127, EP-1141
Ceylan, S. **EP-0808**
Ceyrat, Q. OP-864

Chaban, A. **EP-0182**, EP-0286, EPS-265, **OP-368**, **OP-606**
Chafai El Alaoui, M. EPS-044
Chaib, S. OP-542
Chakragiri, M. S. EP-1013
Chalewska, W. EP-0789
Chamnan, A. EP-0596, **EP-0700**
Champion, L. EP-0217, EP-0297, OP-104
Chan, C. H. TEPS-007
Chan, C. Y. **EPS-008**
Chan, C. **EP-0081**
Chan, K. **EPS-201**
Chan, S. C. **EP-0194**, EP-0281, **EPS-174**
Chandler, H. **OP-624**
Chandra, B. EP-0583
Chandra, K. B. OP-353
Chang, J. OP-216
Chang, P. EP-0899
Chang, T. OP-665
Chang, Y. J. TEPS-002
Chang, Y. **EPS-133**
Chang, Y. H. EP-0823
Chanu, A. R. EP-0371, EP-0372, EP-0373, EP-0764
Chao, C. EP-1427
Chao, Z. OP-457
Chapeau, D. EP-0087, OP-221
Charalambous, P. EPS-254
Chardin, D. EP-1004
Chareonthaitawee, P. OP-679
Charfi, j. **EP-1264**
Charlton, J. EP-0822
Chasseigneaux, S. EP-0093
Chatry, N. TEPS-016
Chatti, K. EP-0447, EP-0465, EP-1231, EP-1264, EP-1390, EPS-284, OP-027
Chattigkezou, D. **EP-0675**
Chatzipavlidou, V. **EP-0820**, OP-557
Chaudhary, A. K. EP-0527
Chaudhary, J. **EP-1084**
Chauhan, A. OP-074
Chauhan, P. EP-0853, **EP-0859**, OP-821
Chaurasiya, K. EP-0481, EP-0482
Chaushev, B. EP-1292, EP-1293, EP-1294, EP-1330, EP-1331, EP-1359, EP-1384
Chausheva, S. EP-1292, EP-1293, EP-1294, EP-1330, **EP-1331**, EP-1359, **EP-1384**
Chauvie, S. **EP-0496**, EPS-298, OP-033, OP-323
Chavdarova, L. **EP-0457**, EP-0563
Cheal, S. M. OP-279
Checcucci, E. EP-0370
Chehrara, M. OP-734
Chelghoum, L. EP-0756, EPS-212
Chen, A.H. EP-0342
Chen, B. OP-458, **EP-0626**
Chen, C. OP-174, EP-0610
Chen, C. C. EP-0051, EP-0120, EPS-046
Chen, C. T. TEPS-002
Chen, C. Y. **OP-793**
Chen, G. **EPS-058**, EP-0964
Chen, H. EP-0256, EP-1038, EP-1049, EPS-171, OP-117, OP-431, OP-781
Chen, H. **EP-1025**, EP-1422, EP-0438, EP-0855
Chen, I. OP-474
Chen, J. **EP-0515**, OP-226, OP-444, **EP-1167**
Chen, K. OP-466
Chen, L. EP-0113, EP-0684, **EP-0056**, EP-0649, EPS-233, EP-1410
Chen, M. EP-1282, TEPS-002
Chen, P. EP-0067
Chen, Q. OP-086, EP-0218, OP-112, OP-167
Chen, S. EPS-130, **EP-0342**, EP-1437, **EP-0469**, **EP-0493,** EP-0429, **EP-0499**, **EP-0799**, EPS-177, **OP-306**, **TEPS-002**
Chen, T. OP-174, **EP-0823**
Chen, W. EPS-049, EPS-152, **EPS-155**, TEPS-002, EP-0469, EP-0493, EP-0621, EPS-169
Chen, X. EP-0518, EPS-123, **EPS-243**, OP-296, EP-0211, **EP-0133**, OP-431, OP-678, **OP-765**, OP-781, EP-0386, OP-733 EP-0649, EP-0975, EPS-101, EPS-113, **OP-230**, EP-0166
Chen, Y. EP-1427, EP-0205, OP-229, OP-308, EP-1148, OP-788 EP-0201, EP-1015, EP-1140, OP-205, OP-545, OP-431
Chen, Z. EPS-006, EPS-014, EP-0978, EP-0995, OP-284, **EP-0111**, **EPS-118**, EP-1079, OP-548, EP-0097
Chêne, S. EP-0812, OP-602, OP-603
Cheng, C. C. EP-0342
Cheng, K.-H. TEPS-007
Cheng, K. EP-0499, EP-0799, EPS-177, OP-306
Cheng, M. EP-1427
Cheng, M. F. EP-0025
Cheng, M. H. Y. OP-094
Cheng, S. EPS-053, **OP-418**
Cheng, W. OP-451
Cheng, X. EP-0174, OP-608
Cheng, Y. EP-0644
Cheng, Z. EPS-033, EPS-025, OP-308
Chequer, R. OP-499
Cherbuin, N. OP-702
Cherchi, V. OP-631
Chérel, M. OP-280
Cherlin, A. **EPS-093**
Chern, Y.-J. EP-0342
Chernov, V. EP-0089, OP-070
Cheung, J. **EP-1193**
Cheung, L. EPS-201
Cheung, P. OP-023
Cheung, S. EP-0429, EP-0499, EP-0799, EPS-177, OP-306
Cheung, Z. OP-876
Chevalley, A. OP-160, **OP-528**
Cheveau, M. EP-0164, **OP-347**
Cheze Le Rest, C. OP-356
Chi, S. S. EPS-174
Chiacchiararelli, L. EP-0263
Chiam, K. EP-1014
Chiang, M. EPS-029, **EP-0284**, **OP-701**
Chiaravalloti, A. EP-0461
Chicklore, S. EP-0916, OP-619
Chierichetti, F. EP-0234, OP-613
Chierici, M. EP-0234
Chiesa, C. EP-0044, EP-1146, **OP-384**
Chiesa, S. OP-776, EP-0497
Chih, S. EPS-075
Chikazoe, J. EP-1059
Chikhradze, M. EP-0929
Chilvers, E. R. OP-697
Chincarini, A. OP-725
Chiola, S. EP-0377
Chiorazzo, T. OP-413
Chirayil, V. OP-861
Chirindel, A. OP-361, **OP-601**, **OP-673**, **OP-677**
Chiti, A. EP-0115, EP-0254, EP-0269, EP-0370, EP-0534, EP-1043, EP-1401, EPS-238, OP-298, OP-326, OP-384, OP-669, OP-706, OP-875
Chiu, C. H. EP-0025
Chiu, K. L. **EP-1284**
Chiumia, P. EP-0824
Cho, H. EP-0795
Cho, S. **EPS-215**
Chodyla, M. K. OP-239
Choi, B. **EP-0655**
Choi, B. EP-0672
Choi, C. OP-284, EPS-179
Choi, H. EP-0161
Choi, J. EPS-214
Chong, W. EP-0097
Chonkar, A. EPS-062
Choo, K. EP-0664
Chopra, S. EP-0009, EP-0064, **EP-0068**, **EPS-043**, **EP-0071**, EP-0159, **EP-1134**, EP-1460
Choudhary, A. EP-0285, EP-0880
Choudhary, J. EP-0750, EP-1210, EP-1235, EP-1236, **EP-1278**, EPS-206, **EPS-277**
Choudhary, S. OP-760
Choudhury, A. OP-604
Choudhury, S. EP-0266, EP-0885, EP-1445
Chow, P. K. H. EP-0847
Chow, T. K. EP-1284
Chowdhury, N. EP-0561
Choyke, P. L. OP-088
Chrétien, B. OP-433
Christ, E. OP-432
Christ, L. OP-552
Christensen, N. **EP-0290**, EPS-223
Christodoulou, S. EP-1417
Chu, X. EP-0517
Chu, Z. EP-0209
Chua, W. OP-031, OP-541
Chuang, C. **EP-0167**

Chuang, P. J. EP-0284, EP-0346, **EPS-029**, **EPS-245**, OP-701
Chudyba, E. EP-0440
Chueh, J. S. EPS-245
Chung, A. EP-0376
Chung, K. EPS-032, OP-222, EP-0466
Chung, T. EP-0033, OP-416
Chunyu, H. **EP-0386**
Ciamarone, A. OP-182, OP-326, OP-327
Ciampi-Dopazzo, J. EP-0846
Ciani, R. OP-042
Ciantar, K. EP-0929
Ciarallo, A. EP-1288
Cichocki, P. **EP-0360**, EP-1232
Cicone, F. EP-0183
Cidda, C. OP-801
Cidemal, M. EP-0354
Cieszykowska, I. EP-0789, EP-1166, EP-1174, EPS-009, OP-518
Ciglar-Hlasc, M. EP-0524
Cik, M. OP-458
Cillero Etxebeste, I. EP-0462, EP-1262, EP-1263
Cilliler, A. EP-1307
Cimic, A. EP-0037
Cimini, A. EP-0345, EP-1212, EP-1281, **EP-1287**
Cinar, A. EP-0222, EP-0273, EP-0749, EP-1216, EP-1249, EP-1307, EPS-260, EP-0232
Cingi Ozdemir, E. OP-856
Cini, O. **EP-0101**
Cinoğlu Karaca, M. EP-0902
Cinquegrani, G. OP-549
Cioffi, M. EP-0681, EP-0683
Ciompi, F. OP-170
Cisero, E. EP-0370
Cistaro, A. EPS-272
Cisternino, S. OP-453, OP-584
Cittanti, C. EP-0461, EP-0893, EP-1254
Ciuciulkaite, I. **OP-247**, OP-383
Civan, C. **OP-329**
Cives, M. EP-0312, EP-0329
Civollani, S. EP-0227, EP-1064, EPS-288
Claesen, K. EP-1041
Claeys, W. EP-0935, EP-1188, OP-096, **OP-097**
Clark, P. OP-767
Claron, M. OP-211, OP-351
Claude, G. **OP-345**
Claudin, M. EP-0800, EP-0827, EP-0829, OP-499
Claus, R. OP-358
Claver-Garrido, E. EP-0618
Clavijo-Umbarila, A. EP-0673, EP-0656
Cleeren, F. EP-0935, EP-1175, OP-179, OP-350, OP-366, OP-656
Cleland, J. **OP-025**
Clement, C. L. EP-0933
Clement, P. EP-0879, EPS-126, OP-366
Clemente, S. EP-0788
Clemmensen, A. OP-166
Clemons, N. EP-0070, EPS-012, OP-217, OP-218, OP-275, OP-517
Clerget, C. EPS-131
Clevert, D.-A. EP-0037
Climent, F. OP-865, EP-0495
Clotagatide, A. EP-1178
Çınar, A. EP-0742
Coates, A. EP-0959
Coban, Ö. **EP-1047**
Coccarelli, A. **EP-0683**
Cocciolillo, F. EP-0665, OP-720
Cochet, A. EP-0096, EPS-044, EPS-186, OP-211, OP-347
Codesido, J. OP-093
Codés Mendez, H. OP-553
Coetzee, A. EP-1250
Cohalan, C. EP-1033
Cohen, D. **EP-0036**
Coşkun, N. EP-1007
Colabufo, N. EP-1399
Colelli, G. OP-706
Colin, T. OP-536
Coliva, A. **EP-0115**
Coll, D. EP-0382, EP-0384
Collado, I. EP-0526
Collamati, F. **EP-1109**, **OP-663**
Collantes, M. EP-0156, OP-700
Collarino, A. EP-0010
Colle, M. TEPS-009
Colley, P. EPS-291
Collin, B. EPS-044, OP-211, OP-347, OP-351
Collins, E. C. EPS-032
Colombo, C. EP-0206, OP-105
Colombo, P. E. EP-0894, EP-1130, EP-0914
Colombo Gomez, L. M. EPS-287
Colpo, N. EP-0160, EPS-021
Comas Rojas, H. EP-0070, EP-0162, EPS-012, OP-217, OP-218, OP-275
Comas-Rojas, H. OP-517
Comber, E. EP-0911
Comelli, A. EP-0369
Comley, R. OP-458
Compte, A. EP-0382, EP-0384, EP-0412
Comtat, C. EP-0083
Comte, V. EP-0671
Cong, E. EP-0694, EP-0695
Cong, S. OP-462
Conlon, S. EP-0389
Connelly, J. P. EP-1397, EP-1044
Constantin, A. **EP-1335**
Constantin, L. EP-0815, EP-0825
Constantinescu, B. **EP-1332**
Constantino, C. EP-1083, EP-0961, OP-158, **OP-527**
Constanzo, J. OP-213, OP-214
Conte, M. EPS-272
Conti, M. EP-0966, EP-0974, EP-0977, EP-0981, EP-1028, EPS-221
Contreras, M. M. EP-1410
Contreras Ameduri, M. EP-0374, EP-0472
Contreras Gutiérrez, J. EP-1308, EP-1311, EP-1312, EP-1315, EP-1305, EP-1289
Cook, B. EP-0116
Cook, G. EP-0916, EP-1093, OP-619, OP-625
Coolkens, A. OP-656
Cools, R. EP-0103
Coosemans, A. OP-150
Coppens, M. OP-121
Coppola, M. OP-059
Corbett, C. OP-825
Corcioni, B. EP-0375, EP-0398, OP-716
Cordero, J. EP-0705
Cordon Avila, A. EP-1145
Cordón del Pozo, J. EP-0776
Corneel, C. OP-604
Cornelissen, B. EP-0011, EP-0061, EPS-195, OP-149, OP-515, EPS-002, OP-452, OP-520
Cornide, M. EP-0775
Cornide Carrallo, M. **EP-0491**, OP-784
Cornide Carvallo, M. EP-0394
Coronado Poggio, M. EP-0705
Corre, J. EP-1055, OP-225
Correia, I. **OP-158**
Cortes Pérez, S. EP-0550
Cortés Romera, M. EP-0731, EP-0758, OP-480, EP-0307, EP-0392, EP-0437, EP-0494, EP-0495, EP-0498, EP-0508, EP-0618, EP-0653, EP-0850, EP-1057, EP-1366, EP-1411, EPS-022, EPS-031, EPS-040, EPS-121, OP-233, OP-865
Cortez, E. EP-1201
Corvo, C. OP-453
Corwin, M. T. EPS-032
Corza Ayala, M. EP-0816, **EP-0909**
Cosby, A. EP-1169
Cos-Domingo, M. EP-0653
Coskun, N. EP-0837, **OP-856**
Costa, C. L. S. EP-1201
Costa, D. C. EP-1133, EP-0814, EP-0905, EP-0961, EP-1083, OP-158, OP-527
Costa, G. EP-0765, EP-0897, EP-1256, EP-1318, EP-1320, OP-379, OP-633, OP-636, **EPS-185**, **OP-180**
Costa, I. V. EP-1409
Costa, L. EP-0701, OP-056, OP-061, OP-372
Costa, M. OP-858, EP-0905, EP-1133, EP-0777
Costa, P. F. EP-1103
Costantini, M. EP-0411, EP-0436, OP-042, OP-068
Costoya-Sánchez, A. OP-440
Cottignoli, C. OP-558
Cotton, J. OP-017
Coudrais, N. EP-0581, OP-500
Coulbault, L. OP-838
Courbon, F. EPS-078, OP-292, OP-599
Courteau, A. EPS-044, OP-211

Coussirou, A. EP-1181
Coussy, F. EP-0217, EP-0297
Couto Caro, R. EP-0394, EP-0491
Couturaud, F. EPS-090
Couture, A. OP-162, OP-164
Cox, B. EP-0160
Cox, C. P. W. **EPS-109**
Crabbe, M. **EPS-020**
Craciun, D. EP-0743
Cralcev, C. EP-0505
Cramon, P. EP-0709
Crapez, E. OP-213
Cras, Y. EP-0786, EP-1019, EPS-199, **OP-098**, **OP-630**
Creisson, A. EP-0202
Cremonesi, M. EP-1159
Crespí-Busquets, M. EP-0850, EP-1366, EP-0495, EP-1411
Creytens, D. OP-522
Crick, E. **EP-1400**
Cristel, G. OP-875
Cristica, T. EP-1316
Cristina Sa De Camargo Etchebehere, E. EP-0337
Crnic Bojkovic, T. **EPS-128**
Crook, L. **TEPS-005**
Cropet, C. OP-331
Croset, A. EPS-055
Cross, D. OP-302, OP-307
Crumbaker, M. EP-1161, OP-323, OP-676, OP-703
Cruz, J. EP-0905
Cruz, N. OP-666
Cruz Garcia, L. OP-425
Cruz Montijano, M. **EP-0328**, EP-0358, EP-0401, EP-1393, **EP-1408**
Csákÿ, A. G. OP-346
Csikos, C. **EP-0450**, EPS-278, OP-501
Cucchi, C. EP-0017, EP-0044
Cuderman, A. **EP-0835**
Cuesta, G. EP-0553, EP-0775
Cuesta Domingo, G. **EP-0339**, **EP-0340**, **EP-0341**, EP-0394, EP-0491
Cueto Cañadas, B. EP-1227, EP-1251
Cuevas, R. EPS-117, OP-378
Cui, B. EPS-118
Cui, C. EP-0554
Cui, F. **OP-207**
Cui, J. OP-477, OP-851, EP-0609
Cui, R. OP-045
Cui, X. Y. **OP-412**, **OP-653**
Cui, Y. EP-0237, EP-1021
Cui, Z. EP-0315, EP-0884
Cullis, P. R. OP-094
Cuneo, A. EP-0461
Cunha, A. OP-061
Cunha, L. EP-1409, EPS-300
Cunha, M. EP-1320
Cuocolo, A. EP-0308, EP-0788, OP-684
Cuocolo, R. EP-0254
Cuomo, M. EP-1146
Cupido, J. EPS-062
Curcio, A. EP-1159, OP-042
Currie, G. EP-0353, OP-316
Curti, A. EP-0504
Custodio, A. OP-430
Cuttone, S. OP-858
Cuzzani, G. **EP-0227**, EP-0444, **EPS-247**, OP-118, OP-168, OP-246, OP-248, OP-798
Cuzzocrea, M. OP-823, **EP-0425**, EP-0889
Cwikla, J. B. OP-429, EP-0320
Cyran, C. C. EP-0037, EP-0309
Czernin, J. EP-0208, EP-0376, EP-1124, EP-1143, EP-1410, EPS-162, EPS-192, OP-714

Daamen, M. OP-303
Da-ano, R. **OP-356**
Daşar, M. EP-1373
Dabbagh, V. EP-0566, EP-0567, EP-1378
Dabin, J. OP-702
Dabiri, S. EP-1296
Dacosta Escobar, A. EP-0758, EP-0618, OP-233, EP-0495
Dadgar, H. **EP-0345**, EP-0348, EP-0413, EP-1281
Dagil, R. OP-760
Dagna, L. EP-1043
D'Agostino, V. EP-0639
Dagrakis, E. EP-0569, EP-1379
Dahlbom, M. EP-1124, EP-1143, EP-1410, EPS-192, OP-824
Dahle, J. EP-0007
Dahlke, P. EP-1092
Dahmen, H. OP-516
Dai, J. **EPS-168**, EP-0276, EPS-176, EP-0386
Dai, Z. EP-0190, **EP-0356**, OP-286
Daignault, M. EPS-139
Daisaki, H. EP-0927, EP-0954, EP-0956, EP-1098, EP-1452
Daisne, J.-F. EP-0183„EP-0879, EPS-126
Dal, M. S. EP-0464
D'Alessandria, C. OP-181, EP-1047
Daley, A. EPS-192
Dallanoce, C. EP-0115
Dall'Olio, D. EP-0145, EP-0270, EP-0421, EP-1064, EP-1268, OP-246, OP-248, OP-293, OP-330, OP-798
Dalm, S. U. EPS-007, EP-0003, EP-0136, **EPS-017**
D'Alò, F. EP-0497
D'Alterio, C. EPS-054
D'Ambrosio, D. OP-669
D'Ambrosio, L. **EP-1115**, EPS-054
Damián, A. OP-302, **OP-307**
Damiani, S. EPS-247
D'Amico, A. EP-0207
Damle, N. A. EP-0285, EP-0559, EP-0746, EP-0880, EP-1387, OP-744, OP-872, EP-0177, EP-0882
Dancheva, Z. EP-1292, EP-1293, EP-1294, EP-1330, EP-1331, EP-1359, EP-1384
D'Andrea, E. EP-1159
D'Andrea, G. EP-1004
D'Andrea, M. EP-0906
Danfors, T. EPS-128
D'Angeli, C. EP-1109
D'Angelo, D. EP-0352
D'Angelo, P. EPS-272
Daniel, S. OP-626
Danieli, R. OP-097, OP-537
Danielsen, H. OP-883
Danila, R. EP-1303
Danilov, G. EP-0992
Dannenberg, M. OP-840
Dános, K. EP-0562
Dansin, E. OP-173
D'Antonio, A. OP-684
Daoud, B. EP-0465, OP-027
Daoust, A. EP-0096, EPS-044
Dapper, H. EP-0331
Darcourt, J. **EP-0671**, EP-1004
Dardiotis, E. EP-0675
Dardouri, T. **EP-0447**, EP-1231
Darian, D. EP-0974
Dario Ramos, C. EP-0262
Darr, C. OP-297, OP-786
Darrigues, L. OP-104
Das, C. J. EP-0371, EP-0372, EP-0373, EP-0764
Das, J. EP-0201
Das, M. EP-0919
Dasar, M. **EP-0443**
Dash, S. **OP-073**
Dasheeva, A. EPS-112, OP-795
Dashti, S. EP-1279
Dassanayake, M. EPS-236
D'Asseler, Y. OP-097
Dassie, A. EP-1120
Daszewska, K. EP-0207
Datres, M. EP-0234
Datseris, I. EP-0875
Datta, P. EP-0118, **EP-0116**
Datta, S. EP-0405
Datz, H. OP-702
Daudén, P. EP-0340, EP-0553, EP-0775
Daudén Oñate, P. EP-0339, EP-0341, EP-0394, EP-0491
Davarci, F. **EP-0925**
Davarpanah, M. EP-0066, EP-0128, EP-0937, EP-1108
Daverio, A. EPS-199
David, D. J. OP-453
David, T. OP-214, OP-213
Davidzon, G. EP-0980, OP-239, OP-539
Davies, L. EP-0974
Davies, P. OP-425
Da Villa, C. OP-467
Davis, C. EP-0942, EP-1116, EPS-086, OP-825
Davis, I. OP-323
Davis, N. **OP-667**
Davis, P. EP-0088

Davoodi, S. EP-1361
Davulcu, C. D. EP-0901
Davydova, E. EP-0286, EP-0402, **EPS-265**, OP-472
Dawson, R. **EPS-179**
D. Chadha, V. EP-1460
Deandreis, D. EP-0306, EP-0786, EP-1019, EP-1075, EPS-199, OP-098, OP-120, **OP-599**, OP-630
De Arcocha-Torres, M. EP-0656, EP-0673
Dearling, J. EPS-062
De Azambuja, E. OP-107
Debacker, J. M. OP-522
De Bakker, M. G. J. EP-1123
Debeir, O. OP-526
Debiossat, M. OP-022
De Blois, E. EP-1185, EPS-017, EPS-196
DeBoni, L. EP-0696
De Bonilla Candau, M. EPS-211
De Bruin, T. EP-1116, OP-825
De Buyst, S.-A. OP-366
De Cabo Ripoll, M. EP-0358
Decaestecker, K. OP-121
de Camargo, R. A. EP-0631
Decazes, P. EP-1017, EP-1114, OP-533
De Cecco, L. OP-384
De Cillis, S. EP-0370
Deckers, W. EP-0391, EP-0935, EP-1188, EPS-126
De Cobelli, F. OP-875
Decock, A. OP-121
Decristoforo, C. EP-0123
De Crop, A. OP-097
Decuadra, P. EP-0140
Dede, A. EP-0718
Dede, F. OP-874
Dedecjus, M. EP-0789
De Dominicis, L. OP-584
De Feo, G. EPS-054
De Feo, M. EP-1281
De Feria Cardet, R. EP-1086
De Francisci, M. EPS-221, OP-771
De Frutos-Seminario, F. EP-0618
De Geus-Oei, L.-F. EP-0010, EP-0334, EP-0948, EP-1086, EP-1395, OP-295, OP-713
De Giovanni, A. EP-0227, EP-0270, OP-168
De Groot, A. **OP-156**
De Groot, M. OP-598
De Groot, T. EP-1175
Degryse, L. EP-0643, **EP-0879**, **EPS-126**
Degueldre, S. EP-1186
Dehghan, M. EP-1163
Dehghani, M. EP-0127, EP-0038, EP-0146
Deibel, A. EPS-041
Dei Cas, A. OP-549, OP-801
Deidda, D. EP-0950, EP-0996
Dejanovic, D. EP-0219
Dejmasu, S. EP-1309, EP-1317
De Jong, H. W. A. M. EP-0907
De Jong, I. OP-598
De Keizer, B. EP-1055, OP-225
De Kemp, R. **EPS-075**, OP-160, OP-528, EP-0977
Dekervel, J. OP-366
DeKeyser, S. EP-0683
Dekker, M. C. EP-1432
De Klerk, J. EP-1395
De Kruijff, R. **OP-587**
Delaby, G. OP-555
De la Cueva Barrao, L. EP-0760
Delage, J. EP-0828, **EP-1404**
De la Rubia Marcos, M. EP-0792, EP-1368, EP-0819, EP-1286, EP-1337, EPS-263, EPS-273
De la Torre, N. EP-0382, EP-0384
De Lauro, F. EP-1115, OP-437
Del Barco Díez Canseco, L. M. EP-0760
Delbridge, C. OP-606
De Leiris, N. EP-0800, EPS-103, OP-787, OP-822
Deleu, A.-L. **OP-169**, OP-470
Delgado-Castro, M. M. EP-0552
Delgado García, A. EP-0774
Delgado Mayenco, N. EPS-195, **OP-515**
Delgado Moreno, J. EP-1227, EP-1251
Del Gaudio, F. OP-484
Del Giudice, E. EP-0255
Delion, M. EP-1189
Delisau, Y. EP-0490, OP-442, EP-0324, **EP-0551**, EP-0762, OP-553
Delker, A. EP-0886, EP-1118, EP-1150, EP-1410, EPS-197, EPS-240, EPS-290
Dell'Acqua, C. OP-055
Della Gala, G. EP-1112
Della Morte, A. OP-059
Della Pepa, R. EP-0507
Dellavedova, L. OP-384
Dellepiane-Clarke, F. EPS-202
Dellovale, T. OP-458
De Loisy, M. EP-0812
Delpassand, E. EP-0088, EP-1143
Del Sol Pérez Lago, M. OP-601
De Luca, S. EP-0370
De Luca, M. **OP-586**
Delucchi, C. OP-868
De Lussanet de la Sabloniere, Q. OP-852, EPS-109
Del Vecchio, A. OP-706
Del Vecchio, S. EP-0233, EP-0393, EP-0507
De Maggi, A. **EPS-298**
De Man, K. OP-782
De Marchi, L. EP-0461
De Marino, R. EP-1115, EPS-054
De Meester, I. OP-156
De Meeus d'Argenteuil, F. OP-344
Demers, A. S. EPS-181
De Mestier, L. OP-429
De Meulenaere, V. **EP-0325**
De Migno, R. EP-1115
Demir, B. EP-0245, EP-0806, EP-1392
Demir, F. **EP-0321**
Demir, O. OP-531
Demir, S. OP-175
Demirdag, C. EP-0355, EP-0368
Demirel, B. B. EP-0464, EP-0808, EP-0851, EP-0225, EP-0335
Demirel, K. EP-0443, EP-0763, EP-1271, EP-1277, EP-1373
Demirkol, M. **OP-386**
Demirtas Senlik, S. **EP-0273**, **EP-0577**
De Monte, F. EPS-287
Demontrond, P. OP-173
Denat, F. EP-0096, EP-0164, EPS-153, OP-211, OP-347, OP-351
Dendukuri, N. OP-551
Den Dunnen, J. EPS-036
Deng, J. OP-174
Deng, Y. EP-0484, **OP-020**, OP-837
Den Hollander, M. E. EPS-081, OP-774
Deniel, P. EP-0093
Denis Bacelar, A. EP-0950, OP-096
Deniz, G. **OP-543**
Denkova, A. G. EPS-015
Dennis, J. EP-0993
de Oliveira Menezes, V. EP-1001
de Oliveira Taveira, M. **EP-0201**
De Paepe, B. TEPS-009
de Paula Faria, D. EPS-232
Depeursinge, A. OP-160, OP-528
Depoortere, V. TEPS-012, OP-317
De Pooter, J. EP-1405
Deportos, J. **EP-0845**, EPS-026
Derdak, Z. EP-1104
Dere, A. B. EP-0511
Dere, A. **EP-0844**, EP-1367, OP-859
Dere, V. EP-1386
De Ridder, C. EP-0087, EPS-017, OP-153
De Ridder, V. EP-0683
Derks, Y. OP-184
Derneden, C. OP-317
Dernjani, N. EP-0014
De Roode, K. E. EPS-048
De Roos, P. EP-1169, EP-1171
Deroose, C. M. EP-0879, EP-0935, EP-1175, EP-1188, EPS-126, OP-067, OP-366
De Rose, F. OP-361
D'Errico, A. EP-0227, OP-168
Derveaux, E. EP-1041
Derwael, C. EPS-084
Desai, P. **OP-658**
Descamps, B. OP-522
Deschavannes, A. **EP-1178**
Deshayes, E. OP-213, **OP-429**
De Simoni, M. EP-1109
Desmidt, T. OP-718

De Souza, C. A. EP-0262, OP-119
De Spirito, M. EP-0665, OP-858
Després, P. EP-1110
D' Este, S. EP-0722
Destro, G. EP-0141
Desuki, A. EP-0532
De Summa, M. EP-1398, **OP-891**
Desvignes, M. EPS-103
De Swart, J. EP-0003
De Tiège, X. EP-0663, EP-0687
De Troyer, B. OP-710
Deurloo, I. S. **OP-289**
Deuschl, C. OP-239
Dev, I. EP-0266, **EP-0885**
Devi, R. **OP-303**
Deville, C. OP-579
Devir-Wolfman, A. EPS-087, OP-103, OP-661
Devisscher, L. OP-522
Devitt, K. OP-323
De Vleeschouwer, S. EP-0879, EPS-126
De Vocht, J. OP-530
De Vos, C. C. OP-870
De Vos, F. OP-522
Devos, G. OP-067
Devous, M. D. OP-440
Devriendt, L. OP-537
De Vries, E. F. J. EP-0061, OP-515
De Vries, E. EP-0011
De Vries, J. J. M. OP-170
Devries, D. EPS-138
De Vries-Huizing, D. M. V. OP-597
Dewaele, F. EP-0325
De Weerd, L. EP-0018
Dewilde, M. OP-656
De Winter, M. **EPS-074**
De Winter, O. OP-107
De With, G. **EPS-285**, EPS-286
De Witte, O. EP-0663
de Witt Hamer, P. C. OP-607
De Wit van der Veen, B. J. OP-597, OP-289, EP-0848, EP-1034
De Wolf, T. OP-221, OP-425
Dewulf, J. OP-152
Deyev, S. EP-0089
Dezső, D. EP-0797
Dhania, S. EP-1459
Dhiantravan, N. OP-676
Dhiman, A. EP-0474, EP-0510, EP-0744
Dhingra, V. K. EP-0259, EP-0877
Dhont, N. TEPS-009
D'Huyvetter, M. OP-152, OP-215, OP-593
Diakakis, A. EP-0675
Dias, A. M. M. OP-211
Dias, A. H. OP-038, OP-769
Dias, J. OP-741
Dias, M. **EP-0905**
Dias, P. EP-0599
Dias Correia, R. EP-1407
Díaz-Alarcón, J.-P. EPS-303
Diaz Brinton, R. EPS-134
Díaz González, L. EP-0364, EP-0378, EP-0200, EP-0931
Diaz Melguizo, J. OP-485
Diaz Moreno, J. EP-0498, **EP-0437**, **EP-0618**, EP-0508, EP-0653, EP-0731, OP-233, OP-480
Díaz-Moreno, J. L. EP-0494, EP-0850, EP-1366, EPS-022, EPS-040
Diaz Vico, T. OP-785
Di Bartolomeo, K. EP-0952
Dibbets-Schneider, P. EP-0948, OP-783
Di Benedetto, S. EP-0115
Dickson, J. OP-096, EP-0996
Di Cristina, L. EP-0406
Didi, N. EPS-087
Di Donato, R. EP-0254, OP-326
Di Donna, E. EP-0507
Didonna, A. EP-0914, **EP-1130**
Diekstra, E. EPS-195, OP-515
Dieplinger, G. EP-0331
Dierckx, R. A. OP-051
Dierickx, L. O. OP-429
Dierks, A. EP-0734, OP-376
Dierneder, J. OP-778
Dietlein, M. EP-0488
Dietze, M. M. A. EP-0907
Dietzel-Schaarschmidt, A. EP-0557
Dieudonné, A. EP-1017, **EP-1114**, OP-533
Diez, M. **EP-0611**
Diez Castro, M. OP-483
Díez-López, C. EP-0618
Di Fazio, P. EP-0854
Di Fiore, F. EP-1114
Di Franco, M. EP-0310, EP-0311, EP-0396, **EP-0502**, **EP-0503**, EP-0504, EP-0514, EP-1064, EP-1268
Di Gennaro, F. EP-1115
Dighero, E. **OP-776**
Di Giorgio, A. **EP-0396**, **EP-0421**, EPS-030, OP-224, **OP-293**
Di Giorgio, E. EP-0639
Di Giuda, D. EP-0665, OP-669, OP-720
Di Grigoli, G. EP-0393
Di Iorio, V. EP-0411, EP-0436, EP-0801, EP-0802, EP-0803, EP-1081, EP-1159, OP-042, OP-068
Di Maiolo, G. EPS-054
Di Maro, S. EP-0044, EPS-054
Di Mauro, F. EP-0255
Dimitrakopoulou-Strauss, A. EP-0485, EP-0506, EP-0520, EP-0525, EP-1022, OP-294
Dinapoli, N. EP-0497
Dinckal, M. EP-0366, EP-0428
Ding, D. **EPS-063**, OP-086, OP-439
Ding, J. **EP-0979**, OP-231
Ding, W. EP-0964
Dinkelaker, J. OP-842
Diogo, L. EP-1318
Dirix, P. OP-710
Di Santo, G. OP-434
Dise, J. EP-0822
Di Sibio, A. EP-1281
Dittmann, H. EP-0229, EP-0351
Divband, G. EP-0888, EP-1149, EP-1151, EP-1152, EP-1351
Dixit, M. EP-1459
Dixon, J. **EP-0993**
Dizdar, K. EP-1007, EP-1008
Dizdar, N. EP-1007, EP-0232, OP-497
Dizdarevic, S. EP-0809
Djaileb, L. **EPS-103**, OP-022, **OP-787**, **OP-822**
Djerroudi, L. EP-0297, OP-104
Djouraev, S. TEPS-013, TEPS-015
Dlugosinska, J. EP-0789
Doğan Yıldız, Ö. OP-715
Dobi, A. EP-0180
Dobra Neacsu, E. EP-1197, EP-1198
Dobson, R. **EPS-023**
Do Carmo, S. EPS-061
Do Carmo Lopes, M. OP-708
Dodel, R. OP-239
Does, L. **OP-890**
Doi, T. OP-729
Doi, Y. EP-0139
Dolezel, L. OP-352
Dolladille, C. OP-433
Doma, A. **EP-0196**, EP-0519
Domingo, A. EP-1219
Domingo Domenech, E. EP-0478, EP-0494, EP-0495
Domínguez-Borrero, C. EP-0999, OP-093
Domínguez Gadea, L. EP-0705
Domínguez Grande, M. EP-0319
Domínguez Polanco, E. **EP-0555**, **EP-0560**, **EP-0867**, EP-0522, EP-0846, EP-0866, EPS-249
Domogalla, L. C. EP-0121, EP-0557
Dondi, F. EPS-272, OP-324
Donegani, M. EP-0377, OP-725
Dong, L. EP-0674
Dong, M. EP-0067, EP-1096
Dong, P. EP-0761
Dong, Y. EP-0492, EP-0667
Dong, Z. **EP-1139**
Donnelly, P. OP-277
Donner, D. EP-0206, OP-105, OP-613, **EP-0234**
Donniaquio, A. OP-725
D'Onofrio, A. M. OP-720
Donswijk, M. **OP-876**
Dooms, C. OP-366
Doornhof, K. **EP-1010**, **EPS-182**
Döring, Y. OP-552
Dorneich, J. S. **EP-0698**, EP-0699, OP-237
Dornish, M. **EP-0007**

Dorothée, G. EPS-131
Doruyter, A. EPS-203
Doruyter, A. G. G. OP-849
Dory, Y. OP-021
Dorzhieva, R. OP-795
Dos Santos Filho, A. EP-1001
Dossat, C. TEPS-016
Dotinga, M. EP-1034, EP-1432
Doudouh, A. EP-1290, EP-1301, EP-1302, EP-1325
Dougall, P. EP-0543, EP-1213, EP-1252, EP-1253, EP-1260
Douillet, A. OP-602
Doukas, M. EPS-017
Doumas, A. EPS-254
Doyen, M. **EP-0692**, OP-049, OP-235, OP-499
Doyeux, K. OP-499
Draganic, K. EP-0045
Dragonetti, V. EP-0389
Draper, M. EP-1400
Dreger, P. EP-0485
Dreher, N. EP-0734, **OP-223**
Drevon, L. EP-1082
Drews, A. EP-0084
Drexler, W. OP-352, OP-354
Driess, D. EP-0532
Drigo, A. EP-1120, OP-631
Driscoll, B. **EP-1100**, OP-423
Droghetti, M. OP-716
Droogers, E. EP-0535, EP-1395
Drouet, C. EPS-186, OP-675
Drozd, S. EP-0178
Drum, T. EPS-138
Drzezga, A. EP-0331, EP-0488, EP-0696, OP-048, OP-381, OP-879
Du, X. EP-1441, EP-1446
Du, Y. EP-0046, **EP-0809**, EP-1037, EP-1048
Duan, X. EPS-032, EP-0043, EPS-016
Duan, Y. **EP-0677**, EPS-025, OP-308
Duarte, A. OP-665
Duarte, H. EP-0199, EP-1205, EP-1243, OP-742
Duarte, I. TEPS-016
Duarte, J. EP-0772, **EP-1255**, **EP-1265**
Duarte, P. EP-1184
Dubart, A. EP-1186
Dubey, V. EP-1445
Dubois, A. EPS-131
Dubois, D. **EP-0377**, OP-324, OP-868
Dubois, J. EP-0589, EP-1082
Dubray-Longeras, P. OP-173
Dubrocq, M. **OP-526**
Duch, J. EP-0324, EP-0490, EP-0551, EP-0762
Duchaj, B. **EP-1006**
Duchstein, L. L. EP-0005, EP-0624
Ducray, F. EP-0183
Ducreux, M. EP-0306
Duezel, E. OP-303
Dührsen, U. EP-0483, EP-0488, OP-032
Dujardin, A. OP-359
Dumas, L. OP-022, OP-787
Dumauthioz, N. **OP-152**, **OP-593**
Dumouchel, A. EP-1114, OP-533
Du Moulinet d'Hardemare, A. OP-022
Dunaykin, M. **EP-0481**, **EP-0482**
Dunckley, C. EP-1169, EP-1171
Dupont, A.-C. OP-718
Dupont, F. EP-0598, EP-0947, EPS-099, EPS-299, OP-496, TEPS-012
Dupont, P. A. OP-838
Dupont, V. OP-227
Durand, A. EP-0787
Durand, E. EPS-207
Durán Poveda, M. OP-785
Durany-Lara, D. EP-0392, EP-0437
Duray, E. EP-1186
Dureja, S. **EP-1402**
Durivault, J. OP-022
Durmaz, S. EP-0368
Durmazer, E. N. EP-0479
Durmo, R. EP-0496, OP-113
D'Ursi, P. OP-776
Durski, J. M. EP-0807
Dursun, A. **EP-0232**, **OP-497**
Dursun Avci, E. EP-0806, EP-0834
Duyar, O. EP-0359
Dvorakova Bendova, K. EP-0148
Dwivedi, P. **EP-1445**
Dyankova, M. **EP-1292**, **EP-1293**, **EP-1294**, EP-1330, EP-1331, EP-1359, EP-1384
Dyczka, A. **EP-0714**
Dyke, J. P. EPS-134
Dzialas, V. **OP-048**
Dziuk, M. OP-679
Ebenau, J. L. OP-607
Eberlein, U. EPS-294, EPS-295, OP-426
Ebert, M. EPS-119
Ebner, R. **EP-0309**
Ebrahimifard, A. EP-0854, **EP-0987**
Echeverri Diaz, J. EP-0388, OP-483
Echeveste, B. EPS-117
Ecke, T. OP-628
Eckenweber, F. EP-0309
Ecsedi, B. EP-1036
Edenbrandt, L. EP-0463, EP-0468, OP-294
Eder, A. C. EP-0121, EP-0135, EP-0557, **EPS-159**
Eder, M. EP-0121, EP-0135, EP-0557, EPS-159
Edet-Sanson, A. EP-1017, EP-1114, EP-1181, OP-533
Edgar, F. EP-0041
Edouard, L. **OP-536**
Edwards, J. EP-0729
Eelkema, R. EPS-015
Eersels, J. OP-593
Effing, J. **OP-884**
Efrati, A. EPS-087
Eftimov, A. EP-0448
Eftychiou, N. **EP-0783**
Egan, G. OP-284
Egger, G. EP-0045
Eggers, K. M. OP-791
Ehret, F. EP-0183
Ehrlichmann, W. OP-017
Eiber, M. EP-1047, EP-1128, EP-1143, OP-181, OP-323, OP-329, OP-363, OP-364, OP-461, OP-789
Eidt, S. OP-628
Eierud, C. EP-0690
Eigler, C. OP-432
Eijkelkamp, N. EPS-036
Eikenes, L. EP-0883
Eilsberger, F. EP-0305, **EP-0854**, EP-0987
Einieh, M. **EPS-278**
Einsele, H. OP-223
Einspieler, H. EP-0408, EP-1241, **OP-325**, OP-820
Einstein, A. OP-679
Eiro, T. OP-301, OP-719
Eismant, A. EP-0784, EP-0790, EP-0881, OP-436, OP-860, OP-862
Ekmekcioglu, O. **EP-0240**
Elahifard, H. EP-1360, EP-1361, **EP-1377**, **EP-1378**, **EP-1380**
Elashoff, D. EP-1410
El-Barkaoui, A. E. OP-049
El Bez, I. **EP-0739**, **EPS-279**
Elboga, U. OP-711, OP-873
Eleftheriadis, V. EPS-198
El Ghalbouni, A. **OP-863**
El-Hage, W. EPS-035, OP-718
El-Hennawy, G. EP-0818
Elhusseiny, G. EP-0810
Elings, E. W. OP-622
Elkanawaty, M. EP-0810
Ells, J. EPS-290
Ells, Z. EP-1124, **EP-1143**, EP-1410, **EPS-192**, EPS-290, OP-824
Ellul, G. EP-1091
Elmenhorst, D. EP-0696
El-Sayed, M. **OP-741**
El Shazly, M. EP-0810
Elsinga, P. EP-0011
Elvas, F. EP-0001, EP-0101, EP-0102, OP-156
Elz, A. EP-0130
Emadzadeh, M. OP-109
Emami, F. EP-1345
Emiliani, S. EP-0227, EP-0270, OP-168
Emmerson, B. EP-0830, OP-605
Emmett, L. OP-323, OP-675
Encina, N. OP-889
Endo, H. EP-0874
Eng, W. OP-206, OP-207
Engbers, P. EPS-196, OP-216, OP-221
Engblom, H. EP-0582
Engel, R. OP-060

Engel-Hills, P. OP-620
Engelsen, O. EP-0807
Engkebølle, C. EP-0172
Engle, J. W. EP-0162, EP-1164, EP-1165, EPS-194, OP-579, OP-583, OP-586
Englert, A. EP-0018
Engur Uyanik, C. EP-1249, EP-0273, EP-0742
Enke, J. **EP-0734**, EP-1009, OP-358, OP-223
Enqvist, O. EP-0463, EP-0468
Entrena Ureña, L. EP-0774
Episkopopoulou, S. EP-0569, EP-1379
Epphard, E. OP-245
Epure, M. **EP-1309**, EP-1317
Eraslan, E. EP-0441
Erba, P. A. OP-326, OP-484, OP-298
Erbil Capci, E. **EP-0197**
Ercan, L. D. EP-0282
Erdem Karaoglu, A. **EP-0222**
Erdil, T. EP-1127, EP-1141, OP-874
Erdim, C. OP-857, EP-0840
Erdogan, A. P. EP-0236
Erdogan, M. F. EP-0441
Erez, O. EP-0837, EP-1127, EP-1141
Erfani, M. EP-0128
Ergün, K. E. EP-0428, EP-0366
Eriksen, C. EP-0722
Eriksson, O. EP-0137, EP-1104, OP-728
Erkek, B. K. EP-0924, EPS-077
Erkoç Ataoğlu, E. EP-0661
Erlandsson, K. EPS-093
Eroglu, A. EP-1141
Eroglu Elden, H. **EP-1271**, **EP-1277**
Erol, A. EPS-260
Erol, B. OP-040
Erol, T. EP-0287
Erro, M. OP-446
Ertay, T. **EP-1420**
Ertekin, C. EP-0282
Ertelt-Delbridge, C. EP-0182
Erturk, S. OP-543
Eryilmaz, Y. EP-0426, **EP-0451**, **OP-804**
Escaleira, J. EP-0701, OP-056
Escalera-Temprado, T. EP-0552
Escola Gil, J. EP-0156
Escorcia, F. E. OP-088
Escrihuela-Vidal, F. EPS-022
Esen Akkas, B. OP-540, EP-0480, EP-0511, EP-0843, EP-1270, EPS-204, OP-856, OP-859
Eseroglou, C. EP-1071
Esfandiari, R. EP-1143
Eskola, O. OP-328
Eskova, D. EP-0089
Esmatinia, M. OP-241
Esnault, M. EP-0581, OP-500
Espigares-Santiago, Á. EP-0731
Espinosa, E. EP-0458, EP-1229
Esposito, A. EPS-054
Esposito, F. EP-0461
Esposito, J. OP-584
Esposto Pirani, P. OP-558
Esquinas, P. EP-0960, OP-102, EP-0160, OP-428, EP-0994
Essler, M. OP-303
Esteban, N. EP-1161
Esteghamat, N. S. EP-0466, OP-222
Estrada Lobato, E. OP-711, EP-0453, OP-873, EP-1396
Estrella, M. EP-0288
Etchebehere, E. EP-1203, EP-1223, EP-1234, EP-1245, EP-1267, EP-1306, EP-1324, EP-1342
Etchebehere, M. EP-1324, EP-1342
Etchegaray, C. EP-0512
Ettala, O. OP-328
Ettema, R. H. OP-876
Etxabeguren Gallo, N. EP-0462, EP-1262, EP-1263
Etxebeste, A. EP-1068
Evangelista, L. EP-0206, EP-0268, EP-0350, EP-0363, EP-0393, EP-0406, EP-0779, EP-1062, OP-105, OP-669
Evenstuen, N. EP-1005
Everaert, H. OP-107
Everaerts, W. OP-067
Exadaktylou, P. EPS-254
Exley, M. EPS-093
Ezzat, S. EP-1100
Ezziddin, S. EP-0780, OP-435
Ezzine, A. EP-0447, EP-1231, EPS-284
Fabbri, L. EP-1159, OP-042
Fabisiak, A. OP-156
Facchinetti, F. EP-0044
Faccini, R. EP-1109, OP-663
Facon, T. EP-1055, OP-225
Fadda, G. OP-380
Fagotti, A. EP-0010
Fagret, D. EPS-103, OP-022, OP-787
Fagundes, M. C. EPS-251
Fahmi, R. EP-0959, EP-1014, EPS-117, OP-234
Faílde Balea, S. EP-0560, **EP-0774**
Faivre, J. EP-0164
Faiz, T. EP-0788
Faizova, R. **EPS-142**
Falasco, G. EP-0100, EP-0157
Falchi, A. EP-0446
Falcini, F. EP-1159, OP-042
Falgás Lacueva, M. EP-0760
Falk, L. EPS-128
Falkenbach, F. EP-1026
Fallanca, F. EP-0496, EP-1043
Fan, D. **EP-0155**
Fan, W. EP-0248, EPS-200
Fan, Y. EP-0385, **EP-0119**, **EP-0211**
Fanetti, G. EP-1120, OP-631
Fang, P. OP-206, OP-207
Fang, T. **EP-0332**
Fang, W. EP-0629, EPS-063, EPS-100, EPS-108, OP-727
Fang, Y. EP-0111
Fangfang, T. EP-0593
Fani, M. OP-361, OP-432
Fanta, O. **EP-0627**
Fanti, S. EP-0145, EP-0227, EP-0270, EP-0310, EP-0311, EP-0375, EP-0396, EP-0398, EP-0421, EP-0444, EP-0502, EP-0503, EP-0514, EP-1064, EP-1112, EP-1238, EP-1268, EP-1372, EPS-030, EPS-247, EPS-288, OP-028, OP-118, OP-168, OP-224, OP-246, OP-248, OP-293, OP-330, OP-437, OP-711, OP-716, OP-798, OP-873
Fantini, L. EP-0206, EP-0411, EP-0436, EP-0803, OP-068, OP-105
Fantuzzi, F. OP-549
Farahi, N. **OP-697**
Farajzadeh, E. **EP-0937**, **EP-1108**
Farasat, M. **EPS-139**
Farina, J. M. EP-0304
Farina Antunes, I. EP-0061
Farncombe, T. EP-1100
Farolfi, A. EP-0389, EP-0145, EP-0270, EP-0375, EP-0396, EP-0398, EP-0421, EP-1064, **EPS-030**, EPS-192, EPS-288, OP-028, OP-224, OP-293, **OP-330**, OP-716, OP-798
Faron, M. EP-0306
Farré Melero, A. EP-0776
Farrher, E. OP-284
Farzanehfar, S. EPS-289
Fasmer, K. E. OP-039
Fassnacht, M. EP-0728
Fasulo, V. EP-0350
Fatima, N. **EP-0293**
Fauci, F. EPS-134
Faure, M. OP-787
Favaretto, C. EPS-137, OP-584
Faviana, P. OP-182
Fayad, H. EP-0383
Fayn, S. **OP-088**
Fearns, N. EP-0699
Feathers, R. **EP-1065**, EP-1156
Federico, A. EP-0010
Fei, G. EP-0357
Fei, K. EP-0042
Fei, M. OP-498, OP-502
Feichtinger, J. OP-778
Feiner, I. EP-0148
Felder, J. OP-284
Feldmann, A. OP-154
Feldwisch, J. EP-0207, EP-0289
Felgenhauer, T. L. M. EP-1105
Feliciani, G. EP-0501
Felix, C. EPS-192
Fendi, R. **EP-1423**
Fendler, W. EPS-190, OP-239, OP-786, OP-818, EP-1103,

EP-1143, OP-329, OP-383, OP-385, OP-538
OP-247, OP-297, OP-779
Feng, H. EP-1441, EP-1446
Feng, J. OP-735
Feng, L. EP-0658, EPS-042, OP-740, EPS-052, EP-0099, **OP-696**
Feng, M. OP-025
Feng, Y. EP-0107, EPS-175, OP-018, EP-0030, EP-0031, OP-276, OP-281, OP-282
Fenter, A. EP-0828
Fenwick, A. **EP-0950**, **EP-1405**
Feraco, P. OP-613
Ferdinandus, S. EP-0331
Feriche, M. EP-0458, **EP-1229**
Fermi, M. OP-798
Fernandes, S. EP-1184
Fernández, E. EP-0553
Fernandez, P. EP-1016
Fernandez, R. OP-471, EP-0783, EP-1400
Fernández-González, A. EP-0156, OP-700
Fernández Iglesias, A. EP-1147
Fernández León, A. **EP-0632**, EP-0490, EP-0762, OP-442, OP-553
Fernández Llana, M. EP-0319
Fernández-Matarrubia, M. EP-0656
Fernández-Zorrilla, E. **EP-0999**
Fernando, P. OP-629
Fernebro, J. OP-596
Ferning, K. H. EP-0007
Feron, J.-G. OP-104
Ferran Sureda, N. EP-1434
Ferrara, D. EP-0230, EP-0968, EP-1079, EP-1089, EP-1093, EP-1097, OP-548
Ferrara, R. EP-0254
Ferrari, C. EP-0206, EP-0312, EP-0329, OP-105
Ferrari, M. OP-702, EP-0227, OP-168
Ferraro, D. **EP-0631**
Ferrat, M. EPS-154
Ferreira, Â. OP-158
Ferreira, B. EP-0729
Ferreira, I. EP-0717, **EP-1247**
Ferreira, K. **EP-0670**, EP-0950
Ferreira, P. EP-0905, EP-1133, OP-315
Ferreira, R. EP-1269, OP-632
Ferreira Mendonça, F. **EP-0140**
Ferreol, L. EP-1075, OP-098, OP-630
Ferrer, L. OP-536, EP-1107
Ferrero, J. M. EP-0202
Ferris, M. R. OP-796
Ferrisi, R. EP-0115
Ferro, J. EP-0199, EP-1205, EP-1269, OP-632
Ferro Flores, G. EP-0086
Ferroni, F. EP-0411, EP-0436, EP-0803, OP-068
Ferrulli, G. OP-113
Fersing, C. **EPS-246**, **OP-343**
Fery, P. EP-0663
Fierro Alanis, M. EPS-297
Fietzek, U. OP-044, OP-046
Figols, M. EP-0382, EP-0384
Figueiredo, S. OP-315
Filho, A. J. S. OP-465
Filice, A. OP-113
Filiks, A. EP-1174
Filipan, D. EP-0264
Filippi, L. EP-0461
Filizoglu, N. OP-874
Filosa, C. EP-1399
Filosofov, D. EPS-150
Findlay, U. EPS-305
Finessi, M. OP-055
Fink, G. OP-458
Finnema, S. OP-457, OP-458
Fiore, G. EP-0175
Fiori, C. EP-0370
Fiorillo, G. **OP-059**
Fiorino, S. EP-0708
Firinu, F. EP-1421, EP-1450
Fischer, B. M. OP-474
Fischer, L. EP-0597, EP-0730
Fischer, S. OP-364
Fischer, T. EP-0331
Fisler, M. EP-0036
Fite-Matamoros, J. EP-0632
Fiz, F. EPS-272
Fizazi, K. OP-599
Flamen, P. OP-111, OP-169, OP-470, OP-526, OP-537
Flamini, M. EPS-235, OP-465
Flaus, A. EP-0787, OP-049, OP-542
Flechon, A. OP-603
Fleck, J. OP-780
Flitter, M. EPS-032
Floch, R. EPS-230
Flodin, V. OP-728
Florea, A. OP-761
Flores, L. EP-0088
Florescu, A. EP-1303
Flores-Moreno, A. OP-581
Florimonte, L. EP-0175, EPS-122, EPS-261
Florit, A. **EP-0010**
Flotats, A. EP-0324, EP-0551, EP-0632, EP-0762, OP-553
Flotats-Giralt, A. EP-0490, OP-442
Foca, F. EP-0411, EP-0436, EP-0801, EP-0802, EP-0803, OP-068
Fodor, M. EPS-149
Fogante, M. OP-558
Fokas, E. EP-0331
Fokem-Fosso, H. OP-173
Fokkema, A. OP-673, OP-677
Fon, D. OP-350
Fonge, H. OP-350
Fongenie, B. EP-0996, **EP-1111**, **EPS-189**, EPS-187
Fonseca, A. I. EPS-061
Fontão de Castro, S. EP-0199, EP-1269, OP-632
Fonteyne, V. OP-710
Fonti, R. EP-0233, EP-0507
Font-Urgelles, J. EPS-026
Forbrig, R. EPS-124, EPS-125, OP-610
Forgács, A. EP-0938, EP-0951
Forgács, G. EP-0562
Forgács, V. EPS-149
Forget, V. **OP-588**
Forlenza, O. V. EPS-232
Förner, L. **EP-1009**, **OP-358**
Fornito, M. **EP-0708**
Forrer, F. EP-0573, OP-601
Forsback, S. EP-1179, OP-328, **EP-1180**
Forsberg Morén, A. EP-0116, EP-0108
Fortea, J. OP-442
Fortin, D. OP-021
Fortunati, E. EP-0145, EP-0227, EP-0310, EP-0311, EP-0444, EP-1064, **EP-1268**, EPS-247, OP-118, **OP-168**, OP-224, OP-246, OP-248, **OP-798**
Fossa, P. OP-776
Fostitsch, J. C. OP-842
Foulon, S. OP-599
Fouque, J. EP-0217, EP-0297, EP-1189
Fourchotte, V. OP-104
Fournier, B. OP-604
Fournier, P. OP-060
Fowler, J. EP-1101, OP-420, **OP-421**
Fraga, D. EP-0521, EP-1409
Fragalà, E. EP-0411, EP-0436, OP-068
Fragkaki, C. **EP-0574**
Fragomeni, S. EP-0010
Fragoso Costa, P. **EPS-190**, OP-247, OP-383, **OP-786**
Fraile, C. EP-0553
Franchini, A. EP-0269, EP-0418, EP-0419, EP-0427, **EP-0470**, EP-0894, EPS-228, OP-556
Franci, X. **EP-1196**
Franciosi, C. EP-1398, EP-1399, OP-708
Francis, R. EPS-119
Francis, R. OP-323
Franco Monterroso, C. EP-0388
Franssen, G. OP-184
Frantellizzi, V. EPS-272
Franzese, C. EP-0393, EP-0406
Franziska, F. EP-0691
Franzmeier, N. EP-0019, EP-0690, OP-044, OP-046, OP-237
Fraschina, S. EP-1421, EP-1450
Fraser, L. EPS-305, **OP-707**
Frasoldati, A. OP-113
Frederiksen, V. M. B. OP-166
Freeman, J. EP-1156
Freire, M. TEPS-021
Freire, T. EP-1324
Freitag, M. T. EPS-159

Frejd, F. Y. EP-0207, EP-0289, EP-1160, EPS-154, OP-764, OP-320
Frenay, J. OP-211
Fricke, J. G. OP-662
Fridsten, S. OP-596
Fried, M. EPS-271
Friedersdorff, F. OP-628
Friedli, R. OP-552
Frigerio, T. **OP-824**
Frijns, D. OP-107
Frille, A. EP-0230, EP-1097, OP-033
Fringuelli, F. M. OP-558
Frisoni, G. B. EP-1072, OP-438, OP-440, OP-443
Fritsch-Medina, A. EP-0618, EPS-040, EP-0495, EPS-031
Frobe, A. EP-1222
Frontzkowski, L. OP-044, OP-046, OP-237
Frood, R. EP-1091
Frost, S. OP-214
Frutos Esteban, L. EP-1308, EP-1311, EP-1312, EP-1315, EP-1289, EP-1305
Fryer, T. D. EP-0216
Fu, C. OP-451
Fu, H. **OP-117**, OP-431, **OP-781**, OP-300
Fu, L. **EP-0644**, EPS-089, **OP-445**, **OP-668**
Fu, P. EP-0650, EP-0654
Fu, W. EP-0097, EP-0338, EP-1046
Fu, X. OP-236
Fu, Y. **OP-463**
Fu, Z. EP-0435
Fuglsang, S. EP-1073
Führer-Sakel, D. OP-247, OP-385
Fujii, H. OP-585
Fujimoto, Y. OP-719
Fujinaga, M. OP-209
Fujino, K. EP-1458
Fukai, S. EP-0927, EP-0954
Fukase, K. EP-0030, EP-0031, EPS-056, OP-276, OP-281
Fukuhara, A. OP-387
Fullerton, N. EP-0993
Fulton, R. EP-0926
Funase, Y. OP-208
Fuoco, V. OP-384
Furey, G. EP-0376
Furini, C. R. OP-051
Furth, C. EP-1092, EPS-024
Furtner, J. EP-0183, OP-609
Furtuna, P. OP-868
Furuya, K. EP-1157
Fusaro, S. EP-1398, OP-891
Fuscaldi, L. EP-0140
Fuseda, R. EPS-141
Fuso, G. A. EP-0444, EP-1238, EPS-247, OP-246, OP-248 **EP-0145**, **EP-1372**, OP-118
Fuster Pelfort, D. EP-0776
Fütterer, C. EP-1047
Fuxjäger, I. **EPS-005**
Fysikopoulos, L. EPS-198
G, K. EPS-219
Gabela, L. **EP-0824**, OP-299
Gabriel, C. OP-121
Gabrielson, S. EP-0381
Gabrys, J. EP-1100
Gabucci, I. EP-1112
Gacitua, E. OP-626
Gadzicki, P. **EP-1336**
Gaertner, F. C. OP-303
Gafà, R. EP-0461
Gafita, A. OP-329, OP-822
Gagliani, C. OP-036
Gagliardi, A. EP-1179, EPS-140, OP-549, OP-801
Gagnon, M. OP-021
Gai, Y. EP-0055, EP-0356, EPS-010, EPS-059, EPS-060, EPS-175, OP-018, OP-286
Gaillard, T. OP-104
Gajate Borau, P. EP-0530
Gajecki, L. OP-204
Galarneau, T. EP-0027
Galassi, R. EP-0255
Galasso, T. EP-0227, OP-168
Galdeano, M. EP-0382, EP-0384
Galeotti, C. OP-321
Galiana Morón, Á. EP-0887
Galindo, C. **EP-0819**, EP-1368
Galindo Fernandez, C. EP-1286, EP-1322, EP-1337, EPS-263, EPS-273
Gallacher, D. EP-1400
Gallamini, A. EP-0496
Gallardo, E. OP-604
Galldiks, N. EP-0183
Galle, V. OP-121
Galli, A. OP-047
Galli, E. EP-0175, EPS-122
Galnaitiene, G. **EP-0361**, **EP-0365**
Gålne, A. EPS-213
Galuppi, F. EP-0503
Gamanagatti, S. OP-861
Gamazo Laherran, C. EP-0550, EP-0613, OP-854, EP-0833
Gambhir, S. EP-0544, EP-0853, EP-0859, EPS-039, OP-554
Gambini, J. EP-1184
Gamenara, D. EP-0134
Gamez, C. EP-0685
Gámez-Cenzano, C. EP-0611, EP-0836, EPS-092, EPS-202, EPS-211, OP-483
Gammel, B. M. EP-0989
Gammel, M. **EP-0989**, OP-363
Gan, C. OP-676
Gan, H. EP-0785, EPS-119, OP-277
Ganapathy, C. EP-0285, EP-0880, OP-872
Gandaglia, G. EP-0370, OP-875
Gandini, A. EP-1173, EP-1199
Gao, J. EP-0644, OP-445
Gao, L. OP-841, **EPS-025**, OP-308
Gao, M. EP-0622
Gao, Y. EP-0050, EP-0316, EP-0400, EP-0969
Gao, Z. EP-0060, EP-0078, EP-0190, EP-0487, EP-0861, OP-463, EP-1164, **EP-1165**
Gape, P. **EP-0084**, EP-0008
Garabedian, N. OP-614
Garai, I. EP-0450, EP-0938, EPS-278, OP-501
Garaventa, A. EPS-272
Garcia, C. EP-0786, EP-1019, EPS-199, OP-630
Garcia, J. EP-0382, EP-0384, EP-0412
Garcia, M. OP-666
Garcia, O. OP-711, OP-873
García-Alcober, C. EP-0307, EP-0494, EP-0618, EP-1366, EP-1411, EPS-022, OP-865
García Alonso, M. EP-1368, EP-0819, EP-1322, EP-1337, EPS-273
Garcia Alonso, P. EP-1286, EPS-263
García Álvaro, J. EP-1431
García Aragón, M. **EP-0549**, **EP-0550**, EP-0612, EP-0613, EP-0833, OP-057, OP-854
Garcia Arevalo, M. **EP-1431**
García Blasco, L. EP-0328
García Bracamonte, B. EP-0887
García Burillo, A. OP-430, EPS-202, EPS-211, OP-483, EP-0792, OP-429
García Cañamaque, L. OP-430, EPS-275, EP-0792
Garcia Carbonero, R. OP-429
García Delgado, R. EP-0387
García de Lucas, Á. **EP-0114**
García Donoso, C. EP-0887
Garcia Granero, M. OP-307, OP-302
García Megías, I. EP-0328, EP-0358, EP-0401, EP-1393, EP-1408
García Muñoz Nájar, A. OP-785
García Otero, X. OP-093
Garcia Perez, F. EP-0086
García Poblete, V. EP-0328
García-Ruiz, A. EP-0656, EP-0673
Garcia-Talavera San Miguel, P. EP-0200, EP-0364, EP-0378, EP-0710, EP-0931, OP-481
García Varela, L. OP-093
García Vicente, A. EP-0328, EP-0358, EP-0401, EP-1393, EP-1408
Garcia Zoghby, L. EP-0328, EP-0358, **EP-0401**, EP-1393, EP-1408
Garelli, G. OP-055, **OP-612**
Garganese, G. EP-0010
Garibotto, V. EP-1072, EP-1122, EPS-226, OP-438, OP-440, OP-443
Gariglio, G. **EP-0123**
Garin, G. OP-331
Garin Rodriguez, A. EP-0462, EP-1262, EP-1263
Garnuszek, P. EP-0360, EP-0789
Garousi, J. EPS-154
Garrido, A. EP-0792
Garrido, I. EP-0288
Garrido, N. EP-0382, EP-0384
Garrote Ordeig, M. EP-0776
Garrou, F. EP-0206, OP-105, OP-324, OP-484

Garufi, C. EP-0263
Gasbjerg, L. EP-0709
Gaschet, J. OP-280
Gascoigne, C. **EP-0996**
Gascón-Bayarri, J. EP-0653
Gasior-Perczak, D. EP-0789
Gaspariunaite, V. OP-593
Gaspar-Sardon, M. EP-0632
Gastreich de Llanes, E. OP-358
Gatón Ramírez, J. EP-0374, EP-0472
Gaudiano, C. EP-0375, EP-0398, OP-716
Gaudieri, V. EP-0308, **EP-0788**
Gaudino, J. EP-0113
Gavriilidis, P. **EPS-227**
Gavriilidis, S. **EP-0477**
Gay, E. EP-0269, EP-0418, EP-0419, EP-0427, EP-0470, EP-0894, EPS-228, OP-556
Gb, P. EP-0265
Ge, J. OP-439
Ge, Q. EP-0209
Ge, S. OP-762
Gebara Garcia de Lima, A. EPS-196
Gebhardt, P. OP-284
Gebhart, G. **OP-107**, OP-111
Gebremariam, A. EP-0260
Gedikli Turgut, G. **EP-0523**
Gegenmantel, E. OP-284
Gehle, P. OP-628
Gehring, A. EP-0967, **EP-0983**, EP-1077
Geibl, F. OP-459
Geier, M. EPS-230
Geiger, H. EP-0573
Geist, B. EP-0968, EP-1093, EP-1097, EP-1089, OP-790
Geistlich, S. OP-673, OP-677
Gelardi, F. **EP-0254**, **EP-0534**, EP-1401, **OP-298**, OP-326, OP-706
Gempt, J. OP-606
Genbrugge, E. EP-0325
Genç, M. **EP-0291**
Gendron, T. EP-1175
Gener-Laquidáin, B. EP-0850
Genest, F. OP-376
Geng, J. EP-0652
Genšor, D. EP-1313
Genova, A. **EP-0826**, **EP-1258**, **EP-1376**, **EP-1383**, **EP-1412**
Gentili, M. EP-0044
Georga, S. **EP-1341**, EP-1370, **EP-1374**, **EPS-027**, EP-1364
George, M. EP-0976
Georgiadis, G. EP-0244
Georgiev, T. OP-182, OP-327
Georgiou, A. EPS-027
Georgoulias, P. EP-0591, EP-0675, OP-557
Gerards, N. R. OP-774
Gerardy, R. EP-1175
Gerhard, A. OP-239
Gerhards, J. W. EP-0109
Gericke, G. OP-658, OP-780
Gerke, O. EP-0403, OP-038, OP-877
Gerlach, I. EPS-131
Gernert, J. A. EP-0691, EP-0698
Gerritsen, W. OP-598
Gervais, P. EPS-131
Gervais, R. OP-173
Gevaert, B. TEPS-009
Gevers, R. EPS-074
Geworski, L. EP-1105
Geza, S. OP-708
Ghadhanfer, L. **EP-0928**, EP-1416
Ghahraman, M. EP-0566, EP-1348, EP-1356
Ghai, K. EP-0784, EP-0790, EP-0881
Ghanaatgar, S. **OP-021**
Ghannem, R. EP-1390
Ghapanvari, M. EP-0038, EP-0127
Gharepapagh, E. **EP-1296**, **EP-1297**
Gharibi, O. EP-1101
Ghassel, S. OP-162, OP-164
Ghedbane, Y. EP-1076
Ghedini, P. OP-324
Ghelardoni, M. OP-776
Gherghe, M. EP-1220, EP-1326, EP-1327, EP-1328, EP-1335
Gheysens, O. EPS-266, OP-317, TEPS-012
Ghezzi, C. EPS-103, OP-022, OP-787
Ghezzo, S. EP-1043, **OP-875**
Ghiani, S. OP-179
Ghidini, A. OP-113
Ghodsirad, M. EPS-220
Ghosh, G. EP-0830
Ghosh, S. EP-0266, EP-0885
Ghujeh, A. **EP-0383**
Ghuzlan, A. OP-120
Giakoumettis, G. EPS-254
Giammarile, F. EP-0453, EP-1396
Giampalma, E. EP-0255
Giani, E. EP-0802, EP-0803
Giannakou, S. EP-0591
Giannoula, E. EPS-254
Giarratana, A. **EP-1211**, **EP-1273**, **EP-1274**, **EP-1280**
Gibson, A. EPS-140
Giehl, K. OP-048
Giesel, F. EP-1116, EP-1200
Giesel, F. L. EP-0154, EP-0703, OP-349, OP-471, OP-825, OP-881
Giesen, A. OP-067
Giglio, J. EP-1184
Gilbert, F. J. EP-0216
Gildehaus, F. J. EP-0793, EP-0936, EPS-248, EPS-290, OP-456, EP-0022
Giles, S. OP-619, OP-625
Gilgen, M. OP-552
Gillen, R. EP-0993
Gillessen, S. EP-0425, OP-604
Gillett, D. OP-697
Gil Santos, S. EP-1269
Giménez, A. EP-0551
Gimenez, M. EPS-207
Giménez Aranda, M. **EP-0221**
Giordano, A. EP-1399
Giordano, G. EP-0708
Giorgi, M. C. P. EP-0631
Giorgio, A. D. OP-329
Giourgouli, S. EP-0875
Giovanella, L. OP-380
Giraldo Gonzalez, L. EP-0705
Girard, N. EP-0251, OP-173
Giraud, P. OP-524
Giraudet, A. OP-599, **OP-331**, OP-603
Giraudo, C. EPS-205
Girault, S. OP-603
Girodon, F. OP-211
Girotto, N. EP-0730
Gissot, V. OP-718
Giunchi, F. EP-0227, OP-168
Giunta, E. EP-0411, EP-0436, EP-0801, EP-0802, EP-0803, OP-068
Giunta, F. EP-0681
Gjukaj, A. OP-526
Gkatzouli, E. EPS-254
Glatting, G. EP-1045, EP-1106, EP-1107, EP-1119, EP-1128, EP-1129, EPS-183, EPS-184, EPS-185, OP-180,
Glaudemans, A. W. J. M. EP-0535, EP-0535, EPS-082, EPS-276, OP-289, OP-760, OP-867, OP-885
Gméling, K. EP-1166
Gnesin, S. EP-0828, EPS-193
Gnörich, J. EP-0018, EP-0019, EP-0699, OP-044, OP-046, OP-237
Gobbi, C. OP-179
Gobbo, A. EP-0893
Gobeil, F. OP-021
Godbert, Y. OP-536, OP-603
Godbole, M. **EP-1394**
Godeau, N. EP-1196
Goel, S. EP-0267
Goenka, v. EP-0474
Goerttler, T. OP-239
Goetghebeur, D. EPS-090
Goetz, C. EP-0838
Goffin, K. EP-0391, EP-0879, EP-1175, EPS-126, OP-067, OP-107, OP-329, OP-366, OP-670, OP-710
Goffinet, S. **EP-0663**
Goh, J. OP-676
Goislard, M. OP-453
Gokdemir, E. EP-1310
Göker, M. OP-782
Göksel, S. EP-1392
Goldman, R. EP-1054
Goldman, S. EP-0687
Goldschmidt, H. EP-0506
Golemi, A. EP-0444, EP-1112, EPS-288, OP-118

Golinucci, M. EP-1081
Golisova, J. EP-0513
Golla, S. S. V. EPS-036
Golshaiyan, S. EP-0937
Gombos, J. EP-1338, EP-1343
Gomes, C. OP-461, EP-0226, OP-665, EPS-061
Gomez, D. EP-0792
Gomez, I. EP-0668, EP-0704
Gómez, J. EPS-236
Gomez Argumosa, E. EP-0086
Gomez-Caminero Lopez, F. **EP-0200**, EP-0378,EP-0710, EP-0931, OP-481
Gómez-De la Fuente, F. EP-0656, EP-0673
Gómez Fernández, I. EP-0798, EP-0841
Gómez Grande, A. EP-0387
Gómez Hidalgo, J. EP-0397, EP-0833, OP-057, OP-854
Gómez-Lado, N. OP-093
Gomez Lopez, A. EP-0462, EP-1262, EP-1263
Gómez-Montesino, G. OP-700
Gómez Rodríguez-Bethencourt, M. EP-0748
Gomez Sanchez, D. OP-430, EP-1147
Goncalves, V. **EP-0164**
Gonçalves, L. F. T. EP-0631
Goñi, E. OP-666, EP-1147
González, A. **TEPS-021**
Gonzalez, B. EP-0157
González-Barca, E. M. EP-0494, EP-0495
González-Cuesta, N. **EP-1057**
González Díaz, J. EP-0538
González Díaz, M. EP-0748
Gonzalez García, F. EP-0319, OP-050
Gonzalez-Montoro, A. TEPS-021
González Roiz, C. EP-0553, **EPS-275**, OP-784, OP-785
Gonzalez Rueda, S. **EP-0086**
González Soto, M. EP-0613, EP-0549, EP-0550, EP-0833
Goorhoo, P. EP-0942, EP-1116, **EPS-086**
Gorbenko, G. EP-0147
Gorczański, T. EP-0440
Gorczewska, I. EP-0207
Görges, R. OP-383
Gorgoni, G. EPS-137, OP-384, OP-584
Gorin, M. EP-0154
Goriparti, L. **EP-0474**, EP-0510, EP-0537, EP-0583, EP-1206
Gormez, A. OP-476
Gormsen, L. C. OP-769
Görtan, F. **EP-0294**
Gotowicz, K. **EP-0013**, OP-679
Gotuzzo, I. **OP-484**
Gouard, S. OP-280
Goudsmit, A. OP-169
Gould, S. OP-625, EP-0916
Gourni, E. EPS-009, EPS-013, EPS-193, OP-417, OP-518
Goussard, P. EPS-203
Goutal, S. OP-453
Gouveia, E. EP-0521
Gowdy, C. OP-029
Goyal, H. EPS-208
Goyal, S. EP-0267, EP-1221
Goyal, V. EP-0267
Gözlügöl, N. EP-0409, **EP-0423**, EP-0614, EP-0933, OP-552, **OP-685**, OP-823
Gracia Sánchez, L. EP-0758, EP-0618, EP-0731
Gràcia-Sánchez, L. M. EP-0495, EPS-022, EPS-031
Grafe, H. OP-385
Graff, J. OP-628
Grah Kple, M. OP-351
Grajeda, M. EP-0288
Grakova, E. OP-795
Grana, C. M. OP-429
Grana, C. OP-434
Granados Alcobendas, M. EP-1393
Granberg, D. EP-0314
Gräni, C. EP-0614
Granvik, A. EP-0934
Grao Torrente, I. OP-785
Grappeja, L. OP-384
Gräslund, T. EPS-050, OP-089
Grassa, M. EP-0447
Grassetto, G. OP-036
Grassi, I. EP-0436, **EP-0801**, **EP-0802**, **EP-0803**, EP-1159, OP-042, OP-068
Grau-Garriga, I. C. EPS-022
Gravand, A. EP-0038, EP-0127
Graven, L. H. EPS-109
Graves, M. J. EP-0216
Gravis, G. OP-599
Grayson, K. **EP-0008**
Graziani, T. OP-801
Greco, E. **EP-0375**, **EP-0398**, **EP-0444**, EP-1238, EP-1372, EPS-247, OP-118, OP-246, OP-248, OP-716
Grecu-Bodnariuc, P.-L. **EPS-216**
Green, H. EP-0153
Green, R. EP-0308, OP-684
Greer, B. OP-817
Greifenstein, L. EP-0784, EP-0790, EP-0881, **EPS-156**, OP-436, OP-628, OP-860, OP-862
Grenier, T. EP-0787
Greuter, H. N. J. M. OP-774
Grierosu, I. EP-1309, **EP-1303**, EP-1317
Grießner, H. EP-0362
Griffiths, M. **OP-290**, OP-676, OP-703
Grigaitytė, G. EP-0365, EP-0361
Grijota-Camino, M. EPS-040
Grill, A. OP-458
Grimaldi, G. EP-1281
Grimaldi, S. OP-055, OP-324
Grimmer, T. OP-232
Grindel, A. L. EP-0083
Grinnemo, K. H. OP-728
Grisay, G. OP-710
Grivet Fojaja, M. EP-1212
Groba-de Antas, S. OP-093
Groener, D. EP-0724, EP-0870, EP-1154, EP-1155,
Grogan, T. EP-1124, EP-1410, OP-714
Gröger, R. **EP-0018**
Grohmann, A. OP-347
Gröhn, H. EP-1442
Gromova, E. **EP-0173**
Grön, G. EPS-135
Gröner, D. OP-385
Groombridge, L. EP-0353
Groos, V. OP-525
Grootjans, W. EP-0958
Gropler, R. J. OP-745
Grosso, G. EP-1173
Grothe, M. EP-0637, **OP-440**
Grozdic Milojevic, I. EP-0898, OP-479
Grözinger, M. EP-0506
Grubbe Hildebrandt, M. OP-106
Gruber, S. EPS-142
Grudzinski, J. EP-0960, EP-1144, EP-1121, EPS-012
Gruenert, S. EP-0230
Grujicic, L. EP-0898, OP-479
Grünberg, J. OP-220
Grundler, P. V. EP-1164, EP-1166
Grundler, P. OP-220, OP-413
Grunwald, D. OP-284
Grünwald, F. EP-0870
Grünwald, V. OP-297, OP-538
Grushka, G. **EP-0871**
Grzmil, M. **OP-220**, OP-413
Gu, B. **EPS-051**, OP-176
Gu, F. EP-0988, **EP-1053**, **EP-1061**, EP-1095
Gu, Y. EP-0209, EP-0241, EP-0629, EPS-063
Gualandro, D. M. EP-0631
Guan, L. EP-1066
Guan, Y. EP-0020, EP-0209, EP-0500, EP-0684, OP-238, OP-439
Guardia Jimena, P. **EP-1300**, EP-1375
Guardiola-Zaragoza, P. **EPS-092**
Guarneri, A. EP-0497
Guarnizo, X. EP-0887
Guarnizo Poma, X. **EP-0387**
Guarrochena, X. EP-0148
Guasch-Jimenez, M. EP-0632
Guazzarotti, G. EP-0534
Guberina, N. OP-329
Gubern, J. EP-0632
Guc, Z. EP-0228, EP-0296
Gückel, B. OP-017
Gudin-De-Vallerin, A. OP-213
Guedj, E. **EPS-035**
Guelfo, R. EP-1187
Guercio, A. EP-1179, EPS-140, OP-549, **OP-801**

Guérin, B. EP-0004, EP-0029, OP-021
Guerra, A. **EPS-207**
Guerra, L. EP-0496
Guerrero Ortiz, M. EP-1227, EP-1251
Guerrero Serrano, P. EP-0530
Guetlin, M. OP-838
Guglielmo, P. EP-0268, EP-0350, **EP-0363**, EP-0393, **EP-0406**, **EP-0779**, OP-105
Gui, J. EP-0438
Guichay, K. EP-0819, EP-1286, EP-1368
Guichay Duran, K. EP-1322, **EP-1337**, **EPS-273**, EPS-263
Guiheneuc, L. EP-1082
Guijarro-Caba, P. **EPS-303**
Guijarro de Armas, G. EPS-263
Guillemin, M. OP-211
Guillen, E. F. EPS-117, OP-378
Guillo, P. EPS-090
Guiot, T. OP-526, OP-537
Guja, K. EP-0980
Gülaldi, N. EPS-218, **OP-257**, **OP-635**
Gülbahar, Ö. EP-0661
Gülbahar Ateş, S. EP-0197, EP-0261, EP-0577, **OP-175**
Gümüş, A. EP-0604
Gümüşer, F. EP-0925
Gumuser, G. EP-0131
Gündoğan, E. EP-0321
Güneş, C. EP-0321
Gunelli, R. EP-0411, EP-0436, OP-068
Guner, A. EP-0912
Güneren, C. **EP-1295**
Gunes, A. EP-0479
Güngör, S. OP-715
Gunneriusson, E. OP-320
Günter, M. OP-159
Günther, E. H. OP-657
Günther, T. **OP-657**
Guntur Ramkumar, P. EP-0908, EPS-034
Guo, B. OP-763
Guo, F. EPS-063
Guo, J. EP-0554, OP-052
Guo, K. EP-0689
Guo, M. EP-0984
Guo, N. OP-277, OP-516
Guo, Q. OP-071
Guo, R. **OP-274**, OP-155, OP-463
Guo, S. **OP-451**
Guo, W. OP-117, **OP-431**, OP-781, EP-1049
Guo, X. EP-0174, OP-608, **EPS-163**, **OP-108**, **OP-052**
Guo, Y. EP-0435, EP-0198, EP-0248
Gupta, A. **EP-0805**
Gupta, G. EP-0267
Gupta, J. EP-0529, OP-482, OP-878
Gupta, M. **EP-0267**, EP-0877, **EP-1221**
Gupta, N. **EPS-219**
Gupta, P. EP-0265, EP-0583, OP-861
Gupta, S. K. EP-0191
Gupta, S. **OP-655**, EP-0177, EP-0882
Gupta, V. EP-1409
Gur, F. **EP-0633**
Gurcay, N. EP-1008
Gurses, I. EP-0355, EP-0368
Gushiken Junior, D. EP-0092
Gustafsson, A. **OP-414**, **OP-519**
Gustafsson, J. EP-0967, EP-0983, EP-1106, OP-099
Gustavsson, T. OP-760
Gutierrez, M. EP-1032, EP-1048
Gutiérrez-Amares, M. EP-0745, EP-0872
Gutiérrez Crespo, A. EP-1408
Gutiérrez Guerrero, M. EP-0530, EP-0565, EP-0821, OP-478
Gutschmayer, S. EP-0968, EP-1067, **EP-1079**, **EP-1089**, EP-1093, EP-1097, OP-033, OP-548
Gutu, M. M. EPS-216
Guven, O. EP-0858
Guyot, J. OP-555
Güzelbey, T. EP-0840, OP-856, OP-857
Guzeloz, Z. OP-040
Guzman, G. EP-0490, EP-0551, EP-0762, OP-553
Guzmán Cruz, J. EP-0798, EP-0841
Guzmán de la Cerda, J. EP-0319, OP-050
Guzman Ortiz, S. EP-0328, EP-0358, EP-0401, EP-1393, EP-1408
Györke, T. EP-0247, EP-0562
H, V. **EP-0804**
Ha, S. EP-0795
Haase, C. OP-817, EP-0018, EP-0047
Haba, H. OP-387
Habbache, M. EP-1076
Habchi, H. **EP-0465**, **OP-027**
Haberkorn, U. EP-0532, OP-371, OP-881
Haberl, D. EP-0252, EP-1011, EP-1040, EP-1071, OP-352, OP-354, OP-468
Haberstroh, J. OP-842
Habibi, N. EP-0937, EP-1108
Habouzit, V. **EP-0787**
Habraken, J. EPS-074
Hacker, M. EP-0230, EP-0280, EP-0408, EP-0528, EP-0609, EP-0725, EP-0811, EP-0815, EP-0825, EP-1040, EP-1071, EP-1089, EP-1093, EP-1097, EP-1241, OP-223, OP-226, OP-231, OP-325, OP-352, OP-357, OP-466, OP-468, OP-600, OP-609, OP-730, OP-731, OP-747, OP-790, OP-820, TEPS-013
Hacker, M. EP-1011
Hadaschik, B. OP-297, OP-538, OP-786, OP-329
Haddad, F. OP-280
Hadebe, B. EP-0824
Hadebe-Chonco, B. **OP-299**
Hadžimusić, S. OP-318
Hadoux, J. EP-0306, EP-0786, EP-1019, OP-120
Hadzimusic, S. **EP-1436**
Haertel, M. **EP-0047**
Hagerman, J. **EP-0607**, **EPS-280**
Hahner, S. EP-0728
Hai, W. EP-0119, EPS-033, OP-367
Haidar, M. OP-711, OP-873
Haj, N. EP-0021
Hajek, R. EP-0513
Hajianfar, G. **EPS-220**
Hajiyianni, M. EP-0506
Hake, R. OP-628
Hakim, A. **EP-1129**
Häkkinen, T. **EP-1457**
Hakulinen, M. EP-1442, EP-1457, EPS-285, OP-702
Halanaik, D. EP-0250, **EPS-208**
Haldorsen, I. S. OP-039
Halil, S. EP-0240
Halilali, M. EP-0787
Halilbasic, E. OP-747
Hall, J. M. OP-474
Halldin, C. EP-0108, EP-0113, EP-0116, EP-0118
Haller, B. OP-789
Hallqvist, A. OP-589
Halme, H. EPS-097, **EP-1000**
Halttunen, J. **EP-1442**
Halvorsen, H. **EP-0958**
Hamacher, R. EPS-190
Hamidpour, R. **OP-034**
Hammadi, A. EP-1404
Hammers, A. EP-0916, EP-1093
Hammouda, S. OP-588
Hamvas, G. OP-552
Han, D. **OP-529**
Han, H. OP-308, EP-0664, EPS-215, OP-532
Han, J. **EPS-151**
Han, K. EP-0629, EPS-108
Han, P. **EPS-089**
Han, Q. **EP-0174**, **OP-608**
Han, S. EP-0572, EP-0576
Han, T. EP-1056, **EP-0278**, **OP-116**
Han, U. EP-1215
Han, W. EP-0650
Han, Y. **EP-0487**, EP-1050, OP-477, **OP-851**, OP-880
Hanáčková, V. EP-0489
Hanan, S. OP-803
Hanaoka, K. EP-0939
Handkiewicz-Junak, D. EP-0782
Hanoun, C. EP-0488, OP-032
Hänscheid, H. OP-043
Hansen, A. EP-1161, OP-290, OP-670, **OP-676**, OP-703
Hansen, C. P. OP-474
Hansen, K. EP-1047, **OP-363**
Hansen, N. **EP-1073**
Hansen, S. EP-0403, OP-877, OP-726
Hansen, T. C. EP-0005
Hansen, T. M. EP-0290, **EPS-223**
Hanyu, M. OP-209

Hao, J. EP-0652, EP-0666, EP-0697, EP-1056, OP-304
Hao, L. **EP-0313**
Hao, X. EP-1037
Happel, C. **EP-0724**, EP-0870, **EP-1154**, **EP-1155**
Haque, A. EP-1208
Harada, M. EP-0459
Harada, T. EP-1237, EP-0991
Hardiansyah, D. **EP-1045**, EP-1107, EP-1119, **EP-1128**, EP-1129, EPS-183
Harding, I. EP-0995
Haresh, K. EP-0177, EP-0882
Hari, V. OP-073
Harish, N. **EP-0539**
Harman, A. OP-664
Harmon, E. S. EP-0918, EP-0920
Harms, H. J. OP-791
Harris, K. EP-1283
Harris, O. EPS-291
Harris, T. EP-0036
Harrison, K. D. OP-745
Harry, L. EP-0824, OP-299
Harsha, T. EP-0539
Harsini, S. EP-0566
Harter, P. OP-610
Harter, P. N. EP-0886, OP-609
Harteveld, A. **EP-0707**, OP-852
Hartikainen, S. EP-0600, **EP-0602**
Hartl, D. OP-120
Hartman, K. EP-0895
Hartmann, S. EP-0195
Hartrampf, P. E. **EP-0794**, EPS-184, EP-0728, OP-043, OP-426, EP-0195
Haruz-Waschitz, S. OP-702
Hasan, T. EP-1208
Hasanzadeh Haddad, E. EP-1362, EP-0570
Hasbek, Z. EP-0224, EP-0291
Hascsi, Z. EP-0450
Hasenauer, N. **OP-043**
Hasenclever, D. EP-0488
Hashimoto, L. EP-1237, **EPS-250**
Hashimoto, S. EP-1157
Hashimura, H. TEPS-020
Hashmi, S. EP-0181
Haslauer, A. OP-291
Hassan, A. **EP-0271**, **EP-0715**, **EP-1406**, OP-026
Hassan, F. EP-0783
Hassan, H. **TEPS-019**
Hassanzadeh, L. EP-1151, EP-1152
Hassel, J. EP-0520, EP-1022, EP-0525, OP-294
Has Simsek, D. EP-0282, OP-110, OP-543
Hassler, L. **EP-1004**
Hassler, M. R. OP-325
Hatano, M. **EP-0676**, EP-1059, OP-301, OP-719
Hatt, M. EP-1036, OP-354
Hautzel, H. **OP-172**, OP-247, OP-383
Havel, M. **EP-0513**, **EP-0586**
Havlova, G. EP-0513, EP-0586
Hawala, I. OP-179
Hawarihewa, P. **EPS-197**
Hawkins, C. EPS-138
Hawotte, M. EP-1186
Hayashi, N. EP-0956
Hazan, T. EP-1088
Hazenberg, B. P. C. OP-053
He, B. EP-0020, EP-0500
He, C. OP-596
He, H. EP-0276
He, J. EP-1039, EP-0158
He, K. OP-238
He, R. EP-0662
He, Y. EPS-151, EP-0186, EP-0187, EP-0515, EP-0546, EPS-060, EPS-158, EPS-164, OP-112, OP-167, OP-547, OP-693
Hebert, K. EP-0800
Hecht, S. EP-0362
Heck, M. EP-1047
Hedeer, F. EP-0582, EP-0607, **EP-0733**, EP-1423, EP-1426, EPS-096, TEPS-004
Hedman, M. EP-0602
Heeger, S. OP-670
Heeman, F. OP-440
Heetun, W. EP-0950
Hegarat, N. OP-173
Heidari, P. EP-0320
Heidenreich, A. OP-628
Heijmen, J. EPS-081
Heijmen, L. EP-0948, EP-1395, OP-713
Heil, R. OP-284
Heilinger, J. EP-0331, OP-381, OP-879
Heimer, M. M. EP-0037
Hein, S. **OP-106**
Heinen, J. **EP-0520**
Heinonen, I. EP-1063
Heinrich, M. EP-0318, OP-043, **OP-376**
Heinzel, A. OP-245
Hejji, N. OP-162, OP-164
Helbling, A. OP-211
Held, C. OP-095
Helfenstein, F. OP-552
Helias, A. EPS-090
Heller, D. EP-0144
Hellmann, J. OP-303
Hellmich, M. OP-381
Hellwig, A. OP-228
Hellwig, D. **OP-228**, OP-591
Helm, A. EP-0080
Hemmingsson, J. **EP-1160**, EPS-180, OP-589, OP-590
Hempel, L. EPS-290
Hemptinne, J. **TEPS-016**
Hendler, A. EP-1100
Hendricks, M. EP-0757, EP-0535
Hendriks, P. EP-0334
Hendrikse, N. H. EP-1185
Hendrikx, J. J. M. A. OP-597
Hendry, F. EP-0993
Hendy, A. F. OP-378
Hendy-Pérez, A. EP-0156
Hendy Pérez-Aranda, F. **OP-700**
Hengstenberg, C. OP-468
Hennenberg, J. OP-468, OP-609
Henrich, M. T. OP-459
Henrich Malizia, L. **EP-0462**, **EP-1262**, **EP-1263**
Henriksen, O. M. EP-0172
Henriksen, O. EPS-120
Henriot, J. **OP-091**
Henrotte, M. **OP-522**
Henry, T. **EP-1075**
Hentzer, M. EP-0108
Henzlová, L. **EP-0489**, EP-0586
Herceg, D. EP-0524
Heredia Genestar, T. OP-216, OP-425, EPS-196
Heringer, V. **EP-0189**, **EP-1203**, **EP-1223**, **EP-1234**, **EP-1245**, **EP-1267**, EP-1306, EP-1324, EP-1342, EP-0262
Herlina, A. EPS-004, OP-089
Herman, R. EP-0712
Hermansen, J. D. EP-0005
Hermine, O. OP-227
Hermosín Peña, A. OP-785
Hernandez, R. EP-0070, EP-0162, EPS-001, EPS-012, EPS-194, OP-217, OP-218, OP-219, OP-275, OP-517, OP-767
Hernandez Cano, L. **EPS-195**, OP-515, OP-520
Hernández Cristancho, O. EP-0611, **EP-0685**, OP-483, EPS-202, EPS-211
Hernandez-Delima, F. J. EP-0807
Hernandez-Falcón, J. EP-0170
Hernandez Fructuoso, A. EP-0388
Hernández Martínez, A. EP-1308, EP-1311, EP-1312, EP-1315, EP-1289, EP-1305
Hernandez Perez, I. EP-0530, EP-0565, EP-0821, OP-478
Hernández Ramírez, R. EP-0816, EP-0909
Hernando, J. EP-0792, OP-430
Hernes, E. OP-427
Herr, F. EP-0037, EP-0309
Herrador-Galindo, L. EP-0618
Herraiz, J. OP-889
Herrera, F. EP-0077
Herrero, A. EP-1368
Herrero Muñóz, A. EP-0819, EP-1286, EP-1337, EPS-263, EPS-273
Herrmann, K. EP-0154, EP-1103, EP-1143, EPS-190, OP-172, OP-239, OP-247, OP-297, OP-329, OP-383, OP-385, OP-538, OP-670, OP-779, OP-780, OP-786, OP-818
Herth, M. M. EPS-146

Hervás Sanz, B. EPS-121, EP-0307, EP-0437, **EP-0494**, **EP-0495**, EP-0498, EP-0508, EP-0618, EP-0653, EP-1366, **EPS-022**, OP-233, OP-480
Herzog, H. EPS-083
Hescheler, D. **OP-245**
Heskamp, S. OP-184, OP-521, OP-796
Hess, S. OP-877
Hesse, J. OP-177
Hesse, M. EP-0598, EP-0947, EPS-099, EPS-299, OP-097, **OP-496**
Hesse, S. EP-0230, EP-1097, OP-033
Hesterman, J. **EP-1135**
Heuschkel, M. EPS-190, OP-779
Heute, A. J. EP-0719
Heute, D. **EP-0719**
Heute, J. D. EP-0719
Heyer, S. EP-0692, EP-0827, OP-235
Hicks, R. OP-817
Hidalgo, J. EP-0777
Hideghety, K. EP-0180
Higashi, T. EP-0139
Hihara, F. EP-0139
Hildebrand, K. OP-358
Hildebrandt, M. G. EP-0292, EP-0403, OP-038, OP-877
Hilmayanti, E. EPS-056
Himmen, S. OP-247
Hindie, E. EP-0069, EP-0512
Hindorf, C. EP-0582, OP-596
Hinge, C. **EP-0766**, **OP-464**
Hinterleitner, M. OP-365
Hioki, T. OP-323
Hippeläinen, E. EP-1000, EPS-097
Hirano, Y. EP-0676, EP-1157
Hiraoka, J. EP-0459
Hirata, K. EP-0303, EP-0796, EP-0860, EP-0874, EP-1237, EPS-250
Hirayama, K. EP-0588
Hirner-Eppeneder, H. EP-0037
Hiroshima, Y. EP-0459
Hirsch, F. OP-237
Hirsch, S. OP-869
Hirschmüller, K. **EPS-117**
Hishimoto, A. EP-0676
Hitzl, W. EP-0326, EP-0688
HJ, P. **EP-0258**, **OP-550**
Hlongwa, K. EP-0367, EP-0379, **EP-0757**, EP-1090, **EP-1250**
Ho, C. EP-0429, EP-0499, EP-0799, EP-1422, EPS-177, OP-306
Ho, C. L. EP-1193, TEPS-007
Ho, I. **EPS-177**
Ho, K. C. EP-0342
Ho, M. OP-088
Ho, W. EPS-201
Hoberück, S. **EP-0483**, OP-032, OP-329, OP-819
Hock, C. EP-0002
Hoehr, C. OP-580
Hofer, F. OP-468
Hoffman, J. OP-824
Hoffmann, C. EP-0943
Hoffmann, F. EP-0696
Hoffmann, P. OP-358
Hofheinz, F. EP-0483, OP-032
Hofland, H. OP-425
Hofman, M. EP-0415, EP-0822, EP-0830, OP-329, OP-605
Hofman, M. OP-323
Hofmann, L. EP-0230
Hofmann, M. EPS-253
Högerman, M. OP-328
Höglinger, G. OP-044, OP-046, OP-237, EP-0691, EP-0699
Hohaus, S. EP-0497
Hohne, R. OP-697
Høi-Hansen, F. E. EP-0766
Høilund-Carlsen, P. F. EP-0627
Holden, D. OP-457
Holdgaard, P. C. EP-0403, EPS-301, OP-877
Höllmüller, I. OP-778
Holm, C. **OP-621**
Holm, J. EP-0403, **OP-038**, OP-877
Holman, B. EP-0729, OP-667
Holmes, I. OP-290, OP-676, OP-703
Hölscher, T. OP-329
Holstensson, M. EP-0260, EP-0275
Holtappels, G. OP-522
Holzgreve, A. EP-0154, EP-0208, EP-0376, EP-0793, **EP-1410**, EPS-162, EPS-248, EPS-290, OP-329, OP-368
Holzleitner, N. EPS-146
Hommen, M. EPS-138
Honda, K. **TEPS-008**
Honda, S. OP-719
Hönemann, J.-N. EP-0696
Hong, I. EP-0995
Hong, J. EP-0346, **EP-0161**, EP-1080, EP-0111, **EPS-162**
Hong, M. EPS-058
Hong, T. C. EPS-029, EPS-245
Hong, X. EP-0413
Hong, Y. EP-0630, **OP-843**
Hongyong, W. **EP-0117**
Honoré d'Este, S. **EP-0219**, **OP-261**
Hooda, M. **OP-072**
Hoogenkamp, D. **OP-597**
Hooijman, E. EPS-196
Hooshyar Yousefi, B. EP-0305, EP-0987, EPS-143, **OP-459**
Hope, T. A. OP-329
Hopfner, F. EP-0691
Hoppin, J. EP-1135
Hopson, N. OP-627
Horikawa, T. EP-1453, EP-1454
Hörmann, L. EP-0168
Horowitz, T. EPS-035
Horsager, J. EP-0998
Horsfall, A. EP-0153, OP-177
Horvatic Herceg, G. **EP-0524**
Hosokawa, S. TEPS-008
Hosse, C. EPS-024
Hossen, L. EPS-224
Hosten, B. EP-0093
Hou, J. **OP-660**
Hou, W. OP-300
Hou, X. **EP-1437**, OP-428
Hou, Y. EP-0059, **EP-0075**, EP-0078, **EP-0861**, **EP-0862**, EPS-259
Houas, J. EP-0447
Houede, N. EP-0812
Houot, R. OP-227
Houting, J. C. OP-622
Hovhannisyan-Baghdasarian, N. **EP-0217**, EP-0251, **EP-0297**, EPS-231, OP-173
Howladar, S. **EP-1242**
Hoye, A. T. EPS-032
Hq, W. **OP-167**
Hrabakova, K. EP-0148
Hribernik, N. EP-0519
Hristova, I. OP-096
Hristova, R. EPS-296
Hrynchak, I. EPS-061
Hsia, C. C. TEPS-002
Hsiao, E. EPS-119
Hsiao, I. T. EPS-229
Hsieh, P. S. EP-0342
Hsieh, R. E. EP-0342
Hsieh, S. EP-1427
Hsu, H. C. EP-0342
Hsu, S. Y. EP-1025
Hsu, Y. J. EP-0342
Hu, B. EP-0622, **OP-845**
Hu, C. EP-0211
Hu, F. EP-0694, EPS-175
Hu, G. OP-226
Hu, J. OP-461, EPS-059, EP-0119, EP-0211, EP-0386, **EPS-033**, EPS-200, **EP-1148**, EPS-033
Hu, K. EPS-057
Hu, L. H. EP-1037
Hu, M. EP-0055, **OP-018**, EPS-049, EPS-152, EPS-155
Hu, Q. EP-0211
Hu, R. OP-763
Hu, S. EP-0124, EP-0215, EP-0430, EP-0517, EP-0658, EP-0706, EP-0727, EP-1080, EP-1214, EPS-042, EPS-132, EPS-160, EPS-165, OP-052, OP-212, OP-296, OP-660, OP-709, OP-712, OP-717, OP-723, OP-740
Hu, T. **OP-238**, EPS-157
Hu, W. OP-018, OP-469, **OP-768**
Hu, X. OP-466, EP-0276, EPS-058
Hu, Y. **OP-053**, EPS-200, **EPS-226**, EP-0650, EP-0654, EPS-118, EPS-243
Hu, Z. EP-0969, EP-1048, EP-1096, OP-236, OP-460, OP-462
Hua, P. EP-0593, OP-544
Hua, T. EPS-123

Huang, C. EP-0129, EP-0167, EPS-029, EPS-062
Huang, F. EP-0666, EP-0167
Huang, G. EP-0652, EP-0682, OP-236, **OP-304**, EP-0212, EP-0533, EP-0652, EP-1233
Huang, H. OP-030, EP-0684
Huang, J. EP-0284, EPS-245, OP-117, OP-781
Huang, L. **EP-0315**, **EP-1039**, EPS-073
Huang, M. **EP-0106**, OP-278
Huang, Q. EP-0684, OP-238, OP-451, EPS-089, EP-0964
Huang, R. EPS-045, **EP-1032**
Huang, S. OP-460, OP-844, **EPS-045**
Huang, W. EP-0052, EP-0054, EPS-006, EPS-014
Huang, X. OP-463, EPS-056
Huang, Y. EP-1427, EPS-164, OP-457, EP-1025, EP-1025
Huang, Z. OP-045, EP-0327, EP-0410, EP-0067
Hubalewska-Dydejczyk, A. EP-0440, EP-0789, EP-0919
Hubele, F. EP-1162
Huber, M. OP-658
Huda, F. EP-0561, EP-0877
Hudomalj, B. EP-1177
Hudson, A. OP-416
Huebner, R. EP-0153
Huebner-Resch, I. EP-0528
Huellner, M. OP-285, EPS-041
Huettges, J. EPS-075
Hugenberg, V. EP-1409
Hughes, S. J. EP-0271, EP-0715, EP-1406
Hughes, T. OP-888
Huglo, D. OP-555
Hui, Y. EPS-201
Huić, D. EP-1389, EP-1023, EP-1230, EP-1298
Huicochea Castellanos, S. EP-0352
Huisman-Siebinga, H. EP-1034
Huitema, A. D. R. EP-1034
Hulin, C. EP-0512, EP-1055, OP-225
Humbert, O. EP-0202, EP-0671, EP-1004
Hume, I. EP-1403
Hung, C. C. EPS-029
Hung, G. U. EP-1032, EP-1037, EP-1048
Hung, R. EPS-075
Huo, L. EP-0174, EP-0327, EP-0410, EPS-242, OP-066, OP-069, OP-206, OP-546, OP-608
Huo, Y. EP-0694, EP-0695
Hurn, L. OP-817
Husevåg, T. **EP-1078**, OP-424
Huseynzade, K. EP-0453
Hüsing, J. OP-329
Husmann, L. EPS-041
Hussain, T. EP-0777
Hustinx, R. EPS-084
Hüttmann, A. EP-0488, OP-032
Hutton, B. EPS-093
Hutton, J. OP-697
Huvelle, S. **EP-0093**
Huvenne, W. J. A. OP-522
Huxley, P. EP-0121
Huxohl, T. **EP-1087**, **OP-159**
Huygen, F. J. M. P. OP-870
Huynh, N. EPS-003
Hvidsten, S. EP-0005
Hyafil, F. OP-499
Hyeong Seok Kim, D. OP-714
Hylle, M. OP-621
Hyppolito, L. T. EP-0631
Hyun, S. EP-0795
Hyväkkä, A. OP-328
Iaccarino, G. EP-0906, EP-1109
Iachetti, G. EP-1398
Iacovitti, C. EP-0425, EP-0889
Iagaru, A. EP-0980, OP-539, OP-670
Iai, R. OP-301
Iakovoglou, D. EP-0820
Iakovou, I. EPS-254
Ialuna, S. EP-0206, EPS-272, OP-105
Iannaccone, V. OP-868
Iannone, M. **EP-1176**
Iaria, S. **EPS-269**
Ibáñez Ibáñez, M. EP-1308, EP-1311, EP-1312, EP-1315 EP-1289, EP-1305
Ibrahim, K. EP-0739, EPS-279
Ibrahim, N. EP-0413
Ibrahim, O. H. EP-0304
Ichijo, S. **OP-301**, OP-719
Icova, V. EP-0586, EP-0489
Iezzi, R. OP-858
Igarashi, C. EP-0139
Ihsan, N. EP-1424, EP-1425, EP-1428
Iida, H. EP-1063, **EPS-234**
Iizuka, Y. **EPS-255**
IJpma, F. F. A. EPS-276, OP-867
Ilan, E. EP-1142, **OP-095**, **OP-369**
Ilangovan, J. **OP-683**
Ilhan, E. EP-0192
Ilhan, H. OP-822
Ilic Tomas, M. **EP-0597**, EP-0730
Imaizumi, N. EP-0927, EP-0954, EP-0956, **EP-1098**, EP-1452
Imakado, R. EP-0634, EPS-111
Imbert, L. EP-0827, EP-0829, EPS-264, OP-049 OP-101, OP-235, OP-499, OP-614
Imbs, D. C. EP-0144, EP-0151
Inaba, H. OP-208
Inácio, I. EP-1269
Inagaki, N. EPS-141
Inaki, A. OP-585
Inal, E. EP-1314
Inal, G. **EP-0359**, **EP-1249,** EP-0232, EP-0806
Inal Cengiz, T. EP-1008
Inan, D. OP-054
Inanir, A. **EP-1007**
Inaoka, Y. EP-0939
Ince, S. EP-0523, EPS-260
Indovina, L. EP-0665, OP-858
Infante, J. EP-0673
Ingenwerth, M. OP-786
Ingham, A. EP-0034, OP-348
Inglese, M. **EP-1052**, OP-047, **OP-669**, OP-725
Ingraito, C. **EP-1146**, OP-384
Inoue, A. EP-0634, EPS-111, **OP-503**
Inoue, K. EP-1435
Inoue Inukai, J. OP-283, **OP-285**
Inui, H. EP-0459
Inui, Y. EP-0939, EP-0956
Ioana, I. A. EP-1220, **EP-1326**
Ion, R. **EP-1317**, EP-1309
Ionescu, D.-M. EP-1327
Ippolito, S. OP-484
Iravani, A. OP-323
Irazoqui, G. EP-0100
Irumva, B. EP-1189
Isabel, C. EP-1318
Isakaj, J. EP-1035, EPS-124, EPS-125, EPS-239, OP-609, OP-610
Isambert, N. EPS-044
Isasi, D. EP-1344
Isayeva, M. EP-0453
Isernia, M. EP-0233
Ishi, Y. EP-1237
Ishii, H. EP-0303
Isik, E. EP-1314, OP-259, OP-110, OP-543, EP-0282
Iskra, I. EP-0597, EP-0730
Islam, M. A. OP-025
Islam, S. EP-1204, EP-1052
Isleyen Çolak, E. **EP-1321**
Isohashi, K. EP-1458, OP-387
Israel, O. EP-1090
Issa, A. **EPS-083**
Istrefi, E. EP-1035, EPS-124, EPS-125, EPS-239
Itagaki, K. EP-0214, EP-0939, **EP-1449**, EPS-255
Italiano, A. OP-120
Ito, K. EP-0956
Ito, M. EP-0028
Ito, R. EP-1453, EP-1454
Ito, S. EP-0939
Itti, E. EP-1055, OP-225, OP-359
Iudicello, A. EP-0206, OP-105, OP-324
Ivanovski, A. OP-479
Ivashchenko, O. V. EPS-082, OP-289, OP-885, OP-886
Ivashkevich, A. **EP-0130**, OP-516
Iversen, P. EP-0807
Iwabuchi, Y. EP-0956
Iwanochko, M. EPS-075
Iwasa, T. EP-0459
Iwasaka, A. EP-1157
Iyer, G. OP-217, OP-218, OP-219, OP-517
Iyer, V. EP-0289

Izawa, Y. TEPS-020
Izoe, Y. **EP-0635**, **EPS-095**
Iztueta Iturbe, A. EP-0462, EP-1262, EP-1263
Jaafar-Thiel, L. OP-361
Jabbarpour, A. **OP-162**, **OP-164**
Jachetti, E. EP-0017
Jäck, A. OP-044
Jacobs, C. OP-170
Jacobs, N. EP-0379, EP-0757
Jacobson, O. OP-088
Jacobsson Svärd, S. OP-095
Jacquet, M. EP-1068
Jäderling, F. EP-0404
Jadoul, A. EPS-084
Jaekel, A. OP-658
Jaeschke, B. OP-436, OP-860
Jafari, E. EP-0038, EP-0878
Jafari Zarrin Ghabaei, F. EP-1339
Jafarvand Giglou, M. EP-0208
Jafperi, N. N. TEPS-019
Jahanbin, M. EP-1138
Jahn, U. OP-369
Jain, A. EP-0181, EP-0414
Jain, B. EP-0300, EP-0558, EP-0839, EPS-270
Jain, K. EP-0750, EP-1207, **EP-1210**, EP-1226, EP-1235, EP-1236, EP-1272, EP-1278, EPS-206, EPS-277, OP-800
Jain, N. **EP-0985**, EP-0986
Jain, S. EP-0559, OP-872, EP-1246
Jain, V. **OP-743**, EP-0559
Jakobsen, N. M. EP-0292, OP-106
Jakobsson, V. OP-860
Jakola, A. S. EP-0183
Jalloul, W. EP-1309
Jamalabadi, S. EP-0038
Jamaludin, S. EP-0416
Jamar, F. EPS-266, EPS-299, OP-317, TEPS-012
James, S. OP-728
Jamet, B. EP-1055, OP-225
Jamieson, E. EP-0160
Jamsek, J. OP-302, OP-307, EP-0835
Jan, B. EP-0811, EP-0815, EP-0825
Jandric, J. EP-0268, **EP-0350**, EP-0363, EP-0393, EP-0406, EP-0779, EP-1062
Janez, A. EP-0712
Janier, M. EP-0787, OP-542
Jankovic, D. EP-0072, EP-1183
Jankulovska, A. EP-0448, EP-0735, EP-0736
Janowitz, D. OP-237
Jansen, S. M. EP-0848, OP-289
Janssen, M. OP-598
Janssen, M. J. R. EP-1123, OP-855
Janssen, Y. F. OP-760
Janssen, Z. OP-150
Januszkiewicz-Caulier, J. EP-0789
Jaramillo López, B. EP-0579, EP-0612, EP-0613, OP-057 EP-0549, EP-0550, **EP-0833**, OP-854
Jaraquemada-Peláez, M. EP-0058, EPS-021
Jareno-Badenas, A. EP-0653
Jarlier, M. OP-213
Járó, I. EP-0247
Jarzab, M. EP-0207
Jauregui Larrea, I. EP-0462, EP-1262, EP-1263
Jayakrishnan, V. EP-0181
Jayasinghe, J. M. A. D. **EP-0921**
Jeanjean, P. **OP-204**
Jedamzik, T. **EP-0318**, EP-0728
Jedidi, S. **EPS-044**
Jeffery, C. OP-817
Jeffry, J. EP-0160
Jehanno, N. EP-0217, EP-0251, EP-0297, EPS-231, OP-104
Jelinek, T. EP-0513
Jensen, A. T. I. EPS-146
Jensen, H. EP-0049, EP-0945, OP-704, OP-092
Jensen, L. EP-0005, EP-0624, EPS-253
Jensen, M. OP-166, OP-579, **EP-0732**
Jensen, P. T. OP-038
Jensen, T. EP-0108
Jensterle, L. EP-0835
Jensterle Sever, M. EP-0712
Jentjens, S. EP-0879, EPS-126, OP-366
Jentzen, W. EP-1103, EPS-190, OP-247, OP-383, OP-385
Jeraj, R. EP-0519
Jerez-Jaimes, M. EP-0872
Jessen, F. OP-303
Jha, A. EP-1445
Jha, P. EP-0009, EPS-043
Jha, S. EP-0543, EP-1213, EP-1252, EP-1260, EP-1261, EP-0259
Jheng, M. J. OP-763
Ji, H. OP-155
Ji, Q. EP-0218, EPS-243
Ji, R. OP-498
Jia, C. OP-045
Jia, J. EP-0186, EP-0187
Jia, K. **EP-0108**
Jia, L. EP-0593, OP-544
Jia, Q. EP-0079, EP-0865, EP-0899
Jia, S. EP-0609
Jia, W. **EP-0212**
Jia, Y. OP-226, **OP-357**, OP-466
Jia, Z. EP-0113
Jiajun, Y. EP-0042
Jianbo, C. **EP-1050**, **OP-880**
Jiang, C. EP-0198, **EP-0276**, EPS-176, OP-030, OP-463
Jiang, D. EPS-052, EP-0099, EP-0107, EPS-053, OP-020, OP-086, OP-090, OP-274, OP-418, OP-419, OP-469, OP-696, OP-768, EP-0209
Jiang, G. EP-0035
Jiang, J. EP-0674, EP-0674
Jiang, L. EP-0239, OP-462, EPS-200, OP-071
Jiang, R. **EP-1096**
Jiang, S. EP-0684
Jiang, T. EP-0727
Jiang, Y. **EP-0186**, **EP-0187**, EP-0662, EP-1441, EP-1446, EP-0695, **EP-0248**
Jiang, Z. OP-030, **EP-0045**, **EP-0252**, EP-1011
Jiao, F. **EP-0657**, OP-439
Jiao, Y. EP-0650, **EP-0654**
Jicheng, L. **EP-1433**
Jilg, C. A. EPS-159
Jiménez-Bonilla, J. **EP-0656**, EP-0673
Jimenez Fonseca, P. EP-0792, OP-430, OP-429
Jiménez-Franco, L. D. EPS-184
Jiménez-Murillo, J. EP-0745
Jimenez-Serrano, S. TEPS-021
Jimeno, R. EP-0288
Jin, S. EP-0916, **OP-664**
Jin, W. OP-178, OP-767
Jin, X. EP-1139
Jin, Y. EPS-033, OP-236, **EP-0517**, **EP-0706**, EP-0727
Jing, H. EP-0327
Jing, W. EP-0042
Jinzaki, M. EP-0676
Jo, S. EPS-023
Jochumsen, K. M. OP-038
Jodeiri, A. EP-1451
Joemon, J. OP-625
Joergensen, P. G. EP-0624
Jögi, J. EPS-213
Johanna Lahdenranta, J. EP-0121
Johansen, H. EP-0883
Johansson, L. EP-1104
Johari Daha, F. EP-0128
Johayem, A. OP-361
John, J. EP-0916, OP-619
John, L. EP-0506
Johnbeck, C. B. EP-0322
Johnsen, R. EP-1030
Johnson, M. OP-710, EPS-032
Johnson, R. R. EP-1409
Johnston, N. OP-791
Jokar, N. EP-0878
Joksch, M. OP-779
Jolly, D. EP-1409
Jonard, E. EPS-266
Jonasson, M. EPS-128
Jones, A. EP-0084, OP-177
Jones, C. EP-0108
Jones, J. EP-0995
Jones, K. EP-0572, EP-0576
Jongsma Wallin, H. OP-458
Joniau, S. OP-067
Jonker, M. OP-598
Jonmarker, O. **EP-0381**, **EP-0404**

Joosten, L. **OP-184**
Jordan, J. EP-0696
Jörg, N. **EP-0936**
Jorge, P. EP-0521
Jorgensen, M. EP-0108
Jørgensen, T. OP-593, OP-708
Jörger, A. K. OP-869
Joseph, E. EP-0062, EP-0691
Jou, J. **OP-687**
Jouanneau, E. OP-542
Joubert, M. OP-838
Jougla, A. EPS-186
Jovanovic, A. OP-479
Jovanovic, R. EP-0448
Jover Díaz, R. OP-485
Jozi, H. **EP-1110**
Jozi, S. **EP-0120**, EPS-046
Jreige, M. EP-0184, EP-1407, OP-160, OP-373, OP-528
Ju, M. **OP-727**
Ju, P. EP-0211
Ju, Z. OP-439
Juarez, B. EP-1223
Juarez Amorim, B. EP-0337
Juel Nissen, H. TEPS-003
Jueptner, M. EP-0080
Juergens, R. EP-1100, OP-423
Juhlin, C. C. EP-0314
Jukic, T. EP-0264, EP-1222
Julian, K. EP-0703
Julia S. Dorneich, J. S. EP-0691
Jullian, N. OP-710
Jun, H. EPS-200
Jun, Y. EP-0664
Juneau, D. EP-1033
Jung, M. EP-1082, EP-1182, EPS-215
Jung, T. EP-0688
Júnior, M. W. P. EP-0223
Junyang, L. OP-544
Juppo, A. M. EP-1180
Jurman, G. EP-0234
Jussing, E. EPS-154
Just-Lauer, I. EPS-024
Jusufbegović, M. OP-318
Jutidamrongphan, W. EP-1148
Juweid, M. **EP-0580**
Juzeniene, A. EP-0014, EP-0016
Kääriä, L. **EP-0946**
Kabasakal, L. EP-0277, EP-0424, EPS-191, OP-434, OP-476
Kabayama, K. EP-0030, EP-0031, EPS-056, OP-276, OP-281
Kabunda, J. EP-1116, OP-825
Kacperski, K. EP-0789
Kaczmarek, K. EP-0440
Kadonaga, Y. EPS-056
Kadoya, Y. EP-0977
Kadymova, N. EP-1304
Kagawa, T. EP-0459
Kagodora, S. **EP-0012**
Kahl, T. OP-786
Kähler, F. **EPS-178**
Kaiafa, G. EP-1341
Kaida, H. EP-0956
Kairemo, K. OP-434
Kaiser, L. EP-0936, EP-1035, **EPS-124**, **EPS-125**, EPS-239, OP-610, OP-773, OP-775
Kajisako, M. EPS-255
Kakkar, A. EP-0559
Kalaeva, D. EP-0178, **EP-0992**
Kalaitzidis, P. EPS-088
Kalaitzoglou, A. EP-1415
Kalasauskas, D. EPS-271
Kalathas, T. OP-557, EP-0820
Kaleemi, R. EP-1424, EP-1425, EP-1428
Kalennik, O. EP-0178
Kalish-Achrai, N. EP-0021
Kalisvaart, G. M. EP-0958
Kaliszczak, M. EP-0116
Kalkan, H. **EP-0605**
Kalkan, R. **EP-0261**
Kallur, K. EP-1455, EP-0539, EP-0258, OP-550
Kalman, B. **EP-0797**
Kalnina, M. **EP-0608**
Kalowa, C. EP-0824
Kamani, C. OP-528, OP-160
Kamat, S. EP-1091
Kamínek, M. EP-0489, EP-0586
Kaminski, G. EP-0782, EP-0789
Kamiya, T. **EP-1458**, OP-387
Kammies, C. **OP-620**
Kamrani, S. **EP-0967**
Kanaan, N. TEPS-012
Kanazawa, N. OP-208
Kandi Dayeni, M. EP-0066
Kandolf, L. EP-0564
Kanellopoulos, P. **EP-0032**, EP-0074, OP-070, OP-087, **OP-659**
Kang, D. EP-0109
Kang, F. EP-0105, EP-0143, EP-0149, EP-0256, EP-0278, EP-0439, EP-0531, EP-0689, EP-0693, EP-0738, EP-1027, EPS-147, OP-114, OP-116, OP-695
Kang, J. EP-0111
Kang, K. EP-0795
Kang, K. EP-0169
Kang, L. **EP-0052**, **EP-0053**, **EP-0054**, **EPS-006**, **EPS-014**, **OP-210**
Kang, S. EP-0664, OP-532
Kang, Y. EP-0795
Kangbin, K. **EP-0112**
Kangxia, Y. EP-0042
Kani, Y. OP-585
Kankara, S. OP-799
Kaoma, C. EP-1116
Kapansahin, K. **EP-1340**
Kapinos, M. OP-457
Kapiteijn, E. EP-0334, OP-295
Kappel, R. H. EPS-301
Kapse, N. A. EPS-302
Kapsoritakis, N. **EP-0242**, **EP-0243**, **EP-0244**, **EP-1031**, EP-1299
Kapucu, H. EP-0840, EP-1367, OP-857, **EPS-204**, **OP-859**
Kar, S. **EP-0283**, **OP-748**
Karabina, J. EP-0801, EP-0802
Karabulut, E. EP-0287
Karabulut, S. EP-0210, EP-0422, **EP-0831**
Karacalioglu, A. O. EP-0523
Karacan, A. OP-257, OP-856
Karaçavuş, S. EP-0321
Karadağ, Ö. EP-1202
Karaivanov, D. EPS-150
Karam, J. OP-213
Karamanlıoğlu, D. EP-0742
Karamanos, D. EPS-027
Karamian, F. EP-1345, EP-1352, OP-242
Karampelas, T. **EP-0065**, EPS-198
Karampina, P. **EP-1417**
Karayel, E. EP-0355, EP-0901
Karbasi, M. EP-1296, EP-1297
Karellis, A. **OP-871**
Karfis, I. OP-537
Karimi, Z. EP-0146, **EP-1168**, EP-1170
Karimzadeh, A. EP-1047
Kariuki, J. EP-0539
Karlberg, A. **EP-0883**, TEPS-010
Karlin, L. EP-1055, OP-225
Karmann, A. EP-0153, EP-1161, OP-177, OP-290, OP-676, OP-703
Karna, R. EP-0474, **EP-0744**, OP-559
Karni-Ashkenazi, S. EP-0021
Karpinski, M. J. OP-329
Kartal, A. EP-0294
Kartal, M. EP-0294, **EP-1386**
Karthikeyan, G. EP-1396
Karyağar, S. EP-0902, EP-0858
Kas, A. EPS-131, OP-611
Kasai, R. **EP-1443**, **EP-1444**, **EP-1447**
Kascakova, G. EP-0513
Kaser, F. **EP-0968**
Kashani, M. EP-0038, EP-0066
Kashi, S. **EP-1163**
Kashiwagi, S. OP-585
Kasivisvanathan, V. EP-0389
Kasraie, N. EP-1137, EPS-289
Kassar, M. **OP-461**
Kassas, M. OP-111, **OP-537**
Kassubek, J. EPS-135
Kastelik-Hryniewiecka, A. EP-0207
Katada, C. EP-0540
Kataev, N. EP-0173
Kataoka, M. EP-0214, EP-0939

Katchel, L. OP-290, OP-676, OP-703
Kater, M. EP-0842
Kato, H. **EPS-056**, OP-058
Kato, S. OP-208
Kato, Y. EP-0939
Katsampoukas, D. EP-1341, EP-1364, EP-1370, EP-1374, EP-1415, EPS-027
Katsuki, A. EP-1449
Katzdobler, S. EP-0691, OP-044, OP-046, OP-609
Kaufmann, E. EP-0698
Kaul, F. OP-361
Kaur, H. EP-0509
Kaur, K. EP-0071, EP-1134, **EP-1460**
Kaur, S. **EP-0090**
Kaushal, S. EP-0371, EP-0372, EP-0373, EP-0764, EP-1084, OP-353
Kaviani, S. EP-1033, OP-162, OP-164
Kavin, M. EP-0371, EP-0372, EP-0764, EP-0373
Kawakami, H. EP-1449
Kawase, S. EPS-255
Kawashima, M. EP-0214
Kaya, E. EP-0480, EP-0486, EP-0511, EP-0844, OP-054, OP-540, OP-856, **EP-0840**, **OP-857**, OP-859
Kaya, E. B. OP-746
Kaya, G. EP-0451, OP-254, OP-386, OP-746, OP-804, **OP-850**
Kaya, M. EP-0480, EP-0486, EP-0840, EP-0844, EP-1270, EP-1310, EPS-204, OP-856, OP-857, OP-859
Kayal, S. EP-0804
Kazemi, A. **EP-1413**
Kazmierczak, W. OP-320
Keefe, S. OP-074
Keereman, V. OP-782
Keerthivasagam, S. EPS-208
Keidar, Z. EP-0336, EP-1088
Keil, T. EP-0883, TEPS-010
Kelemen, N. **EP-0562**
Kellemann Kristensen, L. OP-593
Keller, A. EP-0002
Kelly, E. OP-710
Kelly, J. OP-279
Kendi, A. T. EP-0807
Kengar, A. OP-655
Kennedy, J. EP-0949, EP-1088
Kenner, L. EP-0280, EP-1040
Kenova, A. EP-1131
Keramida, G. EPS-224
Kerckhaert, C. **EP-0907**
Kerleguer, K. EPS-230
Kerminen, E. **EP-1195**
Kero, T. OP-687, OP-791, **OP-794**
Kerro, O. EP-0417
Kersbergen, D. OP-295
Kerschensteiner, M. EP-0691, EP-0698
Kersemans, K. OP-522
Kersting, D. EP-1103, EPS-190, OP-172, **OP-239**, OP-247, OP-297, OP-383, OP-385, OP-468, OP-786
Kertels, O. EP-0182
Kesch, C. OP-538, OP-786
Kesim, S. OP-874
Kessler, L. EP-0696, OP-239
Kettless, K. EP-0957
Khalaf, A. EP-1416
Khalfa, S. EPS-035
Khalili, S. EP-0972
Khalimon, A. EP-0302, **EP-0432**, **EP-0433**, EP-0542, **EP-0932**, EP-0955, EP-1304, EPS-079
Khamadeeva, G. EP-0302, EP-0432, EP-0433, EP-0542, EP-0932, **EP-0955**, EPS-079
Khan, D. EP-0474, EP-0510, **EP-0537**, EP-0583, EP-0721, EP-1042, EP-1235, EP-1236, EPS-209, EPS-217, OP-256
Khan, S. OP-323
Khandelwal, Y. **EP-0300**, EP-0558, EP-0839, EPS-270
Khangembam, B. **EP-0371**, **EP-0372**, EP-0373, EP-0764
Khani, Y. EP-0113
Khani Meynaq, Y. EP-0116, EP-0118
Kharita, M. EP-0383
Khawar, A. **EPS-284a**
Khazaei, M. EP-0878
Khelifa, A. **EP-0756**, **EPS-212**
Kheruka, S. EP-0181, EP-0526, EP-1136
Khezri, S. EP-1362, EP-1363
Khlynin, M. EP-0616
Khobragade, P. EP-1013, **EP-1455**
Khodakova, D. EP-0302, EP-0432, EP-0433, **EP-0542**, EP-0932, EP-0955, EPS-079
Khodzhibekova, M. EP-0302, EP-0432, EP-0433, EP-0542, EP-0932, EP-0955, EPS-079
Khoo, U. S. EPS-008
Khor, Y. OP-031, OP-541
Khorasanchi, A. EPS-220
Khoshhosn, H. EP-0128, **EP-0066**, EPS-136
Khosravifarsani, M. EP-0081, OP-350
Kibar, A. EP-0277, **EP-0475**, EP-0857, **EPS-256**
Kiefer, L. S. EP-0351
Kieffer, Y. EP-0297
Kiener, T. EP-0362
Kienzle, G. OP-017
Kiesel, B. OP-609
Kikunaga, H. OP-585
Kile, E. A. M. **EP-1060**
Kilic, Ö. **EP-0506**
Kim, C. EP-0442, OP-177
Kim, D. EP-0659, EP-0664, OP-163, OP-532
Kim, D. EP-0647, EP-0664, OP-532
Kim, G. EP-0647
Kim, J. EP-0672, EP-0169
Kim, J. Y. **EP-0647**
Kim, M. EP-0868
Kim, Y. I. **EP-0795**
Kimura, H. EPS-141
Kimura, K. OP-719, **EP-0208**, EP-0376, EP-1143, EPS-162, EPS-192, OP-714
Kimura, R. EP-0303, EP-0796, EP-0860, EP-0874, EPS-250
Kimura, S. EP-0991, EP-1157, EP-1453
Kimura, Y. EP-0676, EP-1059, OP-301, OP-719
Kind, F. EP-1045, EP-1129
Kindu, A. OP-243
Kingsmell, Z. TEPS-006
Kinouchi, R. EP-0459
Kinsella, Y. EPS-305
Kinuya, S. EP-0585, EP-1079, OP-548
Kiran, M. Y. **EP-0282**
Kiraz, K. OP-822
Kircher, M. EP-0734
Kircher, S. EP-0318
Kireeva, E. EP-0481, EP-0482
Kirienko, M. **EP-0017**, EP-0044, EP-1146, EP-1401, OP-326, OP-384
Kirjavainen, A. OP-328, EP-1195
Kirk, N. EPS-305
Kirk Lehnskov, T. OP-621
Kirkwood, I. EPS-119
Kis, Z. EP-1166
Kise, S. EPS-141
Kishan, A. U. EPS-192
Kishimoto, Y. EP-0188
Kiss, F. **EP-0247**
Kiss, J. **EP-0938**, **EP-0951**
Kistner, A. EP-0314
Kita, T. EP-0927, EP-0954, **EP-0956**, EP-1098, EP-1452
Kitai, Y. EP-0214
Kitajima, K. EP-0956
Kitamikado, R. A. EP-0631
Kitamura, H. OP-208
Kitano, T. OP-058
Kitano, Y. EP-0214, EP-0540
Kivelä, R. V. EP-1180
Kiyono, Y. OP-283
Kjaer, A. EP-0322, OP-166, OP-818
Kjærnes Øen, S. EP-0883
Kjeldsen, S. A. S. EP-1073
Kjems, J. **EPS-253**
Klain, M. EP-0308, EP-0788
Klauschen, F. EP-0154
Klausen, R. **OP-887**
Kılıçaslan, A. EP-0605
Kleesiek, J. OP-786
Klega, A. OP-436, OP-860, OP-862
Kleiburg, F. **OP-710**, **OP-713**
Klein, G. EPS-131
Klein, O. OP-436, OP-860
Klein, R. EP-0442, EP-1012, OP-160, OP-162, OP-164, OP-528

Klein, S. A. EP-0485
Kleinauskas, A. EP-0016
Kleinendorst, S. **OP-521**
Klenner, M. OP-817
Kleynhans, J. EP-0935, EP-1175, EP-1188, OP-179
Klimek, K. EP-0309, **EP-0870**, EP-1155
Klint, S. OP-320
Klisarova, A. EP-1292, EP-1293, EP-1294, EP-1330, EP-1331, EP-1359, EP-1384
Kloiber, S. EP-0037
Klomp, M. J. EPS-007
Klompenhouwer, E. G. EP-0848
Kloosterboer, L. **EP-0948**
Kluge, A. OP-429
Kluge, K. EP-1011, OP-468
Kluge, R. EP-0488
Knesaurek, K. **EP-1144**, **EPS-237**
Knol, R. J. J. OP-890
Knoop, H. EPS-036
Knuuti, J. EPS-234, OP-595, **OP-679**, OP-794
Ko, C. EP-0645
Ko, C. L. OP-793
Ko, K. Y. **EP-0025**, EP-1427
Kobe, C. EP-0331, OP-879
Kober, L. EP-1085
Koç, Z. **EP-0640**
Koca, G. EP-0443, EP-0763, EP-1271, EP-1277, EP-1373
Kocabas, B. OP-040
Kocabeyoglu, B. **EP-0246**
Kocemba, M. **EP-0702**
Koch, H. EP-0077
Kochebina, O. **EP-0083**
Kocjan, T. EP-0713
Kocsak, E. EP-1338, EP-1343
Kodaz, O. OP-847, OP-850, **EP-0426**, EP-0451, **OP-254**, OP-804
Koefler, M. EP-1011, OP-468
Koehbach, J. EP-0153
Koehler, D. **EP-1026**
Koelewijn, S. OP-183
Koffijberg, H. EP-0334, EP-1086, OP-295
Koga, H. EP-0796, EP-0874, **EP-1237**, EPS-250
Koglin, N. EP-0691
Kogure, T. EPS-111
Koh, E. EPS-119
Kohi, C. EP-1017
Koivula, T. EP-0417
Koizumi, T. EP-0676
Kokalj, M. EP-0895
Kokkini-Paschou, A. EP-0875
Kokkonen, S. E. A. OP-100
Kokufuta, T. OP-209
Kolade, O. EP-0379
Kolck, J. EPS-024
Koley, M. EP-0529, OP-482, OP-878
Kolindou, A. EP-0569, EP-1379
Kolkiran, N. EP-0236
Kollaard, R. EPS-285, OP-702, EPS-286
Kollàr, A. OP-429
Koller, P. EP-0933
Köllermann, J. OP-786
Kolodziej, M. **EP-0782**, **EP-0789**
Kolovcevska Bozinovska, N. EP-0735
Komarova, M. **EP-0253**, **EP-0286**, **EP-0402**, EPS-265, **OP-472**, **OP-473**
Komatsu, A. EP-1453, EP-1454
Kominia, M. OP-452
Koźmiński, P. OP-183
Komoda, T. EP-0028
Konca, C. EP-0441
Kong, C. EP-0964
Kong, G. EP-0830
Kong, Q. EP-0129
Kong, X. EP-0237
Kong, Y. **EP-0020**, EP-0500
Konietzko, U. EP-0002
Konijnenberg, M. EP-1010, EP-1185, EPS-017, EPS-182, OP-184, OP-425, OP-521, OP-764 EP-0074, EPS-048, EP-1119, EPS-183
Konovalova, E. EP-0089
Konstantarogianni, E. A. EP-1430
Koo, S. EP-0847
Kool, W. EP-0535, EP-1395
Koole, M. EP-0641, EP-1126, EPS-227, OP-067, OP-091, OP-096, OP-097, OP-530
Koolen, S. EP-1010, EPS-182
Koopman, T. OP-607
Koopmans, K. P. EPS-082, OP-289
Koosha, F. EPS-289
Kopeva, K. OP-795
Kopka, K. OP-032, OP-154, OP-652
Koppes, J. OP-598
KoppSchneider, A. EP-0485
Korde, A. EP-1396
Korepanov, V. EP-0617
Körholz, D. EP-0488
Korhonen, T. **EP-0600**
Korkmaz, M. EP-0443, EP-0763, EP-1271, EP-1277, EP-1373
Korn, M. J. EP-0809
Korol, P. **EP-0751**, **EPS-281**, **EPS-282**, **EPS-283**
Korsgren, O. EP-0137, OP-728
Korsholm, K. EP-0766, OP-464, OP-474
Kosaka, H. EP-0676
Kösem, H. OP-715
Kos-Kudła, B. EP-0782
Kosmala, A. EP-0318, EP-0794, OP-376
Kosoff, D. EPS-001
Kosovezer, H. EPS-087
Kossatz, S. EP-0161, EPS-146, EPS-185, OP-180, OP-181
Kosta, S. **EP-1430**
Kostadinova-Kunovska, S. EP-0448
Kostashuk, M. EPS-139
Köster, U. **EP-1166**, OP-022
Kostos, L. EP-0830, OP-605
Kostou, T. EP-1379
Kostyal, L. EP-1343
Kostylev, M. EP-0751, EPS-281, EPS-282, EPS-283
Kotake, T. OP-208
Kotasidis, F. EP-1449, EPS-041, OP-285
Kotliarenko, A. OP-584
Kotur, M. EP-0898, OP-479
Kotzerke, J. EP-0082, EP-0483, OP-032
Koudri, F. EP-0756, EPS-212
Koukouraki, S. EP-0242, EP-0243, EP-0244, EP-1031, EP-1299
Koulibaly, M. EP-0671
Koutsikos, J. **EP-0875**
Kovacs, L. **EP-0015**, EP-0114
Kovaleva, N. **EP-0830**
Kovan, B. **EP-0837**
Kowalska, A. EP-0789
Kownacka, A. OP-211, OP-351
Koyama, K. EP-0991
Koyama, T. EP-0768
Koyasu, S. EP-0188, EP-1449
Kozanecki, C. EP-0013, OP-679
Kozanecki, P. OP-679
Kracmerova, T. **EP-1131**
Kraeber Bodéré, F. OP-675, EP-1055, OP-225
Krafft, U. OP-297, OP-786
Krajewski, S. EP-0013, OP-679
Krakauer, M. OP-686
Krakstad, C. OP-039
Kralik, I. OP-708
Krämer, A.
EP-0532
Kramer, C. **EPS-166**, OP-670
Kramer, G. EP-1241, OP-325, OP-820
Kramer, H. EPS-195, OP-515
Kramer, V. OP-471
Kramer-Marek, G. **EP-0207**
Kráčmerová, T. OP-702
Krarup, M. **OP-474**
Krasteva, R. EP-0213
Krasulova, K. EP-0148
Krasznai, Z. T. EP-0450
Kratochwil, C. OP-825, OP-881
Kraus, S. OP-223
Krause, B. OP-779
Krebs, S. OP-204
Kreissl, M. C. OP-245, OP-385
Krenning, E. P. EP-0032
Kretschmer-Chott, E. EP-1241, OP-790, OP-820
Kriari, A. EPS-254
Krishna, D. EPS-119
Krishna, J. EP-1206, EP-1235, EP-1236, EPS-206

Krishna P. J. EP-0474, EP-0510, EP-0537, **EP-0583**, EP-0750, EP-1207, EP-1259, EP-1278, EPS-277
Krishnappa, R. EP-0258, EP-1455
Kristanto, P. OP-470
Kristensen, B. EP-0624, EPS-253
Kristensen Vølund, A. **OP-166**
Kristian, A. EP-0064
Kristóf, E. EP-0562
Krivolapov, S. EP-0616
Krizsan, A. K. OP-501
Kroiß, M. EP-0793
Krokos, G. **EP-0916**, EP-0974, OP-619, OP-664
Krol, A. **EP-0918**, **EP-0920**
Kronberger, J. EP-0148
Krönke, M. OP-789
Krönke, T. **OP-652**
Kroschinsky, F. EP-0483
Krüger, M. OP-017
Kryza, D. OP-331
Kryza, T. EP-0153, EP-1161, OP-177, OP-676
Ku, A. EP-0081
Kuan, K. EP-0153, OP-177, OP-676
Kuba, S. EP-0189, EP-0223, EP-0262, OP-119
Kubeczko, M. EP-0207
Kubeil, M. OP-154
Kubik, A. EP-0789
Kübler, A. EP-0195
Kubo, K. OP-283, OP-285, TEPS-020
Kubota, K. EP-0939
Kucuk, N. Ö. EP-0333, EP-0354, EP-0441, EP-0806, EP-0834
Kucuk, O. OP-711, OP-873
Kucukali, S. B. OP-175
Kucuker, K. EP-0228, EP-0296
Küçüker, C. **OP-746**, OP-846
Kudo, K. EP-0303, EP-0796, EP-0860, EP-0874, EP-1237, EPS-250
Kugelmann, B. OP-773
Kuhar, M. EP-1030
Kukuts, K. EP-0938, EP-0951
Kula, W. OP-679
Kulkarni, K. **EPS-262**
Kullberg, C. **EP-1426**
Kulterer, O. EP-0725
Kumar, A. EP-0071, EP-0177, EP-0882, EP-0559
Kumar, D. EP-0258, EP-0985, OP-550
Kumar, M. OP-655
Kumar, N. EP-0265, **EP-0301**, EP-0558, **OP-861, EPS-009**, **EPS-013**, EPS-193, OP-417, **OP-518**
Kumar, P. EP-1246
Kumar, R. EP-0191, EP-0556, EP-0741, EP-1460, OP-743, OP-797, OP-848, EP-0606, EP-0298, EP-0371, EP-0372, EP-0373, EP-0474, EP-0510, EP-0537, EP-0721, EP-0744, EP-0750, EP-0764, EP-1042, EP-1084, EP-1207, EP-1209, EP-1210, EP-1226, EP-1235, EP-1236, EP-1259, EP-1272, EP-1278, EPS-206, EPS-209, EPS-217, EPS-277, OP-256, OP-353, OP-559, OP-711, OP-800, OP-873
Kumar, S. EP-0153, EP-1084, EPS-208, **EP-0509**
Kumazawa, T. EP-0768
Kumpf, K. OP-468
Kumpf, M. OP-204
Kümpfel, T. EP-0691, EP-0698
Kundu, N. EP-0298, EP-0510, EP-0537, **EP-0721**, EP-0750, **EP-1042**, EP-1207, EP-1209, EP-1210, EP-1226, **EP-1235**, **EP-1236**, EP-1259, EP-1272, EP-1278, EP-1387, **EPS-206**, **EPS-209**, **EPS-217**, EPS-277, **OP-256**, OP-744, OP-800
Kung, H. F. OP-178
Kung, J. EPS-177
Kunikowska, J. EP-0323, EP-0702, OP-711, OP-873
Kunsch, J. EP-0827
Kunst, A. EP-0713
Kunte, S. EPS-248, **EP-0793**, **EPS-290**
Kunz, P. EPS-139
Kunze, L. EP-0019, EP-0022
Kunze, L. H. EP-0047, EP-0062, OP-456
Kuo, C. L. TEPS-007
Kuo, P. S. EP-0346, EPS-245
Küper, A. OP-239, **OP-297**
Kuradia, K. EP-0285, EP-0880
Kurch, L. EP-0488
Kurihara, H. EP-0139
Kurimoto, T. OP-283, OP-285
Kurkowska, S. EP-0960, EP-1016, OP-102, **OP-428**
Kurniawan, A. **EP-0011**, EP-0061, OP-149
Kuromori, I. EP-0956
Kurth, J. EPS-190, OP-779
Kurup, D. OP-074
Kurz, F. T. EP-0485
Kusaka, A. TEPS-020
Kusudo, K. OP-719
Kuttner, S. EP-1060
Kuyumcu, S. EP-0282, EP-0837, OP-110, OP-259
Kuznietsov, P. EP-0147
Kuzucu, M. EP-1420
K V, S. EP-0537, EP-0510
Kvacskay, P. OP-371
Kvarsvik Kristiansen, S. **EP-0014**, EP-0016
Kvassheim, M. EP-1078, EP-1102, EP-1113, **OP-424**
Kvernby, S. EP-0917, EP-1426, **EPS-085**, **EPS-096**, OP-095
Kvistholm, M. **EP-0981**
Kwapisz, M. EP-1336
Kwizera, C. OP-452
Kwon, O. EP-0070, EP-0162, **EP-1121**, EPS-001, OP-217, OP-218, OP-219, OP-517
Laadissi, Z. EP-1290, EP-1301, EP-1302, EP-1325
Laajimi, N. EP-0598, EPS-099, OP-496, **TEPS-012**
Laas, E. OP-104
Labiod, H. EP-0756, EP-1217
Labrador-Espinosa, M. A. OP-440
Lacassagne, P. OP-098, OP-630
Lachachi, B. EP-0787
Lachachi, C. **EP-0812**, OP-429
Lachapelle, C. EPS-084
Lacombe, M. EP-0800
Lacor, P. EPS-032
Lacroix, L. OP-120
Ladefoged, C. OP-261, OP-464, EP-1005
Ladekarl, M. EP-0773
Ladjohounlou, R. **OP-767**
Ladrière, T. OP-433
Laenen, A. OP-067
La Fay, C. EP-1408
Laforest, R. OP-745
La Fougère, C. EP-0809, EP-0229, EP-0351, OP-017, OP-288, OP-365, OP-525
Lafuente Carrasco, S. EPS-026, EP-0845
Lagaki, V. EPS-198
Lagarde, J. EPS-131
Lage, C. EP-0656
Lago, M. EP-0708
Lagrange, A. OP-173
Lahner, H. OP-247
Lahoutte, T. OP-215, OP-593
Lai, Y. OP-178
Laidley, D. EP-1100, OP-423
Laine, M. EP-0934
Laines, N. EP-1344
Laird, A. EP-0572, EP-0576
Lairez, O. OP-060
Laitinen, T. M. EP-0602
Laitinen, T. EP-0600
Laitinen, T. P. EP-0602
Lajkosz, K. EP-1100
Lakes, A. L. EP-1171
Lalia, M. EP-0018, **EP-0019**, EP-0062
Lalitha, G. EP-1207, EP-1259
Lam, M. EP-0535, EP-1395, EP-0907, OP-597
Lam, S. OP-625
Lam, W. EP-0020, OP-031, OP-541
Lamagna, M. EP-0507
Lamali, M. EP-0756, EPS-212
Lamande, M. OP-710
Lamartina, L. EP-0306, EP-0786, EP-1019, OP-120
Lamash, Y. OP-499
Lambert, B. **OP-121**, TEPS-009
Lambert, L. EP-0070, EPS-012, OP-217, OP-218, OP-275
Lambert, R. EPS-210
Lambert-Lepesevich, L. OP-517
Lambidis, E. EP-0065
Lambrecht, M. EP-0879, EPS-126
Lameirão, D. EP-1320
Lamerton, P. **EP-1463**
Lamesa, C. EPS-078

Lammertsma, A. A. OP-051
Lamminmäki, U. EP-0114
Lamprakopoulos, G. EP-1299
Lamy, C. OP-104
Lan, W. EP-0229, OP-288
Lan, X. EP-0055, EP-0099, EP-0107, EP-0190, EP-0356, EP-0484, EP-1024, EPS-010, EPS-053, EPS-059, EPS-175, OP-018, OP-020, OP-086, OP-090, OP-274, OP-286, OP-382, OP-418, OP-469, OP-696, OP-768, OP-837
Lancha Hernández, C. EP-0705
Lanctôt-Bédard, J. **EP-1288**, **EPS-210**
Landau, F. OP-327
Landoni, V. **EP-0263**
Landry, M. OP-023, OP-657
Landvogt, C. EPS-156, OP-436, OP-860, OP-862
Lanfranchi, F. **EP-0370**, EP-0377, **OP-324**, **OP-868**
Lang, M. OP-284
Lang, O. **EP-1285**
Langer, V. OP-770
Langguth, V. OP-228
Langrate, I. K. OP-325
Langrate, I. **EP-1241**, **OP-820**
Langsteger, W. EP-0968, EP-1089
Lanza, A. EPS-298
Lanzafame, H. EPS-190, OP-779
Laoriya, I. EP-0159
Laouafa, A. OP-351
Lapa, C. EP-0734, EP-0811, EP-1009, EP-1111, OP-223, OP-352, OP-358, OP-376, OP-600, OP-863
Lapa, P. EP-0897, OP-633
Lapauw, B. EP-0325
Läppchen, T. EPS-009, EPS-013, EPS-193, OP-417, OP-518
Lara-Hernández, A. EP-0872
Lara Martínez, M. EP-0748
Larcher, A. EP-0534
Larkina, M. EP-0089, OP-070
Laroni, A. OP-725
Larose, T. OP-708
Larrabee, J. EP-1169
Larson, M. EP-1211, EP-1273, EP-1274, EP-1280
Larsson, E. OP-099
Larsson, H. B. W. EP-0172
Larsson, H. EP-0709
Larsson, J. E. EP-0624, **EPS-104**
Larsson, M. EP-0463, EP-0468
Laschinsky, C. **OP-385**
Laske, C. OP-303
Lassmann, M. EP-0967, EP-1077, EP-1143, EPS-184, EPS-294, EPS-295, OP-096, OP-426, EP-0983, EPS-179, OP-590
Lastoria, S. EP-0809, EP-1115, EPS-054, OP-437
Lastrucci, A. OP-321
Latter, M. OP-290
Lattuada, F. OP-484
Latva-Rasku, A. E. EPS-234
Lau, E. EPS-119
Lau, J. EP-0090
Lau, W. EP-0051, EP-0058, EP-0090, EP-0120
Laube, M. **OP-346**, OP-652
Laudicella, R. OP-352
Laurent, G. EPS-153
Lauria, M. EPS-192
Lauricella, E. EP-0312, EP-0329
Lavalaye, J. EPS-074
Laverman, P. OP-184
Lavie-Badie, Y. OP-060
Lavik, J. OP-039
Lavon, B. R. EP-1185
Law, I. **EP-0172**, EP-0709, EP-0957, EP-0990, EPS-120
Lazar, A. EP-0269, EP-1401, EP-0427, **EPS-238**
Lazarenko, S. V. OP-890
Lazarevic, A. EP-1071
Lazaridis, K. EP-1415, EPS-027
Lazutina, T. **EP-0302**, EP-0432, EP-0433, EP-0542, EP-0932, EP-0955, EPS-079
Lazzeri, M. EP-0350
Leal Hernandez, F. EP-0358
Lebedev, A. OP-659
Lebouvier, T. EPS-131
Lebras, F. OP-227
Lebreux, M. E. EP-1404
Lebrun, A. OP-838
Leccisotti, L. EP-0497, EPS-269, OP-858
Lechiara, A. EP-0686
Lecomte, R. EP-0027
Lecorche, P. EP-0088
Lecouvet, F. OP-604
Ledderose, S. EP-0154
Ledoult, E. OP-555
Ledwon, A. EP-0782
Lee, D. **OP-745**, **EP-0169**
Lee, G. EPS-214
Lee, J. **EPS-214**
Lee, K. EPS-062
Lee, P. Y. EP-1193
Lee, S. OP-204, OP-163, EP-0659, EP-0664, EPS-215, OP-163, OP-532, EPS-119
Lee, T. **EP-1427**, EP-0025
Lee, W. EP-0627, EP-0169, OP-088
Lee, Y. G. EP-0664
Leekens, S. OP-350
Leenhardt, F. EPS-246
Leenhardt, J. OP-022, OP-787
Lefaucheur, J. L. OP-284
Lefol, R. EP-1110
Lefranc, F. EP-0663
Le Gal, G. EPS-090
Leger, C. OP-599
Léger, M. A. EP-1033
Legodi, K. EPS-086, EP-0942
Legodi, M. K. EP-1116
Lehmann, P. EP-0957
Lei, P. EPS-060, EPS-158
Lei, Y. EP-0053, EPS-006, OP-210
Leibetseder, A. OP-778
Leidermark, E. **EP-0945**, OP-704
Leimgruber, A. EP-0226
Leiva Montejo, A. **EP-1227**, **EP-1251**
Lejeune, F. OP-718
Lele, V. R. EP-0283, OP-748
Leleu, X. EP-1055, OP-225
Leloux, S. EP-1196
Lemaréchal, Y. EP-1110
Lemes, R. EP-0973
Le Meur, C. EPS-230
Lemos, L. EP-0897, OP-633
Lemoudda, G. EP-0251, OP-173
Lenarz, T. OP-726
Lenda-Tracz, W. EP-0789
Lennartz, M. OP-284
Lenormand, J.-L. OP-022
Lenzo, N. EP-0353
Leo, R. EPS-261
Leonardi, L. EP-1062
León-Jiménez, A. EP-0745
León Ramírez, L. **EP-0553**, OP-784, **OP-785**, EPS-275
Leontev, A. EP-0302, EP-0432, EP-0433, EP-0542, EP-0932, EP-0955, EP-1304, EPS-079
Leon Zubizarreta, I. EP-0462, EP-1262, EP-1263
Leopoldo, M. EP-1399
Leow, N. OP-031
Lepage, M. OP-021
Le Pennec, R. **EPS-090**
Lepore, L. EP-1166
Lerche, C. EP-0929, EP-0943, EPS-083, **OP-284**, EP-0963
Le Rhun, E. EP-0183
Le Roux, A. OP-279
Le Roux, C. EPS-203
Le Roux, P. OP-524
Le Roux, P. Y. EPS-090, OP-864
Leroux, M. EP-0096
Le Saux, L. **EP-0103**
Lesca, A. EP-0681, EP-0683, OP-055, OP-612
Letang, J. M. EP-1068
Leterrier, S. OP-453
Le Tourneau, C. OP-104
Leube, J. EP-0967, EP-0983, EP-1077, OP-590
Leung, E. EPS-090, OP-162, OP-164
Leung, H. M. OP-486
Leung, V. EP-0471, EP-0911
Leung, Y. OP-306
Leupe, H. **OP-366**
Leurquin-Sterk, G. EP-0663, EP-0687

Levasic, V. OP-866
Leveque-El Mouttie, L. EP-1161
Levesque, S. EP-1082, EP-1182
Levillain, H. OP-592, OP-818
Levin, J. EP-0691, OP-044, OP-046, OP-237
Levin, M. D. EP-1055, OP-225
Levine, O. EP-1100
Lewcock, J. W. EP-0047
Lewczuk-Myślicka, A. EP-0782
Lewis, D. Y. EP-0041
Lewold, M. EP-0463, EP-0468
Leyva Vásquez Caicedo, M. OP-784
Lezaic, L. **EP-0712**, **EP-0713**, **EP-0895**, EP-1440, **OP-866**
Lhommel, R. EP-0598, EPS-099, OP-107, OP-496, TEPS-012
Li, B. EP-0119, EP-0211, EP-0386, EP-0964, EPS-033, EPS-130, EPS-200, OP-367, OP-463, OP-765 OP-238, **EP-0050**, **EP-0316**, **EP-0400**, EPS-038
Li, C. EP-0280, OP-477, OP-851, OP-102, EP-1037 EP-0515, EP-0546, OP-112, OP-167, EP-0404, OP-596
Li, D. OP-763
Li, E. EP-0174, OP-608
Li, G. EP-0153, EP-1161, OP-177, OP-149, **OP-452**, **EP-0684**, EP-1027, EPS-147, EP-0693
Li, H. EP-0622, EPS-089
Li, J. EP-0982, **EP-1461**, EPS-158, **OP-693**, EP-0097, **EP-0215**, **EPS-160**, OP-052, EP-0166, EP-1433 EP-0098, EPS-047, EPS-051, OP-024, OP-694 OP-436, OP-862, EP-0111, EP-0097, **EP-0338**, EP-0067, EP-1096, OP-367
Li, K. **EP-1422**, **OP-486**OP-177
Li, L. EP-0087, **EP-0125**, OP-153, EP-0630, OP-732, OP-843, EP-0058, EP-0761, EPS-019, OP-071 **EP-0546**, OP-112, OP-167
Li, M. **EP-0445**, EP-0356, EPS-059, OP-382, **OP-469**, OP-768, EPS-123, OP-439
Li, N. EPS-098, EPS-118, EP-0237, EP-1021, EP-0079
Li, P. OP-763, **EP-0662**
Li, Q. OP-045, EP-1282
Li, R OP-733, EP-1244, EPS-050, OP-089
Li, S. OP-463, **EP-0085**, OP-766
Li, S. EP-0023, EP-0249, EP-0869, EPS-102, OP-732, OP-839, OP-841, EP-0317, **OP-594**, **OP-671**
Li, T. **EP-0399**, EP-0174, OP-608
Li, W. EP-0865, EP-0915, EP-0923, EP-0026, EP-0657, **EPS-053**, OP-545
Li, X. EP-0652, EP-0408, EP-0609, EP-0678, EP-0725, EP-0811, EP-0815, EP-0825, EP-0979, OP-205, OP-223, OP-226, OP-231, OP-300, OP-357, OP-466, OP-600, OP-730, OP-731, OP-790, EP-0129, EP-0554, OP-025, EP-0767, **EP-1275,** OP-069, EPS-100, OP-463, EP-0455, **OP-730**, **OP-731**, EP-0610 EP-0097
Li, Y. **EP-0860**, EP-0690, EP-0315, EPS-167, EP-0357, **EP-0982**, EP-1027, EP-1461, **EPS-080, EP-0430**, **EP-1214**, **EPS-165**, OP-709, OP-712, OP-717, **OP-456**
Li, Z. **EP-0163**, **EPS-268**, OP-692, EP-0067, EP-1096 EP-0085, OP-594, OP-671
Liang, D. **EP-0915**, EP-0923, OP-455, EP-0969, EP-1096, OP-460, OP-462
Liang, G. OP-772
Liang, M. **EP-0554**, **OP-045**
Liang, P. OP-551
Liang, R. OP-869
Liang, S. OP-451
Liang, X. OP-439
Liang, Y. OP-355, OP-460, OP-777
Liang, Z. EP-1024
Liao, EP-0026
Liao, C. K. EP-0342
Liao, K. EP-0657, EP-0680
Liao, X. **EP-0385**
Liapis, V. EP-0130
Liberale, G. OP-470
Librizzi, D. EP-0122, EP-0305, EP-0987, EPS-143, OP-459
Liefhooghe, N. OP-710
Ligeour, M. **EP-0058**
Likar, Y. EP-0755, EP-0481, EP-0482
Lilburn, D. M. L. OP-664
Lilikaki, G. L. EP-0574
Lilja, J. EP-0962
Lilley, L. EP-1169, EP-1171
Lim, C. EP-0471
Lim, D. **OP-031**, **OP-541**
Lim, H. EP-0664
Lim, W. OP-629
Lima, C. EP-1306
Lima, C. S. P. EP-0189, EP-0223
Lima, E. EP-1203
Lima, M. EP-1223, EP-1234, EP-1245, EP-1267, EP-1324, EP-0337
Lima, M. C. L. EP-0536
Lima, M. D. L. EP-0223
Lima, S. K. A. OP-722
Lima, T. **EP-0226**
Limouris, G. S. EP-1429
Limper, U. EP-0696
Lin, C. N. EP-1037, EP-1048
Lin, C. Y. **EP-0645**
Lin, H. EP-0976, **OP-287**, OP-439
Lin, K. J. EPS-229
Lin, K. S. EP-0051, EP-0090, EP-0120, EPS-021, EPS-046
Lin, L. EP-1422
Lin, P. EPS-119
Lin, Q. EP-1038
Lin, S. OP-367, **OP-176**
Lin, X. EP-1096, EP-1056, EPS-101
Lin, Y. EP-1244, EP-1427, EPS-245, EP-0915, EP-0923 EP-0342, EP-0915
Lin, Z. EP-0174, EP-0386, EP-0684, EPS-123, EPS-200, OP-238, OP-287, EP-0107, EP-0484, OP-020, OP-768, OP-837, EP-0484, **EPS-175**
Lindauer, U. EP-0109
Lindberg, U. EP-0172, EP-0709, EP-0981, EP-0990, EP-1005
Lindegren, S. OP-092
Linder, P. M. OP-288
Lindheimer, F. EPS-197
Lindman, H. EP-0289
Lindner, S. EP-0022, EP-0037, EP-0047, EP-0691, EP-0698, EP-0699, EP-0793, EPS-005, EPS-248, OP-237, OP-364, OP-456, OP-773
Lindsey, M. **EPS-001**, EPS-012, **OP-517**
Ling, E. **EP-0380**
Ling, R. EP-0674
Linguanti, F. OP-324
Lio, M. EPS-298
Liolios, C. EPS-153, OP-183
Lira, S. EP-1410
Liss, P. EP-0289
Lita, R. EP-1326
Litvinenko, A. **EP-0077**
Liu, C. EP-0609, **EPS-057**, EP-1096, EPS-243, **EP-0249,** **EP-0205**, EP-0025, EP-0111
Liu, E. OP-462
Liu, F. EP-0035, OP-763, **EP-0153**, **OP-177**, EP-0435
Liu, G. EP-0727, EP-1437
Liu, H. EP-0575, EP-0767, EP-0771, EP-0869, EP-0915, **EP-0923**, OP-455, **OP-155**, **EPS-164**, **OP-362**
Liu, J. EP-0174, OP-608, EP-0587, **EP-0642,** EP-0315, EP-1039, EPS-073, OP-724, EP-0212, EP-0533, EP-0652, EP-0666, EP-0682, EP-0697, EP-1056, EP-1233, OP-236, OP-304, OP-300, EPS-163, OP-155, EPS-163, OP-108, EP-0129, OP-454, OP-594, OP-671, EP-0317
Liu, K. EP-1193
Liu, L. EP-0001, EP-0727, EP-0694, EP-0695
Liu, M. EP-0327, EPS-242, OP-066, OP-546, EP-1027, EP-0410
Liu, N. **EPS-148**
Liu, P. **EPS-145**, OP-412, EP-0124
Liu, Q. EP-0129, EPS-233, OP-762, EPS-157
Liu, R. OP-162, OP-164
Liu, S. OP-030, **EP-0726**, OP-545, TEPS-007, OP-735, **EP-0694**, **EP-0695**
Liu, W. **EPS-107**, OP-051, **OP-840**, EPS-057, EP-0630, **OP-732**
Liu, X. OP-839, OP-841, OP-844, OP-024
Liu, Y. EP-0435, EP-1050, **OP-672**, OP-880, EP-0117, EP-0455, EP-0456, **EP-0237**, EP-1021, OP-439, **EP-1015**, EP-1140, EP-0646, EPS-059, EP-0237, **EP-1021**, EP-0074, OP-089, **OP-764,** EP-0435, EPS-157, OP-030, **EP-0317**
Liu, Z. EP-0085, EP-0110, EP-1167, EPS-145, OP-157, OP-412,

OP-582, OP-653, OP-300, EP-0625, EP-0546, **OP-112**
Liubchenko, G. **EP-1118**, EP-1150
Liukaityte, R. **EP-0016**
Liukkonen, J. OP-708
Livartowski, A. OP-173
Livellara, V. EPS-272
Livieratos, L. EP-0084, EP-1099
Liying, T. **EPS-144**
Ljungberg, M. EPS-088
Lladó-Garriga, L. EP-0850
Llamazares, A. OP-361
Llana, B. OP-430
Llop, J. EP-0002
Lloret-Cano, M. EP-0632
Lo, T. **OP-416**
Lo, W. L. EP-0056
Lobato, L. OP-056, OP-061
Locatelli, M. EP-0175
Lodi, F. EP-0227, EP-0502, OP-168
Lodi Rizzini, E. EP-0444, EP-1112, OP-118, EPS-288
Loewenthal, C. EP-0235
Löfblom, J. EP-0137, OP-766
Loft, A. EP-0219, OP-038, OP-474
Loft, M. EP-0322
Lohith, T. G. EP-1104
Lohmann, P. EP-0183, EPS-083
Löhr, M. EP-0260, EP-0275
Loimaala, A. **EP-0417**
Loirat, D. EP-0217, EP-0297
Loisel, C. **EP-1067**
Loke, K. S. H. EP-0847
Lokhova, A. EP-0302, EP-0432, EP-0542
Lokitz, S. **EP-1283**
Lolli, C. EP-0801, EP-0802, EP-0803
Lomartire, A. EP-1421, EP-1450
Lombardi, C. OP-022
Lombardo, A. EP-0467
Løndalen, A. EP-1102
Long, T. EP-0517, EP-0706, **EP-0727**
Long, X. EP-0438, OP-090, **OP-419**
Long, Y. EP-0055
Longari, V. EPS-261
Longo, M. EP-0306, EP-0786, EP-1019
Lonneux, M. OP-107
Lonnroth, M. OP-818
Lonsdale, M. N. EP-1073
Lopatriello, M. EP-1398, EP-1399
Lopes, L. EP-1090
Lopes de Souza, S. **OP-722**
López, F. EPS-236
Lopez, G. EP-0175
López-Arribas, M. EPS-092
Lopéz-Bermejo García, F. EP-0374, EP-0452, **EP-0472**
Lopez Campos, F. EP-0530
Lopez-Corral, L. OP-229
López-García, S. EP-0656
López Llobet, E. EP-0387, EP-0887
López Martínez, C. **EPS-076**
Lopez Montes, A. **EP-1090**, **EPS-240**, OP-889
López-Mora, D. A. EP-0545
López-Picón, F. EP-0114
Lopez Sanchez, I. EP-0462, EP-1262, EP-1263
Lopez Urdaneta, J. EP-0463, EP-0468
Lopez Villar, I. **OP-485**
Lopo, I. EP-1243
Lorente Fonrodona, C. EP-0760
Lorenz, H.-M. OP-371
Lorenz, K. OP-245
Lorenzini, L. OP-467
Lorenzo, C. EP-0685
Lorenzoni, A. EP-1146, OP-384
Loria, A. OP-706
Loriot, Y. OP-120, OP-604
Losa, M. EP-0683
Losacco, S. OP-776
Löser, R. OP-652
Lötscher, F. OP-552
Lottspeich, C. EP-0793
Lotz, V. OP-697
Lou, J. OP-844
Loudos, G. EPS-198
Loureiro, L. OP-154
Lovibond, S. OP-204
Lovinfosse, P. EPS-084
Low, C. EP-0911, **EP-0471**
Löwik, D. OP-184
Loyal, P. K. EP-0420
Lozada, F. OP-666
Lozada Delgado, F. EP-1147
Lozano, A. EP-0632
Lozano-Murgas, L. EP-0545
L. S., S. EP-0259, EP-1206
Lu, C. **EP-0124**, OP-212, EP-0346, EPS-029, EPS-245, OP-701
Lu, D. EP-1117
Lu, J. EP-0674, **OP-439**, EP-0625, EPS-098, EPS-118
Lu, L. EP-0517
Lu, N. **OP-547**
Lu, Q. EPS-057
Lu, T. EP-0644
Lu, W. EPS-200
Lu, X. EP-0982, EPS-080
Lu, Y. EP-1029, OP-074, OP-367, EP-0097, EP-0594, **EP-0628**, EP-1027, OP-772, EP-0211
Luan, X. EP-0280, EP-0281
Lubberink, M. EP-0275, EP-0289, **EP-1104**, EP-1142, EPS-128, **OP-595**, OP-687, OP-791
Lubrano di Scorpaniello, E. EP-1212
Lucas Lucas, C. EP-0358, EP-0374
Lucchini, R. EP-0393
Lucena Sampaio, I. EP-0199, EP-1243, EP-1269, EPS-267, OP-632
Luciano, A. EPS-054
Lucidi, V. EPS-030
Lucinian, Y. A. OP-162, OP-164
Lucio Baez, O. EP-0816, EP-0909
Lüdemann, W. EPS-024
Ludwig, V. EP-0208, **EP-1124**, EPS-162, EPS-192
Luetzen, U. EP-0080
Lughezzani, G. EP-0350, EP-0363
Luk, W. H. OP-486
Lukas, K. EP-0252
Lumb Morollon, B. **EP-0781**
Luminari, S. EP-0496
Luna Mass, A. **OP-819**
Lunde, L. P. OP-039
Lundgren Mortensen, A. EP-1160, OP-414, OP-519
Lunger, G. EP-0822
Luo, D. EP-1029
Luo, M. **OP-029**
Luo, R. OP-209, **OP-733**
Luo, X. EP-0727, EPS-129
Luo, Y. OP-178, OP-735, EP-1039, **EPS-073**
Luo, Z. EP-1038
Lupi, E. EP-1287
Lupini, A. OP-047
Luporsi, M. EP-0251, EPS-231, OP-173
Luster, M. EP-0122, EP-0305, EP-0854, EP-0926, EP-0987, EPS-143, OP-459
Lusuardi, L. EP-0362
Lütje, S. EP-0109, OP-761
Lutz, F. EP-0794
Luurtsema, G. OP-053, EPS-107, OP-051, OP-840
Luzzago, S. EP-0389, OP-663
Lv, W. OP-206, OP-207
Lv, X. OP-020, OP-837
Lv, Y. **EP-0190**, EP-0356, OP-286, OP-837
Lv, Z. EP-0650, EPS-063
Lyburn, I. EP-1020
Ly-Le Moal, M. EPS-131
Lyo, V. EPS-032
Ma, C. EP-0694, EP-0695
Ma, G. OP-362
Ma, H. EP-0087, EP-0125, EPS-017, **OP-153**, EP-0435
Ma, J. **EP-0410**, EP-0694, EP-0695
Ma, K. M. EP-1284
Ma, L. **EP-0256**
Ma, N. EP-1096
Ma, P. EP-0667
Ma, Q. EPS-160
Ma, R. EPS-089
Ma, T. EP-1027, EPS-063
Ma, W. EP-1284, EP-0915, OP-455, EP-0315, EPS-073, EP-0174, OP-608, EP-0439, OP-114

Ma, X. EP-0646, OP-439
Ma, Y. OP-451
Ma, Z. EPS-062
Maaniitty, T. OP-595, OP-794
Maare, C. EPS-253
Maarsen, J. OP-884
Maas, M. EP-0351
Maas, O. EP-0573
Maccagnani, M. EPS-288
Maccauro, M. EP-0044, EP-1146, OP-384
Maccioni, L. OP-467
Macedo, L. EP-1306
Macedo, L. T. EP-0189
Machado, M. EP-0973, EPS-235, OP-465
Machado, R. OP-665
Machiraju, D. OP-294
Macis, C. EP-1112
Macis, G. EP-0497
MacKewn, J. EP-0916
Mackey, J. EP-0390
Mackowiak, S. EP-1082
Macsuka, M. **OP-423**
Madar, O. EP-1189
Madeddu, G. EP-0446
Madhumali, W. S. N. EP-0921
Madi, N. EP-0824
Madroszyk, A. OP-173
Madsen, J. EP-0709, OP-474, OP-166
Madsen, K. EP-0172, **EPS-120**
Madsen, S. S. OP-877
Maeda, M. **OP-585**
Maeda, Y. EP-0956
Maekawa, Y. EP-0634, EP-0635, EPS-095, EPS-111
Maenhout, A. EPS-302
Maes, J. EP-1175
Maestre Cutillas, R. EP-1431
Maffione, A. M. EP-0206, OP-105
Magalhães, A. L. P. EP-0171
Maggio, S. OP-868
Maggiore, R. OP-384
Magomedbekov, E. EPS-150
Magomedov, G. EPS-150
Mahalik, A. EP-1387, OP-744, **EP-0298**, EP-0510, EP-0537, EP-0721, **EP-0750**, EP-1042, **EP-1207**, **EP-1209**, EP-1210, **EP-1226**, EP-1235, EP-1236, **EP-1259**, **EP-1272**, EP-1278, EPS-206, EPS-277, OP-256, OP-559, **OP-800**
Mahambre, S. **EP-0266**
Mahammedi, H. **OP-675**
Mahamood, M. EP-0416
Mahersi, N. EP-1325
Maheshwari, U. EP-0002
Mahmood, T. EP-1424, EP-1425, EP-1428
Mahrsi, N. EP-1290, EP-1301, EP-1302
Mai, E. K. EP-0506
Maielli, A. OP-298
Maier, A. EP-0965
Maina, T. EP-0074, OP-070
Maina-Nock, T. EP-0032
Maingueneau, C. OP-280
Mainta, I. EP-1122, OP-440
Maiocchi, A. OP-179
Maiolo, E. EP-0497
Mair, M. **EP-0183**, **EP-0886**, **OP-609,** EP-1035, EPS-124, EPS-125, OP-610
Mair, S. EP-0090
Maisto, C. EP-1115, EPS-054
Maitra, S. EP-1091
Majeed, A. EP-0606
Majigsuren, M. EP-0303
Makala, H. OP-088
Makazlieva, T. **EP-0448**, EP-0735, EP-0736, **EP-0754**
Makhdomi, K. EP-0420
Makhloufi-Martinage, S. EP-1266
Makhzoum, J.-P. OP-551
Malachini, M. EPS-137
Malasani, V. OP-073
Malaspina, S. OP-328
Malavolta, L. EP-0140
Malek, H. OP-734
Malek, R. **OP-023**
Malerbi, H. OP-060
Malicet, C. EP-0088
Malicevic Crevar, J. OP-479
Maliha, P. EP-1124, EP-1224
Malik, D. **EP-0529**, **OP-482**, **OP-878**
Malik, P. EP-0556, **EP-0741**
Malito, R. OP-047
Malizia, C. EP-0227, EP-0310, EP-0311, EP-0444, EP-0514, EPS-247,OP-168, OP-224
Mallapura, H. **EP-0137**
Mallem, S. **OP-322**
Mallett, C. EPS-018
Mallia, M. B. OP-861
Mallon Araujo, C. EP-0867
Malovytsia, U. EP-0147
Maltseva, A. EPS-112, OP-795
Malvezzi, F. EPS-055
Malvi, D. EP-0270
Mamach, M. **EP-1105**
Mamlins, E. EP-0154, EP-0703, OP-471, OP-881
Mammadkhanli, Z. **EP-0449**
Mammeri, S. **EP-0903**
Mamoulakis, C. EP-0244
Mañas-Jiménez, M. P. EPS-022
Manavaki, R. **EP-0216**
Mancini-Terracciani, C. EP-1109
Manco, L. EP-0461, EP-0893
Mandal, A. **EP-0606**
Manel, M. EPS-297
Manevska, N. EP-0448, **EP-0735**, EP-0736, EP-1094, EP-1358
Manfrinato, G. EP-1199
Mangia, M. EP-0206, **EP-0681**
Manglani, K. EPS-262
Mangogna, A. OP-631
Manju, R. EP-0250
Mankoff, D. EP-1053
Manley, M. **OP-111**, OP-537
Manna, F. EP-1115, EPS-054
Mannarino, T. OP-684
Manon, A. **EP-0144**, EP-0151
Manoochehry, S. **EP-0326**
Manou, E. EP-1415
Manrique, A. **EP-0581**, **OP-500**, OP-838
Mansi, L. **EP-0639**
Mansouri, Z. EP-0971, **EP-1122**, EPS-220
Mansur, A. J. EP-0631
Mansurov, E. EP-0453
Mantovani, D. **EPS-232**
Mantovani, M. EP-1421, EP-1450
Mantzilas, D. OP-152, OP-593
Manukova, V. **EP-0770**
Manzarbeitia Arroba, B. EP-0387, EP-0887
Manzitti, C. EPS-272
Mao, J. EPS-173
Mao, X. OP-238
Mapelli, P. EP-1043, OP-875
Maradan, R. EP-0148
Marafi, F. EP-0928, EP-1279
Maragkoudakis, S. EP-0574
Marao, R. OP-742, EP-0199, EP-1205, EP-1243, **EP-1269**, EPS-267, **OP-632**
Marcel, M. EPS-013
Marchese, P. OP-293
Marchetti, S. EP-0535, EP-0535
Marchiori, S. EPS-084
Marco Martínez, A. EP-0328
Marconi Porcel, L. OP-483
Marcuartu, J. J. EP-0508
Marcus, H. EP-0045, EP-0252
Marcus, M. EP-0979
Mardan, S. **EP-0759**
Marenco, M. EP-0268, EP-0393, EP-0779
Marengo, M. **EPS-287**
Maresca, K. EP-0113
Margall-Rodriguez, A. EP-0632
Margolin, K. A. OP-796
Mari, A. EP-0668
Mariani, F. OP-307
Mari Aparici, C. OP-074
Maria Veloso Trevisan, J. EP-0716
Maric, M. EP-0072
Marie, P.-Y. EP-0827, EPS-264, OP-101, OP-499

Mari Hualde, A. EP-0798, EP-0841
Marin, A. EP-0743, EP-1323, **EP-1334**
Marin, B. OP-467
Marin, C. OP-169, OP-537, EP-0377, EP-1187, OP-776
Marini, I. EP-0411, EP-0436, EP-0801, EP-0802, EP-0803, EP-1081, EP-1159, OP-042, OP-068
Marino, E. EP-0221
Marino Picciola, V. EP-0893
Marinov, V. EP-1333
Marionneau-Lambot, S. OP-280
Maris, L. **OP-782**
Mariussi, M. EPS-251
Markovska Shterjova, Z. EP-0754
Markus, M. **OP-041**
Marlin, A. OP-586
Marner, L. EP-1073
Marongiu, A. EP-0206, **EP-0446**, OP-105
Maronnier, Q. EP-0949, **EPS-078**
Maróti, B. EP-1166
Marques, A. **EP-0772**, EP-1255, EP-1265
Marques, M. **EP-0235**
Marques, V. EPS-061
Marsden, P. EP-0974, EP-0916, OP-625, OP-664
Martí-Andrés, G. OP-446
Martin, B. EP-0324
Martin, I. **EP-0160**
Martin, M. **EPS-146**, EPS-193
Martin, N. H. OP-457
Martinage, N. **OP-555**
Martin Aguilar, S. EP-1300, EP-1365, EP-1381, EP-1388
Martinelli, E. EP-0010
Martinelli, J. EP-0141, EP-1187
Martinello, C. EP-0425
Martínez, A. EPS-117, OP-378
Martínez, C. **EP-0498**
Martínez Albero, E. EP-0887
Martínez-Amador, N. EP-0656, EP-0673
Martinez-Arias, G. EP-0552
Martínez de Miguel, B. EP-1431
Martínez-Dubarbie, F. EP-0656
Martinez Gomez, G. EP-1308, EP-1311, **EP-1312**, **EP-1315**
Martinez Lorca, A. EP-0530, EP-0565, EP-0821, OP-478
Martínez-Lucio, S. T. OP-890
Martínez Montalbán, E. EP-1431
Martínez Osorio, C. EP-0328
Martínez Osorio, D. **EP-0374**, EP-0452, EP-0472
Martinez-Ramos, C. EP-0478EP-0494, EP-0495, EP-0508, OP-233, OP-480
Martínez-Rodriguez, I. EP-0656, **EP-0673**
Mártínez-Rubio, A. OP-229
Martinez Sanchís, B. TEPS-021
Martínez-Zalacaín, I. EP-1057
Martín Fernández, N. EP-0319
Martin Gallardo, E. EP-0710, OP-481
Martín Gómez, E. EP-0931
Martín Gómez, M. EP-0710, OP-481
Martini, A. **OP-437**
Martini, M. OP-380
Martini, P. OP-584
Martín-Marcuartu, J. J. EP-0307, EP-0392, EP-0850, EP-1366 EP-0437, EP-0618
Martín-Martín, L. OP-229
Martín-Miramón, J. C. EP-0545
Martinovich, A. OP-472, EPS-265, EP-0286, OP-473
Martins, B. OP-035, OP-634
Martlbauer, S. **OP-881**
Marulanda Corzo, V. EP-0352
Marusso Fizzani, M. EP-0611, OP-483
Marvelli, L. OP-584
Marx, T. EP-1054
Marzaro, G. EP-0091
Marzo, K. EP-0268, EP-0779
Marzullo, A. EP-1281, EP-1287
Mas, C. **EP-0458**
Maschio, C. EP-0002
Masikane, S. EP-0824, OP-299
Mason, K. EPS-105
Mas Pascasio, C. EP-1229
Maspero, M. EP-0115, EPS-074
Masri, K. EP-1143, EPS-192
Massa, F. EP-0681, EP-0683, **EP-0686**
Massa, S. OP-152
Massanes, F. EP-0585
Massard, V. OP-603
Massari, F. EP-0421
Masse, M. **EP-0202**
Masseroli, M. EP-1043
Masset, J. EP-1186
Massri, K. OP-384
Masthoff, M. EP-1085
Mastrogiovanni, S. EP-0377
Mastrotto, F. EP-0091
Masubuchi, M. **EP-1157**, EP-1453, EP-1454
Masuda, N. EP-0214
Mat Ail, N. EP-0416
Matamala-Bezmalinović, A. **EP-0324**
Matei, M. **EP-1329**, EP-1355, EP-0743
Mathiazhagan, K. **OP-353**
Mathiyazhagan, P. EPS-219
Mathoux, G. **OP-443**
Matiasek, K. EPS-005
Mat Jusoh, M. EP-0416
Matkovic, M. EP-0733, **TEPS-004**
Matos, T. EP-1394
Matsopoulos, G. K. EP-0525
Matsuda, H. EP-1454
Matsuhara, K. OP-208
Matsumoto, H. EP-0139
Matsuo, Y. EP-0634, EPS-111
Matsushima, S. OP-208
Matsushita, T. EP-0459
Mattana, F. **EP-0389**, OP-663
Mattei, E. EP-1109
Mattern, S. OP-017, OP-365
Mattes-György, K. EP-0703, OP-881
Matteucci, F. EP-0255, EP-0411, EP-0436, EP-0501, EP-0801, EP-0802, EP-0803, EP-1081, EP-1159, OP-042, OP-068
Matthee, B. EPS-048
Matthews, D. C. EPS-134
Mattila, K. OP-328
Mattioli, P. EP-0686
Mauch, T. EP-1111
Mauduit, Z. EP-1082
Maurel, C. EP-0671
Maurer, A. EPS-041, OP-017
Maurer, B. OP-552
Maurer, C. OP-863
Maurer, T. EP-1026
Mauri, F. EP-1052
Maurya, R. **OP-554**
Maus, J. OP-032
Maus, S. EP-0780, OP-435
Mautone, V. EP-1159, OP-042
Mauz-Körholz, C. EP-0488
Mavrinac, M. EP-0730
Mavroeidi, I. EPS-190
Mavrommatis, M. OP-435
Mavuduru, R. OP-072
Maymó Garrido, S. **EP-1411**, EP-0850, OP-865
Mayr, Y. OP-232, **OP-721**
Mayya, A. EP-1451
Mazhoud, A. EP-1390
Mazidi, S. EP-0128, EP-0127, EP-0146, EP-0888
Mazidi Sharaf Abadi, S. EP-0038
Mazilu, C. EP-1355, EP-1316, EP-1329, EP-1332
Mazilu, C. V. EP-0743, EP-1334
Mazzaglia, S. OP-384, OP-669
Mazzarella, C. EP-0497
Mazzola, R. EP-0393, EP-0406
Mazzoletti, A. EP-0206, OP-105
McBride, L.-J. OP-626
McCann, A. OP-702
McClure, T. EP-0352
McCormack, P. **EP-1117**
McCormick, J. EPS-028
McDade, R. EP-0572
McDermott, R. OP-604
McDonald, A. EPS-003, OP-817
McDougall, L. OP-361, OP-432, OP-662, OP-673, OP-677
McGeehan, A. EPS-032
McGovern, A. OP-802
McGowan, D. EP-0962, EP-1030, EP-1099, EP-0670, EP-0958, OP-026, OP-423

McGucken, A. OP-697
McLeavy, L. EP-1052
McMeekin, H. EP-0777, EPS-076, **OP-377**
McNeil, B. OP-580
McNeil, S. W. EP-0034, OP-348, OP-580
Mdanda, S. EP-0942, EP-1116, EP-1200, EPS-086, OP-349, OP-825
Mdlophane, A. EP-0942, EP-1116, EP-1200, EPS-086, **OP-349**, OP-825
Md Safee, Z. EP-0416
Meadows, A. OP-802
Meadows, J. EP-0353, OP-316
Meanhout, A. EP-0718
Mechta-Grigoriou, F. EP-0217, EP-0297
Meddens, M. B. M. EP-0907
Medhurst, E. EP-0830, OP-605
Medici, S. TEPS-001
Medici, V. EPS-032
Medina Guevara, Y. **EP-0070**, **EPS-012**, OP-217, OP-218, **OP-275**
Medina Martínez, J. EP-0328
Medina Romero, F. EP-0748
Medjaher, M. EP-0863
Medvedeva, A. OP-070
Meena, A. **OP-848**
Meena, M. EP-0265
Meens, J. EP-0081
Meeres, H. OP-348, OP-580
Meersschout, S. OP-710
Mehadji, B. **EP-1054**
Mehari, H. OP-766
Mehdi, E. EP-0453
Mehesen, M. **EP-1248**, **EP-1257**
Mehr, S. **OP-074**
Mehra, N. OP-598
Mehra, R. EP-0817, EP-0859, OP-554, **OP-821**
Mehrabi, M. **EP-1158**, EP-1163
Mehrazi, M. EPS-136
Mehri, R. EP-1231, **EP-1390**, EPS-284
Mei, R. EP-0145, EP-0375, EP-0398, OP-118, OP-330, OP-716, OP-798
Mei, S. EP-0684
Meining, A. EP-0318, EP-0794
Meiresonne, L. TEPS-009
Meisner, F. **EP-0838**
Mejia, J. EP-0140
Meles, S. K. OP-051
Mellhammar, E. EP-0733
Melo, L. C. OP-722
Melotti, B. OP-293
Melpomeni, F. OP-601
Melssen, M. OP-523
Meltzer, J. EP-0809
Men, M. EP-0678
Mena Bares, L. EP-1388, **EP-1365**, EP-1381
Mendanha, D. EP-1306
Mendes, A. OP-438
Mendes, J. **EP-0740**, **EP-1382**
Mendes-Arnaud, M. OP-347
Mendi-Barcina, V. EP-0656, EP-0673
Mendibil Esquisabel, B. EP-0462, EP-1262
Mendoza-Ángeles, K. EP-0170
Menedez - Muros, L. EP-0866
Meneghini, C. OP-047
Menéndez, E. EPS-009, EPS-013, EPS-193, OP-417, OP-518
Menendez-Muros, L. EPS-249
Menéndez Sánchez, S. EP-0319
Meneses, P. EP-0288
Meneses Navas, M. EP-0358, EP-0328, EP-0401, **EP-1393**, EP-1408
Menezes, V. **EP-0973**, **EPS-235**, **OP-465**, **OP-665**
Meng, H. EPS-130
Meng, N. **EP-0218**
Meng, Q. OP-733
Meng, R. **EP-0531**
Meng, X. EP-0237, EP-1139, **EP-0738**, OP-880
Mengdan, L. EP-0593, OP-544
Menichini, M. EP-1281, EP-1287
Menke-van der Houven van Oordt, C. EPS-081, OP-774
Mensi, S. EP-0447, EP-0465, EP-1231, OP-027
Menu, Y. EP-0306
Mera, G. EP-0704
Mera, G. EP-0668
Meraldi, M. **EP-0894**, EP-0914
Mera Ovalle, G. EP-0798, EP-0841
Mercier, J. EP-0118
Mercolli, L. EPS-221, OP-771
Mercy Ignatius, P. EP-0004, EP-0029
Merino, C. OP-542
Merisaari, H. EPS-234
Merkens, H. EP-0034, EP-0058, EP-0120, EPS-021, EPS-046, OP-348
Merkt, W. OP-371
Merler, S. EP-0425
Mertens, J. OP-121
Merz, D. OP-726
Mesa, J. EP-0157
Mesbah, Z. **OP-524**
Mesci, E. EP-0333, EP-0441
Mesci, A. EP-1100
Mesci, I. EP-0834
Mesguich, C. EP-0512
Meshcheryakova, N. EP-0253
Mesiani, E. OP-384
Meskens, A. OP-522
Mesotten, L. EP-1041
Mesquita, C. T. EP-1069
Messier, L. OP-094
Messina, C. EP-0369
Messina, N. EP-0497
Mestre Borras, A. OP-766
Mestre Fusco, A. **EP-0545**
Meszaros, L. K. OP-761
Metelkina, M. EP-0770
Metello, L. **EP-1409**
Metherall, P. OP-165
Metser, U. EP-1100, OP-423
Mettier, M. EPS-055
Metzger, G. **EPS-024**
Metzger, K. OP-314
Meurer, T. OP-284
Meyer, B. OP-606, OP-869
Meyer, C. EP-1124, EP-1143, EPS-192, OP-824, EP-1410
Meyer, H. OP-606
Meyer, M. OP-536
Meyer, P. EP-0838, EP-1045, EP-1129, EPS-159, OP-842, EP-0557, EP-0121
Meyer zu Schwabedissen, C. EPS-041
Meyhoff, C. S. EP-1073
Meynen, J. **EP-1041**
Meza, S. EP-0863
Mezher, A. OP-526
Meziane, D. EP-0756
Mezősi, E. EP-0797
Mezzenga, E. EPS-286
Mhiri, A. EP-0571, EP-1239
Miao, L. OP-762
Miao, Q. OP-580
Miao, W. EP-0158, EP-178
Miceli, A. EP-0206, OP-105
Michael, D. OP-888
Michael, M. OP-429
Michalski, K. EP-0318, OP-223, OP-376
Michaud, L. **EP-0828**
Miederer, M. OP-329, OP-819
Mieog, S. EP-0334
Miettinen, T. EP-0934
Migliari, S. **EP-1179**, **EPS-140**, **OP-549**, OP-801
Migliarino, S. OP-059
Migliorini, F. OP-182, OP-326, OP-327
Mignogna, C. EP-0375, EP-0398
Miguel, I. EP-0199
Mihailescu, L. C. EP-1188
Mihailovic, J. **EP-0873**
Mihalic, R. OP-866
Mihalyova, J. EP-0513
Mihaylova, M. **EP-0563**
Mihelcic, A. **EP-1177**
Mijtavila, M. EP-0288
Mikalsen, L. T. G. OP-427
Mikolajczak, J. OP-228
Mikolajczak, R. EP-0360, EP-1166, EPS-009, OP-518, EP-0789, EP-1174, EPS-286
Milà López, M. EPS-297
Miles, B. **EP-0390**, **EPS-105**
Milišic Kelava, L. **EP-1389**
Militaru, A. **EP-0743**, **EP-1323**, EP-1334

Militaru-Minea, D. F. EP-0743
Miljus, B. EP-0564
Millardet, M. EP-0974, EP-0990, EPS-221
Miller, B. W. **OP-279**
Miller, C. TEPS-017
Miller, J. L. EP-0216
Mills, M. K. EPS-274
Mimura, M. EP-0676
Minami, S. S. OP-025
Minarik, D. EP-0917, EPS-085, EPS-213, OP-041
Mindt, T. EP-0148
Minegishi, K. OP-209
Minnema, M. EP-1055, OP-225
Ming, T. **OP-114**
Ming, Z. EPS-144, EP-0011, **EP-0061**, OP-149
Mingels, C. **EP-0466**, EP-0933, OP-222
Minges, P. **EP-0557**
Mínguez, F. EPS-117, OP-378, OP-446
Minn, H. **OP-328**
Minniti, G. EP-0183
Minoshima, S. EP-0648, EPS-274, OP-302, OP-307
Minotti, M. OP-298, OP-326
Minutoli, F. OP-380
Mirabelli, R. EP-1109, OP-663
Miranda, E. EP-0505
Miranda, S. E. M. EP-0171
Mirando, D. EP-1143
Mir Khan, B. EP-0414
Mirkovic, M. EP-0072, EP-1183
Mirshahvalad, S. EP-0326
Mirtti, T. EP-0417
Mirzaei, A. **EP-0004**
Miseo, L. EP-0906
Miserocchi, A. EP-1159, OP-042
Mishkina, A. EP-0616, EP-0617
Mishra, A. OP-860
Mishra, R. EP-0259, **EP-1459**
Mishra, S. EP-0285, EP-0880
Missaoui, Z. EP-1390, **EPS-284**
Mitchell, T. OP-501
Mitea, C. EP-0535
Mititelu, R. EP-1329, EP-1355, EP-0743, EP-1323
Mititelu, R. EP-1385
Mitjavila Casanovas, M. **EP-0792**, **OP-430**
Mitoma, R. EP-0676
Mitova, V. EP-0563
Mitra, I. EP-0718
Mitran, B. EP-1104
Mitrotti, P. OP-047
Mitrovic, G. EP-0895
Mitsikoudi, F. EP-1430
Mitsumoto, K. EP-1449, EPS-255
Mittal, B. OP-743, EP-0071, EP-0159, EP-0191, EP-0556, EP-0741, EP-1134, EPS-110, OP-683, **OP-797**, OP-848, EP-1460
Miwa, K. EP-0939, EP-1157, EP-1453, EP-1454
Mix, M. EP-1045, EP-1129, EPS-159, OP-842
Mixdorf, J. C. OP-579, OP-583, OP-586
Miyaji, N. EP-1157, EP-1453, EP-1454
Miyake, K. **EP-0214**, EP-0540, EP-0768, EP-0939, EP-1449
Miyazaki, T. EP-0676, EP-1059, OP-301, OP-719
Miyazaki, Y. **TEPS-020**
Mizowaki, T. EPS-255
Mizukoshi, Y. OP-208
Mkhize, T. EP-0824, OP-299
Mlesnite, M. EP-1317
Mo, Q. **EP-0609**
Mobilia, E. M. EP-0686
Mochula, A. EPS-112, OP-795
Mock, J. OP-182, OP-298, OP-326, OP-327
Modzelewski, R. EP-1017, OP-524
Moe, F. N. N. EP-0847
Moein, M. M. EPS-154
Mogharrabi, M. EPS-220
Mohajershojai, T. **OP-523**
Mohamad, S. TEPS-019
Mohamed Salem, L. EP-1312, EP-1315, EP-1308, EP-1311, EP-1289, EP-1305
Mohammad Hosseini, H. EPS-304
Mohammadigoldar, Z. EP-0376
Mohammadi Kazaj, P. EPS-220
Mohammed-Gayle, J. EP-1400
Mohan, A. EP-0177, EP-0882
Mohan, H. OP-377
Mohan, R. EP-1100
Mohapatra, P. EPS-161
Mohd Rohani, M. EP-0416
Mohebali, M. EP-0066
Moiseeva, A. **EP-1164**, EP-1165, OP-220
Mok, G. EP-1015, EP-1032, **EP-1037**, EP-1140, EP-1048
Mok, H. EPS-062
Mokhtar, N. OP-243
Mokhtari, M. EPS-136
Mokoala, K. EP-1116, EPS-086, OP-825
Mokoena, M. A. OP-825
Mokri, M. **EP-1033**
Molina, N. EPS-154
Möllenhoff, K. OP-048
Møller, S. EP-0722
Mollica, V. EP-0421
Molnár, S. EP-0450
Moltalvá Pastor, J. EP-0401
Momboisse, D. EPS-090
Momeni, A. OP-094
Momose, M. EP-0634, EPS-111
Monaci, A. EP-1146
Monastero, F. EP-0396
Moneta, C. OP-120
Monroe, K. M. EP-0047
Montalva Pastor, J. EP-0328, EP-0358, EP-1393, EP-1408
Montanini, F. **OP-321**
Mont-Castro, L. EP-0382, EP-0384, EP-0412
Monteiro, M. EP-0897, EP-1256, OP-633
Monteiro, P. OP-056
Montella, M. T. EP-1081
Montellano Fenoy, A. EP-1227, EP-1251
Montemagno, C. OP-022
Montenegro, S. M. OP-422
Monterosso, M. E. EP-0153, OP-177
Montes Fuentes, C. EP-0710, OP-481, OP-229
Montgomery, M. E. OP-261
Monti, M. EP-0801, EP-0802, EP-0803, EP-1159, OP-042
Montorsi, F. EP-0534, OP-875
Moog, S. EP-0306, EP-0786, EP-1019, OP-120
Moon, E. S. EPS-009, OP-518
Moore, A. EPS-119
Moradi, F. **EP-0980**, **EPS-304**, OP-539
Moradi, H. EP-0995
Moradi, S. OP-354
Moragas, G. EP-0845
Moragas Freixa, G. EPS-026
Morais, A. F. OP-465
Moral Cano, M. EP-0549, EP-0550
Moralidis, E. EP-1341, EP-1364, EP-1370, EP-1374, EP-1415, EPS-027
Moratalla Aranda, E. EP-1365, EP-1381, **EP-1388**
Morath, V. EP-0161, EPS-146
Morbelli, S. D. EP-0686, OP-324, OP-725, EP-0683, OP-055, OP-611, OP-669, EP-0141, EP-0681, OP-612
More, S. **EP-0367**, **EP-0379**, EP-0757, EP-1090, EP-1250
Moreau, M. EP-0096, EP-0164, OP-211, OP-347, OP-351
Moreau, P. EP-1055, OP-225
Moreau-Triby, C. OP-864, EPS-090
Moreira, A. EP-0765, EP-1256, EP-1318
Moreira, J. N. EPS-061
Moreira, R. EP-0101
Moreira Siqueira, R. EP-0337
Morén, A. F. EP-0118
Moreno, O. EP-0002
Moreno Monsalve, T. EP-1308, EP-1311, EP-1312, EP-1315, **EP-1289**, **EP-1305**
Moreno Moreno, A. OP-095
Moresco, R. EP-0115
Moretti, A. **EP-0255**, EP-1398, EP-1399
Moretti, I. **EP-0665**, OP-858
Moretti, R. EP-0665, EP-0881, OP-858
Moretto, M. OP-467
Morfesi, A. EP-1341, EP-1364, **EP-1370**, EP-1374, EP-1415, EPS-027
Morgan, D. EP-1099
Morgan, K. OP-277
Morganti, A. G. EP-0234, EP-1112
Morganti, S. EP-1109, OP-663
Morgat, C. EP-0069, EP-0136
Morgenroth, A. OP-761

Morgenstern, A. OP-181, OP-213, OP-280
Mori, R. TEPS-008
Mori, W. OP-209
Mori, Y. EP-0154, OP-471, OP-881
Morin, M. A. EP-1224, EP-1291
Morini, M. EPS-221, **OP-771**
Morisco, A. EP-1115, EPS-054
Morís de la Tassa, G. OP-050
Moriyama, S. OP-719
Mörk, J. EP-0463
Moroni, M. EP-0234
Morris, Z. S. OP-767
Morshhauser, F. OP-227
Mortazavi, N. OP-459, **EPS-143**
Morton, W. EP-1065, **EP-1156**
Morvay, P. OP-425
Mosayebnia, M. EP-0127
Mosconi, C. EP-0375, EP-0398, EP-0503
Mosconi, L. EPS-134
Moscoso, A. EP-0999, OP-440
Mosén, H. EP-0582, EP-1426
Moses, A. OP-023, OP-657
Moskal, P. EP-0919
Mossel, P. EPS-107, OP-051
Mostafa, R. **EP-0818**
Mostert, J. **OP-870**
Motegi, K. EP-0927
Mottaghy, F. M. EP-0109, EPS-227, OP-761
Mou, H. OP-762
Mou, L. OP-584
Mou, T. OP-845
Mouas, D. EPS-212
Moulton, E. OP-160, OP-162, OP-164, OP-528
Moura, A. **EP-1462**, **OP-623**
Mourato, F. EPS-235, **EPS-251**, OP-465
Moustafa, S. **EP-0431**
Moya Alvarado, P. OP-553
Mozaffari, S. **EP-0128**, EPS-136
Mozayani, B. OP-747
Mpalaris, V. EP-1341, EP-1374, EPS-027, EP-1364, EP-1370
Msimang, M. OP-299
Mtazaoui, Y. OP-356
Mu, L. EPS-142
Mu, W. OP-463, EP-0215
Mu, X. **EP-0097**, EP-0338, **EP-1046**
Muchalla, M. EP-0703
Mudd, G. EP-0121
Mueller, A. EP-0691
Mueller, C. EPS-156, OP-436, OP-860, OP-862, OP-818
Mueller, F. OP-284
Mueller, K. J. EP-1035
Mueller, N. EP-0822
Mugnaini, M. **OP-458**
Muhamad, S. A. TEPS-019
Muhic, A. EPS-120
Muin, D. OP-790
Mujahid Bin Muhammad, A. OP-320
Mukai, K. OP-387
Mukhortova, O. EP-0433, EP-0770
Mülazımoğlu, M. EP-0902
Mulders, T. EPS-109
Mulders, T. A. EP-1185
Mülhens, O. OP-284
Mulholland, N. EP-0791
Müller, C. OP-662, OP-673, OP-677
Müller, G. **EP-0168**
Müller, H. EPS-135, EP-0557
Müller, J. EPS-294
Müller, K. J. EP-0886, EPS-124, EPS-125, OP-610
Müller, M. OP-298, OP-043
Mulyukov, Z. EP-1117
Mulzer, J. EPS-024
Munemo, L. EPS-224
Mungai, F. EP-0467
Muni, A. OP-384
Munk, O. L. EP-0998, OP-769
Munoz, C. OP-708
Muñoz de Nova, J. OP-485
Muñoz-González, M. OP-093
Muñoz Pérez, N. EP-0555
Munson, J. OP-217, OP-218
Munuera-Sañudo, C. EP-1411
Muoio, B. **EP-0889**
Muradin, G. S. R. OP-870
Muraglia, L. EP-0363, EP-1062
Murakami, M. OP-208
Murakami, S. EPS-056
Murakami, T. EPS-141, OP-283, OP-285, TEPS-020
Muriana, P. EP-0254
Muriuki, D. EP-0539
Muronova, L. EP-0513
Muros de Fuentes, M. EP-0866, EP-0867, EPS-249
Murru, E. EPS-298
Murthy, N. EP-0981
Muselaers, C. OP-598
Mushaweh, A. **OP-432**
Musi, G. OP-663
Musiałkiewicz, J. EP-0782
Mussetti, A. EP-0498
Mutevelizade, G. EP-0236
Muthu, S. EP-0959, TEPS-005
Muti, G. EP-0269, EP-0894, **EP-0914**, EP-1130
Muto, M. EP-0540
Mutuleanu, M. EP-1326, EP-1328, **EP-1220**
Muzi, M. EP-1053
Mwania, M. EP-0420
Myakova, N. EP-0481, EP-0482
Myrehaug, S. EP-1100, OP-423
Mysliwiec, J. EPS-257, EP-0896
Mzizi, Y. V. OP-825
Nabi, K. EPS-062
Nabih Oueriagli, S. EP-1325
Nabong, R. M. EP-1410
Nacer Khodja, M. **EP-0863**
Nadalin, S. OP-365
Nadeem, M. OP-803
Nader, M. OP-247, OP-297
Nader Marta, G. OP-111
Nadig, V. **EP-0974**
Naeem, F. **EP-0596**, EP-0700
Nag, S. EP-0108, **EP-0113**, EP-0116, **EP-0118**
Nagachinta, S. OP-152, OP-593
Nagai, N. EP-0676, OP-719
Nagao, M. EP-0634, EP-0635, EPS-095, EPS-111, OP-503
Nagaraj, H. EP-0258
Nagarajah, J. EP-1119, EPS-183, OP-184, OP-385, OP-598
Nagel, L. EPS-185, OP-180
Naghavi-Behzad, M. OP-106
Nagral, A. S. EP-0283
Naili, Q. EP-1076
Nak, D. **EP-0245**, **EP-1392**
Naka, S. EP-1458, OP-387
Nakahashi, T. OP-729
Nakajima, K. EP-0585, **OP-058**, **OP-729**
Nakajima, S. EP-0676, OP-719
Nakajima, W. EP-0676, EP-1059, OP-301, **OP-719**
Nakamoto, R. **EP-0395**, EP-0540, EP-1449
Nakamoto, Y. EP-0188, EP-0214, EP-0395, EP-0540, EP-0768, EP-1449
Nakamura, T. EP-1157
Nakano, K. OP-719
Nakao, R. EP-0634, EPS-111, OP-503
Nakashima, R. EPS-255
Nakata, T. OP-729
Nakatani, K. EP-0188, EP-0214, **EP-0768**, EP-1449
Nakro, D. **EP-1266**
Nakuz, T. OP-609, OP-747
Nalbant, H. EP-0466, OP-222
Nalla, S. EP-0949
Nami, R. EP-0038, EP-0066, EP-0127, EP-0128, EP-0146, EP-0888, **EP-1149**, EPS-136
Nanni, C. EP-0145, EP-0227, EP-0396, EP-0502, EP-0503, EP-0504, EP-0514, **EP-1064**, EPS-030, OP-168, OP-224, OP-293, OP-330, OP-798
Nanni, J. EP-0504
Nanni, O. OP-042
Naoi, Y. EP-0939
Napier, P. OP-416
Napolitano, R. OP-584
Nappi, A. EP-0329
Nappi, C. EP-0308, EP-0788
Naranje, P. EP-0558
Naranjo Sancho, S. EP-0319, **OP-050**
Narayan, M. L. EP-0561, OP-743

Nardo, L. EP-0466, EP-1064, EPS-030, OP-222
Narváez, J. A. EP-0508
Narykina, V. EP-0103
Nascimento, L. T. C. EP-1201
Naserbegi, A. EP-1163
Nasir, M. OP-711, OP-873, EP-0038, EP-0146, **EP-0888**, EP-1149
Nasiri, M. EP-0066
Nasr, A. EP-1423
Nasrollahi, H. EP-0362
Nassi, L. EP-0467
Natali, F. EP-0227, OP-168
Natarajan, H. OP-667
Natour, G. OP-284
Nau, M. **EP-0965**
Nausheen, S. EP-1424, EP-1425, EP-1428
Navab, N. OP-461
Naval-Baudín, P. EP-1057
Navales Mateu, I. EP-0388, EP-0836, EPS-092, EPS-211
Navarro, L. OP-152, OP-215, OP-593
Navarro Beltrán, P. EP-0760
Navarro Fernandez, J. EP-1308, EP-1311, EP-1312, EP-1315 EP-1289, EP-1305
Navarro Martínez, T. EP-0530, EP-0565, EP-0821, OP-478
Navarro-Niño, N. EP-0776
Naveau, M. OP-838
Nawaz, R. **EP-1424**, **EP-1425**, **EP-1428**
Nawinne, M. EP-0822
Nawwar, A. EP-1020
Nayak, B. EP-0474, **EP-0559**
Nazar, A. EP-0805, EP-0853, OP-821, **EP-0813**, **EP-0817**, EP-1459
Nazarenko, I. EP-0253, OP-472
Nazari, A. EPS-256
N'Diaye, E. R. **OP-453**
Ndlovu, H. EP-0942, EP-1116, EP-1200, **OP-825**
Ndlovu, N. EP-0824, OP-299
Neelsen, C. EP-0485
Negi, M. EP-0561, EP-0877
Negre, M. EPS-249
Negre Busó, M. EP-1434
Negro, A. EP-0639
Negwer, C. EP-0182
Nejabat, M. **OP-747**
Nejati, S. F. OP-457
Nekolla, S. OP-291, EP-0989
Nemallapudi, M. EP-0976
Nemati, M. EP-0141
Nemati, R. EP-0878
Nemer, U. EP-1045, EP-1129
Nerattini, M. **EPS-134**, OP-321
Neri, D. OP-182, OP-298, OP-326, OP-327
Nero, C. EP-0010
Nespral, P. EP-0775
Nespral Torres, P. EP-0339, EP-0340, EP-0341
Nestor, M. EP-0009, EP-0057, **EP-0064**, EP-0068, EP-1160, EPS-043, OP-414, OP-519, OP-523
Neuber, C. **OP-154**
Neuzilova, B. EP-0148
Nevares, M. EP-0792, OP-430
Newton, B. OP-818
Neyt, S. OP-522
Ng, A. Y. K. C. OP-697
Ng, C. EP-0416
Ng, D. EP-0020, OP-031
Ng, H. **EP-0544**
Ng, N. C. EP-1193
Ng, P. EP-0051, EP-0058, EP-0120, EPS-046
Ng, S. EP-0194, EPS-119
Ng, Y. EP-0677, EPS-025
Ngai, S. EPS-119, **OP-670**, OP-676, OP-703
Ngam, P. **EP-0648**
N'Guessan, E. **OP-022**
Nguku, S. EP-0420
Nguyen, A. EPS-162, OP-323
Nguyen, C. EP-0709
Ni, J. **OP-291**
Ni, R. **EP-0002**, **EP-0500**, EP-1080
Ni, Y. EP-0357, EP-0976, OP-733
Nian, X. OP-419
Nickels, M. L. OP-745
Nicocia, A. OP-380
Nicod Lalonde, M. TEPS-001, EP-0184, EP-1407, OP-315, OP-373
Nicol, A. EP-0993
Nicolanti, F. EP-1109, OP-663
Nicolas, G. **OP-361**, OP-432, OP-601, OP-673, OP-677
Nicolini, S. EP-0411, EP-0801, EP-0802, EP-0803, EP-1159, OP-042, OP-068
Nics, L. EP-0528, EP-1241, OP-325, OP-820
Nie, B. EPS-233, OP-441
Niekaemper, D. OP-284
Niekämper, D. **EP-0943**, EP-0963
Nielsen, M. **EP-0005**, **EP-0624**, EPS-104
Nielsen, N. OP-025
Nienhuis, H. OP-053, EP-0535
Nienhuis, P. H. OP-551
Nieto Margareto, J. EP-1431
Nieves Cabrera, M. EP-0394
Niftaliyeva, K. **OP-874**
Nigam, S. EP-0986
Niimi, T. **EP-0588**
Nijkamp, M. W. EP-0842
Nijkerk, A. J. OP-622
Nijsen, J. F. W. EP-1145, EP-1123, OP-855
Nikiforuk, A. EP-0432, EP-0433, EP-0542, EP-0932, EPS-079
Nikitas, J. EP-1410
Nikkita, K. EP-0643
Nikolajevs, A. EP-0608
Nikolaou, K. OP-365
Nikolic, A. A. EP-0811, EP-0815, EP-0825
Nikolovski, S. **EP-1094**
Nikoukar, L. OP-329
Nikulin, P. EP-0483, **OP-032**
Nilsson, E. OP-099
Nilsson, M. EP-0733
Nilsson, T. EP-0260, **EP-0275**
Nin, J. EP-0535
Ninatti, G. EP-1401
Niñerola Baizán, A. EP-0776
Ning, J. **EP-0280**, EP-1011, **EP-1040**, OP-468
Nioche, C. EP-0251, EPS-230, EPS-231, OP-173
Niorettini, A. OP-584
Nisar, S. OP-169
Nischal, N. EP-0559, OP-872
Nishida, K. OP-585
Nishimura, M. EP-0459
Nissilä, L. EP-0114
Nistor, A. EP-1317, EP-1309
Nistor, M. **EP-1327**
Nitsch, R. EP-0002
Nitsche, C. OP-468
Nitzsche, E. OP-601
Niu, M. OP-695
Niu, Q. EP-0023
Niu, S. **EP-0575**, EP-0767
Niu, W. EPS-158
Niu, X. OP-418
Niyazi, M. EP-0183
Njotu, F. OP-350
Noamen, H. EP-0306, **EP-0786**, **EP-1019**, **EPS-199**, OP-098
Nobashi, T. EP-1449, **EP-0540**
Noben, J. EP-0935
Nock, B. A. EP-0032, EP-0074, OP-070
Noferesti, A. EP-1351
Nogami, M. **OP-283**, OP-285, TEPS-020
Nogareda, Z. OP-430
Nogueira, S. EP-0140, **EP-1403**
Nogueira Lima, E. **EP-1324**, EP-1306, EP-1342
Nogueiras Alonso, J. EPS-258
Nogueira-Souto, D. EP-0552
Nölting, S. EP-0793
Nomizo, T. EP-0540
Nomoto-Takahashi, K. OP-719
Nomura, M. EP-0540
Noncovich, A. OP-416
Nonnekens, J. EPS-196, OP-216, **OP-221**, **OP-425**
Nooij, L. S. OP-783
Noordzij, W. EP-0842, EPS-082, OP-149, OP-289, OP-598, OP-885, OP-886
Noponen, T. EP-0904, EP-0946, **EPS-127**
Nordberg, A. EP-0002
Nordquist, L. EP-0822
Nordström, J. OP-687
Nørgaard, J. EP-1044
Noriega Álvarez, E. EP-0374, EP-0452, EP-0460, EP-0472
Norikane, T. EP-0956

Norouzbeigi, N. EP-0348
Nosaka, H. EP-0939
Noskovičová, L. EP-1006
Notni, J. EP-0077, EPS-146
Noto, A. **EP-1150**
Noto, B. OP-244
Notohamiprodjo, S. OP-363, OP-364, **OP-789**, OP-869
Notta, P. EPS-031, EP-0494, EPS-022, EP-0618, EP-0758
Noudeau, E. EPS-246
Noughabi, A. J. OP-109
Nouhaud, F. X. EP-1266
Nouira, M. EP-1264, EP-1390
Nourouzi, A. EP-1163
Nousch, M. OP-344
Nousiainen, K. EP-0934
Novak, U. OP-220, OP-413
Novelli, P. OP-344
Novi, G. OP-725
Novkovic, A. EP-0898, OP-479
Novruzov, E. **EP-0154**, **EP-0703**, **OP-471**, OP-881
Novruzov, F. **EP-0453**, OP-711, OP-873
Nový, Z. EP-0138, EP-0123
Nowak, E. EP-0711
Nowak Lonsdale, M. OP-686
Ntihabose, C. EPS-017
Nübling, G. OP-046
Nummenmaa, L. EPS-234
Nunes, H. EP-0521
Nunes, R. EP-0716
Nunes Lemos, L. **EPS-211**, OP-483, EPS-202
Nürnberger, M. **TEPS-013**
Nuttens, V. **EP-0641**, **EP-1126**, OP-097
Nuutila, P. EPS-234
Nuvoli, S. EP-0446
Nwangele, E. OP-350
Nxasana, T. EP-0824, OP-299
Nyamari, J. EP-0420
Nygren, P.-Å. EPS-050, OP-089
Nyholm, D. EPS-128
Nyiranshuti, L. OP-416
Nylund, R. EP-0941
Obara, T. EP-0179, OP-614
Obata, H. **OP-282**
Obeid, K. **EP-0074**, OP-659
O'Brain, G. OP-425
O'Brien, J. EP-0940
O'Brien, K. EP-0995
Ochagavia Cámara, S. OP-784
Odalovic, S. EP-0898, EP-1240, OP-479
Oddstig, J. EP-0733, EPS-088, EPS-096, TEPS-004
Odes, Y. EPS-087
Ödling, J. EPS-154
O'Dwyer, E. **EP-0352**
Oehler, S. OP-182, OP-298, OP-326, OP-327
Oei, E. H. G. OP-870
Øen, S. TEPS-010
Oertel, W. OP-459
Oflas, M. **OP-110**
Ofner, H. OP-325
Ogum, A. **OP-501**
Oh, Y. EPS-215
Ohshima, S. **EPS-114**
Ohtani, Y. OP-719
Oikawa, M. EP-0139
Oinam, A. S. EP-0071, EP-1134
Oishi, T. EP-0214
Okazawa, H. EP-0676
O'Keeffe, D. EP-0381
Okkels, N. EP-0998
Okuda, K. TEPS-008
Okudan Tekin, B. EP-1386, EP-1340
Okuyucu, K. EPS-260
Olarte Casas, M. EP-0476
Olazabal Eizaguirre, I. EP-0462, EP-1262
Oldfield, C. **EP-0910**
Olesiński, M. EP-0440
Olhaye, M. **OP-883**
Olianti, C. EPS-272
Olivari, L. OP-384
Oliveira, A. EP-0716, EP-0171, EPS-235, OP-465
Oliveira, B. OP-722
Oliveira, C. OP-527
Oliveira, F. EP-0905, EP-1083, EP-1133, OP-158
Oliveira, F. OP-527, EP-0814, EP-0961
Oliveira, L. C. EPS-232
Oliveira, M. OP-372
Oliverio, F. EP-1421, EP-1450
Olivier, P. EP-0827, EP-0829, OP-603, OP-675
Olivieri, M. EP-0268, EP-0779
Ollarves Carrero, M. EPS-275
Olmedo Chiva, A. M. EP-0760
Olson, A. P. OP-583
Olson, S. EPS-028
Olsson, H. EP-0137
Olsson, J. **EP-1397**
Olsson, M. EP-0404
Olwit, W. **EP-0420**
O'Mahoney, E. **OP-703**, OP-676, OP-290
Omar, Y. EP-0810, EP-1403
Omay, S. **EP-0843**
Omaygenc, M. **EP-0977**
Omer, S. **EPS-154**
Omokawa, M. EPS-141
Omrane, M. A. EPS-159
Onder, S.
OP-110
O'Neill, K. EP-1052
O'Neill, E. OP-520
Ones, T. EP-0837, EP-1127, EP-1141, OP-874
Önner, H. EP-0604
Ono, N. EPS-234
Onoguchi, M. EP-0585
Onuki, K. EP-0991
Ooe, K. EP-1458, EPS-056, OP-387
Ooms, D. EP-0641, EP-1126
Ooms, M. EP-0034, EPS-020, OP-150, OP-350, OP-656, OP-657
Oorschodt, J. OP-323
Oos, R. EP-0037, EP-0062, EP-0168, EP-0936, EPS-005, EPS-197
Oosterwijk, E. OP-521
Opalinska, M. **EP-0440**, EP-0789
Opalińska, M. EP-0919
Ophey, A. OP-048
Oprea-Lager, D. EP-1395, OP-598, OP-876
O. Prior, J. OP-315
Opsomer, T. EPS-020, OP-150, OP-592
Ora, M. EP-0544, EP-0805, EP-0813, EP-0817, EP-0853, EP-1459, EPS-039, OP-554
Orcajo, J. E. EP-0668
Orcajo Rincon, J. EP-0841, EP-0798
Orcutt, K. EP-1135
Ordas, L. OP-215
Orduña Diez, M. EP-0530, EP-0565, EP-0821, OP-478, EP-0792, OP-430
Orhon, P. EP-1082, EP-1182
Orlandi, P. E. EP-1238, EP-1372
Orlandini, G. EPS-275
Orlhac, F. EP-0251, EP-1067, EPS-230, EPS-231, **OP-173**
Orlova, A. EP-0074, EPS-050, **OP-070**, OP-087, OP-089, OP-320, OP-659, OP-764, OP-766
Oroujeni, M. EPS-050, OP-089, **OP-320**
Orso, B. EP-0683
Ország, G. EPS-278, OP-501
Ortega, A. EP-0775
Ortega Candil, A. EP-0339, EP-0340, EP-0341
Ortega Cuadrado, P. EP-1198
Ortega Valle, A. EP-1322, EPS-263, EP-1368, EP-0819, EP-1286, EP-1337, EPS-273
Ortenzi, M. EP-0370
Ortiz Muñoz, C. EP-0460, EP-0328, EP-0374, **EP-0452**
Ortiz Romero, P. EP-0887
Ortolan, N. OP-324
Orujova, N. EP-0453
O Santos, A. EP-0337
Osawa, A. EP-0927
Osborne, J. R. EP-0352
Osellame, L. OP-277, OP-516
Osiowski, M. EP-0440
Osipova, O. OP-778
Osmak, M. EP-1223, EP-1234, EP-1245, EP-1267
Osooly, M. OP-348
Ost, P. OP-710
Ostaszewska, A. EP-0013
O'Sullivan, F. EP-0988, EP-1053, EP-1061, **EP-1095**
Otani, T. EP-0980, **OP-539**

Öter, A. EP-0638
Otero Gonzalez, J. EP-0705
Othman, M. F. TEPS-019
Otomi, Y. EP-0459
Otsuka, H. EP-1443, EP-1444, EP-1447
Ottino, M. OP-478, **EP-0565**, **EP-0821**
Otto, T. OP-628
Oude Wolcherink, M. EP-1086
Oudot, A. OP-351
Oueriagli, S. EP-1302
Ouguirti, S. EPS-264
Oulad Bouchetta, A. EP-0598, EPS-099, OP-496
Ouyang, W. OP-300
Oğuzsoy, T. EP-1276
Overbeck, N. EP-0981, **EP-0990**
Owaki, Y. EP-0956
Oza, Q. EP-0390
Oza, U. EP-0390, EPS-105
Özşahin, M. K. EP-0901
Ozasa, H. EP-0540
Ozcan, P. EP-0640
Ozdemir, A. OP-856
Ozdemir, E. EP-0837
Ozdemir, M. EP-0837, OP-856
Özdemir, S. **EP-1373**
Özden, A. EP-0443
Ozel, A. EP-0837
Ozel, B. EP-0131
Ozel-Yildiz, S. EP-0355, EP-0368
Ozenil, M. OP-325
Özer, M. EP-0901
Özer, Ö. EP-1089
Özge, A. EP-0640
Ozgen Kiratli, P. OP-746, OP-846, OP-254, EP-0451, OP-847, OP-850
Özgüven, S. OP-874
Ozkan, Z. EP-0282, OP-259, OP-110
Ozkara, C. OP-531
Ozkara, M. EPS-260
Ozmen, O. EP-0222, EP-0232, EP-0273, EP-0359, EP-0577, EP-0742, EP-0749, EP-1007, EP-1008, EP-1216, EP-1249, EP-1307, OP-497
Ozsaran, A. A. EP-0924, EPS-077
Ozsarikaya, I. F. OP-040
Öztürk, A. EP-0295, EP-0723, **EP-0272**
Ozturk, I. **EP-1270**, EP-1367
Ozulker, T. EP-0858, EP-0902, EP-1276, EP-1371
Paborji, M. OP-025
Pabst, K. EPS-190, OP-297
Pace, L. OP-059
Pacella, S. **EP-0478**
Pacelli, R. EP-0788
Pack, T. OP-659
Packard, R. R. S. OP-679
Padilha, B. G. EP-0631
Padilla, A. OP-430
Padilla Bermejo, A. EP-0374
Padovani, A. OP-047
Paez, D. EP-0324, EP-0453, EP-1396, OP-302, OP-307, OP-434
Paez Vargas, P. **EP-0552**
Paganelli, G. EP-1159, OP-042
Pages, C. OP-292
Pahlajani, S. EPS-134
Pain, C. **EP-0978**, EP-0995
Pais, B. OP-361
Pais, J. EP-0521
Paisey, S. OP-888
Paiusco, M. EPS-287
Paiva, S. EP-0765, EP-0897, EP-1256, EP-1318, EP-1320, **OP-379**, OP-633, OP-636
Paixão, M. R. EP-0631
Pajares-Vinardell, M. EP-0745, EP-0872, EP-1391
Pakula, V. **EP-0699**
Pala, A. **EP-0778**, OP-254, **OP-847**
Pala, H. **EP-0287**, EP-0778
Palade, E. EP-1317
Palanivel, P. EP-0259
Palard-Novello, X. OP-227
Palazón Palazón, A. EP-0849
Palazzo, M. EP-0467
Palchan Hazan, T. **EP-1088**, EP-0949
Palio, L. EP-1187
Palleis, C. OP-044
Palm, S. EP-0049, EP-0945, **OP-704**
Palma, G. EPS-054
Palmer, E. EP-1104
Palmeri, D. EPS-084
Palomar-Muñoz, A. EP-0611, EPS-202, EPS-211, OP-483
Paloranta, M. EP-0417
Palucci, A. OP-558
Palumbo, D. EP-0254
Palumbo, G. EP-0022, EP-0037, EP-0047, EP-0062, EP-0168, EP-0936, EPS-005, OP-456
Pan, B. EPS-236
Pan, J. EP-0218
Pan, L. EP-0520, **EP-1022**
Pan, Q. OP-071, OP-735
Pan, T. **EP-1029**
Pan, Y. OP-477, OP-851
Panagiotidis, E. EP-0591, **OP-557**
Panareo, S. EP-0206, OP-105, OP-324
Panda, P. EP-0741
Pandey, A. K. EP-1042, EP-1084, EPS-209, EPS-217, OP-256
Pandey, S. EP-0159
Pandit, N. EP-0804
Pandya, K. EPS-233
Paneta, V. EPS-198
Pang, H. EP-0026, EP-0445, EP-0610, EP-0623, EP-0657, EP-0680, EP-0726, EP-0982, EP-1461, EPS-080, EPS-167, OP-545
Pang, Y. EP-1038, EP-1049
Paniagua, C. EP-1368
Paniagua Correa, C. EP-0819, EP-1286, EP-1322, EP-1337, **EPS-263**, EPS-273
Panico, M. OP-684
Panin, V. EP-0970, EP-0990
Pant, V. EP-0596, EP-0700
Pantaleo, D. EP-1399
Pantic, B. EP-0898
Pantic, N. **EP-0898**, EP-1240, **OP-479**
Paolacci, G. EP-1421, EP-1450
Paolino, A. EP-0100, EP-0157
Paone, G. EP-0425, EP-0889, OP-823
Papa, N. EP-0415, EP-0830, OP-323, OP-605
Papadimitroulas, P. EPS-198
Papadopoulos, N. EPS-254
Papadopoulou, K. **EPS-254**
Papagni, I. EP-1421, EP-1450
Papajík, T. EP-0489
Papalanis, E. **EPS-050**, OP-089, OP-320, OP-659
Papanastasiou, E. EPS-254
Papantoniou, I. EP-0875
Papathanasiou, M. OP-239
Papathanasiou, N. EP-1074
Papayannidis, C. EP-0504
Paphiti, M. EP-1429
Papillon, L. OP-536
Papotto, C. EP-0115, EP-1176
Papp, L. EP-1036, **OP-352**, **OP-354**
Parabicoli, S. OP-669
Parach, A. OP-213, OP-215, EP-1138
Parafita, R. EP-0905, EP-1133
Paraiso, P. EP-0087, OP-153
Parakh, N. EP-0583
Pardini, M. EP-0681, EP-0683, EP-0686, OP-725
Parducci, B. OP-384
Paredes Rodriguez, P. EP-0530, EP-0565, EP-0821, OP-478
Pareja, F. OP-378, OP-446
Pareja, F. OP-700
Pareja del Rio, F. **EP-0156**
Paris, A. OP-787
Park, B. N. **EP-0024**
Park, K. **EP-0672**
Park, M. A. OP-163
Park, R. **EPS-028**
Parkar, N. OP-707
Parkar, T. EP-0784, EP-0790, EP-0881
Parkes, E. EPS-008
Parlak, Y. EP-0131, EP-0925
Parodi, K. EP-0936
Parra-Rina, M. EP-0552
Partida-Palma, F. EP-0872
Partin, L. EP-0959, **EP-1014**
Paruta, L. OP-666
Paruta Araez, L. EP-1147

Parwar, R. EP-0347
Pascal, P. OP-864
Pascali, C. EP-0017, EP-0044
Paschali, A. EP-0820, OP-557
Paschke, M. OP-817
Pasciuto, T. EP-0010
Pascual, T. **EP-1414**
Pascual Pascual, V. EP-0319
Pasindu, H. G. D. EP-0921
Pasini Nemir, E. **EP-1230**, EP-1298
Paslawski, W. OP-459
Passamonti, F. EP-0478
Passlick, B. EPS-159
Pastusiak, P. EP-0789
Patel, C. EP-0371, EP-0372, EP-0373, EP-0583, EP-0764, OP-353
Patel, D. EP-0627
Patel, M. EP-0008, EP-0824, OP-299, EP-0822
Patel, R. OP-074
Patel, S. **EP-0299**
Paterson, C. EP-0572, EP-0576
Pathak, A. EP-0267, EP-1221
Pathak, J. EP-0510, EP-0537
Pathania, S. **EP-0051**
Patil, P. **EP-1013**
Patil, S. EP-0627
Patko, Z. **EP-1338**, **EP-1343**
Patronas, E. EP-0528, EP-0045
Patt, M. OP-863
Patterson, A. J. EP-0216
Pattison, D. EPS-119, OP-290, OP-676, OP-703
Paulssen, E. OP-587
Paunescu, M. EP-1328
Paunet, T. EP-0589
Pavaluta, I. EP-0306
Pavel, M. EP-0784, EP-0790, OP-429
Pavics, L. EP-0180
Pavlova, G. EP-0178
Pawar, R. K. EP-0527
Pawlak, D. **EP-1174**, EPS-009, OP-518
Payan, N. **EPS-186**
Pearson, T. OP-314, **OP-626**, **TEPS-017**
Pedersen, K. S. OP-579
Pedersen, K. T. EP-0403, OP-877
Pedrani, M. EP-0425
Peer-Firozjaei, M. EP-0878
Peeters, E. **OP-796**
Peeters, S. OP-156
Pehlivanoglu, H. EP-0355, EP-0901
Pei, J. **OP-454**
Peiris, H. EP-0995
Peiró, I. EP-1366
Pełka, K. EP-0323
Pekedis, H. **OP-540**
Peker Yalcın, H. EP-0523
Pellegrini, C. OP-224
Pellegrino, S. **EP-0233**, **EP-0507**
Pellerino, A. EP-0183, OP-612
Pellet, O. OP-302, OP-307
Pellinen, S. EP-1457
Peltier, C. OP-602
Pelucchi, P. OP-776
Peluso, S. EP-1064
Peña, C. EPS-207
Peña, G. EP-0221
Peñaherrera Cepeda, A. EP-0378, **EP-0364**, EP-0710, EP-0931, OP-481
Pena Pardo, F. EP-0460, EP-0328, EP-0374, EP-0452, EP-0472
Pendharkar, D. OP-073
Penesopoulou, V. EP-1417
Peng, Q. EP-0915, EP-0923, OP-455
Peng, W. **EP-1140**
Peng, X. EP-0198, EP-0276, EPS-176
Peng, X. EPS-037, OP-151
Peng, Y. EP-0211
Pennacchio, L. EPS-137
Penny, R. OP-359
Peñuelas, I. EP-0156, OP-700
Pešorda, M. **EP-1298**, EP-1389
Pepe, G. EP-1173, EP-1199
Pepponi, M. EP-0230
Peralta, S. **OP-378**
Pereira, P. EP-0521
Pereira, S. EP-0916, **OP-619**, OP-625
Perera, W. C. EP-0921, EP-1438
Peretti, D. E. EP-1072, EPS-226, OP-438, OP-443
Perevozcikova, J. EP-0608
Pérez, I. EP-0551
Pérez Beteta, J. EP-1408
Perez de Ciriza Cordeu, M. EP-1263
Pérez de los Ríos, E. EP-0565, EP-0821, **OP-478**
Pérez García, V. M. OP-229
Pérez-Gil, J. OP-700
Pérez Iruela, J. EP-1197, EP-1198
Pérez López, B. EP-0397, EP-0612
Pérez Luque, S. EP-1408
Perez-Martinez, A. OP-229
Perez Quiros, S. EP-1286, **EP-1322**, EP-1337, EP-1368, EPS-263
Pérez-Recio, S. EPS-040
Peric, M. EP-0072, EP-1183
Peric, S. **EP-1120**, OP-631
Peris Conejero, T. EP-0849
Perissi, A. EP-1379
Perissinotti, A. OP-440
Perlaza-Jiménez, M. EP-0618
Perlaza-Jiménez, P. EPS-031, EPS-040
Perneczky, R. EP-0691, OP-237
Perol, D. OP-331
Pérol, M. OP-173
Perovnik, M. OP-307
Perret, P. OP-022
Perret, S. **EP-1017**, EP-1114, OP-533
Perrin, M. EPS-264, OP-499
Perrone, E. **EP-0784**, **EP-0790**, **EP-0881**, OP-860
Perrot, A. EP-1055, OP-225
Perrotta, F. EP-1212
Persijn van Meerten, E. EP-0334
Persson, L. EP-0945
Perucho, J. **OP-234**
Peruzzi, D. EPS-137, OP-584
Pervaiz, N. EP-0414
Peshevska, A. EP-0754
Pesorda, M. EP-1230
Peters, O. OP-303
Peters, S. EP-1119, EPS-183
Peters, S. M. B. EP-1123, EP-1145
Petiet, A. EPS-131
Petřík, M. EP-0123, EP-0138
Petitot, C. **OP-211**, OP-351
Petranovic Ovcaricek, P. OP-380
Petrelli, R. EP-0254, OP-298, OP-326
Petrik, M. **EP-0148**
Petroiu, C. EP-1220
Petropoulos, T. EP-0875
Petrovic, J. EP-0898
Petrovic, K. EP-1240, OP-479
Petrungaro, C. OP-458
Petruzzelli, M. EP-0822
Pettinato, C. EP-0175, EP-0269, EP-0914, **EPS-122**
Petzold, J. **OP-364**, OP-363
Pfaehler, E. EP-0943, **EP-0963**
Pfestroff, A. EP-0854
Pfob, C. H. EP-0734, OP-329
Pham, Q. EP-1169, EP-1171
Philippe, C. OP-747
Philips, J. EP-0718, EPS-302
Piai, A. EP-0534, OP-326, **OP-706**
Piana, S. OP-113
Pianou, N. EP-0477
Piccardo, A. EPS-272
Picchio, M. EP-1043, OP-875
Picciola Bordoni, G. **EP-0262**
Pichard, A. OP-214
Pichler, B. OP-525, OP-017
Pichler, J. EP-0785, **OP-778**
Pichler, R. OP-778
Picola-Brau, N. EP-0437
Picori, L. EP-0234, **OP-613**
Piedelobo Vaquero, C. **EP-1197**, **EP-1198**
Piens, V. TEPS-009
Pieper, L. OP-590
Piermattei, A. EP-0010
Piet, A. EP-0087, EP-0125, OP-153
Piet, B. OP-170
Pietzsch, J. OP-154, OP-346, OP-652

Pigg, D. OP-446, OP-769
Pillay, V. OP-299, EP-0824
Pillon, M. EPS-205
Pilotto, A. OP-047
Pinchuk, A. EP-0070, EPS-012, OP-217, OP-218, OP-275, OP-517
Pineau, C. OP-551
Pineda-Fernández, E. EP-1411
Piñeiro, A. EP-0792, OP-430
Piñeiro Donis, A. EP-0555, EP-0560, EP-0867, EP-0846, EPS-249, EP-0522, EP-0866
Piñero Fernandez- Reyes, M. EP-0872, EP-1391, EP-0745
Piñerúa-Gonsálvez, J. F. EP-0579
Pini, C. EP-0370, **EP-1401**, OP-298, **OP-326**
Pinilla, L. EP-0382, EP-0412, **EP-0384**
Pinkham, M. EPS-119
Pino, A. EP-0973
Pinon, A. EPS-131
Pintão, S. EP-0772, EP-1255, EP-1265
Pinto, C. OP-471, OP-035
Pinto, L. OP-675
Piperkova, E. EP-0457, EP-0563
Piperkova-Slavova, N. EP-0457
Pipintakou, A. OP-557
Piquemal, M. EP-1178
Pirdadeh, M. **EP-0038**, EP-0146
Pires, L. **EP-1184**
Pires, M. EP-0251, EP-0968, EP-1067, EP-1079, EP-1089, EP-1093, **EP-1097**, **OP-033**, OP-548
Pirich, C. EP-0326, EP-0362, EP-0688
Piroska, M. EP-0562
Pirozzi, M. EP-0639
Pirrone, G. EP-1120
Pisani, A. EP-0312, EP-0329
Pisano, G. **OP-783**
Piscopo, L. EP-0308, EP-0788
Piscopo, V. EP-0826, EP-1258, EP-1376, EP-1383, EP-1412
Pitalua Cortes, Q. EP-0086
Pitaud-Renaud, T. EP-1178
Piteo, G. OP-584
Pitzalis, M. EP-0044
Piva, F. **EP-1072**, **OP-467**
Piva, V. EP-0894
Pizzi, M. EP-0611
Pizzuto, D. **EP-0497**, **OP-720**
Placidi, L. OP-858
Plagwitz, L. EP-1085
Planas Roca, A. OP-485
Platsch, G. EP-1013
Plavc, G. EP-0895
Plönes, T. OP-172
Plonkova, H. EP-0513
Plotnikov, E. EP-0089
Plummer, S. OP-888, OP-888
Poblete García, V. EP-0460, EP-0358, EP-0374, EP-0452, EP-0472
Poelaert, F. OP-710
Poelarends, R. **EP-0349**
Poellmann, A. OP-591
Poetter-Lang, S. OP-747
Pohlki, F. OP-458
Pokalchuk, V. EPS-150
Polastro, L. OP-470
Polat, B. OP-043
Polem, T. M. Y. EP-1045
Polgárová, K. EP-0489
Poli, G. OP-669
Polson, L. **EP-0960**, **OP-102**
Pombo Antunes, A. R. OP-152, OP-593
Pomper, M. G. EP-0154
Pompignoli, L. EPS-287
Pomposelli, E. OP-384
Poncet, C. OP-604
Ponnusamy, M. EPS-219
Ponsard, B. EP-1166, OP-657
Pons-Martinez, L. EP-0392
Pontecorvo, M. J. OP-440
Pontone, G. EP-0255
Pool, J. J. OP-622
Poole-Jones, J. EPS-291
Poorbaygi, H. EP-1413
Poot, A. EP-0876, OP-260
Pooth, J. S. OP-842
Pop, S.-G. OP-823
Popescu, C. M. EP-1323
Popkova, T. EP-0513
Popov, S. EP-0616, EP-0617
Popova, E. **EP-0213**
Popovič, P. EP-0835
Porcaro, F. EP-0826, EP-1258, EP-1376, EP-1383, EP-1412
Porfidia, V. EP-1115
Porot, C. EP-1162
Porpiglia, F. EP-0370
Port, M. EPS-294
Portal, C. EPS-140
Portella, L. EPS-054
Portilho, A. EP-1418, **OP-119**
Portilla Merino, P. **EP-0705**
Porto, F. **OP-584**
Posa, A. OP-858
Possanzini, P. EP-1159, OP-042
Postorino, M. EP-0461
Potapov, E. EPS-024
Potier, M. C. EPS-131
Płotka, S. EP-0320
Potocnik, M. EPS-022
Poty, S. EP-0164, OP-215, OP-347
Pouget, J. P. **OP-213**, **OP-214**, **OP-215**
Pouget, N. OP-104
Pougoue Ketchemen, J. **OP-350**
Pouliot, F. OP-534
Poulsen, C. A. **EP-0403**
Poulsen, M. H. OP-877, EP-0403
Pouwels, P. J. OP-607
Poveda, J. **EPS-236**
Powell, A. **EPS-305**, OP-707
Poyanli, A. EP-0837
Pozzi, M. EP-0234
Pozzi, S. EP-1109
Prabash, R. R. K. EP-1438
Prach, A. EP-0089
Pradeep, S. EP-0250
Pradere, C. EP-0288
Pradhan, P. EP-0853, EP-0813, EP-0817, EP-0805, EP-0859, EP-1459
Prakash, B. OP-872
Prakash, V. EP-1091
Pranjatno, N. EPS-139
Prashanth, R. EP-0539
Prati, E. EP-1081
Prats-Cabaces, L. EPS-297
Prchalova, D. EP-1131
Preet, K. OP-797
Prége-Renaud, V. OP-536
Prekopp, P. EP-0562
Presles, B. EPS-044
Pressello, M. EP-0263
Presutti, M. OP-716
Preusser, M. EP-0183, EP-0886, OP-609, OP-610
Prieto, E. EPS-117, OP-446
Prietsch, A. C. EP-0854
Priftis, K. **EP-1429**
Priller, J. OP-303
Primac, I. OP-150
Prinster, A. EP-0639
Prior, A. EP-0153, OP-177
Prior, J. O. EP-1404, EP-0828, EP-1407, OP-373, OP-528, EP-0184, OP-160, TEPS-001
Prisacariu, G. **EP-1355**
Prisco, A. EP-1115
Prisco, M. EP-0826, EP-1258, EP-1376, EP-1383, EP-1412
Pritzkow, M. OP-017
Privé, B. EP-1119, EPS-183, **OP-598**
Priyanka, G. **EP-0285**, EP-0839, OP-872, OP-353, **EP-0880**
Proaño Fierro, M. EPS-258
Procházka, V. EP-0489
Prochowski Iamurri, A. EP-0411, EP-0501, EP-0801, OP-068
Pronello, E. OP-612
Pronin, A. EP-0253, EP-0402, EP-0432, EP-0932, EPS-265, OP-472, OP-473
Pronin, I. EP-0178, EP-0992
Prosotsianiotis, N. EP-0569
Prosperi, E. EP-0270, EP-0270
Próspero, I. OP-632
Proto, S. EP-0514, OP-028, **OP-224**
Provatas, A. EP-0675

Provenzano, E. EP-0216
Provost, C. **EP-1189**
Provost, K. EP-1288
Pryor, M. OP-705
Prządo, J. EP-0320
Psimadas, D. EP-0591, EP-0675
Pu, W. EP-0678
Pu, Y. S. EP-0346
Publicover, J. EP-1100, OP-423
Pubul, V. EP-0792, OP-430
Pubul Nuñez, V. EPS-258
Puca, E. OP-182, OP-327
Puccini, B. EP-0467
Pudis, M. EP-0494, EP-0495, **EP-0508**, EP-0618, EP-0653, **EPS-031**, EPS-121, **OP-233**, OP-480, OP-865
Puhlmann, M. OP-074
Puhr, H. C. OP-609
Puig, A. EPS-207
Püllen, L. OP-786
Pullin, W. EP-0785
Pupi, A. EPS-134
Pupillo, G. OP-584
Purandare, N. EP-0266, EP-0885
Puranik, A. EP-0266, EP-0885
Purpura, P. EP-0369
Puttick, S. EP-0153, EP-1161, OP-177, OP-676
Pylova, I. EP-0302, EP-0432, EP-0433, EP-0542, EP-0932, EP-0955, EPS-079

Qebetu, M. **EP-0942**, EP-1116, EP-1200, EPS-086, OP-349, OP-825
Qi, C. **OP-205**
Qi, H. OP-415
Qi, L. EP-0652, EP-0666, EP-1056, OP-304
Qi, Z. EPS-118
Qiao, Q. OP-455
Qiao, X. EP-0964
Qiao, Z. **EPS-157**, **OP-415**
Qiao, Z. EP-0133
Qin, C. EP-0190, EP-0356, OP-286, OP-837
Qin, R. EP-0625, EPS-098
Qin, S. OP-762
Qin, Z. EP-0023, EPS-102, OP-841
Qing, Y. OP-675
Qiu, F. **EP-0098**, **OP-694**
Qiu, Y. EPS-006, EPS-014, OP-210
Qu, Q. EP-0119, EPS-033
Qu, W. EP-0923
Quan, J. **EP-0039**, EP-0662
Quan, Z. EP-0256, EP-0278, EP-0693, EP-0738, EP-1027, OP-116
Quantin, X. OP-173
Quaranta, D. EP-0665
Quarantelli, M. EP-0639
Quartuccio, N. **EPS-272**
Quattrocchi, C. C. EP-0234
Quazi, S. EPS-003
Queiroz, C. EP-0973, EPS-235, OP-465
Quere, C. OP-173
Quincoces, G. EP-0156, OP-378, OP-446, OP-700
Quinn, L. EP-0586
Quintana-Bolaño, C. EP-0872
Quirce, R. EP-0656, EP-0673

Raab, M. S. EP-0506
Raab, P. OP-376
Raad, S. OP-819
Rabani, F. EP-1378
Rabani, F. **EP-1350**
Rabano, A. EP-0637
Rabbath, X. **EP-1291**
Rabin, G. EPS-087
Rabrenovic, M. EP-0564
Racca, M. OP-324
Radácsi, A. OP-375
Raddi, M. EP-1115
Radermacher, H. OP-284
Radics, A. OP-818
Radivojevic, O. OP-479
Radnia, F. EP-0051, **EPS-046**
Radosavcev, L. **EP-0564**
Radovic, B. EP-0898, OP-479
Radovic, M. EP-0072, **EP-1183**
Radulovic, M. EP-0564
Raeisi, N. **EP-0548**, **EP-0891**, EP-1339, EP-1380, OP-109
Raes, F. OP-022
Raffa, S. EP-0377, EP-0681, EP-0683, EP-0686, OP-669, OP-725
Raffy, L. **EP-0512**
Rafie, S. EP-0217, EP-0297
Rafiei Sardouei, A. EP-1101
Ragot, M. **EP-1082**, **EP-1182**
Rahabi, S. EPS-212
Rahal, S. EP-0863
Rahbar, K. EP-1085, OP-244, OP-327, OP-329
Rahmim, A. EP-0960, EP-0994, EP-1016, EP-1101, OP-029, OP-034, OP-102, OP-420, OP-421, OP-428
Rai, M. OP-554
Rainero, I. EP-0681
Raj, A. OP-073
Rajala, N. EP-1195
Rajkumar, K. EP-0539
Rajovic, M. EP-0564
Raju, S. EP-0584, **EPS-239**, OP-773, OP-775
Rakia, G. **EP-1231**
Rama Alonso, S. EP-0200, EP-0364, EP-0378, EP-0710, **EP-0931**, OP-481
Ramachandra, P. G. EP-0258
Ramaekers, S. OP-657
Raman, S. S. EP-0376, OP-714
Rambabova-Bushljetik, I. EP-0754
Ramírez-Navarro, Á. EP-0774
Ramogida, C. OP-580
Ramolli, A. EP-1104
Ramonaheng, K. EP-0942, **EP-1116**, EP-1200, EPS-086, OP-349, OP-825
Ramos, C. D. EP-0189, EP-0223, **EP-0505**, **EP-0536**, OP-119
Ramos, C. EP-1223, EP-1234, EP-1245, EP-1267, EP-1418, OP-0337
Ramos, D. O. S. EPS-251
Ramos, L. EP-0841
Ramos Barata, S. **EP-0765**, **OP-636**
Ramos-Docampo, E. **OP-093**
Ramos-Font, C. EP-0555, EP-0560
Ramos-Membrive, R. OP-700
Ramos-Polo, R. EP-0618
Ramos Rodríguez, L. EP-0748
Ramos-Rubio, E. EP-0850
Rampi, N. EP-0478
Ramsdal Hol, H. EP-1397
Ramsvik, H. **EP-1102**, OP-424
Rana, N. EP-0529, OP-482, OP-878
Randolph, G. J. OP-745
Rangarajan, V. EP-0266, EP-0885, EP-1445
Rangger, C. EP-0123
Rannikko, A. EP-0417
Rao, N. EP-0471
Raofi, A. K. EP-0908
Rapa, M. EP-0396, EP-0421
Rashki, M. EPS-258
Rashmi, M. EP-1013
Rasinski, P. **EP-0260**, EP-0275
Rasmussen, I. L. EP-1073
Rasmussen, R. EP-0172
Rasoulian, B. EP-0570
Rassaf, T. OP-239
Rasschaert, G. OP-366
Rasschaert, M. EP-0183
Rastogi, A. OP-683
Rastogi, S. EP-0177, EP-0300, EP-0558, EP-0882, EPS-270
Rasul, S. EP-0408, **EP-0528**, EP-1241, OP-325, OP-329, OP-747, OP-820, TEPS-013
Rathod, N. OP-889
Ratola, M. TEPS-006
Ratsakatika, T. OP-825
Rauchmann, B. S. OP-237, EP-0691
Rausch, I. EP-0968, EP-1089, TEPS-015
Rauscher, I. EP-1047, OP-329, OP-363, OP-364, OP-461, OP-789
Ravaioli, M. EP-0270
Raverot, G. OP-542
Ravi Kumar, A. S. EP-0830
Ravina, M. EP-0584
Rawal, S. EP-1221
Rawashdeh, M. EP-1416
Rawat, P. **EP-0561**
Raymond, P. EP-0827
Razali, N. EP-0416
Razansky, D. EP-0002
Razavi, P. EP-0201
Razis, E. EP-0183

Razola-Alba, P. EP-0552
Razzouk-Cadet, M. OP-864
Re, C. EP-0534
Reader, A. EPS-236
Rebella, G. EP-0686
Rebelo, J. **EP-1318**, **EP-1320**, OP-379
Reberšek, M. EP-0519
Reboulet, G. OP-787
Recarte Ortega, P. EPS-275
Recchia, E. EPS-001
Reccia, P. EP-0206
Reche-Perez, F. OP-017
Redondo Moneda, F. OP-711, OP-873
Reed, A. OP-458
Regine, G. EP-0263
Régio Brambilla, C. EP-0929, OP-284
Reguera Berenguer, L. EP-0798, EP-0841
Regupathy, A. EP-0121
Rehacek, T. EP-1131
Reichel, L. **OP-869**
Reichen, C. **EPS-055**
Rei da Cruz Escaleira, J. **OP-061**, **OP-372**
Reijneveld, J. C. OP-607
Reijonen, V. EP-0934, **EP-0941**, **OP-100**
Reilev Møller, H. TEPS-003
Reilly, R. EP-0081, OP-094
Reimand, J. OP-302, OP-307
Reincke, M. EP-0711, EP-0734
Reinert, C. P. EP-0351
Reinhard, A. TEPS-017
Reinke, Z. OP-358
Reis, H. OP-786
Reis, J. EPS-124, EPS-125, OP-609, OP-610
Reis, T. L. EP-0536
Reischl, G. OP-017, OP-365
Reissig, F. EPS-146
Reiter, R. OP-714
Reitsma, N. OP-886
Rekabpour, S. EP-0878
Remde, Y. EP-0132
Rémi, J. EP-0699
Ren, C. **EP-0204**, **EP-0238**, EP-0327, EP-0410
Ren, M. OP-207
Ren, S. EP-0684, OP-238
Ren, T. EPS-235, OP-465
Ren, W. OP-727
Renaud, J. OP-501
Renaud, S. OP-343
Rendl, G. EP-0688
Renzetti, B. EP-0375, EP-0398
Renzulli, M. EP-0255
Rep, S. EP-0712, EP-0713, EP-0913, **EP-1440**
Repaka, K. OP-655
Repáraz, D. EP-0077
Repetto, A. EP-0792
Resch, S. EP-1118, EP-1150
Reschke, P. OP-245
Rescigno, P. EP-0370
Resta, S. EP-1043
Resuello, K. **EP-1219**, **OP-629**
Rettl, R. EP-1011
Reuvers, T. OP-216
Revel, C. EPS-090
Revheim, M.-E. EP-1044
Revilla, E. OP-772
Revy, A. EP-1082, EP-1182
Rey, A. EP-0140, **EP-0134**
Reyes, L. EP-0100, EP-0157
Reymann, M. **OP-422**, EP-0965
Reynaert, N. OP-592
Reynés Llompart, G. EP-0758, EP-0307, EP-0653, EP-0850, EP-1057, EPS-297
Reynolds, S. EP-0791
Reza, H. EP-0688
Rezaei, H. EP-0922
Rezaei, S. EP-0413, EP-1296, EP-1297
Rezaeianpour, M. **EP-0127**
Riana, A. EP-1128
Ribaldi, F. OP-440
Ribeiro, D. **TEPS-006**
Ribelles, M. OP-666
Ribelles Segura, M. EP-1147
Riberio, B. EP-0777
Ricardo, A. EPS-062
Ricart Paredes, E. EP-0758, EP-1411
Ricaurte Fajardo, A. EP-0352
Ricci, C. EP-1268
Ricci, F. EPS-054
Ricci, M. EP-0345, **EP-1212**, EP-1287
Ricci, R. OP-321, OP-227
Richard, P. EP-0581
Richardson, M. OP-707
Richardson, S. OP-416, OP-416
Richter, A. OP-363, OP-364
Ricke, J. EP-0037, EP-0309
Rida, H. **OP-838**
Ridder, C. EP-0125
Rieger, C. OP-628
Riemann, B. OP-244, OP-385
Riera, E. EP-0382, EP-0384, EP-0412
Riesco, M. EP-0792
Riesenberg, S. EPS-055
Rietbergen, D. EP-0334, OP-037, EP-0948, OP-783
Righini, M. EPS-090
Rignanese, F. EP-0234
Rigopoulos, A. EPS-003
Riiabova, M. EP-0008
Rijk, V. EP-1395
Ringler, R. **OP-591**
Rinke, A. EP-0305
Rinne, S. EP-0064, OP-279, OP-414, OP-519, **EP-0057**
Rinscheid, A. EP-1111
Rintala, A. **EP-0934**
Rioja Blanco, E. **OP-413**, OP-220
Riola Parada, C. EP-0397, OP-057
Riondato, M. **EP-0141**, **EP-1187**, OP-776
Rios, A. TEPS-021
Riou, L. EPS-103
Rioufol, C. EP-1178
Ripa, R. S. OP-166
Rischpler, C. EP-0696, OP-239, OP-385
Rissanen, A. EPS-127
Ristikankare, A. EP-0934
Ritawidya, R. EP-1107, EP-1129
Ritt, P. OP-429, OP-662
Ritter, Z. EP-0797, EP-1036, OP-354
Ritzel, K. EP-0711, EP-0734
Rivera-Sanchez, M. EP-0673
Riverol, M. EPS-117
Riveros Frutos, A. EPS-026
Rivombo, M. EP-0367, EP-0379, EP-1090, EP-0757, EP-1250
Rizkallal Monzon, S. EP-0705
Rizza, E. EP-0206, OP-105
Rizzo, A. EP-0370, OP-324
Rizzo, F. EP-0044
Robbrecht, D. EP-0535
Robert, A. OP-670
Robert, S. OP-347
Robert-Ebadi, H. EPS-090
Roberto, E. EPS-298
Robesti, D. EP-0370
Robillard, M. S. EPS-048
Robin, P. EP-0800, EPS-090, OP-602
Robinson, A. EP-0950, EP-0670
Robinson, J. EP-0572, EP-0576
Robles, J. J. **EP-0392**
Robles-Barba, J. EP-0437, EP-0494, EP-0495, EP-0508, EPS-031, EPS-040
Rocamora Blanch, G. EP-0508, OP-865
Roccatagliata, L. EP-0683, EP-0686, OP-725
Roch, V. EPS-264, OP-499
Rodari, M. EP-0268, EP-0350, EP-0393, EP-0779, EP-1062, OP-384
Roddy, D. EP-0950
Rode, M. **TEPS-003**
Rodell, A. B. EP-0957, EP-0981, OP-769
Rodrigo, V. OP-378
Rodrigues, C. EP-1462, OP-623, OP-624
Rodrigues, D. **EPS-061**
Rodrigues, M. OP-434
Rodrigues, P. OP-056, OP-061
Rodrigues Teixeira, A. TEPS-001
Rodríguez, C. EP-0775
Rodriguez, S. EP-0100
Rodríguez-Arce, I. EP-0156, OP-700

Rodríguez-Bel, L. EP-0653, EP-0731, EP-1057, EPS-031, EPS-121, OP-233
Rodríguez Díaz, L. **EP-0319**
Rodríguez-Fernández, A. EP-0846
Rodríguez-Fonseca, O. OP-440
Rodríguez-Fraile, M. OP-378
Rodríguez-Gasén, A. EP-0618
Rodríguez Gómez, J. EP-0374, EP-0452, **EP-0460**, EP-0472
Rodríguez Gómez, M. EP-1198
Rodríguez Locarno, T. EP-1312, EP-1315, EP-1308, EP-1311 EP-1289, EP-1305
Rodriguez Ortega, V. EP-0462, EP-1262, EP-1263
Rodriguez Oviedo, D. EP-0819, EP-1286, EP-1337, EP-1368 EPS-263, EPS-273
Rodriguez Pérez, S. EPS-020, OP-091
Rodríguez-Puig, D. EP-0307, EP-0850, EP-1411
Rodríguez-Revuelto, A. A. EP-0545
Rodríguez Rey, C. EP-0339, EP-0340, EP-0341
Rodríguez-Rodríguez, C. EP-0034, OP-348
Rodríguez-Rodríguez, E. EP-0656
Rodriguez Rodriguez, G. EP-0462, EP-1262, EP-1263
Rodríguez-Rubio Corona, J. **EP-0745**, EP-0872, EP-1391
Rodriguez Vida, A. **OP-604**
Roelants, V. **EP-0598**, **EPS-099**
Roelants, V. OP-496
Roemer-Cassiano, S. EP-0019, OP-044
Roetman, J. **EP-0069**, **EP-0785**, **EP-0810**, **OP-674**
Roganovic, J. EP-0873
Rogasch, J. EP-1092
Rogic, I. **EP-1023**
Rohmah, A. **EPS-229**
Röhrich, M. **EP-0532**, EPS-271, **OP-371**
Roivainen, A. EP-1179
Rokni, M. OP-222
Roll, W. **EP-1085**, **OP-244**
Romagnoli, A. EP-0504
Romagnoli, L. EPS-030
Romagnolo, C. OP-558
Romanò, C. EP-0894, EP-1130, EP-0470, EP-0914
Romanowicz, G. EP-1409
Rombo, D. EP-0521
Romei, F. OP-716
Romeo, A. EP-1238, EP-1372
Romera, M. OP-378
Romero, J. EP-0382, EP-0384
Romero, M. **EP-0394**, EP-0775
Romero, S. EP-0382
Romero Acevedo, S. EP-0748
Romero Otero, M. EP-0849
Romero Porras, M. EP-0491, OP-784
Romero-Zayas, I. **EP-0776**
Romić, M. EP-1222
Romic, M. EP-0264
Rominger, A. EP-0002, EP-0161, EP-0409, EP-0423, EP-0466, EP-0500, EP-0614, EP-0933, EP-0970, EP-0988, EP-1061, EP-1080, EP-1090, EP-1095, EP-1148, EPS-009, EPS-013, EPS-193, EPS-221, EPS-240, OP-222, OP-417, OP-461, OP-518, OP-552, OP-685, OP-770, OP-771, OP-788, OP-823, OP-889
Roncali, E. EP-1054
Roncali, M. **OP-113**
Rontogianni, P. EP-0477
Roosen, J. EP-1123, OP-855
Roque Pérez, A. EP-0611
Rorsman, F. EP-1104
Rosado Hidalgo, M. **EP-0748**
Rosales, J. J. OP-378
Rosar, F. EP-0780, OP-435
Roscales, S. OP-346
Rösch, F. EPS-009, EPS-013, EPS-190, EPS-193, OP-150, OP-417, OP-518
Rose, S. EP-0153, EP-1161, OP-177, OP-290, OP-676, OP-703
Rosenau, A. K. OP-459
Rosenbaum, C. OP-708
Rosenskjold Madsen, J. **OP-769**
Rosenström, U. EP-0009, EPS-043, OP-087
Rosero, A. OP-666
Rosero Enríquez, Á. EP-1147
Rosewarne, D. EP-1091
Rosi, A. OP-708
Rosiek, V. EP-0782
Roskar, S. OP-866
Ross, T. OP-726
Rossetti, C. EP-0269, EP-0418, EP-0419, EP-0427, EP-0470, EP-0894, EP-0914, EP-1130, EPS-228, OP-484, OP-556
Rossetti, V. EP-0411, EP-0436, EP-0501, OP-068
Rossi, A. EPS-054, EP-0436, EP-0501, EP-0802
Rossi, C. OP-211, OP-227
Rossi, F. EP-0478
Rossi, P. EP-0268
Rossin, R. EPS-048
Rossini, A. OP-484
Rota-Roca, M. R. EP-0850
Roteta Unceta Barrenechea, A. EP-0462, EP-1262, EP-1263
Roth, D. EPS-088
Roth, H. OP-025
Roth, K. S. EP-0331, OP-879
Roth, N. OP-499, OP-500
Rotllan Vila, N. EP-0156
Rottey, S. OP-522
Rottiers, M. OP-121
Roubaud, G. OP-536, OP-603
Rouchota, M. EP-0065
Rouet, C. EP-1082
Rousseau, C. OP-675
Rousseau, É. EP-0004, OP-551
Roussopoulos, K. EP-1429
Rout, A. EP-0510
Roux, S. EPS-153
Rouzet, F. OP-499
Rovai, A. EP-0663, EP-0687
Rovera, G. **EP-0306**, EP-0681, EP-0683, OP-055, OP-098, OP-105, **OP-120**, OP-324, OP-611, OP-612
Rovere, M. EP-0018
Roveta, F. EP-0681
Rowe, S. P. EP-0154
Rowley, L. EP-0471, **EP-0911**
Roy, A. EP-0583, EP-0298, EP-0510, EP-0537, EP-0721, **EP-0746**, EP-0750, EP-1042, EP-1207, EP-1209, EP-1235, EP-1259, **EP-1387**, EPS-206, OP-256, **OP-744**, OP-800, OP-162, OP-164, **OP-551**, OP-871
Roy, P. M. EPS-090
Roz, L. EP-0044
Rozenblum, L. OP-611
Ruan, D. **EP-1038**, **EP-1049**
Ruan, W. EP-0356, EP-1024, EPS-175, OP-286
Ruano Pérez, R. EP-0397, EP-0549, EP-0550, EP-0612, EP-0613, OP-057, OP-854, EP-0833, EP-0579
Rubagotti, S. EP-0091
Rubini, D. EP-0312, EP-0329
Rubini, G. EP-0312, EP-0329
Rubino, E. EP-0681
Rubino, F. EP-1146, OP-384
Rubino, M. OP-384
Rubio Álvarez, L. EPS-202, EPS-211
Rubio Alvarez, M. OP-483
Rubio Fernández, G. EP-1197, EP-1198
Rubió Rodríguez, A. EP-1434
Rubira, L. OP-343
Ruchała, M. EP-0782
Rudà, R. OP-612
Rudbeck, A. L. **EP-0292**
Rudolphi, T. EP-0458
Rudolphi Solero, T. EP-1229
Ruediger, M. OP-658
Ruffin, R. OP-351
Ruffinelli, J. C. EP-0307, EP-1366
Ruffini, L. EP-1179, EPS-140, OP-549, OP-801
Rufini, V. EP-0010, EP-0497
Ruggeri, R. M. OP-380
Ruggiero, M. EP-0010
Ruhwedel, T. **EP-1092**
Rui, Z. OP-544
Ruijgrok, L. EP-1185
Ruiter, S. J. EP-0842
Ruiz, S. EP-0384, EP-0412
Ruiz Corbalán, C. EP-1308, EP-1311, EP-1312, EP-1315
Ruiz Gavilanez, E. **EP-0382**
Ruiz-Llama, S. EP-0845
Rumiantcev, M. EP-1118, EP-1150, EPS-197
Rungby, J. EP-1073
Runge, R. EP-0082
Rusaas, M. **EP-0998**

Rusnak, J. EP-1405
Russo, A. EP-0233
Russo, F. **EP-1281**, EP-1287
Russo, T. OP-875
Ruytenberg, T. EP-0948
Ruzzon, K. OP-722
Ryatt, H. EP-0539
Rybina, A. OP-070
Rydén, T. EPS-180, OP-589
Ryer, E. OP-320
Ryhiner, M. EP-0161
Ryser, M. **OP-315**
Ryzhova, O. EP-0253, EP-0402, EPS-265, OP-473
Saad, F. OP-604
Saad, L. EP-0036
Sabaric, V. EP-0524
Sabatella, M. **EPS-196**, **OP-216**, OP-221
Saber Tanha, A. EP-0548, EP-0891, **EP-1339**, EP-1350, EP-1360, EP-1380
Sabet, H. EP-0320
Sabir, S. **OP-229**
Sablin, M.-P. OP-104
Sabot, B. EP-0945
Sabouri, M. **EP-1101**, OP-421
Sabri, O. EP-0230, EP-0488, OP-033, OP-044
Sabuncu, S. EP-0858
Sabzi, R. OP-109
Sachpekidis, C. **EP-0485**, EP-0506, EP-0520, **EP-0525**, EP-1022, **OP-294**
Sachs, J. EPS-087
Sadeghi, M. EP-0937, EP-1108
Sadeghi, R. EP-0566, EP-0567, EP-0568, EP-0570, EP-1345, EP-1347, EP-1357, EP-1362
Sadeghi-Meibodi, N. EP-0663
Sadeghi Panah, M. **OP-383**
Sadeghipour, F. EP-1404
Sadeq, A. EP-0928, **EP-1279**
Sadik, M. **EP-0463**, EP-0468
Sadri, K. EP-0568, EP-0570
Saeed, M. A. EPS-284a
Saeed, S. OP-803, **OP-803**
Saeedi Saghez, B. EPS-139
Sağer, M. S. EP-0901, EP-0857
Saerens, M. OP-522
Sá e Silva, R. **EP-0701**, **OP-056**, OP-061, OP-372
Sæterstøl, J. **OP-039**
Sáez de Gordoa, E. EP-0685
Safari, M. EP-0038, EP-0146
Safarian, A. **EP-0362**, **EP-0688**, **OP-734**
Safazadeh, G. EPS-274
Sagan, K. P. EP-0782
Saganowski, P. EP-1174
Sagar, S. EP-0474, **EP-0510**, EP-0537, EP-0583, EP-0721, EP-1042, EP-1235, EP-1236, EPS-209, EPS-217, OP-256
Sagara, H. **EP-1435**
Sagastegui Alca, A. **EP-1308**, **EP-1311**, EP-1312, EP-1315
Sager, S. EP-0424, EP-0475, EPS-256
Saghebi, J. EP-0830
Sagiroglu, S. EPS-115
Saglam, K. **EP-0277**, EP-0424, EP-0475, **EP-0901**, EPS-256, OP-531
Sah, B. R. **EPS-041**
Sahafi, P. **EP-0566**, **EP-0567**, **EP-0568**, **EP-0570**, EP-1002, **EP-1345**, **EP-1346**, **EP-1347**, **EP-1348**, EP-1349, **EP-1351**, **EP-1352**, **EP-1353**, **EP-1354**, EP-1356, EP-1361, EP-1363, EP-1369
Sahar, M. EPS-284a
Sahebkari, A. EP-0566
Sahin, D. **OP-715**
Sahin, M. C. EP-0858
Sahin, O. **EP-0723**, EPS-256, OP-531, EP-0277, **EP-0424**
Sahm, F. EP-0183
Sahoo, R. K. EP-0371, EP-0372, EP-0373, EP-0764
Said, M. EP-0416
Saidi, A. EPS-055
Saing, S. EP-1086, OP-295
Saini, M. EP-0258
Saini, P. EP-0258
Saini, V. K. EP-0877
Saintigny, P. OP-173
Saiyed, R. OP-823
Saiyed Alsheikh, R. EP-0409
Sajedi, A. EPS-304
Saji, H. EPS-141
Sajjan, R. TEPS-005
Saka, E. EP-0661
Sakai, A. EP-0634, EPS-111, OP-503
Sakai, S. EP-0634, EP-0635, EPS-095, EPS-111, OP-503
Sakamoto, R. EP-0540
Sakellariou, K. EP-0591, EP-0675
Sala, A. EP-0690
Sala, E. OP-818
Salabert, A. S. EP-1082
Salam, S. EP-0596, EP-0700
Salamoun-Feghali, P. EP-0251, OP-173
Salanti, A. OP-760
Salas Ramirez, M. EP-0967, **EPS-295**, EP-0983, EP-1077, EPS-179, OP-590
Salaün, P.-Y. EPS-090, EPS-230, OP-864
Salavati, A. EPS-162
Salcedo, S. EP-0668, EP-0704
Salcedo Cortes, S. **EP-0798**, **EP-0841**
Salcedo Pujantell, M. EPS-026, EP-0845
Saldarriaga Vargas, C. EPS-020, OP-091, OP-592
Salehi, R. EP-0038
Salehi-Moratab, R. EP-0146
Salek, M. **OP-579**
Salgado, L. EP-0521
Salgarello, M. OP-324, OP-384
Salih, A. EPS-062
Salimi, Y. **EP-0971**, EP-1122, EPS-220, OP-034
Salinas Rodríguez, B. EP-0114
Salinas Sanchez, A. EP-0358
Salkica, N. EP-1436, **OP-318**
Saller, T. OP-773
Salles, A. EP-1181
Salmerón Ruiz, A. EP-0555
Salomanina, M. EP-1285
Salomasova, S. EP-0062
Salomón, C. EPS-121, EPS-207, EPS-031
Salomone, F. EP-0233
Salonia, A. EP-0534
Salt, S. A. EP-0321
Salvador, P. OP-666
Salvador Arthur, R. EP-0552
Salvadori, J. EP-1162
Salvanou, E. A. EPS-153, OP-183
Salvarese, N. OP-179
Salvi de Souza, G. **OP-051**
Salvini, A. EP-1173
Samadi, M. EP-1345, EP-1346, EP-1347, EP-1348, EP-1349, EP-1350, EP-1354, EP-1356, EP-1357, EP-1377, **EP-1361**, **EP-1362**, **EP-1363**, **EP-1369**
Samanes Gajate, A. OP-875
Sambuceti, G. EP-0141, EP-0370, EP-0377, EP-1187, OP-324, OP-725, OP-776, OP-868
Samia Ait-Mohand, S. EP-0004
Samizadeh, M. EP-0038
Sampaio, I. OP-742, EP-1205
Sampaio, J. M. EP-1133
Samson, M. OP-551
Samuelsson, C. EP-0381
Sanaat, A. EP-1033, EPS-220, EPS-226
Sanabria, K. OP-666, EP-1147
Sanche, L. EP-0029
Sanchez, D. TEPS-021
Sanchez, O. EPS-090
Sánchez-Artuñedo, D. EP-0611, **EP-0836**, EPS-092, **EPS-297**, OP-483
Sanchez Barba, M. EP-0200
Sanchez Calderón, J. EP-0819, EP-1286, EP-1337, EPS-263, EPS-273
Sanchez Casi, B. EP-1263
Sanchez Catalicio, J. EP-1227, EP-1251
Sanchez-Crespo, A. EP-0404
Sánchez del Pueblo, C. OP-784
Sanchez Eguiguren, S. EP-0462, EP-1262, EP-1263
Sánchez Izquierdo, N. EP-1308, EP-1311, EP-1312, EP-1315, EP-1289, EP-1305
Sanchez-Juan, P. EP-0637
Sanchez-Lajusticia, A. OP-331
Sanchez Oscoz, I. EP-0462, EP-1262, EP-1263
Sánchez-Pelaez, M. EP-0673
Sánchez Rodríguez, A. EP-0673
Sánchez-Rodríguez, I. EP-0618, EP-0731, OP-480, EP-0495, EPS-022

Sánchez-Salmón, A. EP-0656, EP-0673
Sánchez Sánchez, R. EP-0522, EP-0866, EP-0867, EP-0774
Sanchez Torrente, A. EP-1375
Sanchez Torrente, M. EP-1300, EP-1365, **EP-1375**, **EP-1381**, EP-1388
Sánchez-Vega, J. EPS-022
Sánchez Vera, Y. **EP-0476**, **EP-0538**
Sandgren, K. EP-1070
Sandhu, S. EP-1161, OP-323
Sandker, G. EPS-285
Sandmann, P. OP-726
Sandström, M. **EP-1142**, OP-095
Sandu, I. EP-1355
Sang, B. EP-0317
Sanghera, B. EPS-076
Sangrós Sahún, M. J. EP-0760
Sani, G. EP-1399, OP-720
Sanli, Y. EP-0282, EP-0837, EP-1314, OP-110, OP-543
Sanna, P. EP-1159, OP-042
Sano, A. OP-301, OP-719
Sansovini, M. EP-0411, EP-0436, EP-0801, EP-0802, EP-0803, EP-1159, **OP-042**
Santabárbara, J. EP-0382, EP-0384
Santaella-Guardiola, Y. EP-0745, EP-0872
Santiago-Ribeiro, M.-J. **OP-718**
Santiesteban Gutiérrez, M. EP-1434
Santin, M. EPS-040
Santirso Rodríguez, D. OP-050
Santo, G. **OP-434**
Santoro, M. EP-0145, **EP-1112**, EPS-247, **OP-028**
Santoro, P. EP-1161, OP-676, OP-703
Santos, A. EP-1223, EP-1234, EP-1245, EP-1267, EP-1324, EP-0717, EP-1247, EP-1269
Santos, D. A. M. EP-0631
Santos, E. OP-217, OP-218, OP-219, OP-517
Santos, J. EPS-091, OP-061
Santos, M. M. M. EP-0101
Santos, T. P. EP-0505
Santos Bueno, A. EP-1300
Santos García, B. EP-0364, EP-0710, EP-0931, OP-481
Santos Montero, C. EP-0776
Santoso, A. OP-587
Sanverdi, E. EP-0718
Sanz, S. EP-0458
Sanzo, L. EP-0691, EP-0698
Sanz Viedma, S. EP-1229
Sapin, N. EP-0671
Saracoglu, S. EP-0858
Saracyn, M. EP-0789
Saraiva, T. EP-1256
Saran, S. EP-1426
Sarandeses Fernández, P. EP-0387
Saraste, A. OP-794
Saraswat, D. **EP-0556**
Sarathi Choudhury, P. EP-0267, EP-1221
Sarazin, M. EPS-131
Sareshgi, R. A. M. TEPS-015
Sargant, S. EP-0910
Sari, H. EP-0423, EP-0970, EPS-221, OP-685, OP-771, OP-889
Sari Cataldas, Y. EP-1215
Sarikas, A. OP-531
Sarnelli, A. EP-0801, EP-0802, EP-0803, EP-1081, **EP-1159**, EPS-285, **EPS-286**, OP-042
Sağıroğlu, S. EP-0638
Sarpaki, S. EPS-198
Sarrhini, O. **EP-0027**
Sarrut, D. **EP-1068**
Sartor, C. EP-0504
Sartor, H. OP-041
Sartor, O. EP-0807, OP-674
Sartori, F. EP-0893
Sasaki, F. **EP-0927**, EP-0954, EP-0956, EP-1098, EP-1452
Sasaki, H. EP-1458, OP-387
Satake, M. EP-0822, EP-0942, EP-1116, EP-1200, EPS-086, OP-299, OP-349, OP-825
Sathoo, S. **EP-0250**
Sathyamurthi, B. TEPS-005
Sato, M. EP-0927, EP-0954, EP-0956, EP-1098, **EP-1452**
Satoh, Y. EP-0635, **EP-0939**, EPS-095
Satonkiatngam, S. OP-714
Satpati, D. OP-655
Sauchuk, Y. **EP-0473**
Sauer, M. EP-1026
Sauer, S. EP-0506
Sauge, J. EP-0297
Saunavaara, V. EPS-234, OP-328
Saut, O. EP-0512
Sautois, B. OP-710
Savard, M. OP-021
Savchenko, A. EP-0871
Saviatto Nardi, A. EP-0887
Savinainen, A. **EPS-062**
Savio, E. EP-0100, EP-0157, EP-1184
Savio, L. EP-0175, EPS-122
Savvidis, G. **EPS-198**
Saxtoft, E. S. OP-261
Saya, H. EP-0635, EPS-095
Sayit Bilgin, E. EP-0236, EP-0925
Sayman, H. B. EP-0355, EP-0368, EP-0424, EP-0475, EP-0857, EP-0901, EP-1295, EPS-256, OP-531
Sazdova, I. EP-0754
Sazonova, S. EP-0616, EP-0617
Sbraga, F. EPS-022
Sbrozzi Vanni, A. EP-0263
Scala, S. EP-0044, EPS-054
Scalia, I. **EP-0304**
Scalzo, M. **OP-314**
Scarale, A. F. EP-0418, EP-0419, EP-0894, EP-0269, **EP-0427**, EP-0470, EPS-228, OP-556
Scarano, M. OP-059
Scarlattei, M. EP-1179, EPS-140, OP-549, OP-801
Scarpa, E. OP-631
Scarpi, E. EP-1159, OP-042
Scarsbrook, A. EP-1091
Scartoni, D. OP-613
Schabhüttl, T. OP-609
Schaefer, N. EP-0184, EP-0828, EP-1407, OP-373, OP-601
Schaefer, P. **OP-049**
Schaefer, R. EP-0047, EP-0062, EP-0691
Schaefer-Schuler, A. OP-435
Schaefferkoetter, J. EP-0957, EP-0959, EP-0970, **EP-0966**, **EP-1028**, OP-769
Schäfer, L. **EP-0109**, OP-761
Schäfer, M. EP-0015, EP-0132, EP-0138
Schäfers, M. EP-1085, OP-244, OP-327, OP-329
Schaffer, P. OP-580
Schatka, I. EP-1092
Scheffler, M. OP-438, OP-443
Scheiber, C. EP-1409
Scheie, D. EPS-120
Scheifele, M. EP-0793, EPS-290
Scheins, J. EP-0929, EP-0943, EPS-083, OP-284, EP-0963
Schell, C. EPS-159
Schembri, G. EPS-119
Schemmer, B. **EP-0176**
Schepisi, G. EP-0801, EP-0803
Scherer, C. OP-842
Scherthan, H. EPS-197, EPS-294, EPS-295, OP-426
Schiavina, R. EP-0375, EP-0398, OP-716
Schiavini, M. EP-0175, EPS-122
Schiazza, A. EP-0671
Schibli, R. OP-220, OP-413, OP-662, OP-673, OP-677
Schicchi, N. OP-558
Schichor, C. EP-0886
Schilliger, N. EP-0184
Schilling, F. EPS-185, OP-180
Schindelwolf, M. OP-552
Schindler, P. EP-1085, OP-244
Schirrmacher, R. EPS-248, OP-365
Schjesvold, F. EP-1044
Schlapbach, C. OP-220, OP-413
Schlemmer, H.-P. EP-0485
Schlepckow, K. EP-0047
Schleyer, P. EP-0957, EP-0966, EP-0974, EP-0990, EP-1028
Schlosser, T. W. OP-239
Schlötelburg, W. EP-0318, **EP-0728**
Schmid, D. OP-673, OP-677
Schmidinger, M. EP-0528
Schmidt, D. OP-228, OP-591
Schmidt, F. **OP-288**
Schmidt, F. P. EP-0229
Schmidt, J. EPS-090
Schmidt, K. EP-1116, OP-381
Schmidt, M. OP-381, OP-879
Schmidt, T. EPS-239, **OP-773**, OP-775, EP-0109

Schmidt-Graf, F. EP-0182
Schmidtlein, C. R. EP-0918, EP-0920
Schmiedehausen, K. OP-170
Schmitl, S. EP-1241, OP-790, OP-820
Schmitt, A. EP-0512
Schmitt, C. EP-1189
Schmitt, D. EP-0703
Schmitt, L. G. EPS-251
Schmitz, M. EP-0696
Schneider, C. **EP-0848**
Schneider, S. **EP-0135**
Schneller, V. OP-606
Schnitzer, J. EPS-018
Schobert, I. EPS-024
Schöll, M. EP-0793, OP-440
Schomäcker, K. EP-0331
Schott, M. EP-0703
Schottelius, M. EP-0077, EP-1404, EPS-142
Schrader, A. J. OP-327
Schramm, G. EPS-126
Schreckenberger, M. EP-0532, EPS-271, OP-371
Schrik, A. EP-1010
Schubert, M. L. EP-0485
Schubert, N. OP-361
Schug, D. OP-284
Schuler, M. OP-172
Schulga, A. EP-0089
Schuller, B. EP-1135
Schultz, M. K. EP-0008, EP-0084, EP-0169
Schulz, J. OP-721
Schulz, V. OP-284
Schulze, C. OP-261
Schumacher, K. OP-670
Schumann, S. EPS-294, OP-426
Schupps, N. OP-471
Schürrle, N. EP-1127, EP-1141
Schwach, V. OP-840
Schwartz, P. OP-536
Schweiger, L. **EP-0890**
Schweighofer Zwink, G. EP-0688, EP-0326
Schweizer, J. R. O. L. EP-0711
Schwenck, J. EP-0351, **OP-017**, OP-365
Sciagrà, R. EP-0230, EP-0467, OP-033, OP-321
Scifo, P. EPS-238, OP-875
Sciuto, R. EP-0906, OP-105
Scott, A. EPS-003, OP-277, OP-516, **EPS-119**
Scott, F. OP-516
Scott, N. EP-1111, **EPS-187**, EPS-189
Scribano, G. EP-0461
Scuderi, S. EP-0370
Scuffham, J. OP-705
Seban, R. EP-0297, EP-0217, EP-0251, EP-1067, EPS-231, OP-033, **OP-104**, OP-173
Sebastián Palacid, F. EP-0397, EP-0549, EP-0550, EP-0579 **EP-0612**, **EP-0613**, EP-0833, **OP-057**, OP-854
Sebastián-Segura, M. EP-0836
Sebastian Valles, F. OP-485
Seddon, J. A. OP-849
Sedelaar, J. OP-598
Seefried, L. OP-376
Seemann, J. OP-817
Segbers, M. EP-0707, EP-1010, OP-852
Segers, C. EPS-020, OP-656
Sehati, M. EPS-220
Seidel, L. EPS-084
Seifarth, S. OP-458
Seifert, K. E. OP-327
Seifert, R. EP-0161, EP-0409, EP-0933, EP-1148, EPS-240, OP-461
Seimbille, Y. **EP-0087**, EP-0125, EPS-017, OP-153, OP-221
Seitz, L. OP-552
Seitz, P. OP-552
Seker, K. **EP-0224**, EP-0291
Selçukbiricik, F. OP-386
Selivanova, S. V. OP-659
Selva, D. EP-0551
Selvarajoo, T. EP-0416
Selvaraju, R. EP-0068
Selvarasa, V. EP-0297
Semwal, A. EP-0159
Semwal, V. EP-0543
Sen, F. EP-0466, **OP-222**
Sen, I. B. EP-0529, OP-482, OP-861, OP-878
Sendur, M. A. N. OP-856
Senica, K. EP-0913
Senmevsim, O. **OP-040**
Sennung, D. EP-1143, EPS-192
Seo, D. **EP-0659**, EP-0664, OP-532
Seo, S. EP-0659, EP-0664, **OP-532**
Sepehrizadeh, T. EP-0978
Seppänen, M. EP-0904, EP-0946, EPS-127, OP-328
Sequeira, J. A. EP-1247
Serani, F. **EPS-205**, EPS-247, **OP-036**
Serdengeçti, M. EP-0605
Serdons, K. EP-0391, EP-1175
Seregni, E. OP-384
Sereno, J. EPS-061
Seret, A. **EP-0944**, **EP-0952**
Serfling, S. **EP-0195**, EP-0794
Sergeant, C. OP-542
Sergieva, S. EP-0213, EP-1333
Serin, G. EP-0924, EPS-077
Seront, E. EPS-266
Serra, C. EP-1450
Serra, C. EP-1421
Serrallonga, B. EP-0324, EP-0490, EP-0551, **EP-0762**, OP-442, OP-553
Serrano, L. OP-700
Serrano-Alcalá, E. EP-0850
Sertsios, A. EP-0382, EP-0384
Servetto, A. EP-0233
Servian-Vives, P. EP-0392, EP-0437
Sesink, A. EP-0077
Sestini, S. OP-437
Seth, A. EP-0371, EP-0372, EP-0373, EP-0764, OP-353
Seth, M. EP-1221
Seth, R. EPS-209, EPS-217
Sethi, P. OP-872
Settelmeier, S. OP-239
Setterberg, V. OP-319
Setti, L. EP-0206, EP-0406
Sevaslidou, I. EP-0569, **EP-1379**, EP-1430
Severi, F. OP-384
Sevinç, M. M. EP-0272
Seymen, H. OP-386
Seyyedi, N. EP-0972
Sezak, M. EP-0343
Sezgin, C. **EP-0131**
Sfar, R. EP-0447, EP-1264, EP-1390
Sfiligoj Planjsek, D. **EP-0913**
Sgro, C. M. P. EP-0375, EP-0398, EP-0444, EP-1238, EP-1372 EPS-247, OP-246, OP-248, OP-330, **OP-118**, **OP-716**
Shafiee Dastgerdi, S. **EP-1151**, EP-1152
Shafiei, s. EP-1339
Shagera, Q. OP-317
Shagera, Q. **EPS-266**
Shah, J. OP-284, EP-0963
Shah, N. EPS-083, EP-0929, EP-0943
Shah, S. EP-0266, EP-0885
Shah, V. EP-1014, EP-1020
Shaharuddin, S. EP-0203
Shahbazi Feshtali, S. EP-0334
Shahrbabaki Mofrad, M. EP-1003, EP-1137
Shaikh, N. EP-0283, OP-748
Shakirova, A. EP-0432, EP-0932, EP-0955
Shakti, S. EP-0153, EP-1161, OP-177
Shalgunov, V. EPS-146
Shalimar, D. OP-861
Shamim, S. EP-0880, EP-0177, EPS-277, **EP-0265**, EP-0300, EP-0301, **EP-0558**, EP-0839, EP-0882, **EPS-270**, OP-861
Shan, B. EPS-233, OP-441
Shan, F. OP-844
Shang, J. EP-1037
Shanker, A. EP-1013, EP-1455
Shanker, K. EP-0543, EP-1252, EP-1253
Shao, H. EP-0682, EP-0697, OP-236, OP-304
Shao, X. EPS-170, **OP-788**, EPS-033
Shao, Y. EP-0386
Shapiro, S. EPS-139
Sharbatdar, M. EP-1003
Shariat, S. EP-1241, EP-0528, OP-325, OP-820
Sharifi, H. EP-1151, **EP-1152**
Sharifian, F. EP-0326
Sharma, A. OP-072, EP-0159

Sharma, M. C. EP-0559
Sharma, P. D. EP-1084
Sharma, S. OP-323, EP-0371, EP-0372, **EP-0373**, EP-0474, EP-0764, **EP-0853**, EP-0859, EP-0919
Sharmin, S. EP-1204, EP-1208
Shcherbina, O. EP-0751, EPS-281, EPS-282, EPS-283
She, Y. OP-174
Sheikh, G. EP-0154, EP-0309, EP-0793, EP-1118, EPS-248, OP-329, EP-1150, OP-368
Sheikhzadeh, P. **EP-0922**, EP-0967, **EP-0972**, EP-1003, **EP-1137**, EP-1138, **EPS-289**, EPS-304
Shekhar Singh, S. **EP-0347**, **EP-0527**, **EP-0986**
Shen, E. L. EP-0342
Shen, K. EP-0211
Shen, R. OP-839
Shen, X. **OP-174**, EP-1150, **EP-0610**
Shen, Y. EP-0119
Shenas, F. EP-1026
Shenker, N. G. OP-697
Shera, R. EP-1248, EP-1257
Shessel, A. EP-1100
Shestopalov, G. EP-0481, EP-0482
Shi, H. EP-1437
Shi, J. EPS-008
Shi, K. EP-0030, EP-0031, EP-0161, EP-0658, EP-0933, EP-0988, EP-1015, EP-1061, EP-1080, EP-1090, EP-1095, EP-1148, EPS-042, EPS-106, EPS-233, EPS-240, OP-276, OP-281, OP-461, OP-498, OP-502, OP-709, OP-717, OP-723, OP-770, OP-788, OP-889
Shi, S. EP-1049
Shi, Y. OP-594, OP-671
Shi, Z. EPS-094, OP-730, OP-731
Shibutani, T. EP-0585
Shiga, M. EP-0927, EP-0954
Shih, C.-H. EP-1291
Shiiba, T. **EP-1448**
Shim, H. **EP-0868**
Shimada, N. EP-0927
Shimamoto, H. EPS-056
Shimizu, H. OP-208
Shimizu, T. EP-0585
Shimizu, Y. EP-0214, EP-0395, EP-0540
Shimomura, I. OP-387
Shimoyama, A. EPS-056
Shin, B. EPS-179
Shinada, M. **EP-0139**
Shinya, A. EP-0459
Shinya, T. **EP-0459**
Shioji, M. EPS-255
Shirakami, Y. EP-1458, OP-387
Shirasaki, K. OP-585
Shirazi, F. OP-162, OP-164
Shirdel, F. EPS-220
Shiri, I. EPS-220
Shirzadi Golzar, A. EP-0937
Shivani, S. **EPS-032**
Shiyam Sundar, L. EP-0251, EP-0230, EP-1093, OP-548
Shnayien, S. EP-1092
Shooshtari, T. EP-1002
Shou, H. EPS-144
Shovan, S. R. EP-0071, EP-1134
Shridharan, K. OP-743
Shtangel, A. EPS-087
Shukla, J. EP-0071, EP-0159, EP-1134, EP-1460, OP-743
Shungube, M. EP-0942, OP-825
Shvets, B. EPS-079
Shyli, K. EP-0418, EP-0419, EP-0427, **EP-1421**, **EP-1450**
Sibaud, V. OP-292
Sibiya, S. EP-0942, EP-1116, **EP-1200**, EPS-086, OP-825, OP-349
Siciliano, R. F. EP-0631
Sidandy, A. D. EP-0409
Siegmund, T. EPS-290
Siekkinen, R. **EP-1063**, EPS-234
Siepe, G. OP-293, OP-798
Sigfridsson, J. OP-791
Signori, A. EP-0370
Sihotang, V. **EP-0976**
Siikanen, J. OP-596
Sikdar, S. EP-0746, OP-744
Silex, W. OP-284
Sillanmäki, S. EP-0602
Silva, A. **EP-0814**, EP-0905, EP-1133
Silva, D. **EP-0199**, EP-1205, **EP-1243**, EP-1269, EPS-267, OP-632, OP-742
Silva, J. EPS-236,EP-0765, EP-0897, EP-1256, OP-633, OP-636, OP-061, EP-0171, **EP-0961**
Silva, L. C. EP-0814, EP-0905, EP-1083, EP-1133, OP-158
Silva, M. D. S. EP-0505
Silva, M. EP-1342, EP-1324
Silva, N. EP-1203, OP-119
Silva, O. **EP-0717**, EP-1247
Silva, P. EP-0199
Silva, R. EP-1318, EP-1320
Silva Oliveira, A. **EP-1001**
Silva-Ribeiro, F. **OP-035**, **OP-634**
Silva Rodriguez, J. EP-0637, EP-0999, OP-440
Silveira, M. B. **EP-0171**, **EP-1201**
Silveira, N. **EP-0223**, EP-0189
Simanek, M. EP-0892
Simankova, A. EP-0892
Simankova, D. **EP-0892**
Simard, C. OP-838
Sime Loayza, I. EP-1227, EP-1251
Simeone, R. OP-036
Simeonov, F. **EPS-296**
Simmet, M. EP-0691
Simões, M. EP-1247
Simon, S. EP-0615
Simonet, J. OP-211, OP-351
Simonetti, A. **EP-1399**
Simonic, B. EP-0913
Simonnet, J. A. OP-173
Simo Perdigo, M. **EP-0388**
Sin, C. EP-0844, OP-856, OP-859, EP-0840, OP-857
Singareddy, C. **OP-799**
Singer, S. OP-017, OP-365
Singh, A. EP-0527, OP-872, EP-0285, EP-0880, OP-670, **OP-817**, EP-0510
Singh, B. OP-072
Singh, D. **EP-1246**
Singh, G. EP-1134
Singh, H. EP-0741, EP-0191, OP-072, OP-797, OP-848, EP-0592, EP-0741, OP-683
Singh, N. EP-0191
Singh, P. **EP-0191**, OP-797
Singh, S. EP-0584, EPS-018, EP-1259, EP-1278, EPS-277, EP-0750, EP-1210, EP-0985, EP-0267, **EPS-039**
Singh, V. EP-1278, EPS-277, EP-0750, EP-1207, EP-1210, EP-1235, EP-1236, EPS-206
Singhal, A. EP-0177, EP-0882
Singhal, N. EP-0785
Singhal, T. EP-0191
Singla, A. EP-0592
Sinha, S. EP-0877
Sinitsyn, V. EP-0286, OP-472, OP-473
Siokas, V. EP-0675
Sipka, G. **EP-0180**
Sirrenberg, C. OP-516
Sisk, A. OP-714
Sisko Markos, I. **EP-0264**, **EP-1222**
Sitarica, P. EP-0072
Sitek, A. **EP-0320**
Siveke, J. EPS-190
Sivonen, V. OP-328
Six, M. EP-1181
Sjögreen Gleisner, K. EP-1106, EP-1405
Sjöholm, T. OP-095
Skaddan, M. B. OP-458
Skalič, K. EP-0519
Skamagkas, I. EP-0244
Skauge, S. TEPS-010
Skeidsvoll Solheim, T. EP-0883
Skerl, T. EP-0196
Skingley, L. EP-1161, OP-676
Skjødt, M. K. EP-0732
Skjøth-Rasmussen, J. EPS-120
Skopljak-Beganović, A. EP-1436, OP-318
Skoularigis, J. EP-0591
Skoura, E. EP-0875
Skriabina, A. **OP-373**
Slade, D. EP-0822
Slama, H. EP-0663
Slart, R. H. J. A. OP-053, EP-1395, EPS-107, OP-840 EPS-082, OP-289, OP-551, OP-867, OP-885

Slodnjak, I. EP-0712, EP-0913, EP-1440
Slomka, P. J. OP-679
Sluis, J. v. EP-0842
Smerling, C. OP-817
Smit, F. OP-713
Smith, A. L. EP-0996
Smith, C. **EPS-081**, **OP-774**
Smith, F. EP-0757
Smith, K. R. EPS-018
Smith, L. EP-0942, EP-1116, EPS-086, OP-825
Smith, N. OP-416
Smith-Tsibolane, D. EPS-203
Smits, K. **EPS-180**, **OP-589**, OP-590
Smits, M. EP-0907, EP-0183
Smorgon, A. EP-0616
Smout, A. **OP-705**
Snarskis, K. EP-0361, EP-0365
Snijders, T. J. OP-863
So, M. EP-0659, **EP-0664**, OP-532
Soares, A. EP-0199, OP-604
Soares Jr, J. EP-0631
Sobic Saranovic, D. EP-0898, EP-1240, OP-479
Sobral, C. **TEPS-001**
Sobral Torres, L. **EP-0599**, **EP-0716**
Socan, A. EP-0895
Soda, P. EP-0254
Sodemann, E. EPS-024
Soderholm, A. **EP-1161**, OP-676
Soeiro, P. EP-0599, EP-0716, EP-0740, EP-1382
Soeterik, T. OP-329, EP-1051
Sofia, L. EP-0206, EP-0377, EP-0681, EP-0683, OP-105, **OP-725**, OP-776
Sofianidis, I. EP-0675
Sohlberg, A. EP-0962
Sökmensüer, C. EP-0287
Solà, M. EP-0845
Solanich, X. OP-865, EP-0508
Solanki, R. **EP-1218**, **EPS-110**
Solano Caballero, F. EP-0816, EP-0909
Solà Suárez, M. EPS-026
Soldevilla Gallardo, I. EP-0086
Soleimani Bami, H. OP-109
Solfaroli, E. OP-708, EP-1109
Solheim, O. EP-0883
Soliman, A. EP-1013, **EP-1018**, **EP-1020**
Solli, P. EP-0227, OP-168
Sollini, M. EP-0254, EP-0534, EP-1401, OP-298, OP-326
Sollmann, N. EPS-135
Solomon, S. EP-1329, OP-542
Solomons, R. S. OP-849
Solomyany, V. EP-0253, OP-472, OP-473
Solovyev, D. EP-0041
Soltani, E. EP-1348, EP-0570, EP-1349
Soltani, N. EP-0128, EPS-136
Soltani, S. EP-0348, EP-1002, OP-242
Soltanolkotabi, M. **EPS-274**
Soman, P. OP-679
Somasiri, K. K. I. N. EP-1438
Somme, F. OP-602
Sommes, F. EP-0800
Somsen, J. EPS-107, OP-051
Son, H. EPS-214
Sone, M. EPS-141
Soneja, M. EP-0559, OP-872
Song, C. EP-1441, EP-1446
Song, H. **EPS-102**, OP-841, EP-0112, EP-0655, EP-0672 EP-0980, OP-539
Song, J. **EP-0630**, OP-732, OP-843, EPS-243, EP-0587, **EP-0454**
Song, L. EP-0053, EP-0054, EPS-006, EPS-014, OP-210, **EP-0166**
Song, S. EP-0098, EP-0205, EPS-047, EPS-051, OP-024, OP-176, OP-694, EPS-100
Song, W. **OP-382**
Song, X. OP-837, EP-0680, EP-0979
Song, Y. OP-018, EP-0795, EP-1021, **EP-0492**
Sonmezoglu, K. EPS-256, EP-0424, EP-0857
Sonneveld, P. EP-1055, OP-225
Sonni, I. EP-0208, **EP-0376**, **OP-714**
Sonoda, M. OP-301
Sood, A. EPS-110, OP-683
Sopeña Sutil, R. EP-0387
Sorbello, S. OP-105
Sordi, B. EP-0467
Sörensen, J. EP-0289, EPS-128, OP-687, OP-791
Sørensen, M. EP-0709
Sorg, C. OP-721
Soria, M. EP-0384, EP-0412
Soriani, A. EP-0906, EP-1109
Sorin, M. **OP-280**
Sotgiu, A. EP-1421, EP-1450
Soto Muñoz, P. EP-0849
Sousa, A. C. J. OP-722
Sousa, E. EP-0521
Sousa, H. EP-1306, EP-0189
Sousa, J. EP-1306
Sousa, V. OP-035, OP-634, EP-0118
Souto, C. EPS-300
Souza, C. A. EP-0223, EP-0505, EP-0536
Souza, F. C. EP-0505
Souza, G. S. D. EPS-107
Souza, R. F. EP-0631
Sowa-Staszczak, A. EP-0440, EP-0789, EP-0919
Soydal, C. EP-0333, **EP-0354**, EP-0441, **EP-0806**, **EP-0834**
Soydas Turan, B. **OP-846**
Soydemir, E. EP-1127, EP-1141
Soza-Ried, C. OP-471
S P, S. EP-0258, OP-550
Spadafora, M. EP-0639
Spagnuolo, L. EP-1166
Spangler, D. OP-523
Spangler-Bickell, M. OP-285, OP-283
Spanu, A. EP-0446
Sparrelid, E. EP-0260, EP-0275
Spataro, A. EP-0269, EP-0418, EP-0419, EP-0427, EP-0470, EP-0894, **EPS-228**, OP-556
Spear, R. OP-787
Specht, L. EP-0219
Speicher, T. **EP-0780**, **OP-435**
Spektor, A. M. EP-0532, **EPS-271**, OP-371
Spellerberg, S. EP-0943
Speltri, G. OP-584
Spencer, B. EP-0466, EP-1064, EPS-030, OP-222, EPS-032
Spencer, P. EP-0092
Spielvogel, C. EP-1040, OP-354, EP-0609, OP-325, **EP-1011**, **EP-1071**, **OP-468**, OP-790, EP-0252
Spigoni, V. OP-549
Spilioti, M. EP-1341
Spiliotopoulou, M. EP-1074
Spinosa, S. EP-1398, OP-891
Spiridon, P. **EP-1316**
Spirov, G. EP-1094, EP-1358
Spitzweg, C. EP-0793, EPS-248
Spohr, S. M. OP-458
Sponholtz, S. E. OP-038
Spoormans, K. EPS-020
Spottiswoode, B. EP-0326, EP-0959, EP-1013, EP-1014, EP-1018, EP-1020, EP-1455, OP-234
Spottke, A. OP-303
Sprajcer, U. EP-1440
Sprauel, T. **OP-499**
Spreckelmeyer, S. OP-345
Sproule, V. OP-817
Spyridonidis, T. EP-1074
Squame, F. EP-0639
Srinivasan, P. EPS-208
Srirajaskanthan, R. OP-429
Sriramachandran, K. OP-823
Staanum, P. F. EP-0807
Stabile, A. OP-875
Stadlbauer, S. OP-652
Staeb, D. EP-0995
Staelens, L. OP-710
Staelens, S. EP-0001
Staff, R. EPS-028
Stagaard, R. OP-025
Ståhl, S. OP-766
Stähli, P. OP-552
Stanciu, S. EP-1332
Stancu, A. OP-323
Stangl, S. EPS-146
Stankovic, D. EP-0072, EP-1183
Starcevic, I. EP-0873
Stark, T. **OP-886**
Starostka, T. OP-593
Stasiuk, G. EP-0008, EP-0084

Stasolla, M. EP-0502, EP-0503, **EP-0504**, **EP-0514**, EP-1064, OP-224
Statescu, A. M. EP-1309
Stathaki, M. EP-1299
Stathopoulos, K. OP-169
Staudacher, A. H. EP-0130
Stawski, K. EP-0360
Steczek, L. OP-679
Steding-Ehrenborg, K. EP-0582
Steemers-de Boer, M. M. OP-289
Steenhout, C. **EPS-084**
Steenken, D. **EP-0690**
Stefan, P. EP-0866
Stefaneli, P. EP-0324, EP-0551, EP-0762, OP-553
Stefaneli Mormandi, P. **EP-0490**, **OP-442**
Stefanescu, C. EP-1303, EP-1309, EP-1317
Steffann, M. EP-1189
Steffens, L. EP-0381
Steger, V. OP-365
Stein, M. A. OP-551
Steinacker, N. EP-0121, EP-0557
Steinbeisser, C. OP-818
Steinberg, M. L. EPS-192
Steinmetz, A. P. OP-262
Stenberg, V. EP-0016
Stenman, A. EP-0314
Stenman, J. EP-0064
Stenvall, A. EP-0733, **EP-0917**, EPS-085, OP-099, TEPS-004
Stephan, S. EPS-156
Stephens, A. W. EP-0691
Stephens, H. EP-0144, **EP-0151**
Stepien, E. **EP-0919**
Sterrantino, A. EP-0370
Stettler, M. OP-525
Stevens, D. EP-1111, EPS-187, EPS-189
Stien, G. **EP-0179**, OP-611
Stockler, M. OP-323
Stoddard, G. J. EPS-274
Stodilka, R. EP-1100
Stoecklein, S. EP-0691
Stoecklein, V. EP-0886
Stoeva, T. EP-1292, EP-1293, EP-1294, **EP-1330**, EP-1331, EP-1359, EP-1384
Stoilovska Rizova, B. EP-0448, EP-0735, EP-0736
Stojanoski, S. EP-0735, EP-0736, EP-0448
Stojiljkovic, M. EP-1240
Stojkovska, N. EP-0735
Stokke, C. EP-1044, EP-1078, EP-1102, EP-1113, OP-424, OP-427
Stolniceanu, C. R. EP-1309
Stolte, S. **EP-0573**
Stormezand, G. N. OP-053, EPS-082, OP-289
Storms, W. **EP-1175**
Storz, E. OP-628
Strabelli, T. M. V. EP-0631
Stracuzzi, F. EP-0708
Strašek, K. EP-0519
Strandberg, S. EP-1070
Stranz, N. EP-0216
Straub, M. EP-1404
Streefkerk, E. C. **EP-1432**, OP-884
Strigari, L. EP-0145, EP-1112, EPS-247, EPS-288, OP-028
Strijbos, M. OP-710
Strobel, I. **EPS-294**, EPS-295, OP-426
Strobel, J. **EPS-135**
Strobel, K. EP-0423
Stroglio, P. EP-0597
Strojan, P. EP-0196, EP-0895
Strok, A. EP-0913, EP-0835
Strosberg, J. OP-429
Strouhal, P. **OP-802**, EP-1091
Struelens, L. EPS-020, OP-091
Strunz, F. EP-0933
Stucchi, S. EP-1176
Studen, A. EP-0196, EP-0519
Stueckl, J. EP-0037
Stüfchen, I. EP-0711
Stürzl, R. OP-609
Stuschke, M. OP-329
Stuurman, D. EP-0087, EP-0125, EPS-017, OP-153
Su, J. EP-0518, OP-296
Su, K. H. EP-1030
Su, M. EP-1427, EP-0357, EP-0761
Su, R. EP-1038
Su, S. EP-0518
Su, X. EP-0407, EP-1441, EP-1446, OP-608, EP-0578, EP-0163, EPS-173, EPS-268, OP-692
Su, Y. EP-0650
Suarez Mansilla, P. EP-0549
Súarez-Novo, J. EP-0437
Suárez-Piñera, M. EP-0653, EP-0731, EPS-031, **EPS-121**, OP-233
Suazo Montero, Á. EP-0579, EP-0612, EP-0613, OP-057, EP-0549, EP-0550, EP-0833, **OP-854**
Subbotnitskiy, D. EP-1396
Subramani, B. EP-0036
Subramaniam, R. M. EP-0380
Subramaniam, S. OP-323
Subramanian, K. **EP-0330**
Subramanian, S. OP-861
Subramanyam, A. OP-848
Subramanyam, P. EP-0299
Subreville, C. OP-536
Suda, A. EP-0676
Sued, A. S. TEPS-019
Sugiyama, N. OP-283
Suh, H. EP-0795
Suils-Ramón, J. EP-0836, EPS-202
Sukar, S. EP-0416
Sukrithan, V. OP-074
Sulaiman, N. OP-243
Sulewska, M. **EP-0121**, EP-0557
Sulima, I. EP-0896, EPS-257
Sullivan, E. **EP-1093**
Sulsenti, R. EP-0017
Sulski, C. EP-1009
Sultana, N. OP-302, OP-307
Summers, C. OP-697
Sumner, R. EP-1169, EP-1171
Sun, B. EPS-185, OP-180, **OP-181**
Sun, C. EP-0248
Sun, L. EPS-063, EP-1038, EP-1049, **EP-0769**
Sun, Q. EP-1096
Sun, R. **EPS-108**
Sun, S. OP-155, EP-0587, OP-155
Sun, T. EP-0239, **EP-0649**, **EP-0975**, **OP-355**, **OP-777**, **OP-792**
Sun, W. OP-367
Sun, X. EP-0317, EP-1125, **EP-1125**, EP-0053, EP-0054, EPS-006, EPS-014, OP-210, EPS-033, EP-1024
Sun, Y. EP-0186, EP-0187, EPS-113
Sundar, L. K. S. EP-1079, EP-1089, EP-1097, OP-033
Sundaram, P. EP-0299
Sunderland, M. EP-0381
Sundin, A. OP-369
Sundin, T. EP-0289
Sundlov, A. OP-708
Sundriyal, D. EP-0877
Sundset, R. EP-1060
Sundvall, M. OP-328
Sunnemark, D. OP-458
Sunzini, F. OP-697
Suoraniemi, H. **EP-0904**, EPS-127
Surlan Popovic, K. EP-0713
Susin, D. EP-0173
Sutcuoglu, O. EP-0222, EP-0273
Sutton, A. EPS-062
Suzuki, C. EP-0188
Suzuki, H. EP-0139
Suzuki, K. OP-208
Svajger, U. EP-0895
Svanström, P. **OP-791**
Svedberg, H. OP-519
Svendsen, N. **OP-319**
Svenningsson, P. OP-459
Svensson, J. EPS-180, OP-589
Swamy M S, S. EP-0267
Swartling, F. J. EP-0064
Sweeney, C. EP-1161
Sweeney, R. OP-043
Swenson, R. E. OP-088
Swiatkowska-Stodulska, R. EP-0782
Sydes, A. OP-177
Syed, A. OP-377
Sykes, J. EP-1111
Sylvest, C. EP-0773
Synnes Lindseth, S. **OP-427**
Syrenicz, A. EP-0782

Székely, A. **EP-0582**
Szentesi, M. **OP-375**
Szigeti, F. EP-0362
Szigeti, K. EP-0247
Szikra, D. **EPS-149**
Szoboszlai, Z. OP-501
Szolikova, M. EP-0180
Szücs, Z. EPS-149
Szumowski, P. EP-0896, EPS-257
Szuszik, P. EP-0938
Szymanski, W. EP-0011, EPS-195, OP-515
Taş, H. EP-0015, **EP-0138**
Taalabi, A. EP-1290, EP-1301, EP-1302, EP-1325
Tabacchi, E. EP-0145, EP-0310, EP-0311, EP-0444, EPS-247, OP-118, OP-246, OP-248, OP-798
Tabotta, F. EP-0226
Tabuenca, M. EP-0792, OP-430, EP-0387, EP-0887
Tabury, K. OP-150, OP-818
Tachibana, T. EP-0139
Taciuc, A. I. EP-1335
Taciuc, I. EP-1220
Tada, H. OP-729
Tag, N. EP-0380
Tagawa, S. OP-674
Tagliabue, L. OP-669
Tagliatori, M. EP-1368
Tagliatori Nogueira, M. EP-0819, **EP-1286**, EP-1322, EP-1337, EPS-263, EPS-273
Tagliavini, F. OP-669
Tagnin, L. **EP-0691**, EP-0698, OP-237, OP-773
Tago, T. EP-0028
Tagore, S. OP-316
Taheri, F. EP-1357, EP-1377, EP-1378
Tahirovic, S. EP-0018, EP-0019
Tahmazov, A. **OP-235**
Tahmi, D. EP-0756, **EP-1217**, EPS-212
Taibi, A. EPS-212
Taieb, D. **OP-602**
Taillandier, L. EP-0179, OP-614
Tajika, Y. EP-0954
Takács, E. OP-375
Takada, Y. EP-0676, OP-301, OP-719
Takahashi, M. E. EP-0262
Takahashi, M. EP-0505, EP-0536, EP-0223, EP-0139
Takahashi, T. EP-0676, EP-1059, OP-301, OP-719
Takahashi, Y. TEPS-008
Takahiro, H. EP-0195
Takayama, Y. OP-301
Takeda, S. EP-1079, OP-548
Takemoto, S. EP-0991
Takenaka, J. **EP-0303**, EP-0796, EP-0860, EP-0874, EPS-250
Takeuchi, S. EP-0303, EP-0796, EP-0796
Taki, J. EP-1079, OP-548
Takizawa, K. EP-1435
Talarico, M. EP-0502, EP-0503, EP-0514, EP-1064
Talavera Rubio, M. EP-0460, EP-0374, EP-0452, EP-0472
Talbi, A. EPS-212
Talebian, H. **EP-0029**
Talini, V. EP-0496
Tallat-Szczotka, K. **EP-0777**, **EPS-291**
Talwar, V. EP-0267
Tamam, M. Ö. EP-0902
Tamayo Alonso, M. OP-229, EP-0710, OP-481
Tamayo Alonso, P. EP-0364, EP-0378
Tamayo Carabaño, D. OP-485
Tamayo Ossa, D. EP-0758, EP-0307, EP-0494
Tamborino, G. OP-221, OP-425
Tamburini, A. EPS-272
Tamura, S. EP-0676
Tan, H. EP-0500
Tan, J. EP-0079, EP-0865, EP-0899, EP-0861
Tan, K. V. EPS-008
Tan, P. W. **OP-457**
Tan, Z. EPS-163
Tanaka, H. EP-0768
Tandon, S. EP-0347, EP-0527
Tandon, V. EP-0177, EP-0882
Tang, A. **EP-1024**
Tang, C. OP-031, OP-541, EP-1024, EPS-175, OP-486, **OP-530**
Tang, H. EP-0386
Tang, L. EP-0645
Tang, Y. EP-0215, EP-0430, EP-0658, EP-1080, EP-1214, EPS-042, EPS-160, EPS-165, **OP-709**, OP-712, **OP-717**, **OP-723**, OP-740
Tangadanchu, V. EPS-138
Tani, H. EP-0676, OP-719
Tani, K. EP-1435
Tank, J. EP-0696
Tankyevych, O. OP-356
Tantot, F. OP-599
Tanzey, S. EP-1169, EP-1171
Tao, J. OP-455, EP-0915, EP-0923
Taoussi, L. EP-1290, EP-1301, EP-1302, EP-1325
Tapias, C. A. OP-865
Tapias-Mesa, A. EP-0494, EPS-031
Taraji, L. OP-111, OP-169, OP-470, OP-537
Taralli, S. EP-0206
Tarasoutchi, F. EP-0631
Tardin-Cardoso, A. L. EP-0552
Tari, P. EP-1008
Tarullo, G. EP-0779
Tasevski, S. EP-1094, EP-1358
Tashireva, L. OP-070
Taskaev, I. EPS-112
Tassinari, R. OP-584
Tassorelli, C. OP-047
Tatci, E. OP-497, EP-1007, EP-0232, EP-1008, EP-1216, EP-1307
Tate, A. OP-697
Tauber, R. EP-1047
Tavakoli, A. EP-0128
Tavakoli, Y. H. EP-0128
Tavera, L. EPS-062
Tavitian, B. EP-0021
Taylor, J. **OP-165**
Taywade, S. EP-0606
Tchouen, N. EP-1394
Tecame, M. EP-0632
Tegelaar Kuiper, A. G. EP-0349
Tegnebratt, T. EPS-154
Tehlan, K. OP-358, **OP-770**
Teimoorisichani, M. **EP-0970**
Teipel, S. OP-303
Teixeira, J. EP-0199, EPS-267
Teixeira, R. OP-158
Teixeira, T. B. EP-0631
Tejería, M. EP-0134, EP-0140
Tekgul, Z. **EPS-115**
Tekin, M. G. EP-0480
Teles, L. **EP-0876**, EP-0879, EPS-126, **OP-260**
Telli, T. **OP-538**
Tellmann, L. EP-0929, EP-0943, EPS-083, OP-284
Tempier, M. EP-1082, EP-1182
Temsamani, J. EP-0088
Tenace, N. EP-0534
Ten Duis, K. EPS-276
Teng, J. **TEPS-015**
Teng, P. OP-418
Teng, Y. OP-030
Tenhunen, M. EP-0934, EP-0941, OP-100
Terauchi, T. EP-0927
Ter-Pogosyan, A. OP-714
Terreno, E. EP-0141
Terro, A. EP-1114, **OP-533**
Terroir, M. OP-292
Terrone, C. EP-0370
Terry, S. Y. A. EP-0008, EP-0084
Terwinghe, C. EP-0935, EP-1188
Tesic, N. EP-0895
Tessoulin, B. OP-227
Testanera, G. EP-0916, OP-619, **OP-625**
Testard, P. EPS-131
Testart, N. EP-1407, **EP-0184**
Teulé Vega, A. OP-429
Teysir, J. EP-0201
Teyssonneau, D. OP-536
Thakral, P. EP-0529, OP-482, OP-861, OP-878
Thakrani, D. EP-0529, OP-482, OP-878
Thakur, S. EP-0584
Thaler, F. EP-0698
Thalhammer, M. OP-721
Tham, W. OP-031, OP-541
Thang, S. OP-541
Theander, T. G. OP-760
Theegarten, D. OP-172

Theisen, A. L. EP-1077, EPS-179, EPS-180, EPS-184, OP-589, **OP-590**
Thelander, U. OP-728
Theodoropoulou, M. EP-0711
Theodorou, E. EP-0591
Theurer, S. OP-385
Theus, L. EPS-162
Thevis, J. EP-0019, EP-0168
Thickens, A. EPS-001
Thieblemont, C. OP-227
Thielemans, K. EP-0996, EPS-093
Thientunyakit, T. **OP-302**, OP-307
Thiveos, G. EP-0875
Thøgersen, K. **OP-686**
Thomas, B. EP-0557
Thomas, E. EPS-119
Thomas, M. A. EP-1029
Thomas, Q. OP-173
Thomas, W. OP-025
Thompson, M. O. EP-0918, EP-0920
Thompson, N. EP-1020
Thomson, B. EP-0940
Thomson, W. **EPS-292**, **EPS-293**
Thon, N. OP-609, OP-610
Thorlacius-Ussing, O. EP-0773
Thorpe, M. P. EP-0807
Thorsteinsdottir, J. EP-0711
Thureau, S. OP-524
Tian, C. OP-205
Tian, F. EP-0657, **EP-0660**
Tian, J. EP-0280, OP-463
Tian, R. EP-0106, EP-0852, EP-0864, EPS-049, EPS-168, OP-030, OP-278
Tian, T. EPS-045
Tian, Y. OP-845, EP-0187
Tietgen, N. EP-0624
Tietze, K. EP-0082
Tieu, W. EP-0153, OP-177, OP-676
Tilak, A. EP-0510, EP-0537
Timmer-Bonte, A. EP-0535
Timon, G. EP-0377
Tineo, R. EP-1267, **EP-1418**
Tineo, R. N. OP-119
Tingen, H. OP-053
Tinjak, E. OP-318
Tirotta, D. EP-0255
Tissier, M. EP-0828, OP-601
Tissot, H. EP-0217, EP-0297, OP-173
Titu, I. EP-1317
Tjwa, E. T. T. J. OP-855
Tkachenko, M. EP-0751, EPS-281, EPS-282, EPS-283
Tobar, N. EP-0262, EP-1306, EP-1324, EP-1342
Todde, S. EP-1176
Todorov, B. EP-0114
Todorov, T. OP-220
Todorova-Stefanovski, D. **EP-1358**
Togao, O. EP-0676
Togni, C. F. EP-0631
Tokac, R. EP-0344, EP-0246, EP-0343, EP-0428, EP-0516
Tokac, R. **EP-0366**
Toklu, T. EPS-191
Tolboom, N. EP-0183, EPS-036, OP-260, OP-863
Tolmachev, V. EP-0074, **EP-0089**, EPS-004, EPS-050, OP-070, OP-087, **OP-089**, OP-320, OP-659, OP-764, OP-766
Tolvanen, T. OP-595
Tomash, H. OP-074
Tombal, B. EPS-266, OP-604
Tomelleri, A. EP-1043
Tomiyama, N. OP-387
Tomiyama, S. OP-719
Tompuri, T. EP-0602
Tøndel, H. EP-0883
Tondo, A. EPS-272
Tong, A. EP-0847, OP-541, EP-0327
Tong, T. EPS-201
Tong, X. **OP-300**
Tonietto, M. EPS-131
Tonnelet, D. **EP-0800**, EP-1017, EP-1114, EP-1181, EP-1266, OP-533
Too, N. **EP-0847**
Toosi, A. OP-034
Topcuoglu, M. OP-856
Toplutas, K. **EP-0511**, EPS-204, OP-859
Topuz, Ö. V. EP-0633
Toral-Sepúlveda, D. EPS-022
Torchio, J. OP-343
Tormo Ratera, M. EP-0498, **EPS-040**, EP-0307, EP-0494, EP-0618, EP-1366
Törnblom, A. **OP-596**
Toro-Gonzalez, M. EPS-138
Toroi, P. EP-0941, EP-1405
Torralbo Caballero, G. OP-485
Torres, L. EP-1382
Torres Consiglieri, A. EP-0565, EP-0821
Torres Espallardo, I. TEPS-021
Torri, G. B. EPS-251
Torricelli, C. EP-1203, EP-1306, EP-1324, **EP-1342**
Tosato, M. EP-0091
Toschi, N. EP-1052, OP-669
Tosoni, D. OP-706
Tosunoglu, Z. **EP-0295**, EP-0272, EP-0723
Tóth, M. EP-0113
Toucheboeuf, J. EPS-246
Tournier, N. EP-0093, OP-453
Touzeau, C. EP-1055, OP-225
Toyohara, J. **EP-0028**
Toyonaga, T. OP-457
Toyoshima, A. EPS-056, OP-387
Trabelsi, K. EPS-199
Tragardh, E. EP-0463, **EP-0468**, EPS-085, EPS-213, OP-041
Trame, M. EP-0144, EP-0151
Tran, B. EP-0822
Tran, P. N. OP-586
Tran, T. EP-0064, EP-0260, EP-0275, EPS-154
Tran-Gia, J. EP-0734, EP-0967, EP-0983, EP-1077, EPS-179, EPS-180, EPS-184, OP-096, OP-589, OP-590
Trapp, S. OP-587
Traub-Weidinger, T. OP-468
Trauner, M. OP-747
Trautwein, N. OP-017, **OP-365**
Travascio, L. EP-1287
Trebec Lukman, B. EP-0712, EP-1440
Trebse, R. OP-866
Treglia, G. EP-0425, EP-0889
Trender-Gerhard, I. OP-239
Trepel, M. OP-358
Tretyakova, M. EP-0089
Treuveur, E. EP-0812
Triantafillou, M. EP-1417
Trinh-Duc, A. EPS-090
Tripathi, M. EP-0177, EP-0298, EP-0559, EP-0880, EP-0882, EP-1209, EP-1226, EP-1272, OP-302, OP-307, OP-800, OP-872
Triposkiadis, F. EP-0591
Triviño-Ibáñez, E. EP-0555, EP-0560, EP-0774, EP-0846
Trněný, M. EP-0489
Trofimuk-Muldner, M. EP-0440
Trolliet, C. OP-331
Trommer, J. OP-652
Trošt, M. OP-302, OP-307
Trotta, A. **EPS-054**
Trotta, N. EP-0663, EP-0687
Trovato, M. EP-0708
Truillet, C. EP-0083
Trummer, G. OP-842
Trump, L. EP-1175
Truong, D. **EP-0314**
Trusova, V. **EP-0147**
Tsai, C. EP-1427
Tsai, S. P. J. M. EP-1185
Tsai, S. Y. **EP-0346**
Tsangaridi, A. EPS-254
Tsaur, I. EP-0351
Tseng, C. S. **EP-0281**
Tsironis, G. EP-0242, EP-0243, EP-1031
Tsitoura, F. EP-0242, EP-0243, EP-1031
Tsoi, F. EPS-008
Tsoi, T. **EP-0429**
Tsougos, I. EP-0591, EP-0675, OP-557
Tsoumpas, C. OP-051
Tsouris, Z. EP-0675
Tsuchida, S. **OP-208**
Tsuchimoto, S. OP-719
Tsuchitani, T. EP-0956
Tsuda, K. **EP-0991**
Tsugawa, S. EP-0676, EP-1059

Tsuji, A. B. OP-282
Tsuji, S. OP-309
Tsujimoto, M. EP-0956
Tsukada, H. EP-0635, EPS-095
Tsukamoto, S. **EP-0188**
Tsukerman, L. OP-103
Tsvetanova, A. **TEPS-014**
Tually, P. **EP-0353**, **OP-316**
Tudda, A. EP-0534, OP-298
Tuisku, J. EPS-234
Tukić, B. EP-1436
Tulbah, R. EP-0739, EPS-279
Tulik, M. EP-0702
Tulipan, A. OP-427
Tunali, I. EPS-032
Tunc, A. EP-0924, EPS-077, **EP-0479**, **EP-0516**
Tunca, E. **EP-0343**, **EP-0344**
Tuncay Ibis, E. **EP-0669**
Tuncel, M. EP-0287, EP-0426, EP-1202, OP-804
Tuomola, N. EPS-234, EPS-234
Turan, U. EP-0523, **EPS-260**
Turchetta, L. EP-0826, EP-1258, EP-1376, EP-1383, EP-1412
Turgut, B. EP-0228, EP-0296
Turkan, C. **EP-1202**
Turksoy Karaca, H. EP-1225
Turolla, E. EP-1176
Turoğlu, H. OP-874
Turpin, L. OP-599
Turpin, S. EPS-210
Tuscano, J. EP-0466, OP-222
Tuttle, R. M. EP-0854
Tworowska, I. **EP-0088**, EP-1143
Twumasi-Boateng, K. OP-521, OP-767
Tyagi, A. EP-0559
Tzanakis, N. EP-0242, EP-0243
Tzannou, I. EP-0477
Tzavara, C. EP-0591
Tzortzakakis, A. OP-596
Uçar, M. EP-0197
Uccelli, A. EP-0686, OP-725
Uccelli, L. EP-0893, EP-1254, OP-584
Uchida, H. EP-0676, OP-719
Uçmak, G. EP-0335, EP-0464, EP-0808, EP-0851
Ud-Din, M. OP-766
Udholm, P. **EP-0722**
Udugama, J. M. C. EP-1438
Ueno, N. EP-0956
Ueno, Y. OP-585
Ufton, D. **EP-0331**, **OP-879**
Ugena-García, R. EPS-026
Uhlending, A. EP-1409
Ulén, J. EPS-213
Ulin-Briseño, E. Y. TEPS-021
Ullo, M. EP-1212
Ullrich, M. OP-652
Ulucay, M. **EP-1367**
Ulyatt, M. EP-0572, **EP-0576**
Umar, M. OP-559
Umpierrez, D. EP-0100
Umutlu, L. OP-247, OP-297, OP-538
Undas, K. EP-0440
Ungania, S. EP-0906
Ungureanu, A. EP-1317
Unnikrishnan, S. OP-515
Uno, M. EP-0939
Ünsal, N. **EP-0210**, **EP-0422**
Unterrainer, L. EP-1124, EP-1410, EPS-192, EPS-290, OP-329, OP-822, OP-368
Unterrainer, M. EPS-290, OP-822
Upadhyay, N. OP-303
Uppal, A. EP-0529, OP-482, OP-878
Urbano, N. EP-0461
Ureña Lara, M. EP-1388, EP-1300, EP-1365, EP-1375, EP-1381
Urena Poch, J. **OP-779**
Urganci, N. EP-0355
Uribe, C. EP-0960, EP-1016, EP-1101, OP-102, OP-420, OP-421, OP-428, EPS-181, OP-034, EP-0160
Urrutia, L. EP-0100, EP-0157
Urso, L. **EP-0206**, EP-0461, EP-0893, EP-1254, **OP-105**, OP-324
Urtaev, S. EP-0302
Urup, T. EP-0172
Urwin, E. **EP-1099**
Us, A. **EP-0228**
Uslu, H. OP-715
Uslu, R. L. EP-0424, EP-0901, EP-0857, **EP-0355**, **EP-0368**, EPS-256, OP-531
Uslu Biner, I. EP-0192
Usmani, M. **EP-0181**, **EP-0414**
Ussia, R. OP-028
Ustun, F. EP-0449
Usul Afşar, Ç. EP-0272
Uğur, Ö. EP-0287
Uurasmaa, T.-M. EP-1063
Uusitalo, V. EP-1000, **EP-1228**, **EPS-097**
Uyanık, E. EP-0902, EP-1371
Uygur, E. EP-0131
Uzuegbunam, B. EP-0122, EPS-143, OP-459
Vach, W. OP-106
Vadalà, S. OP-484
Vadrucci, M. EP-0791
Vagalis, E. EP-0608
Vagenas, T. P. EP-0525
Vaggelli, L. OP-324
Vagios, I. EP-0569
Vahedi, M. EP-1377, EP-1378
Vaidyanathan, S. OP-458
Vaillant, M. EP-0553, **EP-0775**
Vaillant López, M. EP-0339, EP-0340, EP-0341, EP-0394, EP-0491, OP-784
Vajauskas, D. EP-0361, EP-0365
Vale, J. EPS-300
Valente, E. OP-669, OP-047
Valente, S. EP-0467
Valind, K. **EPS-213**
Valle, L. F. EPS-192
Vallejos, V. EP-0845, EPS-026, EP-0392
Vallin, I. OP-523
Vallis, K. A. OP-423
Vallone, C. **EP-0268**, EP-0350, EP-0363, **EP-0393**, EP-0779, EP-1062
Valotasiou, V. OP-557
Valotassiou, V. EP-0591, EP-0675
Valtorta, S. EP-0115
Valve-Dietz, A. K. EP-0600
Valverde, R. OP-430
Vamshi Naik, B. **EP-0584**
Vanasschen, C. **EP-1186**
Van Asten, D. **EP-1034**
Van Berckel, B. N. M. EPS-036
Van Bergen, T. D. **EP-1051**
Van Brecht, J. W. J. EP-0948
Van Butsele, K. OP-344
Vanbutsele, T. **EP-0687**
Van Cutsem, E. OP-366
Van Dalen, J. A. EP-0349
Van Dam, E. OP-074
Van Dam, G. M. OP-760
Van Damme, P. OP-530
Van de Burgt, A. EP-0707, **OP-852**
Van de Giessen, E. **OP-607**
Van Delft, F. EP-0334
Van de Merwe, I. EP-1185
Van den Berg, C. A. T. EP-1051
Vandenberghe, R. EP-0643
Van Den Bossche, B. OP-121
Van den Broeck, B. OP-782
Vandenbulcke, M. EP-0643
Van Den Haak, C. **OP-622**
Van den Heuvel, M. M. OP-170
Van den Heuvel, Y. E. EP-1051
Van den Hoven, A. EP-0535, EP-1395
Van den Oever, G. C. **EPS-082**
Van den Wyngaert, T. EP-0102
Van der Gaag, S. OP-598
Van der Geest, N. OP-551
Van der Heide, C. D. EPS-007, EPS-017
Van der Heijden, R. A. OP-870
Van der Hoorn, I. A. E. OP-170
Van der Hulle, T. OP-713
Vanderlinden, B. OP-097, OP-169
Vanderlinden, G. EP-0643
Van der Meer, P. OP-053
Van Der Meulen, N. OP-673, OP-677, EP-1164, EP-1165, EP-1166, OP-662, OP-220, OP-413
Vandermeulen, A. OP-710

Vandermeulen, N. OP-818
Van der Poel, H. G. OP-876
Van der Sar, E. C. A. OP-597
Van der Schaaf, I. C. OP-863
Vandertop, W. P. OP-607
Van der Vegt, M. **OP-885**
Van Der Veken, P. OP-156
Van der Voort-van Zyp, J. R. N. OP-597
Van der Wildt, B. EP-0876
Van der Zant, F. M. OP-890
Van der Zwaag, P. A. OP-053
Van de Vijver, K. OP-782
Van de Voorde, M. EP-0034, EP-1166, OP-657
Van De Wiele, C. EP-0085
Van Dijk, J. D. EP-0349
Van Dijk, N. C. **OP-760**
Vandoorne, K. **EP-0021**
Van Duuren, K. OP-713
Van Eetveldt, A. **EP-0001**
Van Eimeren, T. OP-048
Van Epern, L. EPS-138
Van Erp Zeilstra, A. I. OP-885
Van Essen, M. EPS-180, OP-440, OP-589
Van Gemert, W. OP-598
Van Genugten, E. **OP-170**, OP-796
Van Golen, L. W. EP-0848
Vangu, M. EP-0012
Van Haverbeke, C. OP-121
Van Herpe, F. OP-366
Van Herpen, C. M. L. OP-796
Van Hoecke, S. OP-782
Vanhove, C. OP-522, OP-782
Van Kruchten, M. EP-0535
Van Laere, C. OP-350, **OP-656**
Van Laere, K. EP-0391, EP-0643, EP-0879, EP-1175, EPS-126, OP-530
Van Leeuwen, F. OP-037, OP-663, OP-783
Van Leeuwen, P. J. OP-597
Van Lith, S. EP-0164
Van Mechelen, S. **OP-150**
Van Mossel, S. **EP-0334**, **EP-1086**, **OP-295**
Vanneste, M. **EP-0391**
Vanney, J. OP-343
Van Nijnatten, T. EP-1395
Van Noesel, M. EP-0876, OP-260
Vannucchi, A. M. EP-0467
Van Oort, I. OP-598
Van Oosterom, M. N. OP-663, OP-783
Van Oostveldt, T. OP-121
Van Overeem, P. OP-183
Van Rijk, M. EP-0535, OP-598
Van Rijsewijk, N. D. **EPS-276**, **OP-867**
Van Rooij, R. EP-0876, EP-0907, OP-260
Van Ruremonde, N. OP-783
Van Sluis, J. EPS-276, OP-867
Van Snick, J. H. OP-053, EPS-082, EPS-276, OP-289, OP-867
Van Speybroeck, C. D. E. **EP-1145**, EP-1123
Van Stevendaal, M. H. M. Elisabe. **EPS-048**
Van Toorn, R. OP-849
Van Velden, F. H. P. EP-0010, EP-0948, EP-0958, OP-783
Van Vugt, M. EPS-195
Van Waasen, S. OP-284
Van Weehaeghe, D. EP-0325
Van Wijk, M. W. M. **EP-1123**, EP-1145, **OP-855**
Van Winnendael, N. EP-0103
Van Zele, E. OP-227
Van Zele, T. EP-0325
Vanzetto, G. OP-787
Vaqué-Alcázar, L. OP-442
Varallo, A. EP-0788
Varekar, P. EP-1455
Varela, N. OP-378
Varga, A. EP-0450
Vargese, N. EP-1013
Varghese, N. EP-1455
Vargiu, S. EP-0446
Varmenot, N. EP-1107
Varrone, A. EP-0108, EP-0113, EP-0116, EP-0118
Varvashenya, R. EP-0089, OP-070
Varzakis, E. EP-0996
Vasconcelos, N. OP-742, EP-0199, EP-1205, EP-1243, EP-1269, **EPS-267**, OP-632
Vasei, A. OP-242
Vasic, V. **EP-1106**, EPS-184, EPS-185, OP-180
Vasiljevic, A. EP-0471
Vasilyev, A. EP-1410
Vassileva, J. EPS-296
Vasuri, F. EP-0270
Vatalis, A. EP-0820
Vatsa, R. OP-073
Vauchot, F. **EP-0589**
Vaughn, B. OP-279
Vavlas, N. EP-1341, **EP-1364**, EP-1370, EP-1374, EP-1415, EPS-027
Vávrová, L. **OP-096**
Veach, D. OP-204
Vega Perez, D. **EP-0887**
Vegara Fernández, R. EPS-263
Veit-Haibach, P. EP-1100
Vela, J. EP-0382, EP-0384
Vela León, J. **EP-0412**, EP-0748
Velasco, M. OP-430, EP-0792
Velasco Fargas, R. EPS-121
Velasco-Nuño, M. EP-0324, EP-0490, EP-0551, EP-0632, EP-0762, OP-442, OP-553
Velasquez, K. **EP-0288**
Veldhuijzen van Zanten, S. **EP-0535**, EP-0535, EP-1010, EP-1395, **EP-1395**
Velidaki, A. EP-1379, **EP-0569**
Velikyan, I. EP-0289, **OP-728**
Veljkovic, M. OP-479
Velleman, T. EPS-082, OP-289
Velliangiri, S. K. EP-0559
Veltri, P. EP-0254
Veltrup, E. OP-628
Vendel, B. N. EP-0349
Vendelbo, M. H. EP-0290, EPS-223
Venditti, A. EP-0461
Venetsanos, D. EP-1417
Vengadesan, K. **OP-872**
Venkatachalam, M. EP-0266
Ventroni, G. EP-0263
Ventura, C. OP-558
Ventura, D. EP-1085, OP-244, OP-327
Vera, P. EP-1017, EP-1114, EP-1181, OP-524, OP-533
Verabyova, A. OP-320
Vera García, R. EP-1147
Vera Schmülling, U. EP-0565, EP-0821, OP-478, EP-0530
Verbanova, K. **EP-1333**
Verberne, H. J. OP-429, OP-729
Verbrugge, N. EP-1196
Verburg, E. EP-0535
Verburg, F. A. EP-0707, EP-1185, EPS-109, OP-852
Verburg, N. OP-607
Vercauteren, S. OP-169
Vercher-Conejero, J. L. EP-0307, EP-0495, EP-1366
Vercouillie, J. OP-718
Verger, A. EP-0179, EP-0183, EP-0692, EP-0829, EPS-264, OP-049, OP-101, OP-235, OP-611, OP-614
Vergili, A. EP-0902, **EP-1371**
Vergote, T. **OP-344**
Vergucht, V. OP-121, TEPS-009
Verhaar, A. F. S. OP-760
Verhulst, E. OP-156
Verkaik, N. OP-216
Vermassen, T. OP-522
Vermeulen, K. EPS-020, OP-150
Vermeulen, S. EP-0641
Verona, M. EP-0091
Veronese, M. EP-1072, EPS-221, OP-467, OP-721, OP-771
Veronesi, G. EP-0254
Veron Sanchez, A. OP-470
Versari, A. EP-0809
Verschueren, J. OP-710
Verschure, F. **TEPS-009**
Verslype, C. OP-366
Ververs, T. EP-1395
Verwey, N. A. OP-051
Veselý, J. EP-1006
Vessby, J. EP-1104
Vetrone, L. EP-0227, **EP-0270**, EPS-288, OP-118, OP-168
Vezir, O. **EP-0296**
Viala, C. OP-603
Viana, A. OP-818
Viana, A. F. EP-1403

Vidal-Calvo, E. E. OP-760
Vidal-Sicart, S. EP-0553
Vidhya, K. **EP-0259**, **EP-0877**
Viering, O. EP-0734
Viertl, D. EP-0077
Vigário, A. OP-465
Vigário, R. EP-1083
Vigil, O. R. EPS-032
Vigil Díaz, C. EP-0319, OP-050
Viglianti, B. OP-429
Vigne, J. **OP-433**
Vija, A. H. OP-422, EP-0585, EP-0965
Vija, L. OP-603
Vikatmaa, P. EP-0934
Vikentjeva, A. EP-0608
Vikhrova, N. **EP-0178**, EP-0992
Vilaça, A. OP-372
Vilallonga-Puy, R. OP-483
Vilariño Quintela, N. EPS-121
Vilaseca, A. EP-0685
Villamayor Hernández, A. OP-480
Villani, F. EP-0686
Villanueva, J. G. EP-0364
Villanueva Curto, J. EP-0378, EP-0200, EP-0710, EP-0931, OP-481
Villanueva Vázquez, R. OP-670
Villa-Palacios, J. EP-0522, EP-0555, EP-0560, **EP-0846,** EP-0866, EP-0867, **EPS-249**
Villaprado, C. **OP-666**, EP-1147
Vilstrup, M. H. EP-0403, OP-038, OP-877
Vinceneux, A. OP-331, OP-675
Vincent, R. EP-0581
Vincent-Salomon, A. EP-0297
Vinches, M. EPS-246
Vindstad, B. E. EP-0883
Vinga, S. OP-527
Vinicius Gomes, C. EP-1148
Vinjamuri, S. EP-0596, EP-0700
Vinnick, C. EPS-139
Vino, E. EP-1176
Vinuesa Sebastian, M. OP-485
Violante, L. EP-0199, OP-632
Virdone, L. OP-556
Virgolini, I. J. OP-434
Virtanen, K. EPS-234
Vis, A. OP-598
Vis, A. N. OP-876
Visentin, R. **EP-1398**, EP-1399, OP-818
Visser, D. **EPS-036**
Visvikis, D. OP-356
Vita, D. EP-0377, OP-324
Vitale, F. EP-0141, OP-776
Vivar, M. EPS-207
Vivier, D. EP-0096, OP-211, OP-347, **OP-351**
Vizier, R. EP-0164
Vizzuso, A. EP-0255
Vlachopoulos, C. EP-1417
Voelter, F. EP-0734
Vogel, W. EP-0535, EP-1395, OP-289, OP-597
Vogelius, I. R. EP-0219
Vogg, A. OP-761, EP-0109
Vöglein, J. OP-237
Vogler, L. EP-0691, EP-0698, OP-237
Vogsen, M. EP-0292, OP-106
Volkan Salancı, B. OP-804, OP-846, OP-847, OP-850, OP-254
Vollmar, C. EP-0699
Volpe, F. EP-0308, EP-0788
Volpe, G. M. EP-1081
Volpicelli, A. EP-0233
Volschenk, M. OP-620
Völter, F. **EP-0711**, EP-0793
Voltin, C. A. **EP-0488**
Von Baumgarten, L. EP-0047, EPS-124, EPS-125, OP-609, OP-610
Von Beschwitz, S. OP-525
Von Brandenstein, M. OP-628
Von Guggenberg, E. EP-0091
Von Hacht, J. L. OP-817
Von Overeem, P. OP-818
Von Polenz, I. EP-1035
Voorbach, M. OP-458
Vorobyeva, A. EPS-004, OP-766
Vorontsova, O. EPS-043
Vorster, M. EP-0824, OP-299
Voskamp, M. **OP-726**
Vosoughi, H. EP-0038
Vourkas, O. **EP-0637**
Vrachimis, A. OP-598
Vraka, C. EP-0041
Vranjes-Djuric, S. EP-0072, EP-1183
Vreeburg, M. OP-037
Vriamont, C. OP-344
Vriens, D. EP-1086, OP-295
Vries, E. F. J. OP-452
Vrigneaud, J. M. EPS-044, EPS-186
Vu, C. EP-1054
Vugts, D. J. OP-760
Vukadinovic, A. **EP-0072**, EP-1183
Vukelic, S. OP-458
Vultaggio, V. EP-0234
Vural, G. EP-0225
Waagmeester, D. OP-760
Wachi, K. EP-1157, EP-1453, **EP-1454**
Wacker, A. OP-279
Wadhwa, P. EP-0258, EP-0347, EP-0527, EP-0985, EP-0986, OP-550
Wagner, L. EP-0008, **EP-0132**
Wagner, M. EP-0137, OP-303
Wagner, O. E. EP-0219
Wagner, S. EP-0019
Wagner, T. EP-0405, **EP-0729**
Wahab, E. EP-0271, EP-0715, EP-1406
Wail, S. EP-0978, OP-352, OP-529
Wakabayashi, H. EP-1079, **OP-548**, OP-729
Wakabayashi, N. EP-0303, **EP-0796**, EP-0874, EP-1237, EPS-250
Wakankar, R. EP-0371, EP-0372, EP-0373, EP-0583, **EP-0764**
Wakfie, C. EP-0775
Wakfie Corieh, C. OP-784, EP-0339, EP-0340, EP-0341, EP-0491
Wakiran, M. EP-0416
Wakizaka, H. OP-209
Waldman, A. D. EP-1052
Waldner, M. OP-628
Waldschütz, A.-M. EPS-271
Walker, G. **EP-1439**, **EP-1456**, **TEPS-018**
Waller, C. F. EPS-159
Wallner, T. **EP-0082**
Wallon, D. EPS-131
Wallter-Rittel, T. EPS-024
Walter, T. EP-0787
Wan, M. EPS-062
Wan, W. EP-0435
Wang, A. EPS-274
Wang, B. **EPS-158**, EP-1032, EP-1037, **EP-1048**, EP-0205
Wang, C. EP-1056, EP-1025, EP-0410
Wang, E. EP-0158
Wang, F. OP-117, EP-0239, OP-463, EPS-057, OP-733
Wang, G. EP-0652, EP-1050, OP-477, OP-851, OP-880
EP-1064, EPS-030, EPS-032, EP-0158, **OP-178**
Wang, H. OP-672, OP-045, OP-462, **EP-0964**, EPS-130, EP-0241, EP-0023, **EP-0852**, **EP-0864,** EP-0455, EP-0456, EP-0865, EP-0899, EPS-049, EPS-168
Wang, J. OP-458, **EP-0105**, OP-695, EP-1148, EPS-240, OP-788, EP-1027, **EPS-037**, OP-151, **OP-678, EP-0651**, OP-238, **OP-305**, OP-439, EPS-063, EP-0095, EP-0105, EP-0143, EP-0149, EP-0256, EP-0278, EP-0439, **EP-0646**, **EP-0667**, EP-0689, EP-0693, EP-1027, EPS-147, OP-114, OP-116, OP-695, EP-0861, **EP-0099**, EP-0438, **EP-0693**, **EP-1027**, EP-0002
Wang, K. OP-502, **EP-0629**, **EPS-100**
Wang, L. **OP-844**, EP-0051, **EP-0407**, EP-0629, EPS-046, EPS-063, EPS-100, EPS-108, OP-727, EP-0186, OP-300, EP-0674
Wang, M. **TEPS-007**, EP-0218, EP-0649, OP-355, OP-777, OP-792, **EP-0650**, EP-0654, EP-0327, EP-0410, **EP-0674**, OP-439, EP-0435
Wang, P. EP-0869, **EPS-173**, EP-1015
Wang, Q. **EP-0305**, OP-300, OP-445, EP-0500, OP-445, OP-839
Wang, R. EP-0106, OP-278, EP-0667, EPS-037, OP-151, OP-678, EPS-057, EP-0587, EP-0642, EPS-133, OP-155, OP-362, OP-672, TEPS-011, EP-0190 , **OP-582**
Wang, S. EP-0023, EP-0079, OP-454, EP-0649, EP-0975
Wang, T. EP-0053, EP-0054, EPS-006, EPS-014, OP-210, EPS-233, EP-0662, EPS-233, EP-0587
Wang, W. EP-0435, EP-0500, OP-205, EP-0106, **OP-278**, **OP-212**
Wang, X. OP-176, EP-0386, OP-367, **OP-695**, EPS-108, **EP-1282**, EP-0067, **OP-763**, **EP-0149**, OP-018, EP-0435, EPS-101, EPS-113, OP-230, OP-680, OP-681, OP-682,

EP-0678, **EP-1441**, **EP-1446**
Wang, Y. OP-238, **OP-762**, **EP-0619**, **EP-0594**, **EP-0595**, OP-845, EP-0280, OP-851, **EP-1244**, EPS-037, OP-151, EPS-060, EPS-164, EPS-102, EP-0278, EP-0106, EP-1015, OP-278, **EP-0689**, EP-1027, EPS-179, EP-0174, OP-608, EP-0587, OP-355, OP-777, EP-0652, **EP-0682**, **EP-0697**, OP-236, EP-0174, EP-0852, EPS-152, EPS-155, EP-0578, EP-0590, EP-0601, EP-0603, EP-0619
Wang, Z. **EP-0725**, EP-0218, EP-0026, EP-0610, EP-0623, EP-0657, EP-0660, EP-0982, OP-545, EP-0057, EP-0009, EPS-014
Wan Kamal, W. H. B. TEPS-019
Warnier, C. EP-1175, EP-1186
Wartski, M. EP-0812
Warwick, J. OP-302, OP-307, OP-849
Wäschle, A. OP-017
Watabe, T. EP-0030, EP-0031, EP-1458, OP-281, **OP-387**, OP-471,OP-276
Watanabe, M. OP-503, EP-1448, **EP-1103**
Watanabe, S. EP-0635, EPS-095, **EP-0585**, EP-0303, EP-0796, EP-0860, **EP-0874**, EP-1237, EPS-250
Webber, G. EPS-236
Webberley, T. OP-888
Weber, F. OP-385
Weber, M. M. OP-385
Weber, W. EP-0161, EP-1047, EPS-185, OP-180, OP-181, OP-364, OP-459, OP-606, OP-789, OP-869, EP-0989, OP-106, OP-363, OP-368
Wechalekar, K. EPS-224
Wehbe, J. OP-675
Wehn, A. C. EP-0886
Wehner, L. EP-0070, **EP-0162**, EPS-012, **EPS-194**, OP-217, OP-218, OP-275
Wei, C. EPS-157, OP-415, OP-762
Wei, F. OP-451
Wei, H. OP-116
Wei, M. EPS-101
Wei, N. **EP-0055**, OP-018
Wei, S. EP-0190, **OP-286**, OP-837
Wei, W. EP-0209, EP-0212, EP-0533, EP-1233, OP-090
Wei, X. EP-0674
Wei, Y. EP-0386, EPS-123, EPS-200, OP-238, OP-287
Weich, A. EP-0318, EP-0794
Weichert, J. EP-0070, EPS-012, OP-275
Weidinger, E. OP-044
Weidong, Y. EP-0042
Weijs, L. EP-1395
Weiman, M. EPS-139
Weindler, J. **EP-0415**, EP-0830, **OP-605**
Weiner, A. B. EP-0376
Weinhold, N. EP-0506
Weis, H. EP-0331, **EP-0696**, **OP-381**
Weis, S. OP-778
Weiss, K. OP-871
Weissensee, A. **EP-0409**
Weissensteiner, J. **EP-1313**
Weissinger, M. OP-525
Weissler, B. OP-284
Weller, J. OP-609
Weller, M. EP-0183
Wells, K. EP-1091
Wen, H. EP-0346, OP-362
Wen, J. OP-174, EPS-058
Wen, R. **OP-680**, **OP-681**, **OP-682**
Wen, S. EP-0408, EP-0811, **EP-0815**, **EP-0825**, OP-600
Wen, X. EP-0133, OP-151, OP-765
Wen, Y. OP-839
Wendler, T. EP-1009, OP-358, OP-461, OP-770
Wendlinger, L. EP-0077
Wenetr, V. U. EP-0793
Weng, M. C. TEPS-002
Weng, Z. EPS-062
Wenker, S. OP-521
Wennbo, H. EP-1104
Wennmann, M. EP-0506
Wens, V. EP-0663, EP-0687
Wenter, V. EP-0886, EPS-248
Werner, J. M. OP-609
Werner, R. EP-0018, EP-0019, EP-0022, EP-0168, EP-0699, EP-0870, EPS-005, OP-044, OP-046, EP-0037, EP-0047, EP-0062, EP-0154, EP-0195, EP-0309, EP-0318, EP-0698, EP-0793, EP-1118, EPS-197, EPS-248, EPS-290, OP-043, OP-237, EP-1150, OP-368, OP-456
Werner, T. EP-0627
Wesseling, P. OP-607
Wesser, L. EP-0168
Westdorp, H. OP-796
Westerbergh, F. EPS-180, **OP-662**, OP-673, OP-677
Westerman, M. **EPS-224**
Westhead, L. **EP-0930**
Westin, H. EPS-043
Westlund Gotby, L. E. L. EP-1145
Wetz, C. EP-1092
Wetzig, K. EP-0082
Wewer Albrechtsen, N. J. EP-1073
Weymeskirch, M. **EP-1162**
Weyts, K. EP-0800
Wharton, L. EP-0034, EPS-139, **OP-348**, OP-580
Wheatcroft, M. OP-516, OP-521, EP-0130, OP-767
Wheeless, L. EPS-138
White, C. EP-0201
White, L. EP-1283
Wichmann, C. **OP-277**, OP-516
Wickre, P. EP-1121
Widhalm, G. OP-609
Widjaja, L. **EPS-248**
Widström, C. EPS-128, OP-095
Wiegand, L. EP-0886
Wielenberg, C.-F. EPS-159
Wierts, R. EPS-227, OP-702
Wiestler, B. EP-0182, EPS-124, EPS-125, OP-606
Wiesweg, M. OP-172
Wijerama, H. J. K. V. **EP-1438**
Wijethunga, S. P. D. EP-0921, EP-1438
Wijewickrama, P. EP-0729
Wijnen, N. EP-0907
Wilcox, K. OP-457
Wild, D. OP-361, OP-432, OP-601, OP-662, OP-673, OP-677
Wilk, M. OP-661
Wilkens, P. EP-1104
Willaime, J. M. Y. EP-1091
Willem, M. EP-0022, EP-0047
Willemen, H. L. D. M. EPS-036
Williams, H. A. EP-0996
Williams, M. EP-1052
Williams, S. EPS-134
Willowson, K. OP-323
Willson, T. EP-0729
Wilocx, D. OP-156
Wilson, P. OP-323
Wilson, Z. **EP-0962**, **EP-1030**
Wimalarathne, D. D. N. EP-1438, EP-0921
Wimana, Z. OP-111, OP-169, OP-470
Wimmer, S. OP-778
Windhorst, B. EP-1395
Wind-Mark, K. EP-0022, EP-0168
Winter, E. OP-881
Winters, E. EPS-285, EPS-286
Wirtz, R. **OP-628**
Wirtz, S. EP-0838
Withofs, N. EPS-084, OP-710
Witteveen, A. OP-713
Wlodarczyk, M. **EP-0747**
Wodtke, R. OP-652
Woff, E. OP-526, OP-537
Wöhrer, A. OP-609
Wojdowska, W. EP-0360
Wolfert, J. **EP-1185**
Wondergem, M. EP-1395, OP-876
Wong, A. OP-541
Wong, D. EPS-119
Wong, H. K. OP-486
Wong, J. EP-0113
Wong, R. EP-1100, OP-423
Wong, Y. EP-0429, EP-0499, EP-0799, EPS-177, OP-306
Wood, F. EP-0121
Wood, S. EPS-154
Wooten, D. OP-458
Włostowska, J. EP-0013, OP-679
Wouthuyzen-Bakker, M. EPS-276, OP-867
Wozniak, R. EP-0005
Wren, A. EP-0718
Wu, C. EP-0061, **OP-149**

Wu, F. OP-205
Wu, H. EP-0117, **EP-0455**, EP-0456, EP-1049, OP-117, EP-0546, EPS-158, OP-112, OP-693
Wu, J. OP-439, EP-0117, EP-0455, EP-0456
Wu, K. OP-466, EP-0429, EP-0499, EP-0799, EPS-177, OP-306
Wu, L. EPS-062
Wu, M. EPS-290
Wu, P. EPS-102, OP-839, OP-841
Wu, Q. **EP-0988**, EP-1053, EP-1061, EP-1095, **EP-0533, EP-0043**, **EPS-016**, EP-0630, OP-732
Wu, R. EP-0660, **EP-0060**, **EP-0078**, EP-0861
Wu, S. K. OP-486
Wu, T. EPS-113
Wu, V. C. EPS-245
Wu, W. EP-0407
Wu, X. EPS-019, EP-0133, OP-765, **OP-460**, EP-0050, EP-0316, EP-0400, EP-0697
Wu, Y. OP-594, OP-671, EP-0209, **EP-0241**, OP-355, OP-777, OP-792, EP-0129, EP-0248, EP-0085, OP-357, **EP-0438**
Wu, Z. **EP-0107**, **EP-0484**, OP-837, EP-1049, EP-0166, EP-0554, OP-839, OP-841, EP-1157
Wuestemann, J. OP-245
Wurzer, A. EPS-185, OP-180, OP-181, OP-364
Wyld, D. EP-1161, OP-290, OP-676, OP-703
Wyndaele, D. EP-1395
Xanthopoulos, S. EPS-153, OP-183
Xi, H. EP-0842
Xi, Y. **OP-367**
Xia, J. EP-0035
Xia, X. EP-0059, EP-0060, EP-0075, EP-0078, EP-0861, EP-0862, EPS-259
Xiang, J. EP-1244, EPS-037, **OP-151**, OP-678
Xiang, L. EP-0984
Xiang, X. EP-0119
Xiang, Z. **EP-0023**, EPS-102, OP-839, **OP-841**
Xiao, J. EP-0500
Xiao, L. **EP-0658**, **EPS-042**, OP-709, OP-712, OP-717, OP-723, **OP-740**
Xiao, X. EP-1056
Xiao, Y. EP-0609, EP-1096
Xiao, Z. OP-439, EPS-060, EPS-158, EPS-164, OP-547
Xiaoyang, Z. EP-0593, OP-544
Xie, D. OP-174
Xie, F. EP-0209, EP-0241, EP-0684, OP-238
Xie, H. **OP-019**
Xie, L. **OP-209**, OP-733
Xie, S. **OP-232**, EP-0248
Xie, W. EPS-089
Xie, X. EP-0727, **EP-0969**, EP-1096, OP-460, **OP-462**
Xie, Y. **EPS-152**, EPS-242, OP-066, OP-546, OP-763,, EP-0205
Xie, Z. EP-1139, OP-308
Xin, J. **EP-0439**
Xin, L. **EP-0434**
Xin, M. EP-0652, EP-0697, EP-1056
Xing, D. OP-547
Xing, H. EP-0174
Xing, Y. EPS-243
Xinhui, S. EP-0832
Xinzhu, Y. EP-1079
Xiong, M. EP-0137
Xu, A. EP-0020
Xu, B. EP-0280, EP-1050, OP-477, OP-672, OP-851, OP-880, **EPS-015**
Xu, C. EP-0067
Xu, D. EP-0241
Xu, H. EP-0085
Xu, J. EP-0020, EPS-062, OP-030
Xu, K. **EPS-060**
Xu, L. **EP-0680**, **EPS-018**, OP-545
Xu, M. EP-0085, **EP-0110**, **OP-157**
Xu, Q. EP-0652
Xu, R. **OP-308**
Xu, S. EPS-058
Xu, T. EPS-157, OP-415, OP-762, **EP-0009**, EP-0068, EPS-043, OP-414, OP-766, OP-545
Xu, W. **OP-411**, **OP-654**, OP-030
Xu, X. EP-0129, EPS-062, EP-0587, EPS-113, **EP-0622**, OP-845, **OP-444**
Xu, Y. EP-0317, EP-0435, OP-594, EP-0915, **EP-0279**, **EP-0541**, **EPS-172**, **EPS-222**, **EPS-225**, **OP-255**, **OP-258**, OP-696
Xue, R. EP-0280
Xue, S. **EP-0408**, EP-0725, **EP-0811**, EP-0815, EP-0825, EP-1148, OP-223, **OP-226**, **OP-231**, OP-357, **OP-466**, OP-600, OP-730, OP-731
Yaacob, N. EP-0416
Yaşar Belek, S. OP-715
Yabata, I. EP-1458
Yadav, R. EP-0285, EP-0880, OP-872
Yadav, S. EP-0583, OP-323
Yadgarov, M. EP-0481, EP-0482, EP-0755
Yaghoobi, N. OP-734
Yagi, Y. **EPS-141**
Yahiaoui, S. EP-1076
Yahiro, D. **EP-1069**
Yahyaoui, S. EP-0571
Yakupoglu, A. EP-0837
Yakushev, I. EP-0182, EP-0690, OP-232, OP-606, OP-721
Yakymenko, I. EP-0147
Yalcintas Bethune, E. **EP-1169**, EP-1171
Yalçın, S. EP-0287
Yamaguchi, J. EP-0634, EPS-111, OP-503
Yamaguchi, S. EP-1237
Yamamoto, A. **EP-0634**, EP-0635, EPS-095, **EPS-111**, OP-503
Yamamoto, H. OP-058, TEPS-008
Yamamoto, S. EPS-056
Yamao, T. EP-1453, EP-1454, EP-1157
Yamashita, S. OP-058
Yağmur, C. OP-054
Yan, C. EP-0554, EP-0629, EPS-100
Yan, H. **EP-0067**, EP-1096
Yan, M. EP-0220
Yan, S. EPS-118, OP-439
Yan, X. EP-0327, **EPS-242**, **OP-066**, **OP-546**
Yanagida, H. OP-208
Yang, A. F. EP-0304
Yang, B. **EPS-059**, OP-018
Yang, C. EP-0020, TEPS-007
Yang, F. EP-1117
Yang, H. **EP-0984**, EP-0099, **EPS-052**, OP-696, EP-1096, EP-0133, **EP-0034**, EPS-139, OP-348, **OP-580**, EP-0280
Yang, J. EP-0198, EP-0276, EP-1015, EPS-176, OP-205, EP-0317, **EP-0435**, EP-0706, OP-709, **OP-712**, OP-717, OP-723 **EP-0035**
Yang, K. C. EP-0025
Yang, L. **EP-0761**, **EP-1066**
Yang, M. EP-0030, **EP-0031**, EP-0626, EP-0304
Yang, P. **OP-071**, EP-0085
Yang, Q. EP-0052, EP-0053, EP-0054, EPS-006, EPS-014, OP-210
Yang, R. OP-733
Yang, S. OP-668, **OP-086**, **OP-090**, **EP-0152**, OP-206, OP-207, **EPS-170**
Yang, W. EPS-147, OP-074
Yang, X. EP-0601, EP-0603, EP-0435, EP-0674
Yang, Y. EP-0174, EP-0218, EP-0386, EP-0407, EP-0625, EP-0650, EP-0654, EP-0684, EP-1441, EP-1446, EPS-123, EPS-200, OP-238, OP-287, OP-608, EPS-157, OP-415, OP-412, EP-0492, EP-0517, **EP-0518**, EP-0706, **OP-296**, EP-0969, EP-0706, OP-439
Yang, Z. EPS-101, EPS-113, EPS-163, OP-108, OP-155 EP-0662, **EPS-233**, EP-0205
Yanık, H. EP-0640
Yanovich, G. EP-0089
Yao, K. OP-300
Yao, L. **EP-0209**
Yao, S. EP-0587
Yao, X. OP-462, EP-0043, EPS-016
Yao, Y. EP-0237
Yao, Z. OP-355, OP-777, EP-0610
Yaqub, M. EPS-081, OP-774, OP-607
Yar, G. **EP-0995**
Yararbas, U. EP-0343, EP-0344, EP-0366, EP-0428
Yasin, A. I. EP-0240
Yasser, F. **EP-1224**
Yasui, H. EPS-141
Yasumura, S. EP-0214, EP-0540
Yatomi, T. OP-719
Yavari, S. EP-1138
Yazaki, P. J. OP-523
Yeh, C. H. EP-0194
Ye, H. EP-0198, EP-0276, EP-1038, EPS-176, OP-115
Ye, J. **EP-0095**, EP-0143, EP-0149
Ye, Q. **OP-772**
Ye, T. EP-0587
Ye, X. OP-844

Yeh, R. EP-0201
Yen, T. OP-045, OP-439
Yerebakan, H. EP-1013, EP-1018
Yeung, I. EP-1100, OP-423
Yeung, L. EP-0596, EP-0700
Yeyin, N. EP-0901
Yi, H. EP-0454, OP-466
Yi, X. EP-0678, OP-853
Yildiz, H. EP-0321
Yildiz Kabaca, F. **EP-1276,** EP-0902, EP-1371
Yilmaz, A. S. OP-540
Yilmaz, B. **EP-1310**
Yilmaz, F. EP-0604
Yilmaz, G. OP-540
Yilmaz, M. EP-0197, EP-0291
Yilmaz, R. OP-110
Yilmaz, S. A. **EP-0763**
Yilmaz, U. EP-1008
Yilmaztekin, B. **EP-0225**
Yilmaztekin, G. EP-0225
Yin, A. TEPS-011
Yin, L. OP-668
Yin, Y. OP-451, OP-412
Yip, K. EP-0429
Yip, Y. EP-0429, EP-0499, EP-0799, EPS-177, OP-306
Yngve, U. EP-0009, EPS-043
Yoganathan, T. EP-0021
Yokokita, T. OP-585
Yokoyama, K. OP-058, OP-309
Yonezawa, K. OP-719
Yoo, J. EP-0169, EP-1422
Yoon, H. EP-0647, **OP-163**
Yoon, Y. EP-0664, OP-532
Yordanova, T. EP-1292, EP-1293, EP-1294, EP-1330, EP-1331, **EP-1359**, EP-1384
Yoshida, H. EP-0540, EP-0927
Yoshida, K. EP-0459
Yoshida, S. EP-0585
Yoshii, Y. EP-0139
Yoshimoto, M. OP-585
Yoshino, H. EP-0028
Yoshino, K. EP-0768
Yoshita, M. **OP-309**
You, J.-F. EP-0342
Younes, A. EP-1169, EP-1171
Young-Mylvaganan, T. OP-884
Younis, M. OP-803
Yousefi, B. EP-0122, EP-0854
Yousefirizi, F. **EP-1016**, OP-029, OP-034
Yousefzadeh-Nowshahr, E. EP-1045, EP-1106, EP-1128, EP-1129, **EPS-184**, EPS-185, OP-180
Ysaebert, L. OP-227
Yu, A. EP-1427
Yu, B. **EPS-123**
Yu, F. **EP-0030**, EP-0031, EPS-106, **OP-276**, **OP-281**, OP-498, OP-502, **EP-1058**
Yu, H. EP-0158, TEPS-007
Yu, J. OP-454, EP-1139, EP-0230, EP-0252, EP-1011, EP-1089, EP-1093, EP-1097, OP-468
Yu, K. **EP-0143**
Yu, L. EP-1038, EP-1049
Yu, Q. **EP-0102**
Yu, S. **EP-0832**, EPS-173
Yu, W. **EP-0578**, **EP-0590**
Yu, X. EP-0923, **OP-455**, **EPS-147**
Yu, Y. EP-0400
Yu, Z. EP-0186, EP-0187
Yuan, H. **EP-0239**
Yuan, P. EP-0055, EP-0652
Yuan, T. **EPS-101**, EPS-113, OP-230
Yuan, Y. EP-0211
Yücel, B. EP-0291
Yuge, S. EP-0214
Yumoto, A. EP-0927, **EP-0954**, EP-0956, EP-1098, EP-1452
Yun, M. EP-0659, EP-0664, EPS-215, OP-163, OP-532 EPS-094, OP-845
Yun-Viladomat, S. EP-0618
Yushchyshyna, H. EP-0009, EPS-043
Yuzefovich, B. EPS-087
Zaabar, L. EP-0571, EP-1239
Zabalza, A. EP-0685
Zacharioudaki, A. EP-0065
Zacherl, M. EP-0886, EP-1118, EPS-197, EP-0793, EPS-248, EP-1150, EP-0309
Zacho, H. D. EP-0773
Zafeirakis, A. EP-1429
Zafeiridou, G. EP-1341
Zaganjori, M. **OP-046**
Zagaria, L. OP-858
Zagni, F. EP-0145, EP-1112, **EPS-288**
Zagorska, A. EPS-296
Zaharia, T. **EP-1080**
Zaharinov, M. EP-0563
Zahfir, I. EP-1301, EP-1302, **EP-1325**
Zaidi, E. EP-0571
Zaidi, H. OP-034, EP-0971, EP-1122, EPS-220, EPS-226
Zakaria, M. TEPS-019, **EP-0203**
Zakavi, S. OP-242
Zalcman, G. OP-524
Zalutsky, M. R. OP-282
Zamagni, E. EP-0502, EP-0503, EP-0514, EP-1064
Zaman, M. EP-0293
Zamanian, A. **OP-534**
Zambrana Delgadillo, M. **EP-0872**, **EP-1391**
Zambrano Infantino, R. **EP-0579**, OP-854, EP-0612, EP-0613, OP-057, EP-0833
Zamorano Rivas, M. EP-0498, **EP-0758**, EP-0494, EP-0508, EP-0618, EP-1057, EP-1366, OP-233, OP-480, OP-865
Zampella, E. **EP-0308**, EP-0788, **OP-684**
Zamudio Rodriguez, D. EP-0798
Zan, E. **OP-780**
Zananiri, R. **EPS-087**, **OP-103**, **OP-661**
Zanca, R. EP-0363
Zandona, Y. EP-1196
Zang, J. **EP-0158**
Zannoni, G. EP-0010
Zanoni, L. EP-0227, EP-0444, EPS-247, OP-118, OP-168, OP-246, OP-248
Zantut-Wittmann, D. E. OP-119
Zapardiel, M. EP-0553, EP-0775, **OP-784**, EP-0339, EP-0340, EP-0394, EP-0491
Zapata, S. EP-0532
Zaplatnikov, K. **EP-0737**
Zappacosta, A. OP-293
Zaragori, T. EP-0827, EP-0829, OP-101, **OP-611**, OP-614
Zaragoza Ballester, P. EP-0887, EP-0387
Zarate-Morales, A. OP-581
Zarei, A. EP-1091
Zarpelao, F. EP-1418, EP-0262
Zarrelli, F. EP-1212
Zatcepin, A. **EP-0022**, EP-0168, OP-456, OP-773
Zatelli, M. C. EP-0893
Zatti, C. OP-047
Zavadovsky, K. **EPS-112**, **OP-795**
Zavvar, T. EP-0091
Zayabat, B. EP-0459
Zeberio Etxetxipia, I. EP-0462, EP-1262
Zedenius, J. EP-0314
Zeevart, J. EP-1200
Zehfir, I. EP-1290
Zeimpekis, K. EP-0933, OP-889
Zeinaki, M. EP-0691, EP-0698, **OP-237**
Zeiske, G. OP-344
Zeisler, J. EP-0090
Zeiss-Carstens, N. OP-591
Zekioglu, O. EP-0924, EPS-077
Zekri, M. EP-1290, EP-1301, EP-1302, EP-1325
Zelchan, R. OP-070
Zelepukin, I. **EPS-004**, OP-764, OP-766
Zeltser Dekel, C. EP-0021
Zender, L. OP-017
Zeng, D. OP-547
Zeng, F. OP-283, OP-285
Zeng, H. OP-772
Zeng, W. EP-0442, EP-1242, OP-162, OP-164
Zeni, M. EP-0140
Zepina, K. EP-0597
Zerahn, B. EP-0005, EP-0624, EP-0732, EPS-104, EPS-253
Zerbini, F. OP-384
Zetterberg, H. EP-1072, OP-438
Zetterberg, U. OP-818
Zevnik, K. **EP-0519**
Zhai, Z. EPS-089

Zhan, J. EP-0158
Zhang, B. OP-762, EPS-038, OP-444
Zhang, C. EP-0034, EP-0652, EP-0666, EP-0682, EP-0697, **EP-1056**, OP-304, OP-733, EP-1050
Zhang, D. OP-348, EP-0163, OP-692
Zhang, F. **EP-0601**, **EP-0603**, **EPS-047**, EPS-051, **OP-024**, EP-1027
Zhang, H. **EPS-106**, **OP-498**, **OP-502**, **OP-724**, **OP-735**, OP-439
Zhang, J. EPS-007, OP-276, EP-0385, EP-0316, OP-411, OP-654, EP-1050, **OP-477**, OP-851, OP-880, EP-0043, EP-0133, EPS-016, OP-151, OP-431, **OP-436**, OP-678, OP-765, OP-781, **OP-860**, **OP-862**, EP-0023, EP-0435, OP-362, OP-672, EP-0035, EP-0807
Zhang, K. EP-0215
Zhang, L. EP-0097, EP-0338, EP-0099, EP-0438, **EPS-010**, EPS-011, EP-0637, OP-209
Zhang, M. EP-0974, EP-0990, **EP-0220**, EP-0964, **EPS-130, EP-0547**, OP-282, EP-0139, OP-209, OP-733 **EP-1190**, **EP-1191**, **EP-1192**, EPS-147, EP-0500
Zhang, N. EP-0969, EP-1096, OP-236, OP-460, OP-462 EP-0385, EP-0435
Zhang, Q. EP-0500
Zhang, R. EP-0067, EPS-243, **EP-0079**, **EP-0865**, **EP-0899**
Zhang, S. EP-1441, EP-1446, EPS-057
Zhang, T. OP-045, **OP-441**
Zhang, W. **EP-0869**, OP-444, **EP-0046**, EP-0079
Zhang, X. EP-0679, EPS-038, EP-0107, EP-0356, EP-0484, EP-0487, EPS-059, EPS-175, OP-020, OP-382, OP-469, OP-768, EP-0435, OP-155, OP-362, OP-672, EP-0594, EP-0595, EP-0622, EP-0628, EPS-094, OP-730, OP-731, OP-845, OP-853, EP-1461, OP-367, EP-1244, **EP-0129**, EPS-170
Zhang, Y. EP-0023, **EP-0652**, **EP-0666**, EP-0682, EP-0697, EP-1056, **OP-236**, EP-0276, EPS-176, **OP-699**, EP-0662, EP-0106, OP-278, EP-0915, EP-0923, OP-209, EP-0609, EPS-158 EP-0107, EP-0484, EPS-053, EPS-059, OP-018, OP-020, OP-418, OP-419, EP-0386, EP-0469, EP-0493, **EP-0621**, **EPS-169**, EPS-200, EP-0694, **EP-0357**, OP-069, **EP-0327**, EPS-242, OP-066, OP-546, EPS-063, **EP-0679**, **EPS-038**
Zhang, Z. EP-0220, EPS-200, EP-0020, **EP-0771**, **EP-0623**, EP-0657, **OP-030**, EPS-108
Zhao, C. EP-0650, **EPS-019**
Zhao, D. **EP-0587**
Zhao, H. EP-1056, EPS-129, EP-0915, EP-0923, OP-455
Zhao, J. EPS-102, **OP-839**, EPS-243, EP-0979, OP-231
Zhao, K. OP-454
Zhao, L. EP-1038, EP-1049, **EPS-171**, OP-431, EPS-129
Zhao, M. EP-0609, EP-0678, OP-300, **OP-853**
Zhao, Q. EP-0492, EP-0646, EP-0667, EPS-033, OP-439
Zhao, T. EP-0043, EPS-016, OP-436, OP-860, OP-862
Zhao, W. OP-672
Zhao, X. OP-454
Zhao, Y. **EP-0080**, EP-0595, EP-0622, **EPS-094**
Zhao, Z. OP-071, OP-733, EP-0915, EP-0923
Zhelyazkova, Z. EP-0213
Zheng, C. EPS-155, **EP-0625**, **EPS-098**
Zheng, D. EP-0107, EP-0190, EP-0484, OP-018, OP-020, OP-286, **OP-837**
Zheng, F. EP-1125
Zheng, G. EPS-242, OP-066, OP-069, OP-546
Zheng, H. EP-0969, EP-1096, OP-460, OP-462
Zheng, K. EP-0198, EP-0276, EPS-176, **OP-115**
Zheng, L. OP-439
Zheng, M. OP-762, OP-457
Zheng, P. EP-0680
Zheng, W. EP-0865, EP-0899, EP-0918, EP-0920
Zheng, X. **EP-0842**, OP-030
Zheng, Y. EP-0974, EP-0981, EP-0990, EPS-221
Zhengjie, W. **EP-0593**, **OP-544**
Zhi, Y. EP-0195
Zhong, J. **EPS-132**
Zhong, Y. EP-0694, EP-0695
Zhou, B. OP-017
Zhou, C. EP-0248, EPS-200, EP-0693, EP-0609, **EP-0678**, OP-300, OP-853
Zhou, H. **TEPS-011**, EPS-152
Zhou, K. EP-0155
Zhou, M. EP-0124, EP-0727, OP-212, OP-296, OP-709, OP-723
Zhou, N. OP-108
Zhou, W. **EP-0198**, EP-0276, EP-1038, **EPS-176**, EP-0609, EPS-123
Zhou, X. OP-439, **EP-0231**, EP-0237, EP-1021
Zhou, Y. **EP-0059**, EP-0862, **EPS-259**, OP-304, **EP-0997**, OP-463, OP-594
Zhou, Z. EP-0190, OP-286, OP-837, EP-0644, OP-445, EP-0500, **EPS-241**
Zhu, G. EP-0039, EP-0152, EP-0662, EPS-233, OP-699
Zhu, H. EP-0500, EPS-101, EPS-113, EPS-163, OP-108
Zhu, J. EP-0107, EP-0237
Zhu, L. OP-178
Zhu, S. EP-1410, EP-0211
Zhu, W. OP-066, **OP-069**, **OP-206**, EP-0915, OP-455
Zhu, X. OP-357, EP-1046
Zhu, Y. OP-287
Zhu, Z. EP-1244, EPS-037, OP-151, OP-678, EP-0662
Zhuang, Y. OP-458
Ziangas, C. EP-0591, EP-0675
Zidell, A. EPS-062
Zieger, K. E. A. OP-877
Ziegler, S. EP-0168, EP-0936, EP-1035, EPS-005, EPS-124, EPS-125, EPS-197, EPS-239, OP-461, OP-773, OP-775, EP-0022, EP-1118
Zieglmeier, M. OP-818
Zielinski, R. EP-0088
Ziener, C. OP-294
Zihala, D. EP-0513
Zijlmans, L. H. M. EPS-048
Zijlstra, J. OP-774, EPS-081
Zimmermann, A. OP-516
Zimowska, M. EP-0013
Zindler, N. **OP-426**
Zink, J. OP-221
Zinn, K. R. EPS-018
Zinnhardt, B. EPS-131
Zinsz, A. OP-611
Zinzani, P. L. OP-224
Zirbesegger, K. EP-1184
Zisser, L. EP-1071
Ziv, O. EPS-087, OP-661
Zivanovic, J. **EP-0791**, EP-0898, **EP-1240**, OP-479
Zmek, J. O. EP-1131
Zogala, D. EP-0489
Zoglopitou, L. EP-0820
Zoltowska, M. EPS-009, OP-518, EP-1174
Zoppolo, F. EP-0100
Zorraquino, C. EP-0976
Zorz, A. EPS-287, OP-702
Zotta, M. EP-0681, EP-0683, OP-612
Zou, H. EP-0915
Zou, P. EP-0117, EP-0455, **EP-0456**
Zou, R. EP-0118, OP-459
Zou, Y. **EPS-049**
Zouaoui, A. OP-101
Zounek, A. **EP-1035**, EP-0936, EPS-124, EPS-125, EPS-239, OP-773, OP-775
Zuccalà, V. OP-380
Zucchetta, P. EPS-205, OP-036
Zuccotti, G. EPS-122, EP-0175
Zuhayra, M. EP-0080
Zuidgeest, P. OP-713
Zukotynski, K. EP-1100
Zuo, C. EP-0674, OP-287, OP-439
Zuo, J. EP-0111
Zuo, R. **OP-545**
Zuur, L. G. OP-597
Zweegman, S. EP-1055, OP-225
Zwergal, A. EP-0690, EP-0699, EPS-005, OP-044, OP-046
Zwezerijnen, B. EP-1395
Zwezerijnen, G. J. C. EPS-081, OP-774
Zychowicz, Z. **EP-1232**

FOCUSMEETING.EANM.ORG

PALMA DE MALLORCA, SPAIN

FEBRUARY 5-7, 2026



EANM FOCUS 7

MOLECULAR IMAGING FOR A PERSONALISED TREATMENT IN ALZHEIMER'S DISEASE

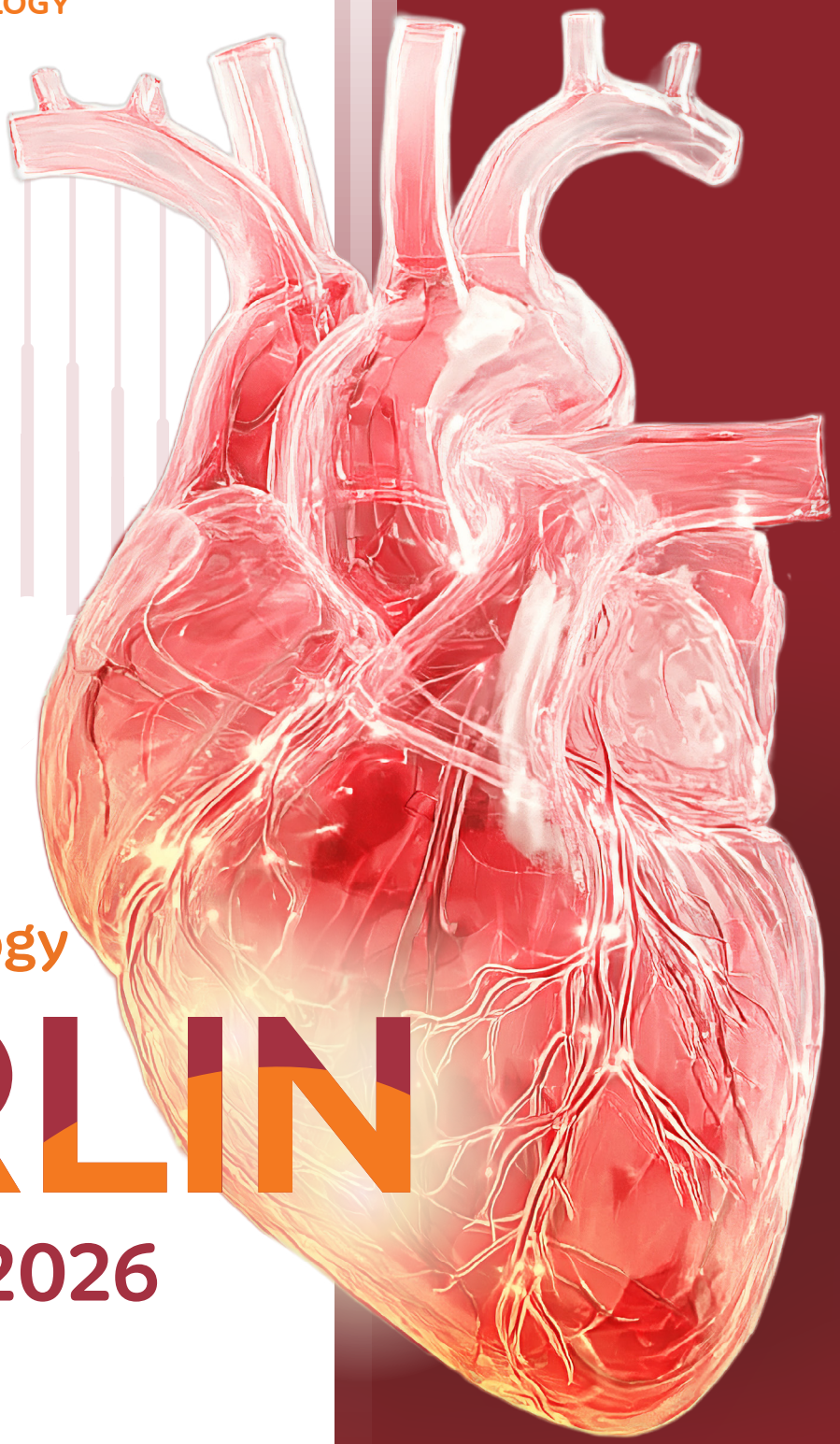
European Association of Nuclear Medicine | e-Mail: office@eanm.org | www.eanm.org

ICNC

May 17-19, 2026 | BERLIN

International Conference on

NUCLEAR CARDIOLOGY



International Conference on Nuclear Cardiology

BERLIN

May 17-19, 2026

With great support

ASNC

American Society of Nuclear Cardiology

EANM

EUROPEAN ASSOCIATION OF NUCLEAR MEDICINE

ICNC.COMMUNITY